SMART GEOTECHNICS FOR SMART SOCIETIES

Edited by
Askar Zhussupbekov
Assel Sarsembayeva
Victor N. Kaliakin

CRC Press
Taylor & Francis Group

SMART GEOTECHNICS FOR SMART SOCIETIES

Smart Geotechnics for Smart Societies contains the contributions presented at the 17th Asian Regional Conference on Soil Mechanics and Geotechnical Engineering (17th ARC, Astana, Kazakhstan, 14-18 August, 2023). The topics covered include:

– Geomaterials for soil improvement
– Tunneling and rock engineering
– Slope, embankments and dams
– Shallow and deep foundations
– Soil dynamics and geotechnical earthquake engineering
– Geoenvironmental engineering and frost geotechnics
– Investigation of foundations of historical structures and monitoring
– Offshore, harbor geotechnics and GeoEnergy
– Megaprojects and transportation geotechnics

Smart Geotechnics for Smart Societies will be of interest to academics and engineers interested or involved in geotechnical engineering.

Taylor & Francis
Taylor & Francis Group
http://taylorandfrancis.com

PROCEEDINGS OF THE 17TH ASIAN REGIONAL ON SOIL MECHANICS AND GEOTECHNICAL ENGINEERING CONFERENCE (17ARC), ASTANA, KAZAKHSTAN, 14-18 AUGUST 2023

Smart Geotechnics for Smart Societies

Edited by

Askar Zhussupbekov

President of Kazakhstan Geotechnical Society, Astana, Kazakhstan

Assel Sarsembayeva

The L.N. Gumilyov Eurasian National University, Astana, Kazakhstan

Victor N. Kaliakin

University of Delaware, Newark, USA

CRC Press
Taylor & Francis Group
Boca Raton London New York Leiden

CRC Press is an imprint of the
Taylor & Francis Group, an **informa** business

A BALKEMA BOOK

Front Cover Image: Bakytzhan Batyrkhanuly

First published 2023
by CRC Press/Balkema
4 Park Square, Milton Park, Abingdon, Oxon, OX14 4RN

and by CRC Press/Balkema
2385 NW Executive Center Drive, Suite 320, Boca Raton FL 33431

CRC Press/Balkema is an imprint of the Taylor & Francis Group, an informa business

© 2023 selection and editorial matter, Askar Zhussupbekov, Assel Sarsembayeva & Victor N. Kaliakin; individual chapters, the contributors

Typeset by Integra Software Services Pvt. Ltd., Pondicherry, India

The right of Askar Zhussupbekov, Assel Sarsembayeva & Victor N. Kaliakin to be identified as the authors of the editorial material, and of the authors for their individual chapters, has been asserted in accordance with sections 77 and 78 of the Copyright, Designs and Patents Act 1988.

The Open Access version of this book, available at www.taylorfrancis.com, has been made available under a Creative Commons Attribution-Non Commercial-No Derivatives 4.0 license.

Although all care is taken to ensure integrity and the quality of this publication and the information herein, no responsibility is assumed by the publishers nor the author for any damage to the property or persons as a result of operation or use of this publication and/or the information contained herein.

British Library Cataloguing-in-Publication Data
A catalogue record for this book is available from the British Library

Library of Congress Cataloging-in-Publication Data
A catalog record has been requested for this book

ISBN: 978-1-003-29912-7 (ebk)
DOI: 10.1201/9781003299127

Smart Geotechnics for Smart Societies – Zhussupbekov, Sarsembayeva & Kaliakin (Eds)
© 2023 The Editor(s), ISBN 978-1-003-29912-7
Open Access: www.taylorfrancis.com, CC BY-NC-ND 4.0 license

Table of contents

Geomaterials for soil improvement

Slope, embankments and dams

Offshore, harbor geotechnics and GeoEnergy

Smart Geotechnics for Smart Societies – Zhussupbekov, Sarsembayeva & Kaliakin (Eds)
© 2023 The Editor(s), ISBN 978-1-003-29912-7
Open Access: www.taylorfrancis.com, CC BY-NC-ND 4.0 license

Preface

The 17th Asian Regional Conference on Soil Mechanics and Geotechnical Engineering is organized by the Kazakhstan Geotechnical Society under the joint guidance favor of International Society for Soil Mechanics and Geotechnical Engineering (ISSMGE) and the L.N. Gumilyov Eurasian National University. The main theme of the 17 ARC is Smart Geotechnics for Smart Societies. A number of subjects in modern geotechnical technology and activities are covered up to match the main theme. In a roll about of 60 years, we sincerely hope that the 17ARC will continue to bring great success following the glories of past ARCs (New Delhi 1960, Tokyo 1963, Haifa 1967, Bangkok 1971, Bangalore 1975, Singapore 1979, Haifa 1983, Kyoto 1987, Bangkok 1991, Beijing 1995, Seoul 1999, Singapore 2003, Kolkata 2007, Hong Kong 2011, Fukuoka 2015, Taipei 2019). 17 ARC is held for the first time in the very heart of Eurasia, in a country located at the junction of 2 continents, and this is its strength and peculiarity. Kazakhstan is located in the geographical center of Central Asia and located in two parts of the world, on the border of Europe and Asia; most of the country is in Asia, the smaller one is in Eastern Europe.

The origin of scientific thought in Kazakhstan goes back to ancient times. Archaeological research and written sources contain information about the culture of cities and settlements that existed in the 6th-11th centuries on the territory of Zhetysu, Central and Eastern Kazakhstan. The founders of this culture are the local Turkic tribes: Oguzes, Karluks, Kimaks, Kypchaks. The medieval cities of Kazakhstan were known throughout the world not only for their bazaars and crafts, but also famous for their poets, scientists, artists, rich libraries, and educational institutions. During the Second World War, many scientific institutions and higher educational institutions of the country were evacuated to the republic of Kazakhstan from Moscow and Saint-Petersburg (Russia). The research carried out by scientists in recent years is aimed at increasing the competitiveness of the science and technology.

In July 1995, the Kazakhstan Geotechnical Society was founded for the first time under the leadership of Doctor of Technical Sciences, Professor Askar Zhussupbekov. Technical Committee of ISSMGE TC305 Megacities Geotechnical Infrastructure for Megacities and New Capitals succefully operates on the basis of Kazakhstan Geotechnical Society and hosted several events annually. At the moment, over 40 scientists from all over the world are permanent members of TC305. Among the events organized: the Eighth Asian Young Geotechnical Engineers Conference (8AYGEC), the KGS-KGS forum, First International Workshop, the ENU-INU forum between the Incheon National University (INU) and the LN Gumilyov Eurasian National University, the Taiwan-Kazakhstan Geotechnical Engineering Seminar, ENU-HIT Scientific forum between the between L.N. Gumilyov ENU (Kazakhstan) and Hachinohe Institute of Technology (Japan), Second Geo-Institute – Kazakhstan Geotechnical Society Joint Workshop (USA) and many others. These events provide an opportunity not only to share information on geotechnical advances and problems and their impact, but also to get a cultural exchange between scientists from different countries: the guests can taste some of the finest cuisine, livestock meat can be cooked in various ways and is usually served with a wide range of traditional bread products, beshbarmak (horse meat). Refreshments often include black tea and traditional dairy drinks such as ayran (source milk), shubat (camel

milk) and kymyz (horse milk), but also experience the hospitality and cultural uniqueness of the formerly nomadic people.

The Conference Proceeding of the 17th Asian Regional Conference on Soil Mechanics and Geotechnical Engineering composes more than 400 scientific papers from 54 countries including the following topics divided by chapters: soil characteristics and properties, underground space and deep excavations, tunneling, slope, debris flow and embankments, dams, shallow and deep foundations, soil dynamics and geotechnical earthquake engineering, soil improvement, geo-environmental engineering, geotechnical reliability, risk assessment and management, geosynthetics and geo-products, engineering geology and rock engineering, forensic engineering, offshore and harbor geotechnics, geotechnical training and education, in-situ testing and monitoring, geo-energy, case history, investigation of foundations of historical structures, buildings and monuments, numerical analysis of soil-structure interaction, geotechnical infrastructures, marine geotechnics, mining and geotechnics, design and modeling, transportation geotechnics, engineering and technology, piling foundations, technologies and testing, press-in piling technology, trenchless technology in underground constructions, pipelines on problematical soil ground, frost geotechnics, BIM technology and geotechnical engineering, megaprojects and megastructures on difficulty soil grounds.

This Conference brought together the achievements of not only 26 Asian countries, but also representatives of Europe, America, Australia, and Africa. We would like to especially note the Japanese Geotechnical Society, Indian Geotechnical Society, Korean Geotechnical Society, Chinese Institution of Soil Mechanics and Geotechnical Engineering-CCES, Chinese Taipei Geotechnical Society, Kazakhstan Geotechnical Society, Iraq Geotechnical Society, and other Asian Geotechnical Societies in participating and assisting in the organization of the review process.

The 17 ARC conference serves as a valuable platform for companies operating in the geotechnical industry to showcase their latest products, technologies, and services to a targeted audience of professionals, researchers, and academics.

On behalf of the 17ARC organizing committee we would like to thank International Society for Soil Mechanics and Geotechnical Engineering and all the Technical Committees, Scientific Committee, International Advisory Board and of course to the Organizing Committee for their constant support and great contribution for making this Conference a success. We would also like to thank our sponsors and exhibitors and all participants of this conference for their active participation in it.

We hope that this Conference proceedings will not only be the conclusion of the research performed, but also motivate for further efforts and collaboration in the field of geotechnical engineering.

Professor Askar Zhussupbekov
President of Kazakhstan Geotechnical Society, Astana, Kazakhstan

Dr. Assel Sarsembayeva
The L.N. Gumilyov Eurasian National University, Astana, Kazakhstan

Victor N. Kaliakin
University of Delaware, Newark, USA

Smart Geotechnics for Smart Societies – Zhussupbekov, Sarsembayeva & Kaliakin (Eds)
© 2023 The Editor(s), ISBN 978-1-003-29912-7
Open Access: www.taylorfrancis.com, CC BY-NC-ND 4.0 license

CONFERENCE ADVISORY BOARDS & COMMITTEES

International Advisory Board
Chairman: Prof. Ken-Jian Shou
Vice-President of ISSMGE for Asia

Members:
Dr. Marc Ballouz *President of ISSMGE*
Prof. Charles W.W. Ng. *Immediate Past President of ISSMGE*
Prof. Yoshinori Iwasaki *Chairman of ATC19, ISSMGE*
Prof. Jun Otani Chair, *15ARC*
Prof. Kenji Ishihara *Past President of ISSMGE*
Dr. Za-Chief Moh *Past Vice-President of ISSMGE for Asia*
Prof. Jean-Louis Briand *Past President of ASCE*
Prof. Seco Pinto *Past President of ISSMGE*
Prof. Der Wen Chang *Chair, 16ARC*
Prof. Fumio Tatsuoka *Past President of IGS*
Prof. Victor Kaliakin *University of Delaware*
Prof. Eun Chul Shin *Incheon University*
Prof. Rolf Katzenbach *Technical University of Darmstadt*

Kazakhstan Advisory Board
Chairman: Prof. Bagdat Teltayev
Joldasbekov Institute of Mechanics and Engineering

Members:
Kassymbek Zhenis
Mayor of Astana
Sayasat Nurbek
Minister of Science and Higher Education of the Republic of Kazakhstan
Prof. Yerlan Sydykov
Rector of L.N. Gumilyov Eurasian National University
Kurmangaliyeva Zhanna
Vice-Rector for Science of ENU
Prof. Rysbek Baimakhan
Kazakh National Women's Teacher Training University
Prof. Zhmagul Nuguzhinov
Kazakhstan Diversified Institute of Reconstruction and Development (KazMIRD)

Prof. Yerkin Isahanov
Academy of Logistics and Transport
Prof. Talgat Baitasov
L.N. Gumilyov Eurasian National University
Prof. Yelbek Utepov
L.N. Gumilyov Eurasian National University
Prof. Baurzhan Bazarov
Karaganda Industrial University

Members of Scientific committee
Prof. Anil Joseph
President of Indian Geotechnical Society
Dr. Muthusamy Karthikeyan
President of Geotechnical Society of Singapore
Ir. Lee Peir Tien
President of Malaysian Geotechnical Society
Prof. Mahdi O. Karkush
President of Iraqi Scientific Society for Soil Mechanics and Foundation Engineering
Dr. Andy Y.F. Leung
Secretary General of Hong Kong Geotechnical Society
Prof. Salah Sadek
President of Lebanese Geotechnical Engineering Society
Dr. Fardin Jafarzadeh
President of Iranian Geotechnical Society
Prof. Netra Prakash Bhandary
President of Nepal Geotechnical Society
Prof. Jian-Min Zhang
President of Chinese Institution of Soil Mechanics and Geotechnical Engineering - China Civil Engineering Society
Prof. Jianye Ching
President of Chinese Taipei Geotechnical Society
Prof. Junichi Koseki
President of Japanese Geotechnical Society
Prof. Kamchibek Ch. Kozhogulov
President of Kyrgyzstan Geotechnical Association
Prof. Suttisak Soralump
President of Thai Geotechnical Society
President of South East Asian Geotechnical Society
Prof. Young Uk Kim
President of Korean Geotechnical Society
Prof. Pulod Aminzoda
President of Tajikistan Geotechnical Society
Prof. Askar Khasanov
President of Uzbekistan Geotechnical Society
Dr. Phung Duc Long
President of Vietnam Society for Soil Mechanics and Geotechnical Engineering

Dr. Talal Awwad
International Secretary of Order of Syrian Engineers and Architects
Prof. Setev Nyamdorj
President of Mongolian Association of Soil Mechanics and Geotechnical Engineering
Prof. Widjojo A. Prakoso
President of Indonesian Society for Geotechnical Engineering
Dr. Sarwar Jahan Md. Yasin
Hon. Secretary General of Bangladesh Society for Geotechnical Engineering
Engr. S. Amjad Agha
President of Pakistan Geotechnical Engineering Society
Prof. Mark Albert H. Zarco
President of Philippine Society for Soil Mechanics and Geotechnical Engineering
Eng. K.L. Srilal Sahabandu
President of Sri Lankan Geotechnical Society
Prof. Askar Zhussupbekov
President of Kazakhstan Geotechnical Society

Organizing Committee
Chairman:
Prof. Askar Zhussupbekov *L.N. Gumilyov Eurasian National University*
Vice-Chairmans:
Dr. Victor Popov *Karaganda GIIZ*
Dr. Zhanbolat Shakhmov *L.N. Gumilyov Eurasian National University*

Members:
Prof. Hoe Ling *Columbia University*
Prof. Faizulla Ikramov *Samarkand State Institute of Architecture and Civil Engineering*
Dr. Yerlan Sabitov *L.N. Gumilyov Eurasian National University*
Dr. Assel Tulebekova *L.N. Gumilyov Eurasian National University*
Prof. Adil Zhakulin *Karaganda Technical Univesity*
Dr. Abdulla Omarov *L.N. Gumilyov Eurasian National University*
Dr. Muzdybayeva Tymarkul *L.N. Gumilyov Eurasian National University*
Dr. Serik Yenkebayev *L.N. Gumilyov Eurasian National University*
Prof. Vitaliy Khomyakov *KazGASA*
Dr. Rauan Lukpanov *L.N. Gumilyov Eurasian National University*
Dr. Gulshat Tleulenova *L.N. Gumilyov Eurasian National University*
Dr. Assem Issina *L.N. Gumilyov Eurasian National University*
Dr. Moon Sung-Woo *Nazarbayev University*
Dr. Ivan Morev *Geostrata, Ltd*
Dr. Iliyas Zhumadilov *Shakarim University*
Dr. Nurgul Alibekova *L.N. Gumilyov Eurasian National University*
Dr. Alfrendo Satyanaga *Nazarbayev University*
Dr. Bazarbayev Daniar *L.N. Gumilyov Eurasian National University*
Yeraly Uralov *"Astana Development Center" LLP*
Lyazzat Taukenova *"Astana Development Center" LLP*

Secretary General:
Dr. Assel Sarsembayeva *L.N. Gumilyov Eurasian National University*

Technical Coordinators:
Bibigul Abdrakhmanova *Geotechnical Institute*
Dr J.S. Dhanya *L.N. Gumilyov Eurasian National University*
Dr Assel Mukhamedjanova *L.N. Gumilyov Eurasian National University*
Assem Abisheva *L.N. Gumilyov Eurasian National University*
Abilkhair Issakulov *L.N. Gumilyov Eurasian National University*
Saltanat Mussakhanova *L.N. Gumilyov Eurasian National University*
Sultan Iskakov *L.N. Gumilyov Eurasian National University*
Askar Yessentayev *L.N. Gumilyov Eurasian National University*

Keynote lectures

Taylor & Francis
Taylor & Francis Group
http://taylorandfrancis.com

Smart Geotechnics for Smart Societies – Zhussupbekov, Sarsembayeva & Kaliakin (Eds)
© 2023 The Author(s), ISBN 978-1-003-29912-7
Open Access: www.taylorfrancis.com, CC BY-NC-ND 4.0 license

Technological and structural methods of construction of the underground part of unique facilities in St. Peterburg built during the last 10 years

R.A. Mangushev & A.I. Osokin
Saint Petersburg State University of Architecture and Civil Engineering, Russia

ABSTRACT: Engineering-geological conditions of St. Petersburg, which are characterized by a large thickness of soft water-saturated lake-glacial deposits, are presented. The main characteristics of soils and examples of static sensing results are given. There are considered the main technical characteristics of the foundations of the compound "Lakhta-Center", including a 462-m-hight skyscraper – the tallest building in Europe and a multifunctional center of 85 to 15 m. The main technical characteristics of the foundations of the unique Gazprom-Arena football stadium with an opening roof and a retractable field are presented.

1 INTRODUCTION

Saint Petersburg is the northernmost city in the world which has the population over one million people. Founded in 1703 in the delta of the Neva River as the capital of Russia, the metropolitan city was developing broadways for almost 300 years - most of the buildings were of 2 to 12 floors. Only in the early 21st century high-rise construction began on the periphery of the city, and now a number of floors reaches 25 and more in the buildings erected on piles. The construction of the Lakhta Center Multifunctional Complex on the coast of the Gulf of Finland was a unique event for the megacity, and the high-rise part of the Lakhta Center was completed in 2018. The unique building structures and technologies were used to construct its substructure.

2 ENGINEERING AND GEOLOGICAL CONDITIONS WITHIN SAINT PETERSBURG AREA

The central historical part of Saint Petersburg is formed by deltaic deposits of fine-grained and silty sands with a thickness of 2 to 5 m underlain by the thick layer of soft lake-glacial and marine deposits. These soils have comparatively high and non-uniform compressibility.

The lake-glacial deposits – clays, loams and sandy loams – are practically pervasive and have the stratified or ribbon structure. These soils are characterized by high natural moisture content and porosity, anisotropic mechanical properties, high compressibility, heaving properties and thixotropy.

In this part of the city, the relatively firm moraine deposits are encountered at a depth of 15 to 30 m from the ground surface.

Within the city area, primary deposits are represented by Proterozoic, Paleozoic and Ordovician deposits covered by Quaternary sediments. The main subway tunnels and sewage headers are located in these deposits. Figure 1 shows an example of the engineering and geological conditions of the northern part of Saint Petersburg.

DOI: 10.1201/9781003299127-1

3 LAKHTA CENTER MULTIFUNCTIONAL PUBLIC AND BUSINESS COMPLEX

3.1 *General information*

The Lakhta Center is a public and business complex located on the coast of the Gulf of Finland in Primorsky District of Saint Petersburg. The Complex includes a 462-m-high skyscraper and a multifunctional building divided by the atrium into the southern and northern blocks[1] (Figure 1).

The total area of the buildings is 400 thousand m². The skyscraper is considered as the northernmost in the world and the tallest in Russia and in Europe. Its height with a spire is 462 m, the total weight is 670 thousand tons, the number of floors is 87. The top floor of the skyscraper is located at the elevation of 372 m.

Figure 1. General view of Lakhta center multifunctional complex.

3.2 *Principal design features of the skyscraper substructure*

During the construction of the Public and Business Complex, a pile field of 2080 drilled cast-in-situ piles was used. In this case 264 piles of the diameter of 2 m were constructed under the tower, 848 piles of the diameter of 1.2 m - under the multifunctional building and arch, and 968 piles of the diameter of 0.6 m - under the stylobate (Figure 2).

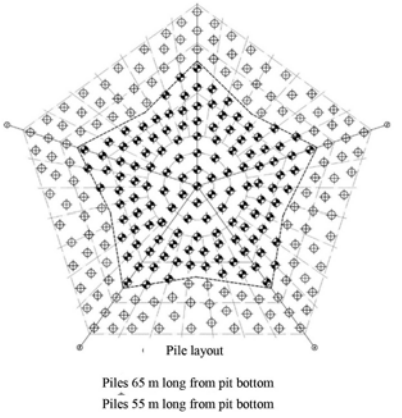

Figure 2. Layout of the pile field under the skyscraper building.

1. The architectural design of the Complex was developed under the guidance of Architect F. Nikandrov. The General Designer was ZAO Gorproekt, the General Contractor was Arabtech (UAE)

The box foundation of the skyscraper consists of three tightly reinforced slabs which are enclosed by a diaphragm wall in the form of a regular pentagon, which penetrates down to undisturbed firm Cambrian clays (Figure 3a).

A space between three slabs of the box foundation is formed by underground floors, in the center of which a reinforced concrete core of the skyscraper is located with 10 radial walls going from it to the external perimeter. The walls are 2.5-m- thick and of the total height of 11 m (Figure 3b).

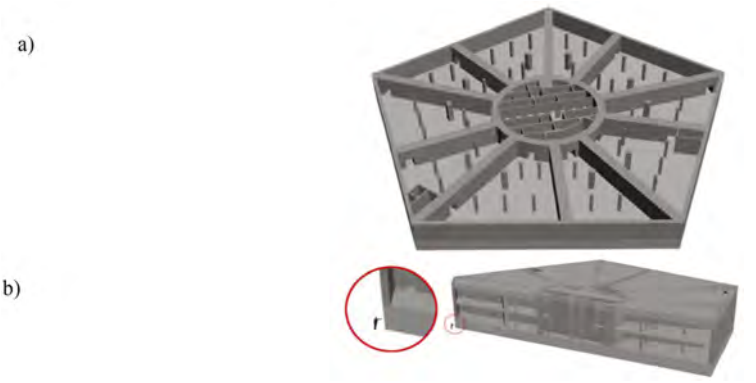

Figure 3. The box foundation and core of tower (a); the model of the box foundation and human scale (b).

The total height of the box foundation is 20 m, the inside diameter of the core is 24.5 m. The bottom reinforced concrete slab of the box foundation is 3.6 m thick, the diameter of its reinforcement bars is 32 mm with the reinforcement bars spaced at 16.5 cm. The total of 15 reinforcement mesh levels are installed in the bottom slab. The top slab is 2-m-thick, the middle slab is 0.4 m thick[2]. The reinforced concrete core, which is the main stability structure of the skyscraper, is made hollow: inside it, there are located utilities, vertical transport, service rooms and safety areas. The core is rigidly connected with the box foundation, which transfers the load from the tower to the piles.

The diaphragm wall is a retaining structure of the excavation pit which protects the excavation pit against underground water and pressure of soil. The disk spacer system held the walls of the excavation pit during the construction of the box foundation (Figure 4).

The total length of the diaphragm wall is 300 m around five sides with the height of 31.5 m and the width of 1.2 m. When the excavation pit was made the stability of the diaphragm wall was provided by 4 spacer disks. In construction of this retaining structure there were used 105 reinforcing cages with the weight of 20 tons. The bottom slab of the skyscraper box foundation is supported by the drilled cast-in-situ piles which were constructed according to the Bauer technology using a protective pipe of 2 m in diameter of two types: in the center of the building, there were 65 m long piles, while along the perimeter, there 65 m long 55 m long long[3]. (Figure 2). This was done in order to compensate a greater settlement produced in the center of the building as compared to the edges. The total number of piles was 264 of each type.

The bearing capacity of one pile is approximately 5 thousand tons, which is 2.5 times higher than the design load. In general, the total bearing capacity of the pile field is over 1,300 thousand ton, and thereby it supports the total load of 670,000 tones.

2. The construction of the diaphragm wall and the box foundation was carried out by ZAO Geostroy
3. The design and monitoring of the pile field was developed and conducted by Gersevanov Research Institute of Soils and Underground Structures (Gersevanov's Institute), the piles were constructed by Bauer (Germany)

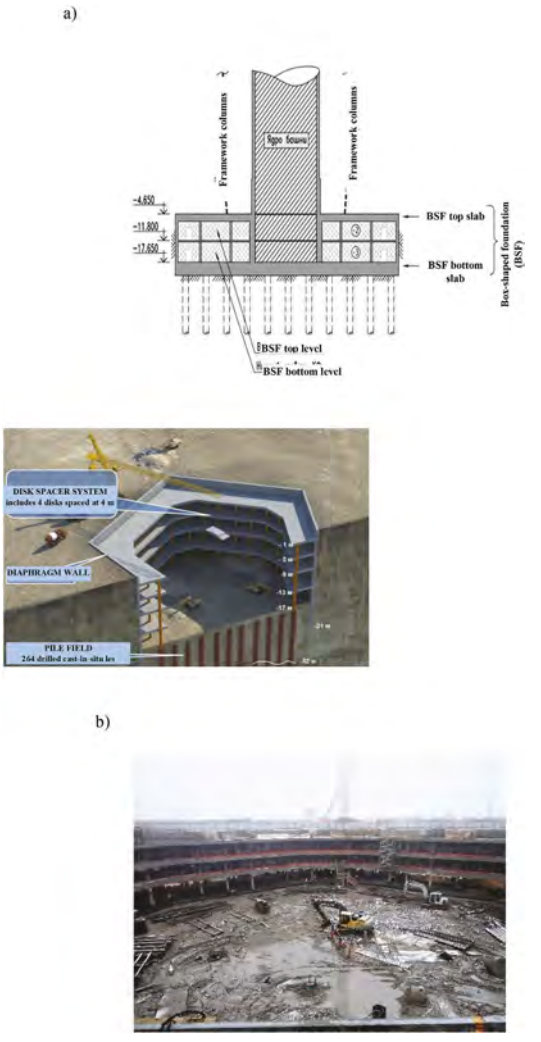

Figure 4. Sectional diagram and axonometric view of the diaphragm wall with spacer disks and pile field (a) and the general view of construction works (b).

3.3 *Specific features of substructure construction for the multifunctional buildings*

Two buildings located on the sides of the high-rise landmark are built with the height difference of 22 to 85 m and they have a two-level underground space (Figures 5 and 6).

Based on the load summary results, pressure was calculated underneath the mat with a thickness greater than 1 m. In order to provide the uniform settlement of the building, it was decided to specify the same diameter of the piles for the entire pile foundation. The piles were taken with D = 1.2 m and the length of 34 m with different spacing between them. The piles were installed at the interval of 3 m under the high-rise part of the building and the interval of 9 m under the foundation that carries a smaller load. The actual load-bearing capacity of the pile was taken equal to 1,400 tons. Thus, the optimum rigidity of each section with a characteristic load has been achieved.

Taking into account that the construction site is adjacent to the water area, as well as the high groundwater level, a retaining wall of the excavation pit (diaphragm wall) 27.5 m deep and 0.8 m thick was constructed and buried into undisturbed clays, whose roof is located at a depth of 25 m from the surface.

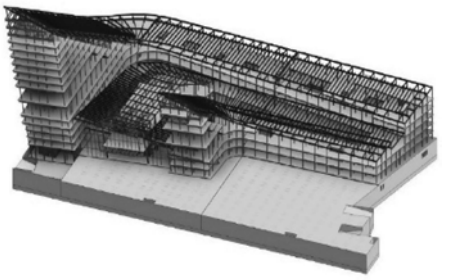

Figure 5. General layout of the load-carrying structure of the multifunctional building.

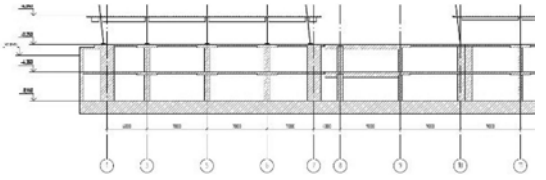

Figure 6. A fragment of substructure (no piles are shown) of the designed multifunctional building across one of sections.

The second purpose of the retaining structure was to secure the walls of the pit during the excavation of the latter and the construction of a zero-level part of the building. Figure 7 shows a fragment of the stage-by-stage excavation of the pit using berms and braces.

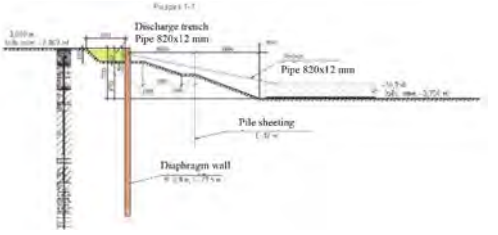

Figure 7. The layout of the diaphragm wall in soil conditions of the construction site.

4 PRINCIPAL STRUCTURAL SOLUTIONS FOR THE SUBSTRUCTURE OF GAZPROM-ARENA FOOTBALL STADIUM

The construction works on Gazprom-Arena Stadium were completed in 2016. The stadium successfully hosted Confederations Cup matches in 2017, 2018 World Cup matches and many other competitions. (Figure 8)

A new stadium was designed as an arena of oval shape in plan, with the 9-storey space which is located on the cone-shaped volume of a man-made hill.

The main functional purpose of the building is a multifunctional football stadium of the highest category, closed-type, year-round use with a retractable field, a sliding roof and viewing stands which accommodate 68,000 seats.

The following piles was used as foundations of the facility:

a) Drilled piles 24-m-long, 520 mm in diameter: 9000 ea. Soil bearing capacity of piles is 2600 kN (Figure 9). Concrete grades B30, B40, W8 and reinforcement A-500C were used for their construction.

Figure 8. General view of Gazprom-arena football stadium.

b) Drilled cast-in-situ piles 28-m-long, 500 mm in diameter: 1440 ea. Soil bearing capacity of piles is 8000 kN. Concrete grade B40, W8 and reinforcement A-500C were taken for their construction. The pile heads were united using reinforced concrete cast-in-situ rafts of variable thickness, H = 900 to 1500 mm.

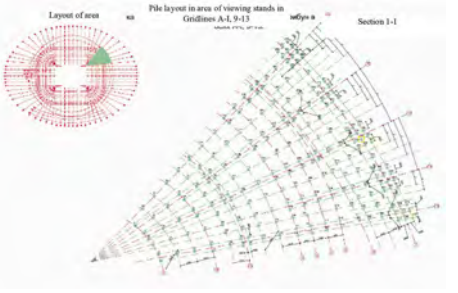

Figure 9. Principle of pile arrangement under viewing stands for one of segments.

The sliding roof is supported by 8 inclined pylons which rest on the structure. Taking into account high horizontal and moment loads which are transferred to the edges of the foundations of the pylons, the pile foundation structures for the roof supports are taken as space systems made of contiguous drilled cast-in-situ piles 1500 cm in diameter and 28-m-long (Figure 10).

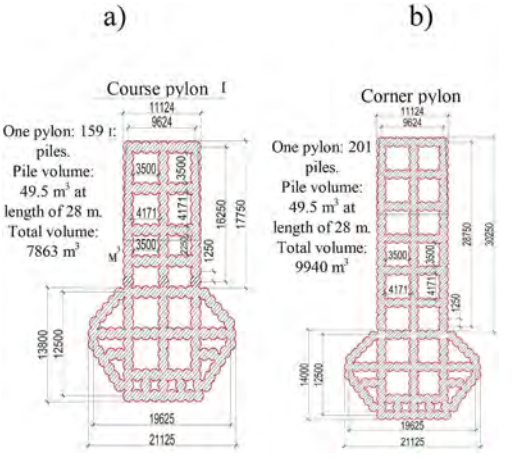

Figure 10. Construction of pile foundations for roof supports: a - course pylon; b - corner pylon.

Rolling out football field of the dimensions 120 x 80 m with the weight of 8,400 tons including the grass turf, heating and blow-off system, engines and the metal frame is moved outside the stadium pit (Figure 11).

Figure 11. General view of the roll-out field fragment.

To meet the above mentioned requirements a pile field was constructed under the slab of the retractable field. The pile field is made of drilled cast-in-situ piles 520 mm in diameter and 24-m-long spaced at 3.0 x 3.0 m; then, additional piles were constructed in the bridge area above the retractable field (Figure 8.30). A thickness of the raft slab was taken equal to 400 mm.

The construction works on Gazprom-Arena Stadium were completed in 2016. The stadium successfully hosted Confederations Cup matches in 2017, 2018 World Cup matches and many other competitions.

5 CONCLUSIONS

The foundations of the unique buildings and structures, which have been recently constructed on the thick layer of soft soils in Saint Petersburg, are made of drilled cast-in-situ piles that were driven to low-compressible primary soils - Cambrian clays – they have shown a high bearing capacity and provided the acceptable absolute and differential settlements.

REFERENCES

EN 1997-1: 2004 (E). Eurocode 7: *Geotechnical Engineering*.

Hanisch, J., Ratzenbach, R., Konig, G. 2002. *Kombinierte Pfahl-Plattegrundunggen*. Erns&Sohn.

Katzenbach, R. 2009. Combined Pile-Raft Foundation and Energy Piles – Recent Trend in Research and Practice. *Inter. Conf. on Deep Foundations – CPRF and Energy Piles*.

Mangushev, R., Ershov, A., Osokin, A. 2015. *Pile Construction Technology*. Stockholm: ASV Construction.

Mangushev, R.A. et al. 2015. *Piles and pile foundations. Engineering. Design. Technologies*. Moscow: ASV Publishing House.

Mangushev, R.A., Osokin, A.I., Sotnikov, S.N. 2018. *Geotechnics of Saint Petersburg. Experience in construction on soft soils. Monograph*. Moscow: ASV Publishing House.

Shulyatev, S.A., Lesnitskii, V.S. 2015. The influence of a rigid wall on soil deflected mode. *Proceedings of the 16 th Europen Conference on Soil Mechaics and Geotechnical Engineering*.

Shulyatiyev, O.A. 2016. Bases and foundations of high-rise buildings. in Ilyichev, V.A., Mangushev, R. A. (eds.) *Geotechnical Engineer's Handbook. Ground beds, foundations and underground facilities*. Moscow: ASV Publishing House.

Smart Geotechnics for Smart Societies – Zhussupbekov, Sarsembayeva & Kaliakin (Eds)
© 2023 The Author(s), ISBN 978-1-003-29912-7
Open Access: www.taylorfrancis.com, CC BY-NC-ND 4.0 license

Undrained instability and fluidization of soft subgrade soils under cyclic rail loading

B. Indraratna, T.T. Nguyen, J. Arivalagan, M. Singh, C. Rujikiatkamjorn & T. Doan
Transport Research Centre, Faculty of Engineering & Information Technology, University of Technology Sydney, Australia

ABSTRACT: The rapidly increasing demand for rail infrastructure to transport passengers and freight has inevitably led to a need for more robust and sustainable track foundations. However, heavy haul rail tracks often run across unfavourable soil conditions (e.g., saturated soft estuarine soils), resulting in frequent track failures accompanied with high maintenance cost. Recent site investigations along the South Coast rail line (NSW, Australia) showed considerable track degradation induced by subgrade mud pumping, requiring urgent attention and studies. This paper thus presents extensive laboratory and numerical investigations on the mechanism and possible solutions for mud pumping. While the effects of mud pumping on track performance are investigated through large-scale permeability and shear tests using the collected fouled ballast, the subgrade soil is subjected to cyclic triaxial and large-scale cyclic testing to understand the soil fluidization and fine particle migration. Transducers are installed at different layers to observe the depth-dependent response of soil foundation under various conditions. The results show that when specimens are subjected to unfavourable cyclic stresses, the fine particles migrate from the lower toward the upper soil layers along with the redistribution of pore water. When the water content of the upper soil layer reaches the liquid limit, the top of the specimen transforms into a slurry. Micro-analysis based on CFD-DEM coupling indicates a serious degradation in soil fabric and strength, thus the formation of mud under rising excess pore water pressure (EPWP). The study indicates that adding reasonable mass of cohesive fines can enhance the resistance of subgrade soils to fluidization, while geotextiles and geocomposites can also be used to mitigate mud pumping. Prefabricated vertical drains (PVDs) can continually reduce the buildup of EPWPs over the time due to the substantial reduction in drainage path, suggesting the efficiency of using the combined PVD-geocomposite system to mitigate mud pumping.

1 INTRODUCTION

1.1 *Subgrade failure under heavy freight trains*

In recent decades, the demand for faster and heavier freight transportation has pressurized geotechnical engineers worldwide to establish more robust and resilient rail track foundations. Alongside countries such as China, the USA, the UK, Canada and other European regions, Australian railways is one of the largest networks with rapid development in transport capacity. For example, the average train length is between 2-4 km, while the axle load is commonly 30 to 40 tonnes on mining and agricultural demands (Indraratna et al. 2014). However, this also results in devastating effects on the stability and longevity of track foundations, causing a greater degree of track deformation and foundation failures. In coastal regions where soft and saturated soils are prevalent, the repeated passage of heavy haul trains with increasing axle loads has been shown to exacerbate the accumulated excess pore water pressure (EPWP) and plastic deformation. When EPWP develops non-uniformly along the depth (localized response), it can stimulate the migration of pore water associated with fines, thus the formation of slurry track, i.e., mud pumping. The

DOI: 10.1201/9781003299127-2

infiltrated fines result in fouling of the ballast, reducing the interlocking between ballast particles (i.e., reduced shear strength) and impeding the drainage capacity (i.e., clogging) of the track foundation (Nguyen et al. 2019). Recent field inspections (Nguyen and Indraratna 2022c) have revealed a significant number of slurry sites along the South Coast (SC) rail line, NSW (Figure 1), many of which often repeat over year despite considerable maintenance cost. In low-lying regions, subgrade soil can be pushed upward (i.e., heave failure) under rising EPWP, seriously deteriorating structure and load bearing capacity of the track foundation. Hence, this phenomenon urgently demands a comprehensive investigation and feasible solutions.

Conventional studies (Selig and Waters 1994) indicated 3 different failure types of subgrade under rail tracks, i.e., (i) massive shear failure, (ii) progressive shear failure and (iii) attrition. However, these do not include the mechanism that transforms subgrade into fluid-like state. Furthermore, the internal migration of fines and moisture along the subgrade depth under repeated loads was not usually attended properly in past studies. Considerable effort has therefore gone to characterizing this phenomenon in the recent years (Duong et al. 2013; Chawla and Shahu 2016; Indraratna et al. 2020a). Past investigations (Hyodo et al. 1994; Indraratna et al. 2020a) indicated that the undrained shear failure can be characterized by the progressive advancement of excess pore water pressure and axial strain until the stress envelope reaches a failure line. On the other hand, when subjected to fluidization, soil becomes softened and fails under internal migration of pore water and fines, followed by the degradation in the stiffness and fabric of the specimens (Indraratna et al. 2020b; Nguyen et al. 2022). Subgrade instability is normally governed by complex combinations of internal and external factors. The internal factors can arise from soil characteristics such as particle size distribution, plasticity index (PI), void ratio and initial fabric (Vucetic and Dobry 1991; Polito and II 2001; Silva et al. 2022), whereas the external influences include the loading state and drainage condition (Sakai et al. 2003; Nguyen et al. 2019). Indraratna et al. (2020a) show that adding cohesive fines as well as increasing compaction degree can enhance soil resistance to fluidization. Despite abundant studies have been conducted to investigate the response of subgrade soils under repeated loads, the mechanism and causative factors that trigger the internal migration of soil particles and moisture still needs further explanation.

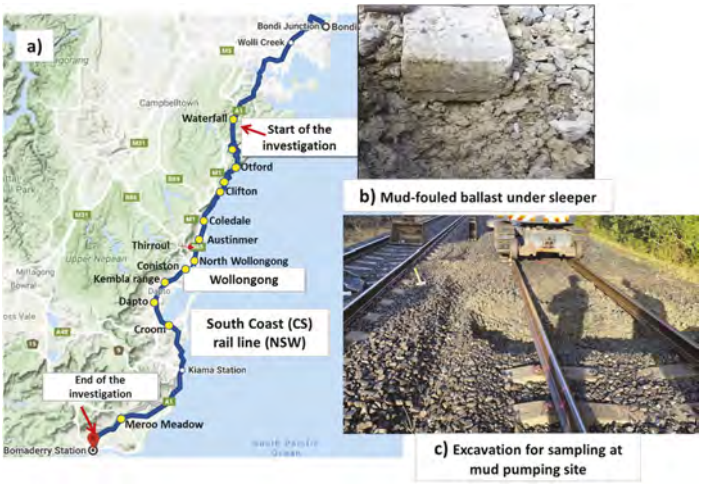

Figure 1. Field inspections of mud pumping sites including (a) locations along the South Coast (SC) line; (b) visual inspection of cohesive fines in ballast layer; and c) excavation for sampling.

1.2 *Use of geosynthetics to stabilize railway foundation*

Although a variety of solutions have been introduced, the most reliable and cost-effective solution for mud pumping and subgrade instability is still a critical question. The common practical method used to remediate a mud pumping track is replacement of the fouled ballast, however, this cannot always prevent the risk caused by subgrade mud pumping (Hudson et al.

2016). Increasing the thickness of ballast or renewing the subgrade (slurry) are expensive, but they are currently used in practice due to the simplicity and long-life effectiveness (Transport for NSW 2016). Additives such as lime and fly ash can also be used to increase the stability and cyclic resistance of substructures, they are time consuming and complex in construction while causing significant environmental impacts (Nguyen et al. 2019).

Geosynthetics are also commonly used to mitigate the migration of soil under railway and highways. Geotextiles have been used as a separation and filter layer under rail tracks for several decades, however, their effectiveness in preventing mud pumping is still now under debate (Raymond 1986; Sharpe et al. 2014; Hudson et al. 2016). Prefabricated vertical drains (PVDs) have been proved as a cost-effective method to shorten drainage path, thus accelerating the dissipation of EPWP as well as mitigating mud pumping (Indraratna et al. 2009; Singh et al. 2020). Short PVDs, i.e., installed in shallow depths within 6-8 m can prevent the accumulation of EPWP induced by the passage of heavy trains, meaning the less susceptibility of subgrade soil to internal instability. Furthermore, horizontal (i.e., transverse) drains can also be installed to facilitate drainage, thereby dissipating EPWP induced by train loads (Ito 1984).

Figure 2 shows the application of geocomposite material to prevent the migration of soil particles and associated mud pumping at Chullora, New South Wales (NSW). Although various geotextiles and geocomposites have been tested in the field and undergone large-scale laboratory testing, their effectiveness to prevent particle migration and fluidization varies widely. Some studies reported that geosynthetics have a limited efficiency and their performance could diminish quite significantly over the years (Selig and Waters 1994; Sharpe et al. 2014). Recent studies show that the installation of effective geosynthetics could prevent particle migration and potential track failures under dynamic loading (Lenart et al. 2018; Kermani et al. 2020). However, the use of geotextile allowed for in-plane drainage and dissipated the rapid development of EPWP. The pore arrangement in geotextiles should be large enough to provide adequate seepage (drainage capacity) and yet small enough to prevent particle migration (filtration) (Giroud 1996). Preventing particles from infiltrating into the overlying layers can increase the permeability of the drainage layer and provide continuous performance under loads.

Figure 2. Geocomposite installation to mitigate the fluidization potential of soft soil at Chullora, New South Wales (an ongoing pilot study supported by Sydney Trains).

This paper aims to review recent state-of-the-art studies around subgrade soil fluidization and the use of geosynthetics and geocomposites to prevent this failure under heavy haul rail tracks. Laboratory investigations from elemental to large scale model tests using real soil samples collected from mud pumping sites in NSW, Australia were extensively carried out at Transport Research Centre (TRC), UTS in recent years. Numerical model was also implemented to provide an insight into the micro-mechanism of soil fluidization under rising internal hydraulic gradient.

2 RESEARCH METHODOLOGY

2.1 *Cyclic triaxial tests*

It is critical to study the cyclic behavior of the subgrade soils prone to undrained instability and fluidization at a fundamental approach such as cyclic triaxial test. Disturbed soil samples were collected from several locations near Wollongong City. Basic geotechnical tests characterized the soils as low plastic clay, CL having a liquid limit less than 30 and a plasticity index of nearly 11. It is anticipated that low-medium plastic soils (PI < 26) are inherently vulnerable to mud pump due to the low cohesion between the soil particles (Duong et al. 2013; Chawla and Shahu 2016; Nguyen et al. 2019; Indraratna et al. 2020b). To achieve uniformity in sample preparation, the soil samples were compacted to a desired density ρ_d = 1600, 1680 and 1790 kg/m^3) using non-linear under-compaction criterion. The ratio of the initial specimen density to the maximum dry density of the soil is defined as Relative compaction (RC). The readers are referred to the following publication (Indraratna et al. 2020b) for further details on sample preparation.

To investigate the cyclic behavior of the reconstituted specimens, a series of stress-controlled undrained cyclic triaxial tests were performed using the GDS ELDYN dynamic triaxial testing equipment. The ELDYN system employs a pneumatic controller to apply the desired confining pressure. The pore pressure response was measured by employing a pore pressure transducer at the bottom of the specimen. Further, site investigations have revealed that mud pumping is a shallow phenomenon, therefore, the specimens were subjected to an effective confining pressure of σ'_{3c} = 15 kPa to simulate the shallow subgrade region. All specimens were back-saturated at a pressure of 400 kPa and then subjected to anisotropic consolidation (k_0 = 0.6).

The effect of varying axle loads was simulated by varying the cyclic stress ratio (CSR) from 0.2 to 1.0. The cyclic stress ratio (CSR) is defined as the ratio of the applied dynamic stress σ_d to twice of the effective confining pressure σ'_{3c}. The loading resulting from the passage of the trains was simulated through a sinusoidal waveform. The specimens were subjected to varying loading frequency (1.0 to 5.0 Hz) and the tests were concluded when the specimens experienced 5% cyclic axial strain or 50000 loading cycles. A generic representation for the fluidized specimen is highlighted in Figure 3 and the formation of a slurry at the top of the specimen at higher CSRs can be visually observed.

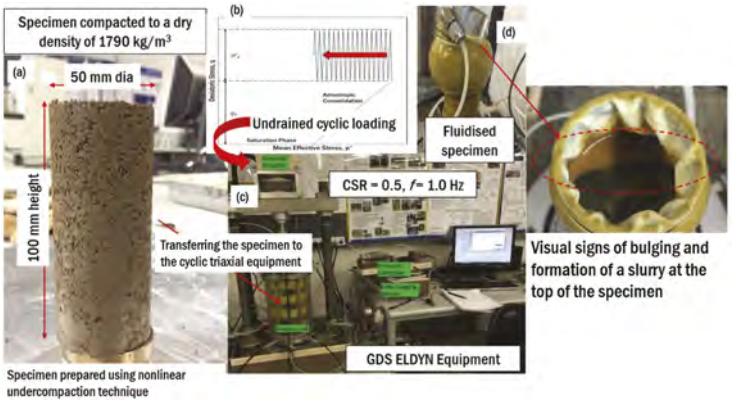

Figure 3. (a) Reconstituted specimen (b) Schematic for undrained loading (c) Cyclic triaxial rig (d) Typical fluidized specimen.

2.2 *Large-scale dynamic tests*

In order to capture the localized behaviour of subgrade soil as well as examining the efficiency of using geocomposite to stabilize subgrade soil under heavy cyclic loading, a series of large-scale dynamic tests were carried out at TRC.

2.2.1 *Testing materials*

Soil samples that had experienced mud pumping were collected from Wollongong, South Coast Rail line (NSW, Australia) for this study. The liquid limit (LL) and plastic limit (PL) of the soil were 42% and 26%, respectively and this soil could be classified as inorganic clay with medium plasticity. The maximum dry density (MDD) and optimum moisture content (OMC) were 1,682 kg/m^3 and 18.5%, respectively. The average water content after saturation was around 32% and the specific gravity was 2.59. A perspex hydraulic cell with a diameter (internal) of 140 mm and a height of 300 mm was used for the permeability tests. D_{cell}/D_{100} is greater than 42 and could avoid the effects of boundary wall friction (i.e. the ratio between the largest particle and the internal diameter of the cell is less than 1⁄6 (ASTM D3999-91 2003)). The compacted soil had a permeability of 8.9x10^{-7} m/s, as determined using the falling head method. Geotextiles and geocomposites with pore opening sizes of 10 to 80 μm, were used for the laboratory experiments. Geocomposite (T1) had a filter which sandwiched between two nonwoven geotextile layers with aperture opening sizes (O_{95}) of <10 μm. Prefabricated vertical drains (PVDs) had an assembled drain width of 100 mm, a thickness of 3.4 mm, and a drain filter pore size of 75 μm. All the properties of the geotextiles and PVD are listed in Table 1.

Table 1. Specification of geosynthetics used in the current.

Geotextile/geocomposite	T1*	T2	PVD	P
Tensile strength (EN ISO 10319 2008)	95 kN/m	22 kN/m	Drain Core and Filter material	PP and PET
CBR resistance (EN ISO 12236 2006)	18 kN	4.3 kN	Assembled drain width (ASTM D3774-96 1996)	100 mm
Pore size – Mean AOS (ASTM F316-03 2011)	<10 μm	60 μm	Assembled drain thickness (ASTM D5199-01 2001)	3.4 mm
Permeability (EN ISO 11058 2019)	0.35 l/m^{2}s	30 l/m^{2}s	Grab strength (ASTM D638-03 2003)	2.5 kN
Thickness (EN ISO 9863-1 2005)	9 mm	2 mm	Drain flow discharge (ASTM D4716-00 2000) at 200 kPa	2800 m^3/yr
Cone drop (EN ISO 13433 2006)	0 mm	22 mm	Drain filter pore size (ASTM D4751-99 1999)	75 μm

* - geocomposite

2.2.2 *Testing apparatus*

The Dynamic Filtration Apparatus (DFA) was designed at the University of Technology Sydney (UTS), Australia, to monitor the local EPWPs, soil porosity, development of excess pore pressure gradients (EPPGs) between different soil layers, and axial deformation under cyclic loading conditions (Figure 4). Four MPs with 1 kPa accuracy were placed on the center-line of the subgrade specimen at depths of 20, 40, 80, and 120 mm from the ballast/subgrade interface. Six pressure transducers (accuracy 0.5 kPa) were placed at the edge of cylinder at depths of 25, 55, 85, 115, 145, and 175 mm away from the ballast/subgrade interface. The local EPPGs that developed inside the specimen was calculated by measuring the differential hydraulic pressure at each layer. Amplitude Domain Reflectometry (ADR) probes were also installed along the subgrade depths and the variations in porosity could be monitored using the dynamic filtration apparatus (Arivalagan et al. 2021).

2.2.3 *Test procedures*

The collected soil from a mud pumping site was sieved through 2.36 mm. The target bulk density (1600 kg/m^3) and moisture content (17%) were achieved by compacting the dry soil and water to the desired volume. The 'nonlinear under-compaction' criterion was adopted to obtain a uniform density for the test specimen. PVDs with a modified size were used in the experiments based on the time factor and the average degree of consolidation for two soil cylinders, as proposed by (Ni 2012; Abeywickrama et al. 2021). Saturation was done with

filtered and de-aired water and monitored continuously by three ADR probes installed at different depths. A uniform vertical pressure of 30 kPa was applied to consolidate the soil specimen. The pore pressure that developed during consolidation process was monitored, and the settlement due to the applied loading was recorded continuously for two days. The geotextile was saturated before being placed onto the subgrade soil. After placing the ballast and/or geotextile, a sinusoidal load was applied through a servo-controlled actuator. In this study, a uniform cyclic stress was applied as a minimum vertical stress (σ_{min} = 30 kPa), and the sinusoidal vertical cyclic stress (σ_{max} = 70 –140 kPa), thus simulates a maximum axle load of 35-40 tonnes. The frequency varied between 1.0 and 5.0 Hz, which represents the train speeds of 40-220 km/h in a typical railway track conditions (Powrie et al. 2007; Indraratna et al. 2020b).

(1) Linear variable differential transformer (LVDT) and load cell,

(2) Miniature pore pressure transducers (MPs),

(3) Body pressure transducers (Ps),

(4) Lab controllers,

(5) Computer and Power supply and

(6) Hydraulic actuator

Figure 4. Dynamic filtration apparatus (DFA) at UTS-TRC.

2.2.4 *Experimental phases*

The laboratory tests were undertaken to simulate (a) undrained conditions where an impermeable boundary was created at the top of subgrade surface, and (b) free drainage conditions where a layer of ballast directly placed over the subgrade specimen. These two tests can be used to evaluate the failure criteria and subgrade fluidization. Dynamic filtration tests were carried out using geocomposite (T1), geotextile (T2) and PVD (P) and laid at the interface between the ballast and subgrade specimens to evaluate how well geosynthetics control the development of EPWP and preventing or delaying the initiation of subgrade fluidization. A series of laboratory experiments were undertaken to investigate the role of geotextiles and PVD under different axle loads and speeds. The loading frequency and amplitude applied varied from 1 to 5 Hz and 20-35 kPa (i.e., σ_{min}= 30 kPa, σ_{max} = 70-100 kPa), respectively. The effectiveness of a combined PVD-geocomposite system was also measured in terms of controlling the development of EPWP and mitigating/controlling the initiation of subgrade fluidization. A horizontal drainage path was created by the inclusion of PVD, and laboratory experiments were carried out to examine how effectively radial drainage could reduce the critical EPWPs that developed under cyclic load.

2.3 *Numerical modeling of subgrade fluidization*

In order to understand how the micro-structure of soil evolves under rising EPWP, a numerical investigation based on discrete element method (DEM) coupled with computational fluid dynamics (CFD) was carried out. In this approach, solid soil particles were modelled by DEM, while fluid flow was described by the CFD. Interactions between two phases, i.e., solid and fluid were governed through fluid-particle interaction models such as the pressure gradient, drag and viscous forces. Variables between the two computation platforms were exchanged regularly to ensure the effects from its counterpart to be captured properly. Details

of theoretical background and numerical algorithm of this method can be found in past studies of the Authors (Nguyen and Indraratna 2020; Nguyen and Indraratna 2022a). In the current paper, a sandy soil which is often used for capping layer under railways was simulated. Fluid went through the soil domain from the bottom to the top under increasing hydraulic gradient, while responses of soil and fluid at micro-scale were captured over time and space (Figure 5). It is important to note that a representative soil element was modelled in this case to enable particle-scale response of soil to be captured. Periodic boundary which simulated the continuous contacts between particles while migrating was used.

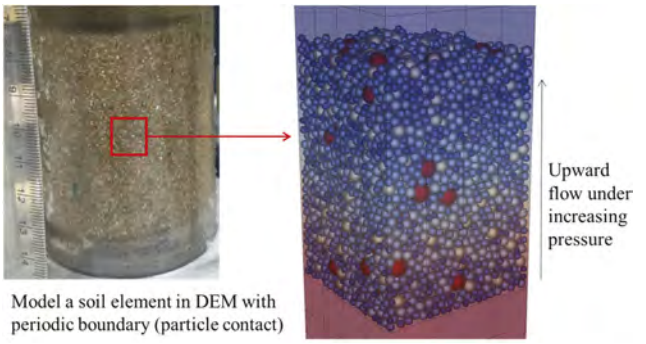

Figure 5. Numerical simulation of soil fluidization using CFD-DEM coupling.

3 RESULTS AND DISCUSSION

3.1 *Build-up of excess pore water pressure and migration of particles under cyclic loading*

When a specimen is subjected to increasing CSR, the specimen experiences larger deformations. However, there lies a critical cyclic stress ratio (CSR_c), wherein the mean excess pore pressure ratio (EPP) and cyclic axial strains shoot up rapidly. This is coupled with a sharp drop in the magnitude of the deviatoric stress q, indicating the onset of fluidization. Based on the test results, the CSR_c is dependent on the initial dry density of the soil specimen and the loading frequency. For example, as can be seen from Figure 6, the CSR_c for a specimen compacted at a dry density of 1790 kg/m^3 at a loading frequency of 1.0Hz lies between 0.4 and 0.5. Similar response was observed with soil samples collected from different mud pumping locations, despite different critical thresholds of load parameters and soil density (Indraratna et al. 2020a; Abeywickrama et al. 2021b).

The accumulation of excess pore water pressure governs the failure of the specimen under undrained cyclic loading. As seen from Figure 6, the increase in the CSR results in the increase in the build-up of excess pore water pressure. To quantify the effect of the EPWP, the incremental rate of EPWP was calculated. It is defined as the ratio between the EPWP and the log(N), where N is the number of cycles. It is observed that the rate of increment in EPWP at different CSRs (0.2, 0.3, and 0.4) is very similar (Figure 7a). The plots stabilize after the specimens reach 5% cyclic axial strain, and there is no considerable change after 2000 loading cycles. This implies that there is no further increase in the excess pore pressure. Figure 7b shows the variation of the incremental rate of EPWP with increasing CSR. When the specimen is subjected to a CSR = 0.5, there is a sudden increase in the excess pore pressure which results in the formation of slurry at the top of the specimen. For example, when the RC is 99%, the CSR_c lies between 0.4 and 0.5 for a frequency of 1.0 Hz. The CSR_c drops as the RC values reduces. It can be attributed to larger pore water pressure accumulation at lower RC as the specimen is in a relatively loose state.

A post-failure analysis was carried out for all fluidized specimens. Representative soil samples were carefully collected from the upper one-third and central region and were examined in the Malvern particle size analyzer. The results indicated an increase in the volume of fines (less than 75 microns) in the upper region of the specimen as opposed to the mid-region. This confirms that during the passage of trains, the fines migrate upwards and are transported by

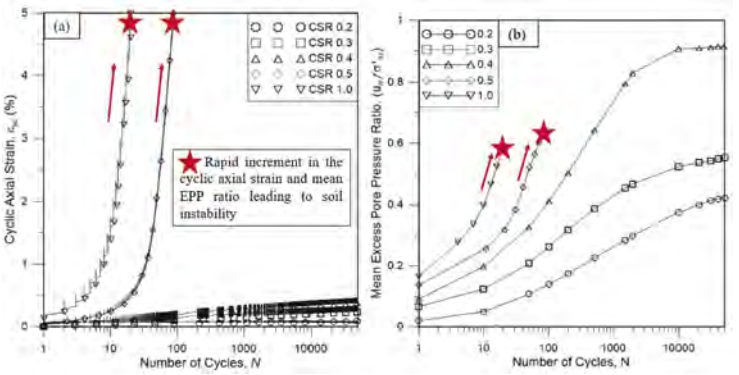

Figure 6. Generation of cyclic axial strains and mean excess pore water pressure (ρ_d = 1790 kg/m^3) (modified after Indraratna et al. 2020a).

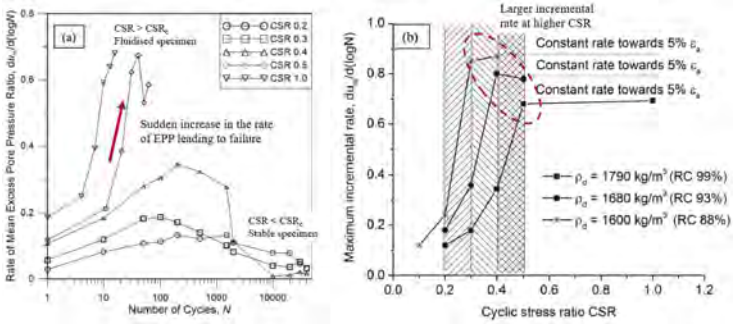

Figure 7. Variation in the incremental rate of EPWP with Number of cycles, N and CSR (modified after Indraratna et al. 2020a).

the displaced water which results in slurry formation or ponding of the slurry. Selig and Waters (1994) suggested that the cyclic nature of loading at the sleep-ballast interface generates a negative pressure which draws the suspended soil slurry from the subgrade level to the top of the ballast. Further, shallow subgrade with high water content (resulting from heavy rainfalls) during continuous railway loading may become susceptible to fluidization.

3.2 *Micromechanics of soil fluidization through numerical investigation*

The numerical results (Figure 8) show that when hydraulic gradient increases, soil particles are displaced under rising hydraulic forces acting on the particles, resulting in broken contact network and expanding porous system. For example, porosity of the simulated soil increases gradually under developing hydraulic gradient *i* before a sharp increase at the critical values of *i.* Meanwhile, the number of particle contacts drop immediately with rising *i* and become severe (i.e., the contact loss jumps from 20 to 35%) when *i* reaches the critical level (i.e., fluidization). While the change in porosity before the onset of fluidization is usually hard to measure in conventional laboratory due to its very sensitive magnitude, the response from particle contact network captured in the current CFD-DEM coupling model is apparent even at a small level of excess pore water pressure gradient or internal *i*. When the effective contacts of particles (i.e., the contacts bear effective stresses) are significantly vanished, soil behaves likes fluid with floating particles, thus fluidization. This microscale analysis indicated that preventing the accumulated EPWP and/or reinforcing contact network of soil are certainly effective approaches to mitigate particle migration and soil softening under rail tracks.

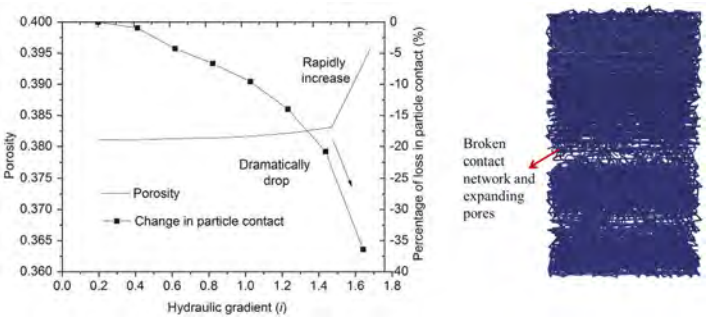

Figure 8. Degradation in micro-structure (porosity and particle contact) of soil under rising internal pore water pressure.

3.3 *Stabilization of subgrade soil using membrane and the composite membrane PVDs*

3.3.1 *Effectiveness of geosynthetics under cyclic loading*

The EPWPs that developed inside the specimen were measured because they were the main cause of instability in soft subgrade under continuous cyclic loading. Figure 9(a) shows the rapid development of EPWPs up to 500 cycles, where all the miniature pressure readings remain above 30 kPa when using geocomposite T1. The transducer MP2 (at 40 mm) measured the maximum EPWP of 37 kPa at 500 cycles. However, geocomposite with a filter membrane (AOS <10 μm) could dissipate the EPWPs below 10 kPa at the end of 75,000 cycles. When only using a geocomposite, the rate of excess pore water dissipation in Test T1 was higher near the ballast/subgrade interface (MP1) than the middle/shallow part of the subgrade (MP2 and MP3). In Test T2, until the test reached 65,000 cycles, the values from MP2 measured 40 mm below the interface were more than 20 kPa for T2 and with a very low rate of dissipation compared to geocomposite T1. As Figure 9(a) shows, T1 dissipated EPWPs by more than 76% and 52%, at 20 and 40 mm below the interface, unlike geotextile T2 at 75,000 cycles. This indicates that geocomposite (T1) dissipated the EPWP better than in comparison to conventional geotextile T2.

Undrained cyclic tests (impermeable boundary created by a geomembrane) indicated that the EPWPs that develops inside the soil specimen without a significant reduction over time might cause subgrade instability (Singh et al. 2020; Arivalagan et al. 2021). As shown in Figure 9(a), the magnitudes of EPWP that developed in Test T1 are more than 30 kPa at 500 cycles at all three depths; however, the presence of PVD (Test P+T1) certainly dissipates the EPWPs, especially in the deeper layers of soil. Therefore, the values of EPWPs from Test P+T1 are less than 15 kPa within 500 cycles and less than 4 kPa after 75,000 cycles. In other words, although a sole geotextile (Test T2) shows a maximum EPWP of more than 15 kPa at 75,000 cycles, there is approximately 80% reduction in EPWPs 40 mm under the interface due to the inclusion of the PVD-geocomposite system as shown in Figure 9(a) (i.e., the EPWPs at MP2 and MP3 remain below

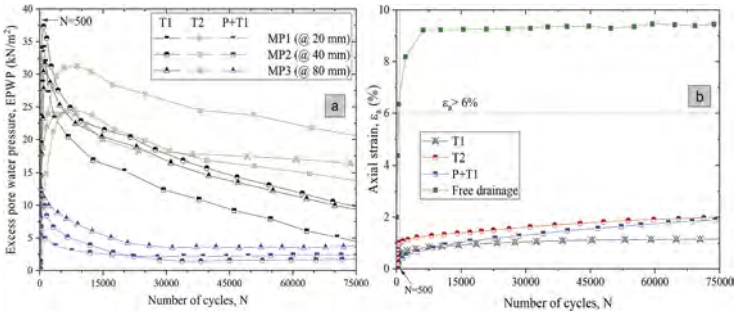

Figure 9. Generation of (a) EPWPs and (b) axial strains with geocomposite (T1), geotextile (T2), and a combined PVD-geocompoite system (after Arivalagan et al. 2022).

5 kPa). This proves that a combined PVD and geocomposite (P+T1) system can reduce the potential for subgrade fluidization during cyclic loading due to the continuous dissipation in EPWPs.

As Figure 9(b) shows, the maximum axial strain (ε_a > 6%) in free drainage tests (35 mm thick ballast was directly placed over the subgrade surface) only occurred after 500 cycles. However, the development of axial strain was controlled due to the inclusion of geotextiles at the interface. Geocomposite (T1) could provide more confinement at the ballast/subgrade interface and prevent the penetration of coarser ballast particles into the subgrade soil in Test T1. However, there was a continual increase in axial deformation due to the migration of fine particles through the pore openings of geotextile (T2) and the residual axial strain after 75,000 cycles remained above 2% for T2. This may lead to differential settlements in railway tracks under repeated cyclic loading conditions.

3.3.2 *Performance of geocomposites under varying cyclic stress*

A set of cyclic deviatoric stresses (i.e., σ_{max} of 70 and 100 kPa) were used to demonstrate how an increased axle load affects the cyclic behaviour of subgrade soil, and to assess the effectiveness of geocomposite T1. There was an expeditious development in EPWPs when the cyclic deviator stress increased up to 100 kPa when a sole geocomposite placed on the subgrade. As shown in Figure 10(a), geocomposite T1 could not reduce the cyclic EPWPs effectively at the middle to the lower region (i.e., the critical layers) when the cyclic stress increased to 100 kPa. The readings from miniature pressure transducers MP2, MP3, and MP4 remained above 35 kPa until the test ended and these results imply that an increased axle load in railway tracks (35-40 tonnes) generates a rapid increase in EPWPs, and the inclusion of geocomposite cannot dissipate them quickly under adverse hydraulic conditions. The increasing trend in axial strain was reported in previous studies when soft subgrade soil is subjected to a higher cyclic stress (Indraratna et al. 2020a). A similar increasing trend was observed at 100 kPa, where ε_a reached 5% before 75,000 cycles, as shown in Figure 10(b). The axial strain for 70 kPa (maximum vertical stress) was less than 1.5% until the test ended, but it rocketed up to 5.3% at 80,000 cycles at 100 kPa maximum vertical stress. Although geocomposite can mitigate the migration of fine particle at 70 kPa, a lot of fine particles accumulated during higher cyclic stress (under 35-40 tonnes axle load), which may induce subgrade instability due to excessive deformation in railway tracks.

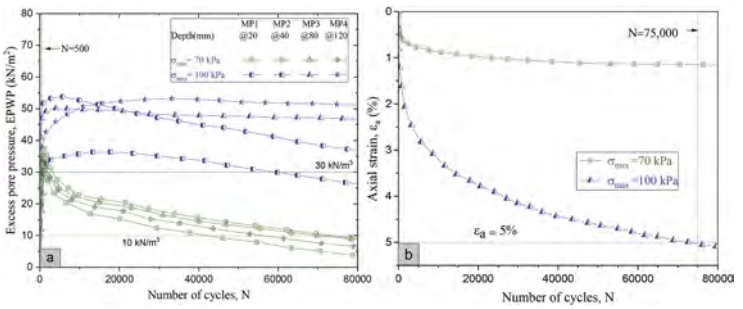

Figure 10. (a) Generation of EPWPs and (b) axial strains due to the inclusion of geocomposite (T1) under different cyclic stress (i.e. σ_{min} = 30 kPa, σ_{max} = 70 - 100 kPa) (modified after Arivalagan et al. 2021).

3.3.3 *The role of PVD-geocomposite system in a typical railway track*

The significant variation in drainage conditions at the interface and inside the soil were studied based on the generation of an excess pore pressure gradient (EPPG) at different depths. The EPWP measured at different soil layers by pressure transducers were used to calculate the EPPG. This can be defined as the ratio between changes in the excess pore water pressure head (unit = m head) and the corresponding distance between two specified locations (unit = m). The generation of critical EPPGs at various locations (inside the subgrade) can also induce instability by dislocating the fines from the original soil matrix. As Figure 11(a) shows, EPPG that developed in undrained tests rocketed above 40 after 500 cycles, and there was no significant reduction until

15,000 cycles. This non-uniform development of EPPGs in the middle and deeper subgrade soil, i.e., Layers (2-1) and (3-2), created a significant upward hydro-dynamic force that dislocated the finer particles towards the top layers. However, a PVD-geocomposite system (P+T1) reduced the EPPG at the top three layers of the soil within 2500 cycles. The EPPGs that developed in Layers (2-1) and (3-2) decreased by 67% and 90% due to the inclusion of PVD and geocomposite (T1), as shown in Figure 11(a). In addition, EPPG that developed at the middle and lower regions (Layer (3-2) and Layer (4-3)) was less than five until the end of cyclic tests.

The increase in the fine percentage and the formation of slurry at the interface (abrupt change in the water of soil) were used to assess the potential for subgrade fluidization in several studies (Indraratna et al. 2020b). Therefore, PSD and moisture content tests were conducted after each cyclic test. Malvern particle size analyzer was used to measure the particle size distributions at the top, middle, and bottom regions at the end of loading. Figure 11(b) shows that fine particles of less the 75μm had accumulated at the top surface in undrained tests where a lot more fines were lost in the middle layers (between 1 and 60μm) compared to the initial PSD. As shown in Figure 11(b), the inclusion of P+T1 prevented the migration of particles from the middle and lower regions. There were no significant variations in PSD, especially at the top and middle layers. This shows that PVD and geocomposite with an effective filter (P+T1) can prevent particle dislocation under critical hydro-dynamic conditions. Similarly, there was a large accumulation of fines (less than 1μm) in the top and middle layers in Test T2. Moreover, the water content for undrained and free drainage tests were close to the liquid limit at the top surface of the subgrade and the amount of high water near the interface causes softening and can induce fluidization as finer particles accumulate below 500 cycles. However, a PVD-geocomposite system helped to reduce the water content where they had a maximum water content of 30% near the interface, which prevented the soil softening under cyclic loading.

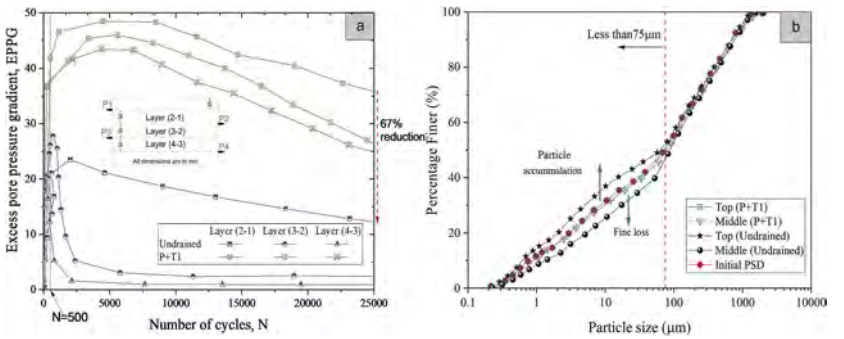

Figure 11. Undrained cyclic test and a combined PVD-geocomposite system (a) EPPGs and (b) variations in PSD (modified after Arivalagan et al. 2022).

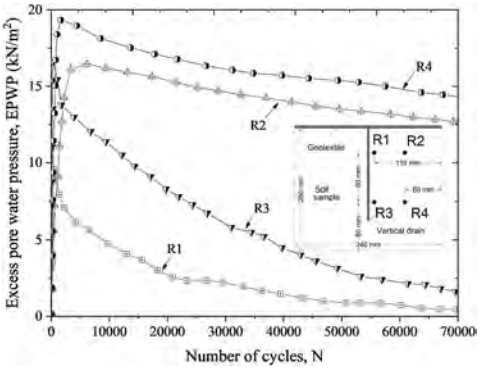

Figure 12. Dissipation of EPWPs due to radial drainage paths (P+T1).

Transducers (MPs) were installed at different locations from the centre (in radial direction 0 and 60 mm from the centre line) to measure how much the prefabricated vertical drains could alleviate the EPWPs (Figure 12). The EPWP measured at R1 (i.e., the shortest radial drainage path) is lower than at R2. Although the EPWPs developed at location R4 may take much longer to dissipate than R3, the PVDs successfully dissipate them before reaching their critical values. Furthermore, the EPWPs that developed at R1 and R3 approached zero after 70,000 cycles. The EPWPs measured at R2 and R4 decreased continuously as the number of cycles increased and were less than 14 kPa at the end of cyclic loading. Furthermore, PVDs can continually alleviate EPWPs during train loading and even during the rest period after each train passes.

3.3.4 *Effectiveness of PVD-geocomposite system under different axle loads and frequencies*
Figure 13(a) shows that the rapid generation of EPWP at 40 mm below the subgrade interface approached 50 kPa prior to reaching 5000 cycles when the maximum vertical stress increased to 100 kPa (approximately 35 tonnes axle loading). However, the EPWPs in the top and middle layers continued to dissipate due to the application of a PVD-geocomposite system. For instance, the EPWPs that developed at MP1 and MP3 were less than 25 kPa under varying cyclic stresses at the end of each cyclic test. In essence, the rapid generation of axial strain was controlled using geosynthetics because the axial strain was only 3% and 2.2% after 100,000 cycles at 30 and 35 tonnes axle loads, respectively. Figure 13(b) shows the effects of two different frequencies with the combination of PVD and geocomposite system. The results indicated that EPWPs that developed at all three locations (MP1, MP2 and MP3) decreased at a lower frequency. An increase in frequency (f=5 Hz) causes a significant increase in EPWPs at MP1 compared to the test under 3 Hz frequency. In addition, the rate of dissipation of EPWP is slightly higher in the test carried out at a lower frequency. The EPWPs that developed at MP1 are 4 kPa and 5 kPa for F=3 and 5 Hz at the end of the cyclic tests (Figure 13(b)). These results confirmed that a PVD-geocomposite system can still prevent critical EPWP generation even under higher frequencies.

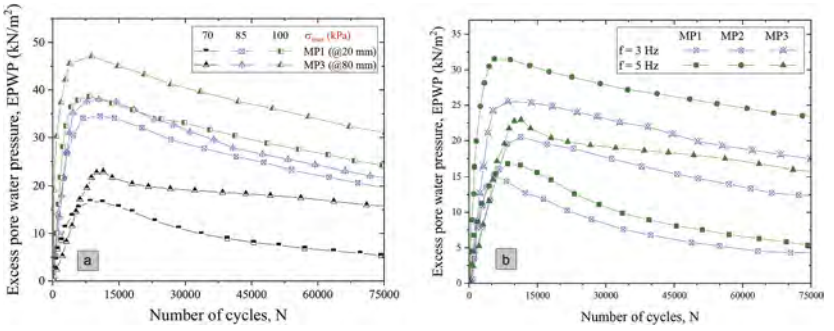

Figure 13. Performance of a combined PVD-geocomposite system under different (a) cyclic stresses (i.e. σ_{min} = 30 kPa, σ_{max} = 70 - 100 kPa) and (b) frequencies (3-5 Hz) (modified after Arivalagan et al. 2022).

4 CONCLUSIONS AND INDUSTRY IMPACT

Comprehensive experimental and numerical studies were carried out to investigate the mechanism and causative factors of subgrade fluidization under heavy haul trains. Geosynthetics and PVD-geocomposite inclusions to mitigate subgrade fluidization were proposed and examined through a large-scale model test. Salient findings of this study can be summarized as follows:

(1) The passage of heavy freight trains can cause a non-uniform accumulation of EPWP over the depth of subgrade soil, resulting in increasing excess pore pressure gradient (EPPG or an internal hydraulic gradient). When this gradient reached a critical level, the internal flows brought moisture and fines upward accompanied with stiffness degradation, thus

mud pumping. The heaver the train, the larger the cyclic stress ratio, the larger the accumulated EPWP and EPPG.

(2) The numerical investigation at micro-scale showed that increasing internal hydraulic gradient meant larger hydraulic forces acting on soil particles that pushed particles away while expanding the pore network (i.e., increasing porosity). As this continued to develop under repeated loading, the soil matrix significantly lost effective contacts between particles that resulted in reduced stiffness and fluidized soil.

(3) Increasing the relative compaction (or density) of soil can enhance the resistance to fluidization, however, when the axle load exceeded very high degree (CSR > 0.5), additional soil stabilization such as inclusion of geosynthetics should be considered.

(4) PVDs combined with a drainage membrane (geocomposite at the interface) facilitated the dissipation of EPWP and EPPG that significantly enhanced track stability by preventing soil softening and fluidization. The test results showed that a combined PVD-geocomposite system can effectively dissipate the pore water pressure even when the axle load and frequency reached high degrees (e.g., equivalent 35-40 tons and 120 km/h train speed over 75,000 loading cycles).

ACKNOWLEDGEMENT

Financial and technical support provided by the Australian Research Council (ARC) funded ITTC-Rail (i.e., LP160101254, LP200200915, DP220102862, IC170100006), and industry partners including TetraTech Coffey, SMEC, ACRI, Sydney Trains and Global Synthetics is gratefully acknowledged. The authors would also like to acknowledge the assistance provided by EngAnalysis for the installation of instrumentation at Chullora Technology Precinct. Some contents of this paper have been published earlier in scholarly journals and reproduced herein with kind permission from Canadian Geotechnical Journal, Geotextiles and Geomembranes Journal, Transportation Geotechnics Journal, among others.

REFERENCES

Abeywickrama, A., Indraratna, B., Nguyen, T.T. and Rujikiatkamjorn, C. 2021b. Laboratory investigation on the use of vertical drains to mitigate mud pumping under rail tracks. *Australian Geomechanics Journal*, **56**(3): 117–126.

Arivalagan, J., Indraratna, B., Rujikiatkamjorn, C. and Warwick, A. 2022. Effectiveness of a Geocomposite-PVD system in preventing subgrade instability and fluidisation under cyclic loading. *Geotextiles and Geomembranes*, **50**(4): 607–617.

Arivalagan, J., Rujikiatkamjorn, C., Indraratna, B. and Warwick, A. 2021. The role of geosynthetics in reducing the fluidisation potential of soft subgrade under cyclic loading. *Geotextiles and Geomembranes*, **49**(5): 1324–1338. https://doi.org/10.1016/j.geotexmem.2021.05.004.

ASTM D638-03. 2003. Standard Test Method for Tensile Properties of Plastics. ASTM International, 100 Barr Harbor Drive, PO Box C700, West Conshohocken, PA 19428-2959, United States.

ASTM D3774-96. 1996. Standard Test Method for Width of Textile Fabric. ASTM, 100 Barr Harbor Drive, West Conshohocken, PA 19428-2959, United States.

ASTM D3999-91. 2003. Standard Test Methods for the Determination of the Modulus and Damping Properties of Soils using the Cyclic Triaxial Apparatus. Annual Book of ASTM standards.

ASTM D4716-00. 2000. Standard Test Method for Determining the (In-plane) Flow Rate per Unit Width and Hydraulic Transmissivity of a Geosynthetic Using a Constant Head. ASTM International, United States.

ASTM D4751-99. 1999. Standard Test Method for Determining Apparent Opening Size of a Geotextile. ASTM, 100 Barr Harbor Drive, West Conshohocken, PA 19428-2959, United States.

ASTM D5199-01. 2001. Standard Test Method for Measuring the Nominal Thickness of Geosynthetics. ASTM, 100 Barr Harbor Drive, West Conshohocken, PA 19428-2959, United States, Pa.

ASTM F316-03. 2011. Standard Test Methods for Pore Size Characteristics of Membrane Filters by Bubble Point and Mean Flow Pore Test. ASTM International, West Conshohocken, PA, 2003.

Chawla, S. and Shahu, J.T. 2016. Reinforcement and mud-pumping benefits of geosynthetics in railway tracks: Model tests. *Geotextiles and Geomembranes*, **44**(3): 366–380. https://doi.org/10.1016/j.geotexmem.2016.01.005.

Duong, T.V., Tang, A.M., Cui, Y.-J., Trinh, V.N., Dupla, J.-C., Calon, N., Canou, J. and Robinet, A. 2013. Effects of fines and water contents on the mechanical behavior of interlayer soil in ancient railway sub-structure. *Soils and Foundations*, **53**(6): 868–878. https://doi.org/10.1016/j.sandf.2013.10.006.

EN ISO 9863-1. 2005. Geosynthetics–Determination of thickness at specified pressures. Part 1: Single Layers. CEN, Brusel.

EN ISO 10319. 2008. Geosynthetics–Wide-width tensile test. International Organization for Standardization, Geneva, Switzerland.

EN ISO 11058. 2019. Geotextiles and geotextile-related products — Determination of water permeability characteristics normal to the plane, without load. ISBN 978 0 580 93628 9, Pa.

EN ISO 12236. 2006. Geosynthetics—Static Puncture Test (CBR Test). European Committee for Standardization, Brussels, Belgium.

EN ISO 13433. 2006. Geosynthetics-Dynamic perforation test (cone drop test). ISO/TC 221 Geosynthetics, ISO 13433:2006.

Giroud, J. 1996. Granular filters and geotextile filters. *Geofilters 96, Proc. of 2nd Int. Conf." Geo-filters"*: 565–680.

Hudson, A., Watson, G., Le Pen, L. and Powrie, W. 2016. Remediation of Mud Pumping on a Ballasted Railway Track. *Procedia Engineering*, **143**: 1043–1050. https://doi.org/10.1016/j.proeng.2016.06.103.

Hyodo, M., Yamamoto, Y. and Sugiyama, M. 1994. Undrained Cyclic Shear Behaviour of Normally Consolidated Clay Subjected to Initial Static Shear Stress. *Soils and Foundations*, **34**(4): 1–11. https://doi.org/10.3208/sandf1972.34.4_1.

Indraratna, B., Attya, A. and Rujikiatkamjorn, C. 2009. Experimental investigation on effectiveness of a vertical drain under cyclic loads. *Journal of geotechnical and geoenvironmental engineering*, **135**(6): 835–839.

Indraratna, B., Korkitsuntornsan, W. and Nguyen, T.T. 2020a. Influence of Kaolin content on the cyclic loading response of railway subgrade. *Transportation Geotechnics*, **22**: 100319. https://doi.org/10.1016/j.trgeo.2020.100319.

Indraratna, B., Nimbalkar, S. and Rujikiatkamjorn, C. 2014. From theory to practice in track geomechanics – Australian perspective for synthetic inclusions. *Transportation Geotechnics*, **1**(4): 171–187. https://doi.org/10.1016/j.trgeo.2014.07.004.

Indraratna, B., Singh, M., Nguyen, T.T., Leroueil, S., Abeywickrama, A., Kelly, R. and Neville, T. 2020b. Laboratory study on subgrade fluidization under undrained cyclic triaxial loading. *Canadian Geotechnical Journal*, **57**(11): 1767–1779.

Ito, T. 1984. Actual situation of mud pumping and its countermeasures. *Quarterly Reports of the Railway Technical Research Institute*, **25**(4): 117–123.

Kermani, B., Stoffels, S. and Xiao, M. 2020. Evaluation of effectiveness of geotextile in reducing subgrade migration in rigid pavement. *Geosynthetics International*, **27**(1): 97–109.

Lenart, S., Bizjak, K.F., Noren-Cosgriff, K., Kaynia, A.M., Kramar, M., Vajdić, M., Chen, K. and Clarke, J. 2018. Guidelines on the use of novel construction and maintenance techniques within the operational railway environment. *DESTination RAIL – Decision Support Tool for Rail Infrastructure Managers*.

Nguyen, T.T. and Indraratna, B. 2020. A coupled CFD-DEM approach to examine the hydraulic critical state of soil under increasing hydraulic gradient. *ASCE International Journal of Geomechanics*, **20**(9):04020138-1:15. https://doi.org/10.1061/(ASCE)GM.1943-5622.0001782.

Nguyen, T.T. and Indraratna, B. 2022a. Fluidization of soil under increasing seepage flow: an energy perspective through CFD-DEM coupling. *Granular Matter*, **24**(3): 80. doi: 10.1007/s10035-022-01242-6.

Nguyen, T.T. and Indraratna, B. 2022b. Rail track degradation under mud pumping evaluated through site and laboratory investigations. *International Journal of Rail Transportation*, **10**(1): 44–71. doi: 10.1080/23248378.2021.1878947.

Nguyen, T.T., Indraratna, B., Kelly, R., Phan, N.M. and Haryono, F. 2019. Mud pumping under railtracks: Mechanisms, Assessments and Solutions. *Australian Geomechanics Journal*, **54**(4): 59–80.

Nguyen, T.T., Indraratna, B. and Leroueil, S. 2022. Localized behaviour of fluidized subgrade soil subjected to cyclic loading. *Canadian Geotechnical Journal*, **59**. https://doi.org/10.1139/cgj-2021-0550.

Ni, J. 2012. Application of geosynthetic vertical drains under cyclic loads in stabilizing tracks. *PhD Thesis*, *University of Wollongong*, *Australia, p.* 210.

Polito, C.P. and II, J.R.M. 2001. Effects of Nonplastic Fines on the Liquefaction Resistance of Sands. *Journal of Geotechnical and Geoenvironmental Engineering*, **127**(5): 408–415. doi: 10.1061/(ASCE)1090-0241(2001)127:5(408).

Powrie, W., Yang, L. and Clayton, C.R. 2007. Stress changes in the ground below ballasted railway track during train passage. *Proceedings of the Institution of Mechanical Engineers, Part F: Journal of Rail and Rapid Transit*, **221**(2): 247–262.

Raymond, G.P. 1986. Geotextile Application for a branch line upgrading. *Geotextiles and Geomembranes*, **3**(2): 91–104. https://doi.org/10.1016/0266-1144(86)90002-6.

Sakai, A., Samang, L. and Miura, N. 2003. Partially-drained cyclic behaviour and its application to the settlement of a low embankment road on sitly-clay. *Soils and Foundations*, **43**(1): 33–46. doi: 10.3208/sandf.43.33.

Selig, E.T. and Waters, J.M. 1994. Track geotechnology and sustructure management. Thomas Telford, London.

Sharpe, P., Roskams, T. and Valero, S.N. 2014. The development of a geocomposite to prevent mud pumping. In *Proceedings of the Conference on Railway Excellence: Railway Transport for Vital Economy (RTSA)*, Adelaide, Australia. pp. 346–353.

Silva, I.N., Indraratna, B., Nguyen, T.T. and Rujikiatkamjorn, C. 2022. Shear behaviour of subgrade soil with reference to varying initial shear stress and plasticity index. *Acta Geotechnica*. https://doi.org/10.1007/s11440-022-01477-w.

Singh, M., Indraratna, B., Rujikiatkamjorn, C. and Kelly, R. 2020. Cyclic response of railway subgrade prone to mud pumping. *Australian Geomechanics Journal*, **55**(1): 43–54.

Transport for NSW. 2016. Track Reconditioning Guidelines, T HR CI 12120 GU. Transport Asset Standards Authority, NSW.

Vucetic, M. and Dobry, R. 1991. Effect of Soil Plasticity on Cyclic Response. *Journal of Geotechnical Engineering*, **117**(1): 89–107. doi: 10.1061/(ASCE)0733-9410(1991)117:1(89).

Smart Geotechnics for Smart Societies – Zhussupbekov, Sarsembayeva & Kaliakin (Eds)
© 2023 The Author(s), ISBN 978-1-003-29912-7
Open Access: www.taylorfrancis.com, CC BY-NC-ND 4.0 license

Deformation of shield tunnels induced by adjacent construction

R.P. Chen, F.Y. Meng, H.N. Wu & H.Z. Cheng
College of Civil Engineering, Hunan University, Changsha, China

ABSTRACT: Shield tunnels are very sensitive to the ground motion. The protection of operating shield tunnels is important during the construction of underground space. This paper introduces three typical soil arching, termed as "upward", "downward" and "lateral" soil arching in light of their developing direction with respect to the ground gravity during the underground construction. Theoretical models are proposed to describe the ground stress and deformation transfer associated with the developing soil arching. The impacts of the nearby construction on the existing shield tunnels are evaluated considering the soil arching. It is found that a significant increase in structural deformation occurs when the loosened zone of soil arching develops to the existing tunnel. Countermeasures regarding protection of the nearby tunnels are developed by mitigating the expansion of the loosened zone and reinforcing the loosened zone. Finally, engineering applications of the countermeasures are also introduced.

1 INTRODUCTION

During the past decades, underground construction has been a promising alternative to extend the space of congested urban cities. More and more shield tunnels are constructed for subways, express roads, and pipe galleries. To further exploit the capacity of the underground space, shield tunneling and upward/lateral excavation nearby operating shield tunnels are frequently encountered. Shield tunnels are fabricated structures assembled by several lining segments and many bolts, featured with long joints, low stiffness and easy to deform. In adverse conditions (weak soil properties, close proximity, insufficient retaining system, and inappropriate countermeasures), the operating shield tunnels would suffer from intolerable deformations and structural damages like lining cracks, dislocations, and leakages at joints (Chen et al. 2016).

In essence, the shield tunnel deformation is determined by the ground deformation and stress change induced by the nearby construction. Soil mass excavation induced by construction could lead to uneven ground deformation, and hence the generation of soil arching. Development of the arching governs the ground stress transfer, deformation propagation, and the tunnel responses. Soil arching is one of the most common phenomena encountered in geotechnical engineering. Terzaghi (1943) proposes an analytical solution for depicting the soil arching above the trapdoor, followed by plenty of studies on the soil arching above the tunnel (Franza et al. 2019; Lin et al. 2022) and piled embankment (van Eekelen et al. 2013; Zhang et al. 2016). These types of soil arching are termed as the upward arching in light of its developing direction. In addition, excavation could also cause arching effect below base level and behind the retaining wall. The developing directions of the soil arching due to shield tunnelling and nearby excavation are different and hence exhibit distinct impacts on the existing tunnels. However, to date, the soil arching induced by the above nearby underground construction has not been well investigated and summarized yet, as well as the associated shield tunnel deformation and countermeasures.

This study introduces three typical soil arching in light of their developing directions. Theoretical models are proposed to describe the ground stress and deformation transfer associated with the developing soil arching. The impacts of the nearby construction on the existing shield tunnels are evaluated considering the soil arching. Countermeasures regarding protection of the nearby tunnels are developed by mitigating the expansion of the loosened zone and reinforcing the loosened zone. Finally, engineering applications of the countermeasures are also introduced.

DOI: 10.1201/9781003299127-3

2 SOIL ARCHING IN UNDERGROUND CONSTRUCTION

2.1 *Understanding and definition*

(1) *Upward soil arching*

Ground volume loss is inevitable during shield tunneling because of overbreak, unbalanced face support pressure, and poor shield tail grouting. The differential ground deformation induced by the volume loss could cause the occurrence of the soil arching above the tunnel, as shown in Figure 1(a). To recognize the characteristics of the arching, experimental and numerical studies have been carried out (Han et al. 2017; Franza et al. 2019; Lin et al. 2019). Lin et al. (2019) find that the shear bands develop obliquely upward from the bottom of the tunnel in sandy ground. Besides, the soil arching develops with the increasing trapdoor displacement (Iglesia et al. 1999), and hence that above the tunnel should develop with the growing ground volume loss.

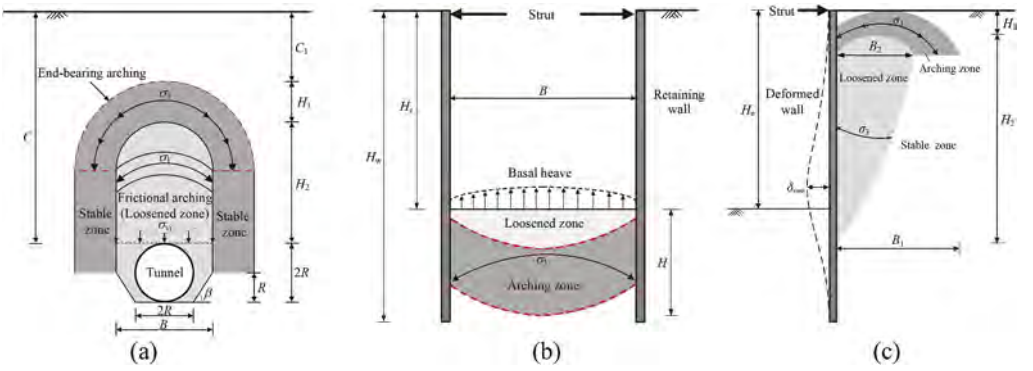

Figure 1. Illustration of the three typical soil arching for underground construction.

(2) *downward soil arching*

Uneven ground deformation occurs below the excavation base and behind the retaining wall, causing downward (Figure 1(b)) and lateral (Figure 1(c)) soil arching, respectively. Numerical simulation (Meng et al. 2022) and centrifuge modeling (Wu et al. 2022) are carried out to get an insight into the downward arching. Similar to the displacement and the width of the trapdoor, the excavation depth and the width are predominant variables influencing the boundary of the downward arching. Furthermore, the soil relative density is also a key factor governing the soil arching (Liu et al. 2022b). The model ground adopted in the centrifuge is dry Fujian sand (D_r=30% in Test 1 and 75% in Test 2), and the widths and final depth of the excavation are 15 m and 24 m, respectively. Figure 2(a) depicts the vertical distribution of the horizontal soil arching ratio (SAR) with varying distances to the excavation centerline, and an inflection point can be found on each curve. Within the loosened zone, the SAR sustainingly increases along with depth, and a steeper slope is found nearby the wall. In comparison, the SAR exhibits negligible change below the arching boundary. In Test 1, a greater distinction among curves in sections and a steeper arching boundary than that in G2 is found, especially in the loosened zone, which indicates that the dense sand layer leads to a more extensive nonuniformity of stress release. Take the inflection points of the curves of the SAR as the arching boundary, the variation of arching zone height with excavation depth is shown in Figure 2(b). The height of arching in the loose sand is larger than that in the dense sand for shallow excavation. This difference decreases with the growing excavation depth, which might be attributed to the similar soil behavior in the loosened zone and the arching zone when the excavation depth reaches a certain value, like the ending of the curve for support pressure versus face displacement for tunnel face stability for loose and dense sand (Kirsch 2010).

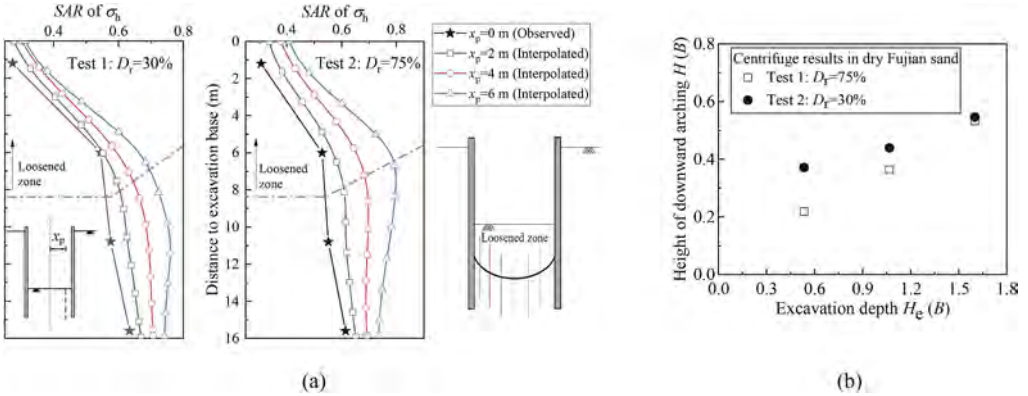

Figure 2. (a) distribution of horizontal soil arching ratio (SAR) below excavation depth; and (b) relationship between height of downward arching and excavation depth.

(3) *Lateral soil arching*

In terms of the ground responses behind the retaining wall, previous studies mostly concentrate on stress transfer and seldom take into account both soil movement and stress transfer (Hashash & Whittle 2002; Ng et al. 2012; Li et al. 2021), which are two key characteristics for lateral soil arching. Furthermore, there is not yet a criterion for determining the arching zone and loosened zone due to lateral excavation. Toward this end, a field test for investigating the lateral soil arching effect behind the retaining wall is carried out in an average 17-meter-deep, braced excavation in clayey ground (Chen et al. 2022a; Liu 2022). The ground movement, lateral earth pressure, and wall deformation are extensively measured, and the shear strain is calculated. It is found that soils behind the wall are predominantly subjected to horizontal extension and vertical compression, especially nearby the area where maximum wall deformation occurs. In comparison, soils neighboring the upper part of the wall experience increases in horizontal stress and hence compression. The soil arching zone and loosened zone are determined by the boundary at which the ratio of lateral earth pressure equals 1, the connected inflection points of lateral earth pressure, the lower sliding plane, and the wall. The arching zone transfers pressure oblique to the well-retained zone and the stable soil, resulting in the formation of horizontal compression zone and vertical extension zone, as well as an increase in lateral earth pressure around the crest of the wall. The major and minor principal stress arching are formed in the arching zone and loosened zone, respectively.

Figure 1(c) depicts the schematic of the lateral soil arching, based upon the above field observation. Similar to other two types of arching, the lateral soil arching develops with the increasing wall deformation. With the growing wall deformation, the height and the width of the loosened zone and arching zone increase. Finally, the arching zone might gradually disappear and the loosened zone would extend to the ground surface, with sharply increased ground movement and cracks along the shear plane. The evolution of the lateral soil arching mainly depends on the ground condition and wall deformation, which needs further investigation.

2.2 *Theoretical model*

To predict the earth pressure on the deep circular tunnel, Lin et al. (2022) propose a multi-arching model incorporating the earlier theories of Terzaghi (1943) and Hewlett & Randolph (1988). Figure 1(a) illustrates the concept and framework of the multi-arching model, which consists of the end-bearing arching, frictional arching, and stable zone. The end-bearing arching with a semi-circular ring shape is located on the upper part of the multi-arching model, whose arch feet act on the stable zone. The cover depth and thickness of this zone are C_1 and H_1, respectively. The inner and outer radius of the semi-circular ring are r and $r+H_1$, respectively. The height and width of the frictional arching are H_2 and B, respectively. The

transferred load q_1 from the end-bearing acting on the top of this zone is partly transferred to the stable zone by the frictional arching effect and the rest of the pressure acts on the top of the tunnel. This zone bears the pressure transferred from the end-bearing arching and frictional arching and provides sufficient support.

To figure out the model, two assumptions are made: (1) the ground loss induced by the tunnel over-excavation is absolutely compensated by the soil mass within the loosened zone, and (2) the frictional arching is composed of a semicircle and a rectangle with two triangles and a circle subtracted. The model geometric parameters include the width and height of the frictional arching, thickness of the end-bearing arching, which are determined based upon the earlier researches as listed in Table 1. On the basis of the geometries of the model, the stress in the end-bearing arching is calculated using the 2D semi-circular ring limit equilibrium model in piled embankments (Hewlett & Randolph 1988). Hence, the horizontal and vertical earth pressure above the tunnel can be calculated, which is verified by centrifuge modeling results (Franza et al. 2019). In comparison with the model of Terzaghi (1943), the multi-arching model yields more reasonable predictions for normalized average earth pressure on the tunnel (Lin et al. 2022).

Table 1. Geometric parameters of the upward arching model.

Parameter	Value	Meaning	Literature
B	$D(1+\cot\beta)$	D = tunnel diameter $\beta = 45°+\varphi/2$	Stein et al. (1989)
H	$D(k(\eta/\alpha)+b)$	$k = \frac{\pi \tan\beta}{4(1+\tan\beta)}$ $b = \frac{(\pi-4)\tan^2\beta + 2(1-\pi)\tan\beta + 4 - \pi}{8\tan\beta(1+\tan\beta)}$ η = ground volume loss α = rebound coefficient (0.1 to 0.24 and 0 to 0.08 for dense and loose sand)	/
H_1	$C\text{-}H>0.4B$, $H_1=0.4B$ $0<C\text{-}H\leq 0.4B$, $H_1=C\text{-}H$ $C\text{-}H\leq 0$, $H_1=0$	C = tunnel cover depth B = width of frictional arching zone	Lai et al. (2018)

Based on the multi-arching model (Lin et al. 2022), Chen et al. (2022b) propose a novel analytical approach to predict the tunneling-induced subsurface settlement on the tunnel centerline (Figure 3). In addition, stress-dependent modulus is adopted to consider the soil mechanical behaviors. This approach assumes that the soil material behaves elastically and isotropically, and the ground movement around the tunnel is oval-shaped. The ground settlement right above the tunnel crown is maximum and equals to the gap parameter g, determined by the physical gap, the over-excavation of the soil around the tunnel, and the 3D elastoplastic deformation of the soil in front of the tunnel face. The tunnel excavation leads to the unloading rebounding deformation within the frictional arching zone u_1 and end-bearing arching zone u_2. To obtain the ground settlement at a certain depth, g can be used to subtract the rebound deformation of the soil at its location. For instance, the ground settlement at the top of the end-bearing arching zone is

$$u_z = g - u_1 - u_2 \tag{1}$$

The magnitudes of u_1 and u_2 can be calculated by the Hooke's law, in which the ground stress change is determined by multi-arching model (Lin et al. 2022) and the stress-dependent elastic unloading modulus (Schanz et al. 1999). The applicability of this methodology is examined by three case histories and one model test, exhibiting satisfying results. Furthermore, the subsurface ground settlement trough can be determined by the calculated settlement at tunnel centerline and empirical settlement trough width coefficient.

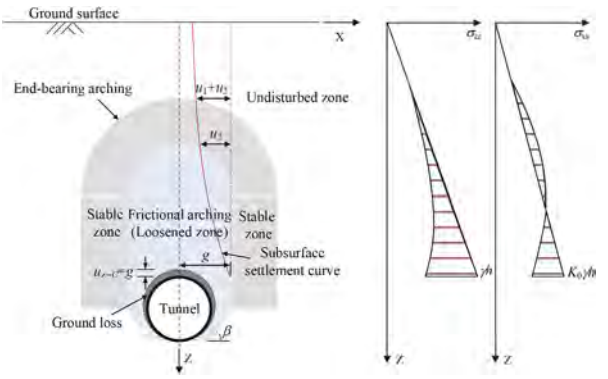

Figure 3. Analytical model for tunneling-induced subsurface ground settlement (after Chen et al. 2022b).

3 APPLICATION OF SOIL ARCHING

3.1 *Prediction of nearby tunnel deformation*

Two-stage method is proposed to predict the nearby tunnel deformation due to adjacent construction, which has been widely employed to solve the problem of tunnel-soil interaction. For tunneling underneath existing tunnel (Figure 4), in the first stage, the vertical unloading stress caused by the underlying tunnel is calculated based on the tunneling-induced subsurface settlement trough considering the soil arching. The maximum settlement of the trough is obtained by the method proposed by Chen et al. (2022b) and the width coefficient of the trough is determined by empirical results. The unloading stress at the level of the tunnel axis is calculated by the corresponding subsurface ground settlement and the coefficient of subgrade reaction. In the second stage, the responses of existing shield tunnel subjected to the corresponding vertical unloading stress are determined by an analytical model. In this analytical model, the existing shield tunnel was treated as a Timoshenko beam (Wu et al. 2015) resting on a Winkler foundation model. The applicability of this method is validated by several case histories in China, and good agreement is achieved in most cases in which soil improvement between the tunnels is not carried out.

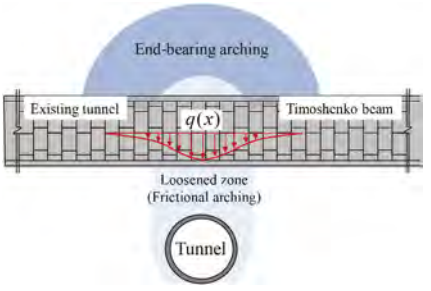

Figure 4. Theoretical upward arching-tunnel interaction model.

3.2 *Mitigating the tunnel deformation*

As aforementioned, nearby excavation-induced tunnel deformation is determined by the ground stress change and soil disturbance degree. The development of the soil arching governs the above two factors. Hence, mitigating the development of the soil arching is an effective alternative for reducing the tunnel deformation. The specific countermeasures for mitigating the tunnel deformation in the cases of downward excavation, upward excavation, and lateral excavation are introduced in the subsequent section associated with engineering application.

(1) *Downward excavation*

The overlying existing tunnel deformation is determined by the upward soil arching. Horizontally grouting above the underneath tunnel could reinforce the ground, avoid the underneath tunnel face instability and prevent the loosened zone from developing vertically. Besides, a key issue involved in this countermeasure is mitigating the disturbance of grouting on the existing tunnel due to the close clear distance between the two tunnels. Spoil discharge jet-grouting (SDJG) technology [S. Nakashima and W. Nakanishi, "Allaround type reinforcing and consolidating method in the ground and apparatus thereof," US Patent No. 5,401,121 (1995)] can erode the soil with mixed cement slurry to generate improved columns and also remove the discharging spoil by negative pressure. The spoils can be discharged synchronously during jet-grouting, and the pressure outside the nozzle can be adjusted to a required value by controlling the discharge in light of the measured pressure in front of the injection rod.

This technology is adopted in the intersection of Metro Line 2 and Metro Line 4 in Changsha, China (Wu et al. 2020). The minimum disturbance between the two lines is 2.9 m, and the main soil encountered is medium sand. The calculated ground settlement above the tunnel crown of Metro Line 2 without ground improvement reaches 22.1 mm, as shown in Figure 5-(a). SDJG is employed in this project to construct horizontal columns to reinforce the soils above the Metro Line 4 (Figure 5(b)). The length of the SDJG column is 42.8 m and the radius is 1.0 m, and the measured average unconfined compressive strength reaches 3.5 MPa. The measured earth pressure change nearby the grouting area ranges from 0.06 to 0.10 MPa and the existing tunnels experienced negligible deformation during SDJG construction. The measured vertical displacement of left tunnel is smaller than 4.0 mm after the shield advancing for Metro Line 4.

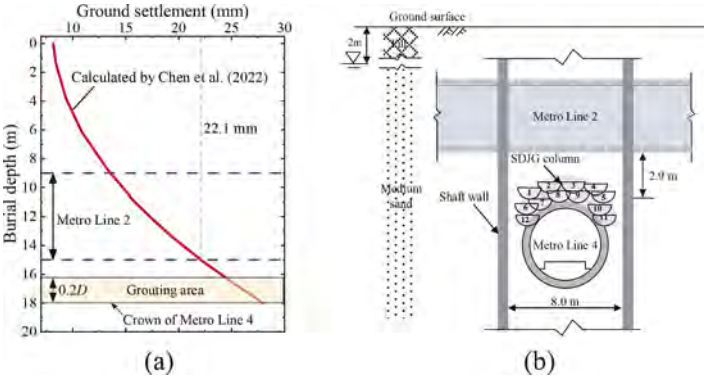

Figure 5. (a) calculated ground surface settlement above the shield tunnel of Metro Line 4 in case of no grouting; (b) SDJG column above Metro Line 4 and relative position of the two metro lines.

(2) *Upward excavation*

Through field observation, Meng et al. (2020) investigates the responses of underlying tunnels of Metro Line 11 subjected to the 3090 m-long collinear overlying excavation in granite residual soil for Guimiao Road in Shenzhen, China. The maximum excavation depth, width, and the minimum residual cover depth of the left tunnel are 18 m, 46 m, and 6 m, respectively. The curve of normalized tunnel heave and unloading ratio, defined as the ratio of excavation depth to tunnel cover depth, is depicted in Figure 6. It is easy to find that the tunnel heave experiences a sharp increase when the unloading ratio reaches about 0.55, which cannot be well estimated by the elastic two-stage solution (Liang et al. 2017) without considering soil arching. Furthermore, based on this case history, Meng et al. (2022) carries out an explicit numerical investigation on the downward soil arching and associated tunnel responses. By changing the tunnel cover depth and keeping a constant excavation depth, the increase of tunnel heave with decreasing tunnel cover depth becomes sharp when the tunnel crown enters into the loosened zone. The

calculated height of the loosened zone is about 14.3 m in the case that the excavation depth is 17.3 m and the width is 49.6 m which are common geometries in this project. The numerical results demonstrate that the tunnel begins to be located in the loosened zone when the unloading ratio reaches 0.55, well agrees with the observed threshold unloading ratio for the sharp increase in tunnel heave.

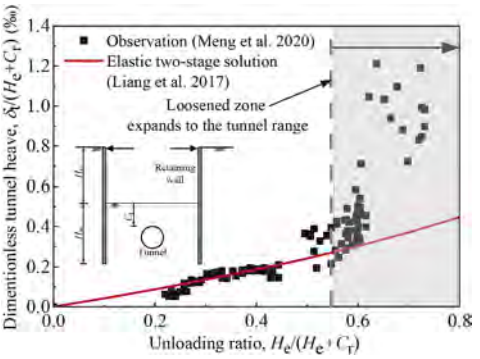

Figure 6. Measured and calculated tunnel heave subjected to upward excavation in granite residual soil.

For an upward excavation with a certain excavation depth, the excavation width and length are key parameters influencing the height of loosened zone. As shown in Figure 7, the loosened zone might extend to the underlying range in case of regular excavation because the excavation width is not well controlled. In cross section, remaining soil method on one-half side of the excavation base is suggested to reduce the height of the loosened zone. The remaining soil can be excavated until the base slab and superstructure of the other half side of the excavation base are constructed. The height of the remaining soil is determined by the aimed value of decreased loosened zone. In terms of longitudinal section, spaced shaft excavation is an effective approach to decrease the excavation length and thus the height of the loosened zone. This approach is carried out in the order of anti-heave pile installation, shaft excavation, anti-heave slab construction, backfill, and finally excavation. The small-sized excavation range could further reduce the ground stress relief and the frictional stress on the interface between the anti-heave pile and the surrounding soils could decrease the tunnel heave during the final excavation stage.

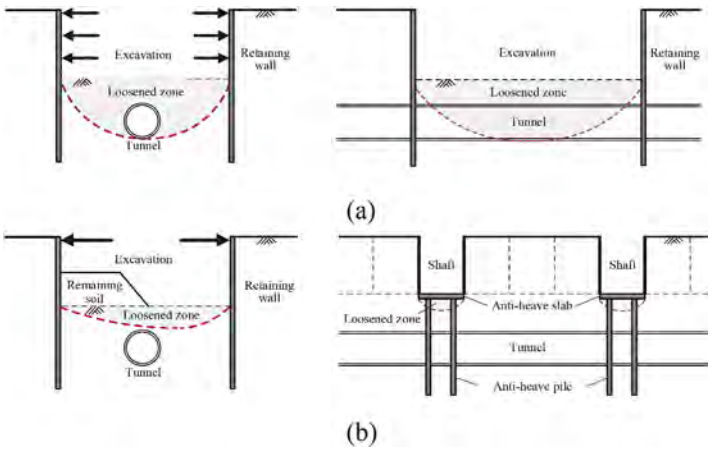

Figure 7. Countermeasures for controlling development of loosened zone: (a) regular excavation in cross section and longitudinal section; (b) remaining soil and spaced shaft excavation with anti-heave structure.

The above countermeasures are adopted in the aforementioned Guimiao Road project. The excavation width, unloading ratio, adopted countermeasures, and measured tunnel heave for different areas are listed in Table 2. For K1+180 to K1+620 with moderate unloading ratio and relatively low excavation width, zoned excavation in longitudinal and transverse directions, and jet-grouting pile reinforcement around the tunnel are adopted. In cross section, the height of the remaining soil is about 2 m to ensure that the surcharge on the excavation base exceeds 30 kPa. The measured tunnel heave in this area does not exceed 9.0 mm. For K2+390 to K2+643 and K3+773 to K4+013, the unloading ratio is moderate and the excavation width is much smaller than K1+180 to K1+620. Hence, no specific countermeasure for controlling the tunnel heave is adopted and the measured tunnel heave is smaller than 8.0 mm. In comparison, for K2+643 to K2+857, the unloading ratio reaches 0.73 and the countermeasures are the same as K1+180 to K1+620, resulting in the significant tunnel heave ranging from 14.8 mm to 23.5 mm. The excavation parameters for K2+857 to K3+476 are about the same as K2+643 to K2+857, but spaced shaft excavation is adopted for decreasing the tunnel heave. The shaft length and width are 15.6 m and 7.2 m, respectively. The thickness of the anti-heave slab and the length of the pile are 1 m and 18 m, respectively. The measured tunnel heave ranges from 1.0 mm to 8.5 mm.

Table 2. Adopted countermeasures and observed tunnel heave in Guimiao Road project.

Area	Unloading ratio	Excavation width (m)	Countermeasures	Tunnel heave (mm)
K1+180 to K1+520	0.58	90	Zoned excavation in longitudinal and transverse directions, and jet grouting pile reinforcement	6.3-8.9
K1+520 to K1+620	0.52	70		5.0-8.5
K2+390 to K2+537	0.54	38	/	1.6-5.1
K2+537 to K2+643	0.64			5.9-7.9
K2+643 to K2+857	0.73	41	Zoned excavation in longitudinal and transverse directions, and jet grouting pile reinforcement	14.8-23.5
K2+857 to K3+476	0.73	40	Spaced shaft excavation with anti-heave structure, in which the depth of anti-heave pile is 18 m and the thickness of the slab is 1.0 m	1-8.5

(3) *Lateral excavation*

The width and height of the loosened zone behind the retaining wall increase with the growing wall deformation. Similar to upward and downward excavations, responses of the lateral tunnel are greatly influenced by its relative position with respect to the loosened zone. Hence, to avoid large tunnel deformation, preventing the loosened zone from extending to the tunnel by decreasing the wall deformation is a promising alternative. Strengthening retaining system, using hydraulic servo strut, zoned excavation, and ground improvement are frequently adopted.

Take a narrow excavation next to the existing shield tunnels of Metro Line 5 in Wuhan, China as an example (Liu 2022; Liu et al. 2022a), the minimum clearance between the excavation and the right tunnel is only 4.6 m. The excavation depth ranges from 16.8 m to 23.4 m, with a total longitudinal length of 132 m. The 6.2 m-diameter shield tunnel has a cover depth of 10.0 m to 13.5 m which is just about the depth with the maximum wall deformation. Strongly weathered silty mudstone is predominantly encountered within the tunnel range. To limit the tunnel deformation, the first three levels of concrete struts and one-level steel struts, combined with longitudinal zoned excavation (a total length of 132 m is divided into 5 sections), are adopted to reduce the wall deformation. The measured maximum deflection of the

retaining wall and horizontal displacement of the right tunnel are only 8.8 mm and 5.8 mm, respectively. Throughout the lateral excavation, the measured lining strain is within the elastic range and no damage are found on the tunnel linings and joints.

4 CONCLUSIONS

This study deals with the deformation of shield tunnels induced by adjacent underground construction. Emphasis is put on the excavation-induced soil arching effect and associated tunnel responses, and corresponding countermeasures for mitigating the tunnel deformation by limiting the development of soil arching. The main conclusions can be drawn as follows.

(1) Underground excavation causes three typical soil arching effect, namely upward, downward, and lateral soil arching according to the developing direction. Arching zone and loosened zone are determined by the ground stress transfer and deformation. The soil arching develops with increasing ground volume loss, excavation size, and retaining wall deformation, respectively. Significant ground deformation would occur when the arching fully develops. Theoretical model for the upward soil arching above the shield tunnel is proposed, as well as the analytical solution for predicting the subsurface ground settlement.
(2) Field observation and numerical simulation all indicate that the tunnel deformation experiences a sharp increase when the loosened zone develops to the existing tunnel. Coupled theoretical model for soil arching and existing tunnel is established, which could yield varying tunnel deformation with different developing statuses of soil arching due to adjacent excavation.
(3) Limiting the development of soil arching is a promising alternative for decreasing the tunnel deformation subjected to nearby excavation. Reinforcing the soils above the tunnel crown by SDJG column, reducing ground stress relief by zoned excavation and spaced shaft excavation and anti-heave structure, and decreasing the retaining wall deformation by longitudinal zoned excavation and strengthening the structs are proved to be effective countermeasures for downward tunneling, upward excavation, and lateral excavation.

REFERENCES

Chen, R.P., Meng, F.Y., Li, Z.C., Ye, Y.H. & Ye, J.N. 2016. Investigation of response of metro tunnels due to adjacent large excavation and protective measures in soft soil. *Tunnelling and Underground Space Technology*, 58: 224–235.

Chen, R.P., Liu, M.C., Meng, F.Y., Li, Z.C. & Wu, H.N. 2022a. Lateral soil arching effect behind diaphragm wall due to braced excavation in clayey ground. *Journal of Geotechnical and Geoenvironmental Engineering*. (under review).

Chen, R.P., Song, X., Meng, F.Y., Wu, H.N. & Lin, X.T. 2022b. Analytical approach to predict tunneling-induced subsurface settlement in sand considering soil arching effect. *Computers and Geotechnics*, 141: 104492.

Franza, A., Marshall, A.M. & Zhou, B. 2019. Greenfield tunnelling in sands: the effects of soil density and relative depth. *Geotechnique*, 69(4): 297–307.

Han, L., Ye, G.L., Chen, J.J., Xia, X.H. & Wang, J.H. 2017. Pressures on the lining of a large shield tunnel with a small overburden: a case study. *Tunnelling and Underground Space Technology*, 64: 1–9.

Hashash, Y. M. & Whittle A.J. 2002. Mechanisms of load transfer and arching for braced excavations in clay. *Journal of Geotechnical and Geoenvironmental Engineering*, 128(3): 187–197.

Hewlett, W.J. & Randolph, M.F. 1988. Analysis of piled embankments. *Ground Engineering*, 22(3): 12–18.

Iglesia, G.R., Einstein, H.H. & Whitman, R.V. 1999. Determination of vertical loading on underground structures based on an arching evolution concept. In *Geo-Engineering for Underground Facilities*. ASCE, pp. 495–506.

Kirsch, A. 2010. Experimental investigation of the face stability of shallow tunnels in sand. *Acta Geotechnica*, 5(1): 43–62.

Lai, H.J., Zheng, J.J., Zhang, R.J. & Cui, M.J. 2018. Classification and characteristics of soil arching structures in pile-supported embankments. *Computers and Geotechnics*, 98: 153–171.
Li, Z. F., Lin, W.A., Ye, J.N., Chen, Y.M., Bian, X.C. & Gao, F. 2021. Soil movement mechanism associated with arching effect in a multi-strutted excavation in soft clay. *Tunneling and Underground Space Technology*, 110: 103816.
Liang, R.Z., Xia, T.D., Huang, M.S. & Lin, C.G. 2017. Simplified analytical method for evaluating the effects of adjacent excavation on shield tunnel considering the shearing effect. *Computers and Geotechnics*, 81: 167–187.
Lin, X. T., Chen, R. P., Wu, H. N. & Cheng, H.Z. 2019. Three-dimensional stress-transfer mechanism and soil arching evolution induced by shield tunneling in sandy ground. *Tunnelling and Underground Space Technology*, 93: 103104.
Lin, X.T., Chen, R.P., Wu, H.N., Meng, F.Y. & Su, D. 2022. Calculation of earth pressure distribution on the deep circular tunnel considering stress-transfer mechanisms in different zones. *Tunnelling and Underground Space Technology*, 119: 104211.
Liu, M.C. 2022. Soil arching effect and mechanical responses of the existing shield tunnel due to lateral braced excavation. *Dissertation for master degree*. Hunan University, China. (in Chinese).
Liu, M.C., Chen, R.P., Meng, F.Y., Cheng, H.Z. & Li, Z.C. 2022a. Ground deformation and mechanical response of shield tunnel due to lateral excavation. *Tunnelling and Underground Space Technology*. (under review)
Liu, Q.W., Wang, H.L., Chen, R.P., Yin, Z.Y., Lin, X.T. & Wu, H.N. 2022b. Effect of relative density of 2D granular materials on the arching effect through numerical trapdoor tests. *Computers and Geotechnics*, 141: 104553.
Meng, F.Y., Chen, R.P., Xie, S.W., Wu, H.N. & Liu, Y. 2020. Observed behaviors of a long and deep excavation and collinear underlying tunnels in Shenzhen granite residual soil. *Tunnelling and Underground Space Technology*, 103: 103504.
Meng, F.Y., Chen, R.P., Xie, S.W., Wu, H.N., Liu, Y. & Lin, X.T. 2022. Excavation-induced arching effect below base level and responses of long-collinear underlying existing tunnel. *Tunnelling and Underground Space Technology*, 123: 104417.
Ng, C.W.W., Hong, Y., Liu, G.B. & Liu, T. 2012. Ground deformations and soil-structure interaction of a multi-propped excavation in Shanghai soft clays. *Géotechnique*, 62(10), 907–921.
Schanz, T., Vermeer, P.A. & Bonnier, P.G. 1999. The hardening soil model: formulation and verification. In: *Beyond 2000 in Computational Geotechnics*. Rotterdam, 1999, pp. 281–290.
Stein, D., Mollers, K. & Bielecki, R. 1989. Microtunnelling. *Ernest & Sohn*, Berlin, Germany, pp. 237–243.
Terzaghi, K. 1943. Theoretical soil mechanics, *John Wiley and Sons*, New York.
van Eekelen, S.J.M., Bezuijen, A. & van Tol, A.F. 2013. An analytical model for arching in piled embankments. *Geotextile and Geomembranes*, 39, 78–102.
Wu, H.N., Shen, S.L., Liao, S.M. & Yin, Z.Y. 2015. Longitudinal structural modelling of shield tunnels considering shearing dislocation between segmental rings. *Tunnelling and Underground Space Technology*, 50, 317–323.
Wu, H.N., Zhang, P., Chen, R.P., Lin, X.T. & Liu, Y. 2020. Ground response to horizontal spoil discharge jet grouting with impacts on the exisiting tunnel. *Journal of Geotechnical and Geoenvironmental Engingeering*, 146(7): 05020006.
Wu, K., Chen, R.P., Meng, F.Y., Wu, H.N. & Cheng, H.Z. 2022. Centrifuge modeling of soil mass excavation in dry sand: inverse soil arching effect below excavation base. In *the 10th International Conference on Physical Modelling in Geotechnics*, KAIST, Daejeon, Korea/19-23 September, 2022.
Zhang, C., Jiang, G., Liu, X. & Buzzi, O. 2016. Arching in geogrid-reinforced pile-supported embankments over silty clay of medium compressibility: Field data and analytical solution. *Computers and Geotechnics*, 77, 11–25.

Smart Geotechnics for Smart Societies – Zhussupbekov, Sarsembayeva & Kaliakin (Eds)
© 2023 The Author(s), ISBN 978-1-003-29912-7
Open Access: www.taylorfrancis.com, CC BY-NC-ND 4.0 license

Monitoring of backward erosion piping in river levees using distribution of surface settlement

M. Okamura
Ehime University, Matsuyama, Japan

M. Imamura
Kajima Corporation, Osaka, Japan

ABSTRACT: River levees occasionally breach during flooding in the mechanics of backward erosion piping and its impact is enormous. Current inspection methods cannot detect the pipe until it manifests at the exterior surface. There is a strong need for non-destructive techniques that can identify progression of the pipe. Okamura et al. (2017) found that small but characteristic deformation appeared on the surface of levees above pipes after a flooding event. They proposed a method for estimating the size and location of the pipes based on the characteristic shape of the deformed slope. In this study, centrifuge tests were conducted to observe evolution of surface deformation as piping progressed. Moreover, this method was applied to a levee along the Naka River, where significant sand boiling occurred at the levee toe during recent flooding events. In addition, a number of penetration tests were conducted at small intervals to identify the pipe locations in a more direct manner. It was found that the penetration tests were effective in detecting the pipe locations. The detected locations compared well with those estimated from the surface topography.

1 INTRODUCTION

Backward erosion piping is a failure mechanism for less-permeable river levees founded on sandy aquifers. The piping initiates in the form of concentrated leaks at the landside soil surface when the hydraulic loads generated by seepage exceed the capacity of the soil to resist the loads. Shallow pipes are formed at the surface of the sandy aquifer by the erosion of sand particles, beginning at the landside ejection holes and progressively extending towards the riverside. The erosion process continues when the river water level is high; eventually, the pipe forms a direct connection between the landside and riverside, which accelerates the widening and deepening of the pipe, resulting in levee collapse and breach (ICOLD, 2015). Once a levee breaches, its impact on the surrounding is enormous (TCYRL, 2013). Meanwhile, a small number of the levees breached in the mechanism of backward erosion piping, although numerous sand boils occur in Japan every year (Yasuda et al., 2016; Okamura et al., 2020). It is important to know how the breaching is imminent.

In the current practice, it is quite difficult to diagnose the severity of backward erosion piping during a flooding event or even after the event (Wang, et al., 2014). Many attempts to detect pipes and loosened zones resulting from the mechanism have been conducted; however, unfortunately, they were mostly unsuccessful even though cutting edge geotechnical site investigation techniques including georadar, seismic exploration, and electric resistivity exploration were used (Okamura et al., 2016). Consequently, many levees with sand boils have been remedied after flooding events without knowing the piping progress.

When a pipe is formed in a levee or foundation soil, stresses of the levee change accordingly, leading to a deformation which may not be sufficiently large to be detected by the eye observation.

DOI: 10.1201/9781003299127-4

Okamura et al. (2017) surveyed levees after flooding events and found that small hollows with the peculiar shape appeared on the surface of the levees near sand boils. The surface subsided several centimeters in a shape of a Gaussian like curve, which is known as a characteristic shape for ground surface subsidence immediately above tunneling (Mair et al. 1993, Mahmound & Magued, 2011). The levee surface settlement could be a good indication of progression of piping.

Technology of land surveying has been rapidly progressing in recent years making it possible to build a digital elevation model (DEM) of the ground surface of a large area in a short time. A laser profiler mounted on an unmanned aerial vehicle (UAV) have been used to build DEM of high resolution, more than 1000 points/m^2, and with an accuracy on the order of a centimeter. Photographing from UAV incorporation with SfM (Structure for Motion) technique are also employed for this purpose. These techniques greatly help to improve understanding of the precise deformation of levees that was not possible before.

This paper describes results of centrifuge tests to investigate evolutions of levee surface settlement as a piping progresses in the mechanism of backward erosion piping. Shape and location of pipe developed below levees and levee surface settlement were closely observed. In addition, the survey technique was applied to a levee where sand boils were observed due to recent flooding events to detect hollows appeared on the surface. Moreover, a small diameter cone was penetrated at a short interval around the detected hollows to identify the locations of pipes or loosened soil because of backward erosion piping, which verified the effectiveness of surface settlement survey as a indicator of pipe progression.

2 CENTRIFUGE TEST

2.1 *Model preparation*

The models were constructed in a rigid container with internal dimensions of 530-mm-long, 120-mm-wide, and 230-mm-high. Figure 1 indicates the model configuration comprising a uniform medium dense sand bed with pervious and impervious retaining walls on the riverside (upstream) and landside (downstream), respectively, and a model levee resting on the bed. A clean silica sands, Keisa #6B, were used in the tests; Figure 2 presents the grain size distributions and physical properties. Dry sand was air-pluviated in the model container to a depth of 60 mm at a target relative density of D_r = 60 %. After the surface of sand bed was carefully levelled using a vacuum device, the model levee was placed on the sand bed. The model levees were either compacted clay or an acrylic block. The clay levee was constructed using a mixture of fine silica sand (d_{50} = 0.06 mm) and Kaolin clay (IP = 23) mixed at 3 : 7 by weight. The material was prepared at a water content of 35 % and compacted to dimensions of L = 190 mm base width and 70 mm high. The acrylic levee of same width was fabricated by gluing acrylic plates, which was transparent for observing the pipes developing on the surface of the sand bed. To prevent the acrylic levee from sliding on the bed during the flooding experiment, a weight was put on the levee.

A high-speed camera was placed on the levee to closely observe sand ejecta appeared at the toe and pipe below the transparent levee during flooding events. An in-flight laser profiler capable of moving on linear ways was mounted to obtain a 3D profile of the surface of the clay levees.

2.2 *Test procedure*

The model was set on the centrifuge platform of a geotechnical centrifuge at Ehime University and spun to 40 g. Water was supplied by a pump to saturate the sand bed prior to flooding events. Table 1 summarizes the test conditions. In the tests, the upstream water head (H) was controlled, whereas the water table was maintained constant at the sand surface on the downstream side, giving rise to the head difference across the levee, H. In test 1 in which acrylic levee was used, the progression gradient (H_l/L), the average gradient across the levee that causes progression of pipe of length l, was observed. The upstream water head was increased

in steps with an ample duration of approximately a few minutes until a pipe was initiated with sand ejecta at the toe of the levee. The head was lowered once and increased stepwise again until the pipe length was extended to a centimeter or two, where the pipe developed just below the levee was observed through the transparent levee using the high-speed camera. This cycle of head change was repeated each time the pipe progressed a few centimeters until the pipe finally went through to the riverside. In the test 2 and 3 with the clay levee used, the cycles of head change similar to the test 1 was applied to the model. In these tests, the pipes were no longer visible by the camera, and progression of piping was inferred from the amount of sand ejecta appeared on the downstream surface. During the interval of each cycle 3D profile of the levee surface was obtained using the laser profiler. For test 2, the cycle was repeated until the pipe reached the upstream toe and direct connection was established. Whereas for test 3, test was halted before the piping tip reached the upstream.

The centrifuge was spun down and levees were carefully removed to expose the surface of foundation soil. The 3D profile of the sand bed surface and the pipe was obtained with the laser profiler.

In this paper, all the results and comparisons are presented in model units without applying any scaling factors commonly used in centrifuge modeling.

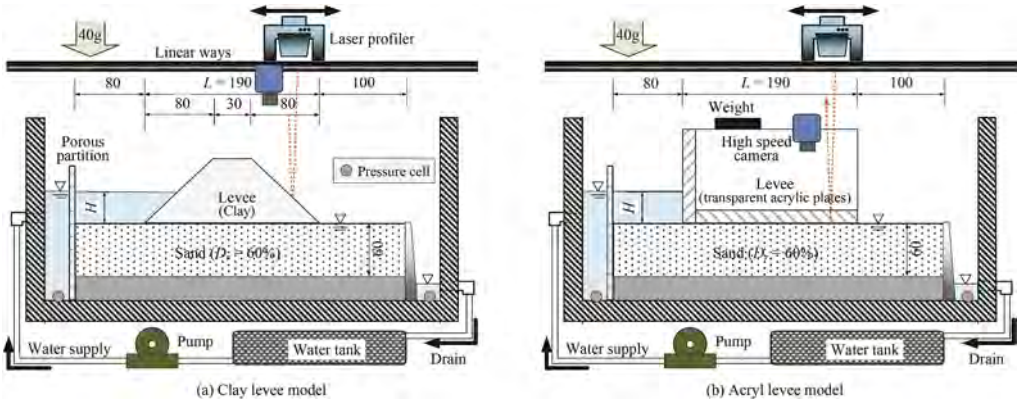

Figure 1. Caption of a typical figure.

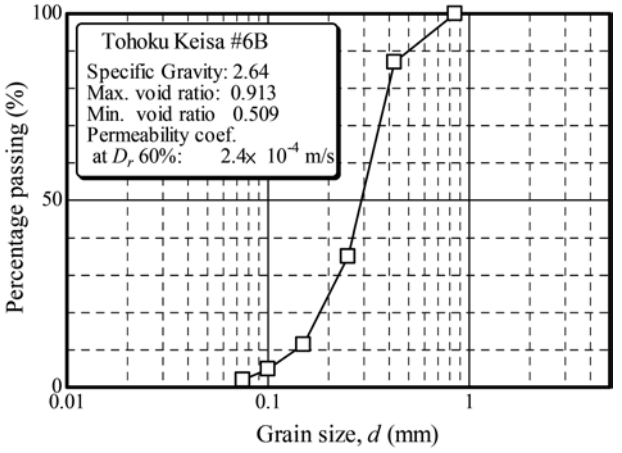

Figure 2. Grain size distribution of sand used.

Table 1. Test conditions.

Test	Sand bed D_r (%)	Material of levee	Unconfined strength of the levee (kPa)	Length of pipe at the end of test (mm)
1	59	Acryl	>50000	190 (breakthrough)
2	62	Clay	54.0	190 (breakthrough)
3	61	Clay	14.5	80

2.3 *Results and discussions*

Figure 3 illustrates the time histories of hydraulic gradient (H/L) and normalized length of pipe (l/L) in test 1. Here, l does not indicate the actual meandering pipe length; it represents the distance from the pipe tip to levee toe. H_l/L remains nearly constant to approximately 0.3 for l/L= 0–0.3, and thereafter, decreases with the increase in l/L. This may be explained by the fact that an increase in l/L resulted in a virtually lower seepage length (distance from the upstream toe to the piping tip) than the original length L. Hence a lower gradient H_l/L would be required to transport the sand grains within the pipe. In fact, in preliminary tests performed on the models similar to those in this study, the pipes developed intermittently until l/L reached approximately 0.3. After the pipe length became longer than, say, $l/L > 0.4$, the rate of pipe development accelerated, leading to failure, while the upstream head was maintained constant throughout the tests.

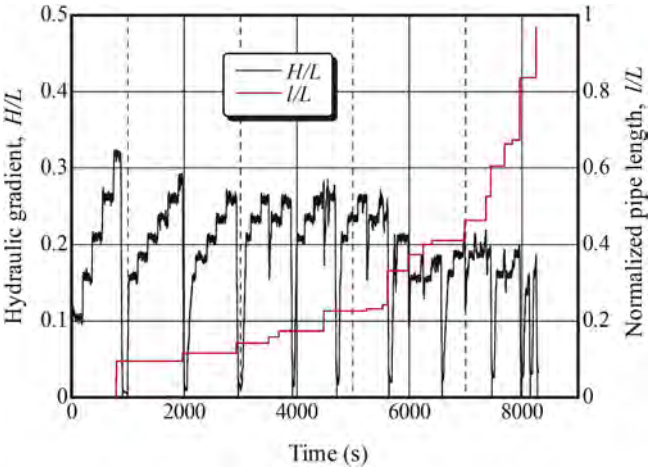

Figure 3. Time histories of hydraulic gradient and normalized length of the pipe (test 1).

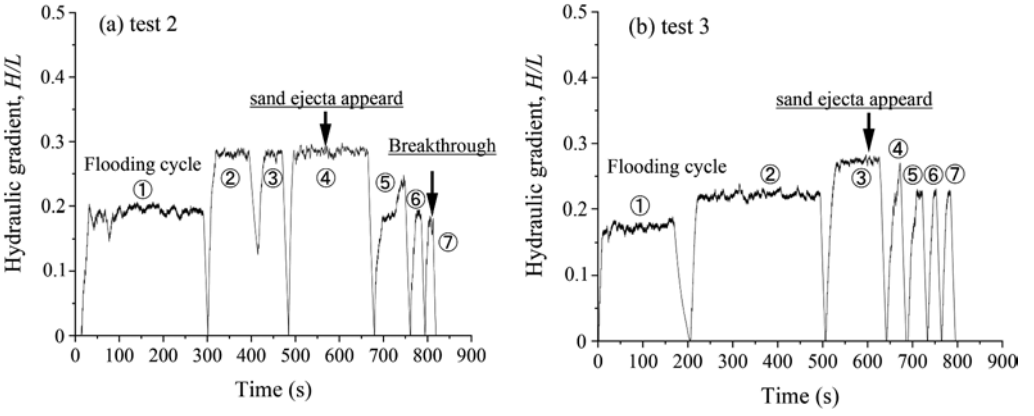

Figure 4. Time histories of hydraulic gradient for test 2 and 3.

Figure 4 presents the time histories of hydraulic gradient for test 2 and 3. For test 2, sand ejecta appeared in 4th cycle (t = 600 s) at the levee toe while keeping the gradient to 0.29. Thereafter amount of sand ejecta increased in 5th and 6th cycles in which the gradients were 0.22 and 0.19, respectively. The pipe broke through the sand bed in 7th cycles at H/L = 0.18; the gradients for the piping initiation and breakthrough are consistent with test 1.

At the end of each cycle the levee surface profiles were obtained with the laser profiler. Figure 5 depicts contours of the surface settlement after the 4th, 5th, 6th and finally 7th cycle for test 2. After the 4th cycle, a very small but clear hollow appears on the levee slope adjacent to the sand ejecta (Figure 5(a)). The hollow increased the depth and extended towards upstream side as the amount of ejecta increased (Figure 5(b) – (c)). After the 7th cycle where rate of water outflow from the exit of the piping suddenly increased during the cycle, the levee largely settled (Figure 5(d)). Figure 6 shows a photo and contours of the surface of foundation sand after removal of the levee for test 2. It is apparent that the hollow of the surface appeared immediately above the pipe. This is also the case for test 3 in which the pipe extended to l = 90 mm from the levee toe and the hollow appeared on the slope immediately above the pipe from the toe to the crest shoulder. It can be concluded that the hollows are good indicator of progression of pipe below levees.

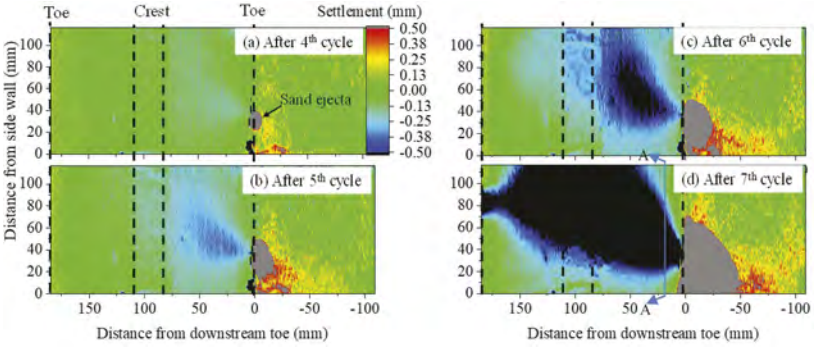

Figure 5. Evolution of settlement appeared at the levee surface (test 2).

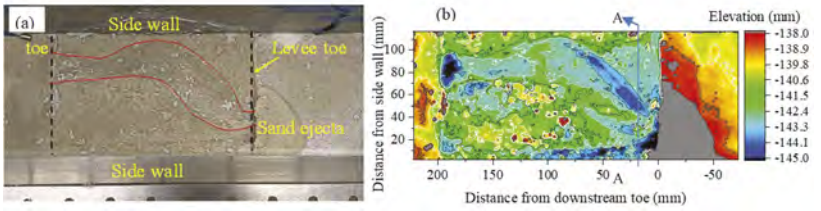

Figure 6. Surface of foundation sand exposed after the test (test 2).

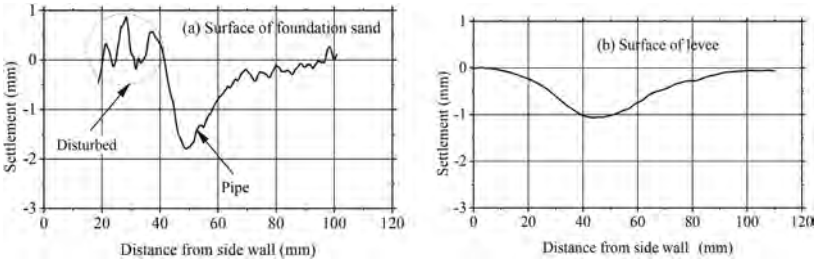

Figure 7. Cross sections of foundation sand exposed after the test and levee slope at l = 20 mm (test 2).

Figure 7(a) depicts cross-sections of the pipe at the distance from the toe l = 20 mm for test 2 (section A-A in Figures 5(d) & 6(b)). Sections of the piping channel are typically 2-mm-deep and 30-mm-wide in the range of l = 0–50 mm. While for test 3, the depth and width of the piping channel are typically 1.5-mm-deep 15-mm-wide, which are smaller than those for test 2. Van Beek et al. (2015) reported the observation of their tests that the pipe depth was approximately 7-14 times the grain size of sand. Considering the fact that their pipe dimension was observed after the pipe broke though the foundation sand and reached upstream water, the pipe depth of test 2 in this study is comparable to those by van Beek et al. Figure 7(b) shows a cross-section of the hollow on the levee surface at l = 20 mm. The hollow with a gaussian-like shape has the maximum depth approximately a half of the pipe, whereas the width is more than double of the pipe. The observed hollows are approximated with gaussian curves and size and depth of the pipes were predicted using the model (Okamura et al., 2017). Not shown in this paper, the prediction agrees well with the observed pipe in test 2 and 3 (Imamura, 2018).

3 APPLICATION TO A LEVEE

3.1 *Test site*

The Naka River in Tokushima prefecture, Japan, has undergone several flooding events during the past decade in 2012, 2014, and 2015. Extensive sand boils appeared near the left bank at 13.4 km from the river mouth. Figure 8 shows an aerial photograph of the levee. The crest is used for local traffic and approach roads to the crest are installed on the hinter land side slope. The levee is 6.7 m high with a riverside slope angle of 1V : 2.5H. In this area, water leakage was observed along the toe over an area of 30 m during the flooding events. Two significant sand volcanos formed in the area at zones A and B as indicated in Figure 8(b). The small circles in the figure indicate locations where the mini-ram sounding was conducted. Four survey lines were set and a total of 47 mini-ram soundings were conducted on lines Aa, Ab, Ac and Ba.

A cross section of the levee and the foundation soil is shown in Figure 8(d). The levee consists mostly of sandy gravel (Bg), with a gravel content of 20–60% and a fines content of 5–20%. The levee soil is medium dense with an SPT- N value of 2–15. Below the levee, a sand layer (As1) 1.5–2.5 m deep lies atop a thick gravel layer (Ag1, Ag2 and Dg). On the river-side slope, an impermeable sheet has been placed to prevent infiltration of river water and rain.

The sand layer As1 is underlain by highly permeable gravel layers. During flooding, a high pore water pressure in the gravel layer on the hinterland side causes a high upward hydraulic

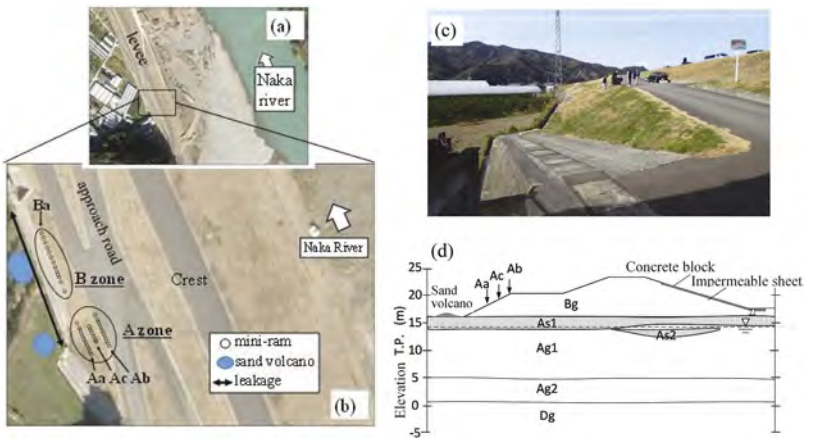

Figure 8. Test site. Location of (a) test site and (b) mini-ram sounding, (c) photo of Zone A and B, and (d) cross section showing soil condition in the levee and foundation.

gradient in the As1 layer. Moreover, the levee is at the foot of a mountain as can be seen in Figure 8(a). The gravel layer is shut off by bed rock, which makes the pore pressure in the gravel layer even higher.

3.2 *Dynamic cone penetration tests*

Mini-ram sounding (JGS, 2017) is an in-situ test in which a 36.6-mm diameter cone is driven by a hammer of 30-kg free falling from a height of 30-cm. The number of blows required to drive the cone 20-cm is recorded as N_{dm}. To remove the effects of skin friction, torque M_v is measured to rotate the rod. The corrected blow count, N_{dc}, is provided in equation (1), which is approximately one-half of the standard penetration test (SPT) N value.

$$N_{dc} = N_{dm}/2 \; - \; 0.14\, M_v \tag{1}$$

Instruments and procedures of the mini-ram sounding were the same as those of Swedish ram sounding except for the smaller cone diameter and driving energy. Because of these differences, the mini-ram was more suitable to identify weak and thin layers. Moreover, in this study, the depth of the tip was recorded and the blow count for every single blow was obtained as follows:

$$N_{d1} = \; 20/d - \; 0.14 M_v \tag{2}$$

where d denotes the penetration depth in decimeter via a single blow.

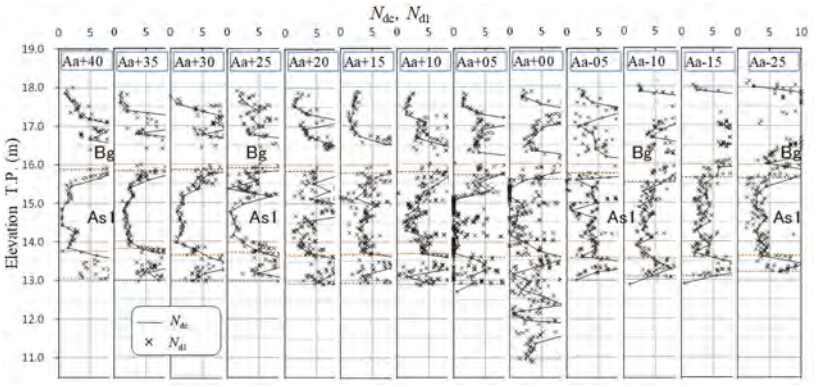

Figure 9. Corrected blow count on line Aa in zone A.

Figure 9 presents the corrected blow counts N_{dc} and N_{d1} along the survey line Aa. The tests were conducted at a very small interval of 0.5 m to better observe the distribution of pipes and loosened zones in the soil. The numbers after "Aa" in the figures denote the horizontal distance (in decimeters) along the survey line from the midpoint. The elevation of the surface of the levee on this survey line is approximately T.P. 18.0 m. N_{dc} increased with depth from the surface and reached approximately 15 at the bottom of the levee (T.P. 15.9 m). The solid lines and cross marks represent N_{dc} (the average corrected blow count for every 20 cm driving) and N_{d1} (the blow count for every single blow), respectively. At three locations from the upstream side, Aa+40, Aa+35 and Aa+30, N_{d1} in the sand layer (As1) was higher than 0.5, while N_{d1} was 0 at a depth at As+25. Because it is unusual to observe N_{d1} = 0 in sand with small fines content, the location where N_{d1} = 0 is considered as either a pipe or loosened sand because of the backward erosion piping. Such extraordinarily low blow counts, and thus loosened sand, was also encountered at Aa+15, Aa+10, Aa+00, and Aa-05.

Figure 10 shows the locations where the zero blow counts were observed. In zone A, the locations are identified by the Aa and Ab lines. It seems that a pipe or loosened zone developed from the location of the sand volcano and branched somewhere between the volcano and Aa line, further extending and reaching to the Ab line. In zone B, four locations with zero blow count were identified along the survey line, Ba, adjacent to the sand volcano.

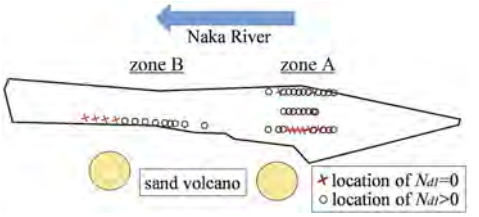

Figure 10. Locations where a zero-blow count was observed.

3.3 *DEM*

A laser profiler was used to obtain DEM of the levee. The profiler was mounted on a UAV and flew at an altitude of approximately 30 m at 20 km/h. The grass on the levee was cut by mowers in advance. Figure 11(a) indicates contours of the site including zones A and B. The slope was divided into 6 area from (i) to (vi) and their elevation was approximated with planes. Deviations in height of each data point of DEM from the plane is shown in Figure 11(b). There are two significant hollows of 10 cm to 20 cm deep on the slope near the locations of sand volcano, i.e. at boundaries between area (i) and (ii), and (ii) and (iii). It should be noted that any significant hollow did not exist except for these two locations.

Figure 12 compares the locations of pipes estimated from the shape of hollows (Okamura et al., 2017) and those identified via the mini-ram sounding. In the plan view (Figure 12(a)), the locations obtained from the two methods agree quite well. The locations of two pipes in zone A, which developed from the sand volcano and reached below the approaching road, were consistently identified by the mini-ram. The estimated pipe location in zone B is approximately 4 m from the locations where the zero blow count (N_{d1}) was observed. However, the N_{d1} estimated from the shape of hollow was also very small, largely less than 1.0. The blow count could be more significantly affected by the skin friction of the penetration rod in this

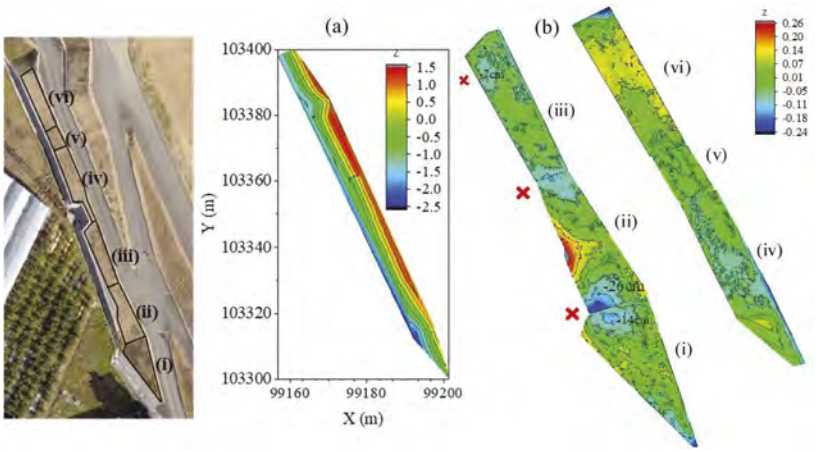

Figure 11. (a) Contours of levee slope, (b) deviation in elevation from the approximated plane.

zone than that in zone A because the thickness of the levee soil along this survey line was relatively large. This indicates that to identify zero blow count locations, careful attention should be paid to the effect of skin friction.

The estimated depth of the pipe is shown in Figure 12(b) and (c). Unlike the horizontal location and width, the estimated depth of the pipes is sensitive to the assumed aspect ratio, H/B, which is assumed in the estimation. Based on the observed shape of pipes in centrifuge test in this study as well as those in Okamura et al. (2022), aspect ratio is approximately 0.1. Considering the con-figuration of the soil layers at this particular site, the thin sand layer immediately below the levee is most susceptible to the backward erosion piping. It should be mentioned that the DEM of the levee surface used in this study was recently obtained after flooding events. The current shape of the levee is not only influenced by recent flooding events but also by such actions as erosion of rain water, weathering, and animal and human activities over a few decades since the levees were finally raised to their current height. A difference in height at two points of time, before and after a flooding event, could be used rather than a point of time for information.

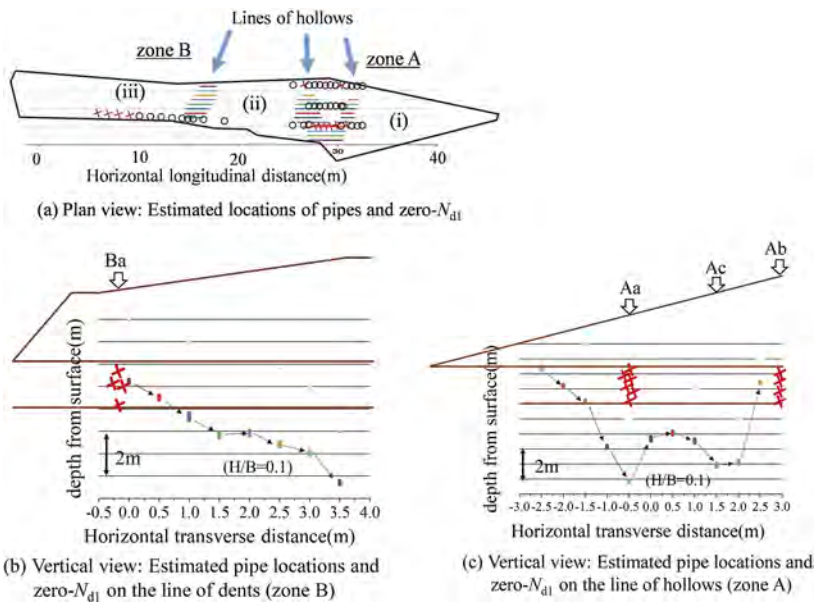

Figure 12. Locations of pipes estimated from the shape of hollows and those identified by the mini-ram sounding.

4 CONCLUDING SUMMARY

Backward erosion piping is a failure mechanism for river levees founded on sandy aquifers. In the current practice it is quite difficult to diagnose the severity of backward erosion piping during a flooding event or even after the event**.** **A**ttempts to detect pipes and loosened zones resulting from the mechanism have been conducted, however, they were mostly unsuccessful. Okamura et al. (2017) have surveyed levees after flooding events and found that small hollows with the peculiar shape often appeared on the surface of the levees near sand boils. This fact suggests that the surface hollows of several centimeters deep in a shape of a Gaussian like curve, which is known as a characteristic shape for ground surface subsidence immediately above tunneling, may be a good indication of progression of piping.

This paper describes results of centrifuge tests to investigate availability of surface settlement as the indicator of progression of backward erosion piping. Evolutions of levee surface

settlement as a piping progresses under the levee was observed in detail. In addition, the survey technique was applied to a levee of Naka river where sand boils were observed due to recent flooding events to detect hollows appeared on the surface. Moreover, a small diameter cone was penetrated (mini-ram sounding) at a short interval around the detected hollows to identify the locations of pipes or loosened soil because of backward erosion piping, which verified the effectiveness of surface settlement survey as a indicator of pipe progression.

In the centrifuge tests, model levees resting on a uniform sand bed were subjected to hydraulic load on the riverside and pipes developed in the mechanism of the backward erosion piping at the surface of sand bed. It was observed that a hollow appeared at the toe when sand begun to eject from the sand bed and the hollow extended towards riverside as the amount of sand ejecta increased. The tip of hollow was immediately above the tip of pipe developed under the levee. It is confirmed that hollows appear on the levee surface immediately above the pipe and are good indicator of progression of pipe below levees.

For the Naka river levee, mini-ram sounding was conducted at 47 locations at a small interval of 0.5 m, which was found effective in detecting pipes. The locations where zero-blow counts were observed were immediately in front of sand volcanos. A 3D profile of the levee surface was obtained using a laser profiler mounted on a UAV. Small hollows in a shape of the Gaussian like curve with a maximum depth of 10– 5 cm and a width of 4–6 m were found on the slope of the levee near the sand volcanos. The hollows are considered to have formed by the loss of sand because of pipe development. The depth and width of the pipes were estimated from the shape of the hollows using the method developed by Okamura et al. (2017) which agreed reasonably well with those detected by mini-ram sounding.

Though the accumulation of further site investigation data is clearly needed, this method has the apparent potential to improve maintenance and health evaluations of levees in which undermining by the mechanism of backward erosion piping is suspected.

REFERENCES

Imamura, M. 2020. On the surface settlement as an indicator of backward erosion piping for river levees, Dissertation for Mater degee, Ehime University.

International Commission on Large Dams (ICOLD). 2013. Internal erosion of existing dams, levees and dikes, and their foundations, Bulletin 164, Paris.

Japanese Geotechnical Society. 2017. Geotechnical and Geoenvironmental Investigation Methods.

Mahmound, A. & Magued, I. 2011. Analysis of Tunneling-Induced Ground movements Using Transparent Soil models, Journal of Geotechnical and Geoenvironmental Engineering 137(5): 525–535.

Mair, R.J., Taylor, R.N. & Bracegirdile, A. 1993. Subsurface settlement profiles above tunnels in clays, Géotechnique 43(2): 315–320.

Okamura, M., Hirao, Y. & Maeda, K. 2017. Profile of induced settlement on river levee due to loss of soil from piping hole, Advances in River Engineering, Japan Society of Civil Engineers 23: 399–404. (in Japanese)

Okamura, M., Tsuyuguchi, Y., Izumi, N. & Maeda, K. 2021. Centrifuge modeling of the scale effect on the hydraulic gradient of backward erosion piping in a uniform aquifer under river levees. Soils Found. 62 (6).

Technical Committee of Yabegawa River Levee (TCYRL), 2013. Technical report on Yabe river levee. Kyushu Regional Development Bureau, MLIT (in Japanese), http://www.qsr.mlit.go.jp/chikugo/site_files/file/torikumi/01-plan_course/tyosa/saisyu/houkokusyo.pdf

Van Beek V.M., Van Essen H.M., Vandenboer K & Bezuijen A. 2015. Developments in modelling of backward erosion piping. Géotechnique 65 (9): 740–754.

Wang, D., Fu, X., Jie, Y., Dong, W. & Hu, D. 2014. Simulation of pipe progression in a levee foundation with coupled seepage and pipe flow domains, Soils and Foundations 54(5): 974–984.

Yasuda, S., Shimizu, Y., Deguchi, K., 2016. Investigation of the mechanism of the 2015 failure of a dike on Kinu River. Soils Found. 56 (4): 581–592.

Smart Geotechnics for Smart Societies – Zhussupbekov, Sarsembayeva & Kaliakin (Eds)
© 2023 The Author(s), ISBN 978-1-003-29912-7
Open Access: www.taylorfrancis.com, CC BY-NC-ND 4.0 license

Energy geotechnology: A new era for geotechnical engineering practice

L. Laloui & M. Sutman
Laboratory of Soil Mechanics, Swiss Federal Institute of Technology Lausanne (EPFL), Lausanne, Switzerland

ABSTRACT: Energy geotechnology provides low carbon, cost-effective and local energy solutions to structures and infrastructures, which opens a new era for the geotechnical engineering practice, by extending the conventional role of structural design to the one of addressing acute energy challenges of our century. The paper initially goes over the idea behind energy geotechnology by highlighting its scope and applications to various geostructures for structural support and energy supply of built environments. Aspects of primary importance for maximizing the energy, geotechnical and structural performance of energy geostructures and solutions to address this challenge are presented. Moreover, analytical solutions and design tools, as well as performance-based design of energy geostructures are introduced. The goal of this paper is to uncover the great potential of energy geotechnology on the path of less dependency on fossil fuels and to emphasize the new critical role of geotechnical engineers to take full advantage of this technology.

Keywords: Energy geostructures, Renewable energy, Thermo-mechanical, Design, Application

1 INTRODUCTION

The residential sector was responsible for 25.4% of final energy consumption in Europe in 2016, of which space heating and hot water production represented 82.6% in total (Eurostat, 2018). Fossil fuel based and conventional electric equipment still dominates the global building market, accounting for more than 70% of space heating and 90% for hot water production, which is also responsible for 28% of global energy-related CO_2 emissions in 2017 (IEA, 2019). Moreover, due to global warming, economic growth and urbanization, the use of energy for space cooling more than tripled between 1990 and 2016 (IEA, 2018), which is mainly covered by electricity. Yet, global energy needs are expected to expand by 30% by 2040 as a result of a global economy growth with an annual rate of 3.4%, a projected population increase by 1.6 billion, as well as an inevitable growing urbanization (IEA, 2017).

Several initiatives and policies at national and international levels are being established in the construction sector (ASHRAE, 2008 and European Directive 2010/31/EU, 2010) for the implementation of zero- or nearly zero-energy buildings. As an example, ASHRAE Vision (2008) presents requirements to enable buildings to produce as much energy as they use by 2030. On the other hand, European Directive 2010/31/EU (2010) requires all new public buildings to be nearly zero-energy by 2018 and all new buildings by the end of 2020. Therefore, the development and the diffusion of reliable, economically viable and environmental-friendly technologies to satisfy a noteworthy part of the energy needs of the building sector is an important challenge.

Conceptually, energy geostructures is a technology enabling the use of renewable energy sources for efficient space heating and cooling. In this technology, any geostructure in contact with the soil and already required for structural support are equipped with geothermal loops,

DOI: 10.1201/9781003299127-5

for heat exchange operations to exploit the near surface geothermal energy. The idea behind energy geostructures comes from the fact that the temperature of the ground remains the same throughout the year below a depth of 6-8 meters. Therefore, with the integration of the geothermal loops and the water-antifreeze mixture circulating within them, the heat is extracted from the ground to heat the buildings during winter. Similarly, during summer, the extra heat coming from the building side is injected into the ground to cool them. In this system, ground source heat pumps (GSHP) are often required which works intermittently in order to adapt the temperature of the circulating fluid to meet the energy demands from the building side.

The heat energy that can be provided by the energy geostructures depends on various factors, including, but not limited to, the thermal and hydraulic properties, and mean temperature of the ground, geothermal and geotechnical design of the geostructures, and the energy demand from the building side. However, 40-150 W/m, 20-40 W/m^2 and 20-60 W/m^2 are achievable energy extraction or withdrawal amounts from energy piles, energy walls and energy tunnels, respectively. As a practical example, a recent numerical investigation was performed at the Laboratory of Soil Mechanics (LMS), considering a five-storey office building, with net heated/cooled area of 2400 m^2, bearing on 32 piles with 0.5 m diameter and 20 m length which were used as energy piles. The results of the analysis show that the energy piles can supply 100% of the heating demands and most of the cooling demands of the office building in Sevilla, Spain. An auxiliary air conditioning system was required only during July and August, to provide the remaining 11% and 6% of the cooling demand (Sutman et al., 2019).

2 ENERGY ASPECT

2.1 *Typical energy problem*

Operation of energy geostructures to meet the heating and cooling demands from the building side involves heat exchange within the three components of the ground source heat pump system, being the primary circuit, the GSHP and the secondary circuit (Figure 1).

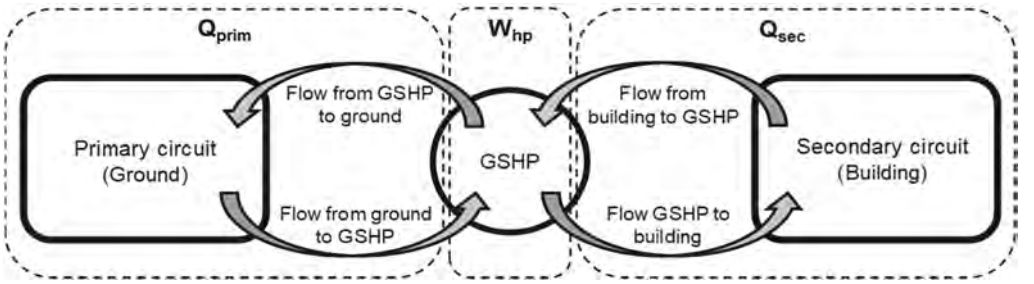

Figure 1. Heat exchange within the three components of ground source heat pump system.

In the primary circuit, the heat exchange occurs between the ground and the GSHP, where the heat is extracted from or withdrawn into the ground for heating or cooling the building side, respectively. The heat exchange mechanism that occurs between the ground and the energy geostructure is shown in Figure 2, through the example of an energy pile, for both building heating and cooling purposes. Regarding the building cooling mode, shown by the white arrows, the temperature of the circulating fluid returning from the building side is warmer than the ground temperature, which results in a thermal gradient. The circulating fluid exchanges heat with the ground loop wall through convection, which is followed by a heat conduction through the wall of the ground loop and the pile until reaching the pile-soil interface. Finally, the heat is transferred within the ground mainly by conduction and partially with convection if a moisture migration takes place. Similarly, during the building heating mode, the returning fluid temperature is colder than the ground temperature and the heat exchange occurs in the reverse direction, as shown by

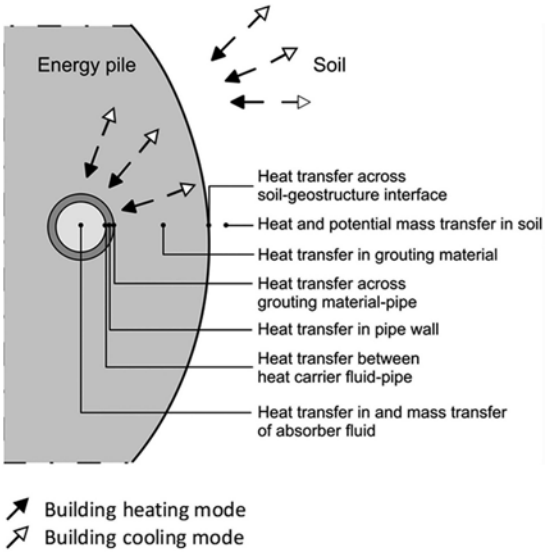

Figure 2. Heat exchange between the energy pile and the ground.

the black arrows. Assuming pure thermal conductivity within the energy pile and the ground, the energy conservation equation reads:

$$\rho c \frac{\partial T}{\partial t} - div(\lambda \boldsymbol{grad} T) = 0 \tag{1}$$

where ρ is the density, c and λ are the specific heat capacity and thermal conductivity, respectively, including both fluid and solid components, T is the temperature, t is the time and *div* and ***grad*** are the divergence and gradient operators, respectively. The energy conservation equation for the incompressible circulating fluid within the loops can be written as:

$$\rho_f A_p c_f \frac{\partial T_f}{\partial t} + \rho_f A_p c_f u_{f,i} \cdot \mathbf{grad} T_f = div\left(A_p \lambda_f \mathbf{grad} \mathrm{T}_f\right) + \frac{1}{2} f_D \frac{\rho_f A_p}{d_h} |u|^3 + q'_w \tag{2}$$

where ρ_f, c_f, and λ_f are the density, specific heat capacity, and thermal conductivity of the fluid, respectively; A_p and d_h are the cross-sectional area and hydraulic diameter of the pipe, respectively; T_f is the temperature of the fluid; $u_{f,i}$ is the velocity vector; f_D is the Darcy friction factor; and q'_w represents the heat flux per unit length that is exchanged through the pipe wall.

In the secondary circuit, the heat is transferred to or from the building side for heating or cooling purposes, respectively. In between the two circuits, there exists the GSHP to transfer the heat between the two circuits. The efficiency of the GSHP is quantified by the coefficient of performance (*COP*) through examining the amount of energy input to operate the GSHP (W_{hp}) and the energy that can be supplied to the building side (Q_{sec}), as shown below:

$$COP = \frac{Q_{sec}}{W_{hp}} \tag{3}$$

2.2 *State of the art on the application of energy geostructures*

To reveal the actual energy performance of energy geostructures, a comprehensive investigation was performed by incorporating information from (i) a survey targeting international construction companies involved in energy geostructures, (ii) available literature on operational energy geostructures and (iii) complementary results by Di Donna et al. (2017). Figure 3 presents the state of the art on energy piles, based on the integration of the

information from 157 energy pile projects, in terms of extracted thermal power with respect to the diameter and length of the piles. On the other hand, Figure 4a and 4b represent extracted and injected heat for heating and cooling purposes for energy walls (17 projects) and energy tunnels (11 projects), respectively.

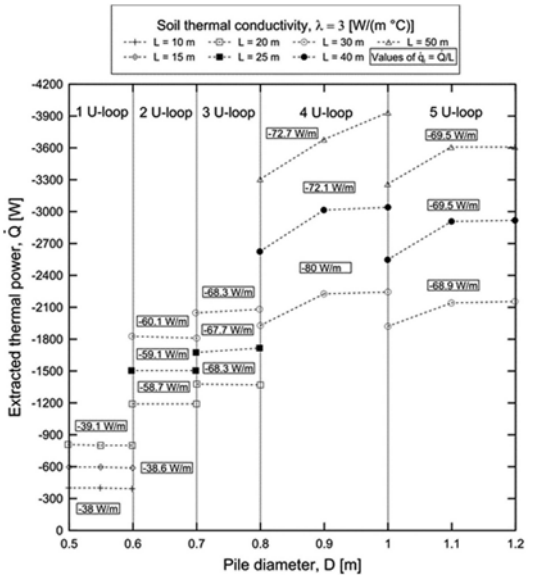

Figure 3. State of the art on application of operational energy piles (Laloui and Rotta Loria, 2019).

3 GEOTECHNICAL ASPECT

As shown in the previous section, energy geostructures concept, a technology capable of exploiting geothermal sources for both space heating and cooling, is undoubtedly an outstanding candidate to cut down the governance of unsustainable resources. Yet, the use of conventional geostructures for heat exchange purposes is associated with temperature changes, hence thermal loads and displacements, along the geostructures and within the surrounding soil, which needs to be taken into consideration in addition to the typical geotechnical design.

In order to understand the extent of temperature change effects on energy geostructures, several in-situ tests were performed on single (Laloui et al., 2006; Bourne-Webb et al., 2009; You et al., 2016; Loveridge et al., 2016; McCartney and Murphy, 2017; Sutman et al., 2017; Sutman et al., 2019) and a group of energy piles (Mimouni et al., 2015; Rotta Loria et al., 2016), energy walls (Xia et al., 2012) and energy tunnels (Adam and Markiewicz, 2009; Frodl et al., 2010; Nicholson et al., 2014; Barla et al., 2019). Moreover, several models or tools with varying complexity were developed for the analysis and design of energy piles (Knellwolf et al., 2011; Bourne-Webb et al., 2014; Salciarini et al., 2013; Rotta Loria and Laloui, 2016; Makasis et al., 2018, Sutman et al., 2018), energy walls (Kürten et al., 2015; Sterpi et al., 2017; Sailer et al., 2019) and energy tunnels (Barla and Di Donna, 2018; Bidarmaghz and Narsilio, 2018). The previous research answered the most fundamental questions on the mechanisms governing the thermal and structural behavior of energy geostructures. These efforts opened a new era for the geotechnical engineering practice, by extending the conventional role of geotechnical design to the one of addressing acute energy challenges of our century.

3.1 *Full-scale experimental analysis on energy piles*

The two pioneering full-scale in-situ tests on energy piles performed at Swiss Federal Institute of Technology in Lausanne (EPFL), investigating (i) the response of a single energy pile to

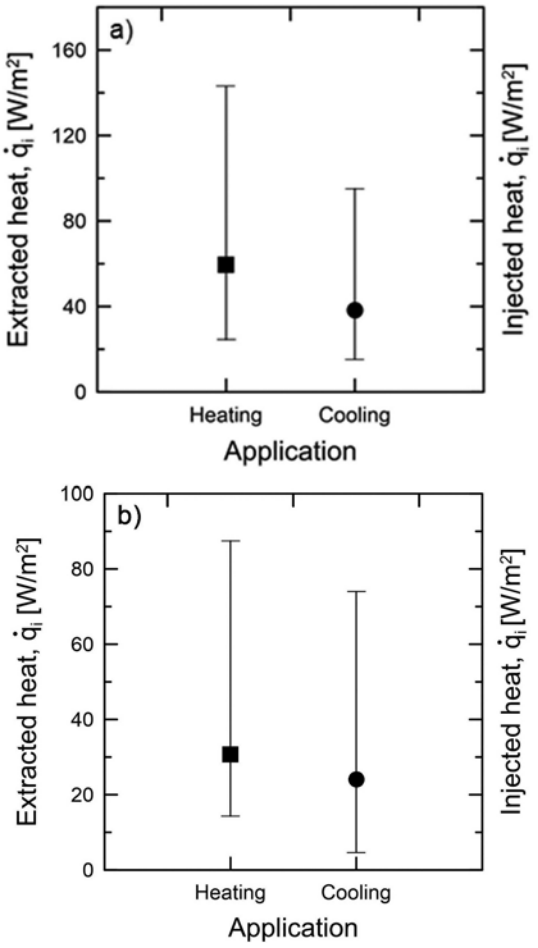

Figure 4. State of the art on application of energy walls and tunnels (Laloui and Rotta Loria, 2019).

combinations of thermal and mechanical loads and (ii) the response of a group of closely spaced energy piles to thermo-mechanical loads are presented in this section. Compressive stresses and upward shaft resistance mobilization are considered positive, according to the adopted sign convention.

3.1.1 *Response of a single energy pile to combinations of thermal and mechanical loads (Laloui et al., 2003)*

A pioneering field test was performed at EPFL campus, on a single energy pile, with a diameter of 0.88 m and length of 25.8 m, under a newly constructed 5-storey building (Bâtiment Polyvalent). The single energy pile was one of the 97 bored piles constructed under the building. Along the test pile, polyethylene (PE) tubes were installed vertically on the reinforcing structure with a U-shaped configuration to permit the passage of the heat-carrying fluid. The test pile was instrumented by a considerable amount of sensors to enable the measurement of temperature, strain and toe load variations during the thermal load applications.

The soil profile at the field test site consists of alluvial soil at the first 12 m (Layers A1 and A2) which is followed by a sandy gravelly moraine (Layer B) and bottom moraine (Layer C) until around 25 m. Finally, a molasse layer (Layer D) is found under the moraine. The ground water table at the test site is located at ground surface. Further information on soil and soil-pile interaction, as well as the test pile and instrumentation can be found in Laloui et al. (2003).

A heating and passive cooling cycle was applied to the test pile following the completion of each storey of the building with the purpose of evaluating the influence of structural load on the development of thermally induced axial stresses and displacements. Figure 5a shows the results of the last test which was performed after the construction had been finalized. The distribution of the mechanical load profile shows the absence of toe resistance which implies that the structural load was entirely carried by the mobilized resistance along the shaft of the test pile. The following temperature increase, with a magnitude of 13.4°C, resulted in generation of thermally induced compressive axial loads with a significant mobilization of the toe (2000 kN) and thermally induced axial loads at the pile head (1000 kN).

Shaft resistance mobilization due to mechanical and thermal loads along the same test pile is shown in Figure 5b and 5c. The mechanical load application resulted in downward displacement of the pile which is associated with positive shaft resistance mobilization. The subsequent temperature increase caused the portion of the pile, above the null point, the depth at which no thermally induced displacement is observed, to possess an upward displacement, resulting in a decrease in corresponding shaft resistance (Figure 5b). On the other hand, the portion below the null point displaced downward, further mobilizing the positive shaft resistance (Figure 5c).

3.1.2 *Response of a group of closely-spaced energy piles to thermo-mechanical loads (Mimouni and Laloui, 2015; Rotta Loria and Laloui, 2017)*

A second field test was implemented at EPFL campus by equipping four out of 20 piles under a water retention tank within the Swiss Tech Convention Center to evaluate the thermally induced group effects among closely-spaced energy piles. The piles were 0.9 m in diameter and 28 meters in length. Each test pile was equipped with four 24 m long U-loops connected in series which were installed 4 m below the pile heads in order to prevent the thermal interaction with the water retention tank. The test piles were instrumented with vibrating wire strain gages at every 2 meters along the length, a pressure cell at the toe and radial optical fibers. Moreover, thermistors and piezometers were installed within boreholes at close proximity to the test piles to monitor the temperature and pore water pressure changes during the field test. The field test site is 200 m away from the single energy pile test location, resulting in similar stratigraphic characteristics (Mimouni and Laloui, 2015).

Heating with maximum temperature increase of 20°C and passive cooling cycles were applied to single (EP1) and the group of four energy piles (EPall) (Rotta Loria and Laloui, 2017). Figure 6 shows (i) thermally induced axial strains and stresses along EP1 when serving as the only operating pile among the group of four piles (20EP1) and (ii) average thermally induced axial strains and stresses along the length of all four piles during full geothermal activation of the group (EPall). The comparison of tests 20EP1 and 20EPall shows that the presence of thermally induced group effects govern the higher development of axial strain when more energy piles operate as geothermal heat exchangers in a closely spaced pile group than when only one energy pile serves this purpose (Figure 6a). Figure 6b shows the comparison in terms of thermally induced axial stresses where an opposite behavior was attained corresponding to a decrease in thermally induced axial stresses as the number of thermally active energy piles increases. This phenomenon is associated with the increased deformation of energy piles operating in a group (Figure 6a) which results in lower thermally induced blocked strains, since the temperature change and hence the free thermal strains are the same for Test 20EP1 and 20EPall, and therefore lower observed axial stresses. Moreover, tensile stresses were observed at the bottom portion of the energy piles during test 20EPall, which is associated with the thermally induced deformation of the molasse layer resulting in a pull-down effect. This effect was less pronounced during the test 20EP1 since the compressive stresses induced by the restrained expansion of EP1 overcame the tensile stresses exerted by the surrounding molasse layer.

Comparison of thermally induced strains and axial stresses per unit temperature change corresponding to geothermal operation of a single energy pile (Test 20EP1) and a group of energy piles (Test 20EPall) is presented in Figure 7a and 7b, respectively, which are average values along the active length of the piles. The figures clearly show greater average vertical strains and lower average axial stresses with increasing number of active energy piles. In terms

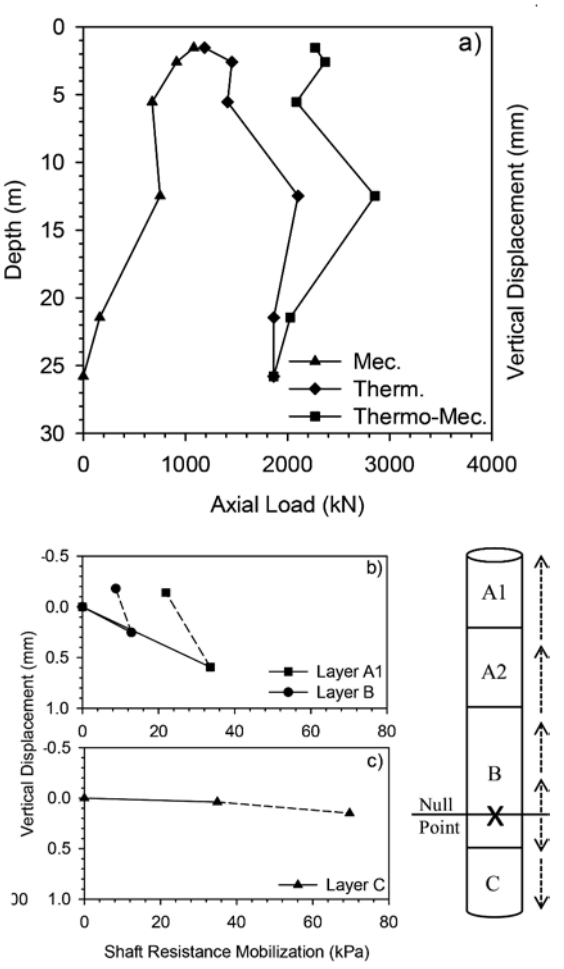

Figure 5. A) Mechanical, thermal and combined thermo-mechanical loads. b, c) Shaft resistance mobilization along the test pile.

of design aspects, analysis of a single pile in a closely-spaced group will lead to a conservative estimate of vertical stresses that can be employed during the preliminary design stages, but is not the case for the vertical strains.

3.2 *Analytical methods for the analysis of energy piles*

Full-scale in-situ tests provided the most fundamental information regarding the response of a single and a group of energy piles to thermo-mechanical actions. Moreover, finite-element methods, the majority of which have been validated by the results of the in-situ tests, were developed, and are considered to be the most rigorous approach for the analysis of energy piles. However, these comprehensive methods require a considerable number of geotechnical parameters, as well as high computational efforts, which renders them more suitable for research purposes rather than for practical piling problems. For the design and wider application of energy piles, a reasonable balance between excessive complexity and unsatisfactory simplicity should be established for the development of practical analytical models. Therefore, several simplified analytical methods have been developed by the Laboratory of Soil Mechanics to serve as preliminary design guidance of single and groups of energy piles.

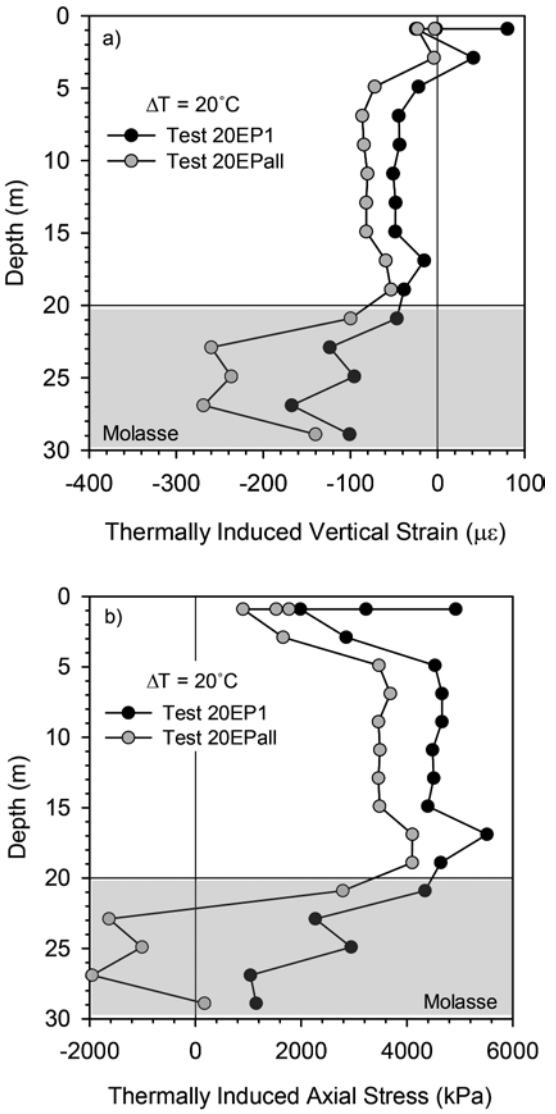

Figure 6. A) Thermally induced axial strains b) Thermally induced axial stresses during tests EP1 and EPall.

3.2.1 *Load-transfer approach for single and group of energy piles (Knellwolf et al., 2011; Ravera et al., 2020)*

The load-transfer approach, where the soil-pile interaction is represented by springs distributed along the pile shaft and toe by neglecting the continuity of the soil domain, is one of the most common analytical methods employed for the analysis of conventional piles (Seed and Reese, 1957; Coyle and Reese, 1966). In this approach, numerous analytical and empirical methods have been proposed to define the load-transfer curves (Randolph and Wroth, 1978; Frank and Zhao, 1982; Kraft et al, 1981). Later on, considering that most piles are implemented in groups in practice, the load-transfer curves have been modified to consider group effects (Randolph and Clancy, 1993; Comodromos et al., 2016). Given the great potential of the load-transfer approach in providing a practical tool for the analysis of axial loaded conventional piles, the approach has been implemented for the analysis of single and groups of energy piles.

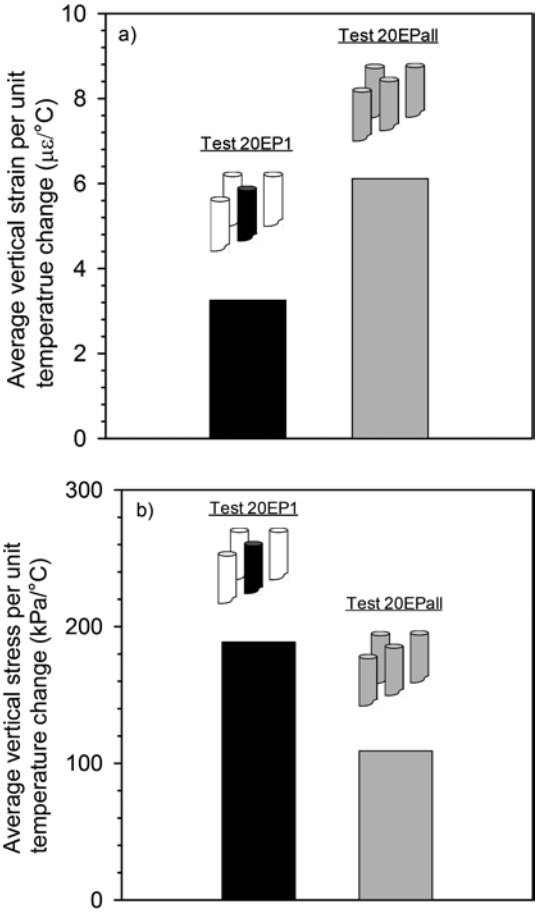

Figure 7. Thermally induced group effects in terms of a) Axial strains and b) Axial stresses (redrawn after Rotta Loria, 2019).

The load-transfer approach has first been modified for single energy piles by Knellwolf et al. (2011), where the pile is divided into rigid elements that are connected to each other and to the surrounding soil by the springs (Figure 8a). In order to define the relationships between the mobilized shaft friction/toe resistance and displacement, the method from Frank and Zhao (1982) was utilized, relating the shaft and toe stiffness to Menard pressuremeter modulus and dividing the load-transfer curve into three main sections: (i) initial linear part characterizing the elastic response, (ii) second linear part associated with the elastoplastic response and (iii) final plateau referring to perfectly plastic response as represented in Figure 8b by full lines for single isolated piles. The presence of a slab above energy piles was considered in a simplified way by introducing an additional spring linked to the pile head. The analytical model is validated by the results of both EPFL single pile in-situ test (Laloui et al., 2006) and Lambeth College in-situ test (Bourne-Webb et al., 2009) and has also been implemented in the Thermo-Pile Software developed by Laboratory of Soil Mechanics for the analysis and design of energy piles.

Following the same logical sequence as the one of conventional piles, the load-transfer approach for single energy piles has subsequently been extended to characterize the response of groups of energy piles to thermo-mechanical loads in a simplified, yet rational manner (Ravera et al., 2020). To represent the interaction between a group of energy piles, a displacement ratio (R_d) was introduced adapting the displacement response of a single isolated energy pile to the one of an energy pile in a group:

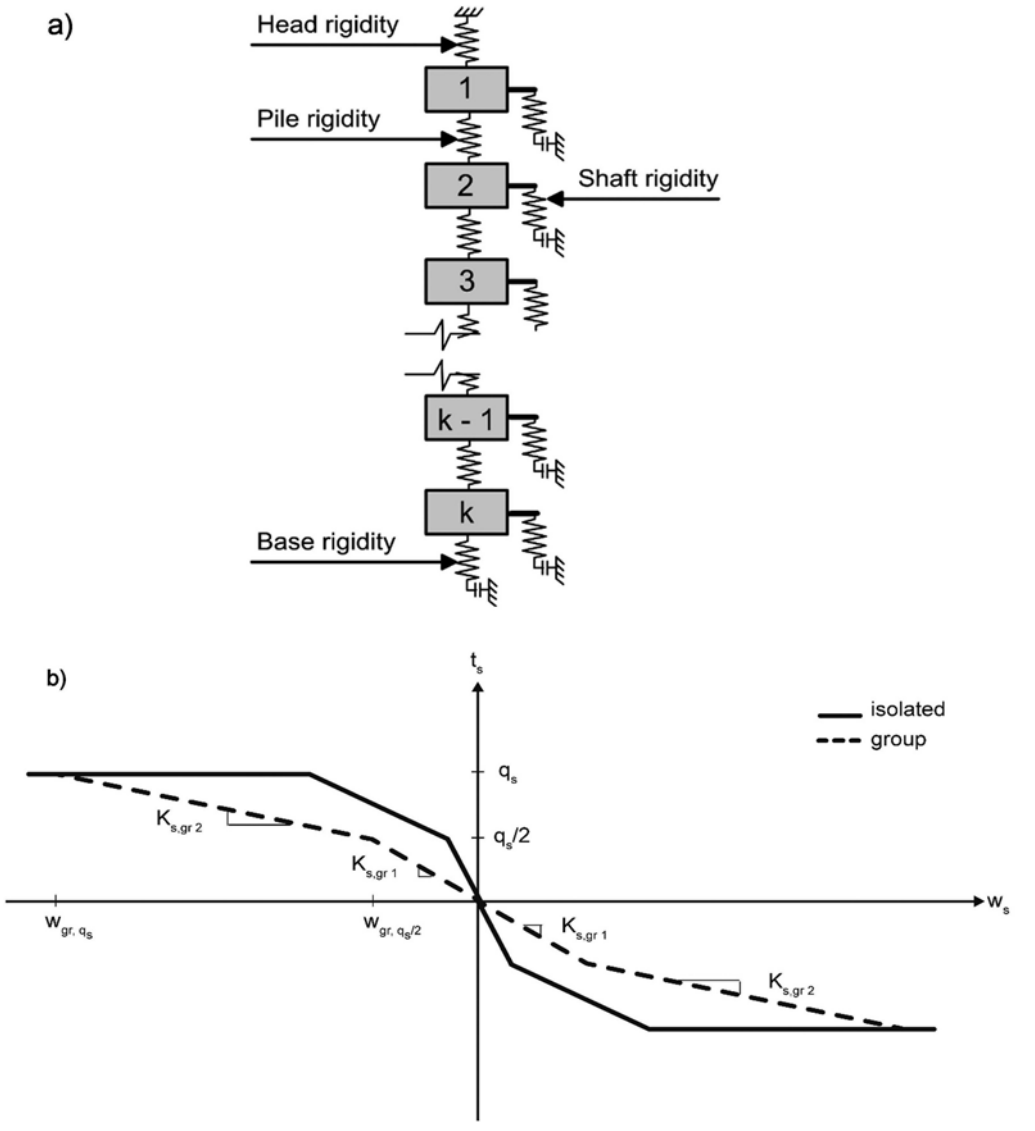

Figure 8. A) Modelling approach b) Load-transfer relationship for single isolated energy pile and energy pile in a group.

$$R_d = \frac{w_{gr}}{w_{is}} \tag{4}$$

Where w_{gr} is the average displacement of group and w_{is} is the displacement of a single pile subjected to same average load. As in the case of the approach proposed for conventional piles (Comodromos et al., 2016), the displacement ratio depends on the geometric configuration as well as the variations in the displacement field introduced by thermal and mechanical loads. In this approach, the ultimate shaft resistance of an energy pile in a group is considered to be the same as the one of a single isolated energy pile, while the displacement ratio is applied to adapt the displacement necessary to mobilize it. The load-transfer curve attained for a single energy pile in a group is represented by dashed lines in Figure 8b and is determined as follows:

$$w_{gr} = R_d w_{is} \tag{5}$$

$$t_{s,gr} = t_{s,is} \tag{6}$$

where w_{gr} and $t_{s,gr}$ are the displacement and shaft resistance of an energy pile in a group, and w_{is} and $t_{s,is}$ are the displacement and shaft resistance of a single isolated energy pile, respectively. The load-transfer curve in Figure 8b is determined using the method proposed by Frank and Zhao (1982), yet, any method developed for single conventional piles can be employed provided that a displacement factor is applied. Finally, since the behavior of a pile in the group highly depends on its location, the displacement ratio may also be corrected by introducing a location weighting factor (Comodromos et al., 2016).

The proposed method has been implemented in Comsol Multiphysics Software and its competence in analyzing the behavior of a group of energy piles has been investigated through the results of the full-scale in-situ test performed at EPFL campus, on a group of four energy piles. The material properties considered in the analysis as well as the development of the load-transfer curves are explained in detail by Ravera et al. (2020). Comparison of experimental data from the full-scale in-situ test (Rotta Loria and Laloui, 2018) and the numerical results obtained through the implemented method is presented in Figure 9a and 9b, in terms of thermally induced axial stress and mobilized shaft resistance, respectively at 20°C temperature increase. The numerical results were attained employing two sets of parameters for the molasses layer in compliance with the ones presented in Knellwolf et al. (2011).

The comparison presented in Figure 9 corresponds only to the geothermal activation of the group of energy piles, excluding the stresses generated by the body load and structural loads. The stress variation corresponds to the average value of the mean temperature variations along the uninsulated portions of all four energy piles in the group and the mobilized shaft resistance is determined by employing the stress variations. A good agreement between the experimental and numerical results is observed in the figure, despite the simplifications inherent in the theory.

It was previously shown in Figure 7 that thermally induced vertical stresses decrease for the same temperature change as the number of geothermally active energy piles increases due to increased vertical strains caused by group interactions. The agreement between experimental and numerical results corroborates the additional value of this method, which allows determination of the thermally induced vertical stress along the depth of an energy pile in a group in a simplified and rational manner.

3.2.2 *Interaction factor method for group of energy piles (Rotta Loria and Laloui, 2016; Ravera et al., 2019)*

A second analytical method was extended from the interaction factor method in the framework of conventional pile groups (Poulos, 1968) to the one of energy pile groups in order to provide a simplified yet rational analysis tool for estimating the vertical displacement of energy pile groups subjected to thermal loads (Rotta Loria and Laloui, 2016). The method allows the estimation of the head displacement of any energy pile in a group by employing the interactions between two energy piles and the superimposition of the individual effects of adjacent piles in the group as follows:

$$w_k = w_i \sum_{i=1}^{i=n_{EP}} \Delta T_i \Omega_{ik} \tag{7}$$

where w_i is the vertical head displacement of a single isolated pile per unit temperature change, ΔT_i is the applied temperature change to pile i, and Ω_{ik} is the interaction factor for two piles corresponding to the center-to-center distance between pile i and k. Interaction factor charts, characterizing a group of two energy piles and taking into consideration pile slenderness ratio and spacing, pile-soil stiffness ratio, Poisson's ratio and non-uniform moduli of the soil have been developed to determine Ω_{ik} (Rotta Loria and Laloui, 2016).

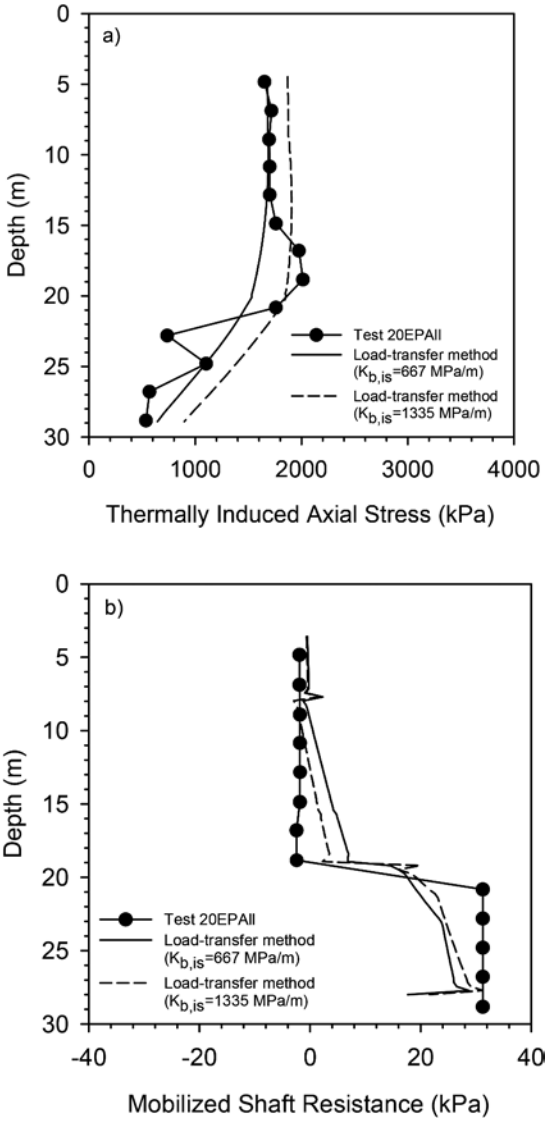

Figure 9. Comparison between experimental data and numerical results for a) Thermally induced axial stresses and b) Mobilized shaft resistance (redrawn after Ravera et al., 2020).

The formulation above provides solutions regarding the displacement interaction for free standing energy pile groups or energy pile groups with a perfectly flexible slab. However, in practice piles are often rigidly attached to a pile cap which stands on the soil (Poulos, 1968). Therefore, it is essential to consider thermally induced mechanical interactions which are governed by the changes in deformation field, due to the interplay between the energy pile-slab-soil responses. With this purpose, the interaction factor method was further extended to take into account the presence of the pile cap (Ravera et al., 2019). 3D steady state finite element simulations were carried out employing Comsol Multiphysics Software to propose a formulation of the interaction factor for energy pile groups under a slab and to propose design charts for the analysis compatible with the former study. The influence of the rigid pile cap is expressed in terms of pile-cap displacement ratio as follows:

$$R_c = \frac{displacement\ of\ pile\ with\ cap}{displacement\ of\ free\ standing\ pile} \tag{8}$$

Employing the pile-cap displacement ratio, displacement determined in free standing conditions can be adjusted to consider the contacting slab as follows:

$$w_k = R_c w_i \sum_{i=1}^{i=n_{EP}} \Delta T_i \Omega_{ik} \tag{9}$$

The combination of the two methodologies (1) interaction factor method for free standing energy piles and (2) extension of the method to consider the presence of the slab yields the following ultimate methodology illustrated in Figure 10. The first three steps belonging to the original methodology (Rotta Loria and Laloui, 2016) and the following two steps corresponding to the extension of the method (Ravera et al., 2019), are as follows:

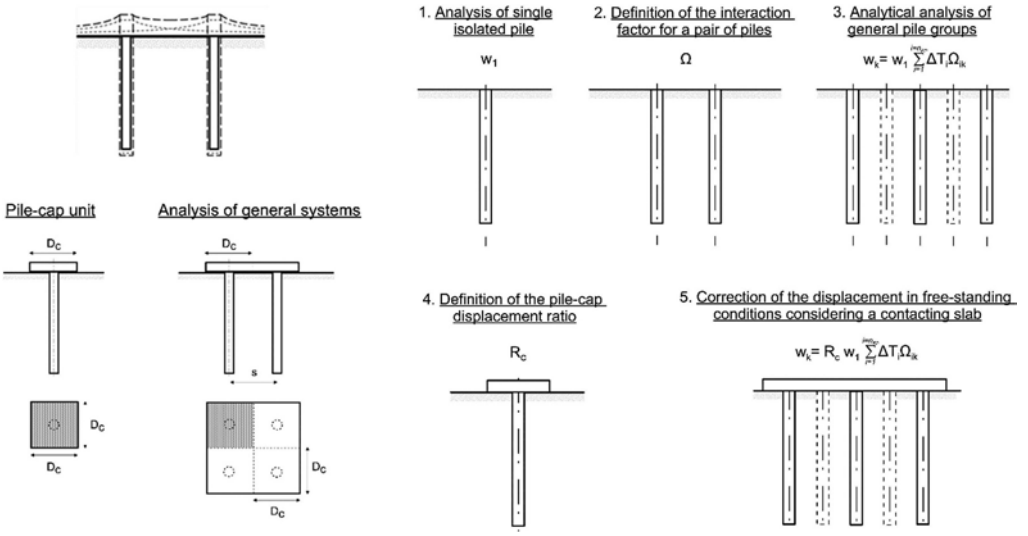

Figure 10. Steps of interaction factor method for the analysis of energy piles with contacting slab.

Step 1: Displacement of an isolated energy pile is computed by employing any suitable practical or sophisticated method as long as it returns representative displacement values for the considered case.

Step 2: Interaction factor is determined for a pair of two energy piles employing the design charts provided by Rotta Loria and Laloui (2016). A sample design chart regarding an energy pile with a slenderness ratio of twenty-five bearing in a soil with a Poisson's ratio of 0.3 is presented in Figure 11a, for various soil-pile stiffness and normalized displacement.

Step 3: Vertical head displacement of any pile in the group in free standing conditions is calculated employing Equation (7).

Step 4: Pile-cap displacement ratio is determined referring to the design charts presented by Ravera et al. (2019). A sample design chart, compatible with the one presented for Step 2, is shown in Figure 11b for pile cap thickness of 0.6 m.

Step 5: Displacement determined in Step 3 for free standing conditions is corrected by employing Equation (9).

The rather approximate yet rational methodology presented above enables the estimation of the head displacement of any energy pile group configuration with a slab supported on soil through the displacement of a single isolated energy pile and superimposition of the individual effects of adjacent piles and the slab in the group, providing a practical tool to perform displacement analysis of energy pile groups in the early stages of the design process.

4 DESIGN OF ENERGY PILES

Full-scale in-situ tests that have been performed on energy piles, as well as the numerical and analytical tools that have been developed over more than two decades, revealed the most fundamental information leading to the recommendations regarding the design of energy piles. According to these findings the design of energy piles at ultimate limit states can be considered as a conventional process by considering that the reactions provided by the soil above and below the null point compensate for each other ensuring equilibrium and, provided that the structural elements are characterized by adequate ductility and rotation capacity (Rotta Loria et al., 2020). However, regarding the serviceability limit states, the effects of both mechanical and thermal loads should be examined by taking into consideration the vertical displacement of single and group of energy piles, as well as the deflection or angular distortion.

Regarding the combinations of actions, Rotta Loria et al. (2020) recommended $\psi_0 = 0.60$, $\psi_1 = 0.50$ and $\psi_2 = 0.50$ for the combination, frequent and quasi-permanent values of variable actions, respectively. Regarding the consideration of thermal loads during cooling of the building side (i.e. temperature increase along the energy piles), two design combinations must be considered, assuming the effects of the thermal loads make them the dominant load ($\Delta T_k = Q_{k,1}$, where $Q_{k,1}$ is the dominant variable load) or if not ($\Delta T_k = Q_{k,i}$, where $Q_{k,i}$ is the i^{th} general variable load), since it is not known if the thermal loads are dominant with respect to the mechanical ones. Regarding the heating of the building side (i.e. temperature decrease along the energy piles) a single design combination must be considered ($\Delta T_k = Q_{k,1}$).

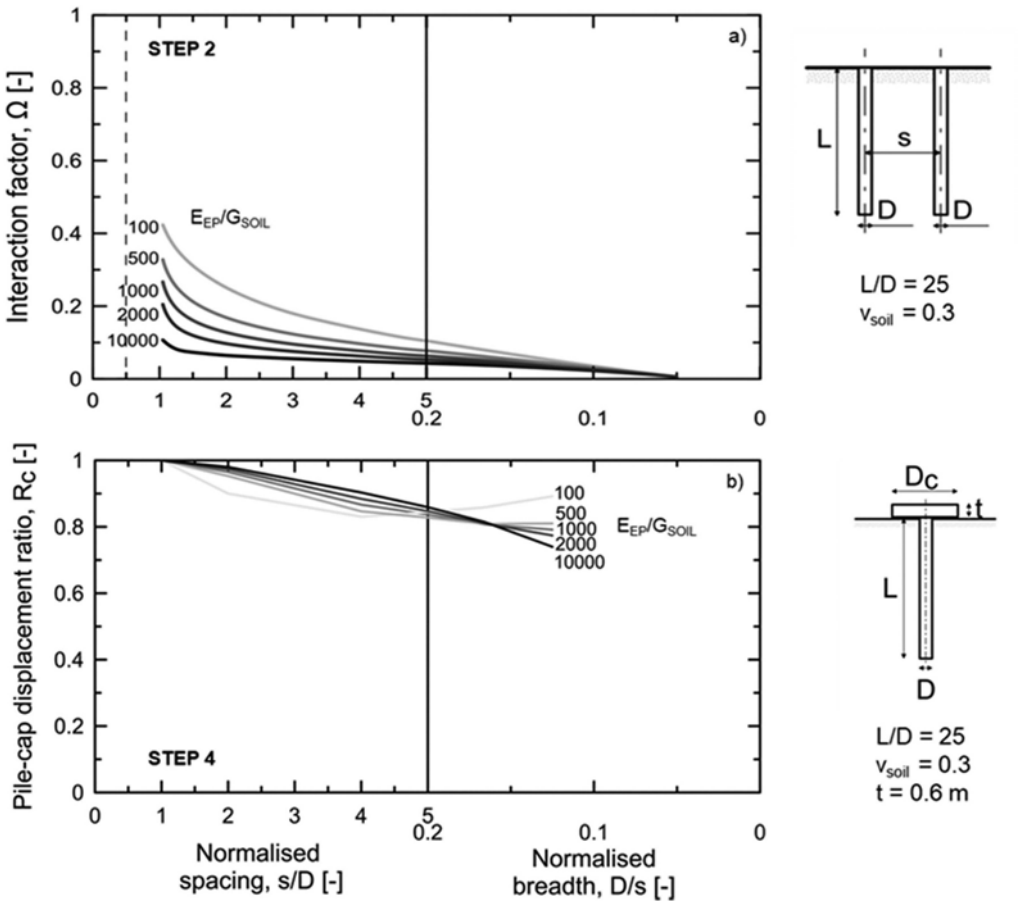

Figure 11. A) Interaction factors, b) Pile-cap displacement ratio for L/D = 25.

Finally, when the influence of thermal loads is analyzed during the design of energy piles, (i) piles free at the head and (ii) piles that are fully restrained should be considered to attain conservative estimations of vertical displacement and stress, respectively.

5 CONCLUSIONS

The fundamental research in the field of energy geostructures, compiled and expanded by the Laboratory of Soil Mechanics over more than two decades, revealed that this emerging technology provides low carbon, cost-effective and local energy solutions to structures and infrastructures, which opens a new era for the geotechnical engineering practice.

The research activities performed by LMS in this field has exclusively covered various elements related to energy geostructures, including but not limited to energy, geotechnical, structural and design aspects. Related to the energy aspect, it has been revealed that typically, 40-150 W/m heat energy can be extracted from and withdrawn into the ground with the use of energy piles, while 20-40 W/m^2 and 20-60 W/m^2 are achievable with energy wall and energy tunnels, respectively. Furthermore, two state-of-the-art in-situ tests have been performed on single and a group of energy piles, which not only revealed the most fundamental knowledge regarding their thermo-mechanical behavior, but also provided invaluable information for the validation of numerical models and analytical tools developed in the area.

To provide satisfactory tools for design and wider application of energy piles, several practical analytical tools have been developed for energy piles including the load-transfer method for the assessment of axial stress, displacement and mobilized shaft resistance along single and groups of energy piles, as well as the interaction factor method for the estimation of vertical displacement of energy pile groups with and without a rigid slab. Incremental research efforts performed in the area, from both experimental and analytical points of view, have eventually led to development of recommendations for the design of energy piles for both ultimate and serviceability limit states. Overall, research outcomes achieved over more than two decades revealed that the energy geostructures concept is a mature and ready-to-be-employed technology.

The questions that remained to be answered now are no longer about how an energy geostructure responds to thermal actions, but rather on how the energy performance, as well as the geotechnical and structural adaptations should be assessed to maximize its cost efficiency.

ACKNOWLEDGEMENT

The financial supports from the Swiss National Science Foundation N. 160117 (Division IIII), Swiss National Science Foundation N. 200021_175500 (Division II), Swiss Federal Office of Energy (contract Nb. 154′426) are greatly appreciated.

REFERENCES

Adam, D. & Markiewicz, R. (2009). Energy from earth-coupled structures, foundations, tunnels and sewers. *Géotechnique*, 59(3), 229–236.

ASHRAE (2008). ASHRAE Vision 2020. https://www.isiaq.org/docs/sponsor%20material/ASHRAE%20Strategic%20Plan%20Jun08.pdf. Last accessed May 2019.

Barla, M. & Di Donna, A. (2018). Energy tunnels: concept and design aspects. *Underground Space*, 3(4), 268–276.

Barla, M., Di Donna, A. & Insana, A. (2019). A novel real-scale experimental prototype of energy tunnel. *Tunnelling and Underground Space Technology*, 87, 1–14.

Bidarmaghz, A. & Narsilio, G. A. (2018). Heat exchange mechanisms in energy tunnel systems. *Geomechanics for Energy and the Environment*, 16, 83–95.

Bourne-Webb, P. J., Amatya, B., Soga, K., Amis, T., Davidson, C. & Payne, P. (2009). Energy pile test at Lambeth College, London: geotechnical and thermodynamic aspects of pile response to heat cycles. *Géotechnique*, 59(3), 237–248.

Bourne-Webb, P. J., Freitas, T. B. & da Costa Gonçalves, R. A. (2016). Thermal and mechanical aspects of the response of embedded retaining walls used as shallow geothermal heat exchangers. *Energy and Buildings*, 125, 130–141.

Bourne-Webb, P. J., Pereira, J. M., Bowers, G. A., Mimouni, T., Loveridge, F. A., Burlon, S., Olgun, C., McCartney, M. & Sutman, M. (2014). Design tools for thermoactive geotechnical systems. *DFI Journal-The Journal of the Deep Foundations Institute*, 8(2), 121–129.

Comodromos, E. M., Papadopoulou, M. C. & Laloui, L. (2016). Contribution to the design methodologies of piled raft foundations under combined loadings. *Canadian Geotechnical Journal*, Vol. 53 (4), 559–577.

Coyle, H. M. & Reese, L. C. (1966). Load transfer for axially loaded piles in clay. *J. Soil Mech. Found. Div. ASCE*. 92 (2), 1–26.

Di Donna, A., Cecinato, F., Loveridge, F. & Barla, M. (2017). Energy performance of diaphragm walls used as heat exchangers. *Proceedings of the Institution of Civil Engineers-Geotechnical Engineering*, 170 (3), 232–245.

Eurostat, (2018) https://ec.europa.eu/eurostat/statistics-explained/index.php/Energy_consumption_in_households (last updated March 2018)

Frank, R. & Zhao, S. R. (1982). Estimation par les paramètres pressiométriques de l'enfoncement sous charge axiale de pieux forés dans des sols fins. *Bulletin de Liaison Laboratoires des Ponts et Chaussees*, No. 119, 17–24.

Frodl, S., Franzius, J. N. & Bartl, T. (2010). Design and construction of the tunnel geothermal system in Jenbach. *Geomechanics and Tunnelling*, 3(5), 658–668.

International Energy Agency, I. E. A. (2017), World Energy Outlook 2017, OECD Publishing, Paris/ IEA,Paris, https://doi.org/10.1787/weo-2017-en.

International Energy Agency, I. E. A. (2018), The Future of Cooling, OECD Publishing, Paris/ IEA, Paris, 92 pp.

International Energy Agency, I. E. A. (2019) https://www.iea.org/tcep/buildings/ (last updated 25 January 2019).

Knellwolf, C., Peron, H. & Laloui, L. (2011). Geotechnical analysis of heat exchanger piles. *Journal of Geotechnical and Geoenvironmental Engineering*, 137(10), 890–902.

Kraft, L. M., Ray, R. P. & Kagawa, T. (1981). Theoretical T-Z curves. *Journal of Geotechnical Engineering, American Society of Civil Engineers*, 107 (11), 1543–1561.

Kürten, S., Mottaghy, D. & Ziegler, M. (2015). Design of plane energy geostructures based on laboratory tests and numerical modelling. *Energy and Buildings*, 107, 434–444.

Laloui, L., Moreni, M. & Vulliet, L. (2003). Comportement d'un pieu bi-fonction, fondation et échangeur de chaleur. *Canadian Geotechnical Journal*, 40(2), 388–402.

Laloui, L., Nuth, M. & Vulliet, L. (2006). Experimental and numerical investigations of the behaviour of a heat exchanger pile. *International Journal for Numerical and Analytical Methods in Geomechanics*, 30 (8),763–781.

Laloui L. & Rotta Loria A. F. (2019). *Analysis and Design of Energy Geostructures: Theoretical Essentials and Practical Applications*. Academic Press.

Loveridge, F. A., Powrie, W., Amis, T., Wischy, M. & Kiauk, J. (2016). Long term monitoring of CFA energy pile schemes in the UK. *Energy Geotechnics*, 585–592.

Makasis, N., Narsilio, G. A. & Bidarmaghz, A. (2018). A machine learning approach to energy pile design. *Computers and Geotechnics*, 97, 189–203.

McCartney, J. S. & Murphy, K. D. (2017). Investigation of potential dragdown/uplift effects on energy piles. *Geomechanics for Energy and the Environment*, 10, 21–28.

Mimouni, T. & Laloui, L. (2015). Behaviour of a group of energy piles. *Canadian Geotechnical Journal*, 52(12),1913–1929.

Nicholson, D. P., Chen, Q., de Silva, M., Winter, A. & Winterling, R. (2014). The design of thermal tunnel energy segments for Crossrail, UK. *Proceedings of the Institution of Civil Engineers-Engineering Sustainability*, 167 (3), 118–134.

Poulos H. G. (1968). Analysis of the settlement of pile groups. *Géotechnique*, 18 (4), 449–471.

Poulos H. G. (1968). The influence of a rigid pile cap on the settlement behaviour of an axially-loaded pile. *Civ. Eng. Trans., Inst. Engrs*, CE10 (2), 206–208.

Randolph, M. F. & Clancy, P. (1993). Efficient design of piled rafts. *Proceedings of 5th International Conference on Deep Foundations on Bored and Auger Piles*, 1-4 June, Ghent, Belgium, 119–130.

Randolph, M. F. & Wroth C. P. (1978). Analysis of deformation of vertically loaded piles. *Journal of Geotechnical Engineering, American Society of Civil Engineers*, 104 (2), 1465–1488.

Ravera, E., Sutman, M. & Laloui, L. (2019). Analysis of the interaction factor method for energy pile groups with slab. *Comput. Geotech*. https://doi.org/10.1016/j.compgeo.2019.103294.

Ravera, E., Sutman, M. & Laloui, L. (2020). Load-transfer method for energy piles in a group with pile-soil-slab-pile interaction. *J. Geotech. Geoenviron. Eng*. https://doi.org/10.1061/(ASCE)GT.1943-5606.0002258.

Recast, E. P. B. D. (2010). Directive 2010/31/EU of the European Parliament and of the Council of 19 May 2010 on the energy performance of buildings (recast). *Official Journal of the European Union* 18, no. 06.

Rotta Loria, A.F. (2019). Performance-based design of energy pile foundations. *DFI J*. 12 (2), 94–107.

Rotta Loria, A. F., Bocco, M., Garbellini, C., Muttoni, A. & Laloui, L. (2020). The role of thermal loads in the performance-based design of energy piles. *Geomechanics for Energy and the Environment*, 21, 100153.

Rotta Loria, A. F. & Laloui, L. (2016). The interaction factor method for energy pile groups. *Computers and Geotechnics*, 80, 121–137.

Rotta Loria, A. F. & Laloui, L. (2017). Thermally induced group effects among energy piles. *Géotechnique*, 67(5),374–393.

Rotta Loria, A. F. & Laloui, L. (2018). Group action effects caused by various operating energy piles. *Géotechnique*, *68*(9), 834–841.

Sailer, E., Taborda, D. M., Zdravković, L. & Potts, D. M. (2019). Fundamentals of the coupled thermo-hydro-mechanical behaviour of thermo-active retaining walls. *Computers and Geotechnics*, 109, 189–203.

Salciarini, D., Ronchi, F., Cattoni, E. & Tamagnini, C. (2013). Thermomechanical effects induced by energy piles operation in a small piled raft. *International journal of Geomechanics*, 15(2), 04014042.

Seed, H. B. & Reese, L. C. (1957). The action of soft clay along friction piles. *American Society of Civil Engineers Society*, 122 (1), 731–754.

Sterpi, D., Coletto, A. & Mauri, L. (2017). Investigation on the behaviour of a thermo-active diaphragm wall by thermo-mechanical analyses. *Geomechanics for Energy and the Environment*, 9, 1–20.

Sutman, M., Brettmann, T. & Olgun, C. G. (2019). Full-scale in-situ tests on energy piles: Head and base-restraining effects on the structural behaviour of three energy piles. *Geomechanics for Energy and the Environment*, 18, 56–68.

Sutman, M., Olgun, C. G., Laloui, L. & Brettmann, T. (2017). Effect of end-restraint conditions on energy pile behavior. *Geotechnical Frontiers*, 165–174.

Sutman, M., Olgun, C. G. & Laloui, L. (2018). Cyclic Load–Transfer Approach for the Analysis of Energy Piles. *Journal of Geotechnical and Geoenvironmental Engineering*, 145(1), 04018101.

Sutman, M., Speranza, G., Ferrari, A., Larrey-Lassalle, P. & Laloui, L. (2020). Long-term performance and life cycle assessment of energy piles in three different climatic conditions. *Renewable Energy*, 146, 1177–1191.

Xia C., Sun M., Zhang G., Xiao S. & Zou Y. (2012). Experimental study on geothermal heat exchangers buried in diaphragm walls. *Energy and Buildings*. 52, 50–5.

You, S., Cheng, X., Guo, H. & Yao, Z. (2016). Experimental study on structural response of CFG energy piles. *Applied Thermal Engineering*, 96, 640–651.

Smart Geotechnics for Smart Societies – Zhussupbekov, Sarsembayeva & Kaliakin (Eds)
© 2023 The Author(s), ISBN 978-1-003-29912-7
Open Access: www.taylorfrancis.com, CC BY-NC-ND 4.0 license

Innovation in dynamic in-situ testing

Jong-Sub Lee, Sang Yeob Kim & Geunwoo Park
Korea University, Seoul, Republic of Korea

Yong-Hoon Byun
Kyungpook National University, Daegu, Republic of Korea

Won-Taek Hong
Gachon University, Seongnam, Republic of Korea

ABSTRACT: Engineering parameters reflecting dynamic responses have been used for reliable subsurface characterization in the field. The objective of this study is to summarize the innovations in in situ devices using dynamic penetration systems. The devices cover the Instrumented Dynamic Cone Penetrometer (IDCP) in small- and large-scale energy-monitoring modules for Standard Penetration Tests (SPT) and Seismic Dynamic Cone Penetrometers (SDCP). For the IDCP, Dynamic Resistance (DR) was experimentally estimated by the F^2, F-V, and F methods and their reliability was compared, while the DR was correlated with the DCPI to assess its applicability in the field. The large-scale IDCP for the deep and dense layer estimates the DR as well, which shows the functions of relationships with the DCPI and static cone resistance. Likewise, an energy monitoring module was installed at the rod head and the SPT sampler. The transferred energy ratios acquired by the energy-monitoring module at the rod head and sampler were compared, and the DR was reasonably correlated with the static cone resistance. Finally, the SDCP simultaneously measured the penetration index and maximum shear modulus, which can characterize both strength and stiffness of the layer. This study suggests that the innovation of dynamic in situ devices may allow for more reliable and efficient subsurface characterization.

1 INTRODUCTION

Dynamic penetration system has been widely used for subsurface characterization because of their applicability to hard layers using simple testing procedures. Among dynamic penetration systems, the dynamic cone penetration test (DCPT) has been adopted for use in fields with low accessibility owing to its mobility (ASTM D6951). Subsequently, the dynamic cone penetration index (DCPI) acquired by the dynamic cone penetrometer (DCP) has been correlated with many engineering parameters, such as the California bearing ratio for pavement design (Kim et al., 2019). However, the dynamic penetration system is limited because energy loss occurs during the driving of the penetrometer (Byun and Lee, 2013; Lee et al., 2019). Therefore, an instrumented dynamic cone penetrometer (IDCP) was developed for the reliable characterization of layers considering dynamic responses (Byun et al., 2014; Kim and Lee, 2020; Kim et al., 2022a).

In addition, a large-scale IDCP was developed for characterization of the deep and dense layers of intermediate geomaterials (Lee and Byun, 2020). When stiffness of the ground gradually increases from very soft to stiff, the subsurface characterization method should be modified from quasi-static for soft soils to dynamic for stiff soils. The standard penetration test (SPT), which is also one of dynamic penetration system, has been applied to ground investigations at deep depths. For accurate strength characterization, the transferred energy into the rod head was evaluated and the N value was corrected to the reference energy ratio of 60% as N_{60}. However, energy correction using the transferred energy into the rod head has a limitation

DOI: 10.1201/9781003299127-6

owing to energy losses at the joints and SPT sampler. An energy-monitoring module was developed to consider these energy losses (Hong et al., 2022; Park et al., 2022).

The stability of the ground subjected to repetitive dynamic and wheel loads is influenced by the stiffness and strength (Clark et al., 2002). DCP has the advantages of portability and profiling the target ground with depth. However, the DCP only produces the strength characteristics of the target ground using the dynamic cone penetration index (DCPI), and the stiffness of the target ground is estimated from the correlations between the stiffness properties and the DCPI suggested by previous studies (Mohammadi et al., 2008; Lee et al., 2014). Therefore, a seismic dynamic cone penetrometer (SDCP) was developed based on the DCP apparatus for direct evaluation of the stiffness properties of the target ground with depth (Hong et al., 2017).

The objective of this paper is to introduce innovations in dynamic in situ tests by measuring the tip or sampler responses or sensing soils near the tip. Dynamic in situ tests include dynamic cone penetration tests, standard penetration tests, dynamic cross-hole tests, and water-content measurements. The device and field tests for these tests are discussed. This manuscript is a summary and reorganization of the research conducted and the articles published by and in the Geo-Engineering (or Geowave) Laboratory, Korea University.

2 INSTRUMENTED DYNAMIC CONE PENETROMETER

2.1 *Device*

The IDCP is composed of guide, hammer, anvil, driving rod, and cone tip, as shown in Figure 1. The hammer with a weight of 78.5 N falls through the guide from a height of 575 mm, which has potential energy identical to that of conventional DCP. The cone tip has an apex angle of 60° and a diameter of 24 mm, and the driving rod is composed of hollow steel pipes with inner and outer diameters of 14 and 24 mm, respectively, to install sensors inside the rod. A load cell composed of four strain gauges was installed at the cone tip and used to measure the force based on a Wheatstone bridge circuit, which amplifies the output voltage and compensates for temperature and bending effects. An accelerometer was installed at the cone tip to acquire the acceleration signals during driving. Note that the dynamic signals can be acquired by calibrating the electrical signals to the force and acceleration. Finally, the dynamic signals were visualized on the oscilloscope through the amplifier and bridge box and stored on a computer (see details in Byun et al. 2014; Kim et al. 2019; Lee et al. 2019).

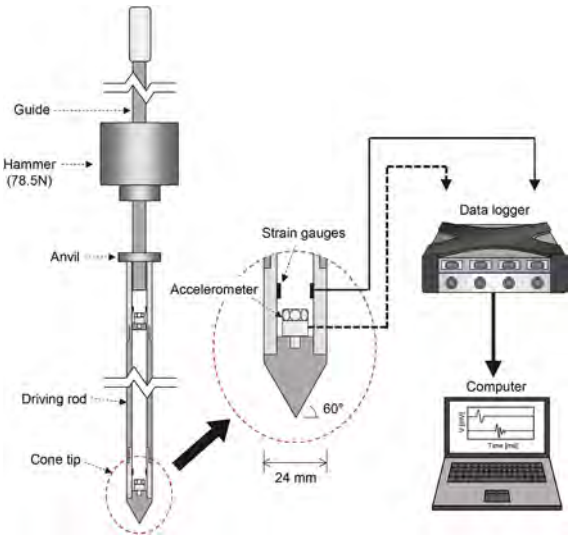

Figure 1. Measurement system of instrumented dynamic cone penetrometer (Lee et al., 2019).

2.2 *Experimental study*

For a direct indication of the soil layer strength, the dynamic resistance (DR) with a unit of stress was used in the DCPT as follows:

$$DR = \frac{1}{A} \times \frac{PE}{\Delta d} = \frac{1}{A} \times \frac{mg \times h}{\Delta d} \tag{1}$$

where A, PE, Δd, mg, and h denote the cross-sectional area, potential energy, displacement, hammer weight, and falling height, respectively. DR allows efficient profiling of hard layers rather than DCPI using conventional DCP.

From the DR concept in Equation (1), DR at the cone tip can be evaluated using dynamic signals. Previous studies have proposed various DR evaluation methods, such as the F2, F-V, and F methods (Kim et al., 2021), as follows:

$$DR_1 = \frac{1}{A} \times \frac{1}{\int_0^t V\,dt} \times \left(\frac{c}{AE} \int_0^t F^2\,dt \right) \tag{2}$$

$$DR_2 = \frac{1}{A} \times \frac{\int_0^t F \times V\,dt}{\int_0^t V\,dt} \tag{3}$$

$$DR_3 = \frac{1}{A} \times \frac{\int_0^t F\,dt}{\Delta t} \tag{4}$$

where F, V, t, c, and E denote the force from the strain gauges, the particle velocity from the accelerometer, time, wave velocity, and Young's modulus, respectively. Typical dynamic signals calculated using the three methods are presented in Figure 2.

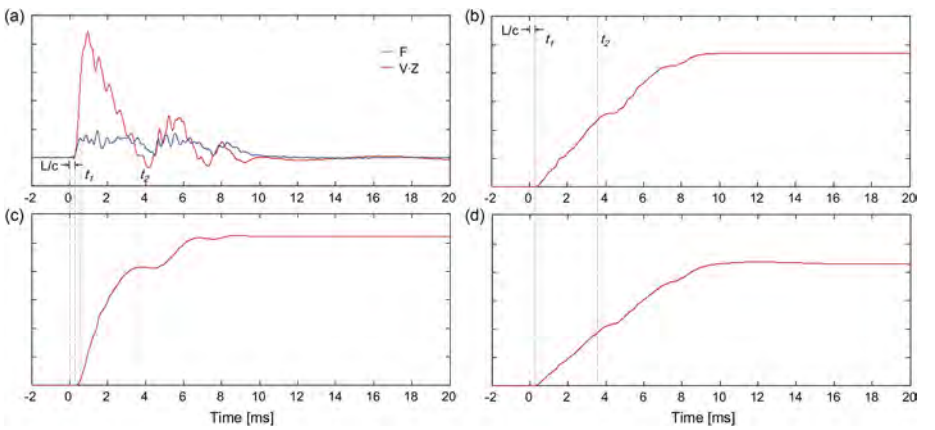

Figure 2. Typical dynamic signals: (a) force-velocity; (b) force square integration; (c) transferred energy; (d) force integration (Kim et al., 2021).

In Figure 2, t_1 and t_2 correspond to L/c and first zero velocity at the cone tip, respectively. Based on the time determination, the F^2, F-V method, and F methods were compared.

The comparative test results show that the relationship between the DRs and estimated t_1 and t_2 using the identical integration method provides an insignificant trend. Among the DR evaluation methods, the F-V method and F–methods present well-matched correlations when t_2 is selected. Compared to the DR estimated by the potential energy method, the F-V and F methods with t_2 show a proportional trend with a high determinant coefficient. For a smaller driving rod length, the F-V method and F methods with t_2 are efficient in acquiring more reliable layer profiles because t_1 is extremely small. Considering the integration interval

effect of the dynamic response obtained from the accelerometer, the F method can be effectively used for DR estimation using IDCP, as previously adopted by Lee et al. (2019).

Laboratory and field tests were conducted to investigate the performance of the IDCP. Byun and Lee (2013) performed lab-scale dynamic cone penetration tests using an IDCP, as shown in Figure 3(a). Weathered soils were compacted in a square-shaped chamber at a depth of 1 m, with two steel pipes grouted with mortar embedded in the compacted soil. The test results showed that the transferred energy at the cone tip was smaller than that at the rod head, regardless of the penetration depth. The energy-corrected cone tip resistances showed better detection of the erratic layers in stiff soils, for which the DCPI may not have been detected. Lee et al. (2019) also used IDCP for dynamic cone penetration tests in a square-shaped chamber filled with soils with three different dry unit weights. The IDCP shows the power function relationship between the DR and DCPI. For stiff soil, the DR varied more sensitively with soil strength than the DCPI. Byun et al. (2014) applied the IDCP to evaluate the strength variation and thickness of the active layer in the Arctic region (see Figure 3(b)).

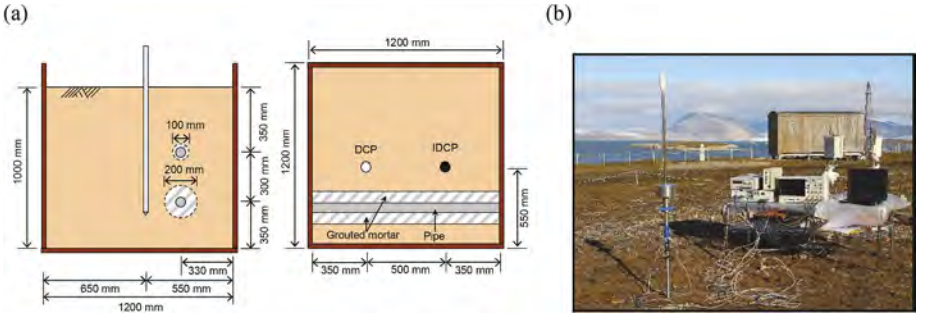

Figure 3. Dynamic cone penetration tests using the IDCP applied in (a) rectangular container and (b) field (Byun and Lee, 2013; Byun et al., 2014).

An in situ modulus detector (IMD) was developed to evaluate the resilient moduli of the subgrades based on the same instrumentation as the IDCP (Byun and Kim, 2022; Kim et al., 2022b). Unlike the IDCP, a rubber buffer was placed on the anvil of the IMD to apply dynamic loads to the subgrade and minimize high-frequency noise in the dynamic signals, as shown in Figure 4. The IMD can provide the resilient modulus profile of the subgrade, which can be affected by hammer drop height, water content, and soil density.

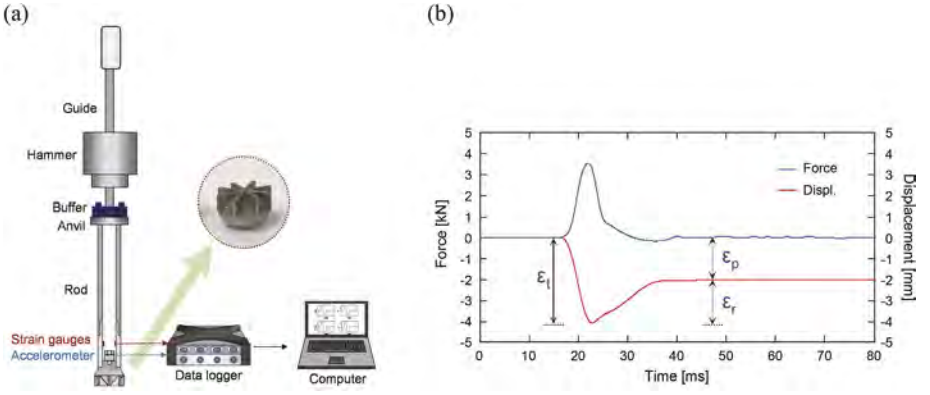

Figure 4. Resilient modulus estimation: (a) in-situ modulus detector; (b) typical tip response (Byun and Kim, 2022; Kim et al. 2022b).

3 LARGE-SCALE INSTRUMENTED PENETROMETERS

3.1 *Device*

The cone tip and rod head of the large-scale IDCP have the same outside diameter of 44.5 mm, and each component includes an accelerometer with a maximum amplitude of 100,000 g and four strain gauges with a resistance of 350 Ω, as shown in Figure 5(a) and (b). Pile driving analyzer (PDA) sensors were installed on the rod head to verify the sensors mounted at the cone tip. Based on the wave propagation, the dynamic response at the cone tip is detected later than that at the rod head, as shown in Figure 5(c).

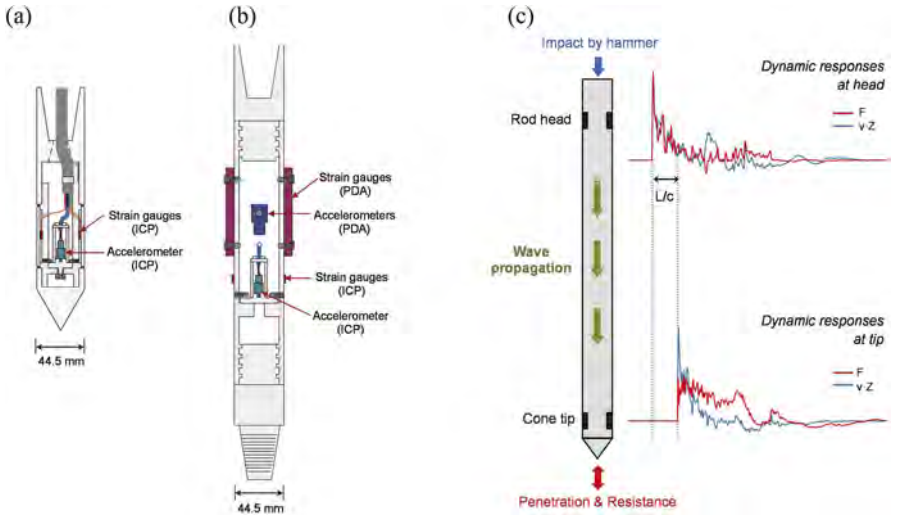

Figure 5. Schematic drawing of large-scale instrumented dynamic cone penetrometer: (a) cone tip; (b) rod head; (c) typical waveforms during driving (Lee and Byun, 2020).

3.2 *Experimental study*

Dynamic cone penetration tests using a large-scale IDCP were performed at two sites with different soil profiles (Lee and Byun, 2020). A previous study reported that the maximum transferred energy estimated at the rod head was the same for IDCP and PDA sensors, showing equally good performance. The force and velocity responses at the cone tip depend on the soil strength, and DR can be correlated with the DCPI and static cone resistance, as shown in Figure 6.

4 ENERGY MONITORING MODULE FOR SPT

4.1 *Device*

An energy-monitoring module was developed to improve the results of the standard penetration test (Hong et al., 2022). The measurement system of the energy-monitoring module is shown in Figure 7. The energy-monitoring modules are connected to the rod head and sampler to estimate the transferred energies. An accelerometer and load cell configured with four strain gauges were installed in the energy monitoring modules. The accelerometer and load cell signals were obtained using a data logger and analyzed using a laptop.

4.2 *Experimental study*

The standard penetration test with energy monitoring modules was conducted until a depth of 14 m (Park et al. 2022). The transferred energy ratios at the rod head and sampler were calculated

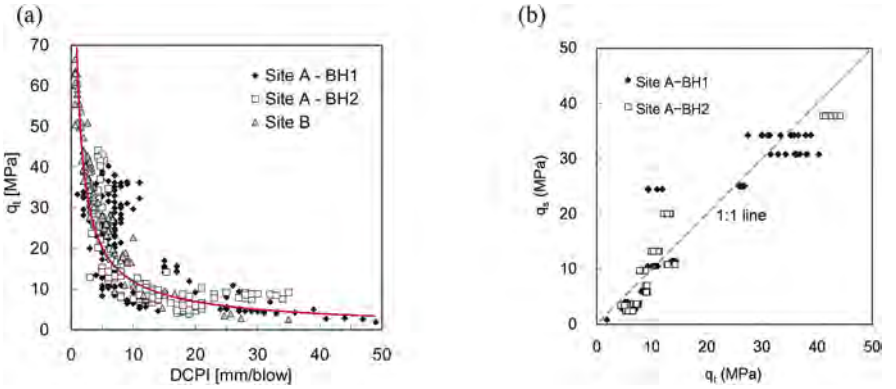

Figure 6. Correlation between the dynamic resistance and soil resistance indices: (a) dynamic cone penetration index; (b) static cone resistance (Lee and Byun, 2020).

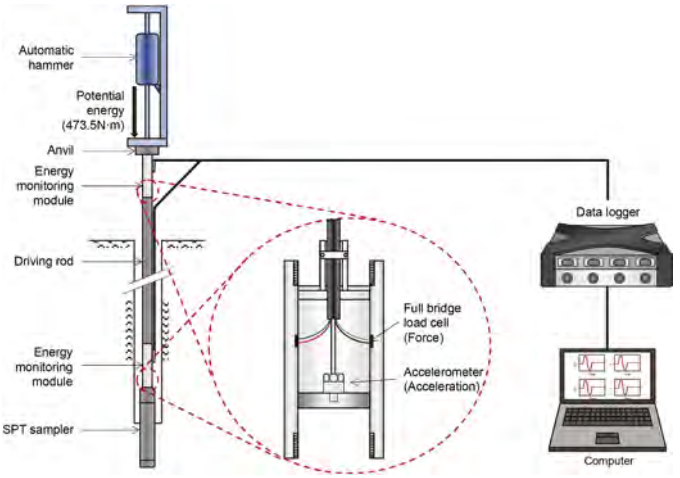

Figure 7. Schematic drawing of energy monitoring module for SPT energy measurement.

based on the potential energy (473.5 N·m) according to the depth, as shown in Figure 8. The average transferred energy ratio was 71.5% at the rod head and 48.2% at the sampler. The transferred energy ratios at the rod head and sampler generally decrease with increasing depth.

DR was calculated based on the energies transferred into the rod head and sampler to estimate the accuracy of the transferred energy ratios. DR is the work done against soil during penetration; thus, the corrected cone tip resistance, which is the result of the cone penetration test, should be similar to the DR in sand. The DR calculated based on the transferred energies is plotted against the corrected cone tip resistance in Figure 8. The DR based on transferred energy into the sampler was more similar to the corrected cone tip resistance than that into the rod head.

5 SEISMIC DYNAMIC CONE PENETROMETER

5.1 *Device*

The seismic dynamic cone penetrometer (SDCP) is composed of a hammer with a weight of 118 N freely falling from a drop height of 575 mm, an extendible driving rod with a diameter of 20 mm, and a cone tip part with a diameter and apex angles of 24 mm and 60, respectively, as shown in Figure 9(a). In the cone tip part, a uniaxial accelerometer with a range of 10,000 g is installed and connected to the data logger.

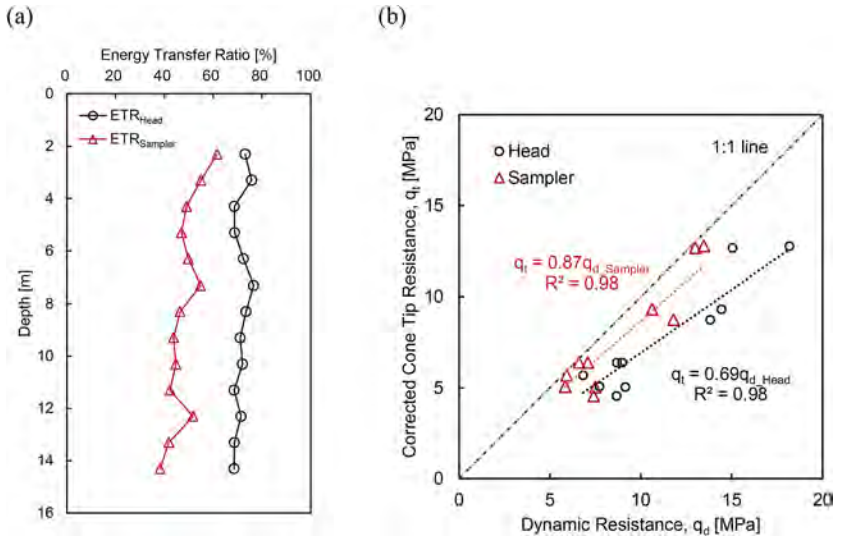

Figure 8. Test results of energy monitoring module in SPT: (a) Transferred energy ratios at the rod head and sampler according to the depth; (b) Relationships between corrected cone tip resistance and dynamic resistances (Park et al. 2022).

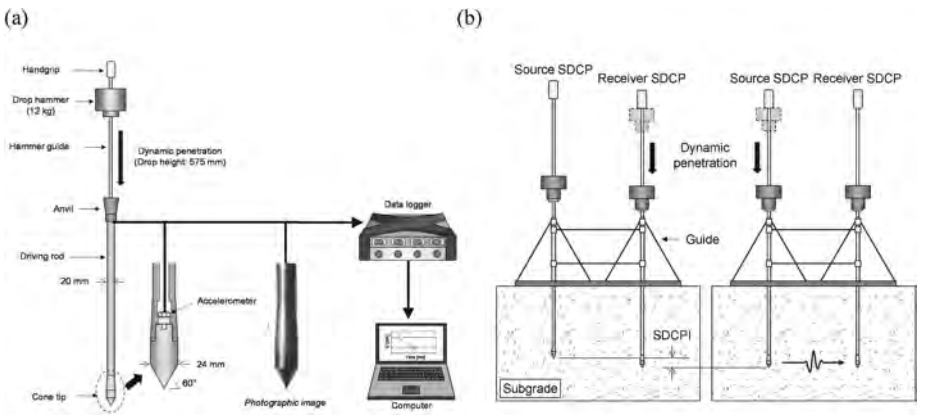

Figure 9. SDCP: (a) Schematic drawing; (b) Test procedure (Hong et al. 2017).

An SDCP test was conducted using two SDCPs. One of the SDCPs generates a seismic wave (source SDCP) while the other SDCP measures the seismic wave (receiver SDCP). The procedure for the SDCP test is illustrated in Figure 9(b). The source and receiver SDCPs and a guide for the vertical alignment of the SDCPs are located on the ground surface, and the receiver SDCP penetrates the ground to the target depths for stiffness evaluation. After the penetration of the receiver SDCP, the dynamic penetration of the source SDCP was conducted while simultaneously recording the blow counts and penetration depths. The recorded blow counts and penetration depths were used to calculate the seismic dynamic cone penetration index (SDCPI) using Equation (5), which indicates the strength characteristics of the target ground:

$$SDCPI\,[mm/blow] = D_{n+1} - D_n \tag{5}$$

where D_{n+1} and D_n are the penetration depths at the $n+1^{th}$ and n^{th} blow counts, respectively.

When the penetration depth of the source SDCP was similar to that of the receiver SDCP, accelerations were measured using both SDCPs during the dynamic penetration of the source

SDCP. The accelerometer in the source SDCP detects the time of hammer impact, which can be considered the generation time of the seismic wave, and the accelerometer in the receiver SDCP measures the seismic wave propagating in the ground. Note that the uniaxial accelerometer was vertically installed in the cone tip part; thus, the seismic wave measured using the receiver SDCP gathered the shear wave corresponding to the shear wave.

The travel time of the shear wave (Δt) is the time difference between the first arrival time of the shear wave and the generation time of the seismic wave as determined by the SDCPs. Therefore, the shear wave velocity (V_s) can be calculated using Equation (6)

$$V_s\,[m/s] = \frac{L}{\Delta t} \tag{6}$$

where L is the distance between the source and receiver SDCPs. Accordingly, the stiffness of the target ground can be profiled based on V_s by adjusting the depths of the SDCPs.

To verify the SDCP test, V_s was measured using both SDCP and bender elements (BE) in a laboratory chamber test, as shown in Figure 10(a). V_s evaluated using the SDCP is directly proportional to that measured by the BE, as shown in Figure 10(b). Therefore, it is considered that the SDCP test produces a reliable V_s profile for the target ground.

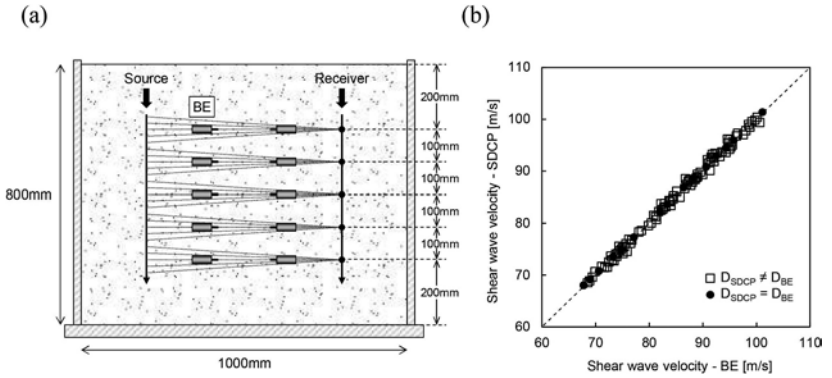

Figure 10. Calibration tests: (a) Schematic drawing of chamber; (b) Shear wave velocity comparison.

5.2 *Experimental study*

For the application of the SDCP, the SDCP test was conducted on a compacted subgrade located in the Republic of Korea (Lee et al., 2021). The distance between the sleeves of the source and receiver SDCPs was set as 576 mm. The receiver SDCP penetrated to a depth of 1,000 mm with a depth interval of 100 mm, and the source SDCP penetrated to a depth of 1,080 mm. Based on the experimental results, the penetration index (SDCPI) and V_s were profiled with depth. In addition, the maximum shear modulus was estimated based on V_s and the density of the subgrade, as shown in Figure 11.

The experimental results show that the SDCPI is measured as 5–7 mm/blow within a depth range of 50–880 mm, and significantly decreases and converges to approximately 2 mm/blow from a depth of 900 mm. V_s was evaluated to be approximately 169 m/s at a depth of 100 mm and gradually increased to 254 m/s at a depth of 800 mm. From a depth of 900 mm, V_s dramatically increases and is approximately 336 m/s at a depth of 1,000 mm, which corresponds to the strength characteristics estimated based on the penetration index.

6 SUMMARY AND CONCLUSIONS

As the test results of dynamic penetrometers are easily affected by energy loss, an innovative method such as an energy monitoring module is required. An energy-monitoring module,

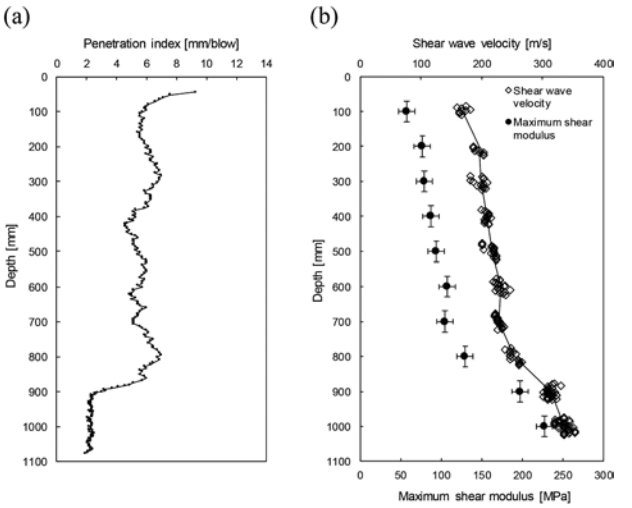

Figure 11. Test results of SDCP: (a) penetration index; (b) Shear wave velocity and modulus.

configured with an accelerometer and load-cell four strain gauges, was installed at the cone tip or near the sampler. The summary and main observations of the new in situ dynamic tests are as follows:

- The instrumentation at the cone tip of the IDCP can provide the force and velocity responses during driving and enable the estimation of the dynamic resistance (DR) suggested as a new soil strength index. Laboratory and field application tests showed that the DR estimated using the IDCP can be used to reliably characterize the soil strength instead of the DCPI. Furthermore, the same instrumentation, with the addition of a buffer to the IDCP device, can provide a resilient modulus estimation of compacted soils.
- The large-scale IDCP showed strong correlations between the DR, DCPI, and static cone resistances. Therefore, the large-scale IDCP and its DR estimation may be used effectively for characterizing dense layers, especially where low DCPI and high static cone resistance occur.
- An energy-monitoring module was developed to correct the standard penetration test. The transferred energies into the rod head and sampler were calculated using the energy monitoring module. Compared with the cone penetration test, the transferred energy into the sampler was more similar to the actual penetration energy than that into the rod head. Therefore, the energy-monitoring module can be effectively used for energy correction in standard penetration tests.
- A seismic dynamic cone penetrometer (SDCP) was developed to characterize the stiffness and strength of the target ground. The SDCP evaluates strength and stiffness based on the penetration index (SDCPI) and shear wave velocity (Vs). The Vs evaluated by the SDCP was verified via comparative analyses with those measured using bender elements, and the applicability of the SDCP was successfully tested in the field test. Therefore, SDCP may be an effective testing method for the investigation of both strength and stiffness of the target ground.

Considering in-situ dynamic penetrometers instrumented with accelerometers and loadcells provided insightful resistances or shear wave velocity profiles, they could be used effectively for subsurface characterization.

ACKNOWLEDGMENTS

This work was supported by a National Research Foundation of Korea (NRF) grant funded by the Korean government (MSIT) (No. NRF-2021R1A5A1032433).

REFERENCES

ASTM D4633, 2005. Standard Test Method for Energy Measurement for Dynamic Penetrometers. ASTM standard D4633-05, *American Society for Testing and Materials*, West Conshohocken, Pa.

ASTM D6951, 2009. Standard Test Method for Use of the Dynamic Cone Penetrometer in Shallow Pavement Applications. ASTM standard D6951, *American Society for Testing and Materials*, West Conshohocken, Pa.

Byun, Y.H. and Kim, D.J. 2022. In-situ modulus detector for subgrade characterization. *International Journal of Pavement Engineering*, 23(2): 297–307.

Byun, Y.H. and Lee, J.S. 2013. Instrumented Dynamic Cone Penetrometer Corrected with Transferred Energy into a Cone Tip: A Laboratory Study. *Geotechnical Testing Journal*, 36(4): 533–542.

Byun, Y.H., Yoon, H.K., Kim, Y.S., Hong, S.S., and Lee, J.S. 2014. Active layer characterization by instrumented dynamic cone penetrometer in Ny-Alesund, Svalbard. *Cold Regions Science and Technology*, 104: 45–53.

Clark, M., McCann, D.M., and Forde, M.C. 2002. Infrared Thermographic Investigation of Railway Track Ballast. *NDT&E International*, 35: 83–94.

DeJong, J.T., Ghafghazi, M., Sturm, A.P., Wilson, D.W., Dulk, J.D., Armstrong, R.J., Perez, A., and Davis, C. A. 2017. Instrumented Becker penetration test. I: Equipment, operation, and performance. *J. Geotech. Geoenviron. Eng*, 143(9): 04017062.

Hong, W.T., Byun, Y.H., Kim, S.Y., and Lee, J.S. 2016. Cone Penetrometer Incorporated with Dynamic Penetration Method for Investigation of Track Substructure. *Smart Structures and Systems*, 18(2): 197–216.

Hong, W.T., Kang, S., Lee, S.J., and Lee, J.S. 2018. Analyses of GPR signals for characterization of ground conditions in urban areas. *Journal of Applied Geophysics*, 152: 65–76.

Hong, W.T., Kim, S.Y., and Lee, J.S. 2022. Evaluation of driving energy transferred to split spoon sampler for accuracy improvement of standard penetration test. *Measurement*, 188: 110384.

Hong, W.T., Kim, S.Y., Lee, S.J., and Lee, J.S. 2017. Strength and stiffness assessment of railway track substructures using crosshole-type dynamic cone penetrometer. *Soil Dynamics and Earthquake Engineering*, 100: 88–97.

Kim, S.Y. and Lee, J.S. 2020. Energy correction of dynamic cone penetration index for reliable evaluation of shear strength in frozen sand–silt mixtures. *Acta Geotechnica*, 15: 947–961.

Kim, S.Y., Hong, W.T., and Lee, J.S. 2019. Role of the Coefficient of Uniformity on the California Bearing Ratio, Penetration Resistance, and Small Strain Stiffness of Coarse Arctic Soils. *Cold Regions Science and Technology*, 160: 230–241.

Kim, S.Y., Kim, D.J., Lee, J.S., Kang, T. H.-K., and Byun, Y.H. 2022-a. Resilient modulus estimation using in-situ modulus detector: Performance and factors. *International Journal of Pavement Engineering*, 23(9): 1–13.

Kim, S.Y., Lee, J.S., and Hong, W.T. 2021. Subgrade assessment using automated dynamic cone penetrometer to manage geo-infrastructures. *Smart Structures and Systems*, 27(5): 861–870.

Kim, S.Y., Lee, J.S., Kim, D.J., and Byun, Y.H. 2021. Comparative Study on Estimation Methods of Dynamic Resistance Using Dynamic Cone Penetrometer. *Sensors*, 21(9): 3085.

Kim, S.Y., Lee, J.S., Tutumluer, E., and Byun, Y.H. 2022-b. Dynamic response of free-end rod with consideration of wave frequency. *Geomechnaics and Engineering*, 28(1): 25–33.

Lee, C., Kim, K. S., Woo, W., and Lee, W. 2014. Soil Stiffness Gauge (SSG) and Dynamic Cone Penetrometer (DCP) tests for estimating engineering properties of weathered sandy soils in Korea. *Engineering Geology*, 169: 91–99.

Lee, J.S. and Byun, Y.H. 2020. Instrumented Dynamic Cone Penetrometer for Dense Layer Characterization. *Sensors*, 20(20): 5782.

Lee, J.S., Kim, S.Y., Hong, W.T., and Byun, Y.H. 2019. Assessing subgrade strength using an instrumented dynamic cone penetrometer. *Soils and Foundations*, 59: 930–941.

Lee, J.S., Tutumluer, E., and Hong, W.T. 2021. Stiffness evaluation of compacted geo-materials using crosshole-type dynamic cone penetrometer (CDP), rPLT, and LFWD. *Construction and Building Materials*, 303: 124015.

Lukiantchuki, J. A., Bernardes, G. P., and Esquivel, E. R. 2015. Efficiency in standard penetration test. *Geotechnical Engineering for Infrastructure and Development*, 6: 2981–2985.

Lukiantchuki, J. A., Bernardes, G. P., and Esquivel, E. R. 2017. Energy ratio (ER) for the standard penetration test based on measured field tests. *Soils and Rocks*, 40(2): 77–91.

Mohammadi, S. D., Nikoudel, M. R., Rahimi, H., and Khamehchiyan, M. 2008. Application of the Dynamic Cone Penetrometer (DCP) for determination of the engineering parameters of sandy soils. *Engineering Geology*, 101(3-4): 195–203.

Park, G., Kim, N., Hong, W.T., and Lee, J.S. 2022. Estimation of Rod Effects on Transferred Energy into Sampler using Smart Measurement System. *Smart Structures and Systems*, 30(2): 159–172.

Smart Geotechnics for Smart Societies – Zhussupbekov, Sarsembayeva & Kaliakin (Eds)
© 2023 The Author(s), ISBN 978-1-003-29912-7
Open Access: www.taylorfrancis.com, CC BY-NC-ND 4.0 license

Contributions of physical modeling and numerical analysis to seismic behavior of reinforced soil retaining structures

Hoe I. Ling
Columbia University, New York, NY, USA

Dov Leshchinsky
University of Delaware, Newark, Delaware, USA
ADAMA Engineering, Clackamas, Oregon, USA

ABSTRACT: This paper summarizes several studies that the authors have been involved in the field of physical modelings and associated finite element analyses for reinforced soil retaining walls under static and earthquake loadings. Full-scale and centrifuge model tests were considered as benchmarks for verifying the numerical models. Material models of different complexities were developed in simulating the monotonic and cyclic behavior of soils and geosynthetic materials. The calibrations of the models and details of finite element analysis were presented. The responses, such as accelerations, wall deformations and geogrid tensile forces obtained from the analyses were compared with the experimental results. The analyses were able to reproduce many aspects of seismic behavior of reinforced soil retaining walls.

1 INTRODUCTION

The conventional design of geosynthetic-reinforced soil retaining walls (GRSRW) has been based on force equilibrium analysis where internal and external stabilities are examined (e.g., Leshchinsky et al., 1995, 2014). The seismic design of GRSRW involves an extension of the static force equilibrium analysis, with the earthquake inertia force considered as a pseudo-static event (Bathurst and Cai, 1995; Ling et al., 1997; Ling and Leshchinsky, 1998; Tatsuoka et al., 1998). The time history of the input motions and its amplifications are not accounted for in a pseudo-static analysis. Moreover, the effects of repeated loadings on the soil behavior cannot be considered through a pseudo-static analysis. Although Ling et al. (1996) proposed a simplistic method that used permanent-displacement limit for design, rigid body motions of reinforced soil typically may not occur during earthquakes.

The use of numerical tools, such as finite element procedures, incorporated with robust soil constitutive models aided to the understanding of the behavior of GRSRW. The past several decades have witnessed a tremendous growth in the applications of finite element method to geotechnical problems involving primarily monotonic loading conditions. Recently, dynamic analyses considering earthquake loading have become feasible. In such analyses, advanced elasto-plastic model is a must for considering realistically the soil behavior subjected to cyclic loading. Several dynamic finite element studies have been reported for reinforced soil retaining walls, but they are based on equivalent linear analyses (Segrestin and Bastick, 1988; Yogendrakumar et al., 1992; Cai and Bathurst, 1995; Helwany et al., 2001).

In this paper, finite element simulations were conducted on a concrete block GRSRW under static loading, and centrifuge models and full-scale GRSRW under earthquake loading. Advanced constitutive models for soils and polymeric reinforcement materials were adopted. The advanced soil models were generalized plasticity model (Ling and Liu, 2003) and unified

DOI: 10.1201/9781003299127-7

generalized plasticity model (Ling and Yang, 2006), which was based on the critical state concept and that considered both the effects of pressure level and density. The physical models, constitutive models, and numerical procedures are summarized in this paper. The results of simulations are presented, compared and discussed.

2 STATIC ANALYSIS: PWRI WALL

A well instrumented full-scale reinforced soil retaining wall that has a block-type facing is selected for comparing a simplistic analysis with an advanced analysis. In the simplistic analysis, the hyperbolic soil and reinforcement models are used with 4-node soil elements. In the advanced analysis, sophisticated plasticity soil and reinforcement models were considered. The wall is first described followed by the descriptions of material models and analysis.

2.1 *Descriptions of test wall and instrumentations*

The wall was constructed and instrumented by the Public Works Research Institute (PWRI) in Tsukuba, Japan. Basic information of PWRI Wall has been reported by Tajiri et al. (1996). The geometry of the wall is shown in Figure 1. It was 6 m high, constructed directly on a concrete floor inside a test pit. A silty sand (mean grain diameter: 0.42 mm) was used as backfill. A uniaxial high-density polyethylene (HDPE) geogrid was used as reinforcement. The strength of the geogrid was 55 kN/m. The wall was constructed using six primary and five secondary geosynthetic layers, each 3.5 m and 1.0 m long, respectively. The geosynthetic layers were bolted to the concrete modular blocks using the nuts and metal frame. A total of 12 concrete blocks were used, each 50 cm high and 30 cm wide, except the top and bottom blocks which were 45 and 55 cm high, respectively.

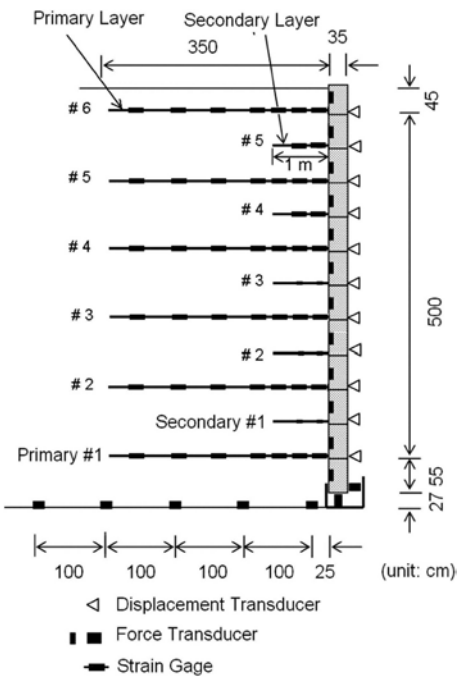

Figure 1. Wall instrumented by PWRI, Japan.

Table 1. Material properties used in simplistic finite element analysis of PWRI Wall.

Soil						
γ (kN/m^3)	ϕ_o (°)	$\Delta\phi$ (°)	K	m	R_f	ν
16.0	45	5	207.2	0.5	0.81	0.42

Concrete			
	γ (kN/m^3)	E (kPa)	ν
Concrete Foundation	-	2.0x10^6	0.17
Modular Block	23	2.0x10^6	0.17

Geogrid Reinforcement		
J_o (kN/m)	T_f (kN/m)	λ
826.45	54.6	0.47

Interfaces		
	δ (°)	T_c (kN/m)
Concrete-Concrete (no slippage)	45	50
Concrete-Concrete (slippage)	19.6	0.5
Concrete -Soil (with Geogrid)	16.5	55
Concrete-Soil only	16.5	0.5

A total of 52 strain gages were used to measure the elongation of the geogrid. The horizontal displacement of the wall face was measured at 12 locations along the height. The lateral force acting on the facing blocks was measured using 11 force transducers. The vertical and horizontal forces acting at the toe of the facing were also measured. The vertical force due to the weight of the backfill soil was measured at 6 locations along the base of the backfill.

2.2 *"Simplistic" finite element analysis*

The "simplistic" analysis has been presented in Ling et al. (2000) using the finite element program M-CANDE (Ling and Tatsuoka, 1992; Ling et al., 1995; Ling and Leshchinsky, 2003), which was modified from program CANDE (Katona et al., 1976). The program simulates time-independent behavior under two-dimensional plane strain conditions. The construction sequence, and inclusion of reinforcement and interface elements was simulated incrementally, and each increment of analysis was iterated until the solution converged at the element level. A nonlinear geosynthetic model was added to CANDE following previous analyses of reinforced soil structures. The soil behavior was expressed using a nonlinear elastic soil model (Duncan and Chang, 1970; Duncan et al., 1980), which has also been used by a number of researchers (see review in Ling and Liu, 2009).

The foundation, backfill and facing blocks were represented by 4-node quadrilateral elements. The two-node beam elements without flexural rigidity were used to represent geosynthetic layers. The interface elements were used to simulate the interactions between different materials at the wall facing. The wall construction consisted of a total of 38 increments. Compaction was not included in the construction simulation.

The nonlinear elastic geosynthetic model is given by Ling et al. (1995). The tangent stiffness J_{tan} is obtained from a hyperbolic load-strain (T - ε) relationships:

$$J_{\tan} = J_o(1 - \lambda\frac{T}{T_f})^2 \tag{1}$$

where J_o, T, T_f and λ are the initial stiffness, reinforcement load, failure strength and failure ratio, respectively.

The 3-node interface element (Katona, 1983) was used in M-CANDE. It was formulated from the constraint approach, and is numerically more stable than the commonly used Goodman interface element, which is based on the stiffness method. The mid-node is used to store the energy of the element during computation. Because of the node-to-node contact assumed in the interface element, the connection strength between the geosynthetic and modular blocks could be simulated using the interface tensile strength.

A linear elastic model was used for the foundation and concrete blocks. The parameters for the soil, concrete and geosynthetic are summarized in Table 1. The comparison between the experimental and fitted results of hyperbolic relationships is given in Ling et al. (2000).

2.3 *"Sophisticated" finite element analysis*

The sophisticated finite element analysis was conducted under two-dimensional plane strain conditions using a modified version of Diana-Swandyne-II (Chan, 1993; Zienkiewicz et al., 1998). Both higher order elements and material models were used in the analysis. The finite element algorithms were modified to also handle the construction sequence together with additional material and element models (Liu, 2003). The soil consisted of 8-node quadrilateral elements and 6-node triangular elements, both calculated using full integration technique (9-point and 6-point integrations, respectively). The geogrid layer was simulated using 3-node one-dimensional elements. A total of 38 increments were used to simulate wall construction. The solution was obtained using a quasi-Newton-Raphson nonlinear iteration scheme. The stiffness matrix was updated every 10 steps and a total of 500 steps was used in each increment with a convergence tolerance of 0.003.

2.3.1 *Generalized plasticity soil model*

A generalized plasticity soil model (Ling and Liu, 2003), which was an improvement over Pastor-Zienkiewicz-Chan model (Pastor et al., 1990), was used to express the soil behavior. Generalized plasticity does not require a prescribed yield surface but uses loading direction vectors for determining the plastic strain increments. Ling and Liu (2003) considered the pressure-level dependency of the stiffness, dilatancy and strength of the sand in the model. The model has been validated against the laboratory test results of several types of sand having different relative densities and under drained and undrained conditions. For the formulation and notations of the model, refer to Ling and Liu (2003).

The generalized plasticity model requires 15 parameters for simulating cyclic loading, whereas 11 are needed for monotonic loading. Table 3 summarizes the parameters and respective values for the backfill sand. Figure 2 shows the comparison between the experimental and simulated results. The model was able to simulate the pressure-dependent stress-strain-dilatancy behavior satisfactorily.

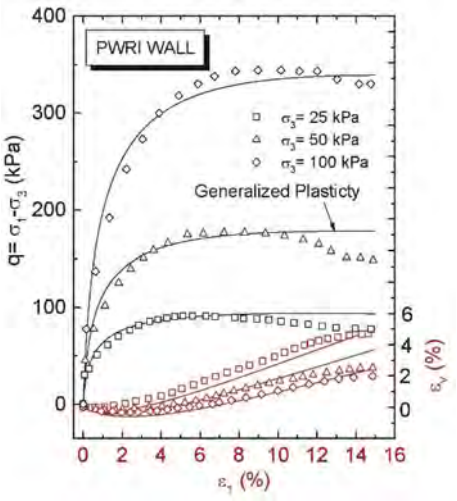

Figure 2. Simulation of backfill sand (PWRI wall) by generalized plasticity model.

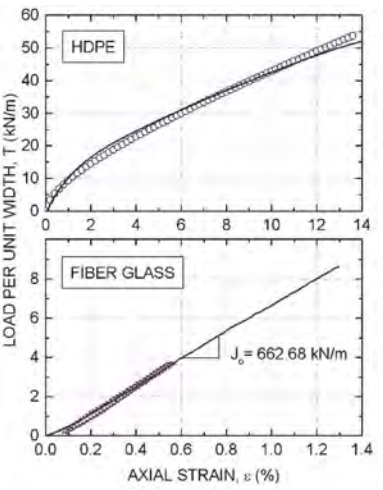

Figure 3. Simulation of HDPE and fiber glass reinforcements by bounding surface model.

2.3.2 *Reinforcements*

Ling et al. (2001) formulated a bounding surface model to simulate the uniaxial cyclic behavior of geogrids. The main features of formulation are:

Total stiffness

$$J_T = \frac{J_p J_e}{J_p + J_e} \tag{2}$$

Bounding line for monotonic loading

$$T_+ = A + J^o_{P+}\, \varepsilon_p \tag{3}$$

Hardening parameters for monotonic loading

$$h^L = h^L_o + h^L_k \sqrt{\varepsilon_p} \tag{4}$$

A total of 9 parameters are required for cyclic loading, whereas in the case of monotonic loading, it is reduced to 5 parameters. For HDPE geogrid (unit: kN/m), *Je* = 2500, A = 28.5, $J^o_{P+} = 2810$, $h^L_o = 150$ and $h^L_k = 900$, where *Je* is the elastic stiffness, A and J^o_{P+} are used to define the bounding line, and h^L_o and h^L_k are for the hardening parameters during loading. Figure 3 shows the results of simulation and comparison with the test results for HDPE geogrid.

2.3.3 *Concrete blocks, interfaces and other materials*

The concrete blocks were assumed linear elastic with typical properties: $E = 2.0\times10^6$ kPa, $\nu = 0.17$, $\gamma = 23$ kN/m^3. The block-block and soil-block interactions were studied using large-scale direct shear tests, from which the interface friction angles were obtained as $\delta = 19.6°$ and 16.5°, respectively (Table 1). The interface between geogrid and sand was modeled for several cases of analysis using a thin interface element. This thin layer element had an elastic (expressed using Young's modulus and Poisson's ratio) followed by a rigid-plastic sliding behavior (expressed using an angle of friction). The elastic properties of the interface were $E = 5{,}000$ kPa and $\nu = 0$. Since the geogrid layers were bolted to the blocks, the connection strength was assumed to be the failure strength of the geogrid and simulated using elastic perfectly plastic interface model. The angle of friction between the soil and geogrid was larger than that of the block-block, block-geogrid and block-soil. The relative displacement should occur between these interfaces before an opportunity for pullout will occur between the soil and geogrid, thus the geogrid layers were assumed to be fully compatible with the soil deformation.

2.4 *Comparison of results*

2.4.1 *Horizontal displacements*

The horizontal displacements of the wall obtained from the analyses are compared with the measured results for the different fill heights during the course of construction (Figure 4). Note that each concrete block was represented by three elements in the analysis, thus the results appeared clustered in sets of three. The measured and analyzed results agreed favorably for the construction height 4 m and above. The trend of deformation is well replicated. It is of interest to see that the results obtained from the simplistic and sophisticated analyses are close to each other, although the results obtained from generalized plasticity model were slightly larger than those of the hyperbolic model.

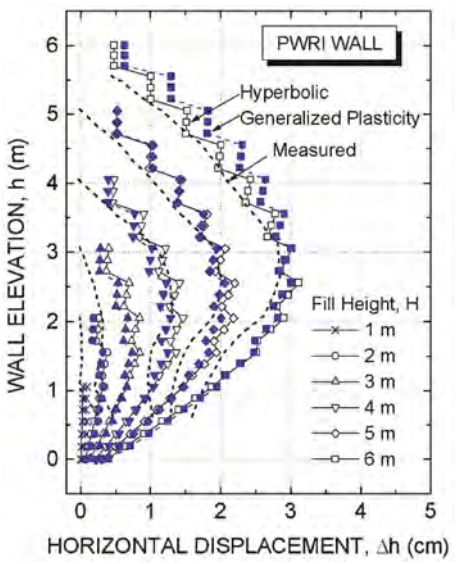

Figure 4. Wall facing block displacements.

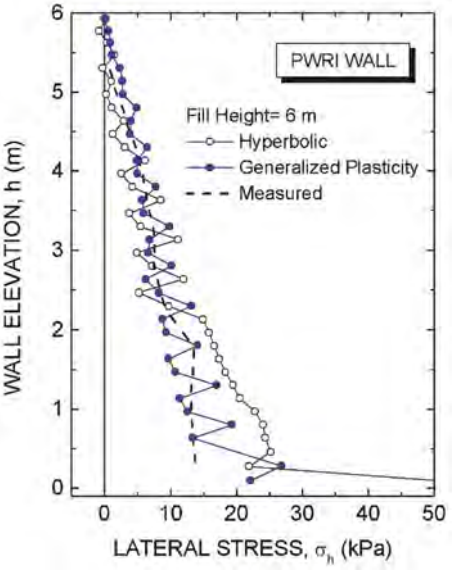

Figure 5. Lateral stress behind the blocks.

2.4.2 *Lateral stress*

The lateral stress distributions behind the blocks at end of construction are shown in Figure 5. The experimental results were obtained from the force transducers, of diameter 20 cm, installed at the backfill side of the blocks. For the plasticity model, the results at different elevations were obtained by averaging the values obtained from the 9 gauss points in the interface elements. The values differed within a soil element, whereas the values obtained from the integration points in the soil element located near to the blocks are close to the average value of the interface elements. The distributions obtained from the analyses are close to the measured values. The results of simplistic and sophisticated analyses fluctuated along the wall height, but the distribution obtained from the nonlinear elastic model is slightly larger than that of the generalized plasticity model toward the bottom of the wall.

2.4.3 *Geogrid tensile strains*

The strain distributions in the six primary geogrid layers, with layer 1 located at the bottom and layer 6 at the top, are shown in Figure 6 for the wall at its completed height. It is seen that the analyzed and measured results gave good agreement. The difference in results at the front end of the reinforcement layers could be attributed to the possible stress concentration due to relative settlement (overhanging) and creep in the geogrid that were not accounted for in the presented study. For the sophisticated analysis, the results at the back of the reinforcement were relatively well simulated. There is only slight difference between the results obtained from the nonlinear elastic analysis and sophisticated analysis. The sophisticated analysis gave larger strain for the bottom reinforcement layers compared to simplistic analysis, and it was the reverse for the top layers, for both primary and secondary reinforcement layers.

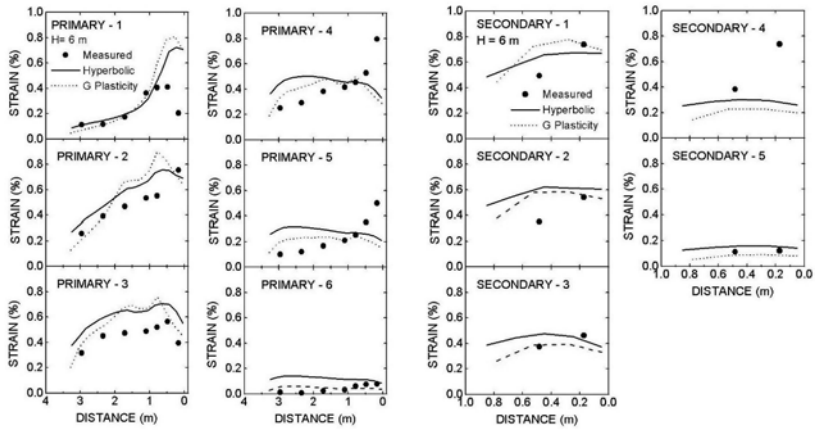

Figure 6. Strains in the geogrid layers.

3 DYNAMIC CENTRIFUGE MODEL TESTS

3.1 *Centrifuge models and instrumentations*

A total of five dynamic centrifuge tests of geosynthetic-reinforced soil retaining walls were conducted using the facilities available at the Tokyo Institute of Technology (Takahashi et al., 1999; Takemura and Takahashi, 2003). The models were 15 cm high that represented a prototype wall of height H= 7.5 m under 50-g acceleration.

The model wall was 21.5 cm long and had a 5-cm deep foundation (Figure 7). The wall model was constructed in an aluminum container having inner dimensions 45 cm (length) × 15 cm (width) × 25 cm (height). The side walls of the container were detachable. Rubber forms were used at the two ends of the model as boundary wave absorber. Note that the curvature of the wall crest surface was introduced to accommodate for the centrifugal acceleration field that varied across the length of model due to the inflight orientation of the centrifuge platform and

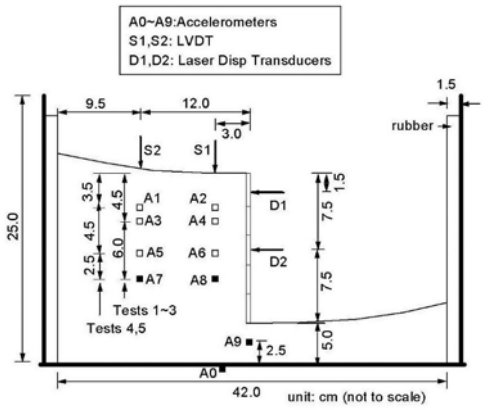

Figure 7. Centrifuge model setup and instrumentations.

Table 2. Reinforcement layout for centrifuge tests.

Test #	Length	Spacing
1	1.0H	0.2H
2	0.8H	0.2H
3	0.6H	0.2H
4	0.8H	0.1H
5	0.6H	0.1H

container. Geosynthetic reinforcement of different lengths (0.6H, 0.8H, 1.0H) and vertical spacings (0.1H, 0.2H) were used. Table 2 summarizes the reinforcement layouts for the tests.

The construction sequence of the reinforced soil wall, such as placement of backfill, geogrid, wall facing and compaction, was not modeled in-flight. In fact, such a modeling technique was found reasonable for earthquake loading where the dynamic effects are more significant than the static effects. The wall model was prepared under 1-g conditions at an upside-down position by first laying down the wooden template in order to produce a curved backfill that met the orientation of the box in the centrifuge. The moist sand with the geogrids and accelerometers were introduced into the box and compacted statically in layers to the required density using a bellofram cylinder. The geogrid layers were attached to the aluminum facing panels of thickness 2 mm. The plates were hinged. At the end of construction, the bottom platen of the box was installed and the container was reversed to the upright position. The top plate was then removed and the displacement transducers were installed in front of the facing and along the wall crest.

A limited number of accelerometers, displacement transducers and strain gages were used because the small size of the model did not allow for intensive instrumentation compared to a full-scale model. In Tests 1-3, five accelerometers were used: two were in the unreinforced backfill (A3, A7) and reinforced soil zone (A4, A8), respectively, and one measured the acceleration in the foundation soil (A9). In Tests 4 and 5, three accelerometers were used in the unreinforced (A1, A5, A7) and reinforced (A2, A6, A8) soil zones, respectively. In addition, the horizontal displacements of the wall facing were measured using two laser displacement transducers (D1, D2) and the settlement of the wall crest was measured at two locations using linear variable displacement transducers (S1, S2). Three geogrid layers were instrumented with strain gages in each test. Four strain gages for each layer were used in Tests 1 and 2, whereas three strain gages were used in Test 3 (layers 1, 3, 5 from the bottom) and Tests 4 and 5 (layers 3, 6, 9 from the bottom). The first strain gage was located 15 mm from the back of the panel, and the other gages were 30 mm apart. However, as discussed later in the results, these strain gages could not measure accurately the strain of the reinforcement because the epoxy used was stiffer than the reinforcement.

The container with the model wall was mounted to the shaking table in the centrifuge. After bringing the centrifuge to 50-g acceleration, shaking was initiated using sinusoidal wave of 100 Hz (prototype frequency of 2 Hz). The input waves were of prototype accelerations 0.2g having 20 cycles of shaking (0.25 second or 12.5 seconds in prototype).

3.2 *Material models*

3.2.1 *Backfill soils*

Inagi sand (D_{50}= 0.4 mm, γ = 17.8 kN/m^3, C_u= 2.3) was used in the backfill and foundation. A generalized plasticity soil model as described in Section 2.3.1 (Ling and Liu, 2003) was used to express the soil behavior.

Two drained triaxial tests (σ_3= 100 kPa and 300 kPa) and a strain-control cyclic triaxial test (σ_3 = 100 kPa, stress amplitude = -50 ~ 85 kPa) were used to calibrate the model. Table 3 summarizes the parameters and respective values for the Inagi sand. Figure 8 shows the comparison between the experimental and simulated results under monotonic and cyclic loadings. The model was able to simulate the pressure-dependent stress-strain-dilatancy behavior satisfactorily.

3.2.2 *Reinforcements, aluminum panels and other materials*

The glass-fiber reinforcement exhibited linear elastic behavior with negligible hysteresis for 10 cycles of loadings (Figure 3), thus the load-strain relationship is defined by the elastic stiffness *Je* (=662.68 kN/m) when using the bounding surface model. The rubber foam and aluminum panel in the centrifuge models were assumed as linear elastic materials having elastic moduli E= 3,000 kPa and 7.0×10^7 kPa, respectively. The joint between the aluminum plates was modeled by assigning a small elastic modulus E= 10.0 kPa. The Poisson's ratios for the rubber, aluminum and panel joint were v= 0.5, 0.3 and 0.0, respectively.

Table 3. Parameters for sands (Generalized Plasticity Model).

	Parameters	PWRI Wall Sand	Centrifuge Inagi sand
ϕ_{p0} (°)	Peak value of the angle of internal friction at atmospheric pressure	39.4	33.0
$\Delta\phi$ (°)	Change of angle of internal friction with 10-fold increase in pressure	0.5	0
M_g	Slope of the critical state line in $p' - q$ plane	1.4	1.32
M_f	Slope of failure line in p'-q plane	0.645	0.4
G_0/p_a	Normalized Elastic modulus	500.0	800.0
K_0/p_a	Normalized bulk modulus	550.0	700.0
k_s	Parameter related to plastic coefficient	0.01	0.07
β_{10}	Parameter related to plastic coefficient	3.1	1.0
β_0	Parameters related to plastic coefficient	20.0	10.0
α	Parameter related to soil dilatancy	0.47	0.25
H_0/p_a	Normalized plastic modulus number	500.0	190.0
H_u0/p_a	Normalized unloading plastic modulus number	-	800.
r	Coefficient related to stress memory factor	-	3.2
r_u	Exponent related to unloading plastic modulus	-	0.0
r_d	Parameter related to densification in unloading plastic modulus	-	350.0

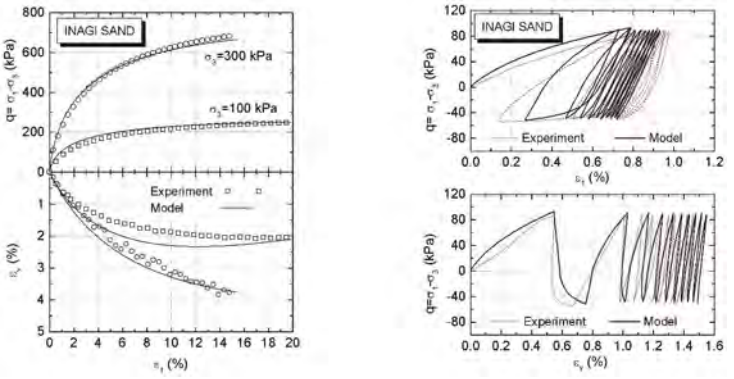

Figure 8. Monotonic and cyclic behavior of Inagi sand.

3.3 *Finite element simulations*

The finite element meshes for the centrifuge models were designed considering the different vertical reinforcement spacings and lengths used in each test. The soil consisted of 8-node quadrilateral elements and 6-node triangular elements, both calculated using full integration technique (9-point and 6-point integrations, respectively). The geogrid layer was simulated using 3-node one-dimensional elements. The base is assumed to be rough/rigidly and the two ends are smooth.

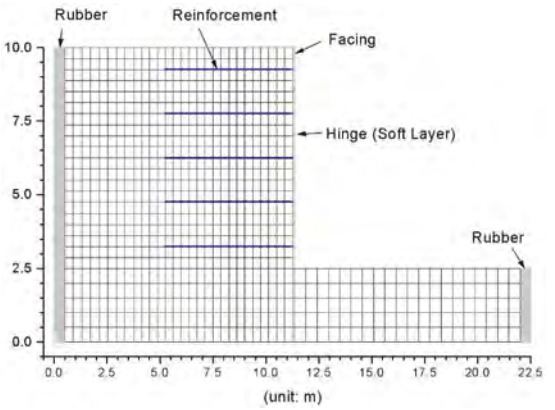

Figure 9. Finite element mesh (Test 3).

Figure 9 shows the mesh used for centrifuge Test 3. A total of approximately 1,000 elements were used, and the number differed slightly in each analysis because of the total number of layers of reinforcement and interfaces. A gravity turn-on analysis was first performed to obtain the initial stress conditions for the walls. The stresses at each Gauss point were used as the initial values for subsequent dynamic analysis. A nonlinear elastic model, whose shear modulus is dependent on the square root of the mean effective stress, was used in computing the initial stresses. A Mohr-Coulomb failure criteria, with tension cut-off, was used to detect soil failure. The soil internal angle of friction and the Poisson's ratio were assumed to be 33° and 0.3, respectively.

The dynamic analysis was initiated using the input motion at the base of the mesh. In the dynamic analysis, the time integration was performed using the generalized Newmark method (Katona and Zienkiewicz, 1985) with coefficients $\beta_1 = 0.6$ and $\beta_2 = 0.605$. In addition to material damping that is simulated by the constitutive models, system viscous damping (Rayleigh damping) was considered in the analyses for the sand and interface (5%), rubber (10%) and aluminum (5%), where the values were determined based on the fundamental frequency of reinforced soil walls. No system damping was assigned to the geogrid. The analysis was iterated to convergence with a tolerance of 0.05 using the norm of relative displacements.

3.4 *Comparison of dynamic analyses*

While the analysis was conducted using the dimensions of the centrifuge model, the results are presented for the prototype full-scale structures. The results obtained from the analysis are compared with the experimental results for the cyclic loading having an amplitude of 0.2g subject to 12 s (20 cycles) shaking. Note that the interfaces between the soil-geogrid and soil-wall panel are not considered in these analyses. Liu (2003) has conducted additional studies that showed that the effects of modeling interfaces were very small for the five tests. Figure 10 shows typical results of acceleration response, wall face deflection and settlement during duration of shaking in Test 3. The results for the four other tests, which are presented in Liu (2002), also gave good agreement.

The results showed that the acceleration amplified slightly with height for both reinforced and backfill zones. Figure 11 shows that the amplification ratio, which is defined as the acceleration at the top of the wall to the input peak acceleration, was less than 1.5 for the tests,

except in Tests 1 and 4 where the measured value was slightly greater than 1.5. There was a little phase lag in acceleration recorded in the reinforced and unreinforced soil zones.

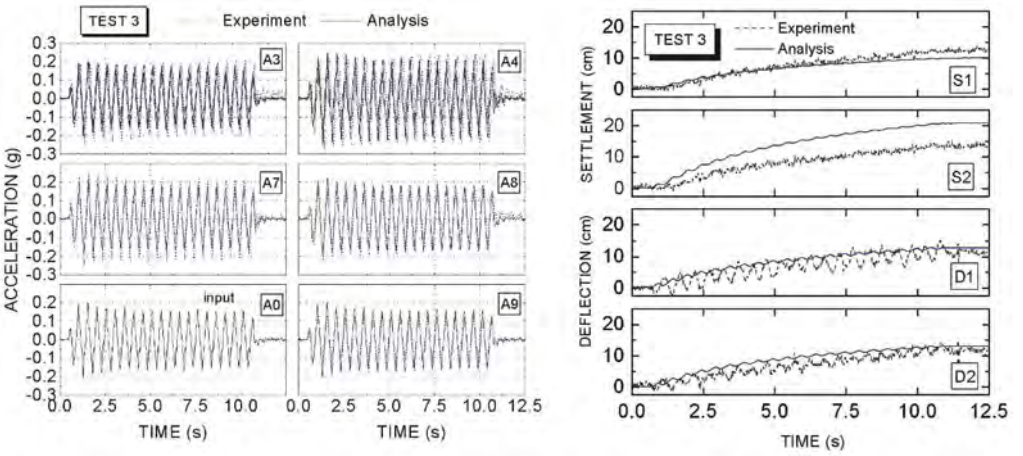

Figure 10. Dynamic response of Test 3.

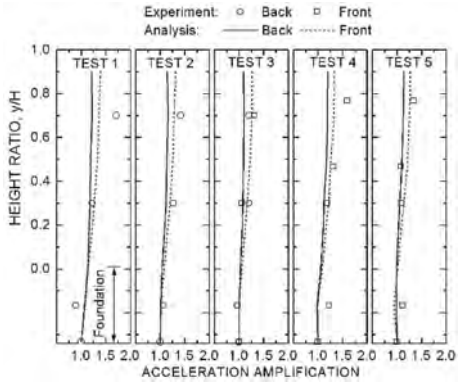

Figure 11. Amplification ratio of acceleration.

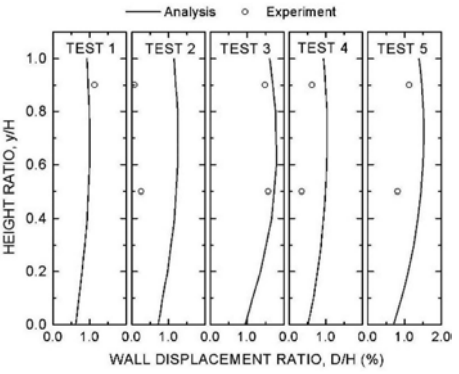

Figure 12. Wall lateral displacements.

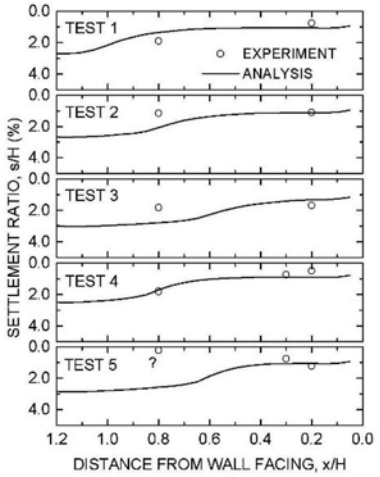

Figure 13. Wall settlements.

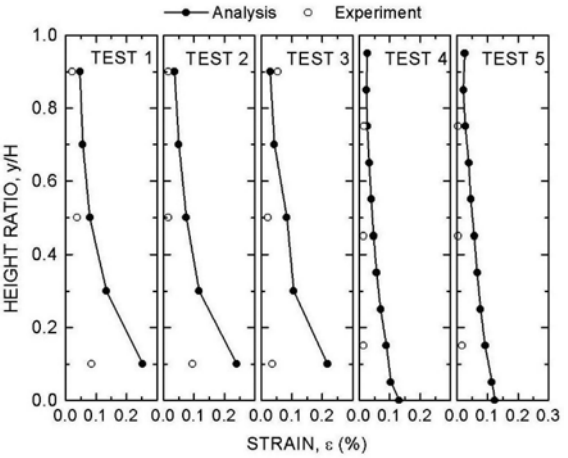

Figure 14. Largest strains in geogrid layers.

The wall face displacements and crest settlements shown in Figures 12 and 13 were accumulations of displacement over a period of 12-second shaking. Figure 12 shows the comparison of wall face displacement at the end of shaking between the analyzed and measured values. There were, however, only two experimental values per wall. Except for Test 2, the experimental results are close to the results of the analyses. Test 3 gave the largest horizontal deformation among the five tests, but it was less than 2% of the wall height.

The results of crest settlement are shown in Figure 13. It is seen that the largest settlement occurred behind the reinforced zone, and was likely due to soil densification and also to the sliding out of the reinforced soil mass. Such results are seen only with the aid of numerical analysis because of the limited number of measurements in the centrifuge tests.

The maximum tensile strain in each geogrid layer was obtained and plotted in Figure 14. The results showed that larger strains were mobilized in Tests 1, 2 and 3. Tests 4 and 5 gave a smaller maximum strain compared to the other tests because of smaller vertical reinforcement spacing. The measured results were smaller than computed due to the problem of strain gage attachment. That is, the epoxy used in attaching the strain gages was stiffer than the geogrid.

Based on the results of wall face deformations, Tests 3 and 5, which had the shortest reinforcement length, rendered the largest deformation. The strain in the reinforcement was also larger for shorter reinforcement length. Thus, an increased length of reinforcement minimizes lateral wall deformations and strains in the reinforcement layers. On the other hand, the acceleration amplification and crest settlement were not affected much by the length and spacing of the reinforcement.

4 FULL-SCALE SHAKING TABLE TESTS

4.1 *Wall layouts and instrumentations*

A total of four full-scale shake table tests with sandy soils were conducted, where the first three tests were reported in Ling et al. (2005a). The walls were 2.8 m high, 2 m wide and 4 m long in the direction of horizontal shaking. They were backfilled with a fine sand (D_{50} =0.27 mm), which was compacted in 10-cm layers at a moisture content of 9.5% to achieve a relative density of 55% (corresponding to a unit weight of 14.3 kN/m^3). The foundation of the wall was 20 cm thick, constructed with the same type of sand. The angle of internal friction of the backfill sand obtained from the triaxial compression tests was 38°.

Several types of geogrid were used as tensile reinforcements: two polyester (PET) geogrid of strengths 35 kN/m and 20 kN/m, respectively, and a polyvinyl alcohol (PVA) geogrid of strength 20 kN/m. They are hereafter denoted as PET-35, PET-20 and PVA-20, respectively. The geogrids were placed at regular vertical intervals (40 cm or 60 cm) between concrete block facing at the front end of the wall. These concrete blocks were hollow, of height 20 cm, depth 30 cm and width 45 cm, and they created a facing of slope angle 78°. The core of the block was filled with gravels and compacted.

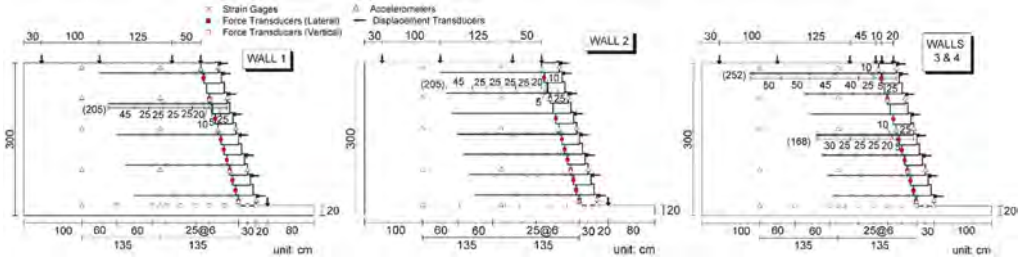

Figure 15. Full-scale shaking table tests (layouts and instrumentations).

The reinforcement layouts are shown in Figure 15, where the lengths of reinforcement were L= 205 cm (0.73H) in Walls 1 and 2, and 168 cm (0.6H) in Walls 3 and 4. In Walls 1 and 2, the length

of reinforcement was constant throughout the height, but in Walls 3 and 4, the top reinforcement layer was a PVA-20 geogrid of length 252 cm (0.9H). In Wall 3, the geogrid layer was grouted to the two top blocks. PET-35 was used in Walls 1 and 2, whereas for Wall 3 the top layer was PVA-20, and the rest of bottom layers were PET-35. The vertical spacings of reinforcement were 60 cm (3 blocks) in Wall 1 and 40 cm (2 blocks) in the other three walls. Walls 3 and 4 were identical except for the types of geogrid used; Wall 1 used single layer PET-35 whereas Wall 4 used double layer PET-20 (a layer of long geogrid overlaid by a short 1-m layer of geogrid).

The motions recorded by the Japan Meteorological Agency during the 1995 Kobe earthquake (North-South and Up-Down components) were used in the tests. For each wall, two shakings were applied. In the first shaking, the motions were scaled to give half the maximum acceleration, and in the second shaking the original motions were used. The first two walls were subjected to only horizontal acceleration, whereas in other walls horizontal and vertical accelerations were applied simultaneously. The instrumentation scheme of the wall is shown in Figure 16, where 20 accelerometers were used to measure the horizontal (and additional 20 accelerometers for vertical accelerations in Walls 3 and 4) at several locations in the backfill soil. The accelerations of the block facing were measured at various heights. The horizontal displacements of the block facing were measured at 8 different heights and the settlements of the backfill were measured at 4 different locations using the laser and linear variable differential transducers, respectively. The strains in each geogrid layer were measured using 8 plastic strain gages. For Wall 4, 5 additional strain gages were installed in the short (1-m) geogrid layers, occupying the same locations as the long layers. The lateral force acting on the blocks and the vertical force at the base of the wall and backfill soil were each measured using 10 force transducers.

4.2 *Finite element analysis*

The dynamic finite element procedure used in the analysis were identical to that of the centrifuge model simulation. However, additional robust soil and geosynthetic models were implemented.

A static analysis was conducted first to obtain the initial stresses for the dynamic analysis. The static analysis used a generalized elastic model, with the shear modulus dependent on the square root of mean effective stress ($p^{0.5}$) and the strength obeying Mohr-Coulomb failure criteria (G at 100 kPa = 60,000 kPa, ν= 0.33, ϕ=38°). The sand model for dynamic loading is described subsequently. The one-dimensional bounding surface model was used for the geogrids, whereas the concrete blocks were assumed as linear elastic material. The interface models were used to simulate soil-structure interactions.

Since each wall was subjected to two shakings, the residual stresses at the end of first shaking acted as the initial stresses for the second shaking. A total of 1,500 steps were used in the static analysis, and 7,000 steps for each dynamic shaking with the time interval of 0.002 seconds. The time stepping parameters were β_1=0.6 and β_2=0.605. The stiffness matrix was updated every 10 steps in the analysis with an incremental displacement convergence criterion of 0.003.

4.3 *Sand model (Unified generalized plasticity model)*

A unified generalized plasticity model based on the concept of critical state was used. In addition to pressure dependent behavior of sand, the effect of density was considered. This is a significantly different model compared to many other sand models, which are valid for only one particular density. Thus, using a single set of 16 parameters, the behavior under different densities and confining pressures can be simulated in this model. Note that the earlier version of model (see Section 2.3.1) proposed by Ling and Liu (2003) requires the same number of parameters for a single density. The formulation of the model is given in Ling and Yang (2006) and the model has been validated against monotonic and cyclic loading test results of several types of sand.

Four drained monotonic and one drained cyclic loading tests were used to calibrate the model. The specimens were prepared at two different void ratios (e= 1.01 or Dr= 55% and e= 0.83 or Dr= 90%) and each subjected to two confining pressure (30 kPa and 70 kPa) under drained monotonic loading. The cyclic test was conducted by Burke et al. (2005) at a confining pressure of 70 kPa and Dr=55%, with the deviator stress varying between -25 kPa and 95 kPa.

The sand parameters are summarized in Table 4. The calibrated results are compared with the experimental results in Figures 16 and 17 for monotonic and cyclic loadings, respectively.

The effects of pressure dependency on the stress-deformation behavior under the medium dense and dense conditions are well simulated. The results for cyclic loading, including hardening behavior under repeated loading, is also well depicted. Note that in the parametric studies (Ling et al., 2005b), it was shown that this hardening behavior affects the dynamic response of the soil structure significantly.

Table 4. Sand parameters and calibration.

Parameters		Values
Elastic Moduli	G_o/p_a	450
	K_o/p_a	480
Critical State Line	e_Γ	1.08
	λ_c	0.037
Phase Transformat-ion Line	M_g	1.6
	m_g	2.0
Plastic Flow	M_f	1.0
	m_f	1.46
Loading Modulus	H_{Lo}/p_a	230
	m_b	4.5
	m_o	1.0
Constant*	α	0.45
Unloading Modulus	H_{Uo}/p_a	80.
	m_U	3.6
Reloading Modulus	B	0.
	κ	0.
	r_{den}	180.

*related to dilatancy, flow direction, and loading modulus

Table 5. Parameters for geogrids.

Parameters	PET-35	PET-20	PVA-20
J_e (kN/m)	680.0	450.0	550.0
A	0.45	0.35	0.28
C	1.0	1.0	-10.0
D	2.4	2.4	2.0
J^0_{p+}	55.	55.0	17.0
J^0_{p-}	-1.0	-1.	-11.0
	36.0	28.0	150.0
h^U_0	2250.0	2250.0	250.0
h^L_k	1800.0	1800.0	1800.0
h^U_k	1.5	1.5	1.0

4.4 *Geogrid model*

The geogrid is modeled using one-dimensional bounding surface concept as described in Section 2.3.2. There are two non-parallel bounding lines and hardening parameters that are different for loading and unloading. This is to account for the fact that polymeric geogrid sustains

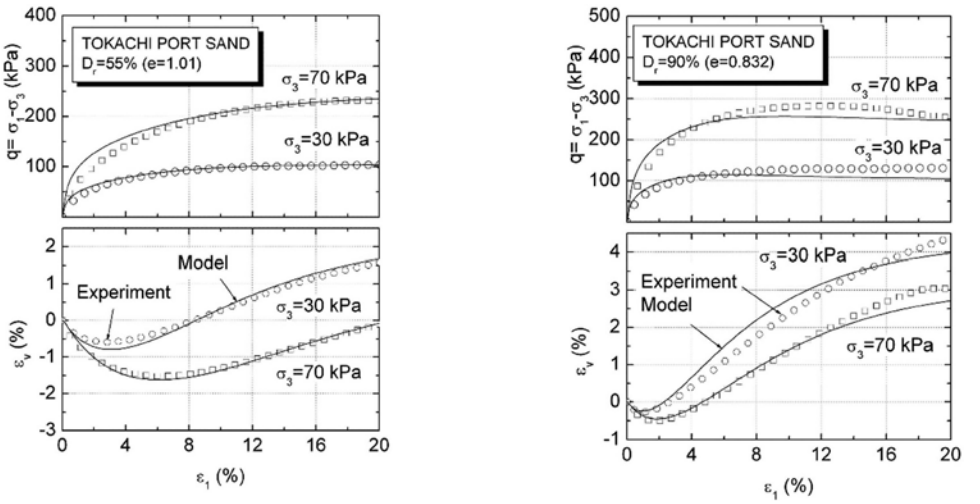

Figure 16. Monotonic behavior of loose and dense Tokachi Port sand.

negligible compression. In this series of analyses, a power function is used to account for the S-shape load-strain relationship of polyester geogrids.

The bounding lines in the tension and compression sides of the load-strain curve in the plastic region are expressed using exponential and linear functions, respectively:

$$T_+ = A + J^0_{p+} \cdot \varepsilon_p^D \tag{5a}$$

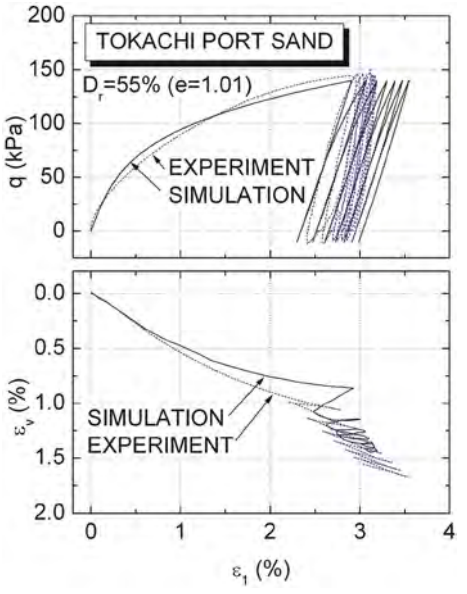

Figure 17. Cyclic behavior of medium dense Tokachi Port sand.

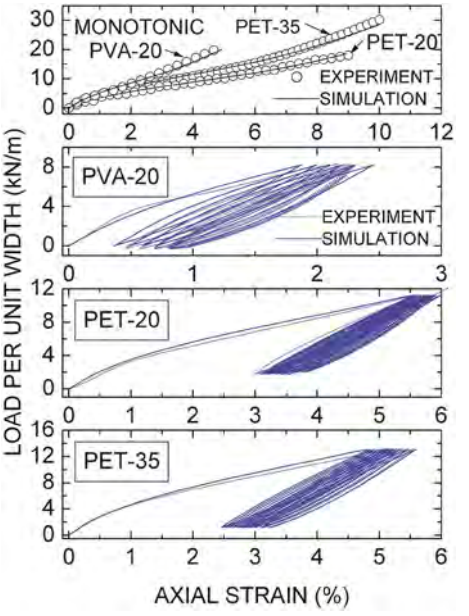

Figure 18. Monotonic and cyclic behavior of geogrids.

$$T_- = B + J^0_{p-} \cdot \varepsilon_p \tag{5b}$$

where A and B are intercepts of the tension and compression bounding lines, respectively, J^0_{p+} and D are the number and exponent for the tension bounding line, and J^0_{p-} is the slope for the compression bounding line.

The hardening functions for loading and unloading are the same as original version of model proposed by Ling et al. (2001):

$$h^L = h^L_o + h^L_k \ \varepsilon_p^{\alpha_L} \tag{6a}$$

$$h^U = h^U_o + h^U_k \sqrt{\varepsilon_p} \tag{6b}$$

where h^L_o, h^U_o, h^L_k, h^U_k, and α_L are constants. Thus, including the elastic stiffness J_e, the modified geogrid model is characterized by a total of 10 parameters, instead of 9 in the original version of model. The parameters for the three types of geogrids are summarized in Table 5. Cyclic loading tests were conducted at 40% load level for PET-35 and PVA-20 geogrids, whereas it was 60% for PET-20 geogrid. The satisfactory comparison between the experimental and simulated load-strain results under monotonic and cyclic loadings are shown in Figure 18.

4.5 *Facing blocks and interfaces*

The concrete blocks are much stiffer and stronger than soils, thus they are assumed as linear elastic material (E= 2.0×10^6 kPa, ν= 0.2). The expanded polystyrene (EPS) boards, which were used as reflective wave absorbers in the tests, are expressed as a linear elastic material (E= 2.0×10^6 kPa, ν= 0.2). The interactions between soil-geogrid (δ=34°), soil-block (27°), block-geogrid (35°) and block-block (35°) were determined from direct shear tests (Burke et al., 2005). The thin-layer interface elements having elastic perfectly plastic behavior were used to simulate the interaction between these materials. The elastic properties of the interface elements are E= 1.5×10^4 kPa and ν= 0.2. In Wall 4, the interaction between the short and long geogrid layers was simulated using a friction angle of 35°.

4.6 *Rayleigh damping*

In addition to the material damping properties, which can typically be handled through an elasto-plastic soil model, the system damping needs to be considered in solving dynamics problems. For a linear system, the use of damping ratio may be straight forward, but for a nonlinear system like soil structure, selection of damping ratio has never been trivial although 5% damping is typically used based on the experience of equivalent linear analysis. The issue of Rayleigh damping has been discussed by several researchers, such as Chan et al. (1993) and Dewoolkar et al. (1999).

The system damping affects the results of response significantly. For shake table tests with a maximum acceleration of 0.4g, 15% damping produced most satisfactory results, while for a maximum acceleration of 0.8g, smaller damping of 5% was sufficient. This is likely due to the fact that less damping is available in the soil model when the material is close to elastic, whereas at large strain the material damping becomes large enough such that a reduced system damping is adequate.

Rayleigh damping (Clough and Penzien, 1975) is used in the dynamic analysis. It is proportional to the mass and stiffness matrices (**M** and **K)**:

$$\mathbf{C} = \alpha\mathbf{M} + \beta\mathbf{K} \tag{7}$$

where α and β are coefficients related to damping ratio ξ and angular frequency ω:

$$\xi = \frac{\alpha}{2\omega} + \frac{\beta\omega}{2} \tag{8}$$

α and β are calculated by selecting a ξ and two frequencies outside which damping is larger than the selected ξ. The fundamental frequency of a wall of height 3 m was about 7.25 Hz (Ling, 2003), thus by setting $\alpha = 0$, β was obtained as 0.0022 for Rayleigh damping of 5%.

4.7 *Finite element mesh and boundary conditions*

Figure 19 shows the finite element mesh of the walls. Note that Walls 3 and 4 share the same mesh, but in Wall 4, the solid line of reinforcement consists of short and long layers of geogrid and interfaces. The solid elements used for soils, concrete and EPS were 8-node quadrilateral and 3-node triangular elements. The interface were 8-node elements. Full integration of 9 and 6 points, respectively, were used for the quadrilateral and triangular elements. The geogrid was simulated using 3-node one-dimensional bar elements, with 3 points of full integration.

The side boundaries of the walls were frictionless but restrained from lateral displacements. The bottom boundary was fixed from lateral and vertical displacements. The earthquake accelerations were input to these nodal points at the bottom of the mesh.

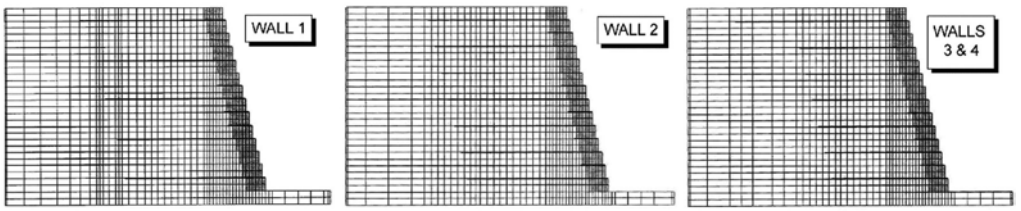

Figure 19. Finite element mesh for full-scale walls.

4.8 *Results of simulation and comparison*

Although two shakings were applied to each of the 4 walls, the deformations induced by the first shaking were negligibly small, in the magnitude of a few mm. Thus, this paper focuses on the presentation and comparison of the results during the second shaking.

4.8.1 *Wall deformations*

The horizontal displacements of the front facing and settlements of the backfill are two most important quantities in examining the wall deformation. From performance or serviceability view point, the residual deformations are quality of concern. Figure 20 show typical time-response of the wall horizontal displacements (Wall 3) and settlements (Walls 2 and 3) during shaking, respectively. Since Walls 3 and 4 included both horizontal and vertical shakings, the response would resemble to that of field earthquake conditions. Note that in the tests, the displacement transducers were attached to the steel frames, which were fixed to the steel box and subjected to shaking. Thus, the time response of the displacement transducers could have been affected by the vibration of the frames, but the residual deformations were unaffected.

The sharp spikes at large displacement, such as that located on the top part of the wall, are not captured in the analysis. The displacement at smaller deformation, say below mid-height of the wall, are simulated. It has to be noted that during strong shaking, deformation recorded through video cameras located directly above the wall showed that the blocks separated from the backfill momentarily. The possibility of separation could not be simulated in this presented numerical procedures. The abrupt settlements at the back of the wall in the experiments are not well depicted. The front part of the walls shows slight heaving in both analyses and experiments.

The residual horizontal displacements and settlements that are critical to wall performance are determined satisfactorily in the analyses (Figure 21). The analysis and experiment give a larger horizontal displacement on the upper part of the wall compared to the bottom part. For the backfill settlement, in addition to the measurements by the laser displacement transducers, rulers were used to measure the settlements at the end of shakings because the targets for the laser transducers were disturbed as the backfill surface deformed largely with the formation of cracks. The results obtained from the ruler measurements for Walls 1 and 2 are included for comparison. There were some discrepancies between the laser and ruler measurements in Wall 1, but the results obtained from the two methods were quite similar in Wall 2.

4.8.2 *Acceleration response and amplifications*

The base accelerations recorded in the experiment was used as input to the finite element analyses. Figure 22 shows the horizontal and vertical acceleration response at different heights of Wall 3. The agreement between the experiment and analysis was very good. It has to be noted that the acceleration response at different locations of the same heights (at the block, in the backfill close to the blocks, in the reinforced zone and in the backfill of the walls) are quite similar for both the analysis and experiment.

The comparison between the experimental and finite element results of maximum horizontal and vertical accelerations are shown in Figure 23. In general, the analysis gave slightly smaller accelerations compared to the experiments for Walls 1 and 2, especially in the blocks. For Walls 3

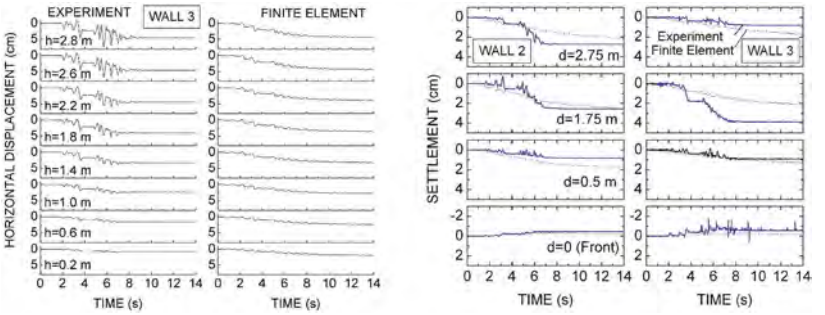

Figure 20. Deformation response of walls.

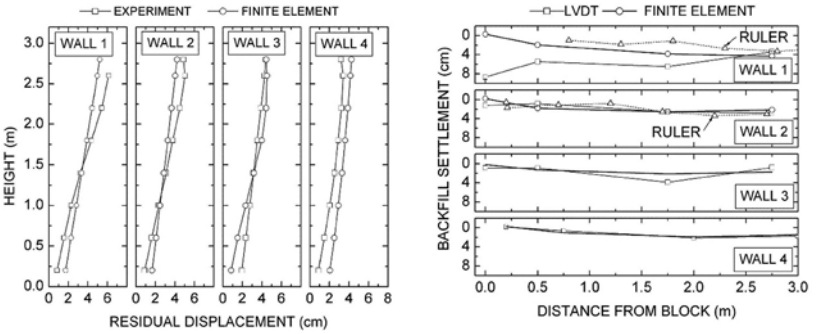

Figure 21. Residual lateral displacements and settlements.

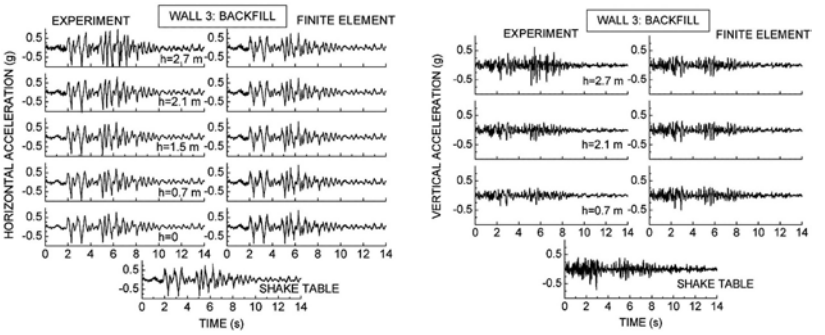

Figure 22. Horizontal and vertical accelration response for Wall 3.

and 4, a slight overestimation was seen in the analysis. Overall the difference was not very large. It has to be mentioned that the top two blocks in Wall 1 were not grouted, thus they tended to respond more vigorously compared to Wall 3 where they were grouted. The acceleration amplification was small in the walls, mostly less than 1.5. For the largest amplification at the top block of Wall 1, the ratio was less than 2.

4.8.3 *Tensile force in geogrid reinforcements*

Figure 24 show the results of measurement and finite element analysis of the tensile force along the geogrid layers. The peak and residual values are compared. In general, the analyses gave slightly higher values than the measurements, but because the tensile forces are relatively small, the difference was about 5 to 10% the strength of geogrids. There were difficulties in interpreting the measurements as the tensile force was converted indirectly from the strain gage readings.

The measurements were affected by other factors such as construction, methods of strain gage attachment, as well as calibration of strains, as discussed in Ling et al. (2005a).

5 SUMMARY AND CONCLUSIONS

This paper documented a series of studies on reinforced soil retaining walls, starting from simple finite element analyses with nonlinear elastic models under static loading conditions to sophisticated dynamic analyses using advanced plasticity models. With the constitutive models that simulated both monotonic and cyclic behavior of soils and geosynthetic reinforcements, the responses of geosynthetic reinforced soil retaining walls could be reproduced satisfactorily. The physical models, both full-scale and centrifuge model testings, provided invaluable results for validation of numerical procedures.

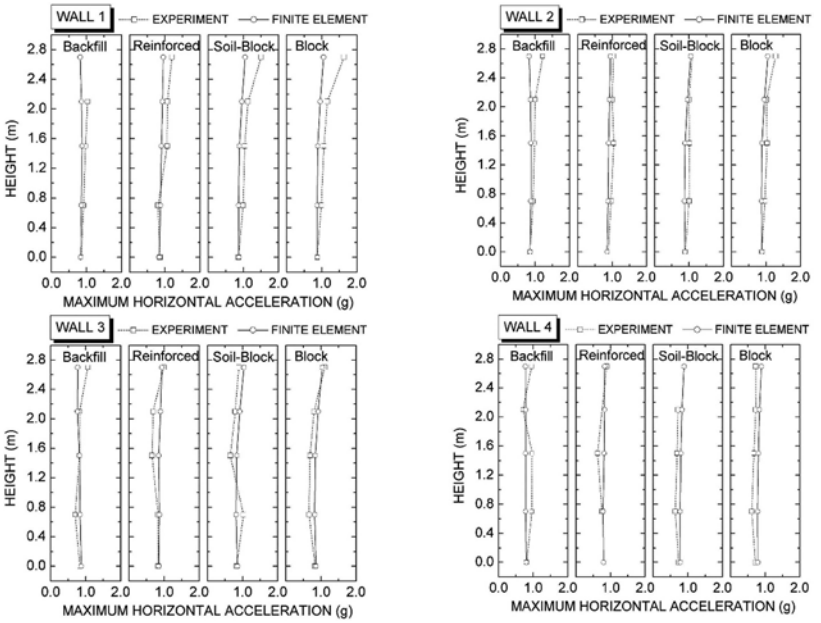

Figure 23. Maximum horizontal accelerations in walls.

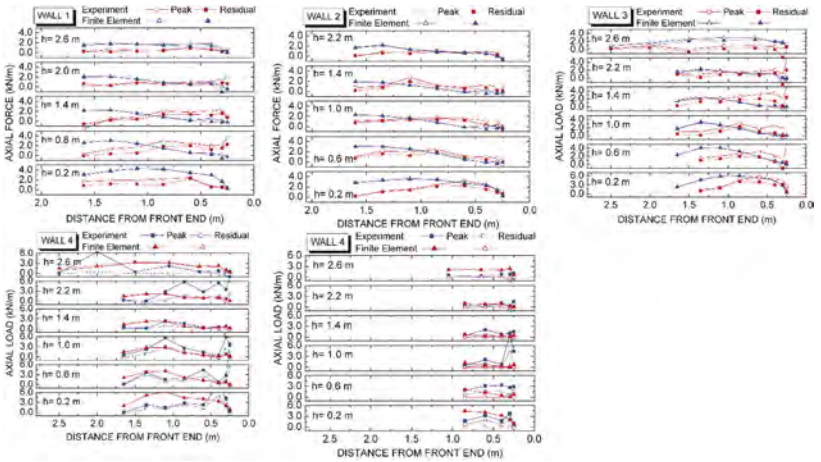

Figure 24. Tensile force in geogrid layers.

ACKNOWLEDGMENTS

The authors would like to acknowledge the collaborations with several researchers over the years, in particular Yoshiyuki Mohri (currently Ibaraki University) and Toshinori Kawabata (Kobe University). H. Hashimoto provided instrumentation data of the PWRI Wall. The centrifuge project was funded by NSF INT-9996230 and JSPS in collaboration with Jiro Takemura and Akihiro Takahashi of the Tokyo Institute of Technology. The major support for the full-scale shaking table study was provided by the National Science Foundation Career Award CMS-0092739, and also the National Institute of Rural Engineering (Japan), Allan Block Corporation (USA), and Huesker Synthetic GmbH (Germany). Former graduate students, Huabei Liu, Christopher Burke, Songtao Yang, and Jui-Ping Wang have been involved in the studies.

REFERENCES

Bathurst, R.J. & Cai, Z. 1995. "Pseudo-static seismic design of geosynthetic-reinforced segmental retaining walls." *Geosynthetics International*, 2(5), 787–830.

Burke, C., Ling, H.I., & Liu, H. 2005. "Seismic response analysis of three full-scale reinforced soil retaining walls." in *Geosynthetics and Geosynthetic-Engineered Soil Structures*, Ling, H.I., Kaliakin, V.N., & Leshchinsky, D., Editors, 147–170. (distributed by Industrial Fabrics Association International, Minneapolis, MN)

Cai, Z. & Bathurst, R.J. 1995. "Seismic response analysis of geosynthetic reinforced soil segmental retaining walls by finite element method." *Computers and Geotechnics*, 17, 523–546.

Chan, A.H.C. 1993. *User Manual for Diana-Swandyne-II*, Department of Civil Engineering, Glasgow University, UK.

Clough, R.W. & Penzien, J. 1975. *Dynamics of Structures*, McGraw-Hill, New York.

Dewoolkar, M.M., Ko, H-Y., & Park, R.Y.S. 1999. "Centrifuge modeling of models of seismic effects on saturated earth structures." *Geotechnique*, 49(2), 247–266.

Duncan, J.M. & Chang, C.Y. 1970. "Nonlinear analysis of stress and strain in soils." *Journal of Soil Mechanics and Foundation Engineering*, ASCE, 96, SM5, 1629–1653.

Duncan, J.M., Byrne, P., Wong, K.S. & Mabry, P. 1980. "Strength, Stress-Strain and Bulk Modulus Parameters for Finite Element Analyses of Stresses and Movements in Soil Masses." *Report No. UCB/GT/80-0*1, Department of Civil Engineering, University of California, Berkeley, CA.

Helwany, S.M.B., Budhu, M., & McCallen, D. 2001. "Seismic analysis of segmental retaining walls. I: Model verification." *Journal of Geotechnical and Geoenvironmental Engineering*, ASCE, 127(9), 741–749.

Katona, M.G., Smith, J.M., Odello, R.S., & Allgood, J.R. 1976. "A modern approach for the structural design and analysis of buried culverts." *FHWA*-RD-77-5, Federal Highway Administration, US Department of Transportation, Washington, D.C.

Katona, M.G. 1983. "A simple contact-friction interface element with applications to buried culverts." *International Journal of Numerical and Analytical Methods in Geomechanics*, 7, 371–384.

Katona, M.G. & Zienkiewicz, O.C. 1985. "A unified set of single step algorithms Part 3: The beta-m method, a generalization of the Newmark scheme." *International Journal for Numerical Methods in Engineering*, 21(9), 1345–1359.

Leshchinsky, D., Ling, H.I., & Hanks, G. 1995. "Unified Design Approach to Geosynthetic Reinforced Slopes and Segmental Walls." *Geosynthetics International*, 2(5), 845–881.

Leshchinsky, D., Kang, B., Han, J., & Ling, H.I. 2014. "Framework for limit state design of geosynthetic-reinforced walls and slopes." *Transportation Infrastructure Geotechnology*, 1(2), 129–164.

Ling, H.I. 2003. "A critical review of full-scale shaking table tests conducted on reinforced soil retaining walls." *Reinforced Soil Engineering: Advances in Research and Practice*." Marcel Dekker, Inc., NY, 491–510.

Ling, H.I. & Tatsuoka, F. 1992. "Nonlinear analysis of reinforced soil structures by Modified CANDE (M-CANDE)." *Geosynthetic-Reinforced Soil Retaining Walls*, Wu, Editor, Balkema, Rotterdam, 279–296.

Ling, H.I., Leshchinsky, D., & Perry, E.B. 1996. "A new concept of seismic design of geosynthetic-reinforced soil structures: Permanent Displacement Limit." *Earth Reinforcement*, Ochiai, Yasufuku & Omine, Eds., Balkema, Rotterdam, 797–802.

Ling, H.I., Leshchinsky, D., & Perry, E.B. 1997. "Seismic design and performance of geosynthetic-reinforced soil structures." *Geotechnique*, 47(5), 933–952.

Ling, H.I. & Leshchinsky, D. 1998. "Effects of Vertical Acceleration on Seismic Design of Geosynthetic-Reinforced Soil Structures." *Geotechnique*, 48(3), 347–373.

Ling, H.I., Liu, H., Y. Mohri, & T. Kawabata 2001. "A bounding surface model for geogrid reinforcements." *Journal of Engineering Mechanics*, 127(9), 963–967.

Ling, H.I. & Liu, H. 2003. "Pressure-level dependency and densification behavior of sand through a generalized plasticity model." *Journal of Engineering Mechanics*, ASCE. 129(8), 851–860.

Ling, H.I., Liu, H., Kaliakin, V., & Leshchinsky, D. 2004. "Analyzing dynamic behavior of geosynthetic-reinforced soil retaining walls." *Journal of Engineering Mechanics*, 130(8), 911–920.

Ling, H.I., Mohri, Y., Leshchinsky, D., Burke, C., Matsushima, K., & Liu, H. 2005a. "Large scale shaking table tests on modular-block reinforced soil retaining wall." *Journal of Geotechnical and Geoenvironmental Engineering*, 131(4), 465–476.

Ling, H.I., Liu, H. & Mohri, Y. 2005b. "Parametric studies on the behavior of reinforced soil retaining walls under earthquake loading." ASCE *Journal of Engineering Mechanics*, 131(10), 1056–1065.

Ling, H.I. & Yang, S. 2006. "A unified sand model based on critical state and generalized plasticity." *Journal of Engineering Mechanics*, ASCE, 132(12), 1380–1391.

Liu, H. 2003. "Finite Element Simulation of the Response of Geosynthethic-Reinforced Soil Walls," *Ph.D*. Thesis, Columbia University.

Pastor, M., Zienkiewicz, O.C., & Chan, A.H.C. 1990. "Generalized plasticity and the modeling of soil behavior." Theme/Feature Paper, *International Journal for Numerical and Analytical Methods in Geomechanics*, 14, 151–190.

Segrestin, P. & Bastick, M.J. 1988. "Seismic design of reinforced earth retaining walls - the contribution of finite element analysis." *Theory and Practice of Earth Reinforcement*, 577–582.

Tajiri, N., Sasaki, H., Nishimura, J., Ochiai, Y., & Dobashi, K. 1996. "Full-scale failure experiments of geotextile-reinforced soil walls with different facings." *Earth Reinforcement*, Ochiai, Yasufuku & Omine, eds., Balkema, Rotterdam, 525–530.

Takashashi, A., Takemura, J. & Izawa, J. 1999. "Dynamic behavior of vertical geogrid-reinforced soil during earthquake." *Proceedings of the International Symposium on Slope Stability Engineering*, 2, 991–996, Balkema, Rotterdam, the Netherlands.

Takemura, J. & Takahashi, A. 2003. "Centrifuge modeling of seismic performance of reinforced earth structure." *Reinforced Soil Engineering: Advances in Research and Practice*, Ling, H.I., Leshchinsky, D., & Tatsuoka, F., Editors, Marcel Dekker, Inc., NY, 417–442.

Tatsuoka, F., Koseki, J., Tateyama, M., Munaf, Y., & Horii, K. 1998. "Seismic stability against high seismic loads of geosynthetic-reinforced soil retaining structures." *Keynote Lecture, Proceedings of 6th International Conference on Geosynthetics*, Atlanta, 103–142.

Yogendrakumar, M., Bathurst, R.J., & Finn, W.D.L. 1992. "Dynamic response analysis of reinforced soil retaining wall." *Journal of Geotechnical Engineering*, ASCE, 118(8), 1158–1167.

Zienkiewicz, O.C., Chan, A.H.C., Pastor, M., Schrefler, B.A., & Shiomi, T. 1998. *Computational Geomechanics with Special Reference to Earthquake Engineering*, John Wiley & Sons, Ltd., Chichester, England.

Smart Geotechnics for Smart Societies – Zhussupbekov, Sarsembayeva & Kaliakin (Eds)
© 2023 The Author(s), ISBN 978-1-003-29912-7
Open Access: www.taylorfrancis.com, CC BY-NC-ND 4.0 license

Temperature and moisture monitoring in pavement and subgrade in Kazakhstan

B.B. Teltayev
"Joldasbekov Institute of Mechanics and Engineering", LLP "Road Research and Production Center", Kazakhstan

ABSTRACT: Some important results of long-term measurement and analysis of temperature and moisture in layers of pavement and subgrade in different regions of Kazakhstan are presented. Most of the measurements in natural conditions were carried out in the period from 2010 to 2022 using specially invented and designed measuring devices, the latest model of which is capable of storing and transmitting the information obtained over distances.The values and peculiarities of the change in temperature and moisture in time and its distribution in depth are established. The processes of freezing and thawing in the subgrade have been studied. A map of the freezing depth of roads has been drawn. The content of unfrozen water was determined. The effect of temperature and moisture on stresses and strains at critical points of the pavement and subgrade was evaluated by calculations. Recommendations have been developed for design of pavement structures, taking into account temperature of an asphalt concrete layers and moisture content in subgrade.

1 INTRODUCTION

The main structural elements of highways, which determine their bearing capacity and durability, are pavement and subgrade. Pavement and subgrade work together, perceiving all kinds of impacts together (Ivanov et al. 1973, Yoder & Witczak 1975, Zolotar et al 1971, Huang 2004).

Back in the second half of the last century, the main principle of landscape design of roads was formulated (Babkov 1980): "Design roads in conjunction with the landscape." The road, designed in relation to the local landscape, and built in compliance with these design requirements, becomes an element of the landscape. Thus, the operated highway, being part of the landscape, is affected by all local complex non-stationary changes in climate, weather, hydrological and other phenomena.

Temperature affects almost all layers of pavement and subgrade. It is known that mechanical (deformation and strength), physical and other characteristics of asphalt concrete strongly depend on temperature. At negative temperatures, the moisture contained in subgrade soil experiences a phase transition (Tsytovich 1973).

From the above, it is clear that it is important to know the qualitative and quantitative characteristics of temperature and moisture changes in the layers of pavement and subgrade for the correct design and efficient operation of roads.

This work contains important for science and practice results of monitoring changes in temperature and moisture in the pavement and subgrade of a number of highways located in different regions of Kazakhstan, carried out by means of special measuring systems. On the example of a section with an asphalt concrete pavement of the Astana-Burabay highway, the influence of temperature and moisture on the mechanical indicators (stresses and strains) that occur in the pavement and subgrade under the act of an automobile load is estimated.

DOI: 10.1201/9781003299127-8

2 SYSTEM FOR MEASURING TEMPERATURE AND MOISTURE

In order to carry out long-term monitoring of changes in temperature and moisture in the structural elements of roads in Kazakhstan, special measuring systems with sensors were invented and created. The first three of them were installed on sections with cement concrete pavement (km 19 +750) and asphalt concrete pavement (km 76+30) of the Astana-Burabai highway in 2010. Then these measuring systems were improved (they can save the measurement results) and in 2013 they were installed on the roads located in four regions of the republic: "Almaty - Bishkek", km 58 +895 (south-eastern region); "Kyzylorda - Shymkent", km 2097 + 00 (southern region); "Atyrau - Astrakhan", km 598+50 (western region); "Oskemen - Zyryanovsk", km 0 + 75 (eastern region). In the future, these measuring systems were improved once again (they could save and transmit measurement results over long distances via wireless communication, power was supplied through solar panels) and in 2021 were installed on roads located in 16 regions of the republic.

3 TEMPERATURE IN PAVEMENT AND SUBGRADE

As one should expect, as the main factor, determining temperature variation in points of pavement and subgrade of a highway, is an air temperature variation. It was stated that, first of all, it should be mentioned that variation in time of air temperature and, as a result, pavement surface temperature has complicated dependence. Both amplitude of daily variation and its distribution in days of months is of random nature. It is seen that graphs of air and pavement surface temperature variation qualitatively coincide well, but there are considerable quantitative differences. Meanwhile, the following common regularity occurs: as a rule, asphalt concrete pavement surface temperature is higher than air temperature. The more absolute value of air temperature the more the difference in values of air and pavement surface temperature is.

The temperature within an asphalt concrete pavement, as well as air temperature, is varied both in "quasi-month" and annual, as well as in daily cycles. However, amplitude of daily temperature variations is decreased with the depth increase. Periods for temperature variation become longer that 24 hours with further depth increase. For bigger depths temperature variation occurs practically only in annual cycle.

Thus, it can be considered that temperature variation on surface and in points of an asphalt concrete pavement occur in daily, "quasi-month" and annual cycles; in the mid depths (30-100 cm) daily harmony disappears, only "quasi-month" and annual cycles remain; in bigger depths (120-140 cm and more) temperature variation occurs practically only in annual cycle.

4 CHARACTERISTICS OF WINTER PERIOD

4.1 *Freezing depth*

The freezing depth is an important characteristic of roads in winter. In many countries of the world and in Kazakhstan, the freezing depth is taken into account when designing pavement structures (ODN 2001, SP RK 2015). It can be noted that the well-known general thesis is that the greater the freezing depth, the more strong the requirements for the design of the pavement and the subgrade soil. Obviously, in the winter (cold) period, the properties of pavement materials (especially asphalt concrete and materials containing organic binders) and subgrade soil change greatly. Some of the moisture contained in them passes from a liquid state to a solid state (ice). Of course, this greatly changes the physical, mechanical, rheological and other characteristics of asphalt concrete, soils and other materials. Therefore, not only scientific, but also important practical interest is the study of the process of freezing of the roadelements.

It has been established (Teltayev & Suppes 2017a) that in the cold regions of the republic in winter, pavement and road subgrade have only one long period of freezing and thawing.

On the highway "Astana - Burabay" (northern region of the republic), the pavement and the upper part of the subgrade are in a frozen state for an average of 130-140 days; the average long-term maximum freezing depth is 253 cm; freezing and thawing rates are 2.11 cm/day and 3.51 cm/day, respectively; the thawing process occurs 1.7 times faster than the freezing process.

According to measurements made in 2017 and 2018 (Teltayev & Suppes 2019a), on the "Oskemen-Zyryanovsk" highway, km 0+75 (eastern region of the republic), the maximum freezing depth was 217 cm; freezing and thawing rates - 1.81 cm/day and 2.18 cm/day, respectively; the thawing rate is 1.2 times greater than the freezing rate.

In warm regions, a "warm" winter may experience two short periods of freezing and thawing (Teltayev & Suppes 2019b, Teltayev et al 2020). It is obvious that in such a casethe maximum freezing depths and duration of the frozen state will be significantly less than in cold (northern) regions. So, on the "Kyzylorda-Shymkent" highway in winter season of 2014-2015 years, the freezing depths and the durations of the frozen states were 75 cm and 82 cm, 18 days and 20 days, respectively (Teltayev et al. 2022).

Based on the results of long-term monitoring of temperature regime in road pavements and subgrade, a map of freezing depth of roads in Kazakhstan has been developed (Figure 1). It is clearly seen that the lines of equal freezing depths are subparallel and directed downward from the northwest to the southeast. As expected, greatest depths of freezing (260-270 cm) occur in the northern part of the republic, and the smallest ones in the south (60-70 cm). According to the distribution of freezing depth, the western region of the republic can be divided into two subregions: the first of them - the northwestern subregion is similar to the central region (130-200 cm); the second subregion - the southwestern one is similar to the southern region (60-130 cm). The eastern region of the republic is slightly softer than the northern one (190-230 cm).

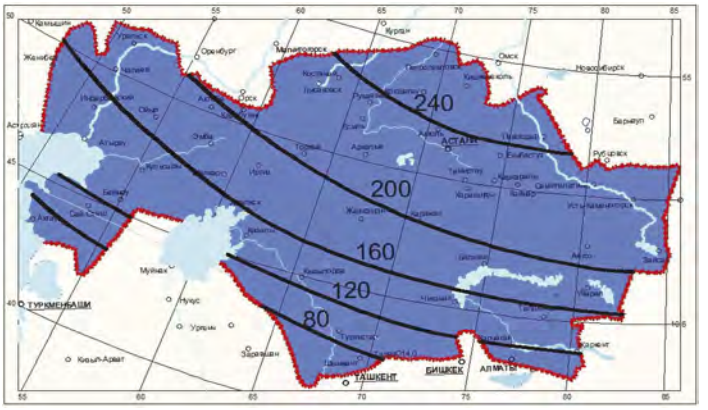

Figure 1. Map of freezing depth of roads in Kazakhstan.

4.2 *Unfrozen water*

Graphs showing changes in moisture at points of the subgrade of the "Oskemen – Zyryanovsk" highway (km 0 + 75) are shown in Figure 2. As you can see, the graphs of moisture changes are complex: there are long periods with stable moisture and short periods in which moisture changes (decreases and increases) sharply. These characteristic sharp changes moisture at different depths were noted at different points in time. It can be seen that the times of a sharp decrease in moisture in the autumn and winter seasons and the times of a sharp increase in moisture in the spring come the later, the deeper the subgrade point is located. These abrupt changes in moisture take place when the temperature passes through 0°C, i.e. these changes show the phase transitions of water from liquid state to solid one (ice) in winter and from solid state to liquid one in spring (Figure 3). The maximum moisture after thawing in spring is greater than before freezing in winter, which can be explained by the movement of vaporous and liquid moisture from below (Sarsembayeva et al. 2022a, Sarsembayeva et al. 2022b) and water infiltration from above.

As can be seen in Figure 4, the dependences of the unfrozen water content on temperature for different depths in the subgrade do not coincide, which can be explained not only by different values of the initial moisture content, but also by different values of pressure, type and characteristics of the soil (density, porosity, granulometric and chemical properties, etc.) at different depths.

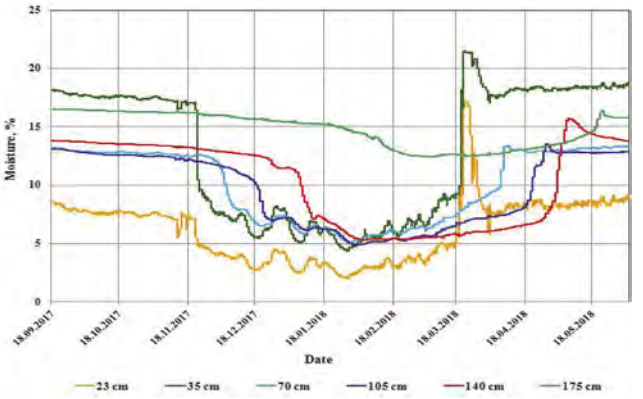

Figure 2. Graphs for moisture changes at points in the subgrade of the “Oskemen - Zyryanovsk” highway.

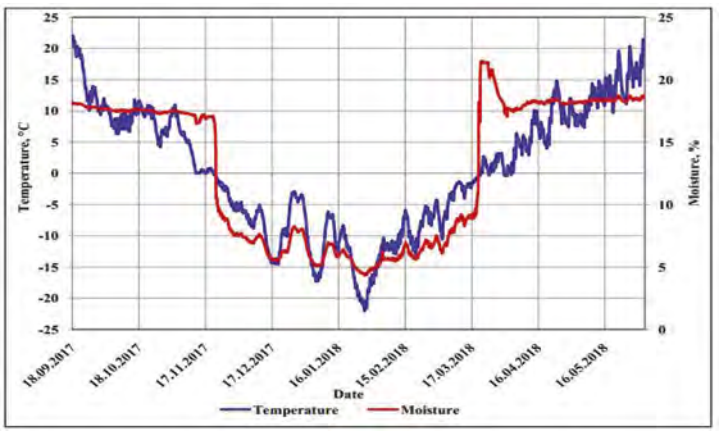

Figure 3. Joint graphs of moisture and temperature changes at a depth of 35 cm in the subgrade of the road “Oskemen - Zyryanovsk”.

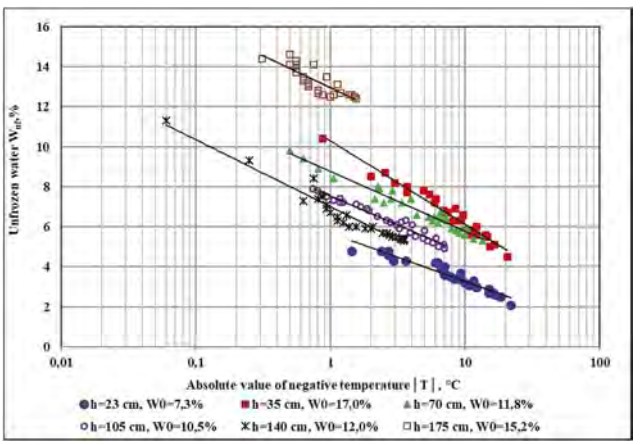

Figure 4. Dependences of unfreezing water content at different depths in the subgrade of the highway “Oskemen - Zyryanovsk”.

5 EFFECT OF TEMPERATURE AND MOISTURE ON STRESSES AND STRAINS

To demonstrate the effect of temperature and moisture on stresses and strains in layers of road pavement and subgrade under acting of an automobile load, the section with an asphalt concrete pavement (km 76 + 30) of the Astana - Burabay highway was selected.

5.1 *Pavement structure*

Pavement structure of the section consists of the following layers: 1- stone mastic asphalt concrete, 6 cm; 2 - dense asphalt concrete, 9 cm; 3 - crushed stone treated with bitumen, 12 cm; 4 - crushed stone and sand mix treated with cement (7%), 18 cm; 5 - crushed stone and sand mix, 15 cm; 6 - sand, 20 cm. Subgrade is constructed from heavy sandy clay loam: moisture in the plastic limit W_P = 18.7 %; moisture in the liquid limit W_T =34.8 %. Underground water is deep (lower than 3.0 m).

5.2 *Calculation scheme*

In order to calculate stresses and strains in the selected structure of pavement and subgrade the calculation scheme with 13 layers was accepted, out of which the first 6 simulate the pavement layers, and the other 7 layers correspond to the layers of subgrade. The materials of all the layers and soil are considered as elastic one. The lowest soil layer (the 13th layer) is considered as an elastic semi-space, which has infinite thickness. Stresses and strains in such multilayer elastic system are determined with the use of the solution of Prof. Privarnikov A.K. (Teltayev & Aitbayev 2015, Teltayev et al. 2018). On the surface of the upper layer there is a load q=0.6 MPa, uniformly distributed within the circle with diameter of D=42 cm. It corresponds to the axial load of 13 tons.

5.3 *Deformation characteristics of asphalt concretes*

Asphalt concrete is a viscoelastic material and its deformation behavior depends on temperature and load duration (Huang 2004, Papagiannakis & Masad 2008, Yoder & Witczak 1975). In this paper the elasticity modulus of stone-mastic and porous asphalt concretes was calculated under the modified formula of Hirsh (Christensen & Bonaquist 2015). Elasticity modulus of the bitumen is calculated under formula, suggested in (Teltayev & Radovskiy 2016). In calculations of the values for elasticity modulus of the asphalt concretes the load duration was set as equal to 0.1 of a second.

Figure 5 Shows the graphs of the mean half-monthly values of temperature for asphalt concrete layers of "Astana - Burabai" ftom December 2013 till December 2014. Figures 6 and 7 show the values of elasticity modulus and Poisson's coefficient of the asphalt concretes, obtained under the above expressions. It should be noted that the mean half-monthly values of the top and bottom layers for the asphalt concretes of the highway are practically the same.

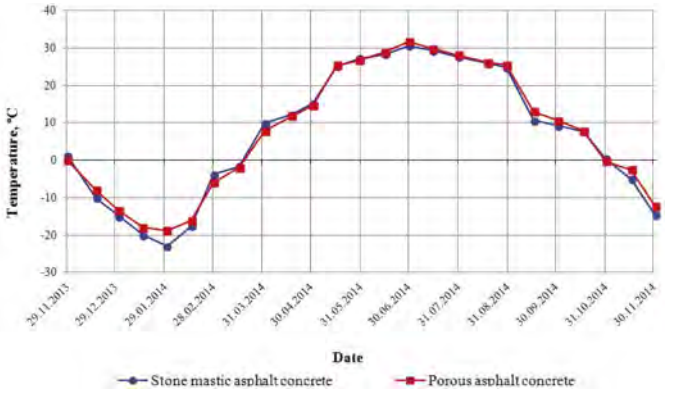

Figure 5. Mean half-monthly values of temperature for asphalt concrete layers.

As one should expect, the character of variation for elasticity modulus of the asphalt concretes is fundamentally opposite to the temperature: the higher the temperature, the lower the elasticity

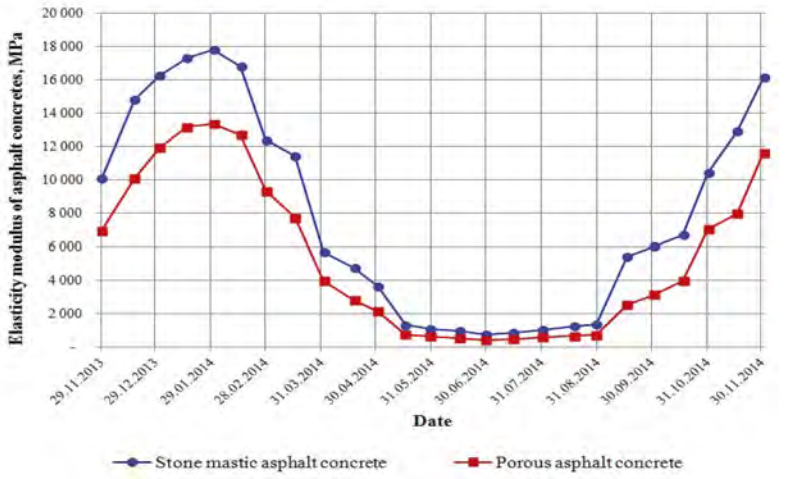

Figure 6. Values of elasticity modulus of asphalt concretes.

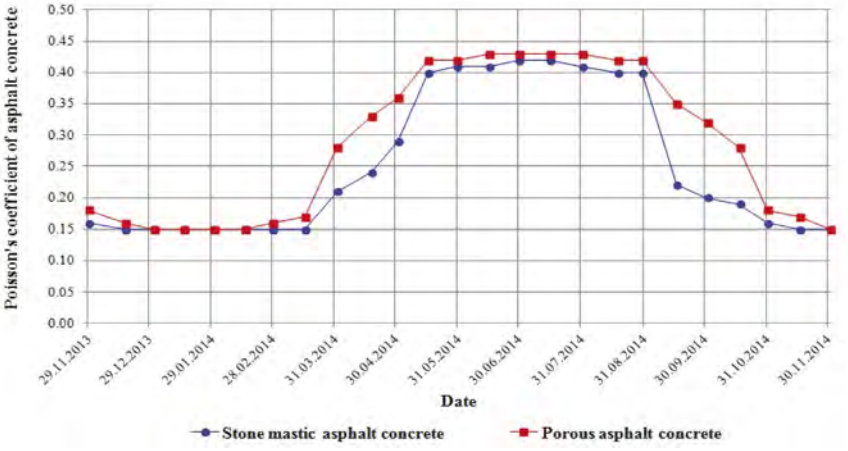

Figure 7. Values of Poisson's coefficient for asphalt concretes.

modulus, and vice versa, the lower the temperature, the higher the elasticity modulus. And qualitative character of variation of the Poisson's coefficient coincides with the temperature: the higher the temperature, the higher the Poisson's coefficient, and vice versa, the lower the temperature, the lower Poisson's coefficient. At high temperatures (in summer) the values of elasticity modulus for both asphalt concretes are practically the same, but at low temperatures (in winter) they are essentially higher for stone mastic asphalt concrete, than for porous asphalt concrete. At high (in summer) and low (in winter) temperatures the values of Poisson's coefficient for both asphalt concretes are practically the same, but at intermediate temperatures (in spring and autumn) they are somewhat higher for the porous asphalt concrete than for stone mastic asphalt concrete.

5.4 *Deformation characteristics of interlayers*

Values of elasticity modulus and Poisson's coefficient of the materials of pavement interlayers (crushed stone, treated with bitumen; crushed stone and sand mix, treated with cement (7%); crushed stone and sand mix; sand) are fixed under the standard document (SP RK 2015).

5.5 *Deformation characteristics of soils*

The values of elasticity modulus for the soil of subgrade (heavy sandy clay loam) at the positive temperatures are set under the standard document (SN RK 2015) depending on soil moisture, and at negative temperatures they are obtained according to the data of the Professor N.A. Tsytovich (Tsytovich 1973) depending on the value of negative temperature and the amount of unfrozen water. The upper part of the subgrade for the highway with thickness of 140 cm (from 80 cm to 220 cm from the asphalt concrete pavement surface) was divided into 7 layers, each of them had the thickness of 20 cm. It was set that for each of those soil layers the temperature and moisture had constant values.

5.6 *Stresses and strains in asphalt concrete layers and subgrade*

Figure 8 represents the graph, showing deflection variation for the surface of the first layer of pavement from stone mastic asphalt concrete. As it is seen, variation of mechanical characteristics for asphalt concrete layers and soil impacts greatly on the deflection value of the pavement surface. Qualitative change of the deflection is of quasi-cyclic nature. It is found that the least deflection values occur from the middle of February to the middle of March, and the biggest ones occur in the beginning of July. The biggest deflection is approximately 5 times more than the least one. Deflection of pavement surface is the only characteristics, which can be measured by non-destructive method. Therefore it is currently used in many countries, including Kazakhstan, for evaluation of strength for the pavement structure (SP RK 2015). It is considered that during spring defreezing of subgrade the pavement structure has the lease strength and the biggest deflection value of the pavement surface. But the graph of deflection shows that the biggest deflection of the pavement surface occurs in the beginning of July, i.e. in summer, but not in spring. In our paper (Teltayev et al. 2018) stated that in the beginning of July the asphalt concrete layers of the pavement have the highest temperature. Therefore, it becomes clear that the biggest pavement deflection in summer season is specified by essential decrease of stiffness (stiffness modulus) of the asphalt concrete layers due to the highest temperatures.

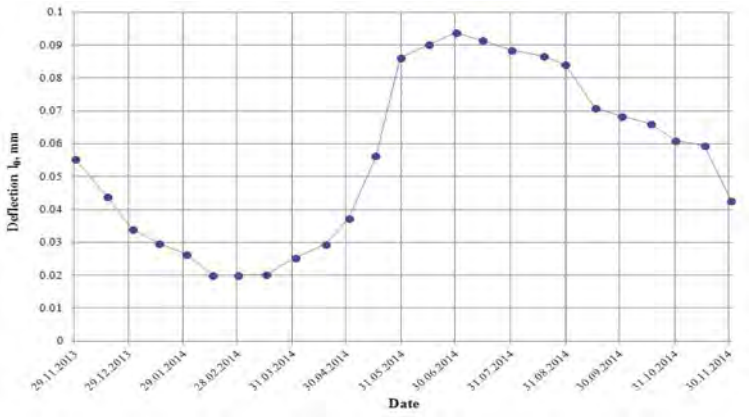

Figure 8. Deflection of the surface for the first pavement layer from stone mastic asphalt concrete.

The next important characteristics for mechanical behavior of pavement are horizontal stress σ_r^2 and strain ε_r^2 in the bottom surface of the second asphalt concrete layer. Stress σ_r^2 and strain ε_r^2 are considered during evaluation of fatigue strength of the asphalt concrete layers. The USA and many other countries include strain ε_r^2 into relevant calculations, but in the countries of the former USSR - the stress σ_r^2. It is found out (Figure 9), the qualitative character of variation for these factors is different. Graph for variation of stress σ_r^2 is identical to the graph for variation of the mean half-monthly temperature of the asphalt concrete: the lower the temperature the higher the stress. In hot period (in summer), when the stiffness

(elasticity modulus) of the asphalt concretes becomes low, the stress changes its sign, i.e. transforms from tension into compression.

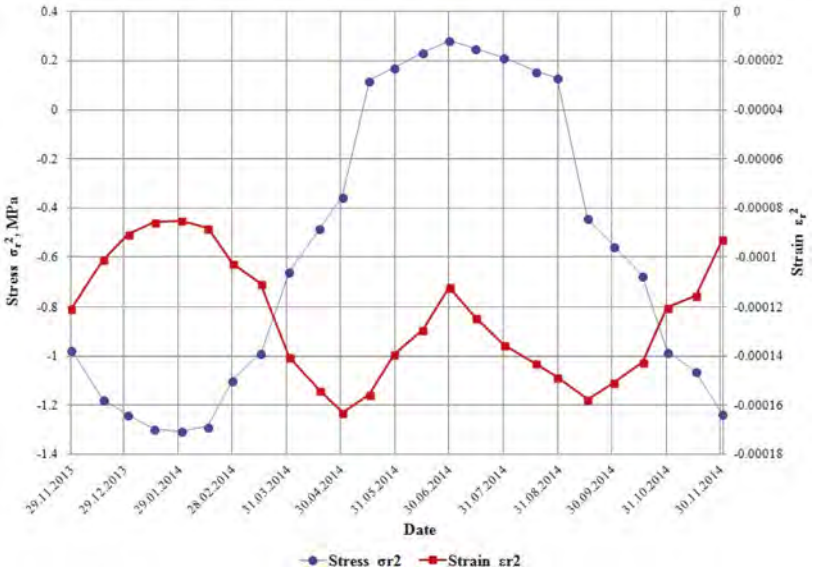

Figure 9. Horizontal stress and strain in the bottom surfaceof the second asphalt concrete layer.

The biggest value of the tensile strength σ_r^2 occurs in the end of January and it is equal to 1.32 MPa, and the biggest value of the compressive strength occurs in the beginning of July and it is equal to 0.28 MPa. The strain ε_r^2 is changed in a more complicated way during annual cycle, but, contrary to the stress σ_r^2, it remains only tensile. Its lowest value, equal to 0.000085 occurs in the end of January, and the biggest values, equal to 0.00016 approximately, occur in the beginning of May and in the middle of September.

The graphs of variation for vertical stress σ_z^{sg} and strain ε_z^{sg} in points of subgrade, located in three different depths, are shown in the Figures 10 and 11. It is seen that freezing of soil impacts greatly on stress and strain in the subgrade. The largest variation of stress and strain during annual cycle occurs on the surface of subgrade and with the increase of the depth the impact of freezing decreases. For example, on the surface of subgrade the biggest vertical

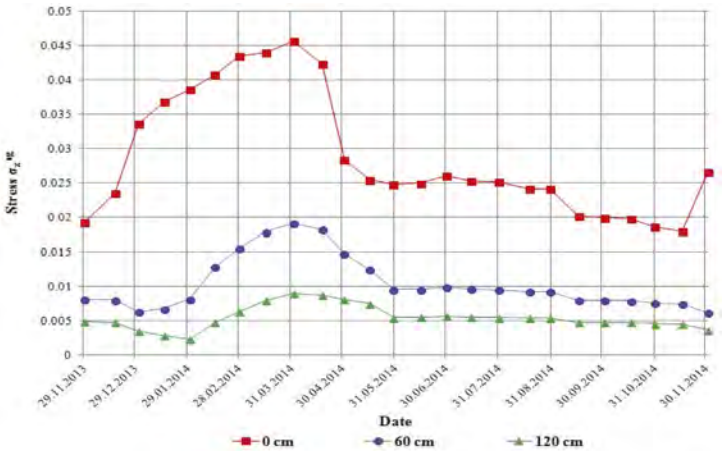

Figure 10. Vertical stress in subgrade.

stress σ_z^{sg} in the end of winter season reaches 0.045 MPa, and in the beginning of winter season it decreases to 0.018 MPa. During freezing the soil becomes stiff and the strain decreases sharply. And with the beginning of defreezing the stiffness of soil decreases sharply, which causes sharp increase of the strain. In the case considered the biggest vertical strain, equal to 0.00043, was registered on the surface of subgrade in the middle of May and it decreases gradually in time before freezing starts.

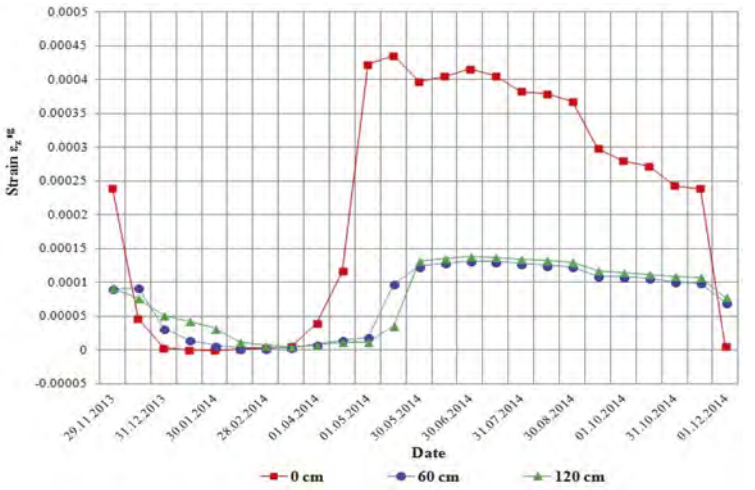

Figure 11. Vertical strain in subgrade.

6 CONCLUSIONS

1. Temperature variation on surface and in points of an asphalt concrete pavement occur in daily, "quasi-month" and annual cycles; in the mid depths (30-100 cm) daily harmony disappears, only "quasi-month" and annual cycles remain; in bigger depths (120-140 cm and more) temperature variation occurs practically only in annual cycle.
2. In cold regions of the republic in wintera pavement and road subgrade have only one long period of freezing and thawing.In warm regions, a "warm" winter may experience two short periods of freezing and thawing.
3. Greatest depths of freezing (260-270 cm) occur in the northern part of the republic, and the smallest ones in the south (60-70 cm); the western region of the republic can be divided into two subregions: the first of them - the northwestern subregion is similar to the central region (130-200 cm); the second subregion - the southwestern one is similar to the southern region (60-130 cm); the eastern region of the republic is slightly softer than the northern one (190-230 cm).
4. In points of subgrade abrupt changes in moisture take place when the temperature passes through 0°C, i.e. these changes show the phase transitions of water from liquid state to solid one (ice) in winter and from solid state to liquid one in spring; the maximum moisture after thawing in spring is greater than before freezing in winter.
5. The dependences of unfrozen water content on temperature for different depths in subgrade do not coincide, which can be explained not only by different values of the initial moisture content, but also by different values of pressure, type and characteristics of the soil (density, porosity, granulometric and chemical properties, etc.) at different depths.
6. Changes in temperature and moisture strongly influence stresses and strains in a pavement and subgrade.
7. When designing pavement structures, it is recommended to divide the entire design period into a number of characteristic sub-periods; in each sub-period, set the calculated values of temperature and moisture, mechanical and all other indicators of materials and soils; apply the principle of damage accumulation.

REFERENCES

Babkov, V.F. 1980. *Landscape Design of Highways*. Moscow: Transport.

Christensen, D.W.& Bonaquist, R.F. 2015. Impoved Hirch model for estimating the modulus of hot mix asphalt. *Journal of the Association of Asphalt Paving Technologists* 84: 527–562.

Huang, Y.H. 2004. *Pavement Analysis and Design*. New Jersey: Pearson Education.

Ivanov, N.N. et al. 1973. *Design and Calculation of Flexible Pavement*. Moscow: Transport.

ODN 218-046-2001. 2001. *Flexible Pavement Design*. Moscow.

Papagiannakis, A.T. & Masad, E.A. 2008. *Pavement Design and Materials*. New Jersey: John Wiley & Sons.

Sarsembayeva, A., Zhussupbekov, A. & Collins, P.E.F. 2022a. Heat and mass transfer by vapour in freezing soils. *Energies* 15 (4): 1515–1531.

Sarsembayeva, A., Zhussupbekov, A. & Collins, P. 2022b. Heat and mass transfer in the freezing soils. *Lect. notes civ. eng.Vol. 230. Adv.geoeng.Belt &Road. BRWSG 2021*. Singapore: Springer Nature.

SP RK 3.03-104-2014. 2015. *Flexible Pavement Design*. Astana.

Teltayev, B. & Aitbayev, K. 2015. Modeling of temperature field in flexible pavement. *Indian Geotechnical Journal* 45 (4): 371–377.

Teltayev, B., Baibatyrov, A. & Suppes E. 2015. Characteristics of highway subgrade frost penetration in regions of the Kazakhstan. *Proc. 15 Asian region. conf. soil mech. geotech. eng., Fukuoka*.

Teltayev, B.B. & Suppes, E.A. 2017a. Regularities for temperature variation in subgrade of highway. *Geomechanics and Engineering* 13(5): 793–807.

Teltayev, B. & Suppes, E. 2017b. Freezing characteristics of a highway subgrade. *Sciences in Cold and Arid Regions* 9(3): 325–330.

Teltayev, B.B., Liu, J. & Suppes E.A. 2018. Distribution of temperature, moisture, stress and strain in the highway. *Magazine of Civil Engineering* 7: 102–113.

Teltayev, B.B. & Suppes, E.A. 2019a.Temperature in pavement and subgrade and its effect on moisture. *Case studies in Thermal Engineering* 13: 1–11.

Teltayev, B.B. & Suppes, E.A. 2019b. Temperature and moisture in a highway in the south Kazakhstan. *Transportation Geotechnics* 21: 1–11.

Teltayev, B.B., Zhussupbekov, A.Zh., Shakhmov&Suppes E.A. 2020. Field experimental investigations of freezing and thawing of highway subgrade. *Lect. notes civ. eng. Proc. TRANSOILCOLD 2019. Transport.soil eng.cold reg. Vol.1. St Petersburg,*2019. Singapore: Springer Nature.

Teltayev, B., Suppes, E., Sarsembayeva, A. & Tileu, K. 2022. Freezing and thawing characteristics in highway pavements and subgrade in conditions of Kazakhstan. *Proc. 20 int. conf. soil mech. geotech. eng., Sydney*.

Teltayev, B. & Radovskiy, B. 2016. Low temperature cracking problem for asphalt pavements in Kazakhstan. Proc.8 RILEM Int. conf.m ech. crack. debond. pavem.

Tsytovich, N.A. 1973. *Mechanics of Frozen Soils*. Moscow: Higher School.

Yoder, E.J. & Witczak, M.W. 1975. *Principles of Pavement Design*. 1975. New Jersey: John Willey & Sons.

Zolotar, I.A. et al. 1971. *Water and Thermal Regime of Subgrade and Pavements*. Moscow: Transport.

Taylor & Francis
Taylor & Francis Group
http://taylorandfrancis.com

Special lectures

Taylor & Francis
Taylor & Francis Group
http://taylorandfrancis.com

Smart Geotechnics for Smart Societies – Zhussupbekov, Sarsembayeva & Kaliakin (Eds)
© 2023 The Author(s), ISBN 978-1-003-29912-7
Open Access: www.taylorfrancis.com, CC BY-NC-ND 4.0 license

On the landslide hazard and resilience with the impact of climate change in Taiwan

K.J. Shou & W.J. Lin
Department of Civil Engineering, National Chung-Hsing University, Taiwan

K.L. Wang
Department of Civil Engineering, National Chi-Nan University, Taiwan

ABSTRACT: This study aims to investigate the landslide susceptibility and resilience of the study area located in Central Taiwan, including the mountain highway and the villages in this area. After calculating the landslide susceptibility values by Logistic Regression model. By considering the core concept of resilience, the control factors were adopted and the data was collected for the study area. In order to explore the temporal behavior of landslide resilience, the population density, electricity consumption per household, and the cost of reconstruction were adopted as the indicators to establish the landslide disaster resilience model. Based on the data layers, the comprehensive linear regression model was established and used for the resilience interpretations, with suggestions on the village human mobility and the rehabilitation budget for resilience enhancement. This study can help for landslide disaster mitigation, especially for the enhancement of landslide resilience of the villages in mountain areas.

1 INTRODUCTION

Following the Hyogo Framework for Action, initiated on the 2005 World Conference on Disaster Reduction (WCDR), Sendai Framework for Disaster Risk Reduction (SFDRR) was presented in 2015, in which the disaster resilience was more clearly defined to improve the capabililty of recovering from a disaster, by the countermeasures in the aspects of social, economy, policy, etc. The most popular definition of resilience could be "the capability of an ecosystem enduring external disturbance and returning to the state before the disturbance". But it is still scarce for the research on the quantitative disaster resilience, including the geohazard-related reslilience. In view of the rainfall induced landslide hazards in Taiwan, quantifying and enhancing the resilience are critical to protect the life, property, and infrastructure in the landslide area. This study comprises two major part, i.e., calculating the landslide susceptibility as a hazard factor, and collecting data of the control factors, then establishing the landslide resilience model of the research area.

2 METHODOLOGIES

The study area is located in the upstream of Wu River watershed in Central Taiwan, with focuses on the mountain highway and the six villages (see Figure 1). Data of the landslide causative factors and the resilience control factors before and after rainfall events in study area were collected, then the landslide susceptibility values were calculated and the landslide disaster resilience models were established.

2.1 *Landslide susceptibility analysis*

This study adopted the Logistic Regression method of Lin (2016), with the nine causative factors, i.e., elevation, slope, slope, dip slope index, distance to fault, distance to road, distance

DOI: 10.1201/9781003299127-9

to river, greenness index, and 72 hour cumulative rainfall. Among them, the hourly rainfall data during 2012~2017 was further analyzed to find the largest 72-hour cumulative in a quarterly basis for each rainfall station, such that we can explore the spatial changing trend of rainfall in the study area.

Considering the villages as the analysis units, the Thiessen's Polygon method was used to obtain the rainfall distribution, as shown in Figure 2. By introducing the seasonal rainfall data to the following Logistic Regression model of Lin (2016), as described in Equation (1), we can obtain the seasonal landslide susceptibility values of each village.

$$\ln[P/(1-P)] = -0.577 \times F_1 + 1.545 \times F_2 + 0.077 \times F_3 - 0.038 \times F_4 - 0.242 \times F_5 - 0.102 \times F_6 - 0.458 \times F_7 - 3.564 \times F_8 + 0.560 \times F_9 - 0.406 \quad (1)$$

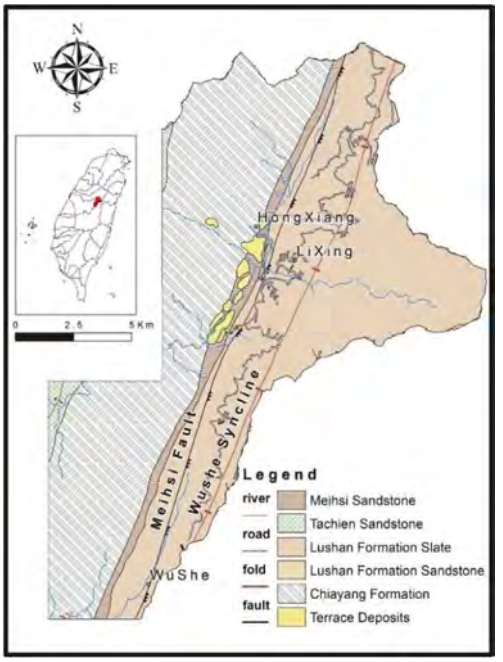

Figure 1. The location and geology of the study area study are in the upstream of Wu River watershed in Central Taiwan.

2.2 *Landslide disaster resilience*

Based on a review of the behavior of landslide hazard, nine control factors were selected for assessing the landslide resilience in the study, including population density, average electricity consumption per household, elder ratio, shelter ratio, fire fighter ratio, medical manpower ratio, income tax, and reconstruction budget.

This study further applied linear regression analysis based on the resilience of landslide disasters defined by Equations (2) and (3). Karen (2011) quantified the resilience of landslide disasters with time dependence, using Equation (2) to define the incremental resilience r(t), as the cost per unit time C(t) multiplying unit time In c(t) and dividing by total time (NI). In Equation (3), by integrating r(t) according to time, the resilience Re can be obtained.

$$r(t) = \frac{C(t)Inc(t)}{NI(t)} \quad (2)$$

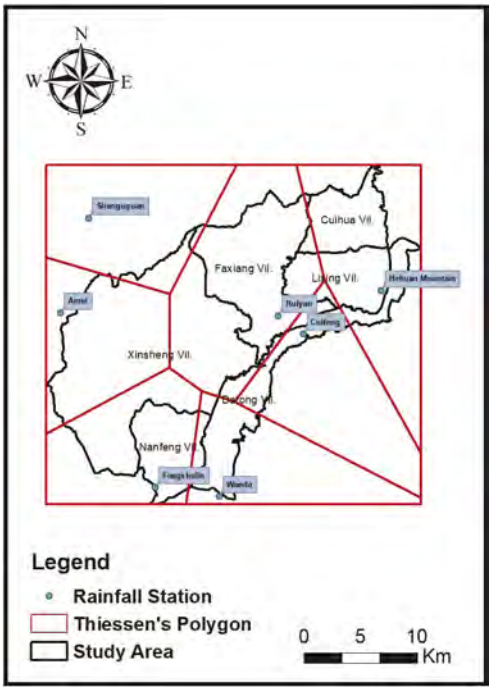

Figure 2. The Thiessen's Polygons to obtain the rainfall distribution of the six villages in the study area.

$$Re(t_s) = \int_{t_0}^{t_s} r(t)dt \tag{3}$$

3 LINER REGRESSION ANALYSIS

In order to more properly establish the landslide resilience model, this study tried to use different control factors and divided the data into high season and low season for linear regression analysis. Before further establishment of resilience model, the correlation of those control factors for the major resilience indicators were analyzed.

3.1 *Population density*

The linear regression analysis was carried out for the high season and low season of different time periods, namely 2012-2016, 2016-2017, 2012-2017, 2012-2015, and 2015-2017. The independent control factors include landslide susceptibility (RI1), elder ratio (RI2), shelter ratio (RI3), fire fighter ratio (RI4), medical manpower ratio (RI5), income tax (RI6), and rehabilitation budget (RI7).

The difference between low season and high season is that the impact of landslide susceptibility on population density is reduced, that is, it shows that the impact of landslides on the study area is relatively lower during the period when the population density is lower. The results suggest that, whether in high season or low season, the best model for forecasting is the 2012-2015 period, as they can properly to predict the population density in 2016-2017. Therefore, the population density could be considered as a dependent factor to assess the recovering from a landslide disaster.

$$Y = -0.731 * RI1 - 0.594 * RI2 + 0.434 * RI3 - .260 * RI4 + 0.820 * RI5 - 0.543 * RI6 - 0.124 * RI7 + 1.879 \tag{4}$$

3.2 *Electricity consumption*

Similarly, the linear regression analysis for the resilience indicator, i.e., electricity consumption, was carried out for the high season and low season of different time periods. Comparing the R^2 coefficients of five models of electricity consumption, i.e., 0.597-0.436, it shows the regression is barely acceptable. The weightings of the control factors on the electricity consumption for the 2016-2017 model (as shown in Equation (5) can be ranked as: landslide susceptibility, medical manpower ratio, shelter ratio, reconstruction budget, income tax, elder ratio, and fire fighter ratio.

$$Y = -0.199 * RI1 - 0.617 * RI2 + 0.419 * RI3 - 1.310 * RI4 + 0.820 * RI5 - 0.505 * RI6 - 0.138 * RI7 + 1.486 \quad (5)$$

Based on the highest R^2 value, it suggested the best mode for both high season and low season is the 2012-2015 model. This model was applied to predict the population density of 2016-2017 with error between 1~53 %, best for Xinshen village and worst for Nanfeng village. For the low season, the error is between 0~66%, 0% for Faxiang village and 66% for Nanfeng village. The results suggest there are variation of error temporally and spatially.

Table 1. The prediction errors of regression models for different seasons in 2016-2017.

		% of Error				
Year	Season	Xinsheng	Lixing	Faxiang	Nanfeng	Cuihua
2016	1	2%	3%	10%	45%	8%
	2	6%	5%	9%	46%	7%
	3	6%	5%	12%	44%	17%
	4	4%	6%	18%	53%	12%
Ave		5%	5%	12%	47%	11%
2017	1	6%	19%	8%	8%	28%
	2	2%	19%	1%	24%	19%
	3	3%	27%	8%	10%	23%
	4	1%	26%	2%	13%	27%
Ave		3%	23%	5%	14%	24%

4 LANDSLIDE RESILIENCE ANALYSIS

This study applied the model of Karen (2011) to study the resilience of landslide disasters, to explore the differences in reconstruction budget in different time scales.

4.1 *Model based on reconstruction budget*

In order to compare the performance of the reconstruction budget on the resilience, the linear regression analysis was carried out by letting reconstruction budget as the dependent variable. The cases of analyses were numbered as shown in Table 2. Case A is for the reconstruction budgets in 2008-2011 and 2012-2016; Case B is for the reconstruction budgets in 2012-2015 and 2016-2017; Case C is based on the reconstruction budget as dependent variable for linear regression, for the periods of 2012-2015 and 2016-2017, and matching with Equations (2) and (3).

The linear regression analysis model with R^2 of 0.623 was used to estimate the 2012-2017 reconstruction budget (see Figure 3); then introduce the data into the formula of Karen (2011) to obtain the resilience, as shown in Figures 4~6. The results show that the resilience of Lihang, Datong, Nanfeng and Cuihua villages changed from negative to positive in the post-2015 period, while that of the remaining two villages (Xinshen and Faxiang) was positive and increasing. In terms of the concept of disaster resilience, the lower the cost of rehabilitation,

the higher the resilience, indicating that its villages do not need too much money to deal with natural disasters. However, it is suggested to have more evidence to support the findings of this study.

Table 2. Different group settings for the resilience analyses.

Case	Groups of data	
A	2008-2011	2012-2016
B/C	2012-2015	2016-2017

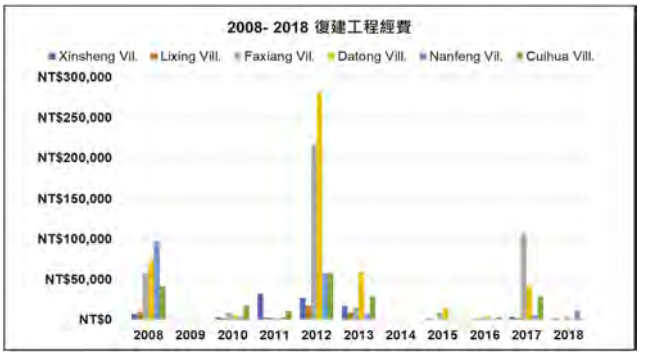

Figure 3. The 2008-2018 reconstruction budgets for the villages in the study area.

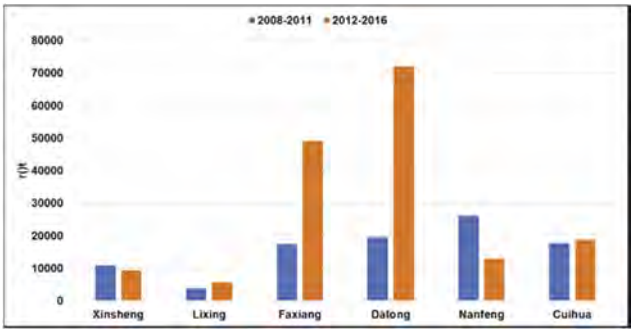

Figure 4. The resilience values of the six villages in the study area, for Case A with the reconstruction budget model.

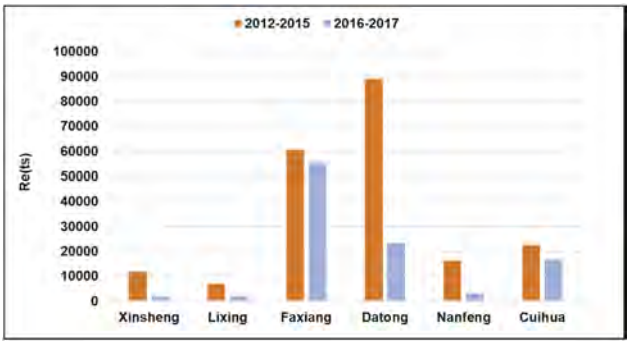

Figure 5. The resilience values of the six villages in the study area, for Case B with the reconstruction budget model.

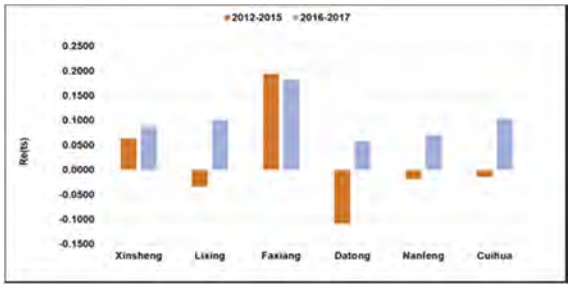

Figure 6. The resilience values of the six villages in the study area, for Case C with the reconstruction budget model.

4.2 *Model based on population density*

For the population density model, the applied data was obtained by the best regression formula, with the largest R^2 value. The seasonal data of 2012-2017 was used as C(t). In order to compare the temporal behavior of population density of each village, two periods of time, i.e., 2012-2015 and 2016-2017, were considered. The unit time of an increment Inc(t) is one season, and the total time (seasons) NI(t) is 16 seasons in 2012-2015 and 8 seasons in 2016-2017.

The results in Figure 7 indicate Nanfeng village is obviously different from the other villages. It could be due to the high regression error of 54%, that also reflects an abnormal behavior of population density. Unlike the other villages, there is no significant variation of population density in Xinsheng and Faxiang villages. Similar to electricity consumption, the population density is an indicator of economic activity. The larger of those two indicators, the larger disaster resilience.

Figure 7. The resilience values of the six villages in the study area, for Case B with the population density model.

4.3 *Model based on electricity consumption*

Similarly, the regression formula with the highest R^2 value is also used to calculate the average electricity consumption per household for each season of 2012-2017 as C(t). The unit time of an increment Inc(t) is one season, and the total time (seasons) NI(t) is 16 seasons in 2012-2015 and 8 seasons in 2016-2017. According to the results of the regression analysis, although the R^2 value is acceptable, but the average error in the performance of the forecast results is up to 68% (Faxiang Village). However, Cuihua village possesses the largest increases in population density and electricity consumption, also has the highest disaster resilience out of the six villages.

Two different interpretations are summarized according to different indicators of disaster resilience. First of all, the reconstruction budgets are as the cost of post-disaster repair, the more budget invested the more time the region needs to return to a stable state. Therefore, as a wayward evaluation value the greater the disaster resilience is lower. Based on the results of Cuihua Village, the population density and electricity consumption are the highest compared with other villages, and the comparison with the calculation results of the village's reconstruction

budget shows that the reconstruction budgets of the village in 2008-2018 were relatively large compared with other villages. In order to compare the performance of the reconstruction budget.

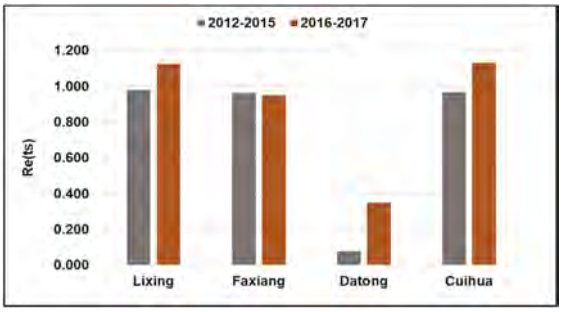

Figure 8. The resilience values of the villages in the study area, for Case B with the electricity consumption model.

5 CONCLUSIONS ANS DISCUSSIONS

This study adopted the upstream of Wu River as the research area, and chose the control factors by to establish the resilience model by linear regression method. In order to incorporate the concept of disaster resilience, population density, electricity consumption, and reconstruction budget were used as the indicators of resiliece. And the following conclusions are drawn from the analysis results:

For the landslide susceptibility, this study adopted the Logistic Regression model of Lin (2016) to produce landslide susceptibility values. The 99% percentile susceptibility value of the grid unit was conservatively considered as the landslide susceptibility of the village. In the establishment of landslide disaster resilience assessment indicators, covering the hazard, preservation, response and reconstruction indicators. The following four groups of control factors were adopted for the resilience analysis, i.e., (i) landslide susceptibility, (ii) population density and electricity consumption, (iii) elder ratio, shelter ratio, fire fighter ratio, and medical manpower ratio, (iv) income tax and reconstruction budget.

Based on the analysis results using the resilience model of Karen (2011), with considering reconstruction budget, population density, and electricity consumption as resilience indicators, it suggests the smaller the value calculated by the reconstruction budget represents higher resilience. On the other hand, for population density and electricity consumption, the smaller the calculated value the smaller the resilience.

Through the analysis of population density as a dependent variable, it is possible to find the time at which the villages return to the pre-event stable state. However, for the quantitative analyses, the number of samples is crucial to obtain promising results. It is suggested to optimize and simplify the resilience model of the most important indicator factor. Such that the error of the model can be reduced and the efficiency of the evaluation can be increased.

ACKNOWLEDGEMENTS

This research was made possible by the financial support of the Ministry of Science and Technology (Project No. 109-2625-M-005-001) of Taiwan. We also deeply appreciate the databases and support from the Central Geological Survey project (Project No. 97-5826901000-05).

REFERENCES

Karen, S.R., 2011. On Landslide Risk, Rresilience and Vulnerability of Mountain Communities in Central-Eastern Nepal, Thesis, University of Lausanne.

Lin, J.F., 2016. On the Rainfall Factor for the Landslide Susceptibility Analysis in Central and Southern Taiwan Areas, Thesis, National Chung-Hsing University.

UNISDR, 2015. Sendai framework for disaster risk reduction 2015–2030.

UN World Conference on Disaster Risk Reduction, 2015 March 14–18, Sendai, Japan.

Smart Geotechnics for Smart Societies – Zhussupbekov, Sarsembayeva & Kaliakin (Eds)
© 2023 The Author(s), ISBN 978-1-003-29912-7
Open Access: www.taylorfrancis.com, CC BY-NC-ND 4.0 license

Geotechnical contribution in Central Asia: Practice and lessons learnt

W. Kwiatkowski & A. Korpach
Keller Central Asia LLP, Atyrau, Kazakhstan

ABSTRACT: Presented is some geotechnical experience of Keller Central Asia LLP based on projects executed since 2014 in the Central Asia region. Only some selected execution experience is shared without detail description of well-known technologies. The wet soil mixing technology deserves special attention as it was implemented in Kazakhstan in year 2020 for the first time by Keller Central Asia LLP. Selected local experience related to concrete precast piles and Deep Soil Mixing (DSM) will be shared in this article.

1 INTRODUCTION

Keller Central Asia LLP is a regional part of Keller Group plc., with its office located in Atyrau, Kazakhstan since 2014. Having the first category construction license, design and testing licenses as well as ISO 9001 certifications, allows Keller to provide the full range of professional geotechnical services at the local market.

Keller Group plc. with its history since 1860, is the world's largest and innovative independent ground engineering contractor. With permanent operations in more than 40 countries across five continents, Keller has the financial strength, know-how, capacity, and the global reach to tackle some of the largest and most demanding projects around the world. The local presence allows Keller to solve geotechnical problems and helps to service our Clients in Central Asia. Keller has successfully developed many of the ground engineering techniques which are now widely accepted in the construction industry, i.e.: ground improvement, special grouting, piling and earth retention, anchors, nails, micropiles, instrumentation, and monitoring.

Keller Central Asia LLP executed its first job in Tengiz Oil&Gas field and that time it was the largest geotechnical project in the region as well as in Keller's history. Subsequent projects followed Tengiz one and required the use of different geotechnical solutions including a first time application of wet soil mixing in Kazakhstan.

Special attention will be put on Deep Soil Mixing (DSM) as this is relatively new technique in Kazakhstan, and design and execution aspects are fundamental for its proper application. So far, DSM has been implemented by Keller Central Asia LLP as soil improvement for infrastructure, residential projects and retaining walls for deep excavations. However, DSM can be also used for bridges, wind turbines foundation systems or filtration barriers when properly designed and executed.

2 CONCRETE PRECAST PILES

Concrete precast piles are well-known and widely used foundation method in Kazakhstan. It is usually the fastest and often the cheapest method which can be used in different soil conditions and typically regardless of the weather conditions. The concrete precast piles are usually square section 300x300, 350x350 or 400x400 mm made of concrete C20/25 or C25/30 with non-prestressed reinforcement and length up-to 16 meters. Concrete precast piles are classified

DOI: 10.1201/9781003299127-10

in the standard catalogue "Series 1.011.1-10" of typical concrete constructions, where working drawings for different types of piles can be found. Based on the market research done in 2014, there are more than 200 piling rigs with hammers for concrete precast pile driving in Kazakhstan. Most of the piling rigs are owned and used by general construction companies where geotechnics is not part of their core company profile.

Keller Central Asia LLP was awarded the contract for procurement and installation of ca. 40,000 concrete precast piles at Tengiz Oil&Gas field (Western Kazakhstan) in 2014. Pile installation was done within a 3,5 year period using owned, as well as locally sourced piling rigs and personnel.

Based on the above mentioned project, the authors would like to share some insights which are often ignored and not taken into consideration during the execution of many smaller projects.

2.1 *Application of bitumen protective coating on the concrete precast piles external surface*

The geotechnical conditions in western Kazakhstan are typically a mixture of sand, clay, loam and sandy loam. The ground level is ca. 24,0 to 25,5 meters below sea level and the ground water table varies, depending on the season, between 1,0 to 2,5 meters below the terrain. The region is located within the Caspian sedimentation basin where the soil and ground water contain chlorides and sulphates, moderate to highly aggressive to concrete and reinforcement steel.

The aggressiveness of the soil and water is the reason for bitumen coating application to the piles. This practice has started in the late 90's and still continues for almost all projects in the region where concrete precast piles are designed. However, Keller's experience shows that bitumen application has significant negative impact on piles bearing capacity, as well as durability problems with the coating during transportation, handling and storage of the coated piles.

During execution of the Tengiz project, 167 vertical static load tests were performed. The first tests showed relatively large final settlement (after complete unloading) as well as significant creeping (lack of settlement stabilization) of tested piles. The discussion with the Client and engineering team brought us to the conclusion that concrete admixture shall be incorporated instead of bitumen coating. The concrete admixtures available now on the market are intended for concrete sealing and cause significant reduction of concrete permeability as well as an increase in resistance to aggressive chemical compounds, such as sulphates or chlorides.

Finally around 40% of piles had bitumen coating and 60% were fabricated with a concrete admixture. The comparison of piles behaviour with bitumen and concrete admixture is shown in the table and figures below. This demonstrates that incorporation of concrete admixture instead of bitumen application was a positive decision.

Table 1. Comparison of pile behaviour under loading (both piles 14 m long at the same area no. 41).

Parameter	Pile 0059 with bitumen coating	Pile 0063 with concrete admixture
Maximum settlement at load 1605 kN	39 mm	4,8 mm
Final settlement (after complete unloading)	35 mm	2 mm
Duration of load test	4000 minutes	1650 minutes

The conclusion is pretty clear, the influence of bitumen coating on pile settlements and creeping is significant. This has been confirmed by a number of other tests done on both types of piles within the project duration.

There are also other practical disadvantages of bitumen coating application compared to concrete admixture. The most important are degradation of coating when exposed to the sun and mechanical damages of coating during transportation and lifting operations, both shown in the Figure 5a and b below.

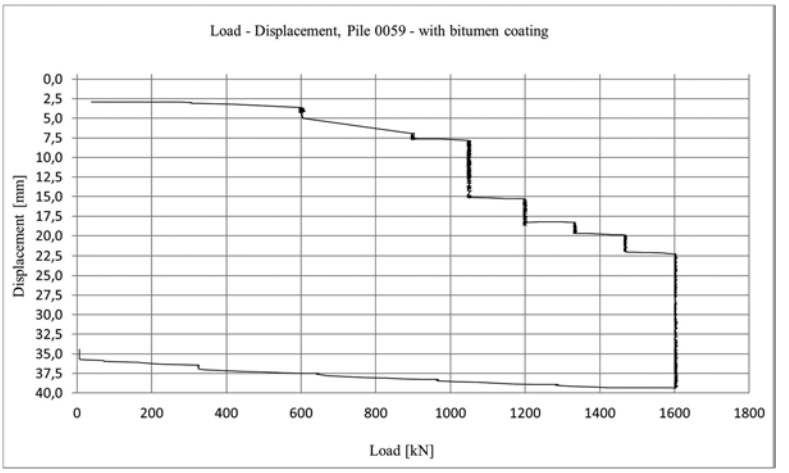

Figure 1. Load – displacement curve for pile 0059 with bitumen coating.

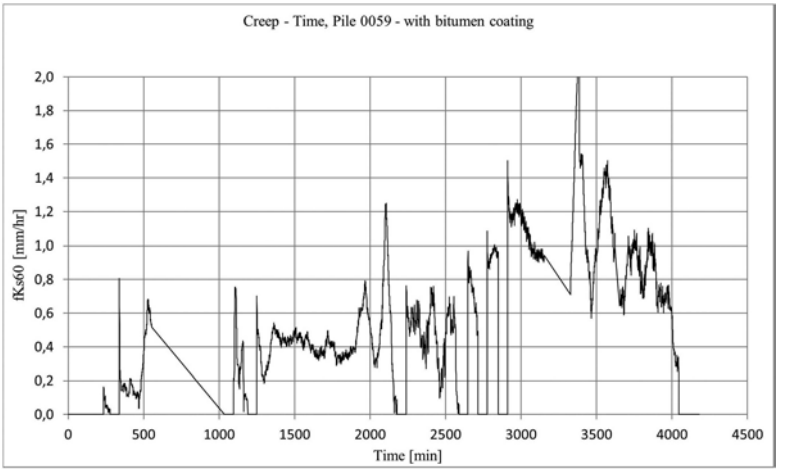

Figure 2. Creep – time curve for pile 0059 with bitumen coating.

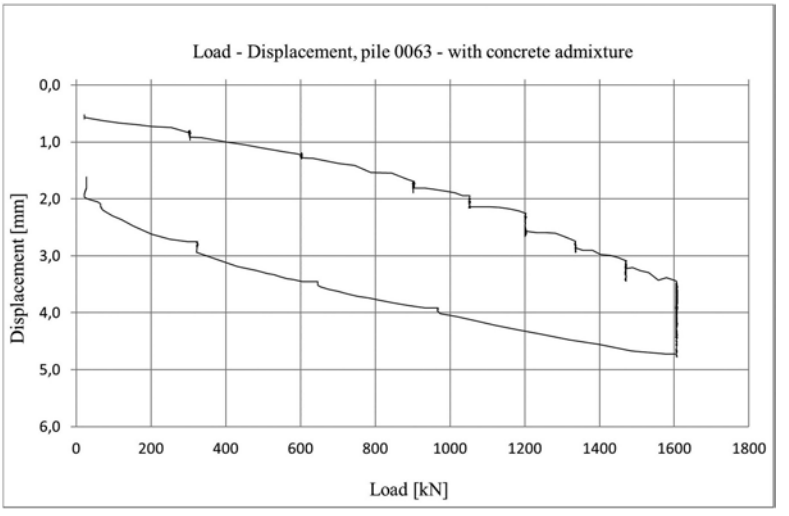

Figure 3. Load – displacement curve for pile with concrete admixture.

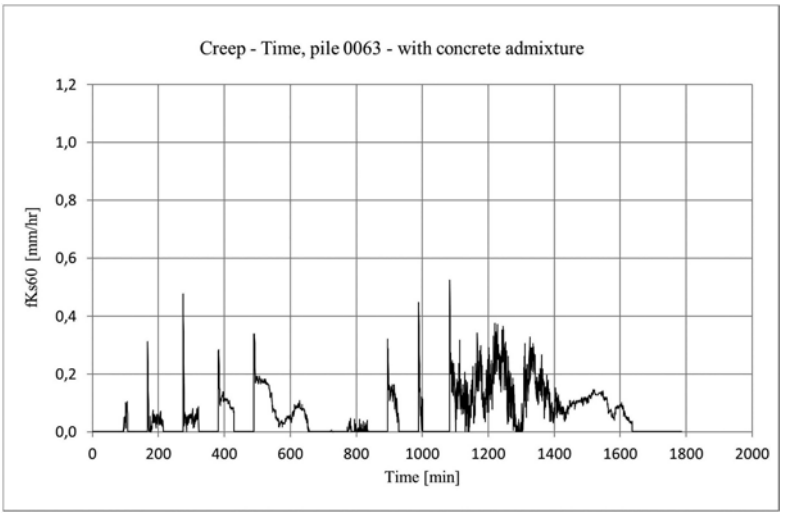

Figure 4. Creep – time curve for pile 0063 with concrete admixture.

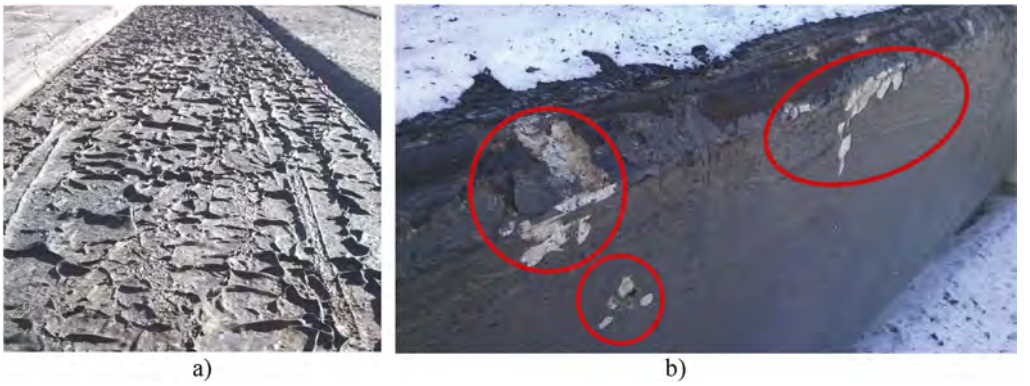

Figures 5. Degradation of bitumen coating a) sun exposition b) during transportation and lifting operations.

2.2 *Concrete precast piles heave and re-tapping (re-striking) of the piles*

Driving of concrete precast piles may initially spear technically straight forward and in many cases piling contractors just drive piles at the designed depth without controlling the driving criteria, internal stresses or pile behaviour after driving. In fact, driving of concrete piles is much more complicated than it seems. One of the aspects regarding concrete precast piles is heave control and potential retapping of the piles.

The phenomenon of piles heave was observed during execution of piles at Tengiz project and it will be presented based on data for Generator 1 (project Area 52) shown in Figure 6.

All piles at Generator 1 met driving criteria before they reach the design depth. Consequently, piles were sticking out above the ground (see Figure 7). This caused additional impediment for post-driving geodetic survey check and later cutting/trimming of the piles.

All elevations of the piles were checked just after driving and later re-checked over some period of time and installation of the adjacent piles. A very dense pattern of the piles (1,2 meters axially between the 400x400 mm cross-section piles) was the reason for pile heave as well as horizontal displacement (moving of already driven pile by the next ones). The geodetic survey showed the heave of practically all piles, with an average value of 26 mm with maximum of 98 mm at Generator 1.

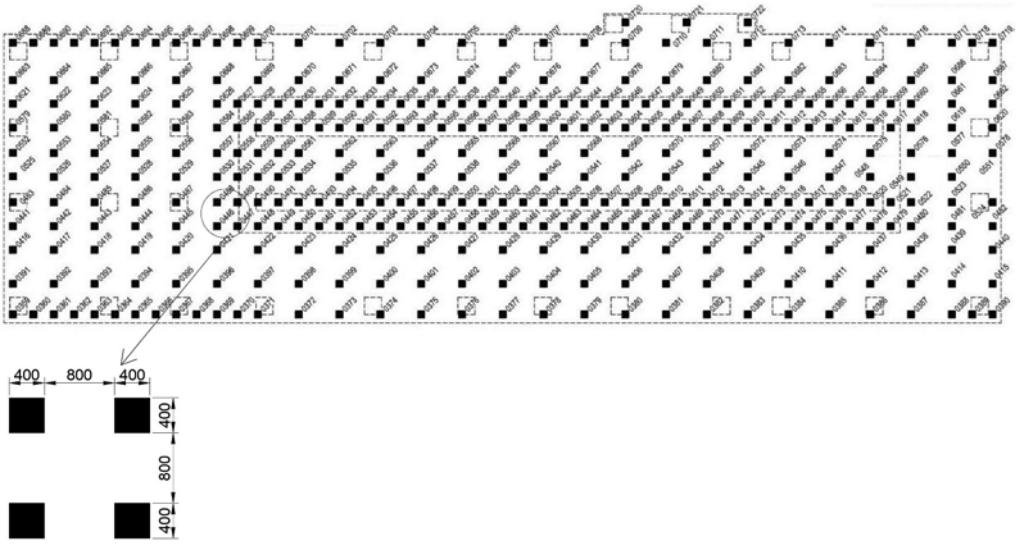

Figure 6. Piling layout, Generator 1, Area 52.

Figure 7. Concrete precast piles at Generator 1, area 52.

Consequently, sequence of piles driving was changed as well as re-tapping of the piles was implemented. The crane suspended hammer was used for re-tapping activity, which is shown in Figure 8.

Figure 8. Retapping activity with crane suspended hammer.

3 DEEP SOIL MIXING (DSM), WET METHOD

Soil mixing is an advanced ground improvement technique requiring considerable expertise in planning, design and execution. The technique leads to significant improvement of the mechanical and physical properties of the in-situ soil, which is mixed with cement or compound binders to form the so-called soilmix (or soil-cement). The resulting stabilised soil generally has a higher strength, lower permeability and lower compressibility than the original soil. The soil to be improved is mixed mechanically in-situ either with a binder in a slurry form (wet method) or with a dry binder (dry method). Slurry jetting can be also used to enhance mechanical mixing, and increase column diameter. The ability to choose between dry and wet processes enables Keller to offer tailored soil mixing applications.

There are many publications where different aspects of soil mixing are described and discussed between professionals including design approach, execution details as well as quality control. The paper describes and presents experience gained with wet deep soil mixing process based on almost 100,000 linear meters of DSM columns done by Keller to date in the Central Asia region.

3.1 *Design of DSM*

The design approach and methods are widely described in many standards and publications, however the most important parameters of DSM soil-cement material are unconfined compression strength *UCS* and deformation modulus E_0 which are based on the local experience, database and statistical analysis.

To determine *USC* and E_0 Keller Central Asia LLP undertook test fields and commissioned laboratory tests for DSM columns performed in Shymkent at 2 projects, in similar soil conditions. The detailed results of laboratory tests are described in the separate report (KazNIISA JSC 2022), however, it will be shortly summarized herein.

The scope of tests covered determination of *UCS* and E_0 (for natural humidity and water saturated) based on 90 tests for determination of *UCS* and 22 tests for determination of E_0 and Poisson ratio *v*. The results are summarized in Table 2.

a) b)

Figure 9. Test DSM columns a) and core samples b).

Table 2. Results of *UCS* and E_0 determination.

Humidity of the core sample	Direction of core sample	Density (kg/m^3)	Characteristic unconfined compression strength *UCS* [MPa]	Deformation Modulus M_0 [MPa]	Poisson ratio *v*
Dry (normal humidity)	horizontal	1721	6,36	424,3	0,287
	vertical	1725	4,68		
Wet (water saturated)	horizontal	1921	3,70	381,5	0,316
	vertical	1907	3,14		

The above presented results were reached for cement content in soil-cement material: 340 kg/m^3 and are valid only for the soils in Shymkent region where DSM technology is now commonly used.

Based on the local standards, calculations of settlements of the objects and bearing capacity of DSM columns system shall be performed for the worst soil parameters, i.e. for water saturated collapsible soils with decreased parameters.

The required design value f_{cd} of the compressive strength of soil-cement material can be calculated as follows (Topolnicki, 2016):

$$f_{cd} = 0,85\frac{f_{ck}}{\gamma_m} \tag{1}$$

where:
0,85 - reduction factor for potential long-term effects affecting strength of the deep mixed soil, γ_m = partial safety factor for the deep mixed soil, applying γ_m = 1.5 for permanent and transient loads, and γ_m = 1.3 for accidental loads, f_{ck} - characteristic compressive strength of soil-cement material.

This practically means that for average f_{ck} = *(3,70+3,14)/2 = 3,42 MPa,* the maximum load on 1000 millimetre diameter DSM column shall not exceed: F_{max} = *1521 kN.*

One of the typical DSM column layouts for a 16-floor residential building located in Shymkent is shown at the Figures 10 and 11.

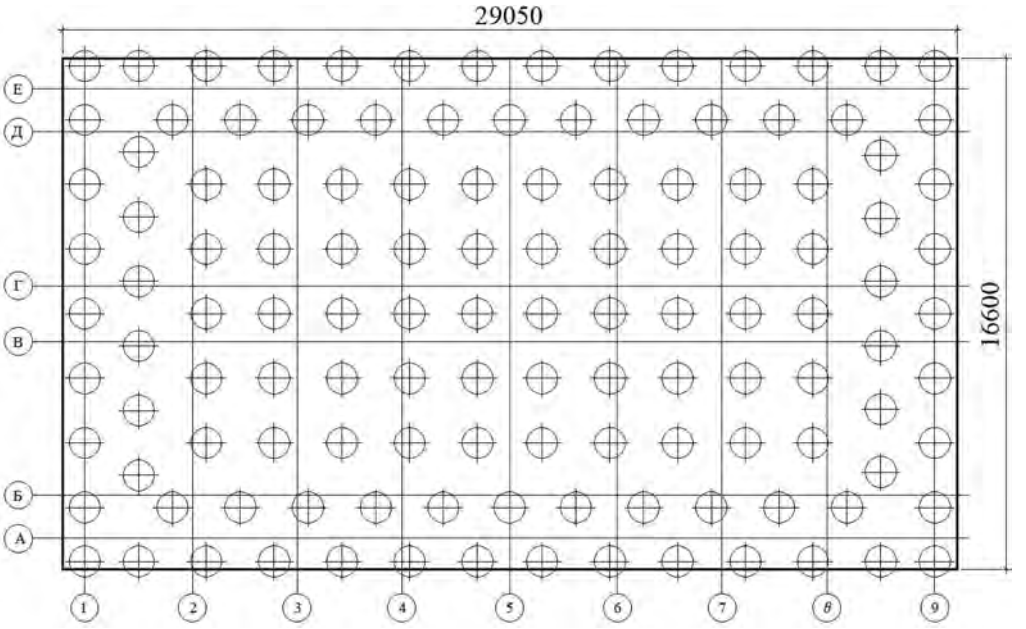

Figure 10. DSM layout, 126 DSM columns, average design pressure under the foundation slab: 398 kPa.

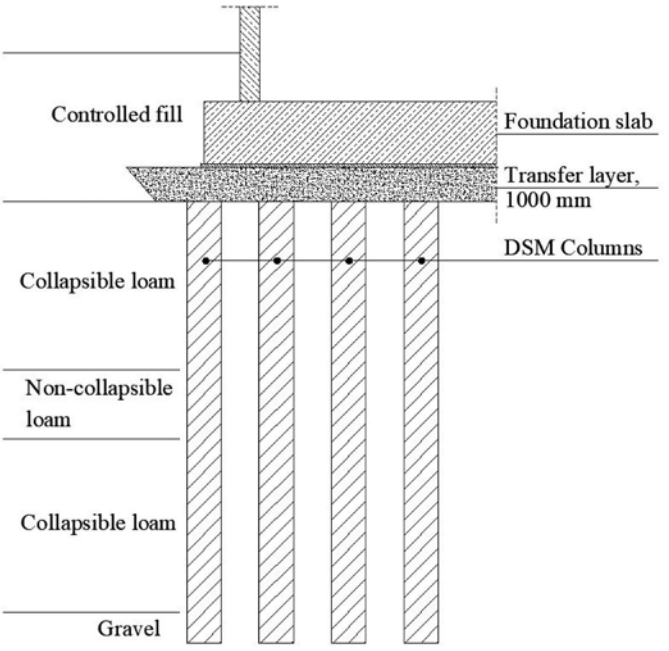

Figure 11. Soil improvement with DSM technology under the 16 floor residential building – cross section.

3.2 *Execution good practice and quality control of DSM columns*

Soil mixing may appear straightforward, however in fact this is advanced technology which requires advanced quality control and know-how based on the experienced gained in the past.

The standard quality control of DSM consist of:

– Control of cement slurry density. For this, computer controlled mixers and areometers are used. Each part of cement slurry prepared in the mixers shall follow the mix design (recipe) as well as a check on the density of slurry for each part shall be performed.
– Volume of cement slurry pumped for each DSM column. Knowledge about volume of cement slurry as well as its density is crucial for each DSM column. This allows calculation of the cement content in the soil-cement mixture, which must be closely controlled.
– Unconfined compression strength of soil-cement mixed material. Collection of the samples is possible from a "fresh" already executed DSM column or/and by core drillings. The samples are usually collected on a daily basis.
– Sometimes, a vertical static load test of single or/and group of DSM columns is performed.
– Real time observation and recording of the following production parameters: - column depth, - execution date and time, - total volume of the cement slurry, - actual flow of the cement slurry and distribution of cement slurry over the time, - distribution of the cement slurry volume along the DSM column - drill pressure, - crowd force, - BRN (Blade Rotation Number)

The quality of the DSM columns depends on many factors but mixing process and consequently homogeneity of the DSM column is one of the most important. For better control of the mixing process the BRN (Blade Rotation Number) shall be observed (Topolnicki, 2018).

$$\mathrm{BRN} = \Sigma \mathrm{M} \left(\frac{R_p}{V_p} + \frac{R_w}{V_w} \right) \cdot n \tag{2}$$

where:
BRN - blade rotation number [rev./m], ΣM- total number of mixing blades (a full diameter blade is counted as two blades), R_p - rotational speed of the mixing tool during penetration [rev./min], V_p - penetration velocity [m/min], R_w – rotational speed of the mixing tool during withdrawal [rev./min], V_w - withdrawal velocity [m/min], n - number of restroking cycles to full depth.

The BRN value is especially important in the soils where the mixing process is difficult (e.g. clays). BRN shall be controlled for every column, and needs to determined by an experienced engineer and piling rig operator for every project individually, however it shall be not less than 400 [rev./m] for well mixed DSM column.

4 CONCLUSIONS

When concrete precast piles are executed, many aspects shall be taken into account. Some of these aspects are: corrosion protection and piles heave, described in this article. The general practice in western Kazakhstan is to use bitumen protection of concrete precast piles, however as described herein, it is considered that this approach is incorrect and concrete admixtures shall be applied instead. The examples and comparison of both solutions are presented in Section 2 where significant negative impact of bitumen coating on bearing capacity and creeping is described.

Concrete precast piles are commonly used within the residential construction sector. Many construction companies don't sufficiently consider the driving process and many instances where external stresses are exceeded or heave becomes apparent have been observed. The heave phenomenon described in Section 2 of this article may have influence on building settlement when not properly controlled.

The DSM technology was implemented in Kazakhstan by Keller Central Asia in 2020 for the first time. The design process differs from the traditional "piling" approach and some other aspects are important. The author has highlighted the very basic issues regarding DSM design, however the experience, real projects and advanced calculations are much more complicated and advanced and it needs to be developed in Kazakhstan.

The DSM execution process requires modern equipment with advanced control and recording system in place. Beside proper design, the high level execution of DSM is needed to obtain safe and cost effective foundation solutions.

REFERENCES

KazNIISA JSC 2022, Kazakh Scientific Research and Design Institute of Construction and Architecture. Technical report for the construction of the foundations of the object: "Construction of the multi-apartment residential complex Arman Qala-1 with built-in premises and parking, located at the address: Shymkent, Karatau district, block 189, Section 513, on the territory of Shymkent City."

Topolnicki M. 2016. General overview and advances in Deep Soil Mixing.

Topolnicki M. 2018. Ground improvement instead of piling – effective design solutions for heavily loaded structures.

Smart Geotechnics for Smart Societies – Zhussupbekov, Sarsembayeva & Kaliakin (Eds)
© 2023 The Author(s), ISBN 978-1-003-29912-7
Open Access: www.taylorfrancis.com, CC BY-NC-ND 4.0 license

Consolidation problem of dredged fill soil for large-scale land reclamation project

E.C. Shin
Incheon National University, Korea Consultant Co., Ltd., Incheon, Republic of Korea

Y.J. Yi
POSCO Engineering and Construction Co., Ltd., Republic of Korea

Y.C. Chang
Mokpo National Maritime University, Jeollanam-do, Republic of Korea

J.K. Kang & J.S. Yoo
Korea Consultant Co., Ltd., Gyeonggi-do, Republic of Korea

ABSTRACT: Land reclamation from the sea is one of best methods to expand the land and obtain the suitable land for the construction of port and harbor, and industrial complex. The man-made land is being normally created along the costal line in the way of sea-dike construction and fill the dredged soil inside the dike by hydraulic method due to the lack of good soil from landside. In this case, the most of dredged soil in west coast of the Korean Peninsular is composed of soft clay, silty, and silty sand. The magnitude of self-weight consolidation settlement level is a great concern for proper estimation of volume of dredged filled soil. The self-weight consolidation tests for the dredged soil obtained from sea were conducted under the conditions of 300%, 600%, and 1000% water contents. The consolidation settlement factors such as void ratio, water content, volume change ratio, and sedimentation consolidation coefficient were determined to propose a self-weight consolidation relationship. The settling factors are derived according to the self-weight consolidation theory by finite strain. In addition, the volume change ratio was derived through the relationship between the interfacial height and the actual soil height, and the settlement amount and the volume change ratio according to elapsed time were predicted. This result is compared with the results of field surveying by using field surveying equipment as well as drone surveying. Based on the results of this study, when the fine-grained soil content (#200 sieve passing) of the dredged soil is 30% or more, the estimation of the settlement amount by the self-weight consolidation theory and experiment work shows a deviation of about 4% compared to the actual value of the field. It is found that the settlement amount of dredged soil by self-weight consolidation theory can be predicted more accurately than that of existing Port and Fishing Port Design method (2015) which gives a deviation of about 8.5%.

1 INTRODUCTION

As the supply of good soil from land for land reclamation project in coastal area is rather limited, therefore the use of sea route dredged soil is being increased. When the reclaimed area is large, there are many errors in the estimation of the settlement amount of the dredging reclaimed land site, and the settlement management at the reclaimed area is not effectively performed due to practical problems. The methods of landfilling are a method of pumping dredged soil to a landfill by pump type dredging ship with the capacity of 20,000 HP. In the dredging process of seabed soil excavating and transporting it to the landfill site through the

DOI: 10.1201/9781003299127-11

discharge pipe, the soil may float out, and some of it may be lost to the outside of the planned landfill site. At this time, the accumulation soil in the planned area with considering soil loss is called the retention volume.

When designing a landfill site, the retention ratio is calculated by the average after self-weight consolidation test or calculating the retention ratio according to the grain size and species of the dredged soil. The settlement rate is expressed by the settlement amount for the ground layer thickness and settlement value by Terzaghi's one-dimensional consolidation theory (1943). Richart (1957) suggested the finite stain theory with the relationship between effective stress and void ratio for one-dimensional consolidation analysis of soft clay. The sedimentation and self-weight consolidation behavior of dredged soil were studied by Mikasa (1963) by using Osaka clay and Gibson et al. (1967) by one-dimensional non-linear finite strain consolidation theory. Imai (1980) conducted sediment experiment work on the Japanese dredged clay and studied the interaction behavior between settling and consolidation.

Yano (1985) predicted the settling volume of dredged soil in the landfill site by using interfacial height change with elapsed time, which is widely used in Korea. Lee & Lee (2011), Lee & Choi (2016) investigated the behavior of self-weight consolidation for the dredged soil in western coastal region in Korea. Shin et al. (2017) presented about the determination of retention ratio by the results of self-weight consolidation test for ship navigation route dredged soil in Incheon region, Korea. Figure 1 shows the location of the ground investigation site in west coast of the Korean Peninsular for this research.

Figure 1. Location of the ground investigation from the ship navigation route in the Gunjang harbor in Mid-west coastal region of Korean Peninsular.

2 SETTLEMENT OF DREDGED SOIL BY SELF-WEIGHT CONSOLIDATIOJN THEORY

The percentage of retention volume against total volume is called the retention ratio. Estimating the dredging volume based on the retention ratio is based on Equation 1:

$$M = \frac{M_0}{R} \tag{1}$$

where, M is the volume of dredged soil for landfill site (m^3), M_0 is the volume of the landfilled soil (m^3) considering the settlement rate and the shrinkage rate, and R is the average retention rate (%) of the landfill by the pump dredger.

Korea Port and Harbor Authority (KPHA) issued the design standard (KDS, 2015) proposed the retention ratio (R) for different types of soils, that is, $R < 70\%$ for clayey soil, $70\% < R < 95\%$ for sand and sandy silt, and $95\% < R < 100\%$ for gravel. Korea Rural Community

Corporation (KRCC, 2011) gives more detail information regarding on the soil loss rate with considering the particle size as described in Table 1. This manual indicates that the soil has a particle size bigger than 1.2 mm, there is no soil loss. However, if the soil has a particle size less than 0.75 mm, then soil loss rate is greater than 35%.

Table 1. Classification of soil loss rate by soil particle size (KRCC, 2011).

Particle size (mm)	Loss rate (%)	Remark
More than 1.2	-	
1.2∼0.6	5∼8	
0.6∼0.3	10∼15	
0.3∼0.15	20∼27	
0.15∼0.075	30∼35	
0.075	30∼100	

The volume of the landfilled soil (M_0) in the land reclamation project can be estimated with the consideration of consolidation settlement at the original soil ground (R_s) as well as compression ratio of dredged filled soil or self-weight consolidation settlement (R_c).

Therefore, the volume of the landfilled soil (M_0, m^3) can be written as Equation 2:

$$M_0 = \frac{M_0}{1 - R_0} \times (1 + R_0) \tag{2}$$

3 SELF-WEIGHT CONSOLIDATION AND RETAIN RATIO

3.1 *Self-weight consolidation theory*

Self-weight consolidation settling curves are classified into sections of flocculation, settling with increasing settling velocity, and consolidation settling. At this time, the starting point of consolidation settlement is generally based on the inflection point at which the settling velocity slows down.

The time of self-weight consolidation is the time corresponding to the intersection point of the tangent line in the settlement section and the consolidation settling step. In the time-settling curve, the point that meets the tangent line at the bottom curve becomes the end point of settling, and this end point can be estimated as the self-weight consolidation time.

Figure 2 shows the method for determining the starting point of self-weight consolidation through the separation of the settling and consolidation step.

When a sample having the same initial water content and different contents of fine particles has settled and consolidated, the dredged soil, which has the form of section settlement, enters the self-weight consolidation step according to the passage of time through the sedimentation and accumulation steps.

In the relation between the interface height and sedimentation time, a linear relationship Equation 1 can be obtained, and the interface can be obtained as Equations 3 and 4:

$$\log H = \log h_1 - C_S \cdot \log t \tag{3}$$

$$H = h_1 \cdot t^{-C_S} \tag{4}$$

where, h_1 is a constant indicating the height at which $H = h_1$ at t = 1 (min), and C_s is the settling consolidation coefficient.

The beginning point of the straight line is the start point of self-weight consolidation, while the end of the straight line is defined as the self-weighted consolidation end point.

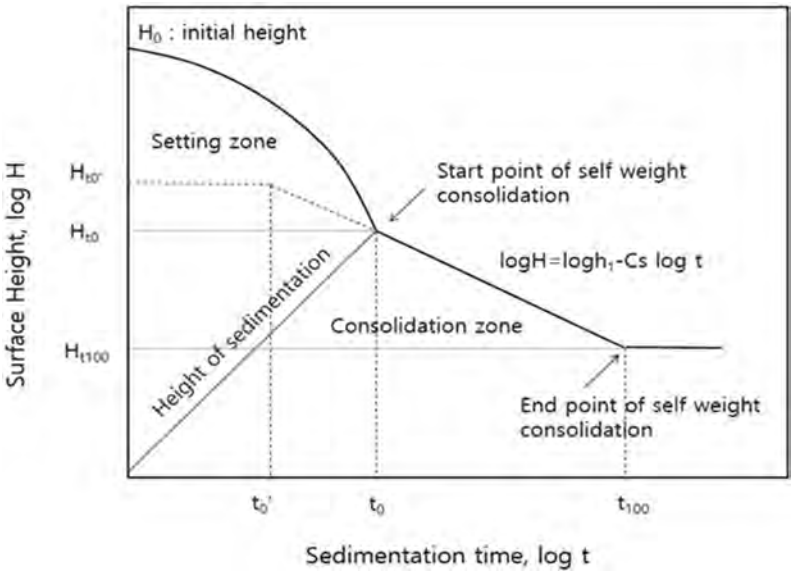

Figure 2. Determination of the starting point of self-weight consolidation.

The coefficient of sedimentation self-weight consolidation can be expressed as the slope between the two points, as expressed in Equation 5:

$$C_s = \frac{\log(\mathrm{H}_{t0}/\mathrm{H})}{\log(t/t_0)} \tag{5}$$

where, H_{t0} is the interface height at time t_0.

The relation between the real soil height and the interface height is given by Equation 6:

$$H_s = \frac{H}{1 + G_s/G_w \cdot \bar{w}} = \frac{H}{1 + \bar{e}} \tag{6}$$

where, H_0 is the initial interfacial height, G_s is the specific gravity of the soil, G_w is the specific gravity of water, $\bar{w}$ is the average water content of the dredged soil, and $\bar{e}$ is the average void ratio of the dredged soil.

The dredged soil with the same initial water content and different heights were settled, then assuming that the consolidation settling start time shown in each settling curve is expressed as t_0, and the time when entering the creep behavior is t_{100}, the self-weight consolidation formulae in the consolidation settling zone between the time (t = $t_0 \sim t_{100}$) and the interface height (H) can be obtained.

Figure 3 shows the height of the real soil height with the interfacial height at time (t_0,t_{100}).

When the self-weight consolidation starts and end point according to the water content ratio are indicated by the real soil height of the logarithmic scale, a linear relationship is established.

From this, it is possible to obtain the real soil height for the initial surface height of the landfill, as shown in Equation 7:

$$\log H = \log h_2 + C_k \log H_s \tag{7}$$

where, h_2 is the surface height, and is the intercept at the real soil height H_s = 1, and C_k represents the slope of the surface height-real soil height graph.

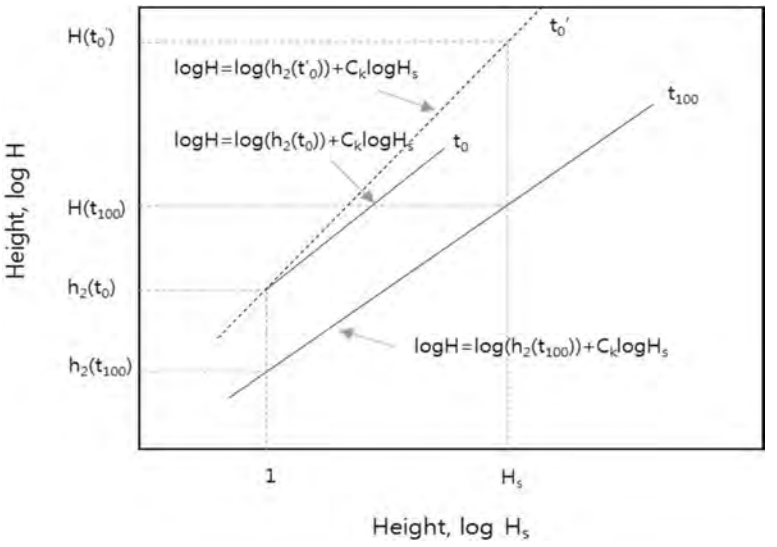

Figure 3. Height of dredged soil with Hs at t=0 and t=100.

The landfill height is estimated using the real soil height calculated from the sedimentation consolidation test. It is possible to finally calculate the volume change ratio by using the relationship between the void ratio and the water content ratio.

4 SELF-WEIGHT CONSOLIDATION AND RETAIN RATIO

4.1 *Sampling and physical properties test of dredged soils*

Dredged soil samples were obtained from the ship navigation route in the Gunjang harbor in Mid-west coastal region of Korean Peninsular to determine the physical properties and to perform the self-weight consolidation test. The dredging equipment was mounded on the self-elevation platform barge at the soil sampling site and drilled the bore hole by using hydraulic drilling machine down to weathered rock layer in the ocean as shown in Figure 4. The detail types of soil sampled with respect to the boring depth of GL-10m is described in Table 2. Total 9 boring holes were drilled under the water depth from 10m to 17m. The thickness of sedimented clay layer ranges from 3m to 10 m with overlying a thinner layer of sandy soil on the top. The situation of offshore boring sites is shown in Figure 4.

Table 2. Each depth of layer by soil type on the offshore drilling area.

Boring No.	Depth of soil layer (m)			Depth of boring (GL.-m)	Depth of water (DL.-m)	Remark
	Sedimentary layer		Weathered granite soil			
	Clayey soil	Sandy soil				
1	8.0	2.0	-	10.0	15.72	
2	3.0	7.0	-	10.0	12.82	
3	-	1.0	2.0	1	17.12	
4	8.0	2.0	-	10.0	10.99	
5	9.0	1.0	-	10.0	12.35	
6	10.0	-	-	10.0	14.03	
7	5.0	-	2.0	5	10.75	
8	2.9	-	1.1	2.9	10.89	
9	4.0	6.0	-	10.0	10.35	

Figure 4. Situation of each boring number on the offshore drilling.

The soil specimens from No. 7 & No. 8, and No. 1, No. 6, No. 9 are classified as Silty soil (ML) and clayey soil (CL) by USCS, respectively. The soil specimens from No. 2-4 and No. 5 are classified as Silty clayey soil (CL-ML) and silty soil mixed with shell fragment (OL) by USCS, respectively. Most of soil specimens from 9 boring holes are consisted of clay and silty soil with a small portion of sand. The proportion of fine-grained soil for given soil specimens is more than 90%, that is, 50% for silty soil, 40% for clayey soil, and 10% is colloid state with grain size less than 0.001 mm. A liquid limit for most of soil gives less than 40% and natural water contents of 31.9-50.9%. The grain size less than 0.005 mm (#200 sieve) is consisted of 75-98% along with grain size less than 0.002 mm is approximately 10~30%. The clayey soil deposited in this area is normally consolidated clay or under-consolidated clay. The physical properties of dredged soil obtained from offshore sites are tabulated in Table 3.

Table 3. Physical properties of dredged soil obtained from offshore sites.

			Atterberg Limits (%)		Grain Size Distribution %, Finer than		
No.	w_n (%)	G_s	LL	PI	0.075mm	0.425mm	USCS
1	31.9	2.62	39.7	17.1	100	100	CL
2	34.4	2.64	25.8	4.0	100	100	CL-ML
3	25.8	2.64	26.5	6.6	-	-	CL-ML
4	50.9	2.65	27.0	5.7	100	100	CL-ML
5	36.2	2.57	41.5	11.9	100	100	OL
6	36.8	2.65	34.3	14.9	100	100	CL
7	50.1	2.61	39.0	13.5	100	100	ML
8	34.7	2.59	31.7	7.0	100	100	ML
9	33.8	2.61	26.0	10.0	100	100	CL

4.2 *Settlement analysis of dredged soils by using the self-weight consolidation test*

In the laboratory self-weight consolidation test through column test, the downward movement of suspended soil particle can be divided into two parts as shown in Figure 3. The first part is categorized as sinking and sedimentation of soil particles which gives concave curve. The second part is a downward linear line between soil elevation height and sedimentation time, that is, self-weight consolidation zone. The gradation of downward linear line is called sedimentation-consolidation coefficient or self-weight consolidation coefficient (C_s) as given in Equation 5. The end point of linear line is indicated that the self-weight consolidation process is terminated.

Table 4 describes the self-weight consolidation test results for soil specimens with the moisture contents of 300%, 600%, and 1000%, respectively. From the soil-water interface height with corresponding sedimentation elapsed time as shown in Figure 3, the self-weight consolidation

coefficient is determined by using Equation 5. The self-weight consolidation coefficient (C_s) is decreased with the increase of water contents of soil. The self-weight consolidation coefficient (C_s) ranges from 0.073 cm/min to 0.127 cm/min. The silty soil gives the higher value of Cs that that of clayey soil. Because the sea water contributes slow-down of sedimentation velocity due to dispersion of clay particle. Therefore, the larger size of soil particle gives a greater sedimentation velocity that that of smaller size of soil particle. The self-weight consolidation coefficient (C_s) of various soil specimens describes with the water contents of 300%, 600%, and 1000%, respectively.

Table 4. Coefficient of self-weight consolidation for various soil specimens.

Soil Type	Water content (%)	Initial height (cm)	Start point		End point		C_s (cm/min)	Ave. C_s(cm/min)
			t_0 (min)	H_0 (cm)	t_{100} (min)	H (cm)		
CL	300	100	1020	43.90	7090	37.25	0.085	0.079
	600	100	760	22.90	2880	20.60	0.079	
	1000	100	280	16.10	4320	13.20	0.073	
CL-ML	300	100	135	13.80	1089	11.05	0.106	0.101
	600	100	115	14.10	910	11.35	0.105	
	1000	100	120	14.00	1200	11.30	0.093	
OL	300	100	307	14.8	1087	12.6	0.127	0.111
	600	100	270	15.45	1270	13.00	0.112	
	1000	100	260	15.40	1440	13.10	0.094	
ML	300	100	300	15.8	1085	13.50	0.122	0.113
	600	100	280	16.1	1280	13.45	0.118	
	1000	100	240	15.9	1440	13.30	0.100	

The relationship between the height of the real soil height and the interfacial height is established as shown in Figure 5 by using the self-weight consolidation test data in Table 5. The heights of dredged soil slurry were varied as 30 cm, 50 cm, and 100 cm during the self-weight consolidation test as described in Tables 5 and 6.

Table 5. Result of H and Hs from initial height of dredged soil (w=1000%).

Initial Height, H_0 (cm)	Specific gravity, G_s	Water content of specimen, w (%)	Void ratio, e (e= $G_s \times w$)	Height, H (cm)	H_s (= H/1+e)
30	2.63	106	2.794	4.35	1.15
50	2.63	106	2.794	7.24	1.91
100	2.63	106	2.794	14.50	3.82

Table 6. Relationship between H and Hs in the soil column of CL (w=1000%).

Soil type	Water content (%)	Initial value (t_0)		Final value (t_{100})	
		A	B	A	B
CL	1000	0.5798	0.9989	0.5441	0.9772

Therefore, this consolidation test data is plotted in Figure 5 for CL soil specimen with 1000% of water content. Similar self-weight consolidation tests were performed for soil specimens, CL-ML, OL, and ML with variations of water contents, 300%, 600%, and 100%, respectively.

Based on the real soil height (H_s) in the graduated cylinder obtained according to the interfacial height (H) due to the variations of heights of dredged soil slurry during the self-weight consolidation tests, determined A and B parameters for various soil types and test conditions and tabulated in Table 7.

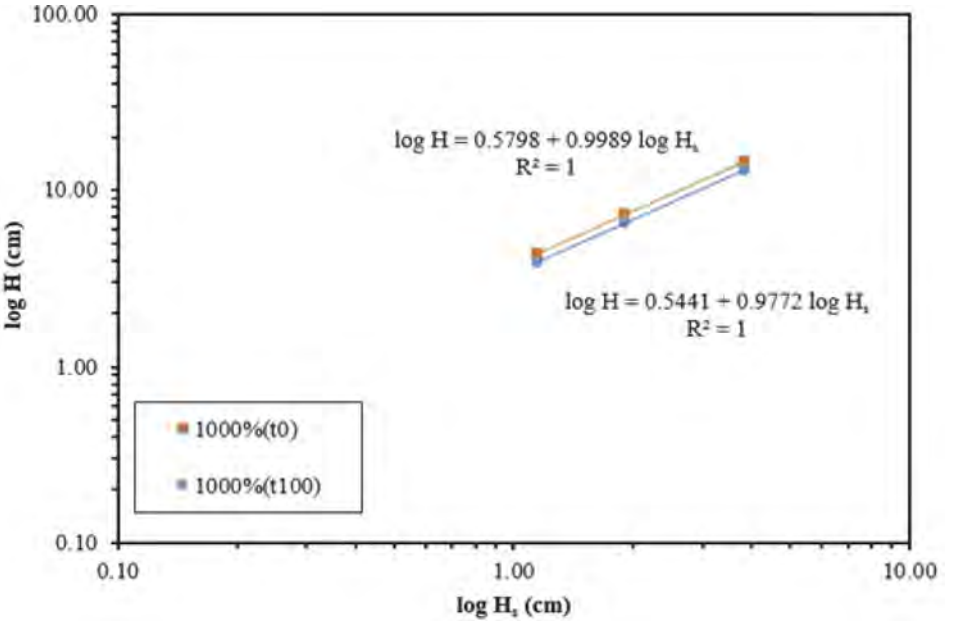

Figure 5. Relationship between H and Hs in the soil column of CL.

The coefficient of self-weight consolidation for clayey soil gives lowest value while the greater water content gives lower value. The intercept value obtained from the relationship between real soil height (H_s) and interfacial height (H) ranges from 1.0 to 1.2 for sandy soil and a little bit higher than 1.0 which contains a bit of fine-grained soil. However, the soil specimen contained more than 70% of clay and silty soils gives an intercept values from 0.59 to 0.65, and hence it caused the low value of actual landfill height.

Table 7. Correlation equation using relationship of H and H_s.

Soil type	Water content (%)	Initial line (t_0)	Final line (t_{100})
CL	300	$\log H = 0.5911 + 0.9946 \log H_s$	$\log H = 0.5682 + 0.8648 \log H_s$
	600	$\log H = 0.5798 + 0.9989 \log H_s$	$\log H = 0.5051 + 0.9802 \log H_s$
	1000	$\log H = 0.5798 + 0.9989 \log H_s$	$\log H = 0.5441 + 0.9772 \log H_s$
CL-ML	300	$\log H = 0.6021 + 0.9978 \log H_s$	$\log H = 0.5315 + 0.9989 \log H_s$
	600	$\log H = 0.6021 + 0.9978 \log H_s$	$\log H = 0.5051 + 0.9991 \log H_s$
	1000	$\log H = 0.6021 + 0.9978 \log H_s$	$\log H = 0.4914 + 1.0059 \log H_s$
OL	300	$\log H = 0.6128 + 1.0073 \log H_s$	$\log H = 0.5563 + 1.0011 \log H_s$
	600	$\log H = 0.6232 + 1.0024 \log H_s$	$\log H = 0.5563 + 0.9914 \log H_s$
	1000	$\log H = 0.3232 + 1.0024 \log H_s$	$\log H = 0.5441 + 0.9922 \log H_s$
ML	300	$\log H = 0.6532 + 1.0002 \text{og} H_s$	$\log H = 0.6021 + 0.9290 \log H_s$
	600	$\log H = 0.6532 + 1.0002 \log H_s$	$\log H = 0.6021 + 0.9875 \log H_s$
	1000	$\log H = 0.6532 + 1.0002 \log H_s$	$\log H = 0.5911 + 0.9929 \log H_s$

5 DETERMINATION OF RETENTION RATE

The self-weight consolidation settlement and ratio of soil volume change after completion of dredged landfill were predicted by using the self-weight consolidation equation. The ratio of soil volume change is defined as soil specimen volume during the self-weight consolidation after dredging against the volume of original ground. When the disturbed soil becomes a same void ratio as original ground, then soil volume change ratio becomes 1.0. The variation of soil

volume change during the self-weight consolidation test for CL soil specimen is described in Table 8. The initial soil volume change ratio was 1.79, and after 4 years later, it becomes 1.51 on the progress of self-weight consolidation. The soil volume change ratio becomes approximately 1.36-1.44 after 8 years later with completion of dredged work. This value gives retention ratio of 69%-74%. The variation of void ratio, water content, and volume change for 300%, 600%, and 1000% of water contents are shown in Figures, 6, 7, and 8, respectively.

Table 8. Volume change ratio of CL material on w=1000%.

No.	Elapsed time		Log H	Height (m)	Void ratio	Water content (%)	Volume change ratio
	Day	Year					
1	1	0.00	0.778	6.00	2.78	106.00	1.79
2	30	0.08	0.772	5.92	2.73	104.17	1.77
3	60	0.16	0.768	5.86	2.69	102.59	1.75
4	90	0.25	0.763	5.80	2.65	101.23	1.73
5	120	0.33	0.760	5.75	2.62	100.04	1.72
6	150	0.41	0.756	5.71	2.59	98.99	1.70
7	180	0.49	0.753	5.67	2.57	98.04	1.69
8	210	0.58	0.751	5.63	2.55	97.19	1.68
9	240	0.66	0.748	5.60	2.53	96.40	1.67
10	365	1.00	0.739	5.49	2.46	93.71	1.64
11	730	2.00	0.722	5.28	2.32	88.68	1.57
12	1460	4.00	0.703	5.05	2.18	83.24	1.51
13	2920	8.00	0.683	4.82	2.04	77.68	1.44

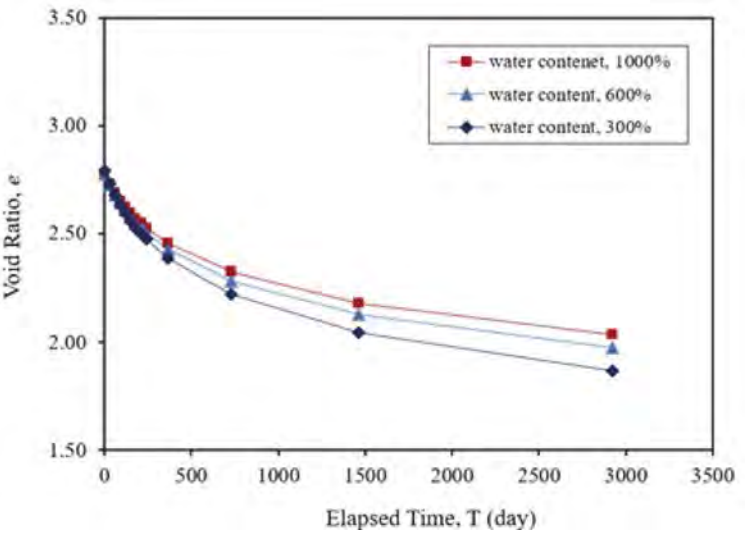

Figure 6. Variation of void ratio with elapsed time for low plasticity clay (CL).

This study was focused on the area where it has a spillway. The sandy soil is deposited near to the discharge pipe which transported dredged soil into the reclamation site. The suspended fine-grained soil particles which passed through #200 sieve is deposited around spillway where the silt pocket is normally formed. The soil specimen obtained in this area is consisted of clayey and silty soils (CL-ML). After the interfacial height was established by the result of self-weight consolidation test, the water content of soil slurry was ranges 100%-135% with the corresponding void ratios of 2.73-3.50. The initial soil volume change ratio was 1.87, and after 4 and 8 years later, it becomes 1.50 and 1.42, respectively, with completion of dredged work. This value gives retention ratio of 70% against the final height of dredged fill site.

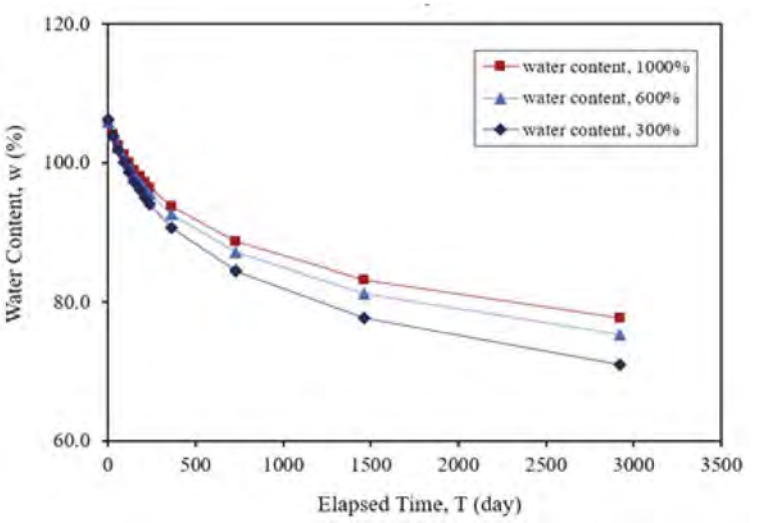

Figure 7. Variation of water content with elapsed time for low plasticity clay (CL).

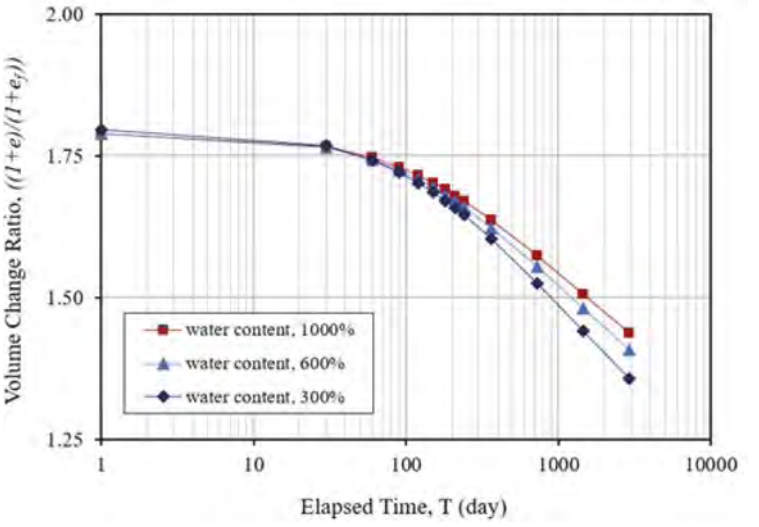

Figure 8. Volume change ratio with elapsed time for low plasticity clay (CL).

The soil specimen contains an organic silty clay (OL) shows the initial soil volume change ratio was 2.01, and after 4 and 8 years later, it becomes 1.61 and 1.44, respectively, with completion of dredged work. This value gives retention ratio of 69% against the final height of dredged fill site.

The soil specimen contains a silty soil (ML) shows the initial soil volume change ratio was 1.48 - 1.58, and after 4 and 8 years later, it becomes 1.68 and 1.48 - 1.58, respectively, with completion of dredged work. This value gives retention ratio of 63% - 68% against the final height of dredged fill site.

The summary of self-weight consolidation tests for the soil specimens of CL, CL-ML, OL, ML in Table 7, after the interfacial height was established by the result of self-weight consolidation test. The water content of soil slurry was ranges 100% - 135% with the corresponding void ratios of 2.73-3.50. The initial soil volume change ratio was 1.79 - 2.13, and after 8 years later, it becomes 1.36 - 1.58, respectively, with completion of dredged work. This value gives overall retention ratios of 63 - 74% against the final height of dredged fill site.

6 COMPARISON ANALYSIS FOR EXTIMATION OF VOLUME OF DREGED FILL SOIL

The volume of dredged fill soil has been estimated by following the design standard (2015) by the Korea Port and Harbor Authority (KPHA). In the process of estimation for dredged fill soil volume, the retention ratio (R) for sand and sandy ranges from 70% to 95%, and for clayey soil gives less than 70% of retention ratio. This means that the retention rates are greatly different depending on the soil particle size. The land reclaimed block for this study is potential deposited area of suspended soil particles among the huge land reclamation project site. The results of ground investigation on offshore area, the sandy soil is deposited in the upstream area of ship navigation route while the fine-grained soil is deposited in the spillway area. Therefore, the study area is deposited more silty soil as well as clayey soil rather than sandy soil. The soil specimens obtained from field is classified as clayey soil. The result of self-weight consolidation test indicates that the real net height of dredged fill soil is lower than that of retention rate (82.5%) given by the design standard of KPHA

In case of average height of dredged fill soil is about 6 m at the reclaimed site, the magnitude of settlements is estimated by using the design standard of KPHA, actual field surveying, and self-weight consolidation test result. The settlement levels with corresponding retention rates given for the design standard of KPHA (82.5%), actual field surveying (74.0%), and self-weight consolidation test result (72.0%) are 105.5 cm, 156.8 cm, and 180.9 cm, respectively. Based on the settlement level by actual field surveying, the deviation rate by KPHA's method can be reduced by 50% if the result of self-weight consolidation test is used.

7 CONCLUDING REMARKS

The proper estimation of volume of dredged fill soil for a large-scale land reclamation project is necessary. Current methodology for estimation of dredged fill soil is rough and not systematic method. The adoption of self-weight consolidation test for the soil specimen obtained from the dredging site is more realistic and reduce the risk of lack of dredged fill soil (approximately 50% at this particular site) at the land reclamation project. The design standard (2015) by the Korea Port and Harbor Authority (KPHA) should be clearly described:

(1) where the soil specimen should be obtained, (2) what kind of soil property tests must be conducted, and (3) the self-weight consolidation test is necessary for the given soil specimen.

The detail plan of construction management for the sea dike construction as well as controlling to avoid silt pocket. The UAV (Unmanned Aerial Vehicle) surveying by using Drone is also a good method to effectively survey the large area in a such short period of time which can help the proper estimation of ground settlement level and predict the level of dredged fill soil at the land reclamation site.

REFERENCES

Gibson, R.E., England, G.L., and Hussury, M.J.L. 1967. The theory of one-dimensional consolidation of saturated clay I: Finite non-linear consolidation of thin homogeneous layers. *Geotechnique* 17(3): 261–273.

Imai, G. 1980. Setting behavior of clay suspension. *Soil and Foundations* 20(2): 61–77.

Mikasa, M. 1963. The consolidation of soft clay – A comparison between two theory and its application. *Japanese Society of Civil Engineering Reprint from Civil Engineering in Japan*: 21–26.

Korea Rural Community Corporation (KRCC) 2011. *Design Report for Semangeum Industrial Complex Development Project, Site 2 Land Reclamation Work*. Gunsan: KRCC.

Lee, C.W. & Choi, H.S. 2016. Experiment and numerical analysis on sedimentation and consolidation characteristics for dredged fill soil in Songdo Incheon. *Korean J. of Geo-environmental Engineering Society* 17(2): 13–22.

Lee, S.H. & Lee, J.H. 2011. Experiment study on sedimentation and consolidation characteristics for dredged fill soil in west coastal area, Korea. *Korean J. of Geo-environmental Engineering Society*: 29–36.

Korean Design Standard (KDS) 2015. *Port and Fishing Port Design method.* Korea: The Ministry of Maritime Affairs and Fisheries.

Richart, F.E. 1957. A review of the theories for sand drains. *Proceedings of ASCE* 83(SM3–1302).

Shin, E.C., Park, Y.J., and Kang, J.K. 2017. Determination of retention rate by self-weight consolidation test for sea navigation route in Incheon coastal area. *J. of Korean Geosynthetics Society* 16(4): 57–66.

Terzaghi, K. 1943. *Theoretical Soil Mechanics*. New York: John Wiley & Sons.

Yano, K. 1985. Properties of very soft ground reclaimed by dredged marine clay and their prediction. *JSCE* 364(III-4): 1–13.

Smart Geotechnics for Smart Societies – Zhussupbekov, Sarsembayeva & Kaliakin (Eds)
© 2023 The Author(s), ISBN 978-1-003-29912-7
Open Access: www.taylorfrancis.com, CC BY-NC-ND 4.0 license

Engineering challenges behind demolition of a highrise structure by delayed detonation techniques at Delhi, India

Anil Joseph
Geostructurals Pvt Ltd, Kochi, India

A. Boominathan
IIT Madras, Chennai, India

ABSTRACT: Delayed detonation techniques by implosion is successfully used in many countries for demolition of high rise structures in heavy urban and densely populated areas without inducing damages to neighboring structures. This paper deals with engineering challenges behind demolition by implosion technology of Supertech Twin Towers at New Delhi, India. After completing 32 floors of Apex and 29 floors of Ceyane tower, work was stopped in 2014 for violating building norms. Buildings were brought down by controlled implosion on 28th August 2022 as per the Supreme Court verdict. The towers were surrounded by numerous adjacent multistoried apartments and a buried gas pipeline passing within the plot of Supertech twin towers. Bringing the building down within the plot without affecting the built environment was the major challenge. After detailed engineering analysis, proper instrumentations, safety measures to prevent flying debris and to control touch down vibration, the demolition was successfully completed.

1 INTRODUCTION

Demolition is the method of deconstruction of structure by manual (non-engineering) or mechanical (engineering) methods. Normally the demolition is carried out on structures which has completed its life span - to replace the existing structure with new development, or when the structure has undergone irreparable damages due to fire, earthquake etc. or when the building is found to violate the rules of construction and the authorities has ordered for demolition. Nowadays demolition by implosion is becoming common in many countries. Implosion is defined as the designed collapse of a building using explosives within its own foot print (McKenzie et al.2019). Explosive demolition is the preferred method for safe and efficient demolition to bring dangerous multistoried structures to ground in comparison to conventional demolition methods (Jalandar et al.2014). Detonation of small quantities of strategically placed explosives can demolish an unwanted high-rise in a matter of seconds (Mark & Douglas. 1995). The ground motion caused by blasting demolition is usually a combination of blasting vibration, backlash vibration and touch down vibration and it could damage nearby structures if the amplitude of these vibrations are high (Wang & Li. 2010). Touch down vibration is caused by the collision of buildings falling to the ground and it has huge energy, long duration and complex function process, hence this vibration has a much harmful impact on the surrounding build environment. Therefore, the touch down vibration due to blasting has become a research focus in hazard control for demolition of buildings (Yang and Shi.1985, Lu et al. 2003, Zhou.2009). During the demolition by blasting techniques, it is to be ensured that the impact of vibration induced by the touchdown of the collapsing structure does not adversely affect the safety of the buildings nearby and delayed detonation techniques are adopted for the same (Akhil et al. 2020). The damage potential of buildings/structures, however, varies widely depending on the type and quality of construction, nature of excitation, the surrounding soil strata, structural resonance, etc. (Anil et al. 2022). This paper discusses the

DOI: 10.1201/9781003299127-12

grounds behind the demolition of Supertech Twin Tower, Noida, Engineering challenges behind its demolition, Evaluation made to study the impact of implosion on adjacent building, Precautionary measures adopted, instrumentation systems carried out and the observation made after the successful completion.

2 ABOUT THE PROJECT

Noida, short for New Okhla Industrial Development Authority, is a planned city located in Gautam Buddha Nagar district of the Indian state of Uttar Pradesh. The Supertech Twin Towers were located in Sector 93A, Noida, Uttar Pradesh and is close to the Noida-Greater Noida Expressway. Figure 1 shows the location of the Supertech Twin Tower, Noida. The Noida Supertech Twin Towers consisted of two buildings, Apex and Ceyane Towers. They were planned to have 40 floors each. The two structures had different heights, Apex had 32 floors and stood at 103 metres (338 ft) tall while Ceyane had 29 floors and stood at 97 metres (318 ft). Both towers together had a built-up area of around 7.5 lakh square feet.

Figure 1. Image of location of Supertech Twin Tower, Noida.

3 BACKGROUND AND TIMELINE – SUPERTECH TWIN TOWER, NOIDA

In the year 2005, the Noida Authority sanctioned the building plan for the construction of Emerald Court comprising of 14 towers, each with ground and nine floors (G+9) and the construction commenced for those 14 towers.The entire amount of leased space given to the corporation was expanded to 54,819.51 sq m in June 2006, and the plan was revised to G+11 with the addition of two new buildings. The architect updated the design in 2009 and added two additional towers with a total height of 24 storeys. The proposal was once more altered in 2012 to increase the height to 40 stories with two basements for parking. The neighborhood's Residence Welfare Association (RWA) filed a lawsuit in Allahabad High Court challenging the illegal addition of towers that were being built in 2012 but were not originally part of the plan. The high court determined the towers to be unlawful in April 2014 and ordered their demolition. The construction works were stopped in the year 2014, when the height of Apex tower was 103 meters and height of Ceyane tower was 94 meters. Figure 2 shows the image of Supertech Twin Tower, Noida before demolition.

4 CHALLENGES BEHIND DEMOLITION OF SUPERTECH TWIN TOWER, NOIDA

Emerald Court and ATS Village, two multistory building complexes, flanked the Supertech Twin Tower. Since Emerald Court and Supertech Twin Tower formerly shared a retaining wall and

Figure 2. Supertech Twin Tower, Noida before demolition.

a basement, separating them prior to the explosion was a crucial undertaking. Over 5000 people and about 2500 vehicles had to be evacuated from the area around the towers before the explosion, which presented additional challenge. It was extremely difficult for the Supertech Twin Tower to collapse and tumble since Aster 2, an apartment in Emerald Court, was only 9 metres away. Implosion has to be carried out without affecting nearby buildings in both ATS Village and Emerald Court. Underground GAIL gas pipelines were passing within the plot area of Supertech twin tower. The pipelines were 4m below the ground level and was located at a minimum distance of 23m from the towers as indicated in Figure 3. The pipeline was crucial as it supplies CNG for Noida and East Delhi. The demolition plan was to make apartment collapse into the open space near ATS Village. The total weight of Apex tower was 41720 tonnes and of Ceyane tower was 18150 Tonnes. 633 flats were booked but since the construction was not completed, the towers were uninhabited.

4.1 *Soil type and the foundation provided*

The region's soil is a medium-density alluvium soil with a predominance of sand and silt and little to no clay. Hard rock strata are followed by extremely dense silty sand deposits as the subsurface layers of these alluviums. 5m below the current ground level, there was a water table. The Super Tech Twin Towers have two basements and a piled raft system as their foundation. Aster-2 has just one basement, and it is built on a raft foundation that rests on medium-density alluvium soil. In the first basement level, the buildings were joined.

4.2 *Prediction of impact of Touch down vibration on Aster -2*

Delay detonation techniques are used to reduce the impact of falls reaching the ground. In both horizontal and vertical planes, the blast is delayed. To lessen the load that hits the ground after the explosion, structures are pre-weakened, and rubble is heaped in the basement to serve as a cushion layer. Pre-weakening entails removing all non-load-bearing walls, fixtures, mechanical devices, plumbing and piping (electrical, water, sewage, and communications), stairways, and facades, including all glazing, from the building while leaving the fundamental structural components, such as columns, beams, and floors, in place. Numerous

Figure 3. Layout of GAIL gas pipeline within the compound of SuperTech Twin Tower.

columns that contain closely pitched spirals or stirrups made of circular or rectangular steel must be exposed and chopped before they can be drilled and loaded with explosives. By removing the concrete matrix surrounding the steel reinforcing, shear walls can be mechanically pre-weakened, creating plastic hinges that will help the structure collapse once the implosion is initiated.

The formula used to determine the size of the explosive charge required to breach concrete is as per Eq. (1) (McKenzie et al.2019):

$$P = R^3 KC \tag{1}$$

Where,
P = TNT required (lbs)
R= Breaching radius (ft)
K= Material factor which reflects hardness and mass of the material to be demolished
C= Tamping factor

Figure 4 shows the layout of primary blast floors where charges will be placed in all columns and the secondary blast floors where the charges in 40% of columns.

Before conducting the implosion, the structure was examined to predict how the touch down vibration of the implosion would affect it. The peak particle velocity within a 10 m radius after the blast was predicted by the UK-based company Vibrock to be between 22 and 34 mm/s, and between 3 and 5 mm/s up to a radius of 100 m. These predictions were based on the implosion time isochrome, collapse time contour, direction of the pull, and the type of soil found at the site. The damage level for peak particle velocities up to 35 mm/sec is none, which is shown in Table 1(Chi En et al.2010). The British Standards BS 5228 advises between 15 and 50 mm/s of vibration frequency to prevent hairline plaster cracking, and when the values surpass 15 mm/s, cosmetic harm is probable. The characteristics of earthquake-induced vibrations and those caused by demolition-induced vibrations differ significantly, according to Vibrock's report. In particular, compared to earthquake vibration, which can persist for many minutes and typically consists of energy at less than 1 Hz, the vibration produced by the demolition event will be of relatively high frequency content (10 to 40 Hz) and brief duration (2-5 seconds).

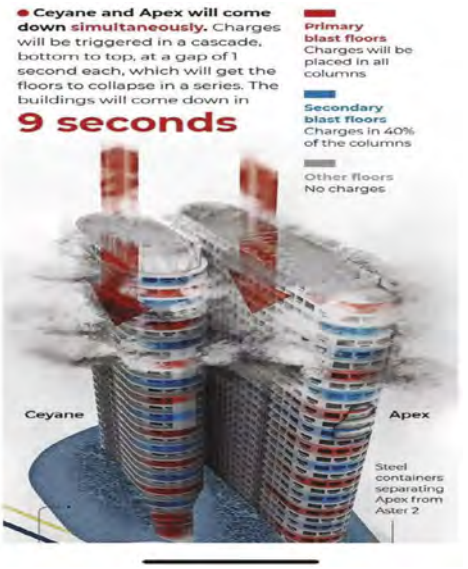

Figure 4. Layout of primary and secondary blast floors of Supertech Twin Tower.

Table 1. The relation between the damage level of buildings and vibration velocity.

Maximum Velocity of Mass Point (mm/s)	Damage Level
35	None
55	Very finest plastering cracking
80	Cracking
115	Severe Cracking

5 EVALUATION MADE TO STUDY THE IMPACT ON ADJACENT BUILDING

5.1 *Structural analysis of adjacent building: Aster -2*

Aster 2 has a basement, ground floor, and 12 floors. The Aster 2 was given top priority and was closely watched throughout deconstruction because it was only 9m from the Supertech Twin Tower. Aster 2's structural performance was assessed and modelled using ETABS, and it was exposed to various load combinations, including blast loading, and earthquake impact.

M20 and Fe 415 were the chosen concrete and steel grades for the analysis. Various load combinations were applied to the structure in accordance with the recommendations in IS 456. The seismic forces were calculated using IS 1893, the dead and live loads were obtained in accordance with IS 875, and the blast loads were acquired from data from Vibrock, UK. The maximum peak particle velocity that is predicted to occur within a 9-meter radius following the blast is 36 mm/s, which is stimulated in the model based on the vibration intensity report. Figure 5 depicts the arrangement of a typical floor, a 3D ETABS model, and a 3D rendered representation of Aster-2.

According to the analysis's findings, the maximum storey drift in the X direction for blast vibration is 720×10^{-6}, while it is 2700×10^{-6} for earthquake vibration. It has been determined that the maximum storey drift in the Y direction for blast vibration is 690×10^{-6} and that it is 2030×10^{-6} for earthquake vibration. The maximum storey displacement in the X direction is 12.5 mm for blast vibration and 95 mm for earthquake vibration. The maximum storey displacement in the Y direction for blast vibration is 16.5 mm, and if an earthquake occurs, it is 71 mm. The maximum allowable storey displacement, according to IS 1893 part 1 2016, is h/250, while the allowable displacement for Aster-2, which has a height of 48m, is 192 mm. It

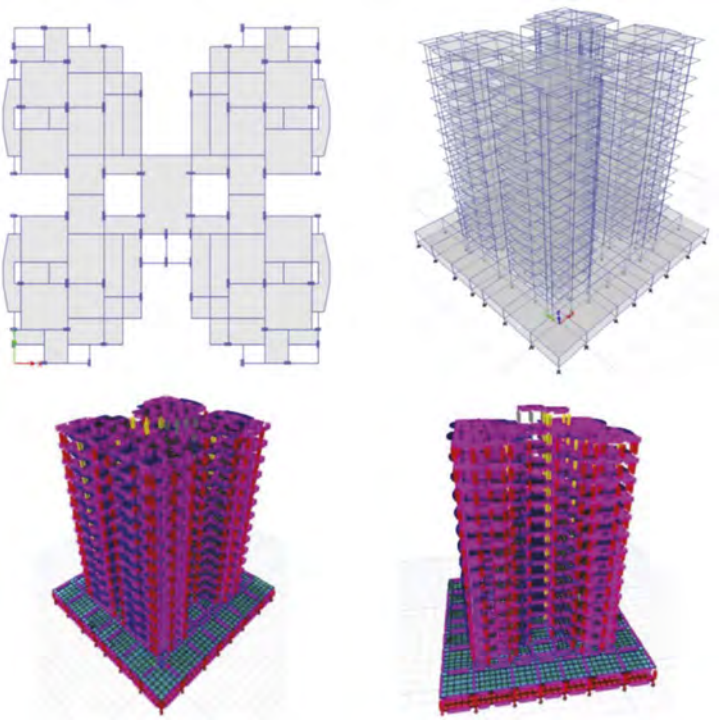

Figure 5. Layout of typical floor, 3D ETABS Model and 3D Rendered view of Aster-2.

was observed that the storey drift and displacement are well within the permitted range according to the codal regulations.

6 PRECAUTIONARY STEPS ADOPTED

6.1 *Test blast*

The test blast was conducted to determine the kind, calibre, and volume of explosives required for the demolition as well as to assess the intensity and blast radius. On April 10, 2022, at 2:30 PM IST, the Supertech Twin towers underwent a test blast. Four pillars in the basements and one on the tower's 14th floor each received test blasts. The implosion time isochrome, collapse time contour, and pull direction for the primary blast were all decided upon in light of the findings.

6.2 *Rapid visual assessment of adjacent building and strengthening*

Prior to the explosion, a visual inspection of the nearby structures, including a door-to-door survey of each apartment within the safety zone of 50 metres, was conducted to ascertain any structural damage. Pictures were also taken and recorded to compare the same after the demolition process. The typical observations made throughout the visual assessment procedure are shown in Figure 6. As illustrated in Figure 7, non-destructive tests were performed on a number of columns to determine the structure's current strength. The typical outcomes are listed in Table 2.

6.3 *Protection work for gas pipe lines, Berms, geotextile wrapping*

The 200mm gas pipeline was 23 m away from the building and was buried at a depth of 4 m. below the surface of the ground. Steel plates that were 2-3 mm thick were placed on the

SUMMARY OF CRACKS SEEN DOCUMENTED DURING RAPID VISUAL TEST						
ASTER-3 Apartment No.- 503						
Defect ID	Location	Orientation	Approx. Width	Approx. Length	Category	Photo ID
1	Balcony	Vertical	0.40 mm	1.00 m	Very Slight	503-01
2	Bed room	Vertical	0.10 mm	0.50 m	Negligible	503-02
3	Balcony	Horizontal	1.00 mm	0.60 m	Slight	503-03
4	Bedroom	Vertical	0.30 mm	0.20 m	Very Slight	503-05
5	Balcony	Horizontal	1.00 mm	1.50 m	Slight	503-07

Figure 6. Typical damages noted during rapid visual assessment of adjacent building.

Figure 7. Conducting NDT tests at Aster 2.

Table 2. Typical rebound hammer test results.

Measurement ID	Direction of Measurement	Rebound Numbers (RN)										Individual Average	Average Rebound Numbers (RN)	Average Estimated Compressive Strength (N/sq.mm)
11	Horizontal	30	38	40	26	26	40	32	40	32	34	33.8	33.8	38.08
80	Horizontal	46	42	42	40	40	44	42	44	46	42	42.8	42.8	45.04

ground above to protect it. Figure 8 (a) illustrates the placement of protection berms over the plates that are about 2 m high, shielded with a geotextile layer, and rubber tyres designed to deflect impacts.

In order to prevent the flying debris, the columns were covered with 4 layers of shown in Figure 8 (b) and then a further layer of non-woven geotextiles. Perimeter curtains were also provided on all blast floors as a second layer of insurance against flying debris as indicated in Figure 8 (c). As seen in Figure 8 (d), the nearby buildings were additionally covered with geotextile fabrics as a precaution against flying debris and dust collection. As shown in Figure 8

(e), a container wall was employed to divide the higher Apex from Aster 2. These containers were secured at the lower basement level, loaded with debris, and raised to the two-story level. Between the containers and columns of Aster 2 and 3, rubber tyres were inserted. A cushion layer formed of demolished waste materials was installed in the basements to control the touch down vibrations caused by the rubble falling on the ground. Figure 8 (f) shows the formation of berms and pits around the structures to lessen the transmission of vibration .

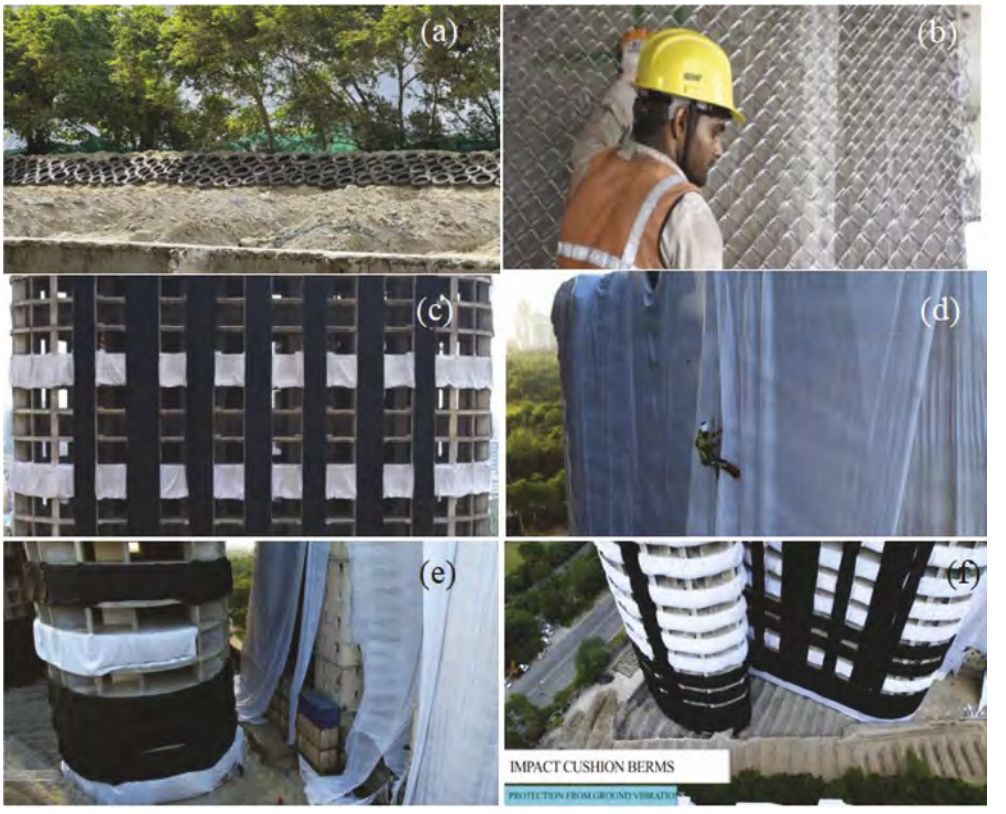

Figure 8. Protection works adopted for demolition of Supertech Twin Tower (a) Berms for protection of gas pipeline (b) Wire Mesh Wrapping around columns (c) Perimeter curtain geotextile walls on blast floors (d) Suspended Geotextile Curtains for adjacent buildings (e) Container wall for protection of Aster 2 (f) Impact Cushion Berms.

7 INSTRUMENTATION SYSTEMS CARRIED OUT

7.1 *Measuring ground vibrations*

Geophones and accelerometers were used to record vibration readings. Accelerometers were installed on top of the GAIL gas pipeline, while geophones were positioned 33 - 62m from the twin tower building's plinth edge and 3 m below ground level in the basement. Due to the equipment being damaged by the fall of buildings, the accelerometer data were lost. According to data gathered from accelerometers and geophones, the peak particle velocity in the vertical direction at the basements of ATS Village and Emerald Court varied from 6.42 mm/s to 7.27 mm/s and 7.25 mm/s to 7.28 mm/s, respectively. Figure 9 depicts the positioning of accelerometers and geophones. The crack meters were installed wherever minor cracks were noted in the structures within the safety zone. Figure 10 displays the standard crack meter positioning.

Figure 9. Measuring ground vibrations by placing Accelerometers and Geophones.

Figure 10. Crack meter reading pre and post blast.

8 POST DEMOLITION WORKS

The demolition of the structure was carried out on 28th of August 2022 at 2.30PM. After the demolition, the post blast survey of the adjacent buildings was carried out. Few superficial cracks were noted to be widened after the blast. Since, these cracks are of superficial in nature, they do not affect the structural elements. The comparison of the readings of crack meter pre and post blast is indicated in Figure 10. The vibration measurements from geophones indicate only minor impact on the structure within the safety zone as explained in Section 7 of Instrumentation system carried out. Some glass and windows were found damaged and was rectified. The demolition waste is used as fill materials for the construction of roads and a minor quantity is recycled as aggregates. The steel components were removed from the debris and is send to steel plants for recycling. Figure 11 shows the structure after the collapse and Figure 12 shows the image of the build environment before and after the blast.

Figure 11. Structure after the collapse.

Figure 12. Build environment before and after the blast.

9 SUMMARY AND CONCLUSIONS

Applying the implosion method in highly populated urban regions presents a number of difficult issues, necessitating appropriate prudence and preventative measures. Based on the implosion time isochrome, collapse time contour, direction of the pull and type of soil identified at the site, the UK-based company Vibrock predicted that the peak particle velocity within a 10 m radius of the blast would be between 22 and 34 mm/s. According to the codal laws, it was determined from the evaluation done to study the influence on nearby buildings that the storey drift and displacement caused by blast-induced loadings are well within the authorised range. According to geophone data collected during the blast, the peak particle velocity in the basements of ATS Village and Emerald Court was lower than expected, demonstrating the effectiveness of the preventative measures taken. There were no discernible differences between the crack meter readings before and after the explosion. Using the controlled implosion with delayed detonation strategy, high rise buildings in urban areas can be successfully brought down with a great level of speed and cost effectiveness, with minimum damage to neighbouring structures and the technology will be used extensively in the near future for redevelopment projects.

REFERENCES

Akhil. A, Chandrasekaran, S.S & Boominathan. A. 2020. Impact of vibrations on a high rise RCC structure due to blast induced demolition of adjacent building. *Proceedings of Indian Geotechnical Conference (IGC 2020)*.

Anil Joseph, Akhil Anil, Ramon Varghese & Boominathan. A. 2022. Monitoring blast induced vibration and structural health assessment of neighbouring building before, during and after implosion of High rise structure using delayed detonation technique at Kochi, India. *Proceedings of 11th International Symposium on Field Monitoring in Geomechanics at Imperial College London*.

BS 5228. (2009 +A1:2014). Code of Practice for Noise and Vibration Control on Construction and Open Sites Part 2 – Vibration.

Chi En-An and Zhang Yi-Ping. 2010. Analysis on control technology for collapsing vibration generated by building demolition blasting. *Journal of Coal Science and Engineering* Vol.16

Graeme McKenzie, Bijan Samali & Chunwei Zhang 2019. Design Criteria for a controlled demolition (Implosion). *International Journal of GEOMATE* 16(53): 101–112

IS 456 (Reaffirmed 2005). Plain and Reinforced Concrete - code of practice.

IS 875 (Reaffirmed 2008). Code of practice for design loads (other than earthquake) for Buildings and Structures.

IS 1893 Part 1 (2016). Criteria for Earthquake Resistant Design of Structures

Kotulkar Poonam Jalandar, G.N. Kanade and Swapnil S. Kulkarni. 2014. Demolition of structure using implosion Technology and reuse waste - a case study. *International Journal of Advanced Engineering Research and Studies* Vol 3: 43–45

Lu S R, Yang J, Liu G Z. 2003. Research on the detection and control of building's oriented blasting vibration effect. Blasting Vol.3: 71–74

Mark Loizeaux, J., & Douglas Loizeaux, K. 1995. Demolition by Implosion. *Scientific American*, 273(4), 146–153.

Yang R G, Shi J Y. 1985. Blasting demolition of buildings, *China Building and Industry Press*, Beijing

Yushi Wang and Xiaojun Li. 2010. Analysis of Strong Ground Motion Caused by Blasting Demolition of a 22-Storey RC Building, *Institute of Geophysics, China Earthquake Administration*, Beijing, 100081, China.

Zhou J H. 2009. Discussion on the formulas for calculating falling vibration velocity of blasting demolition buildings. Project Blasting Vol.1: 1 – 4.

Taylor & Francis
Taylor & Francis Group
http://taylorandfrancis.com

Invited lectures

Taylor & Francis
Taylor & Francis Group
http://taylorandfrancis.com

Smart Geotechnics for Smart Societies – Zhussupbekov, Sarsembayeva & Kaliakin (Eds)
© 2023 The Author(s), ISBN 978-1-003-29912-7
Open Access: www.taylorfrancis.com, CC BY-NC-ND 4.0 license

Study of slope failure in two regions: A comparative study between Penang Island Malaysia and North Sumatera Indonesia

F. Ahmad
School of Civil Engineering, Universiti Sains Malaysia, Engineering Campus, Nibong Tebal, Penang, Malaysia

I. Puji Hastuty
Lecturer, Department of Civil Engineering, Universitas Sumatera Utara, Sumatera Utara, Indonesia

ABSTRACT: Penang and North Sumatra are two of the regions which seldom have cases of slope instability which causes landslides. Two different site for the study are in the Penang Island, Malaysia and the North Sumatera along Medan-Brastagi Road, Indonesia where the condition for both sites seem to be similar where the area are prone to its natural disaster which lead to landslide after the area has been developed either for road construction, building a housing scheme or a resort development. The condition of the area development that took place required to cut and fill along the terrain and usually the hill site are made of rough topography with undulating hill site reliefs and the slope angles are between 60°-90°. The literature on landslide susceptibility analysis will be reviewed in accordance to its geological formation and the rainfall analysis that has shown the triggering factors after rainfall event. The main summary of the incidences will be reviewed and classification approaches that have been developed to study the parameters, methodologies, and tools used to obtain a landslide hazard map. Base on the hazard map, the area can then be identified and verified by identification the main factor that causes the slopes failure/landslides. In summary the numbers of site in hillside development in Malaysia or Indonesia are due to rainfall, storm water activities and poor slope management and maintenance. Therefore, it is important to practice good planning, proper design, sustainable construction and regular maintenance so as to achieve a community safe slope and cost-effective hill site development.

1 INTRODUCTION

1.1 *Locations*

Penang Island and Medan, North Sumatra are the areas where landslides often occurred as in Figure 1 showing the location of the study in the map. Most of the prone area were located alongside the developed area and majority were along the road side. As for both area they can be classified as a landslide prone area where both sites have rough topography with the undulating hillside reliefs where the slope angle can be between 60-90 degree. As in Penang Island the failure has been due to induced rainfall where the data shown almost every year the landslide occurred, same as in Medan, the road along Medan-Berastagi. The record on both landslide susceptibility analysis in Penang Island and Sibolangit - Karo areas, where the two sites as shown in Tables 1 and 2. This article presents summary review and classification of the main approaches that have been developed with the parameters, methodologies, and tools used to obtain a landslide hazard map.

1.2 *Site conditions*

The in-situ behavior of soils is complex because it is heavily dependent on numerous factors. To acquire appropriate understanding, it is necessary to analyze them not only through geotechnical

DOI: 10.1201/9781003299127-13

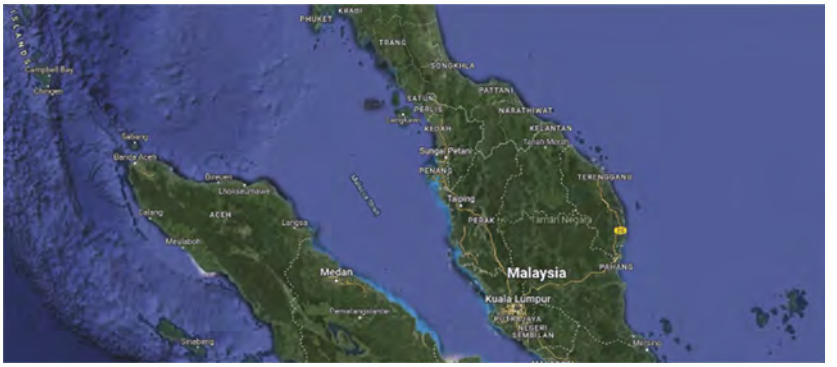

Figure 1. Location of Penang Island and Medan, North Sumera in the Map.

Table 1. Total landslide events in Penang.

State	2010	2011	2012	2013	2014	2015	2016	2017	2018	2019	2020	TOTAL
PENANG	2	2	2	2	2	2	3	3	5	3	5	22

Table 2. Total of landslide events in Sumatera Indonesia.

Province	2010	2011	2012	2013	2014	2015	2016	2017	2018	2019	2020	TOTAL
SUMATERA BARAT	15	6	29	12	22	44	10	8	14	13	18	191
SUMATERA SELATAN	3	6	10	13	8	12	5	5	6	8	6	82
SUMATERA UTARA	5	4	6	5	11	8	5	5	7	9	8	73
Grand Total												**345**

engineering skills but also through other associated disciplines like geology, geomorphology, hydrogeology, climatology and other earth and atmosphere related sciences. However, it is known that the problems, even when tackled within the framework of geotechnical engineering, are huge and arduous. It is understood that geotechnical problems with socio-economic impacts like landslides can only be addressed within a framework that accounts for behavioral features in natural soils. Research is actively taking place in many countries, each focusing on natural deposits of local importance, and a unified framework that can account for all important effects is still being developed [Grove, 1980]. The development of this unified framework requires a huge and joint effort from as many sources as possible taking underway the best of their academic and technical skills and using best possible instruments. Therefore, the study is to summarize the index, strength, compressibility and field properties of tropical residual soils of Penang and North Sumatra base on general conditions and its correlations.

2 METHODOLOGY

2.1 *Data collections*

The study of the slope failure requirements was done as follow:

- To characterize landslide parameters.
- To evaluate slope failure during field study.
- To analyze the factors that trigger landslides.
- To develop risk map using GIS and risk assessment.
- To follow the guideline of hillside development for local government.

The main purpose of this review is to analyze the factors for both sites where the review result will indicate the failure of the slopes concerned were based on the rainfall event and factors affecting the failure which led to land sliding.

2.2 *Risk assessment*

Base on all the parameters of landslide vulnerability analysis that has been carried out in Sibolangit District using Geographic Information System (GIS) (Puji Hastuty et al, 2020) this was observed by the population density and slope angle factors. The data from Badan Pusat Statistik [2018], population density in Sibolangit is around 21.5 – 582.5 people/km2. Final hazard map can be obtained by calculation of total score; the scoring/ weighting method referred to Puslittanak Bogor [2004]:

$$\text{LHI} = (0.4\text{PD} + 0.2\text{JD} + 0.2\text{NW} + 0.1\text{NE} + 0.1\text{NC}) \quad (1)$$

Where, LHI = landslide hazard index, PD = Population Density, JD = Job Description, NW = Number of Women, NE = Number of Elderly, NC = Number of Children.

The parameters used in this study were angle of slope, slope water management, soil conditions, seismicity, constituent rocks, vegetation, and rainfall where scoring and weighting referred to Peraturan Menteri Pekerjaan Umum No.22/PRT/M/2007 [5] which can be formulated as follows:

$$\text{LHI} = (0.1\text{CP} + 0.2\text{SE} + 0.1\text{PC} + 0.1\text{SD} + 0.2\text{BC} + 0.2\text{PD} + 0.1\text{ME}) \quad (2)$$

Where, LHI = landslide hazard index, CP = Cropping Patterns,
SE = Slopes Excavation and Cutting, PC = Pond Construction, SD = Slope Drainage,
BC = Building Construction, PD = Population Density, ME = Mitigation Efforts.

Based on Figure 2 for Medan and Figure 3 for Penang, it can be seen that population density in areas with slopes above 45% affects the level of vulnerability to landslides in Penang island and Sibolangit District and Karo Regency. The reason is that the land has changed its function due to the need for regional infrastructure. From Figure 2(a) and (b); it was concluded that three villages were classified as very high landslide prone areas with a population density of 423.81-582 people/km2 and a slope of > 45%. Study conducted in Penang by Ahmad (2014) described >500 people categorized as very high-density population, developed areas such as residential buildings with no less than 100 units; the number of people at risk is very high. The land is also not suitable for development because it is very risky to humans and the environment and is considered the most likely to experience slope failure. According to Althuwaynee (2017), high population density is directly related to the high density of residential buildings where the population density is between 700-1500 person/acre, but this area is not the riskiest areas to landslide. Slope instability generally occurs due to natural processes, but some of the results of uncontrolled human activities in exploiting nature can also be a factor causing slope instability which can lead to landslides. The

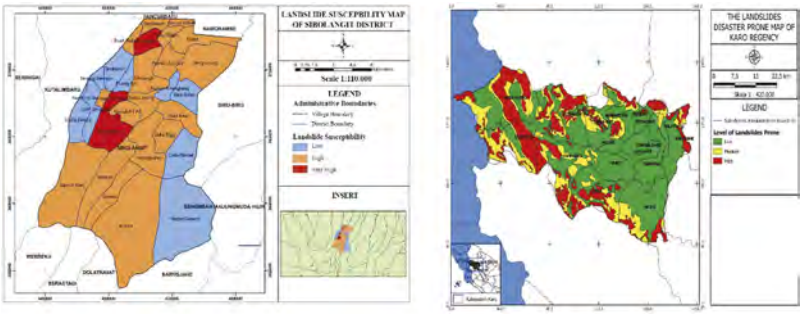

Figure 2. Landslides susceptibility Map; (a) Sibolangit District (b) Karo Regency.

risk is concentrated more of population concerned in terms of direct social impact towards the safe community and safe infrastructure.

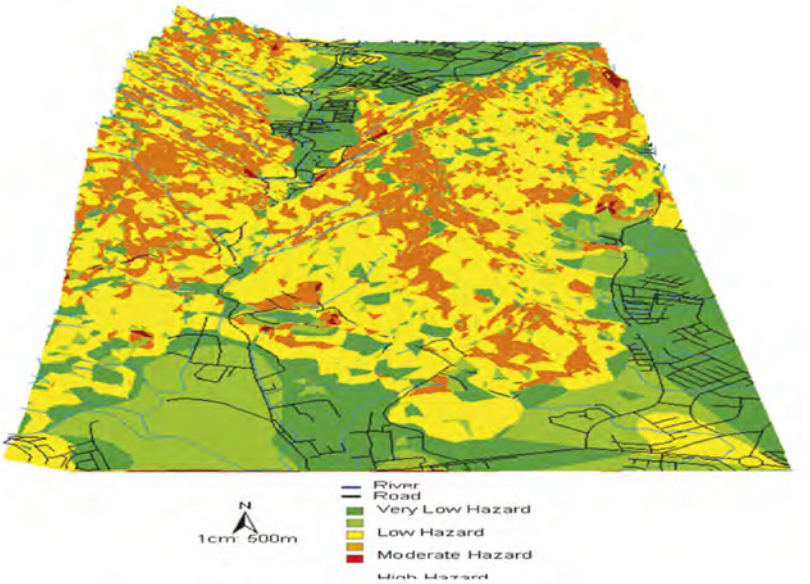

Figure 3. 3D Landslide susceptible map of Penang Island.

3 RESULT AND DISCUSSION

3.1 *Rainfall*

The geography of Penang, Malaysia and Medan is situated in close proximity to the equator, hence exposing this region to the tropical humid and dry climate every year. In addition, this region has received an abundance of tropical rain each year in conjunction with the monsoon or rainy season. This monsoon season usually occurs twice a year (November until March) and (May-September). For the record, in 2017, Peninsular Malaysia recorded an average rainfall of 2702 mm. This indication of high annual rainfall can be a significant factor contributing to a landslide where it shows the significant factors causes landslide. This is due to the presence of sporadic extreme precipitation that triggers the unforeseen slope failure. Therefore, the effect of climate is vital in inducing the occurrence of the landslide (Ahmad, 2018). The rainfall of 30 years show the pattern of rainfall exceed the average rainfall in Penang. Figure 4 shows the time series plot of annual mean total rainfall for all stations from 1984 to 2013. For Sumatera regencies, 90% of the area were having rainfall intensity of 2001-2500mm/year and this were considered extremely high and other of the regencies were between 1500-2000mm/year (high intensity). This shows that the area is exposed to extreme conditions when it comes to rainy season which is almost the same as in Malaysia. The yearly rainfall for Karo Regency as shown in Figure 5.

The study of rainfall thresholds for predicting the landslide for Peninsular Malaysia, which elaborates on the landslide classification, the triggering factor of landslide for Malaysia, the mechanism of intense rainfall induced shallow landslide, the historical development of I-D threshold for estimating the mass movement [Abdul Muaz, 2021]. Then, it will explain the effect of antecedent rainfall that influence the slope failure, and the application of rainfall threshold in the Landslide Early Warning System (LEWS). The 30 days antecedents as in Figure 6, show an example of 15 August till 13 Sept 2013, at Air Itam in Penang that indicate the pattern of rainfall.

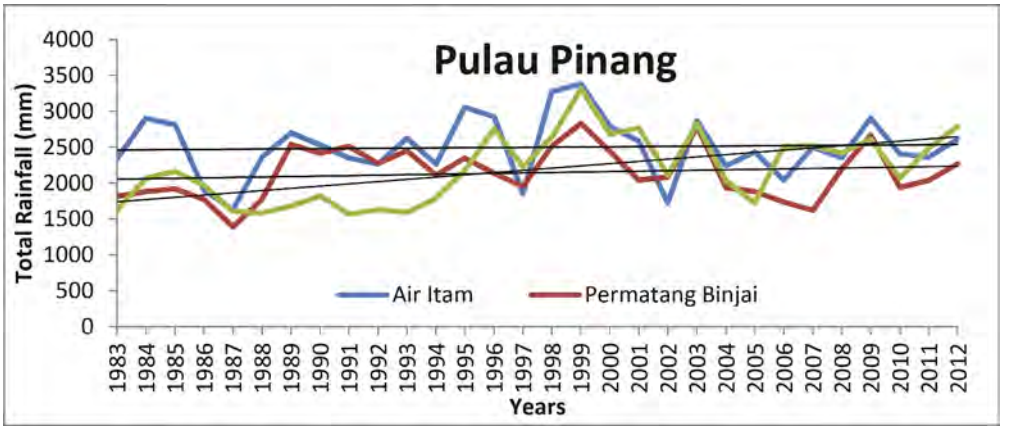

Figure 4. Time series plot for Pulau Pinang.

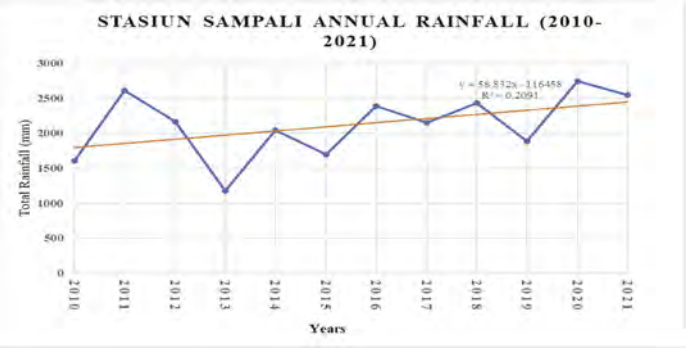

Figure 5. Annual rainfall for Karo regency (2010-2021).

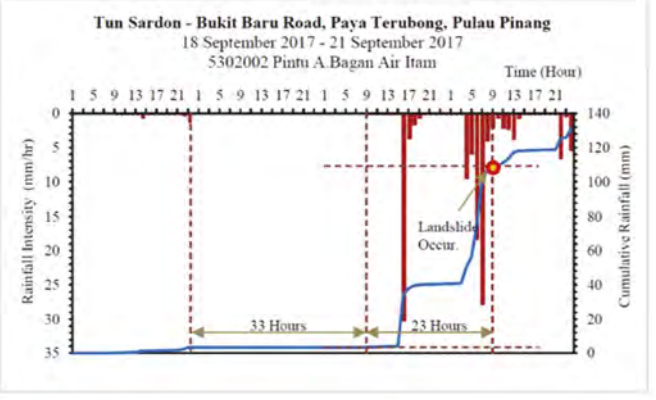

Figure 6. 30 days antecedent rainfall for the landslide at Bendera Hill, Air Itam, Penang [Muaz, 2020].

3.2 *Landslide occurances*

From the Figure 7 at Medan – Berastagi road, Karo Regency; it was concluded that five districts were classified as high landslide prone areas. Uncontrolled human activity in exploiting nature has a big share in the occurrence of landslides. The construction of building,

excavation, and slope cutting are the parameters that influence the occurrence of landslides the most. The reason is because it has an indicator weight by 20%, so that the high landslide hazard level is mostly located in areas that have a high level of construction and slope cutting, Puji Hastuty et al (2021).

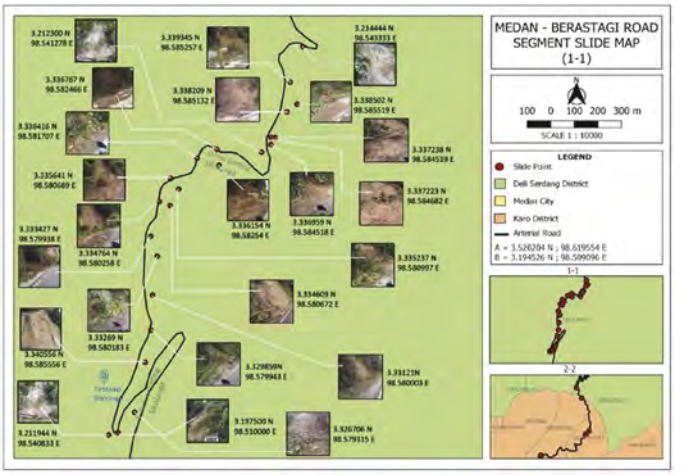

Figure 7. Landslide events along Medan – Brastagi road.

As for Penang Island, the landslide events that were critical cases are as listed in Table 3 and Figure 8 to show the occurrences of the failure after heavy rainfall over long hours during the monsoon season.

Table 3. List of Landslide event in Penang from 2017-2018.

No	Date	Case	Fatalities	Losses
1	7th Sept 2008	Minor Landslide and fallen tress	-	Road closure
2	14th Sept 2013	13 Landslide occurs due to soil erosion at Tanjong Bungah	-	Road damage
3	7th Nov 2016	Debris flow at Teluk Bahang slope causing road damages	-	Road closure
4	14th July 2017	Landslide at Lebuh Rambai, Paya Terubong	-	Road closure
5	21st Sept 2017	Bukit Baru slope failure cut of road access	-	Road closure
6	15th Sept2017	Slope Failure at Universiti Sains Malaysia RST Hostel	-	Road closure
7	21st Oct 2017	Tanjong Bungah Landslide on Lorong Permai3 and collapsed(Design Criteria problem)	14 buried and died, 2 survivor	Injuries and project stopped
8	22nd May2018	Sungai Kelian, Tanjong Bungah	-	-
9	18th Oct 2018	Landslide at road Contruction at Bukit Kukus, Paya Terubong	12 died (construction workers)	Road closure

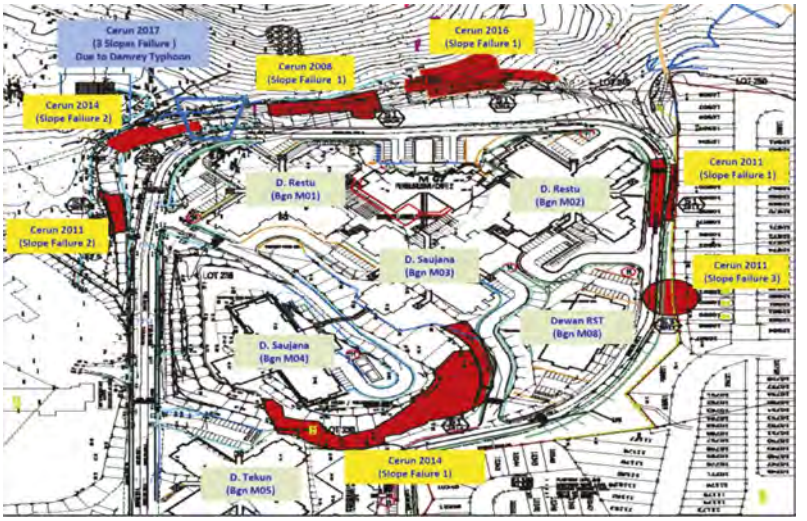

Figure 8. Landslide/Slope failure events at University Sains Malaysia from year 2011 till 2017.

4 CONCLUSION

In Malaysia or in Indonesia we can conclude that the behaviour of landslide due to slope instability are caused by development in hilly area. These activities created the disturbance to the geological and properties of the sites plus the triggering factors that happen after certain durations of rainfall events due to monsoon season and the fact that due to climate change. The unpredictable increase of rainfall intensity does affect the conditions of the slope especially if the slope is exposed and this can cause or triggered ingression of water on the ground.

As for housing development and human activities show that the growth is very significant increase especially to developed at high land or hilly terrain area. Therefore, the right guideline for hillside development needs to be follow and need to design in accordance to the slope stability requirement.

ACKNOWLEDGEMENT

This is a collaboration work done between Universiti Sains Malaysia and Universiti Sumatera Malaysia. The author would like to acknowledge the Universiti Sains Malaysia where a part of the research has been funded by RUI Grants Project 8014094 and the Development Office of Universiti Sains Malaysia under Healthy Campus project.

REFERENCES

Abdul Muaz, A.M.M. 2021, Development of Empirical Rainfall Thresholds For Landslide Forecasting In Peninsular Malaysia, *Master Thesis*, International Islamic University Malaysia.

Ahmad, F., Yahaya, A. S. & Farooqi, M. A. (2006). Characterization and Geotechnical Properties of Penang Residual Soils with Emphasis on Landslides. *American Journal of Environmental Sciences*, *2* (4), 121–128.

Ahmad, F. Yahaya, A.S. Ali, M. & Hairy, S.H.A. 2012. Qualitative risk assessment schemes using selected parameters for hillslope developments: A case study of Penang Island. Landslides, vol. 9, no. 1, pp. 63–74. https://doi.org/10.1007/s10346-011-0275-7.

Althuwaynee, O.F & Pradhan, B. 2017, Semi-quantitative landslide risk assessment using GIS-based exposure analysis in Kuala Lumpur City. Geomatics National Hazards Risk, vol. 8, no. 2, pp. 706–732.

Lembaga Badan Nasional Penanggulangan Bencana (BNPB), 2020. Data Bencana Longsor 2010 – 2020 in Indonesia.

Puji Hastuty, I. Ahmad, F. Roesyanto, Ridwan Anas, M. & Hidayati, Y.R 2020. Vulnerability analysis of landslide at Sibolangit using Geographic Information System (GIS) based on population density and slope gradient, *IOP Conf. Ser. Mater. Sci. Eng*., vol. 801, no. 1.

Puji Hastuty, I. & Ellysses Pratama, O. 2021, Geographical information system and satellite imagery for landslides analysis in Karo Regency based on human factors. *IOP Conferences Series Material Science*. Eng., vol. 1122, no. 1, p. 012019.

Puslittanak. 2004. Laporan Akhir Potensi Bencana Kekeringan, Banjir dan Longsor di Kawasan Satuan Wilayah Sungai Citarum-Ciliwung, Jawa Barat Bagian Barat Berbasis Sistem Informasi Geografis. Bogor.

Majid, N.A. Taha M.R. Selamat, S.N. 2020). Historical landslide events in Malaysia 1993-2019. *Indian Journal of Science and Technology*,13(33): 3387–3399.

Smart Geotechnics for Smart Societies – Zhussupbekov, Sarsembayeva & Kaliakin (Eds)
© 2023 The Author(s), ISBN 978-1-003-29912-7
Open Access: www.taylorfrancis.com, CC BY-NC-ND 4.0 license

Electrokinetic enhancement of microbial induced calcite precipitation used in improving the shear strength of soft clay

Mahdi Karkush & Nawar A. Ali
Department of Civil Engineering, University of Baghdad, Baghdad, Iraq

ABSTRACT: In recent years, and from the principle of sustainable development to reduce chemical pollution, researchers around the world have begun to use microorganisms to induce the precipitation of calcium carbonate which is a biological ground improvement method that has been successfully used to improve sandy soil. Also, the electrokinetic method is a soil improvement technique without excavation, unlike traditional methods. In this study, MICP and electrokinetic techniques were used to improve the geotechnical properties of soft clay. A large bench scale will be used for this purpose. The test model was using graphite electrodes with a voltage gradient of 50 V/m. This study was carried out in two phases. The first phase included using a concentration of prepared Bacillus sonorensis 12×10^{-7} cfu while the second phase was 1×10^{-4} cfu for cementation reagent (0.25M, 0.5M, and 1M) during the period of treatment for each phase. The results showed the following. precipitation of calcite was considered to be the main reason causing a significant increase in shear strength by about (600-1350%) for Bacillus sonorensis 1×10^{-4} and (800-2000%) for Bacillus sonorensis 12×10^{-7} cfu.

1 INTRODUCTION

Electrokinetic is a reliable method for transport under the electrical potential of charged particles and fluid. The EK shows changes in soil pH due to electrolyzes, water flow between electrodes, and cathode migration. This treatment has proved to be less costly than other methods in the processing of organic, toured, and clay silt. Otherwise, this approach also gives a nondestructive advantage to the site. Electrokinetics been proven as hardening technique for soft clay in recent years through the electroosmosis of the pore water in the soft clay and at the same time the injection of a chemical grout into the soft clay, in order to increase the soft clay properties. Laboratory and field studies have confirmed the efficacy of this approach many times (Chien et al., 2009). The techniques of artificial cementation are not always practical and are environmentally friendly. The reduction in the use of artificial cementation techniques can, however, be accomplished by replacing environmental techniques or materials. The Microbial Induced Calcite Precipitation (MICP) is a form of soil stabilization. This technique uses microbes as the primary soil stabilization element. Efficient implementation of MICP can be applied in a wide range of areas of civil engineering, such as wall retaining stability, embankments, and dams, soil erosion management, stabilizing cohesionless soil to promote soil stability, increasing shallow and piled foundation hold capacities and reducing liquefaction potential soil (Ivanov & Chu 2008).

MICP is a soil treatment process based on the urease hydrolysis of bacteria containing the urease enzyme, resulting in calcite precipitation in the presence of dissolved calcium ions. Electrokinetic is a reliable method for transport under the electrical potential of charged particles and fluid. The EK shows changes in soil pH due to electrolyzes, water flow between electrodes, and cathode migration. This treatment has proved to be less costly than other methods in the processing of organic, toured, and clay silt. Otherwise, this approach also gives a nondestructive

DOI: 10.1201/9781003299127-14

advantage to the site. Soft clay is a late alluvial deposit that has probably been formed over the last 10,000 years by its flat terrain (Abbawi 2010). They have high natural moisture levels generally (40%-60%), while plasticity is between (45%-65%). The major problems of soft soil are excessive settlement, low shear strength (bearing capacity), and Liquefaction (Abbawi 2010). Bacterial transportation is limited in fine-grained soils (and thus bacterial activity). Because bacteria are of a typical 0.5 to 5 μm size, they are not conveyed via silty or clayey soil and are not used for the induction of carbonate precipitation in those layers (Mitchell and Santamarina 2005).

Consequently, the Electrokinetic technique can enhance this green technique in fine-grained textured soil. Precipitation of microbiologically induced calcium carbonate (MICP) is a relatively common reaction that has been successfully used to improve sandy soil. Presently, only sandy soils are subject to specific research findings and only small studies are performed with single specimens. Over the past decade, numerous researchers have experimentally studied MICP (Dejong et al. 2006; Whiffin et al. 2007; van Paassen, 2009; Karkush et al. 2022) to provide a fair level of understanding of the processes involved. Nevertheless, soft clay layers also need improvement in the engineering industry to increase their strength. The use of the new microbial-induced soil enhancement technique in practical applications, therefore, depends on whether the technique applies to soft clay layers and can strengthen them effectively. Although few studies have been published on clay soils (Chien et al. 2018, Sharma and Ramakrishna 2016, Karkush & Altaher 2017a,b; Karkush and Ali 2019a,b), results are inconsistent and remain in the laboratory stage due to the uncertainty and complexity of the clay soils, the geochemistry of the soil, bacteria, and environmental factors. The objectives of the present study are to investigate the effect of MICP enhanced with EKs to improve the shear strength of soft clay soil.

2 SOIL AND MATERIALS USED IN TESTS

2.1 *Soil sampling*

A clayey soil sample was brought from Al Nahrawan city which is located 35 km to the east of Baghdad city from a depth of 9 m below the existing soil surface. Standard tests have been conducted to specify the chemical, physical, and mechanical characteristics of the soil samples. The physical and mechanical soil tests were conducted on the soil samples at the Laboratory of soil mechanics at the Department of Civil Engineering/University of Baghdad, while the chemical tests are conducted for both treated and untreated soil samples in the Department of Materials Research/Ministry of Science and Technology. Table 1 shows the results of physical, mechanical, and chemical tests.

Table 1. The physical and chemical properties of natural soft soil.

Index property	Test standard	Value	Index property	Test standard	Value
Liquid limit, %	ASTM D 4318	49	Gypsum content, %	BS. 1377:1990	1.17
Plastic limit, %	ASTM D4318	24	Chloride content, %	BS. 1377:1990	0.628
Plasticity index, %	ASTM D4318	25	Organic Material, %	ASTM D 2974	0.732
Specific gravity	ASTM D 854	2.77	Total soluble salt, %	BS. 1377:1990	2.541
Sand, %	ASTM D 422	6	Classification (USCS)	ASTM D 2487	CL
Silt, %	ASTM D 422	26	Optimum water content, %	ASTM D1557	21.54
Clay, %	ASTM D 422	68	Maximum dry unit weight, kN/m^3	ASTM D 1557	17.13
SO_3 content, %	BS. 1377:1990	0.52	Hydraulic conductivity, cm/s	ASTM D 2434	2.45×10^{-7}
pH Value	ASTM D 4972	8.45			

2.2 *Bacterial selection*

The bacteria selected in this study are previously isolated by Ali et al. (2020) from the Iraqi soil sample. The bacteria obtained from local sources denoted as C11 was identified to be Bacillus sonorensis. These isolates were routinely maintained in a growth media called nutrient agar which was supplemented with 20 g urea substrate, serving as a source of energy and nitrogen. The media was stored at 4°C in the fridge, before being used for subsequent tests of treatment. The bacteria were cultivated in the same way from a bacterial culture not grown for more than one month.

2.3 *Preparing of urea nutrient agar and bacteria culturing*

Urea nutrient agar was generally used to cultivate all the Bacillus spp. that could hydrolyze the urea. Table 2 shows the solid and liquid contents of the media. To prepare this media, the solid components were added to distilled water to bring the volume to 1 L and mixed well. The mixture was then gently heated and brought to a boiling temperature. Later, it was autoclaved for 15 min at 15 kPa pressure at 121°C. After autoclaving, it was cooled to 50–55°C. The urea solution was prepared by dissolving 10 g of urea in 50 mL of distilled water, and then the prepared solution was sterilized using a bacterium filter (diameter of this filter 0.25 μm). A total of 50 mL of sterile urea solution was added to the mixture and mixed well. The urea nutrient agar medium was then immediately poured into approximately 20 culture plates under a laminar flow hood.

Table 2. Details of the solid and liquid contents of the media.

Composition	Quantity
Nutrient agar	28 g/l
Urea solution Add 20 g of urea to distilled water and bring the volume to 100 ml, mix well, filter, and sterilize.	50 mL

2.4 *Purging solutions*

To prepare the bacterial treatment solution, a urea medium was first created. Nutrient broth (3 g), NH_3Cl (10 g), $NaHCO_3$ (2.12 g), and 450 ml of distilled water, as shown in Table 3, were mixed to create the urea medium solution. Each of the solid ingredients was mixed thoroughly in 450 ml of distilled water until it had dissolved. After autoclaving, Distilled water with urea after sterilization using a bacterium filter (diameter of this filter 0.25 μm) was then added to reach the final required volume (500 ml). The tube of diluted culture was added to the flask of the treatment solution. The flasks containing the growth medium were then cultivated for 48 hours with agitation (130 rpm) in an incubation shaker under aerobic batch conditions at 37°C. For injection, after incubation adds sterilized calcium chloride. While for the electrokinetic test the solution of bacteria and urea was added to the Cathode chamber without mixing with urea Cementation reagent was prepared by adding equal molars of Urea and Calcium Chloride ($Ca^{+2} + CO_3 \rightarrow CaCO_3$). The concentration of bacteria and cementation reagent (urea, calcium chloride) was a governing parameter and hence was decided based on the study by Lee et al. (2012) and varied 0.25M, 0.5M, and 1.0M.

Table 3. Bio-cement treatment components.

Component	Amount	Component	Amount	Component	Amount
Nutrient broth powder	3 g	$NaHCO_3$	3 g	Urea ($NH_2(CO)NH_2$)	0.25M, 0.5M, 1M
NH_4Cl	10 g	Distilled water	1 L	$CaCl_2.2H_2O$	0.25M, 0.5M, 1M

3 PHYSICAL MODELLING AND TESTING PROCEDURE

3.1 *Physical model*

The electrokinetic (EK) model was manufactured locally and modified to achieve the objectives of this study. A schematic and the detailed dimensions of the electrokinetic system used in the experiment are shown in Figure 1. The major components of the system are:

1) A power supply: which is used to apply a constant voltage and read a continuous electrical current during the time of the experiment. It is capable of supplying a maximum voltage of 60 Volts and a maximum current of 5 Amps.
2) Electrodes were made from graphite plates (Graphite Laminate SLS) placed into the chambers. The graphite electrodes do not corrode or introduce any secondary products into the system. The electrodes in this work are 20 mm thick, 150 mm long, and 300 mm high.
3) Two Mariotte bottles maintained a constant water level across the specimen and prevented any hydraulic gradient. Any excess fluid transported owing to electro-osmotic flow was collected in cylinders placed at the end of the chambers. Normally, the flow will be from the anode to the cathode. However, as the electro-osmotic flow direction is reversed under the polarity reversal condition, the Mariotte bottles and cylinders were placed on both sides.
4) A voltmeter was used to measure the voltage potential between two points in an electrical circuit across the specimen.
5) Electrokinetics rectangular cell: the electrokinetics cell consists of three compartments, one for the soil sample and two for electrodes (anode and cathode) which was made of a stainless-steel plate with 5 mm thickness braced externally by steel angles at their corners, edges, and each side and inner coated with two layers of fiberglass to prevent electric conduction manufactured of dimensions 800 mm in length, 600 mm in width and 550 mm in height. The dimensions of the soil compartment are (600×600×550) mm; the electrodes (anode and cathode) compartment each is 600 mm in length, 100 mm in width, and

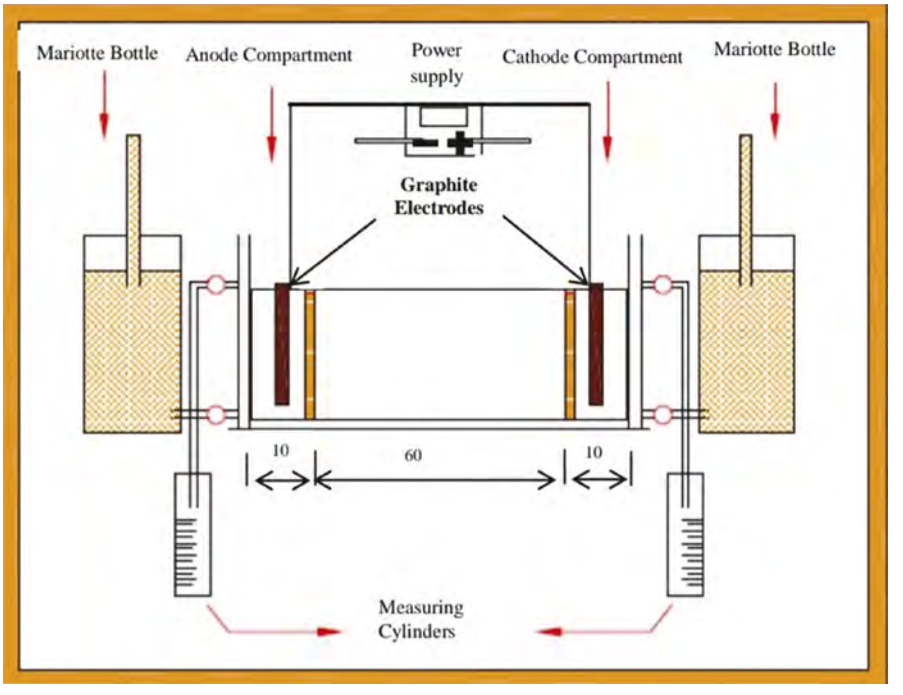

Figure 1. Schematic diagram of the electrokinetic setup.

550 mm in height. Each electrode compartment comprises a valve to manage the flow into the cell, a graphite electrode, and filter paper. The filter paper is used to prevent soil particles from the entrance into the anode reservoir or the cathode reservoirs.

6) Also, a pH meter (HANNA HI 96107) is used to measure changes in the pH of the solution in the cathode and the anode compartment and measure the pH of the soil after treatment. The outflow through the electrode compartment was also monitored to determine the electro-osmotic flow (EOF).

3.2 *Preparation of soil samples*

Trial testing was conducted to control the efficiency of the preparation process before the preparation stage of the bedding soil. Two key aspects of critical importance for preparing the homogenous soft soil bed have been tested via control tests. The first is to depart with various contents of water (or liquidity indexes) the variation of shear strength. Various trials have been done and typical findings are shown in Figure 2. With an increased liquidity index, the shear strength of the soil decreases. The second point, the variation in soil shear strength with time after mixing is determined. Such experiments provided the time required to recover strength in the remolded soil after a period of rest following the mixing process. Six samples have been prepared individually and placed in five layers inside CBR molds to achieve this aim. A special hammer for removing entrapped air was gently tamped on each layer. The samples were then wrapped with a plastic sheet of polythene and left for 8 days. Every day, the van shear system measured the undrained shear strength. Figure 3 demonstrates the effects of the increase in undrained shear strength over time. For the liquidity index range, with an increased liquidity index, the time influence decreases.

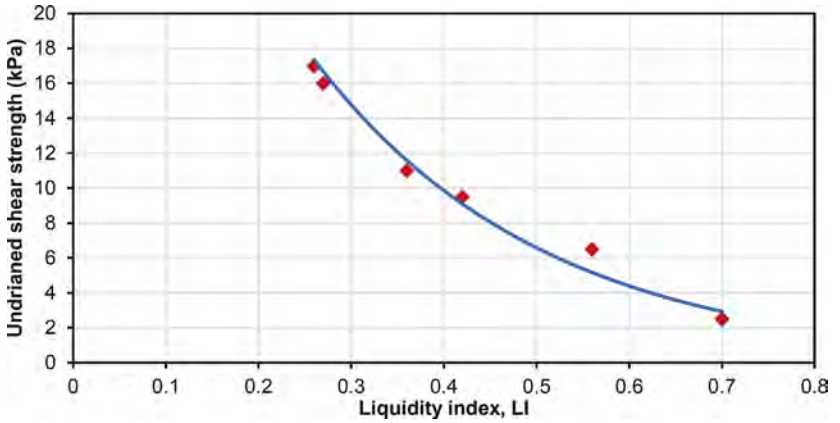

Figure 2. Variation of undrained shear strength with liquidity index for the remolded clay after 96 hrs.

The test was carried out at a liquidity index of 0.4 with c_u equal to 10 kPa. In order to achieve the necessary coherence, 650 kg of natural soil was mixed with enough water. The required water was thoroughly mixed with every 10 kg of soil by hand until the entire volume was completed and saved in plastic bags, not less than four days, to achieve uniform moisture content. The soil was then placed in a container of steel (600×600×400) mm in ten layers; each layer was tamped gently with a manufactured metal hammer of 10 kg and the dimension of (100×100) mm to remove any entrapped air, as shown in Figure 4. This process continues for the ten layers until reaching a thickness of 400 mm of soil in the steel container. The top surface was scratched and leveled after finishing the last layer so that a smooth surface could be made as near as possible, then covered by polythene sheets to ensure no moisture loss. Over the bed was placed a wooden panel of the same size as the floor area of the bed soil (600 to

600) mm and a fixed pressure of 5 kPa was applied. The prepared soil had been permitted to recover its strength (10 kPa) for a maximum of four days.

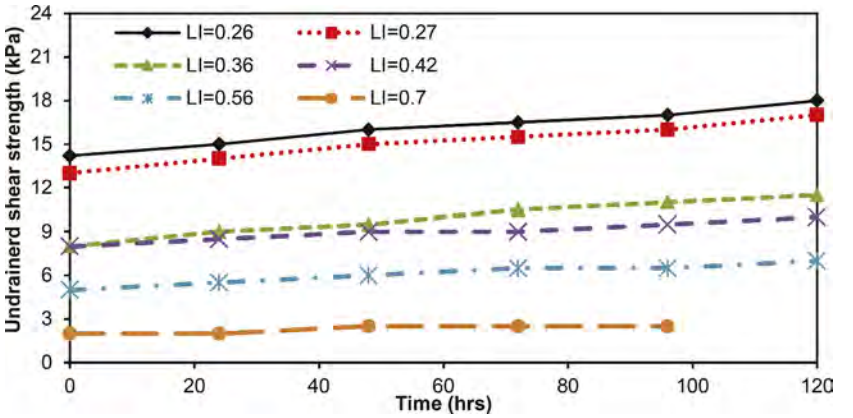

Figure 3. Variation of undrained shear strength versus time for the remolded clay.

3.3 *Testing procedure*

The testing procedure can be summarized by the following points:

1) Prepare the electrokinetic cell with all parts described previously (electrodes, treatment solution, and equipment and device used to control hydraulic and voltage gradients).
2) Putting the soft soil sample in the electrokinetic cell. The filter papers were inserted into the perforated sides of the soil container walls.
3) The electrode compartments are stuffed with a treatment solution. The anode reservoir was filled with calcium chloride solution was injected into the anode chamber for 3 days (T1) at the beginning of the test then add 0.1 M of NaOH was to maintain a pH higher than 2, whilst the cathode reservoir was filled with a solution of bacteria with urea (bacteria culture, urea, Nutrient broth (3 g), NH_3Cl (10 g), $NaHCO_3$ (2.12 g) for 7 days (T2).
4) Then, the electrodes are connected to the power supply with a potential gradient of 50 VDC/m applied to the soil sample.
5) The electric current across the soil sample, the water flow within the cathode compartment, and pH in the anode and cathode compartments were measured every day during the test period.
6) The shear strengths were measured by a vane shear device after 4 days of curing across the soil specimen at the horizontal distance of 0, 150, 300, 450, and 600 mm from the cathode to the anode. In the transverse direction, the vane shear test was conducted at three points at the same level, so the shear strength measured at each distance is the average of three readings.
7) The test is stopped when the current becomes constant or there is no noteworthy change in EO flow was observed.
8) At the end of each experiment, the aqueous solution from the reservoirs and the electrode compartments are gathered and examined. The electrodes, the tubing, and the reservoirs are exchanged at the beginning of each new test; Table 4 shows the main conducted experimental program.

4 RESULTS AND DISCUSSION

Figures 4 and 5 clearly show the undrained shear strength profile of the treated soft soil for soil treated with bacterial concentrations 10^7 and 10^4 cfu/ml with different cementation

Table 4. Main experimental testing program.

Phase 12×10^{-7}					
Code	Test	Anode	Cathode	EK Duration	Purpose
T1	$CaCl_2$-DW	$CaCl_2$	DW	3 Days	Effect of concentration of urea with bacteria and $CaCl_2$ (0.25, 0.5, 1) M
T2	DW-Urea with bacteria	DW	Urea with bacteria	8 Days	
T3	Measurement of Voltage	$CaCl_2$-DW- Urea with bacteria		1-11 Days	
T4	Measurement of the value of UCT and $CaCO_3$			16	
Phase 48×10^{-4}					
Code	Test	Anode	Cathode	EK Duration	Purpose
T1	$CaCl_2$-DW	$CaCl_2$	DW	3 Days	Effect of concentration of urea with bacteria and $CaCl_2$ (0.25, 0.5, 1) M
T2	DW-Urea with bacteria	DW	Urea with bacteria	8 Days	
T3	Measurement of Voltage	$CaCl_2$-DW- Urea with bacteria		1-11 Days	
T4	Measurement the value of UCT and $CaCO_3$			16	

reagent molar concentrations. The value of undrained shear strength for the soil treated with bacterial concentration 10^7 cfu/ml and with a molar concentration of calcium chloride and urea (0.5M) is increased above the control line, raised to about 120 kPa near the anode and then the values increase toward the cathode until it gained a higher strength of about 205 kPa at the proximity of the cathode, while the molar concentration (0.25M and 1M) tests start at a lower value which is around (85 and 90) kPa respectively at the anode. Then starts to increase steadily and reach the maximum value of 145 kPa and 160 kPa for samples treated with 0.25M and 1M respectively. Also, for the soil treated with bacterial concentration 10^4 cfu/ml system, the trend was almost similar with the 10^7 cfu/ml but at a lower value of c_u that is from 60, 80, and 75 kPa to 85, 135, and 100 kPa from the anode to cathode with the molar concentration (0.25, 0.5, and 1) M respectively.

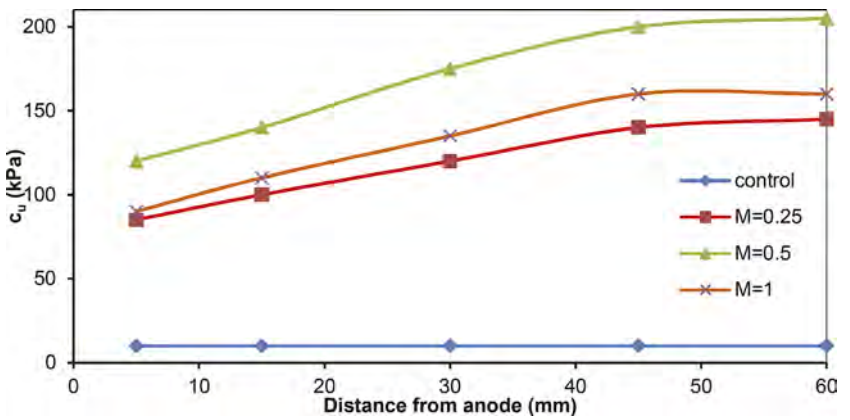

Figure 4. Undrained shear strength of soil treated with bacterial concentration 10^7 cfu/mL system with distance from the anode.

In general, this clearly shows the highest values of the undrained shear strength of all treated soils by 0.5M, whereas for the soil treated with cementation reagent molar concentration 1M, it did less than 0.5M and more than 0. 25M. Therefore, it can be concluded that the

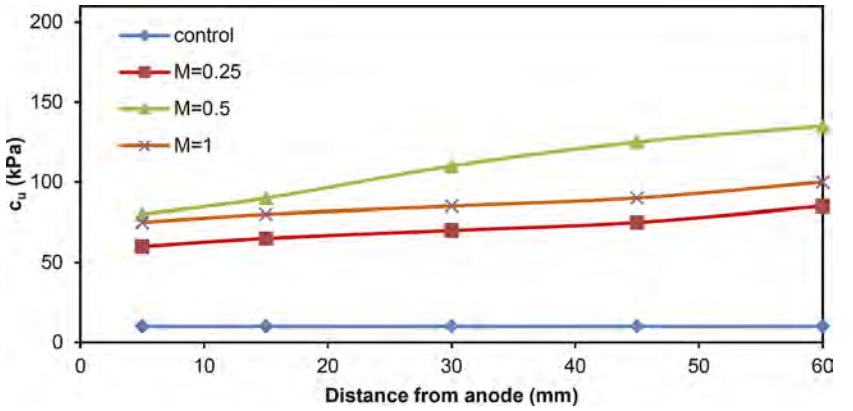

Figure 5. Undrained shear strength of soil treated with bacterial concentration 10^4 cfu/mL system with distance from the anode.

precipitation of calcite has a greater influence on the shear strength of the soil under electrokinetic stabilization treatment and will be validated with the other physical and chemical parameters later on. The soil strengthening at the cathode is attributed to the precipitation of calcium and because of the high concentration of carbonate ions (CO_3^{-2}) form cementing agent that bind the soil particles together. The high cementation reagent molar concentration and bacterial concentration that dominates the ionic concentration of the pore cause numerous electrochemical effects in the soil electrolysis, cations exchange, precipitation of salts, or secondary mineral, physical and chemical adsorption, and fabric change. All these factors are interrelated with each other and contribute to the changes in soil behavior due to electrokinetic stabilization treatment.

5 CONCLUSIONS

The following conclusions are made based on the outcomes of experimental tests:

- The undrained shear strength (c_u) of the treated soil was higher than the soft clay concerning different concentrations.
- The highest value of the undrained shear strength of all treated soils by 0.5M, whereas for the soil treated with cementation reagent molar concentration, 1M did less than 0.5M and more than 0. 25M.
- For the soil treated with bacterial concentration 10^4 cfu/ml system, the trend was almost similar with the 10^7 cfu/ml but at a lower value of c_u.
- The bearing capacity of the square footing increased with the increase of the molar concentration. Soil treated with the 0.5M test showed the highest value. However, the bearing capacity of soft soil treated with by EKs test is higher than soft soil treated with the biocementation test.

REFERENCES

Abbawi, Z.W. 2010. Proposed techniques for improving soft soil underneath a ballasted track. Ph.D. thesis, Building and Construction Engineering Department, University of Technology, Baghdad, Iraq.

Acar, Y.B. & Alshawabkeh, A.N., 1993. Principles of electrokinetic remediation. Environmental science & technology, 27(13), pp.2638–2647.

Acar, Y.B. & Alshawabkeh, A.N., 1996. Electrokinetic remediation. I: Pilot-scale tests with lead-spiked kaolinite. Journal of geotechnical engineering, 122(3), pp.173–185.

Acar, Y.B., Gale, R.J., Putnam, G.A., Hamed, J. & Wong, R.L., 1990. Electrochemical processing of soils: Theory of pH gradient development by diffusion, migration, and linear convection. Journal of Environmental Science & Health Part A, 25(6), pp.687–714.

Ali, N.A., Karkush, M.O. & Al Haideri, H.H., 2020, August. Isolation and identification of local bactria produced from soil-borne urease. In IOP Conference Series: Materials Science and Engineering (Vol. 901, No. 1, p. 012035). IOP Publishing.

Chien, S.C., Ou, C.Y. & Hsieh, P.G., 2018, June. Electro-osmotic with injection of microbial for strengthening clay. In The 28th International Ocean and Polar Engineering Conference. OnePetro.

Chien, S.C., Ou, C.Y. and Wang, M.K., 2009. Injection of saline solutions to improve the electro-osmotic pressure and consolidation of foundation soil. Applied clay science, 44(3-4), pp.218–224.

Chu, J., Stabnikov, V., & Ivanov, V. 2012. Microbially induced calcium carbonate precipitation on surface or in the bulk of soil. Geomicrobiology Journal, 29(6), pp. 544–549.

DeJong, J. T., Fritzges, M. B., & Nüsslein, K. 2006. Microbially induced cementation to control sand response to undrained shear. Journal of Geotechnical and Geoenvironmental Engineering, 132(11), pp. 1381–1392.

Ivanov, V. & Chu, J. 2008. Applications of microorganisms to geotechnical engineering for bioclogging and biocementation of soil in situ. Reviews in Environmental Science and Bio/ Technology, 7(2), pp. 139–153.

Karkush, M. & Ali, S., 2019a. Remediation of clay soil contaminated with lead nitrate using washing-enhanced electrokinetic technique. Journal of Electrochemical Science and Engineering, 9(1), pp.63–73.

Karkush, M.O. & Ali, S.D., 2019b. Remediation of clayey soil contaminated with copper sulfate using washing-enhanced electrokinetics technique. Russian Journal of Electrochemistry, 55(12), pp.1381–1390.

Karkush, M.O. & Altaher, T.A., 2017a. Remediation of contaminated soil of Thi-Qar oil refinery plant. In Proceedings of the 19th International Conference on Soil Mechanics and Geotechnical Engineering (Vol. 1).

Karkush, M.O. & Altaher, T.A., 2017b. Remediation of Contaminated Soil with Petroleum Industrial Wastewater. Journal of Engineering, 23(2), pp.13–20.

Karkush, M.O., Ali, N. & Imran, S., 2022. Using microbial induced carbonate precipitation for improving the undrained shear strength of soft clayey soil. Proceedings of the 20th International Conference on Soil Mechanics and Geotechnical Engineering. pp. 2925–2930.

Lee, L.M., Ng, W.S., Tan, C.K. and Hii, S.L., 2012. Bio-mediated soil improvement under various concentrations of cementation reagent. In Applied mechanics and materials (Vol. 204, pp. 326–329). Trans Tech Publications Ltd.

Mitchell, A.C. & Ferris, F.G., 2005. The coprecipitation of Sr into calcite precipitates induced by bacterial ureolysis in artificial groundwater: temperature and kinetic dependence. Geochimica et Cosmochimica Acta, 69(17), pp.4199–4210.

Sharma, A., & Ramkrishnan, R. 2016. Study on effect of microbial induced calcite precipitates on strength of fine grained soils. Perspectives in Science, 8, pp. 198–202.

Van Paassen LA. 2009. Biogrout: ground improvement by microbially induced carbonate precipitation. Ph.D. thesis, Delft University of Technology.

Whiffin, V. S., Van Paassen, L. A., & Harkes, M. P. 2007. Microbial carbonate precipitation as a soil improvement technique. Geomicrobiology Journal, 24(5), pp. 417–423.

Smart Geotechnics for Smart Societies – Zhussupbekov, Sarsembayeva & Kaliakin (Eds)
© 2023 The Author(s), ISBN 978-1-003-29912-7
Open Access: www.taylorfrancis.com, CC BY-NC-ND 4.0 license

Geomembrane barrier systems for construction and rehabilitation of embankment dams

D. Cazzuffi
Cesi SpA, Milan, Italy

D. Gioffrè
University of Pavia, Pavia, Italy

ABSTRACT: The main goal of this invited lecture is to discuss the use of geomembranes in embankment dams in order to understand and to evaluate the geosynthetic barrier function in different types of applications, both for the new constructions and also for the rehabilitation of existing dams. Presently, in more than 200 embankment dams worldwide, geomembranes are in fact the main waterproofing component, including the Contrada Sabetta rockfill dam in Italy, that dates back to 1959, being recognized from the international literature as the oldest geomembrane application in dams in the world. The use of geomembranes is generally associated with other types of geosynthetics performing various functions, as geotextiles for mechanical protection and local drainage, or also as geonets for more extended drainage, thereby forming a geosynthetic barrier system. In the invited lecture, the uses of geosynthetic barriers in the construction of new dams and also in the rehabilitation of existing dams around the world are critically reviewed. Design and construction aspects are considered, as well as selection and specifications of the various types of geosynthetic materials. In particular, the issue of sustainability matters on the use of geomembranes in embankment dams compared to the use of other traditional materials (as granular and cohesive soils, metallic blankets and bituminous concrete layers) is adequately treated. Finally, the durability aspects are extensively illustrated, with particular reference to the on-site behavior of applications in dams in the Alpine region.

1 INTRODUCTION

The design of embankment dams involves an adequate seepage and stability analysis of the dam's body (see for example Zhussupbekov and Mkilima 2022). Depending on the available materials on site, the embankment dam could be conceived with a central core or with a watertight upstream face (Jappelli 2002).

In particular, the use of geosynthetics as water barrier on the upstream face became widely use in the last sixty years, starting with the first application of Contrada Sabetta dam in Italy in 1959.

The first applications of geomembranes in dams took place in new embankment dams because many of these dams, being too permeable, required a separate element to provide imperviousness. In many cases, it appeared that geosynthetic barrier systems were more economical and easier to install than traditional impervious materials such as clay, cement concrete, bituminous concrete or even metallic blankets (ICOLD 1981).

Geomembranes were used in embankment dams before they were used in concrete or masonry dams probably for two reasons: (i) because geomembrane installation on the slope of an embankment dam is similar to installation on the slopes of a pond, an application where geomembranes has been used since the late 1950s; and (ii) because installation on a gentle slope is less demanding than installation on a vertical face (Cazzuffi et al. 2010).

As already mentioned, Contrada Sabetta dam, constructed in 1959 in Italy, is considered the first example of use of a geomembrane as the only water barrier in a dam (Cazzuffi 1987).

DOI: 10.1201/9781003299127-15

Contrada Sabetta dam is a 32.5 m high rockfill dam with a crest length of 155 m. It is a dam of a special type: rocks were arranged as dry masonry, which made it possible to achieve very steep slopes, 1V:1H upstream and 1V:1.4H downstream. The geomembrane used was 2.0 mm thick and made of polyisobutylene, an elastomeric compound that is no longer used as a geomembrane today, not because of any performance problem, at least when it is covered, but essentially because modern geomembranes are easier to seam. A general cross section of Contrada Sabetta dam is shown in Figure 1 and a detailed cross section is illustrated in Figure 2. Special features of Contrada Sabetta dam included the following:

- The geomembrane barrier consisted of two layers of identical geomembranes placed on top of each other over the entire upstream face of the dam. (It is important to note that two geomembranes (or two liners of any type) placed on top of each other, without a drainage layer in between, do not form a double liner.) A total of 3900 m^2 of geomembrane were used on the 1900 m^2 upstream face. These two geomembrane layers were glued to each other along the edges.
- The lower geomembrane layer was glued using a bitumen adhesive on the 0.1 m thick supporting material made of porous cement concrete. The porous cement concrete rests on 0.25 m thick reinforced concrete slabs, resting on the dry masonry.
- The geomembrane barrier was covered by unreinforced 2 m x 2 m concrete slabs, 0.20 m thick, cast on site. The joints between adjacent slabs were left open, 1 mm wide, and were not filled by any porous material, to allow for free circulation of water and to provide some flexibility in case of settlement. There was also a sheet of bituminous paper-felt between the concrete slabs and the upper geomembrane layer to protect the geomembrane during the casting of the concrete slabs.

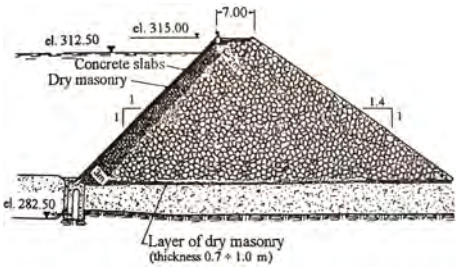

Figure 1. General cross section of Contrada Sabetta dam (modified after Cazzuffi 1987 and ICOLD 1991).

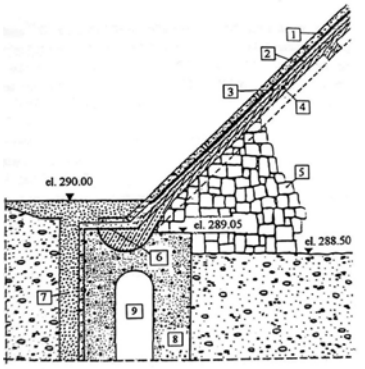

1) 0.20 m thick concrete slabs
2) one sheet of bituminous paper-felt + two sheets of polyisobutylene geomembrane (2.0 mm thick) + bituminous adhesive
3) porous concrete (0.10 m thick)
4) reinforced concrete slabs (0.25 m thick)
5) dry masonry (thickness ranging from 2.00 to 3.00 m)
6) joint be-tween plinth and upstream facing
7) plastic concrete diaphragm wall
8) concrete plinth
9) inspection and drainage gallery

Figure 2. Detailed cross section of upstream toe of Contrada Sabetta dam (modified after Cazzuffi 1987 and ICOLD 1991).

In most of the early projects, the geomembranes were installed during construction of the dam on the upstream slope and covered. The first exceptions were: (1) the first geomembrane used inside a dam was a CPE (Chlorinated Polyethylene) geomembrane used in 1970 on a 1V:0.67H slope (56º) inside a rockfill dam (Odiel dam in Spain) with upstream and downstream slopes of 1V:1.3H; (2) the first geomembrane used for repairing a dam was a 0.9 mm thick PVC (Polyvinyl chloride) geomembrane installed in 1971 at Obecnice dam, an earthfill dam in the Czech Republic; and (3) the first geomembrane used exposed on the face of an embankment dam was a 4 mm thick bituminous geomembrane installed in 1973 at Banegon dam, a 17 m high earthfill dam in France. It was also the first use of a bituminous geomembrane in a dam.

Mission dam (now called Terzaghi dam), a 55 m high rockfill dam constructed in 1960 in Canada, is a special case for both historical and technical reasons. It is a special case for historical reasons because Karl Terzaghi was the designer and because it was one of the first dams including a geomembrane. It was a special case for technical reasons because the geomembrane application was not typical. A detailed description of the construction of the dam was provided by Terzaghi & Lacroix (1964) and a description of the geomembrane installation was provided by Lacroix (1984).

Special features of Terzaghi dam relevant to the geomembrane application are the following:

- The water barrier in the dam was a 1.5 m thick clay layer covered by 2 m of rubble fill.
- Large differential settlement was expected and the clay layer was designed to be convex in order to remain in compression when settlement occurs.
- However, at the transition between the 15º slope and the quasi-horizontal area near the toe of the upstream face, the clay layer was necessarily concave.

In this 10,000 m^2 transition zone, a geomembrane was used to prevent the clay from cracking. The function of the geomembrane can be described as follows. The geomembrane, placed on top of the clay, ensures that a uniform pressure equal to the hydrostatic pressure is applied on the clay. The hydrostatic pressure being higher than the compressive strength of the clay, clay cracking is prevented. Furthermore, if some cracks develop, in spite of the normal pressure applied by the geomembrane, water does not penetrate into the cracks and, therefore, no hydrostatic pressure is applied within the cracks.

In contrast, without geomembrane, as cracks tend to develop as a result of differential settlement, water would penetrate in the cracks. The hydrostatic pressure, acting on both sides of cracks, would open the cracks and cause the cracks to propagate through the entire thickness of the clay layer, thereby impairing the clay barrier function of the clay layer.

A PVC geomembrane was selected because of its large elongation before rupture. The PVC geomembrane selected was 0.75 mm thick, which was considered, particularly in North America, to be a very thick PVC geomembrane at that time. It was smooth on one side and embossed on the other side.

Clearly, Terzaghi dam is an interesting use of a geomembrane in a dam, which can provide an example for some applications in the future. However, it cannot be considered as a precursor of modern applications of geomembranes in embankment dams.

2 EMBANKMENT DAMS

2.1 *Geomembranes and other barriers*

Until 2010, geomembranes have been used in 171 large embankment dams, according to the ICOLD database (ICOLD 2010), both for new construction and for rehabilitation purposes. (Scuero and Vaschetti 2009). In embankment dams, geomembranes are in competition with traditional barriers such as: clay or bituminous central cores, or upstream facings made of cement concrete slabs or bituminous concrete layers or even metallic blankets (Bertacchi et al 1988).

2.2 *Advantages of geomembranes*

Geomembranes are increasingly used because they have numerous advantages over traditional barrier materials: imperviousness, cost, construction, sustainability issues and practical considerations (Cancelli and Cazzuffi 1994).

Geomembranes are significantly less permeable than all other barrier materials. This geomembrane property is essential for the containment of liquids that could contaminate the ground or the ground water, but typically is not considered essential in dams. However, with the growing emphasis on water conservation due to the climatic change, it is likely that the superior imperviousness of geomembranes will be considered to be a significant asset of geomembranes in the future.

Some geomembranes can undergo large strains (e.g., 100% or more) without rupture. A geomembrane with a high elongation capability will maintain watertightness in presence of differential settlements and movements that could cause: (1) cracking of concrete slabs in concrete face rockfill dams and, in extreme cases, could cause failure of the waterstops; and (2) disruption in the connection of the bituminous facing to the concrete structures in the case of bituminous concrete face embankment dams. Concerning dams with clay core, the imperviousness of the core heavily relies on construction quality (too often influenced by weather conditions) and on the skill of the contractor. It can therefore be said that geomembranes can improve safety of embankment dams because they are engineered to maintain imperviousness in presence of events that could impair the performance of other waterproofing systems eventually used in embankment dams.

Geomembrane waterproofing barriers can provide substantial advantages in the construction of embankment dams as compared to traditional waterproofing barriers, because they avoid problems such as lack of suitable materials and deterioration of waterstops. Also, they simplify construction by eliminating the need for installing multiple lines of waterstops and by being easier to connect to ancillary concrete structures than clay cores or bituminous concrete layers.

Construction times and constraints are reduced when geomembrane barriers are used. With traditional barrier materials, the impact that the installation/construction of the face slabs, or the placement/compaction of the impervious core, can have on the overall construction schedule, and the complexity of the techniques needed to construct the waterproofing system, must be taken into consideration when evaluating times of completion. In dams with a central core (made of clay or bituminous material), a crucial point is that, being the construction of the dam body and the construction of the central core related, the constraints imposed by the weather conditions, or any disruption in the placement of the filter material, will affect the rate of construction of the entire dam body. On the contrary, installation of a geomembrane barrier system can be scheduled in function of the general schedule of construction and is not significantly affected by weather.

A variety of types of geomembranes are used in embankment dams (Table 1). Based on the ICOLD database, geomembranes have been used in a total of 171 embankment dams (ICOLD, 2010). In particular, PVC geomembranes have been adopted in 48.5% of dams, while PE (polyethylene) geomembranes (LLDPE, HDPE, CSPE, CPE) have been installed in almost 30% of dams and bituminous geomembranes have been utilized in about 12% of embankment dams.

Table 1. Embankment dams: geomembranes (GM) by types of constituent material.

Type of GM	N	%	Tot exposed	Tot covered	Unknown
PVC	83	48.5	23	57	3
LLDPE	27	15.8	0	26	1
Prefabricated bituminous	20	11.7	7	13	0
HDPE	15	8.8	3	11	1
Elastomeric	11	6.4	5	4	2
CSPE	7	4.1	3	4	0
PP	6	3.5	3	3	0
CPE	2	1.2	0	2	0
Total	171	100.0	44	120	7

PVC: Polyvinyl chloride; LLDPE: Linear Low-density Polyethylene; HDPE: High-density Polyethylene; CSPE: Chloro-sulfonated Polyethylene; PP: Polypropylene; CPE: Chlorinated Polyethylene

3 CONSTRUCTION OF NEW EMBANKMENT DAMS

For new construction of embankment dams, it is possible to define two design concepts: location of the geomembrane and type of liner system.

In an embankment dam, two positions can be considered for the geomembrane barrier: (1) the geomembrane can be at the upstream slope, covered or not; or (2) the geomembrane can be internal, i.e. located inside the dam body, either inclined inside the upstream zone of the dam, or vertical or quasi vertical, in a central position.

Based on the ICOLD database, in approximately 90% of the dams where a geomembrane is used, it is at the upstream slope and in approximately 10% it is internal. Among the geomembranes used at the upstream slope: 70% are covered, and 30% are exposed.

When a geomembrane is used on the upstream slope, it can be exposed or covered (i.e. "protected") by a layer of heavy material such as soil, concrete, etc.

The design of a dam with a liner (any type of liner) should be such that the seepage resulting from a major breach in the liner should not cause the rupture or a major distress of the dam. Therefore, the various zones that constitute a dam should comprise adequate filters to prevent internal erosion of the dam. This is particularly important when the liner is an exposed geomembrane because this type of materials can be breached accidentally. In fact, geomembranes are significantly more waterproof than concrete or clay, but they can be damaged by some mechanical actions.

If the dam does not meet the conditions indicated above and is sensitive to internal erosion in case of seepage, a possible solution consists in minimizing the rate of leakage through the liner system, even in case of a breach in the geomembrane. Two possibilities for minimizing leakage are the use of a double liner, and/or the use of a composite liner.

Even if there are some examples of use of geomembranes in a central position of an embankment dam (Cazzuffi et al 2010), the present invited lecture illustrates mainly the case of applications on the upstream face, both for exposed geomembranes and for covered geomembranes.

3.1 *Upstream exposed geomembranes*

Exposed geomembranes account for approximately 30% of the geomembranes used at the upstream slope of embankment dams, e.g. Bilancino cofferdam in Italy (Figure 3); and the geomembranes used at the upstream slope of embankment dams are approximately 90% of the geomembranes used in embankment dams.

Geomembranes exposed on the upstream face of embankment dams are subjected to a variety of potentially detrimental actions:

- Mechanical damage by ice, floating debris, rocks falling, animals, vandals, and traffic.
- Degradation by exposure to environmental agents (oxygen, UV, heat).
- Displacement by wind, wave action, fluctuations of water level, and gravity (causing creep).

Geomembranes can be used exposed if they have appropriate strength and composition to resist mechanical damage and degradation. Precautions must be taken to prevent or reduce geomembrane displacement by wind, waves and gravity. Generally, the main risk is displacement by wind. Therefore, geomembranes must be anchored against wind uplift.

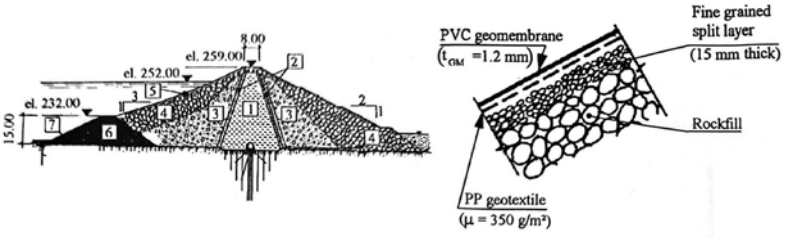

Figure 3. Bilancino zoned embankment dam in Italy, 42 m high, with a cofferdam lined with an exposed PVC geomembrane (modified from Baldovin, 1993): 1. Clayey silt core; 2. Filters, 3. Transitions; 4. Rockfill; 5. Rip-rap; 6. Cofferdam (with upstream face 1V:2H and downstream face 1V:1.5H); 7. PVC geomembrane (t_{GM} = 1.2 mm) and PP geotextile (μ = 350 g/m^3).

3.2 *Upstream covered geomembranes*

If a geomembrane is left exposed on the upstream face of an embankment dam, it could be subjected to a number of actions that could damage it. The reasons for geomembrane protection by a cover layer are:

- Protection of the geomembrane against mechanical damage (by ice, floating debris, rock falling from the sides, animals, vandals, traffic).
- Elimination of exposure to environmental agents (oxygen, UV, heat) that in some cases could cause degradation of the geomembrane.
- Prevention of geomembrane displacement by wind, wave action, gravity (causing creep).

Mechanical protection of geomembranes on slopes is typically ensured by covering the geomembrane with a layer of heavy material such as cement concrete or soil. Considering all of the potentially detrimental actions, a majority (70%) of the geomembranes used at the upstream slopes of embankment dams are covered, based on the ICOLD database.

Several systems have been used, or could be used, to cover geomembranes:

- Interlocking concrete blocks;
- Articulated concrete blocks;
- Concrete slabs;
- Shotcrete on geotextile;
- Geocells or geo-mattresses filled with concrete;
- Soil and rock protection layers.

It is important to note that improperly designed or constructed cover layers can eventually damage a geomembrane during construction or operation. Therefore, a thick needle-punched nonwoven geotextile is generally used between the geomembrane and the cover material.

The placement of the cover layer is possibly the most critical part of construction of a covered geomembrane system. Construction quality assurance activities should not stop after placement of the geomembrane. It should continue during the placement of a geotextile protection layer on the geomembrane and then, during the following placement of the cover layer.

The important role of the geotextile layer during operation is illustrated by the fact that the geomembrane was not damaged despite extensive displacement of articulated concrete blocks at L'Ospedale dam in France, that was built in 1978.

At Codole dam, always in France, a cost analysis at the design stage showed that the solution adopted was cost-effective compared to other solutions even if the geomembrane and the overlying cement concrete slabs had to be re-placed after 25 years of service. Codole dam was built in 1983 and is still in service without any further replacing of cement concrete slabs (Figure 4).

At Codole dam, the cement concrete slabs were reinforced with traditional steel bars. This proved to be a potential problem. Great precautions had to be taken during construction to avoid damaging the geomembrane with the reinforcing bars, in spite of the presence of a geotextile layer above the geomembrane.

Bovilla dam in Albania, is a 91 m high rockfill dam built in 1996 for water supply, flood mitigation and hydropower (Figure 5). The original design of a concrete face rockfill dam was changed to a geomembrane face rockfill dam for the following reasons: (1) concerns about the final quality of the reinforced concrete face and its potential for future cracking; and (2) need to reduce construction time and costs as the project was behind schedule (Sembenelli et al. 1998).

The upstream composite geomembrane installed in 1996 is the only element providing watertightness to the dam: the composite geomembrane consists of a 3 mm thick PVC geomembrane laminated to a 700 g/m^2 polyester geotextile. It was placed directly over a porous cement concrete layer constituted by gravel stabilized with cement slurry (Figure 6). The geomembrane covers the entire upstream slope, from the crest to the massive toe block, i.e. over a difference in elevation of 54 m. The upstream slope is 1V:1.55H in the upper 40% and 1V:1.6H in the lower 60%.

The geomembrane was covered with unreinforced concrete slabs that were placed on an 800 g/m^2 geotextile. The slabs are 6 m long in the slope direction and 3 m horizontally. The slabs

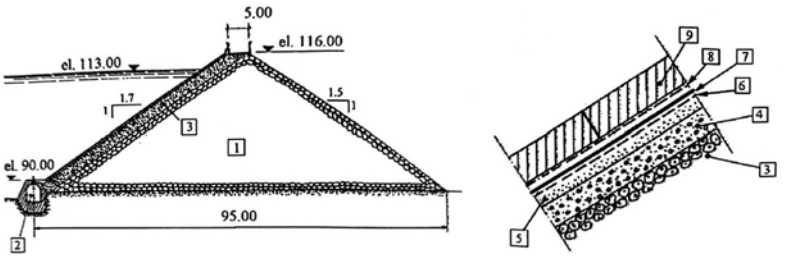

Figure 4. Codole rockfill dam in France, 22 high (modified from ICOLD, 1991): 1. Rockfill (up to 1.00 m size); 2. Inspection and drainage gallery; 3. Sand and gravel layer (2.00 m thick, 25÷120 mm grain size); 4. Gravel layer (0.15 thick, 25÷50 mm grain size); 5. Cold premix layer (50 mm thick, 6÷12 mm grain size); 6. Geotextile (μ = 400 g/m^3) bonded to geomembrane; 7. PVC geomembrane (t_{GM} = 2.0 mm); 8. Geotextile (μ = 400 g/m^3); 9. Cement concrete slabs (0.14 m thick, 4.5 x 5.0 m^2 size).

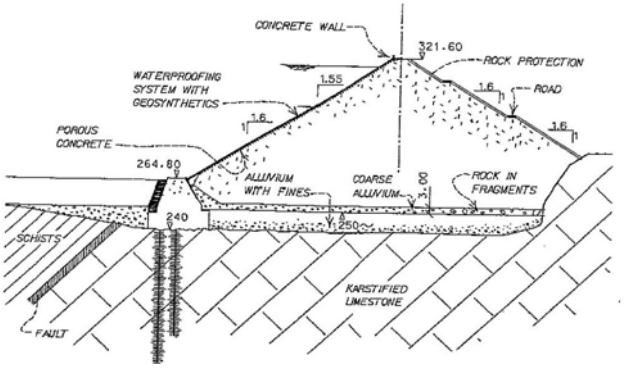

Figure 5. General main cross section at Bovilla dam in Albania.

are 0.20 m thick. The geotextile had a double function: providing anti-puncture protection to the geomembrane against casting of the slabs, and act as a light reinforcement for the slabs themselves.

Figure 6. Bovilla dam: composite geomembrane placing over the porous cement concrete layer.

The decision to adopt cast in place concrete slabs rather than prefabricated concrete blocks was taken because casting slabs was considered less aggressive on the PVC geomembrane than the placement of prefabricated concrete elements, and also considering the problems with articulated concrete blocks previously registered at L'Ospedale dam in France.

At Bovilla dam, the bottom seal of the geomembrane on the toe block was designed to be able to accept differential movements and settlements one order of magnitude larger than the estimated ones. Extra material and protection/decoupling layers were placed for this purpose over the layer of geomembrane at the seal.

La Galaube dam, 43 m high, a rockfill dam built in France in 2000, is one of the highest dam waterproofed with a bituminous geomembrane (Gautier et al,. 2002). The bituminous geomembrane, 5 mm thick, has been laid on a 0.10 m thick cold asphalt mix placed over a layer of non-bounded gravel impregnated with bitumen on the 1V:2.0H slope. The bituminous geomembrane is protected by a geotextile layer (Figure 7) and the final cover layer is constituted by a 0.10 m thick cement concrete slab reinforced with PP (Polypropylene) fibers.

The bottom anchorage is made on the concrete plinth and is of the tie-down type. Installation of 22.000 m^2 of bituminous geomembrane was completed in 2000.

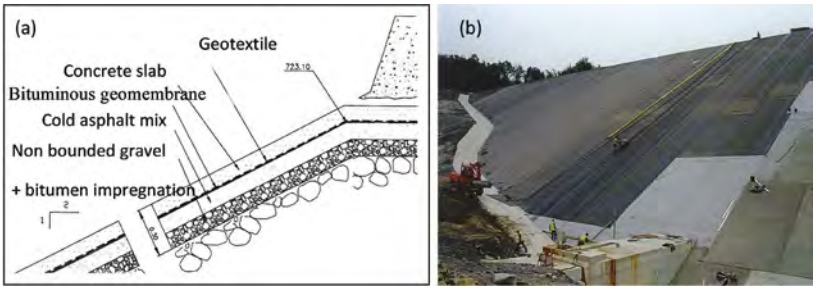

Figure 7. La Galaube dam in France: (a) typical cross section at the top (after Gautier, 2003); (b) placing of geotextile protection layer (in grey) over the bituminous geomembrane layer (in black).

Geomembrane covers using a soil layer cannot be used on the steep slopes typical of rockfill dams because they would not be stable. Soil layers should only be used on slopes less steep than 1V:2.0H, preferably on 1V: 2.5H slopes and less steep. It is essential to check the stability of the soil cover under rapid drawdown conditions, the worst conditions for static stability. In relevant areas, the seismic stability should also be checked.

At Worster dam, Colorado, USA, 22 m high, 215 m long, lined with a 1.5 mm textured HDPE (High-density Polyethylene) geomembrane, the 0.3 m thick soil cover bulged at the toe of the 1V:3.0H slope at the first drawdown of the reservoir, as it was uplifted by water entrapped between the geomembrane and an old concrete slab located a few meters behind the geomembrane.

4 REHABILITATION OF EMBANKMENT DAMS

Geomembranes have been used also for the rehabilitation of embankment dams, and in particular for cement concrete face rockfill dams and for bituminous concrete face rockfill dams.

4.1 *Rehabilitation of cement concrete or bituminous concrete face rockfill dams*

In the rehabilitation of cement concrete face rockfill dam dams or bituminous concrete face rockfill dams, the design should take into account that both are hard surfaces to which geomembranes can be attached. Therefore, the anchorage system of the geomembrane to the dam face is designed depending on the type and strength of the existing facing (cement concrete or bituminous concrete): consequently, the geomembrane is typically left exposed, and maintained to the dam upstream face by face anchorage and perimeter anchorage.

4.2 *Rehabilitation of cement concrete face rockfill dams*

For cement concrete rockfill dams, face anchorage in the past has be made by gluing or by mechanical fixations.

Gluing has been done in the case of in situ geomembranes. In a number of these applications, gluing has resulted in failure, such as at Paradela dam in Portugal and Rouchain dam in France. These failures can be attributed to the nature of the in-situ geomembranes. But, they may also be due to a fundamental conceptual mistake. Two liners should not be located directly on top of each other, unless there is a sufficient load on them to counteract water pressure. Of course, there is no load on a geomembrane glued on a rigid support. Therefore, the ICOLD Bulletin (2010) recommends that gluing "should not be continuous over the entire face to allow drainage behind the geomembrane and release of vapor pressure which would result in uplift pressure which could detach and ultimately damage the geomembrane or the sup-porting layer. Rehabilitation of cement concrete or bituminous concrete facings with a geomembrane glued on the entire surface is not recommended." In fact, gluing has been abandoned since the late 1980s.

A simple mechanical fixation consists of nailing the geomembrane to the supporting layer. This has been done for the partial repair of Heimbach concrete dam in Germany. Conceivably, a nailed geomembrane (or a geomembrane with other types of punctual anchors) could be used for the repair or rehabilitation of cement concrete face rockfill dams.

Mechanical fixations are bolted to the dam with different methods depending on the characteristics of the face. Mechanical fixations are commonly used nowadays and they have the additional advantage of allowing a drainage system behind the geomembrane.

A remarkable example of rehabilitation on the entire facing of cement concrete face rockfill dam is represented by Midtbotnvatn dam in Norway (Figure 8). In this dam, the 2.5 mm thick PVC composite geomembrane was installed in 43 days instead of 2 full summer seasons as required by the second best rehabilitation option (morainic material): this fact is quite important for applications in cold regions where the rehabilitation works could be done only in the summer season.

Figure 8. Rehabilitation of Midtbotnvatn rockfill dam in Norway: placing of PVC composite geomembrane layer over the damaged cement concrete facing.

4.3 *Repair of bituminous concrete face rockfill dams*

If a geomembrane is used to repair dams having a bituminous concrete face, the anchorage system is designed in function of the particular characteristics of the subgrade, which being not a rigid material like concrete does not always allow using the type of anchors used on concrete.

For anchoring the profiles or batten strips that provide face anchorage, typically field testing is made to verify if chemical phials or grouted anchors or deep anchors must be adopted.

Chemical phials require a stronger and not very viscous subgrade. Grouted anchors and deep anchors (Duckbill/Manta Ray type) can be used in alternative.

At Moravka, a 39 meter high earthfill dam in the Czech Republic used for hydropower, potable water supply, and flood control, an exposed PVC composite geomembrane was placed on the bituminous concrete facing that despite several repairs, including a new bituminous concrete layer, continued to exhibit important leakage (Figure 9). An asset of geomembrane systems in this type of dams is that they do not require milling of the deteriorated bituminous concrete, which on the contrary is necessary if a new bituminous concrete layer is installed.

Pull out field testing was carried out at several locations of the facing to ascertain if chemical anchors could be used to fix the tensioning profiles for face anchorage. The tests were successful, but since the resistance of the bituminous concrete could vary over the year depending on atmospheric temperature, the conventional chemical anchors were modified to ensure stability.

Two bottom perimeter seals were installed at the concrete block where the drainage gallery is located (Figure 10). The primary seal confines the drainage system of the upstream face (geomembrane system); the secondary seal confines the drainage system for water coming from foundation/abutments/failing joints in the concrete. The two drainage systems discharge in the gallery with separate discharge pipes to allow a suitable monitoring of the system.

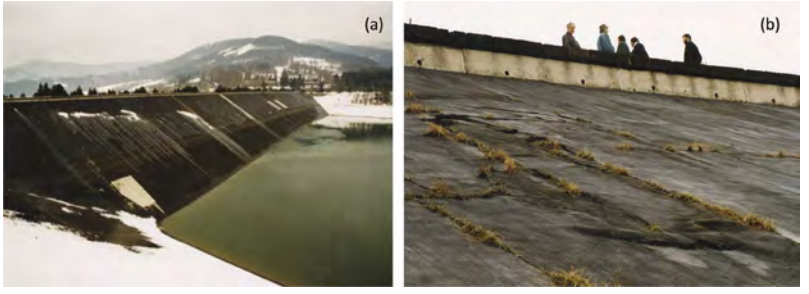

Figure 9. Moravka bituminous concrete face rockfill dam, Czech Republic: (a) original situation of the facing before rehabilitation; (b) detailed of the very important differential settlements in the facing.

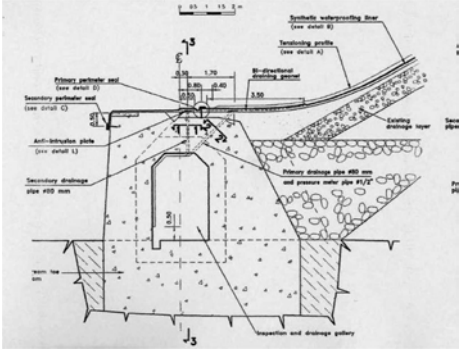

Figure 10. Moravka bituminous concrete face rockfill dam, Czech Republic: the two bottom seals.

The exposed geomembrane system was released in 2009 (Figure 11a). During the following years, the geomembrane system has resisted to important ice impact (Figure 11b).

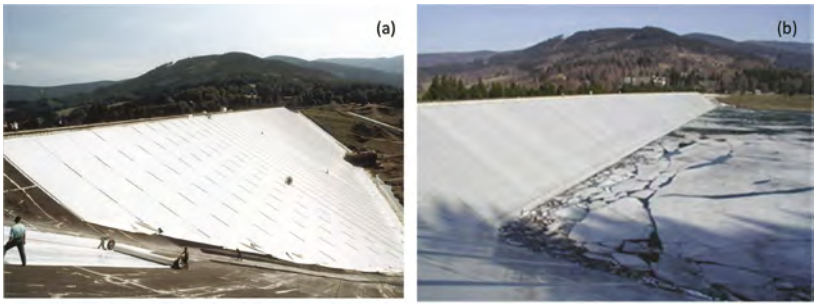

Figure 11. Moravka dam: (a) placing of PVC composite geomembrane layer 2.5 mm thick (b) heavy ice impact did not damage the exposed PVC geomembrane.

5 PERFORMANCE OF EMBANKMENT DAMS WITH GEOMEMBRANES

A typical rate of leakage per unit area observed in the case of large earthfill and rockfill dams constructed with a geomembrane liner on the upstream face and covered is of the order of 1 liter/hr/m^2 (assuming that monitoring is accurate, which is not guaranteed) for the best cases and up to 10 liter/hr/m^2 for dams that do not have the best performance. For the sake of comparison, one defect per 1000 m^2 with a diameter of 2 mm gives a calculated leakage rate of the order of 0.1 liter/hr/m^2 with a typical water head. It is possible that leakage at peripheral connections may explain the difference.

However, in the case of geomembranes anchored on a concrete face rockfill dam, the rate of leakage is of the order of 0.1 liter/hr/m^2 for the best cases. It appears that the typical leakage rate in the case of geomembranes anchored on a concrete face rockfill dam is an order of magnitude times less than the typical rate of leakage through geomembranes installed conventionally in embankment dams. This may be due to better installation on rigid surface.

5.1 *Safety in case of geomembrane failure*

Exposed geomembranes can be damaged by accidental exceptional events (vandalism, terrorism) or by repeated or occasional aggressions from the service environment (animals, ageing). Upstream geomembranes, exposed or covered, can be damaged by extraordinary causes such as earthquakes or falling aircrafts.

The design of a dam with a liner (any type of liner) should be such that the seepage resulting from a major breach in the liner should not cause the rupture or a major distress of the dam itself. Therefore, when a geomembrane liner is considered for an embankment dam, it is essential to check that the appropriate precautions have been taken.

First of all, it is important to monitor and maintain dams. Current defects in geomembranes generally have no detrimental consequences, because a geomembrane - with a small number of small punctures - is still less permeable than any other liners.

Significant defects in geomembranes, due to the exceptional causes mentioned above (earthquakes or falling aircrafts), should be repaired if they are likely to have detrimental consequences. Fortunately, it is generally easy to repair geomembranes. Damage repair, at least for geomembranes having suitable characteristics, is feasible by simple patching if in the dry, or by underwater installation. Of course, the damage repair could be easy for exposed geomembranes.

In the case of internal geomembranes (covered geomembranes), the only cause of significant damage to the geomembrane could be a major earthquake. Therefore, it is important - particularly in seismic areas - to design the dam structure accordingly and to use a geomembrane with high elongation capability and high puncture resistance, since the geomembrane could come in contact with rocks in case of malfunctioning of the protective layers. An internal geomembrane (covered case) with high elongation capability is probably the safest possible liner in case of earthquake.

In conclusion, with an appropriate dam design, and proper geomembrane selection, the geomembrane liners are very safe also in case of important earthquakes.

5.2 *Behavior of geomembranes as a function of time*

Durability is based on the weathering properties, and on the resistance of the geomembrane to specific loads during service (extreme temperatures, frost, freeze/thaw, ice, impacts by floating debris and boats, wind and waves, fauna and flora, vandalism etc.).

Taken for granted that not all geomembranes have the same behavior due to their chemistry, their basic ingredients and their manufacturing process, it is important for dam projects to select a type of geomembrane already adopted in several similar applications or eventually to design a new geomembrane that can best perform according to the type of environment in which it will be used, and that can provide adequate durability for the required application.

Standard accelerated ageing tests are available and are being used all over the world to predict the behavior of geomembranes in service. These tests, although accelerated, would however require too long time to give indication of long-term behavior.

The most practical way to ascertain if a geomembrane will be resistant in the long term to the environmental loading expected in a dam project, is to exhume samples of the same geomembrane that have already been in service, in a similar environment and project, for a period of time that should be as long as possible, ideally as long as the required service life of the geomembrane in the considered dam, and perform tests to determine to which extent their properties have changed. Testing of the physical and mechanical properties of the exhumed samples indicates if the geomembrane properties at the time of the test are within acceptable limits, and extrapolation allows the determination of the expected remaining service life.

This approach has been adopted for applications in the Alpine regions (Cazzuffi 1987; Cazzuffi and Gioffrè 2020; Cazzuffi and Gioffrè 2021; Giroud 2021), using data from several dams rehabilitated with exposed PVC composite geomembrane. The oldest reported application of exposed PVC geomembranes on dams dates back to the mid 1970s, and -since then- many dams have been rehabilitated with exposed geomembranes of the same type, which makes it possible to obtain dependable results. Furthermore, many of these dams are at high elevation (typically higher than 2000 m) where the UV radiation is relevant and the weather conditions are harsh. From this database, it has been provisionally concluded that the service life of PVC composite geomembranes in such extreme environment is around 50 years (Hsuan et al. 2008). It should be noted that geomembranes of the same type installed today are of better quality than the geomembranes installed about 40 years ago and included in the data base used to predict durability. Therefore, the durability of PVC composite geomembranes installed today may be even greater than the predicted durability of at least 50 years.

The approach just described for PVC geomembranes should be eventually used also with other types of geomembranes to evaluate if they have the appropriate durability for use in dams.

5.3 *Evaluation of the residual life of exposed geomembranes*

In order to evaluate the variation over time of the characteristics of the PVC geomembranes installed on 8 dams in Alpine regions, a remarkable number of samples have been taken some periods after application and all of them have been put through the same type of tests.

Samples have been taken both above and under the water level and in different parts of the upstream face, with the aim of studying the different behavior of the same geomembrane in different conditions of exposure.

In the determination of the life expectancy of a geomembrane, it is important to identify the more critical portion of the upstream face, as the first failure will affect negatively the whole waterproofing system. Therefore, here we will present the results of the tests made on samples exhumed above the water level, as this is the area which suffers most from the direct exposure to atmospheric agents. The results obtained are thus referred to the worse conditions for each geomembrane and this helped us to conduct a precautionary analysis of the geomembrane durability.

All the samples taken from the dams' upstream faces have been tested at the Geosynthetics Laboratory of CESI SpA in Italy. The different types of tests (Table 2) allowed the comparison among different samples during the degradation process of the geomembranes.

Table 2. Laboratory tests and reference standards for the evaluation of the determination of the long-term behavior of the exhumed PVC composite geomembrane samples.

Laboratory test	Reference standard
Plasticizer extraction	EN ISO 6427
Nominal thickness	EN 1849-2
Volumic mass	EN ISO 1183-1
Hardness (Shore A)	EN ISO 868
Cold flexibility	EN 495-5
Dimensional stability	EN 1107-2
Tensile properties	EN ISO 527-3
Water vapor permeability	EN 1931

The case of Camposecco masonry dam in Italy is particularly significant, as for this dam also the test results on virgin samples are available; knowing the material's initial conditions, the analysis is more precious as it allows to reconstruct the entire life of the geomembrane on the dam in which it has been applied for rehabilitation of the upstream face (Figure 12).

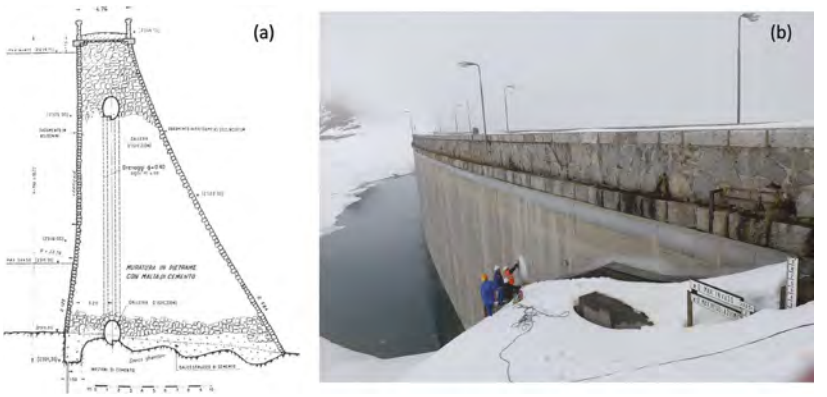

Figure 12. Camposecco dam in Italy: (a) Cross section; (b) PVC composite geomembrane sampling.

The results obtained show a constant small decrease of the plasticizers' content (Figure 13), while temperature of cold flexibility rises with time, and dimensional stability grows longitudinally and declines transversally in the years.

Mechanical parameters derived from the tensile tests show that the geomembrane get a little bit stiffer over time (Figure 14), with some increase of tensile strength and a small reduction of the correspondent strain, both in the longitudinal and in the transversal directions.

With regards to the waterproofing properties, the results of the vapor transmission tests demonstrate in general a negligible decrease of the permeability coefficient, thus a small improvement of the watertightness of the geomembranes, also due to some possible inclusion of particulates and sediments.

Long-term performance of PVC geomembranes depends on several aspects referred to the exposure environment and to the specific polymer and additive formulations. The service life

of PVC geomembranes can be predicted based on experimental results. Through a careful monitoring of the variation over time of the characteristics of the PVC geomembranes in service, it was possible to define a methodology of lifetime prediction of the geomembrane installed in dams when the results on virgin samples are available. In particular, the plasticizer content plays a fundamental role particularly in terms of variation in physical properties of the PVC geomembranes (Giroud, 1995; Giroud and Tisinger, 1993).

In order to evaluate most critical service life of the PVC geomembrane, the curve of plasticizer content versus time is extrapolated until the end-of-service-life plasticizer content is reached.

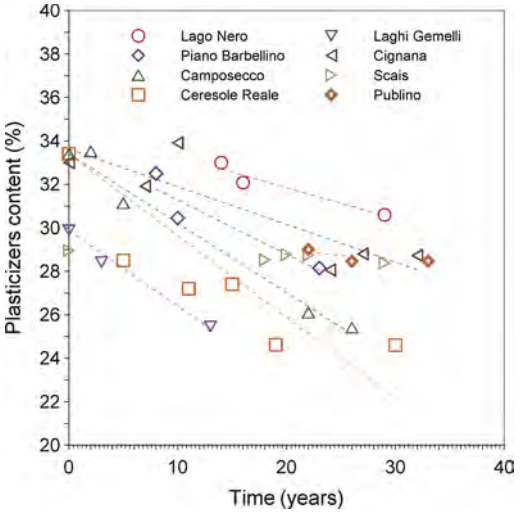

Figure 13. Plasticizers content evolution vs time for PVC geomembrane samples exhumed from different dams on Alps in Italy.

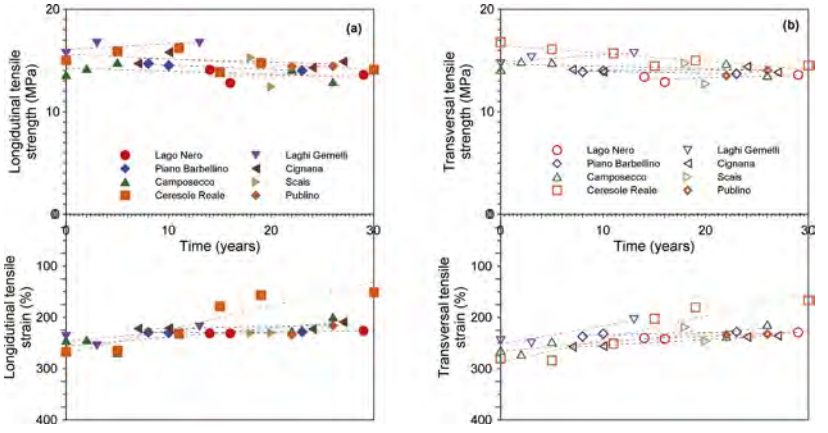

Figure 14. Tensile strength and strain evolution vs time for PVC geomembrane samples exhumed from different dams on Alps in Italy: (a) longitudinal direction; (b) transversal direction.

Based on laboratory tests (Luciani et al. 2019; Luciani et al. 2020) and on data from monitored structures, Giroud (2021) proposes, for the end-of-service-life criterion, a plasticizer content value of 17.5% for PVC composite geomembranes bonded to a nonwoven needle-punched geotextile (which are most frequently used in the considered dams).

Figure 15 shows lifetime assessment of exposed PVC geomembranes for Camposecco dam; vertical lines in Figure 15 shows that the lifetime assessment of the exposed geomembranes for Camposecco dam, assuming a linear decrease of plasticizer loss ratio over time, is approximately 48.5 years, based on the plasticizer content criterion.

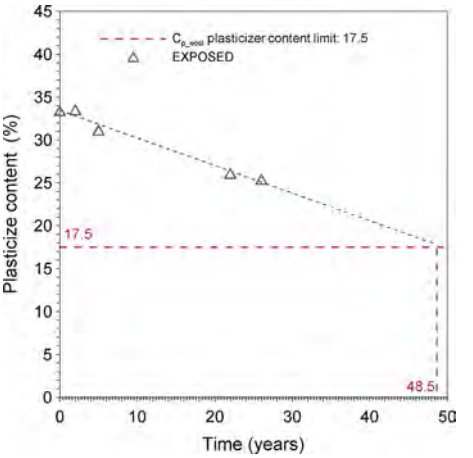

Figure 15. Camposecco dam: Lifetime assessment of exposed PVC geomembranes.

6 CONCLUSIONS

The range of possible applications of geomembranes as water barriers in embankment dams is quite wide. Geomembranes can be applied to all types of dams, in new construction and in rehabilitation.

Design and installation systems of the various components of geomembrane systems according to the type of application have been discussed in this invited lecture.

Geomembrane selection and behavior of geomembrane systems vs. time have been also investigated based on various research projects, and on results from laboratory tests and tests on exhumed samples.

Data on the performance of dams rehabilitated using geomembranes have been provided. These data show a remarkable performance of geomembranes in embankment dams, even when geomembranes are directly exposed to atmospheric agents.

Therefore, this invited lecture could contribute to demonstrate that nowadays the use of geomembranes in embankment dams, both for new constructions and also for rehabilitation purposes, is a well-established technique all around the world, provided that good design, excellent application and careful monitoring are provided.

REFERENCES

Baldovin, E. (1993). New developments of filters in some recent Italian embankment dams. *Filters in Geotechnical and Hydraulic Engineering*, Balkema, Rotterdam, 321–330.

Bertacchi, P., Jappelli, R., Croce, A., Baccini, S., Baldovin, G., Catalano, A., Cazzuffi, D., Di Maio, S., Puccio, M., Sarti, L., Sembenelli, P., Silvestri, T., Tomasi, L., and Travaglini, B. - Working Group of the Italian National Committee on Large Dams - ITCOLD (1988). Embankment dams with impervious upstream facings: an overview of Italian practice, *Proceedings of the 16th International Conference on Large Dams*, Q. 61, San Francisco, USA, 415–454.

Cancelli, A. and Cazzuffi, D. (1994). Environmental aspects of geosynthetics applications in landfills and dams. Keynote Lecture. *Proceedings of the 5th International Conference on Geotextiles, Geomembranes*

and Related Products. Preprint Volume on Special Lecture and Keynote Lectures, Singapore, 55–95, and Vol. 4, 1998, 1299–1338.
Cazzuffi, D. (1987). The use of geomembranes in Italian dams. *Water Power and Dam Construction*, vol. 39, 17–21.
Cazzuffi, D. and Gioffrè, D. (2020). Lifetime assessment of exposed PVC-P geomembranes installed on Italian dams. *Geotextiles and Geomembranes*, 48(2), 130–136.
Cazzuffi, D. and Gioffrè, D. (2021). Reply to the discussion by Giroud on Lifetime assessment of exposed PVC-P geomembranes installed on Italian dams. *Geotextiles and Geomembranes*.
Cazzuffi, D., Giroud, J.P., Scuero, A. and Vaschetti, G. (2010). Geosynthetic barriers systems for dams. Keynote Lecture, *Proceedings of the 9th International Conference on Geosynthetics*, 9 ICG, Guaruja, Brazil, Vol. 1, 115–163.
Gautier, J.L., Lino, L. and Carlier, D. (2002). A record height in dam waterproofing with bituminous geomembrane: La Galaube Dam on Alzeau river, *Proceedings of the 7th International Conference on Geosynthetic*s, 7 ICG, Nice, France, Vol.3, 975–978.
Gautier, J. L. (2003). Etanchéification de masques amont par une membrane bitumineuse, *Colloque du Comité Français des Grands Barrages*, Paris, France. CD Rom.
Giroud, J.P. (1995). Evaluation of PVC Geomembrane Shrinkage Due to Plasticizer Loss. Geosynthetics International, *Special Issue on Design of Geomembrane Applications*, 2 (6), 1099–1113.
Giroud, J.P. (2021). Discussion on "Lifetime assessment of exposed PVC-P geomembranes installed on Italian dams" by D. Cazzuffi and D. Gioffrè. *Geotextiles and Geomembranes*.
Giroud, J.P. and Tisinger, L.G. (1993). The Influence of Plasticizers on the Performance of PVC Geomembranes. *Proceedings of the 7th Symposium of the Geosynthetic Research Institute*, Koerner, R.M. & Wilson-Fahmy, R.F., Eds., Philadelphia, USA, 169–196.
Hsuan, Y.G., Schroeder, H.F., Rowe, R.K., Müller, W., Greenwood, J., Cazzuffi, D. and Koerner, R.M. (2008). Long-term performance and lifetime prediction of geosynthetics. Keynote lecture, *Proceedings of the 4th European Geosynthetics Conference EuroGeo 4*, Edinburgh, UK.
ICOLD, the International Commission on Large Dams (1981). *Bulletin 38. Use of thin membranes on fill dams*, Paris, France.
ICOLD, the International Commission on Large Dams (1991). *Bulletin 78. Watertight geomembranes for dams – State of the art*, Paris, France.
ICOLD, the International Commission on Large Dams (2010). *Bulletin 135. Geomembrane sealing systems for dams – Design principles and review of experience*. ICOLD, France.
Jappelli R. (2002). Terza Conferenza Annuale A. Croce - Le costruzioni geotecniche per le grandi dighe in Italia (in Italian with English abstract). Third Croce Lecture – Earthwork Engineering for Large Dams in Italy *Rivista Italiana di Geotecnica*, Vol. 2, 17–79.
Lacroix, Y. (1984), Use of a geomembrane at Terzaghi Dam, *Proceedings of the International Conference on Geomembranes*, Denver, USA, Vol. 1, pp. 9–14.
Luciani, A., Todaro, C., Martinelli, D., Carigi, A. and Peila, D. (2019) Long-term durability analysis and lifetime prediction of PVC waterproofing membranes. *Proceedings of the WTC2019*. Napoli, Italy.
Luciani, A., Todaro, C., Martinelli, D. and Peila, D. (2020). Long-term Durability Assessment of PVC-P Waterproofing Geomembranes through Laboratory Tests. *Tunneling and Underground Space Technology*, Volume 103.
Sembenelli,P., Sembenelli, G. and Scuero, A. M. (1998). "Geo-synthetic System for the Facing of Bovilla Dam", *Proceedings of the 6th International Conference on Geosynthetics*, 6ICG, Atlanta, USA, Vol. II, 1099–1106.
Scuero, A.M. and Vaschetti, G. (2009). Use of geomembranes for new construction and rehabilitation of hydraulic structures, Keynote lecture, *Workshop on Advanced Methods and Materials for Dam Construction*. Skopje, North Macedonia.
Terzaghi, K. and Lacroix, Y. (1964). Mission dam, an Earth and Rockfill Dam on a Highly Compressible Foundation. *Geotechnique*, London, UK.
Zhussupbekov A. and Mkilima T. (2022). Stability analysis of an old earth Samarkand dam in Kazakhstan under rapid drawdown conditions. *Environmental Engineering - Inženjerstvo okoliša*, Vol. 9 No. 1–2.

Smart Geotechnics for Smart Societies – Zhussupbekov, Sarsembayeva & Kaliakin (Eds)
© 2023 The Author(s), ISBN 978-1-003-29912-7
Open Access: www.taylorfrancis.com, CC BY-NC-ND 4.0 license

Assessments of dimensionless pile stiffness for embedded piled raft foundations in soft clays under vertical loads

D.W. Chang & J.H. Lin
Tamkang University, New Taipei City, Taiwan

Y.K. Lin, F.C. Lu & C.J. Kuo
Ground Master Construction Co., Ltd., Taipei, Taiwan

A.Zh. Zhussupbekov
L.N. Gumilyov Eurasian National University, Astana, Kazakhstan

ABSTRACT: Three-dimensional finite element analysis has been widely used in foundation design. For the efficiency of computations, simplified analysis treating the soils by series of springs were suggested in many design practice. For piled raft foundation, the coefficients of subgrade reactions and the pile stiffness are thus important to the design analysis. This paper intends to discuss the values of coefficients of pile reactions and/or pile stiffness for the embedded piled raft foundations in soft clays subjected to vertical uniform loads. Dimensionless pile displacements, pile reactions, and coefficient of pile reactions were suggested. Their correlations with the ratio of foundation embedment depth to raft size, the slenderness ratio of pile, and the ratio of pile-to-pile spacing distance to pile diameter were examined. Finally the optimized correlation diagrams were reported while a simple modelling was able to verify the suggestion.

1 INTRODUCTION

1.1 *Piled raft foundation analysis*

Piled raft foundation can provide economic and ecologic design solution to mega building structures. The load-response mechanism of such foundation can be deviated from those known for pile foundations. It has been noted that conventional pile foundation is usually designed assuming that the piles are connected to a rigid cap which can yield uniform settlements and rotations under the loads. Soil resistance underneath the cap is typically ignored. In the contrast, piled raft foundation relies heavily on the resistances of soils below the raft. To evaluate the foundation serviceability, the design of piled raft foundation requires computing the structural deformations. Overview of the available analysis methods have been suggested by Poulos (2001). The three-dimensional finite-element (FE) analysis has been known as the most powerful tool to estimate the behaviors of building foundations. The correspondent applications have been reported in numerous engineering projects on high-rise buildings (Katzenbach et al 2016). With the performance based design (PBD) guidelines, Katzenbach & Choudhury (2013) suggested that both the capacity and serviceability performances of the foundation should be taken into account in designing the piled raft foundation (or namely the combined pile raft foundation, CPRF). Figure 1 depicts the qualitative relationships of the settlement ratio (maximum settlement of CPRF to max. settlement of a single raft) versus the load ratio (the load supported by piles to the total foundation load) of the CPRF. It was suggested that both ratios at 50% should be aimed for an efficient design. Chang & Matsumoto (2017) suggested that the serviceability (*i.e.,* deformations) of the foundation is significantly important to modern design practice since the foundation load-response relations became more predictable with the advanced numerical methods, and the foundation deformations are commonly restraint first to avoid inelastic behaviors.

DOI: 10.1201/9781003299127-16

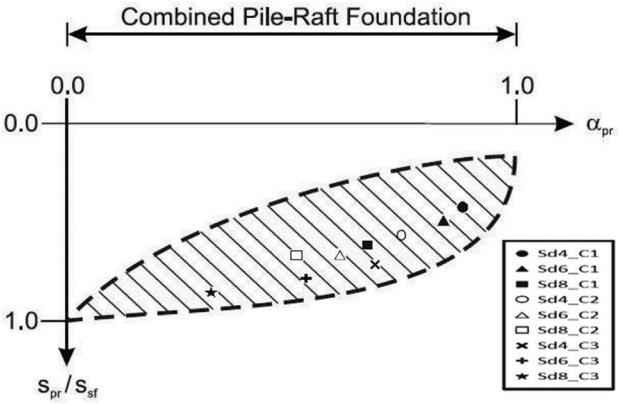

Figure 1. The qualitative relations between the settlements and the load of CPRF (after Katzenbach & Choudhury, 2013).

1.2 *Piled raft foundation analysis in Taiwan*

The current design of pile foundation in Taiwan follows the conventional methodologies. Vertical bearing capacity and uplift capacity of the single pile are analyzed first with presumed pile dimensions and bored-hole data from the field. The factors of safety at different design conditions are applied to ultimate loads in the predictions. In some cases, negative skin frictions are estimated to ensure that the piles are safe under such effects. The pile load test is required to ensure the design. Total capacity of the grouped pile is calculated using either analytical formulas suggested in the design code excluding the interferences of pile-to-pile interactions or the solutions from simplified computer-based analysis. Computer programs such as APILE, LPILE and GROUP (Ensoft, 1987-) are commonly adopted to examine the pile performance. The *t-z*, *Q-z* and *p-y* curves interpreted from the field test and/or available documents are often used for the measurements. The SAP2000 analysis is sometimes utilized by structural engineers to examine the foundation behaviors. Analytical equations suggested by Chang (1937) on single pile subjected to horizontal loads are sometimes used to check the corresponding pile performance. If the site had liquefaction induced problems, both vertical and lateral resistances of the pile will be analyzed with soil stiffness and strength reduced from the empirical liquefaction potential analysis. The soil parameter reduction coefficients suggested by JRA (1996) and AIJ (1988) are recommend for such deductions. According to the design code, lateral resistance of the pile is dominated by an allowable displacement at 10% of the pile diameter. One can refer to Chang et al (2016) for the general report.

Until now, the design of piled raft foundation (or CRPF) is rarely addressed in geotechnical engineering design code in Taiwan. The design of such foundation requires the third-party structure assessments. In order to ensure that the foundation performs safely under the loads, structural deformation analysis of the foundation became rather important. It is normally done by treating the raft as a beam or a plate attached to a series of soil and pile springs. The values of spring constants can be assumed using empirical formulas and/or engineering judgements. Therefore these springs require special attentions.

Chang et al (2022a) recently has reported the variations of the modulus of subgrade reactions for surface raft foundation subjected to short-term vertical loads. For the piled raft foundation at the ground surface, the loads carried out at the piles were found mainly dependent of the soil stiffness and the number of piles installed, however the size of the raft also would interactively affect the results (Chang et al 2022b). For mat foundations with the embedment, a technic paper on dimensionless modulus of subgrade reactions is shared at 17ARC (Chang et al 2023). This paper is aimed to discuss the similar studies for embedded piled raft foundation in clays under short-term vertical loads from three-dimensional finite element analysis. The long-term loading effects including the consolidation influences to the clays would dramatically increase the foundation settlements, therefore the pile stiffness should be further analyzed with cautions.

2 NUMERICAL MODELS

2.1 *Foundation modelling*

The numerical model of the embedded piled raft foundation is illustrated in Figure 2. A square raft with the width varying at 16, 26 and 36 meters was assumed. The thickness of the raft was 1m. Embedded depth of the raft was varying at 8 and 12m. For more realistic modelling, the concrete diaphragm wall was around the raft. The depth of the diaphragm wall was kept as 2 times of the depth for foundation embedment. Round concrete piles with 1m diameter were installed underneath the raft. The pile length was varying at 20m and 30m. The pile-to-pile spacing distance was kept at 3 and 5 times of the pile diameter. Homogeneous soft clay was assumed for the ground soil. The corresponding shear wave velocity, V_s of the soil was varying at 100, 120 and 140 m/s, respectively. Ground water table was temporarily excluded whereas the averaged Poisson's ratio of the soil was kept at 0.4.

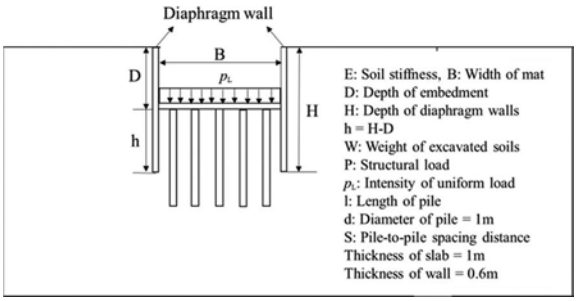

Figure 2. Foundation model of this study.

The Young's modulus of the soil, E_s were thus obtained from elasticity equations. Empirical relations suggested by Hsieh et al (2003) between the Young's modulus E_s and the undrained shear strength of the clays, S_u in Taipei was used to obtain the value of the undrained shear strength. The Mohr-Coulomb soil model was adopted. Note that the structural load, P was taken approximately as 1.5 times the weight of excavated soils. In some studies, the total load was fixed to be independent of embedment depth and size of the slab. The applied uniform load, p_L was decomposed into a series of incremental loads of 10kPa. Iterative procedure was carried out to ensure the equilibriums of the system. Table 1 summarizes the material properties and engineering parameters used in the analysis. Totally 72 numerical cases were analyzed.

Table 1. Foundation geometries, material properties and parameters of the study.

Foundation dimensions and load	FE zone: 350m×350m×150m, Mat width (B): 16m, 26m, 36m, Depth of embedment (D): 8m, 12m Depth of diaphragm (H): 2D Thickness of mat: 1m, Thickness of wall: 0.6m Pile diameter (d): 1m, Cross-section area of pile (a), Pile length (l): 20m, 30m Pile-to-pile spacing distance (S): 3m, 5m Structural load (P): 1.5W, Weight of soils excavated (W):$\gamma_s \times B^2 \times D$
Concrete	γ_c = 24 kN/m^3, E_c =30 GPa, v_c = 0.15
Soil	γ_s = 20 kN/m^3, v_s= 0.4, V_s = 100m/s, 120ms, 140m/s, E_s =57 MPa, 82Mpa, 112Mpa, S_u= 28.5kPa, 41kPa, 56kPa (E_s/S_u =2000) for soils denoted as E1, E2 and E3 soils

2.2 *Discrete mesh and boundaries*

The 3D FE analysis was made using Midas GTX NX package (Midas, 2014). Three dimensional 8-node solid elements were used to model the concrete structure and the soils. The

interface elements were implemented between the concrete and the soils. Normal and tangent stiffness of the interface elements, k_n and k_t were assigned as $10E_s$ and E_s, respectively. Ultimate adhesion of the interface elements was assumed as 2/3 of the undrained shear strength of the clay. Stage-construction feature available in Midas analysis was used. The stability of the foundation displacements was ensured with the FE dimensions at 350m×350m×150m. Essential boundaries such as the rollers were placed. Two- and three-dimensional hinges were resulted at the interfaces of these boundaries. For computational efficiency, 1/4 FE mesh was analyzed based symmetry. The computation time required for the piled raft foundation analysis are around 6~24 hours using PC with Processor 11th Gen Intel® Core™ i7-11700 @2.5 GHz. The required time was mainly found in proportion to the resulted foundation settlement.

3 GENERAL PILE BEHAVIORS

3.1 *Pile displacements*

The largest displacements of the foundations were found appeared at the center in the range of 16~231mm. The pile displacements are the same. They were mainly reduced by the increase of soils stiffness, number of piles, and the length of pile. For similar structural loads, increasing the depth of embedment and the size of mat foundation will reduce the foundation settlements. Figure 3 presents the influences of soil stiffness, the number of piles and the pile length for piled raft foundation where the raft width is 26m. The maximum pile displacements occurred at different locations of the piled raft foundation can be found in Lin (2022).

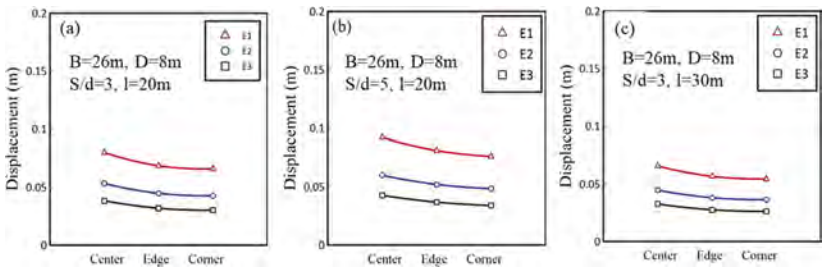

Figure 3. Foundation displacements affected by (a) soil stiffness (b) number of piles (c) pile length.

3.2 *Pile reactions*

The variations of pile reactions were found relatively insignificant in comparison with the pile displacements. The pile reactions (p) at the center pile or the pile near to the center of the foundation were found in between 989~4137kPa. The load sharing of the piles was found influenced by the soil stiffness, the raft dimension, embedment depth, number of piles, and the pile length. The influences of soil stiffness are rather smaller compared to those found at the pile displacements. Figure 4 indicates the influences of the pile reactions by soil stiffness, embedment depth, number of piles and pile length. More details of the discussions can be found in Lin (2022).

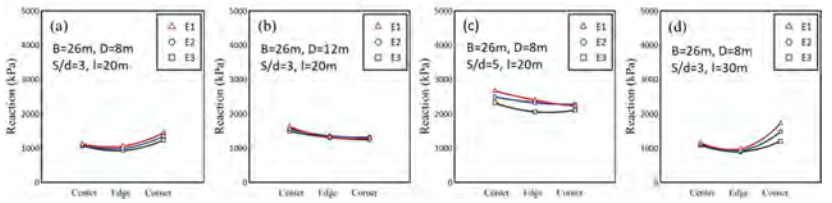

Figure 4. Pile reactions affected by (a) soil stiffness (b) depth of embedment (c) number of piles (d) pile length.

3.3 *Coefficient of pile reaction and corresponding pile stiffness*

The coefficient of pile reaction (k) is able to obtain subtracting pile reactions by pile displacement. The pile stiffness kp is calculated by multiplying k with the cross-section area of the pile. It was found that the coefficient of pile reaction (k) at the center were in the range of 8.7~136MN/m^3. Corresponding pile stiffness is about 6.8~106MN/m. It seems that the increase of soil stiffness, depth of the embedment, and the pile length will help to increase the pile stiffness. Figure 5 reveals the corresponding results. For more information, please see Lin (2022).

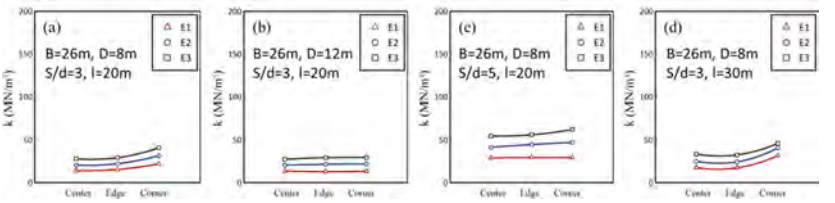

Figure 5. Coefficient of pile reaction affected by (a) soil stiffness (b) depth of embedment (c) number of piles (d) pile length.

4 DIMENSIONLESS MEASURES

4.1 *Pile displacements*

The dimensionless pile displacement in this study was defined as $\gamma_c s/E_c$ and s/B, where s is the real pile displacement. The values of 2D/B, S/d and l/d were taken as the dimensionless characters of the foundation geometry. It was found that the correlations between the dimensionless pile displacements and the dimensionless character of the foundation geometry are more scattered compared to those shown in mat foundation. Therefore the Box Plot was used to find the median values of the dimensionless pile displacements. For example, the dimensionless pile displacements ($\gamma_c s/E_c$) can be plotted against the shear wave velocities (V_s) of the soils considering the variations of raft dimensions and embedment depth. Figure 6 depicts the plots of $\gamma_c s/E_c$ versus V_s varying with the raft dimension (B) and depth of embedment (D). The corresponding plots of medians of $\gamma_c s/E_c$ versus the values of 2D/B are shown in Figure 7 separating the influences of raft dimension. Similarly, the plots for $\gamma_c s/E_c$ versus 2D/B separating the influences of the depth of embedment are shown in Figure 8.

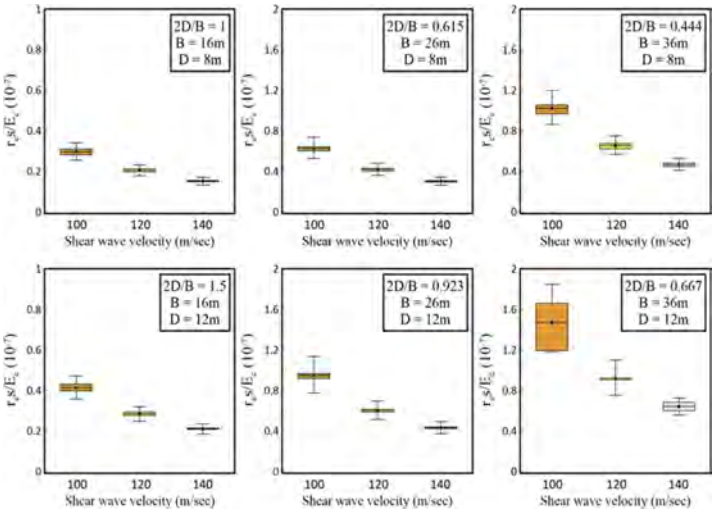

Figure 6. Box plots for dimensionless pile displacements ($\gamma_c s/E_c$) versus shear wave velocities (V_s).

For dimensionless pile displacement defined as s/B, the plots of s/B versus Vs varying with the raft dimension (B) and depth of embedment (D) can be shown in Figure 9. Again, the corresponding plots of s/B versus the values of 2D/B separating the influences of the raft dimension and the depth of embedment are depicted in Figure 10 and Figure 11, respectively. Correlations of the dimensionless pile displacements and the dimensionless character of foundation geometry (2D/B) based on different depths of the embedment were suggested owing to the number of data points presented.

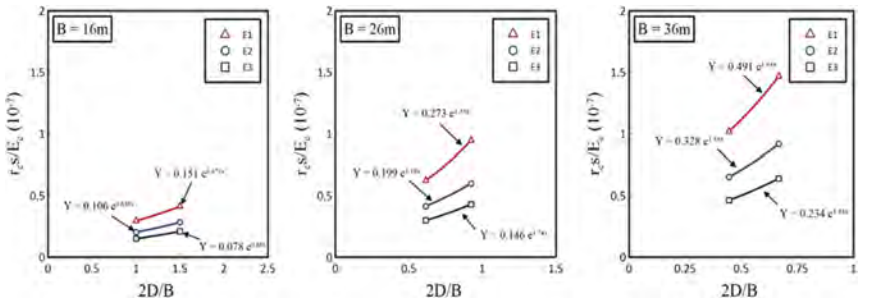

Figure 7. Correlations of dimensionless pile displacements ($\gamma_c s/E_c$) versus 2D/B for various raft dimensions.

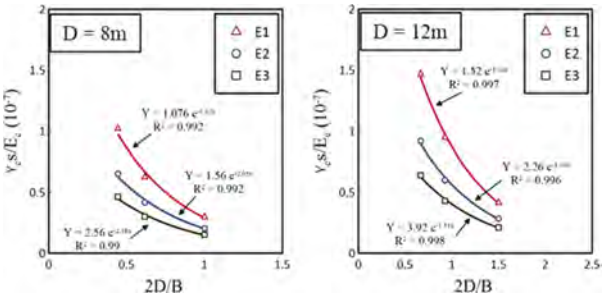

Figure 8. Correlations of dimensionless pile displacements ($\gamma_c s/E_c$) versus 2D/B for various depths of embedment.

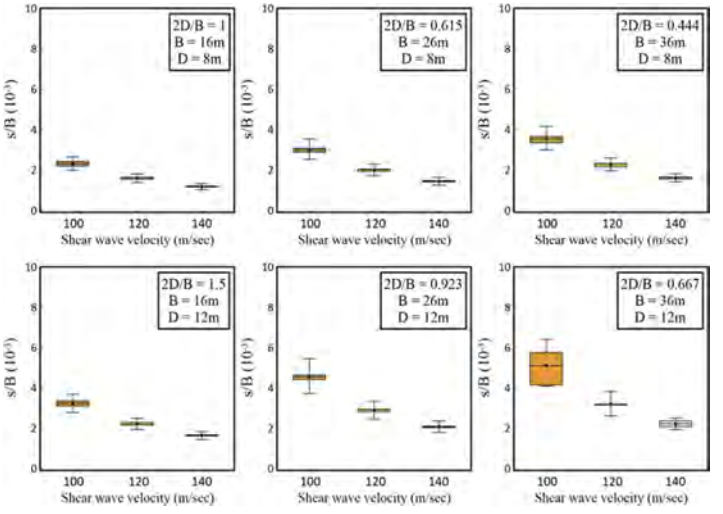

Figure 9. Box plots for dimensionless pile displacements (s/B) versus shear wave velocities (V_s).

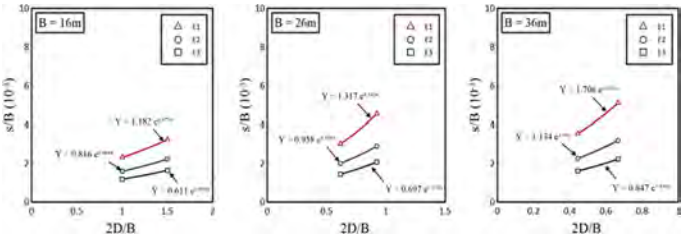

Figure 10. Correlations of dimensionless pile displacements (s/B) versus 2D/B for various raft dimensions.

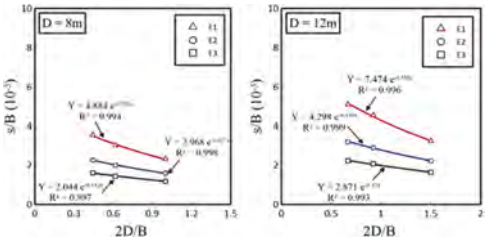

Figure 11. Correlations of dimensionless pile displacements (s/B) versus 2D/B for various depths of embedment.

The similar procedures to plot the dimensionless pile displacements $\gamma_c s/E_c$ and s/B with the dependence of shear wave velocity (V_s) of the ground soils, and subsequently obtain the correlations of the pile displacements versus other characters of the foundation geometry (e.g. S/d and l/d) can be found in Lin (2022). It was generally found that the Box plots made with the dependence of S/d and l/d would have larger deviations in terms of the height of the box and the height difference of the maximum and minimum values. Therefore they were not recommended.

4.2 *Pile reactions*

Following the above definitions of dimensionless pile displacement, the dimensionless pile reaction in this study was defined as p/E_c and $p/\gamma_c B$ respectively, where p is the pile reactions (Units in F/L^2). Figure 12-Figure 15 reveal the Box plots for p/E_c and $p/\gamma_c B$ versus the shear wave velocity of the ground soils with variations of embedment depth, and the correlations of the medians with respect to the dimensionless character 2D/B. The correlations of $p/\gamma_c B$ were not recommended owing to relatively higher deviations.

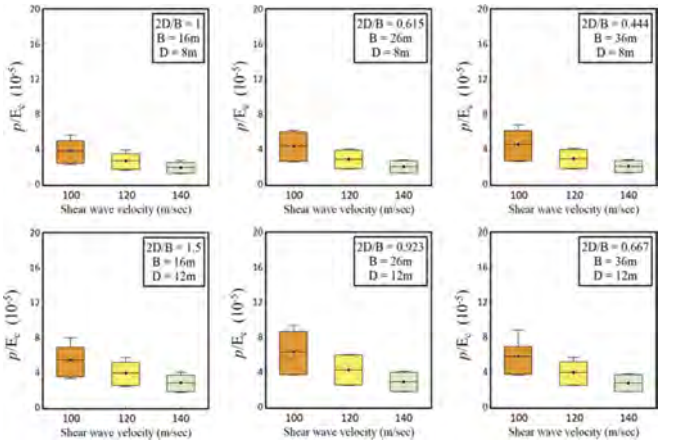

Figure 12. Box plots for dimensionless pile reactions (p/E_c) versus shear wave velocities (V_s).

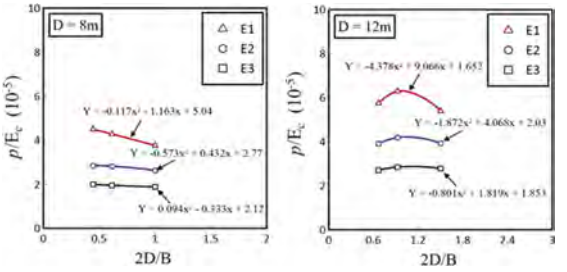

Figure 13. Correlations of dimensionless pile displacements (p/E_c) versus 2D/B for various depths of embedment.

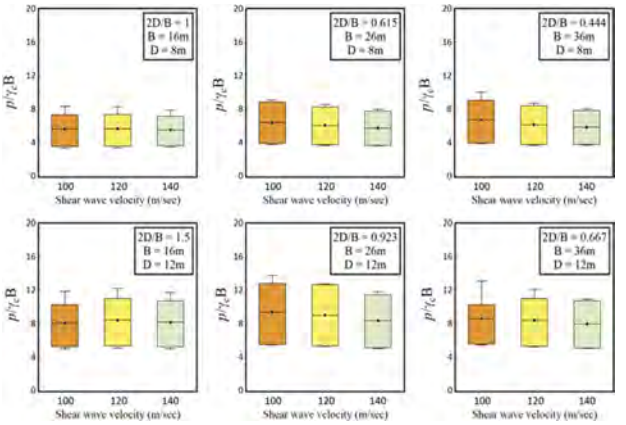

Figure 14. Box plots for dimensionless pile reactions ($p/\gamma_c B$) versus shear wave velocities (V_s).

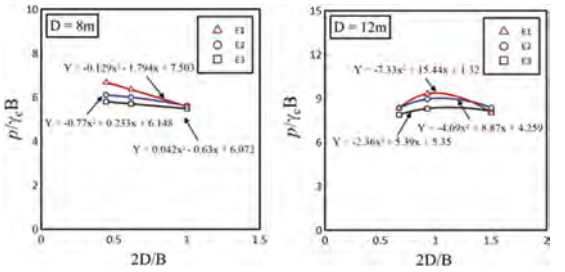

Figure 15. Correlations of dimensionless pile displacements ($p/\gamma_c B$) versus 2D/B for various depths of embedment.

4.3 *Coefficient of pile reactions*

The dimensionless coefficient of pile reactions was denoted as $p/\gamma_c s$ following the above dimensionless quantities of pile displacement and pile reaction. Similarly, the Box plots of $p/\gamma_c s$ versus V_s can be shown in Figure 16. The correlations between the dimensionless coefficient of pile reaction and the dimensionless character of foundation geometry (2D/B) at different depths of embedment are shown in Figure 17.

4.4 *Applications*

Notice that the maximum load pressure applied to the studied foundation is in the range of 240~360kPa. Therefore, if the loading condition can be approximated, engineers can use the

regression curves shown in Figures 8, 13 and 17 to estimate the pile displacement, the pile reactions and the coefficient of pile reactions based on similar soil conditions. For soil stiffness different to the suggested quantities, interpolations should be used to obtain the approximated values. For example, the pile displacement, s can be found as the procedures shown in Figure 18 considering the depth of foundation embedment is in between 8~12m. The pile reactions and the coefficient of pile reaction (or multiplying with a to obtain the pile stiffness) can be found using the similar procedure. Once the pile settlement, s and pile reactions, p are obtained, the coefficient of pile reaction, k can be also calculated as p/s.

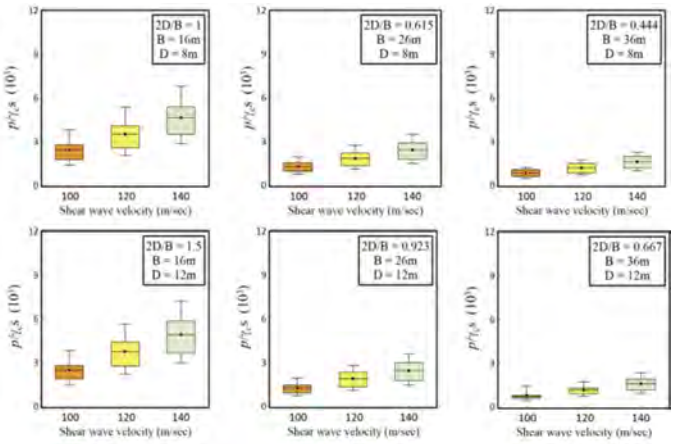

Figure 16. Box plots for dimensionless coefficient of pile reaction ($p/\gamma_c s$) vs. shear wave velocities (V_s).

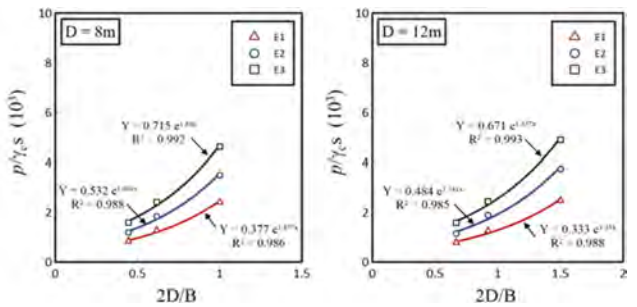

Figure 17. Correlations of dimensionless coefficient of pile reaction ($p/\gamma_c s$) vs. 2D/B for various depths of embedment.

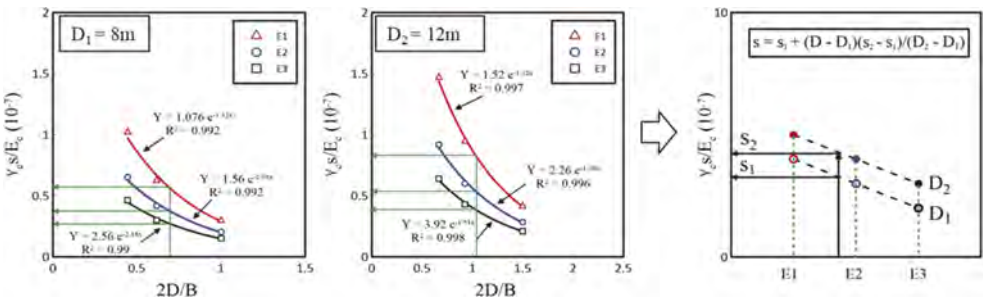

Figure 18. Interpolation procedure to find pile displacement of the piled raft foundation in clays for approximate soil and embedment depth conditions.

5 CONCLUDING REMARKS

The pile displacements, pile reactions, and the coefficient of pile reactions of the embedded piled raft foundation located in soft clays subjected to vertical loads have been analyzed by 3D FE analysis. The influences of soil stiffness, raft dimension, depth of embedment (which affects the applied load), the number of piles installed, and the pile length were studied by seventy-two numerical cases. Enable to use them in routine design, the dimensionless measures were proposed first and then analyzed using Box plot. With the medians, their correlations with the dimensionless characters of the foundation geometry were examined. The correlations of $\gamma_c s/E_c$, p/E_c, and $p/\gamma_c s$ versus 2D/B were finally recommended to design practice. They are suggested as a preliminary design tool for piled raft foundations in soft clays. Further examination with the field measurements is welcomed.

ACKNOWLEDGEMENT

This paper presents a partial result of the technical project supported by Ground Master Construction Co. Ltd. in Taiwan. Sincere gratitude is expressed. The thankfulness is extended to Prof. C.H. Chen (NTU), Dr. C.D. Ou (SEAGS & AGSSEA) and Vice President Mr. C.C. Ko (MAA) for their valuable comments/suggestions in reviewing the project.

REFERENCES

Architecture Institute of Japan (1988). Design guideline for foundations of architectures. (in Japanese).

Chang, Y.L. (1937). Chang on Lateral Pile-Loading Tests. *Transaction of the American Society of Civil Engineers*, 102, 272–278.

Chang, D.W., Chiou, J.S. & Chou, C.R. (2016). Pile foundation design in Taiwan - current practice, developments and prospective", *Procds., Tripartite* Seminar – CIE, HKIE and IEM, November 4, Taipei, Taiwan.

Chang, D.W., Hung, M.H., Lai, Y.Y. & Zhussupbekov, A. (2022b). Finite difference analysis on settlements of pile rafted foundation considering the effects of soil springs and pile-to-pile interactions, 20ICSMGE, Sydney, Australia, May 1-5, 2022.

Chang, D.W., Lu, C. W., Tu, Y.J. & Cheng, S.H. (2022a). Settlements and subgrade reactions of surface raft foundations subjected to vertically uniform load, *Applied Sciences*, 12 (11), 5484.

Chang, D.W., Lin, J.H., Lin, Y.K., Lu, F.C. & Kuo, C.J. (2023). Dimensionless modulus of subgrade reaction for embedded mat foundation in soft clays under vertical load, 17ARC on Soil Mechanics and Geotechnical Engineering, August 14–18, Astana, Kazakhstan.

Chang, D.W. & Matsumoto, T. (2017). Performance based seismic design of pied raft foundations from probability and reliability based methods using approximate numerical analyses, Chapter 11, *Design and Analysis of Piled Raft Foundations-2017*, Tamkang University Press, Taipei Taiwan, 147–166.

Ensoft (1987). APILE, LPILE & GROUP User Manuals, Houston, Texas, US.

Hsieh, P.G., Kung, T.C., Ou, C.Y. & Tang, Y.G. (2003). Deep excavation analysis with consideration of small strain modulus and its degradation behavior of clay, *Procds*., The 12th Asian Regional Conference on Soil Mechanics and Geotechnical Engineering, Singapore, Vo1.1, 785–733.

Japan Road Association (1996). Design specifications of Highway Bridges, Part V Seismic Design (English version is available)

Katzenbach, R. & Choudhury, D. (2013). ISSMGE Combined Pile-Raft Foundation Guideline. Technische Universität Darmstadt, Darmstadt, Germany.

Katzenbach, R., Leppla, S. & Choudhury, D. (2016). Foundation Systems for High-Rise Structures, CRC Press, 314p.

Lin, J.H. (2022). Study on coefficients of subgrade reactions and pile stiffness of piled raft foundations in clays subjected to vertical loads, Master Thesis, Department of Civil Engineering, Tamkang University (in Chinese)

Midas (2014). Midas GTS NX User Manual; Midas Ltd., Co.: Tokyo, Japan.

Poulos, H.G. (2001). Pile-raft foundation: design and applications. *Geotechnique*, 51(2), 95–113

Smart Geotechnics for Smart Societies – Zhussupbekov, Sarsembayeva & Kaliakin (Eds)
© 2023 The Author(s), ISBN 978-1-003-29912-7
Open Access: www.taylorfrancis.com, CC BY-NC-ND 4.0 license

Numerical modelling of complex geotechnical problems - Three examples

Helmut F. Schweiger
Institute of Soil Mechanics, Foundation Engineering and Computational Geotechnics, Graz University of Technology, Austria

ABSTRACT: Over the last decades numerical methods have gained increasing importance in practical geotechnical engineering and have become a standard tool in geotechnical design, widely accepted by the geotechnical profession. In this presentation the application of advanced numerical models for solving practical geotechnical problems is shown whereas the examples have been chosen in such a way that different aspects are highlighted in each case. Results from fibre-optic measurements for a pull-out test of a ground anchor in soft soil could be reproduced by employing advanced constitutive models, in particular for the grout, in the bonded length of the anchor. The back-analysis of a slow-moving landslide is presented next, where the rate of deformation is influenced by water level changes in a reservoir for a pumping power plant, creep of lacustrine sediments and environmental effects such as rainfall infiltration. Finally results of modelling cone penetration testing in silts are presented.

1 INTRODUCTION

Numerical methods have proven to be an extremely powerful tool for solving practical geotechnical problems. This has been possible on the one hand because a number of commercial codes have been developed to a stage that they can be easily operated by geotechnical engineers and complex 3D models can be calculated with reasonable computational effort. On the other hand, constitutive models which are able to describe important features of soil behavior have been implemented in a robust manner in these codes. So, it seems there is no limit with respect to complexity in geometry and/or mechanical/hydraulical behavior which can be modelled today. However, it has to be emphasized that open questions in soil modelling remain and there is still no generally accepted constitutive model for soils available. Figure 1 shows an example of a finite element mesh typically used in the eighties and Figure 2 what is fairly standard today, and the progress made is obvious.

Similar developments can be observed with respect to constitutive models. It is now widely accepted that simple failure criteria such as the Mohr-Coulomb model are a reasonable choice for describing failure under drained conditions (or undrained conditions in terms of total stresses where it becomes the Tresca failure criterion) but are not sufficient to describe the mechanical behavior of soils for stress states well below failure. The latter however is the majority of applications of numerical methods in geotechnics. For this reason, all commercially available software packages offer more advanced constitutive models based on hardening plasticity formulations which consider a non-linear stress-strain behavior under working load stresses and in most cases include the behavior in the very small strain range, usually denoted as "small strain stiffness". An example for such a model which has gained some popularity in recent years is the Hardening Soil Small model (Schanz et al. 1999, Benz et al. 2009) which is implemented, in slightly modified versions, in various commercially available codes.

DOI: 10.1201/9781003299127-17

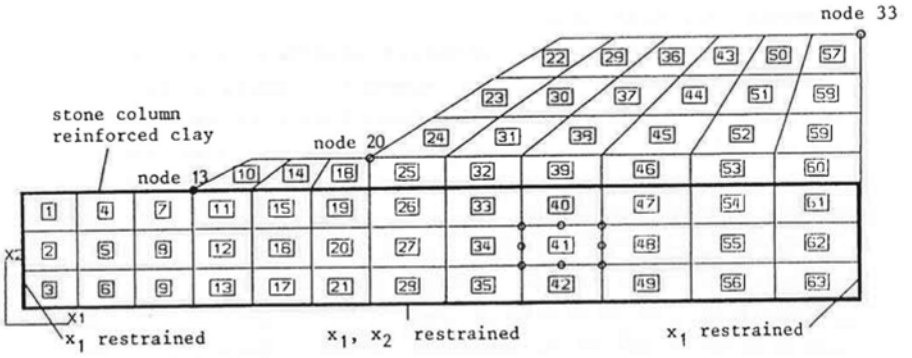

Figure 1. Typical finite element mesh used in the eighties (Schweiger & Pande, 1988).

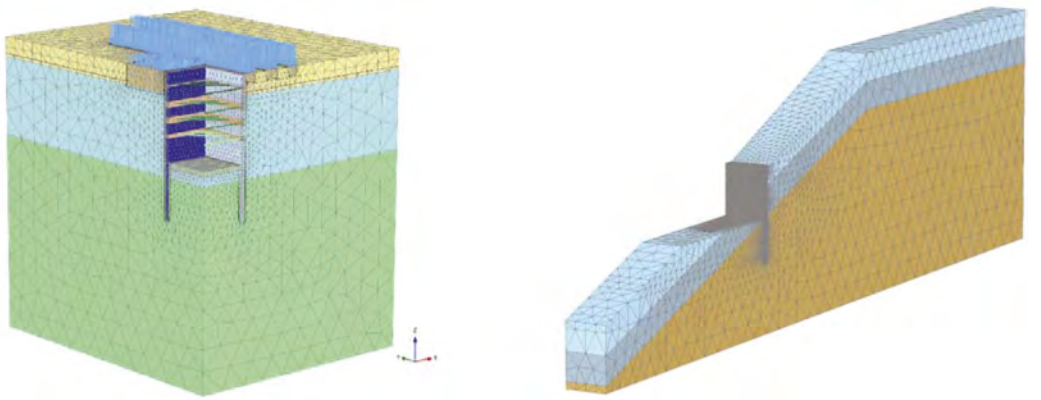

Figure 2. Typical finite element meshes used today in routine analyses.

2 ANCHOR PULL-OUT TEST MONITORED BY FIBRE-OPTIC MEASUREMENTS

2.1 *Soil conditions, constitutive models for soil and grout and numerical model*

The test was performed on a construction site in St. Kanzian, in the southern part of Austria. The anchor was installed vertically, was post-grouted and had a free length of 12 m and a fixed length of 8 m respectively. Laboratory testing of soil samples extracted close to the test area classified the soil as clayey, sandy silt of low plasticity and the grain size distribution was approximately 70% silt, 15% clay and 15% sand. A seismic dilatometer test (sDMT) was conducted to determine the shear wave velocity and the shear modulus at small strains, $G_{0,ref}$. The soil is referred herein as "Seeton". Layers with higher sand content (denoted as sand in the following) were identified in a core drilling performed close to the location where the anchor was installed and were also observed in the sDMT. Oedometer tests and direct shear tests were performed for both soil layers. The constitutive model chosen for both soil layers is the Hardening Soil Small model (Schanz et al. 1999, Benz et al. 2009) as implemented in the finite element code Plaxis (Brinkgreve et al. 2017). Four stiffness parameters are required for this model: a secant stiffness for deviatoric loading ($E_{50,ref}$), a tangent stiffness for oedometer loading ($E_{oed,ref}$), an unloading/reloading stiffness ($E_{ur,ref}$) and the small-strain shear modulus ($G_{0,ref}$). The threshold shear strain $\gamma_{0.7}$ for $G_{0,ref}$ was assumed based on experience. These parameters are related to a reference pressure which is taken here as 100 kPa. The stress level dependency of stiffness values is controlled by parameter m. For parameter determination in-situ, laboratory test and experience have been combined to arrive at the input parameters for the Hardening Soil Small model which are summarized in Table 1.

Table 1. Material parameters for Hardening Soil Small model.

Parameter	Seeton	Sand
$E_{50,ref}$ (kPa)	6 625	16 000
$E_{oed,ref}$ (kPa)	5 300	16 000
$E_{ur,ref}$ (kPa)	48 000	48 000
c' (kPa)	10	5
φ′ (°)	29.5	32
m	0.9	0.6
ν'_{ur}	0.2	0.2
K_0^{nc}	0.51	0.43
$G_{0,ref}$ (kPa)	120 000	120 000
$\gamma_{0.7}$	0.15E-3	0.15E-3

It was expected that the grout material used in the bonded length of the anchor would behave as a nonlinear material and would, at least at higher load levels, exhibit some cracking. Therefore an appropriate constitutive model had to be employed and a model, originally developed for modelling the mechanical behavior of shotcrete, has been selected (denoted as Concrete model in the following). The model is formulated within the framework of elasto-plasticity and for deviatoric loading a Mohr-Coulomb yield surface is employed and, in the tension regime, a Rankine yield surface is assumed. The important feature of the model relevant to the analysis presented in the following is its capability to model the development of cracks by means of a so-called smeared-crack approach. This behavior in tension is linear elastic until the tensile strength is reached. Linear strain softening follows, governed by the major principal plastic strain and the fracture energy G_t (Figure 3). Once the residual strength is reached, no further softening takes place. As follows from Figure 3 the softening parameter H_t takes a value between 0 and 1.0 in the softening regime and a value larger 1.0 once the residual strength in tension is reached. This parameter will be plotted later in order to visualize the occurrence of cracks. More details on the model can be found in Schädlich & Schweiger (2014). Samples of the grout material were taken and uniaxial compressive test (UCS) and the multistage triaxial test (MST) were utilized to determine the required input parameters. However, no tensile tests were available and therefore G_t was chosen based on experience. Key parameters are given in Table 2. E is the Young'smodulus, ν the Poisson's ratio, $f_{c,28}$ and $f_{t,28}$ are the uniaxial compressive and tensile strength, $G_{c,28}$ and $G_{t,28}$ the compressive and tensile fracture energy and f_{tun} is the ratio of residual to peak tensile strength, all values for cured grout. The tendon of the anchor was modelled as a linear elastic material.

Table 2. Key material parameters for Concrete model.

Parameter	Grout Material
E_{28} (GPa)	15.5
ν	0.20
$f_{c,28}$ (MPa)	30.6
$f_{t,28}$ (MPa)	1.5
$G_{c,28}$ (kN/m)	3.06
f_{tun}	0.05
$G_{t,28}$ (kN/m)	0.01

The numerical simulation was performed using the finite element software Plaxis 2D (Brinkgreve et al. 2017). Because the anchor was installed vertically an axisymmetric model could be used. The model geometry including a detail of the anchor is presented in Figure 4. The tendon was considered only in the fixed length and prescribed displacements were applied at the tendon at the top of the fixed length. Grout was considered in the free and fixed length,

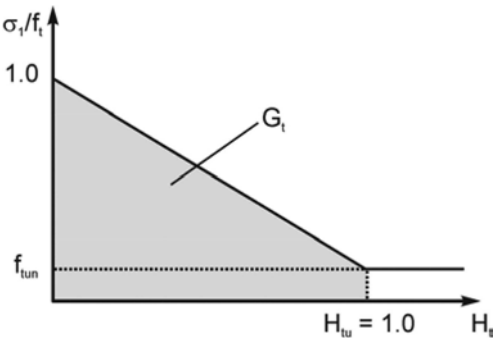

Figure 3. Normalized stress - strain curve in tension, definition of state variable H_t.

whereas pressure grouting was only assumed in the latter. The pressure grouting was taken into account in the numerical model by increasing the radial stresses along the fixed length, i.e. the earth pressure coefficient at rest (K_0) was set equal to one. In addition, the diameter of the bonded section was increased to 280 mm (borehole diameter was 178 mm) based on the amount of grout pumped into the soil.

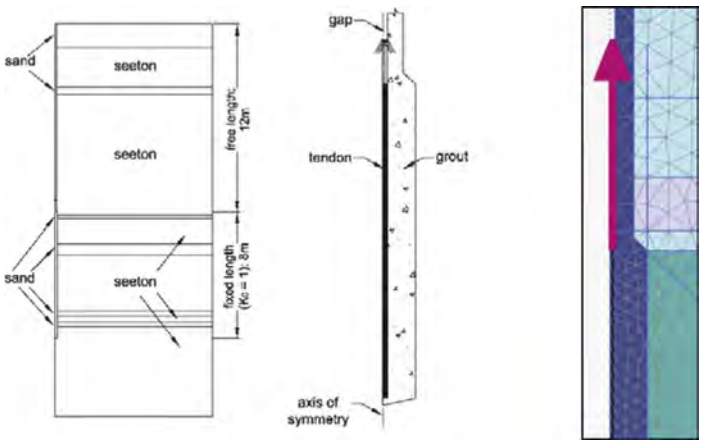

Figure 4. Numerical model: geometry, anchor detail, detail of finite element mesh.

2.2 *Results*

The in-situ measured and the numerically obtained load-displacement curves are compared in Figure 5. Only the displacements at the top of the fixed length are presented. The horizontal bars show the anchor displacement if the creep, developing during the holding stage at each load level, is subtracted from the displacement because creep effects have not been considered in the numerical analysis. Two numerical load-displacement curves are shown. The dashed line corresponds to the class-A prediction done before the test and the solid line to the numerical simulation with slightly refined material parameters after the test. The predicted load-displacement curves showed very good agreement with the in-situ one. The numerical ultimate load was approximately 1100 kN and the failure criteria of the in-situ test was achieved at 1200 kN. The class-A load-displacement curve was slightly stiffer than the in-situ curve and a better agreement was achieved with modified parameters as mentioned above. However, from a practical point of view the agreement between measurements and analysis can be considered excellent.

The numerical strain distribution along the tendon compared with the in-situ measurements, obtained by means of fibre-optic measurements (Monsberger et al. 2016), is presented in Figure 6. The numerical oscillations observed from 280 kN onwards are a result of the snap-

back instability generated when cracking in the grout starts. This is a numerical problem which is however not considered relevant for the purpose of this study. Together with the fact that measurements indicate that some cracks are closing with further loading which cannot be accounted for realistically by the applied constitutive model this leads to some deviations between numerical results and measurements, in particular for higher load levels. Because at residual state the calculated strain values are not meaningful, the tension softening parameter H_t is used as a measure to compare numerical results with in-situ cracking in the grout body. H_t is an output of the model and a value of H_t larger than 0 indicates that softening in tension has started. A value larger than 1 means that the tensile stress has decreased to its residual value (Figure 3). Figure 7 presents the evolution of H_t for selected load stages. In Figure 7 H_t is plotted along the fixed length and compared with the in-situ strain distribution in the grout. The peaks along the H_t profile indicate that cracking is, at least qualitatively, captured very well. A more comprehensive discussion of results can be found in Fabris (2020) and Fabris et al. (2021).

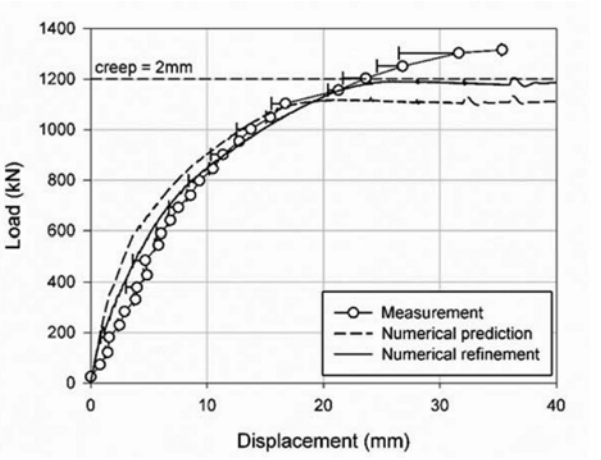

Figure 5. Load displacement curves: measurement vs Class-A prediction vs back-analysis.

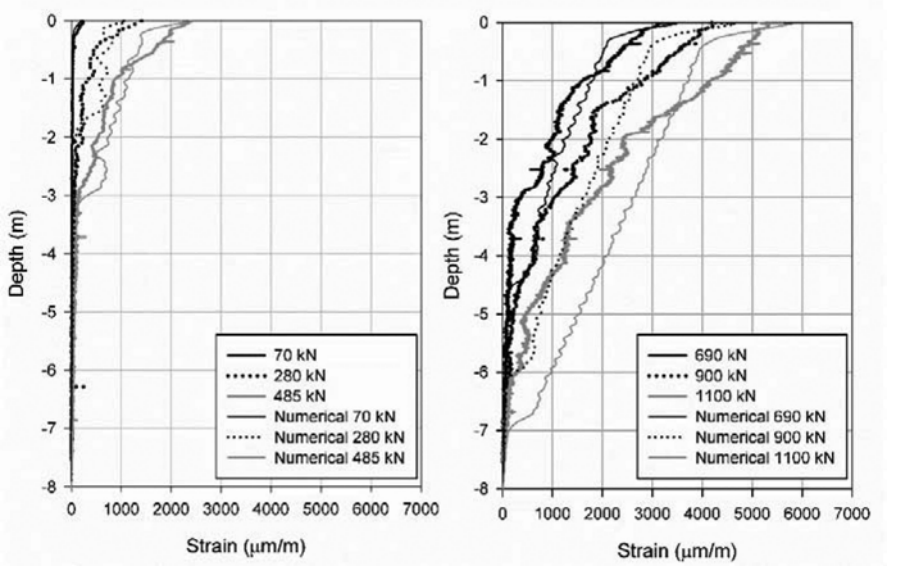

Figure 6. Load displacement curves: measurement vs Class-A prediction vs back-analysis.

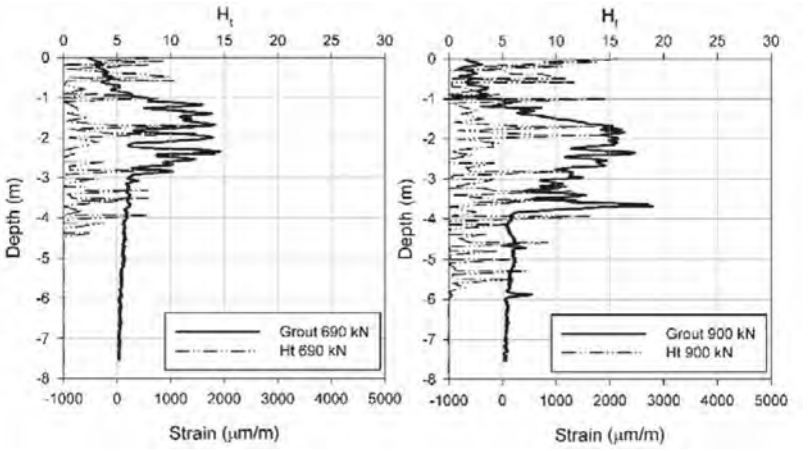

Figure 7. Evolution of H_t in the grout at the fixed length – comparison with in-situ results.

3 SLOW MOVING LANDSLIDE

3.1 *Problem description and measurements*

In the course of extension works for a water storage basin, a slow-moving landslide was identified next to the storage basin. The dimensions of the water storage basin are roughly 400 m in length and 100 m in width with a horizontal length of the landslide of roughly 270 m. The inclination of the slope is 30° on average and inclinometer readings suggested that the sliding surfaces would be between 20 and 40 m below ground surface. The subsurface explorations showed a sliding mass consisting mainly of weathered and sheared rock. Below the sliding mass and below the water storage basin lacustrine fine sediments, mainly silt, are present. A plan view and a layout of the slow-moving landslide and the water storage basin are shown in Figure 8.

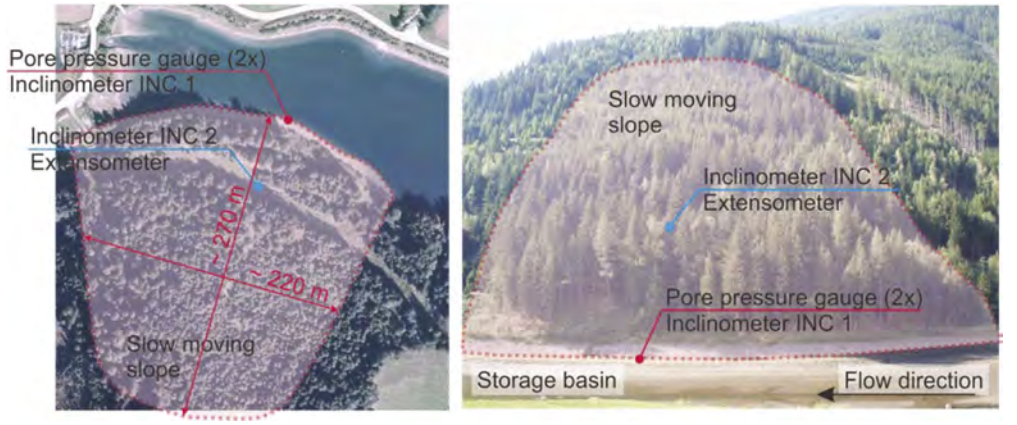

Figure 8. Layout and plan view of water storage basin and slow-moving landslide.

Due to the operation of the pump storage power plant the water level in the basin changes up to three times a day whereas the maximum level change is 7.0 m. A comprehensive monitoring system was installed including additional inclinometers and pore water pressure gauges. The pore pressure measurements showed changes in pore water pressures in the subsoil at the toe of the landslide linked to the water table changes in the water storage basin. However, it was observed that this was not a one-to-one relationship because positive and negative excess

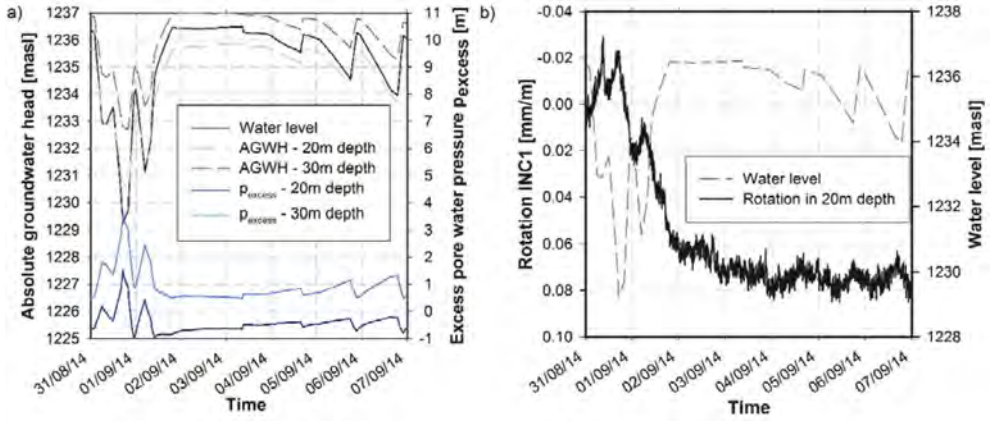

Figure 9. Excess pore water pressures due to water level changes, b) Correlation between deformation rates and water level changes.

pore pressures have been measured, i.e. the pressure level of the pore pressure measurement is above or below the corresponding water level in the water reservoir. Typical measurement results of the pore pressure gauges are shown in Figure 9. For a better understanding of the reasons for these measured excess pore water pressures a numerical study was carried out. These analyses revealed, as expected, that the magnitude of these excess pore water pressures depends on the ratio between drawdown velocity and soil permeability and furthermore on the ratio between pore water compressibility and soil skeleton compressibility (Ausweger & Schweiger, 2017). Also the presence of air bubbles in the water may contribute to this effect (Ausweger & Schweiger, 2016). In Figure 9 the excess pore water pressure p_excess is defined by the difference of measured and hydrostatic pore water pressure. Deformation measurements using in-place inclinometers revealed a correlation between deformation rates and excess pore water pressures at the slope toe. This shows that the slope deformations are influenced by the water level changes in the water storage basin, as these control the excess pore water pressures in the subsoil. A typical comparison of water level changes and rotation of the inclinometer probe in the major sliding zone is shown in Figure 9b.

3.2 *Numerical model for storage basin and results*

Preliminary numerical analyses and careful examination of the measurements indicated that water level changes alone could not explain measured displacements. Therefore a finite element model (Figure 10) was set up incorporating the water level changes from the storage basin but also environmental influences such as rainfall events assuming site specific precipitation and evaporation. Furthermore, the lacustrine fine sediments at the slope toe were modelled with the Soft Soil Creep model (Vermeer & Neher, 1999) to model the creep behavior of these soil layers (see Figure 10). To achieve appropriate initial conditions concerning the stress state and the hydraulic conditions, the geological history was modelled in a simplified way. Afterwards, one year with characteristic precipitation and water level changes was simulated (Ausweger, 2017).

The back-calculation of the pore water pressures was performed for several periods with different types of water level changes. Figure 11 shows a comparison of the measured and calculated excess pore water pressures for the two installed pore water pressure gauges PPG 1 (in 21 m depth) and PPG 2 (in 33 m depth). Furthermore, the water level in the storage basin is plotted in the diagram. From the comparison in Figure 11 it can be seen that a good agreement between calculations and measurements could be achieved. In order to identify the quantitative contribution of the different influencing factors on the total displacements, separate calculation phases were performed. In each phase a new influencing factor was considered. As

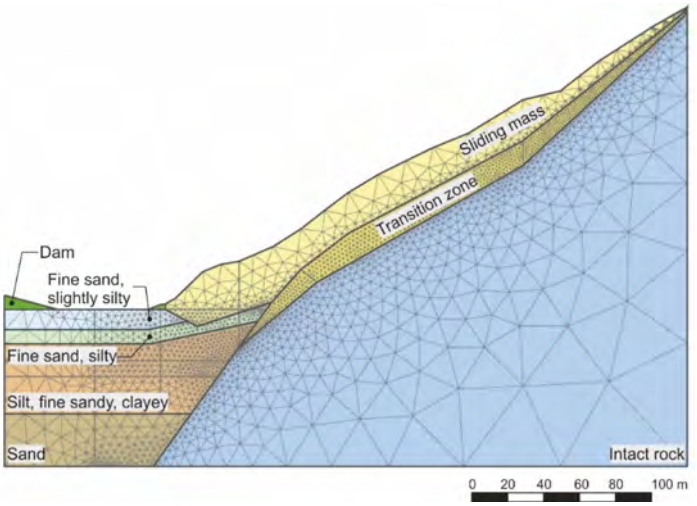

Figure 10. FE-model for numerical back-calculations (Ausweger, 2017).

an example, the results for a point in the middle of the slope are shown in Figure 12. The difference between two time-displacement curves is the influence of each additionally considered factor as indicated by the label of the curves. It follows that for the point considered the influence of water level changes is about 50% of the total displacements (difference between curve labelled "precipitation" and curve labelled "water level changes") but creep behavior of the lacustrine sediments at the base of the slope and precipitation add to the displacements. A comparison between the in-situ measurements and the total calculated displacements including all effects indicates a good agreement. The results were evaluated for several points along the slope. It could be clearly shown that the influence of the creep behavior of the lacustrine fine sediments on the deformations decreases with increasing distance from the slope toe. The influence of precipitation and evaporation is increasing in the middle and upper part of the slope and the influence of the water level changes on the slope deformations is almost constant over the entire slope. Based on the back-calculations of the slope deformations it can be argued that the water level changes are the main reason for the slope movements. However, slope movements would also occur without the storage operation but the magnitude of the deformations would be smaller.

4 NUMERICAL SIMULATION OF CONE PENETRATION TEST

4.1 *Numerical framework and constitutive model*

In-situ site investigation methods, such as cone penetration testing (CPT), are frequently used to derive hydraulic and mechanical soil properties from measured tip resistance, sleeve friction and pore water pressure via empirical correlations. However, there are uncertainties in interpretation of CPT results when e.g. partial drainage has to be considered or the soil exhibits some form of structure and bonding. The latter aspect is addressed in the following. Here numerical methods can play a significant role in obtaining a better understanding of CPT. Recent advances in the numerical simulation of large deformation problems based on a Particle Finite Element Method (PFEM, see Oñate et al. 2011) allow to model this kind of penetration problems. The simulations in this paper are carried out using the platform G-PFEM, short for Geotechnical-Particle Finite Element Method (Monforte et al. 2017a,b), which has been developed within the Kratos framework (Dadvand et al. 2010) at the Polytechnic University of Catalonia (UPC) and the Center for Numerical Methods in Engineering (CIMNE). In G-PFEM, the quasi-static linear momentum and mass balance equations are

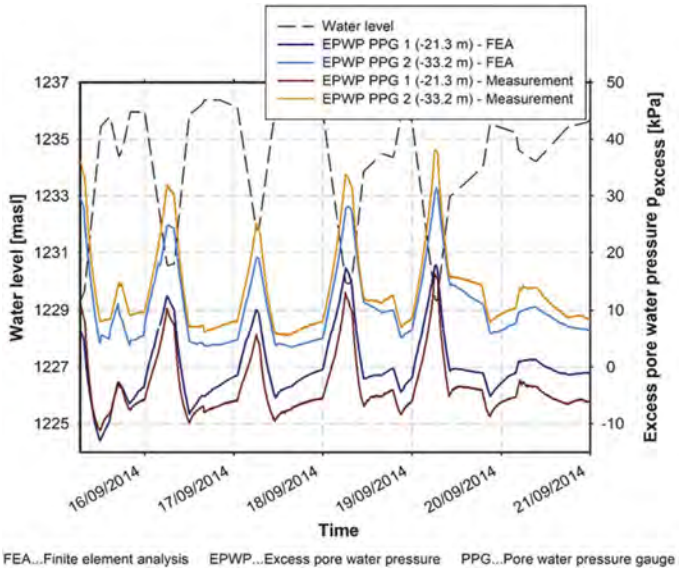

Figure 11. Back-calculated excess pore water pressures (Ausweger, 2017).

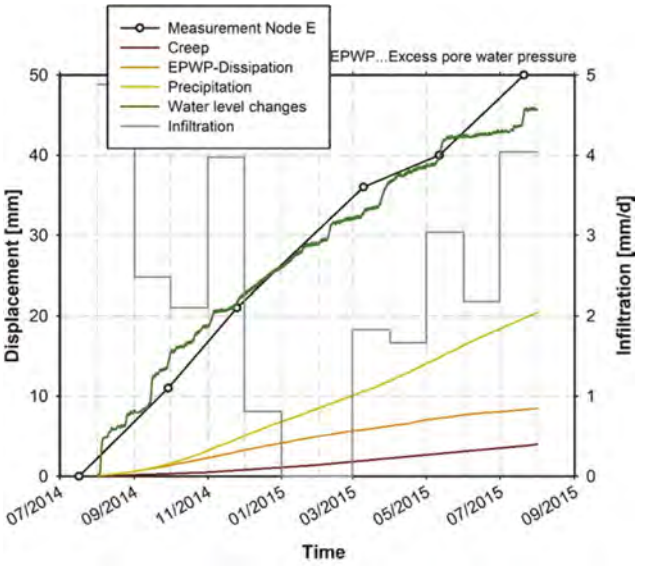

Figure 12. Displacements at node E (in the middle of the slope) due to different factors (Ausweger, 2017).

formulated for a solid and fluid phase adopting an updated Lagrangian description. The basic idea behind the PFEM is a continuous remeshing of critical regions of the domain, where new nodes can be added and old ones removed, in order to deal with large deformations and avoid excessive mesh distortion. This strategy results in an increased computational cost and therefore low order elements in combination with a mixed formulation of the problem are used. In order to avoid locking effects an additional degree of freedom, namely the determinant J of the deformation gradient is introduced on top of the displacement and water pressure fields u and p_w (Monforte et al. 2017b).

Modelling a CPT involves an ideally rigid cone that penetrates a deformable two-phase medium at a constant velocity. This leads to an axisymmetric model consisting of a rectangular

box with a height of 1.1 m and a width of 0.5 m. The cone radius R measures 1.78 cm with a tip angle of 60° corresponding to the standard geometry (base area of 10 cm²). The penetration starts from an initial position where the cone is located at a depth of 10 cm. The lateral and lower boundaries are fixed in normal direction while an overburden pressure can be applied at the top of the domain. Figure 13 shows the basic model. In this work the Clay and Sand Model (CASM) which is a state parameter based, elastic-plastic critical state (CS) model proposed as proposed by Yu (1998) is employed. [2]. The model has been enhanced in order to take into account the effects of bonding and destructuration based on the concepts presented by Gens & Nova (1993), see Figure 14. Undrained conditions have been postulated.

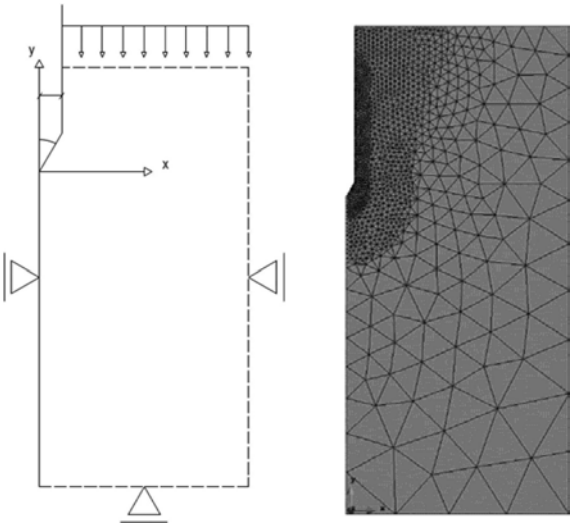

Figure 13. Axisymmetric model (left) and refined mesh during penetration process (right).

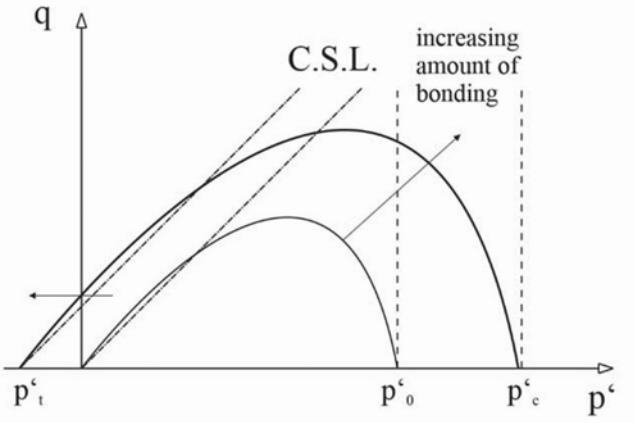

Figure 14. CASM yield surface with bonding.

4.2 *Influence of bonding and destructuration*

In this section the influence of initial bonding and destructuration occurring during the penetration process is evaluated. The parameters for this investigation are taken again for a clayey silt. The coefficient of lateral earth pressure at rest K_0 is taken as 0.5, the effective vertical stress is 160 kPa and the initial water pressure u_0 is 50 kPa. Two different degrees of initial

bonding, defined by the parameter b_0, namely 0.25 and 0.75, are chosen. In addition, different rates for destructuration, controlled by the parameter h are assumed. h = 0 denotes no destructuration at all, i.e. the bonds between particles are not destroyed during penetration whereas higher values for h indicate higher rates of destructuration. It follows from Figure 15 that bonding increases the calculated tip resistance as compared to the soil with b = 0, the higher b the higher q_c, as expected. The increase of tip resistance is significant. If destructuration is taken into account (h > 0), tip resistance decreases, and the values obtained are between the bonded and unbonded case.

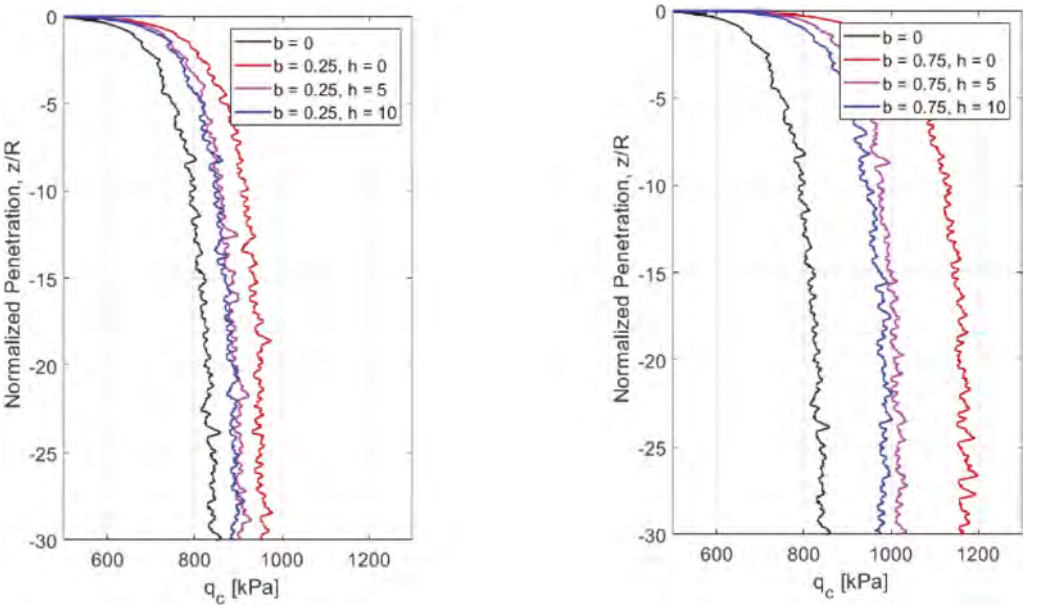

Figure 15. Calculated tip resistance q_c over normalized depth z/R for different degrees of bonding and rate of destructuration.

5 CONCLUSIONS

In this paper three examples have been chosen to illustrate that advanced numerical modelling can contribute to a better understanding of geotechnical problems. The numerical simulation of an anchor pull-out test showed that the predicted load-displacement curve and the one obtained in-situ showed very good agreement proving that accurate predictions are possible when a careful interpretation of in-situ testing and laboratory experiments using engineering judgement and experience is made. The fibre-optic sensors installed led to a better understanding of the behavior of ground anchors. The development of cracks in the grout of the bonded length could be clearly identified. By employing an appropriate constitutive model for the grout in the numerical analysis the development of cracks in the grout could be successfully reproduced in good agreement with the in-situ measurements.

The second example, namely the back-analysis of a slow-moving landslide at a water reservoir, proved that complex mechanisms contributing to slope movement, such as water level fluctuations in the reservoir, creep phenomena in soft lacustrine deposits present at the toe of the slope and environmental effects such as rainfall infiltration can be accounted for in numerical analyses. It is acknowledged that due to significant uncertainties in input parameters the solutions presented are by no means unique but still provide a better insight into the mechanical behavior of such slopes and will help the experienced geotechnical engineer in defining appropriate mitigating measures.

In the last example it is shown that G-PFEM, a finite element framework for analyzing large strain and large deformation problems, is an appropriate tool for simulating CPTu. The

constitutive model CASM has been enhanced in order to take into account bonding and destructuration. It could be clearly shown that tip resistance increases significantly with the degree of bonding and reduces with higher rates of destructuration, as expected. These results can be used for an improved interpretation of CPT results in structured soils.

ACKNOWLEDGEMENTS

The work presented on the pull-out test is part of a FFG-funded research project (Bridge-24 Nr. 858505) and the support of ÖBB-Infrastructure and ASFINAG is gratefully acknowledged. The fibre-optic measurements have been performed by the Institute of Engineering Geodesy and Measurement Systems of the Graz University of Technology (H. Woschitz). The test has been executed by Keller Grundbau (V. Račanský, R. Kulmer). Thanks are also due to Boštjan Pulko, Carla Fabris, Georg Ausweger, Roman Marte and Laurin Hauser.

REFERENCES

Ausweger, G.M. & Schweiger, H.F. 2016. Numerical study on the influence of entrapped air bubbles on the time-dependent pore pressure distribution in soils due to external changes in water level. In: *Proceedings of the 3rd European Conference on Unsaturated Soils*, Paper #16010. Paris.

Ausweger, G.M. & Schweiger, H.F. 2017. Numerical investigation of excess pore water pressures due to external fluctuating water tables. *Proceedings 15th International Conference Computer Methods and Recent Advances in Geomechanics*, Wuhan, China.

Ausweger, G.M. 2017. Influences of water level changes on the behaviour of a slow moving landslide – In-situ measurements, model test and numerical analyses. *PhD Thesis*, Graz University of Technology.

Benz, T., Vermeer, P. A. & Schwab, R. 2009. A small-strain overlay model. *Numerical and Analytical Methods in Geomechanics*, 33(1): 25–44.

Brinkgreve, R. B. J., Kumarswamy, S. & Swolfs, W. M. 2017. Plaxis 2017. Delft, The Netherlands: Plaxis bv.

Dadvand, P., Rossi, R. & Oñate, E. 2010. An Object-oriented Environment for Developing Finite Element Codes for Multidisciplinary Applications. *Arch Comput Methods Eng* 17(3): 253–297.

Fabris, C. 2020. Numerical Study on Pullout Tests of Ground Anchors Monitored with Fibre Optic Sensors. *PhD Thesis*, Graz University of Technology.

Fabris, C., Schweiger, H.F., Pulko, B., Woschitz, H. & V. Račanský, V. 2021. Numerical Simulation of a Ground Anchor Pullout Test Monitored with Fiber Optic Sensors. *J. Geotech. Geoenviron. Eng*., 147 (2):04020163. 1–10.

Gens, A. & Nova, R. 1993. "Conceptual base for a constitutive model for bonded soils and weak rocks", *Proceeding of the International Symposium on Geotechnical Engineering of Hard Soils-Soft Rocks*, Athens, Vol. 1, 485–494.

Monforte, L., Arroyo, M., Carbonell, J.M. & Gens, A. 2017a. Numerical simulation of undrained insertion problems in geotechnical engineering with the Particle Finite Element Method (PFEM). *Computers and Geotechnics* 82: 144–156.

Monforte, L., Carbonell, J.M., Arroyo, M. & Gens, A. 2017b. Performance of mixed formulations for the particle finite element method in soil mechanics problems. *Computational Particle Mechanics* 4(3): 269–284.

Monsberger, C., Woschitz, H., Hayden, M. & Lienhart, W. 2016. Faseroptische Instrumentierung und Deformationsmessung eines duktilen Rammpfahls. In Stahlmann, J. (Hrsg.) *Messen in der Geotechnik. Mittl.Inst.f. Grundbau und Bodenmechanik d. TU Braunschweig*, Heft 101, 195–216.

Oñate, E., Idelsohn, S.R., Celigueta, M.A., Rossi, R., Marti, J., Carbonell, J.M., Ryzakov, P. & Suárez, B. 2011. Advances in the particle finite element method (PFEM) for solving coupled problems in engineering. *Particle-Based Methods* 25: 1–49.

Schanz, T., Vermeer, P.A. & Bonnier, P.G. 1999. The hardening soil model: formulation and verification. *Beyond 2000 in Computational Geotechnics*: 281–290.

Schädlich, B. & Schweiger, H.F. 2014. A new constitutive model for shotcrete. In Hicks, Brinkgreve & Rohe (eds.) *Proceedings Numerical Methods in Geotechnical Engineering*): 103–108.

Schweiger, H.F. & Pande, G.N. 1988. Numerical Analysis of a Road Embankment Constructed on Soft Clay Stabilized with Stone Columns. *Proc. 6th Int. Conf. Numerical Methods in Geomechanics*, Balkema, Rotterdam: 1329–1333.

Vermeer, P.A. & Neher, H.P. 1999. A soft soil model that accounts for creep. *Proceedings of the International Symposium Beyond 2000 in Computational Geotechnics*.

Yu, H.S. 1998. "CASM: a unified state parameter model for clay and sand". *International Journal for Numerical and Analytical Methods in Geomechanics* 22: 621–653.

Smart Geotechnics for Smart Societies – Zhussupbekov, Sarsembayeva & Kaliakin (Eds)
© 2023 The Author(s), ISBN 978-1-003-29912-7
Open Access: www.taylorfrancis.com, CC BY-NC-ND 4.0 license

Creep after surcharge unloading

C.F. Leung
National University of Singapore, Singapore

T.A. Vergote
DEME, Belgium

S.C. Chian
National University of Singapore, Singapore

ABSTRACT: Ground improvement by means of surcharge and vertical drains are often employed to accelerate the consolidation of newly reclaimed lands. However, the long-term performance of the reclaimed land is uncertain as the creep settlement of the land after unloading may exceed the stringent ground settlement limit for the operation of container port with various automated port equipment. A review of published literature reveals that existing methods have limitations on predicting the long-term ground settlement after surcharge unloading. In this article, a theoretical approach is proposed to simulate the long-term ground settlement after unloading. The approach is verified against long term soil consolidation tests subject to different over-consolidation ratios. Finally, the potential applications of the theoretical approach in practice are highlighted.

1 INTRODUCTION

The container port of Singapore is one of the busiest ports in the world. In many countries including Singapore, the container ports are built on reclaimed land underlain by soft compressible materials of the original seabed. Owing to shortage of reclaimed fills in Singapore, the Building and Construction Authority of Singapore (BCA 2008) issued guidelines that all dredged, and construction waste soils should be used for land reclamation to tackle the simultaneous problem of shortage of fill materials and disposal of construction waste soils. The above filling process would produce a highly heterogeneous and less competent fill grounds. Ground improvement employing surcharge and vertical flexible drains are typically employed to accelerate the settlement of such fill grounds and the underlying in-situ compressible soils. Figure 1a shows vertical drains being installed in the reclaimed land and Figure 1b shows the placement of surcharge to accelerate the consolidation of the fill ground and underlying compressible soil strata.

Figure 2 shows the Singapore Pasir Panjang Container port wharf front after completion. In modern days, automatic guided vehicles often operate in the wharf front area and the container stacking yard area behind the wharf front. To ensure that the automated equipment would function properly during the life of port operation (typically minimum 60 years for the case of Singapore), the mechanical engineers would specify stringent residual movement and rotation limits of the reclaimed ground after surcharge removal. As such, the long-term settlement of the reclaimed land after removal of surcharge needs to be evaluated.

Although many studies have reported the creep of soils under constant loading (Grimstad et al. 2017, Mesri 1973, Watabe et al. 2012), there are relatively few existing literatures reporting on the creep of soils after unloading of surcharge (Mesri & Feng, 1991). In view of the above, this invited lecture will present the latest research findings on creep upon unloading from the National University of Singapore. A new theoretical model will be presented in this lecture to predict the long-term ground settlement after removal of the surcharge.

DOI: 10.1201/9781003299127-18

(a) Flexible band drains being installed in reclaimed land (photograph courtesy of Prof. Jian CHU)

(b) Surcharge works on reclaimed land for the construction of Pasir Panjang Container Port Phase 1

Figure 1. Ground improvement work using surcharge and vertical drains in Singapore.

Figure 2. Singapore Pasir Panjang Container Port Phase 1 wharf front after completion.

2 LABORATORY TEST OBSERVATIONS

Vergote (2020) conducted an extensive series of oedometer tests to examine the creep of clay upon unloading with various over-consolidation ratios (OCR). Sample test results are shown in Figure 3. It is evident that soil creep would reappear upon stress relaxation and the clay would respond to unloading by swelling due to dissipation of suction pressures under constant effective stress. The amount of creep of the soil depends on the magnitude of OCR.

Vergote et al. (2019) compared recent constitute models of soil creep upon unloading. They reported that while the models are fitted with parameters to render near-identical compression behavior during loading, the unloading creep behavior varied widely depending on the OCR applied. They also highlighted the limitations of existing strain-based model and established that the isotache strain rate-based models are better suited as the problem of the time origin can

be overcome. However, unloading behavior is characterized by changes in the isotache relation which are not fully consistent with the loading behavior. As such, the more flexible, non-linear strain rate-based models to evaluate the unloading creep behavior should be utilized.

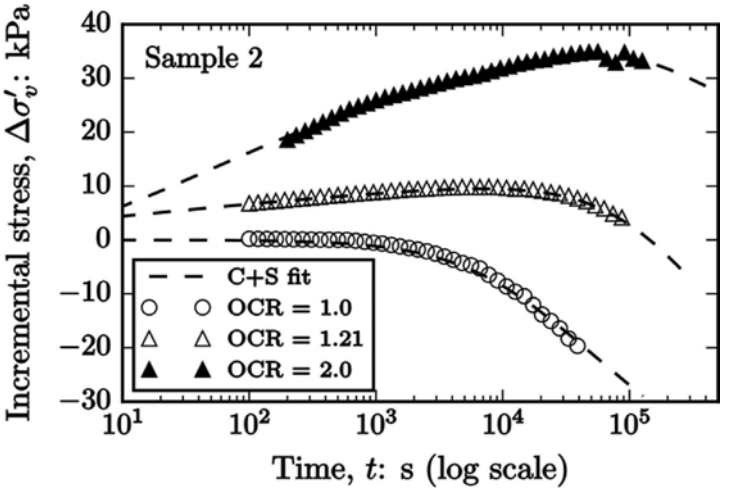

Figure 3. Effect of overconsolidation ratio to relaxation of soil, with increased swelling and reduced creep with increasing overconsolidation, after (Vergote et al., 2022).

Vergote (2020) re-analyzed the oedometer test results of Feng (1991) on creep after unloading using the strain rate-based approach, and the results are shown in Figure 4. The creep after reappearance is non-linear in e-log(t) scale (as reported by Mesri & Feng, 1991). In the present study, it can be interpreted in a consistent way using the strain rate versus accumulated strain ($\dot{e} - \Delta e$). The speed at which creep occurs, $\dot{e}$, goes down gradually with time and as more creep strain Δe occurs. For normally consolidated clay, this results in an approximately linear relation between $e - \log(t)$, but the linearity strongly depends on the selection of a time origin or a reference time. This problem does not occur if strain rate is evaluated relative to strain. Both in loading and after unloading, a linear relation can be found, which can be described by the initial strain rate, $\dot{\varepsilon}_{initial}$, as the intercept and $\hat{C}_\alpha$ as the slope (Figure 4).

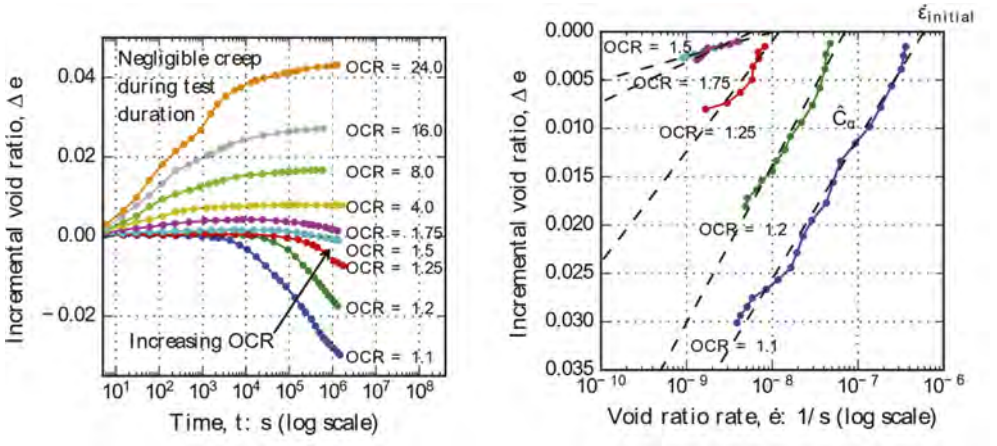

Figure 4. Reinterpretation of the oedometer tests on Berthierville clay (Feng, 1991), following a strain rate approach, after (Vergote et al., 2022).

The interpretation in $\dot{e} - \Delta e$ space linearizes the creep response aligned with the isotache approach. This is illustrated in Figure 5 whereby a normalized best-fit parameters of $\dot{\varepsilon}_{initial}$ and a rate-based secondary compression index $\hat{C}_\alpha$ for different OCR values upon loading can be obtained. The key finding is that the initial creep strain rate after unloading, and hence the secondary compression index, reduce significantly with increasing OCR. In view of this, a simple model is presented here to estimate creep after unloading.

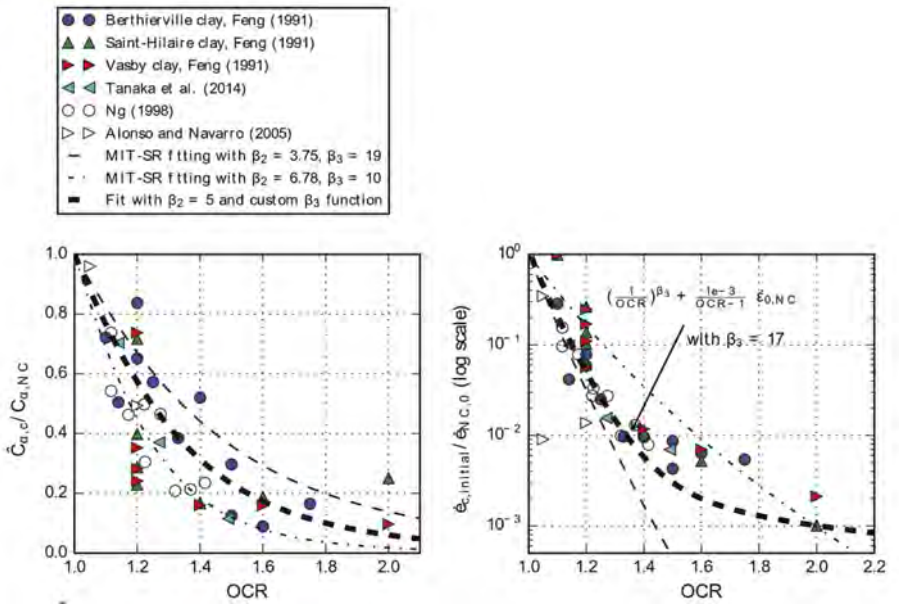

Figure 5. Normalized best-fit creep parameters after unloading for six clays, after (Vergote et al., 2022).

3 C + S MODEL

Existing models only allow to predict creep after unloading but they do not account for the soil swelling behavior. In reality, viscous swelling has a significant effect. It does not only lead to significant deformations (often larger than creep) but also affects the creep response. In view of this, Vergote et al. (2022) proposed a new model tackling creep C and swelling S independently, namely the **C+S model**, to account for this behavior. Figure 6 reveals the principle of the C+S Model. As illustrated in Equation 1, the model considers a decomposition in strain rates as:

$$\dot{e} = \dot{e}_e + \dot{e}_c - \dot{e}_s \tag{1}$$

Where $\dot{e}$ is the total void ratio rate, $\dot{e}_e$ is the elastic void ratio rate, $\dot{e}_c$ is the creep void ratio rate and $\dot{e}_s$ is the viscous swelling rate. The creep and swelling strain rates, respectively, under constant loading are expressed as:

$$\ddot{e}_c = -\frac{\dot{e} \cdot \dot{e}_c}{\hat{C}_{\alpha,c}} \ln(10) \tag{2}$$

$$\ddot{e}_s = \frac{\dot{e}_s^2}{\hat{C}_{\alpha,s}} \ln(10) \tag{3}$$

where $\hat{C}_{\alpha,c}$ and $\hat{C}_{\alpha,s}$ are the secondary compression and swelling indices, and $\dot{e}_{c,init}$ and $\dot{e}_{s,init}$ the initial strain rates for creep and swelling after unloading. These four parameters are a function

of OCR. When considering the overconsolidation, it is important to make a distinction between the applied overconsolidation due to surcharge as defined by:

$$OCR = \frac{\max(\sigma')}{\sigma'} \tag{4}$$

This definition does not consider creep induced increase in the preconsolidation pressure. This is considered within an isotache framework by considering the preconsolidation stress on the reference isotache, leading to a reference overconsolidation ratio (see Figure 7):

$$OCR_{ref} = \frac{\sigma'_{p,ref}}{\sigma'} \tag{5}$$

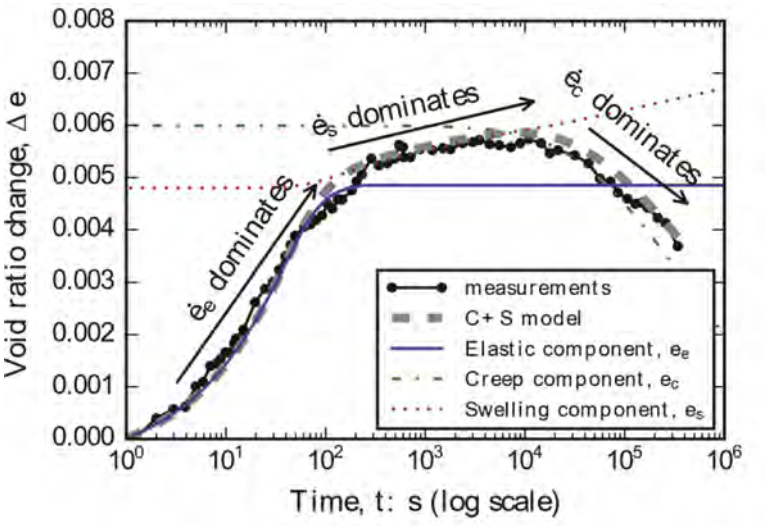

Figure 6. Principle of C + S model: decomposition of strain rates in an elastic, swelling and creep rate component, with sequential dominance of the three components as illustrated in a test at OCR = 1·49 by (Tanaka et al. 2014), after (Vergote et al., 2022).

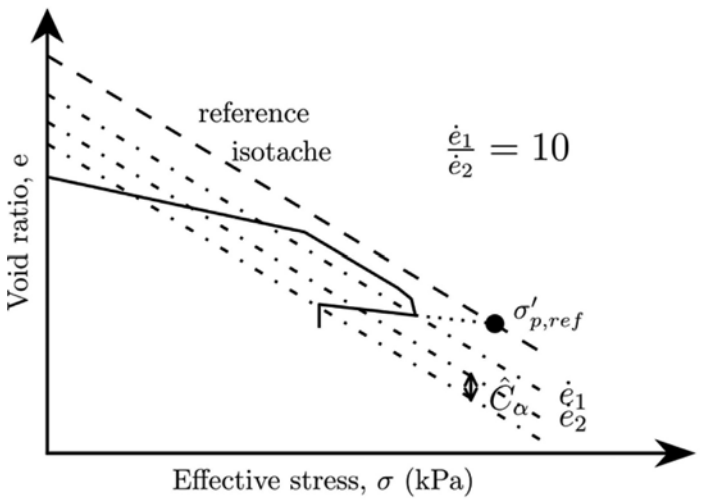

Figure 7. Reference isotache and the derivation of the reference preconsolidation pressure, after (Vergote et al., 2022).

The model is derived for constant loading and for relaxation conditions and used in calibration for previously published test results by others and new results. This was done with a Bayesian parameter updating approach using Markov Chain Monte Carlo simulation, (Hogg & Foreman-Mackey 2018). A clear relation of the normalized parameters, $\hat{C}_{\alpha,c}/C_{\alpha}$, $\hat{C}_{\alpha,s}/C_{\alpha}$, $\dot{e}_{c,init}/\dot{e}_{NC}$ and $\dot{e}_{s,init}$ can be observed. The relation is consistent among the different tests and samples implying that the normalization is appropriate for a wide range of silty and clayey soil types. These are illustrated in Figures 8 to 11. Details of the C+S Model are given in Vergote et al. (2022). A large set of test results is fit to the C+S model and the derived parameters are given in these figures. A clear relation is found between the different test results, including tests on sand, with a general reduction in the creep parameters, $\hat{C}_{\alpha,c}$ and $\dot{e}_{c,init}$ in function of the overconsolidation ratio relative to a reference isotache line, OCR_{ref}. The swelling parameters, $\hat{C}_{\alpha,s}$ and $\dot{e}_{s,init}$ increase with increased preloading and evolve in function of the overconsolidation ratio as calculated from load changes, OCR.

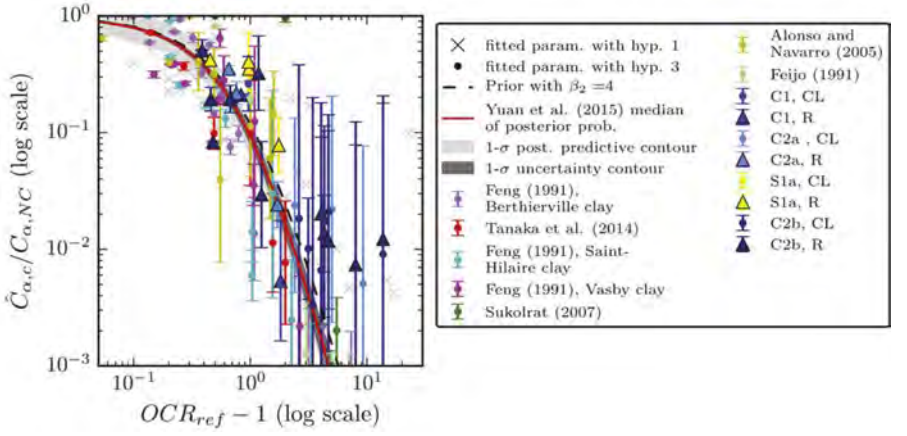

Figure 8. Reduction of $\hat{C}_{\alpha,c}$ with increasing OCR_{ref}, after (Vergote 2020).

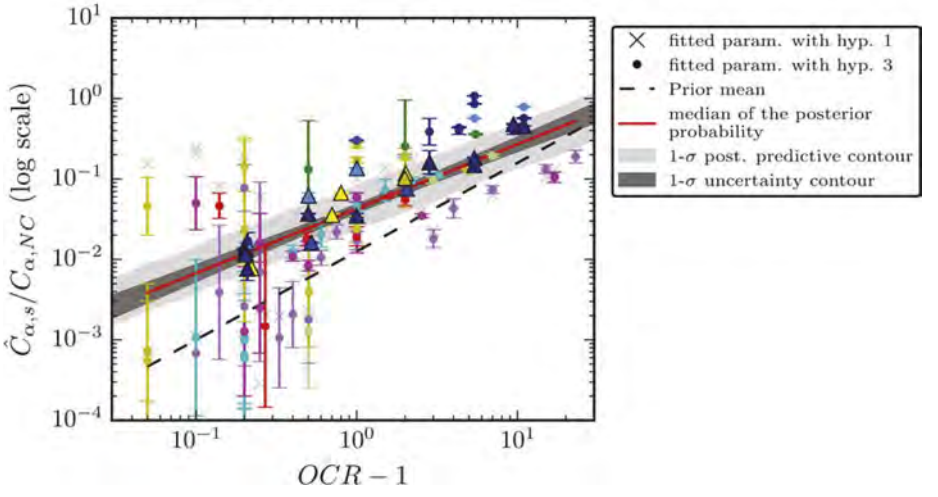

Figure 9. Increase of $\hat{C}_{\alpha,s}$ with increasing OCR, after (Vergote 2020).

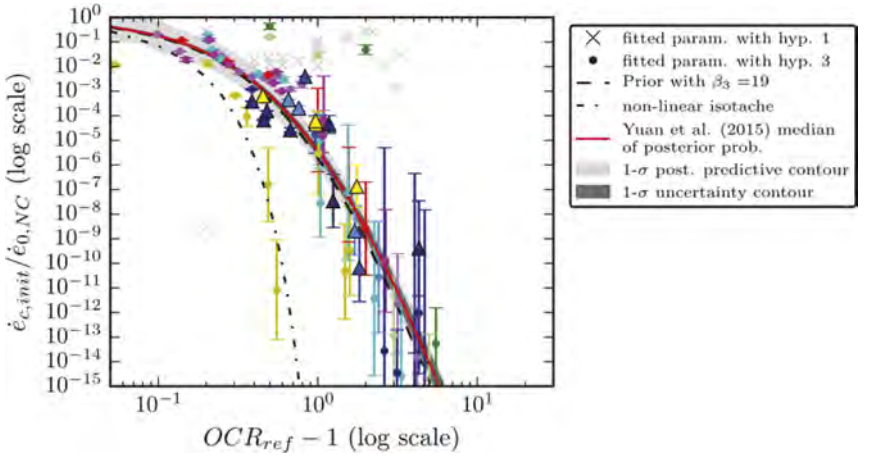

Figure 10. Reduction of $\dot{e}_{c,init.}$ with increasing OCR_{ref}, after (Vergote 2020).

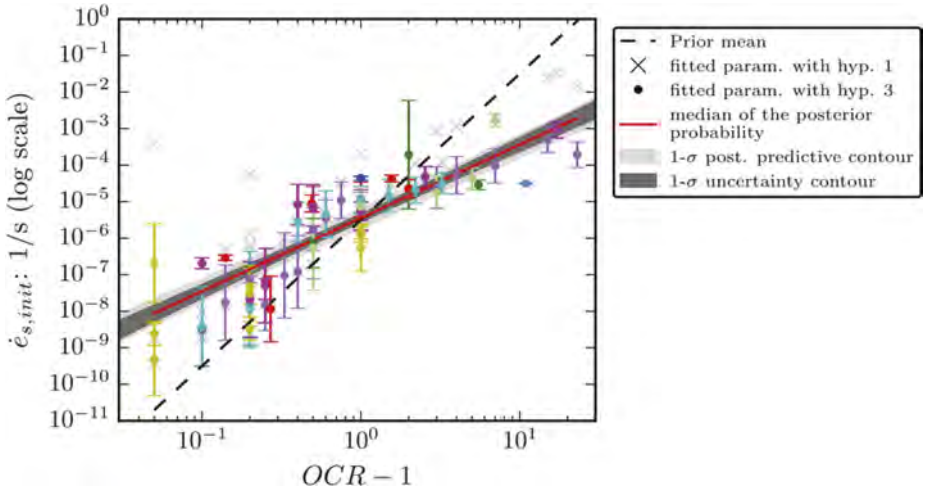

Figure 11. Increase of $\dot{e}_{s,init.}$ with increasing OCR, after (Vergote 2020).

4 DISTORTED ISOTACHE MODEL WITH SWELLING

Vergote et al. (2021) provided further evaluation to examine the validity of C+S Model from the prospective of an isotache model. In general, one can observe that (a) swelling and creep are not mutually exclusive and should be considered in the model, (b) the isotaches are non-linearly spaced, which implies that creep slows down (lower coefficient of secondary compression C_α at higher accumulated creep strain), and (c) after unloading, the isotaches are distorted. An illustration of these non-linear and distorted isotaches is given in Figure 12.

The C+S model allows to model the unloading effect under constant load or relaxation (constant volume) conditions. To simulate the real stress path of the soil in a more general application, one can integrate these features in a new isotache model that considers non-linear isotaches, distortion of isotaches after unloading and viscous swelling. The model is also hydro-mechanically coupled such that it can simulate consolidation correctly. A complex stress path is illustrated in Figure 13.

The model was validated with a constant rate of strain (CRS) compression test involving all the loading and unloading stages, constant loading stages, and relaxation stages. Thanks to the viscous swelling and distorted isotaches, a better fit to the model results was possible, with

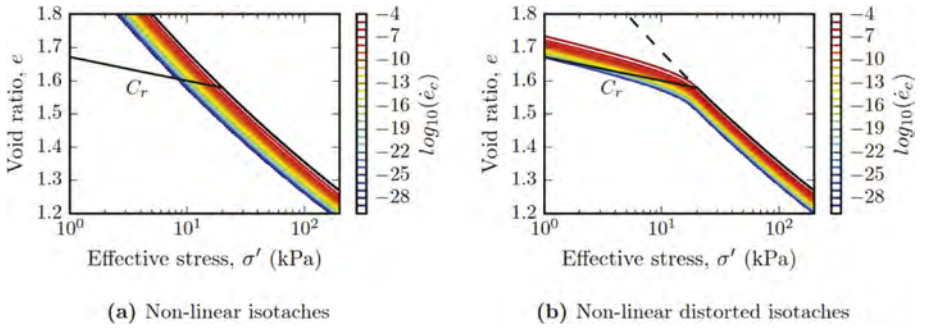

Figure 12. Increase of $\dot{e}_{s,init.}$ with increasing *OCR*, after Vergote et al. (2021).

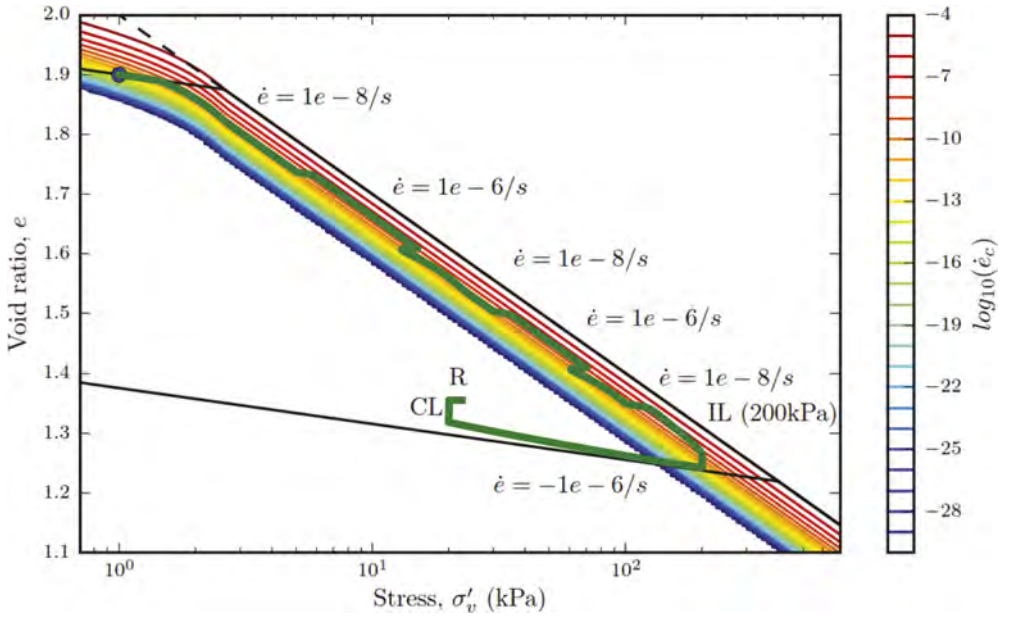

Figure 13. Increase of $\dot{e}_{s,init.}$ with increasing *OCR*, after Vergote et al. (2021).

particular improvement during unloading at low to medium OCRs. Please refer to Figure 14 for illustration.

Experimental results also suggest a rate dependence in the hysteresis effect during unloading-reloading cycles. The model can simulate this, thanks to the viscous effects in the soil, as demonstrated in Figure 15.

4 INDEPENDENT EVALUATION OF C+S MODEL

Dick (2022) evaluated the C+S model for the use of long-term settlements against field data based on the InSAR field measurements. InSAR (Interferometric Synthetic Aperture Radar) is a technique to interpret radar images. The measurements allow to map the relative deformation of surfaces over time, which makes InSAR a promising alternative to field measurements. The measurements were applied to two roads in the Netherlands. He illustrated that the C+S model showed a more realistic settlement rate compared to the linear isotache model, although it still overestimated the settlement rate after 10 years employing default parameters. This was done by comparing the measured strain rate to the predicted strain rate after 10

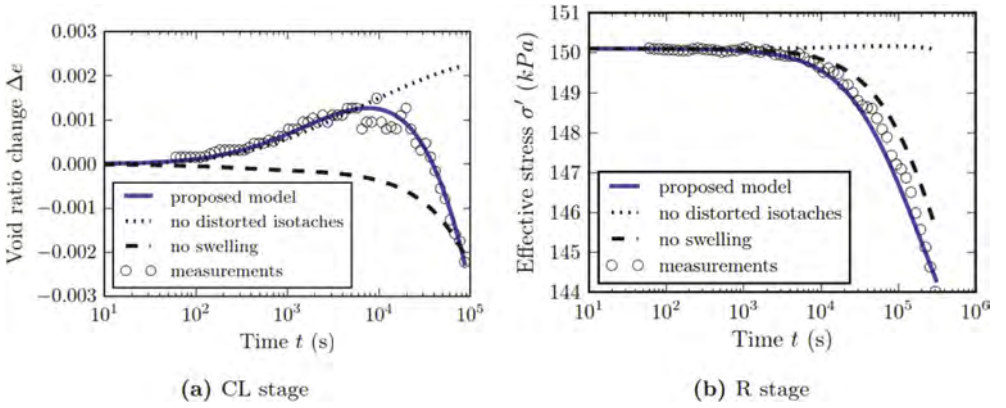

(a) CL stage (b) R stage

Figure 14. Sequential constant load and relaxation tests after unloading at OCR = 1.2, after Vergote et al. (2021).

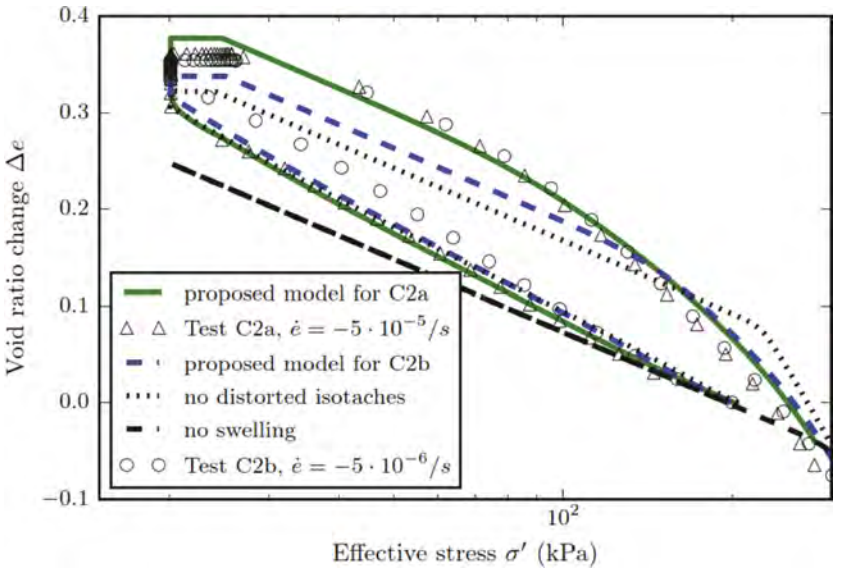

Figure 15. CRS Unloading-reloading cycle at slow and fast rate with a constant load and relaxation phase at OCR = 12, after Vergote et al. (2021).

years. The authors of this article think that it is fairly straightforward to calibrate the parameters of the model with the InSAR measurements to achieve better long-term predictions and retain a good prediction upon loading. This indicates the potential of the model to predict long term settlement of the soil.

In addition, extensive validation using compression tests on Mexico Clay show features as identified in the C+S research: viscous swelling and non-linear creep. The experimental data was used to validate multiple isotache models. The C+S model was compared to linear isotache models and predicted the actual behavior much better, especially after unloading. This can be seen in Figure 16.

5 POTENTIAL PRACTICAL APPLICATIONS OF C+S MODEL

Vergote et al (2021) demonstrated the potential use of C+S model for soil improvement designs presenting some practical phenomena to be considered including the evaluation of

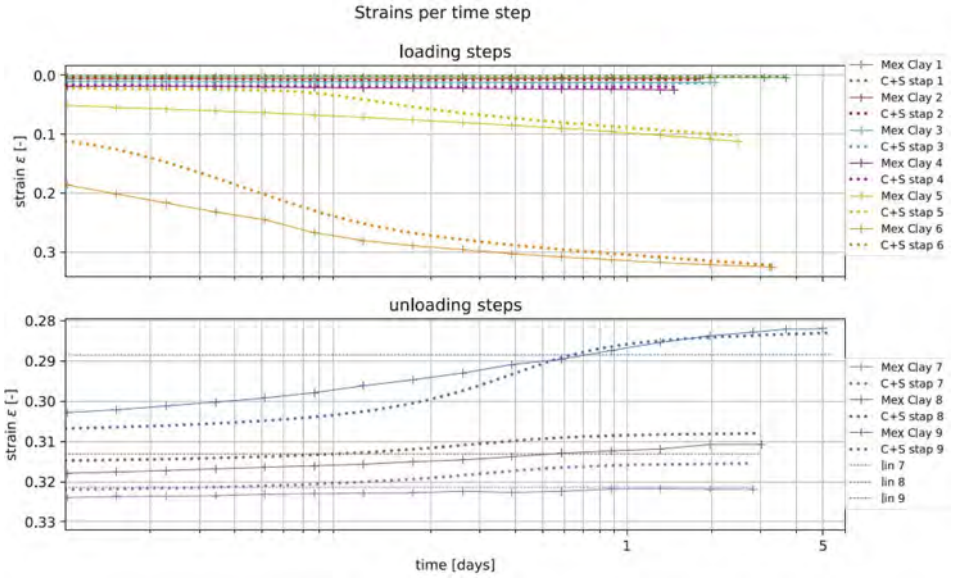

Figure 16. Strain development per loading step for the C+S model and Mexico clay data with a changed value of *cv* upon unloading, after (Dick 2022).

unloading effects. The primary goal of the model is to improve prediction after preloading with surcharge and prefabricated vertical drains (PVD) or vacuum consolidation. The amount of preload stress depends not only on the elastic response of future live loads but also on the long-term time-dependent deformations. By selecting an appropriate preloading height and preload time, the creep deformations can be reduced. Figures 17 and 18 show the effect of increase in preload and increase in preload time on the long-term response of a homogenous clay ($C_c = 0.4,\ C_r = C_c/10,\ C_\alpha = C_c \cdot 0.04$) of 20m.

For a given preload, the overconsolidation ratio will vary over depth, which should be considered in the predictions. In general, it can be observed that creep is reduced to very small values with an OCR > 1.4. Preloading beyond this level will lead to larger long-term swelling. This is function of the design life and the properties of the soil.

The viscous response during unloading is also important for other phenomena, such as long-term swelling estimations after excavation of dredging of soils that serve as foundations for tunnels, for instance for the Fehmarn Belt fixed link, see Kinslev (2021). Highly overconsolidated clays are dredged, leading to significant swelling which impose possible future stresses and deformations to the infrastructure. The current research shows that the swelling is rate-dependent and the C+S approach provides a framework to interpret this and relevant predictions.

Finally, to enable reliable practical predictions, it is important to map the uncertainty of the model to enable probabilistic predictions and reliability-based design. As part of this research, the model calibration was done with a Bayesian updating approach using Markov Chain Monte Carlo, (Foreman-Mackey et al. 2013, Hogg & Foreman-Mackey 2018, Vergote et al. 2022). This allows to create posterior predictive distributions, to derive a probability of a deformation and can be further integrated in an overall framework. An example for drivability predictions in offshore wind is given in Vergote & Raymackers (2022).

6 CONCLUDING REMARKS

This invited lecture first reports the limitations of existing theories on the prediction of soil creep settlement upon removal of surcharge. The conventional strain-based theories are

unable to simulate the laboratory oedometer test results on creep after unloading. In view of the above, a new strain rate-based approach, the C+S Model, is presented to better simulate the creep behavior upon unloading. The overall concept and principle of the model are presented in this lecture. The model can evaluate the creep and swelling phenomena separately in a rational manner. In addition, the model is verified using distorted isotache model considering swelling as well as third-party independent evaluation against existing field data on creep after unloading. Although there are still minor gaps in the verification against field data in the longer term after 10 years, the authors believe that the model can be further fine-tuned to bridge these minor gaps between theoretical and observed field data.

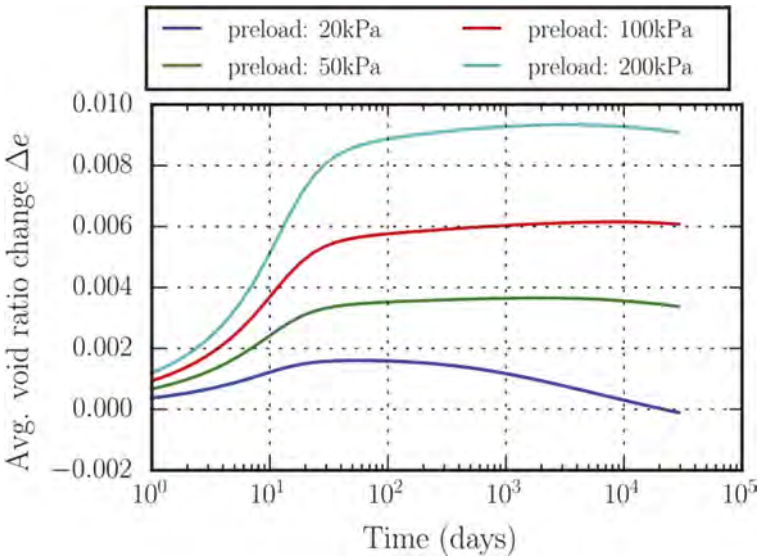

Figure 17. Model sensitivity to preload magnitude.

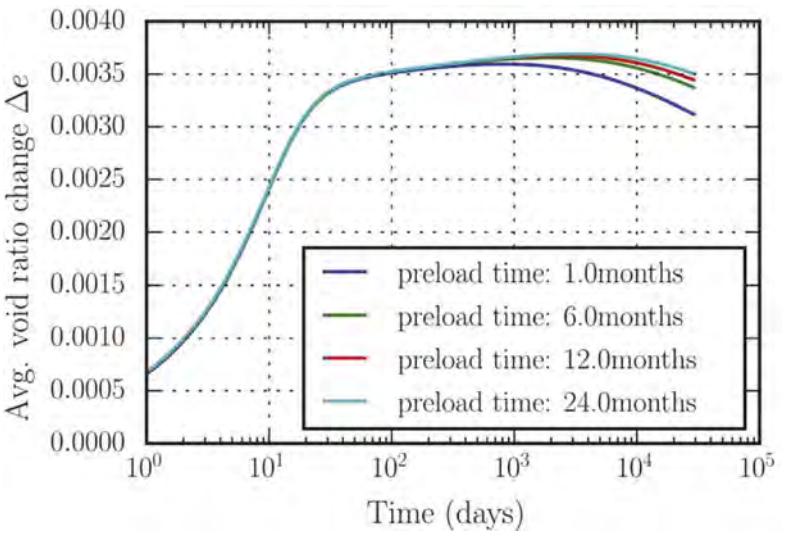

Figure 18. Model sensitivity to preload time (100kPa preload).

Further improvements to the model are planned to be made, both numerically and with availability of more experimental data. For instance, the model should be incorporated in a multi-layered, large strain, axisymmetric model to cater for end-to-end realistic consolidation predictions of land reclamations. Further, while significant experimental work has been done, the data is still rather limited, especially related to rate-dependence of unloading, the effect on reloading and the behavior of sandy soil. A large dataset of long-term field data similar to the InSAR data from the Netherlands would be particularly useful, especially if applied to a reclaimed area from the start of deployment.

7 NOTATION

$\hat{C}_{\alpha,c}$	Secondary compression index for creep, in void ratio (rate-based)
$\hat{C}_{\alpha,s}$	Secondary swelling index, in void ratio, rate-based
C_C	Compression index
C_r	Recompression index
$C_{\alpha.NC}$	Secondary compression index for normally consolidated soils, in void ratio
σ'	Effective stress
$\sigma'_{p,ref}$	Reference preconsolidation stress, relative to reference isotache line
$\dot{e}$	Total void ratio rate
$\dot{e}_c$	Creep void ratio rate
$\dot{e}_s$	Swelling void ratio rate
$\dot{e}_{c,init}$	Initial creep void ratio rate after unloading
$\dot{e}_{s,init}$	Initial swelling void ratio rate after unloading
$\dot{e}_e$	Elastic void ratio rate
OCR	Overconsolidation ratio
OCR_{ref}	Reference overconsolidation ratio

REFERENCES

BCA 2008. Artistic development in autistic children. *Sustainable Construction: A Guide on the Use of Recycled Materials*. Building and Construction Authority of Singapore.

Dick, J. 2022. Long-term settlement behaviour in soft soil areas for stress levels below the yield stress. MSc Thesis, Delft University of Technology, Delft.

Feng, T.W. 1991. Compressibility and permeability of natural soft clays and surcharging to reduce settlements. PhD thesis, University of Illinois at Urbana-Champaign.

Foreman-Mackey, D., Hogg, D.W., Lang, D., and Goodman, J. 2013. emcee : The MCMC Hammer. Publications of the Astronomical Society of the Pacific, **125**(925): 306–312. doi:10.1086/670067.

Grimstad, G., Karstunen, M., Jostad, H.P., Sivasithamparam, N., Mehli, M., Zwanenburg, C., den Haan, E.J., Ghoreishian Amiri, S.A., Boumezerane, D., Kadivar, M., Ashrafi, M.A.H., and Rønningen, J.A. 2017. Creep of geomaterials - some finding from the EU project CREEP. European Journal of Environmental and Civil Engineering, **8189**(January): 1–16. Taylor & Francis. doi:10.1080/19648189.2016.1271360.

Hogg, D.W., and Foreman-Mackey, D. 2018. Data Analysis Recipes: Using Markov Chain Monte Carlo. The Astrophysical Journal Supplement Series, **236**(1): 11. doi:10.3847/1538-4365/aab76e.

Kinslev, E.M. 2021. Efficient performance of large infrastructure. Technical University of Denmark.

Mesri, G. 1973. Coefficient of secondary compression. ASCE J Soil Mech Found Div-v 99, (SM1): 123–137. doi:10.1016/0148-9062(74)91585-x.

Mesri, G., and Feng, T.W. 1991. Surcharging to Reduce Secondary Settlements. *In* Proceedings, International Conference on Geotechnical Engineering for Coastal Development. Theory to Practice, Yokohama, Japan. pp. 359–364.

Tanaka, H., Tsutsumi, A., and Ohashi, T. 2014. Unloading behavior of clays measured by CRS test. Soils and Foundations, **54**(2): 81–93. doi:10.1016/j.sandf.2014.02.001.

Vergote, T.A. 2022. Large strain consolidation parameters by Markov Chain Monte Carlo. *In* 4th International Conference on Information Technology in Geo-Engineering. Singapore.

Vergote, T.A. 2020. Deformation of soils: time and strain effects after unloading. PhD thesis. National University of Singapore.

Vergote, T.A., Leung, C.F., and Chian, S.C. 2019. Creep after unloading: A comparison and validation of constitutive models. *In* Procds. of the 16th Asian Regional Conference on Soil Mechanics and Geotechnical Engineering. Taipei, Taiwan.

Vergote, T.A., Leung, C.F., and Chian, S.C. 2021. Elastoviscoplastic modelling with distorted isotaches and swelling for constant strain rate and incremental loading. International Journal for Numerical and Analytical Methods in Geomechanics, **45**(13): 1920–1933. doi:10.1002/nag.3248.

Vergote, T.A., Leung, C.F., and Chian, S.C. 2022. Modelling creep and swelling after unloading under constant load and relaxation with Bayesian updating. Géotechnique, **72**(6): 496–509. doi:10.1680/jgeot.20.P.106.

Vergote, T.A., and Raymackers, S. 2022. Building a framework for probabilistic assessment accounting for soil, spatial, operational and model uncertainty, applied to pile driveability. Ocean Engineering, doi:10.1016/j.oceaneng.2022.113181.

Watabe, Y., Udaka, K., Nakatani, Y., and Leroueil, S. 2012. Long-term consolidation behavior interpreted with isotache concept for worldwide clays. Soils and Foundations, **52**(3): 449–464. Elsevier. doi:10.1016/j.sandf.2012.05.005.

Taylor & Francis
Taylor & Francis Group
http://taylorandfrancis.com

Bright Spark Lectures

Taylor & Francis
Taylor & Francis Group
http://taylorandfrancis.com

Smart Geotechnics for Smart Societies – Zhussupbekov, Sarsembayeva & Kaliakin (Eds)
© 2023 The Author(s), ISBN 978-1-003-29912-7
Open Access: www.taylorfrancis.com, CC BY-NC-ND 4.0 license

Innovative geotechnical solution for base isolation

J.S. Dhanya
L. N. Gumilyov Eurasian National University, Astana, Kazakhstan

ABSTRACT: Base isolation systems have been widely recognized as a promising solution for mitigating seismic hazards in buildings. This paper explores a novel solution to the problem of earthquake damage to low-rise buildings in developing countries, where traditional base isolation systems are often too costly and difficult to install. The proposed solution is a Geotechnical Seismic Isolation (GSI) system composed of geomaterials beneath the building foundation to act as a seismic filter medium, reducing the intensity of seismic waves by energy dissipation and damping. The present study focuses on using the Sand-rubber mixture (SRM) and geogrid composite as the geomaterials for energy dissipation. The study includes laboratory tests to optimize the geomaterial composition, scaled model tests, and finite element-based numerical studies to assess the performance of the GSI system under static and dynamic loading. It was observed from the element test that SRM with 30% rubber content has adequate shear strength and damping properties to be used as a foundation bed. The results from scaled model tests on a model footing placed on the GSI system show that a geogrid-reinforced GSI layer can increase bearing capacity up to three times with a significant reduction in settlement. Based on finite element studies on a symmetric low-rise framed building placed on the proposed GSI system subjected to seismic excitation, it was found that GSI is effective in reducing peak ground acceleration and decreasing the shear force and interstory drift in the building.

1 INTRODUCTION

Earthquake-resistant buildings have been a focus for the past few decades. Structural control concepts have been implemented by increasing the strength and stiffness of the structure, but damages can still occur. Though the strengthening method leads to safeguarding the structure from collapse at, the functionality of the structure after an earthquake cannot be guaranteed due to excessive damages. A different approach is to decouple the structure from the footing using base isolation techniques to reduce the intensity of the earthquake vibrations transmitted to the structure. The base isolation systems shift the natural period of the structure, reduce the magnitude of energy transferred to it, and increase damping, reducing the spectral displacement. The first rubber bearing isolator was used in 1969, and by the 1980s, seismic isolation gained worldwide popularity and has been refined over the years, using different types of bearings and materials (Kelly 2002).

Rubber bearings were the first modern-era isolation devices, followed by elastomeric bearings made of rubber and steel layers, which exhibit low damping resistance followed by friction pendulum and sliding bearings. However, the procurement and installation can be costly, making it challenging for developing nations to implement the system for regular residential buildings. A potential alternative to conventional base isolation systems involves incorporating damping into the soil up to a specific depth to partially dissipate energy within the soil before it reaches the foundation and superstructure. Compacted sand layers have traditionally been used as an energy dissipating layer. However, due to the decreasing availability of sand in the construction industry, researchers have investigated the use of waste materials such as scrap rubber tires and other polymeric waste products for geotechnical applications (Edil and

DOI: 10.1201/9781003299127-19

Bosscher1994; Ahn and Cheng 2014). Scrap tires with rubber as their primary component have been found to be particularly useful for vibration isolation (Dhanya et al. 2022, 2020, 2019; Forcellini et al.2020). A mixture of sand and shredded rubber tires, referred to as sand-rubber mixture (SRM), has been proposed as a potential solution to the problems of earthquake hazard, unaffordable and ineffective seismic isolation systems, and the rapid generation of scrap rubber tires. This mixture can be used as a vibration mitigation solution and serves as a novel seismic isolation layer, referred to as the Geotechnical Seismic Isolation (GSI) system, placed below building foundations.

In 2007, Tsang proposed using a sand-rubber mixture (SRM) as a geotechnical seismic isolation layer beneath building foundations. Studies by Tsang et al. (2012,2021), Xiong and Li (2013), and Pitilakis et al. (2015) have demonstrated that this method can reduce both horizontal and vertical shaking levels. Similar studies have examined the use of sandbags and synthetic liners as energy-absorbing layers for seismic protection, with Yegian et al. (2004), Jain et al. (2004), and Ansari et al. (2011) reporting lower accelerations compared to fixed-base structures. Pitilakis et al. (2015) noted that SRM layers are particularly effective for mid-rise buildings, reducing design shear force and displacement. Shaking-table experiments conducted by Xiong and Li (2013) and Bandyopadhyay et al. (2015) with shredded rubber-soil mixtures as isolation material placed below concrete blocks confirm the suitability of SRM for seismic isolation. Previous studies have also reported that the damping ratio of SRM increases with an increment in rubber content (Hazarika et al. 2010; Anastasiadis et al. 2012; Senetakis et al. 2012; Ehsani et al. 2015) and that it has low liquefaction potential (Hazarika et al. 2007; Kaneko et al. 2013; Mashiri et al. 2016). The high elasticity, durability, and non-biodegradability of rubber present in SRM make it a sustainable and cost-effective alternative to expensive base isolation techniques.

The previous studies on the use of SRM for seismic isolation have mainly focused on laboratory characterization of the material with varying amounts and sizes of rubber. However, there is still no conclusive study on the optimal percentage of sand-rubber shreds mixture that provides a reasonable shear modulus with a satisfactory damping ratio over a wide range of strains suitable for seismic isolation applications. Furthermore, limited studies have been reported on the use of SRM as a vibration-absorbing layer for buildings, with little emphasis on site-specific conditions and earthquakes with varying peak ground acceleration (PGA) and frequency content. Additionally, the static performance of buildings placed on the GSI system, settlement problems posed by the low stiffness of SRM, and the influence of Soil-Structure Interaction (SSI) on the performance of the base-isolated building have not been adequately addressed in previous studies.

In view of this, the current study aims to investigate the physical and mechanical response of SRM through a series of laboratory tests to determine the optimal percentage of the mixture that offers sufficient stiffness and energy dissipation capacity. Furthermore, scaled model tests were conducted to evaluate the performance of footings resting on GSI systems, with a primary focus on settlement issues in the foundation on the SRM layer. Geosynthetic reinforcement was also explored to enhance the bearing capacity and settlement performance of the GSI system. Further rigorous dynamic analysis was conducted using advanced Finite Element Method (FEM) tools to gain a deeper understanding of the response of a low-rise building resting on the proposed GSI system under seismic loading.

2 CHARACTERIZATION OF SRM AND GEOSYNTHETIC

The study utilized locally sourced river sand of uniformly angular-shaped grains from Chennai city, India. Scrap rubber tyre used in the study was obtained from a local scrap tyre-recycling unit where the steel reinforcements inside the automobile tyres were removed. The tyre base material used for the study is from heavy-duty automobiles such as lorry/trucks which have a higher proportion of natural rubber compared to other non-rubber ingredients like steel and fibres. The final shredded tyre samples are metal and textile fibre-free. The scrap tyres were fragmented into angular shaped granulated tyres of size less than 4.75 mm using the shredding

machine from the tyre-recycling unit. The tyre particles passing 4.75mm size sieve was used in the preparation of sand-rubber tyre mixture samples. For the present study, the sand and granulated rubber were uniformly hand mixed to achieve a homogenous SRM mixture as shown in Figure 1a. Gravimetric proportioning is adopted rather than the volumetric proportioning for the rubber/sand content in the SRM to attain better control and uniformity in the mixture. The physical properties of sand and the granulated rubber tyre are presented in Table 3.1. The geosynthetic reinforcement used in the study is a commercially available planar biaxial geogrid (MACGRID AR) made of glass fibre strands arranged in grid shape having an aperture size of 10 mm x 10 mm (Figure 1b) with a maximum tensile strength of 11.5 kN/m.

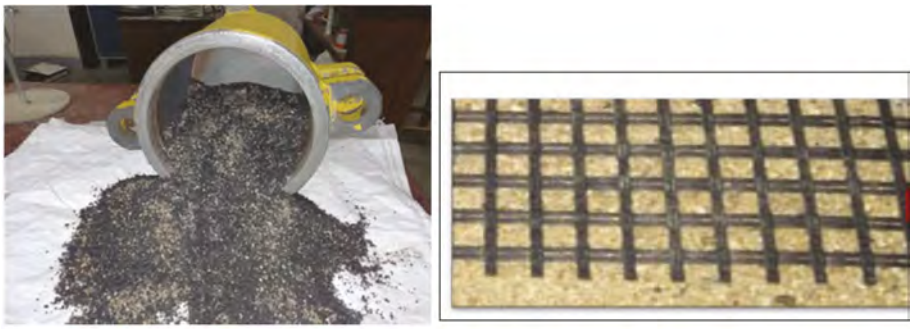

Figure 1. (a) Typical sand-rubber mixture sample (b) Geogrid used for the study.

To determine the gradation of the material, mechanical shakers were used for grain size analysis (Figure 2a). Based on the Indian standard classification system (IS: 1498 1970), the material was classified as poorly graded Sand (SP). The rubber tyre material used in this study is classified as granulated rubber tyre according to ASTM D 6270-08 (2012) since the particle size lies in the range of 425 μm – 12 mm. The granulated tyre for the present study was classified as an equivalent of poorly graded sand (SP) as per IS: 1498 (1970).

To get a better insight into the effect of rubber content on the shear strength response of the mixture, direct shear test is carried out on a standard apparatus with a shear box of 60 mm x 60 mm size. The shear strength of the mixture was normalized with respect to sand for a relative density of 85%. It can be seen from Figure 2b that the decrease in peak shear strength is gradual upto 30% rubber content, beyond which there is a steep decrease in the strength characteristics. Further, increase in normal stress was found to increase the shear strength of the mixture, this could be due to the redistribution of rubber within the voids of sand particles thereby increasing the contact surface and interlocking friction between sand and rubber particles (Foose et al., 1996; Asadi et al., 2018). Hence for the GSI system in the present study SRM with 30% rubber contend was adopted.

3 SCALED MODEL TEST ON FOOTING RESTING ON GSI SYSTEM

To shed insight into the understanding of shallow foundation performance with the presence of reinforced and unreinforced GSI layer, a series of laboratory model tests were carried out on scaled-down model footing. The study employed Wood's (2004) scaling laws of similitude to ensure similarity in both geometry and materials. A scale factor (λ) of 10 was applied to create a model footing that represents a prototype footing of 1 m x 1 m in size. The prototype footing used concrete with E of 20 GPa, while the model footing used steel with E of 200 GPa. The thickness of the model footing was calculated as 10 mm for the study.

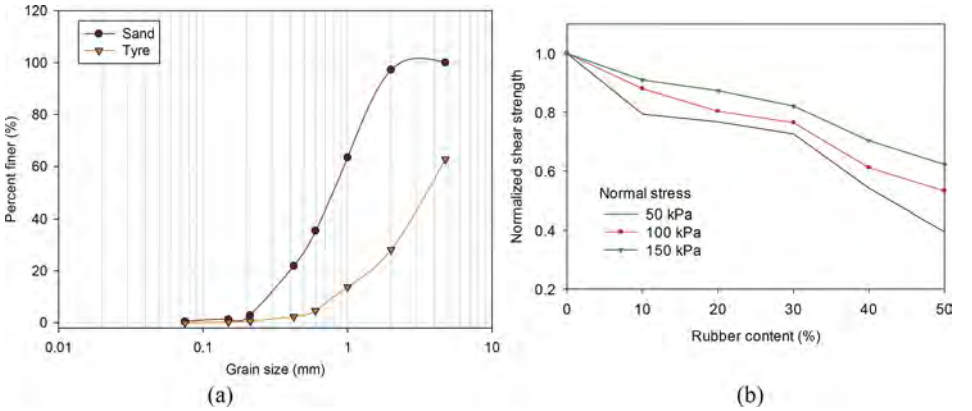

Figure 2. (a) Grain size distribution curve (b) Influence of rubber content on the shear strength of SRM (relative density- 85%).

3.1 *Experimental setup and methodology*

Experiments were conducted using a model square footing of width 0. 1 m (B) placed on top of the GSI layer composed of SRM within a sand bed tank setup (refer to Figure 3). The test tank utilized in this study was made of steel and had inner dimensions of 1 m x 1 m x1 m positioned below a 2m long and 2m high reaction frame. Pneumatic actuators were attached to the reaction frame to apply loads. A steel rod with a height of 1m connected the steel plate for the model footing to the actuator. The pneumatic actuator was used to apply vertical loading in displacement control mode. The load was measured using an electronic load cell with a capacity of 20 kN, and displacement was measured using a linear variable displacement transducer (LVDT) with a capacity of ±30 mm. Calibration of the load cell and LVDT was performed during installation by the equipment providers, and digitalized load-displacement data was automatically saved and available for analysis after testing.

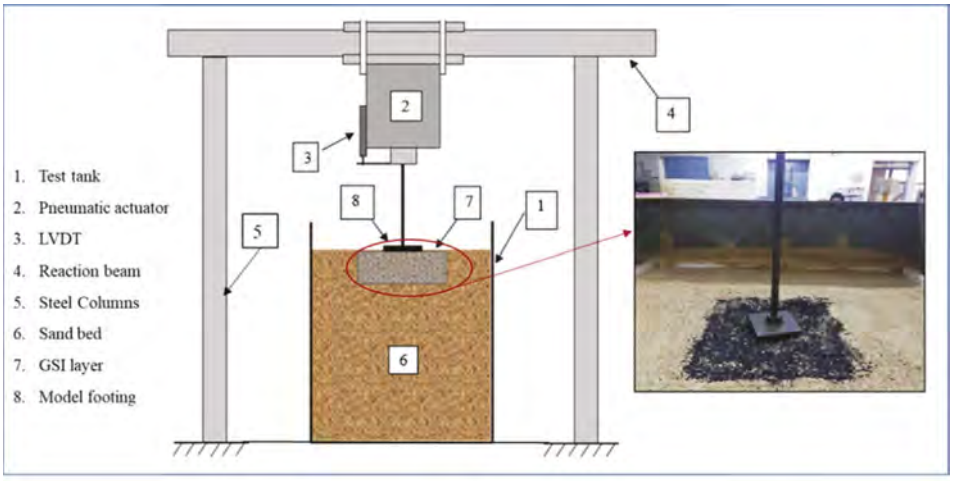

Figure 3. Schematic of the model test setup.

In all experiments, the test tank was filled with sand to a depth of 0.9 meters. A series of tests were conducted on footings resting on different layers of the GSI system to study their behavior under static loading. The first series of tests involved footings on sand beds of 0.9m depth with a relative density of 85% using the sand pluviation technique (Cresswell et al. 1999), where the

sand was poured from a fixed height. The sand was filled in 0.1 m layers and leveled before adding the next layer. Three preliminary trial tests were carried out to confirm the repeatability of load testing. The second series of tests were carried out on footings placed on the SRM-GSI layer. The already-compacted sand bed was excavated for a fixed size of 300 mm x 300 mm with the necessary thickness and backfilled with SRM. Geogrid reinforcement was added to the GSI layers below the footing to increase the bearing capacity and settlement aspect of the system. Hence, the third series of tests were carried out on footings placed on geogrid-reinforced SRM-GSI layer layers. Geogrids were placed at the top of the already compacted sand and SRM layer at a desired depth, and filling was carried out simultaneously to achieve the required relative density. The delicate strain gauges attached to the geogrids were carefully protected throughout the operation to avoid damage. The effective depth of influence is within a range of 2B from the bottom of the footing; hence the geogrids were positioned within a depth of 2B below the footing. In this study, single and double geogrids were used to reinforce the GSI system with layer thicknesses of 1B, 2B and 3B. The single layer of geogrid was placed at a depth of 0.5B, while the double layered geogrids were placed at depths of 0.3B and 0.5B with a vertical spacing of 0.2B. The model footing was placed on the level surface at the center of the GSI layer and sand-bed medium, to which a vertical compressive load was applied until the ultimate bearing pressure was observed. Readings from the load cell, LVDT and strain gauges were collected at a sampling rate of 5s.

3.2 *Response of footing resting on the reinforced and unreinforced GSI layer*

The results obtained from different series of tests are plotted as bearing pressure against the footing settlement (s) in terms of settlement ratios (s/B), as shown in Figure 4. The results revealed that the SRM-GSI layer had a larger settlement compared to the sand layer. The settlement ratio corresponding to the ultimate bearing pressure was 9% for sand and 13% for the SRM-GSI layer. The SRM-GSI layer showed initial compression due to the higher ductility of the rubber content in the mixture. However, there was no significant reduction in the bearing capacity of the GSI layer compared to sand. Interestingly, the SRM-GSI layer with a thickness of 0.5B exhibited a bearing capacity equivalent to that of pure sand. This could be because of the small difference in shear strength between the sand and SRM mixture at lower confining pressure. The bearing capacity of the SRM-GSI layer with a thickness of 1B and 2B increased, but the rate of increment in bearing capacity with settlement ratio reduced by 30% compared to the SRM-GSI layer with 0.5B width. In conclusion, the results suggest that the SRM-GSI layer has a higher settlement than the sand layer.

Figure 4.b Illustrates the load-settlement curves for a footing on the SRM-GSI layer reinforced with geogrid. The results show that the geogrid reinforcement significantly increases the bearing capacity and reduces the settlement of the footing. Additionally, the geogrid-reinforced GSI system exhibits a higher ultimate capacity and fails at higher values of settlement ratio compared to the unreinforced system. The figure reveals that the ultimate bearing capacity of the footing (at an s/B ratio of 20%) on the GSI system increases three times for double geogrids and two times for single geogrid reinforcement. The details of the influence of different parameters of geogrid reinforcement in the GSI system can be found in Dhanya et al. (2019). The studyconfirms that geogrid reinforced GSI system performs well under static loading conditions and can sustain foundation loading sufficiently with adequate bearing capacity and reduced settlement.

4 SEISMIC RESPONSE OF FRAMED STRUCTURE RESTING ON GEOGRID REINFORCED GSI LAYER

A low-rise building with shallow footing is used to numerically analyze the GSI system's dynamic performance using finite element software ABAQUS 6.14. A typical moment resisting framed structure on raft footing is chosen for numerical modeling, with the GSI layer placed below and at the sides of the raft footing. Geogrid reinforcement is added to enhance the GSI system's advantages under static and dynamic loading conditions. The study focuses on a region-specific layered soil domain in the highly seismic Indo-Gangetic plain basin the details of which are presented in Dhanya et al. (2020).

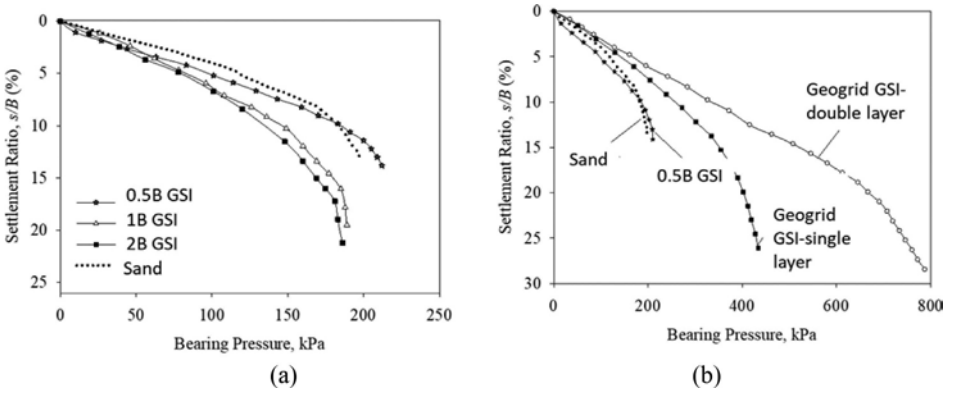

Figure 4. Bearing pressure-settlement response for the GSI system.

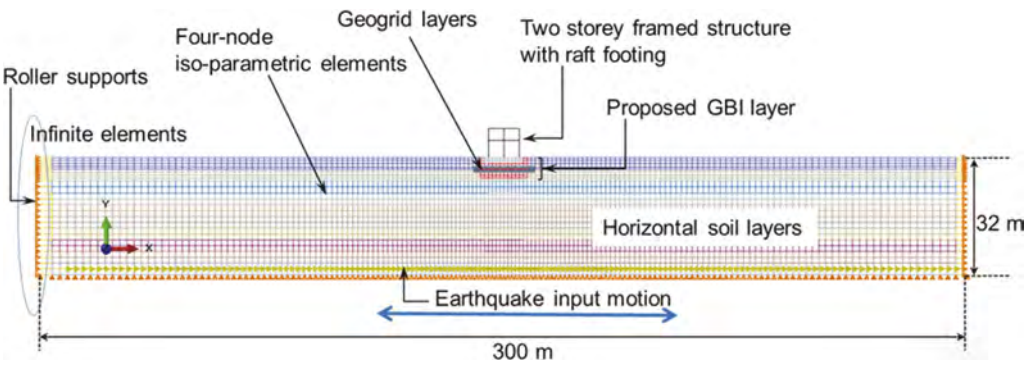

Figure 5. Finite element model adopted for the study.

A-4 type residential apartment buildings with two stories were selected to represent conventional low-rise buildings, based on the National Building Code (NBC) of India (2016). The framed structure used in the study had a height of 4.5 meters at the ground floor (including plinth level) and 3 meters at the top floor, with two equal bays each having a width of 4 m. The beams and columns in the structure were assigned cross-sections of 0.35 m x 0.4 m and 0.35 m x 0.45 m, respectively. The dead load and live load coming on the structure was calculated based on the code provision, IS 875:1987 Part 1& II (2008).

The soil domain of depth 32 m was chosen for the study. Plane strain quadrilateral grids with four-node iso-parametric elements were used to model the soil, GSI layer and footing. Soil is modelled using hypoelstic constitutive model while SRM is modelled using hyperelastic model. Elastic-perfectly plastic material constitutive behaviour was assumed for geogrids modelled using beam elements the details of which can be found in Dhanya et al. (2020). The soil domain was divided into homogenous horizontal layers. The bottom boundary was assumed to be fixed while the side boundaries were given roller supports that restrained horizontal movements but allowed for vertical movements. To simulate unbounded soil media and prevent wave reflections, infinite elements were used to create transmitting boundaries. In the dynamic analysis, the input motions under consideration consist of acceleration-time histories from two major earthquakes that occurred in the Indian subcontinent namely the 2001 Bhuj earthquake (Mw=7.7; PGA=0.1g; predominate frequency= 3.5 Hz) and 2015 Nepal earthquake (Mw=7.8; PGA=0.14g; predominate frequency= 0.2 Hz) obtained from the COSMOS Virtual Data Center as shown in Figure 6.

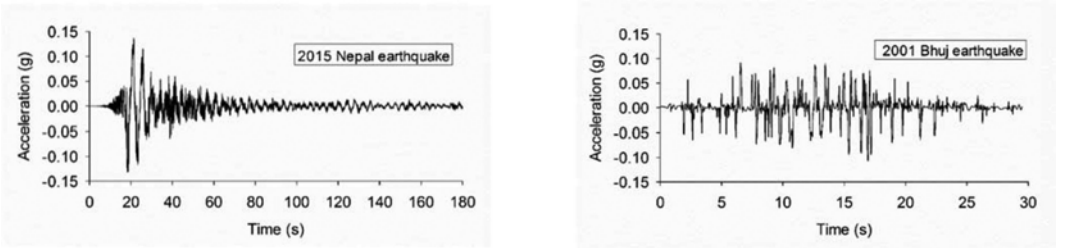

Figure 6. Acceleration-time history of earthquake input motions adopted.

4.1 *Acceleration response of the framed structure on GSI system*

Figure 7a depicts the acceleration-time history obtained at the top of the footing for the natural soil and geogrid reinforced GSI layer of thickness 0.05B when subjected to the 2015 Nepal earthquake motion. The GSI layer shows a significant reduction in the amplitude of acceleration at the footing top compared to the natural soil system. Figure 7b can provide a useful understanding of the characteristics of the acceleration response spectra (with 5% damping) for buildings resting on the geogrid reinforced GSI layer at the footing level. The graph clearly shows a reduction in spectral acceleration for the GSI system compared to the natural sol layer. This reduction is particularly pronounced in the mid-period range of 0.3 s to 1 s, whereas for periods less than 0.3 s and greater than 1 s, the reduction in spectral acceleration is less noticeable. Additionally, the presence of the GSI layer causes a slight shift in the predominant period of the system to a higher value compared to the natural soil system. This shift results in a reduction of spectral acceleration for low-rise buildings, which have a shorter natural period, such as 0.24 s in the current scenario.

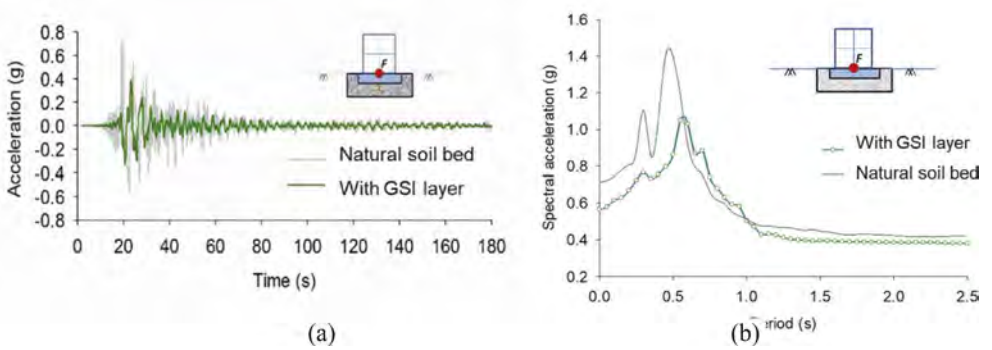

Figure 7. (a) Acceleration time history response (b) Spectral acceleration response at the footing level of the structure.

The thickness of the GSI system has a significant impact on the degree of reduction in earthquake input motion amplification. An optimal thickness of the GSI layer was determined through numerical analysis to ensure satisfactory seismic isolation for the proposed building. The GSI layer thickness was varied at 0.05B, 1B, and 2B, and the system was double-layer geogrid reinforced. The study used the scaled acceleration-time history of the 2015 Nepal earthquake (Mw=7.8) as the input motion and the results were extracted from nodes at the top of the building and footing. The reduction in the peak values of the spectral acceleration due to the presence of GSI was evident for all thicknesses of the GSI layer, as shown in Table 1. The reduction in spectral acceleration values for the GSI system indicates higher energy absorption induced by a thicker layer of the GSI system. For instance, at the top of the building, the isolation efficiency increased by 37% when the thickness of the GSI layer was

increased from 0.05B to 2B. At the footing top, an isolation efficiency of 35% was obtained, indicating that the peak ground acceleration of incoming seismic waves was reduced significantly due to the presence of the GSI layer (thickness=2B). Although the isolation effect initially increases with the increase in thickness of GSI, the isolation efficiency for 0.1B and 0.2B are more or less similar, indicating that using a 0.1B thickness of the GSI layer is enough to achieve the necessary energy dissipation. Additionally, the shift in the fundamental period of the system is more significant for thickness of GSI of 0.1B and 0.2B compared to 0.05B.

Table 1. Effect of thickness of GSI layer on peak spectral acceleration and predominant period (Scaled 2015 Nepal earthquake, Mw=7.8; PGA= 0.24g).

		Peak spectral acceleration (g)		Predominant period (s)	
Description		Footing top	Building top	Footing top	Building top
Natural soil		2.39	2.75	0.47	0.67
Geogrid reinforced GSI layer	$T_{GSI}=0.05B$	1.72	2.27	0.6	0.85
	$T_{GSI}=0.1B$	1.59	1.73	0.67	0.90
	$T_{GSI}=0.2B$	1.46	1.69	0.7	0.95

4.2 *Shear force and interstorey drift*

The effect of seismic isolation on the base shear of the framed structure was investigated and comparison was made between the fixed base structure and structures with seismic isolation, namely, while taking into account the effects of SSI. A constant scaled PGA of 0.24g was maintained for the earthquake input motions during the study. Figure 8 illustrates the base shear ratio, which represents the ratio of shear force developed in the SSI structure to that of the fixed base structure. The figure suggests that the SSI effects are advantageous for the GSI system, as it reduces the base shear when compared to the fixed base system. Additionally, the figure shows that the reduction in base shear is more significant for buildings placed on the SRM-GSI system than on the geogrid reinforced SRM-GSI system. This may be due to the decrease in soil stiffness beneath the building foundation. In contrast, the natural soil layer demonstrated a higher base shear ratio, as it is relatively stiff compared to the GSI system. For example, during the 2015 Nepal earthquake (Mw=7.8), the base shear ratio was 0.47 for the Sur system, which decreased to 0.3 for the GSIur system. Furthermore, the flexible-base provided by the GSI layer influences the SSI effects, resulting in lower base shear when compared to the fixed base system.

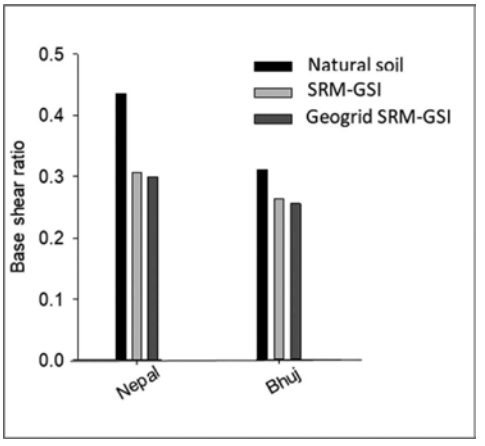

Figure 8. Base shear ratio for different earthquake input motion.

Assessing the performance of GSI isolated structures during earthquakes involves analyzing the maximum lateral displacement experienced by each floor of the building and the corresponding interstorey drift calculated as the difference in lateral deflection of the jth storey and the lateral displacement of the (j+1)th storey, divided by the storey height. The results were summarized in Table 2, which showcases the variation of maximum storey drift for the 1st and 2nd floors of the building for different ground motions (PGA=0.24g). The structure on natural soil had a higher inter-storey drift due to increased lateral displacement in comparison to SRM-GSI layer. This effect is mainly caused by the high amplitude of seismic waves reaching the structure. To further reduce the lateral displacement of GSI layers, the geogrids were introduced, which created a confining effect and restrained the structure's lateral displacement placed on the GSI system.

Table 2. Maximum inter-storey drift of the building for different earthquake motions.

	Maximum storey drift (mm)					
	Natural soil		SRM-GSI		Reinforced SRM-GSI	
Earthquake	1st floor	2nd floor	1st floor	2nd floor	1st floor	2nd floor
2015 Nepal (Mw=7.8)	9.4	10.5	7.7	8.6	6.1	6.6
2001 Bhuj (Mw=7.7)	3.6	5.1	3.2	4.5	3.0	4.2

5 CONCLUSIONS

The present study explores the use of geo-base isolation system made of Sand-Rubber Mixture (SRM) as a vibration isolation layer below the foundation system for seismic protection of buildings using element tests, laboratory model studies and numerical investigation. It was observed that the contribution of sand and rubber to the SRM material matrix is predominant at rubber content below 40% higher than which the influence of rubber matrix prevails. SRM with 30% rubber content possesses adequate stiffness, shear modulus and damping properties ideal for its use as geo-base isolation material. From the model tests, it was observed that the introduction of the proposed GSI layer between the footing and the underlying sandy strata reduces bearing capacity and increases settlement. Provision of geogrids to the geo-base isolation system was found to increase the bearing capacity by two times for single geogrid layer and three times for double geogrid layer. Further, single and double layered geogrid reinforcement reduces the settlement of GSI system up to 30% and 45% respectively. The finite element based numerical studies recommended. It is recommended to adopt the geo-base isolation system for seismic protection of low-rise symmetric buildings in the seismically active Indo Gangetic region of India with the following parameters: GSI layer with a width of 1.2B and thickness of 0.1B reinforced with two layers of geogrid having a spacing of 0.05B and length of 2B.

REFERENCES

Ahn, I. and Cheng, L. (2014). Tire derived aggregate for retaining wall backfill under earthquake loading. *Const. and Building Mat*., 57, 105–116.

Anastasiadis, A., Senetakis, K. and Pitilakis, K. (2012). Small-strain shear modulus and damping ratio of sand-rubber and gravel-rubber mixtures. *Geotech. and Geological Eng*., 30(2), 363–382.

Bandyopadhyay, S., Sengupta, A. and Reddy, G. R. (2015). Performance of sand and shredded rubber tire mixture as a natural base isolator for earthquake protection. *Earthq. Eng and Eng. Vibration*, 14 (4), 683–693.

BIS (Bureau of Indian Standards). 1970. *Classification and identification of soils for general engineering purpose*. IS:1498-1970. Manak Bhawan, New Delhi: BIS.

Cresswell, A., M. E. Barton, and R. Brown. 1999. Determining the maximum density of sands by pluviation. *Geotech. Test. J*. 22 (4): 324–328.

Dhanya, J. S., A. Boominathan, and S. Banerjee. 2019. Performance of geo-base isolation system with geogrid reinforcement. *Int. J. Geo- mech*. 19 (7): 04019073.
Dhanya, J. S., A. Boominathan, and S. Banerjee. 2020. Response of low- rise building with geotechnical seismic isolation system. *Soil Dyn. Earthquake Eng*. 136: 106187.
Dhanya, J. S., A. Boominathan, and S. Banerjee. 2022. Investigation of geotechnical seismic isolation bed in horizontal vibration mitigation. *J. Geotech. Geoenviron. Eng*., 2022, 148(12): 04022108.
Edil, T., and P. J. Bosscher. 1994. Engineering properties of tire chips and soil mixtures. *Geotech. Test. J*. 17 (4): 453–464.
Ehsani, M., Shariatmadari, N. and Mirhosseini, S. M. 2015. Shear modulus and damping ratio of sand-granulated rubber mixtures. *J. Cent. South Univ*., 22, 3159–3167.
Forcellini, D. 2020. Assessment of geotechnical seismic isolation (GSI) as a mitigation technique for seismic hazard events. *Geosciences*, 10 (6): 1–14.
Hazarika H, Yasuhara K, Kikuchi Y, Karmokar AK, Mitarai Y. 2010. Multifaceted potentials of tire-derived three dimensional geosynthetics in geotechnical applications and their evaluation. *Geotext Geomembr*., 28:303–15.
IS 875: 1987 Part 1 (2008). *Code of Practice for Design Loads (Other than Earthquake) For Buildings and Structures. Part 1: Dead Loads-Unit Weights of Building Materials and Stored Materials*. Bureau of Indian Standards, New Delhi.
IS 875: 1987 Part 2 (2008). *Code of Practice for Design Loads (Other than Earthquake) For Buildings and Structures. Part 2: Imposed Loads*. Bureau of Indian Standards, New Delhi.
Jain, S. K. and Thakkar, S. K. (2004). Application of base isolation for flexible buildings. *13th World Conference on Earthquake Engineering*, Vancouver, B.C, Canada, August, Paper no. 1924.
Kaneko, T., Orense, R. P., Hyodo, M. and Yoshimoto, N. (2013). Seismic response characteristics of saturated sand deposits mixed with tire chips. *J. Geotech. Geoenvironmental Eng*., 139(4), 633–643.
Kelly, J. M. (2002). Seismic isolation systems for developing countries. *Earthquake. Spectra*, 18, 385–406.
NBC (2016). *National Building Code of India*. Bureau of Indian Standards (BIS) New Delhi
Pitilakis, K., S. Karapetrou, and K. Tsagdi. 2015. Numerical investigation of the seismic response of RC buildings on soil replaced with rubber– sand mixtures. *Soil Dyn. Earthquake Eng*. 79 (Dec): 237–252.
Rao, G. V., and R. K. Dutta. 2006. Compressibility and strength behaviour of sand-tyre chip mixtures." *Geotech. Geol. Eng*. 24 (3): 711–724.
Senetakis K, Anastasiadis A, Pitilakis K, Souli A. 2012. Dynamic behavior of sand/ rubber mixtures, Part II. *J ASTM Int*., 9(2), 1–13.
Tsang, H. 2008. Seismic isolation by rubber–soil mixtures for developing countries. *Earthquake Eng. Struct. Dyn*. 37 (2): 283–303.
Tsang, H. H., D. P. Tran, W. Y. Hung, K. Pitilakis, and E. F. Gad. 2021. Performance of geotechnical seismic isolation system using rubber-soil mixtures in centrifuge testing. *Earthquake Eng. Struct. Dyn*. 50 (5): 1271–1289.
Tsang, H., Lo, S. H., Xu, X and Sheikh, M. N. (2012). Seismic isolation for low-to-medium-rise buildings using granulated rubber – soil mixtures: numerical study. *Earthquake Eng. Struct. Dyn*., 41, 2009–2024.
Wood, D. M. 2004. *Geotechnical modelling*. Abingdon, UK: Spon.
Xiong, W. and Li, Y. (2013). Seismic isolation using granulated tire–soil mixtures for less-developed regions: experimental validation. *Earthquake Engineering and Structural Dynamics*, 42, 2187–2193
Yegian, M. K. and Kadakal, U. (2004). Foundation isolation for seismic protection using a smooth synthetic liner. *Journal of Geotechnical and Geo-Environmental Engineering*, 130(11), 1121–1130.

Smart Geotechnics for Smart Societies – Zhussupbekov, Sarsembayeva & Kaliakin (Eds)
© 2023 The Author(s), ISBN 978-1-003-29912-7
Open Access: www.taylorfrancis.com, CC BY-NC-ND 4.0 license

Influence of microscale cohesive contacts on the macro-behaviour of soils through DEM investigation

T. Doan
PhD Candidate, Transport Research Centre, Faculty of Engineering & Information Technology, University of Technology Sydney, New South Wales, Australia

B. Indraratna
Distinguished Professor, Transport Research Centre, Faculty of Engineering & Information Technology, University of Technology Sydney, New South Wales, Australia

T.T. Nguyen
Research Fellow, Transport Research Centre, Faculty of Engineering & Information Technology, University of Technology Sydney, New South Wales, Australia

C. Rujikiatkamjorn
Professor, Transport Research Centre, Faculty of Engineering & Information Technology, University of Technology Sydney, New South Wales, Australia

ABSTRACT: Microscale contacts are inherent in most geotechnical failures such as soil liquefaction, landslides and internal instability, thus study of these failures based on microscale concepts can significantly enhance our intrinsic understanding as well as the quality of prediction and designs. Despite rapidly increasing investigation on micro-mechanisms of soil failures, especially based on Discrete Element Method (DEM), cohesive behaviours of particles are usually ignored and simplified, resulting in incomplete and/or inaccurate understanding. My study aims to overcome this imperative limitation and improve our modelling capability by investigating the influence of microscale cohesive contacts on fundamental soil behaviours such as the formation of angle of repose and direct shear. Different degrees of cohesion between particles are incorporated into DEM models and the results are validated against experimental data. The results show cohesive contacts can significantly affect soil behaviour and the predicted outcomes if they are not considered properly. The prediction capability of this DEM model can be further applied to study the cohesive behaviour of geomaterials in various geotechnical problems such as soil clogging and debris flow.

1 INTRODUCTION

Soils are naturally occurring materials composed of constituent grains of varying sizes, shapes and compositions that are in contact with each other. The particulate nature of soils gives rise to complex interactions between particles such as friction and inter-particle cohesion and these particle-scale contacts play a crucial role in determining the overall behaviour of the soil including its strength, stiffness, and deformation characteristics. To understand the macro-response of soils, it is imperative to take their particulate nature and micro-scale contacts into account, and this requires the use of advanced approaches such as the discrete element method (DEM) to capture the particle-scale response. Previous studies have successfully employed DEM techniques to capture a range of complex soil responses; for instance, non-linear stress and strain responses (O'Sullivan, 2011), stress-state dependency (Lommen et al., 2014), critical-state behaviour (Phan et al., 2021), internal instability (Nguyen and Indraratna, 2020a), and many others. However, most previous studies have mainly considered cohesionless frictional materials

DOI: 10.1201/9781003299127-20

whereas cohesive contacts are ignored leading to inaccurate or incomplete analysis. This means increasing effort is needed to simulate the cohesive behaviour of soils more accurately in DEM.

The cohesive behaviour of soils, which refers to the bonding and inter-particle cohesion between soil particles, plays a crucial role in the stability of soils and their resistance to macro-scale failures such as liquefaction, landslides and slope instability (Mitchell and Soga, 2005). At the macro-scale, the classical Mohr-Coulomb theory states that the cohesive strength of soils contributes to the overall shear strength, providing resistance to sliding and shear deformation. At the microscopic level, the cohesive strength is characterised by the presence of cohesive contacts between soil particles, which mainly include van der Waal forces between fine particles (Parteli et al., 2014), electrostatic forces (Endres et al., 2021) and capillary interactions between wet particles (Wang et al., 2018). As these cohesive forces can occur individually or concurrently, the effort to consider these non-linear forces in DEM contacts can be complex and computationally intensive. In addition, measuring the micro-scale cohesive forces between individual particles in laboratory testing is arduous, which makes it more difficult to obtain accurate and reliable data to support the modelling of this behaviour. Moreover, cohesion is often dependent on several factors such as moisture contents and types of soil, making it problematic to develop a comprehensive model to accurately represent this behaviour. In a nutshell, the cohesive behaviour of soils, despite its significant influence on the performance of soils, is often ignored in DEM simulations due to difficulties in modelling and characterising this ambiguous behaviour.

To overcome limitations regarding the computational cost, it is common to use some of the well-established physics models such as the JKR (Johnson-Kendall-Roberts) and the DMT (Darjaguin-Muller-Toporov) to describe the attraction forces between two contacting particles. While JKR theory is developed to capture the short-range, strong surface forces between large and deformable bodies, DMT regime corresponds to an opposite type of materials (i.e., hard, small radius, and long-range attraction forces). Previous studies stated that cohesive forces calculated by the JKR model are closely approximated with experimental measurements by AFM for various materials (Jones, 2003). Therefore, the JKR model has been increasingly used to model fine and wet materials in which cohesive interactions dominate the macroscopic behaviour of materials considerably (Deng and Davé, 2013, Hassanzadeh et al., 2020). In this study, the JKR theory will be incorporated into the DEM contact mechanics to capture the cohesive behaviour of geomaterials.

This study aims to apply DEM model which simultaneously considers frictional (sliding) contact, rolling resistance and micro-scale cohesive forces, with a special emphasis on the modelling the cohesive behaviour of geomaterials. It will also provide a thorough investigation into the micro-cohesive effects on macro-behaviour of soils while flowing and shearing. The application of the current cohesive model is validated against experimental tests such as the angle of repose (AoR) and direct shear tests (DST). Furthermore, extensive analysis is conducted to investigate the effect of cohesive contact forces on the macro- and micro-response of soils. Based on this analysis, a linkage between micro-scale parameter and macro-scale property can be provided to obtain a better understanding of the overall soil responses.

2 DEM COHESIVE MODEL AND NUMERICAL ANALYSIS

2.1 *DEM cohesive model*

For granular materials, the Hertz-Mindlin contact model has been successfully adopted by previous studies (Zhu et al., 2007) to compute the normal and tangential contact forces in relation to elastic deformation between particles, therefore, this model will be employed in the current study. In the Hertz-Mindlin model, the respective contact forces are determined from contact stiffnesses as follows:

$$k_n = \frac{4}{3} E^* \sqrt{R^* \delta_n} \tag{1}$$

$$k_t = 8G^* \sqrt{R^* \delta_n} \tag{2}$$

where E^*,G^* and R^* are the effective Young's modulus, shear modulus, and radius of two particles respectively, and δ_n is the normal overlap or displacement. Further information to determine these input parameters is provided elsewhere (Li et al., 2005, Zhu et al., 2007).

Following most of DEM studies in the literature, spheres are commonly used owing to the modelling simplicity and contact detection efficiency. However, this simplification leads to the loss of shape effects (i.e., angularity and interlocking) and results in discrepancies between numerical and physical results. Hence, to compensate for realistic shapes in DEM, a concept of using rolling resistance model has been developed by several researchers (Ai et al., 2011) to account for a rolling resistance torque opposing the free-rolling tendency of spheres. In this study, a rolling resistance model known as elastic-plastic spring-dashpot model (EPSD2) will be used as this model has been recognised to prevent oscillatory behaviour and provide quasi-static simulations. The rotational resistance torque is a function of a rolling friction coefficient μ_r as follows:

$$\left| M_{ij}^r \right| \leq \mu_r R^* \left| F_{ij}^n \right| \tag{3}$$

For the cohesive behaviour, the cohesive model proposed by Doan et al. (2023) was used to couple the simplified Hertz-Mindlin contact mechanics and JKR theory to capture the elasto-cohesive response between particle contacts. The fundamental concept of JKR theory characterises the attractive forces between solids by an additional tensile stress at the contact boundary leading to a finite contact area even at zero load, as shown in Figure 1.

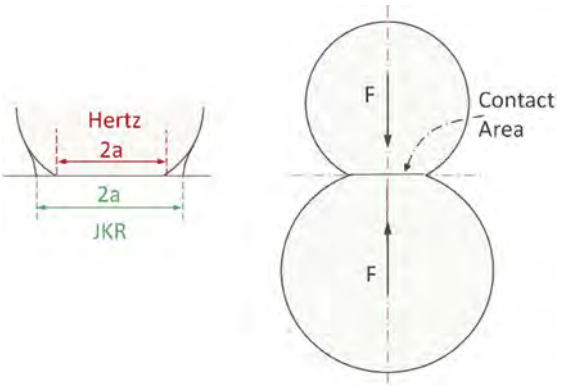

Figure 1. Schematic of the force-displacement relationship in JKR theory (refer to (Roessler and Katterfeld, 2019)).

The JKR theory used a concept of energy balance method to determine the surface attraction forces (i.e., vdW forces) based on their respective surface energies. The application of JKR has been expanding across multi-disciplinary fields to model the cohesive behaviour of powders, micro-scale particles and geomaterials (Deng and Davé, 2013, Barthel, 2008). The contact forces, deformation and radius are derived by JKR theory as follows:

$$\boldsymbol{F_{ij}^{JKR}} = \frac{4E^* a^3}{3R^*} - \sqrt{8\pi E^* \gamma_E a^3} \tag{4}$$

$$\delta_{ij}^{JKR} = \frac{a^2}{R^*} - \sqrt{\frac{2\pi a \gamma_E}{E^*}} \tag{5}$$

$$a = \frac{3R^*}{4E^*}\left[\boldsymbol{F_{ij}^{JKR}} + 3\pi\gamma_E R^* + \sqrt{\boldsymbol{F_{ij}^{JKR}} 6\pi\gamma_E R^* + (3\pi\gamma_E R^*)^2}\right] \tag{6}$$

Where as F_{ij}^{JKR} and δ_{ij}^{JKR} are the cohesive contact force and deformation according to JKR formulations; γ_E is an effective surface energy between two particles and a is the contact radius. As the computation of the contact radius a is prohibitively demanding and not easily obtained, the original JKR model is subjected to some simplifications leading to the development of the simplified JKR model (SJKR). Instead of using the surface energies, the SJKR model employs an empirical and numerical cohesive term named Cohesion Energy Density (CED), which is defined as the volumetric energy needed to separate the attractive interactions between two particles. In this SJKR model, the cohesive force is computed as a function of CED (J/m^3) and the contacting area A as follows:

$$\boldsymbol{F_{ij}^{JKR}} = CED \times A \tag{7}$$

As described by Doan et al. (2023), the term CED can be related to the surface energy which is a physical property and can be theoretically measured for any materials, as follows:

$$CED = \sqrt[3]{\frac{8E^{*2}\gamma_E}{3R^*\pi^2}} \tag{8}$$

2.2 *Numerical validation with experimental tests studying the flowing behaviour of soil (Angle of repose test)*

Prior to further developments, it is crucial to test the proposed DEM model with micro-scale cohesive forces against fundamental tests such as the angle of repose (AoR) test. The angle of repose is defined in Terzaghi (1943) as the steepest slope of angle that a soil can form without external effects such as confining pressures. The AoR test is demonstrated by numerous studies (Li et al., 2005, Derakhshani et al., 2015) to provide valuable information about the interparticle forces and friction angle of materials, both of which are critical for geotechnical designs and analysis. Previous studies have shown that the AoR is highly sensitive with the presence of cohesive forces, hence, a neglect of cohesive contacts results in an underprediction of the AoR value. Therefore, incorporating the cohesive forces in DEM contact mechanics is prominent to capture the macro-response of materials more realistically.

To simulate the AoR test, a lifting cylinder test was chosen due to its simplicity to determine the AoR of geomaterials. Sandy soils in dry and wet states were selected to study the cohesionless and cohesive behaviour of materials in the AoR test. For wet sands, the inter-particle cohesive forces mainly take on a form of liquid-bridging forces which result in the generation of capillary and viscous forces. The SJKR model was used to represent the capillary forces, while the influence of viscous force was deemed insignificant in quasi-static conditions. To simulate the AoR test in DEM, several input parameters which have been consistently provided in previous studies were collated in the Table 1 below. Additionally, as the rolling friction coefficient and micro-scale cohesive forces (i.e., calculated from the Cohesion Energy Density (CED) value) are different among materials, these values will be calibrated to match with the current experimental data. For the calibration of rolling resistance coefficient, this value varies greatly in the literature ranging from 0.1 (i.e., highly spherical particles) to 0.5 (i.e., highly angular shape), hence, this range was used in the current study. The calibration of CED parameter was based on past studies which reasonably captured the cohesive effect of various materials. In the current investigation, CED values were selected from 0 for the cohesionless state to 5 x 10^5 (J/m^3) for the cohesive state. The variations of rolling resistance coefficients and CED were summarised in Table 2.

To verify that the DEM simulations are valid, the numerical results were compared with the experimental tests conducted on wet sands from Roessler and Katterfeld (2019). It is worthy to

Table 1. The input parameters for the current DEM study.

Parameters	Inputs	References
Particle density (kg/m^3)	2650	
Poisson's ratio	0.3	
Shear modulus (Pa)	10x10^7	
Restitution coefficient	0.2	(Behjani et al., 2017)
Particle-wall friction coefficient	0.36	(Roessler and Katterfeld, 2019)
Particle-particle sliding friction	0.5	(Nguyen and Indraratna, 2020a, Phan et al., 2021)
Timestep (s)	10^{-5}	10% Rayleigh time step
Gravitational acceleration (m/s^2)	9.81	

Table 2. The calibrated parameters in DEM.

Parameters	Value range	Value increment
Rolling friction coefficient (μ_r)	0.1 - 0.5	0.1
Cohesion Energy Density (CED) (J/m^3)	0 - 5x10^5	1x10^5

note that instead of comparing the angle of repose (AoR) values which can be highly variable and not appropriate for the characterisation of cohesive materials, the flowability of materials was selected for comparison. The flowability of wet soils was observed to be dependent on a lifting height (h) which was defined as a gap between the bottom of the cylinder and the horizontal base, hence, the flow response of soils was captured in four separate stages (i.e., h = 90 mm, 120 mm, 160 mm and 280 mm for a 375mm-high cylinder). Figure 2 demonstrates that DEM simulations can mimic the flow characteristics of materials in the experiments very well. More specifically, at the initial stage of the tests when the lifting height remains small (h = 90 mm), a solid column of materials is witnessed in both DEM and experiments without any bending or spreading of materials yet as the cohesive and frictional forces are sufficient to counteract with the self-weight of the material. This phenomenon is repeatedly observed in the physical tests by Roessler and Katterfeld (2019). Then, when the gap is increased further, the column of materials starts to collapse, leading to the further spreading of materials to form a convex slope as seen in Stage 2, 3 in Figure 2. Finally, at stage 4 when the cylinder is sufficiently lifted, a quasi-static heap of wet sand materials is formed physically and numerically. To sum up, the DEM simulations incorporating cohesive forces were in good agreement with the experimental results. For a further development, the DEM model can be improved to simulate cracks appearing in the heaps of wet sands owing to difficulties to maintain a uniform and homogenous distribution of moisture content in the experiment.

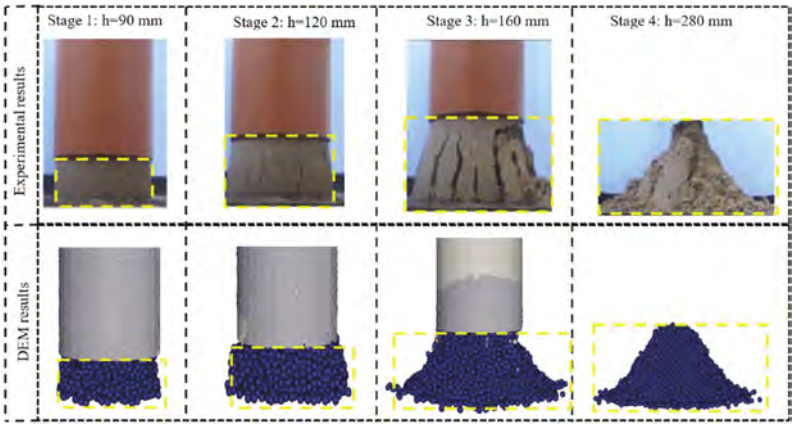

Figure 2. Comparison between DEM models and experimental tests.

The experimental tests from Roessler and Katterfeld (2019) also found out that the bending of the column of materials at different phases was reproducible and can be quantified, hence, this criteria was chosen for a quantitative comparison between DEM and experiments. The bending of material was characterised by a parameter named the relative pile diameters (d_{rel}) to compare between the diameter of the pile d_{pile} and the diameter of the cylinder ($d_{cylinder}$) (i.e., the formulation was given in Doan et al. (2023)). Figure 3 indicates that with a small lifting height h = 80 mm, the pile remains nearly vertical with 2.3 % bending in DEM results and 2.1 % bending in experiments. However, when the cylinder is lifted further, the slope of materials curves more significantly with 25.1 % of convex bending in DEM and 25% in the referenced case. By comparing the DEM results and experiments both qualitatively and quantitatively, DEM simulations represented experimental observations very well. More particularly, the DEM results also captured many important features of the cohesive behaviour of soils; for example, when cohesive forces were present, the flowability of materials was significantly hindered as compared to the free-flowing feature of cohesionless materials.

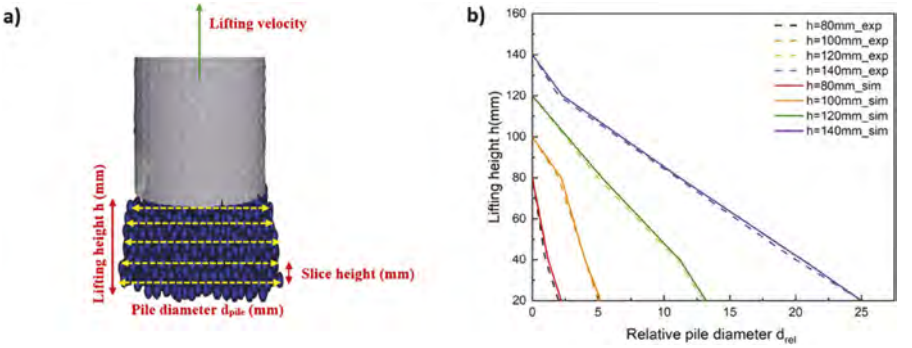

Figure 3. Quantitative comparison of the convex bending between DEM and experimental results from Roessler and Katterfeld (2019) (modified after (Doan et al., 2023)).

2.3 *Numerical calibration and comparison with experimental test for loading condition in Direct Shear Test (DST)*

After the DEM cohesive model was validated against the fundamental angle of repose test, more efforts are needed to test the capability of the cohesive model under external loading. It is critical to study the behaviour of a soil under loading conditions such as the shear strength and deformation of soil in several contexts, namely, the soil bearing capacity and settlement characteristics, the stability of slopes and retaining walls, and soil liquefaction and erosion. This study aims to investigate the underlying mechanics of the cohesive effects on the shear behaviour of soils via the use of the proposed DEM cohesive model and standardised Direct Shear Tests (DST). A validation of the current DEM model is performed by using a series of physical direct shear test to compare with the equivalent numerical results.

A series of direct shear tests were conducted using DEM simulations to capture the effect of microscopic cohesion on the shear strength of cohesive materials. The simulations were carried on a realistic grading of geomaterials with a similar particle size distribution as in the experiment as shown in . The schematic of the direct shear test (DST) is given in Figure 5.

To fill in a numerical shear box as shown in Figure 5, the number of particles was nearly 100,000 particles which by far surpassed the minimum number of 30,000-50,000 particles required for the friction angle and the dilation angle to be captured well in DEM results (Ni et al., 2000). In addition, the ratio between the length of the shear box and the maximum particle size was nearly 50 times, which exceeded the ratio of 10 times empirically defined in ASTM standards to minimize the boundary effects. Besides particle sizes, other microparameters such as the Young's Modulus, Poisson's ratio in DEM simulations were selected based on previous studies (refers to Table 3).

For comparison with experimental results, soils in cohesionless and cohesive states were used to compare with DEM results. For the dry sand without cohesion, the shear strength is primarily controlled by the sliding and rolling friction between two particles. These particle-level parameters are difficult to measure, hence they are often calibrated in numerical procedure. This study varied sliding and rolling friction to match the experimental results with experimental data. As shown in Figure 6, both experimental and numerical results exhibit a strain softening behaviour, where the shear stresses reach a peak value and then gradually decrease. A dimensionless parameter called stress ratio is used to normalise the shear stresses with the applied normal stresses. The maximum stress ratios in DEM simulations for three levels of normal stresses (i.e., 45 kPa, 90 kPa, and 133 kPa) are very close with the experimental values, confirming the accuracy of the strength parameters predicted in DEM simulations. In addition, comparison between dilative behaviour between DEM and experiments indicates a reasonable agreement confirming the predictability of DEM both in terms of strength and deformation of the cohesionless soil.

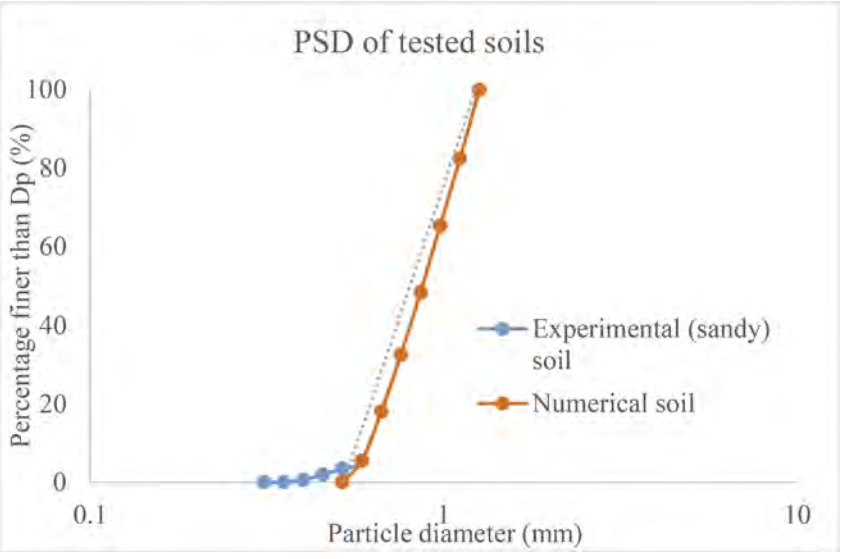

Figure 4. PSD used in DEM and experiments for the direct shear tests.

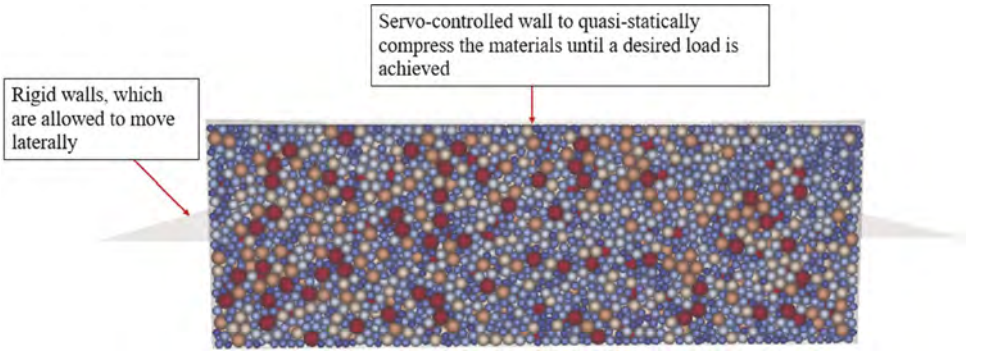

Figure 5. Direct shear test simulated in DEM.

For the cohesive state of materials, the sandy samples were mixed with a certain degree of water (i.e., moisture content 10%) to generate weakly cohesive forces arising

mainly from capillary interactions. Figure 7 demonstrates the stress-strain curves in the experiments with 10 % water content and DEM model introducing cohesive forces from CED value (i.e., CED = 4 x 10^5 J/m^3). Results from DEM simulations show a similar trend as those of the experimental observations. In general, DEM model has successfully captured the main features of the experimental outcomes, such as the peak strength and the softening response under various cohesion levels (i.e., cohesionless and weakly cohesive state).

Table 3. DEM input parameters for the direct shear simulations.

Parameters	Inputs	References
Particle density (kg/m^3)	2650	(Nguyen and Indraratna, 2020b)
Poisson's ratio	0.3	
Shear modulus (Pa)	10x10^7	
Restitution coefficient	0.7	
Particle-wall friction coefficient	0.1	(Cui and O'Sullivan, 2006)
Timestep (s)	10^{-7}	10% Rayleigh time step
Gravitational acceleration (m/s^2)	9.81	

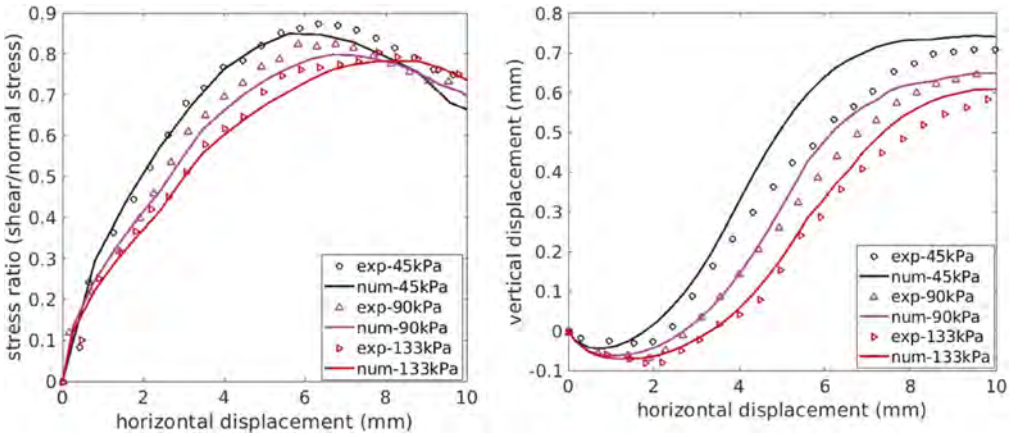

Figure 6. Comparison between DEM and experiments for the referenced cohesionless material.

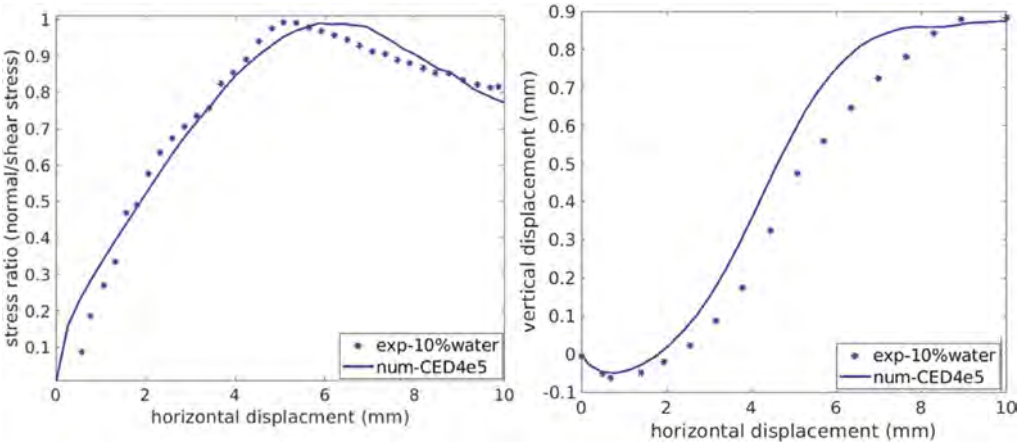

Figure 7. Comparison between the shear behaviours of materials in experiments and DEM under cohesion levels and normal stress of 45 kPa.

3 RESULTS AND DISCUSSION

After completing the calibration process where the DEM results were reasonably validated against fundamental experiment tests such as the Angle of Repose (AoR), and the Direct Shear Test (DST), this section will discuss some of the insights obtained from DEM analysis to demonstrate the effect of micro-scale cohesion on the macro- and micro-responses of soils.

3.1 *The cohesive effect on the macro-response in AoR test*

Figure 8 shows a three-dimensional plot indicating an interactive role between micro-scale friction and cohesion on the angle of repose. It shows that with increasing cohesion levels (from 0 to $5x10^5$ J/m^3), AoR values increase proportionally regardless of the rolling friction value. More importantly, without the effect of cohesion, the AoR is only able to increase up to 31°, however, with the presence of CED values, the AoR values can reach a higher value ranging from 40° to 45°. This finding is supported by experimental observations presented in (Mason et al., 1999, Mitarai and Nori, 2006) implying that the angle of repose of partially saturated materials is generally higher than a cohesionless dry system, nonetheless, these studies did not study how various cohesion levels (i.e., moisture content) affect the forming of this angle. This study also discovers that the numerical AoR values can increase up to 45°, which falls within the range of AoR values for cohesive materials (Beakawi Al-Hashemi and Baghabra Al-Amoudi, 2018). The reason for this rising AoR can be linked to the effect of cohesive forces on the flowing behaviour of soils as with the cohesive presence, the additional tensile forces prevent the separation between particles and consequently, hinder the flowing capacity of the materials.

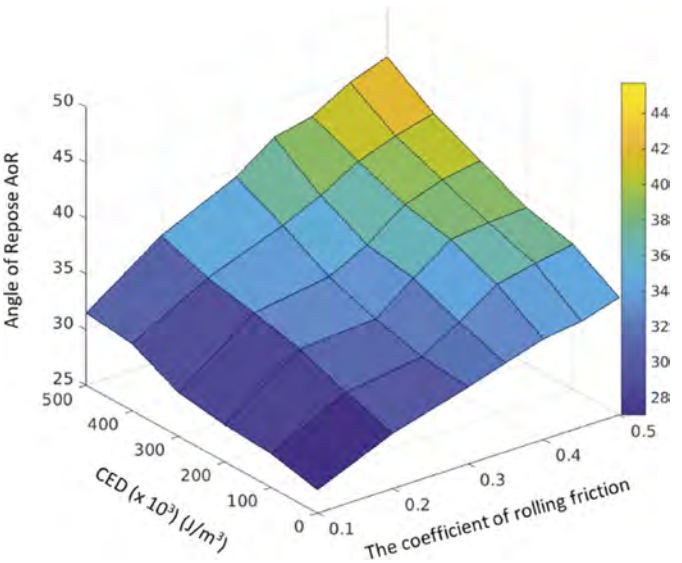

Figure 8. The effect of micro-scale cohesive forces (determined from CED values) on AoR value.

Besides AoR values, the overall porosity is a significant consideration to reflect the microstructure and the compactness of the pile, which is also dependent of micro-scale parameters such as inter-particle cohesion and friction. To compute the porosity value, this study developed a Python program incorporating Monte-Carlo algorithm to approximate the void fraction (i.e., or porosity) within a specific volume of materials. Figure 9 shows the changes of porosity with cohesion and rolling friction levels as when the cohesive and frictional forces increase, the porosity increases as well. For instance, with a given value of rolling friction (for example, 0.1), the porosity value increases from 0.586 to 0.6 when cohesion value CED

increases from 0 to $5x10^5$ (J/m^3). This tendency is due to a fact that when cohesive forces are present, the micro-structure of materials is seen gradually separated with large voids and chain-connected connections (Rognon et al., 2007, Xu et al., 2007). The increased porosity with cohesion content has been observed experimentally by (Gratchev et al., 2006, Goudarzy et al., 2021), indicating that when cohesive fines are present, the structures become separated with open micro-fabrics.

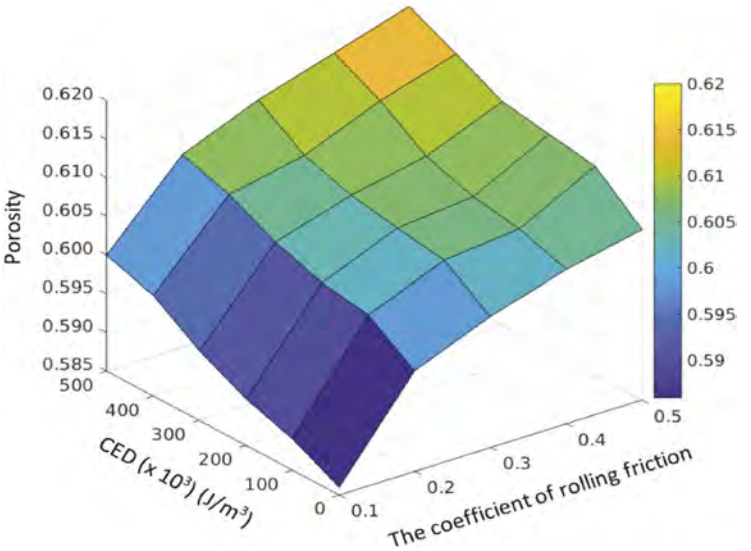

Figure 9. The cohesive effect on the porous structure of the AoR pile.

3.2 *Effect of cohesive contact on the micro-mechanical response of AoR via the analysis of coordination number*

The coordination number CN (i.e., refers to the number of neighbours per particle) is determined with respect to the total number of contacts (n_c) and number of particles (n_p) as follows:

$$CN = \frac{2n_c}{n_p} \tag{9}$$

Figure 10 demonstrates that the coordination number, which is with the spatial arrangement of the particles, was negatively dependent on the values of cohesion and rolling friction coefficients. In the case of cohesive materials as CN values decrease with increasingly cohesive particles (i.e., CED increased from 0 to 5 x 10^5). The similar tendency is also observed in the case of cohesionless material (CED = 0), the CN value experiences a reduction from 8 to 7.3 when the particles become more rotationally resistant. When the values of cohesion and rolling friction are both high, the CN value continuously reduces to reach a small value between 6 and 7. This means when cohesive forces or frictional forces dominate, the system becomes less densified with fewer contacts per particles.

To gain insights into how the cohesive and rolling resistant forces impact the coordination number, the balance of all external and internal forces acting on particles is analysed. According to Yu et al. (2003), cohesionless granules commonly have an average of six contacts per particle to counterbalance the gravitational forces. However, when both cohesion and rolling friction increase, the coupled effect of cohesive and frictional forces is sufficient to resist the driving force of gravity, allowing stability to be achieved with fewer particle-to-particle contacts, as few as two per particle, as demonstrated by Xu et al. (2007).

3.3 *Particle-scale insights into the movement of individual particles in the AoR test*

This study also attempts to track the kinetic energy and the total displacement of particles which have not been provided in previous studies and explores how cohesive forces affect the materials at the particle-scale level. Figure 11a compares the kinetic energy between the cohesionless and cohesive systems and reveals that the with cohesive forces, the KE of the system reaches a smaller peak. In addition, the cohesionless samples peak and stabilise at an earlier stage than the cohesive

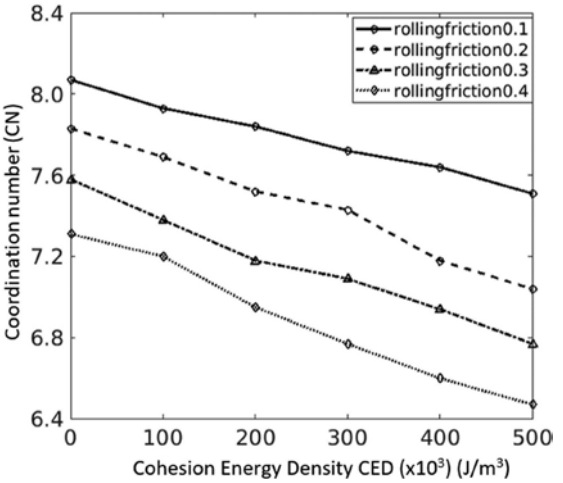

Figure 10. The cohesive influence on the internal fabric of AoR test.

samples, indicating that more time is required for the cohesion-induced materials to dissipate the kinetic energy. This is because as the level of cohesion increases, the interparticle forces become stronger and the particles tend to move together as agglomerates instead of as individual units. As a result, cohesive particles exhibit a more gradual and less brittle response, with a delay in the initiation and dissipation of kinetic energy compared to non-cohesive particles. This is shown in the Figure 11a that the non-cohesive materials take about 17s to reach a stable state, while the cohesive materials need more than 19s to stabilise. Moreover, Figure 11b captures the total displacement of particles with and without cohesion in the forming of the angle of repose AoR. The

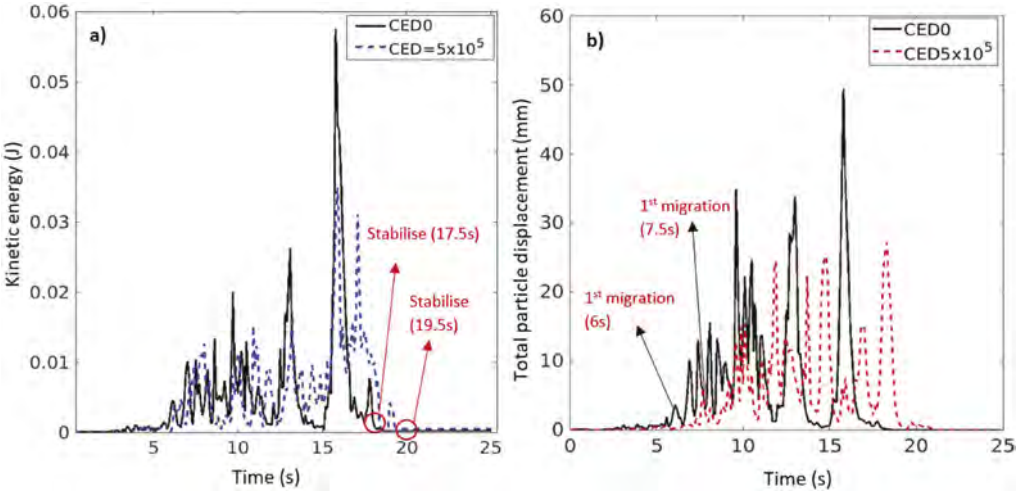

Figure 11. Particle-scale analysis in the AoR test in terms of a) kinetic energy KE and b) particle displacements.

cohesionless particles (i.e., black solid line) experience a much higher displacement (i.e, around 49 mm) than the displacement that the cohesive materials can make (i.e., 35 m). In addition, similar with the evolution of kinetic energy, cohesive samples experience a delay in the migration and stabilisation, compared to the cohesionless samples. Hence, this signifies a less brittle response when cohesion is included.

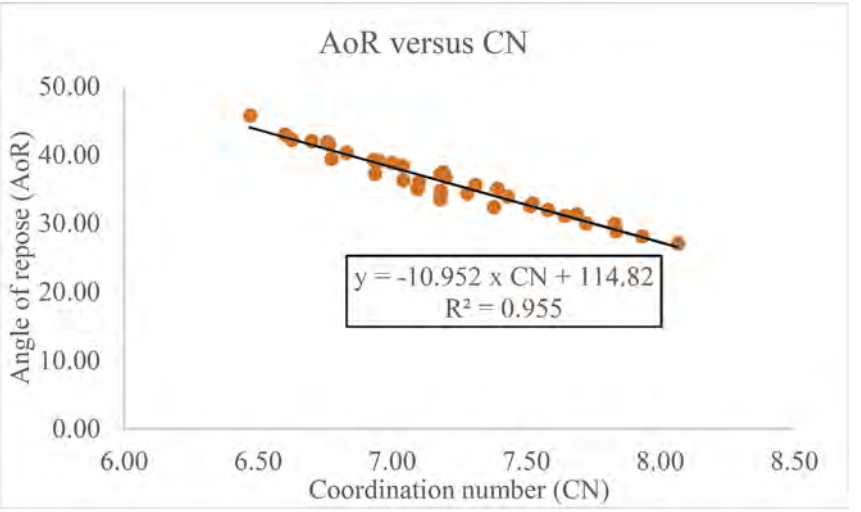

Figure 12. Quantitative relationships between AoR and CN for varying cohesion and rolling friction levels.

3.4 *Linkage between macro-parameters and micro-parameters*

The current study has revealed that both the angle of repose (AoR) and the micro-scale coordination number (CN) are directly affected by the particle-scale parameters such as the cohesion and friction effects. With the data available, this study attempts to propose a linkage between the macro-parameter AoR and the micro-parameter CN for materials for all cohesion and rolling friction levels. The correlations between the AoR and CN values are depicted very well by the fitted regression lines, with an error rate below 5% as shown in Figure 12. Moreover, the proposed equation demonstrates an inverse relationship between AoR and CN, which means a higher CN leads to a lower AoR, indicating increased stability of the slopes. In fact, a higher CN implies that the particles are more densely packed and have more contacts with their neighbours, resulting in a more stable structure. This stability is then reflected in a lower angle of repose. This explanation is also applied in the case of increasing cohesive and frictional forces, the system becomes looser (i.e., smaller CN) and the angle of repose can reach a higher slope without sliding (i.e., higher AoR).

3.5 *The cohesive effect on the strength-deformation behaviour in DST shear test*

Figure 13 shows the evolution of shear stress as observed in DEM simulations during shear tests on cohesionless (CED = 0) and cohesive state of soils with varying levels of cohesion. Compared to the non-cohesive dry sand samples, cohesive effects contribute to an enhanced shear strength, which becomes more pronounced with increasing cohesion levels. For example, when the cohesion energy density CED is low (i.e., CED < 5 x 10^5), the stress-strain curve in the simulations experiences a slight upward shift, reflecting the higher peak shear stresses and residual stresses, which is quite similar with the behaviour of wet samples with 10 % water content from experiments. However, this shift is minimal as the capillary forces, also known as the weak apparent cohesion, have a limited effect on soil strength under external loading.

Figure 13 also shows the dilation characteristics influenced by the cohesive effects in soils in the direct shear test. The results indicate that when cohesive forces increase, the samples displace more substantially in the vertical direction. The reason for this effect is that the addition of cohesion causes particles to behave as agglomerates or clumps, resulting in a larger dilation angle and

a higher friction angle. In order words, with the addition of cohesion, agglomerated particles are mobilised by a larger force and hence, the soil exhibits a greater resistance to shearing.

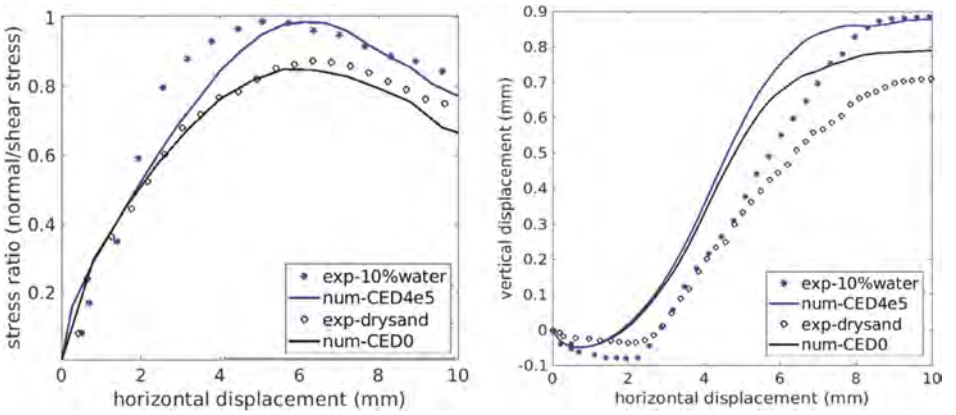

Figure 13. The development of shear stress and vertical movement under varying cohesion levels in DEM a) shear stress versus horizontal displacement at a normal stress 45 kPa, b) vertical displacement versus horizontal displacement.

4 CURRENT CHALLENGES AND FUTURE STUDIES

Although significant efforts have gone to modelling particle contacts in the past years, yet the current state of DEM contact models, especially considering cohesive behaviour still remains considerable challenges that prevent predictions from higher accuracy. Some of them can be pointed out, thus suggestions for future studies as follows:

1. As the generic formulation of the JKR contact radius is mathematically challenging, the simplified JKR (SJKR) model takes on a circular form as proposed in Hertzian theory. More computational efforts are needed to solve the equation of the real contact radius in cohesive contact model, so that more accurate load-deformation behaviour of various materials can be simulated.
2. The cohesion forces provided by JKR model will diminish when the normal deformation δ_n reaches negative values, therefore, this model is applicable to model the short-range attraction forces between particles, whereas the separation distance is minimal, rather than the long-range attraction forces.
3. The current JKR model was developed to extend the Hertz theory to capture the elaso-cohesive contacts, while solutions for modelling visco-elastic and plastic effects are still incomplete. As visco- and elasto-plastic behaviours often exhibit in soils, significant efforts are required to develop more detailed and realistic contact models for DEM simulations.

5 CONCLUSIONS AND PRACTICAL IMPLICATIONS

Advanced numerical DEM studies were conducted to investigate the mechanism and the influences of micro-scale cohesive contacts on the macro-behaviour of soils. Varying degrees of cohesion between particles were incorporated to study the cohesive behaviour of soils under different conditions such as the free-flow and shear. Critical findings of this study can be collated as follows:

1) The cohesive behaviour of soils, despite its significant influence on the stability of soils, remained considerable ambiguity in terms of its microscale mechanism and effects. The current extensive investigation using DEM study to examine the cohesive effect of material found out that when the cohesive effect was ignored, it can lead to the underestimation of the angle of repose. In fact, the AoR value was reported as a function of the micro-scale cohesion since the higher the cohesive forces, the higher AoR values.

2) The results also revealed that increasing cohesion levels led to a higher apparent porosity regardless of the level of friction. Such a response of increasing porosity can be attributed to the tendency to form chain-connected structures, as well as large agglomerates among cohesive particles.
3) The empirical relationships ($R^2 > 0.98$) between the macro-scale AoR and micro-scale coordination number CN were established for the first time considering different levels of cohesion. The equations demonstrated the inverse relationship between AoR and CN, meaning that a higher CN signified a smaller AoR value. As when CN increased, the gravity-induced densification process was enhanced significantly and particles were more vulnerable to moving, leading to a smaller AoR value.
4) This study also demonstrated that not only the interparticle cohesive effects were dominant in the free-flowing condition, but also they can significantly alter shear behaviour of soil under loading. When cohesion was present, the shear strength of the cohesive samples was significantly higher than that in cohesionless state, and this feature was expected to become more pronounced with increasing cohesion levels.
5) Moreover, with the presence of cohesive forces, the samples experienced a greater degree of expansion in the vertical direction (i.e., dilation) than the cohesionless samples. This is because the addition of interparticle cohesion linked particles into agglomerates through increased particle connections and bridging, which were mobilised by a larger dilation angle and friction angle.
6) The practical implication of this study is to promote a better understanding of the micro-cohesive effect on soil behaviour and to use this understanding in geotechnical designs and analysis. For instance, the strengthening effect of the interparticle cohesion on the shear strength of materials can provide significant values to ground improvement in practical applications if they are appropriately combined with frictional components.

ACKNOWLEDGEMENT

This research was supported by Transport Research Centre (TRC, UTS), and the Australian Government through the Australian Research Council's Linkage Projects funding scheme (project **LP160101254**). Technical and financial support from industry partners including SMEC, Sydney Trains, ACRI and Coffey are greatly appreciated. Moreover, the contents of this paper include some critical outcomes that have been published previously. They have been cited where warranted, and the copyright clearance from the original sources has been granted to the authors to reproduce with kind permission.

REFERENCES

Ai, J., Chen, J.-F., Rotter, J. & Ooi, J. 2011. Assessment of rolling resistance models in discrete element simulations. *Powder Technology*, 206, 269–282.

Barthel, E. 2008. Adhesive elastic contacts: JKR and more. *Journal of Physics D: Applied Physics*, 41, 163001.

Beakawi Al-Hashemi, H. M. & Baghabra Al-Amoudi, O. S. 2018. A review on the angle of repose of granular materials. *Powder Technology*, 330, 397–417, https://www.sciencedirect.com/science/article/pii/S0032591018301153

Behjani, M. A., Rahmanian, N., Fardina Bt Abdul Ghani, N. & Hassanpour, A. 2017. An investigation on process of seeded granulation in a continuous drum granulator using DEM. *Advanced Powder Technology*, 28, 2456–2464, https://www.sciencedirect.com/science/article/pii/S0921883117300730

Cui, L. & O'sullivan, C. 2006. Exploring the macro- and micro-scale response of an idealised granular material in the direct shear apparatus. *Géotechnique*, 56, 455–468, https://doi.org/10.1680/geot.2006.56.7.455

Deng, X. L. & Davé, R. N. 2013. Dynamic simulation of particle packing influenced by size, aspect ratio and surface energy. *Granular Matter*, 15, 401–415, https://doi.org/10.1007/s10035-013-0413-0

Derakhshani, S. M., Schott, D. L. & Lodewijks, G. 2015. Micro–macro properties of quartz sand: Experimental investigation and DEM simulation. *Powder Technology*, 269, 127–138, https://www.sciencedirect.com/science/article/pii/S0032591014007888

Doan, T., Indraratna, B., Nguyen, T. T. & Rujikiatkamjorn, C. 2023. Interactive Role of Rolling Friction and Cohesion on the Angle of Repose through a Microscale Assessment. *International Journal of Geomechanics*, 23, 04022250, https://doi.org/10.1061/(ASCE)GM.1943-5622.0002632

Endres, S. C., Ciacchi, L. C. & Mädler, L. 2021. A review of contact force models between nanoparticles in agglomerates, aggregates, and films. *Journal of Aerosol Science*, 153, 105719, https://www.sciencedirect.com/science/article/pii/S0021850220302044

Goudarzy, M., Sarkar, D., Lieske, W. & Wichtmann, T. 2021. Influence of plastic fines content on the liquefaction susceptibility of sands: monotonic loading. *Acta Geotechnica*, https://doi.org/10.1007/s11440-021-01283-w

Gratchev, I. B., Sassa, K., Osipov, V. I. & Sokolov, V. N. 2006. The liquefaction of clayey soils under cyclic loading. *Engineering Geology*, 86, 70–84, https://www.sciencedirect.com/science/article/pii/S0013795206001499

Hassanzadeh, V., Wensrich, C. M. & Moreno-Atanasio, R. 2020. Elucidation of the role of cohesion in the macroscopic behaviour of coarse particulate systems using DEM. *Powder Technology*, 361, 374–388, https://www.sciencedirect.com/science/article/pii/S0032591019305625

Jones, R. 2003. From Single Particle AFM Studies of Adhesion and Friction to Bulk Flow: Forging the Links. *Granular Matter*, 4, 191–204, https://doi.org/10.1007/s10035-002-0122-6

Li, Y., Xu, Y. & Thornton, C. 2005. A comparison of discrete element simulations and experiments for 'sandpiles' composed of spherical particles. *Powder Technology*, 160, 219–228, https://www.sciencedirect.com/science/article/pii/S0032591005004079

Lommen, S., Schott, D. & Lodewijks, G. 2014. DEM speedup: Stiffness effects on behavior of bulk material. *Particuology*, 12, 107–112, https://www.sciencedirect.com/science/article/pii/S1674200113001387

Mason, T., Levine, A., Ertaş, D. & Halsey, T. T. C. 1999. Critical angle of wet sandpiles. *Physical review. E, Statistical physics, plasmas, fluids, and related interdisciplinary topics*, 60, R5044–7.

Mitarai, N. & Nori, F. 2006. Wet granular materials. *Advances in Physics*, 55, 1–45, https://doi.org/10.1080/00018730600626065

Mitchell, J. K. & Soga, K. 2005. *Fundamentals of soil behavior*, John Wiley & Sons New York.

Nguyen, T. T. & Indraratna, B. 2020a. A Coupled CFD–DEM Approach to Examine the Hydraulic Critical State of Soil under Increasing Hydraulic Gradient. *International Journal of Geomechanics*, 20, 04020138, https://doi.org/10.1061/(ASCE)GM.1943-5622.0001782

Nguyen, T. T. & Indraratna, B. 2020b. The energy transformation of internal erosion based on fluid-particle coupling. *Computers and Geotechnics*, 121, 103475, https://www.sciencedirect.com/science/article/pii/S0266352X20300380

Ni, Q., Powrie, W., Zhang, X. & Harkness, R. 2000. Effect of Particle Properties on Soil Behavior: 3-D Numerical Modeling of Shearbox Tests. *Numerical Methods in Geotechnical Engineering*.

O'sullivan, C. 2011. *Particulate discrete element modelling a geomechanics perspective*, London, Taylor & Francis.

Parteli, E. J. R., Schmidt, J., Blümel, C., Wirth, K.-E., Peukert, W. & Pöschel, T. 2014. Attractive particle interaction forces and packing density of fine glass powders. *Scientific Reports*, 4, 6227. https://doi.org/10.1038/srep06227

Phan, Q. T., Bui, H. H., Nguyen, G. D. & Bouazza, A. 2021. Effect of particle rolling resistance on drained and undrained behaviour of silty sand. *Acta Geotechnica*, 16, 2657–2682, https://doi.org/10.1007/s11440-020-01128-y

Roessler, T. & Katterfeld, A. 2019. DEM parameter calibration of cohesive bulk materials using a simple angle of repose test. *Particuology*, 45, 105–115, https://www.sciencedirect.com/science/article/pii/S1674200119300033

Rognon, P., Roux, J.-N., Wolf, D., Naaim, M. & Chevoir, F. 2007. Rheophysics of cohesive granular materials. *EPL (Europhysics Letters)*, 74, 644.

Terzaghi, K. 1943. *Theoretical Soil Mechanics*, Wiley, New York.

Wang, J.-P., Li, X. & Yu, H.-S. 2018. A micro–macro investigation of the capillary strengthening effect in wet granular materials. *Acta Geotechnica*, 13, 513–533, https://doi.org/10.1007/s11440-017-0619-0

Xu, J. Q., Zou, R. P. & Yu, A. B. 2007. Analysis of the packing structure of wet spheres by Voronoi–Delaunay tessellation. *Granular Matter*, 9, 455–463, https://doi.org/10.1007/s10035-007-0052-4

Yu, A., Liu, L., Zhang, Z., Yang, R. & Zou, R. 2003. Computer simulation of the packing of particles. *International Journal of Materials & Product Technology - INT J MATER PROD TECHNOL*, 19

Zhu, H. P., Zhou, Z. Y., Yang, R. Y. & Yu, A. B. 2007. Discrete particle simulation of particulate systems: Theoretical developments. *Chemical Engineering Science*, 62, 3378–3396, https://www.sciencedirect.com/science/article/pii/S000925090700262X

Smart Geotechnics for Smart Societies – Zhussupbekov, Sarsembayeva & Kaliakin (Eds)
© 2023 The Author(s), ISBN 978-1-003-29912-7
Open Access: www.taylorfrancis.com, CC BY-NC-ND 4.0 license

Temperature effect to soil ground and structures in transportation engineering

Zh. Shakhmov
Department of Civil Engineering, L.N. Gumilyov Eurasian National University, Astana, Kazakhstan

S. Kuvakov
Jalal-Abad state university named after B.Osmonov, Jalal-Abad, Kyrgyzstan

T. Awwad
Department of Soils and Foundations, Emperor Alexander I St. Petersburg State Transport University, St. Petersburg, Russia
Geotechnical Engineering Department, Civil Engineering faculty, Damascus University, Damascus, Syria

G. Tleulenova
Department of Civil Engineering, L.N. Gumilyov Eurasian National University, Astana, Kazakhstan

D. Dyussembinov & A. Zhumagulova
Department of Technology of Industrial and Civil Engineering, L.N. Gumilyov Eurasian National University, Astana, Kazakhstan

ABSTRACT: The temperature effects on foundations and structures. The results of calculations of ground bases and structures on temperature influences and loads are given. Conclusions on the obtained results with suggested recommendations are also made in work.

Keywords: temperature, numerical analysis, mosaics, loads

1 INTRODUCTION

Kazakhstan is located in a climatic region with seasonally frozen ground. During the calendar year the temperature varies seasonally from negative to positive values. Temperatures can reach -45 °C in winter and +45 °C in summer. Soil types vary across Kazakhstan due to its large size and varied landscape (Shakhmov et al. 2015; Zhussupbekov at al. 2013; Zhussupbekov at al, 2012; Shakhmov et al. 2016). Many buildings and constructions have been built in Kazakhstan due to urban growth, such as Astana, Almaty and Shymkent. There are also many infrastructure projects such as roads, railways and bridges. Kazakhstan is located at the crossroads between east and west, and historical economic and cultural ties run through this area. Kazakhstan is also a participant in international infrastructure projects such as the Silk Road, One Belt, One Road, and others. The China-Western Europe Westward Project, also known as the New Silk Road by land, is a Chinese initiative to create a network of transport and logistics links between China and Western Europe. One element of this project is the construction of a road that will connect the western and eastern parts of Kazakhstan. The road will be made of cement concrete, which is one of the strongest materials for road construction. It has a high compressive and bending strength which allows it to withstand heavy loads and retain its properties for a long time (Usenov et al. 2022; Kuvakov et al. 2016). But the operation of these rigid roads has resulted in problems with the occurrence of deformation and defects. Defects and deformations such as longitudinal and transverse cracks, through and surface cracks, spalling and warping(blow-up) of boards are common on the road.

DOI: 10.1201/9781003299127-21

2 RESEARCH METHOD

2.1 *Numerical analysis of various temperature stress-strain state of highways in the "Lira" program*

The LIRA-CAD 2017 software package (LIRA-CAD 2017 PC) is a multifunctional software package for calculating, researching and designing structures for various purposes.

PC LIRA-CAD 2017 is successfully used in the calculations of construction, mechanical engineering, bridge construction, nuclear power, oil industry and in many other areas where methods of construction mechanics are relevant.

The software complexes of the LIRA family have a more than 40-year history of creation, development and application in scientific research and practice of design of structures. The software systems of the LIRA family are continuously being improved and adapted to new operating systems and graphical environments. The newest representative of the LIRA family is the LIRA-CAD 2017 PC.

In addition to the general calculation of the object model for all possible types of static loads, temperature, deformation and dynamic effects (wind taking into account pulsation, seismic effects, etc.), the LIRA-CAD 2017 PC automates a number of design processes: determination of calculated combinations of loads and forces, assignment of structural elements, selection and verification of sections of steel and reinforced concrete structures with the formation of sketches of working drawings of columns and beams.

PC LIRA-CAD 2017 allows you to study the overall stability of the calculated model, check the strength of the cross-sections of elements according to various theories of destruction. The LIRA-CAD 2017 PC provides an opportunity to perform calculations of objects taking into account physical and geometric nonlinearities, to simulate the process of erecting a structure taking into account the installation and dismantling of elements.

PC LIRA-CAD 2017 supports information communication with such systems as AutoCAD,ArchiCAD, Allplan, Hypersteel, as well as PC MONOMACH-CAD, FOC-PC.the template file B1ProcA4.dot to the template directory. This directory can be found by selecting the Tools menu, Options and then by tabbing the File Locations. When the Word programme has been started, open the File menu and choose New. Now select the template B1PROCA4. dot and start by renaming the document after clicking Save As in the Files menu.

2.2 *Initial data*

The road was originally taken from the southern regions of Kazakhstan. This region has the highest temperatures in summer. This causes the concrete slabs to warp. In particular, dozens of cases of road warping are recorded every year in these regions. The road consists of 4 lanes of which 2 in the forward direction and 2 in the reverse direction. The slabs are 5 metres long and 25 cm thick.

3 RESULTS

The results for temperature phenomena at 50 degrees Celsius are shown below.

4 CONCLUSION

According to the results obtained on the temperature loads of the central bank of the plates, isofields and VAT plots were identified with the following values: the expansion of concrete by 50 m was 30 mm, while the deformation of the plates during warping was 92 mm. The maximum mosaics voltage according to Mx 1.93e-009 t* m/ m, according to Mu 105 t * m/ m. When pinched on both sides, the maximum mosaics are stressed by Mx 184 t * m/m,

Figure 1. Isofield of movements along the X axis (mm).

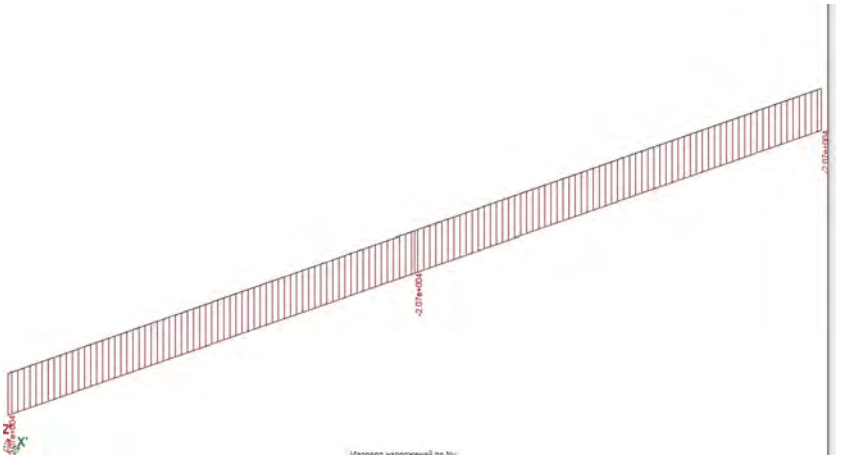

Figure 2. Mx plot.

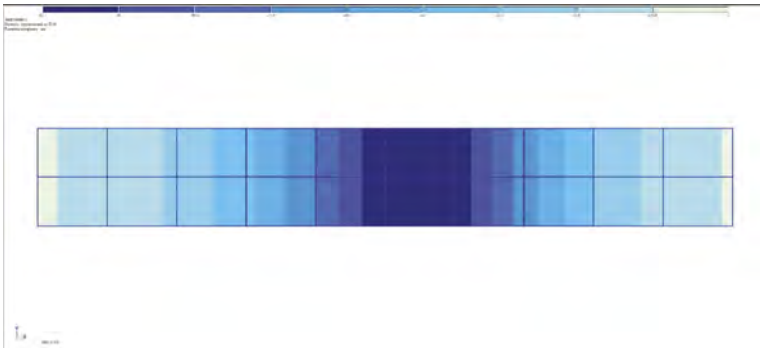

Figure 3. Isofield of movements along the X-axis (mm) with double pinching.

by Mu 231 t * m/m. The mosaic voltage according to Nx is 2.07e-004, and 4.57e-004 (t/m2) with double pinching (Figures 1–10).

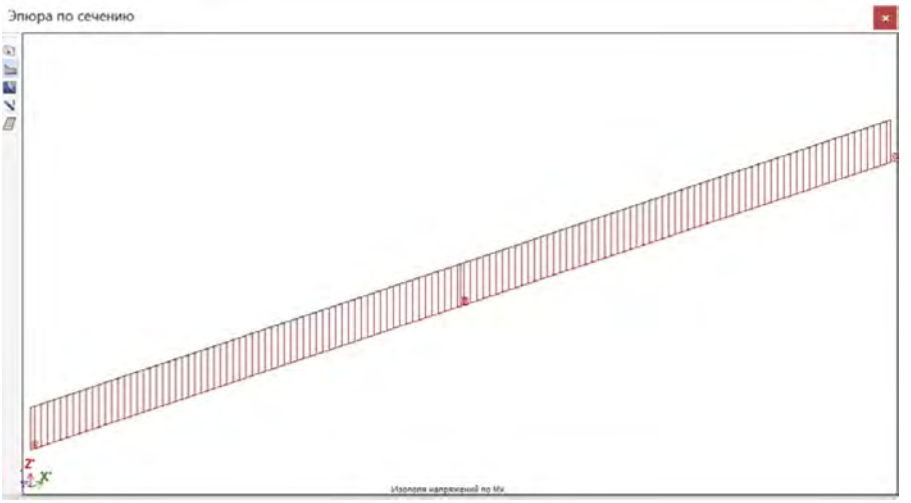

Figure 4. Mx plot.

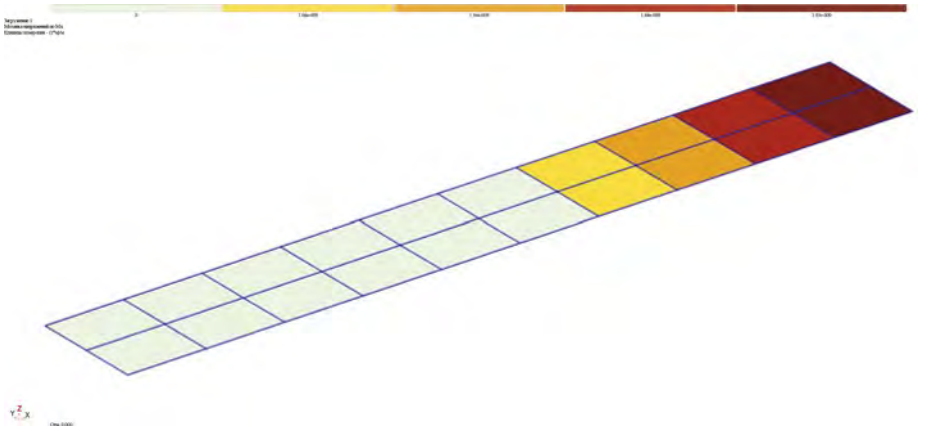

Figure 5. Mosaic voltage by Mx (t*m/m).

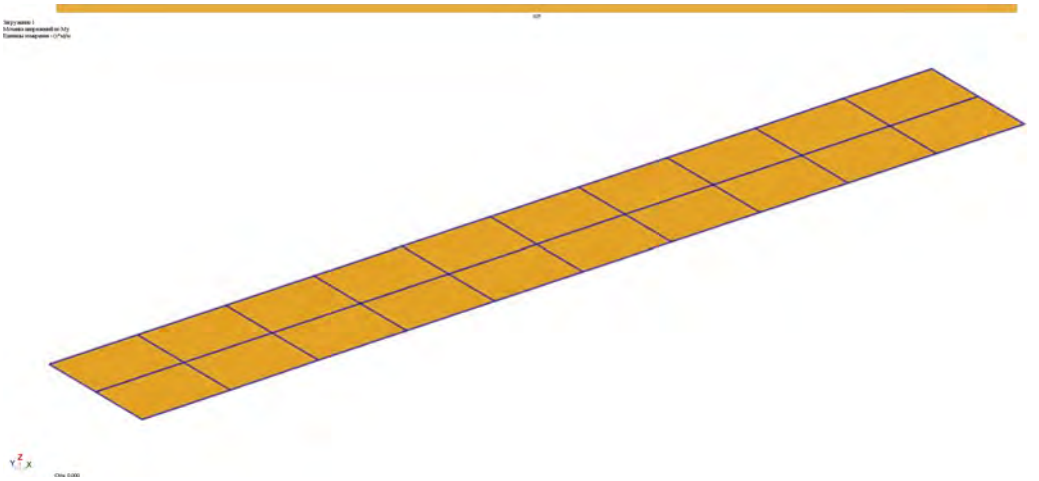

Figure 6. Mosaic of Mu stresses (t*m/m).

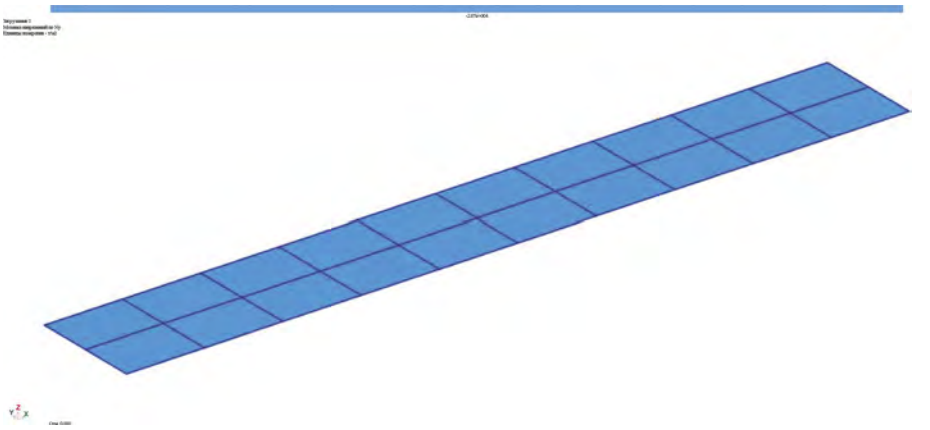

Figure 7. Mosaic of stresses by N (t/m^2).

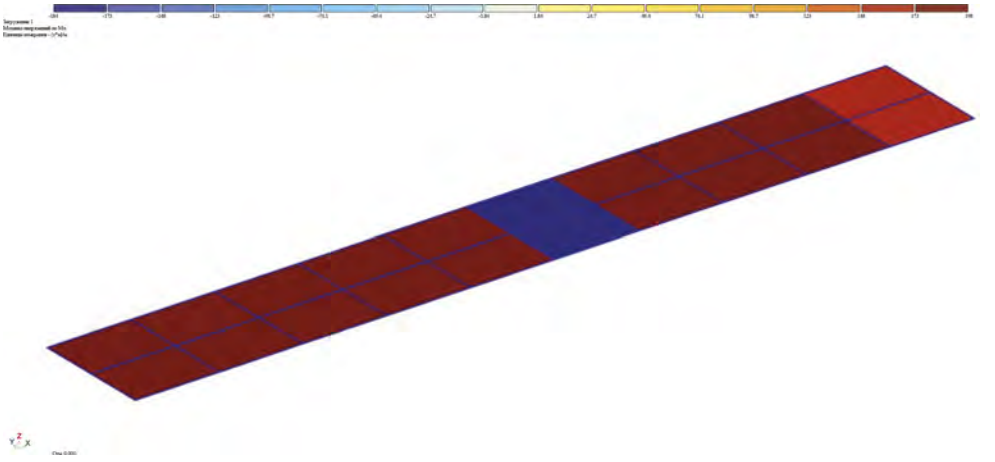

Figure 8. Mosaic voltage according to Mx (t*m/m) 184 pinching on both sides.

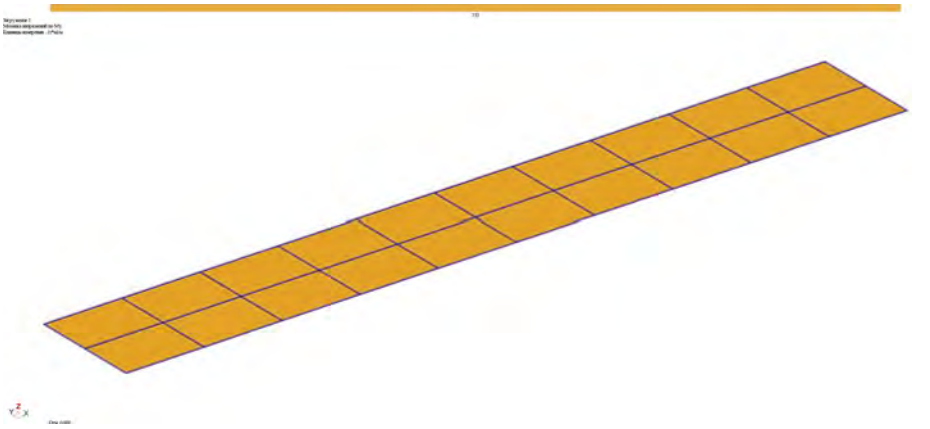

Figure 9. Mosaic of Mu stresses (t*m/m) with pinching on both sides.

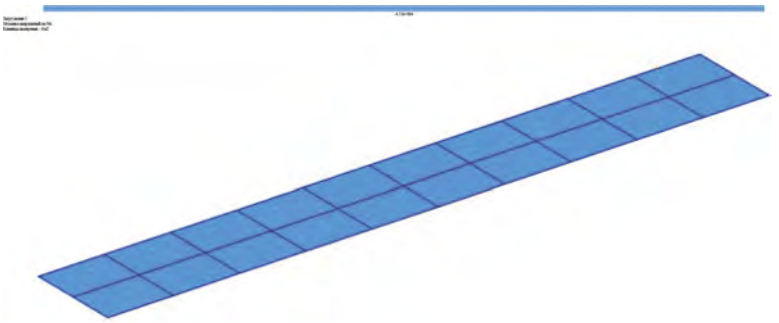

Figure 10. Mosaic of stresses by N (t/m^2).

REFERENCES

Shakhmov, Zh. A., Zhussupbekov, Zh. A. 2015. Frost susceptibility of soil and in-situ monitoring of frost depth in construction. *The 15th Asian Regional Conference on Soil Mechanics and Geotechnical Engineering Proceedings*, 4.

Usenov, K.Zh., Kuvakov, S.Zh., Alibaev, A.P., Kuvakov, Zh.M., Takeeva, A.R. 2022. The change in physical and mechanical properties of rocks in the course of mining in Makmal Mine. *IOP Conference Series: Earth and Environmental Science*. Volume 991. Novosibirsk. Russia.

Zhussupbekov, A.Zh., Utepov, E.B., Ling, H.I., Shakhmov. Z.A. 2013. Model testing of piles in a centrifuge for prediction of their in-situ performance. *Soil Mechanics and Foundation Engineering scientific-technical journal Volume 50*. Moscow. Russia. 92–96.

Kuvakov, S., Kozhogulov, K.C., Kabaeva, G.D. 2016. Mathematical modeling of massif state around the mountain road slopes and highland pit. *The Eighth Asian Young Geotechnical Engineers Conference Proc*., 237–239.

Zhussupbekov, A., Shakhmov, Z., Shin, E.C., Krasnikov, S. 2012. *Challenges for transportation geotechnics in extreme climates of Kazakhstan and Korea*. Hokkaido: CRC Press Taylor&Francis Group.

Utepov, Ye., Aniskin, A., Mkilima, T., Kozina, G., Shakhmov, Zh. 2021. Potential Impact of Land-Use Changes on River Basin Hydraulic Parameters Subjected to Rapid Urbanization. *The Journal Tehnički vjesnik*, 28(5). 1519–1525.

Shakhmov, Zh., Tleubayeva, A., Utepbergenova, L., Togabayev, Y., Bazarbayev, D. 2016. Analyzing of soil ground to frost heaving of structures. *The Eighth Asian Young Geotechnical Engineers Conference Proc*., 47–50.

Taylor & Francis
Taylor & Francis Group
http://taylorandfrancis.com

Thematic lectures

Taylor & Francis
Taylor & Francis Group
http://taylorandfrancis.com

Smart Geotechnics for Smart Societies – Zhussupbekov, Sarsembayeva & Kaliakin (Eds)
© 2023 The Author(s), ISBN 978-1-003-29912-7
Open Access: www.taylorfrancis.com, CC BY-NC-ND 4.0 license

Behavior and modeling of silt-clay transition soils

V.N. Kaliakin
Department of Civil and Environmental Engineering, University of Delaware, USA

P. Anantanasakul
Department of Civil and Environmental Engineering, Mahidol University, Nakhon Pathom, Thailand

ABSTRACT: Natural soil deposits are often composed of particles of different sizes and base minerals. Such variations generally preclude characterization of natural soils into a single soil type such as a gravel, sand, silt or clay. The mechanical behavior of such soils can vary quite considerably spatially within a soil deposit. The soil formation process involves variable particle size distribution from one location to another. This gives rise to the creation of an array of soils that transition from one general soil type to another within essentially similar deposits. Such materials are thus commonly referred to as transition soils and are very abundant in the world. The effect of non-plastic silt content on the behavior of silt-clay soils is not fully understood. This is due to a lack of laboratory tests that isolate silt content from clay mineral type, pre-consolidation histories, loading direction, and loading rate. This paper gives an overview of the experimentally measured behavior of silt-clay transition soils and their characterization using the Generalized Bounding Surface constitutive model.

1 INTRODUCTION

In many parts of the world, natural soil deposits often consist of particles having different sizes and base minerals. Such variations often preclude characterization of natural soils into a single soil type such as a gravel, sand, silt or clay. Instead, such deposits must be characterized as some combination of these four basic soil types. Although natural soils having similar origins typically have similar base materials, the nature of their formation process often results in particle size distributions that vary spatially from one site to another. This results in an array of soils that, within essentially similar deposits, transition from one general soil type to another. Very often, the mechanical behavior of such "transition" soils can vary rather significantly.

Present in several metropolitan areas of the world (e.g., London, greater Bangkok, Shanghai, the islands of Hong Kong, the San Francisco Bay area) are large deposits of silt-clay transition soils. Since a rather significant amount of geotechnical activities are ongoing in these areas, it is imperative for geotechnical engineers to understand the behavior of such soils in which the gradation gradually changes, thus producing essentially different soil types. An improved understanding of the stress-strain, volume change and strength characteristics of silt-clay transition soils will thus allow for more accurate analysis and more robust design of geostructures constructed on such soil deposits.

2 PREVIOUS EXPERIMENTAL STUDIES

Pertinent to better understanding the behavior of silt-clay transition soils are the results of experimental studies performed on low-plasticity silts (Penman 1953; Parry & Nadarajah 1974; Fleming & Duncan 1990; Brandon et al. 2006; Nocilla et al. 2006). One characteristic exhibited by such soils is a sensitivity of undrained stress-strain characteristics to sample disturbance and testing conditions.

DOI: 10.1201/9781003299127-22

A relatively small number of researchers have studied the stress-strain and strength behavior of silt-clay transition soils (Seed et al. 1964; Lupini et al. 1981; Stark et al. 1994; Yin 1999; Cola & Simonini 2002; Yin 2002; Nocilla et al. 2006; Anantanasakul et al. 2012; Wang & Luna 2012; Wong et al. 2017; Anantanasakul & Roth 2018; Anantanasakul et al. 2023). Based on the results of these studies it has generally been concluded that with high silt contents of low clay contents, silt-clay transition soils become less plastic, as quantified by lower values of the plasticity index. The behavior of such soils, which are often characterized as being low-plasticity silts, has been observed to be intermediate between that of clay and fine sand (Penman 1953; Fleming & Duncan 1990; Brandon et al. 2006; Nocilla et al. 2006).

Compared to soils that are primarily clays, silt-clay transition soils are less compressible under both one-dimensional and isotropic consolidation. Such behavior was observed when testing both isotropically (Yin 1999; Cola & Simonini 2002; Anantanasakul & Roth 2018) and anisotropically (Parry & Nadarajah 1974; Anantanasakul et al. 2012) prepared specimens.

Increases in silt content result in stiffer stress-strain response, larger undrained shear strength and effective friction angles (Stark et al. 1994; Yin 2002; Nocilla et al. 2006; Anantanasakul et al. 2012, Anantanasakul & Roth 2018). At higher silt contents, silt-clay transition soils often exhibit dilative volumetric response during shearing under drained conditions (Yin 1999; Brandon et al. 2006). This precludes a straightforward determination of undrained shear strength in a manner similar to clays.

Relatively few studies have investigated the effect of overconsolidation ratio (OCR) on the response of silt-clay transition soils (Henkel 1956; Hvorslev 1960; Ladd & Foott 1974; Fleming & Duncan 1990; Wang & Luna 2012; Anantanasakul & Roth 2018). With increasing OCR, less ductile stress-strain response with more pronounced peak strength has been observed in silt-clay transition soils. In these studies, under drained conditions, the soils exhibited increased dilative volumetric response. The magnitude of such response varied considerably among the different soils tested.

The only study that systematically investigated the effect that variations in silt content have on the mechanical behavior of silt-clay transition soils was that performed by Anantanasakul & Roth's (2018). In this study, the same base clay, specimen preparation procedure, testing methods and conditions were used. Only the amount of silt present in a test specimen was systematically varied. Since the results of this study will be used to illustrate the numerical simulation of silt-clay transition soils, some additional details pertaining to this study are next presented.

3 EXPERIMENTAL STUDY WITH VARYING DEGREES OF OVERCONSOLIDATION

3.1 *Information on soils tested*

In their study, Anantanasakul & Roth (2018) employed two base soils, namely kaolin clay and a non-plastic silt. The silt consisted of ground silica, sieved to obtain a specific particle-size gradation. Three laboratory-prepared soils were studied. In the subsequent development, the pure kaolin clay will be referred to as "Soil 1". The other two soils were created by mixing Soil 1 with different amounts of non-plastic silt. These two silt-clay mixtures will be referred to as Soils 2 and 3.

Table 1 lists the clay (grain diameter < 0.002 mm), silt (0.075 mm > grain diameter > 0.002 mm) and sand (4.75 mm > grain diameter > 0.075 mm) contents of the three soils. The tested silt-clay soils contained small amounts of sand-sized particles (sand contents equal or less than 2%). The effects of such particles on the mechanical response of silt-clay soils were deemed negligible. Table 1 also lists the liquid limits, plastic limits and plasticity indices for the three soils tested. The liquid limits and plasticity indices decrease with increases in the amount of non-plastic silt. According to the Unified Soil Classification System (USCS), Soils 1, 2 and 3 can be classified as MH, ML and ML, respectively.

3.2 *Specimen preparation*

Proper amounts of dry kaolin powder and base silt were mixed with water to produce slurries at water contents twice the liquid limits of the three tested soils. The mixing of slurries was carried out in a commercial-grade stand mixer. The slurries were one-dimensionally consolidated in the double-draining consolidation tank at an effective vertical stress of 150 kPa. Following consolidation, cake samples, 250 mm in diameter and 170 mm high, were obtained from the tank. It is worth mentioning that the consolidation pressure of 150 kPa was employed to produce soil samples which were adequately stiff and could be handled in the subsequent testing procedures without significant disturbance. Cylindrical specimens, 71 mm in diameter and 142 mm tall, were carved from the cake samples and installed into the axisymmetric triaxial apparatus.

Table 1. Properties of soils tested.

Soil Property	Soil 1	Soil 2	Soil 3
Clay content (%)	74	49	30
Silt content (%)	24	50	69
Sand content (%)	2	1	1
Liquid limit (%)	55	42	30
Plastic limit (%)	35	31	24
Plasticity index (%)	20	11	6
Specific gravity	2.64	2.64	2.65

3.3 *One-dimensional compression tests*

A series of one-dimensional consolidation tests was performed on the three soils tested. Table 2 summarizes the initial void ratios (e_0) of the specimens prior to the compression tests, the values of the compression indices (C_c) and, recompression indices (C_r) indices, and the measured preconsolidation pressures (σ'_p) are presented in Table 3.

Table 2. Values obtained from one-dimensional consolidation tests.

Soil Parameter	Soil 1	Soil 2	Soil 3
Initial void ratios (e_0)	0.95	0.77	0.65
Compression index (C_c)	0.290	0.220	0.130
Recompression index (C_r)	0.090	0.040	0.015
C_r/C_c	0.31	0.18	0.12
Preconsolidation pressure (kPa)	160	125	140

3.4 *Consolidated-undrained triaxial tests*

Consolidated-undrained triaxial tests were performed on isotropically consolidated specimens of Soils 1, 2 and 3. These CIUC tests were of deformation control type with an axial strain rate of 0.01% per minute. The triaxial specimens were consolidated at a maximum isotropic effective stress (σ'_0) of 400 kPa. Upon completion of primary consolidation at this stress level, triaxial specimens of Soils 1, 2 and 3 were normally consolidated. In some tests, the specimens were then unloaded to appropriate confining stresses (σ'_c) of 200, 100 and 50 kPa so as to achieve OCRs of 2.0, 4.0 and 8.0 prior to undrained shear.

Based on the results of their experimental study, Anantanasakul & Roth (2018) concluded that the amount of non-plastic silt present rather significantly affected the behavior of silt-clay transition soils. During undrained shearing, such soils exhibited stiffer stress-strain response with increasing silt content. Figure 1 presents graphical evidence that confirms this conclusion for OCR equal to 2.0. Similar trends were observed for the normally consolidated specimens, as well as for ones with OCR equal to 4.0 and 8.0.

The undrained shear strengths and effective friction angles increased with increases in the amount of silt. This was attributed to the increased friction and interlocking among the angular silt particles.

With increasing silt content, in specimens with OCR equal to 1.0, 2.0 and 4.0, the excess pore pressure changes increased, suggesting an increased contractive tendency. However, as evident from Figure 2, this trend reverses for OCR equal to 8.0 in that now the excess pore pressure becomes more negative with increasing silt content, the pore pressure, indicating an increased dilative tendency.

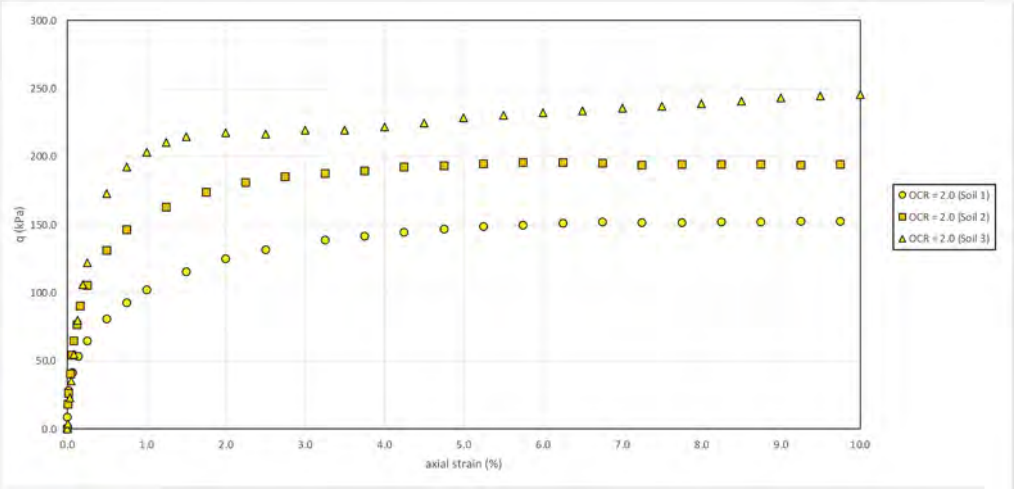

Figure 1. Comparison of experimental principal stress difference-axial strain response for OCR=2.0.

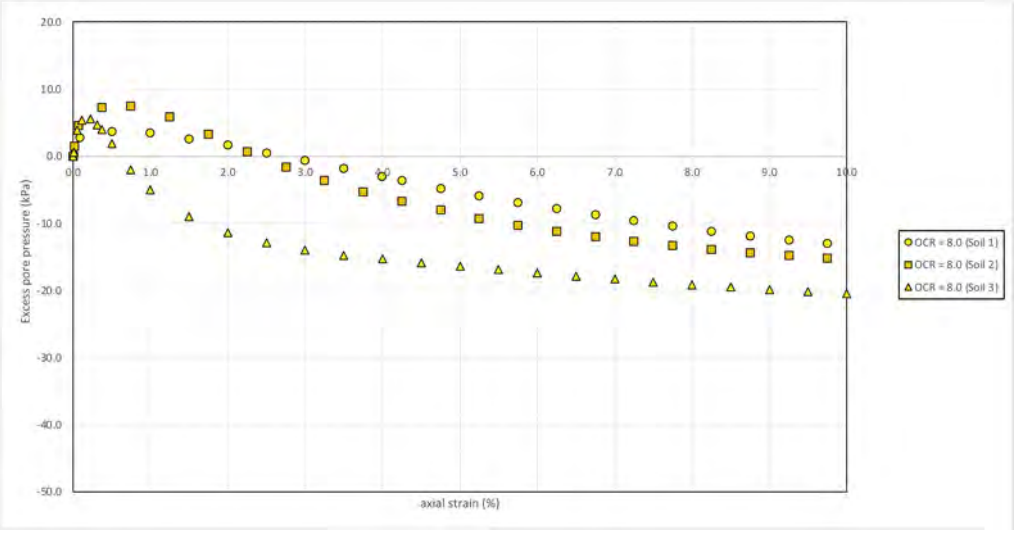

Figure 2. Comparison of experimental excess pore pressure-axial strain response for OCR = 8.0.

The discussion next turns to the the numerical simulation of the silt-clay transition soils tested by Anantanasakul & Roth (2018). Before discussing specifics associated with these simulations, it is timely to briefly review some general aspects related to the mathematical modeling of the response of clays.

4 MATHEMATICAL MODELING OF RESPONSE

Several constitutive models based on classical elastoplasticity theory have been proposed to simulate the behavior clay. A significant milestone in the development of such models was the advent of the critical state theory of soil mechanics (Schofield & Wroth 1968). This theory served as the basis for several isotropically hardening elastoplastic formulations such as the Modified Cam Clay model (Roscoe & Burland 1968) and its variants. Perhaps the biggest drawback of such models is that plastic response is restricted to only those stress states lying on the yield surface; states within the surface are purely elastic. As a consequence, models based on classical elastoplasticity predict excessively "stiff" elastic response for overconsolidated clays; in addition, such models cannot accurately predict hysteretic plastic strains or accumulated excess pore pressures generated by cyclic loading. Finally, the simulations developed using such models are counter to the results of experimental studies indicate that as a saturated cohesive soil is loaded, it continuously develops both elastic and inelastic strains without a distinct yield state that delineates elastic from inelastic response (Roscoe & Burland 1968; Wong & Mitchell 1975).

Beginning in the 1960's one class of "unconventional" constitutive models developed to overcome the aforementioned shortcomings associated with standard elastoplastic models employed kinematic hardening in addition to purely isotropic hardening. In such models, the overall hardening is said to be anisotropic. Extended elastoplastic formulations utilyzing kinematic hardening of a family of "nested" surfaces were developed (Iwan 1967; Mrŏz et al. 1978). Each such surface translates independently in a purely kinematic fashion. The combined effect gives rise to a piecewise linear hardening behavior for the material as a whole.

Although nested surface models have demonstrated flexibility in simulating the complex monotonic response of clays (Darve et al. 1986), their numerical implementation tends to be complicated (Vermeer & De Borst 1984). This shortcoming was overcome by developing models based on the bounding surface in stress invariant space (Dafalias 1979a), which can be viewed as a modification of certain nested surface models (Mrŏz et al. 1978). Bounding surface models involve only two surfaces, namely a current loading surface and an outer "bounding" surface (Figure 3). The intermediate loading surfaces are implicitly defined on the basis of the proximity (δ) of the current stress point to a properly defined "image" stress point on the bounding surface. The prominent features of a bounding surface formulation are 1) the existence of inelastic deformations for stress states within an outer ("bounding") surface, and 2) the existence of a smoothly varying plastic modulus. These features represent definite advantages over classical rate-independent yield surface elastoplastic formulations, especially for "softer" materials such as cohesive soils (Dafalias 1986).

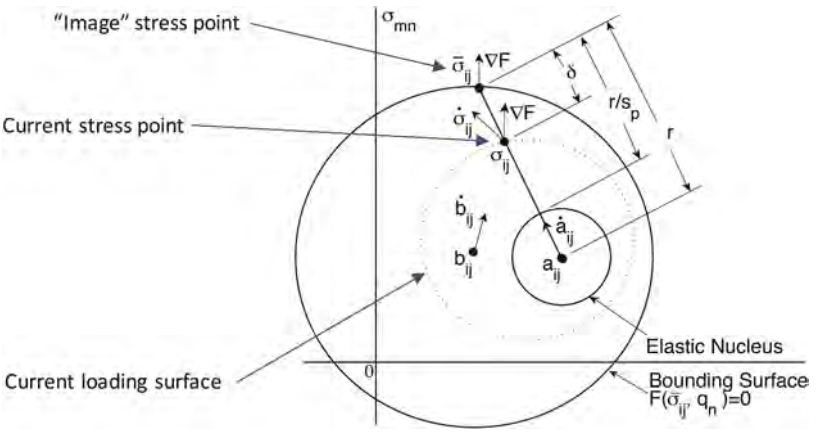

Figure 3. Schematic illustration of a general bounding surface in stress space.

Dafalias (1979a) qualitatively presented a direct bounding surface formulation for rate-independent isotropic soil elastoplasticity for the case of zero elastic range and in conjunction with implied loading surfaces; this model was also extended to include a quasi-elastic range (Dafalias 1979b). The latter model combined the attractive features of simplicity and good predictive capabilities when applied to clays. It was subsequently formulated within the framework of stress invariant space in conjunction with a critical state failure criterion (Schofield & Wroth 1968), which included a three-invariant formulation (Dafalias & Herrmann 1982; Dafalias et al. 1982). This form of the model was synthesized (Dafalias & Herrmann 1986) and then subsequently simplified (Kaliakin & Dafalias 1989).

Dafalias (1982a) was the first to discuss the issue of anisotropy in conjunction with bounding surface models. This led to the progressive development of an anisotropic, rate-independent bounding surface models for cohesive soils (Anandarajah & Dafalias 1986; Liang & Ma 1992).

Dafalias 1982a,b first presented the theoretical basis for a time-dependent version of the bounding surface model for isotropic cohesive soils. This model was subsequently refined, implemented, formally presented and verified (Kaliakin & Dafalias 1990a,b).

Realizing that previous anisotropic time-dependent bounding surface formulations (Al-Shamrani & Sture 1998; Voyiadjis & Kim 2003) were overly complex, Ling et al. (2002) proposed a somewhat more rational model that reduced the total number of parameters without compromising predictive capabilities (Ling et al. 2002, 2003).

Jiang et al. (2012) extended the anisotropic model of Ling et al. (2002) to include a non-associative flow rule, which is typically required in order to more accurately simulate the response of soft cohesive soils that exhibit softening.

The predictive capabilities of bounding surface models for cohesive soils have typically been assessed by comparing numerical results with data obtained from laboratory tests. The majority of these tests were performed under axisymmetric triaxial compression and extension stress states. In a few instances, more complex stress states were considered. This included the centrifuge modeling of the filling and emptying of an oil storage tank (Shen et al. 1986), the simulation of a caisson-retained sand island in the Canadian Beaufort Sea (Kaliakin et al. 1990), sundry simulations of field soils (Jiang et al. 2013), and simulation of complex field excavations in soft soils (Hung et al. 2014; Ling et al. 2016).

5 THE GENERALIZED BOUNDING SURFACE MODEL

Although all of the aforementioned models for cohesive soils were based on the concept of a bounding surface in stress space, they improved upon earlier versions of such models, enhanced the predictive capabilities of earlier models by expanding their features, or accomplished both of these tasks. Missing from the earlier development of bounding surface models for cohesive soils was any attempt to *synthesize* the many previous forms of these models. Such a synthesis has now been realized through the Generalized Bounding Surface Model (GBSM) for cohesive soils (Kaliakin et al. 2018). The GBSM also improves upon many aspects of previous models for cohesive soils and expands the scope of the model to thermo-hydro-mechanical analyses.

In its most general form, the GBSM for cohesive soils is a fully three-dimensional, temperature and time-dependent model that accounts for both inherent and stress induced anisotropy. To better simulate the behavior of cohesive soils exhibiting softening, the model employs a non-associative flow rule. The microfabric-inspired rotational hardening rule associated with the model was developed after a thorough review of past modeling practice. Finally, the shape hardening function used in the GBSM was developed simplifying earlier versions without compromising the model's predictive capabilities. Details pertaining to the GBSM, an investigation of the associated parameters, as well as a discussion describing how potential limitations of the model have been overcome are given in (Kaliakin et al. 2018; Nieto-Leal et al. 2020; Nieto-Leal et al. 2021).

The GBSM has been shown to accurately simulate the stress-strain and strength characteristics of different clays for various stress conditions (e.g., Kaliakin et al. 2018; Nieto-Leal et al. 2021). However, its applicability for cohesive soils with different clay and silt contents and thus

levels of plasticity has not been investigated in a systematic manner. Due to the availability of experimental results obtained from a series of consolidated-undrained triaxial tests on silt-clay transition soils by Anantanasakul & Roth (2018), the present simulations were undertaken.

5.1 *Identification of applicable model parameters*

Since the specimens tested by Anantanasakul & Roth (2018) were all isotropically consolidated, only isotropic forms of the GBSM apply to the present simulations. This reduces the number of applicable model parameters. The isotropic forms employing an associative and non-associative flow rule are referred to herein as the GBSMia and GBSMin forms, respectively, of the model.

Since Anantanasakul & Roth (2018) only tested the aforementioned specimens in axisymmetric triaxial compression, those parameters controlling the response of the GBSM in extension are immaterial. Consequently, the number of model parameters reduces further.

The model parameters associated with the GSBMia and GBSMin forms of the model, as restricted to response in axisymmetric triaxial compression, are grouped by their type as follows: the critical state parameters λ, κ and M_c, the elastic parameter Poisson's ratio (ν), the surface configuration parameters R and N_c (the latter only applies to the GBSMin form of the model), the projection center parameter C, the elastic nucleus parameter s_p, and the shape hardening parameters h_c and a.

5.2 *Determination of parameter values for silt-clay transition soils*

The values of λ and κ were determined from the values of C_c and C_r, respectively, listed in Table 2. With increasing silt content, the values of λ decreased from 0.146 to 0.058; the κ values likewise decreased from 0.045 to 0.007. Table 3 lists the values of λ and κ determined for each of the three soils tested.

Assuming no effective cohesion, the friction angle (ϕ') for each of the three soils was determined from the maximum effective stress ratios (σ'_1/σ'_3), as measured in the CIUC tests on both normally consolidated and overconsolidated specimens. The slope of the critical state line associated with axisymmetric triaxial compression (M_c) is then determined from the following expression:

$$M_c = \frac{6\sin\phi'}{3 - \sin\phi'} \tag{1}$$

With increasing silt content, the values of M_c increased from 0.770 to 1.440. Table 3 lists the values of M_c determined for each of the three soils tested.

Table 3. Values of model parameters used in present simulations.

Model Parameter	Soil 1	Soil 2	Soil 3
λ	0.146	0.105	0.058
κ	0.045	0.015	0.007
M_c	0.77	1.07	1.44
ν	0.18	0.23	0.30
R	2.35	2.20	2.45
C	0.50	0.60	0.55
s_p	1.00	1.50	1.50
h_c	1.75	4.00	4.00
a	3.25	2.25	3.25
N_c	n/a	0.950	n/a

To determine the values of Poisson's ratio, isotropically consolidated drained (CIDC) triaxial compression tests, each with an unload-reload cycle, were performed on normally consolidated

specimens of the silt-clay soils (Anantanasakul & Roth 2018). In these tests, deviator stresses in the vertical direction were applied up to levels equal to 50% of the anticipated maximum principal stress differences $(\sigma_1 - \sigma_3)_{max}$. The specimens were later unloaded to 25% of the maximum value and then reloaded. The Poisson's ratio values were computed from the corresponding changes in axial strains $(\Delta\varepsilon_1)$ and volumetric strains $(\Delta\varepsilon_v = \Delta\varepsilon_1 + 2\Delta\varepsilon_3)$ during reloading as follows:

$$\nu = -\frac{\Delta\varepsilon_3}{\Delta\varepsilon_1} = -\frac{\Delta\varepsilon_v - \Delta\varepsilon_1}{2\Delta\varepsilon_1} \tag{2}$$

where ε_3 is the minor principal strain. Table 3 lists the values of Poisson's ratio so determined for the three soils tested, which ranged from 0.18 to 0.30.

Values of the surface configuration parameter R ($R \geq 2$) were determined by primarily matching the effective stress paths of the normally consolidated specimens of the three soils tested. Suitable values for the projection parameter C ($0 \leq C < 1$) were determined primarily by matching the effective stress paths of tests on overconsolidated specimens with the OCRs of 2.0, 4.0 and 8.0. The values R and C so determined are listed in Table 3.

Values for the "elastic nucleus" parameter s_p ($s_p \geq 1$) were determined by matching the principal stress difference ($q = \sigma_1 - \sigma_3$)-axial strain (ε_1) response for the aforementioned overconsolidated specimens. When $s_p = 1$, the elastic nucleus reduces to a point and plastic strains are predicted within the entire bounding surface. Stiffer q-ε_1 response can be simulated by using s_p values greater than unity. This was the case for Soils 2 and 3 (see Table 3). Figure 4 better illustrates the meaning of the parameters R, C and s_p.

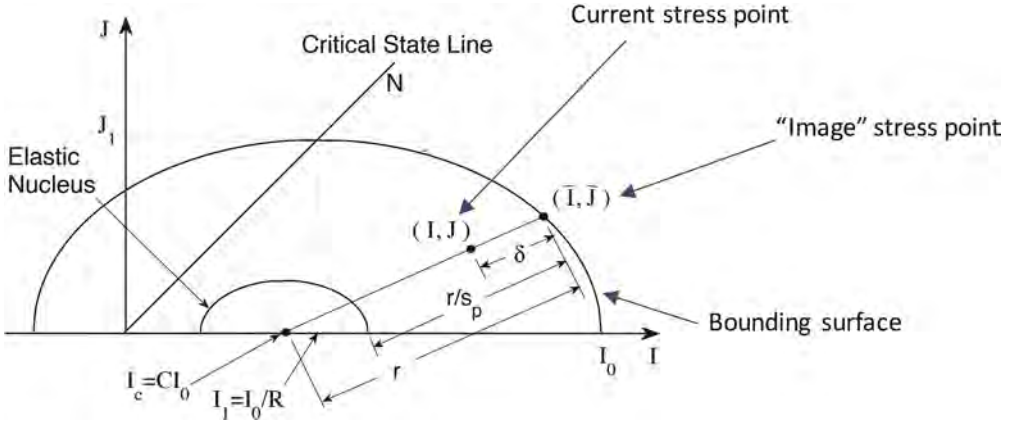

Figure 4. Schematic illustration of elliptical bounding surface in space of stress invariants.

Accurate simulation of Soil 2 required the use of the GBSMin form of the model. The non-associative flow rule used in this form requires the value of the parameter N_c that is used to define the shape of the plastic potential surface. The value of this parameter (0.950) was primarily determined by matching the q-ε_1 curves for specimens with OCRs of 2.0, 4.0 and 8.0.

The values of the shape hardening parameters h_c and a are only active in simulation of tests on overconsolidated specimens. The values of h_c were determined by matching the q-ε_1 curves for specimens with OCRs of 2.0 and 4.0. Finally, the values of a were determined by matching the q-ε_1 curves and effective stress paths for specimens with OCR equal to 8.0. With increasing silt content, the values of h_c increased from 1.75 to 4.0. The values determined for a did not follow this trend. Table 3 lists the values of the shape hardening parameters determined for the three soils tested.

6 SIMULATION OF BEHAVIOR OF SILT-CLAY TRANSITION SOILS

The constitutive relations associated with the GBSM, along with such enhancements as local iteration, sub-stepping and radial return (Herrmann et al. 1987) have been incorporated into

a modular system of FORTAN-77 subroutines. This system consists of a master subroutine clay_UD that is supported by numerous lower-level subroutines. Implementation of the GBSM in such a manner facilitates simple and inexpensive incorporation into existing and new computer programs for the analysis of geo-structures.

For purposes of assessing the characteristics of the GBSM and for simulating experimental results, a means for predicting the results of simple homogeneous tests must be made available. The Fortran-90 computer program CALBR8 (Kaliakin 1992) has been developed for this purpose. CALBR8 evaluates the constitutive relations, as applied to a homogeneous specimen, subjected to arbitrary homogeneous stress, strain and temperature histories, under either drained or undrained conditions. Although CALBR8 has been written to evaluate the time- and temperature-dependent constitutive relations, the formulation can also be used to perform time-dependent and isothermal analyses (Burmister).

In the subsequent figures, the experimental results of Anantanasakul & Roth (2018) are depicted by discrete symbols. The simulations obtained using the GBSM are depicted by solid, dashed, and dot-dashed lines.

6.1 *Simulation of the behavior of Soil 1*

Using the parameter values listed in the second column of Table 3 in conjunction with the GBSMia form of the model, the behavior of Soil 1 was simulated. Figure 5 shows the simulated effective stress paths for the OCRs of 1.0, 2.0, 4.0 and 8.0. The simulated q-ε_1 response is shown in Figure 6. Finally, Figure 7 shows the simulated excess pore pressure-ε_1 response.

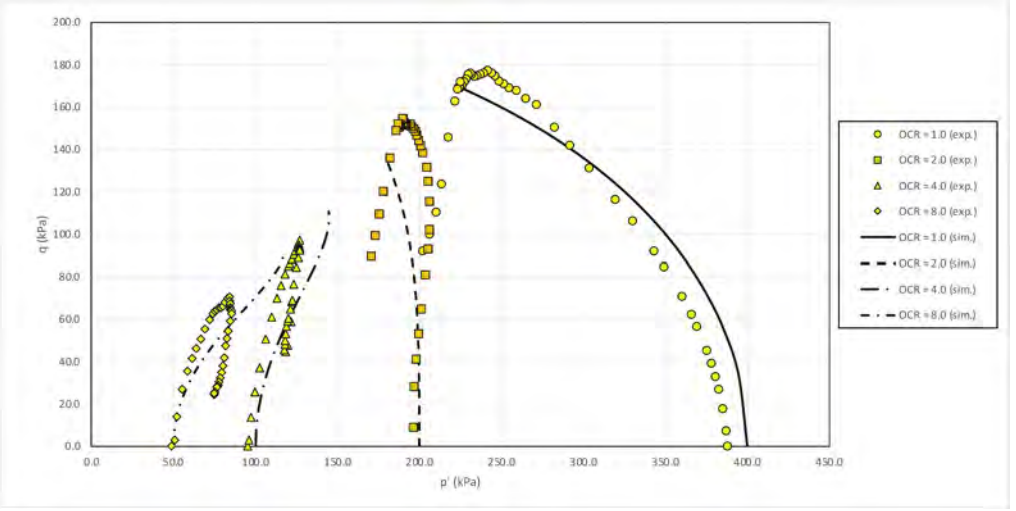

Figure 5. Comparison of simulated and experimental effective stress paths for Soil 1.

Although no single q-ε_1 is simulated exactly, as seen from Figure 6, an overall "best-fit" of the q-ε_1 has been realized. The simulated excess pore pressure-ε_1 for OCRs of 1.0, 2.0 and 4.0 is quite accurate (Figure 7). In the case of OCR equal to 8.0, the excess pore pressure is somewhat over predicted.

6.2 *Simulation of the behavior of Soil 2*

Using the parameter values listed in the third column of Table 3 in conjunction with the GBSMin form of the model, the behavior of Soil 2 was simulated. Figure 8 shows the

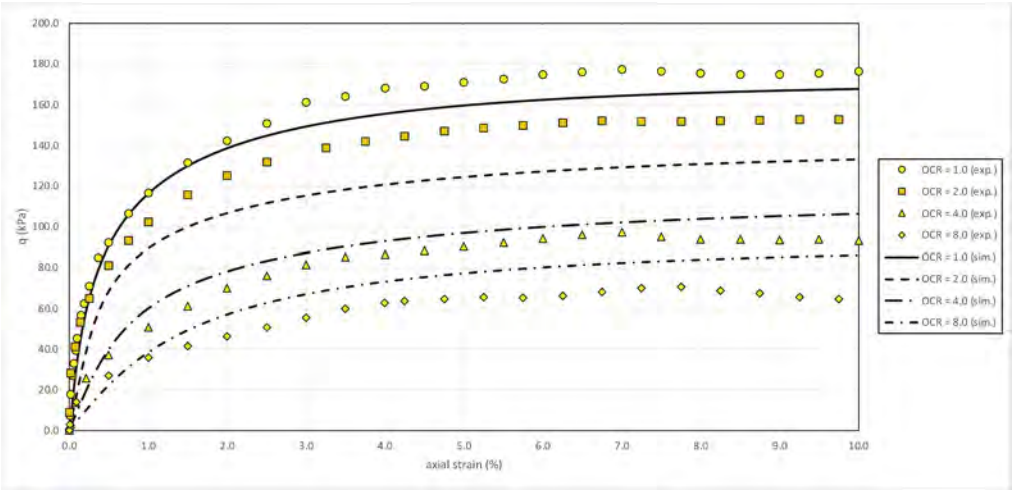

Figure 6. Comparison of simulated and experimental principal stress difference-axial strain response for Soil 1.

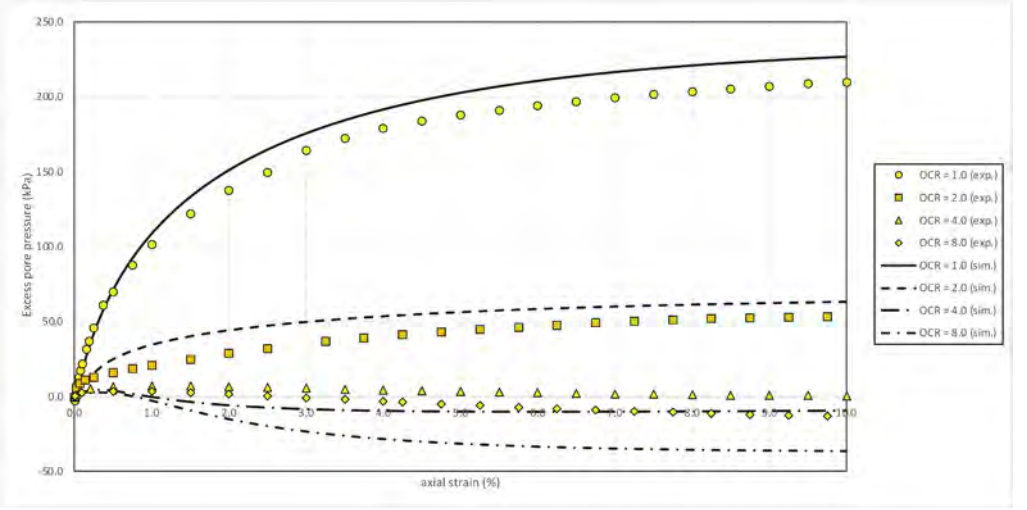

Figure 7. Comparison of simulated and excess pore pressure-axial strain response for Soil 1.

simulated effective stress paths for the OCRs of 1.0, 2.0, 4.0 and 8.0. The simulated q-ε_1 response is shown in Figure 9. Finally, Figure 10 shows the simulated excess pore pressure-ε_1 response.

Initially, the response of Soil 2 was simulated using the GBSMia form of the model. However, the GBSM employs a critical state failure criterion that predicts a constant value of undrained shear strength even as the shear strains continuously increase. As such, the reduction in strength after failure that was exhibited by Soil 2 at high strains could not be simulated. This shortcoming was partially reduced through the use of the GBSMin form of the model. The non-associative flow rule allows for some reduction in strength with continued straining (Nieto-Leal et al. 2018). However, as evident from the simulations of Soil 2, the use of a non-associative flow rule is not a panacea in such simulations.

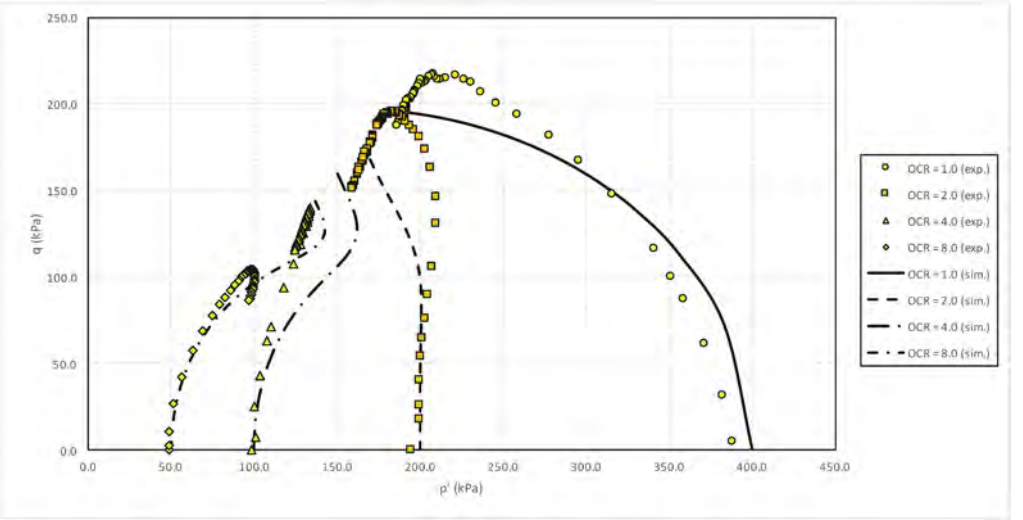

Figure 8. Comparison of simulated and experimental effective stress paths for Soil 2.

As evident from Figure 9, an overall "best-fit" was again obtained for the simulated q-ε_1 response. With the exception of the case for OCRs 1.0 and 8.0, the overall excess pore pressure response was simulated rather accurately (Figure 10).

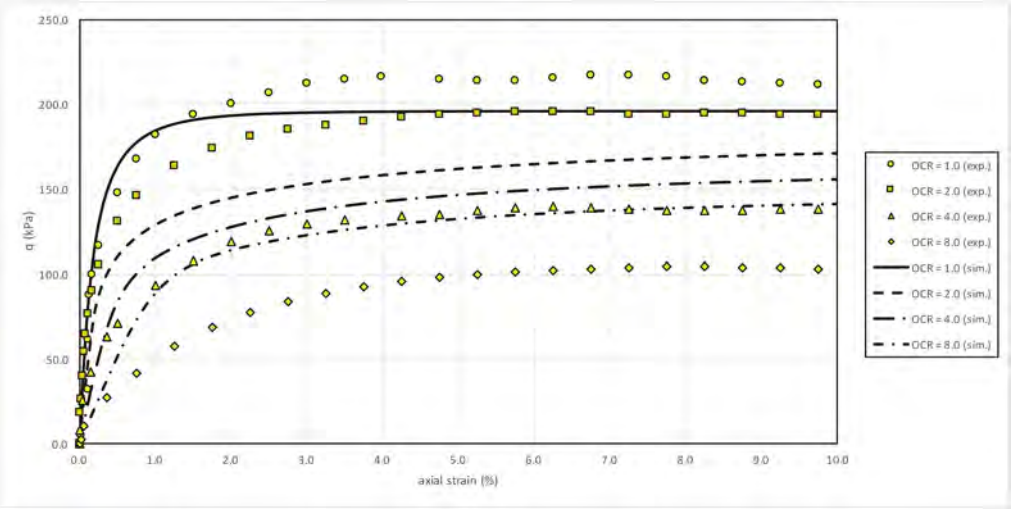

Figure 9. Comparison of simulated and experimental principal stress difference-axial strain response for Soil 2.

6.3 *Simulation of the behavior of Soil 3*

Finally, using the parameter values listed in the fourth column of Table 3 in conjunction with the GBSMia form of the model, the behavior of Soil 3 was simulated. Figure 11 shows the simulated effective stress paths for the OCRs of 1.0, 2.0, 4.0 and 8.0. The simulated q-ε_1

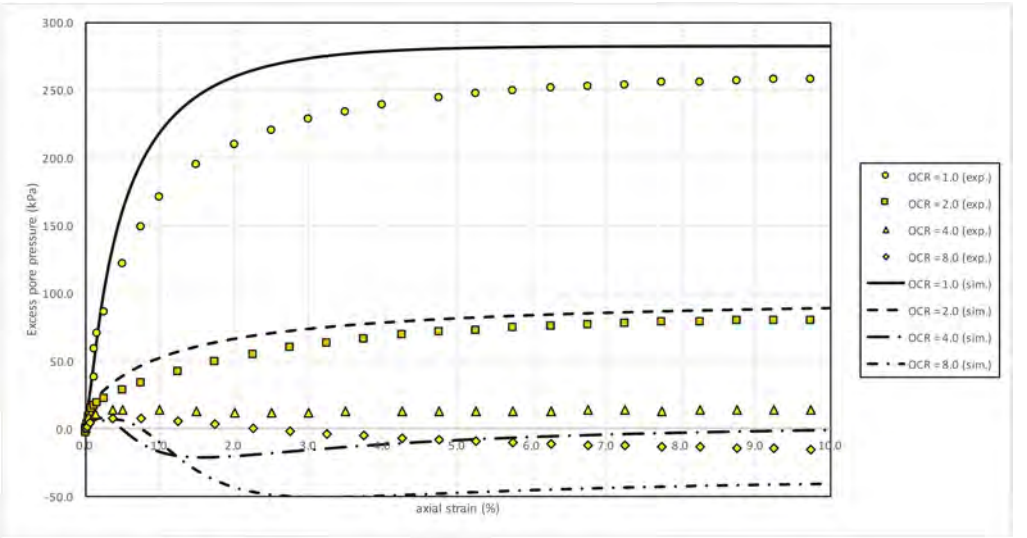

Figure 10. Comparison of simulated and excess pore pressure-axial strain response for Soil 2.

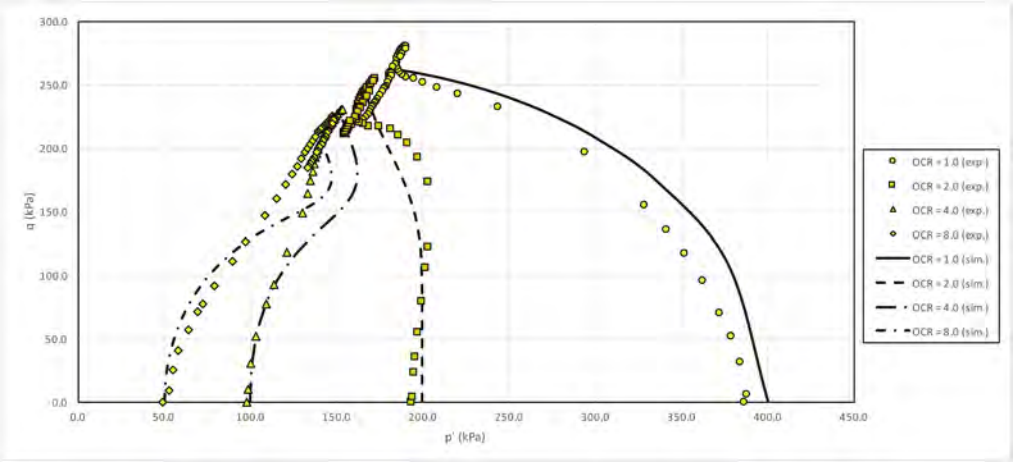

Figure 11. Comparison of simulated and experimental effective stress paths for Soil 3.

response is shown in Figure 12. Finally, Figure 13 shows the simulated excess pore pressure-ε_1 response.

Although Soil 3 contained the largest amount of non-plastic silt, the GBSM simulations obtained for this soil were the most accurate. This is particularly evident in the simulated q-ε_1 (Figure 12) and excess pore pressure-ε_1 response (Figure 13).

7 CONCLUSIONS

The Generalized Bounding Surface Model for cohesive soils was employed to simulate the stress-strain, pore pressure change and strength characteristics obtained from CIUC triaxial tests on normally consolidated and overconsolidated silt-clay transition soils. The soils employed in this study employed the same base clay but systematically varied the amount of non-plastic silt content. It was observed that the isotropic forms of the GBSM, once calibrated properly, was able to simulate the undrained response of silt-clay soils with widely varying silt

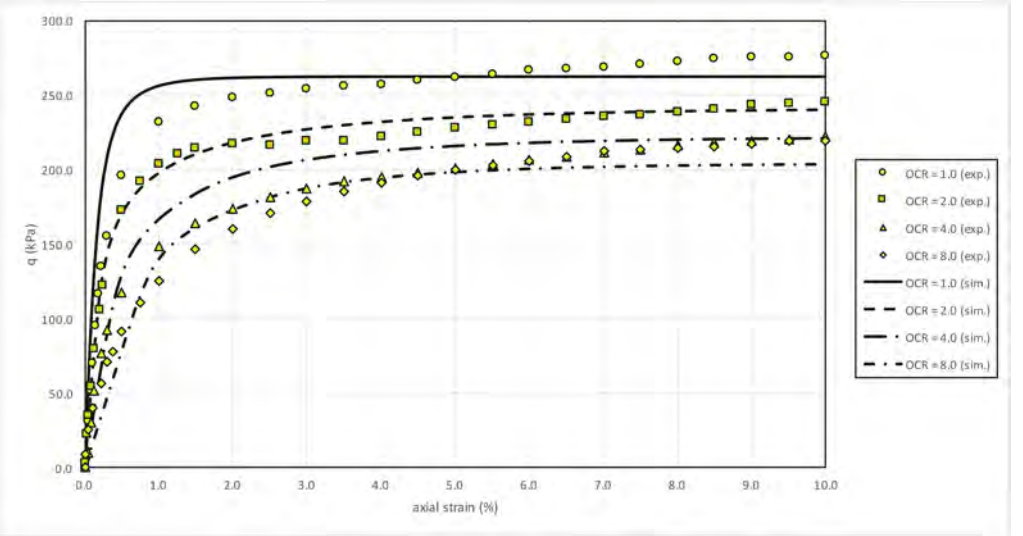

Figure 12. Comparison of simulated and experimental principal stress difference-axial strain response for Soil 3.

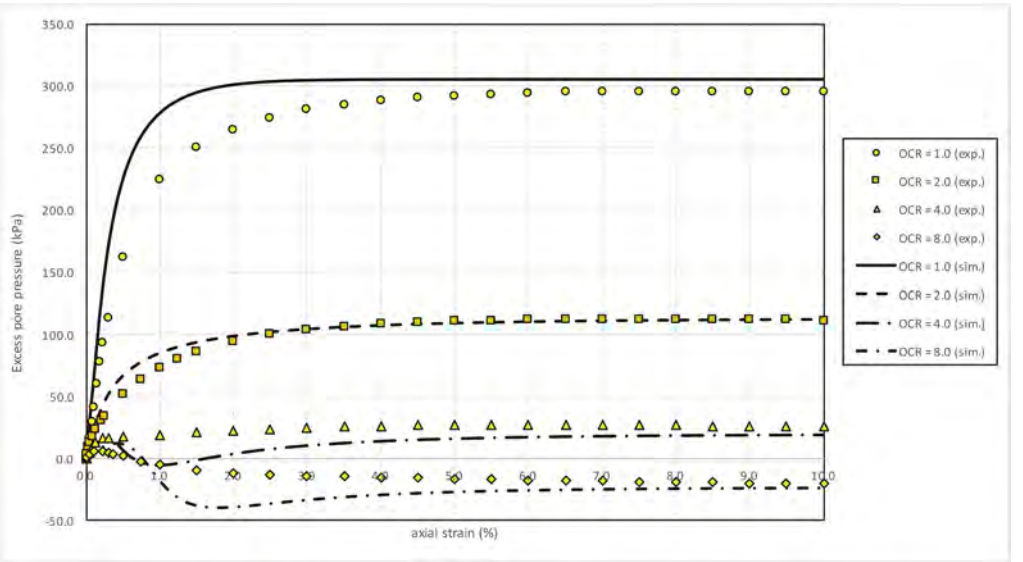

Figure 13. Comparison of simulated and excess pore pressure-axial strain response for Soil 3.

contents and thus values of plasticity index with reasonable accuracy. The trends of material behavior with respect to variation in the silt content can reasonably be simulated. The accuracies of numerical predictions were highest for the soil with highest non-plastic silt content and lowest plasticity index. The model was less accurate, where the experimental stress-strain relations and undrained shear strengths were sometimes over-estimated, for the soils with lower silt contents and with moderate and high OCR values. In the case of Soils 1 and 2, the simulated excess pore pressure-axial strain response was over-predicted.

The reason for such over-predictions may, in part, be attributed to the use of a single elliptical bounding surface (Figure 2). For overconsolidated stress states on the "dry" (or left) side of critical, the predicted effective stress path is unrealistically "pulled" upward. This often results in

prediction of a high peak shear strength and stiff stress-strain response prior to failure. Although this issue has been investigated in detail and a remedy proposed (Nieto-Leal & Kaliakin 2014), this issue may need to be re-visited when simulating the response of silt-clay transition soils.

Finally, the values of several of the model parameters used to simulate each of the three silt-clay transition soils were determined by best matching the associated experimental results. Ideally, however, the values of at least some of these parameters should be determined from index properties, from volume content of non-plastic silt present in a soil, etc. This can, however, only be realized with additional systematic experimental studies of silt-clay transition soils. These should consider time and rate effects, as well the effect of anisotropy.

REFERENCES

Al-Shamrani, M. A. & Sture, S. 1998. *A Time-dependent Bounding Surface Model for Anisotropic Cohesive Soils*. Soils and Foundations. 38(1): 61–76.

Anandarajah, A. & Dafalias, Y. F. 1986. Bounding Surface Plasticity III: Application to Anisotropic Cohesive Soils Journal of Engineering Mechanics, ASCE. 112(12): 1292–1318.

Anantanasakul, P., Yamamuro, J. & Kaliakin, V. N. 2012. *Stress-strain and strength characteristics of silt-clay transition soils*. Journal of Geotechnical and Geoenvironmental Engineering. 138(10): 1257–1265.

Anantanasakul, P. & Roth, C. 2018. *Undrained behavior of silt-clay transition soils with varying degrees of overconsolidation*. Journal of GeoEngineering. 13(1): 1–12.

Anantanasakul, P., Intharachart, P. & Kaliakin, V. N. 2023. *Three-dimensional stress-strain and strength behavior of silt-clay transition soils*. Canadian Geotechnical Journal (in press).

Brandon, T., Rose, A., & Duncan, J. M. 2006. *Drained and undrained strength interpretation for low-plasticity silts*. Journal of Geotechnical and Geoenvironmental Engineering. 132(2): 250–257.

Cola, S. & Simonini, P. 2002. *Mechanical behavior of silty soils of the Venice lagoon as a function of their grading characteristics*. Canadian Geotechnical Journal. 39(4): 879–893.

Dafalias, Y. F. 1979a. A Bounding Surface Plasticity Model. *Proceedings of the Seventh Canadian Congress of Applied Mechanics*. Sherbrooke, Canada: The Congress: 89–90.

Dafalias, Y. F. 1979b. A Model for Soil Behavior under Monotonic and Cyclic Loading Conditions. *Transactions of the Fifth International Conference on SMIRT*. The Netherlands: North-Holland Pub. Co. for the Commission of the European Communities. K 1/8: 1–9.

Dafalias, Y. F. 1982a. On Rate Dependence and Anisotropy in Soil Constitutive Modeling. *Results of the International Workshop on Constitutive Relations for Soils*. Edited by Gudehus, G., Darve, F. & Vardoulakis, I. Rotterdam: Balkema: 457-462.

Dafalias, Y. F. 1982b. Bounding Surface Elastoplasticity-Viscoplasticity for Particulate Cohesive Media. *Deformation and Failure of Granular Materials*, IUTAM Symposium on Deformation and Failure of Granular Materials. Edited by Vermeer, P. A. & Luger, H. J. Rotterdam: Balkema: 97-107.

Dafalias, Y. F. 1986. *Bounding Surface Plasticity. I: Mathematical Foundation and the Concept of Hypoplasticity*. Journal of Engineering Mechanics, ASCE. 112(90): 966–987.

Dafalias, Y. F. & Herrmann, L. R. 1982. A Generalized Bounding Surface Constitutive Model for Clays. *Application of Plasticity and Generalized Stress-Strain in Geotechnical Engineering*. Edited by Yong, R. N. & Selig, E. T. New York: ASCE: 78-95.

Dafalias, Y. F., Herrmann, L. R. & De Natale, J. S. 1982. The Bounding Surface Plasticity Model for Isotropic Cohesive Soils and its Application at the Grenoble Workshop. *Results of the International Workshop on Constitutive Relations for Soils*. Edited by Gudehus, G., Darve, F. & Vardoulakis, I. Rotterdam: Balkema: 273-287.

Dafalias, Y. F. & Herrmann, L. R. 1986. *Bounding Surface Plasticity II: Application to Isotropic Cohesive Soils*. Journal of Engineering Mechanics, ASCE. 112(12): 1263–1291.

Darve, F., Flavigny, E. & Rojas, E. 1986. *Class of incrementally non-linear constitutive relations and applications to clays*. Computers and Geotechnics. 2(1): 43–66.

Fleming, L. N. & Duncan, J. M. 1990. *Stress-deformation characteristics of Alaskan silt*. Journal of Geotechnical Engineering. 116(3): 377–393.

Henkel, D. 1956. *The effect of overconsolidation on the behaviour of clays during shear*. Géotechnique. 6 (4), 139–150.

Herrmann, L. R., Kaliakin, V. N., Shen, C. K., Mish, K. D. & Zhu, Z-Y. 1987. *Numerical Implementation of a Plasticity Model for Cohesive Soils*. Journal of Engineering Mechanics, ASCE. 113(4): 500–519.

Hung, C., Ling, H. I. & Kaliakin, V. N. 2014. *Finite Element Simulation of Deep Excavation Failures*. Transportation Infrastructure Geotechnology.1(3–4): 326–346.

Hvorslev, J. M. 1960. Physical components of the shear strength of saturated clays. *Proceedings of the ASCE Research Conference on Shear Strength of Cohesive Soils*, Boulder, Colorado: 169–273.
Iwan, W. D. 1967. *On a Class of Models for the Yielding Behavior of Continuous and Composite Systems*. Journal of Applied Mechanics, ASME. 34(E3): 612–617.
Jiang, J., Ling, H. I. & Kaliakin, V. N. 2012. *An Associative and Non-Associative Anisotropic Bounding Surface Model for Clay*. Journal of Applied Mechanics, ASME. 79(3): doi: 10.1115/1.4005958.
Jiang, J., Ling, H. I. & Kaliakin, V. N. 2013. *Simulation of Natural Pisa Clay Using an Enhanced Anisotropic Elastoplastic Bounding Surface Model*. Journal of Applied Mechanics, ASME. 80(2): doi: 10.1115/1.4007964.
Kaliakin, V. N. 1992. *CALBR8, A Simple Computer Program for Assessing the Idiosyncrasies of Various Constitutive Models Used to Characterize Soils*. Technical Report. University of Delaware, Department of Civil Engineering. 92–1.
Kaliakin, V. N. & Dafalias, Y. F. 1989. *Simplifications to the Bounding Surface Model for Cohesive Soils*. International Journal for Numerical and Analytical Methods in Geomechanics. 13(1): 91–100.
Kaliakin, V. N. & Dafalias, Y. F. 1990a. *Theoretical Aspects of the Elastoplastic-Viscoplastic Bounding Surface Model for Cohesive Soils*. Soils and Foundations. 30(3): 11–24.
Kaliakin, V. N. & Dafalias, Y. F. 1990b. *Verification of the Elastoplastic-Viscoplastic Bounding Surface Model for Cohesive Soils*. Soils and Foundations. 30(3): 25–36.
Kaliakin, V. N., Muraleetharan, K. K., Dafalias, Y. F., Herrmann, L. R. & Shinde, S. B. 1990. *Foundation-Response Predictions Below Caisson-Retained Island*. Journal of Geotechnical Engineering, ASCE. 116(9):1291–1308.
Kaliakin, V. N., Nieto-Leal, A. N. & Mashayekhi, M. 2018. *Modeling the Time- and Temperature-Dependent Response of Cohesive Soils in a Generalized Bounding Surface Framework*. Transportation Infrastructure Geotechnology. 5(3): 250–286.
Ladd, C. C. & Foott, R. 1974. *New design procedure for stability of soft clays*. Journal of the Geotechnical Engineering Division. 100(7): 763–786.
Liang, R. Y. & Ma, F. 1992. *Anisotropic Plasticity Model for Undrained Cyclic Behavior of Clays. I: Theory*. Journal of Geotechnical Engineering, ASCE. 118(2): 229–245.
Ling, H. I., Yue, D., Kaliakin, V. N. & Themelis, N. J. 2002. *An Anisotropic Elasto-Plastic Bounding Surface Model for Cohesive Soils*. Journal of Engineering Mechanics, ASCE. 128(7): 748–758.
Ling, H. I., Yue, D. & Kaliakin, V. N. 2003. Geosynthetic-reinforced containment dike constructed over soft foundation: numerical analysis. *Reinforced Soil Engineering: Advances in Research and Practice*. Edited by Ling, H. I., Leshchinsky, D. & Tatsuoka, F. New York: M. Dekker, Inc.: 283–295.
Ling, H. I., Hung, C. & Kaliakin, V. N. 2016. *Application of An Enhanced Anisotropic Bounding Surface Model in Simulating Deep Excavations in Clays*. Journal of Geotechnical and Geoenvironmental Engineering, ASCE. 142(11): 10.1061/(ASCE)GT.1943–5606.0001533.
Lupini, J. F., Skinner, A. E. & Vaughan, P. R. 1981. *The drained residual strength of cohesive soils*. Géotechnique. 31(2): 181–213.
Mrŏz, Z., Norris, V. A. & Zienkiewicz, O. C. 1978. *An Anisotropic Hardening Model for Soils and its Application to Cyclic Loading*. International Journal for Numerical and Analytical Methods in Geomechanics. 2(3): 203–221.
Nieto-Leal, A. & Kaliakin, V. N. 2014. *Improved Shape Hardening Function for Bounding Surface Model for Cohesive Soils*. Journal of Rock Mechanics and Geotechnical Engineering. 6(3): 327–337.
Nieto-Leal, A., Kaliakin, V. N. & Mashayekhi, M. 2018. *Improved RH rule for cohesive soils and inherent anisotropy*. International Journal for Numerical and Analytical Methods in Geomechanics. 42(3): 469–487.
Nieto-Leal, A. N., Kaliakin, V. N. & González, R. 2020. *Investigation of Parameters Associated with the Generalized Bounding Surface Model for Cohesive Soils*. Transportation Infrastructure Geotechnology. 7(3): 496–515.
Nieto-Leal, A. N. & Kaliakin, V. N. 2021. *Additional Insight into the Generalized Bounding Surface Model for Saturated Cohesive Soils*. International Journal of Geomechanics. 21(6): doi: 10.1061/(ASCE)GM.1943-5622.0002012.
Nocilla, A., Coop, M.R. & Colleselli, F. 2006. *The mechanics of an Italian silt: an example of 'transitional' behavior*. Géotechnique. 56(4): 261–271.
Parry, R. H. G. & Nadarajah, V. 1974. *Anisotropy in a natural soft clayey silt*. Engineering Geology. 8: 287–309.
Penmen, A. D. M. 1953. *Shear characteristics of a saturated silt, measured in triaxial compression*. Géotechnique. 3(8): 312–328.
Roscoe, K. H. & Burland, J. B. 1968. On the generalized stress-strain behaviour of 'wet' clay. In *Engineering Plasticity*: 535–609. United Kingdom: Cambridge Univ. Press.
Schofield, A. N. & Wroth, C. P. 1968. *Critical State Soil Mechanics*. London: McGraw Hill.

Seed, H. B., Woodward, R. J. & Lundgren, R. 1964. *Clay mineralogical aspects of the Atterberg limits*. Journal of the Soil Mechanics and Foundations Division. 90(4): 107–134.
Shen, C. K., Sohn, J., Mish, K., Kaliakin, V. N. & Herrmann, L. R. 1986. Centrifuge Consolidation Study for Purposes of Plasticity Theory Validation. *Consolidation of Soils: Testing and Evaluation*. Edited by Yong, R. N. & Townsend, F. C. Philadelphia: ASTM. STP 892: 593–609.
Stark, T. D., Ebeling, R. M. & Vettel, J. J. 1994. *Hyperbolic stress-strain parameters for silts*. Journal of Geotechnical Engineering, 120(2): 420–441.
Vermeer, P. A. & De Borst, R. 1984. *Non-associated plasticity for soils, concrete and rock*. HERON. 29(3): 1–64.
Voyiadjis, G. Z. & Kim, D. 2003. *Finite Element Analysis of the Piezocone test in Cohesive Soils Using an Elastoplastic-Viscoplastic Model and Updated Lagrangian Formulation*. International Journal of Plasticity. 19(2): 253–280.
Wang, S. & Luna, R. 2012. *Monotonic behavior of Mississippi River Valley silt in triaxial compression* Journal of Geotechnical and Geoenvironmental Engineering. 138(4): 516–525.
Wong, S. T. Y., Ong, D. E. L. & Robinson, R. G. 2017. *Behavior of MH silts with varying plasticity indices*. Geotechnical Research. 4(2): 118–135.
Wong, P. K. K. & Mitchell, R. J. 1975. *Yielding and plastic flow of sensitive cemented clay*. Géotechnique. 25(45): 763–782.
Yin, J.H. 1999. *Properties and behavior of Hong Kong marine deposits with different clay contents*. Canadian Geotechnical Journal. 36(6): 1085–1095.
Yin, J.H. 2002. Stress-strain strength characteristics of a marine soil with different clay contents. ASTM Geotechnical Testing Journal. 25(4): 459–462.

Smart Geotechnics for Smart Societies – Zhussupbekov, Sarsembayeva & Kaliakin (Eds)
© 2023 The Author(s), ISBN 978-1-003-29912-7
Open Access: www.taylorfrancis.com, CC BY-NC-ND 4.0 license

Application of vertical drains and vacuum preloading for stabilising soft ground for transport infrastructure

Cholachat Rujikiatkamjorn
Professor, Transport Research Centre, University of Technology Sydney, NSW, Australia

Buddhima Indraratna
Distinguished Professor and Director, Transport Research Centre, University of Technology Sydney, NSW, Australia

ABSTRACT: Demand for the development of transportation infrastructure built on soft clays soils has increased in the past decades because of the rapid surge in population density along the coastal belts of many countries. Acceptable ground conditions are also becoming limited. Due to these reasons, ground improvement is pertinent and required as an essential part of infrastructure development. The application of prefabricated vertical drains with vacuum and surcharge preloading can be one of the economical techniques for transportation infrastructure projects. Consoldiation of soft soil by applying a surcharge alone can become lengthy. The application of prefabricated vertical drains (PVDs) with vacuum can reduce the waiting period significantly by decreasing the drainage path length in the radial direction. In this paper, factors affected the performance of the system including (a) drain spacing and partially penetrating drains, (b) smear zone, (c) vacuum systems, (d) application of numerical analysis for multi-drain system, (e) the optimum time for switching off vaccum pump, are discussed with their advantages and limitations.

1 INTRODUCTION

The application of preloading prior to the construction of transport infrastructure is one of the most effective and economical methods for reducing long-term deformation and increasing soft soil shear strength (Johnson 1970). To accelerate the consolidation, prefabricated vertical drains (PVDs) with or without vacuum pressure can be applied with surcharge. The consolidation time can be decreased via (a) shortened radial drainage path facilitated by PVDs and (b) apparent increased preloading pressure due to vacuum pressure (Kjellman, 1948; Qian et al. 1992). The combined vacuum and fill can further increase embankment stability through the reduction of surcharge height and the inward lateral displacement due to suction (Indraratna et al. 2005).

2 APPLICATION OF PVDS: DRAIN SPACING AND PARTIALLY PENETRATING DRAINS

In current practice, prefabricated vertical drains (PVDs) are comprised of a plastic strip with flow channels protected by filter geosynthetics jacket to prevent silt intrusion (Rixner et al. 1986). To reduce environmental footprint, bio-degradable vertical drains were introduced (Lee et al. 1994). Indraratna et al. (2018) showed that the performance of the biodegradable drains is similar to synthetic drains as the influence of the drain degradation becomes minimal at the end of the consolidation. PVD shapes can be either rectangular (100mmx4mm) for a typical fill surcharge or circular for the application of vacuum preloading (35-50mm diameter). They are often installed in a triangular or square pattern using installation machine. The spacing and installation depth range from 0.8-2.5m and 3-30m, respectively.

DOI: 10.1201/9781003299127-23

Partially penetrating vertical drains option where PVDs are installed within impermeable soil layer (Figure 1) can often be observed in practice when (a) the influence of an embankment loading is restricted within a shallow depth of soft clay layer, (b) vacuum consolidation to prevent any leak to bottom permeable layer (Hart et al. 1958; Zeng and Xie 1989; Zhu and Yin 2000; Ong et al. 2012; Geng et al. 2011). Geng et al. 2011 showed that PVD length could be reduced by 10% without considerably affecting consolidation time.

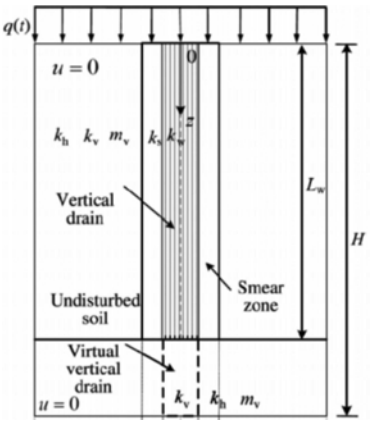

Figure 1. Partially penetrating drain (Geng et al. 2011, Permission obtained from CGJ).

3 ROLE OF SMEAR ZONE

During the installation process of PVDs, surrounding soil properties are disturbed, such as permeability and compressibility. The characterisation of smear zone can be determined using large-scale laboratory testing, back calculation of time-settlement curves and recently soil samples collected after the PVDs installation (Bergado et al. 1991; Indraratna and Redana, 1997; Miura & Chai, 1999; Sharma and Xiao 2000; Hird and Sangtian, 2002; Basu et al. 2007, Sathananthan et al. 2006; Pothiraksanon et al. (2008); Saowapakpiboon et al., 2011; Ghandeharioon et al. 2012; Indraratna et al. 2015; Parsa-Pajouh et al. 2014; Choudary et al. 2016; Sengul et al., 2017). Indraratna et al. (2015) showed that the extent of the smear zone can be determined using a variation of permeability, soil compressibility, or water content. Overlapping of the smear zone can be evidenced due to multiple drains installation (Figure 2). Depending on the installation method and the condition of soil, the extent of the smear zone can vary from 1.3 to 7 times the equivalent mandrel diameter. Based on the observation, Rujikiatkamjorn and Indraratna (2014) incorporated the change of soil compressibility and permeability in a smear zone into an analytical model for a unit cell. The proposed theory was validated with field data from a selected case study in the town of Ballina, New South Wales, Australia.

4 APPLICATION OF VACUUM AND SURCHARGE PRELOADING

After the removal of load application, treated soils become over-consolidated upon the construction of permanent structures (Almeida et al. 2000; Bergado et al. 2002; Indraratna et al. 2000). For conventional fill application, PVDs are often installed through entire clay strata or beyond the loading influence zone imparted by an embankment fill. In an area where embankment's instability is an issue due to soil at a shallow depth having very low shear strength or significant height of surcharge, vacuum in combination with fill preloading can become a desirable option (Cognon et al. 1994; Chu et al. 2000). Apparent preloading pressure created by suction can speed up consolidation process as staged construction can be minimised (Shang et al. 1998; Shen et al. 2005). Vacuum pressure can propagate at the greater depth via PVDs which are often installed within low permeable layer to minimise vacuum loss. Due to the isotropic consolidation effects,

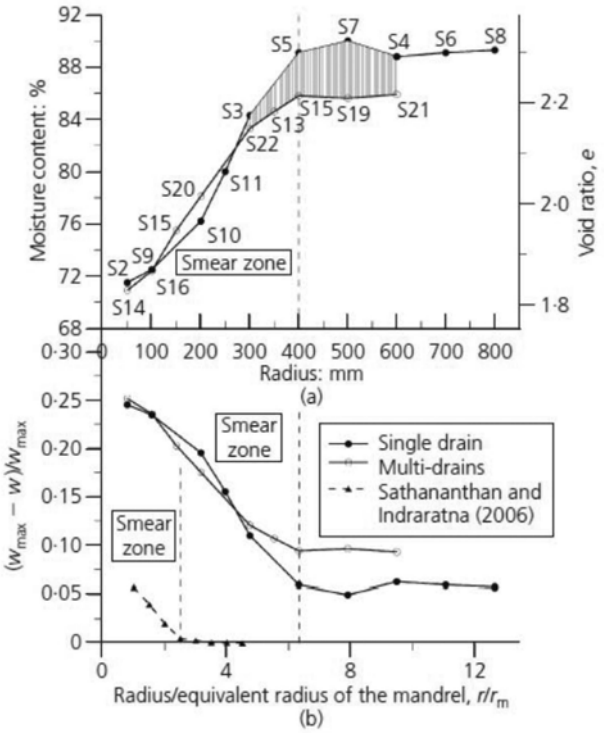

Figure 2. Water content and void ratio variation (Indraratna et al. 2015 with permission obtained from ICE).

the lateral displacement can be controlled using the combination of fill and vacuum preloading (Chai et al. 2008; Indraratna et al. 2012). The systems to apply vacuum pressure can be divided into 2 major systems, namely, membrane and membraneless system.

For the membrane system, the working platform made of a sand layer is placed before an installation of PVDs (Figure 3). Afterwards network of horizontal drainage connected to vacuum pumps is laid, followed by a membrane. The edges of the membrane are submerged under the peripheral bentonite trench. Quality assurance prior to the placement of the fill needs to be performed to prevent any leakage of the membrane. To prevent any leakage at the peripheries of the treated areas due to the presence of an intermittent permeable layer, bentonite slurry walls are often installed to provide vertical impermeable wall adjoining the treated area.

The second approach to apply vacuum pressure is the membranless system (Figure 4). The system is no longer required the membrane as individual drains are connected directly to vacuum pumps via horizontal pipes. Recently some efforts have been made to improve the connection between PVDs and the horizontal pipes to ensure minimum leakage and better propagation of vacuum preloading (Cai et al, 2017; Sun et al. 2017). This system allows smaller portion of an improved area to be treated. The applied vacuum pressure can range from 40-85 kPa. Additional field instrumentation, such as vacuum gauges and in-drain piezometers, is often required to assess the performance of the system.

5 FINITE ELEMENT MODELLING OF VERTICAL DRAINS IN SOFT GROUND UNDER SURCHARGE COMBINED WITH VACUUM PRELOADING

Due to the shape of embankments applicable for transport and port infrastructure, finite element analyses under plane strain condition can be adopted to predict or assess the consolidation behaviour of soft soil beneath an embankment (i.e. multi-drain analysis). Hird et al. (2002);

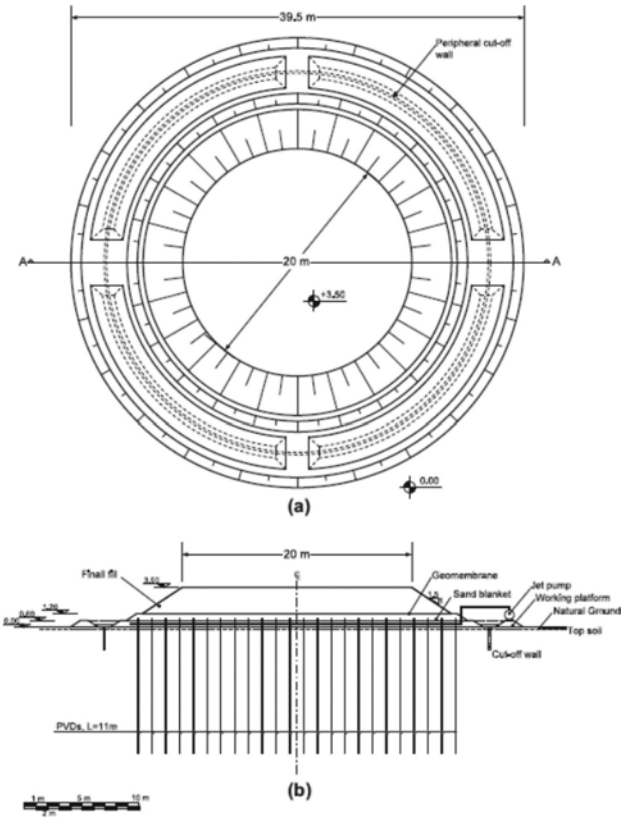

Figure 3. Typical circular embankment plan and cross-section for membrane system (Indraratna et al. 2016 with permission from Computers and Geotechnics).

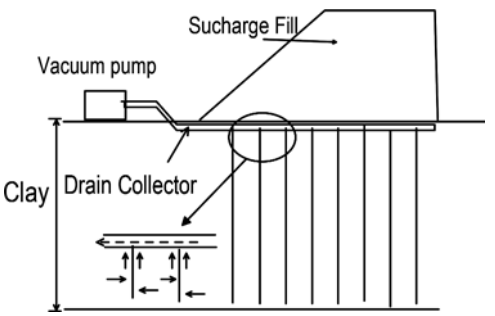

Figure 4. Typical cross section for membraneless system (Indraratna et al. 2015b with permission).

Indraratna and Redana (2000); Chai et al. (2001) showed that conversion techniques are required to ensure the equivalence between axisymmetric (in-situ) and plane strain condition. The equivalent soil permeability in the PVDs zone can be determined based on the drain spacing, in-situ soil permeability, smear zone and the length of the drain. The PVDs zone in finite element modelling can be represented by single equivalent soil permeability with no drain elements. On the other approaches, Hird et al. (2002); Indraratna and Redana (2000) present the permeability conversion by maintaining the geometry of the unit cell. An entire consolidation curve under axisymmetric condition can be captured under equivalent plane strain analysis. In

this approach, individual drains surrounded by smear zone can be modelled explicitly in the analysis. Another advantage of this method is to simulate more realistic consolidation under vacuum preloading. It allows the decayed propagation of the vacuum pressure along the drain and captures inward lateral displacement due to suction (Indraratna et al. 2005).

6 OPTIMUM TIME PERIOD FOR VACUUM PRELOADING APPLICATION

Application of vacuum and fill preloading can further shorten consolidation time. However, extended period of the vacuum application can become uneconomical due to the excessive operation cost of vacuum pumps. Based on laboratory observation supported by field observation at the Port of Brisbane reclamation project in Australia, Kianfar et al. (2015) showed that removal of the vacuum pressure can be decided upon the pore pressure response. In the field, settlement and pore pressure dissipation rates are required through an array of field instrumentation to terminate vacuum pressure (Figure 5)

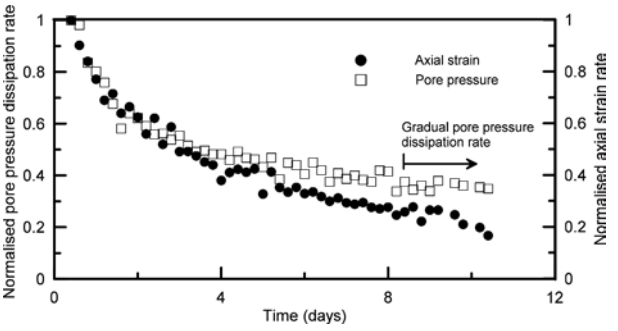

Figure 5. Determination of removal time of vacuum pressure (Kianfar et al. 2015 with permission from CGJ).

7 TIME-DEPENDENT SOIL AND DRAIN PROPERTIES WITH SPECIAL REFERENCE TO BIODEGRADABLE PVDS

In order to analyse the radial consolidation responses due to vertical drains, the unit cell theory representing a single drain surrounded by a soil annulus in axisymmetric condition (3D) was originally proposed by Barron (1948), Richart (1957), Hansbo (1981). Their theories are based on several assumptions including (a) small strain theory, (b) larminar flow (Darcy's law), (c) constant compressibility and permeability, and (d) constant PVDs properties e.g. drain discharge capacity. Indraratna et al. (2011) and (2012) demonstrated that for case studies dealth with larger clay thickness or the application of vacuum preloading, predictions based on conventional redial consolidation theory often deviate from the field observations. Since 2000, several studies have made an attempt to incorporate some features into radial consolidation theory. Indraratna et al. (2017) showed that large strain solution considering non-Darcian flow and variation of compressibility and permeability should be adopted when the vertical strain due to preloading is expected to be more than 15%.

From an environmental point of view, the use of biodegradable natural drains helps to minimise the carbon footprint and improve the environmental sustainability of future infrastructure developments. They also offer a more cost-effective alternative to polymer PVDs and assist rural industries (e.g. jute) in developing Asian nations. The use of biodegradable drains in soft ground is not entirely new. The very first PVD used in Sweden was made of cardboard, while jute drains were trialled in Singapore in the 1970s. This phenomenon of degradation tends to reduce the efficiency of natural drains overtime. Recently, Indraratna et al. (2016) considered the time depedent degaradability of natural

PVDs made from jute, coir and straw in their analytical solution. Figure 6a shows the results of a recent pilot project in Ballina, Australia (2013-2016) where plastic and biodegradable PVDs were installed and monitored in the same condition. It is evident that the settlement and excess pore pressure induced by these two types of PVDs are almost identical, which indicates insignificant influence of biodegradation on soil behaviour. However, this novel type of PVDs can also experience a rapid degradation when subjected to adverse environmental conditions such as surface soils where cellulose degrading bacteria are very active, which can hence hamper considerably the consolidation progress of soil. For example, Figure 1b represents experimental data where an over-degradation of drains causes the dissipation of excess pore pressure severely deviated from the case of normal PVDs. A novel numerical approach where the biodegradation of PVDs is incorporated into the governing equations of soil has been developed, and the results show a good agreement with experimental observation (Figure 6). This finding clearly indicates that attention to biodegradation properties of these fibre drains is seriously needed especially when using them in adverse soil conditions.

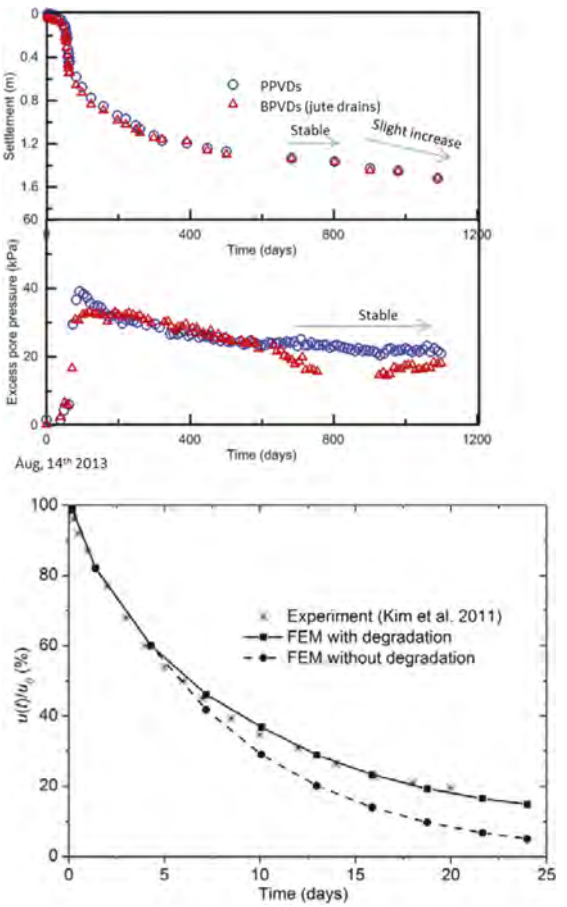

Figure 6. A) Compare the performance of PPVDs and BPVDs in Ballina field and b) Influence of drain degradation on soil consolidation (laboratory observation compared to FEM model) (Indraratna et al. 2018 with permission from Computers and Geotechnics).

8 CONCLUSIONS

In this paper, factors affecting the performance of vacuum preloading with vertical drains were explained and discussed. Salient findings can be summarized as follows:

- Performance of the biodegradable drains is similar to synthetic drains as the influence of the drain degradation becomes minimal at the end of the consolidation.
- PVD length could be reduced by 10% without considerably affecting consolidation time.
- Depending on the installation method and the condition of soil, the extent of the smear zone can vary from 1.3 to 7 times the equivalent mandrel diameter.
- In an area where embankment's instability is an issue due to soil at a shallow depth having very low shear strength or significant height of surcharge, vacuum in combination with fill preloading can become a desirable option.
- Finite element analyses under plane strain condition can be adopted to predict or assess the consolidation behaviour of soft soil beneath an embankment (i.e. multi-drain analysis) with appropriate conversion techniques.
- Removal of the vacuum pressure can be decided upon the pore pressure and time settlement responses.

ACKNOWLEDGEMENT

This research was funded under Australian Research Council (ARC) Linkage scheme s as a collaboration a In this paper, several universities (University of Wollongong, University of Newcastle, Imperial College, London and the University of London) and industry partners (Menard Oceania, Soilwicks, Douglas partners, Coffey geotechnics, National Jute Board of India). The contributions from past research fellows and students including Dr Kirti Choudhar, Prof Geng Xueyu, Dr Ali Ghandeharioon, Dr I Redana, Dr Darshana Perera, Dr Rui Zhong, Dr Pankaj Baral, Dr Kourush Kianfar, is very much appreciated. Most of the content of this paper has already been published in the Canadian Geotechnical Journal, Jorunal of Geotechnical Engineering, ICE, Journal of Geotechnical and Geoenvironmental Engineering, ASCE, Computers and Geotechnics.

REFERENCES

Almeida, M. S. S., Santa Maria, P. E. L., Martins, I. S. M., Spotti, A. P., and Coelho, L. B. M. 2000. Consolidation of a very soft clay with vertical drains. *Geotechnique*, 50, Issue 6, pp633–643.

Barron R.A. 1948. Consolidation of fine-grained soils by drain wells. *Transactions, ASCE*, 113: 718–754.

Basu D, Prezzi M. 2007. Effect of the smear and transition zones around prefabricated vertical drains installed in a triangular pattern on the rate of soil consolidation. *Int J Geomech*;7(1):34–43.

Bergado, D. T., Balasubramaniam, A. S., Fannin, R. J., and Holtz, R. D. 2002. Prefabricated vertical drains (PVDs) in soft Bangkok clay: A case study of the new Bangkok International Airport project. *Can. Geotech. J*., 39(2), 304–315.

Cai, Y., Xie, Z., Wang, J., Wang, P., Geng, X., 2018. A new approach of vacuum preloading with booster PVDs to improve deep marine clay strata. *Can. Geotech. J*. 55, 1359–1371.

Chai, J.-., Shen, S.-., Miura, N. & Bergado, D.T. 2001, Simple method of modeling PVD-improved subsoil, *Journal of Geotechnical and Geoenvironmental Engineering*, vol. 127, no. 11, pp. 965–972.

Chai, J. C., Miura, N., and Bergado, D. T. 2008. Preloading clayey deposit by vacuum pressure with cap-drain: Analyses versus performance. *Geotexiles and Geomembranes*, 26: 220–230.

Choudhary, K., Indraratna, B. & Rujikiatkamjorn, C. 2016, Pore pressure based method to quantify smear around a vertical drain, *Geotechnique Letters*, vol. 6, no. 3, pp. 211–215.

Chu, J. Yan, S.W., and Yang, H. 2000. Soil improvement by the vacuum preloading method for an oil storage station. *Geotechnique*, 50(6): 625–632.

Cognon JM, Juran I and Thevanayagam S 1994, Vacuum consolidation technology – principles and field experience. *Proceedings of the Conference on Vertical and Horizontal Deformations of Foundations and*

Embankments, College Station, TX, USA, (Yeung AT and Felio GY (eds.)). ASCE, New York, NY, USA, Geotechnical Special Publication 40, pp. 1237–1248.
Geng, X., Indraratna, B. & Rujikiatkamjorn, C. 2011, Effectiveness of partially penetrating vertical drains under a combined surcharge and vacuum preloading, *Canadian Geotechnical Journal*, vol. 48, no. 6, pp. 970–983.
Ghandeharioon, A., Indraratna, B. & Rujikiatkamjorn, C. 2012, Laboratory and finite-element investigation of soil disturbance associated with the installation of mandrel-driven prefabricated vertical drains, *Journal of Geotechnical and Geoenvironmental Engineering*, vol. 138, no. 3, pp. 295–308.
Hansbo, S. 1981. Consolidation of fine-grained soils by prefabricateddrains and lime column installation. *Proc., 10th Int. Conf. onSoil Mechanics and Foundation Engineering*, Vol. 3, Balkema,Rotterdam, Netherlands, 677–682.
Hart, E.G., Kondner, R.L., and Boyer, W.C. 1958. Analysis for partially penetrating sand drains. *Journal of the Soil Mechanicsand Foundations Division, ASCE*: 84(4): 1–15
Hird, C.C. & Sangtian, N. 2002, Model study of seepage in smear zones around vertical drains in layered soil: Further results, *Geotechnique*, vol. 52, no. 5, pp. 375–378.
Hird C.C., Pyrah I.C., and Russel D. 1992. Finite element modeling of vertical drains beneath embankments on soft ground. *Geotechnique*, 42(3): 499–511.
Indraratna B, Redana IW. 1997 Laboratory determination of smear zone due to vertical drain installation. *J Geotech Geoenviron Eng* 1998; 124:180–4.
Indraratna, B., and Redana, I. W. 2000. Numerical modelling of vertical drains with smear and well resistance installed in soft clay. *Can. Geotech. J*., 371, 133–145.
Indraratna, B., Rujikiatkamjorn, C., and Sathananthan, I. 2005. Radial consolidation of clay using compressibility indices and varying horizontal permeability. *Can. Geotech. J*., 42(5), 1330–1341.
Indraratna, B., Rujikiatkamjorn, C., Ameratunga, J., and Boyle, P. 2011 Performance and Prediction of Vacuum Combined Surcharge Consolidation at Port of Brisbane. *J. of Geotechnical & Geoenvironmental Engineering*, ASCE, 137 (11), 1009–1018.
Indraratna, B., Rujikiatkamjorn, C., Kelly, R., and Buys, H. 2012. Soft soil foundation improved by vacuum and surcharge loading. *Proceedings of the ICE - Ground Improvement* 165, 87–96.
Indraratna, B., Perera, D., Rujikiatkamjorn, C. & Kelly, R. 2015a, Soil disturbance analysis due to vertical drain installation, *Proceedings of the Institution of Civil Engineers: Geotechnical Engineering*, vol. 168, no. 3, pp. 236–246.
Indraratna, B., Rujikiatkamjorn C., Balasubramaniam, A. S. and Wijeyakulasuriya, V. 2015b. Predictions and observations of soft clay foundations stabilized with geosynthetic drains and vacuum surcharge. *in Embankments with Special Reference to Consolidation and Other Physical Methods*. Elsevier Scientific (UK). Edited by Indraratna, B. Chu, J. and Rujikiatkamjorn, C., pp. 209–240.
Indraratna, B., Kan, M. E., Potts, D., Rujikiatkamjorn, C. and Sloan, S. 2016. Analytical Solution and Numerical Simulation of Vacuum Consolidation by Vertical Drains beneath Circular Embankments, *Computers and Geotechnics*, 80, pp. 83–96.
Indraratna, B., Zhong, R., Fox, P.J. & Rujikiatkamjorn, C. 2017, Large-strain vacuum-assisted consolidation with non-Darcian radial flow incorporating varying permeability and compressibility, *Journal of Geotechnical and Geoenvironmental Engineering*, vol. 143, no. 1, DOI: 10.1061/(ASCE)GT.1943-5606.0001599.
Indraratna, B., Baral, P., Rujikiatkamjorn, C. & Perera, M. 2018. Class A and C predictions for Ballina trial embankment with vertical drains using standard test data from industry and large diameter test specimens. *Computers and Geotechnics*, 93 232–246.
Johnson, S. J., 1970. Precompression for improving foundation soils. *J. of the Soil Mechanics & Foundations Division*, ASCE, 1: 111–114.
Kianfar, K., Indraratna, B., Rujikiatkamjorn, C. & Leroueil, S. 2015, Radial consolidation response upon the application and removal of vacuum and fill loading, *Canadian Geotechnical Journal*, vol. 52, no. 12, pp. 2156–2162.
Kjellman WA. 1948. Discussion: Consolidation of fine-grained soils by drain wells. *Transactions of the American Society of Civil Engineers* 113(2346): 748–751.
Lee, S.L., Karunaratne, G.P., Ramaswamy, S.D., Aziz, M.A., Das Gupta N.C., 1994. Natural geosynthetic drain for soil improvement, *Geotext Geomembr*, 13 (6–7), pp. 457–474.
Miura, N. & Chai, J.-. 1999, Investigation of factors affecting vertical drain behavior, *Journal of Geotechnical and Geoenvironmental Engineering*, vol. 125, no. 3, pp. 216–226.
Ong CY, Chai JC, Hino T 2012. Degree of consolidation of clayey deposit with partially penetrating vertical drains. *Geotextiltes and Geomembranes* 34:19–27. 10.1016/j.geotexmem.2012.02.008
Qian, J.H., Zhao, W.B., Cheung, Y.K. and Lee, P.K.K. 1992. The theory and practice of vacuum preloading. *Computers and Geotechnics*, 13: 103–118.

Parsa-Pajouh, A., Fatahi, B., Vincent, P. & Khabbaz, H. 2014, Trial Embankment Analysis to Predict Smear Zone Characteristics Induced by Prefabricated Vertical Drain Installation, *Geotechnical and Geological Engineering*, vol. 32, no. 5, pp. 1187–1210.

Pothiraksanon, C., Saowapakpiboon, J., Bergado, D.T. & Than, N.M. 2008, Reduction of smear effects around PVD using thermo-PVD, *Proceedings of the Institution of Civil Engineers: Ground Improvement*, vol. 161, no. 4, pp. 179–187.

Richart F.E. 1957. A review of the theories for sand drains. *Journal of the Soil Mechanics and Foundations Division*, ASCE, 83(3): 1–38.

Rixner, J.J., Kraener, S.R., and Smith, A.D. 1986. *Prefabricated vertical drains. Summary and research effort – final report*. Federal Highway Administration. US Department of Commerce, Washington, D. C. Report FHWA-RD-86–169. Vol. 2.

Rujikiatkamjorn, C. & Indraratna, B. 2014, Analytical solution for radial consolidation considering soil structure characteristics, *Canadian Geotechnical Journal*, vol. 52, no. 7, pp. 947–960.

Sengul, T., Edil, T. & Ozaydin, K. 2017, Laboratory determination of smear and transition zones due to prefabricated vertical drain installation, *Marine Georesources and Geotechnology*, vol. 35, no. 7, pp. 895–904

Shang, J.Q., Tang, M., Miao, Z., 1998. Vacuum preloading consolidation of reclaimed land: a case study. *Canadian Geotechnical Journal*, 35, 740–749.

Sharma, J.S. & Xiao, D. 2000, Characterization of a smear zone around vertical drains by large-scale laboratory tests, *Canadian Geotechnical Journal*, vol. 37, no. 6, pp. 1265–1271.

Shen, S.-L., Chai, J.-C., Hong, Z.-S., and Cai, F.-X. 2005. Analysis of field performance of embankments on soft clay deposit with and without PVD-improvement. *Geotextiles and Geomembranes*, 23, 6, pp463–485.

Sun, L., Guo, W., Chu, J., Nie, W., Ren, Y., Yan, S., Hou, J., 2017. A pilot test on a membraneless vacuum preloading method. *Geotext. Geomembranes* 45 (3), 142–148.

Zeng, G.X., and Xie, K.H. 1989. New development of the vertical drain theories. *In Proceedings of the 12th International Conference on Soil Mechanics and Foundation Engineering (ICSMFE)*, Rio de Janeiro, Brazil, 13–18 August 1989. Balkema, Rotterdam, the Netherlands. Vol. 2, pp. 1435–14

Zhu, G. & Yin, J. H. 2000, Finite element consolidation analysis of soils with vertical drain, *International Journal for Numerical and Analytical Methods in Geomechanics*, vol. 24, no. 4, pp. 337–366.

Smart Geotechnics for Smart Societies – Zhussupbekov, Sarsembayeva & Kaliakin (Eds)
© 2023 The Author(s), ISBN 978-1-003-29912-7
Open Access: www.taylorfrancis.com, CC BY-NC-ND 4.0 license

Preservation and restoration of monuments: The authenticity principle in geotechnical interventions

C. Tsatsanifos
Pangaea Consulting Engineers Ltd., Athens, Greece

ABSTRACT: Generally, the authenticity principle has been discussed for the superstructures of historic monuments and not for their foundations. Interventions on the foundations or on the embankments on which some monuments have been built have not usually been deemed necessary, while there are many examples where either the type of the foundation or the embankment was developed in some special way according to regional characteristics, or the foundation or the embankment itself is of historic heritage. In this paper case studies of geotechnical interventions for the preservation and restoration of monuments are presented and discussed and questions are posed regarding the application of the authenticity principle.

1 INTRODUCTION

The principles on the conservation and restoration of monuments were initially set at the 1st and 2nd International Congresses of Architects and Technicians of Historic Monuments held in Athens (1931) and Venice (1964) respectively, which adopted the so-called "The Athens Charter" and "The Venice Charter".

"The Athens Charter" introduced the word anastylosis as defining the conservation method which intends to keep the authenticity of the monuments: "*In the case of ruins, scrupulous conservation is necessary, and steps should be taken to reinstate any original fragments that may be recovered (anastylosis), whenever this is possible; the new materials used for this purpose should in all cases be recognizable*".

Later on, in "The Venice Charter" it was stated that "*The process of restoration is a highly specialized operation. Its aim is to preserve and reveal the aesthetic and historic value of the monument and is based on respect for original material and authentic documents … Where traditional techniques prove inadequate, the consolidation of a monument can be achieved by the use of any modern technique for conservation and construction, the efficacy of which has been shown by scientific data and proved by experience*".

The authenticity principle was concluded in "The Nara Document on Authenticity", drafted by the participants at the Nara Conference on Authenticity in Relation to the World Heritage Convention, held at Nara, Japan, in November 1994. Accordingly, the authenticity should be determined in a manner respectful of cultures and heritage diversity to include any variation of the regional tradition of conservation of heritage.

2 THE AUTHENTICITY PRINCIPLE IN GEOTECHNICAL ENGINEERING

The authenticity principle has been discussed for geotechnical historic monuments (superstructures) like retaining structures, earth/rock fill dams, embankments etc. However, the foundations of historic monuments were not considered as one of the elements that constitute historic monuments and have been changed and modified without any concern for authenticity. The same

DOI: 10.1201/9781003299127-24

applies for the embankments on which some monuments have been built in some special way according to regional characteristics, or for the foundation ground. In these cases, the type of the geotechnical structure might be preferred to keep its originalities.

Based on the above, the International Scientific Committee on the Analysis and Restoration of Structures of Architectural Heritage under ICOMOS (ISCARSAH) had proposed and was accepted to include heritage structures in the ISO 13822:2010 Bases for design of structures – Assessment of existing structures. ISO 13822:2010 has expanded the heritage structure to include foundation as a part of the structure. Furthermore, in paragraph of I.5.3 of the Annex I: Authenticity of Foundation it is stated: *From the point of view of conservation, foundations are not different from the rest of the structure and should be assessed and rehabilitated taking into consideration their heritage value. This involves the requirement to identify their authenticity and character-defining elements.* (Iwasaki et al., 2022).

The foundation ground has not been considered with respect to authenticity, because, over the years of the life of the monument, disrupting natural and anthropic agents introduce changes in the prevailing geotechnical conditions of the site. These agents may strongly affect the foundation system of the monument, or the ground on which the monument has been built, requiring major interventions in order to strengthen the foundation of the structure or the ground. In such cases, the full compliance with the authenticity and anastylosis principles is not possible.

The authenticity principle can be somehow violated in the case of interim or temporary remedial measures.

3 METHODS OF GEOTECHNICAL PRESERVATION AND RESTORATION OF MONUMENTS

The International Society for Soil Mechanics and Geotechnical Engineering promoted, over 30 years ago, an ad hoc Committee on the Preservation of Monuments and Historic Sites, initially numbered TC19 and currently TC301, to study methods of conservation of monuments and historic sites. The committee focuses on the organisation of symposia and workshops with the aim to exchange and compare experiences and to collect case histories of preservation of monuments, as well as well as on the preparation of a set of guidelines on conservation and preservation of monuments and historic sites. However, as stated in the objectives of TC301, considering that each monuments is a "unicum" and taking into account the concept of "integrity", it is rather difficult to apply approaches based on guidelines to the preservation of monuments and the effort is devoted to:

- Framing of the special requirements and constraints to be considered in any rehabilitation intervention on Monuments in order to preserve their cultural and historical integrity;
- Geotechnical methodologies suitable for the interventions on Monuments and Historic sites.

Poulos (2005) and (Ulitsky, 2005) attempted a division of the methods for the geotechnical restoration of monuments, into two broad categories:

i. "Hard" methods, which rely on changes on the foundation of the monument or on the application of some form of direct force to the foundation, like:
– Repair of the existing foundation or strengthen it by its extension,
– Provide additional supports,
– Underpin the foundations by means of piles constructed through the body of the foundation,
– In case of pile foundations extend the pile caps or rafts to provide additional bearing capacity and stiffness,
– In case of uneven settlements application of force by anchor stressing, additional loading, jacking of the foundation on the "low" side.

ii. "Soft" methods, which rely on processes improving the subsoil or produce corrective foundation movements by inducing appropriate ground movements, like:
– Soil extraction and underexcavation,

– Dewatering or inducing changes in the pore water pressures by local injection of water or by electro – osmosis,
– Compensation grouting,
– Removal of soil support,
– Improve the subsoil (cementation, silication, chemical and electro - chemical strengthening, high pressure grouting capable of stabilising the soil mass, deep soil mixing, soil nailing, rock anchoring etc.),
– Isolation or separation trenches between new and existing building – monument.

From the above methods only the isolation or separation trenches seem to fully comply with the authenticity and anastylosis principle. The "hard" methods alter the foundation system, while the other "soft" methods alter the subsoil conditions.

4 CASE STUDIES

4.1 *Retaining walls*

4.1.1 *The treasures retaining wall and the retained upslope at the Ancient Olympia (Egglezos and Karnavezos, 2014)*

The retaining wall of the treasures of the Sanctuary of Olympia (Figure 1a) is the northern part of the sanctuary's enclosure and retains the slope of the Kronian hill. The material of construction of the domes of the wall is bioclastic limestone. A provincial road passes upstream of the wall.

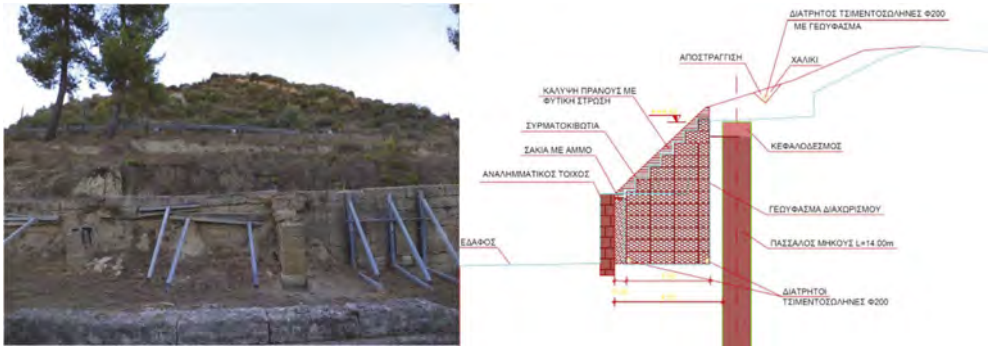

Figure 1. (a) Photo of the Treasures Retaining Wall. (b) Final phase of the restoration measures behind the ancient retaining wall.

The wall was probably constructed in the second half of the 4th century. Many landslides occurred and consecutive repairs, up to and including Roman imperial times. After the destruction of the Sanctuary of Olympia, possibly in 426 A.D., landslides and floods slowly covered with alluvial all the ancient monuments, including the retaining wall of the Treasures, which came to light again during the excavations of the German Archaeological Institute in the years 1875-1881.

The earth pressures and the roots of the trees on the slope have caused deformation of the original geometry of the wall and have damaged blocks of the wall. A detailed field reconnaissance has been conducted, which concluded that there is sliding (or near sliding condition), with the failure surface passing under the wall, the crest under the upstream road and the toe on the northern boundary of the foundations of the Treasures.

Based on these findings, a detailed geotechnical analysis has been conducted in order to investigate the current stability of the retaining wall and the upstream slope. The results of the analysis concluded that:

i. The area of Kronion hill upstream of the road is in a state of surface instability, consistent with the macroscopic observations.
ii. There are no general instabilities under static conditions; however, the safety factors for the historical earthquake loading are marginally inadequate and absolutely inadequate taking into account high water level behind the slope, as well as the regulatory earthquake. Local instabilities upstream of the wall occur systematically for all analysed cross-sections and for all load states (even in the case of static conditions – a favourable case).

To increase the stability of the whole system, the following measures have been designed (Figure 1b):

a. A pile diaphragm (piles Ø120 every 2.40m) to stabilize the upstream slope against sliding.
b. Relief of earth pressures on the wall by placing gabion boxes and sand bags between the wall and the piles.
c. Construction of a drainage system to relieve the wall from the adverse action of the water (surface flowing stormwater upstream of the piles and water moving underground within the soil mass of the slope at the base of the gabions).
d. Cover with topsoil of the restored slope.
e. Reinforcement of the temporary metal retaining structure during the construction phase of the project, to safely take over any additional loads on the wall from the operation of the construction equipment.

According to the authors, the design of the stabilisation measures achieves, at a reasonable financial cost, the desired safety of the upstream slope against an existing slip, the reduction of the earth pressures on the ancient retaining wall (and therefore the wall is not required to act as the main retaining structure of the slope), the possibility of carrying out restoration works of the monument, according to its final restoration design, with safety for employees, as well as the future safe passage of visitors along the base of the slope. In addition, it contributes to the safety of antiquities that extend along the base of the wall (foundations of the Treasures), to the stability of the upstream road, as well as to the prevention of relatively deep slipping surfaces, which could, under certain conditions, emerge, having their crest on the hill upstream of the road.

Regarding the retaining structure, the proposed solution is fully compatible with the authenticity principle; however, the initial ground conditions as well as the loading conditions of the monument are changed (these "initial" conditions have changed many times in the past due to excavations and Kladeos river deposits). Hence, one could argue that the solutions does not totally respect the authenticity principle, since it should reinstate the ground behind the wall. But, maybe this is the only solution to solve the monument without any direct action on it.

4.1.2 *Angkor monuments (Iwasaki et al., 2022)*

The Baphuon Temple

The Baphuon temple was built in mid11th century in Angkor Thom and was dedicated to the Hindu God Shiva. In the late 15th century, the temple was converted to a Buddhist temple.

In 1943, the northeastern side of the slope of the temple failed as a result of excessive water penetration due to rainfall. Figure 2a shows the original structure of a stone masonry retaining wall with thin layers of crushed laterite chips, of 1–2 cm in thickness, embedded in compacted sandy layers for possibly drainage of infiltrated water, extending 4m to 5m behind the wall.

École Française d'Extrême-Orient (EFEO) had started the restoration work in 1958 and tried to reconstruct the original structure but failed when the fill mound reached at 5m in height. They tried three times to replicate the original structure, but in vain. As a result, the stone masonry retaining wall was substituted by a reinforced concrete retaining wall as shown in Figure 2b. The original stones were reused to cover the front face of the concrete wall.

West causeway of Angkor Wat

The west causeway of Angkor Wat is the gateway that overpasses the 190m wide moat, as shown in Figure 3a. The causeway consists of earthen embankment between two stone masonry retaining walls consisting of lateritic blocks. The original structure of retaining wall

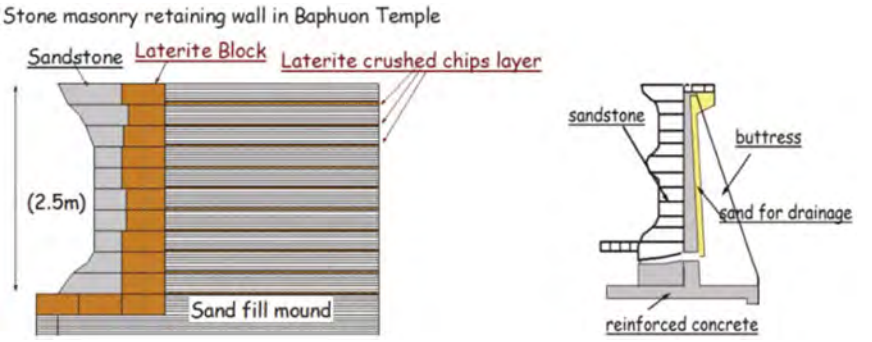

Figure 2. (a) Original masonry retaining wall, (b) Reinforced concrete.

is shown in Figure 3b. After the failure of the causeway in 1952 as a result of infiltration of water due to heavy rain, EFEO performed restoration work for the southern side of the retaining structure using reinforced concrete as shown in Figure 3c.

Figure 3. (a) Retaining wall structure of the west causeway of AngkorWat (south side). (b) Original structure, (c) RC-retaining wall (EFEO) and (d) RC-retaining wall (Sophia Univ.).

The second phase of the restoration work for the northern side of the west causeway of Angkor Wat has been studied by Sophia University as shown in Figure 4d. It is a modification of the EFEO design, using again a concrete retaining structure. The backfilled soil behind the masonry wall is excavated first and the reinforced concrete retaining wall is placed behind the existing retaining wall. The existing weathered and decayed lateritic blocks are anchored to the RC wall and maintained as it is.

In the EFEO design the original wall was removed, the concrete retaining structure was built and the blocks of the original wall were reinstated in front of the concrete wall. In the University of Sophia alternative there was no intervention on the original wall except the anchoring of the blocs on the RC wall.

Prasat Suor Prat

Prasat Suor Prat consists of 12 towers and located on the east side of the Royal Plaza, Angkor Thom. The towers are constructed almost exclusively of lateritic blocks with sandstone accessories and door/window jambs.

N1-tower has inclined 4–5 degrees northward from the vertical, representing the largest inclination in all towers of Prasat Suor Prat. Further to the inclination, its foundation was spreading outwards in all directions.

It was difficult to identify the reason why the tower was inclined and spread out. Therefore, it was decided to dismantle the upper structure as well as the foundation to excavate archaeological trench. The base of the tower is 10m by 10m on a filled mound with lateritic masonry retaining structure.

Figure 4a shows N-S section of foundation of the N1 tower. The surrounding retaining wall was inclined to the north by 0.4m settlement for 10m width. The basement of the retaining structure at the north side was found to have settled and slid outwards as shown in Figure 4a. The vertical weight had caused compression of the fill as well as outward spreading.

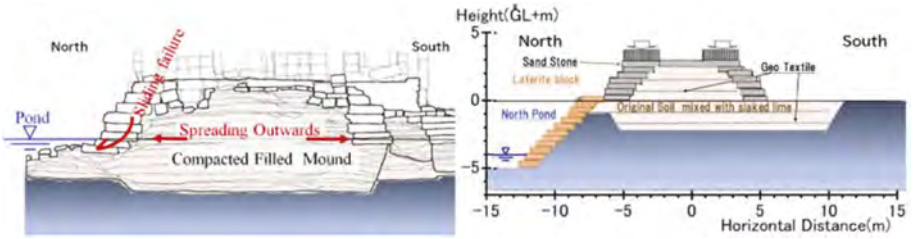

Figure 4. (a) Trenched section of N1 tower. (b) Restoration of foundation of N1 tower.

The Japanese Government for Safeguarding Angkor Team (JSA) had introduced a traditional technology of slake lime mixed with the original sand, which improves the strength characteristics with geo-textile to increase the tension strength of the fill. Adding about 10% of the slaked lime to the original soil resulted in increasing strength with durability against water submersion (Figure 4b).

In all the case studies presented by Iwasaki et al. (2022) practically there was a complete reconstruction of the monuments. In the first two cases new structural members were introduced, but covered with the original blocks of the wall and, consequently, not visible to the visitor, and the original soil was used for backfilling. We could say that the authenticity and anastylosis principles were applied for the visible parts of the monuments (reassembly of existing but dismembered parts), though the material used for integration is hidden and not identifiable.

In the case of the N1 Tower of Prasat Suor Prat the reconstruction did not use new structural members. The original blocks of the wall as well the original soil were used, the latter being compacted with the addition of slake lime (a traditional method) but also with geotextile to increase the tension strength of the fill. At the end, one could say that the authenticity and anastylosis principles were applied for the restoration of the monument, though the addition of geotextile does not conform to them, but it is hidden and not identifiable.

4.2 *Foundations*

4.2.1 *The National Bank of Greece administration building and the acharnian gate of the Ancient Athens circuit wall (Tsatsanifos and Pasqualin, 2013)*

The archaeological excavation prior to the construction of the new administration building of the National Bank of Greece (NBG) at the centre of modern Athens brought to light important antiquities concerning the approach to the Acharnian Gate of the ancient Athens circuit wall.

The preservation and the exhibition of the antiquities were prerequisites for constructing the building at this site. This, combined with the other operational prerequisite that the building should have underground floors formulated a serious geotechnical problem, requiring innovative solution to be overcome.

The building was designed taking into account these requirements. Figure 5a shows a drawing of the building with the antiquities preserved in the ground floor – basement.

The solution involved the temporary excavation and support under the antiquities without any interference with them. Figure 6a shows the plan of the whole temporary support system, i.e. that for the excavation walls and that for the antiquities.

The "Berlin" type wall was used for the temporary support of the vertical slopes of the excavation. This is a rather flexible support system consisting of vertical steel beams (2 steel ∏ or, sometimes, bored reinforced concrete piles), earth anchors and shotcrete.

The method of the forepoles (horizontal micro piles) was used for the support of the antiquities and horizontal steel beams were welded to the steel piles under the forepoles, in order to act as their support after the excavation of the ground under the fore poles (Figure 6b). To ensure the good contact of the fore poles and the steel beams, shotcrete was applied. Finally, steel tube trusses were used for the lateral support of the system.

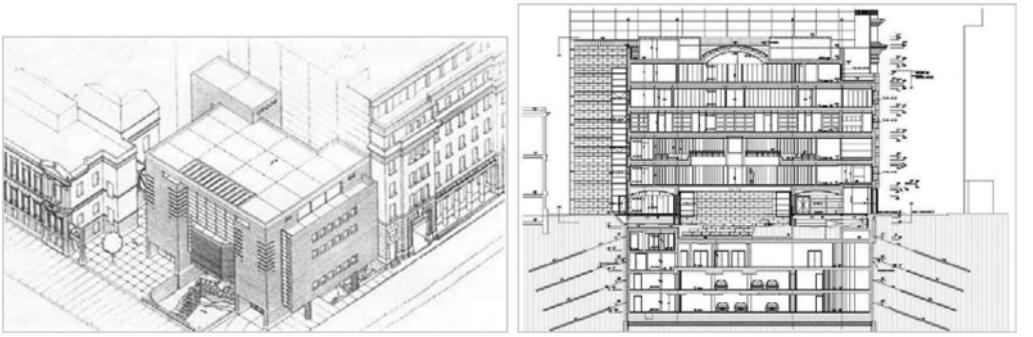

Figure 5. (a) Drawing of the NBG Administration Building with the antiquities preserved in the ground floor – basement. (b) Cross section with the underground floors below the antiquities.

Figure 6. (a) Plan of the temporary support system for the construction of the building. (b) Construction of the fore poles under the antiquities.

In the next stage the ground under the fore poles was excavated and a layer of shotcrete, reinforced with steel wire mesh was applied. The final step was the concreting of the roof slab of the 2nd basement, just under the fore poles supporting the Acharnian Gate.

The method applied did not affect the antiquities or their foundations. Hence, from this point of view the solution is fully compatible with the authenticity principle; however, the initial ground conditions have changed: the monument is resting on a concrete slab instead on the original ground. So, one could argue that the solutions does not totally respect the authenticity principle. But, this is the only solution to retain the monument in place without any direct action on it. The other solution, which has been applied in a number of cases in Greece is the total dismantling of the monument and its re-erection at a different site or on top of the new structure.

4.2.2 *Foundation strengthening of the AEB Bank building in Budapest (Sata, 2003)*

This is again an example where underground space was required under a historical building. The AEB Bank chose a two-storied historic building for its headquarters in Budapest (Figure 7a). The renewal, re-utilisation and enlargement of the building should follow the original architecture. An underground garage had also to be constructed, requiring the deepening of the foundation level. In this case underpinning for strengthening the foundation of the building was used.

The main concern was to minimize the settlements to acceptable for the historic structure levels. It was achieved by inducing a pre-stressing force between the wall and the piles, which acted against the gravitational force of the wall.

In this case, the method has changed completely the foundation of the structure, hence the authenticity principle, regarding the foundation, has not been respected. But again for a building of this size and for the requirement of creating a basement floor, this was the only solution.

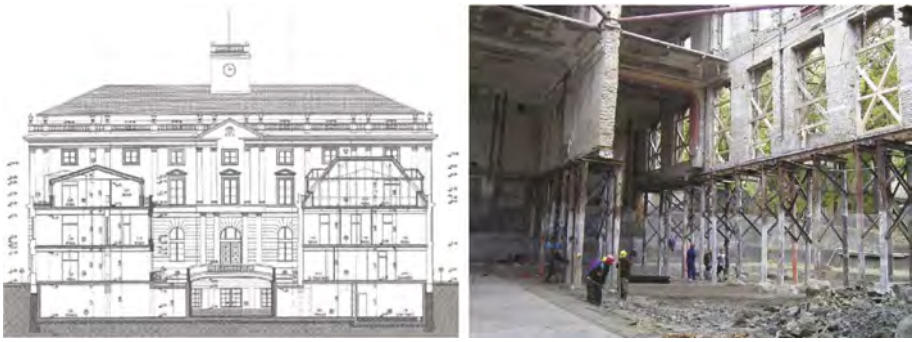

Figure 7. (a) Architectural section of the renewed AEB Bank in Budapest. (b) The building "in the air".

4.2.3 *Underpinning. The cases of the 1st High-School Building of Thessaloniki and the Catholic Church in Giannitsa (Tsotsos and Naskos, 1995)*

According to the authors the problems of the building was the result of the higher applied stresses, compared to the estimated bearing capacity of the ground, combined with the differentiation of the water content under the building, which led to swelling or settlement in different parts of the foundation.

The restoration consisted of seven pairs of micro-piles, along the problematic area and the underpinning of the old foundation with an equal number of perpendicular to the walls beams connected to the pile heads (Figure 8). The whole operation of this intervention was done from the outside and there was no disruption of the operation of the church.

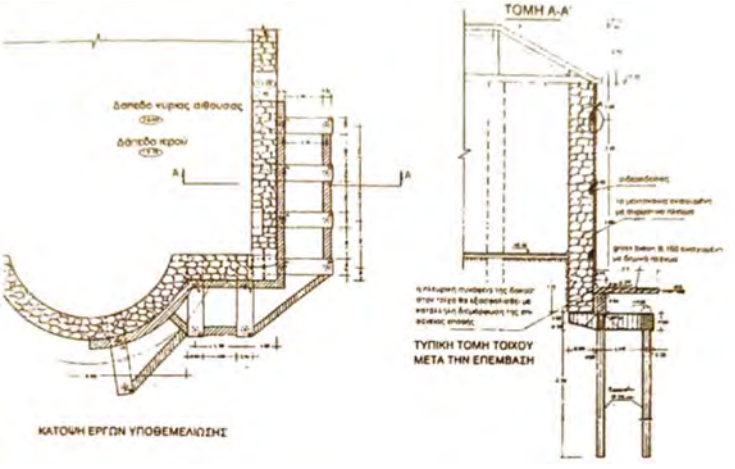

Figure 8. Schematic presentation of the underpinning works in the northeastern part of the Church.

In this case, the method has changed part of the foundation of the structure, hence the authenticity principle, regarding the foundation, has not been respected. However, there was no intervention in the superstructure of the monument.

4.3 *Interventions on the foundation ground*

4.3.1 *The leaning Tower of Pisa (Burland et al., 2003)*

The most famous example of the contribution of geotechnical engineering in the restoration of a monument is that of the Leaning Tower of Pisa, where the soil extraction method has been applied.

The tower is founded on weak, highly compressible soils and its inclination has been increasing inexorably over the years to the point at which it was about to reach leaning instability (about 5.5 degrees to the vertical, see Figure 9).

Since the internationally accepted conventions for the conservation and preservation of monuments and historic sites provided that any intrusive intervention on the Tower had to be kept to an absolute minimum, permanent stabilisation schemes involving propping or visible support were unacceptable and in any case could have triggered the collapse of the fragile masonry. After a careful consideration of a number of possible approaches, the International Committee for the Safeguard and Stabilisation of the Tower of Pisa, appointed by the Italian Government, adopted a controlled removal of small volumes of soil from beneath the north side of the tower foundation (underexcavation).

This technique provided an ultra-soft method of increasing the stability of the tower, which is completely consistent with the requirement of architectural conservation.

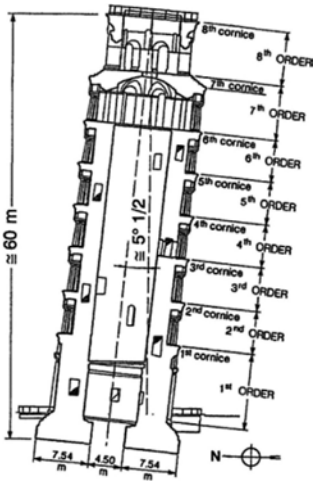

Figure 9. Cross section of the leaning Tower of Pisa.

Different physical and numerical models have been employed to predict the effects of soil removal on the stability. The preliminary underexcavation intervention, only undertaken once the Commission was satisfied by comprehensive numerical and physical modelling together with a large scale trial, has demonstrated that the tower responds very positively to soil extraction. The final underexcavation has attained the target of reducing the tilt of the tower by half a degree, i.e. to bring the tower "back to future" to the time just before the excavation of the catino in 1838.

The application of the method did not change the foundation of the tower; however it changed the subsoil, if we consider the soil extraction as change. The Pisa Tower intervention is the case with the highest respect of the authenticity and anastylosis principles.

4.3.2 *Design of the Stabilisation of the NW wing of the Stavronikita Holy Monastery (Arvanitakis and Monokroussos, 1988)*

The Stavronikita Monastery lies on the northern coast of the Athos peninsula, at the top of a rocky outcrop about 40m above sea level.

The monastery was built in the 16th century and has undergone many additions since then. However, the 1932 Ierissos earthquake cracked many parts the walls of the monastery over the steep slopes, as well as the rock formation, while the 1978 Thessaloniki earthquake accelerated the phenomenon of new cracks on the walls and in the rockmass and widening of their apertures. The cracks in the rockmass resulted in rockfalls, underexcavations and general stability problems.

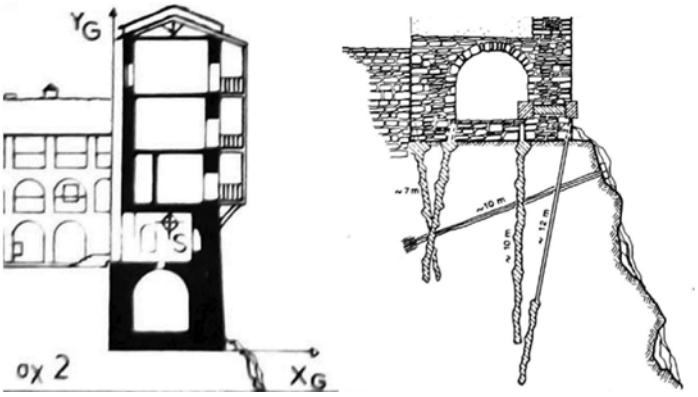

Figure 10. (a) Cross section at the problematic area. (b) Stabilisation measures.

The stabilisation measures proposed by the designers consisted of micropiles, through the existing foundation of the walls, combined with rock anchors in order to increase the stability of the rock slope, as shown in Figure 10a and 10b.

In this case study the method applied for the restoration do not respect the authenticity and anastylosis principles either for the foundation of the monument or for the rockmass; however it seems that it was the only visible solution for the preservation of the monuments.

4.4 *Temporary or permanent Burial of antiquities (Tsatsanifos, 2017)*

Many antiquities have being found during the excavations for the reconstruction of an old 3 storey and a basement building at the Plaka area of central Athens, consisting of parts of marble roman baths and "siroi" (large storage earthen jars in the ground) of the Byzantine era (Figure 11).

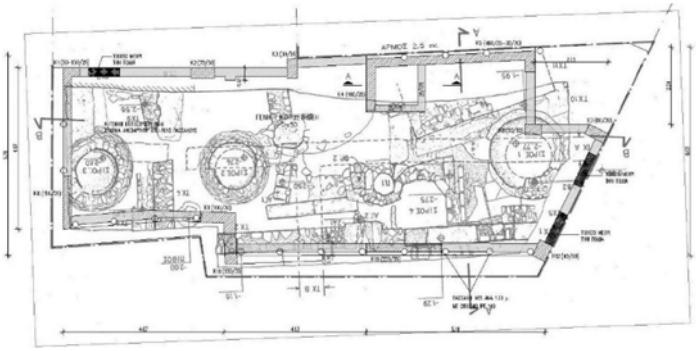

Figure 11. Plan of the foundation of the building at Cherefontos with the antiquities found (Tsatsanifos, 2017).

After the detailed archaeological investigations, the archaeological service decided that the antiquities could be buried and the new structure be built over them. However, since the burial of any ancient monument is considered as intervention to the monument, some rules should be followed, particularly the Articles 9, 10, 11, 12, 13, 14 and 15 of the Venice Charter.

In this particular case the new building will have a raft foundation and the burial would be performed using well graded sand with less than 5% fines.

This is a case where the authenticity and anastylosis principles were fully respected; however, not for us but the future generations.

5 CONCLUSIONS

From the case studies presented from different parts of the world it seems that the full compliance with the authenticity principle is relatively easy for the superstructure of the geotechnical monuments but it is very difficult regarding the foundations of the monuments. However, considering that in almost all the cases the foundations are not visible, we can violate the principle of authenticity and apply any available method in order to succeed in the stability of the monument.

The serious problem arises when we are discussing about the foundation ground. Can the foundation ground been considered as a monument itself? Maybe not. We have accepted that natural and anthropic agents may have reduced the shear strength or increased applied stress leading to bearing capacity failures of the monument on it. For example the rock outcrops, on which many of the Mount Athos monasteries have been built, during the 1,000 years life of the monasteries, have undergone weathering, fracturing, earthquake loading etc. and now they cannot support the structures on them. Hence it is imperative to apply some retaining measures on them. On the other hand the actions of the foundation ground on the monument have been changed and, as D' Agostino said, the stabilizations measures should not modify the soil - structure relation.

Finally, it seems that the soil extraction as well as the support of the monument well below its foundation are the methods with the highest respect of the authenticity and anastylosis principles.

REFERENCES

Arvanitakis, M. and Monokroussos, D. 1988. Design of the Stabilisation of the NW Wing of the Stavronikita Holy Monastery. In *Proc. 1st Panhellenic Conference on Geotechnical Engineering*, 3-5 February, *Athens, Greece 1977*, pp. 307–311 (in Greek).

Burland, J.B, Jamiolkowsky, M. & Viggiani, C. 2003. The Stabilisation of the Leaning Tower of Pisa. In *Soils and Foundations*, Vol. 43, No. 5, pp. 63–80.

Egglezos, D.N. and Karnavezos, C. 2014. Protection measures of the Treasures Retaining Wall and the retained upslope at the Ancient Olympia. In *Proc. 7th Panhellenic Conference on Geotechnical Engineering, Session VII Environmental Geotechnics, Cultural Heritage and Geotechnical Engineering_VII.5*, 7-9 September, *Athens*, *Greece 2014* (in Greek).

Iwasaki, Y., Fukuda, M., Ishizuka, M. McCarthy, R., Akazawa, Y., Nakagawa, T. and Ly, V. 2022. The authenticity and the integrity of the soil and the foundation of heritage structure in Angkor. In *Proceedings 3rd International Symposium on Geotechnical Engineering for the Preservation of Monuments and Historic Sites, TC 301 – IS NAPOLI* 2022, 22 – 24 June, *Naples, Italy 2022*, pp. 325–336.

Poulos, H.G. 2005. Pile Behavior – Consequences of Geological and Construction Imperfections, *Journal Geotechnical and Geoenvironmental Engineering, ASCE*, Vol. 131, No. 5, pp. 538–563 (Terzaghi Lecture).

Sata, L. 2003. Foundation strengthening of a historic building. In *Proceedings 2nd International Young Geotechnical Engineers Conference*, *Mamaia, Romania*.

Tsatsanifos, C. 2017. Building in Ancient Cities: Geotechnical Engineering Challenges. In *Iscarsah Newsletter n. 15-16-17/2017 Scientific Reports*, pp. 3–22 (extract from the XVI Prague Geotechnical Lecture, on May 26, 2008, in the Academy of Science of the Czech Republic).

Tsatsanifos, C. and Pasqualin, C. 2013. The National Bank of Greece Administration Building and the Acharnian Gate of the Ancient Athens Circuit Wall". In *Iscarsah Newsletter n. 4/2013 Scientific Reports*, pp. 14–16.

Tsotsos, S. and Naskos, N. 1995. Underpinning. The cases of the 1st High-School Building of Thessaloniki and the Catholic Church in Giannitsa. In *Proceedings First Scientific Meeting "The restoration of historical buildings in Northern Greece", 1-3 June, Thessaloniki, Greece 1995*, pp. 137–144 (in Greek).

Ulitsky, V. M. (2005) *TC-19 Preservation of Historic Sites/Guidelines – Part II. Specific Problems: Urban Areas* (draft).

Geomaterials for soil improvement

Taylor & Francis
Taylor & Francis Group
http://taylorandfrancis.com

Smart Geotechnics for Smart Societies – Zhussupbekov, Sarsembayeva & Kaliakin (Eds)
© 2023 The Author(s), ISBN 978-1-003-29912-7
Open Access: www.taylorfrancis.com, CC BY-NC-ND 4.0 license

Strength ellipses of induced anisotropy for a compacted sandy material

A. Mochizuki
Tokushima University, Tokushima, Japan

A.Zh. Zhussupbekov & Y. Zharkenov
L.N. Gumilyov Eurasian National University, Astana, Kazakhstan

S. Akhazhanov
Karaganda Buketov University, Karaganda, Kazakhstan

ABSTRACT: This paper presents a study on strength anisotropy in a sandy material with anisotropic fabric formed by press loading. Two series of DS-CD tests (direct shear tests under CD condition) were performed using a developed DS apparatus with a double-jack system. To maintain anisotropic fabric in a sample, a freezing technique was developed. Shear strength of samples in the active shear zone was found to be stronger than that of the passive zone, and the results could be expressed well by an ellipse equation with tilting coordinates of an angle measuring 15° to the horizontal line. To find a reason for the inclination of the axis of strength ellipses, a 2D-DS test was performed by a developed 2D-DS device. The direction of the main shear zone of a sand sample measuring 15° coincided well with that of the ellipses' coordinates, which should be taken into consideration when shear strength from a DS-CD test should be used in a safety analysis of a soil structure.

1 INTRODUCTION

Aiming to evaluate shear strength of a compacted weathered granite with anisotropy for such as safety analyses of an embankment, two series of CDDS tests (direct shear tests under CD condition) on sandy soil samples, in which the inherent anisotropy was induced by press loading, were performed using an improved DS apparatus in this study (Mochizuki *et al.*, 2021).

The first directive articles for research on shear strength anisotropy, it is said, was presented by (Bjerrum, 1973) in the 'State of arts reports' in the 8th-ICSMFE conferences, in which a concept of "an extension mode (TE)" for the shoulder part of a slope, "a simple direct shear mode (SDS)" for the middle part and "a compression shear mode (TC)" for the toe part was presented. After that, Bjerrum's discussion became a road map for the following study of shear strength anisotropy.

The most reliable test data on undisturbed clay samples from Osaka city, Japan were presented by (Mikasa, Takada and Oshima, 1987) using the original type of Mikasa's DS apparatus ((MIKASA, 1965), see Figure 1). Test results on clay samples against the N-S surface showed similar trends of anisotropy on shear strength as those on ones of remolded clay. They compared them to those of the E-W direction, and the possibility of secondary loading of tectonic force in the E-W direction on the Osaka layers was found. Whereas (Nishimura, Minh and Jardine, 2007) tried to quantify the anisotropy of London clay using a torsional triaxial test. An introduction of anisotropic shear strength into stability analysis of a slope was tried by (Shogaki and Kumagai, 2008).

DOI: 10.1201/9781003299127-25

The fabric characteristics and anisotropic nature of granular materials was systematically studied by (Parkin, Gerrad and Willougby, 1968), (Arthur and Menzies, 1972), (Oda, 1972) and (EL-Sohby and Andrawes, 1973), which demonstrated the significance of anisotropic fabric also in cohesionless soils. Regarding the anisotropy of sandy material, however, less publications were published as a study on sand anisotropy appears to be much more difficult to prevent deterioration of anisotropic fabric than that of clay during sampling or forming of them for shear tests.

In this study, to overcome the difficulty to maintain anisotropic fabric induced by press loading a freezing technique was introduced, in which an improved DS apparatus was used ((Ishikawa *et al.*, 2009), see Figure 2). It was found that the test results could be expressed well by an ellipse equation with tilting coordinates of an angle measuring 15° for the strength anisotropy of the sandy material. In order to discuss the inclination of the axis of ellipses, a 2D-DS tests (two-dimensional direct shear tests) were performed using a newly developed 2D-DS device (Ohfuji, Ueno and Mochizuki, 1999).

2 TEST CONDITIONS AND PREPARATION OF SAMPLES WITH ANISOTROPIC FABRIC

2.1 *Improved direct shear apparatus and used material*

Progress of a DS (direct shear) apparatus in Japan was totally different from that in Europe or USA. Figure 1 shows a cross-sectional sketch of the main part of Mikasa's original DS apparatus developed in 1965 (MIKASA, 1965). Vertical stress is applied from the bottom of a sample, the reaction force is supported by the rollers installed at the upper plate, which prevents the upper shear box to lean during shearing. And the resulting function enables performing a CV (constant volume) test as well as a CD test (Takada, 1993). The apparatus was adopted in a code of the Japan Geotechnical Society since 1979 (JGS0561 (Japan Geotechnical Society, 1979)) and has been used widely in Japan.

One shortcoming of the Mikasa's DS apparatus, however, is growing evitable friction between a sample and the shear box wall when performing CD tests on dense sands, which tends to give unexpected over-prediction of shear strength. To eliminate such problems, (Ishikawa *et al.*, 2009) developed a new DS apparatus with a double-jack (DJ) system on the upper shear box, shown in Figure 2. Accuracy of test results on Toyoura sand (standard sand in Japan), was proved to present almost equivalent results obtained by triaxial CD tests.

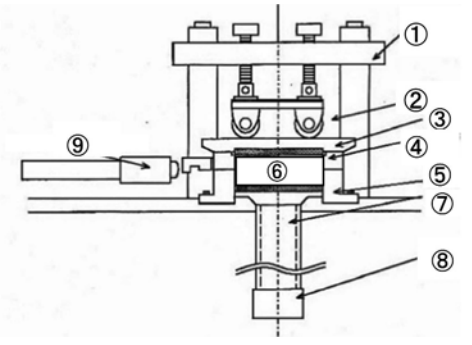

①	Reaction plate
②	Reaction rolers
③	Upper plate
④	Upper shear box
⑤	Lower shear box
⑥	Samaple
⑦	Loading rod
⑧	Load cell for σ_N
⑨	Load cell for τ

Figure 1. Main structure of Mikasa's *DS* apparatus (MIKASA, 1965).

2.2 *Test conditions for CD_{DS} tests and preparing test samples*

Table 1 shows the main properties of the material used for specimens, which was made from strongly weathered granite with 20% of fine grains from Tokushima, Japan. It is normally used

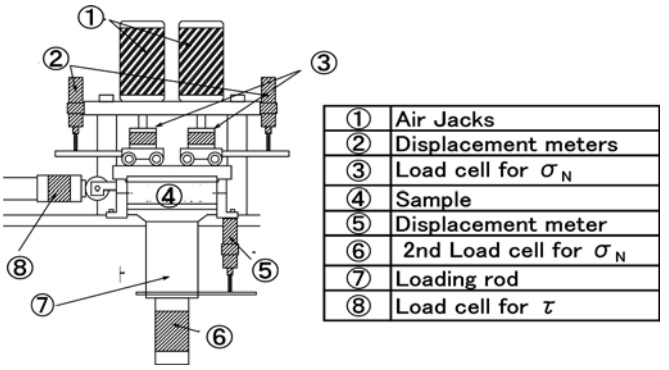

Figure 2. A newly designed DS_{DJ} apparatus with double-jack system (Ishikawa *et al.*, 2009).

for construction of dike, road embankments, earth dams etc. The material was sieved with a 1.2 mm mesh and mixed well. Then, the material was weighted measuring 1 kg each by the quartering method, and water was added to be its optimum water content measuring 14%, which was found from a preliminary compaction test. After forming a sand layer of about 1 cm thickness with 1kg of material in a strong box measuring L52×W19.5×H18cm the layers were pressed with a static load of 600 or 1,200 kN/m^2 for one minute to each layer, which compressed into a 0.5 cm layer of a specimen. Twenty times of press loading was repeated to produce a specimen with about 10 cm thickness, which simulated a road embankment construction by heavy roller weight.

Table 1. Main properties of sand material.

γ_s (g/cm^3)	2.634
d_{max} (mm)	1.2
Sand (%)	79
Silt (%)	8
ρ_{dmax} (g/cm^3)	1.87
w_{opt} (%)	13.4

After the forming of a specimen with twenty sub-layers, the plate for loading was clicked by handy vices to prevent it from heaving. As an anisotropic fabric formed in soil specimen was not free from disruption due to sampling or forming into a sample, a freezing technique to a sample was developed for these tests. The specimen in the strong box was moved into a freezer at a temperature of minus 45 °C. Here, they are referred to as "a 600 kN/m^2 sample or 1,200 kN/m^2 sample" in this paper. The surface of which was covered with aluminum foil to prevent the sublimation of water. Table 2 shows test conditions. The procedure of a CDDS test followed the Japanese code of JGS0561.

Table 2. Test conditions (DS-CD test).

Shear test conditions	
Drain condition	CD
Melting temperature (°C)	21 (15 min)
Time for consolidation (min)	20
σ_N (kN/m^2)	50, 100, 150, 200, 250, 300
Rate of shear (mm/min)	0.25
Shear angle, θ (°)	Active zone: 0, 30, 60, 90 Passive zone: 90, 120, 150, 180
γ_d (g/cm^3)	1.74

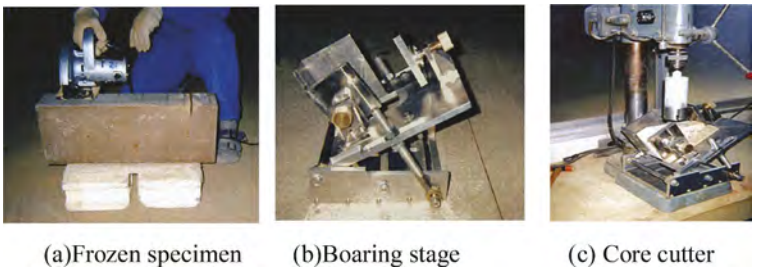

Figure 3. Process of sampling from a frozen specimen.

Then, a frozen specimen was cut into seven blocks of L7×W19.5 ×D10 cm (Figure 3(b)), and cutting direction were designated for each test on a frozen block. Then, a frozen block was moved to a newly designed coring stage (Figure 3(c)).

Figure 4 shows the definition of shearing angle, δ, of a sample, which is d fined against the shearing direction of a sample to the horizontal stratification, in which a zone of δ=0° to 90° is referred to as the active shear zone, and that of δ=90° to 180° is the passive shear zone. A sliced sample measuring about 2.5cm in height was brought into a cutter-ring of φ60×20 mm by a pre-determined press slowly to avoid deterioration of a sample due to over-loading, and a frozen sample was set into a shear box. Then, the sample was heated up to its melting point of 21 □ for 15 min by a band heater around the shear box, that condition was found in a preliminary test. The samples were sheared loading a designed vertical stress, σ_N under CD condition.

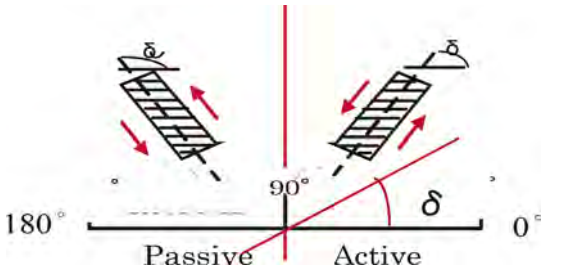

Figure 4. Shearing angleδand Active/Passive zone.

3 TEST RESULTS

Figure 5(a) shows τ (shear strength)∼ D and Δh∼ D relations of CDDS tests sheared to δ = 0° direction for 1,200 kN/m^2 samples. Here, D is horizontal displacement and Δh is a change of height (or volume) of a sample due to dilatancy. Curves of $\tau \sim$ D show a distinct peak strength even though the vertical stress, σ_N, increased. Figure 5(b) shows test results of those sheared to δ=90° direction. Test results of samples of δ = 90° direction did not exhibited such distinct peak strengths.

Figure 6(a) shows test results of 1,200 kN/m^2 samples sheard to different angles of δ under the vertical stress of σN=100kN/m^2. The $\tau \sim$ D curves sheared to $\delta = 0 \sim 60^\circ$ (the active zone) exhibited distinct peak strengths, though samples of δ=90, 120, 150° (the passive zone) did not show such clear peak strengths. These results suggest that 'inherent fabric in a sample' was destructed more during shearing in the passive zone under CD condition than that in active zone.

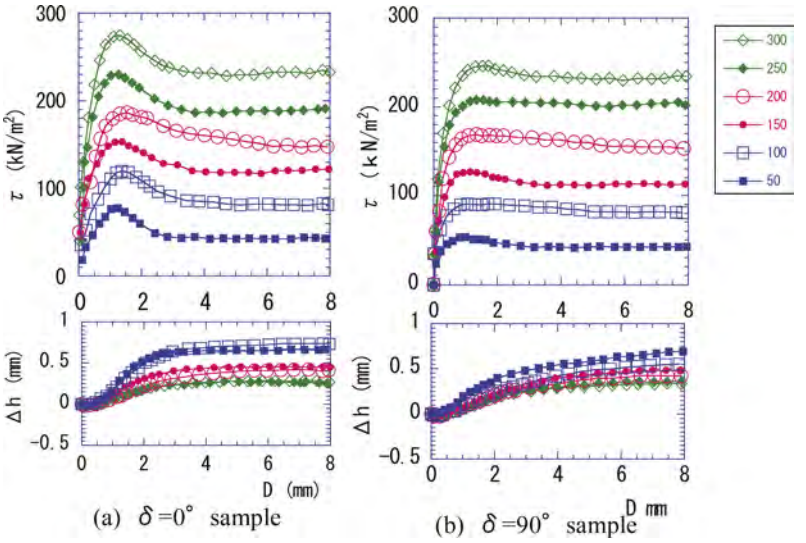

Figure 5. $\tau \sim D$, $\Delta h \sim D$ diagrams of CD_{DS} tests for 1,200 kN/m^2 samples.

Figure 6(b) shows test results of 1,200 kN/m^2 samples tested under the vertical stress of σ_N=200 kN/m^2, which did not exhibit such distinct difference of peak strengths even for δ=0, 30, 60° samples.

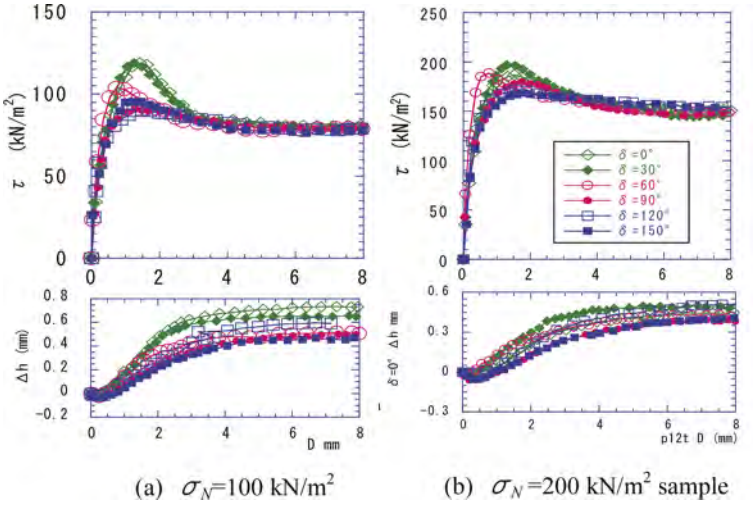

Figure 6. $\tau \sim D$, $\Delta h \sim D$ diagrams of CD_{DS} tests for 1,200 kN/m^2 samples with different angles of δ.

It suggests that anisotropic fabric in samples under σN=200 kN/m^2 was destroyed during shearing more than that in a sample under σN=100 kN/m^2. "An intention ratio of anisotropic fabric/σ_N" will be an index for shear strength of a sample with anisotropic fabric.

4 DISCUSSION OF TEST RESULTS

4.1 *Strength ellipses for anisotropy*

From discussions in the foregoing section, the strength of a sample with anisotropic fabric was found to depend on stress condition and the shearing direction of a sample, δ. When test results of strength anisotropy are introduced into safety analysis of soil structure, formulation of test results of strength anisotropy is a preferable technique. The formulating test data will also work effectively to take an average of data in such a case with un-evitable fluctuating errors. After several preliminary trials, an ellipse equation was found to express the test results of strength anisotropy of samples.

Figure 7(a) shows the resulting elliptical curves for 600 kN/m^2 samples. It should be noted that the axis of ellipses tilted measuring β= -15° to the horizontal coordinate of the chart (in the passive zone: see Figure 7(a)), therefore, the direction of the long axis of ellipses was measuring θ=+15°(=δ-β), and that of the short axis was measuring 105°(θ). The results of CDDS tests are well expressed by the ellipsoidal curves, though some scatters of the test data are detected. It should be noted that the degree of flatness of the ellipses decreases along with increases of vertical stress.

Figure 7(b) is a chart of test data for 1,200 kN/m^2 samples. Results of CDDS tests showed successfully being represented in ellipses, inclined at an angle measuring 15° to the horizontal coordinate. However, the trend of the elliptical curves was different from that of clay samples with the maximum shear strength at θ=45°.

Shear strength, τf in Equation (1), being a formula of ellipse, was calculated in the following processes:

$$\tau_f = \sqrt{\left[a^2\cos^2(\delta-\beta) + b^2\sin^2(\delta-\beta)\right]} \quad \text{Here, } \theta = \delta - \beta \tag{1}$$

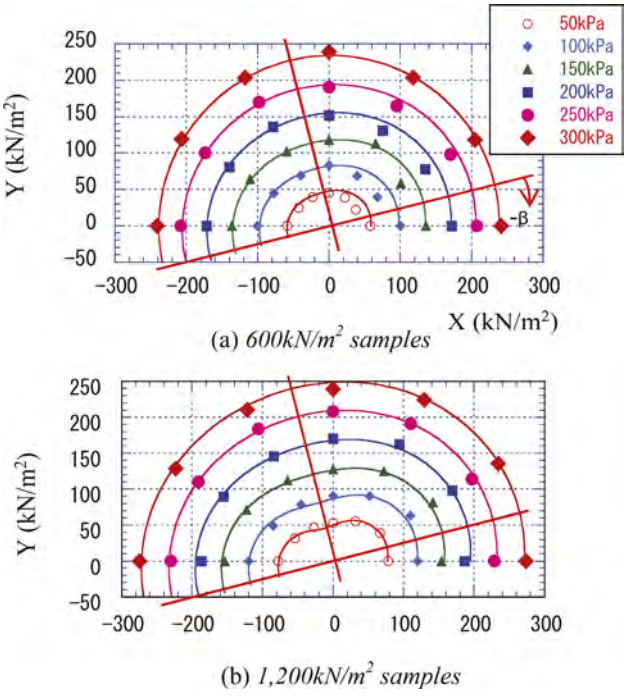

Figure 7. Results of CD_{DS} tests and ellipses of strength anisotropy.

An equivalent radius of the ellipse, Re, is found from Equation (2), and a ratio of flatness, A1 or A2 of an ellipse is calculated from Equation (3), in which parameters, 'a' and 'b' are a short or a long radius of an ellipse, which were found from test data of δ=0° or 90° samples, respectively for the first approximation of the parameters in this study. Then, Re was calculated by Equation (2), and test results were plotted in a polar chart. Then, shear strength, τf is calculated by Equation (4), which was transformed from Equation (1) using parameters, A and Re instead of parameters, a and b.

$$\text{Equivalent radius of an ellipse: } R_e = \sqrt{[a \times b]} \tag{2}$$

$$\text{Ratio of flatness of an ellipse: } A_1 = \frac{(a - R_e)}{R_e} \text{ or } A_2 = \frac{(R_e - b)}{R_e} \tag{3}$$

$$\tau_f = R_e \sqrt{\left[(1+A)^2 \cos^2(\delta - \beta) + (1-A)^2 \sin^2(\delta - \beta)\right]} \quad Here,\ \delta - \beta = \theta \tag{4}$$

4.2 *Discussion on the inclination of the primary axes of ellipses to the horizontal coordinate*

In Section 3, the primary axes of strength ellipses were found to be inclined measuring β= -15° to the horizontal line (in the passive zone). To introduce the effect of strength anisotropy into an analysis of soil structures such as road embankments etc., it is necessary to find a reason about the inclination of the axes of the ellipses.

With this view, the development of the shear zone in a sand sample during a DS test was observed using a newly developed 2D-DS device, a sketch of which was shown in Figure 8 (Ohfuji, Ueno and Mochizuki, 1999). A double jack system was installed on the upper plate of the shear box to keep it horizontally with a constant condition of total vertical force, σ_N. The front surface of the shear box was covered with separated crystal-glass plates to observe the deformation of a sample. The density of sand (ρ_d) was 1.655g/cm^3 and the size of the sample was L30×H20×D4 cm. Photos were taken at each scheduled interval, and the photo image analyzer was used to detect shear zone in a sand sample of Toyoura-sand (Japanese standard sand).

Figures 9(a) ~ (d) show areas where shear strains, γ_{xy}, being over 10% in a sample at each displacement of a 2D-DS test, which exhibited progress of expanding shear zones over 10%. The peak strength of a test was detected at D=10 mm (Figure 9(c). Additional broken lines in the figure were drawn to show the direction of β= -15° to the horizontal (in the passive zone). The direction of the shear zone to the horizon in the sample was found to coincide well with the inclination angles of the axis of strength ellipses, which is a reason for the inclination of strength ellipses in Figure 7.

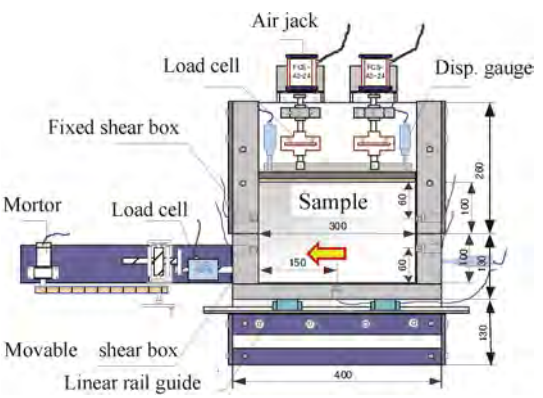

Figure 8. Sketch of a developed 2*D-DS* device (Ohfuji, Ueno and Mochizuki, 1999).

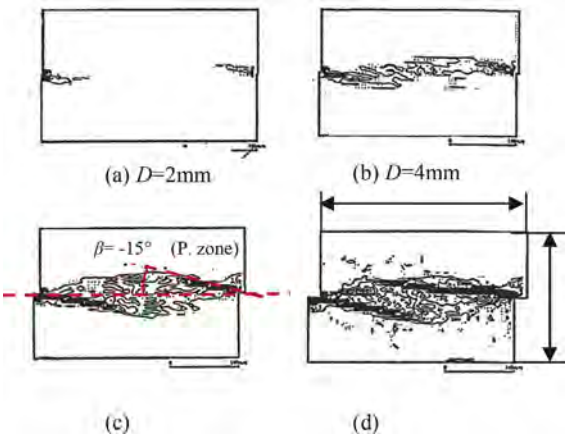

Figure 9. Expanding of a zone over 10% of γ_{xy} (Ohfuji, Ueno and Mochizuki, 1999).

It is concluded that an inclined angle measuring θ=15° (θ=δ - β) of the axis of strength ellipses to the horizontal coordinate must be revised when results of DS tests will be used in safety analysis of soil structures. Someone may think it is a particular kind of a negative problem in a DS test, however, it is not, as the only way to observe strength anisotropy in sandy materials is not test data of a triaxial test, but those of a DS test using the improved DS apparatus with double-jack system.

5 CONCLUSIONS

This paper presented an experimental study on shear strength anisotropy in a compacted sandy material. Two series of CDDS tests (direct shear tests under CD condition) were performed using an improved DS (direct shear) apparatus. To avoid deterioration of the anisotropic fabric of a sample, which was formed by press loading of 600 kN/m^2 and 1,200 kN/m^2, a freezing technique was introduced. The samples and test method were chosen to simulate the construction of an actual road embankment. The main conclusions reached in this study are as follows:

(1) A freezing technique of a sample was attributed to preventing deterioration of the anisotropic fabric induced by press loading in a sandy sample. An improved DS apparatus with a double-jack system worked effectively to observe strength anisotropy in sandy samples under CD condition.
(2) Samples in the active shear zone of δ=0°to 60°showed distinct and high peak strengths, whereas those in the passive zone of δ=90°to 150°showed un-clear peak and low strengths.
(3) Strength gap of δ=0° samples to that of θ=90° samples became smaller along with the increase of vertical stress, σ_N, which was caused by the induced anti-anisotropy behavior or destruction of anisotropic fabric during shearing under CD condition.
(4) It was found that the results can be expressed well by an ellipse equation with tilting coordinates of an angle measuring β= -15° (in the passive zone) to the horizontal coordinate.
(5) Progress of increasing of the shear zone in a sand sample was observed using a newly developed 2D-DS device, and the primary shear zone developed to a direction measuring β= -15° to the horizon in the sample was found, which coincided well with the inclination of the primary axes of strength ellipses for a sample with strength anisotropy induced by press loading. It suggests that the axes inclination of strength ellipses must be revised when the results of the strength anisotropy observed by DS tests will be used in safety analysis of soil structures.

ACKNOWLEDGEMENT:

The authors would like to express the appreciation to Prof. Victor Kaliakin (University of Delaware, *USA*) who discussed and gave much advice to our study. The authors also express our gratitude to Mr. J. Hujisawa for his laboratory works in this study.

REFERENCES

Arthur, J. R. F. and Menzies, B. K. (1972) 'Inherent anisotropy in a sand', *Géotechnique*, 22(1), pp. 115–128. doi: 10.1680/geot.1972.22.1.115.

Bjerrum, L. (1973) 'Problems of soil mechanics and construction on soft clays and structurally unstable soils (collapsible, expansive and others)', in *Proc. of 8th ICSMFE*, pp. 109–159.

EL-Sohby, A. A. and Andrawes, K. Z. (1973) 'Experimental examination of sand anisotropy', *Proc. 8th ICSMFE, 1973*, 1, pp. 103–109. Available at: https://cir.nii.ac.jp/crid/1573105975120231296.bib?lang=ja (Accessed: 5 December 2022).

Ishikawa, H. *et al*. (2009) 'Development of a direct shear apparatus with a double-jacks system and the effect of the double-jacks system', *JGS journal*, 4(1),pp. 11–19 (in Japanese).

Japan Geotechnical Society (1979) *Direct shear test method. JGS0561 (Standard)*.

MIKASA, M. (1965) 'Test apparatus and test procedures of Triaxial and direct shear testing', in *The 10th Symposium on Soil Testing*. Japanese Society of Soil Mechanics and Foundation Engineering, pp. 117–123 (in Japanese).

Mikasa, M., Takada, N. and Oshima, A. (1987) 'In-situ strength anisotropy of clay by direct shear test', *Proc. 8th ARC*, 1, pp. 61–64. Available at: https://cir.nii.ac.jp/crid/1572824501502638592.bib?lang=ja (Accessed: 5 December 2022).

Mochizuki, A. *et al*. (2021) 'Strength Anisotropy of Compacted Sandy Material', *Soil Mechanics and Foundation Engineering*, 57(6), pp. 480–490. doi: 10.1007/s11204-021-09696-1.

Nishimura, S., Minh, N. A. and Jardine, R. J. (2007) 'Shear strength anisotropy of natural London Clay', *Geotechnique*, 57(1), pp. 49–62. doi: 10.1680/geot.2007.57.1.49.

Oda, M. (1972) 'Initial Fabrics and their Relations to Mechanical Properties of Granular Material', *Soils and Foundations*. Elsevier, 12(1), pp. 17–36. doi: 10.3208/SANDF1960.12.17.

Ohfuji, Y., Ueno, K. and Mochizuki, A. (1999) 'Photo-Image analysis of Deformation of a Sand Sample during Shearing under 2D-direct Shear Condition', in *The 54th annual conference of JSCE*, pp. 42–43 (in Japanese).

Parkin, A. K., Gerrad, C. M. and Willougby, D. R. (1968) 'Discussion on deformation of sand in shear', *Journal of Soil Mechanics and Foundation Division*, 94(1), pp. 336–340.

Shogaki, T. and Kumagai, N. (2008) 'A slope stability analysis considering undrained strength anisotropy of natural clay deposits', *Soils and Foundations*, 48(6), pp. 805–819. doi: 10.3208/sandf.48.805.

Takada, N. (1993) 'Mikasa's direct shear apparatus, test procedures and results', *Geotechnical Testing Journal*, 16 (3),pp. 314–322. Available at: https://www.scopus.com/inward/record.uri?eid=2-s2.0-0000965932&partnerID=40&md5=12f1d224ace04e4b4f5a573faf1be1e9.

Smart Geotechnics for Smart Societies – Zhussupbekov, Sarsembayeva & Kaliakin (Eds)
© 2023 The Author(s), ISBN 978-1-003-29912-7
Open Access: www.taylorfrancis.com, CC BY-NC-ND 4.0 license

Consideration of the methods determining a characteristics length of concept model using the new parameter D_{rmv} for volcanic sandy soil

R. Nakajima, K. Sako, S. Ito & R. Kitamura
Kagoshima University, Kagoshima Prefecture, Japan

ABSTRACT: This study investigated the characteristic length (D_{cha}) as a parameter of the concept model for estimating unsaturated seepage behaviors. We aimed to improve the practicality of the model. The model was proposed by Sako and Kitamura (2006) to derive the seepage behavior of unsaturated soil. D_{cha} is a parameter used to determine the pore size distribution in soil specimens. The methods for determining the parameters for each soil were discussed herein. In this study, a new parameter D_{rmv} was proposed to determine D_{cha}. The characteristics of this parameters were analyzed for volcanic sandy soil. The results indicated $D_{rmv} < 10^{-3}$ mm for volcanic sandy soil and D_{rmv} were related to the uniformity coefficient, U_c. The validity of this method was verified by comparing the D_{rmv} calculation with the experimental data for volcanic sandy soil sampled at a natural slope in Kagoshima Prefecture, Japan.

1 INTRODUCTION

The soil-water characteristic curve (SWCC) is an essential characteristic of the soil that controls water infiltration characteristics in unsaturated soil and has been employed to simulate the saturated-unsaturated seepage analysis. As soil water retention tests to obtain SWCCs are complicated and time-consuming, various models have been proposed to estimate SWCCs. Sako and Kitamura proposed a conceptual model for unsaturated seepage behavior using statistics and probabilities (Sako and Kitamura., 2006). In this model, the pore size distribution was correlated with the grain size distribution and void ratio. The SWCCs and unsaturated hydraulic conductivity were derived using the estimated pore size distribution and characteristic length, D_{cha}, which is a crucial parameter for deriving the pore size distribution. However, the value of characteristic length must be modified depending on the soil type. In previous studies, equations for D_{cha} have been proposed and methods for determining D_{cha} for each soil type have been discussed. This study proposed a method for determining D_{cha} for volcanic sandy soil. In this study, D_{rmv} was introduced as a new parameter to determine D_{cha}, which was calculated for 30 samples of volcanic sandy soil. The parameters were characterized and their relationship with the properties of the grain size distribution was also discussed. A method for determining D_{cha} using D_{rmv} was proposed in this study. The validity of the method was verified by comparing D_{rmv} calculation with the experimental data for volcanic sandy soil.

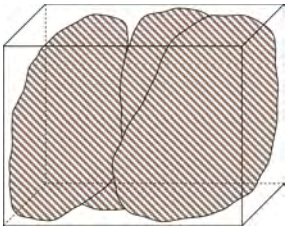

Figure 1. Elementary particulate body (EPB).

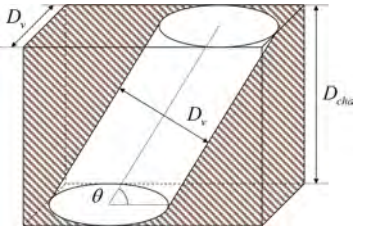

Figure 2. Modeling of pore structure by EPB.

DOI: 10.1201/9781003299127-26

2 OUTLINE OF THE CONCEPT MODEL FOR UNSATURATED HYDRAULIC PROPERTIES AND CALCULATION PROCESS

2.1 *Outline of the concept model for unsaturated hydraulic properties*

A soil element with a few soil particles, called an Elementary Particulate Body (EPB) is shown in Figure 1. The EPB can be modeled as shown in Figure 2. The pore structure in the EPB was modeled using a pipe with diameter D_v and the inclination angle θ. The soil particles in the EPB were modeled by other impermeable parts. D_v and θ were also adapted as random variables to model the complex pore structure of the soil.

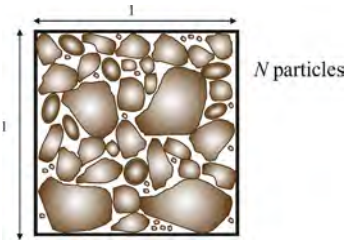

Figure 3. Random packing of particles in unit volume.

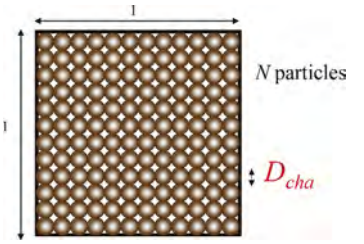

Figure 4. Packing of uniform sphere in unit volume.

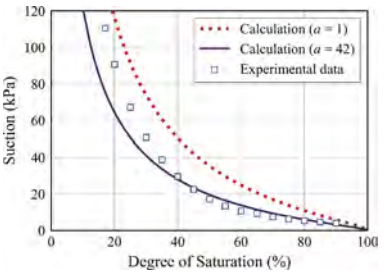

Figure 5. SWCCs obtained from experiments and calculations.

The volumetric water content (W_v) and suction (s_u) were expressed as follows:

$$W_v = \frac{e(d)}{1+e} = \frac{1}{1+e}\int_0^d \int_{-\pi/2}^{\pi/2} \frac{V_p}{V_e - V_p} \cdot P_d(D_v) \cdot P_c(\theta) d\theta \, dD_v \tag{1}$$

$$\text{and} \quad s_u = \gamma_w \cdot h_c = \frac{4 \cdot T_s \cdot \cos\alpha}{d}. \tag{2}$$

Here, V_e and V_p denote the volumes of the EPB and pipe in Figure 2, respectively. $P_d(D_v)$ and $P_c(\theta)$ denote the probability density functions of the pipe diameter (D_v) and inclination (θ), respectively. d denotes the maximum diameter of pipes filled with water. γ_w, h_c, T_s, and α are the unit weight of water, pressure head, surface tension, and contact angle of the meniscus at a contact point of the soil particle, respectively.

In this model, the characteristic length D_{cha} was defined as the particle size representative of the soil. Nakajima et al. (Nakajima, R. et al., 2019) pointed out that D_{cha} varies depending on the soil type and proposed a new equation for D_{cha}, as follows:

$$D_{cha} = \left\{ \sum_{i=a}^{n} \frac{1}{D_{s,i}^3} \cdot f_s(D_{s,i}) \cdot \Delta D_{s,i} \right\}^{-\frac{1}{3}}. \tag{3}$$

Here, $D_{s,i}$, $f_s(D_{s,i})$, $\Delta D_{s,i}$, a, and n denote the i-th grain size, probability density function of grain size distribution, interval increment, minimum value of the integration range of $f_s(D_{s,i})$, and number of divisions (n = 360), respectively.

Since the grain size distribution can be expressed as a log-normal distribution, the probability density function of the grain size distribution $f_s(D_s)$ in Equation (3) can be expressed as

$$f_s(D_s) = \frac{1}{\sqrt{2\pi} \cdot \zeta_s \cdot D_s} \cdot \exp\left[-\frac{\ln(D_s - \lambda_s)^2}{2 \cdot \zeta_s}\right], \quad (4)$$

where, D_s, λ_s, and ζ_s, are the grain size, distribution parameter, and integral range of $f_s(D_s)$ from ($\lambda_s - 4\zeta_s$) to ($\lambda_s + 4\zeta_s$), respectively.

The principle behind Equation (3) can be expressed as follows: Figure 3 shows the random packing of soil particles per unit volume. The N soil particles of random shape and size are packed with a dry density of ρ_d. Figure 3 is modeled as shown in Figure 4. It shows a simple N uniform particles per unit volume. The dry density is equal to that shown in Figure 3. D_{cha} is the diameter of a uniform particle. The value of a in Equation (3) is a parameter related to integration range of $f_s(D_{s,i})$. The optimum value of a is calculated using experimental data of SWCC. Consequently, the D_{cha} is determined for each soil.

2.2 *The calculation process of the concept model*

This section describes how to determine D_{cha} and derive SWCC using Equation (3). The SWCC experimental data of Kushira soil (ρ_s = 2.48 mg/m^3) from volcanic sandy soil were obtained using the simplified evaporation method. Figure 5 shows the SWCC values obtained from the experiments and calculations. The calculation results overestimated the experimental data by a dotted line with a value of a = 1 in Equation (3). This resulted in D_{cha} being 0.85 % finer by weight, denoted as $D_{0.85}$. The equation assumed that particles of random sizes and shapes are uniform particles of equal numbers. A significant number of fine particles resulted in the size of the uniform particles being underestimated. The size of D_{cha} was adjusted by increasing the minimum value of a of the integration range of $f_s(D_{s,i})$. Reducing the integral range of $f_s(D_{s,i})$ from the smallest particles reduces the effect of the fine particles. The solid line shows that the results are close to the experimental data when a = 42. D_{cha} was 3.56% finer by weight, indicating that the grain size of $D_{3.56}$ influences the SWCC of Kushira soil. Using this calculation process, the parameter D_{cha} was determined for each soil. However, to derive a valid D_{cha} experimental data is needed. This study proposed a method to determine D_{cha} for volcanic sandy soil by introducing D_{rmv} as a new parameter. D_{rmv} was calculated for 30 for volcanic sandy soil samples. The characteristics of the parameters are discussed in the following section.

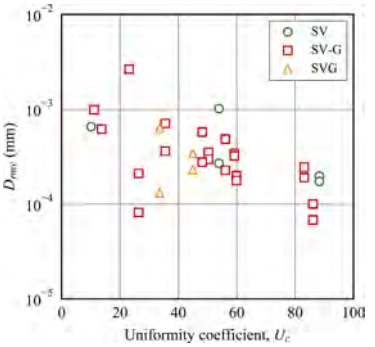

Figure 6. Relationship between D_{rmv} and uniformity coefficient, U_c.

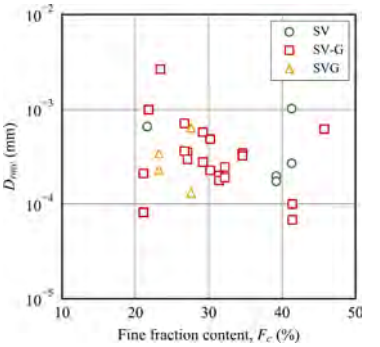

Figure 7. Relationship between D_{rmv} and fine fraction content, F_c (%).

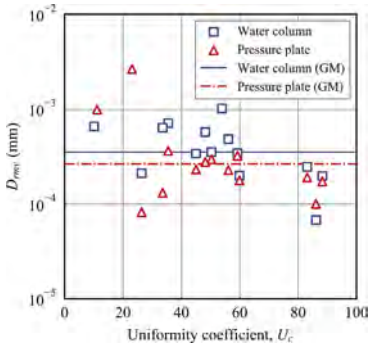

Figure 8. Relationship between D_{rmv} and uniformity coefficient, U_c classified by the test methods.

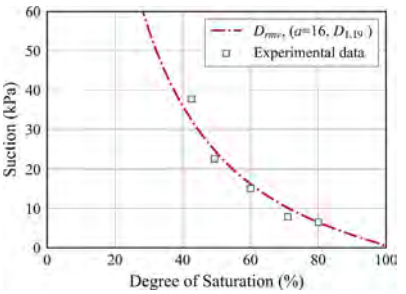

Figure 9. Calculation result and experimental data. (Higashimata soil).

3 NEW PARAMETER AND ITS CHARACTERISTICS

D_{cha} is determined by adjusting the size of D_{cha} and narrowing the $f_s(D_{s,i})$ from the finest particle size. The maximum diameter of the particles removed for determining D_{cha} is defined as D_{rmv} and can be expressed as follows:

$$D_{rmv} = \exp\left[\lambda_s - \left\{4\zeta_s\left(1 - \frac{2}{n}\right) \times (a-1)\right\}\right]. \quad (5)$$

The value of a can be determined without the results of the experimental data if the D_{rmv} is known for each soil. This making it possible to calculate D_{cha} for each soil acceding to Equation (3). In this study, the D_{rmv} was calculated for 30 SWCCs experimental datasets of volcanic sandy soil to obtain the characteristics of D_{rmv}. The soils were classified as sand of volcanic fine fraction nature (SV), sand of volcanic fine fraction nature with gravel (SV-G) and gravelly sand of volcanic fine fraction nature (SVG) according to the Japanese Geotechnical Society (2015). The SWCC experimental data were obtained using pressure plate, water column, centrifuge, and simplified evaporation methods.

The relationship between D_{rmv} and the properties of grain size distribution, such as uniformity coefficient, U_c, and fine fraction content, F_c (%) (percentage of particles with diameter less than 0.075 mm), are discussed. Figure 6 shows the relationship between D_{rmv} and uniformity coefficient U_c. Although the value of SV-G varies, the larger the uniformity coefficient, the smaller the value of D_{rmv}. Most of the value of D_{rmv} were in range $D_{rmv} < 10^{-3}$ mm. Figure 7 shows the relationship between D_{rmv} and F_c (%). The larger the fine fraction content, the smaller D_{rmv} trend to be. However, there is more variation compared to the relationship with the uniformity coefficient.

Owing to the differences in the soil-water retention test results, the D_{rmv} for each experiment is discussed. Of the 30 SWCCs experimental data, 14 were obtained using the pressure plate method and 14 using the water column method. Figure 8 shows the relationship between D_{rmv} and uniformity coefficient, U_c, classified by the soil-water retention test methods. The geometric means (GM) of D_{rmv} were calculated using each test method. Based on the results, the relationships were clarified by classifying the test methods. The geometric means of D_{rmv} for the water column and pressure plate methods were 3.53×10^{-4} mm and 2.64×10^{-4} mm, respectively. For volcanic sandy soil it was suggested that the geometric mean of D_{rmv} for each test method could be used to determine D_{cha}.

4 EVALUATION OF THE VALIDITY OF THE METHOD USING A NEW PARAMETER

A soil water retention test was conducted using pressure plate method to verify the validity of the new method. Volcanic sandy soil collected from natural slopes in Kagoshima, Japan was

used (from now on, this will be referred to a "Higashimata soil") (ρ_s=2.51(mg/m^3). Higashimata soil is classified as Volcanic gravelly sand with fine fraction (SG-V). The void ratio e of the sample was set to 0.98. The initial water content was set to 33.4 %. Figure 9 shows the experimental data and calculation results. The dash-dot line shows the result using the geometric mean of D_{rmv} for pressure plate methods, which is $D_{rmv} = 2.64 \times 10^{-4}$ mm. Using the geometric mean of D_{rmv} and Equation (5), a = 16 was obtained. D_{cha} was calculated to be 1.19% finer by weight ($D_{1.19}$) from Equation (3). The calculated values of SWCC were close to the experimental data. Therefore, an appropriate D_{cha} can be obtained by using the geometric mean of D_{rmv}. The SWCCs can be estimated without soil-water retention tests for volcanic sandy soil.

5 CONCLUSION

In this study, a new method to determine the D_{cha} was proposed using the parameter D_{rmv}. The D_{rmv} values were calculated for 30 volcanic sandy soil samples. The characteristics of the parameters were discussed. A soil-water retention test was conducted to verify the validity of the method. The result indicated a relationship between D_{rmv} and the uniformity coefficient. However, D_{rmv} was found to be less than 10^{-3} mm for volcanic sandy soil. This relationship was clarified by separating the test methods. The geometric mean was calculated for each test method. The methods using the geometric mean could determine D_{cha} The calculation results were close to the experimental data for volcanic sandy soil. Appropriate D_{cha} can be obtained by using the geometric mean of D_{rmv}, and the SWCCs can be estimated without soil-water retention test results for volcanic sandy soil.

REFERENCES

Japanese Geotechnical society. 2015. JAPANESE GEOTECHNICAL SOCIETY STANDRAS Laboratory Testing Standard of Geomaterials Vol.1.

Nakajima, R., Sako, K., Ito, S., and Kitamura, R. 2019. Consideration on a characteristic length in a concept model for Soil-water Characteristic Curve. *Proc. of the Technical Forum on Mitigation of Geo-disasters in Asia*: 162–167.

Sako, K., and Kitamura, R. 2006. A practical numerical model for seepage behavior of unsaturated soil. *Soil and Foundation*, 46(5): 595–604.

Smart Geotechnics for Smart Societies – Zhussupbekov, Sarsembayeva & Kaliakin (Eds)
© 2023 The Author(s), ISBN 978-1-003-29912-7
Open Access: www.taylorfrancis.com, CC BY-NC-ND 4.0 license

Y-Y' Calculus: From soil consolidation to other physical sciences

Sudhir K. Tewatia
Adama Science & Technology University, Ethiopia

Kanishck Tewatia
Loyalist College, Toronto, Canada

Anttriksh Tewatia
Hughes Systique, Gurgaon, India

One Line Summary: Originated from Soil Consolidation, its breakthrough in Calculus to start a new era in physical sciences wherever Newton-Leibniz Calculus applies, gets complicated or fails.

ABSTRACT: Advancements in soil consolidation are discussed and further improvements proposed with particular reference to *Tewatia's Y-Y'* Calculus that is known as Settlement versus Rate of Settlement Approach in consolidation. A branch of calculus named as *Y-Y'* (or *y versus dy/dx*) is suggested (as compared to the common *X-Y', x versus dy/dx, dy/dx versus x* or *Newton-Leibniz* branch) that solves some complicated/unsolved theoretical and practical problems in physical sciences (Physics, Chemistry, Mathematics, Biology and allied sciences) and engineering in amazingly simple and short manner, particularly when independent variable *X* is unknown and *X-Y'* Approach can't be used. Complicated theoretical and practical problems in *1D, 2D, 3D* Primary and Secondary consolidations with non-uniform gradual loading and irregular shaped clays are solved with elementary school level *Y-Y'* Approach. Some particular cases from soil consolidation that are basically creep and diffusion equations in isolation and in combination with each other are taken for comparison with heat and electricity transfer. The *Y-Y' Approach* can similarly be applied in wave equations and other fields wherever normal calculus works or fails.

1 INTRODUCTION

The *Y-Y' Calculus* was invented by Tewatia in 1998 and used in various theoretical and practical problems of soil consolidation [1-20]. In common calculus, differential equations are used for solving problems mostly as below

$$y = f(x); y' = dy/dx = f_1(x) \text{ or } x = f_2(y'); y'' = d^2y/dx^2 = f_3(x) \text{ or } x = f_4(y'') \quad (1)$$

That means differential equations are used as a function of x or vice versa. Very less practice is there to use it as a function of y instead of x. A new approach in calculus, named as *Y-Y'* (or *y* versus *dy/dx*), is suggested (as compared to the common *X-Y'* or *x* versus *dy/dx* or *Newton-Leibniz Approach*) that solves some complicated/unsolved theoretical and practical problems in physical sciences (Physics, Chemistry, Mathematics, Biology and allied sciences) and engineering in amazingly simple and short manner, particularly when independent variable x is unknown and *X-Y'* Approach can't be used. Similar happened in consolidation where all researchers were using δ-t or δ-σ plots; where, δ is settlement, t is time and σ is pressure in primary and secondary consolidation equations. The solution failed when σ or t is unknown at the instant of load increment and it was the common case in the field. Terzaghi [21-22] gave the average loading time concept for continuous uniform loading that, however, was very rough assumption and not true (Figure 1).

DOI: 10.1201/9781003299127-27

The numerical/computer or exact solutions of this problem were suggested by researchers like Leo [23] but they are complicated or require some extra (initial/boundary etc) conditions to be known and fail in case of non-uniform ramp loading and arbitrary shaped clayey soils. A rough (not exact) example is *Pissa* tower where its assumed that it has been sinking due to secondary consolidation since its construction in stages about 8-9 centuries ago so exact time of final/present load increment is not known. However, time settlement data of last 100 years is known. If one wants to predict its past and future settlements due to secondary consolidation and wants to determine the coefficient of secondary consolidation using creep or secondary consolidation equation

$$\delta = a\ log(t) + b \tag{2}$$

then time of load increment (8-9 centuries back), t, should be known. However, its very simple by following $Y\text{-}Y'$ equation [3, 15]

$$\delta = a\ log(d\delta/dt) + b \tag{3}$$

In field, the settlement is due to complex phenomenon like primary and secondary consolidations intermix, non-uniform gradual or ramp loading, multiple stratified layers with different consolidation properties, complex drainage boundaries, unknown initial settlement, time and pressure at the time of load increment etc. In such situations $Y\text{-}Y'$ approach gives easy solutions of some theoretical and practical problems.

Terzaghi [21,22] defined Soil Mechanics as "The Application of the laws of mechanics and hydraulics to engineering problems dealing with sediments and other unconsolidated accumulations of solid particles". That means Geotechnical engineering used laws and mathematical analogies from other physical sciences. Perhaps, Coulomb was the first scientist to use mechanics in soil in slope analysis in 1776. Primary consolidation is basically a *diffusion* (heat) equation [24,25] applied by Terzaghi from thermodynamics to soil mechanics and Secondary consolidation is creep equation of physics, where settlement proceeds linearly with logarithm of time at constant effective stress. Therefore, new developments in consolidation theory on account of $Y\text{-}Y'$ Approach will be beneficial to (diffusion) thermodynamics, electricity, mass transfer etc. For example equations of one, two, three dimensions; radial and combined *radial +vertical* ($R+V$) consolidations are derived very easily without partial differential equations in $Y\text{-}Y'$ approach, similar should follow in other disciplines on similar mathematical analogies. In this paper advancements in soil consolidation are discussed from this point of view with some examples. $Y\text{-}Y'$ calculus (alone or in combination with $X\text{-}Y'$ calculus) can be used not only in creep and diffusion equations but in several other problems also like wave equation etc in all physical sciences and engineering wherever normal calculus works or fails.

2 Y-Y' CALCULUS IN CREEP OR SECONDARY CONSOLIDATION

Illustration, procedure and advantages of new method; generation of δ-t data and its comparison with actual data are given by solved examples [3, 6, 15].

Question 1: Because of secondary consolidation, the rate of settlement of a structure after *1* years is *10 mm/year*. Find the rate of settlement after 3 years.

Answer: In $Y\text{-}Y'$ calculus, product of time and rate of settlement is constant in secondary consolidation. Therefore, the rate of settlement after 30 years will be (10*1/3) i.e. 3.3 *mm/year*.

3 Y-Y' CALCULUS IN COMPRESSIBILITY CHARACTERISTICS

This is similar to previous section as in case of creep except for, t is substituted by σ' and α is substituted by compression index, C_c [3,6,15,17]. In the previous section a method was suggested for obtaining δ-t data of present, past and future from limited δ-$d\delta/dt$ or δ-$dt/d\delta$ data. In this section a method is suggested for obtaining δ-σ' data of present, past and future from limited δ-$d\delta/d\sigma'$ or δ-$d\sigma'/d\delta$ data. Fastest rapid loading methods for vertical, radial and *3D* consolidation are possible only when $Y\text{-}Y'$ Approach is used [17].

4 DERIVATION OF BASIC THEORETICAL EQUATIONS OF CONSOLIDATION

In consolidation literature, equations have been derived, solved and used from simple to more difficult sequence; One dimensional (Vertical), Radial, Combined (*V+R*) and the *3D* consolidation equation (in Cartesian coordinates) does not exist. To show the simplicity and beauty of *Y-Y'* approach let's move from most difficult to simplest one.

4.1 *Carrillo [26] type equations for 3D consolidation in cartesian coordinates*

Using *Y-Y'* Calculus (*Figure 2*), Tewatia [9,10] derived

$$(1 - U_{xyz}) = (1 - U_x)(1 - U_y)(1 - U_z) \tag{4}$$

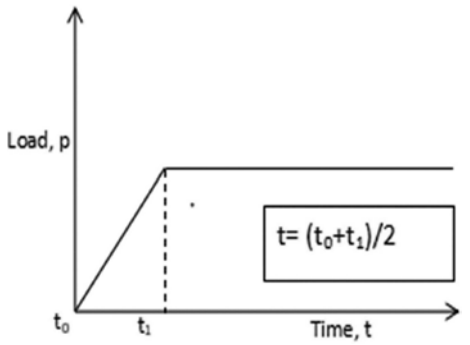

Figure 1. Uniform ramp loading.

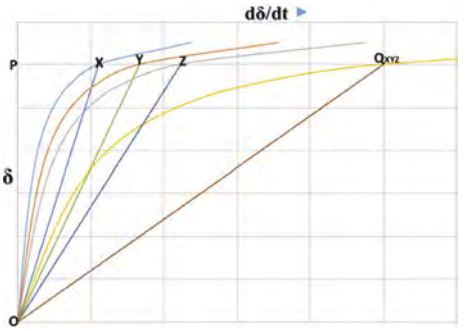

Figure 2. Derivation of *3D* consololidation Eq (4).

Where, U_x, U_y, U_z are degrees of consolidation when drainage is allowed in *X*, *Y* and Z directions only individually and U_{xyz} is the degree of consolidation due to combined drainage in *X*, *Y* and *Z* directions, simultaneously. Eq 4 can be easily modified for *N* number of drainage (Q4), just not *3* only. When the drainage is allowed in radial and vertical directions, it is called combined *vertical+radial* consolidation and Eq 4 reduces to Carrillo's [26] Eq 5

$$(1 - U_{rv}) = (1 - U_r)(1 - U_v) \tag{5}$$

4.2 *Barron's Radial consolidation Equation [27]*

Thiem's [28] *Eq* for flow of water in confined aquifer is used and we get Barron's *Eq 6* [3,16,27]

$$U_r = 1 - e^{-\frac{8}{F_n}T_r} = 1 - e^{T_{rn}} \tag{6}$$

$$F(n) = \frac{n^2}{n^2 - 1}\ln(n) - \frac{3n^2 - 1}{4n^2} \tag{7}$$

Where, F_n is a function of n ($= d_e/d_w$); d_e is the diameter of influence and d_w is the diameter of the drain well. A new variable T_{rn} ($=8T_r/F_n$) is introduced that contains family of U_r-T_r curves for different values of n (in Eq 6) in a single curve [3,16-19].

4.3 *Vertical consolidation Equation*

Similar to radial consolidation, one dimensional or vertical consolidation equation was derived as [16]

$$U = 1 - e^{-T} \tag{8}$$

Newly derived *Eq 8* is somewhat similar to *Eq 9*, later (exponential) part of Terzaghi's *Eq 10* and it does not compare well with first parabolic part of Terzaghi's *Eq 11*.

$$U = 1 - \frac{8}{\pi^2}\varepsilon^{-\frac{\pi^2}{4}T} \tag{9}$$

$$U_v = 1 - \frac{8}{\pi^2}\sum_{N=0}^{N=\infty}\frac{1}{(2N+1)^2}\exp\left(-\frac{(2N+1)^2\pi^2}{4}T\right) \tag{10}$$

$$T = \frac{\pi}{4}U^2 \tag{11}$$

Citing this new derivation and mismatching with initial portion and quoting other researchers Mei and Chen [29] observed that Initial conditions and Boundary conditions of the Terzaghi's [21-22] one dimensional consolidation equation conflict with each other. Therefore, the classical initial-boundary value problem of the equation is not well-posed. However, the exact reasons for this are left to the future researchers and in next articles *Y-Y'* approach is carried out to various other problems of consolidation based on Terzaghi's *Eq 10*.

5 ADVANCED THEORETICAL EQUATIONS OF COMBINED (*V+R*) AND *3D* CONSOLIDATIONS WITH NON-UNIFORM RAMP LOADING AND ARBITRARY SHAPE OF DRAINING CLAY

5.1 *For combined vertical and radial consolidation*

Tewatia [3,9,10,16,17,19] derived

$$\delta = \frac{4H^2}{\pi^2\lambda c_v}\left(\frac{d\delta}{dt}\right) + \delta_{100} \tag{12}$$

Following is the theoretical equation of above experimental *Eq 12*

$$U_{rv} = 1 - \frac{8}{\pi^2}\exp\left(-\frac{\pi^2\lambda T_v}{4}\right) \tag{13}$$

Where,

$$\lambda = 1 + \frac{32k_rH^2}{\pi^2k_vd_e{}^2F_n};\ \frac{c_r}{c_v} = \frac{k_r}{k_v} \tag{14}$$

Installation of vertical drains accelerates the time factor for vertical consolidation within a fixed time by λ times.

Question 2: A clay layer *10m* thick with vertical drains is sandwitched between *2* sand layers. Given: $c_v = 0.6\ m^2/yr$, $c_r = 1.2\ m^2/yr$, $d_e = 1.06m$, $d_r = 0.1m$. Find % settlement of clay in *0.42 years* by ***a***. *Conventional method* and ***b***. *Using Eq 13*.

Solution: $n = 1.06/0.1 = 10.6$, $F_n = 1.634$ using *Eq 7*

a. *Conventional Method*: $U_r = 0.9$ by *Eq 6* (*1st part*), $U_v = 0.12$ by *Eq 10*, $U_{rv} = 91.2\%$ by *Eq 5*.
b. *Using Eq 14*: $\lambda = 89.3$, $U_{rv} = 91.2\%$ by *Eq 13*.

Note: U_{rv} by new method is directly found without using *Eq 6, 10 or 5*.

5.2 *Theoretical Equation of 3D consolidation in cartesian coordinates using Y-Y' Approach*

In *Cartesian co-ordinates* [30]

$$\frac{\partial u}{\partial t} = c_x \frac{\partial^2 u}{\partial x^2} + c_y \frac{\partial^2 u}{\partial y^2} + c_z \frac{\partial^2 u}{\partial z^2} \tag{15}$$

Where, t is time; u is pore pressure; in X, Y and Z directions c_x, c_y, and c_z are the coefficients of consolidation, respectively. Solution of Eq 15 does not exist in literature. However, Tewatia [3,9,10] easily obtained it using *Y-Y' Approach* as

$$U_{xyz} = 1 - \frac{8}{\pi^2} \sum_{N=0}^{N=\infty} \frac{1}{(2N+1)^2} \exp\left(- \frac{(2N+1)^2 \pi^2}{4} \lambda T_v \right) \tag{16}$$

$$\lambda = 1 + \frac{k_y H^2}{k_z B^2} + \frac{k_x H^2}{k_z L^2} \tag{17}$$

Where, k_x, k_y *and* k_z are the permeability's of soil in *X (Length L), Y (Breadth B) and Z (Height H)* directions. *Eq 16-17* (like *Eq 12-14*) can be applied in step and non-uniform ramp loading with unknown time of load increment and can determine that unknown time also.

5.3 *Arbitrary drainage*

A new factor, $\lambda c_H = \lambda c_v / H^2$ is defined [3, 6,19]. The λ_{cH} is the property of in situ clay of definite shape, size and drainage conditions that can be determined in the field itself by *Eq 18* along with δ_{100}) by observing the trend of settlement for some time without knowing any history, shape, size and drainage conditions [3,6].

$$\delta = \frac{4}{\pi^2 \lambda_{cH}} \left(\frac{d\delta}{dt} \right) + \delta_{100} \tag{18}$$

6 SOME PARALLEL ANALOGIES/EXAMPLES IN DIFFUSION EQUATIONS OF PHYSICAL SCIENCES (SAY, THERMODYNAMICS, ELECTRICITY)

Question 3: A solid body of Length L, Breadth B and Height H was allowed to cool for a sufficient time (theoretically infinite) from Temperature $T°C$ to $0°C$ in a an ice box at $0°C$ ice temperature. Total ice melted to $0°C$ water was *100 ml* due to latent heat gained from the body while it cooled. Now suppose, in t minutes time:

1. Total ice melted when the body was insulated along H and B and heat conduction was allowed only along length L from the two ends was *20ml*.
2. Total ice melted when the body was insulated along L and B and heat conduction was allowed only along Height H from the two ends was *80ml*.
3. Total ice melted when the body was insulated along L and H and heat conduction was allowed only along Breadth B from the two ends was *50ml*.

Find the total ice melted in t minutes when the heat conduction is allowed along L, H and B simultaneously (from all *6 faces*) and no insulation is provided.

Solution: Consolidation *Eq 4* is used directly; where, $U_L = 20/100 = 0.2$, $U_H = 80/100 = 0.8$, $U_B = 50/100 = 0.5$. $(1-U_{LBH}) = (1-0.2)(1-0.8)(1-0.5) \Rightarrow U_{LBH} = 0.92$, means *92ml* ice will melt.

Question 4: 5 Electrical wires of different conductivity or resistance are connected to two capacitors with charge or voltage difference U. When connected individually they drain charge 10, 20, 30, 40 and 50% U, respectively, in time, t. How much % charge they will drain in time, t, when all are connected together in parallel? Voltage difference is not constant, it drops as current flows.

***Solution*:** Its similar to *Q3*. From *Eq 4*:

$(1-U_{12345})=(1-U_1)(1-U_2)(1-U_3)(1-U_4)(1-U_5)=(1-0.1)(1-0.2)(1-0.3)(1-0.4)(1-0.5)$
$=0.9\times0.8\times0.7\times0.6\times0.5=0.15120$. => $U_{12345} = 0.84880 = 84.88\%$

Question 5: In *Question 3*, *case 1*, it took *10 minutes* for *20ml* ice to melt. How much time will be taken for *40 ml* ice to melt? If the length of rod, *L* is *2m*, what is diffusivity coefficient of the body conducting heat, κ?

***Solution*:** This is parallel to one dimensional consolidation *Eq 10* and for *U=40%, Eq 11 is valid*. $U_1 = 20/100 = 0.20$; $U_2 = 40/100 = 0.40$; $t_1 = 10$ *minutes*

$$\frac{T_1}{T_2} = \frac{t_1}{t_2} = (\frac{U_1}{U_2})^2 \Rightarrow \frac{10}{t_2} = (\frac{0.2_1}{0.4})^2;$$

That gives, $t_2 = 40$ *minutes*. From *Eq 11: T=0.032* for $U = 0.20$ at $t = 10$ *min*, h = length of drainage path for heat conduction = $L/2 = 2/2$ for double drainage = *1m*. $T = c_v\, t/h^2 = \kappa\, t/h^2$ => $\kappa = 0.0032\ m^2/min$.

It is noted that c_v = coefficient of consolidation, is diffusivity coefficient in consolidation, while in heat equation diffusivity coefficient is κ, that is parallel to c_v in mathematical analogy.

Question 6: In *Question 3*, if κ is same along *L*, *B* and *H*. Find *B* and *H*.

***Solution*:** $T = \kappa\, t/h^2$ => $h = (\kappa t/T)^{0.5}$; For *U=0.8, T=0.567* from *Eq 9* => $h = (0.0032\times10/0.567)^{0.5} = 0.2375$; $H = 2h = 0.475m$. For *U=0.5, T=0.2* from *Eq 10* => $h = (0.0032\times10/0.2)^{0.5} = 0.16$; $B = 2h = 0.32m$

Question 7: A solid body of Length *L=2m*, Breadth *B=0.32* and Height *H=0.475m* was allowed to cool from Temperature *T°C* to *0°C* in a an ice box at *0°C* ice. Total ice melted to *0° C* water was *100 ml*. Diffusivity coefficient, $\kappa = 0.0032\ m^2/min$ is same in *X, Y* and *Z* directions, Find time *t* in minutes when *80ml* ice will melt. The body is draining from all *6 faces*.

***Solution*:** This is the case of *3D* drainage of heat in *Cartesian Coordinates* and *Eq 16-17* are applicable. $U = 80/100 = 0.8$, λT from *Eq 16 is 0.567*. As κ is same in all directions, so thermal conductivity is also same in all directions. Hence, in *Eq 17;* $k_x=k_y=k_z$.

$\lambda = 1 + (H/B)^2 + (H/L)^2 = 1 + (0.475/0.32)^2 + (0.475/2)^2 = 1 + 2.203 + 0.056 = 3.259$. $T = 0.567/3.259 = 0.174 = \kappa t/h^2$, where, $h = H/2$ in double drainage of heat. $t = (0.174/0.0032)(0.475/2)^2 = 3.07$ *min*.

When flow was in *H* direction alone, it was *10 min*, so the time to achieve *80%U* was reduced by λ *(=3.259)* times by addition of heat flow in *L* and *B* directions.

Similar examples may be taken in Electricity (where charge is diffused, producing current), mass transfer etc. One interesting example is *Hubble's law*, where plot of distance versus the speed of galaxies is straight line and slope of that is Hubble constant. Plot of settlement versus rate of settlement in Radial (and later part of vertical) Consolidation is also a straight line (like Eq 23) the slope of which is c_r, the coefficient of radial consolidation [3]. The straight line starts from the beginning and reduces the experimental time to the minimum possible (zero theoretically). Creep examples are found in various engineering and physics. Spreading of communicable diseases like Corona etc is also a diffusion where *Y-Y'* Approach may also have some application. In consolidation, *Y-Y'* Approach is used mostly on *diffusion* and *creep* equations but it may be tried in wave equations also and in all fields.

7 ADVANCEMENTS IN VERTICAL CONSOLIDATION DUE TO Y-Y' APPROACH

7.1 *Terzaghi's Eq 10 is resolved in 3 parts [1,3,15,17,19,31]*

(Figure 3-4): (1) Parabolic *Eq 11* for *0-40% U*, (2). Transition (*Eq 20*) from Parabolic to Exponential for *40-60% U*, (3). Exponential *Eq 9* for *60-100% U*. *U* versus *dU/dT* plot is a symmetrical *S* shaped curve on semi-log plot (Figure 3), having point of inflection at *50%U*.

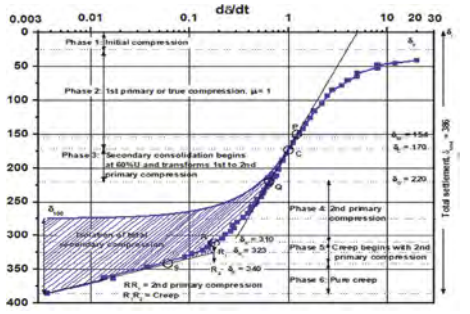

Figure 3. Symmetrical *S-Curve* & 6 Phases.

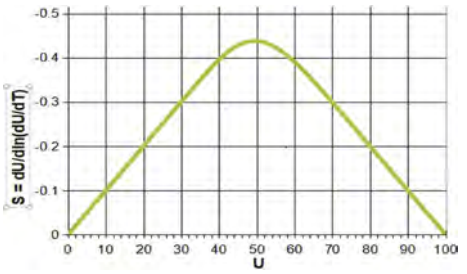

Figure 4. *U* versus Slope of Symmetrical *S-Curve*, *S*.

$$S = U \text{ for } 0 < U < 40\%;\ S = 1 - U \text{ for } 60 < U < 100\%;\\ S = 3.82\left(U - U^2 - 0.1353\right) \text{ for } 40 < U < 60\% \tag{19}$$

$S_{max} = 0.438$ at $U = 0.5$ or *50%* on *ln* scale on *X-axis*. $S_{max} = 1.009 \approx 1$ at $U = 0.5$ or *50%* on log_{10} scale on *X-axis* The slope of this *S-curve*, *S*, varies linearly with *U* from *0-40%* and *60-100%*. *S* has a parabolic relationship with *U* from 40-60% *U*, called transition zone (Figure 4). The equation of transition zone is

$$3.82(U^2 - U - 0.1353)U'' + (U')^2 = 0 \tag{20}$$

Eq 20, does not contain any *T* or *x* term; all variables are in terms of *U, U', U''* only in a simple manner; its *Y-Y' Approach*. Earlier, Eq 10 was resolved in 2 parts only; parabolic Eq 11 from *0-60%U* and Exponential *Eq* 9 from *60-100%U*.

7.2 *Six phases of consolidation (Figure 3)*

The six phases occur due to intermixing of Initial Compression and Secondary compression with 3 parts (parabolic, transition and exponential) of primary compression of *Eq* 10. They are (1) Initial Compression (2) First Primary Compression (3) Transition from first primary compression to second primary compression (4) Second Primary compression (5) Transition from second primary compression to creep and (6) Creep. They are quantitatively isolated in *Figure 3*. In inorganic soils, usually, first primary compression (and transition) part gives *true* c_v. Earlier, only Initial, Primary and Secondary (three) phases of consolidation were known.

7.3 *Fastest method for determination of c_v [1,3,15,17,19,32]*

It can be evaluated at *50% U* only by *Eq 21* (*Figure 3-4*) as compared to minimum *70% U* in other faster methods for the determination of c_v.

$$c_v = -\frac{0.8033\left(\frac{d\delta}{dt}\right)_{50} H^2}{s_{50}} \tag{21}$$

The c_v, δ_0 *and* δ_{100} can be evaluated without knowing the time, settlement and pressure at the instant of load increment, just by observing the δ *versus* $d\delta/dt$ plot for sometime, starting from any arbitrary settlement, δ.

7.4 *The Y-Y' approach gives a simple condition for true c_v:*

In soils following Terzaghi's vertical consolidation theory the product of time and rate of settlement at *50%* consolidation divided by the slope of the tangent at the point of inflection

in *semi-log$_{10}$* plot of *settlement versus rate of settlement* equals *0.245*. In that case, *Eq 21* gives *true* c_v.

$$\mu = \frac{t_{50} \times (\frac{d\delta}{dt})_{50}}{0.245 \times s_{50}} \tag{22}$$

where, μ is a fuzzy logic varying between 0-1, that determines the trueness of c_v [3, 4, 15,31]. Closer is c_v to the *true* c_v, closer is μ to 1. The *true* c_v is devoid of any effect of secondary consolidation. Before the advent of *Y-Y' Approach*, comparison of the calculated values of hydraulic conductivity with the measured ones was required to get the trueness of c_v.

7.5 *From δ-(dδ/dt) Plot, Determination of Instantaneous* c_v, δ_0 *and* δ_{100} *[1, 3, 15]*

$$\delta = \frac{4H^2}{\pi^2 c_v}(\frac{d\delta}{dt}) + \delta_{100} \tag{23}$$

$$c_v = -\frac{4H^2}{\pi^2 m} \tag{24}$$

Eq 23 is straight line in the form: $y = m\,x + c$, where, H is the drainage path, c is intercept on *y-axis* and m is slope. The *δ-(dδ/dt)* plot is a straight line having an intercept on δ axis, $c = \delta_{100}$ and slope, $m = (4H^2)/(\pi^2 c_v)$. The c_v can be evaluated from *Eq 24*.

8 CONCLUSIONS

The *Y-Y'* Calculus is powerful mathematical tool to be used where *X-Y'* calculus fails or becomes complicated. It can be used alone or in combination with *X-Y'* calculus. Analysis and advancements of consolidation problems is carried out with it while comparing it with *X-Y'* calculus in solving the problems. However, consolidation consists of mainly diffusion and creep equations but *Y-Y'* calculus can be used in wave equations and other field also. Soil Consolidation paves the way and marks the beginning of new era in physical sciences and engineering with novel mathematical analogies developed through *Y-Y' Calculus*. Terzaghi's definition of Soil Mechanics, at least in soil consolidation, needs to be re-evaluated.

REFERENCES

1. Tewatia, S.K.: Evaluation of true c_v and instantaneous c_v, and isolation of secondary consolidation. ASTM Geotechnical Testing Journal 21(2), 102–108 (1998).
2. Tewatia, S.K.: Discussion on 'Comparison of the hyperbolic and Asaoka observational method of monitoring consolidation with vertical drains' by Tan and Chew, 1996′. Soils and Foundations, Japanese Geotechnical Society 38 (2), 224–227 (1998).
3. Tewatia, S.K., Tewatia, K.: Consolidation of Soils: Rate of Settlement Approach. 1st edn. Lambert Academic Publishing, LAP, Riga Latvia (2019). https://www.amazon.in/Consolidation-Soils-Rate-Settlement-Approach/dp/6200313016.https://www.researchgate.net/publication/336739313_CONSOLIDATION_OF_SOILS_RATE_OF_SETTLEMENT_APPROACH_RSA_A_Scholarly_book_on_the_State-of-the-Art
4. Tewatia, K., Tewatia, S.K., Rath, S.: Discussion on 'Evaluation of consolidation results by the settlement rate approach' by B.S. Olek, A. Borecka and H. Wozniak (2016). Electronic Journal of Geotechnical Engineering 21 (07), 1-9(2019).
5. Tewatia, K., Tewatia, A., Rath, S.: Discussion of 'Fastest rapid loading methods of vertical and radial consolidations' by S.K. Tewatia, Pratima Rani Bose and Asuri Sridharan (2013). International Journal of Geomechanics 15 (1), 1 (2015).
6. Tewatia, S. K., Tewatia, K., Tewatia, A.: Discussion, 'Consolidation of Clayey Gouge amid Permeating Rock Masses by Trivedi et al'. Environmental Geotechnics, ICE, Vol 2/4, 237–248 (2015)

7. Tewatia, S.K.: Time Dependent Behavior of Clayey Soils. PhD Thesis, Department of Civil Engineering, Delhi College of Engineering, Delhi University, India (2010).
8. Tewatia, S.K.: Trend of settlement in primary and secondary consolidations. Geomechanics and Geo-Engineering 8(2), 125–134 (2012).
9. Tewatia, S.K.: Equation of 3D consolidation in Cartesian co-ordinates. International Journal of Geotechnical Engineering, 7(1), 105–108 (2013).
10. Tewatia, S.K.: Principle of super position of rate of settlement in 2D and 3D consolidations. Geotechnical and Geological Engineering 33(5), 1369–1378 (2015).
11. Tewatia, S.K., Venkatachalam, K.: Closure for discussion on 'Improved √t method to evaluate consolidation test results'. Geotechnical Testing Journal 21(2), 155–156 (1998).
12. Tewatia, S.K., Venkatachalam, K., Sridharan, A.: T-Chart to evaluate consolidation test results. ASTM Geotechnical Testing Journal 21(3), 270–274 (1998).
13. Tewatia, S.K., Bhargav, D.N., Chouhan, G., Sridharan, A.: Velocity method for creep of clayey soils. Electronic Journal of Geotechnical Engineering 7(Bundle B), (2002).
14. Tewatia, S.K., Bose, P.R.: Discussion on 'A study on the beginning of secondary compression of soils' by R.G. Robinson. ASTM Journal of Testing and Evaluation 34(5), 1–6 (2006).
15. Tewatia, S.K., Bose, P.R., Sridharan, A., Rath, S.: Stress induced time dependent behavior of clayey soils. Springer's Geotechnical and Geological Engineering 25(2), 239–255 (2007).
16. Tewatia, S.K., Sridharan, A., Singh, M., Rath, S.: Theoretical equations of vertical and radial consolidations by equating degrees of consolidation by settlement analysis and dissipation of pore pressure. Springer's Geotechnical and Geological Engineering 30(4), 1037–1043 (2012).
17. Tewatia, S.K., Bose, P.R., Sridharan, A.: Fastest rapid loading methods of vertical and radial consolidations. ASCE International Journal of Geomechanics 13(4), 332–339 (2013).
18. Tewatia, S.K., Huat, B., Rath S., Tewatia, K.: U-chart for quick evaluation of radial and 3D consolidation test results. ICE Ground Improvement 166(4), 188–195 (2013).
19. Tewatia, S.K., Bose, P.R., Sridharan, A.: Closure to 'Fastest rapid loading methods of vertical and radial consolidations' by S.K. Tewatia, P.R. Bose, and Asuri Sridharan. ASCE International Journal of Geomechanics 15 (1), 1–3 (2015).
20. Tewatia, S. K., Chetia, M., Nasrin, T. and Tewatia, K.: Consolidation: Critical Appraisal of Settlement versus Rate of Settlement Approach with Fuzzy Logic. Ground Characterization and foundations, CNV Satyanarayan Reddy et al. (eds), Springer Nature Singapore, LNCE 167 (2022). https://doi.org/10.1007/978-981-16-3383-6_37
21. Terzaghi, K.: Mathematisch-naturewissenschaftliche Klasse, Akademie der Wissenschaften in Wien, Sitzungsberichte, Part Iia132(3/4), 125–138 (1923).
22. Terzaghi, K.: Theoretical Soil Mechanics. John Wiley and Sons, Inc., New York, London (1943).
23. Leo, C. J.: Equal Strain Consolidation by Vertical Drains. ASCE Journal of Geotechnical and Geoenvironmental Engineering 130(3), 316–327 (2004)
24. Fick, A. (1855). "On liquid diffusion". Annalen der Physik und Chemie. 94: 59. – reprinted in Fick, Adolph (1995). "On liquid diffusion". Journal of Membrane Science. 100: 33–38. doi:10.1016/0376-7388(94)00230-v
25. Fourier, J. B. J., Théorie Analytique de la Chaleur, F. Didot, Paris, 1822.
26. Carrillo, N.: Simple two and three dimension cases in the theory of consolidation of soils. Journal of Mathematics and Physics **21**(1), 11–18 (1942).
27. Barron, R. A.: Consolidation of Fine Grained Soils by Drain wells. Transactions of ASCE, Vol. 113, 718–724 (1948).
28. Theim, A.:Verfahress fur Naturlicher Grundwasser geschwindegkiten. *Polyt. Notizblatt* **42**, 229 (1906)
29. Mei, G., Chen, Q.: Solution of Terzaghi one-dimensional consolidation equation with general boundary conditions. Journal of Central South University 20(8), 2239–2244 (2013)
30. Biot, M. A. (1941). General theory of three-dimensional consolidation. Journal of applied physics, 12(2), 155–164.
31. Nasrin, T.: Critical Appraisal of Settlement versus Rate of Settlement Approach in Vertical Consolidation. MTech Thesis, Department of Civil Engineering, Assam Science & Technology University, Guwahati, India (2022).
32. Tewatia, S. K., Venkatachalam, K.: Improved √t Method to Evaluate Consolidation Test Results. ASTM Geotechnical Testing Journal, 20(1), 121–125 (1997).

Smart Geotechnics for Smart Societies – Zhussupbekov, Sarsembayeva & Kaliakin (Eds)
© 2023 The Author(s), ISBN 978-1-003-29912-7
Open Access: www.taylorfrancis.com, CC BY-NC-ND 4.0 license

The use of grading entropy in assessing granular soil hydraulic conductivity

S. Feng
Birmingham City University, Birmingham, UK
University of Bristol, Bristol, UK

P.J. Vardanega & E. Ibraim
University of Bristol, Bristol, UK

D. Barreto
Edinburgh Napier University, Edinburgh, UK

E. Imre
Óbuda University, Budapest, Hungary

ABSTRACT: Hydraulic conductivity is an important geotechnical engineering property as it is linked to the performance of many geo-structures. This study used a recently compiled granular soil database (CG/KSAT/7/1278) to evaluate the best fit probability density functions for important parameters in the database. The Loglogistic function was found to be the best-fit probability density function for the parameters from CG/KSAT/7/1278 investigated in this paper. The grading entropy parameters (un-normalised) were used to develop a chart that highlights trends from the effect of changes of the gradation parameters on the estimated soil permeability.

1 INTRODUCTION

Hydraulic conductivity (k) is a fundamental soil mechanics parameter that is closely linked to many geotechnical problems, such as seepage, settlement, and slope stability (e.g. Lambe & Whitman 1969, Taylor 1948). Simple predictive models for k calibrated using laboratory data are often used (e.g. Chapuis 2012).

Feng (2022) assembled a coarse-grained soil database CG/KSAT/7/1278, which consists over 1200 measurements of k (see Feng 2022 and Feng et al. 2023 for full details of the assembled database including the original data-sources). Feng (2022) examined various empirical and semi-empirical transformation models for k of granular soils.

The aims of this study are: (a) Identify the best-fit PDFs for important parameters using CG/KSAT/7/1278; (b) Examine the influence of statistical outliers on the choice of best-fit PDFs from (a) and (c) Investigate if the grading entropy theory can offer insights into the variation of the soil permeability data from CG/KSAT/7/1278. For further details on the establishment and statistical analysis of the database see the thesis of Feng (2022) and Feng et al. (2023).

2 DATABASE STUDY

2.1 *Identifying potential outliers*

In this work the following procedure for identification of potential outliers was adopted: (i) datapoints with a computed standardized residual not within the range of -2 to 2 (cf. Montgomery et al. 2007), or those with a computed leverage value greater than three times the computed mean

DOI: 10.1201/9781003299127-28

leverage (cf. Velleman & Welsch 1981) were identified for all calibrated regression models (see Feng 2022 for a full list of the calibrated models); and (ii) if a datapoint from (i) was identified as an outlier for greater than 75% of the calibrated models it was deemed to be a statistical outlier. This analysis results in 22 datapoints out of 1278 in the CG/KSAT/7/1278 database (approximately 2%) being classified as statistical outliers (a similar procedure for identification of statistical outliers was adopted in Feng et al. 2021, Feng et al. 2022, and the procedure outlined in this paper is also used in Feng et al. 2023 for analysis of CG/KSAT/7/1278).

2.2 *Probability Density Functions (PDFs)*

The best fitting PDFs for the key parameters from the database CG/KSAT/7/1278 were evaluated using the Akaike Information Criterion (AIC) (Akaike 1974) before and after the removal of the statistical outliers as identified in Section 2.1. The AIC is computed as:

$$AIC = -2\log\left(L(\hat{\theta})\right) + 2K_i \tag{1}$$

where $L(\hat{\theta})$ is the 'likelihood function', and K_i is the number of parameters in the PDF fitted to the data. The trialled PDFs were: 'Lognormal', 'Exponential', 'Weibull', 'Loglogistic' and 'Gamma' (Feng and Vardanega 2019 carried out a similar study for a fine-grained soil k database: FG/KSAT-1358), were fitted to the void ratio (e), aperture diameter through which 50% of the material would pass (D_{50}) and k data from CG/KSAT/7/1278. In the following analysis the k data was analysed in the form of the intrinsic permeability K (length^2).

Figures 1–3 show probability plots where the aforementioned PDFs are fitted to the e, D_{50} and K data from CG/KSAT/7/1278 with and without the identified statistical outliers included. Tables 1 and 2 record the computed AIC for the PDFs trialled. The results show that the 'Loglogistic' function is the best-fit PDF for all parameter examined in database either before or after the removal of the identified statistical outliers. The 'Loglogistic' function can be expressed as (e.g. Johnson et al. 1994):

$$f(x|\mu,\sigma) = \frac{e^z}{\sigma x(1+e^z)^2} \text{ , where } z = \frac{\log(x)-\mu}{\sigma} \tag{2}$$

where, μ = mean of the logarithmic values, and σ = scale parameter of the logarithmic values. Table 3 compares the fitted parameters of the best-fit PDFs ('Loglogistic') for the key parameters of the studied database with and without the identified statistical outliers. The effect of outliers on the fitted PDFs was deemed to be negligible.

Table 1. Computed AIC for the fitted PDFs for CG/KSAT/7/1278 (best fits shown in bold).

n =1278	Exponential	Lognormal	Weibull	Loglogistic	Gamma
e	1140	-628	-599	-801	-716
D_{50} (mm)	3810	2800	3313	2762	3524
K (mm^2)	-16736	-25291	-25108	-25388	-24269

Table 2. Computed AIC for the fitted PDFs for CG/KSAT/7/1278 with identified outliers removed (best fits shown in bold).

n =1256	Exponential	Lognormal	Weibull	Loglogistic	Gamma
e	1131	-716	-656	-880	-791
D_{50} (mm)	3582	2610	3127	2565	3331
K (mm^2)	-17532	-24883	-24701	-24972	-23946

Table 3. Best fit PDF (Equation 2) for key parameters of CG/KSAT/7/1278.

Fitted parameters	with the outliers included (n = 1278)			with outliers removed (n = 1256)		
	e	D_{50} (mm)	K (mm^2)	e	D_{50} (mm)	K (mm^2)
μ	-0.59	-0.71	-12.49	-0.59	-0.74	-12.48
σ	0.18	0.69	1.74	0.17	0.67	1.66

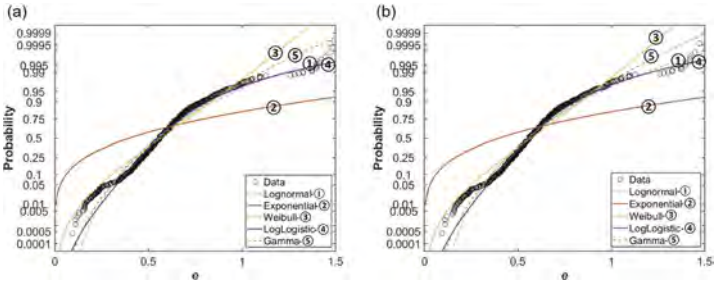

Figure 1. (a) Probability plot with PDFs fitted to data of e from CG/KSAT/7/1278 (n =1278), (b) Probability plot with PDFs fitted to data of e from CG/KSAT/7/1278 with identified statistical outliers removed (n =1256).

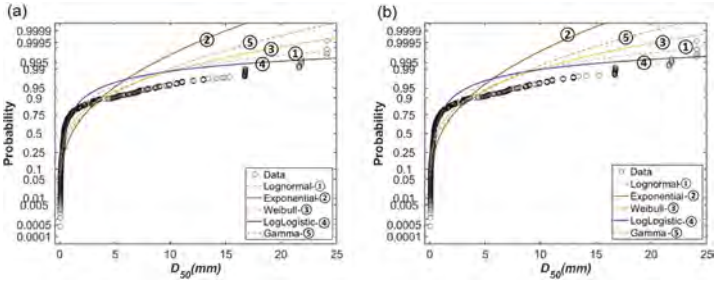

Figure 2. (a) Probability plot with PDFs fitted to data of D_{50} (mm) from CG/KSAT/7/1278 (n =1278), (b) Probability plot with PDFs fitted to data of D_{50} (mm) from CG/KSAT/7/1278 with identified statistical outliers removed (n =1256).

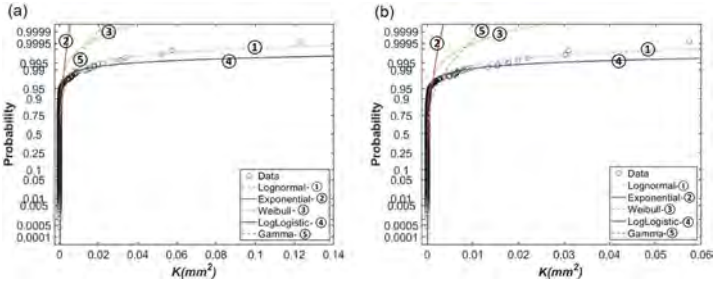

Figure 3. (a) Probability plot with PDFs fitted to data of K (mm^2) from CG/KSAT/7/1278 (n =1278), (b) Probability plot with PDFs fitted to data of K (mm^2) from CG/KSAT/7/1278 with identified statistical outliers removed (n =1256).

3 GRADING ENTROPY

The grading entropy approach was presented to investigate granular soil dry bulk density (e.g. Lőrincz 1990) and has subsequently been used to study a range of geotechnical problems (e.g. Lőrincz et al. 2005, Imre et al. 2009, Imre et al. 2012 and McDougall et al. 2013). Lőrincz

et al. (2005) and Imre et al. (2009) give a detailed introduction of the framework (which characterizes disorder in soil particle size distributions) and full derivation of grading entropy parameters. The grading entropy S of a soil mixture is given by (form of the equations are shown as in Singh 2014, pp. 324-328):

$$S = S_0 + \Delta S \tag{3}$$

where S_0 = base entropy:

$$S_0 = \sum_{i=1}^{N} x_i \log_2 C_i \tag{4}$$

where N = number of fractions, x_i = relative frequency of fraction i, C_i = number of elementary statistical cells contained in fraction i. The entropy increment ΔS is:

$$\Delta S = -\sum_{i=1}^{N} x_i \log_2 x_i \tag{5}$$

the base entropy S_0 and the entropy increment ΔS helps explain the relative spread of the grain sizes and explains the relative distribution of the particles. The normalised grading entropy coordinates A and B are:

$$A = \frac{\sum_{i=1}^{N} x_i(i-1)}{N-1} \tag{6}$$

$$B = -\frac{\sum_{i=1}^{N} x_i \log_2 x_i}{\log N} \tag{7}$$

Feng et al. (2019) used the normalised grading entropy parameters (A, B) to assess the hydraulic conductivity for a granular soil mixture. O'Kelly & Nogal in their discussion of Feng et al. (2019) proposed the addition of the e alongside A and B for hydraulic conductivity prediction (Feng et al. 2020). O'Kelly & Nogal (2020) applied their three-parameter approach to test data on a wider range of granular materials than was presented in Feng et al. (2019, 2020). Feng et al. (2021) then investigated the influence of using the grading entropy parameter (S) along with the percentage air voids to assess asphalt concrete hydraulic conductivity using a large database. Imre et al. (2021) used the un-normalised grading entropy coordinates and determined iso-lines for the saturated k.

The grading entropy parameters for data from CG/KSAT/7/1278 were calculated with the width of the elementary cell (d_0) assumed to be 2^{-22}mm following Imre et al. (2009). Figures 4 and 5 present the normalised and non-normalized grading entropy diagram for the database CG/KSAT/7/1278. Figure 4 shows that the permeability levels exhibit an increasing trend with higher S_0 value and lower ΔS value. Such variation of permeability level is less distinct on the normalised grading entropy diagram (Figure 5). It was observed that datapoints with lower permeability level (i.e. categories 'very low', 'practically impermeable') mostly are aggregated around the A = 2/3 on the normalised grading entropy diagram, which according to Lőrincz (1990) represent mixtures with the maximum density for a given fraction number N, concerning a fixed distribution type (e.g., fractal distribution, non-fractal distribution).

4 CONCLUSIONS

Some statistical analysis of the coarse-grained soil database CG/KSAT/7/1278 has been presented in this paper. The main findings from this study are:

(a) the 'Loglogistic' function is the best fit PDF (of those trialled) for the e, D_{50} and K data from CG/KSAT/7/1278.
(b) The influence of the identified statistical outliers was found to be minimal on the best fit PDFs.

(c) On the normalised grading entropy diagram (A versus B), the K categories are less distinguishable than on the un-normalised grading entropy diagram (ΔS versus S_0) for the studied data.

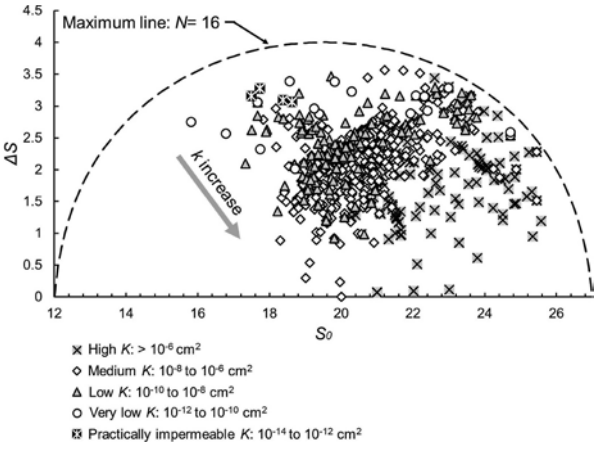

Figure 4. Grading entropy diagram; K categorization based on the categorization system given in Lambe & Whitman (1969, p. 288).

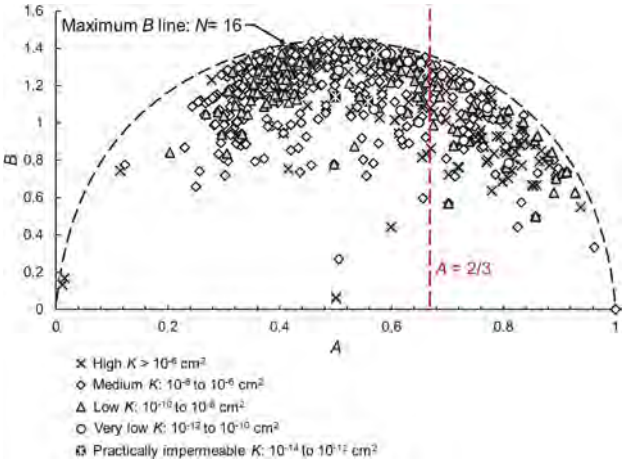

Figure 5. Normalised grading entropy diagram; K categorization based on the categorization system given in Lambe & Whitman (1969, p. 288).

ACKNOWLEDGEMENTS

SF acknowledges support from the China Scholarship Council (Grant Number 201708060067) for funding her doctoral studies at the University of Bristol. Data availability: This study has not generated new experimental data.

REFERENCES

Akaike, H. 1974. A new look at the statistical model identification. *IEEE Transactions on Automatic Control* 19(6): 716–723.

Chapuis, R.P. 2012. Predicting the saturated hydraulic conductivity of soils: A review. *Bulletin of Engineering Geology and the Environment* 71(3): 401–434.

Feng, S. & Vardanega, P.J. 2019. A database of saturated hydraulic conductivity of fine-grained soils: probability density functions. *Georisk: Assessment and Management of Risk for Engineered Systems and Geohazards* 13(4): 255–261.
Feng, S., Vardanega, P.J., Ibraim, E., Widyatmoko, I. & Ojum, C. 2019. Permeability assessment of some granular mixtures. *Géotechnique* 69(7): 646–654.
Feng, S., Vardanega, P.J., Ibraim, E., Widyatmoko I., Ojum, C., O'Kelly, B.C. & Nogal, M. 2020. Discussion: permeability assessment of some granular mixtures, *Géotechnique* 70(9): 845–847.
Feng, S., Vardanega, P.J., James, M. & Ibraim, E. 2021. Studying hydraulic conductivity of asphalt concrete using a database. *Transportation Engineering* 3: [100040].
Feng, S. 2022. *Hydraulic Conductivity of Road Construction Materials: with a focus on freeze-thaw effects*. PhD thesis, University of Bristol, Bristol, UK.
Feng, S., Ibraim, E. & Vardanega, P.J. 2022. Databases to assess the hydraulic conductivity of road construction materials. In M.M. Rahman & M. Jaksa (eds), *Proc. of Twentieth International Conference on Soil Mechanics and Geotechnical Engineering (ICSMGE 2022)*, *Sydney*, *1-5 May 2022*. Australian Geomechanics Society, Sydney, Australia, pp. 4547–4552.
Feng, S., Barreto, D., Imre, E., Ibraim, E. & Vardanega, P.J. 2023. Use of hydraulic radius to estimate the permeability of coarse-grained materials using a new geodatabase. *Transportation Geotechnics*, https://doi.org/10.1016/j.trgeo.2023.101026
Imre, E., Bálint, Á., Nagy, L., Lőrincz, J., Illés, Z., Barreto, D., Csini, F., Guida, G. & Feng, S. 2021. Examination of saturated hydraulic conductivity using grading curve functions. In *Proc. of 6th International Conference on Geotechnical and Geophysical Site Characterisation, Budapest*, 26-29 September 2021. https://doi.org/10.53243/ISC2020-373
Imre, E., Lőrincz, J., Szendefy, J., Trang, P.Q., Nagy, L., Singh, V.P. & Fityus, S. 2012. Case studies and benchmark examples for the use of grading entropy in geotechnics. *Entropy* 14(6): 1079–1102.
Imre, E., Lőrincz, J., Trang, Q.P., Fityus, S., Pusztai, J., Telekes, G. & Schanz, T. 2009. A general dry density law for sands. *KSCE Journal of Civil Engineering* 13(4): 257–272.
Johnson, N.L., Kotz, S. & Balakrishnan, N. 1994. *Continuous univariate distributions*. New York: John Wiley & Sons.
Lambe, T.W. & Whitman, R.V. 1969. *Soil Mechanics*. New York: John Wiley & Sons.
Lőrincz, J. 1990. Relationship between grading entropy and dry bulk density of granular soils. *Periodica Polytechnica Civil Engineering* 34(3): 255–265.
Lőrincz, J., Imre, E., Gálos, M., Trang, Q.P., Rajkai, K., Fityus, S. & Telekes, G. 2005. Grading entropy variation due to Soil crushing. *International Journal of Geomechanics* 5(4): 311–319.
McDougall, J.R., Imre, E., Barreto, D. & Kelly, D. 2013. Volumetric consequences of particle loss by grading entropy. *Géotechnique* 63(3): 262–266.
Montgomery, D.C., Runger, G.C. & Hubele, N.F. 2007. *Engineering Statistics* (4th ed.). New York: John Wiley & Sons Inc.
O'Kelly, B.C. & Nogal, M. 2020. Determination of soil permeability coefficient following an updated grading entropy approach. *Geotechnical Research* 7(1): 58–70.
Singh, V.P. 2014. *Entropy Theory in Hydraulic Engineering*. Reston: American Society of Civil Engineers.
Taylor, D.W. 1948. *Fundamentals of Soil Mechanics*. New York: John Wiley & Sons.
Velleman, P.F. & Welsch, R.E. 1981. Efficient Computing of Regression Diagnostics. *The American Statistician* 35(4): 234–242.

Smart Geotechnics for Smart Societies – Zhussupbekov, Sarsembayeva & Kaliakin (Eds)
© 2023 The Author(s), ISBN 978-1-003-29912-7
Open Access: www.taylorfrancis.com, CC BY-NC-ND 4.0 license

Preparing CO_2 hydrate-bearing sand specimens using dissolved gas and its properties

S. Kimoto
Osaka Sangyo University, Osaka, Japan

Y. Yoshida
Toyota Tsusho Corporation, Tokyo, Japan

ABSTRACT: Various projects related to gas hydrate, such as methane hydrate resource development and carbon dioxide underground storage using gas hydrate, are attracting attention. Various laboratory tests have been conducted using artificially prepared hydrate-containing sand samples to investigate the mechanical properties of gas hydrate-containing ground. In this study, we focused on the hydrate formation process and morphologies, and prepared CO_2 hydrate-bearing sand specimens by the dissolved gas method. In addition, undrained triaxial compression tests were performed using the prepared specimens. From the test results, hydrate-bearing specimens with the value of hydrate saturation ranged from 3.4% to 8.8% were made. The stress-strain behavior and the effective stress path were almost the same as that of the hydrate-free specimen.

1 INTRODUCTION

Various laboratory tests have been carried out on the mechanical properties of gas-hydrate-containing ground. Since the data of the mechanical test using the natural hydrate-containing samples collected by the pressure core is limited, various mechanical tests using the gas hydrate-containing specimens artificially prepared are carried out. Several methods can form hydrates artificially in ground materials in a laboratory. The most commonly used method is the partial water saturation method, which can prepare a specimen with high hydrate saturation in a short time (Waite et al., 2009). However, the formation process may be different from that in nature because it produces hydrates in excess gas condition. In this study, we attempted to prepare sand specimens containing CO_2 hydrate by the dissolved gas method. In this method, the formation process is similar to that in nature in the sense that hydrate is formed from the gas aqueous solution in excess water condition. In addition, undrained triaxial tests were conducted for understanding the mechanical properties.

2 TESTING PROCEDURE

2.1 *Dissolved gas method and testing apparatus*

In the dissolved gas method, hydrate is formed by passing a saturated CO_2 aqueous solution through the specimen and cooling it to the temperature in the hydrate stable region. In this method, hydrate is formed by utilizing the fact that the gas solubility in the presence of hydrate decreases with decreasing temperature. Figure 1 shows the temperature dependence of CO_2 solubility in each phase at 2.0 MPa. As shown in the figure, the solubility of CO_2 decreases at low temperatures in the presence of hydrate, so the excess dissolved gas precipitates as hydrate. To

DOI: 10.1201/9781003299127-29

increase the hydrate saturation rate, it is important to cool the CO_2 saturated aqueous solution to increase gas concentration.

A schematic view of a low-temperature and high-pressure triaxial apparatus (Iwai et al. 2018), used in this study is shown in Figure 2. In this study, a circulation tank (No. (13) in

Table 1. Test conditions, collected gas volume, and hydrate saturation.

Case-No	Temperature of CO_2 solution [°C]	Temperature of specimen [°C]	Time for formation [hour]	Amount of water flow [cm^3]	Collected gas volume [cm^3]	Hydrate Saturation [%]
Case-MDO	8	1	-	-	520	0
Case-MD1	8	1	64	142	x	x
Case-MD3	8	1	80	263	692	3.4
Case-DO	20	1	-	-	301	0
Case-D1	20	1	69	332	554	4.8
Case-D4	8	1~4	293	755	960	8.8

* In Case-MD1, CO_2 gas could not be collected (denoted by ×).

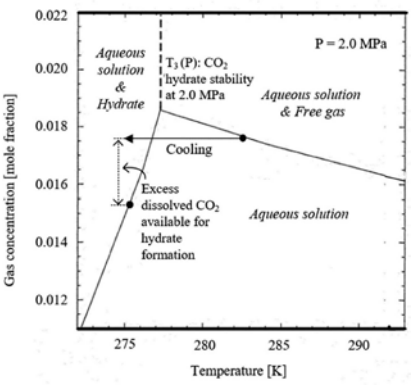

Figure 1. CO2 solubility at 2.0 MPa and hydrate formation mechanism of dissolved gas method (modified from Buffet and Zatsepina (2000)).

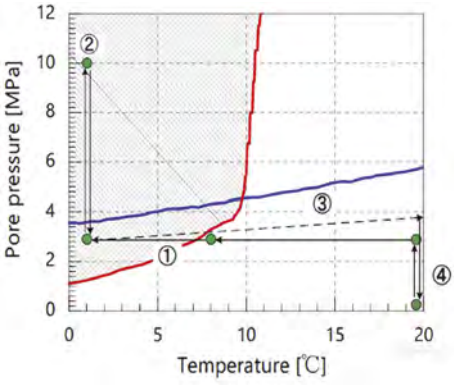

Figure 3. CO_2 hydrate equilibrium curve and temperature-pressure paths during test.

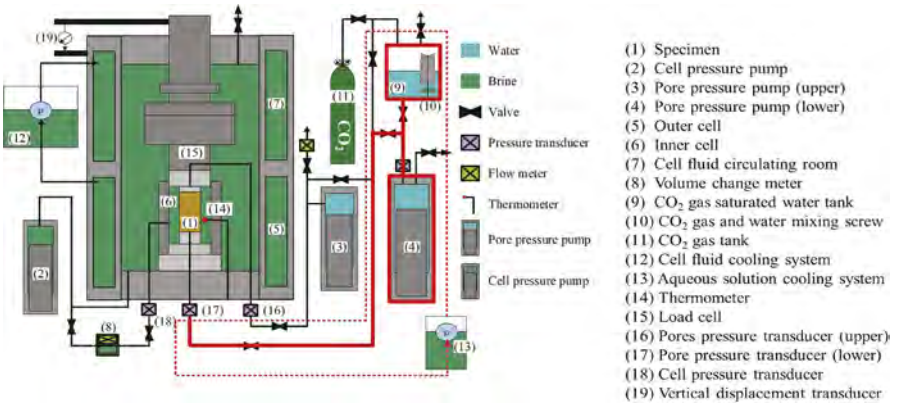

Figure 2. Schematic diagram of how-temperature and high-pressure triaxial apparatus (Red lines indicate route of CO_2 aqueous solution to be cooled by the cooling system indicated by No. (13)).

Figure 2) was newly added as a cooling system for the containers and routes involved in the preparation and water flow of the CO_2 aqueous solution indicated by the red line in the figure.

2.2 *Sample preparation*

Toyoura sand with a water content of 16.0% is used as the host soil. The specimen is molded to a diameter of 35 mm and a height of 70 mm and frozen for 24 hours. The initial void ratio is 0.75. After the specimen is placed in the cell, the void is replaced with a saturated aqueous CO_2 solution under the conditions of a temperature of 8 °C or 20 °C and a pressure of 2.8 MPa. After that, hydrate is formed by continuing to pass the aqueous solution from the lower part (tank (4) in Fig. 1) to the upper part (tank (3) in Fig. 1) of the specimen while keeping the specimen temperature at 1 to 4 °C and the gap pressure at the upper part of the specimen at 2.8 MPa. Table 1 shows the preparation conditions for the specimen. The tests were conducted with different the cooling temperature and the water flow time. Case-MD represents a case where a monotonic loading test and a thermal dissociation test are performed, and Case-D represents a case where only a thermal dissociation test is performed.

After hydrate formation, in the series of Case-MD, shear is performed under undrained conditions at a pore pressure of 10 MPa, a cell pressure of 12 MPa, and a strain rate of 0.1%/min. After that, the pore pressure is adjusted to 2.8 MPa and the cell pressure is adjusted to 3.3 to 4.8 MPa, and the temperature of the cell water is raised from 1 °C to 20 °C in an isotropic state to dissociate the hydrate in the specimen. CO_2 hydrate equilibrium curve and temperature-pressure paths is shown in Figure 3.

2.3 *Calculation of hydrate saturation*

After the test is completed, the CO_2 gas generated from the specimen is collected and the hydrate content is calculated from the volume. In order to consider the amount of dissolved gas, the hydrate content was calculated from the difference from the recovered gas volume of Case-D0 and Case-MD0, in which hydrate formation process were not carried out after replacing the void with an aqueous solution. To describe the hydrated contest in the pore space, hydrate saturation, S_r^H, is defined as the ratio of hydrate volume to void volume. The recovery volume and the calculated hydrate saturation, S_r^H, is shown in Table 1. The value of hydrate saturation, S_r^H, ranges from 3.4% to 8.8%.

3 TEST RESULTS

Figure 4 shows the change in the amount of water flow of the aqueous solution and the change in the hydraulic conductivity during the hydrate formation process. It was confirmed that the hydraulic conductivity decreased with the passage of the aqueous solution. This is the effect of solid hydrate blocking the flow path of the aqueous solution. In Case-MD1 and MD3 using an aqueous solution saturated at 8 °C, the decrease in hydraulic conductivity was remarkable. The reason why the hydraulic conductivity increases and decreases repeatedly in Case-D4 is that the water flow is continued while the obstruction is cleared each time by the backflow of the aqueous solution. Figure 5 shows the pore pressure-temperature relationship and axial strain-temperature relationship during dissociation by thermal stimulation. With the hydrate equilibrium curve as the boundary, the interstitial pressure increased sharply, and at the same time, the axial strain increased significantly in the expansion. This is because CO_2 gas was generated by the dissociation of hydrate.

Figure 6 shows the stress-strain relationships and effective stress paths in the shear process. No change in mechanical properties was confirmed with or without hydrate formation. The increase in strength due to the inclusion of hydrate has not been confirmed under the hydrate saturation, S_r^H, of 3.4 %.

4 CONCLUSIONS

In this study, CO_2 hydrate-bearing sand specimen was prepared by the dissolved gas method. From the test results, hydrate was formed in the void of sand specimen and the value of hydrate saturation ranged from 3.4% to 8.8%. From the triaxial tests, the increase in strength due to the inclusion of hydrate has not been confirmed. Hydrates may be formed in the void of sand grain and did not affect mechanical properties in the range of hydrate saturation.

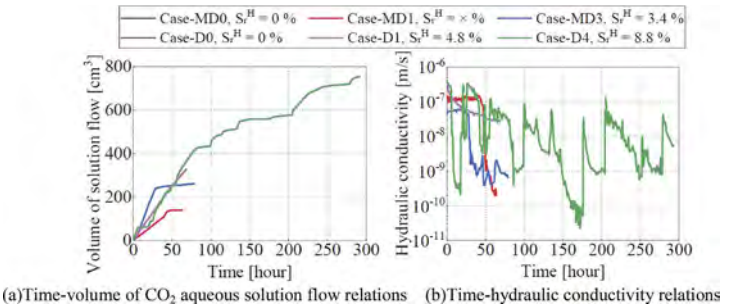

Figure 4. Change of solution flow volume and hydraulic conductivity during hydrate formation.

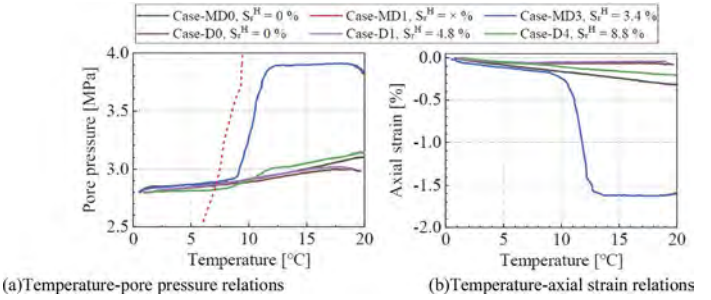

Figure 5. Change of pore pressure and axial strain during hydrate dissociation by thermal stimulation.

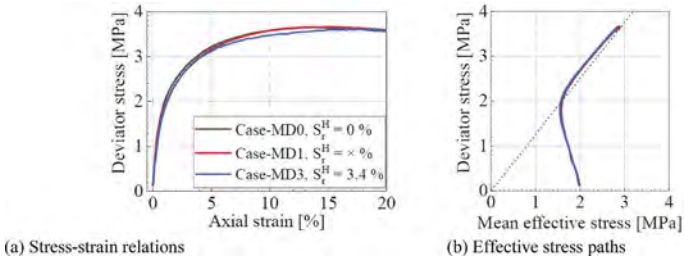

Figure 6. Undrained triaxial tests on saturated sand and CO_2 hydrate-bearing sand.

REFERENCES

Waite, W. F., Santamarina, J.C., Cortes, D. D., Dugan, B., Espinoza, D. N., Germaine, J., Jang, J., Jung, J. W., Kneafsey, T. J., Shin, H., Soga, K., Winters, W.J. and Yun, T. S. 2009. Physical properties of hydrate-bearing sediment. *Reviews of Geophysics*, RG4003: 1–38.

Buffett, B. A. and Zatsepina, O. Y. 2000. Formation of gas hydrate from dissolved gas in natural porous media. *Marine Geology*, 164 (1-2): 69–77.

Iwai, H., Konishi, Y., Saimyou, K., Kimoto, S. and Oka, F. 2018. Rate effect on the stress-strain relations of synthetic carbon dioxide hydrate-bearing sand and dissociation tests by thermal stimulation. *Soils and Foundations*, 58 (5): 1113–1132.

Smart Geotechnics for Smart Societies – Zhussupbekov, Sarsembayeva & Kaliakin (Eds)
© 2023 The Author(s), ISBN 978-1-003-29912-7
Open Access: www.taylorfrancis.com, CC BY-NC-ND 4.0 license

Reconstruction of isotropic Cam-clay model based on finite deformation theory

Y. Abe, S. Yamada & T. Kyoya
Tohoku University, Sendai, Japan

ABSTRACT: This study reconstructs isotropic Cam-clay model based on multiplicative decomposition of the deformation gradient. The aim of the reconstruction is a formulation considering the existence of the state boundary surface in Cauchy stress – specific volume space, which is a basic experimental fact of Cam-clay model. For this purpose, we define a hyperelastic strain energy function per unit volume in the intermediate configuration and formulate using zeta stress and Eshelby-zeta stress derived by considering the non-negativeness of plastic dissipation. This study also constructs an implicit stress update algorithm for the model and derives the tangent modulus consistent with the algorithm to incorporate the proposed model into a finite element analysis code. Moreover, this study demonstrates the significance of the proposed model by comparing an existing model using Kirchhoff stress, and verifies the stress update algorithm.

1 GENERAL INSTRUCTIONS

In the framework of finite deformation elastoplasticity, several researchers (Borja et al. 1998, Yamakawa et al. 2010) have formulated the Cam-clay model using multiplicative decomposition of the deformation gradient and a hyperelastic constitutive law. However, these pioneering works have not fully considered the volume change of the intermediate configuration. Due to this, the formulations in the previous studies cannot guarantee the existence of the state boundary surface, which plays an important role in the derivation of the Cam-Clay model.

Therefore, this study reconstructs the isotropic Cam-clay model that can explain the existence of state boundary surface using zeta and Eshelby-zeta stresses, which are derived by considering the volume change of the intermediate configuration in terms of the non-negativeness of plastic dissipation with referring to Bennett et al. (2016). To verify the validity of the proposed model, numerical analysis using a finite element analysis code that implements the constructed model is performed.

2 FORMULATION OF THE ISOTROPIC CAM-CALY MODEL BASED ON FINITE DEFORMATION THEORY

2.1 *Definition of main kinematic quantities*

The formulation is given in the framework of finite deformation elastoplasticity based on the multiplicative decomposition of the deformation gradient. The deformation gradient is multiplicatively decomposed into elastic and plastic components $\boldsymbol{F} = \boldsymbol{F}^e\boldsymbol{F}^p$.

The elastic left Cauchy-Green tensor $\boldsymbol{b}^e \left(= \boldsymbol{F}^e(\boldsymbol{F}^e)^T\right)$ referring to the current configuration can be spectrally decomposed as follows:

DOI: 10.1201/9781003299127-30

$$\boldsymbol{b}^e = \sum_{\alpha=1}^{3} (\lambda_\alpha^e)^2 \boldsymbol{n}_\alpha \otimes \boldsymbol{n}_\alpha \tag{1}$$

where $(\lambda_\alpha^e)^2$ and $\boldsymbol{n}_\alpha$ are the eigenvalues and eigenvectors of $\boldsymbol{b}^e$, respectively. $\varepsilon_\alpha^e = \ln \lambda_\alpha^e$ is defined as the elastic principal logarithmic strain.

The elastic logarithmic volume strain $\varepsilon_{\mathrm{v}}^e = \varepsilon_\alpha^e \delta_\alpha$ ($\delta_\alpha = 1$) and the elastic logarithmic shear strain $\varepsilon_{\mathrm{s}}^e = \sqrt{2/3 \varepsilon_{\mathrm{dev},\alpha}^e \varepsilon_{\mathrm{dev},\alpha}^e}$ are defined as invariants of the elastic principal logarithmic strain. Note that $\varepsilon_{\mathrm{dev},\alpha}^e = -\left(\varepsilon_\alpha^e - (1/3)\varepsilon_{\mathrm{v}}^e \delta_\alpha\right)$ is the elastic deviatoric principal strain.

2.2 *Hyperelastic constitutive law and plastic flow rule*

To formulate using the hyperelastic constitutive law, a special form of the hyperelastic model proposed by Houlsby et al. (2005) is applied to the elastic part. A hyperelastic strain energy function per unit volume in the intermediate configuration $\bar{\Psi}$ is defined as follows:

$$\bar{\Psi} = \tilde{\kappa}^* p_r \exp\left[\frac{1}{\tilde{\kappa}^*}\left(\varepsilon_{\mathrm{v}}^e + \frac{3}{2}\tilde{\mu}\left(\varepsilon_{\mathrm{s}}^e\right)^2\right)\right] \tag{2}$$

where $\tilde{\kappa}^*$ is the swelling index in the $\ln \mathrm{v} - \ln p^\zeta$ plane and there is a relationship $\tilde{\kappa}^* = \tilde{\kappa}/(1-\tilde{\kappa})$ using the swelling index $\tilde{\kappa}$ in the $\ln \mathrm{v} - \ln p$ plane. p_r is the reference stress and $\tilde{\mu}$ is the dimensionless shear modulus. A hyperelastic constitutive law is defined as follows:

$$\zeta = 2\frac{\partial \bar{\Psi}}{\partial \boldsymbol{b}^e}\boldsymbol{b}^e \tag{3}$$

where $\boldsymbol{\zeta}$ is defined as $\boldsymbol{\zeta} = J^e \boldsymbol{\sigma}$ and referred to as zeta stress.

To satisfy the non-negativeness of plastic dissipation, the plastic velocity gradient tensor $\boldsymbol{l}^p \left(= \boldsymbol{F}^e \dot{\boldsymbol{F}}^p (\boldsymbol{F}^p)^{-1} (\boldsymbol{F}^e)^{-1}\right)$ is specified by the associated flow rule as follows:

$$\boldsymbol{l}^p = \dot{\gamma}\frac{\partial f}{\partial \xi} \tag{4}$$

where $\dot{\gamma}\,(\geq 0)$ is the plastic multiplier. ξ is defined as $\xi = \zeta - \bar{\Psi}\boldsymbol{I}$ and referred to as Eshelby-zeta stress.

2.3 *Hardening rule and yield function*

To make the normal consolidation line straight on the $\ln \mathrm{v} - \ln p^\zeta$ plane, the isotropic hardening rule is given by using the yield mean stress p_{c}^ξ and the plastic logarithmic volumetric strain $\boldsymbol{\varepsilon}_{\mathrm{v}}^p$:

$$p_{\mathrm{c}}^\xi = p_{\mathrm{c0}}^\xi \exp\left[\tilde{\theta}^*\left(\varepsilon_{\mathrm{v}}^p - \varepsilon_{\mathrm{v0}}^p\right)\right] \tag{5}$$

where $\tilde{\theta}^* = 1/(\tilde{\lambda}^* - \tilde{\kappa}^*)$. $\tilde{\lambda}^*$ is the compression index on the $\ln \mathrm{v} - \ln p^\zeta$ plane and has the relationship $\tilde{\lambda}^* = \tilde{\lambda}/(1-\tilde{\kappa})$ with the compression index $\tilde{\lambda}$ on the $\ln \mathrm{v} - \ln p$ plane. Note that the subscript 0 indicates the initial value.

The yield function of the modified Cam-Clay model is adopted in the Eshelby-zeta stress space

$$f(\xi, p_{\mathrm{c}}^\xi) = \frac{p^\xi}{p_{\mathrm{r}}}\frac{\left(\mathrm{M}^\xi\right)^2 + \left(\eta^\xi\right)^2}{\left(\mathrm{M}^\xi\right)^2} - \frac{p_{\mathrm{c}}^\xi}{p_{\mathrm{r}}} \tag{6}$$

where p^{ξ} and η^{ξ} are the mean stress and stress ratio with respect to the Eshelby-zeta stress, respectively. M^{ξ} is expressed as $M^{\xi} = (1 - \tilde{\kappa})M$ using the critical state constant M in the Cauchy stress space.

This study formulates the constitutive model by describing the above basic lows/rules using principal values and axes of several tensors. For finite element analysis, an implicit stress updating algorithm is developed and tangent modulus consistent with the algorithm is derived.

2.4 *State boundary surface*

The state boundary surface can be obtained from the above basic laws/rules as follows:

$$\ln v = \ln N - \tilde{\lambda} \ln \frac{p}{p_r} - \frac{\tilde{\lambda} - \tilde{\kappa}}{1 - \tilde{\kappa}} \ln \frac{M^2 + \eta^2}{M^2} + (1 - \tilde{\lambda}) \frac{\eta^2}{6\tilde{\mu}} \tag{7}$$

i.e. the specific volume v is uniquely determined for the current Cauchy stress during yielding.

3 NUMERICAL ANALYSIS EXAMPLES

3.1 *Comparison with existing model: Isotropic compression*

In this verification, a soil is isotropically compressed with initial specific volume varying from 2.7 to 2.4 in increments of 0.1. Figures 1a and 1b indicate that in both the Eshelby-zeta stress - specific volume and Cauchy stress - specific volume spaces, the normal consolidation line of the proposed model is uniquely determined regardless of the difference in the initial specific volume. In contrast, Figures 1c and 1d illustrate that the normal consolidation line of the

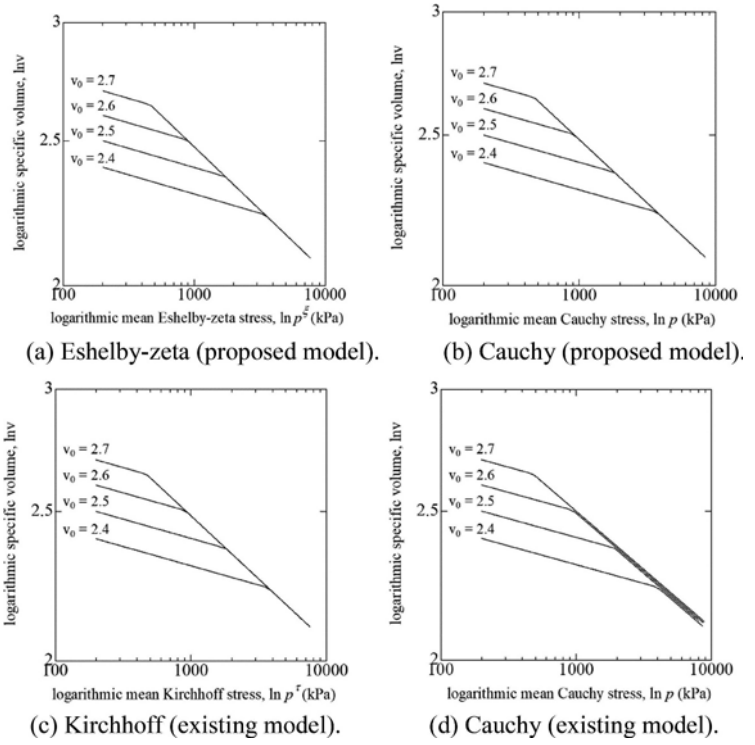

Figure 1. Mean stress - specific volume relationship.

existing model is uniquely determined in Kirchhoff stress - specific volume space, but not in Cauchy stress - specific volume space.

3.2 *Comparison with existing model: Drained and undrained triaxial compression shear*

In this verification, a drained triaxial compression shear is first applied to a normally consolidated clay until the axial strain reaches 50% under constant lateral pressure in a uniform deformation field. Next, undrained shear is performed separately, setting the initial specific volume to the specific volume when the axial strain reaches 50% in the drained triaxial compression shear.

Since the specific volume is constant during undrained shear, the specific volumes at the critical states of the two analyses coincide under such conditions. The stress states at the critical state of the two models are compared. Figures 2a and 2b indicate that the critical states for the drained triaxial compression and undrained shear coincide in both Eshelby-zeta and Cauchy stress spaces in the proposed model. On the other hand, as shown in Figures 2c and 2d, in the existing model, the critical states for both tests coincide in the Kirchhoff stress space, but not in the Cauchy stress space. This difference emerges depending on the existence of the state boundary surface in Cauchy stress - specific volume space.

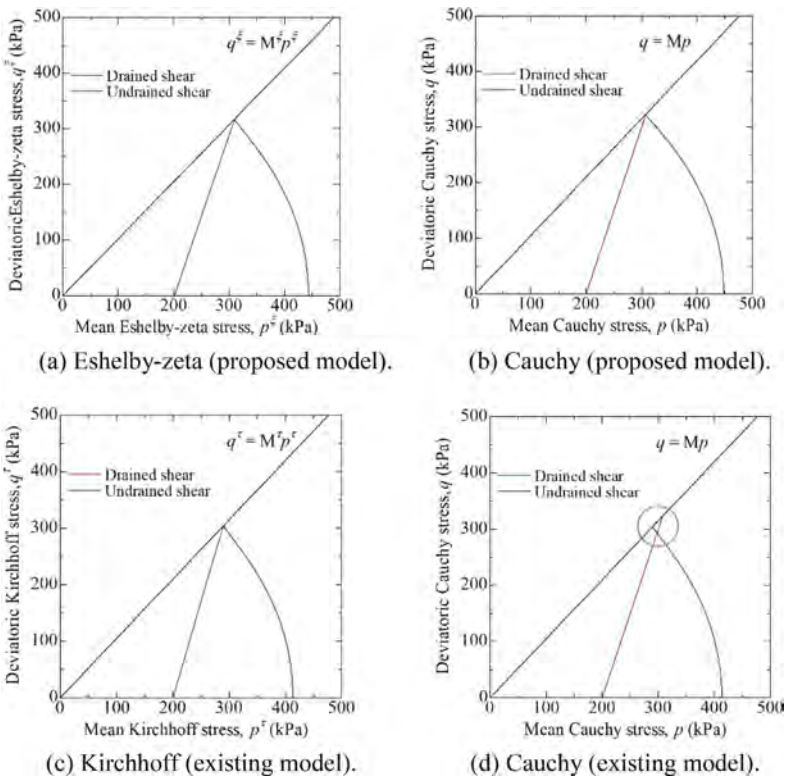

Figure 2. Mean stress - shear stress relationship.

4 CONCLUSION

This study has formulated the isotropic Cam-Clay model based on the multiplicative decomposition of the deformation gradient and using zeta and Eshelby-zeta stresses so that the model has the state boundary surface. Comparison with the existing model using Kirchhoff stress shows the necessity of the state boundary surface in the Cauchy stress - specific volume space.

REFERENCES

Bennett, K.C., Regueiro, R.A. and Borja, R.I. 2016. Finite strain elastoplasticity considering the Eshelby stress for materials undergoing plastic volume change, *International Journal of Plasticity* 77: 214–245.

Borja, R.I., and Tamagnini, C. 1998. Cam-Clay plasticity PartIII: Extension of the infinitesimal model to include finite strains, *Computer Methods in Applied Mechanics and Engineering* 155: 73–95.

Houlsby, G.T., Amorosi, A., and Rojas, E. 2005. Elastic moduli of soils dependent on pressure: a hyperelastic formulation, *Geothechnique* 55: 383–392.

Yamakawa, Y., Hashiguchi, K., and Ikeda, K. 2010. Implicit stress-update algorithm for isotropic Camclay model based on the subloading surface concept at finite strains, *International journal of Plasticity* 26(5): 634–658.

Smart Geotechnics for Smart Societies – Zhussupbekov, Sarsembayeva & Kaliakin (Eds)
© 2023 The Author(s), ISBN 978-1-003-29912-7
Open Access: www.taylorfrancis.com, CC BY-NC-ND 4.0 license

Critical state parameters for a saturated lateritic clay

D.B. Akinniyi & M. Bagheri
Coventry University, UK

ABSTRACT: The critical state soil mechanics is the most useful framework for understanding responses of different soil type to mechanical stress. For lateritic soil, widely distributed soil in the tropics and well recognized for its rich composition in oxides of iron and aluminum (sesquioxide), its mechanical behaviour has not been well studied within this framework. Therefore, a good understanding of the compressibility and shear strength properties of the lateritic soil would improve the designs of structures built on it. This paper presents experimental data from isotropic compression and consolidated undrained triaxial tests on saturated samples of lateritic soil from Nigeria. The data from these tests are presented and interpreted within the critical-state framework. Effects of sesquioxide composition on the compressibility and dilatancy is reported and discussed.

1 INTRODUCTION

The critical-state concept is a very important framework for interpreting the behaviour of saturated soils (Schofield & Wroth, 1968). When a soil undergoes shearing, it reaches a state where it continues to deform at constant stress and constant void ratio. This state is the critical state and for most soils, the critical state is reached at large strains above 25%. The conventional understanding is that when a soil is sheared to such a large strain i.e. above 25%, the effects of fabric on the soil behavior should have been erased. Therefore, the strength parameters obtained at this critical state is independent of soil fabric and is unique for each soil type (Atkinson, 1993). The determination of the critical state line for a soil can aid the interpretation of its mechanical behavior especially during shearing. For instance, a soil specimen whose initial state lies above the critical state line in the v-ln p' compression plane is considered wet/loose and according to critical state soil mechanics, a strain-hardening and contraction behavior is expected during drained shearing. For soil specimen whose initial state falls below the critical state line in the same plane, a strain softening and a dilative behavior is expected during drained shearing (Atkinson, 1993).

The critical state theory has been used to interpret the mechanical behavior of many soil type and their unique parameters has been determined (Ng & Chiu, 2001 & 2003; Wheeler & Sivakumar, 1995; Gan & Fredlund, 1996). However, for lateritic soil, a type of soil that is found in many region of the world, there are very few studies investigating its behavior within the critical state framework. Although, there has been several studies on the mechanical behavior of the lateritic soil (Ng et al., 2019; Otalvaro et al., 2015; Futai & Almeida, 2005; Toll, 1990), still there is a wide variation in the shear strength parameters available in the literature. While most authors stop shearing the test at a small strain between 1% and 5%, others adopt the Mohr Coulomb theory for interpretation of the shear result. In Africa, unconfined compression test is one of the most common shear test conducted on lateritic soil and the maximum shear strain is generally less than 10% (Owolabi & Aderinola, 2014; Ola, 1978;). In Brazil, some authors conducted undrained and drained triaxial testing on both compacted and intact lateritic soil specimen (Fagundes & Rodrigues, 2015; Futai et al. 2004). However, majority of these authors studying lateritic soil adopted Mohr-Coulomb theory rather than the critical state framework. As such, the strength parameters in the literature are mostly peak state parameters which are dependent on the initial fabric, (water content and

DOI: 10.1201/9781003299127-31

sample preparation technique) of the specimen. To understand the behavior of lateritic soil more explicitly, determining unique critical state parameters is therefore important.

Furthermore, the lateritic soil is also well recognized for its rich composition in oxides of iron and aluminum (sesquioxide) (Gidigasu, 1976). The soil, even though a fine material, contains large particles which results from the aggregation influence of its sesquioxide content (Zhang et. al., 2014). Thus, the lateritic soil is a highly structured material depending on the quantity of the sesquioxide content. Previous researchers working on highly structured soil found that the critical state may be impossible to reach even if shearing exceeds 25%. According to previous researchers (Ferreira & Bica, 2006; Martins et al. 2001), the fabric of highly structured soil maybe difficult to erase and therefore no unique parameter may be determined and determining critical state parameters may be unrealistic. There are very few authors who have sheared the lateritic soil to such large strain, therefore, it is still not clear if critical state parameters could be determined for lateritic soil.

In this paper, a compacted and saturated lateritic clay from Nigeria undergoes isotropic compression and undrained shearing test at three different confining stresses. The results were interpreted within the critical state framework, a critical state line and its parameters were determined.

2 TEST MATERIAL

Disturbed sample of lateritic clay from Southwest, Nigeria was collected and tested in this study. Large aggregates in the collected samples were broken down and the soil was sieved through 2mm ASTM standard sieve. Particles larger than 2mm were discarded and not used for the determination of the geotechnical index properties and the shearing test. The index properties of the soil were determined following the ASTM standard (ASTM, 2011). Due to possible aggregation as a result of the sesquioxide content in lateritic soil, wet sieving and hydrometer method were used to determine the particle size distribution and a sodium hematophospate was added to the solution as dispersant to separate soil aggregates. The coarse and fine fractions of the tested soil are 42% and 58% respectively. Details of other index properties of the soil are summarized in Table 1. The soil was classified as a sandy lean clay (CL) (ASTM D2487, 2011). The sesquioxide content in the tested soil was determined using X-ray fluorescence test and quantified to be 38%.

3 SPECIMEN PREPARATION AND TEST PROGRAMME

A total number of 6 specimens was prepared for the isotropic compression and undrained shearing tests using static compaction method. Each specimen was compacted in 10 layers at 19% compaction water content to a dry density of 74% of the proctor maximum. Specimen uniformity was ensured by adopting the under-compaction method of preparation proposed by Ladd (1978).

Two series of tests were carried out in a triaxial apparatus, the first series is isotropic loading and unloading tests to obtain the compressibility parameters. The second series is consolidated undrained (CU) shear test to investigate the shear behaviour and obtain the critical state strength parameters. For the shear test, normally consolidated specimen and over-consolidated specimen were tested in order to understand the influence of stress history on the shear behaviour of the tested material. The normally consolidated specimen were sheared at three different confining stresses (50, 100 and 200 kPa). The over-consolidated specimen were sheared at 50kPa confining stress after been loaded and unloaded to achieve over-consolidation ratio of 5 and 7. Details of the test are summarized in Table 2.

4 TEST PROCEDURES

After specimen preparation, a porous stone was placed underneath and on top of the specimen and carefully placed on the base pedestal of the triaxial apparatus. The specimen was flushed with

Table 1. Classification and mineral composition of studied material.

Index test	Lateritic soil
Standard compaction Test	
Maximum dry density: kg/m^3	1696
Optimum water content: %	20
Grain size distribution	
Percentage of sand: %	42
Percentage of silt: %	16
Percentage of clay: %	42
Coefficient of uniformity	35
Coefficient of gradation	1.6
Atterberg limits	
Liquid limit: %	44
Plastic limit: %	24
Plasticity index: %	20
Specific gravity	2.67
Soil classification based on USCS (ASTM,2011)	CL (sandy lean clay)
Chemical composition (%)	
Silicon oxide (SiO_2)	60
Iron oxide (Fe_2O_3)	10
Aluminum oxide (Al_2O_3)	28
Sesquioxide (Fe_2O_3 + Al_2O_3) content	Lateritic soil = 38%

Table 2. Testing conditions for CU shear test on saturated specimens of lateritic clay.

Series	Specimen ID*	Confining stress (kPa)	Initial void ratio	Void ratio after consolidation	Ψ after consolidation*
	L50	50	0.948	0.912	0.06
I	L100	100	0.942	0.872	0.09
	L200	200	0.956	0.803	0.09
II	L50 - OC5	50	0.945	0.821	-0.02
	L50 - OC7		0.962	0.765	-0.07

CO_2 and de-aired water respectively, then back pressure was applied to fully saturate the specimen. The minimum back pressure used in all the test was 250 kPa and minimum B value achieved for all the saturated specimen is 0.97. There was no measurement of volume change during saturation.

For the isotropic loading test, the following confining pressures were applied in stages: 15, 25, 50, 100, 200, 300, 400 kPa. Unloading was done at 250 and 350 kPa respectively to take the specimen back to 50 kPa given a OCR value of 5 and 7 respectively. After isotropic compression test, consolidated undrained shearing test was carried out. After bringing each specimen to the design effective stresses, drainage valves were closed after the excess pore water pressure has been dissipated, then an undrained shearing test was performed. The strain rate was 0.04 mm/min during the shearing process.

5 DISCUSSION OF RESULTS

5.1 *Isotropic loading and unloading*

Figure 1 shows the response of the lateritic specimen to isotropic loading and unloading. At first, a gradual change in specific volume is observed as the effective mean stress increases. Then, a yield point is reached and the specific volume begins to reduce abruptly. The yield stress corresponding to the yield point is estimated to be 80 kPa using Casangrande's graphical method. At 100 kPa effective stress, the specimen is unloaded in stages to 50 kPa and a very slight increase in the specific volume is observed. The specimen is compressed again

from 50 kPa in stages to 300 kPa effective mean stress and then unloaded back to 50 kPa. A post yield isotropic normal compression line (NCL) is determined and its slope (usually denoted as λ) is estimated as 0.07. The slope of the unloading curve is also estimated to be 0.013. The value of λ obtained in this study is compared with the saturated compressibility of some other compacted lateritic soils reported in the literature and summarized in this study are summarized in Table 3. It is clear that the compressibility of lateritic soils varies significantly with particle sizes. The lateritic soil in this study have the least compressibility even though it contains significant amount of clay compared other soils in the Table 3.

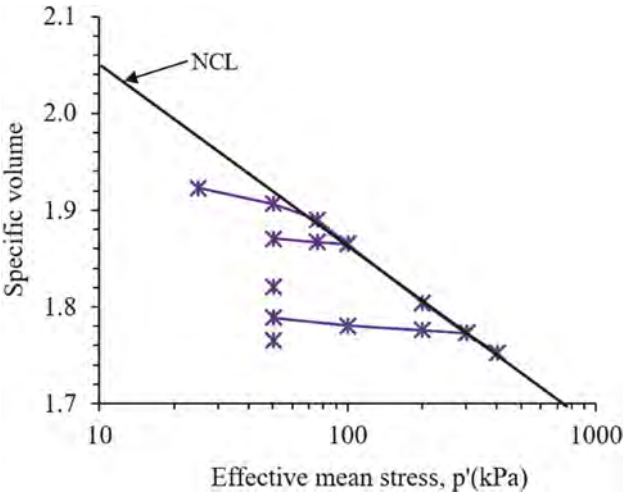

Figure 1. Isotropic compression behavior of the tested specimen.

The reason for this low compressibility of the lateritic soil in this study may be due to the influence of its 38% sesquioxide composition. The sesquioxide content in most lateritic soils is not often quantified, thus, comparing compression behavior may be misleading. The sesquioxide enhances aggregation, hence larger particles are formed and specimen may behave as a coarse grained material (Zhang et al., 2016).

Table 3. Comparison of compression index of compacted lateritic soils.

Lateritic soil types	λ	Parent rock
Sandy lean clay (this study)	0.08	Granitic (Igneous)
Gravel (Toll, 1990)	0.11	Basalt (sedimentary)
Clayey silt (Otalvaro et al., 2015)	0.16	Paranoá (meta-sedimentary)
Clayey sand 1 (Bennatti et al., 2013)	0.15	Colluvium (sedimentary)
Clayey sand 2 (Futai & Almeida, 2005)	0.18	Gneiss (sedimentary)

Figure 2 shows the initial condition of the specimen before shearing. It is noted that all the normally consolidated (NC) specimen lies close to the NCL line determined during isotropic compression. The over-consolidated specimens lies farther away from the NCL compared to the NC specimens.

5.2 *Shear behavior of the normally consolidated specimen*

Figure 3a shows the stress-strain relationship during undrained shearing of the lateritic specimens at three confining stresses. At 50 kPa confining stress, the deviator stress increases monotonically with the axial strain and no sign of softening is observed till the end of the test. The behavior at

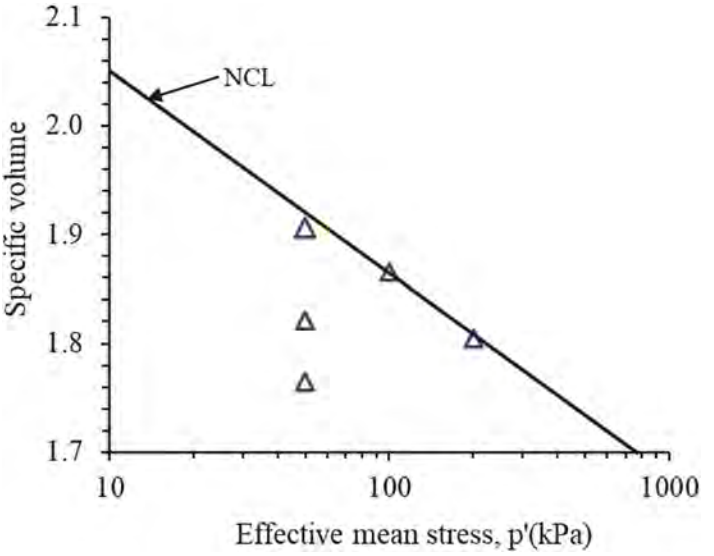

Figure 2. States of all saturated specimens before shearing.

50 kPa is generally referred to as a strain hardening behaviour and this is consistent with the critical state framework for normally consolidated specimen. At 100 kPa and 200 kPa confining stress, a similar strain hardening behaviour with no evidence of softening is observed. As expected, maximum deviator stress increases with confining stress. It can also be observed that the deviator stresses at the three confining stresses are still changing slightly towards the end of the test suggesting a true critical state has not been reached. However, the rate of increase in deviator stress at 50 and 100 kPa towards the end of the test has reduced significantly. The behaviour of the studied soil may be due to the influence of the sesquioxide content which may enhance aggregation of particles (Zhang at al., 2004). Due to aggregation, the fabric of the soil may require larger shear strain to fully reach critical state.

Figure 3b shows the relationship between the excess pore water pressure and the axial strain during the undrained shearing test at all confining stress. At 50 kPa, the specimen shows initial build-up of positive excess pore water pressure, it reaches a peak and then a slight drop from peak is observed till the end of the test. The initial build-up of the pore pressure indicate that specimen exhibit a contractive tendency while the slight reduction indicates a dilative tendency. At other confining stresses, similar behavior observed at 50 kPa is observed in all the specimen. A barreling type of failure was observed in all the specimen after testing. All these observations are consistent with critical state framework for soils sheared at normally consolidated state (Atkinson, 1993).

5.3 *Shear behavior of the over-consolidated specimen*

The stress strain relationship of the over-consolidated specimen sheared at confining stress of 50 kPa is shown in Figure 4a. All the specimen showed a strain hardening behaviour despite having different stress histories. It can be seen that the deviator stress increases monotonically with the axial strain and no peak nor sign of softening is observed. As expected, the maximum deviator stress increases with increasing OCR. Most of the specimen are still showing significant change in deviator stress at the end of the state. This indicates that the specimen have not reached the critical state. Lateritic soil may require shearing to a larger strain (above 25%) in order to reach a true critical state. In Figure 4b, the relationship between the excess pore water pressure and the axial strain is shown. It can be seen that positive excess pore water pressure was initially generated in all the specimen. As shearing continues, a reduction in pore water pressure is observed in all the specimen but only the specimen with OCR of 1 and 5 appears to have reached a plateau at the end of the test.

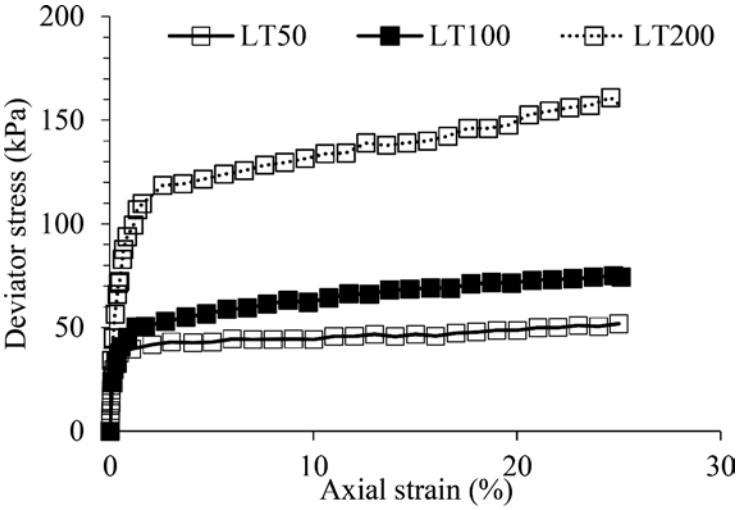

(a)

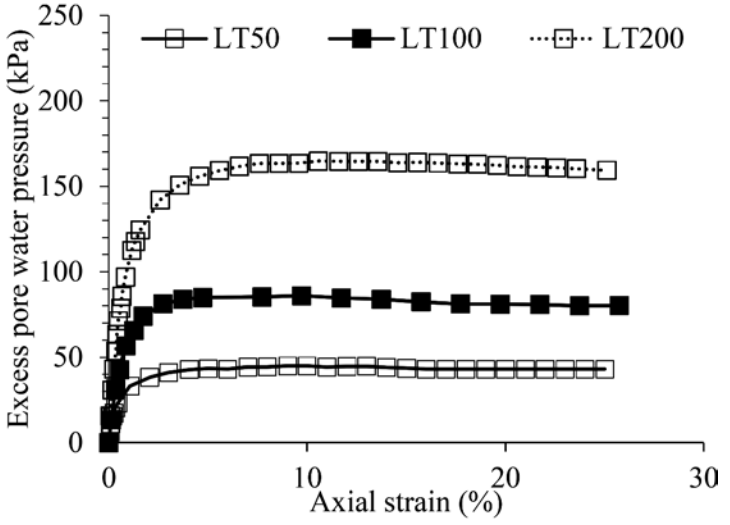

(b)

Figure 3. (a) Triaxial stress strain and (b) Pore pressure vs strain responses from undrained tests for the normally consolidated saturated lateritic specimen.

5.4 *Phase transformation behaviour*

Figure 5 shows the stress paths of the normally consolidated lateritic specimen during undrained shearing in the q – p′ plane. For all the specimen, the effective mean stress initially reduces (showing a tendency of contraction), then at a later stage, a turning point is reached and phase transformation occurs. Under subsequent shearing, the effective mean stress increases (showing a tendency of dilation, accompanied by an increase in deviator stress) and soil state finally reaches the CSL. The initial contraction is likely attributed to the collapse of large inter-aggregate pores. The subsequent dilative behaviour is due to re-arrangement and interlocking of the large-sized aggregates. Futai & Almeida (2004) also observed a phase

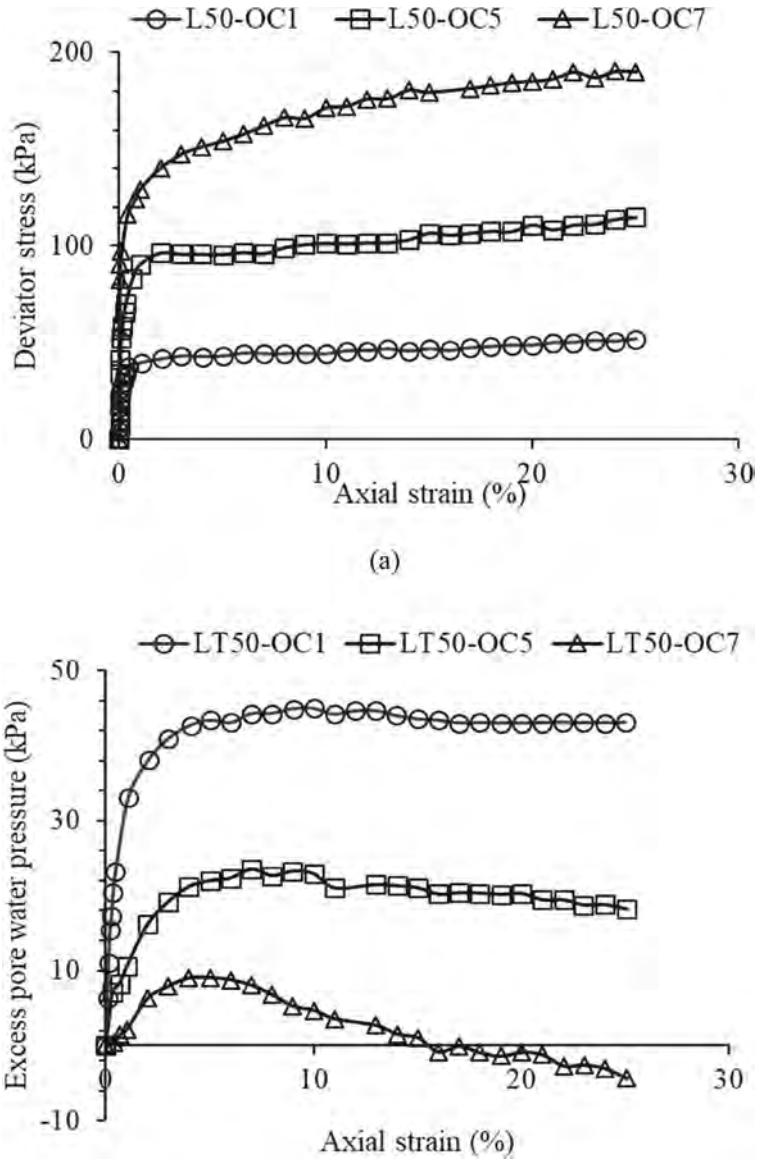

Figure 4. Influence of stress history on the shearing response of the studied lateritic soil (a) stress strain and (b) pore pressure vs strain responses from undrained tests.

transformation behaviour on a saturated and compacted lateritic clay from Brazil. This is likely due to the effect of the aggregates giving the specimen a behaviour typical of coarse-grained material.

Figure 6 shows the stress paths of the specimen at OCR of 1, 5 and 7 during undrained shearing in the q – p′ plane. At 50 kPa confining stress, the effective mean stress of the specimen at OCR of 1 initially reduces indicating a tendency of contract. Under subsequent shearing, the effective mean stress increases (showing a tendency of dilation, accompanied by an increase in deviator stress) and soil state finally reaches the CSL. For the specimens at OCR of 5 and 7, the effective mean stress initially increases indicating a tendency of dilate. Under subsequent shearing, the effective mean stress decreases (showing a tendency of contract, accompanied by an increase in deviator stress).

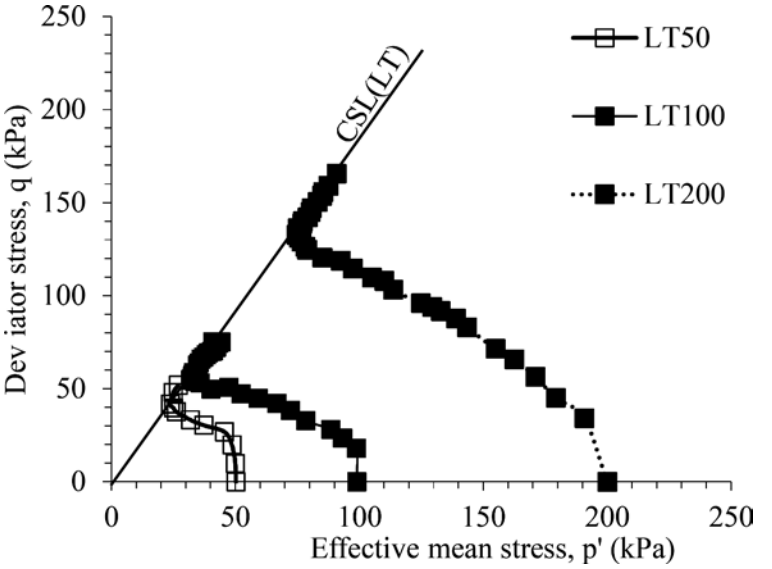

Figure 5. Stress paths of normally consolidated saturated lateritic specimen in q - *p*' space.

According to the stress path shown in Figure 7, the final states of all specimens fall on a single line. The slope of the critical state line, M (commonly referred to as the stress ratio of the critical state) line, is estimated to be 1.73. The corresponding critical state angle of internal friction φ′ is 42° for the studied specimen. The high friction angle is due to the influence of large particles and aggregates in their microstructure.

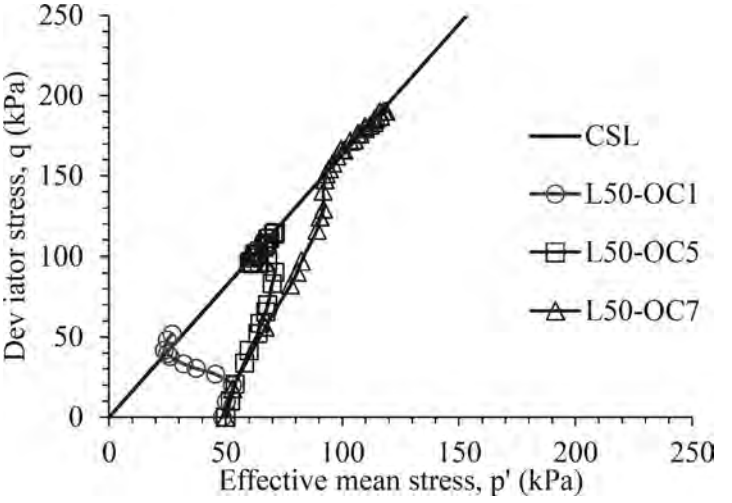

Figure 6. Stress paths of the saturated lateritic specimen at different stress history in q - *p*' space.

Figure 8 presents the stress path of the specimen in the v-ln p' compression plane. The effective mean stress of the normally consolidated specimens shift to the left at the end of shearing indicating a reduction in effective mean stress. On the other hand, the over consolidated specimen shifts to the right indicating an increase in the effective mean stress after shearing. For all the specimen tested in this study, a unique line is determined which is parallel to the slope of the NCL. This line is the critical state line in the compression plane. The slope of the CSL (λ) in this plane, the specific volume (Γ) at p'=1kPa were determined. These two parameters are

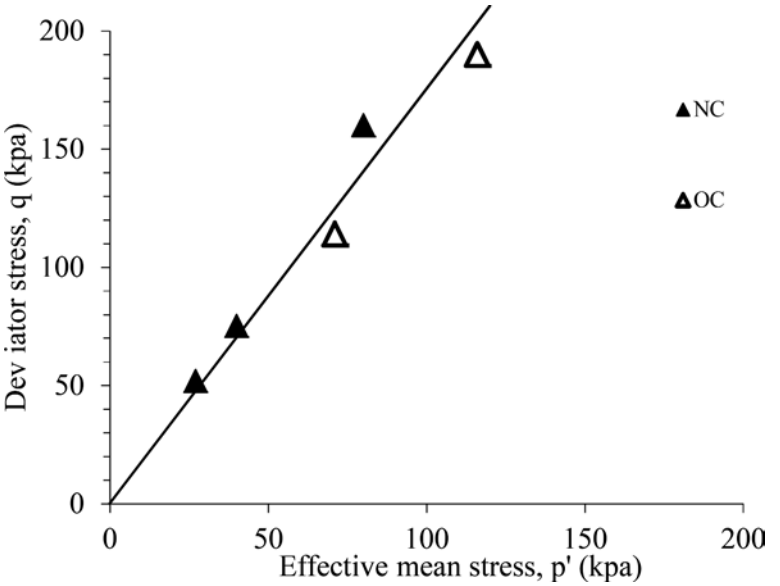

Figure 7. The critical state line of the studied lateritic soil in q – p' space.

critical state parameters and are unique to the soil tested in this study. The critical state parameters obtained for the saturated lateritic specimen tested in this study are summarized in Table 4. These parameters are useful for interpreting the behaviour of lateritic soils.

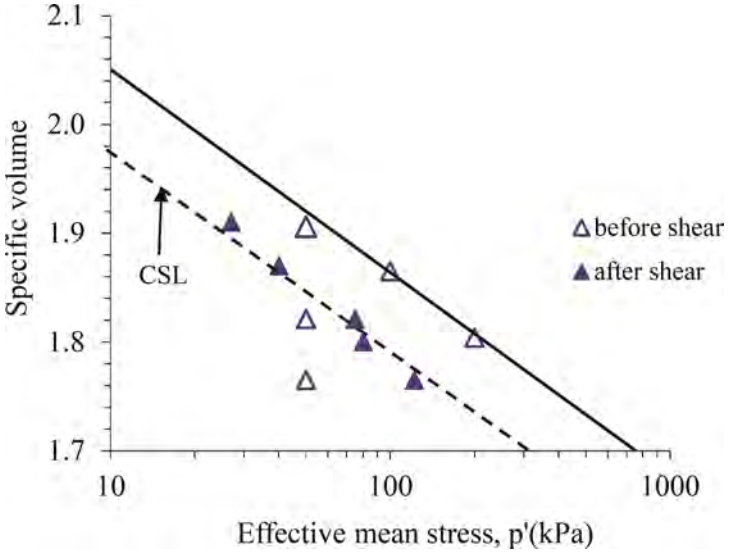

Figure 8. States of all saturated specimens before and after shearing in v – ln p' space.

6 CONCLUSION

In this study, the critical-state parameters for a saturated sample of a lateritic clay were experimentally determined using the conventional triaxial test apparatus. Isotropic compression and consolidated undrained shearing test were carried out on both normally consolidated and

Table 4. Summary of the critical state parameters obtained in this study for the tested lateritic specimen.

*CSL parameters	Lateritic Soil
λ	0.07
Γ	1.98
N	2.05
M	1.733

* where M is the slope of the projection of the critical-state line in q– p' space, Γ and N are the intercept of the CSL and NCL respectively (at p' = 1 kPa in the v – ln p' space), λ and M are the slope of the projection of the critical-state line in v – ln p' space and q – p' space respectively.

over consolidated specimen. Specimen were fully saturated with a back pressure not less than 200 kPa. At the end of shearing, most of the specimen did not reach the true critical state as the deviator stress is still increasing at the end of the test. Unlike most clays where the critical state is often reached at about 25% axial strain, the lateritic soil needs to be sheared to a larger strain in order to erase the effects of fabric on the strength parameters. The behaviour of lateritic soil is attributed to the influence of its highly aggregated microstructure which is due to the influence of its sesquioxide content. Even though a true critical state was not reached by some of the specimen, critical state parameters were still derived at the end of the test. The test results have shown that the slope of the NCL and CSL lines for the saturated lateritic specimens are parallel to each other. The parameters of M and λ have been determined and it was found that the lateritic clay has a larger friction angle which is not typical for a sandy clay material. The large friction angle is therefore attributed to the influence of its sesquioxide content which enhances formation of large grain sizes through aggregation of soil particles. The intercept of the critical state line in the compression plane was also determined which is unique to the studied soil. Considering the variability in the microstructure of different lateritic soil owing to the presence of sesquioxide, it is impossible to generalize the critical state parameters in this study for all lateritic soil. Therefore, the result of this study could be useful for interpreting lateritic specimen with similar grain size distribution and sesquioxide content.

REFERENCES

ASTM D2487 (2011). Standard Practice for Classification of Soils for Engineering Purposes (USCS). *American Society of Testing and Materials, West Conshohocken, PA*.

Atkinson, J. (1993). An introduction to the mechanics of soils and foundations: through critical state soil mechanics. *McGraw-Hill Book Company (UK) Limited*.

Benatti, J. C. B., Rodrigues, R. A., & Miguel, M. G. (2013). Aspects of Mechanical Behavior and Modeling of a Tropical Unsaturated Soil. *Geotechnical and Geological Engineering*, *31*(5), 1569–1585.

Fagundes, L. S., & Rodrigues, R. A. (2015). Shear strength of a natural and compacted tropical soil. *Electronic Journal of Geotechnical Engineering*, *vol. 20*, *No. 1*, p47–58.

Ferreira, P. M. V. & Bica, A. V. D. (2006). Problems in identifying the effects of structure and critical state in a soil with a transitional behaviour. *Ge´otechnique 56, No. 7, pp* 445–454

Futai, M. M., & Almelda, M. S. S. (2005). An experimental investigation of the mechanical behaviour of an unsaturated gneiss residual soil. *Géotechnique*, *55*(3), 201–214.

Futai, M. M., Almeida, M. S. S., & Lacerda, W. A. (2004). Yield, strength, and critical state behavior of a tropical saturated soil. *Journal of Geotechnical and Geoenvironmental Engineering*, *130*(11), 1169–1179.

Gan, J. K., & Fredlund, D. G. (1996). Shear strength characteristics of two saprolitic soils. *Canadian Geotechnical Journal*, *33*(4), 595–609.

Ladd, R.S. (1978). Preparing test specimens using undercompaction. Geotech. Test. J. 1, 16–23.,
Martins, F. B., Bressani, L. A., Coop, M. R., & Bica, A. V. D. (2001). Some aspects of the compressibility behaviour of a clayey sand. *Canadian Geotechnical Journal*, *38*(6), 1177–1186.
Ng, C. W. W., Akinniyi, D. B., Zhou, C., & Chiu, C. F. (2019). Comparisons of weathered lateritic, granitic and volcanic soils: Compressibility and shear strength. *Engineering Geology*, *249*, 235–240.
Ng, C. W. W. & Chiu, A. C. F. (2001). Behavior of a loosely compacted unsaturated volcanic soil. *Journal of Geotechnical and Geoenvironmental Engineering*, *vol. 127*, *No. 12*, pp1027–1036.
Ng, C. W. W. & Chiu, A. C. F. (2003). Laboratory Study of Loose Saturated and Unsaturated Decomposed Granitic Soil. *Journal of Geotechnical & Geoenvironmental Engineering*, vol. *129, No*. 6, pp 550–559.
Ola, S.A. (1978). Geotechnical Properties and behavior of some stabilized Nigerian Lateritic Soils. *Quaterly Journal of Engineering Geology, vol. 11,* 145–160.
Otalvaro, I. F., Neto, M. P. C., & Caicedo, B. (2015). Compressibility and microstructure of compacted laterites. *Transportation Geotechnics, 5,* 20–34.
Owolabi, T. A., & Aderinola, O. S. (2014). Geotechnical Evaluation of Some Lateritic Soils in Akure South, South-western Nigeria. *Electronic Journal of Geotechnical Engineering*, *19*, 6675–6687.
Schofield, A. W. and Wroth, C. P. (1968). Critical state soil mechanics. London: McGraw-Hill.
Toll, D. G. (1990). A framework for unsaturated soils behavior. *Geotechnique 40, No. 1, pp* 31–44.
Wheeler, S. J., & Sivakumar, V. (1995). An elasto-plastic critical state framework for unsaturated soil. *Géotechnique*, *45*(1), 35–53.
Zhang, X. W., Kong, L. W., Cui, X. L., & Yin, S. (2016). Occurrence characteristics of free iron oxides in soil microstructure: evidence from XRD, SEM and EDS. *Bulletin of Engineering Geology and the Environment*, *vol. 75*, *No. 4*, *pp* 1493–1503.

Smart Geotechnics for Smart Societies – Zhussupbekov, Sarsembayeva & Kaliakin (Eds)
© 2023 The Author(s), ISBN 978-1-003-29912-7
Open Access: www.taylorfrancis.com, CC BY-NC-ND 4.0 license

Liquid limit and density of high plastic clays

J. Frankovska & M. Brcek
Slovak University of Technology in Bratislava, Slovakia

ABSTRACT: Laboratory tests to determine the limits of the liquid and plastic are by far the most widely used index tests and are often adopted to assess the mechanical behaviour of clay. The laboratory investigation results for determining liquid limits using the Fall-cone method and method based on Casagrande-type devices for high-plastic clays were analysed. The density of the soil particles was determined by the pycnometer method by fluid displacement and the pycnometer method by gas displacement. Helium was used as the measurement gas. Significant differences were observed based on the laboratory method used. The range of differences in the geotechnical properties of high plastic clays was 10 to 30 %. The impact of the testing methods on the intrinsic properties of high plastic clays is analyzed in the paper.

1 INTRODUCTION

The basic physical properties of soils also referred to as intrinsic properties, are those that we need to describe and classify soils. These are mainly grain size and consistency (Atterberg) limits for fine-grained soils. The descriptive properties are constant for a given soil, independent of stress, strain, time, etc. Geotechnical parameters that characterise the physical state of the ground (state parameters) and are not constant for the soil are, for example, the soil's moisture content and bulk density in its natural state. Fine-grained soils it is mainly the consistency of the ground. Thus, the initial condition of the soil (soil in its natural state) can be characterised by two sets of geotechnical parameters: descriptive and state parameters. The basic physical properties of soils are also referred to as intrinsic properties in geotechnical engineering. Based on these, significant physical, strength-strain or hydraulic properties of soils, which are the geotechnical parameters of strength, compressibility or coefficient of filtration, can be determined by using appropriate correlations in cases where direct field or laboratory tests are not possible. These geotechnical parameters directly enter analytical or numerical models in the design of geotechnical structures.

Consistency limits include liquid, plasticity and shrinkage limits. These limits are also called Atterberg limits after the Swedish engineer Albert Atterberg, who defined them in the early 20th century and published their determination in 1911. They are important characteristics of fine-grained soils because they determine their geotechnical properties. Atterberg limits are empirically determined moisture contents that represent changes in soil behaviour. The liquid and plasticity limits provide important information on the character of fine-grained soils and are determined by relatively simple laboratory tests.

Atterberg limits are extensively used to identify, describe, and classify fine grained soils and as a basis for preliminary assessment of their mechanical properties.

The consistency limits depend on the mineralogical composition and the more smectites the soil contains, the greater the value they reach (Mitchell & Soga, 2005, Tiwari & Ajmera, 2011). Consistency limit values for selected clay minerals are given in Table 1.

Eurocode 7 and STN 72 1014 define two methods for determining the liquid limit: the Casagrande method and the fall cone method. The cone penetration method is based on the measurement of soil penetration by a standardized cone of a specified mass. It has been used in

DOI: 10.1201/9781003299127-32

Table 1. Consistency limits based on clay minerals (Mitchell & Soga, 2005).

Mineral	Liquid limit (%)	Plasticity limit (%)	Shrinkage limit (%)
Montmorillonit	100 – 900	50 – 100	8.5 – 15
Kaolinite	30 – 110	25 – 40	25 – 29
Illite	60 – 120	35 – 60	15 – 17

Scandinavia since 1915 (Bjerrum & Flodin, 1960). Two types of cones are recommended for determining the liquid limit. They differ in the angle of the cone, its mass and the depth of penetration at which the liquid limit is determined. They are designated the British cone (30°/80 g) and the Swedish cone (60°/60 g). Based on the results of a study comparing the results in five laboratories in Europe: TCD Ireland, BAW Germany, RGD Netherlands, SGI Sweden and BRE UK, it was shown that the two cone types give essentially the same values of flow limit for geotechnical practice (Farrell et al., 1999).

Density of solid particles - specific gravity can be defined as the density that expresses the mass per unit volume of the solid phase of a soil, i. e. excluding pores, voids and fractures.

It is determined in the laboratory most commonly in a Gay-Lussac type pycnometer (a container with a special stopper that has an accuracy of volume determination to the thousandth of a millilitre) with a volume of 50 ml or 100 ml. In the case of problematic soil types (e.g. expansive soil) or where higher accuracy requirements are required, the specific gravity is determined in a gas pycnometer, most commonly using helium.

2 MATERIALS

Tests were performed on 22 specimens of high plastic clays. Test samples of fine-grained soils were taken on bentonite deposits, the Western Carpathians, Slovakia (Kopernica, Stará Kremnička - Jelšový potok, Lutila I, Stará Kremnička III, Bartošová Lehôtka II, Lastovce and Kuzmice). All samples were classified as clays with very high and extremely high plasticity.

3 METHODS

3.1 *Liquid limit determination*

Two methods: the Casagrande method and the fall cone method, were used for the liquid limit determination. The British cone (30°/80 g) was used for cone penetration testing. The sample preparation is the same for both methods. However, the amount of soil required to perform the test is greater for the cone test, which requires about 200 g of soil.

3.2 *Density of solis particles determination*

Two methods were compared for the determination of density (bulk density) - using a Gay-Lussac pycnometer with water and gas (helium) pycnometer (type ULTRAPYC 1200e, Quantachrome Instrument, procedure according to ASTM D6093-97:2011, DIN 18121-2:2010). The equipment allows the determination of the volume of the solid phase of the soil. The gas pycnometer method uses the property of expansion and compression of gases with pressure change at a constant temperature. Helium is a suitable gas for use because it is an inert gas and because of the small size of the molecules, which makes it capable of penetrating even the smallest pores and capillaries of an apparently compact material. The values of the resulting specific gravity of soils are most often in the range of 2400 to 3000 $kg.m^{-3}$. The measurement duration is limited by the time required to reach thermal stability.

4 RESULTS

4.1 *Liquid limits of high plastic clays*

For fine-grained soils with a liquid limit of 30% to 50%, the results of testing using the two methods are comparable (Frankovská & Dananaj, 2006, Farrell et al., 1999). For soils with w_L higher than 50 %, the liquid limit determined by the cone method is lower than the liquid limit determined by the Casagrande method (Figure 1).

The variance of the values of the liquid limit determined by the two methods increases linearly with increasing liquid limit value and reaches a difference of 70% for soils with a liquid limit up to 350%.

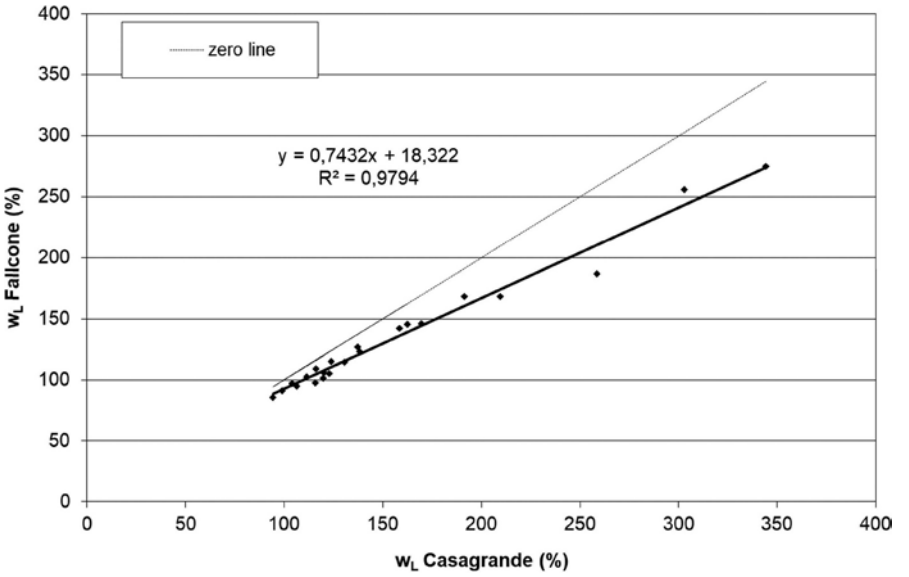

Figure 1. Casagrande and fall cone methods for soils with w_L > 90%.

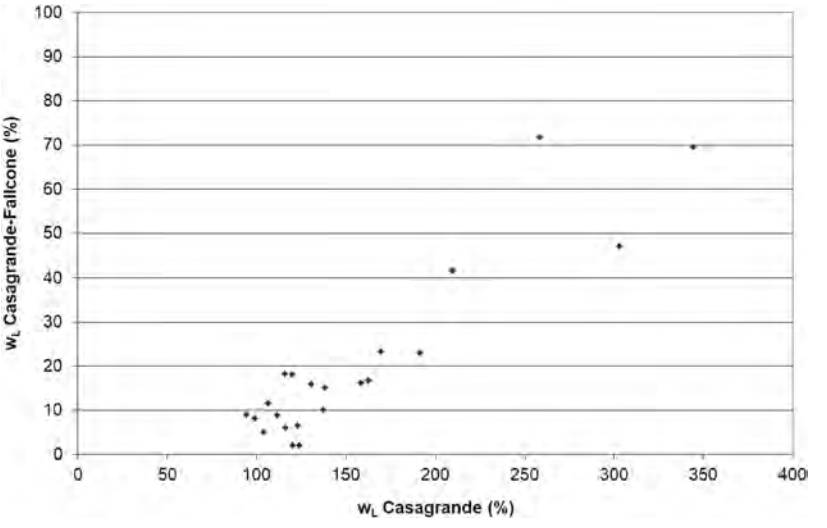

Figure 2. Differences between liquid limits determined by Casagrande and fall cone methods.

The cone test is not faster, but it is more reliable because the test mechanism depends directly on the static shear strength of the soil. Casagrande's method introduces a dynamic element to the test that does not depend on the shear strength in the same way for all soil types. The unconfined shear strength of soils at the yield stress decreases as the yield stress increases, which is the reason for the different yield stress values determined by the Casagrande and cone methods.

Results obtained by the fall cone method have been proven to be more consistent and less liable to experimental and personal errors than those obtained by the Casagrande method. Comparing the time necessary for the test, both methods are equally time-consuming. The estimate of liquid limit either by the cone test or by the Casagrande´s method, requires very good laboratory skills.

4.2 *Results of density measurement*

For twelve bentonite test samples, significant differences were found in the results - evaluation of the solids particle densities due to the methodology used.

The resulting values ranged from 2.63 g/cm^3 to 2.83 g/cm^3 for the water pycnometer determination and from 2.31 g/cm^3 to 2.39 g/cm^3 for the helium ultrapycnometer determination.

5 CONCLUSION

Both the liquid limit of the soils and the density of solid particles depend mainly on the mineralogical composition of the soils. The correct determination of the liquid limit is important because of the use of this basic geotechnical parameter of soils for correlations with other parameters characterizing the strength, compressibility and hydraulic properties of soils, which directly enter the computational models for the design of geotechnical structures.

Experimental investigations based on laboratory tests of samples of highly plastic soils from different locations in Slovakia have indicated significant differences in the values of the liquid limit determined by the Casagrande apparatus and the 80g/30° cone, ranging from 10 to 70 % for soil samples with a liquid limit above 90 %.

A significant difference was also found for the determination of the solid particle density of highly plastic soils. The indication of the method used for the determination of the liquid limit of the soils in the geotechnical investigation report or is therefore necessary.

ACKNOWLEDGEMENT

This article was supported by the Grant Agency of the Ministry of Education, Science, Research and Sport of the Slovak Republic, VEGA, grant project No. 1/0745/21 and APVV-20-0175.

REFERENCES

Bjerrum, L. & Flodin, N., 1960: The development of soil mechanics in Sweden 1900-1925, Geotechnique, 16 (1), 1–18.

Farrell E., Schuppener, B., Wassing, B.: ETC 5 Fall-cone study. In Recommendations of the ISSMGE for Geotechnical Laboratory Testing, ISSMGE, DIN 1999, p. 103–110.

Farrell, E.: Workshop Liquid and plastic limits, In: Proc. 11th ECSMFE, Copenhagen 1995, DGS, Bulletin 11, Vol. 10, p. 161–168.

Frankovská, J. & Dananaj, I., 2006: Determination of liquid limits. of fine grained soils, Slovak Geological Magazine, Vol. 12, No. 1, p. 69–75.

Mitchell, J.K., 1993. Fundamentals of Soil Behavior. Univesity of California, Berkley, USA. 560 p.

Tiwari1, B., Ajmera, B. 2011: Consolidation and Permeability of Clay Minerals - Expansive to Non-expansive, Geo-Frontiers 2011, ASCE 2011, s. 2414–2423.

Smart Geotechnics for Smart Societies – Zhussupbekov, Sarsembayeva & Kaliakin (Eds)
© 2023 The Author(s), ISBN 978-1-003-29912-7
Open Access: www.taylorfrancis.com, CC BY-NC-ND 4.0 license

Effect of different pore structure in sandy soil on monotonic and cyclic shear behavior

M. Nakano & T. Sakai
Nagoya University, Nagoya, Aichi, Japan

ABSTRACT: This study investigated the effect of pore structure due to suffusion on the behavior of soil specimens by replacing some of the fine-grain content of the specimens with a chemical fertilizer that dissolves in water. In monotonic shear behavior, the fertilizer-replaced samples showed a greater degree of plastic compression in early shear. In cyclic undrained shear behavior, the fertilizer-replaced sample exhibited more shear strain development with fewer cycles. It can be inferred that the pore structure due to the dissolution of fertilizer in water has a different soil structure from that of the basic specimens.

1 INTRODUCTION

Internal erosion, a phenomenon in which fine particles move and flow out of river levees and earth-fill dams due to seepage, is one of the causes of instability of these structures. Ishimaru et al. (2020) categorized and organized previous studies on internal erosion based on the Initiation-Continuation-Progression-Breach/Failure process described by Foster & Fell (1999). Some studies to investigate the Breach/Failure process, i.e., the cause of instability of levees, have been conducted by triaxial tests simulating suffusion, which was shear tests using specimens with fine-grain removed beforehand (e.g., Kodaka et al. 2016), or shear tests by revised triaxial apparatus reproducing suffusion from the specimen (Ke & Takahashi 2014, Prasomsri & Takahashi 2020)

The objective of this study is to investigate the effect of pore structure due to fine-grain loss on the behavior of soil specimens by replacing some of the fine-grain content of the specimens with a chemical fertilizer that dissolves in water, and then to provide basic data for research on suffusion. In the future, we aim to describe the soil skeleton structure of soils with the same specific volume but different pore structure based on the mechanical behavior of soils.

2 PHYSICAL PROPERTIES OF THE SAMPLES USED IN THE TEST

The samples used in the tests were three types of Tohoku silica sand: 'basic sample', 'fine-grain-removed sample', and 'fertilizer-replaced sample'. Figure 1 shows the grain size distribution for the basic and fine-grained samples, and Table 1 shows their physical properties.

Table 1. Physical property of sand.

	Particle density ρ_s(g/cm^3)	Maximum void ratio e_{max}	Minimum void ratio e_{min}
Basic sample	2.650	0.885	0.486
Fine-grain-removed sample	2.650	0.908	0.486

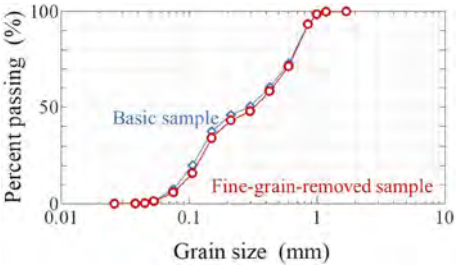

Figure 1. Grain size distribution.

DOI: 10.1201/9781003299127-33

The fine-grain removal sample is a sample removed 5% fine fraction of 106 μm or less in grain size from the basic sample. The fertilize-replaced sample is obtained by adding 5% of fertilizer grains of 106 μm or less in grain size to the fine-grain removal sample. The grain size distribution is the same as that of the basic sample. When the fertilizer is fully dissolved by water, the distribution is equal to that of the fine-grain removal sample.

3 SPECIMEN PREPARATION FOR THE THREE SAMPLES AND TESTING METHODS

The specimens were cylindrical specimens with a diameter of 50 mm and a height of 100 mm. The basic and fertilizer-replaced samples were prepared by air-dropping method to achieve a relative density *Dr* of 80%. On the other hand, the fine-grain removal sample was *Dr* of 60%. The reason for this is that the *Dr* of the fertilizer replacement sample is 60% when the fertilizer is sufficiently melted in water.

Each specimen was set in a triaxial apparatus and saturated by water flow to ensure that the B-value was greater than 95%. After isotropic consolidation was completed at an isotropic pressure of 98.1 kPa, various shear tests were conducted. The saturation process time for the fertilizer-replaced specimens was 2 hours and 30 minutes. It was confirmed that the fertilizers in the specimens were completely dissolved during this water flow time by preliminary experiments. Both the fine-grain-removed and fertilizer-replaced specimens had *Dr* of 60% after saturation process, but the pore structure is considered to be different in the specimens.

4 EXPERIMENTAL RESULTS

4.1 *Shear behavior of specimen simulating suffusion*

Figure 2 shows the undrained shear behavior for the basic sample and the fertilizer-replaced sample. The fertilizer-replaced sample simulated that the basic sample with a *Dr* of 80% has a *Dr* of 60% due to suffusion. Fertilizer dissolves to form pore space, which represents suffusion.

The basic sample exhibited remarkable hardening behavior with plastic expansion, with a maximum deviator stress *q* of approximately 1600 kPa. On the other hand, the fertilizer-replaced specimen also exhibited hardening behavior with plastic expansion, but the maximum *q* was below 600 kPa. A significant reduction in strength occurred due to suffusion. Figure 3 shows a comparison of drainage shear behavior. The basic sample shows more pronounced plastic expansion and a clear peak of *q* (approximately 450 kPa). On the other hand, the fertilizer-replaced sample did not show a clear peak, and the maximum *q* was about 330 kPa.

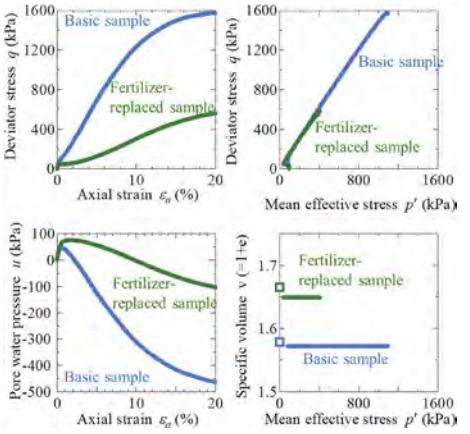

Figure 2. Undrained shear behavior for the basic sample and the fertilizer- replaced sample.

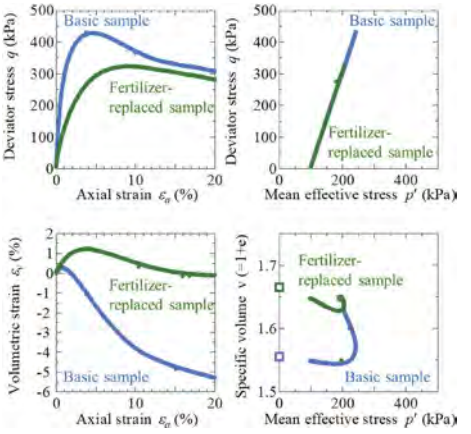

Figure 3. Drained shear behavior for the basic sample and the fertilizer- replaced sample.

4.2 *Comparison of fine-grain-removed and fertilizer- replaced samples - Monotonic undrained shear test*

To investigate whether the voids created by the dissolution of fertilizer by water supply created a special soil skeleton structure, a comparison was made between the fine-grain removal sample and the fertilizer replacement sample, which had the same *Dr* and particle size distribution.

Figure 4 shows the undrained shear test results. For $q \sim \varepsilon_a$, the fertilizer-replaced specimens had lower q and lower maximum q than the fine-grain-removed specimens. The mean effective stress p' in the early shear phase decreased and the positive excess pore pressure u increased, which means larger plastic compression. The excess pore pressure in the fine-grain-removed sample was higher in the latter half of the shear period.

Figure 5 shows the drained shear test results. For $q \sim \varepsilon_a$, the fertilizer-replaced sample had a smaller initial stiffness and a slightly larger peak than the fine-grain-removed sample. The dilatancy properties showed that the fertilizer-replaced sample exhibited a large compression in the early shear phase, followed by expansion, but did not exhibit negative volumetric strain throughout the shear phase. On the other hand, the fine-grain removal sample showed a small positive volumetric strain at the beginning of shearing and negative the latter half of the shear period.

Both undrained and drained shear behavior showed differences between specimens, with different pore formation and soil structures.

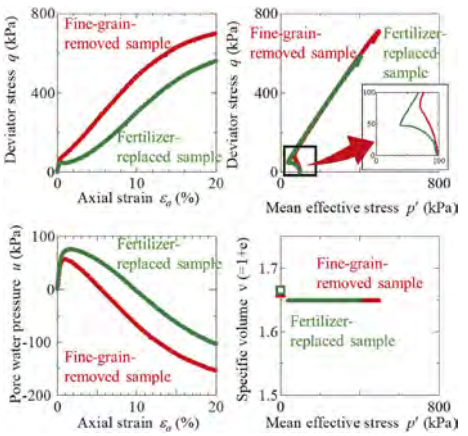

Figure 4. Undrained shear behavior for the fine-grain-removed sample and the fertilizer-replacedsample.

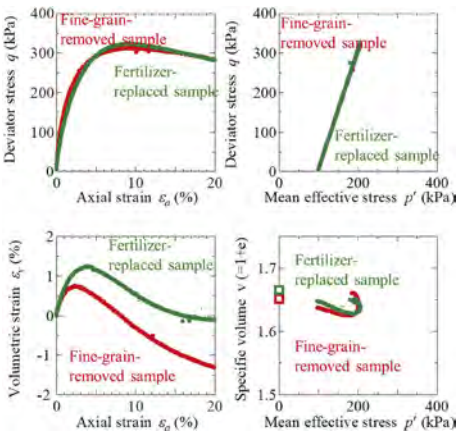

Figure 5. Drained shear behavior for the fine-grain-removed sample and the fertilizer-replaced sample.

4.3 *Comparison of fine-grain-removed and fertilizer- replaced samples - Monotonic undrained shear test - Cyclic undrained shear test*

The difference between both specimens was also investigated in cyclic undrained shear tests. The stress amplitudes were 25.0 kPa and 30.0 kPa.

Figures 6 and 7 show the undrained cyclic shear results for the fine-grain-removed and fertilizer-replaced samples, respectively. Both samples liquefied more easily as the amplitude increased, and the strain gradually increased after liquefaction. However, for the same amplitude, the fertilizer-replaced sample liquefied more easily and showed greater strain development after liquefaction. This is because the p' of the fertilizer-replaced sample decreased more significantly during the first iteration (black circles in the figure). This may be due to the greater reduction in stiffness and shear resistance of the fertilizer- replaced specimens.

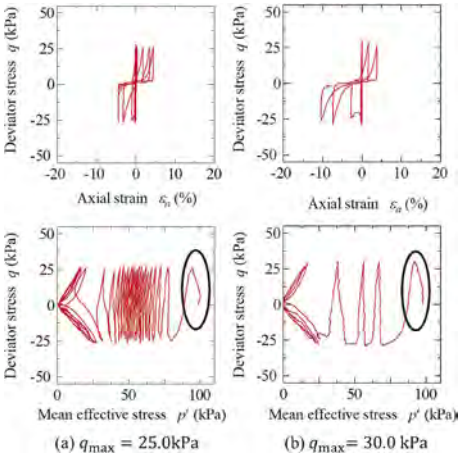

Figures 6. The undrained cyclic shear results for the fine-grain-removed samples.

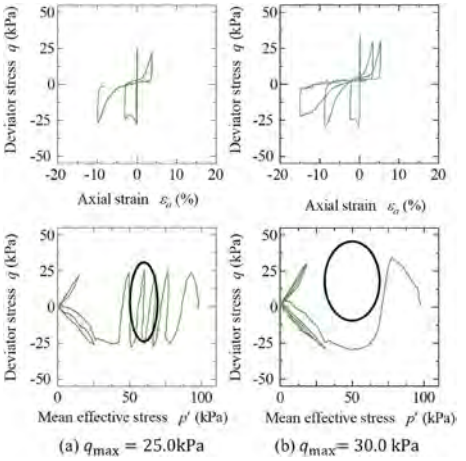

Figures 7. The undrained cyclic shear results for the fertilizer-replaced samples.

5 CONCLUSIONS

In this study, the effects of different pore structures on monotonic and cyclic shear tests of sand specimens were investigated using a triaxial compression test apparatus. The following conclusions are drawn.

1) The fertilizer in the fertilizer-replaced sample was dissolved with water to reproduce the sample with suffusion. When undrained shear was performed on these samples, the maximum q decreased compared to the basic sample.
2) In monotonic undrained shear behavior, the fertilizer- replaced samples showed a greater degree of plastic compression in early shear. In drained shear, the fertilizer- replaced specimens had lower initial stiffness and greater positive volumetric strain. It can be inferred that the pore structure due to the dissolution of fertilizer in water has a different soil structure from that of the basic specimens.
3) In cyclic undrained shear behavior, both samples were more prone to liquefaction as the stress amplitude ratio was increased. However, the fertilizer-replaced sample exhibited more shear strain development with fewer cycles.

We have not found evidence that fertilizer-induced pore formation is the same as actual pore formation due to suffusion. However, it is suggested that the pore formation in the sample from which the fine particles have been removed, i.e., the fine-grain-removed sample, is not the same as the actual pore formation. This should be taken into account when conducting future experiments to reproduce suffusion.

REFERENCES

Foster, M. & Fell, R. 1999. A framework for estimating the probability of failure of embankment dams by internal erosion and piping using event tree methods. *University of New South Wales*, Kensington.

Ishimaru, T., Suzuki, M. & S. Takano, S. 2020. Particle size composition of migrating soil particles and the time change in water-passing experiments for reproducing suffusion using turbidity. *Japanese Geotechnical Journal*, 17(1): 47–60 (in Japanese).

Ke, L. & Takahashi, A. 2014. Experimental investigations on suffusion characteristics and its mechanical consequences on saturated cohesionless soil. *Soils and Foundations*. 54(4): 713–730.

Kodaka, T., Cui, Y., Lee, K., Mitarai, S. & Takagi, R. 2016. Degradation of a sandy embankment soil due to outflow of fine particles. *28th Chubu Geotechnical engineering symposium*: 101–106 (in Japanese).

Prasomsri, J. & Takahashi, A. 2020. The role of fines on internal instability and its impact on undrained mechanical response of gap-graded soils. *Soils and Foundations*. 60(6): 1468–1488.

Smart Geotechnics for Smart Societies – Zhussupbekov, Sarsembayeva & Kaliakin (Eds)
© 2023 The Author(s), ISBN 978-1-003-29912-7
Open Access: www.taylorfrancis.com, CC BY-NC-ND 4.0 license

Progressive formation of concentrated seepage path in gap-graded sand due to suffusion and its influence on permeability change

R. Kido & Y. Higo
Kyoto University, Kyoto, Japan

ABSTRACT: Suffusion, which is classified as one of internal erosion, causes change in physical and hydraulic properties of soils during permeation, while the mechanism of permeability change for sands due to suffusion is not sufficiently clear. In the present study, permeability tests of gap-graded sand are performed by increasing levels of hydraulic gradient. During the tests, X-ray micro CT is applied to observed internal structure of sand specimens, and then the progressive formation of concentrated seepage path caused by suffusion is visualized by image analysis. It is found that permeability of gap-graded sand increases until a concentrated seepage path completely goes through the sand along a direction of seepage due to suffusion.

1 INTRODUCTION

Degradation and failure of soil structures, such as embankment subsidence, are often caused by the generation and development of microcavities due to internal erosion, in which particles are expelled by seepage forces and other actions. In general, internal erosion can be classified into four types: 1) pile or crack internal erosion, 2) backward internal erosion, 3) internal contact erosion and 4) suffusion (internal stability of a soil, or volume erosion) (Fry, 2012). In this study, suffusion, i.e., the internal erosion in which only fine particles are expelled from the pore spaces composed of coarse grains due to the seepage flow.

Once a suffusion occurs and develops, the physical and hydraulic properties of the soil change. Such changes in soil properties are caused by the formation of concentrated seepage path and clogging in the process of changing the grain size distribution and void ratio. Some studies observed internal structural changes in soil caused by suffusion using Scanning Electron Microscopy (SEM) (Sato and Kuwano, 2018) and X-ray micro Computed Tomography (CT) (e.g., Nguyen et al., 2019). They focus on the change in pore structure and its associated settlement caused by suffusion, while the mechanism of permeability change of the eroded sand is not sufficiently clear.

In the present study, permeability tests of gap-graded sand are performed by increasing levels of hydraulic gradient. X-ray micro CT is applied during the tests to observed inner structure of sand specimens, and then the progressive formation of concentrated seepage path caused by suffusion is visualized by image analysis. The influence of the formation of concentrated seepage path on the permeability change due to suffusion is discussed.

2 EXPERIMENTAL METHODS

2.1 *Materials and specimen preparation*

Figure 1 shows the test apparatus used in the present study, which was developed to conduct permeability test, triaxial compression test and X-ray micro CT scan. The downward seepage flow is applied by the water head difference between the upper tank connected to the top of the specimen and the lower tank connected to the bottom of the specimen. The lower tank has an outlet hole to maintain a constant water level, and the water flow rate from this hole is

DOI: 10.1201/9781003299127-34

measured by a gravimeter. The triaxial cell is made by an acrylic that allows us not only to support the loading force, but also to obtain high resolution images using X-ray micro CT apparatus, KYOTO-GEO μXCT (TOSCANER-32250mhdk).

Two levels of confining pressure, 10 kPa and 50 kPa, were applied to the specimen during the permeability test. The permeation was performed at a specified level of hydraulic gradient for three hours and then, the inner structure of the specimen was visualized using the X-ray micro CT. Such permeation and visualization were repeated with a step-by-step increase of the hydraulic gradient. The rest specimen was made dried and the mass of the dry sand was measured to calculate the mass of the eroded sand particles after completing the permeability test. In the present study, Erosion Rate (ER) is defined as a ratio of the amount of fine particles in the specimen before the permeability test to that of eroded fine particles after the permeability test. Water flow rate was measure by 10 seconds and permeability was calculated based on Darcy's law.

2.2 *Test apparatus and test methods*

Silica sand No. 3 was used for the coarse particle and silica sand No. 8 was used for the fine particle. These sand materials were mixed with a weight ratio of 7:3, similar to Ke and Takahashi (2014). The fine content F_c is 12.87%. A maximum void ratio and a minimum void ratio of the mixed sand is 0.782 and 0.390, respectively.

Silica sand No. 3 and No. 8 were mixed to obtain a relative density D_r of 30% as the mixed sand. Desaturated water with a water content of 3% was added to the mixed sand to make an uniform specimen by a moist tamping method. A perforated plate with a diameter of 34.9 mm, a thickness of 5.0 mm, a hole diameter of 1.0 mm, and a hole center spacing of 2.0 mm was placed at the top of a pedestal. The hole diameter of the perforated plate is large enough to allow only silica sand No. 8 to pass through. The moist-mixed sand was compacted in ten layers to make the specimen with a diameter of 35.0 mm and a height of 70.0 mm. After placing a porous stone and cap with bearing on the top of the specimen, the specimen was saturated by passing desaturated water through the specimen using a double-suction method.

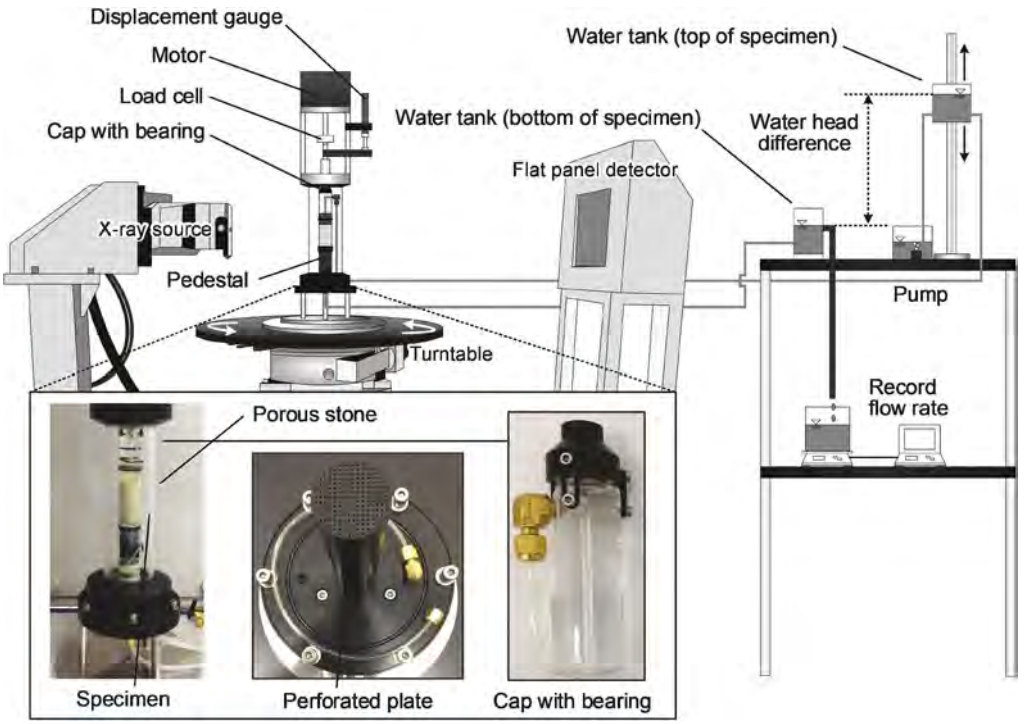

Figure 1. Apparatus of permeability test.

3 RESULTS AND DISCUSSIONS

3.1 *Change in permeability*

Test cases are listed in Table 1. The change in permeability and appearance of tube connected to the bottom of the specimen after the permeability test are shown in Figure 2. In Case 1, the permeability is kept almost constant at i=4, and then the permeability is increased monotonically with an increase of hydraulic gradient. In this process, the amount of eroded fine particles is increased as shown in Figure 2b. In other words, permeability is increased due to suffusion. As shown in Table 1, Case 3 shows smaller value of ER than Case 2; namely, a larger amount of fine particles is eroded in Case 3 than Case 2. Nevertheless, the permeability of Case 3 becomes higher than that of Case 2 beyond i=12.

3.2 *Development of local concentrated seepage path by suffusion*

Since the specimen is in an almost water-saturated condition, water fills the pore spaces where fine particles are expelled when suffusion occurs. Such pore spaces will locally occur and then connect with each other forming a concentrated seepage path, through which water will selectively flow. In the present study, the progressive formation of the seepage path in the specimen during permeability test is visualized using image analysis techniques.

Figure 3a shows a procedure of image analysis. At first, a binary image for pore water phase is obtained by a simple threshold method using a three-dimensional image processing software VGstudioMax3.1 (Volume Graphics). The binary image includes voxels of the pore water phase related to the seepage path, absorbed water around soil particles of silica sand No. 3, and partial volume effect (Higo et al., 2014). In order to extract the voxels for the pore water phase related to only the seepage path, Morphology analysis (Kido et al., 2020) that performs two kinds of image processing, i.e., Erosion and Dilation, is performed.

Figures 3b-3d show the concentrated seepage path at each hydraulic gradient visualized by the image analysis. In Case 1, the pore water phase is limited until i=4, and then it progressively increases with an increase of hydraulic gradient, forming a concentrated seepage path that goes through from top to bottom of the specimen. The similar tendency for development of such a concentrated seepage path is also observed in Case 3. On the other hand, it is found from Figure 3c that the concentrated seepage path for Case 2 is locally formed at the lower part of the specimen.

Table 1. Permeability test cases.

Case	σ_3 (kPa)	e_0	ER (%)	Hydraulic gradient i
Case 1	10	0.66	11.33	4, 8, 12
Case 2	50	0.67	6.08	4, 8, 12
Case 3	50	0.66	4.56	4, 8, 12, 16

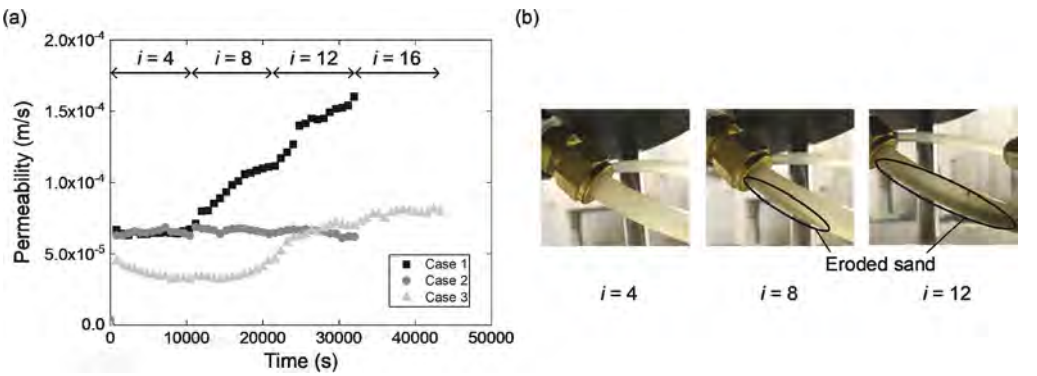

Figure 2. Results of permeability test: (a) permeability change and (b) eroded sand for Case 1.

3.3 *Effect of suffusion on permeability change*

The permeability change is compared with the tendency for the development of the concentrated seepage path. For Case 2, the seepage path is limited at the lower part of the specimen and the permeability is not changed. These results probably indicate that the suffusion occurs mainly at the lower part of the specimen, and the fine particles clogged in the middle part of the specimen that becomes a bottleneck, resulting in almost constant permeability. A reduction of permeability for Case 3 up to i=8 may be also caused by such clogging phenomenon because the seepage path is only seen in the bottom part of the specimen. On the other hand, the values of permeability for Cases 1 and 3 tend to gradually increase with an increase of hydraulic gradient. In this process, a clear concentrated seepage path is progressively formed for both the two cases.

The above results confirm that permeability of gap-graded sand increases until a concentrated seepage path completely goes through the sand along with a direction of seepage due to suffusion.

4 CONCLUSIONS

Permeability tests of gap-graded sand were conducted, and pore water phase in specimens at each level of hydraulic gradient was observed using X-ray micro CT and image analysis. The progressive formation of concentrated seepage path caused by suffusion was successfully visualized. It was found that permeability of gap-graded sand increases until a concentrated seepage path completely goes through the sand along a direction of seepage due to suffusion.

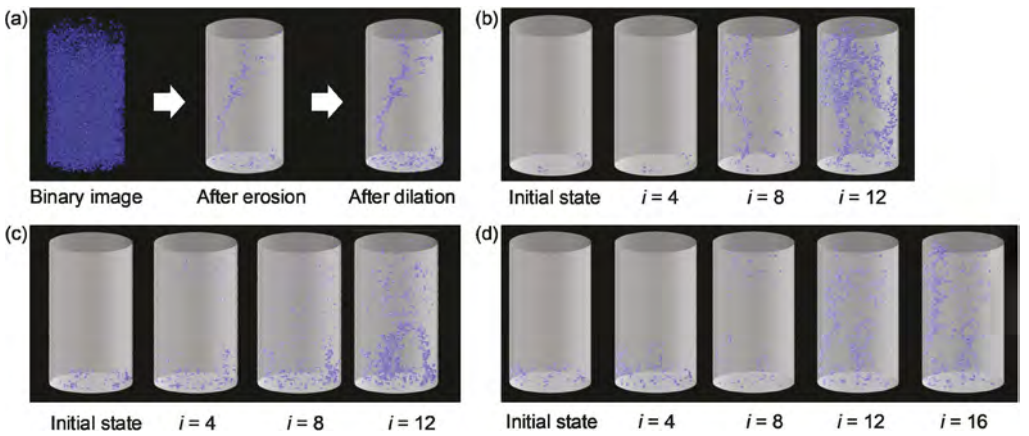

Figure 3. Visualization of concentrated seepage path: (a) method, (b) Case 1, (c) Case 2 and (d) Case 3.

REFERENCES

Fry, J. J. 2012. Introduction to the process of internal erosion in hydraulic structures: embankment dams and dikes. In Bonelli S (ed.), *Erosion of Geomaterials, Chapter 1*: 1–36. London, UK: ISTE-Wiley.

Higo, Y., Oka, F., Morishita, R., Matsushima, Y. & Yoshida, T. 2014. Trinarization of μX-ray CT images of partially saturated sand at different water retention states using a region growing method. *Nuclear Instruments and Methods in Physics Research B* (324): 63–69.

Ke, L. & Takahashi, A. 2014. Experimental investigations on suffusion characteristics and its mechanical consequences on saturated cohesionless soil. *Soils and Foundations* 54(4): 713–730.

Kido, R., Higo, Y., Takamura, F., Morishita, R., Khaddour, G. & Salager, S. 2020. Morphological transitions for pore water and pore air during drying and wetting processes in partially saturated sand. *Acta Geotechnica* 15: 1745–1761.

Nguyen, C.D., Benahmed, N., Andò, E., Sibille, L. & Philippe, P. 2019. Experimental investigation of microstructural changes in soils eroded by suffusion using X-ray tomography. *Acta Geotechnica* 14: 749–765.

Sato, M. & Kuwano, R. 2018. Laboratory testing for evaluation of the influence of a small degree of internal erosion on deformation and stiffness. *Soils and Foundations* 58: 547–562.

Smart Geotechnics for Smart Societies – Zhussupbekov, Sarsembayeva & Kaliakin (Eds)
© 2023 The Author(s), ISBN 978-1-003-29912-7
Open Access: www.taylorfrancis.com, CC BY-NC-ND 4.0 license

Evaluation of density of consolidated clay during desiccation using X-ray CT scanner

M. Tanaka, T. Kawamura & T. Umezaki
Shinshu University, Nagano, Japan

ABSTRACT: X-ray CT imaging was conducted for a consolidated clay in air-dry test, which is defined as the element test. It was found that the distribution of CT values in the specimen was not uniform during desiccation. Then the representative CT value, CT^*, of the entire specimen was computed during the desiccation process, during which the specimen transitioned from saturated to unsaturated state. The relations of w–CT^* and ρ_t–CT^* can be evaluated as bilinear relations, which bend near the shrinkage limit, w_s. Before or after w_s, there are conditions where the value of CT^* is the same even though the values of w and ρ_t are different. The relationship of ρ_t–CT^* during clay desiccation differs from that of solid materials and aqueous solutions.

1 INTRODUCTION

X-ray CT scanner is widely used for medical and industrial purpose. It is also used for geotechnical engineering purpose, for example, to visualize movement of soil particles and changes in density in a given region. The authors have studied to evaluate the state change of soil due to shrinkage and freezing, respectively, by using an X-ray CT scanner (Computerized tomography scanning equipment NAOMi-CT, RF Co., Ltd.). This scanner is 650 mm in width, 310 mm in depth, and 300 mm in height does not require shielded space to avoid X-ray exposure. Therefore, it can be transportable and is expected to be employed in not only laboratory tests but also outside work.

In this paper, X-ray CT scanning was conducted for the consolidated clay specimen during desiccation. The state change of the whole specimen from the saturated condition of the two-phase structure of soil particle and pore water to the unsaturated condition of three-phase structures adding pore air was discussed. The representative CT value for the entire specimen in the element test was generated from CT images using image analysis and averaging, and wet density was evaluated using CT value.

2 REPRESENTATIVE CT VALUE OF WHOLE SPECIMEN IN ELEMENT TEST

Image analysis for CT images and averaging procedure were conducted, to calculate the representative CT value of not local part of the specimen but the whole specimen. Figure 1 shows a flow diagram for calculating the representative CT value. The diagram consists of three phases. In phase (a), one vertical cross sectional CT image was captured for each CT scanning. The CT image is converted to local CT values within the specimen, which are subsequently translated to pixel values. In phase (b), the CT image was binarized using a threshold determined by the CT value at the border between air and the specimen. Then the part of air was eliminated from the CT image and the cross section of only the specimen was extracted as the target area. In phase (c), the CT-value distribution of the specimen was output. The CT values were averaged and finally, the representative CT value, CT^*, of the whole specimen, was calculated.

DOI: 10.1201/9781003299127-35

3 SAMPLES AND TEST PROCEDURE

Air-dry test was performed on NSF(C) clay specimen (soil particle density ρ_S = 2.723 g/cm^3, liquid limit w_L = 57.5%, plastic limit w_P = 35.7%, and shrinkage limit w_S = 37.6%). The value of w_s is larger than that of w_p. Toyoda et al. (1996) compared the shrinkage limits and the plastic limits of 17 soils. Results show that the values of w_s in seven soil samples were $w_s \geq w_P$. After de-airing slurry sample (water content, $w \approx 2\ w_L$), one-dimensional consolidation was performed at the fixed pressure. The consolidation time was determined using the 3t method and four saturated consolidated clay samples (w_0 = 0.87–0.89 w_L) were prepared. Then, cylindrical specimens (initial diameter and height, d_0 =3.5 cm and h_0 =5.0 cm) was fabricated using a trimming method with a thin wire saw. The specimen was placed on a glass plate and an air-dry test was performed in a thermostatic chamber with a room temperature of 23°C ± 1°C. X-ray CT scanning and measuring the specimen mass, height, and diameter were conducted at a fixed interval. And the values of water content, w, volume, V, void ratio, e, degree of saturation, S_r, and wet density, ρ_t, were calculated.

4 TEST RESULTS AND DISCUSSIONS

Table 1 shows the distribution of CT values in the vertical cross sectionals of the specimen during the air-dry test and the representative CT value, CT^*, derived from the process shown in Figure 1. The air-dry test is defined as the element test. However, it was found that the distribution of CT values within the specimen was not uniform during desiccation. Red color points, where CT value is larger than about 30,000, increase with elapsed time. The CT value in the specimen increases from the side area due to desiccation. However, at t = 360 min, w is almost equal to the shrinkage limit, and then red points decrease, as shown in Table 1(c)–(e).

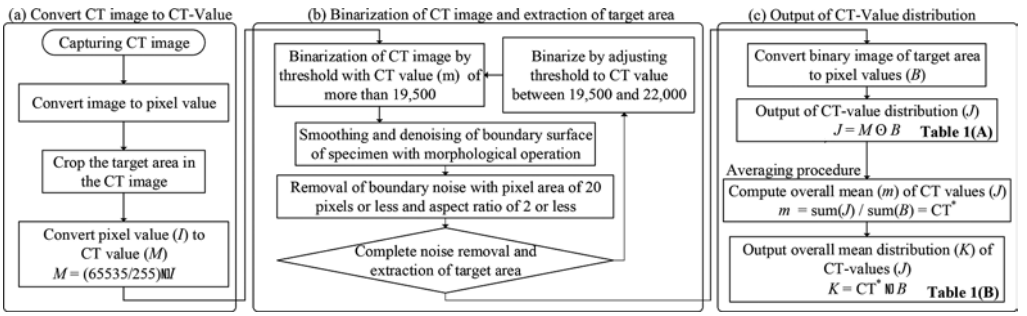

Figure 1. Flow diagram of extraction of CT value from CT image.

Figure 2 shows the relation of w–e. The relation decreases through S_r = 100% line, which is the normal shrinkage line. Then, when w gets lower than w_s, the value of e approaches a constant value, and the volume does not decrease even if moisture decreases. Because the volume is constant in $w < w_s$, it is assumed that the soil structure is formed.

Figure 3 depicts the relation of w–S_r. The value of S_r is about 100% until the value of w decreases to w_s and the saturated condition is maintained. When the value of w becomes smaller than w_s, the relation becomes almost a unique straight line through the origin, S_r = 0%, and the specimen becomes unsaturated and finally dry. Based on the findings of vacuum evaporation tests for six different types of reconstituted cohesive soil, Umezaki et al. (2013) reported that the relations of w–e and w–S_r bend near w_s.

Figure 4 shows the relation of w and CT^* of the whole specimen. The relation is not a straight line, but can be evaluated as bilinear relation, which bends near w_s. This is a similar tendency to the relations of w–e and w–S_r. When the value of w decreases under the saturated condition, CT^* increases and becomes maximum near the shrinkage limit, w_s. The initial and maximum values of CT^* are about 29,000 and 31,000, respectively. Then the value of w decreases further, the specimen transitioned to the unsaturated condition. During the

Table 1. CT-values distribution and representative CT value of consolidated clay in the air-dry test.

(a) t = 0 min (Initial) (w = 50%)	(b) t = 180 min (w = 44%)	(c) t = 360 min (w = 38% ≈ w_s)	(d) t = 540 min (w = 32%)	(e) t = 720 min (w = 26%)
(A) CT-Values distribution inside of specimen during desiccation.				
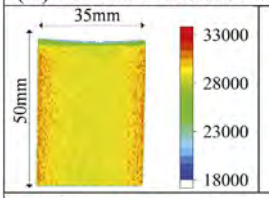				
(B) Representative CT-value, CT^*, of whole specimen after averaging procedure.				
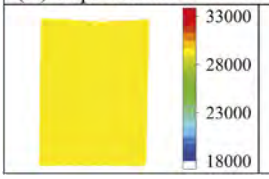				

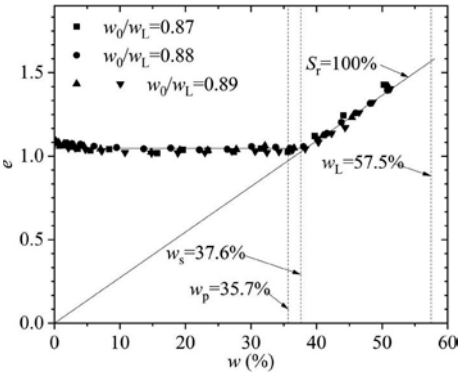

Figure 2. Relation of w and e.

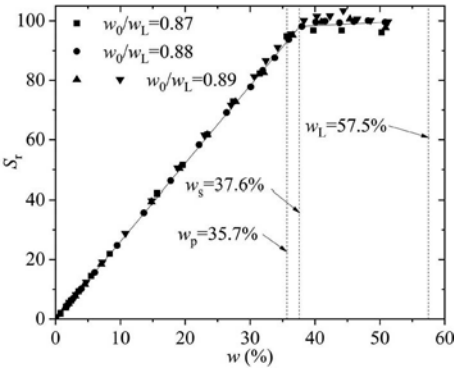

Figure 3. Relation of w and S_r.

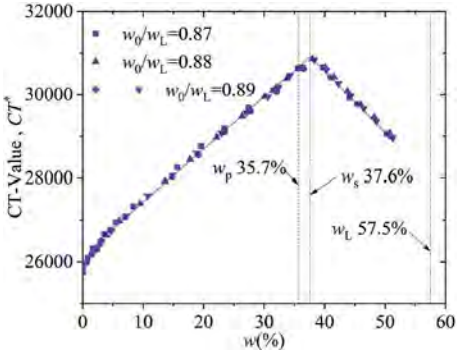

Figure 4. Relation of w and CT^*.

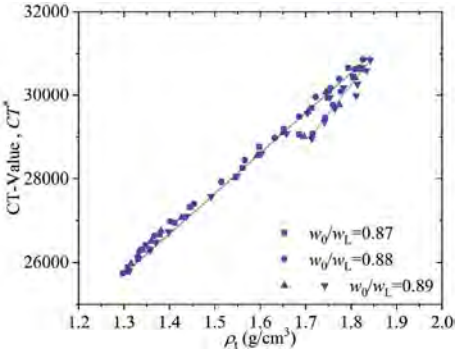

Figure 5. Relation of ρ_t and CT^*.

process, the value of CT^* decreases and becomes minimum at dry condition. The minimum value is about 25,500. There are the conditions where the value of CT^* is the same before or after w_s even if the values of w are different. The shrinkage limit is considered to be a particular point concerning degree of saturation and soil structure.

Figure 5 shows the relation of ρ_t and CT^*. The relation is not a straight line, but can be evaluated as bilinear relation, which is one straight line in saturated condition from the initial to w_s and another straight line in unsaturated condition from w_s to dry condition, as well as w–e, w–S_r, and w–CT^* relations. Furthermore, as well as the w–CT^* relation, before or after the shrinkage limit, there are the conditions where the value of CT^* is the same even though the values of ρ_t are different. The inclination of two straight lines is larger than in the saturated condition.

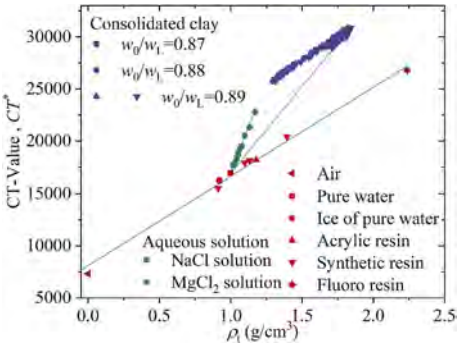

Figure 6. Relation of ρ_t and CT^* for synthetic resin, aqueous solution, and consolidated clay.

Figure 6 shows the relation of ρ_t and CT^* and added the measured values of other homogeneous samples: air, pure water, ice of pure water, solid materials of synthetic resin and aqueous solutions. Three distinct types of synthetic resin and two different types of aqueous solutions with varying concentrations of NaCl and $MgCl_2$ were employed. The CT values of pure water and aqueous solution were measured by pouring them into a glass container. Except for clay, CT value distributions were almost uniform for all materials, and the procedure in Figure 1 was not used. The relation of ρ_t and CT^* for homogeneous samples except for clay becomes a straight line as widely known. The relationship for aqueous solutions is a different straight line with pure water as an initial point. The relation for consolidated clay differs from the others and becomes bilinear. The source of the relationship under saturated conditions appears to be pure water. It is considered that the reason why the relation of ρ_t and CT^* of clay during desiccation becomes bilinear is the influence of soil structure.

5 CONCLUSIONS

X-ray CT imaging was performed for the consolidated clay in the air-dry test, which is defined as the element test. The representative CT value, CT^*, of the whole specimen was calculated during desiccation and state change of clay was discussed. The main conclusions are as follows.

(1) The relations of w–CT^* and ρ_t–CT^* are not straight lines, but can be evaluated as bilinear relations, which bend near w_s.
(2) Before or after the shrinkage limit, there are the conditions where the value of CT^* is the same even though the values of w and ρ_t are different.
(3) The relation of ρ_t and CT^* during desiccation of clay differs from the other homogeneous samples of solid materials of synthetic resin and aqueous solutions. The origin of the relation in saturated clay seems to be pure water.

ACKNOWLEDGMENT

The X-ray CT scanner was presented by RF Co., Ltd. Mr. Kazumi Kodaira, a researcher in RF Co., Ltd., supported the image analysis. Mr. Kouya Matsuda, a former student of Shinshu University, supported a part of the air-dry test. The authors are deeply grateful to them.

REFERENCES

Toyoda, T., Kawakami, H. & Takagi, R. 1996. Consistency limits in soils and soil moisture characteristics, *Proc. 31st Japanese Geotechnical Society Annual Meeting*, 523–524 (in Japanese).

Umezaki, T. & Kawamura, T. 2013. Shrinkage and desaturation properties during desiccation of reconstituted cohesive soil. *Soils and Foundations* 53(1): 47–63.

Smart Geotechnics for Smart Societies – Zhussupbekov, Sarsembayeva & Kaliakin (Eds)
© 2023 The Author(s), ISBN 978-1-003-29912-7
Open Access: www.taylorfrancis.com, CC BY-NC-ND 4.0 license

Closed-form solution for the consolidation of unsaturated soils considering semi-permeable boundary

L.S. Zhao & S.L. Shen
MOE Key Laboratory of Intelligence Manufacturing Technology, Department of Civil and Environmental Engineering, College of Engineering, Shantou University, Shantou, China

W.H. Yuan
Department of Civil and Environmental Engineering, College of Engineering, Shantou University, Shantou, China

ABSTRACT: The consolidation of unsaturated soils is commonly encountered in real practice. In contrast to saturated soils, the additional air phase in the void of the soil stratum complicates the consolidation process of unsaturated soils. In this study, a closed-form solution was established for the consolidation of unsaturated soils considering a semi-permeable boundary. A series of cases were conducted to show the characteristics associated with the consolidation of unsaturated soils commonly happened in in-situ projects. Compared with the existing analytical solutions, the derivation process is much simpler without using complicated mathematical methodologies. The proposed solution is verified to be accurate by comparing it with an analytical solution in the literature. This study reveals that, with a semi-permeable boundary, there exist some impeded effects on the excess pore water and air pressures at corresponding boundaries. The excess pore water and air pressures closed to the semi-permeable boundary exhibit an impeded feature.

1 INTRODUCTION

The consolidation of unsaturated soils is commonly encountered in real practice (Chiu et al., 2003; Ho and Fatahi, 2016; Huang et al., 2021; Lei et al., 2001; Ng et al., 2016). In contrast to the saturated soils (Terzaghi, 1943), the additional air phase in the void of the soil stratum complicates the consolidation process of unsaturated soils. This feature may cause a large discrepancy when approximating the settlement associated with the consolidation process (Huang et al., 2020; Li et al., 2021). In recent decades, researchers made a great effort in the consolidation of unsaturated soils (Lo et al., 2021; Wang et al., 2017; Wang et al., 2020). For instance, Ho et al. (2016) considered the permeable characteristics both in horizontal and vertical directions and proposed a new model under the 2D plain strain assumption. Wang et al. (2019) took the partial drainage boundary conditions into account and the proposed models are more flexible in the real application. Moradi et al. (2019) extended the governing equation from a one-layer system into a multi-layer system.

These analytical solutions were commonly applied to verify the numerical solutions and were used to study the influence of parameters with physical meanings through a parametric study. Nevertheless, plenty of these analytical or semi-analytical solutions were based on ideal boundary conditions, which have remarkable differences from the scenarios in real practice. The boundary in real practice cannot be absolutely permeable or impermeable due to the movement of fine particles towards the boundaries and the variation of temperature at the ground surface. The semi-permeable boundary condition describes the partial drainage properties at the

DOI: 10.1201/9781003299127-36

boundaries and can mitigate the discrepancy between the predictions and the measurements in real practice. With the scholars' great efforts, some great progress has been made in the consolidation of unsaturated soils considering semi-permeable boundary conditions. (Wang et al., 2017) used Laplace transform and Crump's method to solve the consolidation problem with semi-permeable boundary conditions. Huang and Zhao (2020) further evaluated the different permeable properties for both water and air phase at boundaries and presented a general analytical solution. To obtain corresponding analytical solutions, some complicated mathematical algorithms were inevitable to be introduced into these methods. Such as Laplace transform and inverse Laplace transform (Zhao et al., 2020), Crump's method (Wang et al., 2017), conjugate complex number (Niu et al., 2021), etc. This is reasonable when dealing with complex mathematical problems. However, this may decrease the widespread application of these proposed analytical or semi-analytical solutions by engineers in real practice.

Thus, the present study aims to propose an analytical solution considering partial drainage boundary conditions with simple mathematical derivation, which is more user-friendly in real practice. Besides, the proposed solution will be validated by comparing it with other solutions considering impeded boundary.

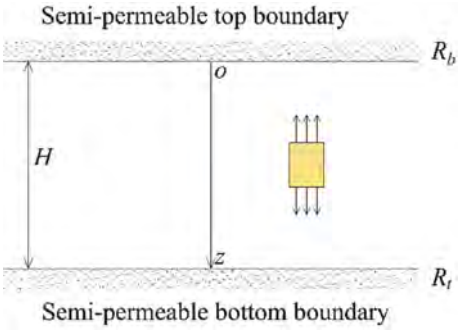

Figure 1. One dimensional consolidation of unsaturated soil layer with a semi-permeable boundary.

2 MATHEMATICAL MODELLING

Figure 1a illustrates a soil stratum of unsaturated soil with semi-permeable upper and lower boundary conditions. The thickness of the soil layer is H and the parameters, R_t and R_b, which are related to the semi-permeable boundary will be discussed later. The flows of air and water were assumed in the vertical direction only. To obtain the analytical solution considering the semi-permeable boundary properly, some assumptions were made to facilitate the derivation. Most of these assumptions are aligned with those assumptions made in the consolidation theory of unsaturated soils.

According to Fredlund and Hasan (1979), the governing equations for the consolidation of unsaturated soils can be expressed as follows,

$$\frac{\partial u_a}{\partial t} + C_a\left(\frac{\partial u_w}{\partial t}\right) + C_v^a\left(\frac{\partial^2 u_a}{\partial z^2}\right) = C_\sigma^a\left(\frac{\partial q}{\partial t}\right) \tag{1}$$

$$\frac{\partial u_w}{\partial t} + C_w\left(\frac{\partial u_a}{\partial t}\right) + C_v^w\left(\frac{\partial^2 u_w}{\partial z^2}\right) = C_\sigma^w\left(\frac{\partial q}{\partial t}\right) \tag{2}$$

where C_a, C_v^a, C_w, C_v^w, C_σ^a, C_σ^w are parameters used to get neat and uniform forms of Equations (5) and (6). These six parameters can be written as the following formulas based on the consolidation properties of unsaturated soils.

$$C_a = \frac{m_2^a\left(u_a^0 + u_{atm}\right)}{\left[\left(m_1^a - m_2^a\right)\left(u_a^0 + u_{atm}\right) - n(1 - S_r)\right]} \tag{3}$$

$$C_v^a = \frac{k_a R\Theta}{gM\left[\left(u_a^0 + u_{atm}\right)\left(m_1^a - m_2^a\right) - n(1 - S_r)\right]} \tag{4}$$

$$C_w = \left(\frac{m_1^w}{m_2^w} - 1\right) \tag{5}$$

$$C_v^w = \frac{1}{m_2^w}\left(\frac{k_w}{\gamma_w}\right) \tag{6}$$

$$C_\sigma^a = \frac{m_1^a\left(u_a^0 + u_{atm}\right)}{\left[\left(m_1^a - m_2^a\right)\left(u_a^0 + u_{atm}\right) - n(1 - S_r)\right]} \tag{7}$$

$$C_\sigma^w = m_1^w / m_2^w \tag{8}$$

3 BOUNDARY CONDITION

To meet the real drainage feature at boundaries of unsaturated soils, some researchers made a great effort to develop the theory of partial drainage boundary. As stated by Huang et al. (2020), there exist two hypotheses about partial drainage conditions. One is about time-dependent boundary conditions which are used to show the change of drainage properties at boundaries with time (Zhou et al., 2017). The other one is associated with an additional impeded layer at the boundary (Wang et al., 2017, Zhao et al., 2019). The current study is based on the assumption with impeded layers and they can be written as:

Top boundary

$$\frac{\partial u_a(0,t)}{\partial z} - \frac{R_a^t}{H} u_a(0,t) = 0 \tag{9}$$

$$\frac{\partial u_w(0,t)}{\partial z} - \frac{R_w^t}{H} u_w(0,t) = 0 \tag{10}$$

Bottom boundary

$$\frac{\partial u_a(1,t)}{\partial z} + \frac{R_a^b}{H} u_a(1,t) = 0 \tag{11}$$

$$\frac{\partial u_w(1,t)}{\partial z} + \frac{R_w^b}{H} u_w(1,t) = 0 \tag{12}$$

where R_a^t, R_w^t, R_a^b, R_w^b are four parameters related to the impeded layers at the top and bottom boundaries. Some researchers related these parameters with the permeability ratio and thickness ratio between the impeded layer and the target unsaturated soil layer. This hypothesis is reasonable and has explicit physical meaning. It should be noted the initial condition is assumed as a uniform distribution, which was adopted by many researchers.

4 CLOSED SOLUTION

In this study, the separation of the variable method was adopted to obtain the closed-form solution. The solution related to the governing Equations (1) and (2) can be written as,

$$\phi_i(\bar{z}, T) = \sum\nolimits_{m=1}^{\infty} A_m Z^m(\bar{z}) f_i^m(T) \ (i = \ 1, 2) \tag{13}$$

where $Z^m(\bar{z})$ is the eigenfunction associated with the depth of the soil layer. $f_i^m(T)$ is generalized Fourier coefficients with the variable of time factor T. A_m are coefficients related to $f_i^m(T)$, which can be obtained on basis of the initial distribution of excess pore pressures.

The excess pore water and air pressures can be calculated as,

$$\bar{u}_a(\bar{z}, T) = \frac{e_{21}\phi_2(\bar{z}, T) - \phi_1(\bar{z}, T)}{e_{12}e_{21} - 1} \tag{14}$$

$$\bar{u}_w(\bar{z}, T) = \frac{e_{12}\phi_1(\bar{z}, T) - \phi_2(\bar{z}, T)}{e_{12}e_{21} - 1} \tag{15}$$

where e_{21} and e_{12} are parameters related to the properties of unsaturated soils and can be calculated using the coefficients in Equations (1) and (2). Once, the average degree of consolidation for both water and air phases subjected to instantaneous loading can be obtained according to the consolidation theory proposed by Fredlund and Hasan (1979).

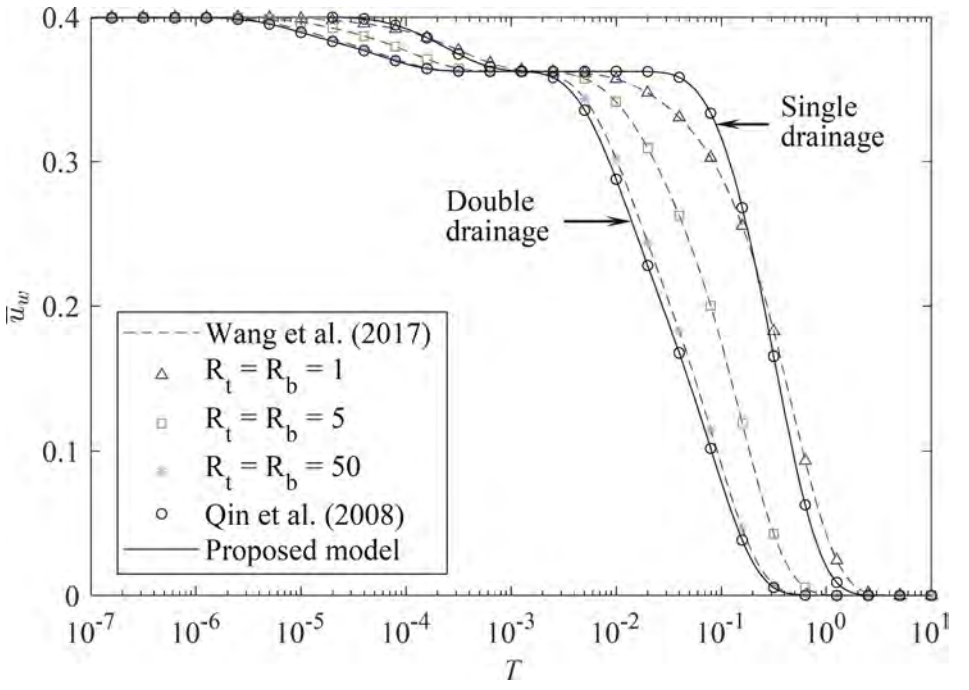

Figure 2. Normalized excess water pore pressures versus time compared with existing analytical solutions.

5 CASE STUDY AND VALIDATION

In this study, the following case was used to validate the accuracy of the proposed analytical solution for unsaturated soils with impeded boundaries. The thickness of the unsaturated soil stratum is assumed as 10 m, the initial porosity is 0.50 and the initial degree of saturation is 80%. The hydraulic conductivity for the water phase, k_w, and air phase, k_a, are $10^{-1\circ}$ m/s and 10^{-9} m/s, respectively. The coefficient of volume change with respect to a change in net normal stress under K_0 loading is m_{1k}^s. The coefficient of volume change with respect to a change in matric suction under K_0 loading is m_2^s. The coefficients of volume changes are: $m_{1k}^s = -2.5 \times 10^{-4} kPa^{-1}$, $m_2^w = -2.0 \times 10^{-4} kPa^{-1}$, $m_{1k}^w = -0.5 \times 10^{-4} kPa^{-1}$, $m_2^s = -1.0 \times 10^{-4} kPa^{-1}$. In the cases presented by Wang et al. (2017), the uniform initial distributions of excess pore air and pore water pressures were assumed as 5 kPa and 40 kPa, respectively. To prove the reasonableness of the proposed solution, Figure 2 presents the variations of excess pore water pressure at the depth of

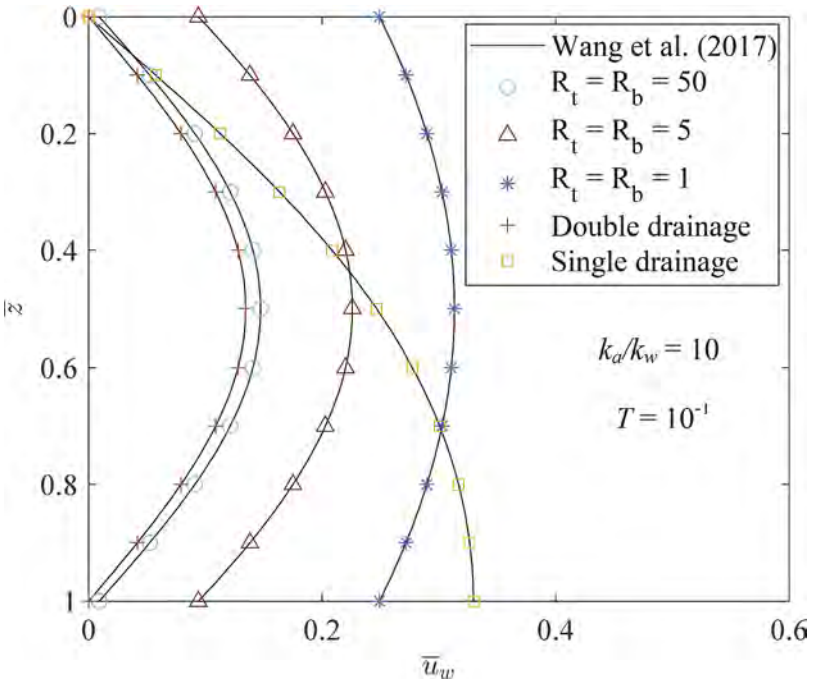

Figure 3. Isochrones of excess water pore pressures compared with existing analytical solutions.

8 m considering different semi-permeable boundary conditions. The analytical solutions presented by Wang et al. (2017) with the same semi-permeable boundary conditions were plotted in these two figures as well and they are identical to the proposed solutions. Furthermore, this figure shows another two scenarios with ideal double drainage ($R_t = R_b = \infty$) and single drainage ($R_t = \infty$, $R_b = 0$) and they are the same as the solutions obtained from the analytical solution proposed by Qin et al. (2008). To further validate the proposed analytical solution, the isochrones of excess pore water and air pressure are shown in Figure 3. At the time step of $T = 10^{-4}$, Figure 3 shows the influence of the semi-permeable boundary on the isochrones of excess pore water pressures at $T = 10^{-1}$. In the same way, the results were compared with the existing analytical solutions in the literature (Lei Wang et al., 2017). The above discussion indicates the accuracy of the proposed analytical solution from different aspects.

6 CONCLUSION

In this study, an analytical solution is presented to show the consolidation characteristics of unsaturated soils considering semi-permeable boundary conditions. The present work reveals a simple derivation process involving semi-permeable boundary conditions. The solutions illustrate that the semi-permeable boundary can impede the dissipation of excess pore pressures at the corresponding boundary and can increase the excess pore pressures to some certain value. The permeability ratio between the air and water phases has the main impact on the consolidation of the air phase and the early stage of consolidation for the water phase.

ACKNOWLEDGEMENTS

This research has been supported by the National Natural Science Foundation of China (Grant No. 42102308), and the Research Funding of Shantou University for New Faculty Member (Grant No. NTF21008-2021).

REFERENCES

Chiu, C.F. & Ng, C.W.W. 2003. A state-dependent elasto-plastic model for saturated and unsaturated soils. *Géotechnique*, 53, 9, 809–829.

Fredlund, D.G., Hasan, J.U., 1979. One-dimensional consolidation theory: unsaturated soils. *Can. Geotech. J.*, 16, 521–531.

Ho, L., Fatahi, B., 2016. One-dimensional consolidation analysis of unsaturated soils subjected to time-dependent loading. *Int. J. Geomech.*, 16, 1–19.

Huang, M. hua, Zhao, M. hua, 2021. Semi-analytical solutions for two-dimensional plane strain consolidation of layered unsaturated soil. *Comput. Geotech.*, 129, 103886.

Huang, M. hua, Zhao, M. hua, 2020. A general analytical solution for one dimensional consolidation of unsaturated soil incorporating impeded drainage boundaries. *Comput. Geotech.*, 128, 103801.

Huang, Y., Li, T., Fu, X., Chen, Z., 2020. Analytical solutions for the consolidation of unsaturated foundation with prefabricated vertical drain. *Int. J. Numer. Anal. Methods Geomech.*, 44, 2263–2282.

Lei, G.H., Ng C.W.W. & Rigby, D.B. (2001). Stress and displacement around an elastic artificial rectangular hole. *J. Eng. Mech.*, 127, No.9, 880–890.

Li, L., Qin, A., Jiang, L., 2021. Semianalytical Solution of One-Dimensional Consolidation of Multilayered Unsaturated Soils. *Int. J. Geomech.*, 21, 06021017.

Lo, W.C., Chang, J.C., Borja, R.I., Deng, J.H., Lee, J.W., 2021. Mathematical modeling of consolidation in unsaturated poroelastic soils under fluid flux boundary conditions. *J. Hydrol.*, 595, 125671.

Moradi, M., Keshavarz, A., Fazeli, A., 2019. One dimensional consolidation of multi-layered unsaturated soil under partially permeable boundary conditions and time-dependent loading. *Comput. Geotech.*, 107, 45–54.

Ng, C.W.W., Ni, J., Leung, A.K., Zhou, C. & Wang, Z. (2016). Effects of planting density on tree growth and induced soil suction. *Géotechnique*, 66, No. 9, 711–724.

Niu, J., Ling, D., Zhu, S., Gong, S., Shan, Z., 2021. Solutions for one-dimensional consolidation of unsaturated soil with general boundary conditions subjected to time-dependent load. *Int. J. Numer. Anal. Methods Geomech.*, 1–17.

Qin, A., Sun, D., Yang, L., Weng, Y., 2008. A semi-analytical solution to consolidation of unsaturated soils with the free drainage well. *Comput. Geotech.*, 37, 867–875.

Terzaghi, K., 1943. Theoretical soil mechanics. John Wiley & Sons, New York.

Wang, L., Sun, D., Li, L., Li, P., Xu, Y., 2017. Semi-analytical solutions to one-dimensional consolidation for unsaturated soils with symmetric semi-permeable drainage boundary. *Comput. Geotech.*, 89, 71–80.

Wang, L., Zhou, A., Xu, Y., Xia, X., 2020. Consolidation of unsaturated composite ground reinforced by permeable columns. *Comput. Geotech.*, 125, 103706.

Zhao, X., Ng, C.W.W., Zhang, S., Ni, J., Zhou, C., 2020. An explicit one-dimensional consolidation solution with semi-permeable drainage boundary for unsaturated soil. *Int. J. Numer. Anal. Methods Geomech.*, 44, 2241–2253.

Zhou, W.-H., Zhao, L.-S., Garg, A., Yuen, K.-V., 2017. Generalized analytical solution for the consolidation of unsaturated soil under partially permeable boundary conditions. *Int. J. Geomech.*, 17, 04017048.

Smart Geotechnics for Smart Societies – Zhussupbekov, Sarsembayeva & Kaliakin (Eds)
© 2023 The Author(s), ISBN 978-1-003-29912-7
Open Access: www.taylorfrancis.com, CC BY-NC-ND 4.0 license

Direct and indirect methods in determination of water retention curve of residual soils

A. Satyanaga*, A.S. Mohammad & A.B. Ibrahimi
Department of Civil and Environmental Engineering, Nazarbayev University, Nur-Sultan, Kazakhstan

M. Wijaya
Department of Civil Engineering, Parahyangan Catholic University, Bandung, Indonesia

S.-W. Moon & J. Kim
Department of Civil and Environmental Engineering, Nazarbayev University, Nur-Sultan, Kazakhstan

ABSTRACT: Many steep slopes are associated with deep groundwater table so they are located within unsaturated zone. Therefore, it is important to incorporate the unsaturated soil properties in the analysis of slope and design of slope preventive measures. The main property of the unsaturated soil is Water Retention Curve (WRC) describing the relationship between suction and water content. Many researchers developed technologies and methods in the determination of WRC which are associated with certain theory and assumption. The establishment of WRC can be performed using direct and indirect method. This paper focuses on the comparison of three different laboratory testing methods as direct methods to generate WRC. In addition, the paper summarizes the advantages and disadvantages of different methods in the determination of the air-entry value which is the important variable of WRC. The estimation of WRC using indirect method is presented as the practical approach for rapid determination of WRC.

Keywords: Rainfall-induced landslides, unsaturated soil, water retention curve, air-entry value

1 INTRODUCTION

In classical soil mechanics (e.g., excavation and foundation), geotechnical problems have been solved based on the saturated shear strength principles from Terzaghi (1936). This is admissible because of its conservative approach. Saturated condition can only be found below the groundwater table. For residual soils, unsaturated conditions need to be considered (Satyanaga and Rahadjo, 2020). Unlike saturated soil, an unsaturated soil has negative pore water pressures (Rahardjo et al., 2016). Therefore, understanding on unsaturated soil mechanics is required in solving geotechnical issues.

The water retention curve (WRC) describes the relation between the water content and the suction of the unsaturated soil (e.g., Satyanaga et al., 2017). The determination of WRC is merely done in the laboratory whereby the mathematical modelling is of huge importance to reduce the efforts in the laboratory. The WRC is highly depended on the soil type, but it has usually the form of a sigmoid function. The water content can be displayed as degree of saturation, gravimetric water content or volumetric water content. The soil suction has a range between nearly 0 and 10^6 kPa (Rahardjo et al., 2019). The boundary effect zone is the zone between zero suction and the air-entry value (AEV) (Satyanaga and Rahardjo, 2019). Basically, this zone represents the capillary fringe of groundwater in an unsaturated soil. The

*Corresponding author: alfrendo.satyanaga@nu.edu.kz

DOI: 10.1201/9781003299127-37

transition zone is the zone between the AEV and the residual condition. The air-entry value marks the suction where air begins to penetrate into the largest pores. The determination of the AVE can be done deterministic (Zhai & Rahardjo, 2012) or graphically (Zhai et al., 2020). On the WRC, the AEV is the interception of the tangent at the point of the maximal water content and the tangent at the point of the maximum gradient called inflection point.

This paper focuses on the comparison of different laboratory test methods as direct methods and different estimation methods to generate WRC. The scope of works includes the WRC testing in laboratory using Tempe cell, pressure plate, Fredlund cell, modified triaxial cell.

2 APPLICABLE THEORY

Laboratory experiments deliver a series of data for defining the WRC. For a practical usage, simple mathematical description of the WRC is needed. This description are empirical formulations, which can be fitted at most exactly to the measured data. Over the past century, investigators presented a whole variety from simple to sophisticated mathematical models. Statistical assessment from Sillers and Fredlund (2001) with the Akaike Information Criterion (AIC) and Leong and Rahardjo (1997) with a residual analysis concluded that Fredlund and Xing (1994) model as the best model in best fitting WRC data. Therefore, the model from Fredlund and Xing (1994) (Equation 1) was used in this study.

$$\theta(\psi,\ a,\ n,\ m) = C(\psi) * \frac{\theta_s}{\left\{ ln\left[e + \left(\frac{\psi}{a}\right)^n \right] \right\}^m} \tag{1}$$

whereas *a,n ,m* are unknown fitting parameters, ψ is the matric suction (u_a - u_w), θ_s is the saturated water content, *e* is the natural number (≈2.72) and $C(\psi)$ is a correction factor defined as follow:

$$C(\psi) = \frac{ln\left(1 + \frac{\psi}{\psi_r}\right)}{\left[ln1 + \left(\frac{1'000'000}{\psi_r}\right) \right]} + 1 \tag{2}$$

The parameter ψ_r is a fitting parameter related to the residual suction. However, Leong and Rahardjo (1997) favour to use C(ψ) = 1 and this was applied in this study as well. The fitting parameters a,n and m are empirical in nature and they can be fitted with the method of the least squares whereas the parameters need to be reasonable (Fredlund & Xing, 1994). Parameter *a* is related to the AEV and basically defines the "position" of the curve. Parameter *n* expresses the ratio of drain of a soil and could be regarded as slope of the SWCC. Parameter *m* is related to the residual stage of the curve and is an indicator for the logarithmic symmetry of the curve. Zhai and Rahardjo (2012) proposed deterministic approach (Equations 3 and 4) to calculate AEV.

$$\psi_{AEV} = a * 0.1^{\frac{3.72 * 1.31^{m+1} * \left(1 - e^{-\frac{m}{3.67}}\right)}{n * m * \ln(10)}} \tag{3}$$

for correction factor = 1

$$\psi_{AEV} = a * 10^{\frac{\theta_i - \theta_s}{s_1}} \tag{4}$$

for correction factor is not equal to 1

where the parameters *a, m* and *n* are the fitting parameters from D. G. Fredlund and Xing (1994). The parameter s_1 is the slope, θ_i the volumetric water content at the inflection point a_f and θ_s the saturated residual water content.

To avoid time consuming and expensive laboratory experiments, some researchers came up with estimations for the SWCC. Such estimations can also be useful for planning the laboratory experiments (i.e., define the suction to be measured). M. D. Fredlund et al., (2002)

presented an estimation based on the grain-size distribution. This method is implemented in the software SoilVision and it is rather difficult to calculate by hand but it delivers reasonably reliable results for sands and silts. However, it has some weaknesses for clays, tills and loams.

A straight forward estimation for plastic soil is proposed by Zapata (1999) and further developed by Perera et al., (2005). This method is based on the grain-size distribution and the plasticity index (PI). The method predicts WRC based on a weighed Plasticity index, *wPI* for non-plastic soils (Equation 5), respectively. Equations 6 to 8 can be used to determine WRC of plastic soils.

$$wPI = PI * P_{200} \ (expressed\ as\ a\ decimal) \tag{5}$$

$$a = 32.835\{ln(wPI)\} + 32.438 \tag{6}$$

$$n = 1.421(wPI)^{-0.3185} \tag{7}$$

$$m = -0.2154\{ln(wPI)\} + 0.7145 \tag{8}$$

The parameter *a, n, m* and ψ_r representing the fitting parameters from the Fredlund & Xing equation in Equation 3 and 4 where ψ_r = 500.

3 APPLICABLE THEORY RESEARCH METHODOLOGY

The soil used in the laboratory test was obtained from a borehole at Orchard Boulevard site located at the central of Singapore which is a part of residual soil from Bukit Timah Granite. In this study undisturbed samples from a depth between 6 to 7 meters were used. The index properties tests were performed based on ASTM standard. The grain-size distribution was determined based on ASTM D422-63. The tests to obtain Atterberg limits were performed based on ASTM D4318-00. The specific gravity was carried out based on ASTM D854-02.

Three sets of WRC tests were determined in the laboratory with three different methods (Satyanaga et al., 2019): (i) Tempe cell and pressure plate; (ii) Fredlund cell and (iii) modified Triaxial device. The Tempe cell in Figure 1 was used for measurement of WRC at suction < 100 kPa. A 1 bar high entry disk was used in this experiment. A schematic diagram of a cross sectional view of Tempe cell is shown in Figure 2. The pressure plate (Figure 3) was measurement of WRC at suction > 100 kPa. A 5-bar high entry disk was applied in this experiment. The image of the open pressure plate is shown in Figure 4. A cross sectional view of pressure plate is shown in Figure 5.

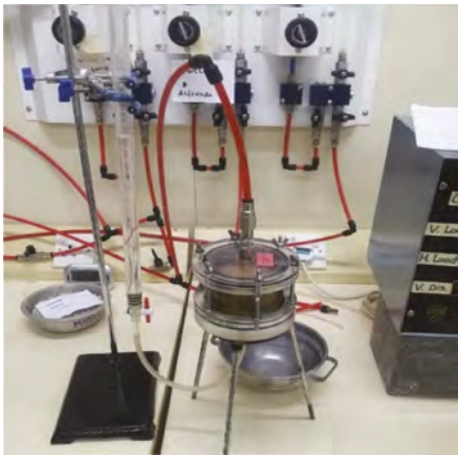

Figure 1. Tempe cell set up during WRC testing.

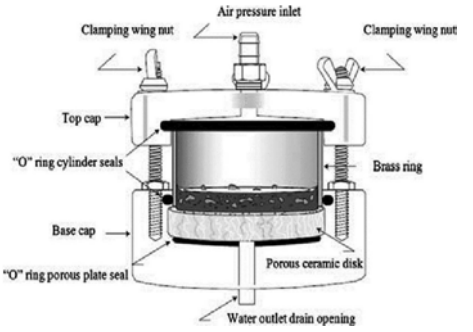

Figure 2. Cross sectional view tempe cell from Satyanaga et al. (2021a).

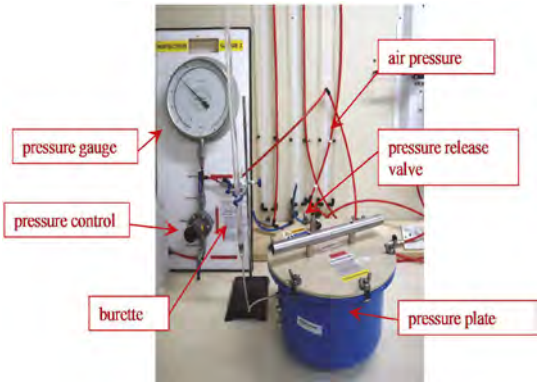

Figure 3. Pressure plate set up during WRC testing.

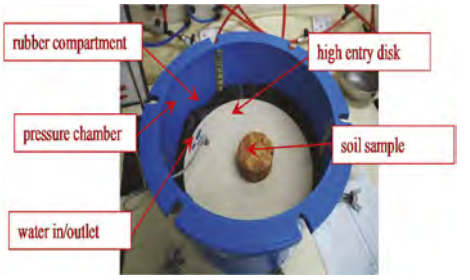

Figure 4. Open pressure plate during WRC testing.

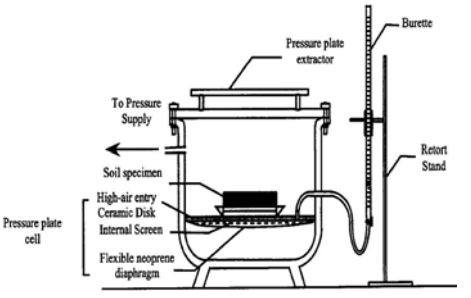

Figure 5. Cross sectional view pressure plate from Satyanaga et al. (2021b).

The previous WRC estimation from M. D. Fredlund et al. (2002) was used to define the applied matric suction, based on the grain-size distribution. The following suction stages were applied in the measurement of WRC: 1 kPa, 2 kPa, 5 kPa, 10 kPa, 20 kPa, 25 kPa, 50 kPa, 75 kPa, 90 kPa for Tempe cell testing and 200 kPa, 300 kPa, 400 kPa for pressure plate testing. The high entry disc (or porous ceramic disc) was connected via a tube to a burette filled with de-aired and distilled water. The purpose of this connection was to keep the disc during the experiment saturated. Air pressure was applied from the top of the cell. The matric suction resulted from the difference between the applied air pressure and the piezometric head in the burette. The equalization was controlled by measuring the mass of the sample by weighting the closed cell.

The Fredlund cell set up during the WRC testing is shown in Figure 6. A 5-bar high entry disk was applied in the experiment. The set-up of the open Fredlund cell is shown in Figure 7. A schematic diagram of a cross sectional view is shown in Figure 8.

Figure 6. Fredlund cell set up during WRC testing.

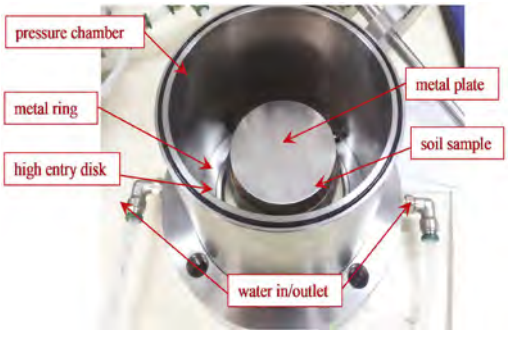

Figure 7. Open Fredlund cell before WRC testing is started.

The different suction stages were estimated according to the findings of the first suction measurements of the Tempe cell. The following suction stages were used in the measurement of WRC: 5 kPa, 10 kPa, 25 kPa, 50 kPa, 75 kPa, 100 kPa, 150 kPa, 200 kPa, 300 kPa, 400 kPa and 500 kPa. Before the testing, the water volume tube was calibrated for determining. the following correction factors. They are the ratio between mass water and the height in the tube, and the volume change in the tube which can directly be converted into water mass or water volume. Air pressure was applied from the top of the cell. The matric suction resulted from the difference between the applied air pressure and the piezometric head in the volume tube. The equalization was controlled by reading the volume change.

The modified triaxial device for the WRC testing is shown in Figure 9. A 5-bar high entry disk was applied in this experiment. The image of open cell is shown in Figure 10.

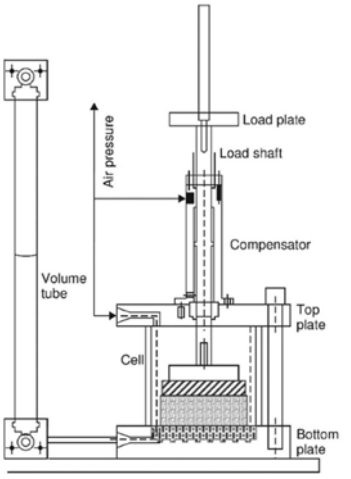

Figure 8. Cross sectional view Fredlund cell (after Fredlund et al., 2012).

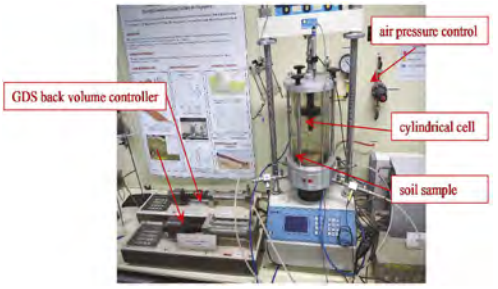

Figure 9. Modified triaxial apparatus set up during WRC testing.

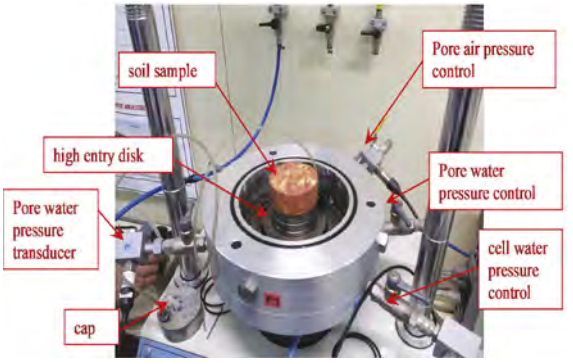

Figure 10. Open triaxial apparatus prior to WRC testing.

The different suction stages were estimated according to the findings of the suction measurements of the Tempe cell and Fredlund cell. The following suction stages were used in the measurement: 10 kPa, 25 kPa, 50 kPa, 75 kPa, 100 kPa, 150 kPa, 200 kPa, 300 kPa, 400 kPa and 500 kPa. Soil suction could be applied to the sample by reducing the pore water back pressure and keeping the air pressure on 490 kPa. As soon as no significant change in the back pressure volume change was observed, the sample was regarded as equalized, and the soil suction could be increased. The different readings were done automatically by transducers attached to the air pressure control, pore water pressure and cell pressure control. Since the

specimen was from a depth of 6 to 7m, confining pressure of 90 kPa was applied to the specimen to simulate the conditions in such depth.

4 RESULTS AND DISCUSSIONS

The WRC from direct and indirect method are displayed in Figure 11. The duration of WRC test using Tempe cell and pressure plate are around 5 weeks. Totally, 175 measurements were made at 8 different matric suctions. The curve was fitted with Fredlund and Xing (1994) by the sum of the least square with the correction factor $C = 1$ on the degree of saturation points. In order to get reasonable results, the fitting parameter were limited with the values $a = 500$, $n \leq 6$ and $m \leq 6$. Following parameter were determined a = 500, n = 0.716, m = 2.475, θ_s = 49%. The duration of WRC test using Fredlund cell are around 6 weeks. Totally, 152 measurements were made at 11 different matric suctions. a = 500, n = 1.048, m = 0.974, θ_s = 51%. The duration of WRC test using modified Triaxial cell test are around 5 weeks. Totally, 6 different matric suctions were measured. a =500, n = 1.030, m = 1.472, θ_s = 50%. The estimation based on Zapata resulted in following SWCC. a = 131, n = 0.548, m = 0.070, θ_s = 50%, C_r = 500. The estimation based on Fredlund & Wilson was done with the software SoilVision and resulted in following SWCC. a = 583, n = 0.722, m = 0.988, θ_s = 50%, C_r = 500.

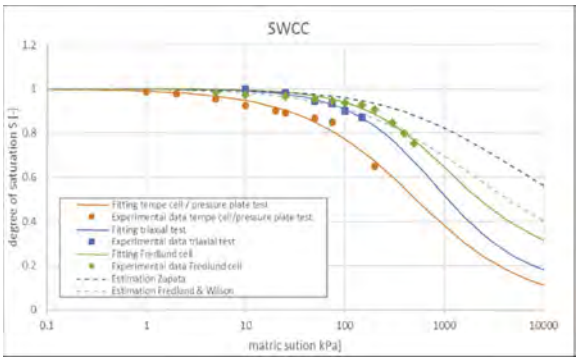

Figure 11. Overview of determined and estimated SWCC.

Figure 11 shows that different methods result in different curves. It shows that the application of confining pressure has a significant influence on the SWCC. The water content is higher on the same suction when confining pressure is applied. The two estimations perform up to 200 kPa quite well compared with the experimental data from the Fredlund Cell and the triaxial test. It seems that estimation based on Perera et al. (2005) overestimates the data. However, both curves seem to be too flat. This has a significant influence on the bending point and therefore on the AEV and on higher suctions.

As the determination of the WRC with the Fredlund cell could be done without any problems, this WRC is assumed to be the most accurate. Therefore, the air entry value (114 kPa) was determined based on Zhai and Rahardjo (2012). In order to show the variability and uncertainties, which comes with the AEV determining with a fitting by Fredlund and Xing (1994) and C=1, the AEV of different methods and different parameters were analyzed. Then, the comparisons of AEV were made with the following methods: (i) Determination (Zhai & Rahardjo, 2012)/ graphically estimation (Vanapalli et al., 1998); (ii) Fitting methods: least square / R^2 / least absolute deviation/sum of weighted least squares; (iii) SWCC determination/estimation: Tempe cell & Pressure plate / Fredlund cell / Triaxial device / Zapata estimation / Fredlund & Wilson estimation; (iv) Fitting degree of saturation / volumetric water content; (v) Fitting limits. The obtained value above (114 kPa) and the applied approach (i.e., determination from the Fredlund & Xing fitted saturated water content based on a least square fitting with given limits) were regarded as standard. The AEVs were analyzed by

varying one element. The AEV was determined mathematically. The other, more classical, approach is a graphical estimation and is described by Vanapalli et al. (1998). The AEV is the interception of the tangent at the point of the maximal water content (i.e., S=1) and the tangent at the inflection point (a_f). The method is illustrated in Figure 12, whereby the dotted line is the function of the slope. The determined AVE from graphical method is 143 kPa. All the different AEV are summarized in Figure 13.

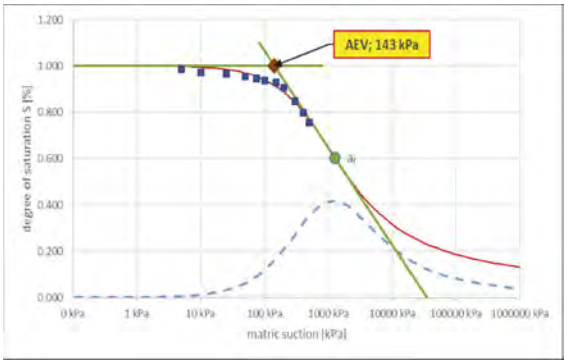

Figure 12. Determination of AEV based on graphical method.

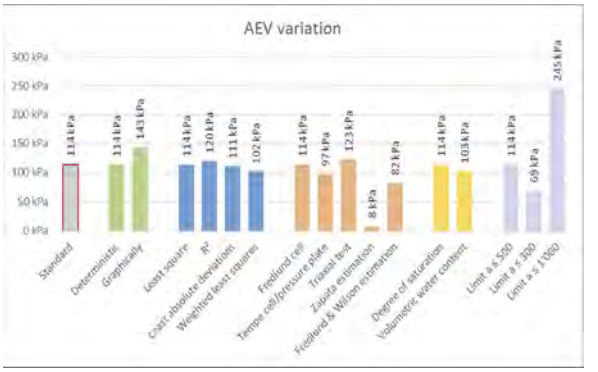

Figure 13. AEV from different method.

5 CONCLUSIONS

The following conclusions can be deduced from this study

- The biggest influence on the AEV seems to have a variation of the limits, whereby as described above, the variation is much higher if the AEV is determined mathematically.
- There is a significant difference between determining the AEV mathematically and graphically.
- The variation due to different fitting methods is the smallest and does not have an influence on the shape of the SWCC.
- With different laboratory methods, the AEV varies. Whereby an applied confining pressure results in a higher AEV.
- The estimation methods in this study underestimated the AEV. The shape of the SWCC estimated by Perera et al. (2005) cannot lead to a reliable estimation of the AEV.
- The AEV determined based on a volumetric water content fitting is smaller than the AEV obtained from a degree of saturation fitting.

ACKNOWLEDGEMENT

This research was supported by the Nazarbayev University Research Fund under Grants 11022021CRP1512 and Social Policy Grant. The authors are grateful for this support. Any opinions, findings, and conclusions or recommendations expressed in this material are those of the author(s) and do not necessarily reflect the views of the Nazarbayev University.

REFERENCES

ASTM D422-63. Standard Test Method for Particle–Size Analysis of Soils; *ASTM International*: West Conshohocken, PA, USA, 2002.

ASTM D4318-00. Standard Test Methods for Liquid Limit, Plastic Limit, and Plasticity Index of Soils; *ASTM International*: West Conshohocken, PA, USA, 2000.

ASTM D854-02. Standard Test Methods for Specific Gravity of Soil Solids by Water Pycnometer; *ASTM International*: West Conshohocken, PA, USA, 2002.

ASTM D698-12E1. Standard Test Methods for Laboratory Compaction Characteristics of Soil Using Standard Effort (12 400 ft-lbf/ft3 (600 kN-m/m3)); *ASTM International*: West Conshohocken, PA, USA, 2012.

ASTM D2487-00. Standard Practice for Classification of Soils for Engineering Purposes, Unified Soil Classification System; *ASTM International*: West Conshohocken, PA, USA, 2000.

Fredlund, D. G., & Xing, A. (1994). Equations for the soil-water characteristic curve. *Canadian Geotechnical Journal*, Vol. 31(3), 521–532.

Fredlund, D. G., Rahardjo, H., & Fredlund, M. D. (2012). *Unsaturated Soil Mechanics in Engineering Practice*. Hoboken, New Jersey: Wiley.

Fredlund, M. D., Wilson, G. W., & Fredlund, D. G. (2002). Use of the grain-size distribution for estimation of the soil-water characteristic curve. *Canadian Geotechnical Journal*, 39(5), 1103–1117.

Leong, E. C., & Rahardjo, H. (1997). A review on soil-water characteristic curve equtions. *Journal of Geotechnical and Geoenvironmental Engineering*, ASCE, 123(12), 1106–1117.

Perera, Y. Y., Zapata, C. E., Houston, W. N., & Houston, S. L. (2005). Prediction of the Soil-Water Characteristic Curve Based on Grain-Size-Distribution and Index Properties. Paper presented at the Geo-Frontiers Congress.

Rahardjo, H., Satyanaga, A., Mohamed, H., Ip., C.Y., Rishi, S.S. (2019). "Comparison of Soil-Water Characteristic Curves from Conventional Testing and Combination of Small-Scale Centrifuge and Dew Point Methods". *Journal of Geotechnical and Geological Engineering*, April, Vol. 37, No. 2, pp. 659–672. https://doi.org/10.1007/s10706-018-0636-2.

Rahardjo, H., Satyanaga, A. & Leong, E.C. (2016). "Effects of rainfall characteristics on the stability of tropical residual soil slope." Proceedings of E-UNSAT 2016, E3S Web of conferences 9, Sep 2016, 15004, 1–6, DOI:10.1051/e3sconf/20160915004.

Satyanaga, A. and Rahardjo, H. (2020). "Role of Unsaturated Soil Properties in The Development of Slope Susceptibility Map", *Geotechnical Engineering* (Accepted in Jul 2020) https://doi.org/10.1680/jgeen.20.00085; ISSN 1353-2618; E-ISSN 1751-8563.

Satyanaga, A. and Rahardjo, H. (2019). "Unsaturated Shear Strength of Soil with Bimodal Soil-water Characteristic Curve". Geotechnique. September 2019. Vol. 69, No. 9, pp. 828–832. https://doi.org/10.1680/jgeot.17.P.108.

Satyanaga, A., Wijaya, M., Zhai, Q., Moon, S.-W., Pu, J., Kim, J.R. (2021a) "Stability and Consolidation of Sediment Tailings Incorporating Unsaturated Soil Mechanics." Fluids, 6, 423.

Satyanaga, A., Moon, S.-W., Kim, J.R. (2021b) "Stability Analyses of Dual Porosity Soil Slope." Geomechanics and Engineering. Accepted in 23 Dec 2021.

Satyanaga, A., Rahardjo, H., Koh, Z.H. and Mohamed, H. (2019) "Measurement of a Soil-water Characteristic Curve and Unsaturated Permeability using the Evaporation Method and the Chilled-Mirror Method". *Journal of Zhejiang University-SCIENCE A*. May 2019, Vol 20, No 5, pp. 368–375. https://doi.org/10.1631/jzus.A1800593.

Satyanaga, A., Zhai, Q., Rahardjo, H. (2017) "Estimation of Unimodal Water Characteristic Curve for Gap-graded Soil" *Soils and Foundations*, October, Vol. 57, No. 5, pp. 789–801. DOI: 10.1016/j.sandf.2017.08.009

Sillers, W. S., & Fredlund, D. G. (2001). Statistical assessment of soil-water characteristic curve models for geotechnical engineering. *Canadian Geotechnical Journal*, 38(6), 1297–1313.

Terzaghi, K. (1936). The shear strength of saturated soils. Paper presented at the First International Conference on Soil Mechanics and Foundation Engineering.

Zapata, C. E. (1999). *Uncertainty in soil soil-water characteristic curve and impacts on unsaturated shear strenght predictions*. (PhD), Arizona State University, Tempe AZ.

Zhai, Q., Rahardjo, H., Satyanaga, A. and Dai, G. (2020) "Estimation of tensile strength of sandy soil from soil-water characteristic curve" *Acta Geotechnica*. Vol 15, pp. 3371–3381 (Published online on 30 Jun 2020) https://doi.org/10.1007/s11440-020-01013-8.

Smart Geotechnics for Smart Societies – Zhussupbekov, Sarsembayeva & Kaliakin (Eds)
© 2023 The Author(s), ISBN 978-1-003-29912-7
Open Access: www.taylorfrancis.com, CC BY-NC-ND 4.0 license

Filling missing soil data using machine learning

S.C. Chian
National University of Singapore, Singapore

J. Bi
SEA Ltd, (formerly National University of Singapore), Singapore

H.D. Halai
University of Southampton, (formerly National University of Singapore), UK

N.G.L.H. Lee
University of Cambridge, (formerly National University of Singapore), UK

C.F. Leung
National University of Singapore, Singapore

ABSTRACT: Missing soil parameters are common in soil investigation and published literature due to the fact that undisturbed soil samples used in a laboratory test cannot be used for another testing as the soil has been disturbed and no longer representative of the actual field condition. The issue of missing soil parameter is further exacerbated in the event of high heterogeneity of the ground, where soil parameters obtained from a specific depth in the ground may not be reflective of another depth in the same borehole. Therefore, soil parameters without direct measurements have to be inferred from other available soil parameters. This is the part where machine learning becomes useful. However, many machine learning models do not handle missing data automatically. This paper presents the attempt to modify existing machine learning algorithms to achieve the ability of filling missing values in soil datasets.

1 INTRODUCTION

1.1 *Nature of geotechnical engineering*

In the modern geotechnical engineering, sophisticated numerical software and wide range of insitu and lab testing are available to model the behavior of soil. However, in practice, soil parameters needed for numerical modelling are often inadequate for design. Comprehensive site investigation to complete these missing parameters may also be constrained due to time and cost limitations. Sometimes, despite carrying out what was deemed sufficient site investigations, design engineers may occasionally encounter cases where adjacent boreholes may provide ground conditions that are not consistent. This highlights the essence of the key challenge in geotechnical engineering: Inadequate, incomplete and sometimes conflicting information.

Inadequate information may be a result of too few boreholes with wide spacing at an unexpectedly heterogeneous site. Too few lab tests provisioned for each borehole may also surface such issues of inadequate information. Incomplete information can arise from the limited undisturbed samples at each depth interval. Design engineers would have to decide whether to conduct a triaxial, oedometer, vane shear or shearbox test. Different tests can produce slightly different results for the same parameter. In making matters worse, large variation in soil proile and properties between adjacent boreholes can lead to conflicting information when

DOI: 10.1201/9781003299127-38

determining the ground profile and properties. All these issues with information can have significant repercussion to numerical modeling of geotechnical problems.

1.2 *Overcoming limited soil information*

In order to overcome cases of limited soil data, design engineers resort to making certain assumptions and interpolation of missing soil parameters based on the typical values for similar soil. For design engineers with rich depository of records from past projects and literature, an alternative is to acquire complementary information from trends and relationships of these local and global soil databases. This is known as machine learning, or in broader terms, data driven methods.

In data driven approach, decisions are made based on data, rather than intuition. Machine learning is an attempt to make machines learn from experience. In the recent years, such use of data-driven methodologies in research and field trials have been adopted, especially to characterise soil properties in site investigation (Ching and Phoon, 2014; Christensen et al., 2021; Javadi and Rezania, 2009; Wang and Liang, 2020; Xiao et al. 2021; Shen et al., 2023; Lo et al. 2023).

In this paper, the focus would be on the use of data driven machine learning, where learning is based on data, to fill missing soil data in site investigation.

2 MISSING VALUE IMPUTATION

2.1 *Database*

Data from a total of 77 compressibility related publications were compiled to form the database. The 12 parameters collated were: compression and recompression indices C_c and C_r, initial void ratio e_0, initial moisture content w_0, specific gravity G_s, plastic limit PL, liquid limit LL, plasticity index PI, percentage of sand, silt, clay as well as fines (silt + clay) content.

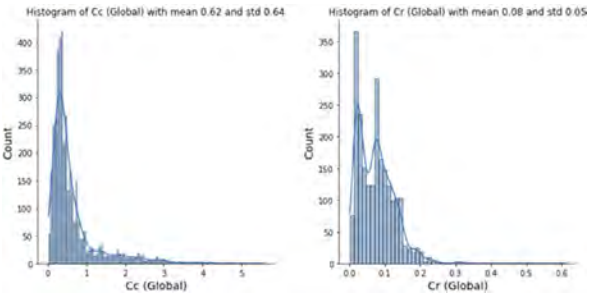

Figure 1. Histograms of input parameters.

Figures 1 and 2 show the histograms of the compressibility indices and input parameters collated, respectively. These publications were selected having provided sufficient information with respect to both oedometer test results as well as sample properties and conditions. These scope of these papers therefore largely included the evaluation and investigation of empirical correlations between compression indices and soil properties, detailed oedometer analyses of soils with varying compositions or structural conditions, and reviews of the classifications and engineering properties of a particular soil. For conciseness, the full list of these publications would not be listed in the references. They are available upon request from the authors.

Table 1 presents the missing percentages of missing data for each input parameter in the C_c and C_r training set. Missing values have to be filled by imputation in order for machine learning to be carried out in order for input parameters to be complete for proper design in numerical modeling. In machine learning, parameters are often referred to as features.

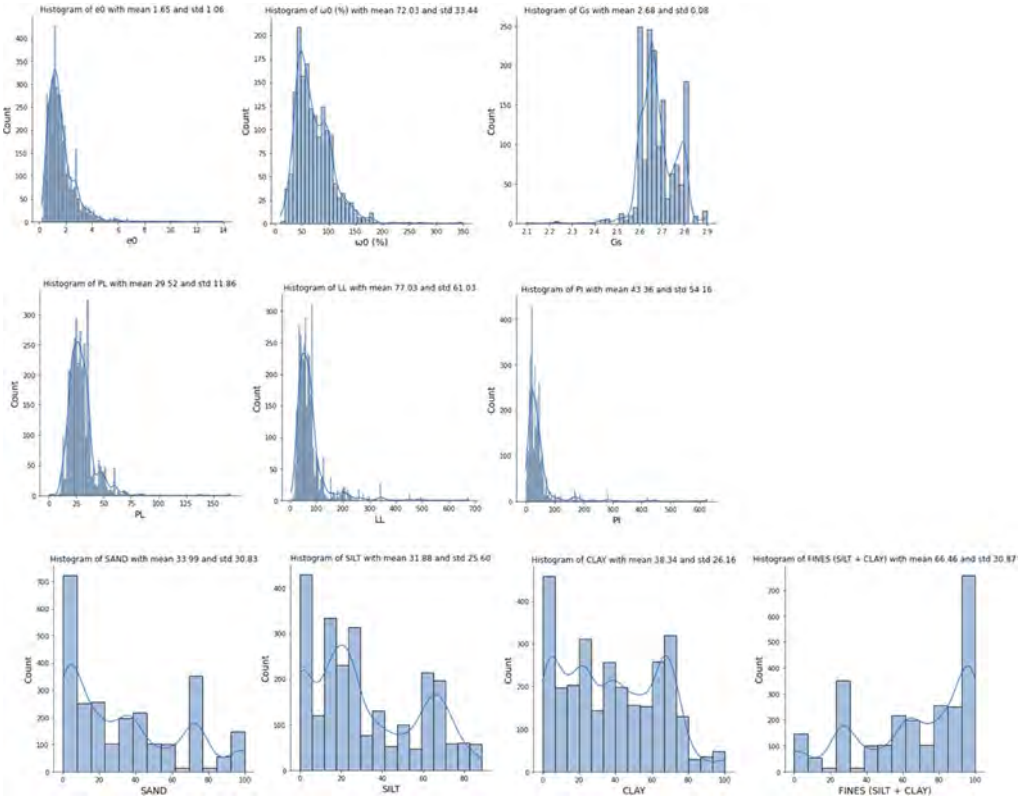

Figure 2. Histograms of compressibility indices.

Table 1. Percentage of missing data (by feature) in training set.

Features	% of missing data	
	C_c	C_r
e_0	10.0	2.6
w_0	30.1	13.0
G_s	80.3	18.7
PL	30.5	11.6
LL	24.7	11.6
PI	30.5	11.6
Sand	68.7	0.9
Silt	71.0	8.3
Clay	55.2	8.3
Fines	68.4	0.7

2.2 *Machine learning model*

Our machine learning analysis adopts the XGBoost model as it is capable of handling missing values relatively better than the other models due to a built-in algorithm. Conventional machine learning approaches may simply neglect the row of data with missing inputs, resulting in a small dataset to work with. In XGBoost, Chen and Guestrin (2016) described the sparsity-aware split finding in the approach. When searching for the best split, XGBoost first

considers the non-missing values. Then, the missing values would be classified into one default direction, either left or right. The optimum default direction is determined by the one that gives the maximum gain in the similarity score after classifying the missing values into that direction.

XGBoost (eXtreme Gradient Boosting) is a tree boosting method originated from "Gradient Boosting" introduced by Friedman (2001). XGBoost predicts the results using K additive regression trees. The decision function can be written in following form:

$$\hat{y}_i = \sum_{k=1}^{K} f_k(x_i),\ f_k \in \mathcal{F}$$

where f is a regression tree in the functional space $\mathcal{F}$.

The objective function of XGBoost consists of 2 terms: loss term (l) and model complexity term (Ω):

$$L(\phi) = \sum_i l(\hat{y}_i, y_i) + \sum_k \Omega(f_k)$$

where $\Omega(f_k) = \gamma T + \frac{1}{2}\lambda \|w\|^2$. T is the number of leaves, w is the vector of scores on leaves, γ and λ regularization hyper-parameters. The objective function is minimized in an additive manner.

Figure 3 shows an example of predicting whether someone likes a hypothetical computer game using XGBoost regressor.

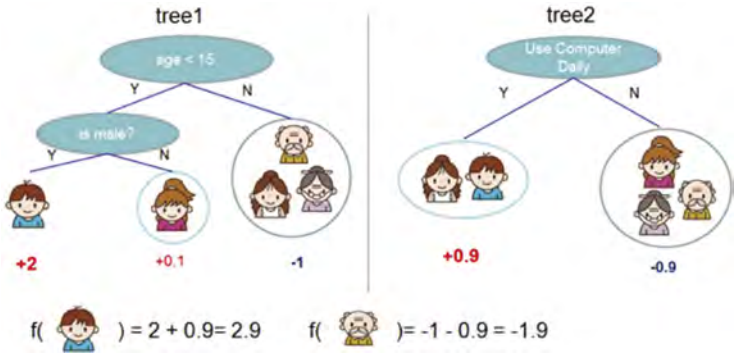

Figure 3. Example of XGBoost regressor (Chen & Guestrin, 2016).

2.3 *Imputation methods*

According to Rubin (1976) and Little & Rubin (1987), missing data can be classified into 3 mechanisms: missing completely at random (MCAR), missing at random (MAR), and missing not at random (MNAR). For MCAR, the probability of data missing is independent of any data. An example is a data logger missing a data point due to random connection problem. For MAR, the probability of data missing is independent of that feature, but is dependent on other features. For example, a data logger produces more missing value on a soft ground. For MNAR, the probability of data missing is dependent on the value of the missing data. An example is a data logger that always fails to record large numbers. In this study, the missing data issue is akin to the MAR assumption. Three imputation methods were considered: 1) mean and median, 2) KNN, and 3) iterative imputation.

Mean and median use the mean or median value of a certain feature to fill in any missing value in that feature. They are the simplest and fastest imputation method. However, the distribution of the features and the relations between features are often distorted after imputation.

KNN imputation fill in missing data using the weighted average k-Nearest Neighbors approach (Troyanskaya et al., 2001). Euclidean distance is used to measure the distance between 2 samples. Stekhoven & Buhlmann (2012) proposed a cross-validation KNN method to determine k. The original dataset is first imputed using mean imputation, and is then introduced with artificial missing values. After that, KNN imputation is conducted using a range of k values, the error between the imputed and the complete dataset is obtained for each k. Repeat the above steps for l times, and k is determined by the value that has the lowest average error across the l repetitions.

Iterative imputation is a multivariate imputation method. Each feature with missing values are predicted using the remaining features. Some popular iterative imputation methods include MissForest (Stekhoven & Buhlmann, 2012) and MICE (van Buuren & Oudshoorn, 1999). Since the focus of this study is not to measure the uncertainty caused by missing values, multi-imputation method like MICE is not adopted.

For each method considered, the performance of the unimputed (for XGBoost) and imputed datasets (via the various imputation methods) were assessed in terms of cross validated mean squared error (CVMSE). The option giving the lowest CVMSE was then adopted as the optimal dataset for that model, and would be selected to undergo further evaluation through the feature selection process. An example of this assessment is shown in Figure 4, where the original dataset still resulted in the best performance for C_c prediction on a untuned XGBoost model against the various imputed datasets. OriginalData refers to the original dataset with missing data. Bayesian_sample_asc refers to iterative imputation using Bayesian Ridge Regression; the order of imputation is from features with fewest missing values to most. Bayesian_desc refers to iterative imputation using Bayesian Ridge Regression; the order of imputation is from features with most missing values to fewest. et_asc adopts iterative imputation using extra tree; the order of imputation is from features with fewests missing values to most. mf_asc adopts Miss-Forest imputation; the order of imputation is from features with fewest missing values to most. knn refers to K-Nearest Neighbors imputation. cvknn is the cross-validated KNN. Median is filling the missing data with the median value, while mean is fills the missing data with the mean value.

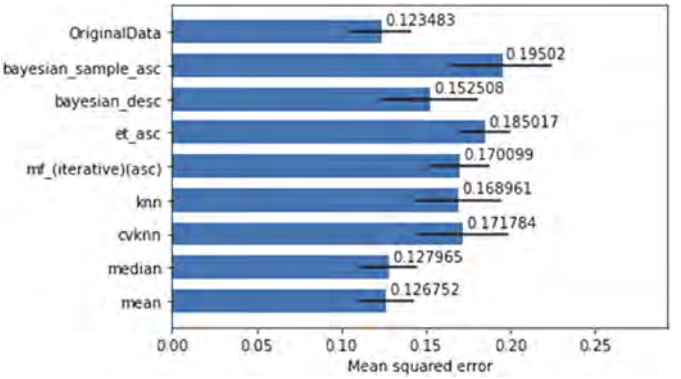

Figure 4. Comparison of unimputed (for XGBoost) and imputed (via various imputation methods) datasets.

According to findings from Figure 4, the imputation methods performed appear to provide no significant improvement on the performance of the model. Some imputation methods have shown to cause an increase in the means squared error instead. This suggests that the XGBoost model can already handle the missing values reasonably well and suitable for use in this database with the soil parameters mentioned earlier.

3 CONCLUSION

Missing soil parameters is a common issue in practice, which can hamper good quality numerical modeling of geotechnical problems. Data driven machine learning techniques can enable statistically robust and efficient filling of missing soil parameters. XGBoost was adopted in this study which showed its ability to fill these missing soil parameters with low mean squared errors comparable or better than existing imputation methods. Therefore, design engineers new to imputation approaches may consider attempting techniques similar to XGBoost as a start to overcoming issues with missing soil parameters in their modeling.

ACKNOWLEDGEMENT

The authors are grateful to the Singapore Maritime Institute (SMI) and Maritime and Port Authority of Singapore (MPA) for their financial support to this study via the research project ID and title, SMI-2018-MA-01 Evaluation of In-situ Consolidation of Dredged and Excavated materials at Reclaimed Next Generation Tuas Port.

REFERENCES

Chen, T., & Guestrin, C. 2016. XGBoost: a scalable tree boosting system. *Proceedings of the 22nd ACM SIGKDD International Conference on Knowledge Discovery and Data Mining*, 785–794. New York, NY, USA: ACM.

Ching, J. & Phoon, K. K. 2014. Transformations and Correlations among Some Clay Parameters – the Global Database, *Canadian Geotechnical Journal* 51 (6), 663–685.

Christensen, C. W., Harrison, E. J., Pfaffhuber, A. A. & Lund, A. K. 2021. A Machine Learning–Based Approach to Regional-Scale Mapping of Sensitive Glaciomarine Clay Combining Airborne Electromagnetics and Geotechnical Data, *Near Surface Geophysics* 19 (5), 523–539.

Friedman, J.H. 2001. Greedy function approximation: a gradient boosting machine. *The Annals of Statistics* 29(5): 1189–1232.

Javadi, A. & Rezaniam, M. 2009. Applications of Artificial Intelligence and Data Mining Techniques in Soil Modeling, *Geomechanics and Engineering* 1(1), 53–74.

Little, R. J. A. & Rubin, D. B. 1987. *Statistical analysis with missing data*. New York: John Wiley & Sons.

Lo, M. K., Loh, D. R. D., Chian, S. C. & Ku, T. 2023. Probabilistic Prediction of Consolidation Settlement and Pore Water Pressure Using Variational Autoencoder Neural Network, *Journal of Geotechnical and Geoenvironmental Engineering* 149 (1), 04022119.

Rubin, D. B. (1976). Inference and missing data. *Biometrika*, 63(3), 581–592.

Shen, Z., Tian, Y., Chian, S. C. & Tan, Z. 2023. Improving the estimation of soil spatial variability by considering transformation uncertainty based on LDRFE analysis, *Computers and Geotechnics* 156, 105299.

Stekhoven, D. J. & Bühlmann, P. 2012. MissForest—non-parametric missing value imputation for mixed-type data, *Bioinformatics*, 28(1), 112–118.

Troyanskaya, O. G., Cantor, M., Sherlock, G., & Brown, P. O. 2001. Missing value estimation methods for DNA microarrays. *Bioinformatics*, 17(6), 520–525.

van Buuren, S. & Oudshoorn, K. 1999. *Flexible multivariate imputation by MICE* (Report No. PG/VGZ/99.054). TNO Prevention and Health. Available at: <https://stefvanbuuren.name/publications/Flexible%20multivariate%20-%20TNO99054%201999.pdf>

Wang, H., Wang, X. & Liang, R. 2020. *Study of AI Based Methods for Characterization of Geotechnical Site Investigation Data*, FHWA/OH-2020-3. Ohio Department of Transportation.

Xiao, T., Zou, H. F., Yin, K. S., Du, Y. & Zhang, L. M. 2021. Machine Learning-Enhanced Soil Classification by Integrating Borehole and CPTU Data with Noise Filtering, *Bulletin of Engineering Geology and the Environment* 80(12), 9157–9171.

Smart Geotechnics for Smart Societies – Zhussupbekov, Sarsembayeva & Kaliakin (Eds)
© 2023 The Author(s), ISBN 978-1-003-29912-7
Open Access: www.taylorfrancis.com, CC BY-NC-ND 4.0 license

Clay soil deformations under regime long-term triaxial compression taking into account initial defects

I.T. Mirsayapov & N.N. Aysin
KSUAE, Kazan, Russia

ABSTRACT: The arrangement of deep pits leads to a change in the stress-strain state of the soil mass within the radius of the zone of influence. When entering the zone of existing buildings, there is a need for an assessment and geotechnical forecast of the behavior of the soils under foundations of existing buildings and structures. At the same time, it is necessary to take into account existing and new defects and cracks in soils. For determine the main dependences of clay samples deformation characteristics with existing defects experimental studies with triaxial compression of samples with cracks and without cracks were carry out. Based on the results of the study, new data were obtained on the effect of defects in soil samples on the deformation of clay soil. Based on the research results, the dependences of the main deformation characteristics of clay soil are constructed.

1 INTRODUCTION

Constructing a deep pit located in a built-up area makes necessary to perform a geotechnical forecast (assessment) of the impact of construction on the change in the stress-strain state of the surrounding soil mass, including the foundations of the surrounding buildings. The geotechnical forecast of the impact should take into account the technological settlement of the foundations of the surrounding buildings from the "wall in the soil" device. At the same time, it is necessary to take into account the horizontal movements of the enclosing structure of the pit and the unloading of the subgrade from the excavation in the pit, loads from the newly erected structure or additional loads from the reconstructed structure and other factors, taking into account the sequence of the underground part of the structure, using analytical and numerical calculation methods. Depending on the category of technical condition of existing buildings, the permissible additional settlement of buildings is 20-50 mm. At the same time, the unevenness of the settlements is no less, sometimes even more dangerous. Pronozin et al (2019, 2020) considered the amount of additional stresses in the structure of the building with uneven settlement.

The process of destruction and development of nonlinear deformations of clay soil under triaxial compression is accompanied by the formation and development of micro- and macrocracks in the planes of ultimate equilibrium. Micro- and macro-cracks in the soil structure affect the deformation and strength of the soil under prolonged loading. Melnikov et al. (2021) studied the change in the physical and mechanical characteristics of the soil under the building when the structure of soil changes.

Emil Soból et al. (2020) studied 15 different Warsaw clays. The collected data allowed the authors to create empirical models describing the characteristics of rigidity with high reliability. Combined empirical models allow us to estimate the value of the shear modulus of a connected soil in a wide range of shear deformations with high accuracy. As a result of the study, it was found that the maximum shear modulus increases with the average effective pressure. The plasticity number had a negligible effect on the G_{MAX} value, and depends on the effective stress p' and the void ratio e. Shear deformation had the greatest impact on the shear

DOI: 10.1201/9781003299127-39

modulus and normalized shear modulus degradation curves. With an increase in both plasticity and effective stress, the nonlinear threshold strain shifted to a higher shear strain. However, the average effective stress (p') had a noticeably smaller effect on the elastic range of shear deformation than the plasticity index (P_I).

Clay soils have pronounced rheological properties, which vary depending on the degree of damage to the structure with initial defects and damages. A relatively small number of works study the influence of defects in the form of micro- and macro-cracks on the rheological properties of soils. The issues of changing the strength and deformability of clay soils with initial defects and damages under prolonged regime static loading have not been practically studied (Xianzhang 2017, Kutergin 2015, Hussein 2020, Mirsayapov 2020, Mirsayapov & Koroleva 2019).

When designing and building, it is necessary to avoid uneven settlement. In the article by Heng Zhang et al. (2021), an analytical solution based on the Laplace integral transformation method has been developed for predicting long-term uneven settlement of buildings on soft soil foundations. The methodology is based on Laplace integral transformation and the theory of viscoelasticity. It combines an analytical solution with a finite element method for a solution taking into account the sequence of construction and loading. The accuracy of the analytical solution based on the integral Laplace transform is confirmed by the monitoring results.

In clay soils under triaxial compression, stresses and deformations vary depending on the stress level, the ratio of vertical and horizontal stresses, the duration of the load, the trajectory and the size of the initial structural defects (Wang Y. 2017, Hicher P. Y. 2016, Hu C. & Liu H. 2015, Wang Y. 2017, Mirsayapov, I.T. & Koroleva, I.V. 2019). Therefore, the stress to strain ratio is not constant, and changes, even if one of these quantities does not change over time and the other (stress or strain) changes. In connection with the above, there is a need to establish patterns of changes in the strength and deformability of clayey soils, taking into account changes in long-term loading modes and the influence of existing defects and damages

2 MATERIALS AND METHODS

Complex modeling of the stress-strain state and numerical studies have made it possible to establish that the construction of a deep pit with a depth of 13.0 m with vertical walls without proper fastening in the immediate vicinity of the building led to simultaneous vertical and horizontal movement of the soils of the foundations of the building. There were a lot of shear lines of the soil mass under the foundations (Figure 1), indicating the achievement of the first limit state of the foundations and the formation of cracks in the soil mass.

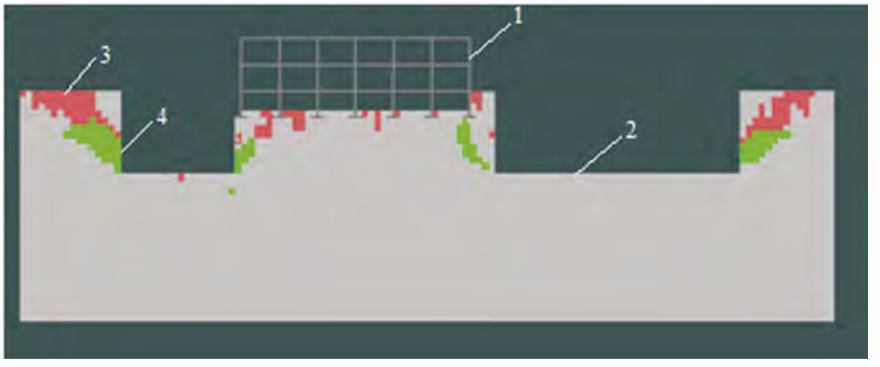

Figure 1. The general condition of the soil after digging the pit to a depth of 13 m: 1 – existing building, 2 – deep pit, 3 – the zone of soil failure, 4 – the zone of soil starching.

To assess the further behavior of the soil, it is necessary to establish the physical, mechanical and deformation characteristics of the soil, taking into account the cracks and defects that

have appeared. For this purpose, this stress-strain state of the soil was recreated in laboratory conditions. The tests were carried out on a true triaxial compression device with rigid walls. The device was developed at the department (Mirsayapov et al 2012, 2015). The soil sample loaded using mechanical levers, which ensures constant pressure when the sample is deformed. The tests were carried out at the same lateral pressure. Vertical σ_1 stresses were applied to the sample with a given step.

Artificially prepared samples of clay soil were used for testing, having the shape of a cube with dimensions of 10 x 10 x 10 cm, with the specified characteristics: density p = 1.91 g/cm^3; humidity W = 0.2. To determine the effect of the formation and development of defects on the strength and deformation of clay soil, artificial cracks of two types were created (Figure 2) with the line with the diameter 0.8 mm: 1 – one crack in the assumed ultimate equilibrium surface of the soil; 2 – in the form of two intersecting cracks in two surfaces of ultimate equilibrium.

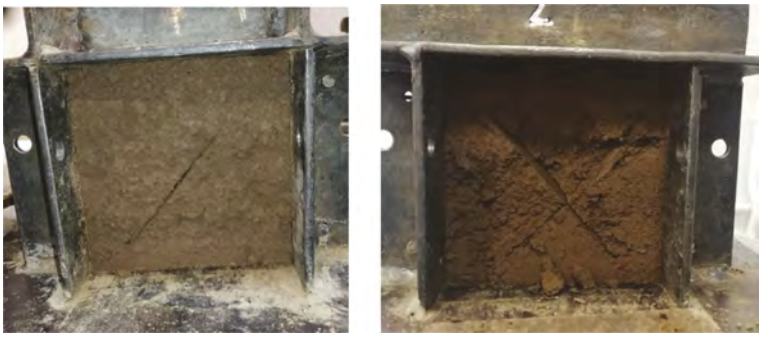

Figure 2. Samples with cracks in the equilibrium planes: a) with one crack; b) with two intersecting cracks in two equilibrium planes.

The design of the equipment includes five loading dies, which are displaced in pairs relative to each other. It is assumed that during loading, only the main stresses are applied to the edges of the soil sample, and the shear stresses are equal to zero. Movements, coaxial with the applied loads, were measured by indicators. The values of deformations were determined by calculation. At the initial stage, the soil sample was subjected to comprehensive compression $\sigma_1 = \sigma_2 = \sigma_3$ = 160 kPa. After stabilization of axial deformations at constant values of lateral stresses $\sigma_2 = \sigma_3$ = 160 kPa, a vertical load was applied to the sample. Each loading stage was sustained, then the next load level was applied until the ultimate deformation was reached.

3 RESULTS

Within each block of regime long-term static loading, there was an increase in linear vertical deformations, shear deformations, as well as a change in the intensity of shear deformations, the modulus of vertical deformations and the shear modulus, indirectly characterizing the change in the strength and deformation characteristics of soils during loading.

At the stage of comprehensive compression lateral deformations grow more intensively than vertical ones. The maximum value of lateral deformations is reached at the moment when vertical deformations make up 25-30% of the maximum deformations during fracture. A noticeable increase in vertical linear deformations begins at $\sigma_z > 0.3\ \sigma_{ult}$. In the blocks of regime long-term loading, there was an increase in vertical deformations both at the stage of comprehensive and at the stage of deviatory loading. Analysis of the development schedule of vertical deformations shows that they develop throughout the tests with varying intensity. At this interval of deviatory loading, the maximum vertical deformations were in samples with two cracks, the minimum deformations were in samples without cracks.

Horizontal deformations ε_x and ε_y also developed throughout the long-term deviatory loading with different intensity. The highest value of horizontal deformations is observed in

samples with two cracks, the minimum deformations are observed in samples without cracks. The results of experimental studies show that the biggest values of the intensity of shear deformations were in samples with one crack and the minimum values of the intensity of shear deformations in samples without cracks.

At the stage of deviatory loading, the linear modulus of *AER* vertical deformations, the shear modulus and the volumetric modulus of deformations decreased on all blocks of regime loading. The most intensive decrease in the modulus of vertical deformations occurred in samples without cracks. In the samples with one and two cracks, the decrease in the modulus of vertical deformations occurred more smoothly than in the samples without cracks. The same situation can be seen with the volumetric modulus of deformations. Due to the fact that the initial cracks led to a more intensive growth of all components of deformations, the decrease in the volume modulus of deformations was smooth with an increase in the stress deviator.

Numerical modeling, taking into account the results of laboratory studies, showed that the construction of a three-storey underground parking in a deep pit led to a further deterioration of the geotechnical situation:

- vertical and horizontal movements of soils in the foundations increased to 42.5 mm and 23.7 mm;
- the zone of the first limiting state of the soil under the foundations has spread in the axes A-D, 9-15;
- the forces in the elements of the frame increased up to 60%.

4 DISCUSSIONS

The construction of a deep pit with a depth of 13 m with vertical walls without proper fastening in the immediate vicinity of the building caused horizontal movement of the subgrade. There were signs of deformations of the reinforced concrete frame of the building between the axes A-B due to additional settlement of the foundations of the columns of the frame of the building due to the horizontal movement of the walls of the deep pit, which led to simultaneous vertical and horizontal movement of soils outside the deep pit, i.e. the soil under the foundations of the building. A cracks appeared in the concrete floor of the basement floor along the wall along the A axis with an opening width of up to 6 mm at a distance of 1 m from the inner surface of the wall along the A axis, while the vertical movement of the floor in the wall area was about 20 mm. There were also cracks with an opening of up to 1 mm in the interplate seams of the basement floor and vertical cracks with an opening of up to 0.5 mm in the support zone of the basement floor crossbar (between axes A-B). In the future, these defects were further developed and other defects appeared, which indicates the continuation of the development of deformations of the soil under the foundations of the building. The technical condition of the foundations and the building at the moment is difficult to predict and requires research taking into account the development of additional deformations of soils in the pit and beyond.

5 CONCLUSIONS

The performed experimental studies of clay samples in a cubic stabilometer under conditions of long-term regime static loading and numerical calculation of building deformations allowed us to establish the following basic patterns of behaviour of clay soils under load:

1. The rate of crack development depends on the rate of change of the vertical stress deviator and the change in the lateral pressure.
2. The initial defects of clay soil samples in the form of one or two cracks located in the ultimate equilibrium surfaces led to an increase in vertical, horizontal deformations and the intensity of shear deformations, regardless of the loading regime, compared with samples without initial defects.

3. The numerical studies performed on the basis of the calculation model showed that the construction of a deep pit with a depth of 13 m led to simultaneous vertical and horizontal movement of the soils of the foundations of the building. There were a lot of shifting lines of the soil mass under the foundations. The results of geotechnical monitoring for 4 months confirmed the results of numerical studies.

REFERENCES

Hicher P. Y. 2016. Experimental study of viscoplastic mechanisms in clay under complex loading. *Geotechnique* 66: 661–669.

Hussein, H. K. et al. 2020. Behaviour of soft clayey soil improved by fly ash and geogrid under cyclic loading. *Civil engineering journal* 6: 225–237. DOI: 10.28991/cej-2020-03091466.

Hu C. & Liu H. 2015. A new bounding-surface plasticity model for cyclic behaviors of saturated clay. Commun. *Nonlinear Sci. Numer. Simul*. 22: 101–119. DOI.10.1016/j.cnsns.2014.10.023.

Kutergin, V.N. et al. 2015. Assessment of soil strength changes under cyclic loads simulating the impact of storm waves on the structure. *Geoecology. Engineering geology, hydrogeology, geocryology* 5: 450–459.

Melnikov, R et al. 2021. Soil areas numerical determination aimed at correction of a building tilt. *J. Phys. Conf. Ser*. 1928: 012009.

Mirsayapov, I. T. et al. 2012. Low cycle endurance and deformation of clay soils under triaxial cyclic loading. *Housing construction* 9:, 6–8. DOI: 18083643/0044-4472. 2012. 9. 6–8.

Mirsayapov, I. T. & Koroleva, I. V. 2015. Bearing capacity of foundations under regime cyclic loading. *15th Asian Reg. Conf. Soil Mech. Geotech. Eng. ARC*: 1214–1217.

Mirsayapov, I.T. & Koroleva, I.V. 2019. Studies of the water migration effect on changes in the clay soil physicomechanical characteristics under triaxial loading conditions. *News KSUAE* 2 (48): 168–174.

Mirsayapov Ilizar T. 2020. Punching settlement of raft-pile foundation under cyclic loading. *News KSUAE* 4 (54): 6–14.

Pronozin, Y. A. et al. 2020. Analytical determination of well parameters while eliminating uneven settlement of foundations by drilling soil. *Construction and geotechnics* 11: 40–48. DOI: 10.15593/2224-9826/2020.2.04.

Pronozin, Y. A. et al. 2019. Structural safety of buildings in excess values of differential settlements. *IOP Conf. Ser.: Mater. Sci. Eng*. 481: 012013. doi:10.1088/1757-899X/481/1/012013.

Sobol, E. et al. 2020. Laboratory Studies of Small Strain Stiffness and Modulus Degradation of Warsaw Mineral Cohesive Soils. *Minerals* 10: 1127. DOI: 10.3390/min10121127.

Wang Y. 2017. Cyclic response of natural soft marine clay under principal stress rotation as induced by wave loads. *Ocean eng*. 129: 191–202. DOI:10.1016/j.oceaneng.2016.11.031.

Xianzhang, L. et al. 2017. Permanent deformation characteristics of coarse grained subgrade soils under train-induced repeated load. *Hindawi advances in materials science and engineering* 15: 15. DOI: 10.1155/6241479. 2017. 15.

Zhang, H. et al. 2021. The Rheological Analytical Solution and Parameter Inversion of Soft Soil Foundation. *Symmetry* 13: 1228. DOI: 10.3390/sym13071228.

Smart Geotechnics for Smart Societies – Zhussupbekov, Sarsembayeva & Kaliakin (Eds)
© 2023 The Author(s), ISBN 978-1-003-29912-7
Open Access: www.taylorfrancis.com, CC BY-NC-ND 4.0 license

DEM modeling mechanical behaviors of remolded and structured clays under constant stress ratio compression tests

M.Y. Niu
Department of Geotechnical Engineering, College of Civil Engineering, Tongji University, Shanghai, China

M.J. Jiang
School of Civil Engineering, Suzhou University of Science and Technology, Suzhou, China
Department of Geotechnical Engineering, College of Civil Engineering, Tongji University, Shanghai, China
Department of Civil Engineering, Tianjin University, Tianjin, China

ABSTRACT: By a novel approach, this paper simulates the mechanical behaviors of clays under constant stress ratio compression tests using three-dimensional Discrete Element Method (DEM), and different cement contents and principal stress ratios (CSR $= \sigma_3/\sigma_1$) are included. The DEM remolded/structured clay sample is generated using spheres of a certain grade, which characterize an assembly of bonded/unbonded clusters of the highest level, and the cluster crushing is further employed to simulate the structural degradation and gradual deformation of clays. The simulation results qualitatively agree with available experimental observations. As the CSR increases, the deviator strain decreases while the structural yield stress increases generally on the macro scale; and the fabric anisotropy of total contact normal and ratios of inter-cluster bond breakage and cluster crushing all decline, and the contact force chains tend to be more uniformly distributed on the micro scale. The structural yield surface enlarges with the increasing cement content.

Keywords: remolded and structured clays, discrete element method, constant stress ratio compression test, structural yield stress, clay cluster crushing

1 INTRODUCTION

Due to the physico-chemical reactions in sedimentary environments, the precipitated amorphous or crystalline cementitious (e.g. free oxides, soluble salts) bridges gradually connect the clay particles, which creates an open-type microstructure with multilevel water-stable clusters (aggregates) in the structured (i.e. natural, artificial cemented) clays [Liu et al. 2012, Nguyen et al. 2017, Jiang et al. 2017], as presented in Figure 1. The interaction between multilevel clusters instead of clay platelets controls the structural strength as well as macro behaviors of clay (Figure 1e). Taken the microstructural properties into account, many researchers explored the mechanical behaviors (e.g. compressibility, fabric anisotropy, rate-dependence, overconsolidation, swelling, etc.) of clays using various micro numerical approaches, including Discrete Element Method (DEM), molecular dynamic simulations and micromechanical method. These published studies facilitate the understandings of inter-particle complex physico-chemical forces [Anandarajah & Chen 1994, 1997] and aggregation process [Boton et al. 2014, Liu et al. 2015] in clays. However, most of them were mainly performed based on the clay platelets of various shapes for remolded state (i.e. rigid/flexible line segments in two-dimensional (2D) simulations [Anandarajah 2000, Khabazian et al. 2018]; and flat cuboid, flat ellipsoid, irregular flat polygon and clumps for them in three-dimensional (3D) simulations [Yao & Anandarajah 2003,

DOI: 10.1201/9781003299127-40

Katti et al. 2009, Ebrahimi et al. 2014, Luo et al. 2021, Jaradat & Abdelaziz 2019]), and cannot consider the cluster characteristics of structured clays, which needs further explorations.

Only a few studies were carried out based on the rigid or flexible clay clusters. Hattab & Chang (2015) proposes a micromechanical modeling technique for clay behaviors by regarding clay as an assembly of rigid spherical clusters, in which the deformability of individual cluster as well as intra/inter-cluster cementations cannot be considered. Suzuki & Matsushima (2015) further utilized a variety of irregular clusters with different shapes, voids and flexibilities to simulate clay sediments with a more realistic microstructure by DEM, in which the deformation (destruction) of individual cluster can be simply quantified by interparticle movements within it, while the cluster number is limited by computational efficiency and the cementation effect remains unknown.

On this basic, this paper breaks out clay platelet-based modeling frame, and proposes a novel DEM approach by considering cementation mechanism and multilevel clusters characteristics of structured clay. A 3D micro contact model accounting for various physico-chemical interactions between spherical clusters is adopted. The remolded/structured clay sample is regarded as an assembly of unbounded/bonded clusters of highest level following certain grade, and the cluster crushing is employed to simulate the gradual structural destruction and deformation in clays. The proposed numerical approach was utilized to investigate the macro/micro-mechanical behaviors of remolded and structured clays of three cement contents under constant stress ratio compression tests, which can coincide with relevant laboratory results qualitatively.

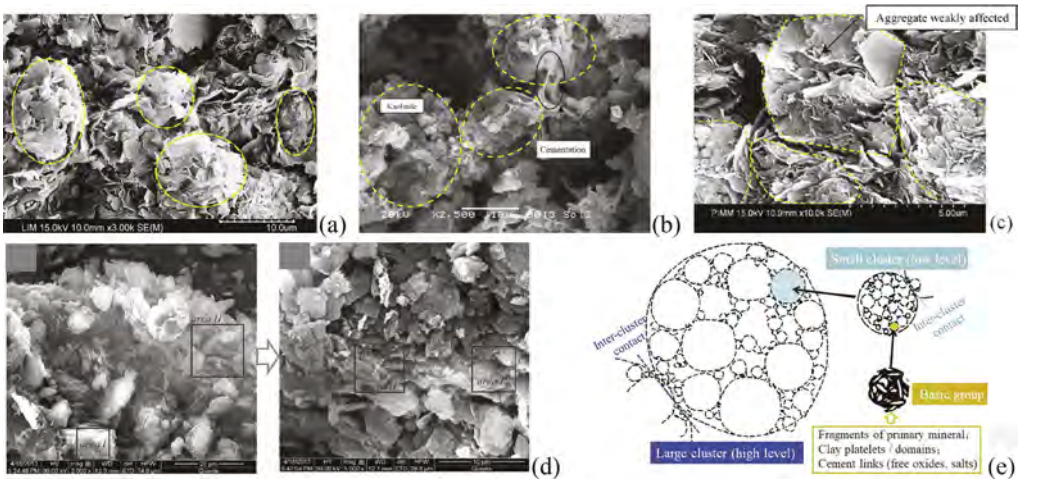

Figure 1. The cluster feature observed by scanning electron micrographs (SEM) of clays and its schematic: (a) mix-clayey material composed of 35% kaolinite and 65% montmorillonite [Hattab & Chang 2015]; (b) (c) natural marine clay in Guinea [Liu et al. 2012]; (d) natural Zhanjiang clay and Zhanjiang clay with free iron oxides removed [Zhang et al. 2016]; (e) schematic of natural clay structure based on multi-level clusters (modified from [Tan & Kong 2001]).

2 DEM SIMULATION PROGRAM

2.1 *Contact model for clay and cluster crushing execution in DEM*

By using well-graded spheres as a simplification on the clay clusters of highest level, a 3D micro contact model for clay was adopted, and the cluster crushing was implemented. Details will be given in other relevant studies, and here only the crucial information are elaborated.

In this contact model, two cutoff distances (i.e. physico-chemical cut-off distance d_{pc}, and mechanical cut-off distance d_{mc}) [Anandarajah 2000] are taken into account in the inter-cluster contact detection criterion (i.e. gap $\leq d_{pc}$ for contact) and bond formation criterion

(i.e. gap $\leq h_0^b = g_c R_b$ for bond formation). At the inter-cluster contact, the bridged bond force and three micro phyisco-chemical forces (i.e. diffused double-layer repulsive force F_{DDL}, van der Waals attractive force F_{VD}, and Born mechanical repulsive force $F_B = f(E_p, d_{mc}, \text{gap})$) are considered in the normal direction. Based on the Hamaker-de Boer and Gouy-chapman theories, the physico-chemical forces $F_{VD} = A \cdot f(\beta, R, d_{mc}, \text{gap})$ and $F_{DDL} = f(\beta, \kappa, \psi_0, R, d_{mc}, \text{gap})$ between two coarse spheres are calculated respectively as power and exponential functions by the Derjaguin approximation [Jiang et al. 2013], which meet the classical DLVO colloid stability theory. While in the tangential/rolling/twisting directions, only the Born mechanical and bond forces are calculated. Note that, the rational assignments of two cutoff distances are crucial, which need to consider several factors, i.e. the significant (long/short term) range of each physico-chemical force, relative magnitude of repulsive barrier/attractive valley for normal net force and the DEM computation efficiency. Generally, d_{mc} ranges in 0.5nm ~ 2nm [Yao & Anandarajah 2003, Jaradat & Abdelaziz 2019, Luo et al. 2021], and d_{pc} is 3 ~ 5 times the electrical double-layer thickness $1/\kappa$ [Anandarajah 2000, Bayesteh & Mirghasemi 2013]. On this basis, Figure 2 illustrates the variations of three physico-chemical forces and their net force in the normal direction with proper values of relevant parameters, which coincide with the numerical investigations by Lu et al. (2008), Jaradat & Abdelaziz (2019) and Luo et al. (2021). As presented, F_{VD} and F_{DDL} begin to act when inter-cluster separation gap decreases to d_{pc} from infinity, and for gap less than d_{mc} these two physico-chemical forces are assumed to remain contant and F_B begins to dominate.

Cluster crushing is further executed every certain steps to simulate the gradual deformation of local stable aggregates in the remolded clay and successive bond breakages between multi-level clusters in the structured clay. Based on the investigation of Ciantia et al. (2015), the cluster crushing criterion of structured clay is established by using correction factors (i.e. A_k and B_k) to identify the influences of cluster size and bond strength/size on the cluster crushing strength. The broken cluster is deleted and replaced by two or fourteen (bounded by the median diameter d_{50}) non-overlapping tangent spherical sub-clusters with different smaller sizes. The remaining bonds associated with the broken cluster are all removed automatically by default [De Bono & Mcdowell 2014].

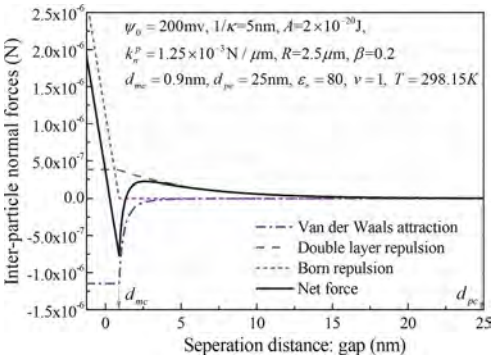

Figure 2. Variations of inter-particle physico-chemical and net forces.

2.2 *Sample preparation and DEM programs*

Based on the SEM observations [Lu et al. 2008] and numerical studies of clay cluster [Hattab & Chang 2015], the adopted DEM assembly is composed of 20870 clay clusters of highest level, with the diameters uniformly ranging from 4.8 um to 16.5 um given d_{50} of 10um, as presented in Figure 3. The clay sample was accomplished by the following step in PFC3D. (1) A homogenous and loose cubic assembly with the target void ratio of 1.50 was generated by the multi-layer under-compaction method [Jiang et al. 2003]. (2) A vertical stress of 12.5kPa was then applied to the top and bottom walls with the side walls stationary to reproduce an in-situ stress state (i.e. 'k_0' state), and the void ratio was 1.25 after precompression. (3) For the structured clay sample, the bonds at inter-cluster contacts were finally assigned when the gap

is smaller than $g_c\lambda_b R$. The cement content (cc) can be geometrically calculated based on inter-particle separation distance (gap), bond radius coefficient λ_b (i.e. ratio of bond radius R_b to the common particle radius R) and critical bond thickness coefficient g_c (i.e. ratio of the critical bond thickness h_0^b to bond radius R_b). In the DEM study four cement contents were considered, including cc = 0% (i.e. remolded clay) and cc = 2.5%, 5% and 10% (i.e. structured clay) by varying the bond radius coefficient λ_b only. The values of contact and crushing parameters are illustrated in Table 1, among them the proper parametric values for physico-chemical forces are essential to obtain the high void ratio.

In the subsequent step-loading stage, six rigid walls were servo-controlled to maintain a constant ratio of the minor and major principal stresses (i.e. CSR $=\sigma_3/\sigma_1$). A series of constant stress ratio compression tests on four clay samples were simulated, including CSR= 0.3, 0.35, 0.4, 0.5, 0.6, 0.7, 0.9 (i.e. anisotropic compression) and 1.0 (i.e. isotropic compression).

Table 1. Micro parameters for the remolded and structured clays.

Particle parameter	Intercluster effective modulus E_p (MPa)	70	Bond parameter	Compressive bond strength σ_c^b (Mpa)	25
	Normal-to-shear stiffness ratio ξ_p	1.5		Tensile-to-compressive strength ratio η_σ	2.5
	Intercluster frictional coefficient μ	0.5		Critical bond thickness coefficient g_c	0.1
	Electrical double-layer thickness $1/\kappa$ (nm)	5		Bond radius coefficient λ_b	0.429/ 0.506/ 0.597
	Surface electric potential ψ_0 (mv)	10	Crushing parameter	Reference cluster diameter d_0 (um)	10
	Hamaker constant A (10^{-20}J)	7.5		Reference cluster crushing strength $\sigma_{d,0}$ (GPa)	1.25
				Cluster size effect index m	0.25
	Contact radius coefficient β	0.1		Correction factor by bond strength/size A_k	2.57e2
	Physico-chemical cutoff distance d_{pc} (nm)	25		Correction factor by cluster size B_k	10
	Mechanical cutoff distance d_{mc} (nm)	0.9		Minimum cluster crushing size $d_{\lim}$ (um)	2.5

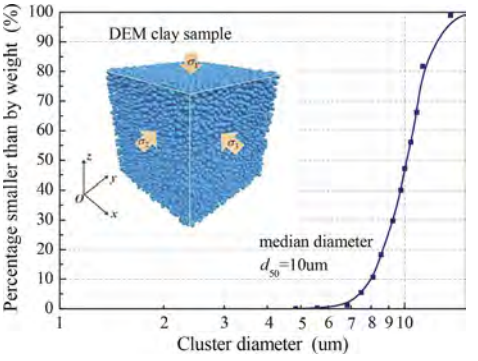

Figure 3. Cluster size distribution of highest level in the DEM clay sample.

3 ANALYSES OF SIMULATION RESULTS

3.1 *Macro mechanical behaviors*

In this section, the macro mechanical behavior of numerical clay samples are first analyzed and compared with experimental data for remolded, natural and artificial cemented clayey soils.

Figures 4a and 4c present the compression curves of remolded and structured clay (cc = 5%) samples under different constant stress ratios respectively, which qualitatively agree with the laboratory results by Shi et al. (2015) and Jiang et al. (2017) (Figures 4b and 4d). Due to the gradual microstructure evolution (e.g. cluster deformation, inter-cluster displacement, variation of water film thickness, etc.), the void ratio of remolded clay exhibits an almost uniform decrease without a distinct consolidation yield point, and its magnitude increases with the increasing CSR when the same effective mean stress p is reached (Figure 4a). In comparison, the apparent structural yield characteristic can be observed in the structured clays, and the yield stress p_y (determined by the bi-linear method, as depicted in Figure 5(a)) increases basically as CSR increases (Figure 4c). For the structured clay, initially only elastic deformation occurs and the beneficial contribution of cementation make the variation of void ratio negligible. While beyond the yield stress, plastic deformation associated with cementation degradation (i.e. structure damage) gradually accumulates, and thus the void spaces of inter/intra-cluster reduce significantly. At the ultimate state, the compression curves under different CSRs tend to be parallel.

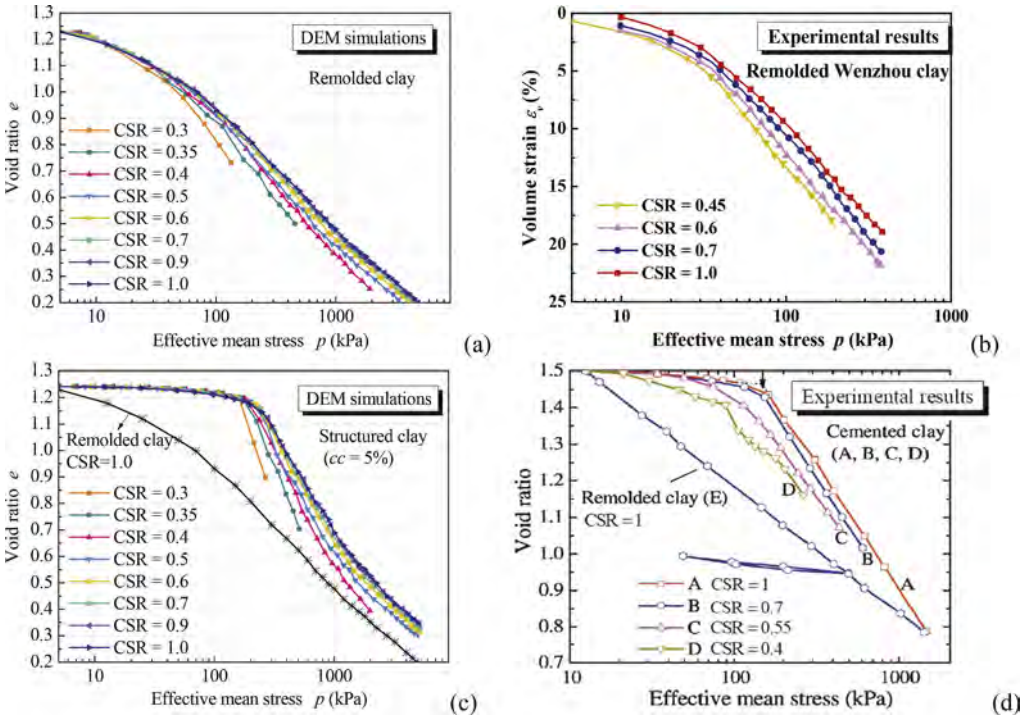

Figure 4. Compression curves under different CSRs: (a) DEM results of the remolded clay; (b) experimental results of the remolded Wenzhou clay [Shi et al. 2015]; (c) DEM results of the structured clay (cc = 5%); (d) experimental results of the artificial cemented clay [Jiang et al. 2017].

To study the cementation effect, Figure 5a provides the isotropic compression (i.e. CSR = 1.0) curves as well as their unloading-reloading curves at p = 500kPa of each clay sample, and Figure 5b further gives the structural yield surface of all structured clays. As shown, increasing the cement content can lead to an increase in the yield stress aas well as an enlargement of structural yield surface. In addition, at a high stress level, the void ratio of structured clay is gradually approaches that of remolded clay, and their ultimate void difference suggests the residual cementation effect (i.e. the incompletely destroyed cementations and the cumulative fabric changes), whose magnitude also tends to increase with the increasing cement content. Moreover, it can be observed from the unloading-reloading curves that (Figure 5a), the higher the cement content is contained (i.e. the stronger the clay structure is), the more the elastic

deformation accumulates during loading, and thus the more distinct the swelling exhibits. These features are basically consistent with the experiment observations of natural clays [Adachi et al. 2008, Delage 2010] and artificial cemented clays [Miura et al. 2001, Kamruzzaman et al. 2009, Nguyen et al. 2017]. Note that, the simulated increasing yield stress cannot be exactly captured as CSR ranges from 0.7 to 1.0 (i.e. the yield surfaces rotate anticlockwise slightly), as described in Figures 4c and 5b,which can be explained by the slight initial anisotropy of 'k_0' generated clay samples.

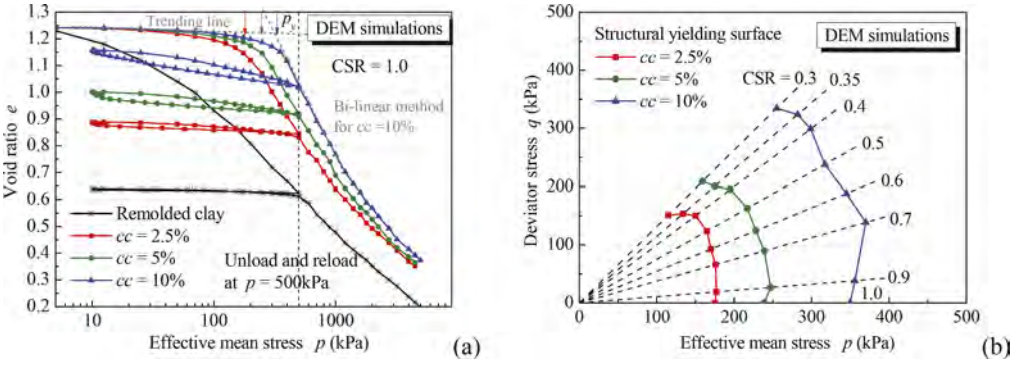

Figure 5. Yielding in the DEM structural clay samples with different cement contents: (a) isotropic compression (CSR = 1.0) curve and its unloading-reloading curve; (b) structural yielding surface.

Figure 6a and 6b present the deviator strain versus log p relationships of remolded and structured clay (cc = 5%) samples respectively under different CSRs. These figures reveal that, the higher the CSR is, the lower the deviator strain incurs (its irregularity at CSR = 0.9 is attributed to the initial anisotropy, as aforementioned) by the remolded and structured (at post-yielding stage) clays at the same effective mean stress. Similar behavior can be found by the experimental researches of cemented Bangkok clay [Bergado et al. 2006], as given in Figure 6c.

3.2 *Microstructure evolutions*

The microscopic information, including the inter-cluster bond breakage, cluster crushing, contact force chain and contact orientation, will be analyzed and linked to the macro features.

Figure 7 illustrates the evolutions of inter-cluster bond breakage and cluster crushing ratios in structured clay samples (cc = 5%) under different CSRs, as a reflection of the microstructure degradation. It can be observed from Figures 4c and 7 that, at each CSR condition, the macro structural yielding corresponds to the stress state in which the significant inter-cluster (at highest level) broken bonds commence (Figure 7a), while the start point of distinct cluster crushing (i.e. bond breakages between sub-level clusters) lags behind it slightly (Figure 7b). Hence, the phenomenon that the higher the clay cluster level is, the easier the inter-cluster bonds break can be simulated by a set of rational parameters (Table 1). These figures also reveal that the broken bond ratio of multilevel clusters decreases with increasing CSR in structured clays.

In addition, to study the cementation effect, Figure 8 provides the evolutions of inter-cluster bond breakage and cluster crushing ratios in three structured clays under isotropic compression test (i.e. CSR = 1.0), as well as their normalization curves by p/p_y. As presented, given a specific p beyond p_y, the ratios of broken bond between highest-level clusters and themselves crushing all decrease with the increasing cement content, while their normalizations in different structured clays all coincide approximately.

To visualize the microstructure, Figure 9 illustrates the cluster distribution and contact force chains for the remolded and structured (cc = 5%) clay samples under CSR = 0.4, 0.6 and 0.9. As observed from Figures 9a and 9c, the deviator strain, the total number of clay cluster and the

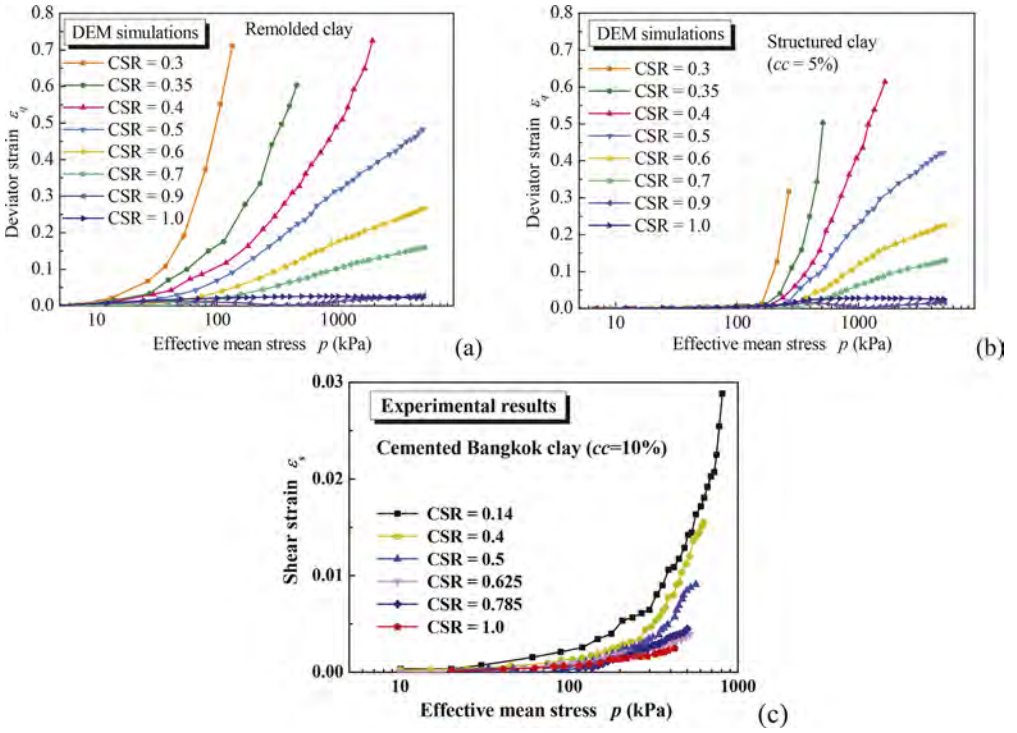

Figure 6. Deviator strain evolution under different CSRs: (a) DEM results of the remolded clay; (b) DEM results of the structured clay (cc = 5%); (c) experimental results of cemented Bangkok clay [Bergado et al. 2006].

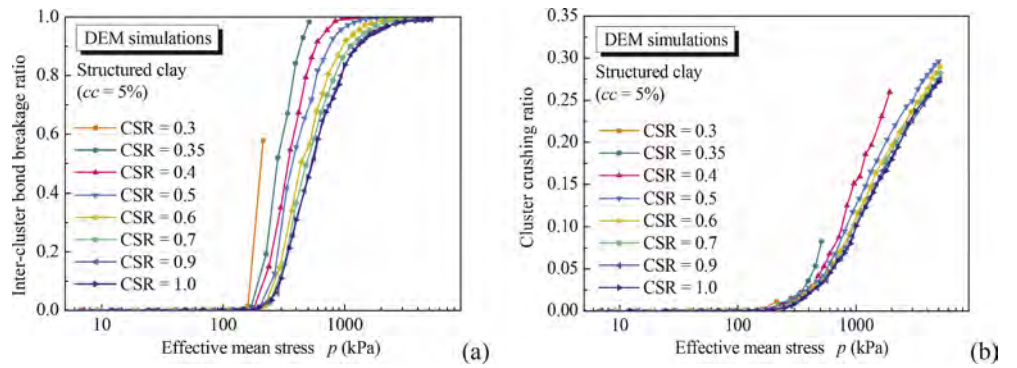

Figure 7. Structural degradation in the DEM structured clay (cc = 5%) samples under different CSRs quantified by: (a) evolutions of inter-cluster bond breakage ratio; (b) evolutions of cluster crushing ratio.

proportion of smaller clusters all increase significantly with the decrease of CSR (or cement content). Due to the structural resistance, the coarser strong contact force chains in the structured clay are more distributed than those in the remolded clay, as described in Figures 9b and 9d. Moreover, as CSR increases from 0.4 to 0.9, the distribution of stronger contact force chains tends to be from mainly along the vertical to more uniform in all directions.

To quantify the variation of contact orientation during loading, the fabric anisotropy curves of total contact normal as well as the contact orientation rose diagrams of CSR = 0.4 /0.6 /0.9 at p = 1000kPa (i.e. projected onto the xy, xz and yz planes) in remolded and structured (cc = 5%) clay samples are given in Figure 10. For the deviator fabric of contact normal, its initial small value of around 0.06 suggests the slightly initial anisotropy of clay samples after 'k_0'

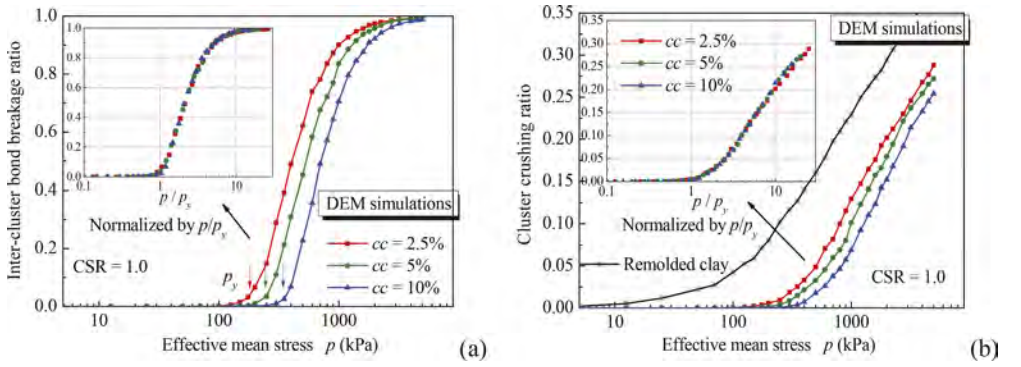

Figure 8. Structural degradation in the DEM structured clay samples with different cement contents (under CSR = 1.0) quantified by: (a) evolution of the inter-cluster bond breakage ratio and its normalization by p/p_y; and (b) evolution of the cluster crushing ratio and its normalization by p/p_y.

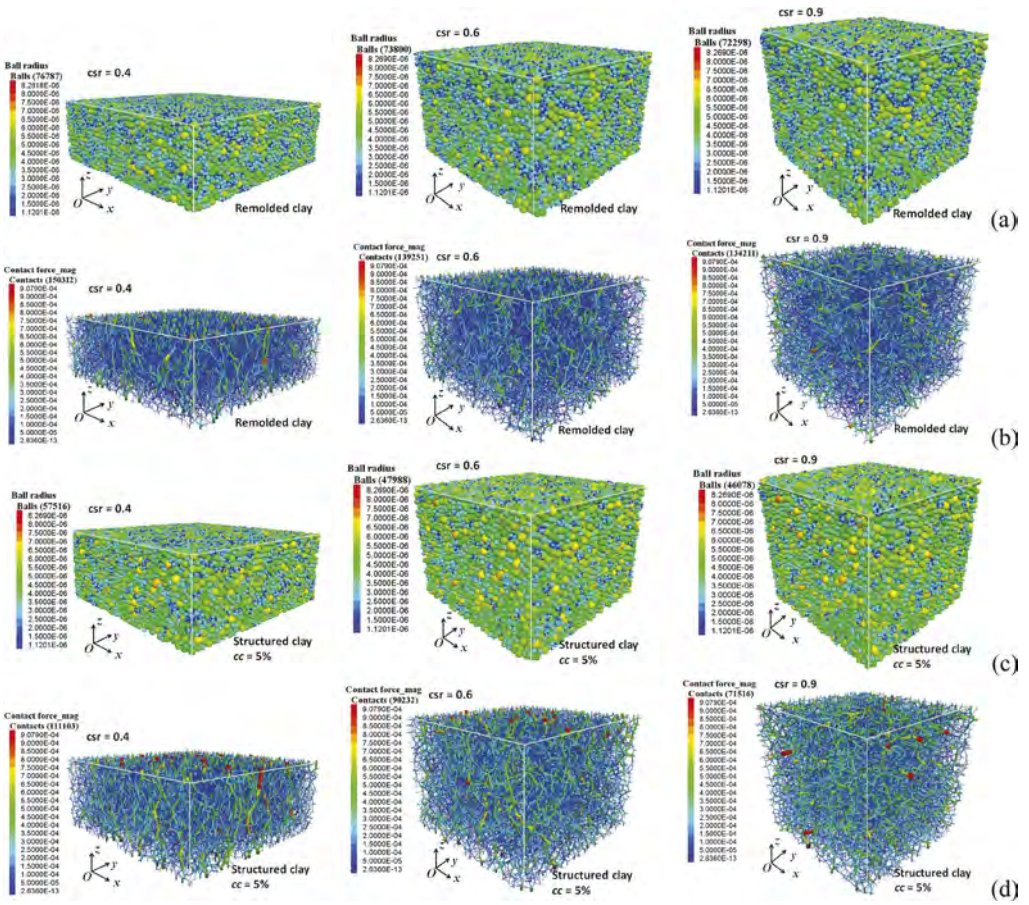

Figure 9. DEM micro observations under CSR = 0.4/0.6/0.9: (a) (b) cluster composition of deformed sample and contact force chain in the remolded clay; (c)(d) cluster composition of deformed sample and contact force chain in the structured clay (cc = 5%).

precompression, and it keeps almost constant until reaching the structural yielding state for the structured clay, suggesting the significant fabric resistance. Beyond the structural yielding, the micro bonds gradually degrade, and thus the fabric anisotropy of contacts is affected obviously by the stress anisotropy of different CSR compression tests. That is, the deviator fabric of total contact normal gradually decreases when the stress ratio is high (i.e. CSR $\geq$ 0.5), while it tends to first increase and then decrease as CSR < 0.5. It can be also observed from the rose diagrams that, the clay samples are approximately isotropic in the *x*-*y* direction, while some degree of anisotropy is exhibited in *x*-*z* and *y*-*z* directions. The final steady fabric anisotropy of clay samples with different cement contents is similar, which reduces with the increasing CSR.

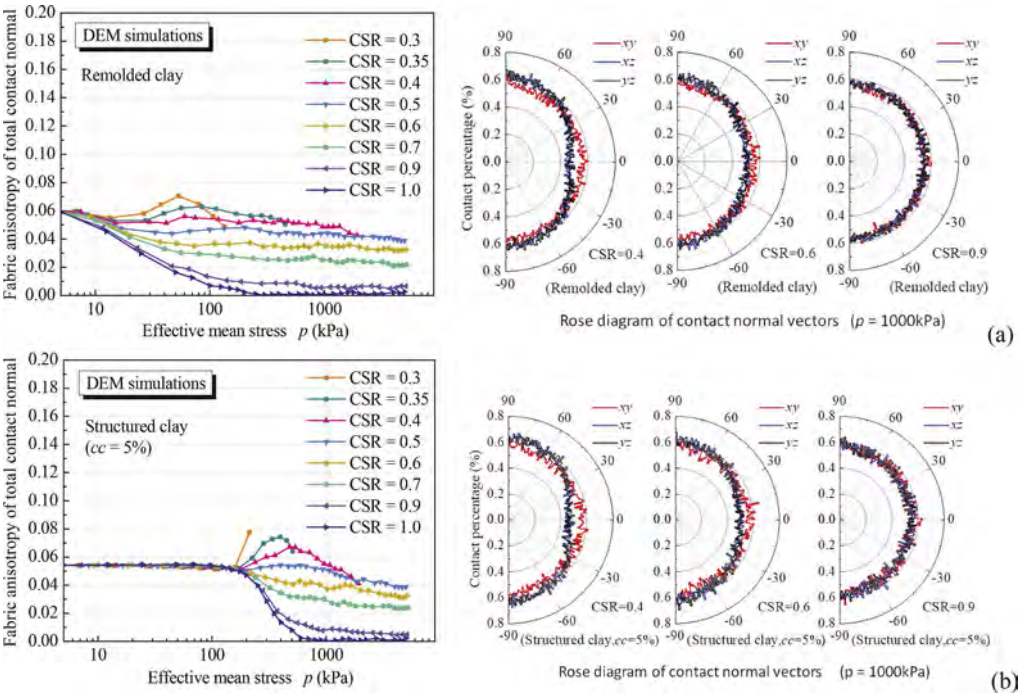

Figure 10. DEM results of fabric anisotropy of contact normal under different CSRs and contact orientation rose diagram under CSR =0.4 /0.6 /0.9: (a) for remolded clay; (b) for structured clay (*cc* = 5%).

4 CONCLUSIONS

This paper investigates the influences of cement content and stress ratio on the macro/micro-mechanical behaviors of remolded and structured clays under CSR compression conditions by utilizing a novel 3D numerical approach. The main conclusions can be drawn as follows:

(1) The DEM materials incorporating the proposed contact model as well as cluster crushing can capture the mechanical characteristics of clay in the CSR compression tests. For structured clays, the distinct structural yield stress can be captured, and its ultimate void difference from the remolded clay suggests the residual cementation effect, which all increase with the increasing cement content. The yield stress basically raises as CSR increases except CSR = 0.7 ~ 1.0, which is mainly due to the initial anisotropy of 'k_0' generated clay samples.

(2) With the increasing CSR (or cement content), the deviator strain, the broken bond ratio of multilevel clusters and the proportion of smaller clusters all decrease significantly. The final steady fabric anisotropy of clay samples with different cement contents is similar, which decreases with the increasing CSR.

ACKNOWLEDGEMENTS

The project presented in this article is supported by the National Natural Science Foundation of Grant Nos. 51639008 and 51890911, all of which are sincerely appreciated.

REFERENCES

Adachi, T., Oka, F., Hirata, T., et al. 2008. Stress-strain behavior and yielding characteristics of Eastern Osaka clay. *Journal of the Japanese Geotechnical Society* 35(3):1–13.

Anandarajah, A. 2000. Numerical simulation of one dimensional behaviour of a kaolinite. *Géotechnique* 50(5): 509–519.

Anandarajah, A., Chen, J. 1994. Double layer repulsive force between two inclined platy particles according to the Gouy Chapman theory. *Journal of Colloid and Interface science* 168(1): 111–117.

Anandarajah, A., Chen, J. 1997. Van der Waals attractive force clay particles in water and contaminants. *Soils and Foundations* 37(2): 27–37.

Bayesteh, H., Mirghasemi, A. A. 2013. Procedure to detect the contact of platy cohesive particles in discrete element analysis. *Powder Technology* 244: 75–84.

Bergado, D. T., Taechakumthorn, C., Lorenzo, G. A., et al. 2006. Stress-deformation behavior under anisotropic drained triaxial consolidation of cement-treated soft Bangkok clay. *Soils and Foundations* 46(5): 629–637.

Boton, M., Estrada, N., Azéma, E., et al. 2014. Particle alignment and clustering in sheared granular materials composed of platy particles. *European Physical Journal E* 37(11): 1–8.

Ciantia, M. O., Aproyo, M., Calvetti, F., et al. 2015. An approach t o enhance efficiency of DEM modelling of soils with crushable grains. *Géotechnique* 65(2): 91–110.

De Bono, J. P., Mcdowell, G. R. 2014. Discrete element modelling of one dimensional compression of cemented sand. *Granular Matter* 16(1): 79–90.

Delage, P. 2010. A microstructure approach to the sensitivity and compressibility of some Eastern Canada sensitive clays. *Géotechnique* 60(5): 353–368.

Ebrahimi, D., Pellenq, J. M., Whittle, A. J. 2016. Mesoscale simulation of clay aggregate formation and mechanical properties. *Granular Matter* 18(3): 49.

Hattab, M. & Chang, C. S. 2015. Interaggregate forces and energy potential effect on clay deformation. *Journal of Engineering Mechanics* 141(7): 04015014.

Jaradat, K. A., Abdelaziz, S. L. 2019. On the use of discrete element method for multi scale assessment of clay behavior. *Computers and Geotechnics* 112: 329–341.

Jiang, M. J., Konrad, J. M., Leroueil, S. 2003. An efficient technique for generating homogeneous specimens for DEM studies. *Computers and Geotechnics* 30(7): 579–597.

Jiang, M. J., Li, T., Cui, Y., et al. 2017. Mechanical behavior of artificially cemented clay with open structure: Cell and physical model analyses. *Engineering Geology* 221: 133–142.

Jiang, M. J., Shen, Z. F., Thornton, C. 2013. Microscopic contact model of lunar regolith for high efficiency discrete element analyses. *Computers and Geotechnics* 54: 104–116.

Kamruzzaman, A. H., Chew, S. H., Lee, F. H. 2009. Structuration and destructuration behavior of cement treated Singapore marine clay. *Journal of Geotechnical and Geoenvironmental Engineering* 135: 573–589.

Katti, D. R., Matar, M. I., Katti, K. S., et al. 2009. Multiscale modeling of swelling clays: A computational and experimental approach. *KSCE Journal of Civil Engineering* 13(4): 243–255.

Khabazian, M., Mirghasemi, A. A., Bayesteh, H. 2018. Compressibility of montmorillonite/kaolinite mixtures in consolidation testing using discrete element method. *Computers and Geotechnics* 104: 271–280.

Liu, X., Hammad, T., Saiyouri, N., et al. 2012. Physical chemical analysis of marine sediment cementation from the Gulf of Guinea. *Comptes Rendus Géoscience* 344(9): 461–470.

Liu, J., Lin, C., Miller, J. D. 2015. Simulation of cluster formation from kaolinite suspensions. *International Journal of Mineral Processing* 145: 38–47.

Lu, N., Anderson, M. T., Likos, W. J., et al. 2008. A discrete element model for kaolinite aggregate formation during sedimentation. *International Journal for Numerical and Analytical Methods in Geomechanics* 32(8): 965–980.

Luo, L. S., Shen, Z. F., Gao, H. M., et al. 2021. Macroscopic behavior and microscopic structure evolution of marine clay in one dimensional compression revealed by discrete element simulation. *Processes* 9: 2259

Miura, N., Horpibulsuk, S., Nagaraj, T. S. 2001. Engineering behavior of cement stabilized clay at high water content. *Soils and Foundations* 41(5): 33–45.

Nguyen, L. D. Fatahi, B. Khabbaz, H. 2017. Development of a constitutive model to predict the behavior of cement-treated clay during cementation degradation: C3 Model. *International Journal of Geomechanics* 17(7): 04017010.

Shi, J., Qian, S., Zeng, L.L., et al. 2015. Influence of anisotropic consolidation stress paths on compression behaviour of reconstituted Wenzhou clay. *Géotechnique Letters* 5: 275–280.

Suzuki, A., Matsushima, T. 2015. Meso scale structural characteristics of clay deposit studied by 2D Discrete Element Method. *In Geomechanics from Micro to Macro edited by Soga et al. Taylor & Francis Group*. London. 33–40.

Tan, L. R., Kong, L. W. 2001. Fundamental property and microstructure model of red clay. *Chinese Journal of Geotechnical Engineering* 23(4): 458–462 (in Chinese).

Yao, M., Anandarajah, A. 2003. Three dimensional discrete element method of analysis of clays. *Journal of Engineering Mechanics* 129(6): 585–596.

Zhang, X. W., Kong, L. W., Cui, X. L., et al. 2016. Occurrence characteristics of free iron oxides in soil microstructure: evidence from XRD, SEM and EDS. *Bulletin of Engineering Geology and the Environment* 75(4): 1493–1503.

Smart Geotechnics for Smart Societies – Zhussupbekov, Sarsembayeva & Kaliakin (Eds)
© 2023 The Author(s), ISBN 978-1-003-29912-7
Open Access: www.taylorfrancis.com, CC BY-NC-ND 4.0 license

Statistical analysis based geotechnical characterization of Kathmandu soils

Mandip Subedi & Indra Prasad Acharya
Department of Civil Engineering, Pulchowk Campus, IoE, TU, Lalitpur, Nepal

Keshab Sharma
BGC Engineering Inc., Fredericton, NB, Canada

Kalpana Adhikari
Department of Roads, Government of Nepal, Kathmandu, Nepal

Rajan KC
Department of Civil Engineering, Pulchowk Campus, IoE, TU, Lalitpur, Nepal

Netra Prakash Bhandary
Ehime University, Japan

ABSTRACT: Kathmandu Valley, the capital of Nepal, is a highly populated and rapidly urbanised area of the country built upon lacustrine and fluvial origin deposits. Because the valley deposit is located in an earthquake-prone zone with a long history of catastrophic earthquakes, it is vulnerable to numerous geohazards like liquefaction. Although a few localized geotechnical studies have been conducted in the valley, holistic understanding, modelling, and geotechnical soil characterisation are seldom documented. This study attempts to characterize the Kathmandu soil based on geotechnical properties using statistical analysis approach. We have collected and analysed more than 400 geotechnical investigation reports and bored 10 test locations. Statistical analysis and representation of index properties, consolidation parameters, shear strength, SPT-N value, and shear wave velocity have been assessed in this paper. These findings can aid structural and foundation engineers in studying foundations, cost estimation of geotechnical investigations, and planning and implementing various civil engineering projects.

Keywords: Geotechnical properties, Characterization, Statistical analysis, Index properties, Shear strength, Kathmandu Valley

1 INTRODUCTION

The capital city of Nepal, Kathmandu, is located in the valley and is the largest city in the country, serving as an important center of politics, business, and tourism. It is considered the cultural and economic hub of Nepal, and is home to numerous UNESCO World Heritage sites, including temples, palaces, and stupas. The valley's rich history and cultural heritage, combined with its vibrant city life, make it an essential destination for anyone visiting Nepal. It is located in central Nepal and is the most populous metropolitan area in the country.

Kathmandu Valley is characterised by lacustrine and fluvial deposition in origin with a maximum thickness of 650 m (Sakai, 2001). The deposited sediments consist of interbedded clay, silt, sand, and gravel (Mugnier et al., 2011) with a temporal and spatial variable shallow groundwater table (Shrestha et al., 2016).

DOI: 10.1201/9781003299127-41

The valley's urbanisation has been fast, and all of the urban communities exhibit rapid expansion on their peripheral (Chaulagain et al. 2016). Additionally, the Kathmandu Valley is located in an earthquake-prone zone with a long history of deadly earthquakes. Being formed of lacustrine sediments with a strong capability for amplifying seismic waves, the valley is highly susceptible to damage if not given proper care during geotechnical investigations or subsoil characterisation of the site.

Subsoil characterisation is vital for geotechnical and geological designing associated with earthworks, structure foundations, forecast and comprehension of natural hazards, and environmental issues (Ahmed et al., 2020). Due to inadequate or incompetent subsurface characterisation and assessment of soil strength, possible foundation-related failures or structure collapses may occur. As a result of the variety and variance in subsurface conditions, thorough geotechnical evaluations of a building site are required in designing earthworks and structural foundations (Oyeyemi et al. 2017).

This research aims at collecting and analysing more than 400 previous geotechnical investigation data from different projects and boring 10 SPT-N boreholes with laboratory experiments. Statistical analysis and representation of index properties, consolidation parameters, shear strength, SPT-N value, and shear wave velocity have been assessed in this paper. This study can help urban planning, preliminary and feasibility studies, and land-use policies. It also assists the geotechnical engineers beforehand to plan the comprehensive geotechnical investigation based on the provided geotechnical map and soil properties data.

2 GEOLOGY

Surrounded by mid-height mountains and drained by a river system called Bagmati, a bowl-shaped Kathmandu Valley has a more or less flat terrain except for a few gorges created by the river network. As a deep sediment-filled ancient lake, the valley deposit mainly consists of materials transported from the peripheral mountains. Figure 1 shows the geological map of the valley deposit (redrawn after Dhital (2015)). The sediment deposits are mostly a mixture and alteration of clay, silt, sand, and gravel layers (Subedi et al. 2021) and relatively shallow groundwater table (Shrestha et al., 2016). Moreover, materials in the northern side of the valley are riverbed stratified deposits of all soil types. In contrast, alluvial fan facies are evident in the south end. Additionally, middle part of the valley is mostly thick layers of black clay and organic mud. All this makes it clear that relatively coarse material (i.e., coarse silt, sand, and fine gravel) deposited areas in the Kathmandu Valley are particularly prone to liquefaction (Okamura et al., 2015; Sharma et al., 2019) (Subedi & Acharya 2022).

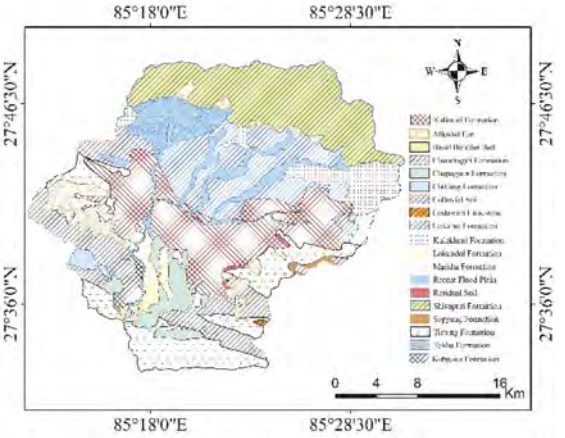

Figure 1. Geological formation map of Kathmandu Valley redrawn after Dhital (2015).

3 DATABASE

In Kathmandu Valley, the standard penetration resistance test (SPT) is the most often utilised in-situ test. In Nepal, other approaches such as the cone penetration test (CPT) have not been deployed due to resource and technical constraints (Sharma et al. 2019). Thus, for this study, most of the data include borehole logs prepared for a different purpose. The uncorrected SPT numbers are corrected using the strategy proposed by Robertson and Wride (1998). For this study, both primary and secondary data were used. As primary data, geotechnical investigations (boreholes and SPT test) were conducted at ten different locations in Kathmandu Valley, five boreholes from the core city area and five from the 2015 Gorkha earthquake-induced liquefaction zones. As secondary data, about 400 soil investigation reports for various projects, including residential and public buildings, bridges, slope stability works etc., were collected. The total number of boreholes collected for this study were more than 1500. All these boreholes were up to 20 m from ground surface.

4 RESULT AND DISCUSSION

4.1 *Stratigraphy*

The geotechnical investigations reveal that the top 20m of soil in the valley contains a complex and stratified profile. A depth up to 20m was considered for this study as this depth is good enough for the shallow foundation for residential buildings and low story commercial or public buildings. Mostly grey to dark, silty sand and clayey silt are abundant throughout the valley, with wide variations in soil characteristics. Up to 1m depth, organic clay, fine sand beds, and peat layers are commonly termed a crust layer on the surface. Dark grey sandy silt dominates the majority of the investigation locations just under the crust layer. Below this layer comes silt with low plasticity followed by silt with medium plasticity; the resultant layer is often composed of stiff clay with low-to-medium plasticity. Typical soil profiles with SPT-N values are presented in Figure 2.

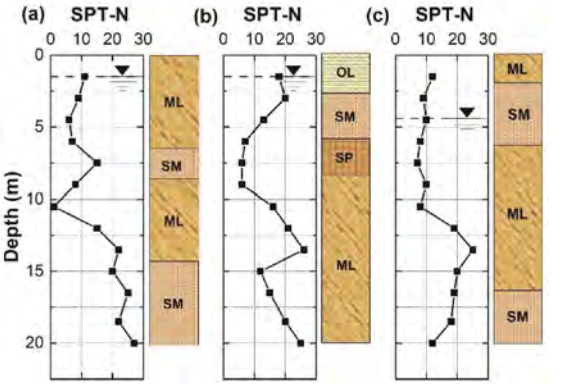

Figure 2. Typical stratigraphy profiles observed GWT and SPT of (a) Manamaiju, (b) Ramkot, and (c) Tundikhel.

4.2 *Statistical analysis*

The soil in Kathmandu Valley is diverse and layered at shallow depths. The heterogeneity results from lithological variation, natural soil variability, and exposure to varying overburden forces in different places. Thus, if the probability distribution for any measurable characteristic is known, it is critical to do statistical analysis to identify their geotechnical properties. According to prior research, the normal distribution fits most of the index, consolidation, and shear strength parameters of many natural soils (Kim et al., 2012). As a result, the current analysis used the standard distribution to provide a general characterisation for Kathmandu

soils. The number of data (n), minimum value, maximum value, mean value (μ) and standard deviation (σ) were calculated for each soil property. The list of geotechnical properties, number of data, minimum and maximum value with μ and σ are summarised in Table 1.

Table 1. Variability and statistical representation of Geotechnical properties of Kathmandu soils.

Property	Number of Data (n)	Min.	Max.	Mean (μ)	Standard deviation (σ)
Bulk density, γ (kN/m^3)	166	9.8	22.34	18.14	1.83
Specific gravity, G_s	302	1.89	2.89	2.59	0.15
Natural water content, w_n (%)	455	5.38	98	39.94	20.08
Plastic limit, PL (%)	239	15.2	50.98	29.12	7.84
Liquid limit, LL (%)	239	22.8	69.12	44.29	11.29
Plasticity index, PI (%)	239	1.73	34	15.13	6.26
Standard penetration test, SPT (N)	1167	0	50	15.5	11.14
Undrained shear strength, C_u (kPa)	119	1.3	178.48	61.50	33.65
Cohesion, C (kPa)	102	0	29	11.63	7.11
Friction angle, ϕ (°)	120	6.2	40	22.60	8.42
Coefficient of consolidation, C_v (cm^2/s)	67	0.0002	1	0.18	0.271
Shear wave velocity, V_s (m/s)	108	65	432	208.37	88.72
Primary wave velocity, V_p (m/s)	26	246	1677	999.58	449.29

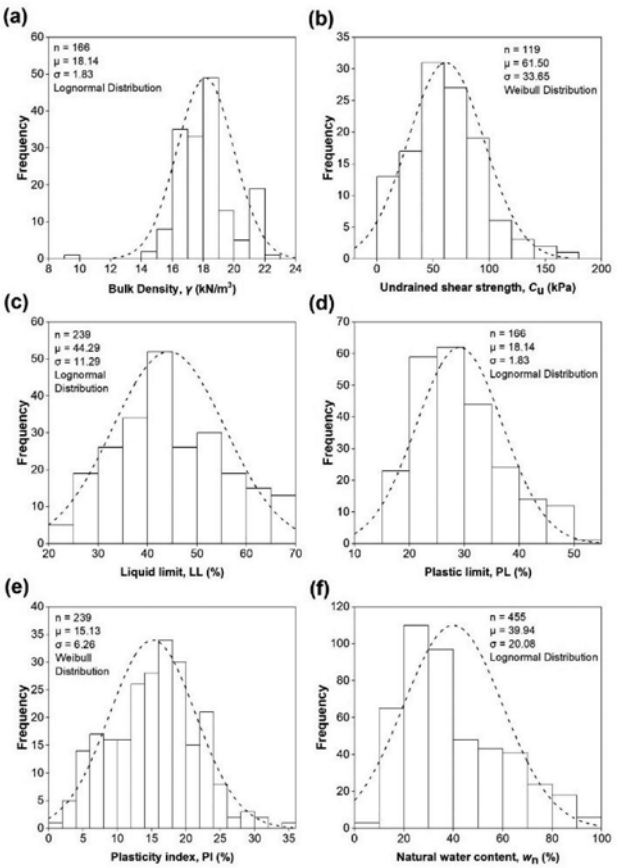

Figure 3. Histogram and distribution function of the Kathmandu soil properties (a) γ, (b) $C_{u,}$ (c) LL, (d) PL, (e) PI, and (f) w_n.

As illustrated in Figure 3, the statistical details and histograms were created with depth to determine the variance of soil properties with depth.

4.3 *Particle size distribution*

The percentage of various sizes of soil particles was determined utilising particle size analysis. The particle size distribution graph shown in Figure 4 shows that silty sand is abundant in Kathmandu soil. In addition to this, two sets of grain size curves showing the particle size distribution ranges for most liquefiable and potentially liquefiable soils proposed by Tsuchida and Hayashi (1972) are also plotted. The majority of the gradation curves are seen to fall inside the border of possibly liquefiable soil. It strongly suggests that the soil in Kathmandu is highly susceptible to liquefaction considering high GWT.

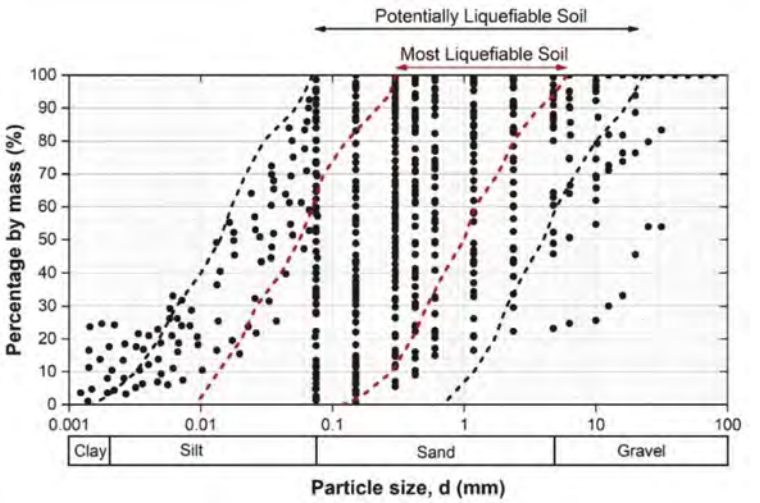

Figure 4. Particle size distribution with a range of Liquefiable soils given by Tsuchida and Hayashi (1972).

4.4 *Index and strength properties*

The SPT-N values of soil layers lying in the central part were found less than the outer part of the valley. It might be due to the presence of hard rock in the outer part of the valley. Most of the shallow depth soil is silt and silty sand. The SPT-N values of about 85% of the borehole test data were found less than 20, and more than 50% have SPT-N values less than 10 in shallow depth in the core area of the valley. The average SPT-N value of Kathmandu soil at depths 1.5m, 3m, 6m, 9m and 15m were 12, 15, 18, 20 and 23, respectively, with overall μ=15.5 and σ=11.14. Typical SPT profiles at three different locations in the study are presented in Figure 2, whereas the variation of SPT-N with depth for Kathmandu Valley is shown in Figure 5(a).

Specific gravity (G_s) is a critical parameter in evaluating the engineering behaviour of the soil. The value of G_s is used to calculate the void ratio, compressibility coefficient, degree of saturation and other soil parameters. In general, a higher value of G_s indicates mineral soil and higher strength. In the study area, the value of the specific gravity of soil is between 1.89 to 2.89 (μ=2.59, σ=0.15) (Figure 5(b)). The low specific gravity (<2.5) might be attributed to the organic soil at the top. The average value of G_s as 2.59 indicates the high presence of silty sand in the valley.

The fines content (FC) of sandy soils is critical in the engineering design of geotechnical buildings, particularly in earthquake-prone areas. The quantity of FC in soil has

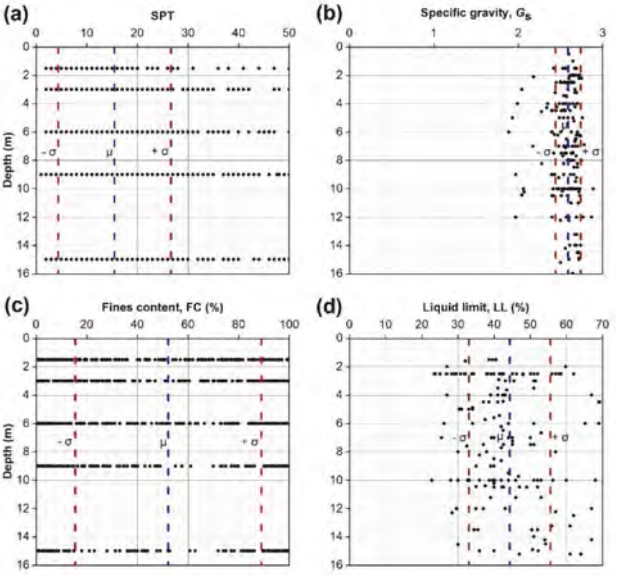

Figure 5. Index and strength properties of soil vs. depth: (a) SPT, (b) G_s, (c) FC, and (d) LL.

a considerable effect on its relative density and liquefaction potential. The variation of FC with depth in Kathmandu soils is shown in Figure 5(c). The value of FC ranges from 0 to 100 %, with a mean of 52.24 and standard deviation of 36.69. Sand and silt with low FC might be attributed to liquefaction at several locations in Kathmandu Valley during 2015 Gorkha, Nepal, even though the peak ground acceleration (PGA) earthquake (~0.18g) was much smaller than that expected (i.e. 0.30g).

The lowest water content at which soil transitions from a plastic to a fluid state is the liquid limit (LL). More than 40% of the borehole locations considered in this study have less or equal 35% with μ=44.29 and σ=11.29. Sandy soil with LL less than 35 indicates the high probability of liquefaction (Bray and Sancio, 2006). The variation of LL with depth is presented in Figures 5(d).

5 CONCLUSIONS

Following are the major conclusions of this study:

1. From ground surface to a depth of around 20 metres, the Kathmandu Valley has a complicated and layered profile. The majority of the gathered database exhibited lithological heterogeneity. The valley was primarily composed of clayey silt and silty sand. Fine sand beds, organic clay, and peat layers were prevalent in the 1 m top layers.
2. After analysing particle size distribution and the Plasticity chart, it was evident that Kathmandu soil deposits are very susceptible to liquefaction.
3. The SPT values of soil layers lying in the central part were much lesser than the outer. It might be due to the presence of hard rock bedding in the outer part of the valley. About 85% of the borehole test data had SPT less than 20, and more than 50% have SPT less than 10 in shallow depth in the core area of the valley. Most of the samples had a moisture content ranging from 20 to 40% with an average of 39.94%, whereas the specific gravity value was mainly between 1.89-2.89 with an average value of 2.59.
4. More than 40% of the boreholes locations taken for this study had a liquid limit (LL) less or equalled 35% (μ=44.29). Most of the soils in this study possessed undrained shear strength at failure (Cu) ranging from 30 to 90 kPa. After plotting a total of 120 ring shear

tests, cohesion was found from 0 kPa to 20 kPa (μ=11.63 kPa), and friction angle varied from 6.2° and 40° with an average of 22.6°. It was observed that most of the soil samples had a shear wave velocity lesser than 360 m/s, which indicates the extensive presence of stiff soil.

The analytical findings apply to future research and studies on the subsurface state of the Kathmandu Valley and civil engineering techniques. This work is the first comprehensive investigation on the geotechnical characterisation of Kathmandu soil to the authors' knowledge. It will have a substantial impact on land use planning. These study findings might help prioritise sites with geotechnical concerns or high total costs for civil engineering projects. It may aid in selecting more appropriate foundation types and building designs, as well as in the forecasting of changes in geological engineering conditions and the prediction of hazardous geological events. Finally, despite the abundance of boreholes in the Kathmandu valley, direct shear wave observations are pretty rare. To better understand the Kathmandu soil's geotechnical properties, more investigations and studies are required to obtain more accurate results.

ACKNOWLEDGEMENT

Soil Test Pvt. Ltd., Pashupati Drillers, Multi Lab Pvt. Ltd., Clay Engineering, Archiplan Pvt. Ltd., Adarsha Design and Solutions Pvt. Ltd., Department of Mines and Geology, Department of Civil Engineering, Tribhuvan University, Institute of Engineering, Pulchowk Campus, and Nepal Academy of Science and Technology (NAST).

REFERENCES

Ahmed C, Mohammed A, Tahir A. 2020. Geostatistics of strength, modeling and GIS mapping of soil properties for residential purpose for Sulaimani City soils, Kurdistan Region, Iraq. Model Earth Syst Environ.:1–15.

Akbarzadeh Kasani H, Eslami A. 2019. Geotechnical properties of Rasht clay and silt in Northern Iran. Int J Geotech Eng. 13(6):566–580. http://doi.org/10.1080/19386362.2017.1374496.

Atalar C. 2011. A review of the origin and properties of the soils of Nicosia, Cyprus. Int J Geotech Eng 5(1):79–86. https://www.tandfonline.com/doi/abs/10.3328/IJGE.2011.05.01.79-86.

Bray JD, Sancio RB. 2006. Assessment of the liquefaction susceptibility of fine-grained soils. J Geotech geoenvironmental Eng. 132(9):1165–1177.

Chaulagain H, Rodrigues H, Silva V, Spacone E, Varum H. 2016. Earthquake loss estimation for the Kathmandu Valley. Bull Earthq Eng. 14(1):59–88.

Dhital M. 2015. Geology of the Nepal Himalaya: Regional perspective of the classic collided orogen. [place unknown].

Jones NL, Wright SG. 1993. Subsurface characterization with solid models. J Geotech Eng. 119(11): 1823–1839.

Kim D, Kim K-S, Ko S, Choi Y, Lee W. 2012. Assessment of geotechnical variability of Songdo silty clay. Eng Geol. 133:1–8.

Mugnier J-L, Huyghe P, Gajurel AP, Upreti BN, Jouanne F. 2011. Seismites in the Kathmandu basin and seismic hazard in central Himalaya. Tectonophysics. 509(1–2):33–49.

Okamura M, Bhandary NP, Mori S, Marasini N, Hazarika H. 2015. Report on a reconnaissance survey of damage in Kathmandu caused by the 2015 Gorkha Nepal earthquake. Soils Found. 55(5): 1015–1029.

Oyeyemi KD, Aizebeokhai AP, Adagunodo TA, Olofinnade OM, Sanuade OA, Olaojo AA. 2017. Subsoil characterization using geoelectrical and geotechnical investigations: Implications for foundation studies. Int J Civ Eng Technol. 8(10):302–314.

Polito C. 2001. Plasticity based liquefaction criteria.

Robertson PK, Wride CE (Fear). 1998. Evaluating cyclic liquefaction potential using the cone penetration test. Can Geotech J. 35(3):442–459. https://doi.org/10.1139/t98-017.

Sakai H. 2001. Stratigraphic division and sedimentary facies of the Kathmandu Basin Group, central Nepal. J Nepal Geol Soc. 25(Sp. Issue):19–32.

Sharma K, Deng L, Khadka D. 2019a. Reconnaissance of liquefaction case studies in 2015 Gorkha (Nepal) earthquake and assessment of liquefaction susceptibility. Int J Geotech Eng. 13(4):326–338. https://doi.org/10.1080/19386362.2017.1350338.

Sharma K, Deng L, Khadka D. 2019b. Reconnaissance of liquefaction case studies in 2015 Gorkha (Nepal) earthquake and assessment of liquefaction susceptibility. Int J Geotech Eng. 13(4):326–338.

Shrestha S, Semkuyu DJ, Pandey VP. 2016. Assessment of groundwater vulnerability and risk to pollution in Kathmandu Valley, Nepal. Sci Total Environ. 556:23–35. http://dx.doi.org/10.1016/j.scitotenv.2016.03.021.

Subedi M, Acharya IP. 2022. Liquefaction hazard assessment and ground failure probability analysis in the Kathmandu Valley of Nepal. Geoenvironmental Disasters 9(1):1–17. https://geoenvironmental-disasters.springeropen.com/articles/10.1186/s40677-021-00203-0.

Subedi M, KC R, Acharya IP. 2021. SPT-based seismic soil liquefaction potential evaluation of Kathmandu Valley using first-order second-moment method. In: GeoNiagara Conf 2021. Canada.

Subedi M, Sharma K, Upadhayay B, Poudel RK, Khadka P. 2013. Soil liquefaction potential in Kathmandu Valley. Int J Landslide Environ. 1(1):91–92.

Tsuchida H, Hayashi S. 1972. Estimation of liquefaction potential of sandy soils. Publ Mcgraw Hill B Co. 14.

Smart Geotechnics for Smart Societies – Zhussupbekov, Sarsembayeva & Kaliakin (Eds)
© 2023 The Author(s), ISBN 978-1-003-29912-7
Open Access: www.taylorfrancis.com, CC BY-NC-ND 4.0 license

Minimum dry density in terms of grading entropy coordinates

E. Imre
EKIK HBM Research Centers and Bánki Donát Faculty of Mechanical and Safety Engineering, Óbuda University, Budapest, Hungary

D. Barreto
Edinburgh Napier University, UK

M. Datcheva
Institute of Mechanics and Institute of Information and Communication Technologies, Bulgarian Academy of Sciences, Sofia, Bulgaria

V.P. Singh
Texas A & M University, USA

W. Baille
Ruhr-Universität Bochum, Germany

S. Feng
Birmingham City University, UK
University of Bristol, UK

T. Firgi
Ybl Miklós Faculty of Architecture and Civil Engineering, Óbuda University, Budapest, Hungary

ABSTRACT: In this paper, the grading entropy method is applied together with advanced interpolation methods in order to establish empirical relationships between grading entropy coordinates and minimum dry density of sands. Three databases consisting of 94 samples (in total) of artificial mixtures of natural sands with fractal or continuous grain size distributions were used to evaluate three different types of empirical relationship. Whilst some databases have been previously published, recently acquired data has also been considered. The results show that there is a strong relationship between grading entropy coordinates and the minimum dry density.

1 INTRODUCTION

The experimental works by Kabai (1968, 1972, 1974) in relation to the dry density of sands from the Danube river concluded that the ratio of the minimum to the maximum dry density was basically constant, although it decreased as the soil became slightly plastic. Lőrincz (1986) also observed that a mixture of spheres with various radii can be denser if the radii values are selected from a larger size interval. Consequently, the dry density of the soil increases with the maximum particle diameter d_{max}. Furthermore, if the number of size fractions (N) in a sand mixture increases density is also expected to increase. Lőrincz (1986) tested both fractal and gap-graded grain size distribution with fixed N between 1 and 5 using grading entropy coordinates and found that the minimum dry density had a minimum value at around $A = 2/3$ (A is the relative base entropy, one of the grading entropy coordinates). This minimum value

DOI: 10.1201/9781003299127-42

occurred for gap-graded mixtures. The aim of the present study is to extend the findings of these pioneering works with new experimental work (referred to as the new Óbuda-Bochum database) as well as other theoretical work by Imre et al (2009, 2011, 2013 and 2017). A key aspect is that a relationship between grain size distribution and dry density cannot be generally determined empirically due to the large number of possible grading curves hence an interpolation technique is used (Imre et al, 2009, 2017) to assess the success of various statistically derived PSD-density relationships in terms of grading entropy coordinates. The grading entropy concept is described in detail by Lőrincz (1986) and characterises any grading curve using an abstract system of N fractions. Each fraction (which may represent the weight of material collected in a given sieve during an experimental test) has a diameter (d) range that doubles in size (e.g. $d_0 \leq d < 2d_0$, …, $2^{22}d_0 \leq d < 2^{23}d_0$, $2^{23}d_0 \leq d < 2^{24}d_0$, where d_0 may be 2^{-22} mm, the size of a silica tetrahedron). The relative frequencies of the fractions fulfil that:

$$\sum_{i=1}^{N} x_i = 1, x_i \geq 0, N \geq 1 \tag{1}$$

where the integer variable N is the number of the fractions between the finest and coarsest non-zero fractions, and x_i is the relative frequencies of fraction i (i.e. it may be the mass percentage retained in each sieve) The grading entropy can be separated into the base entropy (S_0) and the entropy increment (ΔS), defined as follows:

$$S_0 = \sum x_i S_{0i} = \sum x_i i \text{ and } \Delta S = \frac{-1}{\ln 2} \sum_{x_i \neq 0} x_i \ln x_i \tag{2}$$

where S_{0i} is the i^{th} fraction entropy ($=i$). The normalised forms of S_0 and ΔS are the relative base entropy (A) and the normalised entropy increment (B), respectively:

$$A = \frac{(S_0 - S_{0min})}{(S_{0max} - S_{0min})} \text{ and } B = \frac{\Delta S}{\ln N} \tag{3}$$

where S_{0max} and S_{0min} are the entropies of the largest and smallest fractions, respectively. Any grading curve can be represented as a point in terms of the non-normalised or normalised entropy coordinates. The inverse image of the maximum line of the diagram (critical values of the map) is the optimal line. The optimal point or grading curve has finite fractal distribution with the following relative frequencies:

$$x_1 = \frac{1}{\sum_{j=1}^{N} a^{j-1}} = \frac{1-a}{1-a^N}, \; x_j = x_1 a^{j-1} \tag{4}$$

where a is the root of equation (5) as defined by Imre, et al (2009):

$$y = \sum_{j=1}^{N} a^{j-1}[j - 1 - A(N-1)] = 0 \tag{5}$$

The optimal grading curve with finite fractal distribution is a kind of mean grading curve of the grading curves for a given A. The inverse image of a regular value of the diagram with a given A and B ordinate is an "N-3 dimensional sphere" in the N-1 dimensional, closed simplex. The mean grading is the optimal one related to the given A.

2 MEASUREMENTS AND DATABASE - MINIMUM DRY DENSITY

The soils and testing methods are described in Imre, et al (2009, 2013, 2017). For this preliminary study three different databases were used. They are here referred to as the (i) Lőrincz, (ii) Kabai

and (iii) Óbuda-Bochum databases, respectively. For the present analysis 50, 23 and 21 data samples were used from the databases (i), (ii), and (iii), respectively. In all databases, artificial mixtures of sand with different gradations were tested for dry density according to DIN 18126, and using various sample sizes. Values of the minimum solid volume ratio (s_{min}) were evaluated in terms of these dry density tests. The rationale for using such databases is as follows:

The Lőrincz (1986) database includes mixtures with optimal gradings with particle sizes varying between 0.07 and 4 mm with different values of relative base entropy (A); the Kabai (1972) database includes continuous data considering a slightly different value of d_0; the Óbuda-Bochum database (with data produced from ongoing research) includes unpublished results consisting of optimal gradings with $A = 2/3$. In summary, the databases have been chosen/developed in order to consider a wide range of particle sizes and distributions.

3 RESULTS AND ANALYSIS

In order to assess the effectiveness of using the grading entropy coordinates to estimate the minimum solid volume ratio (s_{min}), three types of empirical equation were tested on the basis of the experimental data. These are as follows:

$$s_{min} = C_3 S_0^{C_1} \Delta S^{C_2} \tag{6}$$

$$s_{min} = C_3 S_0^{C_1} (\Delta S + 1)^{C_2} \tag{7}$$

$$s_{min} = C_1 S_0 + C_2 \Delta S + C_3 \tag{8}$$

According to the results shown in Table 1 and Figure 1, the fitting parameters for each of the equations used were similar and it may be argued that additional statistical tests are required. The evaluation of these relationships must also be made within the context of their range of validity (which differs for each of the databases used). Note that despite its relative simplicity, Equation 8 provided the best fit for all databases. Similarly, amongst the three databases used, the Lőrincz database produced the best R^2 values.

4 SUMMARY AND CONCLUSIONS

The grading entropy method was applied using some experiments made on artificial mixtures of natural sands with fractal or continuous grain size distribution to determine a relationship between grading curves and dry density values in terms of solid volume ratio. Results indicated that there is a strong relationship between grading entropy coordinates and density. Despite its simplicity a fully linear relationship provided the best fit. Results however are dependent on the database used and must also be considered within the context of their range of validity.

A linear relation was found for the tested fractal distributions or continuous mixtures which supports the idea raised in Edwards' Statistical Mechanics approach that the dry density and the entropy are closely related. Therefore, by means of further research, a link between minimum solid volume ratio and the statistical mechanics approach (Baule et al. 2016) may be established. Further research is also suggested on gap-graded mixtures

ACKNOWLEDGEMENTS

The work by Prof. M. Datcheva is supported by Grant No BG05M2OP001-1.001-0003, financed by the Science and Education for Smart Growth Operational Program (2014–2020) and co-financed by the European Union through the European Structural and Investment Funds. The authors also appreciate the fruitful discussions between Dr. E. Imre and Dr. J. Török at Budapest University of Technology and Economics.

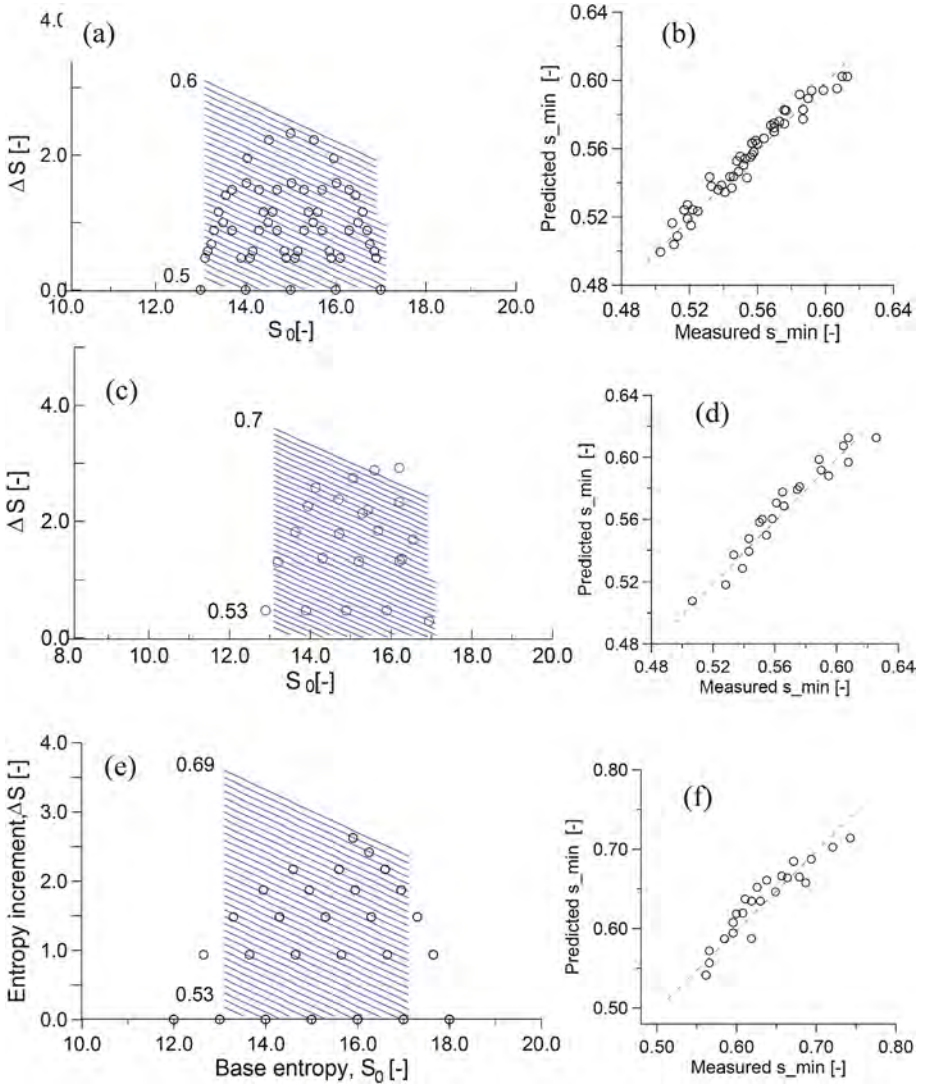

Figure 1. (s_{min}) isolines shown with gradings of experiments using on the non-normalised entropy diagram (left) and scatter plots for Equation. (8) (right.) for databases (a, b) Lőrincz; (c, d) Kabai and (e, f) Óbuda-Bochum.

Table 1. Fitting parameters and R^2 values for each of the empirical relationships and databases.

	Equation 6				Equation 7				Equation 8			
Database	C_1	C_2	C_3	R^2	C_1	C_2	C_3	R^2	C_1	C_2	C_3	R^2
Lőrincz	0.46	0.06	0.17	0.92	0.53	0.12	0.12	0.94	0.02	0.03	0.23	0.96
Kabai	0.41	0.08	0.21	0.76	0.38	0.18	0.19	0.82	0.02	0.05	0.32	0.87
Óbuda-Bochum	0.32	0.11	0.22	0.90	0.32	0.18	0.20	0.92	0.01	0.04	0.33	0.94

REFERENCES

DIN 18126. 1996. *Determination of minimum and maximum dry densities of non-cohesive soil*

Baule, A., Morone, F., Herrman, H.J., Makse, H.A. 2018. Edwards Statistical Mechanics for Jammed Granular Matter. *Rev. Mod. Phys* 90(1):015006

Imre, E., Lőrincz, J., Trang, Q.P., Fityus, S., Pusztai, J., Telekes, G. Schanz, T. 2009. Some dry density transfer function for sands. *KSCE Journal of Civil Engineering* 134:257–272.

Imre, E; Fityus, S; Keszeyné, E; Schanz T. 2011. A comment on the ratio of the maximum and minimum dry density for sands. *Geotechnical Engineering* 42:77–82.

Imre, E., Lőrincz, J., Gerendai, E., Szalkai, R., Lins, Y., Schanz, T. 2013. Some notes concerning the dry density testing standards. *18th ICSMGE*. Paris. 349–352.

Imre, E., Schanz, T., Firgi, T., Hegedus, C. 2017. Properties of sand mixtures with identical entropy coordinates. In: *Proceedings of the 19th International Conference on Soil Mechanics and Geotechnical Engineering*, Seoul 2017. 1163–1166.

Kabai, I. (1968). The compactibility of sands and sandy gravels. *Acta Technica Acad. Sci. Hung.*, 113–124.

Kabai, I. (1972). *Relationship between the grading curve and the compactibility*. University doctoral thesis TU of Budapest, Hungary (in Hungarian).

Kabai, I. (1974). The effect of grading on the compactibility of coarse grained soils. *Periodica Polytechnica*. 18 (4) 255–275.

Lőrincz, J. 1986. *Grading entropy of soils*. Doctoral Thesis, TU of Budapest (in Hungarian).

Lőrincz, J. 1990. Reletionship between grading entropy and dry bulk density of granular soils. *Periodica Polytechnica Civil Engineering*, 34(3),255–265.

Smart Geotechnics for Smart Societies – Zhussupbekov, Sarsembayeva & Kaliakin (Eds)
© 2023 The Author(s), ISBN 978-1-003-29912-7
Open Access: www.taylorfrancis.com, CC BY-NC-ND 4.0 license

Determination of shear and deformation parameters of coarse-grained soils

E. Kucova & J. Frankovska
Slovak University of Technology in Bratislava, Slovakia

ABSTRACT: The determination of soil properties is highly affected by its spatial variability. Furthermore, in many cases, it is impossible to extract undisturbed soil sample for laboratory testing. Regarding coarse grained soils, their mechanical parameters are mostly determined directly in situ as conventional shear and oedometric apparatus do not have the capacity for its measurement. In Slovakia, the dynamic penetration test is one of the most widely used field tests for these purposes. The test is primarily used for testing the resistance of coarse-grained soils, but using proper correlations, it is possible to determine other selected properties, including deformation modulus and angle of shear strength. These parameters can also be tested in the laboratory with a large-scale shear box and oedometric apparatus. In this article, the analysis of the results of deformation modulus and angle of shear strength measured in situ and in laboratory is presented.

1 INTRODUCTION

In geotechnical engineering, soil and rock properties are essential knowledge for the design of structures. However, the determination of these properties is more complicated than the determination of manmade materials properties due to their natural condition. In many cases, geotechnical engineers are met with the situation, when it is hard to obtain undisturbed representative samples for laboratory testing and therefore, many soil/rock tests are conducted directly in the field.

In Slovakia, besides common field tests used in engineering-geological survey (Schnaid 2009, Marchetti 2006, Yu 2000), the dynamic penetration (DP) is frequently used for soil testing. It is used for investigation of the soil resistance against the dynamic penetration of the rod. The test is primarily intended for testing of coarse-grained soils, because of the less friction between the soil particles and the penetration rod. Using appropriate correlations, it is possible to derive specific geotechnical parameters: relative density (I_D), angle of shear strength (ϕ_{ef}), deformation modulus (E_{def}) of coarse-grained soils. To obtain these properties, there exist many correlations published in foreign and domestic literature (EN 1997-2:2007, DIN 4094-3:2002, STN 72 1032:1997, Matys et al.1990). However, these correlations should be chosen with caution as not all of them are direct (do not represent direct relation between DP results and property), thus the applicability of them may vary.

Regarding the relation between DP results and soil property, foreign standards (EN 1997-2:2007, DIN 4094-3:2002) mention mostly the direct correlations between the results of the number of blows and relative density. Correlations for mechanical properties (e.g., ϕ_{ef} and E_{def}) are expressed indirectly. It means that in the foreign standards ϕ_{ef} and E_{def} are derived from I_D. The applicability of these correlations was discussed by Vrettos & Papamichael (2018), who concluded that the correlations are reliable for determining the medium density. Furthermore, they observed that the accuracy for determination of other geotechnical parameters is questionable, and they recommended using direct correlations.

Direct correlations for mechanical parameters of coarse-grained soils are published in the Slovak literature (STN 72 1032:1997, Matys et al.1990). These correlations are derived from

DOI: 10.1201/9781003299127-43

the results of dynamic penetration resistance (q_{dyn}), which considers the friction on the rod and the change in rod´s weight with increasing depth, therefore, is considered as more reliable (Vrettos & Papamichael, 2018).

Other important factor, necessary for choosing appropriate correlation, is soil composition and genesis of the soil. The fact is that from all the available correlation in Slovakia only some correlations specify type or genesis of the soil. This creates significant gap for evaluation of geotechnical properties (especially the mechanical ones) from DP test. The genesis of soil is critical for the evaluation of geotechnical properties, especially in gravels, where mechanical properties are affected by interlocking forces between grains. In general, it is known that between angular grains the interlocking is greater, which means better geotechnical parameters than in the soils with round particles.

On the other hand, in Slovakia there exist some recommended values of mechanical properties for coarse-grained soils (STN 73 1001:1989) assessed from comparable experience. But, in previous study, comparing them with field test results, we found out that these values are a bit optimistic for fluvial gravels, therefore cannot be completely followed.

In order to analyze the mechanical properties of fluvial coarse-grained material, this paper presents results from a series of heavy dynamic penetration tests performed in fluvial soils near Bratislava, the capital of Slovakia. These results were consecutively used for the determination of mechanical properties of coarse-grained soils by applying selected direct correlations. The results are furthermore compared with the results of laboratory tests to analyze mechanical properties and assess the applicability of selected correlations.

2 GEOLOGY AND TESTING METHODS

In our study, we analyzed the results of mechanical properties of coarse-grained soil collected from the field and laboratory testing. The field test was performed in southwestern Slovakia near the capital city. This area is characterized by the large deposits of quaternary fluvial coarse-grained soils. In the past, these deposits were accumulated by the Danube River in form of river terraces. The most represented soils in the area are well (GW) and poor (GP) graded gravels, that are occasionally intersected with layers of fine-grained gravel (G-F, GC). The grains of fluvial gravels are well rounded with smooth round or cylindrical shapes with size of 1-5 cm.

These soils were tested by heavy dynamic penetration (DPH). Penetrations were performed to depths of 7-25 meters. Groundwater was observed at depths of 0.4 - 4 meters below the surface. The investigation shows that the area is mostly represented by medium dense to dense poor-grade gravels (GP), alternatively by layers of sandy soils - see typical geological profile (Figure 1). During the execution of DPH tests (example of DP test recording is shown in Figure 1), the number of blows N_{10} were recorded, from which the dynamic penetration resistance q_{dyn} (MPa) was subsequently derived. Afterwards, using selected correlations (Table 1), the mechanical properties of coarse-grained soils were derived from the q_{dyn} results.

Table 1. Correlations for determination of mechanical properties.

Soil property	Correlations	Soil	Coefficients	
Angle of shear strength (°)	$\varphi_{ef} = p \times (q_{dyn})^r$	Fine grained sand	p	24
		Gravely soils	r	0.16
Deformation modulus (MPa)	$E_{def} = n \times (q_{dyn})^m$	Silty sand	n	2.0
			m	0.83
		Fine-grained sand	n	3.5
			m	0.83
		Medium/ coarse-grained sand	n	5.5
			m	0.83
		Gravely sands	n	8.8
			m	0.83

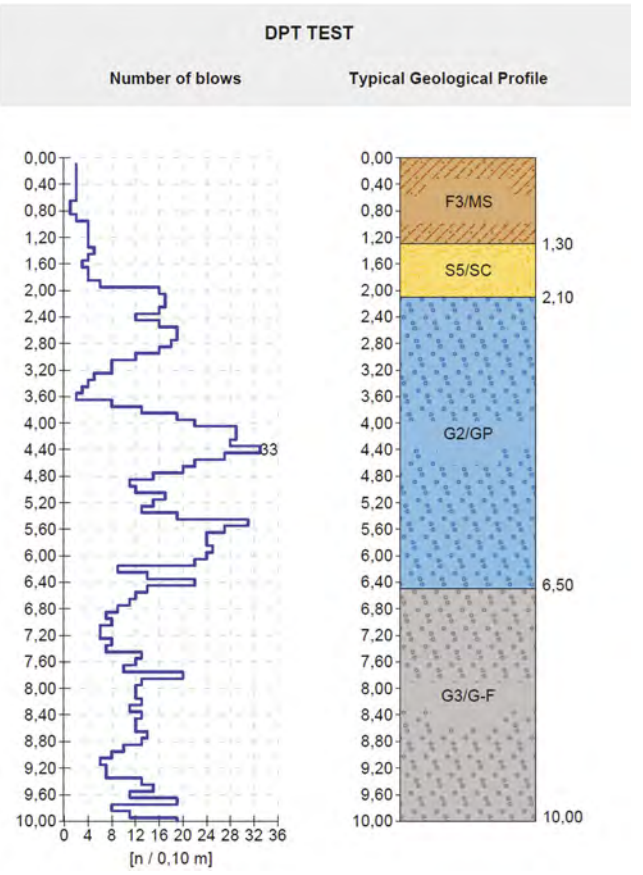

Figure 1. Typical geological profile with DPT results in tested area.

For comparison, mechanical properties of dense poor-graded gravel were also tested in labo-ratory. Shear parameter (ϕ_{ef}) was tested by using large-scale shear box machine with shear box of 300 x 300 x 200 mm and maximal horizontal displacement 60 mm. Two series of tests with normal stress of 50 kPa, 100 kPa, 150 kPa and 200 kPa were conducted on this machine. First series of tests were performed with shear velocity of 1 mm/min, while for second series of tests the shear velocity was set to 0.25 mm/min.

Before testing of shear parameters, it is important to determine the relative density of coarse-grained soil as it affects the shear strength of the sample. During our tests, we used dense gravel meaning that the sample had bigger shear strength and effect of initial shear strength, caused by grain interlocking, was observed.

Second parameter, deformation modulus, was tested on the large-scale oedometric test. The oedometric test was simulated by using the triaxial apparatus and Proctor test mold, which allowed us to test coarse-grained soil with maximum grain size of 16 mm. The soil was filled into a Proctor mold with a diameter of 150 mm and height of 125 mm. To obtain a dense sample, gravel was compacted in three layers according to the rules for the Proctor test. The mold with the soil was placed in a triaxial apparatus in which different load stages were simulated in two load cycles. The maximum applied load for the test series was 0.6 MPa.

3 RESULTS

The paper analyzes the results of mechanical properties of dense poor-graded gravel of fluvial origin obtained from field and laboratory testing. Firstly, during the field testing there were

collected about 110 results of q_{dyn} for poor-graded gravel. Consecutively, mechanical properties (e.g., ϕ_{ef} and E_{def}) were derived from these results and afterwards were statistically processed (Figure 2). For further analysis the mean values were used.

Secondly a series of laboratory tests were performed on dense poor-graded gravel using large-scale shear box test and large-scale oedometric test. For the evaluation of ϕ_{ef}, a series of shear tests with different maximal load were carried out on the dense gravel soil sample. The result of the shear test is a diagram of shear strength, which shows its development against horizontal displacement. In order to determine the angle of shear strength, the maximum values of shear strength from each load step were overlayed by straight line that indicates the angle (Figure 3).

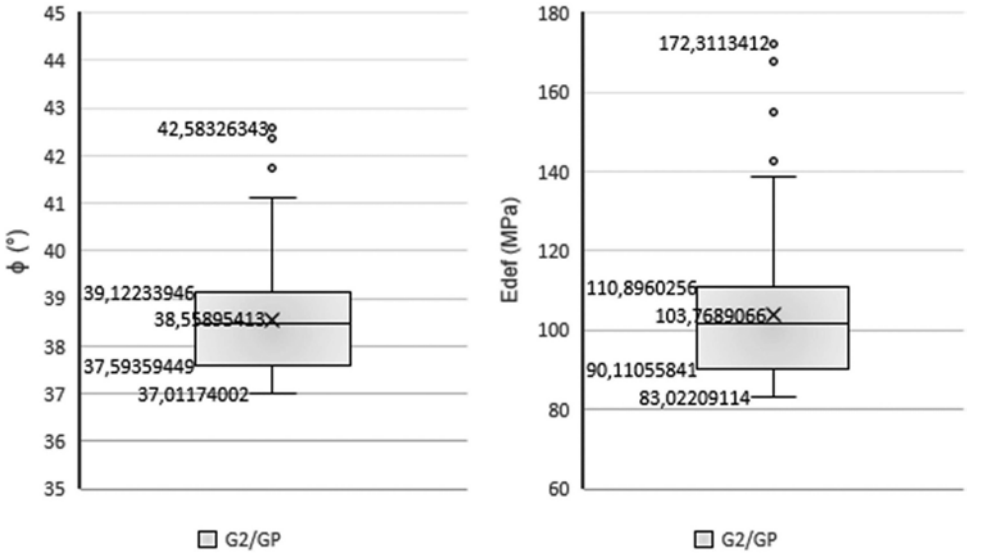

Figure 2. Statistical evaluation of mechanical properties derived from DP results.

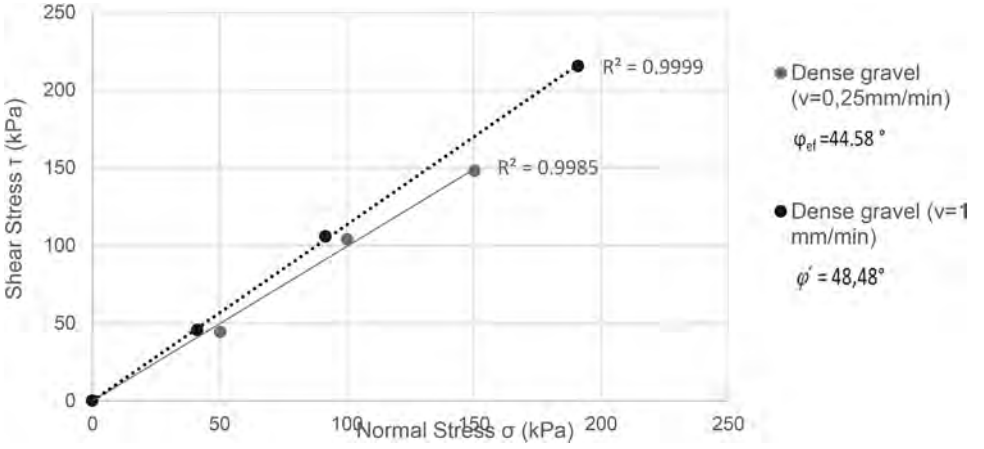

Figure 3. Angle of shear strength of dense poor-graded gravel measured in laboratory.

Furthermore, 3 compressibility tests of poor-graded gravel were carried out in the laboratory using a large-scale oedometer to determine the deformation modulus of dense gravel soil sample. During the test, the gravel was gradually loaded with a normal stress from 25 kPa to 600 kPa. Subsequently, the sample was unloaded. In total, 5 loading and 2 unloading stages with a duration of 1 hour were simulated in one loading cycle. Figure 4 shows the results of compressibility tests of poor-graded gravel.

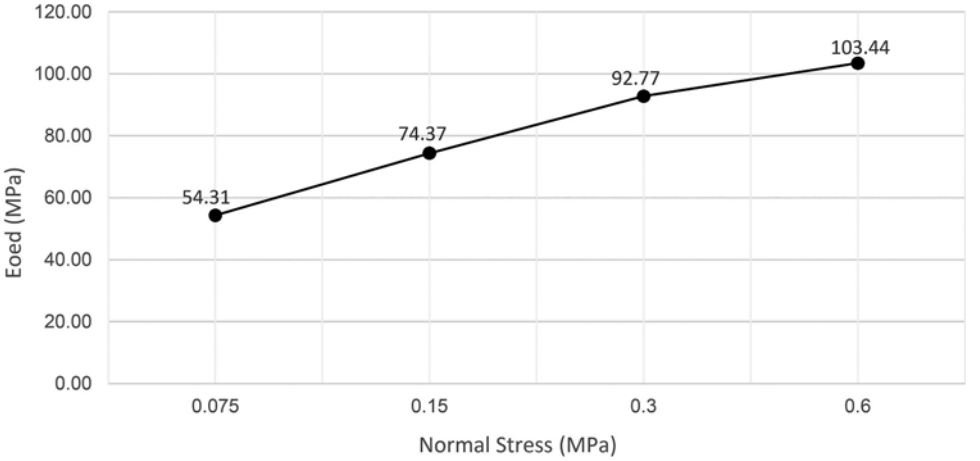

Figure 4. Deformation modulus of dense poor-graded fluvial gravel.

4 DISCUSSION

The results of the shear and oedometric tests were compared with the results of the mechanical properties derived from the dynamic penetration tests. The angle of shear strength derived from DP test using the selected correlation (Table 1) is 38.6°. Compared to the results of large-scale shear tests (Figure 2), the value is lower. However, applied correlation considers the type and class of coarse-grained soils, but do not consider its genesis (grain shape), which also affects the evaluation of geotechnical properties. Tested soil was coarse-grained soils of fluvial origin with rounded grains that have a smaller tendency for grain interlocking. Thus, this could be a cause of the lower values measured in the field.

The deformation modulus of dense gravels (Figure 4) shows a good match only for the loading step of 0.6 MPa. Nonetheless, the chosen correlation between DP results and E_{def} is more critical and gives lower values. On the other hand, in Slovak literature there exist other correlations that gives more optimistic values (STN 72 1032:1997, Matys et al.1990). However, it should be emphasized that the chosen correlations do not consider the genesis of the soil, therefore we cannot determine the accuracy of the results. In contrary, during laboratory tests, it is necessary to know the relative density of the soil, which significantly affects the determination of strength parameters. Since it is more difficult for coarse-grained soils to achieve the natural relative density, different results can be measured by laboratory tests.

5 CONCLUSION

Determining the properties of soils and rocks is a key aspect in the design of geotechnical structures. However, their determination is largely influenced by spatial variability (Pohl, 2011), and therefore in many cases it is difficult to take a representative and undisturbed sample suitable for further laboratory testing. For this reason, many tests are carried out directly in the field (Schnaid, 2009). In Slovakia, dynamic penetration (DP) is one of the most widely used field tests for the exploration of coarse-grained soils. Using appropriate correlations, it is possible to derive selected geotechnical parameters including angle of shear strength (ϕ_{ef}) and deformation modulus (E_{def}). In the laboratory, these parameters can only be determined using large-scale oedometric and shear tests, as standard tests do not have a capacity for testing soils with a large fraction of grains (Pavlík & Račanský, 2019). In laboratory conditions, it is difficult to restore original density of coarse-grained soil, especially gravels. Therefore, in most cases, field testing is used.

In this article, we present the determination of mechanical properties of coarse-grained soils from DP results using selected correlations. Coarse-grained soils in the Southwestern part of Slovakia were tested by heavy dynamic penetration. Using selected correlations, the mechanical parameters of poor-graded gravels were derived. The poor-graded gravel was further tested in the laboratory using large-scale oedometric and shear tests.

A series of shear and oedometric tests were carried out on dense gravel. A large-scale shear apparatus, (shear box dimensions 300 x 300 x 200 mm), was used for the tests. For the tests, 2 normal speeds of horizontal displacement were set – 0.25 and 1 mm/min. The angle of shear strength derived from the DP results using selected correlation is 38,6°. Compared to the results of large-scale shear tests, the value is lower. Given that tested soil is fluvial gravel with rounded grains, the smaller results of the angle of shear strength can be explained by the lateral pushing of grains during dynamic penetration.

Furthermore, a series of compressibility tests were carried out in the laboratory using a large-scale oedometer. The large-scale oedometric test was simulated by a combination of a triaxial device and a Proctor cylindrical mold with a diameter of 150 mm and a height of 125 mm. The soil samples were subjected to two loading cycles with a maximum normal stress 600 kPa. The deformation modulus (103.44 MPa) of dense gravel obtained during maximal loading stage shows a good match with the mean value (103,77 MPa) of the deformation modulus derived from DP tests. The chosen correlations for the derivation of ϕ_{ef}f and E_{def} do not consider the genesis of the soil, so the accuracy of the results is uncertain.

On the other hand, dynamic penetration is relatively often used for soil exploration in Slovakia. Therefore, it is worth to reevaluate and reconsider the use of existing correlations regarding the genesis of soils, since many of the used correlations do not take it into account.

ACKNOWLEDGEMENT

This article was supported by the Grant Agency of the Ministry of Education, Science, Research and Sport of the Slovak Republic, VEGA, grant project No. 1/0745/21.

REFERENCES

DIN 4094-3:2002. Subsoil. Field testing. Part – 3: Dynamic probing.

EN 1997-2:2007. Eurocode 7. Geotechnical design. Part 2: Ground investigation and testing.

Marchetti, S. 2006. Origin of the flat dilatometer. *Proc. 2nd Int. Flat Dilatometer Conf*., Washington DC, 2–4.

Matys, M., Ťavoda, O., Cuninka, M. 1990. *Field testing* [in Slovak], Alfa, Bratislava, Slovakia,

Pavlík, I., Račanský, V. 2019: *Evaluation methodology of laboratory shear and oedometric tests of gravels and other coarse-grained materials*. [in Czech language] - Brno 2019, 47th Conference. Proceedings. Praha: Czech geotechnical society ČSSI, p. 43–50. ISBN 978-80-87920-07-7.

Pohl, C. 2011. *Determination of characteristic soil values by statistical methods*. In: Vogt, Norbert; Schuppener, Bernd; Straub, Daniel; Bräu, Gerhardt (Hg.): Geotechnical Safety and Risk. ISGSR 2011. Karlsruhe: Bundesanstalt für Wasserbau, p. 427–434

Schnaid, F. 2009. *In Situ Testing in Geomechanics*, The *main tests*. London, New York: Taylor & Francis. 328 p. ISBN 0-203-93133-5.

STN 72 1032:1997. Dynamic penetration test (Slovak National Standard).

STN 73 1001:1989. Geotechnical structures. Foundation (Slovak National Standard).

Vrettos, C., Papamichael, S. 2018. *Relative density of cohesionless soils from dynamic probe and cone penetration test – An update assessment of empirical relationship*. Geotechnik 41, p. 186–196

Yu, H.S. 2000. *Cavity Expansion Methods in Geomechanics*. Kluwer Academic Publishers, UK, 385 p.

Smart Geotechnics for Smart Societies – Zhussupbekov, Sarsembayeva & Kaliakin (Eds)
© 2023 The Author(s), ISBN 978-1-003-29912-7
Open Access: www.taylorfrancis.com, CC BY-NC-ND 4.0 license

Shear wave evolution in granular materials - role of wave oscillation direction

J. Liu
Department of Civil Engineering, The University of Tokyo, Tokyo, Japan

M. Otsubo
Public Works Research Institute, Tsukuba, Ibaraki, Japan

R. Kuwano
Institute of Industrial Science, The University of Tokyo, Tokyo, Japan

ABSTRACT: This study investigates the influence of S-wave oscillation direction on the evolution of S-wave signals in granular materials using the flexible boundary cubical cell and disk-shaped shear plates, by which S-waves with a fixed propagation direction and varied oscillation directions can be generated and received. Comparisons of wave signals show that S-wave oscillation direction can reflect the inner fabric of granular materials. In addition, strong directivity of particle orientation within the depositional plane was observed to have obvious influence on S-wave propagation.

1 INTRODUCTION

Shear wave (S-wave) propagation, as the most versatile and portable method to obtain the small-strain stiffness of soils, has been widely used in both laboratory testing (e.g. bender element and shear plate) and field investigation (e.g. cross-hole and surface waves) to monitor and characterize soil seismic behaviors (Minsu et al. 2014). S-waves are transverse waves, meaning that the direction of oscillation of a S-wave is perpendicular to its propagation direction. Some previous studies successfully made use of S-waves to characterize the small-strain stiffness anisotropy of soils in both principle and oblique directions by changing S-wave propagation directions (Bellotti et al. 1996; Fioravante et al. 2001). However, little attention has been paid to the effects of S-wave oscillation direction on the received wave signals, thus the measured S-wave velocities (V_s). In addition, accurate determination of S-wave traveling time is still a challenge.

In this contribution, the disk-shaped piezoelectric shear plate was used to conduct S-wave propagation tests in granular materials, by which the plate can generate and receive S-waves with various oscillation directions and the same propagation direction. The effects of oscillation direction on the S-wave signal evolution and the determination of S-wave traveling time are discussed.

2 TESTED MATERIALS

Discussions in this contribution are based on the results of tests on two granular materials: Toyoura sand (TS) and wild rice (WR). Their physical properties are listed in Table 1, and images of each material are provided in Figure 1. TS grains are sub-angular in shape, whereas WR grains are elongated, having their aspect ratios be about 0.16 as detailed in Liu et al. (2022).

DOI: 10.1201/9781003299127-44

Apart from natural TS, the WR was introduced in this research to explore some extreme fabrics of granular materials. Referring to Figure 1, the image of WR, obtained from micro-computed tomography (μCT), reveals that no obvious air voids exist inside the grains.

Table 1. Physical properties of tested materials.

Material	Median particle size (D_{50}) mm	Specific gravity (G_s)	e_{max}	e_{min}
Toyoura sand (TS)	0.24	2.64	0.943	0.574
Wild rice (WR)	11.27 (major axis)	1.47	0.951	0.612

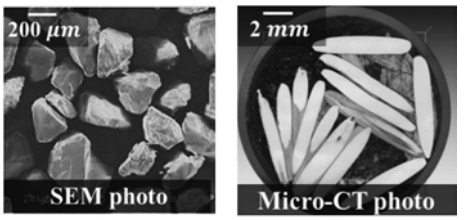

Figure 1. Images of tested materials: (a) Toyoura sand (TS) and (b) wild rice (WR).

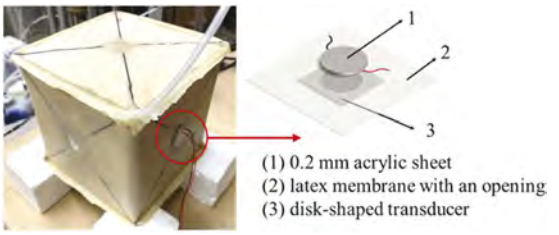

Figure 2. Flexible boundary cubical cell and transducer attachment method (Liu et al. 2022).

3 APPARATUS AND TESTING PROGRAM

3.1 *Flexible boundary cubical cell and specimen preparation*

The TS and WR were air-pluviated vertically (Z-axis) into the cubical cell (Figure 2) and tamped using a wooden hammer layer by layer for ten layers. In particular, another WR specimen was prepared by arranging the major axes of rice particles parallel to the Y-axis within the horizontal plane (Figure 3a), which is referred to as the unidirectional particle orientation specimen. Accordingly, the WR specimen prepared by the air-pluviation followed by tamping is referred to as the random particle orientation specimen (Figure 3b). All three cubical specimens had a dimension of 125 × 125 × 125 mm at dense states and were isotropically confined by the negative pressure of 50 kPa. At the center of each membrane face, a circular opening with a diameter of 20 mm was cut before the specimen preparation, and a 0.2 mm thick acrylic sheet was pasted inside the opening. The disk-shaped S-wave transducers were attached to the sheet directly by double-sided adhesive tape. By rotating a pair of transducers at the same axis (Figure 4), S-waves with a fixed propagation direction but various oscillation (shearing) directions were inserted and received.

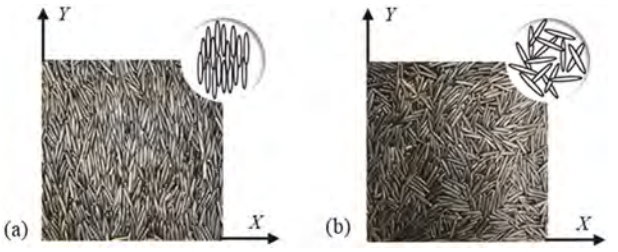

Figure 3. WR specimens with different particle orientations in XY plane: (a) dominated in Y-axis and (b) random.

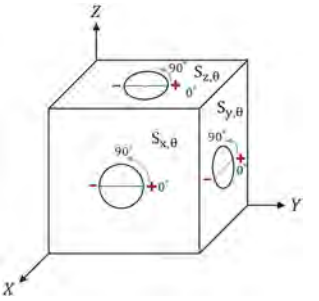

Figure 4. Change of oscillation direction of transducers.

3.2 *S-wave measurements*

A single period of sinusoidal pulse with a double amplitude voltage of 140 V was used to generate S-waves from the transmitter transducer. The input frequency f_{in} = 10 kHz was selected for the TS specimen, while f_{in} = 5 kHz was chosen for the two WR specimens. The first peak of the received S-wave was considered for the following discussions.

4 EXPERIMENTS RESULTS

4.1 *S-wave evolution in the vertical propagation direction (Z-axis)*

In the TS and WR specimens with random particle orientations, particles were assumed mostly oriented within the horizontal plane after the air-pluviation and tamping in the Z-axis. There is little difference in the S-wave arrival times when S-waves propagated in the Z-axis regardless of their oscillation directions (Figures 5a and 5b), confirming that Z-axis is the axis of symmetry according to the cross-anisotropy assumption of granular materials. However, in the WR specimen with dominated particle orientation along the Y-axis, a discontinuous change of the first major peaks can be observed (Figure 5c) when the oscillation direction was rotated from 20° to 40°. The possible explanation for this is that the WR particles can rotate easier in the XZ plane compared with the YZ planes, where elongated particles orientating along the Y-axis resist against rotation or oscillation in the YZ plane. S_{zy} is faster than S_{zx}, indicating greater stiffness in the YZ plane.

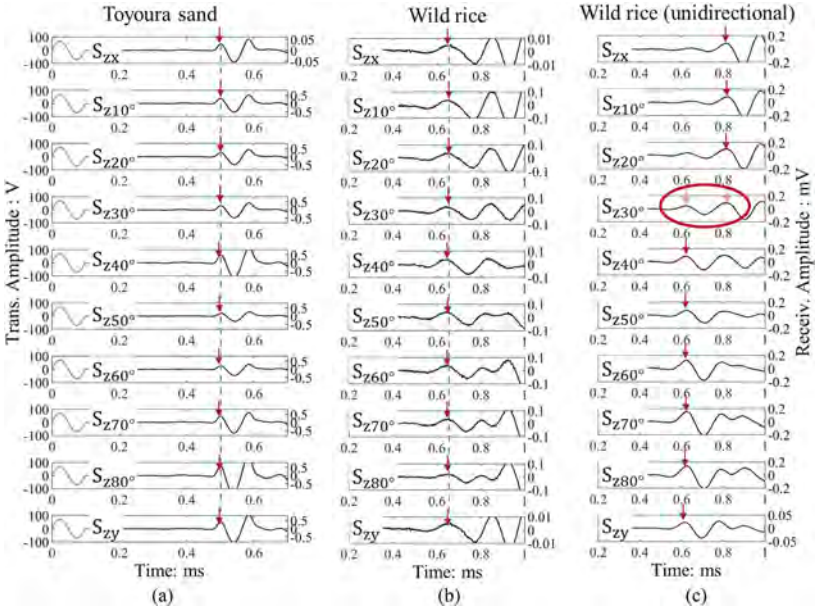

Figure 5. S-wave evolution Z-axis (vertical) propagation direction in: (a) Toyoura sand specimen, (b) wild rice specimen, and (c) wild rice specimen with unidirectional particle orientation.

4.2 *S-wave evolution in the horizontal propagation direction (X- or Y-axis)*

Figure 6a shows the S-wave evolution in the Y-axis propagation for the TS specimen (a similar response was observed for the case of propagation in the X-axis); there is a little difference in the arrival times of S-waves when the oscillation direction was varied systematically, indicating a small degree of anisotropy. Referring to Figure 6b, a discontinuous change in the arrival times of the first major peaks occurred (same for the X-axis propagation) when the oscillation direction was varied from 40° to 60°. Similarly, such phenomena may be explained by the change of dominant particle orientation within vertical planes. A gradual change of the

first arrivals of S-waves was observed in the WR specimen with dominant particle orientation in the Y-axis (Figure 6c). Liu et al. (2022) reported that for the same material with unidirectional particle orientation, S-wave travels the fastest when the propagation direction coincides with dominant particle orientation. Therefore, the gradual change in Figure 6c may result from the consistency of the S-wave propagation direction and the dominant particle orientation within the XY plane.

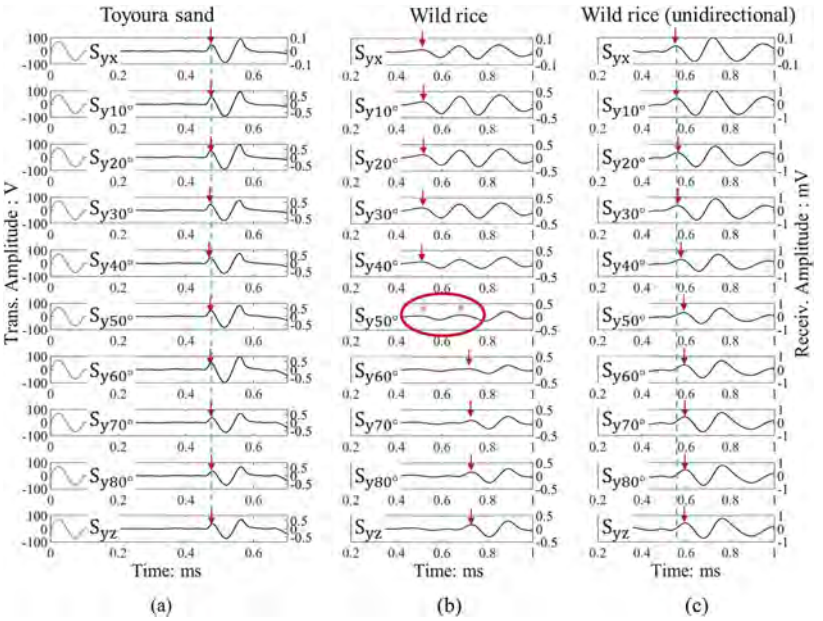

Figure 6. S-wave evolution in Y-axis (horizontal) propagation direction in: (a) Toyoura sand specimen, (b) wild rice specimen and (c) wild rice specimen with unidirectional particle orientation.

5 CONCLUSIONS

This study investigated the significance of the S-wave oscillation direction. S-waves of the TS and WR specimens with different particle orientations within the horizontal plane were measured using the flexible boundary cubical cell equipped with disk-shaped shear plates. S-waves with a fixed propagation direction but systematically varied oscillation directions were successfully measured. The S-wave oscillation direction does reflect the inner fabric of granular materials to some extent. In addition, particle orientation has an obvious influence on the S-wave propagation.

ACKNOWLEDGEMENT

This work was supported by JSPS KAKENHI Grant Number 19K15084 and 22K14322.

REFERENCES

Bellotti, R., Jamiolkowski, M., Presti, D. L. & O'neill, D. A. 1996. Anisotropy of small strain stiffness in Ticino sand. *Géotechnique* 46(1): 115–131.

Cha, M., Santamarina, J.C., Kim, H.S. & Cho, G.C. 2014. Small-strain stiffness, shear-wave velocity, and soil compressibility. *Journal of Geotechnical and Geoenvironmental Engineering* 140(10): 06014011.

Fioravante, V. & Capoferri, R. 2001. On the use of multi-directional piezoelectric transducers in triaxial testing. *Geotechnical Testing Journal* 24(3): 243–255.

Liu, J., Otsubo, M. Kawaguchi, Y. & Kuwano, R. 2022. Anisotropy in small-strain shear modulus of granular materials: Effects of particle properties and experimental conditions, *Soils and Foundations* 62(1): 101105.

Smart Geotechnics for Smart Societies – Zhussupbekov, Sarsembayeva & Kaliakin (Eds)
© 2023 The Author(s), ISBN 978-1-003-29912-7
Open Access: www.taylorfrancis.com, CC BY-NC-ND 4.0 license

Influence of initial defects on the strength of clay soil under triaxial compression

I.T. Mirsayapov & I.V. Koroleva
Kazan State University of Architecture and Engineering, Kazan, Russia

ABSTRACT: Clay soil is the most fragile element of the "building above – ground part – foundation – soil base" system. This is especially important in cases where the base has received deformations during operation and micro- and macro-shear zones have formed in the soil, but the building is not subject to demolition. This loaded soil has different physical-mechanical characteristics than the data obtained from the geotechnical surveys results before the building construction start. The authors carried out studies of changes in the soil strength, which has a "history of loading". A soil sample with a disturbed structure was first loaded in a triaxial compression device of a cubic shape, and then destroyed in a stabilometer. Data were obtained on the change in soil strength depending on time and the influence of humidity on this process. Analytical equations have been developed that describe the process of changing the soil strength with a loading history.

Keywords: clay soil, triaxial tests, soil model, cracks in the ground, loading history

1 INTRODUCTION

In modern construction, a person uses high-strength concrete, steel and other materials for the supporting frame of the building, while the strength and deformability parameters of these materials are determined in advance at the stage of their manufacture. However, the strength and modulus of deformation of the soil base is significantly less than that of the materials from which the main structures of the building are made. Clay soil is the most fragile element of the "above-ground part of the building – foundation – soil base" system, while the safety of the building depends most of all on its reliability. This is often written about (Travush et al, 2019, Petrukhin, 2010). This is especially important in cases where the base has received deformations during operation, but the building is not subject to demolition. This loaded soil has other physical and mechanical characteristics, different from the data obtained from the results of engineering and geological surveys before the construction of the building (Mirsayapov & Aysin, 2019, Mirsayapov & Sharaf, 2017). However, there is very little research on this. The aim of the work is to study the effect of initial defects and damage on the soil strength under triaxial loading and to develop calculation methods. To achieve this goal, experimental studies of soils "without loading history" and "with loading history" were carried out in cubic and stabilometric triaxial compression devices according to the scheme of an unconsolidated undrained (UU) test (Leong et al, 2013, Nguyen et al, 2018). Theoretical studies of the influence of defects and damages on the change in the strength of clay soil from the point of view of fracture mechanics have been carried out.

2 LABORATORY TESTS OF CLAY SOIL

Under laboratory conditions, clay soils with a disturbed structure were tested, including two stages of loading. At the first stage, a "loading history" was created. At this stage, the sample

DOI: 10.1201/9781003299127-45

either underwent destruction, that is, it reached the limiting vertical or horizontal deformation for its size from the effect of an external static load, or only a few loading steps were applied in a cubic triaxial compression device with dimensions of 100 mm x 100 mm x 100 mm. It should be noted that the "load history" was created both by static (Series 1 and Series 2) and cyclic loads (Series 3). The value of all-round reduction in Series 1 was 100 kPa, in Series 2 – 300 kPa, and in Series 3 – 100 kPa, while the amplitude of the cycle – 100 kPa, and the number of cycles applied to the sample was 30 and 50. At the second stage, a cylindrical sample with a height of 76 mm and a diameter of 38 mm was cut out of the cube and subjected to static destruction in a stabilometer according to the "crushing" scheme. Unconsolidated-undrained loading (UU) was used. To evaluate the influence of the "loading history", tests only in a stabilometer were carried out without the first stage. Loading regimes are shown in Figure 1.

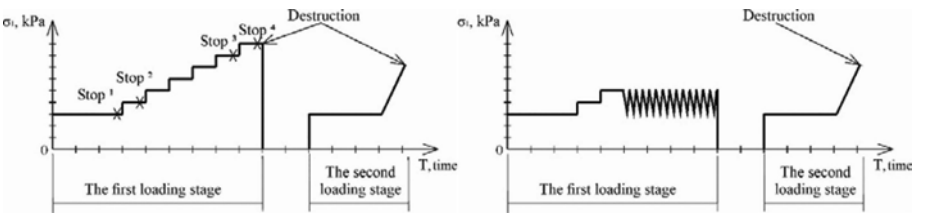

Figure 1. Loading regimes: Series 1 and Series 2 (left), Series 3 (right).

The initial characteristics of the disturbed clayey soil are shown in Table 1.

Table 1. Initial characteristics of clay soil.

Characteristic	Designation, Unit	Arithmetic mean value
Desired humidity	W,%	22
Plasticity number	J_P	17.5
Yield index	J_L	-0.03
Soil density	ρ, g/cm^3	1.95
Angle of internal friction at W	φ,^{o}	20.6
Specific adhesion at W	C, kPa	67.5

The test results are shown in Figure 2. For the "zero" regime, a three-axis test without a "loading history" is taken.

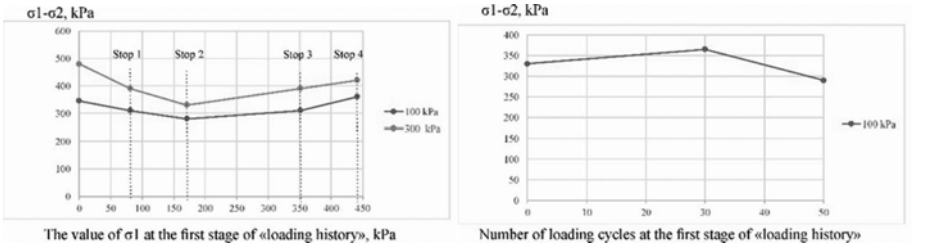

Figure 2. Change in the strength of a clay soil sample: Series 1 and Series 2 (left), Series 3 (right).

The test results made it possible to establish that, depending on the magnitude of the load and the number of cycles applied at the "load history" stage, a clayey soil sample of a disturbed structure can demonstrate an increase in the bearing capacity (strength), for example, Series 3 – after 30 cycles, the strength of the soil increased by 15% and Series 1 Stop 4 – up to 5%, and its decrease by 20%. This process is explained by the formation and

accumulation of defects in the body of the soil sample at the first stage and further softening at the second stage or hardening at the first stage and a further increase in strength at the second, depending on the magnitude of the applied load or the number of cycles that create the "loading history".

Tests of the first stage made it possible to set the soil to varying degrees of structural change. The first sample (Stop 1) had additional soil compaction by 3% in the integral volume.

Based on the results of experimental studies, it is assumed that under triaxial regime loading of a soil sample, various zones (Figure 3) of the stress-strain state arise, i.e. with a gradual increase in load, compacted zones are formed in the form of pyramids of various sizes and shapes, depending on the loading mode: from above, in the lower part of the sample and at the side faces. The sample deformation occurs due to the movement of these pyramids as rigid bodies. In these compacted zones, there is no deterioration in the physical and mechanical characteristics of soils, but their improvement (increase in density, φ and c). Negative processes that reduce the physical and mechanical characteristics of the soil are localized in the zone between these "pyramids" and the soil in this zone is subjected to simultaneous separation and shear with the formation of micro- and macro- cracks in the limiting equilibrium plane, which is used by the authors when developing a theoretical model.

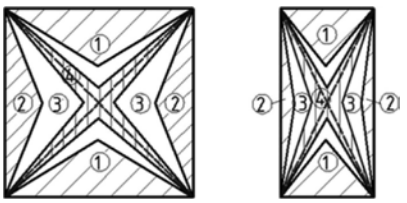

Figure 3. Location scheme of local zones of different density in the sample: 1 – vertical compacted pyramids; 2 – compacted pyramids at the side faces; 3 – zone of uniform stress state; 4 – zone of dilatancy.

3 THEORETICAL RESEARCH

According to the results of studies previously presented by the authors (Mirsayapov & Koroleva, 2011, Mirsayapov & Koroleva, 2015, Mirsayapov & Koroleva, 2016), in a cubic sample, during loading, soil compaction occurs at the first stages, and then zones of formation of limit equilibrium planes appear, and with further loading, shear zones and the shear of one part of the soil relative to another, while on strength and deformation are affected by soil moisture and load application time. Based on the above model and the results of experimental studies, the strength condition under triaxial regime compression is represented as:

$$4 \cdot [\ \sigma_V(t,N,t_1) \cdot A_{sh} \cdot cos\ \alpha_1(t,N,t_1) + \tau_V(t,N,t_1) \cdot A_{sh} \cdot sin\ \alpha_1(t,N,t_1)\ ] \geq \sigma_1 \cdot A_1 \qquad (1)$$

where $A_{sh}=b^2/(4cos\alpha_2(t,N,t_1))$ is the surface area of the side faces of the pyramid; $A_1=b^2$ is the area of the cube face; $\alpha_1(t,N,t_1)$ is the time-varying slope of the limit equilibrium area; $\alpha_2(t,N,t_1)$ is the time-varying angle of inclination of the shear area; $\sigma_v(t,N,t_1)$ are normal stresses; $\sigma_d(t,N,t_1)$ are dilatant stresses; $\tau_V(t,N,t_1)$ are shear stresses on the area of limit equilibrium.

Thus, the strength of the soil both on the first and on the second loading blocks depends on the change in the angle of internal friction, specific adhesion and the angle of inclination of the limit equilibrium plane.

The initiators of the formation of microcracks are structural defects - pores and shrinkage microcracks. Micro- and macrocracks in the planes of limit equilibrium develop unstably: the stages of nucleation, accumulation of submicrocracks, their transformation into micro- and macrocracks and abrupt development to a critical value are distinguished.

The process of crack development can be conditionally divided into three periods.

The first period - soil loosening - begins with the appearance of submicroscopic cracks after the appearance of limit equilibrium planes. Cracks occur at the pores or in the continuation of shrinkage microcracks (structural defects). At this stage, the crack sizes are small and it is most correct to speak of the formation of local plastically deformed areas. These locally plastically deformed areas near pores or shrinkage microcracks unite many submicrocracks, which are localized in certain zones of the structure, and then gradually form a loosening chain, preparing the microcrack path. In the initial stage of loading, several loosening zones are formed distributed throughout the volume. Loosening chains turn into microcracks only at a certain concentration of submicrocracks in a certain characteristic volume of the soil structure. The formation of large-sized microcracks or macrocracks occurs only in those areas where the deformation energy is sufficient to unite individual links of the loosened soil. In other, less stressed areas, individual microfractures are gradually excluded from the chain process of damage accumulation due to a decrease in stress concentration in the places where microcracks form. As the load increases, submicrocracks and microcracks grow and join, gradually turning into large microcracks. This stage can be called incubation. The duration of the incubation stage depends on the level of applied load: the higher the load level, the shorter the incubation period.

The second period begins when one of the microcracks, which is in the most unfavorable conditions, grows into a macrocrack. At the front of a developing macro-crack, a zone of plastically deformed material (loosening zone) is always formed, and a further increase in length occurs due to this end zone. The processes of material loosening in the end plastic zone and the formation of a new macrocrack section alternate. The development of a macrocrack is preceded by a relatively long period of loosening of the material in the end plastic zone. Then, depending on the stress level, a macrocrack develops by means of a stable or abrupt advance by the length of the loosening zone. This process is then systematically repeated. The second period ends when the macrocrack reaches a critical size. In the future, the crack develops unstably due to the deformation energy of the calculated volume of soil.

The duration of the third period is usually negligible compared to the previous ones, and it appears on the descending branch of the soil deformation diagram. The transition between stages is abrupt and represents a link in a continuous chain. Each period has its own crack development mechanism, but there are basic processes.

The criterion of "breakaway" (the beginning of the increase in length) is the condition of critical opening of the crack tip:

$$\delta(x, t, l) = \delta_{cr} \tag{2}$$

The development of a crack occurs stepwise by the value Δl_n as the stress increases until the total length reaches the value d_0:

$$\Delta l_n = l_0 \cdot c_0(t) \cdot (1 + \chi_0) \div (\pi \cdot K_0) \cdot ln\ (cos\ ek\alpha) \tag{3}$$

where $c_0(t) = 2K_0 \cdot \varepsilon_2/(1 + \chi_0)$; $\chi_0 = (3 - \nu_0)/(1 + \nu_0)$; $K_0 = E(\tau_1)/(2(1 \cdot \nu_0))$ is bulk modulus of soil deformation; Δl_n is crack length increment (increment of the elementary zone of plastic deformation at $\varepsilon_{gr} \geq \varepsilon_{gr,u}$).

After this, the development of a macrocrack begins. In this case, it is assumed that cracks develop in stages as deformations at the apex reach a critical value. The crack length increment Δl_n at each stage is determined from the condition:

$$\sum \left[\Delta W_i - \Delta W_r \left(\frac{\Delta W_i}{W_r} \right)^{\beta} \right] = const = W_{pl} \tag{4}$$

According to the results (Zaretskii, 2002), failure occurs when the degree of microcrack damage in the limiting equilibrium zone reaches a critical value. Therefore, the decrease in soil strength occurs mainly due to a decrease in cohesive forces.

Using the technique proposed in (Panasyuk et al. 1976), after transformations and simplifications, we obtain the function of soil strength reduction (specific cohesion) during regime loading:

$$\eta(t,\tau_1) = m(t,\tau_1)\cdot\lambda(t,\tau_1)\times\sqrt{\frac{K(\tau_1)}{K(t)}\cdot\frac{1}{1+\mathrm{K}(\tau_1)\cdot C(t,\tau_1)}}. \quad (5)$$

Then the specific cohesion between particles, taking into account the time factor, will be represented as:

$$\mathrm{C}_0(t,\tau_1) = \mathrm{C}_0(\tau_1)\cdot m(t,\tau_1)\cdot\lambda(t,\tau_1)\times\sqrt{\frac{\mathrm{K}(\tau_1)}{\mathrm{K}(t)}\cdot\frac{1}{1+\mathrm{K}(\tau_1)\cdot C(t,\tau_1)}}. \quad (6)$$

where $C(t,\tau 1)\chi_0 = (3-\nu_0)/(1+\nu_0)$ is measure of soil volumetric creep; $C_0(\tau_1)$ is initial value of specific soil cohesion at "zero" loading; $m(t, \tau_1)$ is soil strengthening function due to the restoration of water-colloidal bonds; $\lambda(t, \tau_1)$ is strengthening function due to the restoration of the structural bonds of the soil, taking into account the combination of different blocks in the process of two stages of loading.

The functions $m(t, \tau)$ and $\lambda(t, \tau)$ take into account the effects of delaying the development of micro and macro cracks and the effects of self-hardening and self-healing of clay soil due to the restoration of structural and coagulation bonds in the process of creating a "loading history".

4 CONCLUSION

Studies have been carried out on changes in the strength of soil having a cyclic and static "loading history". Data were obtained on the change in soil strength depending on the number of loading cycles, as well as the level of deviatoric load at the first stage of loading, taking into account the accumulation of structural defects in the form of micro- and macro-cracks and their self-healing.

A computational model of clay soil under triaxial compression has been developed, which makes it possible to take into account the "loading history", the processes of hardening and restoration of structural bonds, as well as dilatancy from the point of view of fracture mechanics.

REFERENCES

Leong, E.C., Nyunt, T.T., and Rahardjo, H. 2013. Triaxial testing of unsaturated soils. *Springer Series in Geomechanics and Geoengineering* 3:33–44. doi:10.1007/978-3-642-32492-5_3.

Mirsayapov, I.T., Aysin, N.N. 2019. Influence of a deep construction pit on a technical condition of surrounding buildings. In: Geotechnics Fundamentals and Applications in Construction: New Materials, Structures, Technologies and Calculations - Proceedings of the International Conference on Geotechnics Fundamentals and Applications in Construction: New Materials, Structures, Technologies and Calculations, GFAC 2019, 197–201.

Mirsayapov, I.T., Koroleva, I.V. 2011. Designed model of long nonlinear deformation of clay soil in a complex stress state. *NEWS KSUAE* 2(16): 121–128.

Mirsayapov, I.T., Koroleva, I.V. 2015. Clayey soils rheological model under triaxial regime loading. In: Geotechnical Engineering for Infrastructure and Development - Proceedings of the XVI European Conference on Soil Mechanics and Geotechnical Engineering, ECSMGE 2015, 6: 3249–3254.

Mirsayapov, I.T., Koroleva, I.V. 2016. Strength and deformability of clay soil under different triaxial load regimes that consider crack formation. *Soil Mechanics and Foundation Engineering* 53(1): 5–11.

Mirsayapov I.T., Sharaf Hani M.A. 2017. Strength and deformation of clay soils in the conditions of the triaxial compression under block regime cyclic loading. *NEWS KSUAE* 4(42): 221–227.

Nguyen, H.B.K., Rahman, M.M., and Fourie, A.B. 2018. Characteristic behavior of drained and undrained triaxial compression tests: DEM study. *Journal of Geotechnical and Geoenvironmental Engineering* 144(9):1–13. doi:10.1061/(ASCE)GT.1943-5606.0001940.

Panasyuk, B.B. et al. 1976. *Stress distribution around cracks in plates and shells*. Naukova dumka. Kiev.

Petrukhin, V.P. 2010. Geotechnical problems of construction in Moscow – the largest metropolis of Russia. Proceedings of the international. Conference – Geotechnical problems of megacities, GEOMOS2010, Moscow, Russia.

Travush, V.I et al. 2019. Analysis of the Results of Geotechnical Monitoring of "Lakhta Center" Tower. *Soil Mechanics and Foundation Engineering* 56: 98–106. https://doi.org/10.1007/s11204-019-09576-9.

Zaretskii, Yu. K.2002. Two Failure Mechanism and a Unified strength Condition for Geomaterials. *Soil Mechanics and Foundation Engineering*39(6): 193–201.

Smart Geotechnics for Smart Societies – Zhussupbekov, Sarsembayeva & Kaliakin (Eds)
© 2023 The Author(s), ISBN 978-1-003-29912-7
Open Access: www.taylorfrancis.com, CC BY-NC-ND 4.0 license

Design aspects of a soil improvement in saturated clay - requirements for the material properties of an innovative composite

C. Boley & P. Pratter
Institute for Soil Mechanics and Geotechnical Engineering, Bundeswehr University Munich, Germany

ABSTRACT: Clayey soils represent a challenge in geotechnical engineering worldwide, which is dealt with using soil improvements. In particular, the choice of a suitable soil improvement method requires expertise already in the design phase. In addition to the planning aspects that must be considered for foundations in saturated clayey soils, the results of laboratory tests on an innovative composite material are presented. The research focuses on an innovative composite material made of gravel and polymer, whose mechanical and hydraulic properties are suitable for dealing with the difficult soil conditions in saturated clayey soils. Among other things, it is shown that the load-bearing capacity of the composite material is comparable to concrete, but the material has an effective pore space and remains permeable. These drainage properties are a great advantage in soils otherwise characterized by low permeability.

1 INTRODUCTION

The challenges of foundation work in saturated clay are the low load-bearing capacity of the soils and the settlement behavior. Basically, the permeability of the soils is of central importance. Experience has shown that permeability of saturated clay lies in the range from very low to practically impermeable. In geotechnical engineering, the challenges associated with saturated clay are met with

- foundation work that allows large settlements over many years, for example a spread foundation with a rigid raft foundation,
- or soil improvements.

For soil improvement, ground column technologies are used in many cases and transmit the load from the structure through the surrounding soil by side friction or lateral confinement in a comparatively flexible way. Alternatively, the load is transmitted into the deeper load-bearing soil layers by rigid vertical support elements. The different ground column technologies are presented in detail by Han (2015). The challenges and risks associated with foundations in saturated clay are pointed out by several researchers, for example Gyger et al. (1996) or Yazdani et al. (2021). Thus, driving of displacement piles into a cohesive soil causes large excess pore pressures close to the pile and at the pile-soil interface (Bałachowski & Konkol 2021, Sagaseta & Whittle 2001, Simonsen & Sørensen 2016). This increase in pore water pressure can be counteracted with an adapted design and vertical drainage (Suleiman et al. 2016, Kirstein & Wittorf 2013).

This research focusses a composite material that is semi-rigid and represents a load-bearing behavior between the above-mentioned flexible and rigid behavior. The innovative composite material has a load-bearing capacity comparable to that of concrete, but nevertheless features excellent drainage properties.

2 COMPOSITE MATERIAL

Composites are combinations of materials, where the individual constituents retain their separate identities. These separate constituents act together to give the necessary mechanical strength or stiffness to

DOI: 10.1201/9781003299127-46

the composite material (Jose et al. 2012). In this research work synthetic polymers and gravel are used. The polymers form a strong adhesive bond with the gravel and are waterproof so that an application below the groundwater level is possible. Characteristics of the intact adhesive bond of the composite material are the grain-to-grain contacts of the gravel and the polymer menisci that form on it, as well as the wetting of the entire grain surface with the polymer, see Figure 1. The polymer menisci can develop because the pore space of the gravel is not completely saturated with the polymer and air voids remain. These air voids are mainly linked and form the effective pore space, which is available for the flow processes (Fuchs et al. 2017) and significantly determines the permeability. Figure 1 (b) shows a microscopic image of the composite material. The areas with polymers are highlighted in yellow, by image processing/segmentation, and the effective pore space is marked in blue.

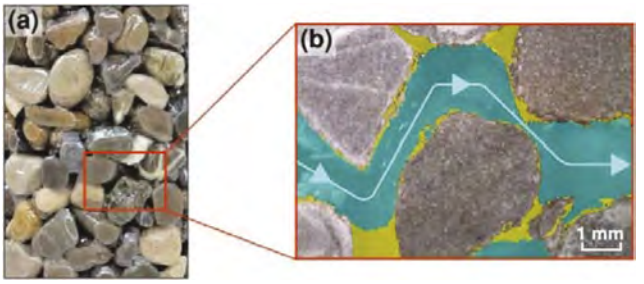

Figure 1. Composite material (a) and microscopic analysis of the pore space (b).

2.1 *Hydraulic properties*

The hydraulic properties were determined in a cylindrical permeameter with a rigid wall and at a constant hydrostatic pressure head. The test specimens were pure gravel and the composite material with different mass fractions of polymer. The mass fraction of polymer was continuously increased in three steps. At least nine individual tests were carried out for each composite material. Figure 2 shows the essential hydraulic properties. With increasing mass fraction of the polymer, the permeability of the material decreases since more pores are now filled with the polymer and less effective pore space is available for flow processes (Anagnostopoulos 2005). Although the permeability is reduced, the composite material still has a high permeability of 6.7E-03 m/s, see Figure 2. compared to pure gravel, the addition of polymer has reduced the permeability by less than one power of ten.

Consequently, soil improvement with composite material in the normally very low to practically impermeable clay, less than 10E-09 m/s (Terzaghi et al. 1996), creates a drainage path that contributes significantly to the reduction of pore water pressure.

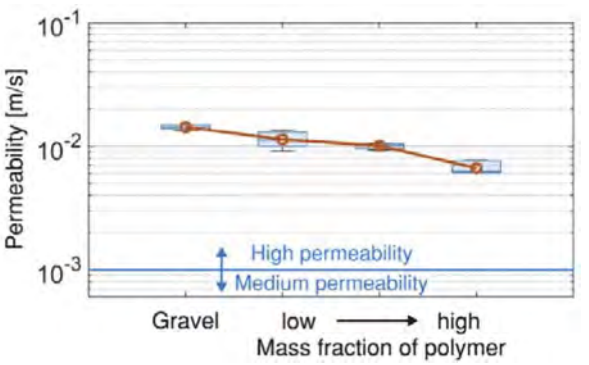

Figure 2. Permeability of pure gravel and composite material depending on the mass fraction of the polymer.

2.2 *Mechanical properties of the composite material*

Previous work with grouting material has shown that the shear behavior of grouted bodies can be correctly described using the nonlinear failure criterion according to Hoek-Brown (Boley et al. 2019). In addition to the principal stresses, the Hoek-Brown failure criterion uses the uniaxial compressive strength σ_{ci} and the material constants s, a, and m_b. The material constants depend on the geological strength index *GSI* and the disturbance factor *D* (Hoek & Brown 2019).

The results of the uniaxial compression tests show the load-bearing capacity of the composite material can increase up to 12 MPa, equal to the strength of concrete. As a grouting material, polymers can have a compressive strength of this size and even significantly higher, as the compressive strength tests by Shi et al. (2010) demonstrate. Material with a strength in this order of magnitude must be tested using rock mechanical testing equipment.

For compact and intact rock, the parameters are chosen to $s = 1$ and $a = 0.5$. The laboratory tests have shown that these values can also be used for the grouted body. The Hoek-Brown constant m_b of the composite material is determined by curve fitting from the data of the uniaxial compression tests and triaxial tests. For a composite based on polymer 01 and gravel, m_b was determined to 7.7 (R^2 0.99).

$$\sigma_1' = \sigma_3' + 11.9\ (MPa) \cdot \left\{ \left(\frac{7.7 \cdot \sigma_3'}{11.9\ (MPa)} \right) + 1 \right\}^{0.5} \tag{1}$$

The high cohesion value of 3.3 MPa can be verified by analyzing the microstructure of the composite material, see Figure 1 (b). The gravel grains are held together by the polymer, because the entire surface of the gravel, except for the grain-to-grain contact points, is wetted with the polymer and polymer menisci are formed.

In contrast to cohesion, the addition of the polymer causes a reduction in the angle of friction. In the example, the angle of friction is reduced from 39° to 35°. The decline is due to the full-surface wetting of the grains with polymer and the associated loss of grain roughness. The angle of friction and the cohesion in this example were evaluated for a normal stress of around 5.0 MPa, see Figure 3.

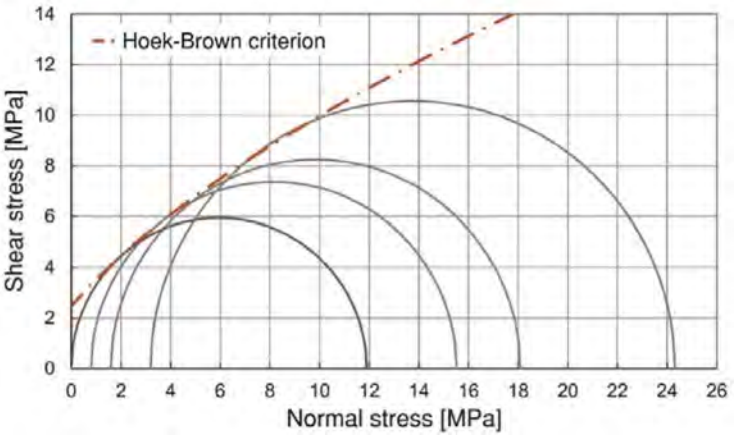

Figure 3. Fractional envelope according to Hoek-Brown for the composite material.

3 CONCLUSIONS

Based on the results of the research work, the innovative composite material has potential for application as a soil improvement. Thus, even the difficult ground conditions in saturated clay can be handled with it. Essentially, the findings of the present research work can be summarized as follows:

- The composite material has an effective pore space through which water can drain.
- Even for a high mass fraction of polymer, the composite material, with a permeability coefficient of 6.7E-03 m/s, can be classified as high permeable.
- The final strength of the high permeable composite material can be increased up to 12 MPa.
- Material behavior can be described as being well approximated by the Hoek-Brown failure criterion.
- The increase in cohesion is due to the adhesive and cohesive forces of the polymer, see polymer menisci in the microscopic analysis in Figure 1 (b).
- In contrast to cohesion, the addition of polymer causes a reduction in the angle of friction.

The presented research work is part of a currently ongoing research project. Furthermore, the research work focuses on the detailed numerical simulation of the composite material, by using the discrete element method, and on aspects from construction practice, such as durability and workability. Basically, the composite material appears to be suitable for permanent ground improvement.

ACKNOWLEDGMENTS

We are grateful to Keller Grundbau GmbH and TPH Bausysteme GmbH for the financial support of this research.

REFERENCES

Anagnostopoulos, C.A. 2005. Laboratory study of an injected granular soil with polymer grouts, *Tunnelling and Underground Space Technology* 20: 525–533.

Bałachowski, L. & Konkol, J. 2021. Pore Water Pressure Development in Soft Soil due to Installation and Loading of Controlled Modulus Columns. *J. Geotech. Geoenviron. Eng*. 147(12): 06021014.

Boley, C., Forouzandeh, Y., Wagner, S. & Pratter, P. 2019. Scherverhalten von acrylatischen Injektionskörpern. *geotechnik* 43(1): 31–39.

Fuchs, S., Ziesche, M. & Nillert, P. 2017. Estimation of porosity from hydraulic conductivity and uniformity coefficient: A review. *Grundwasser* 22: 83–101.

Gyger, M., Kuhn, B. & Werder, F. 1996. Probleme mit Verdrängungspfählen in wassergesättigtem Seebodenlehm. *Schweizer Ingenieur und Architekt* 114(8): 4–8.

Han, J. 2015. Recent research and development of ground column technologies. *Proc. of the Institution of Civil Engineers - Ground Improvement* 168(4): 246–264.

Hoek, E. & Brown, E.T. 2019. The Hoek-Brown failure criterion and GSI – 2018 edition. *Journal of Rock Mechanics and Geotechnical Engineering* 11(3): 445–463.

Jose, J.P., Malhotra, S.K., Thomas, S., Kuruvilla, J., Goda, K. & Sreekala, M.S. 2012. Advances in Polymer Composites: Macro- and Microcomposites – State of the Art, New Challenges, and Opportunities. *Polymer Composites* 1. Weinheim: Wiley-VCH Verlag & co. KGaA.

Kirstein, J.F. & Wittorf N. 2013. Improvement of soft fat clay using rigid inclusions and vertical drains. *Proc. of the 18th International Conference on Soil Mechanics and Geotechnical Engineering, Paris 2013*: 1–4.

Sagaseta, C. & Whittle, A.J. 2001. Prediction of ground movements due to pile driving in clay. *J. Geotech. Geoenviron. Eng*. 127(1): 55–66.

Shi, M., Wang, F. & Luo, J. 2010. Compressive Strength of Polymer Grouting Material at Different Temperatures. *Journal of Wuhan University of Technology* 25(6): 962–965.

Simonsen, T.R. & Sørensen, K.K. 2016. Field measurements of pore water pressure changes in very high plasticity stiff clays adjacent to driven piles. *Proceedings of the 17th Nordic Geotechnical Meeting Challenges in Nordic Geotechnic 25th – 28th of May, Reykjavik*: 257–266.

Suleiman, M.T., Ni, L., Davis, C., Lin, H. & Xiao, S. 2015. Installation Effects of Controlled Modulus Column Ground Improvement Piles on Surrounding Soil. *J. Geotech. Geoenviron. Eng*. 142(1): 04015059.

Terzaghi, K., Peck, R.B. & Mesri, G. 1996. *Soil Mechanics in Engineering Practice*, third edition. New York: John Wiley & Sons, Inc.

Yazdani, E., Wang, J. & Evans, T.M. 2021. Case study of a driven pile foundation in diatomaceous soil. II: Pile installation, dynamic analysis, and pore pressure generation. *Journal of Rock Mechanics and Geotechnical Engineering* 13(2): 446–456.

Smart Geotechnics for Smart Societies – Zhussupbekov, Sarsembayeva & Kaliakin (Eds)
© 2023 The Author(s), ISBN 978-1-003-29912-7
Open Access: www.taylorfrancis.com, CC BY-NC-ND 4.0 license

New method of mechanical research of soils and use of it in design practice

A.N. Alekhin
A.N. Alekhin Ural State University of Railway Transport, Yekaterinburg, Russian Federation

ABSTRACT: Soil base is a basic, often the most pliable, load-bearing element of the building. Not being, as a rule, a constructive element of the building (except maybe artificially created reinforced soil massifs geomassifs) soil base takes on entire load from building, affecting operational and strength parameters of the building. This situation certainly requires inclusion of a soil base model into computer model of the building. In this case the problem of determining the mechanical parameters of a physically nonlinear soil from in-situ tests arises, because laboratory tests for these purposes are complex and on various reasons their results are unreliable The paper presents an algorithm of the method of determination of the design mechanical soil parameters for the physically nonlinear Botkin model. Examples of practical application of the method for the design of real objects are given.

1 INTRODUCTION

In the 1940s Russian scientist Botkin experimentally determinated and investigated physically nonlinear type of deformation for non-rocky soils (clays and sands); then this fact was confirmed by other geotechnicians (Klein, Kriegel, Alekhin). Currently researches on various aspects of this fundamental reality are being actively and successfully developed. One of the most important aspect is development of methods for determining design parameters of nonlinear soil model from in-situ test data including geometric nonlinearity as well as soil rheological properties. If the question of geometric nonlinearity, which importance for soil deformation has not yet been fully elucidated, is solved rather simply, mainly by a small adjustment of formulas for relative strains, while very complex but important investigations of rheological properties with physical nonlinearity is now beginning at some laboratories, maybe effective in-situ method will allow for rheological theory to be corrected taking into account initial stress state in soils; application of this method will also may help to asses more accurately geometric nonlinearity influence, for example, at designing neighboring buildings. Thus, the validity to solve problem of using in-situ test data was predetermined both by unique physical properties of nonrocky soil itself as specific kind of solid medium with specific internal bonds and fixed of soil structure initial stress state (both of them are inevitably destroyed during sampling) and by soil mathematical model with complex nonlinear relationships. At present Botkin's model is the only systematically and consistently verified, including practical application of physically and geometrically nonlinear soil model. Moreover, so far this is the only soil model with complex nonlinear relationships for which it was possible to develop a convenient method for determining true values of design mechanical parameters from in-situ test data that much increase reliability and accuracy of geotechnical design. The general principles of the proposed method, in particular the method of solving revers unstable problems can be applied for determining mechanical parameters of other types of physically nonlinear models. Below algorithm for the determination of mechanical parameters of physically nonlinear soil model in relation to the Botkin's model is presented. As for the way of derivation of constitutive relations for the Botkin's model as well as the formula of less general physically linear Young-Hook's model are referred to the, so called, phenomenological form obtained as a result of approximation of data

DOI: 10.1201/9781003299127-47

of actual and presentable in general parameters of the stress-strain state (SSS) of mechanical tests on deformation. Phenomenological difference between physically linear (Hooke) and physically nonlinear (Botkin) deformation types of a solid medium is shown at Figure 1.

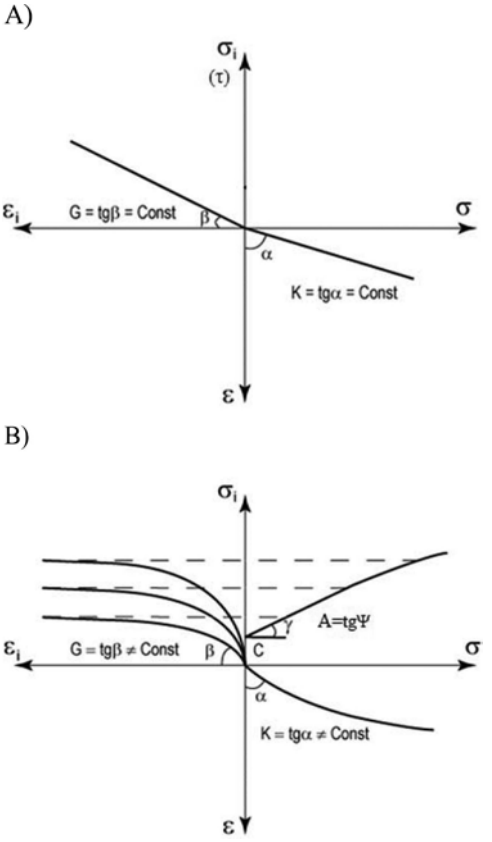

Figure 1. A) physically linear type of deformation (solid materials and rocks) B) physically nonlinear type of deformation (non-rocky soils: sands and clays); K and G – bulk modulus and shear modulus respectively; σ and ε – first invariants of the stress and strain tensors (bulk deformation); σ_i and ε_i – second invariants of the stress and strain deviators shape deformation).

2 METHODOLOGY

Main and defining difference between the less general Hooke's type of deformation salient for solid materials (primarily for metals and rubber) in relation to the more general Botkin's type of deformation salient, as was shown by Botkin for non-rocky soils (clays and sands) is in independence of stiffness and corresponding stiffness characteristics on the SSS for linear type and in their significant dependence on the SSS and also on the initial SSS for nonlinear type of deformation, especially for nonrocky soils. That is why in contrast to the stiffness constants E (Young-Hooke/s modulus) and ν (Poisson's ratio), which are convenient for determining and using for solid materials, but absolutely unsuitable for soils due to serious insurmountable problems with their definition and application, Botkin proposed simple and at the same time physically substantiated, but objectively nonlinear (with SSS parameters) formulas for stiffness characteristics, that are more convenient for soils and at the same time more fundamental for the phenomenon of solid medium deformation and hence for soil mechanics theory: for bulk modulus $K=\sigma^{1-\sigma}/A_0$ and for shear modulus $G=(A\sigma+C)/(B+\varepsilon_i)=(\sigma U-\sigma_i)/B$; here $\sigma_U=A\sigma+C$ is Mises-Botkin's criterion for soil strength which is a private version and analogue to the classical Coulomb's version of soil strength criterion, and A, B, C, A_0, α are model constants which must be determined from test data. But true values of these parameters that

allow to do geotechnical design with required accuracy both for naturally and artificially formed soil massifs can be determined only from in-situ test data since they depend on initial structural and stress states due soil physical nonlinearity. Of the complexity of nonlinear formulas describing deformation of non-rocky soils determination it is possible to determine soil design mechanical parameters values for nonlinear model only by special methods for solving inverse weakly conditioned problems, namely by minimizing discrepancy between the actual S_{fi} and numerically simulated soil displacements S_{mi}. Algorithm of the developed method was developed by analog with the method of academician Tikhonov applied for solving some nontrivial geophysical problems. In the case of determining a set of soil mechanical parameters $z_k = \{A, B, C, A_0, \alpha\}$ the objective minimization function has general form:

$$min\rho_{\alpha zk}\left[\sum_{i=1}^{n}\left(S_{mi}-S_{fi}\right)^2\right] \tag{1}$$

Here i is number of pressure stage, n is total quality of stages; to rationalize the procedure the regulatory factor α can be used in the form of a procedure or of a function that must optimizes a search for a global minimum at any stage of minimizing procedure.

The specific implementation of this method depends on the type of resolving relations of the problem being solved and on the features of physical problem being analyzed. In presented method parameters are determined by minimizing residual discrepancy $\rho\alpha_{zki}$ according to general formula (1) after applying in procedure previously determined true values. In this procedure values of S_{mi} are determined as a result of solving direct stable problem and values of S_{fi} are determined from standart in-situ static tests with usual accuracy (loading of soil by round shtamp and pressuremeter test). High speed of computational procedure is also of great importance for the efficiency of the method. Determination of true values of parameters of Botkin's model must begin on its key parameter B since this parameter though soil resistance to shape-shear deformation G affects directly soil strength. Integration on compressible zone of vertical relative soil deformations ε_z made it possible to obtain formula for vertical soil settlement with linear dependence on the parameter B:

$$S = \sqrt{3}B/2\int_0^1 y_z d_z \tag{2}$$

(Here y_z is a function of vertical stresses in soil massif which due to Henky's relations depends on mechanical soil parameters. Hypothetical representation of actual settlements (marked with individual index "f") as one of variant of numerically simulated settlements (marked with common index "m"): $S_m=F\ (p,\ A_m,\ B_m,\ C_m,\ A_{m0},\ \alpha_m) \rightarrow$ (formal rename indexes from the common index "m" to the individual index "f") $S_f=F\ (p,\ A_f,\ C_f,\ B_f,\ A_{f0},\ \alpha_f)$ allowed to write the ratio $S_f/S_m=B_f/B_m$, that after use it in formula (1) made it possible to derive statistically valid formula for true value of the parameter B: $B_f=B_m\Sigma S_{fi}/\Sigma S_{mi}$. Thus, algorithm of the method is actually based on the comparing two identical functions with different values of their identical parameters. Another very effective procedure using the regulating factor α in the form of technically meaningful interval of 100 for soil internal friction angle φ was used to determine true values of parameters A and C, connected with this angle by Botkin-Malyshev's formulas:

$$A=\frac{\sqrt{2(3+\mu^2)\mathrm{SIN}\varphi}}{3+\mu\mathrm{SIN}\varphi};\ C=\frac{\sqrt{2(3+\mu^2)\mathrm{COS}\varphi}}{3+\mu\mathrm{SIN}\varphi}\ c; \tag{3}$$

here φ and c are soil strength parameters on Coulomb's version of soil strength. These formulas made it possible to use the simplest minimization procedure with single result being obtained by looking over different angle values of angle φ.

To determine true values of parameters A_0 and α was used well-known Himmelblau's program Flexiplex for search global minimum on two parameters.

3 RESULTS AND CONCLUSION

Using physically nonlinear Botkin's model several geotechnical objects were designed and built in Ekaterinburg, namely: strip foundations of 6-storey neighboring buildings instead of pile foundations, retaining wall close to 9-storey building and spread-slab foundation of

35-storey high-rise building (see Figure 2a and 2b). In all these cases Botkin's soil model with design parameters values from in-situ test data were used for design of foundations. At all cases the cost of geotechnical constrictions was about $1 million less than the cost in original project on the base of Hooke's linear theory and with significant increase in reliability of the design solution on the base of true soil model: for example, in the case of 35-storey high-rise building on eluvial hard silty-argillaceous loam and sandy loam actual settlements differ from design one for about 25%, that is discrepancy coincides with discrepancy due to replacing in design real soil by ideal continuous medium.

Figure 2a. High-rise buildings in Ekaterinburg city: left building on the spread slab foundation is $1 cheaper than others of the same kind.

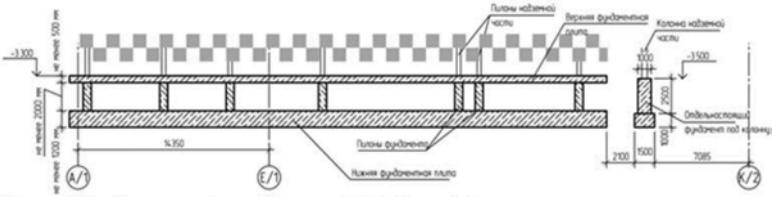

Figure 2b. Cross section of spread slab foundation.

REFERENCES

Alekhin, A. 1983. Nonlinear analysis of stress-strain state of soil mass under static loading: Thesis of cand. techn. degree. – Sverdlovsk: UPI.

Alekhin A. 2015 Substantiation of the method of determination of nonlinear soil model parameters from in-situ test data, Proceedings UralNIIproject RAASN. – Ekaterinburg: UralNIIproject RAASN.

Botkin, A. 1939. Investigation of stress state at cohesionless and cohesive soils. Moscow: RIIG.

Klein G. 1956. Inhomogeneities, tensile deformations and other mechanical properties of the soil when designing structures on the soil massif. Moscow: MISI.

Kriegel H., Wiesner H. 1973. Problems of Stress-Strain Conditions in Subsoil Proceedings of VIII-th ICSMFE. Moscow.

Himmelblau D. 1972 Applied nonlinear programming. Austin: University of Texas.

Malyshev V. 1994. Strength of soils and stability of soil bases of the structures. – Moscow,

Tikhonov, A., Arsenin, V. 1979. Methods for solving ill-conditioned problems. Moscow: Nauka.

Smart Geotechnics for Smart Societies – Zhussupbekov, Sarsembayeva & Kaliakin (Eds)
© 2023 The Author(s), ISBN 978-1-003-29912-7
Open Access: www.taylorfrancis.com, CC BY-NC-ND 4.0 license

Measurement of field hydraulic conductivity for a Quito soil

C. Zapata
University of Bristol, Bristol, UK
College of Social Sciences and Humanities, Universidad San Francisco de Quito, Ecuador

S. Feng
Birmingham City University, Birmingham, UK
University of Bristol, Bristol, UK

E.A. Holcombe & P.J. Vardanega
University of Bristol, Bristol, UK

E. Jiménez
Facultad de Ingeniería en Geología y Petróleo, Escuela Politécnica Nacional, Ecuador

ABSTRACT: In Quito, Ecuador, landslides present a significant threat to communities settled on hillsides and ravine slopes, and geotechnical data is needed to assess slope stability. Saturated hydraulic conductivity is a key input parameter for mechanistic modelling of rainfall infiltration and the pore water pressure conditions that can trigger landslides. This paper presents field data of in-situ saturated hydraulic conductivity by working with communities to conduct field measurements on the cemented volcanoclastic soils found in Quito. The new field data is then compared with predictions from recently established geodatabases of hydraulic conductivity obtained from laboratory tests on fine-grained and granular soil.

1 INTRODUCTION

Rapid urbanisation is predicted to increase landslides worldwide in the coming decades (e.g. Holcombe *et al.* 2016 & Ozturk *et al.* 2022). However, slope stability assessment and urban landslide risk reduction presents a challenge in regions with limited financial and technical resources for geotechnical data gathering and meeting slope design standards (e.g. Anderson & Holcombe 2006, 2013). In Quito, Ecuador, landslides often occur in the volcanic ash Cangahua soils that are found in the inter-cordillera valley from southern Colombia to central Ecuador at altitudes of 2200 to 3000 metres (Winckell & Zebrowski 1992). This is a multi-hazard environment in which rainfall can trigger cascading landslides, debris flows, and floods. Hydraulic conductivity (k) is an important soil parameter for geotechnical engineers. Saturated hydraulic conductivity (k_{sat}) is used to calculate rainfall infiltration and saturated groundwater seepage and to derive unsaturated hydraulic conductivity, for example using the Millington–Quirk formulation (Millington & Quirk 1959) in slope hydrology and stability models (e.g. CHASM, see Wilkinson *et al.* 2002).

To support the investigation of rainfall infiltration and landslide initiation, this study has the following aims: (i) present new field data of k_{sat} obtained via citizen science activities; (ii) compare the new data with values predicted from previously established transformation models. The study is part of the Tomorrow's Cities project on urban disaster risk reduction (see Galasso *et al.* 2022 for a discussion of the aims of the wider project).

DOI: 10.1201/9781003299127-48

2 MATERIAL AND METHODS

2.1 *Geological setting of the study site*

The study site is part of the Conocoto Giant Landslide (CGL) located on the eastern flank of the Puengasí anticline, uplifted by a segment of the Quito reverse fault system, in the southwestern part of the Metropolitan District of Quito. This relict landslide is estimated to have occurred between 165ka to 10ka and has a 3700 metre semi-circular scarp (Noroña Muñoz 2021). The deep colluvial strata are comprised of Cangahua – a volcanic ash soil produced by partial diagenesis of fine explosive volcanic material cemented primarily by amorphous clayey material, silica, iron oxides or calcite (see Vera & Lopez 1992, for a detailed description of Cangahua).

2.2 *Soil sampling and index testing*

In collaboration with community residents, undisturbed soil samples were taken from a continuous Cangahua material layer. The soil samples were denoted as S1 and S2 from 200mm and 500mm sample depths respectively. Granulometric analysis and SUCS classification were carried out on both samples, following the standard ASTM D2487 (ASTM 2011). To carry out the soil classification tests of the soil samples (using ASTM 2017a), the laboratory used the material that passed through Sieve No 40 (see ASTM D6913 for the ASTM sieve sizes) (ASTM 2017b).

2.3 *Estimation of saturated hydraulic conductivity using a double ring experiment*

In this study ASTM D3385 (ASTM 2018) was used to measure k_{sat} at the sampling point located on the ridge of the CGL, in collaboration with community residents. The experiment was carried in a half-metre deep pit during the rainy season. The double ring system was filled with water for two hours to allow saturation conditions to develop. A long-term test was then carried out in which infiltration measurements were taken every 15 minutes for 2 hours, and then every 24 hours for the following three days. The soil conditions were assumed to be near saturation. For natural Cangahua, O'Rourke & Crespo (1988) indicated a natural degree of saturation (S_r) ranging from 32% to 56%.

3 TEST RESULTS

The k_{sat} measurements obtained from the field testing show an order of magnitude range (Table 1). The soil samples (S1 and S2) collected for this study have a SUCS classification of type CL (following ASTM 2011), with a predominance of fines (see Tables 2 and 3). Table 3 also shows the computed specific surface area per volume (S_A) which can be computed using the soil grading curve (see Chapuis & Légaré 1992, Feng 2022).

Table 1. Double-ring infiltrometer test results for three-day experiment.

Time (min)	0	60	90	120	150	1590	3030
Infiltration (cm)	0	0.4	0.2	0.2	0.2	9.4	5.8
k_{sat} (m/s)	0	4.72×10^{-6}	3.61×10^{-6}	2.78×10^{-6}	2.50×10^{-6}	1.09×10^{-6}	6.71×10^{-7}

Table 2. Laboratory grain size analysis results.

ASTM sieve no.	3"	2"	1½"	1"	3/4"	3/8"	4	10	40	200
Aperture (mm)	75.0	50.0	37.5	25.0	19.0	9.5	4.75	2.0	0.425	0.075
% passing (S1)	100.0	100.0	100.0	100.0	100.0	100.0	99.5	99.2	92.5	60.7
% passing (S2)	100.0	100.0	100.0	100.0	100.0	100.0	100.0	99.8	94.6	64.0

Table 3. Laboratory results for soil samples.

Sample	Moisture content, w (%)	Liquid limit, w_L (%)	Plastic limit, w_p (%)	S_A (1/mm)
S1	35	37	23	110.57
S2	25	32	20	113.95

4 ESTIMATIONS OF HYDRAULIC CONDUCTIVITY

Feng (2022) reported a new database CG/KSAT/7/1278, with over 1200 k measurements on soils with over half of the soil grain particles larger than 0.075mm in diameter (i.e. coarse-grained soils). Equations (1a) and (1b) are a k transformation model calibrated using CG/KSAT/7/1278:

$$K = 1.693 \times 10^{-2} e^{2.283} / {S_A}^2 \tag{1a}$$

$$k_{sat} = K(\gamma_w / \mu_w) \tag{1b}$$

where K = intrinsic permeability of the porous medium (mm^2 in Equation 1a, and m^2 in Equation 1b), e = void ratio, S_A = specific surface area per volume (1/mm), k_{sat} = saturated hydraulic conductivity (m/s), μ_w = dynamic viscosity of the permeant = 1.002×10^{-3} kg/(m.s) (Kestin *et al.* 1978, assuming a testing temperature of 20°C) and γ_w = unit weight of the permeant = 9.81 (m/s^2) × 998 (kg/m^3) (density value from Kestin *et al.* 1978, assuming a testing temperature of 20°C).

Feng & Vardanega (2019) assembled a fine-grained soil database FG/KSAT-1358, which contains over 1300 k measurements soils with more than half of the particles smaller than 0.075mm in diameter and with a measurable w_p (i.e. fine-grained soils). The FG/KSAT-1358 database was used to develop a transformation model of the form presented in Feng & Vardanega (2019) and further refined in Feng *et al.* (2022) (after removal of statistical outliers), shown as Equation 2:

$$k_{sat} = 1.86 \times 10^{-9} (w / w_L)^{4.226} \tag{2}$$

where k_{sat} is in units of m/s and w/w_L = the water content ratio (where w = the water content).

By using Equations 1a, 1b and 2, predictions of k_{sat} for S1 and S2 for a range of porosities (n) quoted in various publications were made and compared with the test results. Tables 4 and 5 summarise the predicted k_{sat} values. For all the calculations, S_r is taken as equal to 1.0 and specific gravity (G_s) is taken as 2.585 (the average value from the data in O'Rourke & Crespo (1988)).

Table 4. k_{sat} at 20°C predicted using Equation 1.

Reference	S1 (w_L = 37%)			S2 (w_L = 32%)		
	$e = n/(1-n)$	S_A (1/mm)	k_{sat} (m/s)	e	S_A (1/mm)	k_{sat} (m/s)
This study	0.905	110.57	1.08×10^{-5}	0.646	113.95	4.70×10^{-6}
Podwojewski & Germain (2005) (n = 40%)	0.667	110.57	5.36×10^{-6}	0.667	113.95	5.05×10^{-6}
Crespo (1987) (n = 43%)	0.754	110.57	7.11×10^{-6}	0.754	113.95	6.69×10^{-6}
Crespo (1987) (n = 56%)	1.273	110.57	2.35×10^{-5}	1.273	113.95	2.21×10^{-5}

Table 5. k_{sat} at 20°C predicted using Equation 2.

Reference	S1 (w_L = 37%)			S2 (w_L = 32%)		
	$e = n/(1-n)$	w (%)	k_{sat} (m/s)	e	w (%)	k_{sat} (m/s)
This study	0.905	35	1.47×10^{-9}	0.646	25	6.54×10^{-10}
Podwojewski & Germain (2005) (n = 40%)	0.667	25.8	4.05×10^{-10}	0.667	25.8	7.47×10^{-10}
Crespo (1987) (n = 43%)	0.754	29.2	6.82×10^{-10}	0.754	29.2	1.26×10^{-9}
Crespo (1987) (n = 56%)	1.273	49.2	6.22×10^{-9}	1.273	49.2	1.15×10^{-8}

Compared with the measured k_{sat} data from the field testing (Table 1), the coarse-grained soil hydraulic conductivity transformation model (Equation 1) gives a significantly better prediction of k_{sat} than the fine-grained soil hydraulic conductivity transformation model (Equation 2). This may be because that while the Cangahua soil samples tested have a measurable w_P, the data in FG/KSAT-1358 are mostly pure laboratory fine-grained clays and silts and thus might not be representative for the samples testing in this work which contain a combination of fine and coarse material (see Table 2).

5 SUMMARY

This paper has presented the results of a citizen-science based project to assess saturated hydraulic conductivity in data-limited locations where rainfall-triggered landslide hazard assessment is required. New field k_{sat} measurements were made using a double-ring infiltrometer. The new data were compared with predictions from two transformation models developed from databases of coarse-grained and fine-grained soils. The field values are closer to the predictions from the coarse-grained transformation model – this is possibly because Cangahua is not a pure clay and comprises a large component of coarse-grained material.

ACKNOWLEDGEMENTS

Funding from UKRI GCRF under grant NE/S009000/1, Tomorrow's Cities Hub is acknowledged. *Data availability*: The field data is available from the first author upon reasonable request.

REFERENCES

Anderson, M.G. & Holcombe, E.A. 2006. Sustainable landslide risk reduction in poorer countries. *Proceedings of the ICE – Engineering Sustainability* 159(1): 23–30.

Anderson, M.G. & Holcombe, E.A. 2013. *Community-based Landslide Risk Reduction: Managing Disasters in Small Steps*. Washington DC: World Bank.

ASTM International (ASTM). 2011. Standard Practice for Classification of Soils for Engineering Purposes (Unified Soil Classification System) *D2487–11*, West Conshohocken: ASTM International.

ASTM 2017a. Standard Test Methods for Liquid Limit, Plastic Limit, and Plasticity Index of Soils *D4318−17*, West Conshohocken: ASTM International.

ASTM 2017b. Standard Test Methods for Particle-Size Distribution (Gradation) of Soils Using Sieve Analysis *D6913/D6913M −17*, West Conshohocken: ASTM International.

ASTM 2018. Standard Test Method for Infiltration Rate of Soils in Field Using Double-Ring Infiltrometer *D3385-18*, West Conshohocken: ASTM International.

Chapuis, R. & Légaré, P.-P. 1992. A Simple Method for Determining the Surface Area of Fine Aggregates and Fillers in Bituminous Mixtures. In R.C. Meininger (ed.) *Effects of Aggregates and Mineral Fillers on Asphalt Mixture Performance*: 177–186. West Conshohocken: ASTM International.

Crespo, E. 1987. Slope stability of the Cangahua Formation, a volcaniclastic deposit from the Interandean Depression of Ecuador. *M.S. thesis*, Ithaca, NY: Cornell University.

Feng, S. 2022. Hydraulic Conductivity of Road Construction Materials: with a focus on freeze-thaw effects. *Ph.D. thesis*, Bristol, UK: University of Bristol.

Feng, S., Ibraim, E. & Vardanega, P.J. 2022. Databases to assess the hydraulic conductivity of road construction materials. In: M.M. Rahman & M. Jaksa (eds), *Proc. of Twentieth International Conference on Soil Mechanics and Geotechnical Engineering (ICSMGE 2022)*, *Sydney*, 1-5 May 2022. Australian Geomechanics Society: vol. 2, 4547–4552, Sydney: Australian Geomechanics Society.

Feng, S. & Vardanega, P.J. 2019. Correlation of the hydraulic conductivity of fine-grained soils with water content ratio using a database. *Environmental Geotechnics* 6(5): 253–268.

Galasso, C., McCloskey, J., Pelling, M. Hope, M., Bean, C.J., Cremen, G., Guragain, R., Hancilar, U., Menoscal, J., Mwang'a, K., Phillips, J., Rush, D. & Sinclair, H. 2021. Editorial. Risk-based, Pro-poor Urban Design and Planning for Tomorrow's Cities. *International Journal of Disaster Risk Reduction* 58: [102158].

Holcombe, E.A., Beesley, M.E.W., Vardanega, P.J. & Sorbie, R. 2016. Urbanisation and landslides: hazard drivers and better practices. *Proceedings of the ICE - Civil Engineering* 169(3): 137–144.

Kestin, J., Sokolov, M. & Wakeham, W.A. 1978. Viscosity of liquid water in the range −8 °C to 150 °C. *Journal of Physical and Chemical Reference Data* 7(3): 941–948.
Millington, R.J. & Quirk, J.P. 1959. Permeability of porous media. *Nature* 183(4658): 387–388.
Noroña Muñoz, E.M. 2021. Modelo Geológico del Macro Movimiento en Masa Conocoto-La Armenia, asociado al Sistema de Fallas de Quito, DMQ, Quito: EPN.
O'Rourke, T.D. & Crespo, E. 1988. Geotechnical properties of cemented volcanic soils. *Journal of Geotechnical Engineering* 114(10): 1126–1147.
Ozturk, U., Bozzolan, E., Holcombe, E.A., Shukla, R., Pianosi, F. & Wagner, T. 2022. How climate change and unplanned urban sprawl bring more landslides. *Nature* 608(7922): 262–265.
Podwojewski, P. & Germain, N. 2005. Short-term effects of management on the soil structure in a deep tilled hardened volcanic-ash soil (cangahua) in Ecuador. *European Journal of Soil Science* 56(1): 39–51.
Vera, R. & Lopez, R. 1992. Tipologia de la cangahua. In C. Zebrowski, *et al*. (eds), *Terra, Numero Especial Suelos Volcánicos Endurecidos*, vol. 10: 113–119.
Wilkinson. P.L., Anderson, M.G. & Lloyd, D.M. 2002. An integrated hydrological model for rain-induced landslide prediction. *Earth Surface Processes and Landforms* 27(12): 1285–1297.
Winckell, A. & Zebrowski, C. 1992. La cangahua en Equateur: le contexte paléogéographique de sa formation. In C. Zebrowski, *et al*. (eds), *Terra, Numero Especial Suelos Volcánicos Endurecidos*, vol. 10: 107–112.

Smart Geotechnics for Smart Societies – Zhussupbekov, Sarsembayeva & Kaliakin (Eds)
© 2023 The Author(s), ISBN 978-1-003-29912-7
Open Access: www.taylorfrancis.com, CC BY-NC-ND 4.0 license

Research of the physical-mechanical properties of soils in a landslide-prone area along the Kugart river basin in the Suzak region

A.R. Takeeva
Jalal-Abad State University named after B. Osmonov, Jalal-Abad, Kyrgyzstan

M.A. Imankulov
Researcher, Jalal-Abad, Kyrgyzstan

S.Zh. Kuvakov & K.Zh. Usenov
Jalal-Abad State University named after B. Osmonov, Jalal-Abad, Kyrgyzstan

K.Zh. Kozhogulov
Institute of geomechanics and subsoil development, Bishkek, Kyrgyzstan

ABSTRACT: The paper describes the terrain of the landslide-prone area and the geological condition and factors affecting stability. Reflected the results of the research of the physical and mechanical properties of the constituent soils.

Keywords: soils, physical and mechanical properties, subsidence, Kara-Mart village, Kugart river basin, landslide

1 INTRODUCTION

The structure and state of the mountain massive is changing under the influence of endogenous and exogenous factors, arising naturally or under the influence of the structure of man-made structures. Based on the statistical data, it can be observed that landslides are mainly for an untouched massif accompanied by natural factors in mountainous areas. The terrain, seasonal changes in the hydrological and climatic conditions of the area, the physical and mechanical properties of the constituent soils are the main factors affecting the stability of the slopes [Shakhmov, 2015; Shakhmov, 2012; Shakhmov, 2016; Kuvakov, 2022]. With the transition from winter to summer and an increase in air temperature, leading to intensive melting of snow cover, expected precipitation and seismic activity in the spring-summer period, landslides are expected to intensify in the south of the republic. At the moment, out of the data of the Ministry of Emergency Situations of the Kyrgyz Republic, 1204 landslide areas threaten settlements, objects with a possible descent, which make up 80% of all landslides in the republic. The beginning of the Kugart river basin and their numerous tributaries start from the southwestern slopes of the Ferghana Range. In the river basin, 529 landslides have been described and systematized, of which 260 landslides were formed on slopes close to the northern exposure. A total of 225 landslides pose a threat to settlements, various objects of social and cultural life and infrastructure. Landslides have a large capture depth, reaching 20m. On the territory of the Suzak region, about 80% of the territory belongs to mountain structures, and 20% to flat relief types. The map-scheme for predicting emergency situations shows the location of areas of possible activation of landslide processes (Figure 1).

DOI: 10.1201/9781003299127-49

Figure 1. Location of areas of possible activation of landslide processes in the Suzak region.

It should be noted that the Kugart river basin covers many landslide-prone areas, and according to previous static studies, the number of landslides in the river section was established. Kugart has a close correlation with the amount of total annual precipitation (Figure 2) [Beksultanov, 2013].

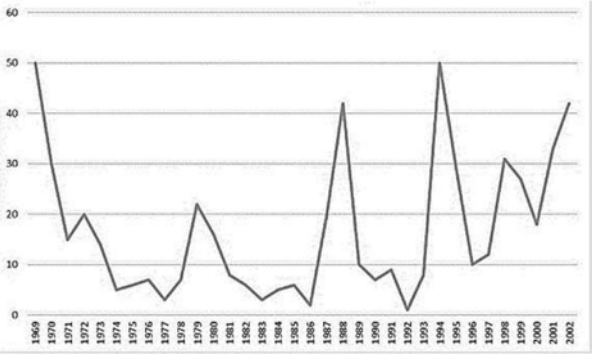

Figure 2. The number of landslides in the Kugart river basin by years.

he landslide-prone areas of the Karamart village are one of the most dangerous, located in the Kugart river basin.

2 METHODOLOGY AND RESULTS OF THE RESEARCH

In the research of soil properties, well-known state standards were used: 30416-96 - Laboratory tests. General provisions, 51-84 - Physical characteristics, 12248-96 - Strength and deformability, 12536-79 - particle size distribution. The physical and mechanical properties of soils were determined in laboratory conditions (specific gravity, density, moisture in nature, porosity, plasticity number, cohesion and angle of internal friction.) [Beksultanov, 2013].

3 MAIN RESULTS

The average relative error is 5%, which complies with the regulatory requirements specified in state standards. As a result of laboratory studies, averaged physical and mechanical data were obtained, which are shown in Table 1.

Table 1. The number of officially reported plague cases in the world.

№	pit	weight	Density	natural humidity	porousness	Plasticity number	cohesion	Angle of internal friction
1	P-1	2,71	1,78	21,5	46,2	12,2	0,033	21
2	P-2	2,72	1,72	20	42,3	12,4		
3	P-3	2,71	1,76	21	45,4	10,6		
4	P-4	2,73	1,61	19,5	44,8	11,6		

Based on the results of a visual inspection of the site, identified that subsidence lines (20 cm) with a length of 79 meters were. (Figure 3)

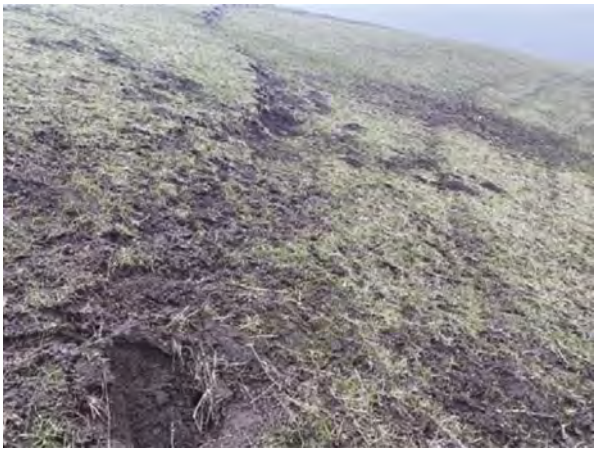

Figure 3. Line of subsidence on the surface of a landslide slope.

Also, as a result of the research of subsidence, we obtained averaged following data. Similar researches were carried out by the open joint-stock company "KYRGYZGIIZ" Osh branch [Mombekov, 2017], the results of which are shown in Figure 4.

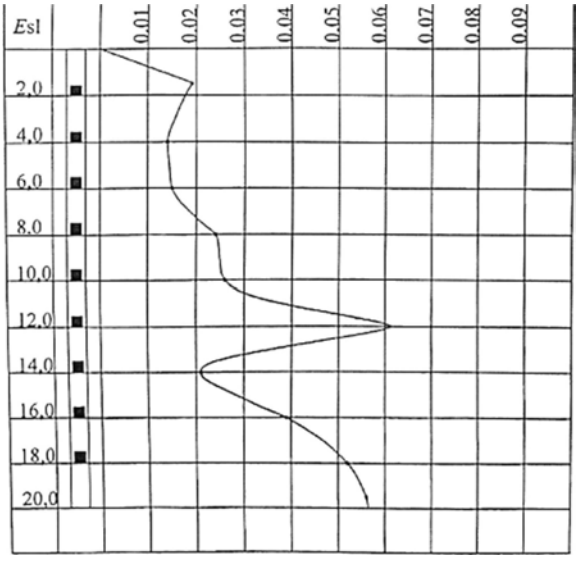

Figure 4. Graph of change in subsidence values depending on the depth of occurrence.

4 CONCLUSIONS

The obtained indicators of physical and mechanical properties are within the normal range, except for porosity. We can notice a high porosity, which reaches up to 45 As can be seen in Figure 4, the subsidence index increases with depth and shows a maximum subsidence value of 0.06 mm at depth. According to the results of the study by vertical electrical sounding, soils of semi-solid loam, moist loam and loam with gravel inclusions were identified. Note that up to 25 meters of depth, the corrosive activity is both low and medium, and the electrical resistivity varies from decreases from 120 to 10 Ohm-m. Taking into account the data obtained, it is necessary to carry out a number of measures for the geomechanical assessment of slope stability taking into account various factors. On the basis of a visual research, lines of slope subsidence were identified, which can serve as manifestations of landslide processes.

REFERENCES

Beksultanov Zh. Dissertation. Methods of mathematical modeling for the analysis and forecast of landslides of hydrodynamic type in the territory of the Kyrgyz Republic, Bishkek, 2013, P. 20–33.

Kuvakov Zh.M., Alimamatov A., Kuvakov S.Zh. Calculation of the stability of the sides of mountain ridges with a complex structure in the tension-deformation state based on the stress program. Bulleten of Jalal-Abad state university 4(53), Jalal-Abad 2022, P.189–193.

Mombekov O.M., Mirzaliev M., Baratov E.R. Report on the engineering-geological survey to assess the stability of the slope in the village of Karamart, Suzak district, Jalal-Abad region. Osh, 2017. Page – 39.

Shakhmov Zh., Tleubayeva A., Utepbergenova L., Togabayev Y., Bazarbayev D. Analyzing of soil ground to frost heaving of structures, The Eighth Asian Young Geotechnical Engineers Conference, Challenges and Innovations in Geotechnics, 5-7 August, 2016, Astana, Kazakhstan, P. 47–50.

Shakhmov Zh.A., Zhussupbekov Zh.A. Frost susceptibility of soil and in-situ monitoring of frost depth in construction, The 15th Asian Regional Conference on Soil Mechanics and Geotechnical Engineering. – Fukuoka (Japan), 9-12 September 2015. P. 4 pages.

Zhussupbekov A., Shakhmov Z., Shin E.C., Krasnikov S. Challenges for transportation geotechnics in extreme climates of Kazakhstan and Korea, Advences in Transportation Geotechnics II: CRC Press Taylor&Francis Group, a Balkema book.- Hokkaido(Japan), 10-12 September 2012.

Smart Geotechnics for Smart Societies – Zhussupbekov, Sarsembayeva & Kaliakin (Eds)
© 2023 The Author(s), ISBN 978-1-003-29912-7
Open Access: www.taylorfrancis.com, CC BY-NC-ND 4.0 license

Development of innovative designs of drainage pipes that increase their stability in difficult geotechnical conditions

F.G. Gabibov
Azerbaijan Research Institute of Construction and Architecture, Baku, Azerbaijan

H.B. Salayeva
Azerbaijan University of Architecture and Civil Engineering, Baku, Azerbaijan

ABSTRACT: Studies of drainage pipes with different cross-sections have been carried out. Designs of drainage pipes with cross sections constructed using cycloid shapes have been developed. Analytical and model studies have shown increased stability of the arches of these pipes. The latter makes it possible to achieve a sharp reduction in the risk of loss of stability of drainage pipes under complex static, seismic and dynamic loads.

1 INTRODUCTION

Application in the practice of industrial, urban, transport and hydraulic engineering horizontal tubular drains are a combination of drainage pipes with loose filter sprinkles. The structural forms of tubular drains and their main elements are determined by the hydrogeological and hydrochemical features of the drained area, and also depend on the layout of the protected structures, their purpose and conditions of work. Ceramic, asbestos cement, polymer, concrete and reinforced concrete pipes are used as drainage pipes. The studies of Tulaev (1980), Abramov, Degtyarev & Korinchenko (1976), Storozhuk (1987), Razumov (1988), Gabibov & Salaeva (2022 a,b) and others are devoted to the constructions of horizontal tubular drainage. The monographs of Prevo (1964), Babin, Bykov & Volokhov (1979), Vinogradov (1980), Borodavkin & Sinyukov (1984), Dimov & E.M.Bogushevskaya (2010) are devoted to the calculation of horizontal pipeline (including closed drainage).] and others. Many computer programs have been developed to calculate horizontal pipelines Awoshika & Tokano (1972), Trautman & O'Rourke (1985). Currently, a very urgent task for engineers is to identify the most stable cross-sections of horizontal drainage pipes, which are often laid in difficult ground conditions.

2 INVESTIGATION OF NATURAL AND ARCHITECTURAL ANALOGIES TO IDENTIFY THE MOST STABLE DRAINAGE PIPE SECTIONS

To identify the most rational and stable vaults for drainage and collector pipes, it is undoubtedly useful to use natural analogies found in mining and underground construction, as well as analogies from the experience of designing and constructing vaults, domes and arches of famous architectural structures. In mining and underground construction, one of the costly items is fixing the arch of the workings to prevent its collapse. In order to reduce the material costs associated with carrying out this kind of work, various forms of workings were proposed at different times, ensuring the formation of a "natural balance" vault.

Thus, in the work of Stajevsky (1986), the results of field and experimental studies of the stability of underground workings, depending on the shape of their cross-section, are presented. It has been established that workings with a cross-section close in shape to a triangle and with walls deviated from the vertical by an angle $\alpha \leq 15 \div 30^{\circ}$ have their own high load-bearing capacity, and if necessary, they require insignificant costs to strengthen them.

DOI: 10.1201/9781003299127-50

A significant increase in the strength of soils and rocks in the vicinity of the triangular section is due to the fact that in the zones adjacent to the apex of the triangle, the vertical and horizontal stress components reach significant values that have very close numerical values (the effect of all-round compression).

Protodyakonov (1931) notes: "Based on observations of old abandoned drifts, the fastening of which has long rotted and has not been renewed, and over which, with the appropriate lateral rocks, a natural vault is formed, which holds for years and decades without further fixing, it was decided to achieve directly obtaining the same vault." Further in the work it is noted: "... the drifts have the form of a very high arch ..." and "... can stand for many years without repair."

Kilesso (1983) cites the fact that there are triangular drifts, which are without any repairs from the IV century BC.

To the conclusion that the production cross section close to the triangular are the most optimal for large depths, based on field data and results of calculations, came and the authors Baryshnikov, Mashukov & Pirlya (1982). Figure 1 shows the arches of natural equilibrium.

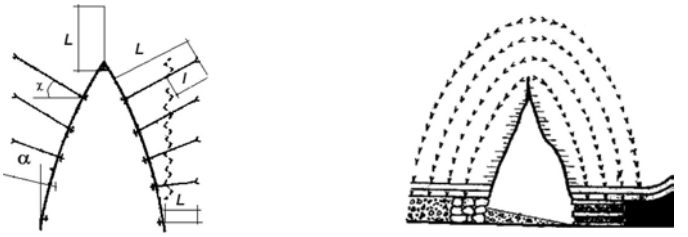

Figure 1. Vaults of natural equilibrium: *a)* – a vault obtained experimentally; *b)* – a vault in an abandoned tunnel.

The history of the development of arched structures in the general history of construction reflects the process of changing the relationship between the growing material and cultural needs of people and the growing possibilities of meeting these needs.

The arch as a load-bearing structure, simultaneously perceiving and transmitting the load, has brought its unique charm to our days through millennia. As Buettner & Hampe (1983) note: "It was already known to the architects of antiquity that if a stone beam was given an arched shape, then it acquires new bearing properties that can significantly increase the overlapped span with the same building material."

Torroja (1961) gives the following characteristic of the arch as a bearing element of a building structure: "From the point of view of stress distribution, the arch is the biggest find in the history of classical architecture. Even today, it has not lost its significance, although humanity has been getting used to the idea for quite a long time that it is the arch that is the element that increases the strength of the structure."

In the era of ancient Greek civilization, "false arches" were mostly erected. The most famous and oldest arched structures are the gateway arch and the arched vault, preserved from the Mycenaean culture. We find these curved systems with a continuous arched line of protruding cantilever elements in almost all ancient cultures.

In numerous works on the history of construction equipment by scientists of the past and modern specialists, the evolution of arched structures is described in detail. Adler (1926) points out that "even before the appearance of arched structures in ancient Greece, they were already known to the Etruscans living in the territory later conquered by Ancient Rome. Therefore, it is the Etruscan arches that can be considered the forerunners of Roman arches and vaults."

The desire of the masters of Gothic cathedrals to reduce the mass of structures and preserve the load-bearing capacity of arched structures led to the creation of giant lattice arched loops (Figure 2). In the arched loops obtained by medieval architects, who at that time solved not only artistic but also design problems, empirically, in vertically interacting paired arches, elements of modern reloid structures are viewed.

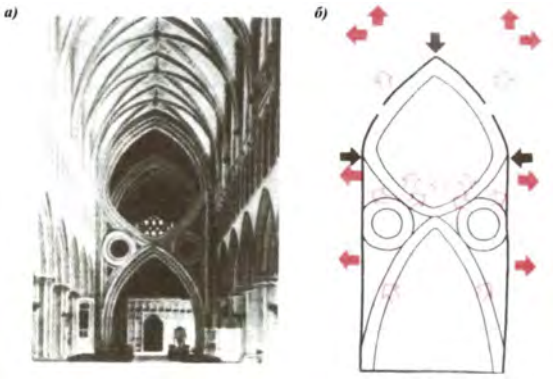

Figure 2. Reinforced arched hinges of the Cathedral in Wales (Great Britain), the end of the XII century: *a)* – type of arched hinges of the cathedral; *b)* – the scheme of the arched loop.

3 DEVELOPMENT OF DRAINAGE PIPES WITH ARCHES OF INCREASED STABILITY

The design of the drainage pipe (Figure 3) in cross-section in the form of a Reulot triangle, which has a bottom part 1 and side parts 2, has been developed. There is a perforation 3 along the entire surface of the drainage pipe. One of the corners 4 of the cross-section of the pipe is located in its upper consolidated part. Ground water passing through the protective drainage sprinkling, through the perforation of the bottom 1 and side parts 2 of the drainage pipe, enters its inner cavity and flows to the collector along a given slope. Compared to pipes with a circular cross-section, the considered design has higher indicators of stability, strength and water absorption capacity Gabibov, Habibova & Hasanov (2017).

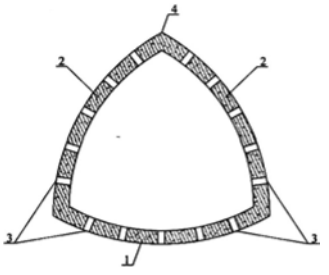

Figure 3. Drainage pipe with a peppered cross section in the form of a Reulot riangle with an angular arch: 1 – bottom part of the pipe; 2 – side parts of the pipe; 3 – perforation; 4 – upper arch corner of the pipe.

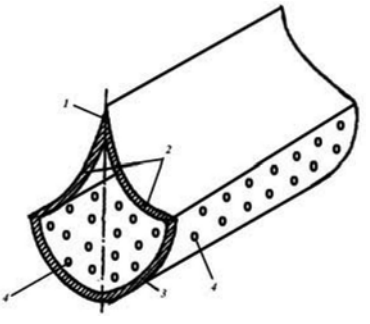

Figure 4. A drainage pipe with a clapboard formed by the intersection of hyperbolas; 1 – canopy; 2 – hyperbolas; 3 – semicircular lower part of the pipe; 4 – perforation.

Model studies Gabibov, Bogomolov & Salaeva (2022) show that the greatest stability is observed in the development with a vault in the form of half an astroid. A new design has been developed (Figure 4) of the drainage pipe, in which the arch 1 with intersecting hyperbolas 2 practically corresponds to half of the astroid. At the same time, in the lower semicircular part 3 of the pipe section, due to perforation 4, during the period of elevated groundwater level, pressure micro-streams will occur, which will erode the formed silty deposits.

4 CONCLUSIONS

1. Natural and architectural analogies have shown that triangular and arched arches are the most stable;
2. A new design of a drainage pipe with a cross-section in the form of a Reulot triangle with an angular arch has been developed, relating to cycloidal structures and increased stability;
3. Based on model studies, it was revealed that the arches in the form of half of the astroid are the most stable, in this regard, a new design of a drainage pipe with a vault in the form of intersecting hyperbolas has been developed, which practically corresponds to half of the astroid.

REFERENCES

Abramov, S.K., Degtyarev B.M., Korinchenko I.V. 1976. Horizontal drains with porous concrete pipe filters. Moscow: Stroyizdat, 80 p.

Adler, L. 1926. Vom Wese n der Baukunst. Leipzig Im Yerlag der Asia Major.

Awoshika, K., Tokano, M. 1972. Analysis of pipelines subjected to differential ground settlement. Nippon kokan Techn. Rept., №14.

Babin, L.A., Bykov, L.I. Volokhov, V.Ya. 1979. Typical calculations for the construction of pipelines. M.: Nedra, 176 p.

Baryshnikov, V.D., Mashukov, V.I., Pirlya, K.V., 1982. Analysis of the stress state of rocks in the vicinity of preparatory workings. FTPRPI, No. 4 pp. 114–116.

Borodavkin, P.P., Sinyukov, A.M. 1984. The strength of trunk pipelines. M.: Nedra, 245 p.

Buettner, O., Hampe, E. 1983. Structure – Bearing structure – Bearing structure. Moscow: Stroyizdat, 340 p.

Dimov, L.A., Bogushevskaya, E.M. 2010. Main pipelines in swamps and flooded areas. Moscow: Publishing House "Mountain Book", Publishing House "Moscow State Mining University", 392 p.

Gabibov, F.G., Bogomolov, A.N., Salaeva, H.B. 2022. Determination of the most stable arches of drainage and collector pipes by analog and model studies. "Architecture and Construction in Azerbaijan", No. 1, Baku, pp.2–9.

Gabibov, F.G., Habibova, L.F., Hasanov, S.T. 2017. Drainage pipe. Patent of the Russian Federation for invention No. 2611803,

Gabibov, F.G., Salaeva, H.B. 2022. Engineering analysis of round drainage pipes and their complementary technical elements in horizontal drainage structures. Materials of the XII National Scientific and Practical Conference "The bowels of Kalmykia are unique and interesting", Elista: Kalmyk University Publishing House, pp.173–182.

Gabibov, F.G., Salaeva, H.B. 2022. Research, analysis and refinement of round drainage pipe designs with structural additions for the development of their individual functions. Collection of articles of the XXII International Scientific and Technical Conference "Effective building structures: theory and practice", Penza: Privolzhsky House of Knowledge, pp.38–48.

Kilesso, S.K. 1983. Architecture of the Crimea. Kiev: Budivelnik, 96 p.

Prevo, R. 1964. Calculation of the strength of pipelines laid in the ground. M.: Stroyizdat, 123 p.

Protodyanov, M.M. 1931. Rock pressure and various fastening. M.-L: OGIZ, 186 p.

Razumov, G.A. 1988. Design and construction of horizontal water intakes. Moscow: Stroyizdat, 240 p.

Stajevsky, S.B. 1986.To the choice of form and fixing of workings. FTPRPI, No.5, pp. 27–32.

Storozhuk, S.I. 1987. Porous drainage in the arid zone. Moscow: VO "Agropromizdat", 103 p.

Torroja, E. 1961. Logik der Form. München. Verlag G. D. W. Callwey,

Trautman, C.H., O'Rourke, T.O. 1985. Lateral force-displacement of buried pipe. Geotechn. Eng. J. 111, №9, p.1077–1092.

Tulaev, A.Ya. 1983. Drainage of the roadbed of urban roads. Moscow: Stroyizdat, 132 p.

Vinogradov, S.V. 1980. Calculation of underground pipelines for external loads. Moscow: Stroyizshchdat, 135 p.

Smart Geotechnics for Smart Societies – Zhussupbekov, Sarsembayeva & Kaliakin (Eds)
© 2023 The Author(s), ISBN 978-1-003-29912-7
Open Access: www.taylorfrancis.com, CC BY-NC-ND 4.0 license

Dangerous geological processes and reasons of the development of landslides. (on the example of the landslides of the Zarafshan oasis, Uzbekistan)

F.A. Ikramov & M.M. Yakubov
Samarkand State Architectural and Civil Engineering Institute, Samarkand, Uzbekistan

ABSTRACT: Violation of the stability of the massifs, dangerous geological processes (land-slides, land-slips, subsidence, suffusion, karst) are widely developed in the mountain and foot-hill areas (Urgut) of the Zarafshan oasis, Republic of Uzbekistan. Especially, in recent years, due to abundant of atmospheric precipitation earthquakes and active human intervention in the environment create emergency situations and are accompanied by large material losses, often by human losses.

The main reason of the development and descent of landslides is the over moistening of loan at the contact with bedrock surface and groundwaters, as well as, the formation of land-slides caused by seismic effects. At present, more then 20 landslide hazardous and 60 potential landslide plots are under observation. In the zone of acting landslides, there are 57 children's recreation camps within the mountains and foothills areas.

Ongoing permanent observations for especially dangerous five landslide, located in the Urgut district (the villages: Sayguss, the Guss Upper, the Guss Lower, the Aktash Upper, the Aktash Lower, the Khodjaabdal village) of the Samarkand region of Uzbekistan. The above – mentioned landslides were activated by the landslide that came about and were provoked by a forced explosion on November 13, 1994. The results of long – term observations testify, that heavy rainfall and as wall as high seismic activity have a huge effect on the formation of land-slides. Landslides are most intensively developed along high-way. This makes it clear, that developing of mountainous and foothill areas without pre-liminary studies to determine the degree of stability of the slopes and the implementation of protective recommendations becomes one of the main factors in the formation of land-slides.

1 INTRODUCTION

1.1 *Dangerous geological process (as landslides)*

There are wide develops in mountain and plain areas in the Republic of Uzbekistan. Their displacing near the populated stations, different national economic objects now ever makes extraordinary situation, and it is accompanies by huge financial waits, and frequently by human loses.

Handstand's phenomena and theirs study with registration of the seismic dangerousness of our region id being very important. For solving global problems, which is arises in the result of landslides, it is necessary right value of the development reasons of landslides and effective elaboration of the engineering methods of protection, and also projecting construction against landslides.

The practice which is direct against landslides testifies with most obvious about the reasons of mistaken value and methods of the solving facts which is connected natural phenomena, often just with fallings out from the field of vision of engineers.

DOI: 10.1201/9781003299127-51

2 CONFORMITY OF DEVELOPMENT LANDSLIDES OF THE GEOLOGICAL PROCESS

Wide development and originality of displaying form of landslides and other dangerous forms of the geological process in the mountain and plain areas creates definitizes difficulties on the mastering of the territory. Mostly intensive they develop in last 2-3 thousands years, that is connected not just with intensive influence of the natural landslides factors, but with active interference of human in natural environment.

Regional conformity of displacing of landslides as in previous years, was formed for huge landslides by geological structural peculiarities of the lot, and for not so dup drifts, smelting and collapses, on the slopes of the motor-ways characters of the dropping out of precipitations.

One of the factors which is determines intensity of development and displacing landslides are atmosphere precipitations which are promotes humidity of the soil on the slopes, and increases debits of the ground water. A whole development of dangerous geological process in connected with wide spreading on the slopes of loess rock's, is under humidity characterizes with instant distorting with transitional structure in the liquid condition.

3 BASIC INFORMATION ABOUT INVSETIGATION OF THE LANDSLIDES

At present there are 20 landslides is being under the observation, and 60 potentially landslides lots. In the zone of the active landslides there are 57 children camps in the bound of the mountains and plain areas.

Nowadays we are keeping the observation of the five particularly dangerous landslides, which is in the Urgut district (of the village Sayguss, Upper-Guss, lower-Guss, upper-Actash, lower-Actash, Khodjabdal) of the Samarkand region of the Republic of Uzbekistan. Above mentioned landslide was activated with came down landslide which was provoke by the compulsory explosion on the 13th of November 1994.

3.1 *Sayguss landslide*

Landslide area is situate on the right bank of the middle flow of river Sayguss, which is timed to the diluvial slope with the steepness up to 30 degree, from the Northern- Western exposition. The height of the slope is 150-200 meter, the shape of slop is in the plan of building, in the profile is buildingly-concaved. The leigh of dislocation zone is 3 000 m2, breadth is 12 000 m, area of zone is 36 000 m2, development zone of the landslides is 8 000 m2.

In the lower part, slope is pass to the alluvial terrace, which is follows along both sides of the basic river-beds, 80-110 m wide. In the upper part, slope pass in to the gently watershed. On the character of breaking up the slope conditionally may devoid on to two parts.

The erosional cut from 1 to 3 m, is services as a natural board, between them.

Southern part of the slope is smoothed, with separate bares of the carbonated rocks. In the geological structure of the slope there are limestones of the Devonian age, which is covered from surface with the scaffolding loamy soil, with capacity in the upper part to two meter in the middle part to the 8 m and in the lower part 5 m.

3.2 *Landslide actash (upper)*

The lot is situated on the left side of Actashsay. In the geomorphological attitude the lot is situated on the diluvial slope with the steepness of 30-35 degree with height to 200 meter from the Northern-Western exposition.

At the limits of the landslides slope in the relief of the spreading under of rocks is clean stands out two hollow-figurative drops, which is divided by the doomily figurative block, capacity of the cover on the domes does not rise to 2 meters.

The 1st drop was noted in the Eastern part of the lot, and in the upper part of the slope, which is limit by the wall of frustration of the landslides, there is a spring which is wedge in the center. The spring was timed to the zone of the break. The breadth of the hollow on the lot to 40-50 meters.

The 2nd drop in the relief of the under spreading rock there is a control line in the upper part of the slope of the landslide crack, which is displayed after the compulsory explosion. Lower on the slope there is an observation of the drop. In the middle part of the slope there is an observation of the supply with watered crash, which is under the control by regime springs. Breadth of the zone dropping zone to 190 m.

3.3 *Guss landslide*

Landslide area is situated on the Northern slope of mountain range of the Chakil-Kaliyan and joins to the Guss. The buildings of the villages are locates on the gently-wavy surface of the alluvially-diluvial train on the absolute note from 1050 to 1160 meters. The body of the landslides lot-on the note from 1100 to 1250 meter.

Development of the landslides process on the slope is continued and displays more intensive in the rainy period, and still keeps the threat for the dwelling buildings which is under this landslides, of the village Guss.

4 THE RESULTS OF THE ENGEENERIAN -GEOLOGICAL INVESTIGATIONS AND PHYSICS-MECANICAL QUALITY OF THE SOILS LANDSLIDES (MASSIFS) SOLID MASS

As the engineer-geological results show, that the lithology of the locality landslides massifs is very similar. For definition of physics-mechanical qualities of the soils of covered deposits on the lot goes hole, with depth from 1,5 to 5 meter, with the selection of the assay. In the geological construction of the slope hire is limestone of the Devonian age, floored from the surface of the cover of losses with capacity in upper part to 2 meter, in the middle part to 8 meter in the lower (part) to 5 m (picture number 1).

Loamy soils by their structure are easy, middle, dusty of being definition in face metric structure of slope undifferenced. Maintenance of dusty particles with depth gradually increase with 60-62% till 70-75%, maintenance of clayey particles with depth are decrease gradually from 4-8% till 22-23%.

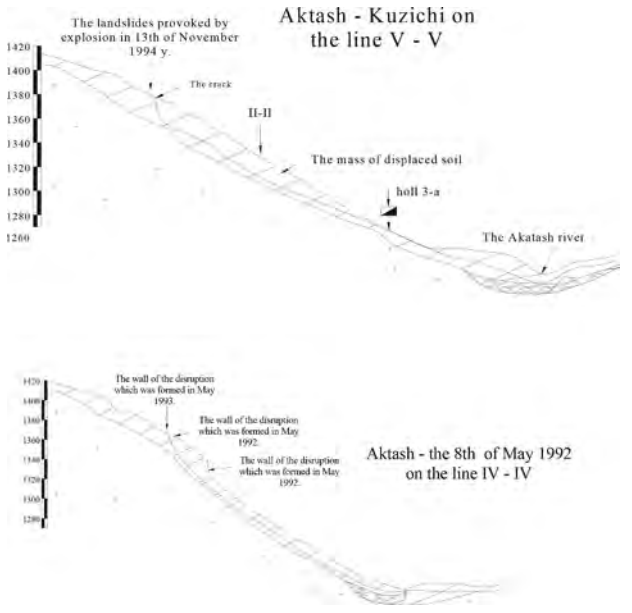

Figure 1. Engineering - geological cuts (rips) of the lots: (upper) Aktash, (Lower) Aktash, Aktash - Kuzichi.

The volume mass of rock at the break part of slope has less meaning 14,1-15,7 kH/m 3, than in natural bed 15,7-16,3% kH/m3, it testifies about some its loosen by moving of landslides. The porous of landslide soil is equally 48,7-52%. The coefficient of filter of break soil consist 0,026-0,06 m/day, with differ of feebly water stability at the first minute. After water saturation it soaks till 70% mass of soil. The soils of unbreak slope have porous 48,3-50,2% at 5 minute wets only 5% mass of soil.

Underground waters at the research lot (Saygus) everywhere accustomed to a contact of covered loamy soils with root brads. The depth of bed underground waters is changes and depends from relief's roof root's brads. At the down part of slope in the place of projection timely water flowing is wedged in spring to 0,001-0,5 l/sec.

Specific coupling under the natural humidity makes up 0,014-0,065 Mpa under the angle of the inside friction 27-32 degree, under the water-saturation - specific coupling 0,0015-0,22 Mpa, and angle of the inner (inside) friction 21-25 degree.

5 REASONS AND CONFORMITY OF DISPLAING OF THE LANDSLIDES

Peculiarity and places of displacing of the dangerous geological process is determines by the geological-tectonically structure of the region's area.

The basic reason of development and getting down of the landslides is being the presence of over humidity of the loamy soil on the contact with rooted rocks, surfaced and underground water, and also formation of the landslides, which was evoke by the seismic action, provoked by explosion.

The surface of the side served for the irrigation of the wooden-road-metal of deposit on contact with over humidity of the loamy soil.

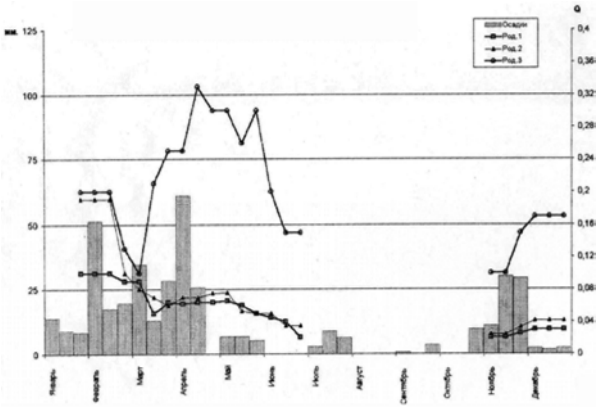

Figure 2. Graphic of subordination of springs (courses) from the amount of the atmospheric – precipitations (Lower) Aktrash 1998.

The formation and similar of landslides coming at the period of rains at the ending of months February and May. At the picture (2,3) derived graphs of dependence of amount falling precipitations up to months and water's expenditure of spring (the landslide Aktash). As you see from graphs (pic 4) the amount of landslides and their similar are confirming by facts of Samarkand meteoritical station. Last year at the first quartier falling precipitations consisted 146,1 and 173 mm.

At the landslides lots putted 30 dephonometers and at the main landslide crack putted 12 tensiometers. The value of displacement from tensiometers consisted about 9-62 mm.

At the result of observing topo geodesic repress, at the landslides gradually shows the formation mound of getting out at the down part of zone arty crack. Negative meaning of

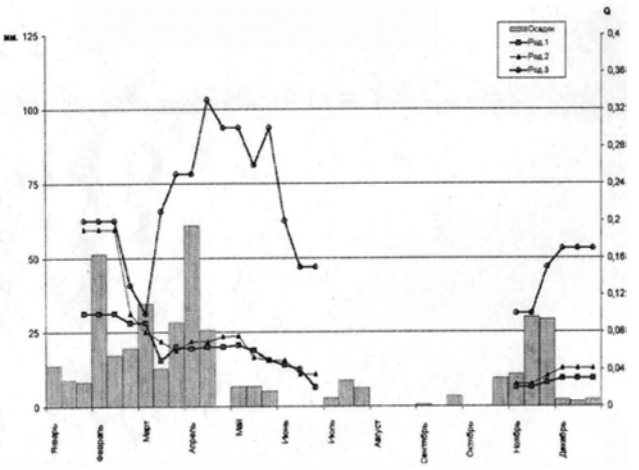

Figure 3. Graphic of subordination of springs (courses) from the amount of the atmospheric – precipitations (Lower) Aktrash 1999.

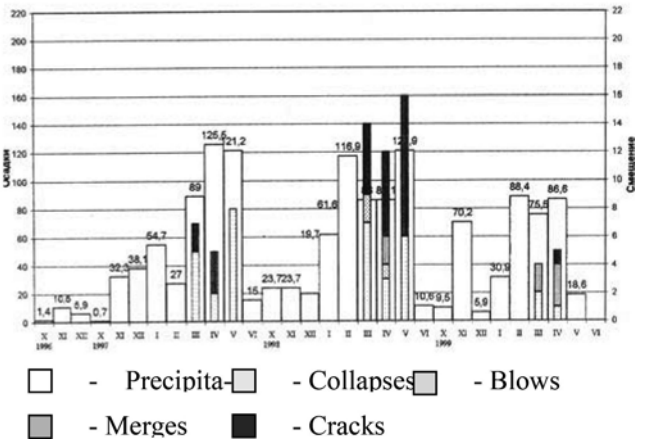

Figure 4. Graphic of subordination of the amount of landslides from the amount of atmospheric – precipitations. Samarkand Region meteorological station of the Yangiariq.

vertical reaper's moving able to evidence about the possible forming of the crack on the depth and gradually precipitate of the surface.

6 CONCLUSIONS AND ADOPTED ENGINEERING DECISIONS

The results of long observing tells, that big influence on appear of landslides gives economical activity of human. Analyze of landslides appearing tells that more 50% registrational landslides was appear by influence of building and exploitation different buildings.

More intensive landslides are develop along of auto roads. It gives notion, that mastering of mountainous and around mountainous districts without preliminary investigations by definition of degree of stability of the slopes and execution of the protection recommendations, is being one of the main factors of formation of the landslides.

At the same time, high elevated seismic activity of exploratory zone, is aggravates the dangerous of the catastrophic consequences from their influence.

On the basis of results which was spend on research works. There is an establishment four particularly dangerous landslides blocks, the capacity of the displacement mass which is makes up from 30 thousand m3 to 250 thousand m3.

In the case of displacement of the whole landslides massif the river-bed of the Say can be covered on the height 6-7 m with formation of the flooding zone on the horizon 1230 m. in the dangerous zone.

There are 44 economy (farms) of the landslides dangerous. For the dangerous landslides liquidation was recommended:

1. Unloading the unsteady mass of the slope, with the following planning and porching - terracered where are the landslides develops- the capacity of flow 150-300 thousand m3 with the straightforward direction on the house-construction.
2. After completion of the unloading in the middle part of the slope for it interception of the subterranean waters on the contact of the soils and clay it is necessary to drain ditch and restore of the exists drain-pine as a natural drains.
3. There are recommendation for construction of the water-fall of extinguished walls, the regulate dam for challenge of the landslides mass from the settlement under the formation of the huge landslides-streams.

REFERENCES

Maslov N.N. Mechanics of soils in the practice of construction. (landslides and their control) training. "Stroyzdat", 1977. 320 p.

V.I. Presnukhina Landslides of Tajikistan. Dushanbe. "Nauka" Publishing House 1988. 106 p.

Ikramov. F.A. Study of the causes of resurgence and features of landslide phenomena Proceedings of the I Central Asian Geotechnical Symposium. Astana May 2000 "Geotechnical problems of construction, architecture and geology at the turn of the XXI century" 2, pp. 889–901.

Reasons of damages of buildings on loess soils of. The III Central Asia International Conference on Geotechnical Engineering and Soil Mechanics, .Tehran December 9-11, 2002.

Ikramov F.A. "Investigation of the causes and features of landslide phenomena" Proceedings of the I Central Asian Geotechnical Symposium .Astana May 2000.

Kezdi Árpád Manual of Soil Mechanics Academy Kiado, Budapest,1976. Translation into Russian. Moscow. "Stroyizdat" 1978.

Ikramov F.A. Z.A. Khasanov "Study of landslide processes and the mechanism of combating them (on the example of the Samarkand Oasis)". Proceedings of the XIX international conference, St. Petersburg, Russia 2001.

Smart Geotechnics for Smart Societies – Zhussupbekov, Sarsembayeva & Kaliakin (Eds)
© 2023 The Author(s), ISBN 978-1-003-29912-7
Open Access: www.taylorfrancis.com, CC BY-NC-ND 4.0 license

Semi experimental Thermo-Hydro-Mechanical model for maximum shear modulus of unsaturated soils

Shaya Banar
Ph. D. Candidate, Department of Civil Engineering, Sharif University of Technology, Tehran, Iran

Fardin Jafarzadeh
Associate Professor, Sharif University of Technology & President of Iranian Geotechnical Society, Tehran, Iran

ABSTRACT: Soils in geotechnical engineering are in different mechanical and environmental conditions. What is very important in evaluating unsaturated soils is the study of environmental processes that occur in the soil. Due to the fact that soils are exposed to different climatic conditions in different seasons, its temperature and matrix suction are variable. Also, the study of soil stiffness behavior in dynamic conditions is one of its important parts. Therefore, in this paper, an attempt is made to provide a semi-experimental model for evaluating the maximum shear modulus of unsaturated soils under different temperatures and mechanical conditions, using Thermo-Hydro- Mechanical principles and various laboratory results. Laboratory results are used to validate the proposed model.

1 INTRODUCTION

Shear modulus is a key parameter to evaluate the dynamic response of geotechnical structures under various loading (i.e. machine vibration and earthquakes). Near-surface soils can be placed in different climate conditions and therefore these soils can be placed in different hydraulic and temperature conditions. Soils in different seasons behave differently due to the changes in matric suction or temperature. One of the influencing parameters on the value of maximum shear modulus (G_{max}) of unsaturated soils is matrix suction and net normal stress. For this reason, the evaluation of the maximum shear modulus in Thermo-Hydro-Mechanical (THM) conditions becomes important.

The value of the maximum shear modulus represents the elastic behavior of the soil in small strains and the effect of sliding between the soil particles is negligible, and its deformation occurs due to the elastic behavior of the soil (Hardin & Kalinski 2005). One of the important parameters for evaluating the shear modulus is the amount of shear strain level. For measuring the shear modulus different laboratory and in-situ methods are used. Most of the maximum shear modulus measurements have been done by researchers using laboratory methods such as bender element, resonant column or triaxial tests that can be conducted in small strains.

Initial studies (Hardin 1978) show that effective stress and pre-consolidation stress are principle parameters on shear modulus in saturated and dry soils (Equation 1). In the next step, researchers' studies on unsaturated soils show that the matric suction and net normal stress have a significant effect on the maximum shear modulus. Considering that measuring the maximum shear modulus in unsaturated soils requires advanced laboratory equipment. In addition, there is a long time (a couple of days or weeks) to reach equilibrium for unsaturated soils, so various researchers have given empirical and semi-empirical relationships to evaluate the shear modulus.

DOI: 10.1201/9781003299127-52

$$G_{\max} = AP_a\left(\frac{P'_c}{P'}\right)^k\left(\frac{P'}{P_a}\right)^n \quad (1)$$

where A and n = stress-dependency fitting parameters, vary for different soils; P'_c = mean pre-consolidation stress, P' = mean effective stress; P_a = atmospheric press.; k = hardening parameter.

In the last decade, more researchers try to understand the effect of temperature on soil behavior. By continuing the studies on the maximum shear modulus of unsaturated soils, the researchers found that temperature has a significant effect on the maximum shear modulus (Vahedifard et al. 2021, Zhou et al. 2015). So far, very limited studies have been done to measure the maximum shear modulus of unsaturated soils in non-isothermal conditions. But these results show that temperature has a significant effect on the shear modulus. In fact, with the increase in temperature, the shear modulus of the soil has decreased, which depends on various factors that will be discussed below.

For this reason, this research tries to evaluate the effect of THM factors on the shear modulus by providing a comprehensive model. In this model, the effect of various factors such as effective stress, pre-consolidation stress, degree of saturation, net normal stress, and temperature on the shear modulus has been seen. Finally, the evaluated value of the maximum shear modulus is compared with the results available in the literature for validation.

2 BACKGROUND

The maximum shear modulus, G_{max}; is considered in shear strains smaller than $\gamma < 10^{-5}$. Considering the importance of shear modulus evaluation, researchers have presented different experimental relationships in different conditions. In the first step (Hardin 1978) evaluated the effect of factors such as soil porosity, stress history, plastic index, and effective stress. In the next step, other researchers (Hardin & Black 1968, Vucetic & Dobry 1991) presented several relationships to evaluate the shear modulus in dry and saturated conditions.

Soil behaves differently in environmental and seasonal conditions. For this reason, researchers investigated the shear modulus of unsaturated soils in the next step. In these studies, the degree of saturation (or matric suction) and net normal stress were identified as parameters affecting the dynamic behavior of the soil (Banar et al. 2019, Mancuso et al. 2002, Inci et al. 2003, Sawangsuriya et al. 2009). Also, various researchers have tried to provide an experimental model to determine the shear modulus (Khosravi & McCartney 2012, Ghayoomi et al. 2017). In each of these models, the degree of saturation and net normal stress were considered important soil components in hydraulic conditions. Also, effective soil stress is considered the main parameter of soil mechanical behavior. In addition, all these models are suitable for isothermal conditions, and they never consider the effect of temperature on their models. Uchaipichat & Khalili 2009 confirms that temperature affects pre-consolidation stress. As the temperature increases, the pre-consolidation stress decreases (Salager et al. 2008). Various studies in this field show that temperature affects the volume change behavior of soil. It is evident that the tendency of highly overconsolidated soils to expand and normally consolidated to contract, is common for both saturated and partially saturated soils. Temperature effects on compressibility indexes are investigated, where no specific trend is identified in saturated (Campanella & Mitchell 1968, Di Donna & Laloui 2015) and unsaturated conditions (Uchaipichat & Khalili 2009, Coccia & McCartney 2016).

3 PROPOSED MODEL

In this study, an attempt is made to evaluate the maximum shear modulus value of silty soil in different Thermo-Hydro-Mechanical (THM) conditions by presenting a semi-experimental model. There are limited studies to understand the G_{max} in different THM conditions especially for unsaturated soils. In this semi-empirical model, the effect of three factors of temperature,

degree of saturation and mechanical stress loading on the maximum shear modulus is obtained. In the following, the presented model is validated using the results in previous studies.

3.1 *Semi-empirical model in Thermo-Hydro-Mechanical*

Liu et al (2021) has been proposed a fully coupled constitutive model for the Thermo-Hydro-Mechanical behavior of unsaturated soils. In this model, they consider three constitutive variables: 1- Bishop's effective stress (Equation 2) 2- Modified suction (Equation 3) 3- Temperature (T).

Liu et al (2021) employed four yield surfaces to govern the plastic behavior in Thermo-Hydro -Mechanical conditions: 1-Loading surface (LS) 2- Temperature Surface (TS) 3- Suction Increase (SI) 4- Suction Decrease (SD). LS yield surface is the extension of the Loading collapse (LC) yield line in the Hydro-Mechanical (HM) model of Wheeler et al. (2003) to non-isothermal conditions. Also, thermal contraction deformation of normally consolidated soils and lightly over-consolidated soils are attributed to LS yield surface. The thermal expansion corresponds to an elastic behavior while the thermal contraction corresponds to an elastoplastic behavior. Also, the transition temperature between thermal expansion and contraction increases with an increasing consolidation ratio. Thus, the transition temperature can be defined as the yield temperature. The third and fourth yield surfaces, suction increase/decrease are the extensions of SI/SD yield lines in the HM model of Wheeler et al. (2003) to non-isothermal conditions.

$$\sigma_{ij}^{*} = (\bar{\sigma}_{ij} - u_a) + s \times S_{r.} \tag{2}$$

$$s^{*} = ns \tag{3}$$

where $\overline{\sigma}_{ij}$= total stress tensor, u_a= pore air pressure, s=matric suction, S_r= degree of saturation, n=porosity.

Liu et al (2021) have offered that the hardening of the LS is jointly controlled by the sum of the hardening caused by yielding on the LS itself and the couple hardening produced by yielding on the TS. Also, and hardening in LS controlled by double-hardening mechanism for unsaturated soil introduced by wheeler et al. (2003) which is related to the yielding on SI/SD (Equation 4). Therefore, the hardening of the LS can be presented as follows:

$$\frac{dp_c}{P_c} = \frac{1}{\lambda - \kappa}(d\varepsilon_{VL}^{p} + d\varepsilon_{VT}^{p}) + k_1 \frac{ds_r^{p}}{\lambda_s - \kappa_s} \tag{4}$$

where λ_s= slope of the primary drying/wetting lines in the S_r-*ln S**, κ_s= slope of the scanning lines in the S_r-*ln S** plane, k_1= control the coupled movement of the LS and TS when yielding on only SI, dS_r^{p} = Plastic degree of saturation increment, $d\varepsilon_{vl}^{p}$ = plastic strain increment by mechanical loading, $d\varepsilon_{vt}^{p}$= Thermal plastic strain when yielding occurred on the TS during the heating process, v = Specific volume, P_c = Preconsolidation stress at room temperature, λ = Slope of normally consolidated line in the v-*lnP* plane, and κ= Slope of swelling curve in the v-*lnP* plane.

To drive the hardening Equation 4 can be integrated from the initial conditions into general values of these parameters (Equation 5). Then both sides can be divided by P' to yield a definition that was used in Hardin's Equation (Equation 6). Then Equation 6 directly insert into Equation 1 to define the general formulation of G_{max} in different THM conditions. Equation 7 can be split into three dimensionless terms: 1- Represent the hardening because of mechanical loading (first bracket) 2- Represent the thermal softening (second bracket) 3- Represent the hardening because of changes in saturation (third bracket). *k, k', k''* are the hardening fitting parameters that are related to the mechanical, hydraulic, and thermal conditions respectively.

$$\ln\left(\frac{dp_c^{*}}{P_c^{*}}\right) = \frac{\Delta e_L^{P} + \Delta e_T^{P}}{\lambda - \kappa} + \frac{k_1 \Delta s_r}{\lambda_s - \kappa_s} \tag{5}$$

$$\frac{P_c^*}{P'} = \frac{P_{c_0}^*}{P'} \exp\left(\frac{\Delta e_L^P}{\lambda - \kappa}\right) \exp\left(\frac{\Delta e_T^P}{\lambda - \kappa}\right) \exp\left(\frac{k_1 \Delta s_r}{\lambda_s - \kappa_s}\right) \tag{6}$$

$$G_{\max} = AP_a \left(\left[\frac{P_{c_0}^*}{P_n} \exp\left(\frac{\Delta e_L^P}{\lambda - \kappa}\right) \right]^k \times \left[\exp\left(\frac{\Delta e_T^P}{\lambda - \kappa}\right) \right]^{k'} \times \left[\frac{P_n}{P'} \exp\left(\frac{k_1 \Delta s_r}{\lambda_s - \kappa_s}\right) \right]^{k''} \right) \left(\frac{P'}{P_a}\right)^n \tag{7}$$

4 VALIDATION AGAINST EXPERIMENTALLY MEASURED DATA

4.1 *Soil type and specimen preparation*

Zhou et al. 2015 used the Completely Decomposed Tuff (CDT) to measure shear modulus at various shear strains, matric suction, and temperature. For the present study, the result of the small strain shear modulus of CDT soil is used to verify the model that is proposed. The index tests of this soil are according to Table 1 (Zhou et al. 2015). The Soil-Water Retention Curve (SWRC) at 20°C of this soil is shown in Figure 1. After the soil is statically compacted, its initial suction value is approximately equal to 95 kPa. Then this sample reaches 1, 150, and 300 kPa respectively in different hydraulic paths. Also, these samples reach equilibrium at different temperatures of 20°C and 60 °C.

Finally, after the soil sample reaches equilibrium, dynamic loading is performed on it using a modified triaxial test that has the ability to control matrix suction and temperature, and the value of the shear modulus in different strains is obtained. What is used in the current research is the results of the maximum shear modulus which is in the strain range of 0.003 %, which is considered in the range of small strains.

Table 1. Index tests of CDT soil.

Index test	Measured value
Standard compaction tests	
Max Dry density: kg/m^3	1760
Optimum water content: %	16.3
Grain size distribution:	
Percentage of sand: %	24
Percentage of silt: %	72
Percentage of clay: %	4
Specific gravity	2.73
Atterberg limits:	
Liquid limit: %	43
Plastic limit: %	29
Plasticity index: %	14

4.2 *Model parameters*

A parametric evaluation was performed to highlight the behavior of the model during the THM condition. Soil specimen had the following initial conditions: P_n=100 kPa, e_0 =0.573, s_0 =95 kPa, P'= 100 kPa, λ_s=0.254, κ_s=0.0251, λ=0.055, κ=0.005, and P'_c= 500 kPa. The value of P_n does not change during the tests. The changes in P' define based on the Bishop effective stress (Equation 2).

Soil matric suction changes from the initial condition (i.e. 95 kPa) to 1, 150, and 300 kPa. For measuring the differences in the degree of saturation in different hydraulic path use the SWRC curve. Differences for T=60 °C are similar to the T= 20°C. There is little difference between the degree of saturation in different temperatures (Uchaipichat & Khalili 2009). Also, in the non-isothermal condition, the value of λ and κ are constant and the changes of these parameters due

to the temperature effect are negligible. For measuring the changes of Δe_t^p result of normal isotropic compression test has been used. Also, for measuring the Δe_t^p the data of the non-isothermal normal isotropic compression test has been used (Uchaipichat & Khalili 2009).

Figure 2 provide a comparison between measured G_{max} value and those predicted using the Thermo-Hydro-Mechanical shear modulus in this study (i.e. Equation 7). The fitting parameters A, n, K, K', K'', and K_1 provided the most reasonable estimates and are summarized in Table 2 for the CDT soil.

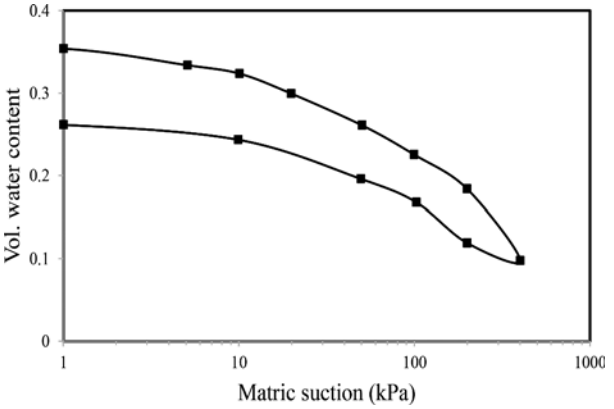

Figure 1. Soil-Water Retention Curve of CDT soil at 20°C (Zhou et al. 2015).

Table 2. Fitting parameters value.

Fitting parameters	Value	
	T=20°C	T=60°C
A	0.9	0.9
n	1.5	1.4
k	2.9	2.85
k'	0.2	0.1
k''	0.1	0.15
k_1	0.3	0.5

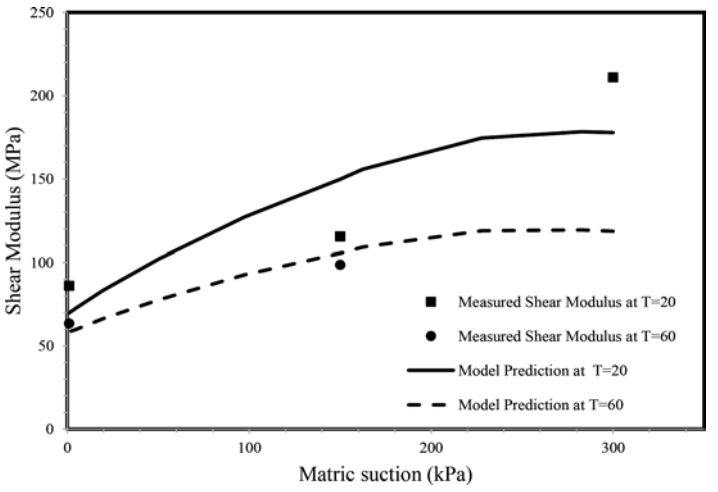

Figure 2. Comparison between the measured value and model prediction.

5 CONCLUSION

A new model was presented to represent the effect of Thermo-Hydro-Mechanical conditions on maximum shear modulus (G_{max}). Most of the previous models were in the isothermal condition and the effect of temperature was not considered. The effect of various parameters like net normal stress, degree of saturation, pre-consolidation pressure, effective stress, and temperature are considered in this model. The model was found to fit the trends in the available G_{max} data in the literature. There are limited studies to measure the G_{max} of soils at various suction and temperature, so further experimental tests are required to validate the proposed model for different conditions.

REFERENCES

Banar, S., Haeri, S.M., Khosravi, A. and Khosravi, M., 2019. Evaluation of strain dependent shear modulus and damping ratio of unsaturated silty soil during drying path with resonant-column-torsional shear. In Earthquake Geotechnical Engineering for Protection and Development of Environment and Constructions (pp. 1281–1288). CRC Press.

Campanella, R.G. and Mitchell, J.K., 1968. Influence of temperature variations on soil behavior. Journal of the Soil Mechanics and Foundations Division, 94(3),pp.709–734.

Coccia, C.J.R. and McCartney, J.S., 2016. Thermal volume change of poorly draining soils I: critical assessment of volume change mechanisms. Computers and Geotechnics, 80, pp.26–40.

Di Donna, A. and Laloui, L., 2015. Response of soil subjected to thermal cyclic loading: experimental and constitutive study. Engineering Geology, 190, pp.65–76.

Ghayoomi, M., Suprunenko, G. and Mirshekari, M., 2017. Cyclic triaxial test to measure strain-dependent shear modulus of unsaturated sand. International Journal of Geomechanics, 17(9), p.04017043.

Hardin BO, Kalinski ME. 2005. Estimating the shear modulusof gravelly soils. J Geotech Geoenviron Eng 131(7):867–875.

Hardin, B.O. and Black, W.L., 1968. Vibration modulus of normally consolidated clay. Journal of the Soil Mechanics and Foundations Division, 94(2),pp.353–369.

Hardin, B.O., 1978, June. The nature of stress-strain behavior for soils. In From Volume I of Earthquake Engineering and Soil Dynamics–Proceedings of the ASCE Geotechnical Engineering Division Specialty Conference, June 19-21, 1978, Pasadena, California. Sponsored by Geotechnical Engineering Division of ASCE in cooperation with: (No. Proceeding).

Inci, G., Yesiller, N. and Kagawa, T., 2003. Experimental investigation of dynamic response of compacted clayey soils. Geotechnical Testing Journal, 26(2), p.125.

Khosravi, A. and McCartney, J.S., 2012. Impact of hydraulic hysteresis on the small-strain shear modulus of low plasticity soils. Journal of Geotechnical and Geoenvironmental Engineering, 138(11), pp.1326–1333.

Liu, Y., Cai, G., Zhou, A., Han, B., Li, J. and Zhao, C., 2021. A fully coupled constitutive model for thermo-hydro-mechanical behaviour of unsaturated soils. Computers and Geotechnics, 133, p.104032.

Mancuso, C., Vassallo, R. and d'Onofrio, A., 2002. Small strain behavior of a silty sand in controlled-suction resonant column torsional shear tests. Canadian Geotechnical Journal, 39 (1),pp.22–31.

Salager, S., Francois, B., El Youssoufi, M.S., Laloui, L. and Saix, C., 2008. Experimental investigations of temperature and suction effects on compressibility and pre-consolidation pressure of a sandy silt. Soils and Foundations, 48(4),pp.453–466.

Sawangsuriya, A., Edil, T.B. and Bosscher, P.J., 2009. Modulus-suction-moisture relationship for compacted soils in postcompaction state. Journal of Geotechnical and geoenvironmental engineering, 135 (10), p.1390.

Uchaipichat, A. and Khalili, N., 2009. Experimental investigation of thermo-hydro-mechanical behaviour of an unsaturated silt. Géotechnique, 59(4),pp.339 353.

Vahedifard, F., Thota, S.K., Cao, T.D., Samarakoon, R.A. and McCartney, J.S., 2020. Temperature-dependent model for small-strain shear modulus of unsaturated soils. Journal of Geotechnical and Geoenvironmental Engineering, 146(12),pp.04020136–04020136.

Vucetic, M. and Dobry, R., 1991. Effect of soil plasticity on cyclic response. Journal of geotechnical engineering, 117(1),pp.89–107.

Wheeler, S.J., Sharma, R.S. and Buisson, M.S.R., 2003. Coupling of hydraulic hysteresis and stress–strain behaviour in unsaturated soils. Géotechnique, 53(1),pp.41–54.

Zhou, C., Xu, J. and Ng, C.W.W., 2015. Effects of temperature and suction on secant shear modulus of unsaturated soil. Géotechnique Letters, 5(3),pp.123–128.

Smart Geotechnics for Smart Societies – Zhussupbekov, Sarsembayeva & Kaliakin (Eds)
© 2023 The Author(s), ISBN 978-1-003-29912-7
Open Access: www.taylorfrancis.com, CC BY-NC-ND 4.0 license

Liquefaction potential in the upper reaches of River Ravi, Pakistan

Sohail Kibria
Head R&D, NESPAK, Lahore, Pakistan

Tahir Masood
Managing Director, NESPAK, Lahore, Pakistan

Sadaf Saeed
Principal Engineer, NESPAK, Lahore, Pakistan

ABSTRACT: Pakistan has several regions of seismic activity, having low to high seismic potential. Similarly, a variety of soil deposits exist in the country; some of which are known to have significant liquefaction potential. Liquefaction potential of a certain site is generally a trade-off between the state of denseness of saturated sand deposits and the peak ground acceleration (PGA) at that site. River Ravi flowing through the Punjab province, has its flood plain in the upper Punjab. The soil deposits in its flood plain consist of fine sand with variable silt content (upto to 15%). The PGA in these plains ranges from 0.16 to 0.24g with an average of 0.20g for 475 years return period earthquake having 10% probability of exceedance in 50 years. At an important project site located in the upper reaches of river Ravi, recently loose Sand deposits were encountered up to 10-12m depth below the ground level. Light to moderately heavy structures were planned over the site. The evaluation of free-field liquefaction potential using the Cyclic Stress Approach based on SPT blows (Youd, Seed et al., 2001) with due adjustment for the moment magnitude of 6, indicated sands to be liquefiable up to 12 m depth. The mitigation of liquefaction risk at this site consisted of providing long R.C. drilled shafts (ignoring skin friction in the upper 10 to 12 m zone) under the moderately heavy loads and providing earthen platforms (raising the ground level) under the light structures. A Factor of Safety of 1.1 was taken as the threshold of liquefaction in terms of ratio of the cyclic stress ratio required to cause liquefaction to the one induced by earthquake of average PGA of 0.22g. The project structures stand constructed safely at the site. This paper provides a complete account of the process of evaluation of liquefaction potential and its effective mitigation using simple means. These type of mitigation measures can be adopted for the structures in similar ground and seismic conditions.

1 INTRODUCTION

The project site under discussion lies at India-Pakistan border in the northern Punjab in Pakistan. It is of great religious importance to a particular community of people. The facilities included light to moderately heavy buildings and a 772m long bridge.

The site is located between rivers Chenab and Ravi, about 100 m away from a tributary of Ravi on its right bank. The area is underlain by thick alluvial deposits consisting of clays, silts and sand lain by the Chenab and Ravi rivers, which flow from northern to southern sides of the project area.

2 SEISMIC Z ONATION OF PUNJAB

The Punjab plains are located near the foothills of the Himalayan range, which is seismically very active. The main active tectonic features of the Himalayan range are Main Boundary Thrust (MBT) and Riasi thrust which are passing at the closest distance of about 93 km and 80 km, respectively northeast of the project area. Both these features have potential to generate damaging earthquakes and can cause appreciable ground motion at site.

DOI: 10.1201/9781003299127-53

The part of Punjab Plain, in which the Project site is located, shows low to moderate level of seismicity which is associated with the faulting in the Basement rocks covered by the alluvial deposits.

As per Seismic Zoning Map of Pakistan included in the Revised Seismic Provisions (2007) of Building Code of Pakistan, the project falls in Zone-2B having PGA varying from 0.16 to 0.24g. This Seismic Zoning Map is based on the probabilistic evaluation of tectonic and seismicity data of the region and represents ground motion having 10% probability of exceedance in 50 years (i.e. for a return period of 475 years). Building Code of Pakistan Seismic Provisions (2007) show that the project area falls on the contour value of 0.22g on PGA contour map.

The de-aggregation of the probabilistic seismic hazard analysis for the project area shows that the most critical seismic source is a magnitude 6 earthquake occurring at a distance of 10 km from the site in the Punjab plain. The liquefaction analysis is based on this most critical seismic source.

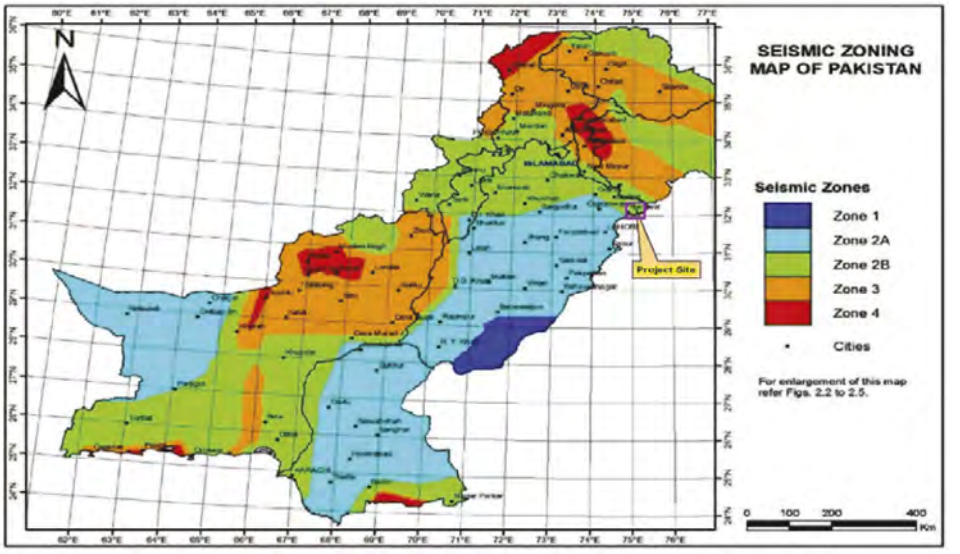

Figure 1. Seismic zoning map of pakistan.

3 GEOTECHNICAL STUDIES AND SITE CONDITIONS

Two (2) boreholes up to a maximum depth of 40 m and four (4) boreholes up to a maximum depth of 50 m below River Bed Level (RBL) were executed by using straight rotary drilling method along the proposed alignment of bridge over river Ravi. In addition, twelve boreholes up to 20m depth were drilled at structural facilities sites. Four boreholes of 10 m depth were also drilled at minor facilities sites.

3.1 *Bridge site*

At bridge site, the on-site soils comprised silty sand/poorly graded sand/poorly graded sand with silt, in very loose to medium-dense state as per SPT-N value were present from river bed level (RBL) to maximum depth of 15 m. This was followed by lean clay/silty clay, in very stiff to hard state as per SPT-N values, measured up to maximum depth of 34 m. This layer was followed by silty sand/poorly graded sand with silt, in dense state from 34 m to maximum investigated depth of 50 m. Groundwater table was encountered in all the boreholes at depth varying from 1.0 to 3.3 m below RBL.

3.2 *Main facilities sites*

At the sites for main facilities, silt/silty sand, in very loose to loose state was present to a depth of 4 m below Natural Surface Level (NSL). Silty sand/poorly graded sand with silt, in loose to

Table 1. Geotechnical characterization at bridge site.

Soil Type	H Elevation below RBL From (m)	To(m)	γ_b kN/m^3	$(N_1)_{60}$	c kPa	Φ Degrees
silty sand/poorly graded sand with silt	242.0	234.0	17.5	8	-	29
silty sand/poorly graded sand with silt	234.0	227.0	18.5	14	-	31
lean clay/silty clay	227.0	208.0	19.0	-	125	-
silty sand/poorly graded sand with silt	208.0	192.0	19.0	20	-	33

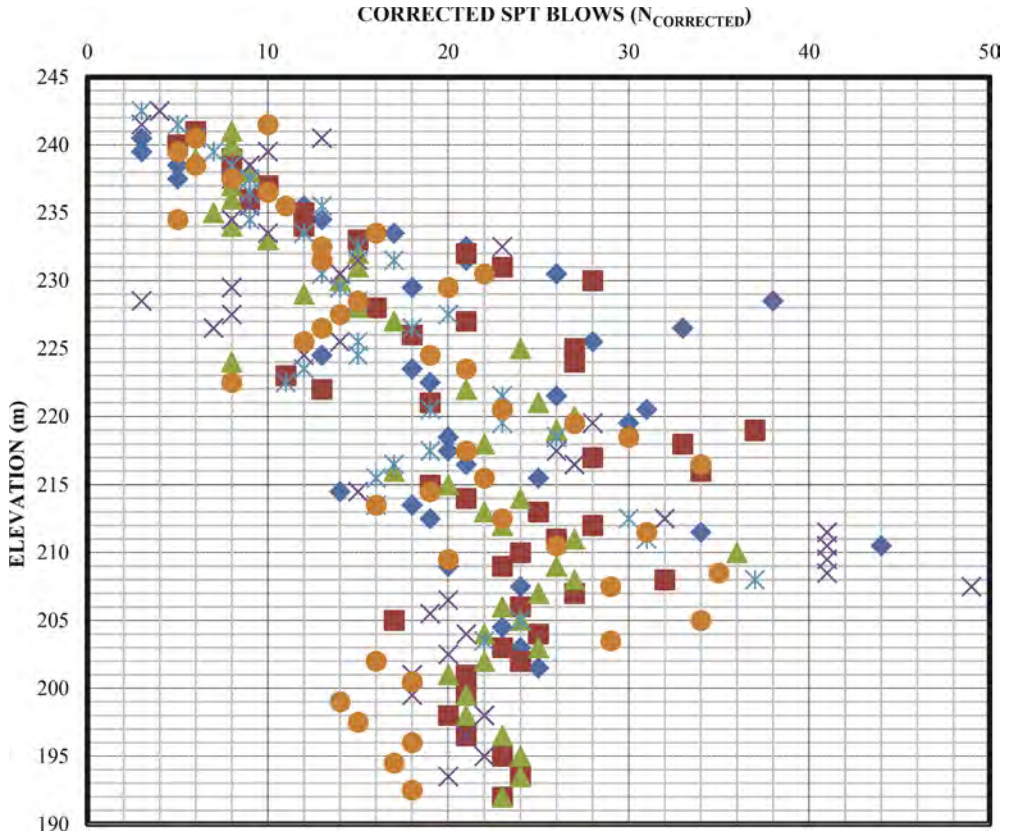

Figure 2. Corrected SPT blows at bridge site.

medium-dense state was present upto maximum investigated depth of 8 m below NSL. Poorly graded sand in medium-dense condition was encountered upto 19 m depth. This layer was followed by lean clay/silty clay in very stiff to hard state upto maximum investigated depth. Groundwater table was encountered in all the boreholes at depth varying from 3.0 m to 5.0 m below NSL.

3.3 *Minor facilities sites*

Loose to medium-dense silty sand/poorly graded sand with silt was encountered upto the maximum investigated depth of 10 m below NSL at the minor facilities sites. Groundwater table was encountered at depth varying from 3.0 m to 4.0 m below NSL.

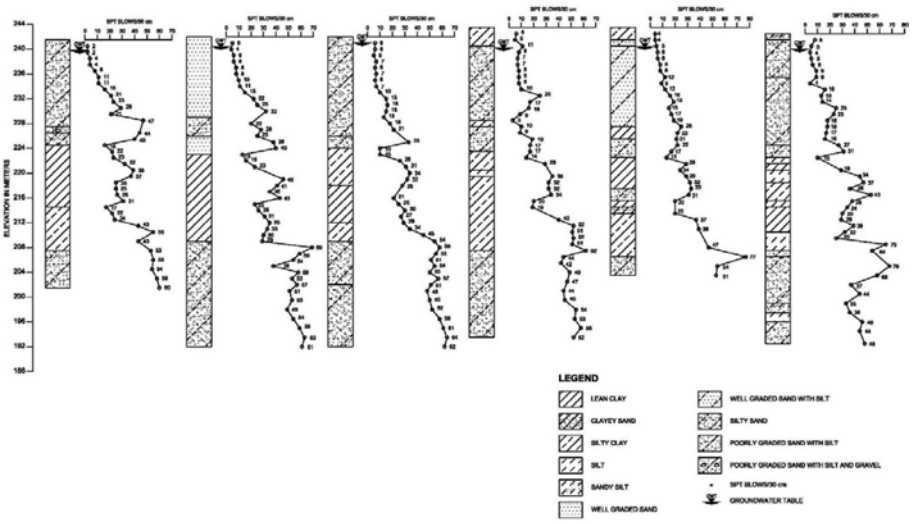

Figure 3. Subsurface soil profile at bridge site.

Table 2. Geotechnical characterization at main facilities sites.

Soil Type	H Elevation below NSL From(m)	To(m)	γ_b kN/m^3	$(N_1)_{60}$	c kPa	Φ Degrees
silty sand/poorly graded sand with silt	244.0	237.0	16.0	5	-	26
silty sand/poorly graded sand with silt	237.0	233.0	17.5	10	-	28
silty sand/poorly graded sand with silt	233.0	224.0	18.5	16	-	32
silty clay	224.0	223.0	19.0		125	-

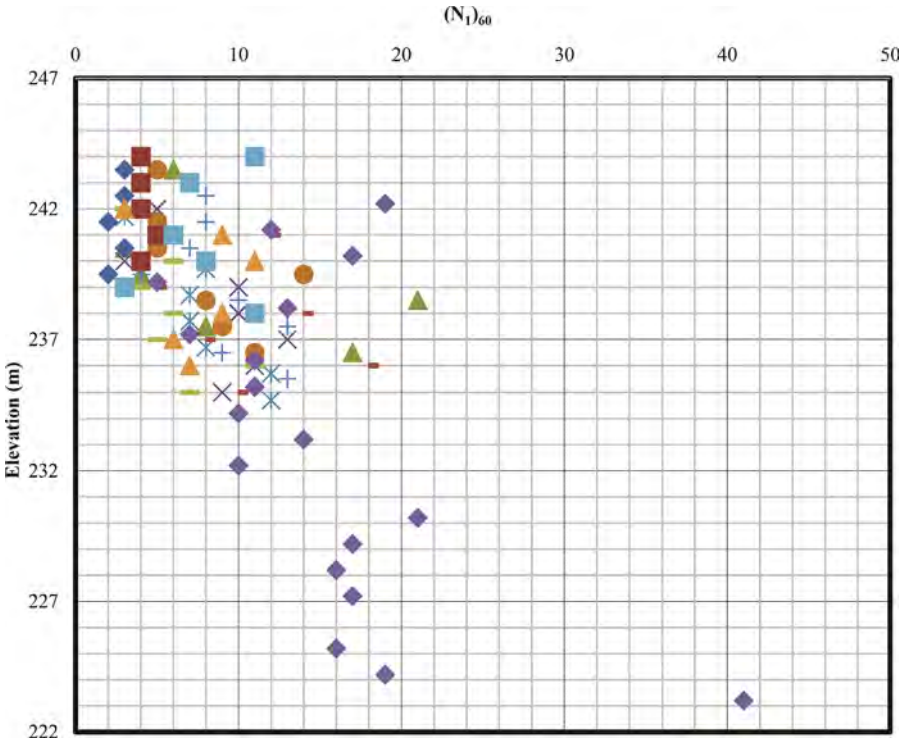

Figure 4. Corrected SPT blows at main facilities sites.

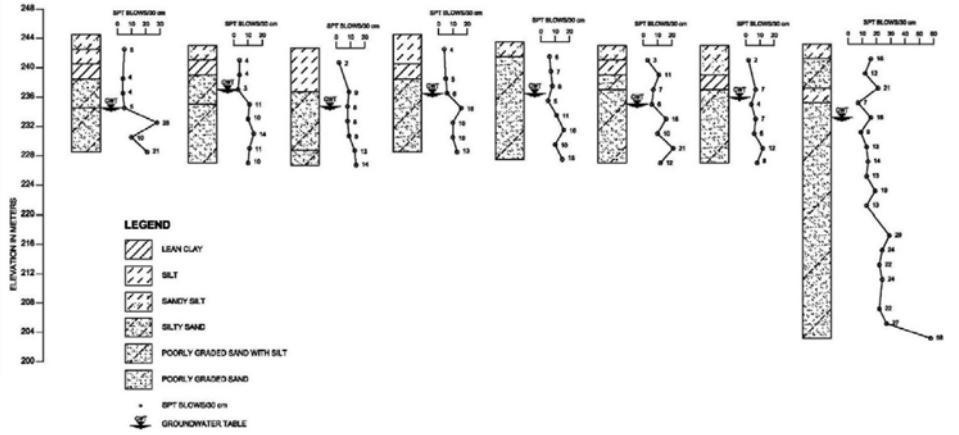

Figure 5. Subsurface soil profile at main facilities site.

Table 3. Geotechnical characterization at minor facilities sites.

Soil Type	H Elevation below NSL From(m)	To(m)	γ_b kN/m^3	$(N_1)_{60}$	Φ Degrees
Silty Sand/Poorly Graded Sand with Silt	242.0	238.0	17.5	6	27
Silty Sand/Poorly Graded Sand with Silt	238.0	232.0	18.0	8	29

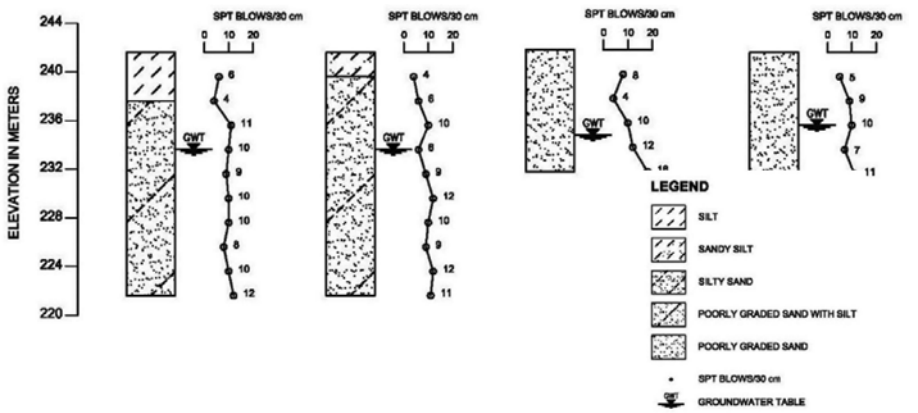

Figure 6. Subsurface soil profile at minor facilities site.

4 SPT-BASED LIQUEFACTION POTENTIAL EVALUATIONS OF SITE

When saturated sand deposits are subjected to earthquake-induced shaking, pore water pressure in the soil progressively builds-up with each loading cycle, which eventually leads to the significant loss of effective shear strength. Total liquefaction is the extreme manifestation of this phenomenon. At the commencement of soil liquefaction, the effective stress in the soil becomes zero and pore water pressure in the soil becomes equal to the initial static effective stress, i.e., the present total stress becomes zero.

Keeping in view the site subsurface conditions, the liquefaction potential of the subsurface strata was determined using Seed's cyclic stress approach based on SPT (Youd et al, 2001,

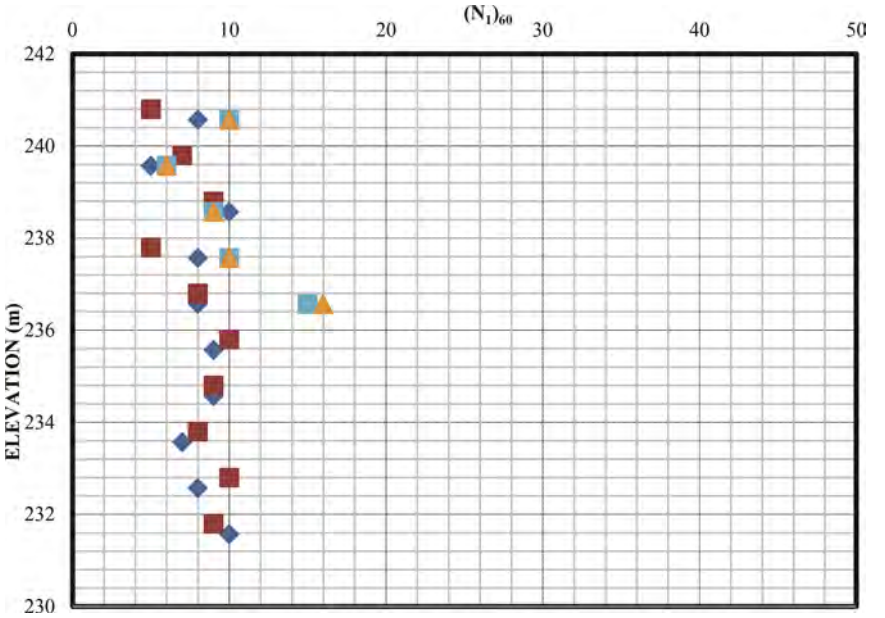

Figure 7. Corrected SPT blows at minor facilities sites.

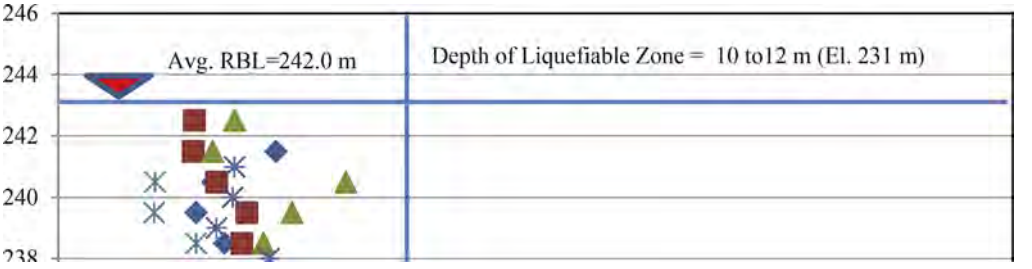

Figure 8. Bridge site – FOS.

Rauch, 1997) for free-field condition. Factor of Safety (FOS) of 1.10 was kept as the acceptance criterion against the risk of liquefaction; FOS being the ratio of cyclic stress required to cause the liquefaction using soil resistance to the cyclic stress ratio induced by earthquake. PGA value of 0.22g has been used in the liquefaction evaluations. Liquefaction analysis have been carried out considering all borehole data for the three categories of structures. The results are shown in Figures 8, 10 and 11.

FOS against liquefaction is defined as $(CRR_{7.5}/CSR).MSF.K_{\sigma}.K_{\alpha}$

$$CSR = \tau_{av}/\boldsymbol{\sigma}'_{v0} = 0.65 r_d [\boldsymbol{\sigma}_{v0}/\boldsymbol{\sigma}'_{v0}][a_{max}/g]$$

$$r_d = 1.0 - 0.00765z \quad \text{for } z \leq 9.15\text{m}$$

$$r_d = 1.174 - 0.0267z \quad \text{for } 9.15\text{m} < z \leq 23\,\text{m}$$

$$CRR_{7.5} = \left[1/\left(34-(N_1)_{60}\right)\right] + \left[(N_1)_{60}/135\right] + \left[50/\left[10\,.\,(N_1)_{60}+45\right]^2\right] - [1/200]$$

$$(N_1)_{60cs} = \alpha + \beta.(N_1)_{60}$$

where
$\alpha = 0$ for FC ≤ 5%
$\alpha = \exp[1.76 - (190/FC^2)]$ for 5% < FC < 35%
$\alpha = 5.0$ for FC ≥ 35%
$\beta = 1.0$ for FC ≤ 5%
$\beta = [0.99 + (FC^{1.5}/1{,}000)]$ for 5% < FC < 35%
$\beta = 1.2$ for FC ≥ 35%
to calculate MSF from M_w, use equation below or Figure 9.

$$MSF = (M_w/7.5)^{-2.56}$$

$$K_\sigma = (\sigma'_{v0}/P_a)^{(f-1)}$$

for relative densities between 40 and 60%, $f = 0.7$–0.8;
for relative densities between 60 and 80%, $f = 0.6$–0.7

$$K_\alpha = \tau_{st}/\sigma'_{v0}$$

where
a_{max} = peak horizontal acceleration at ground surface;
$CRR_{7.5}$ = cyclic resistance ratio for $M_w = 7.5$ earthquakes;
g = acceleration of gravity
H = thickness of layer in meters
NSL = Natural Surface Level in meters
RBL = River Bed Level in meters
γ_b = Bulk Density in kN/m^3
c = cohesion in kPa
Ø = angle of internal friction in degrees
CSR = cyclic stress ratio induced by earthquake
CRR = cyclic stress ratio required to resist liquefaction for magnitude 7.5 earthquake
r_d = stress reduction coefficient
FOS = Factor of safety
z = depth below ground surface in meters
$(N_1)_{60cs}$ = SPT blows considering clean sand effect
$(N_1)_{60}$ = Corrected SPT blows
α and β = coefficients, that are functions of fines content, used to correct $(N_1)_{60}$ to $(N_1)_{60cs}$;
FC = Fine sand content in percentage
σ_{v0} = total vertical overburden stress
σ'_{v0} = effective vertical overburden stress
MSF = Magnitude Scaling Factor to adjust the clean-sand curves to magnitudes smaller or larger than 7.5, to convert CRR (M7.5) to CRR [Figure 9]
M_w = Magnitude of earthquake
K_σ = Correction Factor for Effective Overburden Pressure larger than 100 kPa
P_a = Atmospheric pressure and f is the function of site conditions, including relative density, stress history, aging, and over consolidation ratio
K_α = Correction Factor for pre-existing shear stress in the ground
τ_{st} = Static shear stress
f = exponent estimated from site conditions used in calculation of *K*s

5 MITIGATION OF LIQUEFACTION POTENTIAL

Separate considerations of the liquefiable behavior have been made for various structure categories, for assigning different mitigation measures.

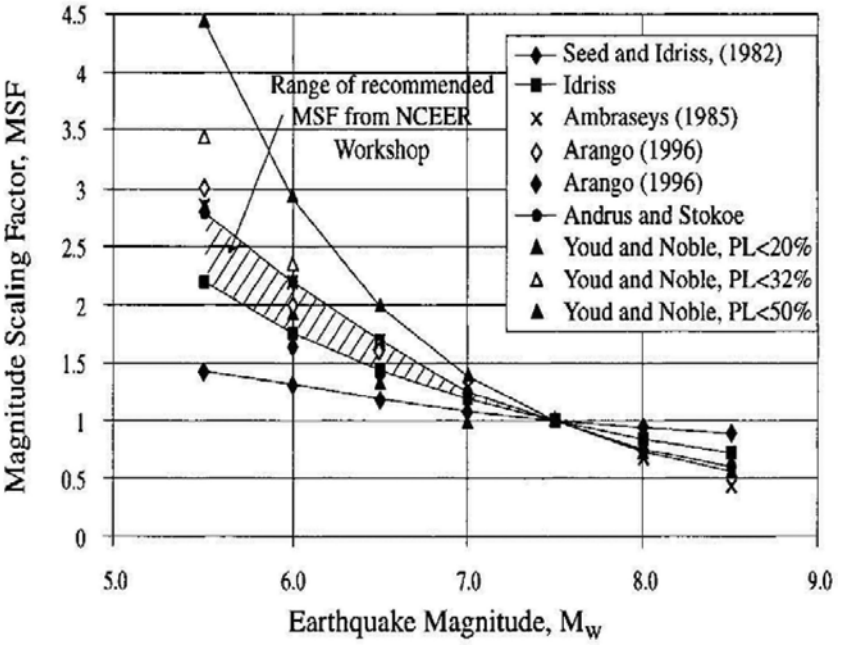

Figure 9. Magnitude scaling factors derived by various investigators (Reproduced from Youd and Noble 1997a).

Keeping in view the specific loading requirements, scour conditions, liquefaction potential of subsoil and the strata encountered at the foundation level 1500 mm diameter and 48m, drilled shafts have been provided for supporting the bridge. The shaft friction has been ignored in the upper 10 to 12 m zone to simulate liquefaction of the upper soil deposits.

All buildings of main and minor facilities have been constructed on a raised platform comprising 1 to 3.5 m thick select fill placed over existing ground. Liquefaction analyses had been carried out for all the structures with natural condition as well as placed over NSL upto Finished Floor Level (FFL) with fill. The cyclic stress ratio induced by the design earthquake has been effectively.

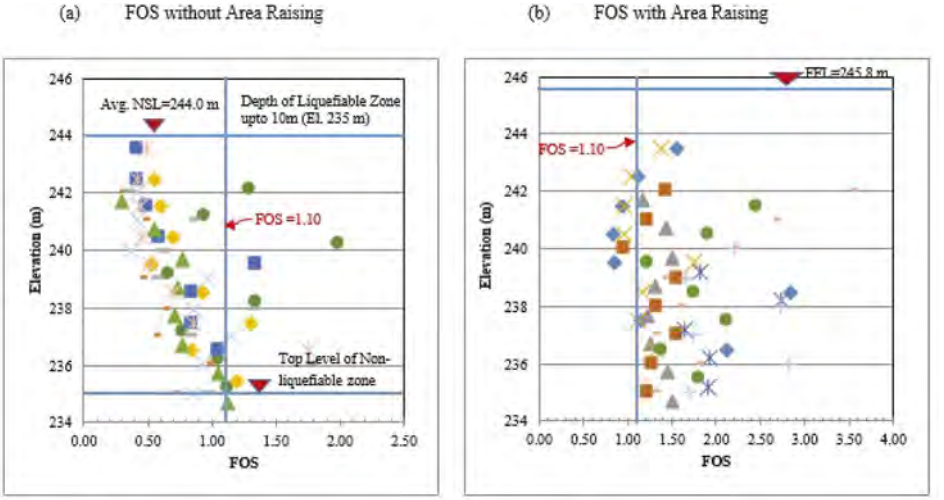

Figure 10. Main structures – FOS before and after raising NSL to FFL.

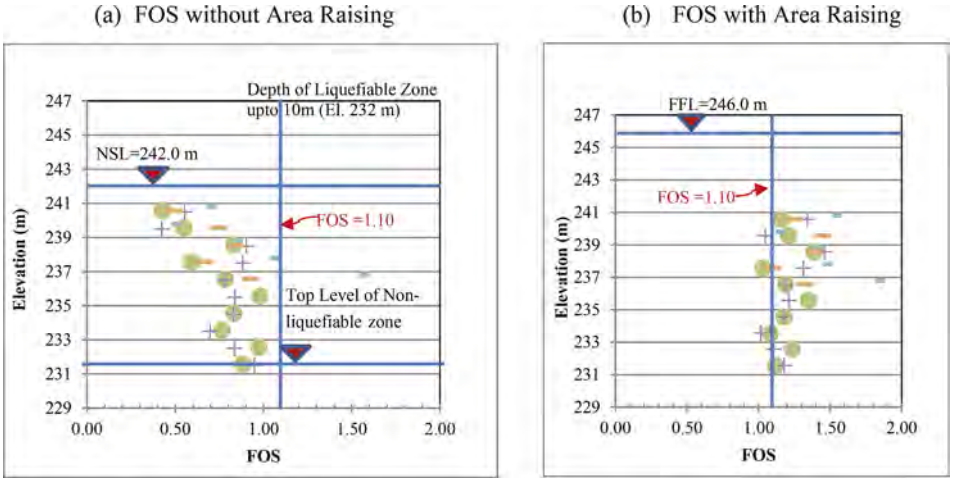

Figure 11. Minor facilities – FOS before and after raising NSL to FFL.

Deep foundations have also been provided for those main facilities where FOS was less than 1.1 and shallow foundations have been provided for other structures. The minor structures have been constructed on a raised platform comprising upto 4.0 m thick select fill placed over natural ground as shown in Figure 8. The results show FOS value as more than 1.1 after raising the area.

6 CONCLUSIONS & RECOMMENDATIONS

1. Sand deposits in the upper reaches in the north of Pakistan of river Ravi are liquefiable, under the expected seismic activity in the area, under free-field condition.
2. Drilled shafts serve as a good solution to mitigate liquefaction potential under the moderately heavy structures, whereas provision of earthen platforms works effectively by lowering the cyclic stress ratio generated by earthquake.
3. The conclusions and mitigation measures adopted at this site can be utilized for other structures too with similar ground conditions; subject to independent evaluations.

REFERENCES

NESPAK, 2019, Geotechnical Investigation Report of the project.

Skempton, 1986. "Standard Penetration Test Procedures and the Effects in Sands of Overburden Pressure, Relative Density, Particle Size, Aging, and Overconsolidation." *Ge´otechnique, London*, 36(3),425–447.

Youd, Idrees, 2001. Liquefaction Resistance of Soils Summary Report from the 1996 NCEER and 1998 NCEER/NSF *Workshops on Evaluation of Liquefaction Resistance of Soils*, Journal of Geotechnical and Geoenvironmental Engineering/April 2001.

Seed, and Idriss, 1982. "Ground Motions and Soil Liquefaction During Earthquakes." *Earthquake Engineering Research Institute Monograph*, Oakland, Calif.

Youd and Noble, 1997a. "Magnitude Scaling Factors."Proc., NCEER *Workshop on Evaluation of Liquefaction Resistance of Soils*, Nat. Ctr. for Earthquake Engrg. Res., State Univ. of New York at Buffalo, 149–165.

Youd and Noble, 1997b. "Liquefaction Criteria Based on Statistical and Probabilistic Analyses." Proc., NCEER Workshop on *Evaluation of Liquefaction Resistance of Soils*, Nat. Ctr. for Earthquake Engrg. Res., State Univ. of New York at Buffalo, 201–215.

Smart Geotechnics for Smart Societies – Zhussupbekov, Sarsembayeva & Kaliakin (Eds)
© 2023 The Author(s), ISBN 978-1-003-29912-7
Open Access: www.taylorfrancis.com, CC BY-NC-ND 4.0 license

The method for determining the designed resistance of soils with considering the theory of soil strength proposed by the authors

A.Z. Khasanov
Samarkand State Architecture Construction University, Samarkand, Uzbekistan

U.Z. Shermukhamedov & A.R. Abdullayev
Tashkent State Transport University, Tashkent, Uzbekistan

ABSTRACT: The paper deals with theoretical issues of determining the design resistance of soils. The main postulates of the well-known theory of the ultimate stress state condition are analyzed. The results of theoretical solutions presented by the authors of the article are given.

Keywords: Ultimate stress transmitted to the ground, Design soil resistance, Contact stresses, Shear surface deflection angle, Methods for determining the design soil resistance

1 MAIN INFORMATION

1.1 *Introduction*

The design soil resistance R is the safe pressure transmitted to the soil base through the foundation. At the same time, it is assumed that, the expected settlement of the base at such a pressure should not exceed the calculated allowable settlement for this structure S_u. It is known that the theoretical solution for determining the design resistance of soils is based on the joint solution of the equation of the plane stress state problem proposed by Flaman and the Mohr-Coulomb strength theory. The solution to this problem was obtained by N.P. Puzerevsky [1].

1.2 *Theoretical foundations for determining the magnitude and criteria for the design resistance of soils*

At present, this expression in a modified form is included in the normative documents SNiP. The main idea of this theory is that the ultimate stress state under the foundation is allowed only along its edges with a depth of its development up to $z \leq B/4$. The second, more realistic way to determine this important criterion is through the results of plate load tests. In this case, the calculated soil resistance is determined within the boundaries of the linear dependence of the graph $f(s,P)$ (Figure 1).

Below we consider a method for determining this important characteristic according to the theory of soil strength proposed by the authors based on expression (1) of the theory of limit equilibrium [3]

$$\sigma_u = cM_c + 2b\gamma M_\gamma + q_2 M_g \tag{1}$$

Where $M_\gamma = \frac{\pi * \left(\frac{\beta}{360}\right) tg^2\theta^*}{cos^3\theta^* k_a}$; $M_g = \frac{tg\theta^*}{cos^3\theta^* k_a}$ and

DOI: 10.1201/9781003299127-54

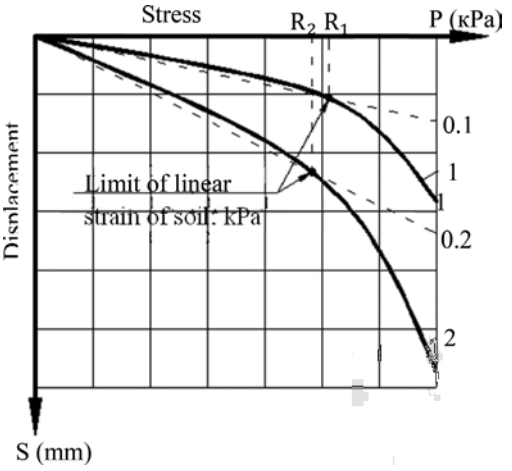

Figure 1. The relationship between the pressure under the stamp and its vertical movements: 1-soil of natural moisture and 2-in a water-saturated state.

$$M_c = \frac{1}{cos^4\theta^*(tg\theta - tg\varphi)}$$

In accordance with this theory, along the edges of the foundation of higher rigidity, contact stresses of a parabolic shape arise with a maximum at its edges:

$$\sigma_z = \frac{2\sigma_m}{\pi\sqrt{1 - \left(\frac{kx}{(b-a)}\right)}} \tag{2}$$

where $0,94 \leq k \leq 0,99$ is the coefficient regulating the maximum boundary stresses. Condition $\sigma_z = \sigma_u$ is satisfied for $(b-a) \leq x \leq b$ and condition $\sigma_z = \sigma_{min} -$ for $x = 0$, a is determined from condition $z \leq 2b/4$ (Figure 2)

$$a = \frac{b}{vtg\varphi^*}$$

where is v = (5 - 10) the scaling factor characterizing the depth of plastic zones propagation; $\varphi^* = \theta^*$- angle of deviation of the shear platform.

From the equilibrium condition corresponding to the limit state condition, we determine the average stresses under the base of the foundation

$$N = 2\sigma_m(b-a) + 2\sigma_u a \tag{3}$$

On the other hand, from equation (2) for x = (b - a) and $\sigma_z = \sigma_u$ we determine the value of σ_m

$$\sigma_m = \sigma_u \frac{\pi\sqrt{1 - \left(\frac{kx}{(b-a)}\right)^2}}{2} = \sigma_u \frac{\pi\sqrt{1-k^2}}{2} \tag{4}$$

For x = 0

$$\sigma_{xmin} = \frac{2\sigma_m}{\pi} \tag{5}$$

Finally, substituting σ_m (4) into expression (3), we get the allowable load on the foundation

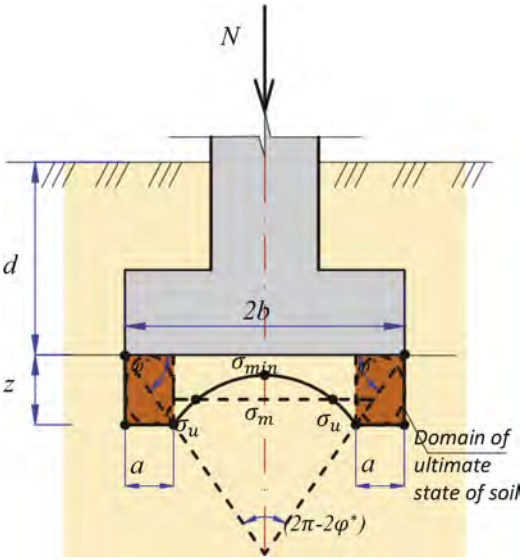

Figure 2. Design scheme for determining values of calculated soil resistance.

$$N = 2\sigma_m(b-a) + 2\sigma_u a = \sigma_u\left[\pi\sqrt{1-k^2}(b-a) + 2a\right]$$

Dividing both parts of the equation by the width of the foundation, we determine the value of the calculated soil resistance

$$R = \sigma_u \frac{\left[\pi\sqrt{1-k^2}(b-a) + 2a\right]}{2b} = \sigma_u \frac{\left[\pi\sqrt{1-k^2}\left(b-\frac{a}{b}\right) + 2\frac{a}{b}\right]}{2} \tag{6}$$

where

$$m = \frac{a}{b} = \frac{1}{vtg\varphi^*}$$

Contact stresses, considering the ultimate stress state arising along the edges, are determined by the following expression (2)

$$\sigma_x = \frac{2\sigma_m}{\pi\sqrt{1-\left(\frac{kx}{(b-a)}\right)^2}} \tag{7}$$

2 EXAMPLE

Determination of the value of the calculated soil resistance. The ultimate stress transferred to the soil is $\sigma_u = 500$ kPa. The foundation width is $2b$ = 1.4 m. The angle of deflection of the shear surface is $\varphi^* = 50^0$, $v = 10$ and $k = 0,96$, then

$$\theta^* = \kappa(atg\xi + \varphi) = 1,1(atg0,23 + 37) = 1,1 * 50 = 55$$

$$a = \frac{b}{vtg\varphi^*} = \frac{0,7}{5 * 1,19} = 0,12m$$

$$R = \sigma_u \frac{\left[\pi\sqrt{1-k^2}(b-a)+2a\right]}{2b} = 500\frac{3,14(0,7-0,12)\sqrt{1-0,96^2}+0,24}{1,4} = 266 \text{ kPa}$$

3 CONCLUSIONS

1. The well-known theory for determining the design resistance of soils, proposed by N.P. Puzerevsky [1] is based on the theory of plane stress state and Mohr-Coulomb theory of strength.
2. In the proposed theory for determining the design resistance of soils, the expression of the ultimate load $\sigma_u$on the soil and the function of contact stresses for rigid foundations proposed by the authors are used.
3. The expression proposed by the authors does not depend on the stress state of the mass in the active region of the base deformation and is a certain function of the limit stress state.

REFERENCES

Tsytovich N.A. Soil mechanics. M. 1981, p. 117–120.

Khasanov A.Z. Khasanov Z.A. Theory of soil strength. Ed. Sam GU. Samarkand 2021, p. 162–163.

State Standards KMK "Foundations of buildings and structures".

Кузнецова, И. О., Уздин, А., Шермухамедов, У. З., & Ван, Х. Б. (2010). Использование упругого полупространства для моделирования оснований при оценке сейсмостойкости больших мостов. Вестник гражданских инженеров, (3), 91–95.

Rashidov, T. R., Tursunbay, R., & Ulugbek, S. (2020). Features of the theory of a two-mass system with a rigidly connected end of the bridge, in consideration of seismic influence on high-speed railways. European Journal of Molecular and Clinical Medicine, 7(2), 1160–1166.

Ulugbek Shermukhamedov, Ibrakhim Mirzaev, Anora Karimova, Abdurakhim Abdullaev A.R. The influence of the type of rubber-metal bearings on the vibrations of monolithic bridges and overpasses, based on the records of real earthquakes. Proceedings of the 5th Central Asian Conference on Soil Mechanics and Geotechnical Engineering, Samarkand 2022.

Smart Geotechnics for Smart Societies – Zhussupbekov, Sarsembayeva & Kaliakin (Eds)
© 2023 The Author(s), ISBN 978-1-003-29912-7
Open Access: www.taylorfrancis.com, CC BY-NC-ND 4.0 license

Optimal design scheme and probabilistic analysis of soil-water characteristic

Zhang Xuejuan, Tan Xiaohui, Fei Suozhu, Dong Xiaole & Xiao Ying
Hefei University of Technology, Hefei, China

ABSTRACT: Soil-water characteristic curve (SWCC) is an important curve in unsaturated soil mechanics. A SWCC can be obtained by curve fitting for a group of data points of suctions and water contents. The lower and the higher part of suction can be measured by the osmotic method and the filter paper method, respectively. Based on the results of a lot of laboratory tests of suctions and water contents of clay, four combinations of data points measured from the osmotic method and the filter paper method are employed to perform the curve fitting for SWCC. Results show that the statistics of SWCC parameters can be accurately obtained by curve fitting all data points of the osmotic method plus only one data point with high suction of the filter paper method. This finding can save a lot of laboratory effort for the measurement of SWCC of unsaturated soils.

1 INSTRUCTION

Soil water characteristic curve (SWCC) is a primary curve to study the behavior of unsaturated soil in geotechnical engineering (Han et al. 2016; Zhai et al. 2017). It is used to characterize the relationship between matrix suction and water content of soils.

There are many methods to measure the SWCC (Nam et al. 2010). However, most SWCC tests can measure soil suction range only in a limited range. It is difficult to obtain a SWCC in the whole suction range by a single test method. Therefore, some scholars proposed to use the combination of several SWCC test methods to obtain the SWCC in the whole suction range. For example, the osmotic method and the filter paper method were usually adopted to measure the low suction part and the high suction part of a SWCC, respectively (Tan et al. 2020).

Although the osmotic method and the filter paper method are simple to operate, measurement of one suction requires at least 10 days using these two methods (Nam et al. 2010), which is very time-consuming. Therefore, reducing the number of suction measurement can save the laboratory workload greatly (Li et al. 2017). Generally speaking, accuracy of the curve fitting of a SWCC decreases with the decrease of the number of data points of (ψ, w) (Ren et al. 2020). According, reducing the number of data points of (ψ, w) without decreasing the accuracy of the curve fitting of SWCC is a very important issue for investigating the behavior of unsaturated soils.

To this end, the osmotic method and the filter paper method were adopted to measure the low and the high suction part of SWCCs of clay in Hefei, China, respectively. Sixty-three groups of SWCCs were measured. Four combinations of data points (all data points of the osmotic method plus different selection of data points of filter paper method) are employed to perform the curve fitting for SWCCs. Statistics of SWCC fitting parameters of different combinations of data points were compared, and an optimal test design for obtaining a SWCC is proposed.

2 MATERIALS AND METHODS

2.1 *Properties of tested soil*

Sixty-three soil columns were collected in a construction site in Hefei, China. These soil samples are all drilled from the same unsaturated clay layer, which is about 10 m below the

DOI: 10.1201/9781003299127-55

ground surface. Basic properties of the soil are measured in the laboratory and their values are listed in Table 1.

Table 1. Basic properties of the tested soil.

Index	Water content w_0 (%)	Density ρ_0 (g/cm^3)	Specific density G_s	Plastic limit ω_P (%)	Liquid Limit ω_L (%)	Plastic index I_P
Value	23.4	2.03	2.73	26.0	53.0	27.0

2.2 *Measurement of the low suction part of SWCC - osmotic method*

The suction range measured by the osmotic method is 0 – 1500 kPa. The principle and operation steps of the osmotic method in details can be found in the reference (Shen et al. 2013). In the paper, as one of the materials used in the osmotic method, the suction of the polyethylene glycol (PEG) solution was setting as 0, 3, 8, 22, 65, 200, 550 and 1600 kPa, respectively. The relationship between the suction of the soil and the concentration of PEG solution can be expressed as follows:

$$PEG = \frac{90}{\sqrt{11/\psi + 1}} \tag{1}$$

2.3 *Measurement of the high suction part of SWCC - filter paper method*

The filter paper method is used to measure the SWCC within the high suction part of 1500 kPa – 30000 kPa. The principle and operation steps of the filter paper method can be found in the reference (Li et al. 2017). In order to obtain different suction points, the water content of the soil sample is set in the range of 13% – 23.5% in the paper. The relationship between the suction of the soil (ψ) and the water content of filter paper (w) can be expressed in Equation (2):

$$\begin{cases} \log \psi = 5.493 - 0.0767w & (w \le 47\%) \\ \log \psi = 2.470 - 0.0120w & (w > 47\%) \end{cases} \tag{2}$$

2.4 *SWCC fitting model and data combination scheme*

There are many SWCC fitting model (Brooks & Corey 1964; van Genuchten. 1980; Fredlind & Xing 1994), among which the van Genuchten model (VG model) is popularly used in Geotechnical engineering. The expression of the VG model is shown in Equation (3):

$$w = \frac{w_s - w_r}{[1 + (\psi/a)^n]^m} + w_r \tag{3}$$

where w, w_s, and w_r are the water content, the saturated water content, and the residual water content, respectively; a, n, and m are model parameters. The parameter a is related to the air entry value of soil. The parameter n is related to the pore size distribution of soil and control the gradient of the curve. The relationship between m and n is considered as m=1-1/n. ψ is matrix suction.

As described in Sections 2.2 and 2.3, eight and three data points of (ψ, w) were measured using the osmotic method and the filter paper method, respectively, for obtaining one SWCC. To obtain an optimal test design for these data points, four combination schemes of these data points are used for the curve fitting of SWCCs. The four data combination schemes are illustrated in Table 2.

Table 2. Data combination schemes for fitting SWCCs.

No.	Osmotic method	Filter paper method
1	All data points	All data points
2	All data points	No data points
3	All data points	The lowest suction point
4	All data points	The highest suction point

3 RESULTS AND DISCUSSIONS

3.1 *SWCCs of the four data combination schemes*

According to Table 2, four data combination schemes were adopted for fitting a SWCC. Therefore, a total of 63 groups of SWCCs were obtained, and each group has 4 SWCCs. Take any two groups (e.g., Group 1 and 2) for example, the comparison of four SWCCs corresponding to the four data combination schemes are shown in Figure 1, in which the squares and the circles represent the data points measured by the osmotic method and filter paper method, respectively. It is apparent that the combination of all data points controls the shape of the whole SWCC, but the data points of the osmotic method or filter paper method can only control the lower or higher part of the SWCC. Therefore, data combination 1 is necessary for accurately obtaining the entire SWCC.

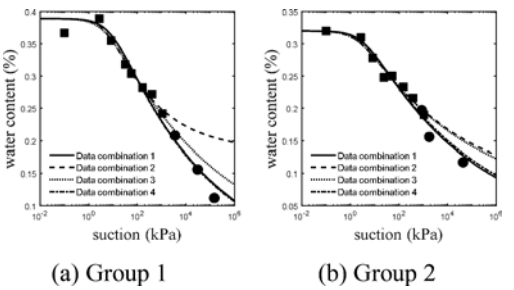

Figure 1. Comparison of SWCCs.

It can also be observed from Figure 1 that all the curves are close to each other for the low suction part of SWCCs, and the curves gradually diverge when the suction increases. For the entire suction range, the SWCCs of data combinations 1 and 4 are nearly overlapped, but the SWCCs of data combinations 2 and 3 are far from those of data combinations 1 and 4. Similar phenomena can be observed for the rest groups of SWCCs, which are not shown here. This indicates that data combination 2 (i.e., the osmotic method) and data combination 3 (i.e., the osmotic method plus the smallest suction point of the filter paper method) are not suitable for accurately measuring the SWCC. On the contrary, the data combination 4 can be obtained the SWCC accurately. Therefore, by using data combination 4 to replace data combination 1, only the highest suction data need to be measured using the filter paper method, which can greatly save the laboratory test time and effort.

3.2 *Statistical characteristics of SWCC parameters*

To further compare the features of the four data combination schemes, the statistical characteristics of SWCC parameters of each data combination of all the 63 groups of SWCCs are calculated and compared. The frequency distribution histogram and the corresponding fitted distribution curve of the four data combination schemes for the 63 SWCCs are shown

in Figures 2 and 3 for parameter a and parameter n. It is apparent that parameters a and n obey lognormal distribution for all the four data combinations. The mean and coefficient of variation (COV) in these figures are the statistical values of SWCC parameters a and n. The skewness and the kurtosis represent the degree of asymmetry and steepness of parameters frequency distribution, respectively.

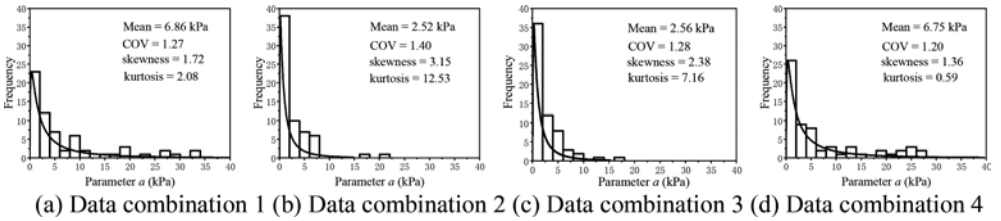

Figure 2. Probability distribution curve of parameter a.

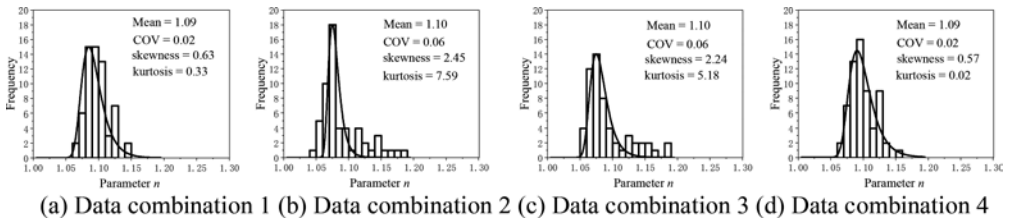

Figure 3. Probability distribution curve of parameter n.

For Figures 2 and 3, the sub-figures (a) and (d) are similar both in shape and in the values of statistics. On the contrary, the shapes and statistics of sub-figures (b) and (c) are apparently different from those of sub-figures (a) and (d). This proves again that data combination 4 can be used to substitute data combination 1 for obtaining the SWCC.

4 CONCLUSIONS

The osmotic method and filter paper method are adopted together to measure the data points of suction and water content. Many groups of data points of unsaturated clay in Hefei were measured for obtaining the SWCCs, and four data combination schemes for data points of the osmotic method and the filter paper method are investigated to select an optimal test design which can save the laboratory test effort without decreasing the accuracy of the SWCC fitting. Results show that data combination 4, including all data points of the osmotic method and the highest suction point of the filter paper method, is a best choice for obtain the entire SWCC accurately and efficiently.

REFERENCES

[1] Brooks, R.H. & Corey, A.T. 1964. Hydraulic properties of porous media. Colorado State University. *Hydrolology Paper* No. 3.
[2] Fredlind, D.G. & Xing, A. 1994. Equations for the soil-water characteristic curve. *Canadian Geotechnical Journal* 31: 521–532.
[3] Han, Z. & Vanapalli, S.K. 2016. Relationship between resilient modulus and suction for compacted subgrade soils. *Engineering Geology* 211: 85–97.
[4] Li, P. Tan, X.H. Xin, Z.Y. et al. 2017. Numerical simulation of determination of equilibrium time for osmotic technique. *Rock and Soil Mechanics* 38(11): 3363–3370.

[5] Nam, S. Gutierrez, M. Diplas, P. et al. 2010. Comparison of testing techniques and models for establishing the SWCC of riverbank soils. *Engineering Geology* 110(1–2): 1–10.
[6] Ren, X. Kang, J. Ren, J. et al. 2020. A method for estimating soil water characteristic curve with limited experimental data. *Geoderma* 360: 114013.
[7] Shen, M.F. Tan, X.H. Li, D. et al. 2013. Experimental research of Soil-Water Characteristic Curve by using osmotic technique. *Chinese Journal of Underground Space and Engineering* 9(2): 241–245.
[8] Van Genuchten, M.T. 1980. A closed-form equation for predicting the hydraulic conductivity of unsaturated soils. *Soil science society of America journal* 44(5): 892–898.
[9] Tan, X.H. Li, P. Shen, M.F*. et al. 2020. Evaluation of the spatial variability characteristics of the unsaturated clay in Hefei, China. *Soils and Foundations* 60(2), 454–465.
[10] Zhai, Q. Rahardjo, H. & Satyanaga, A. 2017. Effect of bimodal soil-water characteristic curve on the estimation of permeability function. *Engineering Geology* 230: 142–151.

Smart Geotechnics for Smart Societies – Zhussupbekov, Sarsembayeva & Kaliakin (Eds)
© 2023 The Author(s), ISBN 978-1-003-29912-7
Open Access: www.taylorfrancis.com, CC BY-NC-ND 4.0 license

Determination of elastic-visco-plastic parameters of soils based on the results of torsional shear tests

Z.G. Ter-Martirosyan, A.Z. Ter-Martirosyan, V.V. Sidorov & A.S. Almakaeva*
NRU MGSU, REC Geotechnics, Moscow, Russia

ABSTRACT: The article considers the possibility of determining soil viscosity parameters that are used for rheological soil models. These models allow to take into account the development of deformations over time and to describe the deformation curve with a high degree of accuracy. Nine shear tests were carried out on a torsional shear device at three normal stresses: 100, 200 and 400 kPa. The shear proceeded at a constant rate of 0.1138°/min and a constant vertical pressure. The soils for shear tests were selected from the construction site of the city of Moscow and are loams of a solid consistency. According to the results of laboratory experiments, the parameters of the strength and viscosity of the soil were determined. Using the new universal rheological model of Ter-Martirosyan A.Z. plots of shear stress versus time $\tau = f(t)$ were obtained. The authors in the article compare the experimental curves obtained from the results of the torsional shear test and the analytical curves obtained on the basis of the rheological model.

Keywords: shear stress, consolidation, torsional shear, viscosity, soil rheological model

1 INTRODUCTION

Clay soils, as a rule, are multiphase systems consisting of soil particles and pores filled with water and air. Clay soils have extremely low permeability coefficient. The application of loads on the soil base of a structure, composed of such soils, leads to the development of deformations in time. This is due to two processes: primary filtration consolidation which occurs due to the squeezing of water from the pores and secondary consolidation or, in other words, creep, which occurs due to the rheological properties of the soil skeleton and depends on the interstructural bonds of the particles. Both of these processes occur simultaneously in clayey soils but if filtration consolidation ends when the pore pressure increment is zero then secondary consolidation does not end with it but can proceed after a sufficiently long time. As a rule, the settlements of the construction are of a damping nature which is explained by the compaction of the soil under load. However, if shear deformations occur the creep process may redevelop. Such soil behavior is called elastoviscoplastic and models that describe the behavior of soils with regard to viscosity are called rheological. One of the main input parameters of such models is the viscosity parameter η. Rheological models make it possible to describe the soil behavior during shear with a high degree of accuracy and to obtain curves that almost completely repeat the curves based on experimental studies of soils.

The purpose of this article is to present the possibility of obtaining a viscosity parameter that allows you to more accurately describe the curve of dependence of shear stresses on time $\tau = f(t)$, in addition to the strength and deformation properties of soils. To determine the effective shear stresses laboratory tests were carried out on a torsional shear device. The experiments were carried out in accordance with the current regulatory document GOST R 59937-2021 Soils. Method for laboratory determination of strength characteristics by ring shear.

*Corresponding author: totilas96@mail.ru

DOI: 10.1201/9781003299127-56

2 LITERATURE REVIEW

The formation of rheology as a separate science was initiated by the research of Bingham Yu. (1922) who was the first to introduce the term "rheology" and who made valuable studies of the rheological properties of liquids and dispersed systems. But the prerequisites for the formation of rheology as a science appeared long before that when Newton proposed the law of viscosity (internal friction) for liquid and gaseous media.

In 1874, L. Boltzmann used a linear relationship between stresses and strains and proposed the theory of hereditary creep deformation. According to this theory, stresses will depend not only on the deformation at a given point in time but also on the previous history of deformation. The theory of Boltzmann L. was further developed in the works of Volterra V.

In 1948, Yu.N. Rabotnov invented the theory of plastic heredity of creep deformations for solids and extended the Boltzmann-Volterra theory to the area of nonlinear creep.

Rheology studies have become important in solving soil mechanics problems associated with long-term loads leading to the accumulation of significant creep deformations. A great contribution to the development of soil rheology was made by the works of Terzagi K., Khvorostlev M., Tsytovich N.A., Vyalov S.S., Goldstein M.N., Casagrande A., Florin V.A., Meschan S.R., Reiner M., Maslov N.N., Ter-Stepanyan G.I., Zaretsky Yu.K., Ter-Martirosyan Z.G. and etc.

First of all, research on rheology spread in clayey soils. The first mention of the creep of clay soils is in the well-known work of Terzaghi K. (1925) [1]. The first results of long-term tests of clay soils were carried out on an annular shear device and were described by M. Khvorslev in 1937-1939. He tried to apply Newton's law for ideally viscous liquids to soils. However, later studies of the rheological properties of clay soils showed that soil flow is observed not under any load, as in a viscous Newtonian fluid but under a certain one, so Bingham's theory of viscoplastic flow began to be applied to soils. Experimental evidence of the applicability of his theory to soils was obtained by Maslov N.N. However, the theory of viscoplastic flow describes the process of steady flow at a constant speed while soils tend to change the flow speed. A modified Bingham law which takes into account the nonlinear relationship between stress and soil flow velocity was proposed by Vyalov S.S. in 1959.

Further studies by Vyalova S.S., Casagrande A., Goldstein M.N. et al. 1950 - 1970 which were summarized in the monograph by Meschyan S.R. [2] it was proved that the behavior of soils under long-term loads is more consistent with the creep of solids because similar stages of creep develop in the soil, namely damped creep, creep at a constant rate and progressive creep.

Rheology developed most intensively in the mechanics of frozen and permanently frozen soils where the soil due to the presence of water and ice in it was considered as a classical rheological body. Researches of Tsytovich N.A. [3] in frozen soils made it possible to discover the property of fluidity. In 1950 - 1955 Vyalov S.S. found that frozen soils are characterized by all manifestations of classical creep, i.e. damped and undamped deformations can develop in soils under load and the creep curve describing them has all the typical stages of creep development: unsteady creep, plastic-viscous flow, and progressive creep [4]. As a result of his research, Vyalov S.S. Introduced the term "ultimate strength" which means the stress before exceeding which progressive creep does not occur leading to destruction.

For the first time, the Boltzmann-Volterra theory was applied to soils by Florin V.A. in 1958 [5]. He developed a generalized theory of soil consolidation which could take into account primary and secondary consolidation taking into account hereditary creep. Maslov G.N. continued further research on this topic. [6, 7].

Reiner M. [8] in his book considered the basic simplest models of Hooke, Saint-Venant and Newton and described methods for determining the rheological properties of real materials.

Research Vyalova S.S. and Pekarskaya N.K. in 1966 showed that in the process of creep of clay soils the shear resistance under long-term loads is always less than the instantaneous one. Therefore, the researchers divided the instantaneous strength at the beginning of the application of loads, temporary strength which can destroy the soil in a certain period of time and long-term strength below which the resistance does not decrease.

Goldstein M.N. thought [9] that the soil has two types of bonds between particles: brittle and viscous which are destroyed when the soil is deformed. However, new viscous contacts

are formed at the site of broken bonds due to which creep damping occurs. This process is called soil hardening. If the stage of progressive creep begins during shear then soil softening occurs which was also noted in the works of Vyalov S.S., Goldstein M.N., Maslov N.N., Ter-Stepanyan G.I., Meschan S.R. and Ter-Martirosyan Z.G. [10-13].

To describe the behavior of soil under load, taking into account creep, rheological soil models are used. The simplest rheological model describing the purely viscous behavior of a material represented by a liquid or gas is Newton's law which relates shear stress to a change in strain rate:

$$\dot{\gamma}_i = \tau_i / \eta(\sigma_m, t), \tag{1}$$

where $\eta(t)$ – variable shear viscosity.

To describe the behavior of solids more complex two- or more-component models should be used. These models include the Maxwell body, the Kelvin-Voigt model, the Bingham-Shvedov model, etc. As a rule, they are combinations of the simplest models: an elastic body (Hooke model), a plastic body (Saint-Venant model) and a viscous body (Newton model).

The model of a viscoelastic body with stress relaxation which is called the Maxwell body is a series-connected elastic and viscous elements. Thus, under loading the body can elastically deform and flow at the same time. Mathematically, the model looks like this:

$$\dot{\varepsilon} = \frac{\dot{\sigma}}{E} + \frac{\sigma}{\eta}, \tag{2}$$

A model that describes the strain-relaxing behavior of a viscoelastic material also known as the Kelvin-Voigt model describes elastic strains over time that increase when a load is applied and decrease when it is removed, as well as the creep of a material under constant stress. In the scheme of the Kelvin–Voigt model the elastic and viscous elements are connected in parallel:

$$\sigma(t) = \varepsilon E(t) + \dot{\varepsilon}\eta(t), \tag{3}$$

The study of the rheological properties of concentrated clay suspensions led Bingham and Green to postulate a viscoplastic body [14]. This model is characterized by the fact that at stresses less than the critical σ_T, it does not deform and obeys Hooke's law and when this stress is exceeded it flows like a Newtonian fluid:

$$\sigma = \varepsilon E \text{ at } |\sigma| \prec |\sigma_T|, \tag{4}$$

$$\sigma - \sigma_s = \varepsilon\eta \text{ at } |\sigma| \succ |\sigma_T|, \tag{5}$$

Investigating the rheological properties of solutions, Shvedov proposed a model of a plastic-viscous material in which stress relaxation will proceed according to an exponential law up to a certain value of residual stress [15]. Mechanically, the model is a parallel connection of the elements of the Maxwell body and the Saint-Venant body with an elastic spring connected in series to them:

$$\eta\dot{\varepsilon} = (\sigma - \sigma_s) + \frac{\eta}{E}\sigma, \tag{6}$$

The Bingham equation is a degenerate Shvedov body. Comparing Equations (4), (5) and (6) it is possible to obtain the Bingham-Shvedov equation which can describe the behavior of the soil.

The rheological equation of the hardening material Rabotnov Yu.N., applicable to soils, has the following form:

$$\dot{\gamma} = \tau/(G \cdot t) \tag{7}$$

where G – soil shear module.

In the dissertation [16] Ter-Martirosyan A.Z. proposed a new universal rheological equation obtained on the basis of the Timoshenko model to describe the rate of shear deformation of a hardening and softening clay soil in the form:

$$\dot{\gamma} = \frac{\tau - \tau^*}{\eta_0}\left(\frac{e^{-\alpha\gamma}}{a} + \frac{e^{\beta\gamma}}{b}\right) + \frac{\dot{\tau}}{G} \tag{8}$$

where τ^* – ultimate shear stress;
τ – effective shear stress;
η_0 – initial viscosity;
γ – shear strain rate;
$\dot{\tau}$ - initial shear stress;
α, β, a, b – parameters of hardening and softening of clay soil determined by the results of the experiment.

Using Equation (8), the authors of [17] made graphs of the dependence of shear stresses on time $\tau = f(t)$. The parameters for the rheological model were obtained from simple shear tests. The results of comparing the experimental and analytical curves showed good convergence because Equation (8) allows one to accurately describe the double curvature of the graphs obtained experimentally on a simple shift device.

3 METHODS

In this work, a modification of the torsional shear device developed by Ter-Martirosyan Z.G. was used to test soils. This modification was combined with a certified and calibrated control and measuring device manufactured by LLC NPP Geotek which includes a set of pneumatic loading device GT 2.0.7 10 kN and control units. The general view of the installation is shown in Figure 1.

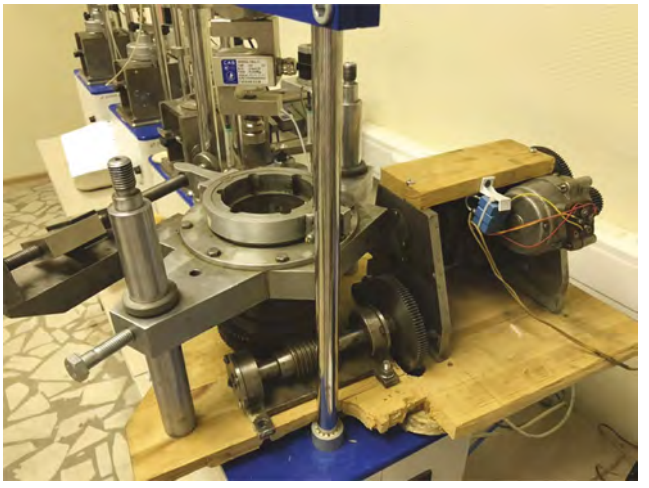

Figure 1. General view of the torsion shear device.

This device performs a kinematic torsional shear by rotating the lower part of the soil sample box at a predetermined speed. Shear resistance is measured with a horizontal force transducer connected by a lever to the top of the soil sample box and preventing it from

rotating with the bottom. The engagement of the sample which excludes its rotation inside the box during torsional shear is provided by blades located in the side parts, in the upper and lower parts of the box. A view of the box with blades is shown in Figure 2.

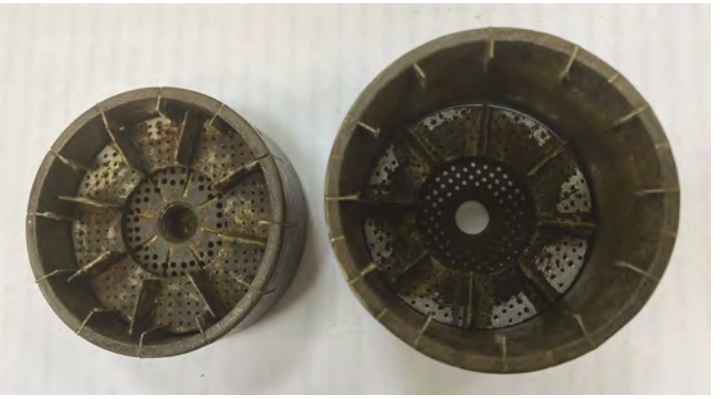

Figure 2. General view of the soil sample box.

Laboratory tests were carried out according to the consolidated-drained scheme in accordance with GOST R 59937-2021 Soils. Method for laboratory determination of strength characteristics by ring shear. Loams were used in this study. They were taken from a depth of 34-36 m. The dimensions of the samples were 71.4 mm in diameter and 35 mm in height which corresponds to the dimensions of the inside of the box. Before the start of each experiment the soil samples were under a vertical load corresponding to the normal pressure during the shear test: 100, 200 and 400 kPa for at least 8 hours. The shear was carried out at a constant speed of 0.1138°/min and a constant vertical load until a rotation angle of 17° was reached. The main physical properties of the tested soil are shown in Table 1.

Table 1. Physical properties of the soil.

Type of soil	Humidity of the lower plastic limit W_P, %	Humidity of liquid limit W_L, %	Plasticity number I_P
Loam	28	44	0.16

4 RESULTS

Using the results of laboratory experiments test reports were obtained containing an array of data on measured stresses and strains. However the shear stress is not constant in the shear plane, it changes according to a linear law: in the center of the section the shear stress is zero and at the points of the outer contour it reaches its maximum values. Therefore, it is necessary to determine the average shear stress in accordance with 9.1 of GOST R 59937-2021 using the formula:

$$\tau = 10\frac{3M_t}{2\pi(R_a^3 - R_i^3)} \tag{9}$$

where M_t moment of rotational force applied to the sample, kN· cm;

R_a – outer radius of the ring sample, cm;

R_i – inner radius of the ring sample, cm.

A similar formula was described by Boldyrev [18]. Based on the test results and using equation (4.1), graphs of shear stresses versus time $\tau = f(t)$ were plotted. These graphs are shown in Figure 3. Nine tests were carried out at three vertical stresses of 100, 200 and 400 kPa. The shear stress was determined only in the resulting shear plane. The friction of the soil along the side surface against the box and blades was not taken into account.

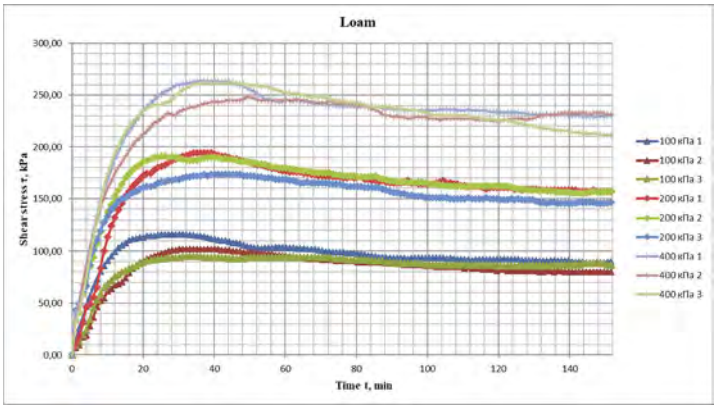

Figure 3. Plots of shear stress versus time $\tau = f(t)$.

As shown in Figure 3 an increase in vertical load leads to an increase in shear resistance: at a vertical pressure of 100 kPa peak shear stresses vary from 90 to 120 kPa, residual stresses from 70 to 90 kPa; at a vertical pressure of 200 kPa peak values of shear stresses vary in the range from 170 to 200 kPa, residual - from 140 to 160 kPa and at a vertical pressure of 400 kPa peak stresses ranged from 240 to 260 kPa, residual vary in the range from 210 to 230 kPa. It should be noted that there is a decrease in strength by 25-30% after the shear stresses reach peak values while most of the graphs plotted have pronounced peaks. Upon reaching shear deformations approximately equal to 6-7 mm shear stresses reach constant values, i.e. for residual strength. The figure shows graphs of the dependence of shear stresses on normal stresses $\tau = f(\sigma)$ which are built as a result of statistical data processing using the least squares method.

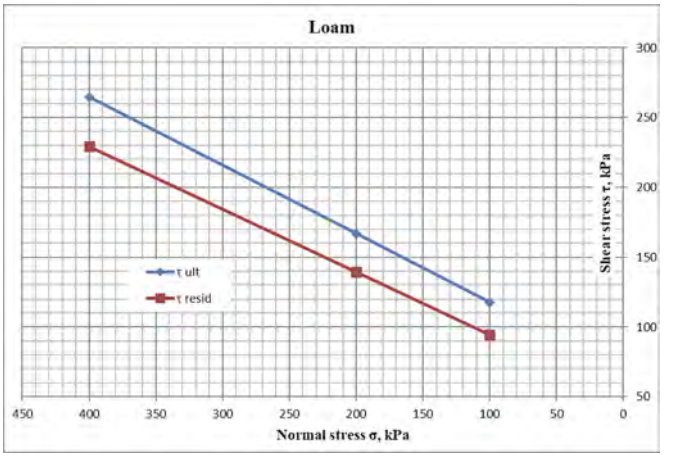

Figure 4. Graphs of dependence of shear stresses on normal stresses $\tau = f(\sigma)$.

Figure 5 shows a tested sample of loamy soil. Furrows formed in the shear plane indicating the nature of the shear - rotation. In addition, it should be noted that the shear is not smooth because there are depressions and elevations which can be one of the reasons for the appearance of peaks in the graphs. This effect was more pronounced for hard clays. The presence of irregularities in the shear plane was in direct proportion to the appearance of one or even two pronounced peaks in the graphs [19].

Figure 5. Tested soil sample (loam).

The calculation of the strength characteristics of soils is carried out by standard well-known methods presented in section 9 of GOST 12248.1-2020. Therefore, they are not of scientific interest and were not determined in this article. The viscous characteristics of soils are an integral part of describing the behavior of soils over time. In some cases, taking into account rheological properties can greatly affect the results. However there are no requirements and recommendations for their determination in the regulatory documentation. For this reason, in this article more attention is paid to determining the rheological properties of soils rather than strength parameters.

Using the shear creep Equation (8) of Ter-Martirosyan A.Z. in the *MathCAD* program graphs of the dependence of shear stress on time $\tau = f(t)$ were analytically plotted which, due to the selection of hardening and softening parameters a, b, α and β allow more accurately describe laboratory shear test curves. Other components of Equation (8) were determined from the results of laboratory tests for torsional shear. In this case, to obtain the values of the initial viscosity η_0 Newton's law (1) was applied. The calculated parameters of the shear creep Equation (8) for describing the laboratory shear test curves are presented in Table 2. The hardening and softening parameters a, b, α and β, selected by enumeration, are presented in Table 3.

Table 2. Parameters of the shear creep equation.

Normal stress σ, kPa	№	Ultimate shear stress τ*, kPa	Shear deformation y	Time t, min	Shear rate Ý, 1/min	Initial shear stress τ, kPa	Initial shear modulus G, kPa	Initial viscosity η_o, kPa*min
100	1	116,4	0,00320	2	0,00160	26,46	8269	16538
	2	102,3	0,01122	6	0,00187	36,05	3213	19278
	3	95,4	0,01122	6	0,00187	36,05	3213	19278
200	1	194,2	0,00801	4	0,00200	24,42	3049	12195
	2	190,8	0,00160	1	0,00160	32,62	20388	20388
	3	173,3	0,00160	1	0,00160	43,03	26894	26894
400	1	264	0,00160	1	0,00160	40,70	25438	25438
	2	248,8	0,00160	1	0,00160	32,62	20388	20388
	3	261,7	0,00481	3	0,00160	55,82	11605	34815

Table 3. Hardening and softening parameters.

Normal stress σ, kPa	№	a	b	α	β
100	1	5,5	2,5	30	1
	2	0,15	0,53	15	0,24
	3	0,4	0,47	12	0,12
200	1	1,8	2,2	19	0,32
	2	26	6,5	50	1,6
	3	10	4,7	35	1,6
400	1	14	7	65	1,2
	2	16	8,5	35	1
	3	1,6	1,7	24	0,4

Analytically obtained plots of shear stress versus time $\tau = f(t)$ were built and compared with the corresponding plots obtained from the results of laboratory tests (Figure 6). Comparison of the experimental and analytical curves shows their high convergence because a new universal rheological model of Ter-Martirosyan A.Z. was used which takes into account the hardening and softening of loamy soil.

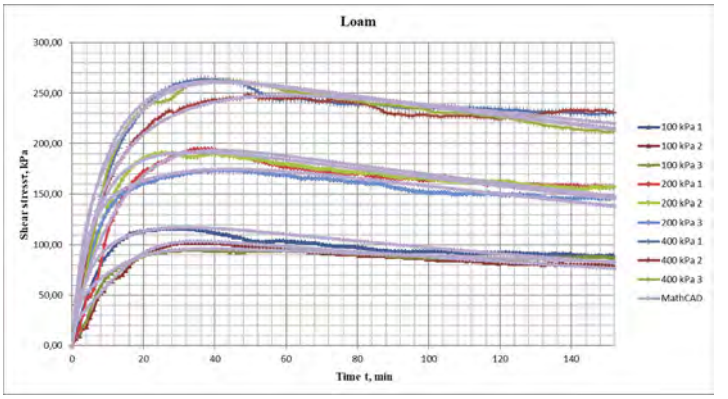

Figure 6. Comparison of experimental and analytical plots of shear stress versus time $\tau = f(t)$.

5 CONCLUSIONS

1. Based on the test results for loam on a torsional shear device plots of the dependence of shear stresses on time $\tau = f(t)$ were plotted at three normal stresses (100, 200 and 400 kPa) at a constant rate of 0.1138 °/min. These plots showed that the increase normal load the shear stress increases too and upon reaching the peak valu, the shear stresses decrease by 25-30% when the shear deformations reach 6-7 mm.
2. Due to the fact that during the transfer of loads to the soil base, deformations develop in time, caused by primary and secondary consolidation, soils are characterized by elastic-viscoplastic behavior. It is most correct to use rheological models to describe the behavior of soils under load over time. Viscosity parameters for such models can be obtained from laboratory shear tests.
3. In this paper for the analytical description of the behavior of soils in a torsional shear a new universal model by Ter-Martirosyan A.Z. is used which due to the parameters a, b, α and β makes it possible to take into account the processes of hardening and softening of the soil. Comparison of plots of shear stress versus time $\tau = f(t)$ obtained analytically and

experimentally showed that the new universal rheological model allows one to describe the behavior of the soil during shear with a sufficient degree of accuracy and obtain dependence curves that almost completely repeat the curves built on the basis of experimental studies of soils using the torsional shear method.

REFERENCES

1. Terzagi K. Fundamentals of soil mechanics. M.: N.K.P.S. Transprint. 1925. 85 p.
2. Meschyan S.R. Creep of clay soils. M.; L.: Publishing House of the Academy of Sciences of the ArmSSR. 1967. 318 p.
3. Tsytovich N.A., Sumgin M.I. Foundations of mechanics of frozen soils. M.: Publishing House of the Academy of Sciences of the USSR. 1937. 432 p.
4. Vyalov S.S. Rheological properties and bearing capacity of frozen soils. M.: Publishing House of the Academy of Sciences of the USSR. 1959. 190 p.
5. Florin V.A. Fundamentals of soil mechanics. Gosstroyizdat Leningrad-Moscow. Volume I. 1958. 356 p.
6. Maslov N.N. Long-term stability and displacement deformation of retaining walls. M.: Energy. 1968. 124 p.
7. Maslov N.N. Fundamentals of soil mechanics and engineering geology. M.: Higher school. 1982. 511 p.
8. Reiner M. Rheology. M.: Science. 1965. 224 p.
9. Goldstein M.N. Mechanical properties of soils. Moscow: Gosstroyizdat. 1977. 256 p.
10. Vyalov S.S. Rheological foundations of soil mechanics. M.: Higher school. 1978. 447 p.
11. Maslov N.N. Fundamentals of engineering geology and soil mechanics. M.: Higher school. 1982. 511 p.
12. Meschyan S.R. Experimental bases of rheology of clayey soils. Moscow: Gitutyun Publishing House. 2008. 788 p.
13. Ter-Martirosyan Z.G. Soil mechanics. M.: ASV. 2009. 552 p.
14. Bingham E.C., Green H. Paint, a plastic material and not a viscous liquid // Proc. amer. assoc. Testing Materials, II. 1919. pp. 640–676.
15. Schwedoff T.N. Recherches experimentales sur la cohesion des liquides. I. Rigidité des liquids // J. de Physiqul. Vol. 8.1889. pp. 341–359.
16. Ter-Martirosyan A.Z. Interaction of foundations of buildings and structures with a water-saturated base, taking into account the nonlinear and rheological properties of soils. Diss. . . doc. tech. Sciences. Moscow. 2016. 324 p.
17. Ter-Martirosyan A.Z., Manukyan A., Ermoshina L.Yu. Experience of determining the parameters of the elastoviscoplastic soil model // E3S Web. Conf. 2021 Vol. 263, 02051. DOI: 10.1051/e3sconf/202126302051.
18. Boldyrev G.G. Methods for determining the mechanical properties of soils with comments on GOST 12248-2010. 2nd ed., add. and correct. Moscow: Prondo LLC. 2014. 812 p.
19. Ter-Martirosyan A.Z., Sidorov V.V., Almakaeva A.S. Peculiarities and difficulties in determining the contact strength of soil and structural materials // Journal of Geotechnics. 2019, Volume 11, Number 4, p. 30–41.

Smart Geotechnics for Smart Societies – Zhussupbekov, Sarsembayeva & Kaliakin (Eds)
© 2023 The Author(s), ISBN 978-1-003-29912-7
Open Access: www.taylorfrancis.com, CC BY-NC-ND 4.0 license

Tunnel and swelling analysis of expansive bedrock considering multiphysics between crystal layers

K. Hoshi, S. Yamada & T. Kyoya
Tohoku University, Sendai, Miyagi, Japan

ABSTRACT: This research proposes a new model targeting expansive bedrock by means of combining an elastoplastic model considering electro-chemo-mechanical phenomena with the Cam-clay model introducing cementation and its degradation due to plastic deformation. Tunnel excavation and swelling analyses are demonstrated by incorporating the proposed model into a finite element analysis code. The simulation results indicate that swelling occurs in narrowed area such as the bottom of the tunnel and swelling phenomena suddenly develops likewise real observation although ion-concentration change is uniformly given in the entire analysis area. This research unraveled the mechanism of the swelling phenomenon with the object of interaction between electro-chemo-mechanical phenomena on the surface of expansive clay mineral crystal and yield of bedrock skeleton accompanied with degradation of cementation.

1 INTRODUCTION

Pore fluid composition affects the mechanical behavior of bedrock containing expansive clay minerals. Moreover, swelling of expansive bedrock often causes problems during tunnel excavation and earth cutting. Thus, it is necessary to elucidate the mechanism behind the emergence of bumps and cracks as well as quantitatively evaluate the deformation caused by swelling. To simulate the issues regarding swelling behavior, a constitutive model that considers the electro-chemo-mechanical phenomena on the surface of expansive clay mineral crystal, stiffness of bedrock, and the degradation of the internal structure is required.

2 MODELING THE MECHANICAL BEHAVIOR OF SWELLING BEDROCK

2.1 *Electro-chemo-mechanical phenomena in crystal layers of clay minerals*

An elastoplastic model considering electro-chemo-mechanical phenomena in the crystal layers of clay minerals (Kyokawa et al. 2019) is used to investigate swelling bedrock. This model assumes swelling soils are composed of expansive clay minerals and non-expansive soil as well as possess a double-porous structure consisting of soil skeleton and interlaminar, as shown in Figure 1.

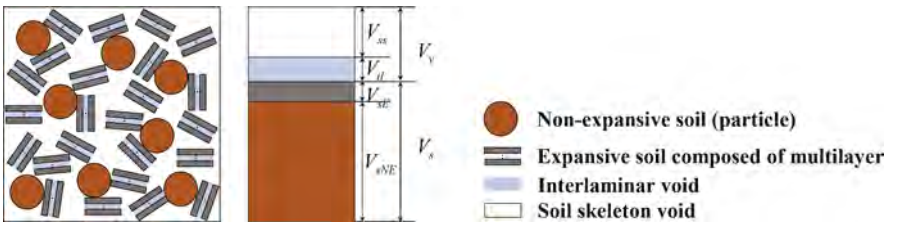

Figure 1. Schematic of expansive soil and its volumetric structure.

DOI: 10.1201/9781003299127-57

In this model, the void ratios (total void ratio e, interlaminar void ratio e^{il}, and soil skeleton void ratio e^{ss}) and the volumetric strain $\varepsilon_v$are defined as

$$\varepsilon_v = -\frac{V - V_0}{V_0} = -\frac{\Delta V_{ss} + \Delta V_{il}}{V_{s0} + V_{ss0} + V_{il0}} = \varepsilon_v^{ss} - \theta^* \frac{d - d_0}{d_0} \tag{1}$$

where θ^*, e^{il}, $e^{ss}$is defined as follows:

$$\theta^* = \frac{V_{il0}}{V_{s0} + V_{ss0} + V_{il0}} = \frac{e_0^{il}}{1 + e_0^{ss} + e_0^{il}}, \ e = \frac{V_v}{V_s}, \ e^{il} = \frac{V_{il}}{V_s}, \ e^{ss} = \frac{V_{ss}}{V_s} \tag{2}$$

where d is the distance of the interlaminar space, d_0 is its initial value.

The swelling behavior is determined by the following equilibrium equation of the electro-chemo-mechanical forces between the crystal layers:

$$F^{il}(c, d, \boldsymbol{\sigma}) = f_a(d) - f_r(c, d) - f_h(d) + f_e(\boldsymbol{\sigma}) = 0 \tag{3}$$

where c is the ion concentration of the pore fluid, f_a is the van del Waals force, f_r is the osmotic pressure from the double diffusion layers, f_h is the hydration force, and f_e is the force from the (mean) effective stress $\boldsymbol{\sigma}$. The osmotic pressure, van del Waals force, and hydration force are monotonically decreasing functions with respect to the interlaminar distance; moreover, the osmotic pressure changes with ion concentration. The osmotic repulsive pressure increases with decreasing ion concentration and vice versa. Therefore, increasing or decreasing interlaminar distance can describe swelling or osmotic compression. In addition to the above equilibrium model, bedrock skeleton behavior is described with Cam-clay model considering cementation and its degradation in Section 2.2.

2.2 *Cementation and internal degradation of swelling bedrock*

A method that considers the cementation effect and its degradation proposed by Yamada et al. (2022) is introduced into the Cam-clay model to describe the degradation of internal structure due to swelling. This model determines the tensile strength due to the cementation effect of the material in soil skeletons, such as cement-treated soil and bedrock, by translating the yield surface to the tensile side, as shown in Figure 2. It can also express high cementation because confining pressure virtually increases by treating translations of the yield surface as modifications of the effective stress. Moreover, it describes the transition from cement-treated soil and bedrock into normal soil by eliminating the deviation of the yield surface from the origin due to progressive plastic deformation. Specifically, the model is expressed with modified effective stress $\bar{\boldsymbol{\sigma}}$, which is the effective stress $\boldsymbol{\sigma}$plus the amount of isotopically parallel shifts of the yield surface Ψ.

$$\bar{\boldsymbol{\sigma}} = \boldsymbol{\sigma} + \Psi \boldsymbol{I} \tag{4}$$

This study applies the Cam-clay model considering cementation and its degradation due to plastic deformation in the soil skeleton aspect of the elastoplastic model that satisfies the interlaminar equilibrium for a double-porous structure.

3 TUNNEL EXCAVATION AND SWELLING ANALYSIS METHODS

Tunnel excavation and swelling analyses are demonstrated by incorporating the proposed model into a finite element analysis code. Excavation analysis is performed by unloading the surface forces acting on circular hole were calculated based on the initial stress state. After that, swelling analysis is conducted by lowering ion concentration uniformly in the entire

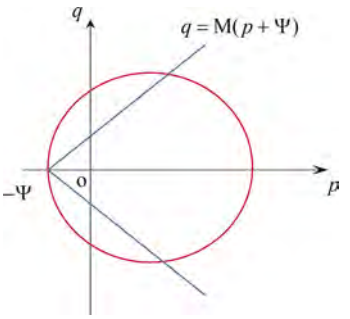

Figure 2. Parallel shift of the yield function.

analysis area assuming that groundwater is supplied from the surrounding ground toward the tunnel-cavity under the influence of excavation. Calculations are performed assuming plane strain conditions and the analysis conditions are given assuming tunnel excavation in bedrock with 100 m of earth cover.

4 COMPUTATIONAL RESULTS AND DISCUSSION

Figure 3 shows the distributions of cementation Ψ and volumetric strain in an interlaminar void after excavation and swelling analyses. cementation degradation and swelling progresses in a limited area, such as just below the tunnel bottom, even though the ion concentration is reduced uniformly in the entire analysis area.

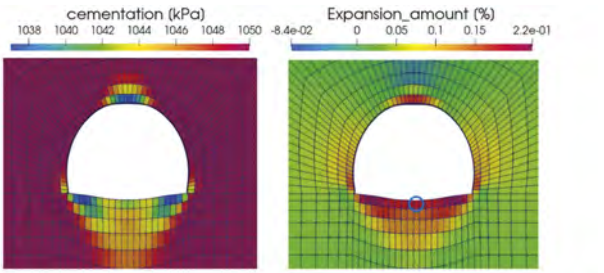

(a) Cementation distribution. (b) Expansion amount distribution.

Figure 3. Cementation distribution and expansion amount distribution.

Figure 4a shows distributions of vertical displacement and expansion amount in bedrock just below the tunnel bottom. Depth from the bottom is plotted on the vertical axis, and the cumulative values are plotted at a fixed point approximately 10 m from the bottom. Note that the expansion and vertical displacement increase remarkably from approximately 5 m just below the bottom. These tendency in the vertical displacement distribution matches the observed results at swelling bedrock.

Next, we investigate this remarkable swelling behavior that occurs approximately 5 m below the tunnel bottom. Figure 4b shows the shear stress distribution just below the tunnel bottom after excavation. The shear stress reaches a minimum at 7 m below the bottom and increases rapidly from approximately 5 m below the bottom. This distribution of the shear stress is similar to that of the expansion amount after swelling analysis in Figure 4a.

This correlation suggests that the greater is the shear stress generated during tunnel excavation, the greater is the swelling when ion concentration decreases.

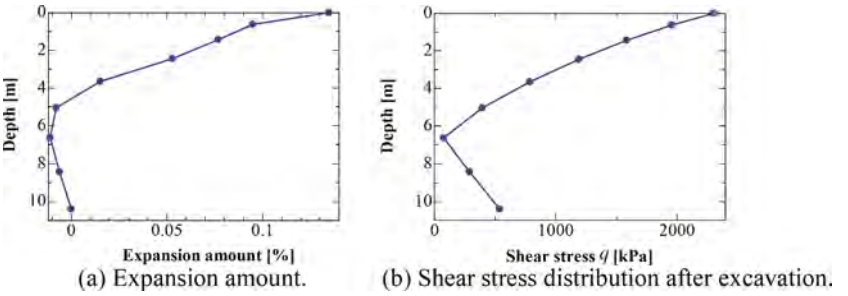

(a) Expansion amount. (b) Shear stress distribution after excavation.

Figure 4. Distributions of expansion amount and shear stress distribution after excavation.

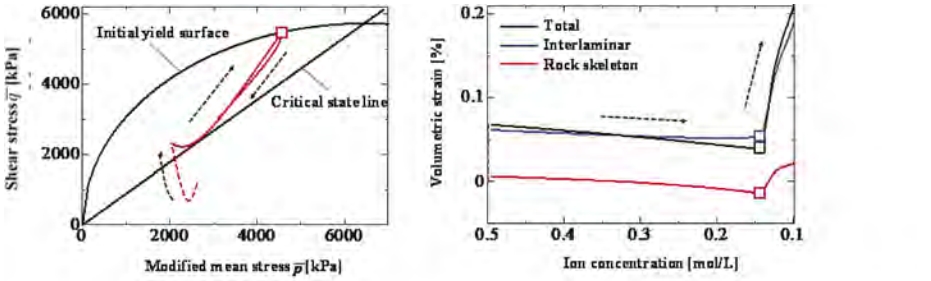

(a) Stress path. (b) Ion concentration versus expansion amount.

Figure 5. Behavior of Element A.

Considering the stress paths of an element shown in Figure 3b, Element A indicated by a blue circle is located at the bottom of the tunnel where swelling is significant. Figures 4 shows the stress path and relationship between ion concentration and volumetric strain in Elements A. Here too, the dashed and solid lines show the excavation and swelling processes, respectively.

In the stress paths, Element A (Figure 5a) achieves a stress state above the critical state line at the initiation of swelling analysis already owing to the influence of the large shear stress caused by excavation. During swelling analysis, the effective stress increases because of interlayer spreading as the ion concentration decreases and the bedrock skeleton yields above the critical state line. In the Cam-clay model, the area above the critical state line is the softening zone with plastic expansion (Asaoka et al. 1994). In the stress path of Element A, the shear and mean effective stresses decrease after yielding, which indicates that softening occurs in the region with pronounced swelling. As the mean effective stress decreases due to softening, the distance between the crystalline layers also increases according to the mechanism described by Equation (3), resulting in significant swelling just below the tunnel base.

Moreover, Figure 5b shows that the expansion amount increases rapidly when the ion concentration falls below a certain value. Considering changing ion concentration as equivalent to evolving time, this figure suggests that deformation due to swelling develops in a short time when the ion concentration falls below a certain value. Here, it becomes clear that the rapid swelling begins when the bedrock skeleton reaches yield after comparing Figure 5a and 5b. This illustrates that the changing ion concentrations induce the bedrock skeleton to yield; moreover, the softening initiated by the yielding of the bedrock skeleton leads to significant swelling of the interlaminar layers. Consequently, the yielding of the bedrock skeleton triggers rapid expansion.

5 CONCLUSION

This paper proposes a novel model targeting expansive bedrock considering multiphysics in crystal layers and degradation of internal structure. The proposed model is incorporated into a finite element analysis code; moreover, tunnel excavation and swelling analyses describe the characteristics of the observed deformations. The results clarify the characteristics of and mechanism behind tunnel deformation in swelling bedrock.

REFERENCES

Asaoka, A., Nakano, M. & Noda, T. 1994. Soil-water coupled behaviour of saturated clay near/at critical state. *Soils Found* 34(1): 91–105.

Kyokawa, H., Ohno, S. & Kobayashi, I. 2019. A method for extending a general constitutive model to consider the electro-chemo mechanical phenomena of mineral crystals in expansive soils. *Int. J. Numer. Anal. Meth. Geomech*. 44: 749–771.

Yamada, S., Sakai, T., Nakano, M. & Noda, T. 2021. Method to introduce the cementation effect into existing elasto-plastic constitutive models for soils. *J. Geotech. Geoenv. Eng*. 148(5): 04022013.

Smart Geotechnics for Smart Societies – Zhussupbekov, Sarsembayeva & Kaliakin (Eds)
© 2023 The Author(s), ISBN 978-1-003-29912-7
Open Access: www.taylorfrancis.com, CC BY-NC-ND 4.0 license

Investigation of the stability of clay slopes under various types of their loading

F.G. Gabibov & A.Z. Zeynalov
Azerbaijan Research Institute of Construction and Architecture, Baku, Azerbaijan

ABSTRACT: It was found that a change in the angle of inclination of the load from 0 to 30° leads to a decrease in the slope stability coefficient K; for clays by 2.8 times; for sandy loams by 2.5 times. The triangular distributed load was applied so that the smaller triangle cathet was at the base of the slope perpendicular to the daytime surface, the hypotenuse of the triangular load coincides with the slope surface. With an increase in the load of 0.40 MPa, the values of the resistance coefficients. To increase for clays in the range of 8.2-21.3%, for sandy loams in the range of 7.7-15.7%. The slope was divided into 10 equal sections. The load is applied simultaneously in Sections 1, 6 and 10. At q = 0.33 MPa, the stability coefficient for clay is 1.066, and for sandy loam 1.79.

1 INTRODUCTION

The study of the stability of clayey slopes is an actual problem of geotechnics. This is due to the fact that most of the landslide slopes are represented by clay soils. Hill (1950), Morgenstern & Tchalenko (1967), Bjerrum & Landva (1966) and others are devoted to the development of methods for studying shear deformations of clay soils. Bishop & Bjerrum (1960), Lo (1970), Skempton & Petley (1967), Kulchitsky & Usyarov (1981), Osipov (1979), Kazarnovsky (1985) and others are devoted to the study of shear deformation patterns and strength parameters of clay soils.

It is of great interest to study the stability of a clay slope under various variants of surface loading.

For analytical studies, a calculation model of a clayey landslide-prone slope with geometric characteristics of the Bailovsky slope in Baku (slope height h = 80 m, slope angle β = 30°) was chosen. When solving the problem, the models and programs for a personal computer (PC) developed at VolgGASU based on the finite element method were used, including the results of studies given in the works of Tsvetkov (1993) and Bogomolov (1996), which allow, based on the solution of plane problems of elasticity theory determine the stresses at various points of the soil mass from the impact of the own weight of the soils and various surface loads, as well as the most probable fracture surfaces (MPFS) and the magnitude of the slope stability coefficients.

In the work of Tsvetkov (1993), based on the exact solution of the problem of elasticity theory for a weighty half-plane with a curvilinear boundary and the use of the technique for constructing the most probable fracture surface, the shape and location of which in the slope zone depend on the stress state and physical and mechanical characteristics of soils, formulas were obtained for determining the stability coefficients K of homogeneous slopes and slopes: at $\lambda \geq 0,1$

$$K = \frac{4}{7}(1+\mu)(a\lambda + b)\ \ tg\phi \tag{1}$$

at $0 < \lambda < 0,1$

DOI: 10.1201/9781003299127-58

$$K = \frac{4}{7}(1+\mu)\sqrt{10\lambda(d^2 + ctg^2\beta) + ctg^2\beta}\ \ tg\,\phi. \tag{2}$$

Here: stability parameter

$$\lambda = \frac{2c}{\gamma\ h\ tg\ \phi}; \tag{3}$$

c – adhesion; γ- density; ϕ- angle of internal friction; μ- soil lateral pressure coefficient; h- height; β- slope angle; *a, b, d* - dimensionless coefficients determined by the graphs.

The dimensions of the computational model are taken on the basis of the well-known position of the theory of elasticity that the boundary conditions practically do not affect the stress distributions if the boundaries of the region are removed from the considered part of the region by at least six of its largest dimensions.

The study area is divided into 17900 triangular elements connected at 9138 nodes. The breakdown was carried out in such a way that the elements had the smallest dimensions in the studied part of the area (Figure 1).

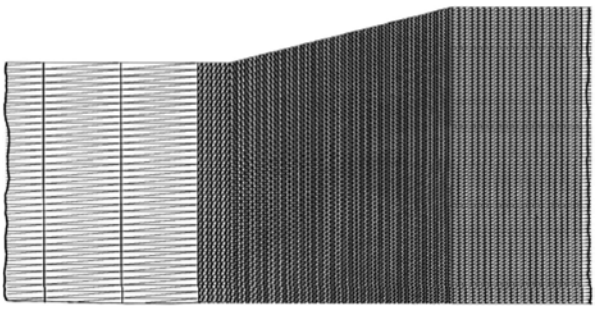

Figure 1. Breakdown of the studied slope into triangular elements.

The boundary conditions are set as follows: 1) there are no movements in the horizontal direction along the vertical boundaries of the design model; 2) there are no vertical movements along the lower horizontal boundary; 3) no restrictions are imposed on the movements of other points.

The initial data for solving the problem under consideration include soil properties (bulk weight γ, deformation modulus E, lateral pressure coefficient μ, cohesion c and internal friction angle φ of the soil), surface loads and boundary conditions.

In calculations, the average values of the physical and mechanical characteristics of soils with a change in their relative humidity from 0.6 to 0.9, based on approved Russian standards, are taken equal to: 1) for clays and loams - $\gamma = 1{,}9 \cdot 10^4$ N/m^3, $E = 48$ MPa, $\mu = 0{,}75$, $c = 0{,}019$ MPa, $\varphi = 20^o$; 2) for sandy loam - $\gamma = 1{,}8 \cdot 10^4$ N/m^3, $E = 49$ MPa, $\mu = 0.65$, $c = 0.011$ MPa, $\varphi = 34.5^o$.

In this case, the values of the loads q applied to individual sections of the slope surface varied from 0.2 to 0.4 MPa.

Figure 2 shows the design scheme, as well as the MPFS of the slope at $q = 0$ (unloaded slope) with the width b of a possible collapse prism.

According to the results calculated on a personal computer in tabular form, the coordinates X and Y (m) at the points of the MPFS are obtained; and at these points: angles α (degrees) between the tangents to the fracture line and the horizontal; horizontal, vertical and tangential stress components; holding and shearing forces; horizontal and vertical movements, as well as work produced by holding and shear forces. At the end of the tables, the areas of the diagrams of the holding and shear forces, as well as the sums of their work and the coefficients of slope stability K are given.

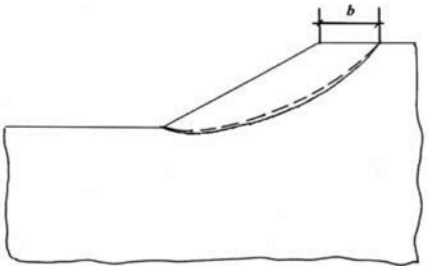

Figure 2. Calculation scheme of a loaded slope with an MPFS - (solid line for clays and loams, dotted line for sandy loam); *b* - width of possible collapse prism.

It should be noted that for the PC program used in this work, the slope stability coefficient *K* is calculated as the ratio of the holding and shear forces acting along the MPFS, and as the ratio of the work performed by these forces during the movement of soil massifs.

2 INVESTIGATION OF THE STABILITY OF CLAY SLOPES UNDER DIFFERENT FORMS OF LOAD DISTRIBUTION ON THEIR SURFACES

The influence of the direction of a uniformly distributed load on the stability of clay slopes was studied. It was revealed that changing the load slope angle from 0 to 30º leads to a decrease in the slope stability coefficient *K*; for clays (loams) 2.8 times; for sandy loam by 2.5 times. Therefore, a vertical uniformly distributed load reduces slope stability minimally.

The stability of clay slopes loaded with a triangular vertical load has been studied. The triangular distributed load was applied in such a way that the smaller triangle was at the base of the slope perpendicular to the day surface, the hypotenuse of the triangular load coincided with the slope surface. With an increase in the load *q* to 0.40 MPa, the values of the stability coefficients increase for clays and loams in the range of 8.2-21.3%, for sandy loams in the range of 7.7-15.7%. Thus, if, during the development of clay slopes, individual objects create a load identical to the triangular load on the slope surface, then the stability of the slope will increase.

3 INVESTIGATION OF THE STABILITY OF CLAY SLOPES UNDER VARIOUS VARIANTS OF APPLICATION OF A DISTRIBUTED LOAD IN LOCAL AREAS

Let us consider the influence of the vertical distributed load applied to local equal sections of the slope surface. We will divide the slope surface 160 m long into 10 sections 16 m long and sequentially apply a load with intensity $q = 0.25$ to each section; 0.33; 0.40 MPa.

In Figures 3–5, as examples, design schemes and MPFS are shown for a slope composed of clays (loams, sandy loams) and loaded in Sections 1, 5, 10 (the sections are numbered from bottom to top). The results of determining the stability coefficient of the considered slope for all 60 options are summarized in Table 1.

If we take into account that the coefficient of stability of an unloaded slope for clays and loams is 1.059, and for sandy loams - 1.792 (Table 1), then the following follows from the analysis. With the movement of the load from the bottom up, the slope stability coefficient decreases for clays (loams) by 7.9-9.9%, for sandy loams by 7.6-11.8%. The slope is most stable at the lower and least stable at the upper load positions, the stability coefficient in the first case is greater for clays (loams) by 3.8-6.0%, and for sandy loams by 4.9-8.1%, in the second case less than the similar coefficient K of an unloaded slope for clays (loams) by 4.4-5.0%, and for sandy loams by 3.1-4.6%. The stability of unloaded and loaded slopes is almost the same if the load is applied approximately in the middle of the slope.

The change in the stability of clay slopes was studied when their surface was loaded with a uniformly distributed load in several areas. The slope was divided into 10 equal sections, the

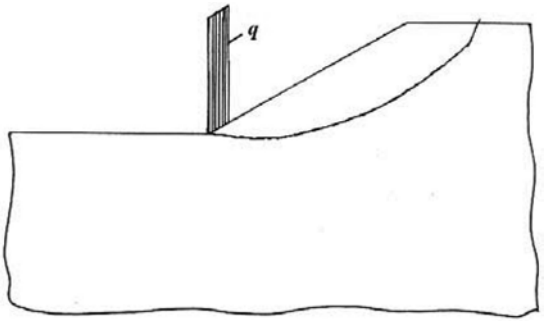

Figure 3. Calculation scheme under the influence of a load applied in section No. 1.

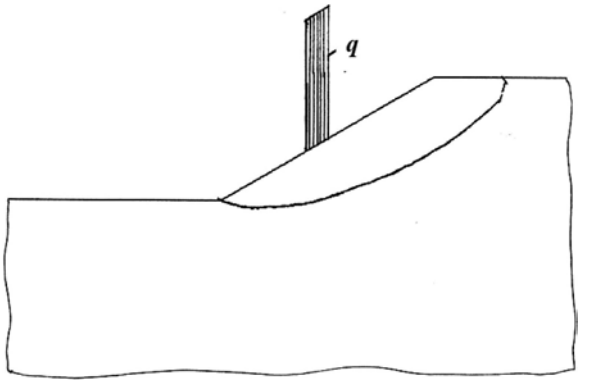

Figure 4. Calculation scheme under the influence of a load applied in section No. 5.

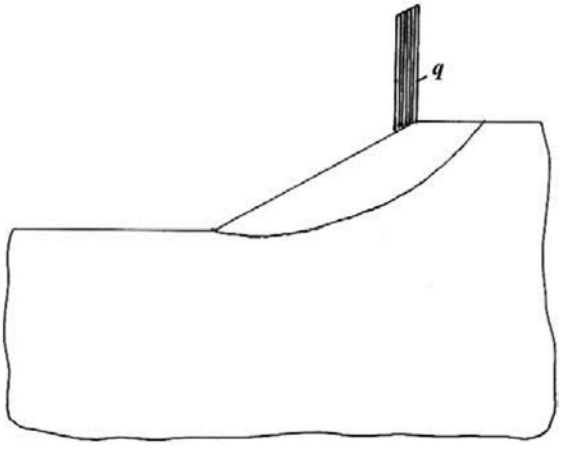

Figure 5. Calculation scheme under the influence of a load applied in section No. 10.

lower section - Section 1, the upper section - section 10. In Figure 6 shows the calculation scheme of the MPFS when the load is applied simultaneously in Sections 1, 6 and 10. At q = 0.33 MPa, the stability coefficient for clay (loam) is 1.066, and for sandy loam 1.79, i.e. compared to the unloaded slope, the stability coefficients remained practically unchanged.

Calculations have shown that at q = 0.25-0.40 MPa, the stability coefficients of the loaded slope are practically the same as compared to the unloaded slope (the difference does not even

Table 1. The dependence of the coefficient of stability of the slope, folded clay soils, on the position and magnitude of the local uniformly distributed load.

	K					
	Clays, loams			Sandy loam		
	q (MPa)			*q* (MPa)		
No. site	0,25	0,33	0,40	0,25	0,33	0,40
1	1,099	1,114	1,123	1,880	1,883	1,937
2	1,080	1,090	1,100	1,849	1,850	1,855
3	1,074	1,080	1,083	1,816	1,844	1,850
4	1,084	1,078	1,077	1,819	1,806	1,803
5	1,069	1,066	1,080	1,809	1,825	1,804
6	1,047	1,040	1,052	1,795	1,802	1,804
7	1,049	1,042	1,046	1,792	1,808	1,806
8	1,042	1,040	1,014	1,789	1,786	1,777
9	1,039	1,028	1,031	1,783	1,739	1,751
10	1,012	1,006	1,012	1,737	1,712	1,709

reach 1%). The results obtained allow us to conclude that the intermittent uniform loading of the slope practically does not change the stability coefficients of clay slopes. With intermittent uniform loading of the slope, each loaded section works according to an independent scheme. The load of the lower 1st section and the potential increase in the coefficient of stability of the slope caused by it compensates for the negative potential of the decrease in the coefficient of stability of the slope caused by the loads of the upper 10th section. The load of the central section 6 is neutral in relation to the stability of the slope.

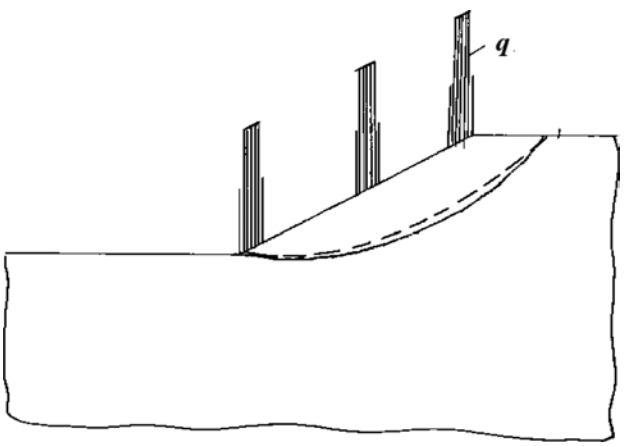

Figure 6. Calculation scheme, as well as the MPFS of a clay slope loaded with a uniformly distributed load in three sections (1, 6 and 10): solid line – clays (loams); dotted line - sandy loam.

Figure 7 shows the scheme and MPFS when the load is applied to Section 1 (q = 0.4 MPa) and to section 6 (q = 0.2 MPa). The calculations showed that the stability coefficient for clays (loams) is K = 1.125, and for sandy loams K = 1.909, i.e. with the last design scheme, the slope stability coefficient is on average 6.3% higher than that of the stability coefficients of an unloaded slope and a slope loaded according to the scheme shown in Figure 6.

These studies have confirmed the expediency of loading clay slopes with a triangular vertical load.

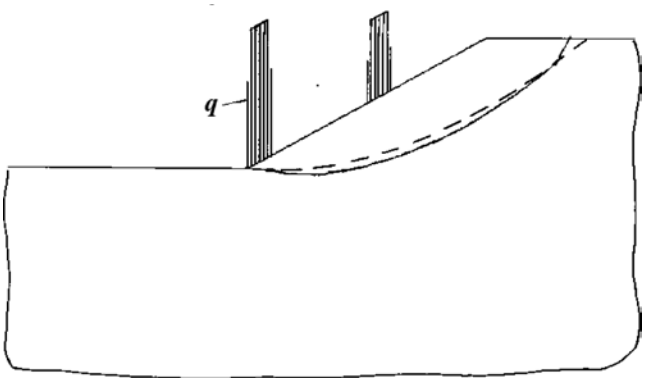

Figure 7. Calculation scheme, as well as the MPFS of a clay slope loaded evenly distributed load in the lower (Section 1) section q = 0.4 MPa and in the middle (section 6) section q = 0.2 MPa, solid line - clay (loam); dotted line - sandy loam.

4 CONCLUSIONS

1. Changing the angle of inclination of the load from 0 to 300 leads to a decrease in the coefficient of slope stability K; for clays (loams) 2.8 times; for sandy loam by 2.5 times.
2. Vertical uniformly distributed load minimally reduces slope stability.
3. A triangular distributed load, in which the hypotenuse of the triangular load coincides with the slope surface, increases the value of the stability coefficients K increase for clays and loams.
4. Intermittent uniform loading of the slope practically does not change the stability coefficients of clay slopes.
5. With the movement of the local load from the bottom up, the stability coefficient of the clay slope decreases.

REFERENCES

Bogomolov, A.N. 1996. Calculation of the bearing capacity of the foundation of structures and the stability of soil massifs in an elastic-plastic formulation. Perm, PSTU, 150 p.

Tsvetkov, V.K. 1993. Calculation of rational parameters of workings. M., Nedra, 251 p.

Hill, R. 1950. The Mathematikal Theory of Plasticity. Oxford Univ. Press. London, 355 p.

Morgenstern, N.R., Tchalenko, J.S. 1967. Microscopic Structure in Kaolinite Subjected to Direct Shear. Geotechnique, 17, №4, p.309–328.

Bjerrum, L., Landva, A. 1966. Simple-Shear Tests on a Norwegian Quick Clay. Geotechnique, 6, №1, p.1–20.

Bishop, A.W., Bjerrum, L. 1960. The Relevance of the Triaxial Test to the Solution of Stability Problems. Proc. Research Conference on Shear Strength Cohesive Soils. Boulder, American Society of Civil Engineers, New York, p.437–501.

Lo, K.J. 1970. The Operational Strength of Fissured Clays. Geotechnique, 20, №1, p.57–74.

Skempton, A.W., Petley, D.J. 1967. The Strength Along Structural Discontinuities in Stiff Clays. Proc. Geotechnical Conference on Shear Strength Properties of Natural Soils and Rocks. Norwegian Geotechnical Institute, Oslo, 2, p.29–46.

Kulchitsky, L.I., Usyarov, O.G. 1981. Physical and chemical bases of formation of properties of clay rocks. Moscow, Nedra, 1981, 178 p.

Osipov, V.I. 1979. The nature of the strength and deformation properties of clayey rocks. Moscow, Moscow University Press, 235 p.

Kazarnovsky, V.D. 1985. Evaluation of shear stability of cohesive soils in road construction. Moscow, Transport, 168 p.

Smart Geotechnics for Smart Societies – Zhussupbekov, Sarsembayeva & Kaliakin (Eds)
© 2023 The Author(s), ISBN 978-1-003-29912-7
Open Access: www.taylorfrancis.com, CC BY-NC-ND 4.0 license

Acceleration of consolidation of water-saturated loess subsidence massifs during their compaction by deep explosions

V.S. Shokarev
Research Institute Of Building Structures, Zaporozhye, Ukraine

F.G. Gabibov
Azerbaijan Research Institute of Construction and Architecture, Baku, Azerbaijan

ABSTRACT: The authors have developed technologies that significantly reduce the time of filtration consolidation of loess subsidence arrays during their compaction by deep explosions. According to the first new technology, explosive charges are installed in an array of moistened subsidence soil. The moment of sharp attenuation of the precipitation of the soil mass is determined, which makes it possible to determine the time for the initiation of the second series of explosions of charges installed above the charges of the first series. The number of series of exploding charges is accepted from 3 to 5. The duration of the period between explosions, depending on the composition of the soil, is taken from 1 to 15 days. The consolidation time is reduced by 4-5 times. According to the second new technology, the loess subsidence layer is divided into several separate layers.

1 INTRODUCTION

Trofimov (2003), Rendell (1989), Rozycki (1991), Pecsi (1993), Sajgalik (1991), Zarate & Blasi (1991) and others are devoted to research on the properties of loess subsidence soils.

The works of Abelev & Abelev (1979), Klepikov, Tregub & Matveev (1987), Mustafayev (1989), Aliyev (2005), Krutov, Kovalev & Kovalev (2013) and others are devoted to the development of effective construction methods on subsiding loess soils.

One of the cost-effective methods of deep compaction of subsiding massifs with a thickness of more than 10 m, in combination with other methods, is the hydraulic explosive method of deep compaction of subsiding soils. Litvinov (1977), Ryzhov (1995), Gabibov (2011) and others are devoted to the hydraulic explosive method of compaction of subsiding massifs.

2 INFLUENCE OF DEEP EXPLOSIONS ON THE PROCESS OF SOIL CONSLIDATION

Numerous experimental studies carried out on field sites in Zaporozhye (Ukraine) indicate that any violation of the structure of soft soil leads to one degree or another of accelerating the process of filtration consolidation. A particularly effective method of accelerating filtration consolidation is multi-series deep explosions in soaked loess subsidence soil.

The filtration consolidation equation is generally described by the equation

$$\frac{\partial \varepsilon_0}{\partial t} + na\frac{\partial \sigma_\mu}{\partial t} = \frac{k_f}{\rho_w}\nabla^2\sigma_\mu, \tag{1}$$

where is ε_0 - volumetric deformation of the soil; a - coefficient of volumetric compressibility of soil; n - soil porosity; k_f - filtration coefficient; ρ_w - density of water; ∇ - Laplace operator; σ_μ- pore pressure; t- time.

DOI: 10.1201/9781003299127-59

In the case of a plane problem, the consolidation equation is significantly simplified

$$\frac{\partial \sigma_\mu}{\partial t} = \frac{k_f}{\rho_w . a} \cdot \frac{\partial^2 \sigma_\mu}{\partial_{z^2}} . \tag{2}$$

Soil compressibility coefficient is determined from the experimental compression curve

$$e_f = e_s - a\, \ell n \frac{\sigma}{\sigma_s}, \tag{3}$$

where is e_s - initial value of the porosity coefficient; e_f - final value of the porosity coefficient.

Taking the mentioned coefficients constant, it is easy to determine that with two-way water drainage

$$k_f = \frac{0,2 \rho_w\ ah^2}{(1 - e_s)\, t_{50}}, \tag{4}$$

where is h - thickness of the soil sample in the device; t_{50} - time corresponding to 50% filtration consolidation.

The calculation data indicate that the process of filtration consolidation stretches for several years. So, with a subsiding soil thickness of 10-12 m, the estimated time of filtration consolidation is 4.8 years.

It has been experimentally established that the performance of one series of deep explosions reduces the time of filtration consolidation to several months, and two or three series of filtration consolidation to several weeks (Figure 1). Thus, it is achieved that the time of filtration consolidation practically does not hold back the pace of construction.

It remains to estimate the time of secondary consolidation. If the density of the soil in the process of multiple hydraulic explosive compaction changes from initial to critical, then the stabilization of the soil settlement will be more and more complete as the number of series of deep explosions increases (Figure 1).

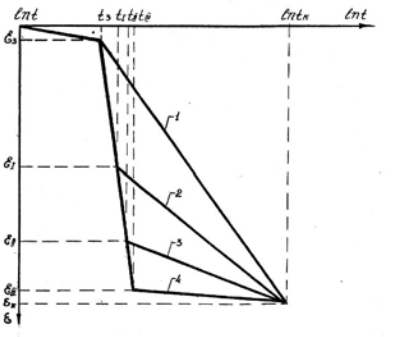

Figure 1. Acceleration of filtration and secondary consolidation of water-saturated loess loams by the energy of deep explosions: 1 – corrected curve of primary and secondary consolidation (before the explosion); 2 - acceleration of consolidation after the first series of deep explosions; 3 - acceleration of consolidation after the second series of deep explosions; 4 - acceleration of consolidation after the third series of deep explosions.

According to Buisman, the process of secondary consolidation of water-saturated structurally unstable soils is quite reasonably described by the equation

$$\varepsilon = \varepsilon_s + tg\, \alpha_1\, \ell n \frac{t}{t_s}, \tag{5}$$

where is ε_s - initial deformation of the soil; ε - current soil deformation; t_s, t - initial and current values of time; $tg\,\alpha$- coefficient of soil compressibility.

The same equation describes with acceptable accuracy the nature of the flow of soil sediment in time after deep explosions. After the first, second and subsequent series of deep explosions, we get

$$\begin{aligned} \varepsilon_1 &= \varepsilon_{s_1} + tg\,\alpha_1\, \ell n \frac{t_1}{t_{s_1}}, \\ \varepsilon_2 &= \varepsilon_{s_{21}} + tg\,\alpha_2\, \ell n \frac{t_2}{t_{s_2}}, \\ &\cdots\cdots\cdots\cdots\cdots\cdots \\ \varepsilon_n &= \varepsilon_{sn} + tg\,\alpha_{n1}\, \ell n \frac{t_n}{t_{sn}}, \end{aligned} \tag{6}$$

If in the initial period (before explosions) the process of filtration consolidation prevailed, then due to a series of deep explosions, the specific effect of filtration consolidation can be almost imperceptible. Then the time of filtration consolidation from soil soaking will be obtained in the form

$$\Delta \ell n\, t_w = \ell n\, t_w - \ell n\, t_s. \tag{7}$$

The time during the transition of the soil from the initial to the final density, spent on plastic deformations of the secondary consolidation, is determined from the formula

$$t_p = t - t_f - t_w, \tag{8}$$

where is t - time of final deformation.

The increment of filtration consolidation time after each new series of explosions rapidly decreases and tends to zero, and the total filtration consolidation time becomes much less than the time spent on plastic deformations of secondary consolidation.

In Figure 1, attention is drawn to the absence of a smooth transition from the filtration area to the secondary consolidation area. This is due to a sharp increase in water loss from the soil in the initial period of time after deep explosions. A sharp inflection of the filtration and secondary consolidation areas indicates that not only the filtration area is reduced, but also part of the non-linear area of the secondary soil consolidation.

3 DEVELOPMENT OF TECHNOLOGY FOR DEEP COMPACTION OF SUBSIBLE LOESS SOILS BY SEVERAL SERIES OF EXPLOSIONS

The authors have developed a new technology for compacting loess subsidence soil by several series of deep explosions. Wells are being drilled in which explosive charges are installed for the first series of explosions.

By leveling the sediment of the soil according to the established marks, the change in the rate of sedimentation of the soil and its individual layers in time is fixed. According to the graph (Figure 2) $S(t)$, the moment of sharp attenuation of the sedimentation of the massif and the time of sedimentation from the explosion of the next series of deep explosions are determined. Then, deep charges of the second series of explosions are installed above the charges of the first series and explosions of the charges of the second series are performed. In the future, all operations are repeated.

By comparing the sinking between series of deep blasts, we determine the sufficient degree of compaction of the soil massif and the time for completion of blasting. For example, if with two explosions the precipitation reached 60%, and with three explosions 80% of the potential, then blasting is stopped after the condition is met

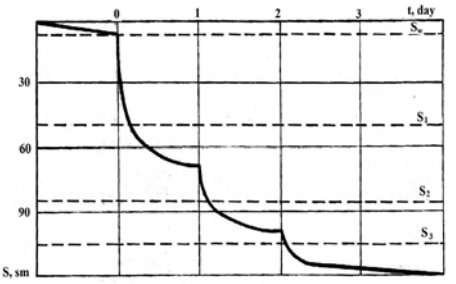

Figure 2. Graph of subsidence of the subsidence soil surface in time during successive blasting of explosive charges in three series: S_W, S_1, S_2, S_3 - precipitation after soaking, the first, second and third series of explosions.

$$S_n = 0,25\, S_{n-1}, \tag{9}$$

where is S_n - *sinking of the final series of deep explosions;* $S_{n\text{-}1}$- sinking of the previous series of deep explosions.

In the example shown in Figure 2, the condition $S_n < 0.25\ S_{n\text{-}1}$ is satisfied by the result of soil sinking after the third series of explosions. The time intervals between series of single deep explosions are taken equal: from 3 to 7 days for light and medium loams; from 7 to 15 days for loess clays.

4 DEVELOPMENT OF A TECHNOLOGY FOR DEEP COMPACTION OF SLOWING LESS SOILS BY EXPLOSIONS IN INDIVIDUAL LAYERS OF THE MASSIF

New technology for deep compaction of a subsiding massif includes the formation of contour trenches, waterproofing the compacted soil massif along the perimeter of the contour trenches, the formation of wells, the placement of explosive charges in these wells, filling the wells with coarse-grained material, soaking the soil to a state of fluid consistency, and explosions of explosive charges with soil sinking under its own weight. The soil mass is divided into several layers by thickness. The soaking of the soil and the initiation of explosions are carried out in separate layers, starting from the bottom layer. After the formation of wells, their walls are fixed with casing pipes, and before explosions, the walls are freed from fastening to the height of the compacted layer. The thickness of each layer of soil in the massif is taken equal to its depth, at which the rock pressure increases to 0.9 - 0.975 kg/cm^2. When compacting the lower layers, water is squeezed out of them and partially moistens the overlying layer. As you can see, the number of series of explosions is equal to the number of installed layers of compacted soil. The time to decrease the consolidation approximately corresponds to the decrease in the time of consolidation according to the first technology.

5 CONCLUSIONS

1. A particularly effective method of accelerating filtration consolidation is multi-series deep explosions in soaked loess subsidence soil.
2. It has been experimentally established that the performance of one series of deep explosions reduces the time of filtration consolidation to several months, and two or three series of filtration consolidation to several weeks.
3. On the basis of analytical studies, it was revealed that the increment of filtration consolidation time after each new series of explosions rapidly decreases and tends to zero, and the total filtration consolidation time becomes much less than the time spent on plastic deformations of secondary consolidation.

4. A new technology has been developed for compacting loess subsidence soil by several series of deep explosions. Graphically determine the moment of sharp attenuation of sedimentation of the array and the time of precipitation from the explosion of the next series of deep explosions. The time intervals between series of single deep explosions are taken equal: from 3 to 7 days for light and medium loams; from 7 to 15 days for loess clays.
5. According to the second new technology, the soil mass is divided into several layers by thickness, and the soaking of the soil and the initiation of explosions are carried out in separate layers, starting from the bottom layer. The thickness of each layer of soil in the massif is taken equal to its depth, at which the rock pressure increases to 0.9 - 0.975 kg/cm^2.

REFERENCES

Abelev, Yu.M., Abelev, M.Yu. 1979. Fundamentals of design and construction on subsidence macroporous soils. Moscow: Stroyizdat, 271 p.

Aliev, S.K. 2005. Roadbed of highways on loess subsidence soils. Baku: Elm, 633 p.

Gabibov, F.G. 2011. Theory and practice of improving the properties of structurally unstable clay soils in solving geotechnical and engineering geoecological problems. Baku: Elm, 422 p.

Klepikov, S.N., Tregub, A.S., Matveev, I.V. 1987. Calculation of buildings and structures on subsidence soils. Kyiv: Budivelnik, 200 p.

Kriger N.I. Loess. Formation of subsidence properties. Moscow: Nauka, 1986, 132 p.

Krutov, V.I., Kovalev, A.S., Kovalev, V.A. 2013. Design and installation of bases and foundations on subsidence soils. Moscow: DIA Publishing House, 544 p.

Litvinov, I.M. 1977. Strengthening and compaction of subsidence soils in housing and industrial construction. Kyiv: Budivelnik, 288 p.

Mustafaev, A.A. 1989. Foundations of subsidence and swelling soils. Moscow: Visshaya Shkola, 590 p.

Pecsi, M. 1993. Nedyedkor es loszkutatas. Budapest. Akademiai Kiado.

Rendell, H.M. 1989. Loess deposition during the Late Pleistocene in Northern Pakistan. Zeits chrift fur Geomorphologie. Neue Folge, 76: p.247–255

Rozycki, S.Z. 1991. Loess and loess-like deposits. Wroclaw. Polish Academy of Science.

Ryzhov, A.M. 1995. Introduction to non-linear soil mechanics and physical modeling of foundations. Zaporozhye: RIP "Vidavets", 446 p.

Sajgalik, J. 1991. Geotechnical Properties of the Danubian Lowland Loess soils in the Slovak Carpathians. GeoJournal. vol.24. B.2, p.165–174

Trofimov, V.T. 2003. Theory of formation of subsidence loess rocks. Moscow: GEOS, 275 p.

Zarate, M. & Blasi, A. 1991. Late Pleistocene and Holocene Loess Deposits of the Southeastern Buenos Aires province, Argentina. GeoJurnal.Vol. 24. №2, p.41–47

Smart Geotechnics for Smart Societies – Zhussupbekov, Sarsembayeva & Kaliakin (Eds)
© 2023 The Author(s), ISBN 978-1-003-29912-7
Open Access: www.taylorfrancis.com, CC BY-NC-ND 4.0 license

Evaluating the shear strength of agar gum-treated gypseous soil

Ahmed Hammad Hussein
Department of Civil Engineering, College of Engineering, University of Samarra, Samarra, Iraq

Farouk M. Muhauwiss, Naser A. Hassan & Arwa Faaeq Theyab
Department of Civil Engineering, College of Engineering, Tikrit University, Salah Al Deen, Iraq

ABSTRACT: Gypseous soil is strong in its dry state but has real problems when exposed to water, and this requires an effort to improve it and reduce these problems. Soil chemical improvement is a well-known method and leads to environmental problems related to the emission of greenhouse gases and the impossibility of recycling the improved soil in the future. This encouraged the creation of alternatives to stabilizers with a large carbon footprint. Biopolymers are environmentally friendly materials because of their low carbon footprint, resulting in the creation of improved and sustainable geo-structures. Recently introduced as soil improvement materials, they provide significant reinforcement and in lower quantities than conventional binders such as cement. Agar biopolymer was used to analyze the strengthening properties of gypsum soil. Four gypsum contents were used for soil, which are 8, 25, 45 and 59%, agar content by adding (1, 2, 3)%, The curing time for the prepared samples is 14 days before the tests and obtaining the results. The results showed that the resistance of gypsum-agar mixtures was significantly increased even under water saturated conditions compared to pure soil. The value of (Φ) increased by 24.4% and 32.33% for the soil samples improved by 3% agar in the dry and wet conditions, respectively, while the percentage increase in the cohesion (C) of the improved gypsum soil increased by 67.89% and 45.95% for the dry and wet samples respectively.

1 INTRODUCTION

Gypsum soil is regarded as one of the most challenging unsaturated soils to work with while constructing roads and structures. The presence of gypsum (Hydrated Calcium Sulphate (CaSO4.2H2O)) in the soil alters its mechanical and physical qualities, as well as making it more susceptible to water. When water from a strong rain falls on this type of soil, it causes a reconfiguration and a change in volume (reduction). Because the soil loses the bond between the particles and becomes weak to withstand and resist the load applied to it, based on the soil nature and geological structure, the primary soil density, soil structure, the imposed formal stress, and the amount of wetting, this change in volume significantly causes structural failure (Ahmed, Al-Hadidi, & Mohammed, 2020). In civil engineering, soil is classed as Gypsum soil based on the quantity of gypsum content in it, independent of soil color or form. Some scholars suggested that a particular percentage of gypsum should exist, such as 3%, 4%, or 6% as a lower limit (H, 2007). These gypsum rates have a significant impact on the physical and mechanical properties of soil, and this impact varies depending on the quantity of gypsum present.

Problem soils are treated to enhance the engineering properties of the soil. Conventional chemical and mechanical stabilizers to enhance soil properties. Among these stabilizers are lime, cement, chemical plaster, epoxy, phenoplast, polyurethane and acrylamide with the improvement and reinforcement offered by these technologies but these additives have a significant negative impact on the ecosystem (Worrell et al., 2001),(Afolabi, Francis, & Adejompo, 2012),

DOI: 10.1201/9781003299127-60

(Latifi et al., 2017), (Joga & Varaprasad, 2019). The production of the most widely used stabilizers such as lime and cement causes significant emissions of carbon dioxide and nitrogen oxides. In addition to disturbing the ecosystem by changing and increasing the acidity of the soil, it can cause desertification to its low, degrading nature. In addition to chemical germs that have been reported to be toxic and/or dangerous, except for sodium silicate (Smitha & Sachan, 2016). These disadvantages, make stabilization of problem soils with environmentally friendly, harmless alternative stabilizers very necessary and important. Researchers (Mitchell, Santamarina, & engineering, 2005); (Ivanov, Chu, & Bio/Technology, 2008); (Cole, Ringelberg, Reynolds, & engineering, 2012) present attempts to stabilize soils with biotechnical techniques for geotechnical purposes. Presented new stabilizers for soils and gave important results that are biopolymers of a biological nature. Agar, xanthan, chitosan, guar etc. have been used as biopolymers that provide a water-insoluble gel provided by organisms such as algae, bacteria and fungi and prepare hydrogen bonds that form the branched structure of polymeric chains within the soil structure (Smitha & Sachan, 2016); (Joga & Varaprasad, 2019).

A few researchers have used biopolymers to enhance the shear strength and hydraulic conductivity of erosive soils and sandy clays (Orts et al., 2007); (Nugent & Zhang, 2010); (Smitha & Sachan, 2016). (Chang, Cho, & Materials, 2012) and Chang (Chang, Prasidhi, Im, Cho, & Materials, 2015b). Show biopolymers of agar, gellan and beta-glucan have been used successfully to improve the Cheonan sandy soil and the strength of the remaining Korean clay soil. However, the stability of expansive soils has not been examined using the biopolymer mixture. Expansive soil cause serious problems for geotechnical structures due to their excessive collapse and shrinkage behavior due to the dissolution of gypsum salts. In addition, the shear resistance decreases when saturated with water to a higher degree. Hence, in this study an attempt was made to stabilize gypsum soil treated with biopolymer agar. The biopolymer Agar was chosen, because it gives the highest mechanical strength (Khatami & O'Kelly, 2013),(Kantesaria, Chandra, & Sachan, 2021). Agar provides a dense covering and coating that envelops soil particles resulting from the generation of a dense gel network, and this also ensures less biodegradability (Khatami & O'Kelly, 2013). From the above scientific literature, we note the lack of studies on the problems of gypsum soil in the field of biopolymer treatment.

This experimental research was conducted to study the shear strength of gypsum soil treated with agar gum. A solution of 1%, 2% and 3% By soil weight of agar gum which was prepared at optimum water content was added to the soil with different gypsum content. The treated mixture cured for 24 days. Shear properties were evaluated by a series of tests. The microstructure of the treated mixture was explored by scanning electron microscopy (SEM) testing.

2 MATERIALS

2.1 *Soil*

Gypsum soil samples were taken at a depth of one meter in an area of 18 km west of Ramadi city, Anbar, Iraq from places southwest of Lake Tharthar, north of Ramadi city in Iraq, between N43° 15'E32'33°, Anbar, Iraq. Four gypsum contents were used for soil, which are 8, 25, 45 and 59%, which were designed with 1, 2, 3 and 4 soils, respectively. All soils were classified as Poorly graded sand (SP) according to the standard soil system (ASTM D2487-17e1). The chemical composition of gypsum soil was analyzed as shown in Table 1. A modified Proctor test was performed to determine the maximum unit weight (MDD) and the ideal moisture content (OMC) as shown in Table 2.

Table 1. Chemical properties of soil samples.

Properties	Soil 1	Soil 2	Soil 3	Soil 4
Gypsum content %	8	25	45	59
Total soluble salts (T.S.S)%	28	37.13	52.34	64.28
Organic matters (O.M)%	0.45	0.38	0.28	0.13
pH value	8.06	7.8	8.1	8.07

Table 2. Physical properties of soil samples.

	Grain size distributions (ASTM D422, 2007)			Atterberg limits (ASTM D4318)		Compaction test (ASTM D1557)		
Soil type	USCS	uniformity coefficient (Cu)	Curvature coefficient (Cc)	LL%	PL%	γ_{field} (kN/m³)	γ_{dry} max (kN/m³)	OMC(%)
1	SP	6.3	0.64	35	N.P	14.3	17.3	11
2	SP	7.8	0.55	34	N.P	13.5	16.7	12
3	SP	6	0.58	29	N.P	14.8	15.8	11
4	SP	7	0.78	27	N.P	13.2	15.5	12

2.2 *Agar*

Agar is a biopolymer, which form a dissolved suspension at a high temperature (ie 85-90 °C) and coagulated at lower temperature (ie <50 °C) as a gelatinous structure. Agar is a naturally growing polysaccharide, frequently found in the cell walls of some species of red algae such as Gelidium and Gracilleria, which belong to the family Rhodophycae of red marine plants (Smitha and Sachan 2016). Agar gum is a mixture of agaropectin and agarose. Agarose which is responsible for gel formation, when heated and mixed with soil. Agar biopolymer powder used in the study is bacteriological grade bought from local mar-kets.

2.2.1 *Physico-chemical properties*

The physicochemical activities of guar galactomannan and other polysaccharides are determined by how they behave in water. On dispersion, guar gum swells and/or dissolves in polar solvents, forming strong hydrogen bonds. It only forms weak hydrogen bonds in non-polar solvents. The rate of guar gum solubility and viscosity progress generally increases as particle size, pH, and temperature decrease. In the presence of soluble salts and other water-binding agents such as sucrose, hydration rates are reduced. Table 3 General composition of guar gum (Mudgil, Barak, & Khatkar, 2014).

Table 3. General composition of guar gum.

Constituent	Percentage
Galactomannan	75–85
Moisture	8.0–14
Protein (N x 6.25)	5.0–6.0
Fiber	2.0–3.0
Ash	0.5–1.0

3 PREPRATION OF SAMPLES

Agar gum solution was prepared with the optimum moisture content by adding (1, 2, 3)% By soil weight and mixing it properly in the magnetic device. It is added to the soil to make a mixture treated with agar-biopolymer. Then the mixture is transferred to molds 50 * 50 mm (length * width) and 20 mm high with two layers of compaction to obtain the Max dry density Prepared for the direct shear test. Samples were extracted and dried at room temperature for 14 days, while half of the dried samples were soaked in distilled water for 24 hours before being subjected to direct shear tests to represent the “soak condition”. Also, reference samples were remolded without treatment for each of the four types of gypsum soils for the purpose of comparison with the improved samples. All samples were wrapped in plastic bags during the treatment period. All specimens were prepared at optimum moisture content and maximum soil Dry unit weight. To study the interaction in the structure of the soil-agar mixture, Small cubic samples of side length of 10 mm were taken from cylinder molds with 100mm height and 50 mm diameter. After the curing period 14 day was checked by SEM.

4 RESULTS AND DISCUSSION

4.1 *Shear strength*

Figure 1a-d shows the relationship between maximum shear and normal stresses by direct shear test. From these figure, it is noticed that the shear strength of the agar-treated mixture increases in the dry and wet conditions with the increase of the agar content, and the highest increase in strength was when 3% agar was added to all four contents of gypsum. The value of (Φ) increased by 24.4% and 32.33% for the soil samples improved by 3% agar in the dry and wet conditions, respectively, while the percentage increase in the cohesion (C) of the improved gypsum soil increased by 67.89% and 45.95% for the dry and wet samples respectively at the same agar content 3% Table 4. These strengthening mechanisms may be due to particulate interaction and conductance of the pore area. The agar gum modified the bonding features of the treated soil granules because the agar solution encapsulated the soil granules and bridged them by electrical bonding, and/or provided a biofilm. As a result, the shear cycles required to overcome the bridging of soil grains increased (Chang et al., 2020).

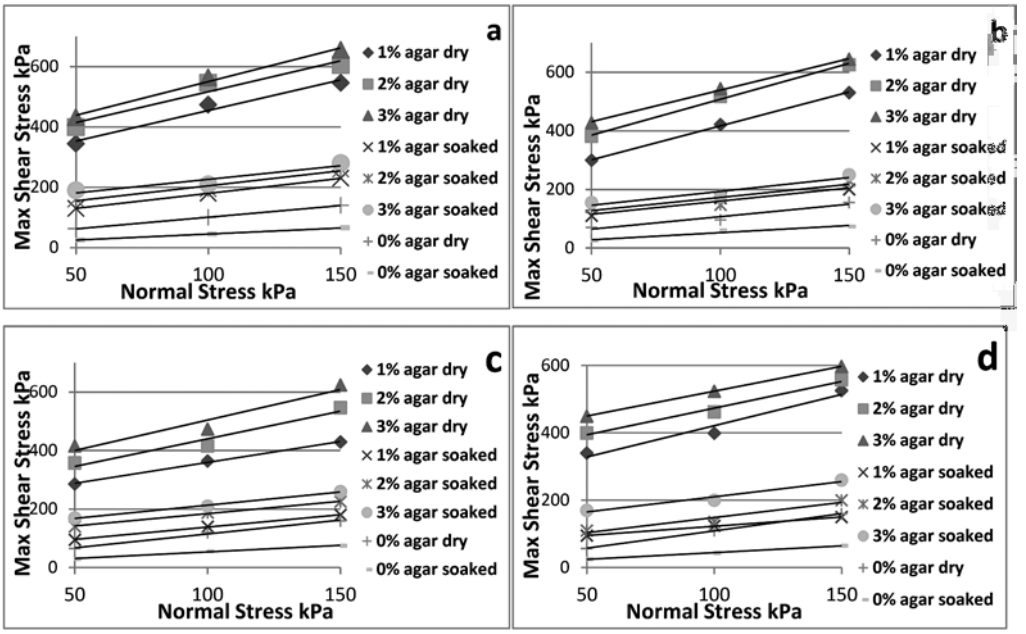

Figure 1. The relationship of shear stress with Normal stress in the dry and soaking condition and with different Agar contents: (a) soil 1, (b) soil 2, (c) soil 3 and (d) soil 4.

In the wet state, the biopolymers absorb moisture and develop hydrogels, and increase the viscosity of a liquid between the pores. This absorption property increases the shear strength of the soil. In addition, the biopolymer hydrogels reduce soil permeability and promote pore blockage, and this reduces seepage and surface erosion. The above mechanisms are involved in enhancing the erosion shear stress in addition to increasing the cohesion and contact between the soil grains (Kantesaria et al., 2021).

When the agar content increases, the internal friction angle in dry conditions Figure 2 a,b and the cohesion Figure 3 and Table 4 increases. This is because drying, which occurs as a result of the drying of the biopolymer hydrogel increases the angle of friction between soil particles that is similar to saturated conditions due to the condensation of agar biofilms, which enhances soil agglomeration by surface coating and antiparticle bridging (Smitha & Sachan, 2016).

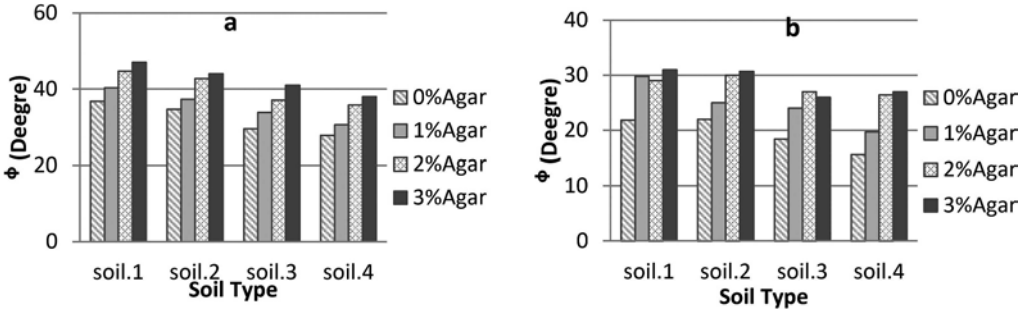

Figure 2. The relationship angle of internal friction and soil type for agar-treated samples after 14 days curing: (a) dry condition and (b) wet condition.

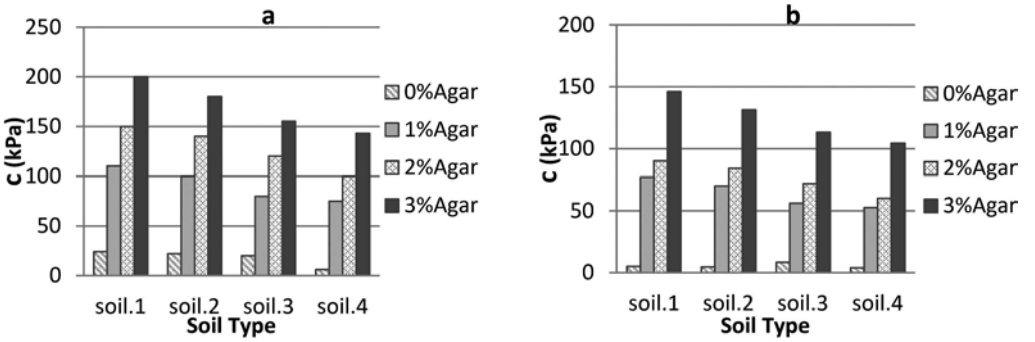

Figure 3. Cohesion and soil type relationship for agar-treated samples after 14 days curing: (a) dry condition and (b) wet condition.

Table 4. Shear parameters for reference and treated samples by Agar.

Parameter	Agar ratio %	soil.1		soil.2		soil.3		soil.4	
		Dry	Wet	Dry	Wet	Dry	Wet	Dry	Wet
Φ (Degree)	0	36.8	21.8	34.65	22	29.53	18.4	27.8	15.6
	1	40.3	29.8	37.3	25	33.8	24	30.6	19.7
	2	44.7	29	42.7	30	37.1	27	35.8	26.4
	3	47	31	44	30.65	41	26	38	27
C (kPa)	0	24	5	22	4.66	20	8.33	6	4
	1	110	77	100	70	80	56	75	52.5
	2	150	90	140	84	120	72	100	60
	3	200	146	180	131.4	155	113.15	143	104.39

4.2 *Scanning electronic microscopy (SEM)*

The microstructure changes of samples treated with agar observed by SEM images. Microscopic analysis was performed on soil 3 only that a gypsum content of 45%. Figure 4a shows the natural state of the soil 3. The compacting of the soil at the optimum moisture content leads to the movement of soil particles inside the pores and their aggregation without any clear physical bonds due to the lack of cohesion between the particles, so the particles move on each other without restrictions.

The pores were more compact in Figure 4a and there is a more dense soil mass, but there is no special bond between the fine particles. In Figure 4b with the addition of 2% agar

biopolymer make an agar hydrogel layer on soil mass. In the case of compacted cohesive soils, the soil particles unite in the form of aggregates. A hydrogel coating on this aggregate binds the soil and provides reinforcement between two sets of aggregates (Kantesaria et al., 2021), which were not initially in contact. Thus, the increase in the total contact area due to the formation of a matrix of sand and biopolymer leads to an increase in the shear strength of the soil.

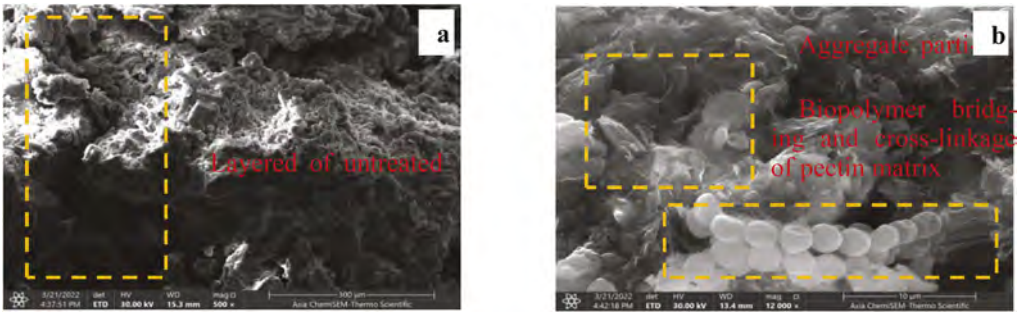

Figure 4. SEM of (a) untreated soil and (b) soil-pectin mixture with 2% pectin after 14 day curing.

5 CONCLUSIONS

The study determined the shear strength, properties and characteristics of the reinforcement after conducting a series of tests to check the direct shear. The structural modification of the treated soil was also studied by assay and SEM. Then it was concluded from the following study:

- Shear coefficients (c, Φ) decrease with increasing gypsum content, and the decrease is greater with water soaking in the soil. Φ decrease 36.8, 34.65, 29.53 and 27.8 for soil 1, 2, 3 and 4 respectively for dry condition and were 21.8, 22, 18.4 and 15.6 for for soil 1,2,3 and 4 respectively at wet condition. C decrease 24, 22, 20 and 6 for soil 1, 2, 3 and 4 respectively at dry condition and 5, 4.66, 8.33 and 4 for soil 1, 2, 3 and 4 respectively at wet condition.
- The shear strength of the treated samples improved and increased with the increase of the agar content, and the improvement efficiency ranged between 3.5 to 5.4 times at a concentration of 3% agar and according to the gypsum content as a result of the interplay of granular cohesion provided by the agar gum biogels. The curing stage of the biopolymer-fixed models is important to obtain the best reinforcement resulting from the addition of biopolymers in different concentrations.
- The value of (Φ) increased by 24.4% and 32.33% for the soil samples improved by 3% agar in the dry and wet conditions, respectively, while the percentage increase in the cohesion (C) of the improved gypsum soil increased by 67.89% and 45.95% for the dry and wet samples respectively at the same agar content 3%.
- Through pictures (SEM) it was concluded that the contact area increased between the gypsum soil particles provided by the sand matrix and the biopolymer as a result of the agar gum hydrogel, which enhanced the physical bonding within the improved soil structure.

REFERENCES

Afolabi, A., Francis, F. A., & Adejompo, F. J. A. J. o. H. E. (2012). Assessment of health and environmental challenges of cement factory on Ewekoro community residents, Ogun State, Nigeria. *1*(2), 51–57.

Ahmed, B. A., Al-Hadidi, M. T., & Mohammed, D. W. (2020). *Improvement of the Gypseous soil properties by using Copolymer and Styrene-butadiene rubber*. Paper presented at the IOP Conference Series: Materials Science and Engineering.

Chang, I., Cho, G.-C. J. C., & Materials, B. (2012). Strengthening of Korean residual soil with β-1, 3/1, 6-glucan biopolymer. *30*, 30–35.

Chang, I., Lee, M., Tran, A. T. P., Lee, S., Kwon, Y.-M., Im, J., & Cho, G.-C. J. T. G. (2020). Review on biopolymer-based soil treatment (BPST) technology in geotechnical engineering practices. *24*, 100385.

Chang, I., Prasidhi, A. K., Im, J., Cho, G.-C. J. C., & Materials, B. (2015b). Soil strengthening using thermo-gelation biopolymers. *77*, 430–438.

Cole, D. M., Ringelberg, D. B., Reynolds, C. M. J. J. o. G., & engineering, G. (2012). Small-scale mechanical properties of biopolymers. *138*(9), 1063–1074.

H, A.-E. O. (2007). *Collapsibility of gypseous soil under fluc-tuation of ground water table*. (M.Sc), University of Technology, University of Technology, Iraq.

Ivanov, V., Chu, J. J. R. i. E. S., & Bio/Technology. (2008). Applications of microorganisms to geotechnical engineering for bioclogging and biocementation of soil in situ. *7*(2), 139–153.

Joga, J. R., & Varaprasad, B. J. C. E. J. (2019). Sustainable improvement of expansive clays using xanthan gum as a biopolymer. *5*, 1893–1903.

Kantesaria, N., Chandra, P., & Sachan, A. (2021). Stabilization of expansive soil using Agar biopolymer. In *IFCEE 2021* (pp. 272–281).

Khatami, H. R., & O'Kelly, B. C. J. A. J. G. G. E. (2013). Improving mechanical properties of sand using biopolymers. *139*.

Latifi, N., Horpibulsuk, S., Meehan, C. L., Abd Majid, M. Z., Tahir, M. M., & Mohamad, E. T. J. J. M. C. E. (2017). Improvement of problematic soils with biopolymer—an environmentally friendly soil stabilizer. *29*(2), 04016204.

Mitchell, J. K., Santamarina, J. C. J. J. o. g., & engineering, g. (2005). Biological considerations in geotechnical engineering. *131*(10), 1222–1233.

Mudgil, D., Barak, S., & Khatkar, B. S. (2014). Guar gum: processing, properties and food applications-A Review. *J Food Sci Technol*, *51*(3), 409–418. doi:10.1007/s13197-011-0522-x

Nugent, R., & Zhang, G. (2010). *The effects of exopolymers on the erosional resistance of cohesive sediments*. Paper presented at the Proceedings 5th International Conference on Scour and Erosion (ICSE-5), November 7-10, 2010, San Francisco, USA.

Orts, W. J., Roa-Espinosa, A., Sojka, R. E., Glenn, G. M., Iman, S., Erlacher, K., & Pedersen, J. S. J. J. o. m. i. c. e. (2007). Use of synthetic polymers and biopolymers for soil stabilization in agricultural, construction, and military applications. *19*(1), 58–66.

Smitha, S., & Sachan, A. (2016). Use of agar biopolymer to improve the shear strength behavior of sabarmati sand. *International Journal of Geotechnical Engineering*, *10*(4), 387–400. doi:10.1080/19386362.2016.1152674

Worrell, E., Price, L., Martin, N., Hendriks, C., Meida, L. O. J. A. r. o. e., & environment, t. (2001). Carbon dioxide emissions from the global cement industry. *26*(1), 303–329.

Smart Geotechnics for Smart Societies – Zhussupbekov, Sarsembayeva & Kaliakin (Eds)
© 2023 The Author(s), ISBN 978-1-003-29912-7
Open Access: www.taylorfrancis.com, CC BY-NC-ND 4.0 license

Study of geotechnical conditions of the city of Pavlodar

N.T. Alibekova & A. Abisheva
Department of Construction, L.N. Gumilyov Eurasian National University, Astana, Kazakhstan

A.K. Aldungarova
School of Architecture and Construction, D. Serikbayev East Kazakhstan Technical University, Kazakhstan

M. Mimura
Graduate School of Engineering, Kyoto University, Kyoto, Japan

ABSTRACT: Pavlodar is one of the main industrial regions of Kazakhstan, with a historically formed territorial and production complex, which is an important part of the national wealth of our country. Increasing volumes of construction of all forms of ownership of this city predetermine further increase of engineering design and survey works. However long-term observations show that technogenic impacts of buildings and structures on the geological environment cause changes in it is elements, which are manifested in the development and activation of such engineering and geological processes as erosion and destruction of the coastal slope, gullying, waterlogging and salinization of soil. Therefore, in order to minimize the damage caused by these processes, it is necessary to develop in a timely development scientifically based urban and architectural planning solutions, where the task of generalizing the results of the current engineering and geological surveys with the purpose of typing geotechnical conditions of the city. The presence of the typing will allow to carry out a more rational study, identification of features and assessment of geotechnical conditions for such issues as, reduction of engineering and geological surveys, increase of economic efficiency. The article considers questions of typification of engineering and geological conditions of the city territory, as the main factor is studied geological structure. An analysis of the physical and mechanical properties of the soils with the study of strength and deformation characteristics of the soils located in the territory of the city of Pavlodar was also performed.

1 INTRODUCTION

As it is well known that any construction begins with the construction of the most important part – the base. The reliability of the building in the processes of construction and operation on foundation which perceives external influences and transfers to the foundation, and the reliability of the foundation and base depends on physical and mechanical properties of foundation soils, which are studied and analyzed in detail engineering and geological surveys.

The territory of the Republic of Kazakhstan is characterized by a wide variety engineering and geological conditions. The issues of designing, construction and operation buildings and structures in difficult engineering and geological conditions are becoming increasingly relevant, taking into account the decrease in the area with favourable soils. However engineering and geological data of surveys in the regions of our country are almost not generalized and are most often in paper form. As a rule, companies engaged in engineering research accumulating impressive archives, most often not very open in the exchange of data.

All this complicates the conduct of survey works, it is more difficult for prospectors to predict development engineering and geological processes, and most importantly, there are cases of duplicate works, sometimes full exploration in the same territories [Zhussupbekov et al. 2021].

DOI: 10.1201/9781003299127-61

Therefore, the timely development of scientifically new urban and architectural planning solutions for the territory of our country on the example of Pavlodar city will be a relevant decision.

2 CHARACTERISTICS OF THE OBJECT OF STUDY

2.1 *Characteristics of the object*

Pavlodar – the largest city of North Kazakhstan located between 41°57′-54°27′ northern latitude and 73°25′-79°20′ eastern longitude from Greenwich and covers an area of 127.5 thousand square kilometers. It is bordered by four regions of the Republic of Kazakhstan (North Kazakhstan, Akmola, Karaganda, East Kazakhstan) and two entities of the Russian Federation (Omsk region, Altai region). The territory of the region, stretching more than 450 km from north to south and over 420 km from west to east, is crossed by the Irtysh River, the main waterway of the region. Currently, there are 10 rural districts, 3 cities of regional subordination, 4 villages, 169 rural districts in the region [Smailov 2015].

Here, in addition to traditional industrial enterprises and the extraction of hydrocarbon raw materials, large-scale industry is developed, with which the Pavlodar city acts as one of the major industrial centers of the Commonwealth of Independent States. The region accounts for 7% of industrial production, 70% of coal production, 3/4 ferroalloys smelting, 40% of electricity generation and oil products processing from the level of the republic [Zhakupov et al. 2014]. Increasing volumes of construction of all forms of ownership of this city predetermine further increase of engineering design and exploration, it is enough to note, renovation and construction of new neighborhoods, such as Saryarka and Dostyk.

2.2 *Characteristics of engineering and geological conditions*

In geological and structural terms, the area of the Pavlodar region is located in the zone of junction of two large geological structures - the Kazakh folded country (Saryarka), which occupies about 25% of the area of the region, and the West Siberian lowland.

Geomorphologically, the location of the territory at the edge of the extensive accumulation of the southern plain of the West Siberian Lowland has led to it is long-term development as a lacustrine, lacustrine-alluvial and alluvial plain since the middle of the Oligocene. The main features of the relief of the territory were created by erosive and accumulative processes of the middle and upper Quaternary time, as well as the modern stage of geological history. The main genetic groups of relief forms are identified: alluvial, lacustrine-alluvial and lacustrine, of various geological ages, from the middle section of the quaternary system to the modern one. The alluvial group includes two terraces above-floodplain and the floodplain of the Irtysh River. Most of the territory is occupied by the second floodplain terrace of the Irtysh river, which is the next oldest relief element. The first terrace above-floodplain of the Irtysh River is covered by a cloak of cover deposits and is characterized by the still quite preserved relief of the former floodplain. It is all indented by numerous lowers, which have the form of a channel bend.

The *geological* structure of the territory of Pavlodar city involves lacustrine-alluvial deposits of the Neogene age (N), which are subdivided into deposits of the Pavlodar suite ($N_{1\text{-}2}$pv), Aral suite (N_1ar) and Kulunda suite (al$N_{1\text{-}2}$kln), overlain from the surface by the upper Quaternary and modern deposits of alluvial-deluvial (ad$Q_{II\text{-}IV}$) and technogenic (tQ_{IV}) genesis.

The *groundwater* of the above-floodplain terraces occurs at a depth of 1 to 17 m (usually 2-5 m). In the last 25-30 years on the territory of Pavlodar city, in particular in the area of the industrial zone of the city, there has been a systematic rise in the level of groundwater. Groundwater depth - 3-5 meters or more.

Physical and geological processes in an urban area are appear processes as erosion and destruction of the coastal slope, gullying, waterlogging and salinization of soil, which in turn cause the changes elements of geological structure. Therefore, in order to minimize the damage, caused by these processes it is necessary to timely development scientifically based urban planning and architectural and planning decisions in order to typify engineering and geological conditions of the city. Engineering and geological typing is one of the practically significant

procedures in the assessment of the conditions building and structures. It allows a more rational study, identification of features and assessment engineering and geological conditions to solve many issues of planning, design and rational use of natural resources [Astvacaturova 2009].

In the course of the study the construction zoning was performed according to the floors and residential buildings and facilities. Three main building areas were identified for residential development in Figure 1:

– building zone of multi-storey residential buildings;
– building zone low-rise residential buildings up to 4 floors;
– building zone with individual residential buildings.

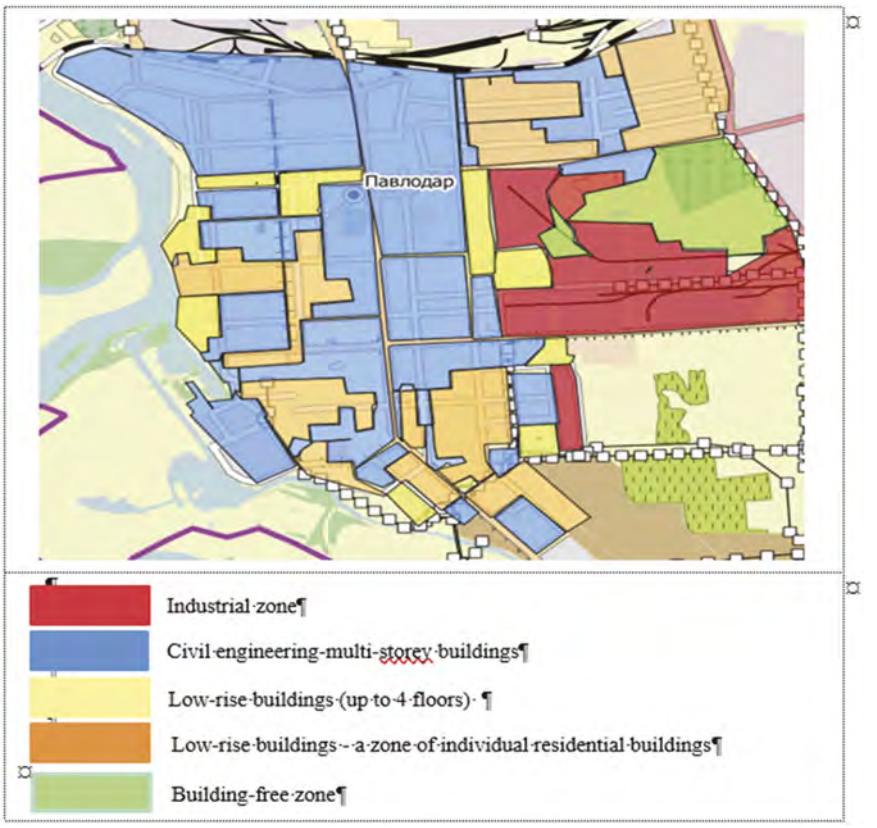

Figure 1. Scheme of construction zoning of the territory of Pavlodar city.

In order to objectively assess of the urban development taking into account various geotechnical conditions geoinformation database program was created, with the help which the regional soil conditions of Pavlodar city were analyzed before a detailed study. In the process of developing Geoinformation Database, the built-up area of multi-storey buildings was investigated.

3 STUDY OF GEOTECHNICAL CONDITIONS OF PAVLODAR CITY USING GEOINFORMATION DATABASE PROGRAM

3.1 *Methodology for the creation geoinformation database*

To create the "Geoinformation Database of Pavlodar city" (Figure 2) published and stock materials of engineering and geological surveys initially were collected and analyzed. Results of boring

of 523 engineering and geological boreholes in 2014-2021 were selected as sources. Composition and physical-mechanical properties studied for 2147 soil samples surface to depth 25 m.

The geoinformation database has a hierarchical structure consisting of two levels and including the following main four functions:

1) General management function (Host DB).
2) Input data management function (Local DB).
3) Data extraction and processing (AP) function.
4) Data augmentation function (Layer DB).

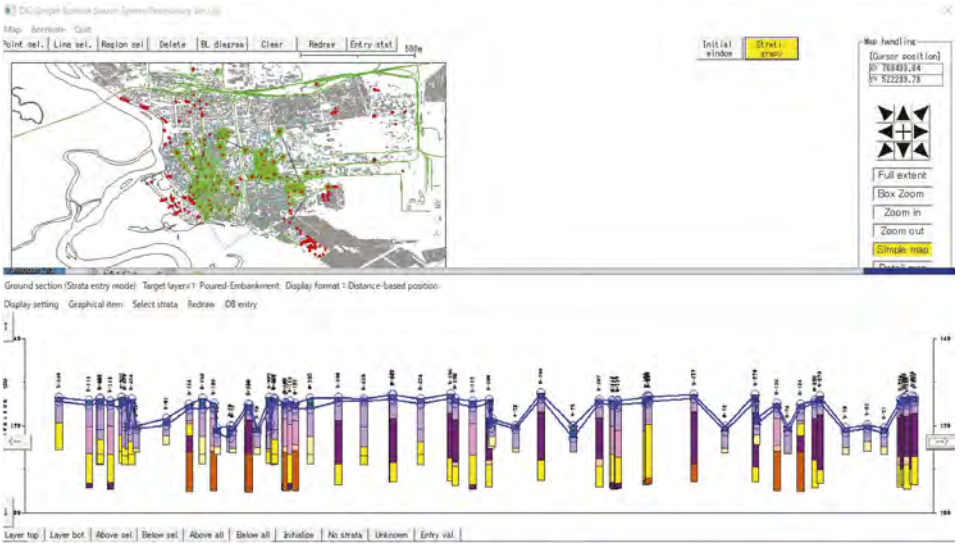

Figure 2. General view of the "Geoinformation Database program of Pavlodar city".

The first level of the hierarchical structure is responsible for the general management function, which provides general management and organization of the graphic process. The second level of the hierarchy includes the remaining three functions that perform preliminary processing of the initial information and ensure the organization of the graphic process [Alibekova 2009].

In the process of executing the initial information of the second level, the following stages of work can be distinguished:

1. The survey area was determined, and a map of the survey area is created in CAD program, i.e., AutoCAD.
2. The location of each borehole was indicated and labeled on the survey area map.
3. The exact X and Y coordinates were determined for each borehole.
4. A set of data was collected in the Excel table to log the information about each borehole.
5. Data on all layers, depth of occurrence, age of rocks are indicated [Zhussupbekov et al. 2019].

3.2 *Research of geotechnical environment of the Pavlodar city*

With the help "Geoinformation Database of Pavlodar city" geotechnical conditions were analyzed, in particular, 5 main engineering-geological elements were identified [Abisheva 2021] and special geotechnical maps of the occurrence of soils of Quaternary deposits and deposits of Neogene age with physical-mechanical characteristics were built in Figure 3:

EGE-1 — *technogenic deposits* (tQ_{IV}) represented by the topsoil (EGE-1a) and backfill (EGE-1b). Topsoil is represented by humus sandy loam with plant roots, the backfill is composed of sandy loam with sand and construction debris of 20%.

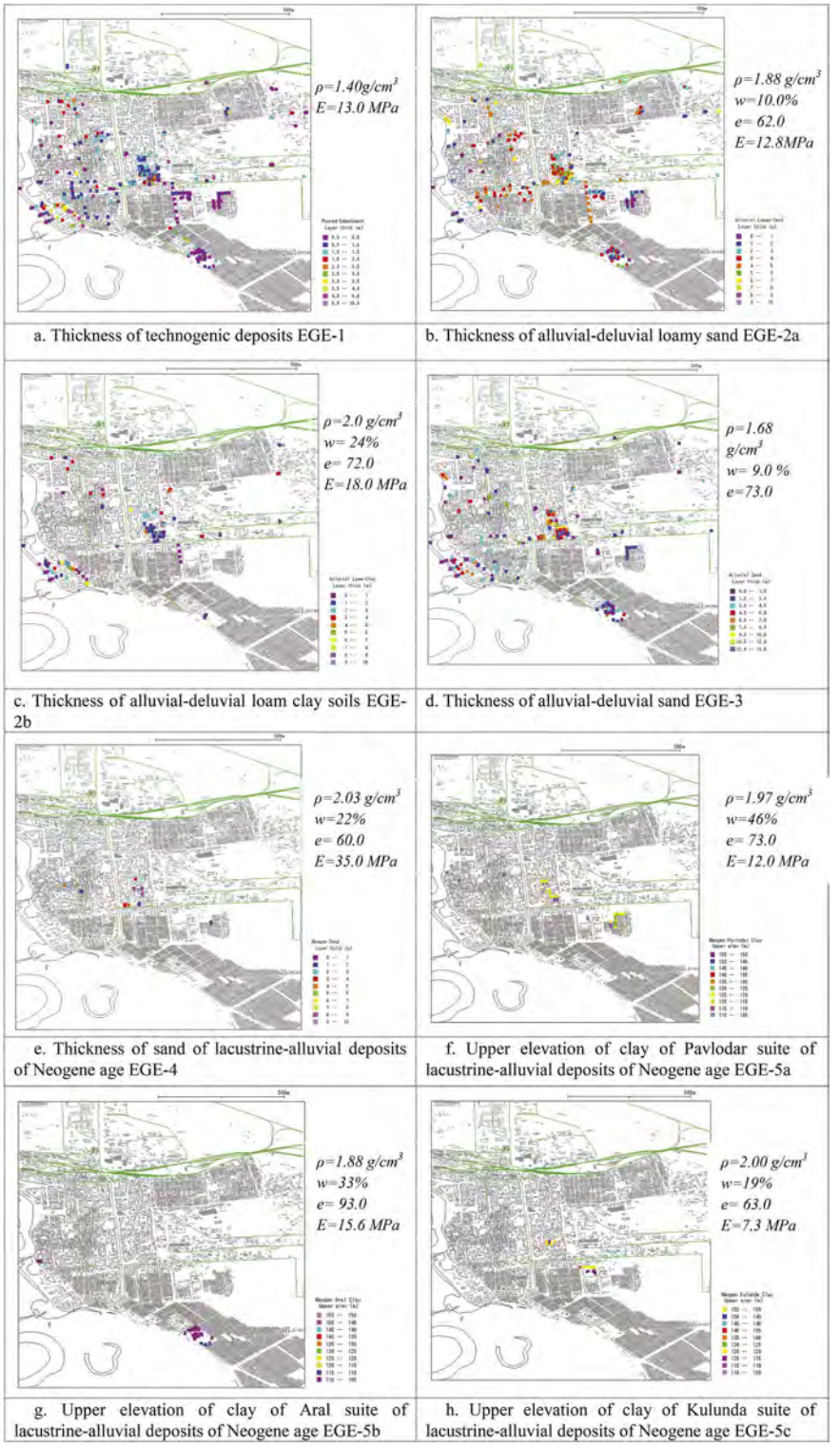

Figure 3. Special geotechnical maps of Pavlodar city.

EGE-2 — *alluvial-deluvial deposits of Upper Quaternary and modern ages* (adQ_{II-IV}), consisting of carbonated, subsident sandy loam (EGE-2a) from solid to fluid consistency and clay loam (EGE-2b). According to [SP RK 1.02–102-2014], the sandy loam in this layer is a specific soil, when soaked with water it has subsidence properties under household and additional loads. Capacity of this soil is measured from 0.9 up to 10.3 m.

EGE-3 — *alluvial-deluvial deposits of Upper Quaternary and modern ages of sand* (adQ_{II-IV}) is located at the depth of 2,5 to 8.0 m. According to the field description, all sands are similar in color, mostly yellow-brown, dense, saturated with water, with single layers of soft-plastic clay, differ only in the amount of the determining fraction according to the granulometric composition.

EGE-4 — *lacustrine-alluvial deposits of neogene age (N)* represented by sand of various size. According to the granulometric composition, the sands of the deposits are medium-sized, coarse. The thickness of the sands increases from south to north and varies from 0.6 to 9.7 m.

EGE-5 — *lacustrine-alluvial deposits of neogene age* includes clays that are represented by lacustrine-alluvial deposits of the Pavlodar suite (EGE-5a), the Aral suite (EGE-5b), the Kulunda suite (EGE-5c). Lacustrine-alluvial deposits of the Pavlodar suite are represented by brown clay and loam, with a thickness of 1.6 to 5.2 m. Lacustrine-alluvial deposits of the Aral suite represented by clay from light gray to gray green, from hard-plastic to semi-hard, ferruginous, manganese, with inclusions of gypsum up to 10% and marl up to 5%. The thickness of clays varies from 2.5 to 16.2 m. Lacustrine-alluvial deposit of the Kulunda suite are represented brownish-gray, greenish-brown, greenish-gray clays, containing calcareous-marl nodules ranging in size from 0.1 to 0.2 cm and interlayers of sand. Clay thickness varies from 0.5 to 7.6 m.

4 CONCLUSIONS

The assessment of the geotechnical conditions of the territory of Pavlodar city served as the basis for the creation of a geoinformation database program. This geoinformation database system allows the development of engineering and geotechnical maps on geotechnical zoning of the city according to the classification of soils and the criteria of homogeneity formed areas. The economic efficiency of a geoinformation system and developing engineering and geotechnical maps will significantly reduce the time and costs during the survey and design work, as well as in the construction of foundations for buildings and structures in difficult ground conditions. Implementation of geoinformation database ensures sustainable development of megacities, models and approaches in urbanistic development of geo infrastructure megapolises and small cities of the new generation.

REFERENCES

Abisheva, A.K. 2021. Engineering and geological conditions of Pavlodar. *Materials of the 77th Student Scientific and Technical Conference, section "Geotechnics and construction Mechanics", Proc. intern. conf., Minsk, Belarus national technical university,* 30 April 2021: 8–15 (in Russian).

Alibekova, N.T. 2009. Analysis of geotechnical properties of soil in Astana city for optimization of length of piles. Thesis for the academic degree of Doctor of Philosophy (PhD), Astana.

Astvacaturova, K.A. 2009. Typification of engineering-geological conditions of urban areas for their construction development and justification of engineering protection schemes. Moscow (in Russian).

Smailov, S. 2015. Peculiarities of regional nature management in Pavlodar region. *Bulletin of Kemerovo State University*, (2-5): 59–65 (in Russian).

SP RK 1.02–102-2014. *Engineering-geological survey for construction*. State standards in the field of architecture, urban planning and construction. Codes of Rules of the Republic of Kazakhstan.

Zhakupov, A., Dzhanaleeva, G., Berdenov, Zh. 2014. Geographical aspects of Pavlodar city and regional development. *Natural and mathematical sciences in the modern world*, 16: 208–219 (in Russian).

Zhussupbekov, A.Z., Alibekova, N.T., Akhazhanov, S.B., Shakirova, N.U., & Alpyssova, A.B. 2019. Geotechnical Geo-Information System of Astana. *Soil Mechanics and Foundation Engineering*, 55(6): 420–424.

Zhussupbekov, A., Alibekova, N., Akhazhanov, S., Sarsembayeva, A. 2021. Development of a Unified Geotechnical Database and Data Processing on the Example of Nur-Sultan City. *Applied Sciences*, 11, 306: 1–19.

Smart Geotechnics for Smart Societies – Zhussupbekov, Sarsembayeva & Kaliakin (Eds)
© 2023 The Author(s), ISBN 978-1-003-29912-7
Open Access: www.taylorfrancis.com, CC BY-NC-ND 4.0 license

Typification of engineering and geological conditions of the city territory using GIS

N.T. Alibekova, A.K. Tleubayeva & A. Abisheva
L.N. Gumilyov Eurasian National University, Astana, Kazakhstan

ABSTRACT: The relevance of the study is due to the rapid growth of construction of buildings and structures in large cities of the Republic of Kazakhstan over the past thirty years. An engineering-geological assessment of the area is necessary to support the decision-making process on the location of structures, as well as to ensure that the construction of facilities is carried out with less negative environmental impact, accompanied by a reduction in danger and damage to both construction, society, and the economy. As a result, it is necessary to systematize and analyze previously obtained data using modern geoinformation systems (GIS). The relevance of the introduction of GIS in geotechnical research is due to the fact that geoinformation systems and technologies allow creating, storing, analyzing, processing and providing the consumer with spatially distributed information, where the main means of communication for visualizing geotechnical data are special geotechnical maps, so how modern GIS have a wide arsenal of basic methods of spatial analysis that can and should be used to solve the problems of typification of engineering-geological conditions. The results of this work demonstrate the ability of GIS technologies to analyze engineering and geological conditions and zoning development areas according to the types of bases and foundations in such cities of Kazakhstan as Astana and Pavlodar.

1 INTRODUCTION

The formation of an information engineering-geological model of the terrain is the main task of engineering-geological research. This kind of model should contain in an analytical or synthetic form all the data necessary to solve problems related to the placement of building complexes and structures, assess the impact of engineering and geological measures on the natural environment and plan measures for its transformation. At the present stage of development, engineering-geological maps of zoning are used for this purpose, supplemented by engineering-geological sections, an explanatory note, and various tables. The methodology of creation of maps of engineering-geological zoning, developed in the main theoretical positions of N. Nikolaev & F. Savarensky (1939), I. Popov (1951, 1969), is based on consistent zoning of the studied territory on the area, increasingly homogeneous in terms of engineering and geological conditions [Tsotsur 1976].

Zoning is the main tool for flexible regulation in cities when planning urban development, which is a sustainable form of control over the use of land in settlements. Construction zoning of urban space is the division of the residential area of the city into zones with different number of storeys. One of the main goals of construction zoning is the correct placement of the main types of buildings in the city, considering the relief and engineering-geological conditions, the most economical use of the territory both in new construction and in the reconstruction of residential areas. To take into account engineering-geological factors in zoning, it is necessary to know the history of the

DOI: 10.1201/9781003299127-62

development of the territory in the anthropogeny and the current state of the rocks, the main engineering-geological features of the territory that have been created throughout the history of its geological development. Today, the study and use of natural resources, rational economic development, environmental protection, and monitoring, making practical decisions related to the geological environment are impossible without reliable information support [Kozlovskii 2010].

Since the beginning of the twenty first century, there has been a tendency to use digital materials in working with paper primary sources. The problems of the accumulation, processing and storage of geological engineering information should be addressed through the introduction and improvement of automation processes and computer facilities and their subsequent development.

2 BASES OF CONSTRUCTION OF THE GEOINFORMATION DATABASE

GIS in engineering-geological surveys is considered, first, as a means of processing spatial data of the geosystem for obtaining new knowledge and presenting them in the form of special geotechnical maps. According to several authors, the introduction of formal procedures in cartographic work makes it possible to automate the daily and labor-intensive stages of mapping, thereby freeing up time for experimentation and creativity in the field of cartographic modeling and map design [Dyshlyuk et al. 2015].

GIS capabilities applicable in engineering and geological surveys:

- input, accumulation, storage and processing of digital cartographic and geotechnical information;
- construction of thematic maps based on the obtained data, reflecting the current state of the geosystem;
- study of the dynamics of changes in the geotechnical situation in area and time;
- construction of graphs, tables, diagrams;
- modeling the development of the geotechnical situation in various environments and studying the dependence of the state of the geosystem on engineering and geological conditions, characteristics of foundations and construction objects;
- obtaining comprehensive assessments of the condition of construction facilities based on various data [Alibekova 2009].

The development of the "Geoinformation Database program" provides for the collection of geotechnical survey data with its own inherent format that expands the concept of communication of databases [Zhussupbekov & Alibekova 2013].

The main management system of the Geoinformation Database program (DIG-system) has a hierarchical structure consisting of two levels and including the main functions:

1) general management function; 2) input control data function; 3) function of data extraction and processing; 4) data augmentation function.

The first level of the hierarchical structure is responsible for the general management function, which provides general management and organization of the graphic process. The second hierarchical level includes functions that perform preliminary processing of source information and provide organization of the graphic process.

The initial information used in the program is divided into the two main sections:

1. Constant datasets (local data base), included directly in program text (for example, a city map, coordinates and characteristics for obtaining graphic files) (Figure 1).
2. Initial data, prepared directly by the user from the materials of engineering and geological surveys and entered during the execution of the program (Figure 2).

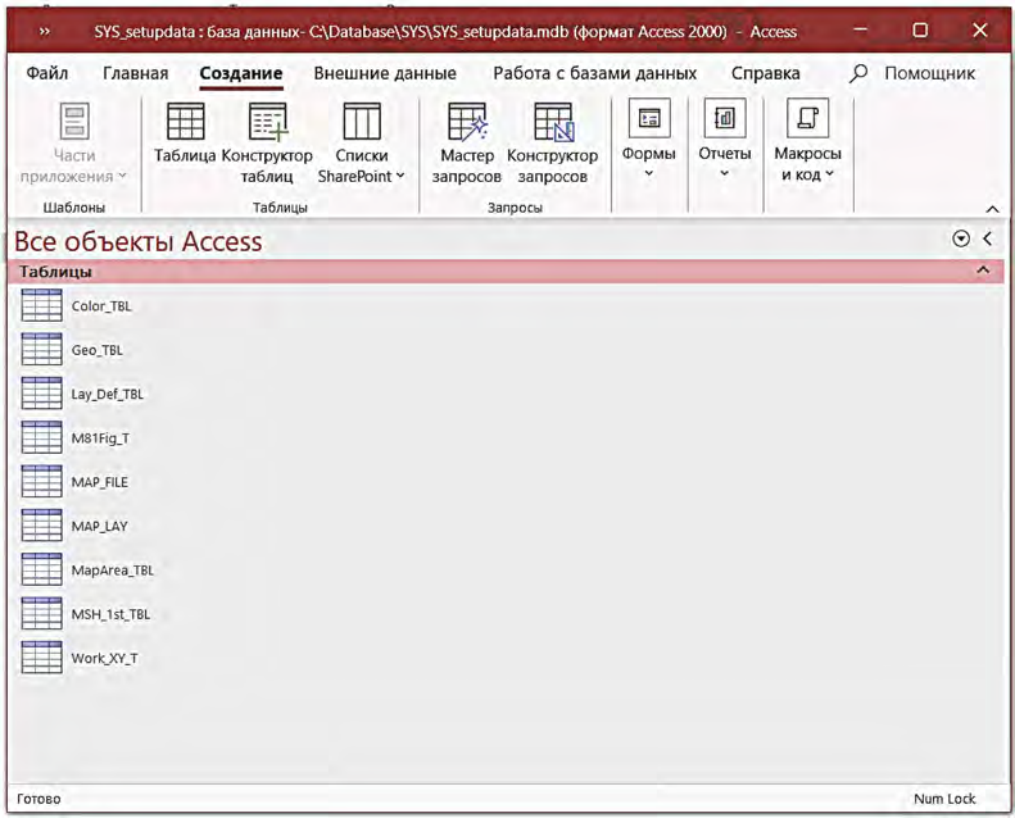

Figure 1. Local data base.

3 TYPIFICATION OF ENGINEERING AND GEOLOGICAL CONDITIONS IN KAZAKHSTAN USING GIS

3.1 *Geoinformation system for Astana*

Astana is a city in the north–east of Kazakhstan, which in 1997 received the status of the capital of the Republic of Kazakhstan and is one of the youngest capitals in the world. For less than 30 years, a modern Euro-Asian-style city has grown up on the site of a provincial town in the middle of the steppe, with skyscrapers, original architectural structures, broad avenues, and spacious areas. The super-accelerated pace of design and construction of the young capital of Kazakhstan requires targeted study, forecasting and management of geological aspects of both existing and planned buildings and structures.

In 2008, the program "Geoinformation Database of Astana" was created for the first time to evaluate engineering and geological studies of Astana (Figure 3), which allowed analyzing regional soil conditions before a detailed study. On the territory of Astana there are six main engineering-geological elements (EGE), diverse in origin and age (Figure 4) [Zhussupbekov et al. 2012].

In addition, with the help of the program "Geoinformation Database of Astana", special geotechnical zoning maps were created by types of foundation and optimization of the lengths of driven piles for buildings of the 2nd (normal) level of responsibility, taking into account the type of foundation (Figure 5) [Zhussupbekov et al. 2012].

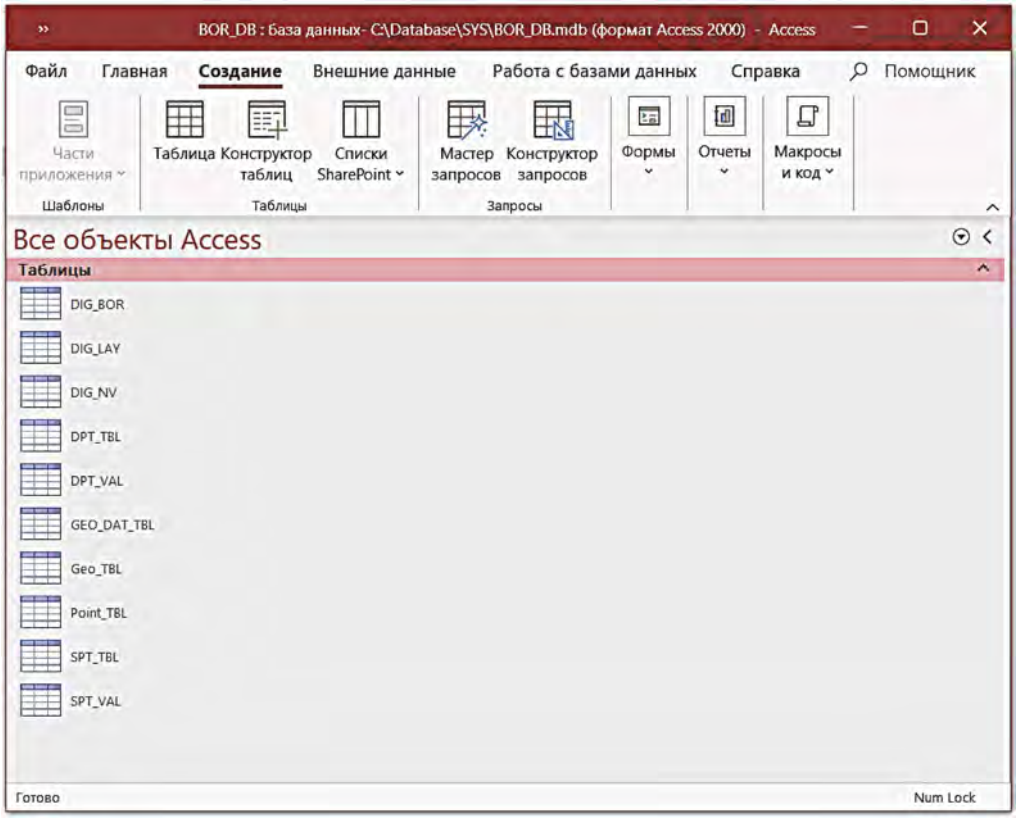

Figure 2. Source data base.

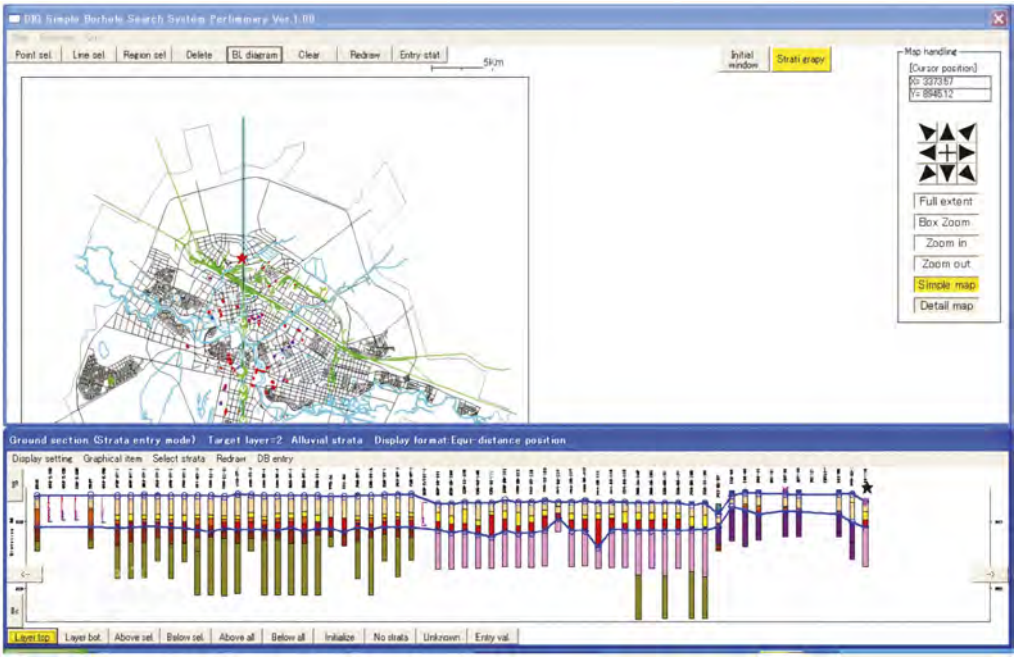

Figure 3. General view of the program “Geoinformation database of Astana”.

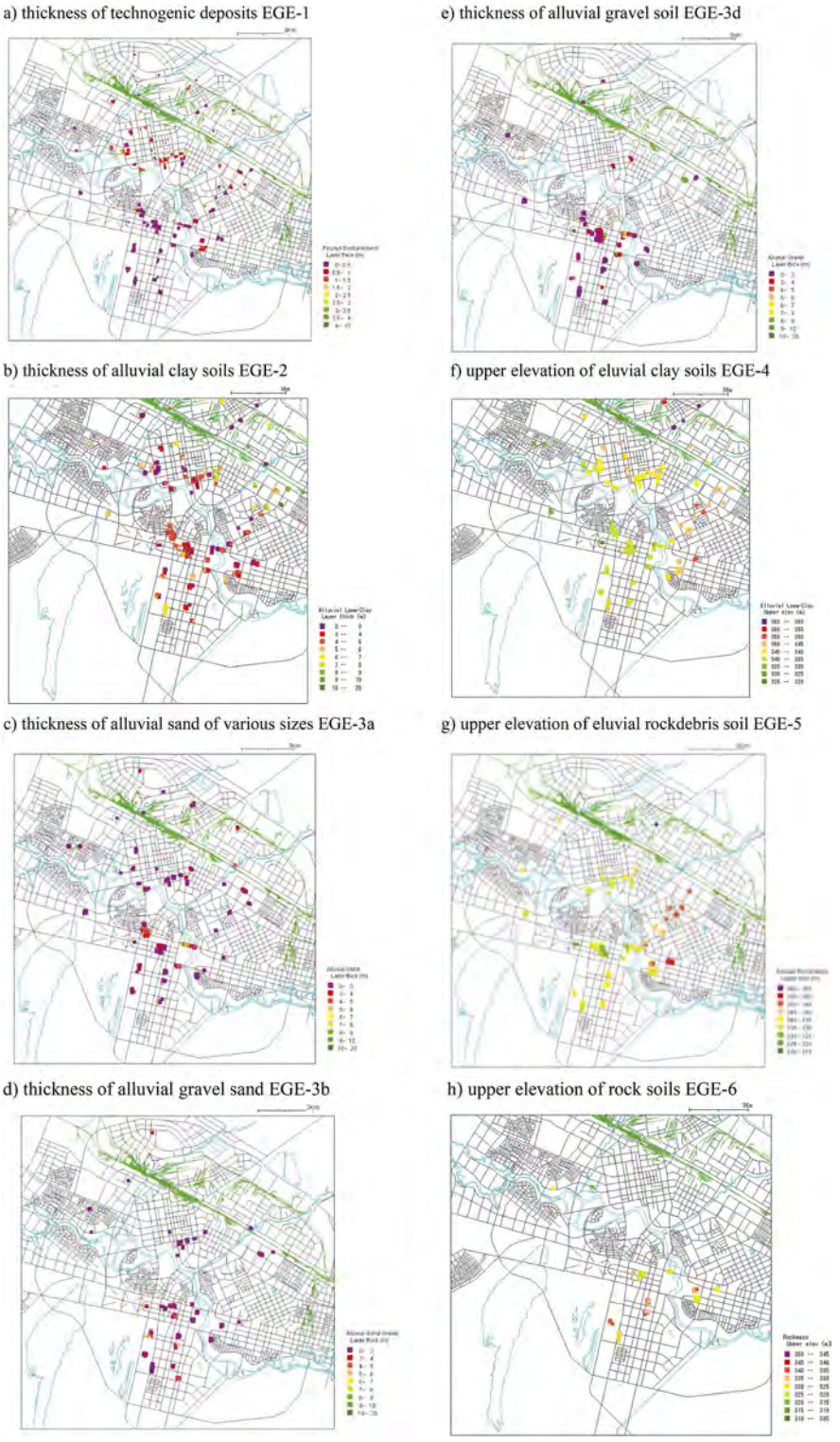

Figure 4. Engineering and geological maps of Astana.

a) geotechnical zoning map by type of foundation

b) geotechnical zoning map for optimizing the lengths of driven piles

Figure 5. Special geotechnical maps of Astana.

3.2 *Geoinformation system for Pavlodar*

Pavlodar is the center of industrial and cultural development in the Republic of Kazakhstan. It is located 450 km northeast of national capital Astana.

In 2022, for the evaluation of engineering and geological research in Pavlodar, the program "Geoinformation Database of Pavlodar" was created for the first time (Figure 6), which also made it possible to analyze regional soil conditions before a detailed study.

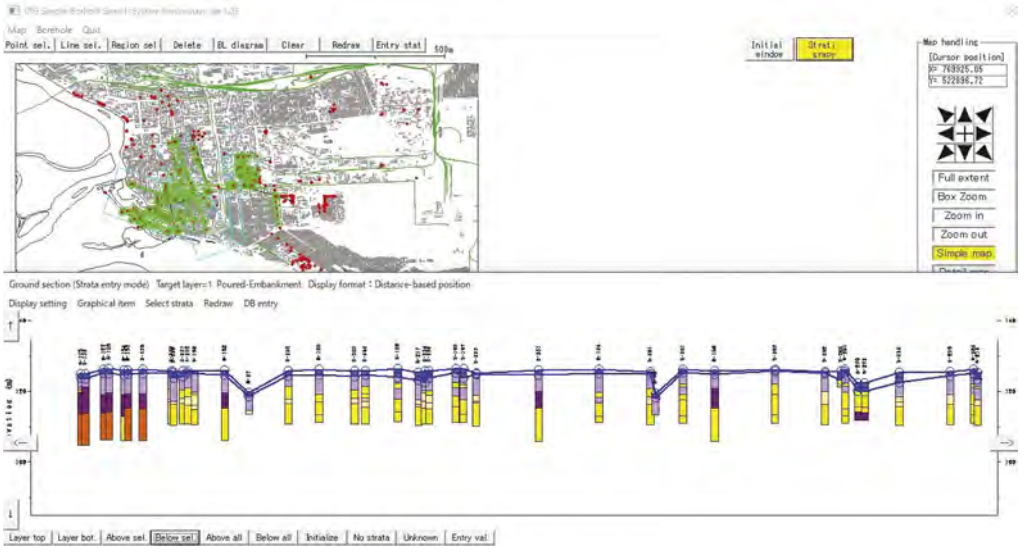

Figure 6. General view of the program "Geoinformation database of Pavlodar".

With the help "Geoinformation Database of Pavlodar" geotechnical conditions of the city territory were analyzed five main engineering-geological elements (EGE) were identified [Abisheva 2021] and special geotechnical maps of the occurrence of soils of alluvial-deluvial deposits and lacustrine-alluvial deposits of Neogene age were built in Figure 7:

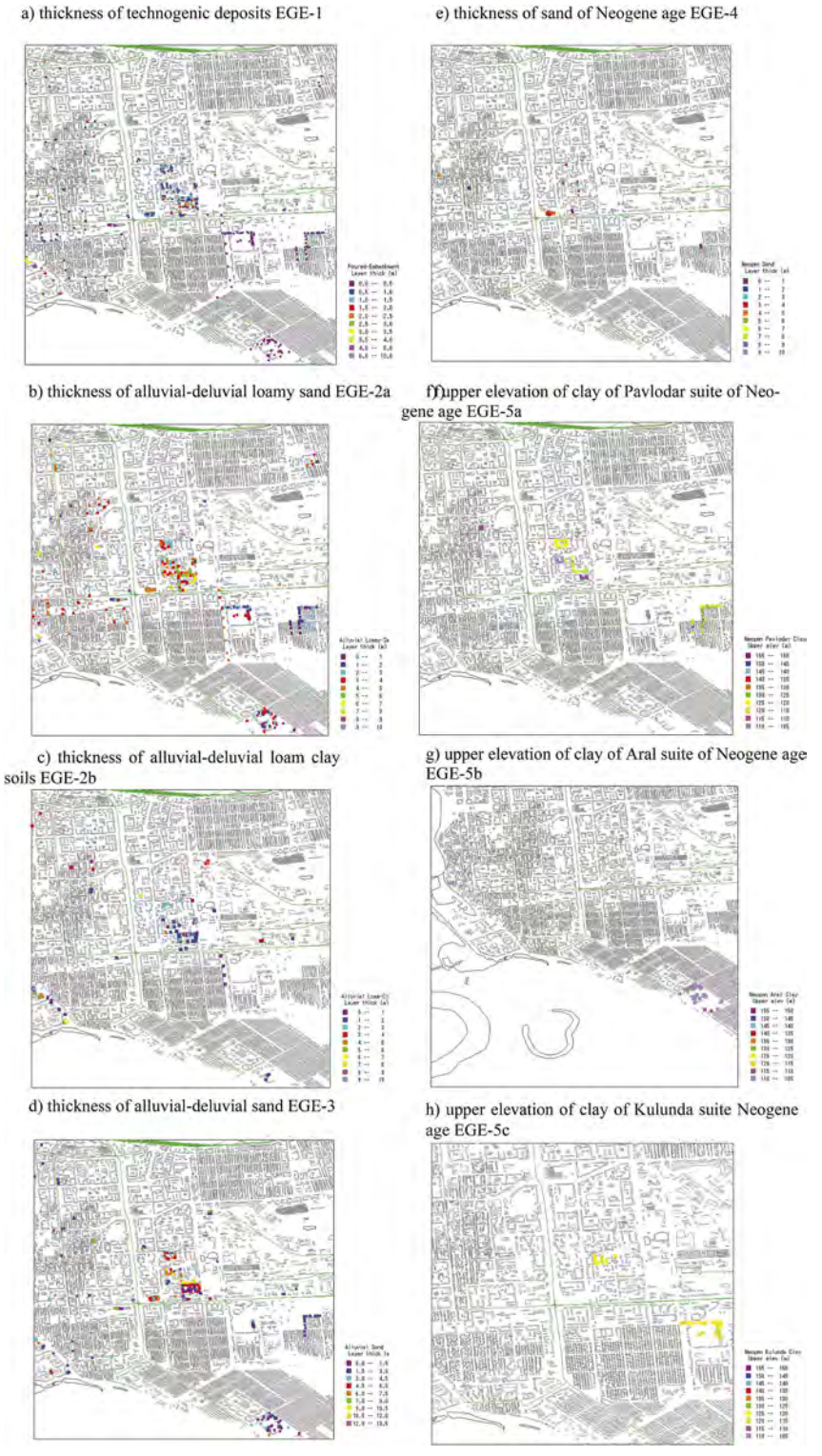

Figure 7. Engineering and geological maps of Pavlodar.

4 CONCLUSIONS

The results of the study suggest that the engineering and geological conditions of the two cities are different. The territory of Astana is represented by a diverse complex of soils, such as loams with interlayer of sandy clay loam and clays, gravel sands, medium-sized sands, silty soils, clays with lenses and layers of sandy loams, gravelly sands and gravel soils, as well sandstones, which are inter bedded with siltstones and mudstones. At the same time, it should be emphasized that groundwater in the undeveloped territories of the capital is at a depth of 5 m, and in most of the built-up areas at a depth of 0 to 2 m. From what has been said, it becomes obvious that most of the city's territory is in a flooded state, which is one of the reasons for the use of pile foundations in the construction. In turn, subsidence soils are most common in the territory of the city of Pavlodar, where the specific soil is a swelling sandy loam, from solid to fluid consistency. The groundwater of the above-floodplain terraces of the city's territory lies at a depth of 1 to 11 m, most often at a depth of 3 to 5 m.

As a result of consideration of this issue, it was found that with the help of special geotechnical maps obtained as a result of the development of geoinformation databases for the city of Astana and Pavlodar, it is possible to quickly obtain the necessary information for the purpose of substantiation when solving problems of industrial and civil construction, namely, typification of engineering-geological conditions and planning of urban development. These data not only systematize already known information, but also significantly accelerate the processing and analysis time for creating new projects, as well as significantly reduce the time and cost of exploration and design work.

REFERENCES

Abisheva, A.K. 2021. Engineering and geological conditions of Pavlodar. *Materials of the 77th Student Scientific and Technical Conference, section "Geotechnics and construction Mechanics", Proc. intern. conf., Minsk, Belarus national technical university,* 30 April, 2021: 8–15 (in Russian).

Alibekova, N.T. 2009. Analysis of geotechnical properties of soil in Astana city for optimization of length of piles. Thesis for the academic degree of Doctor of Philosophy (PhD), Astana.

Dyshlyuk, S.S., Nikolaeva, O.N., Romashova, L.A. 2015. Formalization of thematic map-making for public at large. *Interexpo-GEO-Siberia*, 2: 10–16.

Kozlovskii, S.V. 2010. The principal structure of a geoinformation system for solving the problems of engineering and geological surveys. *Engineering survey*, 5: 12–16 (in Russian).

Tsotsur, E.S., 1976. Typification of engineering-geological conditions of the Aleksandrovsky Ob region. *Proceedings of the Tomsk Polytechnic Institute*, 281: 107–109 (in Russian).

Zhussupbekov A., Alibekova N., Morev I., Iwasaki Y., Mimura M. 2012. Geotechnical issues of geodata base of soil ground of new capital Astana. *Advances in ground technology and geo-information*, 175–181.

Zhussupbekov, A. Zh., Alibekova, N.T. 2013. Geotechnical zoning territory of new capital Astana. *Geotechnical and Geophysical Site Characterization* 4, 1:1537–1542.

Smart Geotechnics for Smart Societies – Zhussupbekov, Sarsembayeva & Kaliakin (Eds)
© 2023 The Author(s), ISBN 978-1-003-29912-7
Open Access: www.taylorfrancis.com, CC BY-NC-ND 4.0 license

Comprehensive study of the mutual influence of closely erected foundations of reconstructed buildings

A.Zh. Zhussupbekov & A.T. Mukhamejanova
Eurasian National University, Nur-Sultan, Kazakhstan

K.A. Abdrakhmanova
NJC "KarTU named after Abylkas Saginov", Karaganda, Kazakhstan

ABSTRACT: A complex of studies of the mechanism of interaction of closely erected foundations with a soil base has been carried out. Based on the generalization of the obtained results of field experiments and field observations, a universal method for calculating the precipitation of foundations of reconstructed buildings has been developed.

The results of complex studies of the mechanism of interaction of closely erected foundations with the ground base are presented. A universal method is proposed for calculating the sediment of foundations that are being built closely, which allows for the design to take into account local changes in compressibility and the stress state of the base due to mutual influence. Comparison of the results of theoretical and experimental studies showed acceptable reliability of the proposed methodology.

1 INTRODUCTION

The existing methods for calculating sediments based on the theory of linearly deformable bodies are designed to calculate idealized soil, do not allow predicting the actual size of the active (compacted) zone of the foundation, and therefore are unacceptable for determining the sediment foundations of reconstructed buildings designed taking into account local hardened and overlapping stress zones in the base caused by compaction and mutual influence of foundations [1].

Let us consider the nature of the development of sediments of the bases of neighboring foundations for three cases of their interaction (Figure 1.), where lpr is the permissible distance between them.

Case 1, when at l = epr (Figure 1a) the isolation of the active zones of the base 1 and 1′ of both foundations is ensured, and their sediment S develops independently of each other.

Case 2 corresponds to the condition l < lpr (Figure 1b) and the simultaneous construction of adjacent foundations, which leads to their roll towards the overlap of active zones 1 and 1′.

Case 3 corresponds to the condition l < lpr (Figure 1c) and the sequential loading of adjacent foundations, which will lead to their roll towards the foundation being erected in the second turn.

One of the main drawbacks of the methods for determining precipitation regulated by building codes is the uncertainty in the choice of compressibility characteristics of the foundation soils, namely the use of an increasing coefficient mk = 2 . . . 6 for the transition from the compression module (Ec) to the die module (S), which significantly reduces the reliability of the results of the calculations performed [2].

Our research has shown that the straightening of the compression curve adopted during the surveys in the area of compacting loads of 0.1. . .0.3 MPa leads to significant errors, in particular, to a decrease in the foundation precipitation by 28%, and the deformation of the base in various zones by 20%, 34% and 51%.

DOI: 10.1201/9781003299127-63

Based on the generalization of the results of complex studies of the mechanism of interaction between the foundation and the foundation, the authors proposed a computational model based on the idea of volumetric compression of soils under the action of the greatest main normal stresses forming a compacted zone in the base. The essence of this approach to the prediction of deformations of the soil base is, as noted above, to use for this purpose solutions of the theory of linearly deformable bodies to determine stresses. At the same time, precipitation is calculated without the use of a deformation modulus, taking into account the real law of compaction of a particular soil by using porosity coefficients along the compression curve corresponding to the actual stress state of the base of the projected object.

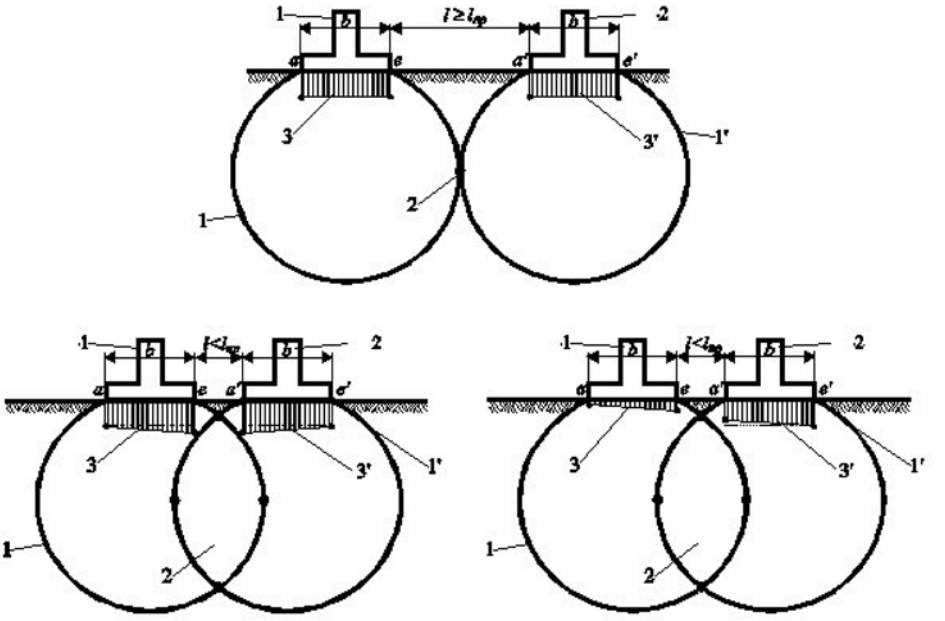

Figure 1. Mutual influence of neighboring foundations on the precipitation of their bases. a - the foundations are not affected by the neighboring; b and c – the foundations are affected by the neighboring, are built simultaneously and sequentially, respectively; 1 and 1′ – the boundaries of the active zones of the bases of neighboring foundations; 2 – the area of overlap of the active zones of the foundations; 3 and 3′ – the assumed plots of the sediment of the bases of neighboring foundations.

2 EXPERIMENTAL STUDIES

Experimental studies of the nature of the mutual influence of neighboring foundations were carried out by simulating their operation in the field by sequentially loading closely spaced two rigid round dies with a diameter of 0.8 m. Stamp experiments were carried out on two sites composed of relatively homogeneous clay soils, significantly differing in compressibility.

The purpose of the experiments is to study the patterns of mutual influence of two adjacent stamps during their sequential loading.

To achieve this goal, the following tasks were set during the experiments: 1) assessment of the size of the soil compaction zone under stamp 1, loaded in the first place; 2) study of the influence of the compaction factor of the stamp base 1 on the nature of the development of precipitation of the adjacent stamp loaded in the second place 2; 3) study of the nature of the development of the roll of the previously loaded stamp 1 in connection with the additional loading of part of its base by the neighboring stamp 2, loaded in the second turn; 4) measurement of the precipitation of the soil surface near the stamps; 5) investigation of the stress-strain state of the bases of adjacent stamps during their sequential loading.

The solution of the tasks of the experiment required conducting experiments on bases composed of homogeneous clay soils. Therefore, when choosing experimental sites, special attention

was paid to the factor of uniformity of the soil composing the assumed compressible thickness under the experimental foundations. The analysis of the data of engineering-geological studies presented in Table 1 showed that the soils of the base of the studied neighboring stamps for experimental sites No. 1 and No. 2 differ significantly in the quality of their physical and mechanical properties. In the experiment at site No. 1, the stamps are based on reliable soils - refractory loams with relatively good construction properties. Site No. 2 is composed of weak soils - ribbon loams in a fluid state, characterized by low strength and high compressibility.

Table 1. Physical and mechanical characteristics of the soils of experimental sites No. 1 and No. 2.

Experimental site	Name of soils	γ gs/cm^3	W	I_L	c, MPa	φ, degree	E_o, MPa
№ 1	The loam is refractory	1,98	0,25	0,36	0,015	17	8,2
№ 2	Fluidplastic loam	1,87	0,36	1,09	0,005	20	4,6

In the course of studies, deformations (stamp deposits and deep movements of the foundation soil) were measured at 37 points (site No. 1) and at 18 points (site No. 2). In addition, in the experiments conducted at site No. 2, vertical normal stresses were measured at 10 points of the base of neighboring stamps by means of the design of B.I. Dalmatov, A.V. Golly and the movement of soils using screw marks with indicators and deflection meters [3].

The stamps were located at a distance of 1.25 D between their centers and were loaded with steps up to pressures along their soles of 0.2 and 0.12 MPa, respectively, at sites No. 1 and No. 2. To assess the size of the soil compaction zone under stamps 1, screw stamps in the base were installed at different depths from the level of the stamp sole and distances from its vertical axis along the grid in increments of 0.125D and 0.25D.

Analysis of the test results of stamp No. 1 according to the "full loading and unloading" scheme at both sites allowed us to establish the actual dimensions of the soil compaction zone at sites No. 1 and No. 2, respectively: depth Ha = 1.25D and 1.60D; width Ba = 1.58D and 1.98D; removal of zone la = 0.29D and 0.49D. It was found that even with a lower load in conditions of weak soils, the size of the studied zone is much larger.

Full loading of stamps 2 at sites No. 1 and No. 2 led to their rolls away from stamps 1, respectively: 0.0030 and 0.0035. At the same time, in turn, stamps 1 received a roll towards stamps 2, respectively: 0.0028 and 0.0030. The measurement of stress under the edge of stamp 1 from the side of stamp 2 at site No. 2 showed an additional increase in stress in the foundation soils up to 30% due to the influence of the neighboring foundation.

Comparative analysis of the results of a test problem for calculating the sediment and depth of the compressible thickness of the base of the ribbon foundation, solved by different methods (Table 2) shows that the proposed sediment calculation scheme models well the patterns of deformation of real soil foundations, the calculated data for the determination of the new method for the ribbon foundation are close to the actual (less than 2.25 b), which is confirmed by the results of experiments [4].

Table 2. Comparative analysis of the results.

Methods for calculating the sediment of the foundation foundations	Initial data				Calculation results				
					precipitation, cm taking into account			compressible thickness, m	
	b, m	p, MPa	E_k, MPa	$E_s=m_k \cdot E_k$, *MПa*	E_k	E_s	$e_i = f(p_i)$	H_d/b	H_a
Layer - by - layer summation	2,0	0,2	6,0	12,0*	8,9	4,5	-	4,2	8,4
Linearly deformable layer	2,0	0,2	6,0	12,0*	10,3	5,0	-	6,0	12,0
Equivalent layer	2,0	0,2	6,0	12,0*	31,0	15,7	-	5,2	10,4
Finite Elements (FEM)	2,0	0,15	6,0	-	4,7	-	-	2,0	4,0
		0,2	6,0	-	6,6	-	-	2,0	4,0
Proposed (model-free)	2,0	0,2	-	-	-	-	5,53	2,25	4,5

The wide potential possibilities of the proposed calculation model (see Figure 2) of the foundation in comparison with the existing ones and its versatility make it possible to determine the precipitation of neighboring foundations of reconstructed buildings, taking into account the distance between them, the sequence of their loading, the size of the sole, the magnitude of loads and the compaction of the foundation soils.

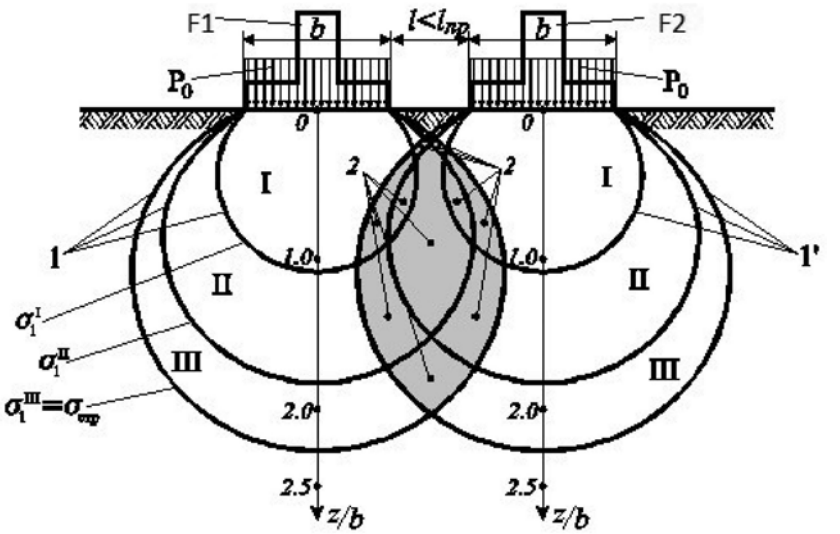

Figure 2. Calculation scheme of the foundation of neighboring foundations: 1 and 1′ – boundaries of various stress zones I, II and III of the foundations of neighboring foundations F1 and F2; 2 – areas of superposition of the stressed zones of the base of both foundations, taken into account when calculating precipitation.

Based on the analysis of the results of the experimental studies carried out, the following can be concluded:

1. A complex of studies of the mechanism of interaction of closely erected foundations with the soil foundation has been carried out by field experiments, field observations, numerical analysis of the FEM. Based on the generalization of the results obtained, a universal method for calculating the sediment of neighboring foundations has been developed.
2. The use of a new technique allowed us to establish the features of the behavior of neighboring foundations erected simultaneously and sequentially. To a greater extent, the mutual influence of neighboring foundations is manifested when they are loaded simultaneously. Sequential loading leads to a significant reduction in additional sediments of both foundations due to the influence of soil compaction at the base of the existing foundation.

REFERENCES

1. U. S. Utenov, A. Zh. Zhusupbekov, S. N. Sotnikov, A. T. Mukhamedzhanova, B. O. Kaldanova. Interaction analysis of adjacent foundations of renovated builidngs// Soil Mechanics and Foundation Engineering, Vol. 54, No. 1, March, 2017. Pp. 17–23. https://doi.org/10.1007/s11204-017-9427-7 https://www.scopus.com/record/display.uri?eid=2-s2.0-85017584872&origin=resultslist&sort=plf-f
2. E. S. Utenov, Subsoil Analysis of Renovated buildings, KarSTU, Karaganda (2013).
3. B. I. Dalmatov, Soil Mechanics, Subsoils and Foundations, Stroiizdat, Leningrad (1988).
4. Utenov, Y.S., Zhusupbekov, A.Z., Abildin, S.K., Mukhamedzhanova, A.T., Abdrakhmanova, B.G. Calculation of Building Settlement on Flood-Prone Foundations by Using the Modulus-Free Method// Soil Mechanics and Foundation Engineering, 2022, 59(1). https://doi.org/10.1007/s11204-022-09783-x https://www.scopus.com/record/display.uri?eid=2-s2.0-85129896184&origin=resultslist&sort=plf-f.

Smart Geotechnics for Smart Societies – Zhussupbekov, Sarsembayeva & Kaliakin (Eds)
© 2023 The Author(s), ISBN 978-1-003-29912-7
Open Access: www.taylorfrancis.com, CC BY-NC-ND 4.0 license

Water characteristic curve and permeability function of steel slag

Gulnur Pernebekova, Alfrendo Satyanaga, Rezat Abishev, Sung-Woo Moon & Jong Kim
Department of Civil and Environmental Engineering, Nazarbayev University, Kazakhstan

ABSTRACT: Waste arising from construction and demolition constitutes one of the largest waste streams globally. Construction and maintenance of roads require a large volume of aggregates for use as base and sub-base material. Because of the cost of virgin aggregates, government and local companies are encouraging the use of recycled material in old pavement and construction material. One type of recycled material, steel slag could be used for several construction purposes, such as concrete, road subgrade, and railway ballast materials. In order to utilize steel slag in these constructions, the engineers need to understand the properties of material appropriately including its unsaturated properties. The objective of this project is to study the soil-water characteristic curve, unsaturated permeability and unsaturated shear strength of steel slag. Advanced laboratory testing was conducted to obtain these unsaturated properties. The results of study indicated that the steel slag has the same unsaturated properties as natural aggregate or gravel.

1 INTRODUCTION

One of the main waste streams in the EU and many other countries is waste produced during construction and demolition (C & D). For instance, it is estimated that core C&D waste, defined as items originating from demolished structures or civil engineering infrastructure, amounts to about 180 million tons annually, or 480 kg per person, in Europe (Aggregates Advisory Service-UK, May 1999). Aggregates are needed in huge quantities for base and sub-base material during road construction and maintenance. Because of the cost of virgin aggregates, government and local companies are encouraging the use of recycled material in old pavement and construction materials.

Recycling of material is the process of turning used construction or industrial waste into raw materials that are suitable to be reused again. Natural resource preservation and pollution reduction are its primary goals. Recycling also lowers energy use because it often requires less energy to make a product through recycling than it does to create a new one. Similar to how recycling conserves raw materials and produces less pollution than producing new products. Additionally, less waste is disposed away or burned in incinerators. The term "water content" describes how much water is contained in a material's pores. The amount of water in unsaturated soil depends on the soil's suction. The soil-water characteristic curve (SWCC), which depicts the change of water storage capacity inside the micro and macro pores of the soil with respect to soil suction, can be used to show the relationship between water content and suction.

The properties of recycled materials in saturated conditions have been the subject of numerous studies. However, there haven't been many studies done on the permeability of recycled materials and the water characteristic curve in unsaturated conditions. The shear strength of recycled materials in unsaturated environments has also not been thoroughly studied. Thus, this project aims to investigate the unsaturated permeability and soil-water characteristic curve of steel slag.

DOI: 10.1201/9781003299127-64

2 STEEL SLAG

Researchers found that steel slag might be utilized for a variety of construction purposes, including the production of concrete, road subgrade, and railroad ballast materials (Koh et al., 2018). Li et al. (2022) provided a description of the steel slag's characteristics and talked about how they affected the properties and microstructure of cement concrete. Their research indicates that the volume stability and workability of concrete are adversely affected by steel slag. It improves compressive strength, frost resistance, and wear resistance, although its effects on flexural strength and permeability are questionable. Meanwhile, steel slag can be utilized in road construction since it has qualities that are compatible with unbound and asphalt layers (Motz and Geiseler, 2001). Steel slag may create high-quality aggregates of a level that is comparable to natural aggregates, making its use in road construction plausible due to its great strength and durability. Additionally, characteristics like its high abrasion and rough texture make it appropriate for hydraulic construction (Yi et al., 2012). In their analysis, Yi et al. (2012) note that the Nippon Slag Association in Japan has been investigating the use of steelmaking slag as a material for ground improvement in port and harbour construction since 1993. The study of powdered steel slag was done by Akinwumi (2014). Related experimental results show that it was effectively applied to improve the drainage, plasticity, and uncured strength of lateritic soil without exhibiting any unfavourable swell behaviour.

3 LABORATORY TESTING

Grain size examination of the specimen was performed in accordance with ASTM D422-63. A water pycnometer was used in the test by ASTM D854-06 to estimate the specific gravity. A triaxial permeameter with two back pressure systems was used to obtain the saturated coefficients of permeability from the constant head permeability test (Head, 1986). The best method for figuring out slow flow rates is to do a constant head triaxial permeability test. This test may be executed under real confining stress at pore pressures that are relevant to the site circumstances, and a variety of hydraulic gradients can be applied and precisely quantified.

Three stages—saturation, consolidation, and permeability—of the triaxial test were used to determine the specimen's permeability. The saturated permeability test applied back pressure and water pressure to the specimen while it was inside a specific cell. Water would flow when the drainage intake was opened because of the pressure difference caused by the water pressure that was applied. The water volume change and the passing of time were gauged as the water passed through the specimen. Darcy's Law can then be used to compute the saturated permeability (ks).

An average value of the ks was then determined after several saturated permeability tests under various water pressures.

Using a typical 250 ml sample ring, the HYPROP fully automated laboratory apparatus (Figure 1) can be used to obtain unsaturated hydraulic parameters of soil samples, such as SWCC and unsaturated hydraulic conductivity. When using HYPROP equipment, the phases of the experimental technique include saturating the soil sample, setting up the device with the specimen inside, starting the measurement, and analyzing the results (Satyanaga et al., 2019).

Effective cohesion (c') and effective friction angle (') of soils are measured using the Consolidated-Drained (CD) Triaxial Test. It's a compression test where the sample is allowed to consolidate to its equilibrium moisture content during the application of the cell pressure prior to shearing and the drainage taps are opened during shearing where water is free to flow out of or into the test specimen (Powrie, 2004). Drainage is allowed throughout the test to ensure that consolidation happens fully under the all-around load and that there is no buildup of pore pressure when the deviator stress is applied (Bishop and Henkel, 1962).

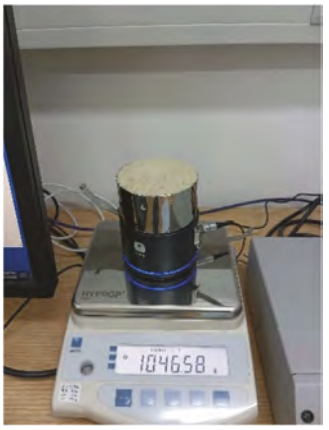

Figure 1. Measurement of SWCC using Hyprop.

4 RESULTS AND DISCUSSION

Based on the grain size analysis, steel slag appeared to have 98.11% of gravel content larger than 4.75 mm. A complete composition can be seen in Table 1, which shows the index properties of the steel slag.

Table 1. Index properties of Steel slag.

	Steel Slag
USCS Classification	GP (Poorly-graded gravel)
Specific gravity, G_s	3.5
Gravel content,% (more than 4.75mm)	98.11
Sand content, %	1.89
Fines content, % (Less than 0.075mm)	0
Saturated permeability, k_s (m/s)	0.98

From the conducted laboratory works, SWCC of steel slag was generated. Accordingly, the relationship between volumetric water content and matric suction can be observed in Figure 2. Equation (1) was used to fit the experimental data of SWCC best. The best fitting parameters of Equation (1) can be seen in Table 2.

Table 2. Best fitting parameters of Satyanaga et al. (2022) equation.

θ_s=	0.27
θ_r=	0
ψ_m=	1.034308
σ=	1.601103
ψ_{aev}=	0.3
ψ_r=	137489.9
r2	0.992052

In order to use Equation (1) for modelling SWCC, each parameter must have a proper initial value (Satyanaga et al. 2017). To best fit the laboratory data of the SWCC, all the parameters can be adjusted via an iterative non-linear regression approach offered in the Microsoft Excel software (Satyanaga et al. 2019b; Dodge and Stinson, 2007). Eventually, SWCC data are applied in subsequent seepage analyses.

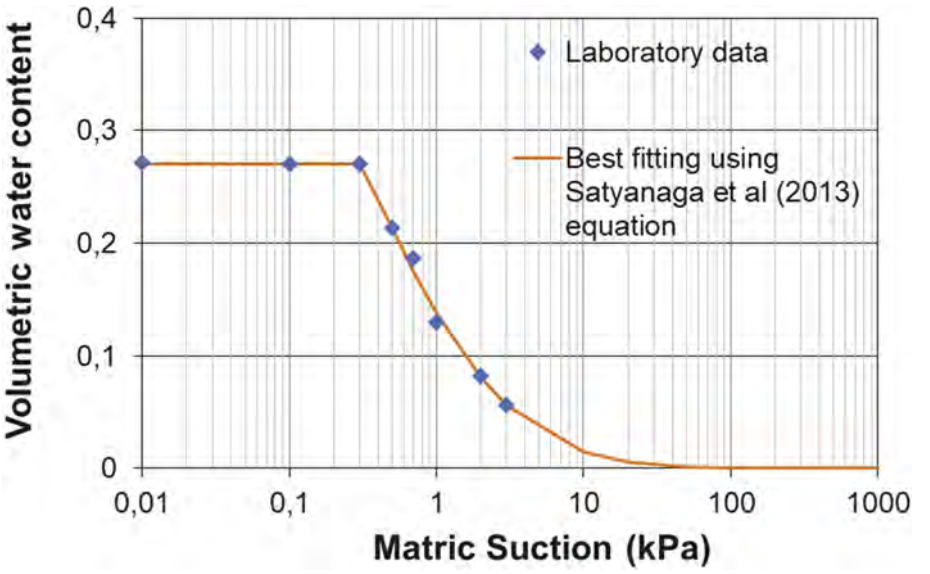

Figure 2. SWCC of Steel Slag.

The permeability function of steel slag was determined from SWCC and saturated permeability using the statistical method following the procedure explained by Satyanaga et al. (2022b) (Figure 3). The permeability function was also incorporated in the numerical analysis together with the best fitted SWCC data.

Figure 3. Unsaturated permeability of Steel Slag.

5 CONCLUSIONS

The results of the study indicated that the properties of steel slag are similar to gravel. The air-entry value of steel is 3 kPa which is corresponding to its saturated permeability (1 m/s).

REFERENCES

Akinwumi, I. (2014). "Soil modification by the application of steel slag." *Periodica Polytechnica Civil Engineering*, *58*(4), pp. 371–377.

Bishop A. W., and D. J. Henkel, The measurement of soil properties in the triaxial test, 2nd ed. London: E. Arnold, 1962.

Dodge, M., and Stinson, C., 2007. Microsoft Office Excel 2007 Inside Out.Microsoft Press, Washington (USA), p. 1088 pp.

Koh, T., Moon, S.W., Jeong, H, Jeong, Y., Pyo, S. (2018) A Feasibility Study on the Application of Basic Oxygen Furnace (BOF) Steel Slag for Railway Ballast Material, Sustainability, 10(2), 284

Li, Y., Satyanaga, A., Rahardjo, H. (2021) "Characteristics of unsaturated soil slope covered with capillary barrier system and deep-rooted grass under different rainfall patterns." International Soil and Water Conservation Research, Sep, 9(3):405–418

Motz, H., & Geiseler, J. (2001). "Products of steel slags an opportunity to save natural resources." *Waste Management 21*, pp. 285–293

Satyanaga, A., Rahardjo, H., and Zhai, Q. (2017). Estimation of unimodal water characteristic curve for gap-graded soil. *Soils and Foundations*, *57*(5), 789–801.

Satyanaga, A. and Rahardjo, H. (2019). "Unsaturated Shear Strength of Soil with Bimodal Soil-water Characteristic Curve". Geotechnique. Vol. 69, No. 9, pp. 828–832.

Satyanaga, A., Bairakhmetov, N., Kim, J.R., Moon, S.-W. (2022) "Role of Bimodal Water Retention Curve on The Unsaturated Shear Strength." Applied Sciences.12(3):1266.

Yi, H., Xu, G., Cheng, H., Wang, J., Wan, Y., & Chen, H. (2012). "An Overview of Utilization of Steel Slag." *Procedia Environmental Sciences*, *16*, 791–801.

Smart Geotechnics for Smart Societies – Zhussupbekov, Sarsembayeva & Kaliakin (Eds)
© 2023 The Author(s), ISBN 978-1-003-29912-7
Open Access: www.taylorfrancis.com, CC BY-NC-ND 4.0 license

An assessment of transversely isotropic elastic constitutive models for geomaterials

V.N. Kaliakin
Department of Civil and Environmental Engineering, University of Delaware, USA

ABSTRACT: Due to the manner in which natural soils are deposited, it is logical to expect them to exhibit approximately transversely isotropic response. While this realization is not new, the lack of suitable experimental apparatus to accurately measure the five elastic constants associated with transverse isotropy has, in the past, precluded the use of such idealizations. More recently, substantial progress has been made in experimental techniques that facilitate the measurement of the aforementioned elastic constants. The development of elastic constitutive relations for transversely isotropic geomaterials is complicated by the fact that the elastic material parameters are usually not constant. The elastic strain increments will thus be related to the stress increments through compliance matrices that are functions of the instantaneous stress state, the stress history and so forth. Since the response is thus rendered stress path-dependent, only hypoelastic constitutive models are thought to be relevant. Some of these models are reviewed and assessed in this paper.

1 INTRODUCTION

Gravitationally deposited natural sedimentary soils possess different properties in the direction of deposition as opposed to the planes normal to this direction. Mathematically, such soils are classified as being anisotropic. For a general homogeneous, anisotropic linear elastic (Hookian) material, in the absence of initial strains and stresses, the constitutive relations, in "direct" vector-matrix form, are given by

$$\boldsymbol{\delta\varepsilon}^{e} = \mathbf{A}\,\boldsymbol{\delta\sigma}' \tag{1}$$

where $\mathbf{A}$ is a symmetric (N_{rowb} * N_{rowb}) matrix of compliance coefficients characterizing the material, $\boldsymbol{\delta\varepsilon}^{e}$ and $\boldsymbol{\delta\sigma}'$ are (N_{rowb} * 1) vectors of infinitesimal elastic strain and effective stress increments, respectively, and N_{rowb} is the number of stress and strain components (Kaliakin 2001). For three-dimensional analyses,N_{rowb} = 6, with

$$\boldsymbol{\delta\varepsilon}^{e} = \left\{ \delta\varepsilon^{e}_{11} \quad \delta\varepsilon^{e}_{22} \quad \delta\varepsilon^{e}_{33} \quad \delta\gamma^{e}_{12} \quad \delta\gamma^{e}_{13} \quad \delta\gamma^{e}_{23} \right\}^{T} \tag{2}$$

$$\boldsymbol{\delta\sigma}' = \left\{ \delta\sigma'_{11} \quad \delta\sigma'_{22} \quad \delta\sigma'_{33} \quad \delta\sigma'_{12} \quad \delta\sigma'_{13} \quad \delta\sigma'_{23} \right\}^{T} \tag{3}$$

where γ^{e}_{12}, γ^{e}_{13}, and γ^{e}_{23} are engineering shear strains, and the superscript T denotes the operation of vector transposition. For torsionless axisymmetry, N_{rowb} = 4, while for plane strain analyses, N_{rowb} = 3.

Although some experimental findings (Kirkgard & Lade, 1991) suggest that natural soils are elastically orthotropic, the difficulty associated with determining values for the nine elastic

DOI: 10.1201/9781003299127-65

constants precludes the adoption of such an idealization. Instead, transversely isotropic elasticity is commonly assumed, thus reducing the number of elastic parameters to five.

Although transversely isotropic elastic material characterizations for soils are not new (Barden 1963, Pickering 1970, Atkinson 1975, Graham & Houlsby 1983, Sivakumar et al. 2001), in the past the lack of suitable experimental apparatus to accurately measure the five elastic constants associated with transverse isotropy has precluded the use of such idealizations. More recently (Hoque & Tatsuoka 1998, Lings et al. 2000, Kuwano & Jardine 2002, Arroyo et al. 2003, Nishimura 2014a), substantial progress has been made in experimental techniques that facilitate the measurement of the aforementioned elastic constants.

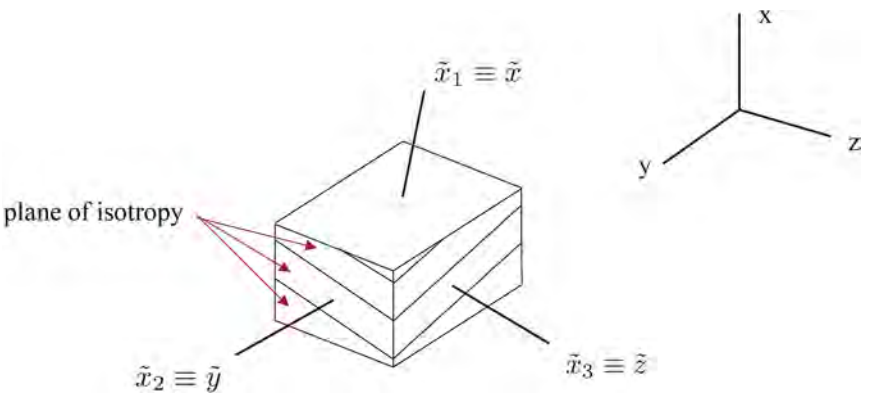

Figure 1. Schematic illustration of an element of transversely isotropic material.

The importance of elastic anisotropy in geotechnical engineering applications has been noted in conjunction with predicting ground deformations associated with tunneling (Lee & Rowe 1989, Simpson et al. 1996, Addenbrooke et al. 1997, Wongsaroj et al. 2007). It is, however, equally relevant to simulating the small-strain response of any two- or three-dimensional geotechnical problem.

2 TRANSVERSELY ISOTROPIC ELASTIC IDEALIZATIONS

Through all points of a transversely isotropic material there pass parallel planes of elastic symmetry in which all directions are elastically equivalent (i.e., planes of isotropy). Thus at each point there exists one principal direction and an infinite number of principal directions in a plane normal to the first direction (Lekhnitskii 1981).

For the present development, assume that the local material axes $(\tilde{x}_1, \tilde{x}_2, \tilde{x}_3) \equiv (\tilde{x}, \tilde{y}, \tilde{z})$ coincide with the global x, y and z coordinate axes (Figure 1). In addition, assume that the global $x_1 \equiv x$-axis is taken normal to the planes of isotropy, with the global y and z axes directed arbitrarily in such planes.

Associated with the definition of a transversely isotropic material are five elastic constants. E_n' is the elastic modulus for compression or tension in a direction normal to the plane of isotropy. E_t' is the elastic modulus for compression or tension in the plane of isotropy. Since the y - z plane is a plane of isotropy, ν_{tn}' is the Poisson's ratio characterizing the lateral contraction normal to the plane of isotropy when tension is applied in the plane. The quantity ν_{tt}' is the Poisson's ratio characterizing transverse contraction in the plane of isotropy when tension is applied in the same plane. Finally, G_{nt} is the modulus associated with shearing involving $\delta\gamma_{12}^e$ and $\delta\gamma_{13}^e$.

The modulus G_{tt}, which characterizes shearing in the plane of isotropy, is obtained from $1/G_{tt} = 2\left(1 + \nu_{tt}'\right)/E_t'$. It is thus evident that G_{tt} is not an independent material constant.

The compliance matrix, given in Equation (1), thus becomes

$$\mathbf{A} = \begin{bmatrix} 1/E_n' & -\nu_{tn}'/E_t' & -\nu_{tn}'/E_t' & 0 & 0 & 0 \\ -\nu_{nt}'/E_n' & 1/E_t' & -\nu_{tt}'/E_t' & 0 & 0 & 0 \\ -\nu_{nt}/E_n' & -\nu_{tt}/E_t' & 1/E_t' & 0 & 0 & 0 \\ 0 & 0 & 0 & 1/G_{nt} & 0 & 0 \\ 0 & 0 & 0 & 0 & 1/G_{nt} & 0 \\ 0 & 0 & 0 & 0 & 0 & 2\left(1+\nu_{tt}'\right)/E_t' \end{bmatrix} \tag{4}$$

Since $\mathbf{A}$ is symmetric, $A_{12} = A_{21}$, implying that $\nu_{tn}'/E_t' = \nu_{nt}'/E_n'$ or $\nu_{tn}' = \nu_{nt}'\left(E_t'/E_n'\right)$. Several key issues related to anisotropic elastic material idealizations for soils in general, and transversely isotropic idealizations in particular, are presented elsewhere (Kaliakin 2019).

2.1 *Limiting values for elastic material parameters*

For isotropic elastic material idealizations, the drained Young's modulus (E') is related to the shear modulus (G) and to the drained Poisson's ratio (ν') through the relation $E' = 2G(1+\nu')$. No such relations are possible for anisotropic elastic materials, as the moduli and Poisson's ratios become dependent upon the directions of stretch, lateral strain, and the directions of shear (Love 1927).

Nevertheless, certain limits of the possible values attained by the elastic constants have been derived. For the special case of transverse isotropy, expressions derived by Lempriere (1968) for orthotropic materials reduce to

$$\left|\nu_{tt}'\right| < 1 \;\Rightarrow\; -1 < \nu_{tt}' < 1 \tag{5}$$

In addition,

$$-\left(\frac{E_t'}{E_n'}\right)^{1/2} < \nu_{nt}' < \left(\frac{E_t'}{E_n'}\right)^{1/2} \quad ; \quad -\left(\frac{E_n'}{E_t'}\right)^{1/2} < \nu_{tn}' < \left(\frac{E_n'}{E_t'}\right)^{1/2} \tag{6}$$

For the special case of transverse isotropy, it can also be shown that

$$\frac{1}{2} > \frac{1}{2}\left[1 - \left(\nu_{tt}'\right)^2 - 2\left(\nu_{tn}'\right)^2\left(\frac{E_n'}{E_t'}\right)\right]\nu_{tt}'\nu_{nt}'\nu_{tn}' \tag{7}$$

Considering the left inequality in Equation (7) gives the following relation:

$$\left(\nu_{tt}'\right)^2 < 2\left(\nu_{tn}'\right)^2\left(\frac{E_n'}{E_t'}\right) \tag{8}$$

Adopting a more rigorous form of analysis, Pickering (1970) noted that, similar to Lempriere (1968), the necessary and sufficient condition for the quadratic form $\frac{1}{2}\dot{\sigma}'^T\mathbf{A}\dot{\sigma}'$ to be positive definite is that all of the principal minors of $\mathbf{A}$ should be positive. This leads to the requirements that $E_t' > 0$, $E_n' > 0$, $G_{nt} > 0$, $G_{tt} > 0$. Pickering (1970) also confirmed Equation (5), and from one of the principal minors of $\mathbf{A}$, obtained the following relation:

$$\frac{E_t'}{E_n'}\left(1 - \nu_{tt}'\right) - 2\left(\nu_{tn}'\right)^2 > 0 \tag{9}$$

Finally, Pickering (1970) noted that, similar to G_{nt}, E_t' and E_n' are independent; only the Poisson's ratios are bounded by the ratio E_t'/E_n'.

In commenting on an earlier paper by Barden (1963), Raymond (1970) stated that, from a zero-strain energy function,

$$1 \geq \nu'_{tt} + 2\left(\frac{E'_t}{E'_n}\right)\left(\nu'_{nt}\right)^2 \tag{10}$$

which, except for the case of equality, is identical with Equation (9) given by Pickering (1970).

By requiring the dilation to be the same sign as the applied stress, Raymond (1970) also stated that $\nu'_{nt} \leq 1/2$, and noted that the shear modulus G_{nt} is bounded by the following inequality:

$$G_{nt} \leq \frac{E'_n}{2\nu'_{nt}\left(1+\nu'_{tt}\right) + 2\sqrt{\frac{E'_n}{E'_t}\left[1-\left(\nu'_{tt}\right)^2\right]\left[1-\frac{E'_t\left(\nu'_{nt}\right)^2}{E'_n}\right]}} \tag{11}$$

Additional details pertaining to the limiting values for orthotropic and transversely isotropic elastic material idealizations are discussed elsewhere (Kaliakin 2020).

2.2 *Experimental determination of material parameter values*

The values of the small strain moduli and Poisson's ratios in soils characterized by transversely isotropic elastic material idealizations can be determined from the results of field or laboratory tests. Commonly used field tests include the pressuremeter and in-situ seismic surveys consisting of cross-hole and down-hole techniques. When transversely isotropic shear moduli are determined in the field, the value of G_{nt}, is obtained from a down-hole survey in which the shear wave propagates in the vertical direction and the particles move horizontally; in such tests, the shear wave velocity v_{nt} is measured. By contrast, the vale of G_{tt} is determined from a cross-hole survey, in which the shear wave velocity v_{tt} is measured. Due to the difference in the modes of shear deformation, the results obtained using field tests can, however, be different from laboratory values (Yimsiri & Soga 2002).

Laboratory tests commonly used to determine the small strain moduli and Poisson's ratio values include axisymmetric triaxial, torsional shear, resonant column, and ultrasonic tests. Such tests must be suitably modified in order to determine the values of all five independent parameters associated with a transversely isotropic elastic material idealization. The small-strain probe loadings in such tests are typically applied quasi-statically. The multiaxial body wave measurements in such tests are made using either piezoelectric transducers such as bender elements (e.g., Lings & Greening 2001, Kuwano & Jardine 2002, Nishimura 2014a) or other P- and S-wave transducers (Bellotti et al. 1996). Using such laboratory tests allows for either direct measurement (e.g., Hoque & Tatsuoka 1998) or indirect determination (e.g., Lings et al. 2000) of all five independent parameters associated with a transversely isotropic elastic material idealization.

Additional details pertaining to the experimental determination of material parameter values for transversely isotropic material idealizations are beyond the scope of the present paper. For additional details, the interested reader is directed to the references cited above.

The inclusion of transversely isotropic elastic material idealizations into existing and new elastoplastic and/or elastoviscoplastic constitutive models for soils requires a specific analytical form for the anisotropic idealization, as well as suitable empirical expressions for the associated elastic material constants. These two topics are thus next discussed.

3 DEVELOPMENT OF CONSTITUTIVE RELATIONS

The development of elastic constitutive relations for transversely isotropic geomaterials is complicated by the fact that the elastic material parameters are usually not constant.

Indeed, test results (Hoque & Tatsuoka 1998) indicate that these parameters are a function of the stress state, density, and stress history. The elastic strain increments will thus be related to the stress increments through compliance matrices (**A**) that are functions of the instantaneous stress state, the stress history and so forth. Since the elastic response is thus rendered stress path-dependent, only hypoelastic constitutive models are thought to be relevant (Hoque & Tatsuoka 1998). Some of these models are described in the subsequent sub-sections.

A key assumption underlying the development of hypoelastic models is that the elastic modulus (E_i) associated with a particular coordinate direction is a unique function of the normal stress acting in this direction, and is independent of the other two orthogonal directions (Hardin 1978, Hardin & Bladford 1989). This important assumption has subsequently been supported by data from body wave velocity measurements (Jamiokowski et al. 1991, Lo Presti et al. 1991, Stokoe et al. 1991), as well as by micromechanics-based simulations (Yimsiri & Soga 2000).

3.1 *Hypoelastic model of Yu and Dakoulas*

In their transversely isotropic hypoelastic model, (Yu & Dakoulas 1993) assumed the elastic moduli $E_h \equiv E_t^{'}$ and $E_v \equiv E_n^{'}$ to be functions of the stress state. The two Poisson's ratios were, however, assumed to be constant. Finally, although $E_t^{'}$ and $E_n^{'}$ increase with increasing confining stress, the ratio $E_t^{'}/E_n^{'}$ was assumed to remain constant. The same model was subsequently presented and further discussed by Dakoulas & Yu (1995).

Motivated by the work of Lade & Nelson (1987), Yu & Dakoulas (1993) proposed the following expressions for the elastic moduli $E_t^{'}$ and $E_n^{'}$ associated with a transversely isotropic elastic material idealization:

$$E_t^{'} = MP_a\left[\left(\frac{I_1^*}{P_a}\right)^2 + \frac{6\left(1+\nu_{tt}^{'}\right)}{\left(1-2\nu_{tt}^{'}\right)}\frac{J_2^*}{(P_a)^2} + \frac{3\left(n-m^2\right)}{\left(1-2\nu_{tt}^{'}\right)}\left(\frac{\sigma_{11}{}'}{P_a}\right)^2\right]^{\lambda} \tag{12}$$

$$E_n^{'} = nMP_a\left[\left(\frac{I_1^*}{P_a}\right)^2 + \frac{6\left(1+\nu_{tt}^{'}\right)}{\left(1-2\nu_{tt}^{'}\right)}\frac{J_2^*}{(P_a)^2} + \frac{3\left(n-m^2\right)}{\left(1-2\nu_{tt}^{'}\right)}\left(\frac{\sigma_{11}{}'}{P_a}\right)^2\right]^{\lambda} \tag{13}$$

where M and λ are model parameters, and

$$n = \frac{E_t^{'}}{E_n^{'}} = \frac{\nu_{tn}^{'}}{\nu_{nt}^{'}} \quad ; \quad m = \frac{E_t^{'}\nu_{nt}^{'}}{E_n^{'}\nu_{tt}^{'}} = \frac{\nu_{tn}^{'}}{\nu_{tt}^{'}} \tag{14}$$

$$I_1^* = m\sigma_{11}^{'} + \sigma_{22}^{'} + m\sigma_{33}^{'} \tag{15}$$

$$J_2^* = \frac{1}{2}\left(m\sigma_{11}^{'}\right)^2 + \frac{1}{2}\left(\sigma_{22}^{'}\right)^2 + \frac{1}{2}\left(\sigma_{33}^{'}\right)^2 + \left(\alpha\sigma_{12}\right)^2 + \left(\alpha\sigma_{13}\right)^2 + \left(\sigma_{23}\right)^2 \tag{16}$$

In Equation (16), $\alpha^2 = G_{tt}/G_{nt} = E_t^{'}/\left[2\left(1+\nu_{tt}^{'}\right)G_{nt}\right]$. No explicit expression for G_{nt} is, however, given.

In their paper, Dakoulas & Yu (1995) give the following values for the model parameters associated with a "remolded cross-anisotropic marine clay" from the Gulf of Mexico: M = 3.60, $\lambda = 1.29$, $\nu_{tt}^{'} = 0.18$, n = 1.26, m = 1.39 and $\alpha = 2.39$.

3.2 *Hypoelastic model of Tatsuoka and Co-Workers*

The results of extensive axisymmetric triaxial tests performed on various uncemented sands and gravels (Tatsuoka & Kohata 1995, Jiang et al. 1997, Hoque & Tatsuoka 1998) demonstrated that such soils are inherently transversely isotropic. Based on these results,

a hypoelastic constitutive model was proposed by Tatsuoka & Kohata (1995) and then subsequently refined by Hoque et al. (1996), Jiang et al. (1997), Hoque & Tatsuoka (1998), and Tatsuoka et al. (2001). This model is based on the aforementioned assumptions of Hardin (1978) and Hardin & Bladford (1989) that the Young's modulus (E_i) associated with a particular coordinate direction is a unique function of the normal stress acting in this direction, and is *independent* of the other two orthogonal directions.

For a transversely isotropic elastic material idealization, the following moduli are proposed:

$$E_n^{'} = E_1^{*} F(e) \left(\frac{\sigma_{11}^{'}}{\sigma_{ref}^{'}} \right)^{m_1} \tag{17}$$

$$E_t^{'} = E_1^{*} R_E F(e) \left(\frac{\sigma_{22}^{'}}{\sigma_{ref}^{'}} \right)^{m_2} \tag{18}$$

$$E_t^{'} = E_1^{*} R_E F(e) \left(\frac{\sigma_{33}^{'}}{\sigma_{ref}^{'}} \right)^{m_3} \tag{19}$$

where $E_1^{*} = \left(E_1^{'}\right)_{ref} / F\left(e_{ref}\right)$. The exponents m_1, m_2, and m_3 represent the pressure dependency of the elastic stiffness; this is consistent with the general power law relationship proposed by Hardin & Black (1968). If $m_1 = m_2 = m_3 = 0.0$, the elastic material characterization will be linear. To avoid an overly large number of model parameters being associated with just the definition of the elastic response, the three exponents are commonly assumed to be equal; i.e., $m_1 = m_2 = m_3 = m$. In addition, m is typically assumed to be equal to 0.50 (Hoque & Tatsuoka 1998).

In Equations (17)–(19), the quantity $F(e)$ is the following function of the void ratio (e):

$$F(e) = \frac{(2.17 - e)^2}{1 + e} \tag{20}$$

which was proposed for sands with rounded grains by Hardin & Richart (1963) and Hardin & Black (1966).

The quantity $\left(E_1^{'}\right)_{ref}$ is the value of $E_1^{'}$ for $\sigma_{11'} = \sigma_{ref'}$, and $F(e_{ref})$ is the value of $F(e)$ for $e = e_{ref}$; i.e., the void ratio associated with $\sigma_{11'} = \sigma_{ref'}$. Finally, the quantity $R_E = E_t^{'}/E_n^{'}$ represents the degree of inherent anisotropy ($R_E = 1.0$ implies an inherently isotropic material).

It is timely to note that, since, in general, $\sigma_{22}^{'} \neq \sigma_{33}^{'}$, equations (17) to (19) will not necessarily predict transversely isotropic elastic response. Only under axisymmetric triaxial conditions do these equations predict such response. In particular, under axisymmetric triaxial conditions, $\sigma_{22}^{'} = \sigma_{33}^{'}$. For $m_2 = m_3 = m$, equations (18) and (19) are identical. Thus,

$$E_n^{1} = E_1^{*} F(e) \left(\frac{\sigma_{11}^{'}}{\sigma_{ref}^{'}} \right)^{m} \quad ; \quad E_t^{'} = E_1^{*} R_E F(e) \left(\frac{\sigma_{33}^{'}}{\sigma_{ref}^{'}} \right)^{m} \tag{21}$$

and

$$\frac{E_n^{'}}{E_t^{'}} = \frac{1}{R_E} (R_\sigma)^m \quad \text{or} \quad n = \frac{E_t^{'}}{E_n^{'}} R_E (R_\sigma)^{1/m} \tag{22}$$

where $R_\sigma = \sigma_{11}^{'}/\sigma_{33}^{'} = \sigma_n^{'}/\sigma_t^{'}$. In equation (22), the term $1/R_E$ represents the inherent anisotropy, while the term R_σ represents the stress-induced anisotropy.

Attention is next turned to defining the Poisson's ratios for the material idealization. Assuming symmetry of **A**, $\nu_{tn}^{'} = \nu_{nt}^{'}\left(E_t^{'}/E_n^{'}\right)$. Substituting equations (21) into this expression gives

$$\nu'_{tn} = \nu'_{nt} R_E \left(\frac{1}{R_\sigma}\right)^m \tag{23}$$

Although equation (23) is consistent with equations (21), it does not give explicit expressions for either ν'_{tn} or ν'_{nt}. To overcome this shortcoming, Hoque & Tatsuoka (1998) developed alternate functional forms for ν'_{tn} and ν'_{nt}. They noted that, based on the results of axisymmetric triaxial tests performed on different sands at various stress states in the range $0.5 \leq R_\sigma \leq 2.0$, the Poisson's ratio ν'_{nt} did not vary greatly. Within the range of pressures investigated, the value of ν'_{nt} was not sensitive to the change in σ'_n or σ'_t at a fixed ratio R_σ. This Poisson's ratio did, however, gradually increase with R_σ.

To account for this fact and to include the effect of inherent anisotropy (via R_E) while also satisfying the relation $\nu'_{tn}/E'_t = \nu'_{nt}/E'_n$ that comes form the symmetry of **A**, Hoque & Tatsuoka (1998) proposed the following functional forms:

$$\nu'_{nt} = \nu_0 \sqrt{\frac{1}{R_E}} (R_\sigma)^{m/2} \; ; \; \nu'_{tn} = \nu_0 \sqrt{R_E} \left(\frac{1}{R_\sigma}\right)^{m/2} \tag{24}$$

When

$$\sqrt{\frac{1}{R_E}} (R_\sigma)^{m/2} = 1 \;\Rightarrow\; R_\sigma = (R_E)^{1/m}$$

then $\nu_0 = \nu'_{nt}$ in the first of equations (24). When

$$\sqrt{R_E} \left(\frac{1}{R_\sigma}\right)^{m/2} = 1 \;\Rightarrow R_\sigma = (R_E)^{-m}$$

then $\nu_0 = \nu'_{tn}$ in the second of equations (24).

Regarding the Poisson's ratio ν'_{tt}, Hoque & Tatsuoka (1998) proposed that $\nu'_{tt} = \nu_0$. Then, for isotropic materials (i.e., $R_E = 1.0$) subjected to isotropic stress states, $\nu'_{nt} = \nu'_{tn} = \nu'_{tt} = \nu_0$. Clearly, this choice of ν'_{tt} is somewhat arbitrary.

In light of the assumed expression for ν'_{tt}, the shear modulus associated with the place of isotropy is thus $G_{tt} = E'_t / \left[2\left(1 + \nu'_{tt}\right)\right]$.

Unlike the case of isotropic elastic materials, there is no unique relationship between G_{nt} and the other elastic parameters. Based on equations (21), Tatsuoka et al. (2001) derived the following functional form:

$$G_{nt} = \left(\frac{1 - \nu_0}{1 + \nu_0}\right) \frac{1}{\frac{1-\nu'_{nt}}{E'_n} + \frac{1-\nu'_{tn}}{E'_t}} \tag{25}$$

In summary, as evident from the present development, the hypoelastic model of Tatsuoka and co-workers is useful only under axisymmetric triaxial conditions and is somewhat complex.

3.3 *Hypoelastic model of Lings et al.*

Lings et al. (2000) performed high-quality axisymmetric triaxial tests on samples of natural Gault Clay. The tests involved multiple drained stress excursions and orthogonal determination of horizontal shear wave velocity using bender elements. Small-strain data from both engineering strain and shear wave velocity measurements were combined to derive values for all five material parameters associated with a transversely isotropic elastic material idealization.

Based on the results of their tests, Lings et al. (2000) proposed the following expressions for the elastic moduli:

$$E_n^{'} = 550p' \; ; \; E_t^{'} = 2186p' \tag{26}$$

where p', and thus $E_n^{'}$ and $E_t^{'}$, have units of kPa.

The Poisson's ratios were assumed to be constant; viz., $\nu_{nt}^{'} = 0.00$ and $\nu_{tt}^{'} = -0.04$. No value was reported for $\nu_{tn}^{'}$.

Finally, the independent shear modulus was represented by $G_{nt} = 507p'$. Using the above expression for $E_t^{'}$ and the assumed value of $\nu_{tt}^{'}$ gives $G_{tt} = E_t^{'}/\left[2\left(1+\nu_{tt}^{'}\right)\right] = 1140p'$. The small-strain stiffness anisotropy is thus quantified as follows: $n = E_t^{'}/E_n^{'} = 2186/550 = 3.97$, $G_{tt}/G_{nt} = 2.25$, and $\nu_{nt}^{'}/\nu_{tt}^{'} = 0.0$.

3.4 *Hypoelastic model of Kuwano and Jardine*

Kuwano & Jardine (2002) determined that, although the overconsolidation ratio (OCR) and the recent stress history had no discernible independent effect on the moduli measured in any tests performed on Ham River sand, these factors strongly influenced the extent of the linear strain range. Extending the earlier formulations of Roesler (1979), Yu & Richart (1984), and Bellotti et al. (1996), Kuwano & Jardine (2002) proposed the following expressions for the elastic moduli associated with a transversely isotropic material idealization:

$$E_n^{'} = C_v F(e)\left(\frac{\sigma_v^{'}}{p_{ref}}\right)^{a_v} \; ; \; E_t^{'} = C_h F(e)\left(\frac{\sigma_h^{'}}{p_{ref}}\right)^{b_h} \tag{27}$$

$$G_{nt} = C_{vh} F(e)\left(\frac{\sigma_v^{'}}{p_{ref}}\right)^{a_{vh}}\left(\frac{\sigma_h^{'}}{p_{ref}}\right)^{b_{vh}} \; ; \; G_{tt} = C_{hh} F(e)\left(\frac{\sigma_v^{'}}{p_{ref}}\right)^{a_{hh}}\left(\frac{\sigma_h^{'}}{p_{ref}}\right)^{b_{hh}} \tag{28}$$

where the reference pressure p_{ref} was assumed to be equal to the atmospheric pressure P_a = 101.3 kPa. In *equations (27)* and (*28*), C_v, C_h, C_{vh}, C_{hh} are model parameters that describe the inherent anisotropy of the material. The quantities a_v, b_h, a_{vh}, b_{vh}, a_{hh}, b_{hh} are model parameters that dictate the stress dependency of the cross-anisotropic moduli. For sands, the indexes a_v and b_h, and the sums $a_{vh} + b_{vh}$ and a_{hh}+b_{hh} typically vary from 0.5 to 0.6 (Schadlich & Schweiger 2013). Finally, $F(e)$ accounts for variations of void ratio; Kuwano & Jardine (2002) assumed the void ratio function proposed by Hardin & Richart (1963) and given by equation (20).

Kuwano & Jardine (2002) determined the following model parameter values for Ham River sand: C_v = 204.0 MPa, C_h = 174.0 MPa, C_{vh} = 72.0 MPa, C_{hh} = 81.0 MPa, a_v = 0.52, b_h = 0.53, a_{vh} = 0.32, b_{vh} = 0.20 ($a_{vh} + b_{vh}$ = 0.52), a_{hh} = -0.04, and b_{hh} = 0.53 (a_{hh}+b_{hh} = 0.49). The Poisson's ratios for this material, measured at various stress levels, exhibited substantial scatter.

Nishimura (2014b) used expressions similar to equations (27) to (28) to simulate the small-strain response of six different clays. Schadlich & Schweiger (2013) used such expressions to simulate the stiffness anisotropy of coarse-grained soils.

3.5 *Hypoelastic model of Yimsiri and Soga*

Yimsiri & Soga (2011) used a special triaxial testing apparatus that incorporates local strain measuring system and elastic wave velocity measurement system to determine the five material parameters associated with a transversely isotropic elastic material idealization. The materials tested consisted of two heavily overconsolidated clays, namely London Clay and Gault Clay. Isotropically consolidated drained compression tests and shear wave velocity measurements were undertaken on both vertically and horizontally cut specimens.

Based on the results of their tests on London clay, Yimsiri & Soga (2011) proposed the following expressions for the elastic moduli:

$$E_n^{'} = 5.5F(e)(p')^{0.38} \; ; \; E_t^{'} = 12.0F(e)(p')^{0.38} \tag{29}$$

The values of $\nu_{tt}^{'}$ and $\nu_{tn}^{'}$ measured exhibited some scatter, and but there was no evident relationship with confining pressure. Consequently, Yimsiri & Soga (2011) assumed these Poisson's ratios to be *constant* and *independent* of the confining stress. In particular, ν'_{nt} = 0.07, $\nu_{tn}^{'} = 0.15$ and $\nu_{tt}^{'} = 0.18$.

The independent shear modulus was represented by the following expression:

$$G_{nt} = 4.25F(e)(p')^{0.38} \tag{30}$$

Finally, using equation (29) gives $G_{tt} = E_t^{'}/\left[2\left(1+\nu_{tt}^{'}\right)\right] = 5.10F(e)(p')^{0.38}$. In the above expressions, p', and thus the elastic moduli, are expressed in units of MPa. The void ratio function is assumed to be that proposed by Hardin & Black (1968) for cohesionless soils; viz., $F(e) = (2.973 - e)^2/(1+e)$.

The small-strain stiffness anisotropy is thus quantified as follows: $n = E_t^{'}/E_n^{'} = 12.0/5.5 = 2.18$, G_{tt}/G_{nt} = 1.20, and $\nu_{nt}^{'}/\nu_{tt}^{'} = 0.39$.

Symmetry of the compliance matrix **A** requires that $\nu_{tn}^{'}E_n^{'} = \nu_{nt}^{'}E_t^{'}$. Substituting the values determined by Yimsiri & Soga (2011) gives, in units of MPa,

$$\nu_{tn}^{'}E_n^{'} = 0.825F(e)(p')^{0.38} \;\; ; \;\; \nu_{nt}^{'}E_t^{'} = 0.840F(e)(p')^{0.38}$$

Thus, $\nu_{tn}^{'}E_n^{'} \neq \nu_{nt}^{'}E_t^{'}$, rendering **A** non-symmetric. Yimsiri & Soga (2011) attributed this result partly to the fact that $\nu_{nt}^{'}$ was the most unreliable parameter in this study due to the difficulty in placing the proximity transducer to align exactly to the in-situ vertical direction when horizontally cut specimens were tested.

Based on the results of their tests on Gault clay, Yimsiri & Soga (2011) proposed the following expressions for the elastic moduli:

$$E_n^{'} = 12.5F(e)(p')^{0.34} \; ; \; E_t^{'} = 29.0F(e)(p')^{0.34} \tag{31}$$

The Poisson's ratios were again assumed to be constant; viz., $\nu_{nt}^{'} = 0.13$, $\nu_{tn}^{'} = 0.30$ and $\nu_{tt}^{'} = 0.21$. The independent shear modulus was represented by the following expression:

$$G_{nt} = 7.15F(e)(p')^{0.34} \tag{32}$$

Finally, using equation (31) gives $G_{tt} = E_t^{'}/\left[2\left(1+\nu_{tt}^{'}\right)\right] = 12.0F(e)(p')^{0.34}$. In the above expressions, the void ratio function is as previously defined. The small-strain stiffness anisotropy is thus quantified as follows: $n = E_t^{'}/E_n^{'} = 2.32$, G_{tt}/G_{nt} = 1.68, and $\nu_{nt}^{'}/\nu_{tt}^{'} = 0.62$.

Checking symmetry of the compliance matrix **A** gives

$$\nu_{tn}^{'}E_n^{'} = 3.75F(e)(p')^{0.34} \;\; ; \;\; \nu_{nt}^{'}E_t^{'} = 3.77F(e)(p')^{0.34}$$

As in the case of London clay, $\nu_{tn}^{'}E_n^{'} \neq \nu_{nt}^{'}E_t^{'}$, rendering **A** non-symmetric.

3.6 *Hypoelastic model of Ratananikom et al.*

Ratananikom et al. (2012) performed high-quality axisymmetric triaxial tests on samples of natural Bangkok Clay with OCR≈1.2. The experimental program used an axisymmetric triaxial device that was equipped with local strain measuring systems and bender elements. The latter

were used to measure the small-strain shear modulus (G_{max}). A set of isotropically consolidated CIUC/CIDC tests was performed on vertically and horizontally cut undisturbed specimens.

Ratananikom et al. (2012) used an optimization procedure that assumed that the transversely isotropic elastic parameters for natural Bangkok Clay comply with the simplified model of Graham (1983). Following the approach used by Rampello (1997), they also assumed that all elastic moduli to be power functions of the mean effective confining stress $p_0^{'}$; viz.,$E_n^{'}/P_a = A\left(p_0^{'}P_a\right)^n$, where A and n are dimensionless model parameters, and P_a is the atmospheric pressure (assumed to approximately equal to 100 kPa), which must be expressed in the same units as $p_0^{'}$.

Based on the results of their tests, used in conjunction with an optimization scheme, Ratananikom et al. (2012) proposed the following expressions for the elastic moduli (in units of MPa):

$$E_n^{'} = 23.1\left(\frac{p_0^{'}}{P_a}\right)^{0.62} \; ; \; E_t^{'} = 30.0\left(\frac{p_0^{'}}{P_a}\right)^{0.62} \tag{33}$$

The Poisson's ratios were assumed to be constant; viz., $\nu_{nt}^{'} = 0.068$, $\nu_{tn}^{'} = 0.088$ and $\nu_{tt}^{'} = 0.077$. The independent shear modulus was represented by the following expression:

$$G_{nt} = 12.2\left(\frac{p_0^{'}}{P_a}\right)^{0.62} \tag{34}$$

Thus, $G_{tt} = E_t^{'}/\left[2\left(1+\nu_{tt}^{'}\right)\right] = 13.9\left(p_0^{'}/P_a\right)^{0.62}$. The small-strain stiffness anisotropy is thus quantified as follows: $n = E_t^{'}/E_n^{'} = 300/231 = 1.30$, $G_{tt}/G_{nt} = 1.14$, and $\nu_{nt}^{'}/\nu_{tt}^{'} = 0.88$.

Using equation (33), a check of the symmetry of the compliance matrix **A** gives

$$\nu_{tn}^{'}E_n^{'} = 2.033F(e)(p')^{0.34}\left[P_a\left(\frac{p_0^{'}}{P_a}\right)^{0.62}\right] \; ; \; \nu_{nt}^{'}E_t^{'} = 2.040F(e)(p')^{0.34}\left[P_a\left(\frac{p_0^{'}}{P_a}\right)^{0.62}\right] \tag{35}$$

Thus, $\nu_{tn}^{'}E_n^{'} \neq \nu_{nt}^{'}E_t^{'}$, rendering **A** non-symmetric.

4 CONCLUSIONS

This paper has presented and assessed several transversely isotropic hypoelastic constitutive models that have been proposed for geomaterials. Although the progress in the development of such models is notable, additional work is required before such models can be reliably used in the simulation of geomaterials.

In particular, not all models are complete. That is, they do not necessarily provide explicit functional forms for all five parameters associated with such models. In addition, some models render the compliance matrix **A** is non-symmetric.

Finally, values of the parameters associated with such models are only available for select soils. No attempts have been made to apply a given model to more than one or two specific soils.

REFERENCES

Addenbrooke, T. I., Potts, D. M. & Puzrin, A. M. 1997. *The influence of pre-failure soil stiffness on the numerical analysis of tunnel construction*. Géotechnique. 47(3): 693–712.

Atkinson, J. H. 1975. *Anisotropic Elastic Deformations in Laboratory Tests on Undisturbed London Clay*. Géotechnique. 25(2): 357–374.

Arroyo, M., Muir Wood, D. & Greening, P. D. 2003. *Source Near-Field Effects and Pulse Tests in Soil Samples*. Géotechnique. 53(3): 337–345.

Barden, L. 1963. *Stresses and Displacements in a Cross-Anisotropic Soil*. Géotechnique. 13(3): 198–210.
Bellotti, L., Jamiokowski, M., Lo Presti, D. C. F. & O'Neill, D. A. 1996. *Anisotropy of small strain stiffness in Tocino sand*. Géotechnique. 46(1): 115–131.
Dakoulas, P. & Yu, S. 1995. *Stress-Dependency of Elastic Moduli for Cross-Anisotropic Soils*. Géotechnique. 45(2): 325–332.
Graham, J. & Houlsby, T. 1983. *Anisotropic Elasticity of a Natural Clay*. Géotechnique. 33(2): 165–180.
Hardin, B. O. & Richart, F. E. 1963. *Elastic wave velocities in granular soils*. Journal of the Soil Mechanics and Foundations Division, ASCE. 89(SM1): 33–65.
Hardin, B. O. & Black, W. L. 1966. *Sand stiffness under various triaxial stresses*. Journal of the Soil Mechanics and Foundations Division, ASCE. 92(SM2): 27–42.
Hardin, B. O. & Black, W. L. 1968. *Vibration Modulus of Normally Consolidated Clay*. Journal of the Soil Mechanics and Foundations Division, ASCE. 94(SM2): 353–369.
Hardin, B. O. 1978. *The Nature of Stress-Strain Behavior for Soils*. Proceedings of the Specialty Conference on Earthquake Engineering and Soil Dynamics. Pasadena, CA: ASCE. 1: 3–90.
Hardin, B. O. & Bladford, G. E. 1989. *Elasticity of particulate materials*. Journal of Geotechnical Engineering, ASCE. 89(6): 788–805.
Hoque, E., Tatsuoka, F. & Sato, T. 1996. *Measuring Anisotropic Properties of Sands Using a Large Triaxial Specimen*. ASTM Geotechnical Testing Journal. 19(4): 411–420.
Hoque, E. & Tatsuoka, F. 1998. *Anisotropy in the Elastic Deformation of Materials*. Soils and Foundations. 38(1): 163–179.
Jamiokowski, M., Lerouell, S. & Lo Presti, D. C. F. 1991. *Design parameters from theory to practice*. Geo-Coast '91.Yokohama, Japan: 1: 877–917.
Jiang, G-L., Tatsuoka, F., Flora, A. & Koseki, J. 1997. *Inherent and stress-induced anisotropy in very small strain stiffness of a sandy gravel*. Géotechnique. 47(3): 509–521.
Kaliakin, V. N. 2001. *Approximate Solution Techniques, Numerical Modeling and Finite Element Methods*. New York: Marcel Dekker, Inc.
Kaliakin, V. N. 2019. *Anisotropic Elasticity for Soils: A Synthesis of Some Key Issues*. Bulletin of L.N. Gumilyov Eurasian National University, Technical Science and Technology Series. 127(2): 49–63.
Kaliakin, V. N. 2020. *Some Observations Regarding Poisson's Ratios for Anisotropic Soils*. Bulletin of L. N. Gumilyov Eurasian National University, Technical Science and Technology Series. 132(3): 83–100.
Kirkgard, M. M. & Lade, P. V. 1991. *Anisotropy of Normally Consolidated San Francisco Bay Mud. ASTM Geotechnical Testing Journal*. 14(3): 231–246.
Kuwano, R. & Jardine, R. J. 2002. *On the Applicability of Cross-Anisotropic Elasticity to Granular Materials at Very Small Strains*. Géotechnique. 52(10): 727–749.
Lade, P. V. & Nelson, R. B. 1987. *Modelling the Elastic Behaviour of Granular Materials*. International Journal for Numerical and Analytical Methods in Geomechanics. 11(5): 521–542.
Lee, K. M. & Rowe, R.K. 1989. *Deformations caused by surface loading and tunneling; the role of elastic anisotropy*. Géotechnique. 39(1): 125–140.
Lekhnitskii, S. G. 1981. *Theory of Elasticity of an Anisotropic Body*. Moscow: Mir Publishers.
Lempriere, B. M. 1968. *Poisson's ratio in orthotropic materials*. American Institute of Aeronautics and Astronautics Journal. 6(11): 2226–2227.
Lings, M. L., Pennington, D. S. & Nash, D. F. T. 2000. *Anisotropic Stiffness Parameters and their Measurement in a Stiff Natural Clay*. Géotechnique. 50(2): 109–125.
Lings, M. L. & Greening, P. D. 2001. *A novel bender/extender element for soil testing*. Géotechnique. 51 (8): 713–717.
Lo Presti, D. C. F. & O'Neill, D. A. 1991. *Laboratory investigation of small strain modulus anisotropy in sands*. Huang, A. -B. (ed.). Proceedings of the International Symposium on Calibration Chamber Testing. New York: Elsevier: 2: 213–224.
Nishimura, S. 2014a. *Assessment of anisotropic elastic parameters of saturated clay measured in triaxial apparatus: Appraisal of techniques and derivation procedures*. Soil and Foundations. 54(3): 364–376.
Nishimura, S. 2014b. *Cross-anisotropic deformation characteristics of natural sedimentary clays*. Géotechnique. 64(12): 981–996.
Pickering, D. J. 1970. *Anisotropic Elastic Parameters for Soil*. Géotechnique. 20(3): 271–276.
Ratananikom, W., Likitlersuang, S. & Yimsiri, S. 2012. *An investigation of anisotropic elastic parameters of Bangkok Clay from vertical and horizontal cut specimens*. Geomechanics and Geoengineering. 8(1): 15–27.
Raymond, G. P. 1970. *Discussion: Stresses and displacements in a cross-anisotropic soil, by L. Barden.* Géotechnique. 20(4): 456–458.
Roesler, S. K. 1979. *Anisotropic shear modulus due to stress anisotropy*. Journal of Geotechnical Engineering, ASCE. 105(GT7): 871–880.

Schädlich, B. & Schweiger, H. F. 2013. *Influence of Anisotropic Small Strain Stiffness on the Deformation Behavior of Geotechnical Structures*. Journal of Geomechanics, ASCE. 13(6): 861–868.

Simpson, B., Atkinson, J. H. & Jovičić, V. 1996. *The influence of anisotropy on calculation of ground settlements above tunnels*. Geotechnical Aspects of Underground Construction in Soft Ground. Rotterdam: Balkema. 1: 591–595.

Sivakumar, V., Doran, I. G., Graham, J. & Johnson, A. 2001. *The Effect of Anisotropic Elasticity on the Yielding Characteristics of Overconsolidated Natural Clay*. Canadian Geotechnical Journal. 38 (1):125–137.

Stokoe, K. H. H., Lee, J. N. K. & Lee, S. H. H. 1991. *Characterization of soil in calibration chambers with seismic waves*. Huang, A. -B. (ed.). Proceedings of the International Symposium on Calibration Chamber Testing. New York: Elsevier: 2: 363–376.

Tatsuoka, F. & Kohata, Y. 1995. *Stiffness of hard soils and soft rocks in engineering applications*. Shibuya, et al. (eds.). Proceedings of the International Symposium on Pre-Failure Deformation of Geomaterials (IS-Hokkaido). 2: 947–1063.

Tatsuoka, F., Uchimura, T., Hayano, K., Di Benedetto, H., Koseki, J. & Siddique, M. S. A. 2001. *Time-Dependent Deformation Characteristics of Stiff Geomaterials in Engineering Practice*. Proceedings of the Second International Conference on Pre-Failure Deformation Characteristics of Geomaterials. Balkema. 2: 1161–1262.

Wongsaroj, J., Soga, K. & Mair, R. J. 2007. *Modelling of long-term ground response to tunnelling under St. James's Park, London*. Géotechnique. 57(1): 75–90.

Yimsiri, S. & Soga, K. 2000. *Micromechanics-based stress-strain behaviour of soils at small strains*. Géotechnique. 50(5): 559–571.

Yimsiri, S. & Soga, K. 2011. *Cross-anisotropic elastic parameters of two natural stiff clays*. Géotechnique. 61(9): 809–814.

Yu, P. & Richart, F. E. 1984. *Stress Ratio Effects on Shear Modulus of Dry Sands*. Journal of Geotechnical Engineering, ASCE. 110(3): 331–345.

Yu, S. & Dakoulas, P. 1993. *General Stress-Dependent Elastic Moduli for Cross-Anisotropic Soils*. Journal Geotechnical Engineering Division, ASCE. 119(10): 1568–1587.

Smart Geotechnics for Smart Societies – Zhussupbekov, Sarsembayeva & Kaliakin (Eds)
© 2023 The Author(s), ISBN 978-1-003-29912-7
Open Access: www.taylorfrancis.com, CC BY-NC-ND 4.0 license

Feasibility study on the controlled low-strength material using co-firing fly ash from bubbling fluidized bed boiler

A. Cheng
National Ilan University, Ilan, Taiwan

Kinga Korniejenko & Michał Łach
Cracow University of Technology, Cracow, Poland

W.T. Lin, S.J. Chao & H.M. Hsu
National Ilan University, Ilan, Taiwan

ABSTRACT: This study aims to investigate the reuse of resources of the co-firing fly ashes from a bubbling fluidized boiler to produce controlled low-strength material (CLSM). First, we made a pozzolanic-activity test to confirm if the fly ash can be used as a raw material for making cementitious materials. After that we make samples of cementitious materials with the co-firing fly ashes taking different percentages of weights in them (5%, 10%, 15% and 20% for each) and use them to undergo the various tests including initial set time, slump flow, compression, X-ray diffraction experiments and SEM microstructure of mercury.

The result shows that the strength activity index (SAI) of the co-firing fly ashes is greater than 75 percent of the materials that can be used as the raw materials and meet the ASTM C311 standard. The results above show that co-firing fly ashes from a bubbling fluidized bed boiler can be utilized as substitution materials for cementitious materials in the controlled low-strength materials. The best substitution percentage is 15 percent.

1 INTRODUCTION

Taiwan is moving towards the era of circular economy and converting waste into renewable resources [1], which clearly shows that circular economy and waste recycling have become important issues in Taiwan's current development. According to the 2016 statistics from the Environmental Protection Agency's Sustainable Materials Management Database, about 70% of the various types of materials are imported into Taiwan from other countries. Among them, 100% of metals, 99.8% of fossil fuels, 66.3% of biomass and 32.7% of non-metals [2].

Taiwan's per capita consumption of materials is very high, and the amount of various types of waste generated is also staggering. According to the 2016 National Waste Quantity Statistics of the Environmental Protection Agency, the total amount of waste in Taiwan is 26.43 million metric tons [3]. Due to the implementation of the International Basel Convention [4], waste should be disposed in an environmental sound area as much as possible. However, the co-firing fly ash produced by the co-firing of fuels in the commercial waste Bubble Fluidized Bed Boiler (BFBB) in this research cannot be directly for reuse, it can only be disposed of as industrial waste for burial or solidification. The research results are used as supporting materials for other manufacturers who intend to reuse this material to apply for reuse. Let the circular economy continue to move forward.

DOI: 10.1201/9781003299127-66

2 LITERATURE REVIEW

2.1 *Controlled low-strength backfill material*

Controlled Low-Strength Materials (CLSM) is a kind of cementitious composite material with tamping-free self-filling properties. This material currently has many different names, such as fluid backfill, controlled low-strength backfill, fluid mortar, plastic soil cement or soil cement mud. . .etc. [5].

CLSM is defined in accordance with ACI 116R as a material that produces a compressive strength of 8.3 MPa (1200 psi) or less, the lower compressive strength specification being dictated primarily in response to possible future excavation needs. Also as stated in ACI 230.IR CLSM should not be confused with compacted cement. CLSM typically does not require compaction (consolidation) or curing to achieve the required strength and the long-term compressive strength of compacted cement typically exceeds the 8.3 MPa (1200 psi) maximum limit of the CLSM specification [6].

2.2 *The use and specification of controlled low-strength backfill materials in Taiwan*

According to Chapter 03377 of the Construction Outline Specification of the Public Construction Commission, Executive Yuan, CLSM is made by mixing cement (including cement-based treatment agent), pozzolanic admixture, granules and water in a set proportion, and chemical admixtures must be used if necessary. In addition to the special inspection items specified by the engineering department according to the special needs of the project, the basic properties such as pipe fluidity or slump flow, falling strength, 28-day compressive strength and chloride ion content should meet the requirements [7].

It is also specified in the construction specification that the cement (binder) used in CLSM should comply with the specifications of CNS61 "Portland Cement" [8] or CNS15286 "Hydraulic Mixed Cement" [9], and the specifications of pozzolanic admixtures must comply with Specification of CNS3036 "Fly ash and natural or pozzolanic for concrete" [10].

2.3 *Characteristics of co-firing fly ash in a Bubble Fluidized Bed Boiler (BFBB)*

Due to the co-combustion of fuels, the co-combustion fly ash produced by BFBB will have different chemical compositions depending on the type of fuel co-combustion. BFBB usually adds limestone ($CaCO_3$) as a desulfurizing agent. In order to maintain the desulfurization effect continuously, limestone ($CaCO_3$) will be continuously added during the process of fuel addition, so calcium sulfate ($CaSO_4$) and desulfurization will be continuously produced. The intermediate product of the sulfur reaction is calcium oxide (CaO) and the final limestone ($CaCO_3$) that does not react with sulfur. In view of the above and the characteristics of the bubble fluidized bed boiler, the characteristics of BFBB co-firing fly ash are as follows:

(1) High content of calcium oxide (CaO) and limestone ($CaCO_3$) [11]
(2) High calcium sulfate ($CaSO_4$) content [12].
(3) Fewer glassy.

3 RESEARCH RESULTS AND DISCUSSION

3.1 *Pozzolanic activity index test*

Pozzolanic strength activity index (Strength Activity Index, SAI) value to evaluate whether BFBB co-firing fly ash has cementing ability, and BFBB co-firing fly ash replaces 10% and 20% of the cement material in CLSM for cement mortar mixing and preparation of test specimens, and the compression test was carried out when the age of the test body reached 7 days and 28 days.

According to the requirements of ASTM C311 test specification, the SAI value of the test group should be greater than 75% of the strength of the control group. The test results show

that when the age of the test body reaches 7 days, 10% and 20% of the cement material is replaced by co-fired fly ash. SAI is 101.5% and 94.0% respectively; when the test specimens age reaches 28 days, the co-firing fly ash replaces 10% and 20% of the cement material, and the SAI values are 107.6% and 93.4%, respectively, as shown in Table 1. The test results confirmed that the BFBB co-fired fly ash has the activity of Pozzolanic and can be used as a cementitious material.

Table 1. Test results of Pozzolanic strength activity index.

	Compressive strength (kgf/cm^2)		SAI (%)	
Replacement ratio	7 days	28 days	7 days	28 days
0%	31.7	39.3	100.0	100.0
10%	32.5	42.3	101.5	107.6
20%	29.8	36.7	94.0	93.4

3.2 *Slump flow test*

From the slump flow test results (see Table 2), it can be found that the slump flow does not change significantly when the amount of cement replaced by BFBB co-firing fly ash is less than 10%, but the slump flow begins to deteriorate with the increase of the substitution amount. When it reaches 20%, its slump flow is only 85.9% and 87.9% of the original according to Table 2.

Table 2. Summary of slump test results.

Replacement ratio	slump flow (cm)	Average slump flow (cm)	%	Standard (cm)
0%	57 × 58	57.5	100	≧ 40
5%	54 × 57	55.5	96.5	
10%	55 × 59	57.0	99.1	
15%	52 × 54	53.0	92.2	
20%	49 × 51	50.0	87.0	

3.3 *X-ray diffraction test*

This test is mainly based on the spectrum obtained by X-ray diffraction analysis to compare whether the crystalline composition of samples with different substitution ratios and different sample ages after hydration reaction and curing period is different. The results are compared and discussed.

In this experiment, 3 groups of different proportions of specimens (substitution ratios of 0%, 10% and 20%) were selected and made, and the 7th and 28th days of the specimen age were used as the benchmarks, respectively, and were analyzed by X-ray diffractometer as shown in Table 3.

Table 3. XRD analysis results.

Ages	7 days			28 days		
Replacement ratio	0%	10%	20%	0%	10%	20%
Calcite ($CaCO_3$)	3.29	3.04	2.5	4.57	3.51	2.86
Quartz (SiO_2)	63.05	63.54	65.7	53.14	58.84	54.7
Dolomite (Carbonate minerals)	1.67	3.11	4.12	1.31	1.36	0.78
Portlandite ($Ca(OH)_2$)	1.85	2.18	1.57	3.96	3.58	3.49

Comparing the proportions of minerals between the samples with different substitution ratios at 7-day age, it is found that the proportions of carbonates increase proportionally with the increase of the substitution ratios. This is mainly due to the proportion of calcium carbonate ($CaCO_{3)}$ in the BFBB co-firing fly ash reaches 14.39%, the proportion increases with the increase of the substitution ratio.

3.4 *Compressive strength test*

In this test, the compressive strength test of the specimen was carried out according to the CNS1232 specification [14]. According to the data of the test results, it is found that this ratio design meets the requirements of compressive strength (including 1day, 7day and 28day) under different BFBB co-firing fly ash substitution additions. It was found that the compressive strength was the highest when the amount of substitution was 15%, and the compressive strength decreased rapidly if the amount of substitution was increased. The compressive strength values are shown in Table 4.

Table 4. Compressive strength results.

	Compressive strength (kgf/cm^2)
Replacement ratio	28 days
0%	64.9
5%	66.6
10%	74.8
15%	81.8
20%	58.7

4 CONCLUSIONS AND RECOMMENDATIONS

1. Combining the above tests, it can be known that the co-firing fly ash in a bubble fluidized bed can be used to replace the cement material in the controlled low strength material, and the optimal ratio of replacement is 15%. If it exceeds 15%, the performance will drop significantly.
2. In this study, the proportion of BFBB co-firing fly ash to replace cement material in CLSM is only 20%, and the various properties (such as slump flow or compressive strength) are much higher than the CLSM specification. It is recommended to continue to explore the largest replacement in the future.

REFERENCES

[1] Lai Yingying (2018). Environmental Protection Agency of the Executive Yuan-Promoting recycling economy waste recycling. The 3587th session of the Executive Yuan, P1.
[2] The Environmental Protection Agency of the Executive Yuan, the Environmental Resource Analysis System, the four major categories of imports over the years (2010-2016).
[3] Environmental Protection Agency of the Executive Yuan, Industrial Waste Reporting and Management System, 2016 National Industrial Waste Reporting Statistics Form.
[4] The Basel Convention Promotion Website, Environmental Protection Agency, Executive Yuan, introduction to the Convention. Retrieved from https://basel.epa.gov.tw/basel (June, 27, 2021).
[5] Taiwan Iron and Steel Industry Association (2019), Application Manual of Controlled Low Strength Backfill Material (CLSM) in Electric Arc Furnace Steelmaking Oxidized Ballast (Stone), Taipei City.
[6] Controlled Low-Strength Materials Reported by ACI Committee 229 (ACI 229R-99 Reapproved 2005).
[7] Executive Yuan Public Construction Commission (2019), "Chapter 03377 Controlled Low-Strength Backfill Materials for Construction Outline Specifications of Executive Yuan Public Works Committee," V.8.0, revised February 25, 2019.

[8] National Standard of the Republic of China, CNS61: 2021 R2001, Portland Cement, revised on January 15, 2021.
[9] National Standard of the Republic of China, CNS15286: A2290, Hydraulic Mixed Cement, revised on July 30, 2014.
[10] National Standard of the Republic of China, CNS3036: 2021 A2040, Coal-fired fly ash and unburned or burnt natural Pozzolanic materials for concrete, revised on May 7, 2021.
[11] Zhu Xuede (2015), Research on the effect of adding circulating fluidized bed co-combustion fly ash and fly ash on the properties of cementitious composites, Master's Thesis, Institute of Materials Engineering, National Taiwan Ocean University, pp. 4–80.
[12] Qian Jueshi, Zheng Hongwei, Wang Zhi, Song Yuanming, Yang Juan, Method for assessing the activity of fluidized bed coal-fired sulfur-fixing ash, Journal of China Coal Society, August 2006 (Volume 31, Issue 4), pp.506–510.
[13] Yang Shifeng, Comparative Study on the Characteristics of Coal-fired Fly Ash and Co-fired Fly Ash in Fluidized Bed Boilers - Taking Textile Sludge as an Example, Master's Thesis, Department of Civil Engineering, National Central University, 2019.
[14] National Standard of the Republic of China, CNS1232 A3045, Test Method for Compressive Strength of Concrete Cylindrical Specimens, Revised on December 9, 1991.

Smart Geotechnics for Smart Societies – Zhussupbekov, Sarsembayeva & Kaliakin (Eds)
© 2023 The Author(s), ISBN 978-1-003-29912-7
Open Access: www.taylorfrancis.com, CC BY-NC-ND 4.0 license

Comparison of design methods for ground improvement by dry concrete columns

T.V. Tronda
Belarusian National Technical University, Minsk, Belarus

ABSTRACT: Nowadays, admixtures and inclusions are widely used as ground improvement. Variety of inclusions is used for this purpose all over the world. One of the effective types is dry concrete columns which were applied at construction sites in Belarus. For ground improvement design, there are different design methods. However, there is no one for dry concrete columns. Therefore, comparison of existing design methods for ground improvement was carried out in order to determine the most suitable for dry concrete columns design. Moreover, the methods were compared with results of field tests. The comparison and its analysis are described in the paper.

1 INTRODUCTION

Nowadays, there are many ground improvement methods which are used worldwide, also in Belarus. Some methods are described in codes, standards, and recommendations. However, dry concrete columns are quite a novel ground improvement method and there is no special design method for it.

Dry concrete columns (geomassif, vertical reinforcement and drainage elements) are used for upper soft water-saturated clayey soils to reinforce and drain them at the same time. The columns are installed together with a transfer layer under a shallow foundation, e.g. a mat foundation, but they can also be used for ground improvement in other cases. Dry concrete columns have been investigated in the laboratory (Tronda 2017, 2019, Sernov & Tronda 2019) and in-situ (Tronda 2016a, b, Tronda & Sernov 2020), successfully applied at construction sites in Belarus (Tronda 2013, 2016a, b, Sernov & Tronda 2019). The previous studies have proven dry concrete columns to be an efficient ground improvement method.

As dry concrete columns are mainly used for soft clayey soils layered under a foundation, the principal design comes to determination of vertical deformation, which must be less than limit settlement.

Design methods on determination of vertical deformations are described in Belarusian national normative documents for different types of foundation. Ground improvement methods and types of foundation alike dry concrete columns and their design are mentioned in four documents (P6-2000, R 1.02-133-2014, TKP 45-5.01-268-2012, TKP EN 1997-1-2009).

Therefore, the main purpose of the study was to learn design methods mentioned in the normative documents, check these methods for dry concrete columns and compare results with a field test in order to determine the most appropriate method for dry concrete columns design, specifically, for settlements estimation.

2 DESIGN METHODS

In this study, six Belarusian national normative documents were considered.

Initially, the following normative documents which describe similar to dry concrete columns types of foundation and their design were selected for consideration:

DOI: 10.1201/9781003299127-67

– P6-2000 to SNB 5.01.01-99 “Technogenous geomassifs from sand-gravel and crushed stone piles” (P6-2000);
– R 1.02-133-2014 “Recommendations for the design and installation of vertically reinforced foundations (geomassifs) for slab foundations of buildings and structures in the soil conditions of the Republic of Belarus” (R 1.02-133-2014);
– TKP 45-5.01-268-2012 “Bases and structures from the reinforced earth. Rules of designing and device” (TKP 45-5.01-268-2012);
– TKP EN 1997-1-2009 “Eurocode 7. Geotechnical design. Part 1. General rules” (TKP EN 1997-1-2009).

P6-2000, R 1.02-133-2014 and TKP 45-5.01-268-2012 include detailed description of methods for settlements calculation. The methods are based on the layer-by-layer summation method, which is commonly used in Belarus. Moreover, the documents use equivalent modules of deformation for improved ground (technogenic geomassif).

The last one, TKP EN 1997-1-2009 “Eurocode 7. Geotechnical design. Part 1. General rules” (TKP EN 1997-1-2009), is a version of translation of DIN EN 1997-1:2008 “Eurocode 7: Geotechnical design – Part 1: General rules” (DIN EN 1997-1:2008). There are basic geotechnical design approaches similar to national ones (Kravtsov 2019) but the code does not include a detailed design method for technogenic geomassifs or similar structures. Therefore, it will not be considered in this study.

However, two more documents were taken for comparison. These are:

– TKP 45-5.01-67-2007 “Slab foundations. Rules of designing” (TKP 45-5.01-67-2007);
– TKP 45-5.01-254-2012 “Bases and foundations of buildings and structures. The basic rules. Construction standards of designing” (TKP 45-5.01-254-2012).

TKP 45-5.01-67-2007 was considered to determine settlement of a slab on natural ground as if any reinforcement or improvement was not applied. TKP 45-5.01-254-2012 was selected additionally to determine settlement as if it was a pile foundation. For settlement calculation, the mentioned documents are also based on layer-by-layer summation method.

Limit general settlements are given in TKP 45-5.01-254-2012 and must be under 80-150 mm depending on building.

3 FIELD TEST

Ground improvement with dry concrete columns was applied under a foundation slab of a multi-storey building at a construction site in Minsk. In order to determine the accessibility of the improvement method, a set of field tests was fulfilled. One of the tests was static load tests of improved ground massif under each building section. In this study, one of static load tests results was taken for comparison with existing design methods.

Engineering geological conditions of the site included soft sandy clays, peaty soils, chalk, marl and sands. Soil properties are given in Table 1.

Table 1. Sub-surface conditions at the test site.

Unit	γ_{II}, kN/m^3	c_{II}, kPa	φ_{II},°	E, MPa	q_s, MPa	f_s, kPa
Sand transfer layer	17.0	–	–	30	–	–
Technogenic formation						
1 fill-up soil	16.8	–	–	18	5.9	40
Lacustrine, alluvial, swamp deposits						
3 sandy clay	19.7	26	25	8	1.2	45
9 medium-coarse sand	17.9	2	37	21	14.0	102
10 medium-coarse sand	17.9	2	38	33	19.1	113
3 sandy clay	19.7	26	25	8	1.9	41
10 medium-coarse sand	17.9	2	38	33	26.2	115
5 marl, chalk, peaty soil	13.3	28	5	12	2.8	71

The test area included dry concrete columns installed into the ground and a sand transfer layer under a reinforced concrete slab (see Figures 1-2).

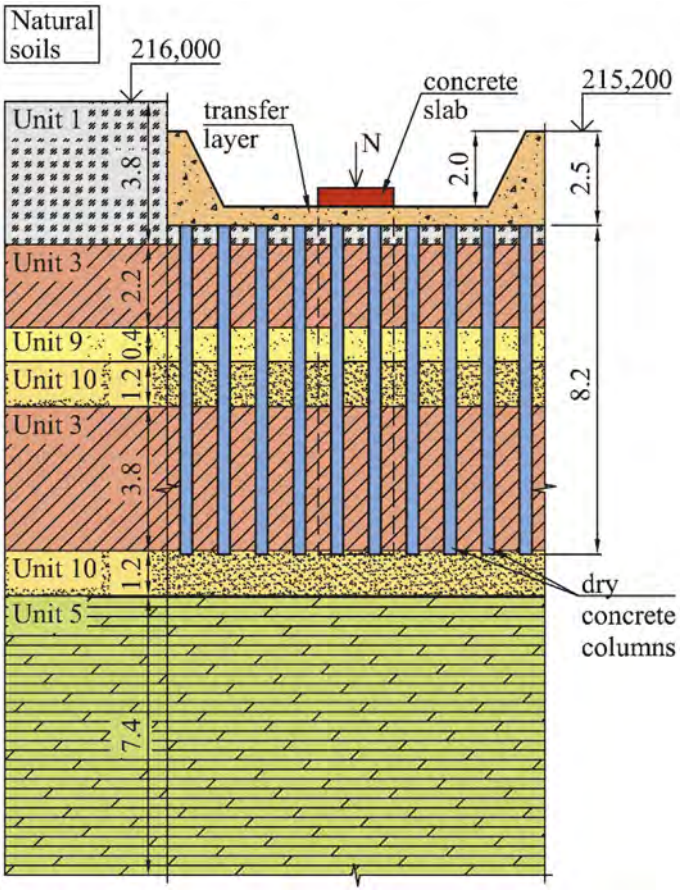

Figure 1. Geotechnical cross section at the test site.

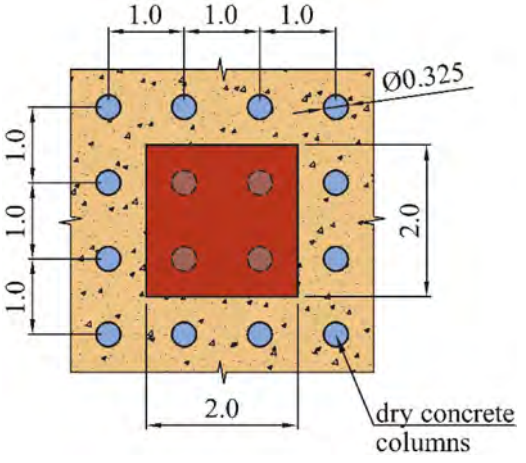

Figure 2. Top view of the test fragment.

The static load test was carried out according to GOST 20276-99 "Soils. Field methods for determining the strength and strain characteristics" (GOST 20276-99) (see Figure 3). Loads were applied to the slab by hydraulic jack step by step beginning from pressure of 50 kPa to 350 kPa. Vertical displacements of the slab were measured with four deflection gauges. Settlements of the slab were stated after each step stabilisation.

Figure 3. Field static load test.

4 STUDY RESULTS

Results of the field test and calculations according to normative documents mentioned above are shown in Table 2 and Figure 4.

Table 2. Settlements *s*, mm received in-situ and calculated according to different methods.

	Pressure *P*, MPa						
Method	50	100	150	200	250	300	350
Field test	1.4	2.8	4.0	5.4	6.8	8.3	9.8
P6-2000	3.8	8.3	13.0	17.8	22.7	27.6	32.6
TKP 45-5.01-268-2012	3.8	8.4	13.3	18.1	23.1	28.1	33.2
R 1.02-133-2014	4.3	9.6	15.1	20.6	26.3	32.0	37.8
TKP 45-5.01-67-2007	5.5	12.0	18.3	24.6	31.1	37.9	44.9
TKP 45-5.01-254-2012	3.8	13.5	23.7	33.9	44.5	55.5	66.5

Thus, field test results show lower settlements at all steps of loading than results of analytical calculations according to reviewed regulations.

The closest method is one described in P6-2000 to SNB 5.01.01-99. The difference between field test results and calculations was from 2.7 to 3.3 times. Similar values were obtained according to TKP 45-5.01-268-2012 but considering calculation of additional stress in the ground according to layer-by-layer summation method. Both methods use equivalent modulus of deformation.

Additionally selected TKP 45-5.01-67-2007 considered only a slab on natural ground without an improvement, and TKP 45-5.01-254-2012 determined settlements as for a pile foundation. The methods did not consider ground improvement, but loads transfer into soft layers. Consequently, high settlements were received.

In general, the difference between field test results and calculations amounted up to 6.8 times. The difference can be explained by the fact that the design methods do not take into account changes on natural soils caused by installation of dry concrete columns. As it was proved in

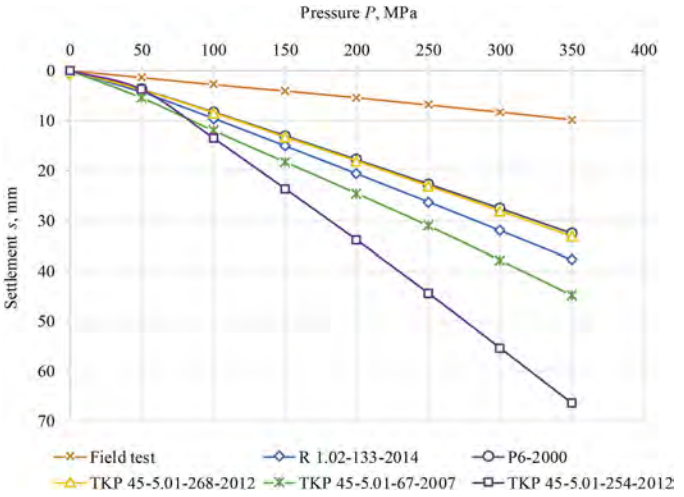

Figure 4. Graphs $s = f(P)$ according to different methods.

earlier study, dry concrete of columns absorbs pore water that leads to decreasing water saturation, the installation method allows natural soils to be compacted that leads to decreasing porosity and strengthening soils. As the result, deformation properties of natural soils improve and settlements decrease.

Moreover, the layer-by-layer summation method for settlement calculation used in all mentioned regulations is not extremely accurate (but quite easy to use) that leads to differences between field test results and analytical calculations.

Therefore, special design methods for dry concrete columns should be developed and implemented into design practice.

5 CONCLUSIONS

Field test of dry concrete columns show lower settlements at all steps of loading than results of analytical calculations according to existing national regulations.

The closest to field test results method is one described in P6-2000 to SNB 5.01.01-99 "Technogenous geomassifs from sand-gravel and crushed stone piles". The difference between field test results and calculations is from 2.7 to 3.3 times.

The difference between field test results and calculations can be explained by the fact that the design methods do not take into account changes on natural soils caused by installation of dry concrete columns.

Not only national normative documents but also unofficial methods should be taken into consideration to find a more suitable one as a base for special design method for dry concrete columns.

Special design method for dry concrete columns should be developed. The method should consider changes on natural soil properties caused by installation of dry concrete columns.

REFERENCES

DIN EN 1997-1:2008. *Eurocode 7: Geotechnical design – Part 1: General rules*. Brussels: CEN.

GOST 20276-99. *Soils. Field methods for determining the strength and strain characteristics*. Minsk: Ministry of Architecture and Construction of the Republic of Belarus.

Kravtsov, V. 2019. Practice in the application of Eurocode 7 in the Republic of Belarus and the comparison results of the geotechnical calculation of bases foundation according to European and national standards. *Vestnik of Polotsk State University. Part F, Constructions. Applied sciences* 8(22): 79–86.

P6-2000 to SNB 5. 01.01-99. *Technogenous geomassifs from sand-gravel and crushed stone piles*. Minsk: Ministry of Architecture and Construction of the Republic of Belarus.

R 1.02-133-2014. *Recommendations for the design and installation of vertically reinforced foundations (geomassifs) for slab foundations of buildings and structures in the soil conditions of the Republic of Belarus*. Minsk: Ministry of Architecture and Construction of the Republic of Belarus.

Sernov, V.A. & Tronda, T.V. 2019. Model researches and practical application of vertical reinforcing-draining elements for improvement of soft clay soils in Minsk. *Vestnik of Polotsk State University. Part F, Constructions. Applied sciences* 18(16): 45–52.

TKP 45-5.01-254-2012 (02250). *Bases and foundations of buildings and structures. The basic rules. Construction standards of designing*. Minsk: Ministry of Architecture and Construction of the Republic of Belarus.

TKP 45-5.01-268-2012 (02250). *Bases and structures from the reinforced earth. Rules of designing and device*. Minsk: Ministry of Architecture and Construction of the Republic of Belarus.

TKP 45-5.01-67-2007 (02250). *Slab foundations. Rules of designing*. Minsk: Ministry of Architecture and Construction of the Republic of Belarus.

TKP EN 1997-1-2009 (02250). *Eurocode 7. Geotechnical design. Part 1. General rules*. Minsk: Ministry of Architecture and Construction of the Republic of Belarus.

Tronda, T. 2013. Actual experience with the geo-massive in complicated soil conditions. *Proc. of the 5th International Young Geotechnical Engineers' Conference, Paris, 31 August – 1 September 2013*, 2: 151–154.

Tronda, T. 2016a. Ground improvement by dry concrete columns. *Deep Foundations, Seepage Control and Remediation*; *Proc. of the International Conference*, *New York*, 12-15 October 2016: 225–231.

Tronda, T. 2016b. Improvement of soft soil characteristics through application of dry concrete mix pillars. In Askar Zhussupbekov (ed.), *Challenges and Innovations in Geotechnics*; *Proc. of the 8th Asian Young Geotechnical Engineers Conference*, *Astana*, 5-7 August 2016: 155–158. London: Taylor & Francis Group.

Tronda, T. 2017. Improvement of soft clay soils with vertical reinforcing drain elements. *Proc. of the 6th International Young Geotechnical Engineers' Conference, Seoul, 16-17 September 2017*: 111–112.

Tronda, T. 2019. Experimental research of ground improvement using dry concrete. *Proc. of the XVII European Conference on Soil Mechanics and Geotechnical Engineering*; *Reykjavík*, 1-6 September 2019.

Tronda, T.V. & Sernov, V.A. 2020. In-situ research of foundation soils reinforced with cylindrical and conical vertical elements of dry concrete. In D.N. Lazovsky (ed.), *Architectural and construction complex: problems, prospects, innovations*; *Proc. of the II International scientific conference*, *Novopolotsk,* 28-29 November 2019: 47–51.

Smart Geotechnics for Smart Societies – Zhussupbekov, Sarsembayeva & Kaliakin (Eds)
© 2023 The Author(s), ISBN 978-1-003-29912-7
Open Access: www.taylorfrancis.com, CC BY-NC-ND 4.0 license

Effect of alkali activated materials in stabilizing sabkha soil

Wagdi M. Hamid, Ahmed M. Alnuaim* & Abdulhafiz O. Alshenawy
Department of Civil Engineering, College of Engineering, King Saud University, Riyadh, Saudi Arabia

ABSTRACT: Sabkha soil is one of the most problematic and hazardous soils in arid areas. Due to the geotechnical concerns connected with sabkha soil an appropriate treatment method must be implemented before using it as a construction material. Ordinary Portland cement (OPC) is one of the major chemical additives utilized to minimize the geotechnical issues of sabkha soil. However, OPC manufacturing is a significant source of carbon dioxide (CO_2) emissions globally. Consequently, environmental issues are gaining prominence around the world, prompting the immediate need for new sustainable solutions. Hence, this paper aims to investigate the potential of alkali-activated material as a promising alternative to OPC. The results show that the geopolymer treatment significantly increase the UCS compared to untreated sabkha soil, and the highest value is obtained when using the molarity of NaOH of 8 M.

Keywords: Sabkha soil, problematic soil, alkali-activated material, chemical stabilization

1 INTRODUCTION

Sabkha sediments have low dry densities and high void ratios. As a result, when wet, sabkha soil is recognized for having a very compressible nature with low bearing resistance and is hence regarded as one of the worst foundation materials. The existing condition of sabkha soil renders it unsuitable as a foundation material and incapable of supporting the vast majority of construction projects. This leads to enhancing the soil's engineering properties prior to applying structural loads (Alnuaim and El Naggar, 2014; Alnuaim, Alsanabani and Alshenawy, 2020; Alshenawy, Hamid and Alnuaim, 2021).

Damage to roads and other infrastructure built on sabkha soil has been documented in many sites around the world, especially in arid and hot areas, resulting in major financial losses. Ordinary Portland cement (OPC) and lime are the most widely used stabilizing binders. However, in the past several decades, the carbon footprint associated with the production of these conventional binders has led to significant environmental risks. The use of alkaline activated aluminosilicate minerals to make binders for soil stabilization is an ecologically friendly and low-energy alternative to the common soil stabilization methods (e.g., OPC and lime) since it permits the efficient recycling of industrial by-products (e.g., fly ash (FA), mine tailing, and granulated ground blast furnace slag). Numerous studies have investigated the potential of geopolymers based on FA in stabilizing various types of soils (Cristelo *et al.*, 2013; Parhi *et al.*, 2017; Teing *et al.*, 2019). There are a number of potential building dangers when working with sabkha soils because of their variability and poor natural strength capacity. The limited bearing capacity of sabkha soils is the main reason for these issues. Also, sabkha soils are extremely water sensitive. Contact with water results in a decrease in bearing capacity and a complete collapse. The objective of this study was to stabilize sabkha soil samples using geopolymerization with sustainable and environmentally friendly raw materials (such as FA). In this study, an FA-based geopolymer that is activated by sodium hydroxide and sodium silicate solutions was utilized. Various laboratory tests, including sieve analysis, standard compaction tests, unconfined compressive strength tests (UCS), and X-ray fluorescence (XRF) tests, were conducted.

*Corresponding author: alnuaim@ksu.edu.sa

DOI: 10.1201/9781003299127-68

2 EXPERIMENTAL METHOD

2.1 *Materials*

Samples of sabkha soil were collected in Ras-Al-Ghar, Eastern Province of Saudi Arabia. Figure 1 displays the particle size distribution curves of the sabkha soil. The percentage of soil that went through the #200 sieve was 6.8%, and the USCS and AASHTO soil classifications are SP-SM and A-3, respectively. In order to synthesize geopolymer, FA class F was utilized as a precursor. Table 2 displays the chemical compositions of the sabkha soil and FA as revealed by X-ray fluorescence (XRF) analysis. sabkha soil was composed primarily of CaO (40.43%) and SiO_2 (16.81%), while FA was composed primarily of SiO_2 (58.196%) and Al_2O_3 (27.78%). The alkaline activator solution was a combination of sodium silicate (SS) (Na_2SiO_3) and sodium hydroxide (SH) in a ratio of 2:1. (NaOH). The chemical composition of the SS solution is 8.7% Na_2O, 28.73% SiO_3, 60 ppm Fe, and 37.43% total solids. At 27°C, the specific gravity of the SS solution was 1.38 and its viscosity was 158 CPS. SH was originally a flake with a molecular weight of 40 g/mole and a purity of 99.9%.

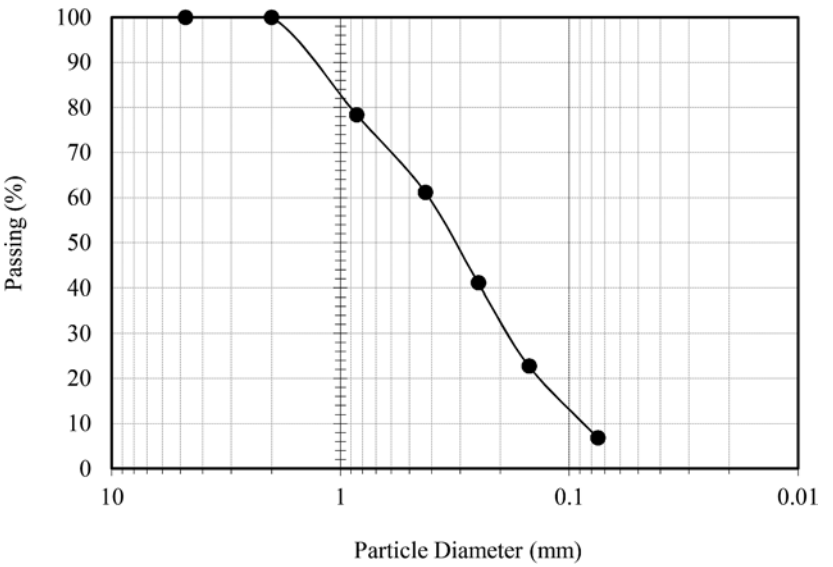

Figure 1. Grain size distribution of sabkha soil.

Table 1. Physical properties of sabkha soil.

Properties	Parameters
Specific gravity, G_s	2.78
Passing through #200 (%)	6.786
D_{10} (mm)	0.09
D_{30} (mm)	0.19
D_{60} (mm)	0.42
C_u	4.67
C_c	0.96

2.2 *Specimens' preparation and testing procedures*

The SH solution was produced by dissolving a certain amount of SH in distilled water, based on its molarity (e.g., 4, 8, 12). SH flakes were dissolved in water, and the resulting

Figure 2. Procedure for preparation of geopolymer-treated samples.

Table 2. XRF analysis of FA, and sabkha soil.

Elemental Oxide	Sabkha	FA
Na_2O	1.408	0.260
MgO	6.519	0.711
Al_2O_3	1.304	27.78
SiO_2	16.814	58.196
P_2O_5	0.03	0.483
SO_3	5.065	0.697
K_2O	0.329	1.505
CaO	40.43	3.948
TiO_2	0.072	1.615
MnO	0.012	0.031
Fe_2O_3	0.503	4.145
Cl	1.659	0.122
CuO	-	0.013
LOI	25.80	0.30

solution was cooled to room temperature before being combined with SS solution. In a cylindrical metal mold with a diameter of 36 mm and a height of 72 mm, the UCS specimens were formed. The needed amounts of dry ingredients (sabkha soil and FA) were weighed and hand-combined to create a dry mixture. An adequate amount of the alkaline activator with a predetermined molar concentration was added to the mixture and thoroughly mixed until it was homogeneous. A predetermined quantity of the mixture was poured in three equal levels into the metal mold. Immediately following compaction, the specimens were extruded and cured at room temperature (23°C). Figure 2 shows the procedure for preparation of geopolymer-treated samples. By conducting UCS tests in accordance with ASTM D2166, the strength performance of untreated and geopolymer-treated sabkha soil samples was determined. The stress–strain curves were created by applying a constant loading rate of 0.5 mm/min to the specimens. The UCS values were derived from these curves as the peak axial stresses.

3 RESULTS AND DISCUSSION

3.1 *Effect of standard compaction test*

The results of the standard proctor compaction test on untreated and geopolymer-treated soil are shown in Figure 3. The results of optimum moisture content (OMC) and maximum dry density (MDD) for 0% of FA represent the untreated soil. The geopolymer-treated soil was found to have a higher MDD and a lower OMC than the untreated soil. Due to the solution's lubricating properties, which reduce repulsive forces and improve soil particle sliding, the OMC was found to have decreased (Abdullah, 2020). However, the increase in MDD was attributed to the fact that FA had finer particles than sabkha soil and that MDD is influenced by grain size distribution. MDD is affected by the grain size distribution because FA has finer particles than sabkha soil (Osinubi, Yohanna and Eberemu, 2015; Ojuri, Adavi and Oluwatuyi, 2017; Murmu, Jain and Patel, 2019).

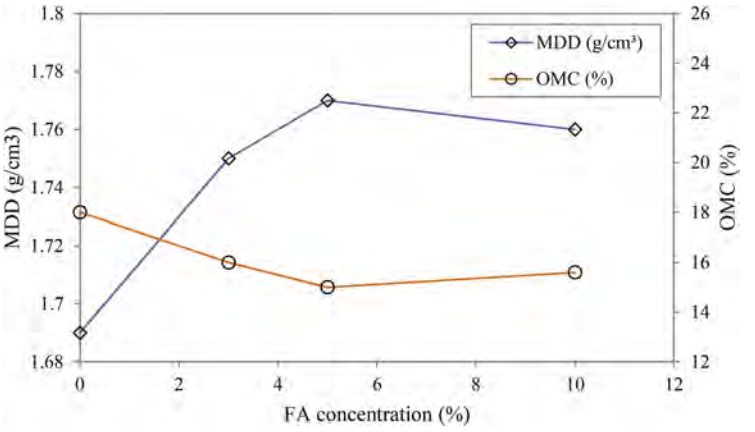

Figure 3. Results of standard proctor compaction tests on untreated and treated sabkha soil.

3.2 *Effect of FA concentration on UCS*

Figure 4 depicts the UCS results at different FA concentration (3%, 5%, and 10%) and different curing periods (1, 7, and 28 days) compared to the untreated UCS values. The UCS was increased by 535%, 536% and 697% compared to untreated soil specimens after 1 day of curing. The strength improvement behavior was also observed clearly for samples cured at 7 and 28 days. The improved binding of soil particles by geopolymer gels is most likely responsible for the higher strength.

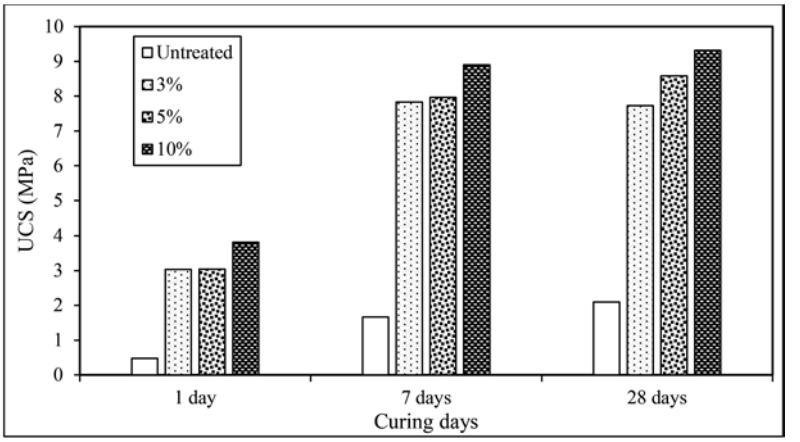

Figure 4. Effect of FA concentration and curing period on the improvement of UCS.

3.3 *Effect of NaOH molarity on UCS*

Figure 5 illustrates the effects of NaOH molarity in the alkaline solution on the UCS of the treated sabkha soil. When the concentration of NaOH was increased, the UCS of the treated soil was considerably enhanced. This performance is due to the effect of SH concentration on the dissolution of silica and alumina, which strengthens the geopolymeric link and increases UCS (Manjarrez and Zhang, 2018; Noolu et al., 2020). Figure 6 displays the effect of FA concentration and NaOH molarity on UCS after 7 days of curing. It is clearly shown that the higher UCS values were obtained when the molarity of NaOH is 8 M. This conclusion was also reported by previous researchers (Ghadir and Ranjbar, 2018; Noolu et al., 2020).

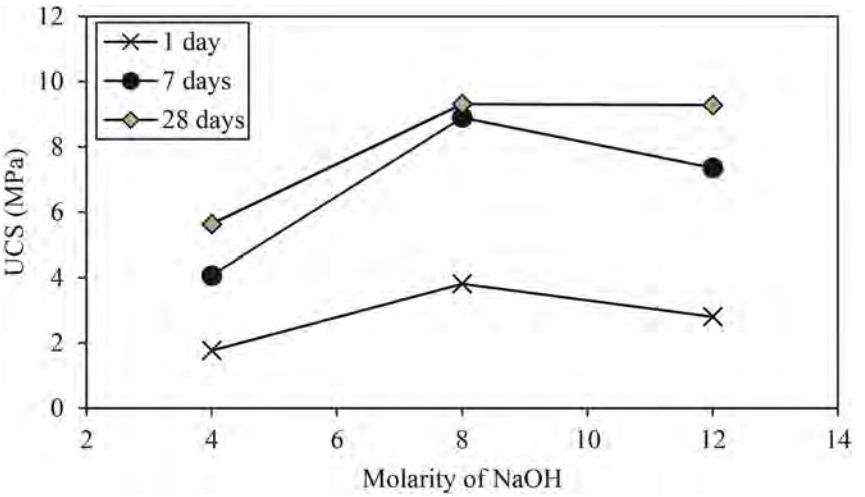

Figure 5. Effect of molarity of NaOH and curing period on UCS.

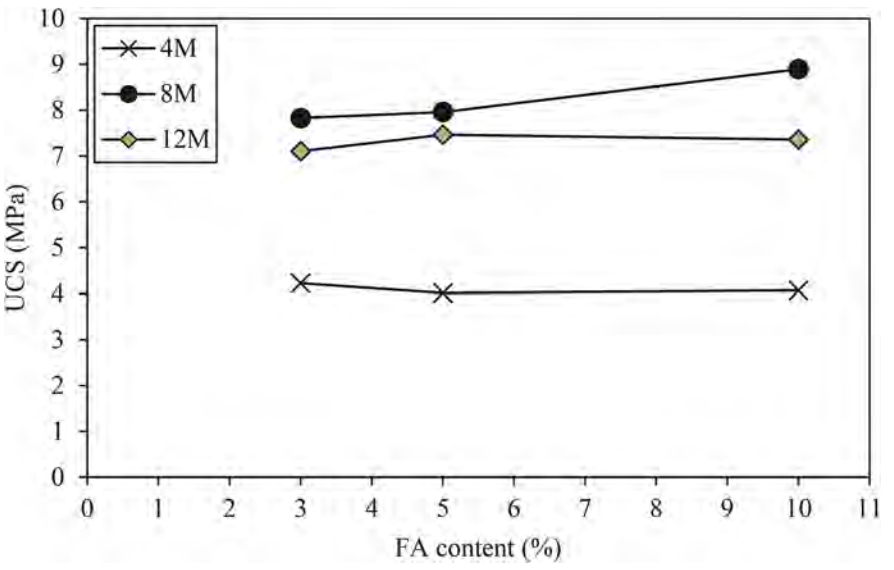

Figure 6. Effect of FA concentration and NaOH molarity on UCS after 7 days of curing.

4 CONCLUSION

This work highlights the ability of alkali-activated materials as an environmentally sustainable solution as a sabkha soil stabilizer. In comparison to untreated sabkha soil, the soil samples treated with geopolymer had higher MDD and lower OMC. In comparison to untreated soil, FA-based geopolymer increases the strength by more than 500%. The maximum value of UCS was measured when using the molarity of NaOH of 8 M and a concentration of FA of 10%. It is expected that the outcomes of the research would motivate geotechnical engineers to employ novel sustainable ways of stabilizing saline sabkha soil, such as stabilization based on geopolymers.

REFERENCES

Abdullah, H. H. 2020. An experimental investigation on stabilisation of clay soils with fly-ash based geopolymer. PhD thesis, Curtin University.

Alnuaim, A., Alsanabani, N. and Alshenawy, A. 2020. Monotonic and cyclic behavior of salt-encrusted flat (Sabkha) soil. *International Journal of Civil Engineering*. Springer International Publishing, 0. doi: 10.1007/s40999-020-00561-0.

Alnuaim, A. M. and El Naggar, M. H. 2014. Performance of foundations in sabkha soil: numerical investigation. *Geotechnical and Geological Engineering*. 32(3), pp. 637–656. doi: 10.1007/s10706-014-9739-6.

Alshenawy, A. O., Hamid, W. M. and Alnuaim, A. M. 2021. A review on the characteristics of sabkha soils in the Arabian Gulf Region. *Arabian Journal of Geosciences*, 14(19). doi: 10.1007/s12517-021-08275-w.

Cristelo, N. et al. 2013. Effects of alkaline-activated fly ash and Portland cement on soft soil stabilisation. *Acta Geotechnica*, 8(4), pp. 395–405. doi: 10.1007/s11440-012-0200-9.

D2166, A. 2016. ASTM D2166, Standard test method for unconfined compressive strength of cohesive soil, ASTM, West Conshohocken, PA, USA'.

Ghadir, P. and Ranjbar, N. 2018. Clayey soil stabilization using geopolymer and Portland cement. *Construction and Building Materials*. Elsevier Ltd, 188, pp. 361–371. doi: 10.1016/j.conbuildmat.2018.07.207.

Manjarrez, L. and Zhang, L. 2018. Utilization of copper mine tailings as road base construction material through geopolymerization. *Journal of Materials in Civil Engineering*, 30(9), p. 04018201. doi: 10.1061/(asce)mt.1943-5533.0002397.

Murmu, A. L., Jain, A. and Patel, A. 2019. Mechanical properties of alkali activated fly ash geopolymer stabilized expansive clay, *KSCE Journal of Civil Engineering*, 23(9), pp. 3875–3888. doi: 10.1007/s12205-019-2251-z.

Noolu, V. et al. 2020. Strength and durability characteristics of GGBS geopolymer stabilized black cotton soil, *Materials Today: Proceedings*. Elsevier Ltd., 43, pp. 2373–2376. doi: 10.1016/j.matpr.2021.01.939.

Ojuri, O. O., Adavi, A. A. and Oluwatuyi, O. E. 2017. Geotechnical and environmental evaluation of lime–cement stabilized soil–mine tailing mixtures for highway construction, *Transportation Geotechnics*. Elsevier Ltd, 10, pp. 1–12. doi: 10.1016/j.trgeo.2016.10.001.

Osinubi, K. J., Yohanna, P. and Eberemu, A. O. 2015. Cement modification of tropical black clay using iron ore tailings as admixture, *Transportation Geotechnics*. Elsevier Ltd, 5, pp. 35–49. doi: 10.1016/j.trgeo.2015.10.001.

Parhi, P. S. et al. 2017. Stabilization of an expansive soil using alkali activated fly ash based geopolymer', in International Congress and Exhibition" Sustainable Civil Infrastructures: Innovative Infrastructure Geotechnology. Cham: Springer, pp. 36–50. doi: 10.1007/978-3-319-61931-6.

Teing, T. T. et al. 2019. Effects of alkali-activated waste binder in soil stabilization, *International Journal of GEOMATE*, 17(59), pp. 82–89. doi: 10.21660/2019.59.8161.

Smart Geotechnics for Smart Societies – Zhussupbekov, Sarsembayeva & Kaliakin (Eds)
© 2023 The Author(s), ISBN 978-1-003-29912-7
Open Access: www.taylorfrancis.com, CC BY-NC-ND 4.0 license

Plastic materials waste for improvement gypseous soil

L.N. Snodi
Department of Civil Engineering, Tikrit University, Tikrit, Iraq

ABSTRACT: Large quantities of plastic waste are released into the environment in an undesirable way, these waste causes many environmental problems. The current research presents an attempt to improve the properties of gypseous soil by using plastic. Different percentages of plastic (2%, 4% and 6%) were mixed with a soil of gypsum content of 57%. The results showed that adding (6%) of plastic leads to a reduction in the maximum dry unit weight by (21.48%), and the optimum moisture content increases by (20.68%). The angle of internal friction decreased by (17.45%) when adding (6%) plastic, and the soil cohesion decreased by (266.125%) when adding (6%) plastic . Overall, the plastic had positive effect on some geotechnical properties of soil and it can be used as admixture in soil.

1 INTRODUCTION

Gypseous soils are considered as collapsible soils, which contain high proportion of hydrated calcium sulfate ($CaSO_4.2H_2O$). Gypsum, dissolves due to water infiltration into soils leading them to be soft and highly compressible causing severe foundation problems due to collapse of soils structure and the formation of cavities (Al-Mohammadi et al. 1987).

Gypsum present in soil structure acts as a binder (cementing material) between soil particles and causes the soil to be very hard when it is dry. The bond between soil particles of fine materials and salts is washed away during saturation process and consequently this results in the general soil collapse. It is well known that many damages are recorded in several projects located in particular regions in Iraq due to presence of gypseous soils underneath the base of foundation. Problems associated with structures constructed on gypseous soils can be summarized as: settlement, collapse due to soaking, collapse due to leaching, delayed compression and shear failure Al-Neami.(2006).

The amount of wastes has increased and the disposal becomes a serious problem. Particularly, recycling ratio of the plastic wastes in life and industry is low and many of them have been reclaimed for the reason of unsuitable ones for incineration. It is necessary to utilize the wastes effectively with technical development in each field**.** For the construction of any kind of structure resting on collapse soil, there are many methods used to improve this soils, such as mixed with other materials lime, bentonite, ashes and chemicals ..etc. Thakur & Yadav (2018).

Rao & Dutta (2004) assessed the overall influence of waste plastic as a reinforced material on the bearing capacity improvement of granular trench. The results of tests concluded that inclusion of waste plastic strips in sand improves the bearing capacity.

This paper studying the ability of plastic waste to improve Gypseous soil.

2 MATERIALS USED

2.1 *Soil*

Soil used in this study is poorly graded (SP) as classified according to USCS. The soil used was brought from Tikrit city, which located in Salah-Aldeen Governorate, in the middle of Iraq at 1m depth Figure 1. The basic properties of soil was listed in Table 1.

DOI: 10.1201/9781003299127-69

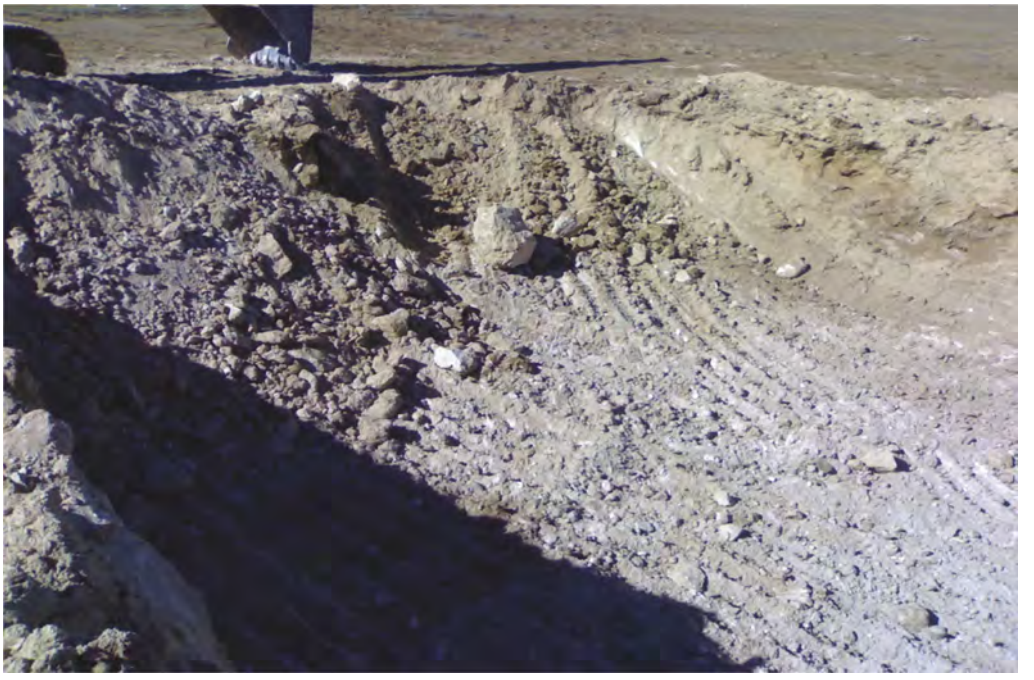

Figure 1. Gypseouse soil depth 1m.

Table 1. Basic Properties of soil used.

Properties	values
Specific gravity, (Gs)	2.46
Liquid limit (L.L)%	N.P.
Plastic limit (P.L)%	N.P.
Maximum dry unit weight (γ_{max}) kN/m^3	16.4
Optimum moisture content %	14.5%
Gypsum content (Gc)%	57%

2.2 *Plastic waste material*

Plastic is an easy-to-form material in various forms that mainly consists of chains called polymers. Since the world knew the Industrial Revolution, societies are still witnessing development from the age of coal to the era of black gold (petroleum), which contributed to the emergence of many new industries that developed over time. The plastic industry appeared and flourished and is today at the forefront of the current industries due to its many uses in daily life, because it is involved in the installation of things and tools surrounding us. Figure (2) shown the plastic used in this study cut from bottle of water each piece was 1cm

3 EXPERIMENTAL WORK

Many tests were done in this study to complete the experimental program, Physical Tests (Particle Size Distribution, Atterberg Limits Test, Specific Gravity, Gypsum Content) and Engineering Properties (direct shear test to obtain the shear parameters (C and φ) and compaction test).

3.1 *The particle size distribution*

The particle size distribution of the tested samples for gypseous soils were determined according to (ASTM D - 422) (dry sieving). The results shows that for gypseous soil the percentages

Figure 2. Pieces of plastic.

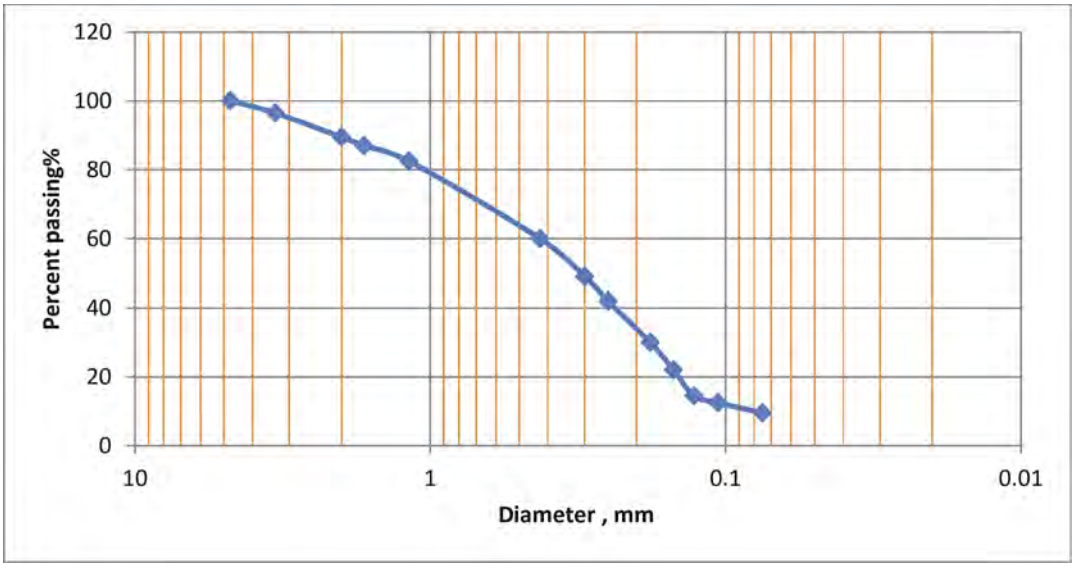

Figure 3. Grain size distribution of gypseous soil.

of gravels, sand and fines were (3.5, 87 and 9.5) respectively. Figure 3 shows the particle size distribution.

3.2 *Gypsum content*

The gypsum content determination Al - Mufty & Nashat method (2000) depending on the heating process. They described that gypsum content could be easily estimated by oven drying of the soil specimen at (45°C) temperature until the specimen weight becomes constant, the weight is recorded. Then the specimen is dried at (105°C) temperature, and the weight is rerecorded. The gypsum content was calculated according to the following equation.

$$Gc\% = \frac{W45^{\circ}C - W105^{\circ}C}{W45^{\circ}C} \times 4.778 \times 100\% \quad (1)$$

Where:
Gc = Gypsum content by weight%
W45°C = Weight of sample at 45°C
W105°C = Weight of sample at 105°C
4.778 = Inverse ration of molecular weight of hydration water to the molecular weight of gypsum. The result are tabulated in Table 1.

3.3 *Direct shear test*

The test is applied on the soil and soil/plastic mixture (2, 4, and 6% plastic/soil mixture) to obtain the shear strength parameters (cohesion c and internal friction angle φ) according to the ASTM specification D3080-72.

3.4 *Compaction tests*

Standard compaction test applied on the original soil and soil/plastic mixture (2, 4, and 6% plastic/soil mixture) to evaluate the effect of plastic percentages on the density of soil. This test applied according to ASTM D 698 – 12 clauses 2.

4 RESULTS AND DISCUSSION

Direct shear test are carried out on dry condition for samples treated with (2%, 4% and 6%) plastic content, Figure 4 shows the relationship between the normal stress and shear stress for treated and untreated samples in dry condition. The maximum shear stress versus normal stress was drawn, and both shear strength parameters, that angle of internal friction (ϕ) and cohesion (c) were calculated. A summary of the test results is given in Table 2. The results show that the cohesion of soil (c) and angle of internal friction (ϕ) decreased as the plastic content increased from (2%) to (6%). The reason behind this behavior is due to the plastic effect which did not create a high bonding force between the soil particles and the plastic which led to a decrease in the strength of the plastic mixture and the gypsum soil.

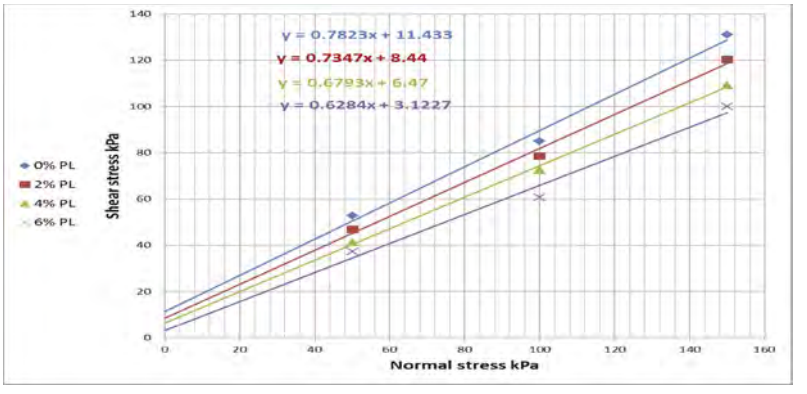

Figure 4. Direct shear results for gypseous soil treated with plastic.

For compaction tests the soil mixtures, with and without additives, were thoroughly mixed. The first series were aimed to determine the compaction properties of the untreated soils. Secondly, tests were carried out to determine the Proctor compaction properties of the treated

Table 2. Summary of the direct shear result of gypseous soil treated with plastic.

Plastic Content%	Cohesion (kN/m^2)	Internal angle of friction(ϕ)
0	11.43	38.6
2	8.44	36.73
4	6.47	34.43
6	3.12	32.87

soils with varying amounts of plastic .It is worth to mention that in this research used the soil which passes on sieve No. 4 for all of the tests.

The addition of plastic affected the compaction parameters of soil-plastic mixtures. It was observed that the maximum dry unit weight decreased and optimum moisture content increase with the addition of plastic and the reason for that the specific gravity of plastic is less than the specific gravity of the soil used. On the other hand, the reason behand the increase in optimum moisture content and decrease in maximum dry unite weight with the increase in plastic proportions because the plastic created large gaps inside the mixture of soil and plastic .

Figure 5 shows the relationship between the maximum dry unit weight and optimum moisture content increase for treated and untreated samples for gypseous content (57%).

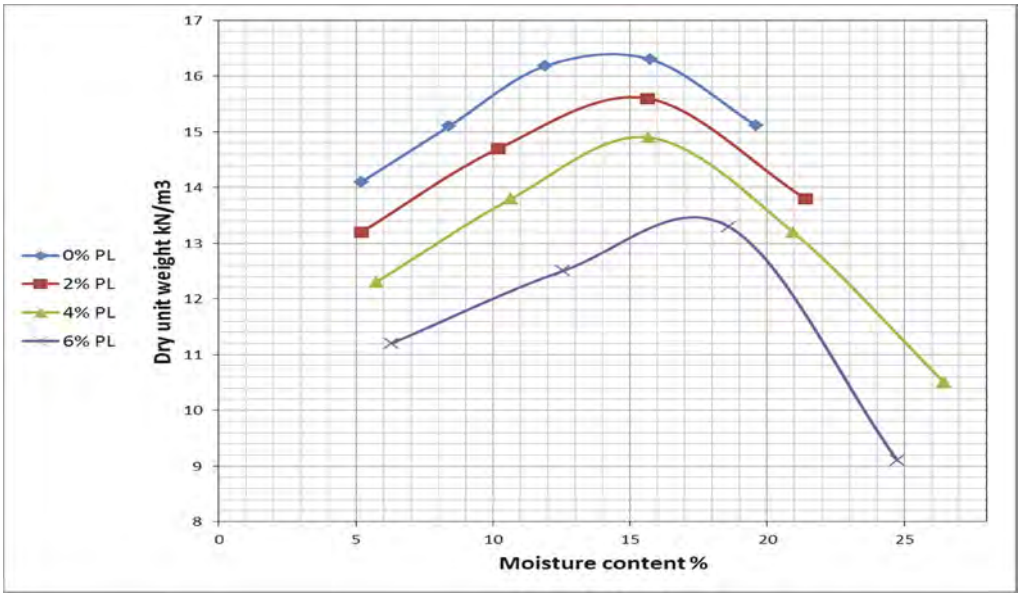

Figure 5. Compaction test results for gypseous soil with plastic.

5 CONCLUSIONS

Based on the results following conclusions can be drawn:

1- Adding plastic decreases the maximum unit weight of the Gypseous soil and also it increases the optimum water content.

2- plastic works as not good filler material to fill the voids between particles of a gypseous soil passes on sieve No. 4.

3- Adding plastic to the Gypseous soil decreases the cohesion value and decreases the internal friction angle when increasing the plastic to (6%).

REFERENCES

Al-Mufty, A.A. and Nashat, E. H. 2000. Gypsum Content Determination in Gypseous Soils and Rocks. Proceedings of the 3th Jordanian International Mining Conference, Amman. (2): 485–492.

Al-Mohmmadi, N. M., Nashat, I. H. and Bako, G. Y. 1987. Compressibility and Collapse of Gypseous Soils. In Proc. 6th Asian Conf. on Soil Mechanics. (1): 51-54. Tokyo.

Al-Neami, M. A. M. 2006. Evaluation of Delayed Compression of Gypseous Soils with Emphasis on Neural Network Approach. Ph.D Thesis, Department of Civil Engineering of Al-Rasheed, College of Engineering and Science, University of Technology, Baghdad, Iraq.

ASTM D422. 2002. Standard Test Method for Particles Size Analysis of Soil.

ASTM D3080. 2000. Standard Test Method for Direct Shear Test of Soils under Consolidated Drained Conditions.

ASTM 698. 2000. Standard Test Methods for Laboratory Compaction Characteristics of Soil Using Standard Effort.

Rao V., G. and Dutta, R.K. 2004. Ground Improvement with Waste Plastic. Proceedings of 5th International Conference on Ground Improvement Techniques, 22 – 23 March, Kaula Lumpur, Malaysia, 321–328

Thakur, Y. and Yadav, R.K., 2018. Effect of bentonite clay on compaction, CBR and shear behavior of Narmada sand. International Research Journal of Engineering and Technology (IRJET), 5(3), 2087–2090

Smart Geotechnics for Smart Societies – Zhussupbekov, Sarsembayeva & Kaliakin (Eds)
© 2023 The Author(s), ISBN 978-1-003-29912-7
Open Access: www.taylorfrancis.com, CC BY-NC-ND 4.0 license

Assessment on the improvement of liquefiable ground by stone-column, micro-pile and densification measures

M. Chang, H.J. Lin & R.R. Rayhansah
Department Civil & Construction Engineering, National Yunlin University of Science and Technology (YunTech), Taiwan, ROC

M.H. Fansuri
Universitas Pertahanan RI (UNHAN), Bogor, Indonesia

T.C. Upomo
Graduate School of Engineering Science and Technology, National Yunlin University of Science and Technology (YunTech), Taiwan, ROC

R. Kusumawardani
Universitas Negeri Semarang (UNNES), Semarang, Indonesia

ABSTRACT: Soil liquefaction is an important issue in geotechnical engineering that would cause damages as a result of bearing loss, lateral spreading, or even flowsliding in a mildly sloping ground. Mitigation of excess pore pressure generation and lateral deformation thus become major concerns for liquefiable deposits. This paper examines three commonly adopted mitigation measures (stone-column/SC, micro-pile/MP, and densification/DS) on their effectiveness in reducing the influences of soil liquefaction. A numerical tool is employed and a real soil deposit of liquefaction concern is assumed for the assessment. In this study, we investigate the improvements for each of the mitigation measures, with their usual ranges of design specifications, on liquefaction phenomena of the original deposit. The study indicates both SC and DS options could effectively reduce the generation of excess pore pressure in soil. However, in reducing the lateral deformation of sloping ground, MP option would be superior than the other two options.

1 INTRODUCTION

Soil liquefaction is a key problem in geotechnical engineering, in particular for lateral spreading or liquefaction-induced flow sliding, which could sometimes be devastating and damaging; such as the case of Petobo flow failure causing significant movements in a mildly sloping ground due to 2018 Palu-Donggala Indonesia earthquake (Kusumawardani et al. 2021). Accordingly, mitigation or prevention of liquefaction disasters would be a primary concern in engineering practice. This paper addresses the numerical assessment of several liquefaction mitigation measures, including stone-column (SC), micro-pile (MP) and densification (DS), with an aim to provide a clearer understanding on the effectiveness of these methods.

2 ANALYSIS METHOD

The assessment adopts a numerical tool, OpenSees, through a graphical user interface for conducting 3D ground-structure finite element analysis (http://opensees.berkeley.edu). A 20-8-node brick element is assumed, where 20 nodes are for solid translational degrees of freedom and 8 corner nodes for fluid pressure. Multi-yield conical surfaces with considering phase transformation are applied for soils. The coupled solid-fluid option of the software enables the performance of liquefaction studies. Details of theoretical background are referenced to the manual (Lu et al. 2011).

DOI: 10.1201/9781003299127-70

Figure 1 indicates a typical soil column of the improved ground with a depth of 30 m, where a periodic boundary condition is assumed for the vertical faces and a fix end at the base of column. Due to symmetry, only one half of the soil column is assumed in the numerical analysis. As indicated, the seismic shaking is assigned at the base of the soil column and acting in X-direction.

A liquefaction-prone area at Chuoshui river alluvial fan-delta of Taiwan (CRAFD; Chang et al. 2012) is selected as the target site, where the log of Borehole W5-3, as shown in Figure 2, is adopted as the soil deposit with improvements by several mitigation measures in current study. It is noticed that nearly top 25m of the deposit comprises of sandy soils which are prone to liquefaction due to seismic shaking. Table 1 indicates the assumed material parameters of soil deposit and mitigation measures in the numerical simulations.

The input motion of this study adopts the recorded motion at CHY002 station during 1999 Chi-Chi earthquake (M_w = 7.6) of Taiwan. The recorded motion, however, should be scaled to the design earthquake of the site (M_w =7.1 & PGA=0.308g) based on local building code (MOI 2011), and then deconvoluted from ground surface to a depth of 30m of the site for OpenSees analysis. Figure 3 shows the deconvoluted input motion for this study (a_{max} = 0.250g).

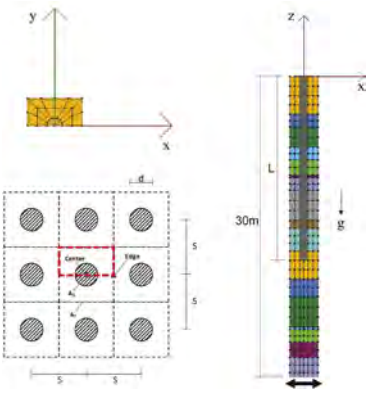

Figure 1. Finite element meshes of representative soil column for numerical simulations.

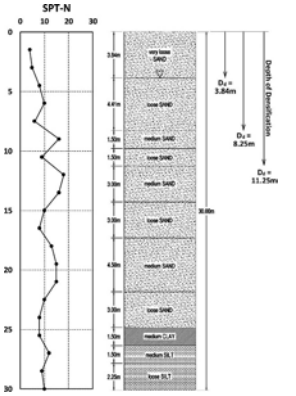

Figure 2. Typical soil/SPT-N profile, based on Borehole W5-3 in CRAFD, for current analysis.

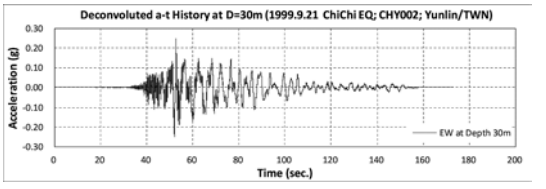

Figure 3. Deconvoluted input motion originally recorded at Station CHY002 (ground surface), in the proximity of Borehole W5-3 with a distance <2 km, during the 1999 Chi-Chi earthquake of Taiwan.

3 ASSESSMENT RESULTS

Three mitigation options are considered, including stone-column (SC), micro-pile (MP) and densification (DS), and the results are compared with the original deposit (i.e., original ground, OG; without improvement). Typical ranges of design specifications for each of the options are selected, as indicated in the relevant figures, with varied spacing (s) for SC option, embedment depths (L) for MP option, and depths of densification (D_d) for DS option.

Table 1. Adopted material parameters for original soil deposit (original ground; OG) and for liquefaction mitigation options of stone-column (SC) and micro-pile (MP).

Parameters	Original Ground (OG)						Stone Column (SC)	Micro Pile (MP)
	Very Loose SAND	Loose SAND	Medium SAND	Loose SILT	Medium SILT	Medium CLAY		
γ (kN/m^3)	16.7	16.7	18.6	16.7	18.6	14.7	18.5	24.5
ϕ (deg.)	29	29	33	29	33	0	33	-
c (kPa)	-	-	-	-	-	37	-	-
ϕ_{PT} (deg.)	29	29	27	29	27	-	27	-
G_r (kPa)	5.5E4	5.5E4	7.5E4	5.5E4	7.5E4	6.0E4	7.5E4	1.4E7
B_r (kPa)	1.5E5	1.5E5	2.0E5	1.5E5	2.0E5	3.0E5	2.0E5	-
K_{soil} (m/s)	6.6E-5	6.6E-5	6.6E-5	1.0E-7	1.0E-7	1.0E-9	-	-
K_{SC} (m/s)	-	-	-	-	-	-	1E-4, 1E-2, 1E0	-
E_r (kPa)	-	-	-	-	-	-	-	3.5E7
v	-	-	-	-	-	-	-	0.2
σ_{py} (kPa)	-	-	-	-	-	-	-	5.2E4

Note: γ = unit weight; ϕ = friction angle; c = cohesion; ϕ_{PT} = phase transformation friction angle; G_r = shear modulus at a reference effective confining pressure of 80kPa; B_r = bulk modulus at a reference effective confining pressure of 80kPa; K_{soil} = hydraulic conductivity of soil; K_{SC} = hydraulic conductivity of stone-column; E_r = Young's modulus at a reference effective confining pressure of 80kPa; v = Poisson's ratio; σ_{py} = yield stress.

3.1 *Excess pore pressure time history*

For level ground, the computed excess pore pressures at a depth of 7m of deposit are shown in Figure 4. As seen, the SC option would appear most effective in preventing excess pore pressure generation, hence reducing liquefaction potential. The DS option would also be effective in delaying the pore pressure generation if the depth of densification becomes deeper.

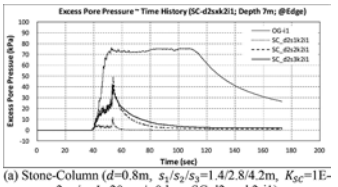

(a) Stone-Column (d=0.8m, $s_1/s_2/s_3$=1.4/2.8/4.2m, K_{SC}=1E-2 m/s, L=20m, i=0deg.; SC-d2-sx-k2-i1)

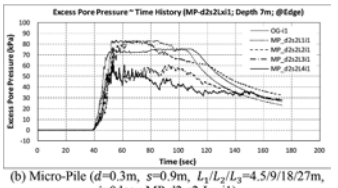

(b) Micro-Pile (d=0.3m, s=0.9m, $L_1/L_2/L_3$=4.5/9/18/27m, i=0deg.; MP-d2-s2-Lx-i1)

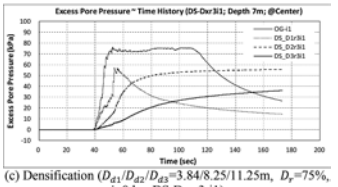

(c) Densification ($D_{d1}/D_{d2}/D_{d3}$=3.84/8.25/11.25m, D_r=75%, i=0dg.; DS-Dx-r3-i1)

Figure 4. Computed excess pore pressure time histories at a depth of 7m (loose SAND) of the level ground ($i = i_1$ = 0deg.) for various liquefaction mitigation options. (Note: OG – original ground; SC – stone-column; MP – micro-pile; DS – densification).

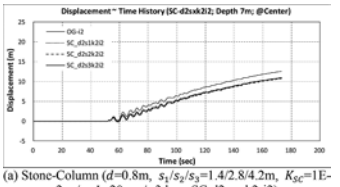

(a) Stone-Column (d=0.8m, $s_1/s_2/s_3$=1.4/2.8/4.2m, K_{SC}=1E-2 m/s, L=20m, i=3deg.; SC-d2-sx-k2-i2)

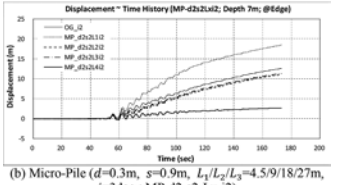

(b) Micro-Pile (d=0.3m, s=0.9m, $L_1/L_2/L_3$=4.5/9/18/27m, i=3deg.; MP-d2-s2-Lx-i2)

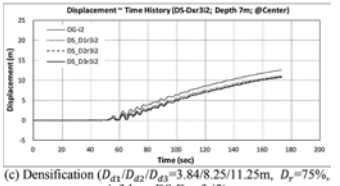

(c) Densification ($D_{d1}/D_{d2}/D_{d3}$=3.84/8.25/11.25m, D_r=75%, i=3deg.; DS-Dx-r3-i2)

Figure 5. Computed lateral deformation time histories at a depth of 7m (loose SAND) of the inclined ground ($i = i_2$ =3deg.) for various liquefaction mitigation options. (Note: OG – original ground; SC – stone-column; MP – micro-pile; DS – densification).

3.2 *Lateral deformation time history*

Figure 5 shows lateral deformation time histories computed at a depth of 7m of a mildly sloping ground (i=3deg.). As seen, Both SC and DS options would appear not effective in holding lateral deformation of the ground. For MP option, however, if the embedment depth of micro-pile is long enough, penetrating through the liquefiable zone of deposit, then the lateral deformation of the ground would be significantly reduced.

3.3 *Lateral deformation profile*

Figure 6 illustrates the lateral deformation profiles of soil deposit with a slightly inclined ground (i = 3deg.). Similarly, Both SC and DS options would appear ineffective, while MP option with an embedment depth greater than the liquefiable zone would substantially hold the deformation.

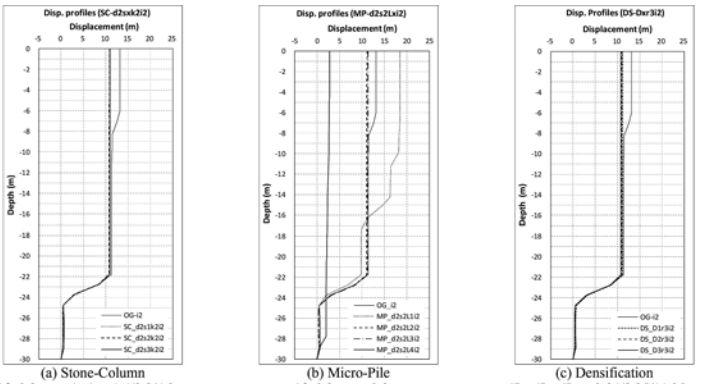

(a) Stone-Column (d=0.8m, $s_1/s_2/s_3$=1.4/2.8/4.2m, K_{SC}=1E-2 m/s, L=20m, i=3deg.; SC-d2-sx-k2-i2)

(b) Micro-Pile (d=0.3m, s=0.9m, $L_1/L_2/L_3$=4.5/9/18/27m, i=3deg.; MP-d2-s2-Lx-i2)

(c) Densification ($D_{d1}/D_{d2}/D_{d3}$=3.84/8.25/11.25m, D_r=75%, i=3deg.; DS-Dx-r3-i2)

Figure 6. Computed lateral deformation profiles of an inclined ground (i = i_2 = 3deg.) for various liquefaction mitigation options. (Note: OG – original ground; SC – stone-column; MP – micro-pile; DS – densification).

4 CONCLUDING REMARKS

The numerical assessment of various liquefaction mitigation options indicates the stone-column (SC) and densification (DS) options would be effective in reducing or delaying the excess pore pressure generation, hence the risk of soil liquefaction. The micro-pile (MP) option could substantially reduce lateral deformation if the embedment depth is deeper than the liquefiable zone.

ACKNOWLEDGEMENTS

Financial support by MOST, Taiwan (Grant: MOST110-2221-E-224-054) is acknowledged.

REFERENCES

Chang, M., Kuo, C.P., Hsu, R.E., Shau, S.H., Lin, T.M. 2012. Liquefaction potential and post-liquefaction settlement evaluations of Chuoshui River Allluvial Fan in Taiwan, *Bulletin of Engineering Geology and the Environment*, Springer, doi 10.1007/s10064-011-0390-7.

Kusumawardani, R., Chang, M., Upomo, T.C., Huang, R.C., Fansuri, M.H., Prayitno, G.A. 2021. Understanding of Petobo liquefaction flowslide by 2018.09.28Palu-Donggala Indonesia earthquake based on site reconnaissance. *Landslides*, Springer-Verlag GmbH Germany, doi 10.1007/s10346-021-01700-x.

Lu, J., Elgamal, A., Yang, Z. 2011. *OpenSeesPL: 3D Lateral Pile-Ground Interaction - User Manual*, http://cyclic.ucsd.edu/openseepl/.

Ministry of the Interior (MOI), Construction and Planning Agency, Taiwan. 2011. *Seismic Resistance Design of Buildings – Code and Explanations* (in Chinese).

Smart Geotechnics for Smart Societies – Zhussupbekov, Sarsembayeva & Kaliakin (Eds)
© 2023 The Author(s), ISBN 978-1-003-29912-7
Open Access: www.taylorfrancis.com, CC BY-NC-ND 4.0 license

Soil stabilization with Basic Oxygen Furnace (BOF) slag

A. Mustafayeva, A. Bimykova, J. Kim & S.-W. Moon
Nazarbayev University, Nur-Sultan, Kazakhstan

ABSTRACT: The number of problems regarding the weak foundation and subgrade profile to support overlaying weight addresses mainly clay soils. Clay soils usually tend to be problematic and exhibit unsustainable infrastructure due to their low stiffness, strength, and high compressibility. In this study, the stabilization of kaolin clay with an iron by-product called Basic Oxygen Furnace (BOF) slag is considered. The aim of this study is to treat the problematic soil and promote the waste disposal of steel waste material. Soil treatment with BOF slag content of 10, 20, and 30% was assessed by an unconfined compressive strength test (UCS) for soil samples cured for 3, 7, 14, and 28 days. This technique would contribute to a sustainable and green environment in road construction.

1 INTRODUCTION

One of the essential aspects of geotechnical engineering is lying on soil stabilization. Soil stabilization means improving soil properties to make it suitable for further application. Soft soils represent weak soil with low stiffness, high compressibility, and inefficient bearing capacity. BOF slag is a steel by-product produced during pig iron transformation in a basic oxygen furnace (Fisher & Barron 2019; O'Connor et al. 2021). There is a tremendous amount of steel production worldwide because it is one of the most demanded materials in the engineering industry.

The chemical binders such as lime, ordinary Portland cement (OPC), and calcium sulfoaluminate cement (CSA) has been generally used as a soil stabilizer due to its high bonding properties when added to the soil (Bazarbekova et al. 2021; Jumassultan et al. 2021; Moon et al. 2020; Ocheme et al. 2023; Sagidullina et al. 2022; Subramanian et al. 2018; Subramanian et al. 2023). However, processing BOF slag to powder-form cementitious material would take only about 10% of the energy needed to produce OPC, releasing a substantial amount of CO_2 (O'Connor et al. 2021; Shi & Qian 2000). Furthermore, because of the similar mineralogical composition of BOF slag and OPC, BOF slag is considered a weak OPC by several researchers (Poh et al. 2006; Shi & Qian 2000). However, BOF slag contains mainly slowly hydrating C_2S, and OPC contains specifically faster hydrating C_3S (Poh et al. 2006). Additionally, it was reported that even a small share of fines (<5%) cannot be ignored in cement-treated sand (Vinoth et al. 2018). Thus, higher BOF content and longer curing time would be recommended for clay soil stabilization with BOF slag (Cikmit et al. 2019; Goodarzi & Salimi 2015; Kang et al. 2019; Poh et al. 2006; Salimi & Ghorbani 2020).

BOF slag has already been used as a primary stabilizing agent for soft clays such as dredged marine clay, English China clay, Mercia Mudstone, dispersive smectite clay, and in combination with Ground granulated blast furnace slag (GGBFS) for kaolin clay. (Cikmit 2019; Cikmit et al. 2019; Goodarzi & Salimi 2015; Kang et al. 2019; Poh et al. 2006). However, the stabilization of kaolin clay with BOF slag as a primary stabilizer has not been researched yet. Therefore, this study examines the stabilization of kaolin clay with BOF slag.

DOI: 10.1201/9781003299127-71

2 EXPERIMENTAL PROGRAM

2.1 *Materials*

The soil used in this study is kaolin clay. It has white color and powder texture. According to the Unified Soil Classification System, this soil has been classified as MH. Basic soil characteristics of kaolin clay are shown in Table 1, specified with corresponding ASTM standards. The soil was dried in the oven before conducting any tests. Particle size distribution (PSD) analysis was performed using the QICPIC (M7) particle size and shape analyzer tool. Fresh BOF slag obtained from a steel company near Karaganda in Kazakhstan is evaluated in grain size, unit weight, chemical composition, and mineralogical composition, which define its basic properties (Table 2).

Table 1. Basic characteristics of kaolin clay.

Property	Value	Standard
Plastic Limit, %	33.1	ASTM D4318
Liquid Limit, %	53.6	ASTM D4318
Plasticity Index, %	20.5	ASTM D4318
Fine, %	> 80	QICPIC
USCS classification	MH	ASTM D1921
Specific gravity	2.4	ASTM D854
Optimum Moisture Content, %	19.3	ASTM D698
Maximum Dry Density, kN/m^3	12.1	ASTM D698

Table 2. Basic characteristics of BOF slag.

Property	Value	Standard
Specific gravity of fine aggregate	3.14	ASTM C188
Absorption rate of fine aggregate, %	3.05	ASTM C128
Free CaO, %	4.51	XRD analysis
Coarse aggregate (>0.075mm), %	99.5%	ASTM C136
Fine aggregate (<0.075mm), %	0.5%	ASTM C136

2.2 *Mixture design and sample preparation*

The standard proctor compaction test (ASTM D698) was used to define the optimum moisture content (OMC) and maximum dry density (MDD) of the future samples. There were three different mixtures according to BOF addition rate. Table 3 demonstrate how OMC and MDD increase with the increase of BOF content. However, the difference in OMC-MDD between BOF content of 10, 20, and 30% is not substantially huge.

Table 3. MDD-OMC of the BOF-stabilized soil.

BOF	Maximum Dry Density, kN/m^3	Optimum Moisture Content, %
BOF D 10%	14.27	27.7
BOF D 20%	14.35	28.9
BOF D 30%	14.48	29.0

Samples were prepared using the ratio of BOF slag mass to the mass of dry soil, and water content was taken as the ratio of water to the total mass of solids (mass of kaolin clay and slag). Initially, dry ingredients were mixed thoroughly, and then water was added. After manually mixing for about 5 minutes, the mixture was mixed with Hobart mixer for another 5 minutes to make a uniformly mixed texture. Cylindrical molds with dimensions 50x100mm, greased with oil inside, were used to prepare specimens. Samples were prepared with manual compaction of 3 layers with 25 blows. Samples were extruded from the mold on the third day of curing to obtain

enough hardening without breaking the specimen. After extrusion, the diameter and height of samples for further testing were recorded. Then, samples were carefully wrapped into polyethylene and rubber bands to avoid moisture loss. The curing period for all samples is 3, 7, 14, and 28 days. Five samples were prepared for each curing day and mix design.

2.3 *Unconfined compressive strength (UCS) and Bender element (BE) tests*

One of the critical parameters of the stabilized soil is increasing the resistance to compressive forces. An unconfined compressive strength test (UCS) was conducted to see the stabilization effect on strength gain. Test was performed according to ASTM D2166 with a standard compressive speed of 1mm/min.

Bender Element (BE) test was conducted according to ASTM D8295, using a peak-to-peak method to determine shear wave velocity at small strains. Two piezoelectric materials are placed on the top and bottom of the tested sample. The height of the sample is measured and input into the GDS Bender Element software. By the signal transmitted from the source (top) and receiver (bottom) of the specimen, the shear wave velocity can be calculated using the wave travel time through the length of the specimen.

It was reported that the maximum stress of the cemented sand has a direct relationship with the shear strength of its particles (Bisserik et al. 2021). This means that with increasing the UCS, the BE also should increase.

3 RESULTS AND DISCUSSION

3.1 *Unconfined Compressive Strength (UCS)*

Figure 1 (a) shows the impact of BOF content on the strength of stabilized soil with 10, 20, and 30% fine BOF particles (i.e., BOF 10%, BOF 20%, and BOF 30%). At an early age, there was no strength development (3 and 7 days), which means that 3-7 days are not enough for strength improvement. The increase in strength occurs only after seven days. Moreover, BOF 30% shows a considerable strength gain compared to BOF 20% and BOF 10%. However, BOF 10% was consistent throughout the whole curing period. BOF 20% has a moderate rate of strength improvement. Furthermore, the difference is also insignificant in regard to 14 and 28 curing days. Consequently, BOF 30% replacement tends to be the most prominent one.

3.2 *Shear wave velocity (Vs)*

According to Figure 1 (b), shear wave velocity starts to gradually increase only after the 7 days. BOF 10% and BOF 20% did not show any substantial difference throughout 28 days. Only BOF 30% started to rise apparently after 7 days. The highest Vs increase is obtained with BOF 30% for approximately 100m/s during the whole curing period. Hence, with an increasing curing period, the shear wave velocity also increases due to the prevalence of fine BOF slag rate. It was reported that with the increasing of curing days the stiffness of the soil is also increasing (Di Sante et al. 2022). It means that Vs increases with the increasing of the soil stiffness.

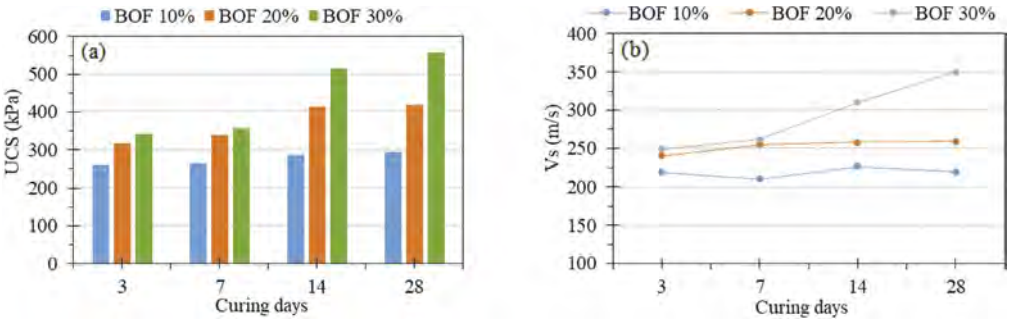

Figure 1. UCS (a) and BE (b) test results of BOF 10%, BOF 20%, and BOF 30%.

4 CONCLUSION

This research's main aim is to stabilize kaolin clay with BOF slag. A considerable strength increase is acquired for BOF 30% after seven days of curing. On the other hand, BOF 10% saved a consistent trend throughout 28 days. Compared to BOF 30% and BOF 10%, BOF 20% showed a moderate strength improvement. However, 3-7 days are insufficient to improve the soil properties in all cases. The highest strength increase is seen in the transition from 7 to 14 days. Bender Element test showed a similar trend with UCS test. BOF 10% and BOF 20% did not increase substantially from 3 to 28 days. Only BOF 30% showed the maximum strength increase after 7 days. It is assumed that shear wave velocity is linked with the soil stiffness, as well as with the strength of the soil sample. To sum up, BOF slag has excellent potential to be used as a stabilizing agent. Although there is a strength development to the maximum value of 557 kPa on the 28th day of curing with 30% of BOF D, it is not enough to stabilize kaolin clay. Therefore, long-term stabilization is needed to see the stabilization behavior of BOF slag. If the results from long-term stabilization (56 and 112 days) will be the same as 28 days, then other calcium-based materials should be added to improve the stabilization effect of BOF slag.

REFERENCES

Bazarbekova, A., Shon, C.-S., Kissambinova, A., Kim, J. R., Zhang, D. & Moon, S.-W. 2021. *Potential of limestone powder to improve the stabilization of sulfate-contained saline soil*. IOP Conference Series: Materials Science and Engineering: IOP Publishing.

Bisserik, A., Kim, J., Satyanaga, A. & Moon, S.-W. 2021. *Characterization of CSA cemented-treated sands via discrete element method*. AIP Conference Proceedings: AIP Publishing LLC.

Cikmit, A. A. 2019. *Engineering Properties of Stabilized Marine Clay Using Basic Oxygen Furnace Steel Slag: Strength Development and Expansion Behaviour*.

Cikmit, A. A., Tsuchida, T., Kang, G., Hashimoto, R. & Honda, H. (2019). Particle-size effect of basic oxygen furnace steel slag in stabilization of dredged marine clay. *Soils and Foundations*, 59 (5): 1385–1398.

Di Sante, M., Bernardo, D., Bellezza, I., Fratalocchi, E. & Mazzieri, F. (2022). Linking small-strain stiffness to development of chemical reactions in lime-treated soils. *Transportation Geotechnics*, 34: 100742.

Fisher, L. V. & Barron, A. R. (2019). The recycling and reuse of steelmaking slags—A review. *Resources, Conservation and Recycling*, 146: 244–255.

Goodarzi, A. & Salimi, M. (2015). Stabilization treatment of a dispersive clayey soil using granulated blast furnace slag and basic oxygen furnace slag. *Applied Clay Science*, 108: 61–69.

Jumassultan, A., Sagidullina, N., Kim, J., Ku, T. & Moon, S.-W. (2021). Performance of cement-stabilized sand subjected to freeze-thaw cycles. *Geomechanics and Engineering*, 25 (1): 41–48.

Kang, G., Cikmit, A. A., Tsuchida, T., Honda, H. & Kim, Y.-s. (2019). Strength development and microstructural characteristics of soft dredged clay stabilized with basic oxygen furnace steel slag. *Construction and Building Materials*, 203: 501–513.

Moon, S.-W., Vinoth, G., Subramanian, S., Kim, J. & Ku, T. (2020). Effect of fine particles on strength and stiffness of cement treated sand. *Granular Matter*, 22 (1): 1–13.

O'Connor, J., Nguyen, T. B. T., Honeyands, T., Monaghan, B., O'Dea, D., Rinklebe, J., Vinu, A., Hoang, S. A., Singh, G. & Kirkham, M. (2021). Production, characterisation, utilisation, and beneficial soil application of steel slag: A review. *Journal of Hazardous Materials*, 419: 126478.

Ocheme, J. I., Olagunju, S. O., Khamitov, R., Satyanaga, A., Kim, J. & Moon, S.-W. 2023. *Triaxial shear behavior of calcium sulfoaluminate (CSA)-treated sand under high confining pressures*. Geomechanics and Engineering: Techno-Press, Ltd.

Poh, H., Ghataora, G. S. & Ghazireh, N. (2006). Soil stabilization using basic oxygen steel slag fines. *Journal of materials in Civil Engineering*, 18 (2): 229–240.

Sagidullina, N., Abdialim, S., Kim, J., Satyanaga, A. & Moon, S.-W. (2022). Influence of Freeze–Thaw Cycles on Physical and Mechanical Properties of Cement-Treated Silty Sand. *Sustainability*, 14 (12): 7000.

Salimi, M. & Ghorbani, A. (2020). Mechanical and compressibility characteristics of a soft clay stabilized by slag-based mixtures and geopolymers. *Applied Clay Science*, 184: 105390.

Shi, C. & Qian, J. (2000). High performance cementing materials from industrial slags—a review. *Resources, Conservation and Recycling*, 29 (3): 195–207.
Subramanian, S., Moon, S.-W., Moon, J. & Ku, T. (2018). CSA-treated sand for geotechnical application: microstructure analysis and rapid strength development. *Journal of Materials in Civil Engineering*, 30 (12): 04018313.
Subramanian, S., Khan, Q., Moon, S.-W. & Ku, T. 2023. *A Review of Mix Design Terminologies for Cement-Admixed Sandy Clay*. 8th International Symposium on Deformation Characteristics of Geomaterials.
Vinoth, G., Moon, S.-W., Kim, J. & Ku, T. 2018. *Effect of fine particles on cement treated sand*. Proceedings of China-Europe Conference on Geotechnical Engineering: Volume 1: Springer.

Smart Geotechnics for Smart Societies – Zhussupbekov, Sarsembayeva & Kaliakin (Eds)
© 2023 The Author(s), ISBN 978-1-003-29912-7
Open Access: www.taylorfrancis.com, CC BY-NC-ND 4.0 license

A laboratory investigation of using enzyme induced calcite precipitation for soil strength improvement

A.G.R. Kennedy
National Taiwan University, Taipei Taiwan

Y.S. Jhuo
National Taiwan University, Taiwan

L. Ge
National Taiwan University, Taipei, Taiwan

ABSTRACT: Enzyme Induced Calcite Precipitation (EICP) is an innovative bio-inspired ground improvement technique that promotes calcite ($CaCO_3$) precipitation. This helps in the clogging of pore spaces and increases the strength of the soil. In this paper, a series of consolidated drained triaxial tests were carried out to investigate the effect of EICP treatment on the strength characteristics of soil. Two urease enzymes were adopted for the EICP treatment with different activity rates of 3g/l (5000 Units/g and 3500 Units/g) and mixed with cementation solution (1M Urea and 0.67M $CaCl_2$). The stress-strain curves after a curing of 7 days are presented herein. The volumetric strain response curve demonstrated a more dilative tendency in the EICP-treated specimens than in the untreated. Mohr-Coulomb failure criteria were adopted to determine the shear strength parameters at peak and residual stages. Finally, acid digestion was performed on the specimens to evaluate the calcite precipitation.

1 INTRODUCTIONS

Calcite-induced precipitation methods (CIPMs) are promising techniques for enhancing the strength of the soil. CIPMs include Enzyme induced calcite precipitation (EICP), Microbial-induced calcite precipitation (MICP), and chemical stabilization methods (Pratama et al., 2021). The application of green and eco-friendly techniques has gained attention in recent times. These bio-cementation techniques include using ureolytic bacteria for the ureolysis process in MICP (Wu et al., 2021) and free urease enzymes in EICP(Gao et al., 2018), which are mixed with urea and calcium chloride solution. The calcite precipitation from this technique binds the soil grains together by increasing the particle roughness and promotes the stiffness, dilatancy, and strength of the soil, reducing in hydraulic conductivity of the soil. Enzyme-induced calcite precipitation is adopted in this research. EICP is an innovative, bioinspired ground improvement technique. EICP bio-cementation includes the mixture of free urease, urea, and calcium carbonate. The primary chemical constituents involved in the EICP process are the urease enzyme, urea ($CO(NH_2)_2$), and calcium chloride ($CaCl_2$).

$$CO(NH_2)_2 + 2H_2O \xrightarrow{\text{Urease}} 2NH_4^+ + CO_3^{2-} \quad (1)$$

$$Ca^{2+} + CO_3^{2-} \rightarrow CaCO_3 \quad (2)$$

The urease enzyme catalyzes the hydrolysis of urea ($CO(NH_2)_2$ into carbon dioxide (CO_2) and ammonia (NH3). The process of ureolysis increases the pH and alkalinity of the reagent

DOI: 10.1201/9781003299127-72

solution from the production of carbonate and ammonium ions. The presence of Ca^{2+} cations from the calcium chloride cementation solution combined with the carbonate ions leads to the precipitation of calcium carbonate (Sun et al., 2021). The precipitated calcite gels between void spaces of soil particles and improved the soil's engineering properties. The effectiveness of EICP can be achieved by using additives in the EICP solutions like dried non-fat milk, xanthan gum, magnesium chloride ($MgCl_2$), magnesium sulfate ($MgSO_4$) and zeolite (Ahenkorah et al., 2021). EICP applications in soil improvement include soil strength, liquefaction resistance, remediation of soil contamination, slope stabilization, and surface erosion control (Meng et al., 2021).

2 MATERIAL USED

2.1 *Sand*

Crushed silica sand was purchased from Singapore. Sand properties are derived from preliminary laboratory tests. The coefficient of uniformity Cu is 1.403 and coefficient of curvature Cc is 0.977, and the specific gravity is 2.66. Some of the other geotechnical parameters are D_{60} = 0.205mm, D_{30} =0.171 mm, D_{10} = 0.146 mm, e max = 0.911, e min = 0.574 and γ at 50% Relative Density = 1527 kg/m^3.

2.2 *Characteristics of urease enzyme and reagents*

The cementation solution consisting of Calcium chloride dihydrate ($CaCl_2.2H_2O$) and Urea ($CO(NH_2)_2$) with 99% purity was purchased from Bioman Scientific Co. Ltd. This experimental study uses two urease enzymes (powder form) derived from an agricultural source (jack bean). The urease enzyme was purchased from Sigma-Aldrich Company Ltd. The activity rate of this enzyme in the research is 5000 Units/gram. The urease enzyme was purchased from CDH chemicals Pvt Ltd, India. The enzyme activity rate used in the study is 3500 Units/gram. After the use of the enzyme, it is stored in the refrigerator at 4ºC for future use.

3 METHODLOGY

The paper mold for triaxial specimen with a diameter of 73mm and height of 150mm for the preparation of EICP treated soil specimens. EICP solutions were prepared with 1M Urea, 0.67M $CaCl_2$, and 3g/l urease enzyme with 5000 Units/gram and 3500 Units/gram, respectively. The pure sand is compacted in the paper mold with a relative density of 50%. One cycle of EICP biocementation solution is added from top to bottom in the closed retained columns. After the curing of 7 days, the sample is shifted to the triaxial apparatus for consolidated drained triaxial testing. Consolidated Drained (CD) triaxial tests were conducted to evaluate the influence of biocementation on the sand by the stress-strain behavior. Two types of saturation, manual saturation and backpressure saturation, were performed in the sample to achieve a B value higher than 0.95. The samples were subjected to three different confining pressure – 50 kPa, 100 kPa, and 200 kPa. The samples were monotonically sheared with a shear rate of 0.185mm/min. When the axial strain reached 20%, the test was made to stop, and the data were extracted.

3.1 *Determination of calcium carbonate*

The process of acid digestion of the calcium carbonate precipitation in the following equations

$$CaCO_3 + 2HCl \rightarrow CaCl_{2(aq)} + H_2O_{(l)} + CO_{2(g)} \quad (3)$$

After the completion of each triaxial test, three samples of 10 grams were collected at the top, middle, and bottom. 4M HCl was used to digestion precipitation calcium carbonate over the soil grains. After 24 hours, the sample is washed thoroughly with DI water. The acid

digested specimens were dried. The percentage of calcium carbonate content of 3 illustrations from the top, middle, and bottom is calculated.

$$\% \; CCC = \frac{W_1 - W_2}{W_1} \times 100 \tag{4}$$

W_1= weight of the crushed soil sample before acid washing. W_2 = weight of the oven-dried crushed soil sample after acid washing.

4 RESULTS & DISCUSSION

Table 1. Test scheme.

Tests	Combination	Curing Days	Peak Deviatoric Stress (kPa)	Calcium carbonate content (%)
PS 50 kPa			189.05	0
PS 100 kPa			359.95	0
PS 200 kPa			629.11	0
Sigma 50 kPa	1M Urea	7 days	199.483	1.87
Sigma 100 kPa	0.67M $CaCl_2.2H_2O$		362.862	2.13
Sigma 200 kPa	3g/l urease		686.581	2.13
CDH 50 kPa			173.011	0.37
CDH 100 kPa			275.76	0.34
CDH 200 kPa			575.54	0.4

4.1 *Stress-strain response*

Uncemented and EICP cemented consolidated drained triaxial shear response curves are shown at 50 kPa, 100 kPa, and 200 kPa effective confining pressures at 7 days curing time. The bio-cemented specimens failed in brittle behavior with peak deviatoric stress at 3–5% axial strain, and further shearing led to the reduction of deviatoric stress. After 10-12% of axial straining, the deviatoric pressure falls to a residual state. Treated EICP sand generally has a higher peak deviatoric stress than untreated sand. The higher deviatoric stress is due to the high calcium carbonate content. The urease enzyme with 3g/l urease of 5000 Units per gram showed a higher peak deviatoric stress with 199.483 kPa, 362.862 kPa, and 686.581 kPa at 50kPa, 100kPa, and 200 kPa effective confining pressure. In contrast, the urease enzyme with 3500 Units per gram showed a lesser peak deviatoric stress with 173.011 kPa, 275.76 kPa, and 575.54 kPa at 50kPa, 100kPa, and 200 kPa effective confining pressure. The lesser peak deviatoric stress may be due to the lower amount of CCC in 3500 Units per gram urease enzyme. The weak calcite bonds in the soil particles increase the initial stiffness and are later destroyed by the shear stress, which leads to a decrease in peak deviatoric stress. The peak deviatoric stress is highly influenced by EICP particle-particle contact (Wang et al., 2019). The failure of pure sand and EICP-treated sands showed brittle failure (dilative behavior) at 20% axial shear strain, as shown in the Figure 1.

4.2 *Volumetric strain response*

The volumetric strain in EICP treated specimens with 3500 Units per gram urease enzyme have shown a slightly higher volumetric strain rate compared to untreated pure sand whereas the urease enzyme with 5000 Units per gram have shown higher dilation. The dilation rate decreases with an increase in effective confining pressure (Safdar et al., 2021). The volumetric strain response showed an initial contraction followed by significant dilation. The amount of initial contraction has increased the EICP bio-cemented sand, which can be seen in the repeatability of consolidated triaxial tests at varying confining pressures and curing times. All the EICP-treated specimens transition from contractive behavior to dilative behavior after a certain stage of initial

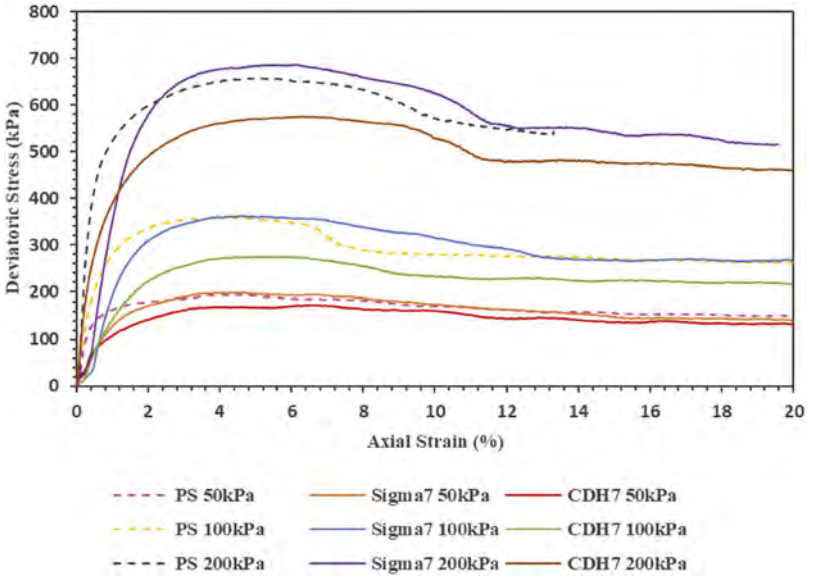

Figure 1. Shear Response curve at 7 days curing in two different urease enzymes at 50 kPa, 100 kPa and 200 kPa confining pressure.

shearing. The increase of CCC in EICP-treated specimens induces dilative behavior compared to the untreated specimens. The EICP bio-cementation enhances the particle interlocking capacity between the soil grains by gelling calcite precipitation between the soil particles. EICP-treated specimens with 5000 Units per gram have shown a higher volumetric strain than untreated pure sand, whereas 3500 Units per gram have shown a slightly higher volumetric strain. One cycle of bio-cementation has shown a lesser amount of calcite precipitation in the EICP treated specimens

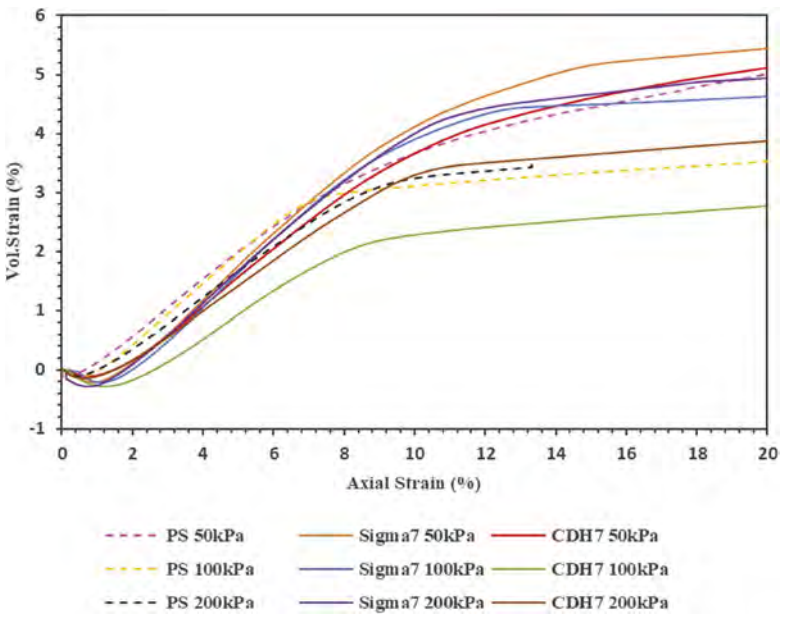

Figure 2. Volumetric strain response curve at 7 days curing in 50 kPa, 100 kPa and 200 kPa effective confining pressure.

with 3500 Units per gram of urease enzyme. Hence, multiple cycles of bio-cementation may increase the calcite precipitation in the treated specimens. High the CCC, higher stiffness and dilations of the bio-cemented specimens. The EICP bio-cementation enhances the particle interlocking capacity between the soil grains by gelling calcite precipitation between the soil particles.

4.3 *Shear strength envelope*

The effective stress strength parameter is derived from the shear strength envelope, which is widely used in the geotechnical field for the quantification of the strength of the soil. The shear strength parameters are measured at peak, and residual strength is determined for each EICP treated specimen at 7 days curing in 5000 Units per gram and 3500 Units per gram urease enzyme. The increase in bio-cementation has increased the cohesion in the EICP-treated specimens (Feng and Montoya, 2016). The EICP treatment increases the soil's residual strength along with the soil's peak strength, which can also be observed from the Table 2.

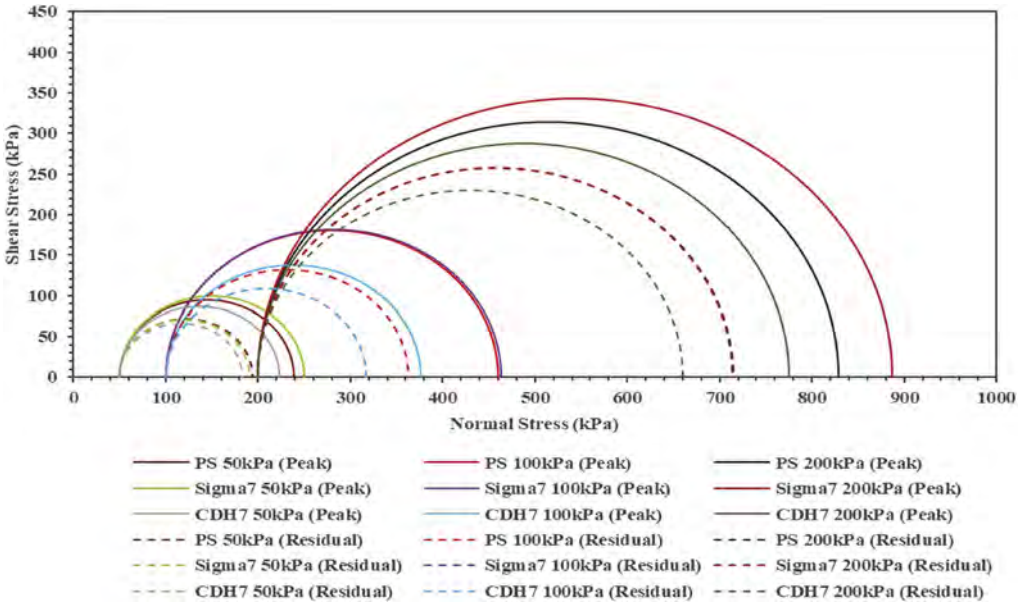

Figure 3. Mohr circles of EICP treated and untreated (Peak and Residual strength) in two different urease enzymes at 50kPa, 100kPa and 200 kPa effective confining pressure.

Table 2. Shear strength parameters (Peak and Residual strength).

	Peak Strength Parameters		Residual Strength Parameters	
Samples	c_p (kPa)	φ_p (deg)	c_r (kPa)	φ_r (deg)
Pure Sand	0	38.35	0	34.43
Sigma	9.13	38.22	2.88	34.32
CDH	5.63	35.32	2.81	31.79

5 CONCLUSIONS

The following conclusions are derived from the research study. The increase of bio-cementation by EICP has increased the higher deviatoric stress and volumetric strain in 5000 Units per gram urease enzyme due to high calcium carbonate content in the specimens. One

cycle of bio-cementation has precipitated lesser calcium carbonate content, leading to lesser deviatoric stress and small amounts of increased volumetric strain in 3500 Units per gram urease enzyme. Higher peak deviatoric stress and higher stiffness of the treated specimen can be achieved by multiple cycles of treatment. The number of treatment cycles directly influences the precipitation rate in the soil particles. The EICP-treated specimens showed an increase in effective cohesion. The influence of % CCC over the friction angle was negligible from the shear strength parameter in peak and residual strength. Increased treatment cycles may significantly improve effective cohesion. The higher CCC from the number of treatment cycles improves the sand's mechanical behavior. The weak cemented bonds can be transformed into stronger calcium carbonated bonds in the treated specimen with treatment cycles. With the inclusion of additives such as powder milk, the conventional EICP solution (urea, calcium chloride, and free urease enzyme) can be changed to produce improved strength in a weakly cemented sand or low calcium carbonate environment ($CaCO_3$).

REFERENCES

Ahenkorah, I., Rahman, M.M., Karim, M. & Beecham, S. 2021. Enzyme induced calcium carbonate precipitation and its engineering application: A systematic review and meta-analysis. *Construction and Building Materials*, 308, 20.

Feng, K. & Montoya, B.M. 2016. Influence of Confinement and Cementation Level on the Behavior of Microbial-Induced Calcite Precipitated Sands under Monotonic Drained Loading. *Journal of Geotechnical and Geoenvironmental Engineering*, 142.

Gao, Y., Hang, L., He, J. & Chu, J. 2018. Mechanical behaviour of biocemented sands at various treatment levels and relative densities. *Acta Geotechnica*, 14, 697–707.

Meng, H., Shu, S., Gao, Y., Yan, B. & He, J. 2021. Multiple-phase enzyme-induced carbonate precipitation (EICP) method for soil improvement. *Engineering Geology*, 294.

Pratama, E.M., Putra, H. & Syarif, F. 2021. Application of calcite precipitation method to increase the shear strength of peat soil. *Earth and Environmental Science* 871.

Safdar, M., Newson, T. & Shah, F. 2021. Consolidated drained (CID) behavior of fibre reinforced cemented Toyoura sand in triaxial loading conditions. *International Journal of Geo-Engineering*, 12.

Sun, X., Miao, L., Wang, H., Wu, L. & Zhang, J. 2021. Enzymatic calcification to solidify desert sands for sandstorm control. *Climate Risk Management*, 33, 1–9.

Wang, Y., Liu, H., Zhang, Z., Xiao, P., He, X. & Xiao, Y. 2019. Study on Low-Strength Biocemented Sands Using a Temperature-Controlled MICP (Microbially Induced Calcite Precipitation) Method. *New Prospects in Geotechnical Engineering Aspects of Civil Infrastructures*.

Wu, S., Li, B. & Chu, J. 2021. Stress-Dilatancy Behavior of MICP-Treated Sand. *International Journal of Geomechanics*, 21.

Smart Geotechnics for Smart Societies – Zhussupbekov, Sarsembayeva & Kaliakin (Eds)
© 2023 The Author(s), ISBN 978-1-003-29912-7
Open Access: www.taylorfrancis.com, CC BY-NC-ND 4.0 license

Stabilization of organic soil with CSA cement

Nazerke Sagidullina, Aiym Muratova, Jong Kim, Alfrendo Satyanaga & Sung-Woo Moon
Nazarbayev University, Nur-Sultan, Kazakhstan

ABSTRACT: Problematic soils, especially organic soils, are not usually suitable for engineering construction purposes due to their high compressibility. The infrastructures built on organic soil can be easily damaged by causing many problems, such as foundation settlement, cracking in the structure, and corrosion. Therefore, this study aims to investigate the effectiveness of CSA cement for the stabilization purposes of organic soil by conducting comprehensive laboratory work for the improvement of organic soil properties. For this purpose, Unconfined Compressive Strength (UCS) and free swell testing were performed on the stabilized soil specimens cured for 3, 7, and 14 days. Samples were prepared at optimum moisture content using different cement content, 0%, 10%, 15%, and 20%. Overall, the use of CSA as a stabilizer for silty would be useful to achieve sufficient strength and meet the requirements subgrade.

1 INTRODUCTION

The problematic soil, especially in severe weather conditions of Kazakhstan, is usually not applicable for geotechnical engineering purposes. Therefore, investigating the characteristics and performance of problematic soil is of great importance. Generally, the soil stabilization method is adopted to improve ground properties. For the treatment of problematic soil properties, chemical soil stabilization has been implemented for several decades due to a potential reduction in the construction and maintenance costs of pavement infrastructure built on problematic grounds. Chemical stabilization generally involves mixing or injecting the soil with a chemical stabilizer (Güllü &Fedakar 2017, Yilmaz &Fidan 2018, Bazarbekova et al. 2021, Subramanian et al. 2023). Cement and lime stabilization are commonly used methods for improving ground properties among the existing soil stabilization techniques.

Ordinary Portland Cement (OPC) is popularly used as a binding admixture, whose behavior has been well investigated by many researchers. On the other hand, using OPC poses environmental problems due to the significant emission of CO_2. Hence, considering global warming and climate change, there has been a strong need for replacing OPC with low CO_2-emitting binders.

Calcium Sulfoaluminate cement (CSA), which releases less carbon than OPC cement, can be used to treat problematic soil since several research works were carried out to assess CSA binder effectiveness. The previous research results showed the rapid strength gain of CSA-treated soil (Ocheme et al. 2022, Bisserik et al. 2021, Subramanian et al. 2018, Vinoth et al. 2018, Moon et al. 2020). Also, the effect of cyclic freezing and thawing was tested, where the addition of CSA cement considerably reduced the effect of cyclic freezing and thawing by improving the performance (Jumassultan et al. 2021, Sagidullina et al. 2022). Therefore, the CSA cement will be tested for the treatment of organic soil by conducting different experimental tests, such as unconfined compressive strength (UCS) and free swell tests.

DOI: 10.1201/9781003299127-73

2 EXPERIMENTAL WORK

2.1 *Materials*

The materials used in this experimental work are natural soil, calcium sulfoaluminate (CSA) cement, gypsum, and water. Table 1 shows the main physical properties of natural soil, which was received from the open-cut excavation in Nur-Sultan. Natural soil is defined as organic soil since it contains 18% of organic matter. The organic content of the soil is determined based on ASTM D2974 standard (2000). Applying the USCS classification, the soil type is classified as poorly graded sand with silt [SP-SM]. The gypsum was used to partially replace CSA cement since previous research by Subramanian et al. (2019) has shown that CSA cement with 30% of gypsum will have a high strength gain in treated soil.

Table 1. Physical properties of the soil.

Property	D_{10} (mm)	D_{30} (mm)	D_{60} (mm)	C_c	C_u	Organic content (%)	LL (%)	PL (%)	PI (%)	USCS
Value	0.08	0.18	0.45	0.90	5.63	18	83.99	74.01	9.99	SP-SM

2.2 *Sample preparation*

The received organic soil is oven dried for 24 hours at 105ºC to be further used in cement-soil mixtures. The mixture should be prepared at the optimum moisture content (OMC) and maximum dry density (MDD) conditions. These conditions are defined by the standard Proctor test, conducted according to ASTM/D698 standard (2007). The results of the testing for 0, 10, 15, and 20% CSA content mixture are given in Table 1. From the results of the Proctor test, it can be seen that with the increase of cement content, the maximum dry density decreases, and optimum moisture content increases. Using the OMC, soil mixtures were prepared, and samples were placed into the mold applying the undercompaction technique in three layers, where each layer was compacted 25 times. Mold with a diameter of 50 mm and a height of 100 mm was used. After the sample preparation step, the samples were cured at room temperature for 3, 7, and 14 days.

Table 2. Standard proctor test results.

Cement Content	0%	10%	15%	20%
OMC	36.0%	41.0%	44.0%	45.5%
MDD	1.148	1.114	1.101	1.062

2.3 *Experimental methods*

After each curing period, samples were tested for expansion and strength by conducting free swell and UCS element tests. A one-dimensional free swell test was performed according to ASTM D4546 standard (2008). The 1-D free swell test was conducted to observe changes in the volume of cement-treated soil. Problematic soils, especially expansive soils, with the change of moisture content, could have considerable changes in volume, which leads to the development of wide cracks with the decrease of moisture and swelling with the increase of moisture. The samples were assembled in an oedometer and inundated until the value of the dial gauge becomes constant. This wetting-induced deformation was measured continuously by setting the dial indicator. As the samples were already in the optimum moisture, content precautions should be applied to avoid test water absorption. The dial gauge reading was taken after 0.5, 1, 2, 4, 8, 15, 60, 120, 240, 480, 960 minutes, and so on until the dial gauge showed constant value over a significant period.

A UCS test was conducted to evaluate the cement-soil mixture's mechanical properties (ASTM/2166 2003). The samples were compressed at 1 mm per minute until the sample breakage. Five samples were tested for each cement content and curing time to get more reliable data.

3 RESULTS AND DISCUSSIONS

Figure 1 illustrates the UCS test results for 3, 7, and 14 days cured samples. It can be observed that the strength of the treated soil sample increases with the increase of cement content, mainly after 7 and 14 curing days. For example, in the case of samples treated with the 10% CSA cement, the compressive strength increased only by 18%, from 3 to 14 curing days, whereas samples with 15% and 20% cement content showed an 82% and 106% increase in strength, respectively.

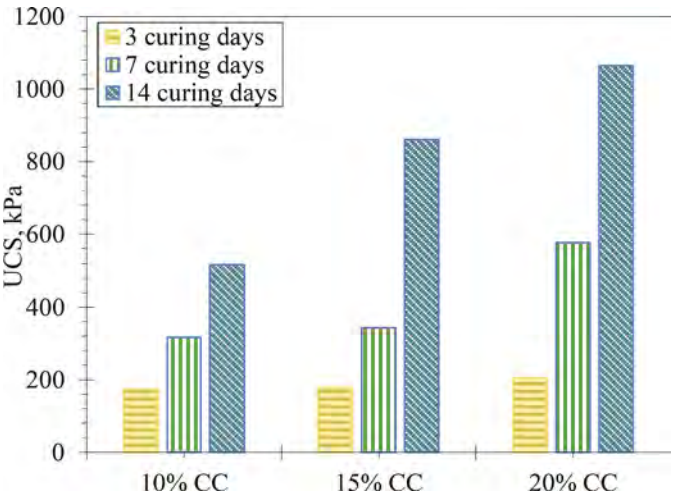

Figure 1. UCS test results.
Note: CC – cement content.

Figure 2 shows the results of 1D free swell testing for the 3, 7, and 14 curing days. Figure 2 shows that with the addition of more cement, the swelling percentage considerably decreased.

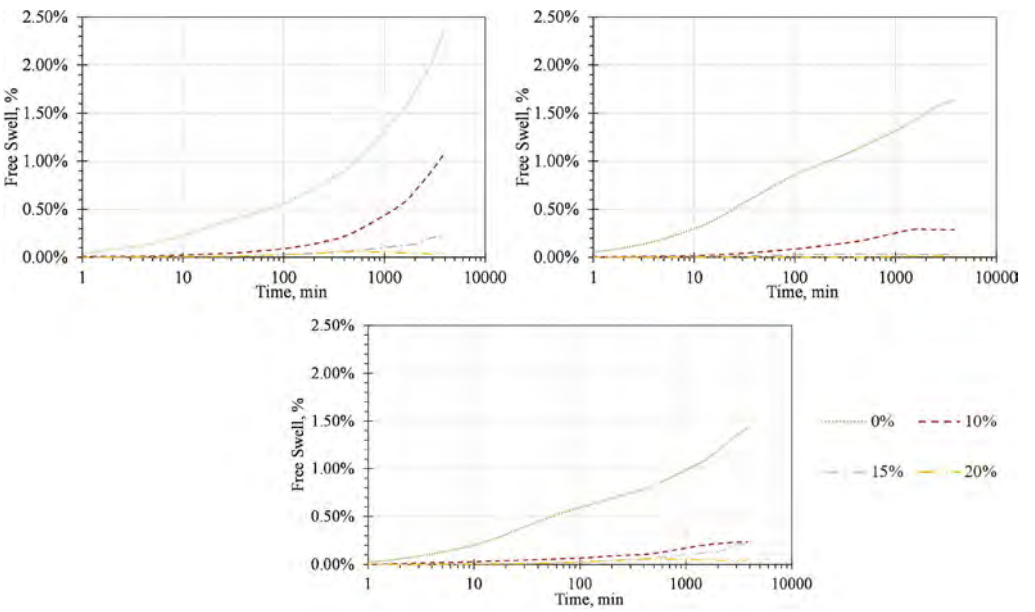

Figure 2. Free Swell test results: (a) 3 curing days, (b) 7 curing days, (c) 14 curing days.

For example, in the free swell test results after 3, 7, and 14 curing days, the swelling percentage decreased from 2.36% to 0.04%, from 1.63% to 0.01%, and from 1.44% to 0.04%, respectively.

Moreover, an increase in the curing period showed a reduced swelling percentage. For the untreated sample, the free swell value decreased by 61% from 2.4% to 1.4% when the curing period increased from 3 to 14 curing period. Overall, the CSA cement effectively reduced the swelling percentage of the soil. The decrease of free swell value depends on the percentage of additive and curing period.

4 CONCLUSIONS

This study is conducted to evaluate the effect of CSA cement used to stabilize problematic soil, categorized as expansive soil with organic content. For the assessment of the CSA cement treatment method, 1-D free swell and UCS tests were performed. The main findings of the research are listed below.

- Adding more cement improved the soil performance and cement-treated soil samples gained more strength with the increase of the curing period.
- The reduced swell percentage of soil can be achieved with an increase in cement content.

Further research will include assessing other parameters of stabilized soil, such as 3-D volume expansion and shear velocity. SEM pictures of soil will also be taken to see the changes in the microstructure of soil. Moreover, the long-term performance of CSA-treated soil will be tested. In addition, the determination of the efficiency of the soil stabilization technique with the CSA cement and other traditional chemical additives will be tested.

REFERENCES

Astm 2000. Standard test methods for moisture, ash and organic matter of peat and other organic soils, method ASTM D2974-00. ASTM International.

Astm, D. 2008. 4546, Standard Test Methods for One-Dimensional Swell or Collapse of Cohesive Soils. *ASTM International, United States*.

Astm/2166 2003. Standard test method for unconfined compressive strength of cohesive soil *American Society for Testing and Materials*. Philadelphia.

Astm/D698 2007. Standard Test Methods for Laboratory Compaction Characteristics of Soil Using Standard Effort. *American Society for Testing and Materials*. Philadelphia, PA.

Bazarbekova, A., Shon, C.-S., Kissambinova, A., Kim, J. R., Zhang, D. & Moon, S.-W. Year. Potential of limestone powder to improve the stabilization of sulfate-contained saline soil. *In:* IOP Conference Series: Materials Science and Engineering, 2021. IOP Publishing: 012016.

Bisserik, A., Kim, J., Satyanaga, A. & Moon, S.-W. Year. Characterization of CSA cemented-treated sands via discrete element method. *In:* AIP Conference Proceedings, 2021. AIP Publishing LLC: 030001.

Güllü, H. & Fedakar, H. I. 2017. Unconfined compressive strength and freeze-thaw resistance of sand modified with sludge ash and polypropylene fiber. *Geomechanics and Engineering*, 13: 25–41.

Jumassultan, A., Sagidullina, N., Kim, J., Ku, T. & Moon, S.-W. 2021. Performance of cement-stabilized sand subjected to freeze-thaw cycles. *Geomechanics and Engineering*, 25: 41–48.

Moon, S.-W., Vinoth, G., Subramanian, S., Kim, J. & Ku, T. 2020. Effect of fine particles on strength and stiffness of cement treated sand. *Granular Matter*, 22: 1–13.

Ocheme, J. I., Khamitov, R., Satyanaga, A., Kim, J. & Moon, S.-W. Year. Triaxial Test Behavior of CSA-treated Sand with High Confining Pressure. *In:* The 2022 World Congress on Advances in Civil, Environmental, & Materials Research, 2022.

Sagidullina, N., Abdialim, S., Kim, J., Satyanaga, A. & Moon, S.-W. 2022. Influence of Freeze–Thaw Cycles on Physical and Mechanical Properties of Cement-Treated Silty Sand. *Sustainability*, 14: 7000.

Subramanian, S., Khan, Q., Moon, S. W. & Ku, T. 2023. A Review of Mix Design Terminologies for Cement-Admixed Sandy Clay. *8th International Symposium on Deformation Characteristics of Geomaterials*. Porto, Portugal.

Subramanian, S., Moon, S.-W. & Ku, T. Year. Effect of Gypsum on the strength of CSA treated sand. *In:* 16th Asian Regional Conference on Soil Mechanics and Geotechnical Engineering, 2019.
Subramanian, S., Moon, S.-W., Moon, J. & Ku, T. 2018. CSA-treated sand for geotechnical application: microstructure analysis and rapid strength development. *Journal of Materials in Civil Engineering*, 30: 04018313.
Vinoth, G., Moon, S.-W., Moon, J. & Ku, T. 2018. Early strength development in cement-treated sand using low-carbon rapid-hardening cements. *Soils and Foundations*, 58: 1200–1211.
Yilmaz, F. & Fidan, D. 2018. Influence of freeze-thaw on strength of clayey soil stabilized with lime and perlite. *Geomechanics and Engineering*, 14: 301–306.

Smart Geotechnics for Smart Societies – Zhussupbekov, Sarsembayeva & Kaliakin (Eds)
© 2023 The Author(s), ISBN 978-1-003-29912-7
Open Access: www.taylorfrancis.com, CC BY-NC-ND 4.0 license

Experimental and numerical modeling of load settlement behavior of gypseous soils improved by MICP

Alaa D. Almurshedi
Department of Surveying Engineering, University of Baghdad, Baghdad, Iraq

Mahdi Karkush
Department of Civil Engineering, University of Baghdad, Baghdad, Iraq

ABSTRACT: In this paper the load-settlement of gypseous soils improved by microbial induced calcite precipitation (MICP) have investigated experimentally and numerically. Tests were carried out on two sandy soils collected from two different sites in Iraq, Najaf city and Samawa city. The soil samples were injected with two ratios of bacteria solution (4 and 8%). The load-settlement of gypseous soils were investigated in both cases dry and soaking. A numerical model is developed using PLAXIS software. Finite element analysis is carried out using Mohr coulomb failure criteria to represent 2D soil model. Foundation is modelled as square footing and load increment is applied till the soil model fails. Ultimate bearing capacity is identified as that minimum pressure on footing at which the foundation soil experiences shear failure. The stress distribution in soil and displacement experienced at different locations are obtained. Also, the ultimate bearing capacity of square foundation was computed by Terzaghi's equation to know the preliminary values of bearing capacity of gypseous soil and loading frame which was successfully compared with PLAXIS software. Based on the results of tests, PLAXIS software can be used worthily to understand the load-settlement behavior of gypseous soils in dry and soaking conditions and Mohr-Coulomb model can be considered the best to estimate the ultimate bearing capacity of a foundation constructed on gypseous soils. The difference between the maximum settlement measured from experimental tests and calculated from the numerical analysis was 20% in dry condition and 30-40% in soaked condition. The bearing capacity obtained from experimental tests were identical with results of Terzaghi's equation.

1 INTRODUCTION

The collapsible soil is defined as any soil suffering from volume changes upon wetting which resulted from the radical rearrangement of particles of soil without change in loading (Karkush et al. 2008, Abid Awn 2010, Karkush et al. 2022). The wetting or soaking of gypseous soils causes dissolution the calcite silicate cementing the particles of soil consequently reduces the bonds among soil particles (Al-Mufty 1997, Al-Morshedy 2001). In the past few years, the use of microbial induced calcite precipitation (MICP) has become popular as a ground improvement technique. It is presented as a new and environmentally friendly method (DeJong et al. 2006). This new method has an advantage over conventional chemical treatments, which can be toxic and environmentally harmful and have a limited injection distance ((Karkush et al. 2022). The MICP method is also cost-effective in comparison to chemical treatments. Many studies in the literature have reported that the microbial-induced calcite precipitation technique is very effective in increasing the shear strength and in decreasing the permeability of sandy and gravelly soil (van Paassen et al. 2010, Van Wijngaarden et al. 2011, Martinez et al. 2013). Scaled-up studies were also performed on sandy soil and successful results were obtained (van Paassen et al. 2010).

DOI: 10.1201/9781003299127-74

The main role of bacteria in the calcite precipitation process has been to generate an alkaline environment through different physiological actions (Weaver et al. 2011). Bacillus pasteurii, a highly urease active bacteria, plays an important role in $CaCO_3$ precipitation (DeJong et al. 2014). The main nutrient solution that is commonly used to provide the necessary nutrition for the bacteria, as well as the chemical compounds that are needed for soil cementation, contain $NaHCO_3$, NH_4Cl, $CaCl_2$, urea, and a nutrient broth (mixture of peptone, yeast extract, beef extract, and NaCl). Under favorable environmental conditions, S. pasteurii uses urea as an energy source, producing ammonia (NH_3) and carbon dioxide (CO_2), which tend to increase the pH in the proximal environment. The chemical reaction is given in Equation (1). The calcite bonds tend to form at the particle-to-particle contacts in the soil matrix, which has an overall cementing effect between soil particles (Chou et al. 2011, Qabany & Aziz 2011, Qabany & Soga 2014).

$$Ca^{2+}+HCO_3^- + OH^- \rightarrow CaCO_3+H_2O \quad (1)$$

In the present study the effects of injection bacteria solution (BS) on the load-settlement behavior of two types of gypseous soils collected from two Iraqi cities have been studied experimentally and modeled theoretically using PLAXIS software. Two ratios of bacterial solution injected in the gypseous soils and tested in both cases dry and after soaking.

2 MATERIAL AND METHODS

2.1 *Gypseous soils*

The soil samples used in this study is obtained from Najaf Sea located 10 km from the center of Najaf city and Sawa Lake located 30 km from the center of Samawa city. The soil samples are taken from a depth of (0.5-1.5) m depth below the existing ground level and have gypsum content of 42 and 54% respectively. The results of physical and chemical tests for natural gypseous soils samples are given in Table 1 (Karkush et al. 2020).

Table 1. Physical and chemical properties of the gypseous soils.

Property	Najaf	Samawa	Property	Najaf	Samawa
Specific gravity, Gs	2.54	2.48	Sand, %	80.0	90.5
Maximum dry unit weight, $\gamma_{d,max}$	14 kN/m^3	13.4 kN/m^3	Silt, %	17.0	9.5
Optimum moisture content, ω_{opt}	18%	18%	Clay, %	3.0	-
D_{10}, D_{30}, D_{60}, mm	0.018, 0.175, 0.5	0.075, 0.11, 0.3	Soil type (USCS)	SM	SP-SM
Organic matter content, %	2.15	0.45	pH value	6.8	6.5
Electrical conductivity, μS/cm	2.43	15	SO_3, %	20	24.5
ESP (Exchange sodium), %	13		$CaCO_3$, %	4.6	6.0
TSS (Total soluble salts), %	34.1	63	Cl^-, mg/l	0.04	0.09
CEC (Cation exchange capacity), meq/100g	6.54	5.33	Gypsum content, %	42	54
			$CaCO_3$, %	4.6	6.0

2.2 *Bacterial treatment solution preparation*

To prepare the bacteria treatment solution, urea medium was first created. Nutrient broth (4 g), urea (25 g), NH_4Cl (15 g), $NaHCO_3$ (3 g), and 500 ml of distilled water, were mixed to create the urea medium solution. Each of the solid in gradients was mixed thoroughly in 500 mL of distilled water until it had dissolved, and the pH of the resulting urea medium solution was adjusted to 6.0 with the use of 5 N HCL prior to autoclaving. Distilled water was then added to reach the final required volume (1 L). After autoclaving, the pH of the urea medium was measured to be 7. The pH value of the resulting1Lof solution was adjusted by aerating the solution to increase the initial pH value from 7 to 8. In this way, the solution became suitable for biological activity for bacteria (Ali et al. 2020).

3 MODELING OF PROBLEM

The large-scale model consisting of steel container of dimensions (600×600×500) mm containing gypseous soil, rigid steel foundation is (100×100×20) mm installed in the gypseous soil, Figure 1. illustrates the schematic diagram of the model. The use of PLAXIS 2020 software to solve problems involves the construction of a 3D model consisting of points, lines, surfaces, and volumes by the finite element method. It also requires the properties of materials and the boundary conditions to be defined. The problem geometry is determined using the first two-tab sheets of the program input data. In the last three-tab sheets of the program input data, the mesh generation, description of the boundary conditions, and calculations are done. The physical and mechanical properties of the sandy soil Foundation plate properties used in tests are given in Table 2. The sand's shear strength and stiffness parameters are obtained from a direct shear test conducted according to ASTM (D3080-72) and the triaxial test. The foundation plates are modeled as a plate element and behave as an elastic material, while the steel shaft is modeled with elastic behavior.

Table 2. Inputs parameters of the sandy soils and foundation.

Parameter	Soil	Parameter	Foundation
Material model	Mohr-Coulomb	Material	Rigid steel
Drainage type	Drained	Material model	Liner-elastic
Unit weight, γ (kN/m^3)	✓	Drainage type	Nonporous
Internal friction angle	✓	Young's modulus, E (Pa)	20×10^6
Cohesion	✓	Unit weight, γ (kN/m^3)	78.0
Dilatancy angle	✓	Poisson's ratio	0.3
Coefficient of earth pressure at rest	✓		
Young's modulus, E (kPa)	✓		
Poisson's ratio	✓		

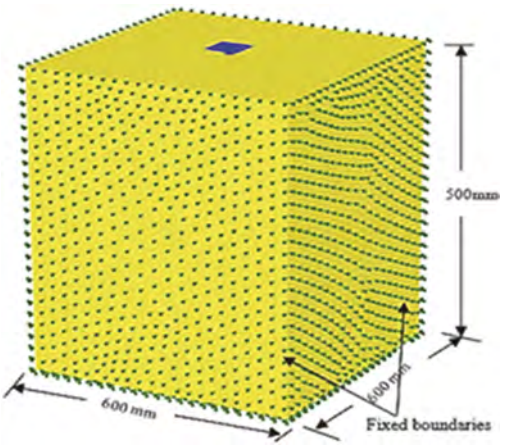

Figure 1. Finite element model (PLAXIS 3D 2020).

4 RESULTS DISCUSSION

4.1 *Load –settlement test*

Using PLAXIS 2020 finite element analysis is conducted using Mohr-coulomb failure criterion in this study numerical model to represent the three-dimensional soil model. The foundation is designed as a square base (100 mm) and the increase in load is applied before the soil model fails. Ultimate bearing capacity is known as the lowest footing pressure at which shear failure is

experienced by the foundation soil. The validity of PLAXIS 2020 software in the analysis foundation is approved by comparing the load-settlement curve, where good agreement noted with the same curve obtained experimental works as shown in Figures 2 to 5. PLAXIS is a program based on the finite element mechanism (FEM) used to achieve deformation. Geotechnical research programs and flow analysis. A simple strain or axisymmetric model may be modeled for 3D analysis.

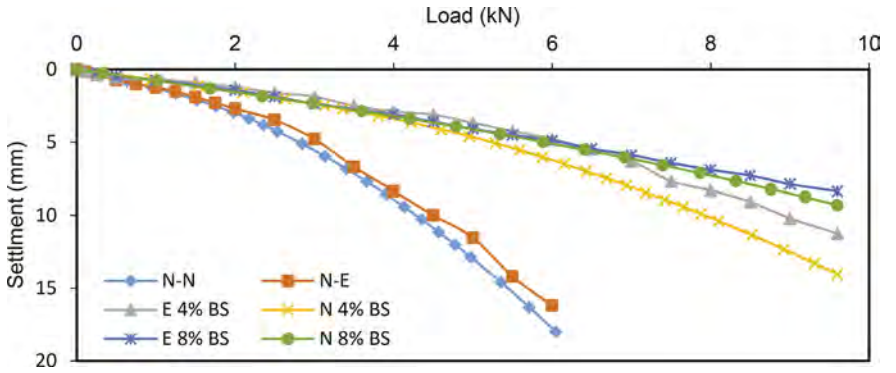

Figure 2. Load versus settlement of Najaf gypseous soil treated with BS.

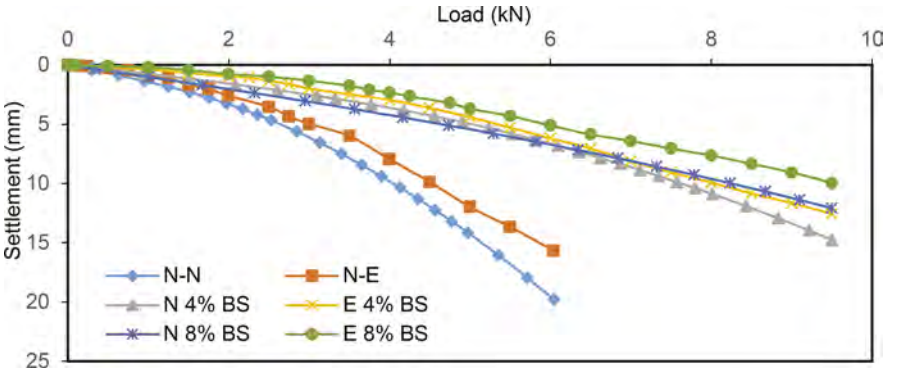

Figure 3. Load versus settlement of Najaf gypseous soil treated with BS in soaking condition.

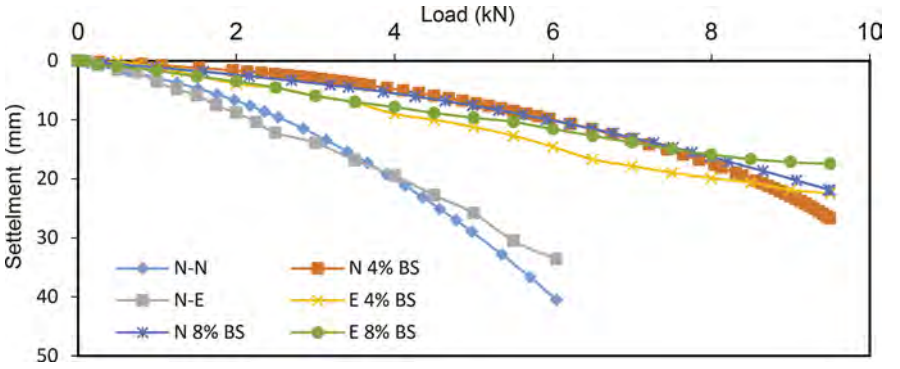

Figure 4. Load versus settlement of Samawa gypseous soil treated with BS.

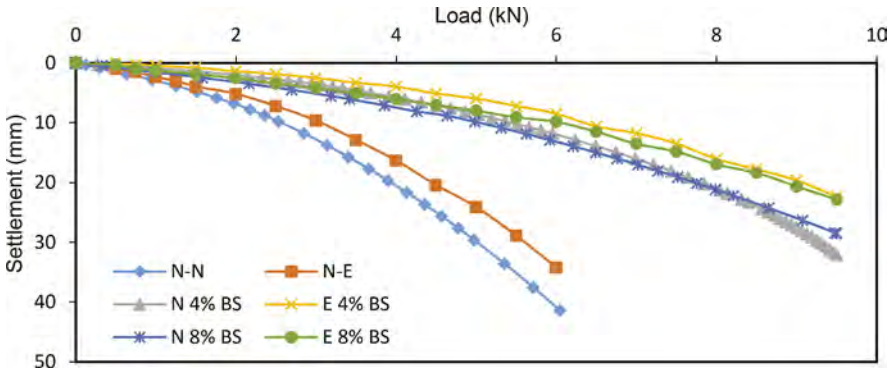

Figure 5. Load versus settlement of Samawa gypseous soil treated with BS in soaking condition.

4.2 *Bearing capacity*

The bearing capacity in this work was calculated according to the failure method. The calculated bearing capacity is higher than the estimated bearing capacity which considered the soil as fully saturated. The results show that the calculated bearing capacity is (5-15) % lower than the estimated by Terzaghi equation (Equation 2) in dry condition and (20-40) % lower than the estimated by Terzaghi equation in soaked condition. Also, the rate of increase in bearing capacity in the soil treated with MICP technique. The bearing capacity of footing is considered as the stress at failure condition. The bearing capacity of square footing increased with the increasing the concentration of the bacteria solution, so the bearing capacity of gypseous soils treated with bacterial solution is higher than untreated gypseous soils. It can be noticed that the soil with a high value of shear strength is affected more by the variation of the moisture content change than the soil with a low value of shear strength.

$$q_{ult} = cN_c + qN_q + \frac{1}{2}B\gamma N_\gamma \tag{2}$$

Where

q_{ult}: ultimate bearing capacity (kPa),

Nc, Nq, Nγ: bearing capacity factors, B: foundation width, c: cohesion, d: depth of foundation = 0, γ: the unit weight of soil, and q =γ×d= 0 (Bowels 1996).

Table 3 shows that the bearing capacity of square footing increased in soil treated by the MICP technique. In both condition of tests (dry and soaked), an increase in soil strength can be attributed to the calcite precipitates produced, which strengthened the bonding between the soil particles. This result is due to the large amount of calcite precipitation that accumulates in the soil. The bearing capacity of the foundation is a primary concern in the field of foundation engineering. The load at which the shear failure of the soil occurs is called the foundation's ultimate bearing capacity. In this study, a numerical model is developed using PLAXIS 2020. Finite element analysis is carried out using Mohr-coulomb failure criteria to represent a 3D soil model. Foundation is modeled as square footing, and load increment is applied till the soil model fails. Ultimate bearing capacity is identified as that minimum pressure on footing at which the foundation soil experiences shear failure. The stress distribution in soil and settlement experienced at the surface location is obtained. In PLAXIS 2020, effective stress is considered as an ultimate bearing capacity. Figures 6 and 7 show the comparison between the results obtained from Terzaghi's equation and PLAXIS software. The results obtained from PLAXIS software are very close to the results of experimental model tests rather than Terzaghi's equation results. Mostly, the same trend of bearing capacity for soil treated with bacterial solution. Also, the soaking causes lowering the bearing capacity of soil.

Table 3. The estimated and calculated bearing capacity for treated gypseous soils.

	Bearing capacity (kPa)											
	Najaf soil						Samawa soil					
	Dry			Soaked			Dry			Soaked		
Condition	Exp.	Equation 2	PLAXIS	Exp.	Equation 2	PLAXIS	Exp.	Equation 2	PLAXIS	Exp.	Equation 2	PLAXIS
Natural	450	612	530	210	160	260	436	534	444	301	144	260
4% BS*	878	1100	930	438	543	580	790	1089	790	564	608	545
8% BS	1000	1228	1000	523	764	629	1000	1201	1000	630	765	562

* Refer to bacteria solution (BS).

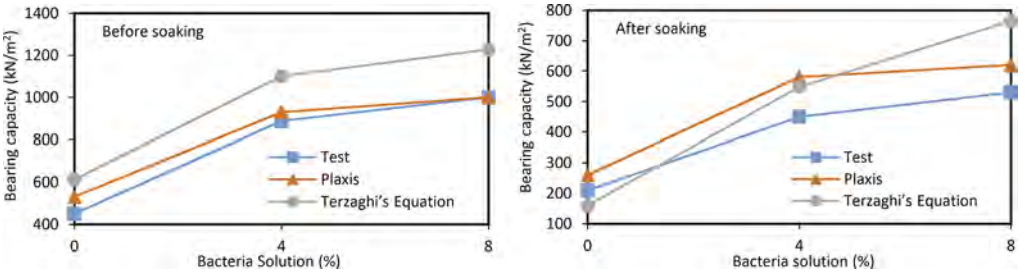

Figure 6. Ultimate bearing capacity for Najaf gypseous soil treated by BS.

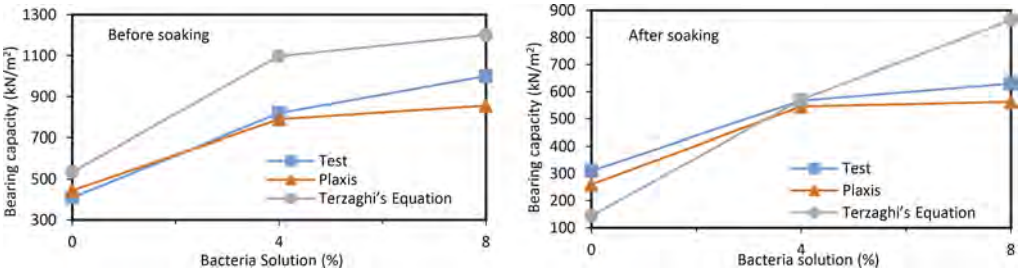

Figure 7. Ultimate bearing capacity for Samawa gypseous soil treated by BS.

5 CONCLUSIONS

Based on the obtained results, the following conclusions can be made:

- PLAXIS 2020 software can be used worthily to understand the load-settlement behavior of gypseous soils in dry and soaking conditions.
- Mohr-Coulomb model can be considered the best to estimate the ultimate bearing capacity of a foundation constructed on/in gypseous soils.
- The difference between the maximum settlement measured from experimental tests and calculated from the numerical analysis was 20% in dry condition and 30-40% in soaked condition.
- The test and Terzaghi's equation values for ultimate bearing capacity are almost identical.

REFERENCES

Ali, N.A., Karkush, M.O. and Al Haideri, H.H., 2020, August. Isolation and identification of local bactria produced from soil-borne urease. In IOP Conference Series: Materials Science and Engineering (Vol. 901, No. 1, p. 012035). IOP Publishing.

Al-Morshedy, A.D., 2001. The use of cut-back MC-30 for controlling the collapsibility of gypseous soils. M.Sc. Thesis, Building and Construction Department, University of Technology.

Al-Mufty, A.A., 1997. Effect of gypsum dissolution on the mechanical behaviour of gypseous soils. Ph. D. Thesis, Civil Engineering Department, University of Baghdad, Baghdad, Iraq.

Awn, S.H., 2010. A modified collapse test for gypseous soils. Diyala Journal of Engineering Sciences, pp.299–309.

Bowels, J.E. 1996. Foundation Analysis and Design. 5th Edition, McGraw-Hill Book Company.

Chou, C.W., Seagren, E.A., Aydilek, A.H. and Lai, M., 2011. Biocalcification of sand through ureolysis. Journal of Geotechnical and Geoenvironmental Engineering, 137(12),pp.1179–1189.

DeJong, J.T., Fritzges, M.B. and Nüsslein, K., 2006. Microbially induced cementation to control sand response to undrained shear. Journal of Geotechnical and Geoenvironmental Engineering, 132(11), pp.1381–1392.

DeJong, J.T., Soga, K., Kavazanjian, E., Burns, S., Van Paassen, L.A., Al Qabany, A., Aydilek, A., Bang, S.S., Burbank, M., Caslake, L.F. and Chen, C.Y., 2014. Biogeochemical processes and geotechnical applications: progress, opportunities and challenges. In Bio-and chemo-mechanical processes in geotechnical engineering: géotechnique symposium in print 2013 (pp. 143–157). Ice Publishing.

Karkush, M.O., Ali, N.A. and Imran, S., 2022. Using microbial induced carbonate precipitation for improving the undrained shear strength of soft clayey soil. Proceedings of the 20th International Conference on Soil Mechanics and Geotechnical Engineering, Pp. 2925–2930.

Karkush, M.O., Al-Murshedi, A.D. and Karim, H.H., 2020. Investigation of the impacts of nano-clay on the collapse potential and geotechnical properties of gypseous soils. Jordan Journal of Civil Engineering, 14(4).

Karkush, M.O., Almurshedi, A.D. and Karim, H.H., 2022. Investigation of the Impacts of Nanomaterials on the Micromechanical Properties of Gypseous Soils. Arabian Journal for Science and Engineering, pp.1–11.

Karkush, M.O., Al-Shakarchi, Y.J. and Al-Jorany, A.N., 2008. Theoretical modeling and experimental investigation of leaching behavior of salty soils. In Conference on Construction and Building Technology, Pp. 123–138.

Martinez, B.C., DeJong, J.T., Ginn, T.R., Montoya, B.M., Barkouki, T.H., Hunt, C., Tanyu, B. and Major, D., 2013. Experimental optimization of microbial-induced carbonate precipitation for soil improvement. Journal of Geotechnical and Geoenvironmental Engineering, 139(4),pp.587–598.

Qabany, A. and Aziz, A.A., 2011. Microbial carbonate precipitation in soils (Doctoral dissertation, University of Cambridge).

Qabany, A.A. and Soga, K., 2014. Effect of chemical treatment used in MICP on engineering properties of cemented soils. In Bio-and Chemo-Mechanical Processes in Geotechnical Engineering: Géotechnique Symposium in Print 2013 (pp. 107–115). ICE Publishing.

van Paassen, L.A., Ghose, R., van der Linden, T.J., van der Star, W.R. and van Loosdrecht, M.C., 2010. Quantifying biomediated ground improvement by ureolysis: large-scale biogrout experiment. Journal of geotechnical and geoenvironmental engineering, 136(12),pp.1721–1728.

Van Wijngaarden, W.K., Vermolen, F.J., Van Meurs, G.A.M. and Vuik, C., 2011. Modelling biogrout: a new ground improvement method based on microbial-induced carbonate precipitation. Transport in porous media, 87(2),pp.397–420.

Weaver, T.J., Burbank, M., Lewis, A., Lewis, R., Crawford, R. and Williams, B., 2011. Bio-induced calcite, iron, and manganese precipitation for geotechnical engineering applications. In Geo-Frontiers 2011: Advances in Geotechnical Engineering (pp. 3975–3983).

Smart Geotechnics for Smart Societies – Zhussupbekov, Sarsembayeva & Kaliakin (Eds)
© 2023 The Author(s), ISBN 978-1-003-29912-7
Open Access: www.taylorfrancis.com, CC BY-NC-ND 4.0 license

Physical and numerical modeling of strip footing on geotextile reinforced foundation beds

M. Kapor & A. Skejić
Faculty of Civil engineering, University of Sarajevo, Bosnia and Herzegovina

ABSTRACT: The paper presents insights from small-scale physical model tests on statically loaded strip footing resting on dense base sand supported by a single geotextile layer on soft subgrade soil. The benefits of the geotextile were assessed by comparing the results obtained for the improved soil model to the unreinforced beds. Experimental testing was conducted in a steel tank with inside dimensions 120/50/80 cm (width/ length/ height). The images were collected by recording the 120×80 cm transparent front side and analyzed by DIC software. Results confirm the contribution of reinforcement inclusions to the improved behavior of base and subgrade layers. A numerical simulation of the strip footing on reinforced and unreinforced sand was applied to assess the geotextile's influence. Independent laboratory tests were performed to obtain the parameters of numerical models. The FEM results were compared with the experimental observations, and a good agreement with measurements was confirmed.

1 INTRODUCTION

Geosynthetic inclusions can enhance the behavior of loose soft soils when surcharged by foundation loads (Guido et al., 1985, Demir et al., 2014). The different geosynthetic products were used to investigate the reinforcement effect, most being planar geogrids and geotextiles or geocells. Lateral confinement and membrane action of geosynthetics contributes to the reduction of footing settlements and increment of ultimate bearing capacity compared to unreinforced foundation beds. The benefits of planar reinforcement installed in variously compacted sands were investigated by small-scale physical modeling (Latha et al. 2009, Cicek et al. 2015), full-scale tests (Adams and Collin 1997), and numerical modeling (Love et al. 1987, Wang et al. 2019).

Small-scale models with a transparent side of the box were recognized as a powerful tool for observing the displacements at the total foundation soil area. The digital photos collected at the different stages of the footing pressure were implemented in different digital (or velocity) image correlation software, and the displacement of foundation soils with a failure mechanism was declared. The displacement patterns and failure mechanism of reinforced and unreinforced foundations soils were usually compared to understand the soil-reinforcement interaction mechanism in detail (Michalowski, 2003, Gedela et al., 2021). Michalovski (2003) used a very small strip footing (3.2 cm) and reinforced the foundation soil with a single layer of geosynthetic strips. The results arrived at from this study show that the deformation of sand reinforced with one long layer of reinforcement retained many of the features found in the sand without reinforcement. Michalowski (2003) also showed that a single reinforcement layer slightly modifies the failure mechanism compared to the well-known Prandtl mode typically obtained for dense unreinforced beds. This observation is not in agreement with the result reported by Yetimoglu et al. (1994), who obtained typical punching-shear failure for geogrid located at depths below 0.25B the footing, similar to Akinmasuru and Akinbolade (1981), Guido et al. (1987) and Adams and Collin (1997).

DOI: 10.1201/9781003299127-75

Consequently, an additional investigation on the soft subgrade and base layer response is performed in the present study to investigate the displacement pattern and failure mechanism of geotextile reinforced foundation beds on the loose subgrade. Digital image correlation was implemented to assess the loose subgrade and base layer response (displacements and failure mechanism) for different footing surcharge pressures. A complex 3D numerical modeling in Plaxis software was also formed to compare measured and numerically predicted results, and a good agreement was obtained.

2 PHYSICAL AND NUMERICAL MODELS

2.1 *Physical model*

Figure 1 shows the box dimensions and the geometry of a small-scale physical model test performed to investigate the non-woven geotextile reinforcement influence on the behavior of the loose subgrade sand and dense base sand under the strip load surcharge. The same box was used by Skejic et al. (2018) for the small-scale models of the reinforced earth wall. The two different types of sand (loose subgrade sand and dense base sand) were installed in a box with inside dimensions of 120.0 cm (width), 50.0 cm (length), and 80.0 cm (height). A transparent sidewall is made of 5.1 cm thick glass, whereas a thin 0.4 cm thick glass is glued to the opposite stiff wooden wall side to enable the low friction characteristics at the interface. Sidewall surfaces were not lubricated because transparency was requested for a digital image collection during footing pressure application. A 16.0 cm wide, 49.5 cm long, and 2.0 cm thick steel plate was used to simulate the strip footing. The box and steel plate dimensions were adopted to eliminate the influence of box side boundaries on displacements and strains filed.

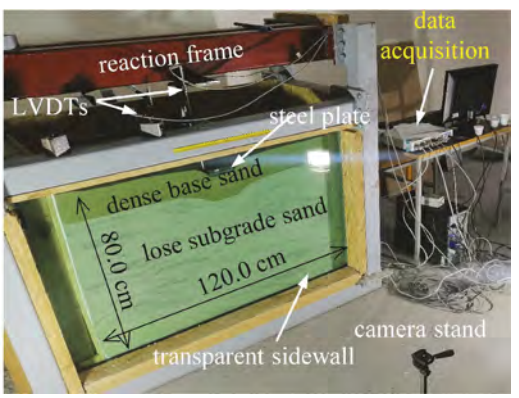

Figure 1. Details of the physical model – deformed sand configuration at the end of the test.

The loose subgrade material was quartz sand of uniform size (SP in the Unified Soil Classification System) with a mean diameter D_{50}=0.22 mm, a coefficient of curvature C_c=0.95, and a coefficient of uniformity C_u=1.9. A small fine particle content and a very low coefficient of uniformity make this material a good choice for the simulation of loose subgrade soils. The dry unit weight of the subgrade sand was 13.4 kN/m3, resulting in D_r = 10%. The base layer was composed of river sand of uniform size (SP in the Unified Soil Classification System), with a mean diameter D_{50}=0.35 mm, a coefficient of curvature C_c=1.0, and a coefficient of uniformity C_u=2.9. The dry unit weight of the base layer was 16.3 kN/m^3, resulting in D_r = 80%.

The non-woven geotextile was used for single-layer reinforcement at the subgrade-base sand interface. This reinforcement (L=2.5B=40.0 cm) was placed 6.0 cm below the surface, which is equal to the thickness of the base sand layer. The subgrade sand layer was 74.0 cm thick, resulting in the total height of the model of 80.0 cm. The manufacturer reported that the in-air tensile characteristics of the 100 g/m^2 non-woven, needle-punched UV-stabilized polypropylene geotextile are: a geotextile strength of 7.0 kN/m and geotextile stiffness of 14.0 kN/m.

The physical model was prepared by installing the dry sand in seven layers with equal thickness, with each layer weighing the equal weight of the installed dry sand. The 74.0 cm tick subgrade sand was installed without compaction to simulate loose soil conditions. After that, the reinforcement was placed and covered by the base sand layer. Compaction of this layer was performed with a 5.0 cm diameter steel rammer weighing 2.0 kg. After the model had been completed, a hydraulic press was placed on a steel plate to simulate a strip footing surcharge. The surcharge was applied in increments of 5.0 kPa/min. After each load increment, the settlement was measured with displacement transducers (LVDT), and images of sand deformation were collected for DIC analysis.

2.2 *Numerical model*

3D numerical model of the test, shown in Figure 2, was formed in Plaxis 3D finite element program (Brinkgreve et al., 2012). Details of the numerical model are described for particular model components, which include: boundary conditions, subgrade and base soil layers, reinforcement, construction phases, and loading program. The model's lateral vertical and bottom boundaries were assumed fixed in all directions. Interface elements are introduced between stiff sidewalls and soil to account for friction. Namely, the direct use of interface strength reduction by applying a reduction factor value ($R_i < 1$) to backfill significantly reduces the normal stiffness, resulting in misleading displacements perpendicular to the sidewall surface. In order to prevent this, an additional material with high stiffness and small strength is introduced for defining a side wall-sand interface. It is found that the glass sidewall-sand friction does not influence the reinforcement behavior significantly if the model width is larger than 0.6H (Skejić et al., 2017). The values of 7° for interface internal friction angle and 0.1 kPa for interface cohesion are adopted for this numerical model since the reported friction angles between glass and sand ranged from 6° to 9° (Tatsuoka and Haibara, 1985).

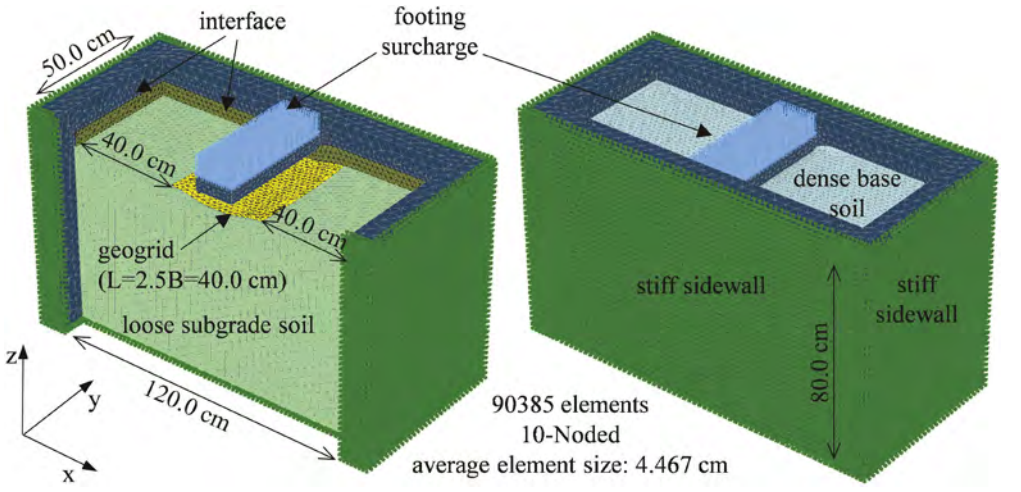

Figure 2. 3D numerical model details.

The base and subgrade sand soil is modeled with the Hardening soil constitutive model. Strength and stiffness parameters are determined following conventional laboratory tests for appropriate relative density. Poisson ratio and empirical m coefficient were adopted according to the suggested values from the literature (Benz, 2007). Reinforcement (non-woven geotextile) was modeled as a linear elastic, ideally plastic material (geogrid). Reinforcement stiffness is defined as the force per unit width ratio at 50% of ultimate strength (F_{ult}) and corresponding axial deformation measured during the in-air tensile test (EA = 14 kN/m and F_{ult} = 7.0 kN/m). The parameters of numerical model components are given in Table 1.

According to the model test setup, a surcharge load is applied as a uniform load applied through a steel plate 49.5/16.0/2.0 cm, with the following properties: unit weight, γ = 78.5 kN/m^3, Young's modulus, $E_{ref}=2\cdot10^8$ kPa and Poisson ratio, ν=0.15. The load is applied following the physical model test procedure, and the load is incrementally increased up to pressure, resulting in a 2.5 cm settlement.

Table 1. Material properties for the numerical model.

Parameter	Base sand HS model	Subgrade sand HS model	Soil-glass interface MC model
Unit weight, γ [kN/m^3]	16.30	13.40	14.0
Internal friction angle, ϕ [°]	40.0	31.0	7.0
Cohesion, c [kN/m^2]	1.0	0.1	0.1
Dilatancy angle, ψ [°]	8.0	0.0	0.0
Reference stress, p_{ref} [kN/m^2]	100.0	100.0	
Tangent oedometer stiffness, E_{oed}^{ref} [MPa]	15.0	7.0	
Secant triaxial stiffness, E_{50}^{ref} [kN/m^2]	15.0	7.0	50.0
Unloading/reloading stiffness, E_{ur}^{ref} [kN/m^2]	45.0	21.0	
At-rest lateral earth coefficient, K_0 [-]	0.35	0.48	
Stress-level dependency factor, m [-]	0.5	0.5	
Poisson ratio, for unloading/reloading, υ_{ur} [-]	0.2	0.2	0.4

3 TEST RESULTS, COMPARATIONS, AND ANALYSIS

Figure 3 shows typical curves for footing pressure (q) vs. footing settlement (s) for the physical and numerical model with and without reinforcement. A notable contribution of reinforcement was confirmed by comparing reinforced to unreinforced foundation bed response, both for the numerical and the physical model.

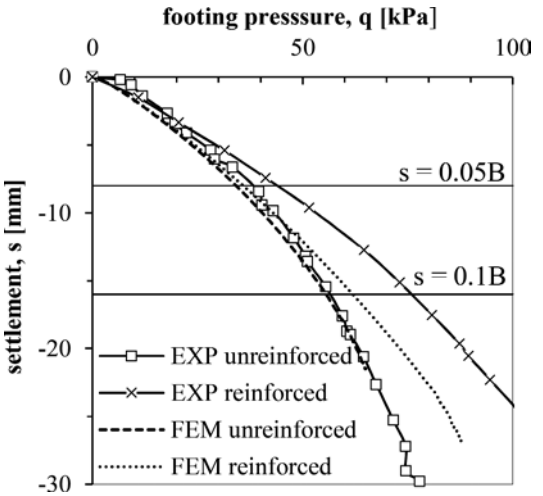

Figure 3. Footing pressure vs. settlement curves for reinforced and unreinforced models.

This improvement is especially noticeable for higher vertical displacements in the physical model. A good agreement on the results was obtained noting that more improvement by geotextile was obtained by experiment (EXP) compared to numerical model results (FEM). Images of the transparent sidewall collected at different stages of the vertical footing pressure were

analyzed using the GOM Correlate digital image correlation software to discuss the influence of reinforcement on displacement field and failure mechanisms. Vertical displacement obtained for the reinforced and unreinforced physical and numerical models at q=60.0 kPa is shown in Figure 4a. The selected load approximately corresponds to the unreinforced model's mobilized load for a 1.6 cm settlement (s=0.1B). Vertical upward movements are considered positive. The numerically obtained settlement bulb corresponds to the measured. The depth of the settlement bulb was generally lower in the case of reinforced soil, compared to the unreinforced bed.

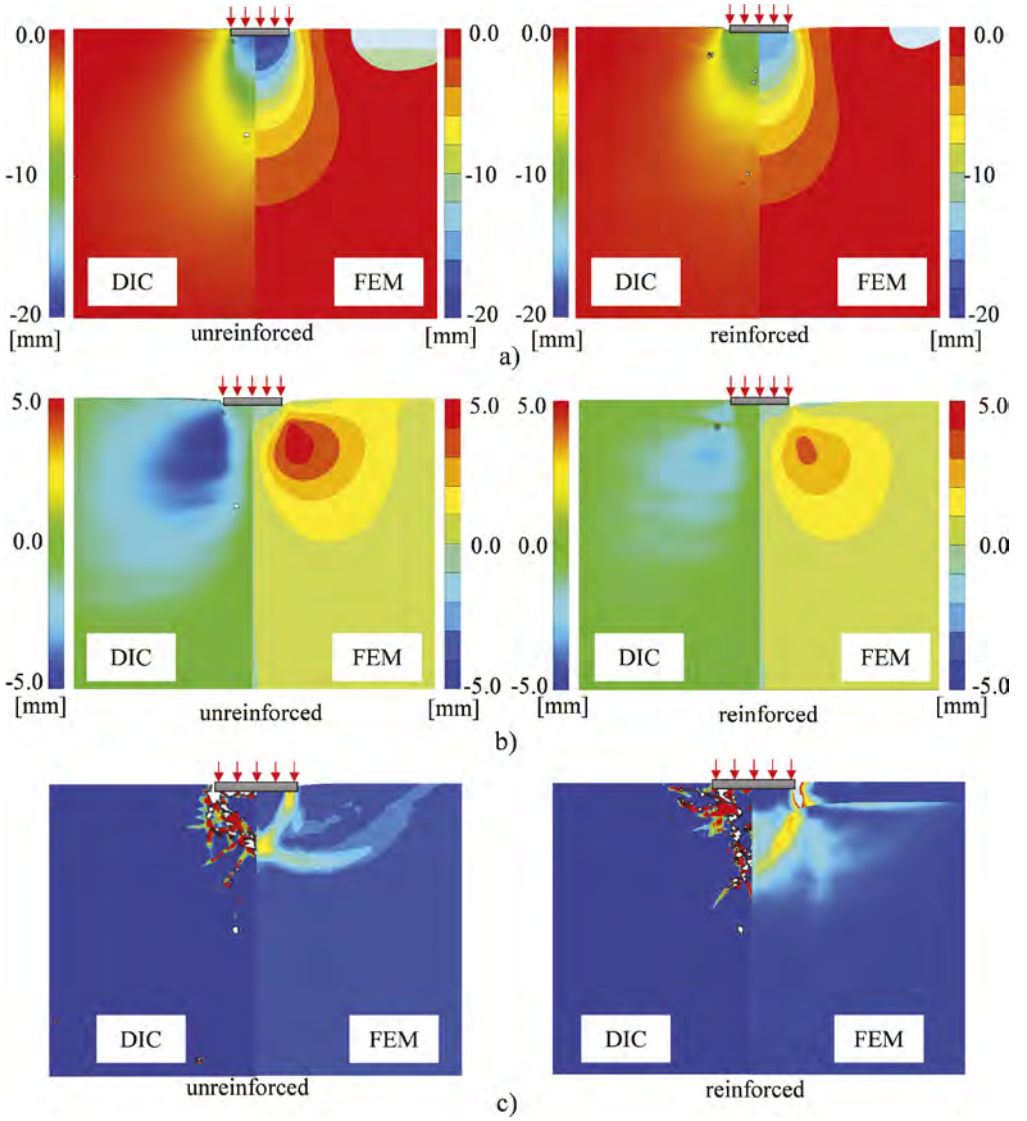

Figure 4. DIC and numerical model results for unreinforced and reinforced foundation bed: a) Vertical settlements at 60.0 kPa footing pressure; b) Horizontal displacements at 60.0 kPa footing pressure; c) Failure mechanism at approx 2.5 cm footing settlement.

An additional set of DIC and numerical model results showing horizontal displacements for reinforced and unreinforced models at 60.0 kPa footing pressure is given in Figure 4b. Rightward movements are considered positive. The geotextile reduces the horizontal displacement

above and below the reinforcement indicating the inclusion confinement effect in both experimental and numerical model results. Figure 4c shows the failure pattern obtained from the major principal shear strains for physical and numerical reinforced and unreinforced models. The obtained results show punching-shear failure without significant heave of the ground surface n both experimental and numerical models. This result was expected due to a very loose, high compressibility subgrade soil located at a relatively shallow depth under the strip footing, illustrating the importance of the sand density influence on the resulting failure mechanism. The failure mechanisms show that shear bands spread deeper under the strip footing in reinforced models compared with unreinforced models in both physical and numerical models.

4 CONCLUSION

This paper uses the physical and numerical models to analyze the benefits of using the one-layer geotextile reinforcement placed at the loose subgrade sand–dense base sand interface. The FEM results were compared with the experimental observations, and a good agreement with measurements was confirmed with some notable deviations in load-settlement response and failure mechanism.

Based on the results of this study, the following conclusions are stated:

a) The reduction of vertical displacement was obtained in reinforced models compared with unreinforced models.
b) The geotextile reduced the horizontal soil displacement in the vicinity of the reinforcement, and this confining effect was recognized by physical and numerical modeling.
c) The punching failure mode is obtained by physical and numerical modeling since very loose subgrade soil was analyzed.
d) The reinforcement affects the failure mechanism in a way that shear bands spread deeper under the strip footing at reinforced models compared with unreinforced models.

REFERENCES

Adams, M. T., & Collin, J. G. (1997). Large model spread footing load tests on geosynthetic reinforced soil foundations. Journal of geotechnical and geoenvironmental engineering, 123(1), 66–72.

Akinmusuru, J. O., & Akinbolade, J. A. (1981). Stability of loaded footings on reinforced soil. Journal of the Geotechnical Engineering Division, 107(6), 819–827

Benz, T. (2007). Small-strain stiffness of soils and its numerical consequences(Vol. 5). Stuttgart: Univ. Stuttgart, Inst. f. Geotechnik.

Brinkgreve, R. B. J., Engin, E., Swolfs, W. M., Waterman, D., Chesaru, A., Bonnier, P. G., & Galavi, V. (2012). Plaxis 3D 2012. Plaxis bv.

Cicek, E., Guler, E., & Yetimoglu, T. (2015). Effect of reinforcement length for different geosynthetic reinforcements on strip footing on sand soil. Soils and Foundations, 55(4), 661–677.

Demir, A., Yildiz, A., Laman, M., & Ornek, M. (2014). Experimental and numerical analyses of circular footing on geogrid-reinforced granular fill underlain by soft clay. Acta Geotechnica, 9(4), 711–723.

Gedela, R., Kalla, S., Sudarsanan, N., & Karpurapu, R. (2021). Assessment of load distribution mechanism in geocell reinforced foundation beds using Digital Imaging Correlation Techniques. Transportation Geotechnics, 31, 100664.

Guido, V. A., Chang, D. K., & Sweeney, M. A. (1986). Comparison of geogrid and geotextile reinforced earth slabs. Canadian Geotechnical Journal, 23(4), 435–440

Latha, G. M., & Somwanshi, A. (2009). Bearing capacity of square footings on geosynthetic reinforced sand. Geotextiles and Geomembranes, 27(4), 281–294.

Love, J. P., Burd, H. J., Milligan, G. W. E., & Houlsby, G. T. (1987). Analytical and model studies of reinforcement of a layer of granular fill on a soft clay subgrade. Canadian Geotechnical Journal, 24(4), 611–622.

Michalowski, R. L., & Shi, L. (2003). Deformation patterns of reinforced foundation sand at failure. Journal of Geotechnical and Geoenvironmental Engineering, 129(5), 439–449.

Skejić, A., Kapor, M., Medić, S., & Čerimagić, Đ. (2017, May). 3D Numerical Study of Sidewall Friction Influence on Small Scale Reinforced Earth Wall Behavior. In International Symposium on Innovative and Interdisciplinary Applications of Advanced Technologies (pp. 449–457). Springer, Cham.

Skejic, A., Medic, S., & Dolarevic, S. (2018). Influence of wire mesh characteristics on reinforced soil model wall failure mechanisms-physical and numerical modelling. Geotextiles and Geomembranes, 46(6), 726–738.

Tatsuoka, F., & Haibara, O. (1985). Shear resistance between sand and smooth or lubricated surfaces. Soils and Foundations, 25(1), 89–98.

Wang, Z., Jacobs, F., Ziegler, M., & Yang, G. (2020). Visualisation and quantification of geogrid reinforcing effects under strip footing loads using discrete element method. Geotextiles and Geomembranes, 48(1), 62–70.

Yetimoglu, T., Wu, J. T., & Saglamer, A. (1994). Bearing capacity of rectangular footings on geogrid-reinforced sand. Journal of Geotechnical Engineering, 120(12), 2083–2099.

Smart Geotechnics for Smart Societies – Zhussupbekov, Sarsembayeva & Kaliakin (Eds)
© 2023 The Author(s), ISBN 978-1-003-29912-7
Open Access: www.taylorfrancis.com, CC BY-NC-ND 4.0 license

Improvement of soil mechanical properties by biomass-derived chitosan and carboxymethyl cellulose

T. Sakai & M. Nakano
Nagoya University, Nagoya, Aichi, Japan

ABSTRACT: In order to investigate the effectiveness of ground improvement methods using chitosan (CS) and carboxymethyl cellulose (CMC), which are biomass-derived polymeric materials, unconfined compression test and triaxial compression test were conducted on specimens compacted after mixing CS and CMC with soil. The results showed that the improved soil had much greater strength than the untreated soil. The dilatancy properties were also found to be different, suggesting that the critical state constant was different. The greater the concentration of CMC solution, the greater the strength; and the most effective mass ratio of CS to CMC was 2 to 3 times CS to CMC.

1 INTRODUCTION

Polymeric materials have been widely used to solve various environmental problems. Solid polymer-ion complexes (polyion complexes, PIC) were used to prevent the dispersion of radioactive materials in soil contaminated by the nuclear power plant accident in Chernobyl (Zezin et al. 2015). In the Fukushima nuclear power plant accident, PIC were used to immobilize the soil surface layer and to detach soil contaminated with radioactive cesium (Kumazawa 2011). The mechanisms of soil immobilization of contaminants are as follows. Strong electrostatic interactions between positively charged polymers (polycations) and negatively charged polymers (polyanions) form PIC (Figure 1, top). In the soil, PIC polymers further bind to soil particles, immobilizing the soil and radioactive materials (Figure 1, bottom). PIC have been actively explored as soil improvement formulations in the agricultural field during several past decades (e.g., Izumrudov et al. 2019).

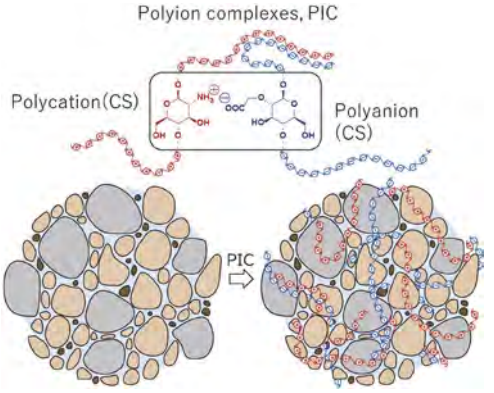

Figure 1. Schematic diagram of polyion complex formation.

DOI: 10.1201/9781003299127-76

In this study, chitosan (CS) was used as a polycation and carboxyl methyl cellulose (CMC) was used as a polyanion to improve soil. CS and CMC are naturally derived polymers and are low cost. Therefore, they are suitable for industrial-scale applications and satisfy the needs of "carbon neutral" and "circular economy". The soil improvement method proposed in this study using biomass-derived CMC and CS is a "green" and sustainable approach and is expected to be a more flexible soil improvement method compared to previous studies.

To investigate the effectiveness of soil improvement methods using CS and CMC, unconfined compression test and triaxial compression test were conducted on specimens compacted after mixing CS and CMC with soil. First, the mixing method of CS, CMC, and soil was investigated, and then the effects of CS and CMC concentrations on the strength were examined. The curing period of the specimens was also investigated.

2 EFFECT OF SAMPLE PREPARATION ON THE STRENGTH OF IMPROVED SOIL

Figure 2 Shows the particle size distribution of the soils used in this study. The soil particle density ρ_s was 2.716 g/cm^3. The maximum dry density ρ_{dmax} was 1.864 g/cm^3 and the optimum water content w_{opt} was 13.5% from compaction test using the A-b method. CS and CMC were mixed with 350 g dry weight of the soil in four methods. Method 1 is to add 0.7 g of CS powder and GDL solution, a pH adjuster, to 70 g of CMC solution and mix them before adding them to the soil. Method 2 is to add 35 g of CS solution to the soil and then mix it with 35 g of CMC solution. Method 3 is to add 35 g of CMC solution to the soil and then mix it with 35 g of CS solution. Method 4 is to first divide the soil into two parts and then mix the two parts with 35 g of CS solution and 35 g of CMC solution, respectively. In all of methods 1 through 4, 0.7 g of CS and 0.7 g of CMC were mixed.

The mixed sample were compacted in the mold in three layers using rammers to prepare the specimens. The density was adjusted to 90% of the maximum dry density, with a water content of approximately 20%. The specimens were cured in the mold for four days.

Figure 3 shows the results of unconfined compression tests conducted in accordance with JIS A 1216:2020. Figure 3 also shows the results for untreated soil adjusted to the same density and water content as the improved soil. Method 1 has the highest strength, with a compressive strength of approximately 140 kPa, about 1.5 times stronger than the other methods and three times stronger than the case with distilled water mixed in. The reason for the small strength in Methods 2-4 was assumed to be that soil particles had a negative charge and wasn't able to form a PIC well when mixed with CS, which had a positive charge in advance.

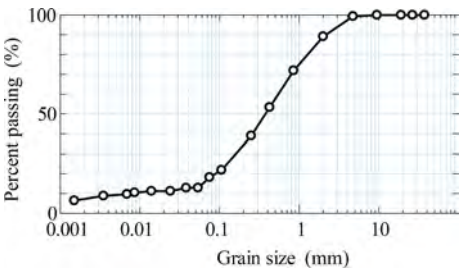

Figure 2. Grain size distribution.

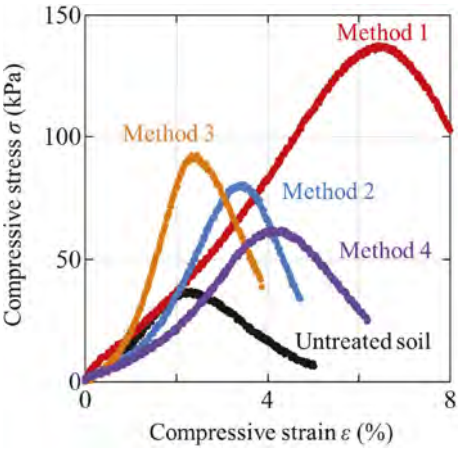

Figure 3. Effect of mixing method on the strength.

3 EFFECT OF CS AND CMC CONCENTRATIONS ON THE STRENGTH OF IMPROVED SOIL

All specimens in this and subsequent section were prepared by Method 1. In this section, specimens were prepared with varying concentrations of CMC and varying mixing ratios of CS and CMC. Figure 4 shows the stress-strain relation for each case. In all cases, peak strength was observed at approximately 5-6% strain. The specimens with higher strength also had higher stiffness. The larger the concentration of CMC solution, the greater the unconfined compressive strength. On the other hand, the optimum ratio of CS to CMC changes depending on the concentration of CMC solution. The unconfined com-pressive strength of the soil was greater when CS is mixed more than CMC. This is be-cause soil particles have a negative charge, and it is important to mix more CS with a positive charge. The case of the highest strength was 560 kPa, which was about 10 times stronger than the untreated soil.

Curing periods were studied for cases with a CMC solution concentration of 1% and a CS:CMC ratio of 2:1. Four cases were tested: 4 days, 1 week, 2 weeks, and 3 weeks of curing after specimen preparation. For the curing method, the specimens were left in the mold, sealed to prevent drying, and left at room temperature. Figure 5 shows the strength increased up to 2 weeks of curing period, with the same strength at 2 and 3 weeks, indicating that 2 weeks of curing was sufficient for improvement. Because the increase in strength after 4 days of curing is not significant, it is possible to design the mix ratio of CS and CMC using specimens with a curing period of 4 days.

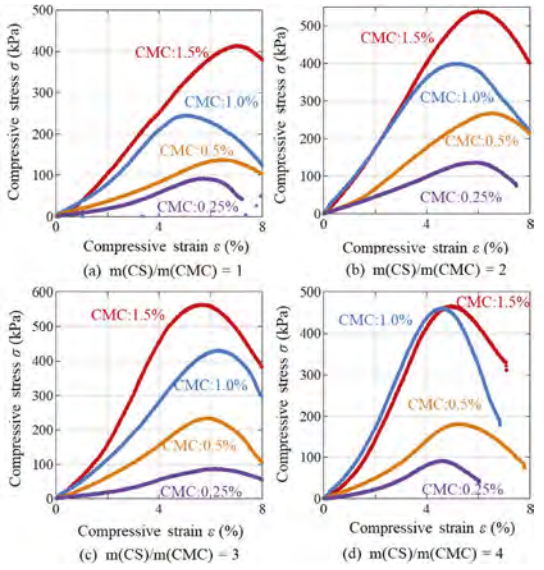

Figure 4. Unconfined compression test results of improved soil with different amounts of CMC and CS.

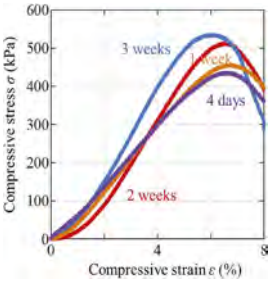

Figure 5. Effect of curing period.

4 TRIAXIAL COMPRESSION TEST FOR IMPROVED SOIL

Triaxial compression tests were conducted in accordance with JGS 0523-2020 with a CMC solution concentration of 1% and a CS:CMC ratio of 2:1. Untreated soil was also tested for comparison. The specimens were saturated using the double-suction and back-pressure method. After confirming that the B-value was larger than 0.95, isotropic consolidation was performed for 24 hours under a confining pressure of 100 kPa. Then, monotonic shear was applied at an axial strain rate of 20%/day under undrained condition.

Figure 6 shows the triaxial compression test results for improved soil and untreated soil. The two specimens were prepared at the same density. The relation between deviator stress q and axial strain ε_a shows that the maximum deviator stress was about 2.5 times higher than that of the untreated soil, even though the densities were the same. The untreated soil exhibited almost constant deviator stress after 5% axial strain ε_a, whereas the improved soil exhibited an increase in q with increasing ε_a. The q-mean effective stress p' relation indicated that the improved soil exhibited a remarkable hardening behavior with plastic expansion. The stress ratio ($\eta = q/p'$) at the transformation point and the η at ε_a of 20% were different, suggesting that the critical state index changes. The relation between excess pore water pressure u_e and ε_a showed that positive excess pore water pressure at the beginning of shear and negative excess pore water pressure at the end of shear for the improved soil were larger than ones for the untreated soil.

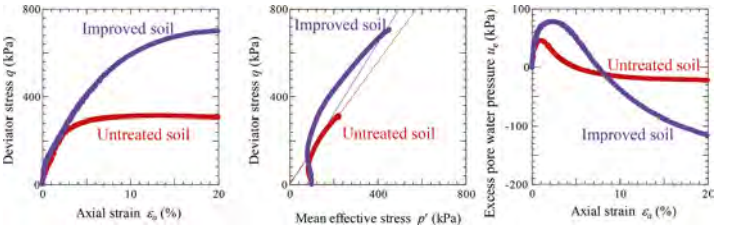

Figure 6. Triaxial compression test results for improved and untreated soil.

5 CONCLUSION

In this study, unconfined compression test and triaxial compression test were conducted on specimens compacted after mixing CS and CMC with soil to investigate the effectiveness of soil improvement methods using CS and CMC. The conclusions are as follows.

1) The most effective improvement was achieved by mixing the CMC solution with CS powder and GDL solution before mixing them with soil. In this method, the strength of the improved soil is clearly increased.
2) The larger the concentration of CMC, the greater the strength. The most effective mass ratio of CS to CMC also depends on the concentration of CMC; mixing two to three times as much CS as CMC was most effective. The greatest unconfined compressive strength of all cases was about 560 kPa, which was approximately 13 times greater than that of untreated soil.
3) The strength increased up to 2 weeks of curing period, with the same strength at 2 and 3 weeks, indicating that 2 weeks of curing was sufficient for improvement. Because the increase in strength after 4 days of curing is not significant, it is possible to design the mix ratio of CS and CMC using specimens with a curing period of 4 days.
4) Triaxial compression test results also indicated that the strength of the improved soil is much greater than that of the untreated soil. The dilatancy properties were also different. The stress ratio at the transformation point and ε_a of 20% were different, suggesting that the critical state index changed.

REFERENCES

Izumrudov, V.A., Mussabayeva, B.K., Kassymova, Z.S., Klivenko, A.N. & Orazzhanova, L.K. 2019. Interpolyelectrolyte complexes: advances and prospects of application, *Russ. Chem.* Rev. 88(10) 1046–1062.

Kumazawa, N. 2011. From the decontamination site in Iitate village - What should chemists do now? Toward the decontamination of radioactive materials caused by the Fukushima Daiichi Nuclear Power Station accident., *Chemistry Today*, 484, 34–38 (in Japanese).

Zezin, A.B., Mikheikin, S.V., Rogacheva, V.B., Zansokhova, M.F., Sybachin, A.V. & Yaroslavov, A.A. 2015. Polymeric stabilizers for protection of soil and ground against wind and water erosion, *Adv. Colloid. Interfac.* 226, 17–23.

Smart Geotechnics for Smart Societies – Zhussupbekov, Sarsembayeva & Kaliakin (Eds)
© 2023 The Author(s), ISBN 978-1-003-29912-7
Open Access: www.taylorfrancis.com, CC BY-NC-ND 4.0 license

Impulse compaction - one of the most economical methods in soil improvement

M. Bissmann
Ing., Terra-Mix Bodenstabilisierungs GmbH

ABSTRACT: Impulse Compaction also known as Rapid Impact Compaction (RIC) is a relatively new method of soil improvement and at the same time in principle one of the oldest methods in soil compaction. Already in ancient times, people improved their soil with the help of muscle strength or with small falling weights. In this paper, the origin, the historical roots, the current state of the art practice, and the various possibilities of Impulse Compaction use and application will be discussed. Furthermore, it will be shown how the impulse compaction with some modifications can also be used on weaker soils. Current documentation and quality assurance standards will be shown. Some selected projects will then underline the potential and attractiveness of Impulse Compaction.

1 INTRODUCTION

To improve the subsoil in terms of its load-bearing capacity, soil compaction is still the most economical method because, in general, little to no foreign material is added and instead the inherent load-bearing capacity of the soil material is stimulated and optimized. Stomping is the oldest type of compaction (Figure 1): already in ancient times, people improved their soil with the help of muscle strength or with small falling weights creating dynamic soil compaction. The modern impulse compactor (Figure 1) takes this old principle and adapts it to the demands of modern projects by being much more time efficient and providing better quality results.

Figure 1. Compacting in the past, stomping (left), and now, impulse compactor (right).

DOI: 10.1201/9781003299127-77

Modern Impulse Compaction, also known as Rapid Impact Compaction (RIC), is the action of compacting the ground with a so-called impulse compactor, in which a defined weight falls freely from a height of up to 1.2 m onto a steel plate that is resting on the ground. The dropped weight is hydraulically lifted and this can be done so quickly as to perform up to 60 blows per minute, while the steel plate, the so-called compactor foot, always remains in contact with the ground. Within the family of soil improvement methods, Impulse Compaction can be seen as the "missing link" between near-surface compaction (rolling) and deep compaction (vibro-compaction, dynamic deep compaction) (Figure 2).

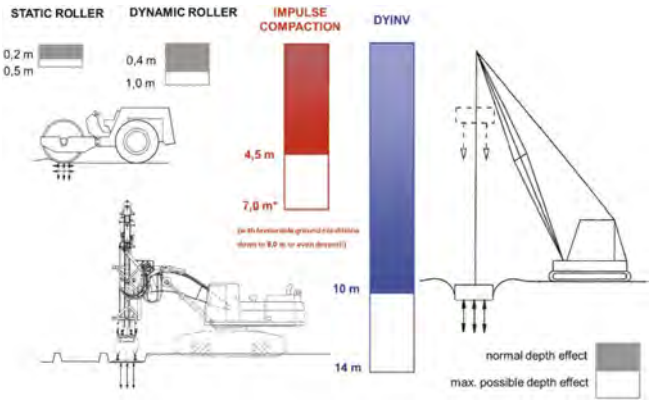

Figure 2. Depth effect of various methods of subsoil improvement: near-surface, impulse and deep compactions.

Impulse Compaction has many advantages when compared to the other compaction methods. Due to the fact that usually no or very little foreign material has to be introduced, Impulse Compaction is not only economically advantageous, it also generates by far the smallest carbon footprint compared to the other processes. Furthermore, compared to dynamic intensive compaction, Impulse Compaction generates far fewer vibrations, which may be of advantage in certain scenarios. However, in some urban settings, the vibrations from Impulse Compaction can still be too high.

To the author's knowledge, modern Impulse Compaction is only commercially done using freely falling weights: companies that use hydraulically accelerated hammers, as opposed to freely falling weights, only use them for driving piles of wood, steel or precast concrete and not for ground improvement as such. There have been attempts and considerations on the part of Terra-Mix to accelerate the falling weight by means of a rocket propulsion system in order to reduce costs by reducing the weight, but these have not yet come to any useful results.

2 TECHNICAL DESCRIPTION OF IMPULSE COMPACTION

The impulse compactor is a dynamic compaction device based on a piling hammer technology and is used to increase the bearing capacity of soils through controlled impacts. A drop weight of 5 to 16 tonnes is dropped onto the compactor foot assembly 40–60 times a minute. The foot, which remains in contact with the ground at all times, has a diameter that can range from 80 cm to 2 m, but 1.5 m is common. The compaction results in a rearrangement of the solid material in the soil, because as the water and air pores are displaced, the solid particles are brought into an even denser positioning. In coarse-grained or mixed-grain soils, water in the soil can be squeezed out of between the grains by pressing the grains together and creating a higher contact pressure. In cohesive soils, instead of reducing the soil volume by displacing pore spaces, the result of the mechanical compaction action is rather to have a constant

displacement of the material, as the (almost) incompressible water pushes the impermeable grain material in front of it. This effect can also be seen occasionally when material bulges out laterally during Impulse Compaction. In such cohesive soil cases, a soil improvement with Impulse compaction can still be achieved by compacting in (time order) primary and secondary grid patterns or by including longer waiting times between the passes. Due to the hammering action and the soil rearrangement below, the compactor foot can penetrate up to 1 m into the soil, and when using a special construction, it can penetrate even deeper (which is desired in that case). During the compaction process, each individual impact is measured and documented by a depth sensor. Data monitoring during the compaction process and the online monitoring display in the operator's cab enable the operator to have detailed compaction control. The total impact depth of the compactor foot, the number of blows, and the "Final Set" of the compactor foot (resulting settlement from each particular blow) all contribute to making the decision to stop a hole. The resulting compaction craters (Figure 4) are usually filled with the site material, and the process is repeated until a previously defined 'stop code' is reached. Alternatively, external stone material can also be used to fill the holes in order to increase the stiffness of the soil. The 'stop code', in particular the 'Final Set' parameter, provides indirect information about the soil improvement. A measurable correlation between the indirect soil improvement information and the direct measurement of the improved soil usually takes place via a soil penetration test, such as the Dynamic Probing Heavy (DPH), which is carried out in the course of the so-called calibration field phase.

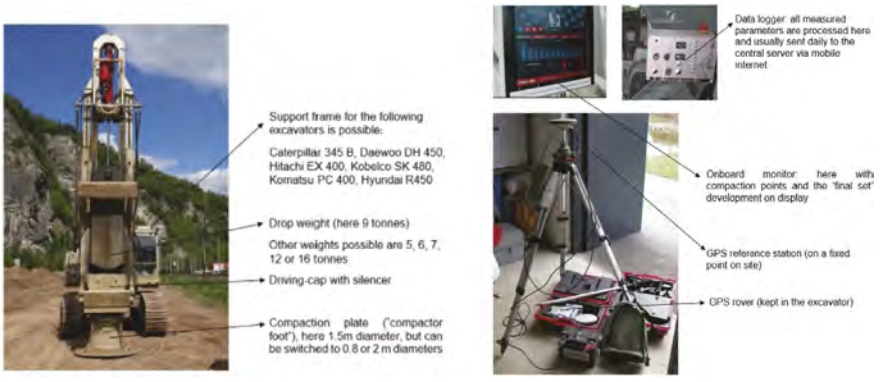

Figure 3. Components of an impulse compactor (standard version in Europe).

The following soil parameters and characteristics can be improved with the Impulse Compaction method:

- compactness of the soil particle packing (bulk density)
- soil stiffness (soil modulus, modulus of subgrade reaction),
- bearing capacity (friction angle, cohesion),
- settlement behaviour
- uniformity of the soil parameters
- weak zones identified
- shear wave modulus (thus mitigating the liquefaction risk)

In Europe, the nine tonne drop weight and the 1.5 m diameter foot, as shown in Figure 3, have proven to be the most economical combination. A heavier drop weight provides relatively little further depth effect, but it does speed up the compaction process because fewer blows are required per pass. Further equipment used in the Impulse Compaction process are shown in Figure 3: the onboard monitor, the data logger and the rover of the GPS system are all installed in the excavator cabin, while the GPS reference station is placed in a secure location on site.

3 LIMITS OF STANDARD IMPULSE COMPACTION

Originally, Impulse Compaction was only intended for sandy and gravelly or mixedgrained soils, in which there can be a deep compaction effect of up to 7 m. In certain sandy soils in Northern Germany or in coastal areas in Southeast Asia, compaction depth effects of up to 9 m have been documented, using the common drop weight of 9 tonnes and the 1.5 m foot. A heavier drop weight and a larger foot diameter allow for a significantly higher compaction speed, but the soil improvement effect at depth is rather small. In certain fine-grained soils, the compaction effect at depth decreases to 4.0–4.5 m. Table 1 can be used as a guideline for the use of Impulse Compaction technology in various soil types. The following values describe general limits of Impulse Compaction application in soft soils:

- coefficient of water permeability (Kf-value): max 10–6 m/s
- silt (grain size < 0,063 mm) content: max 15%

As the soil becomes more fine grained (the yellow cells in Table 1), it generally becomes required to undertake a more thorough soil investigation in order to ascertain the suitability of Impulse Compaction for those soils. In clayey and organic soils, consideration of Impulse Compaction without any additional measures should be rejected from the outset.

Originally, Impulse Compaction was only intended for sandy and gravelly or mixedgrained soils, in which there can be a deep compaction effect of up to 7 m. In certain sandy soils in Northern Germany or in coastal areas in Southeast Asia, compaction depth effects of up to 9 m have been documented, using the common drop weight of 9 tonnes and the 1.5 m foot. A heavier drop weight and a larger foot diameter allow for a significantly higher compaction speed, but the soil improvement effect at depth is rather small. In certain fine-grained soils, the compaction effect at depth decreases to 4.0–4.5 m. Table 1 can be used as a guideline for the use of Impulse Compaction technology in various soil types. The following values describe general limits of Impulse Compaction application in soft soils:

- coefficient of water permeability (Kf-value): max 10–6 m/s
- silt (grain size < 0,063 mm) content: max 15%

As the soil becomes more fine grained (the yellow cells in Table 1), it generally becomes required to undertake a more thorough soil investigation in order to ascertain the suitability of Impulse Compaction for those soils. In clayey and organic soils, consideration of Impulse Compaction without any additional measures should be rejected from the outset.

4 DOCUMENTATION AND QUALITY CONTROL

For an Impulse Compaction soil improvement program to be considered successful, an increase in soil stiffness and the homogenization of the soil under individual foundations are required. In Europe, the soil stiffnesses are thus far mostly measured indirectly with Dynamic Probing Heavy (DPH), but Cone Penetration Test (CPT) or Standard Penetration Test (SPT) can also be used. Sometimes, the soil improvement measurements are also carried out by means of geophysics, for example, Continuous Surface Wave (CSW) analysis or similar. DPH soundings, taken before and after Impulse Compaction, show the resulting increase in soil stiffness (Figure 4)

In order to be able to prove a successful soil improvement program, an exact documentation of the effects on the soil is required. During soil compaction, the following data of each point can be recorded continuously and stored daily on the central server:

- local or transferred GPS coordinates (X, Y, Z) (with an assigned point ID)
- date and time
- number of compaction blows

Table 1. Guideline for application of Impulse Compaction in various soil types.

Main group	General group	Abbreviation Group symbol	Replacement base layer System	Impulse Compaction Effective depth	Hybrid Foundation System	RIC Stone Columns Without pre-drilling	RIC Stone Columns Without pre-drilling
Coarse-grained soil	Coarse gravel	cGr		max.6-8m			
Coarse-grained soil	Medium gravel	mGr		max.6-8m			
Coarse-grained soil	Fine gravel	fGr		max.6-8m			
Coarse-grained soil	Coarse sand	cSa		max.7-9m			
Coarse-grained soil	Medium sand	mSa		max.7-9m			
Coarse-grained soil	Fine sand	fSa		max.7-9m			
Mixed-grained soil	Silty gravel	siGr		max.5-7m		aprox. 3m	aprox. 3m
Mixed-grained soil	Gravelly silt	grSi		max.4-7m		aprox. 3m	aprox. 3m
Mixed-grained soil	Clayey gravel	clGr		max.4-7m		aprox. 3m	aprox. 3m
Mixed-grained soil	Silty sand	siSa		max.4-7m		aprox. 3m	aprox. 3m
Mixed-grained soil	Sandy silt	saSi		max.3-6m		aprox. 3m	aprox. 3m
Mixed-grained soil	Clayey sand	clSa		max.4-5m		aprox. 3m	aprox. 3m
Fine-grained soil	Silt	CSi		max.3-5m		aprox. 3m	aprox. 3m
Fine-grained soil	Silt	MSi, FSi				aprox. 3m	aprox. 3m
Fine-grained soil	Clay	Cl				aprox. 3m	aprox. 3m
			tecnically possible		tecnically eventually possible		tecnically NOT possible

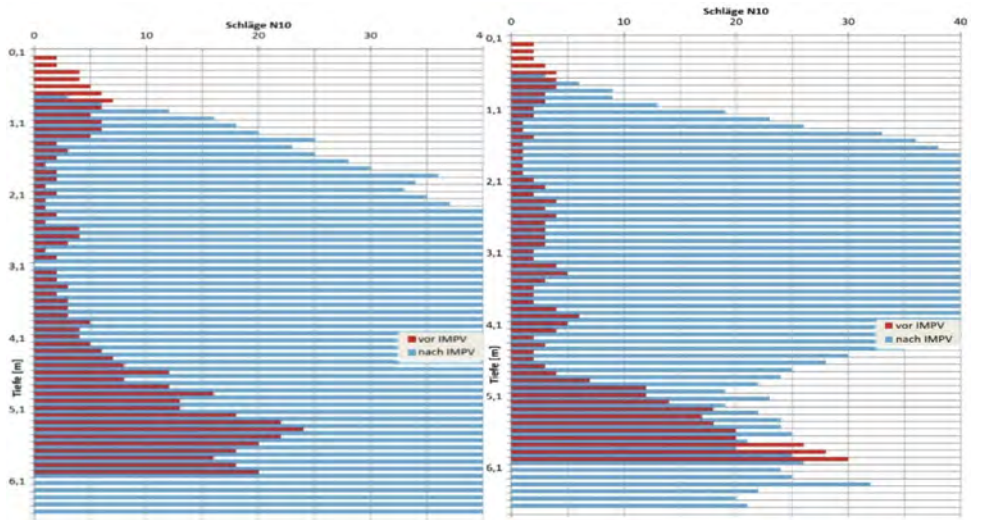

Figure 4. Examples of DPH soundings before (red) and after (blue) Impulse Compaction.

- number of passes (if within certain criteria (depth, time, number of strokes) the desired target is not reached, the hole must be filled again and a new pass from the working plane must be started)
- the penetration depth into the ground per blow
- the total (summed) penetration depth per pass and per point ("Deep Total")
- possibly also vibration and noise measurements

With the recording of these parameters, one of the most important tasks of Impulse Compaction can be verified directly: the homogenization of the subsoil. In practice, this means that every single point is worked on until the same "answer" from the ground can be documented in the form of the 'Final Set'. Furthermore, the choice of the grid of compaction points, or the distance between points under individual or strip foundations, as well as the compaction plate diameter play a big role in the resulting quality of the Impulse Compaction program. These are usually determined beforehand in the geotechnical design according to empirical values and geotechnical calculations and later re-evaluated so that the soil mechanical properties such as stiffness and packing density are improved to the desired levels.

For quality control, the impulse compactor must be "calibrated" to each soil before starting work. This is done in a so-called "calibration field", where a field of at least 3 × 3 points is defined on the construction site, and in which geotechnical investigations are first carried out. After the initial testing, the calibration field is compacted with the impulse compactor according to the preliminary geotechnical plan. Then the same geotechnical soil investigations are carried out again to determine soil improvement and to check that the required improvement has been reached. Depending on the results, the machine parameters are then confirmed or adjusted if necessary. These become the "stop codes", as the on-board computer automatically stops the compaction work at that point once these parameters are reached.

After the calibration process, compaction can be rolled out over the entire construction site.

Compaction quality control continues with regular checks using the investigation methods used in the calibration phase. The continuous recording and documentation of the machine parameters usually means a significant reduction in control testing.

5 DISCUSSION/CONCLUSIONS

Impulse Compaction or RIC is now considered "state of the art" when it comes to economical solutions for soil improvement and homogenisation of non-cohesive soils. In its most basic application, the idea is to improve the ground, primarily the soil stiffness, such that it can support the structural loads with a shallow foundation only. This would help to avoid needing more expensive deep foundation solutions. Therefore, the geotechnical conception and calculation for Impulse Compaction are relatively simple, as improving soil stiffness is the main desired outcome. However, thorough preparatory work (including subsoil investigation) is still essential in order to undertake a successful Impulse Compaction program.

This paper has shown that Impulse Compaction works very well in granular soils to reduce pore spaces and create a stiffer ground. In softer, more cohesive soils, it is also possible to work with this technology, but this requires more detailed preliminary investigations, a greater geotechnical understanding and the selection of an appropriate Impulse Compaction application or combination, such as the variant that combines Impulse Compaction with predrilled stone columns. The calculation and verification of the Impulse Compaction method can be carried out analogously to the recognized method of Priebe [6], which is often used for the dimensioning of vibro compaction. An interesting aspect of Impulse Compaction is that the soil is usually reduced in volume as a result of the compaction. This can lead to additional savings in the cost of excavating a construction pit, especially if the material is contaminated but compactable.

Finally, the noise and vibration of the Impulse Compaction method do not necessarily exclude it from ground improvement choices in sensitive areas. It is important to know the

country-specific regulations and to take the correct precautionary measures. A problemsolving mindset may also find solutions before a problem comes up. For example, in the construction of a building with a planned future expansion, an extra 10–20 m wide strip can be pre-compacted in the direction of the planned expansion so that future compaction work does not have to be undertaken close to the existing building. In conclusion, Impulse Compaction has already established itself as a particularly economical method for improving medium-deep soils. Looking forward, current ongoing research into noise and vibration reductions, into a more direct determination of the improved soil stiffness, and into a reduction of the system's weight will likely find innovations to make Impulse Compaction even more attractive as a soil improvement method.

REFERENCES

1. Adam, D., Herrmann, R.A.: Vortragsband Baugrundverbesserung in der Geotechnik. In: Symposium TU Siegen, s.111–176. Eigenverlag (2010)
2. Adam, D., Paulmichl, I.: Rapid impact compactor-an innovative dynamic compaction device for soil improvement. Improvement of Soil Properties, Bratislava, 4–5 June 2007 (2007)
3. Bißmann, M.: Die Impulsverdichtung- eine wirtschaftliche und ökologische Alternative in der Bodenverbesserung. In: Baugrundverbesserung Méthodes de confortation en géotechnique 170 MITTEILUNGEN der GEOTECHNIK SCHWEIZ, s. 77–88. Frühjahrstagung vom 7 Mai 2015 Luzern (2015)
4. Yanulova, D.: Master Thesis Auswertung und Interpretation von Messdaten zur Erfassung des Verdichtungserfolgs (2015)
5. Bißmann, M.: DIE IMPULSVERDICHTUNG IM EINSATZ IN ERDBEBENREGIONEN IN INDONESIEN. In: D-A-CH Tagung Erdbebeningenieurwesen & Baudynamik (D-A-CH 2019) am 26. und 27. September 2019 Univ
6. Priebe, H.: Die Bemessung von Rüttelstopfverdichtungen. Die Bautechnik 72(3),183–191 (1995)

Smart Geotechnics for Smart Societies – Zhussupbekov, Sarsembayeva & Kaliakin (Eds)
© 2023 The Author(s), ISBN 978-1-003-29912-7
Open Access: www.taylorfrancis.com, CC BY-NC-ND 4.0 license

Imparting soil water repellency with polymeric microcapsules

R. Qi & S.D.N. Lourenço
Department of Civil Engineering, The University of Hong Kong, Hong Kong S.A.R., China

ABSTRACT: Hydrophobized soils, which have a functional hydrophobic coating, can restrict water infiltration and thus have various engineering applications. Microencapsulation approaches, developed for self-healing applications emerge as a potential solution to switch the hydraulic properties of soil. In soils, microcapsules have been successfully implemented in agriculture to improve plant nutrition, based on the release of fertilizers into the soil from the microcapsules. The aim of this study is to impart soil water repellency with polymeric microcapsules by releasing hydrophobic cargo into soil. In this research, the hydrophobic cargo was encapsulated and mixed with soil. The released hydrophobic cargo and the soil hydrophobicity change was measured. The results show that the polymeric microcapsule could impart water repellency in soils.

1 INTRODUCTION

Natural hydrophobic soils originate from fungi and microorganisms, certain types of vegetation, and burning by wildfires, and are known to reduce the rate of wetting and the affinity of soil to water (Olorunfemi et al., 2014). Thus, they have been suggested to be used as an impermeable barrier for landfill cover systems, improving slope stability, and improving drainage in porous pavements (Beckett et al., 2016). Hydrophobic soils could be synthesized artificially by forming a hydrophobic coating on the surface of soil particles, which could adjust the level of soil water repellency and allow their use in infrastructure. Soil hydrophobicity can be quantified by the contact angle (CA) and water drop penetration time (WDPT) (Ng and Lourenço, 2016). The contact angle is a physical expression of the wettability of a surface. Through the Young-Laplace equation, 90° is used as a threshold. CA>90° indicates a hydrophobic surface and CA<90° indicates a hydrophilic surface (GOEBEL et al., 2011). The water drop penetration time (WDPT) measures the persistence of water repellency on the soil surface and classifies the water repellency according to the infiltration time (Olorunfemi et al., 2014). With different infiltration times (<5s, 5-60s, 60-600s, 600-3600s, >3600s), the soil is classified into wettable, slightly water repellent, strongly water repellent, severely water repellent, and extremely water repellent.

There has been an ongoing interest in applying polymeric microcapsules to enhance the performance and duration of various types of infrastructure. Microcapsules typically have a shell and cargo, which can store healing agents inside the microcapsules and release the stored agents to improve the properties of the matrix. They have been successfully implemented in cementitious materials including concrete and asphalt. For microcapsules mixed in concrete, microcapsules were proved to release cargo and fill fissures and thus improve the strength of the concrete (Kanellopoulos et al., 2016, Kanellopoulos et al., 2017). In asphalt pavements, it was found that by mixing with microcapsules, the cracked asphalt mixture recovered 52.9% of its initial strength (Al-Mansoori et al., 2017). For the application of microcapsules in soil, previous studies in agriculture have shown that microcapsules release nutrients into the soil slowly and contribute to plant growth (Cesari et al., 2020). Polymeric microcapsules are a suitable candidate for imparting water repellency in soils. In this study, we test whether polymeric microcapsules with hydrophobic cargo can release hydrophobic substances and impart soil water repellency.

DOI: 10.1201/9781003299127-78

The aim of this study is to induce water repellency in soils by polymeric microcapsules. Specific objectives are (1) to synthesize microcapsules with hydrophobic cargo, (2) to investigate the physical properties of the microcapsules, and (3) to verify the effectiveness of imparting soil water repellency with polymeric microcapsules by measuring the CA and WDPT of the soil.

2 METHOD

2.1 *Materials*

Fujian sand was used in the experiments. The particle size ranged from 150 to 300μm. Polydimethylsiloxane (PDMS) was used as the hydrophobic cargo as past studies show that the PDMS can induce high and stable hydrophobicity in sands (Lin and Lourenço, 2020). Calcium alginate was used as the shell of the microcapsules. Alginate has the advantage of being biodegradable, biocompatible, and non-toxic.

2.2 *Microcapsules encapsulation*

Microencapsulation is a process to produce a protective shell and isolate the cargo material from the surrounding environment (Kanellopoulos et al., 2017). The ionic gelation method was applied to encapsulate the PDMS cargo into a calcium alginate shell. This encapsulation mechanism is the emulsification of PDMS with sodium alginate solution, formation of cross-linking between sodium alginate and calcium ion, and encapsulation of the cargo. The encapsulation process is shown in Figure 1. Firstly, 1.5g of sodium alginate is dissolved in 100g of water. Secondly, PDMS emulsified with a homogenizer (Benchmark, D1000). The PDMS and sodium alginate emulsion was then dripped into calcium chloride solution (1.0 M) and the microcapsules was produced. The mass of PDMS used per 100g sodium alginate solution was defined as PDMS loading. In this study, three different PDMS loadings (5, 10, 20) were used to produce microcapsules with three different PDMS contents.

Figure 1. Encapsulation of hydrophobic cargo with the ionic gelation method.

2.3 *Microcapsules characterization*

The size and shape of microcapsules and sand were measured by a dynamic image analyser (QicPic™, Sympatec GmbH); 0.5 g of microcapsules and sand samples were analyzed to obtain the particle size distribution and the particle shape. Three parameters (aspect ratio, sphericity, convexity) that indicate particle shape were measured. The aspect ratio is defined as the ratio of particles minimum to the maximum Feret diameter indicating the elongation of the particle. sphericity is the ratio between equivalent and real perimeters of the particle profile, and convexity refers to the ratio of the whole area of a particle profile to its convex hull area. The microcapsules surface was characterized by an optical microscope (Leica, CH-9435).

2.4 *Imparting soil water repellency with microcapsules*

The microcapsules with different PDMS loading were mixed with soil. In this study, the number of microcapsules mixed was not studied and 4% mass content of microcapsules were

used. After mixing for 12 days, the microcapsules and the soil were separated, and the released amount of hydrophobic cargo and the soil hydrophobicity were measured.

The released PDMS amount was measured based on the different decomposition temperature points of PDMS and silica sand. Past studies showed that there is 85% mass loss when PDMS was heated to 800°C ((Camino et al., 2001, Sethy et al., 2019) while the silica sand was stable and there was no mass change for silica sand when the heating temperature was below 900°C (Ranjan and Brittain, 2007). In this study, the sand samples with PDMS were heated to 800°C, the mass loss was recorded, and the PDMS amount in soil was calculated.

The contact angle was measured with the sessile drop method, which is an accurate and direct measurement of soil hydrophobicity (Bachmann et al., 2000). The contact angle of the soil samples was tested with the following steps: (1) a layer of sand particles was placed onto a microscopic glass slide. (2) 10 μL of distilled water was dropped and dispensed on the sand surface. (3) the CA was recorded with a drop shape analyzer (DSA100, KRÜSS GmbH).

The WDPT was measured by recording the infiltration time of water into the soil. The soil samples were flattened and then 50 μL of distilled water drops were dispensed onto the surface of the sand with a pipette. The entire water infiltration process was recorded with a digital camera. The time duration of complete water drop infiltration was recorded as WDPT. For each soil sample, six water droplets were tested and the average penetration time was calculated.

3 RESULTS AND DISCUSSION

3.1 *Microcapsules properties*

The physical properties of the microcapsules are shown in Figure 2. Figure 2 (a) shows the particle size distribution curve of calcium alginate-PDMS microcapsules and sand. The majority (approximately 95%) of the capsules were distributed between 1.5mm and 2.0mm. The size of sand is distributed in the range of 0.3mm to 0.6mm. The average particle size of the capsules was 1.6mm. Figure 2 (b) showed the shape and surface features of the capsules. The microcapsules had a spherical shape with a rough surface. The spherical shape of the microcapsules and the sand host were further characterized and shown in Table 1. The aspect ratio, sphericity, and convexity of microcapsules were 0.81, 0.84, and 0.95, respectively. The aspect ratio and convexity of the microcapsules were larger than that of sand, which were 0.73 and 0.91, indicating that the roundness of the capsules is larger than that of the sand.

Table 1. Attributes of calcium alginate-PDMS composite microcapsules.

	Aspect ratio	Sphericity	Convexity
Fujian sand	0.73	0.86	0.91
Microcapsules	0.81	0.84	0.95

*For Microcapsules with 10 PDMS loading.

3.2 *Cargo release*

The released amount of hydrophobic cargo from microcapsules was measured. Figure 3 showed the content of PDMS in soil after mixing with 5, 10, and 20 PDMS loading microcapsules for 12 days. With the increase of PDMS loading in microcapsules, the released cargo amount increased. For soil mixed with 5 PDMS loading microcapsules, the PDMS content in soil was 0.02%. As the PDMS loading of microcapsules increased to 10 and 20, the PDMS content in soil increased to 0.26% and 0.34%, respectively. The increase of PDMS loading in microcapsules leads to a decrease in the proportion of sodium alginate solution, which forms the shell by cross-linking. The decrease of sodium alginate results in a weaker crosslinking structure and increased leakage of the hydrophobic cargo.

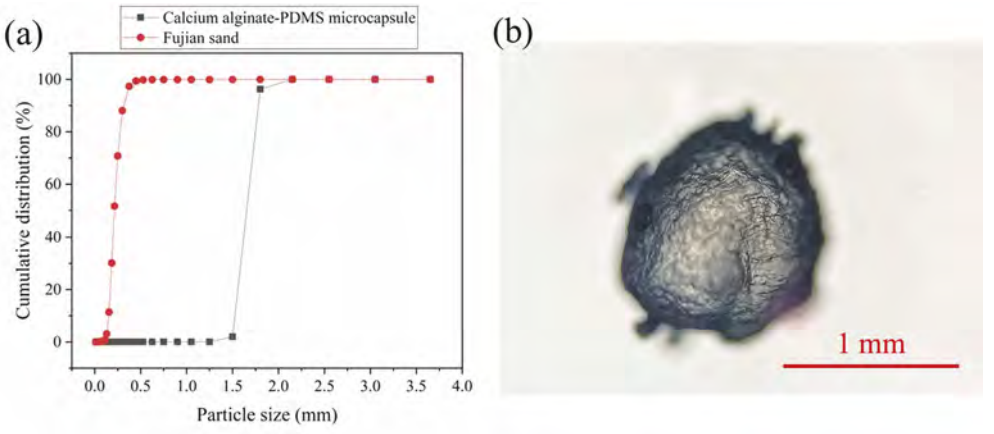

Figure 2. Physical properties of microcapsules: (a) particle size distribution of Fujian sand and calcium alginate-PDMS composite microcapsules; (b) Microphotograph of single calcium alginate-PDMS composite microcapsule.

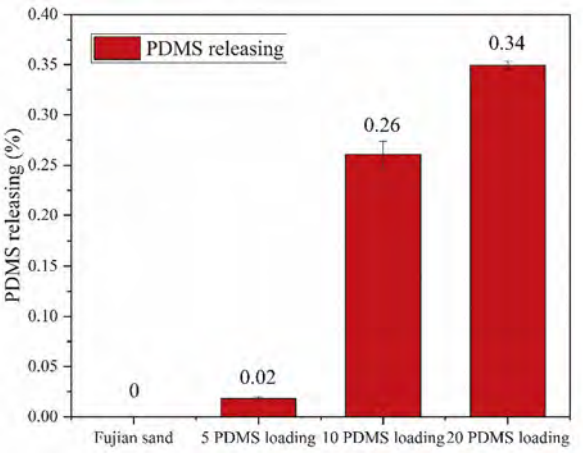

Figure 3. Hydrophobic cargo (PDMS) release amount.

3.3 *Soil water repellency*

The soil hydrophobicity is shown in Figure 4. Figure 4 (a) shows the CA of the soil while Figure 4 (b) shows the WDPT of soil after mixing with 5, 10, and 20 PDMS loading microcapsules for 12 days. After mixing with microcapsules, the CA of the soil increased. Besides, the CA of the soil increased with the increasing PDMS loading of the microcapsules. As shown in Figure 4 (a), the CA of the soil was 29.7° while the soil mixed with the microcapsules increased to 89.5°, 92,8°, and 115.1°, respectively (5, 10, and 20 PDMS loading microcapsules). Past studies have shown that before a critical concentration, the CA of soil increased with the increasing percentage of hydrophobic substances (Ng and Lourenço, 2016). The CA of the soil increased with PDMS loading as more hydrophobic cargo released into soils. With the criteria of CA = 90°, the soil surface was originally hydrophilic. By mixing with calcium-alginate PDMS microcapsules with the loading of 10 and 20, the soil switched to hydrophobic.

The WDPT of soil was smaller than 5s, which also suggested a hydrophilic state. For soil mixed with 5 and 10 PDMS loading microcapsules, the WDPT was also smaller than 5s. When the PDMS loading of the microcapsules increased to 20, the WDPT of sand increased to 3600s, which was an extremely water-repellent state. With the criteria of WDPT, the calcium alginate-PDMS microcapsules with 20 PDMS loading imparted soil water repellency.

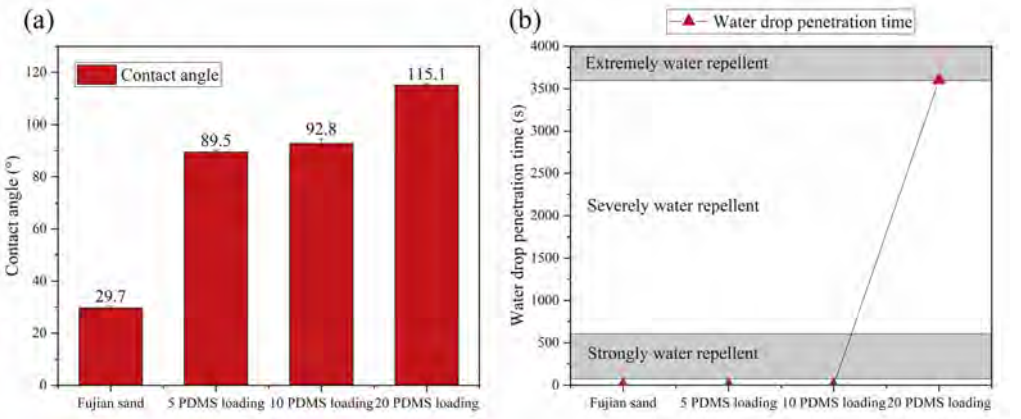

Figure 4. Soil hydrophobicity: (a) contact angle; (b) water drop penetration time.

4 CONCLUSIONS

This study demonstrates that polymeric microcapsules with hydrophobic cargo made of PDMS here, can be used to impart soil water repellency. PDMS was encapsulated with calcium alginate shell and proved capable to release cargo after mixing with soils. The released hydrophobic substances induced soil water repellency which was indicated by increased soil CA and WDPT. The PDMS loading of microcapsules affects the release amount and soil hydrophobicity increase. Higher microcapsule PDMS loading results in a higher amount of released PDMS. Based on the criteria of CA and WDPT, the microcapsules PDMS loading should be large than 20 in order to switch the soil from a hydrophilic state into water repellent state.

ACKNOWLEDGEMENTS

This work was supported by a Collaborative Research Fund from the Research Grants Council Hong Kong (C6006-20GF).

REFERENCES

Al-Mansoori, T., Micaelo, R., Artamendi, I., Norambuena-Contreras, J. & García, A. 2017. Microcapsules for self-healing of asphalt mixture without compromising mechanical performance. *Construction and Building Materials*, 155, 1091–1100.

Bachmann, J., Horton, R., Van der ploeg, R. & Woche, S. 2000. Modified sessile drop method for assessing initial soil–water contact angle of sandy soil. *Soil Science Society of America Journal*, 64, 564–567.

Beckett, C., Fourie, A. & Toll, D. Water repellent soils: the case for unsaturated soil mechanics. E3S Web of Conferences, 2016. EDP Sciences, 11011.

Camino, G., Lomakin, S. & Lazzari, M. 2001. Polydimethylsiloxane thermal degradation Part 1. Kinetic aspects. *Polymer*, 42, 2395–2402.

Cesari, A., Loureiro, M. V., Vale, M., Yslas, E. I., Dardanelli, M. & Marques, A. C. 2020. Polycaprolactone microcapsules containing citric acid and naringin for plant growth and sustainable agriculture: physico-chemical properties and release behavior. *Sci Total Environ*, 703, 135548.

Goebel, M. O., Bachmann, J., Reichstein, M., Janssens, I. A. & Guggenberger, G. 2011. Soil water repellency and its implications for organic matter decomposition–is there a link to extreme climatic events? *Global Change Biology*, 17, 2640–2656.

Kanellopoulos, A., Giannaros, P. & Al-Tabbaa, A. 2016. The effect of varying volume fraction of microcapsules on fresh, mechanical and self-healing properties of mortars. *Construction and Building Materials*, 122, 577–593.

Kanellopoulos, A., Giannaros, P., Palmer, D., Kerr, A. & Al-Tabbaa, A. 2017. Polymeric microcapsules with switchable mechanical properties for self-healing concrete: synthesis, characterisation and proof of concept. *Smart Materials and Structures*, 26, 045025.

Lin, H. & Lourenço, S. D. N. 2020. Physical degradation of hydrophobized sands. *Powder Technology*, 367, 740–750.
Ng, S. & Lourenço, S. 2016. Conditions to induce water repellency in soils with dimethyldichlorosilane. *Géotechnique*, 66, 441–444.
Olorunfemi, I. E., Ogunrinde, T. A. & Fasinmirin, J. T. 2014. Soil hydrophobicity: An overview. *J. Sci. Res. Rep*, 3, 1003–1037.
Ranjan, R. & Brittain, W. J. 2007. Combination of living radical polymerization and click chemistry for surface modification. *Macromolecules*, 40, 6217–6223.
Sethy, N. K., Arif, Z., Mishra, P. K. & Kumar, P. 2019. Synthesis of SiO2 nanoparticle from bamboo leaf and its incorporation in PDMS membrane to enhance its separation properties. *Journal of Polymer Engineering*, 39, 679–687.

Smart Geotechnics for Smart Societies – Zhussupbekov, Sarsembayeva & Kaliakin (Eds)
© 2023 The Author(s), ISBN 978-1-003-29912-7
Open Access: www.taylorfrancis.com, CC BY-NC-ND 4.0 license

A model test and 3D coupled analysis of vacuum consolidation method using vacuum well

T. Noda
Nagoya University, Nagoya, Japan

S. Takahashi, Y. Umehara & S. Sugie
Obayashi Corporation, Tokyo, Japan

T. Takaine
GEOASIA Research Society, Nagoya, Japan

ABSTRACT: In offshore reclamation works using dredged soil containing soft soil with high water content ratio, consolidation settlement of the ground is the main problem. In the present study, a large scale model test on a vacuum consolidation method using vacuum well, permeable layer and drains, which was developed to promote early consolidation of such reclaimed ground, was analyzed using a three-dimensional soil-water coupled finite deformation analysis code that can accurately describe the large compression of unconsolidated soil. The analysis accurately reproduced the test results, and showed clearly how the negative pressure propagated efficiently and accelerated settlement due to the effect of the underlying permeable layer and vertical drain.

1 INTRODUCTION

Since dredged soil contains soft clayey soil with high water content ratio, consolidation settlement of the ground is a major problem in offshore reclamation works using the dredged soil. A vacuum consolidation method (Figure 1a) using vacuum well, permeable layer, and vertical drains (Umehara et al. 2020) has been developed to achieve early consolidation of reclaimed ground and control residual settlement. This paper first outlines a large scale model test (Figure 1b, Umehara et al. 2020) on the vacuum consolidation method. Next, since the unconsolidated soil shows large compression in this consolidation problem, a three-dimensional soil-water coupled finite deformation analysis (Noda et al. 2008) employing the elastoplastic constitutive model, SYS Cam-clay model (Asaoka et al. 2002), was conducted to show that the test results were well reproduced (Validation). Through these results, this paper also emphasizes the need for the analytical features shown in the following (1)-(3). (1) Use of the elastoplastic constitutive model which allows to describe the mechanical behavior of unconsolidated (colloidal) soils with high voids ratio and pore pressure greater than the hydrostatic pressure before consolidation begins; (2) use of the soil-water coupled finite deformation analysis that can accurately calculate the amount of large compression from moment to moment while also considering supernatant water; (3) introduction of a permeability change model (Taylor 1948) associated with large compression of the soil.

2 OVERVIEW OF A LARGE-SCALE MODEL TEST OF VACUUM CONSOLIDATION METHOD USING VACUUM WELL

This consolidation method is a ground improvement method that aims to promote consolidation more efficiently by installing vacuum wells in the bottom drainage layer of clayey soil and propagating the negative pressure applied to the vacuum wells through the bottom of the clayey soil

DOI: 10.1201/9781003299127-79

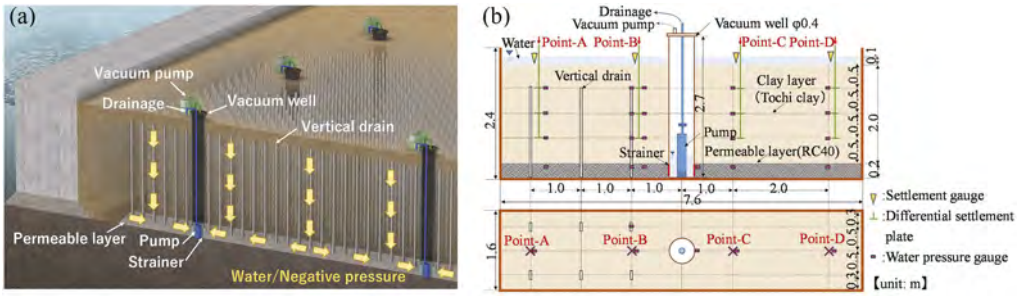

Figure 1. Vacuum consolidation method using vacuum well and a large scale model test.

using vertical drains that do not penetrate the ground surface. This chapter presents an overview of a large scale model test conducted to confirm the effectiveness of this improvement (Umehara et al. 2020). Figure 1b shows a cross-sectional and plan view of a 28 m^3 test soil tank (W7.5 m × D1.6 m × H2.4 m) that reproduces a clay layer 2.0 m thick, as well as the measuring points of settlement gauge, differential settlement plate, and water pressure gauge. The main components of the model are the clay layer to be improved (Tochi clay: plasticity index I_p = 10.0, initial water content w_0 = 38.8% = 1.3w_L, w_L: liquid index), a permeable crushed stone layer (RC40) placed below the clay layer, a vacuum well (φ400mm steel pipe) placed at the center of the soil tank, and vertical drains (plastic board drain, 94 mm wide and 3.6 mm thick) were installed only on the left side of the tank shown in Figure 1b. The vacuum well is a φ400 mm steel pipe with a lid that can be sealed inside, and a vacuum pump installed outside can provide negative pressure inside the well. A strainer installed at a depth equivalent to the crushed stone layer at the bottom of the well and a pump inside the well can pump up water from the clay layer.

In this test a negative pressure of -70 kPa was applied to the well after the pumping in the well was started. Pumping was controlled in the range of GL-1.7 - -2.0m where the water level in the well did not reach the bottom of the pump. The pressure in the well and the amount of water pumped were controlled by a pressure gauge and a flow meter installed at the top of the well. The vacuum pressure loading time was approximately 80 days.

3 A SOIL-WATER COUPLED FINITE DEFORMATION ANALYSIS CONSIDERING LARGE COMPRESSION OF UNCONSOLIDATED SOIL AND ANALYSIS CONDITIONS

In order to understand the mechanism of this test, a numerical analysis was performed using the analysis code, *GEOASIA* (Noda et al. 2008). The reasons for this are as follows. This analysis code employs the SYS Cam-clay model (Asaoka et al. 2002) as an elastoplastic constitutive model that can describe the mechanical behavior of soil in a colloidal state with a high water content ratio, especially the large compression behavior caused by the vacuum consolidation method, and it is a finite deformation analysis code that can sequentially and exactly calculate the large compression behavior and the geometrical nonlinearities that lead to it. In this analysis, the permeability is also greatly reduced by the large compression, and to evaluate this, the permeability was expressed as $k = k_0 \exp(\Delta e / C_k)$, $\Delta e = e - e_0$ (Taylor 1948). Here, e and e_0 are the voids ratio at the present and reference times, k, k_0 are the coefficients of permeability at the present and reference times, and C_k is the material constant.

Figure 2 shows the analytical conditions of three-dimensional finite element mesh and material constants. The analytical model is a one-half range model, considering the symmetry in the depth direction for the large test. The clay layer of the Tochi clay was determined using the SYS Cam-clay model with reference to the existing material constants (Nakai et al. 2017). The underlying drainage layer (crushed stone layer) and vertical drains were modeled as two-phase elastic materials. For the vertical drain, the compressive stiffness was made smaller than that of the clay layer, and actual permeability values were given.

The pore pressure distribution of unconsolidated clayey soil in the unconsolidated state immediately after soil tank input is almost equal to the total stress distribution. Therefore, as an initial condition for vacuum consolidation, the mean effective stress distribution of the soil skeleton was determined by subtracting the pore water pressure in the vertical direction immediately after clay input from the overburdened soil pressure (total stress distribution) calculated using the unit volume weight of the input clay. The unconsolidated clayey soil in colloidal state was assumed to be a highly structured soil in a normally-consolidated and isotropic stress state. In other words, structure R_0^* in the SYS Cam-clay model was distributed in the vertical direction with normal consolidation, $R_0 = 1$, and anisotropy, $\eta_0 = 0$ (isotropic) while assuming the structure (bulk) is developed equivalent to the pore water pressure.

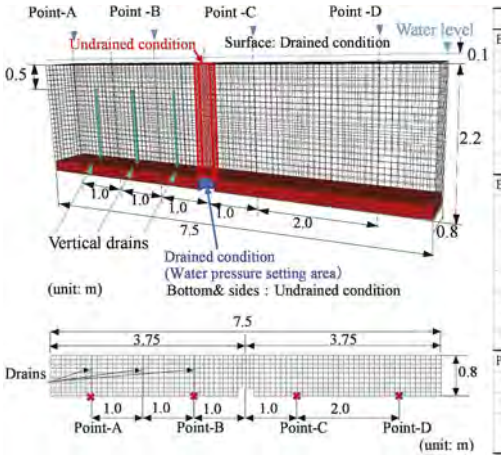

Tochi clay	
Elasto-plastic parameters	
Compression index $\tilde{\lambda}$	0.07
Swelling index $\tilde{\kappa}$	0.01
Critical state index M	1.2
Void ratio at q=0 and p'=98.1(kN/m^2) on NCL-1 N	1.62
Poisson's ratio ν'	0.3
Evolution rule parameters	
Degradation index of overconsolidation m	2.00
Degradation index of structure a (b=c=1)	1.00
Ratio of $-D_v^p$ to $\lvert D_s^p \rvert$ c_r	0.60
Evolution index of rotational hardning br	1.00
Limit of rotational haradning m_r	0.50
Physical properties	
Permiability k (cm/s)	8.0×10^{-7}
Slope of e-ln$k$ C_k	0.16
Density of soil particles ρ_s (g/cm^3)	2.717

Tochi clay	
Initial conditions	
Specific volume v_0	2.033
Degree of structure $1/R^*_0$	250.0
Stress ratio K_0	1.00
Degree of anisotropy K_p	1.00

Permeable layer and drain		
	RC40	Plastic board drain
Elastic modulus E(kN/m^2)	2.1×10^7	1.0×10^3
Poisson's ratio ν	0.3	0.3
Permiability k(cm/s)	1.0×10^{-2}	1.0

Figure 2. Finite element mesh and material constants used in this analysis.

4 COMPARISON BETWEEN TEST AND ANALYTICAL RESULTS

Figure 3 shows the measured and calculated results of stratified settlement over time in the areas where a vertical drain was placed (left side in Figure 1b or 2) and no drain was placed (right side). In the test the lower layer (GL-1.0 - -1.5 m) of the drain-placed area settled about 6.0 cm at 70 days, while the upper layer (the area not penetrated by the drain) GL0.0 - -0.5 m settled about 3.0 cm, indicating that the effect of the drain was larger in the lower layer. The analysis shows that after 30 days, the progress of consolidation settlement in the lower layer (GL-1.0 - -1.5 m), where the drain was placed, was slightly faster than in the test, but the effect of drain drainage, which promotes consolidation more in the lower layer than in the surface layer, was well reproduced.

Figure 4 shows the measured and calculated isochrones of pore water pressure at measuring Points-B and C. In the test, the initial pore water pressure starts near the total stress because of the unconsolidated condition at the start of consolidation, and then it decreases with time. The test results show that the negative pressure develops over time and approaches each of the assumed values. In the analysis, the SYS Cam-Clay model was used to simulate the unconsolidated state of the clayey soil. As a result, the initial pore water pressure was set close to the total stress, and the subsequent changes toward the final state of vacuum loading were reproduced.

Figure 5 shows the comparison of pore water pressure over time in the clayey soil layer. In the test, the pore water pressure decreased by -40 kPa at GL-1.5m and -15 kPa at GL-1.0 m, indicating that the greater the depth, the larger the negative pressure changes, and the greater the settlement promotion effect appears at deeper depths. This is the drainage effect of the bottom drainage layer in addition to drainage near the bottom drainage layer. The analysis reproduces the test results quantitatively well, and confirms that negative pressure propagates to the upper layer due to the installation of the drain, and that consolidation progresses even in the unpenetrated area.

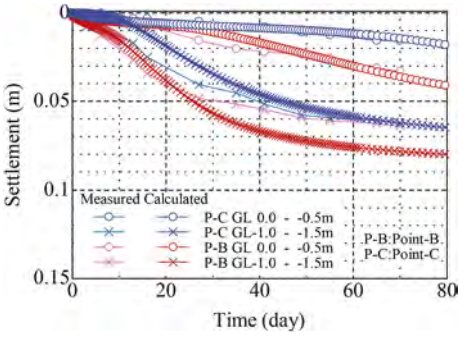

Figure 3. Comparison of stratified settlement.

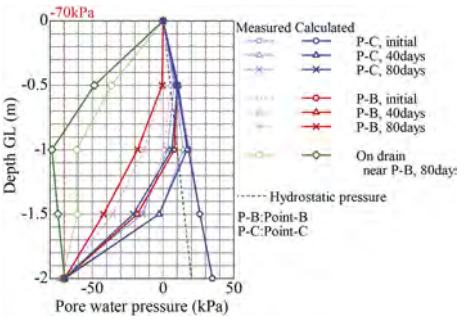

Figure 4. Isochrones of pore water pressure.

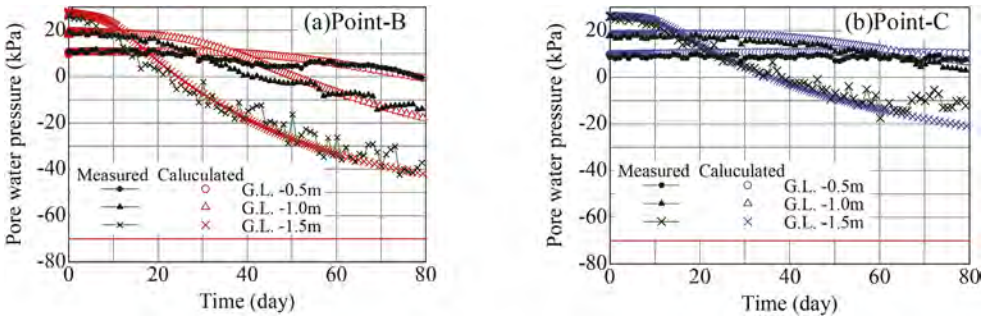

Figure 5. Temporal change of pore water pressure at two measuring points, P-B and P-C.

Figures 6-8 show the contours of pore water pressure (40 days after the vacuum start), deviator stress (40 days) and voids ratio change from the initial state (20 and 80 days), respectively. From these figures, it can be seen that the negative pressure is transmitted to the entire drain section and propagates at each depth as described above, and that the soil around the drains begins to compress subject to significantly high shear stress as a result.

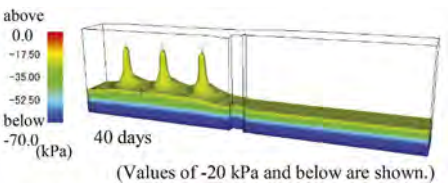

Figure 6. Distribution of pore water pressure.

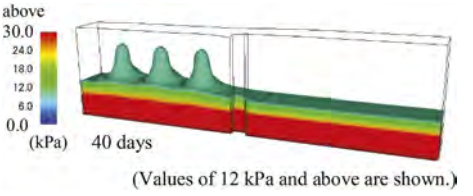

Figure 7. Distribution of deviator stress ratio.

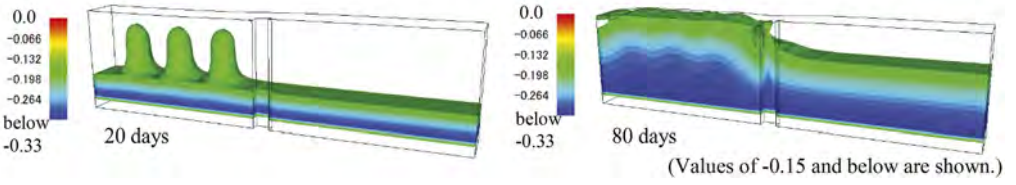

Figure 8. Distribution of voids ratio change from the initial state.

5 CONCLUSION

The soil-water coupled finite deformation analysis, which can accurately track the large compression behavior of soil in an unconsolidated state, was performed for a large model test of vacuum consolidation method using vacuum well. The analysis shows that the test results can be reproduced with high accuracy while clearly showing the mechanism by which the negative pressure is efficiently propagated and settlement is accelerated by the effect of the underlying permeable layer and vertical drain.

REFERENCES

Asaoka, A., Noda, T., Yamada, E., Kaneda, K. & Nakano, M. 2002. An elasto-plastic description of two distinct volume change mechanisms of soils. *Soils and Foundations* 42(5): 47–57.

Nakai, K., Noda, T., Kawamura, S. & Shiratori, Y. 2017. Soil-water coupled finite deformation analyses on subgrade reaction of pile which were embedded into naturally deposited foundation, *Japanese Journal of JSCE* A2 (Applied mechanics), 73 (2): I_535-I_544. in Japanese.

Noda, T, Asaoka, A. & Nakano, M. 2008. Soil-water coupled finite deformation analysis based on a rate-type equation of motion incorporating the SYS Cam-slay model. *Soils and Foundations* 45(6): 771–790.

Taylor, D.W. 1948. *Fundamentals of soil mechanics*, New York: John Wiley & Sons.

Umehara, Y., Takahashi, S. & Yamada, Y. 2020. Model test on vacuum consolidation method using vacuum well, *55th Japan national conference on geotechnical engineering*. in Japanese.

Smart Geotechnics for Smart Societies – Zhussupbekov, Sarsembayeva & Kaliakin (Eds)
© 2023 The Author(s), ISBN 978-1-003-29912-7
Open Access: www.taylorfrancis.com, CC BY-NC-ND 4.0 license

The application and benefit of pilot test for ground improvement on reclaimed land

K.S. Sheu & C.R. Chou
Moh and Associates, Inc., New Taipei City, Taiwan

ABSTRACT: Application of ground improvement methods mostly relies on semi-empirical design approaches. Before the construction is commenced, the design is always verified and improved based on the feedback of the pilot test with various on-site monitoring results. This paper presents the pilot test results of dynamic compaction and sand drains and discusses the on-site monitoring results and effectiveness. In the dynamic compaction case, the vibration induced by the falling weights is monitored to determine the impact on the adjacent structures. The observation of piezometer showed that the induced excess pore water pressure dissipated faster than the estimated time based on the permeability of the sand layers. In the sand drains case, the design was assessed by rechecks of the empirical charts and correction of fine grain contents to obtain the optimal spacing that meet engineering economy requirement and improved the construction time and effectiveness of ground improvement.

Keywords: Pilot test, Dynamic compaction, PPV, Sand Compaction Pile

1 INTRODUCTION

This paper takes the dynamic compaction pilot test of the geological improvement of the reclaimed land in Taipei Port as an example, and discusses the influence of different experimental variables such as tamping configuration, tamping energy, and formation conditions on the peak particle velocity (PPV) in the test. To propose construction disposal measures to avoid damage to existing harbor structures caused by construction vibration.

The southern boundary of the reclaimed land in Taipei Port is adjacent to the permanent revetment; sand compaction piles are used for soil improvement. A pilot test is carried out before construction in the formal area, and evaluate the construction distance of the sand compaction piles to meet the requirements of engineering economy, reasonable construction period and improvement effect.

2 SITE CONDITIONS OF THE STUDY AREA

The Taipei Port's South Wharf District A is a large-scale land reclamation project of the north coast of New Taipei County, Taiwan. The reclaimed land in the Taipei Port's District A is created through hydraulic filling. The filling material comes from sediments under the sea, which consists mainly of silty sand to fine sand. The thickness of the hydraulic fill is approximately 9 to 11 m.

This paper collects a total of three groups of pilot test results, including two groups of dynamic compaction (DC) tests and one group of sand compaction pile (SCP) tests as shown in Figure 1. The dynamic compaction pilot test is divided into test zone I and test zone II according to the location of the work area. Because this project is a new land for hydraulic backfilling (the backfilling is completed for half a year), the test zone I is located in the water

DOI: 10.1201/9781003299127-80

end of sand pumping and filling, and fine particles such as silt and clay are easily mixed during the backfilling process, so the strata of test zone I and test zone II are slightly different.

The pilot test site of sand compaction pile (test zone III) is located on the south side of the project site, and the upper half of the stratum is dominated by silty fine sand. The soil conditions of the project site are arranged according to the geological survey results as shown in Table 1. According to the geological survey results, the groundwater within the scope of the project is about 1.18 to 3.45m below the surface.

Figure 1. Layout of the pilot tests.

Table 1. Soil profile of pilot test site.

Pilot test site	Improvement method	Depth (m)	Soil description	SPT-N value	Soil physical property
Test zone I	Dynamic compaction	0~5	Silty clay interbedded with silty fine sand	4	$w_n = 22 \pm 3\%$ FC = 53 ± 8%
		5~10	Silty clay interbedded with silty fine sand	7	$w_n = 22 \pm 4\%$ FC = 54 ± 17%
Test zone II	Dynamic compaction	0~5	Silty fine sand with little sandy silt	10	$w_n = 22 \pm 4\%$ FC = 28 ± 8%
		5~10	Silty fine sand with little sandy silt	15	$w_n = 22 \pm 2\%$ FC=23 ± 2%
Test zone III	Sand compaction pile	0~5	Silty fine sand	8	$w_n = 23 \pm 3\%$ FC = 19 ± 7%
		5~10	Silty fine sand with some clay	7	$w_n = 32 \pm 12\%$ FC = 46 ± 35%

3 TEST AND DESIGN OF DYNAMIC COMPACTION

The dynamic compaction method uses a special construction crane to pull a tamper with a weight of 26.4T and a size of 1.5×1.5×1.6m (length, width and height) according to different energy per drop (396T-M and 600T-M).

3.1 *Test zone I (DC)*

The test area is located in the center of the project scope. The two groups of test areas A and B are arranged up and down about 25 meters apart. The construction plane configuration is shown in Figure 3. The main strike is divided into three stages of tamping. In the first stage, 1-1~1-9 (circle) will be applied first; in the second stage, 2-1~2-4 (hexagon) will be applied; in the third stage, 3-1~3-12 (square) will be applied; as shown in Figure 2.

The test zone I is divided into I-A group and I-B group test. The construction parameters are shown in Table 2. Parameter assumptions in the design stage, and feedback from the test results are applied to the formal construction.

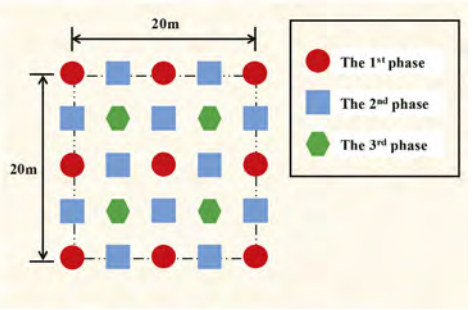

Figure 2. Layout of dynamic compaction procedure (Test zone I).

Table 2. Detail of dynamic compaction (Test zone I).

Test zone I	Group I-A			Group I-B		
Phase	I	II	III	I	II	III
No. of impact point	9	4	12	9	4	12
Energy per drop (T-M)	600	600	600	600	600	600
No. of drops per phase	25	25	19	35	35	25

3.2 *Test zone II (DC)*

The test area is located at the upper edge of the project scope. The two groups of test areas A and B are arranged at a distance of about 25 meters from left to right. The construction plane configuration as shown in Figure 3.

The test zone II includes the tests of group A and group B: group II-A was subjected to three-stage strikes, and group II-B was subjected to two-stage strikes. There was little difference in the total tamping energy between the two groups of test areas.

The idea of this configuration is to compare the relationship between the number of tamping stages and the improvement effect, and obtain the optimal configuration between the improvement effect and the work period. The construction parameters are shown in Table 3.

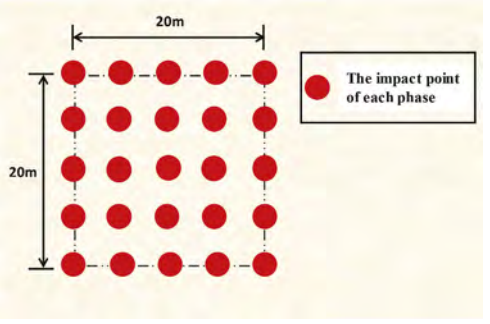

Figure 3. Layout of dynamic compaction procedure (Test zone II).

Table 3. Detail of dynamic compaction (Test zone II).

Test zone II	Group II-A			Group II-B	
Phase	I	II	III	I	II
No. of impact point	25	25	25	25	25
Energy per drop (T-M)	396	396	600	396	396
No. of drops per phase	15	10	6	15	15

3.3 *Dynamic compaction construction monitoring configuration*

The purpose of construction monitoring is to record the effectiveness of the pilot test plan on the improvement area, such as the dissipation time of excess pore water pressure excited by tamping and the measurement of vibration caused. Under the conditions of safety, economy and efficiency, to achieve the expected improvement goals, the related equipment configuration is shown in Figure 4.

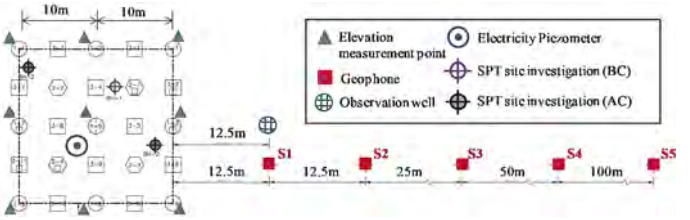

Figure 4. Layout of monitoring instrumentation.

4 TEST AND DESIGN OF SAND COMPACTION PILE

The design method of sand compaction piles was developed in Japan and gradually established by feedback from on-site construction cases. There are three commonly used methods, namely, the Table Lookup method, the N-Dr-e relationship curve method (Gibbs and Holtz, 1957) and the fine particle content correction method (Mizuno et al.,1987). This project is for hydraulic backfilling of new land (backfilling is completed for half a year), and fine-grained materials such as silt and clay are easily mixed in the backfilling process. Considering the chart method and the N-Dr-e relationship curve method, its scope of application is limited to sandy soils with a fine particle content less than 20%, and the influence of fine particle content is not considered. Therefore, in this case, the fine particle content correction method was used to design the pilot test of the SCP (Figure 5).

The test zone III is planned at the south edge of the project scope. It is divided into three areas with 20m×20m. The sand pile spacing of pilot tests are 1.9 meters, 2.1 meters and 2.3 meters as shown in Figure 6. The improvement depth is 10 meters and the pile diameter is 70 cm in equilateral triangle configuration.

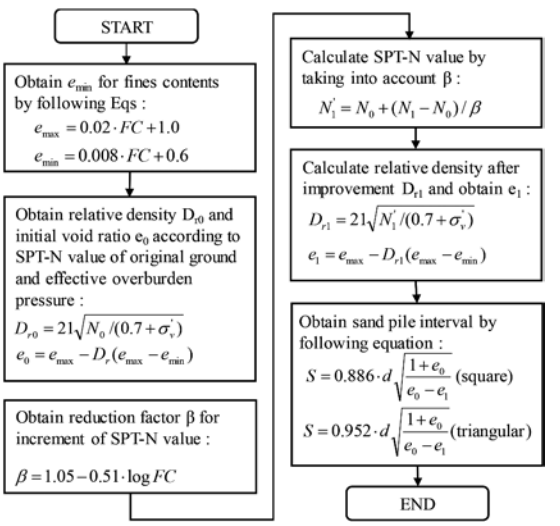

Figure 5. Flowchart of SCP design procedure.

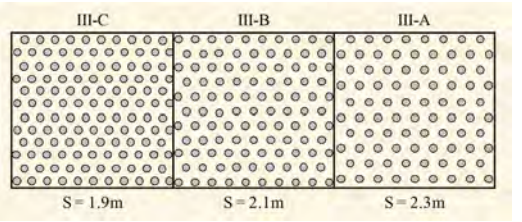

Figure 6. Layout of sand compaction pile (pilot test III).

5 RESULTS OF THE CASE STUDY ON THE EFFECT OF DYNAMIC COMPACTION

In this paper, a case study of ground improvement project to demonstrate the benefits of DC through both the increase in soil strength and the reduction in the variation of the soil strength. In this section, the results of this case study are presented and discussed.

5.1 *Ground water level measurement*

Figure 7 shows the groundwater level measurement data in Zone I-B. During the dynamic tamping operation (1/6 to 1/12), the water level depth is affected by the vibration of the tamping impact, and the water level depth is raised to between 2m and 1.7m underground. After about 12 hours of standing after the daily tamping, the water level returns to the initial level. After the completion of dynamic compaction (after 1/13), the groundwater level returned to stability.

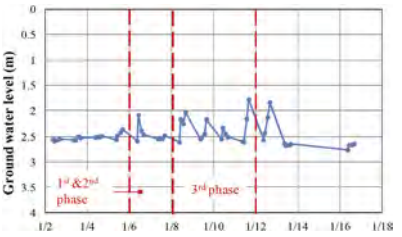

Figure 7. Ground water level during the I-B pilot test.

5.2 *Excess pore water pressure induced by dynamic compaction*

The test results of water pressure measurement with a buried depth of 5m in Zone I-B show that, during the tamping period (1/6~1/12), the excess pore water pressure is excited from 3.5 t/m2 to 7.5 t/m2 maximum, the increase range is about 115%, and within 6 hours after the end of the tamping, the water pressure gradually dissipated to 3.6 t/m2~3.8 t/m2 and returned to the initial state (Figure 8).

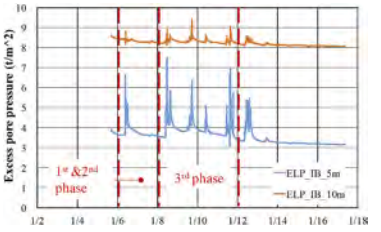

Figure 8. Excess pore pressure during the I-B pilot test.

The water pressure returns to the initial state within 6 hours after the end of tamping. During the test process, the dissipation time of excess pore water pressure is significantly faster than the estimated time of general permeability. A radial drainage path is formed to improve soil permeability and greatly reduce the dissipation time of excess pore water pressure.

5.3 *Ground vibrations induced by dynamic compaction*

Figure 9 shows the attenuation relationship of PPV with distance of two pilot test results. It was found that dynamic compaction has a greater vibration but a slightly faster attenuation rate with distance. The surface vibration decreases most significantly within 25m, and when the distance from the ramming pit is about 20~25m, the PPV value can be less than 20mm/sec, which meets the requirements of relevant regulations.

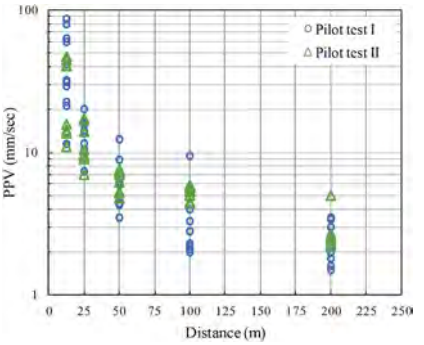

Figure 9. PPV measured at DC pilot tests.

Regarding the measurement results of PPV value and construction distance, considering the drop energy used in each group of cases and the difference in the measurement distance of monitoring instruments, the square root of the measurement distance and click energy is standardized, and the measurement is carried out according to multiple groups of construction cases. Mayne et al (1984) proposed the following formula as a conservative upper limit to the ground vibration levels as shown in formula (1):

$$\mathrm{PPV} = 7\left(\frac{\sqrt{\mathrm{WH}}}{\mathrm{D}}\right)^{1.4} \tag{1}$$

Where PPV is the peak particle velocity (in cm/s), W is the mass of the hammer (in tones), H is the fall height (in meters), D is the distance from the point of impact (in meters).

In this paper, the PPV measurement results o in zone I and zone II are compiled and compared with the upper limit value of the empirical formula and the lower limit value of foreign cases proposed by Mayne et al (1984). The results show that it falls roughly between the upper limit of the empirical formula and foreign cases (Figure 10), and the average PPV of this project can be regressed to an empirical formula as shown in formula (2):

$$\mathrm{PPV} = 2\left(\frac{\sqrt{\mathrm{WH}}}{\mathrm{D}}\right)^{1.4} \tag{2}$$

The engineer can easily estimate the PPV value caused by the tamping energy in the design stage, but the actual PPV value may be different due to the site conditions and construction methods. The adoption of the parameters can achieve a more economical tamping configuration.

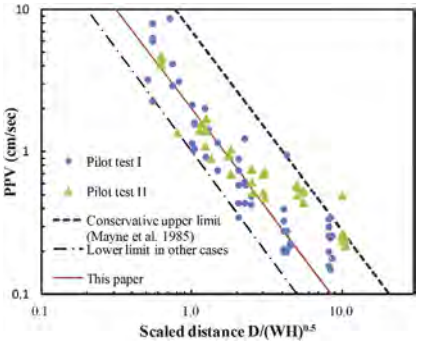

Figure 10. Relationship between measured PPV and scaled distance.

6 RESULTS OF THE CASE STUDY ON THE EFFECT OF SAND COMPACTION PILE

The design of the sand compaction pile is discussed by the method of Table lookup method and the correction method of fine particle content The design details of the pilot test as shown in Table 4. The comparison of SPT-N values with N_0(before SCP) and N_1(after SCP) are shown in Figure 11. The solid line in the figure is the average replacement ratio empirical curve drawn according to the Table lookup method. And the dashed line is drawn according to the fine particle content correction method, which is corrected by considering the average reduction factor ($\beta = 0.28$). The reduction factor β is a correction parameter related to fines content as shown in Figure 8. The increase of the N value between the sand piles after the improvement of the pilot test is positively correlated with the sand pile density, and the improvement effect of the sand pile spacing S = 1.9m is the most significant. In the three groups of tests, the improved SPT-N values of the sand pile spacing S=1.9m and S=2.1m can all meet the design requirements of the fine particle content correction method (dotted line),

Table 4. Detail of sand compaction pile (test zone III).

Group	Pile spacing	Replacement ratio a_s	FC (%)	Reduction factorβ
III-A	2.3m	0.084	29	0.304
III-B	2.1m	0.101	38	0.244
III-C	1.9m	0.123	33	0.276

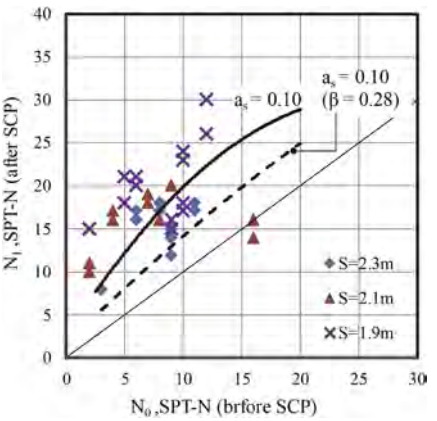

Figure 11. Comparison of SPT-N values with N_0(before SCP) and N_1(after SCP).

only the sand pile spacing S=2.3m at some depths SPT-N value does not meet design requirements.

According to the configuration of this case, the number of sand piles required for geological improvement and the construction period are discussed as shown in Table 5. In summary, comparing the improvement effect, construction quantity and construction period, the sand pile spacing S=2.1m can meet the requirements of construction economy, reasonable construction period and improvement effect.

Table 5. Benefit assessment of SCP in different spacing.

Pile spacing	No. of columns/ha	Working day/ha	Construction cost	Improve performance
S=2.3m	2200	14	High	Δ
S=2.1m	2600	16	Medium	O
S=1.9m	3200	20	Low	O

7 CONCLUSIONS

Through the pilot test results of DC, the water pressure dissipation rate is faster than the estimated time given the permeability of the sand layer. In the future, the dynamic compaction of the whole area can shorten the preset resting time and improve the engineering efficiency. The surface vibration decreases most significantly within 25m, and when the distance from the ramming pit is about 20~25m, the PPV value can be less than 20mm/sec, which meets the requirements of relevant regulations. And the engineer can easily estimate the PPV value caused by the tamping energy with the empirical formula proposed in this paper. The difference between the PPV generated by zone I and zone II configurations is not significant, but in terms of construction efficiency, zone II has the better efficiency

Through the pilot test results of SCP, the improved SPT-N values of sand pile spacing S=1.9m and sand pile spacing S=2.1m can meet the design requirements. A smaller spacing can achieve better improvement results, but the smaller spacing will increase the construction cost and schedule. Economical and effective improvement ratio can be obtained by the pilot test.

Before carrying out large-scale geological improvement, one should select the appropriate construction method according to the local conditions and assist in the review of the pilot test, so as to facilitate the evaluation of the formal area to meet the needs of construction economy, reasonable construction period and improvement effect.

ACKNOWLEDGMENTS

Permission for publishing this paper from Moh and Associates, Inc. and Port of Keelung, Taiwan International Ports Corporation, Ltd is gratefully appreciated.

REFERENCES

1. Gibbs, H.J., Holtz, W.G. (1957). Research on determining the density of sand by spoon penetration testing. In: Proceedings, 4th international conference on soil mechanics and foundation engineering, London, pp 35–39.
2. Mayne, P. W., Jones, J. S. & Dumas, J. C. (1984). Ground response to dynamic compaction. J. Geotech. Engng, ASCE 110, No. 6, 757–774.
3. Mizuno, Y., Suematsu, N. and Okuyama, K. (1987). Design method of sand compaction pile for sandy soils containing fines, Tsuchi-to-Kiso, Japanese Society of SMFE, Vol. 35, No. 5, pp. 21–26.

Smart Geotechnics for Smart Societies – Zhussupbekov, Sarsembayeva & Kaliakin (Eds)
© 2023 The Author(s), ISBN 978-1-003-29912-7
Open Access: www.taylorfrancis.com, CC BY-NC-ND 4.0 license

Evaluation of jet grouting design and construction methods for TBM launching and arrival

Wittawat Tueyot & Kuo Chieh Chao
Asian Institute of Technology, Bangkok, Thailand

Ricky K.N. Wong
Sanshin Construction (Thailand) Co., Ltd., Bangkok, Thailand

Morris Wang
ISEKI Engineering (Thailand) Co., Ltd., Bangkok, Thailand

ABSTRACT: In Bangkok, Thailand, the soils consist of a layer of soft clay underlain by interlayers of stiff clay and sand. The groundwater level is often observed a few meters below the ground surface. Unexpected incidents, such as water inflow from the sand aquifers and excessive deformation from the soft clay, could occur during TBM breakthroughs in such soil conditions. The jet grouting technique is commonly utilized for ground improvement to avoid these issues. This paper focuses on an evaluation of jet grouting design and construction methods related to water leakage issues for TBM breakthroughs. The design and construction data collected from the MRTA Orange Line East Project in Bangkok, Thailand, were used to evaluate key jet grouting design and construction parameters for TBM launching and arrival. A large-diameter jet grouting technique was used to form jet grouted blocks at the TBM launching and arrival areas. Regarding the design method, it was found that the cohesion of the jet grouting mixture is one of the key parameters that affect the jet grouted block dimension. The permeability and dimension of the jet grouted block are also essential design parameters when the tunnel is subjected to high water pressure at a greater depth. Regarding the construction method, it was concluded that to minimize construction issues a combination of many construction techniques, such as jet grouting, sealing rings, concrete blocks and flood of the chamber, should be applied to provide safer TBM breakthroughs.

1 INTRODUCTION

The high density of a population can be expected in capital cities such as Bangkok, Thailand. The traffic has become a problem as people have been using their personal cars. Hence, the mass rapid transit (MRT) system is a proper solution to solve the traffic problem. An underground transit system is a common MRT system in cities. However, underground space utilization is subjected to many local conditions, such as existing underground facilities, structure foundations, and especially soil conditions.

Groundwater issues and the associated stability of the soil resulting from high groundwater pressure is a common issue for the underground transit system. The groundwater is a significant factor that can lead to water inflow and surface settlement when the underground wall is excavated. The tunnel face can also collapse as it is unsupported. The potential for these problems to occur becomes higher when the tunnels are constructed at a greater depth. Normally, the earth pressure balance (EPB) shield, which is one type of tunnel boring machine (TBM), is chosen for tunneling in soft ground conditions. This EPB shield is capable of minimizing ground loss, and there is a sealing device to prevent groundwater. Besides, jet grouting

DOI: 10.1201/9781003299127-81

is also used to avoid the problems caused by groundwater and ground loss during TBM launching and arrival. However, the water leakage problem sometimes occurs even if jet grouting is constructed according to the design and construction guidelines. Therefore, this paper focuses on an evaluation of jet grouting design and construction methods related to water leakage issues for the TBM breakthroughs.

2 LARGE DIAMETER JET GROUTING TECHNIQUES

A large-diameter jet grouting technique was conducted to improve the soft soils for the MRTA Orange Line East Project. The large diameter jet grouting technique utilizes high-pressured grout slurry to erode and mix the in-situ soil to form soil-cement mixture columns with a diameter up to approximately 4.5 m (Cheng et al. 2021; Chao et al. 2020). This technique is capable to reduces the number of grout holes. Since there are a small number of grout holes, the construction time and cost can be minimized, which is preferable in congested areas. The large-diameter jet grouting techniques are described in Table 1.

Table 1. Large diameter jet grouting techniques.

Technique	Description
Rapid jet grouting (RJG)	This method is a double fluid system with two nozzles placed oppositely on the monitor (Chu et al. 2012).
V-Jet method	This method is a double fluid system. The two nozzles of this method are placed opposite each other and located at different levels (Cheng et al. 2013; Shinsaka et al. 2018).
Rodin jet pile (RJP)	This method is the same as the V-Jet method, whereas this method is a triple fluid system. The cutting nozzle, which is used to inject a water jet shrouded by an air jet, is located above the jet grout nozzle (Wang et al. 2013).
X-Jet method	The X-Jet method is a triple fluid system. The soil is disaggregated under the action of cross-water jets enveloped by an air jet, and the grout jet is injected at low pressure from another nozzle (Njock et al. 2018).

3 METHODS FOR TBM LAUNCHING AND ARRIVAL

Many techniques and methods are used to ensure the safety of TBM breakthroughs. These methods aim to stabilize a tunnel face behind a cutting wheel and prevent groundwater issues. Also, a vertical shaft or diaphragm wall should be delicately removed to provide the safety of launching and receiving processes. Ground improvement techniques and some special techniques for TBM breakthroughs are used to control ground movement and groundwater. The methods for TBM launching and arrival are presented in Table 3. Among the methods described in Table 3, the most common methods that are used for the TBM construction are the ground improvement methods and sealing rings.

4 CONSTRUCTION EVALUATION

The jet grouting soil improvement is commonly applied for TBM construction to prevent water leakage issues. However, water leakage issues could occur due to construction and environmental issues. Examples of the methods that were used to prevent water leakage issues and to ensure the safety of the TBM breakthrough for projects in Thailand are listed in Table 2. A detailed description of the methods shown in Table 2 is provided in Table 4.

Table 2. Examples of the methods applied to prevent water leakage for projects in Thailand.

Project	Permeation grouting	Jet grouting	Sealing rings	Concrete blocks	Flood of the chamber
River crossing water tunnels (Dung 2002)	✓	✓	✓	✓	✓
Blue Line ISP (Homburg, 2001; Suwansawat 2002)	✓	✓	✓	✓	✓
Orange Line East	✓	✓	✓	✓	✓

Table 3. Methods for TBM launching and arrival.

Method	Description
Dewatering	Dewatering can lower the groundwater table to provide dry conditions at the tunnel face and along the tunnel alignment. The drawdown causes an increase in the effective stress of the soil. This increase in the effective stress could result in a consolidation settlement in cohesive soils and elastic compression in granular soils. As a result, dewatering may not be suitable for urban areas where surface settlement is a significant concern. Moreover, in fine-grained layers which are low permeability, dewatering may not be applicable (Kuesel et al. 2012).
Ground freezing	This technique is usually applied in areas with considerable pore water in soils. The pore-water will be converted to ice which strengthens the soil and reduces the soil permeability. However, this technique could result in the ground being stronger than necessary for tunnel excavations. Also, the surface heave can be found due to water freezing, and thawing can lead to subsidence (Kuesel et al. 2012).
Fiberglass nailing	The nails are installed in the excavation face to reinforce and be temporary excavation support. The mesh or series of pins is applied in loose soils to stabilize and control the ground displacements. However, this technique cannot prevent the flow of groundwater (Valle et al. 2017).
Grouting	Grouting has advantages in groundwater control and soil stabilization. Also, grouting can be applied in various soil conditions. Grouting is used to strengthen the loose soil to prevent ground flow. The groundwater inflow can be minimized because of the low permeability of grouted soil. The subsidence due to water drainage and ground loss can be decreased (Kuesel et al. 2012).
Sealing ring	The sealing rings are used to limit the water flow through the annular gap during the entry and exit of TBMs. The gap between a tunnel wall and either the shield or erected segmental rings will be sealed by a rubber device that is pressed against two interfaces. The primary caution is the misplacement between a sealing ring and a cutting wheel during the launching and arrival. The sealing rings are mainly used for launching and are usually combined with other techniques (Valle et al. 2017).
Fake tunnels	This method can be used for TBM launching and arrival, but this technique is commonly used for arrival cases. This technique is used to solve the problems related to site dimension and geotechnical and hydrological conditions. The TBM will be assembled inside a steel sleeve (fake tunnel) for the launching procedure. In arrival cases, the end cap will be installed at the end of a steel sleeve, and the steel sleeve is filled with water to balance forces (Valle et al. 2017).
Concrete blocks	This technique is mainly used for TBM arrival. However, cement concrete blocks may be used for TBM launching. The concrete block is built inside the arrival station to keep the face pressure until the cutting head touches the wall and will be demolished after the TBM crosses (Valle et al. 2017).
Flood of a chamber	This technique is only used for arrival cases of TBMs. The reception station will be filled with water to balance the pressure from the soil and groundwater. This technique is commonly applied when the other common methods cannot be carried out due to limited space or construction difficulties. However, the flooding technique can cause a delay in other construction works (Valle et al. 2017).

5 DESIGN EVALUATION

The jet grouted block design extracted from the MRTA Orange Line East Project for TBM launching and arrival was reviewed and compared with the design manuals (JJGA 2017; Rapidjet Association 2019). Also, the parametric study was carried out to observe the design parameters, which mainly influence the water flow at the opening face. A comparison of jet grouting design for TBM launching and arrival of the MRTA Orange Line East Project was summarized and discussed in the subsequence section. The results of the parametric study are also provided and discussed in the following section.

The typical subsoil along the MRTA Orange Line East Project is the altered layers of clay and sand layer. The uppermost layer is a fill material layer. The following layer is a clay layer, which consists of soft clay, medium stiff clay, and stiff clay, respectively. The layer below these clay layers is the sand layer, and the following subsoil is the altered layers of clay and sand layer till approximately 35 m depth below the surface according to the boreholes.

Table 4. Detailed description of the methods used to prevent water leakage for projects in Thailand.

Method	Description
Permeation grouting	The chemical proportion is a significant parameter and directly controls the setting time of grouting materials. Also, the grain size of soils is a primary concern. As the soil particles are tiny, a grouting mixture may not seep into the ground. In the water transmission tunnel project, the chemical proportion was improperly used, and the opening face was not treated entirely by this grouting. As a result, the water leakage problem might come from these aspects.
Jet grouting	The integrity of jet grouted blocks is a concern. The untreated zone due to a rod inclination can cause the seepage issue. The corrosion should be considered for permanent purposes. In the MRTA Orange Line East Project, the quality control of the jet grouting method is mentioned in the method statement. The core samples are collected at an intersection point for the unconfined compressive and permeability test. Also, the diameter of a jet grouting column is checked by the jet wave monitoring method (JWM). However, the coring and JWM are carried out in the trial test.
Sealing ring	The sealing ring was mounted on the diaphragm wall to limit the water flow during a breakthrough. The sealing ring was installed for the launching of the TBMs. However, in the MRTA Blue Line Initial System project, the sealing ring was also applied for the TBM arrival.
Concrete block	As the length of the jet grouted block was limited by the utilities, the concrete block was built as an additional jet grouted block inside a station to prevent water inflow in both the MRTA Blue Initial System and Orange Line East projects. The TAM grouting was also applied with the concrete block for water prevention at the MRTA Orange Line East Project.
Flood of a chamber	This method is selected when other techniques cannot be carried out. In the water transmission tunnel project, the arrival station was filled with the backfill soil and water to facilitate the TBM arrival because the permeation grouting did not provide suitable treatment. Furthermore, this method was carried out at the IVS shafts to allow the TBM to drive continuously through the shaft in the MRTA Orange Line project.

5.1 *Jet grouted block design*

The procedure to determine the grouted block dimensions for the MRTA Orange Line East Project was evaluated in this study. The design procedure for the MRTA Orange Line East Project, in general, follows the jet grouting design manual by the Japanese guidelines (JJGA 2017). The design is also described in (Duangsano et al. 2021). The calculations use the same equations for the required length (t), the side thickness (B), the top thickness ($H1$), and the bottom thickness ($H2$) of the grouted block. However, there are some minor differences between the design methods. For example, firstly, the minimum dimensions of the jet grouted

block are different. This is because the Japanese guidelines were developed based on a - 25 m depth of tunnels. As the tunnels in the MRTA Orange Line East Project are located approximately 15 – 35 m in depth, the minimum dimensions of the MRTA Orange Line East Project are higher than the minimum dimensions specified in the Japanese guidelines. Secondly, the criteria to determine the required length of the block are different. In the MRTA Orange Line East Project, the required length of the block is determined based on the maximum value out of the values calculated from the following three equations: bending stress equation, arc sliding equation, and punching shear equation. The minimum required length of the block used for the MRTA Orange Line East Project is 1 m. In contrast, the required length of the block in the Japanese guidelines is obtained separately using the following different equations: bending stress equation for sandy soils and arc sliding equation for clayey soils. Lastly, the additional length for the jet grouted blocks in sandy soils is one segmental ring (1.4 m) for the MRTA Orange Line East Project, whereas the Japanese guideline suggests the additional length to be three rings (4.2 m).

Furthermore, the cohesion of a jet grouting material is a significant input parameter that controls the dimension of the jet grouted block. Figure 1 shows the effect of cohesion on the dimensions. According to equations provided in the Japanese guidelines, the dimensions are shorter when the cohesion is higher, and the required length is less sensitive than the rest of the dimensions. Also, the value of bottom thickness is equal to the side thickness if the minimum dimensions by the guidelines and the water pressure condition are ignored.

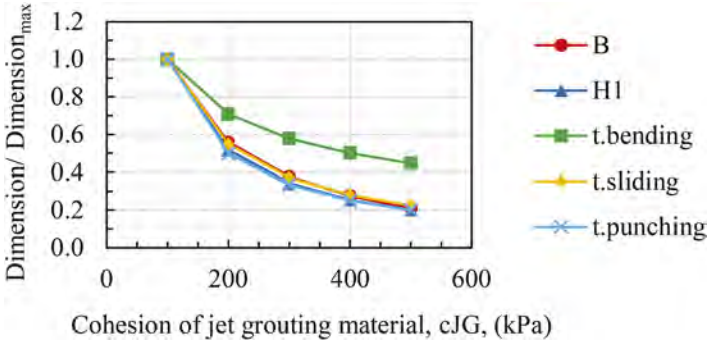

Figure 1. Relationship between dimension and cohesion of jet grouting material.

5.2 *Parametric study*

The parametric analysis was performed by the finite element software for the following two scenarios: (1) the launching cases in the clayey soil (LC) and (2) the launching cases in the sandy soil (LS). The considered design parameters are the length, side thickness, and permeability coefficient of the jet grouted block. The results of the analysis give the same trend of the water discharge in both cases (see Figure 2). The side thickness of the jet grouted blocks has a negligible effect on the water discharge at the opening face, because the changes in water pressure at the opening face are insignificant. The water pressure only dissipates around the opening face even though the side thickness increases. However, at a longer time, the water discharge drops as the side thickness increases. It also shows a little change when the side thickness is equal to the minimum side thickness, which is 2 m according to the Japanese guideline.

The length of the jet grouted blocks has a significant effect on the water discharge at the opening face. The discharge sharply decreases when the length is elongated, and it gives a minor effect when the length reaches the minimum dimension, which is 3.3 m, as suggested by the Japanese guidelines. The permeability coefficient of the jet grouted block also has a significant effect on the water discharge. The water discharge gradually rises as the permeability coefficient is lower.

6 CONCLUSIONS AND RECOMMENDATIONS

6.1 *Conclusions*

1. Among the methods that are used to provide the safety of TBM breakthroughs, jet grouting is commonly used as it can be applied in various ground conditions. The concern of this method is the integrity of a jet grouted block. The untreated zone can cause the seepage issue. Also, the corrosion should be considered for permanent purposes. Based on the subsoil conditions at the MRTA Orange Line East Project, the rapid jet grouting gave the successful treatment for TBM launching and arrival.
2. The results of the construction evaluation in this study indicate that the sealing ring is generally applied to launching cases. However, it can be used for arrival cases. The concern is the position of a sealing ring. The concrete block is built as an additional jet grouted block to ensure that the TBM is covered entirely. Otherwise, water can seep into the station from the TBM rear section when the TBM exposes to the ground. Also, the flood of a chamber method is selected when the other techniques cannot be carried out. This method may cause a construction delay. Also, this method is suitable for a small chamber to allow TBM to drive through continuously.
3. The results of the design evaluation in this study show that the design procedure to determine the grouted block dimensions for the MRTA Orange Line East Project generally follows the Japanese jet grouting design manual. However, there are some minor differences between the design methods, as outlined in Section 5.1 of this paper. The cohesion of a jet grouting material is a significant parameter. The dimensions are directly reduced as the cohesion is high. The side thickness has a negligible impact on the water discharge. However, the side thickness must exist to resist the lateral earth pressure. The water discharge can be reduced by a lower permeability, an extended length, and a large side thickness of the jet grouted block.

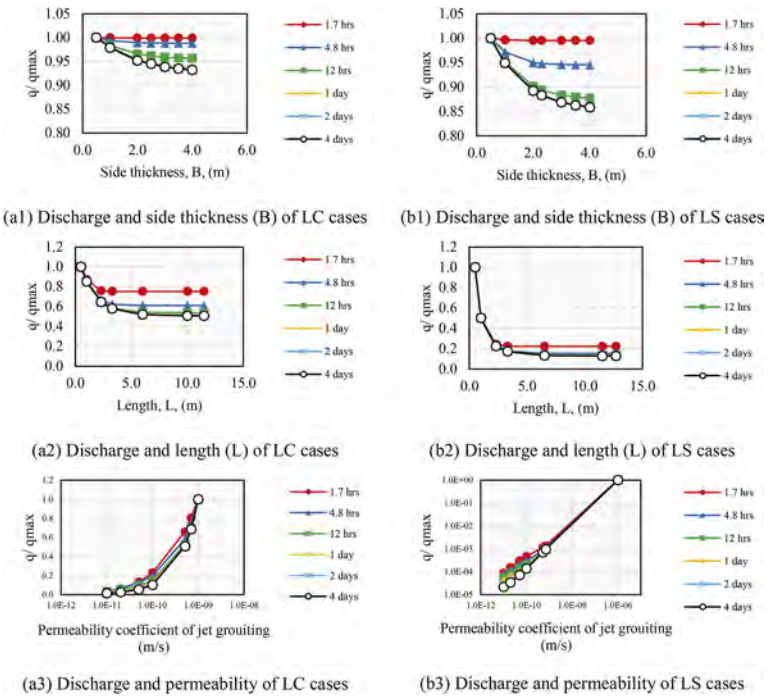

Figure 2. Relationship between discharge and design parameters.

6.2 *Recommendations*

1. The integrity of jet grouted blocks, such as the strength, permeability, and diameter, is only verified in the trial test. Therefore, the combination of many techniques in the construction, as outlined in Section 4 of this paper, should be applied to provide a safer TBM breakthrough.
2. Because of the gap between a tunnel wall and a shield, the additional length for sandy soils should be the three-ring length according to the Japanese guidelines to ensure that the backfill grouting completely seals the gap and prevent the water from the TBM rear section. Also, chemical grouting can be applied to fill the gap along the shield.
3. The cohesion of the jet grouting mixture is a significant parameter. Thus, cohesion should be determined based on local soils to design the dimension of the jet grouted block appropriately.
4. At a greater depth, the tunnel is possibly subjected to high water pressure. Therefore, besides the permeability of a jet grouted block, the dimension should not be overlooked, especially the length. The water discharge at the opening is reduced with an extended dimension of the block, resulting from a longer flow path of water in the structure.

REFERENCES

Chao, K. C., Surachet L., Prasert C., Wong, R. K. N., Iwakubo, T., & Takeshima, H. 2020. Evaluation of Large Diameter Jet Grouting Technique Used for Tunnel Construction in Bangkok. *International Symposium on Evolving Jet Grouting Technology*, Tokyo, Japan.

Cheng, S. H., Liao, H. J., Wong, R. K., Takeshi, I., & Hsieh, Y. H. 2013. Performance of V-JET method for arrival of shield tunnelling machine. *Geotechnics for Sustainable Development–Geotech Hanoi 2013*, 28–29.

Cheng, S. H., Wong, Ricky K. N., Liao, H. J., & Hsieh, Y. H. 2012. A Large Diameter Jet Grouting Method for Arrival of Shield Tunnelling Machine. *ISSMGE - TC 211 International Symposium on Ground Improvement IS-GI*, Brussels.

Chu, H. C., Wong, K. N., Yu, C. F., Liao, H. J., & Cheng, S. H. 2012. Large Diameter Rapid Jet Grouting in Taipei Silty Soil. *Geotechnical Special Publication*, 228 GSP, 2132–2141.

Duangsano, O., Jangjit, W., Asanprakit, A., Chanchaya, C., & Muangsaen, K. 2021. Application of Ground Improvement for Launching and Arrival of TBM Shield Machine on MRT Orange Line (East Section) Project. *The 26th National Convention on Civil Engineering: NCCE*

Dung, N. A. 2002. Performance Evaluation of Soft Ground Tunneling at The Tha Chin River Crossing. Asian Institute of Technology.

Homburg, S. 2001. Shield Tunneling and Associated Ground Movements in Bangkok MRT Blue Line ISP. Asian Institute of Technology.

JJGA. 2017. Jet Grouting: JSG Method, Column Jet Grouting Method. Technical Information of the Japanese Jet Grouting Association (25th ed.).

Kuesel, T. R., King, E. H., & Bickel, J. O. 2012. Tunnel Engineering Handbook. *Springer Science & Business Media*.

Njock, P. G. A., Chen, J., Modoni, G., Arulrajah, A., & Kim, Y. H. 2018. A Review of Jet Grouting Practice and Development. *Arabian Journal of Geosciences*, 11(16).

Rapidjet Association. 2019. Rapidjet Method: Jet Grouting Guideline (1st ed.)

Shinsaka, T., Yamazaki, J., Nakanishi, Y., & Komiya, K. 2018. Quality Control and Shape Control Techniques in Jet Grouting. *Geotechnical Special Publication*, 2018-March (GSP 296), 294–304.

Suwansawat, S. 2002. Earth Pressure Balance (EPB) Shield Tunneling in Bangkok: Ground Response and Prediction of Surface Settlements Using Artificial Neural Networks. In Department of Civil and Environmental Engineering: Vol. Doctor of Massachusetts Institute of Technology.

Valle, N. Della, Haro, P. G. De, Sáenz, I., & María, D. S. 2017. TBM Shield Machines Break in and Break out. December, 2–3.

Wang, Z. F., Shen, S. L., Ho, C. E., & Kim, Y. H. 2013. Jet Grouting Practice: An Overview. Geotechnical Engineering, 44(4), 88–96.

Smart Geotechnics for Smart Societies – Zhussupbekov, Sarsembayeva & Kaliakin (Eds)
© 2023 The Author(s), ISBN 978-1-003-29912-7
Open Access: www.taylorfrancis.com, CC BY-NC-ND 4.0 license

Linear regression to predict the unconfined compressive strength of biopolymer-based soil treatment (BPST)

Haejin Lee
Graduate student, Department of Civil Systems Engineering, Ajou University, Korea

Jaemin Lee
Graduate student, Department of Mechanical Engineering, Korea Advance Institute of Science and Technology, Korea

Seunghwa Ryu
Associate Professor, Department of Mechanical Engineering, Korea Advance Institute of Science and Technology, Korea

Ilhan Chang*
Associate Professor, Department of Civil Systems Engineering, Ajou University, Korea

ABSTRACT: Biological soil treatment methods have recently been actively promoted for sustainable and ecofriendly geotechnical engineering. Biopolymer-based soil treatment (BPST) is recognized as a low-carbon footprint ground improvement approach with appropriate pore clogging and strengthening properties. BPST is typically applied as a combination of soil, biopolymer, and water; however, depending on the hydrogel phase and soil type, varied results can be produced. In this study, Decision Tree, a machine learning approach, was used to predict the unconfined compressive strength (UCS) of BPST. The model performed successfully, and the determinant accuracy was more than R^2=0.99. And through permutation feature importance, it was confirmed that biopolymer content and water content act as determinants for the prediction of UCS of BPST.

1 INTRODUCTION

Biopolymers are becoming increasingly popular as a means of improving soil via bioengineering perspectives. Biopolymers are environmentally friendly polymers made from natural resources such as microbial activities or proteins and are widely used in food and pharmaceuticals (Chang et al. 2020, Choi et al. 2020). According to recent studies, due to the hydrogen bonding between soil particles and biopolymer chains, biopolymer-based soil treatment (BPST) increases the soil shear strength as well as the unconfined compressive strength. Moreover, the biopolymer is regarded as a material with low impact on the ground and groundwater environments due to its low CO_2 footprint and natural decomposition (Chang et al. 2019). As a result, BPST is considered a possible method in ground improvement practices, where the commonly used cement is concerned as a high CO_2 emitting material (Worrell et al. 2001).

There are several types of biopolymers that are applicable in geotechnical engineering. In particular, gel-type biopolymers (e.g., xanthan gum, gellan gum) form hydrogel structures that fill intergranular pore spaces which results in interparticle shear strength increase and hydraulic conductivity decrease (Chang et al. 2015, Bueno et al. 2013, Lee et al. 2019, Kwon et al. 2019, Coutinho et al. 2010). Furthermore, the mechanism of BPST varies depending on the type of soil. In general, biopolymers form biopolymer-clay matrices via direct ionic bonding between biopolymers and electrically charged clay surfaces, where it seems to have an optimal biopolymer-to-clay content in mass depending on biopolymer and clay mineral types

*Corresponding author: ilhanchang@ajou.ac.kr

DOI: 10.1201/9781003299127-82

(Chang & Cho 2019). Despite the fact that BPST-related research has been conducted over the past 10 years and is actively ongoing, it is still insufficient to conclude the exact strengthening efficiency of BPST. Thus, a decision tree method was attempted to analyze the unconfined compressive strength (UCS) of BPST from existing literature and to predict the UCS of BPST by integrating existing experimental data achieved over the past 10 years.

2 CHARACTERISTIC OF BIOPOLYMER-BASED SOIL TREATMENT

2.1 *Soil strength improvement*

When gel-type biopolymers dissolve in water, they form viscous hydrogels that transform into condensed biofilms through dehydration (Kulicke & Nottelmann 1989). Poorly graded sand (SP) generally does not have intergranular cohesion, whilst BPST on SP soil provides interparticle adhesion which results in significant strengthening. Furthermore, the strengthening of BPST becomes more effective for clayey soils (e.g. kaolinite, montmorillonite), due to the biopolymer-clay matrix formation via ionic bonding between the biopolymer and clay particles (Chang & Cho 2019).

2.2 *Hydraulic conductivity control*

By altering the soil-water retention characteristics and pore-clogging characteristics, BPST is reported to reduce the soil hydraulic conductivity in orders of 10^{-4} or more (Cabalar et al. 2017, Chang et al. 2020). According to Chang et al. (2016), when BPST is exposed to water, condensed biofilms absorb water and swell to viscous hydrogels due to the hydrophilicity of biopolymers which results in a significant soil hydraulic conductivity reduction.

2.3 *Soil erosion control*

Surface soil erosion is a serious problem in agriculture, climatology, hydrology, natural hazards (e.g. landslides), and human safety. The interparticle bonding enhancement of BPST has the proper function of increasing the erosion resistance of erosion-prone soils and geotechnical engineering structures (e.g., earth dams and levees) (Kwon et al. 2019). In the laboratory, BPST's erosion response was evaluated, and it was observed that BPST was effective in reducing surface erosion. Biopolymers such as xanthan gum, chitosan, and beta-glucan, in particular, exhibit significant erosion resistance, with a cumulative erosion rate of less than 1% (Chang et al. 2015).

3 DATA AND METHOD

3.1 *Target data*

In this study, experimental data was used to perform machine learning-based analysis in order to predict the UCS of BPST, herein eight published articles related to BPST were used. The feature data for the strength of BPST are summarized in Table 1. The target data is unconfined compressive strength (UCS). This is because UCS data was able to account for the majority of the data, and the analysis was concise. Normally, UCS is influenced by biopolymer type, soil type, soil composition, water content, and dry unit weight, etc.

3.2 *Decision tree*

Decision Tree is one of the most commonly used, practical approaches for supervised learning. It can be used to solve both Regression and Classification problems (Pekel 2020). However, Since the UCS data analyzed in this study are continuous data, regression was used.

Table 1. Feature values for machine learning.

Categorization	Feature data
Biopolymer condition	BP type
	BP concentration for total soil mass (m_b/m_s)
Soil condition	Soil type
	Soil source
	clay content ratio to total soil (m_c/m_s)
	50% passing grain-size (D_{50})
	dry density
Water content	initial water content
	test water content
Test condition	BP mixing temperature
	condition (wetted or dried)
	drying time
	specimen size

4 RESULTS

The prediction result of decision tree regression is shown in Figure 2. For analysis, the entire 453 UCS data were split into 407 train data and 46 test data. As a result of finding the condition in which the determinant coefficient (R^2) becomes the maximum while changing the value of Max depth (Figure 1), each train data and test data showed good performance with R^2 values of 0.9997 and 0.9863 (Figure 2).

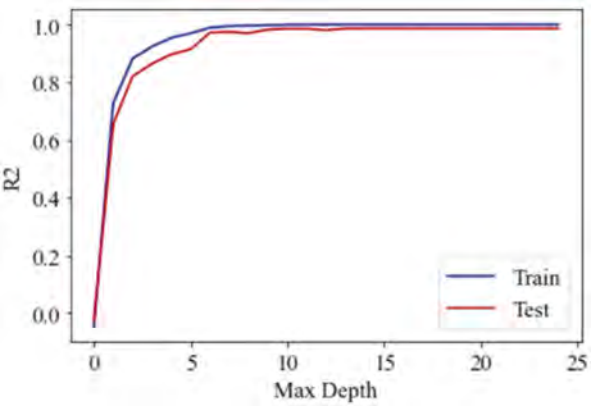

Figure 1. Optimizing hyperparameter (max depth) with the highest R^2.

Additionally, the importance of the feature was determined by comparing the size of the error by substituting a random value for each feature. The most important feature was biopolymer content (m_b/m_s), followed by test water content (Figure 3).

5 CONCLUSIONS

Machine learning analysis is a technique for understanding the behavior of biopolymer-based soil treatment (BPST). It is significant because BPST research period is short (approximately 10 years) and the specific mechanism has not been elucidated. Future BPST experiments or field

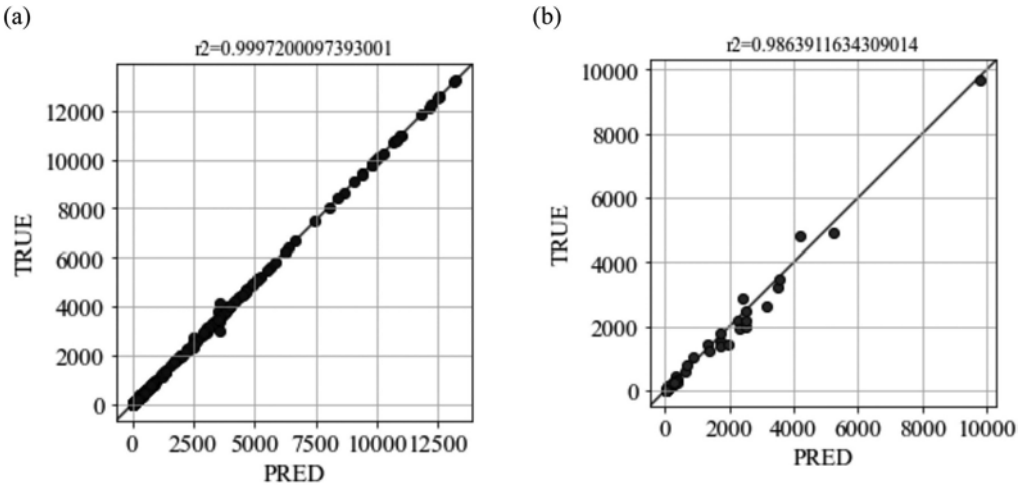

Figure 2. UCS prediction result of decision tree. (a) prediction accuracy of train data; (b) prediction accuracy of test data.

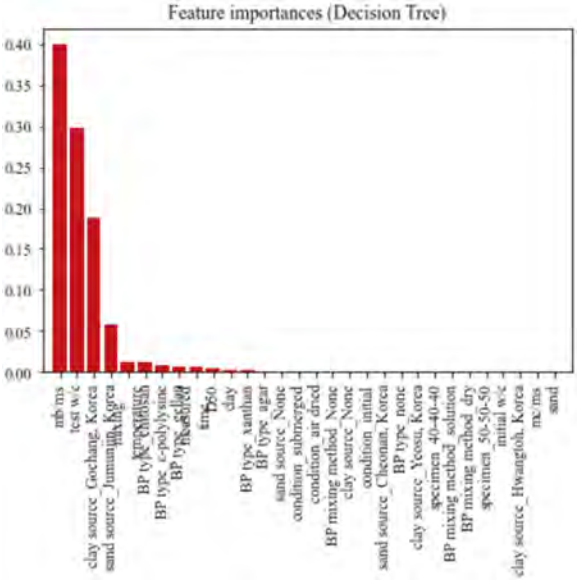

Figure 3. Permutation feature importance.

applications will be less expensive if machine learning can be used to estimate the strength of each material. The prediction accuracy R^2 of the model was 0.99 or better as a result of estimating the strength with decision tree regression. Furthermore, it appears that the biopolymer content and water content are significant. Because the higher the biopolymer concentration, the thicker the hydrogel and matrix are produced. The biopolymer becomes more rigid in the dry state than in the wet state, BPST is thought to have a higher UCS at low water content than at high water content. It can be shown that more exact recording and control of the water content during the test, as well as reducing the water content to enhance strength, will be necessary for future UCS tests.

ACKNOWLEDGEMENT

This work was supported by the National Research Foundation of Korea (NRF) grant funded by the Korea government (MSIT) (No. 2022R1A2C2091517).

REFERENCES

Bueno, V.B. Bentini, R. Catalani, L. H. & Petri, D. F. S. 2013. Synthesis and swelling behavior of xanthan-based hydrogels. *Carbohydr.Polym*. 92(2): 1091–1099.

Cabalar, A.F. Wiszniewski, M. & Skutnik, Z. 2017. Effects of xanthan gum biopolymer on the permeability, odometer, unconfined compressive and triaxial shear behavior of a sand. *Soil Mechanics and Foundation Engineering* 54(5): 356–361.

Chang, I. Im, J. Prasidhi, A. K. & Cho, G. 2015. Effects of Xanthan gum biopolymer on soil strengthening. *Construction & Building Materials* 74 65–72.

Chang, I. Im, J. & Cho, G. 2016. Introduction of microbial biopolymers in soil treatment for future environmentally-friendly and sustainable geotechnical engineering. *Sustainability* 8(3): 251.

Chang, I. & Cho, G. 2019. Shear strength behavior and parameters of microbial gellan gum-treated soils: from sand to clay. *Acta Geotechnica* 14(2): 361–375.

Chang, I. Lee, M. & Cho, G. 2019. Global CO2 emission-related geotechnical engineering hazards and the mission for sustainable geotechnical engineering. *Energies* 12(13): 2567.

Chang, I. Lee, M. Tran, A. T. P. Lee, S. Kwon, Y. Im, J. & Cho, G. 2020. Review on biopolymer-based soil treatment (BPST) technology in geotechnical engineering practices. *Transportation Geotechnics* 24 100385.

Choi, S. Chang, I. Lee, M. Lee, J. Han, J. & Kwon, T. 2020. Review on geotechnical engineering properties of sands treated by microbially induced calcium carbonate precipitation (MICP) and biopolymers. *Constr.Build.Mater*. 246 118415.

Coutinho, D.F. Sant, S. V. Shin, H. Oliveira, J. T. Gomes, M. E. Neves, N. M. Khademhosseini, A. & Reis, R. L. 2010. Modified Gellan Gum hydrogels with tunable physical and mechanical properties. *Biomaterials* 31(29): 7494–7502.

Kulicke, W. & Nottelmann, H. 1989. "Structure and swelling of some synthetic, semisynthetic, and biopolymer hydrogels." ACS Publications.

Kwon, Y. Chang, I. Lee, M. & Cho, G. 2019. Geotechnical engineering behavior of biopolymer-treated soft marine soil. *Geomechanics and Engineering* 17(5): 453–464.

Lee, S. Chung, M. Park, H. M. Song, K. & Chang, I. 2019. Xanthan Gum Biopolymer as Soil-Stabilization Binder for Road Construction Using Local Soil in Sri Lanka. *J.Mater.Civ.Eng*. 31 (11): 06019012.

Pekel, E. 2020. Estimation of soil moisture using decision tree regression. *Theoretical and Applied Climatology*. 139(3): 1111–1119.

Worrell, E. Price, L. Martin, N. Hendriks, C. & Meida, L. O. 2001. Carbon dioxide emissions from the global cement industry. *Annu.Rev.Energy Environ*. 26(1): 303–329.

Smart Geotechnics for Smart Societies – Zhussupbekov, Sarsembayeva & Kaliakin (Eds)
© 2023 The Author(s), ISBN 978-1-003-29912-7
Open Access: www.taylorfrancis.com, CC BY-NC-ND 4.0 license

A DEM study on the degree of mixture of soil particles stirred by rotation of rods

A. Naqi & R. Kuwano
Institute of Industrial Science, The University of Tokyo, Tokyo, Japan

M. Otsubo
Public Works Research Institute, Tsukuba, Ibaraki, Japan

H. Nagatani, K. Kawano & W. Liu
Kajima Corporation, Tokyo, Japan

ABSTRACT: This contribution aims to propose a simple method to quantify the degree of mixture of soil particles stirred by rotation of rods. Discrete element method (DEM) is used to simulate the stirring process and evaluate the degree of mixture at each rotation based on the initial positions of particles. To reduce complexity in the mixing process of actual soil, this study focuses on monodispersed spherical particles where inter-particle cohesion is not considered. The DEM results reveal spatial variation of the degree of mixture (d_m) in the given volume; however, its mean ($\overline{d_m}$) increases with the rotation number of stirring rods. Besides, $\overline{d_m}$ depends on the size of stirring rods whereas the mixing rate is insensitive to $\overline{d_m}$ for the non-cohesive sandy particles.

1 INTRODUCTION

Geotechnical engineering deals with mixing of soil, e.g. deep soil mixing (DSM) and tunnel boring machines, i.e. earth pressure balance (EPB) shields. It is important to evaluate the extent of mixing to confirm the required performance of such phenomenon. The extent of soil mixing in DSM is usually estimated by measuring the permeability or unconfined compression strength of the material at different curing periods (Bruce et al. 2013). Another index to assess the quality of mixing is blade rotation number (Yoshizawa et al. 1996). Moreover, mixing phenomena have been studied in fields other than civil engineering (Khosropour et al. 2000; Bothe 2010). This study aims to define a parameter for calculating the degree of mixture of soils mixed by the rotary action of two stirring rods in a cylindrical soil specimen using discrete element method (DEM).

2 MATERIAL

The DEM simulations were performed using a modified version of LAMMPS (Plimpton 1995) and the model test simulation broadly follows Ali et al. (2020). Spherical particles were used (Young's modulus = 71.6 GPa; Poisson's ratio = 0.23, particle density = 2650 kg/m^3; diameters = 2 to 2.2 mm). The simplified Hertz-Mindlin contact model was used with an inter-particle friction coefficient of 0.05. The wall-particle friction was set to zero.

3 SAMPLE PREPARATION

Table 1 shows the four test cases conducted in this study. Referring to Figure 1, the generated particles were pluviated inside a rigid box from a height exceeding 100 cm. A cylindrical region with rigid walls (diameter = 30 cm, thickness = 2 cm) was created inside the box and extra particles

DOI: 10.1201/9781003299127-83

Table 1. Test cases and specifications.

	Mixing rate	Diameter of stirring rod (φ)	
Case	RPM	cm	Number of particles
1	20	3	165,919
2	100	3	165,919
3	500	3	165,919
4	100	1	169,398

were removed around this region. After this, two rigid stirring rods having their diameters (φ) of 1 or 3 cm (Table 1) and thickness = 2 cm were provided by deleting the particles in the two given regions. The material was mixed by rotating these rods at 20, 100 or 500 RPM (Table 1).

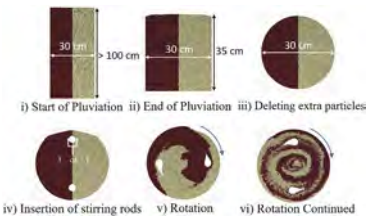

Figure 1. Simulation steps.

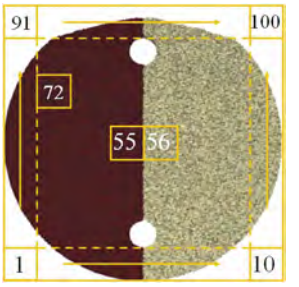

Figure 2. Grid system (not on scale).

4 DEFINITION OF DEGREE OF MIXTURE

4.1 *Local degree of mixture*

For the calculation of local degree of mixture (d_m), the particles in the ground were divided into the two regions (type 1 and type 2) based on their initial coordinate as shown by two different colors in Figure 2. The ground was divided into one hundred equal-sized grids (10×10) over the specimen. For each grid, the d_m value was defined based on the difference in the numbers of type 1 and type 2 particles as follows.

$$d_m = \left(1 - \frac{|n_1 - n_2|}{n_1 + n_2}\right) \times 100\ [\%] \tag{1}$$

where n_1 and n_2 are the numbers of type 1 and type 2 particles, respectively. Equation 1 implies that d_m becomes the highest (i.e. 100%) when $n_1 = n_2$ for each grid. If there are no particles in any grid, that grid was omitted from the calculations.

Figure 3 illustrates a snapshot of the ground after 25 rotations along with the variation of d_m where the color bar corresponds to the magnitude of d_m. Figure 4a provides an example (Case 2) for the variation of d_m for grid number 72 (Figure 2) with the rotation number.

4.2 *Mean degree of mixture ($\overline{d_m}$)*

In this study, the rods are given twenty-five rotations. For each rotation, the mean degree of mixture ($\overline{d_m}$) is defined by calculating the mean of d_m of all the grids, that contain non-zero particles, at the given rotation number using the following equation.

$$\overline{d_m} = \frac{\sum(d_m \text{ for all grids})}{\text{Total number of grids}} \tag{2}$$

The evolution of $\overline{d_m}$ with the rotation number for Case 2 is given in Figure 4b.

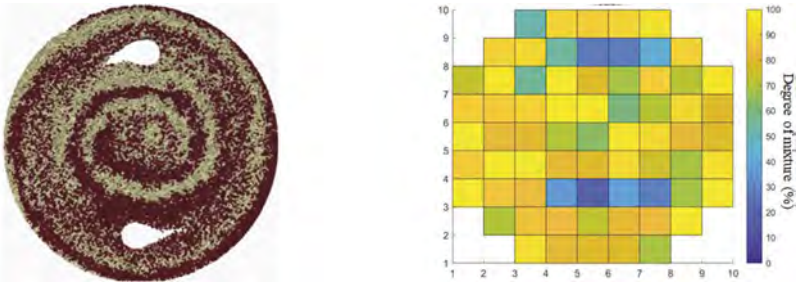

Figure 3. Mixed condition and spatial distribution of d_m at 25 rotations with φ = 3 cm (Case 2).

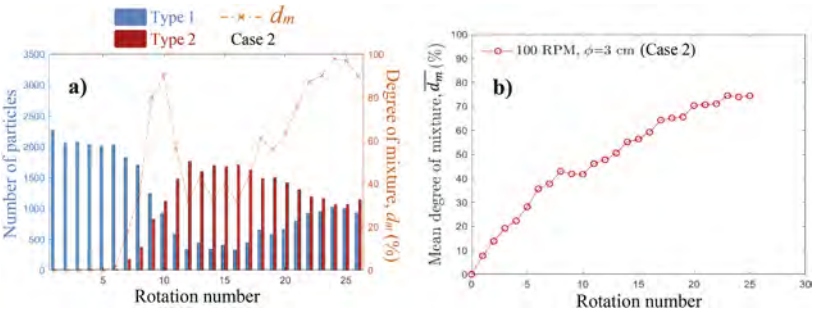

Figure 4. Evolution of degree of mixture with the rotation number (Case 2) (a) Numbers of two types of particles and d_m for grid number 72 (b) Mean degree of mixture ($\overline{d_m}$) of all the grids.

5 DISCUSSIONS

5.1 *Effect of the mixing rate of stirring rods*

Figure 5 compares the mixing conditions after 25 rotations with different mixing rates. It is not easy to differentiate the degree of mixture by eyes. Figure 6 compares the evolution of $\overline{d_m}$ with the rotation number. The mixing rate appears less sensitive to $\overline{d_m}$ where there is no clear dependency of the mixing rate in the given results. It is noteworthy that the current simulation study focuses on coarse particles and does not consider the effect of viscosity or cohesion which can be an influential factor for the mixing phenomenon of finer particles like plastic silt or clay.

5.2 *Effect of the size of stirring rods*

Figure 6 also shows the effect of rod diameter (φ) on $\overline{d_m}$. The larger rods (i.e. φ = 3 cm) are more effective to achieve higher $\overline{d_m}$ for a given rotation number at the same rate of rotation. Figure 5 indicates some locally concentrated zones for the two different colors in Case 4 (φ = 1 cm), probably due to the less influenced zone generated by the motion of smaller rods during rotation.

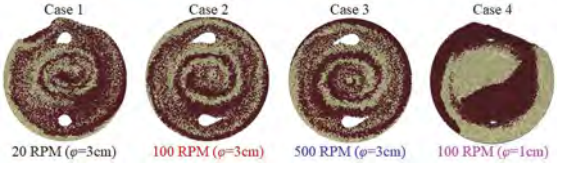

Figure 5. Effects of mixing rate and size of stirring rods on the mixing condition after 25 rotations.

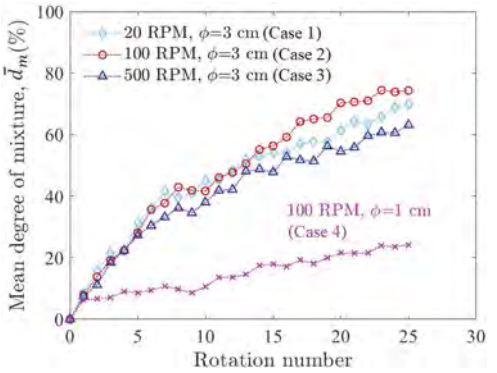

Figure 6. Evolution of the mean degree of mixture ($\overline{d_m}$) with the rotation number for all test cases.

6 CONCLUSIONS

This contribution proposed a simple method to quantify the degree of mixture of soil particles stirred by rotation of rods. Based on a series of DEM simulations using monodispersed coarse spherical particles, the following conclusions can be drawn:

- A new parameter for the calculation of degree of mixture (d_m) has been defined. The results show that the parameter performs well for each grid at given number of rotations.
- The mean degree of mixture ($\overline{d_m}$) increases with the rotation number up to 25.
- Mixing rate is less sensitive to the degree of mixture for non-cohesive sandy particles.
- Larger diameter of stirring rods tends to mix the material well as compared to smaller rods in this study since the smaller rods generate locally concentrated zones.

This study is eventually aimed at enhancing the in-situ mixing and monitoring techniques. Therefore, additional DEM simulations using more realistic material properties are being examined. Besides, some model tests are being performed to validate the results of DEM simulations.

ACKNOWLEDGEMENT

This research was conducted using the Fujitsu PRIMERGY CX400M1/CX2550M5 (Oakbridge-CX) at the Information Technology Center, The University of Tokyo.

REFERENCES

Ali, U., Otsubo, M., Ebizuka, H. & Kuwano, R. 2020. Particle-scale insight into soil arching under trapdoor condition. *Soils and Foundations*, 60(5), 1171–1188.

Bothe, D. 2010. Evaluating the quality of a mixture : degree of homogeneity and scale of segregation. *Micro and Macro Mixing. Heat and Mass Transfer*, 17–35.

Bruce, C., Collin, J., Berg, R., Filz, G., Terashi, M., & Yang, D. 2013. Federal Highway Administration Design Manual: Deep Mixing for Embankment and Foundation Support. *FHWA-HRT*, 13–046.

Khosropour, R., Valachovic, E. & Lincoln, B. 2000. Flow and pattern formation in a binary mixture of rotating granular materials. *Physical Review E - Statistical Physics, Plasmas, Fluids, and Related Interdisciplinary Topics*, 62(1 B), 807–812.

Plimpton, S. 1995. Fast parallel algorithms for short-range molecular dynamics. *Journal of Computational Physics*, 117(1), 1–19.

Yoshizawa, H., Okumura, R., Hosya, Y., Sumi, M. & Yamada, T. 1996. JGS TC Report: Factors affecting the quality of treated soil during execution of DMM. *Proc. the 2nd Intern. Conf. on Ground Improvement Geosystems, Tokyo, Japan (IS-Tokyo'96)*.

Smart Geotechnics for Smart Societies – Zhussupbekov, Sarsembayeva & Kaliakin (Eds)
© 2023 The Author(s), ISBN 978-1-003-29912-7
Open Access: www.taylorfrancis.com, CC BY-NC-ND 4.0 license

Behaviour of randomly distributed fibre reinforced clay

Narendra Kumar Samadhiya
Department of Civil Engineering, Indian Institute of Technology Roorkee, Roorkee, India

ABSTRACT: Various soil improvement techniques have been developed to improve soil properties. One of the soil strengthening technique is mixing of randomly distributed discrete fibres to the soil, termed as a "ply soil". In the present investigation, polypropylene fibres have been chosen as the reinforcement material and were randomly mixed in the soil at 0.1, 0.2 and 0.3% by dry weight of soil. Three different lengths of fibre i.e. 6mm, 10mm and 20mm have been considered as one of the parameters of this study. An intermediate compressible clay (CI) has been used as a soil material in experimental work. The randomly distributed fibre reinforced clay samples were subjected to different types of tests viz. IS: Light compaction tests, unconfined compression tests, consolidation tests, triaxial tests and C.B.R. tests. The results of these tests have clearly shown a significant improvement in the strength properties of the clay.

1 INTRODUCTION

Vidal (1969) demonstrated that the introduction of reinforcing elements in a soil mass increases shear resistance of the medium. The mechanical interlock effect of the fibres provides increased tensile strength and cohesion to the soil matrix. However, as a modification of the same conventional technique, random inclusion of various types of fibres is also considered as a soil reinforcement material. (Prabakar and Sridhar, 2002). The main advantage of randomly distributed fibred soil (RDFS) is the strength isotropy and absence of potential planes of weakness that can develop parallel to the oriented reinforcement. McGown et. al (1978) classified the reinforcements into two major categories viz. a) ideally inextensible inclusions (i.e. metal strips and bars) and b) ideally extensible inclusions (i.e. natural and synthetic fibres, plant roots and polymeric fabrics). The soil reinforced with extensible inclusions is termed as 'plysoil'. Fretaig (1986) investigated the effect of fibre on strength of fine-grained soil which was mixed with 1% by volume of 20-mm-long synthetic fibers. Specimens compacted wet of optimum were found to have somewhat greater strength (up to 25%) and strain to failure with fibers in comparison with specimens without fibers. Reinforcement of micaceous, silt significantly enhanced (65% to 133%) the California Bearing Ratio (C.B.R.). The micaceous silt mixed with fibrillated fibres yielded 16% higher C.B.R. than soil with monofilament fibres (Fletcher and Humphries, 1991). Al-Wahab and Al-Qurna (1995) observed practically no change in the compaction behaviour due to inclusion of fibres in silty clay. The fibre content of approximately 1% of dry unit weight of the soil and a fibre length of 25 mm, maximize the strength, workability and homogeneity of the soil-fibre matrix. Fibre reinforced soil comes under ideally extensible earth reinforcement category. The main advantage of RDFS is the strength isotropy and absence of potential planes of weakness that can develop parallel to the oriented reinforcement. The technique of reinforcing soil increases the stiffness and load carrying capacity of soil through frictional interaction between soil and reinforcement (Chakraborty and Dasgupta, 1996). The other qualities of RDFS are its flexibility, no reduction in permeability, small loss of post peak strength etc. This technique has been effectively used as

DOI: 10.1201/9781003299127-84

ground improvement technique with respect to embankment slopes, slope failure repairs, sports turf, reinforced grass, retaining structures, bridge abutments, foundation slabs and especially in case of subgrade/subbase as well as built and maintained roads.

Nataraj and McManis (1997) achieved optimum values of maximum dry unit weight at a fibre content of 0.2 % for the clay and 0.1 % for the sand. The addition of fibres resulted in an increase in peak shear strength, a reduction in post peak strength loss, substantial increase in peak friction angle and cohesion, signficant increase in compressive strength, and significant increase in CBR values. Ranjan and Charan (1998) reported that the inclusion of fibres to silty sand and clay results in significant increase in cohesion and though the angle of internal friction, φ remains almost unaffected yet there is always an overall gain in strength.

Michalowski and Cermak (2002) concluded that the fibres in the direction of largest extension contribute most to the strength of the composite. Yetimoglu et. al (2005) observed that adding fibre inclusions in sand fill results in an appreciable increase in the peak piston load in C.B.R. test. The effect of treated coir fibres on the shear strength behaviour of clay is presented by Khatri et. al (2016). A series of consolidated undrained test were performed on soil reinforced with untreated, sodium hydroxide treated and carbon tetrachloride treated fibres. The coir fibre content was varied from 0.4% to 1.6%. A significant increase was observed in shear strength parameters of clay reinforced with coir fibres at different percentages.

Suffri et. al (2019) found that increasing the percentage inclusion increases the undrained shear strength of the soil, only up to a certain amount. Wang et. al (2019) have shown that the addition of the fibre leads to a significant increase in CBR strength and stiffness. In addition, samples reinforced with shorter fibres show better behaviour than those reinforced with longer fibres. Valipour et. al (2021) studied the effects of recycled tire polymer fibers (RTPF) and glass fibers (GF) on enhancing the strength/deformation properties of clays. Concerning the shear strength parameters, i.e. cohesion intercept and internal friction angle, the fiber inclusion was particularly influential in increasing cohesion, whereas changes in internal friction angle were minimal. Moreover, the shorter fibers (5 mm) were generally more efficient in reinforcing the clay.

2 EXPERIMENTAL PROGRAMME

The main objective of the study presented herein was to investigate the strength and deformation characteristics of clay reinforced with randomly distributed fibrillated fibres. The properties of the clay used in this study are shown in Table 1. The unconfined compressive strength (UCS) as well as shear strength parameters (c and φ) obtained for clay compacted at maximum dry density (MDD) and optimum moisture content (OMC) are presented in Table 2.

Table 1. Properties of clay used in the experimental investigation.

Liquid limit (%)	Plastic limit (%)	Classification (IS: 1498-1970)	Maximum dry density (g/cc)	OMC (%)
42.5	20.5	CI	1.69	19.0

Table 2. Strength parameters of unreinforced clay.

Strength parameters unconfined compression test		Effective strength parameters (CU) Triaxial Test	
UCS (kPa)	c (kPa)	c' (kPa)	Φ'(°)
118.3	59.1	49.7	29.4

UCS: unconfined compression strength; c': effective cohesion; Φ': effective friction angle of soil

Fibrillated polypropylene fibres with 6 mm, 10 mm, and 20 mm in lengths manufactured by "Zenith Fibre Limited", Baroda, Gujarat, India were used as reinforcement. Fibrillated polypropylene fibres with 6 mm, 10 mm, and 20 mm in length were used as reinforcement. The characteristics of fibres are shown in Table 3. The fibre content in all of the soil test specimens varied from 0.1% to 0.3% of dry unit weight of the soil with fibre length varying from 6mm to 20mm. All test samples were prepared at maximum dry density (MDD) and optimum moisture content (OMC).

Table 3. Fibre characteristics.

Fibre type Fibrillated	Specific gravity,Gf	Fibre Avg Denier	Fibre Diameter microns	Avg. Breaking Elongation, %	Avg. Breaking Tenacity (gm/denier)	Melting point,°C
Polypropylene	0.91	3	21.6	45.0	5.2	162-170

3 ANALYSIS OF RESULTS

3.1 *Effect of fibre on compaction characteristics*

Figure 1 shows the variation of maximum dry unit weight with fibre length. For all samples, the dry unit weight increases with an increase in water content upto optimum moisture content beyond which it reduces. For a particular percentage of fibre content, the dry unit weight increases with increase in fibre length. However beyond a fibre length of about 10 mm, the maximum dry unit weight has got reduced. The reduction has been found to be more for longer fibres. In the case of 20 mm fibre, maximum dry unit weight has reduced by approximately 3% to that of the unreinforced clay. The maximum dry unit weight has been found to increase with increase in fibre content except for fibres having 20 mm length, as is presented in Figure 2 The optimum moisture content has been found to decrease for all the combinations of length and fibre content (FC) except for 20 mm fibre with 0.3%. F.C. where it is slightly more, as shown in Figure 3. The reduction has been more for 6 mm fibres. Figure 4 shows the variation of OMC with fibre content.

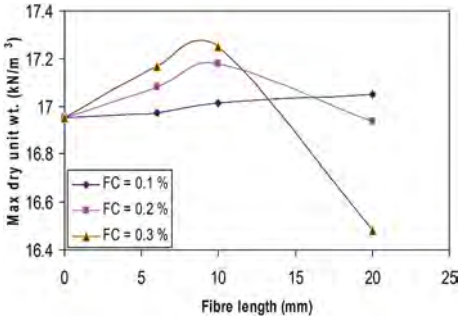

Figure 1. Effect of fibre length on maximum dry unit weight.

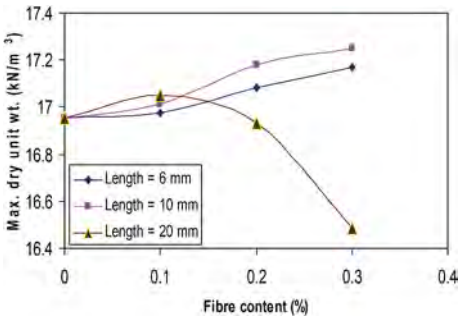

Figure 2. Effect of fibre content on maximum dry unit weight.

3.2 *Effect of fibre on unconfined compressive strength*

The results of the unconfined compression tests are presented in Table 4. The unconfined compression strength increases with increase in fibre length as well as fibre content (FC). It is clear that for all fibre contents, RDFS has got maximum unconfined compressive strength for 20 mm fibre length. It may also be noted that at 0.3% fibre content with 20mm fibre, the

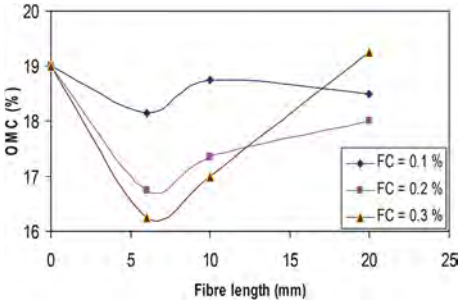

Figure 3. Effect of fibre length on optimum moisture content.

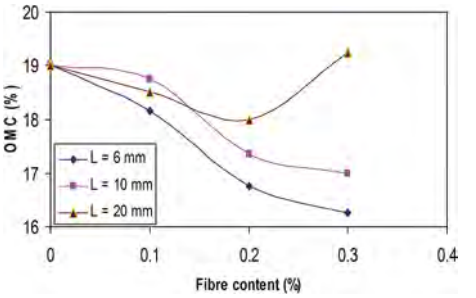

Figure 4. Effect of fibre content on optimum moisture content.

RDFS achieved maximum percentage increase in UCS which is about 95% which is nearly two times as that of unreinforced clay.

Table 4. Effect of fibre length and fibre content on unconfined compressive strength.

Fibre length mm	Fibre content (%)	UCS kPa	Failure strain (%)	Increase in UCS (%)
Unreinforced	0.0	118.3	17.7	-
6	0.1	131.8	17.1	11.4
	0.2	142.0	15.8	20.0
	0.3	184.5	15.1	56.0
10	0.1	168.4	15.8	42.4
	0.2	178.0	15.1	50.5
	0.3	207.1	14.8	75.0
20	0.1	201.9	15.1	70.7
	0.2	217.3	14.5	79.2
	0.3	231.1	13.8	95.4

3.3 *Effect of fibre on compressibility characteristics*

Table 5 shows the effect of fibre length as well as fibre content on compression index and percentage reduction in compression index. It may be observed that there is a significant effect on compressibility of clay due to the fibre content as well as fibre length. The increase in fibre content reduces compressibility of RDFS.

Table 5. Effect of fibre length and fibre content on compression index and % reduction in compression index (Cc).

Fibre length mm	Fibre content (%)	Compression index, Cc	Reduction in Cc (%)
Unreinforced	0.0	0.243	-
6	0.1	0.165	32.1
	0.2	0.144	40.7
	0.3	0.133	45.3
10	0.1	0.148	39.1
	0.2	0.130	46.5
	0.3	0.114	53.1
20	0.1	0.138	43.2
	0.2	0.122	49.8
	0.3	0.106	56.4

3.4 *Effect of fibre on triaxial strength behaviour*

CU triaxial tests with pore water pressure measurement were conducted. The unreinforced clay specimens revealed a shear failure and with the increase in reinforcing fibres, the specimens failed due to bulging at different confining pressures. Increase in deviator stress at failure has been observed for all combination of fibre length and fibre contents. Table 6 shows the effective cohesion (c') and effective angle of internal friction (φ') of the reinforced clay.

3.5 *Effect of fibre on California bearing ratio (C.B.R.)*

A series of C.B.R. tests was conducted in 4 days soaked condition. Table 7 shows C.B.R. values and percentage increase in C.B.R. for different fibre content and fibre length.

It is clear from Table 7 there is a significant percentage increase in C.B.R. as fibre content increases from 0.1% to 0.3%. It can be observed that, at 0.1%, 0.2%, and 0.3% fibre content the percentage increase in C.B.R. are 23%, 35.5% and 51.97% respectively for 20 mm fibre. The percentage increase in the C.B.R. with increase in fibre content is almost linear. So it may be concluded that at 0.3% fibre content (FC) and 20 mm fibre length gives maximum C.B.R. value to RDFS. After each C.B.R. test, the fibres were inspected and showed no signs of breakage.

Table 6. Effect of fibre length and fibre content on strength parameters.

Fibre length mm	Fibre content (%)	Effective cohesion, c',(kPa)	Angle of friction Φ'(°)
Unreinforced	0.0	49.7	29.4
6	0.1	67.7	28.2
	0.2	71.7	28.0
	0.3	94.4	27.4
10	0.1	85.1	27.8
	0.2	88.2	27.5
	0.3	104.6	26.6

It may be observed from Table 6 that there is significant increase in the cohesion value due to increase in fibre content. The influence of fibre length on the cohesion is also significant. However, there is not much variation in the friction angle due to addition of fibres.

Table 7. Effect of fibre length and fibre content on strength parameters.

Fibre length mm	Fibre content (%)	CBR (%)	Reduction in CBR (%)
Unreinforced	0.0	3.04	-
6	0.1	3.39	11.5
	0.2	3.74	23.0
	0.3	4.17	37.1
10	0.1	3.56	17.5
	0.2	3.91	29.0
	0.3	4.43	46.0
20	0.1	3.74	23.0
	0.2	4.12	35.5
	0.3	4.62	51.9

4 CONCLUSIONS

Various parameters namely maximum dry density, unconfined compression strength, compression index, strength and deformation characteristics and C.B.R. were studied with different fibre content and fibre length. Following conclusions may be mde:

i. The compaction characteristics of the fibre reinforced clays were found similar to that of the unreinforced clays. The maximum dry unit weight reached a maximum value at a fibre content of 0.3% with 10 mm fibre length for clay specimens.
ii. The addition of fibres to the clay specimens increased the peak shear strength of the soil and reduced, in some cases, the post peak strength. Also, there is a substantial increase in unconfined compression strength of clay at 0.3% fibre content with 20 mm fibre length.
iii. Due to inclusion of polypropylene fibre, compressibility of clay substantially decreases. At 20 mm fibre with 0.3% fibre content compression index of clay has decreased to the maximum extent.
iv. The inclusion of fibres in clay significantly increases cohesion of soil. However, there is no specific trend in the variation of friction angle with fibre length as well as fibre content. In fact, it is confirmed that reinforcement does not have a significant influence on the improvement of angle of shearing resistance.
v. California Bearing Ratio (C.B.R) increases significantly with the addition of fibres. The maximum C.B.R. value has been found for 20 mm fibre with 0.3% fibre content.
vi. Finally, results indicated that by reinforcing soil with 20 mm long fibrillated fibres, the optimum fibre content is 0.3% of the dry unit weight of soil.

REFERENCES

Al-Wahab, R. M. & Al- Qurna, H. H. 1995. Fibre reinforced cohesive soils for application in compacted earth structures. *Proceedings of Geosynthetics 95, IFAI, vol. 2, Nashville, Tennessee, USA, February 1995 :* 433–446.

Chakraborty, T. K & DASGUPTA, S. P. 1996. Randomly reinforced fly ash as foundation material. Proceedings of the Indian Geotechnical Conference (IGC-96), Madras, India, 231–235.

Fletcher, C. S. & Humphries, W. K. 1991. California bearing ratio improvement of remolded soils by the addition polypropylene fibre reinforcement. *Proceedings of seventieth Annual Meetings, Transportation Research Board*. Washington, DC, USA: 80–86.

Fretaig, D. R. 1986. Soil randomly reinforced with fibres. *Journal of Geotechnical Engineering, ASCE*, 112 (8)8: 823–826.

Khatri, V. N., Dutta, R. K., Venkataraman, G. & Shrivastava, R. 2016. Shear strength behaviour of clay reinforced with treated coir fibres", Periodica Polytechnica, Civil Engineering, 60(2): 135–143.

McGown A., Andrawes, K. Z. & Al-Hasani, M. M. 1978. Effect of inclusion properties on the behaviour of sand. *Geotechnique* 28(3): 327–346.

Michalowski, R. L. & Cermak, J. 2002. Strength anisotropy of fibre reinforced sand. *Computers and Geotechniques* 29(4): 279–299.

Nataraj, M. S. and McManis, K. L. 1997. A technical note on strength and deformation properties of soils reinforced with fibrillated fibers. *Geosynthetics International* 4(1): 65–79.

Prabakar, J. & Sridhar, R. S. 2002. Effect of random inclusion of sisal fibre on strength behaviour of soil. *Construction and Building Materials* 16:123–131.

Suffri N., Jeludin M. & Rahim S. 2019. Behaviour of the undrained shear strength of soft clay reinforced with natural fibre. *IOP Conference Series: Materials Science and Engineering, Volume 690, 2nd International Conference on Civil Engineering and Architecture 21–23 September 2019, Seoul, South Korea*

Valipour, M. Shourijeh P. T. & Mohammadinia, A. 2021. Application of recycled tire polymer fibers and glass fibers for clay reinforcement. *Transportation Geotechnics*, 27 100474 https://doi.org/10.1016/j.trgeo.2020.100474

Vidal, H. (1969). The principle of reinforced earth. *Highway research record no. 282*. 1–16.

Yetimoglu, T., Inanir, M. & Inanir, O. 2005. A study on bearing capacity of randomly distributed fibre reinforced sand fills overlying soft clay. *Geotextile and Geomembranes* 23: 174–183.

Wang, J.Y., Hughes, P. N. & Augarde, C. E. 2019. CBR strength of London clay reinforced with polypropylene fibre. *Proceedings of the XVII ECSMGE-2019 Geotechnical Engineering foundation of the future, Reykjavik*, Iceland 1st - 6th of September 2019, doi: 10.32075/17ECSMGE-2019-0296.

Smart Geotechnics for Smart Societies – Zhussupbekov, Sarsembayeva & Kaliakin (Eds)
© 2023 The Author(s), ISBN 978-1-003-29912-7
Open Access: www.taylorfrancis.com, CC BY-NC-ND 4.0 license

Stabilization of clay soil using ground granulated blast furnace slag and banana fibres

K. Gayathridevi
Research scholar, School of Civil Engineering, Vellore Institute of Technology, Vellore, Tamil Nadu, India

Divya Priya Balasubramani*
Assistant Professor (Senior), College of Engineering Guindy Campus, Anna University, Chennai, India

ABSTRACT: Numerous studies have been carried out to improve the strength characteristics of clay soil using various admixtures and mechanical methods. This study focuses on the influence of Ground Granulated Blast Furnace Slag (GGBS) and banana fibres in improving the strength characteristics of clay soil. GGBS is a known by-product of iron manufacturing industries and banana fibre is a locally available, economic, and eco-friendly agricultural waste produced from the banana plantation. Virgin soils and various combinations of clay soil with GGBS and banana fibres are evaluated by analysing their index properties, compaction, permeability, and strength characteristics. Scanning electron microscopy (SEM) and X-ray diffraction (XRD) analysis have been carried out to understand the physical and mechanical behaviours of soil samples before and after treatment. Based on the results the optimal percentage of GGBS and banana Fibre mixture in clay soil is recommended indicating its suitability as a sustainable stabilizing material.

Keywords: Stabilization, Clay soil, GGBS, Banana fibres, Sustainability

1 INTRODUCTION

Due to the increase in population and urbanization, there is a significant need for the provision of infrastructure facilities and an increase in the construction of superstructures and substructures. With the growing demand due to technological development, the only option is to carry out construction on problematic soils. The Problematic soils are unsuitable without treatment, especially the expansive clays, which swell and shrink with annual moisture changes, affecting the structures built on them. To accommodate loads of the superstructures, these soils must be excavated, replaced, or enhanced (Wei & Huang 1996, Kolias et al 2005, Bhavanna Rao R 2006, Horpibulsuk et al 2012, Saravanan et al 2017,). Hence there is a need to stabilize this type of soil to increase its bearing capacity. On the other hand, industrialization leads to the generation of industrial wastes like, fly ash, phospho-gypsum, blast furnace slags, lime kiln dust, cement kiln dust, red mud, jarosite, steel slags, copper slags, plastic wastes, rubber wastes, rice husk ash, etc. in large quantities. The improper management of these wastes will leads to health and environmental hazards. The use of these industrial wastes as a stabilizing agent to improve problematic soil characteristics is considered the most sustainable solution (Joe & Rajesh 2015). However, carbon dioxide emission from these wastes especially from cement and lime manufacturing unit will lead to environmental degradation and increased global warming (Horpibulsuk et al 2012, Ayeldeen & Kitazume

*Corresponding author: divyapriya.b@vit.ac.in

DOI: 10.1201/9781003299127-85

2017). In recent times, additives with fewer CO_2 emissions and locally available fibres are used as a stabilizing material to improve the mechanical properties of soil (Sharma et al. 2015, Wu et al. 2019). In this study, an attempt has been made to stabilize the clay soil using Ground Granulated Blast Furnace Slag (GGBS) and banana fibres produced from industrial waste and agricultural waste respectively. The use of GGBS and banana fibres will be an economical and sustainable solution and also the addition of fibre in soil act as a reinforcement replacing the cement & lime which in turn reduces carbon dioxide emissions by improving the strength and deformation characteristics of the soil.

2 STUDY AREA

Vellore district is one of the 38 districts of Tamil Nadu state in southern India. It is located between 12°15'23"–13°12'32"N latitude and 78°24'13"–79°54'56"E longitude covering a land area of 5920.18 square kilometers. Geologically the entire area can be classified into hard rock and sedimentary formations. Hard rock covers 90% of the region which is Azoic, Crystalline, and extremely contorted and these are the oldest rocks for the earth's crust. Gneisses and Charnockites are the most common hard rock formations whereas Gneisses are found in nearly all the taluks of the district.

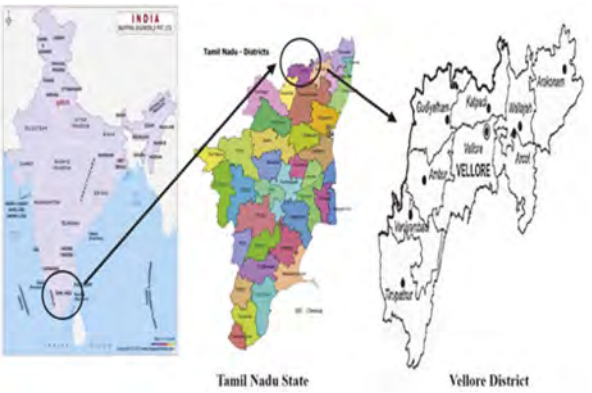

Figure 1. Study area.

3 MATERIAL AND METHODS

3.1 *Material*

3.1.1 *Soil*

The soil in the study (as shown in Figure 1) is collected from the local villages in and around Vellore city at a depth of 2 m from the ground level. Based on the laboratory test the basic properties of the soil are determined and tabulated as shown in Table 1. Based on the index properties, the collected soil is classified as Inorganic clay of low compressibility as per IS 1498:1970. From the free swell index value (see Table 1), the soil can be categorized as highly expansive clay.

3.1.2 *Ground Granulated Blast Furnace Slag (GGBS)*

The Ground Granulated Blast Furnace Slag (GGBS) as shown in Figure 3, is collected from the coal & steel industries located in Ambattur, Chennai city of Tamil Nadu state. In this study, GGBS is used as a basic additive for stabilization with a specific gravity of 2.64. The X-ray diffraction analysis of GGBS indicates the presence of calcite (as shown in Figure 4) which has the potential to improve the engineering properties of soil. GGBS is added to the soil at the percentage of 10%, 20%, and 30% respectively.

Figure 2. Collected soil sample.

Table 1. Properties of soil.

Soil Property		Values
Specific gravity		2.57
Particle size	% Gravel (>4.75 mm)	2.12
	% Sand (4.75-0.075mm)	23.00
	% Silt and clay (<0.075mm)	74.87
Index values	Liquid limit, %	35
	Plastic limit, %	25.17
	Plasticity index, %	9.83
Classification (as per IS 1498:1970)		CL
OMC, %		20.05
Max dry density, g/cc		1.828
Free swell Index (%)		40
Permeability cm/s		$4.46x10^{-5}$

Figure 3. Ground granulated blast furnace slag.

3.1.3 *Banana fibre*

The banana fibre (as shown in Figure 5), is collected from locally available sources. Banana fibre has an average length of 350 mm and an average diameter of 0.11mm. In this study, the banana fibres are uniformly cut into an average length of 2cm and mixed with soil at a percentage of 0.25 0.50, and 0.75 respectively. The properties of banana fibres were

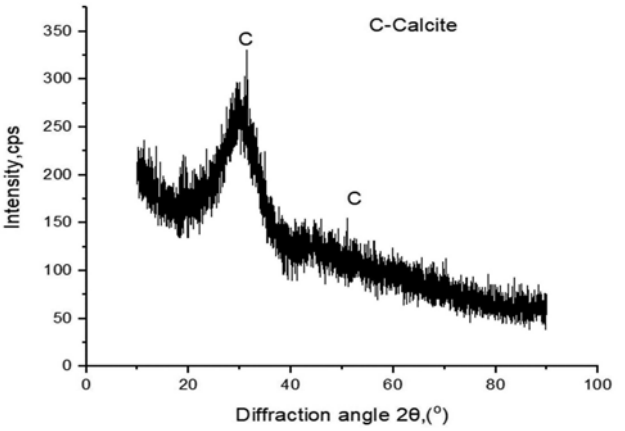

Figure 4. XRD pattern for GGBS.

determined in their natural form as presented in Table 2. The banana fibre when added to soil, will act as a reinforcement material, and interlocks the soil particles.

Figure 5. a. Banana fibre collected from local sources. b. Banana fibre after cut into 2 cm.

Table 2. Properties of banana fibre.

Property (%)	Banana Fibre
Ash content	4.58
Wax content	0.31
Moisture content	11.75
Cellulose Content	71.11
Lignin Content	7.86
Density g/cc	1.23
Hemi cellulose	34.79
Pectin	5.21

3.2 *Methods*

A series of laboratory tests are conducted in the present study in three stages. At stage-I, the virgin soil i.e., without any additives is used. At stage II, GGBS is added in various proportions i.e. 10%, 20%, and 30% of soil. At stage III, the various proportions of banana fibre

(0.25%, 0.50%, and 0.75%) are blended into the soil mixture with different percentages of GGBS. At all the above-mentioned three stages, i.e. the virgin soil and soil mixtures are subjected to basic tests like Specific gravity, Free Swell index, Sieve analysis, and Atterberg limits test. The compaction characteristics are determined using Standard proctor compaction tests at three stages. Then the soil sample is prepared at the respective optimum moisture content and compacted at a maximum dry density to conduct the unconfined compressive strength test. The stepwise procedure from the preparation of soil mixture to failure of soil samples at various compositions is shown in Figure 6. Also, permeability tests for treated and untreated soil at different proportions are conducted using the Falling head permeability test apparatus.

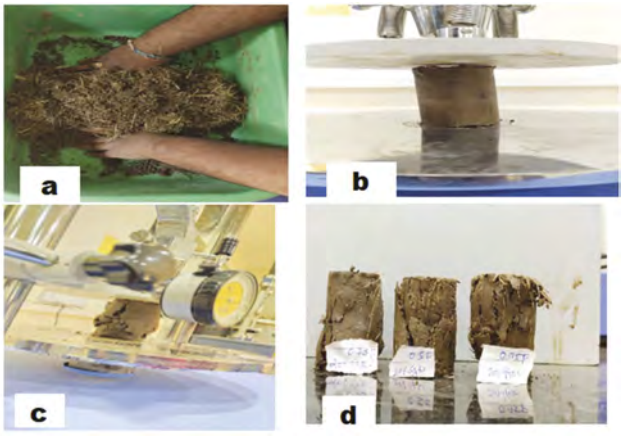

Figure 6. UCS sample preparation a) Mixing of soil+ GGBS+ Banana fibre b) Prepared sample c) Sample under testing d) Samples failed under UCS test.

4 RESULTS AND DISCUSSIONS

As a result of laboratory tests conducted at three stages in this study, the basic properties are obtained for virgin soil and soil mixed with GGBS at various percentages as presented in Table 3. The results indicate that the soil with 30% GGBS shows a decreasing percentage of the free swell index compared to virgin soil. Thus the addition of GGBS reduces the swelling characteristics of the clay soil.

Table 3. Results of the laboratory tests of soil mixed with GGBS.

Sample	LL (%)	PL (%)	PI (%)	Free swell Index (%)
Soil +0 % GGBS	35	25.17	9.83	40
Soil + 10% GGBS	33.15	17.77	15.38	40
Soil + 20% GGBS	26	20.30	5.7	20
Soil + 30% GGBS	24.8	19.50	5.30	15

4.1 *Effect of GGBS and banana fibre on compaction characteristics of soil*

The compaction curves of the virgin soil and soil mixed with variable percentages of GGBS i.e (10%, 20% and 30%) are obtained as shown in Figure 7. The graph indicates that the addition of GGBS into the soil increases the dry density and decrease in optimum moisture decreases. This may be due to the presence of fine particles in GGBS which reduce its affinity with water and replaces the voids in the soil increasing its dry density. From Figure 6, it can be seen that the max dry density with minimum OMC can be obtained when soil is mixed with 30% of GGBS.

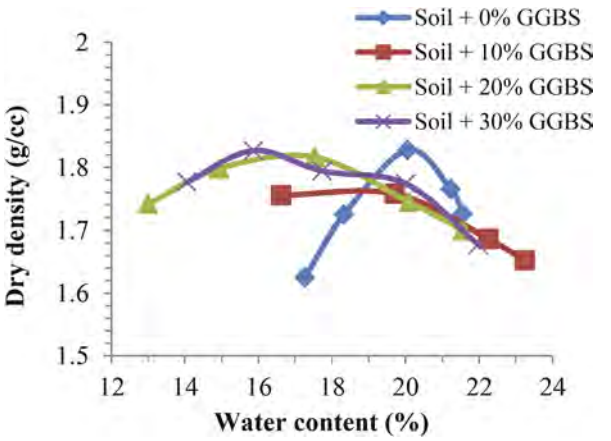

Figure 7. Compaction curves for soil modified with GGBS.

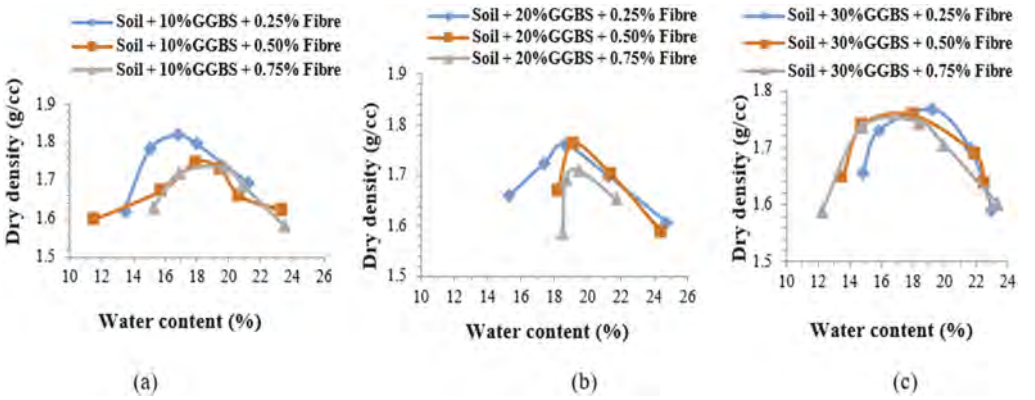

Figure 8. Compaction curves for soil modified with GGBS and Banana fibre (a)10% GGBS with proportions of 0.25%,0.5%,0.75% Banana fibre (b) 20% GGBS with proportions of 0.25%,0.5%,0.75% Banana fibre (c) 30% of GGBS with proportions of 0.25%,0.5%,0.75% Banana fibre.

The compaction characteristics of the soil mixed with GGBS and banana fibre in various proportions are determined as shown in Figure 8. From the Figures 8a, b, c it can be seen that the soil+10%GGBS+0.25% banana fibre is optimum. Similarly, the soil+20% GGBS +0.25% banana fibre is optimum and the soil +30% GGBS+0.75 fibre is taken as an optimum combination as the max dry density with minimum OMC and minimum compactive effort.

4.2 *Effect of GGBS on strength characteristics of soil*

The stress-strain graphs for virgin soil and soil with combinations of GGBS are obtained from UCS tests as shown in Figure 9. It is observed that virgin soil attained a low peak at high strain whereas soil+30%GGBS mix shows a high peak at low strain. The peak stress and the corresponding strain are low for soil with 30% of GGBS. This is due to the higher binding proportion of GGBS which improves the strength of the soil. The strength of the soil is increased to 82.23% by the addition of 30% of GGBS to the virgin soil. In comparison with other proportions of GGBS to the virgin soil, the elevated rise in the strength characteristics is observed at 30% of GGBS hence the combination of soil +30% GGBS is determined as optimum.

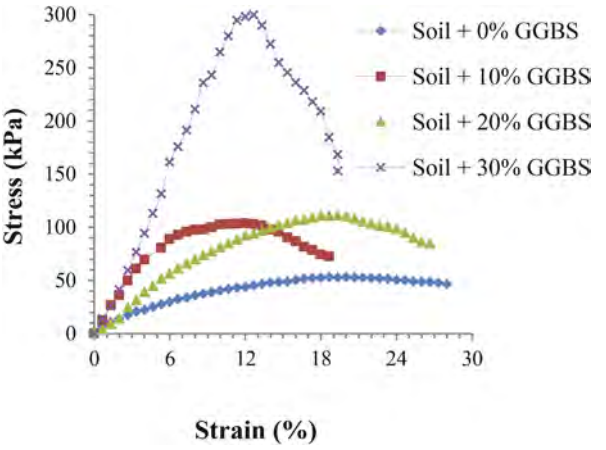

Figure 9. Stress-strain plots for Soil + GGBS mixes.

4.3 *Effect of soil with GGBS and fiber on UCS*

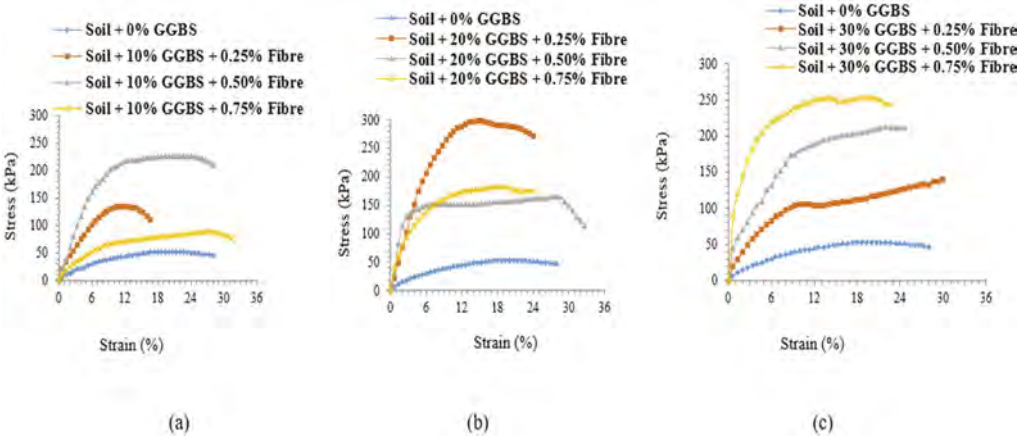

Figure 10. Stress-strain plots for soil modified with GGBS and Banana fibre (a) 10% GGBS with proportions of 0.25%,0.5%,0.75% Banana fibre (b) 20% GGBS with proportions of 0.25%,0.5%,0.75% Banana fibre (c) 30% of GGBS with different proportions of 0.25%,0.5%,0.75% Banana fibre.

The banana fibre is added to the soil and GGBS in various proportions and UCS tests are conducted to determine its strength characteristics. Figure 10 illustrates the stress-strain characteristics of various combinations of soil + GGBS+ banana fibres. Overall, the combination of soil + 30% GGBS + 0.75% fibre is found to be the optimum mixture as it shows an 85% increase in strength characteristics of the soil compared to virgin soil.

4.4 *Effects of permeability*

The soil samples are prepared with respective optimum moisture content and the falling head test is conducted as per IS 2720-17(1986) to determine the permeability of virgin soil and soil treated at an optimum percentage i.e. soil+30%GGBS+0.75 banana fibre. The treated soil increases the permeability by 7.85% compared to virgin soil. This is due to the enlargement of voids by fibres causing an improved permeability which in turn increases the rate of consolidation.

5 MICROSCOPIC STUDIES

Scanning electron microscopy (SEM) and X-ray diffraction (XRD) analysis have been carried out to understand the physical and mechanical behaviors of soil samples before and after treatment. Figure 11–15 illustrates the results of Scanning electron microscopy (SEM) of the virgin soils and combinations of soils with GGBS and banana fibres.

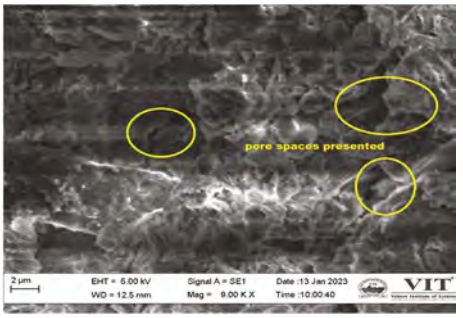

Figure 11. SEM images of soil.

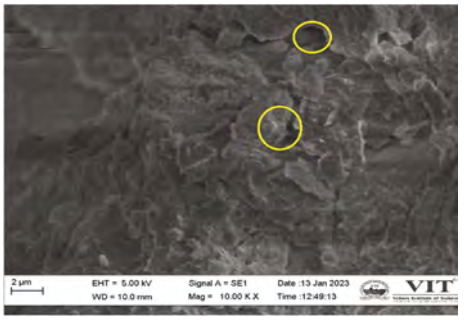

Figure 12. SEM images of soil+ 30%GGBS.

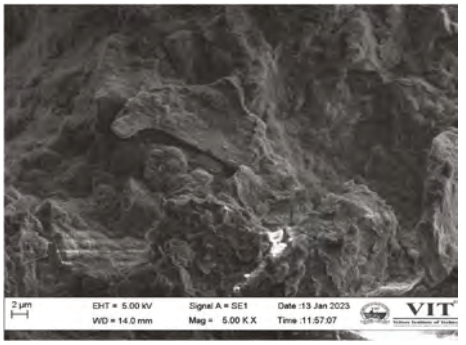

Figure 13. SEM images of soil+30%GGBS +0.25 fibre.

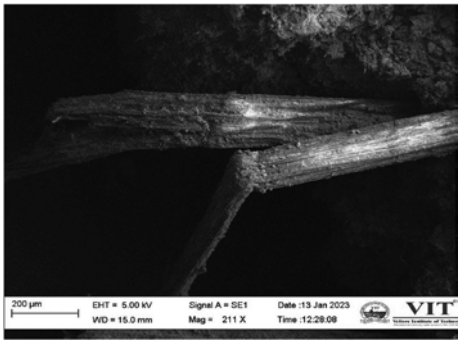

Figure 14. SEM images of soil+30%GGBS+0.5 fibre.

The SEM images of the virgin soil (refer Figure 11) indicates the presence of voids in the soil mass. When GGBS and banana fibres are added to the soil, they act as a binding material interlocking the soil particles as seen in Figures 12–15. Especially addition of fibres at 0.75 % to the soil and 30% GGBS mixture reduces the porous structure of the soil decreasing the soil's compressibility and increasing strength.

5.1 *EDX-analysis*

Energy Dispersive X-ray analysis is carried out for virgin soil and soil+30%GGBS which is an optimum percentage and various combinations of banana fibres like 30%GGBS+0.5F and 30% GGBS+0.75F. The results of the EDX analysis are illustrated in Figures 16–18 respectively.

Figure 16 indicates the presence of the highest peak values of silica and alumina in virgin soil. When the optimum percentage i.e.30% of GGBS is added to the soil, there is an increase in alumina and silica content resulting in the formation of calcium silicate enhancing the soil properties (see Figure 17). The addition of banana fibres to soil + 30% GGBS mixture leads to the formation of cementitious material (Figure 18) and also it acts like a composite material in which fibres withstand tension providing greater resistance to the soil.

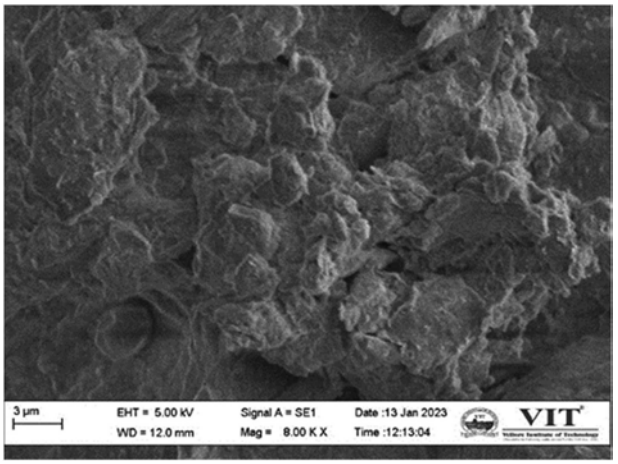

Figure 15. SEM images of soil +30%GGBS+0.75 fibre.

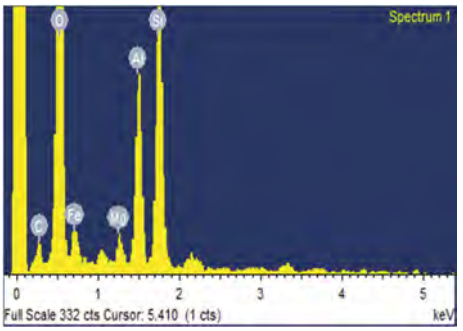

Figure 16. EDX of virgin soil.

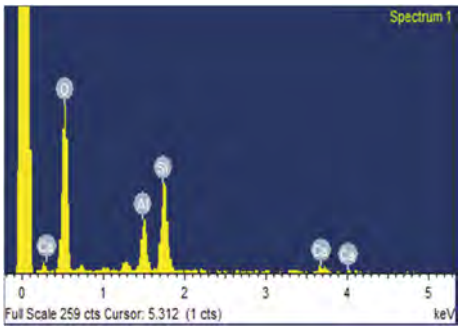

Figure 17. EDX of soil+30%GGBS.

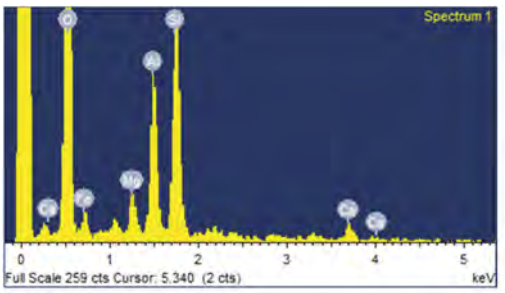

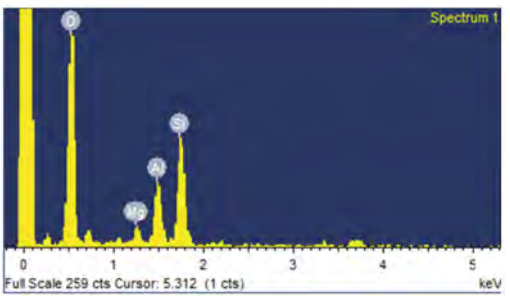

Figure 18. EDX for soil+30%GGBS+ fibre.

6 CONCLUSIONS

In this study, the influence of Ground Granulated Blast Furnace Slag (GGBS) and banana fibres in improving the strength characteristics of highly expansive clayey soil as a stabilizing agent is investigated in detail. From the results, it is concluded that

- The addition of Ground Granulated Blast Furnace Slag to the soil decreases the plasticity of the clayey soil and reduces the swelling characteristics to more than 50% curtailing its expansive nature.

- Based on the results obtained for the various tests to determine compaction and strength characteristics of the various proportions of soil +GGBS+ Banana fibre mixture, it is found that the plasticity (PI) of the untreated soil decreased by 42% and 46% by the addition of 20%GGBS and 30%GGBS respectively.
- Similarly, the strength and drainage characteristics increased by 85% and 10% when the soil is treated with 30% GGBS and 0.75% banana fiber. Thus, proving that the soil + 30% GGBS + 0.75% banana fibre is an optimum combination for stabilizing the expansive clay.
- The formation of Calcium carbonate due to cementitious reactions between GGBS and soil increases the strength properties of soil.
- The addition of GGBS and banana fibres binds the soil particles together along with the reinforcement to bear the tensile stress contributing to the strength improvement of treated soil.

Thus, the Ground Granulated Blast Furnace Slag and banana fibres can be effectively used as a sustainable stabilizing material for clayey soils.

REFERENCES

Ayeldeen, M., & Kitazume, M. (2017). Using fibre and liquid polymer to improve the behaviour of cement-stabilized soft clay. *Geotextiles and Geomembranes*, *45*(6), 592–602.

Bhavanna Rao R, D. S. (2006). Poor condition of roads on B.C soils and steps to improve their condition. *National Conference on Corrective Engineering Practices in Troublesome Soils*, 101–103.

Horpibulsuk, S., Phetchuay, C., & Chinkulkijniwat, A. (2012). Soil Stabilization by Calcium Carbide Residue and Fly Ash. *Journal of Materials in Civil Engineering*, *24*(2), 184–193.

Kolias, S., Kasselouri-Rigopoulou, V., & Karahalios, A. (2005). Stabilization of clayey soils with high calcium fly ash and cement. *Cement and Concrete Composites*, *27*(2), 301–313.

Saravanan, R., Udhayakumar, T., Dinesh, S., Venkatasubramanian, C., & Muthu, D. (2017). Effect of addition of GGBS and lime in soil stabilisation for stabilising local village roads in Thanjavur region. *IOP Conference Series: Earth and Environmental Science*, *80*(1), 012060.

Sharma, V., Vinayak, H. K., & Marwaha, B. M. (2015). Enhancing compressive strength of soil using natural fibres. *Construction and Building Materials*, *93*, 943–949.

Wei, M. S., & Huang, K. H. (2001). Recycling and reuse of industrial wastes in Taiwan. *Waste management*, 21(1), 93–97.

Wu, Y., Lu, B., Bai, T., Wang, H., Du, F., Zhang, Y., Cai, L., Jiang, C., & Wang, W. (2019). Geopolymer, green alkali-activated cementitious material: Synthesis, applications, and challenges. *Construction and Building Materials*, 224, 930–949.

IS, B. 1498 Classification and Identification of Soils for General Engineering Purposes (1970).

IS, B. 2720 Methods for Tes for Soils Part -17 Laboratory Tests for Permeability (1986)

Smart Geotechnics for Smart Societies – Zhussupbekov, Sarsembayeva & Kaliakin (Eds)
© 2023 The Author(s), ISBN 978-1-003-29912-7
Open Access: www.taylorfrancis.com, CC BY-NC-ND 4.0 license

A case study of the ground improvement works for the TBM tunneling in composite stratum

S.H. Cheng
National Taiwan University of Science and Technology, Taipei, Taiwan

Ricky K.N. Wong, H.Y. Hsu & Isaac T.Y. Wong
SANSHIN Corporation Ltd., Taipei, Taiwan

C.H. Chen & C.J. Chen
Department of Rapid Transit Systems, Taipei City Government, Taipei, Taiwan

ABSTRACT: This paper presents a case study of the ground improvement works on TBM tunneling for Taipei MRT in the east district of Taipei City. The TBM tunnel is mainly drilled in the composite strata which consist of alluvial deposits, colluvium deposits, and rock formation. The upper half of the improvement zone is a soft soil layer and the lower half of the improvement is a hard rock layer (Sandstone or Shale). The soft soil layers outside of the tunnel-shaft interface require jet grouted body to increase their strength and decrease their permeability. Also, in order to tunnel through the composite stratum, it needs to carry out jet grouting in the soft ground to increase the strength of the soil layer to homogenize the excavation section. Since the hard rock cannot be used by jet grouting, permeability grouting is used to decrease its permeability. In this case, the jet grouting and the permeability grouting were used to overcome the strata with different geological conditions to meet the strength (self-supporting) and to reduce the permeability of the ground. The ground improvement results show that for the jet grout zone, the total core recovery is greater than 90%, the in-situ permeability tests and the laboratory uniaxial compression strength meets the specification requirements. For the TAM grouting zone, the permeability coefficient k carried out by in-situ permeability tests was less than 1×10^{-5} cm/sec. Before breaking the cutter face on the diaphragm wall for the TBM to enter from the shaft, the horizontal leakage tests of the up track and down track at the west side station have been completed. Without supplementary grouting, the permeability coefficient k of all horizontal permeability tests is less than 1×10^{-5} cm/sec.

1 INTRODUCTION

Various ground improvement methods have been adopted in the construction of the Taipei Mass Rapid Transit system (Taipei MRT system). The jet grouting and the chemical grouting technique have been widely used in the tunnel-shaft interface for the TBM launching and arrival works. This study reports the ground improvement works for the Taipei MRT Xinyi East Extension Line in the east district of Taipei City. The TBM tunnels pass through the composite stratum when the TBM arrives at the shaft of the station. The soft soil layers of the tunnel-shaft interface require jet grouted to increase their strength and decrease their permeability. Also, to tunnel through the composite stratum, it needs to carry out jet grouting in the soft ground layer to increase the strength of the soil layer to homogenize the excavation section. Since the hard rock cannot be used by jet grouting, chemical grouting is used to decrease its permeability. In this study, the commercial Rapidjet jet grouting method and the TAM grouting with chemical grouting are used to overcome the strata with different geological conditions to meet the self-supporting and water-proofing required for TBM tunneling. The grouting results show that the total core recovery in the jet grouting zone is greater than

DOI: 10.1201/9781003299127-86

90%, the permeability coefficient k is less than 1×10^{-5} cm/sec and the uniaxial compression strength (UCS) meets the specification requirements (28-days UCS of sand and clay layers is not less than 2.0 MPa and 1.2 MPa). In addition, in-situ permeability tests were carried out in the TAM grouting zone, and the permeability coefficient k was found to be less than 1×10^{-5} cm/sec. The performance and the results of the jet grouting and the TAM grouting works are presented in the following sections.

2 SITE CONDITIONS

The location and layout for the study case of Taipei MRT are shown in Figure 1. It consists of the R03 station, the cross-over, the R03 tail rail ventilation shaft with the cut and cover method, and the shield tunnels with shield machines. The shield tunnel in this study adopts a circular section with an inner diameter of 5.6 m and an outer diameter of 6.1 m. The shield machine adopts the earth pressure balance critical, in which the total length of the shield machine is 8.5 m with an outer diameter of 6.24 m as shown in Figure 2. The lengths of the shield tunnels from the east side of the R03 station to the R03 tail rail ventilation shaft are about 524 m, and the overburden depth is about 20.8 m to 22.0 m. The shield tunnel is mainly drilled in the composite strata which consist of alluvial deposits, colluvial deposits, and rock formations.

The soil condition near the ground surface mainly consists of fill material (SF), alluvial deposit (CL/CH/ML/SM) with a thickness of 10-20 m and a very soft to weak consistency, and underneath is soft to medium-hard, moderately weathered to fresh sandstone (SS), shale (SH). The soil-rock interface is occasionally mixed with colluvial deposits; the main components are gravel and rock blocks. The physical properties of soil near the east side/west side of the R03 station and R03 tail rail ventilation shaft are shown in Table 1. Additionally, the soil and rock properties along the R03 station to the R03 tail rail ventilation shaft are shown in Figure 3. It indicates that the q_u value of the rock formation is > 1000 kgf/cm^2, and the RQD of the rock formation is between 0 and 100. The groundwater level was about 0 ~ 1.8 m below the ground surface.

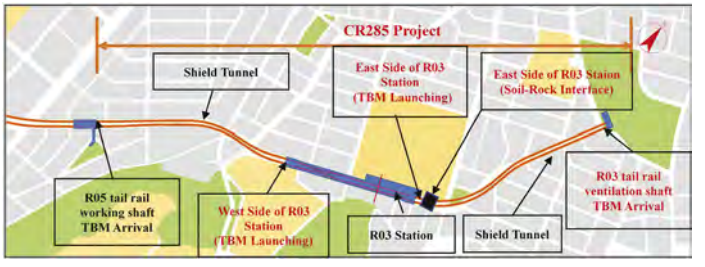

Figure 1. The location and layout for the study case of Taipei MRT.

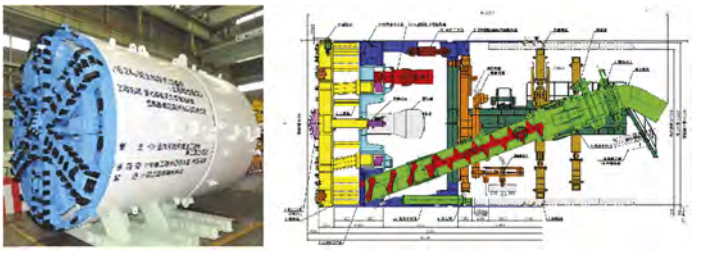

Figure 2. The TBM shield machine of this study case (Chen et al., 2020).

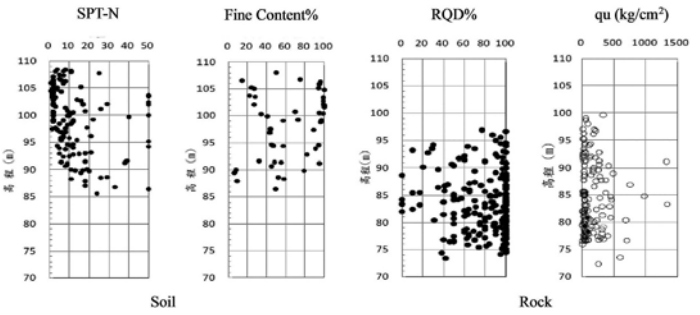

Figure 3. Soil and rock properties along R03 station to R03 tail rail ventilation shaft (Chen et al., 2020).

Table 1. The soil properties at the west side, east side, and tail rail ventilation shaft of R03 station.

at the west side:					
Soil Layer	Depth (m)	Soil Type	SPT-N (Avg.)	Unit Weight (kN/m^3)	Water Content (%)
1	1.6	SF	-	-	-
2	16.5	CH-CL	2.2	15.89~17.85	41~52
3	21.4	CL	4.5	18.05~18.34	31~37
4	22.8	SM	53	17.95~18.25	29~32
5	35.0	SS/SH	100	-	-
at the east side:					
Soil layer	Depth (m)	Soil type	SPT-N (Avg.)	Unit weight (kN/m^3)	Water content (%)
1	1.6	SF	-	-	-
2	8.3	CH	2.5	16.30	61
3	15.0	ML-SM	8.8	18.24~19.72	24~34
4	23.3	CL	6.7	16.38~17.10	42~49
5	33.5	SS	100	-	-
at the tail rail ventilation shaft:					
Soil layer	Depth (m)	Soil type	SPT-N (Avg.)	Unit weight (kN/m^3)	Water content (%)
1	1.6	SF	-	-	-
2	11.8	CH~CL	5.1	16.48~18.25	28~43
3	20.0	SM-CL-ML	65	19.32~21.29	16~23
4	35.0	SS/SH	100	-	-

3 GROUTING WORKS

3.1 *Grouting for tunnel launching and arrival*

For the grouting works of this study case, the soft soil layers outside of the tunnel-shaft interface for tunnel launching and arrival require jet grouting to increase soil strength and decrease ground permeability, but the hard rock layer cannot be performed with jet grouting. Therefore chemical grouting is used to reduce the permeability. In this case, jet grouting (Rapidjet Method) and chemical grouting (TAM method) were used to overcome the strata with different geological conditions and meet the strength and reduce the permeability of the ground. The grouting work and improved zone for the launching and the arrival shield of the presented case as shown in Figure 4 and Table 2.

3.2 *Grouting for soil-rock interface*

When the TBM tunnels pass the interface of the alluvial layer and a colluvial layer or rock formation, it increases the possibility of over-excavation. This is because the stratum on the shield machine's cutting blade disk is soft at the top and hard at the bottom, so the TBM becomes liable

to offset when drilling and digging. The strength of mixed strata varies significantly in some areas of this study case. To minimize the impact of drilling on the surrounding area, ground improvement is carried out for these areas. This study introduces the grouting method of the soil-rock interface located on the east side of the R03 station as shown in Figure 5. The soil layer above the soil-rock interface is performed by jet grouting (Rapidjet method) to ensure that the shield machine does not shift up or cause the ground to collapse due to improper digging. Figure 5 shows the position of the soil-rock interface, grouting zone, and adopted grouting method. However, the TAM grout of the soil-rock interface area is always for building protection.

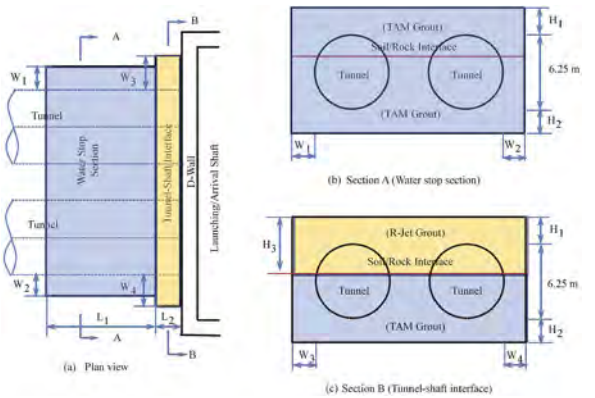

Figure 4. Grouting plan and profile for launching and arrival shield of the study case (Chen et al.,2020).

Table 2. Grouting method and improved zone for launching and arrival shield of the study case.

Location	Center of tunnel EL (m)	Grouting method	Improved range (m)								
			L_1	L_2	H_1	H_2	H_3	W_1	W_2	W_3	W_4
East Tunnel	Launching 85.6	R-Jet/ TAM Grout TAM Grout	7.8	2.2	4	2	6.5	2	2	2.7	0.5*
	Arrival 84.6	R-Jet/ TAM Grout TAM Grout	8.8	2.2	2.5	2	5.5	2	2	2.7	2.7
West Tunnel	Launching 85.6	R-Jet/ TAM Grout TAM Grout	8.8	2.2	2.5	2	4.4	2	2	2	2
	Arrival 89.9	JSG **	-	10.5	2.5	2	10.8	-	-	2	2

Noted: * Close to D-Wall of Entrance C; ** Not included in this report

4 GROUTING METHOD

4.1 *Jet grouting*

4.1.1 *Working procedure*

The jet grouting method used in this study is a double-fluid jet grouting system, commercially named the Rapidjet method. Considering that part of the clay layer has occasionally mixed with a colluvial deposit, and the subsequent construction of double tube double packer grouting requires drilling of sandstone and shale, the jet grouting adopts a rotatable percussion

drilling machine to drill first. The drilling is used directly in the subsequent double tube double packer grouting. The construction process of Rapidjet is shown in Figure 6.

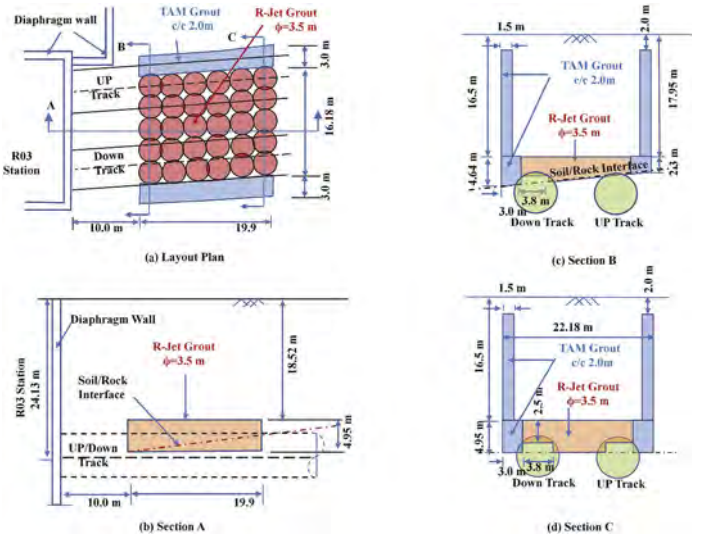

Figure 5. The soil-rock interface, grouting zone, and adopted grouting method the at east side of R03 station.

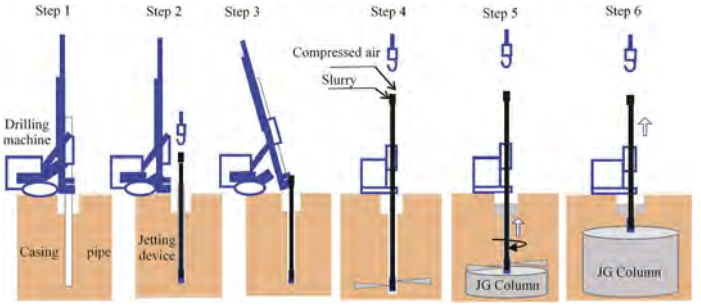

Figure 6. Rapidjet working procedure (Rapidjet association, 2019).

4.1.2 *Material and grouting parameters*

The jet grouting parameters of this method are similar to those proposed by Burke (2004) and Lunardi (1997). The grout jet was shrouded with compressed air (pa = 0.7–1 MPa) and grouting pressure (p_g = 33–37 MPa). The grout flow rate (q_g) was increased to 540 liters/min to enhance its cutting ability and cutting distance while also enhancing the mixing of cement grout with the soil in situ. In the drilling of jet grout holes, rotary drilling and water jet are used to pre-drill the holes. The rotation force provided by the drilling machine is then transferred to the drill bits at the tip of the drill rod. Two nozzles were mounted on the opposite side of the monitor with a 25 mm difference in elevation. The parameters used in this grouting are listed in Table 3. Materials required for Rapidjet are as follows: (1) groundwater is required, and it must not contain oil, acid, alkali, organic matter, or other harmful substances that affect solidification, durability, and strength; (2) cement binder HSC301 material for jet grouting.

Table 3. Jet grouting parameters used in the Rapidjet grouting.

Parameter	Value
Water cement ratio, W/C	1.4
Jetting pressure of air, p_a (MPa)	0.9
Jetting pressure of grout, p_g (MPa)	35±10%
Flow rate of grout, q_g (liters/min)	180 per nozzle
Nozzle diameter, d_0 (mm)	4.24
Number of nozzles on the monitor	2
Rotation speed of the rod, R_s (rad/s)	0.52
Lift up or withdrawal rate of rod, v_s (m/s)	1.19×10^{-3}
Lift up step, ΔS_t(cm/step)	2.5

4.2 *TAM grouting*

4.2.1 *Working procedure*

TAM grouting can be applied to any grouting material in any grouting hole, which is one of its irreplaceable advantages. Generally speaking, when the grouting zone, location of grouting holes, and grouting ratio are decided, pressure control or quantity control can be used for grouting practice. Influenced by non-uniform and anisotropy of soil, pressure control grouting as well as quantity control grouting, can perform better grouting efficiency. It is especially apparent when the value of grouting pressure itself is not so influential and relative change in pressure is essential. Relevant construction procedures are shown in Figure 7:

Step1: Boring

The hole was bored with a 125 mm diameter casing using a high-efficiency rotary percussion boring machine. To prevent disturbance of the surrounding ground, double pipe boring was used and the spoil was withdrawn through the space between the inner and outer pipes. Meanwhile, to ensure the reliability of ground investigation, we also keep track of drilling slag to understand the ground condition more clearly.

Step2~Step 4: Sealing compound injection grouting and external pipe placing

After boring the holes, the inner pipe of the double pipe withdrew, and after injecting the sealing compound the TAM tube was driven into the hole. In order not to cause obstruction when carrying out the drilling work and to withstand the grouting pressures, a TAM tube made of PVC was used. The axial spacing of injection openings in each TAM tube was maintained at 33 cm, and fitted with a packer to seal and prevent the inflow of groundwater/the flow of grout.

Step5~Step 6: The grouting operation

An internal inner pipe, at the end of which is fitted two stages of packing, was inserted into the TAM tube, and step grouting was carried out at predetermined depths.

4.2.2 *Material and grouting parameters*

Two stages of grouting were used in the grouting work: the first-stage grouting used cement and bentonite grout (CB grout) with an injection volume of 5~8 % soil porosity for interlayer. Similarly, a solution-type sodium silicate grout (with MK reagent) with a volume of 30~32 % soil porosity was injected during the second stage. The first-stage CB grouting was aimed to fill and compact the voids in the ground (mix proportions as shown in Table 4). The grouting was not stopped until the mentioned design grouting quantity was reached. Such grout intrusions compress the sandy soil, and make the improved zone homogenization. In comparison, the injection of sodium silicate grout into the sandy layer was for low-permeability purposes and increased its overall strength. TAM Grout injection parameters, grout ratio, and grout volume for the project as shown in Table 5 to Table 7.

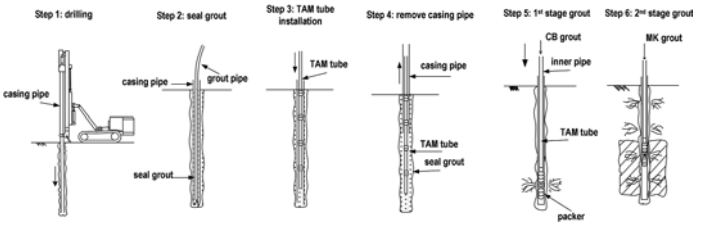

Figure 7. TAM grouting procedure.

Table 4. Summary of mix proportions for CB grout and MK grout.

CB grout	Mix proportion	MK grout	Mix proportion
Cement binder	150~250 kg	Sodium silicate	250 L
bentonite	40 ~ 80 kg	MK reaction	35 ~ 65 L
Water	888~937 L	Water	685~715 L
Total	1000 L	Total	1000 L

Table 5. TAM grouting parameters.

Grouting method		TAM Grout (Double packer method)
Grouting mode		1 shot
Grouting length per step		1 step=0.33 m
Grout flow		q =4 ~15 L/min
Gel Time	CB	-
	MK	≈ 60 min
Quantity control		Flow rate and pressure
Grout type	1st Grout	CB
	2nd Grout	MK

Table 6. TAM grouting ratio.

		Grout ratio %		
Grouting zone	Soil type	1st Grout	2nd Grout	Total
Tunnel-shaft interface	SS/SH	5	10	15
Water-stop section	CL/ML	10	10	20
	SM	15	20	35
	SS/SH	5	10	15
East side of R03 station (Soil-Rock Interface)	CL/ML	10	15	25

Remark: If the filling is completed according to the grouting rate but the pressure is low, the MK material will be used to inject about 3 to 5% of the inspection and supplement grouting.

5 QUANTITY CONTROL AND QUALITY ASSURANCE

5.1 *TAM grout pressure recorded*

Although the value of grouting pressure observed at each step is not so meaningful, the relative change itself is essential. It proves it's helpful to record the 1st and 2nd grouting pressure at the injection hole in each step (33 cm) by comparing them with each other to evaluate the grouting effects and detect the insufficiently-improved areas (Hayashi and Matsubayashi, 1996). TAM

grout pressure was recorded for 1st grout, 2nd grout, and supplement grout as shown in Table 8. The average pressures on the clayey, sandy, and sandstone/shale range from 6.4~8.0, 11.8~13.0 and 7.0~13.3 kg/cm^{2,} respectively.

Table 7. TAM Grouting volume.

Location	Soil volume (m^3)	Grout ration (%)	Nos	Grout volume (m^3) Design	Actual	Soil type
West side of R03 station	853.6	20	53	170.7	186.6	CL/ML
	1569.9	15		235.5	250.4	SS/SH
East side of R03 station	1086.2	20	51	217.2	224.0	CL/ML
	1257.4	15		188.6	191.8	SS
Tail rail ventilation shaft	960.2	35	49	336.2	349.4	SM
(Arrival)	1180.6	15		177.1	182	SS/SH
East side of R03 station (Soil-Rock Interface)	591.0	25	38	147.8	148.2	CL/ML

Table 8. Results of TAM grout pressure recorded.

Location	Soil type	Average grout pressure (kgf/cm^2) 1st Grout (CB)	2nd Grout (MK)	Supplement grout (MK)
West side of R03 station	CL/ML	6.5	7.3	7.7
(Launching)	SS/SH	7.0	8.1	7.6
	Remark: When the pressure is lower than 6.5 kgf/cm^2, apply about 3.0% MK supplementary grouting, and most of the grouting pressure at this position has increased.			
East side of R03 station (Water-Stop Section)	CL/ML	8.0	7.5	8.0
	SS/SH	9.0	9.7	11.4
	Remark: When the pressure is lower than 6.5 kgf/cm^2, apply about 3.0% MK supplementary grouting, and most of the grouting pressure at this position has increased.			
Tail rail ventilation shaft	SM	12.7	11.8	13.0
(Arrival)	SS/SH	13.2	13.3	13.3
	Remark: When the pressure is lower than 9.0 kgf/cm^2, apply about 3.5% MK supplementary grouting, and most of the grouting pressure at this position has increased			
East side of R03 station	CL/ML	6.4	9.1	-
(Soil-Rock Interface)	Remarks: The purpose of the improvement of the low-pressure zone on both sides of the soil-rock interface is to protect the adjacent buildings, and no supplementary grouting is applied.			

5.2 *Permeability test of TAM grout zone*

According to the construction specification, every 100 grout holes should be tested with at least 3 holes. The permeability coefficient k $\leq 1\times10^{-5}$ cm/sec. Table 9 shows the results of the permeability of the TAM grout zone. All test results meet the design requirement.

5.3 *Core sampling and permeability test of the jet grouted zone*

According to the construction specification, every 100 grout holes should be sampled with at least 3 holes. The total core recovery (TCR) of sampling was ≥ 90%, the 28-day uniaxial compressive strength (UCS) of each sample ≥ 20.0 kgf/cm^2 for sandy soil, and ≥ 12.0 kgf/cm^2 for clayey(silty)

soil, and the permeability coefficient k $\leq 1\times10^{-5}$ cm/sec. Table 10 shows the results of coring, UCS, and permeability of the Jet grout zone. All test results meet the design requirement.

Table 9. Permeability test results of TAM grouted zone.

Location	Test No	Depth, E.L. (m)	Permeability k, (cm/sec)
Tail rail ventilation shaft (Arrival)	T-1	87.75~88.75	2.36×10^{-07}
	T-2	84.30~85.30	2.66×10^{-07}
	T-3	81.00~82.00	1.90×10^{-06}
West side of R03 station (Launching)	T-1	88.69~89.75	3.92×10^{-07}
	T-2	85.01~86.01	3.50×10^{-07}
	T-3	82.00~83.00	2.04×10^{-07}
East side of R03 station (Launching)	T-1	89.9~90.9	2.25×10^{-06}
	T-2	86.0~87.0	9.78×10^{-08}
	T-3	82.0~83.0	1.95×10^{-07}

Table 10. The core sampling and permeability test results of jet grouted zone.

Location	Test No	TCR %	Age (Day)	UCS (kgf/cm^2) Top/ Mid./Bot.	Permeability k, (cm/sec)
West side of R03 station (Launching)	T-1	100.0	28	26.0/40.0/26.0	6.40×10^{-06}
	T-2	96.0	28	36.0/28.0/46.0	2.58×10^{-06}
	T-3	94.0	27	12.0/20.0/28.0	6.75×10^{-06}
East side of R03 Station (Water-Stop Section)	T-1	97.9	28	31.8/22.4/45.8	5.20×10^{-06}
	T-2	96.1	28	27.5/34.0/39.3	8.15×10^{-06}
	T-3	94.6	27	42.0/44.0/33.0	5.65×10^{-06}
Tail rail ventilation shaft (Arrival)	T-1	98.9	28	18.2/25.9/34.2	5.79×10^{-07}
	T-2	98.5	28	19.6/26.6/35.6	1.89×10^{-06}
	T-3	97.0	27	17.4/30.0/48.4	2.37×10^{-06}
East side of R03 station (Soil-Rock Interface)	T-4	98.6	28	27.0/32.5/23.3	-
	T-5	96.5	26	31.9/16.5/28.8	-
	T-6	95.0	27	17.5/29.9/48.3	-

5.4 *Horizontal leakage tests in the grouting zone*

Before breaking the mirror face on the diaphragm wall for the shield machine to enter or from the shaft, it is critical to conduct leakage tests for the grouted zone behind the wall. Typically, horizontal boreholes were drilled at the mirror-face location, through the wall into the grouted zone to the desired length. Then the valve attached to the horizontal borehole is opened to measure the groundwater inflow rate through the grouted zone into the working shaft. The supplement of the grout will achieve the purpose of safely breaking the mirror. According to the construction specification, with five holes within the mirror frame, and nine holes outside the mirror frame, the depth is at least 2 m into the grouted zone. The depth of the hole is at least 1 hole must reach the front edge of the outermost row of the grouted zone or the position 1m before the grouted zone. After drilling the leaking amount of each test, the hole is measured by the measuring cup with a meter after the water leakage is stable. The permeable field test uses a spherical flow method to determine the permeability coefficient. The design permeability coefficient k $\leq 1\times10^{-5}$ cm/sec. The horizontal leakage tests of the up track and down track at the west side of the R03 station for launching as shown in Figure 8. The depth of the center hole was 8.6 m into the grouted zone, and the depth of the other holes was 2 m. There were 5 holes inside the mirror frame that were equally distributed in the center diameter of 4.4 m, and the 9 holes outside the mirror frame distributed the hole positions evenly within the center diameter of 7.2 m. A total of 28 horizontal leakage tests were carried out in the up and down track grout zone, test results of permeability k range 0.0~9.19×10-7 cm/sec, and the maximum quantity of water was 20 cc/min at the center hole. All tests met the design requirement and were without supplementary grouting.

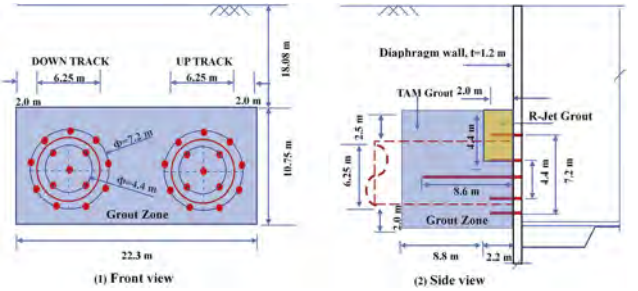

Figure 8. Horizontal leakage tests at the west side of the R03 station for launching.

6 CONCLUSIONS AND RECOMMENDATIONS

This study reports the grouting works for the Taipei MRT Xinyi East Extension Line in the east district of Taipei City. The TBM tunnels through the composite stratum at the east side of the R03 station. The upper half of the improvement zone is a soft soil layer and the lower half of the improvement is a hard rock layer (Sandstone or Shale). The Rapidjet Method and the TAM grouting were used to overcome the strata with different geological conditions to meet the self-supporting and water-proofing required for the TBM break-in and break-out. The following conclusions can be drawn:

1) All the tests carried out in the jet grouted and TAM grouted zone meet the design requirement. For the jet grouted zone: the 28-day uniaxial compressive strength (UCS) of each sample was ≥ 20.0 kgf/cm^2 for sandy soil, and ≥ 12.0 kgf/cm^2 for clayey (silty) soil, and the permeability coefficient k ≤1×10^{-5} cm/sec. For TAM grouted zone: the permeability coefficient k ≤1×10^{-5} cm/sec. For the horizontal leakage test in the grouting zone at the west side of the R03 station, the permeability coefficient k was ≤1×10^{-5} cm/sec.
2) The TBM at the west side of the up-track tunnel of the R03 station was launched smoothly and without supplementary grouting. Therefore, careful planning of grouting methods can significantly shorten construction time and reduce construction costs.
3) In addition, the construction of the diaphragm wall for the TBM launching and arrival works may have an adverse effect on the grouting works (such as the verticality of the grout holes, the impermeability of grouting, etc.), a row of low-pressure inspection grout (TAM grout) can be accessional at the interface between the diaphragm wall and the ground, it can let the grouting works effect more perfect.

REFERENCES

Burke, G.K., 2004. "Jet Grouting Systems: Advantages and Disadvantages." *GeoSupport 2014: Drilled shafts, Micropiling, Deep mixing, Remedial method, and Specialty foundation systems*, Orlando, Florida, American Society of Civil Engineers, New York, pp. 218–234.

BES Engineering Corporation/DAIHO Corporation Taiwan Branch (2018)," Shield tunnel launching and arrival/soil-rock interface ground improvement works for Xinyi East Extension Line CR285" (In Chinese).

Chen Jian Ren, Zhang Zheng Lin, Yang Gwo Rong, Guo Jin Wei 2020, "Design Consideration and Construction Plan of Shield Tunneling Through Composite Stratum in Edge of Taipei Basin", *Rapid Transit Systems and Technology*", N0.55, pp. 99–119 (In Chinese).

Hayashi K. and Matsubayashi Y. 1996. "Chemical grouting contributed to the urban development in Hiroshima city", *Proceedings of Grouting and Deep Mixing, Japan, pp. 299-302*.

i-Grout association 2020. *4. Chemical Grouting Guideline (Version 1)*. Japan: i-Grout association.

Lunardi, P., 1997. "Ground Improvement by Means of Jet-Grouting." *Proc. Inst. Civ. Eng. Ground Improv.*, Vol. 1, Issue 2, pp. 65–85. https://doi.org/10.1680/gi.1997.010201

Rapidjet association 2019. *Rapidjet Method Jet Grouting Guideline (Version 1)*. Japan: Rapidjet association.

Smart Geotechnics for Smart Societies – Zhussupbekov, Sarsembayeva & Kaliakin (Eds)
© 2023 The Author(s), ISBN 978-1-003-29912-7
Open Access: www.taylorfrancis.com, CC BY-NC-ND 4.0 license

Monitoring-based approach for stability prediction of embankments on port-said clay

Mohamed H. Mahmoud
WSP Dubai, U Bora Tower Residence Parking, Dubai, UAE

Mohamed F. Mansour
Department of Structural Engineering, Ain Shams University, Cairo, Egypt

ABSTRACT: This paper presents the results of a numerical study carried out to investigate the stability of preloading embankments on the very soft to firm Port-Said Clay deposit in north-eastern Egypt. Characteristic stability assessment charts were developed to predict the factor of safety against deep-seated failure of preloading embankments based on routine field measurements such as the vertical and horizontal displacements. The results were compared with well-established methods. A new chart is also developed in this study to predict the preloading embankment stability based on horizontal displacement measurements at the embankment toe.

1 INTRODUCTION

Soft clays are often classified as one of the most problematic soil types in terms of their engineering behaviour. Preloading is one of ground improvement methods that induces significant improvement to soft clay. Upon unloading followed by reloading to the operational loads, the compressibility would be governed by the unloading-reloading, rather than the primary compression index. In order to accelerate the consolidation process, particularly for thick clay deposits, sand drains or Prefabricated Vertical Drains (PVD) are installed.

Preloading embankments are monitored for vertical and horizontal displacements in order to control stability and observe any signs of approaching failure. Matsuo and Kawamura (1977) developed a chart to determine the failure load ratio of an embankment resting on soft ground. It based on field measurements during construction of preloading embankments on different types of soft ground and backed by numerical analysis. It should be noted, however, that Matsuo and Kawamura (1977) considered the non-linear elastic analysis to simulate shear deformations in the undrained condition, and an elastic analysis based on Biot's equations to simulate the behaviour during consolidation. These constitutive models were relatively simple in terms of simulation of the soft clay behaviour. Advanced constitutive models based on the critical state theory (Roscoe et al., 1963; Burland, 1965) have been developed over the last decades to better simulate the constitutive behaviour of soft clay materials such as the Modified Cam Clay (MCC) Model (Roscoe and Burland, 1968), the Soft Soil (SS) Model, and the Soft Soil Creep (SSC) Model. The use of advanced constitutive models would have contributed to a more reliable modelling of the soft clay behaviour.

El-Tina plain, located to the east of Port-Said City on the Mediterranean Sea shore in Egypt, consists of a thick deposit of very soft to firm clay known as Port-Said Clay (Hamed et al., 2017a; and Hamed, 2017). The very soft to firm Port-Said Clay represented the delta of an old tributary of the Nile River that dated back to the Holocene Period. The Port-Said Clay was deposited in a marine environment due to the transgression and regression of the Mediterranean Sea shoreline (Ibrahem, 2002; Abdallah, 2006). Geotechnical characterization of Port-Said Clay

DOI: 10.1201/9781003299127-87

and its interaction with quay walls and tunnels were investigated in previous studies (Hamed et al., 2017(a, b); Mansour et al., 2021).

In this paper, the behaviour of a preloading embankment on Port-Said Clay is investigated by numerical analysis. The main objective is to develop characteristic stability assessment charts for preloading embankments resting on Port-Said Clay. The charts would relate the displacement routinely measured in projects involving an embankment on soft clay to the factor of safety against deep-seated failure of the embankment slopes. The numerical study is carried out using the characteristic properties of Port-Said Clay (Hamed et al., 2017a) and the critical state theory-based SSC Model to simulate the constitutive behaviour of Port-Said Clay.

2 PROBLEM CONFIGURATION

The ground conditions in the East of Port-Said region generally consist of an upper crust layer ranging in thickness from 0.5 to 7.4 m followed by the very soft to firm Port-Said Clay deposit to a depth of up to 50 m. The Port-Said Clay layer is underlain by very dense sand with intrusions of very stiff clay. The groundwater table depth ranged from 0.0 to 4.3 m below the ground surface (Hamed et al., 2017b; Rizos et al., 2018). The ground profile considered in this study consisted of an upper 0.5m-thick layer of fill underlain by Port-Said Clay to a depth of 50 m below ground surface where a very dense sand layer was encountered. The groundwater table was taken at 1.3 m below the ground surface (Hamed et al., 2017b).

Preloading embankments are designed such that a minimum overconsolidation ratio (OCR) of 1.1 is achieved after unloading of the preloading embankment and application of the operational loads. This requirement in preloading design ensures that the settlement due to operational loads will be governed by the unloading-reloading/swelling index rather than the primary compression index. The preloading embankment considered in the present study had a height of 6 m, crest width of 65 m and side slopes of 2H: 1V, and consisted of sand fill.

3 METHODOLOGY

The numerical analysis was carried out using the plane strain two-dimensional finite element program PLAXIS (Brinkgreve et al., 2018). Different soil layers were modelled using the 15-node triangular elements. A sensitivity analysis was carried out to determine the appropriate distance to the lateral and bottom boundaries of the model so as to ensure negligible effects of the boundaries on vertical and horizontal displacements. Hence, the model depth and width were taken 60 and 215 m, respectively. The model considered symmetric plane strain configuration. The vertical boundaries of the model were assigned zero lateral movements. A closed flow boundary was defined along the embankment centre. The bottom boundary was restrained against movement in the vertical and horizontal directions and was considered permeable (sand formation).

The embankment fill and lower dense sand, which were modelled using the Hardening Soil Model. While, the upper crust, which was modelled using the elastic perfectly-plastic constitutive model with Mohr-Coulomb failure criterion. Ali et al. (2016) pointed out to the inability of the SSC Model to reasonably predict actual deformations at shallow depths, where the surficial layers are usually overconsolidated. The Port-Said Clay was modelled using the SSC Model, which is an elastic-plastic strain hardening model based on the principles of the critical state soil mechanics (Roscoe et al., 1963; Burland, 1965). The different SSC Model parameters for Port-Said Clay were determined based on the characterization carried out by Hamed et al. (2017a). The primary compression and swelling indices (C_c and C_s) were taken 0.75 and 0.105, respectively. The initial void ratio (e_o) was taken 2.0 (Hamed et al., 2017b). The coefficient of secondary consolidation ($C_{\alpha e}$) was taken 0.011. The drained friction angle (ϕ') was determined from consolidated drained triaxial tests, and was equal to 22 degrees. The Port-Said clay layer was divided into nine (9) sublayers in order to account for the variations with depth of the plasticity index, which affects the at-rest earth pressure coefficient, and hydraulic conductivity (Hamed et al., 2017a; Hamed, 2017).

Six lifts were considered for the embankment construction. Each lift had a thickness of 1.0 m except the first one which had a thickness of 2.0 m, since this height was found to fulfil a factor of safety against embankment slope failure of more than 1.1. The time increments considered in the analysis for each lift are illustrated in Table 1. The time increments corresponding to each lift represent the durations at which the results were extracted.

Table 1. Time increments corresponding to each construction lift.

	Time increments considered in analysis (days)																
Lift	Δ T0	Δ T1	Δ T2	Δ T3	Δ T4	Δ T5	Δ T6	Δ T7	Δ T8	Δ T9	ΔT 10	ΔT 11	ΔT 12	ΔT 13	ΔT 14	ΔT 15	ΔT 16
L2 (2 m)	0.5																
L3 (3 m)		2	10	20	40												
L4 (4 m)					10	15	30	60	120								
L5 (5 m)									0.5	30	60	120	240				
L6 (6 m)													0.5	60	120	240	350

4 NUMERICAL MODEL VERIFICATION

A full-scale earth embankment (TS1) was designed, constructed and monitored at the proposed Second Bangkok International Airport in Nong Ngu Hao, East Bangkok, Thailand (Bergado et al., 2002). A numerical model is developed in this study to verify and validate the use of the SSC Model to predict the vertical and horizontal displacements of embankments constructed on soft clay deposits. The field monitoring program, documented by Bergado et al. (2002), involved measurement of the development with time and embankment construction stages of the vertical displacement at the embankment centre and the horizontal displacement at the crest.

A two-dimensional plane strain model, based on the finite element method, was developed in the present study to simulate the different stages of the TS1 embankment construction over the very soft to stiff Bangkok Clay deposit. The commercial program PLAXIS (Brinkgreve et al., 2018) was employed to carry out the analysis. Different soil layers were modelled using the fifteen node triangular elements. The installed PVD's were modelled using the drain option offered in the utilized program (Brinkgreve et al., 2018). The elastic perfectly plastic model with Mohr-Coulomb failure criterion was adopted to simulate the behaviour of the TS1 embankment fill, sand blanket, clayey sand and the lower dense sand layer. All Bangkok Clay layers were modelled using the SSC Model. The parameters adopted for different soil layers were based on the engineering properties presented in Bergado et al. (1995) and Samieh et al. (2010). Figure 1 presents the measured and predicted vertical displacement (settlement) at the embankment centre. It can be observed that the predicted settlement exceeded the measured settlement during intermediate stages of the embankment construction. However, the final settlement at the end of the monitoring period, i.e. at about 400 days, was in good agreement with the measured settlement. This overestimation by the numerical model during consolidation could be attributed to the presence of low-permeability sublayers within the main Bangkok Clay formation causing some delayed consolidation, which might not have been considered in the primary consolidation parameters reported by Bergado et al. (1995) and, hence, was not captured by the numerical model. Figure 2 presents the measured and predicted horizontal displacement at the embankment crest. The available horizontal displacement measurements were available at a time of about 240 days. Hence, the numerical analysis results were extracted at the same time. The results indicate that the maximum lateral displacement occurred within the very soft Bangkok Clay layer at a depth of about 3.5 m below the ground surface. In general, the horizontal displacement significantly increased within the very soft and soft Bangkok Clay layers. The numerical model underestimated the maximum horizontal displacement by about 14%. The results of the numerical verification indicated that the SSC Model can be utilized to reasonably predict the vertical and horizontal displacement of embankments resting on soft clay deposits.

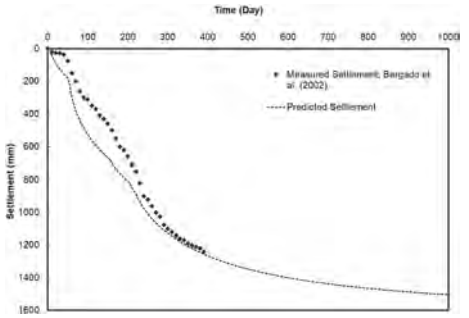

Figure 1. Measured and predicted settlement at the TS1 embankment centre (point A).

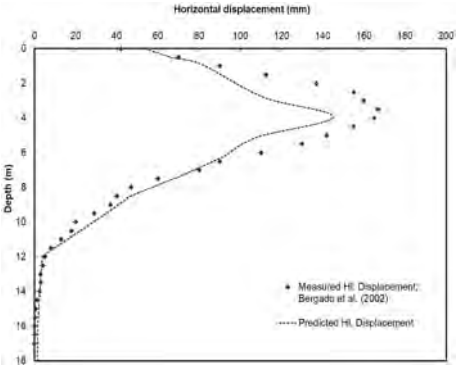

Figure 2. Horizontal displacement profile at the TS1 embankment crest (along line A-A).

5 PRELOADING EMBANKMENT ON PORT-SAID CLAY

This section presents the results of the numerical study carried out on Port-Said Clay in order to assess the stability of the preloading embankment described in the PROBLEM CONFIGURATION Section by developing relationships between the factor of safety against deep-seated failure and routine field measurements including the vertical and horizontal displacements at the embankment centre and toe, respectively.

5.1 *Analysis procedure*

The numerical analysis was carried out in different phases as follows:

- Undrained analysis: This analysis type was adopted in the short-term condition right after placement of the preloading lift in order to calculate the excess pore water pressure.
- Consolidation analysis: This analysis type was adopted to simulate the dissipation with time of the excess pore water pressure during the consolidation process.
- Slope stability analysis: Stability analyses were carried out in each of the above analysis phases. The factor of safety against deep-seated failure was calculated using the c-phi reduction technique in the short-term condition (Brinkgreve et al., 2018).

5.2 *Analysis results and discussion*

The results were interpreted by calculating the factor of safety against deep-seated failure in the preloading embankment and the Port-Said Clay for different preloading lift heights and durations. The analysis results showed that, for lift heights of less than two meters, the critical slip surface was borne by the preloading embankment fill, and did not extend to the Port-Said Clay. Lift heights of two meters or more caused the critical slip surface to be deep-seated. Figure 3 shows a typical geometry of the slip surface, represented by incremental displacement contours, for an embankment height of 5 m. For each embankment height, the factor of safety, vertical displacement at the embankment centre and horizontal displacement at the embankment toe were calculated right after placement of the preloading lift and after different time increments representing different degrees of consolidation. The vertical and horizontal displacements were determined from the respective total displacement contours. Figure 4 shows a typical output of the horizontal displacement contours corresponding to an embankment height of 5 m.

The results are displayed in the same format of Matsuo and Kawamura (1977) and they are presented in Figure 5. The line connecting different data points represents the variation of the factor of safety (FS) since placement of each embankment lift until the end of the time period corresponding to each lift. This figure also shows the variation of the FS due to application of

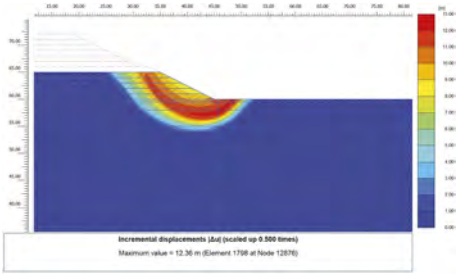

Figure 3. Contours of incremental displacement for one of the intermediate stages (embankment height = 5 m).

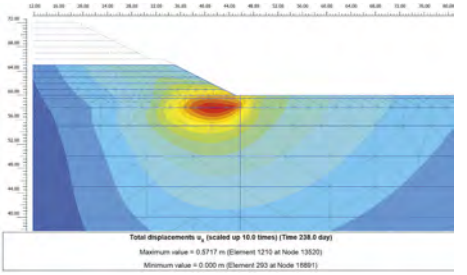

Figure 4. Horizontal displacement contours showing the location of maximum horizontal displacement (embankment height = 5 m).

a new preloading lift. As expected, the minimum FS for each preloading lift occurs in the initial stage right after placement of the additional lift (undrained stage). The FS increases with time due to dissipation of excess pore pressure with the ongoing consolidation process. The commercial software DPlot® was utilized to develop FS contours for different combinations of the horizontal to vertical displacement ratio and vertical displacement, as shown in Figure 6. The developed contour lines represent FS ranging from 1.05 to 1.35. Preloading embankments are typically designed to achieve short-term stability during construction where the target FS is in the order of 1.1 or 1.2. Hence, the developed FS contours will enable the design engineer to predict the preloading embankment stability based on field measurements of vertical displacement at the embankment centre and horizontal displacement at the embankment toe. The developed contours are considered characteristic to Port-Said Clay. A comparison is carried out between the Port-Said Clay-characteristic FS contours, shown in Figure 6, and the contours developed by Matsuo and Kawamura (1977), referred to herein as the MK FS contours. The comparison is shown in Figure 7. It can be observed that the FS contours characteristic to Port-Said Clay spanned over a bigger range of horizontal to vertical displacement ratio compared to the MK contours. Therefore, the use of the well-established MK contours for Port-Said Clay would require some judgement for δ/d values outside the range of FS contours. It is believed that Port-Said Clay exhibits high lateral displacements in the toe area due to the very soft to soft consistency in the upper twenty meters (Hamed et al., 2017a). It can be also observed that the Port-Said Clay FS contours are narrower than the MK FS contours. In other words, the variation of the FS for preloading embankments on Port-Said Clay is more sensitive to changes in the vertical and horizontal displacements than the predicted values based on Matsuo and Kawamura (1977) diagram. Furthermore, the Port-Said Clay contours are more optimistic in terms of the corresponding FS against deep-seated failure.

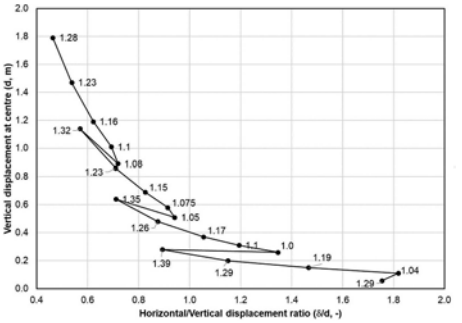

Figure 5. Variation of the FS against deep-seated failure for an embankment on Port-Said Clay.

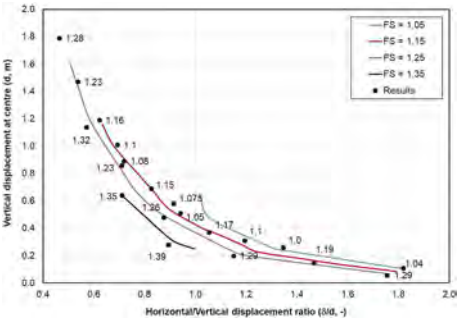

Figure 6. Characteristic factor of safety (FS) contours for Port-Said Clay.

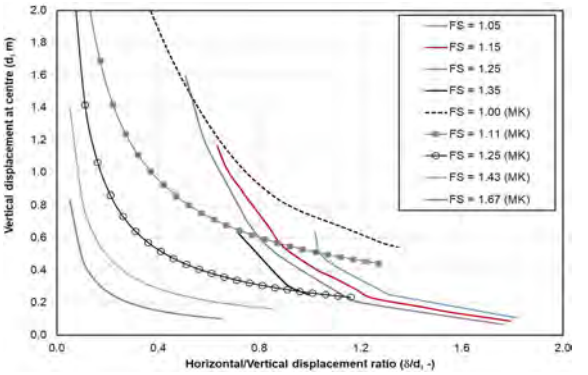

Figure 7. Comparison between the Port-Said Clay FS contours and the Matsuo-Kawamura (MK) FS contours.

The observed discrepancy between the contours developed in this study and the Matsuo and Kawamura (1977) contours could be attributed to the difference in modelling the constitutive behaviour of soft clay. Matsuo and Kawamura (1977) adopted the elastic nonlinear (hyperbolic) model to simulate the behaviour in undrained conditions. The consolidation behaviour was modelled by formulating Biot's multi-dimensional consolidation theory using the finite element method. These constitutive models could have represented the latest development at that time in terms of modelling the constitutive behaviour of soft soils. The comparisons provided in Matsuo and Kawamura (1977) indicated differences between the measured and predicted displacements of up to 250 and 70 mm in the vertical and horizontal displacement, respectively. On the other hand, the more robust SSC Model was utilized in this study, which enabled better agreement between the measured and predicted displacements of a soft soil deposit, i.e. Bangkok Clay, with similar geotechnical properties, as explained in detail in section 4.

The analysis results showed that the horizontal displacement reached a maximum value at a depth of about two (2) m below the toe level, which corresponded to a depth of about 1.5 m inside the Port-Said Clay layer. The pore water pressure should be measured at the same level of maximum horizontal displacement. Hence, the excess pore water pressure can be calculated, and the FS can be estimated.

6 CONCLUSIONS

This paper presents the results of a numerical study to develop a monitoring-based approach to predict the stability of preloading embankments on the very soft to firm Port-Said Clay deposit in north-eastern Egypt. The conclusions of the study can be summarised in the following points:

- Characteristic stability prediction charts have been developed to predict the factor of safety against deep-seated failure for preloading embankments resting on Port-Said Clay.
- The developed chart has a similar form to the chart developed by Matsuo and Kawamura (1977). However, the factor of safety prediction is different, which is attributed to the lack of advanced constitutive models at the time the Matsuo and Kawamura (1977) chart was developed. The Port-Said Clay characteristic chart is more optimistic in terms of the factor of safety against deep-seated failure.
- Characteristic charts should be developed for each soft clay deposit due to the uniqueness of deposition environment and engineering characteristics of each deposit.
- The critical-state-theory-based SSC Model can reasonably predict the deformation behaviour of Port-Said Clay.

REFERENCES

Abdallah, G. 2006. Management of groundwater aquifers along the Mediterranean Sea in Sinai Peninsula. *2nd international conference on water resources and arid environment, King Saud University, Riyadh, Saudi Arabia,* November 2006.

Ali, H.E., Elkateb T. & Fernandes D. 2016. Practical Aspects of Numerical Modelling of Soft Clays Treated with Prefabricated Vertical Drains. In *19th Southeast Asian Geotechnical Conference & 2nd AGSSEA Conference*. Dorsett Grand Subang, Subang Jaya, Malaysia, pp. 1033–1039

Bergado, D.T., Balasubramanian, A.S., Fannin, R.J. & Holtz, R.D. 2002. Prefabricated vertical drain (PVDs) in soft Bangkok clay: a case study of the new Bangkok International Airport project. *Canadian Geotechnical Journal* (39): 304–315.

Bergado, D.T., Chai, J. & Miura, N. 1995. FE analysis of grid reinforced embankment system on soft Bangkok clay. *Computers and Geotechnics* 17(4): 447–471.

Brinkgreve, R.B.J., Kumarswamy, S., Swolfs, W.M. & Foria, F. 2018. *PLAXIS Finite Element Code for Soil and Rock Analysis*. Delft: A.A. Balkema.

Burland, J.B. 1965. The yielding and dilation of clay. *Geotechnique* 15(2): 211–214.

Hamed, O.M. 2017. *Modeling and Laboratory Testing of Port Said Marine Clay and Applications on Geotechnical Design of Ports*. Ph.D. Thesis, Department of Structural Engineering, Ain Shams University, Cairo, Egypt.

David, H. 2018. DPlot User Manual. Mississippi: HydeSoft Computing.

Hamed, O.M., Mansour, M., Abdel-Rahman, A. & El-Nahhas, F. 2017a. Geotechnical Characterization of Port-Said Clay. In *Proceedings of the 19th International Conference on Soil Mechanics and Geotechnical Engineering, Seoul, South Korea*, pp. 2991–2994.

Hamed, O.M., Mansour, M., Abdel-Rahman, A. & El-Nahhas, F. 2017b. Investigating the Behavior of an Existing Quay Wall Using the Characteristic Parameters of Port-Said Clay, Egypt. *World Applied Sciences Journal* 35 (3): 483–499.

Matsuo, M. & Kawamura, K. 1977. Diagram for Construction Control of Embankment on Soft Ground. *Soils and Foundations* 17 (3): 37–52.

Samieh, A.M., Mansour, M.A., Elgendy, A.A. & Mahmoud, M.H. (2010). Analysis of an earth embankment constructed on a soft clay formation stabilized by prefabricated vertical drains. In *Proceedings of 8th International Conference on Civil and Architecture Engineering, Cairo, Egypt*, Article 16, Vol. 8, pp. 1–10. DOI: 10.21608/ICCAE.2010.44416.

Mansour, M.F., El-Nahhas, F.M. & Elshanawany, A.M. 2021. Short and Long-term Behaviours of Bored Tunnels in Port-Said Clay. *Geotechnical and Geological Engineering Journal* (39): 4563–4580.

Roscoe, K.H., Schofield, A.N. & Thurairajah, A. 1963. Yielding of clays in state wetter than critical. *Geotechnique* 13(3): 211–240.

Roscoe, K.H & Burland, J.B. 1968. In J. Heyman & F.A. Leckie (eds), *On the generalized stress-strain behavior of 'wet' clay. Engineering Plasticity (Papers for a Conference held in Cambridge)*: 535–609. London: Cambridge University Press.

Smart Geotechnics for Smart Societies – Zhussupbekov, Sarsembayeva & Kaliakin (Eds)
© 2023 The Author(s), ISBN 978-1-003-29912-7
Open Access: www.taylorfrancis.com, CC BY-NC-ND 4.0 license

Study on reinforcement of existing retaining walls with small diameter steel pipes

M. Ogawa
Hokoku Engineering Co. Ltd., Chiba, Japan

M. Hyodo
Yamaguchi University, Ube, Yamaguchi, Japan

ABSTRACT: In this paper, the authors investigated the effectiveness of three types of small diameter steel pipe reinforcement on the reduction of horizontal displacement of soil and stability of a retaining wall, using a soil tank and simulated house on land with a sloped retaining wall. Horizontal and vertical loads were applied to the base of the house and images taken with a digital camera were used in 2D image correlation analysis in order to measure the amount of horizontal displacement of the soil and retaining wall. It was found that the pattern of slip failure was different for unreinforced and reinforced soil. Also, out of the three types of reinforcement, the Λ-type reinforcement was most effective in restraining the horizontal displacement of the soil and increasing stability of the retaining wall.

1 INTRODUCTION

During recent major earthquakes, there has been an increase in the collapse of retaining walls on sloped land and consequent damage to houses located behind the retaining walls (Okimura, et al。 1999) (Hashimoto 2017). As the retaining wall itself is not strong enough to remain standing, it collapses, leading to damage of residential properties due to ground deformation. Therefore, there is an urgent need to reinforce such existing retaining walls, to ensure the stability of residential foundation soils.

In this study, the behaviour of simulated residential land with a retaining wall under vertical and horizontal loads was investigated. In addition, the effectiveness of three different types of reinforcement placed behind the retaining wall was also investigated.

2 LOADING TESTS

2.1 *Outline of the tests*

An overview of the apparatus used in the tests is shown in Figure 1. The soil tank is 1,500 mm (length) x 1,000 mm (depth) x 200 mm (width) with five sides made of 30 mm thick acrylic boards. Air-dried Toyoura sand (ρ_{dmax}=1.652 g/cm^3, ρ_{dmin}=1.369 g/cm^3) was used as the soil material. In order to observe the behaviour of the ground behind the retaining wall up to failure and the effect of loading on the retaining wall, as well as the effect of reinforcement, the upper layer of sand was loosely packed with a relative density of D_r = 30% (ρ_d = 1.443 g/cm^3), whilst the lower layer was medium-dense packed with D_r = 50% (ρ_d = 1.497 g/cm^3). The two layers were prepared using the air-pluviation method (Toki, et al。 1979).

Eight 40 mm x 40 mm x 195 mm aluminium bars, stacked at an angle of 70°, were used to represent the retaining wall and the house was simulated by placing a 140 mm x 195 mm x 12 mm steel plate (hereafter referred to as the load plate) on the ground behind the retaining

DOI: 10.1201/9781003299127-88

wall. This set-up simulated a house constructed behind a block retaining wall. Vertical loading was carried out by stacking one 22 N steel plate on top of another, on top of the load plate, and horizontal loading was carried out by pulling the load plate horizontally with a load of roughly 0.2 times the vertical load.

In this study, images taken by a digital camera were analysed using 2D image correlation, and the displacement was measured over the entire target area (Demizu, 2012). The digital camera was installed 1.5 m away from the front of the tank and images were taken at each step of vertical loading, until the retaining wall collapsed or until the loading capacity of the apparatus was reached.

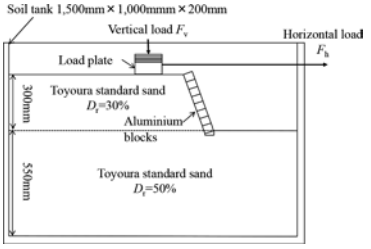

Figure 1. Outline of the test.

2.2 *Test results*

The results for horizontal displacement obtained through image analysis at the final load before failure, for vertical loading only and for simultaneous vertical-horizontal loading, are shown in Figure 2. As can be seen, compared with only vertical loading, failure occurs under a smaller total load during simultaneous vertical-horizontal loading, indicating the more severe influence of horizontal loading on ground stability compared with vertical loading.

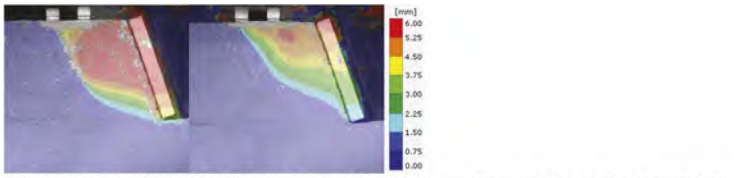

Figure 2. Horizontal displacement at final load before failure.

3 COMPARISON OF REINFORCEMENT TYPE

3.1 *Reinforcement types*

Aluminium pipes with a diameter of 5 mm, a wall thickness of 0.5 mm, a specific gravity of 2.7 and a tensile strength of 185 N/mm^2 were used as the reinforcing material. The following three types of reinforcement were tested in this study, as shown in Figure 3.(i) a single row of pipes parallel to the retaining wall, placed at the midpoint between the wall and the load plate with 40 mm spacing (hereafter referred to as Type I); (ii) two staggered rows of pipes with 20 mm spacing (hereafter referred to as Type II); and (iii) a row of pairs of pipes in a Λ-shape with an internal angle of 20°, spaced 40 mm apart (hereafter referred to as Λ-type). Note that for (iii), the heads of each pair of two pipes were joined using a nut and bolt. The reinforcement passes through the upper layer (D_r=30%) and is set into the lower layer (D_r=50%). For each type of reinforcement, as well as with no reinforcement, vertical and horizontal loads were applied to the foundation soil through the same load plate, and the displacement of the soil was measured at each loading stage.

3.2 *Effect of reinforcement on horizontal displacement*

Figure 4 shows the amount of horizontal displacement for each type of reinforcement, at the same load step as that of the final load before failure during the unreinforced test (vertical load 231.9 N, horizontal load 48.8 N). The dotted red lines represent the position of the reinforcements.

It can be seen that the amount of displacement decreases with increasing depth from the load plate. In the case of unreinforced soil, displacement appears in the form of an arc, whilst in the case of reinforced soil, the shape of the arc changes to become almost horizontal in the area of the reinforcement. Comparing the areas of horizontal displacement above 3.75 mm, the difference between Type I and Type II is not significant.

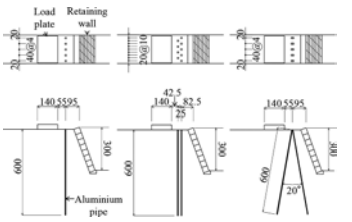

Figure 3. Types of reinforcement.

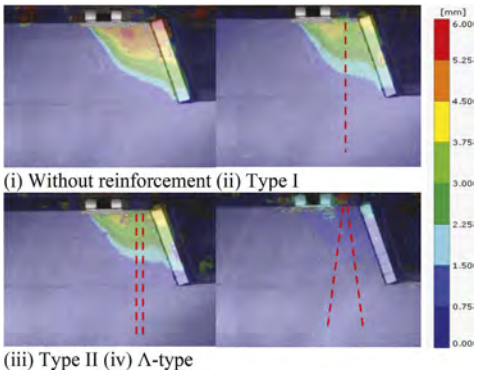

Figure 4. Horizontal displacement at vertical load of 231.9N and horizontal load of 48.8N.

On the other hand, in the case of the Λ-type, the maximum horizontal displacement is 2.25 mm at the same vertical load, indicating that the Λ-type is most effective at restraining the soil movement behind the retaining wall. The amount of horizontal displacement of the retaining wall based on image analysis was in the following order: no reinforcement > Type I ≈ Type II > Λ-type, when compared at the top of the retaining wall. Figure 5 shows the amount of horizontal displacement at final load before collapse of the retaining wall for the cases of no reinforcement, Type I and Type II, and at maximum load capacity of the apparatus for Λ-type. The grey areas immediately below the load plate show where large displacement occurred and the arrangement of the soil particles changed significantly, such that the amount of displacement could no longer be measured through image analysis. The red dotted lines represent the reinforcements and how much they have tilted due to ground deformation, assuming that the base of the reinforcement remains in the same position as in the initial loading stage.

In the case of no reinforcement, the grey area extends to the bottom of the retaining wall, showing the aspect of slip failure. On the other hand, in reinforced soil, a triangular soil "mass" appears between the reinforcement and the retaining wall, indicating the mitigating effect of the reinforcement on soil deformation. A comparison of the these "masses" clearly shows a size relationship of Type I < Type II < Λ-type, which is consistent with the results shown previously. From this, it can be seen that although for Type II, the increase in number of pipes does not give

a significant change in results compared to Type I, in setting the pipes in a Λ-shape, the resistance to horizontal displacement increases greatly.

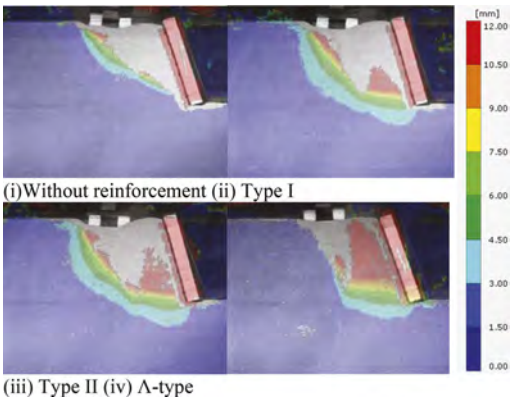

Figure 5. Horizontal displacement before collapse of retaining wall (at maximum load for Λ-type).

4 CONCLUSIONS

The displacement of the retaining wall and the deformation of the soil due to the application of vertical and horizontal loads on a simulated house on land behind a retaining were investigated using image analysis and the effectiveness of three types of reinforcement were compared. The findings are summarised as follows:

1) Simultaneous vertical and horizontal loading caused the retaining wall to collapse under a smaller total load than vertical loading alone. This is due to the predominant horizontal movement of the soil from under the load plate towards the retaining wall and the horizontal force due to soil displacement on the retaining wall.
2) In the case of unreinforced soil, displacement appeared in the form of an arc, whilst in the case of reinforced soil, the shape of the arc changed to become almost horizontal in the area of the reinforcement.
3) In the case of no reinforcement, an area of large deformation extended to the bottom of the retaining wall, showing the aspect of slip failure. On the other hand, in reinforced soil, a triangular soil "mass" appeared between the reinforcement and the retaining wall, indicating the mitigating effect of the reinforcement on soil deformation.

ACKNOWLEDGEMENTS

The authors would like to thank Professor Nakata of Yamaguchi University for his guidance, Mr. Kawasaki of Misawa Homes and Dr. Kuroyanagi of Hokoku Engineering for their assistance in this research. We hereby express our gratitude.

REFERENCES

Hashimoto, T. 2017. Damage analysis of damaged residential retaining walls by the 2016 Kumamoto Earthquake, In Kokushin University (ed.), *Bulletin of the Faculty of Science and Technology* 11: 97–105.

Demizu, A., Matsuda, H., Hetsugi, S., Morisaki, M., Uchino, M., Ito, M., & Morita, C. 2012. Fundamental study on improvement of strain measurement by digital image correlation method. In *Journal of JSCE A2* 68(2):683–690.

Okimura, T., Futaki, M., Okamoto, A., & Nambu, M. 1999. Characteristics and causes of damage to housing site retaining walls by the Hyogo-ken Nambu Earthquake. In *Journal of JSCE* 637/VI-45: 63–77.

Toki, S., Miura, S., Asami, H. 1979. On the preparation of sand specimens by the multiple sieve pluviation method. In *14th JGS Annual Meeting* 193–196.

Smart Geotechnics for Smart Societies – Zhussupbekov, Sarsembayeva & Kaliakin (Eds)
© 2023 The Author(s), ISBN 978-1-003-29912-7
Open Access: www.taylorfrancis.com, CC BY-NC-ND 4.0 license

Effect of incorporating kaolinite geopolymer on some mechanical properties of subgrade soil

A.H. Abdulkareem & T.M. Ahmed
Department of Civil Engineering, University of Anbar, Anbar, Iraq

N.F. Kwad
College of Engineering, University of Anbar, Anbar, Iraq

ABSTRACT: Subgrade soil is a critical element in the pavement system and can be considered as one of the major challenges for civil engineering applications. This paper investigates the efficiency of geopolymer material in sandy silt soil stabilization in terms of the strength and durability. Various proportions of the kaolinite (5, 10, 15, 20, 25, and 30%) by weight were used as a raw material to produce the geopolymer. The alkaline liquid consists of the NaOH at 8M and Na2SiO3 liquid, at 1.5 ratio of the NaOH:$Na2SiO_3$. Laboratory investigation involves the compaction and mechanical properties of the natural and stabilized soil mixtures. The results showed a great improvement in the strength of the soil in terms of the unconfined compressive strength (UCS) and the indirect tensile strength (ITS). The optimum content of the kaolinite was 15%, which achieved the maximum UCS and ITS values. The CBR index of the soil significantly increased with the kaolinite-based geopolymer. Specimens stabilized using the optimum content of the kaolinite-based geopolymer did not pass the durability test in terms of the weight loss and volume change. The microstructural analysis of the stabilized specimens showed a poor distribution of the geopolymer binder. Moreover, pores were clear in the structure and this may indicates the poor behavior during the durability test.

1 INTRODUCTION

The subgrade layer is a foundation for the pavement structure, which represents the in situ or the modified soil that provides the support to upper layers of pavement system and distributes traffic loads within the soil. The subgrade impact is a critical for the pavement design and long-term performance, where the strength and stiffness of the subgrade soil are the most important factors to define the quality of the subgrade material. High-quality subgrade reduces the thickness of the upper layers, especially the pavement layer. This leads to a significant cost reduction in road construction. The strength and stiffness of the subgrade can be determined by conducting common tests such as the California Bearing Ratio (CBR), Resilient Modulus, Unconfined Compressive Strength, Indirect Tensile Strength and Modulus of Subgrade Reaction [1].

Kaolinite is a clay mineral and produced naturally through weathering or by hydrothermal process of aluminosilicates-rich rocks such as granite. Kaolinite as a clay mineral is generally composed of $Al_2Si_2O_5(OH)_4$. Kaolin terminology comprises both of the raw clay and the net commercial kaolin [2]. The white color and the fine particles distinguish the kaolin from the other types of clay. Kaolinite clay is a suitable raw material for geopolymer production. The kaolinite is aluminosilicate material can be activated by the alkali solutions to produce the geopolymer binder. Many researchers utilized the kaolinite in geopolymer production. The compressive strength of kaolinite-based geopolymer was studied by [3]. Various concentrations of NaOH (6-14 mol/L) was used and cured at 80°C. Three periods of curing, i.e. 1, 2, and 3 days were tested in the study. It was reported that NaOH concentration of 12 mol\L is sufficient for strength development. The compressive strength also showed a proportional trend with the increasing curing period, where the samples cured for three days in oven achieved the highest compressive strength.

DOI: 10.1201/9781003299127-89

Synthesis of kaolinite-based geopolymer at various conditions was studied by [4] through the calcined kaolinite to produce the reactive metakaolin by heating the kaolinite at several temperatures, i.e. 550, 700, 900, and 1100°C. The produced material was used to form the geopolymer binder. The Potassium hydroxide (KOH) and NaOH were used at a molarity ranges between 5 to 18 mol\L. It can be noticed that 700°C is the temperature required to produce metakaolin with the highest level of reactivity. At this temperature and at a base concentration of 13 M, the various physical characteristics reached their ideal levels. Moreover, the physical and mechanical properties of the geopolymer were evaluated. The results showed that the compressive strength of geopolymer samples were extensively low for samples activated by NaOH and KOH solution below 10M concentrations. Further increase in the molarity, i.e. 13M of NaOH and 15M of KOH maximized the strength and the density. While the porosity showed an adverse behavior to the compressive strength. The relatively low porosity was observed for the specimens at the maximum compressive strength and optimum density. However, water absorption was low. The influence of the alkali solution concentration in the kaolin-based geopolymer was studied by [5] . The outcomes revealed that 8M is the optimum molarity for NaOH solution, which provided the highest compressive strength. Also, the scanning electron microscope (SEM) images confirmed the presence of geopolymer binder as a dense structure. The results obtained showed that the temperature required to obtain a metakaolin with the highest degree of reactivity is approximately 700°C. The various physical properties reached optimum values at this temperature and for base concentration equal to 13 M. These values decreased at higher temperature and concentration.

The results indicate that 700°C is the temperature required to produce metakaolin with the highest level of reactivity. At this temperature and at a base concentration of 13 M, the various physical characteristics reached their ideal levels. At higher temperatures and concentrations, these values decreased.

The study aims to investigate the strength and durability of soils in the subgrade layer after the incorporation of kaolinite - geopolymer mixture. The main interest of the study is the incorporation of a chemical stabilizing agent and kaolinite with the soil. This may produce high-quality material that can be used as a roadbed or stiff foundation for the road. The kaolinite and the chemical agent used in the study are available and can be utilized in Iraq.

2 MATERIALS AND METHODS

2.1 *Soil*

One type of soil was used in this study and collected from Msheheeda quarry in Ramadi city. The soil consists of 60% of silt, 9 % of clay and 31% of fine sand. Due to the high content of silt, the soil is classified as sandy silt according to the USCS system. The physical and chemical properties of the soil are presented in Tables 1 and 2 respectively. The chemical composition shows that the soil is composed mainly of the silicon, aluminum, and calcium oxide. The result of the X-Ray Diffraction (XRD) test is presented in Figure 1, which describes the crystalline structure and the mineral compounds of the soil. The soil has a lamellar composition and exhibited loosely structure as shown in the SEM image in Figure 2.

2.2 *Kaolinite (kao)*

Kaolinite is the alumina-silicate material used to produce the geopolymer. It was dried at ambient temperature as shown in Figure 2. More than 71% of the kaolinite particles passed No.200 sieve. The chemical composition through the X-Ray Fluorescence test is listed in Table 2. The specific gravity of the kaolinite is 2.35. The chemical analysis showed that the amount of silica and alumina are high, while it has a low content of CaO.

2.3 *Alkaline activator solution*

The alkaline activator solution consists of 99% pure sodium hydroxide (NaOH) pellets and sodium silicate (Na_2SiO_3) liquid. The concentration of NaOH was 8 molar, as 40 g/mole is the NaOH molecular weight. The liquid form of the sodium silicate (Na_2SiO_3) contains 32.5% of SiO_2, 13.4%

of Na_2O, and 54% of water. The NaOH:Na_2SiO_3 ratio was 60:40. The UCS test was performed to assess the variation in the strength with different molarity of NaOH and NaOH:Na_2SiO_3 ratios.

Table 1. Physical properties of soil.

LL (%)	PL (%)	PI (%)	G_s	AASHTO	USCS	Description	OMC (%)	MDD (gm/cm^3)
38	27	11	2.66	A-6	ML	Sandy silt	15.5	1.73

Table 2. Chemical composition of soil and kaolinite.

ELEMENT	SIO_2	AL_2O_3	CAO	FE_2O_3	MGO	NA_2O	K_2O	SO_3	MNO
SOIL	37.64	6.50	23.43	4.06	3.90	1.30	1.10	0.70	0.10
KAOLINITE	51.40	26.23	5.38	5.64	2.41	1.28	1.20	-	-

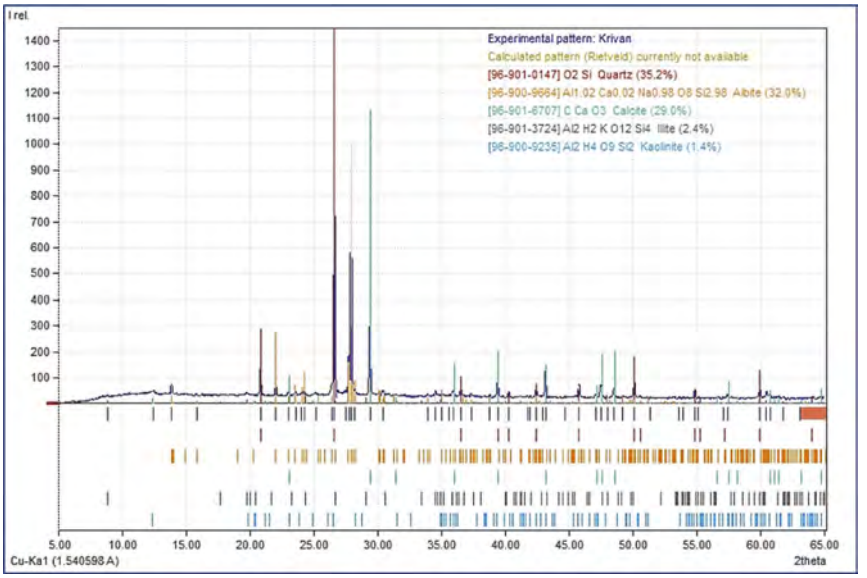

Figure 1. X-ray Diffraction (XRD) pattern of soil.

Figure 2. (a) Dried soil (b) SEM image of soil (c) Kaolinite.

2.4 *Sample preparation*

The oven-dried soil was mixed with the kaolinite and the alkali solution to produce the geopolymer material. The mechanical mixing was used to ensure a homogeneous mixture. Specific

weights of soil and kaolinite were mixed prior to the alkaline solution addition. As estimated by the compaction test, the alkali content corresponds to the optimum moisture content of the mixture. The extra weight of the alkali liquid was added to the blend to compensate the dissolved NaOH weight in the solution. The extra weight is approximately 30 % at 8 M of the NaOH concentration [6]. The UCS test specimens were compacted into steel molds with a diameter of 100 mm and a height of 200 mm according to the requirements of the ASTM D4219-08. The alkaline solution has been used as a replacement for the OMC of the soil-kaolinite mixtures. For each mixture, three samples were prepared. UCS test was carried out at a constant loading rate of 0.1 kN/sec. The ITS test involves preparing soil specimens compacted under the modified effort method. The ITS value can be calculated by:

$$\sigma_t = (2P/\pi dt) \tag{1}$$

Where:
σ_t = Tensile strength (MPa)
P = Maximum load at failure (N)
d = Diameter of specimen (mm)
t = Thickness of specimen (mm)

The percentages of kaolinite in the UCS and ITS tests were (5, 10, 15, 20, 25, and 30 %) by weight of the soil. CBR test involves applying gradual loads using cylindrical piston (Plunger) having 50 mm diameter at constant penetration rate of 1.3 mm/minute according to ASTM D1883-14. CBR index is given by Equation 2 [10]:

$$CBR\% = (X/Y)100 \tag{2}$$

Where:
X: The load (pressure) required to have a penetration of 2.54 mm or 5.08 mm
Y: Standard load (pressure) of the well-graded crushed stone, which are:
6.9 MPa for 2.54 mm penetration
10.3 MPa for 5.08 mm penetration

The CBR specimens were soaked in water for 96 hours before the test. Mixing time was 10 minutes, dry mixing by hand for 3 minutes and mechanical mixing for 7 minutes to ensure the uniform distribution of the alkaline solution and the mixture components. The stabilized samples were molded and cured in the oven for 48 hours at 65°C for the UCS, ITS and CBR tests. After the heat-curing which depending on previous study, the specimens were removed from the oven and covered by cling film and kept at room temperature to be tested after 7 and 28 days. The modified proctor test was performed according to ASTM D 1557-12 in order to obtain the moisture-density relationships.

3 RESULT AND DISCUSSION

3.1 *Compaction test*

Figure 3 presents the moisture-density curves of the soil-kaolinite blends. It can be seen that the maximum dry density increased from 1.73 g/cm^3 for the natural soil to 1.94 g/cm^3 for soil +30% kao. While the optimum water content decreased from 15.5% for the natural soil to 13% for the soil+30% kao mixture. Also, Figure 3 shows a noticeable increase in the maximum dry density of the soil at the various kaolinite percentages and obvious decrease in the optimum moisture content at the same percentages. The clear trend of compaction curves reveals that adding more of kaolinite to the soil leads to higher MDD and less OMC. The higher MDD may be attributed to the role of the fine particles of kaolinite, which are likely to fill the pores in the soil as a filler material resulting in a denser state in the soil. In addition, there is no evidence of kaolinite reaction with the water; this justifies the OMC decrease at the high content of kaolinite. It is also known that the compaction results are highly affected by the compaction energy, where the modified proctor method is likely to result in higher densities due to the higher energy applied to the soil.

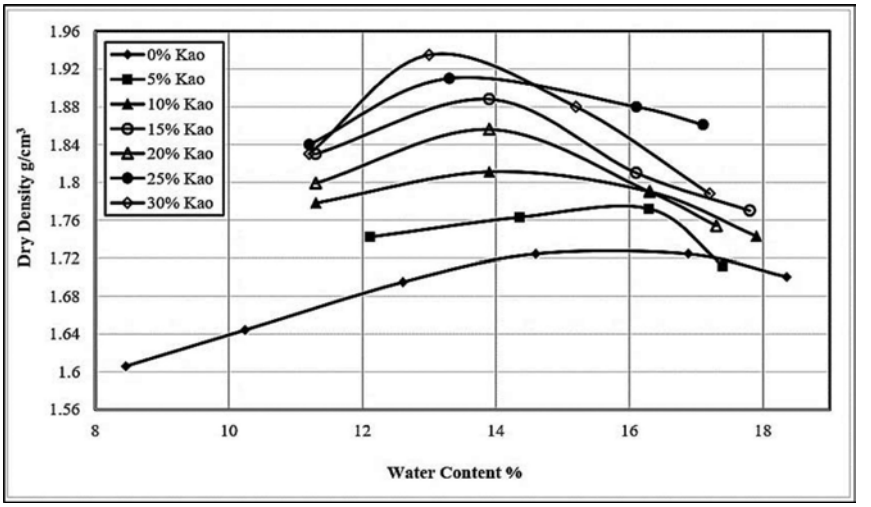

Figure 3. Moisture-density relationship of soil-kaolinite mixtures.

3.2 *Unconfined Compressive Strength (UCS) test*

The UCS is one of the major mechanical properties to be considered in the soil. UCS test was conducted to evaluate the effectiveness of the kaolinite-based geopolymer as a soil stabilization agent. The results of the UCS test at 7 and 28 days of curing time are shown in Figure 4. It can be noticed that the kaolinite-based geopolymer significantly improved the UCS of the soil and the maximum strength observed at 15% of the kaolinite percentage by weight of the soil irrespective of curing period. By inspecting Figure 5, it can be observed that low percentages of kaolinite (10% and 15%) provided the highest strength at the early ages in comparison with the other percentages. In addition, there was no big variation between 7 and 28 days cured specimens except the specimens that contain 20% of the kaolinite content which exhibited a noticeable gap in the strength. This behavior is related to the fact that 48 hours of curing at 65°C corresponds to 28 days of curing at the room temperature as found by [7].

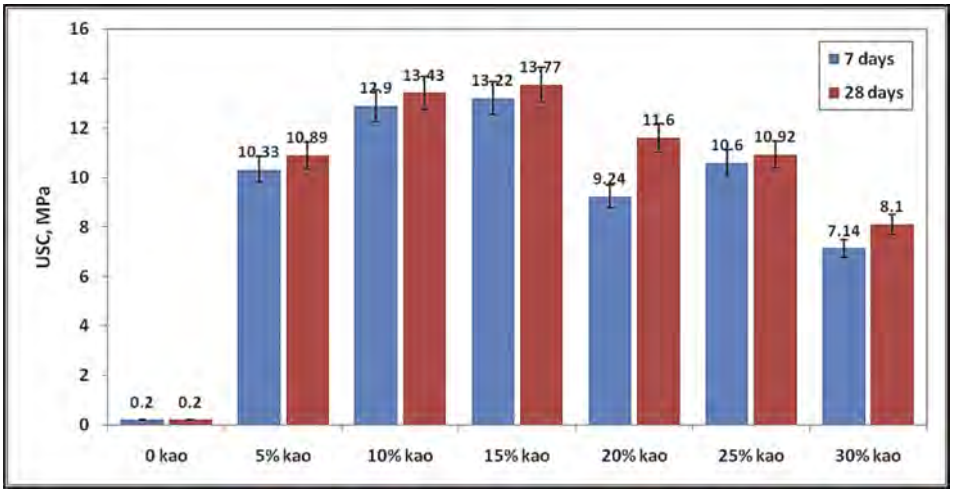

Figure 4. UCS test results of the soil–kaolinite geopolymer at 7 and 28 days.

This behavior may be attributed to the curing time, as 48 hours of curing at 65°C corresponds to 28 days of curing at the ambient temperature as found by [7]. Brittle failure was observed in the stabilized specimens as shown in Figure 6. This pattern of cracks points out the stiff structure within the soil. The kaolinite has a chemical composition of silica and alumina particles which make it proper material in geopolymer synthesis. However, there is no clear study investigated the results of kaolinite-based geopolymer in the silty soil stabilization.

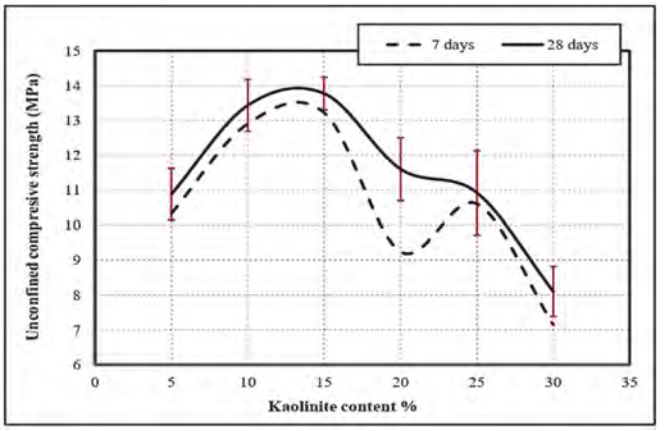

Figure 5. Variation of UCS with Kaolinite content for soil- kaolinite geopolymer mix.

Figure 6. Failure of soil-kaolinite geopolymer UCS test specimen.

3.3 *Indirect Tensile Strength (ITS) test*

The interest in tensile property of the stabilized soil due to concerns related to cracking behavior in the fully bonded materials. The soil is very weak in tension and may easily collapse under the light tension stresses.

Figure 7 shows ITS test results of soil with kaolinite geopolymer at 7 and 28 days of curing period . It can be seen that there was no significant variation in the tensile strength between 7 and 28 days cured specimens at the low content of kaolinite. The noticeable variation occurs at the higher content of the kaolinite. This behavior may be attributed to the continuous geopolymerzation reactions of the kaolinite particles with the alkali liquid. These reactions take place in the soil structure at ambient temperature. However, this increase insignificant for the long-term performance, where the geopolymer material gains most of the compressive strength by heat-curing at 70-80°C [8]. Figure 8 shows the clear splitting of the stabilized specimens in the longitudinal plane after conducting the ITS test.

3.4 *California Bearing Ratio (CBR) test*

CBR index provides significant information about the bearing capacity of the soil and compare it with the strength of the well graded crushed stone which possess a high strength and CBR index by 100% [9].

All CBR tests were performed according to (ASTM D1883-14). Kaolinite percentage used in the CBR test was the optimum proportion estimated from the UCS and ITS tests which is 15% by weight. The CBR index of the natural soil is 3.8% at the soaked condition. The load-penetration curve of the soaked soil-Kaolinite geopolymer mixture is shown in Figure 9. It can be seen that 2.54 mm of penetration into the soil surface requires corresponding load of 19.24 kN, while a penetration of 5.08 mm requires 31.54 kN. The CBR index was 143% at 2.54 mm and 162% at the 5.08 mm penetration. The CBR value for the stabilized soil is 162% according to the ASTM D1883-14. This means that the CBR index has improved to 40 times

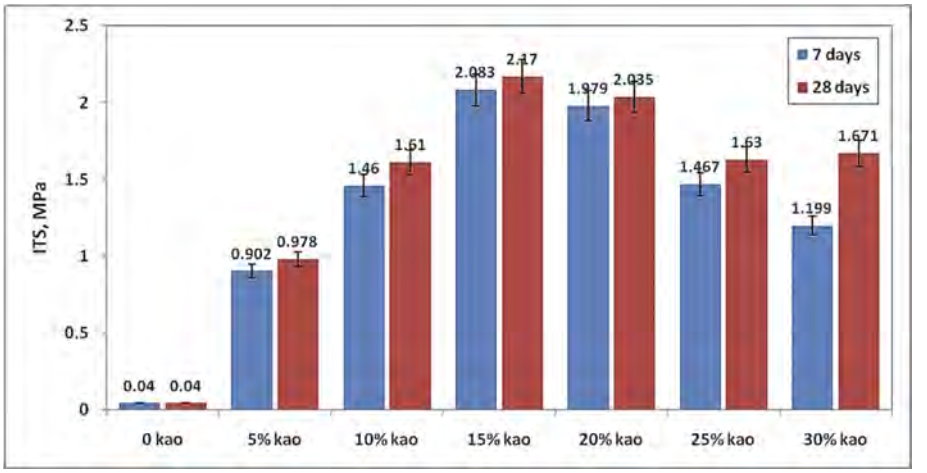

Figure 7. Effect of soil–kaolinite geopolymer on ITS test with curing period at 7 and 28 days.

Figure 8. Failure of ITS test specimens of soil-kaolinite-based geopolymer mixture.

after adding the kaolinite-based geopolymer to the soil, which is significant improvement in the soil strength. The increase in the CBR index indicates that the bearing capacity and the shear strength of the stabilized soil were highly improved [11]. The chemical composition of the kaolinite is the key factor in the geopolymer synthesis. The high amount of the silica and alumina in the kaolinite material determines the nature of the new products in the soil. In addition, the heat curing at 65°C accelerates the geopolymer reactions and synthesis, consequently, rapid strength gain in the stabilized soil.

3.5 *Durability test*

Long-term performance of the stabilized soil is one of the important concerns in the chemical stabilization methods. The new chemical components in the soil may be affected by water, especially the effect of chemical leaching of the new chemical products. The test was conducted according to the method outlined in ASTM D559-15. This method can be applied by subjecting accelerated moisture fluctuations to simulate the actual conditions in the field during the seasonal variation. The optimum mixture of the kaolinite (15%) was also adopted in the test. Wetting and drying conditions were subjected on the same specimens size that used in the UCS and ITS tests. One cycle of the test involves immersing the specimens in the water for 5 hours followed by 42 hours of drying in the oven at 70°C and one hour for stroking and taking weight and volume records. The test results are listed in Table 3. The specimens could not sustain its stability after two cycles of wet/dry conditions, and it collapsed after taking it out from the water in the second cycle as shown in Figure 10. This rapid collapse of specimens may be attributed to the weak bonds of the alkali activated material inside the soil. Also, the leaching of the

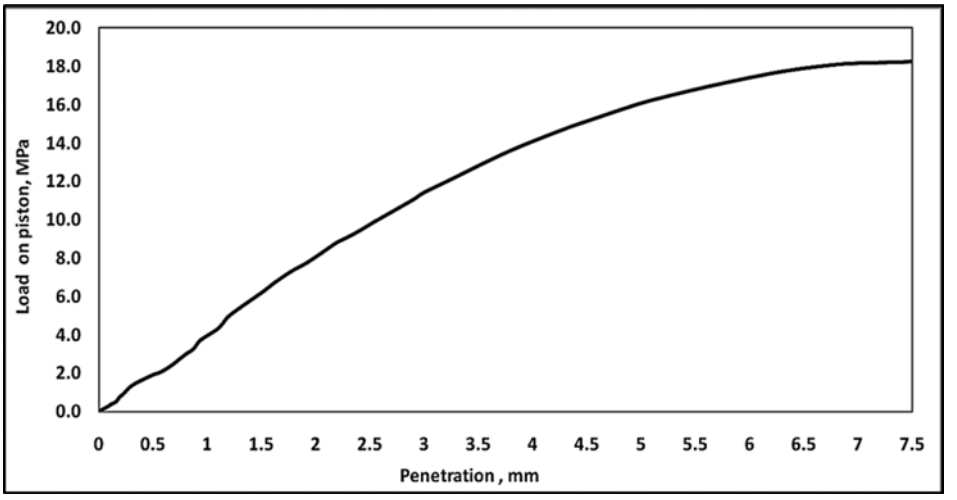

Figure 9. Load – Penetration curve of CBR test for the soil +15 Kao mixture.

alkali material due to water infiltration inside the voids may be one of the factors that affected the stabilization efficiency. The rapid loss of consistency in kaolinite geopolymer stabilized specimens may be due to the small cracks in the mixture. These cracks caused by the reaction between the reactive-silica in the soil and kaolinite with the hydroxide from the alkali liquid. This reaction increases the volume of the specimen and cracks formation due to the new products [12]. The collapse of the specimens may be considered as an indicator of the calcium role in the geopolymer reactions, as the calcium may prevent the formation of the geopolymer binder at the early ages of the alkaline activation resulting in weaker structure in the soil.

Table 3. Wet-dry test results after 28 days of curing period.

Mixture	Weight loss %	Volume change %	Durability against W-D conditions
Soil+15Kao geopolymer	Collapsed	Collapsed	Failed

Figure 10. Soil stabilized using kaolinite geopolymer after two cycles of W-D conditions test.

3.6 *Microstructure*

The microstructural analysis presents valuable evidence on the new transformations after the geopolymer addition to the soil. Figure 11 shows the SEM image for the natural soil. It is

obvious that the soil has a laminar composition and loosely structure. Also, the soil composition was inhomogeneous and contains scattered voids as shown in Figure 11.

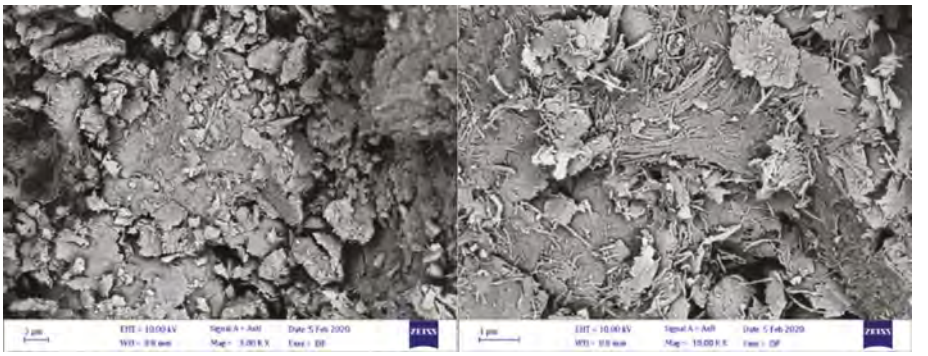

Figure 11. SEM images of the natural soil.

The SEM image of the soil and kaolinite geopolymer mixture is shown in Figure 12 and the size analysis is shown in Figure 13. The analysis of these images indicates the formation of the geopolymer binder in nanometers size. However, it can be observed that the microstructure of this blend has a lot of connected pores distributed randomly in the structure. These pores explain the poor performance of the stabilized soil in the durability test as the geopolymer binder did not fill the soil voids and bind it strongly. The structure of kaolinite geopolymer was likely to be a plate-like structure as shown in Figure 12. The particles act as combined plates to form layered texture with small surface area [13]. The SEM images confirm the loose state of the kaolinite geopolymer in the soil and the presence of unreacted kaolinite particles accumulated around the soil particles. In addition, the lamellar texture was observed in the microstructure, which results in weak composition and performance. In addition, accumulated C-S-H gel was observed with high intensity in the microstructure of the soil-kaolinite geopolymer mixture as shown in Figure 13.

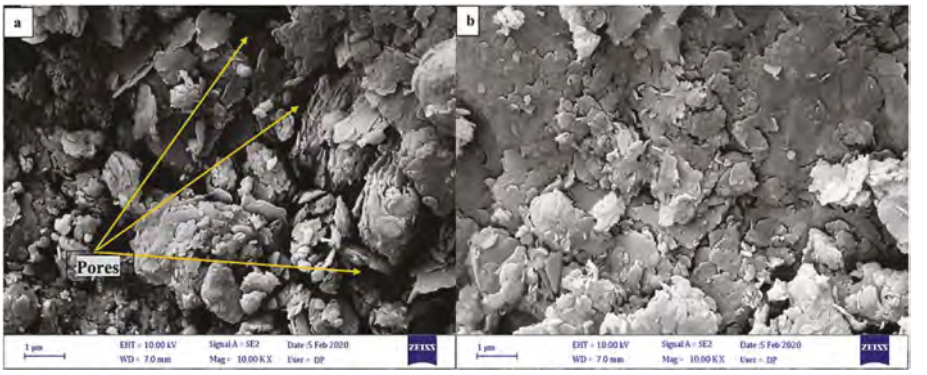

Figure 12. SEM image of soil+15Koalinite geopolymer mixture at 1μm magnification, a) micro pores b) Plate-like structure.

4 CONCLUSIONS

The study proves the efficiency of using kaolinite based geopolymer in weak subgrade soil stabilization. The following conclusions are drawn:

- As kaolinite content in the soil increased, the MDD increased while the OMC reduced in the same proportions. When kaolinite was 15% of the soil's weight, the MDD increased from 1.73 g/cm^3 of natural soil to 1.93 g/cm^3.

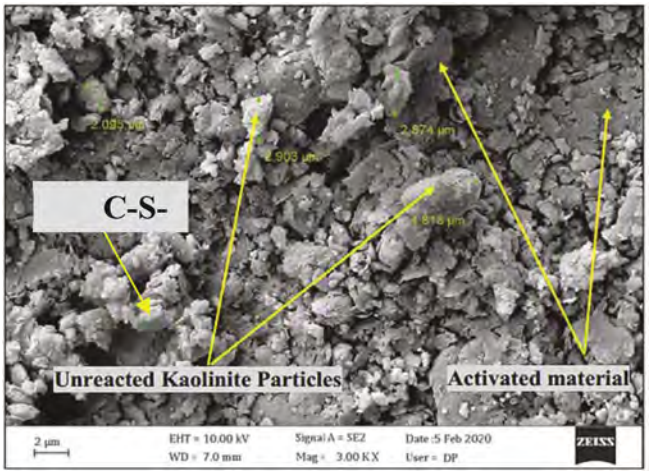

Figure 13. Size analysis using SEM image for the soil with kaolinite geopolymer mixture.

- The UCS strength of the stabilized soil was improved significantly at the optimum content of the kaolinite compared to the natural soil at both 7 and 28 days of curing time.
- The tensile strength of the stabilized soil increased significantly after the addition of the kaolinite based geopolymer.
- CBR index was highly improved due to the kaolinite geopolymer addition. The stabilized soil exhibited high CBR index by 162%.
- The stabilized specimens by the kaolinite-based geopolymer did not pass the durability test and exhibited bad performance in the initial cycles.
- When the soil's microstructure was analyzed using SEM images, weak and random geopolymer binder was found in the kaolinite-based geopolymer stabilized soil.
- It is recommended to study the influence of the low temperatures below 25°C on the strength development of the stabilized soil by the geopolymer. This is important to reduce the curing temperature and period of the geopolymer as it one of the most critical challenges in the site applications when it used with the soil or as a geopolymer concrete.

ACKNOWLEDGEMENTS

The authors thank University of Anbar, Engineering College, Civil engineering laboratory for their support.

REFERENCES

[1] D. Jones, A. Rahim, S. Saadeh, and J.T. Harvey, Guidelines for the stabilization of subgrade soils in California. University of California Pavement Research Center, Guideline: UCPRC-GL-2010-01.
[2] A. J. Bloodworth, D. E. Highley, and C. J. Mitchell, "Industrial minerals laboratory manual: kaolin," British Geological Survey, Technical report WG/93/1,Mineralogy and Petrology Series, 1993.
[3] C. Y. Heah et al., "Kaolin-based geopolymers with various NaOH concentrations," Int. J. Miner. Metall. Mater., vol. 20, no. 3, pp. 313–322, 2013.
[4] A. Nmiri, N. Hamdi, M. Duc, and E. Srasra, "Synthesis and characterization of kaolinite-based geopolymer: alkaline activation effect on calcined kaolinitic clay at different temperatures," J. Mater. Environ. Sci., vol. 8, no. 2, pp. 276–290, 2017.
[5] C. Y. Heah, H. Kamarudin, A. M. Mustafa Al Bakri, B. Abdullah, M. Bnhussain, M. Luqman, I. Khairul Nizar, & Y. M. Liew, "Effect of alkali concentration on mechanical properties of kaolin geopolymers," Romanian Journal of Materials, 42 (2), 179 – 186, 2012.
[6] S. Adhikari, Mechanical Properties of Soil-RAP-Geopolymer for the Stabilization of Road Base/Subbase. Thesis, University of Louisiana at Lafayette, 2017.

[7] P. Sukmak, S. Horpibulsuk, S.-L. Shen, P. Chindaprasirt, and C. Suksiripattanapong, "Factors influencing strength development in clay–fly ash geopolymer," Constr. Build. Mater., vol. 47, pp. 1125–1136, 2013.
[8] E. Arioz, Ö. Arioz, and Ö. M. Koçkar, "The effect of curing conditions on the properties of geopolymer samples," Int. J. Chem. Eng. Appl., vol. 4, no. 6, p. 423, 2013.
[9] R. E. Link, N. Pandian, A. Sridharan, and P. Raju, "California Bearing Ratio Test Simplified," J. Test. Eval. - J TEST EVAL, vol. 27, Jan. 1999.
[10] A. D1883, "Standard test method for California bearing ratio (CBR) of laboratory-compacted soils." ASTM International West Conshohocken, PA, 2016.
[11] R. S. Kesharwani, A. Sahu, and N. U. Khan, "CBR value of sandy subgrade blended with coarse aggregate," Int. J. Geomate, vol. 10, pp. 1743–1750, Jan. 2016.
[12] F. Slaty, H. Khoury, H. Rahier, and J. Wastiels, "Durability of alkali activated cement produced from kaolinitic clay," Appl. Clay Sci., vol. 104, pp. 229–237, 2015.
[13] Y. M. Liew et al., "Processing and characterization of calcined kaolin cement powder," Constr. Build. Mater., vol. 30, pp. 794–802, 2012.

Smart Geotechnics for Smart Societies – Zhussupbekov, Sarsembayeva & Kaliakin (Eds)
© 2023 The Author(s), ISBN 978-1-003-29912-7
Open Access: www.taylorfrancis.com, CC BY-NC-ND 4.0 license

Effects of fly ash on sand behaviour in monotonic triaxial tests

E. Angelova & V. Angelov
Geohydroconsulting, Skopje, North Macedonia

V. Sheshov, J. Bojadjieva, K. Edip, T. Kitanovski & D. Ivanovski
Institute of Earthquake Engineering & Engineering Seismology, Skopje, North Macedonia

S. Dimitrijević
Mining and Metallurgy Institute Bor, Bor, Serbia

ABSTRACT: Taken the environment into consideration, in geotechnical engineering waste materials are tested to prove their compatibility for soil improvement. One such product is fly ash, being waste of the coal burning process. Fine-grained soils enhanced with fly ash have shown to have better strength and deformation properties, as well as benefits as fill material. However, the properties of sandy soil mixtures have not been extensively investigated. Therefore, research has been started by determining the chemical properties of the fly ash samples, followed by specialized tests in the field of soil mechanics, on samples of fly ash and Skopje sand, in order to identify the benefits of such mixtures. This paper has the purpose to present the obtained results from monotonic triaxial tests on Skopje Sand – fly ash mixtures with different percentage of fly ash, namely 5, 10 and 20%, tested under effective stress of 100 kPa.

1 INTRODUCTION

As the term "Environmental Geotechnics" is becoming more popular, globally there is an intensive tendency for use of waste materials instead of their deposition in landfills. One such product is the fly ash, being waste or secondary industrial product of the coal burning process. Fly ash has been greatly examined for use in civil engineering, especially for soil improvement in road construction. Additives as fly ash can improve the mechanical and chemical properties of the soils such as strength, swelling, plasticity index and compressibility (Amiralian et al., 2012). Its compaction properties have been widely studied for road construction (Beeghly, 2003; Senol et al, 2006; McCarthy et al., 2009; Santos et al, 2011; Vukićević et al, 2019), as use of fly ash in practice has been frequently reported (Beeghly, 2003; Parsons and Kneebone, 2005; Edil and Benson, 2007; Jackson et al, 2007; Lin et al, 2009; Trast et al, 2011). However, there are less studies for mixtures of sand and fly ash, such as those by Keramatikerman et al. (2017) and Kolay et al. (2019). This paper presents the results from monotonic triaxial tests done on mixtures of the natural Skopje Sand and fly ash.

The chemical properties of fly ash depend on the composition of coal, as well as the technology of burning. Therefore, the chemical composition of fly ash must be examined first for its suitability. The chemical characterization of the used fly ash is also presented in this paper accompanied by classification of the used sand and mixtures.

2 PROPERTIES OF THE USED MATERIALS

2.1 *Fly ash (FA)*

The used fly ash in this study is from location of freshly deposited fly ash. Therefore, the properties of fly ash are in relation to the composition of the coal burnt at the time of sampling as well as the

DOI: 10.1201/9781003299127-90

current burning technology in the power plant. Table 1 presents the chemical composition of the fly ash, which classifies the fly ash in Class F, according to the standard for definition of the fly ash class ASTM C618 (2019). It should be noted that the used fly ash does not contain organic toxic elements and compounds, or any excessive trace elements, so it can be further used.

Table 1. Chemical composition of the used fly ash.

Oxide	(%)
Al_2O_3	23.85
BaO	0.073
CaO	3.49
Fe_2O_3	8.14
K_2O	3.00
MgO	1.95
MnO_2	0.31
Na_2O	0.89
P_2O_5	0.20
SO_3	0.60
SiO_2	54.61
SrO	0.035
TiO_2	0.84
LOI	2.875

Additionally, microscope imaging was done for the fly ash using Scanning Electronic Microscopy (SEM). This test is useful to discover the shape of the particles as well as the range of their size. As it can be observed in Figure 1, the fly ash does is not consisted only of spherical particles called cenospheres. Despite irregular particles being present, also there are groups of particles attached to each other forming groups of particles called flocculations, which could not be dispersed by the method of ultrasound. Also, the particle size distribution was determined for the fly ash, being classified as sandy silt with a little clay (Figure 2).

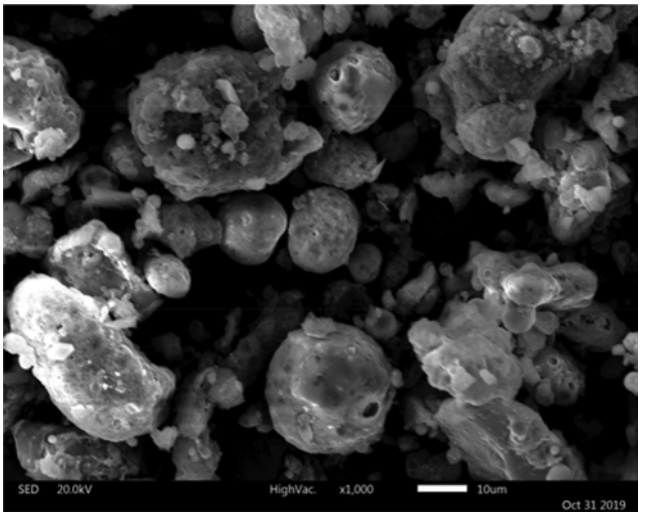

Figure 1. SEM image of fly ash with magnification 1000x.

2.2 *Skopje Sand (SS)*

The sand used in this study is called Skopje Sand. It is a natural sand from the alluvial deposit from river Vardar in the region of the city Skopje. It has been used in previous studies

(Bojadjieva, 2014 et al; Bojadjieva, 2015; Kitanovski et al, 2018; Bojadjieva, 2019) as clean sand, however this is the first extensive study for mixtures of Skopje Sand and fly ash. This sand is classified as poorly graded sand with silt (Figure 2).

2.3 *Skopje Sand – fly ash mixtures*

The main tests in this study are done on samples of Skopje Sand mixed with fly ash. The percentage of fly ash was chosen to be 5, 10 and 20% in order to be able to observe the influence of low but also high percentage of fly ash in the sand. According to the results from the particle size distribution test, the mixture with 5% fly ash is poorly graded sand with silt, the mixture with 10% fly ash is well-graded sand with silt, whereas the mixture with 20% fly ash is silty sand (Figure 2).

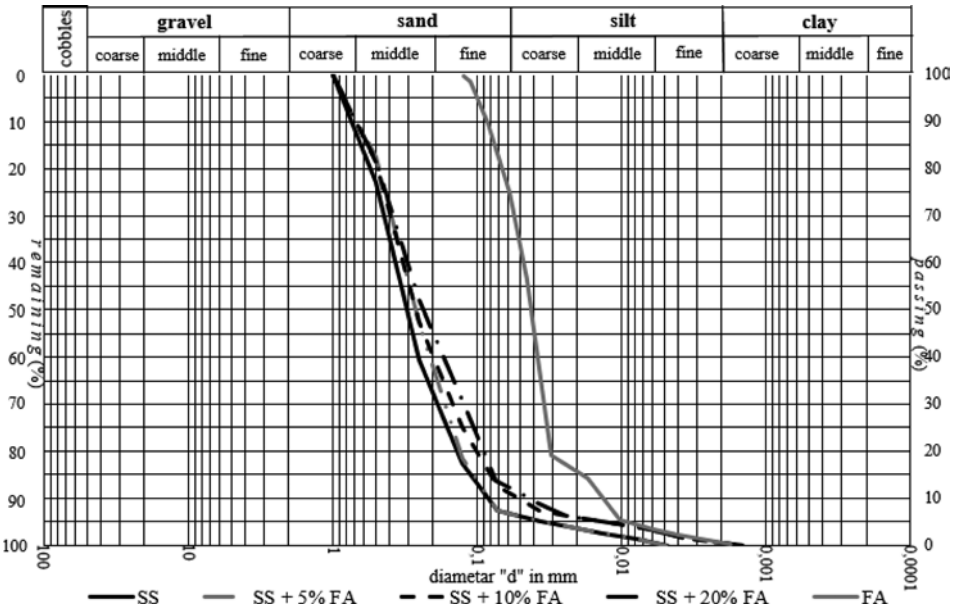

Figure 2. Particle size distribution of Skopje Sand, fly ash and their mixtures.

3 MONOTONIC TRIAXIAL TESTS

The possibility to use fly ash for soil improvement or soil replacement is studied through element tests such as triaxial tests. It was decided to perform triaxial tests on samples with relative density around 50%, with effective stress of 100kPa, using the same sample preparation procedure with wet tamping as in the work by other authors (Edip, 2013; Bojadjieva, 2015; Edip et al, 2018; Bojadjieva et al, 2018). The monotonic compression drained tests are performed with loading rate 0.2mm/min and axial strain limit of 15%. Considering that Bojadjieva (2015) performed an extensive testing program on Skopje Sand, this study is continuation of her work. It is used as referent for comparison of her results for clean Skopje Sand and the results of this study for mixtures of Skopje Sand with different amount of fly ash. The results from monotonic triaxial tests performed on clean Skopje Sand by Bojadjieva (2015) and on mixtures of Skopje Sand and fly ash done in this study are presented in Figure 3.

It can be noticed that the mixture with 5% fly ash shows the highest peak deviatoric stress which supersedes the peak strength of clean Skopje Sand, referring to soil improvement. It can be noticed that this mixture follows the referent Skopje Sand after the peak value with almost parallel trend towards the residual strength. As the amount fly ash increases the peak strength drops, so the Skopje Sand with 10% fly ash mixture has slightly lower peak strength than clean Skopje Sand. The effect is more drastic for the Skopje Sand - 20% fly ash mixture in which case the deviatoric stress requires higher axial strains to reach peak value.

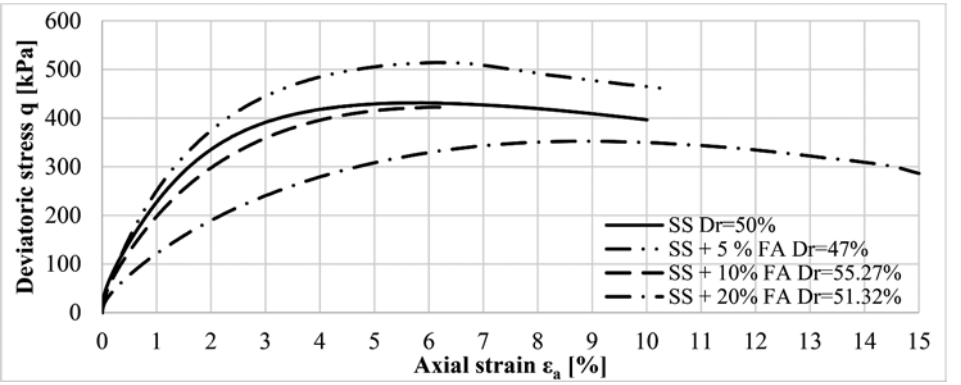

Figure 3. Deviatoric stress versus axial strain for clean Skopje Sand and mixtures with fly ash.

4 CONCLUSIONS

From environmental aspect the use of fly ash is of high importance. This paper presents the results from monotonic triaxial test on mixtures of natural Skopje Sand and fly ash with different percentage.

The strength properties of Skopje Sand can be improved with low quantities of fly ash, around 5%. If fly ash is mixed with Skopje Sand for soil replacement purposes, at higher percentage of fly ash the mixtures have to be with higher relative density in order to retain the referent strength properties of Skopje Sand at certain relative density.

Based on these initial results, it is recommended that the further work should be in direction of testing mixtures with different percentage of fly ash in order to establish correct mathematical correlation between the percentage of fly ash and the peak strength. Also, field tests or large scale laboratory tests can be performed and compared to the laboratory results from the element tests in order to validate the proposed assumptions.

REFERENCES

ASTM International. 2019. ASTM C618-19 *Standard Specification for Coal Fly Ash and Raw or Calcined Natural Pozzolan for Use in Concrete*, West Conshohocken, PA, ASTM International.

Amiralian, S., Chegenizadeh, A. and Nikraz H. (2012) A Review on The Lime and Fly ash Application in Soil Stabilization. *International Journal of Biological, Ecological and Environmental Sciences (IJBEES)* Vol. 1, No. 3, 2012 ISSN 2277 – 4394. pp. 124–126.

Beeghly, J. (2003). Recent Experiences with Lime- Fly Stabilization of Pavement Subgrade Soils, Bas, and Recycled Asphalt. *International Ash Utilization Symposium (Paper No. 46). Kentucky: University of Kentucky*.

Bojadjieva, J. 2015. *Dynamic behaviour of 15 saturated cohesionless soils based on element and 1-G experiments*. PhD Thesis. University "St. Cyril and Methodius", Institute of Earthquake Engineering and Engineering Seismology, Skopje.

Bojadjieva, J., Sesov, V., Edip, K., Gjorgiev, I. 2014 Some important aspects in experimental setup for liquefaction studies on shaking table tests. *Second European Conference on Earthquake Engineering and Seismology*, *Proc. Intern. Symp., Istanbul* 25-29 August 2014. New York: Curran Associates, Inc.

Bojadjieva, J., Sheshov, Vl., Edip, K., Kitanovski, T., Chaneva, J. 2018 In-situ and laboratory methods for liquefaction hazard assessment. *XVI Danube – European Conference on Geotechnical Engineering; Proc. Intern. Symp., Skopje 7-9 June 2018*. Berlin: Ernst & Sohn.

Bojadjieva, J., Sheshov, V., Edip, K., Kitanovski, T., Chaneva, J. and Ivanovski, D. 2019 Comparison of cyclic simple shear and triaxial tests on natural sand. *XVII European Conference on Soil Mechanics and Geotechnical Engineering; Proc. Intern. Symp.*, *Reykjavik* 1-6 September 2019.

Edil, T.B. and Benson, C.H. (2007) Sustainable Construction Case History: Fly ash Stabilization of Road-Surface Gravel. Paper presented at the World of Fly ash (WOCA), Lexington, KY, USA.

Edip, K. 2013. *Development of Three Phase Model with Finite and Infinite Elements for Dynamic Analysis of Soil Media*. PhD Thesis. University "St. Cyril and Methodius", Institute of Earthquake Engineering and Engineering Seismology, Skopje.

Edip, K., Sheshov, Vl, Bojadjieva, J., Kitanovski, T., Chaneva, J. 2018 Numerical simulation of triaxial tests. *XVI Danube – European Conference on Geotechnical Engineering; Proc. Intern. Symp.,* Skopje 7-9 June 2018. Berlin: Ernst & Sohn.

Jackson, N.M., Mack, R., Schultz, S. and Malek, M. (2007) Pavement Subgrade Stabilization and Construction Using Bed and Fly Ash. Paper presented at the World of Fly ash (WOCA), Lexington, KY, USA.

Keramatikerman, M., Chegenizadeh, A. and Nikraz, H. (2017) Experimental study on effect of fly ash on liquefaction resistance of sand. *Soil Dynamics and Earthquake Engineering* vol. 93, pp1–6.

Kitanovski, T., Sheshov, Vl., Edip, K., Bojadjieva, J., Chaneva, J. 2018 Laboratory model tests on natural sand from Skopje region. *XVI Danube – European Conference on Geotechnical Engineering; Proc. Intern. Symp., Skopje* 7-9 June 2018. Berlin: Ernst & Sohn.

Kolay, P. K., Puri, V. K., Lama Tamang, R., Regmi, G. and Kumar, S. (2019) Effects of Fly Ash on Liquefaction Characteristics of Ottawa Sand. International Journal of Geosynthetics and Ground Engineering 5: 6.

Lin, L., Tuncer, E., Benson, C. (2009). Properties of Pavement Geomaterials Stabilized with Fly Ash. Paper presented at the World of Fly ash (WOCA), Lexington, KY, USA.

McCarthy, M. J., Csetenyi, L. J., Sachdeva, A., and Jones, R. (2009). Role of Fly Ash in the Mitigation of Swelling in Lime Stabilised Sulfate Bearing Soils. Paper presented at the World of Fly ash (WOCA), Lexington, KY, USA.

Parsons, R. L., and Kneebone, E. (2005). Field performance of fly ash stabilised subgrades. Proceedings of the Institution of Civil Engineers. Ground improvement, 9(1), 33–38.

Santos, F., Li, Lin., Li, Y. and Amini, F. (2011) Geotechnical Properties of Fly Ash and Soil Mixtures for Use in Highway Embankments. Paper presented at the World of Fly ash (WOCA), Denver, CO, USA.

Senol, A., Edil. T.B., Acosta, Bin-Shafique, M.S. and Benson, C.H. (2006). Soil stabilization by using the sorts of fly ash at various sites in Wisconsin. Resources, conservation, and recycling, 46 (4),365. *87 Proc. INTERMAG Conf.*, pp. 2.2-1–2.2-6.

Trast, J.M., DeJardin D.M. and Skrzypchak, G.M. (2011) Beneficial Use of Fly Ash for an Airport Safety Way Extension over a Multiple Year Project. Paper presented at the World of Fly ash (WOCA), Denver, CO, USA.

Vukićević, M., Marjanović, M., Pujević, V. and Jocković, S. (2019) The Alternatives to Traditional Materials for Subsoil, Stabilization and Embankments. Materials, 12, 3018; doi: 10.3390/ma12183018

Smart Geotechnics for Smart Societies – Zhussupbekov, Sarsembayeva & Kaliakin (Eds)
© 2023 The Author(s), ISBN 978-1-003-29912-7
Open Access: www.taylorfrancis.com, CC BY-NC-ND 4.0 license

Prediction of undrained shear strength in soil-cement columns constructed with dry mixing method for Bangkok soft clay

Bipin Singh Karki & Kuo Chieh Chao
Asian Institute of Technology, Bangkok, Thailand

Suman Manandhar
Global Institute for Interdisciplinary Studies, Kathmandu, Nepal

Ricky K.N. Wong
Sanshin Construction (Thailand) Co., Ltd., Bangkok, Thailand

ABSTRACT: The undrained shear strength is a critical design parameter in the design of soil-cement columns for ground improvement projects. This paper presents an evaluation of undrained shear strength in soil-cement columns constructed with the dry mixing method for Bangkok soft clay. The relationships between undrained shear strength and design parameters including cement content, total water-cement ratio, curing time, and natural moisture content were established using machine learning (ML) techniques in this study. Soil samples of soil-cement column (SCC) were obtained from two sites including the AIT site and Highway No. 35 site. Different varieties of cement contents were mixed using the dry method to prepare laboratory SCC samples with curing times of 7, 14, and 28 days. The SCC samples were utilized to develop models including the multivariate regression (MLR) model, random forest (RF) model, and artificial neural network (ANN) regression model for prediction of the undrained shear strength. The coefficient of determination (R^2), mean absolute error (MAE), and root mean square error (RMSE) were used as performance detectors for different models. It was found that R^2 values for all models ranged from 0.70 to 0.99 for the training data and from 0.5 to 0.94 for the testing data. A linear equation using the MLR model to predict undrained shear strength was proposed using cement content, natural moisture content, and curing time as the primary parameters. Various graphs to predict undrained shear strength were also proposed using the RF and ANN models.

1 INTRODUCTION

Soil cement column is the application of deep mixing for ground improvement projects. It is a technique in which the grout is injected using the tip of a mechanical icer consisting of a basic drilling head and separated horizontal blades. It is generally used with lime or cement in soft soil. The main purpose of this method is to improve the soil, physical and mechanical characteristics. The wide range of applications that address a variety of geotechnical issues includes road and railway subgrade reinforcement, supporting deep excavations and protecting surrounding structures, slope stabilization retaining walls, cut-off walls, seepage control, improving the ground under existing construction, applying shallow foundations for future construction, and remediation of pollutant soil (P. G. Nicholson, 2014) and (Porbaha, 1988). There are two type of soil cement mixing methods; dry mixing method (DMM) and wet mixing method (WMM). In this study the DMM was used to improve the soft clay in Bangkok, Thailand.

There are fewer control elements in the DMM, such as cement content (C), curing time (CT), machine execution, and so on, making the task more difficult than in other types of mixing

DOI: 10.1201/9781003299127-91

methods. Because the natural moisture content (NMC) and the cement mixture are not regulated during the process, it is more complicated in the DMM to estimate the strength. Most construction firms encounter these challenges. So, to improve the projects using this technique, the most appropriate way of prediction is required. Permeability, compressibility, and shear strength are the key mechanical characteristics of the soil to be determined before use. In soft soils, like Bangkok clay, these characteristics fail to perform, so improvement is needed to increase its workability. In soil cement columns the shear strength plays a vital role, and the prediction for that is a difficult task in a laboratory and in a field. In this study, certain parameters which influence the shear strength of the soil cement columns were considered to predict the undrained shear strength. Empirical equations developed by utilizing statistical methods and data from extensive laboratory or filed testing are commonly used in geotechnical engineering practice to estimate undrained shear strength. Prediction of the undrained strength with multivariate parameters is a complex work. Therefore, machine learning (ML) was used in this study to conduct the prediction of the undrained shear strength efficiently and accurately.

The use of ML in geotechnical engineering has developed significantly in recent years (Shahin M. A., 2004); (Zhang, 2021); (Jin Y. F., 2019), (Jin Y. F., 2019), (Jin Y. F., 2019) to assist in estimating geotechnical engineering parameters. There are three major categories of ML algorithms, Supervised learning; Unsupervised learning, and Reinforcement learning. In this study, supervised learning algorithms is more highlighted than the others.

In this study, the supervised learning technique was used as Random Forest (RF), a model to predict the undrained shear strength. Random Forest, a well-known supervised ML algorithm, is a nonparametric methodology evolved from classification and regression trees (CART) that solves problems using the ensemble learning method (Breiman, 2001). The term "RF" refers to the building of multiple trees, each of which is created by bootstrap samples (H-B., 2020). Then, a specific number of samples are maintained for validation, which is referred to as out-of-bag predictions (OOB).

A random procedure was used to produce a subset of the predictors at each node of the tree. The ultimate output of RF is the average of all the trees' findings (Breiman, 2001). The data set was separated into two parts: training and testing. Model learning was implemented using a training set, and the correctness of the model is determined using a test set (Kulkarni, 2013). The training test was used to produce a tree, and a random vector that is independent of previous random vectors with the same distribution (Breiman, 2001) has presented a randomization method that is more effective than bagging or the random space method.

2 METHODOLOGY

2.1 *Sampling and testing*

The soil test samples were collected GTE's testing field at AIT and the Highway No. 35 Bang-Khun-Thain-Ekachai intersection (part-1) in Bangkok, Thailand. The obtained samples were used to evaluate physical properties and prepare specimens using the dry method of deep mixing. The base clay in this study is Bangkok soft clay. A rotary driller was used to extract undisturbed samples up to 8.5 m below the ground surface. Atterberg limit, uniaxial compression (UC) test, total unit weight, and dry unit weight were determined. The dry method was used for the preparation of the SCC specimen. After mixing was completed, the treated soil was immediately used to prepare for testing.

Cement amounts of 150, 175, 200, and 250 kg/m^3 were tested. The mold of the specimen was wrapped in plastic foil and stored in a humid condition box for 7, 14, and 28 days of curing. The water content and unit weight of the sample were determined before testing in accordance with the guidelines from (ASTM-D2216, 1998) and (ASTM-D7263, 2021), respectively. The UC test was performed following (ASTM-D2166-00., 2000) recommendations. The same method was used to prepare samples obtained from the Highway No. 35 site, with slight variation in curing times of 1, 3, 7, 14, and 28 days and cement amounts of 150, 175, 200, and 250 kg/m^3. Compressive strength data were compiled from both sites.

A total nine parameters including natural moisture content, plasticity index, unit weight, maximum dry unit weight, cement content by amount, curing time, total water-cement ratio, undrained shear strength and cement content by weight were determined for samples obtained from the two study locations The laboratory and field shear strengths were separated from both sites and compiled together. The total number of data points is 92. The compilation was completed with the goal in mind. Separate data compilation was performed for prediction models and correlation analysis. The laboratory data obtained from both sites were used to create prediction models.

Using the deep machine learning method, the relationship between strength and other parameters was chosen. For this process, the 'seaborn' library was chosen, and a heat map was generated using 'SciPy' Stats library. The function "Pearson r" was used to evaluate the R^2 value between two variables. The heatmap shows each R^2 value for the correction. The input parameters were then chosen by observing the highest value.

Three models were proposed for the prediction of the strength of the SCC constructed by DMM. A trial-and-error method was conducted for each method to improve the accuracy of the model, considering the most effective input parameter. The following section describes the detailed execution of each model.

2.2 *Multiple linear regression model*

The general model of MLR used in this study is presented in the equation below.

$$Y = a + b_1 V_1 + b_2 V_2 + \ldots . + b_n V_n$$

where Y =the dependent variable (strength); a =constant; b_1 to b_n = partial regression coefficients for V_1 to V_n; V_1 to V_n = independent variables.

The trial-and-error were done with changing input parameters for the best R^2 value. The best input parameters are then trained and tested in the model for the prediction of strength.

2.3 *Random forest machine learning algorithm model*

Random Forest Machine Learning Algorithm was developed for a quick estimation of the undrained shear strength of SCCs. In this algorithm, parameters were fed to predict the strength of the column. Various libraries like pandas, NumPy, 'Sklearn' were imported for this model. Random forest regressor was used for the regression process. The dataset was split into training and testing data. A total of 80% of data were used as the training and 20% of data were used as the testing dataset. These data sets were kept in the model for the prediction.

2.4 *Artificial Neuron Network (ANN)*

ANN is mainly utilized for the resolution of difficult issues. The issues are regarded in engineering as tough if the link between independent variables and dependent variables is extremely non-linear. Therefore, it will be a difficult task to develop a closed-form solution. Nevertheless, a feedforward neural network is the most often utilized family of neural networks (A. R. Bunawan, 2018). Some investigators, such as (Shahin & Jaksa, 2004) and (Macmillan, 1999) revealed that the multilayer perceptron network is one of the most common feedback ANNs. Multilayer perceptron ANNs typically consist of at least three layers, which are joined by connection weights known as the input, hidden, and output layers.

3 RESULTS AND DISCUSSION

The results of the UC test from the two sites with curing times of 7, 14, and 28 days are presented in Table 1. The influencing factors to affect strength in gaining strength are shown in detail. The deep machine learning models were generated to predict the strength in the laboratory for DMM.

Table 1. Unconfined compressive test from the sites.

Cement content (kg/m^3)	UCS 7 days (kPa)	UCS 14 days (kPa)	UCS 28 days (kPa)
0	28.08(undisturbed)	-	-
150	893.718	1441.251	1479.49
200	1403.197	1636.65	1764.86
250	1859.579	1899.63	2018.021
300	2928.54	3235.5	3600.94

3.1 *Influencing parameter for undrained shear strength*

NMC of the soil directly influences the strength development in SCC. Further analysis was carried out for to find the factors influencing the strength development using the Pearson correlation coefficient by deep machine learning. A total of 9 parameters were used in this study. Among them trial-and-error approach was carried out to find the most affecting factors for strength. Using the Pearson correlation coefficient analysis (PCA), it was found that cement content (C), total water-cement ratio, and curing time (CT) are mostly correlated. Cement content and curing time are positively correlated with R^2 values of 0.77 and 0.5, respectively, whereas the total water- cement ratio is inversely correlated with an R^2 value of 0.79.

3.2 *Prediction using multiple linear regression*

After the compilation of data from the two sites, MLR was set up. A total number of 92 data points were taken from the laboratory work. The undrained shear strength (S_u) is the dependent variable and the independent variables selected from previous sections were cement content (C), water-cement ratio, curing time (CT), and NMC. Although, trial-and-error approach was conducted to check the reliability of parameters in the multiple regression model. Different models with a selection of different parameters along with the selected parameters were run. The training and testing predicted data were evaluated with an R^2 correlation value. A total of six models were created & ran, and R^2 values less than 0.7 were neglected. Previously analyzed parameters which were C, CT and NMC gave the best R^2 values, 0.90 (train) and 0.92 (test). The outcome of this model was a linear equation which is:

$$Su = 5.12 + 0.05x_1 - 0.12x_2 + 0.13x_3$$

Where:-, Su = Undrained shear strength in ksc; x_1 = Cement Content in kg/m^3; x_2 = NMC in %; and x3 = CT in days

3.3 *Prediction model using Random Forest algorithm (RF)*

The models were trained and tested, using 80 % of training data and 20 % of testing data from the total data. Cement content, curing time, and NMC gave the best results with 0.99 (training R^2), 0.94 (testing R^2), 0.47 MAE, and 0.59 as RMSE. Figure 1 shows the results of the prediction using the Random Forest model. Obtaining lower values of RMSE and MAE indicates better prediction capability of the model, and the higher the value of R^2 the better the performance.

Due to the space limitation of the paper only four graphs representing the NMC are presented in this study, as shown in Figure 1. NMC of Bangkok soft clay ranges from 76 – 84%, but can differ from plain. In this study, a maximum of 95.5 % water content and a minimum of 75% water content have been used. For the prediction of undrained shear strength, we can have a prediction relying on these NMC. In practice, usually average NMC is used as NMC before mixing cement. So, the range in this model fits the average NMC of the Bangkok clay.

Figure 1 provides information about the relationship between the required amount of cement and the resulting undrained shear strength. The graphs mentioned in Figure 1 can be directly used to predict the undrained shear strength of SCC in the laboratory. With the NMC

which is the easiest property that can be obtained in any project, the undrained shear strength can be predicted. The right amount of cement required for the design strength can be predicted and, thus, reduce the laboratory works. This approach can make the project more economical from the initial phase.

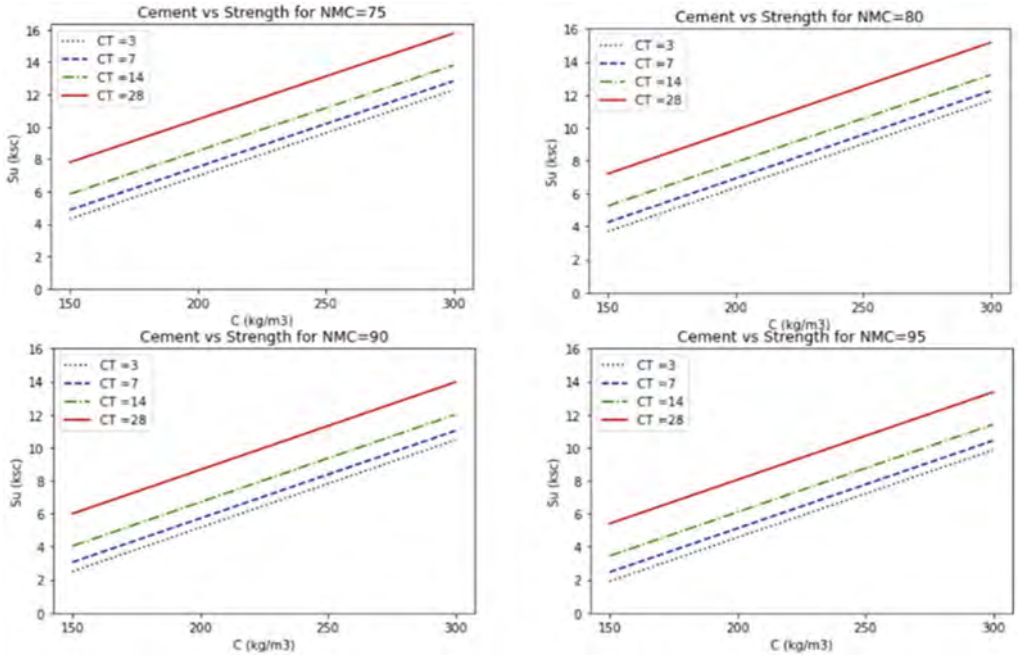

Figure 1. Graphical representation of prediction model using Random Forest model.

3.4 *Prediction model using Artificial Neuron Network (ANN)*

This model is different from other previous models as it can perform non-linear regression. The model was set up with various parameters such as optimizer, normalizer, learning rate, features splitting ratio, hidden layers, nodes, and epochs. The number of input parameters in this model makes it more complicated than other previously mentioned models. The input features were selected as before and run in the model for the trial-and-error process. The best results with various input parameters were noted for further investigations and analysis.

Several models were discarded due to low performance in prediction by, observing R^2 values of the trained and tested datasets. These models used different parameters and different settings in neuron networks. In this study, ANN performance was not satisfactory compared with other models. A multilayer perceptron was used in this analysis with one input layer, one hidden layer, and one output layer. This network architecture gave the best result, compared to others.

Three independent input variables were used, and one output dependent variable was used, like in the previous models. The R^2 values of 0.96 and 0.87 for the training and testing datasets, respectively, were achieved using the ANN model. The difference in R^2 values between the training and testing datasets is signidicant, which is not a good scenario in a neuron network.

4 CONCLUSIONS

In this study, a total of nine parameters including moisture content, plasticity index, unit weight, maximum dry unit weight, cement content by amount, curing time, total water-cement ratio,

undrained shear strength and cement content by weight were selected to predict the undrained shear strength of the treated samples. It was found that the undrained shear strength can be predicted with a reasonable accuracy when at least three parameters were used in all the models. Among those nine parameters, it was concluded that the natural moisture content, cement content, and curing time has the most significant impact on the strength of Bangkok soft clay using the deep mixing method.

Conventional prediction methods were replaced by deep machine learning for predicting the strength using the most influencing factors in this study. This methodology of a prediction model using ML makes the work more effective and is recommended to be widely used in the geotechnical engineering field. The R^2 values of 0.91 and 0.87 for the MLR model and 0.99 and 0.94 for the RF model were obtained from the models which indicate strong correlation results for prediction purposes. The linear equation has the advantage of predicting the wide range of data outside the fed dataset in this study, whereas the random forest is the best within the fed dataset. So, if both prediction methods are used, a good prediction of the undrained strength of Bangkok soft clay can be obtained in a cost and time- efficient way. The results of the analysis indicate that using multiple linear equations and random forest model graphs can predict laboratory strength with higher accuracy.

REFERENCES

A. R. Bunawan, E. M. (2018). Experimental and Intelligent Techniques to Estimate Bearing Capacity of Cohesive Soft Soils Reinforced with Soil-Cement Columns. *Measurement: Journal of the International Measurement Confederation*, 529–538.

ASTM-D2166-00. (2000). Standard Test Method for Unconfined Compressive Strength of Cohesive Soil. *ASTM International*.

ASTM-D2216. (1998). Standard Test Method for Laboratory Determination of Water (Moisture) Content of Soil and Rock by Mass. *ASTM International*, 1–5.

ASTM-D7263. (2021). Standard Test Methods for Laboratory Determination of Density and Unit Weight of Soil Specimens. *American Society for Testing and Material*.

Breiman, L. (2001). Random Forests. *Machine Learning*, 5–32.

H-B., L. &. (2020). Prediction of Shear Strength of Soil Using Direct Shear Test and Support Vector Machine Model. *The Open Construction and Building Technology Journal*, 268–277.

Jin, Y. F. (2019). A Single-Objective EPR Based Model for Creep Index of Soft Clays Considering L2 Regularization. *Engineering Geology*, 242–255.

Jin, Y. F. (2019). Identifying Parameters of Advanced Soil Models Using An Enhanced Transitional Markov Chain Monte Carlo Method. *Acta Geotechnica*, 1925–1947.

Jin, Y. F. (2019). Multi-Objective Optimization-Based Updating of Predictions During Excavation. *Engineering Applications of Artificial Intelligence*, 102–123.

Kulkarni, V. (2013). Random Forest Classifiers: A Survey and Future Research. *Researchgate*.

Lee, J. G.–5. (2017). Deep Learning in Medical Imaging: General overview. *Korean Journal of Radiology, Vol. 18*, 570–584.

Lorenzo, G. A. (2006). Fundamental Characteristics of Cement-Admixed Clay in Deep Mixing. *Materials in Civil Engineering*, 161–174.

Macmillan, S. H. (1999). Neural Networks: A Comprehensive Foundation. *The Knowledge Engineering*, 409–412.

N. Miura, S. H. (2001). Engineering Behavior of Cement Stablized Clay at High Water Content. *Soil and Foundations*, 33–45.

P. G. Nicholson. (2014). Soil Improvement and Ground Modification Methods. *Butterworth-Heinemann, Elsevier*.

Porbaha, A. (1988). State of the Art in Deep Mixing Technology: Part I. Basic Concepts and Overview. *Institution of Civil Engineers* (pp. 81–92). Proceedings of the Institution of Civil Engineers - Ground Improvement.

Shahin, M. A. (2004). Data Division for Developing Neural Networks Applied to Geotechnical Engineering. *Journal of Computing in Civil Engineering*, 105–114.

Shahin, M. A., & Jaksa, H. R. (2004). Data Division for Developing Neural Networks Applied to Geotechnical Engineering. *Journal of Computing in Civil Engineering*, 105–114.

Zhang, P. Y. (2021). Intelligent Modelling of Clay Compressibility Using Hybrid Meta-Heuristic and Machine Learning Algorithms. *Geoscience Frontiers*, 441–452.

Smart Geotechnics for Smart Societies – Zhussupbekov, Sarsembayeva & Kaliakin (Eds)
© 2023 The Author(s), ISBN 978-1-003-29912-7
Open Access: www.taylorfrancis.com, CC BY-NC-ND 4.0 license

Pavement design improvement through implementation of processed admixture in subgrade

F. Hakimzadeh Zargar, M.A. Zarco & A.P. Acacio
Institute of Civil Engineering, University of the Philippines, Diliman, Quezon City, Philippines

ABSTRACT: This study presents a new approach for further improving the strength and compressibility characteristic of soils using Type I Portland Cement (PC) and Class F Fly Ash (FA) by processing the individual components of the admixture through ball milling. Unconfined Compression Strength (UCS) and California Bearing Ratio (CBR) Tests were performed on improved soils using 5% PC+5% FA and 10% PC+10% FA. Using 5% PC+5% FA resulted in a 46% and 31% increase in UCS and CBR values, respectively, for improved soils using processed admixtures versus improved soils using unprocessed (commercial) admixtures. Using 10% PC+10% FA resulted in a 55% and 80% increase in UCS and CBR values, respectively, for improved soils using processed admixtures versus improved soils using unprocessed admixtures. The flexible pavement design of a typical 4-lane expressway with 110,000,000 ESALs was used to illustrate the potential cost savings from processing PC and FA components before deep mixing.

1 INTRODUCTION

In every pavement construction, to avoid bearing capacity failure and excessive settlement while ensuring a stable, long-lasting, and maintenance-free roadway, a subgrade that carries the imposed load of the whole pavement section must be constructed using specific established procedures that provide satisfactory results. Moreover, an enhanced subgrade with a higher resilient modulus (M_r) reduces the Structural Number (SN) and thickness (D) of the required pavement resulting in economic savings in terms of construction materials, power, and labor costs.

Among the many approaches for improving subgrades in roadway projects, the most commonly used technique is chemical stabilization through admixtures. In this study, the efficacy of a stabilizing admixture consisting of Portland Cement (PC) and Class F Fly Ash (FA) was enhanced by grinding each component individually through ball-milling. The approach of stabilization in this study involved blending soils and additives thoroughly with a Rotary Mixer Drum (RMD) *in situ* before compaction to achieve a more homogenous layer and attain the desired gradation, maximum dry density (MDD), and optimum moisture content (OMC) of the admixture closest to laboratory conditions.

The flexible pavement design for a 4-lane expressway, 30.7 km in length and 60 m in width having a 110,000,000 Equivalent Standard Axle Load (ESALs), was considered. Tests included specific gravity, compaction, UCS, and CBR tests for both unimproved and improved subgrades with unprocessed (commercial) and processed soil additives were examined; and then resilient modulus correlation (M_r) was obtained before determining the Structural Number (SN) of the pavement. Following the American Association of State Highway and Transportation Officials (AASHTO) Guide for Design of Pavement Structures, the most economical approach was considered for each unimproved and improved structure in the pavement design.

DOI: 10.1201/9781003299127-92

2 MATERIALS

2.1 *The subgrade soil*

Before mixing the admixture, sieve analysis (ASTM D6913M-17), sedimentation (ASTM D7928-17), Atterberg limits (ASTM D4318-17), and specific gravity (ASTM D854-14) were conducted on excavated soil of the subgrade. The laboratory tests' results are shown in Tables 1 and 2.

Table 1. Sieve analysis and sedimentation (hydrometer) tests' results.

Sieve size mm	4.75	2	0.85	0.425	0.25	0.105	0.075	0.0537	0.039	0.0284	0.0184	0.011	0.008	0.0057	0.0041	0.0029	0.0021
Pass finer %	100	92	81	70	62	55	51	45	42	39	35	31	27	26	24	23	21

Table 2. Atterberg limits and specific gravity tests' results.

LL	PL	PI	USCS	specific gravity
44	29	15	CL (lean clay)	2.63

2.2 *Commercial (unprocessed) and processed cement*

The usual Type I Portland Cement was used as the commercial soil additive, while the processed cement was produced after 4 hours of grinding by ceramic ball-milling. Through laser diffraction technique (USP 429 standard), within three trials, the mean values of the particle size distribution from D0.02 (min.) to D100 (max.) for both commercial and processed cement were obtained, as reflected in Table 3.

Table 3. Particle size distribution of commercial and processed cement.

Material	D0.02	D10	D20	D30	D40	D50*	D60	D70	D80	D90	D100
Commercial (μm)	0.04	1.54	3.5	5.63	7.4	9.18*	11.23	14.17	23.93	40.21	74.98
Processed (μm)	0.04	0.6	1.11	1.67	2.43	3.42*	4.53	5.83	7.5	10.56	65.615

* 50% of the commercial sample had a size of 9.18 μm or finer, while it was decreased to 3.42 μm or finer for the processed sample.

2.3 *Commercial (unprocessed) and processed fly ash*

Class F Fly Ash taken from the coal power plants in Batangas, provided by Pozzolanic Philippines, Inc., was used as another commercial soil additive. Processed fly ash, the same as processed cement, was produced after 4 hours of grinding by ceramic ball-milling. Via the same mentioned technique and standard (laser diffraction, USP 429) also undergoing three trials, the mean values of the particle size distribution from D0.41 (min.) to D100 (max.) were obtained for both commercial and processed fly ash as shown in Table 4.

Table 4. Particle size distribution of commercial and processed fly ash.

Material	D0.41	D10	D20	D30	D40	D50	D60	D70	D80	D90*	D100
Commercial (μm)	0.04	0.75	1.44	2.38	3.36	4.33	5.36	6.62	8.5	27.97*	66.98
Processed (μm)	0.04	0.73	1.27	1.97	3	4.09	5.27	6.53	8.23	11.61*	61.47

* 90% of the commercial sample had a size of 27.97 μm or finer while it was decreased to 11.61 μm or finer for the processed sample.

3 GEOTECHNICAL TESTS AND RESULTS

3.1 *Laboratory tests*

Using the above materials, a series of compaction (ASTM D1557-12e1), UCS (ASTM D2166), and CBR tests (ASTM D1883–16) was conducted on subgrade for both unimproved and improved designs of subgrade. A modified proctor (AASHTO proctor) test indicated the maximum dry density (MDD) and optimum moisture content (OMC) of the unimproved and improved subgrade soil before conducting any UCS (after 7-day curing) and CBR test (after 96-hour soaked condition) at 95% MDD.

3.2 *Results*

Table 5 shows the results for unimproved (compacted subgrade soil) and improved designs (compacted subgrade in a certain percentage of commercial and process ed soil additives).

Table 5. MDD, OMC, UCS, CBR, and M_r* values of all subgrade designs.

Material	Design	MDD g/cc	OMC %	UCS psi	CBR %	MR psi*
0% PC+0% FA	unimproved	1.697	17.86	43.08	6.01	6800
5% PC+5% FA	commercial	1.404	23.41	60.33	32.29	21000
5% PC+5% FA	processed	1.564	21.36	88.08	63.24	33000
10%PC+10%FA	commercial	1.333	22.41	104.84	116.17	53500
10%PC+10%FA	processed	1.633	19.61	162.02	196.31	75000

* Established from AASHTO correlation chart relationship between CBR and M_r values of the subgrade. (AASHTO interim guides, 1972).

4 PAVEMENT STRUCTURE COMPUTATION

The basic Equation 1 was applied for flexible pavement design (AASHTO,1993):

$$\log_{10}W18 = Z_R \times S_0 + 9.36 \times \log_{10}(SN+1) - 0.20 + \frac{\log 10\left(\frac{\Delta PSI}{(4.2-1.5)}\right)}{0.4 + \left(\frac{1094}{(SN+1)^{5.19}}\right)} + 2.32 \times \log_{10}M_r - 8.07 \quad (1)$$

where *W18* = designed ESALs; Z_R = standard normal deviation for a given reliability (R = 85%); S_0 = overall standard deviation; and ΔPSI = Present Serviceability Index.

Given *W18* = 109, 620, 118; Z_R = -1.037; S_0 = 0.45; ΔPSI = 1.7; and = values in Table 5; the structural number (*SN*) for each pavement could be computed and shown in Table 6, where the sum of designed structural numbers in every layer above the subgrade shown in Figure 1 should not be any value less than the computed *SN* for the entire pavement.

5 FLEXIBLE PAVEMENT DESIGN

Targeting the most economical pavement consideration: applying the material's minimum allowed thickness (D), coefficient ($a_{sandy\ gravel\ subbase}$ = 0.11, $a_{crushed\ stone\ base}$ = 0.14, $a_{cement\ treated\ base}$ = 0.2, $a_{HMA\ binder}$ = 0.4, $a_{HMA\ surface}$ = 0.44) (SUDAS, 2019) and drainage factor of each layer (m_{base} = 1and $m_{subbase}$ = 0.7) the entire pavement structure for each design is summarized in Table 6. (Richardson, et al. 1996).

To evaluate the significance of this study, processed designs versus commercial and unimproved designs were compared geotechnically and economically, as shown in Table 7.

Table 6. Minimum pavement SN and layer thickness in each design.

Material	Design	SN min.	subgrade cm	treated-subgrade* cm	subbase cm	base cm	CTB cm	binder cm	surface cm	cost** USD
0%PC +0%FA	unimproved	9.45	30.48	N/A	49.7	49.3	49.3	5	3.8	125.51M
5%PC +5%FA	commercial	5.3	30.48	52.6	49.2	22.9	15.2	5	3.8	99.54M
5%PC +5%FA	processed	4.1	30.48	25.9	23.5	15.2	15.2	5	3.8	83.93M
10%PC +10%FA	commercial	3.17	30.48	22.5	0	15.2	15.2	5	3.8	79.95M
10%PC +10%FA	processed	2.76	30.48	7.7	0	0	17.9	5	3.8	70.88M

* Treated subgrade is where the proposed materials/admixture is used.
** Includes materials, equipment, processing, hauling, power, and labor costs for the entire pavement. (1USD = PHP56.00)

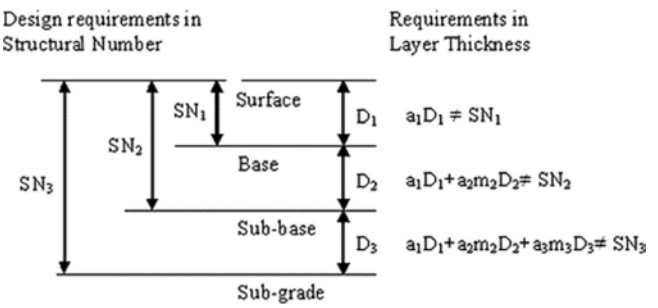

Figure 1. AASHTO structural number equation (AASHTO,1993).

Table 7. Processed designs *vs*. commercial and unimproved designs.

Comparison	MDD	OMC	UCS	CBR	M_r	SN	savings
5% PC+5% FA (processed *vs*. commercial)	+11%	-9%	+46%	+31%	+57%	-23%	+16%
10%PC+10%FA (processed *vs*. commercial)	+23%	-12%	+55%	+80%	+40%	-13%	+11%

6 CONCLUSION

Based on the evaluation summarized in this study, it can be seen that the processed designs for the described improved subgrade could significantly increase MDD, UCS, CBR, M_r and correspondingly decrease OMC and SN. The study showed that a processed admixture of 10% PC+10% FA could save $9.07M compared with the cost of 10% PC+10% FA commercial admixture. Moreover, the processed admixture of 10% PC+10% FA could save $54.63M compared to the unimproved design.

Similarly, for a 4-lane expressway, 30.7 km long and 60 m wide with 110,000,000 ESALs, 5% PC+5% FA processed material indicated an economic achievement of $15.61M and $41.58M compared to the cost of 5% PC+5% FA commercial and unimproved designs, respectively.

REFERENCES

AASHTO guide for design of pavement structures 1993, Washington, D.C., *American Association of State Highway and Transportation Officials*.

Evaluation of AASHTO interim guides for the design of pavement structures 1972. Highway research Board, National Research Council, *National Academy of Engineering*.

Iowa Statewide Urban Design and Specifications (SUDAS). Chapter 5, Section 5F-1, Pavement Thickness Design, 2019. *Iowa Statewide Urban Design Manuals*.

Richardson, D., Morrison, W., et al. l. 1996. *Determination of AASHTO drainage coefficients*, Missouri highway, and transportation department. In corporation with the U.S. department of transportation federal highway administration.

Smart Geotechnics for Smart Societies – Zhussupbekov, Sarsembayeva & Kaliakin (Eds)
© 2023 The Author(s), ISBN 978-1-003-29912-7
Open Access: www.taylorfrancis.com, CC BY-NC-ND 4.0 license

Investigation of combined support structures under complex geological conditions

R.K. Zhanakova & A.O. Sagybekova
Kazakh Automobile and Road Institute named after L.B. Goncharov, Almaty, Republic of Kazakhstan

ABSTRACT: At present, the construction of mine and underground structures is intensively growing in our country. In the mining industry and transport systems, the role of horizontal and inclined mine workings is very large. In their length they cross a rock mass with different stability characteristics. In general, for the support of the workings, they account for 30-40% of the funds spent on driving the workings, therefore, the provided new, inexpensive, innovative design of the lining is relevant. It is especially necessary to carry out scientific work to create a rational innovative technology for the passage of underground workings in an array with complex mining and geological conditions. This paper considers a new approach that will allow to fix the workings, to divide the workings into separate sections along the working route, suitable for specific geomechanical conditions, with fasteners of various designs. As a result, it is possible to achieve an improvement in the technical and economic indicators of tunneling and an increase in labor productivity. The presented reasoned method and fastening methods can be widely applied in the mining industry.

Keywords: Support structure, Combined structures, Mine workings, Massif

1 INTRODUCTION

At present, for fixing complex development workings (drift, crosscut), only one type of fixing is used without taking into account the frequent change in the mining and geological conditions of the massif along its length.

For the object of study, monolithic concrete lining is used as the main permanent support at the Beskempirsky and Akbakaysky mines. At the same time, unreasonable safety margins of the lining are often created in areas with favorable mining and geological conditions. All this leads to a deterioration in the indicators of tunneling, an increase in the labor intensity of underground work and the estimated cost of driving underground workings [1,2,11,13,20].

Existing and used in the complex mining and geological conditions of the Beskempir mine, when the designed drifts cross the zones of geological faults, traditional types and methods of fixing and maintaining mining developments become expensive and laborious.

To do this, it is necessary to simulate the stress-strain state of the massif of the Beskempir mine (+230 m) and determine the stability of the rocks using several alternative methods. Based on the results of the study, it is very important to determine the boundaries of sections along the drift route, consisting of unstable sections with high cracks, the stability and stress properties of which have changed due to the influence of tectonic disturbances [3-15].

This innovative approach makes it possible to fix sections of workings, dividing them along longitudinal sections, with fixation by various structures suitable for specific tectonic conditions. As a result, it is possible to improve the technical and economic indicators of underground mining and increase labor productivity. The fixing methods proposed by the research results of the dissertation work can be used in other mines.

DOI: 10.1201/9781003299127-93

2 LITERATURE REVIEW AND PROBLEM STATEMENT

Research specialists like: M.M. Protodyakonova, P.M. Tsimbarevich, V.D. Slesarev, V. Fenner, A. Labas, K.V. Ruppeneita, J.S. Erzhanova, Yu.L. Lieberman et al. gave hypotheses about rock pressure. Which at present, all known theories of rock pressure, depending on the methods underlying them, can be divided into three groups:

- methods for calculating the load;
- calculation methods for given deformations;
- calculation methods for given deformations and loads.

The third method of rock pressure calculation combines the advantages of the first two calculation approaches. Which is taken to calculate the magnitude of the load on the support of the object under study [12-22].

3 THE AIM AND OBJECTIVES OF THE STUDY

At present, for fixing complex development workings (drift, crosscut), only one type of fixing is used without taking into account the frequent change in the mining and geological conditions of the massif along its length (Table 1).

Table 1. Initial data of the object under study.

Excavation size, m		Fault zone size, m	Distribution size Voltage, m	Max stress MPa
Working area	S=10,9м^2	a=138	от 0-183	от 30 до -60
Entry length	L=1300	b=138	от 0 до 52	от 30 до 90
Fault zone size, m	B=3,2	c=138	От 0 до 152	от 30 до 120

For the object of study, monolithic concrete lining is used as the main permanent support at the Beskempirsky and Akbakaysky mines. At the same time, unreasonable safety margins of the lining are often created in areas with favorable mining and geological conditions. All this leads to a deterioration in the indicators of tunneling, an increase in the labor intensity of underground work and the estimated cost of sinking underground workings (Figure 1).

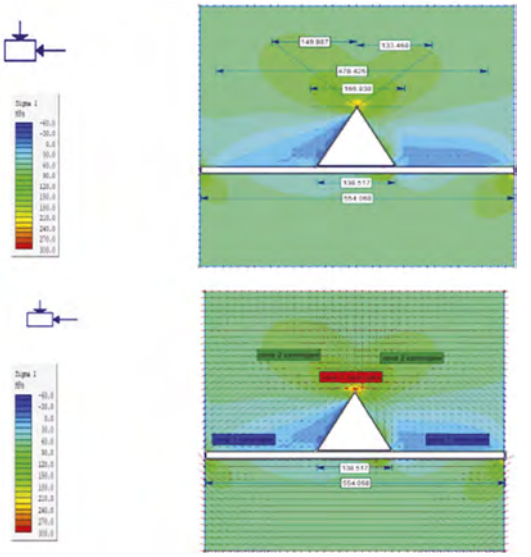

Figure 1. The results of modeling the stress-strain state of the massif, taking into account the tectonic fault.

Existing and used in the complex mining and geological conditions of the Beskempir mine, when the designed drifts cross the zones of geological faults, traditional types and methods of fixing and maintaining mining developments become expensive and laborious.

To do this, it is necessary to simulate the stress-strain state of the massif of the Beskempir mine (+230 m) and determine the stability of the rocks using several alternative methods. Based on the results of the study, it is very important to determine the boundaries of the sections along the drift route, which consist of unstable sections with high cracks, the stability and stress properties of which have changed due to the influence of tectonic disturbances (Figure 2).

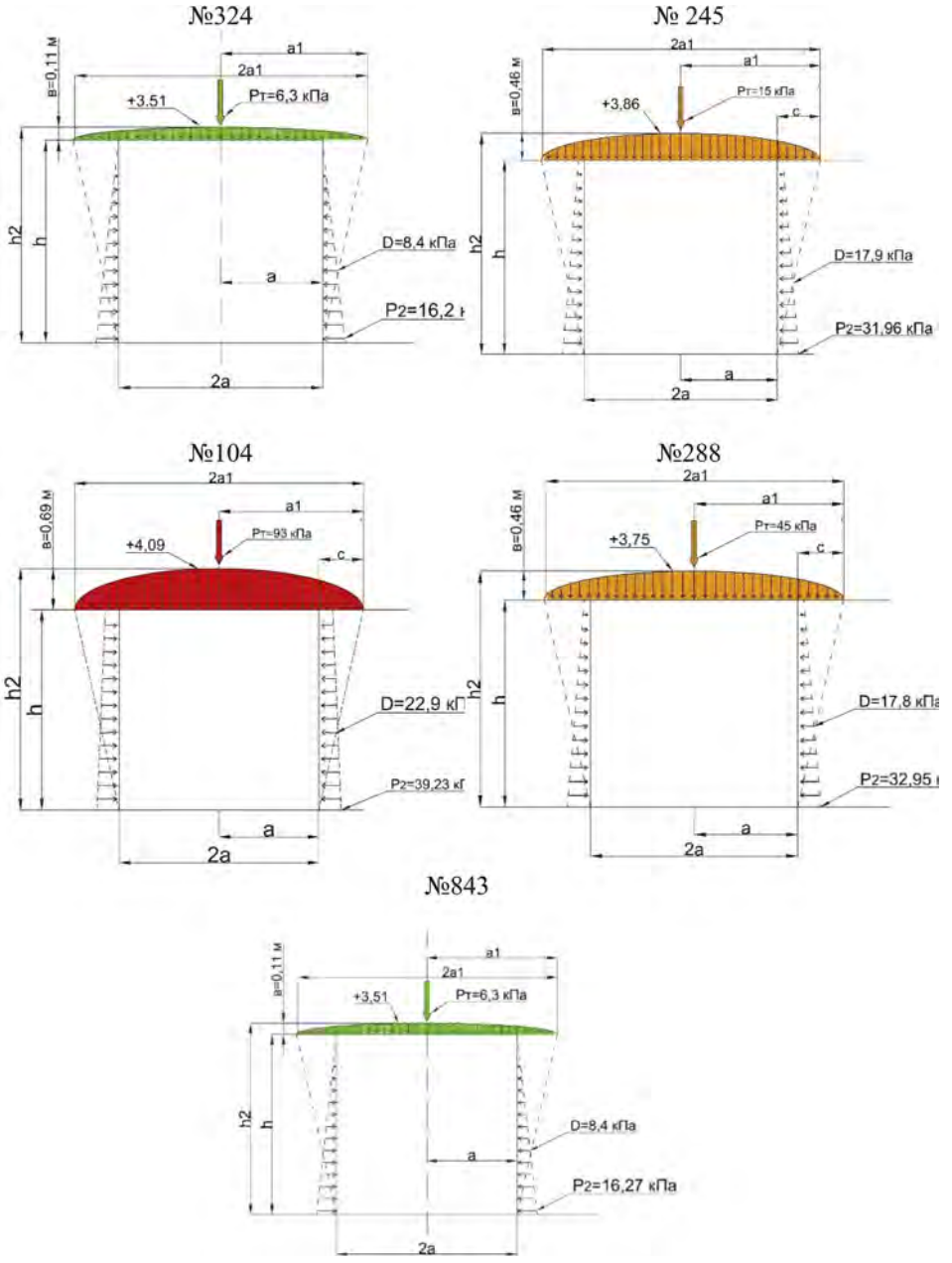

Figure 2. Results of rock pressure calculation for wells No. 324, No. 245, No. 104, No. 288 and No. 843.

4 MATERIALS AND METHODS

Studied the stability of rocks at rest in three alternative ways in accordance with the specific mining and geological conditions of development:

- official traditional method
- according to the rating (RMR) of Z. Benyavsky and according to the drawing up of the diagram by E. Hook (E. Noak);
- Empirical method of N. Barton (Q-rating)

The types of rational fastenings and their designs are determined, suitable for fastening each section of the roadway, their parameters, in accordance with the stability of rocks.

5 RESULTS OF RESEARCH

This innovative approach makes it possible to fix sections of workings, dividing them along longitudinal sections, with fixation by various structures suitable for specific tectonic conditions. As a result, it is possible to improve the technical and economic indicators of underground mining and increase labor productivity. The fixing methods proposed by the research results of the dissertation work can be used in other mines [21-27].

To solve these problems, research and analysis of actual geological data and test materials and performed laboratory work experiments. To determine the digital estimates of the stress-strain state, a numerical simulation of the studied mass was created.

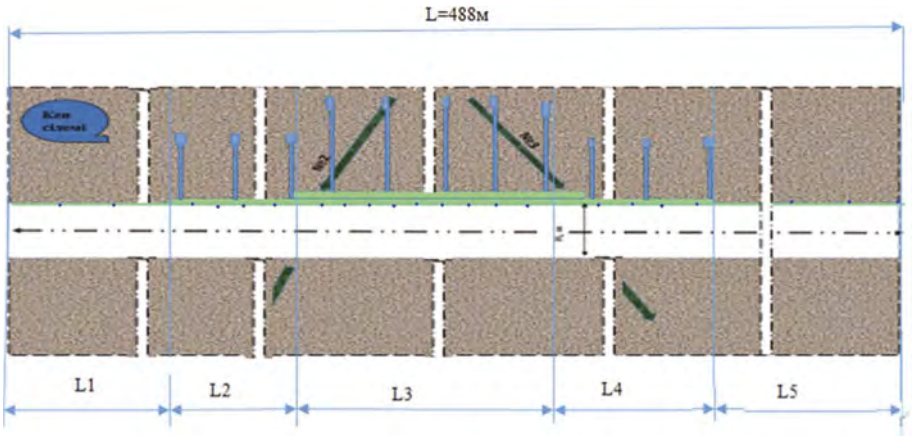

Figure 3. Recommended support design.

Based on the modeling of specific values of stress-strain loads that occur in the working area in the "Rocks-massif-working" system, it is determined with a breakdown by sections in accordance with the distribution zones of the state of the massif (Figure 3).

Based on the obtained data, it was determined that the drift can be fixed with fastening structures having different bearing capacity and design, which can withstand geomechanical processes in the massif. A new method of fastening horizontal workings is proposed, in which the methods of fastening (sprayed concrete) are justified in areas with high stability of the workings, as well as in unstable areas with high load-bearing fasteners, i.e. load-controlled fastening system.

As a result of a special study of stress-strain states in the rock mass intersected by the working route, taking into account the influence of tectonic faults, it was found that the stability of rocks in the vicinity of the working was determined using several new methods and, as a result, a system of combined supports with various designs was reasonably presented, managed and regulated by the values of the bearing capacity of the mine

REFERENCES

1. R. Zhanakova, A. Pankratenko, T. Almenov, V. Bektur. Rational selection of the form of support for the formation of genetic composition of rocks in the conditions of the Beskempir field. NEWS of National Academy of Sciences of the Republic of Kazakhstan. Volume 1, Number 439. 2020, ISSN 2224-5278 Pages:106-113. Q3/0.21.
2. Begalinov, T. Almenov, R. Zhanakova B. Bektur Analysis of the stress deformed state of rocks around the haulage roadway of the Beskempir field (Kazakhstan). Mining of Mineral Deposits. Volume 14 (2020), Issue 3, 2020, UDC 622.281, 622.012.2 Pages: 28-36. (percentile 60%, Q2/0.24).
3. Zhanakova R.K., Elzhanov E.A. Influence of engineering-geological conditions on the construction of mine workings on the example of the Beskempirsky deposit. Bulletin of the scientific journal KazGASA, No. 4 (70), Almaty, 2018, ISSN 1680-080X, pp. 145–150
4. Sagybekova A.O., Abiev B.A., Zhanakova R.K. Determination of the strength of foundation soils. Industry of Kazakhstan No. 3 2019, ISSN 1814-5787, pp. 163–166
5. Tulendiev T.T., Sagybekova A.O., Abiev B.N., Zhanakova R.K. experimental studies of coarse-grained soils. Industry of Kazakhstan No. 3 2019, ISSN 1814-5787, pp. 60–64
6. Zhanakova R.K., Sagybekova A.O. Development of underground space in megacities. Vestnik KazGASA, No. 3, Almaty, 2019, ISSN 1680-080X, pp. 199–204
7. Sagybekova A.O. Nauruzbaev K.A. Kabylgazy A., Zhanakova R.K., Abiev B.A. Practical use of the obtained results of testing coarse clastic soils in construction. "Bulletin" of the Kazakh Humanitarian-Legal Innovation University. No. 3 (43), 2019, ISSN 2519-2338, pp. 130–134
8. Sagybekova A.O., Abiev B.N., Rustemov I.A., Zhanakova R.K., Belov A.G. Application of experimental results of soil tests in the calculations of some building structures. Bulletin of science and education. 2019, No. 20 (74). Part 1 Moscow, ISSN 2312-8089, p. 31–34
9. Sagybekova A.O., Zhanakova R.K., Nauruzbaev K.A. Comparison of the influence of sandy and clay aggregates on the strength characteristics of coarse-grained soils. "POIS" International scientific journal-application of the Republic of Kazakhstan 2019, ISSN 1560-1722, pp. 148–152
10. Zhanakova R.K. Application of intensive technology of strengthening of rocks. Science Innovators. International Conference on European Science and Technology. Materials of the XX International research and practice conference. March 21th -22th Munich, Germany, 2018, ISBN 978-3-946227-19-9, P.82–86
11. Zhanakova R.K., Elzhanov E.A. Beskempir kenshogyrynyn tau-ken sileminde opyrylyska beyim zharykshakty aimakta zherasty kazbalaryn bekitu turin negizdeu. Collection of materials of the Joint International Scientific and Practical Conference dedicated to the Year of Uzbekistan in Kazakhstan. "Actual problems and prospects for the development of building structures, innovations, modernization and energy efficiency in construction." Almaty. UDC 622.261, 2018.sr.217-220
12. Dukhovnaya G.M., Sarybaev T.T., Zhanakova R.K. Analysis of the mining and geological conditions for the construction of the second stage of the "10th Anniversary of Independence of Kazakhstan". Proceedings LV International scientific-practical conference "N innovations in science". Novosibirsk, 2016. UDC 622.261 pp. 135–141
13. Zhanakova R.K., Dukhovnaya G.M. Analysis of the mining and geological conditions of the Beskempir deposit. Collection of Satpaevsky Readings. "Innovative Solutions to Traditional Problems: Engineering and Technology". Almaty. April 12, 2018. ISBN 978-601-323209-6, pp. 895–899
14. Zhanakova R.K., Almenov A.T. Zhanabaeva, K.M. Akhmetzhanov. Justification of the choice of the type of rational lining in the construction of mine workings in difficult mining and geological conditions. International Scientific and Practical Conference "Satpayev Readings-2020". Satbaev University. Almaty, 2020. ISBN 978-601-323209-6, pp. 380–383.
15. Zhanabaeva A.T., Akhmetzhanova K.M., Zhanakova R.K. The impact of complex mining and geological conditions for the rational choice of lining design. International Scientific and Practical Conference "Satpayev Readings-2020". Satbaev University. Almaty, ISBN 978-601-323209-6, 2020, pp.36–38
16. Zhanakova RK, Kaliakpar AK Rational choice of the type of support for the formation genetic structure in complex mining and geological conditions. The road that we chose a collection of materials of the XIX interuniversity scientific and practical conference of undergraduates and students, held as part of the implementation of the New Economic Policy of Kazakhstan "Nurly Zhol- the way to the future" Kazakh Automobile and Road Academy named after L.B. Goncharova. Almaty, ISBN 978-601-08-1108-9, 2021, pp.14–16
17. Zhanakova R.K., Lesbay A. Peculiarities of the choice of support type in the construction of mine workings in difficult mining and geological conditions. The road that we chose a collection of materials of the XIX interuniversity scientific and practical conference of undergraduates and students, held as part of the implementation of the New Economic Policy of Kazakhstan "Nurly Zhol- the

way to the future" Kazakh Automobile and Road Academy named after L.B. Goncharova. Almaty, ISBN 978-601-08-1108-9, 2021, p.22–25.
18. Zhanakova R.K., Ataeva G.K. Tau-ken salasyn zhetildiru barysyndagy akparattyk tekhnologicnyn roli. Kazakh-Amerika univessitetinin gylymi enbekteri. Transactions of Kazakh-American University № III (41) Almaty 2018 p.78–82
19. Zhanakova R.K. Kurdeli geologiyalyk zhagdaidagy bekitpe kurylymyn tandaudyn tiimdiligi. Collection of scientific papers of the eighth international scientific-practical conference "Automotive roads and transport equipment: Problems and development prospects", dedicated to the 80th anniversary of R.A. Kabashev and the 20th anniversary of KazADI. Almaty, ISBN 978-601-7166-27-4, 2019 p.56–61
20. Sagybekova, A., Khomyakov, V. (2013). Analytical and experimental decisions to ensure stability of slopes. The 1st Taiwan-Kazakhstan Joint Workshop in Geotechnical Engineering. Taipei, 328–331.
21. Sagybekova, A., Zhanakova, R. K. (2019). Development of underground space in metropolitan areas. Bulletin KazGASA, 3 (73), 199–204.
22. Bek A., A. Sagybekova, A. Observations of deformations of engineering structures with the help of modern high-precision geodetic devices. AD Alta: Journal of Interdisciplinary Research. 2019.
23. Yessentay, D. (2021). Reliability criterion for calculation of the optimum driving speed on road in winter. International Journal of GEOMATE, 21 (83). https://doi.org/10.21660/2021.83.j2115
24. Zhussupbekov, A., Tulebekova, A., Zhumadilov, I., Zhankina, A. (2020). Tests of Soils on Triaxial Device. Key Engineering Materials, 857, 228–233. doi: https://doi.org/10.4028/www.scientific.net/kem.857.228
25. Tulebekova, A., Zhussupbekov, A., Zhumadilov, I., Bukenbaeva, D., Drozdova, I. (2020). Laboratory tests of soils on triaxial compression apparatus. 16th Asian Regional Conference on Soil Mechanics and Geotechnical Engineering, ARC 2019.
26. Zhussupbekov, A. (2020). Assessment of soils deformability under vertical load. International Journal of GEOMATE, 18 (70), 221–228. https://doi.org/10.21660/2020.70.12174
27. Tulendiev, T., Sagybekova, A., Abiev, B., Zhanakova, R. (2019). Experimental studies of coarse soils. Industrial transport of Kazakhstan, 3 (64), 221–228.

Smart Geotechnics for Smart Societies – Zhussupbekov, Sarsembayeva & Kaliakin (Eds)
© 2023 The Author(s), ISBN 978-1-003-29912-7
Open Access: www.taylorfrancis.com, CC BY-NC-ND 4.0 license

Investigation on mechanical behavior of MICP cemented sands in undrained cyclic triaxial tests with the CFD-DEM method

Y.X. Lu
School of Civil Engineering, Tianjin University, Tianjin, China

M.J. Jiang
School of Civil Engineering, Suzhou University of Science and Technology, Suzhou, China
College of Civil Engineering, Tongji University, Shanghai, China
School of Civil Engineering, Tianjin University, Tianjin, China

P.M. Jiang
School of Civil Engineering, Suzhou University of Science and Technology, Suzhou, China

ABSTRACT: Microbially Induced Calcite Precipitation (MICP) has emerged as an innovative and sustainable soil improvement technique, which can improve liquefaction resistance. This paper presents a numerical study on the mechanical behavior of MICP cemented sands in cyclic triaxial shear tests by CFD-DEM simulations. Firstly, a novel three-dimensional cyclic contact model for cemented sand was proposed, associated with the time-dependent relationship describing the microbial denitrification reaction, and employed into a commercial DEM software, PFC3D 5.0. Secondly, undrained cyclic triaxial tests were simulated respectively on clean and cemented sands using the CFD-DEM coupling method. Finally, liquefaction resistance of specimens microbially-treated with different times were analyzed macroscopically and microscopically. The results show that the liquefaction resistance of MICP cemented sand is larger than that of clean sand. The increases of pore pressure ratio are suppressed significantly with decreases of mechanical coordination number and bond coordination number, due to different amounts of MICP cementation.

1 INTRODUCTION

Liquefaction of sand manifests itself as the reduction of the effective stress of soil, and the increase of the pore water pressure, which eventually results in the insufficiency of the shear strength of soil. It causes uneven settlement of building foundations and structural damage, even leads to serious disasters and casualties. Since the traditional methods enhancing liquefaction resistance have lots of disadvantages, microbial geotechnical approaches have become a better choice. Among traditional chemical soil modification technology, the microbially induced calcite precipitation (MICP) technology is simpler and has less impact on the environment (Tang et al., 2020), which is extensively studied for soil improvement in geotechnical engineering (Wang et al., 2019, Liu et al., 2020).

In recent years, most studies on liquefaction resistance of MICP cemented sand has been analyzed through laboratory tests, paying more attention to the influence of biological bond. Inagaki et al. (2011) conducted consolidated-drained triaxial compression tests and centrifuge tests on MICP cemented sand. Gao et al. (2019) used triaxial consolidated drained tests and K0 consolidation tests to understand the mechanical behavior of bio-cemented sand at various cementation levels and relative densities. Liu et al. (2018) investigated the evolutions of the

DOI: 10.1201/9781003299127-94

dynamic characteristics under different degrees of bio-cement as well as the micromechanism of the MICP-treated calcareous sands by dynamic triaxial tests and SEM tests.

However, laboratory tests suffer from the shortcomings of long time-consuming, high cost, and poor repeatability, so it is necessary to use numerical simulation methods for analysis. The distinct element method (DEM), which was firstly developed by Cundall and Strack (1979), provides an effective approach describing the micromechanical behaviors of particle assemblies. Previous studies simulated the triaxial test of MICP cemented sand by DEM, and analyzed the characteristics of strength and stiffness of cemented and uncemented samples (Evans et al., 2015, Khoubani et al., 2016). Feng et al. (2017) used three-dimensional discrete element software PFC3D (Particle Flow Code) to simulate the mechanical properties of MICP cemented sand, analyzing the macro and micro mechanical responses, and the shear band phenomenon was observed.

The existing simulation results fail to consider the influence of water and cannot reflect the interaction between particles and fluid in the whole liquefaction process, while the influence of water flow cannot be ignored. So, coupling methods is a good choice to research on macroscopic and microscopic mechanism of the effect.

The computational fluid dynamics (CFD) is the method of replacing the governing partial differential equations of fluid flow with numbers, and advancing these numbers in space and/or time to obtain a final numerical description of the complete flow field of interest (Anderson and Wendt, 1995).DEM can be coupled with CFD to describe fluid-particle interaction systems, and using this type of coupled simulation can get an effective description of the interaction between particles and pore water during liquefaction (Zeghal and El Shamy, 2008). Jiang and Zhang (2014) established CFD-DEM codes to simulate the porous media with weakly compressive fluid introduced the fluid state equation considering the weak compressibility of the fluid, and used FISH language to couple CFD and PFC2D discrete element calculation to simulate the undrained consolidated shear test of saturated sand.

Based on the theoretical framework of geomechanics from micro to macro (Jiang, 2019), employing the CFD-DEM coupled model, this paper aims to simulate MICP cemented sands of different reaction time under undrained consolidated cyclic triaxial tests, tracing and analyzing the changes of some mechanical parameters during the simulation procedure to study mechanical properties from macroscopic and microscopic scales. And finally, get some conclusions about the effect and possible mechanism of the presence of cementation on anti-liquefaction capacity.

2 CONTACT MODEL AND MICROBIAL TREATMENT PROCESS

The contact model of this paper is on the basis of the three-dimensional (3D) contact model incorporating rolling and twisting resistances at inter-particle contact (Jiang et al., 2015b) and 3D bonded aluminum ball tests (Jin, 2016) of our team's previous work, and takes the cyclic load effect on microbial cementation and mechanical properties of MICP cemented sands into further consideration.

2.1 *Contact model*

Like the regular discrete element bond contact model, the bond contact between MICP cemented sand particles can be simplified as thick cementation and non-thick cementation. Soil particles with radius R_1 and R_2 are connected by calcareous cementation. The minimum thickness of cement is h_{min} and the width is B, as shown in Figure 1. The thickness cementation refers to the formation of cementation between two separated particles, which means the minimum thickness $h_{min}>0$; while the non-thick cementation means cementation between two contact particles with the minimum thickness $h_{min}\leq 0$. The cement is simplified to two cylinders with spherical ends. The mechanical model of non-thick cementation can be simplified as a parallel connection between particle spring and cementation spring, while that of thickness

cementation can be regarded as a series connection of particle spring and cementation spring. Since the particle stiffness of MICP cemented sand is much larger than that of bond stiffness, the contact stiffness is approximately equal to the bond stiffness. It is considered that the thickness bond only has bond forced.

The particle part of DEM contact model is based on the 3D contact model for granulates incorporating rolling and twisting resistances (Jiang et al., 2015b). In order to consider the small plastic deformation under cyclic loading (Thornton et al., 2013), this paper adopts the linear hysteretic contact model in the normal contact component, that is, different loading and unloading stiffness, so that the plastic deformation dissipation energy caused by the collision of particles under cyclic loading can be considered. The ideal elastic-plastic model is still used in tangential, rolling and torsional directions. The mechanical response of the particle part can refer to previous study (Tan, 2018).

The law of force and displacement of the bond part of 3D contact model is derived by formula (Shen et al., 2016). It is considered that the two ends of the cement are spherical, and the bond cylinder between spheres is dissected into hollow cylinder elements for integration operation. The stiffness of cementation is obtained by integral calculation. Similar to the particle part, the mechanical response of the bond part can be divided into normal, tangential, rolling and torsional directions.

The strength criterion used in the bond part of the model is extracted by previous experiments (Jiang et al., 2015a). The bond strength criterion is obtained by combining the simplified elliptic formula with the indoor 3D microscopic contact mechanics test, and the tensile strength R_{nt}, compressive strength R_{nc}, shear strength R_s, bending strength R_r, and torsional strength R_t of bond are gotten. Based on the test results under complex loading conditions of indoor tests, the spherical failure envelope controlled by peak shear load, bending moment and torque is established, and the size of failure envelope is controlled by normal force, as shown in Figure 2, where F_s is the bond shear force, M_r is the bond rolling moment, and M_t is the bond twisting moment.

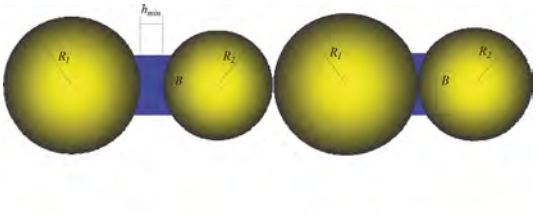

(a) thickness cementation. (b) non-thick cementation.

Figure 1. DEM diagram of MICP cemented contact.

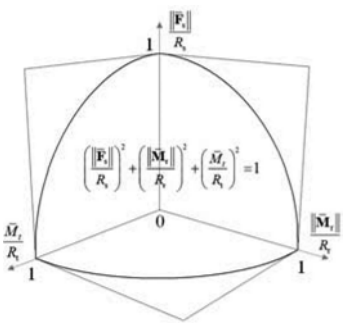

Figure 2. Cemented failure criterion.

In addition, since the mechanical behavior of granular materials has obvious rate correlation (Peng et al., 2007, Yamamuro et al., 2011, Svoboda, 2013, Sheahan et al., 1996), to consider the rate correlation of MICP cemented sand under cyclic loading, viscous damping is added to the contact model. The viscous damping at contact is determined by the dash pot element and can also be divided into normal, tangential, rolling and twisting direction (Thornton et al., 2013).

This improved microstructural bond model is implemented into the commercial DEM code PFC3D via C++ coding. Then a set of micro parameters are calibrated by the laboratory data and experience, the micro parameters of MICP cemented sand are shown in Table 1 (Tan, 2018).

Table 1. Micro parameters of MICP cemented sand.

	Model micro parameters	Value
Particle part	Particle modulus E_p (MPa)	3×10^8
	Normal tangential stiffness ratio ξ	1.5
	Friction coefficient μ	0.5
	Anti-rotation coefficient β	0.2
	Local crushing coefficient ζ_c	2.1
	Normal contact loading and unloading stiffness ratio e_n	0.95
Bond part	Slenderness ratio δ	0.05
	Radius proportional coefficient η	(0.5)*
	Elastic modulus E_b (Pa)	2×10^8
	Poisson's ratio v_b	0.2
	Tensile strength σ_t (Pa)	1.6×10^6
	Compressive strength σ_c (Pa)	8×10^7
Viscous damping	Normal critical damping ratio β_n	0.6
	Tangential critical damping ratio β_s	0.6

* Radius proportional coefficient takes 0.5 during parameter calibration, and it takes the calculated parameter that controls the cementation content in the subsequent simulation.

2.2 *The time-dependency characteristic of microbial treatment process*

The microbial treatment process is a new type of foundation treatment technology, it has many advantages over traditional methods, but it is necessary to require considerable time and economic costs in the early cultivation and reinforcement process. So, the time-dependency characteristic was established by summarizing the data of precipitation rate and gas generation rate in the laboratory biological denitrification tests. The microbial denitrification was chosen in this paper to consider MICP reaction, for the reason that denitrification was chemically inert, non-toxic, and potential (Hamdan et al., 2017).

According to previous studies (Van Paassen et al., 2010, He, 2013), the formation rate of denitrifying cementation is 91mmol/day in laboratory tests. Using this formation rate, this paper recorded the number of the sample cementation with 2-, 3- and 5-day reaction separately. Then the corresponding parameters were chosen and calculated in the numerical simulation, applying to the following undrained cyclic shear simulation. The calculated volume growth rate of calcium carbonate cementation of denitrification reaction is 0.359mm^3/day. So, after 2-, 3-, 5-day reaction, the cementation volume is respectively 0.718mm^3, 1.077mm^3, 1.795mm^3, and the proportional coefficient of cementation radius (η) is separately 0.273, 0.3, 0.34. The final calculation results are shown in Table 2.

Table 2. Cementation formation of microbial treatment.

Reaction time (day)	Cementation volume (mm^3)	Proportional coefficient of cementation radius η
0	0	0
2	0.718	0.273
3	1.077	0.3
5	1.795	0.34

3 CFD-DEM SIMULATION

3.1 *Specimen*

Figure 3 provides the grain size distribution of Ottawa 50-70 sand used in this study (Feng and Montoya, 2016). The DEM sample was prepared using the Multi-layer with the Undercompaction Method (UCM) (Jiang et al., 2003). 10-layer preparation was used

with the initial void ratio of 0.73. Then the sample was pre-compressed to a vertical load of 12.5 kPa by servo system.

After precompression was stable, the servo system was used in the isotropic consolidation stage, the average effective principal stress of the consolidated sample is 100 kPa. The figure of sample consolidation is illustrated in Figure 4. Then apply model cementation parameters provided in Table 1, and the parameters for clean sand refer to the particle part in Table 1.

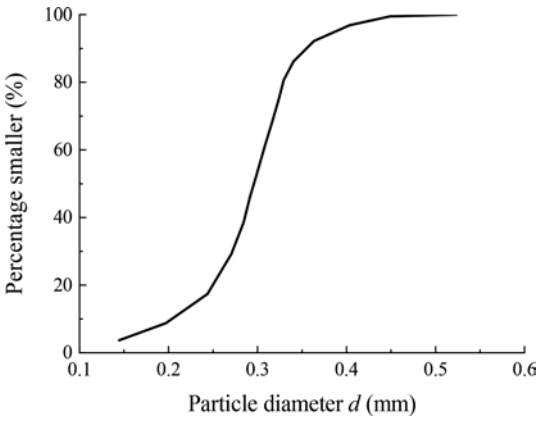

Figure 3. Grain size distribution.

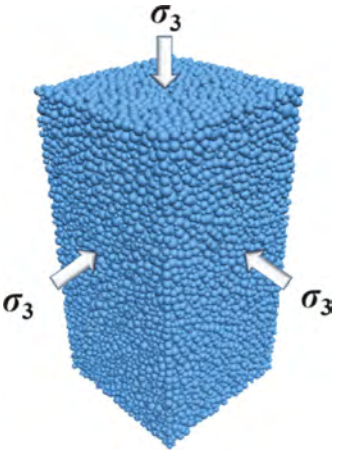

Figure 4. Schematic diagram of sample consolidation.

3.2 *Shear test*

The CFD-DEM coupling method is developed by Zhang et al. (2020). The DEM calculation adopts PFC3D, and the CFD calculation is carried out by OpenFOAM to simulate the fluid including the pore water and possible microbial bubble. The data exchange of CFD-DEM is realized by Python using TCP socket programming.In this cyclic shearing stage, the CFD module was added for coupling simulation of cyclic shear. The DEM time step is 1×10^{-6}s/cycle, the exchange frequency between DEM and CFD is 25, and the CFD time step is 2.5×10^{-5}s/cycle. The initial density of the fluid is 1000 kg/m^3 and the compression coefficient is 4.5×10^{-7}. The number of fluid grids is 6×6×12, and the CFD grid boundaries are consistent with the coordinates of the six walls in the DEM. Before cyclic loading, the backpressure of 100kPa was applied. The upper and lower walls were loaded at a uniform speed. When the deviator stress reached the stress amplitude q_{cyc}, the upper and lower walls continued to move in the opposite direction. Then, until the stress amplitude q_{cyc} in the opposite direction was reached, the moving direction reversed again. The sidewall was still controlled by servo system, and the servo stress is the effective stress of confining pressure minus pore pressure. The fluid boundary uses a velocity boundary, which is consistent with the velocity of the wall.

3.3 *Simulation scheme*

To investigate the liquefaction resistance of MICP cemented sand specimens with different degrees of cementation, specimens were selected for comparative analysis at 2, 3, and 5 days after microbial treatment. MP2/3/5 represents MICP cemented sand specimens after microbial treatment for 2/3/5 days, and MP2-1/2/3 represents the cyclic triaxial tests of specimens with different cyclic stress ratios after microbial treatment for 2 days, respectively. The cyclic results showed that the failure modes of specimens are initial liquefaction failure (I. L.), except for specimen MP5-1, which did not fail. And L0 represents the pure sand specimens. Detailed parameters and basic results are shown in Table 3.

Table 3. Working condition list of MICP cemented sand cyclic triaxial tests.

	Simulated conditions			Cyclic results	
Test number	Days	η	Cyclic stress ratio CSR	Failure vibration frequency N_L	Failure mode
L0	0	0	0.15	0	I.L
MP2-1	2	0.273	0.5	37	I.L
MP2-2	2	0.273	0.6	5	I.L
MP2-3	2	0.273	0.75	3	I.L
MP3-1	3	0.3	0.6	55	I.L
MP3-2	3	0.3	0.75	5	I.L
MP3-3	3	0.3	0.9	3	I.L
MP5-1	5	0.34	0.75	(132+)*	/
MP5-2	5	0.34	0.8	60	I.L
MP5-3	5	0.34	0.9	10	I.L
MP5-4	5	0.34	1.0	5	I.L

* + represents the specimen undestroyed.

4 SIMULATION RESULTS

4.1 *Liquefaction resistance*

The liquefaction vibrations N_L and CSR of MICP specimens with different days of microbial treatment were plotted in semi-logarithmic coordinates, to obtain the anti-liquefaction strength curve of MICP cemented sands shown in Figure 5. At the same time, a comparison is made with the clean sand specimen without microbial treatment.

The liquefaction resistance of MICP cemented sands after microbial treatment gets a significant rise than pure sand. And with the increase of treatment time, the development of cementation content leads to a gradual increment of the liquefaction resistance. When CSR is the same value 0.75, the specimen with 2 days treatment reaches liquefaction after 3 vibrations, the specimen with 3 days treatment needs 5 vibrations, and the specimen with 5 days treatment does not fail after 132 vibrations.

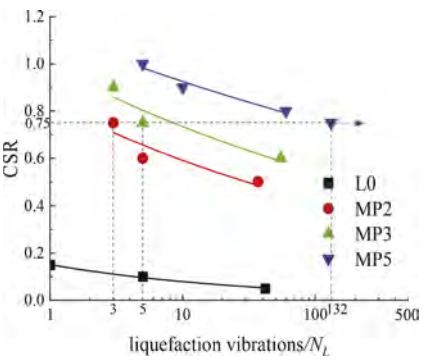

Figure 5. Cyclic stress ratio - liquefaction vibration times curves ratio.

(The arrow represents that the specimen of this vibration has not been destroyed.)

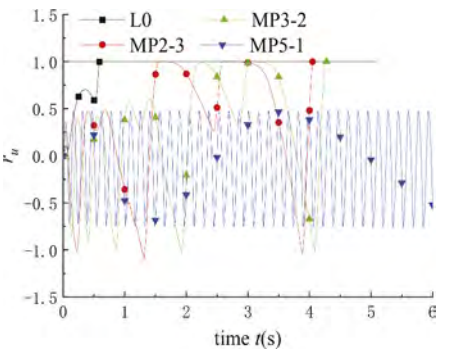

Figure 6. Development curve of pore water pressure of different specimens.

4.2 *Excess pore water pressure ratio*

The water pressure ratio is the ratio of pore water pressure increment to lateral effective consolidation stress under cyclic stress. Figure 6 shows the evolution of pore water pressure ratio of specimens with different cementation contents under same CSR=0.75 and the pure sand

specimen with CSR=0.15. For the pure sand specimen, the specimens with 2 days, and 3 days microbial treatment, the pore pressure ratio increases to 1 after several loadings, with soil reaching the initial liquefaction state. The cementation of microbial treatment has an obvious inhibitory effect on the development of pore pressure ratio, even when CSR is 5 times higher than that of the pure sand, it still takes more time to reach liquefaction. Moreover, the longer the microbial treatment time is, the longer the liquefaction time required. When CSR is 0.75, the pore pressure ratio of the specimens with 5 days treatment changes periodically with no upward trend, and soil does not reach the initial liquefaction.

4.3 *Mechanical coordinate number*

The mechanical coordination number is the average coordination number of particles without the particles with 0 or 1 contact, which can characterize the contact state of particles. (Thornton, 2000).

Figure 7(a) gives the evolutions of mechanical coordination number of specimens with different cementation contents under the same CSR=0.75, which are compared with that of the clean sand specimen L0. The mechanical coordination numbers of the specimens with 2 days and 3 days treatment decrease rapidly, and the decreasing tendency of 2 days' is much faster. At the end of loading, the mechanical coordination numbers of these two specimens are about 3.4, which is close to the pure sand. Whereas the value of the specimen with 5 days treatment decreases from 5 to 4.6, then fluctuates around 4.6.

Figure 7(b) demonstrates the evolutions of bond mechanical coordination number of different cemented specimens when CSR is 0.75. The decline is sharper and more obvious than that of mechanical coordination number. The bond mechanical coordination number before loading is 4.8, which is slightly smaller than the value of the mechanical coordination number. The fall decreases with the increase of processing time. Contrast 2 days' and 3 days' specimens, the descending speed of bond mechanical coordination number is much quicker than that of mechanical coordination number. The value of the specimen with 5 days treatment decreases to 3.7, then remains unchanged.

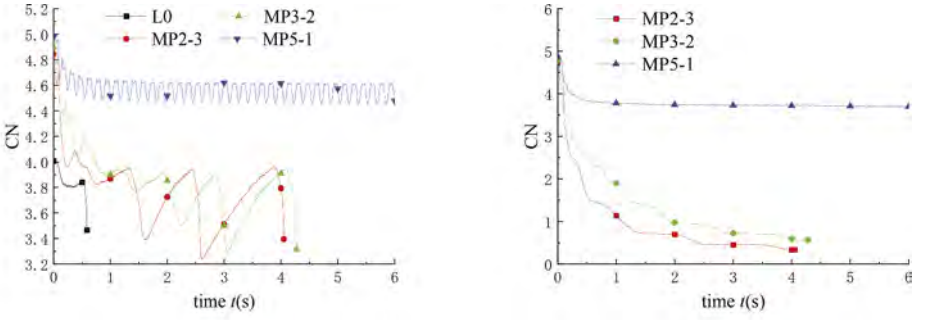

(a) Mechanical coordination number. (b) Bond mechanical coordination number.

Figure 7. Development curve of (bond) mechanical coordination number of different specimens.

5 CONCLUSIONS

This paper introduced a coupled CFD-DEM simulation of MICP cemented sands under undrained cyclic triaxial shear tests to consider the liquefaction resistance. The main conclusions can be drawn as follows:

1) The presence of cementation has a great improvement on the liquefaction resistance. The anti-liquefaction capacity of MICP cemented sands is higher than that of clean sand. The failure mode of MICP cemented sands is initial liquefaction.

2) With the increase of treatment time, the cementation content grows gradually, leading to stronger liquefaction resistance. And the development of excess pore water pressure ratio is suppressed more significantly, the downward trend of (bond) mechanical coordinate number becomes weaker.

ACKNOWLEDGMENTS

The research was financially supported by the National Nature Science Foundation of China with Grant Nos. 51890911, 51639008.

REFERENCES

Anderson, J. D. & Wendt, J. 1995. *Computational fluid dynamics*, Springer.

Cundall, P. A. & Strack, O. D. 1979. A discrete numerical model for granular assemblies. *geotechnique*, 29, 47–65.

Evans, T., Khoubani, A. & Montoya, B. Simulating mechanical response in bio-cemented sands. computer methods and recent advances in geomechanics: Proceedings of the 14th International Conference of International Association for Computer Methods and Recent Advances in Geomechanics, 2014 (IACMAG 2014), 2015. Taylor & Francis Books Ltd, 1569–1574.

Feng, K. & Montoya, B. 2016. Influence of confinement and cementation level on the behavior of microbial-induced calcite precipitated sands under monotonic drained loading. *Journal of Geotechnical and Geoenvironmental Engineering*, 142, 04015057.

Feng, K., Montoya, B. M. & Evans, T. M. 2017. Discrete element method simulations of bio-cemented sands. *Computers and Geotechnics*, 85, 139–150.

Gao, Y. F., Hang, L., He, J. & Chu, J. 2019. Mechanical behaviour of biocemented sands at various treatment levels and relative densities. *Acta Geotechnica*, 14, 697–707.

Hamdan, N., Kavazanjian JR, E., Rittmann, B. E. & Karatas, I. 2017. Carbonate mineral precipitation for soil improvement through microbial denitrification. *Geomicrobiology journal*, 34, 139–146.

HE, J. 2013. *Mitigation of liquefaction of sand using microbial methods*. Nanyang Technological University.

Inagaki, Y., Tsukamoto, M., Mori, H., Nakajima, S., Sasaki, T. & Kawasaki, S. 2011. A centrifugal model test of microbial carbonate precipitation as liquefaction countermeasure. *Jiban Kogaku Janaru (japanese Geotechnical Journal*), 6, 157–167.

Jiang, M. J. 2019. A new paradigm for modern soil mechanics-–Geomechanics from micro to macro. *Chinese Journal of Geotechnical Engineering*, 41, 195–254.

Jiang, M. J., Jin, S. L., Liu, W. & Liu, J. 2015a. Three-dimensional experimental study of mechanical behaviors of bonded granules. *Rock and Soil Mechanics*, 36.S1, 9–13.

Jiang, M. J., Konrad, J. & Leroueil, S. 2003. An efficient technique for generating homogeneous specimens for DEM studies. *Computers and geotechnics*, 30, 579–597.

Jiang, M. J., Shen, Z. F. & Wang, J. F. 2015b. A novel three-dimensional contact model for granulates incorporating rolling and twisting resistances. *Computers and Geotechnics*, 65, 147–163.

Jiang, M. J. & Zhang, W. C. 2014. Coupled CFD-DEM method for soils incorporating equation of state for liquid. *Chinese Journal of Geotechnical Engineering*, 36, 793–801.

JIN, S. L. 2016. *Three dimensional experimental and numerical study on micro- and macro- mechanical behaviors of structural sands*. Tongji University.

Khoubani, A., Evans, T. & Montoya, B. 2016. Particulate simulations of triaxial tests on bio-cemented sand using a new cementation model. *Geo-Chicago 2016*.

Liu, B., Zhu, C., Tang, C. S., Xie, Y. H., Yin, L. Y., Cheng, Q. & Shi, B. 2020. Bio-remediation of desiccation cracking in clayey soils through microbially induced calcite precipitation (MICP). *Engineering geology*, 264, 105389.

Liu, H. L., Xiao, P., Xiao, Y., Wang, J. P., Chen, Y.-M. & Chu, J. 2018. Dynamic behaviors of MICP-treated calcareous sand in cyclic tests. *Chinese Journal of Geotechnical Engineering*, 40, 38–45.

Peng, F. L., Li, F. L., Li, J. Z. & Tatsuoka, F. 2007. Loading rate effects on stress-strain relation of sandy soils. *Rock and Soil Mechanics*, 28, 16–20.

Sheahan, T. C., Ladd, C. C. & Germaine, J. T. 1996. Rate-dependent undrained shear behavior of saturated clay. *Journal of Geotechnical Engineering*, 122, 99–108.

Shen, Z. F., Jiang, M. J. & Thornton, C. 2016. DEM simulation of bonded granular material. Part I: contact model and application to cemented sand. *Computers and Geotechnics*, 75, 192–209.

Svoboda, J. 2013. *Impact of strain rate on the shear strength and pore water pressure generation of clays and sands*. University of Colorado at Boulder.
Tan, Y. 2018. *A novel three-dimensional bonded contact model incorporation the effect of cyclic loads and CFD-DEM simulation of microbially treated sands under undrained consolidation cyclic triaxial tests*. University of Shanghai for Science and Technology.
Tang, C. S., Yin, L. Y., Jiang, N. J., Zhu, C., Zeng, H., Li, H. & Shi, B. 2020. Factors affecting the performance of microbial-induced carbonate precipitation (MICP) treated soil: a review. *Environmental Earth Sciences*, 79, 1–23.
Thornton, C. 2000. Numerical simulations of deviatoric shear deformation of granular media. *Géotechnique*, 50, 43–53.
Thornton, C., Cummins, S. J. & Cleary, P. W. 2013. An investigation of the comparative behaviour of alternative contact force models during inelastic collisions. *Powder technology*, 233, 30–46.
Van Paassen, L. A., Daza, C. M., Staal, M., Sorokin, D. Y., Van Der Zon, W. & Van Loosdrecht, M. C. 2010. Potential soil reinforcement by biological denitrification. *Ecological Engineering*, 36, 168–175.
Wang, Y., Soga, K., Dejong, J. T. & Kabla, A. J. 2019. A microfluidic chip and its use in characterising the particle-scale behaviour of microbial-induced calcium carbonate precipitation (MICP). *Géotechnique*, 69, 1086–1094.
Yamamuro, J. A., ABRANTES, A. E. & LADE, P. V. 2011. Effect of strain rate on the stress-strain behavior of sand. *Journal of Geotechnical and Geoenvironmental Engineering*, 137, 1169–1178.
Zeghal, M. & El Shamy, U. 2008. Liquefaction of saturated loose and cemented granular soils. *Powder Technology*, 184, 254–265.
Zhang, A., Jiang, M. J. & Thornton, C. 2020. A coupled CFD-DEM method with moving mesh for simulating undrained triaxial tests on granular soils. *Granular Matter*, 22, 1–13

Smart Geotechnics for Smart Societies – Zhussupbekov, Sarsembayeva & Kaliakin (Eds)
© 2023 The Author(s), ISBN 978-1-003-29912-7
Open Access: www.taylorfrancis.com, CC BY-NC-ND 4.0 license

Geotechnical properties and embankment construction of crushed solidified soil

A. Sato & H. Hayashi
Civil Engineering Research Institute for Cold Region, Sapporo, Japan

ABSTRACT: One method of improving soft soil materials generated at construction sites is to use a solidifier. The authors focused on solidified crushed soil, which is a compactable material produced by strengthening crushed soil with a solidifier using this method, and studied its geotechnical properties as an embankment material. This paper presents the results of the study and an example of embankment construction using solidified crushed soil.

1 INTRODUCTION

For the effective use of resources, soft soil materials generated during road and river works can be improved for use as an embankment material (CERI 2013). One of the improvement methods involves mixing the materials with cement, lime or other solidifiers. The aim of improvement is to ensure both sufficient strength for construction work and stability of the embankment, while the elution amount of hexavalent chromium is within the standard value range. All of these conditions must be satisfied. Improvement using a solidifier can ensure increased strength. However, the strength of the embankment may exceed the required level if an amount of solidifier that provides adequate strength for trafficability of construction machinery is mixed. It may also complicate re-excavation of the embankment for the installation of median strips or guardrails, since the strength of material improved with a solidifier increases over the course of time. In case of construction on soft ground, there is also a risk of slip failure because the embankment cannot follow ground deformation. The authors have therefore focused on crushed solidified soil as a material of which strength development can be minimized or reduced when mixed with a solidifier. This paper presents the geotechnical properties of crushed solidified soil as an embankment material (Sato, A. & Hatakeyama, O. 2021), and the results of the construction of a river embankment using this material.

2 CRUSHED SOLIDIFIED SOIL

Crushed solidified soil is produced by mixing a solidifier with the soil subject to improvement (original soil) and crushing the solidified soil after some time to allow compaction. Figure 1 shows the definitions of terms used in the paper. Crushed solidified soil means a material produced by crushing a mixture of original soil and a solidifier (solidified soil) after some time (standby time). The time until the implementation of testing and research on crushed solidified soil samples and the embankment is defined as the curing time. The strength of crushed solidified soil at the time of compaction is low if the standby time is short, as it is crushed when solidification has not progressed much. However, the strength further increases with a longer

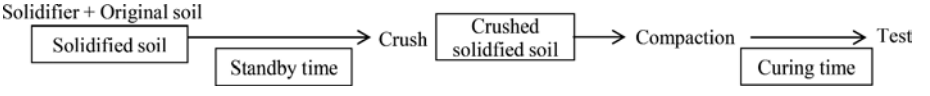

Figure 1. Definition of the terms.

DOI: 10.1201/9781003299127-95

curing time, because of its remaining solidification capacity. If the standby time is long, the material is crushed when the solidifying capacity is expressed, resulting in higher strength at the time of compaction, but less increase in strength, even if the curing time is long.

3 TEST METHOD

In this study, a laboratory test was conducted to investigate the geotechnical properties of crushed solidified soil as an embankment material (Sato, A., Hatakeyama, O. & Chujo, G. 2021). An embankment was also constructed using the material. The original soil used for the laboratory test and the construction of the embankment is different. The basic physical properties are shown in Table 1. Since the original soil materials were soft and the cone index (Japanese Industrial Standard 2020) with a natural water content was too low to ensure trafficability of swamp bulldozers, they could not be used for earthworks without improvement.

Table 1. Physical properties of original soil.

No.	Laboratory test	Construction of embankment	Standard number
Soil particle density ρ_s (g/cm^3)	2.675	2.662	JGS 0111-2009
Natural water content w_n (%)	34.5	54.2	JGS 0121-2009
Grain size characteristics 2mm-(%)	0.0	0.0	JGS 0131-2009
75μm-2mm(%)	34.0	7.7	
-75m(%)	66.0	92.3	
Liquid limit w_L (%)	N.P.	60.9	JGS 0141-2009
Plastic limit w_P (%)	N.P.	28.9	
Ground material classification	ML	MH	JGS 0051-2009
Cone index q_c (kN/m^2)	64	34	JGS 0716-2009
Maximum dry density ρ_{dmax} (g/cm^3)	1.665	1.359	JGS 0711-2009
Optimum moisture content w_{opt} (%)	19.1	29.4	(A-c)

3.1 *Laboratory test*

In the laboratory test, crushed solidified soil samples were prepared on site by setting a standby time of 0, 7, 28 and 91 days. The sample with a standby time of 0 days was solidified soil. The solidified soil and the crushed solidified soil were brought to the laboratory immediately from the site to conduct a compaction test and cone index measurement. The unconfined compression test was conducted by setting a curing time of 0, 7, 28, 91 and 183 days. For a curing time of 0 days, samples were collected immediately after preparation. For 1 m^3 of the original soil, 70, 110 and 150 kg of solidifier, respectively, was used to prepare solidified soil and crushed solidified soil.

3.2 *Embankment construction*

Figure 2 shows embankment construction procedures using crushed solidified soil. The most economical combination of the type and the amount of solidifier to satisfy the requirements for embankment construction was found based on the laboratory test. The requirements for crushed solidified soil are a cone index of 400 kN/m^2 or higher to allow trafficability of a 3.5-ton combined roller, a 90% or higher degree of compaction (Japan Road Association 2001), which is the standard value for embankments in Japan, and an elution amount of hexavalent chromium of 0.05 mg/liter (Ministry of the Environment 1991), which is the standard

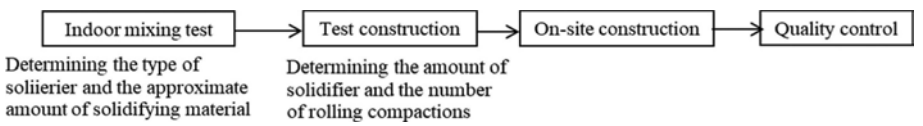

Figure 2. Embankment construction procedures using crushed solidified soil.

value for soil improved with a cement-based solidifier in Japan. Since the compaction, curing and other procedures differ between the laboratory test and the on-site construction, test construction was conducted to determine the mixing proportions for actual construction. In test construction, the soil and solidifier were mixed and compacted using the actual construction machines. Based on the test results, an actual embankment was constructed and managed.

4 RESULTS

4.1 *Laboratory test*

Figure 3a shows the relationship between the standby time and the cone index of crushed solidified soil. The cone index, which was 64 kN/m^2 for the original soil, increased when it was made into crushed solidified soil. The index increased as the amount of solidifier increased and the standby time increased. The solidified soil had to be mixed with 150 kg/m^3 of solidifier to achieve the target value of 400 kN/m^2. However, the target value could be achieved with crushed solidified soil using only 70 kg/m^3 of solidifier by setting a standby time of seven days. By preparing crushed solidified soil, the amount of solidifier can be reduced to less than half the amount needed for solidified soil.

Figure 3b shows a case of 110 kg/m^3 of solidifier as an example of the relationship between the curing time of crushed solidified soil and unconfined compressive strength. The unconfined compressive strength increased with a longer curing time. When the curing time was the same, the unconfined compressive strength of crushed solidified soil was lower than that of solidified soil, indicating that it is possible to suppress the development of strength.

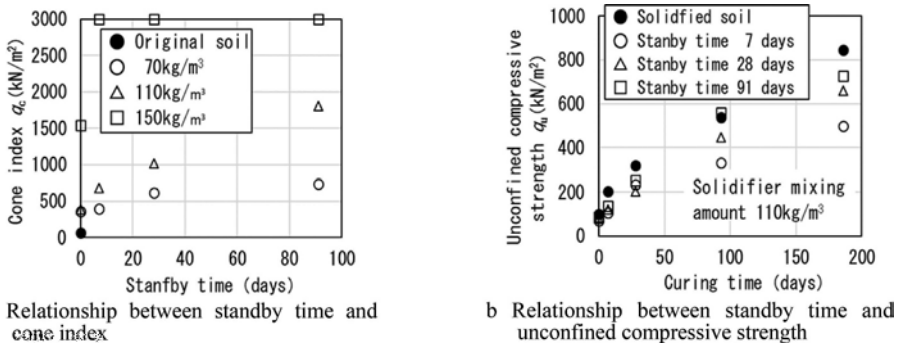

a Relationship between standby time and cone index

b Relationship between standby time and unconfined compressive strength

Figure 3. Strength properties of crushed solidified soil.

Figure 4a shows the compaction curves of crushed solidified soil with a standby time of seven days. The maximum dry density of crushed solidified soil was lower than that of the original soil, and its compaction curve was different from that of the original soil. Figure 4b shows the relationship between the standby time and the maximum dry density. When the amount was 70 kg/m^3, the maximum dry density of the crushed solidified soil was higher than that of the solidified soil. When the amount was 110 kg/m^3, the maximum dry density was almost the same for both materials, regardless of the curing time. When the amount was 150 kg/m^3, the maximum dry density of crushed solidified soil was lower than that of solidified soil, and tended to decrease with a longer standby time. The maximum dry density of crushed solidified soil seems to be affected more by the amount of solidifier than by the standby time.

4.2 *Embankment construction*

At the embankment construction site, the standby time of crushed solidified soil was set as seven days, based on accumulated past knowledge about the material, the preparation amount and the size of the construction yard. Based on the results of the indoor mixing test for embankment construction, it was found that mixing 95 kg/m^3 of blast furnace cement Type B was the most

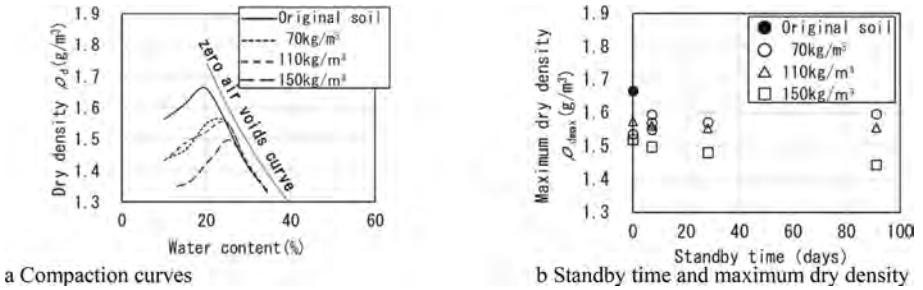

a Compaction curves b Standby time and maximum dry density

Figure 4. Compaction characteristics of crushed solidified soil.

economical. By using this mix proportion as a reference, test construction was conducted with 90, 100 and 110 kg/m^3 of solidifier. The original soil and solidifier were mixed using a fixed-type soil improvement plant. Rolling compaction of the embankment was conducted 4, 6 and 8 times, using a 3.5-ton compound roller (cone index: 400 kN/m^2). Figure 5 shows the relationship between the rolling compaction frequency and the cone index/dry density. The degree of compaction was 90% or higher regardless of the total amount of solidifier. The cone index was 400 kN/m^2 or more, except for 70 kg/m^3. Based on these results, it was decided to construct an embankment by mixing 90 kg/m^3 of solidifier and applying compaction four times. It has been confirmed that the standard value of the elution amount of hexavalent chromium is satisfied with this mix proportion.

As the degree of compaction of the constructed embankment was 90% or higher, it was confirmed that the embankment satisfied the quality standard.

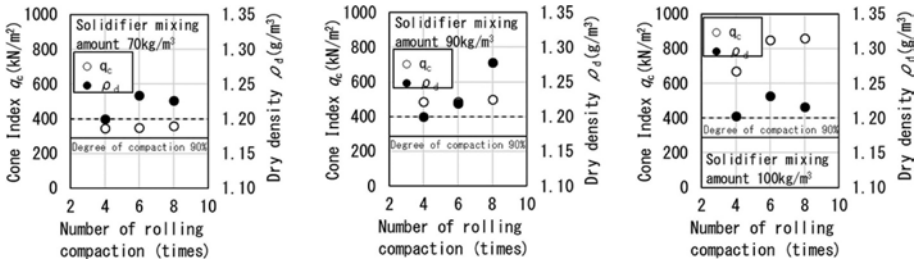

Figure 5. Results of test construction.

5 CONCLUSION

It was confirmed that crushed solidified soil has the required geotechnical properties for embankments, and that its strength development was smaller than that of solidified soil. It was successfully used for the construction of an embankment.

REFERENCES

Civil Engineering Research Institute for Cold Region 2013. The Manual of Measures against Unsuitable Soil in Hokkaido (in Japanese).

Sato, A. & Hatakeyama O. 2021, Influence of preparation conditions on solidified crushed soil characteristics and strength, *International Journal of GEOMATE*, 20 (79): 48–55.

Sato, A., Hatakeyama O. & Chujo G. 2021, Example of construction embankment of Kitamura retarding basin by crushed solidified soil, *Japanese Geotechnical Society Hokkaido Branch Technical Report* No. 61: 229–236 (in Japanese).

Japanese Industrial Standard 2020. JIS A 1228-2020, Test method for cone index of compacted soils (in Japanese).

Japan Road Association 2009. Road Construction Summary: 287 (in Japanese).

Ministry of the Environment 1991. Environmental Quality Standards for Soil Pollution", Notice of the Environmental Agency No. 46, https://www.env.go.jp/en/water/soil/sp.html

Smart Geotechnics for Smart Societies – Zhussupbekov, Sarsembayeva & Kaliakin (Eds)
© 2023 The Author(s), ISBN 978-1-003-29912-7
Open Access: www.taylorfrancis.com, CC BY-NC-ND 4.0 license

The technology of strengthening waterlogged foundation soil in the construction of shallow foundations

A.S. Montayeva
Korkyt Ata Kyzylorda University

S.A. Montayev & N.S. Montayeva
West Kazakhstan Agrarian Technical University

ABSTRACT: The article presents the results of scientific and experimental research on the strengthening of waterlogged soil on the foundation during the construction of shallow foundations. Efficient implementation of technological operations to strengthen soils is possible only when the moisture content of the treated soil does not exceed the optimal standard compaction, at which the soil is in a semi-solid state, capable of crumbling and compacting. However, in engineering practice, there are often cases when cohesive (clayey), fine sands, sandy loams, loams and other soils are in an overmoistened state, i.e. have moisture content above the optimum. Waterlogged soils cannot be compacted. loosen, and therefore excludes the use of binder materials such as cement, bitumen, silicate mortar and polymer components for their strengthening. Natural drying of waterlogged soils, especially clay ones, occurs very slowly. The currently used artificial methods of drying are ineffective and require large expenditures of money and time. To increase the bearing capacity and reduce the deformation of soil foundations, there are many ways to artificially fix soils. They are divided into physical - strengthening the soil mass with the help of physical fields, mechanical - placing reinforcing elements with high tensile strength in the soil, chemical - improving the properties of soils by injecting special solutions into their thickness. As a result of the analysis of research and practical work in the field of strengthening waterlogged soils, it was found that the most effective treatment of such soils with chemicals that, along with dehydration, can change the physical and chemical properties.It has been established the effectiveness of dehydration and strengthening of waterlogged soil by introducing quicklime through the use of the heat generated (T = 1000C) when interacting with water and their ability to harden due to chemical interaction with the mineral part of the soil. The patterns of change in the duration of dehydration and the state of aggregation of waterlogged soil from the amount of quicklime have been established. It has been proven that the introduction of quicklime in the amount of 20-25% into waterlogged soil radically changes the properties of these soils, enlarges the state of aggregation and creates workability for fixing by cementation, silicification and resinization.

1 INTRODUCTION

During the construction and operation of buildings and structures on weak water-saturated soils, the problem of transforming their physical and mechanical properties inevitably arises in order to increase the bearing capacity and reduce deformability. On the one hand, this is a problem, but on the other hand, it is an opportunity for innovation and modernization of existing methods for strengthening the foundation soils.

Artificial soil stabilization is the impact on the soil with the help of various structural and technological measures, which increases its bearing capacity and reduces deformations.

DOI: 10.1201/9781003299127-96

Currently, there are many methods of soil stabilization, each of which has its own advantages and disadvantages. Most often, the scope of the method is somehow limited by the type of soil.

To increase the bearing capacity and reduce the deformation of soil foundations, there are many ways to artificially fix soils.

Conventionally, they can be divided into physical - strengthening the soil mass with the help of physical fields, mechanical - placing reinforcing elements with high tensile strength into the soil, chemical - improving the properties of soils by injecting special solutions into their thickness.

The fixing method is chosen based on the soil conditions of the construction area, as well as the production capabilities of its implementation.

Thermal fixing of the soil - the transformation of structural bonds in the soil under the influence of high temperatures. It is carried out either by injection into the soil under pressure of air heated to a temperature of 600–800 ° C, or as a result of burning fuel (solar oil, fuel oil, natural gas, etc.) in hermetically sealed wells drilled for this purpose.

After fixing, the strength and water resistance of soils increase, and their subsidence properties are eliminated [1]. In accordance with the technology, it is necessary to maintain a pressure in the well from 15 to 50 kPa, which is achieved by supplying hot air to enhance the filtration of hot gases in the soil and maintain the required temperature. The diameter of the wells is assumed to be 10–20 cm, while the depth varies from 6 to 15 m or more. Depending on the loads and their distribution over the building spot, the distance between the axes of the wells is determined.

Roasting of the soil lasts from 5 to 10 days. An array of thermally fixed soil with a diameter of 1.5–3 m is formed around the well when 80–180 kg of liquid fuel is burned per 1 m of the well depth. To avoid the penetration of groundwater or water-saturated unstable soils into the mine under construction, artificial freezing of soils is used, which creates a solid fence that has a circular or rectangular shape in plan from frozen soil. To freeze soils, a refrigerant or refrigerant is usually used (most often a chilled aqueous solution of calcium chloride - brine). The main function of the brine is the ability to remain liquid at low temperatures.

The second group under consideration is the mechanical methods of fixing the foundation soils. The methods are considered the most popular, since they do not involve changes in soil properties under the action of solutions or physical fields, which is quite difficult to control. Mechanical methods involve soil reinforcement with ready-made elements from various materials with high tensile strength.

The most common method of soil compaction is tamping or layer-by-layer compaction. For compaction, hammers are used, which are mechanized and manual.

Mechanized compaction with special construction equipment significantly increases the estimated cost of construction, but for large volumes of work, the use of only manual mechanisms is impractical.

Compaction of soils with the help of hammers is carried out until the surface of the soil, with each subsequent fall, drops by the same amount, called “failure”. The size of the failure is approximately taken equal to 1–1.5 cm for dusty clay soils, and 0.5–1 cm for sandy soils.

Failure is achieved after 8–12 hits on one track. The compaction mode is set experimentally and depends on the soil conditions at the construction site.

The use of fibrous materials, namely geosynthetics, to strengthen soil foundations has now become popular. This is facilitated by their great variety, simplicity and efficiency of technology. There are several types of geosynthetic materials used to reinforce soil foundations: geotextile, geogrid, geomatrix. Depending on the manufacturing method and, as a result, the final technical characteristics, woven and non-woven geotextiles are distinguished. Nonwoven geotextile is a flat structure, which consists of synthetic fibers, fastened together by a mechanical method. Such material does not rot, plant roots do not grow through it, and the structure provides good strength and filtering properties. [2-4].

Of greatest interest is the use of geogrids, which is a honeycomb structure made of polyethylene tapes, which are interconnected by high-strength welds and have a staggered arrangement. They are used primarily for reinforcing soil foundations for the purpose of strengthening, given

their special structure, when the soil sandwiched between the cells of the geogrid cannot move from acting loads and all tensile stresses are transferred to the geogrid. One of the novelties for soil stabilization is the use of a geomatrix. Structurally, geomatrices are a box without a top cover, to the walls of which geotextile tapes are attached. Intersecting, they form rectangular cells inside the box [5–10].

When arranging the foundation and foundations of a building and construction, a certain problem exists in construction sites where the groundwater level is high. Due to the high levels of groundwater, the soil under the base of the foundation has increased water saturation. In many cases, special dewatering works are carried out to solve the problem. The essence of the method of dewatering is based on the fact that the surface of the water in the soil acquires a funnel-shaped shape with a slope towards the pumping point of groundwater that enters the well. The funnel-shaped (lowered) surface of groundwater is called the depression surface, and the depression funnel is the space between this surface and the non-lowered surface of the ground flow. The soil below the groundwater level experiences the weighing effect of water, therefore, the specific gravity of the soil decreases. In this case, artificial dewatering is used, as a result of which the soil is above the groundwater level, the specific gravity of the soil increases, and the base is compacted. The depression funnel increases as the water is pumped out. The development of the depression funnel does not occur, stabilization occurs if the pumping intensity remains constant. With the cessation of pumping, the groundwater level is restored. The main purpose of dewatering is to maintain depression funnels in a drained state during the entire period of construction of the structure.

In some cases, dewatering is used to relieve excess pressure in the underlying aquifers, separated from the bottom of the pit by a layer of water-resistant soil. When dewatering, several methods are used: using light and ejector wellpoints and the vacuum method.

Currently, of particular interest is the chemical methods of fixing soils. All chemical processes occur due to the chemical interaction of the reagents introduced into the soil, among themselves, as well as with mineral particles.

On the territory of Kazakhstan there are regions where the level of groundwater is high. These regions include Akmola, Kyzylorda, Atyrau regions. Currently, along with the construction of large civil and industrial buildings and structures, low-rise residential complexes are also being actively built up.

The use of pile foundations for these complexes is technically and economically inexpedient.

Therefore, during the construction of such complexes, the construction of shallow foundations is mainly adopted in design decisions.

Typically, the depth of the foundation in such cases is taken in the range from 1.0 -1.5 m. In these regions, the groundwater level is within these limits, which predetermines waterlogging of the soil.

Waterlogged soils cannot be compacted. Waterlogged soils cannot be loosened, and therefore, cement, bitumen, silicate mortar, polymeric and other binders cannot be used to strengthen them. Natural drying of waterlogged soils, especially clay soils, occurs very slowly, and artificial drying methods currently used are ineffective or require large expenditures of money and time.

Therefore, strengthening waterlogged soil under the foundations of shallow foundations, taking into account technological and economic feasibility, is an urgent task.

An analysis of possible ways to improve the workability of waterlogged fine sandy, sandy loam, loam and clay soils for further strengthening them with binders, including cement, silicate mortar and polymer suspensions, showed that the most effective treatment of such soils with chemicals that, along with dehydration, can change the physical - Chemical properties.

The purpose of the work is to carry out scientific and experimental work on the use of quicklime to strengthen waterlogged soils with the study of changes in their physical and mechanical properties.

1.1 *Materials and research methods*

When examining the soil, standard methods were used to determine the physical and mechanical properties of the samples.

Ground quicklime is of particular interest as the main material for solving the tasks set.

Lime is the most common material. Its main active components - CaO, when interacting with water, turns into Ca (OH) 2. The rate of hydration of these components depends on the degree of their dispersion and the temperature of limestone firing. The process of lime slaking occurs according to the reaction: CaO + H2O \u003d Ca (OH) 2 + 15.5 kcal., Where 1 kcal \u003d 4.1868 10^3 J. The lime slaking reaction proceeds rapidly, with a large release of heat - 15.5 kcal per gram-molecule or 277 kcal per 1 kg of lime. Water, penetrating into the depths of the lime grains, enters into a chemical interaction with CaO, and the heat released in this case turns the water into steam.

For scientific and experimental work, standard powdered slow-extinguishing quicklime of the 1st grade was used according to GOST 9179-2018 "Building lime. Specifications" (EN 459-1:2010, NEQ). The content of active CaO + MgO, not less than 90%.

Soil (loam) was chosen as the object of research for the construction of a residential building in Kyzylorda (Kazakhstan). At the initial stage of the research, scientific and experimental work was carried out to study the physical and mechanical properties of the soil, the results of which are given in Table 1.

Table 1. Physical and mechanical properties of soil for the construction of a residential building in Kyzylorda.

Soil name	Depth sampling, m	Density particles, Ps g/cm3	Humidity natural, W%	Plasticity number, Ip	Fluidity	Coefficient porosity, e	Coeff. water saturation, Sr
Loam	1,0	2,7	23,2	9,9	-0,52	0, 722	0,40

Samples of waterlogged loam soil had the following technical characteristics: particle specific gravity γs =26,3 kN/m^3; specific gravity before compaction γ=14,6 kN/m^3, after compaction γ′= 18,5 kN/m^3; optimal moisture content for standard seal Wo = 0,14 is between the maximum molecular moisture capacity Wm = 0,11 and rolling limit Wp = 0,15; yield strength WL = 0,25 for this type of soil. Granulometric composition, content of fractions: d > 2 mm; d = 0,1..2 mm – 34 %; d = 0,1..0,25 mm – 27 %; d = 0,05. . .0,002 mm – 14 %;loss on ignition 4,3 %; pH < 5,0 water extract.

2 RESULTS AND DISCUSSIONS

To establish the maximum temperature of the heat generated when interacting with water, laboratory studies were carried out according to the following method: quicklime in the amount of 100 g was poured into a transparent plastic dish. Then water at room temperature (t = 20-22 C) was added to the dish with quicklime in the amount of 150 g. To measure the temperature of the heat generated in the center of the plastic dish, a thermometer was installed to a depth of half the height of the poured quicklime, as shown in Figures 1 and 2.

The results of the study demonstrate that the reaction of interaction of calcium oxide with water is a transient process with a large release of heat. During the first 5 minutes, the temperature rises sharply to 100 0C, after which there is a slow decline to room temperature over 90 minutes.

At this stage of the study, it was proved that water, penetrating into the depths of lime grains, enters into a chemical interaction with CaO, and the heat released in this case turns the water into a boiling state, which leads to the release of steam. It is this effect of heat release with the release of steam that is planned to be used to drain and strengthen the waterlogged soil caused due to the high level of groundwater.

Figure 1. Temperature readings during the reaction 5 min.

Figure 2. Temperature readings during the reaction 45 min.

Table 2. Temperature readings over time.

Time (minute)		5	10	15	20	25	30	35	40	45	50	55	60
Temperature (°C)	test №1	98	96	86	82	75	70	63	61	58	55	50	48
	test №2	97	95	88	82	76	71	65	62	56	53	49	45
	test №3	98	95	87	81	75	69	64	60	57	54	52	49

For scientific and experimental work, four batches of prototypes of loamy soil with a moisture content of 20 to 40% were prepared. Figure 3.

Figure 3. The process of preparing soil with different moisture content in laboratory conditions.

After preparing the soil with different moisture content, quicklime was added to it in an amount from 5 to 25%. Quicklime was poured onto the surface of wet soil and the ongoing processes were visually observed. Figure 4.

Figure 4. The process of adding quicklime to the soil surface.

In the process of mixing the soil with quicklime, intensive adsorption of moisture contained in the soil was observed, and the process of slaking the lime with the release of heat was observed.

In addition, moisture evaporation was observed in parallel due to the heating of the mixture associated with the processes of chemical reactions. Figure 5.

At the same time, it was found that after a certain time the mixture of soil with lime acquires the ability to clot and harden.

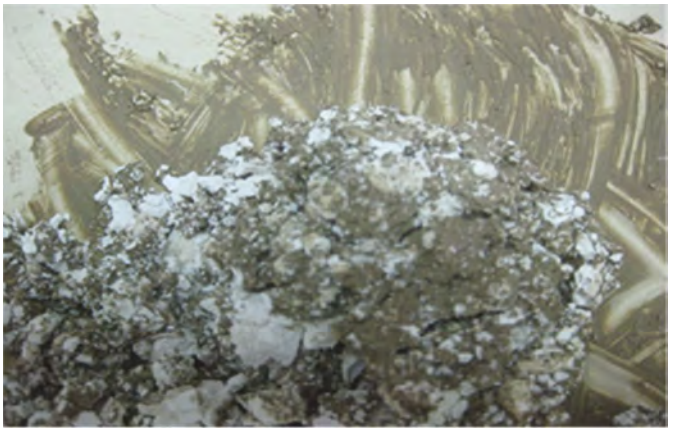

Figure 5. A mixed mixture of soil and quicklime, where the process of slaking lime takes place with the release of heat and evaporation of moisture.

The next stage of the study was the study of the duration of dehydration of wet soil from the content of quicklime. The studies were carried out until the soil moisture reached 8-10%. The results of the study are presented in Figure 6.

As the results of scientific and experimental studies show, with an increase in the content of quicklime, a decrease in the duration of soil dehydration is observed. The longest dehydration time was recorded at a soil moisture content of 20% and a quicklime content of 5%. In this case, the duration reaches up to 70 minutes. However, with an increase in the amount of quicklime from 10% to 25% (with a soil moisture content of 20%), the dehydration time is gradually reduced to 20 minutes.

It should be noted that with an increase in soil moisture, even with a minimum amount of quicklime (5%), a significant reduction in dehydration time is observed. So, with an increase in soil moisture up to 25% and with an amount of quicklime of 5%, the dehydration time is

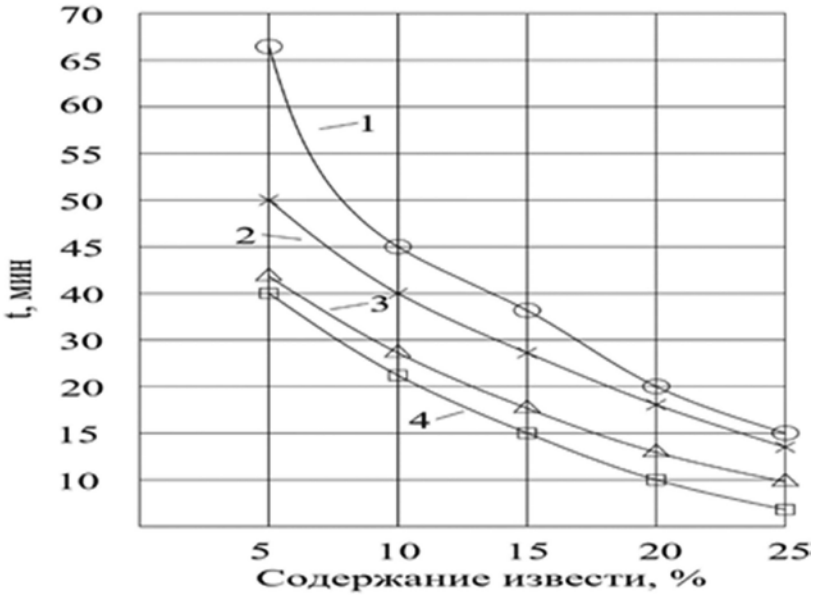

Figure 6. Dependence of the duration of soil dehydration depending on the content of quicklime. 1 - at soil moisture 20%, 2 - the same 25%, the same 30%, the same 40%.

55 minutes. The maximum reduction in the dehydration time of drying up to 15 minutes was recorded at a soil moisture content of 40% and with an amount of quicklime of 25%.

This pattern is explained by the fact that a decrease in the moisture content of waterlogged soils when lime is applied occurs as a result of the following factors:

a) in the process of lime slaking, the released heat (T=100 0C) raises the temperature of the soil, so the evaporation of moisture from the treated layer increases. In this case, the degree of activity of the quicklime quenching reaction directly depends on the amount of moisture;
b) when lime is added to the soil, part of the moisture enters into a chemical interaction with its active components and passes into a solid state due to the binding and hardening properties of quicklime.;
c) quicklime in the form of a dry powder added to the waterlogged soil increases the weight of its dry mass due to the addition of dry material and due to the weight of water chemically bound by calcium oxide.

Thus, it has been established that the addition of quicklime is capable of dehydrating waterlogged soils due to the release of heat generated as a result of chemical reactions.

The main physical properties that determine the workability of waterlogged soils are: maximum molecular moisture capacity Wm, yield strength WL, rolling limit Wp, optimum moisture content with standard compaction Wo.

The optimum moisture content of a standard seal, Wo, depends on the magnitude of the sealing load and can vary over a wide range.

After the introduction of quicklime into waterlogged soil, the physical properties of these soils change dramatically. Depending on the dosage of quicklime, two stages of change in physical properties are distinguished, such as WL, Wp, Wo and Wm.

At stage I, additions of quicklime or MgO at a dosage of 5.0 to 25% act as reagents that radically change the properties of waterlogged soil, in which the number of particles $d<0.005$ mm decreases almost to zero, the value of WL, Wp, Wo and Wm increases sharply.

At stage II, additions of quicklime from 5.0 to 25% no longer act as chemical reagents, but as mechanical components of the mixture, affecting only the increase in the strength of the mixture, since quicklime, when interacting with waterlogged soil, has the ability to harden.

The change in the properties of waterlogged soils when ground quicklime is introduced is associated with the coagulation of fine particles due to the compensation of their charges. Soil particles are charged by double electric layers of soil micelle with a negative electric charge, and these charges are compensated by cations, which, being adsorbed on the surface of negatively charged particles, reduce their charge. Ions of higher valencies cause coagulation at lower concentrations than ions of lower valences.

The amount of lime or magnesia required to change the properties of waterlogged soils depends on the composition of the soil. Therefore, for the processing of light sandy loams, loams and clayey soils with carbonate inclusions, additional scientific and experimental studies are required.

Lime pre-treatment of waterlogged soils significantly improves their workability by fixing them by cementation, silicification, claying and polymerization. At the same time, the number of dust-like particles sharply decreases and the number of aggregates with a diameter of more than 5 mm and more than 10 mm increases. Figure 7.

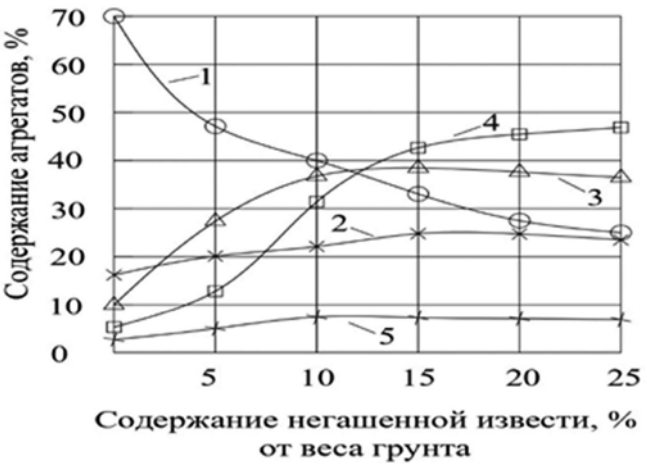

Figure 7. The influence of quicklime on the nature of the change in the content of soil aggregates from loam with the content of aggregates in size: 1 - more than 10 mm; 2 - 10-5 mm; 3 - 5-3 mm; 4 - 3-1 mm; 5 - less than 1 mm.

Influence of lime on the nature of the change in the content of soil aggregates and standard compaction for loamy soil with a specific gravity of soil γ=14.6 kN/m^3, in which, after the introduction of lime and compaction, the specific gravity became 18.5 kN/m^3, with the optimum moisture content of the standard compaction Wo= 0.14.

The influence of lime on the nature of the change in soil aggregates is carried out by thoroughly mixing them, since when lime is applied to waterlogged soil, crusts form on the surface of the soil, and lime cannot penetrate deep into. The thickness of the crust can reach 10 mm.

The optimal doses of quicklime for the waterlogged studied loam can be taken 15-20%. At these doses, the strength of waterlogged soils reaches from 0.5 to 2.0 MPa and the deformation modulus Eo - from 40 to 80 MPa.

3 CONCLUSIONS

1. As a result of the analysis of research and practical work in the field of strengthening waterlogged soils, it was found that the most effective treatment of such soils with

chemicals that, along with dehydration, can change the physical and chemical properties.

2. It has been established the efficiency of dehydration and strengthening of waterlogged soil by introducing quicklime through the use of heat generated (T = 1000C) when interacting with water and their ability to harden due to chemical interaction with the mineral part of the soil.
3. The patterns of change in the duration of dehydration and the state of aggregation of waterlogged soil from the amount of quicklime have been established.
4. It is proved that the introduction of quicklime in the amount of 20-25% into waterlogged soil radically changes the properties of these soils, enlarges the state of aggregation and creates workability for fixing by cementation, silicification and resinization.

REFERENCES

Injection chemical fixation of soils. Thermal stabilization of soils: a typical technological map. - St. Petersburg, 2009.

The use of synthetic materials in the highway engineering in the Urals / A. Bartolomey, A. Bogomolov, V. Kleveko, A. Ponomarev, V. Ofrikhter // Proceedings of the twelfth European conference on soil mechanics and geotechnical engineering. - Amsterdam, Netherlands, 1999. - Vol. 2. - P. 1197–1202.

Kleveko V.I. The use of geosynthetic materials in road construction in the conditions of the Perm region // Bulletin of the Perm National Research Polytechnic University. Construction and architecture. - 2013. - No. 1. - P. 114–123.

Mashchenko A.V., Ponomarev A.B. Analysis of changes in the strength and deformation properties of soil reinforced with geosynthetic materials at different degrees of water saturation // Bulletin of the Perm National Research Polytechnic University. Construction and architecture. - 2014. - No. 4. - P. 264–273.

Ponomaryov A., Zolotozubov D. Several approaches for the design of reinforced bases on karst areas // Geotextiles and Geomembranes. – 2014. – No. 42.–P. 48–51.

Methods of construction of reinforced soil structures: textbook.-method. allowance / V.G. Ofrichter, A. B. Ponomarev, V.I. Kleveko, K.V. Reshetnikov. - Perm: Publishing House of Perm. state tech. un-ta, 2010. - 145 p.

Sokolova V.D., Kleveko V.I. Application of the finite element method for modeling the work of pavement of a city square from paving stones on a reinforced soil base // Transport. Transport facilities. Ecology. - 2014. - No. 4. - P. 77–89.

Kleveko V.I. Evaluation of the value of foundation settlement on clay bases reinforced with horizontal layers // Bulletin of the Perm National Research Polytechnic University. Environmental protection, transport, life safety. - 2012. - No. 1. - P. 89–98.

Igosheva L.A., Kleveko V.I. Geosynthetic materials in the construction of pavements for car parks in difficult engineering and geological conditions // Geology in the Developing World. - 2015. - T. 2. - S. 33–37.

Igosheva L.A., Petreneva O.A., Kleveko V.I. The use of geosynthetic materials in the design of car parks in complex engineering and geological conditions [Electronic resource] // Construction and architecture. Experience and modern technologies. - 2015. - Issue. 4, part 1. - URL: http://sbornikstf.pstu.ru/council/?n=4&s=243.

Smart Geotechnics for Smart Societies – Zhussupbekov, Sarsembayeva & Kaliakin (Eds)
© 2023 The Author(s), ISBN 978-1-003-29912-7
Open Access: www.taylorfrancis.com, CC BY-NC-ND 4.0 license

Numerical study on stress-strain characteristics of the deep cement mixing column improved soil

M.J. Singh & S. Choudhary
Indian Institute of Technology Indore

Lalit Borana
Associate Professor, Indian Institute of Technology Indore

ABSTRACT: Infrastructural development on soft and marine soil is challenging owing to its time-dependent behaviour. Different ground improvement techniques are used to improve the naturally available soft and marine soil. Among different techniques, Deep Cement Mixing (DCM) is an efficient approach to enhance the engineering characteristics of the ground. Researchers have attempted to investigate the behaviour of the DCM-improved soil and mainly focused on the strength and stiffness characteristics of composite soil. it is noted that not much emphasis has been given to examining the time-dependent consolidation behaviour of DCM-improved clay soil. In this study, efforts are been made to investigate the time-dependent consolidation behaviour of the DCM-improved clay soil and discussed in detail through numerical simulation. Further, the distribution of the creep behaviour of the DCM column and surrounding soil with depth is also discussed in detail.

Keywords: Ground improvement techniques, Deep cement mixing, Consolidation behaviour

1 INTRODUCTION

Good-quality constructional geomaterials are becoming scarce due to limited space and continuous constructional activities, in the last few decades. Therefore, in developing countries, several infrastructural projects are being constructed on marine and soft soil (Geng 2008; Singh et al. 2022). The soft soils are characterized by their low permeability and exhibit time-dependent consolidation settlement, swelling shrinkage behaviour, and strength changes behaviour (Feng et al. 2017; Singh et al. 2021). The settlement of the soft/marine soil poses a severe threat to various engineering structures, including railways, and airport runways and damages the foundation of coastal engineering projects (Johnson Singh et al. 2022; Park and Lee 2011). Different researchers suggest several ground improvement techniques including sand drains, wick drains, stone columns, removal and replacement of soil, grouting and deep mixing of soil and many more (Andromalos et al. 2001; López-lara et al. 2017; Mitchell 2008). Among these techniques, deep cement mixing (DCM) columnar inclusion is one of the effective techniques, due to its cost-effectiveness, technologically simple, and allowing fast construction (Alhamdi and Albusoda 2021; Turner et al. 2017).

DCM method is the injection of cement additive either in powder or slurry form into soft soil and mixed together by using a mixing blade. After the completion of the curing period, this mixture converts to a soil cement column (Voottipruex et al. 2019). Bruce (Bruce and Geosystems 2000) investigated the influence of the mixing factors such as installation rate, water/cement ratio, and rate of rotation that affected the strength development of soil-cement columns. Different researchers investigated the influence of different quantities of cement content and consolidation behaviour of the soft soil with different area ratios of DCM column under different vertical stresses (Horpibulsuk et al. 2012b; Suebsuk et al. 2010). The stabilization of clayey soil with cement

DOI: 10.1201/9781003299127-97

mixing is due to the cementitious bond developed between the hydration products of the cement in aluminate and silicate form and the soil particles. Due to this interaction, the interlayer and inter-micellar swelling of the clayey soil particles reduced significantly (Fang and Yin 2007; Horpibulsuk et al. 2012a; Jamsawang et al. 2017). Horpibulsuk et al. (Horpibulsuk et al. 2010) employed finite element methods to investigate the consolidation behaviour of the composite ground and designed a practical method to predict the estimated settlement. Wijerathna et al. (Wijerathna et al. 2016) investigate the behaviour of DCM column-improved soil during the breakdown of the soil-cement structure and subsequent consolidation. The study considered the strain-softening behaviour of cement-mixed soils beyond yield. Several factors can influence the strength of the soil-cement-treated clayey soil like characteristics of soil, characteristics of the binder, curing conditions and mixing conditions (Kitazume and Terashi n.d.; Yin et al. 2022).

Few researchers have conducted several experimental and numerical analyses on DCM-improved soft soil. However, the time-dependent stress-strain characteristics of DCM-improved composite soil, especially the creep behaviour are neglected. In this study, a parametric study is conducted using finite element simulation to assess the time-dependent stress-strain behaviour of DCM-improved composite soil.

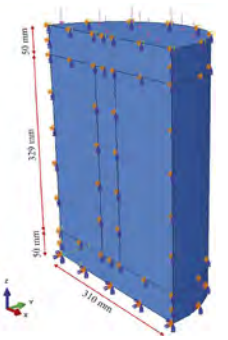

Figure 1. The boundary condition and model development.

2 MODEL DEVELOPMENT AND BOUNDARY CONDITION

In this study, the modified Drucker-Prager/Cap plasticity/creep model is used as this model is able to simulate creep in geomaterials exhibiting long-term inelastic deformation through a cohesion creep mechanism and a consolidation creep mechanism in the cap region (as suggested in ABAQUS User's Manual). A finite element model was developed in the ABAQUS/Standard to simulate the time-dependent settlement of the soil, as illustrated in Figure 1.

Table 1. Material properties and different parameters.

Parameters	Clay soil	DCM column	Sand
Density (kg/m^3)	1791	2039.43	1835.49
Void ratio, e_o	1.93	1.98	2
Permeability m/sec	$1.12x10^{-7}$	$1x10^{-7}$	$1x10^{-5}$
Poisson's ratio, v	0.2	0.2	0.2
Young's modulus of elasticity, MPa	20	40	30
The angle of internal friction	24	57.5	30
Cohesion, kPa	35	87	-
Cap eccentricity, β	0.4	0.4	-
Initial yield surface position	0	0	-
Transition surface position	0	0	-
Flow stress	1	1	-

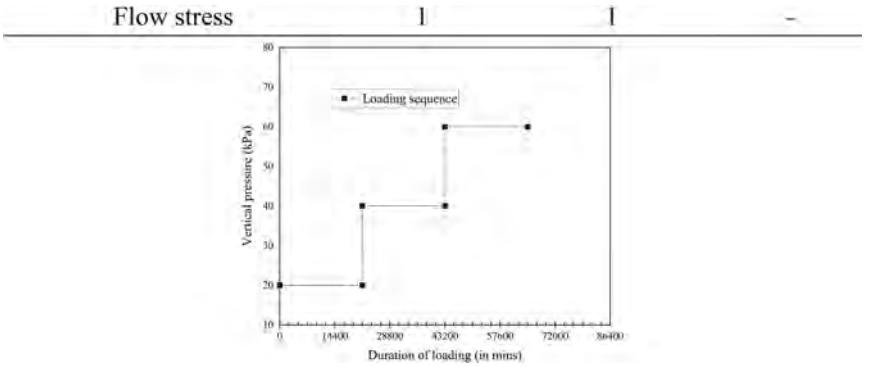

Figure 2. Loading sequences and duration of loading. (not included in theory).

Different properties of the DCM column, sand and clay soil are presented in Table 1. The parameters used in the simulation are taken from the relevant literature (Aza-Gnandji and Kalumba 2014; Gupta and Sharma 2016; Peeters 2017; Yapage et al. 2014). In this study, both the DCM column and surrounding clay soil were simulated using the Cap plasticity model, this arrangement reduces the interaction relevant problems between the soils. Drainage was allowed at the top surface of the DCM column and soft clay through the sand layers. Thus pore pressure dissipation takes place only on the upper surface of the model. To maintain the symmetry at the centre of the model, lateral displacement was restricted throughout the study. The bottom surface is constrained in both lateral and vertical displacement. The interaction between the DCM and surrounding soil is simulated using the normal behaviour and tangential behaviour with friction formulation in the penalty subsection and uses a 0.3 friction coefficient. The mesh size of the DCM column and surrounding soil sample are respectively 0.009 and 0.0095. A smaller mesh size was provided to simulate the DCM column without possible errors. There were three different stages of the loading, and each load were applied for 1296000 seconds with a magnitude of 20 kPa as illustrated in Figure 2.

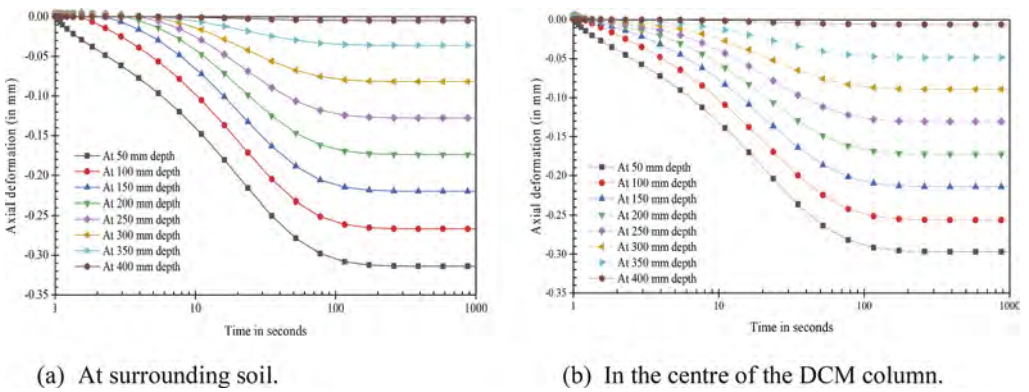

Figure 3. Axial deformation behaviour of the soil and DCM column.

3 RESULT AND DISCUSSION

The variation of axial deformation behaviour surrounding clay and the DCM column with depth during the application of 20 kPa is illustrated in Figure 3 (a) and (b). It is observed that during the application of 20 kPa effective stress the surrounding clay soil exhibits 5.69%

higher axial deformation with respect to the DCM column at 50 mm below the soil surface. Similarly, the relative settlement behaviour of the surrounding soil with depth is observed to decrease with respect to the settlement in the DCM column. A similar pattern is observed during the application of remaining effective stress. During the application of 60 kPa, the reconstituted soil exhibits a maximum settlement of 0.91 mm during the whole loading period. In this study, a small loading was applied which is below the failure of the column. The overall settlement of the DCM-improved soil is observed to be small. Different factors might be responsible and some of the probable factors may include the coefficient of consolidation, the length of the drainage path and the permeability of the soil.

Further, an attempt was made to investigate the time-dependent creep behaviour of the soil using the power law model proposed by Briaud and Garland (Briaud and Garland 1985). It considered the creep behaviour of the soil during the primary consolidation stage also. It has been extended by the author to present the time-dependent behaviour of various sources of soils on diversified data. The model is written as below:

$$\frac{s}{s_1} = \left(\frac{t}{t_1}\right)^n$$

where, s and t signify the deformation (settlement, strain, etc.) and corresponding time respectively. The s_1 is usually chosen to be the value of deformation s observed at reference time t_1. The reference time could be either 1 second, 1 minute, 1 day or onwards, and n is the viscous exponent (Bi et al. 2019; Singh et al. 2022).

Using the relationship between $\log(s/s_1)$ and $\log(t/t_1)$, the slope is used to represent the viscous time-dependent component. After the end of the primary consolidation, the slope can be regarded as a creep parameter of the soil (Bi et al. 2019). Taking the DCM-improved soil as a whole, the creep parameters are determined for every 50 mm depth from the upper soil surface. The first 50 mm which is just below the sandy layer has a creep parameter of 0.025. Similarly, the creep parameter of remaining layers 100 mm, 150 mm, 200 mm, 250 mm, 300 mm, and 350 mm are respectively 0.0259, 0.029, 0.0142, 0.0152, 0.0159 and 0.0162. For the natural clay soil, the creep coefficient is reduced with depth as reported by other researchers (Le and Fatahi 2016). But during the installation of the DCM column, it changes the drainage behaviour, soil column interaction, stress distribution and many more (Fang and Yin 2007; Turner et al. 2017). All these factors may influence the distribution of creep parameters with depth, therefore a particular trend is cannot derive. However, in this study, it is observed that the time-dependent behaviour of DCM-improved soil composite is significantly varied with the depth.

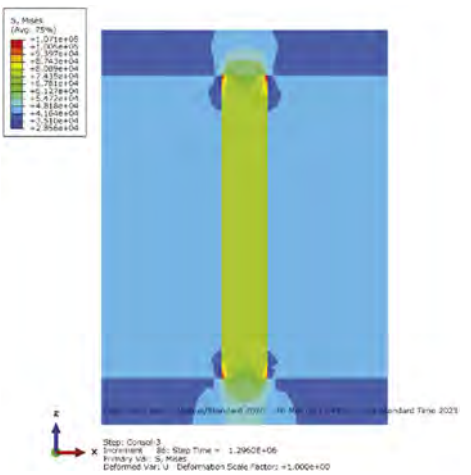

Figure 4. The stress-distribution behaviour of the DCM-installed clay soil.

The stress-distribution behaviour of the DCM-installed clay soil is illustrated in Figure 4. From this figure, it is observed that the top and bottom portion of the column carries the maximum stress compared to the other portions. Therefore, these locations may be the responsible portions for the failure of the column as maximum stress distribution takes place in these portions. The failure portion of the DCM improved soil is well agreed with the findings of other researchers (Wijerathna et al. 2016). The crushing of the soil structures is also the responsible factor for the failure of the DCM column in the laboratory (Horpibulsuk et al. 2012a). During the numerical simulation, lateral deformations are not observed in the DCM column while applying the pressure.

4 CONCLUSION

DCM columnar inclusion is a potential ground improvement technique to stabilize soft or marine soil. In this study, a numerical study is utilized to investigate the time-dependent stress-strain behaviour of DCM columns. Based on the findings, the following conclusions are drawn.

1. It is observed that the surrounding soil exhibits 5.69% higher axial deformation behaviour with respect to the DCM column at 50 mm below the soil surface. With depth, the surrounding clay exhibits higher axial deformation behaviour compared to the DCM column.
2. The distribution of the time-dependent creep parameter of composite soil is varied with depth. This might be due to changes in drainage behaviour, soil column interaction, stress distribution etc.
3. Maximum stress distribution takes place in the top and bottom edges of the DCM column play compared to the other portions. Therefore, these are the expected locations for the failure of the DCM column.

REFERENCES

Alhamdi, M. K., and Albusoda, B. S. (2021). "A Review on Deep mixing method for soil improvement." *IOP Conference Series: Materials Science and Engineering*, IOP Publishing, 12110.

Andromalos, K. B., Hegazy, Y. A., and Jasperse, B. H. (2001). "Stabilization of soft soils by soil mixing." *Soft ground technology*, 194–205.

Aza-Gnandji, R., and Kalumba, D. (2014). "Experimental and numerical analysis of the behaviour of rammed stone columns installed in a South African soft soil." *International Journal of Engineering Science and Innovative Technology*, 3(6), 477–499.

Bi, G., Ni, S., Wang, D., Chen, Y., Wei, J., and Gong, W. (2019). "Creep in Primary Consolidation with Rate of Loading Approach." *Scientific Reports*, Springer US, (December 2018), 1–9.

Briaud, J.-L., and Garland, E. (1985). "Loading rate method for pile response in clay." *Journal of Geotechnical Engineering*, American Society of Civil Engineers, 111(3), 319–335.

Bruce, D. A., and Geosystems, E. C. O. (2000). *An introduction to the deep soil mixing methods as used in geotechnical applications*. United States. Federal Highway Administration. Office of Infrastructure.

Fang, Z., and Yin, J.-H. (2007). "Responses of excess pore water pressure in soft marine clay around a soil–cement column." *International Journal of Geomechanics*, American Society of Civil Engineers, 7(3), 167–175.

Feng, W., Lalit, B., Yin, Z., and Yin, J. (2017). "Long-term Non-linear creep and swelling behavior of Hong Kong marine deposits in oedometer condition." *Computers and Geotechnics*, Elsevier Ltd, 84, 1–15.

Geng, X. (2008). "Non-linear consolidation of soil with vertical and horizontal drainage under time-dependent loading." *2008 International Conference on Advanced Computer Theory and Engineering*, IEEE, 800–804.

Gupta, C., and Sharma, R. K. (2016). "Black cotton soil modification by the application of waste materials." *Periodica Polytechnica Civil Engineering*, 60(4), 479–490.

Horpibulsuk, S., Chinkulkijniwat, A., Cholphatsorn, A., Suebsuk, J., and Liu, M. D. (2012a). "Consolidation behavior of soil-cement column improved ground." *Computers and Geotechnics*, Elsevier Ltd, 43, 37–50.

Horpibulsuk, S., Liu, M. D., Liyanapathirana, D. S., and Suebsuk, J. (2010). "Behaviour of cemented clay simulated via the theoretical framework of the Structured Cam Clay model." *Computers and Geotechnics*, Elsevier Ltd, 37(1–2), 1–9.

Horpibulsuk, S., Phojan, W., Suddeepong, A., Chinkulkijniwat, A., and Liu, M. D. (2012b). "Strength development in blended cement admixed saline clay." *Applied Clay Science*, Elsevier B.V., 55, 44–52.

Jamsawang, P., Nuansrithong, N., Voottipruex, P., Songpiriyakij, S., and Jongpradist, P. (2017). "Laboratory investigations on the swelling behavior of composite expansive clays stabilized with shallow and deep clay-cement mixing methods." *Applied Clay Science*, Elsevier, 148(March), 83–94.

Johnson Singh, M., Feng, W., Xu, D., Dubey, M., and Borana, L. (2022). "Long-Term Elastoviscoplastic Behavior of Fly Ash–Blended Indian Montmorillonite Clay in Oedometer Conditions." *International Journal of Geomechanics*, American Society of Civil Engineers, 22(3), 4021306.

Kitazume, M., and Terashi, M. (n.d.). *The Deep Mixing Method*.

Le, T. M., and Fatahi, B. (2016). "Trust-region reflective optimisation to obtain soil visco-plastic properties." *Engineering Computations*, Emerald Group Publishing Limited.

López-lara, T., Hernández-zaragoza, J. B., Horta-rangel, J., and Rojas-gonzález, E. (2017). "Expansion reduction of clayey soils through Surcharge application and Lime Treatment." *Case Studies in Construction Materials*, Elsevier, 7(June), 102–109.

Mitchell, J. K. (2008). "Recent developments in ground improvement for mitigation of seismic risk to existing embankment dams." *Geotechnical Earthquake Engineering and Soil Dynamics IV*, 1–20.

Park, H. Il, and Lee, S. R. (2011). "Evaluation of the compression index of soils using an artificial neural network." *Computers and Geotechnics*, Elsevier, 38(4), 472–481.

Peeters, B. (2017). "Two-dimensional analysis of the failure mechanisms of an embankment supported by rows of dry deep mixing columns."

Singh, M. J., Borana, L., Weiqiang, F., and Xu, D.-S. (2021). "Long-Term Swelling Characteristics of Montmorillonite Clay with and without Fly Ash: Wetting–Drying Cycle Influence in 1D Oedometer Condition." *Journal of Testing and Evaluation*, ASTM International, 51(1).

Singh, M. J., Feng, W. Q., Xu, D. S., and Borana, L. (2022). "Time-dependent compressibility characteristics of Montmorillonite Clay using EVPS Model." *Geomechanics and Engineering*, 28(2), 171–180.

Suebsuk, J., Horpibulsuk, S., and Liu, M. D. (2010). "Modified Structured Cam Clay: A generalised critical state model for destructured, naturally structured and artificially structured clays." *Computers and Geotechnics*, Elsevier Ltd, 37(7–8), 956–968.

Turner, B., Huang, J., and Kelly, R. (2017). "Long-term strength of soil-cement columns in coastal areas." *Soils and foundations*, Elsevier, 57(4), 645–654.

Voottipruex, P., Jamsawang, P., Sukontasukkul, P., Jongpradist, P., Horpibulsuk, S., and Chindaprasirt, P. (2019). "Performances of SDCM and DCM walls under deep excavation in soft clay: Field tests and 3D simulations." *Soils and Foundations*, Elsevier, 59(6), 1728–1739.

Wijerathna, M., Liyanapathirana, D. S., and Leo, C. (2016). "Consolidation behaviour of deep cement mixed column improved ground during breakage of soil-cement structure." *Australian Geomechanics Journal*, 51(2), 35–42.

Yapage, N. N. S., Liyanapathirana, D. S., Kelly, R. B., Poulos, H. G., and Leo, C. J. (2014). "Numerical modeling of an embankment over soft ground improved with deep cement mixed columns: case history." *Journal of Geotechnical and Geoenvironmental Engineering*, American Society of Civil Engineers, 140(11), 4014062.

Yin, K. S., Zhang, L. M., Zou, H. F., Luo, H. Y., and Lu, W. J. (2022). "Key Factors for Deep Cement Mixing Construction for Undredged Offshore Land Reclamation." *Journal of Geotechnical and Geoenvironmental Engineering*, 148(8), 1–11.

Smart Geotechnics for Smart Societies – Zhussupbekov, Sarsembayeva & Kaliakin (Eds)
© 2023 The Author(s), ISBN 978-1-003-29912-7
Open Access: www.taylorfrancis.com, CC BY-NC-ND 4.0 license

Microcapsules retention behavior in granular materials

K. Chen & Q. Rui
Department of Civil Engineering, The University of Hong Kong, Hong Kong S.A.R., China

S.D.N. Lourenço
Department of Civil Engineering, The University of Hong Kong, Hong Kong S.A.R., China

ABSTRACT: Due to the advantages of protection and controllable releasing of chemical materials, microcapsules have been widely used to self-heal cementitious materials. However, their applications in granular materials like soils remains to be unexplored. An initial challenge to tackle is the microcapsules retention in open porous media. From laboratory results, a distinctive demarcation between effective and ineffective gravel-microcapsules mixtures was identified in considering the washout of microcapsules. An attempt has been made to develop a design criterion in terms of the relationship of d_{85} (a representative size of microcapsules being protected) and D_{15} (a representative size of gravel), following the approach from filter design. The criterion can be adopted for both gravels and microcapsules with different particle sizes and gradations.

1 INTRODUCTION

Different functional materials can be stored and protected by polymers inside at micro-scales without reducing their functionality (Bah et al. 2020). This fabricated microcapsule is generally a sphere with its wall called a shell and the material inside termed a core. Microcapsules were initially developed for self-healing polymeric composites (White et al. 2001) and have been widely used in cementitious construction materials to self-heal cracks triggered by mechanical loadings and environmental changes (Yang et al. 2009). For cementitious materials, the size of microcapsules should be designed considering the size of cracks to achieve high level of healing (Kanellopoulos et al. 2016), otherwise microcapsules will either fail to survive the mixing process or not be ruptured when a crack forms due to inappropriate size design. Up to now, the application of microcapsules on granular materials like soils still remains unexplored. As microencapsulation method has been successfully exploited in cementitious materials, it then emerges as a potential prospect to switch and enhance the physical properties (e.g. strength and permeability) of granular materials.

Regardless of specific utilizations and encapsulation techniques, the first challenge to be solved is the microcapsules retention in voids. Generally, the particle size distribution of microcapsules (MSD) and particle size distribution of soil (PSD) should match after mixing, so that microcapsules will break and release core materials only under external stimuli such as compression, which results in decreasing void ratio of soil. The size of microcapsules should be large enough to make microcapsules retain in voids even under seepage, and meanwhile small enough to keep microcapsules from being ruptured by soil particles. These two competing design purposes coincide with the dual role of soil filters, which play a significant part in the performance of embankment dams. The PSD of filter soil (i.e. soils having a gradation designed to prevent movement of fine base soil by flowing water) is required to be sufficiently small to prevent the migration of base materials (i.e.

DOI: 10.1201/9781003299127-98

the soil adjacent to a filter through which water may pass), whilst sufficiently large to allow the seeping water to flow through the filters without the generation of pore water pressure (Terzaghi 1922).

The effectiveness of filter design, dependent on gradation of the filter and the base material, was investigated experimentally by filter-base combination tests for ascertaining washout of base soil and permeability change (Sherard et al. 1984; Indraratna et al. 1996; Lone et al. 2005). The experimental data were used to develop empirical criteria for designing suitable filters for base soils of various gradations. Most empirical relations were originated from that developed by Terzaghi (1922) and concentrated on given size ratios of base and filter, such as D_{15}/d_{85} (USBR 1987; NRCS 1994). Here, D and d represent the size of filter and base respectively, and D_a or d_a exhibits the percentage by mass the material that is finer than D_a or d_a.

In this study, similar flushing tests are conducted on microcapsules and gravel with different gradations to assess the microcapsules retention in granular materials. The effectiveness of different gravel-microcapsules combinations is validated by acceptable washout amount of microcapsules. An empirical criterion capable of describing microcapsules retention in granular materials is presented and compared with Terzaghi (1922)'s one aimed for successful filter design.

2 MATERIALS, APPARATUS AND TESTING PROGRAM

2.1 *Materials*

Calcium alginate/polydimethylsiloxane (PDMS) microcapsules were selected and synthesized. PDMS were encapsulated in calcium alginate shell by the ionic gelation method (Benavides et al. 2016). Sodium alginate and calcium alginate were utilized to form the shell. PDMS is in a liquid form and its density is 965 kg/m^3. The microcapsules were produced by the following steps: (1) sodium alginate was firstly dissolved in 100 g deionized water. (2) PDMS was added into the sodium alginate solution and emulsified with a homogenizer until a stable oil-water emulsion was formed. The mass of PDMS to water is 10%. (3) The emulsion droplets were then dripped into a calcium chloride solution through a PTFE tube by a syringe pump. (4) The microcapsules were produced and immersed in calcium chloride solution for 24 hours, then rinsed with distilled water and filtered. The microcapsules size distributions (MSDs) were characterized by a dynamic iamge analyzer (Qicpic^{TM}, Sympatec GmbH). Microcapsules range from 0.35-1.80 mm were produced, with specific gravity of approximately 0.965 (BS 1377-2:1990).

Clean granite gravel ranging in size from 2.36 mm to 11.20 mm was mixed with microcapsules for sample preparation. The wide range of size selection was aiming to have different coefficient of uniformity (i.e. C_u). The specific gravity of the granite gravel was 2.65 (BS 1377-2:1990).

2.2 *Apparatus*

The experimental set-up (Figure 1) consists of a cylinder of 180 mm in diameter and 400 mm in height to ensure the internal diameter of the cylinder is at least 12 times the maximum particle size of the soil to be tested (BS 1377-5:1990). A wire mesh (i.e. sieve) of 180 mm in diameter and 2 mm in mesh size was placed at the bottom of the cylinder to support the mixture, and separate gravel and flushed microcapsules. A flowmeter was connected between the inlet and water tank for regulating the inflow of water.

2.3 *Testing program*

Testing was conducted in well-graded and uniform gravel. Both uniform and well-graded gravel was prepared by mechanical sieving to obtain the desired coefficient of uniformity of 1.25 and 2.58-3.82, respectively. The mixtures of gravel and microcapsules were compacted in

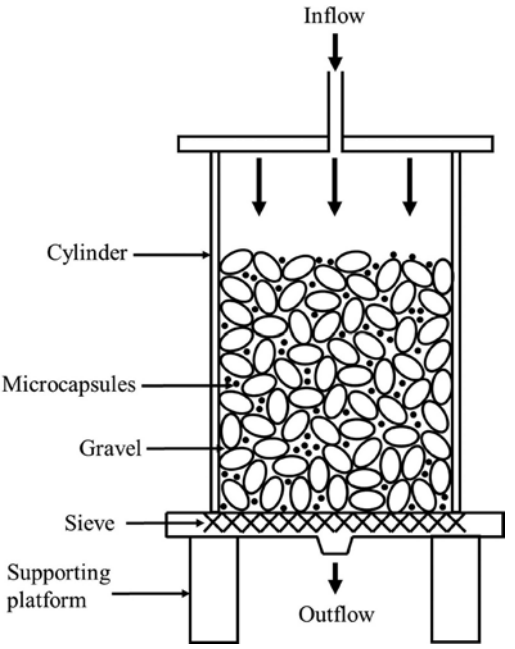

Figure 1. Schematic diagram of flushing test apparatus.

the cylinder in several light tamped layers to reach a required relative density of 50% for ease of comparison. The main gradation features of microcapsules and gravel are presented in Figure 2. As shown in Figure 2(a), only one MSD was matched with three different PSDs of well-graded gravel, in order to keep the size of microcapsules isolated while only changing the sizes of gravel. Conversely, as plotted in Figure 2(b), only one uniformly graded gravel was selected and mixed with three different microcapsules. In total, 4 groups of gravel and 4 groups of microcapsules were combined in the above-mentioned manner to form 6 experimental groups.

The ratio of mass of microcapsules to the mass of gravel was set as 2%, which provided a measurable washout amount. Average water temperature at the time of testing was 24.1°C with a density of 0.9973 g/cm^3, its average pH was 6.35 and its viscosity was approximately 1.0 mPa·s.

The tests were started by a constant downward flow of 9 L/min, with the washout of microcapsules collected at around 20-minute intervals and later weighed after air drying. The test was continued until the washout became constant with time, which usually lasted for 2 hours. After completion, the mixtures were removed and optical microscopy was used to investigate if microcapsules were cracked during sample preparation, flushing and drying. The results of all tests were classified as effective or ineffective. Effective gravel-microcapsules combinations were defined as those able to retain most of the microcapsules under downward flow for 2 hours, with washout of microcapsules less than 5% of the total weight of microcapsules mixed. Conversely, ineffective combinations were stated as those lost excessive amounts of microcapsules after flooding (larger than 5%). This specific value was determined with reference to the washout amount in filter design (Indraratna et al. 1996; Lone et al. 2005). However, it is challenging to establish a critical value of washout for microcapsules due to no previous study conducted on microcapsules retention to data, as well as no clear description of allowable washout of base materials in filters.

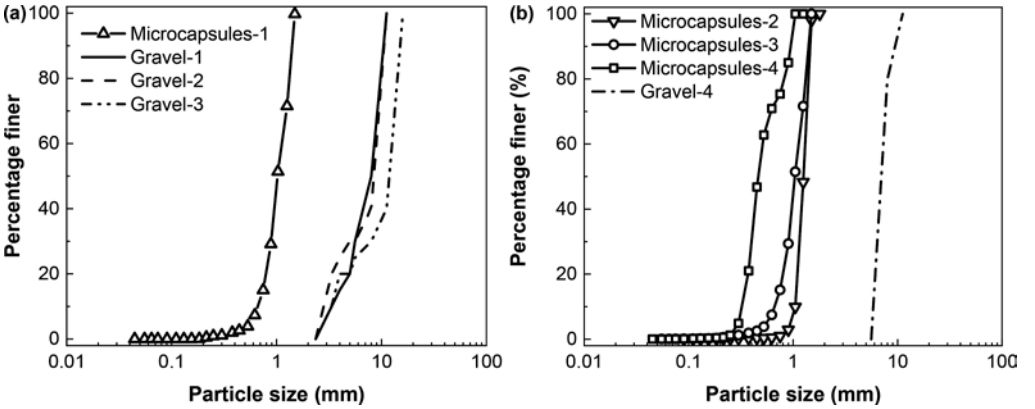

Figure 2. Particle size distributions of microcapsules and gravel for (a) different gravel gradations; (b) different microcapsules gradations.

3 RESULTS AND DISCUSSION

3.1 *Washout and time relationship*

As no obvious cracks of microcapsules were observed for all the mixtures after testing, only the loss of microcapsules was taken into consideration in this study. The relationship of microcapsules washout percentage and elapsed time is drawn in Figure 3, where *M* stands for microcapsules and *G* for gravel. The numbers (i.e. 1, 2, 3 and 4) are in accordance with those shown in Figure 2. In general, a constant washout was attained with time, which demonstrated that a stable mixture structure was established. In Figure 3(a), when the MSD was kept unchanged, gravel with larger D_{15} would result in more washouts of microcapsules, which explained why *M1G2* owned the least washout, while *M1G1* and *M1G3* would have washout larger than 5% (i.e. 5.03% and 6.93% respectively). In Figure 3(b), when the PSD of gravel was kept constant, microcapsules with smaller d_{85} would cause more washout. Also, for all the 6 experiments, the final washout percentage of microcapsules was not remarkable, with values all smaller than 11%. This may be attributed to the low specific gravity of microcapsules, making them difficult to be flushed away compared with heavier base soil in filter.

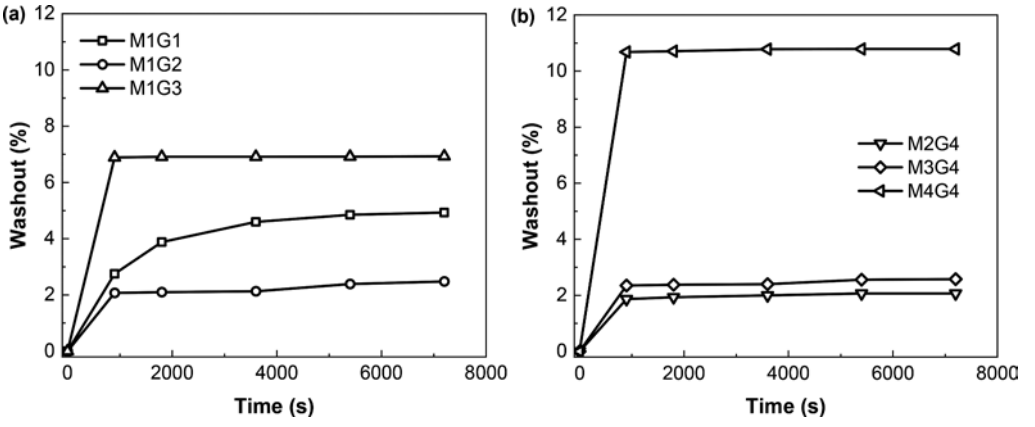

Figure 3. Percentage of washout of microcapsules against time for (a) different gravel gradations; (b) different microcapsules gradations.

3.2 *Empirical criterion*

Both effective and ineffective cases of microcapsules-gravel mixture were drawn in Figure 4 for establishing an empirical criterion to account for microcapsules retention behavior in granular media. The traditional Terzaghi's criterion (i.e. $d_{85}/D_{15} > 4$) could not fit very well with the experimental data, with two effective cases evaluated to be ineffective. If the equation was modified (i.e. $d_{85}/D_{15} > 4.3$), more effective/ineffective cases would locate on both sides of the borderline. The little inaccuracy of this criterion may be due to the judgement of effective/ ineffective cases based on this specific washout amount (i.e. 5%). It is worth mentioning that more experimental data could be conducted to more precisely validate the effectiveness of this empirical equation.

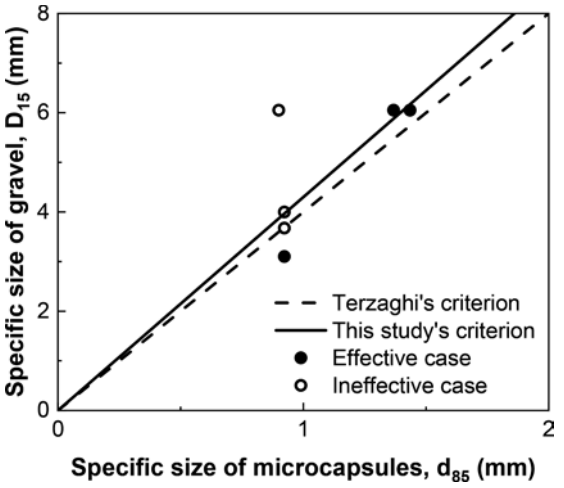

Figure 4. Application of retention criteria to distinguish between effective and ineffective filters.

4 CONCLUSION

Washout tests by changing solely the d_{85} of microcapsules and D_{15} of gravel, were conducted to experimentally investigate the microcapsules retention behavior in gravel by monitoring the loss of microcapsules during water flushing. For this microcapsules-gravel mixture, $d_{85}/D_{15} > 4.3$ is proposed to separate effective and ineffective cases, in order to make more microcapsules retain completely in pores of granular materials for further use. Note that further investigation is needed on well-graded granular materials, and microcapsules of various origins will be required to validate this design criterion.

ACKNOWLEDGEMENT

This work was supported by a Collaborative Research Fund from the Research Grants Council Hong Kong (C6006–20 GF).

REFERENCES

Bah, M.G., Bilal, H.M. and Wang, J., 2020. Fabrication and application of complex microcapsules: A review. *Soft Matter*, 16(3),pp.570–590.

Benavides, S., Cortés, P., Parada, J. and Franco, W., 2016. Development of alginate microspheres containing thyme essential oil using ionic gelation. Food chemistry, 204, pp.77–83.

Indraratna, B., Dilema, E.L.G. and Vafai, F., 1996. An experimental study of the filtration of a lateritic clay slurry by sand filters. Proceedings of the Institution of Civil Engineers-Geotechnical Engineering, 119(2), pp.75–83.

Kanellopoulos, A., Giannaros, P. and Al-Tabbaa, A., 2016. The effect of varying volume fraction of microcapsules on fresh, mechanical and self-healing properties of mortars. Construction and Building Materials, 122, pp.577–593.

Lone, M.A., Hussain, B. and Asawa, G.L., 2005. Filter design criteria for graded cohesionless bases. Journal of geotechnical and geoenvironmental engineering, 131(2), pp.251–259.

Natural Resources Conservation Services (NRCS). 1994. Gradation design of sand and gravel filters. National engineering handbook, Chap. 26, Part 633, USDA, Washington, D.C

Sherard, J.L., Dunnigan, L.P. and Talbot, J.R., 1984. Basic properties of sand and gravel filters. Journal of Geotechnical Engineering, 110(6), pp.684–700.

United States. Bureau of Reclamation. 1987. *Design of small dams*. US Department of the Interior, Bureau of Reclamation.

White, S.R., Sottos, N.R., Geubelle, P.H., Moore, J.S., Kessler, M.R., Sriram, S.R., Brown, E.N. and Viswanathan, S., 2001. Autonomic healing of polymer composites. Nature, 409(6822), pp.794–797.

Yang, Z., Hollar, J., He, X. and Shi, X., 2009, October. Feasibility investigation of self-healing cementitious composite using oil core/silica gel shell passive smart microcapsules. In Second International Conference on Smart Materials and Nanotechnology in Engineering (Vol.7493, pp. 1260–1271). SPIE.

Smart Geotechnics for Smart Societies – Zhussupbekov, Sarsembayeva & Kaliakin (Eds)
© 2023 The Author(s), ISBN 978-1-003-29912-7
Open Access: www.taylorfrancis.com, CC BY-NC-ND 4.0 license

The use of neural networks in the practice of jet-grouting

N. Ovchinnikov
Post graduate student, Perm National Research University, Perm, Russian federation

I. Gladkov
Techical director, GeoSpecTechnology, Perm, Russian federation

A. Zhemchugov
Product director, GeoSpecTechnology, Perm, Russian federation

ABSTRACT: The technology of jet grouting has been used for ground stabilization during construction of various structures for quite a long time. However, the task of developing effective methods of predicting actual geometric and physical-mechanical parameters of soil-cement columns is still urgent. Application of neural networks for assignment of ground-cement column diameters at the design stage can significantly increase the accuracy of assignment of design parameters of ground-cement columns and reduce the cost of design solutions

1 INTRODUCTION

Jet-grouting technology has been used since the 80s of the last century. The essence of the jet grouting technology is to use the energy of a high-pressure jet of cement slurry to destroy and simultaneously mix the soil with the cement slurry in the "mix-in-place" mode. A soilcrete with high strength and deformation characteristics is formed.

Jet grouting technology is widely used to strengthen soils at the base of foundations. Numerical modeling is used. A reinforced base is most often modeled homogeneous, with the given effective characteristics of the deformation modulus, the value of which is largely determined by the deformation modulus of the soil cement and the proportion of the fixed soil mass. These parameters are laid down at the design stage and determine the final constructive and economic efficiency of the selected solution (Modoni et al, 2019; Bayesteha & Sabermahani, 2020).

Figure 1 shows soilcrete columns in the base of the foundation slab at the site in Nizhny Novgorod.

Figure 1. Jet-grouting columns.

DOI: 10.1201/9781003299127-99

2 DESIGN OF JET-GROUTING COLUMNS

One of the main problems in the design of foundations reinforced by the technology of jet grouting is the problem of matching the design parameters of the fixed soil mass to the actual results The strength and diameter parameters of the soilcrete columns are assigned according to the reference tables, as well as based on the experience of the designer.

This method of assigning the design diameter of the soil-cement element has a number of significant drawbacks. The recommended diameter values have a fairly large variation within one type of soil, the effect of the strength characteristics of the soil at the construction site on the diameter of the ground concrete columns is not described. There is also a need to apply large stock coefficients, which leads to an increase in the cost of a technical solution. There is no universal method for calculating the diameter of soil-cement elements. The existing dependencies are empirical in nature and differ significantly from each other (Alexandre Pinto et al., 2016; Zuev et al., 2021).

3 NEURAL NETWORKS TO PREDICT THE DIAMETER

Neural networks can be used to predict the diameter of soil cement columns. Neural network training can be performed based on the results of work on implemented construction projects.

An artificial neural network is a subset of machine learning algorithms that arose when trying to simulate the processes occurring in the human brain during the transmission of signals between biological neurons. Each node (artificial neuron) is connected to other nodes with a certain weight and threshold value. If the output of any node exceeds the threshold value, then this node is activated and sends data to the next level of the network. Otherwise, the data is not transmitted to the next level of the network. Training data is used to train and gradually improve the accuracy of neural networks. The structure of the artificial neuron is shown in Figure 2.

Artificial neural networks consist of nodes forming layers: an input data layer, one or more hidden layers and an output data layer (Yasnitsky, 2016; Milad & Golamreza, 2018).

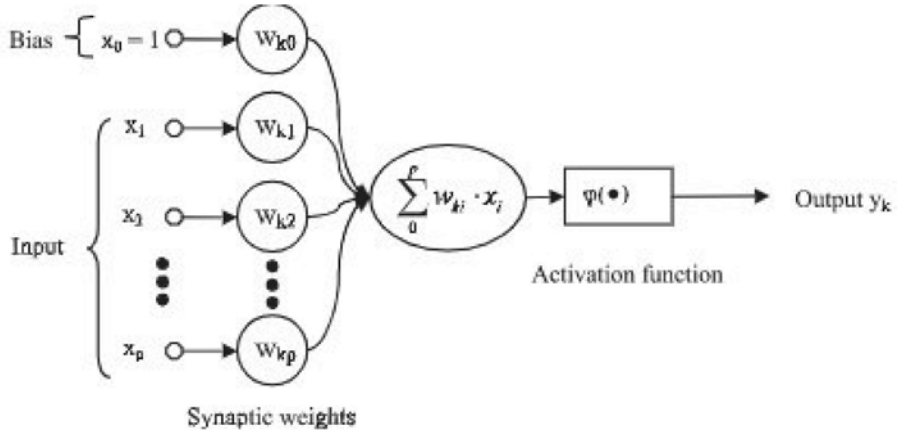

Figure 2. The structure of an artificial neuron.

In general terms, the structure of the designed artificial neural network is shown in Figure 3. We used the following as input parameters:

– Friction angle of soil at the construction site;
– Cohesion of soil at the construction site
– Specific energy of destruction of a jet of cement slurry during jet grouting Eg (MJ/m).

The diameter of the soil-cement element was chosen as the output parameter. The parameters of the physical and mechanical parameters of soils are determined based on the results of standard engineering and geological surveys. The value of the specific fracture energy can be determined by formula (1).

$$E_g = \frac{0.1PQ}{V} \tag{1}$$

where Q – solution consumption (l/min);
P – discharge pressure (Mpa);
V – monitor lifting speed (cm/min).

As part of writing this work, three neural networks were created: using EXCEL software complexes (Neural Excel) and MATLAB, as well as written in the PYTHON programming language.

Data from 38 real objects were selected for neural network training.

The structure of the neural network is shown in Figure 3

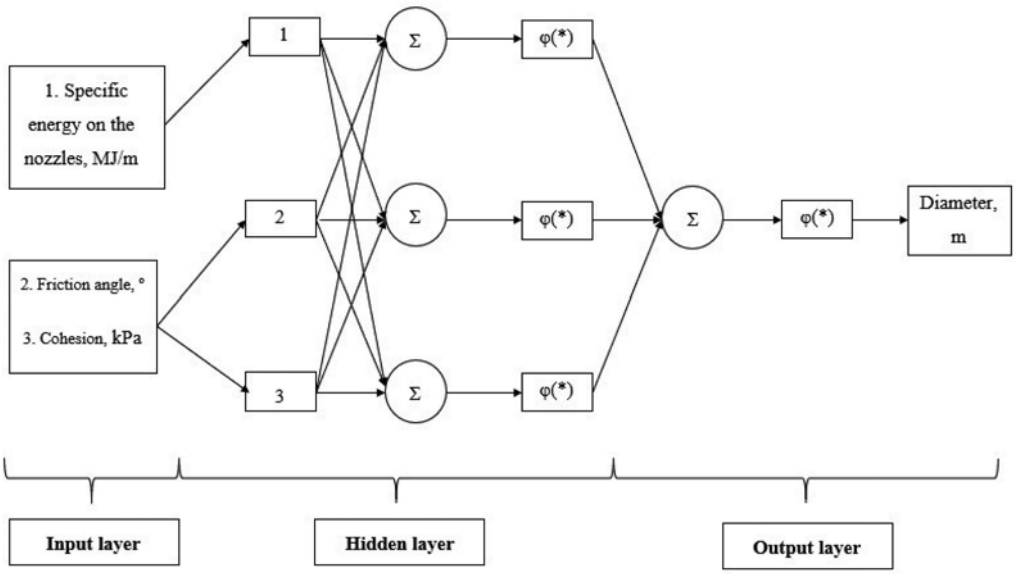

Figure 3. The structure of the designed neural network.

A fragment of the sample of the source data is presented in the Table 1.

The values were normalized in the range from 0 to 1 by interpolation methods relative to the maximum values of the output data. A fragment of the normalized learnings of the training set is presented in Table 2.

Table 1. Multitude of experimental data for neural network training.

№	Types of soil	C, kPa	ϕ, °	Specific energy of destruction, MJ/m	Measured diameter, m
1	Sandy loam plastic	10	16	59,85	2,49
2	Soft-plastic loam	13	13	47,88	1,40
37	Clay semi-hard	20	15	59,85	2,09
38	Dusty sand	1	31	59,85	2,20

Table 2. Multitude of experimental data for neural network training.

		Training set				Result		
		Input			Output			
№	Types of soil	C, kPa	ϕ, °	Specific energy of destruction, MJ/m	Measured diameter, m	EXCEL	MATLAB	PYTHON
1	Sandy loam plastic	0,4	0,52	1,0	0,87	0,88	1,00	0,91
2	Soft-plastic loam	0,52	0,42	0,80	0,49	0,55	0,65	0,61
37	Clay semi-hard	0,8	0,48	1,00	0,73	0,73	0,83	0,75
38	Dusty sand	0,04	1,00	1,00	0,77	0,78	0,90	0,79

4 DISCUSSION

The results of the forecast are shown in Figure 4.

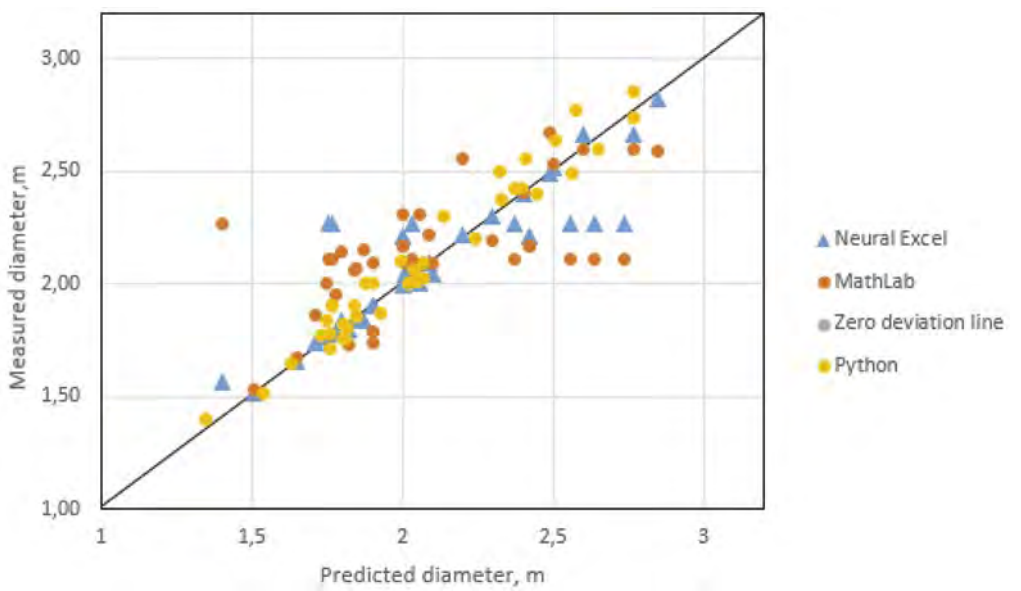

Figure 4. Obtained results.

Based on the results of the performed calculations, a comparative graph was built to evaluate and compare the results (Figure 4)

According to the results of the study, the following conclusions can be drawn

1. The average deviation when using Neural EXCEL was 0,11 m.
2. The average deviation when using MATLAB was 0,22 m.
3. The average deviation when using PYTHON was 0,07 m.

In most cases, the accuracy of the forecast is sufficient to make a project decision. Significant deviation of individual values can be caused by insufficient training of the neural network. A neural network written in Python is the most accurate among those presented.

5 CONCLUSION

Neural networks can be used to assign the diameter of soil-cement columns made by jet grouting technology in the geological conditions of the Russian Federation.

This work can be the basis for the development of new design schemes for strengthening soils using jet grouting technology.

REFERENCES

Modoni et al. 2019. Strength of sandy and clayey soils cemented with single and double fluid jet grouting. *Soils and Foundations, Volume 59, Issue 4*, *2019*, P. 942–954,

H. Bayesteha, M. Sabermahani. 2020. Field study on performance of jet grouting in low water content clay. 2020. *Engineering Geology; Vol. 264*, *2020*;

Alexandre Pinto, Rui Tomásio, Gonçalo Marques. 2016. Ground Improvement with Jet Grouting Solutions at the New Cruise Terminal in Lisbon, Portugal. *Procedia Engineering. Advances in Transportation Geotechnics; The 3rd International Conference on Transportation Geotechnics, 2016:* P.1495–1502.

Zuev, Zaitseva, Makovetsky. 2021. The device of a modified soil layer with specified physical and mechanical characteristics in the construction of multi-storey buildings *Housing construction; 2021. No. 9*: P. 17–27.

Yasnitsky L.N. 2016. Intelligent systems. *Laboratory of Knowledge*.

Milad F., Golamreza A.2018. Review of the application of genetic programming and artificial neural networks in pile foundations. 2018. *International Journal of Geoengineering. Vol. 9. 2018*

Smart Geotechnics for Smart Societies – Zhussupbekov, Sarsembayeva & Kaliakin (Eds)
© 2023 The Author(s), ISBN 978-1-003-29912-7
Open Access: www.taylorfrancis.com, CC BY-NC-ND 4.0 license

Time-dependent settlement behaviour of clayey soil treated with deep cement mixed column

S. Choudhary, M.J. Singh & L. Borana
Indian Institute of Technology, Indore, India

ABSTRACT: In soft and clayey soils, application of deep cement mixing (DCM) columns as an effective ground improvement technique is gaining popularity in comparison to other conventional methods for several reasons such as simple methodology, cost effectiveness, rapid construction and high stiffness end products. However, past studies pertaining to DCM improved composite soil reported limited information about the time-dependent consolidation settlement behaviour. To develop a better understanding of the time-dependent settlement behaviour of the DCM improved composite soil, an experimental setup is developed in this study. From the results, it is found that the creep parameters determined during the primary and secondary stage of consolidation decrease with increase of the loading period. Further observations and results of the distribution behaviour of creep parameters before and post failure of DCM column are presented and comprehensively discussed in this study.

Keywords: Bearing capacity, consolidation settlement, creep parameters, deep cement mixing

1 INTRODUCTION

Expansive clay soils create severe problems for civil infrastructures and geotechnical structures due to the swelling and shrinkage behaviour of the minerals present in them. To mitigate or reduce the severity of the mentioned problems, various soil improvement techniques were employed by the researchers. Out of all the conventional methods, in situ soil-cement mixing has gained a lot of popularity recently and it is said to be one of the most suitable and effective techniques owing to its easy, economic, and rapid construction methodology (Kitazume and Terashi n.d., Chai et al. 2006, Fang and Yin 2007, Yin et al. 2022). The Deep Cement Mixing (DCM) technique was first employed at the Port and Harbour Research Institute (PHRI) in Japan in the 1970s. The PHRI developed the technique as a solution to improve the stability of soft soils for port and harbor facilities. DCM involves injecting cement slurry into soft soil to create columns of cement-stabilized soil. Several researchers attempted to study the behavior of strength gain and stiffness of the cement-stabilized soil columns created through DCM. These studies have examined various factors such as the curing time, the properties of the injected cement slurry, the spacing between the columns, and the effect of environmental conditions on the strength and stiffness of the soil columns (Fang et al. 2001, Jamsawang et al. 2017, Pham et al. 2017, Yin et al. 2022). However, very little emphasis was given to the time-dependent settlement behaviour of the DCM-treated clayey soil.

In this study, a small-scale physical model was developed and laboratory tests were carried out with varying vertical stresses, cement content, and area ratio to analyze the time-dependent settlement behaviour of the clayey soil treated with a DCM column installed at the centre of the model. The settlement behaviour of the composite soil and the stress distribution is recorded and monitored by using Linear Variable Differential Transformers (LVDT) installed at a specific location in the strongbox and analyzed the settlement behaviour of the composite soil using the power law proposed by (Venda Oliveira et al. 2011) Clay 1985.

DOI: 10.1201/9781003299127-100

2 LITERATURE STUDY

The DCM method comprises of mechanical mixing of soil present in the field at a natural state with cementing agents either in wet form or powder form, as per the requirement, to form a soil-cement column with high stiffness and strength qualities (Kitazume and Terashi n.d., Horpibulsuk et al. 2012b). The stabilization of clayey soil with cement mixing is due to the cementitious bond developed between the hydration products of the cement in aluminate and silicate form and the soil particles. Due to this interaction, the interlayer and inter-micellar swelling of the clayey soil particles reduced significantly (Fang and Yin 2007, Horpibulsuk et al. 2012a, Jamsawang et al. 2017). However, several factors can influence the strength of the soil-cement-treated clayey soil like characteristics of soil, characteristics of the binder, curing conditions, and mixing conditions (Kitazume and Terashi n.d., Yin et al. 2022) which directly affects the strength and stiffness properties of the DCM columns, but there has been very limited research done to understand the long-term deformation of the DCM columns and settlement of the surrounding grounds (Fang et al. 2001, Chai et al. 2006, Fan et al. 2018). Some researchers (Mesri and Choi 1987, Yang 2019) emphasized creep as a progressive and continuous deformation under constant effective stress whereas some other researchers (Yin 1999, Yin et al. 2017, Bi et al. 2019) suggested that creep phenomena occur during the entire consolidation process (including primary and secondary consolidation both). Consolidation is defined as a combined effect of both stress and time-dependent deformation, in which saturated soil exhibits a continuous volumetric reduction under static loading (Singh et al. 2020).

3 MATERIALS AND SAMPLE PREPARATION

3.1 *Soil preparation*

3.1.1 *Clayey soil*

The natural soil used in this study was procured from an excavation site in Indore which has a specific gravity of 2.6 and a liquid limit of 73.4 % respectively. Based on the Unified Soil Classification System (USCS) and AASHTO soil classification system, the soil is classified as highly expansive clay. This soil was passed through a 2 mm sieve size and oven dried for 24 hours. Water was added to this soil and mixed thoroughly to obtain a homogenous slurry consistency by adding 20.32 litres of water in 20.07 kg of oven-dry soil to make water content about 1.45 times the liquid limit.

3.1.2 *Sand for drainage purpose*

The sand was used in this study to provide drainage at the top and bottom of the experimental setup. The sand used was procured from the Narmada basin with a specific gravity of 2.45. The sand was kept saturated so that no moisture loss takes place from the clay slurry.

3.2 *DCM column preparation*

In DCM columns, dry PPC cement having a specific gravity of 3.10 is added at 20 % by weight of the dry soil and then mixed with appropriate water content to obtain slurry-type consistency. The mix design of soil cement is based on mixtures developed in previous studies (Chai et al. 2006, Horpibulsuk et al. 2010, 2012a, Fan et al. 2018, Yin et al. 2022). The prepared soil-cement slurry is poured into a cylindrical high-density polymer split mold (HDPSM) having an internal diameter of 50 mm and thickness and kept overnight to get matured and achieve appreciable strength to get de-mold further. The sample is wet-cured for 30 days in the water tanks and then it was installed in the cylindrical strongbox after the completion of the pre-consolidation period of the clay slurry.

4 METHODOLOGY

A cylindrical strongbox made of stainless steel having an internal diameter of 310 mm and height of 665 mm is used for this experimental research. 11kg of saturated sand was placed in the cylindrical strongbox up to the height of 50 mm placed in the upper and lower portion clay slurry. It acts as a uniform bed and also prevents moisture change between sand and the clay slurry during the experiment. The sand layer was lightly compacted by using a rammer and leveled with the help of a palette knife. One hollow casing of the same dimensions as the HDPSM is placed at the centre of the strongbox to create space for the installation of the DCM column in the later stage. A layer of geo-membrane filter was applied on top of the clay slurry before placing another layer of saturated sand of the same height so that there was no intermixing of sand and clay slurry. The sand layer was leveled and static loads are applied for pre-consolidation for 44 days. A rigid perforated plate is placed on the top of the soil sample for uniform distribution of load to the soil sample and soil-cement column. After the completion of the pre-consolidation period, the loads were removed and the recorded height of the clay is 329 mm. Further, the hollow casing is pulled out carefully without disturbing the surrounding soil. The DCM column was placed in the same place and covered with a sand layer. LVDT was also installed at a certain location above the upper sand layer as observed in Figure 1. Further loads are applied for 15 days, 10 days, and 15 days with an increment of 10 kPa.

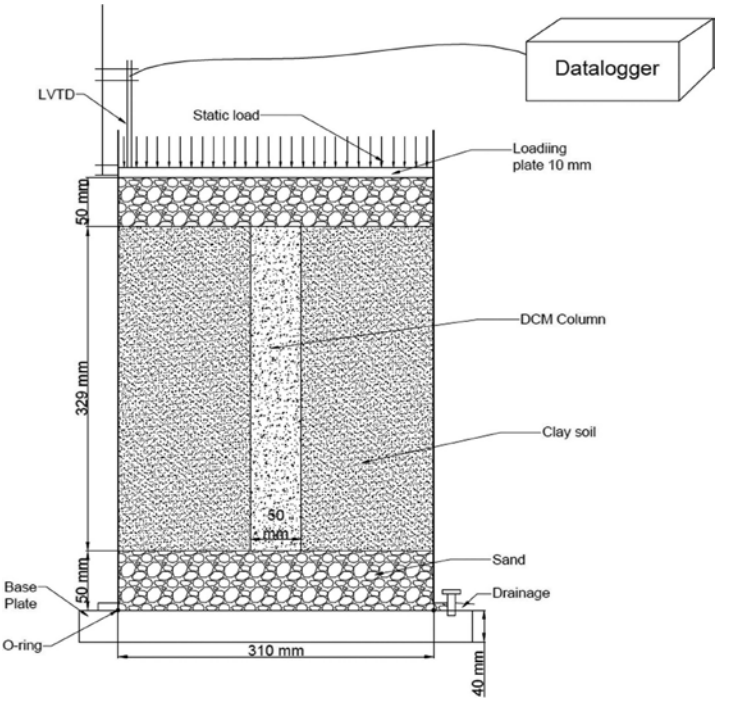

Figure 1. Physical model setup.

5 RESULT AND DISCUSSION

A power law model was proposed by Briaud and Garland (1985) to describe the rate of loading behaviour on piles of clay. It has been extended by the author to present the time-dependent behaviour of various sources of soils on diversified data. The model is written as below:

$$\frac{s}{s_1} = \left(\frac{t}{t_1}\right)^n$$

where, s and t signify the deformation (settlement, strain, etc.) and corresponding time respectively. The s_1 is the value of deformations observed at reference time t_1. The reference time could be either 1 second, 1 minute, or 1 day or any specific time, and n is the viscous exponent (Bi et al. 2019, Johnson Singh et al. 2022, Singh et al. 2022).

In the above equation, the viscous exponent can be derived from the slope of the settlement curves as illustrated in Figure 2. It is considered that after the completion of the primary consolidation, only creep settlement takes place. Therefore, the slope of the secondary line i.e., n_{cr} includes only creep and the corresponding angle can be denoted by β. However, during the primary consolidation, both creep and expulsion of excess pore water pressure take place. Therefore, the slope of the primary consolidation i.e., n_{both} includes both consolidation and creep. If the angle corresponding to n_{both} is α, the n value only including consolidation (n_{con}) during the primary consolidation will be (α − β). The n value n_{con} can be calculated by Equation 1.

$$\begin{aligned} n_{con} &= \tan(\alpha - \beta) \\ &= \frac{\tan(\alpha) - \tan(\beta)}{1 + \tan(\alpha) * \tan(\beta)} = \frac{n_{both} - n_{cr}}{1 + n_{both} * n_{cr}} \end{aligned} \tag{1}$$

Here, the parameters n_{both} and n_{cr} are small quantities and their products are quite small and negligible therefore, the above equation can be simplified as follows;

$$n_{con} = \frac{n_{both} - n_{cr}}{1 + n_{both} * n_{cr}} \approx n_{both} - n_{cr}$$

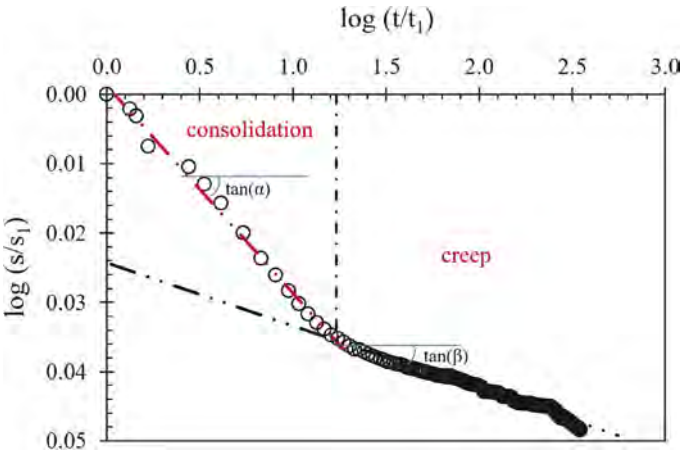

Figure 2. Different phases of settlement behaviour.

A reference time of 180 mins is assumed in this study, other reference time below 180 mins is also tried, however, a representable slope of the primary consolidation period is not obtained. During the pre-consolidation period the n_{both}, $n_{cr,}$ and n_{con} are respectively 0.0299, 0.0091, and 0.0208. After the installation of the DCM column, the n_{both}, $n_{cr,}$ and n_{con} are 0.098, 0.021, and 0.077 respectively. In the next loading period, failure of the DCM column takes place, therefore significant reduction settlement is observed. Therefore, the n_{both}, $n_{cr,}$ and n_{con} are observed to be 0.209, 0.079, and 0.130 respectively. During the last load

increment, the corresponding values of the n_{both}, $n_{cr,}$ and n_{con} are respectively 0.0083, 0.0034, and 0.00049. It is observed that after the installation of the DCM column, the creep parameters are observed to be increased and maximum values are observed during the failure period of the DCM column. After the failure of the DCM column, a significant reduction of void ratio is observed in a short period as illustrated in Figure 3. This might be due to enhanced excess pore water pressure dissipation by the DCM column (Fang and Yin 2007, Pham et al. 2017).

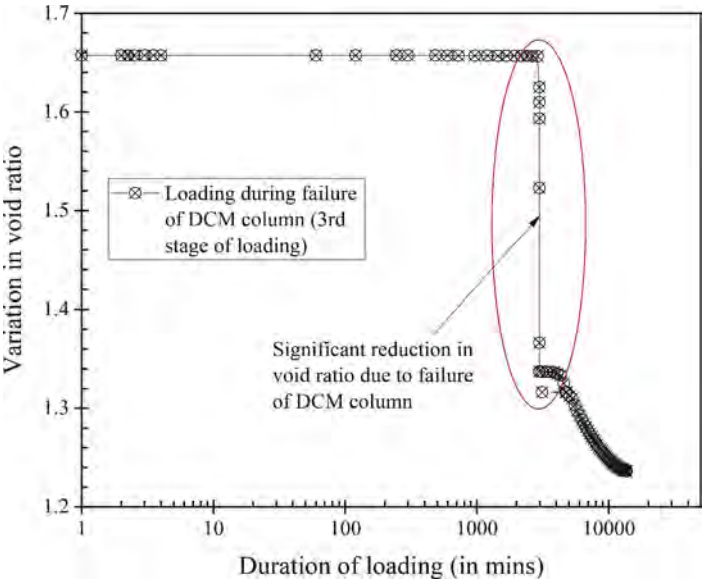

Figure 3. Significant reduction of void ratio during the third stage of loading due to DCM column breakage.

6 CONCLUSION

In this study, an indoor physical model of the DCM column installed in the clayey soil is developed to perform the experimental analysis of the time-dependent settlement behaviour at different phases for the clayey soil treated with a DCM column. Based on the experimental results achieved, the following conclusions are drawn.

1. The creep parameters determined during the primary, and secondary stages of consolidation are observed to be reduced with the increase of the loading period. However, with the failure of the DCM column, there is a sudden rise in these parameters, which might be due to the sudden transfer of load from the DCM column to the surrounding soil.
2. It can be noted that the proposed power law model can assess the creep parameters during the primary consolidation and secondary consolidation. However, the selection of proper reference time is a prerequisite for getting a representable slope of the primary consolidation period. Additionally, it can represent the concept of "creep as the rate of loading" in which the viscous exponent of the model represents the process of time-dependent settlement behaviour of soil under applied external loadings.
3. In this study, major emphasis is given to the time-dependent settlement of the composite soil. However, there are opportunities to enhance the current understanding and investigation of various parameters, such as friction, settlement behavior of column and overlying soil, the effect of rate of mixing, long-term durability, and effectiveness of soil-cement

columns. Further investigation into the suitability of the model for predicting the settlement behavior of DCM columns also needs to be investigated.

REFERENCES

Bi, G., Ni, S., Wang, D., Chen, Y., Wei, J., and Gong, W. 2019. Creep in Primary Consolidation with Rate of Loading Approach. Scientific Reports, (December 2018): 1–9. Springer US. doi:10.1038/s41598-019-45498-0.

Chai, J.C., Onitsuka, K., and Hayashi, S. 2006. Physical modelling of consolidation behaviour of a composite foundation consisting of a cement-mixed soil column and untreated soft marine clay. Geotechnique, **56**(8): 579–580. doi:10.1680/geot.2006.56.8.579.

Clay, R.I.N. 1985./Loading Rate Method/ Fori Pile Response/in Clay. **I**(3): 319–335.

Fan, J., Wang, D., and Qian, D. 2018. Soil-cement mixture properties and design considerations for reinforced excavation. Journal of Rock Mechanics and Geotechnical Engineering, **10**(4): 791–797. Elsevier Ltd. doi:10.1016/j.jrmge.2018.03.004.

Fang, Y.S., Chung, Y.T., Yu, F.J., and Chen, T.J. 2001. Properties of soil-cement stabilised with deep mixing method. Ground Improvement, **5**(2): 69–74. doi:10.1680/grim.5.2.69.39982.

Fang, Z., and Yin, J.-H. 2007. Responses of Excess Pore Water Pressure in Soft Marine Clay around a Soil–Cement Column. International Journal of Geomechanics, **7**(3): 167–175. doi:10.1061/(asce)1532-3641(2007)7:3(167).

Horpibulsuk, S., Chinkulkijniwat, A., Cholphatsorn, A., Suebsuk, J., and Liu, M.D. 2012a. Consolidation behavior of soil-cement column improved ground. Computers and Geotechnics, **43**: 37–50. Elsevier Ltd. doi:10.1016/j.compgeo.2012.02.003.

Horpibulsuk, S., Liu, M.D., Liyanapathirana, D.S., and Suebsuk, J. 2010. Behaviour of cemented clay simulated via the theoretical framework of the Structured Cam Clay model. Computers and Geotechnics, **37**(1–2): 1–9. Elsevier Ltd. doi:10.1016/j.compgeo.2009.06.007.

Horpibulsuk, S., Phojan, W., Suddeepong, A., Chinkulkijniwat, A., and Liu, M.D. 2012b. Strength development in blended cement admixed saline clay. Applied Clay Science, **55**: 44–52. Elsevier B. V. doi:10.1016/j.clay.2011.10.003.

Jamsawang, P., Nuansrithong, N., Voottipruex, P., Songpiriyakij, S., and Jongpradist, P. 2017. Laboratory investigations on the swelling behavior of composite expansive clays stabilized with shallow and deep clay-cement mixing methods. Applied Clay Science, **148**(March): 83–94. Elsevier. doi:10.1016/j.clay.2017.08.013.

Johnson Singh, M., Feng, W., Xu, D., Dubey, M., and Borana, L. 2022. Long-Term Elastoviscoplastic Behavior of Fly Ash–Blended Indian Montmorillonite Clay in Oedometer Conditions. International Journal of Geomechanics, **22**(3): 1–14. doi:10.1061/(asce)gm.1943-5622.0002290.

Kitazume, M., and Terashi, M. (n.d.). The Deep Mixing Method.

Mesri, G., and Choi, Y.K. 1987. Settlement analysis of embankments on soft clays. Journal of Geotechnical Engineering, **113**(9): 1076–1085. doi:10.1061/(ASCE)0733-9410(1987)113:9(1076).

Pham, V.N., Turner, B., Huang, J., and Kelly, R. 2017. Long-term strength of soil-cement columns in coastal areas. Soils and Foundations, **57**(4): 645–654. Japanese Geotechnical Society. doi:10.1016/j.sandf.2017.04.005.

Singh, M.J., Feng, W.Q., Xu, D.S., and Borana, L. 2022. Time-dependent compressibility characteristics of Montmorillonite Clay using EVPS Model. Geomechanics and Engineering, **28**(2): 171–180. doi:10.12989/gae.2022.28.2.171.

Venda Oliveira, P.J., Pinheiro, J.L.P., and Correia, A.A.S. 2011. Numerical analysis of an embankment built on soft soil reinforced with deep mixing columns: Parametric study. Computers and Geotechnics, **38**(4): 566–576. Elsevier Ltd. doi:10.1016/j.compgeo.2011.03.005.

Yang, Z. 2019. Consolidation of Soils. Material Modeling in Finite Element Analysis,: 149–156. doi:10.1201/9780367353216-21.

Yin, J.H. 1999. Non-linear creep of soils in oedometer tests. Geotechnique, **49**(5): 699–707. doi:10.1680/geot.1999.49.5.699.

Yin, K.S., Zhang, L.M., Zou, H.F., Luo, H.Y., and Lu, W.J. 2022. Key Factors for Deep Cement Mixing Construction for Undredged Offshore Land Reclamation. Journal of Geotechnical and Geoenvironmental Engineering, **148**(8): 1–11. doi:10.1061/(asce)gt.1943-5606.0002848.

Yin, Z.Y., Zhu, Q.Y., and Zhang, D.M. 2017. Comparison of two creep degradation modeling approaches for soft structured soils. Acta Geotechnica, **12**(6): 1395–1413. Springer Berlin Heidelberg. doi:10.1007/s11440-017-0556-y.

Smart Geotechnics for Smart Societies – Zhussupbekov, Sarsembayeva & Kaliakin (Eds)
© 2023 The Author(s), ISBN 978-1-003-29912-7
Open Access: www.taylorfrancis.com, CC BY-NC-ND 4.0 license

The effect of lime additives on the improvement of swelling soils in geotechnical conditions of Syrian Arab Republic

L. Awwad
Department of Geotechnical Engineering, Saint-Petersburg State University of Architecture and Civil Engineering, Russia

ABSTRACT: Clay soils are widespread in Syria. Due to their shortcomings, the need for stabilization is becoming increasingly urgent. The improvement of swelling soils is becoming very important for the archaeological sites belonging to the ancient civilizations of Syria. These buildings are mostly lightly loaded structures, consisting of domes and stone walls based on strip foundations. Therefore, expansive soils can cause significant damage to these structures. This paper presents some historical monuments in Syria with a description of their typical foundations and the main geotechnical parameters. In this paper, the effect of additives of mixtures of polypropylene fibers with lime on improving the building properties of swelling soils will be discussed. The aim of using this type of material is to improve the performance of the ground without affecting the historical mission of the building. Additives of mixtures of polypropylene fibers with lime reduce plasticity index, increases workability and shrinkage limit, reduces shrinkage cracking, eliminates almost all swelling problems, and increases the soil strength.

1 INTRODUCTION

The Syrian Arab Republic is located on the west wing of the Fertile Crescent in an important location between the East and the West. Syria has seen some of the oldest and most important civilizations as evidenced by the enormous archaeological discoveries, some of which date back to over 8,000 years BC. In Syria, there are more than 4,500 archaeological sites dated back to different periods of history. Archaeologists consider Syria the center of one of the oldest civilizations on earth, wherein was the beginning of human settlement, the first urban planning, and the development of the alphabet. In Syria were the first cities in history, such as the ancient kingdom of Ebla, from 2500 to 2400 BC, the Kingdom of Mary about 2900 BC, and Palmyra which flourished in the second half of the first century BC.

2 CONSTRUCTION AND FOUNDATION TYPES OF BUILDINGS

Most of the historic buildings and monuments in Syria are lightly loaded structures and consist mainly of domes, arches, and stone walls based on strip stone foundations that are seated directly on the soil, therefore, expansive soils are widely spread in Syria could cause considerable damage to these structures.

The main reason for soil movement is a change in soil moisture, which is occurred either artificially by construction works, or naturally because of a change in rainfall between summer and winter (Corley. J.B, Dietz. and Schürmann 2006, Ulitsky 2017, Awwad, Gruzin 2019). We will set some examples of historic buildings and monuments in Syria, and how they expose to damage because of soil movement.

DOI: 10.1201/9781003299127-101

2.1 *Al-Azem Palace*

Al-Azem Palace is located south of the Umayyad Mosque, Beside Albzoriah market, and it is one of the most important archaeological palaces in Syria. It was built by Asaad Pasha Al-Azem in 1749 when he was the ruler of the territory of Damascus and its extension in the Ottoman period.

This palace is one of the most important huge historic buildings in the old city of Damascus, and one of the best examples of early architecture for large Damascene houses where it extends over an area of 5500 square meters.

The Azem palace was divided into Haramlik (private family aria), Salamlik (business public reception area for the male head of the house and his clients or guests), Khadamlik (servants), and Hammam (baths), each with relating courtyards, fountains, and gardens. Within these spaces, the palace hosted approximately sixteen great halls, nineteen rooms on the ground floor, nine rooms on the second story, three Iwans, a basement for storage, a praying wing, Stable, and carriage parking.

Figure 1. Al-Azem Palace.

Figure 2. Waves in the soil surface under slabs.

2.1.1 *Structural description*

Al-Azem Palace walls of the interior and exterior faces were built with lime-colored stone as telescopic rows separated by basalt black stone rows which its dimension about 80 cm. The lime mortar was used to bond the stones. Roofs are made from wood and mud. Stone walls, stone arches, stone cupolas, and stone columns were used to make the palace spaces and transfer roofs loads to the foundations. Stone walls and columns are based on strip stone foundations that are seated directly on the soil. It is the only remaining palace of rulers palaces of Damascus, which is considered the oldest continuously inhabited city in history.

2.1.2 *Cracks appearance*

It was observed in the recent few years the appearance of cracks in the walls of some Al-Azem Palace halls. Engineering analysis and evaluation of this phenomenon stated that there were two kinds of cracks: vertical cracks resulted from a change in temperatures, and cracks resulted from soil movement, they are inclined and not stable in width.

The Ministry of Culture - General Directorate of heritage and Museums who is responsible for the palace implemented a project for maintenance and restoration of the Al-Azem Palace (Study of Al-Azem Palace 2010). Vertical movement of the Palace was observed during (2009-2010), there were inhomogeneous vertical movements in most of the palace parts and most of these movements are settlements with a total value of movement is between 7 mm to 2.3 mm.

2.1.3 *Maintenance and restoration*

Geotechnical situation: Al-Azem Palace was constructed of load-bearing walls based on strip stone foundations seated directly on the soil. The stone foundations are consisting of rectangular stones bond by lime mortar. Its depth is 3.25 m. Soil investigations showed that the soil in Al-Azem Palace is clayey gravel (GC) and was affected by wastewater.

Figure 3. Cracks in Al-Azem Palace.

Figure 4. Cracks in the cupolas.

It was predicted that the main reasons for the appeared cracks are both of reduction in the groundwater level in the valley of the Barada River, which is close to the Al-Azem Palace, and water or wastewater leakage from surrounding areas.

The implemented method of restoration and maintenance of foundation in Al-Azem Palace was by micro reinforced concrete piles with a diameter of 8 cm, which is connected to the foundation stone by metal bars and concrete.

Although this method of restoration and maintenance of foundations is supporting the foundation and transferring the loads to another layer of soil, which is more depth from the ground, surface and lesser exposure to the effect of water content changes. But it used modern materials (metal and concrete) which is different from the foundation materials and it could lead to detract the building's historical character (Zhussupbekov 2013, Awwad L 2016, Awwad T, Chekaeva R 2019).

3 SOIL IMPROVEMENT

3.1 *Suggested methods of soil improvement with lime (lime stabilization)*

Clay soils are widespread in Syria. Due to their shortcomings, the need for stabilization is becoming increasingly urgent. The improvement of swelling soils is becoming very important for the archaeological sites belonging to the ancient civilizations of Syria. These buildings are mostly lightly loaded structures, consisting of domes and stone walls based on strip foundations. Therefore, expansive soils can cause significant damage to these structures.

Lime is an excellent choice for short-term modification of soil, and it can modify almost all fine-grained soils, but the most dramatic improvement occurs in clay soils of moderate to high plasticity. Modification occurs because calcium cations supplied by the hydrated lime replace the cations normally present on the surface of the clay mineral, promoted by the high pH environment of the lime-water system. Thus, the clay surface mineralogy is altered, producing the following benefits: additives of mixtures of polypropylene fibers with lime reduces plasticity index, increases workability and shrinkage limit, reduces shrinkage cracking, eliminates almost all swelling problems, and increases the soil strength. The aim of using this type of material is to improve the performance of the ground without affecting the historical mission of the building.

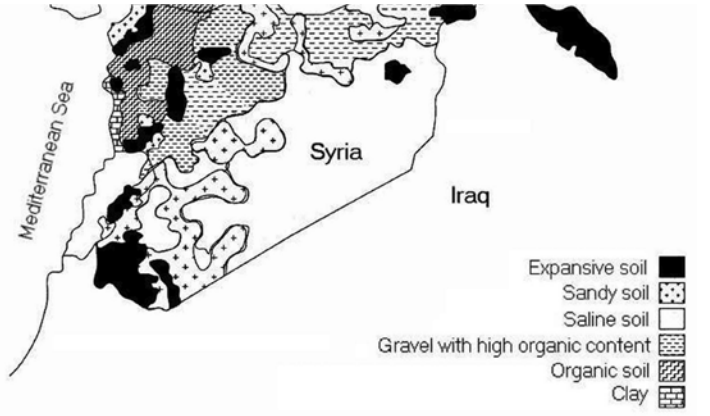

Figure 5. Location of clayey soils in Syria.

3.2 *Laboratory experiments*

A series of laboratory experiments was made on the influence of additives of mixtures of polypropylene fibers with lime on improving the building properties of swelling clay soil.

Figure 6. Laboratory experiments.

Lime was brought from the lime quarries in the province of Hama as limestone and ground with a ball mill at the Adra cement plant, and it was packed in tightly closed bags to isolate it from moisture and transported to the study site.

Table 1. Lime properties (local limestone).

Chemical analysis	
CaO	85.74 %
Ca(OH)2	13.49 %
CaCO3	0,17 %

The soil was mixed with additives in various weight ratios of both materials. Experiments on the physical and mechanical properties of the soil were made on 12 soil samples with different proportions of polypropylene fibers and lime as shown in the table.

Table 2. Laboratory experiment program.

№	1	2	3	4	5	6	7	8	9	10	11	12
lime %	2	5	8	2	5	8	2	5	8	8	0	0
Fibers %	0,05	0,05	0,05	0,15	0,15	0,15	0,25	0,25	0,25	0	0,25	0

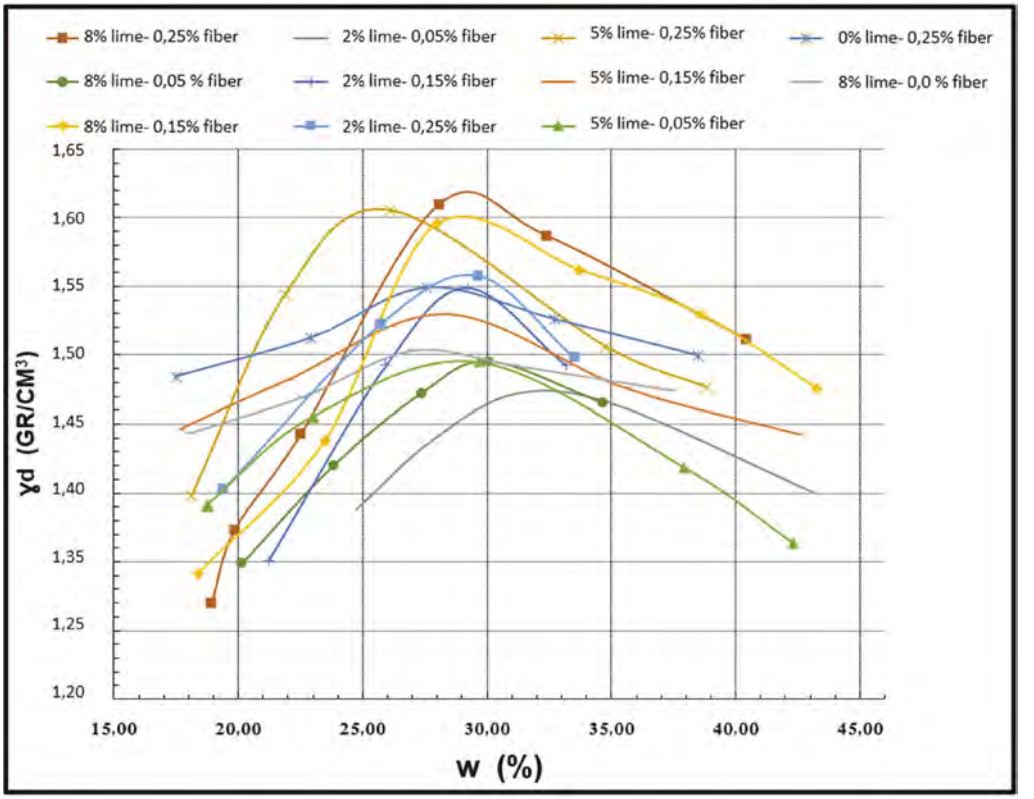

Figure 7. Maximum dry density and optimum moisture content of the soil.

4 CONCLUSIONS

Deciding the best method to improve the soil should take these following steps; a full architecture study for the building, geological and geotechnical surveys, historical study, and constant consultant support to choose the best method for restoring the building without changing its task or character. Using additives of mixtures of polypropylene fibers with lime to improve the soil considered one of the important ways to support and strengthening without harming the historical value.

Using additives of mixtures of polypropylene fibers with lime piles lead to reduce the variation of stress in soft soil after installation the materials and increase the soil strength. Besides the strength, the aspect of swelling and shrinkage improved expansive soil need to be studied in detail.

REFERENCES

Al Kodsi, S., Oda, K., & Awwad, T. 2018. Viscosity effect on soil settlements and pile skin friction distribution during primary consolidation. International Journal, 15(52), 152–159. https://doi.org/10.21660/2018.52.52744

Al-Gharbawi S.A., Ahmed & Najjem, Ahmed & Fattah, Mohammed. 2022. Expansive Soil Stabilization with Lime, Cement, and Silica Fume. Applied Sciences. 13. 1–15. Doi: 10.3390/app13010436.

Al-Rawas. A.A and Goosen. M.F.A 2006 Expansive soils recent advances in characterization and treatment.

AL-Soudany, K. 2018 Improvement of expansive soil by using silica fume. Kufa Journal of Engineering, vol. 9, no. 1, Jan. 2018, pp. 222–39, doi:10.30572/2018/KJE/090115.

Awwad L, Rahme N, Awwad T 2016. The rehabilitation of historic buildings - Case study Al-Thakana Al- Hamidieh in Syria. Proceedings of the Eighth Asian Young Geotechnical Engineering Conference in Astana, Kazakhstan, August 5-7, 2016. pp 297–302.

Awwad T, Chekaeva R, Chekaev M, Seisekeeva A & Awwad L 2019. Reconstruction and methods to protect stone buildings of the early 19th century. Geotechnics Fundamentals and Applications in Construction: New Materials, Structures, Technologies and Calculations, 1st Edition, CRC Press/Balkema, pp.21–25.

Awwad T., Gruzin V., Kim V. 2019 Sustainable Reconstruction in Conditions of Dense Urban Development. In: Weng MC., Lee J., Liu Y. (eds) Current Geotechnical Engineering Aspects of Civil Infrastructures. GeoChina 2018. Sustainable Civil Infrastructures. Springer, Cham, pp 13–23

Awwad Talal, 2016. Problems of Syrian Historical Monuments, Destroyed by Military Action: Diagnostics, Strengthening and Reconstruction. Proceedings of the Eighth Asian Young Geotechnical Engineering Conference in Astana, Kazakhstan, August 5-7, 2016. pp 21–27.

Awwad, T., & Al Kodsi, S. 2017. A comparison of numerical simulation models to determine the location of neutral plane. In ICSMGE 2017-19th International Conference on Soil Mechanics and Geotechnical Engineering (pp. 1947–1950). EID: 2-s2.0–85045455209

Awwad, T., & Donia, M. 2016. The efficiency of using a seismic base isolation system for a 2D concrete frame founded upon improved soft soil with rigid inclusions. Earthquake Engineering & Engineering Vibration, 15(1). pp 49–60. https://doi.org/10.1007/s11803-016-0304-6

Awwad, T., Donia, M., & Awwad, L. 2017. Effect of a stiff thin foundation soil layer's depth on dynamic response of an embankment dam. Procedia Engineering, 100(189), 525–532. https://doi.org/10.1016/j.proeng.2017.05.084

Awwad, T., Kodsi, S. A., & Shashkin, A. 2019. Negative Skin Friction Distribution on a Single Pile-Numerical Analysis. Sustainable Civil Infrastructures, 36-48. https://doi.org/10.1007/978-3-030-01902-0_4

Awwad, T., Yenkebayev, S. B., Tsigulyov, D. V., & Lukpanov, R. E. 2019. Analysis of driven pile bearing capacity results by static and dynamic load tests. In Sustainability Issues for the Deep Foundations: Proceedings of the 2nd GeoMEast International Congress and Exhibition on Sustainable Civil Infrastructures, Egypt 2018–The Official International Congress of the Soil-Structure Interaction Group in Egypt (SSIGE) (pp. 77–84). Springer. https://doi.org/10.1007/978-3-030-01902-0_8

Corley. J.B, Marsh. J.H and Quiring. S.M. Maintenance of existing foundations on expansive clay soils. Texas

Dietz K. and Schürmann A. 2006. Foundation Improvement of historic buildings by micro piles, Museum Island, Berlin, and St. Kolumba, Cologne. 7th ISM workshop, Schrobenhausen 2006,

Muntohar. A.S & Jiun-Liao H. 2007 Strength distribution of soft clay surround lime-column. Soft Soil Engineering – Chan & Law (eds.)© 2007 Taylor and Francis Group, London, pp 315–319.

Ulitsky V., Shashkin, A., Shashkin, K., Lisyuk, M., Awwad, T. 2017. Numerical simulation of new construction projects and existing buildings and structures taking into account their deformation scheme. Proceedings of the 19th International Conference on Soil Mechanics and Geotechnical Engineering. Seoul, Korea, September 2017, pp 2061–2065

Wong. P.K (2001). Ground improvement case studies chemical lime piles and dynamic replacement. Malaysia and Egypt.

Zhussupbekov A, Zhunisov T, Issina A, Awwad T 2013. Geotechnical and structural investigations of historical monuments of Kazakhstan. Proceedings of Second International Symposium on Geotechnical Engineering for the Preservation of Monuments and Historic Sites, Naples, Italy, 2013. PP 779–784.

Smart Geotechnics for Smart Societies – Zhussupbekov, Sarsembayeva & Kaliakin (Eds)
© 2023 The Author(s), ISBN 978-1-003-29912-7
Open Access: www.taylorfrancis.com, CC BY-NC-ND 4.0 license

Insights into 3D printing of polypropylene geocells

Prerana Krishnaraj
Research Scholar, Indian Institute of Science, Bangalore, India

G.M. Latha
Professor, Indian Institute of Science, Bangalore, India

ABSTRACT: Geocells are three-dimensional interconnected polymeric cells filled with soil. 3D printing of geocells has several benefits including control on surface features and tensile strength of the geocells. This helps in controlled laboratory testing of scaled-down geocells and geocell reinforced soil to better quantify their performance benefits. In this study, laboratory-scale geocells of smaller dimensions and low strength were manufactured through 3D printing and ultrasonic welding and tested for their mechanical response. Polypropylene sheets were printed using Fused Deposition Modelling (FDM) based 3D printer. These polypropylene sheets were then ultrasonically welded to form geocells. A horn and table mounting apparatus were designed to facilitate the welding of the sheets. The effects of angle of printing and speed of printing on material tensile strength and geocell-sand interface properties were studied. Results showed that angle of printing is the most influencing parameter on the mechanical properties of the geocells.

1 INTRODUCTION

Geocells were initially developed by US Army of Corps in 1975 (Webster (1979)). They are the class of geosynthetics which are three-dimensional in nature. Geocells consist of interconnected cells filled with soil. The improvement in the properties of the soil due to the inclusion of the geocells can be attributed to interlocking, friction and confinement. The shear strength improvement in the soil, when reinforced with geocells, is superior to that of planar reinforcements and fibre reinforcements (Latha and Somwanshi (2009); Latha and Murthy (2007); Dash et al. (2004)). Hence, numerous experimental analyses were carried out to understand the behaviour of the geocell reinforced soil. Experimental analyses were carried out through laboratory element tests and model tests.

In conducting scaled model tests or laboratory tests of geocell reinforced geomaterial, the unavailability of geocell material of desired scaled strength properties to represent the field conditions is a major drawback. 3D printing can provide a very efficient and time saving method for obtaining geocell material of desired strength characteristics. If the sensitivity and relation of various printing parameters with respect to the strength and friction characteristics of the fabricated material are established, it can be a very useful technique to aid model testing of geosynthetic reinforced geomaterials.

3D printing is the process of manufacturing material using 3D model data one layer at a time (Campbell et al. (2011)). 3D printing involves drawing the 3D sketch of the model using any appropriate software and converting it into an STL (Stereolithography language) file (Wong and Hernendez (2012)). The printer will print one layer at a time to form the required model. The 3D printing of the polymeric components is mostly carried out using the Fused Deposition Method (FDM) based printers (Vaezi et al. (2013)). It works on extrusion principle where the extruded material is deposited on the flat base to form a 2D layer deposition one over the other to form a 3D object. In this technique, the filaments of the thermoplastics are melted and extruded through the heated nozzle.

DOI: 10.1201/9781003299127-102

2 METHODOLOGY

2.1 *3D printing*

Fused Deposition Modelling (FDM) based 3D printer was used to manufacture polymer sheets used to form the geocells. The Polypropylene filaments were used to print polypropylene sheets of the required dimensions. The polypropylene filaments were heated and were ejected through an ejector of circular shape. The printing angle, printing speed and number of layers of filament deposition could be controlled. In this study, single layer of deposition 0.2 mm was considered. Figure1 gives the schematic representation of the different angles of printing considered in this study.

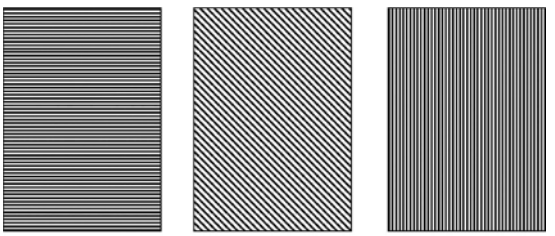

Figure 1. Orientation of printing (a) 0° (b) 45° (c) 90°.

2.2 *Ultrasonic welding*

The 3D printed polypropylene sheets were then ultrasonically welded to form geocell pockets of required dimensions. The ultrasonic welding technique was incorporated instead of stitching or glueing to better represent the actual field geocells. The seam strength could be varied by controlling the input air pressure and also welding time and hold time of the horn of the ultrasonic welding machine

2.3 *Tensile strength tests*

The tensile strength tests were conducted using the Universal Testing Machine (UTM) according to the ASTM D882-18 on the 3D printed sheets of width 0.05 m and grip length of 0.1 m. The samples were strained at a rate of 10% per minute. The tests were conducted to understand the effects of angle of printing and speed of printing on the tensile strength of sheets. The tests were conducted until the axial strain reaches 30 % or until the sample fails, whichever occurs first.

3 RESULTS

3.1 *Effects of printing parameters on tensile strength of the material*

3.1.1 *Effect of speed of printing*

The variation of the tensile strength per unit length with axial strain was plotted. Figure2 shows the variation of the tensile strength with axial strain for the sheets formed at the angle of printing of 45 degrees for different values of the printing speed. It can be seen that the peak tensile strength obtained for the speed of printing of 30 mm/s is higher as compared to that of 20 mm/s and 40 mm/s. Further, Young's modulus obtained from the graph were 378 MPa, 411 MPa and 346 MPa for printing speeds of 20 mm/s, 30 mm/s and 40 mm/s respectively. From the results, it can be seen that the speed of printing of 30 mm/s is very effective in producing polypropylene sheets of high tensile strength. Further analyses were carried out considering the speed of printing of 30 mm/s.

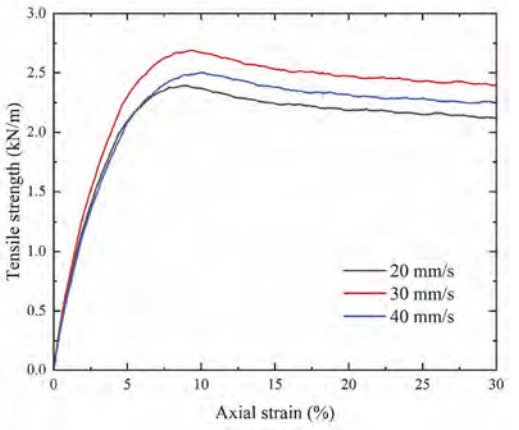

Figure 2. The variation of the tensile strength with axial strain for different printing speeds.

3.1.2 *Effect of angle of printing*

The printing angles considered in the study were 0°, 45° and 90° printed at a speed of 30 mm/s. The variation of the tensile strength with axial strain for different angles of printing is plotted in Figure3. It can be seen that the peak tensile strength is highest for the sheets obtained from the angle of printing of 45°. Young's modulus of 278 MPa, 411 MPa and 314 MPa were obtained for the angle of printing of 0°, 45° and 90° respectively.

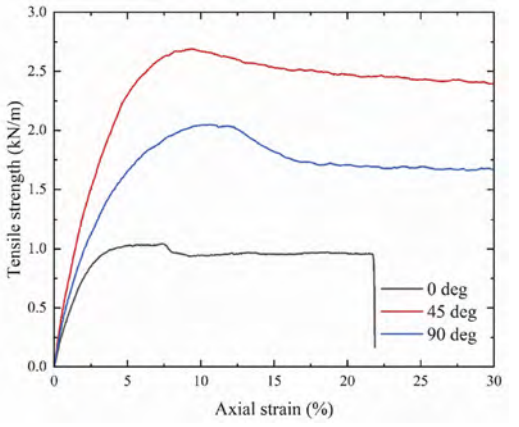

Figure 3. The variation of the tensile strength with axial strain for different printing angles.

3.2 *Interface shear tests*

Interface shear tests were conducted to understand the effects of printing parameters on the interface cohesion and interface friction properties. The polypropylene sheet is fixed to the base plate of the shearing apparatus. A movable shear box of dimensions 17 cm by 17 cm was filled with sand and placed over the 3D printed polypropylene sheet. The box was moved at a rate of 1mm/min over the polypropylene sheet. The peak shear stress for different values of the normal stresses was calculated. The variation of the peak shear stress with normal stress was plotted for three different values of the normal stress. The intercept of the plot gives the interface cohesion value, and the slope of the plot gives the value of interface friction. The interface direct shear tests were conducted on the 3D printed polymeric sheet obtained by maintaining the speed of printing of 30 mm/s as the tensile strength test results show that they

have the highest tensile strength. Table1 gives the values of the cohesion and the friction angle of the sand as well as the interface cohesion and friction angle of the sand-polypropylene sheet interface for different printing angles.

Table 1. Interface cohesion and Interface cohesion for different interfaces.

Interface	Cohesion(kPa)	Friction angle (deg.)
Sand-Sand	0.6	37.4
Sand-A0PP	1.5	25.45
Sand-A45PP	3.73	35.2
Sand-A90PP	3.32	34.04

A0PP: Printing angle 0° A45PP: Printing angle 45° A90PP: Printing angle 90°

3.3 *Peel strength of ultrasonically welded joint*

The ultrasonic welding of polypropylene sheets was carried out. The peel strength of the ultrasonically welded joints was carried out in the UTM. It was found that the peel strength of the welded joints was 90% to 95% of the ultimate tensile strength of the parent material indicating that the welding process was able to produce joints of sufficient strength.

4 CONCLUSIONS

- The effect of speed of printing on the ultimate tensile strength of the polypropylene sheets was found to be not very significant. The sheets printed at a speed of 30 mm/s displayed the highest ultimate tensile strength.
- The sheets printed at 45° angle showed higher ultimate tensile strength as compared to the ones printed at 0° and 90°. The variation in the ultimate tensile strength of the polypropylene sheet was significantly controlled by the angle of printing.
- The interface shear tests results show that the interface cohesion and friction angle between the sand and the polypropylene sheet was highest for the sheets printed at an angle of 45°
- The ultrasonically welded joints had a peel strength ranging between 90% to 95% of the ultimate tensile strength of the parent material.

REFERENCES

ASTM, D., 1995. Standard test method for tensile properties of thin plastic sheeting. *Annual Books of ASTM Standards: Designation 882-95*.

Campbell, T., Williams, C., Ivanova, O. and Garrett, B., 2011. Could 3D printing change the world. Technologies, Potential, and Implications of Additive Manufacturing, Atlantic Council, Washington, DC, 3.

Dash, S.K., Rajagopal, K., Krishnaswamy, N.R., 2004. Performance of different geosynthetic reinforcement materials in sand foundations. Geosynth. Int. 11, 35–42.

Latha, G.M., Murthy, V.S., 2007. Effects of reinforcement form on the behavior of geosynthetic reinforced sand. Geotext. Geomembranes 25, 23–32.

Madhavi Latha, G., Somwanshi, A., 2009. Effect of reinforcement form on the bearing capacity of square footings on sand. Geotext. Geomembranes 27, 409–422

Vaezi, M., Seitz, H. and Yang, S., 2013. A review on 3D micro-additive manufacturing technologies. The International Journal of Advanced Manufacturing Technology, 67(5),pp.1721–1754.

Webster, S.L., 1979. Investigation of Beach Sand Trafficability Enhancement Using Sand-Grid Confinement and Membrane Reinforcement Concepts. IEE J. Comput. Digit. Tech.

Wong, K.V. and Hernandez, A., 2012. A review of additive manufacturing. International scholarly research notices, 2012.

Smart Geotechnics for Smart Societies – Zhussupbekov, Sarsembayeva & Kaliakin (Eds)
© 2023 The Author(s), ISBN 978-1-003-29912-7
Open Access: www.taylorfrancis.com, CC BY-NC-ND 4.0 license

Field pullout testing of geogrid embedded in pond ash at a low normal stress

B.K. Karnamprabhakara
Post-Doctoral fellow, IIT Hyderabad, Kandi, Sangareddy

U. Balunaini
Professor, IIT Hyderabad, Kandi, Sangareddy

ABSTRACT: Pullout interaction between the geogrid reinforcement and the fill material is one of the key factors in the design of Mechanically Stabilised Earth (MSE) walls. It is even more intriguing to understand the pullout interaction behavior when the fill material is a non-conventional fill material such as pond ash. The pullout resistance of the geogrid is typically defined in terms of the pullout resistance factors (F^*) and obtained from laboratory testing. Though it is uncommon to conduct field pullout testing on geogrids, it is ideal to study the pullout resistance of the geogrids in the field conditions. This case study presents field pullout testing conducted using a polyester uniaxial geogrid embedded at a depth of 0.8m (i.e., corresponding to a normal stress of ~12 kPa) in pond ash as fill material at a MSE wall construction site near Vijayawada, Andhra Pradesh, India. The field pullout resistance was found to be closer to laboratory test result under the normal stress of ~17 kPa at a normalized pullout displacement of 4%.

1 INTRODUCTION

The interaction of geogrid with the fill material varies with the orientation of geogrid connected to the facia of the reinforced retaining wall. The two commonly used facia are precast modular block facia and precast concrete panel facia. In block facia, one layer of geogrid are rolled over continuously and connected with the block facia over the fill material for the required length. In concrete panel facia, a given width of geogrids are connected through tie-hook arrangement within the facia and rolled over it to a certain length or the entire length. When geogrids are rolled over the entire length, they form an overlapping arrangement (refer to Figure 1). During the rolling over of geogrids through the hook, the width of the geogrid varies from 1B at the hook side to 2B at the other end. However, it is a common practice to conduct laboratory pullout testing on one-layer of geogrid embedded in the backfill according to ASTM D6706 (as shown in red dotted lines in Figure 1). This methodology may result in over conservatism in the estimation of pullout resistance of the geogrids used in the backfill behind the retaining walls with concrete panel facia as this procedure does not account for the overlapping effect of geogrid reinforcement (as shown in green dotted lines in the Figure 1), but simply considers the average width of the reinforcement.

There are no studies available on the effect of overlapping of geogrid reinforcement behind the concrete panel facia. On the other side, there is a significant rise in the number of mechanically stabilized structures using pond ash as a backfill material in India (Karnamprabhakara et al. 2021, Pant 2019a, b). Authors of this study have extensively worked on the feasibility of using pond ash from the same source as a backfill material, and the effect of tensile strength and aperture opening on the pullout resistance of the geogrid as per ASTM D6706 (Karnamprabhakara et al. 2021). However, the effect of overlapping of geogrids behind the concrete panel with pond ash as backfill material is yet to be explored.

DOI: 10.1201/9781003299127-103

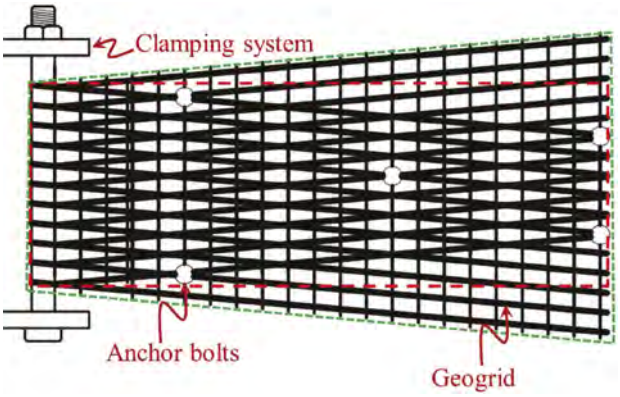

Figure 1. Schematic view of the spread geogrid behind the concrete panel.

In the present study, a field pullout testing was conducted on a uniaxial, polyester geogrid embedded in pond ash with an overlapping arrangement under an overburden stress of ~12 kPa. The variation of pullout resistance along the front-end pullout displacement was monitored and the pullout resistance factor (F^*) was determined.

2 EXPERIMENTAL DETAILS

2.1 *Materials*

2.1.1 *Pond ash*

Pond ash used in the field was collected from ash pond that belongs to Narla Thatharao Thermal Power Station (NTTPS), which is at a lead distance of 20 kms from the construction site. Preliminary studies including grain-size distribution, compaction characteristics, and the engineering properties like shear strength, permeability, and compressibility were performed and reported in Karnamprabhakara et al. (2021). Table 1 presents the properties of pond ash used in the construction site.

Table 1. Properties of pond ash used in the construction site.

Property	Value	Units
D_{10}	0.075	mm
D_{50}	0.2	mm
Soil classification	SP	-
% fines	<10	%
Optimum moisture content	30	%
Maximum dry unit weight	11.6	kN/m^3
Apparent cohesion, c	7.7	kPa
Angle of shearing resistance, φ	42	0
Secant constraint modulus, D	8.3	MPa
Hydraulic conductivity, *k*	2.3e-6	m/s

2.1.2 *Reinforcement*

Geogrids were used as a reinforcing material in the construction of MSE walls with pond ash as backfill material. Different number of geogrids with varied tensile strengths were used in the construction based on the design.

Table 2 gives the details of the geogrid used in the present study. Henceforth, the geogrid used in the study is referred as UXG. More details of the geogrid like longitudinal and transverse rib widths, thickness and so on can be found in Karnamprabhakara et al. (2021). The geogrid UXG of the present study corresponds to UXG2 in Karnamprabhakara et al. (2021).

Table 2. Manufacturer details of the geogrid (UXG) used in the study (adopted from Karnamprabhakara et al. 2021).

Detail	Value	Units
Material	Polyester (PET)	-
Tensile strength		
MD	200	kN/m
CMD	30	kN/m
Aperture size		
MD	30	mm
CMD	23	mm

2.2 *Pullout setup*

Figure 2a shows the photograph of the vibratory compactor and the panel walls used in the construction site, and Figure 2b shows the field pullout test setup with the key components. The key components of the test setup include hydraulic cylinder, hand pump, and pressure gauge. Two number of hydraulic jacks (or) cylinders of capacity 250 kN each were used in the testing. The ram diameter of the jacks was equal to 54 mm. The valves present in hand pump line helps in slow mobilization of oil flow into the cylinders.

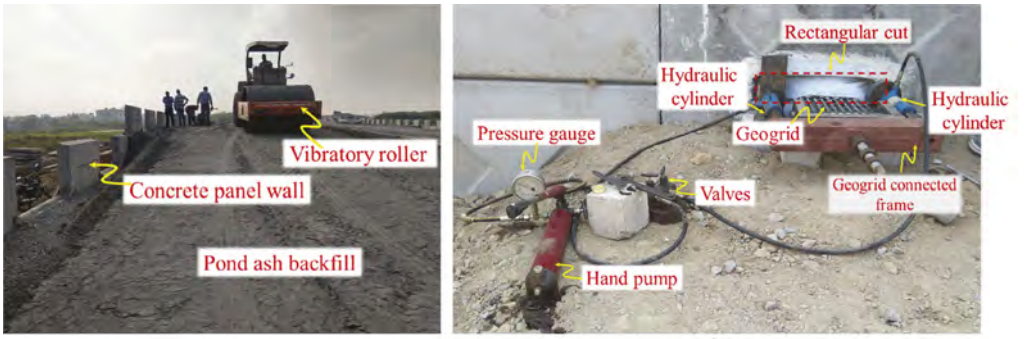

Figure 2. Construction site photographs showing (a) the vibratory roller compactor and panel walls, (b) field pullout test setup with its key components.

3 TESTING PROCEDURE

To perform a field pullout testing on the geogrid, a prefabricated concrete panel with a rectangular cut of width 600 mm and depth of 100 mm, as shown in Figure 2 was installed. Pond ash was used as the backfill material and compacted using vibrating rollers for about 0.8 m above the sacrificial geogrid. The achieved compacted bulk unit weight of the pond ash behind the precast concrete panel was equal to 14 kN/m^3. It was connected to the cylindrical-shaped rod of diameter 50 mm in the geogrid connection frame unit. The hydraulic cylinders were arranged such that the cylinders get a reaction force from the concrete panel wall when

the pistons try to pull the geogrid out from the backfill. The effective overburden stress on the sacrificial geogrid laid at a depth of 0.8m from the top was ~ 12 kPa. During the pullout testing, the loads were applied incrementally up to 50 kN. At every application of load, the geogrid was allowed to get pulled for 5-10 minutes of duration and then subsequent loads were applied. The movement of pistons in both the hydraulic cylinders was measured using a 30 cm-long steel ruler, and the average value was noted as the front-end axial pullout displacement, at every load application.

4 RESULTS AND DISCUSSION

Figure 3a shows the variation of normalized axial pullout resistance along the normalized front-end axial pullout displacement of the geogrid from the field testing. It was also compared with the normalized pullout resistance from the laboratory study (Figure 3b) (adopted from Karnamprabhakara et al. 2021). The lowest normal stress under which the pullout testing data was available corresponded to 17 kPa and the same was presented. From field testing, it could be observed that the pullout resistance of the geogrid increased continuously with the increase in the front-end pullout displacement of the geogrid. This behavior indicates that the shear stress along the reinforcement was not fully mobilized within the front-end pullout displacement of 130 mm. However, the laboratory pullout test result showed a constant pullout resistance beyond 3% of normalized pullout displacement indicates that the shear stress was mobilized along the entire geogrid. The pullout resistance corresponding to maximum front-end pullout displacement of 130 mm (i.e., normalized pullout displacement of ~4%) was considered to define the pullout resistance factor for the field pullout test. Ideally, Federal Highway Authority (FHWA) suggests considering the pullout resistance corresponding to the rear-end displacement of 15 mm for extensible reinforcements like geogrids.

FHWA (Elias et al. 2001) suggests an empirical formula to estimate the ultimate pullout resistance (P_a) of the geogrids.

$$P_a = F^*.\alpha.\sigma_n.C.B.L_e \tag{1}$$

where, F^* is the pullout resistance factor, α is the correction factor for non-linear shear stress mobilization (=0.8 for geogrids, in general), σ_n is the overburden stress on the geogrid (~16 kPa in the present study), C is the effective unit perimeter (=2 in general), B is the average width of the geogrid in the overlapping condition with 0.3 m at the hook end and 0.6 m at the other end (=0.45 m in the present study), L_e is the effective length of the reinforcement (=3.5 m).

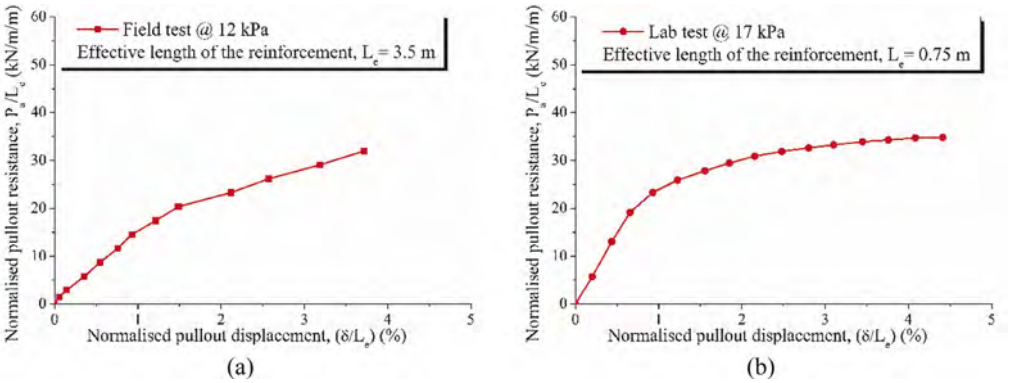

Figure 3. Variation of axial pullout resistance along the front-end pullout displacement under (a) field conditions, and (b) laboratory conditions.

The pullout resistance factor (F^*) from the field pullout test was equal to 1.11 as per Eq. 1 for the considered normalized pullout displacement of ~4%. However, it is to be noted that the effect of spread (overlapping) area of the two-layer geogrid was not considered in the analysis, but just the average width of the geogrid was used in the analysis. The calculated pullout resistance factor for the field pullout testing was closer to the reported pullout resistance factor (=1.25 corresponding to the same equivalent normalized pullout displacement of ~4%) for the same geogrid tested in the laboratory with pond ash as a fill material (Karnamprabhakara et al. 2021). However, the normal stress differs by an amount of 5 kPa between laboratory testing and field testing. This indicates a possibility of higher pullout resistance factors for field pullout testing at the same normal stress. It was expected that the high pullout resistance was anticipated in the field case owing to the increase in the frictional resistance of the geogrid and the pond ash particles and passive resistance against transverse ribs with increase in the spread area of the geogrid. In addition, the continuous increase in the pullout resistance in field testing indicates that the rear-end displacement of the geogrid is considerably lesser than 15 mm, and higher resistance can be expected.

It is inarguably acceptable that the increase in the spread area of the geogrid behind the precast concrete panel would exhibit a considerable increase in the pullout resistance. This study paves towards creating interest to study the factors in terms of increase in the pullout resistance with the increase in the spread area of the geogrid, particularly when it is embedded in non-conventional fill material like pond ash. Thus, a comprehensive study that covers the effect of overlapping (spread) area of geogrid embedded in pond ash, under different possible overburden stresses in the field and model testing for the same case in the laboratory is required to understand the realistic behavior.

5 CONCLUSIONS

Field pullout testing of geogrids behind the mechanically stabilised earth walls for the conditions discussed in the paper can provide realistic behavior of geogrid pullout and to define pullout resistance factors. The pullout resistance factor observed for the geogrid, UXG in the field pullout testing was equal to 1.11 under a normal stress of 12 kPa, which is lower to the laboratory test result (~1.25). This factor is defined at a normalized pullout displacement of ~4%. However, there is a need for a comprehensive study of field and laboratory pullout testing on geogrids in overlapping conditions, and this is suggested as the further scope of the study.

ACKNOWLEDGEMENTS

Authors would like to acknowledge SoilSol Projects, Hyderabad, for their cooperation in conducting field pullout testing in one of their projects near Vijayawada, Andhra Pradesh.

REFERENCES

ASTM D6706. 2001. Standard test method for measuring geosynthetic pullout resistance in soil. pp 1–8. https://doi.org/10.1520/D6706-01R13.2

Elias V, Christopher B, and Berg R. (2001) Mechanically stabilized earth walls and reinforced soil slopes design & construction guidelines, *FHWA-NHI-00-043 Report*.

Karnamprabhakara, B. K., B. Umashankar, A. Arulrajah, & R. Evans. 2021. Axial Pullout Resistance and Interface Direct Shear Properties of Geogrids in Pond Ash Materials. *International Journal of Geosynthetics and Ground Engineering*, 1–14.

Pant, A., M. Datta, & G. V. Ramana. 2019a. Bottom ash as a backfill material in reinforced soil structures. *Geotextiles and Geomembranes*, 47 (4): 514–521. Elsevier. https://doi.org/10.1016/j.geotexmem.2019.01.018.

Pant, A., G. V. Ramana, M. Datta, & S. K. Gupta. 2019b. Coal combustion residue as structural fill material for reinforced soil structures. *Journal of Cleaner Production*, 232: 417–426. Elsevier Ltd. https://doi.org/10.1016/j.jclepro.2019.05.354

Smart Geotechnics for Smart Societies – Zhussupbekov, Sarsembayeva & Kaliakin (Eds)
© 2023 The Author(s), ISBN 978-1-003-29912-7
Open Access: www.taylorfrancis.com, CC BY-NC-ND 4.0 license

Multiple linear regression analysis of foundation soil reinforced with geogrid using wraparound ends technique

Satyanarayana Murty Dasaka
Professor, Civil Engineering Department, Indian Institute of Technology Bombay, Mumbai, India

Sagar Jaiswal
Research Scholar, Civil Engineering Department, Indian Institute of Technology Roorkee, Roorkee, Uttarakhand, India

Vinay Bhushan Chauhan*
Assistant Professor, Civil Engineering Department, Madan Mohan Malaviya University of Technology, Gorakhpur, Uttar Pradesh, India

ABSTRACT: The present study aims to generate generalized equations for the determination of ultimate load-bearing capacity (*ULBC*) of geogrid reinforced foundation (*GRF*) soil using the wraparound ends technique. Firstly, the *ULBC* of the reinforced soil is investigated by employing the two-dimensional FEM tool, and then a multiple linear regression (*MLR*) analysis is performed to obtain the generalized equations for the determination of the same. A series of solutions have been generated by performing a parametric study on the geometrical configuration of the wraparound ends configuration along with the geogrid's axial elastic stiffness (*EA*). The results recommend that the generated equations are reliable as the coefficient of determination (R^2) ranges nearly 1 for *EA* up to 2000 kN/m. However, beyond certain values of stiffness parameters, some qualitative intervention is needed to interpret the *ULBC*.

1 INTRODUCTION

The use of geosynthetics to reinforce the shallow foundation is now being considered the most viable and sustainable approach for construction. In the last few decades, various studies have been performed which have proven the efficiency of geosynthetics to improve the ultimate load-bearing capacity (*ULBC*) and decrease the footing's settlement. The very first concept of soil reinforcement was put forward by (Vidal, 1969), and (Binquet & Lee, 1975) performed the first systematic study of shallow foundations resting on reinforced soil. Since then, various experimental studies have been performed to investigate the *ULBC* and settlement of the footing (Khing et al., 1993; Adams & Collin, 1997; Dash et al., 2004; Azzam & Farouk, 2010; Aria et al., 2021). The experimental test methods, such as plate load tests are time-consuming, very expensive, and require skilled labor to create the exact in-situ field condition for the test, requiring heavy machinery and tools. Researchers have conducted analytical studies to examine the *ULBC* and tried to eliminate the discrepancy in the results due to field limitations (Binquet & Lee, 1975; Chen & Abu-Farsakh, 2015; Huang & Tatsuoka, 1990). In order to eradicate the cumbersome calculations and saving in time and money, researchers have utilized the concept of finite element analysis (*FEA*) to perform the various test on the footing lying over the reinforced soil mass (Bindlish et al., 2013; Kazi et al., 2015b; Jaiswal & Chauhan, 2021a, 2021b).

Earlier, researchers had studied the improvement in the bearing capacity of soil reinforced with horizontal reinforcing layers (Adams & Collin, 1997; Shin et al., 2002; Basudhar et al., 2007)

*Corresponding author: chauhan.vinaybhushan@gmail.com

DOI: 10.1201/9781003299127-104

which requires larger space to lie geogrid beneath the footing. However, a wraparound ends technique came into the picture, which requires less space to sufficiently enhance the bearing capacity and correspondingly imparts lateral confinement to the soil strata in addition to pseudo confinement (Shukla, 2015). This technique has been researched analytically, experimentally, and numerically by various researchers in the recent past (Kazi et al., 2015; Raja & Shukla, 2020; Jaiswal et al., 2021a), and various reinforcing parameters have been recommended.

The abovementioned literatures discussed the characteristic improvement of the reinforced soil in terms of *ULBC* and settlement, yet no generalized equation for the wraparound ends technique is available for the direct estimation of the *ULBC* for varying stiffness parameters of the geogrid on the basis of the requirement of footing and soil conditions.

This study aims to develop generalized equations for the direct determination of *ULBC* of foundation soil reinforced with geogrid using the wraparound ends technique for the mentioned ground conditions. To achieve the abovementioned aim, an *FEA* has been performed using the 2D FEM tool, and a series of solutions is obtained by performing the parametric study on the geometrical parameters of the wraparound ends technique of reinforcement. Further, these solutions were utilized as input parameters for the multiple linear regression (*MLR*) analysis.

2 SCOPE OF THE PRESENT STUDY

2.1 *Problem statement*

The present study aims to perform a finite element analysis (*FEA*) of strip footing (width = *B*) resting on a *GRF* soil using the wraparound ends technique using the Optum G2 FEM tool (Krabbenhoft et al., 2020) and to develop generalized equations for the prediction of *ULBC* employing the multiple linear regression (*MLR*) analysis. The *ULBC* is dependent on the geometrical parameters of the wraparound ends technique i.e., placement of reinforcing layer near the footing (*u*), width of the geogrid (*b*), lap length (*l*), vertical distance of overlapping ends (*d*), and vertical spacing between two layers of reinforcement (*h*), which are considered as independent parameters for *MLR* analysis. A total of 405 solutions are tabulated and used for further analysis. The problem definition considered in the present study is shown in Figure 1 and the details of the study performed for deterministic study are presented in Table 1.

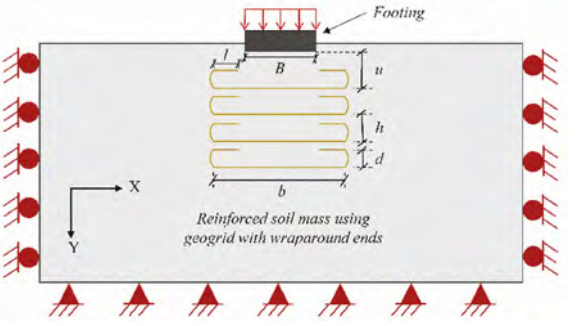

Figure 1. Problem definition.

Table 1. Details of the parametric study.

Footing Width	Width of reinforcement	Depth of first reinforcing layer	Vertical spacing between two layers of reinforcement	Vertical distance of overlapping ends	Lap length
(*B*)	(*b*)	(*u*)	(*h*)	(*d*)	(*l*)
B	3B	0.25B		0.20B	0.50B
	4B	0.30B	0.30B	0.25B	0.60B
	5B	0.35B	0.40B	0.30B	0.70B

2.2 *Methodology*

A two-dimensional finite element analysis (*FEA*) is performed for modeling a strip footing on cohesionless *GRF* soil. The material properties and modeling consideration correspond to the study of Jaiswal & Chauhan (2021a). The soil material is modeled using the Mohr-Coulomb failure criterion following the associated flow rule. The shear strength parameters are maintained invariably during the study for better comparison of the findings. The footing is considered rigid concrete material. The reinforcement is modeled using geogrid material defined in the tool having varied axial elastic stiffness, i.e., EA = 1000 kN/m, 2000 kN/m, and 5000 kN/m. A plane strain condition is considered in the present study. The interface parameters are considered in accordance with the recommendation of (Kazi et al. 2014; Srivastava et al. 2020; Jaiswal et al. 2021b). The sensitivity analysis is performed and noted that 10000 elements are enough for the considered mesh.

The multiplier elastoplastic analysis is performed in the present study and the *ULBC* is obtained by applying the double tangent method (Jaiswal & Chauhan, 2021c). The illustration of mesh deformation of unreinforced foundation and wraparound ends geogrid reinforced foundation is shown in Figure 2, which demonstrates the associated failure mechanisms during the analysis. The progressive potential failure of the *GRF* soil with wraparound ends is shown in Figure 3.

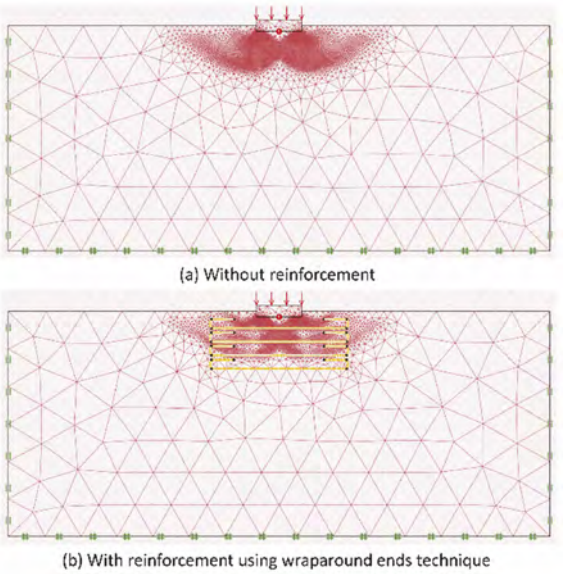

Figure 2. Deformed mesh of footing (a) without reinforcement; (b) with reinforcement using wraparound ends technique.

3 RESULTS AND DISCUSSION

3.1 *Multiple linear regression (MLR) analysis*

Empirical estimation of various significant parameters in almost all problems lying within the civil engineering discipline is a common method. Generally, for the estimation of the relationship between the dependent and independent variables, a function is assumed. An elementary model used for *MLR* analysis is postulated in Equation (1):

$$y = \alpha_1 x_1 + \alpha_2 x_2 + \alpha_3 x_3 + \ldots + \alpha_n x_n \tag{1}$$

where, y is the dependent variable, $x_1, x_2, x_3, \ldots, x_n$ are n independent variable, $\alpha_1, \alpha_2, \alpha_3, \ldots, \alpha_n$, are the unknown parameters and n is the number of independent variables.

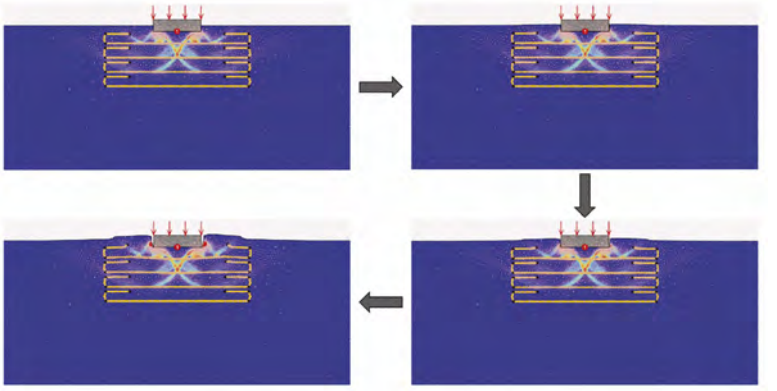

Figure 3. Progressive potential failure obtained during the FEM analysis.

Therefore, m number equations can be written in the form of Equation (1), for each observation, to study the effect of as many parameters as required. Basically, m number of equations will be solved for the n unknown parameters by using multiple linear regression. The m equations for the discussed case can be written more generally in the following way:

$$\begin{aligned} y_1 &= \alpha_1 x_{11} + \alpha_2 x_{12} + \alpha_3 x_{13} + \ldots + \alpha_n x_{1n} \\ y_2 &= \alpha_1 x_{21} + \alpha_2 x_{22} + \alpha_3 x_{23} + \ldots + \alpha_n x_{2n} \\ &\vdots \\ y_m &= \alpha_1 x_{m1} + \alpha_2 x_{m2} + \alpha_3 x_{m3} + \ldots + \alpha_n x_{mn} \end{aligned} \tag{2}$$

Equation (2) can be further generalized as:

$$y_i = \sum_{j=1}^{n} \alpha_j x_{ij}, \text{ for } i = 1 \text{ to } m \tag{3}$$

where, y_i is the i^{th} observation on y and x_{ij} is the i^{th} observation on the j^{th} independent variable.

For Equation (3) to have an intercept term, it is necessary that $x_i = 1$ for $i = 1$ to m, while α_1 becomes the intercept (Bera et al., 2005). For the development of the linear equation, it is assumed that $x_{i1} = 1$ for $i = 1$ to m. The equation thus obtained is a special case of Equation (3), and can be written in the form of:

$$y_i = \alpha_1 + \alpha_2 x_{i2} + \alpha_3 x_{i3} + \ldots + \alpha_n x_{in}, \text{ for } i = 1 \text{ to } m \tag{4}$$

Following the above procedure, an *MLR* analysis has been performed from the combination of simulations as shown in Table 1. The values of *ULBC* are determined from the present numerical study illustrated that it is not significantly affected by the l/B and the d/B ratios, although, for higher accuracy of *ULBC*, these are taken into account while performing the multiple linear regression analysis. The findings unveil that the improvement in the *ULBC* is majorly dependent on the u/B ratio, h/B ratio, and elastic stiffness (EA) of the geogrid. In line with the scope of the present study, a multiple linear regression model was developed to estimate the *ULBC* for various EA values corresponding to u/B, h/B, d/B, and l/B respectively, and represented as follows:

$$ULBC = \alpha_1 + \alpha_2 (u/B)_{i2} + \alpha_3 (h/B)_{i3} + \alpha_4 (d/lB)_{i4} + \alpha_5 (l/B)_{i5}, \text{ for } i = 1 \text{ to } m \tag{5}$$

where, α_1 = intercept; and α_2, α_3, α_4, and α_5 = partial regression coefficients.

Table 2 shows the results of the multiple linear regression analysis, in which the values of α_1, α_2, α_3, α_4, and α_5 are presented together with the coefficient of determination (R^2) corresponding to *EA* and *b*/*B*.

The results presented in Table 2 illustrate the expected change in *ULBC* for a unit change in one parameter when all the other parameters are kept constant. The numerical value of coefficients; α_1, α_2, α_3, α_4, and α_5 evaluated the sensitivity of *ULBC* to the parameters considered in Equation (5). The magnitude of the coefficient of determination (R^2) shows the significance of the generated regression model, and also depicts the variation in outcome when the value of independent variables fluctuates. For *EA* up to 2000 kN/m, R^2 ranges near 0.97, which demonstrates that the regression model (Equation 5) is more reliable. Moreover, R^2 for *EA* = 5000 kN/m ranges near 0.82 which shows that although the predicting variables are affecting the dependent variable (*ULBC*), despite some qualitative interference is required to interpret the *ULBC*.

Table 2. Constants in Equation (5) and the coefficient.of determination (R^2).

Elastic stiffness, *EA* (kN/m)	*b*/*B*	α_1	α_2	α_3	α_4	α_5	R^2
1000	3	648.694	-287.056	-276.687	6.714574	-3.63023	0.976605
	4	644.6981	-287.837	-265.437	3.077017	-4.53544	0.961192
	5	649.455	-298.874	-263.423	-9.56076	-1.82925	0.97835
2000	3	838.4548	-513.514	-446.475	-2.53179	-3.67802	0.959988
	4	839.6996	-513.299	-449.063	-4.28498	-6.02171	0.955031
	5	834.3687	-503.872	-436.922	-15.0534	-2.16956	0.963175
5000	3	1214.368	-1149.28	-654.977	-15.0812	-8.59681	0.818582
	4	1216.515	-1127.42	-667.106	-39.7242	-7.92012	0.822537
	5	1205.114	-1120.9	-657.615	-24.0494	-2.76067	0.812619

4 CONCLUSIONS

An *MLR* analysis has been performed in order to determine the ultimate load-bearing capacity (*ULBC*) of a foundation reinforced with geogrid using the wraparound ends technique based on the outcomes of *FEA* outcomes. The coefficient of determination (R^2) has been calculated for varying stiffness of the reinforcement at various geometrical parameters of the wraparound ends technique. The outcomes indicated that the equations generated during the *MLR* analysis are reliable up to the axial elastic stiffness, *EA* = 2000 kN/m. The generated equations can be directly used in the field for a similar ground condition; however, attention is required for the varying ground conditions.

REFERENCES

Adams, M. T., & Collin, J. G. 1997. Large model spread footing load tests on geosynthetic reinforced soil foundations. *Journal of Geotechnical and Geoenviromental Engineering, ASCE*, 123(1): 66–72.

Aria, S., Shukla, S. K., & Mohyeddin, A. 2021. Behaviour of sandy soil reinforced with geotextile having partially and fully wrapped ends. *Proceedings of the Institution of Civil Engineers - Ground Improvement*, 174(1): 29–41.

Azzam, W. R., & Farouk, A. 2010. Experimental and numerical studies of sand slopes loaded with skirted strip footing. *Electronic Journal of Geotechnical Engineering*, 15 H: 1–18.

Basudhar, P. K., Saha, S., & Deb, K. 2007. Circular footings resting on geotextile-reinforced sand bed. *Geotextiles and Geomembranes*, 25: 377–384.

Bera, A. K., Ghosh, A., & Ghosh, A. 2005. Regression model for bearing capacity of a square footing on reinforced pond ash. *Geotextiles and Geomembranes*, 23(3): 261–285.

Bindlish, A., Singh, M., & Samadhiya, N. K. 2013. Modeling of Ultimate Bearing Capacity of Shallow Foundations resting on Jointed Rock Mass. *Indian Geotechnical Journal*, 43(3): 251–266.

Binquet, J., & Lee, K. L. 1975. Bearing capacity analysis of reinforced earth slabs. *Journal of Geotechnical and Geoenvironmental Engineering*, 101(12): 1257–1276.

Chen, Q., & Abu-Farsakh, M. 2015. Ultimate bearing capacity analysis of strip footings on reinforced soil foundation. *Soils and Foundations*, 55(1): 74–85.

Dash, S. K., Rajagopal, K., & Krishnaswamy, N. R. 2004. Performance of different geosynthetic reinforcement materials in sand foundations. *Geosynthetics International*, 11(1): 35–42.

Huang, C. C., & Tatsuoka, F. 1990. Bearing capacity of reinforced horizontal sandy ground. *Geotextiles and Geomembranes*, 9(1): 51–82.

Jaiswal, S., & Chauhan, V. B. 2021a. Evaluation of Optimal Design Parameters of the Geogrid Reinforced Foundation with Wraparound Ends Using Adaptive FEM. *International Journal of Geosynthetics and Ground Engineering*, 7(77): 1–18.

Jaiswal, S., & Chauhan, V. B. 2021b. Response of strip footing resting on earth bed reinforced with geotextile with wraparound ends using finite element analysis. *Innovative Infrastructure Solutions*, 6(2): 1–9.

Jaiswal, S., & Chauhan, V. B. 2021c. Ultimate bearing capacity of strip footing resting on rock mass using adaptive finite element method. *Journal of King Saud University-Engineering Sciences*.

Jaiswal, S., Srivastava, A., & Chauhan, V. B. 2021a. Improvement of bearing capacity of shallow foundation resting on wraparound geotextile reinforced soil. *International Foundations Congress and Equipment Expo 2021 (IFCEE 2021)* (pp. 65–74).

Jaiswal, S., Srivastava, A., & Chauhan, V. B. 2021b. Performance of strip footing on sand bed reinforced with multilayer geotextile with wraparound ends. *Ground improvement and reinforced soil structures* (pp. 721–732). Springer, Singapore.

Kazi, M., Habibi, D., Shukla, S. K., & Habibi, D. 2014. Behaviour of an embedded footing on geotextile-reinforced sand. *Proceedings of the Institution of Civil Engineers: Ground Improvement*, 169 (2): 1–14.

Kazi, M., Shukla, S. K., & Habibi, D. 2015. Effect of Submergence on Settlement and Bearing Capacity of Surface Strip Footing on Geotextile-Reinforced Sand Bed. *International Journal of Geosynthetics and Ground Engineering*, 1(4): 1–11.

Khing, K. H., Das, B. M., Puri, V. K., Cook, E. E., & Yen, S. C. 1993. The bearing-capacity of a strip foundation on geogrid-reinforced sand. *Geotextiles and Geomembranes*, 12(4): 351–361.

Krabbenhoft, K., Lyamin, A., & Krabbenhoft, J. 2020. Optum computational engineering <www.optumce.com>.

Raja, M. N. A., & Shukla, S. K. 2020. Ultimate bearing capacity of strip footing resting on soil bed strengthened by wraparound geosynthetic reinforcement technique. *Geotextiles and Geomembranes*, 48 (6): 867–874.

Shin, E. C., Das, B. M., Lee, E. S., & Atalar, C. 2002. Bearing capacity of strip foundation on geogrid-reinforced sand. *Geotechnical and Geological Engineering*, 20: 169–180.

Shukla, S. K. 2015. *Core concepts of geotechnical engineering*. ICE Publishing.

Srivastava, A., Jaiswal, S., & Chauhan, V. B. 2020. The Behavior of Multi-Tiered Mechanically Stabilized Earth (MSE) Retaining Wall. *Proceedings of Indian Geotechnical Conference 2020* (pp. 180–191).

Vidal, H. 1969. The principle of reinforced earth. *Geotechnical Special Publication*, (282): 1–16.

Smart Geotechnics for Smart Societies – Zhussupbekov, Sarsembayeva & Kaliakin (Eds)
© 2023 The Author(s), ISBN 978-1-003-29912-7
Open Access: www.taylorfrancis.com, CC BY-NC-ND 4.0 license

Anisotropic behavior of fiber-reinforced sand in undrained triaxial compression and extension tests

J. Ganiev
Nagoya University, Nagoya, Aichi, Japan

ABSTRACT: A series of undrained triaxial experiments for compression and extension were conducted on unreinforced and fiber-reinforced. Three fiber contents of 0.0, 0.2, and 0.4% by dry weight of host soil have been utilized to investigate the trend of fiber-reinforcement. The samples were prepared in medium loose condition with approximately 40% relative density to fully reveal the effect of fibers on pore water pressure generation in a range of 20% axial strain. Experimental results showed that the fibers were more effective in compression compared to extension at a higher axial strains. However, a smaller initial stiffness in compression was observed with the increase in fiber content. A possible mechanism for such kind of behavior were proposed through the consideration of the interaction mechanism between fibers and sand particles, and the influence of fibers on the initial anisotropy of sandy soil.

1 INTRODUCTION

Reinforcing soils with tension resisting elements has raised a high interest for a long time. A lot of studies have performed both experimental and numerical investigations to comprehensively analyze the effectiveness of fiber-reinforcement (Gray & Ohashi 1983, Michalowski & Zhao 1996, Consoli et al. 2009, Diambra et al. 2013, Ganiev et al. 2022a). Despite a huge number of existing literature, there are still a lot of contentious issues and shortage of consistent data to properly describe the fiber-reinforcement mechanism.

In this study consolidated undrained triaxial compression and extension tests were performed to investigate the effect of fibers on a shear strength with simultaneous analysis of the pore water pressure (PWP) generation with the shear progress. Additionally, a mechanism of the fiber – sand particles interaction and influence of fibers on the anisotropic behavior of sand was analyzed by the comparison of the stress paths in compression and extension under several confining pressures. Compared to previous studies, where mainly the anisotropic orientation and distribution of fiber itself was considered, in this study the main attention was paid to the effect of randomly distributed fiber on the degree of anisotropy of sand specimens and the influence of fibers on the spatial distribution of sand particles.

2 MATERIALS AND METHODS

2.1 *Materials and sample preparation*

The standard sand for laboratory testing in Japan – Toyoura sand, was used for all the experiments. Grain size distribution of sand is given in Figure 1a. Its physical properties are: specific gravity G_s = 2.65; maximum and minimum void ratios e_{max} = 0.985 and e_{min} = 0.639, respectively.

As a reinforcing material polyvinyl alcohol (PVA) fibers (Figure 1b) were used with 0.2 and 0.4 percent of the dry weight of sand. The fibers with a circular cross – section have a length

DOI: 10.1201/9781003299127-105

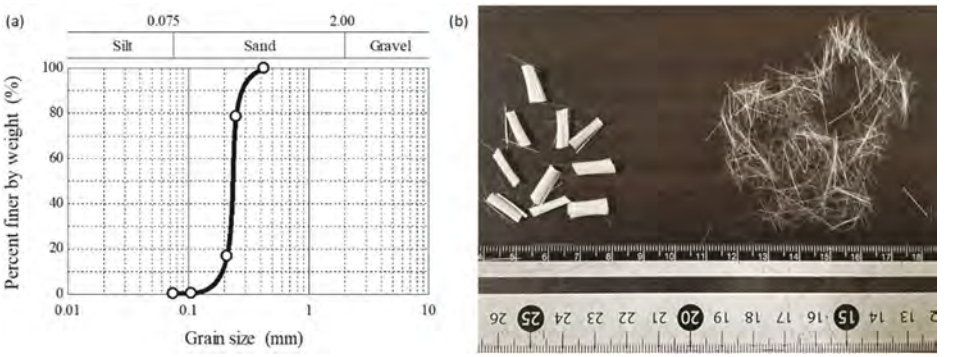

Figure 1. Grain size distribution of Toyoura sand (a) and photograph of PVA fibers (b).

of l_f = 12 mm and diameter of d = 0.04 mm; specific gravity G_f = 1.3; tensile strength 1560 MPa; and elastic modulus E_f = 41 GPa.

Reinforced samples were prepared by mixing fibers and sand with a scoop in a dry condition. All specimens, including unreinforced sand, were placed in one layer by side tapping in a dry condition. Distribution of fibers were considered to be random. The homogeneous distribution was checked by the exhumed sample analysis and the reproducibility of test results was controlled in all series of experimentations (Ganiev et al. 2022a).

2.2 *Testing conditions*

Consolidated undrained ($\overline{CU}$) triaxial compression and extension tests with the pore water pressure (PWP) measurement were performed on unreinforced, 0.2% and 0.4% fiber-reinforced sand specimens placed in a medium loose condition with a relative density of D_r = 40 %. Specimen were consolidated and sheared under p'_0 = 50, 100, 200 kPa confining pressures in compression and under p'_0 = 100, 200kPa in extension. The shearing was performed until 25 % axial strain in compression and 20% axial strain in extension with the rate of 0.5 % strain per minute.

3 TEST RESULTS AND DISCUSSIONS

3.1 *Undrained triaxial compression*

Figures 2 to 4 show the $\overline{CU}$ compression test results performed under p'_0=50, 100, 200kPa confining pressures, respectively. In q–ε_a curves, with the increase in fiber content, fiber-reinforced specimens experienced a higher deviator stress q at the end of shearing compared to unreinforced sand. However, fiber-reinforced specimens experienced smaller initial stiffness with the increase in fiber content for all confining pressures. The difference in the initial stiffness became more obvious at a higher confining pressure (Figures 2a,3a and 4a). This behavior can also be observed in stress paths curves (Figures 2b,3b and 4b), where fiber inclusions caused a higher drop of mean effective stress p'. Despite having a lower initial stiffness and a higher drop of p' until the phase transformation point, the fiber-reinforced specimens reached higher stress ratios. Furthermore, the stress ratio increased with the increase in fiber content, and even fiber-reinforced sand speci-mens, same as unreinforced sand, reached to their definite stress ratio value at the end of tests despite being sheared under different confining pressures. The higher value of initial stiffness of unreinforced sand specimens is related to the higher degree of the initial anisotropy condition with deposition method by side tapping (vibration) which created a highly anisotropic sample with more preferred orientation of sand particles. In turn, fiber inclusions prevent preferred orientation of sand particles and created

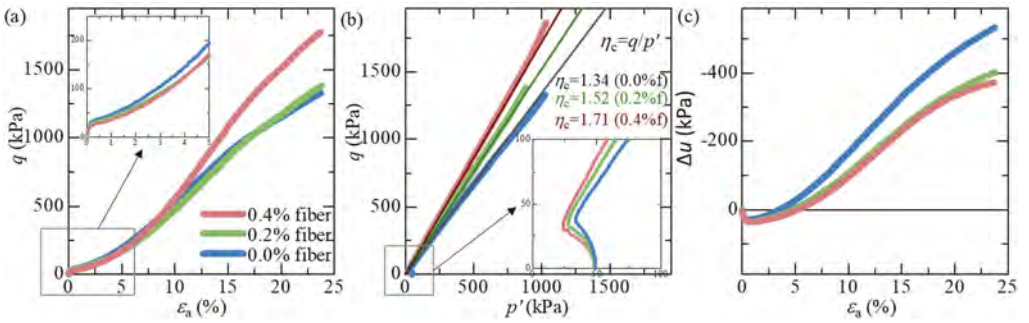

Figure 2. Undrained triaxial compression tests performed under p_0'=50kPa: (a) deviatoric stress – axial strain response, (b) stress paths and (c) excess pore water pressure – axial strain response.

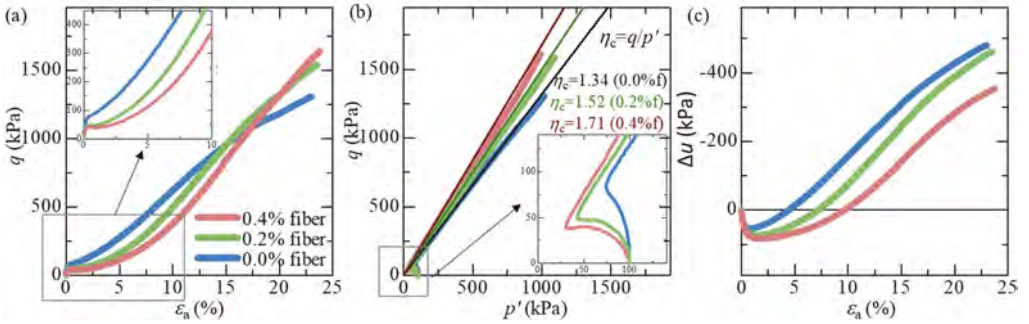

Figure 3. Undrained triaxial compression tests performed under p_0'=100kPa: (a) deviatoric stress – axial strain response, (b) stress paths and (c) excess pore water pressure – axial strain response.

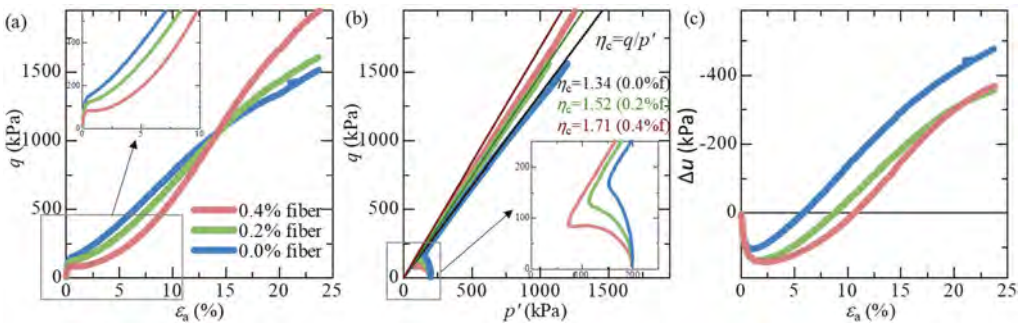

Figure 4. Undrained triaxial compression tests performed under p_0'=200kPa: (a) deviatoric stress – axial strain response, (b) stress paths and (c) excess pore water pressure – axial strain response.

less anisotropic specimens. Similar outcomes were presented in drained compressive behavior of fiber-reinforced sands (Ganiev et al. 2022b).

On the Δu–ε_a curves in Figures 2c,3c and 4c there is a clear tendency for a higher positive PWP at a lower axial strains and a less generated negative PWP at the end of shearing (hardening interval) as fiber content increased. Furthermore, a negative PWP decreased with the increase in confining pressure for all fiber contents including unreinforced sand, i.e., the higher the confining pressure the higher the initial positive PWP and the smaller the final

negative PWP. According to the results, it can be assumed that fibers act as contracting agents, positively contributing to the confining pressure by producing tensile forces in them at higher strains.

3.2 *Undrained triaxial extension*

Figures 5 and 6 show the consolidated $\overline{CU}$ extension test results performed under p'_0=100, 200kPa confining pressures, respectively. Tensile strength of fiber-reinforced sand was higher compared to unreinforced sand under both confining pressures, and fiber-reinforced specimens reached to higher residual stress ratios. In deviatoric stress-axial strain curves (Figures 5a and 6a), there was no initial stiffness decrease in fiber-reinforced specimens compared to unreinforced sand as in compression experiments. Furthermore, reduction of mean effective stresses of fiber-reinforced sand during the softening stage was smaller compared to unreinforced sand. Therefore, considering stress paths in compression and extension experiments under the same confining pressure simultaneously, it can be concluded that unreinforced specimens prepared by dry vibration resulted in a higher initial anisotropy, whereas the increase in fiber contents led to decrease of the anisotropy. Reduction of the deviator stresses q approximately at ε_a=15% was due to the shear band formation, while no explicit strain localization observed in compression.

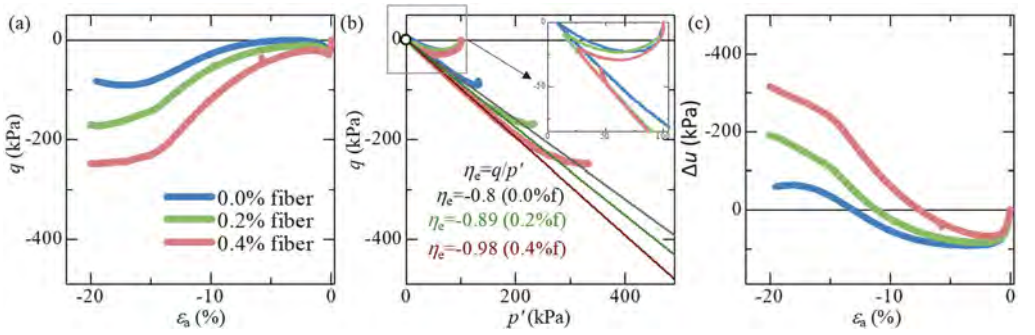

Figure 5. Undrained triaxial extension tests performed under p_0'=100kPa: (a) deviatoric stress – axial strain response, (b) stress paths and (c) excess pore water pressure – axial strain response.

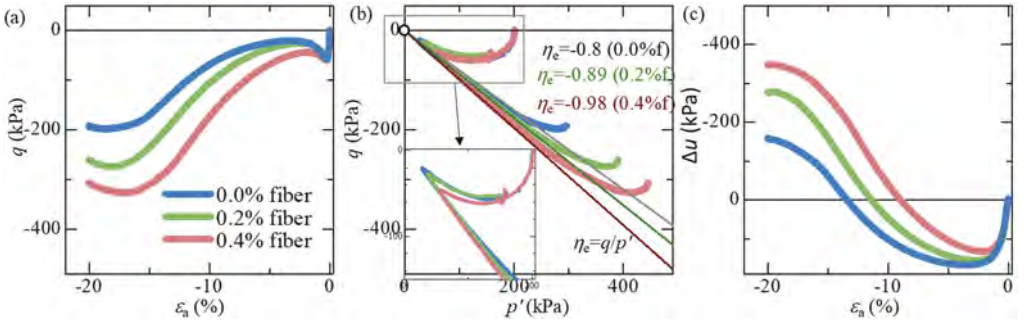

Figure 6. Undrained triaxial extension tests performed under p_0'=200kPa: (a) deviatoric stress – axial strain response, (b) stress paths and (c) excess pore water pressure – axial strain response.

4 CONCLUSION

The followings are main conclusions from the presented results and discussions:

Dry deposition of sand specimen by side tapping (vibration) created a highly anisotropic sample with more preferred orientation of sand particles. In case of fiber-reinforced sand, fiber inclusions prevented preferred orientation of sand particles and reduced the degree of initial anisotropy.

In undrained triaxial test fibers were effective in both compression and extension resulting in the increase of compressive and tensile strength with the increase in fiber contents. Also, there was a clear tendency for the increase in residual stress ratio with the increase in fiber content. Furthermore, the higher positive PWP generation at the softening stage and smaller value of negative PWP at the end of shearing clarified the contractive role of fibers.

Finally, the smaller difference in stress paths in compression and extension of fiber-reinforced sand compared to unreinforced sand might be one of the evidence that fibers reduce the initial anisotropy.

REFERENCES

Consoli, N.C., Festugo, L. & Heineck, K.S. 2009. Strain-hardening behaviour of fibre-reinforced sand in view of filament geometry. *Geosynth. Int*. 16 (2), 109–115.

Diambra, A., Ibraim, E., Russell, A.R. & Muir Wood, D. 2013. Fibre reinforced sands: from experiments to modelling and beyond. *Int. J. Numer. Anal. Meth. Geomech*. 37 (5), 2427–2455.

Ganiev, J., Yamada, S., Nakano, M. & Sakai, T. 2022a. Effect of fiber-reinforcement on the mechanical behavior of sand approaching the critical state. *J. Rock Mech. Geotech. Eng*. 14(4), 1241–1252.

Ganiev, J., Nakano, M. & Sakai, T. 2022b. Numerical analysis of drained compression behavior of fiber-reinforced sand based on a soil skeleton structure concept. *Comput. Geotech*. 148:104789.

Gray, D.H. & Ohashi, H. 1983. Mechanics of fiber reinforcement in sands. *J. Geotech. Eng. ASCE* 109 (3), 335–353.

Michalowski, R.L. & Zhao, A. 1996. Failure of fiber-reinforced granular soils. *J. Geotech. Eng. ASCE* 122(3), 226–234.

Smart Geotechnics for Smart Societies – Zhussupbekov, Sarsembayeva & Kaliakin (Eds)
© 2023 The Author(s), ISBN 978-1-003-29912-7
Open Access: www.taylorfrancis.com, CC BY-NC-ND 4.0 license

Scaled model test on cyclic response of footing on geotechnical seismic isolation layer

Dhanya JS.
L. N. Gumilyov Eurasian National University, Astana, Kazakhstan

Subhadeep Banerjee & A. Boominathan
Indian Institute of Technology Madras, Chennai, India

ABSTRACT: Sand-rubber mixture (SRM) is widely considered as an energy-dissipating layer for vibration mitigation in soils. The present study is focused on using the SRM as an energy dissipation layer below building foundation referred to as the Geotechnical Seismic Isolation layer (GSI) which acts as a buffer to incoming vibrations. Geosynthetic reinforcement is included in the above GSI system to accentuate the damping mechanism and prevent seismic settlements during shaking. The present study aims to experimentally evaluate the dynamic response of the geogrid reinforced SRM-GSI system through scaled model tests. Model footing resting on the geogrid reinforced SRM-GSI system was subjected to continuous cyclic loads and the results are evaluated in terms of load-settlement response for different cycles of loading. It was observed that the geogrid reinforced SRM-GSI system is crucial in reducing the seismic settlement at various loading cycles and the soil-foundation system's overall dynamic response.

1 INTRODUCTION

Geotechnical seismic isolation is a recent trend in earthquake geotechnical engineering that aims to protect buildings and structures from the detrimental effects of earthquakes using a low-stiffness isolation layer beneath the building. The basic principle behind this method is to isolate the structure from the ground, so that the vibrations of an earthquake do not transfer to the building. In conventional base isolation systems, energy dissipation is achieved through the use of isolation bearings (made of natural rubber and lead) are placed between the building structure and foundation. On the other hand, geomaterials such as rubber, geosynthetics, sand, and gravel are often used in GSI method as they provide a flexible and durable barrier between the building foundation and the ground, and they offer a cost-effective and sustainable alternative to traditional isolation systems (Tsang 2008; Pitilakis et al. 2015; Dhanya et al. 2020; Forcellini 2020). One common practice is the use of sand mixed with rubber particles from crushed recycled tires, referred to as Sand-Rubber Mixture (SRM), for seismic isolation. The SRM provides a combination of low stiffness, high flexibility, and damping that helps to dissipate the energy of seismic waves below the foundation level (Tsang 2021).

The use of rubber particles from scrap tires is becoming increasingly popular in civil engineering applications due to its environmental advantages and the large amount of scrap tires produced worldwide. Research have showed that using shredded scrap tires mixed with soil is an effective solution as a lightweight back-fill material for retaining walls, highway embankments, and as vibration absorption layers for underground structures and foundations (Kirzhner et al. 2006; Hazarika et al. 2010). The damping ratio of SRM at small strains is higher than that of pure granular soils and it increases with higher rubber fractions and larger shearing strain amplitudes making it an ideal choice for vibration mitigation studies (Senetakis et al. 2012). Studies

DOI: 10.1201/9781003299127-106

have also shown that increasing the rubber fraction in a granular sand-rubber mixture beyond 30% leads to a decrease in the mobilization peak and large-strain angle of friction of the mixture, making the mechanical response more rubber-like (Zornberg et al.2004).

In general, SRM exhibits a higher degree of compressibility compared to pure sand due to the presence of elastic and deformable rubber particles. This results in immediate settle-ment similar to that of sand during static loading. However, the settlement response under repeated loading needs to be thoroughly examined when SRM is utilized as GSI layer be-low foundations when considering building safety under seismic and other ground borne vibrations. Several researchers have conducted extensive laboratory studies to investigate the cyclic behavior of SRM and the influence of rubber content and particle size on the shear strength and deformation of the mixture (Ehsani et al. 2015; Senetakis et al. 2012). However, model studies on the response of footings resting on GSI layers under repeated loading are limited. Therefore, the current study aims to experimentally investigate the be-havior of a scale model footing on a sand-rubber mixture GSI bed under cyclic loading conditions in terms of load-settlement response.

2 SCALED MODEL STUDY

2.1 *Materials*

In this study, river sand sourced from Chennai, India that was classified as poorly graded sand (SP) per IS: 1498 (BIS 1970) was used. The scrap rubber tyre with steel reinforcements removed and fragmented into angular-shaped granulated tire particles with a size less than 4.75mm and were also classified as an equivalent of poorly graded sand (SP). Research has shown that a rubber content of 20% to 35% (gravimetric) mixed with soil is optimal for achieving maximum shear strength (Edil and Bosscher 1994; Rao and Dutta 2006). Additionally, SRM with a 30% rubber content has been found to exhibit a high damping ratio and adequate stiffness compared to higher rubber contents (Senetakis et al. 2012; Dhanya et al. 2019, 2022). Therefore, in this study, SRM with a rubber content of 30% was used. Undrained triaxial test results on the sand the SRM samples showed peak internal friction angle of 37.5° and 28.5 ° respectively.

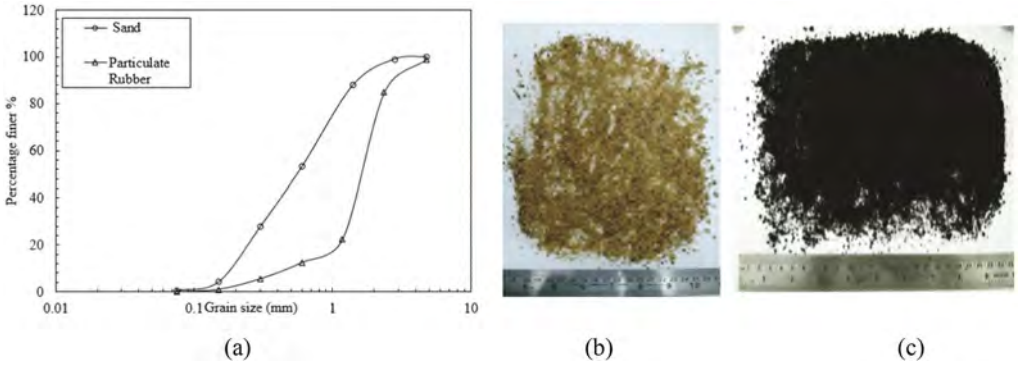

Figure 1. (a) Grain size distribution for sand and rubber (b) sand (c) rubber granules.

2.2 *Test setup and procedure*

Figure 2 presents a general overview of the laboratory test, including the testing tank and test bed. Load tests were performed on a model footing that was placed on a GBI layer made of SRM, in a laboratory setup that simulates a sand-bed tank. The test tank was made of steel and had dimensions of 1m x 1m x 1m. The model square footing was constructed using a square steel plate with a dimension of 100mm and a thickness of 10mm based on model scaling laws of similitude by Wood (2004). The steel plate was connected to pneumatic actuators

that were attached to a reaction frame composed of steel beams and columns. The loading was applied on the load plate in a displacement-control mode using a computer-controlled pneumatic actuator. The load was measured using an electronic load cell with a capacity of 20 kN and the displacement was measured by a displacement transducer (LVDT). For more detailed information on the arrangements of the testing apparatus and procedure, please refer to the work of Dhanya et al. (2019).

Initially, the load tests were conducted on a footing resting on a sand bed compacted at a relative density of 85%. The sand bed was prepared in layers of 0.1m each, using the sand pluviation/rainfall technique (Cresswell et al. 1999) where the sand was poured from a fixed height to achieve the desired density. The next series of tests were conducted on a footing placed on a GSI layer, which was prepared by excavating the required depth and size of the GSI layer in the sand bed and backfilling it with SRM. An aluminium sheet box of the plan size of the GSI bed was placed inside the sand bed to prevent caving in and control compaction during the preparation of the GSI layer. The excavated space was filled with SRM mixture and compacted in layers of 25mm to achieve a relative density of 85%. The depth of the GSI layer was varied as 0.1 B and 0.2 B, where B is the width of the footing while the width of the GSI layer was kept constant as 3B.

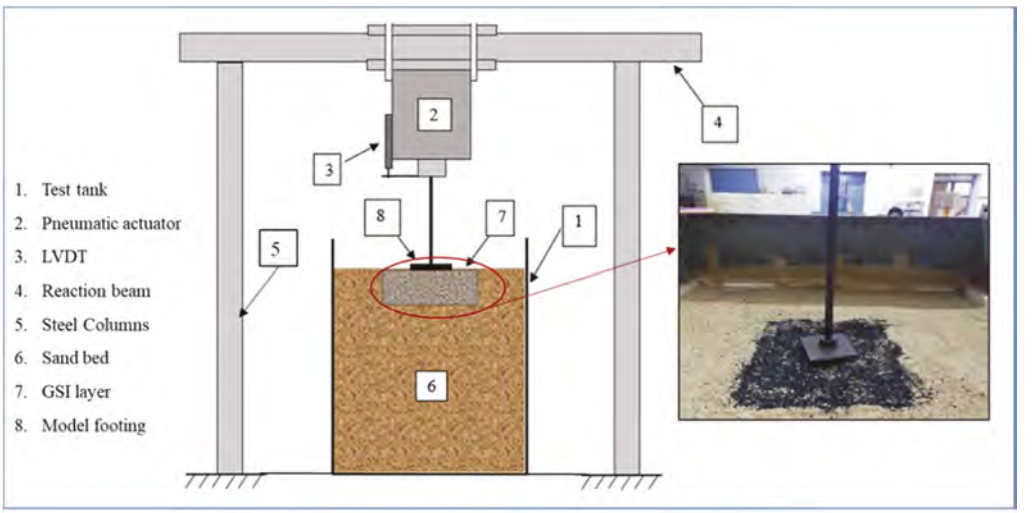

Figure 2. Experimental setup of model footing placed on GSI bed in the test tank.

During the testing phase, the following loading pattern is applied to the soil bed: first, a static load is applied at a gradual rate until it reaches 100 kPa. The static load is then maintained until no further settlement occurs or the rate of settlement is negligible. Next, a cyclic load, which is sinusoidal with a frequency of 1 Hz and is applied until the rate of settlement becomes negligible. The static load of 100 kPa was chosen as it simulates the weight of a low-rise structure, which is often the minimum factor of safety adopted in the field. The ratio of dynamic load amplitude to the static load amplitude is maintained as 0..3 as it is commonly found in seismic and machine vibration problems, as reported in Tafreshia & Dawson (2012).

3 RESULTS AND DISCUSSION

The focus of this study is to examine the settlement of a foundation specifically caused by cyclic loading. An initial monotonic loading is applied to simulate the weight of the structure and foundation, but elastic settlement from static loading is not considered. Figure 3 presents the variation of peak cyclic settlement of footing (S_c) normalized with the footing width (B)

with the number of load cycles under cyclic loading for the footing with and without GSI cases. The general characteristics of loading can be categorized into three zones: a rapid settlement in the initial cycles, a secondary slow settlement until a critical point, and a minimal rate of settlement (Zone C). It is observed that there is a significant increase in settlement in the first few cycles of loading, particularly in the GSI layers, and it is noted that the cyclic settlements are higher for GSI layers of greater depth. However, the rate of settlement decreases and becomes minimal around 1000-1500 cycles of loading. In general, it can be inferred that the stiffness of the GSI layer increases as the number of loading cycles increases, mainly due to particle reorientation and densification of the sand-SRM matrix. This is caused by the deformation of rubber particles in the SRM matrix which fill in the voids in the sand skeleton.

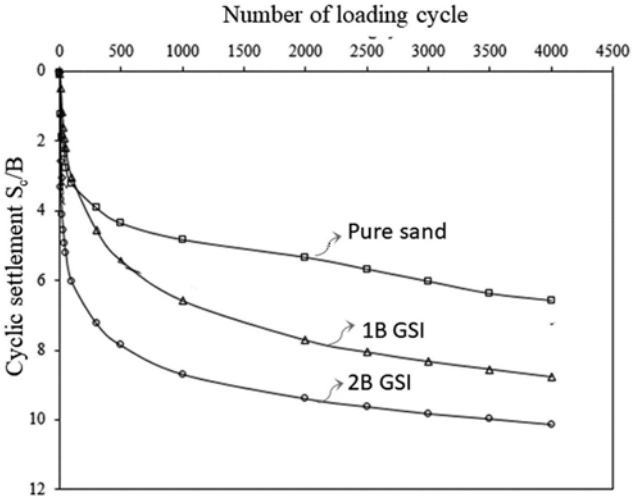

Figure 3. Variation of footing settlement (Sc/B) with number of load cycle for Sand and GSI.

Figure 4 presents the variation of load with the cyclic settlement under cyclic loading for the footing with and without GSI cases. The figure illustrates that the footing response on the sand bed demonstrated a narrow hysteresis loop, indicating hardening of the sand bed with minimal energy dissipation and no plastic deformation. On the other hand, the GSI system exhibited a broader hysteresis loop compared to the sand bed, which suggests higher energy dissipation by the GSI layer during the cyclic loading phase. Furthermore, the hysteresis loop of the GSI bed shows that the loop becomes consistent after a certain number of cycles, indicating densification of the GSI bed and a decrease in plastic deformation.

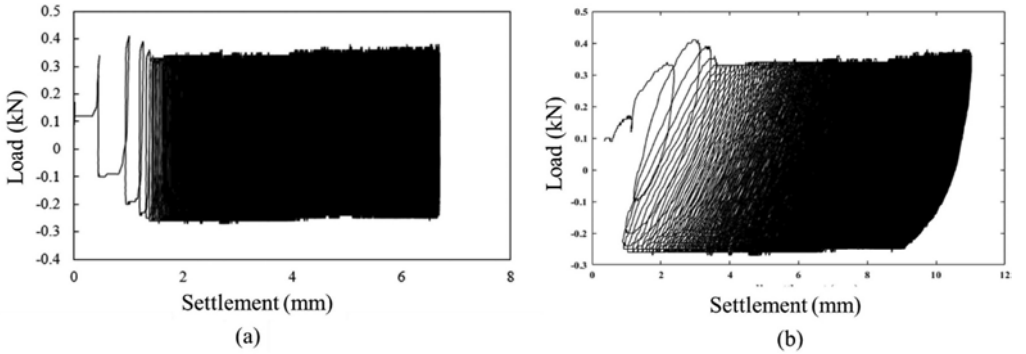

Figure 4. Load vs settlement hysteresis loop: a) Sand bed (b) GSI bed of 2B depth.

4 CONCLUSIONS

The research presented demonstrates the performance of the sand-rubber mixture (SRM) GSI system under both static and repeated loads. The results show that during the initial phase of loading, the cyclic settlement is more prevalent in the GSI system compared to the case without GSI. It is also observed that while the settlement increases with the thickness of the GSI bed, it eventually stabilizes at higher cycles of loading. The high hysteris damping mechanism of GSI that facilitates energy dissipation and vibration mitigation is evident during the cyclic loading, making it critical for vibration isolation applications. When choosing low stiffness materials for the GSI bed, such as the sand-rubber mixture layer, it is important to consider the compressibility response of the material and optimize the thickness accordingly.

The future scope of this research includes assessing the cyclic response of the SRM GSI system reinforced with geosynthetics such as geogrid and geocells which can greatly reduce cyclic settlements and enhance the applicability of SRM-GSI systems without compromising its serviceability and performance. Additional cyclic load testing on the model footing should be performed to evaluate the combined response of the geosynthetic reinforced SRM-GSI system in vibration mitigation studies in selecting appropriate parameter values for the design of footings on GSI systems.

REFERENCES

BIS (Bureau of Indian Standards). 1970. *Classification and identification of soils for general engineering purpose*. IS:1498-1970. Manak Bhawan, New Delhi: BIS.

Cresswell, A., M. E. Barton, and R. Brown. 1999. Determining the maximum density of sands by pluviation. *Geotech. Test. J*. 22 (4): 324–328.

Dhanya, J. S., A. Boominathan, and S. Banerjee. 2019. Performance of geo-base isolation system with geogrid reinforcement. *Int. J. Geo- mech*. 19 (7): 04019073.

Dhanya, J. S., A. Boominathan, and S. Banerjee. 2020. Response of low- rise building with geotechnical seismic isolation system. *Soil Dyn. Earthquake Eng*. 136: 106187.

Dhanya, J. S., A. Boominathan, and S. Banerjee. 2022. Investigation of geotechnical seismic isolation bed in horizontal vibration mitigation. *J. Geotech. Geoenviron. Eng*., 2022, 148(12): 04022108.

Edil, T., and P. J. Bosscher. 1994. Engineering properties of tire chips and soil mixtures. *Geotech. Test. J*. 17 (4): 453–464.

Ehsani, M., Shariatmadari, N. and Mirhosseini, S. M. 2015. Shear modulus and damping ratio of sand-granulated rubber mixtures. *J. Cent. South Univ*., 22, 3159–3167.

Forcellini, D. 2020. Assessment of geotechnical seismic isolation (GSI) as a mitigation technique for seismic hazard events. *Geosciences*, 10 (6): 1–14.

Hazarika H, Yasuhara K, Kikuchi Y, Karmokar AK, Mitarai Y. 2010. Multifaceted potentials of tire-derived three dimensional geosynthetics in geotechnical applications and their evaluation. *Geotext Geomembr*., 28:303–15.

Kirzhner F, Rosenhouse G, Zimmels Y. 2006. Attenuation of noise and vibration caused by underground trains, using soil replacement. *Tunn Undergr Space Technol*., 21(5):561–7.

Moghaddas Tafreshia, S.N., Dawson, A.R., 2012. A comparison of static and cyclic loading responses of foundations on geocell-reinforced sand. *Geotext. Geomembranes*, 32 (32), 55–68.

Pitilakis, K., S. Karapetrou, and K. Tsagdi. 2015. Numerical investigation of the seismic response of RC buildings on soil replaced with rubber– sand mixtures. *Soil Dyn. Earthquake Eng*. 79 (Dec): 237–252.

Rao, G. V., and R. K. Dutta. 2006. Compressibility and strength behaviour of sand-tyre chip mixtures." *Geotech. Geol. Eng*. 24 (3): 711–724.

Senetakis K, Anastasiadis A, Pitilakis K, Souli A. 2012. Dynamic behavior of sand/ rubber mixtures, Part II. *J ASTM Int*.,9(2), 1–13.

Tsang, H. 2008. Seismic isolation by rubber–soil mixtures for developing countries. *Earthquake Eng. Struct. Dyn*. 37 (2): 283–303.

Tsang, H. H., D. P. Tran, W. Y. Hung, K. Pitilakis, and E. F. Gad. 2021. Performance of geotechnical seismic isolation system using rubber-soil mixtures in centrifuge testing. *Earthquake Eng. Struct. Dyn*. 50 (5): 1271–1289.

Wood, D. M. 2004. *Geotechnical modelling*. Abingdon, UK: Spon.

Zornberg, J. G., A. R. Cabral, and C. Viratjandr. 2004. Behaviour of tire shred-sand mixtures. *Can. Geotech. J*. 41 (2): 227–241.

Smart Geotechnics for Smart Societies – Zhussupbekov, Sarsembayeva & Kaliakin (Eds)
© 2023 The Author(s), ISBN 978-1-003-29912-7
Open Access: www.taylorfrancis.com, CC BY-NC-ND 4.0 license

Modeling of sub-ballast and geogrid interaction

A.F. Kolos & A.V. Petriaev
St. Petersburg State Transport University, St. Petersburg, Russia

E.V. Fedorenko
LLC NIP Informatics, St. Petersburg, Russia

ABSTRACT: The article presents the modeling results of the soil and geosynthetics interaction. To achieve this goal, a mathematical model was developed and FEM calculations were performed using the Plaxis program. The results of the calculations showed the coincidence of the soil behavior in the course of physical and mathematical modeling. The results of calculations using the Plaxis software package confirmed the influence of the angle of internal friction and the angle of dilatancy on the increase in the pulling force due to the attachment of a larger volume of soil. The influence of the geogrid ribs on the stress-strain state of the stabilized soil massif was estimated. Reducing the number of ribs leads to the concentration of shear zones along the web of the geogrid in close proximity to it, which reduces the pull-out resistance.

1 INTRODUCTION

The laying of geosynthetic materials is one of the effective stabilizing methods for sleeper bearing with minimal time for all types of track work. Previous studies have shown that the effect of using geosynthetic material is to increase the bearing capacity and reduce the deformability of the railway track (Gobel and Weisemann, 1994; Kolos et al., 2021; Brown et al., 2007; Indraratna et al., 2011; Petriaev, 2019; Esmaeili et al., 2017).

The approach to designing a foundation reinforced by geosynthetics depends on understanding the function and mechanism of mechanical stabilization of granular materials. The geosynthetics property such as stiffness, size and shape of cells, ribs shape and nodes, etc., has a great importance (Petriaev, 2020; Alagiyawanna et al., 2012). The interaction mechanisms will vary depending on the properties of the geosynthetics, as well as the properties of the stabilized aggregate, loading conditions, etc. (Hossain et al., 2012; Liu et al., 2009; Biabani and Indraratna, 2015; Fedorenko and, 2017).

The mathematical model complications leads to the need to obtain additional soil parameters during an engineering and geological survey (Petriaev, 2017; Penkov and Fedorenko, 2020). The natural variation of the foundation soils properties leads to a decrease in the reliability of the substructure behavior prediction in natural conditions. If a new model of soil behavior describes the features of its operation, which significantly affect the design calculation results, then its development can be considered justified. Numerical analysis is an alternative way to study stresses and deformations in the sub ballast, stabilized by geosynthetics.

The purpose of this study is to propose an approach to modeling a geogrid in confined by soil conditions. This is achieved in two stages. First of all the numerical model is verified by the test results, and then it is used to study the detailed behavior of the geogrid in the soil massive.

DOI: 10.1201/9781003299127-107

2 MATERIALS AND METHODS

The models presented in this study were performed by using Plaxis finite element software.

The design scheme shown in Figure 1 is presented in the form of a box with soil inside and a compressive load applied on the top.

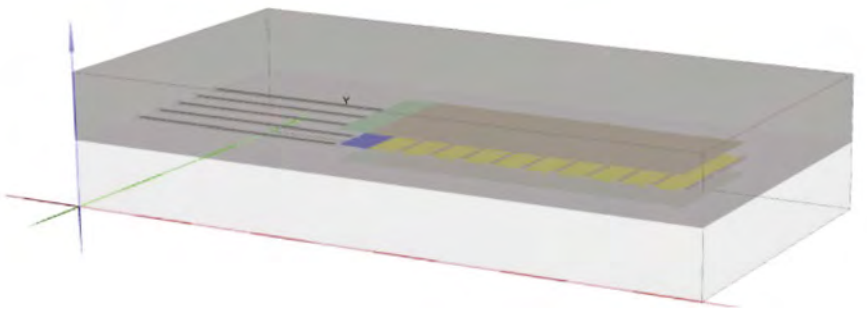

Figure 1. The scheme for study the interaction of geosynthetic material and soil during pulling.

To implement the process of pulling out, the method of fastening the geogrid element using the node-to-node anchor element is considered with the wall of the box, which in PLAXIS is a boundary condition with the prohibition of moving points horizontally (only vertical movements). The anchor as an element has only two contact points with the finite elements grid, so changing its length will have an effect only at the point at the other end, i.e. at the point of contact with the geosynthetic material. The change in the length of the anchor (compression) is set using the pre-tension function. For convenience, the pre-tension is set to 1000 kN.

The geosynthetic is attached to an inextensible plate (plate element with high rigidity and low thickness), which can be pulled by one or more rod elements (node-to-node element) due to the pre-tension set by it. The plate element allows you to transfer a uniform force from the rods to the geotextile. The ground is located on top and bottom of the geosynthetic and contact interaction is carried out due to the interface element. Moreover, zero friction is set for the interface above the plate. Such a system makes it possible to circumvent the problem of geomaterial going beyond the boundary conditions when modeling stretching. Additionally, transverse ribs of plate elements with a height of 5 cm and with distance of 10 cm are set on the web of geosynthetic material. Thus, the design considered below, will allow us to assess the reliability of such a simplification in relation to real tests and it will provide information about the geogrid elements forces and deflections, the the parameters of which are set in the traditional way for these materials and taking into account specific features. This approach is more feasible in practice, compared with the way to model a geogrid with rod elements on a grid. To model the soil, an elastic-plastic model with HardeningSoilSmall hardening was used, the yield surface of which is not fixed in the space of the main stresses and can expand due to plastic deformation (Hardin and Drnevich, 1972; Schanz et. al., 1999).

The interface element is used to simulate contact interaction. The surface contact roughness is modeled by selecting a suitable value of the strength reduction coefficient *Rinter*.

The geogrid particles friction coefficient is an important input parameter, which is the interaction between the geogrid and the ground. In numerical tests, it was adjusted iteratively until satisfactory results were obtained in comparison with the corresponding experimental data. The geogrid particles friction coefficient was found in this study to be equal to 1.0 and this parameter was used in further numerical tests. The parameters of the HSS model given in Table 1 were used for modeling.

Table 1. HSS model parameters.

E_{50}^{ref}, MPa	E_{oed}^{ref}, MPa	E_{ur}^{ref}, MPa	m	C, MPa	φ, °	ψ	$\gamma_{0,7}$	G_0^{ref}, MPa
30	30	150	0,5	0,2	30	0	$1 \cdot 10^{-4}$	70

3 RESULTS AND DISCUSSION

The boundary conditions were defined in such a way that nodes along the vertical boundaries can move freely only in the vertical direction. The nodes in the base are fixed against displacement in all directions.

The dependences of displacements on pulling forces was obtained as a result of numerical analysis and laboratory tests, which show a relatively close match for comparative purposes.

For small displacements, both numerical and experimental results were the same. However, with displacement of more than 10 mm, the results begin to diverge. The proximity of the results shows the suitability of the developed model.

The effect of the ribs placement step is considered by the example of dilatant behavior along the isofield of the porosity coefficient and is shown in Figures 2, 3. At the initial stage, e = 0.5, internal friction angle 50°, angle of dilatancy 20°. The pre-tension is set to 1000 kN. Further, only soil decompression is shown, i.e. e>0.5. Two variants of the ribs placement step are considered: 10 and 30 cm. The figures show the frontal area in front of the first edge, in which the flattening zone is formed (on the left). This zone has values of porosity coefficient less than 0.5, so it is excluded from the color display.

The maximum values of the porosity coefficient correlate with the areas of shear deformations and are concentrated above the ribs. Dilatant properties of compacted soil lead to volumetric expansion of the soil at these points, its decompression with an increase in shear deformations.

Reducing the number of ribs leads to the concentration of shear zones along the geogrid web in close proximity to it, which reduces the resistance to pulling.

The dependence of the pulling force on the ribs number is shown in Figure 4. With an increase in the number of transverse elements, the tensile forces at the loaded ends increase, which clearly shows the contribution of the transverse elements to the overall resistance to pulling.

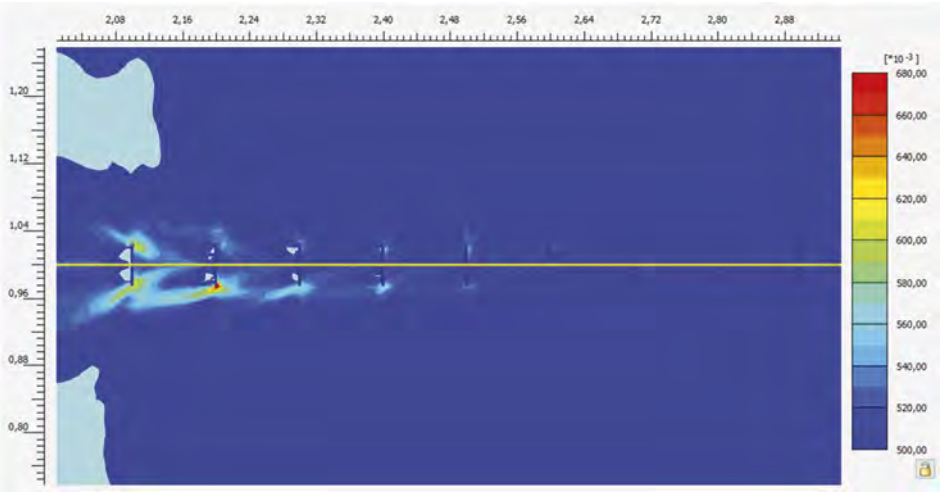

Figure 2. Distribution of porosity coefficient more than 0.5 along the geogrid for ribs step 10 cm.

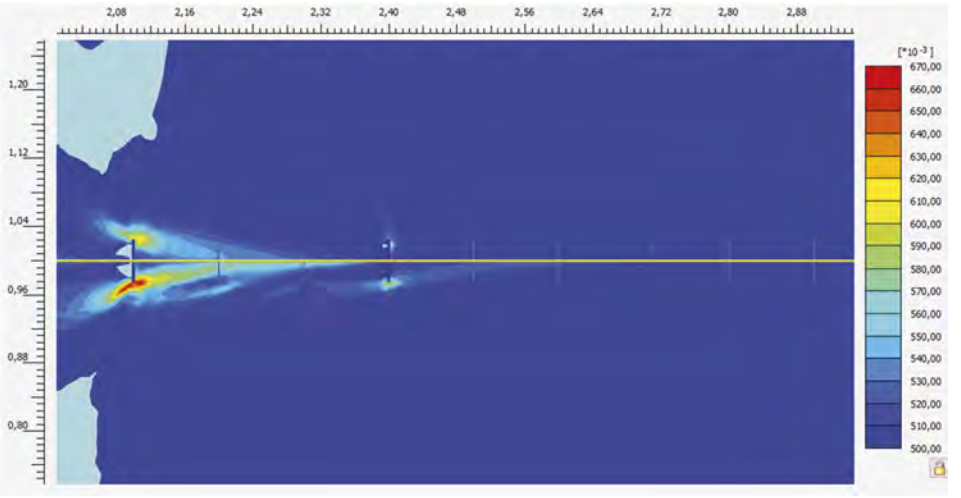

Figure 3. Distribution of porosity coefficient more than 0.5 along the geogrid for ribs step 30 cm.

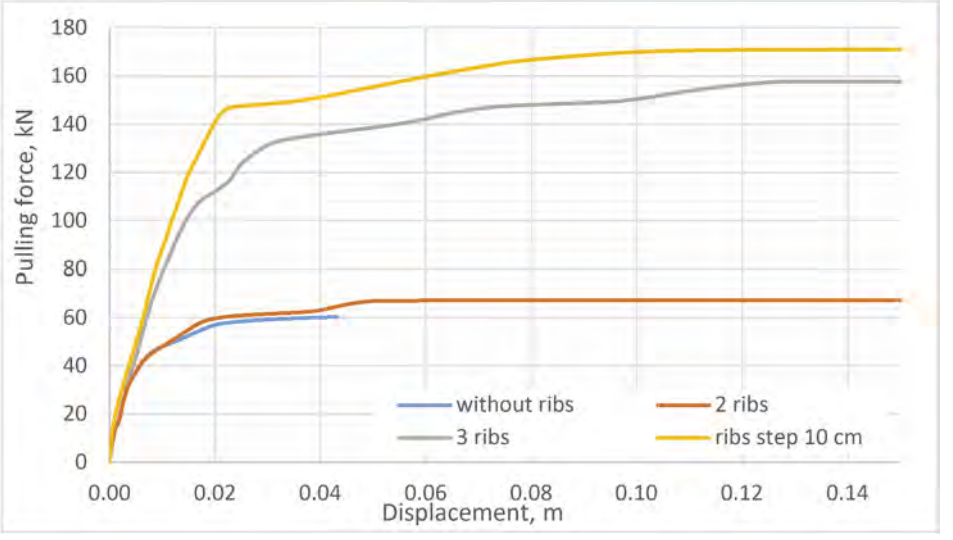

Figure 4. Shear deformations of the variant with 30 cm step.

4 CONCLUSIONS

The conducted studies have shown the possibility of using the developed model to analyze the mechanisms of interaction between the geogrid and the soil.

The results of calculations using the Plaxis software package confirmed the influence of the angle of internal friction and the angle of dilatancy on the increase in the pulling force due to the attachment of a larger volume of soil.

Reducing the number of ribs leads to the concentration of shear zones along the web of the geogrid in close proximity to it, which reduces the pull-out resistance.

REFERENCES

Alagiyawanna, A.M.N., Sugimoto, M., Sato, S., Toyota, H., 2001. Influence of longitudinal and transverse members on geogrid pullout behavior during deformation. *Geotextiles and Geomembranes 19*: 483–507.

Biabani, M., Indraratna, B., 2015. An evaluation of the interface behaviour of rail subballast stabilised with geogrids and geomembranes. *Geotextiles and Geomembranes 43*: 240–249.

Brown, S.F., Kwan, J., Thom, N.H., 2007. Identifying the key parameters that influence geogrid reinforcement of railway ballast. *Geotextiles and Geomembranes 25*: 326–335.

Esmaeili, M., Zakeri, J.A., Babaei, M., 2017. Laboratory and field investigation of the effect of geogrid-reinforced ballast on railway track lateral resistance. *Geotextiles and Geomembranes 45*: 23–33.

Fedorenko, E., Tiep, V., 2017. A comparison of options for determining pseudo-coupling in reinforced soil. *Roads and bridges*. Publishing house: Russian Road Research Institute, Moscow. ISSN: 1815-896X, 38: 218–230.

Gobel, C.H., Weisemann, U.C., 1994. Effectiveness of a Reinforcing Geogrid in a Railway Subbase under Dynamic Loads. *Geotextiles and Geomembranes 13*: 91–99. https://www.sciencedirect.com/science/article/abs/pii/0266114494900418

Hardin, B., Drnevich, V., 1972. Shear modulus and damping in soils: Design equations and curves. *Proc. ASCE: Journal of the Soil Mechanics and Foundations Division*: 667–692.

Hossain, M.B., Hossain, M.Z., Sakai, T., 2012. Interaction Properties of Geosynthetic with Different Backfill Soils. *International Journal of Geosciences:* 1033–1039.

Indraratna, B., Ngo, N.T., Rujikiatkamjorn, C., 2011. Behavior of geogrid-reinforced ballast under various levels of fouling. *Geotextiles and Geomembranes 29*: 313–322.

Kolos, A., Petriaev, A., Kolos, I., Konon., A., 2021. Reducing of negative heavy axle load impact on the railway track structure. *Scientific Conference on Railway Transport and Engineering*. AIP Conference Proceedings 2389 (1). DOI 10.1063/5.0063962

Liu, C., Ho, Y., Huang, J., 2009. Large scale direct shear tests of soil/PET-yarn geogrid interfaces. *Geotextiles and Geomembranes 27*: 19–30.

Penkov, D., Fedorenko, E., 2020. On the issue of obtaining initial data for the hardening soil model. *Soil Science 2(15)*.

Petriaev, A., 2017. Modeling the behavior of geosynthetic material in a railway roadbed. *Transport of the Urals 1(52)*: 61–66.

Petriaev, A., 2019. Laboratory and Field Investigation of Railway Ballast, Stabilized by Geosynthetics. Ebook: *Geotechnical Engineering in the XXI Century: Lessons learned and future challenges. Proceedings of the XVI Pan-American Conference on Soil Mechanics and Geotechnical Engineering (XVI PCSMGE)*, IOS Press: 1611–1618.

Petriaev, A., 2020. Modeling railway roadbed reinforcement. *Lecture Notes in Civil Engineering*, 27–35.

Rowe, P., 1969. The stress-dilatancy relation for static equilibrium of an assembly of particles in contact. *In Proc. Roy. Soc. A*. 269:500–527.

Schanz, T., Vermeer, P.A., Bonnier, P.G., 1999. The hardening soil model: Formulation and verification, *Beyond 2000 Comput. Geotech. Ten Years PLAXIS Int. Proc. Int. Symp*. Amsterdam: 281–296, doi: 10.1201/9781315138206-27

Smart Geotechnics for Smart Societies – Zhussupbekov, Sarsembayeva & Kaliakin (Eds)
© 2023 The Author(s), ISBN 978-1-003-29912-7
Open Access: www.taylorfrancis.com, CC BY-NC-ND 4.0 license

Case study of geotextile tubes infilled with recycled excavated soft soil for coastal bund

S.H. Chew & J.M. Soh
National University of Singapore, Singapore

Y.C. Tan, H.M.A. Yim, J.W.A. Quek, D.J. Lim & S. Kee
Housing & Development Board, Singapore

ABSTRACT: Geotextile tubes are increasingly used in coastal protection structures. Typically, sand material is used as infill material in geotextile tubes as they provide good strength and stability. An alternative and sustainable solution is to use excavated soft soils to fill these geotextile tubes. Challenges to the use of soft soils are its low strength and its potential loss from the geotextile tube through the openings in the geotextile material. Thus, a small amount of flocculant or cement is needed. This paper presents the case study of a field trial where 6 geotextile tubes, infilled with lightly cemented recycled excavated soils, were installed onto the seabed using a high-capacity crane barge. Instrumentation such as strain gauges and shape array accelerometers were installed to monitor the performance of the bund during installation. Analysis of instrumentation data showed that lightly cemented recycled excavated soils is a viable infill material in geotextile tubes.

1 INTRODUCTION

Geotextile tubes are increasingly used for coastal protection structures such as breakwaters, revetments and coastal bunds. Geotextile tubes have certain advantages over conventional structures (e.g., concrete seawalls and sand bund revetments), such as the ease of construction and less environmental impact around the construction area (Siew et al., 2014; Hidayat., 2018). Typically, sand material is used as the infill material of geotextile tubes as it provides sufficient strength and stability, and is cost efficient (Lawson, 2008).

However, where sand resources are limited, excavated soft soils as an alternative infill material is explored. The use of recycled excavated soft soils presents a more sustainable construction practice. There are, however, some challenges of using soft soils as an infill material. The fine-grained particles of the soft soil may result in escaping (or piping) of infill material through the geotextile material, leading to wastage of materials and excessive settlement of geotextile tube (Leshchinsky et al., 1996) as well as contaminating the surrounding waters. Another concern with using soft soil is its low shear strength and high compressibility compared to sand material, which may affect the overall stability of the fully constructed coastal bund. One solution to the above concerns is to add a small amount of cement into the excavated soft soil to reduce piping of infill material, minimize settlement of the geotextile tube and provide sufficient overall strength.

A field trial was conducted to investigate the effectiveness of using lightly cemented excavated soft soils as an infill material for geotextile tubes. Six geotextile tubes were fully filled with lightly cemented soft soil, then lowered onto the seabed using a high-capacity crane to form into a bund. A bearing layer foundation was constructed as a bearing layer, using lightly treated excavated soft soils, prior to the lowering of geotextile tubes on top of it.

DOI: 10.1201/9781003299127-108

2 FIELD TRIAL

2.1 *Lightly cemented excavated soft soil*

The excavated soft soils used were dredged on site which contains previously dumped soil that originated from excavation activities from various land-based construction projects. The particle size distribution of the soil is shown in Figure 1. The soil consists largely of silt, with small amounts of sand and clay present.

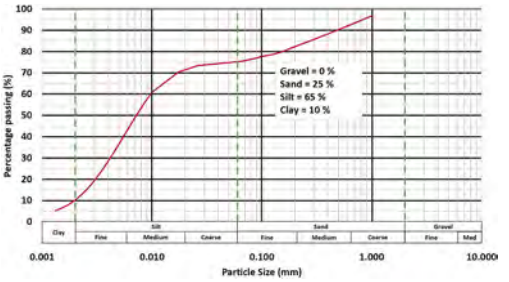

Figure 1. Particle size distribution of excavated soft soils.

To ensure stability of the bund, a target 28-day unconfined compressive strength design value of 60 kPa was determined for both the bearing layer foundation and geotextile tubes. A sufficiently high "flow" value (i.e., low viscosity value) was specified to ensure the ease of pumping. Cement content of 8% (by bulk unit weight of untreated soil) was used for the first two tubes B1 and B3, and 6% for the subsequent geotextile tubes. Cement content of 6.5% was used for the bearing layer foundation construction. The excavated soil has an initial moisture content between 175-190%, and a bulk density of 1.30 g/cm^3 before mixing with cement. After addition of Ordinary Portland Cement (OPC), the bulk density of the mixture was observed to be 1.34 - 1.36 g/cm^3.

2.2 *Construction of geotextile tube bund and bearing layer foundation*

A 30x20 m bearing layer foundation of 1 m thickness was constructed at seabed to provide a sufficiently strong foundation for the geotextile tube bund. The laying of the bearing layer foundation was done in a systematic manner to ensure a uniform and flat surface for the geotextile tube bund to rest on (Figure 2). The geotextile tubes used in the site trial were made from high tension polypropylene woven geotextile sheets with a wide width tensile strength of 200 kN/m in warp and weft direction. During the field trial, significant effort was placed on the QA/QC measures to ensure that the lightly cemented soft soil mixture was prepared properly. This mixture was then pumped into the geotextile tube via its inlet port. Geotextile tube was observed to inflate gradually. After infilling is complete, the fully filled geotextile tube was left in place for a few hours to allow for cementation and curing of infilled material to gain some initial strength. The geotextile tube was then lifted using a high-capacity crane and lowered onto the seabed. Field setup of the high-capacity crane barge is shown in Figure 3. Geotextile tube preparation process is illustrated in Figure 4 and construction sequence is illustrated in Figure 5.

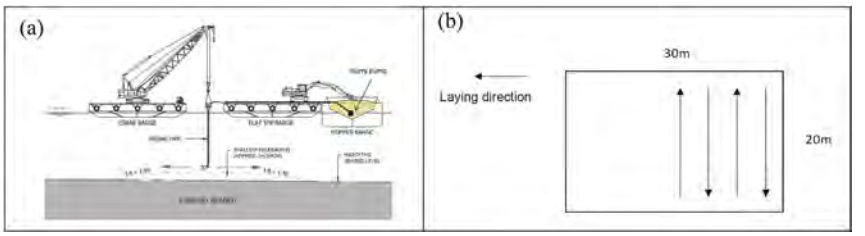

Figure 2. (a) Field setup for laying of bearing layer foundation; (b) Bearing layer foundation laying sequence.

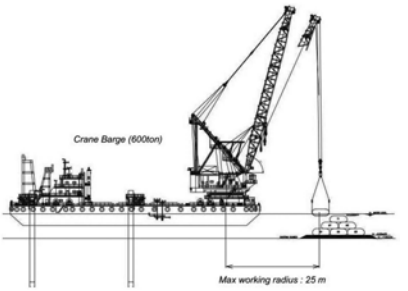

Figure 3. Field setup of high-capacity crane barge lowering geotextile tubes onto seabed.

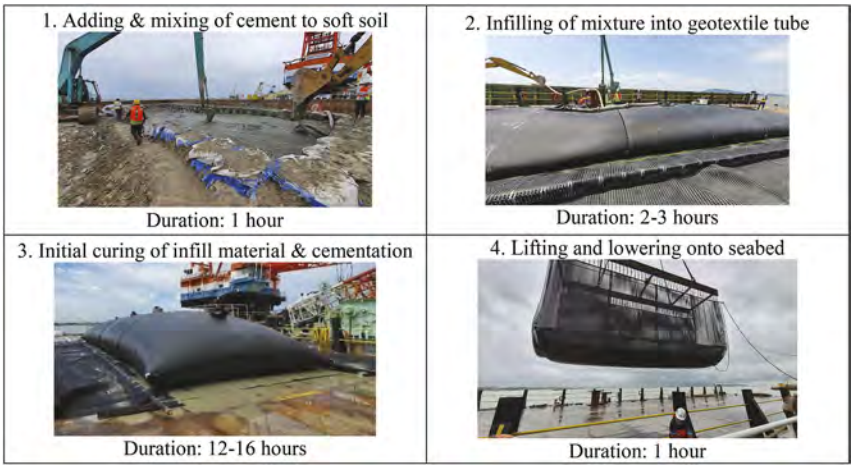

Figure 4. Preparation process of geotextile tube.

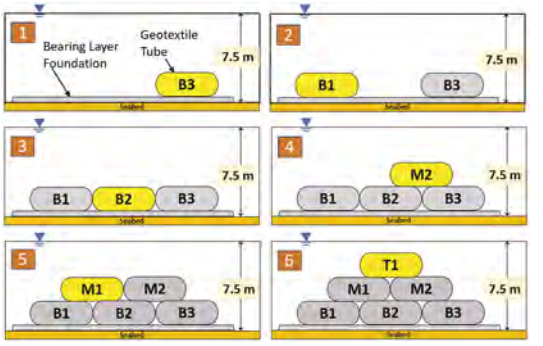

Figure 5. Construction sequence of geotextile tubes forming into a bund (Cross-Sectional View).

2.3 *Instrumentation*

Many instrumentations were installed to monitor the performance of the geotextile tube bund during the installation process. Strain gauges, Total Pressure Cells (TPC) and Pore Pressure Transducers (PPT) were installed in three (3) of the six (6) geotextile tubes. Shape Array Accelerometers (SAA) were installed at various positions to monitor the settlement of the bearing layer foundation and bottom layer geotextile tubes. The positions of the strain gauges and SAA are illustrated in Figures 6(a) and (b) respectively.

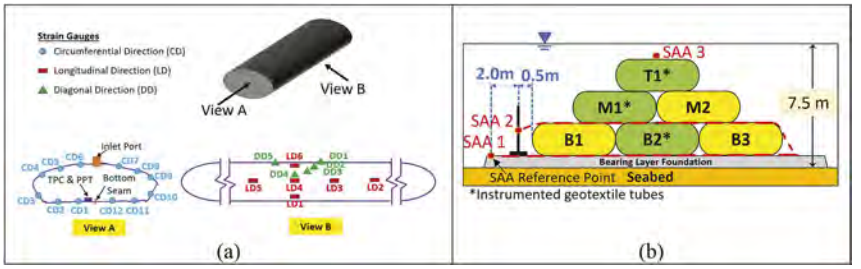

Figure 6. (a) Geotextile tube instrumentation details; (b) Positions of SAA for settlement measurement.

3 RESULTS & DISCUSSION

3.1 *Survey of bearing layer foundation and completed bund*

Bathymetry survey was conducted 14 days after the laying of the bearing layer foundation (Figure 7 (a)). The survey results show that the surface of the bearing layer foundation is relatively uniform and even. After the bund of 6 geotextile tubes were successfully installed, a bathymetry survey was conducted and showed that they were all in exact intended positions as shown in Figure 7(b).

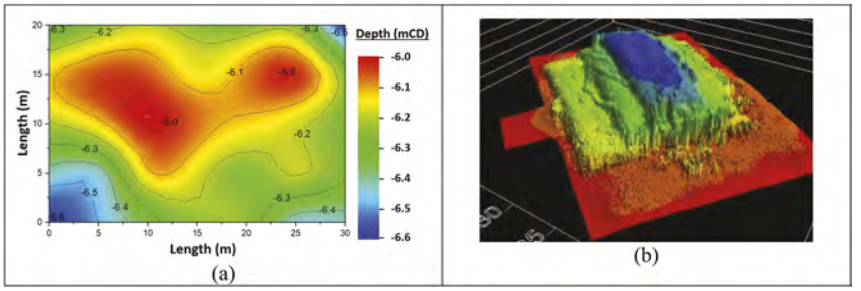

Figure 7. Bathymetry survey of the (a) Bearing layer foundation; (b) Completed geotextile tube bund.

3.2 *Strain gauge readings*

Figure 8(a) shows the strain gauge readings of geotextile tube B2 during the infilling, and 8(b) shows the strain gauge readings of tube B2 during stacking of upper layer tubes on top of it.

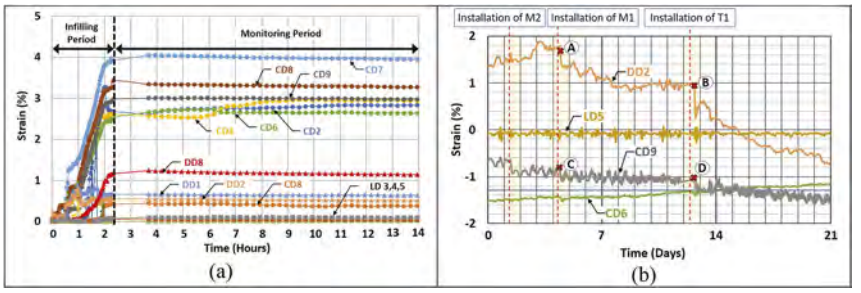

Figure 8. Strain gauge data of geotextile tube B2: (a) During infilling; (b) When upper layer tubes were stacked on it.

It was observed during infilling that the strain gauge readings increased gradually (up to ~4% in CD direction) during infilling as the geotextile tube gradually took shape and the geotextile material experienced tension. During the monitoring period, a minor decrease in strain

was registered (~0.2%) and the shape of the geotextile tube on-site was observed to remain relatively uniform and unchanged. In addition, minor piping of infilled lightly cemented excavated soft soil was observed only at the start of infilling period, and quickly stopped around 15-20 minutes. From Figure 8(b), strain gauges DD2 and CD9 experienced a reduction in tension (at A, B, C and D) while CD6 experienced increase in tension. LD5 strain readings remain relatively constant, suggesting that there was minimal deformation along the longitudinal length of tube B2. Overall, changes in strain readings were quite small, which suggests that during the loading of upper layer tubes, the shape of tube B2 remained largely uniform.

3.3 *Settlement of bearing layer foundation*

The Shape Array Accelerometer (SAA) readings from SAA 1 indicates the settlement of the bearing layer foundation as geotextile tubes were gradually lowered on top of it (Figure 9). After the installation of the bottom layer geotextile tubes was complete at day 0, the maximum settlement observed was 120 mm at the location below center of tube B2. Lightly cemented excavated soft soils (at 6% cement content) was infilled in the spaces between the three bottom layer geotextile tubes (B1, B2 & B3) in preparation for the stacking of the middle and top layers of geotextile tubes. The middle layer tubes (M1 & M2) were lowered onto the bottom layer tubes 34 days later after the completion of the bottom layer, and an almost parallel settlement of about 60 mm was observed across the whole width of the bottom layer. Eight (8) days later (i.e. 42nd day), the top layer tube was installed. An additional settlement of about 30 mm was observed at the center of the bund, directly below the geotextile tube T1. After the completion of all 6 geotextile tubes, SAA 1 readings were monitored for another 42 days and only small additional settlements of around 10-30 mm were observed during this 6-week period.

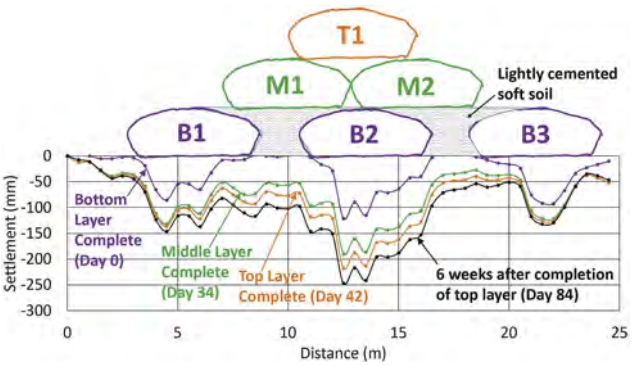

Figure 9. Settlement profile of bearing layer foundation as geotextile tubes were lowered onto it.

3.4 *Thickness of bottom layer geotextile tubes*

Using readings from SAA 1 and SAA 2, the change in the thickness of bottom layer geotextile tubes B1, B2 & B3 can be estimated, as shown in Figure 10. The thickness of bottom layer tube B2 decreases by 30 mm after stacking of the middle layer tubes M1 & M2 on top of it. There was no change in the thickness of bottom layer tube B2 after the top layer tube T1 was stacked on top of the middle layer tubes. A larger settlement of 160 mm towards the left edge and 110 mm towards the right edge of tube B2 was observed, which may be due to the tubes from the middle layer tubes (M1 & M2) deforming slightly to conform to the gap of the bottom geotextile tubes. There was also no change in the thickness of tube B2 six weeks after the completion of the bund.

These observations show that the lightly cemented soft soil infill material was able to ensure sufficient strength and stability of the bund, with only very small settlement observed in the bottom layer geotextile tubes during the stacking of geotextile tubes onto it.

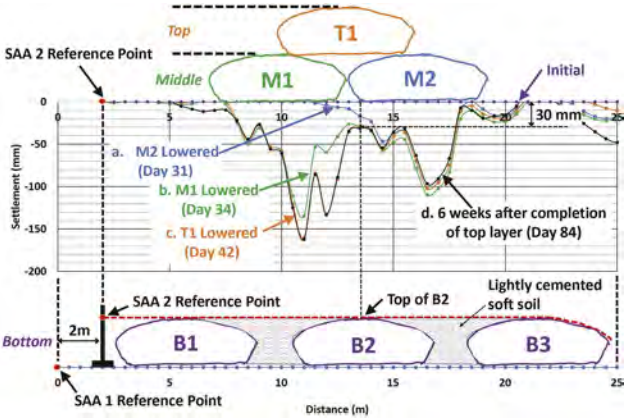

Figure 10. Thickness of bottom layer geotextile tubes as upper layer tubes were stacked onto it.

4 CONCLUSION

In this field trial, six geotextile tubes were successfully infilled with specially designed lightly cemented soft soils and were subsequently lowered onto the seabed forming a bund. Strain gauge results indicate that geotextile tube material and design is adequate in withstanding the pumping pressure and installation stress during the whole installation process. Visual observations on site also showed that only minor piping of lightly cemented soft soils was observed during a very early and brief period in the infilling stage. SAA readings showed that the bearing layer foundation only experienced minor settlement during the lowering of geotextile tubes onto it. In addition, analysis of SAA 1 and SAA 2 showed that there was only a very small settlement observed in the bottom layer geotextile tubes when the middle and top layer geotextile tubes were stacked on top of it. Thus, the results from this field trial shows that lightly cemented soft soil can be an effective alternative infill material within geotextile tubes, providing sufficient strength and stability to the geotextile tube and hence the bund.

ACKNOWLEDGEMENT

This research is supported by the National Research Foundation, Singapore, and Ministry of National Development, Singapore, under its Cities of Tomorrow R&D Programme (CoT Award No. CoT-V4-2019-4). Any opinions, findings, conclusions, or recommendations expressed in this material are those of the author(s) and do not reflect the views of National Research Foundation, Singapore, and Ministry of National Development, Singapore. The authors also gratefully acknowledge the assistance of numerous personnel from Toa-Samsung Joint Venture, Surbana Jurong Consultants Pte Ltd and Geoharbour Co., Ltd for facilitating and supporting the field trial.

REFERENCES

Lawson, C.R. (2008) Geotextile Containment for Hydraulic and Environmental Engineering. Geosynthetics International 15, 2008: 382–427.

Leshchinsky, D., Leshchinsky, O., Ling, H.I., Gilbert, P.A. (1996). Geosynthetic Tubes for Confining Pressurized Slurry: Some Design Aspects. Journal of Geotechnical Engineering, 122 8.

Hidayat, H. and Andrianto, S. (2018). Utilisation of Geotextile Tube for Sandy and Muddy Coastal Management: A Review. Coastal Engineering Proceedings, 1 (36), p.80.

Siew, C.L., Hashim, R., Motamedi, S., Song, K. (2014). Utilization of Geotextile Tube for Sandy and Muddy Coastal Management: A Review. The Scientific World Journal

Smart Geotechnics for Smart Societies – Zhussupbekov, Sarsembayeva & Kaliakin (Eds)
© 2023 The Author(s), ISBN 978-1-003-29912-7
Open Access: www.taylorfrancis.com, CC BY-NC-ND 4.0 license

Comparative assessment of single and double interface shear strength properties: A case study of a landfill project in the Western Cape Province, South Africa

V. Sylivery & D. Kalumba
Department of Civil Engineering, University of Cape Town, Cape Town, South Africa

B. Mawer
Associate, JG Afrika (Pty) Ltd., Cape Town, South Africa

ABSTRACT: Incorporation of multi-layered series of geosynthetics and geomaterials has presented new potential interfaces for shear failure of lining systems in engineered municipal solid waste (MSW) landfills. In the laboratory, interface shear strength parameters used in the design of lining systems especially side-slopes and bases are determined through single interface testing configuration according to ASTM D5321-20 and ASTM D6243-20 standards. This testing configuration, however, gives a limited understanding of shear strength transfers between the lining components when a multi-layered lining system has been proposed. Multi-interface testing configuration has been sought as an alternative by several scholars to address the above limitation. However, there is little information available as it is not stipulated in any official standard. This study was thus, conducted to ascertain the potential use of multi-interface testing methods through a case study of a proposed lining system for a new landfill cell in South Africa. It was found that single and multi-interface testing on specimens that involved geosynthetics only in the setup, similar results were observed. However, a dissimilarity in interface shear results was observed on those that involved geomaterials and geosynthetics.

1 INTRODUCTION

An engineered MSW landfill is a sensitive geo-environmental barrier system that achieves a maximum disposal capacity by increasing the side-slope gradient while limiting leachate migration to ground and surface water reserves (Rowe, 2011). The lining systems used in these structures usually constitute a multi-layered band of numerous geosynthetics and geomaterials that are project and site specific (De Brito Galvão et al., 2008). Since their inception, geosynthetics have been used extensively in different geotechnical projects fulfilling various functions including acting as pollution or contaminant barrier, reinforcement, separation, filtration, drainage and protection (Kalumba & Scheele, 1999; Mawer & Kalumba, 2014; Kiptoo et al., 2017). Thus, playing an important role in the lining system of an engineered MSW landfill. However, as several layers of geosynthetics and geomaterials are being introduced in MSW landfills' lining systems, their interaction becomes pertinent when identifying possible interfaces for shear failure mobilization (Lopes & Silvano, 2010; Zamara et al., 2012; Bacas, Cañizal & Konietzky, 2015; Feng & Lu, 2016; Cen, Wang & Sun, 2018).

To establish interface shear strength properties in the laboratory, single interface shear strength tests of soil-geosynthetic or geosynthetic-geosynthetic are typically conducted following ASTM D5321-20 and ASTM D6243-20 standards for non-cohesive materials and geosynthetic clay liners (GCLs), respectively (ASTM, 2020a,b). Previous studies on multi-interface testing found that, when similar interfaces were tested through this configuration, peak strength envelopes and

DOI: 10.1201/9781003299127-109

interface shear strength parameters were determined to be similar to those of the weakest interface under a single interface configuration (Stark, Niazi & Keuscher, 2015; Khilnani, Stark & Bahadori, 2017; Sikwanda, Kalumba & Nolutshungu, 2019). In contrast, at large displacement (LD), interface shear strength parameters obtained were very dissimilar, with the single interface configuration achieving higher values than multi-interface configuration. Observations by these scholars suggested that tests conducted under the multi-interface arrangement were still uncertain as it was difficult to pinpoint the interface facilitating failure, even though there was a certain degree of comparability to the single interface configuration. In this study, multi-interface testing was further investigated through a systematic comparison of interface shear results generated from single and multi-interface testing configurations through a case study of the proposed lining system for a new landfill cell in the Western Cape Province in South Africa.

2 METHODOLOGY

2.1 *Proposed lining system*

The proposed landfill cell was classified as a general waste landfill (classifying as a Type 2 waste stream as per South African regulations). It also had a net positive water balance during winter months due to Cape Town's seasonal rainfall pattern, therefore creating the potential to generate significant amounts of leachate at certain times of the year (Department of Water Affairs and Forestry, 1998). This landfill cell was planned to be built in a "piggyback" fashion on top of a pre-existing 7-8m thick wastefill deposit which was previously dumped on an unlined area. A multi-layered basal lining design was proposed, as shown in Figure 1.

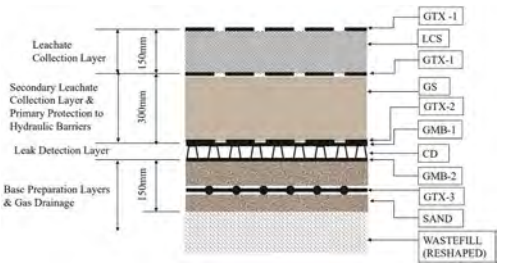

Figure 1. Proposed Basal Lining System for General Waste Landfill (Sylivery, 2022).

2.2 *Description of lining materials*

2.2.1 *Geosynthetics*

Based on the above arrangement, the two nonwoven geotextiles used were bidim® A5 (GTX-1) and bidim® A7 (GTX-2). These geotextiles were locally manufactured from 100% polyester resulting in high-performance nonwoven geotextiles whose continuous filaments were bonded by needle-punching. These geotextiles performed separation and protection functions. Furthermore, a high-strength woven geotextile-based geogrid, RockGrid®PC (GTX-3), was used in a reinforcement function thereby minimizing differential settlement within the underlying historic waste deposit.

Two smooth-sided geomembranes, i.e., 2.00mm thick HDPE geomembrane (GMB-1) and 1.5mm thick LLDPE geomembrane (GMB-2) were also proposed to form part of the lining system. These geomembranes were manufactured through a calendered flat-die extrusion process. Lastly, a durable and heat-formed multiple-cuspated synthetic drain (CD) sheet that provided a high capacity and non-restricted drainage path that was compatible with GMB-1 & GMB-2 was used. The cusps of the CD were symmetrical, thus, providing high resistance to crushing when exposed to heavy loads. Wedged between the two geomembranes the CD formed part of the primary leak detection system.

2.2.2 *Geomaterials*

This study utilized three geomaterials, namely: sand, gravelly sand (GS), and leachate collection stone (LCS). The GS and LCS were products of crushed building waste materials and were abundantly available in the old section of the landfill. The use of these geomaterials was motivated by their availability, the need to re-use building waste, and in the case of the LCS, the high permeability, allowing for easy leachate collection. The mechanical properties which were conducted in the Geotechnical Engineering Laboratory at the University of Cape Town are presented in Table 2.

Table 1. Properties of geosynthetics.

Geosynthetic	Label	Type[a]	Raw material[c]	Mass/area or density	Thickness [mm]
Geotextiles	GTX-1	NW[a]	Bidim PET/continuous filament	270g/m^2	2.60[d]
	GTX-2	NW[a]	Bidim PET/continuous filament	550g/m^2	4.60[d]
	GTX-3	W[b]	PET/staple fibres	150g/m^2	1.00[d]
Geomembranes	GMB-1	Smooth	HDPE	>0.94g/cm^3	2.00
	GMB-2	Smooth	LLDPE	>0.94g/cm^3	1.50
Synthetic Cuspate Drain	CD	Cuspate	HDPE	958g/m^3	4.75

a NW=nonwoven geotextile
b W=woven geotextile/geogrid
c PET=Polyester, HDPE=High Density Polyethylene & LLDPE=Linear Low-Density Polyethylene
d Thickness measured at 2kPa

Figure 2. Geotextiles; (a) GTX-1, (b) GTX-2, (c) GTX-3S1 & (d) GTX-3S2.

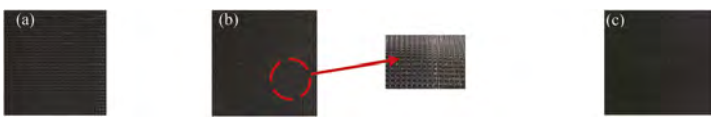

Figure 3. Synthetic Cuspate Drain (CD); (a) Smooth side, (b) Cusps side & (c) GMB-1/2.

Table 2. Properties of geomaterials.

Property	Units	Test Method	Sand	GS	LCS
Cohesion (c')	kPa	ASTM D3080-11	0	0	-
The angle of Internal Friction (ϕ')	°		35.18	35.55	-
Optimum Moisture Content (OMC)	%	ASTM D698-12	3.80	7.60	-
Maximum Dry Density (MDD)	Mg/m^3		1.77	2.12	-
Fine Gravel (4.75 - 75 mm)	%	ASTM C136-19	0	24.78	100
Medium sand (0.075 - 4.75 mm)			99.94	75.20	0
Silt (0.002 - 0.075 mm)			0.06	0.04	0
Clay (<0.002 mm)			0	0	0
Coefficient of Uniformity (C_u)			2.13	4.67	1.03
Coefficient of Curvature (C_c)			1.09	0.60	1.00
USCS Classification		ASTM D2487-17	SP	SP with Gravel	GP

Figure 4. Geomaterials; (a) Sand, (b) Gravelly Sand & (c) Leachate Collection Stone.

2.3 *Testing procedure and program*

A total of 45 single and double interface shear tests were conducted on the lining components for the proposed landfill cell to achieve the objectives of this study. The test conditions included 60 minutes for hydration and consolidation of specimens at their respective applied normal pressures of 150, 300 and 450 kPa. The shear tests were also conducted using a shearing rate of 1mm/min as recommended by the ASTM D5321-20 standard for non-cohesive materials. Table 3 summarizes all lining components tested with their testing configurations.

2.3.1 *Single interface configuration*

In the single interface configuration, two interface setups were facilitated involving soil-geosynthetic and geosynthetic-geosynthetic interactions. In the soil-geosynthetic setup, the geosynthetic component was clamped on the lower shear box and the soil was compacted to the target density in the upper shear box. While, in the case of the geosynthetic-geosynthetic setup, the respective geosynthetic specimens were clamped on the upper and lower shear boxes.

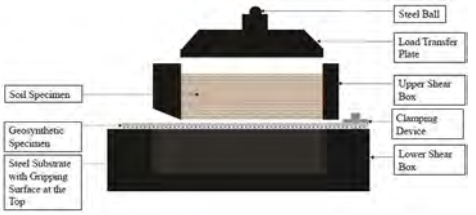

Figure 5. Soil-Geosynthetic Interface.

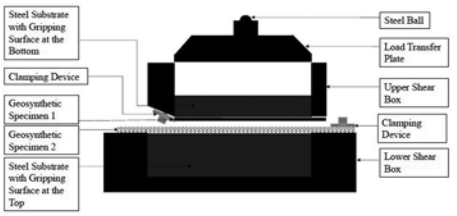

Figure 6. Geosynthetic-Geosynthetic Interface.

2.3.2 *Double interface configuration*

In the double interface configuration, testing was implemented through three setups i.e., soil-geosynthetic-soil, soil-geosynthetic-geosynthetic and geosynthetic-geosynthetic-geosynthetic interactions. The modification to the single interface configuration was an addition of a third soil/geosynthetic specimen in the setup.

In the soil-geosynthetic-soil setup, the soil was firstly compacted to the target density in the lower shear box followed by geosynthetic specimen placement on top of the lower box without any clamping mechanisms and finally, the second soil specimen was compacted on the upper shear box. A similar approach was used for the soil-geosynthetic-geosynthetic setup, except that a geosynthetic specimen was clamped on the top of the lower shear box to replace soil specimen. For a geosynthetic-geosynthetic-geosynthetic setup, two geosynthetics were clamped to the ends of the upper and lower shear boxes while one geosynthetic specimen was placed freely in the middle.

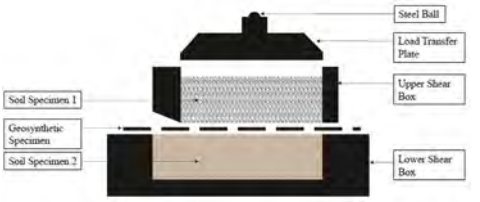

Figure 7. Soil-Geosynthetic-Soil Interface.

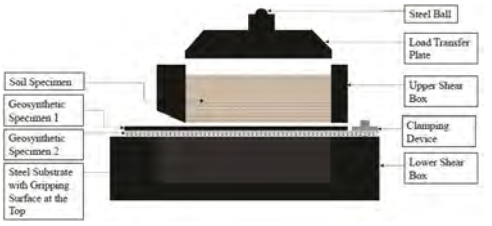

Figure 8. Soil-Geosynthetic-Geosynthetic Interface.

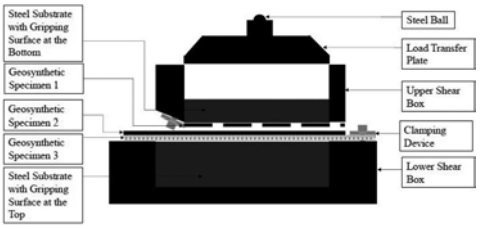

Figure 9. Geosynthetic-Geosynthetic-Geosynthetic Interface.

Table 3. Testing configurations.

Single Interfaces	Double Interfaces
1. LCS | GTX-1	1. LCS | GTX-1 | GS
2. GTX-1 | GS	2. GS | GTX-2 | GMB-1
3. CM | GTX-2	3. GTX-2 | GMB-1 | CD
4. GTX-2 | GMB-1	4. GMB-1 | CD | GMB-2
5. GMB-1 | CD	5. CD | GMB-2 | SAND
6. CD | GMB-2	6. SAND | GTX-3 | SAND
7. GMB-2 | SAND	
8. SAND | GTX-3S1[a]	
9. GTX-3S2[b] | SAND	

a GTX-3S1=Geotextile 3 with rough surface (reinforcing staple fibres)
b GTX-3S2=Geotextile 3 with a smooth surface

3 RESULTS & DISCUSSION

3.1 *Soil-geosynthetic-soil interactions*

Two interface test series in the double interface configuration involved soil-geosynthetic-soil interactions. The recorded interface shear strength parameters, however, were observed to vary across all sets. For instance, the shear strength parameters obtained in the single interfaces LCS |

GTX-1 and GTX-1 | GS were lower than those determined in the double interface LCS | GTX-1 | GS. Whereas the peak interface angle of friction recorded by the single interface SAND | GTX-3S2 was similar to that obtained in the double interface configuration of SAND | GTX-3 | SAND. Other strength parameters including those of SAND | GTX-3S1 were completely different. The inconsistency of this test setup was observed due to soil ploughing or soil blistering in the lower shear box attributed to the size difference with the upper shear box.

3.2 *Soil-geosynthetic-geosynthetic interactions*

There were two test series that involved soil-geosynthetic-geosynthetic interactions in the double interface configuration. The recorded interface shear strength parameters were similar to those of the weakest interfaces for the individual single interfaces. For example, in the single interfaces of GS | GTX-2 and GTX-2 | GMB-1, the weakest peak angle of friction was 11.27° with 4.30kPa apparent adhesion and these were similar to the peak parameters in the double interface configuration of GS | GTX-2 | GMB-1 which recorded 13.55° and 4.46kPa. The other set involved single interfaces CD | GMB-2 and GMB-2 | SAND with the former recording weakest interface parameters at peak of 24.04° and 9.27kPa which were similar to those observed in the double interface configuration of CD | GMB-2 | SAND of 24.51° and 0kPa. This setup suggested that the interface shear strengths of the weakest interface will prevail in the multi-interface configuration provided test conditions are the same.

3.3 *Geosynthetic-geosynthetic-geosynthetic interactions*

For the geosynthetic-geosynthetic-geosynthetic test series, the interface shear strength parameters were in between those observed in the constitutive single interfaces. For instance, the double interface configuration of GTX-2 | GMB-1 | CD recorded a peak angle of interface friction of 13.45° which was in between those recorded for single interfaces of GTX-2 | GMB-1 and GMB-1 | CD as seen in Table 4. However, the interface friction recorded at LD of 9.34° was similar to that of GTX-2 | GMB-1 and lower than that of GMB-1 | CD, partly because GTX-2 | GMB-1 was the overall weakest interface in all test series for this project. A similar trend was also observed at the peak for the double interface GMB-1 | CD | GMB-2 as seen in Table 4

Table 4. Summary of interface shear strength parameters.

		Interface shear strength parameters			
		at Peak		at Large Displacements	
Interface Configuration		δ_p [°]	$c_{\alpha\text{-}p}$ [kPa]	δ_{LD} [°]	$c_{\alpha\text{-}LD}$ [kPa]
Single-	LCS | GTX-1	17.05	65.42	10.85	29.71
	GTX-1 | GS	33.16	29.66	12.23	112.00
	GS | GTX-2	38.06	13.32	35.50	21.32
	GTX-2 | GMB-1	11.27	4.30	10.24	2.40
	GMB-1 | CD	18.45	0.00	18.45	0.00
	CD | GMB-2	24.04	9.27	23.99	8.33
	GMB-2 | SAND	29.07	0.00	22.74	0.00
	SAND | GTX-3S1	37.71	24.66	36.99	24.66
	SAND | GTX-3S2	31.21	44.99	12.95	125.00
Double-	LCS | GTX-1 | GS	42.11	30.50	41.90	24.17
	GS | GTX-2 | GMB-1	13.55	4.46	9.37	6.77
	GTX-2 | GMB-1 | CD	13.45	14.48	9.34	8.05
	GMB-1 | CD | GMB-2	20.30	10.00	20.54	5.13
	CD | GMB-2 | SAND	24.51	0.00	24.00	0.00
	SAND | GTX-3 | SAND	31.11	85.71	31.11	85.71

δ_p and δ_{LD} = peak and large displacement (LD) angles of interface friction
$c_{\alpha\text{-}p}$ and $c_{\alpha\text{-}LD}$ = peak and large displacement (LD) apparent adhesions

4 CONCLUSION

The following conclusions have been established from this study:

- For interfaces that involved geomaterials, i.e., soil and stone in their setups, for instance, LCS | GTX-1 | GS, GS | GTX-2 | GMB-1, CD | GMB-2 | SAND & SAND | GTX-3 | SAND; higher interface friction angles and apparent adhesion parameters were observed at peak with a decline at LD.
- For the interfaces that involved only geosynthetics in their setups, such as GTX-2 | GMB-1 | CD & GMB | CD | GMB-2 interfaces; similar interface friction angles and apparent adhesion parameters at peak and LD were generally observed. This testing configuration presents a success of multi-interface testing when compared to single interface testing.
- This study also found that some of the lining components could potentially improve shear resistances when tested concurrently in the non-standardized double interface testing configuration. For instance, due to a GS layer in the double interface configuration GS | GTX-2 | GMB-1, the shear resistances observed, were 18% higher than the constitutive single interfaces.

Finally, for both testing configurations, the critical or weakest interface involved an interaction between a smooth geomembrane (GMB-1) and nonwoven geotextile (GTX-2). This observation was noted to be similar to observations by other scholars (Buthelezi, Kalumba & James, 2016; Adeleke, Kalumba & Hardie, 2019; Adeleke, Kalumba & Oriokot, 2019).

REFERENCES

Adeleke, D., Kalumba, D. & Hardie, P. 2019. Effects of asperities on the geotextile-geomembrane interface shear characteristics. In *Proceedings of the 13th Australia New Zealand Conference on Geomechanics. H.E. Acosta-Martínez & B.M. Lehane, Eds. Perth, Western Australia: Australian Geomechanics Society, 1–3 April 2019, ISBN: 978-0-9946261-0-3 pp. 699–704*.

Adeleke, D., Kalumba, D. & Oriokot, J. 2019. Asperities effect on polypropylene & polyester geotextile-geomembrane interface shear behaviour. *E3S Web of Conferences (7th International Symposium on Deformation Characteristics of Geomaterials: IS-Glasgow 2019*). 92:5. DOI: 10.1051/e3sconf/20199213017.

Adeleke, D., Kalumba, D., Nolutshungu, L. & Oriokot, J. 2021a. Assessment of Asperities Geometry Influence on MSW Landfill Critical Interface Side-Slope Stability Using Probabilistic Analysis. In *Proceedings of The Evolution of Geotech - 25 Years of Innovation, 20–21 April 2021*, *pp. 196–201.*

Adeleke, D., Kalumba, D., Nolutshungu, L. & Oriokot, J. 2021b. Assessment of asperities geometry influence on MSW landfill critical interface side-slope stability using probabilistic analysis. In *Proceedings of The Evolution of Geotech - 25 Years of Innovation, 20–21 April 2021, pp.196-201. 196–201*.

ASTM. 2020a. *ASTM D5321/D5321M - 20, Standard Test Method for Determining the Shear Strength of Soil-Geosynthetic and Geosynthetic-Geosynthetic Interfaces by Direct Shear*. West Conshohocken, PA, USA.

ASTM. 2020b. *ASTM D6243/D6243M - 20, Standard Test Method for Determining the Internal and Interface Shear Strength of Geosynthetic Clay Liner by the Direct Shear Method*. West Conshohocken, PA, USA.

Bacas, B.M., Cañizal, J. & Konietzky, H. 2015. Frictional behaviour of three critical geosynthetic interfaces. *Geosynthetics International*. 22(5):355–365. DOI: 10.1680/jgein.15.00017.

De Brito Galvão, T.C., Kaya, A., Ören, A.H. & Yükselen, Y. 2008. Geomechanics of landfills - Innovative technology for liners. *Soil and Sediment Contamination*. 17(4):411–424. DOI: 10.1080/15320380802146693.

Buthelezi, S., Kalumba, D. & James, G. 2016. Comparison of interface shear strength characteristics of HDPE and LLDPE geomembrane interfaces. In *Proceedings of the 6th EuroGeo Conference (EuroGeo6), Ljubljana Exhibition and Convention Centre, Ljubljana, Slovenia, 25–28 September, 2016, pp. 1067–1076*.

Cen, W.J., Wang, H. & Sun, Y.J. 2018. Laboratory investigation of shear behavior of high-density polyethylene geomembrane interfaces. *Polymers*. 10(7). DOI: 10.3390/polym10070734.

Department of Water Affairs and Forestry. 1998. *Minimum requirements for waste disposal by landfill*. 2nd ed. Pretoria, Republic of South Africa: Department of Water Affairs & Forestry.

Feng, S.J. & Lu, S.F. 2016. Repeated shear behaviors of geotextile/geomembrane and geomembrane/clay interfaces. *Environmental Earth Sciences*. 75(3):1–13. DOI: 10.1007/s12665-015-4994-2.

Kalumba, D. & Scheele, F. 1999. Friction Characteristics of Sand/Geotextile Interfaces for Three Selected Sand Materials. In *12th African Regional Conference: Conference Proceedings, Durban, South Africa*.

Khilnani, K., Stark, T.D. & Bahadori, T.M. 2017. Comparison of Single and Multi-Layer Interface Strengths for Geosynthetic/Geosynthetic and Soil/Geosynthetic Interfaces. *Geotechnical Frontiers*. 42–51. DOI: 10.1061/9780784480434.005.

Kiptoo, D., Aschrafi, J., Kalumba, D., Lehn, J., Moormann, C. & Zannoni, J. 2017. Laboratory Investigation of a Geosynthetic Reinforced Pavement under Static and Dynamic Loading. *American Society for Testing and Materials (ASTM) Journal of Testing and Evaluation*. Volume 45(ISSN 0090–3973: Issue 1). DOI: https://doi.org/10.1520/JTE20160170.

Lopes, M.L. & Silvano, R. 2010. Soil/Geotextile Interface Behaviour in Direct Shear and Pullout Movements. *Geotechnical and Geological Engineering*. 28(6):791–804. DOI: 10.1007/s10706-010-9339-z.

Mawer, B. & Kalumba, D. 2014. The potential for reinforcement of soft clay soils with geotextiles to resist construction loads. In *Proceedings of the 8th Young Geotechnical Engineers Conference (YGE 2014) on Cultivating the Future of Geotechnics, Spier Conference Centre, Stellenbosch, Western Cape, South Africa, 17–19 September, pp.* 13–23.

Rowe, R.K. 2011. Systems engineering: The design and operation of municipal solid waste landfills to minimize contamination of groundwater. *Geosynthetics International*. 18(6):391–404. DOI: 10.1680/gein.2011.18.6.391.

Sikwanda, C., Kalumba, D. & Nolutshungu, L. 2019. Comparison of Single and Multi-Interface Strengths for Geosynthetic/Geosynthetic. In *Proceedings of the 17th African Regional Conference: Soil Mechanics and Geotechnical Engineering (XVII ARCSMGE), Cape Town, South Africa, 6–9 October 2019, pp. 77–81*.

Stark, T.D., Niazi, F.S. & Keuscher, T.C. 2015. Strength Envelopes from Single and Multi Geosynthetic Interface Tests. *Geotechnical and Geological Engineering*. 33(5):1351–1367. DOI: 10.1007/s10706-015-9906-4.

Sylivery, V. 2022. Comparative Assessment of Single & Double Interface Shear Strength Properties : A Case Study of a Landfill Project in the Western Cape Province, South Africa. MSc Thesis submitted to the University of Cape Town, South Africa.

Zamara, K.A., Dixon, N., Jones, D.R. V. & Fowmes, G. 2012. Monitoring of a landfill side slope lining system: Instrument selection, installation and performance. *Geotextiles and Geomembranes*. 35:1–13. DOI: 10.1016/j.geotexmem.2012.06.003.

Smart Geotechnics for Smart Societies – Zhussupbekov, Sarsembayeva & Kaliakin (Eds)
© 2023 The Author(s), ISBN 978-1-003-29912-7
Open Access: www.taylorfrancis.com, CC BY-NC-ND 4.0 license

Experiment on reducing lateral earth pressure with a biopolymer-treated layer and geogrid-reinforced sand backfill

Gi-Yun Kim & Hwijae Lee
Graduate student, Department of Civil Systems Engineering, Ajou University, Korea

Ilhan Chang*
Associate Professor, Department of Civil Systems Engineering, Ajou University, Korea

ABSTRACT: In general, the common active earth pressure theory used for retaining wall design has several limitations which render ineffective over estimation and conservative design. Recently, biopolymer-based soil treatment (BPST) is considered as a new ground improvement practice in terms of sufficient shear strength enhancement via hydrogel induced interparticle bonding. In this study, an experimental setup which allows wall rotation subjected to the bottom toe is used to monitor the lateral earth pressure variation with wall rotation. Different backfill conditions were considered to assess the BPST effect on the active lateral earth pressure behavior. Experimental results indicate that a dehydrated BPST layer embedded in the backfill reduces the active lateral earth pressure which is similar to the reinforcement effect of a geogrid layer installation.

1 INTRODUCTION

Active earth pressure theories (Coulomb 1776, Rankine 1857,) commonly used in retaining wall design have limitations which can either overestimate or underestimate the earth pressure level in practice. The magnitude of the lateral earth pressure influences the retaining wall cross-sectional dimension. Geosynthetics, lightweight materials (Arrefnia et al. 2021), compressible geofoam (Xie et al. 2020), and retaining wall relief shelves (Khan et al. 2016) are being researched to reduce earth pressure. Furthermore, in cohesive soil, the cohesive force works in the direction of sliding resistance, and friction and cohesion resistance occur along the sliding failure line, reducing active earth pressure.

Biopolymer-based soil treatment (BPST) has recently been introduced into geotechnical engineering as an ecofriendly and sustainable method for soil improvement practices. Through particle surface accumulation and interparticle bonding network formation, BPST enhances interparticle adhesion which results to overall shear strength increment (Lee et al. 2017, Chang et al. 2020). In this study, a soil tank apparatus which has a rotatable wall on the side is used to assess the lateral earth pressure of different backfill conditions with wall rotation.

2 EXPERIMENTAL SETUP AND INSTRUMENTATION

2.1 *Materials*

This study used dried Jumunjin sand to form the model ground. Basic properties of Jumunjin sand are listed in Table 1.

In this study, xanthan gum (Sigma-Aldrich, CAS No. 11138-66-2) biopolymer is used to form a BPST layer placed in the backfill behind the wall. In addition, a geogrid embedded condition was considered to compare the lateral earth pressure distributions between xanthan gum BPST layer containing backfill and typical geogrid installed backfill. Detail dimensions of the geogrid member used in this study is displayed in Figure 1. Table 2 summarizes the

*Corresponding author: ilhanchang@ajou.ac.kr

DOI: 10.1201/9781003299127-110

xanthan gum biopolymer mixing ratio (m_s: soil weight, m_w: water content, m_b: biopolymer weight) and test conditions. Table 3 shows the basic mechanical properties (interparticle cohesion and friction angle) of different soil conditions used in this study.

Table 1. Jumunjin sand properties.

	$\gamma_{d,max}$	$\gamma_{d,min}$	γ_d	D_r	
USCS	kN/m^3	kN/m^3	kN/m^3	%	G_s
SP	18.1	14.6	17.2	78.2	2.65

Table 2. Test conditions.

CASE	Biopolymer treated (UT/BP)	State (W/D)	Number of BPST layer (L0/L3)	Number of geogrid (G0/G3)	Test name
1	Untreated (UT)	Dry (D)	- (L0)	- (G0)	UT(D)-L0-G0
2	Untreated (UT)	Dry (D)	- (L0)	3 (G3)	UT(D)-L0-G3
3	m_w/m_s = 15%	Wet (W)	3 (L3)	- (G0)	BP(W)-L3-G0
4	m_b/m_s = 1% (BP)	Dry (D)	3 (L3)	- (G0)	BP(D)-L3-GO

Table 3. Direct shear test results.

		Untreated	BP(Wet)	BP(Dry)	Wall friction
Internal friction angle	°	37	34	48	15
Cohesion	kPa	0	10.1	269.8	0

2.2 *Experimental details and testing procedure*

The soil tank was fabricated with a size of 980 mm in length × 300 mm in width × 900 mm in height. A transparent acrylic plate was attached at the front.

The rotatable wall was made of acryl with a dimension of 300 mm in length × 100 mm in height × 20 mm in thickness, and consisted 7 separate plates where two load transducers and an earth pressure gauges were installed on each plate to measure the lateral earth pressure acting on the corresponding section. The vertical was corrected and a model ground was formed by installing a hinge at the bottom of the wall.

Model ground (i.e. backfill) has formed via sand pluviation. The model ground in the tank has shown a relative density of D_r = 78.2%. A xanthan gum BPST layers as well as geogrids were installed at the designated positions (Figure 2). The lateral earth pressure acting on the wall during wall rotation was continuously measured by the load transducers and earth pressure transducers. The rotation rate was set at 0.01°/min using a gear box.

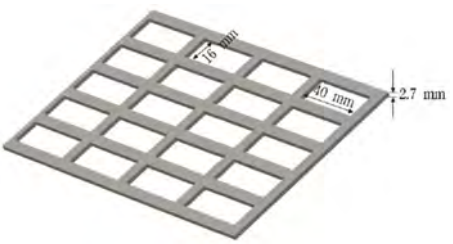

Figure 1. Geogrid detail dimension.

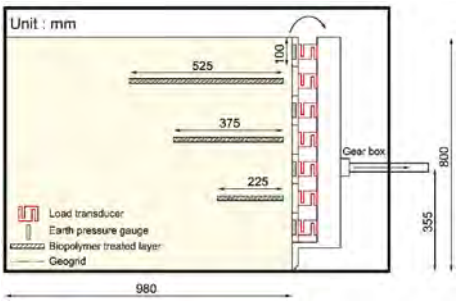

Figure 2. Soil tank.

3 EXPERIMENTAL RESULTS AND DISCUSSION

The effect of reducing earth pressure was verified by measuring lateral earth pressure according to wall rotation and installing BPST layers and geogrids in the model ground. The lateral earth pressure ratio (active earth pressure Ea/earth pressure at rest E0) and wall displacement (Δx: wall lateral displacement, h: wall height) are plotted to analyze the lateral earth pressure distribution and reduction effect by wall rotation (Figure 3). Figure 3(a) shows the total lateral earth pressure acting on the entire wall, and Figure 3(b-f) shows the lateral earth pressure acting on each measurement plate (No. 2-6). (wall number 1 from the top of the wall). In the center of walls No. 2, 4, and 6, BPST layers and geogrids were installed. An arrows indicate the effect of reducing lateral earth pressure in the dehydrated (dry) BPST condition rather than the untreated condition.

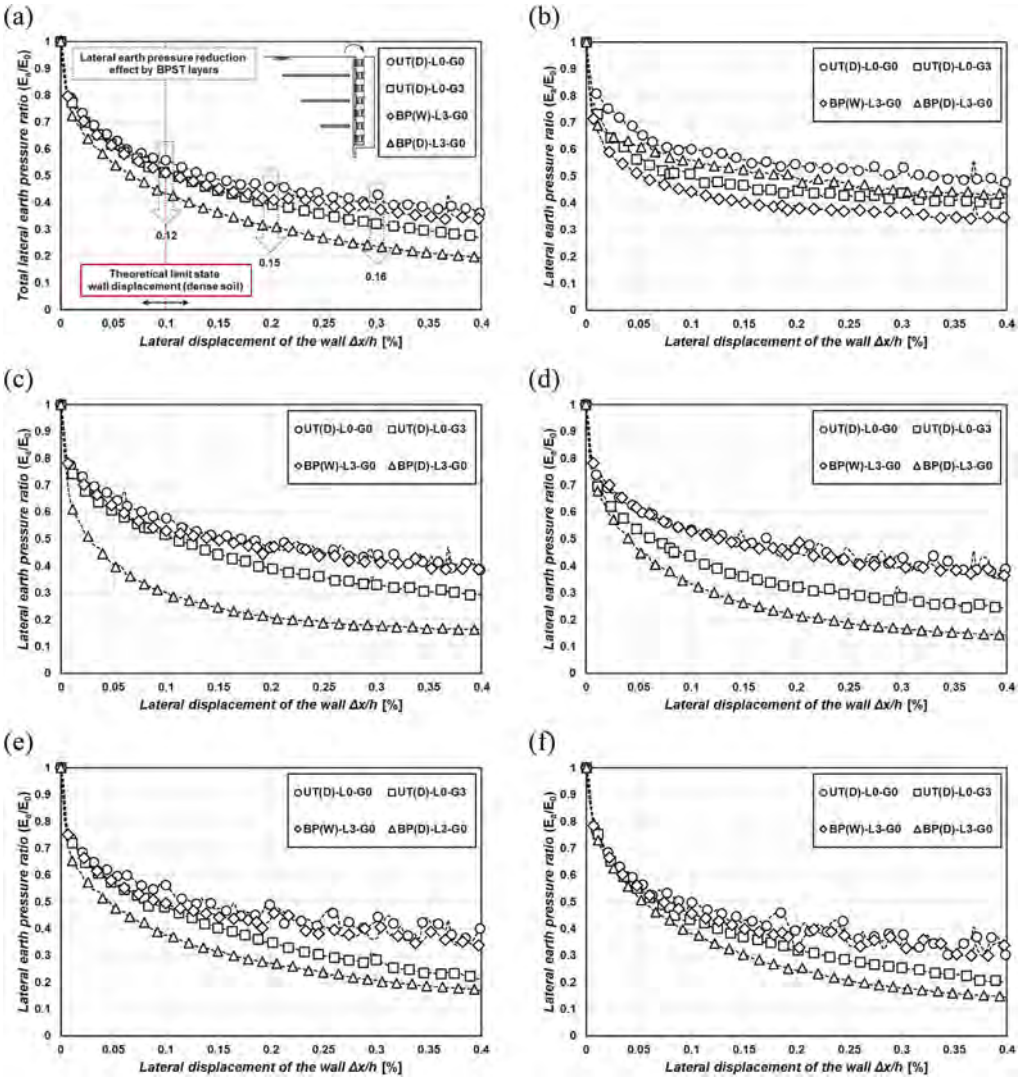

Figure 3. Lateral earth pressure ratio (E_a/E_0) according to wall rotation ((b-f) is No. 2-6 wall) .

Regardless of the backfill conditions, the lateral earth pressure reduces rapidly when the wall begins to rotate. The lateral earth pressure does not converge and decreases linearly after the active earth pressure is generated by the rotation of the wall in each condition due to wall friction and the cohesive force of the BPST layers. Shear resistance occurs when a geogrid is installed in the ground due to surface friction at the soil-soil and soil-geogrid contact surfaces. Because the geogrid was inserted into the ground without being affixed to the wall in this study, the lateral movement of the soil particles was restrained due to the surface friction of the geogrid, resulting in a slight earth pressure reduction effect. Because of the weak structure of the xanthan gum hydrogel, the initial state (wet) condition of the BPST layer (BP(W)-L3-G0) led an earth pressure reduction effect (slightly enhanced cohesion and decreased internal friction angle (Table 3)). However, as BPST layers dehydrate (drying), the strengthening effect promotes the lateral earth pressure reduction, where condensed BPST layers seem to have similar effect on lateral earth pressure reduction when compared to geogrid embedded cases. Because of the improvement in the shear parameter in the dried xanthan gum treated layer, lateral movement restraint occurs at the treated position similar to the time of geogrid installation. Furthermore, the dried xanthan gum treated layer works as a retaining wall relief shelf, reducing the lateral earth pressure under the shelf and restricting soil dis-placement. As a result, it had a little greater lateral earth pressure reduction effect than before the geogrid was installed. The effect of BPST treatment interval should also be considered in order to verify the application of BPST to retaining wall backfill. Furthermore, additional research is needed to combine the backfill of BPST with geogrid to mitigate for the BPST initial (wet) weak hydrogel structure. However, xanthan gum biopolymer has a problem in that it is difficult to dry in the ground, requiring research into materials that may overcome this.

4 CONCLUSION

In this study, a rotatable was constructed and a physical modeling test was performed to obtain the following results on the BPST influence on the backfill of the retaining wall. The lateral earth pressure rapidly decreased as the wall started to rotate. In the case of the BPST layer, the wet (initial) xanthan gum treated layers improve shear strength but does not significantly effect on lateral earth pressure behavior. However, because the BPST layers are dehydrated (dry), the improving effect of the shear strength parameter promotes lateral earth pressure reduction. This demonstrated the effect of restricting lateral movement on reducing lateral earth pressure at a position treated similar to the installation of the geogrid. Furthermore, the dried xanthan gum treated layers work as a retaining wall relief shelf, reducing lateral earth pressure under the shelf and restricting soil displacement. As a consequence, the effect of reducing lateral earth pressure was little greater than the effect of installing a geogrid.

ACKNOWLEDGEMENT

This work was supported by the National Research Foundation of Korea (NRF) grant funded by the Korea government (MSIT) (No. 2022R1A2C2091517).

REFERENCES

AREFNIA, A., DEHGHANBANADAKI, A. and KASSIM, K.A., 2021. Sustainable Implementation of Recycled Tire-Derived Aggregate as a Lightweight Backfill for Retaining Walls. *KSCE Journal of Civil Engineering*, 25(11), pp. 4196–4206.

CHANG, I., LEE, M., TRAN, A.T.P., LEE, S., KWON, Y., IM, J. and CHO, G., 2020. Review on biopolymer-based soil treatment (BPST) technology in geotechnical engineering practices. *Transportation Geotechnics*, 24, pp. 100385.

COULOMB, C.A., 1776. Sur une Application des regles de maximis et minnis a quelque problems de statique, relatif a l'architecture. *Mem.Math.Phys., Acad.Royal Sci., par divers Sevans, Annee 1773, Paris*.

KHAN, R., CHAUHAN, V.B. and DASAKA, S.M., 2016. Reduction of lateral earth pressure on retaining wall using relief shelf: A numerical study, *Proc Int Conf Soil Environ, Bangalore, India, Paper No-117* 2016.

LEE, S., CHANG, I., CHUNG, M., KIM, Y. and KEE, J., 2017. Geotechnical shear behavior of xanthan gum biopolymer treated sand from direct shear testing. *Geomechanics and Engineering*, 12(5), pp. 831–847.

RANKINE, W.J.M., 1857. II. On the stability of loose earth. *Philosophical transactions of the Royal Society of London*, (147), pp. 9–27.

XIE, M., ZHENG, J., SHAO, A., MIAO, C. and ZHANG, J., 2020. Study of lateral earth pressures on nonyielding retaining walls with deformable geofoam inclusions. *Geotextiles and Geomembranes*, 48 (5), pp. 684–690.

Smart Geotechnics for Smart Societies – Zhussupbekov, Sarsembayeva & Kaliakin (Eds)
© 2023 The Author(s), ISBN 978-1-003-29912-7
Open Access: www.taylorfrancis.com, CC BY-NC-ND 4.0 license

Displacement field measurement of stacked geotextile tubes by digital image correlation

Dong-Ju Kim, Jong-Sub Lee & Jun Hyung Bae
Korea University, Seoul, Republic of Korea

Dong Geon Son, Yong-Hoon Byun & Yoon Geom Heo
Kyungpook National University, Daegu, Republic of Korea

ABSTRACT: Displacements often need to be measured to evaluate the stability of earth dams. Various instruments for measuring the displacement exist, but most contacting position sensors can measure the displacement only at a certain position. Digital image correlation is a promising technique for measuring a displacement field through a camera without any contact with the measurement points. In this study, variations in the displacement fields of stacked geotextile tubes with the water level are evaluated using digital image correlation. Experimental results show that the vertical and horizontal displacements of the bottom layers are larger than the top layers with an increased water level. The top layer mainly moves backward and then moves upward and forward. In contrast, the bottom layer consistently moves upward and forward after an initial downward and backward movement. Thus, the digital image correlation method suggested in this study may be effectively used to evaluate the behavior of a temporary dam structured with geotextile tubes.

1 INTRODUCTION

Geotextile tube has the characteristics of permeability, and the geotextile tubes can be filled with sandy soil on site. After the filling, the geotextile tubes behave as a mass-gravity unit, showing high stability (Lawson, 2008). Accordingly, geotextile tubes have been widely used for coastal protection, beach restoration, and embankments.

Geotextile tubes are often stacked in multi-layers to protect structures and slopes in various hydraulic and marine applications. Stacked geotextile tubes have various failure modes, including sliding, global slope stability, bearing capacity, settlement, and skin rupture (Zhu et al., 2014). Zhu et al. (2010) evaluated the global stability of stacked geotextile tubes using numerical analyses. However, there are few studies to characterize the behaviors of each layer of the stacked geotextile tube structure at various water levels.

Digital image correlation (DIC) is a non-contact optical measurement method based on digital image processing and numerical computation. DIC is used to investigate the displacement and strain fields of a specimen by comparing the image patterns before and after the deformation of the specimen. In the geotechnical engineering field, various studies have applied the DIC technique to observe the displacement field and failure mechanisms (Arshad et al., 2014; Wang et al., 2020; Segaline et al., 2022). However, the DIC technique has not been applied to monitor the displacement pattern of stacked geotextile tubes at various water levels.

The purpose of this study is to evaluate the displacement field of stacked geotextile tubes using the DIC technique. Geotextile tubes are filled with sandy soil for stacking. Using the DIC technique, the vertical and horizontal displacements of stacked geotextile tubes with various water levels are evaluated. Finally, the displacement patterns of the stacked geotextile tubes is discussed.

DOI: 10.1201/9781003299127-111

2 MATERIALS AND METHODS

2.1 *Materials*

The geotextile tube used in this study had a theoretical diameter of 38 mm and comprised a woven geotextile fabricated using polyester fabric. The geotextile tubes are manufactured with a length of 600 mm, and a width of 200 mm. The fill material is prepared by mixing silica sand and clay to evaluate the stability of the stacked geotextile tubes. The index properties of the sandy soils are summarized in Table 1. The mean diameter (D_{50}) of the sandy soil is 0.1.

Table 1. Index properties of sandy soil.

D_{10} [mm]	D_{30} [mm]	D_{50} [mm]	D_{60} [mm]	C_u	C_c	#200 [%]	PI [%]	LL [%]	PL [%]	G_s	USCS
0.04	0.10	0.20	0.27	6.75	0.93	20	12.5	23	10.5	2.88	SC

D_{10} = 10% cumulative passing; D_{30} = 30% cumulative passing; D_{50} = 50% cumulative passing; D_{60} = 60% cumulative passing; C_u = coefficient of uniformity; C_c = coefficient of curvature; #200 = percent passing No.200 sieve; PI = plasticity index; LL = liquid limit; PL = plastic limit; G_s = specific gravity; USCS = unified soil classification system; SC = clayey sands

2.2 *Digital image correlation system*

The DIC system consists of two industrial cameras and dual light emitting diode (LED) illumination to acquire the images. The two cameras have a 2.3 megapixel resolution. The measurement areas of the cameras range from 10×6 mm^2 to 1350×850 mm^2. A speckle pattern is applied to the specimen to obtain a high accuracy displacement field in the acquired image. Therefore, a black-on-white random speckle pattern is uniformly applied to each specimen using spray paint. The LED illuminations provide an appropriate brightness and contrast to the speckle pattern applied to the specimen. The DIC system is calibrated according to the software process. For calibration, two cameras simultaneously captured the same calibration object. The captured images were used to estimate the intrinsic (center point, lens distortion coefficients, focal length of each camera) and extrinsic parameters (translation and rotation between the two cameras) through software. The estimated intrinsic and extrinsic parameters were used to correlate the two-dimensional images captured by the cameras into three-dimensional coordinates.

2.3 *Experimental setup*

A schematic of the model test for the stacked geotextile tube is shown in Figure 1. An acrylic tank with a length of 1020 mm, a width of 420 mm, and a height of 600 mm is prepared to conduct the model test. In the acrylic tank, valves are installed on the wall on the upstream side at intervals of 30 mm in height to maintain a constant water level. A hole with a diameter of 50 mm has been installed at the bottom of the acrylic tank on the downstream side for drainage. Each geotextile tube is filled with a weight of 58.8 N of dry sandy soil. The geotextile tubes are stacked in four layers in the triangular. The voids between the stacked geotextile tubes are filled with sandy soil with the same particle size distribution as the fill material. To capture the images, the cameras are placed above the geotextile tube of the downstream side to which the speckle pattern is applied. The test program includes four different water levels. The water level on the upstream side increased from 90 mm to 240 mm. Each water level is maintained for 15 minutes. Each image is captured every 10 seconds.

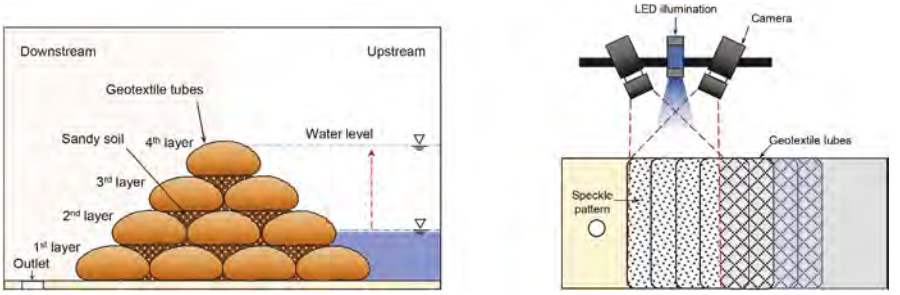

Figure 1. Schematic drawing of a model test using stacked geotextile tube.

3 EXPERIMENTAL RESULTS

3.1 *Vertical and horizontal displacement*

Vertical and horizontal displacements in each layer of the geotextile tube are evaluated from the images obtained from using the DIC technique. Figure 2 shows the vertical and horizontal displacements in each layer with elapsed time. Once the water level increases, the vertical and horizontal displacements show negative values and then converge to a constant value. Note that the negative values of vertical and horizontal displacements denote the downward and backward movements, respectively. After the first water level, the vertical displacement consistently increases up to the fourth water level, and the first and second layers of geotextile tubes show higher vertical displacements than other layers. In the horizontal displacement, all layers initially move to the upstream side in the first water level. After the second water level, the first and second layers of geotextile tubes start to move forward. After the third water level, all layers slightly move to the downstream side.

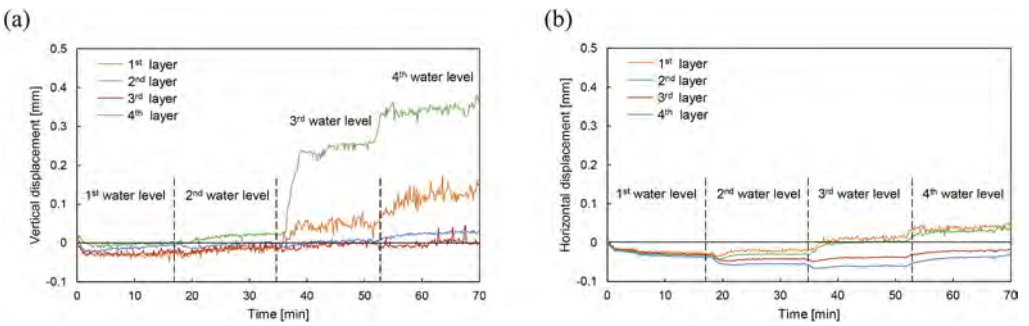

Figure 2. Evolution of displacements with water level: (a) vertical displacement; (b) horizontal displacement.

3.2 *Displacement pattern*

The displacement patterns on a two-dimensional plane estimated from measuring the vertical and horizontal displacements are shown in Figure 3. For the first and fourth layers, the final vertical and horizontal displacements in each water level are presented. In the first layer, the geotextile tubes initially move downward and backward. After the first water level, the first layer of geotextile tubes consistently moves upward and forward. In contrast, the fourth layer of geotextile tubes consistently moves backward up to the third water level and then moves upward and forward.

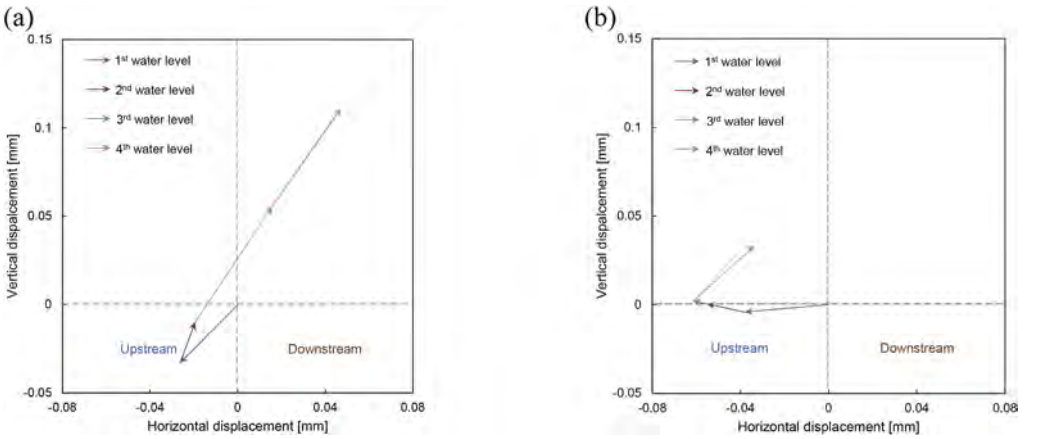

Figure 3. Evolution of displacements with water level: (a) 1st layer; (b) 4th layer.

4 CONCLUSIONS

Displacement evaluation of stacked geotextile tubes is needed for its global stability analysis. The DIC technique, a non-contact optical measurement method, was used to evaluate the displacement of stacked geotextile tubes according to the water level change. The movement of each layer of the stacked geotextile tube depended on the water level. The displacement patterns on a two-dimensional plane were obtained from the evaluated vertical and horizontal displacements. As the water level increased, the first layer of the geotextile tubes moved upward and forward more than the fourth layer. The DIC technique suggested in this study may be effectively used to evaluate the displacements of stacked geotextile tubes.

ACKNOWLEDGEMENTS

This work was supported by the National Research Foundation of Korea (NRF) grant funded by the Korean government (MSIT) (No. NRF-2021R1A5A1032433) and the Korea Institute of Planning and Evaluation for Technology in Food, Agriculture and Forestry (IPET) through the Agricultural Foundation and Disaster Response Technology Development Program, funded by the Ministry of Agriculture, Food and Rural Affairs (MAFRA) (320045032HD020).

REFERENCES

Arshad, M. I., Tehrani, F. S., Prezzi, M., Salgado, R. 2014. Experimental study of cone penetration in silica sand using digital image correlation. *Géotechnique*, *64*(7): 551–569.

Lawson, C. R. 2008. Geotextile containment for hydraulic and environmental engineering. *Geosynthetics International*, *15*(6): 384–427.

Segaline, H., Saez, E., Ubilla, J. 2022. Continuous characterization of dynamic soil behavior by Digital Image Correlation in a transparent shear laminar box. *Acta Geotechnica*, *17*(6): 2395–2414.

Wang, P., Guo, X., Sang, Y., Shao, L., Yin, Z., Wang, Y. 2020. Measurement of local and volumetric deformation in geotechnical triaxial testing using 3D-digital image correlation and a subpixel edge detection algorithm. *Acta Geotechnica*, *15*(10): 2891–2904.

Zhu, M., Kulasingam, R., Beech, J., Brussel, L. 2010. Modeling stability of stacked geotextile tubes. In *GeoFlorida 2010: Advances in Analysis, Modeling & Design*, 1777–1785.

Zhu, M., Viswanath, M., Ebrahimi, A., Beech, J. F. 2014. Slope-stability charts for stacked geotextile tubes. In *Geo-Congress 2014: Geo-characterization and Modeling for Sustainability*. 3082–3091.

Tunneling and rock engineering

Taylor & Francis
Taylor & Francis Group
http://taylorandfrancis.com

Smart Geotechnics for Smart Societies – Zhussupbekov, Sarsembayeva & Kaliakin (Eds)
© 2023 The Author(s), ISBN 978-1-003-29912-7
Open Access: www.taylorfrancis.com, CC BY-NC-ND 4.0 license

A pre-earthquake signal detection by the Eötvös torsion balance

L. Völgyesi, Gy. Tóth & Cs. Égető
Department of Geodesy Surveying, Faculty of Civil Engineering, Budapest University of Technology and Economics, Budapest, Hungary

Gy. Szondy
Society for the Unity of Science and Technology, Hungary

B. Kiss
Department of Control Engineering and Information Technology, Budapest University of Technology and Economics, Budapest, Hungary

G.G. Barnaföldi, E. Fenyvesi & P. Lévai
Department of Theoretical Physics, Institute for Particle and Nuclear Physics, Wigner Research Centre for Physics, Budapest, Hungary

P. Kovács
Department of Space Physics and Space Technology, Institute for Particle and Nuclear Physics, Wigner Research Centre for Physics, Budapest, Hungary

E. Imre
EKIK HBM and Bánki Donát Faculty of Mechanical and Safety Engineering, Óbuda University, Budapest, Hungary

M. Pszota
Faculty of Science, Eötvös Loránd University, Budapest, Hungary

P. Ván
Department of Theoretical Physics, Institute for Particle and Nuclear Physics, Wigner Research Centre for Physics, Budapest, Hungary
Department of Energy Engineering, Faculty of Mechanical Engineering, Budapest University of Technology and Economics, Budapest, Hungary

ABSTRACT: An important goal of seismological research is to predict earthquakes, but despite efforts, short-term earthquake prediction has not yet been achieved. On 9 January 2022, our upgraded Eötvös torsion balance in Budapest, Hungary, detected predictive signals 32 minutes before the earthquake in Florina, Greece, 770 km away, that were not detected by seismometers. Our measurements, in agreement with previous observations in Kazakhstan (Vol'fson et al. 2011), suggest that torsion balances can be effective in detecting earthquake precursors from a considerable distance.

1 MEASUREMENTS BY EÖTVÖS TORSION BALANCE

Our original goal was to repeat the EPF experiment in better circumstances, with at least one or two order higher precision using the original method of Eötvös. At the beginning of last century, *Loránd Eötvös* and his colleagues carried out their famous equivalence experiment by a torsion balance (known as *Eötvös-Pekár-Fekete* (EPF) measurement) for validating the equivalence of gravitational and inertial mass (Eötvös 1922). The original measurements contain tiny regular differences, so we decided to repeat the experiment under modern technical

DOI: 10.1201/9781003299127-112

conditions (Völgyesi et al. 2018). After long preparations, we started our measurements in 2019 (Tóth et al. 2019, Völgyesi et al. 2019), which are still ongoing.

The site of our experiment is the Jánossy Underground Research Laboratory (JURLab) unit of the Vesztergombi Laboratory of High Energy Physics (VLAB) at Wigner Research Center for Physics. On Figure 1 the Eötvös-Pekár torsion balance and the Güralp 3T three-axis broadband seismograph placed next to it can be seen in the laboratory corridor at a depth of 30 meters below ground. The temperature stability of this site is satisfactory, the daily change is only a few hundredths of degrees, and the amplitude of the microseismic ground vibrations is also sufficiently small. Environmental factors are continuously recorded with several temperature, pressure, humidity, infrasound sensors.

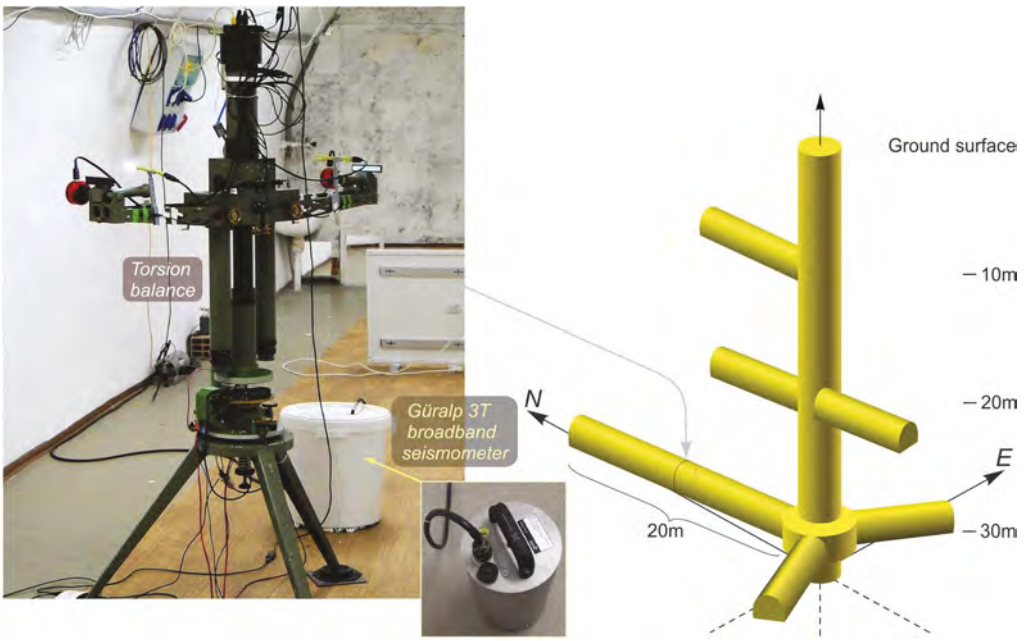

Figure 1. The location of Eötvös-Pekár torsion balance and the Güralp 3T seismometer at the Jánossy Underground Research Laboratory (JURLab).

In addition to temperature variations, measurements are most disturbed by microseismic ground vibrations. The "technogenic" noise (mainly ground vibrations caused by traffic) can be reduced, but earthquakes, free vibrations and natural sources are constantly present. In order to take these into account and to filter them out, we use a Güralp 3T seismograph, continuously recording ground vibrations and earthquakes.

2 EARTHQUAKE REGISTRATION BY TORSION BALANCE

Our torsion balance is also an excellent tool for recording earthquake waves. In the last 2 years we have recorded around 60 earthquakes of greater or lesser magnitude.

Among these earthquake records recently we have found an extremely surprising and interesting observation, namely the torsion balance registered an unusual strange vibrations approximately half hour before the internationally recognized earthquake. Furthermore, the Güralp 3T seismograph, located 1 m from the Eötvös torsion balance did not register this preactivity, it registered signal only at the official time of the earthquake.

This earthquake occurred in Greece on 9 January 2022, (the parameters: t_o = 21:43:47/UTC/, 40°43′48.0″N, 21°21′36.0″E, Richter magnitude M = 5.6, focal depth h = 9km). Several seismograms of this earthquake were registered at different seismological observatories around our measurement site. These are regular seismograms, one cannot see anything special on them.

In contrast to the usual seismograph recordings, the Eötvös torsion balance shows unusual and peculiar vibrations. The earthquake pushed the pendulum of the torsion balance out of equilibrium and then disturbance was damped and the equilibrium restored (top of the Figure 2). However,

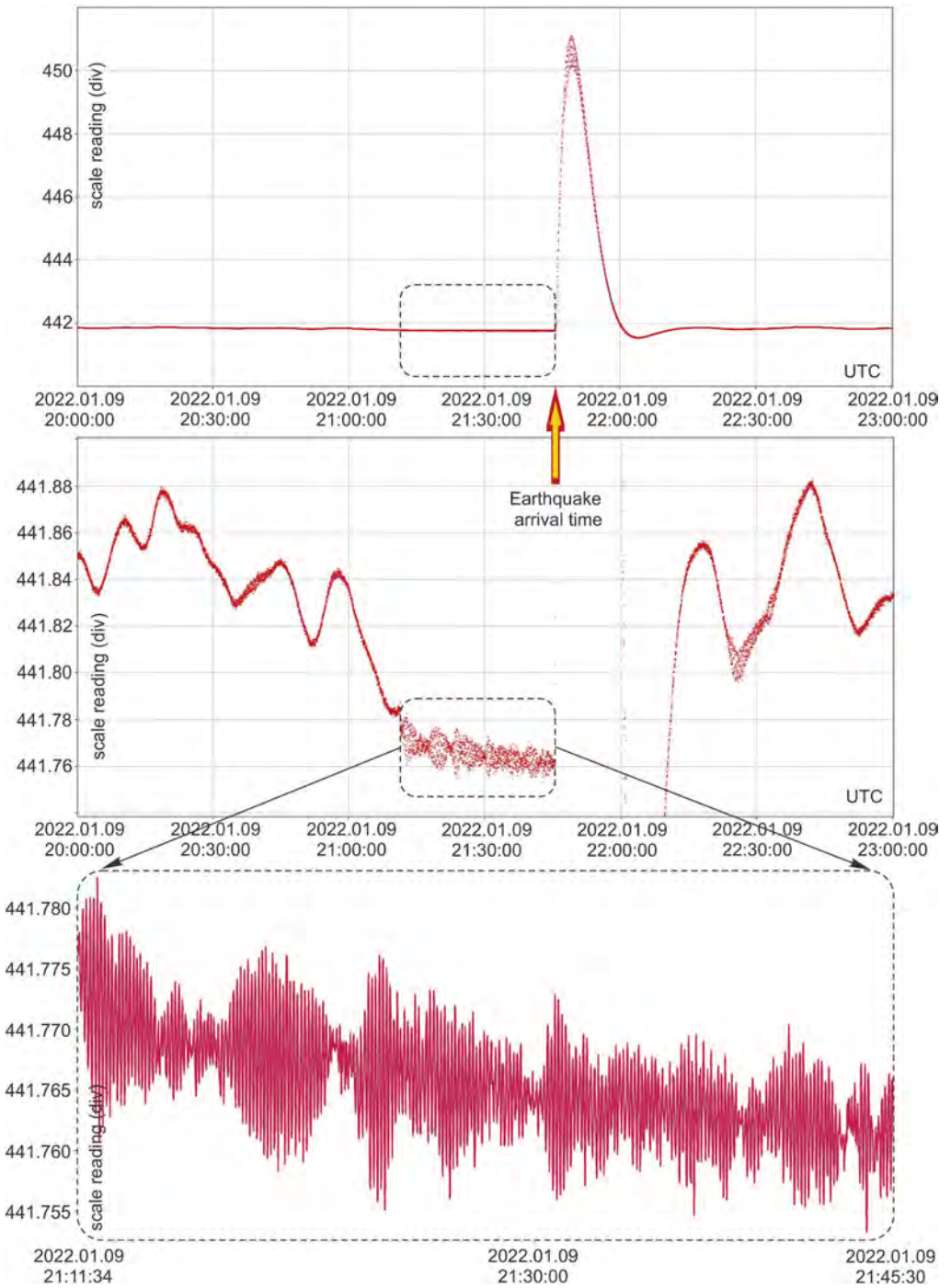

Figure 2. Earthquake in Greece on 9 January 2022, registration and enlarged images by the pendulum II of the torsion balance.

with higher resolution one can see that a characteristic signal appeared about 32 minutes before the earthquake (in the middle part of Figure 2). The lower part of Figure 2 shows a high magnification picture of the shaking of the pendulum in the half hour before the earthquake.

It is very important to note that prior to the earthquake, the Güralp 3T seismograph installed in the immediate vicinity of the Eötvös torsion balance did not indicate any unusual waves.

Further detailed investigation of the circumstances of our observation would be necessary. Neither the thermometers, barometers and the neighboring seismograph indicated any external disturbances that could be correlated to the unusual signal. The torsion balance was all the time at rest, it was not rotated.

3 DISCUSSION

Eötvös balance is a unique device that is sensitive to the force difference of its test masses with extreme sensitivity. Due to its characteristic dipole construction and the suspension system it is a sensitive frequency selective amplifier of the microseismic noise (Speake & Gillies 1987; Kalinnikov et al. 1994). This feature of the balance is available only with continuous registration of the position and high sensitivity. Similar instruments were developed in the Institute of Experimental Geophysics, Russian Federation, motivated by the possibility of earthquake prediction (Kalinnikov et al 2011, Vol'fson et al. 2010; Vol'fson et al. 2011).

Further studies are needed to clarify and understand this phenomenon. Our signal differs from the signal of the previous observations, but the structure of Eötvös balance is also different of their instruments, except the dipole construction. There are a lot of unanswered questions, a clarification requires further observations and modeling.

Our further research goal is to reproduce this observation, and also to understand the origin and the conditions of the detection. To this end we should explore the environmental, geophysical and technological factors that influence the modernized torsion balance. It is remarkable that the detection of signals, like in bottom of Figure 2 required sensitivity an order of magnitude higher than the sensitivity of the original device.

REFERENCES

Eötvös, R., Pekár, D., Fekete, E. 1922. Beiträge zum Gesetze der Proportionalität von Trägheit und Gravität, *Annalen d. Physik*, 11–66.

Kalinnikov, I.I., Matyunin, V.P., Nyunina, N.A. 1994. A property of weakly damped torsion balance with vertical suspension, *Izvestia phisics of the solid Earth C/C of fizika Zemli*, 30: 321–334.

Kalinnikov, I.I., Manukin, A.B., Koneshov, V.P., Matyunin, V.P., Karagioz, O.V., Vol'fson, G.B. 2011: Investigation of variable gravitational gradients and specific features of the microseismic background with torsion balance. *Physics of the Solid Earth*, 47(5): 456–463.

Speake, C.C., Gillies, G.T. 1987. Why is G the least precisely known physical constant?, *Zeitschrift für Naturforschung A*, 42(7): 663–669.

Tóth, G., Völgyesi, L., Szondy, G., Péter, G., Kiss, B., Barnaföldi, G., Deák, L., Égető, C., Fenyvesi, E., Gróf, G., Somlai, L., Harangozó, P., Lévai, P., Ván, P. 2019. Remeasurement of the Eötvös-experiment, status and first results, *PoS*(FFK2019)042.

Vol'fson, G.B., Evstifeev, M. I., Kazantseva, O.S. Kalinnikov, I.I., Manukin, A.B., Matyunin, V.P., Scherbak, A.G. 2010: Gradiometric seismoreceiver with a magnetic suspension int he problems of operative eathquake forecasting. *Seismic instruments*, 46(3): 265–274.

Vol'fson, G.B., Evstifeev M.I., Scherbak A.G. 2011. Gravity gradiometric seismic sensor for early prediction of earthquakes. *Gyroscopy and navigation*, 2(3): 192–196.

Völgyesi, L., Szondy, G., Tóth, G., Péter, G., Kiss, B., Deák, L., Égetõ, C., Fenyvesi, E., Gróf, G., Ván, P. 2018: Preparations for the remeasurement of the Eötvös-experiment. *Magyar Geofizika* 59(4): 165–179. (In Hungarian).

Völgyesi, L., Szondy, Gy., Tóth, Gy., Kiss, B., Fenyvesi, E., Péter, G., Somlai, L., Égető, Cs., Deák, L., Barnaföldi, G., Gróf, Gy., Harangozó, P., Lévai, P., Ván, P. 2019. Torsion Balance and Remeasurement of the Eötvös Experiment, *PoS*(FFK2019)041.

Smart Geotechnics for Smart Societies – Zhussupbekov, Sarsembayeva & Kaliakin (Eds)
© 2023 The Author(s), ISBN 978-1-003-29912-7
Open Access: www.taylorfrancis.com, CC BY-NC-ND 4.0 license

Challenges in design of earthen reservoir in a rocky ground profile

B.V. Sushma
Assistant General Manager, TATA Consulting Engineers Ltd., Bangalore, India

Manos Kumar De
Senior General Manager, TATA Consulting Engineers Ltd., Jamshedpur, India
ORCID ID: 0000-0002-2451-2647

Kailasa Rahul
Trainee Engineer, TATA Consulting Engineers Ltd., Bangalore, India

ABSTRACT: Rock formations are generally perceived as favorable and good bearing stratum. However, there are many challenges in design of earthen reservoir foundation on a rocky profile. Geological mapping coupled with comprehensive geotechnical investigation is a vital requirement for such studies. The geological mapping needs to encompass the study of active folds, faults and any other geological concerns. The geotechnical data need to be detailed covering the permeability, compressive strength, water absorption etc. which are critical in the achieving the reservoir water tightness. This paper outlines the various challenges confronted in earthen reservoir design in a rocky landscape and the solutions provided for a project case.

1 INTRODUCTION

Generally, encountering of the rock as out crops, or at shallow depths is perceived as very favourable condition for the foundation system. However, while designing foundation of earthen embankments in a rocky landscape, there are many challenges to achieve watertight and stable foundation system. Adequate factor of safety against base pressure is not the only criteria that determines the suitability of the founding stratum of earthen reservoir. It calls for exhaustive geotechnical investigation clubbed with geological mapping for arriving at the requisite data to satisfy various other stability aspects for successful design of earthen embankment. The current project is in the Cuddapah region, and earthen embankments are planned to be designed for providing impoundment for a raw water reservoir of a process plant. Rigorous design tools are to be used for checking the stability analysis, drainage arrangements, overall integrity and functioning of the raw water reservoir. The degree of water tightness of foundation strata predicts the containment of the hydraulic head for the specific time length. Further, earthen embankments can undergo breaching that is caused by internal erosion actions of undermining and seepage. *(Foster et al., 2000; Fell et al., 2003)*.

2 GEOTECHNICAL AND GEOLOGICAL ATTRIBUTES

2.1 *Geological mapping of the project site*

The site is located in Cuddapah basin which consists of sedimentary deposits that overlay gneiss and granite formations *(Sukanta Goswami et al., 2017)*, Basic geological studies of the site reveal that rocks with predominantly arenaceous and argillaceous materials form major part whereas rocks with calcareous and dolomitic materials occur as subordinate constituents.

DOI: 10.1201/9781003299127-113

Quartzite, Shale, Sandstone, Limestone, variegated shale, and dolomite are various types of rocks prevailing in the site.

2.2 *Geotechnical information*

In the raw water reservoir area, 9 boreholes and 4 field permeability tests were carried out. Sub- surface soil/rock profile indicates rock outcrops of highly weathered rock underlain by jointed/fractured medium hard rock to jointed rock. In only one borehole (BH-1) silty sand with gravel is encountered as topsoil up to 0.5m depth. The types of rock encountered are Limestone, Shaley limestone, Quartzite, weathered quartzite, and Fresh quartzite. The rock present at shallow depth possess CR (core recovery) ranging from 21% to 84%, RQD (Rock Quality Designation) ranging from 10% to 78 % and Permeability values ranging from 1.69x10-06 cm/sec to 6.39 x 10-06 cm/sec.

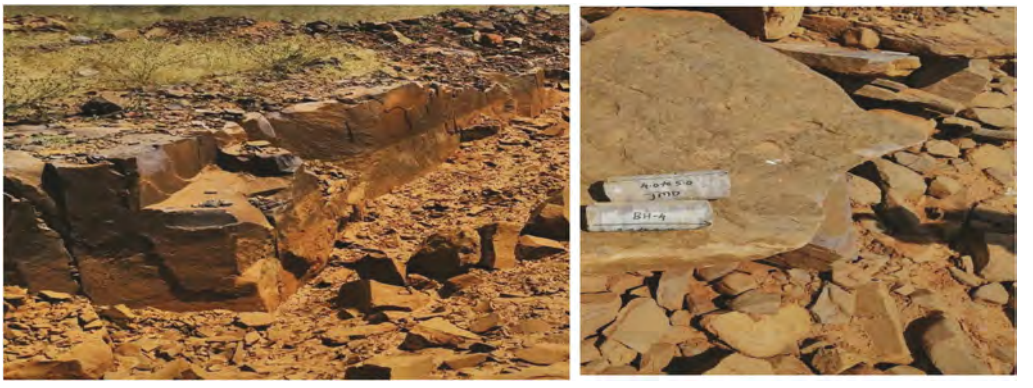

Figure 1. Rock outcrops at site.

2.3 *Topography variation*

As per the contour drawing in the Raw water reservoir area, the reduced Ground levels, are varying from RL 179 m towards the northern side and increasing to RL 203 towards the southern side. The 3D map of the entire reservoir area is hereby attached as Figure 2. As the ground topography is highly varying and site grading is not carried out in the reservoir area to avoid large earthwork volumes, the embankment top level was maintained uniformly at RL 203, this resulted in embankment heights ranging from 4 to 21m along the periphery of the reservoir.

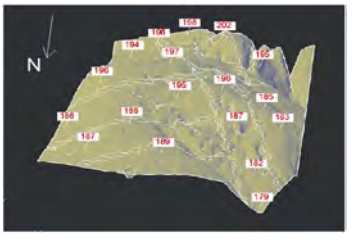

Figure 2. The 3D Topographic view of the entire reservoir area.

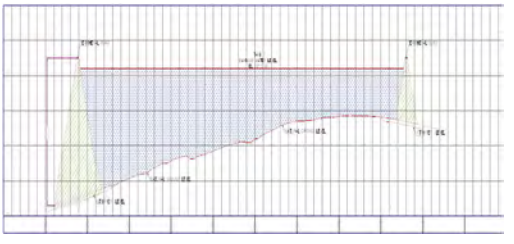

Figure 3. Profile of reservoir area.

3 COMPONENTS OF EARTHEN EMBANKMENT

The earthen embankment of symmetrical section was considered for the reservoir area. The whole area of the reservoir catchment was stripped up to 0.5m below natural ground level to exclude roots, vegetation, and other organic matter.

The design of earthen embankment for raw water reservoir was carried out with all rigorous analysis and checks for the critical aspects which can be anticipated during functionality of the design life period of the reservoir.

- Stability of earthen embankment (Slope stability and overall stability for static and seismic conditions)
- Internal and external erosion control of embankment
- Internal drainage arrangements of embankment
- Water tightness of the foundation system of embankment

The components of the Earthen embankment are categorized based on functional aspects of the reservoir and detailed as below:

3.1 *Stability of earthen embankment (Slope stability and overall stability)*

3.1.1 *Positive cut-off*

The Permeability values of the bed rock are found to be ranging from 1.69×10^{-06} cm/sec to 6.39×10^{-06} cm/sec. Hence the relatively impermeable soil of CL/ CI type soil is provided as the positive cut-off at the junction of embankment and founding strata.

3.1.2 *Core*

Core is constructed with low permeability material of 10^{-06} to 10^{-08} cm/s at center of embankment. In the considered section, central core is provided with top width 3 m and core top level fixed at 1 m above MWL (Maximum water level). Core thickness is not less than 50% of max. water head at any section and slope of 1V:0.5H is provided.

3.1.3 *Casing*

In considered section casing with slope of 1V:2H is provided on both upstream and downstream sides, using SC/SM/GC type of soil with higher permeability of 10^{-03} to 10^{-06}cm/s.

3.1.4 *Berm*

Berms are provided to provide to increase the stability of the earthen embankment. The berms of 3 m width are provided at every 5 m vertical height of the embankment in the considered section.

3.2 *Internal and external erosion control*

3.2.1 *Stone pitching*

Stone pitching is provided on upstream face over filter layer as per *IS 9429*, permeability of filter material to be $< D_{15}$ (F) and $\geq D_{15}$ with respect to base soil and not less than 0.1mm. The soil gradation used for coarse and fine filter are 40mm and 20mm down sized particles respectively. Header stones is provided extending through stone pitching by 150 mm and are spaced at 1.5 m centre to centre.

3.2.2 *Turfing*

The downstream slope is protected against the erosive action of rain and its run-off by providing wild grass turfing with provision for irrigation sprinklers.

3.2.3 *Road*

The road of 3.75m is provided on top width of the embankment for the movement of inspection vehicles.

3.3 *Internal drainage arrangements*

3.3.1 *Inclined filter*

Inclined filter made of fine sand particles passing 2mm IS sieve is provided on downstream side of core. It is provided of 1m thickness for embankment height of up to 10m and increased to 1.5m thickness for sections of embankment height 10-21m.

3.3.2 *Horizontal filter*

The Horizontal filter connecting inclined filter is made of fine sand particles passing 2mm IS sieve. It is provided of 1m thickness for bund height of up to 10m and increased to 2m thickness for sections of bund height 10-21m, with length of three times embankment height.

3.3.3 *Rock toe*

The 'rock toe or toe filter' comprises stones ranging in size from 15 to 20 cm over toe filter composed of graded cohesionless material. Toe filter generally consist of three layers of fine sand, coarse sand, and gravel. In considered section rock toe is provided at toe of downstream slope at the end of horizontal filter. Rock toe height is kept as 2.0m, above the tail/ dead water reservoir level which is 1.5m above the lowest ground elevation.

3.3.4 *Toe drain*

Toe drain of stone masonry of 0.6 m depth is provided in trapezoidal shape on all around the embankment. Toe drain connected to the rock toe to lead the rain/ surface drainage water to nearby identified nalla or water body.

3.4 *Water tightness of the foundation system*

3.4.1 *Clay bedding*

Clay bedding of low permeability of 600 mm thickness is provided on the bed of the raw water reservoir as per *IS 9451*.

3.4.2 *Curtain grouting*

The field permeability test results of the site indicate values in the range 10^{-6} to 10^{-7} cm/s respectively. The RQD (Rock Quality Designation) is found to be around 30% at these depths. The lugeon value is arrived as 0.19 and 0.39 at 2 m and 5 m respectively. Based on field permeability results as lugeon value is less than 3, curtain grouting is not envisaged.

4 SLOPE STABILITY ANALYSIS AND CHECKS

Earthen embankment is susceptible to failure due to various operational and structural reasons.

Overtopping, structural failures in foundation, and piping are the major causes for failure of earthen embankments. There may also be additional causes of failure depending on specific site conditions and embankment structures. (*Journal of Hydraulic Engg. ASCE 2011*).

The various causes leading to failure of earth embankments are listed as 1. Hydraulic Failure 2. Seepage Failure and 3. Structural Failure.

Stability analysis was performed to ensure that reservoir embankment is safe against all possible failure conditions.

In order to check the stability of reservoir against all the possible failure conditions, 3 types of analyses were performed as below:

- Seepage Analysis
- Slope Stability Analysis
- Sliding/ Overall Stability analysis

The stability analysis is carried out for the most critical section of height 21m.

4.1 *Seepage analysis*

Seepage analysis was carried out in SEEP/W module of GeoStudio 2018.

Seepage analysis is performed to check stability against following failure conditions.

- Piping through embankment body
- Piping through Foundation

4.1.1 *Critical exit gradient*

Critical hydraulic Gradient of foundation soil is calculated as $=(G-1)/(1+e)=0.95$ (1)

Figure 4 Shows pressure head variation in embankment under steady seepage condition. It can be seen that phreatic line passes below rock toe. Therefore, embankment is safe against piping through body.

Figure 5 Shows Total head variation in embankment section under steady seepage condition.

Head drop at exit (dh) = 0.25 -0 =0.25m

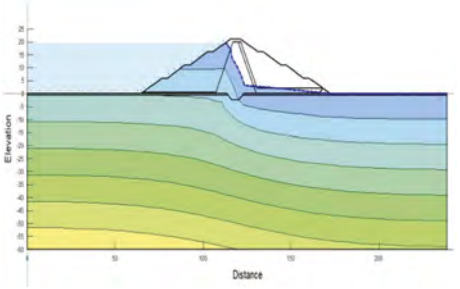

Figure 4. Phreatic line.

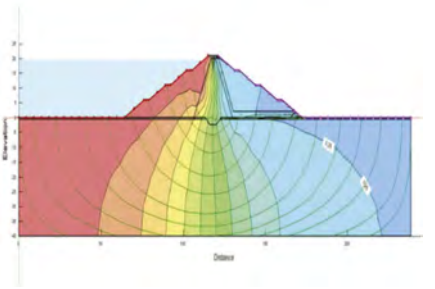

Figure 5. Total head distribution.

Average distance at between the pressure drops at exit (ds) = 5.53 m

Exit gradient = dh/ds = 0.0452

$$\text{Factor of Safety} = \text{Exit Gradient}/\text{Critical exit gradient} = 21 > 6 \text{ (as per IS 6966)} \quad (2)$$

Therefore, embankment is safe against piping through foundation

4.2 *Slope stability analysis*

The loading conditions including all likely combinations of reservoir and tailwater levels, seepage conditions, both after and during construction that could be critical for causing instability were investigated. Based on that, 3 conditions as listed below were checked.

- Immediately after Construction Condition
- The Steady Seepage Condition and
- The Rapid Drawdown Condition in the reservoir (*EJGE Vol. 18 [2013], Bund. Z 6022*)

Sliding of a large soil mass along a curved surface is the usual mode of failure of an embankment.

The stability analysis was carried out using 'GeoStudio 2018′ software by limit equilibrium method per *IS 7894* for critical conditions, which may be anticipated during the service life of the reservoir sections.

The summary of the slope stability analysis is shown by a flowchart in Figure 6. The materials considered for slope stability analysis is tabulated in Table 1.

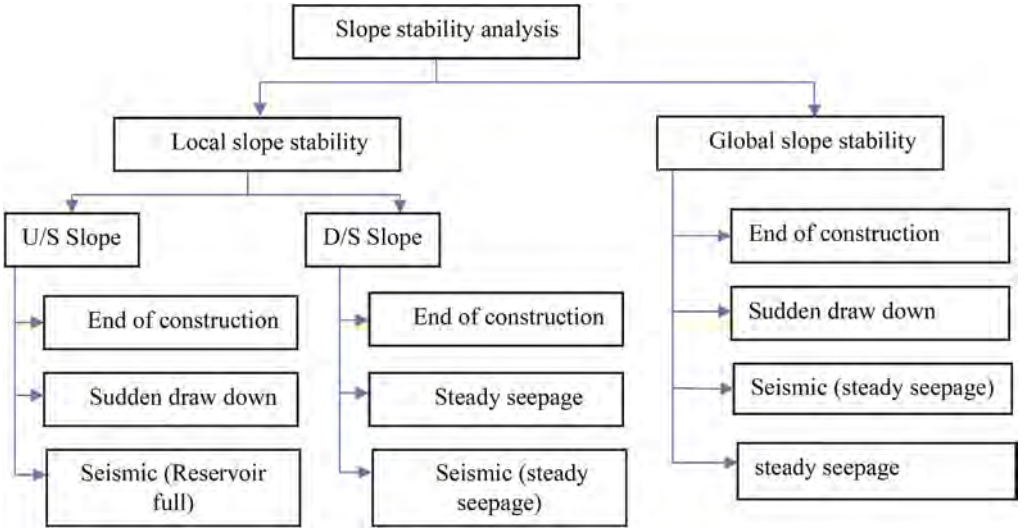

Figure 6. Flowchart for slope stability analysis.

Table 1. Material properties used for stability analysis.

SL. No.	Material	Dry density (kN/m^3)	Saturated density (kN/m^3)	Total strength		Effective strength	
				Cohesion (kpa)	Friction angle (°)	Cohesion (kpa)	Friction angle (°)
1	Casing	17.51	18.6	1.13	29	1	31.5
2	Core	16.3	19.36	37.57	23	35.94	25.67
3	Filter	18	20	0	30	0	30
4	Toe drain	18	20	0	30	0	30
5	Rock toe	20	22	0	40	0	40
6	Cutoff	16.3	19.36	37.57	23	35.94	25.67
7	Foundation soil	18	19.5	0	30	0	32
8	Foundation rock	20	22	0	40	0	40

Table 2. Calculation of seismic coefficients (IS 1893- 1984).

Location	Cuddapah
Seismic horizontal coefficient $A_h = \alpha \times I \times \beta$	0.06
Vertical seismic coefficient ($A_v = 0.5 \times A_h$)	0.03

The summary of slope stability analysis performed, and the factor of safeties obtained for local and global stability condition along with acceptable factor of safety for each condition are listed in Table 3.

From Table 3 it can be concluded that the obtained factor of safeties is within acceptable limits and the raw water reservoir embankment is safe under all critical conditions.

The input and few cases of output sketches of the stability analysis are enclosed below from Figures 7–12.

Table 3. Summary of factor of safeties obtained for various cases.

Condition	Slope	Local FOS	Global FOS	Acceptable FOS
End of construction	Upstream slope	1.53	17.23	1.0
	Downstream slope	1.53		1.0
Steady seepage	Downstream slope	1.55	5.21	1.5
Sudden drawdown	Upstream slope	1.65	18.64	1.3
Seismic (Reservoir full)	Upstream slope	1.33	3.58	1
Seismic (Steady seepage)	Downstream slope	1.44		1

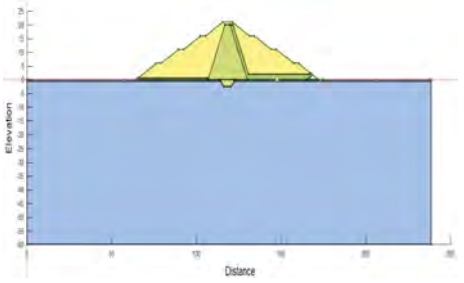

Figure 7. Input model.

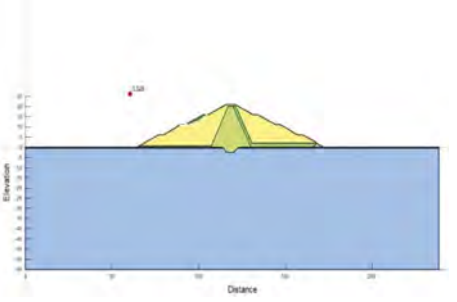

Figure 8. End of construction (upstream slope).

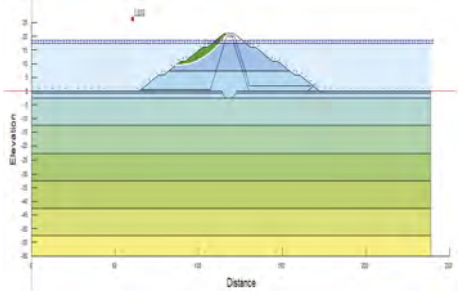

Figure 9. Sudden drawdown (upstream slope).

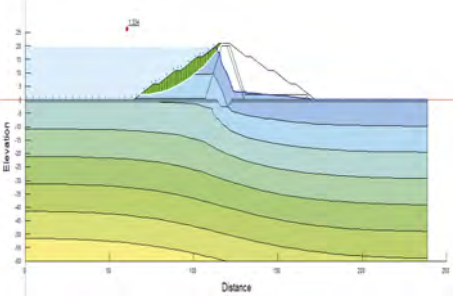

Figure 10. Seismic (Reservoir full for upstream side).

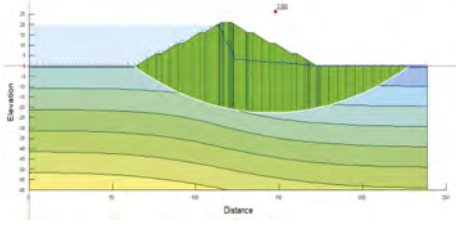

Figure 11. Seismic (Global stability).

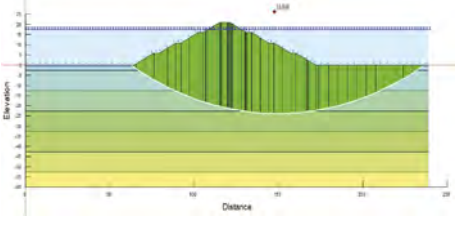

Figure 12. Sudden drawdown (Global stability).

4.3 *Sliding/ Overall stability analysis*

The soil foundations are generally weak in shear and hence the shear stresses developed should be within limits. The stability of embankment is checked against sliding failure (*Irrigation engineering and hydraulic structures by S K Garg*) for following failure conditions.

- Overall stability of embankment
- Stability of U/S slope of embankment
- Stability of D/S slope of embankment
- Stability of Foundation Soil

The acceptable FOS safety for various cases as per *IS 7894* are summarized as below:

Table 4. Summary of sliding stability.

Condition	FOS	Acceptable FOS
Embankment as a whole	1.59	1.3
Downstream Slope	2.01	2.0
Upstream Slope	5.27	2.0
Stability of foundation soil	3.01	2.0

It can be noted that the reservoir embankment is safe for the sliding stability.

4.4 *Embankment settlement criteria*

The dimensions of the embankment are base width =110m, top width = 6m and maximum section height= 21m. The average compressive stress at the base of foundation from the embankment is noted to be around 200kpa and settlement arrived was in the order 10mm. The permissible settlement is around 300-600mm for the embankments as per *IRC 75* (Indian Road Congress) code and 200mm (1-2% of dam height as settlement allowance) as per *IS 8826 (Guidelines for design of large earth and rockfill dams)*. The arrived settlement as above is within permissible limits.

5 CONSTRUCTION ASPECTS OF THE EARTHEN EMBANKMENT

The Construction materials and the aspects are very critical in achieving the requisite functionality as per design. The construction materials are categorized based on the functionality and elaborated accordingly.

5.1 *Water tightness of embankment and to ensure against piping failure*

Detailed packer permeability testing of reservoir embankment is carried out to finalize the depth of cut-off and necessity of curtain grouting.

5.1.1 *Grouting and grout holes below positive cut-off*

Curtain grouting and grout holes below positive cut off are not envisaged at the design phase based on the permeability test results.

5.1.2 *Positive Cut-off*

Borrow material from lakes of classification CI /CL and having permeability less than around 10^{-6} to 10^{-8} cm/s are considered for impervious cut-off.

5.2 *Internal stability and drainage arrangements*

5.2.1 *Core and Bed lining*

The material for core and bed lining considered of impervious material is same as that of the positive cut off.

5.2.2 *Soil in casing*

The soil conforming to classification SM/SC/GC/SC is considered from the nearby identified lakes for the casing material. The permeability of these materials ranging from 10^{-4} to 10^{-6} cm/s.

5.2.3 *Stone pitching*
Stone Pitching of 300mm thickness is laid on upstream slope by hand placing stones along the edge. Stones used for pitching are rounded or sub-angular river cobbles or rock pieces with sufficient base area to be stable. Stones should be of uniform size, not less than 15cm in any direction, sound, hard, durable and should be able to sustain weathering and water action. Stones are laid in compact manner with staggered joints starting from the bottom of the slope. The joints are matched and interlocked so that they are keyed together with a minimum of voids.

Stone pitching placed over a graded fine and coarse filter (for a course of 150mm). The graded material for stone pitching is considered from the nearby quarry. The filter materials are considered by grading of the existing topsoil available at site.

5.2.4 *Rock toe*
Hard stone 25 to 50 kg weight wrapped in geo grid Netlon C.153 or equivalent shall be used for construction of Rock toe. The geo grid shall be impaled to the soil at spacing of 5 m. Stones used are free from lamination, soft spots, cracks, and seams. The graded material for rock toe is considered from the nearby quarry.

5.3 *External drainage arrangements*

5.3.1 *Road on top of embankment*
The road section is provided in accordance with Section 400 of MORTH (Ministry of Road Transport and Highways) specification.

5.3.2 *Chute drains*
Semi-circular precast concrete pipes of 200/225 mm diameter is considered for chute drains at 90m C/C is provided on downstream face as shown in the Figure 13.

5.3.3 *Longitudinal drains*
The longitudinal drain with M15 concrete of 300 mm deep and 300mm wide with thickness of 100 mm are provided connected to the chute drains at berm level to achieve network of external drainage leading to toe drain as shown in the Figures 14 and 15.

Figure 13. Semi-circular chute drain.

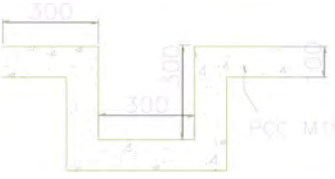

Figure 14. Longitudinal drain.

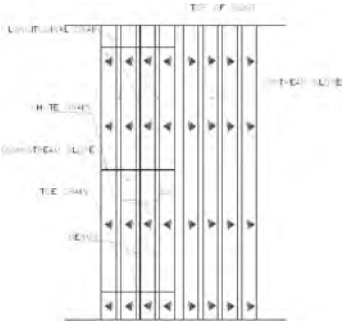

Figure 15. Drain arrangement on downstream slope.

5.4 *Compaction*

The compaction is carried out to achieve minimum 95 % maximum dry density under modified proctor conditions for clayey soil and minimum 75 % relative density for subgrade/sandy soil respectively.

The compaction is considered with a 10 to 12ton sheep foot or padfoot rollers for clayey soil and 10 to 12ton vibro roller for subgrade/sandy soil.

During compaction it is required to check that the specified layer thickness of the materials has been laid, the specified number of passes of roller of specified type and weight have been applied and there is no excessive rutting or weaving of the fill.

The embankment components core, casing, positive cut off and clay bedding are laid with layer wise compaction. Necessary sampling before and after compaction are carried out so that effectiveness checks on fill operations are maintained.

5.5 *Inspection and testing*

The scheme of field tests is considered as a part of quality control for soils used for embankment (before compaction) and on compacted layer (after compaction) is based on provision of clause 903.2.1 and 903.2.2 of MORTH.

5.6 *Construction sequence*

The embankment was proposed to be constructed as per construction sequence elaborated below

- Centre line of raw water reservoir to be marked on site as shown in Figure 16.
- The reservoir bed area was cleared including uprooting rank vegetation, grass, bushes, shrubs, sapling.

Figure 16. Plan and profile view of reservoir.

- The embankment area was stripped up to 500 mm depth to exclude the loose/soft patches, vegetation, plant root, organic material etc. and other objectionable matter.
- From centre line of reservoir, the foundation line was marked.
- Stripped surface was excavated for the construction of positive cut-off. Excavation was carried out with side slope of 1:1. The excavation in rock was carried out using hydraulic breaker etc. to avoid mechanical fracturing of rock.

- Before construction of positive cut-off, lugeon value to be checked based on the packer permeability test along with geologist's visual inspection. If the lugeon value is found to be more than 3 and considering geologist feedback too, the curtain grouting needs to be considered and grout holes to be designed accordingly.
- For construction of positive cut off the soil was laid in layers of 300 mm compacted to 95% of MDD using handheld pneumatic compactor.
- Rock toe was constructed along the toe of the reservoir. The graded filter was laid to correct profile followed by placing of the geonet filled with rocks along the toe portion.
- After construction of positive cut-off and rock toe, core was constructed up to the top level of first layer then horizontal filter, casing, clay bed lining up to the same level.
- Sheep foot roller was used for compaction of core and vibro roller was used for compaction of casing.
- The 600 mm thick clay bed lining is provided as initial layer below casing material along upstream side of embankment and compacted using sheep foot roller.

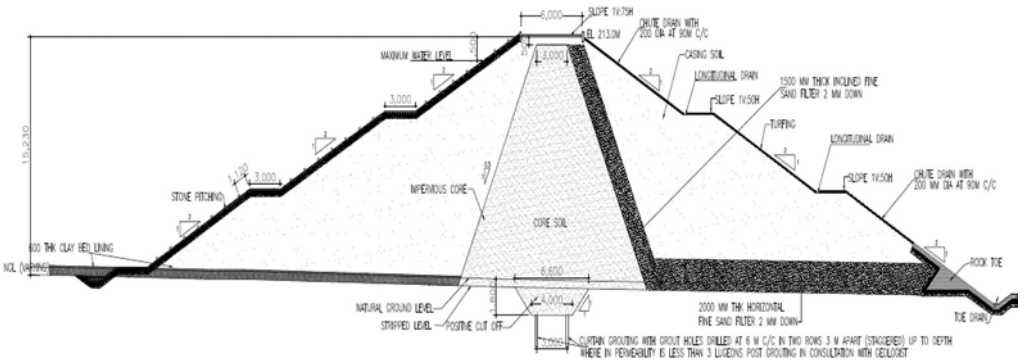

Figure 17. Cross section details.

- Inclined and horizontal filters are placed immediately downstream of the core zone within embankment. The filter layer was installed along with the adjacent core material and downstream shell in one of two ways. The first method is to lay the filter layer one lift ahead of the adjacent zones and in the second method it is laid one lift behind.
- Stone pitching was provided on upstream side of embankment and turfing was provided on downstream side of embankment.
- Toe drain was provided outside the rock toe all along the periphery of the embankment to lead the rain/ surface drainage water to nearby identified nalla or water body.

6 CHALLENGES FACED COMPARED TO EARTHEN SUB PROFILE

- Many challenges were faced due to the rocky landscape at site compared to construction on soil. The below points highlight the comparison and challenge faced in rocky profile compared to soil profile.
- As competent rock is present at shallow depth, the excavation by any machinery is not possible and blasting is the only technique which can be adopted here. Hence general concept of cut and fill could not be adopted here. Various material to be used in dam body was considered from borrow area. If rocky profile would not have encountered, excavation and use of same material for embankment construction would have been adopted, leading to reduced borrow material there by huge cost savings on the project.

- Positive cut- off is provided to increase the path of drainage and curtain grouting is done, for sealing the rock in case of low permeability and fractured rocks. This needs to be carried out to achieve water tightness of the embankment foundation. During construction packer permeability tests are carried to check the permeability of foundation rock to further assess the requirement of grouting. If the rocky profile was not encountered the need for such exhaustive tests in rock would have been avoided achieving less complex design and thereby cost savings.
- Geological mapping and geotechnical studies to carried out check permeability in case of bedding planes, rock joints, folds, and faults which are critical for safety of the embankment. The need of such rigorous foundation strata geological study is not required for foundations on soil profile. In soil profile it only calls for settlement analysis for embankment which will not be critical unless very soft strata is encountered.
- Due to limitations in excavation, higher height embankment had to be designed to achieve the same capacity. In case of soil profile, the design can be planned by using the excavated soil in embankment thereby leading to competitively lower height embankment for same capacity.
- During construction, excavation of the rock calls for rock blasting which requires careful planning. Such aspects do not arise in soil profile.
- If fractured rock with discontinuities, orientation of bedding planes in horizontal direction is encountered, the measure for overcoming the seepage problems is robust and cost effective.

7 CONCLUSIONS

a. Encountering of rock at shallow levels cannot be considered fully favorable for an earthen embankment design.
b. Comprehensive Geotechnical investigations along with geological mapping is required to completely ascertain and design structures in a undulating rocky terrain
c. In an earthen embankment, owing to the various components and materials involved, the design shall be carried out critically considering all the stability and seepage aspects.
d. The stability analysis shall be carried out considering overall embankment stability, slope stability of upstream and downstream slopes in static and seismic condition.
e. The construction materials & aspects to be in in line with the design requirement and consideration.
f. There are many challenges in design, construction and execution which leads to substantial cost increase in rock terrain compared to soil profile.

REFERENCES

Davachi, M.M., Sinclair, B.J., Hartmaier, H.H., Baggott, B.L. and Peters, J.E., 1991. Determination of the Oldman River Dam foundation shear strength. Canadian Geotechnical Journal, 28(5), pp.698–707.

ASCE/EWRI Task Committee on Dam/Levee Breaching, 2011. Earthen embankment breaching. Journal of hydraulic engineering, 137(12), pp.1549–1564.

Bhattacharjee, N. and Mohanty, S.P., 2018. Geological and geotechnical studies around Kaswati dam, Kachchh, India: implications on tectonic stability, rock mass property and water retention capacity. Quarterly Journal of Engineering Geology and Hydrogeology, 51(3), pp.338–351.

Bièvre, G., Lacroix, P., Oxarango, L., Goutaland, D., Monnot, G. and Fargier, Y., 2017. Integration of geotechnical and geophysical techniques for the characterization of a small earth-filled canal dyke and the localization of water leakage. Journal of Applied Geophysics, 139, pp.1–15.

Ghafoori, M., Lashkaripour, G.R. and Tarigh Azali, S., 2011. Investigation of the geological and geotechnical characteristics of Daroongar Dam, Northeast Iran. Geotechnical and Geological Engineering, 29(6), pp.961–975.

IS 9429, Drainage system for earth and rockfill dams - code of practice.
IS 9451, Guidelines for lining of canals in expansive soils.
IS 6966, Hydraulic design of barrages and weirs – Guidelines.
IS 7894, Code of practice for stability analysis of earth dams.
Sukanta, G., Atanu, M., Purnajit, B. and Syed, Z., 2017. Primary sedimentary structures and MISS in Gulcheru quartzite along SW part of Cuddapah Basin. Journal of the Geological Society of India, 89 (5), pp.511–520.
Sachpazis, C.I., 2013. Detailed slope stability analysis and assessment of the original Carsington earth embankment dam failure in the UK. Published in, 18.
Umaru, A., Ogedengbe, K. and Omobowale, M.O., 2010. Structural failures of earth dams in Nigeria: A case study of Cham Dam in Gombe State. ARPN Journal of Engineering & Applied Sciences, 5 (11), pp.47–52.
Fell, R., Wan, C.F., Cyganiewicz, J. and Foster, M., 2003. Time for development of internal erosion and piping in embankment dams. Journal of geotechnical and geoenvironmental engineering, 129(4), pp.307–314.
Foster, M., Fell, R. and Spannagle, M., 2000. The statistics of embankment dam failures and accidents. Canadian Geotechnical Journal, 37(5), pp.1000–1024.
Garg, S K. Irrigation engineering and hydraulic structures.

Smart Geotechnics for Smart Societies – Zhussupbekov, Sarsembayeva & Kaliakin (Eds)
© 2023 The Author(s), ISBN 978-1-003-29912-7
Open Access: www.taylorfrancis.com, CC BY-NC-ND 4.0 license

Fracture initiation and propagation in rocks with pre-existing flaws

M. Yogeshwar
Department of Civil Engineering, IIT Madras, India

G. Sivakumar
Department of Civil Engineering, IIT Jammu, India

V.B. Maji
Department of Civil Engineering, IIT Madras, India

ABSTRACT: Failure behaviour of rock mass is dependent upon the rock fracturing process and that in-turn dependent upon the crack initiation and propagation. The analysis of crack growth on a rock with pre-existing flaws is mostly carried out in open flaw configurations whereas limited study can be found for narrow flaw configurations. Unlike open flaw, narrow flaws are initially open and subsequently gets closed during loading. It also experiences friction which needed to be accounted for. Very few studies are available, to understand the effect of friction between the flaw surfaces. Additionally, the lateral confinement due to the biaxial confinement state would influence the crack initiation and their subsequent growth. In the present study, an experimental investigation is conducted to understand the crack growth behaviour of narrow flaws under uniaxial and biaxial stress environments. The tests were conducted using gypsum with a single flaw at varying orientation. The change in the behaviour of crack growth and stresses with respect to initiation and peak stress level was studied for different flaw angles. Subsequently, the numerical analysis was performed using the Extended Finite Element Method (XFEM) in conjunction with the Cohesive Zone Model (CZM). The model systematically validated with the laboratory experiments. The crack pattern was found to be influenced by various factors namely flaw angle, frictional coefficient between the flaw surface, the confinement stress level.

1 INTRODUCTION

Due to the existence of pre-existing flaws in rocks varying from micro to macro size formed by initial stage of formation of rock or due to stress induced by tectonic plates movement there pre-exist a weak point in rocks from which newly formed cracks can propagate when the stress at the flaw due to loading exceeds its material limit on microscopic level and leads to a nonlinear failure which makes it complicated to predict. But the failure can be analyzed by studying the crack pattern and the factors that cause the cracks to propagate. But the failure process gets more complicated when the flaw is narrow. Initially the narrow flaw is open but due to loading the flaw gets closed and the effect of friction between the flaw surfaces gets added. There is very little studies conducted on narrow flaws. The experimental results indicated that the crack initiation stress was higher in case of narrow flaws compared to open flaws when subjected to compressive loading. The numerical results indicate that the crack initiation stress was caused due to friction in case of narrow flaws (Steif 1984; Horri & Nemat-Naseer 1985; Ashby & Hallam 1986; Baud et al. 1996; Li et al. 2018). In order to get a deeper understanding on the behaviour of narrow flaws both experimental and numerical studies are needed. For the present study, Gypsum specimens containing narrow flaw configurations with single inclined flaw are chosen. The effect of crack initiation stress and its corresponding peak stress for uniaxially and biaxially loaded gypsum rock

DOI: 10.1201/9781003299127-114

were investigated experimentally. The specimens were investigated until the material underwent complete degradation and the crack stresses had been observed at initiation, coalescence, and peak strength. Subsequently, a numerical simulation using finite element (FE) software, ABAQUS, (version 6.14) was done with systematic validation using laboratory experiments.

2 EXPERIMENTAL STUDIES

2.1 *Preparing the specimen and its properties*

Gypsum is chosen as the specimen in both uniaxial (Sivakumar. G & V. B. Maji. 2018) and biaxial loading (Sivakumar. G & V. B. Maji 2022) because it can represent a wide range of brittle rocks and has decent similarities with respect to tensile and shear cracks development. Large number of samples can be prepared in a short amount of time and introduction of flaws is much easier. A gypsum slurry prepared with 35% water content is poured into the above-mentioned mould shown in Figure 1. After removing the sample from mould, it is further air dried for 24h and oven dried at 40°c for 4 days. The specimen is tested in 5th day to determine its properties by following the ISRM suggested methods (ISRM 1978a, b, 1979) and its properties are given in Table 1. The size of the specimen with a H/W ratio of 2 is decided in order to limit bucking effect and end friction. Due to this size of the specimen the tensile cracks growth during loading is vertical and shear cracks is horizontal. Also, the growth of cracks (both primary and secondary) from flaw tips does not get affected by these surface cracks and hence the material strength shows true behaviour. The geometric properties of the specimen are shown in Table 2

Figure 1. a) Specimen preparation mould with prepared gypsum specimen with single flaw of different angles.

Table 1. Material properties of Gypsum.

Material parameters	Gypsum
Uniaxial compressive strength (MPa)	15.50
Young's modulus (GPa)	1.04
Poisson's ratio	0.39
Tensile strength (MPa)	1.11

Table 2. Geometric properties of Gypsum sample.

Geometry of the specimen	Gypsum
Width (mm)	76.2
Height (mm)	152.4
Thickness (mm)	30
Flaw length, 2a (mm)	12.7
Flaw angle (β°)	15°–75°

2.2 *Testing apparatus*

For Uniaxial testing a compression testing machine of 500kN capacity is used. A low rate of loading of 0.031mm/min is adopted in order to capture the crack growth. To measure the crack initiation, stress a load cell is used along with a data logger and linear variable differential transformer to capture the load and displacement of the specimens at every second to get stress-strain plot as shown in Figure 2(a).

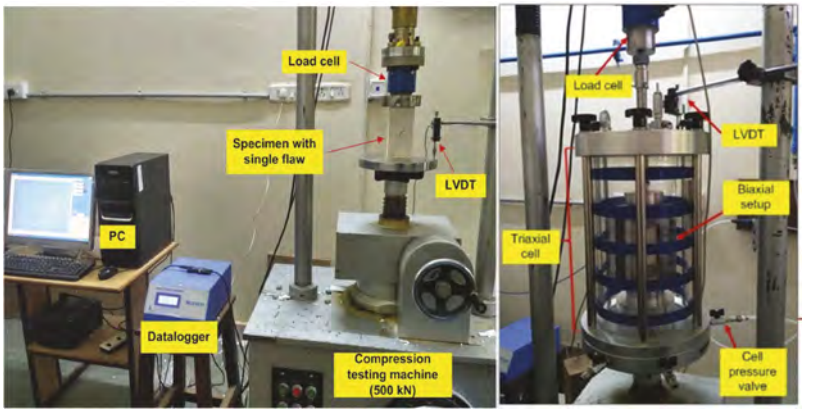

Figure 2. a) Compression testing machines for uniaxial test and its components b) Modified triaxial setup for biaxial loading.

For Biaxial loading, a heavy-duty large-diameter triaxial cell for 150 mm diameter sample sizes with maximum working pressure up to 2000 kPa is used as shown in Figure 2(b). Confining pressure is applied by air pressure regulator fitted with air filter to avoid water formed by condensation inside the PVC pipe getting into the air pressure regulator and also with the help of air booster to double the existing pressure. Two different confinement pressures are applied (0.65 MPa) and (1.24 MPa). In order to simulate biaxial condition in a triaxial apparatus a small arrangement using an acrylic plate fixed on either side of the specimen is made as shown in Figure 3. Due to this arrangement, the confinement stress is allowed to act through the specimen thickness and deviatoric stress acts along the height of the specimen. Due to Poisson's effect, a lateral deformation would enforce additional stress on the acrylic plate. An open-cell rubber foam membrane of thickness 5 mm was provided in-between the specimen and acrylic plate to absorb these stresses.

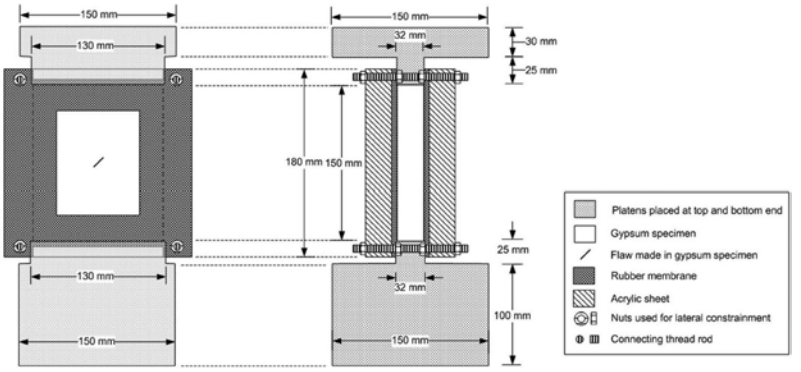

Figure 3. Modified biaxial setup to be kept inside the triaxial cell (Front view cross-sectional view).

2.3 *Experimental results*

2.3.1 *Crack growth and stress analysis in uniaxial loading*

During uniaxial loading (Sivakumar. G & V. B. Maji. 2018), the first crack formed was a tensile crack, which initiates from both the flaw tips in a direction oblique to the flaw surface for all flaw degrees. As the loading continues another crack of shear nature initiated in the quasi-planar direction from the flaw surface is formed. By further loading, the shear crack propagates along with the tensile crack until the material reaches its peak limit and extends in the direction of loading. Finally, the tensile crack grows in an unstable manner and later orients in the direction of major principal stress terminating at the boundary for 15° and 75°. The growth of the tensile crack subsided at a certain length for specimens with flaw angles of 30°, 45°, and 60°. The final failure pattern represents tensile splitting failure/shear failure, where the failure plane usually makes an angle of 0° to 45° concerning the vertical plane. The effect of closure between the flaw surfaces were found to vary at different flaw angles. The flaw surfaces were observed to be closed up to flaw angle 45°. For specimens with flaw angles of 60° and 75°, the flaw surface remained open. Surface spalling was observed at the tip of the flaw for low flaw angles. Peak stress was observed after crack initiation and followed a similar trend to crack initiation stress. There was a significant difference between the crack initiation- and peak stress for flaw angles ranging from 30° to 60°, and the maximum was observed for specimens with a 45° flaw angle as shown in Figure 4. The crack initiation stress decreases with an increase in flaw angle and attains a minimum value for the flaw angle of 45°, and subsequently increases with an increase in the flaw angle as shown in Figure 4. Furthermore, the curvilinearity of the wing crack was relatively high compared with other angles. For flaw angles of 15° and 75°, the wing crack initiated from the flaw tip and directly propagated in the direction of loading with a lesser curvilinear path. This caused the peak stress to occur immediately after the crack initiation stress.

2.3.2 *Crack growth and stress analysis in biaxial loading*

For Biaxial loading (Sivakumar. G & V. B. Maji 2022) due to the complicity in crack trajectory, there are four types of wing crack trajectories formed curvilinear wing-like tensile crack (T1), straight tensile crack (T2), mixed tensile/shear crack (T3) and anti-wing tensile crack (T4) [Wong and Einstein (2009)]. Tensile cracks were observed to appear in all the specimens irrespective of flaw angle and confinement levels and are generally open and their path is smooth. Shear crack follows a similar trend as uniaxial loading, but the shear crack surfaces are generally rough with an indication of slip between the face of the surface. T1 crack initiates from oblique to flaw surface, T2 crack initiates at quasi coplanar to flaw surface, T3 crack propagates in coplanar direction to shear cracks and finally T4 crack propagates parallel and opposite to T1 crack direction. Except for the T4 crack all other cracks shifts their alignment to the

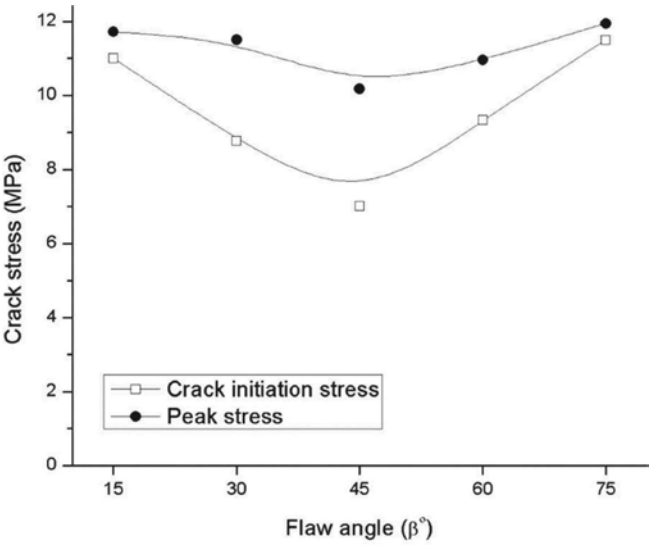

Figure 4. Crack initiation stress, coalescence stress, and peak stress observed in uniaxial loading.

direction of major principal stress. In all specimens, the crack is initiated by tensile cracks but the crack trajectory changes depending on the flaw angle. For the confinement of 0.65 MPa, T1 type and T3 type cracks are observed at both flaw tips for the lowest flaw angle of 15°. Similarly, a flaw angle of 75° T2 type wing crack is commonly observed. The crack grows further towards a nearby boundary and possibly gets linked with an external field crack (F) causing it to fail under lateral shear crack growth. For the confinement of 1.24 MPa, the propagated tensile crack does not completely reach the material boundary for 15° and 45°. Shear crack is also observed in 60° and 75° specimens but the propagated length limits within the material boundary and does not influence the material failure. Peak stress occurs immediately after the crack initiation stress for flaw angles ranging from 15° to 45°. The crack initiation stress was found to initiate sooner for a flaw angle of 45° in both confinements.

3 NUMERICAL STUDIES

3.1 *Modelling the laboratory condition*

To extend the behaviour of crack growth for other flaw configurations and to get a better understanding of the factors of unconfinement and the frictional coefficient for biaxial loading numerical simulation using XFEM in ABAQUS is done. In the present numerical model, rock is expected to behave in an elastoplastic manner. Rock behaves as elastic before the peak and as plastic post-peak. The presence of flaws is taken into account. Flaw is discontinuous and modelling it in a continuum is a challenge which can be overcome by the use of the Cohesive Zone Model. In CZM the pre-existing flaw is assumed to behave accordingly to the concept of traction–separation law, where a new crack is expected to initiate and propagate as per the assigned failure criterion along with the existing Elastoplastic model. Also, the growth of cracks initiated and their propagation accounting for the frictional behaviour influences the stress behaviour for narrow flaw specimens.

3.2 *Governing equations*

For Elastoplastic Model the following Equation 1 is used. The Elastic behaviour of rock is given by Hooke's law

$$\sigma = D^{el}\varepsilon^{el} \tag{1}$$

where σ = total stress, D^{el} = elastic constitutive matrix and ε^{el} = total elastic strain.

The Plastic behaviour is given by Equation 2

$$\sigma^{pl} = \sigma\left(\varepsilon^{pl}\right) \tag{2}$$

where (σ^{pl}) = plasticity stress, (σ) = material's yield stress, ε^{pl} = equivalent plastic strain

For CZM to describe the crack initiation of brittle materials such as rock and concrete the widely adopted maximum principal stress criteria were chosen for the current study. According to these criteria, the onset of crack initiation can be described by Equation 3

$$f = (\sigma_{max})/\left(T_{n,s}\right) \tag{3}$$

where f =maximum principal stress ratio, (σ_{max}) = assigned maximum principal stress value

($T_{n,\,s}$) = Traction in Tension/shear

To describe the dissipation of fracture energy, (Gd), after crack initiation, the term relative displacement (δ_m) was adopted which is given by Equation 4

$$\delta_m = \left((\delta_n)^2 + (\delta_s)^2\right)^{1/2} \tag{4}$$

where δ_n = separation of the discontinuity due to tension, δ_s = separation of the discontinuity due to shear.

To reduce the computational effort the concept of partition of unity, where nodes with discontinuity are enriched with additional degrees of freedom supplementing existing nodal shape functions is used in the Extended Finite Element Method. The approximate formulation of enriched displacement is given by Equation 5

$$u = {}_{I=1}{}^{n=1}\Sigma N_I(x)[u_I + H(x)a_I] \tag{5}$$

where $N_I(x)$= usual nodal shape functions, u_I = usual nodal displacement vector associated with the continuous part of the FE solution, a_I = second term is the product of the nodal enriched degree of freedom vector, H(x) = discontinuous jump function across the crack surface

3.3 *Input parameters*

The size of the specimen, Flaw length, properties of gypsum and loading rate is the same as experimental values. CZM requires two main parameters crack initiation stress and fracture energy dissipated after initiation to describe traction–separation behaviour. The value of the input parameters used are given in Table 3

Table 3. Input parameters in ABAQUS.

Material parameters	Values
Traction for Mode I (MPa)	1.217
Traction for Mode II (MPa)	1.465
Relative displacement under mixed mode (μm)	8.616
Damage stabilization cohesive	1×10^{-5}
Kinetic friction coefficient	0.28
Penalty stiffness	1.04 10^2

4 COMPARING EXPERIMENTAL AND NUMERICAL RESULTS

4.1 *Uniaxial loading*

The failure pattern of the experimental and numerical model under uniaxial loading is compared by Sivakumar. G & V. B. Maji. 2018 and shown below in Figure 5. During Uniaxial loading there was a higher concentration of tensile stress in the path of wing crack propagation and the shear stress concentration was higher in the direction of coplanar to the flaw surface for flaw angles 30°, 45° and 60° but in flaw angles of 15° and 75° they were absent. With an increase in flaw angle, the stress concentration is reduced due to the reduction in flaw closure and slippage between the surfaces. Crack initiation stress was found to be in good agreement with the experimental results and follows the similar behaviour of a decrease in crack initiation stress with an increase in flaw angle obtaining a minimum value for flaw angle of 45°. And then increasing again with the increase in flaw angle.

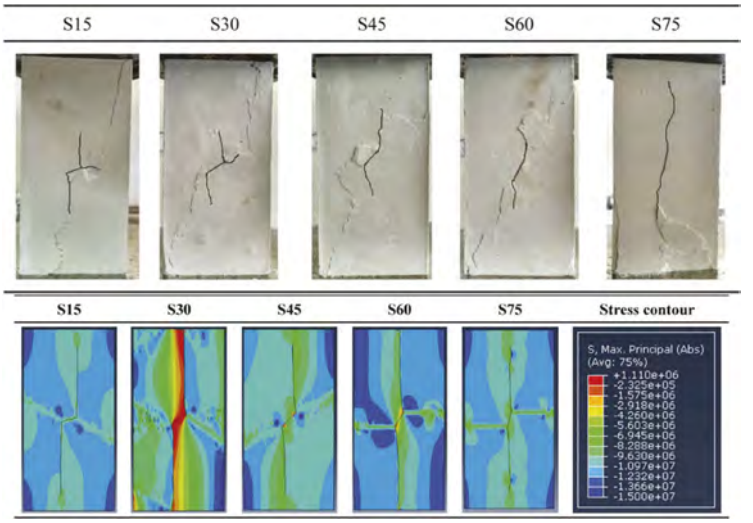

Figure 5. Failure pattern of uniaxially loaded specimen experimentally and numerically.

4.2 *Biaxial loading*

In the numerical simulation, the effect of confinement and friction coefficient can be changed in order to understand its effect clearly which is done by Sivakumar. G & V. B. Maji 2022. For no confinement by increasing the friction coefficient, the length of the tensile crack is relatively smaller, the path of the tensile crack is less curvilinear, and a sharper initiation is observed. On increasing confinement to 1.24 MPa, the crack initiates similarly as the perpendicular changes to an oblique direction, forming a type 1 tensile crack (T1). At a high friction coefficient, the crack initiates in a coplanar direction to the flaw surface and forms a type 3 tensile crack (T3) instead of (T2). The change of crack pattern due to the increase in confinement is shown experimentally and numerically for gypsum specimens of flaw angle 45° is shown in Figure 7. The effect of lateral confinement also alters the trajectory of crack propagation for different friction values. At a lower friction value, the initiated crack takes a curvilinear path for a smaller length and with the increase in confinement, their length reduces similar to the uniaxial condition. Unlike the uniaxial case, the propagated crack does not grow directly towards the major compressive loading direction. Instead, the crack takes a curvilinear outward direction and later near to the material peak, it aligns towards the major loading direction. Change of crack initiation stress, Peak stress with respect to confinement is shown in Figure 6

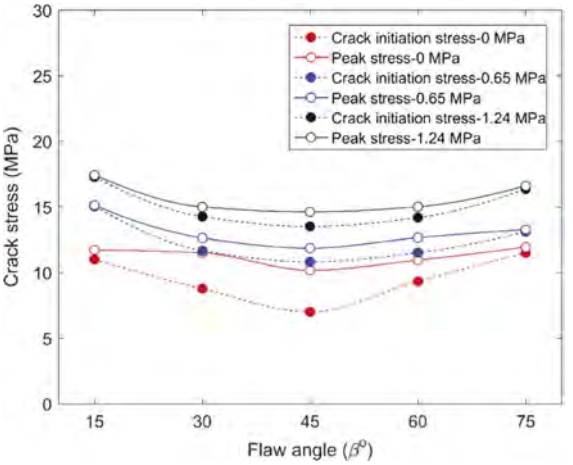

Figure 6. Crack initiation stress and peak stress observed in biaxial loading.

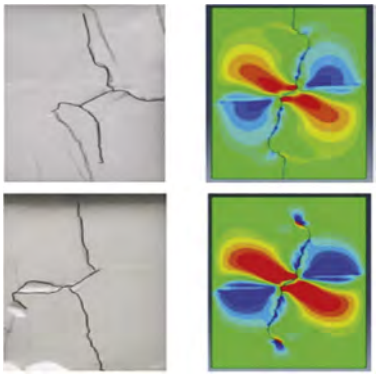

Figure 7. Crack growth pattern observed for 45° subjected to confinement of 0.65 MPa and 1.24 MPa experimentally and numerically.

5 CONCLUSIONS

Fracture initiation and propagation in rocks with pre-existing flaws under uniaxial and biaxial loading are studied both experimentally and numerically. The following conclusions can be drawn from the studies.

- Comparing open flaws to narrow flaws, the effect of closure differs with different flaw angles. The flaw surfaces were observed to be closed up to flaw angle 45°. For specimens with flaw angles of 60° and 75°, the flaw surface remained open. For uniaxial loading the crack initiation stress decreases with an increase in flaw angle obtaining a minimum value for flaw angle of 45°. And then increasing again with an increase in flaw angle.
- The adopted XFEM-based CZM was able to predict the crack growth and crack initiation stress for both uniaxial conditions and bi-axial conditions. CZM requires two main parameters crack initiation stress and fracture energy dissipated after initiation to describe traction-separation behaviour.
- For biaxial loading the favourable flaw angle to initiate the crack sooner is found to be closer to 45° for the lower confinements. Similar to the uniaxial loading, the crack stresses decrease and reach a minimum value and later increase making an undulant behaviour at

the intermediate flaw angles (30°-60°). But with increased confinements, the crack stresses at an intermediate angle the behaviour is relatively linear.

- Based on the shear force distribution monitored across the flaw surfaces, the shear force distribution is lower at a 30° flaw angle compared to a 45° flaw angle. Hence, the favourable flaw angle to initiate the crack mostly shifts closer to 30° at the higher confinements.
- Coefficient of friction and lateral confinement plays an important role in the crack length and propagation path. There can also be a change of crack type due to interference of these factors.

ACKNOWLEDGEMENTS

The authors acknowledge the financial support to extend this study by the Science and Engineering Research Board, Department of Science and Technology, Government of India through core research grant (CRG/2021/008105).

REFERENCES

Ashby, M. F. A., and S. D. Hallam. 1986. *The failure of brittle solids containing small cracks under compressive stress states*. Acta Metall. 34 (3): 497–510, from https://doi.org/10.1016/0001-6160(86)90086-6.

Baud, P., T. Reuschlé, and P. Charlez. 1996. *An improved wing crack model for the deformation and failure of rock in compression*. Int. J. Rock Mech. Min. Sci. Geomech. Abstr. 33 (5): 539–542, from https://doi.org/10.1016/0148-9062(96)00004-6.

Horri, H., and S. Nemat-Naseer. 1985. *Compression-induced microcrack growth in brittle soilds: Axial splitting and shear failure*. J. Geophys. Res. 90 (B4): 3105–3125, from https://doi.org/10.1029/JB090iB04p03105.

ISRM (International Society for Rock Mechanics). 1978a. *Suggested methods for determining tensile strength of rock materials*. Int. J. Rock Mech. Min. Sci. Geomech. Abstr. 15 (3): 99–103, from https://doi.org/10.1016/0148-9062(78)90003-7.

ISRM (International Society for Rock Mechanics). 1978b. *Suggested method for the quantitative description of discontinuities in rock masses*. Int. J. Rock Mech. Min. Sci. Geomech. Abstr. 15 (6): 319–368, from https://doi.org/10.1016/0148-9062(78)91472-9.

ISRM (International Society for Rock Mechanics). 1979. *Suggested methods for determining the uniaxial compressive strength and deformability of rock materials*. Int. J. Rock Mech. Min. Sci.Geomech. Abstr. 16 (2): 135–140, from https://doi.org/10.1016/0148-9062(79)91451-7.

Li, X., C. Qi, and Z. Shao. 2018. *Evaluation of strength and failure of brittle rock containing initial cracks under lithospheric conditions*. Acta Geophys. 66: 141–152, from https://doi.org/10.1007/s11600-018-0123-4.

Steif, P. S. 1984. *Crack extension under compressive loading*. Eng. Fract. Mech. 20 (3): 463–473, from https://doi.org/10.1016/0013-7944(84)90051-1.

Sivakumar, G. and V. B. Maji. 2018. *A study on crack initiation and propagation in rock with pre-existing flaw under uniaxial compression*. Indian Geotech. J. 48 (4): 626–639, from https://doi.org/10.1007/s40098-018-0304-8.

Sivakumar G. and V. B. Maji. 2021. *Crack growth in rocks with preexisting narrow flaws under uniaxial compression*. Int J Geomech 21 (4):04021032,from https://doi.org/10.1061/(ASCE)GM.1943-5622.0001960.

Sivakumar G. and V.B. Maji. 2022. *Study on crack growth behaviour in rocks having pre-existing narrow flaws under biaxial compression*. Geotech and Geological engg, from https://doi.org/10.1007/s10706-022-02272-w.

Wong, L. N. Y. and H. H. Einstein. 2009. *Systematic evaluation of cracking behavior in specimens containing single flaws under uniaxial compression*. Int. J. Rock Mech. Min. Sci. 46 (2): 239–249, from https://doi.org/10.1016/j.ijrmms.2008.03.006.

Smart Geotechnics for Smart Societies – Zhussupbekov, Sarsembayeva & Kaliakin (Eds)
© 2023 The Author(s), ISBN 978-1-003-29912-7
Open Access: www.taylorfrancis.com, CC BY-NC-ND 4.0 license

Physical properties of Tabriz gray marlstone, NW of Iran

N. Dadadszadeh, M. Hashemi & A. Gazifard
Department of Geology, University of Isfahan, Isfahan

E. Asghari-Kaljahi
Department of Earth Sciences, University of Tabriz, Tabriz

ABSTRACT: Tabriz is one of the largest cities in Iran, with a population of more than 2 million. Marlstone is the bedrock of most areas of the city. These marls, consisting of lime and clay, are found in different colors such as yellow, olive, and gray, which mostly belong to Baghmishe and Upper Red Formations. These marls have different amounts of organic materials and in high percentages cause the formation of lignite. The physical characteristics of the marl are different and the gray marl has a high density and strength. Another important characteristic of marls is the high rate of weathering which in excavations, changes over several months and turns into soil. Therefore, marl is considered both a weak rock and a hard soil. This study, by sampling and conducting experiments, presents the physical and mechanical characteristics of gray marls in different parts of Tabriz city. The carbonate content of the mentioned marls is between 30 and 60% and their dry unit weight is between 17.5 and 20.0 kN/m^3. The clay minerals in these marls also include illite, montmorillonite, etc.

1 INTRODUCTION

Marl is a term to describe the mixture of calcium carbonate and clay, normally between 35 and 65 percent (Pettijohn, 1975). Terzaghi and Peck (1967) have defined marl as a hard to very hard marine carbonate soil in green color. Sowers and Sowers (1979) introduced marl as a sandy deposit with silt and clay containing gray or green calcite and McCarthy (1977) stated that marl is soft limestone. Mitchell (1976), considers marl a soft, carbonated, and clay-rich material, and Bell (1981), has pointed out that marl is a term with different meanings, which is used for rocks with 35-65% carbonate and a large amount of clay. Qahvash (1989) introduced limestone sediments with 55 to 80 percent carbonates as marl.

In engineering geology and geotechnical engineering, terms such as colored soils, carbonate, and marl soils are used to specify the composition of fine-grained soil with carbonate minerals. The most important studies conducted on marls are: Bell (1981) conducted a study on the physical and resistance properties (unit weight, specific gravity, porosity and Young's modulus) of marls in the Middlebrook region of England. Qahvash (1989) conducted research on plastic properties, granulation, specific gravity, porosity, etc. in the Dhahran region of Saudi Arabia. El-Amrani et al. (1998), measured the uniaxial strength, deterioration index, carbonate percentage, dispersion index, water absorption, sulfate percentage, specific gravity, etc. in the Grande region of Spain. Hooshmand et al. (2012) studied parameters such as point load index, SPT, Young's and shear modulus, plasticity properties, specific gravity, porosity, and shear strength, in some areas of Tabriz city. Amirali and Katebi (2016) tested the carbonate content, color, strength, shear wave speed, and physical properties of Tabriz marls. Asghari-Kaljahi et al. (2019), studied parameters such as mineralogy, creep, and swelling behavior of marls in the Baghmisheh area of Tabriz.

Tabriz is one of the largest cities in Iran (Figure 1), with a population of more than 2 million. Marlstone is the bedrock of most areas of the city. The old area of Tabriz was

DOI: 10.1201/9781003299127-115

formed on smooth topographic surfaces and alluvial deposits. Still, with the growth and development of the city in the eastern side, a large part of the city's development in areas such as Valiasr town, Baghmisheh, Roshdieh, Marzdaran, and its extension to Ahar road in rough topographic, it is mostly placed on marlstone (NGDIR, 2004). Due to the development of the city on marl layers and the desire to build high-rise buildings and the need to place foundations in deeper layers, huge excavations have taken place in these layers and the future will be more than now will be required. To design the foundations of high-rise buildings, assess the risk of heavy constructions against possible earthquakes, and landslides, as well as guardian structures in deep excavations, it is necessary to exhaustively understand these layers from a physical and mechanical point of view. For this purpose, samples were taken from different parts of Tabriz tested for identification. The performed tests generally include moisture content, Atterberg limits, unit weight, specific gravity and uniaxial strength. On a group of samples, tests were performed to determine the percentage of calcium carbonate, percentage of organic matter, and mineral identification.

Figure 1. The location of Tabriz city on the Iran map.

2 GEOLOGY OF TABRIZ REGION

Marls of Tabriz are the carbonate sediments of lakes that are exposed in the eastern, northern, and southern areas of the city. Some pictures of these marls are illustrated in the Figure 2. The geology map of Tabriz region is showed on Figure 3. They form the bedrock in most areas of the city and are located under the alluvial sediments.

Considering that marls are often formed in warm and shallow lake areas, it can be concluded that such an environment prevailed in the current location of Tabriz city and the continental sediments in this area contained Lignite, shale, and fossil. The presence of gypsum and coal veins reduces the resistance characteristics of these deposits. In many marls, thin layers of gypsum are also observed. It seems that part of the carbonate materials required for the formation of marls in Tabriz is supplied from the limestone springs caused by the presence of Lake Urmia, and the presence of minerals and fossils such as coal, diatomite, sinerite, chlorite, and ferrous iron (Hooshmand, 2012). The marl layers are horizontal in most of the different areas, but in the northern parts of the city, due to the proximity to the Tabriz North fault and tectonic activities, it is inclined. From the point of view of soil mechanics, these materials are classified as clay or silty type with high plastic properties (Babazadeh and Ghobadi, 2013).

Figure 2. Some pictures of marlstone outcrops in the around of Tabriz city.

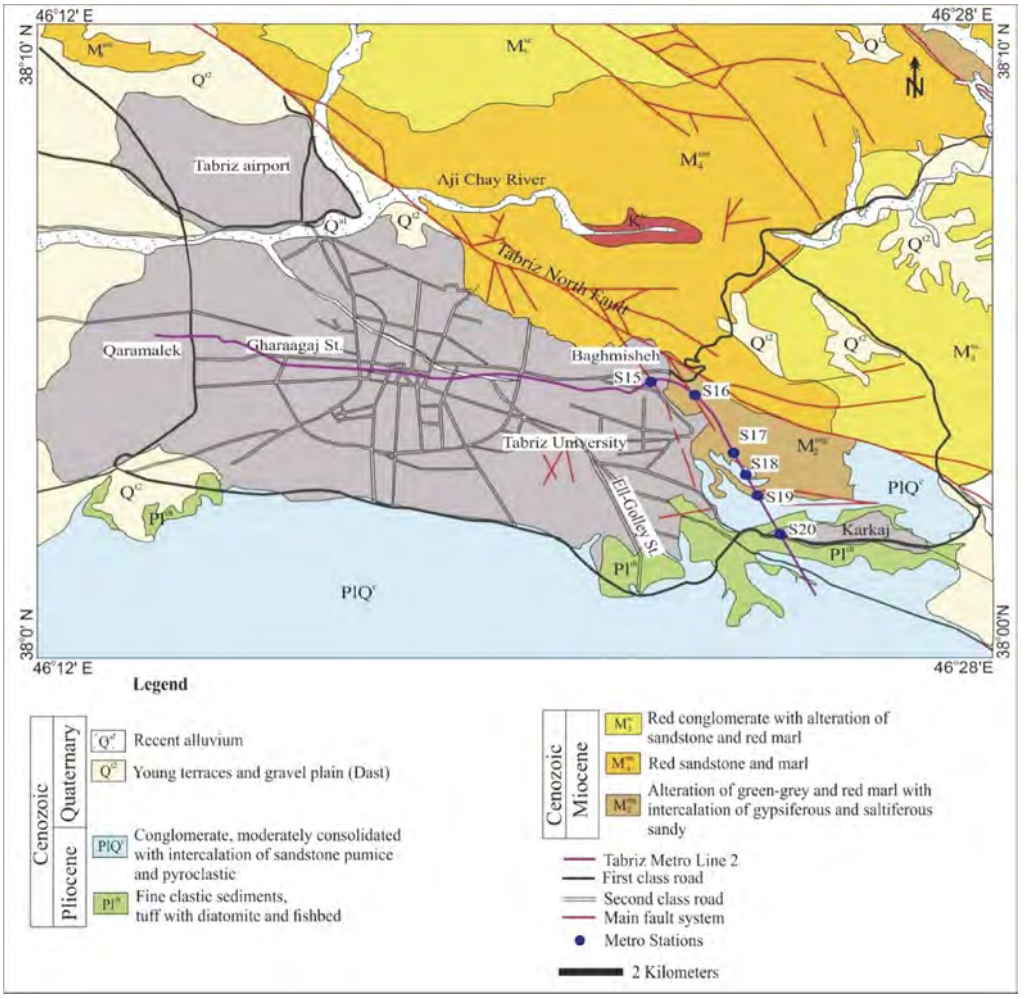

Figure 3. Geological map of Tabriz region (adapted from the geology map of GSI, 1996).

3 RESEARCH METHOD

During the visits to different areas of the city, taking pictures and taking samples in the places where geotechnical excavations were carried out, core samples were taken. Marls can be seen under the alluvial sediments in the central area of the city. In the reconnaissance excavations for the Tabriz metro project, gray marl layers have been observed at depths of 10 to 50 meters in the central areas of the city (Figure 4).

Figure 4. Outcrop of green and gray marls around Baghmisheh town.

4 TEST RESULTS AND DISCUSSION

The physical tests that have been performed on most of the samples include grading, Atterberg limits, specific gravity, and dry density. The test results are presented in Table 1. It can be seen that the soil unified classification of marls are MH, CL and CH. Atterberg limit tests performed on these marls have determined different liquid limits from 39 to 69.5% for yellow marls, 60 to 72% for olive green marls, and 40 to 80% for different types of gray marls. Their plastic index is from 17 to 46% for yellow marls, 38.5 to 42.5% for green marls, and 32 to 60% for different types of gray marls. Therefore, they have medium to high plastic properties. This is due to the change in their calcium carbonate content, the type and amount of clay minerals in them. Based on the Holtz and Kovacs diagram and comparing the results of the Atterberg limit test, it can be seen that the marl clay minerals of the studied area are illite, kaolinite and montmorillonite (Figure 5).

The different characteristics of marls in Tabriz are mostly related to the sedimentary environment and the conditions of their formation, so that layers of gray marl related to Baghmisheh Formation indicate their formation in a sweet lake environment and a large amount of

Table 1. The results of some physical tests.

Type of test	Upper limit	Lower limit	Average
Liquid limit (%)	80	39	52
Plastic limit (%)	58	15	35
Plastic index (%)	60	17	33
Dry density (kN/m^3)	19.0	15.0	15.6
Specific gravity	2.85	2.42	2.56

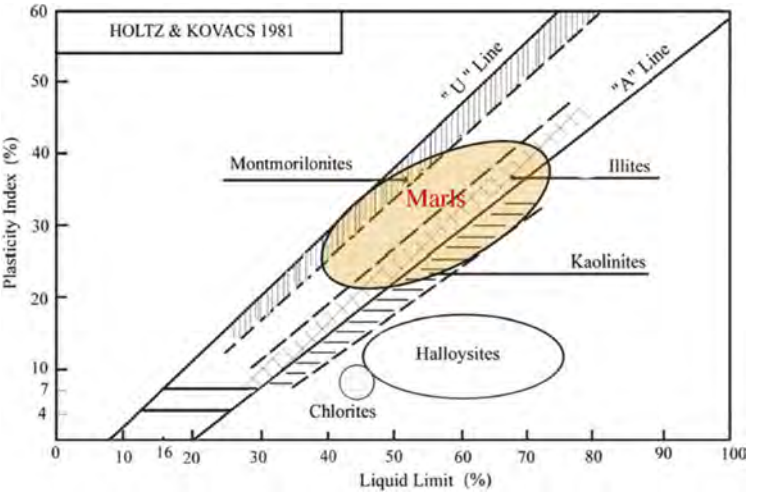

Figure 5. The relationship between the liquid limit and the plasticity index of marls on the Holtz and Kovacs) 1981) chart.

organic matter. Gray marl is an indication of reduced sedimentary environment and their formation next to joints and faults as a porous environment or reduction of iron due to changes in organic matter.

The gray marls of Tabriz contain a relatively large amount of calcium carbonate compared to the yellow and green marls, and by forming at greater depths due to the increase in confining pressure and the decrease in the porosity ratio with the depth and overburden pressure, they show the highest amount of resistance and the least deformation.

The minerals that makes Tabriz marls are not the same due to the difference in the way and time of formation, the way of deposition, the thickness of the layer, weathering conditions, as well as the conditions of the of the parent soil, and similar things. The main minerals in the X-ray diffraction test are quartz, albite, calcite, dolomite, chamosite, anorthite, and albite, and secondary minerals are illite, kaolinite, montmorillonite, hematite, and aragonite

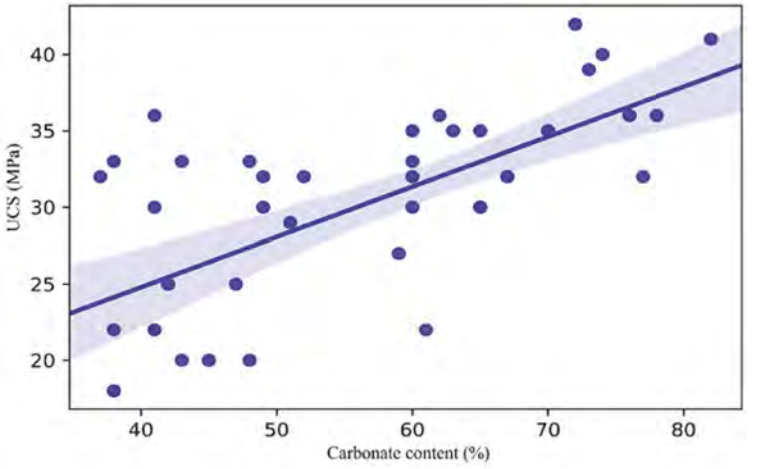

Figure 6. Relationship between calcium carbonate content and compressive strength in marlstone (Azarafza et al., 2019).

(Soleimani et al., 2019). From the geotechnical point of view, the presence of organic materials has a negative effect on soil characteristics. For example, they reduce the mechanical resistance of the soil and increase its settlement and creep. The maximum percentage of weight loss in the loss on ignition (LOI) test for organic matter is 2.6% for Tabriz gray marl, which can be concluded that the percentage of organic matter in Tabriz marl is very low and this value will not have much effect on properties (El Howayek et al., 2012). The amount of calcium carbonate can also affect the physical and mechanical characteristics of the soil. There is an inverse relationship between carbonate content and swelling behavior. Marls with high carbonate and high sulfate content as well as granular particles are easily compacted and their resistance parameters increase dramatically. Also, in these marls, the resulting compaction is irreversible (Figure 6).

Clay content appears to affect the maximum dry density in the case of the standard compaction test. This is attributed to adsorption of water by the clay minerals, whereas other clay-sized minerals such as carbonate do not have such an effect. The amount of calcium carbonate in Tabriz marl is between 10% and 30%, obtained during previous research, and this amount of carbonate does not have much effect on the behavior of marl and can be affected by the parent soil (Khamechian et al., 2000). Since the gray marl is known as the bedrock of Tabriz and continues to the thickness of 100 meters and more, the olive and yellow marl generally includes the surface layers of the soil. Practical experiments have shown that gray marl has more suitable characteristics in terms of resistance than olive marl. Regarding the resistance properties, there is a huge difference between the gray, olive, and yellow marls, and the results of the SPT and uniaxial compression tests are shown in Table 2.

Table 2. Results of SPT and uniaxial compressive strength tests.

Marl Type	SPT	UCS (MPa)	Modulus of elasticity (MPa)
Yellow Marl	7-25	0.25-1.0	<8
Green Marl	25-40	0.4-1.1	8.0-20.0
Gray Marl	28-50	0.65-1.9	10.0-30.0
Solid gray marl	>50	>1.9	>30.0

The above results and practical experiences in construction projects show that gray marl is in the very dense category in terms of SPT and at lower depths, it is like weak rock. The modulus of deformation in gray marl is higher than olive and yellow marl. This issue will cause high confidence in placing foundations of heavy structures in gray marl layers. Marlstones are among strong soil and weak rocks in engineering and behavior. This behavior depends on the amount of clay and calcium carbonate. By increasing the percentage of calcium carbonate and depth, the engineering behavior of marls is similar to weak rock, and by increasing the percentage of clay, this behavior is similar to hard soil. Marlstones are strongly affected by the conditions of their environment; for example, when they are exposed to moisture their primary structure disintegrates; in this situation, it is no longer possible to describe the stone's behavior based on its primary characteristics. The most important determining factor in the design of structures on marl is elastic, plastic, and ultimately rupture deformation. Due to rapid weathering and erosion, marls cause problems such as foundation and slope rupture, tensile cracks in streams, expansion of instabilities in natural slopes and trenches, and geotechnical projects. Dry and wet cycles has important effects on the behavior of marl soils. In a way that most ruptures occur after long rains. The strength and stability of structures in Tabriz city due to the extent of marl formations and weather conditions are associated with settlement and creep issues. So that the marl masses have caused severe landslides in the steep paths (Figure 7), Parsa et al., 2021).

Figure 7. Some pictures of the landslides that occurred in the marl layers in the east of Tabriz.

The results of mineralogical tests show the presence of very little quartz, calcite, dolomite, and feldspar minerals. Muscovite and gypsum are in the mineralogical composition of all marl samples. The color of green marls is mostly attributed to the presence of Hematite and the color of yellow marls is also attributed to the presence of yellowish brown limonite. The color of gray marls is also attributed to the presence of organic matter in them. The clay minerals of the studied marls are mostly Illite and in the next categories, montmorillonite and Kaolinite. Because the mineral type determination test provides only qualitative and descriptive results, it is not possible to obtain the percentage of minerals from its results, only the presence of minerals is mentioned. (Figure 8).

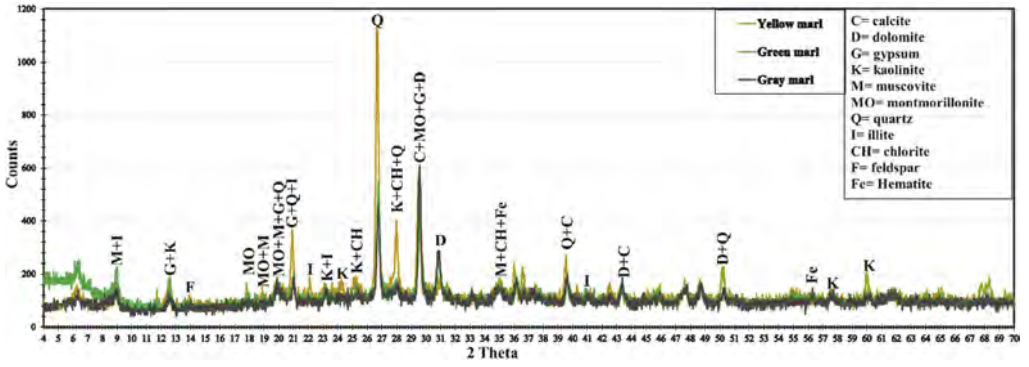

Figure 8. XRD for three types of Tabriz marls (Jalali-Milani et al., 2017).

5 CONCLUSION

Gray marlstone is the bedrock of most areas of the city. According to X-ray diffraction tests, the dominant minerals of Tabriz marls include quartz, illite, calcite, albite, and the dominant clay minerals are illite, montmorillonite, and kaolinite, but these minerals are not the same in different samples. The USCS of marly soils of Tabriz are CH, CL and MH. The percentage of organic matter in Tabriz marls is limited and generally less than 3% and is not included in the organic soil group in terms of classification.

According to the uniaxial compressive strength tests, yellow marls show the lowest strength and the most ductility due to stress and within the range 0.25-1.0 MPa, gray marls show the highest strength (0.65-1.9 MPa) and the least ductility. Green marls are intermediate between these two types and have uniaxial strength 0.4 to 1.1 MPa. The unit weight of marls increases with increasing depth, but this characteristic shows a decreasing trend with increasing moisture percentage. Dry density for the studied marls are between 15.0 and 19.0 kN/m^3.

The SPT values for yellow marl are between 7 and 25, green marl 25-40 and gray marl 28-50, which shows the high strength of gray marls.

REFERENCES

Amirali, M. and Ketabi, H. 2016. Classification of Carbonated Soils from Geotechnical Point of View (Case study: Marly Soils of Tabriz). *Journal of Civil and Environmental Engineering*, 3(48).

Asghari-Kaljahi, E. Barzegari, G. and Jalali-Milani, S. 2019. Assessment of the swelling potential of Baghmisheh marls in Tabriz, Iran, *Geomechanics and Engineering, An International Journal*, Techno press, 18(3), 267–275, doi: 10.12989/gae.2019.18.3.267

Azarafza, M. Akgun, H. and Asghari-Kaljahi, E. 2019. Geotechnical characteristics and empirical geo-engineering relations of the South Pars Zone marls, Iran. *Geomechanics and Engineering, Techno press*, 19(5), 393–405, doi: 10.12989/gae.2019.19.5.393.

Bell, F.G. 1981. A survey of the physical properties of some carbonate rocks, *Bulletin International Association Engineering Geology*, 24, 105–110.

El Amrani, N. Lamas, F. Irigaray, C. and Chacon, J. 1997. Engineering geological characterization of Neogene marls in the Southeastern Granada Basin, Spain, 50, 165–175.

El Howayek, A. Bobet, A. Dawood, S. Ferdon, A. Santagata, M. and Siddiki, N.Z. 2012. Classification of organic soils and classification of marls training. Publication FHWA/IN/JTRP- Joint Transportation Research Program, *Indiana Department of Transportation and Purdue University*, West Lafayette, Indiana.

GSI, Geological and mineral exploration organization of Iran. 1996. Tabriz geological map on a scale of 1:100000.

Babazadeh, R. and Ghobadi, M. 2013. Engineering geological investigations along the Tabriz subway extension focusing on ground surface settlement, northwestern Iran. *Journal of Engineering Geology*, Kharazmi University, 2(6), 1501–1524.

Holtz, R.D. and Kovacs, W.D. 1981. An Introduction to Geotechnical Engineering, *Prentice Hall*, Englewood Cliffs, NJ.

Hooshmand, A. Aminfar, M. Asghari, E. and Ahmadi, H. 2012. Mechanical and physical characterization of Tabriz marls, Iran. *Journal of Geotechnical and Engineering*, Springer Netherlands Publishers, 30(1), 219–232.

Jalali-Milani, S., Asghari-Kaljahi, E., Barzegari, G. and Hajialilu-Bonab, M. 2017. Consolidation deformation of Baghmisheh marls of Tabriz, Iran. *Geomechanics and Engineering, An International Journal*, Techno press, 12(4), doi: 10.12989/gae.2017.12.4.561.

Khamechian, M. Rezaei, H. and Nikodel, M. 2000. Investigation of swelling potential of Marlstones of Bitter Water Formation, *4th Conference of Geological Society of Iran*, Tabriz, Geological Society of Iran, University of Tabriz.

McCarthy, D.F. 1982. Essential of soil mechanics and foundations, 2 ed., *Reston Publishing Company*. Reston, Virginia, 632 pp.

Mitchell, J. K. 1976. Fundamental of soil behaviour, *John Wiley and Sons*, New York.

NGDIR. 2004. Azerbaijan-e-Shargi General Geology. National Geoscience Database of Iran, www.ngdir/States/StateDateil.

Parsa, Z., Asghari-Kaljahi, E. and Hajialilu-Bonab, M. 2021. Study of marl and filling soils problems of the Negin Park area in Tabriz for deep excavation projects. *New Finding in Applied Geology journal*, 15 (30) (in Persian).

Qahvash, A.A. 1989. Geotechnical Properties of fine grained calcareous sediments for engineering purposes. *Eng. Geology*, 26, 161–169.

Pettijohn, F.J. 1975. Sedimentary Rocks, *Harper and Row*, New York, NY, USA, 628 p.

Soleimani Qaragol, M. Asghari, E. and Kiyani, M. 2009. Investigation of Uniaxial Stress-Strain Behavior of Tabriz Marls. 4*th International Conference on Geotechnical Engineering and Soil Mechanics of Iran*, Tehran, Geotechnical Society of Iran (in Persian).

Sowers, G.B. and Sowers, G. F. 1979. Introductory soil Mechanics and Foundation. *McMillan. New York*. N.Y.

Terzaghi, K. and Peck, R. 1967. Soil Mechanics in Engineering Practice. 2ed., *John Wiley and sons*, New York.

Smart Geotechnics for Smart Societies – Zhussupbekov, Sarsembayeva & Kaliakin (Eds)
© 2023 The Author(s), ISBN 978-1-003-29912-7
Open Access: www.taylorfrancis.com, CC BY-NC-ND 4.0 license

Study of pore orientation in compacted crushed mudstone by SEM image

D.X. Sun, H. Komine, H. Wang, D. Ito & M. Takagi
Waseda University, Tokyo, Japan

ABSTRACT: Preferred orientation of pores result in the macroscopic anisotropy of soil. In this study, the SEM images of compacted crushed mudstone with different dry densities were analyzed and the orientation of pores were investigated. The results show that with the increase of dry density, the orientation distribution of pores appear anisotropy: the pore orientation distribution gradually concentrates on the direction which is perpendicular to and parallel to compacting direction.

1 INTRODUCTION

Clay-bearing rocks, mudstones and some other soft rocks including clay stones, siltstones and shales represent more than 60% of the sedimentary rocks exposed on earth's surface (Blatt, 1982). In Japan, crushed mudstone has been used in dam and highway embankment in recent years, which may sometimes cause disasters during earthquakes, such as the dam burst and slope failure (Kiyota et al. 2011, Takagi et al. 2010). Mechanical behavior of mudstone may lead to these disasters mentioned above. Recently, It has been proved that anisotropic mechanical behavior is affected by the anisotropy of soil structure (Hattab et al. 2015, Mitaritonna et al. 2014, Yimsiri & Soga, 2011). Scanning Electron Microscope (SEM) has been used in soil microstructure observation (Hattab & Fleureau, 2011, Tang et al. 2020). However, two-dimensional SEM images obtained from three-dimensional soil structures are difficult to be quantitatively analyzed due to coverage (Wang et al. 2008). Therefore, a resin injection method was introduced into SEM tests to obtain a plane in the section of specimen for quantitative analysis (Bai & Smart, 1997). In this study, SEM images of compacted crushed mudstone after resin injection is obtained and analyzed.

2 MATERIALS, EQUIPMENTS, PROCEDURES AND IMAGE PROCESS

A mudstone was used in this study and Table 1 shows its fundamental properties. The soil particles density is 2.729 Mg/m^3. Liquid limit and plasticity index of mudstone is 19.2% and 7.0 respectively. After completely drying in the oven, the mudstone was crushed and passed the sieve with an opening size of 425μm. Then, the mudstone was placed in a plastic ring and

Table 1. Fundamental soil properties.

Soil properties	Soil particle density (Mg/m^3)	Natural water content (%)	Liquid limit (%)	Plastic limit (%)	Plasticity index
Value	2.729	4.2	19.2	12.2	7.0

DOI: 10.1201/9781003299127-116

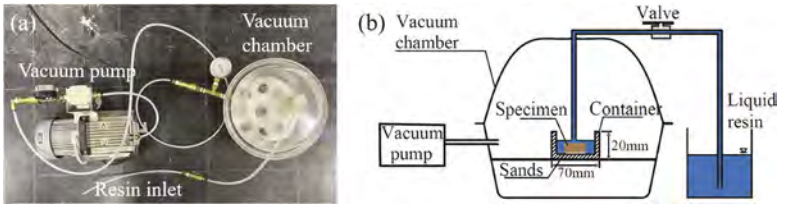

Figure 1. (a) picture and (b) schematic diagram of resin injection equipment.

compacted at 10kN pressure for 5min. Finally, the competed specimens (28 mm in diameter and 5mm in height) with dry densities of 1.60, 1.84, and 1.96Mg/m^3 were obtained.

As shown in Figure 1, compacted specimen was placed in a container with some coarse sands at the bottom, which can allow the resin to enter the sample pores more easily during injection process. The container with specimens was placed in a vacuum chamber and then kept vacuum for 10 min. After that, liquid resin was filled into the container at a uniform speed. Finally, the specimens were removed from the vacuum chamber and prepared for SEM tests. The SEM (JSM-IT100LA, JEOL) with magnification of ×50 (for specimens with dry density of 1.60 and 1.84 Mg/m^3) and ×70 (for specimen with dry density of 1.96 Mg/m^3) was used in observation. The acceleration voltage is 20kV, and the SEM image consists of 5120×3840 pixels.

A new pore orientation evaluation method is applied in this study. The specimen preparations for SEM tests and image processes can be seen in Figure 2. Specimen injected with resin were cut and sanded. The area close to the cross-section center of the specimen was observed using SEM (see Figure 2a). Some common image processes including Median Filter, Opening, and Closing were applied for denoising before thresholding process (Tang et al. 2020). After these, one thresholding value determined by artificial vision was performed on the SEM image for pores extraction. Skeletonization was carried out to create the skeleton of pores represented by a line and two nodes, where one line and two ending nodes are called a segment (Figure 2b). The length and orientation of skeleton were calculated by coordinates of two ending nodes. Details of skeletonizing can be seen in Figure 2c. Finally, skeleton orientations weighted by skeleton length were calculated for pore orientation analysis. Since the edges of the image gather skeletons, sheared round images (as shown in Figure 2b) instead of square ones were used for analysis in order to eliminate the affection of image edge. Due to the resolution of SEM image, extremely small pores consist of several pixels, resulting in orientation calculations of 0° or 90°. Therefore, pores with area larger than 12.6μm^2 were analyzed in this study.

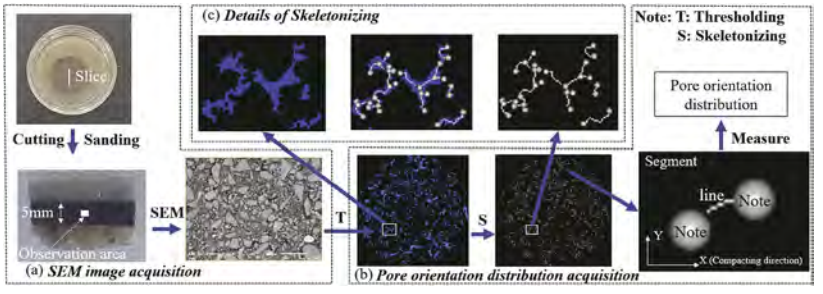

Figure 2. Typical image processing and data acquisition: (a) SEM image acquisition; (c) pore orientation obtained from skeletonized model; and (c) details of skeletonizing.

3 RESULTS AND DISCUSSION

In this study, the structure of mudstone was analyzed by energy dispersive X-ray spectroscopy (EDS) which can recognize the element contents in certain point or area. The SEM image of specimen after sanding can be seen in Figure 3.

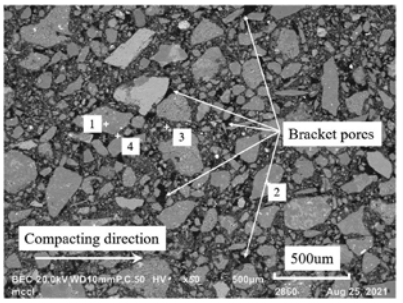

EDS results

Points	Element (mass%)				
	Si	Al	Mg	Na	Ca
1	87.45	10.68	0.99	0.88	-
2	99.86	-	0.07	-	0.07
3	69.70	23.66	6.64	-	-
4	74.13	18.89	2.37	2.93	1.68

Figure 3. SEM image and EDS analysis of specimen with dry density of 1.60Mg/m^3.

There are large particles distributed in the specimen and the bracket pores can be seen between large particles. It can be seen from the EDS results that the silicon content of the large particles (Point 1 and 2 in Figure 3) is higher than that of the areas among large particles (Point 3 and 4 in Figure 3), while the clay element content in the area among large particles is higher than the large particles. Thus, the large particles should be quartz particles. In summary, the conclusion can be drawn from SEM image: structure of compacted crushed mudstone is composed of large particles, bracket pores and clay mineral. This conclusion will support the subsequent discussion of pore compression.

Skeletons with different orientation should represent different specific gravity in statistics due to different lengths. Therefore, the ratio of the sum of the skeleton length in each orientation interval to the total skeleton length is taken as the frequency of different directions (see Figure 4). The statistical orientation with the range of 180° are transformed into distribution results within the orientation range of 360° after common data processing (Hattab et al. 2015, Tang et al. 2020).

The orientation distribution of three specimens with different dry densities were shown in Figure 4. For the specimen with lowest dry density (ρ=1.60 Mg/m^3), the main orientation of the pores is not clearly visible. The frequency is distributed between 4.97% and 3.49% for different pore orientations. When the dry density of the specimen reaches 1.84 Mg/m^3, the orientations of pores are concentrated at 0°, 90°, 180° and 270°, reaching around 5% of frequency. Whereas the orientations of 0°, 90°, 180° and 270° have the smallest frequency, about 3%. The pore orientation distribution of specimen with dry density of 1.96 Mg/m^3 become not as obvious as that in specimen with medium dry density. This may be due to pores being squeezed into smaller ones which are beyond the observation range in the specimen with the highest dry density.

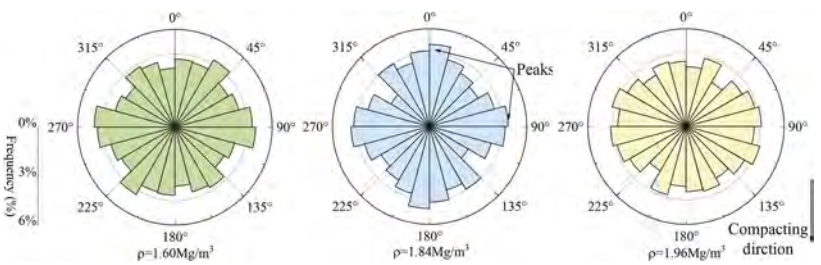

Figure 4. Rosette histogram of pore orientation distribution.

As can be seen in Figure 5, the pore orientation gradually concentrates on two orientations during the increase of dry density: perpendicular to and parallel to compacting direction. While the pore proportion in other directions decreases. In the process of compaction, particles were oriented and perpendicular to the compaction direction (Shi et al. 1998). Due to the rearrangement of particles and squeeze during compaction, the width of the bracket pores parallel to the compaction direction was reduced, thus forming pores perpendicular to the

compaction direction (see Figure 5b: Horizontal pores). Whereas, the pores parallel to the compaction direction are formed due to pores between oriented particles (see Figure 5b: Vertical pores). The conclusion can be used in the study of anisotropic mechanical behavior as mentioned in the introduction.

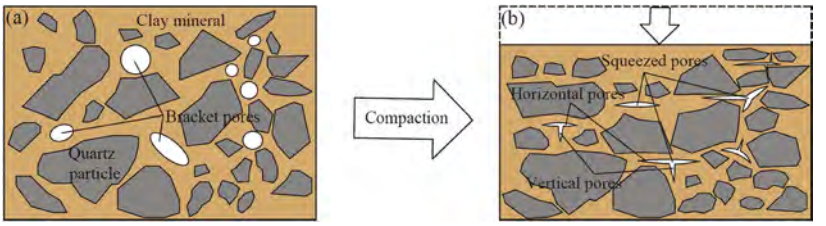

Figure 5. Evolution of pore orientation during compaction.

4 CONCLUSION

The results of SEM images show that with the increase of dry density, the pore orientation distribution gradually concentrates on the direction which is perpendicular to and parallel to compacting direction due to the squeeze of pores and the rearrangement of particles.

ACKNOWLEDGEMENTS

This work was the result of using research equipment (JSM-IT100LA: Material Characterization Central Laboratory) shared in MEXT Project for promoting public utilization of advanced research infrastructure (Program for supporting construction of core facilities) Grant Number JPMXS0440500021. This study is supported by China Scholarship Council (No. 202007000004).

REFERENCES

Bai, X. & Smart, R. 1997. Change in microstructure of kaolin in consolidation and undrained shear. *Geotechnique* 47(5): 1009–1017.

Blatt, H. 1982. *Sedimentary petrology*.

Hattab, M., Hammad, T. & Fleureau, J. M. 2015. Internal friction angle variation in a kaolin/montmorillonite clay mix and microstructural identification. *Geotechnique* 65(1): 1–11.

Hattab, M. & Fleureau, J. 2011. Experimental analysis of kaolinite particle orientation during triaxial path. *International Journal for Numerical and Analytical Methods in Geomechanics* 35(8): 947–968.

Kiyota, T., Sattar, A., Konagai, K., Kazmi, Z. A., Okuno, D. & Ikeda, T. 2011. Breaching failure of a huge landslide dam formed by the 2005 Kashmir earthquake. *Soils and Foundations* 51(6): 1179–1190.

Mitaritonna, G., Amorosi, A. & Cotecchia, F. 2014. Experimental investigation of the evolution of elastic stiffness anisotropy in a clayey soil. *Geotechnique* 64(6): 463–475.

Shi, B., Murakami, Y. & Wu, Z. 1998. Orientation of aggregates of fine-grained soil: quantification and application. *Engineering Geology* 50(1-2): 59–70.

Takagi, M., Yokata, S., Suga, K., Yasoda, S. & Ota, H. 2010. The actual situation of the slope of earthfill that collapsed by an earthquake disaster in the Tomei Expressway Makinohara district. *Proc. of 55th Geotechnical Engineering Symposium*: 193–196.

Tang, C.S., Lin, L., Cheng, Q., Zhu, C., Wang, D.W., Lin, Z.Y. & Shi, B. 2020. Quantification and characterizing of soil microstructure features by image processing technique. *Computers and Geotechnics* 128: 103817.

Wang, B. J., Shi, B., Cai, Y. & Tang, C. S. 2008. 3D visualization and porosity computation of clay soil SEM image by GIS. *Rock and Soil Mechanics* 29(1): 251–255.

Yimsiri, S. & Soga, K. 2011. Effects of soil fabric on behaviors of granular soils: Microscopic modeling. *Computers and Geotechnics* 38(7): 861–874.

Smart Geotechnics for Smart Societies – Zhussupbekov, Sarsembayeva & Kaliakin (Eds)
© 2023 The Author(s), ISBN 978-1-003-29912-7
Open Access: www.taylorfrancis.com, CC BY-NC-ND 4.0 license

Constitutive model of expansive soft rock considering cementation and swelling nature

H. Kyokawa
The University of Tokyo, Tokyo, Japan

M. Kikumoto & Y. Cui
Yokohama National University, Yokohama, Japan

ABSTRACT: A novel constitutive modeling method which assumes expansive soft rock as the parallel composite mixture of rock matrix and expansive soil is proposed in this study. The rock matrix is modeled as the elastic damage model to represent the cementation on mechanical characteristics. The expansive soil is modeled by the double structure model for expansive soil to describe the mineralogical swelling due to wetting. The proposed model reasonably considers the interaction between cementation and mineralogical swelling on the mechanical characteristics of expansive soft rock and its transition.

1 INTRODUCTION

Expansive soft rocks become brittle due to the wetting/drying history because of the degradation of cementation on rock matrix, which is caused by the mineralogical swelling/shrinking of the contained clay minerals such as montmorillonite. Such swelling embrittlement (weathering) of soft rock causes slope failure and heave of tunnel (Pimentel, 2015), and its characteristic would depend on rock and ground water qualities, namely microscopic mineral properties (Chai et al., 2014). The design and construction on an expansive soft rock ground are comprehensively done based on several macroscopic index such as competence factor, slaking index, and montmorillonite content. Some numerical investigations especially on a tunneling in an expansive soft rock have also been conducted (Li et al., 2022). However, the most of them consider the mechanical characteristics at the predefined damaged area at the final weathered state, thus they cannot give a quantitative information on the deformation area and its transition due to surrounding environment such as the drying and wetting cycles.

In this study, a novel constitutive modeling method which assumes expansive soft rock as the mixture of rock matrix and expansive clay is proposed. The rock matrix is modeled as the elastic damage model to represent the influence of degradation of cementation on mechanical characteristics. Moreover, an expansive clay is modeled by the double structure model for expansive soil (Kyokawa, 2021) to describe mineralogical swelling due to wetting. The model validation is carried out by comparing with the observed results of the soaking and consolidation test in oedometer. It is indicated from the simulation of soaking under anisotropic stress state that the mineralogical swelling causes degradation of cementation and it results the failure with large deformation.

2 ISOTROPIC HETEROGENEOUS MATERIAL MODEL FOR SWELLING SOFT ROCK

2.1 *Modeling framework*

It can be seen from Figure 1 (after Cai et al., 2020) that swelling layered clay mineral, e.g., smectite, in sand stone (soft rock) causes the internal cracks at the cemented rock matrix, for

DOI: 10.1201/9781003299127-117

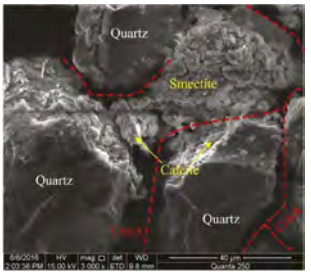

Figure 1. SEM image of Kunming sand stone (after Cai et al., 2020).

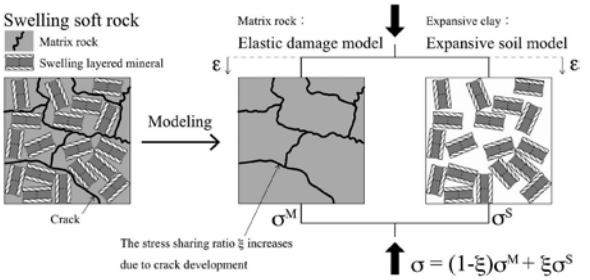

Figure 2. Modeling framework of expansive soft rock the isotropic heterogenous mixture.

instance, due to the drying-wetting cycles and it results the change in mechanical characteristics. In this study, swelling soft rock, which is the mixture of rock matrix and expansive clay, is modelled as the isotropic heterogeneous material shown in Figure 2.

The Bishop's effective stress is used for formulation of the proposed model to treat the unsaturated state and soaking (saturation) process. Assuming the spatially isotropic distribution of the matrix part (denoted by "M") and the expansive soil part (denoted by "S") in the soft rock, the total net stress is shared by each part. Then, adding a scalar state variable ξ to evaluate current stress sharing ratio, the total net stress is given by

$$\sigma_{\text{net}} = (1-\xi)\sigma^{\text{M}}_{\text{net}} + \xi\sigma^{\text{S}}_{\text{net}} \quad \text{where} \quad \boldsymbol{0} \le \xi \le \boldsymbol{1} \tag{1}$$

Considering same strain causes on both the matrix and expansive soil parts. Suction is independent from the stress sharing ratio ξ on the Bishop's effective stresses of each part, namely suction is the intensive property on stress. Assuming the effective stress parameter χ is equal to the degree of saturations of each part, the effective stresses are defined as

$$\sigma^{\text{M}}_{\text{net}} = \sigma''^{\text{M}} - S^{\text{M}}_r s\delta, \quad \sigma^{s}_{net} = \sigma''^{\text{S}} - S^{\text{S}}_r s\delta \tag{2,3}$$

For simplicity, the degree of saturations of each part are identical and it is given as a function of suction (van Genuchten model) in this study.

$$S^{\text{M}}_r = S^{S}_r = S_r(s) \tag{4}$$

The behavior of matrix part is described by the elastic damage model. Assuming the isotropic linear elasticity, namely Hooke's law, the relationship between the effective stress of matrix part and strain is given by

$$\boldsymbol{\sigma}''^{\text{M}} = \boldsymbol{D}^{\text{M}}_{\boldsymbol{e}}\varepsilon \tag{5}$$

In the first term on the right side of Equation (1), the stress sharing ratio ξ is equivalent to the damage index D in general damage theory. As the stress sharing ratio ξ approaches to 1, an apparent reduction of stiffness occurs, namely the degradation of cemented matrix is described. The stress sharing ratio is given by the following equation referring to Kurumatani et al. (2016).

$$\xi = 1 - \frac{\kappa_0}{\kappa}\exp\left(-\frac{E\kappa_0 h_e}{G_f}(\kappa - \kappa_0)\right) \quad \text{where} \quad \kappa(\varepsilon) \tag{6}$$

κ is the equivalent strain given as a function of the strain invariants. κ_0, E, G_f, h_e are the material parameters.

The behavior of expansive soil part is modeled by the double structure model for expansive soils (Kyokawa et al., 2021). Combining the behaviors of soil skeleton and clay mineral

crystals, this double structure model describes the hydro-mechano-chemical coupling behaviors of expansive soils. In particular with regard to the mineralogical swelling, both the crystalline swelling due to the adsorption of water molecule on a crystal, and the osmotic swelling due to the diffusion double layer of cations are considered in the model. Since the elastoplastic model is applied for the soil skeleton behavior, an increment type constitutive relationship of the double structure model is generally given as.

$$\delta\sigma''^{S} = \delta\sigma''^{S}(\delta\varepsilon, \delta \boldsymbol{S}_r^S, \delta \boldsymbol{s}, \delta \boldsymbol{d}), \quad \delta \boldsymbol{d} = \delta \boldsymbol{d}\left(\delta\sigma''^{S}, \delta \boldsymbol{c}, \delta \boldsymbol{S}_r^S\right) \tag{7,8}$$

d is the distance between mineral crystals, which is similar to the basal spacing. $\boldsymbol{c}$ is cation concentrations in pore fluid. Summarizing above equations, the total net stress is given by the following hydro-mechano-chemical coupling equation, in which strains, suction, cation concentrations are variable.

$$\delta\sigma_{\text{net}} = \delta\sigma_{\text{net}}\left(\delta\sigma_{\text{net}}^{\text{M}}, \delta\sigma_{\text{net}}^{\text{S}}, \delta\xi\right) = \delta\sigma_{\text{net}}\left(\delta\varepsilon, \delta\kappa(\delta\varepsilon), \delta \boldsymbol{s}, \ \delta \boldsymbol{S}_r^S(\delta \boldsymbol{s}), \delta \boldsymbol{c}\right) \tag{9}$$

3 MODEL VALIDATION

3.1 *Soaking and consolidation test*

To verify the applicability of the proposed model, the soaking and consolidation test on an expansive soft rock is simulated. The specimens were a natural (undisturbed) expansive soft rock rich in the smectite group mineral, and its disturbed specimen, which is reconstituted by compacting the crushed sample, for comparison. The initial air-dried specimens were loaded to a certain stress level in oedometer, and subsequently soaked by supplying the distilled water in the cell. After the soaking, a further consolidation process was conducted.

Material parameters for the matrix part are set by referring to the literature (Kurumatani et al., 2016) and a fitting. The parameters for the expansive soil part are basically same with those for the bentonite in previous study (Kyokawa, 2021), and the compression index and some parameters controlling swelling behavior are determined from a fitting. To consider the initial specimen disturbance in the simulation, the initial sharing stress ratio (the damage index) ξ_0 was calibrated. To reproduce soaking process in which the degree of saturation increases from almost zero at the air-dried condition to fully saturated condition, while suction was decreased in the water retention characteristic model, the cation concentration was also decreased from the saturated solution to the distilled water.

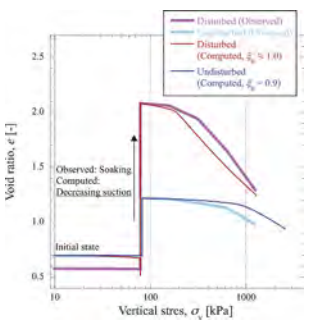

Figure 3. Observed and computed results of the swelling and consolidation tests.

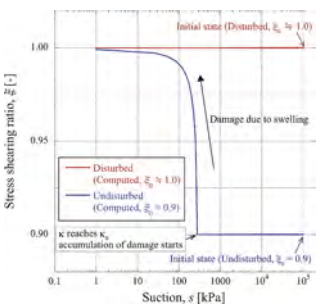

Figure 4. Transition of the stress shaering ratio during soaking process.

Figure 3 shows the relationship between vertical stress and void ratio, and Figure 4 shows the transition of the sharing stress ratio ξ during soaking process. It can be seen from Figure 3 that the proposed model can properly consider the influence of initial disturbance of specimen

not only on the magnitude of swelling due to soaking but also subsequent compression behavior. In Figure 4, the sharing stress ratio ξ of the undisturbed specimen accumulates as suction decreases, since the equivalent strain κ increases due to swelling (tension) strain.

It is indicated in Figure 2 that the stiffness of the proposed model can be regarded as the parallel composite stiffness of the rock matrix and expansive soil parts. Swelling of the expansive soil part due to soaking is initially suppressed by the stiffness of rock matrix. However, such expansive (tension) strain causes damage, and it results that the sharing stress of the matrix part decreases. As expansive strain accumulates, therefore, the behavior of the proposed model gradually becomes that of the expansive soil part.

3.2 *Soaking under anisotropic stress state*

Considering an actual ground condition, the simulation of soaking under anisotropic stress state was conducted. The undisturbed and disturbed soils, of which material parameters and initial conditions are same with those of above soaking and consolidation test, are sheared under the conventional triaxial compression. Moreover, another disturbed soil is sheared up to 100 kPa of deviatoric stress, and subsequently soaking under constant stress state is simulated.

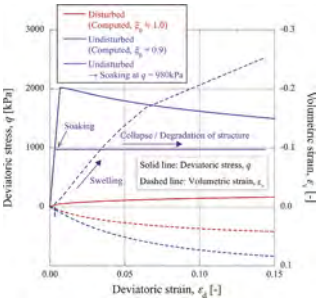

Figure 5. Simulation results of the monotonic compression tests and the soaking test under anisotropic stress state.

Figure 5 shows the stress-strain relationship (deviatoric strain – deviatoric stress – volumetric strain). The disturbed soil exhibits low strength and stiffness, which is equal to the behavior of expansive soil without the cementation effect. On the other hand, the undisturbed soil shows initially higher stiffness and strength. However, since accumulation of strain causes an increase in the sharing stress ratio ξ, namely the degradation of cementation on the matrix part, thus strain softening occurs from a certain strain level. In the case of soaking, development of deviatoric strain with large volume expansion can be observed. The mineralogical swelling of the expansive soil part due to soaking causes the degradation of cementation on the matrix part, and it is followed by the reduction of peak strength and the destabilization of soil structure. This soaking deformation process seems to capture the failure mechanism of expansive soft rock ground due to the drying-wetting cycles, namely swelling and squeezing.

4 CONCLUSIONS

The constitutive modeling method considering expansive soft rock as the parallel composite mixture of the rock matrix and expansive soil parts was proposed. Through the simulation of element test, it was indicated that the proposed model can reasonably describe the interaction between cementation and swelling nature of expansive soft rock. Conducting several element tests and analysis, the verification of model and setting the material parameters and initial condition will be discussed in future work.

ACKNOWLEDGMENT

This study is partially supported by the Ueda Memorial Foundation.

REFERENCES

Cai, X. et al. (2020). Fracture behavior and damage mechanisms of sandstone subjected to wetting-drying cycles, *Engineering Fracture Mechanics*, 234(April), 107109.

Chai, Z. Y., Kang, T. H., & Feng, G. R. (2014). Effect of aqueous solution chemistry on the swelling of clayey rock. *Applied Clay Science*, 93–94, 12–16.

Kyokawa, H. (2021). A double structure model for hydro-mechano-chemical behavior of expansive soils based on the surface phenomena of mineral crystals, Engineering Geology, Vol. 294.

Kurumatani, M., Terada, K., Kato, J., Kyoya, T., & Kashiyama, K. (2016). An isotropic damage model based on fracture mechanics for concrete. Engineering Fracture Mechanics, 155, 49–66.

Li, Y., Ma, C., Zhang, L., & Li, B. (2022). Influence Research for Softening and Swelling of Weakly Cemented Soft Rock on the Stability of Surrounding Rock in Roadway. Geofluids, 2022.

Pimentel, E. (2015). Existing Methods for Swelling Tests - A Critical Review. Energy Procedia, 76, 96–105.

Smart Geotechnics for Smart Societies – Zhussupbekov, Sarsembayeva & Kaliakin (Eds)
© 2023 The Author(s), ISBN 978-1-003-29912-7
Open Access: www.taylorfrancis.com, CC BY-NC-ND 4.0 license

Strength and deformability of large-scale clastic soils

K. Ibragimov, Zh.A. Ussenkulov, B.T. Yerimbetov, K.S. Baibolov & Y.B. Kunanbayeva
M. Auezov South Kazakhstan University, Shymkent, Kazakhstan

S.Zh. Ussenkulova
Kazakh University of Technology and Business, Astana, Kazakhstan

ABSTRACT: This paper presents the results of determining the actual strength and deformability of large-block soils in laboratory conditions on model mixtures. The strength deformative properties of large-block soils were determined on a large-sized device, the minimum size of which should be five times larger than the maximum size of the fraction. The main factors influencing the results of the experiments include: soil characteristics, loading characteristics and device characteristics. At the same time, the large-scale effect associated with the decompression of the end and side surfaces of the soil samples, as well as the friction of the samples on the side surfaces of the device, resulted in more accurate determination of the actual properties of large-block soils.

In recent decades, coarse-grained soils have been increasingly used as a material for the construction of dams in hydraulic engineering and road construction. And at present, the share of coarse-grained soils in hydraulic engineering construction is 75 percent or more (Kazakbaev, 1978).

Coarse clastic soils include soils containing more than 50% of fragments with dimensions of more than 2 mm. These include boulders, stones, crushed stone, pebbles, gruss, gravel; to boulders (rounded) and stones (not rounded) rocks with a particle size of more than 200 mm. Pebble (rounded), crushed stone (not rounded) are fragments of rocks with a fraction size of 200=10 mm. Gravel (rounded), gruss (not rounded) rock fragments with a particle size of 10-2 mm (Ibragimov, 1997).

Although coarse-clastic soils have low deformability and high strength and resistance to external loads, their physical and mechanical properties have not been fully studied due to the significant size of the fraction, which requires labor-intensive, expensive experiments on large-sized installations and devices (Orman, 2003, Ibragimov, 2000).

Therefore, the analysis of data on the study of the physical and mechanical properties of coarse clastic soils is of considerable interest.

As is known, the property of such soils in laboratory and field conditions is determined approximately on instruments and equipment intended for fine-grained soils.

One of the possible ways to solve this problem is modeling, in which smaller model mixtures are used instead of natural soils.

The model mixture is made from natural soil material by reducing the fraction by several times, while maintaining porosity and density.

The strength properties of coarse-grained soils are determined on a large-sized shear device, subject to the following condition:

$$Dpr^{min} \geq 5d_{max} \quad (1)$$

DOI: 10.1201/9781003299127-118

where $_{Dpr}^{min}$ - minimum diameter or height of the fixture; d_{max} - maximum soil particle diameter.

As a result of numerous experiments in laboratory and field conditions, in the general case, factors affecting the strength of coarse clastic soils can be divided into three groups:

1. Soil characteristics
2. Loading characteristics
3. Characteristics of devices

Soil characteristics mainly include soil type, mineralogical composition, particle size and shape, composition, density and moisture (Ibragimov, 2017).

With regard to the characteristics of soil loading, there are two fundamentally different load schemes: static and dynamic.

It is well known that the behavior of soils in these two cases is significantly different. However, the experiments of P.L. Ivanov, L.R. Stavnitser, Yu.K. Zaretsky, it is shown that under dynamic loading, the Coulomb formula can be used, where the normal stress is taken into account together with additional stresses arising from the dynamic application of the load.

Under dynamic loading, the Coulomb equation is written in the following form:

$$\tau_{din} = (\sigma_c - \Delta\sigma_r)\text{tg}\gamma \tag{2}$$

where $\Delta\sigma_s$ -additional stresses arising from the dynamic application of the load; tgγ- friction angle corresponding to static loading conditions.

In construction practice, to determine the strength characteristics of coarse-grained soils, two flat shear devices and stabilometers are mainly used. As experiments performed by many authors show, that if the corresponding condition (1) is observed, where scale effects are not manifested, the results obtained on both devices are practically the same.

In plane shear devices, the parameters are directly normal б and shearing τ stresses in the shear plane, from which the shear coefficient is determined.

In stabilometers, two main voltages are measured: the maximum б1 and the minimum б3. In this case, the shear coefficient is determined taking into account these two principal stresses, i.e. maximum and minimum.

Normal and shear stresses are determined from the following expressions:

$$\begin{aligned} \sigma &= \frac{2\sigma_1 * \sigma_3}{\sigma_1 * \sigma_3} \\ \tau &= \frac{\sigma_1 - \sigma_3}{\sigma_1 + \sigma_3}\sqrt{\sigma_1 * \sigma_3} \\ K_c &= \frac{\sigma_1 - \sigma_3}{2\sqrt{\sigma_1 * \sigma_3}_1} \end{aligned} \tag{3}$$

To determine the deformability of coarse clastic soils, it is necessary to take into account several types of systematic errors associated with scale effects that significantly affect the results of experiments.

These are the following three types of scale effects related to coarse clastic soils:

1. Scale effect associated with the decompaction of the end surfaces of soil samples.
2. Scale effect associated with the presence of zones located on the side surfaces of the samples.
3. Scale effect associated with the friction of the samples on the side surfaces of the samples.

When determining the deformability of coarse-grained soils on conventional compression devices, scale effects are not taken into account. In this case, the error is 50 percent or more..

The deformative properties of coarse-grained soils are determined using a large-sized compression device, subject to the condition:

$$Dpr^{min} \geq 5d^{fr}{}_{max} \quad (4)$$

The deformation characteristics of gravel-pebble soils are determined taking into account the under-stamp effects and lateral friction along the device walls according to the following formula:

$$S_{tr}=S_{exp} + \Delta_1 - \Delta_2 \quad (5)$$

where S_{tr} – true sample deformation; S_{exp} – deformation of the sample measured in experiments; Δ_1 – error due to friction losses along the device walls; Δ_2 – error due to under-stamp effects, independent of sample height.

At present, there are two different approaches to take into account lateral friction along the device walls: constructive and computational-experimental.

The most well-known constructive solution that makes it possible to exclude the influence of lateral soil friction on the measurement results is the device designed by Ya.L. Kogan, which is an odometer consisting of individual metal rings separated by compressible soft rubber gaskets. This should ensure the joint deformation of the walls of the odometer and the ground, respectively, the exclusion of any additional stresses in the ground associated with friction on the side surfaces of the device (Teptsky, 2020).

Calculation and experimental methods for taking into account lateral friction in compression tests of soils in odometers were developed by G.I. Pokrovsky, H.A. Rakhmatulin. According to the method of H.A. Rakhmatulin, it is necessary to conduct parallel tests of two soil samples of different heights h and 2h. If there is a noticeable systematic error associated with under-stamp effects, the relative value of which is inversely proportional to the height of the sample, this can lead to a significant error in the calculations. H.A. method Rakhmatulina gives good results when tested with fine-grained soils (Ibragimov, 2017, Ibragimov, 2020).

The deformation of coarse-grained soils, taking into account the scale effect associated with lateral friction along the walls of the device and decompaction along the side surfaces of the sample, is determined by the following method.

Compression testing of specimens of the same size is carried out in parallel in two types of rigid wall odometer. One of the odometers is a conventional design with a hard bottom and a movable top die. The second odometer instead of a hard bottom has the same movable stamp as on top.

As a result, in the first odometer, the load is applied to the upper stamp, while the stress along the height of the soil sample continuously decreases towards the base, and in the second odometer, the load is applied simultaneously to both stamps (upper and lower) and the stress decreases in the same way towards the middle of the sample. As a result, the second sample can be represented as if it consists of two samples with a height reduced by half. In this case, it will be possible to use the same scheme as that of H.A. Rakhmatulin, which differs in that with the same total height of the samples in the first and second odometers, the influence of the under-stamp effect in them is the same and therefore does not affect the results of calculating the stress state of the sample (Ibragimov, 2017, Ibragimov, 2019).

Accounting for lateral friction along the walls of the device is carried out according to the method of Kh.A. Rakhmatulin with the solution of the differential equation of equilibrium.

The solution of the differential equation gives, to construct a curve of the true compressibility of the soil.

Experimental determinations of compressibility show that lateral friction has a very significant effect on test results. The true compressibility of coarse-grained soils can be 1.5-2.0 times higher than directly observed in odometers with rigid instrument walls.

The second group of errors in determining the compressibility in odometers is the scale effect associated with the decompaction of the end surfaces of soil samples.

To determine the deformation, taking into account the under-stamp effect, two experiments are carried out. The first experiment is the same as discussed above, with a fixed bottom and a movable stamp at the top.

In the second experiment, the sample in the odometer is divided into two identical layers between which an additional stamp is placed, resulting in four contact zones.

In this case, the total deformation, in each of the two experiments, is determined by the sum of the soil deformation in the central part and the soil deformation in the zones in contact with the stamp, and they can be written as:

For the first case;

$$\varepsilon_1 = \varepsilon_{tr} + 2\Delta\varepsilon$$

For the second case:

$$\varepsilon_2 = \varepsilon_{tr} + 4\Delta\varepsilon \quad (6)$$

where ε_{tr} – true deformation of the soil sample corresponding to the selected stress; $\Delta\varepsilon$ – additional deformation (error) due to the under-stamp decompression zone.

Then the relative deformation, taking into account the under-die effect, is determined from the following formula:

$$\varepsilon_{tr} = 2\varepsilon_1 - \varepsilon \quad (7)$$

where ε_1 - relative strain of a sample in a hard-bottom odometer; ε_2 - relative deformation of a sample in an odometer with a hard bottom and a stamp in the middle.

The final actual relative deformation (settlement), taking into account the above errors, is determined from the following expression:

$$\varepsilon_r = \varepsilon_{tr} - \varepsilon_1 + \varepsilon_{tr} \quad (8)$$

where ε_{tr} – true relative deformation taking into account the under-die effect; ε_{tr} – true relative deformation, taking into account lateral friction along the device walls and decompression of zones along the side surfaces of the sample.

Table 1 below shows the results of calculating the actual compressibility performed jointly with Petrov G.N. In this calculation, first, the correction for friction is determined, after which corrections for the influence of under-die effects are introduced to the obtained intermediate calculation. Simultaneously with the calculation of the actual compressibility values, the friction coefficients were also determined.

Table 1. The actual compressibility.

Experienced Data			Estimated data				
	Odometer voltage						
ε	With moving bottom σ_3, kg/*cm^2	Standard σ_1, kg/*cm	$\Delta\varepsilon$ substamp correction	K_{tr}	$\sigma_д$, kg/*cm^2	ε_D	Notes
0,02	4,0	5,0	0,010	0,260	3,13	0,010	
0,04	10,0	14,0	0,012	0,431	6,75	0,028	
0,06	16,0	20,5	0,014	0,294	12,15	0,046	
0,08	24,5	30,0	0,016	0,233	19,66	0,064	$R_{од}$ = 17,9 cm;
0,10	34,5	42,5	0,018	0,240	27,51	0,082	$h_{обр}$ = 35,15 cm;
0,12	46,0	57,5	0,018	0,260	36,02	0,102	p_o = 1,55 t/m^3
0,14	61,5	76,5	0,019	0,256	48,42	0,121	(extremely loose
0,16	81,0	100,0	0,19	0,243	64,41	0,141	state)
0,18	103,0	129,0	0,020	0,263	80,45	0,160	
0,20	132,5	170,0	0,021	0,296	100,48	0,179	
0,22	172,0	220,0	0,018	0,282	130,90	0,202	

1 CONCLUSION

1. In the presence of sufficiently developed methods for calculating structures from coarse-grained soils, their physical and mechanical properties are currently determined quite approximately, with significant errors. Also, the methods of preparing and laying such soils in construction have not been sufficiently developed.
2. The physical models proposed taking into account the scale effects of the interaction of coarse-grained soils with the rigid walls of the devices make it possible to develop metrologically substantiated methods for determining the physical and mechanical characteristics of soils, as well as to obtain calculated dependencies and nomograms for determining the latter.

REFERENCES

Ibragimov K.I., Baidilla I.O., Akhmedov A.B., Sayymkulov E.B. 2019. Modeling of coarse-grained soils during the construction of blast dams: 59–62. Kazakhstan: Shymkent.

Ibragimov K.I., Karabaev A.A., Karabaev N.A. 2017. Theoretical foundations for determining the density of coarse clastic soils. *Materials of the international scientific and practical conference, topical problems of the trend of innovation in modern science and education dedicated to the 60th anniversary of T.A. Turmambekova*: 87–89. Kazakhstan: Turkestan.

Ibragimov K.I., Kasymbekova K.T., Baydilla I.O. 2017. Graph-analytical method for determining the density of coarse-grained soils. M.O. *Proceedings of the international scientific conference dedicated to the 120th anniversary of the birth of Auezov "Auezov readings-15" 3rd revival of Kazakhstan, new concepts and modern solutions*: 50–55. Kazakhstan: Shymkent.

Ibragimov K.I., Kurasbek B.K., Baidilla I.O. 2020. Quality control of coarse-grained soils in the construction of earthen dams. *Proceedings of the XXIII – Republican student scientific conference on the topic of Scientific views of young people to the global challenges of our time in natural, technical, social, humanitarian and economic sciences*. Kazakhstan: Shymkent.

Ibragimov K.I., Nazarov K.I. 1997. Strength of coarse clastic soils of the 21st century. *International Youth Scientific and Technical Conference*. Uzbekistan: Tashkent.

Ibragimov K.I., Nazarov K.I. 2000. Strength and deformability of coarse clastic soils. *Proceedings of the 1st Central Asian geotechnical symposium of Geotechnical problems of construction, architecture and geoecology at the turn of the XXI century*. Kazakhstan: Astana.

Kazakbaev K.K., Petrov G.N., Ibragimov K.I. 1978. Building properties of coarse soils. Uzbekistan: Tashkent.

Orman A.O., Ibragimov K.I., Kerimkulov B.K. 2003. Research of the actual compressibility of coarse clastic soils. *Proc. intern. geotechnical symp. Foundation construction in difficult engineering and geological conditions*. Russia: St. Petersburg,

Teptsky A.Kh., Roberman S.R. 2020. Method for determining the density of coarse-grained soils. Russia: Moscow.

Smart Geotechnics for Smart Societies – Zhussupbekov, Sarsembayeva & Kaliakin (Eds)
© 2023 The Author(s), ISBN 978-1-003-29912-7
Open Access: www.taylorfrancis.com, CC BY-NC-ND 4.0 license

Calculation of the parameters of the base of waste rock dumps on a mountain slope

K.Ch. Kozhogulov & B.T. Djakupbekov
Institute of Geomechanics and Subsoil Development of the National Academy of Sciences of the Kyrgyz Republic, Bishkek, Kyrgyzstan

ABSTRACT: In calculations, the formation of waste rocks of upland deposits and the determination of the parameters of the base of the dumps is a rather difficult problem. Such parameters as the relief of the surface, the storage of a sufficiently large volume of waste rock and with small occupied areas, the steepness of the slope, as well as the minimum distance to the quarry are considered for the planning of dumps. The waste rock dump is the final product in the development of rocks in quarries. A prerequisite for dumping and warehousing is to ensure industrial and environmental safety.

Calculation of the volume of the stored dump in the minimum area. For this task, Google Earth aerial photographs were used and a 3D terrain model was created using the google sketchup software product.

When planning rock dump formations of upland deposits and determining the parameters for the foundations of dumps is a rather difficult problem. Such parameters as the complexity of the terrain, the storage of a sufficiently large volume of overburden and with small occupied areas, the steepness of the slope, as well as the minimum distance relative to the contour of the quarry are considered for the planning of dumps.

In a limited occupied area and a certain volume of the dump is poured into one or more tiers. The parameters of the height of the tier are determined by the stability, which depends on the properties of the base for the dump and the stored rocks, the relief of the surface, the length and speed of movement of the dump front, the rate of dumping of the dump.

The filling schemes define the process of compaction of rock masses of dumps and their strength properties.

A prerequisite for dumping and warehousing is to ensure industrial and environmental safety, as it is the final product in the development of rocks in quarries.

The stored dump on an inclined base is in a stable state as long as there is sufficient internal coupling in the medium forming them and the shear resistance exceeds the shear forces. The main condition for the successful solution of the problem of the stability of dumps is to understand the physical nature of shear resistance, which is a consequence of friction between individual particles of bulk material and between the particles and the solid base of the dump. Krasnoselsky. & Kalabin. 1975. Dumps. . .

For this task, where exact parameters of the surface area of the stored dump are needed, satellite images obtained from the Google Earth software product were used. For this example, we calculated the dumps of the Kumtor mine Figures 1 and 2.

In Google sketchup, based on the satellite images obtained, a 3D model of the surface relief of the selected section of the saved dump is automatically created. Based on the created 3D model, we start designing the placement of dumps taking into account the required conditions, such as the volume of dumps and the area of placement, Figure 3. Dzhakupbekov. 2016. Determination of dump. . .

DOI: 10.1201/9781003299127-119

Figure 1. Satellite image of the dumps of the Kumtor deposit of Kyrgyzstan.

Figure 2. Storage of the Kumtor mine dump.

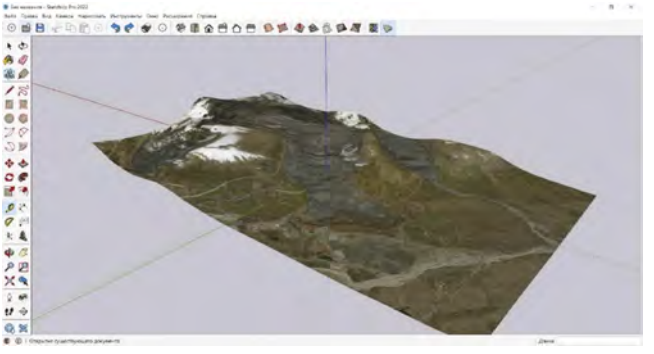

Figure 3. Based on satellite images, a 3D model has been created, a place for a dump.

Based on the 3D model, we obtain the required number of longitudinal and cross sections to calculate the stability coefficient taking into account the geometric parameters of the blade Figure 4.

To calculate the stability coefficient of the dumps, a study was also done to determine the physical and mechanical properties of the base rocks and the rocks of the dumps. The provided samples in laboratory conditions were determined the properties necessary for calculating the stability coefficient.

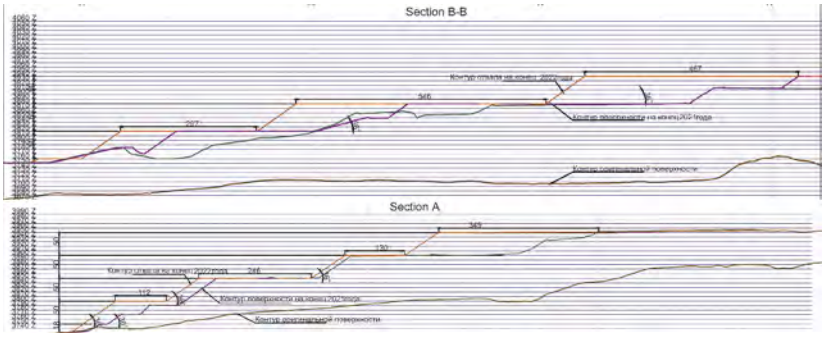

Figure 4. Cross section of dumps.

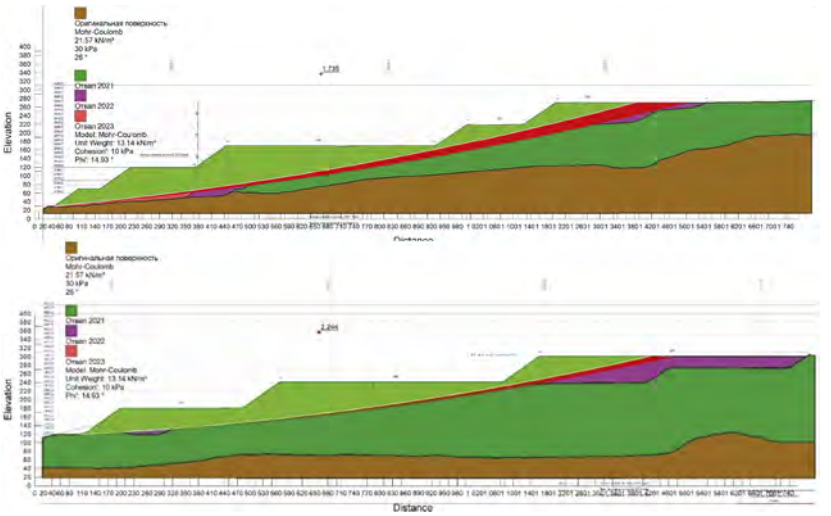

Figure 5. Cross-section stability coefficient calculations, GeoStudio slope/w software was used.

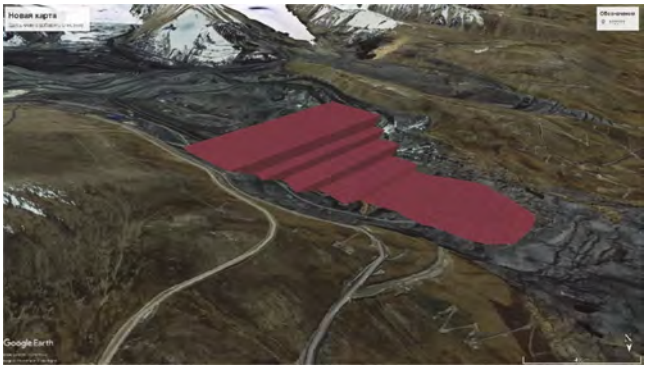

Figure 6. The final view of the 3D model of the dump on the slope, taking into account all Google Earth calculations.

According to the results of the obtained laboratory data, it was revealed that the average value of the bulk weight of the base rocks is $\gamma_н$ = 21.57 kN/m3. According to the results of determining the strength characteristics of rocks, it was found that the angle of internal friction of the base rock is φ = 260, and the adhesion is C = 30kPa.

Also, according to the results of the data obtained, the average value of the bulk weight of the dump rocks is un = 13.14 kN/m3. The angle of internal friction of the dump rock is φ = 14.930, and the adhesion C = 10kPa. Below are the results of calculating the stability coefficient, Figure 5.

You can also import the projected 3D model of the dump into the Google Earth software application with attached geo-positions to view the location of the dumps relative to the quarry, Figure 6.

1 CONCLUSIONS

This method of obtaining the parameters of the 3d model and the base for the dump allows you to calculate the minimum area occupied by the dump and calculate the stability coefficient in a short time.

1. Laboratory studies all the necessary work was carried out to calculate the stability of the dumps.
2. Based on the results of studying the satellite images, all the necessary 3D geometric constructions were made.
3. As a result of the performed studies of the state of the dumps, the calculation of the stability coefficient and the assessment of the stability of the dumps, it was established:
   - newly poured dumps are generally stable;
   - the overall stability of the dumps is within the generally accepted values: the value of the stability coefficient is more than Ky = 1.5.

REFERENCES

Dzhakupbekov B.T. 2016. Determination of dump parameters on mountain slopes using the google SketchUp software application. (eds), Modern problems of mechanics. Issue twenty-sixth, 2016. Bishkek.

Krasnoselsky E.B. & Kalabin G. V. 1975. Dumps on the mountainside. NAUKA Publishing House, Leningrad Branch: 47–53.

Smart Geotechnics for Smart Societies – Zhussupbekov, Sarsembayeva & Kaliakin (Eds)
© 2023 The Author(s), ISBN 978-1-003-29912-7
Open Access: www.taylorfrancis.com, CC BY-NC-ND 4.0 license

Simulate the in-situ direct shear test of gravel and systematic evaluation its mechanical properties parameters based on the discrete element method

P.Y. Shu
Postdoctoral Fellow, Department of Civil Engineering, National Taiwan University, Taipei, Taiwan (R.O.C.)

T.T. Wang*
Professor, Department of Civil Engineering, National Taiwan University, Taipei, Taiwan (R.O.C.)

ABSTRACT: Because the particle size of gravel exceeds the scale of conventional laboratory test equipment, its mechanical properties often obtain by in-situ direct shear tests. Several factors affect the mechanical properties of the gravel layer, including the particle size distribution, the particle arrangement and its stacking. However, due to the high cost and limited number of tests on site, it is difficult to acquire representative mechanical properties parameters of the gravel layer. In this study, discrete element particle flow software is used, and the design of experiments (DOEs) method is applied to determine combinations of microscopic parameters. The microproperties affects the mesoscale mechanical properties of gravel and its regression equations are obtained by the statistical analysis of variance (ANOVA). Combined with the in-situ direct shear tests, the range of the mechanical properties parameters of the gravel formation can be described.

1 INTRODUCTION

Gravel typically has particle sizes that range widely, on average exceeding 10 cm, and are easily impacted by the size effect. According to Marsal (1973), the size effect will have a considerable impact when the ratio of the specimen's diameter to its maximum particle size is less than six. Since the particle size of gravel exceeds the range of common, laboratory test equipment, larger-scale tests (Xu et al., 2011) or the use of numerical analytical software are more appropriate for examining the mechanical properties of gravel.

There are two different types of large-scale tests for gravel: large-scale triaxial tests and large-scale direct shear tests. Because of the limitation of equipment and space, the large-scale triaxial test is more difficult to carry out among them, so the large-scale direct shear test is the one that is most frequently utilized (Yagiz, 2001; Kuenza et al., 2004; Hamidi et al., 2012; He et al., 2021).

Large-scale direct shear experiments can be used to determine the mechanical properties of gravel, but they are expensive, few in number, and unable to measure contact number or force. As a result, the numerical analysis method has been rapidly developing in recent years. Researchers simulate biaxial compression testing by creating gravel models in MATLAB and importing them into Particle flow code (PFC) software (Ding et al., 2010; Liu et al., 2013; Lu et al., 2017).

Although previous research indicates that large-scale tests of gravel primarily rely on direct shear tests, the numerical simulation primarily uses the biaxial test to study the mechanical properties of gravel. As a result, this study simulates in situ direct shear tests by PFC-FLAC coupled numerical modeling.

*Corresponding author: ttwang@ntu.edu.tw, taitienwang@gmail.com

DOI: 10.1201/9781003299127-120

2 NUMERICAL MODEL

This study simulates in situ direct shear tests by PFC-FLAC coupled numerical modeling. Figure 1a shows the layout of the in situ direct shear test. In order to reduce computation time, FLAC is used to generate the mesh to simulate the reinforced concrete, and the gravel specimen is simulated using PFC. (Figure 1b). To investigate the influence of particle shape, a model with elliptical gravel is adopted. A clump is employed to produce 2:1 axial ratio elliptical particles, each clump has three round particles. According to the design of experiment (DOE), the fixed ratio of round particles is replaced to simulate the gravel sample.

The microscopic parameters, particle size, number of particles, packing, and loading rate have an impact on the PFC simulation outcomes. Therefore, to reduce the influence of the particle size, number of particles, packing, and loading rate, a particular particle size distribution curve (Figure 2) and packing are selected, and a specific loading rate is chosen. A constant normal force is applied vertically on the top of the reinforced, while the whole reinforced travels from left to right at a preset rate along the shear plane to imitate in situ direct shear test. The normal force is set at 0.1, 0.2, 0.3, and 0.4 MPa, per the experiment data.

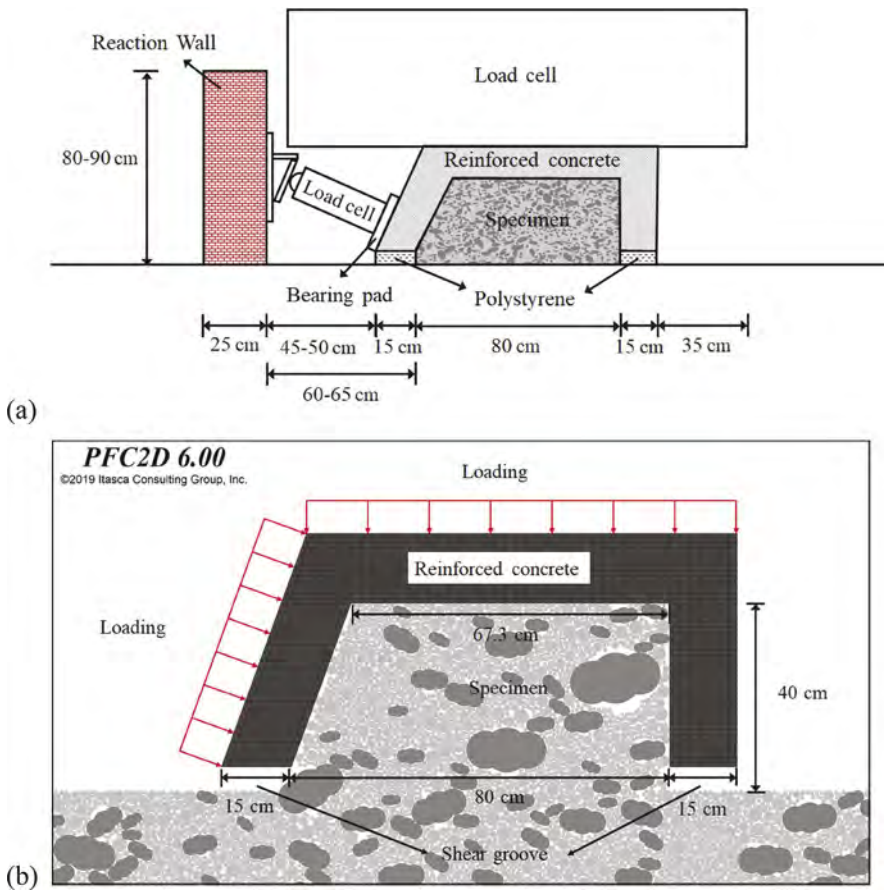

Figure 1. Schematic diagram (a) in-situ direct shear test, (b) numerical model.

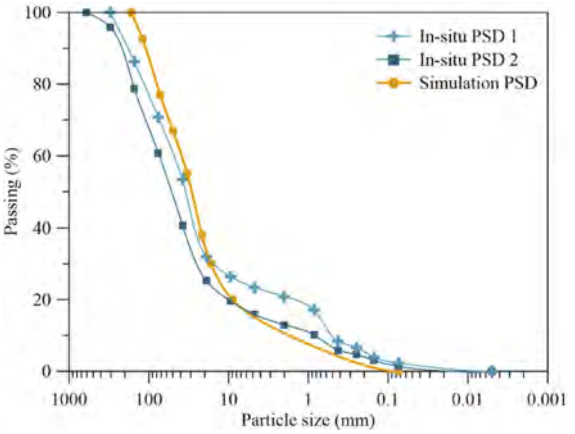

Figure 2. In-situ and numerical model particle size distribution curve.

3 MICROPROPERTIES BASED ON DOES

The input microscopic parameters are set using the DOE and orthogonal array (OA) tables to assess the effects of altering particular microproperties on the dependent variables, which are the mechanical properties. DOE is used to investigate the relationship between multiple input variables (factors) and output variables (responses), and the OA table is used to reduce the number of simulations. A statistical analysis of variance (ANOVA) is carried out to find the significant parameters that affect simulated cohesion (c) and friction angle (ϕ), which are then used for regression analyses and discussion.

3.1 *Two-level factorial experiments*

There are more than ten microscopic parameters needed for the PFC2D simulation. According to Potyondy and Cundall (2004), ten parameters are chosen in this investigation as the main microproperties that may affect the mesoscale c and ϕ of specimens. The Young's moduli of the particles (E_c) and bonds ($\bar{E}_c$) as well as the normal-to-shear stiffness ratios of the particles (k_n/k_s) and bonds ($\bar{k}_n/\bar{k}_s$) affect the deformation properties of specimens. The friction coefficient of particles (μ), the tensile strength of the bonds ($\bar{\sigma}_c$), the cohesion of the bonds ($\bar{c}$), and the friction angle of the bonds ($\bar{\phi}$) affect the strength properties of specimens. The geometry of specimens is influenced by the ratios and rotation angles (α) of clumps.

A full three-level and two-level factorial design of ten microscopic parameters require 59,049 and 1,024 distinct parameter combinations, respectively, which is numerous. However, many of which have a minimal impact on the simulated mechanical properties. Thus, this study employs the orthogonal table $L_{32}2^{10\text{-}5}$ setup factor to decrease the number of simulations and generate 32 sets of various parameter combinations in order to increase analysis efficiency.

According to statistical ANOVA results E_c $\bar{\sigma}_c$, $\bar{c}$ and μ are identified as the main factors that significantly influence the specimen's c and $\bar{E}_c$, μ, α and ratios of clump are identified as the main factors that significantly influence the specimen's ϕ since they are greater than the corresponding critical values at the 90% confidence level (P<0.1).

3.2 *Three-level factorial experiments*

To determine the nonlinear effects of independent variables on dependent variables, three-level factorial experiments are carried out using an orthogonal table. Seven microscopic parameters, E_c, $\bar{E}_c$, μ, $\bar{\sigma}_c$, $\bar{c}$, α and ratios of clump, are chosen as the primary components in

the factorial design per the findings of two-level factorial experiments. The orthogonal table $L_{81}3^{6\text{-}2}$ is used; the magnitudes of the parameters that are used in 3-level DOEs are listed in Table 1. The other three microscopic parameters, k_n/k_s, $\bar{k}_n/\bar{k}_s$, and $\bar{\phi}$ are set to 1.33, 1.00, and 12, respectively. The three-level factorial experiment involves 27 combinations of microproperties. The upper bounds and lower bounds of the simulated cs and ϕs of specimens are the same as those in the two-level experiment. According to statistical ANOVA results E_c are identified as the main factors that significantly influence the specimen's c and ratios of clump are identified as the main factors that significantly influence the specimen's ϕ.

Table 1. Microproperties for use in 3-level DOEs.

		Level			
Effect on the specimen	Items	-1	0	1	Unit
Deformation properties	E_c	$4.00*10^8$	$1.20*10^9$	$3.60*10^9$	Pa
	(k_n/k_s)	-	1.33	-	-
	$\bar{E}_c$	$6.67*10^6$	$2.00*10^7$	$6.00*10^7$	Pa
	$(\bar{k}_n/\bar{k}_s)$	-	1.00	-	-
Strength properties	μ	0.22	0.67	2.00	-
	$\bar{\sigma}_c$	$9.00*10^4$	$2.70*10^5$	$8.10*10^5$	Pa
	$\bar{c}$	$8.00*10^4$	$2.40*10^5$	$7.20*10^5$	Pa
	$\bar{\phi}$	-	12	-	°
Geometry	Ratios of clump	62	70	80	%
	α	0	45	90	°

4 DISCUSSION

Table 2 shows that, in addition to the one microproperties, E_c, μ interaction with E_c and $\bar{E}_c$, and $\bar{\sigma}_c$ interactions with $\bar{c}$, significantly affect the mesoscale c of specimen. Multiple linear regression is used to determine the relationships between the mesoscale c and the two microproperties and their interaction terms, yielding

$$c = 0.7380E_c * \mu + 0.3728\bar{\sigma}_c * \bar{c} - 0.3641\bar{E}_c * \mu - 0.2066E_c \tag{1}$$

with a coefficient of determination $R^2 = 0.786$.

Table 3 shows that, in addition to the one microproperties, Ratios of clump, $\bar{E}_c$ interaction with α, and μ interactions with Ratios of clump, significantly affect the mesoscale ϕ of specimen. Multiple linear regression is used to determine the relationships between the mesoscale ϕ and the two microproperties and their interaction terms, yielding

$$\phi = -0.5424\mu * \text{Ratios of clump} + 0.4102\text{Ratios of clump} + 0.2484\bar{E}_c * \alpha \tag{2}$$

with a coefficient of determination $R^2 = 0.665$.

Table 2. ANOVA based on three-level factorial experiment to determine influence of microproperties on simulated c.

	Coef.	SE Coef.	$t(22)$	p-Level(<0.1)
Residual	0.0000	0.0198	0.0000	1.0000
(1) E_c	-0.2066	0.0632	-3.2677	0.0035
(1) E_c*(5) μ	0.7380	0.0973	7.5862	0.0000
(3) $\bar{E}_c$*(5) μ	-0.3641	0.0775	-4.6984	0.0001
(6) $\bar{\sigma}_c$*(7) $\bar{c}$	0.3728	0.0697	5.3466	0.0000

Figure 3 plots associated 95% confidence level. The range of simulation results of cohesion (c) and friction angle (ϕ) includes the in situ data, and the in situ data are all within the 95% confidence interval, indicating that the formula obtained in this study can be used to predict the in situ data.

Table 3. ANOVA based on three-level factorial experiment to determine influence of microproperties on simulated ϕ.

	Coef.	SE Coef.	$t(21)$	p-Level(<0.1)
Residual	0.0000	0.0308	0.0000	1.0000
(9) Ratios of clump	0.4102	0.0806	5.0889	0.0000
(3) $\bar{E}_c$*(10) α	0.2484	0.0984	2.5239	0.0190
(5) μ*(9) Ratios of clump	-0.5424	0.1013	-5.3518	0.0000

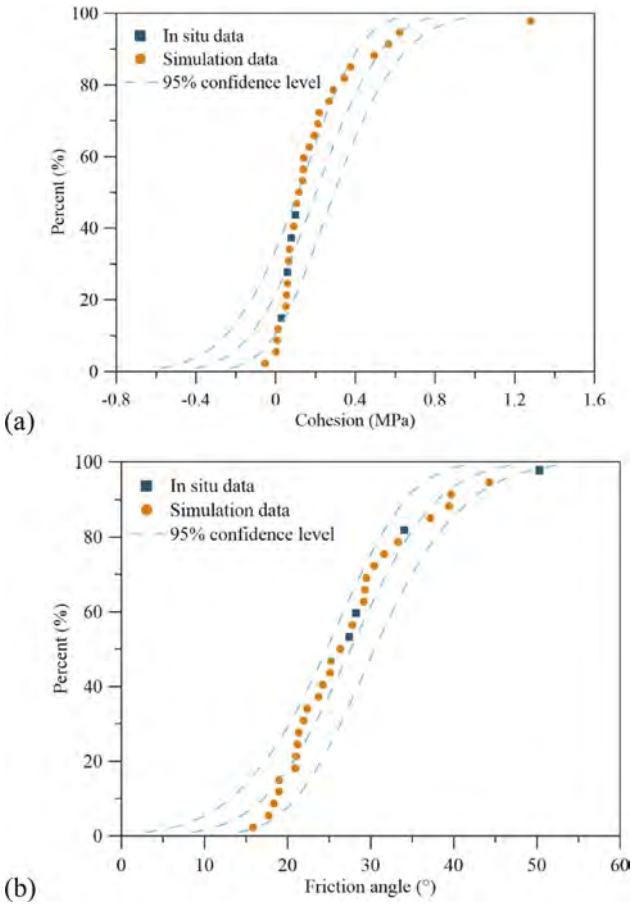

Figure 3. 95% confidence level of corresponding cohesion (a) and friction angles (b).

5 CONCLUSION

The design of experiment (DOE) method is used to determine the relationship between the microproperties and simulate mesoscale mechanical parameters of a rock specimen. Two- and

three-level factorial designs with related analyses of variances (ANOVA) are successively used to identify the microproperties that significantly affect the cohesion (c) and friction angle (ϕ) of a specimen. The following conclusion are drawn.

1. One microproperties, the Young's moduli of the particles (E_c) and μ interaction with E_c and $\bar{E}_c$, and $\bar{\sigma}_c$ interactions with $\bar{c}$, significantly affect the mesoscale c of a rock specimen.
2. One microproperties, the Ratios of clump and $\bar{E}_c$ interaction with α, and μ interactions with Ratios of clump, significantly affect the mesoscale ϕ of specimen.
3. Two multivariate regression equations (Equations (1) and (2)) are proposed to describe the relationships between the cohesion (c) and friction angle (ϕ), of a specimen and its aforementioned microproperties, with coefficients of determination of 0.786 and 0.665, respectively.

REFERENCES

Ding X, Li Y, Wang X. Particle flow modeling mechanical properties of soil and rock mixtures based on digital image. Chinese J Rock Mech Eng. 2010;29:477–484.

Hamidi A, Azini E, Masoudi B. Impact of gradation on the shear strength-dilation behavior of well graded sand-gravel mixtures. Sci Iran. 2012;19:393–402. https://doi.org/10.1016/j.scient.2012.04.002

He L, Feng C, Yang L, Liang Y. Experimental study of influence of particle arrangement angle on shear properties of sand. J Hohai University. 2021;49:447–454. https://doi.org/10.3876/j.issn.1000.1980.2021.05.010

Kuenza K, Towhata I, Orense RP, Wassan TH. Undrained torsional shear tests on gravelly soils. Landslides. 2004;1:185–194. https://doi.org/10.1007/s10346-004-0023-3

Liu Z, Zhou N, Zhang J. Random gravel model and particle flow based numerical biaxial test of solid backfill materials. Int J Min Sci Technol. 2013;23:463–467. https://doi.org/10.1016/j.ijmst.2013.07.001

Lu Y, Tan Y, Li X, Liu C. Methodology for Simulation of Irregularly Shaped Gravel Grains and Its Application to DEM Modeling. J Comput Civ Eng. 2017;31. https://doi.org/10.1061/(ASCE)CP.1943-5487.0000676

Marsal RJ, Mechanical properties of rockfill. in Embankemnt-Dam Engineering, R.C. Hirschfeld and S. J. Poulos, Eds. A Wiley Interscience Publication; 1973: 110–200.

Potyondy DO, Cundall PA. A bonded-particle model for rock. Int J Rock Mech Min Sci. 2004;41:1329–1364.

Xu WJ, Xu Q, Hu RL. Study on the shear strength of soil–rock mixture by large scale direct shear test. Int J Rock Mech Min Sci. 2011;48:1235–1247. https://doi.org/10.1016/j.ijrmms.2011.09.018

Yagiz S. Brief note on the influence of shape and percentage of gravel on the shear strength of sand and gravel mixtures. Bull Eng Geol Env. 2001;60:321–323. https://doi.org/10.1007/s100640100122

Smart Geotechnics for Smart Societies – Zhussupbekov, Sarsembayeva & Kaliakin (Eds)
© 2023 The Author(s), ISBN 978-1-003-29912-7
Open Access: www.taylorfrancis.com, CC BY-NC-ND 4.0 license

Assumptions and reality in ground models – the case of drift-filled hollows and associated subsurface features in London, United Kingdom

A.L. Flynn
Robert Bird Group, London, UK

P.E.F. Collins
Department of Civil and Environmental Engineering, Brunel University London, UK

ABSTRACT: The subsurface of London is often assumed to be relatively simple, with Late Cretaceous and Palaeogene strata sitting within and forming a synclinal structure (the London Basin). The surface has been modified by mostly fluvial processes during the Quaternary.

More recently, a picture of more complex conditions has begun to be developed, largely driven by the need for deeper foundations, groundwater control and tunnelling. One group of significant features are referred to as 'drift-filled hollows' (DFH). These are commonly closed depressions in the surface of the bedrock (typically the London Clay Formation), that are infilled by later deposits. Adjacent and underlying strata is sometimes disturbed

A new database shows that DFH are more widespread than previously thought, but also highlights issues in how they are classified. It also raises questions about the validity of the 'simple' geological model of London and highlights the danger of using assumptions when planning development, and for reconstructing past events.

1 INTRODUCTION

Understanding subsurface conditions is essential for infrastructure development and is integral to design codes such as Eurocode, where structures must "sustain all actions and influences likely to occur during execution and use" (BSI 2010, p26). Frequently, this understanding is expressed as a ground model that incorporates a range of site geological, hydrogeological and geotechnical information. Importantly, as proposed in the current draft of Eurocode 7 (under review, BSI 2022), the degree of ground variability and uncertainty must be acknowledged. This paper explores how ground variability and uncertainty can be affected by assumptions, particularly in contexts such as the London region in southern England where there is a long history of ground investigation and ground conditions are sometimes *believed* to be predictable. To aid this, a new compilation and assessment of data is presented.

2 STUDY AREA

2.1 *The assumed regional geological model*

The geological model that forms the start point of many ground investigations in the London region was first developed in the 19th Century (e.g. Reynolds 1849), and subsequently added to by many authors (e.g. Wooldridge and Linton 1939; Sumbler 1996; Royse et al. 2012).

DOI: 10.1201/9781003299127-121

This was originally based on surface exposures, small quarries and water wells. More recently, boreholes have been drilled for water and increasingly as part of site investigations, with around 80,000 records now available within the London area.

The generally-followed regional model is of a Palaeozoic basement, unconformably overlain by Cretaceous clays, sands and permeable Chalk. Overlying these is a suite of Palaeogene and Neogene strata, the most widely known of which is the London Clay. The Cretaceous and Palaeogene/Neogene strata form a syncline-like structure, with Chalk hills to the north, south and west, while the Chalk generally occurs at depth in the central London area. The current geological structure is traditionally interpreted as being the result of fairly gentle compression and folding between the later Cretaceous and the Miocene.

During the later Neogene, and particularly during the Quaternary, denudation formed the valley of the river Thames and its tributaries. The northern margin of the area was glaciated approximately 0.45 Ma before present but the area has experienced a periglacial climate for much of the past million years or so. River deposits, principally sand and gravel, are widespread as a series of terrace units (Gibbard 1985, Bridgland 1994). During warmer periods, a range of finer alluvial soils and peat was deposited. These occur locally within the river terrace deposits and beneath the modern floodplain. The modern surface is often characterized by human modification and is often referred to as 'made ground'.

2.2 *Recent modifications to the geological model*

Progressive improvement in ground investigation methods, and the availability of evidence, has permitted additional, principally local, detail to be added to the general geological model. For example, a significant number of high-quality borehole, tunnel and groundwater records have been collected as part of the Crossrail project (see e.g. Davis 2016). This has particularly improved understanding of the stratigraphy, showing that the Palaeogene strata under central London are spatially and vertically complex (e.g. Edgar et al. 2022).

The new attention paid to the detail of borehole and other data has also shown that there is, at least locally, structural complexity (e.g. Newman 2022) with a variety of faults that affect ground properties and drainage.

2.3 *Anomalous near surface features – drift-filled hollows*

Variability in the thickness of superficial deposits resting unconformably on Palaeogene strata in and beyond central London is well known (Berry 1979; Hutchinson 1980, 1991). There have been several investigations of individual features where an apparently closed depression in the basal Quaternary unconformity is infilled by an anomalously thick sequence of superficial deposits (e.g. Hawkins 1952; Collins et al. 1996; Lee and Aldiss 2012; Davis et al. 2018). Some, but not all of these features include significance disturbance of the Cretaceous and Palaeogene strata that they overlie, including diapiric structures, or are close to faulting. Some are known to penetrate through some or all of the Palaeogene strata to reach the Cretaceous Chalk. The term 'drift-filled hollows' (DFH) is generally used when this type of feature is encountered in London.

Potential risks associated with drift-filled hollows are due to significant horizontal and vertical variability in ground properties, including permeability and bearing capacity. There is also uncertainty over whether the features are all the result of past processes, or whether some are still actively developing, or could be reactivated in the future. As exploitation of deeper geology increases for deep foundations, excavations, tunnelling, and geothermal energy, it is important that the current uncertainty around these features is addressed.

Although many drift-filled hollows have been reported, detailed studies have been typically based on individual features, with different researchers dealing with apparently unique features. There is a need to consider them more holistically to see if there are common patterns.

Berry (1979) identified several drift-filled hollows in central London and attributed them to river scour. A similar scour hypothesis was proposed by Rose et al. (1980). In contrast, Hutchinson (1980, 1991) proposed a more complex suite of processes including artesian pressure, valley

bulging and particularly ground ice growth and decay (i.e. pingos). In a study to the west of London, Collins et al. (1996) considered a series of drift-filled hollows underlying the modern floodplain and valley-side river terrace deposits, and concluded that localized subsidence, possibly linked to passive (and possibly active) tectonic control was the dominant process. The robustness of evidence for massive ground ice in the hollows in central London was questioned by Collins (2013; also Banks et al 2015) as typical and unambiguous diagnostic features had not been found.

The review by Banks et al. (2015) of drift-filled hollows in central London identified some geographical clustering which supported Hutchinson's (1980) identification of areas most likely to have a drift filled hollow present i.e. areas where impermeable strata are thinner, and a confined/artesian aquifer.

New evidence continues to add to understanding, with the most recent compilation first reported in Flynn et al. (2020) and completed by Flynn (2022).

3 APPROACH

In the most recent work (Flynn 2022), a rigorous re-evaluation of existing evidence was completed with a deliberately non-genetic methodology that minimized the risk of interpretive bias. The bulk of the data was retrieved from the British Geological Survey's GeoIndex database (BGS 2020), with supplementary evidence provided through new site research, industry collaboration and a limited number of published studies e.g. Davis et al. (2018) who provided tunnel face logs.

Data quality was variable and required critical assessment and, where appropriate and possible, confirmation with other evidence. Records that did not meet strict quality criteria were excluded. A new database was established to manage the data and analysed using the ArcGIS 10.5.1 software. Features identified through this new analysis were named using a numbering system to a) maintain interpretative distance from previous work and b) retain confidentiality for sites where required.

4 RESULTS

Collation of the results confirm that the near surface stratigraphy of London is complex. Around 90 features that meet one or more of the commonly-used criteria used to identify a DFH were identified. The detail of the validated evidence collated has allowed the frequency of particular structures often associated with DFH to be assessed (Table 1).

Table 1. Number of features identified with the given characteristic (total of 87 features).

	Present	Absent	Unknown
Diapir	13 (15%)	14 (16%)	60 (69%)
Faulting	18 (21%)	6 (7%)	63 (72%)
Hollow penetrates through Palaeogene strata	25 (29%)	51 (59%)	11 (12%)
Full depth of feature known	34 (39%)	29 (33%)	24 (28%)

What is clear is that, even with higher than normal levels of site investigation evidence, potentially significant information is frequently absent in the assessment of ground conditions for development.

Where DFH depth can be reasonably reliably established, most appear to occur a continuum between a few metres to around 30 m depth. A number are noticeably deeper, with the deepest being in excess of 70 m.

The majority of the DFH occur beneath the floodplain and later Pleistocene river terraces, with the majority of the infilling materials including river gravels and alluvium, sometimes featuring disturbance since deposition. Known DFH hollows are spatially clustered mainly in central London, with a second group in eastern London and fewer in West London (Figure 1).

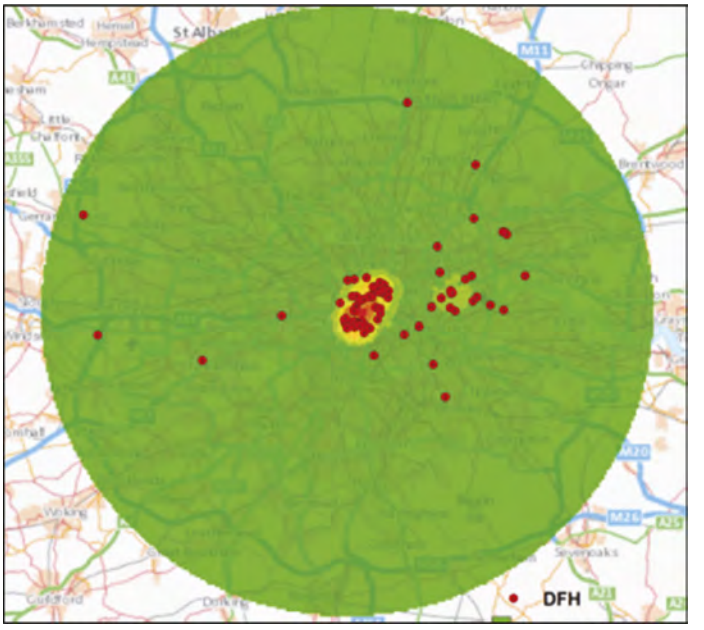

Figure 1. Heat map showing the distribution of known Drift Filled Hollows. The map is centered on central London.

5 CONCLUSIONS

The new, extended dataset confirms that Drift-filled Hollows are a common feature of near-surface geology in London. Sampling bias, due to the overall distribution of data points may mean that areas which show low frequency of features may simply reflect a paucity of data. This is most likely to be the case in the outer parts of the circle shown in Figure 1, where development has been less intense, but is probably a less significant factor for much of the mapped area.

There is some indication that the features are clustered, suggesting one or more spatial controls. Single climate influences, such as hypothesized permafrost and ground ice, or controls such as scour at river confluences might be expected to create a more uniform distribution, particularly along the valley floor. Similarly, simple geological controls such as the thickness of the impermeable London Clay might be expected to produce linear strips of DFHs.

A more likely explanation is that the distribution of DFH is, in part, controlled by linear geological structures, such as faults. Detailed investigations, often related to tunnelling e.g. Linde-Arias et al. (2018) and Morgan et al. (2021), show that such structures are more common than previously thought. These may have interacted with factors such as ground ice, localized erosion and geological material characteristics to allow, in an active or passive fashion, for hollow formation.

The identification of large number of drift-filled hollows, particularly in geographical clusters, provides a useful step forward in helping site developers and engineers assess likely hazards and risk in London. More work is required on the nature and origin of the features to better understand their impact on urban infrastructure and how they generate and influence the "actions and influences" which must be addressed under the Eurocode system.

The presence of such a large number of hard-to-predict ground features in an area such as London, with it's substantial volume of ground data has implications for other regions globally where current assumptions of ground predictability may be masking the true nature of risk.

REFERENCES

Banks, V.J., Bricker, S.H., Royse, K.R. and Collins, P. 2015. Anomalous buried hollows in London: development of a hazard susceptibility map. *Quarterly Journal of Engineering Geology and Hydrogeology*, 48, 55–70, doi: 10.1144/qjegh2014-037.

Berry, F.G. 1979. Late Quaternary scour-hollows and related features in central London. *Quarterly Journal of Engineering Geology and Hydrogeology*, 12, 9–29, doi: 10.1144/GSL.QJEG.1979.012.01.03.

BGS 2020. GeoIndex (onshore). Web tool available at https://mapapps2.bgs.ac.uk/geoindex/home.html (last accessed 11- 09-2022)

Bridgland 1994. *Quaternary of the Thames*. Geological Conservation Review Series, Joint Nature Conservation Committee.

Collins P.E.F., Fenwick I.M., Keith-Lucas D.M. and Worsley P. 1996. Late Devensian river and floodplain dynamics and related environmental change in northwest Europe, with particular reference to a site at Woolhampton, Berkshire, United Kingdom. *Journal of Quaternary Science* 11, 357–375. Doi: 10.1002/(SICI)1099-1417(199609/10)11:5%3C357::AID-JQS250%3E3.0.CO;2-U.

Davis J. 2016. A *geology of London for tunnellers and engineers*. https://learninglegacy.crossrail.co.uk/documents/geology-london-tunnellers-engineers/ last accessed 11- 09-2022.

Davis, J., Soler, R., Hill, N. and Stark, A. 2018. Tunnelling out of a drift filled hollow under Moorgate. Crossrail Project. *Infrastructure Design and Construction*, 5, 237–250.

Edgar J., Ghail R.C., Lawrence J., Skipper J, Mason P.J. 2022. *The impact of facies variability within the Harwich Formation on ground engineering in the London area, UK*. Quarterly Journal of Engineering Geology and Hydrogeology 55. doi: 10.1144/qjegh2020-136.

Flynn A.L. 2022. Drift-filled hollows in the London Basin: Characteristics, Origins and Assessment of Risk. PhD thesis, Brunel University London.

Flynn A.L., Collins P.E.F., Skipper J. A., Pickard T., Koor N., Reading P., Davis J. A. 2020. Buried (drift-filled) hollows in London – a review of their location and key characteristics. *Quarterly Journal of Engineering Geology and Hydrogeology* doi: 10.1144/qjegh2019-145.

Gibbard 1985.

Hawkins, H. 1952. A pinnacle of chalk penetrating the Eocene on the floor of a buried river-channel at Ashford Hill, Near Newbury, Berkshire. *Quarterly Journal of the Geological Society*, 108, 223–260, doi:10.1144/GSL.JGS.1952.108.01-04.11.

Lee, J.R. and Aldiss, D.T. 2012. *Possible Late Pleistocene pingo development within the Lea Valley: Evidence from Temple Mills. Stratford, East London*. CR/11/033 N, British Geological Survey. https://nora.nerc.ac.uk/id/eprint/508854/1/CR11033N.pdf

Linde-Arias E, Harris D, Ghail R. Engineering geology and tunnelling in the Limmo Peninsula, East London. *Quarterly Journal of Engineering Geology and Hydrogeology* 51, 23–30 doi: 10.1144/qjegh2016-116.

Morgan T. Ghail R., Lawrence J. 2021. Major faulting in London: evidence for inherited basement faults in the London Basin. *Quarterly Journal of Engineering Geology and Hydrogeology* 54 doi: 10.1144/qjegh2018-193.

Newman T.G. 2022. Construction geological logging of the Thames Tideway Tunnel beneath central London: unearthing the ground truth. *Quarterly Journal of Engineering Geology and Hydrogeology* 55, doi: 10.1144/qjegh2021-154

Reynolds J. 1849. *Splendid new map of London showing the grand improvements of 1847*. Reynolds, Strand.

Rose J., Turner C., Coope G.R. and Bryan M.D. 1980. Channel changes in a lowland river catchment over the last 13,000 years. in Cullingford R.A., Davidson D.A. and Lewin J. (editors) *Timescales in Geomorphology*. John Wiley & Sons, Chichester. 159–175.

Royse, K.R. de Freitas, M. Burgess, W.G. Cosgrove, J. Ghail, R.C. Gibbard, P. King, C, Lawrence, U. Mortimore, R.N. Owen, H. Skipper, J. Geology of London, UK. *Proceedings of the Geologists' Association* 123 (2012) 22–45

Sumbler M.G. 1996. *London and the Thames Valley*. British Geological Survey.

Wooldridge, S.W. & Linton, D.L. (1939), *Structure, Surface and Drainage in South-east England*. Institute of British Geographers, Publication, 10.

Smart Geotechnics for Smart Societies – Zhussupbekov, Sarsembayeva & Kaliakin (Eds)
© 2023 The Author(s), ISBN 978-1-003-29912-7
Open Access: www.taylorfrancis.com, CC BY-NC-ND 4.0 license

Deep learning for microscopic rock image classification

W. Seo & T.S. Yun
Yonsei University, Seoul, Republic of Korea

ABSTRACT: The optical observation of rock thin section images leads to rock classification, which requires expertise in mineralogy. To overcome the subjectiveness and uncertainty inherent in conventional rock classification practice, this study introduces a deep learning-based classification procedure with a convolutional neural network (CNN). The microscopic images of six igneous rock types were prepared and processed for network model training. Transfer learning was implemented to train the ResNet152 model whose performance was investigated with classification methods at patch and image-levels. The trained model achieved a high accuracy of more than 90%. The results also showed that image-level classification from patches demonstrated the best performance depending on the spatial characteristics of comprising minerals. Based on this approach, it was shown that the CNN model can effectively identify the features in microscopic rock images, leading to reliable rock classification.

1 INTRODUCTION

The conventional rock classification is generally conducted via optical observation of rock thin sections using polarizing microscopic images, but this approach requires expertise in mineralogy. Recently, rock thin section analysis such as pore or grain characteristic extraction and mineral identification are being automated by image processing techniques. Asmussen et al. 2015 used seeded region growing algorithm to determine pore and grain parameters. Borazjani et al. 2016 extracted pore space and textural characteristics to classify carbonate rock using multi-layer perceptron (MLP) as a texture identifier. Ma & Gao 2017 identified pores and the rock skeleton with K-means clustering and support vector machine. Baykan & Yılmaz 2010 used MLP for mineral identification, and Izadi et al. 2013 also identified minerals with MLP based on texture features.

Recent studies have also used computer vision techniques to automatically classify rocks from microscopic images. Cheng & Guo 2017 classified coarse, medium granular, and fine feldspar sandstones using convolutional neural network (CNN). Su et al. 2020 used Concatenated-CNN to classify 13 rock types. Pires de Lima et al. 2020 used pretrained CNNs as backbone networks for transfer learning to classify five types of siltstones. Polat et al. 2021 also used transfer learning with pretrained CNN models for volcanic rock classification, and Seo et al. 2022 classified igneous rocks. By using pretrained CNN models, images can be analyzed without requiring manual extraction of features and parameters. Hence, the aim of this study is to classify six types of igneous rocks from their microscopic images using deep transfer learning with ResNet152 model as a convolutional backbone network.

DOI: 10.1201/9781003299127-122

2 MATERIALS AND METHODS

2.1 *Image dataset*

Six igneous rock types were selected to be classified: granite, diorite, gabbro, rhyolite, andesite, and basalt. Granite, diorite, and gabbro are plutonic rocks with larger mineral grain sizes and rhyolite, andesite, and basalt are volcanic rocks with smaller grain sizes. A total of 352 images with both open and cross nicol polarization were prepared (Table 1) from various sources. The original images were then resized to 896 × 672 pixels, preserving their aspect ratios, and we randomly divided the resized images for each rock type into training, validation, and test datasets in a 7:1:2 ratio. Images in each dataset were then cropped into 224 × 224 pixels to generate 12 image patches. Additionally, images in training dataset were augmented by 8 times by flipping and rotating.

Table 1. Number of images for each rock type.

Rock type	Open nicol	Cross nicol	Total
Granite	23	32	55
Diorite	20	26	46
Gabbro	25	36	61
Rhyolite	25	46	71
Andesite	37	18	55
Basalt	33	31	64
Total	163	189	352

2.2 *Deep transfer learning with CNN*

A CNN is a deep learning network widely used in computer vision tasks, and generally consists of convolutional, pooling, and fully connected (FC) layers. Convolution filters slide over the input images to extract features in convolutional layers, and parameters are updated by the error backpropagation. The pooling layers reduce the size of the input, and outputs from convolutional and pooling layers becomes the feature maps which are used as inputs to nonlinear activation function and the next layers. As a classifier, FC layers connect the flattened data from the final feature map to the final output.

When the size of the original image datasets is relatively small, transfer learning is an effective method to train the network model. Transfer learning adopts backbone networks pretrained with large datasets to optimize the model. Various types of the convolutional backbone networks for transfer learning have been proposed, and ResNet152 (He et al. 2016) were chosen in this study. ResNet152 model uses shortcut connections between convolutional layers to solve degradation problem of deep CNNs. ResNet152 has several convolution blocks which contain convolutional layers with shortcut connections. Global average pooling is applied after the last convolutional layer to collapse the spatial dimensions into a single dimension, instead of flattening.

Commonly, deeper layers of the CNN extract high-level global features of the input images. Therefore, to effectively optimize the model, the deeper parts of the convolutional layers and the FC layers were retrained (fine-tuned) to update parameters, while the parameters in the initial part were frozen. Since the model's purpose is the classification, cross-entropy loss was chosen for the loss function, and Adam was used as the optimizer. The sequences for the training and the architecture of ResNet152 is illustrated in Figure 1.

2.3 *Patch and image-level classification*

The trained model was tested by three different classification methods A, B, and C: the method A is patch-level classification, and the method B and C are image-level classification

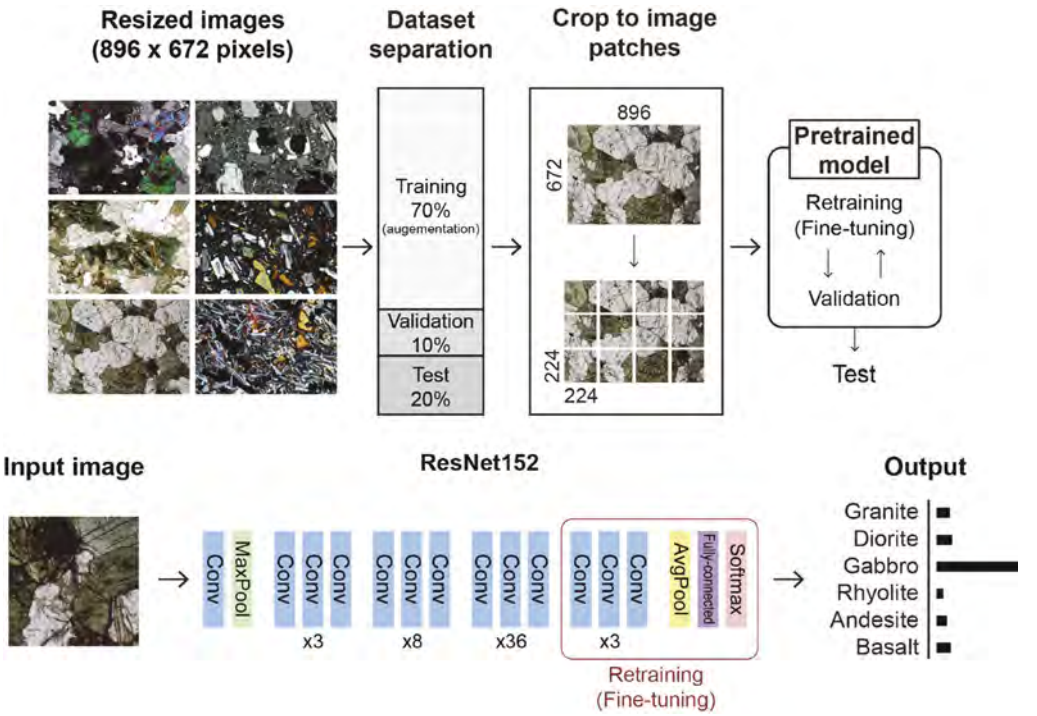

Figure 1. Sequences for image training, and the architecture of image classification network model (ResNet152) in this study.

(Figure 2). Each patch of an image is classified individually at patch-level by method A. In method B, each image patch is classified independently, followed by a majority voting procedure to classify the original image at image-level. In method C, the classification score, the output of the last softmax layer of the model, is first calculated. Calculated scores for each rock type are added up, and the original image is classified as the rock type with the highest summed score.

3 RESULTS AND DISCUSSION

3.1 *Patch-level classification*

The confusion matrix from the classification method A is shown in Figure 3. The overall classification accuracy was 86.90%, and the accuracy for gabbro was the lowest. In comparison to other rock types, classification for diorite and gabbro were relatively inaccurate, presumably because they are plutonic rocks with large mineral grain sizes. As they had relatively large grain sizes to fit in a single image patch, identifying them accurately was challenging for the model. Since the images from the same origin (plutonic rocks or volcanic rocks) share similarities in terms of texture and color, the model mostly misclassified images as belonging to the same origin. The result exhibited that the CNN model can adequately identify inherent features within rock microscopic images.

3.2 *Image-level classification*

The confusion matrix from the classification method B and C are shown in Figure 4. The overall classification accuracy for method B and C were 92.86% and 95.71%, respectively.

Both methods B and C classified more accurately than method A, while the accuracy for gabbro was the lowest similar to method A. Methods B and C are able to compensate for the misclassified image patches by using majority voting scheme and summing the classification scores, respectively, resulting in more accurate classification.

Rock thin section microscopic images often show the characteristics of several rock types in one image. Accordingly, method C, which uses the classification scores of all rock types within one image patch, was more accurate than method B, which only uses the highest classification score. In addition, unlike method B, where voting of compositional image patches can be tied, method C could always classify one rock type for one original image.

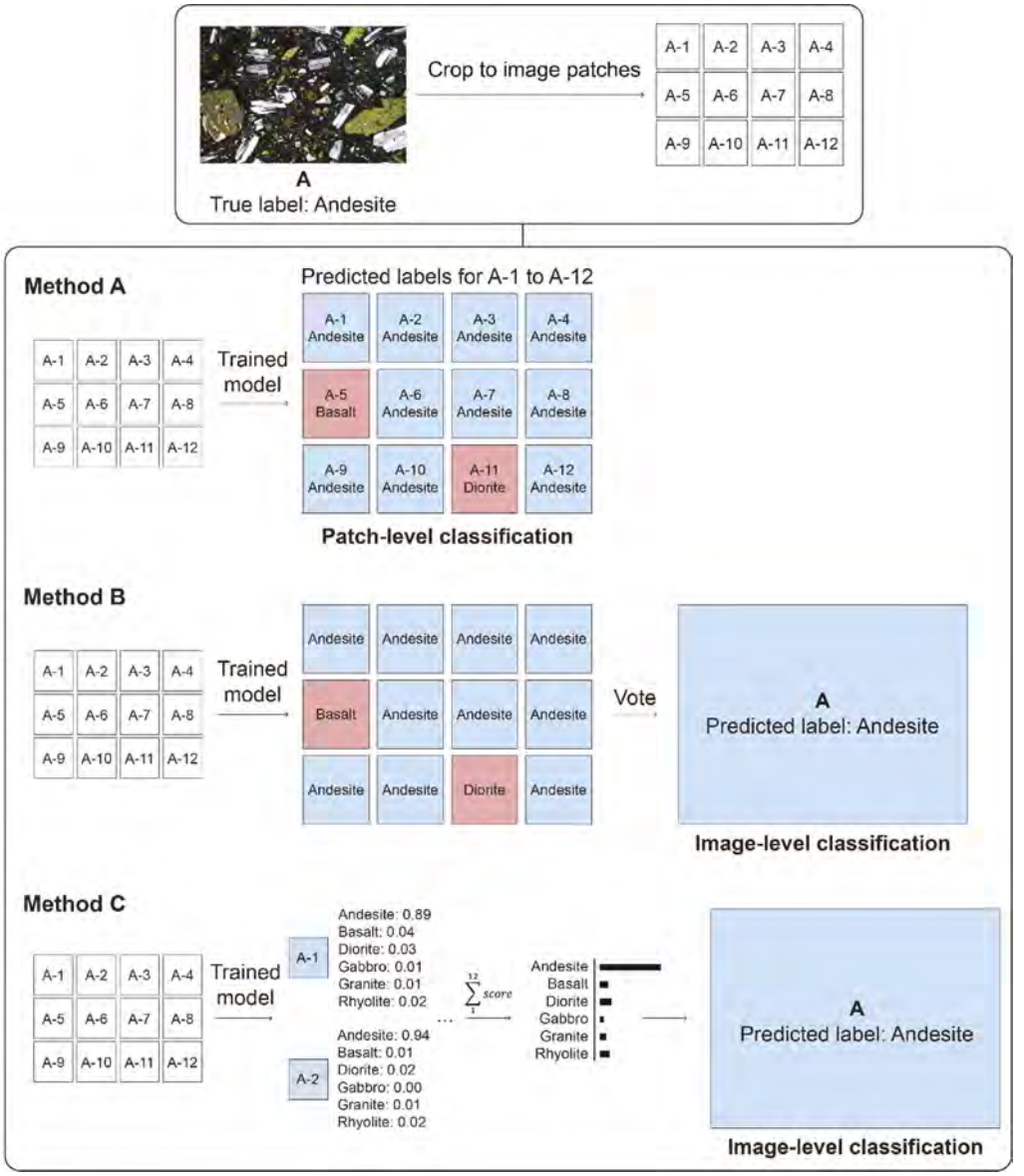

Figure 2. Process of classification methods A, B, and C.

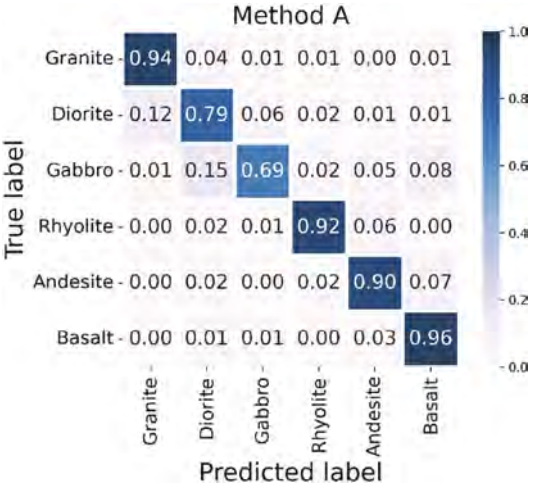

Figure 3. Confusion matrix for patch-level classification: method A.

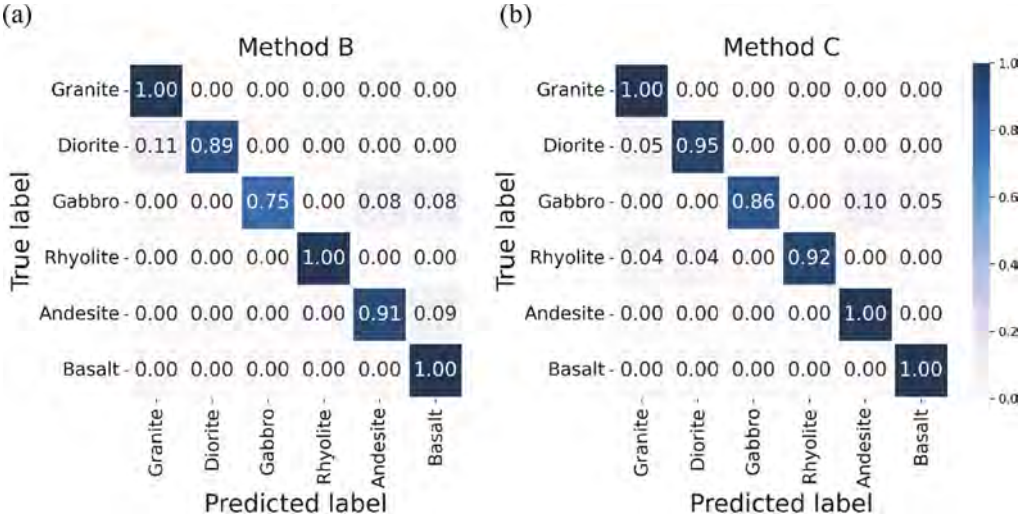

Figure 4. Confusion matrix for image-level classification: methods (a) B and (b) C.

4 CONCLUSIONS

This study conducted classification of igneous rock microscopic images using CNN-based deep learning model. Prepared original images were cropped into several image patches, and the model was retrained with transfer learning based on pretrained ResNet152 structure. The trained model was tested with three different classification methods A, B, and C at both patch- and image-levels and has been proven successful in classifying rock types.

Compared to the patch-level classification, the image-level classification produces better results since the effect of misclassified image patches can be mitigated. It appears that classification method C, which sums up the classification scores of image patches to make image-level decisions, is the most accurate classification method, since it considers the classification scores of all rock types.

Despite the limited database, the use of a CNN-based deep learning model for rock microscopic image classification was found to be valid from the perspective of objective decision regardless of the operator. This approach has the potential to be applicable to other rock types by overcoming ambiguities in conventional rock classification.

ACKNOWLEDGEMENTS

This work was supported by the Land and Housing Institute (LHI) grant funded by the Korea Land and Housing Corporation, and the National Research Foundation of Korea (NRF) Grant funded by the Korea government (MSIT) (Nos. 2020R1A2C1014815, NRF-2021R1A5A1032433).

REFERENCES

Asmussen, P., Conrad, O., Günther, A., Kirsch, M. & Riller, U. 2015. Semi-automatic segmentation of petrographic thin section images using a "seeded-region growing algorithm" with an application to characterize wheathered subarkose sandstone. *Computers & Geosciences* 83: 89–99.

Baykan, N. A. & Yılmaz, N. 2010. Mineral identification using color spaces and artificial neural networks. *Computers & Geosciences* 36(1): 91–97.

Borazjani, O., Ghiasi-Freez, J. & Hatampour, A. 2016. Two intelligent pattern recognition models for automatic identification of textural and pore space characteristics of the carbonate reservoir rocks using thin section images. *Journal of Natural Gas Science and Engineering* 35: 944–955.

Cheng, G. & Guo, W. 2017. Rock images classification by using deep convolution neural network. *Journal of Physics: Conference Series* 887(1).

He, K., Zhang, X., Ren, S. & Sun, J. 2016. Deep residual learning for image recognition. *Proceedings of the IEEE Computer Society Conference on Computer Vision and Pattern Recognition 2016-Decem* 770–778.

Izadi, H., Sadri, J. & Mehran, N.A. 2013. A new approach to apply texture features in minerals identification in petrographic thin sections using ANNs. *2013 8th Iranian Conference on Machine Vision and Image Processing (MVIP)* 257–261.

Ma, Z. & Gao, S. 2017. Image analysis of rock thin section based on machine learning. *International Geophysical Conference, Qingdao*, *China*, *17-20 April 2017* Society of Exploration Geophysicists and Chinese Petroleum Society 844–847.

Pires de Lima, R., Duarte, D., Nicholson, C., Slatt, R. & Marfurt, K. J. 2020. Petrographic microfacies classification with deep convolutional neural networks. *Computers and Geosciences* 142(June): 104481.

Polat, Ö., Polat, A. & Ekici, T. 2021. Automatic classification of volcanic rocks from thin section images using transfer learning networks. *Neural Computing and Applications* 1–10.

Seo, W., Kim, Y., Sim, H., Song, Y. & Yun, T. S. 2022. Classification of igneous rocks from petrographic thin section images using convolutional neural network. *Earth Science Informatics* 15(2): 1297–1307.

Su, C., Xu, S., Zhu, K. & Zhang, X. 2020. Rock classification in petrographic thin section images based on concatenated convolutional neural networks. *Earth Science Informatics* 13(4): 1477–1484.

Smart Geotechnics for Smart Societies – Zhussupbekov, Sarsembayeva & Kaliakin (Eds)
© 2023 The Author(s), ISBN 978-1-003-29912-7
Open Access: www.taylorfrancis.com, CC BY-NC-ND 4.0 license

AI-based back analysis of multiphysics processes in unconventional resource extraction practice

M. Zhou
Department of Geotechnical Engineering, Tongji University, China

M. Shadabfar
Department of Civil Engineering, Sharif University of Technology, Iran

Y.F. Leung
Department of Civil and Environmental Engineering, The Hong Kong Polytechnic University, China

S. Uchida
Department of Civil and Environmental Engineering, Rensselaer Polytechnic Institute, Troy, USA

ABSTRACT: Mulitphysics processes have been commonly identified in geotechnical engineering practice. Researchers and field engineers often carry out multiphysics simulations to understand complex engineering responses. In field practice, a back analysis is typically required along with the simulations to calibrate the most representative model parameters. This would intensify the problem as it requires further simulations to assess the parameter sensitivity. Therefore, an efficient back analysis for multiphysics processes still remains a challenge in practice due to the numerical complexity and the low computational efficiency. With recent advances in AI techniques, opportunities have opened up for meta-model development for problems involving multiphysics processes associated with a large number of properties. This study entails a meta-model developed based on Artificial Neural Networks (ANN) that intelligently learn the correlations between model parameters and the reservoir responses. This efficient meta-model is combined with Genetic Algorithm-based back analysis to report the optimal case that provides the closest output to the target time histories. The results show that the AI-based metamodel can reproduce outputs of heavy computation of the multiphysics processes and thus efficiently perform back-analysis.

1 INTRODUCTION

Mulitphysics processes have been commonly identified in unconventional resource extraction practice (Guo et al., 2019; Mahdi et al., 2017). However, such complex processes are often difficult to model in the field or in the laboratory due to the coupling of multiphysics (Touran et al., 2017; Keyes et al., 2013). Therefore, researchers and field engineers in the oil and gas industry often carry out numerical simulations to understand the complex engineering responses during production. Such simulation practices are conducted via multiphysics numerical simulators (Moridis et al., 2011; Klar et al., 2013; White et al., 2020; Zhou et al., 2020).

In the rise of unconventional energy resources, one of the multiphysics complex processes is gas production from gas hydrate reservoir. production of gas from hydrate-bearing sediments involves change in pressure, temperature and also mechanical behavior, leading to coupled thermo-hydro-mechanical (THM). However, modelling of this complex processes is often computationally demanding and requires a large number of model parameters to represent multiple facets of the hydrate reservoir behavior (Uchida et al., 2016). Even when measurement of

DOI: 10.1201/9781003299127-123

gas and water production history is available, conducting back analysis to calibrate these parameters is significantly time-consuming and also confirming that the calibrated parameters are the best representatives of the site condition is challenging because of potential existence of multiple local optima. Therefore, there is a need for an efficient tool to assess the hydrate reservoir production potential and the complex sediment responses with minimal time cost and computational complexity.

With recent advances in artificial intelligence (AI) techniques (e.g., machine learning and data analytics), opportunities have opened up for meta-model development for problems involving multiphysics processes associated a large number of properties (Tripoppoom et al., 2020; Li et al., 2021; Park et al., 2021; Xu et al., 2020). The main goal of the meta model is to provide an alternative tool to replace a conventional THM simulator in a more timely and computationally effective way. Once this computational tool is provided, the uncertainty in data can be assessed through varying the input parameters and investigating the uncertainty propagation through the sensitivity study.

This study entails a meta-model developed based on ANN that deep learn the correlations between model parameters (i.e., hydrologic and geomechanical parameters of hydrate-bearing sediments) and the reservoir response (i.e., gas and water production), and is capable of reproducing the production results with much higher computational efficiency than coupled numerical simulators based on finite element or finite difference methods. An optimization network based on genetic algorithm (GA) is then proposed and combined with the trained ANN to conduct the back-analysis of the site measured production data, and thus the optimum model parameters can be obtained.

The capabilities of the proposed machine learning approach are demonstrated through the application to the 2013 Nankai offshore gas production test. The training and testing data for the ANN are produced by a series of coupled THM simulations. The assumed ranges of material properties of the simulations are based on the production site conditions and are varied across the multi-dimensional sample space. The ANN predictions suggest good agreement with the measured production data, while the obtained model parameters from back analysis can be regarded as important properties for researchers and field engineers to focus on for reservoir characterization.

2 SYNTHETIC DATASET

This study creates synthetic data numerically through varying 19 material properties and obtaining the corresponding reservoir responses, namely, the amount of produced gas, produced water and vertical strain (Figure 1). A THM numerical simulator, originally developed by (Klar et al., 2013), is adopted to create synthetic data. The simulator is based on a finite difference software, FLAC, and solves the multiphysics processes through the implemented coupled THM formulation derived for hydrate reservoir simulations by (Uchida et al., 2016).

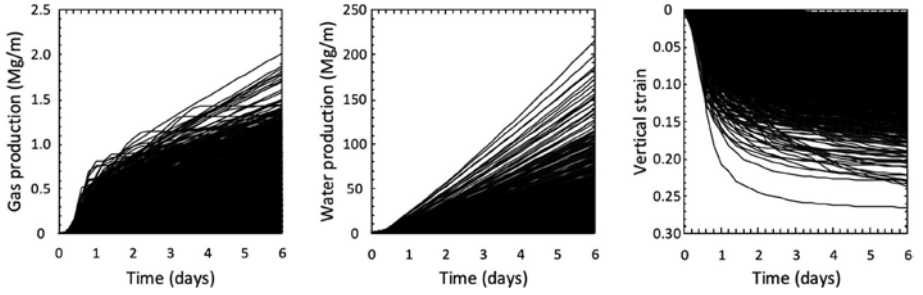

Figure 1. Synthetic data created by the THM analyzes.

Based on the Eastern Nankai Trough production site geometry, the targeted perforation region is between 280.7 m and 318.7 m below the seabed and the seabed is 998 m below the sea level. Figure 2 presents a hydrate reservoir considered for the creation of the synthetic dataset. It would be ideal if the model could explicitly simulate the heterogeneity of in-situ THM properties along the vertical direction, but that would impose a significant computational demand. Therefore, this study simplifies the complexity into a homogenized single radial layer. This simplification has a few shortcomings associated with the lack of thermal or fluid flow in the vertical direction, but the variations in the THM properties are considered in the form of the parameter range, while the most representative homogenized properties will be later determined through back analyses.

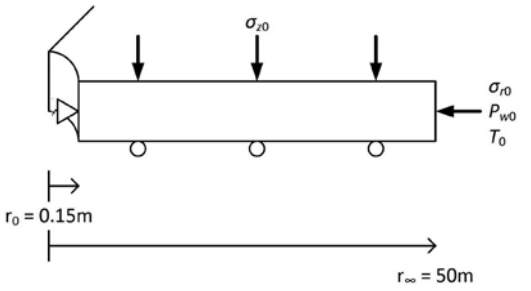

Figure 2. Hydrate reservoir model considered in this study.

The depth of the considered layer is assumed to be at 1297.7 m below sea level and 299.7 m below seafloor, which is the mid-depth of the production region and corresponding to the initial pore water pressure of 13 MPa and the initial effective vertical stress to be 3 MPa. The initial effective horizontal stress is assumed to be 1.5 MPa, which corresponds to the at-rest earth pressure coefficient of K0 = 0.5. The initial porosity is 0.4, the initial temperature is 285 K and the initial hydrate saturation is 61.3%, which is the average value over the production zone based on logging data (Konno et al., 2017). Under the initial temperature, the phase equilibrium pressure is 9.8 MPa. Depressurization is applied according to the measured bottom hole pressure during the 2013 test (Konno et al., 2017).

At the well boundary in the model, a free movement is assumed in the vertical direction while no radial displacement is allowed. The bottom boundary is fixed in the vertical direction and free in the radial direction. The top boundary has the constant total stress applied to facilitate vertical deformation. The outer model boundary is set at 50 m, where the pore pressure, the total radial stress and temperature remain unchanged. The layer is radially discretized into 35 elements with a size of 0.15 m adjacent to the well and increasing at a ratio of approximately 1.1.

This study utilizes the Latin hypercube sampling method (McKay et al., 1979) to ensure the multi-dimensional sampling domain is evenly explored with a relatively small number of simulations, resulting in 1000 simulation cases. Table 1 shows the maximum and minimum values of the 18 parameters adopted. The parameters are assumed to follow lognormal distribution, except the van Genuchten parameters, *b* and *c*, which are assumed to be normally distributed in the synthetic dataset. These simulation cases provide a history of reservoir production responses (gas production and water production), recorded at every 0.2 days for a 6-day period. Therefore, at every recorded time, there are 18000 data points regarding material properties (1000 times 18), which are "inputs" for the ANN. Meanwhile, there are also 2000 data points regarding reservoir production responses (1000 cases times 2) at each recorded time step, which are "outputs" for the ANN.

The established synthetic dataset is normalized, and 80% of the normalized data is selected as the training data and the remaining 20% is selected as the testing data. The normalization process facilitates the calculation by making all the data dimensionless. Additionally, it limits

Table 1. 18 model parameters selected for this study.

name	symbol	max	min
Hydrologic (8)			
initial intrinsic permeability	$\|\|K\|\|$	$10^{-4.8}m^2$	$10^{-7.2}$ m^2
effective permeability power	N	10.0	2.0
air entry pressure	P_0	12kPa	8kPa
van Genuchten parameter	a	1.00	0.80
van Genuchten parameter	b	2.00	-1.00
van Genuchten parameter	c	2.00	-1.00
residual water saturation	S_{rw}	0.60	0.00
residual gas saturation	S_{rg}	0.20	0.00
Mechanical (10)			
critical state stress ratio	M	1.56	1.40
slope of swelling line	k	0.014	0.003
Poisson's ratio	v	0.40	0.20
slope of compression line	λ	0.25	0.14
initial preconsolidation stress	P'_{cs0}	6.0MPa	3.0MPa
hydrate dependent strength	α	100MPa	10MPa
hydrate dependent strenght	β	1.8	0.8
subloading ratio evolution	u	exp(5.52)	Exp(1.61)
hydrate dependent modulus	E_{h0}	12GPa	8GPa
hydrate degradation factor	m	21	1

the range of data to only vary between [-1,1] and consequently controls the algorithm search domain, which results in less complexity and higher accuracy of the ANN predictions.

3 AI-BASED BACK ANALYSIS

The ANN is developed to approximate the gas production and water production time histories. In this study, a multi-layer perceptron (MLP) is used to implement the ANN. The ANN consists of the dataset, two hidden layers of neurons, and the predictions of the reservoir responses. The prediction consists of 2 classes, each with 30 neurons, which represent the simulation results of gas production and water production at the 30 time intervals (0.2-day intervals for 6 days). Two hidden layers are implemented in this study to accomplish accurate predictions. By adopting a trial-and-error method to change the number of neurons in each hidden layer, the MLP model with ten neurons in the first hidden layer and five neurons in the second hidden layer reveals the best performance of the data set analyzed in this study.

The initial MLP model is then generated using the training dataset with the proposed layer structure. The training data is introduced into the ANN to train the network by determining the biases and weights by minimizing the mean squared error (MSE). Once the minimum MSE is obtained, the network training process is completed and can be used to make predictions and evaluate the accuracy using the testing dataset.

The established ANN provides a computationally light method to predict the gas and water production from the 18 input model parameters. An optimization problem is defined for the back analysis, in which the objective function is the difference between the optimal production resulted from the ANN and the actual site measured production values. Conventional optimization techniques often involve determining the gradient of the objective function. Due to the complexity of this optimization problem, it is challenging to calculate the partial derivatives of the objective function because the established ANN is not an explicit function of the input variable. Therefore, derivative-based methods may not be able to solve this problem. As such, GA is used as an alternative solution in this study.

GA is an intelligent optimization method inspired by the theory of evolution by natural selection. This algorithm improves the initial population in the form of an iterative process

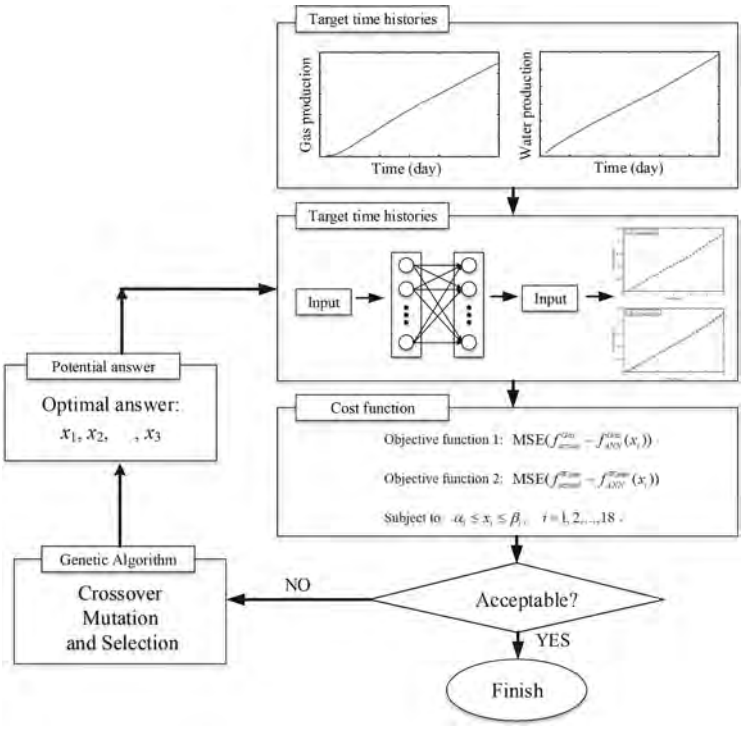

Figure 3. The schematic diagram of the proposed approach.

according to a quality criterion. In this respect, three operators of mutation, crossover, and selection are used to drive the evolution of candidate solutions towards the optimum in each generation. Because the algorithm is population-based and does not require the derivatives of objective function or constraint, it is widely used with implicit function, such as the ANN utilized in this paper. In addition, GA has the ability to search a large number of candidate solutions to converge to the global optimum. As with any iterative method, GA needs a set of termination conditions to determine when to stop and complete the analysis. The termination criteria used in this paper are as follows:

1. when the difference of optimum response in each two subsequent steps is less than 0.1%.
2. when the number of generations reaches 100.
3. when the algorithm reaches the time limit (5 minutes) set for the analysis.

When one of the above three conditions is met, the analysis considers the results as the optimal solutions.

4 RESULTS

The performance of the ANN was evaluated by comparing its predictions with the results of THM simulations, across the whole set of 1000 simulations (Figure 4). The error of the prediction results for both the training and the testing data are relatively small, which suggests that the proposed ANN can make accurate predictions. Hence, by selecting appropriate input model parameters, the established ANN can be used for history matching of the site measured production responses.

The back analysis was implemented in the form of an optimization problem and GA was utilized to provide a solution. It is worth noting that two objective functions are involved in this problem since both gas and water productions are considered in this study. In this study,

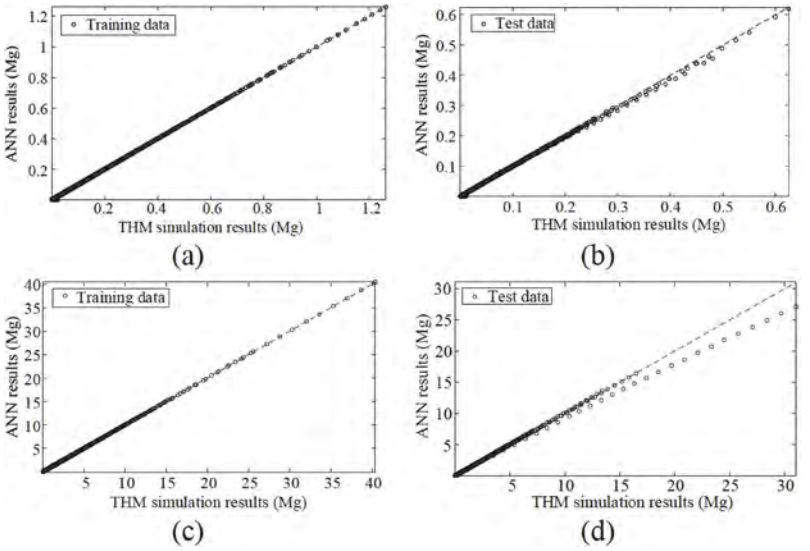

Figure 4. Comparison of the ANN predictions and the THM simulation results of (a) gas production comparison for training data, (b) gas production comparison for testing data, (c) water production comparison for training data, (d) water production comparison for testing data.

the gas and water production values per unit volume are used as the optimization target of the back analysis. Based on the site measured gas and water production rate, the total gas and water production values per unit volume for the first six days are computed and shown in Figure 5. Using the 18 input model parameters, the gas and water production per unit volume can be derived from the established ANN, and the predicted results are plotted in Figure 5 to compare with the target values. The comparison suggested a good match. Therefore, the proposed back analysis method works well for the history matching purpose.

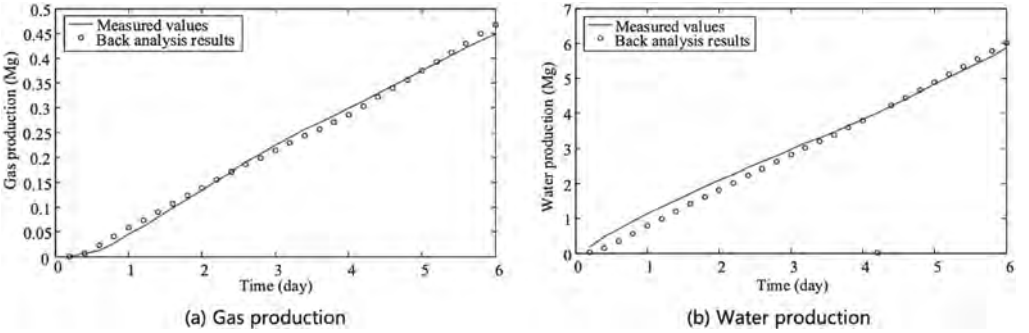

Figure 5. Comparison of the site measured production data and the predicted data based on the back analyzed input parameters: (a) gas production, (b) water production.

The computational efficiency of the proposed meta-model is demonstrated by comparing its processing time with the THM simulator for three specific reservoir cases (Case 300, 600, and 900). The numerical experiments for 8-day gas production were carried out on a desktop equipped with two GeForce GTX 1080 graphics processing units (GPUs), 64 GB of random access memory (RAM), and one Intel Core i7-5820K central processing unit (CPU). For 6-day gas production prediction, the execution time of the ANN and the FLAC THM simulator for three specific reservoir cases are shown in Table 2. It is seen that a typical calculating

of the FLAC THM simulator for 6-day gas production takes on average more than 1000 seconds while the ANN only takes less than 0.1 seconds.

Table 2. For 6-day gas production prediction, the execution time of the ANN and the FLAC THM simulator for Case 300, 600, and 900.

Prediction method	Case 300	Case 600	Case 900
First-block ANN	0.071 seconds	0.069 seconds	0.067 seconds
FLAC THM simulator	1400 seconds	7000 seconds	540 seconds

5 CONCLUSION

This paper utilizes a combination of an ANN and an optimization model for simulation of gas production operations in methane hydrate-bearing reservoir. The combined model enables back analyses of site response in order to obtain the corresponding site properties. The site measured production data in 2013 Eastern Nankai Trough production test is adopted in this study. The ANN successfully learns the relationship between the material properties and reservoir productions, while the optimization model demonstrated the capability of finding the optimum combinations of material properties to characterize the reservoir production.

The main advantage of the proposed approach lies on its computational efficiency for history matching and model parameter calibration, which can be ten thousands of times faster than the numerical analysis conducted via the thermo-hydro-mechanical simulator.

It should be noted that the proposed machine learning approach only learns what it is being taught. The effectiveness of the back analyses clearly depends on the geometries of the specific problem, and the site-specific hydrate and stratigraphy conditions. Nevertheless, the proposed framework allows real-time prediction to be made and adjusted according to the observed reservoir response as the process evolves with time at the production site.

REFERENCES

X. Guo, D. Hu, Y. Li, J. Duan, X. Zhang, X. Fan, H. Duan, W. Li, Theoretical progress and key technologies of onshore ultra-deep oil/gas exploration, Engineering 5 (3) (2019) 458–470. https://doi.org/10.1016/j.eng.2019.01.012.

M. McKay, R. Beckman, W. Conover. A comparison of three methods for selecting values of input variables in the analysis of output from a computer code. Technometrics, 21 (1979) 239–245.

D. E. Keyes, L. C. McInnes, C. Woodward, W. Gropp, E. Myra, M. Pernice, J. Bell, J. Brown, A. Clo, J. Connors, et al., Multiphysics simulations: Challenges and opportunities, The International Journal of High Performance Computing Applications 27 (1) (2013) 4–83.

A. Klar, S. Uchida, K. Soga, K. Yamamoto, Explicitly coupled thermal flow mechanical formulation for gas-hydrate sediments, SPE Journal 18 (02) (2013) 196–206. doi:10.2118/ 162859-PA.

H. Li, H. Yu, N. Cao, H. Tian, S. Cheng, Applications of artificial intelligence in oil and gas development, Archives of Computational Methods in Engineering 28 (3) (2021) 937–949.

Y. Konno, T. Fujii, A. Sato, K. Akamine, M. Naiki, Y. Masuda, ... & J. Nagao. Key findings of the world's first offshore methane hydrate production test off the coast of Japan: Toward future commercial production. Energy & Fuels, 31(3), (2017) 2607–2616.

S. Mahdi, X. Wang, N. Shah, Interactions between the design and operation of shale gas networks, including co2 sequestration, Engineering 3 (2) (2017) 244–256. https://doi.org/10.1016/J.ENG.2017.02.007.

G. Moridis, S. Silpngarmlert, M. Reagan, T. Collett, K. Zhang, Gas production from a cold, stratigraphically-bounded gas hydrate deposit at the Mount Elbert gas hydrate stratigraphic test well, Alaska north slope: Implications of uncertainties, Marine and petroleum geology 28 (2) (2011) 517–534.

T.-R. Park, H. Park, K. Kim, C.-N. Im, J.-H. Cho, Heat and weight optimization methodology of thermal batteries by using deep learning method with multi-physics simulation, Energy Conversion and Management 236 (2021) 114033. https://doi.org/10.1016/j.enconman.2021.114033.

N. W. Touran, J. Gilleland, G. T. Malmgren, C. Whitmer, W. H. Gates, Computational tools for the integrated design of advanced nuclear reactors, Engineering 3 (4) (2017) 518–526. https://doi.org/10.1016/J.ENG.2017.04.016.

S. Tripoppoom, J. Xie, R. Yong, J. Wu, W. Yu, K. Sepehrnoori, J. Miao, C. Chang, N. Li, Investigation of different production performances in shale gas wells using assisted history matching: Hydraulic fractures and reservoir characterization from production data, Fuel 267 (2020) 117097. https://doi.org/10.1016/j.fuel.2020.117097.

S. Uchida, A. Klar, K. Yamamoto, Sand production model in gas hydrate-bearing sediments, International Journal of Rock Mechanics and Mining Sciences 86 (2016) 303–316. doi:10.1016/j.ijrmms.2016.04.009.

M. White, T. Kneafsey, Y. Seol, W. F. Waite, S. Uchida, J. Lin, E. Myshakin, X. Gai, S. Gupta, M. Reagan, et al., An international code comparison study on coupled thermal, hydrologic and geomechanical processes of natural gas hydrate-bearing sediments, Marine and Petroleum Geology 120 (2020) 104566. doi:10.1016/j.marpetgeo.2020.104566.

H. Xu, J. Ma, P. Tan, B. Chen, Z. Wu, Y. Zhang, H. Wang, J. Xuan, M. Ni, Towards online optimisation of solid oxide fuel cell performance: Combining deep learning with multi-physics simulation, Energy and AI 1 (2020) 100003. https://doi.org/10.1016/j.egyai.2020.100003

M. Zhou, K. Soga, K. Yamamoto, Upscaling techniques for fully coupled thm simulation and application to hydrate gas production tests, Computers and Geotechnics 124 (2020) 103596. https://doi.org/10.1016/j.compgeo.2020.103596.

Smart Geotechnics for Smart Societies – Zhussupbekov, Sarsembayeva & Kaliakin (Eds)
© 2023 The Author(s), ISBN 978-1-003-29912-7
Open Access: www.taylorfrancis.com, CC BY-NC-ND 4.0 license

Deformation properties and mechanism of destruction of a block structure rock mass

G.A. Kadyralieva, K.Ch. Kozhogulov & N.A. Aitkuliev
Institute of geomechanics and development of subsoil of the National Academy of Sciences of the Kyrgyz Republic, Bishkek, Kyrgyzstan

ABSTRACT: The management of the state of natural and man-made massifs during the open-pit mining of mineral deposits consists in a set of measures to maintain ledges, sides of quarries and dumps in a stable, close to the limit state by changing the geometric parameters of the slopes during the development process, which ensures economical and safe mining operations. The block structure of the side array is one of the parameters affecting the strength of the rock mass, and the fillers between the block spaces are the main factor in their deformation and destruction. In the sides of the upland quarries, not only individual blocks fall out, but also massive collapses are observed. This indicates that the filler between the block cracks has less strength than the level of the acting shear forces near the surface of the outcrop.

The development of mineral deposits by the open method is associated with the need to ensure safe mining conditions, in particular, the stability of the sides of quarries, where one of the main problems of upland quarries is the calculation of the geometric parameters of the side, taking into account the structure and parameters of the slope on which the quarry is being built.

The design schemes for assessing the condition of the side array used for flat, deepening quarries often leads to unreasonably underestimated parameters of the side of the quarry due to the high value of the structural attenuation coefficient, which leads to an increase in the volume of overburden, and applying the parameters of the quarry for an isotropic array – to the development of irreversible deformations of the side array and the collapse of the side.

The currently existing theoretical approaches to geomechanical substantiation of the possibility of increasing the slope angles of the sides of quarries do not take into account the real stress-strain state of rock massifs, believing that it is caused only by the own weight of the overlying rocks and the structure of rock massifs, equating the influence of structural disturbances of various ranks on the stability of the sides of the quarry as a whole and individual ledges.

The stress state of the rock mass is assumed to be due only to its own weight, although to date there is evidence that excessive horizontal stresses of a tectonic nature operate within the rock masses of more than 60% of ore deposits. As a result, a conclusion is made about the limiting angle of slopes of the sides of quarries on the final contour, which often does not exceed the angle of the natural slope of the fragmented mass of rocks 30^0-40^0, i.e. the real resource of the stability of rock massifs is not fully used.

The development of upland deposits in tectonically active areas, as in the conditions of Kyrgyzstan, is invariably accompanied by a change in the geological and, accordingly, geomechanical environment: the deformation and strength indicators of rocks change, vertical and horizontal stresses increase with depth, the stress concentration zone on the contour of the side of the quarry increases. All this leads to a deterioration of the mining conditions for the extraction of minerals and a decrease in the efficiency of the quarry. In this regard, the development of the theory of geomechanical substantiation of rational designs of quarry sides on the final contour during

DOI: 10.1201/9781003299127-124

open-pit mining based on the creation of geomechanical models of rock massifs is an important scientific and technical problem. (Kadyralieva, G.A., Kozhogulov, K.C., 2022)

In recent years, unplanned rock collapses have become more frequent at mining enterprises in Kyrgyzstan. Typical for upland deposits in the zones of influence of tectonic disturbances is the block structure (Figure 1) and to date, due attention has not been paid to ensuring the safety of mining operations in such fields. Stability assessment for such arrays is carried out according to existing methods, the block array is not acceptable for isotropic media.

Figure 1. Block structure of a rock mass of rocks.

Geomechanical models should take into account the real stress-strain state, hierarchical block structure and physical properties of rock massifs. The result of the geomechanical substantiation of the stability of the sides of the quarry is the creation of methods for controlling the state of the instrument array for each specific deposit.

The results of studies conducted at the gold deposits of Kyrgyzstan such as Makmal, Kumtor, Jeruy, Chaarat, Terekan, indicate a complex geological structure, block structure, properties of rocks and massif. The side array of these quarries has a block structure, the filler of the interblock space is weak, often represented by calcites with low strength characteristics.

In recent years, Kyrgyzstan has been paying more and more attention to the study of slow deformation events: the movement of glaciers, landslides in block-fractured rock massifs. At the same time, the structure and the ratio between the filler components have a strong influence on the distribution of deformation rates. Installations of the slider model type are used for laboratory research. Therefore, the assessment of the impact of the block structure of the rock mass on the development of geomechanical processes is a new approach to solving the problems of ensuring the safety of mining operations during the development of upland deposits in the zones of influence of tectonic disturbances.

Based on the analysis of foreign literature, it has been established that the assessment of the block structure and fracturing of the rock mass is a priority in mining geomechanics. However, the issues of influence on the development and management of geomechanical processes during the development of upland deposits in the mountainous-folded regions, to which Kyrgyzstan belongs, have not been given due attention to date.

In the applied methods for substantiating the parameters of stable sides of quarries developed by VNMI institutes (Methodological guidelines for determining...1972, Rules for ensuring the stability of slopes...1998, Temporary guidelines for managing the stability of the sides...1989), all factors acting in the array at the time of formation of the side are taken into account as much as possible: the physical and mechanical characteristics of the rocks composing the side array; the intensity of fracturing; the geometry of the side; hydrogeological conditions; indicators of shear resistance along the planes of cracks. According to these factors, the state of the array is estimated at the calculated value of the angle of inclination of the side.

In this case, the stability assessment is reduced to the calculation of the stability margin coefficient by the ratio of holding forces to shear forces for several variants of the calculated sliding surfaces, i.e. the calculation and assessment of the stability of the side array of fractured and block structure is performed as for an isotropic array, taking into account the structural attenuation coefficient. With this approach, only the weight of rocks is taken into account when assessing stability.

The high intensity of tectonic movements during the formation of the block structure of the massif can be evidenced by the steep fall of ore bodies with shale elements in contact with rocks of the hanging or recumbent sides. The extended rectilinear contacts of the ore body with the host rocks are very favorable for shear tectonic deformations in the side array due to the low strength properties of these contacts. Conversely, the complex morphology of the ore deposit creates tangible obstacles for inherited tectonic movements along the contacts.

The presence of dikes in the deposit indicates destructive deformation of the massif in the geological past under the influence of compressive stresses in the massif. Due to the limited permeability of the massif with the heterogeneity of the stress field, the magma of deep horizons was able to reach the upper floors of the earth's crust only with the development of large-scale destructive zones. Hence, the vein mass in a foreign rock mass is the result of high- and medium-temperature processes of mineral deposition. With a certain modern spatial distribution of tectonic forces, the process of formation of new or opening of healed cracks in the side array may resume, which will lead to the disintegration of the array and, as a consequence, to a decrease in its strength properties. (Miroshnikova, L.K., Mezentsev, A.Yu., Kadyralieva, G.A., Perepelkin, M.A., 2021)

So, it can be stated that almost every geological element in the structure of the massif emphasizes the predisposition of the massif to tectonic deformations in an anisotropic stress field, that is, each disjunctive reflects the sensitivity of a section of the massif to the shear form of deformations. In this case, the sensitivity is selective with respect to such parameters as the ratio of the main components of the stress field, the angle between the direction of the maximum component and the plane of the seam, the angle of friction and adhesion along the contact.

The disturbance of the array by cracks also affects its elastic properties. With an increase in fracturing, the elasticity of rocks decreases. It is revealed that the elasticity of a fractured rock mass is always less than the modulus of elasticity of a rock sample by about 5 – 15 times. The elastic modulus will be different for different sections of the array.

Geomechanical classifications of rock massifs are the basis of an empirical approach to assessing their stability and are widely used in the design of various objects in various foreign countries.

Based on the results of studying the stability of a block structure rock mass, the mechanism of destruction of blocks if there is a soft filler between them, a test experiment was conducted in laboratory conditions, the purpose of which was to establish the dependence of the resistance of blocks on separation at different types of block filler.

Artificial fillers between block cracks were prepared for laboratory tests. Clay and sand and their different ratios were chosen as aggregates (Table 1).

Table 1. Ratios of clay and sand for laboratory tests selected as a crack filler.

№	Clay	Sand
1	100%	100%
2	50%	50%
3	70%	30%
4	30%	70%

For testing, two marble blocks of the correct shape of the prism were taken, with dimensions:
length – 5cm,
width – 4.7cm
height – 9.7cm
weight – 662.85g (Figure 2)

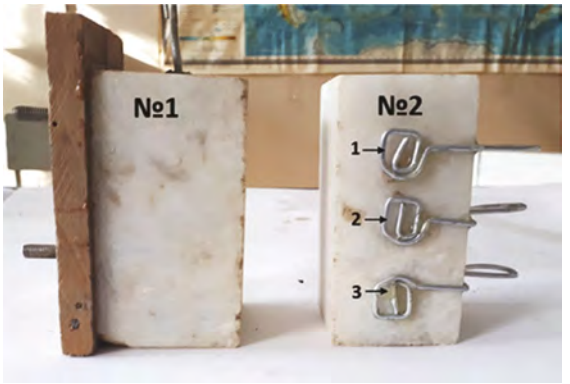

Figure 2. Marble blocks used for laboratory tests.

No. 1 – the first fixed block, No. 2 – the second fixed block, 1 – the first (upper) point of separation, 2 – the second (middle) point of separation, 3 – the third (lower) point of separation.

For testing, a wooden structure was made (Figure 3), with a fixed wall for fixing the 1-fixed block, with the possibility of removal and reverse fastening with nuts.

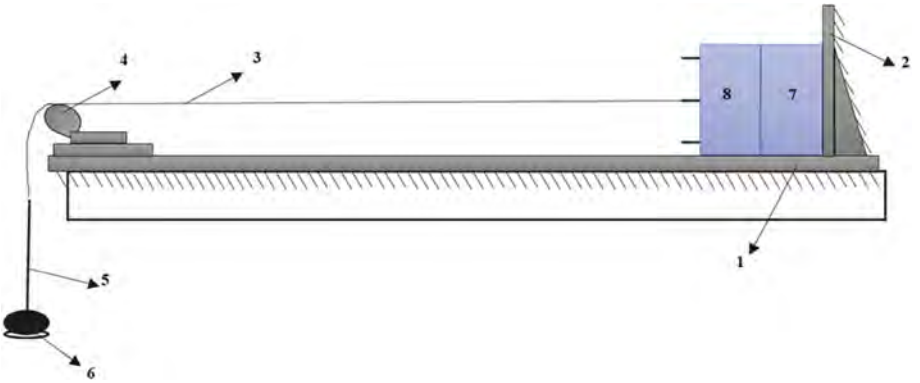

Figure 3. Design for testing blocks for separation.

1-the base of the structure, 2-the vertical supporting wall, 3-the cable for detaching the block, 4-the drum for the cable, 5-the attachment for the load, 6-the load of 100g, 7-the first fixed block, 8-the second movable block.

The results of the data obtained are shown in Figure 4, the dependence of the block separation resistance on the types of filler.

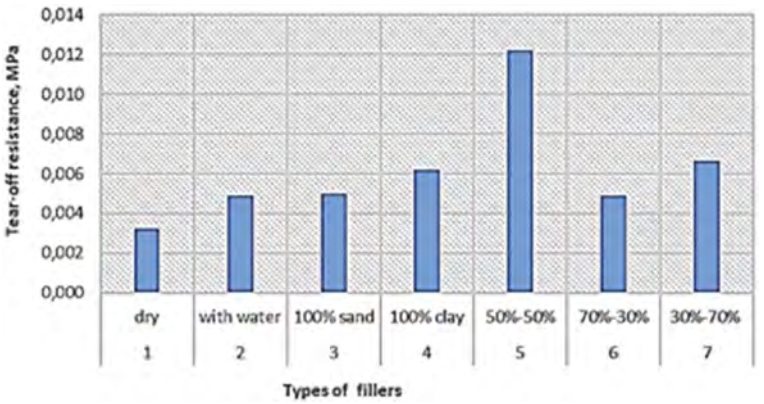

Figure 4. Dependence of the block's resistance to separation from different fillers.

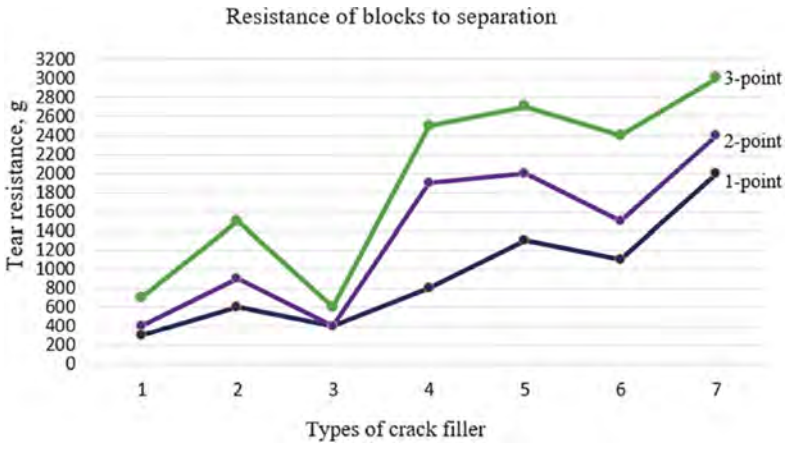

Figure 5. Design for testing blocks for separation.

1 – dry filler, 2 – water filler, 3 – sand filler 100%, 4 – filler clay 100%, 5 – filler sand 50% and clay 50%, 6 – filler sand 70% and clay 30%, 7 – filler sand 30% and clay 70%.

CONCLUSIONS

Based on the obtained laboratory data, it was revealed that:

1. The resistance of the block to separation depends on the type of aggregate, with the greatest resistance being provided by the aggregate, where the ratio is 50% sand to 50% clay.
2. The resistance to the separation of rock blocks depends on the type of filler, while clay fillers have the greatest resistance to separation in a ratio of 70% x30% with sand.
3. The resistance to the separation of rock blocks depends on the point of separation. The third (lower) point has the greatest resistance to separation.

When assessing the stability of the sides of the quarry and choosing their geometric parameters in the rock massifs of the block structure, it must be taken into account that the main factor in this is the filler between the block cracks, their strength, composition, humidity. Based on the results of a test laboratory experiment of the resistance of blocks to separation, it was decided to test the resistance of blocks to shear. In order to identify the main cause of the violation of the mechanism of the block structure rock mass.

REFERENCES

Kadyralieva, G.A., Kozhogulov, K.C. 2022. 1. Features of the Rock Massif in the Influence Zones of Tectonic Disturbances in the Gold Deposits of Kyrgyzstan, *Lecture Notes in Civil* Engineering *230 LNCE*: 155–160.

Miroshnikova, L.K., Mezentsev, A.Yu., Kadyralieva, G.A., Perepelkin, M.A. 2021. 2. Geodynamic zoning of the southwestern part of the Talnakh Orogenic System, *Gornaya Promyshlennost, Moscow, 2021 (6)*. 103–109

Rules for ensuring the stability of slopes at coal mines 1998. *approved by Gosgortehnadzor of Russia on 16. 03.98*. - St. Petersburg: VNIMI, 65(1): 13–16.

Temporary guidelines for managing the stability of the sides of non-ferrous metallurgy quarries 1989 Unipromed. - Sverdlovsk, 25

Smart Geotechnics for Smart Societies – Zhussupbekov, Sarsembayeva & Kaliakin (Eds)
© 2023 The Author(s), ISBN 978-1-003-29912-7
Open Access: www.taylorfrancis.com, CC BY-NC-ND 4.0 license

Coupled CFD-DEM simulation of progressive failure of tunnel face

C. Zhou & J.G. Qian*
Tongji University, Shanghai, China

Z.Y. Yin
The Hong Kong Polytechnic University, Hong Kong, China

ABSTRACT: Extensive studies have been conducted to investigate the face stability of tunnelling by the discrete element method (DEM). However, the DEM simulation of tunnel face's failure considering water-soil interaction has not yet been available. In this paper, the coupled CFD-DEM method was adopted to simulate the progressive failure of the shield tunnel face in saturated sand, and the tunnel's failure in dry sand was also simulated for comparison. The dynamic mesh method was introduced to accurately simulate the CFD domain's variation due to the movement of the tunnel's face. The excavation face was moved forward or backward at a uniform displacement rate to simulate a passive or active failure, respectively. The ground surface movement and supporting force of tunnel face were analyzed to investigate the feature of tunnel face failure in saturated and dry sandy soils.

1 INTRODUCTION

The shield tunneling method is widely used in urban underground tunneling projects. Inadequate or excessive support forces on the tunnel face may cause tunnel destabilization(Peila, 1994; Mollon, Dias and Soubra, 2011). In the vicinity of the tunnel face, where soil deformation or even soil collapse may take place, it greatly challenges traditional continuous medium methods to reproduce the process of such a progressive failure. Thus the discrete element methods (DEM) were introduced to simulate the large deformation and soil transport. Nevertheless, previous discrete element numerical simulations fail to enable us to well understand water-soil interaction and commonly simulate tunneling in dry sand. The saturated soil involves water-soil interaction, which is a multidisciplinary process governed by the principles of soil mechanics and hydraulics. Therefore, a combination of computational fluid dynamics (CFD) and the discrete element method (DEM) is more appropriate to consider saturated sandy soils.

This paper simulates the progressive failure of shield tunnel face in saturated sand using coupled CFD-DEM method. By analyzing the surface displacement and face support force, the different failure behaviors of tunnel face in saturated and dry ground are revealed.

2 METHODOLOGY AND MODEL SETUP

2.1 *Governing equations*

In CFD-DEM method, the motion of the solid particles is governed by Newton's laws, while the velocity and pressure of fluid are calculated by the volume-averaged Navier-Stokes equations (Kloss *et al.*, 2012):

*Corresponding author:

DOI: 10.1201/9781003299127-125

$$m_i \frac{dv_i}{dt} = \sum_{j=1}^{j=n} F_{ij}^n + \sum_{j=1}^{j=n} F_{ij}^t + F_i^f + F_i^g \tag{1}$$

$$I_i \frac{d\omega_i}{dt} = \sum_{j=1}^{j=n} M_{ij} \tag{2}$$

$$\left(\partial \alpha_f\right)/\partial t + \nabla \cdot \left(\alpha_f u_f\right) = 0 \tag{3}$$

$$\frac{\partial \alpha_f u_f}{\partial t} + \nabla \cdot \alpha_f u_f u_f = -\alpha_f \nabla \frac{p}{\rho_f} - R_{pf} + \nabla \cdot \left(\alpha_f \tau\right) \tag{4}$$

where the particle index is denoted by subscript i; m_i is the particle's mass; v_i and ω_i represents the translational and angular velocity; F_{ij} is the inter-particle contact force while F_i^f is the particle-fluid force; F_i^g is the gravity of each particle; α_f is the fluid volume fraction; u_f and p denotes the fluid velocity and pressure, respectively; ρ_f is fluid density; τ represents the shear stress tensor of the fluid cell; R_{pf} is the exchange of momentum with the particulate phase.

2.2 *Model setup*

Spherical particles are adopted in the DEM simulation. The particle size distribution refers to that used in the previous study (Yin, Wang and Zhang, 2020). The particle size is enlarged by ten times to reduce the number of particles and satisfy computional power requirements, which is commonly adopted in DEM simulations. The largest and smallest particle sizes in the simulation are 30.7mm and 12.2mm, respectively. Some of the particle-related parameters are shown in Table 1. Four tests are carried out with the same model size, and both the dry and saturated surrounding soils are considered in this study. The excavation of the tunnel is simulated by the forward and backward movement of a rigid wall in the DEM. Due to the simulation situation's symmetry, half of the tunnel model is used to save computational resources (as shown in Figure 1). In addition, the gravitational acceleration used in the simulation has been magnified by a factor of 10, with reference to the centrifuge test method (Yin, Wang and Zhang, 2020). The actual size of the prototype is ten times the size set in the model. According to the similarity criterion, the corresponding fluid viscosity coefficients are scaled up by the same. Due to the complexity of excavation speed control in actual projects, this paper simplifies active and passive failure into two cases: tunnel backward and forward. As with previous numerical simulations and tests, the tunnel excavation speed is set to a constant speed of 0.01m/s for forward and backward movement to meet the quasi-static requirements. The total simulation time is the 20s, and the total distance of the forward and backward movements is 200mm.

Table 1. Parameters used in the simulations.

Particle density (kg/m^3)	2650
Young's modulus (MPa)	5×10^8
Poisson's ratio	0.3
Inter-particle friction coefficient	0.5
Rolling friction coefficient	0.1
Timestep (s)	2×10^{-5}
Restitution coefficient	0.3

3 RESULTS ANALYSIS

3.1 *Soil displacement field*

Figure 2 shows the particle displacement distribution in four tests with different tunnel movements (40mm, 100mm, 170mm, and 200mm). The particles with displacement less than a certain value (0.04m) are hidden in the figure. Firstly, for the active failure mode of the tunnel face, it can be seen from Figure 2(a)-(b) that the shapes of the displacement field in the dry sand and saturated sand cases are similar while the area of the destabilization zone in the dry sand is larger than that in the saturated sand. The destabilization angle in saturated sand (57.89°) is slightly larger than that in dry sand (52.56°). For passive failure, as shown in Figure 2(c)-(d), the destabilization zone reaches the ground surface in both cases of dry and saturated sand soils. In addition, it's found there is little difference in the size of the instability zone at the beginning of the tunnel face movement (40 mm, 100 mm). As the test proceeds, a significant difference occurs and the destabilization zone in the saturated sand is significantly larger than that in the dry sand.

3.2 *Ground surface displacement*

Surface displacements caused by tunnel excavation may affect nearby buildings, which has been one of the main concerns for urban tunnel construction. Figure 3(a)-(b) shows the surface displacements corresponding to backward movement (the selected location is X=0, -1.25<Y<1.25). It can be observed that the surface settlement increases with the movement of the tunnel and reaches its maximum value at the end of the test. The maximum settlement in dry sand occurs at -0.117 m from the initial position of the tunnel excavation surface (Y=0.95m), and the settlement value decreases rapidly on both sides of the maximum settlement, showing a "V" shape in the figure. The maximum settlement in saturated sand occurs at Y=1.054m, which is not significantly different from that of dry sand. In contrast, both sides' settlement decreases more slowly, and the overall settlement is greater than dry sand. Under the influence of water flow, the surface displacement at the end away from the tunnel face (Y<0m) shows a certain degree of fluctuation. Figure 3(c)-(d) shows the surface uplift when the tunnel moves forward. The amount of surface uplift is small at both ends and large in the middle, and the maximum uplift point is located in the center of the model. Meanwhile, the surface uplift in dry sand is smaller than that in saturated sandy soil.

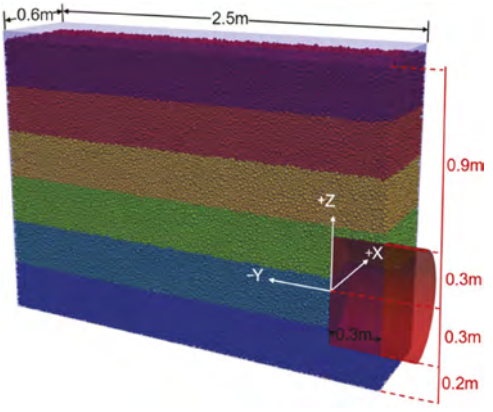

Figure 1. The DEM-CFD model to simulate the progressive failure of tunnel face.

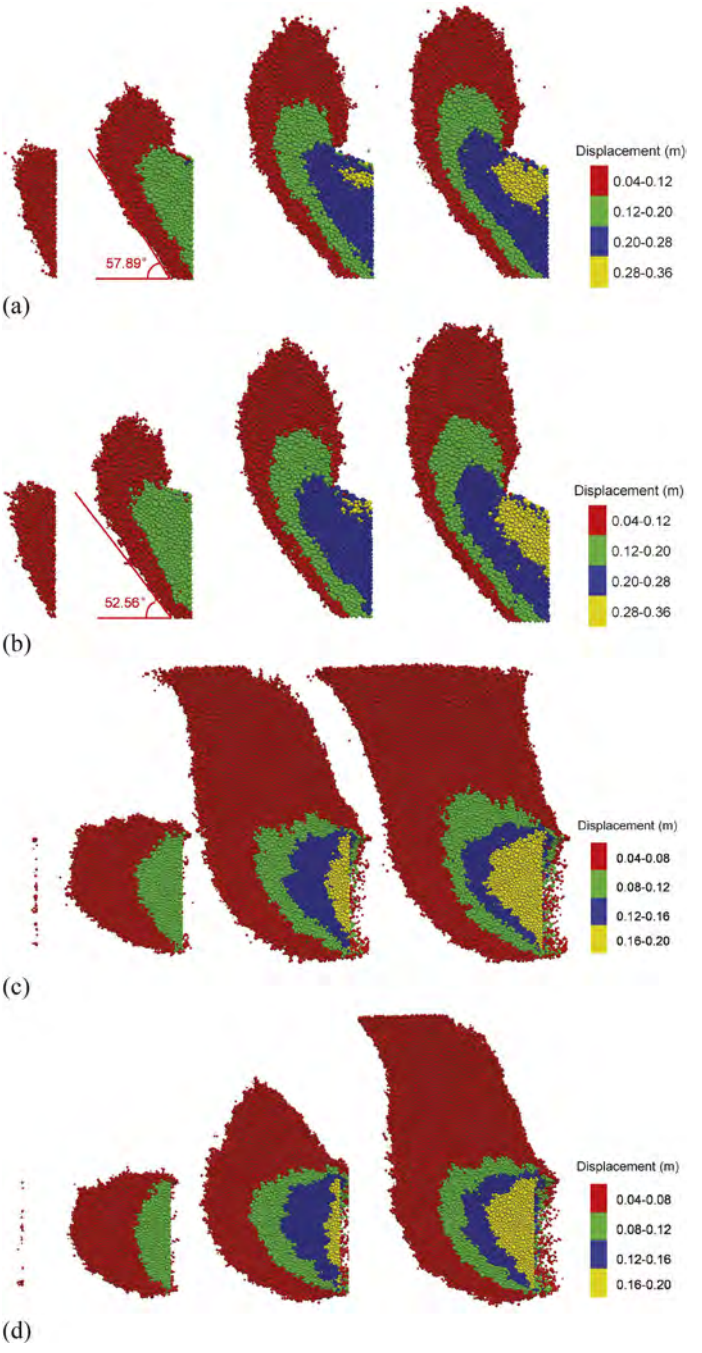

Figure 2. Particle displacement fields from left to right for 40mm, 100mm, 170mm, and 200mm tunnel displacements: (a) Backward displacement in saturated sand (b) Backward displacement in dry sand (c) Forward displacement in saturated sand (d) Forward displacement in dry sand.

3.3 *Supporting force-displacement curve*

The curve of the tunnel face support force versus tunnel displacement is shown in Figure 4, from which it can be seen that under the active damage case, the curve has two stages: the

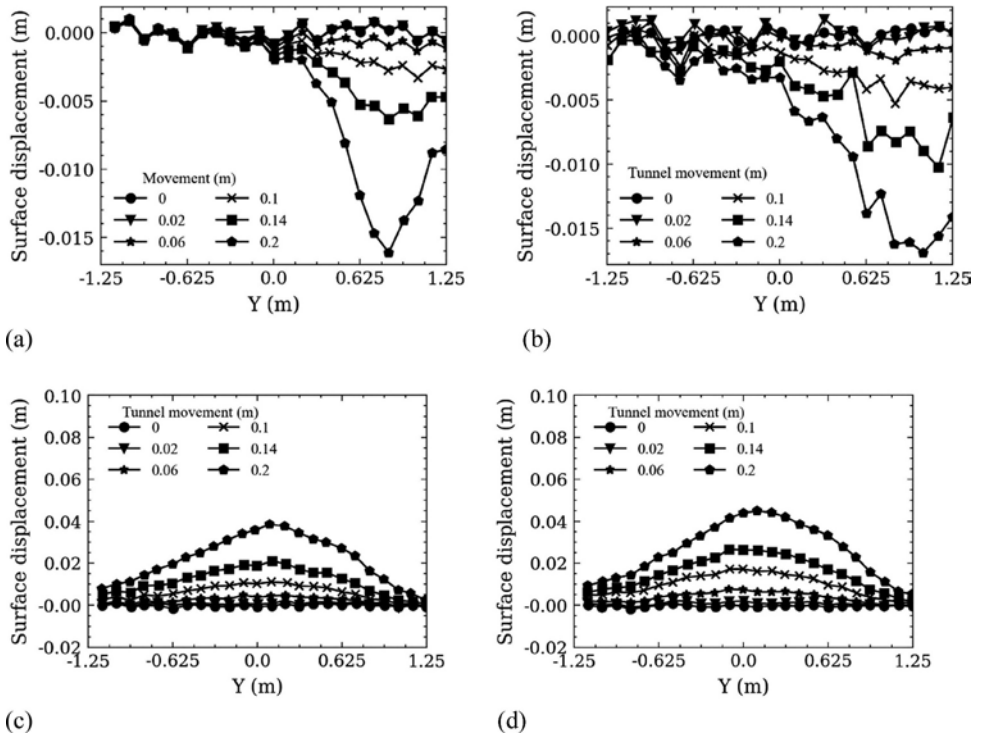

Figure 3. The surface settlement caused by tunnel face: (a) backward movement in dry sand; (b) backward movement in saturated sand; (c) forward movement in dry sand; (d) forward movement in saturated sand.

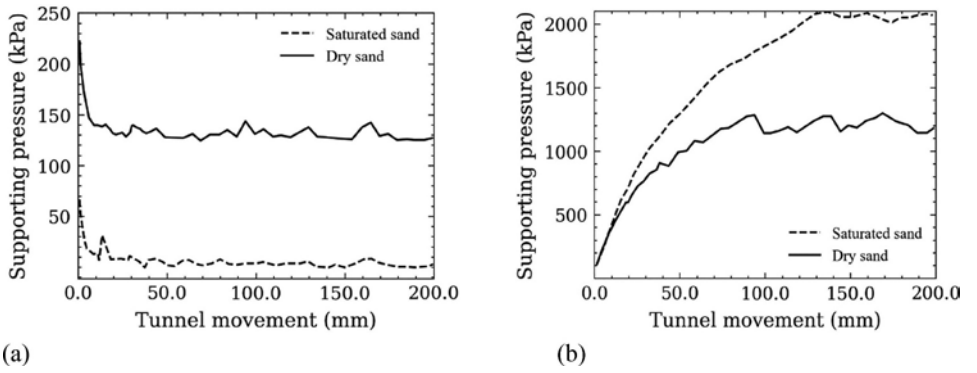

Figure 4. The surface uplift caused by tunnel face: (a) backward movement; (b) forward movement.

support force decreases rapidly with the increase of excavation face displacement in the first stage, and then maintains relative stability in the second stage to reach the ultimate support force. By comparing the two curves corresponding to saturated sand and dry sand, it is found that the ultimate supporting force in saturated sand is significantly higher than that in dry sand. In addition, the support force of dry sand almost decreases to zero, indicating that an arch has formed in the soil. As for the curve of passive damage, the support force is much greater than that for active damage. Unlike the active damage mode, there is no significant steep change in support force but rather a gradual increase to a limiting value as the displacement of the tunnel face increases.

4 CONCLUSION

In this paper, the coupled CFD-DEM method is used to simulate the progressive failure of the tunnel face in saturated sand. Meanwhile, the tunnel face in dry sand is also conducted using DEM as a comparison. Results show that the destabilization angle in saturated sand is slightly larger than that in dry sand for active failure. While in the case of passive damage, the destabilization zone extends to the surface and is significantly larger in saturated sands than in dry sands. In addition, the ultimate support force of the tunnel face for active damage is significantly higher in saturated sand than in dry sand. For passive damage, however, the ultimate support force at the excavation face is higher in dry sand than in saturated sand.

REFERENCES

Kloss, C. *et al*. (2012) 'Models, algorithms and validation for opensource DEM and CFD-DEM', *Progress in Computational Fluid Dynamics*, 12(2–3): 140–152.

Mollon, G., Dias, D. and Soubra, A. (2011) 'Rotational failure mechanisms for the face stability analysis of tunnels driven by a pressurized shield', *International Journal for Numerical and Analytical Methods in Geomechanics*, 35(12): 1363–1388.

Peila, D. (1994) 'A theoretical study of reinforcement influence on the stability of a tunnel face', *Geotechnical & Geological Engineering*, 12(3): 145–168.

Yin, Z. Y., Wang, P. and Zhang, F. (2020) 'Effect of particle shape on the progressive failure of shield tunnel face in granular soils by coupled FDM-DEM method', *Tunnelling and Underground Space Technology*, 100: 103394.

Smart Geotechnics for Smart Societies – Zhussupbekov, Sarsembayeva & Kaliakin (Eds)
© 2023 The Author(s), ISBN 978-1-003-29912-7
Open Access: www.taylorfrancis.com, CC BY-NC-ND 4.0 license

Prediction of tunneling-induced surface settlement using a Bi-LSTM model with high generalization performance

R.P. Chen, N. Zou, H.Z. Cheng & H.N. Wu
Research Center for Advanced Underground Space Technologies, Hunan University, Changsha, China
Key Laboratory of Building Safety and Energy Efficiency of Ministry of Education, Hunan University, Changsha, China
College of Civil Engineering, Hunan University, Changsha, China

ABSTRACT: Using Machine Learning (ML) and Deep Learning (DL) algorithms to predict ground surface settlement caused by shield tunneling has being a hot topic. However, previous developed models are general weakness in the generalization performance when solving the problem in multi-regions. Because the data were usually collected based on a certain project, resulting in the limitations of the data in quantity and representativity. In this study, numerous data were collected from shield tunnels derived in various stratum conditions from different cities of China. Then, the improved models were proposed to identify the relationship between shield tunneling and the settlement. The efficiency of a DL algorithm Bi-directional Long Short-Term Memory (Bi-LSTM), ML algorithms Back-propagation Neural Network (BPNN) and Random Forest (RF) were compared. The results indicated that the accuracy of the proposed models have superior performance on the prediction accuracy of surface settlement, compared with dedicated model trained using individual city data. Furthermore, Bi-LSTM is demonstrated as a better algorithm to predict surface settlement than BPNN and RF.

1 INTRODUCTION

Shield tunnels are widely used in lifeline projects such as underground transportation and public facility construction in China, which not only can construct quickly but also reduce the impact on the ground surface. However, surface settlement is inevitable leading to serious accidents in severe cases. Thus, the prediction of surface settlement has been an important work. Traditional surface settlement prediction methods are based on empirical formulations (Peck 1969, Attewell & Hurrell 1985), analytical and semi-analytical solutions (Sagaseta 1987, Verruijt & Booker 1998), and numerical simulations (Kasper & Meschke 2004, Meng et al. 2018). Shield tunneling-induced surface settlement can be seen as a time series processing problem. It should be predicted based on a section of data from many factors, including geological conditions and shield operation parameters. Previous studies have been proved that there is a complex interaction between surface settlement and these factors (Li et al. 2015). However, the characteristics of these complex relationships were be simplified in traditional methods. As a result, it is desire to develop a more high-accuracy of the predictive model for surface settlement.

With the rapid development of Artificial Intelligence in recent years, BPNN was first applied in the prediction of tunnel settlement by Suwansawat & Einstein (2006), in which three factors were taken into consideration, namely tunnel geometry, geological conditions, and shield operation factors. Base on the public database of Suwansawat & Einstein (2006), Pourtaghi & Lotfollahi-Yaghin (2012) and Kohestani et al. (2017) found that the prediction accuracy of surface settlement would be significantly improved using Wavelet Neural Network (WNN) and RF compared to BPNN. However, these studies still had some shortcomings, such as using numbers to simply distinguish strata. To provide a more adequate

DOI: 10.1201/9781003299127-126

representation of the geological information, Chen et al. (2019) proposed a new method to consider both the strength and distribution of the strata. Furthermore, the selection of shield operation parameters was also discussed (Boubou et al. 2010, Zhang et al. 2019). As well, when other important influencing factors, such as karst cave (Zhang et al. 2020a, Zhang et al. 2021) and shield stoppage (Zhang et al. 2020b), have been chosen as input parameters, the performance of the settlement prediction model will be further improved. However, the current studies are primarily based on data from an individual project (Goh et al. 2018), the performance of the settlement production model in other projects, which generally have various geological conditions, is rarely discussed.

To solve this problem, this study collected data from shield projects in three cities (i.e. Changsha Metro Line 4, Tianjin Metro Line 7 and Zhengzhou Metro Line 3). Several algorithms, including BPNN, RF and Bi-LSTM, were used for a comprehensive comparative study. Then, the performance of the proposed model based on the best-performing algorithm is assessed.

2 METHODOLOGY

2.1 *Bi-directional long short-term memory neural network*

Bi-LSTM was upgraded from LSTM, which is a modification of recurrent neural network (RNN). While RNN is a deep learning algorithm that can capture and store information in time dimension. LSTM based on RNN, enables it to capture events with longer intervals and delays in time series by introducing the structure of forget gate, input gate and output gate, which avoids the problems of weight matrix dimensionality explosion and disappearance of propagation gradient, as is quite common in RNN. Compared to LSTM, Bi-LSTM allows working in both forward and backward direction through two independent hidden layers, which means Bi-LSTM can save both past and future information at any point (Wang et al. 2021). In this way, Bi-LSTM solves the problem that LSTM is susceptible to the last set of input parameters and the influence of the first set is too low.

2.2 *Back-propagation Neural Network*

BPNN is a kind of Multilayer Feedforward Neural Network (FNN), one of the most commonly used machine learning algorithms. Its structure mainly consists of an input layer, one or more hidden layers and an output layer. The input layer is used to obtain the input parameters, then adjust the number of hidden layers and the weights and thresholds among the layers to perform inter-layer operations, eventually using the activation function to derive the output value and error. Moreover, the number of hidden layers and neurons is adjusted by backpropagation until the error is reduced to the set range.

2.3 *Random Forest*

RF is an integrated learning algorithm consisting of multiple decision trees, often used to solve classification and regression problems. The decision trees are generated non-parametric stochastically, and each decision tree is an independent predictor, employing averaging and voting to derive results for the regression and classification problems, respectively. When dealing with problems with a small database, RF has a greater advantage in handling problems such as classification and regression.

2.4 *Particle swarm optimization*

Particle swarm optimization (PSO) is an optimization algorithm designed to find the optimal value of a target, with the characteristics of fast search speed and small memory consumption (Chen et al. 2022). By defining the hyperparameters of the algorithm as particles, PSO can be used to reduce the error of the settlement prediction model through constant updating of the particles.

3 PROJECT OVERVIEW

The database used in this paper is collected from three earth pressure balance (EPB) shield projects (i.e. Changsha Metro Line 4, Tianjin Metro Line 7 and Zhengzhou Metro Line 3). Note that the surface settlement collected in this study was caused by the first one during the excavation of the double-line tunnel. The outer diameter and inner diameter of the segmental lining are 6.0m and 5.4m in Changsha, 6.6m and 5.9m in Tianjin, as well as 6.2m and 5.5m in Zhengzhou. The width of the segmental lining in all three projects is 1.5m.

Figure 1 shows the geological profiles of the three tunnels in this study. The selected Changsha Tunnel is 5.44 km long and consists of 6 stations and 5 sections. In comparison, the tunnels in Tianjin and Zhengzhou both consist of only 2 stations and 1 section, which are 1.90 km and 0.71 km long, respectively. The tunnel burial depths are range from 10 to 28m in Changsha, 9.5 to 21m in Tianjin, and 12 to 23m in Zhengzhou. The average groundwater depth of the Changsha project is about 3m, Tianjin is about 2m, and Zhengzhou is below 15m. During the excavation of the 5-section tunnel from LGL to FBH station in Changsha, the shield machine passed through a complex stratum, which mainly included weathered slate, tuff, weathered mudstone, and sandstone, with a few places crossing chalky clay and gravels. In MJN to WLZ station of Tianjin Metro Line 7, the shield machine mainly excavates in the water-rich silt sand stratum, crossing the silt sand, silty clay, clayey silt and clay, with low strength and high-water content overall. The geological conditions of Zhengzhou Metro Line 3 are quite similar to those of Tianjin Metro Line 7. From LGL station to FBH station, in about half of the distance, the soil type at the tunnel face is fine sand, while the other half is sandy silt and clayey silt. For more details, it can be referred from Chen et al. (2019) and Zhang et al. (2020b). In summary, the tunnel was mainly driven through weathered rock layers in Changsha Metro Line 4, while through soft geological chalk and sandy soils, a more uniform stratum in Zhengzhou Metro Line 3 and Tianjin Metro Line 7.

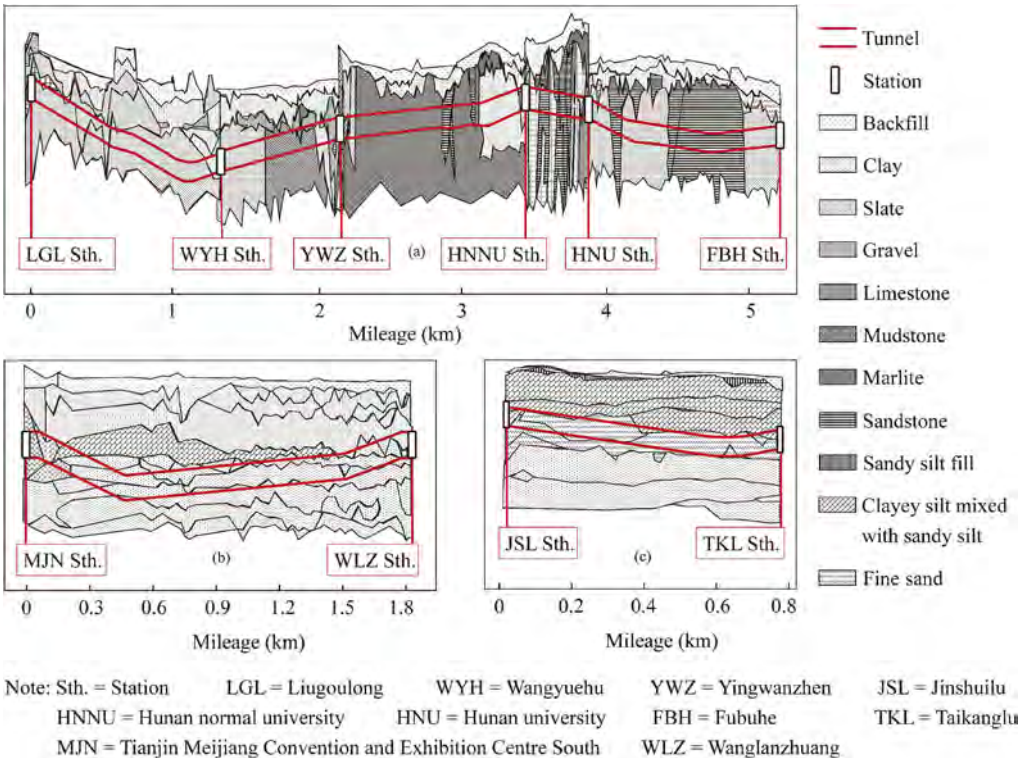

Figure 1. Geological profile of study area: (a) Changsha; (b) Tianjin; (c) Zhengzhou. (modified from (Zhang et al. 2020c)).

4 DEVELOPMENT OF PRODICTION MODEL

4.1 *Inputs and outputs*

The factors that influence surface settlement can be divided into 3 main categories: geometric factors, geological factors and shield operational parameters. Since the tunnel diameters in this study are basically the same, the burial depth of the tunnel is taken as the only geometric factor.

Regarding to the geological factors, in addition to the water table and the soil types at tunnel face (Zhang et al. 2020c), a method based on the correction for the depth and thickness of strata was used (Chen et al. 2019), where the modified standard penetration test blow count (MSPT), modified dynamic penetration test blow count (MDPT), modified uniaxial compressive strength (MUCS) were also chosen to represent the geological conditions in which they are located, expressed in Equations 1~3:

$$N'_{63.5} = \sum_{i=1}^{n} \frac{t_i}{h} \cdot \frac{h_i}{h} \cdot N_{63.5} \tag{1}$$

$$N' = \sum_{i=1}^{n} \frac{t_i}{h} \cdot \frac{h_i}{h} \cdot N \tag{2}$$

$$U' = \sum_{i=1}^{n} \frac{t_i}{h} \cdot \frac{h_i}{h} \cdot U \tag{3}$$

In which $N_{63.5}$ is the blow count of standard penetration test, N is the blow count of dynamic penetration test, U is the unconfined uniaxial compressive strength. As shown in Figure 2, $\frac{t_i}{h}$is the thickness index, representing the ratio of the thickness of the strata i to the tunnel depth h; $\frac{h_i}{h}$ is the depth index, representing the ratio of the depth of the strata i to the tunnel depth h. With these two indices, the thickness of each stratum and the distance between each stratum to the tunnel crown are concerned, which represents the influence of each stratum on the surface settlement.

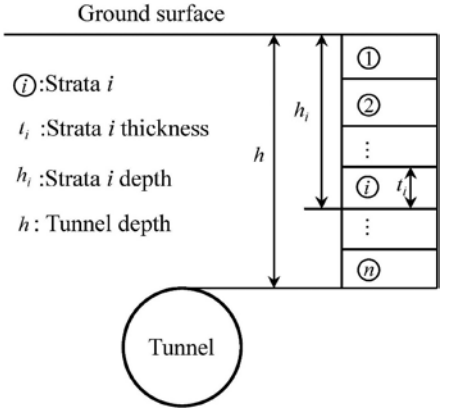

Figure 2. Illustration for the thickness index and depth index. (modified from (Chen et al. 2019)).

The shield operation generates many tunneling parameters, and the parameters most closely related to the magnitude of ground deformation are torque, penetration rate, thrust, chamber pressure and rotational speed (Chen et al. 2022). In addition, whether the shield machine is

stopped over 24 hour or not is also an input parameter, as the stoppage is strongly correlated with the surface settlement (Zhang et al. 2020b).

The histograms of the settlement data collected from the metro projects in Changsha, Tianjin and Zhengzhou are shown in Figure 3, respectively. There were 4215 field settlement records collected from Changsha, 535 from Tianjin, and 2028 from Zhengzhou. Settlement less than 10 mm accounted for most of the database in all projects, while 5 to 10 mm settlement was relatively high in the database of the Zhengzhou project. About 23% of the data in the Tianjin project are small ground uplifts. In comparison, settlement more than 10 mm occurred much frequently in Changsha than in Tianjin and Zhengzhou.

In summary, this paper constructs a database based on 6778 sets of settlement, geometric factors, geological factors and shield operational parameters, and the database structure, statistics of all parameter are listed in Table 1. It should be note that the training set accounted for 80%, and the test set accounted for 20%.

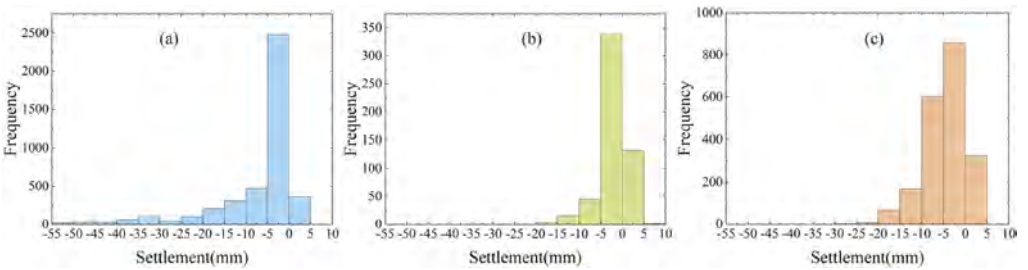

Figure 3. Settlement histograms of each city: (a) Changsha; (b) Tianjin; (c) Zhengzhou.

Table 1. Statistics of all used parameters.

Parameters	Parameter type	Minimum	Maximum	Average	Unit
Cover depth	Input	9.09	31.65	17.58	m
Torque	Input	0.14	4.82	2.41	MN·m
Penetration rate	Input	3.11	76.00	39.73	mm/min
Thrust	Input	1.77	23.80	11.99	MN
Chamber pressure	Input	0.39	2.84	1.15	bar
Rotational speed	Input	0.29	2.16	1.39	rpm
Water table	Input	0	25.11	6.10	m
Soil types at tunnel face	Input	1	4	/	/
MSPT	Input	0	37.92	7.96	/
MDPT	Input	0	22.17	0.25	/
MUCS	Input	0	39.42	4.90	MPa
Stoppage	Input	0	1	/	/
Settlement	Output	-89.13	6.97	-5.62	mm

4.2 *Performance analysis*

In order to demonstrate the accuracy of the constructed shield excavation surface settlement prediction model, three performance evaluation indexes were selected for this study, which is root mean square error (RMSE), mean absolute error (MAE) and Pearson correlation coefficient (R).

$$RMSE = \sqrt{\left(\frac{1}{n}\right)\sum_{1}^{n}(r_i - p_i)^2} \tag{4}$$

$$MAE = \left(\frac{1}{n}\right)\sum_{1}^{n}|r_i - p_i| \tag{5}$$

$$R = \frac{\sum_{i}^{n}(r_i - \bar{r})(p_i - \bar{p})}{\sqrt{\sum_{i}^{n}(r_i - \bar{r})^2(p_i - \bar{p})^2}} \tag{6}$$

where r_i and $\bar{r}$mean the actual and average values of surface settlement, respectively. The MAE and RMSE represent the magnitude of the mean error and the standard deviation between the predicted and measured values, respectively.

4.3 *Optimum hyper-parameters*

The selection of hyperparameters is strongly related to the performance of the ML and DL models. In the selection of BPNN and RF model's hyper-parameters, using 10-fold cross-validation with PSO, setting the MAE of the validation set to the fitness value, and conducting 300 generations, respectively (Zhang et al. 2020b). While the previous study has shown that using the PSO algorithm to find the optimal hyper-parameters of the LSTM model will result in an extremely rapid increase in computational cost (Zhang et al. 2020c). So the optimal hyper-parameters of the Bi-LSTM model in this paper are searched by the trial-and-error method. As shown in Figure 4, the iterative process of both the BPNN and RF models is completed within 25 generations, which indicates that PSO has a strong search capability and converges extremely fast. And the fitness value of the RF model is significantly smaller than that of the BPNN model, suggesting that the prediction performance of the RF model is noticeably better. The optimal hyper-parameters of BP, RF and Bi-LSTM are listed in Table 2.

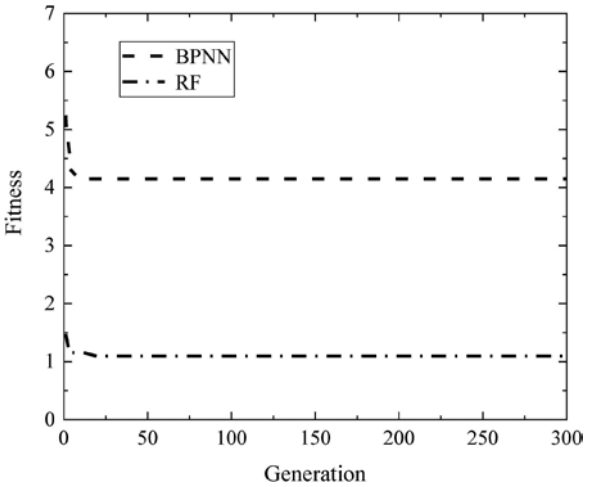

Figure 4. Optimized results of BPNN and RF.

5 RESULTS

Based on the previously mentioned database, three settlement prediction models were constructed using the BPNN, RF, and Bi-LSTM, respectively. The settlement prediction results are shown in Figure 5. The BPNN based model is unsuitable for predicting surface settlement because of its poor performance in R, RMSE and MAE. Meanwhile, the predicted settlement

Table 2. Values of optimum hyper-parameters in five machine learning algorithms.

Algorithm	Optimum hyper-parameters
BPNN	hidden_layer_neuron_num=12
RF	ntree=150
Bi-LSTM	hidden_layer_num=8 hidden_layer_LSTM_cell_num=60 time_step=3

is generally smaller than the measured settlement. The RF based model performs better, while R is above 0.9, and the RMSE and MAE in the test set are 3.01 and 1.67, respectively. The Bi-LSTM based model has the best performance among all, with the highest correlation coefficient and the lowest RMSE and MAE, which can not only accurately predict small settlement but also provide precise warning for excessive settlement even it is up to 90mm. It can be explained that the settlement of a predicted point depends on the tunneling information of the surrounding section, and the Bi-LSTM could capture this long interval information. When Bi-LSTM gives the output through the output gate, it can consider not only the current input but also the information beyond the current input through the forget and input gates, i.e., it considers the tunneling information of the surrounding sections at the same time. While at the same time, its bi-directional structure gives it a better ability to capture information that are closely connected before and after, making it possible to ensure that the influence of the tunneling at distant locations is not ignored.

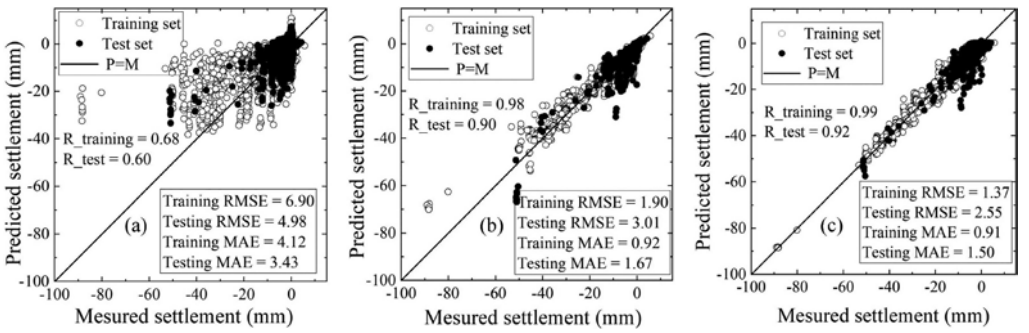

Figure 5. Settlement prediction results of each algorithm-based models: (a) BPNN; (b) RF; (c) Bi-LSTM.

Based on the results above, Bi-LSTM was chosen to construct two settlement prediction models respectively. Figures 6a, b, and c show the results of the dedicated model, which is built with data from Changsha only. Note that the data from Tianjin and Zhengzhou are used as the test set only in Figures 6b and c. The results of the improved model are shown in Figures 6d, e, f.

Even though the dedicated model performs well in Changsha, the predicted values of the Tianjin metro project are generally small, poorly correlated, and unable to provide effective guidance. The predictions for the Zhengzhou metro project are even worse, with almost no correlation between the predicted and measured settlement. The distribution of the predicted values is chaotic and hardly provides any reference meaning. This can be attributed to two possible reasons: 1) as described in Section 3, the geological conditions crossed by the Changsha project in this study are significantly different from those crossed by the Zhengzhou and Tianjin projects; 2) each project uses a different brand or model of earth pressure balance shield machine, which means that the shield operating parameters in different projects may not be compared directly.

As shown in Figures 6e and f, adding the data of the Tianjin and Zhengzhou projects to the database, Bi-LSTM has captured their features successfully. In the improved model, not only

the prediction results of Tianjin and Zhengzhou projects have been improved substantially, but also the accuracy of Changsha project has been further improved. The addition of new data not only increases the generalization ability of the model, but also allows the model to perform better in the part of original database. However, compared to the Zhengzhou project, the prediction model is relatively ineffective in the Tianjin project, with the correlation between the predicted and measured settlement in the test set only 0.79. This may be explained by the fact that the database size in the Tianjin part is 535, which is only 8% of the total database size, while the database size in Zhengzhou is 2028.

Such results suggest that the size of the database still plays a crucial role in the current research on surface settlement prediction. When the improved model in this paper is applied to a project where the geological conditions are significantly different from the current database, it may not always give an excellent result. To improve the generalization ability of the model, the increase of the database size, especially for different types of data, is highly recommended. Alternatively, building a physics-informed machine learning model is an important solution that is getting more and more attention.

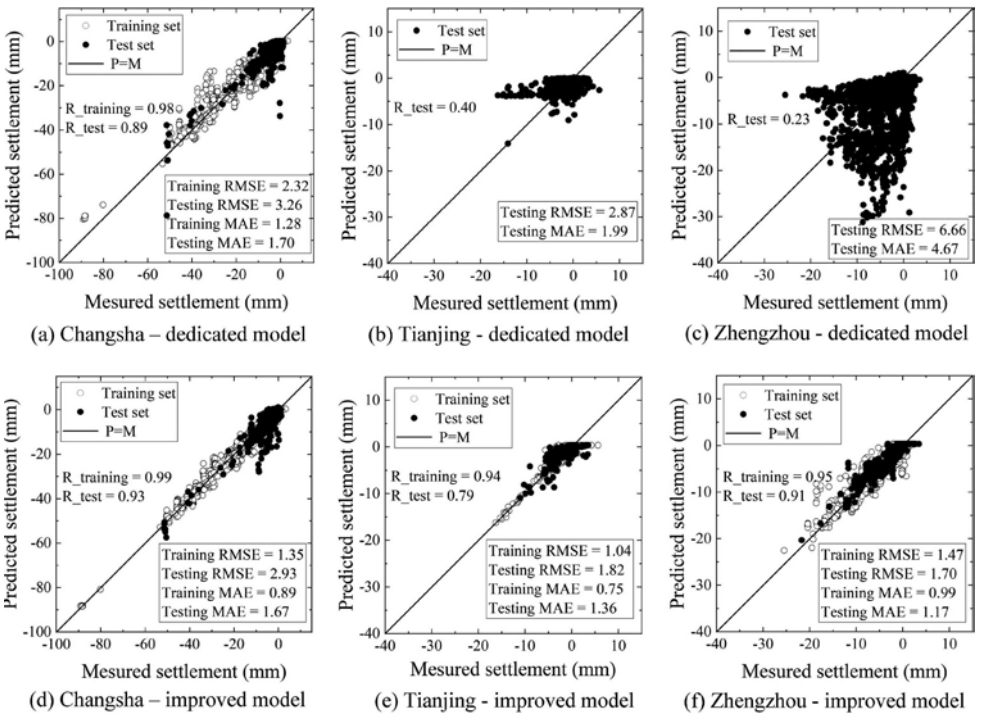

Figure 6. Settlement prediction results of dedicated model and improved model.

6 CONCLUSIONS

In this study, 6778 data from settlement monitoring points were collected based on Changsha Metro Line 4, Tianjin Metro Line 7 and Zhengzhou Metro Line 3. Bi-LSTM, BPNN and RF algorithms were used to establish 4 surface settlement prediction models. Comparing the three algorithms, it is found that the surface settlement prediction model constructed by the Bi-LSTM algorithm has the smallest error and can capture the intrinsic connection between each parameter and surface settlement accurately. Therefore, based on the overall performance of the prediction result, Bi-LSTM is more appropriate for the construction of the surface settlement model. Compared with the dedicated model based on the Changsha data, the improved

model not only has better prediction results in the Changsha metro project but also performs well in the Tianjin and Zhengzhou metro projects.

REFERENCES

Attewell, P. B. & Hurrell, M. R., 1985. Settlement development caused by tunnelling in soil. *Ground Engineering* 18, 17–20.

Boubou, Rim & Emeriault, Fabrice & Kastner, Richard, 2010. Artificial neural network application for the prediction of ground surface movements induced by shield tunnelling. *Canadian Geotechnical Journal* 47, 1214–1233.

Chen, Ren-Peng & Zhang, Pin & Kang, Xin & Zhong, Zhi-Quan & Liu, Yuan & Wu, Huai-Na, 2019. Prediction of maximum surface settlement caused by earth pressure balance (EPB) shield tunneling with ANN methods. *Soils and Foundations* 59, 284–295.

Chen, Ren-Peng & Zou, Nie & Wu, Huai-Na & Cheng, Hong-Zhan, 2022. Review of prediction and control for surface settlement caused by shield tunneling based on machine learning. *Journal of Huazhong University of Science and Technology (Natural Science Edition)* 50, 56–65. (in Chinese)

Goh, A. T. C. & Zhang, Wengang & Zhang, Yanmei & Xiao, Yang & Xiang, Yuzhou, 2018. Determination of earth pressure balance tunnel-related maximum surface settlement: a multivariate adaptive regression splines approach. *Bulletin of Engineering Geology and the Environment* 77, 489–500.

Kasper, Thomas & Meschke, Günther, 2004. A 3D finite element simulation model for TBM tunnelling in soft ground. *International Journal for Numerical and Analytical Methods in Geomechanics* 28, 1441–1460.

Kohestani, V. R. & Bazarganlari, M. R. & Marnani, J. Asgari, 2017. Prediction of maximum surface settlement caused by earth pressure balance shield tunneling using random forest. *Journal of AI and data mining* 5, 127–135.

Li, Zhong-Chao & Chen, Ren-Peng & Meng, Fan-Yan & Ye, Jun-Neng, 2015. Tunnel boring machine tunneling-induced ground settlements in soft clay and influence of excavation parameters. *Journal of Zhejiang University (Engineering Science)* 49, 1268–1275. (in Chinese)

Meng, Fan-Yan & Chen, Ren-Peng & Kang, Xin, 2018. Effects of tunneling-induced soil disturbance on the post-construction settlement in structured soft soils. *Tunnelling and Underground Space Technology* 80, 53–63.

Peck, Ralph B., 1969. Deep excavations and tunneling in soft ground. *Proc of the 7th International Conference on Soil Mechanics and Foundation Engineering.*, *1969*, Mexico City, 225–290.

Pourtaghi, A. & Lotfollahi-Yaghin, M. A., 2012. Wavenet ability assessment in comparison to ANN for predicting the maximum surface settlement caused by tunneling. *Tunnelling and Underground Space Technology* 28, 257–271.

Sagaseta, C., 1987. Analysis of undrained soil deformation due to ground loss. *Geotechnique* 37, 301–320.

Suwansawat, Suchatvee & Einstein, Herbert H., 2006. Artificial neural networks for predicting the maximum surface settlement caused by EPB shield tunneling. *Tunnelling and Underground Space Technology* 21, 133–150.

Verruijt, A. & Booker, J. R., 1998. Surface settlements due to deformation of a tunnel in an elastic half plane. *Geotechnique* 48, 709–713.

Wang, Ruo-Han & Li, Dian-Qing & Chen, Elton J. & Liu, Yong, 2021. Dynamic prediction of mechanized shield tunneling performance. *Automation in Construction* 132, 103958.

Zhang, Kun & Lyu, Hai-Min & Shen, Shui-Long & Zhou, Annan & Yin, Zhen-Yu, 2020a. Evolutionary hybrid neural network approach to predict shield tunneling-induced ground settlements. *Tunnelling and Underground Space Technology* 106, 103594.

Zhang, Ning & Zhou, Annan & Pan, Yutao & Shen, Shui-Long, 2021. Measurement and prediction of tunnelling-induced ground settlement in karst region by using expanding deep learning method. *Measurement* 183, 109700.

Zhang, Pin & Chen, Ren-Peng & Wu, Huai-Na, 2019. Real-time analysis and regulation of EPB shield steering using Random Forest. *Automation in Construction* 106, 102860.

Zhang, Pin & Wu, Huai-Na & Chen, Ren-Peng & Chan, Tommy H. T., 2020b. Hybrid meta-heuristic and machine learning algorithms for tunneling-induced settlement prediction: A comparative study. *Tunnelling and Underground Space Technology* 99, 103383.

Zhang, Pin & Wu, Huai-Na & Chen, Ren-Peng & Dai, Tian & Meng, Fan-Yan & Wang, Hong-Bo, 2020c. A critical evaluation of machine learning and deep learning in shield-ground interaction prediction. *Tunnelling and Underground Space Technology* 106, 103593.

Smart Geotechnics for Smart Societies – Zhussupbekov, Sarsembayeva & Kaliakin (Eds)
© 2023 The Author(s), ISBN 978-1-003-29912-7
Open Access: www.taylorfrancis.com, CC BY-NC-ND 4.0 license

Discrete element analysis on failure of composite rock induced by tunnel excavation

Z. Li
School of Civil Engineering, Tianjin University, Tianjin, China

M.J. Jiang
School of Civil Engineering, Suzhou University of Science and Technology, Suzhou, China
College of Civil Engineering, Tongji University, Shanghai, China
School of Civil Engineering, Tianjin University, Tianjin, China

H.N. Wang
School of Aerospace Environment and Applied Mechanics, Tongji University, Shanghai, China

Y.B. Liao
School of Environment and Architecture, University of Shanghai for Science and Technology, Shanghai, China

ABSTRACT: Composite rock stratum is commonly encountered during tunnel excavation, where the structural planes can easily cause large squeezing deformation, rock burst and other major disasters. Therefore, in order to reduce the risk of tunnel excavation, the discrete element method (DEM) with a new size-dependent contact model is employed to simulate the failure process of composite rock induced by tunnel excavation. Seven inclinations of structural plane are considered. The bond breakage, distribution of maximum principal stress, area ratio of surrounding rock disturbance area, and bond breakage ratio are analyzed. The results show that the bond breakage ratio decreases with the increase of inclination of the soft-hard interbedded rock structural planes. When the angle of the soft-hard interbedded rock structural plane is 0°, the tunnel excavation is found of the most risk.

1 INTRODUCTION

In response to the development needs, a series of long tunnels such as transportation and water conservancy are being constructed or are intended to be constructed in China. In these projects, it is inevitable to encounter the tunnel construction in composite rock mass. The structural planes in rock mass can easily cause disasters such as cutter ring crack, eccentric wear of cutters, TBM jamming and rock bust. Through discrete element simulation, Gong et al.(Gong et al., 2005, Gong et al., 2006a, Gong et al., 2006b) found that structural plane inclination has significant influences on cracking and propagation of fractures, and then on rock breaking mode of TBM. In the past few decades, many studies have been carried out on the influence of structural plane inclination on tunnel excavation.

As for experiments, Park and Adachi (Park et al., 2017) analyzed the distribution of pressure under different inclinations of structural plane. Zheng et al.(Zheng et al., 2019) and Han et al.(Han et al., 2018) studied the mechanical properties of rock mass under various inclinations of structural planes through uniaxial and triaxial compression tests. Sagong et al. (Sagong et al., 2011) simulated and studied the crack development mode and deformation mode under various joint inclinations. Although the laboratory tests can obtain the more

DOI: 10.1201/9781003299127-127

realistic responses of the rock during the tunnel excavation, only macroscopic failure can be achieved, meanwhile, it costs a lot.

The discrete element method (DEM), proposed by Cundall(Cundall and Strack, 1979) in 1971, can reproduce the failure process of materials and has been widely used in various aspects of geotechnical engineering. Wang et al.(Wang et al., 2017) used the jointed rock mass in laboratory tests and PFC2D to analyze the crack development and deformation modes around tunnel under the influence of joint inclinations. Jiang et al.(Jiang et al., 2009) used EDEM to study the impacts of different joint inclinations and joint spacing on tunnel excavation. Geng(Geng, 2015) used discrete element software UDEC^{2D} to study the stress redistribution and the rock deformation after tunnel excavation considering the following three factors, i.e., bedding with different inclinations, faults with different inclinations and different lateral pressure coefficient.

At present, the development of three-dimensional (3D) discrete elements is relatively mature, and the simulation results are more close to the actual situation. However, a large number of particles have to be created when studying boundary value problems such as tunnel excavation using 3D discrete elements. Based on the above studies and computational efficiency of the computer, in this study, we established a two-dimensional tunnel excavation DEM model implanted with a new size-dependent contact model(Jiang et al., 2005, Jiang et al., 2006). From the macro and micro perspective, the stability of surrounding rock of a tunnel excavated in deep composite strata with different inclinations of structural planes is explored, which provides a theoretical basis for reducing the damage risk of tunnel excavation in composite strata.

2 MICROSCOPIC CONTACT MODEL OF ROCK

2.1 *Mechanical response*

In general, according to the microstructure characteristic of a specific rock, thick bond or zero-thickness bond are adopted in DEM simulation. The mechanical response of cemented contact model is shown in the Zhang(Zhang, 2014). Figure 1 shows the bond and its failure state during the discrete element simulation. In the discrete element simulation, bond breakage means that the bond no longer bears any stress, that is, the calculation of the contact force is no longer takes into account the stress borne by the bond.

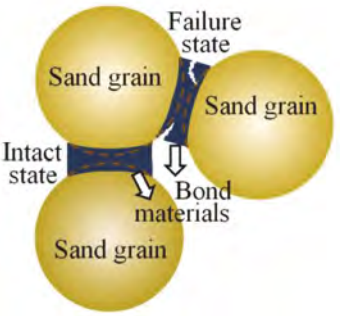

Figure 1. Bond state in discrete element simulation.

2.2 *Parameter calibration*

This paper takes the composite rock mass composed of granite (Martin, 1993) and limestone (Ciantia et al., 2015, Nova and Parma, 2011) as object. The micromechanical parameters of the two rocks are shown in Table 1.

Table 1. Microscopic parameters of rock samples.

Type	Microscopic parameters	Granite	Calcarenite
Particle part	Particle density ρ (kg/m^3)	2700	2700
	Particle normal stiffness k_n (N/m)	6.5×10^{10}	9.0×10^{8}
	Particle shear stiffness k_s (N/m)	4.33×10^{10}	3.6×10^{8}
	Particle friction coefficient μ	1.0	0.7
	Particle anti-rotation coefficient β	1.5	0.6
Bond part	Maximum bond thickness h_{max} (m)	1.30×10^{-4}	1.30×10^{-4}
	Bond tensile strength σ_t (Pa)	1.00×10^{9}	2.18×10^{7}
	Bond compression strength σ_c (Pa)	3.00×10^{10}	2.30×10^{8}
	Bond elastic modulus E_b (N)	3.75×10^{9}	1.10×10^{7}
	Bond elongation rate sp	0.15	0.15

3 DISCRETE ELEMENT SIMULATION OF TUNNEL EXCAVATION

This simulation is built on the deep-buried tunnel of Jinping secondary hydropower station (Zhang et al., 2010).The influence of the support structure is not considered. Discrete element simulation is mainly divided into 5 steps:

(1) Specimen preparation. In order to prepare uniform samples efficiently, the Layered Under Compaction Method proposed by Jiang et al.(Jiang et al., 2003) was adopted. The gradation curve is shown in Figure 2(a). The sample with 300 000 particles were prepared in eight layers, where 37 500 particles are in each layer, and the final void ratio was 0.2.
(2) Preload. Keep the left and right walls unmoved, through the servo mechanism of the upper and lower walls, the sample is consolidated and stabilized under the vertical pressure of 38.02 MPa to simulate the deep burial position of the rock sample.
(3) Add bond. Give the calibrated microscopic parameters of granite and limestone to the sample until equilibrium to simulate the real composite rock mass.
(4) Apply horizontal pressure. According to the actual in-situ stresses, the horizontal pressure of 30 MPa is applied to the rock sample until the sample reaches the equilibrium state, and the displacement and velocity of the particles are cleared.
(5) Tunnel excavation. Based on the principle of centrifuge test, a 200 g gravity field is applied before the excavation of the tunnel to simulate the real size of the tunnel 200 times larger than the discrete element sample, as shown in Figure 2(b). The tunnel with a radius of 0.035 m is excavated in the center of the sample. What needs illustration is that the green part represents soft rock and the blue part represents hard rock in Figure 2(b).
(6) Tunnel stability. Set local and global measuring circles to monitor macro and micro information, which is shown in Figure 3. When the number of bond breakage does not increase, the tunnel is balanced and the calculation is ended.

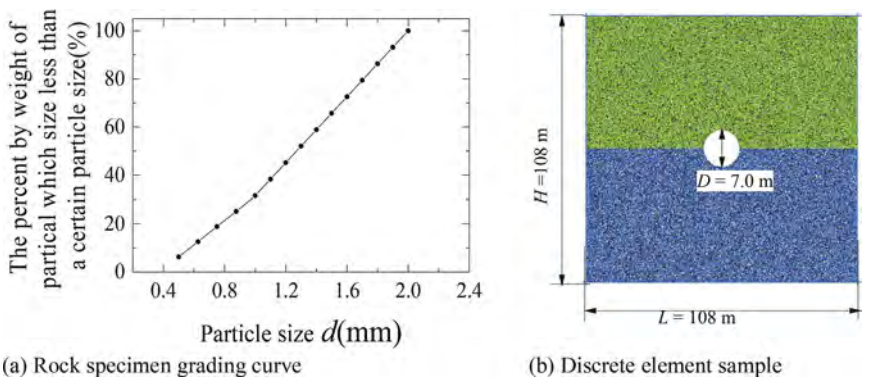

(a) Rock specimen grading curve (b) Discrete element sample

Figure 2. Rock specimen grading curve and discrete element sample.

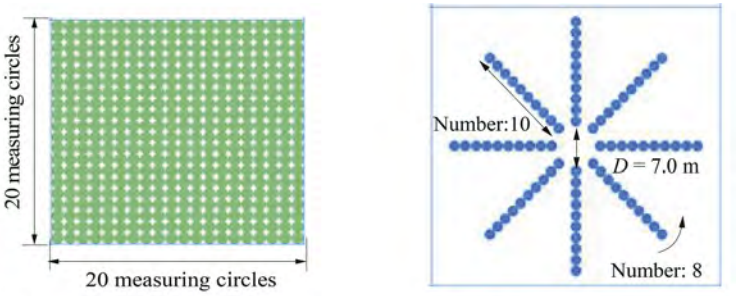

(a) Distribution of global measuring circles (b) Distribution of local measuring circles

Figure 3. Positions of measuring circles in DEM specimen.

4 RESULTS AND ANALYSIS

In order to study the influence of structural plane inclination on the stability of tunnel excavation, the failure mechanism of tunnel excavation is analyzed by discrete element method under seven inclinations (0°, 15°, 30°, 45°, 60°, 75°, and 90°) of structural plane.

4.1 *Bond breakage*

Figure 4 shows the bond breakage number versus time caused by tunnel excavation under different structural plane inclinations. Limited to the space, This paper takes 30°, 45°, 60° and 90° as examples. It should be noted that the initial number of bond is approximately 1,000,000. When the inclination of the structural surface is larger than 45°, the number of tensile-shear bond breakage is more than that of compression-shear bond breakage. Based on the order of bond breakage number, strong and weak failure are classified. Strong failure occurs when the inclinations of soft-hard interbedded rock structural plane are 30° and 45°. In these cases, the number of bond breakage is over 10,000 and reaches the peak at a very slow speed. Weak failure occurs when the inclinations of soft-hard interbedded rock structural plane are 60° and 75°, and the number of bond breakage is less than 2000, and quickly reaches the peak value and becomes stable. The type of bond breakage is mainly the tensile-shear failure.

Through the above analysis, it can be observed that with the decrease of the inclinations of the structural plane, the bond breakage number increases, and the required time that achieves the failure stability is longer.

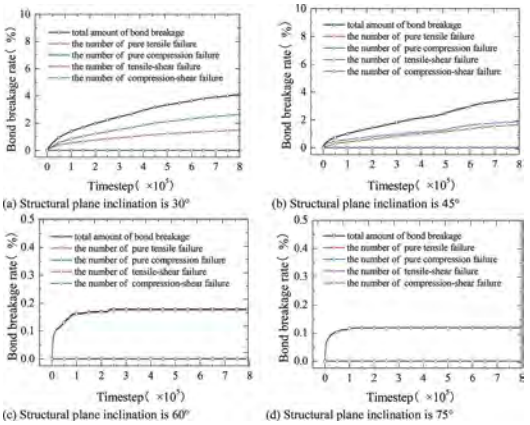

Figure 4. The relationship between the number of bond breakage and time step under different inclinations of the structural plane.

4.2 *Maximum principal stress*

Figures 5 and 6 shows the circumferential and radial distribution of maximum principal stress caused by tunnel excavation under different structural plane inclinations. Limited to the space, This paper takes 30°, and 60° as examples. In Figures 5(a) and 6(a), the longitudinal coordinate represents the magnitude of the maximum principal stress, and the polar coordinate represents the direction of the maximum principal stress. When the inclination of the structural plane is 30°, the circumferential direction of 150° to 330° is the area of hard rock, and when the inclination of the structural plane is 60°, the circumferential direction of 120° to 300° is the area of soft rock. The distribution of the maximum principal stress along the circumferential direction is teardrop-shaped and its cone tip is directly related to structural plane, mainly because the direction of maximum principal stress mainly exists in hard rock. From the radial distribution, the maximum principal stress increases with the distance to the tunnel center when the inclinations of structural plane is 30°. The main reason is the unloading effect of tunnel excavation(Jiang and Yin, 2012). For the structural plane inclinations of 60°, the maximum principal stress at 180° and 225° decreases gradually with the increase of the distance to the tunnel center, and the maximum principal stress at other angles increases gradually with the increase of the distance to the tunnel center.

Through the above analysis, it can be observed that the inclination of structural plane influences the failure form of rock by influencing the location of the maximum principal stress.

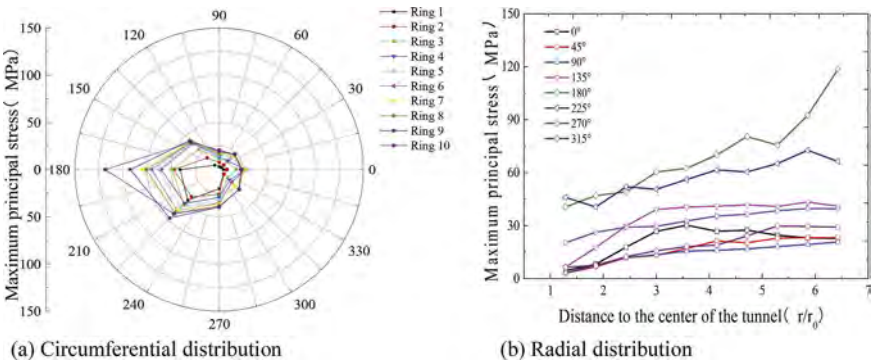

Figure 5. Distribution of maximum principal stress when structural plane inclination is 30°.

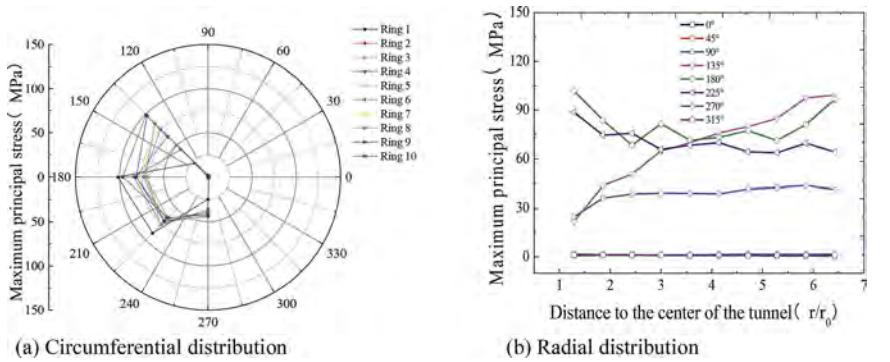

Figure 6. Distribution of maximum principal stress when structural plane inclination is 60°.

4.3 *Bond breakage ratio and area ratio of surrounding rock disturbance area*

Figure 7 shows the bond breakage ratio and the area ratio of surrounding rock disturbance area caused by tunnel excavation under different inclinations of the structural plane. The

larger the bond breakage ratio is, the more serious the micro-damage of surrounding rock. The larger the area ratio of surrounding rock disturbance area is, the more likely the large squeezing deformation occurs. With the increase of inclinations of soft-hard interbedded rock structural planes, microscopic bond breakage ratio decreases. This is mainly because different inclinations of structural planes represent different pressure perpendicular to structural plane. Due to the vertical pressure on the tunnel is larger than horizontal pressure, when the surrounding rock is soft on the top and hard on the bottom, the pressure perpendicular to structural plane is larger than that of the surrounding rock is soft on the right and hard on the left.

As can be seen from the Figure 7, when the inclination of structural plane is 0°, the micro bond breakage ratio is largest, and the area ratio of surrounding rock disturbance area is also large. At this time, the damage inside the tunnel is the most serious, that is, the tunnel excavation is found of the most risk.

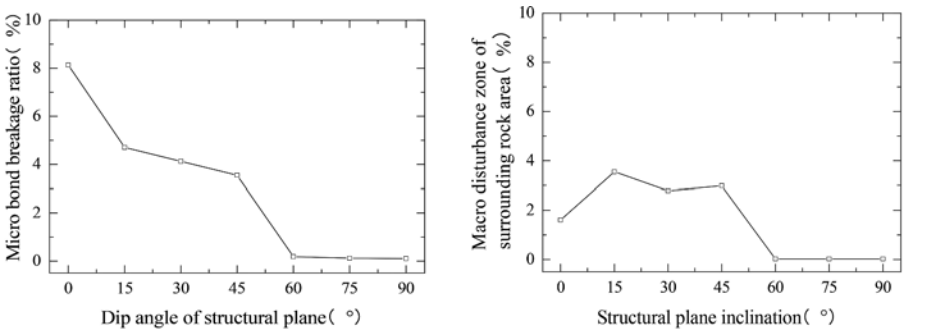

(a) Micro bond breakage ratio (b) Area ratio of surrounding rock disturbance area

Figure 7. Micro bond breakage ratio and area ratio of surrounding rock disturbance area under different inclinations of structural plane.

5 CONCLUSIONS

In this paper, the failure of composite rock induced by tunnel excavation is analyzed by DEM implanted with size-dependent contact model. Various inclinations of soft-hard rock structural plane are considered. The following conclusions are obtained:

(1) The bond breakage ratio decreases with the increase of the inclination of the soft-hard rock structural planes. When the inclinations of the soft-hard interbedded rock structural plane is 0°, the tunnel excavation is found of the most risk.
(2) The distribution of the maximum principal stress along the circumferential direction is teardrop-shaped and its cone tip is directly related to structural plane. From the radial distribution, the maximum principal stress increases with the distance to the tunnel center when the inclinations of structural plane are small. When the inclination of the structural plane is large, the maximum principal stress at 180° and 225° decreases with the increase of the distance from the center of the tunnel, while the other angles are opposite.
(3) When the inclination of the structural surface is smaller than 45°, the bond breakage number is over 10,000 and reaches the peak at a very slow speed, while when the inclination is larger than 45°, the bond breakage number is less than 2,000, and the bond breakages happened mainly due to tensile shear.

ACKNOWLEDGMENTS

The authors gratefully acknowledge the research funding from National Nature Science Foundation of China with grant No. 51890911.

REFERENCES

Ciantia, M.O., Castellanza, R. & Di Prisco, C. 2015. Experimental study on the water-induced weakening of calcarenites. *Rock Mechanics and Rock Engineering* 48(2): 441–461.

Cundall, P.A. & Strack, O.D.L. 1979. A discrete numerical model for granular assemblies. *Geotechnique* 29(1): 47–65.

Geng, X.Y. 2015. Analysis of secondary stress distribution and deformation characteristics of surrounding rock during excavation of cavern with faulted layered strata. *Tongji University*.

Gong, Q.M., Zhao, J., Jiao, Y.Y. 2005. Numerical modeling of the effects of joint orientation on rock fragmentation by TBM cutters. *Tunnelling and Underground Space Technology* 20(2): 183–191.

Gong, Q.M., Zhao, J. & Hefny, A.M. 2006a. Numerical simulation of rock fragmentation process induced by two TBM cutters and cutter spacing optimization. *Tunnelling and Underground Space Technology* 21(3-4).

Gong, Q., Jiao, Y.Y. & Zhao, J. 2006b. Numerical modelling of the effects of joint spacing on rock fragmentation by TBM cutters. *Tunnelling and Underground Space Technology* 21(1): 46–55.

Han, G.S., Jing, H.W., Jiang, Y.J., Liu, R.C., Su, H.J. & Wu, J.Y. 2018. The effect of joint inclinations on the mechanical behavior of infilled jointed rock masses under uniaxial and biaxial compressions. *Processes* 6(5): 49.

Jiang, M.J., Konrad, J.M. & Leroueil, S. 2003. An efficient technique for generating homogeneous specimens for DEM studies. *Computers and geotechnics* 30(7): 579–597.

Jiang, M.J., Yu, H.S. & Harris, D. 2005. A novel discrete model for granular material incorporating rolling resistance. *Computers and Geotechnics* 32(5): 340–357.

Jiang, M.J., Yu, H.S. & Harris, D. 2006. Bond rolling resistance and its effect on yielding of bonded granulates by DEM analyses. *International Journal for Numerical and Analytical Methods in Geomechanics* 30(8): 723–761.

Jiang, M.J. & Yin Z.Y. 2012. Analysis of stress redistribution in soil and earth pressure on tunnel lining using the discrete element method. *Tunnelling and Underground Space Technology* 32: 251–259.

Jiang, Y.J., Li, B. & Yamashita, Y. J. 2009. Simulation of cracking near a large underground cavern in a discontinuous rock mass using the expanded distinct element method. *International Journal of Rock Mechanics and Mining Sciences* 46(1): 97–106.

Martin, C.D. 1993. The strength of massive Lac du Bonnet granite around underground openings. *University of Manitoba*.

Nova, R. & Parma, M. 2011. Effects of bond crushing on the settlements of shallow foundations on soft rocks. *Géotechnique* 61(3): 247–261.

Park, S.H., Adachi, T., Kimura, M., Kishida, K. & Kikumoto, M. 2017. Experimental study on tunneling in the ground with inclined layers and its simulation. *Modern tunneling science and technology*.

Sagong, M., Park, D., Yoo, J. & LEE, J.S. 2011. Experimental and numerical analyses of an opening in a jointed rock mass under biaxial compression. *International Journal of Rock Mechanics and Mining Sciences* 48(7): 1055–1067.

Wang, X.S., Jiang, Y.J. & LI, B. 2017. Experimental and numerical study on crack propagation and deformation around underground opening in jointed rock masses. *Geosciences Journal* 21(20): 291–304.

Zhang, C.S., Chen, X.R., Hou, J. & Chu, W. J. 2010. Study of mechanical behavior of deep-buried marble at Jinping II hydropower station. *Chinese Journal of Rock Mechanics and Engineering* 29(10): 1999–2009.

Zhang, N. 2014. The microscopic mechanism of petrochemical weathering and the discrete element analysis of rock slope stability.

Zheng, Q.S., Liu, E.L. & Liu, M.X. 2019. Influence of inclinations of structural planes on mechanical properties of artificial rock samples under triaxial test conditions. *Rock and Soil Mechanics* 40: 1854.

Smart Geotechnics for Smart Societies – Zhussupbekov, Sarsembayeva & Kaliakin (Eds)
© 2023 The Author(s), ISBN 978-1-003-29912-7
Open Access: www.taylorfrancis.com, CC BY-NC-ND 4.0 license

Pilot project: Applying the tunnel-in-tunnel method on DB electrified routes

Dietmar Mähner
Institute for Underground Construction, FH Münster, Germany

Bodo Tauch
DB Netz AG, Frankfurt a. M., Germany

ABSTRACT: This report deals with the refurbishing of the Petersberg Tunnel. In this connection, for the first time within the scope of a pilot project, the tunnel-in-tunnel method was applied on an electrified line belonging to the DB. The tunnel cross-section was enlarged within the scope of the excavation. These activities were executed with the aid of a tunnel enlargement system (TES). Towards this end, the existing overhead line for electrification of the route had to be integrated in the excavation. Once the driving operations had been completed, the tunnel inner shell made of reinforced concrete was produced. Thanks to this project the spectrum of refurbishing tunnels has been considerably expanded, as the method can be deployed for other projects on the electrified route network.

1 DEPLOYING THE TUNNEL-IN-TUNNEL METHOD FOR DEUTSCHE BAHN

The tunnel-in-tunnel method has already been successfully tried out and further developed on several non-electrified routes in regional transportation. In this method, the tunnel cross-section is expanded by drill+blast or cutting tools with trains services still operating and a new reinforced concrete inner shell installed according to the valid requirements of the code of practice.

When construction starts, the track is relocated to the centre of the tunnel and services run in alternating directions for the duration of the scheme. Once refurbishing is over, the tunnel is once again provided with two running tracks. However, work on the track at the start and end of the tunnel enlargement scheme is undertaken during a scheduled complete closure phase; the route is kept open for traffic throughout the entire residual construction period.

Traffic must only be occasionally rerouted if at all. The tunnel-in-tunnel method has now been deployed on an electrified route for the first time to refurbish the Petersberg Tunnel (Figure 1).

2 PROJECT PRESENTATION

2.1 *Koblenz–perl rail route*

The Petersberg Tunnel lies near Bullay on the twin-track line from Koblenz to Perl, catering for mainline and commuter traffic. The route is of great significance for passenger transportation, linking Koblenz and Trier. It is also a vital artery for goods traffic as the most important link in the direction of Luxembourg.

As a result, it rates very highly on the DB's route network. The DB Netz AG's long-term objective is to maintain the Koblenz–Perl rail line as an integral part of the Trans-European Network (TEN). Thus, enhancing the safety level as well as maintaining the route for goods and passenger traffic is of great public interest.

DOI: 10.1201/9781003299127-128

Figure 1. The Petersberg rail tunnel will be refurbished by late 2019 by the tunnel-in tunnel method while rail services continue.

2.2 *Petersberg tunnel*

The Petersberg Tunnel is 368 m long and was completed in 1879. The existing masonry consists of slate and quarrystone some 0.85 m thick. The thickness is reduced to around 0.70 m at the portals. The tunnel masonry structure is designed with a mouth-shaped cross-section; the tunnel is drained at present.

The Petersberg Tunnel is located in the vicinity of the Moselle syncline, part of the Rhenish Uplands. The area consists of a thick geological sequence of sandstones, siltstones and mudstones. The rocks are in part intensively fissured and contain numerous faults due to the impact of tectonic activity. The maximum overburden height is to be found roughly at the tunnel centre and amounts to ca. 95 m.

The existing masonry of the tunnel has been redeveloped and improved on many occasions in the course of recent decades. During past maintenance operations, the masonry was provided with an extensive thin shotcrete shell. Prior to refurbishment, among other things, broken masonry, loose joints, spalling and cracks in the shotcrete as well as various moist patches were documented. Within the scope of regular controls, it became evident that the quality of the structure was deteriorating, which could not be rectified economically.

Furthermore, the Deutsche Bahn's valid code of practice calls for the track centre distance to be increased from its present 3.50 to 4.00 m. In addition, prior to renovation, there were merely individual emergency bays available rather than continuous escapeways. The task of refurbishing the Petersberg Tunnel was carried out in conjunction with maintaining train services as far as possible even while enlarging the tunnel cross-section and installing a new tunnel inner shell. Minor interruptions were only permissible for blasting operations during the enlargement phase and for lifting and lowering structural parts above the overhead line.

For this reason, the tunnel was enlarged by applying the tunnel-in-tunnel method. Construction activities began in 2017. The actual tunnel drive commenced in January 2018 and wound up in October of the same year.

3 THE TUNNEL ENLARGEMENT SYSTEM (TES)

3.1 *Concept*

Throughout the application of the Tunnel Enlargement System (TES) during construction operations, the running track was provided with a continuous protective housing. This was to ensure safe electrified train services and at the same time, separate rail traffic from ongoing

construction. Within this protective housing, a conductor rail is installed in the roof to carry the overhead line. The overbreak for the additional housing is largely compensated for by deploying the conductor rail and the related low installation height of the overhead line system. The TES is a steel structure and runs within two guide rails, which are installed on the strip foundation, supporting itself above the protective housing (Figure 2).

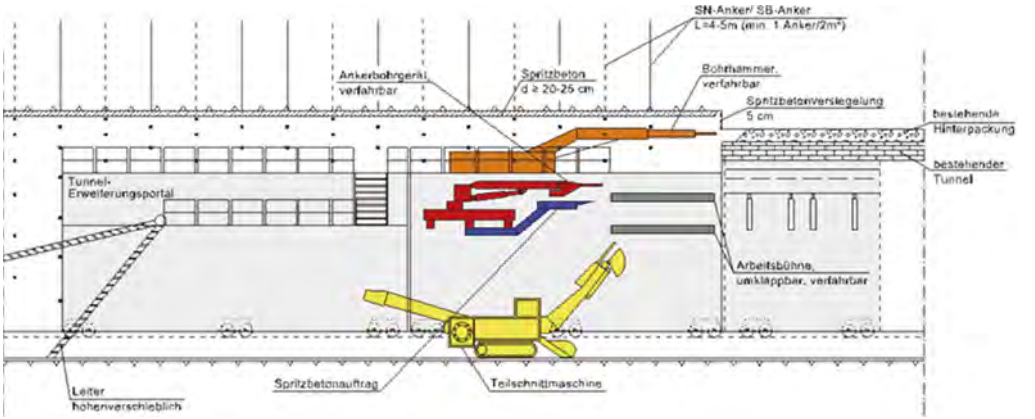

Figure 2. Longitudinal section of the tunnel enlargement system (TES).

The TES possesses an additional vault protective device that can be raised by hydraulic means. By deploying this structure, the objective is to prevent the masonry of the existing tunnel from loosening. For other projects a bolting system was installed in the existing tunnel to secure it in advance. However, this entails a considerable amount of extra work, something that was avoided by introducing the hydraulically raised vault protection device for the Petersberg Tunnel. The TES had to be devised in such a way that it was possible to excavate using a drill hammer at the roof.

Two roadheaders, which move along the tunnel base at abutment height, tackle the side walls (Figures 3–5). The support arches and mats can be installed by means of mobile, foldable work platforms. Two shotcrete manipulators and drilling rigs located at the sides of the TES place the shotcrete and create the drill holes for the anchoring system and the spiles. It must be observed here that the possibility of anchoring involving larger anchor diameters had to be taken into consideration when designing the anchor drilling rigs with regard to their effective capacity during the tendering stage.

The excavated material was removed by special dumpers behind the roadheaders, which must operate in very constricted conditions. The protective housing as well as the TES is set up on strip foundations, running in the longitudinal direction of the tunnel. These strip foundations must be capable of transferring the weight of the TES (approx. 225 t) and the housing safely into the subsurface.

Owing to the local circumstances in the Petersberg Tunnel, driving was carried out by excavators and blasting (Figures 6 - 7). This meant that the TES had to sustain all effects from drilling and blasting. Towards this end, the auxiliary foundations had also to be dimensioned accordingly. Figure 8 shows schematically how the TES was impacted by the effects of blasting. Owing to the high horizontal loads (blasting pressure on the TES) the foundations had to be back-anchored using pretensioned GEWI bars.

The work needed to accomplish this task took some considerable time, leading to the construction cycle being interfered with. Alternative concepts for sustaining this horizontal load should thus be scrutinised properly in advance and resolved.

Figure 3–5. Mobile TES installed on fixed housing.

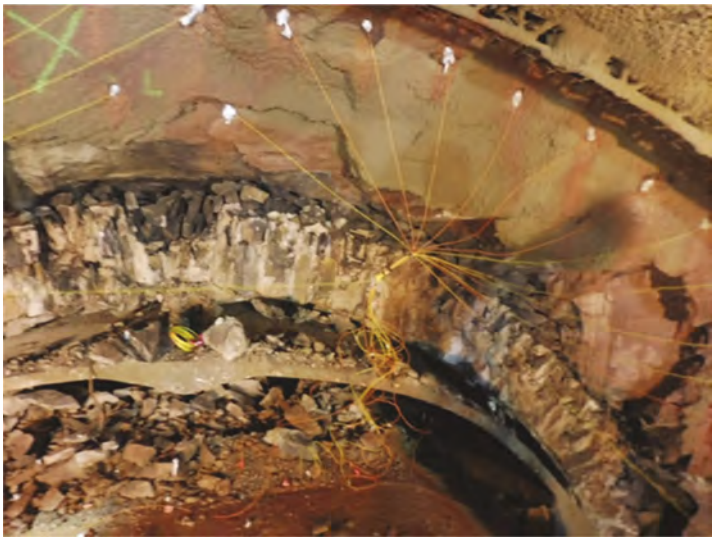

Figure 6. Excavation with drill hammer.

Figure 7. Drill+blast exavation.

3.2 *Construction phases*

Prior to the construction scheme, the route leading through the Petersberg Tunnel ran on two tracks. Within the scope of a four-week long closure of the route in May 2017, first of all the overhead line, the rails and the superstructure in the tunnel were removed. This was followed by the installation of the auxiliary foundations for the TES as well as the protective housing. In addition, the rail bed was produced with a track at its centre in order to enable rail traffic to pass through the tunnel in alternating operation during the entire construction phase.

The protective housing was set up at the end of the shutdown. In August 2017, the TES was hoisted from the construction site installation yard next to the tunnel portal on to the auxiliary foundations during an additional night-time shutdown. In February 2018, driving operations began from the south portal. Towards this end, the tunnel was extended upwards by some 2.5 m (roof) and by roughly 3 m at the side (abutment zone) protected by the TES and subsequently secured with shotcrete (20–30 cm), anchors, support arches and matting.

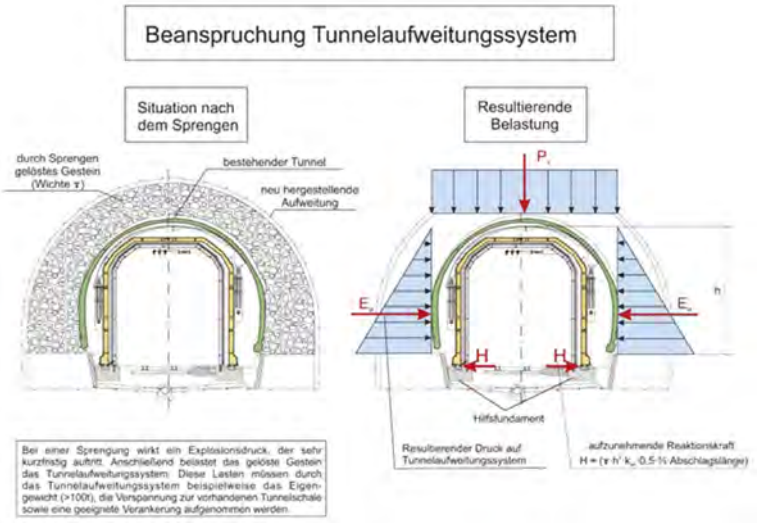

Figure 8. TES impacted by blasting: During blasting explosion pressure acts, which only lasts briefly. Subsequently, the loosened rock impacts the Tunnel Expansion System. These loads must be sustained by the TES, e.g. the dead weight (> 100 t), the bracing against the existing tunnel shell as well as by appropriate anchoring.

The lengths of advance varied between 0.75 and 1.75 m. The excavation over a distance of 330 m was concluded in October 2018. After the TES had been retrieved, the base was prepared for the foundations. Subsequently, the strip foundations were created as from January 2019.

After setting up and positioning the reinforcement carriage, the formwork carriage and three curing carriages, work on the vault blocks started from north to south. Within the framework of a four-week long total closure as from November 2019, among other things, the protective housing will be removed and the auxiliary foundations dismantled prior to producing the rail ballast with two tracks. During the same period, the rail engineering, installation of the drainage pipes and the overhead line will take place. After the shutdown, the tunnel will once again be ready for two-track operation. Figure 9 shows the described construction phases.

4 EXCAVATION CLASSES

The tunnel enlargement has been undertaken commensurate with the principles of the shotcrete method. During planning, a total of six excavation classes (EC = VKL) were devised. Installation of the supporting agents essentially had to be carried out from the TES. This actually meant that the placing of shotcrete, drilling of anchors and spiles as well as the installation of matting and support arches in the entire excavation area had to be accomplished from the TES.

The length of advance in the six excavation classes varied between 1.75 m (VKL 4A1) and 1.00 m (VKL 6A4). The thickness of the shotcrete ranged from 20–30 cm depending on the prevailing rock stresses. Q188 and Q257 mats were used to reinforce the shotcrete shell. These were always installed facing towards the rock and at the airside. During the excavation, spiles were used at certain places as advance supports; they are some 3–5 m long and possess a diameter of 32 mm. The spiles were set up at ≤ 25 cm gaps. The working face was sealed at certain points with 3–5 cm thick supportive layers of shotcrete. Face anchors were also placed in definitive fault zones. SN bolts or self-drilling anchors (anchor length 4–5 m, supporting force ≥ 245 kN, anchor pattern: one anchor every 2 or 3 m²) were deployed for securing the shotcrete shell.

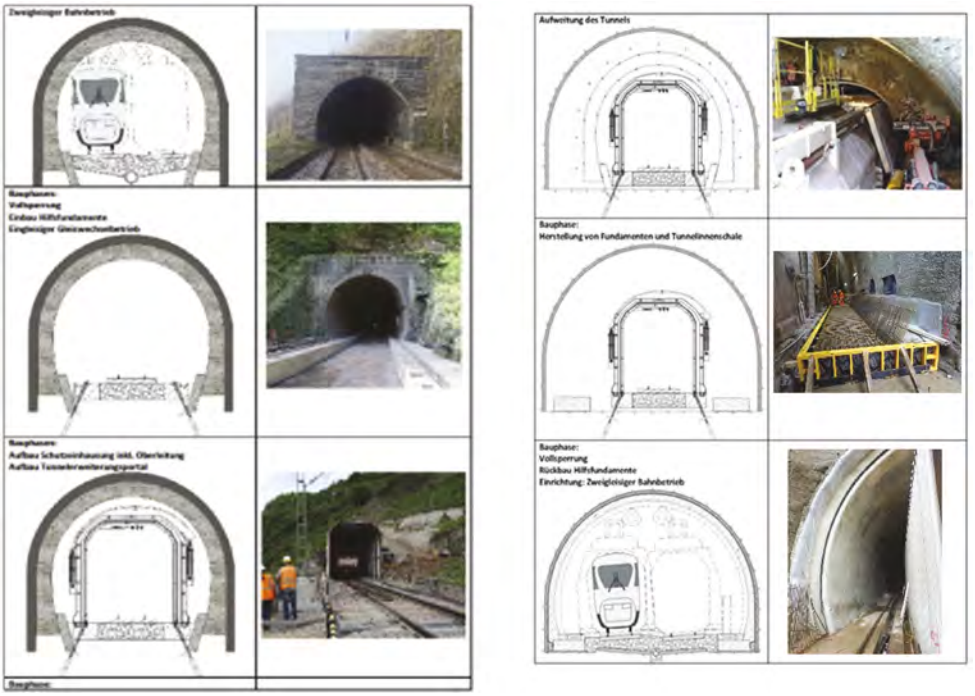

Figure 9. Individual construction phases during the application of the tunnel-in-tunnel method.

Self-drilling anchors up to 10 m in length were foreseen for back-anchoring to minimise the growth of deformations. The support arches were devised as 3-bar lattice girders. The driving concept initially foresaw the vault (height of excavation up to approx. 8.56 m) being tunnelled in advance. Subsequently the abutment (height of excavation approx. 1.00 m) was tackled once the intervening gap was sufficient (> 10 m). The length of advance for the abutment amounted to twice the length for the vault.

Once the first reference values had been accrued for this type of excavation, the method was optimised to such an extent that the vault could be tunnelled at the same time as the abutment without the need for a staggered approach. The support arches were extended to the base of the abutment so that the loads imposed by the rock could be transferred immediately (Figures 10 - 11). The loads imposed by the rock were monitored metrologically.

A daily measurement at up to five points per measuring cross-section was undertaken in the immediate working face area. On account of the low rate of advance, the measuring interval was increased as from roughly 30 m behind the working face. The maximum distances of the measuring cross-sections at the portal zones were restricted to 5 m in each case; in the tunnel, the gap amounted to ≤ 10 m. The outer shell was calculated and dimensioned in keeping with the finite element method. The deformations for the shotcrete shell determined accordingly were listed as permissible displacement values for the individual excavation classes.

In this connection, a warning value (2/3rds of the permissible value) was defined. It was agreed that if this warning value was reached, all involved parties were to be informed for a joint appraisal of the situation and to decide on how to proceed. It was observed that the deformations of the shotcrete shell determined in the FEM calculation were never actually attained during tunnelling. It should be noted here that for the calculation, a pre-reduction factor of the working face, i.e. a reduction of the E-module was applied. This pre-reduction value was set at 0.6.

Two main reasons are provided for the reduction. Firstly, the tunnel was initially completed back in the late 1870s. At the time, a massive masonry shell backfilled in the roof and wall areas served as the supporting structure. It seems probable that while building the tunnel, redistribution of the rock in conjunction with the formation of a protective zone around the tunnel cross-section took place.

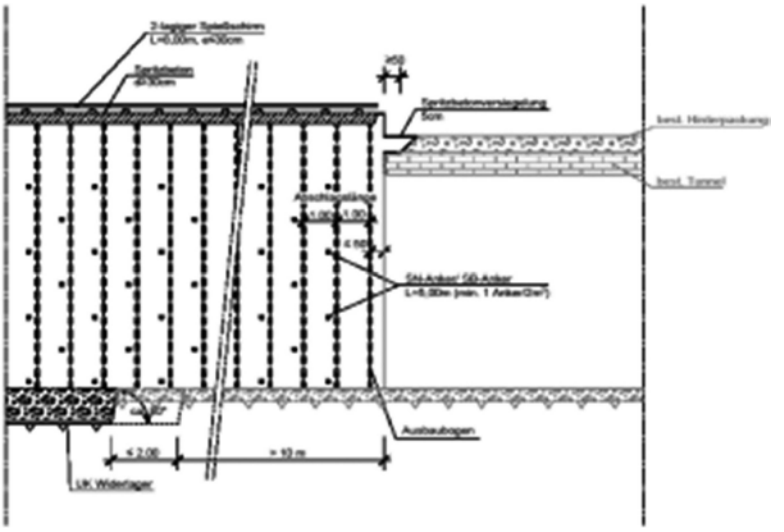

Figure 10. Excavation class 6A4 (staggered excavation of vault and abutment.

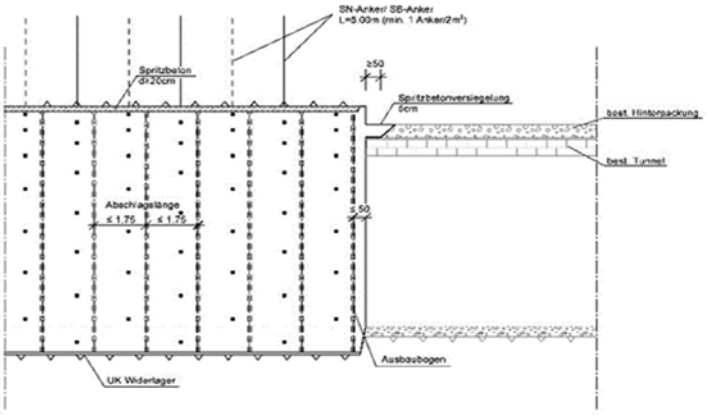

Figure 11. Excavation class 4A1 (simultaneous excavation of vault and abutment).

The tunnel enlargement by up to 3 m probably failed to change this state of tension existing in the rock to any major extent. Secondly, the geotechnical characteristic values for the rock had been so conservatively set that the determined deformations were influenced accordingly.

5 TUNNEL INNER SHELL

Once tunnelling had been completed, the reinforced concrete abutment was produced from the north portal. Then the tunnel inner shell was concreted, also using reinforced concrete. The inner shell is 40 cm thick and is produced from watertight concrete.

The block joint comprises internal FMS 350 joint strips with central hose and steel lugs. The block length amounts to ≤ 10 m in each case. A sliding layer is placed between the inner shell and the outer one. The tunnel is provided with lateral wall drainage and a longitudinal drainage system beneath the floor. After finishing the tunnel inner shell, it has to be furnished.

Towards this end, the route must be closed completely for a four-week period so that the protective housing together with the overhead line can be removed and the auxiliary

foundations as well as the central temporary track can be dismantled prior to reinstalling the overhead line and the tracks including ballast for two-track train services.

6 OUTLOOK, DISCUSSION

The pilot project was successfully completed. The experience gained shows that the method described here can also be used successfully for future tunnel renewals. More tunnels will be renovated in Germany in the next few years. However, it also turned out that some details could be solved even better. Various further investigations are currently underway.

REFERENCES

[1] STUVA-Arbeitskreis „Tunnelsanierung“: Sachstandsbericht 2011, Bauverlag BV GmbH, 2011.
[2] West, T.: Erneuerung elektrifizierter Bahntunnel „über“Eisenbahnbetrieb, EI-Eisenbahningenieur, November 2011.
[3] STUVA-Arbeitskreis „Tunnelsanierung“: Tunnelerneuerung unter Betrieb, Forschung + Praxis“, Band 57, 2021.
[4] Maidl, B.: Handbuch des Tunnel- und Stollenbaus, Band 1+2, Verlag Glückauf, 2004.
[5] Müller L.: Der Felsbau, Dritter Band: Tunnelbau, Ferdinand Enke Verlag Stuttgart, 1978.

Smart Geotechnics for Smart Societies – Zhussupbekov, Sarsembayeva & Kaliakin (Eds)
© 2023 The Author(s), ISBN 978-1-003-29912-7
Open Access: www.taylorfrancis.com, CC BY-NC-ND 4.0 license

Influence of True Triaxial Unloading (TTU) strength on rockburst: An experimental study

D. Deshpande
Master Student, Department of Civil Engineering, IIT Delhi, New Delhi, India

P. Venkateswarlu
Research Scholar, Department of Civil Engineering, IIT Delhi, New Delhi, India

K.S. Rao
Emeritus Professor, Department of Civil Engineering, IIT Delhi, New Delhi, India

ABSTRACT: True Triaxial Unloading (TTU) strength has utmost importance to study the actual behavior of intact rocks upon excavation as compared to traditional triaxial tests. It can be used to understand the mechanisms behind spalling and rockburst in construction of underground structures. The objective of the article is to derive unloading strength envelopes of different kinds of Indian rocks by unloading the minor principal stress (σ3), keeping the intermediate stress (σ2) constant from triaxial loading condition till failure and its influence on rockburst potential using poly axial strength testing machine at Rock Laboratory IIT, Delhi. Three different kind of rocks i. e, Jalore granite (Igneous), Makrana marble (Metamorphic) and Jodhpur sandstone (Sedimentary) were selected and tested for their triaxial loading and unloading strength envelopes in the laboratory to study the behavior of rocks under poly axial confinements. This research shows that the area between the true triaxial loading and unloading strength envelopes depict the zone of confinement in which rockburst will be observed. The results indicate that the potential of the rocks for strainburst increases with increase in separation of the failure envelopes mentioned above.

1 INTRODUCTION

Going underground is the way to the future, providing plethora of opportunities towards a faster and economical way of life. But every opportunity comes with its own set of challenges. As the structures going deep and under high stresses, the dynamic threat of rockburst, also quoted as "cancer of geomechanics" (Suorineni et al., 2014), is increasing with each step, threatening workers and equipment. Substantial research has been conducted emphasizing the mechanism and prediction of rockbursts (Akdag et al., 2020; Kaiser et al., 1996; Salamon, 1984; Zhao et al., 2014). Starinbursts are the most common type of rockbursts which occur under high overburden and low confinement (Diederichs, 2000) will be the focus of this research. Before excavation, rock is in a triaxial state of stresses in equilibrium and the stability of the rock under this stress state is estimated by true triaxial laboratory testing ($\sigma_1>\sigma_2>\sigma_3$) of rocks initially carried out by Mogi (1971) by utilizing a high pressure true triaxial test apparatus for hard rocks using rectangular prismatic specimen (Mogi, 1971). Many researchers since then improved and modified the true triaxial testing techniques and equipment realizing the influence of intermediate principal stress in the strength of the rock in in situ equilibrium condition (Chen & Feng, 2006; Wawersik et al., 1997).

Upon excavation, the principal stress in the direction of excavation axis becomes negligible and the stresses in other two directions significantly increase. These high stress concentrations increase the strain energy stored in rocks which is expelled instantaneously in the form of acoustic emissions, kinetic energy of rock fissile and seismic waves, giving rise to rockbursts in massive, strong, and brittle rocks. Li et al. (2015) depicted this mechanism in terms of radial (σ_r) and tangential stresses (σ_θ) where upon

DOI: 10.1201/9781003299127-129

excavation, radial stress on the free face is relieved completely and tangential stress increases gradually (Li et al., 2015). In conventional true triaxial tests, the study of mechanism upon laboratory true triaxial unloading of intact rocks is difficult. He et al (2010) developed a true triaxial test system through which dynamic unloading of loads from a true triaxial state in any of the principal stress direction independently (He et al., 2010). It allows to study the actual underground excavated surface behavior along with its stress state. He experimentally provided with a zone of confinement under the failure envelope where rockbursts are observed in intact rocks (Figure 1). Many researchers conducted true triaxial unloading tests on intact rocks for laboratory simulation of rockbursts and study the potential of rocks for rockbursts with acoustic emissions (He et al., 2010), infrared thermography (Sun et al., 2017), high speed cameras and decibel meters (Su et al., 2017).

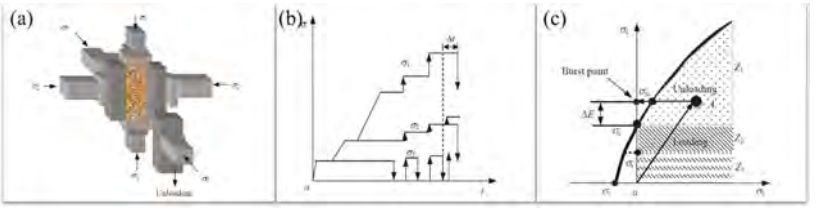

Figure 1. (a) Pictorial depiction of rockburst experiment, (b) Stress paths followed for unloading test, and (c) Zone (Z1) under H-B curve depicts the rockburst zone (He et al., 2012).

In this research, we focused on the stress state under which rockbursts will be observed in different Indian rocks by deriving the loading and unloading failure envelopes. A polyaxial testing machine designed and installed at rock laboratory IIT Delhi is used to conduct true triaxial strength testing and derive the H-B failure envelope (Rao & Tiwari, 2008). Then a series of true triaxial unloading tests have been performed under different confinement by unloading the minor principal stress axis to derive an unloading strength envelope and both have been compared to predict a rockburst zone. This study also involves the observation of free face of the rock specimen to understand the mechanical response of excavated surface of tunnels.

2 MATERIALS AND METHODS

2.1 *Sample selection*

Rajasthan is in the north-western part of India between Latitude 23°03'-30°12' N and Longitude 69° 29'- 78°17'E. It is the largest state in the country with an area of 342,239 sq. km., encompassing about 11% of the total geographical area of the country (Figure 2a). The state is the largest producer of rocks used in construction in the country, including the marble used in renowned Taj Mahal.

The three different rocks selected for the purpose of this research were Jalore granite (Igneous), Makrana marble (Metamorphic) and Jodhpur sandstone (Sedimentary) (Figure 2a). This varied selection of rocks enables us to understand the failure mechanisms in rocks with varying strength, brittleness, process of formation and granular structure. Rockburst is observed in high strength brittle rocks. Granites are igneous rocks of high strength due to the slow crystallization of minerals. SEM images shows surface morphology of granite rock with good interlocking of particles of sharp edges (Figure 2b). Irregular angular arrangement of particles gives higher strength on loading results in high capacity to store strain energy on rockburst. Marble is a metamorphic rock subjected to high pressure and temperature offering high strength. The surface morphology shows that the surface fracture marks are very rough. The particle lumps on the surface upon loading causes rough fracture on failure. The strength directly depends on the orientation of the grains. The grains are elongated and columnar as shown in Figure 2c, representing the direction of pressure acted on it in the past. Sandstones are sedimentary rocks with grain shapes semi rounded to rounded (Figure 2d). The grain boundaries are filled with clayey cementing material with ferrous minerals responsible for the red color. The strength in these rocks mostly depends on the cementation. The grain boundaries roll on over loading and utilize the energy imparted due to external loading in straining of rock. This phenomenon reduces the storage of strain energy hence the rockburst intensity is less compared to other brittle rocks.

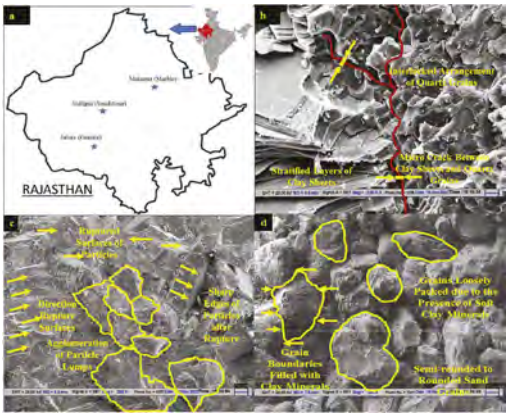

Figure 2. Rock samples selected, (a) Sites of rock collection in Rajasthan, (b) SEM image of Jalore granite, (c) SEM image of Makrana marble, and (d) SEM image of Jodhpur sandstone.

2.2 *Specimen preparation*

The specimen prepared for physical and mechanical testing after determining the number of tests required. The UCS and triaxial tests required 12 specimens of diameter 38 mm for each type of rock with L/d ratio of 2 as specified by ASTM standards C39 for cylindrical specimen. For Brazilian test 5 specimen for each rock were prepared for testing the tensile strength of the rocks. For strength testing cores were drilled from the block samples to prepare specimen with rock drilling using 38 mm drilling bit. For true triaxial unloading (TTU) tests using poly axial testing machine, rectangular prismatic specimen was required as per the machine specifications. The TTU tests were conducted on rectangular prismatic specimens of dimensions 55×55×110 mm as per the machine specifications (Figure 6a, a1, and a2).

2.3 *Polyaxial testing machine*

A servo controlled polyaxial testing machine has been designed and installed at the rock laboratory of IIT, Delhi which facilitates the loading and unloading of intact prismatic rock specimen in three different principal stress directions independently (Rao & Tiwari, 2008). The vertical loading fame can apply a load of 5000 kN through a hydraulic pumping unit, also equipped with a load cell (1000kN, sensitivity 0.1 kN) and a linear variable differential transformer (LVDT) (±20 mm, least count 0.01) for measuring load and axial deformation, respectively.

Figure 3. (a) Polyaxial testing machine installed at IIT Delhi, and (b) True triaxial loading setup of rock specimen.

The confining load is applied by a horizontal rigid frame fabricated by joining a pair of octagonal frames, can apply horizontal loads of 300 kN (Figure 3). Various plates can accommodate square and rectangular prismatic rock specimens of dimensions 55×55×110 mm, 60×60×60 mm and, 55×55×55 mm. A gap of 5 mm on each side of edges on platens are ensured for provision of

micro adjustments of platens during loading and straining of specimen. For the data acquisition three load cells and five LVDTs convert the mechanical signals into digital data through a data acquisition system and can be displayed and stored in a connected display unit.

3 TESTING OF ROCK SAMPLES

3.1 *Physical and strength testing*

The physical properties such as dry densities, porosity, void ratio, and specific gravity were determined for all rock types in their natural state following the standard IS test procedures suggested (IS13030, 1991). The specific gravity calculated as per standard procedures (IS1122, 1974). The results of the physical properties are listed in Table 1.

Table 1. Physical properties.

Property	Jalore Granite	Makrana Marble	Jodhpur Sandstone
Dry Density (g/cc)	2.78	2.84	2.16
Saturated density g/cc)	2.79	2.85	2.27
Porosity (%)	0.23	0.41	11.18
Void ratio	0.08	0.08	4.37
Specific gravity	2.85	2.67	2.62
Index quality (IQ)	99.30	98.08	87.48

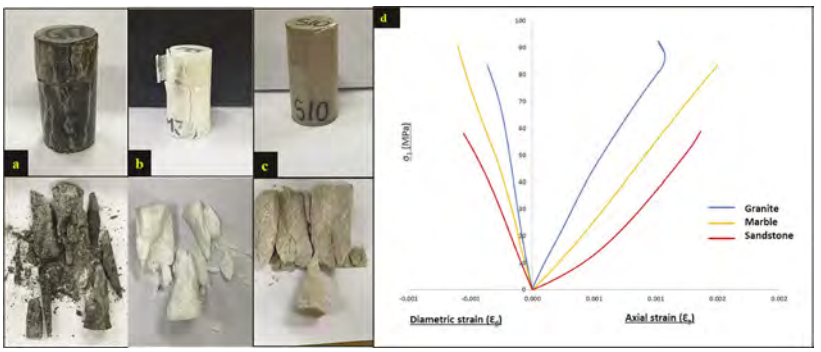

Figure 4. UCS testing, (a) Jalore granite, (b) Makrana marble, (c) Jodhpur sandstone, (d) Stress vs strain curves.

Table 2. Summary of parameters obtained from tests.

Parameters	Granite	Marble	Sandstone
UCS (MPa)	116.8	89	46.52
Elastic modulus (GPa)	78.8	55.61	41.72
Poisson's ratio	0.195	0.243	0.32
Cohesion (MPa)	17.3	11.78	7.65
Friction angle (ϕ)	52.6	55.5	50.90
σ_{ci} (MPa)	102.5	85	44.70
m	23.52	21.38	17.23
s	1	1	1

Strength characterization of rock samples is an important part of the investigation to predict the behavior of the in-situ rock mass under different stress conditions. The failure pattern and failure strains by the rock specimen hint us towards the brittleness of the sample. The

tests results are summarized in Table 2. The stress strain curves, and the failure pattern of the rock specimen are presented in Figure 4.

3.2 *True triaxial unloading (TTU) tests*

In the present research, the behavior of the rock specimen upon unloading of minor principal stress axis (σ_3) from a true triaxial equilibrium state has been observed. Here σ_1, σ_2 and σ_3 have been considered as major principal stress, intermediate principal stress and minor principal stresses respectively. For the test, rectangular prismatic specimen of rocks has been prepared with dimensions 55×55×110 mm. The cuboidal shape has less radial confinement due to the friction of the machine platens along the horizontal axis as compared to a cube specimen. Large radial stress increases the ductility of the specimen which takes the failure from strainburst to fault slip bursts (Diederichs, 2000). Figure 3b, shows the alignment of the specimen between the platens before loading. The specimen has been marked with stress directions for ease in studying the failure pattern. Before commencement of the tests, the failure envelope had to be adjusted for a rectangular prismatic specimen as the previous strength tests were performed of cylindrical specimen. There was a strength reduction of 10-20% observed in the rocks. The bigger specimen has more preexisting flaws than a smaller specimen. Also, the failure patterns observed in a prismatic specimen were mostly slabbing as the effect of slenderness is more in a larger specimen. Hence the failure envelope was derived accordingly.

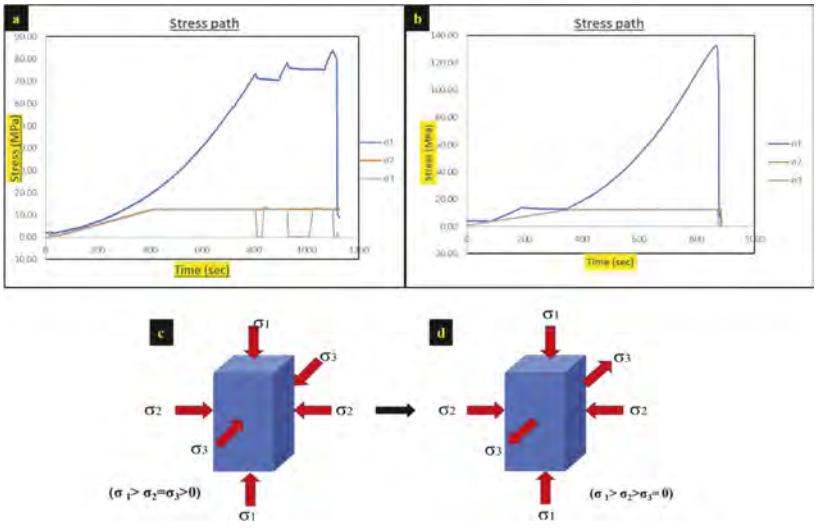

Figure 5. True triaxial unloading (TTU) test, (a) Stress path, (b) Improved confirmatory stress path, (c) Stress state before unloading, and (d) Stress state after unloading.

Stress paths were prepared from the failure envelopes and the decided confinement as shown in Figure 5. At first, all principal stress were increased simultaneously till it reaches the minimum principal stress (σ_3). After that keeping σ_2 and σ_3 constant loading for major principal stress (σ_1) was increased. The loading for σ_3 is removed from a predefined stress state as shown (Figure 5a) and kept for 120 seconds and then re applied the load if the specimen did not fail. The procedure is repeated till the failure of the specimen. Confirmatory tests were done upon improving the stress paths accordingly as Figure 5b and a minimum unloading stress state was derived at the specimen fails in the time frame (Figure 5c, d). Series of tests were done for different confinement for all three rocks and failure envelopes were prepared.

4 RESULTS AND DISCUSSIONS

4.1 *Failure pattern*

When a uniaxial load is applied on a specimen the grain boundaries tend to split in tension in the direction normal to the applied load showing brittle failure. With the increase in confinement the tensile splitting is restricted as it works against the splitting mechanism increasing the strength of the rock. In a UCS condition, there are four failure planes due to lack of confinement, the specimen tend to expand in the four unconfined face directions as shown in Figure 6b (Billings, 1972). This failure can be seen in mine pillars in case of pillar bursts.

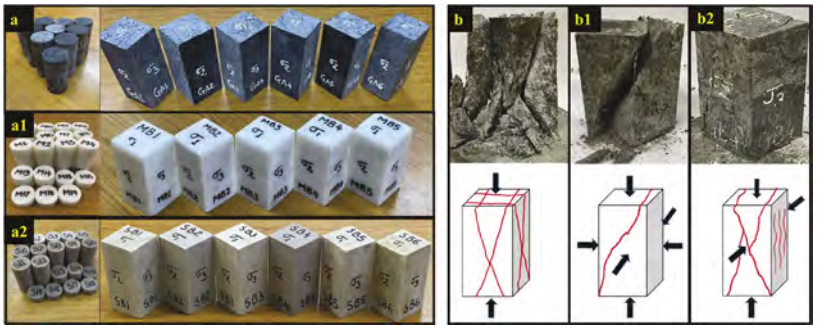

Figure 6. (a) Specimen preparation for strength testing, Jalore granite, (a1) Makrana marble, (a2) Jodhpur sandstone, (b) Effect of confinement of failure of granite specimen in UCS test (4 unconfined faces), (b1) True triaxial loading (no free face), (b2) true triaxial unloading (2 free faces).

In the true triaxial loading test the failure planes reduce to one (Figure 6b1) due to confinement from all the six faces and all the strain energy available is utilized in creation of a shear failure plane instead of tensile failure with expulsion of excess of kinetic energy giving rise to violent fault slip bursts as seen in deep mines with large confinement. In case of triaxial unloading tests, the rock tends to expand towards the unloaded faces and two failure planes form normal to the major and intermediate principal directions. On the unloaded faces, minor tensile cracks are observed. These splinters gain kinetic energy with an increase of σ1 and σ2 similar to the immediate strainbursts from excavated surface of a tunnel. (Figure 6b2).

4.2 *Failure envelopes*

He et al. (2010) identified a zone Z1 (Figure 1c) under H-B failure envelope for instantaneous rockburst and expressed a rockburst criteria in equation:

$$\Delta E = E(\sigma_{1c}) - E(\sigma_c) > 0 \tag{1}$$

Where, ΔE is the excess energy contributing towards the kinetic energy of the rockburst, E(σc) is Strain energy at UCS of the rock and E(σ1c) is the strain energy due to major principal stress. In this work, the influence of intermediate principal stress is not considered. Li et al. (2015) performed the unloading strength tests on Miluo granite, Shandong sandstone and cement mortar (Li et al., 2015). In this paper, materials were tested for both true triaxial loading (TTL) and unloading (TTU) strength and efforts have been made to compare them and identify an actual zone of confinement which depicts strainbursts considering intermediate principal stress. Figure 7a-c, show the fitted TTL and TTU curves of the three rocks.

In Figure 7(d), the plot area has been divided into three different zones. Zone U shaded in yellow above the TTL envelope depicts the unstable stress zone. In this zone, an intact rock will not be stable in situ and will utilize the stored strain energy (ΔE) in creation of cracks and

formation of new surfaces (Cook, 1965b) till a state of stress equilibrium is achieved. In the zone S depicted green shaded area under the TTU strength curve, an intact massive rock will be stable and will be able to withstand the increase in stress concentration in σ_1 and σ_2 direction due to excavation in σ_3 loading direction. The zone represented by red shading depicted as R is the zone of concern for the construction as the rock is stable till the excavation is conducted (unloading). The lower limit of the R zone closer to TTU curve is having less excess energy (ΔE) and hence the intensity of rockburst is minimum and slabbing is observed. The upper limit of the zone closer to TTL curve will be having the maximum stored strain energy (ΔE) which upon excavation will be expelled in the form of projectiles, acoustic emissions (AE), and seismic waves. This part of the stress state will produce severe violent rockbursts.

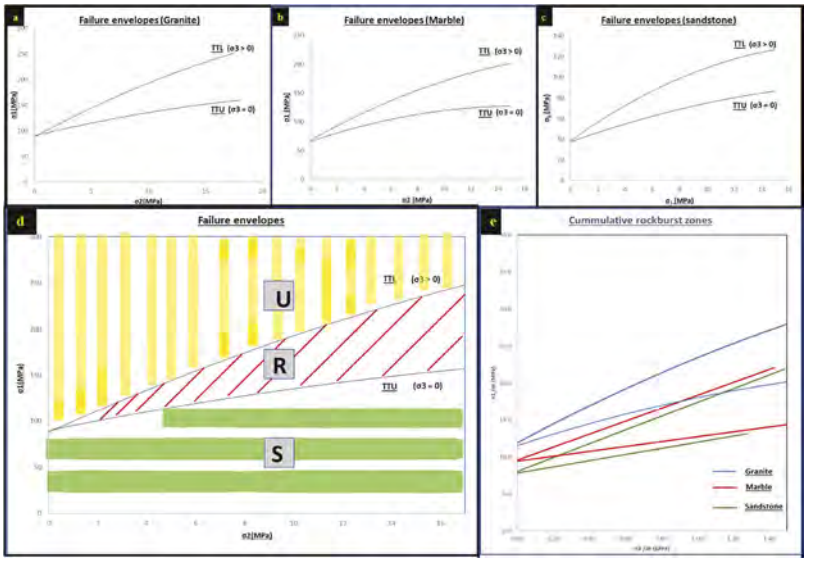

Figure 7. True triaxial loading (TTL) and unloading (TTU) failure envelopes (a) Jalore granite, (b) Makrana marble, (c) Jodhpur sandstone, (d) Stability zones for stress state, (e) Cumulative normalized rockburst zone plot.

Figure 7(e) represents the normalized rockburst zones of all three rocks by the tensile strength of the rocks (σ_t) so that the y-axis represents the brittleness of the rock. The rock with the highest σ_c/σ_t ratio displays high storage of strain energy hence more prone to rockburst. Upon cumulative plotting of the normalized curve, it is observed that when the ratio σ_3/σ_t is below 0.5, the rockburst zones of the three rocks are distant making the rockburst probability low. When this ratio is between 0.5 to 1 the curves start to overlap hinting towards medium rockburst and after this value exceeds 1 all the zones overlap. Here the probability of rock burst can be considered as the maximum

5 CONCLUSIONS

An experimental study has been conducted to identify zones of starinbursts for different Indian rocks on polyaxial testing machine designed and installed at IIT Delhi. Series of both true triaxial loading and unloading tests were conducted in attempt to understand the mechanics of strainburst. The plots of the failure curves were divided into three parts as per their stability conditions considering the effect of intermediate principal stress (σ_2). The failure patterns and rockburst potential were investigated in detail. Hence this experimental study provides a reference for the design and stability of tunnels against strainburst by deriving and comparing both the TTL and TTU curves.

REFERENCES

Akdag, S., Karakus, M., Nguyen, G. D., & Taheri, A. (2020). Strain burst vulnerability criterion based on energy-release rate. Engineering Fracture Mechanics, 237, 107232.

Akdag, S., Karakus, M., Taheri, A., Nguyen, G., & Manchao, H. (2018). Effects of thermal damage on strain burst mechanism for brittle rocks under true-triaxial loading conditions. Rock Mechanics and Rock Engineering, 51(6), 1657–1682.

Billings, M. (1972). Structural geology.

Chen, J., & Feng, X. (2006). True triaxial experimental study on rock with high geostress. Yanshilixue Yu Gongcheng Xuebao/Chinese Journal of Rock Mechanics and Engineering, 25(8), 1537–1543.

Cook, N. G. W. (1965a). A note on rockbursts considered as a problem of stability. Journal of the Southern African Institute of Mining and Metallurgy, 65(8), 437–446.

Cook, N. G. W. (1965b). The failure of rock. International Journal of Rock Mechanics and Mining Sciences & Geomechanics Abstracts, 2(4), 389–403.

Diederichs, M. S. (2000). Instability of hard rockmasses, the role of tensile damage and relaxation.

Du, K., Tao, M., Bing, L. X., & Zhou, J. (2016). Experimental Study of Slabbing and Rockburst Induced by True-Triaxial Unloading and Local Dynamic Disturbance. Rock Mechanics and Rock Engineering, 49, 3437–3453. https://doi.org/10.1007/s00603-016-0990-4.

He, M. C., Miao, J. L., & Feng, J. L. (2010). Rock burst process of limestone and its acoustic emission characteristics under true-triaxial unloading conditions. International Journal of Rock Mechanics and Mining Sciences, 47(2), 286–298.

He, M., Xia, H., Jia, X., Gong, W., Zhao, F., & Liang, K. (2012). Studies on classification, criteria and control of rockbursts. Journal of Rock Mechanics and Geotechnical Engineering, 4(2), 97–114. https://doi.org/10.3724/sp.j.1235.2012.00097

IS1122. (1974). IS 1122 (1974): Method of test for determination of true specific gravity of natural building stones. Buero of Indian Standards.

IS13030. (1991). IS 13030 (1991): Method of test for laboratory determination of water content, porosity, density and related properties of rock material. Bureau of Indian Stanards.

Kaiser, P. K., McCreath, D. R., & Tannant, D. D. (1996). Canadian rockburst support handbook. Geomechanics Research Center.

Li, X., Du, K., & Li, D. (2015). True triaxial strength and failure modes of cubic rock specimens with unloading the minor principal stress. Rock Mechanics and Rock Engineering, 48(6), 2185–2196.

Miao, J. L., He, M. C., Li, D. J., Zeng, F. J., & Zhang, X. (2009). Acoustic emission characteristics of granite under strain rockburst test and its micro-fracture mechanism. Chinese Journal of Rock Mechanics and Engineering, 28(8), 1593–1603.

Michelis, P. (1985). A true triaxial cell for low and high pressure experiments. International Journal of Rock Mechanics and Mining Sciences & Geomechanics Abstracts, 22(3), 183–188.

Mogi, K. (1971). Fracture and flow of rocks under high triaxial compression. Journal of Geophysical Research, 76, 1255–1269. https://doi.org/10.1029/JB076i005p01255

Rao, K. S., & Tiwari, R. P. (2008). A polyaxial system for testing of jointed rock mass models. Geotechnical Testing Journal, 31(4), 1–10.

Salamon, M. D. G. (1984). Energy considerations in rock mechanics: fundamental results. Journal of the Southern African Institute of Mining and Metallurgy, 84(8), 233–246.

Su, G., Chen, Z., Ju, J. W., Zhao, B., Yan, S., & Yan, Z. (2019). Experimental study of the dynamically induced rockburst of a rock wall with double free faces. International Journal of Damage Mechanics, 28(4), 611–637.

Su, G., Jiang, J., Zhai, S., & Zhang, G. (2017). Influence of tunnel axis stress on strainburst: an experimental study. Rock Mechanics and Rock Engineering, 50(6), 1551–1567.

Sun, X., Xu, H., He, M., & Zhang, F. (2017). Experimental investigation of the occurrence of rockburst in a rock specimen through infrared thermography and acoustic emission. International Journal of Rock Mechanics and Mining Sciences, 93, 250–259.

Suorineni, F. T., Hebblewhite, B., & Saydam, S. (2014). Geomechanics challenges of contemporary deep mining: a suggested model for increasing future mining safety and productivity. Journal of the Southern African Institute of Mining and Metallurgy, 114(12), 1023–1032.

Takahashi, M., & Koide, H. (1989). Effect of the intermediate principal stress on strength and deformation behavior of sedimentary rocks at the depth shallower than 2000 m. ISRM International Symposium.

Wawersik, W. R., Carlson, L. W., Holcomb, D. J., & Williams, R. J. (1997). New method for true-triaxial rock testing. International Journal of Rock Mechanics and Mining Sciences, 34(3–4), 330–e1.

Zhao, X. G., Wang, J., Cai, M., Cheng, C., Ma, L. K., Su, R., Zhao, F., & Li, D. J. (2014). Influence of unloading rate on the strainburst characteristics of Beishan granite under true-triaxial unloading conditions. Rock Mechanics and Rock Engineering, 47(2), 467–483.

Smart Geotechnics for Smart Societies – Zhussupbekov, Sarsembayeva & Kaliakin (Eds)
© 2023 The Author(s), ISBN 978-1-003-29912-7
Open Access: www.taylorfrancis.com, CC BY-NC-ND 4.0 license

Finite element analysis of unlined parallel twin tunnels under impact loads in stratified rockmass

Asifa Bano
M. Tech Student, Department of Civil Engineering, IIT Delhi, New Delhi, India

Shipra Sinha
Research Scholar, Department of Civil Engineering, IIT Delhi, New Delhi, India

K. Seshagiri Rao
Emeritus Professor, Department of Civil Engineering, IIT Delhi, New Delhi, India

ABSTRACT: Most urban tunnels are located at shallow depths which pass through stratified rockmass and are extremely vulnerable to impact loads such as falling heavy objects and projectiles. The present study aims to comprehend the behaviour and deformation pattern of twin tunnels in stratified rockmass under impact loads using finite element method (FEM) based numerical simulation. The analysis was carried out for various stratified rockmasses such as homogeneous, stratified horizontal layers of two, and three at an impact load of 20kg, 30kg, and 40kg. Deformation at the crown of a homogeneous rockmass is less than that at the spring line, and similar behaviour is observed in stratified horizontal layers of two and three. In comparison to stratified rockmass, homogeneous model exhibits the most damage and deformation. In the case of stratified horizontal layers of three, there was relatively less damage and deformation. This paper establishes that rockmass properties and formation thickness influences deformation under impact loads.

1 INTRODUCTION

Due to rising population and land scarcity, the demand for underground transportation, particularly metro tunnels in urban areas, has increased significantly. These frequently have to withstand both static and impact loads. Numerous studies on single tunnels in homogeneous rockmass have been conducted to investigate the effects of overburden, shape of tunnel, uniaxial compression, impact loading, blast loading, and varying geological conditions such as the presence of a weak interlayer and jointing orientations. Most urban tunnels are built at shallow depths and in layered rockmass. As a result, tunnels in layered rockmass must be protected from impact loading. Twin tunnels or new tunnels adjacent to existing ones can be built horizontally, vertically, or inclinedly.

Few researchers conducted an analysis for quantitative and reasonable estimation of general safety and local instability zones for underground structures such as multi-tunnels or caverns(Jiang et al., 2021). Several numerical and experimental studies (Mishra et al., 2022), (Mishra & Rao, 2017), (Sinha et al., 2021) have concentrated on single tunnels in anisotropic rockmass for various dynamic loads such as impact and blast loads. Several researchers conducted scale model studies to estimate the stability of twin tunnels with small clearances and discovered that models with wider pillars cracked under higher pressure than models with narrow pillars (Kim & Kim, 2013). A parametric study was conducted to predict the interaction of tunnel construction and piled foundations, and it was discovered that tunnelling can increase the axial and flexural loads on piles (Khabbaz et al., 2019).

The present study is an effort to understand the behavior and damage pattern of twin tunnels in stratified rockmass under impact loads using FEM-based numerical simulation.

DOI: 10.1201/9781003299127-130

2 GEOMETRY, MATERIALS AND METHODS

2.1 *Geometry of the model*

The current work employs finite element analysis with the ABAQUS/CAE 2017 software. The overburden depth is 5cm and pillar width is also 5cm (Figure 1a). The surrounding rockmass model measures 30cm in length, 30cm in height, and 40cm in width (Figure 1b). Twin tunnels of 5cm diameter each are extruded in the length direction. The numerical model is built with homogeneous rockmass, stratified horizontal layers of two and three, and unlined twin tunnels (Figure 1c-e).

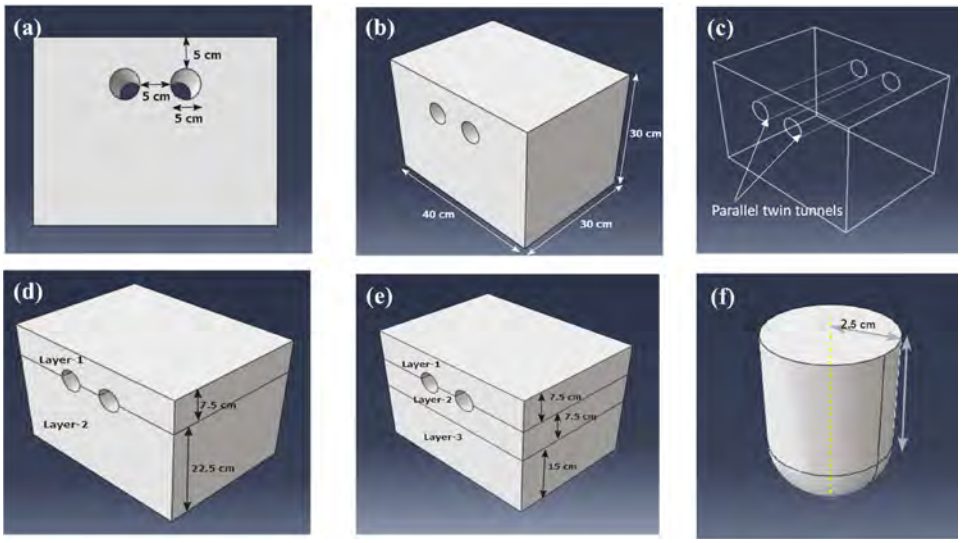

Figure 1. (a) Dimensions of tunnels, (b) Dimensions of rockmass model, (c) Alignment of tunnels (parallel twin tunnels), (d) Stratified horizontal layers of two, (e) Stratified horizontal layers of three, and (f) Hammer dimensions.

The hammer with a hemispherical nose is used to strike the twin tunnels. The hemisphere has a radius of 2.5cm and a height of 5cm (Figure 1f). The current study considered three impact hammer weight of 20kg, 30kg, and 40kg. The sizes of models have been selected as 30cm×40cm×30cm established by a boundary convergence study (Mishra, 2019).

2.2 *Model material properties*

Three geo-materials are modelled in this work, covering the spectrum of low strength rockmass. Geo-materials are synthetically modelled in the laboratory from distinct materials such as Plaster of Paris (POP), Kaolinite clay, Badarpur sand and Mica, and the resulting mixtures are known as geo-synthetic material: GM1, GM2, and GM3 (Mishra et al., 2021). Table 1 shows the composition and properties of various geomaterials. Steel hammer is used for impact loading and striking is done at the center of the top surface of the rockmass. The properties of the hammer are shown in the Table 1 (Mishra et al., 2021).

The GM3 material is used in the case of a homogeneous rockmass model (Figure 2a). Layer-1 is 7.5cm thick and made of GM3, while layer-2 is 22.5cm thick and made of GM2 (Figure 2b) and layer-1 is 7.5 cm thick and made of GM3, layer-2 is 7.5 cm thick and made of GM2, and layer-3 is 15 cm thick and made of GM3 (Figure 2c) In the case of stratified horizontal layers of two and three respectively.

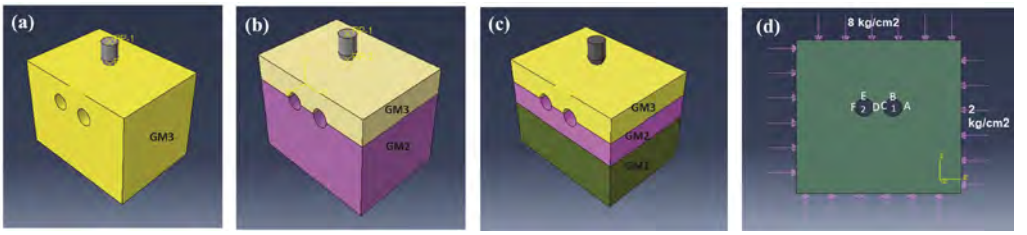

Figure 2. (a) Homogeneous model, (b) Two layered model, (c) Three layered model, and (d) Homogeneous rockmass FEM model subjected to static loading.

Table 1. Properties of geo-material and hammer (Mishra et al., 2021).

Property	GM1	GM2	GM3	Impact Hammer
Density (g/cc)	1.22	1.09	1.10	7.80
Modulus of elasticity, E_{t50} (MPa)	3675.24	2809.46	2480.84	200000
Poisson's ratio, υ	0.16	0.21	0.27	0.30
Sonic wave velocity (m/s)	1724.55	1555.16	1505.89	-
Tensile strength, σ_t (MPa)	0.97	0.59	0.35	-
Uniaxial Compressive Strength, σ_c (MPa)	3.52	1.97	1.14	-
Cohesion, c (MPa)	0.79	0.62	0.40	-
friction angle, ϕ (°)	39.12	31.40	22.65	-

2.3 *Loading, boundary conditions and meshing*

As shown in the Figure 3a, the model's base has been restrained in all directions while remaining sides and top surface are kept free. The dimensions of the rock model are considered larger than the size of the tunnel to minimize wave reflection from the boundaries (Rao et al., 2018.). The layer interaction is rough in the tangential direction and hard in the normal direction. General contact is used with the hammer. At the lower point of the hammer, a speed of 4.68m/s is employed for impact.

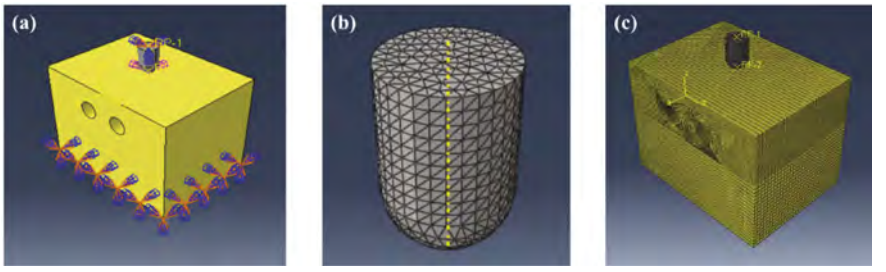

Figure 3. (a) Boundary conditions and loading, (b) Meshing of hammer, and (c) Messing of rockmass model.

The eight-node brick element (C3D8R) with reduced integration and hourglass control is used in the FE mesh for the rock model in Abaqus/Explicit. C3D8R linear hexahedral element type is used for rockmass. Linear tetrahedral elements of size 0.005 and type C3D4 are used for hammer (Figure 3b). Element sizes of various components have been established based on mesh convergence study of the finite element model. The global size of elements for rockmass is 0.01 and structured meshing technique is used (Figure 3c). The rock-mass is modelled using the Mohr-Coulomb plasticity model (Dhamne et al., 2018) whereas, hammer is modelled using linear elastic model.

3 VALIDATION

To ensure validity of the numerical modelling approach, a twin -tunnel problem was numerically modelled. It is validated using existing experimental, numerical, and theoretical results of mechanical behaviour of a twin tunnel in multi-layered formation(Chu et al., 2007). The material is made by combining different proportions of sand, plaster, and water (1.5:1:0.86), and the properties used are the same as those mentioned in the paper by Chu et al., 2007 (Figure 2d).

Table 2. Tunnel in homogeneous formations.

Points	Experimental (kg/cm^2)	FEM result(kg/cm^2)	% Error
Tunnel-1 at A	24.50	24.08	1.69
Tunnel-2 at B	26.60	25.80	3.01

It is important to note that the magnitude of stresses at different points from the numerical model (FEM model) agrees well with that of the physical model, as shown in Table 2.

4 RESULTS AND DISCUSSION

When an impact load with an impact velocity of 4.68m/s is applied at the centre of the top surface for 8 milliseconds, deformation is observed at different points. The spring line and crown (Figure 4a,b) of both tunnels are the most affected.

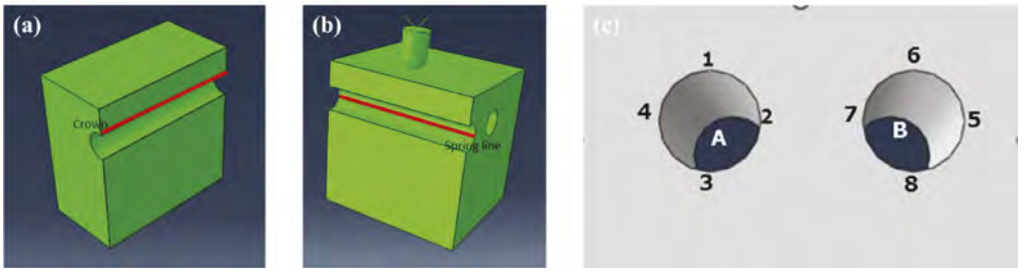

Figure 4. (a) Crown along tunnel length, (b) Spring line along tunnel length, and (c) Locations of crown (1 and 6), and spring (2,4,5, and 7) of tunnels A and B.

Due to loading and geometrical symmetry, both tunnels will have the same deformation and damage zone. Therefore, deformation is measured only in tunnel 'A' (Figure 4c).

4.1 *Homogenous*

The spring line has more deformation than the crown (Figure 5a). Deformation at the crown and spring line increases as impact energies increase (Figure 5b).

The damage zone is closer to the spring line because of the greater impact effect in this region. This material GM3 is relatively weak in comparison to GM1 and GM2, resulting in a lower modulus of elasticity and more damage and deformation. Large stress waves generated during impact will cause more damage.

4.2 *Stratified horizontal layers of two*

Deformation is greater at the spring line than at the crown (Figure 6a). As we increase impact energies, deformation at the crown and spring line increases (Figure 6b)

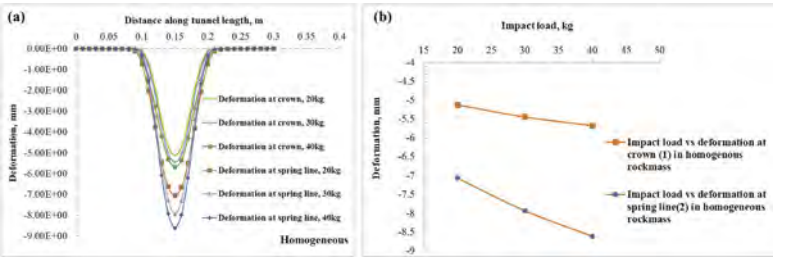

Figure 5. Deformation along tunnel length for crown and spring line, (a) Homogeneous rockmass, and (b) Impact load vs deformation.

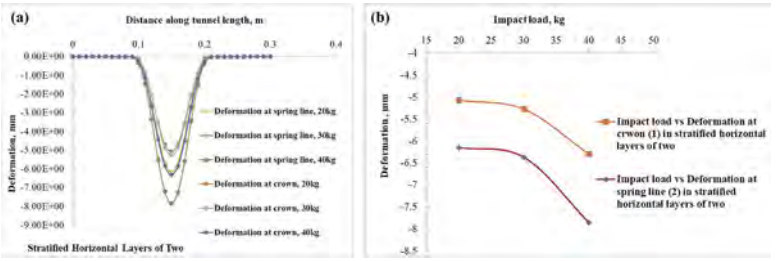

Figure 6. Deformation along tunnel length for crown and spring line, (a) Stratified horizontal layers of two, (b) Impact load vs deformation.

Comparatively weak material (GM3) is above, and hence, more deformation occurs in this layer. In stratified horizontal layers of two, the lower layer provides resistance to upper layer penetration, resulting in less deformation than in homogeneous rock mass.

4.3 *Stratified horizontal layers of three*

The spring line has more deformation than the crown (Figure 7a). As we increase impact energies, deformation at the crown and spring line increases (Figure 7b).

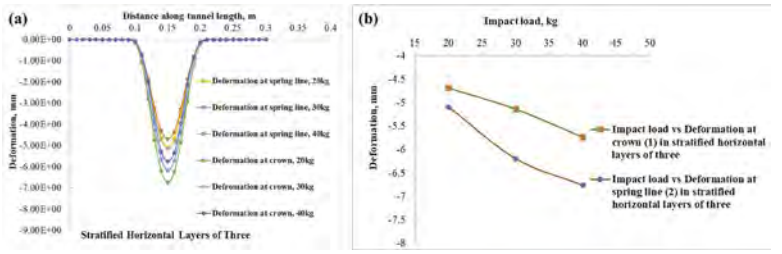

Figure 7. Deformation along tunnel length for crown and spring line, (a) Stratified horizontal layers of three, (b) Impact load vs deformation.

The effect of impact load is limited to the upper layers in this case because the other two layers provide support to the upper layer against deformation. In horizontal layering, lower layers provide more uniform resistance to upper layer deformation.

5 CONCLUSIONS

The current study is an effort to comprehend the deformation and damage in twin tunnels models under impact loading for various formations such as homogeneous rockmass,

stratified horizontal layers of two and three made of different materials (i.e., GM1, GM2, and GM3). The analysis has been carried out using finite element method.

- ✓ The results indicate that maximum deformation and damage occur at the spring line in all three cases. Deformation is less at the crown than at the spring line, and it varies between 38-52%, 20.8-24.8%, and 17.77-20.44% for homogeneous rockmass, stratified horizontal layers of two, and three, respectively.
- ✓ As the impact load is increased, deformation at both points (crown and spring line) increases in all the three cases. At crown, it varies between 4.22-6.25%, 3.94-19.35%, and 9.6-11.6%, and for spring line 8.56-12.30%, 3.57-23.23%, and 9.21-21.61% for homogenous rockmass, stratified horizontal layers of two, and three, respectively.
- ✓ Deformation at both points (crown and spring line) decreases as the number of stratified layers increases and it is 8.74-10.93% at crown and 8.93-13.88% at spring line. The reason is lower layers provide more uniform resistance to upper layers deformation.

The present study implies that the tunnels passing through weaker homogenous layer is more vulnerable to impact than the case where the tunnels pass through layered formations where weaker formation is overlain by stronger formations. The cases analyzed are useful to predict damage zone and deformation due to impact loads in existing tunnels. Deformation behavior can be predicted for different combination of impact load and number of stratified layers which will help to analyze a large amount of design problems and will help to improve the new guidelines generations. Combination of numerical and experimental study gives better understanding of tunnel behavior and tunnel designers can make engineering judgement in complex situations.

REFERENCES

Chu, B. L., Hsu, S. C., Chang, Y. L., & Lin, Y. S. (2007). Mechanical behavior of a twin-tunnel in multi-layered formations. *Tunnelling and Underground Space Technology*, *22*(3), 351–362. https://doi.org/10.1016/j.tust.2006.06.003.

Dhamne, R., Mishra, S., & Rao, S. K. (2018). *Numerical Study of the Cross Sectional Shape of Shallow Tunnels Subjected to Impact and Blast Loading Rohtang Tunnel South Portal Stability View project Behaviour of anisotropic rocks and rockmasses View project*. https://www.researchgate.net/publication/329670763

Jiang, Q., Liu, X., Yan, F., Yang, Y., Xu, D., & Feng, G. (2021). Failure Performance of 3DP Physical Twin-Tunnel Model and Corresponding Safety Factor Evaluation. *Rock Mechanics and Rock Engineering*, *54*(1), 109–128. https://doi.org/10.1007/s00603-020-02244-7

Khabbaz, H., Gibson, R., & Fatahi, B. (2019). Effect of constructing twin tunnels under a building supported by pile foundations in the Sydney central business district. *Underground Space (China)*, *4*(4), 261–276. https://doi.org/10.1016/j.undsp.2019.03.008

Kim, P. G., & Kim, J. W. (2013). Scale Model Studies for Stability Estimation of Twin Tunnels with Small Clearance. *Journal of Korean Society For Rock Mechanics*, *23*(2), 130–140. https://doi.org/10.7474/tus.2013.23.2.130.

Mishra, S. (2019). *Physical and numerical modeling of tunnels under impact and blast loads*.

Mishra, S., Kumar, A., Rao, K. S., & Gupta, N. K. (2021). Experimental and numerical investigation of the dynamic response of tunnel in soft rocks. *Structures*, *29*, 2162–2173. https://doi.org/10.1016/j.istruc.2020.08.055

Mishra, S., & Rao, S. K. (2017). *Numerical Analysis Of the Tunnels Subjected To Impact Loading*. https://www.researchgate.net/publication/320685629

Mishra, S., Zaid, M., Rao, K. S., & Gupta, N. K. (2022). FEA of Urban Rock Tunnels Under Impact Loading at Targeted Velocity. *Geotechnical and Geological Engineering*, *40*(4), 1693–1711. https://doi.org/10.1007/s10706-021-01987-6

Rao, S. K., Gupta, N. K., Sharma, H., Mishra, S., & Rao, K. S. (n.d.). Effect of Cover Depth on Deformation in Tunnel Lining When Subjected to Impact Load. In *10 th Asian Rock Mechanics Symposium*. https://www.researchgate.net/publication/328853194

Sinha, S., Mishra, S., Rao, K. S., & Chakraborty, T. (2021). Analysis of Twin Circular Tunnels Subjected to Impact Loads. *Lecture Notes in Civil Engineering*, *137 LNCE*, 683–694. https://doi.org/10.1007/978-981-33-6466-0_63

Smart Geotechnics for Smart Societies – Zhussupbekov, Sarsembayeva & Kaliakin (Eds)
© 2023 The Author(s), ISBN 978-1-003-29912-7
Open Access: www.taylorfrancis.com, CC BY-NC-ND 4.0 license

A sink hole and caves caused by earth balance shield and digital twin observational method to control face stability

Y. Iwasaki
Geo Research Institute, Kobe, Japan

H. Ito
JIP Techno Science, Osaka, Japan

Y. Koyama
Ritsumeikan University, Kyoto, Japan

A.Zh. Zhussupbekov
L.N. Gumilyov Eurasian National University, Nur Sultan, Kazakhstan

ABSTRACT: A sink hole was found at ground surface in a residential area in Tokyo in October 2020. The site was above a construction line of earth pressure balance shield tunnel with16.1 m in diameter and the crown at the depth of GL-47m. Further study revealed the dense sand layer above the tunnel has been loosened along the tunnel for about 200m length from the tunnel face.

3DFEM simulation based upon the site conditions showed a possibility of the loosing stability of the face when the ground is dense sand with little fine component.

A digital twin observational method is proposed to discuss the face stability and to keep digging safe.

1 UNEXPECTED ACCIDENT BY EARTH PRESSURE BALANCED SHIELD

1.1 *A sink hole above 47m of earth balanced pressure shield of 16.1m in diameter*

A sink hole was reported by East Nippon Expressway Co. Kanto Regional Head Office on October 18, 2020(ENE). A depression of ground surface appeared on a narrow road in front of a private house on Sunday around 12:30 October 18, 2020 in Chofu-city, Tokyo. It was reported the location was just above the tunneling site of the Tokyo Outer Ring Road (Tomei-Kan-etsu) main line tunnel (southbound). The size of the depression was 5m x 2.5m on the ground surface as shown "Sink hole" in Figure 1.

The shield had passed below the sink point with about 47m below the surface on September 14, 2020, about one month earlier than the sink hole appeared. Based upon razer scanning and seismic survey along the shield line, additional void zones were identified as shown in Figure 1.

1.2 *Loosening ground above the shield tunnel*

Based upon borings before the construction, the area was recognized as thick dense sand ground with a thin gravel layer of Pleistocene with SPT N>50 covered by alluvium soft loam Holocene layer.

After the sink was found, several borings were performed to study the geotechnical conditions. The depth distributions of the SPT, N values for these borings are shown in Figure 2. The

DOI: 10.1201/9781003299127-131

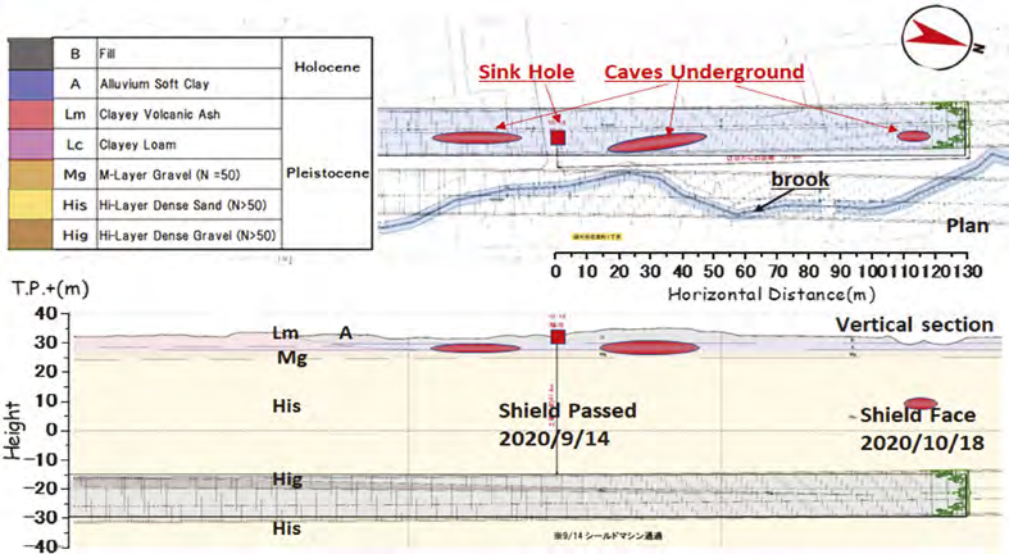

Figure 1. A sink hole and caves underground above a shield tunnel in Chofu-city, Tokyo.

N-values above the shield tunnel for the His Sand layer shows significantly decreased values compared to those before the construction. The N-values in the zone above the shield tunnel shows less than 50 (N<50) not only below the sink and the caves but also other points where no sink or cases was identified. The decreased N-values from N>50 to N<5-50 are found along the tunnel line of 200m from the face. The loosening of the dense sand ground above the shield tunnel was caused by tunneling and induced to create caves and sink holes just above the shield tunnel.

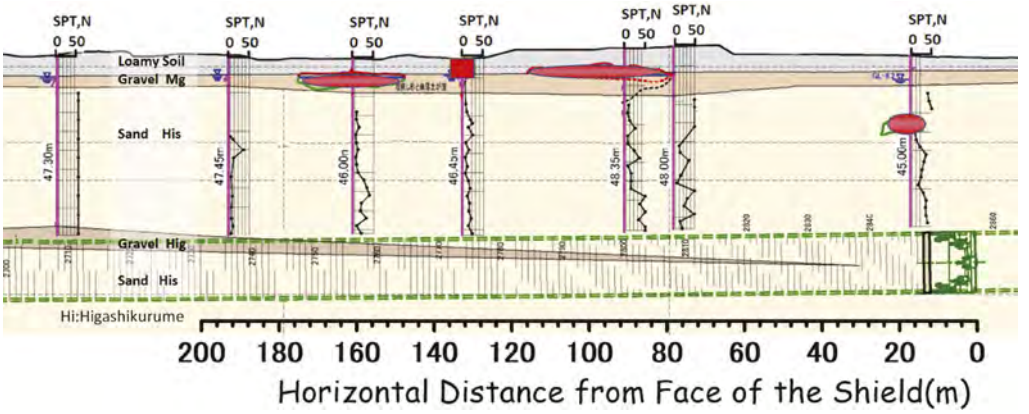

Figure 2. The loosened dense sand layer above the shield about 200m from the face.

1.3 *Chamber pressure*

To keep the stability of the face, the chamber pressure should be kept within some safety range as well as the mud in the chamber under liquid plastic state for the pressures to be distributed smoothly all over the face with a large diameter of 16.1 m.

Monitoring mud pressures in the chamber is a common practice in the earth balanced pressure tunneling. Figure 3 shows the position of the earth pressure sensors. Outer pressure sensors and inner pressure sensors were installed to monitor the chamber pressure.

Figure 4 shows earth pressure distribution near the face of shield machine. Distribution of pressures in front of the face consists of horizontal earth pressure σ_h and water pressure σ_w. On the other hand, the chamber pressure that should be balanced against the earth pressures.

1.4 *Monitored chamber pressure*

Monitored chamber pressures during the process of tunneling in the area where the sink surface and caves underground were found are plotted in Figure 5. Monitored data are found to be grouped into two types of digging and stopping phases.

The chamber pressures at the crown level are the same of the water pressure for both groups. The pressure increment with depth is 12 to 14 kN/m2 for digging phase, which is the same as the unit mass density of mud in the chamber. When the shield machine is under stopping phase, no mixing of the mud in chamber and the pressure increase with depth is the same as the density of water.

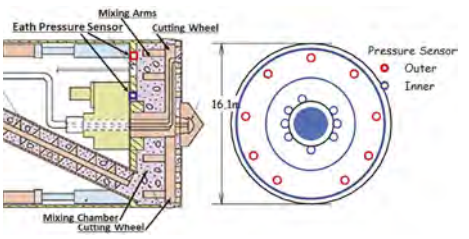

Figure 3. Positions of earth pressure sensors in chamber.

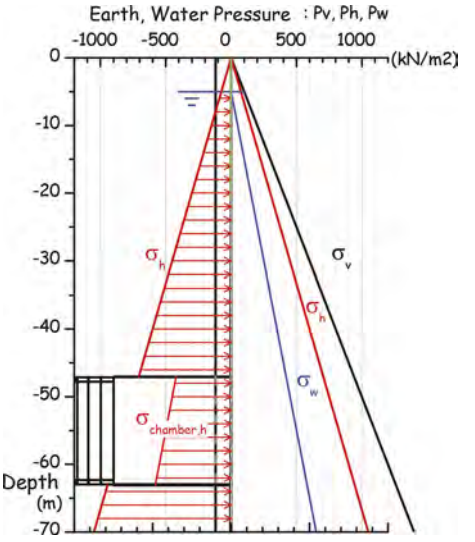

Figure 4. Earth and chamber pressures.

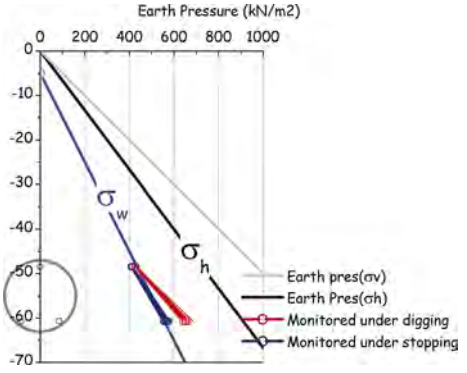

Figure 5. Monitored chamber pressures.

Table 1. Monitored chamber pressure.

Phase	Digging	Stopping
Pressure at crown(kN/m2)	38	38
dp/dz(kN/m3)	12~14	10

Water pressure at the crown = 42(kN/m2)

2 ESTIMATION OF FACE STABILITY

2.1 *Analytical model*

An analytical model for discussion of face stability of the pressure balanced shield of the site as 3D FEM model by Plaxis is shown in Figure 6. The half sectional model of the dimension of 200m in width, 100m in length, and 90m in depth.

2.2 *Properties of ground for analysis*

The ground at the level of the shield and about more than 30 m above the shield consists of dense sand or dense gravel formations of Hs and Hg which shows SPT, N>50. The internal friction angle of sand and gravel was proposed to have a relationship with SPT, N1 as shown in Figure 7 (Hatanaka). N1 is a function of SPT, N as follows,

$$N1 = N/\left(\sigma_v'/98\right)^{0.5}$$

The effective vertical stress at the mid-level of the face (d=55m) under water level of WL=GL-5m and unit mass of sand of 20kN/m3 is obtained as

$$N1 = 50/((20 \times 55 - 10 \times 50)/98)^{0.5} = 20.4$$

The internal friction angle is obtained as

$$\phi = 40^{o} \text{ for } N1 = 20.4$$

The cohesion of sand and gravel soil is a function of the contents of fine soil of clay and silt. The change of the grain size distributions which were obtained by soil test of the excavated mud soils is shown in Figure 8. The fine content of the sand layer in the loosened zone for dense sand above the shield is less than 7.5-5%. The relationship between the cohesion and the fine contents of sand and gravel soil (Kim) as shown in Table 2. The estimated cohesion is around C' = 0 (kN/m2).

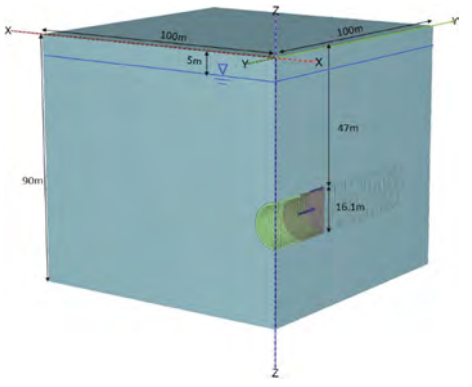

Figure 6. FEM model.

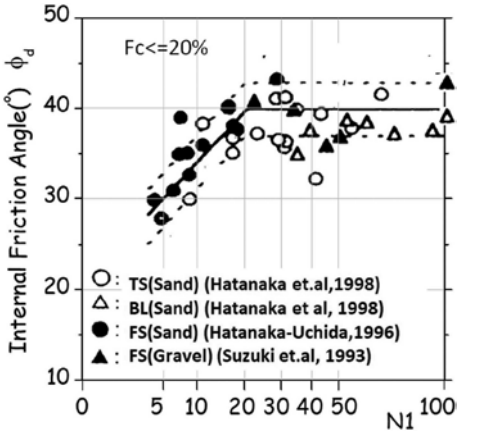

Figure 7. Relationship between N1 and friction angle.

2.3 *3D FEM simulation on face stability for stopping phase*

The force of the shield machine against the face is the sum of the thrust force and the chamber pressure. During the stopping phase of installing of tunnel segments after digging 1.6m of the

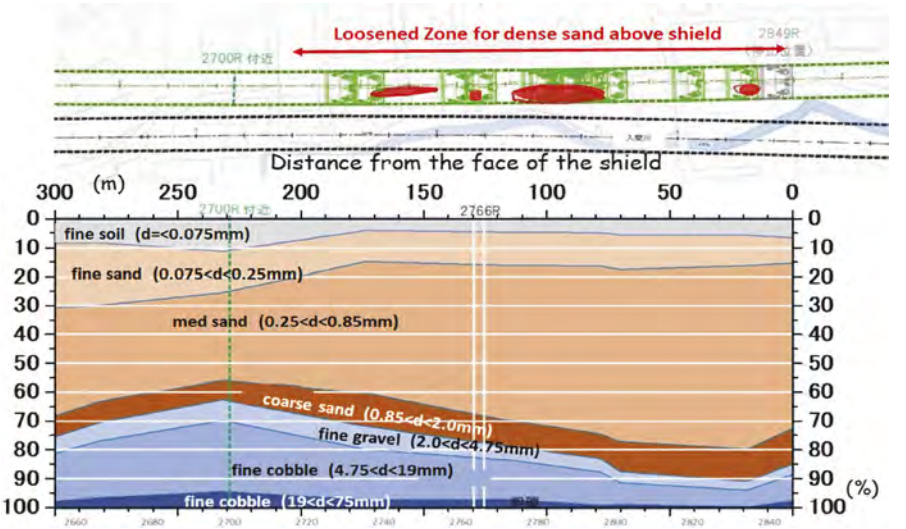

Figure 8. Change of the grain size distribution of the excavated mud.

Table 2. Cohesion of sandy soil and fine contents ratio.

Fine contents Ratio Fc(%)	10	25	40	50
Cohesion C'(kN/m2)	0.0	10.0	13.1	16.0

segment length, the monitored chamber pressure was smaller than digging phase and was used as the model pressure for the analysis.

Young's modulus is estimated as E=2800N(kN/m2), where N is a value of SPT, N for the ground and N=50 for the sand ground above the shield.

3D FEM simulation is performed for different parameters as shown in Table 3. The results for the Model F40C20 are shown in Figure 9. The yielding zone is mainly concentrated at the face and the horizontal displacement is concentrated at the center of the face. When the cohesion is greater than C≥10(kN/m2), the plastic deformation is stable. However, the cohesion is decreased to less than about C<10 (kN/m2), the plastic deformation becomes unstable, and the numerical solution was found to become uncontrolled condition of unlimited deformation. The plastic zones for C=10 (kN/m2) as stable and for C=7.5 (kN/m2) as unstable cases are shown I n Figure 10. As far as the plastics zones are concerned, the zones are rather limited very near the tunnel face, which is due to the confinement condition of the shield machine. The relationship between the cohesion of the sand layer and displacement is plotted in Figure 11.

Table 3. Ground property.

Model	E	ν	ϕ	C	dUy	stress state, stable or unstable
	(kN/m2)		(°)	(kN/m2)	(cm)	
Elastic	140,000	0.3		.	2.71	elastic
F40C40	140,000	0.3	40	40.0	4.90	plastic, stable deformation
F40C20	140,000	0.3	40	20.0	5.72	plastic, stable deformation
F40C10	140,000	0.3	40	10.0	12.5	plastic, stable deformation
F40C75	140,000	0.3	40	7.5	>24.5	plastic, unstable deformation
F40C05	140,000	0.3	40	5.0	>304.2	plastic, unstable deformation
F40C00	140,000	0.3	40	0.0	>500.	plastic, unstable deformation

In the zone of 200m from the face shown in Figure 8 and Table 2, the cohesion is expected as C=0.0. The face stability was anticipated as unstable and induced unlimited displacement for stopping phase.

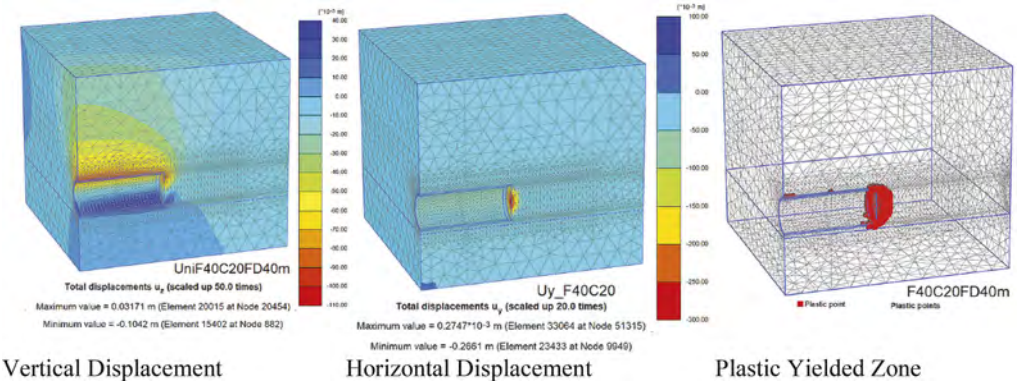

Figure 9. Results of the simulation for F40C20.

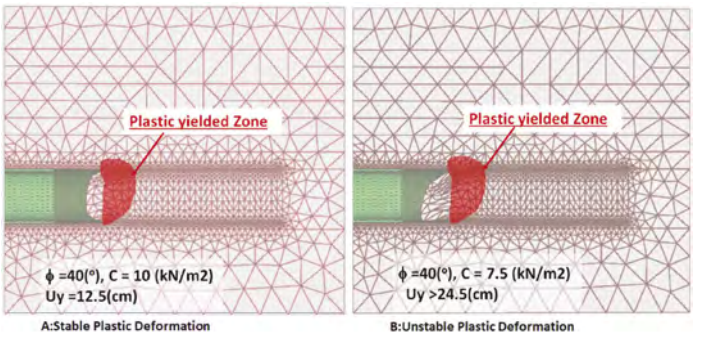

Figure 10. Stable and unstable yielded failure.

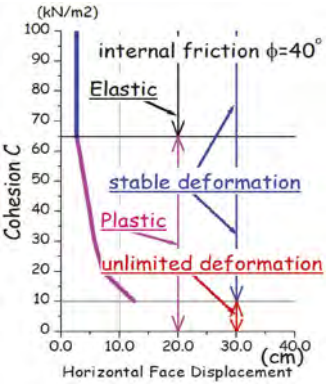

Figure 11. Face stability and cohesion.

Since no free space in front of the shield machine, the unstable plastic condition does not imply the direct failure of the face. However, Once the shield machine begins to dig, the rotation of cutting wheel easily allows for the plastic soil to come out without any control with water flow into the face, which finally results in loosening dense sand ground.

3 DIGITAL TWIN OBSERVATIONAL METHOD TO CONTROL FACE STABILITY

3.1 *Face loading/unloading tests*

To obtain proper chamber pressure for the site, face loading/unloading test may be performed. If displacement around face with changes of chamber pressure, possible sets of the geotechnical parameters of the ground can be estimated. Based upon these parameters, digital simulation can be performed and can be used to predict the shield tunnel performance. Digital observation of the shield tunneling shall be compared with digital simulation. A flow chart is shown in Figure 12 to show the general approach of the digital twin observational method to control face stability.

3.2 *Digital twin observational method*

One of the key factors for the face stability is to control the chamber pressure. Direct in-situ method and evaluation is proposed to obtain the appropriate range of the chamber pressure and to modify them by digital twin method of the Flow chart as shown in Figure 11.

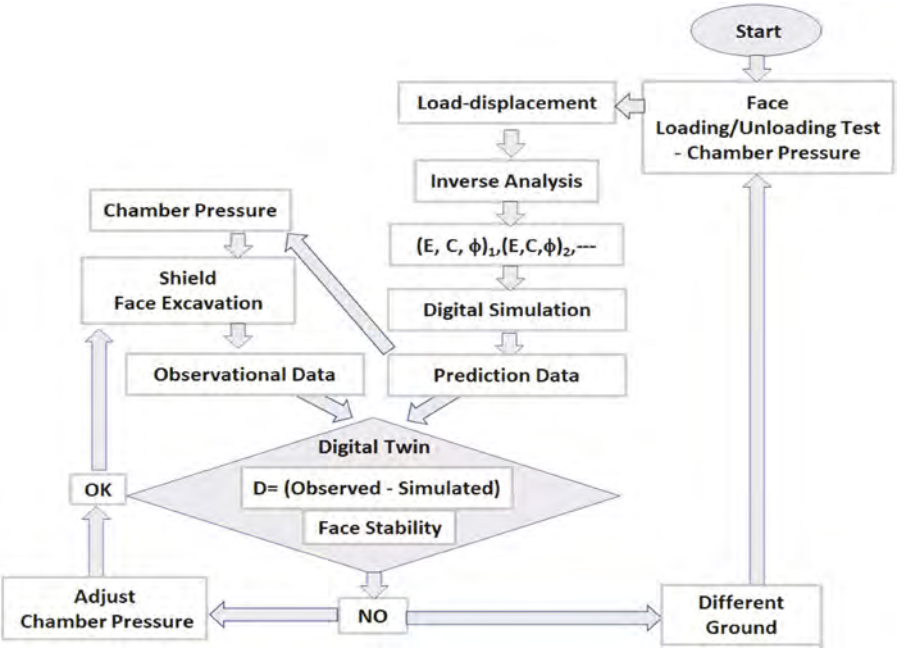

Figure 12. Flow chart of digital twin observational method.

4 CONCLUSIONS

Loosening of dense sand layer above shield tunneling for 200 m length is due to the strength characteristics of no cohesion which induced in unstable shield face and resulted in sink hole as well as caves underground. It may be estimated the appropriate range of the chamber pressure but it is much more practical and straight forwards to carry out face loading/unloading test at the site.

For the safety of face stability, digital twin observational method is proposed by face loading and face unloading tests to obtain the appropriate chamber pressure. Geotechnical parameters shall be obtained by inverse analysis for the tests and further used for simulation of tunnel performance in the next step with different boundary conditions.

REFERENCES

E-Nexco, 2020, https:www.e-nexco.jp/en/pressroom/kanto/2020/1018/00008605.html

Kim et.al, 2017, Effect of Fine Fraction Content in Soil Materials on Stability of River Dike, Ground and Construction, Vol.35, No.1, pp 37–44, Chugoku-Branch, JGS.

Hatanaka, M. et.al, 1999, Empirical Correlation between Internal Friction Angle and Normalized SPT value(N1) for Sandy Soils, Journal of Soils and Foundations, Vol.47-8 pp. 5–8, JGS.

Smart Geotechnics for Smart Societies – Zhussupbekov, Sarsembayeva & Kaliakin (Eds)
© 2023 The Author(s), ISBN 978-1-003-29912-7
Open Access: www.taylorfrancis.com, CC BY-NC-ND 4.0 license

Face-less tunnelling with monitoring and control system of friction cut plates

K. Komiya & M. Endo
Chiba Institute of Technology, Japan

K. Funakoshi & T. Nakamura
Uemura Engineering Co., Ltd, Japan

ABSTRACT: The Face-Less Tunnelling Method (FLTM) is a new simple tunnel construction method without a working face excavation. In FLTM, the sliding steel plate called Friction Cut Plate (FCP) is placed between a box culvert and its surrounding soil to reduce frictional forces during the jacking process of the box culvert. In this study, the FCP monitoring and control system (FMCS) that is a real time control system to fix the FCP automatically during the box culvert advancement is developed. The system restrains the FCP by monitoring the displacement of FCP and controlling tensile forces acting between control jacks and the FCP. The FCP is systematically controlled via the solenoid valve control unit while switching between high pressure and low pressure states for each control jack based on the measurement of stroke sensors. The FMCS was applied to FLTM tunnelling work in Nagano, Japan. The measured horizontal displacements of locations along the railway track due to the construction showed less than plus/minus 3 mm.

1 INTORODUCTION

The face-less tunnelling method (FLTM), is one of non-excavation methods used for constructing an underpass tunnel underneath a railway line or road without disrupting traffics for shallow earth coverage (Funakoshi, 2015). In this method, square-shaped steel elements called guide boxes are placed along the outer periphery of a box culvert into the ground across the existing railway/road to protect the tunnel face and railway/road. Subsequently, a box culvert placed behind the guide boxes is pushed forward and replaced with the box culvert in place. An advantage of this method is that it can construct an underpass tunnel with shallow earth coverage without leaving guide boxes as a protective shield in the ground. A sliding steel plate called friction cut plate (FCP) is placed between a box culvert and its surrounding soil to reduce frictional forces during the jacking process of the box culvert. Further, the FCP plays an essential role in suppressing ground deformation. The FCP needs to be fixed in the construction yard of the launch side because the drag force acts on the FCP during the advancement of the box culvert.

In order to effectively perform the box jacking operation while minimizing railroad track displacement during the advancement of the box culvert, the guide boxes incorporating automatic controlled system including the railroad track monitoring, construction operation and mitigation measures is developed.

This study presents construction cases for adopting a FCP fixing method called an automatic friction plate monitoring and control system (FMCS) comprising stroke sensors, hydraulic pumps, solenoid valve control unit, FCP control jacks and control computer. FMCS is a real time control system that automatically controls to restrain the FCP by monitoring the behaviour of the FCP and tensile forces acting between control jacks and the FCP. The FMCS is used to a FLTM construction work of a four span rectangular tunnel under passing a railway track in Nagano prefecture, Japan.

DOI: 10.1201/9781003299127-132

2 OVERVIEW OF FLTM AND FMCS

2.1 *Face-less tunnelling method (FLTM)*

The FLTM is a refined the box jacking tunnelling method and it is a simple tunnel construction method without a working face excavation.

As shown in Figure 1, the guide boxes and FCP are placed along the outer periphery of a box culvert so that soil is enclosed by these elements in the undercrossing area. Then, the guide boxes connected with the box culvert is pushed out towards the arrival side. During the advancement of the box culvert, the FCP is separated from the guide boxes and anchored to the arrival shaft to reduce friction between the box culvert and soil. After the guide boxes and soils enclosed within the guide boxes are pushed towards the arrival shaft, guide boxes are disassembled and soils are removed.

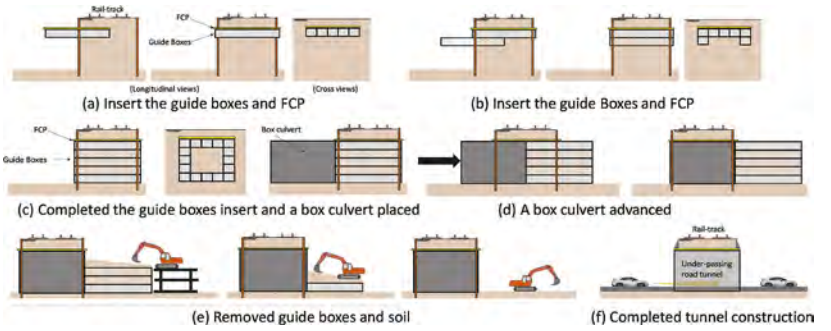

Figure 1. Schematic diagram for FLTM.

2.2 *Friction cut plate monitoring and control system (FMCS)*

FMCS is the automated control system to restrain the FCP by monitoring the displacement of the FCP and tensile forces acting between control jacks and the FCP. FMCS comprises stroke sensors to measure the horizontal displacement of FCP, hydraulic pumps, solenoid valve control unit, FCP control jacks and control computer. The FCP is automatically controlled via the solenoid valve control unit while switching between high pressure state and low pressure state for each control jack based on the measurement of stroke sensors. When the displacement of the FCP exceeds the control value defined in advance, each control jack is automatically switched to high pressure control.

In the high pressure state, the pressure required for the control jack to correct the displacement of the FCP is estimated using the dead load above the FCP. In the low pressure state, the control jack to apply constantly transmits the tensile force to the FCP during the advancement of the box culvert and to maintain the horizontal position of the FCP. In this way, FMCS repeatedly switches to the low pressure state for maintaining the horizontal position of the FCP and the high pressure sate for correcting the displacement of the FCP if it exceeds the control value.

3 FIELD INVESTIGATIONS

3.1 *Construction overview*

A construction work was conducted in Nagano prefecture, Japan. In this project, a single layer four span box culvert was constructed at the intersection of a rail track and a road. In this construction site, a total of 56 rows of guide boxes with a 12m long (3m * 4 pieces) culvert was arranged (Figure 2), and guide boxes integrated with the box culvert was moved forward. Using the FLTM, a cast-in-place RC structure with a width of 24.4 m and a height of 7.7 m was placed 0.66m deep under the earth's surface at a section of 11.604 m.

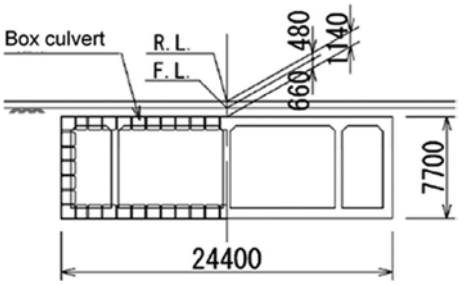

Figure 2. Cross section of box culvert.

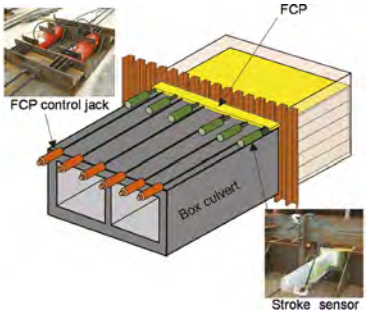

Figure 3. Schematic diagram for FLTM.

3.2 *Implementation of FMCS*

3.2.1 *FMCS equipment*

The FMCS is to restrain the FCP by measuring relative displacement of the FCP with respect to the main girder connected to the FCP using stroke sensors. The displacement of the FCP is adjusted by FCP control jacks when the FCP slides over the setting value during the advancement of the box culvert (see Figure 3).

3.2.2 *Setting value for low pressure*

A setting value for low pressure is calculated using the following equation based on the idea that the frictional resistance as the tensile force acts on the FCPs due to the dead load above the advancing box. Table 1 presents the values calculated using Equation. 1.

$$T = W \cdot A \cdot \mu \tag{1}$$

where T: Tensile force acting on FCP (kN)
W: Dead load acting on FCP (kN/m^2)
A: Top surface area of box culvert (m^2)
μ: Coefficient of friction (0.5 for assumed value)

Table 1. Calculated value of tensile force action on FCP.

	Calculated value	Note
Dead load acting on FCP: Z	20.56 kN/m^2	Railway truck structure + Earth coverage
Top surface area of box culvert: A	243.83 m^2	Width 24.4 m x Length 9.993 m
Tensile force acting on FCP: T=2,506.6 kN		

Since 12 control jacks were used in this site, the setting value for low pressure X becomes X ≧6.83 (MPa). During the construction, the value of 8 MPa was used as the initial setting and the degree of pressure was adjusted as the construction progressed.

3.3 *Horizontal displacement of railway track*

During the advancement process of box culvert, the railway line inspection was conducted to check rail gauge, vertical and horizontal level and rail distortion. Additionally, the lateral displacement of the railway track was measured at the construction site. The main purpose of this measurement was to compensate for the horizontal displacement of the railway track due to the movement of the FCP controlled by FMCS. A total of 12 measurements located 5 m apart (6 locations/railway line × 2 lines) were selected along the inbound and outbound railway lines where the box culvert crossed (Figure 4).

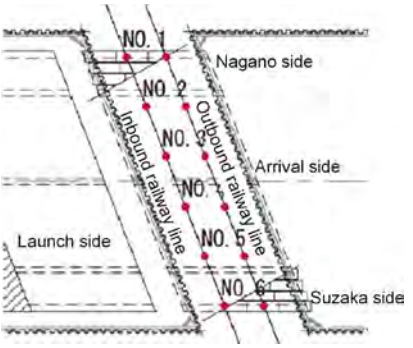

Figure 4. Measurement locations for horizontal displacement of railway track.

Table 2 lists the measurement results for the inbound railway line during the advancement process of the box culvert. Since the construction site was located within the straight railway section, the reference line of 190 mm apart from the rail was set along the railway track. The horizontal distance of the railway track for each location was measured on the basis of the reference line. The initial values presented in the table were measured before the advancement of the box culvert; these values were used as the reference values.

Table 2. Measurement results for inbound railway line during the advancement process of the box culvert.

				Before advancement (mm)		After advancement (mm)		Direction of displacement To launching side → To arrival side ←
Measurement location		Control value (mm)	Initial value α (mm)	Measurement value β	Difference from α	Measurement value	Difference from β	
Nagano side	No.1	190	187	186	1	185	1	←
	No.2	190	180	179	1	180	-1	→
Centre	No.3	190	180	181	-1	182	-1	→
	No.4	190	184	184	0	186	-2	→
Suzaka side	No.5	190	180	180	0	182	-2	→
	No.6	190	186	185	1	185	0	0

4 CONCLUSIONS

This study described a new face-less tunnelling method with the friction cut plate monitoring and control system. The face-less tunnelling method was used to in the construction work of four span rectangular tunnel under passing a railway track in Nagano prefecture, Japan. The integrated friction cut plates were adjusted via six control jacks attached to the top of the box culvert and the railway line inspection was also conducted to check rail gauge, horizontal level and rail distortion during the advancement of the box culvert. Overall, in most of the measurement locations over 108 locations, horizontal displacements along the railway track indicated less than plus/minus 3 mm. So far, the adoption of the friction cut plate monitoring and control system can be anticipated to control displacements of the Friction cut plates and railway track effectively in the face-less tunnelling method.

REFERENCES

Funakoshi, K. 2015. Displacement control method, Journal of Japan Micro tunneling Association, 29 (12): 42–44 (in Japanese).

Smart Geotechnics for Smart Societies – Zhussupbekov, Sarsembayeva & Kaliakin (Eds)
© 2023 The Author(s), ISBN 978-1-003-29912-7
Open Access: www.taylorfrancis.com, CC BY-NC-ND 4.0 license

The reaction of the Earth's surface to twisting and normal loads moving through the tunnel

V.N. Ukrainets, S.R. Girnis, G.A. Zhukenova & K.T. Sakanov
Toraighyrov University, Pavlodar, Kazakhstan

S.T. Mussakhanova
L.N. Gumilyov Eurasian National University, Astana, Kazakhstan

ABSTRACT: The problem of the action on the surface of a circular cylindrical cavity located in an elastic half-space (array) uniformly moving along its forming normal and twisting loads is solved. Dynamic equations of elasticity theory are used to describe the motion of the array. On the basis of the obtained solution, the stress-strain state of the Earth's surface is investigated under the action of axisymmetric loads of this type uniformly moving along an unsupported tunnel of shallow laying.

1 INTRODUCTION

The stress-strain state (SSS) of the earth's surface under the action of a twisting load uniformly moving along an unsupported tunnel is investigated in the article [1]. In this paper, a similar study was carried out in the case when, in addition to the twisting load, a normal load moving at the same speed acts on the tunnel. Such an impact occurs, for example, when cleaning devices are operating in a circular tunnel.

2 MATERIALS AND METHODS

The research uses the method of mathematical modeling involving models of the theory of elasticity.

Formulation and analytical solution of the problem.

For research, we will present the design scheme of the tunnel in the form of an extended circular cylindrical cavity with radius R, located in a linearly elastic, homogeneous and isotropic half-space (array), assigned to fixed Cartesian x,y,z and cylindrical r,θ,z coordinate systems, the z axis of which coincides with the axis of the cavity and is parallel to the load-free horizontal boundary of the half-space (Earth's surface), the x – axis – perpendicular to this boundary: $x \le h$ (Figure 1), where h – is the distance from the axis of the cavity to the boundary of the half–space (earth's surface). The physical and mechanical properties of the array are characterized by the following constants: v – Poisson's ratio, μ – shear modulus, ρ – density.

In the direction of the z axis, the normal $P_r(\theta, \eta)$ and twisting $P_\theta(\theta,\eta)$ loads move along the surface of the cavity with the same constant velocity c

$$\sigma_{rr}|_{r=R} = P_r(\theta, \eta), \quad \sigma_{r\theta}|_{r=R} = P_\theta(\theta, \eta), \quad \sigma_{r\eta}|_{r=R} = 0. \tag{1}$$

where $r, \theta, \eta = z - ct$ – movable cylindrical coordinate system, σ_{rj} – components of the stress tensor in the array, $j = r, \theta, \eta$.

DOI: 10.1201/9781003299127-133

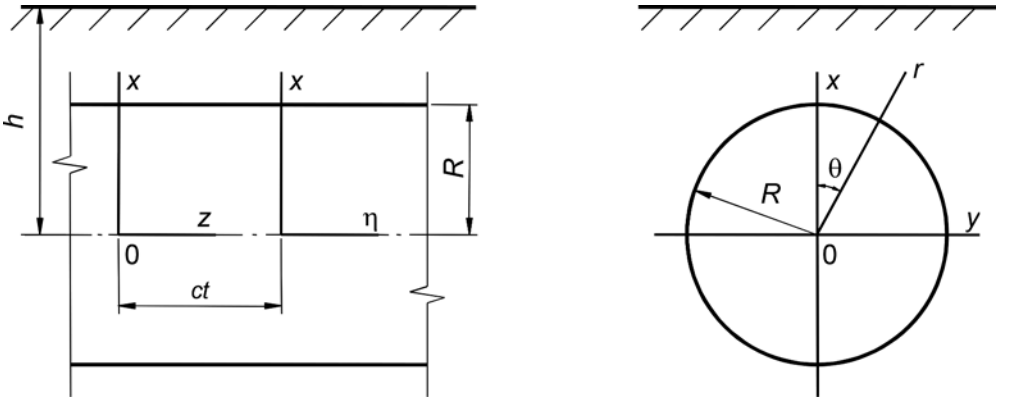

Figure 1. Design diagram of an unsupported tunnel.

Since the boundary of the half-space is free of loads, then, for $x = h$

$$\sigma_{xx} = \sigma_{xy} = \sigma_{x\eta} = 0 \tag{2}$$

To describe the motion of the half-space, we use the dynamic equations of the theory of elasticity in a moving coordinate system [2]

$$\left(M_p^{-2} - M_s^{-2}\right)\text{grad div}\mathbf{u} + M_s^{-2}\nabla^2\mathbf{u} = \partial^2\mathbf{u}/\partial\eta^2, \tag{3}$$

where $\mathbf{u}$ – displacement vector of elastic medium; $M_p = c/c_p,\ M_s = c/c_s$ – Mach numbers, $c_p = \sqrt{(\lambda + 2\mu)/\rho},\ c_s = \sqrt{\mu/\rho}$ – velocities of expansion-compression and shear waves in the medium, $\lambda = 2\mu\nu/(1 - 2\nu)$, ∇^2 – Laplace operator.

We transform equation (3) by expressing $\mathbf{u}$ in terms of Lame potentials [3]

$$\mathbf{u} = \text{grad}\,\varphi_1 + \text{rot}\left(\varphi_2\mathbf{e}_\eta\right) + \text{rot}\,\text{rot}\left(\varphi_3\mathbf{e}_\eta\right), \tag{4}$$

where $\mathbf{e}_\eta$ – ort of the η axis.

It follows from (3) and (4) that the Lame potentials φ_{jj} satisfy the equations

$$\nabla^2\varphi_j = M_j^2\frac{\partial^2\varphi_j}{\partial\eta^2},\ j = 1,\ 2,\ 3,$$

where $M_1 = M_p,\ M_2 = M_3 = M_s$.

Applying the Fourier transform with respect to η to the last equations, we obtain

$$\nabla_2^2\varphi_j^* - m_j^2\xi^2\varphi_j^* = 0,\ \ j = 1,\ 2,\ 3, \tag{5}$$

where ∇_2^2– two-dimensional Laplace operator, $m_j^2 = 1 - M_j^2,\ m_1 \equiv m_p,\ m_2 = m_3 \equiv m_s$, $\varphi_j^*(r, \theta, \xi) = \int\limits_{-\infty}^{\infty}\varphi_j(r, \theta, \eta)\ e^{-i\xi\eta}d\eta$.

By expressing the components of the stress-strain state of the medium through the Lame potentials and applying the Fourier transform according to the η, it is possible to obtain expressions for stress σ_{lm}^* and displacement u_l^* transformants in cylindrical $(l, m = r, \theta, \eta)$ and Cartesian $(l, m = x, y, \eta)$ moving coordinate systems as a function of φ_j^*. To determine the stress-strain state of the array, you need to find φ_j^*.

If we limit ourselves to the case when the speed of movement of loads is less than the speed of propagation of shear waves in the array ($c < c_s$), then $M_s < 1$ $(m_s > 0)$ and the solutions of equations (5) can be represented as follows [2]

$$\varphi_j^* = \Phi_j^{(1)} + \Phi_j^{(2)}, \tag{6}$$

where $\Phi_j^{(1)} = \sum\limits_{n=-\infty}^{\infty} a_{nj} K_n(k_j r)\, e^{in\theta}$,

$\Phi_j^{(2)} = \int\limits_{-\infty}^{\infty} g_j(\xi,\zeta) \exp\left[iy\zeta + (x-h)\sqrt{\zeta^2 + k_j^2}\right] d\zeta$.

Here $K_n(k_j r)$ – MacDonald functions, $k_j = m_j\xi$; $g_j(\xi,\zeta)$, a_{nj} – unknown, to be determined, functions and coefficients, j = 1,2,3.

It follows from [2] that when representing potentials in the form (6), expressions for transformants of potentials in the Cartesian coordinate system have the form

$$\varphi_j^* = \int\limits_{-\infty}^{\infty} \left[\frac{e^{-xf_j}}{2f_j} \sum_{n=-\infty}^{\infty} a_{nj}\Phi_{nj} + g_j(\xi,\zeta) e^{(x-h)f_j}\right] e^{iy\zeta} d\zeta, \tag{7}$$

where $f_j = \sqrt{\zeta^2 + k_j^2}$, $\Phi_{nj} = \left(\frac{\zeta + f_j}{k_j}\right)^n$, $j = 1, 2, 3$.

The functions $g_j(\xi,\zeta)$ are expressed in terms of coefficients a_{nj} from the boundary conditions (2), rewritten for voltage transformers taking into account (7). To do this, it is necessary to allocate the coefficients at $e^{iy\zeta}$ and equate them, due to the arbitrariness of y to zero. Then:

$$g_j(\xi,\zeta) = \sum_{k=1}^{3} \frac{\Delta_{jk}}{\Delta} e^{-hf_k} \sum_{n=-\infty}^{\infty} a_{nk}\Phi_{nk},\ j = \ 1,\ 2,\ 3. \tag{8}$$

Here $\Delta = \left(2\rho_0^2 - \beta^2\right)^2 - 4\rho_0^2\sqrt{\rho_0^2 - \alpha^2}\sqrt{\rho_0^2 - \beta^2}$, $\alpha = M_p\xi$, $\beta = M_s\xi$, $\rho_0^2 = \xi^2 + \zeta^2$. The type of algebraic complements Δ_{jk} is defined in [2].

It should be noted that $\Delta(\rho_0)$ – is the Rayleigh determinant, which, as is well known, has two real roots: $\pm\rho_R = \pm\xi M_R$. Here $M_R = c/c_R$ – Mach number, c_R – Rayleigh surface wave velocity ($c_R < c_s$) in an elastic half-space. Since the corresponding $\pm\zeta_R = \pm\xi\sqrt{M_R^2 - 1}$, Z, then $\Delta(\rho_0)$ does not turn to zero on the real axis if $M_R < 1$, or $c < c_R$ (Dorelean speeds of movement of loads). In this case, all integral functions in (6) are continuous and tend to zero rather quickly at infinity. Therefore, integrals exist and satisfy the conditions of attenuation at infinity. To calculate integrals (7), you can use one of the numerical integration methods, having previously determined the coefficients a_{nj}.

For $c < c_R$, taking into account (8), the relations (7) will take the form

$$\varphi_j^* = \int\limits_{-\infty}^{\infty} \left[\frac{e^{-xf_j}}{2f_j} \sum_{n=-\infty}^{\infty} a_{nj}\Phi_{nj} + e^{(x-h)f_j} \sum_{k=1}^{3} \frac{\Delta_{jk}}{\Delta} e^{-hf_k} \sum_{n=-\infty}^{\infty} a_{nk}\Phi_{nk}\right] e^{iy\zeta} d\zeta. \tag{9}$$

Using the known decomposition $e^{ikr\cos\theta} = \sum\limits_{n=-\infty}^{\infty} i^n J_n(kr) e^{in\theta}$, can get $\exp\left[iy\zeta + (x-h)\sqrt{\zeta^2 + k^2}\right] = \sum\limits_{n=-\infty}^{\infty} I_n(kr) e^{in\theta} \left(\frac{\zeta + \sqrt{\zeta^2 + k^2}}{k}\right)^n e^{-h\sqrt{\zeta^2 + k^2}}$ and, using (8), represent (6) in a cylindrical coordinate system:

$$\phi_j^* = \sum_{n=-\infty}^{\infty} \left[a_{nj} K_n(k_j r) + b_{nj} I_n(k_j r)\right] e^{in\theta},$$

where $b_{nj} = \sum\limits_{k=1}^{3} \sum\limits_{m=-\infty}^{\infty} a_{mk} A_{nj}^{mk}$, $A_{nj}^{mk} = \int\limits_{-\infty}^{\infty} \frac{\Delta_{jk}}{\Delta} \Phi_{mk}\Phi_{nj} e^{-h(f_k + f_j)} d\zeta$.

The coefficients a_{nj} Z are found from the boundary conditions (1), rewritten as

$$\sigma^*_{rr}\big|_{r=R} = P^*_r(\theta,\xi), \cdots \sigma^*_{r\theta}|_{r=R} = P^*_\theta(\theta,\xi), \quad \sigma^*_{r\eta}|_{r=R} = 0,$$

where $P^*_j(\theta,\xi) = p_j(\theta)p^*_j(\xi)$, $p_j(\theta) = \sum\limits_{n=-\infty}^{\infty} P_{nj}e^{in\theta}$, $p^*_j(\xi) = \int\limits_{-\infty}^{\infty} p_j(\eta)\, e^{-i\xi\eta}d\eta$, $j = r, \theta$.

When the coefficients of the Fourier-Bessel series are equated at $e^{in\theta}$, an infinite system of linear algebraic equations with a determinant of normal type is obtained, for the solution of which the reduction method or the method of successive reflections (approximations) can be used [2]. Moreover, as calculations show, the determinant of this system can turn to zero only when $c \geq c_R$.

After determining the coefficients a_{nj}, applying the inverse Fourier transform to the displacement and stress transformants, it is possible to calculate the components of the stress-strain state of the array in cylindrical and Cartesian coordinate systems.

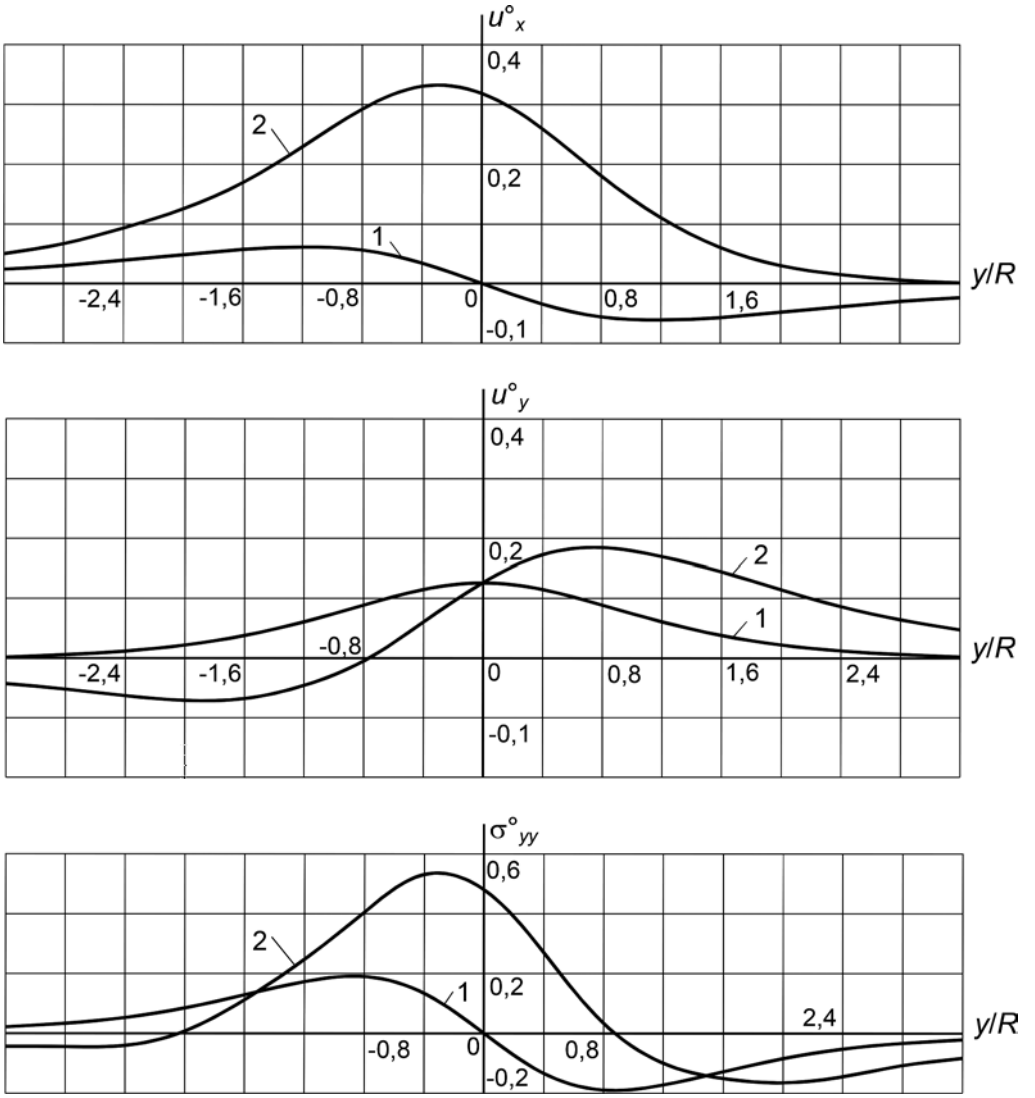

Figure 2. Change u°_x (м), u°_y (м) and σ°_{yy} on the Earth's surface in the coordinate plane xy (η=0).

3 RESULTS AND DISCUSSION

To study the dynamic effect of the loads discussed above on the stress-strain state of the Earth's surface, consider a circular cylindrical tunnel with a radius of R = 1 m and a depth of laying $h = 2R$ H in a siltstone massif (ν = 0,2, μ = 2,532·10^9 Pa, ρ =2,5·10^3 kg/m^3, c_p = 1643,4 m/c, c_p = 1643,4 m/c, c_R=917 m/c).

Axisymmetric compressive normal P_r and twisting P_θ loads of intensity q (Pa), uniformly distributed over the tunnel surface in the interval $|\eta| \leq l_0 = 0,2R$ Z=G, move in the direction of the z Y axis with a constant Dornel velocity c = 100м/с. The intensity q of each of the loads is selected in such a way that the total load along the entire length of the loading section $2l_0$ is equal to the equivalent concentrated ring load intensity $P^{\circ\circ}$ (N/m), that is, $q=P^{\circ\circ}/2l_0$.

Let 's introduce the notation: $u_x^\circ = u_x\mu/P^\circ(\text{M})$, $u_y^\circ = u_y\mu/P^\circ(\text{M})$, $\sigma_{yy}^\circ = \sigma_{yy}/P^\circ$, where $P^\circ = P^{\circ\circ}$/m (Pa).

Figure 2 shows the curves of change u_x° (м), u_y° (м) and σ_{yy}° on the Earth's surface in the coordinate plane xy (η=0). Curves 1 correspond to the action of a twisting moving load only on the tunnel, curves 2 correspond to the joint action of moving twisting and compressing normal loads.

As follows from the analysis of the behavior of curves, with the combined action of twisting and compressing normal moving loads on the tunnel, the maximum displacements and stresses on the earth's surface are significantly greater than with the action of twisting loads alone. Therefore, in the case of calculating the stress-strain state of the Earth's surface on the load from the work of cleaning devices moving along the axis of the tunnel and rotating relative to it, it is possible to represent their impact on the tunnel as a moving twisting load only when the pressure exerted on its surface is much less than the intensity of the twisting load.

4 CONCLUSION

In a strict mathematical formulation, the problem of the action of normal and twisting loads uniformly moving along its generatrix on the surface of a circular cylindrical cavity located in an elastic half-space is solved. The solution obtained for the Dorelev speeds of the movement of loads and the software package developed on its basis allows using mathematical modeling methods to study the dynamics of the rock mass under the influence of these loads at different depths of the tunnel laying.

REFERENCES

Ukrainets V.N. Reakciya zemnoj poverhnosti na begushchuyu vdol' tonnelya skruchivayushchuyu nagruzku [Reaction of the earth's surface to a torsional load running along the tunnel] Bulletin of Kazakh Leading Academy of Architecture and Construction. 2006, 1, 219-223. (In Russ.)

Erzhanov Zh.S., Aitaliev Sh.M., Alekseyeva L.A. (1989) Dinamika tonnelej i podzemnyh truboprovodov [Dynamics of tunnels and underground pipelines] − Alma-Ata: Nauka, 240. (in Russ.)

Novaczkij V. (1975) Teoriya uprugosti. [Theory of elasticity] − Moscow: Mir, 872. (in Russ.)

Smart Geotechnics for Smart Societies – Zhussupbekov, Sarsembayeva & Kaliakin (Eds)
© 2023 The Author(s), ISBN 978-1-003-29912-7
Open Access: www.taylorfrancis.com, CC BY-NC-ND 4.0 license

Assessment of the state of ventilation of high-Mountain Road Tunnels in Kyrgyzstan

S.U. Isagalieva & Zh.M. Ganiev
Kyrgyz Mining and Metallurgical Institute named after Academician U. Asanaliev at the Kyrgyz State Technical University named after I. Razzakov, Bishkek, Kyrgyzstan

ABSTRACT: The article describes the current state of ventilation of high-mountain road tunnels at the Too-Ashuu and Kok-Art passes. The natural factors affecting the mode of air movement through automobile tunnels in high altitude conditions are indicated. The features of the conditions of the highlands are extremely peculiar and are distinguished by a complex relief, a sharp change in climate and seismicity. An assessment was made of ventilation systems for automobile tunnels, based on the actual flow of vehicles today. As a result of the tunnel ventilation calculation, the amount of air required to ensure normal movement through the tunnel, it is necessary to switch to a more efficient way of ventilating high-mountain road tunnels. Safe, productive and high-quality ventilation is one of the main conditions for the operation of road tunnels. Tunnel traffic must be safe, comfortable and reliable.

The territory of Kyrgyzstan covers powerful mountain systems like the Tan Shan and Pamir. Almost 60% of the country's territory is located more than 1500 meters above sea level, with complex types of relief and a rarefied atmosphere. Currently, over 95% of domestic transportation in Kyrgyzstan is provided by passenger and freight vehicles. Roads connecting individual regions of the country pass through high mountain passes such as Too-Ashuu, Ala-Bel, Otmok, Kok-Art, Dolon and others.

At present, the Bishkek-Osh road is the only road in the country connecting the north with the south. In fact, it connects the capital with the western, southwestern and southern regions to maintain the economic, social and political integrity of the country.

On 129-132 km of the Bishkek-Osh highway, the K.Kolbaev tunnel passes on the Too-Ashuu lane. Its construction began in 1957, and it was commissioned in 1964. The tunnel will be 58 years old this year. The tunnel was reconstructed for the first time in 2001 and for the second time in 2003. In addition to the Kolbaev tunnel, four more tunnels have been constructed on the Bishke-Osh highway in the area between the city of Kara-Kul and Tash-Kumyr. Unlike the Kolbaev tunnel, these tunnels have a small length, and they are ventilated due to natural traction. The parameters of the road tunnels of the Bishkek-Osh highway are given in Table 1.

In 2014, the construction of an alternative North-South highway began. The construction of an alternative North-South route along the route Balykchi-Kochkor-Chaek-Aral-Kazarman-Jalal-Abad, 433 kilometers long, with the acquisition of a place by Kyrgyzstan, independence determines the place as the country's top priority project, 200 kilometers along these roads pass through where there are no transport messages. The total cost of the project is estimated at 850 million dollars.

The benefits that the Kyrgyz Republic will receive from the construction of the alternative North-South road are as follows:

1. An additional continuous road transport route will be created between the North and South of the country, which is geographically separated from the existing Bishkek-Osh

DOI: 10.1201/9781003299127-134

route by the mountain range. This route will run at a great distance from the line of state borders with neighboring states, which is important for the country's security.
2. Access to mineral deposits and development of land and agricultural land in Toguz-Toro, Ak-Tala, Jumgal, Kochkor regions will be provided, which is of great interest to the local population and investors who are interested in processing agricultural products.
3. The connection of this road with the roads of Kazakhstan and Russia in the north of the country and Tajikistan in the south will create a through transit along the route Russia-Kyrgyzstan-Tajikistan, which is of particular relevance to fulfilling obligations within the CIS, the Eurasian Economic Union, the CSTO and the Customs Union.

The automobile tunnel is located on the Kok – Art pass at an altitude of 2500 meters above sea level. The tunnel will be 3890 meters length, 10 meters width, and 9 meters height. The tunnel com-plex includes a road tunnel with a longitudinal service (multifunctional) tunnel. Upon completion, the tunnel will be the longest tunnel in Kyrgyzstan. Completion is planned by the end of 2022, and it is planned to be commissioned in 2023. Figure 1 shows a map of the main operating and alternative highway of Kyrgyzstan.

The problem associated with the ventilation of the Kolbaev automobile tunnel is important because of its strategic location and because it is the only road that currently connects the regions of the country. Almost 60 years have passed since the operation of the tunnel, the tunnel ventilation project was not designed for the flow of cars that we see to-day. According to the project, the tunnel is intended for the passage of passenger cars and small trucks, but now numerous multi-ton trucks are moving along it. In 2001, after reconstruction, 11 jet fans were installed in the tunnel by Samsung company (see Reconstruction of the K. Kolbaev tunnel. 1999). The fans are located in the roof of the tunnel as shown in Figure 2. After 12 years in 2013, the fans were replaced with new fans by The best company, but the ventilation system remained the same. The technical characteristics of the fan SDS-7,1-2P-6-30 are given in Table 2.

Table 1. Parameters of road tunnels of the Bishkek-Osh highway.

		Tunnel parameters		
Tunnel name	Location	Length, m	Height, m	Width, m
Tunnel named after K.Kolbaev	At 129-132 km of the Bishkek-Osh highway to the pass Too-Ashuu pass 3201 m above sea level	2510	5	6,2
Tunnel #1	On 409 km of Bishkek-Osh highway, Jalal-Abad region, Kara-Kul city	313	5,5	8,4
Tunnel #2	On 410 km of Bishkek-Osh highway Jalal-Abad region	355	5,5	8,4
Tunnel # 3	On 427 km of Bishkek-Osh highway Jalal-Abad region	694	5,5	8,4
Tunnel # 4	On 455 km of Bishkek-Osh highway, Jalal-Abad region, Tash-Kumyr city	260	5,5	8,4

Table 2. Technical characteristics of the fan.

Fan Type	SDS-7,1-2P-6-30
Air flow, m3/s	16,5
Engine rotation speed in min, rpm	2900
Output air velocity, m/s	41,6
Engine power, kW	30
Food	380v/50Hz
Wire cross section (copper)	3/14
Release date	2012/08

The calculation of emissions of pollutants from vehicles located in the tunnel is carried out according to the value adopted for 2010 (see Code of Rules. 2017).

Emissions Q of pollutants CO, (in terms of), g/h, and soot,, for light cars and light trucks with gasoline and diesel engines are calculated by the formula

$$Q = q \cdot f_h \cdot f_\tau \cdot f_{cm} + q_{BB} \quad (1)$$

where $q_{баз}$ = the basic value of CO and soot emissions for passenger cars and light trucks with gasoline and diesel engines, depending on the average speed and road slope of tunnel i, g/h or (see appendices A-B) (see Code of Rules. 2017);

$q_{вв}$ = emissions of suspended particles formed as a result of the destruction of the road-way, brake pads, (see appendix D) (see Code of Rules. 2017).

The correction factor is determined according to appendix D (see Code of Rules. 2017).

Then Q=192,8·1,0·1,0·1,5+0,56=289,76 g/h.

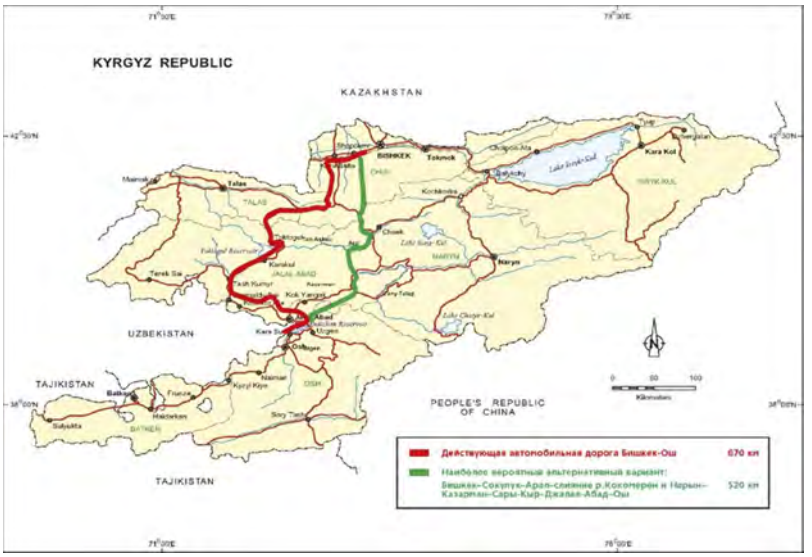

Figure 1. Map of the main highways of Kyrgyzstan.

Gas contamination inside the tunnel occurs due to a large flow of trucks that are passed unilaterally due to the size. When trucks enter the tunnel against the natural draft of the air inside the tunnel, trucks pull the gas blown by fans in the opposite direction and create an obstacle for timely cleaning of the air inside the tunnel. Due to the large flow of motor vehicles, namely trucks, they are passed along the reverse direction Bishkek-Osh-Bishkek. When trucks pass through the tunnel, exhaust gases are emitted in the tunnel. Since the traffic in summer time per day is from 3500 cars to 4500 cars per day, and in winter from 1500 cars to 2500 cars. There is clearly an excess of the maximum permissible concentration of carbon monoxide in the tunnel. Driving through it, drivers must necessarily close the windows and turn off the air conditioners. If the CO norm is exceeded by 17%, a gas contamination sensor is triggered in the tunnel in these cases, the tunnel service operators stop the cargo vehicles, thereby turning on the fans to output exhaust gases in the direction of the wind to output exhaust gases from the tunnel, these cases create long traffic jams of trucks on several serpentines of the highway pass, thereby creating inconvenience to other motor vehicles. the funds move freely.

Having studied the disadvantages of this method of ventilation, we have considered the main ones available. The first drawback in the tunnel is there is no clear separation of polluted air from fresh, the second is the suction and blowing of air occurs through the same channel, that is,

through the tunnel, clean and polluted air are mixed. Since jet fans are in-stalled, they supply the same amount of air that they receive from the outside. The third disadvantage is the wind rose, winds blow from both portals in the mountainous area, due to the lack of a third exit in the tunnel, frequent air reversal occurs, and a stagnant zone forms inside the tunnel.

The fourth disadvantage is the sequential ventilation connection (see Figure 2). With such a connection, each fan passes the same amount of air that it receives from the previous one, because of this we have a smaller amount of air for a larger amount. If one of the intermediate fans fails, the ventilation system is disturbed and a stagnant zone is formed.

The power of each of the 11 fans is 30 kW, then a total of 330 kW of electricity is consumed per hour, and the required amount of air will still not be supplied. The calculation of electricity consumption is shown in Table 3. If viewed from an economic point of view, the operating and capital costs for fan maintenance and subsequent replacement of fans with new ones at the end of their service life increase.

Table 3. Calculation of electric power consumption by fans.

Per hour, kW	Per day, kW	Per month, kW	Per year, kW	Price per 1 kW, som	Total cost of electricity per year, som
330	7920	237600	86724 000	3,4	294 861 600

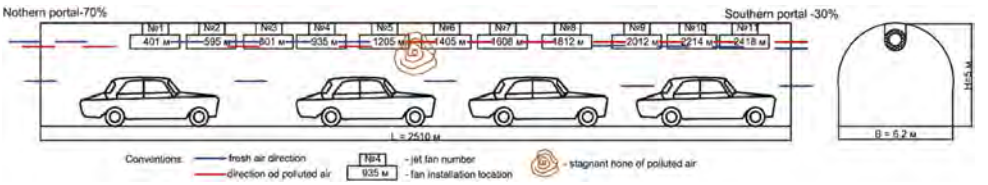

Figure 2. Ventilation scheme of the tunnel at the Too-Ashuu pass with the movement of vehicles in opposite directions using jet fans.

As can be seen from Figure 2, a fresh stream of air moves from both portals at the bot-tom of the portal, with the help of natural traction, exhaust gases in the form of warm polluted air rises to the top and a stagnant exhaust gas zone is formed.

Jet axial fans are multifunctional: they are designed for both normal ventilation and smoke removal during a fire. Composed of axial fans in a special configuration, they are mainly used in longitudinal ventilation and extract air. Jet fans are used in tunnels with bi-directional traffic or when the wind can have a significant effect on the airflow in the tunnel. Jet fan designs. It is based on an axial fan equipped with inlet and outlet pipes. Advantages: 1. Compact design for efficient ventilation; 2. High thrust with low power consumption; 3. Low noise; 4. Excellent corrosion resistance; 5. According to the signals from the sensors, switching to the smoke removal mode occurs immediately after a fire occurs. The disadvantages of jet fans include an increase in the concentration of harmful impurities along the length of the tunnel, susceptibility to natural draft, which depends on thermal and wind pressure, and insufficient fire safety. The amount of ventilation air required depends mainly on the conditions within the tunnel.

Recently, cases of fires of passenger cars running on gas have become more frequent in the tunnel. One of the reasons is the strong gas contamination of the tunnel. Due to the fire, the electrical cables that fed the fans failed and the tunnel was closed for repairs with partial admission of only passenger cars, and cargo vehicles were not allowed to pass. They stood in the cave for a long time in the summer due to this, vegetables and fruits brought from the south of the country deteriorated.

The above disadvantages of tunnel ventilation showed that it is necessary to radically change the tunnel ventilation system, since the existing system does not cope with the main tasks of ventilation systems in the tunnel.

The main tasks of ventilation systems in the tunnel are:

- provide the working environment with fresh air;
- ensure fire safety;
- elimination of exhaust gases;
- elimination of the risk of an explosion of a cloud of the fuel-air mixture, the release of poisonous gases, liquids and biological agents.

The above disadvantages of tunnel ventilation have shown that it is necessary to radically change the tunnel ventilation system.

Having assessed the ventilation conditions of the automobile tunnel, we offer two options for the ventilation scheme of the tunnel. The first option, based on the location of the tunnel (see Figure 1) on the Bishkek-Osh highway, it can be seen that 70% of the air is blown from the northern portal, and 30% of the air is blown from the southern portal, approximately in the zone marked in the diagram (see Figure 2.) the greatest stagnation occurs. Therefore, it is possible to drill a large-diameter well in the specified location with the installation of a powerful VOD-11P fan to the wellhead that will work for suction. The depth of the well at this point will be about 300 meters, the layout of the well is shown in Figure 3. This method has its advantages, we know that exhaust gases are much lighter than atmospheric air and therefore they accumulate in the roof of the tunnel, and thanks to natural traction they themselves will rise up. Since the direction of the flow of natural thrust coincides with the direction of the air created by the fan that works for suction. Table 5 shows the calculation for the consumption of electricity by the VOD-11P fan. Specifications of the VOD-11P fan are shown in Table 4.

Table 4. Technical characteristics of the VOD-11P fan.

Impeller diameter, mm	1100
Air flow, m3/s	7-33
Rated feed	21
Pressure, daPa	110-370
Rated pressure	338
Efficiency static	0,8
Electric motor power, kW	132
Voltage, V	380/660
Impeller speed, min-1	1500
Length, mm	6690
Width, mm	1870
Height, mm	1860
Fan weight with electric motor, kg	4560

Table 5. Calculation of electricity consumption by the VOD-11Pfan.

Per hour, kW	Per day, kW	Per month, kW	Per year, kW	Price per 1 kW, som	Total cost of electricity per year, som
132	3168	95040	34689600	3,4	117944600

Figure 3 shows the movement of clean and exhaust air. The exhaust air is sucked out of the well by the VOD-11P fan. Based on the calculation of electricity, it can be concluded that one powerful fan is more profitable and the performance is high compared to local jet fans, and the stagnant zone is eliminated with the reduction of CO_2 emissions to the MPC. The second option is the method of drilling two wells due to natural traction, polluted air will be removed through the wells without installing fans.

Axial fans are the technology of choice for large air volumes and are ideal for lateral or semi-transverse tunnel systems. They are also suitable for collecting smoke.

The advantages of axial fans include several factors:

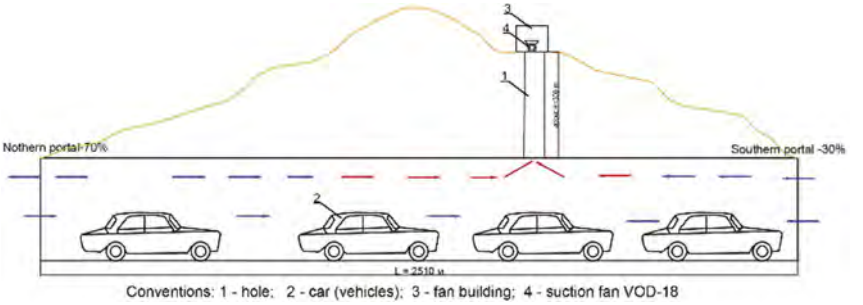

Figure 3. The layout of the hole.

- low noise level during operation;
- high efficiency;
- easy to operate;
- low cost and simplicity of design;
- low power consumption;
- long service life;
- engine protection against overloads, sparks, moisture;
- the ability to change the speed of rotation of the blades by changing the speed of the engine.

Conclusion: Based on the fact that at this stage a fresh stream of air enters and exits through the mouth of the tunnel, fresh and polluted air stream mix with each other (see Figure 2), which complicates the ventilation of the tunnel and provides fresh air. For the above reasons, there is always poor visibility in the stagnant zone, the smell of exhaust gases gets inside vehicles even through closed windows and doors. The methods we have considered change the existing method of tunnel ventilation by separating a fresh stream of air from a polluted one. Our proposed option is shown in Figure 3, the essence of this scheme is that it is necessary to conduct a vertical well on the mountainside, taking into account the terrain. Capital costs for drilling a well and building a building for a fan. We plan to come up with an idea at a meeting at the Ministry of Transport and Communications of the Kyrgyz Republic. According to the plan, ventilation reconstruction and replacement of fans is planned for 2023.

REFERENCES

Code of Rules. 2017. SP298.1325800.2017. Ventilation systems of road tunnels. Design rules. 85. Moscow.

Fomichev, V.I. 1991. Ventilation of tunnels and underground structures. L.: Stroyizdat: Leningrad branch.

Kaledina, N.O. 2016. Ventilation design in the construction of underground structures. Moscow: Gornaya kniga.

Makovsky, L.V., Trofimenko, V.Yu. Evstigneeva, N.A. 2009. Ventilation of road tunnels. Moscow: MADI.

Reconstruction of the K. Kolbaev tunnel. 1999. Bishkek.

Shuvalov, Yu.V. 2007. Ventilation of mines, mines and underground structures. Study guide St. Petersburg State Mining Institute (Technical University), St. Petersburg.

Smart Geotechnics for Smart Societies – Zhussupbekov, Sarsembayeva & Kaliakin (Eds)
© 2023 The Author(s), ISBN 978-1-003-29912-7
Open Access: www.taylorfrancis.com, CC BY-NC-ND 4.0 license

Experimental study on the feasibility assessment of using biopolymer-treated clays as a slurry material for TBM excavation

Sojeong Lee
School of Engineering and Information Technology, University of New South Wales, Canberra, Australia

Ilhan Chang
Department of Civil Systems Engineering, Ajou University, Republic of Korea

ABSTRACT: Bentonite-based slurry is commonly used for tunnel boring machine (TBM) excavation practices. However, the use of bentonite-based slurry accompanies environmental concerns and expansive after-use treatments. Meanwhile, biopolymer-based soil treatment (BPST) has been recently introduced to geotechnical engineering and has shown promising effects including shear strength increase, hydraulic conductivity decrease. In a previous study, xanthan gum biopolymer was attempted as a possible slurry substitute for mechanical tunneling. Biopolymer-based hybrid slurry mixtures were tested through a series of experimental programs including rheology assessment, hydraulic conductivity measurement, and swelling behavior assessment. As a result, biopolymer-based hybrid slurry has shown high competitiveness and feasibility to be used as a slurry material during TBM excavation.

1 INTRODUCTION

1.1 *Research background*

Tunnel Boring Machine (TBM) has been widely utilized in recent days due to its advantages such as adjacent ground disturbance minimization, and higher tunneling efficiency (Liu et al., 2016). While different types of TBM have been invented depending on the ground conditions, TBMs could be mainly classified into two categories (Park et al., 2021). They are 1) earth pressure balance (EPB) TBM and 2) slurry shield TBM, which are grouped from the manner of maintaining pressure at TBM face. Thus, EPB TBM is mainly applied at granite- or rocky ground while tunnelling at the ground with higher moisture content is commonly performed by slurry shield TBM. For EPB TBM, a bentonite-based conditioner is injected to improve excavated muck transportation efficiency. In contrary, bentonite is mixed with slurry, for slurry shield TBM. The excavated muck, consequently, contains high amounts of bentonite, which renders higher possibility to absorb hazardous materials during excavation and after excavation (Ren et al., 2016). This study aims to reduce the amount of bentonite usage among TBM excavation in order to ease the environmental concern related to muck disposal.

1.2 *Introduction of xanthan gum*

Xanthan gum biopolymer is recently introduced in geotechnical engineering, with its soil coagulation effect and natural degradation feature (Kwon et al., 2019, Lee et al., 2019). In details, xanthan gum biopolymer enhances shear strength when the xanthan gum – soil matrix is developed (Cabalar and Canakci, 2011, Soldo et al., 2020, Soldo and Miletić, 2019). Another previous study proved that xanthan gum biopolymer hydrogel effectively decreases hydraulic permeability (Cabalar et al., 2017, Tran et al., 2019). Meantime, xanthan gum has shown its economic efficiency with decreasing trend of the unit price (Mendonça et al., 2020). In this study, xanthan gum is chosen as a target

DOI: 10.1201/9781003299127-135

biopolymer since it has a high workability within a wide range of temperature (García-Ochoa et al., 2000), as well as the shear strength and compressive strength improvement with soil, and economic efficiency in practice.

2 MATERIALS AND METHOD

2.1 *Xanthan gum*

Xanthan gum biopolymer is an extracellular biopolymer cultivated from the bacteria, *Xanthomonas campestris*. Xanthan gum is a compose of repeating units including a main glucuronic backbone structure and a side chain which consists two mannoses and a glucuronic acid (García-Ochoa et al., 2000). When xanthan gum is dissolved in water, its phase renders a hydrogel form. The xanthan gum hydrogel renders pseudoplasticity and shear thinning properties (Ong et al., 2019).

2.2 *Bentonite and Kaolinite*

Bentonite and kaolinite are the representative clayey soil types in geotechnical engineering. Bentonite contains montmorillonite minerals and other smectite minerals. It has repeated 2 silica: 1 alumina layer structure. It has a strong water adsorption capacity owing to its structure. Kaolinite clay has repeated 1 silica: 1 alumina layer structure and each layer is connected via hydrogen bonding. In this study, research-grade bentonite and kaolinite are used (Sigma-Aldrich, CAS number: 1302-78-9, CEC = 64.1 meq/100gl Sigma-Aldrich, CAS number: 1332-58-7, CEC = 6.1 meq/100g).

2.3 *Sample preparation*

All tested samples are hydrated and, heretofore, each sample is referred as a slurry in this study. 7.5% bentonite slurry is set as a control group because 3 – 8% of bentonite is contained in the ordinary TBM slurry (Swartz, 2021). The hybrid slurry candidates are suggested in this study. They are 5% bentonite + 0.5% xanthan gum, 2.5% bentonite + 0.75% xanthan gum, 10.0% kaolinite + 0.5% xanthan gum, and 5.0% kaolinite + 0.75% xanthan gum. Each slurry candidate is prepared by mixing powder type- clay and biopolymer and then dissolved into deionized water. An electronic hand mixer is used to ensure homogeneous mixing.

2.4 *Experimental methods*

Referring that plastic viscosity is commonly used to assess the properties of drilling mud (American Petroleum Institute, 2020), rheological properties are measured from steady state measurement, using a rheometer (Malvern Kinexus Pro Rheomoter). Shear rate is controlled between 0.001 to 1000 s^{-1}. Hydraulic conductivity is tested by measuring the extracted water amount from the slurry containing reservoir under 250 kPa condition. After 30 minutes of duration, filtrate volume is measured.

3 RESULTS

3.1 *Rheology measurement*

7.5% bentonite shows distinctive shear thinning property which decreases viscosity with increasing shear rate as shown in Figure 1. The shear thinning behaviors are similarly monitored when bentonite content is decreased under existence of xanthan gum (Figure 1). While plastic viscosity of 7.5% bentonite is estimated as 0.0486 Pa·s, 5% bentonite + 0.5% xanthan gum and 2.5% bentonite + 0.75% xanthan gum are calculated as 0.0499 Pa·s and 0.0496 Pa·s, respectively. The difference between pure bentonite slurry and bentonite-based hybrid slurries is less than 2.7%. Interestingly, kaolinite-based hybrid slurries show the accordant shear thinning behavior to bentonite 7.5% (Figure 1). The shear thinning behavior is not obviously affected by kaolinite and xanthan gum contents. Their plastic viscosities are approximated as 0.0315 Pa·s and 0.0188 Pa·s, resulting the

relative error less than 61.3% (0.0298 Pa·s). The shear rejuvenation is clearly monitored in all cases, as shown in Figure 2. Yield point could be adjudged from approximation of critical point starting the shear rejuvenation. Although the yield point of bentonite 7.5% is higher than other hybrid slurry candidates, a little difference less than a dozen shear stress pascal is appeared between bentonite slurry and hybrid slurry candidates. In addition, the difference between bentonite-based hybrid slurries and kaolinite-based hybrid slurries is mimic.

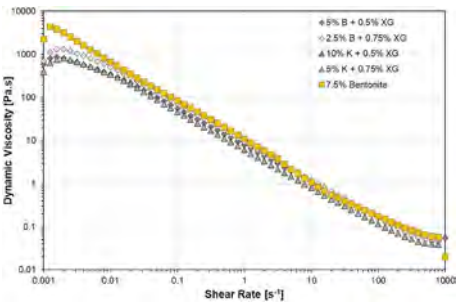

Figure 1. Shear thinning behavior of bentonite and hybrid slurries.

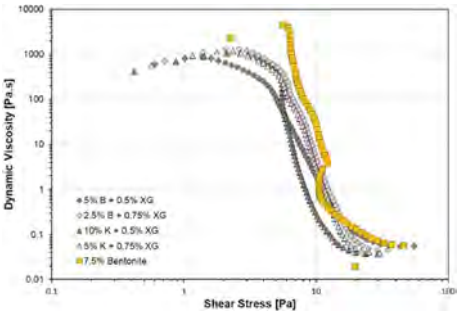

Figure 2. Shear rejuvenation of bentonite and hybrid slurries.

3.2 *Hydraulic conductivity*

As shown in Figure 3, the filtrate volume is decreased under existence of xanthan gum. Regardless of clay content, decrement of filtration is higher in case of higher amount of xanthan gum. Hydraulic conductivity of bentonite 7.5% is calculated as 4.7×10^{-6} m/s whereas bentonite-based hybrid slurries show 1.20×10^{-6} m/s (5% B 0.5% XG) and, 1.56×10^{-6} m/s (2.5% B 0.75% XG), respectively. Moreover, hydraulic conductivity of kaolinite-based hybrid slurries is found as 1.41×10^{-6} m/s (10% K 0.5% XG), and 1.36×10^{-6} m/s (5% K 0.75% XG).

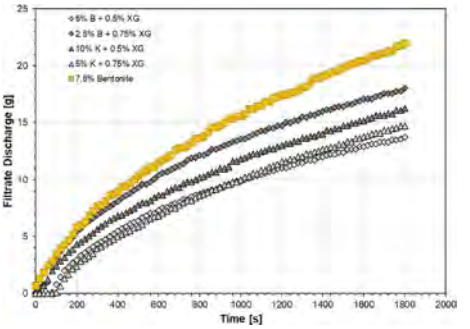

Figure 3. Hydraulic conductivity of bentonite and hybrid slurries.

3.3 *Inferential statistical analysis*

In this study, plastic viscosity and yield point are assessed as rheological properties. In addition, hydraulic conductivity is measured as a physical property. For inferential statistical analysis, these measured values are normalized based on 7.5% bentonite. Under importance order of measured properties is not revealed, random weight factor of units of integer (from 1 to 10) is applied to each measured property. Thereafter, closest slurry candidate condition to bentonite 7.5% is counted as a best case, and secondary closest condition is allocated to a second-best case. This procedure is repeated until all random combinations of weight factors are analyzed. The inferential statistical analysis shows

that 2.5% B 0.75% XG and 5.0% K 0.75% XG are the most feasible slurry candidates. For best case counting, 2.5% B 0.75% XG records 46.75% while 5.0% K 0.75% XG accounts 46.3%. Both configurations are enumerated as 26.0% and 48.7% respectively.

4 CONCLUSION

This study aimed to assess feasibility of sustainable slurry candidates containing xanthan gum. Through a series of laboratory assessment of bentonite-based and kaolinite-based hybrid slurry candidates are verified to be highly feasible in practices. The shear thinning properties of hybrid slurry candidates are similar to bentonite 7.5% regardless of clay and xanthan gum content, and hydraulic conductivity is decreased under existence of xanthan gum in all slurry configurations. This indicates that xanthan gum amends the engineering properties of slurry with less amount of bentonite than common content. Additionally, the inferential statistical analysis shows that 2.5% B 0.75% XG and 5.0% K 0.75% XG are the most feasible as a sustainable slurry alternative. While further studies are necessitated to implement tunnelling with sustainable hybrid slurry containing xanthan gum, this study proves the potential of xanthan gum in TBM excavation, through engineering property assessment.

ACKNOWLEDGEMENT

This work was supported by the National Research Foundation of Korea (NRF) grant funded by the Korea government (MSIT) (No. 2022R1A2C2091517).

REFERENCES

American Petroleum Institute 2020. API Specification 13A. *Drilling Fluids Materials*. Washington, DC, USA.

Cabalar, A. F. & Canakci, H. 2011. Direct shear tests on sand treated with xanthan gum. *Proceedings of the Institution of Civil Engineers - Ground Improvement*, 164, 57–64.

Cabalar, A. F., Wiszniewski, M. & Skutnik, Z. 2017. Effects of xanthan gum biopolymer on the permeability, odometer, unconfined compressive and triaxial shear behavior of a sand. *Soil mechanics and foundation engineering*, 54, 356–361.

Garcïa-Ochoa, F., Santos, V., Casas, J. & Gomez, E. 2000. Xanthan gum: production, recovery, and properties. *Biotechnology advances*, 18, 549–579.

Kwon, Y.-M., Chang, I., Lee, M. & Cho, G.-C. 2019. Geotechnical engineering behaviors of biopolymer-treated soft marine soil. *Geomechanics and Engineering*, 17, 453–464.

Lee, S., Im, J., Cho, G.-C. & Chang, I. 2019. Laboratory triaxial test behavior of xanthan gum biopolymer-treated sands. *Geomechanics and Engineering*, 17, 445–452.

Liu, Q., Huang, X., Gong, Q., Du, L., Pan, Y., Liu, J. J. T. & Technology, U. S. 2016. Application and development of hard rock TBM and its prospect in China. 57, 33–46.

Mendonéa, A., Morais, P. V., Pires, A. C., Chung, A. P. & Oliveira, P. V. J. A. S. 2020. A review on the importance of microbial biopolymers such as xanthan gum to improve soil properties. 11, 170.

Ong, E. E., O'byrne, S. & Liow, J. L. 2019. Yield stress measurement of a thixotropic colloid. *Rheologica Acta*, 1–19.

Park, B., Choi, S.-W., Lee, C., Kang, T.-H., Do, S., Lee, W.-Y. & Chang, S.-H. J. A. S. 2021. An Operating Model for an EPB Shield TBM Simulator by the Correlation Analysis of Operational Actions and Mechanical Responses. 11, 11443.

Ren, D.-J., Shen, S.-L., Cheng, W.-C., Zhang, N. & Wang, Z.-F. J. E. E. S. 2016. Geological formation and geo-hazards during subway construction in Guangzhou. 75, 1–14.

Soldo, A., Miletić, M. & Auad, M. L. 2020. Biopolymers as a sustainable solution for the enhancement of soil mechanical properties. *Scientific Reports*, 10, 267.

Soldo, A. & Miletić, M. J. S. 2019. Study on shear strength of xanthan gum-amended soil. 11, 6142.

Swartz, S. 2021. MDOT Question on Slurry Containment: Slurry systems with excavation by TBM. *In:* Transportation, M. D. O. (ed.).

Tran, A. T. P., Chang, I. & Cho, G.-C. 2019. Soil water retention and vegetation survivabiity improvement using microbial biopolymers in drylands. *Geomechanics and Engineering*, 17, 475–483.

Smart Geotechnics for Smart Societies – Zhussupbekov, Sarsembayeva & Kaliakin (Eds)
© 2023 The Author(s), ISBN 978-1-003-29912-7
Open Access: www.taylorfrancis.com, CC BY-NC-ND 4.0 license

Analysis of tunnel GPR image based on Convolutional Neural Networks with single-stage and two-stage detections

ByongKyu Bae & Jaehun Ahn
Department of Civil and Environmental Engineering, Pusan National University, Busan, Republic of South Korea

DuHwoe Jung
Department of Civil Engineering, Pukyong National University, Busan, Republic of South Korea

Hyunjun Jung
Department of DX, Korea Authority of Land & Infrastructure Safety (KALIS), Jinju, Republic of South Korea

Changkyoon Yoo
Department of Tunnel, Korea Authority of Land & Infrastructure Safety (KALIS), Jinju , Republic of South Korea

ABSTRACT: Maintenance of tunnel structure involves investigation of tunnel wall with Ground Penetration Radar (GPR). By analyzing GPR investigation images, engineers determine the locations of steel ribs, thickness of concrete lining and the location and size of void if any. The identification of defects, however, requires experience and also is a time-consuming work. YOLO (You Only Look Once) and Mask R-CNN are CNN (Convolutional Neural Network) algorithms with single-stage detection and two stage detection, respectively. In this study, a model based on YOLO was trained to detect the steel ribs in GPR images and Mask R-CNN was trained to detect the concrete lining, and tested. Overall, both of the CNN algorithms provided satisfactory results; however, the images with severe scattering resulted in lower accuracy.

Keywords: GPR, Convolutional Neural Network, YOLOv5, Mask R-CNN, Image Detection

1 INTRODUCTION

Tunnels are built to pass through mountains or the sea in the shortest distance. As of 2020, there are 2,472 tunnels in Korea, and the number is gradually increasing. Tunnel maintenance survey is conducted often by the ground penetrating radar (GPR), a non-destructive method to investigate the lining conditions. GPR data analysis often requires experienced engineers. If GPR data can be analyzed by deep learning algorithms, it would increase the easiness and rapidity of the maintenance tasks. In this study, YOLO (You Only Look Once) and Mask R-CNN are CNN (Convolutional Neural Network) algorithms with single-stage detection and two stage detection, respectively, are used to analyze tunnel GPR data.

2 BACKGROUND

2.1 *Principle of Ground Penetrating Radar (GPR)*

Exploration using GPR is conducted by emitting electromagnetic waves from the surface of the structure to the inside in frequencies of several MHz to GHz. When electromagnetic waves

DOI: 10.1201/9781003299127-136

are radiated into a structure to be probed, reflection and diffraction occur due to the difference in permittivity between media. Through the interpretation of these data, it is possible to distinguish the steel support, lining, underground cavity, pipeline, and soft layer of the tunnel (AL-Qadi & Lahouar, 2005). An example of tunnel GPR image is presented in Figure 1.

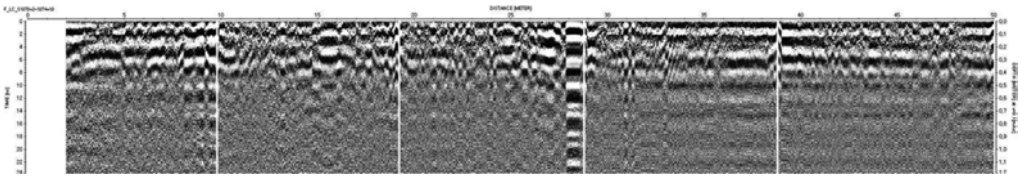

Figure 1. Tunnel GPR image.

2.2 *Convolutional Neural Networks (CNN)*

It is a neural network technique that detects the characteristics of an image by applying a filtering function to the artificial neural network. It classifies images by automatically learning each filter represented by a matrix to be suitable for data processing. In this classification method, the layer next to the input layer extracts low-level features, and the layer behind uses the low-level features obtained earlier to predict successive target values or class labels (Girshick et al., 2014). CNN that performs these functions is largely divided into three structures. Convolutional layer, pooling layer, fully connected layer.

2.3 *You Only Look Once (YOLOv5)*

Yolov5 is an object detection algorithm based on CNN. One-stage object detection is a deep learning technique that predicts objects by segmenting them in a grid form from the entire image, rather than predicting objects step by step, enabling high-speed prediction while maintaining high precision (Ieamsaard et al., 2021).

2.4 *Mask R-CNN*

Mask R-CNN detects an object through bounding box and proceeds with segmentation for each case. The final goal of Mask R-CNN is instance segmentation, which is an activity that identifies each object's area as a rectangular bounding box and then narrows it down more precisely to determine whether it belongs to a class in pixel units (He et al., 2020).

3 EXPERIMENTS

Figures 2 and 3 show the overall flow of analyzing images and deriving feature points using YOLOv5 and Mask R-CNN, respectively. Data labeling is the task of setting feature points required for learning. Labeling types used in this experiment are bounding box labeling and polygon labeling. YOLOv5 uses bounding box labeled data to detect steel ribs. Mask R-CNN uses polygon labeled data to detect concrete lining.

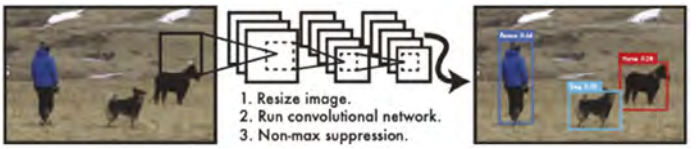

Figure 2. YOLO detection system (Redmon et al., 2016).

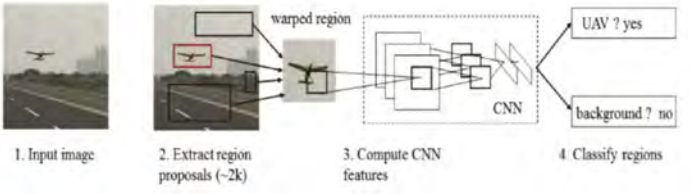

Figure 3. Mask R-CNN detection system (Yang et al., 2017).

Total number of data used in the experiment is 220. Among 220 datasets used, 200 datasets were randomly assigned for training, 10 for validation, and the rest for test. Experiments to detect steel rib and concrete lining were conducted three times each.

Figure 5 is the YOLOv5 detection accuracy graph. It was confirmed that the y value representing the accuracy in the graph converged to a value close to 95.7% accuracy when the x value was 250 epochs or more. Therefore, In the analyses presented here, the maximun epoch was set to be 300. The average time for the detecting steel ribs were 41 minutes. The average of image detection accuracy was about 95.7%. Figure 4 is the result of the steel rib detected from the GPR data.

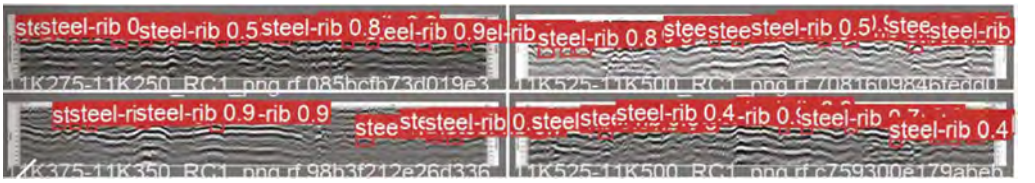

Figure 4. Detecting steel ribs using YOLOv5.

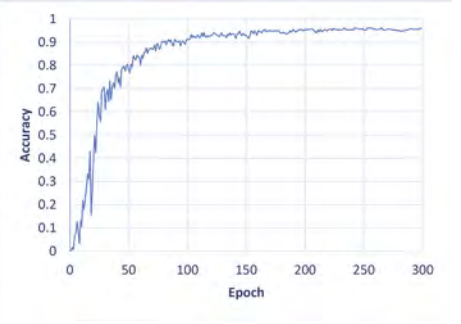

Figure 5. YOLOv5 detection accuracy graph.

Figure 7 is Mask R-CNN detection accuracy graph. Iterations are the number of mini batches required to complete 1-epoch. For the sizes of image and batch used in the analyses,100 iterations corresponds to 1 epoch in this case. It was confirmed that the y value representing the accuracy in the graph converged to a value close to 96% when the x value was 25000 iterations or more. In the analyses presented here, the maximun iteration was set to be 30000. The average time for the detecting concrete lining was 3 hours 25 minutes. The average of image detection accuracy was about 96%. Figure 6 is picture of concrete lining detected using Mask R-CNN. Red line is the concrete lining detected by the experienced engineer, and the purple area is the section detected by Mask R-CNN.

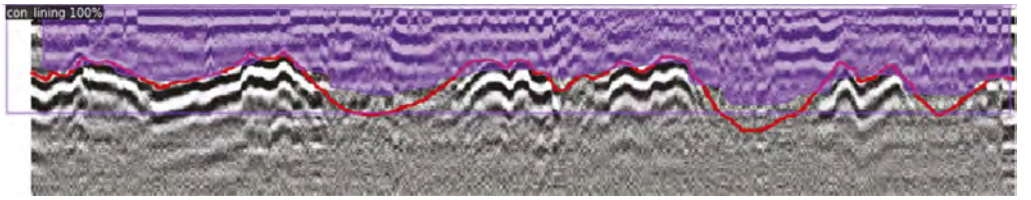

Figure 6. Detecting concrete lining using mask R-CNN.

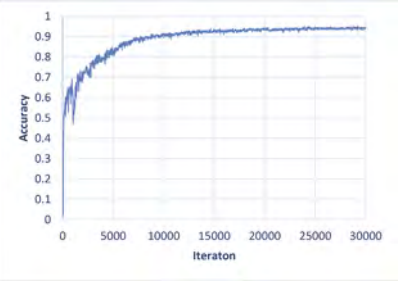

Figure 7. Mask R-CNN detection accuracy graph.

4 CONCLUSION

Experiments were conducted to detect steel ribs and concrete linings in tunnel GPR images based on CNN based algorithms. Steel rib was detected by YOLO, resulting in an average accuracy of about 96%. Concrete lining detection was performed by Mask R-CNN, again with a satisfactory accuracy of 96%. Concrete lining detection using Mask R-CNN was very close to the decision of experienced engineer; however, it predicted smoother curve than engineer's work. Follow-up study would be necessary to have better accuracy for the images with high scattering.

ACKNOWLEDGMENT

This research was supported by Korea and by Basic Science Research Program through the National Research Foundation of Korea (NRF) funded by the Ministry of Education (No. 2022R1I1A3069043).

REFERENCES

Al-Qadi, I. L., & Lahouar, S. (2005). Measuring layer thicknesses with GPR–Theory to practice. *Construction and building materials*, *19*(10), 763–772.

Girshick, R., Donahue, J., Darrell, T., & Malik, J. (2014). Rich feature hierarchies for accurate object detection and semantic segmentation. In *Proceedings of the IEEE conference on computer vision and pattern recognition* (pp. 580–587).

Ieamsaard, J., Charoensook, S. N., & Yammen, S. (2021, March). Deep learning-based face mask detection using yolov5. In *2021 9th International Electrical Engineering Congress (iEECON)* (pp. 428–431). IEEE.

He, K., Gkioxari, G., Dollár, P., & Girshick, R. (2017). Mask r-cnn. In *Proceedings of the IEEE international conference on computer vision* (pp. 2961–2969).

Redmon, J., Divvala, S., Girshick, R., & Farhadi, A. (2016). You only look once: Unified, real-time object detection. In *Proceedings of the IEEE conference on computer vision and pattern recognition* (pp. 779–788).

Yang, Y., Gong, H., Wang, X., & Sun, P. (2017). Aerial target tracking algorithm based on faster R-CNN combined with frame differencing. *Aerospace*, *4*(2), 32.

Smart Geotechnics for Smart Societies – Zhussupbekov, Sarsembayeva & Kaliakin (Eds)
© 2023 The Author(s), ISBN 978-1-003-29912-7
Open Access: www.taylorfrancis.com, CC BY-NC-ND 4.0 license

Investigation of micro cracks evolution around an opening in artificial rock samples: Inclined shear test with acoustic emission and DEM simulations

A.A. Owayo
Technical University of Kenya, Kenya

F. Teng
National Taiwan University of Science and Technology, Taiwan

W.C. Chen
National University of Kaohsiung, Taiwan

ABSTRACT: This research aimed to study micro-cracking in cement mortar made of hollow artificial rock. Via the new discrete element modeling (DEM) technique, ambiguity associated with the excavation damaged zone (EDZ) definition was meant to be clarified. Additions relating to the stress state were meant to be annexed to the EDZ definition. The influence of aggregate shape and water binder (w/b) ratio on the crack behavior of cement-based materials was also investigated. Inclined shear test (IST) was conducted on scaled hollow samples made of differently shaped aggregates (angular, A, and rounded, R) at varying w/b ratios. Further DEM simulations of the tests were carried out and the output both from tests and simulations were compared. New definitions of the EDZ incorporating the stress state have been proposed. The crack mechanism under varying shear angles, w/b ratio, and differently shaped aggregates have been studied.

1 INTRODUCTION

Over the years several methods of crack analysis have been proposed. Continuum-based analysis methods are perhaps the oldest numerical tools in this regard. Continuum-based analysis methods consist of finite element method (FEM) and finite difference method (FDM). They inherit advantages of classical continuum theory, while the constitutive law of elements allows for simulation of objects with complex geometry, these methods cannot solve discrete element (DEM) problems (Lisjak et al., 2014; Pietruszczak and Haghighat, 2015; Owayo et al., 2021). Over the last two decades,other methods such as discrete element methods, DEM (Gálvez et al., 2002; Bono, 2013; Owayo et. al, 2021; University of Edinburgh, 2022) have been introduced. Several authors have investigated the crack evolution of brittle materials (Martin, 1997; Blair and Cook, 1998; Tham et al., 2005; Lisjak et al., 2013; Choinska et al., 2017; Ghamgosar et al., 2017) using various analysis methods and tests. However, the recently introduced DEM modeling technique is yet to be well understood. In fact, so far, the qualitative descriptive method is still the best way to present the comparison between the DEM model with experimental results (Momozu et al., 2000; Tanaka et al., 2000; Owayo, 2022). Chen et al. (2018) developed a novel inclined shear test (IST) coupled with the acoustic emission (AE) technique to investigate the crack evolution of cementitious material from the microscale to the macroscale. The shear test apparatus has an open shear box design to allow for crack growth visualization. In this study, inclined shear test (IST) and acoustic emission (AE) experiments were conducted on hollow artificial rock samples to investigate the effects of crack evolution in brittle materials.

DOI: 10.1201/9781003299127-137

Several studies have analyzed concrete damage in numerical simulations with the finite element method (FEM) (Hu et al., 2004; Miller et al., 2011; Mackie, 2015; Liu et al., 2015; Moharrami and Koutromanos, 2017; Wu et al., 2017; Forti et al., 2020). FEM methods are often based on continuity principles (continuum mechanics), in which meshes cannot disjoin, even when the limiting stresses are attained. Some modified FEMs, such as the extended FEM (XFEM) framework, can have meshes that disjoin; however, these modified FEMs involve procedures that are computationally very expensive. Crack evolution thus cannot be analyzed using FEM. Currently, DEM, which takes into account discontinuity principles, has been used. (Wang and Gutierrez, 2010) conducted a DEM study of the micromechanics of granular materials via a direct shear test. (Nguyen et al., 2017) using DEM provided insight into the fracturing of concrete-like materials, and (Nitka and Tejchman, 2020) performed mesoscale mechanical modeling of damage in concrete, while (Ma and Huang, 2021) looked into the effect of shear bond failure on the strength of quasi-brittle materials.The discrete element contacts of the DEM can be disjointed to enable the visualization of crack initiation, growth, and development. Therefore, it was adopted to analyze the crack evolution of IST in this study in order to enhance the understanding of the crack evolution behavior of brittle materials.

2 INCLINED SHEAR TEST (IST)

Traditional direct shear test (DST) is applicable in studying shear behavior and determining strength parameters, such as cohesion (c) and friction angle (ϕ). To improve the DST, a novel shear apparatus with an open-shear-box design for IST was developed by (Chen et al., 2019) for application, in conjunction with AE technique, in identifying the distribution of micro-cracks in samples. In IST, normal and shear-force components varied during the process. Open-shear box design facilitates installation of extensometer and AE sensors, producing a complete loading curve with accompanying AE events.

A hollow sample with no support on its walls undergoing inclined shear test is shown in Figure 1a. Figure 1b shows a hollow sample with its walls supported undergoing inclined shear test. Figure 2 shows the relationship between the load and the sample faces. The test method was extensively discussed by (Chen et al., 2013). IST's design allows for the installation of AE sensors; which is unachievable in DST, due to its closed-box design. The sample measured 70 mm x 70 mm x 40 mm and were tested at various shear angles; 25°,45°, and 65°. The positions of micro-cracks were located with high precision, thanks to a set-up of eight AE sensors.

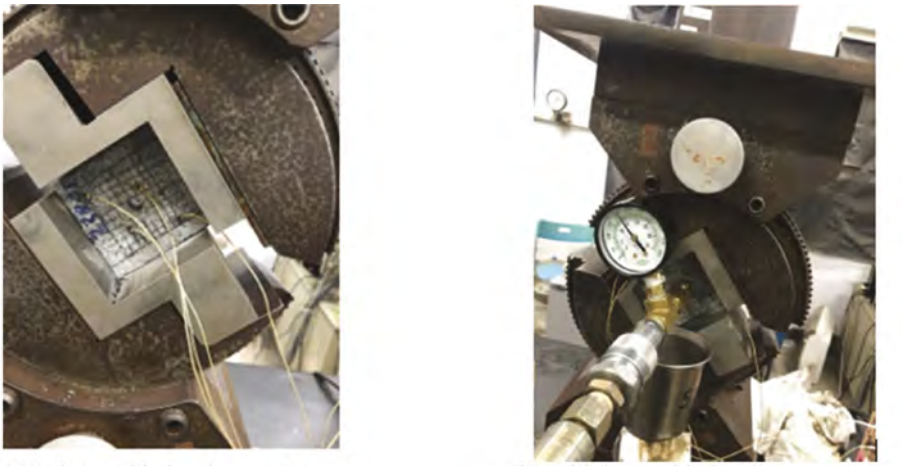

(a) No internal balancing pressure, p_i (b) With internal balancing pressure, p_i

Figure 1. IST set-up used for the EDZ study on hollow samples.

3 DEM SIMULATION

3.1 *Numerical model setup*

The numerical specimens measured 70 mm x 70 mm x 40 mm, similar to the physical samples. In general, for the sake of reducing computational cost, the DEM shear rate is usually considerably higher than those in the test (Brown, 2013; Fakhimi and Hemami, 2017; Owayo et al., 2021; Owayo, 2022). Figure 3(a) and (b) exhibit the numerical setup for non-hollow and hollow sample models respectively. Figure 4(a) shows a triple sphere representation of angular aggregates in DEM and Figure 4(b) shows a single sphere representation of rounded aggregates in DEM. To ensure computational efficiency, the sizes of the particles in the simulation should not be too small. Reasonably compact samples were produced, when particles particle constituting the numerical models were produced using normal distribution statistical technique. The mean size and standard deviation of the generated particles had to be related to the actual particle size distribution of the sand particles in the physical samples. The loading plates were simulated as steel plates.

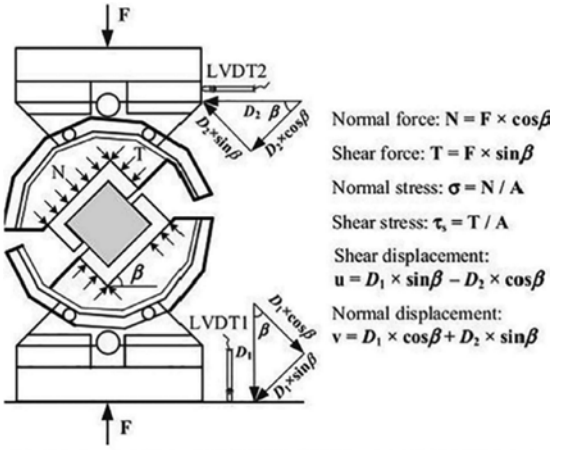

Note: β is the shear angle, **F** is loading force provided by MTS, **A** is the contacted area between specimen and shear box, $\mathbf{D_1}$ is the displacement measured by LVDT1 and $\mathbf{D_2}$ is the displacement measured by LVDT2

Figure 2. Relationship between load and sample faces in the novel test on a hollow sample.

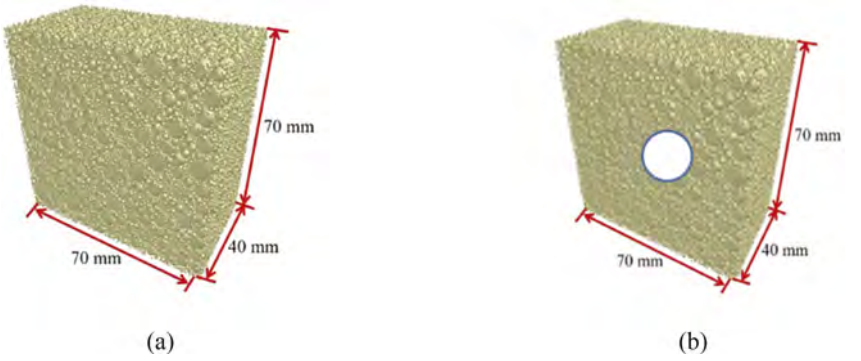

Figure 3. DEM simulation models: (a) Setup with no opening (b) Setup with opening.

Figure 4. (a) Triple-sphere representation of angular aggregates; (b) single-sphere.

3.2 *Macroparameters in the simulation*

Table 1 shows the macroparameters used in the simulation, these values are consistent with those set in the previous work (Owayo et al. 2021). The coefficient of restitution was judged to be near zero for civil engineering, whose calculations revolve around equilibrium of static forces. The values of the coefficient of static friction, coefficient of rolling friction, Poisson's ratio, mean particle bulk density, and Young's modulus were obtained from the literature, as reported in reference (Owayo et al. 2021) or experiments, in addition to recommendations by software. Other values, such as the shear modulus, were automatically computed by software based on Young's modulus and Poisson's ratio inputs. The porosity of the sample is implied in the bond parameters (Owayo et al. 2021).

Angular aggregates have a greater interlocking effect than their rounded aggregate counterparts, and as a result, the coefficient of static friction for the cement-angular aggregate mixture ought to be higher, see Table 1. A higher value of the coefficient of friction was chosen to cater to the additional interlocking effect in the angular aggregates. In addition, just like in the test, in order to minimize the end-bearing effect, the coefficient of static friction for steel-cement interaction has to be quite low.

Table 1. DEM macroparameters.

Macroparameter	w/b ratio and aggregate type				Steel	Cement-steel interaction
	0.35R	0.35A	0.23R	0.23A		
Coefficient of restitution	0	0	0	0	0	0
Coefficient of static friction	0.7	10	0.7	10	0.5	0.01
Coefficient of rolling friction	0.01	0.01	0.01	0.01	0.01	0.01
Poisson's ratio (v)	0.17	0.17	0.15	0.15	0.3	-
Mean particle bulk density (kg/m^3)	2100	2100	2120	2120	7800	-
Young's modulus, E (GPa)	25.4	25.4	28	28	205	-

3.3 *Calibration of the variable bond property model*

Cement mortar made of rounded aggregates with a w/b ratio of 0.35 was chosen for calibration purposes. Eq. sets 1a to1d were initially established from a sample tested at a shear angle of 80°, and confirmed by the results of samples tested at 70° and 65°. Later on, a new set of materials were used as a new set of materials against which the calibrated data were compared. These new set of materials were: cement mortar made of angular aggregates and rounded aggregates with a w/b ratio of 0.23 and cement mortar made of angular aggregates with a w/b ratio of 0.35. A simplified linear variable bond parameter model proposed in the previous work of (Owayo et al., 2021; Owayo, 2022) for use in DEM was applied in this work.Tests and simulations were done at shear angles of; 25°,45°, and 65° respectively.

The previous work (Owayo et al. 2021) showed that microparameters can be computed via the equation set Eq. (1a-1d). Table 2 displays the values of the coefficients and the constants

of equation set Eq. (1a-1d), based on aggregate type. Peak confinement stresses (see (Owayo et al., 2021; Owayo, 2022)) are divided into incremental values over the number of time steps for use in the entire simulation. Afterward, the confinement stresses are applied incrementally throughout the simulation time steps and substituted in equation set Eq. (1a-1d), thereby obtaining the respective microparameters for each time step. Further details of the model can be obtained from (Owayo et al., 2021).

$$bp_\tau = \left[c_1 e^{c_2\beta}\sigma_n + b_\tau\right] \times 10^6 \tag{1a}$$

$$bp_\sigma = \left[c_1 e^{c_2\beta}\sigma_n + b_\sigma\right] \times 10^6 \tag{1b}$$

$$bp_{ss} = \left[c_1 e^{c_2\beta}\sigma_n + b_{ss}\right] \times 10^{10} \tag{1c}$$

$$bp_{ns} = \left[c_1 e^{c_2\beta}\sigma_n + b_{ns}\right] \times 10^{11} \tag{1d}$$

c_1 and c_2 are constants dependent on aggregate shape. bp_τ is the bond parameter associated with the critical shear strength in Pa, compared with bp_σ as the bond parameter associated with the critical normal strength in Pa, bp_{ss} as the bond parameter associated with the shear stiffness per unit area in N/m^3, bp_{ns} as the bond parameter associated with the normal stiffness per unit area in N/m^3, β as the shear angle in degrees, and σ_n as the normal confinement stress in MPa. b_τ is a 'cohesion-like' term related to the critical shear strength in Pa, compared to b_σ, as the critical normal strength in Pa, and b_{ns} is a 'cohesion-like' term related to the normal stiffness per unit area in N/m^3 and b_{ss}, as the shear stiffness per unit area in N/m^3.

Table 2. Coefficients and constants in Equation (1a-1d) according to aggregate type.

	R.- aggregates	A.- aggregates
c_1	0.15	1.1
c_2	0.0326	-0.01
b_τ	1.0	3.0
b_σ	1.0	3.0
b_{ss}	1.0	3.4
b_{ns}	1.0	3.4
bdr (mm)	1.0	1.2

4 RESULTS & DISCUSSION

4.1 *Stress-strain characteristics*

4.1.1 *Tests without internal balancing pressure, pi*

In this set of results (Figure 5a), the samples were loaded in order to achieve a constant value of stress (7.7 MPa) on one of the sample's faces (the face experiencing shear stress). Displacement-controlled loading was used for this particular set of results. The phenomenon already reported by (Chen et al., 2018) i.e., low w/b ratio and low shear angles lead to stiffer sample response in test, are can be seen in curves in Figure 5.

An interesting observation can be made in Figure 5(b); most curves in tests, at the same shear angles coincide, despite the samples being constituted with different aggregate shapes. Figure 5(b) suggests that samples made of w/b=0.23, are strongly anisotropic (Figure 5(a)) for both A and R-aggregate constituted samples. On the other hand, samples made of w/b=0.35 regardless of whether A or R-aggregate seems to approach isotropic behavior. Samples made of w/b ratio of 0.23 contain less water and more cement and the mix is likely to be less homogenous due to an expected strong cement-aggregate bond. Samples constituted in w/b ratio, of 0.35 has more water and less cement, therefore, the resultant mix is likely to be more homogeneous regardless of its aggregate constituent as shown in the figures due to a relatively weak cement-aggregate bond.

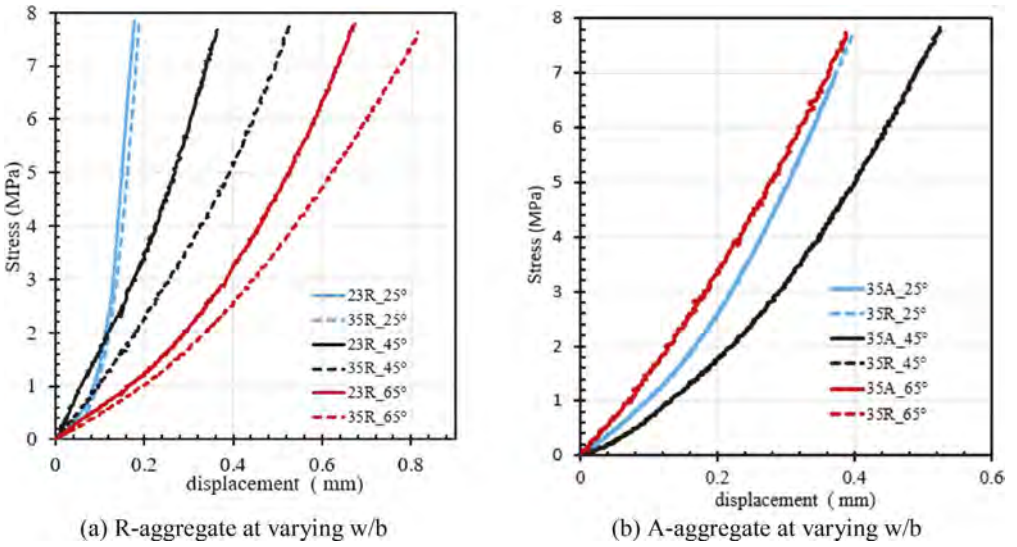

Figure 5. Stress-strain relationship in samples with no internal balancing pressure.

4.1.2 *Tests with internal balancing pressure, pi*

In this set of results (Figure 6), a fixed vertical force was applied to the sample through force-controlled loading in the test, and the maximum value of stress on the samples faces was controlled by the shear angle. Figure 6 indicates the stress-strain curves for cases where internal balancing pressure, p_i. was applied to balance the walls of the hollow opening during the tests. This was meant to simulate scenarios of different K_0 in-situ conditions. With these samples, the trend of stiff response with lower shear angles and low w/b ratio is only partially clear. It appears the presence of the internal support pressure, p_i. on the opening seems to enunciate the anisotropic behavior associated with A-aggregate constituted cement mixes and samples constituted at w/b ratio, 0.23. Furthermore, the presence of the opening in the sample with or without the internal balancing pressure, p_i on the hollow opening walls under tests, seems to have more profound effects on the A- aggregates constituted samples as opposed to their R-aggregate constituted counterparts. The findings regarding the A-aggregate constituted samples largely agree in behavior and mechanics however the presence of factors such as the opening, seems to have some effects. The said effects are thought to be a result of the uniformity of rounded aggregates and non-uniformity of their angular counterparts. The uniformity of rounded aggregates results in uniform stress distribution under loading therefore the behavior of a wide range of samples is bound to remain fairly consistent despite introduction of imperfections (like the opening) in the sample. The irregularity in shape of angular aggregates, on the other hand, may lead to stress concentrations under loading, therefore, imperfections (like the opening) introduced in samples may lead to some variations/inconsistencies in behavior as has been pointed out.

4.2 *Macrofracture pattern behavior around the opening*

The aim was to simulate cases of realistic fixed in-situ loads under varying values of K (K is synonymous with varying values of K_0 in in-situ site conditions) which typically do not reach failure loads (peak strength). Figure 7 shows cracks highlighted at a distance ranging between 3R-5R from the opening (R is the radius of the opening).

4.3 *DEM Simulations of cracking around the hollow opening*

EDEM's broken bonds were digitized and plotted together with the AE events. The analytical solution when the sample was tested with no p_i was obtained from the Kirsch solution while the solution for the sample tested with pi, was obtained from FEM. Figure 8 represents a comparison between EDEM's broken bonds and AE events in samples made of R and

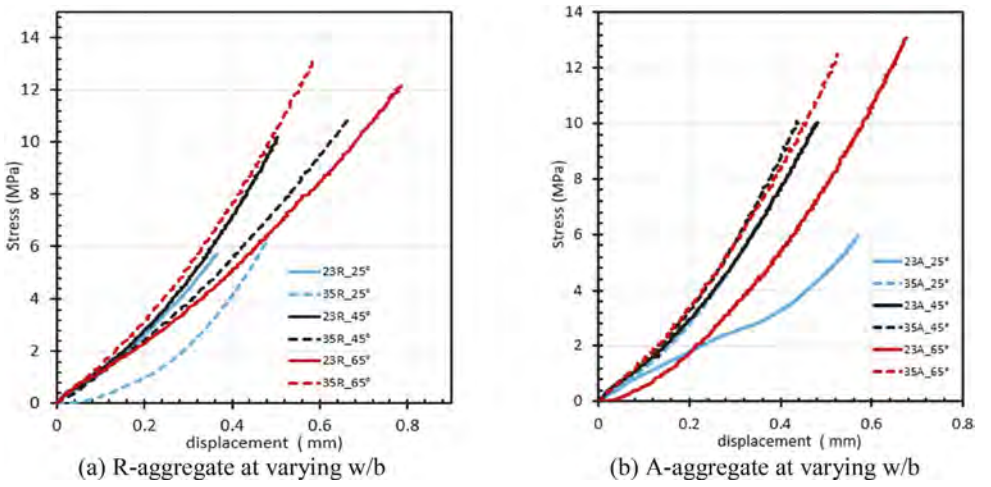

Figure 6. Stress-strain relationship in samples with internal balancing pressure.

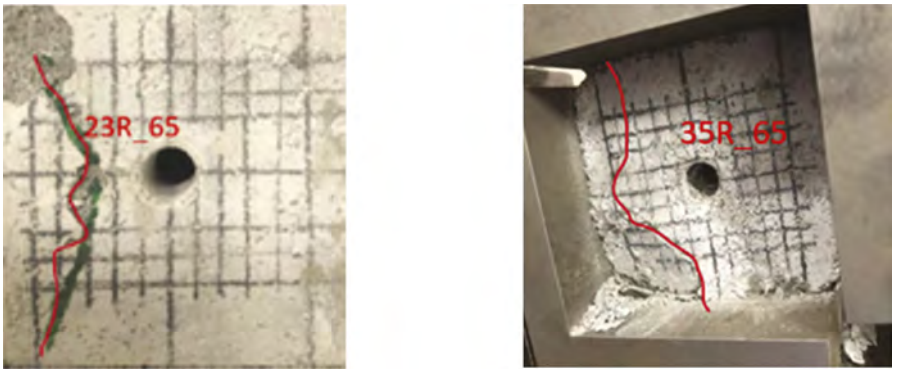

Figure 7. Macro-cracks on the tested samples.

A-aggregates respectively. Also shown alongside the figures is a typical stress state in the material element expressed in MPa. For the anisotropic loading cases, EDZ in the minor principal directions seems to extend more than that in the major principal directions by between 10-30% as indicated in the figures.

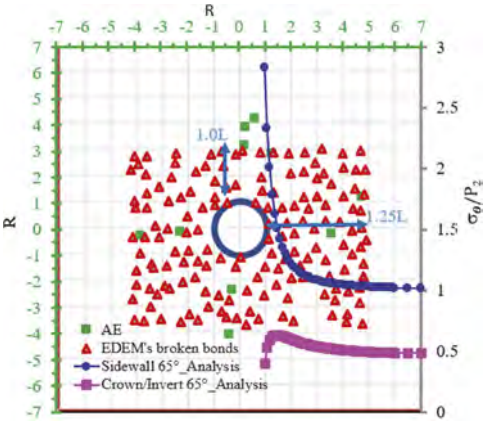

Figure 8. Comparison between EDEM's broken bonds and AE events in samples made of R -aggregates (w/b=0.23 tested at 65°) with no internal balancing pressure, p_i during the tests.

EDZ extent in the minor principal stress direction is between (1-1.3) times longer than the extent in the major principal stress direction. For unsupported opening, the average of the ratio of current stress to the major principal stress associated with the EDZ in the minor principal stress (P1) direction (EDZ1) ranges between 1.5-3.8 (Figure 9), on the other hand, the average of the ratio of current stress to the major principal (P2) stress associated with the EDZ in the major principal stress direction (EDZ2) ranges between 0.45-1.5. The reference values presented in this section are the average values in the reported range. For supported opening, the average of the ratio of current stress to the major principal stress associated with the EDZ in the minor principal direction ranges between 1.09, while the average of the ratio of current stress to the major principal stress associated with the EDZ in the major principal direction, on the other hand, ranges between 0.5-1.09.

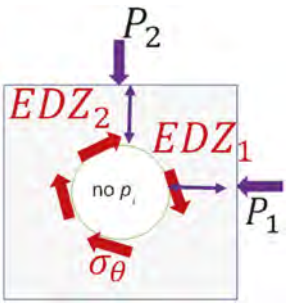

Figure 9. EDZ without internal balancing pressure.

5 CONCLUSIONS

- In anisotropic loading cases ($K \neq 1$), cracks around the opening, in samples with supported walls (with p_i), are less severe.
- The EDZ for all cases (tests and simulations) lies between 4 times the radius of the opening to 6 times the radius of the opening ($4R$-$6R$).
- Cracking in cement mix with rounded aggregates is relatively more intense and widespread around the opening, while the cracking around the opening in cement mix made of angular sand/aggregates is more concentrated and relatively sparse.
- EDZ extent in the minor principal stress direction is between (1-1.3) times longer than the extent in the major principal stress direction.
- For unsupported opening, the average of the ratio of current stress to the major principal stress associated with the EDZ in the minor principal direction ranges between 1.5-3.8; on the other hand, the average of the ratio of current stress to the major principal stress associated with the EDZ in the major principal direction ranges between 0.45-1.5.
- For supported opening, the average of the ratio of current stress to the major principal stress associated with the EDZ in the minor principal direction ranges between 1.09-3.5, while the average of the ratio of current stress to the major principal stress associated with the EDZ in the major principal direction, on the other hand, ranges between 0.5-1.09.

REFERENCES

ASTM 1999. Standard Guide for Determining the Reproducibility of Acoustic Emission Sensor Response [Online]. Available from: iso.org/obp/ui/#iso: std:iso:12714:ed-1:v1:en.

Blair, S.C. and Cook, N.G.W. 1998. Analysis of compressive fracture in rock using statistical techniques: Part I. A non-linear rule-based model. International Journal of Rock Mechanics and Mining Sciences. 35(7), pp.837–848.

Bono, J.P. de Bono, John Patrick (2013) Discrete element modeling of cemented sand and particle crushing at high pressures. PhD thesis, University of Nottingham.
Brown, N.J. 2013. Discrete Element Modelling of Cementitious Materials The University of Edinburgh. Edinburgh: University of Edinburgh.
Chen, L.-H.H., Chen, W.-C.C. and Chen, Y.-C.C. 2019. Shear fracture evolution in rocks examined using a novel shear device associated with acoustic emissions. Engineering Fracture Mechanics. 210 (July 2018), pp.42–53.
Chen, L.H., Lin, G.Z., Chen, Y.C. and Yang, W.X. 2013. Using acousto-optic coupling technology to investigate the fracture evolution of rock-like materials during inclined shear tests In: Applied Mechanics and Materials.
Chen, W.C., Chen, L.H. and Chen, Y.C. 2018. Using a novel shear apparatus coupled with acoustic emission to investigate shear fracture evolution of cement-based materials in macro- and micro-views. Construction and Building Materials. 187, pp.665–673.
Cheng, J., Song, G., Sun, X., Wen, L. and Li, F. 2018. Research Developments and Prospects on Microseismic Source Location in Mines. Engineering. 4(5), pp.653–660.
Choinska, M., Khelidj, A., Chatzigeorgiou, Georges, Choinska, M., Khelidj, A., Chatzigeorgiou, Georges, Effects, G.P., Choinska, M., Khelidj, A., Chatzigeorgiou, George and Pijaudier-cabot, G. 2017. Effects and interactions of temperature and stress-level related damage on permeability of concrete To cite this version : HAL Id : hal-00354323 Effects and interactions of temperature and stress-level related damage on permeability of concrete., pp.0–10.
Fakhimi, A. and Hemami, B. 2017. Rock Uniaxial Compression Test and Axial Splitting. Procedia Engineering. 191, pp.623–630.
Forti, T., Batistela, G., Forti, N. and Vianna, N. 2020. 3D Mesoscale Finite Element Modelling of Concrete Under Uniaxial Loadings. Materials. 13(20), pp.1–14.
Gálvez, J.C., Červenka, J., Cendón, D.A. and Saouma, V. 2002. A discrete crack approach to normal/shear cracking of concrete. Cement and Concrete Research. 32(10), pp.1567–1585.
Ghamgosar, M., Erarslan, N. and Williams, D.J. 2017. Experimental Investigation of Fracture Process Zone in Rocks Damaged Under Cyclic Loadings. Experimental Mechanics. 57(1), pp.97–113.
Hu, H.T., Lin, F.M. and Jan, Y.Y. 2004. Nonlinear finite element analysis of reinforced concrete beams strengthened by fiber-reinforced plastics. Composite Structures. 63(3–4), pp.271–281.
Lagos, S.R. and Velis, D.R. 2018. Microseismic event location using global optimization algorithms: An integrated and automated workflow. Journal of Applied Geophysics. 149, pp.18–24.
Liang, D., Qin-ya, L., Er-gen, G., Wei, Q. and Shou-cai, S. 2020. Locating microseismic sources based upon L-shaped single-component geophone array: A synthetic study. J]. Journal of Central South University. 27(9), pp.2711–2725.
Lisjak, A., Grasselli, G. and Vietor, T. 2014. Continuum-discontinuum analysis of failure mechanisms around unsupported circular excavations in anisotropic clay shales. International Journal of Rock Mechanics and Mining Sciences. 65, pp.96–115.
Lisjak, A., Liu, Q., Zhao, Q., Mahabadi, O.K. and Grasselli, G. 2013. Numerical simulation of acoustic emission in brittle rocks by two-dimensional finite-discrete element analysis. Geophysical Journal International. 195(1), pp.423–443.
Liu, J. Po, Li, Y. Hui, Xu, Shi Da, Xu, Shuai, Jin, C. Yu and Liu, Z. Sheng 2015. Moment tensor analysis of acoustic emission for cracking mechanisms in rock with a pre-cut circular hole under uniaxial compression. Engineering Fracture Mechanics. 135, pp.206–218.
Ma, Y. and Huang, H. 2021. Effect of shear bond failure on the strength ratio in DEM modeling of quasi-brittle materials. Acta Geotechnica. 0123456789(N m).
Mackie, R.I. 2015. Finite element modelling of structural concrete, by M.D Kotsovos: Review. Computers and Structures. 160(June), pp.40–41.
Martin, C.D. 1997. Seventeenth Canadian geotechnical colloquium: The effect of cohesion loss and stress path on brittle rock strength. Canadian Geotechnical Journal. 34(5), pp.698–725.
Miller, T.H., Potisuk, T., Higgins, C.C. and Yim, S.C. 2011. Finite element analysis of reinforced concrete beams with corrosion subjected to shear. Advances in Civil Engineering. 2011.
Moharrami, M. and Koutromanos, I. 2017. Finite element analysis of damage and failure of reinforced concrete members under earthquake loading. Earthquake Engineering and Structural Dynamics. 46 (15), pp.2811–2829.
Momozu, M., Oida, A. and Koolen, A.J. 2000. Analysis of soil cutting process bu the distinct element method In: Proceeding of the international agricultural engineering conference. Bangkok, Thailand.
Nguyen, N.H.T., Bui, H.H., Kodikara, J., Arooran, S., Nguyen, G.D. and Jitsangiam, P. 2017. Discrete element modelling of fracture in quasi-brittle materials. Mechanics of Structures and Materials:

Advancements and Challenges - Proceedings of the 24th Australasian Conference on the Mechanics of Structures and Materials, ACMSM24 2016. (December), pp.329–336.
Nitka, M. and Tejchman, J. 2020. Meso-mechanical modelling of damage in concrete using discrete element method with porous ITZs of defined width around aggregates. Engineering Fracture Mechanics. 231(March), p.107029.
Owayo, A.A. 2022. Investigation of Micro Cracks Evolution in Non-Hollow and Hollow Artificial Rock Samples: Inclined Shear Test with Acoustic Emission and DEM Simulations. The National Taiwan University of Science & Technology PhD Thesis.
Owayo, A.A., Teng, F.C. and Chen, W.-C. 2021. DEM simulation of crack evolution in cement-based materials under inclined shear test. Construction and Building Materials. 301, p.124087.
Pietruszczak, S. and Haghighat, E. 2015. Modeling of Fracture Propagation in Concrete Structures Using a Constitutive Relation with Embedded Discontinuity. Studia Geotechnica et Mechanica. 36(4), pp.27–33.
Sun, H.-M., Yu, J.-Z., Zhang, X.-L., Wang, B.-G. and Jia, R.-S. 2019. Technique for solving for microseismic source location parameters based on adaptive particle swarm optimization. Nonlinear Processes in Geophysics Discussions. (April), pp.1–17.
Tanaka, H., Momozu, M., Oida, A. and Yamazaki, M. 2000. Simulation of soil deformation and resistance at bar penetration by the distinct element method. Journal of Terramechanics. 37, pp.41–56.
Tham, L.G., Liu, H., Tang, C.A., Lee, P.K.K. and Tsui, Y. 2005. On tension failure of 2-D rock specimens and associated acoustic emission. Rock Mechanics and Rock Engineering. 38(1), pp.1–19.
University of Edinburgh 2022. Discrete Element Method Analysis Of Lateral Earth Pressure. Available from: http://demlateralearthpressure.weebly.com/contact-models.html.
Wang, J. and Gutierrez, M. 2010. Discrete element simulations of direct shear specimen scale effects. Geotechnique. 60(5), pp.395–409.
Wang, Y., Shang, X. and Peng, K. 2020. Locating mine microseismic events in a 3d velocity model through the gaussian beam reverse-time migration technique. Sensors (Switzerland). 20(9).
Wu, K., Pizette, P., Becquart, F., Rémond, S., Abriak, N.E., Xu, W. and Liu, S. 2017. Experimental and numerical study of cylindrical triaxial test on mono-sized glass beads under quasi-static loading condition. Advanced Powder Technology. 28(1), pp.155–166.
Zhou, Z.L., Zhou, J., Dong, L.J., Cai, X., Rui, Y.C. and Ke, C.T. 2017. Experimental study on the location of an acoustic emission source considering refraction in different media. Scientific Reports. 7(1), pp.1–13.

Smart Geotechnics for Smart Societies – Zhussupbekov, Sarsembayeva & Kaliakin (Eds)
© 2023 The Author(s), ISBN 978-1-003-29912-7
Open Access: www.taylorfrancis.com, CC BY-NC-ND 4.0 license

Intelligent prediction of excavation-induced retaining wall deformation

L.L. Mu, K. Liu & M.X. Zhu
Department of Geotechnical Engineering, Tongji University, Shanghai, China
Key Laboratory of Geotechnical and Underground Engineering of Ministy of Education, Tongji University, Shanghai, China

J. Jiang
School of Civil Engineering and Architecture, Guangxi University, Guangxi, China

ABSTRACT: Many excavations are made adjacent to existing foundations, especially in urban areas. In order to prevent the damage of the adjacent structures induced by the excavation, it is important to predict the retaining wall deformations caused by excavations. However, the uncertainty of subsurface conditions and the nonlinear interactions between multiple agents (e.g., soils, groundwaters, excavation support structures, and excavation activities) make the prediction of the response of retaining wall induced by excavation a rather difficult and complex task. This paper proposes a method to solve this problem by using machine learning techniques, where information is generated from the interaction processes between soils, structures, and excavation activities for predicting retaining wall deformations. First of all, an artificial neural network (ANN) model is proposed, and the soil properties, groundwaters, excavation support structures and excavation activities are considered. Then a mixed sample database of retaining wall deformations is generated based on high-fidelity numerical simulations and field measurements in Shanghai. Finally, the model is trained by the mixed database to recognize the patterns of the complex interactions between retaining wall deformations, excavation geometries, support structures, and soil properties. The results show that the accuracy of predicting the retaining wall deformations is less than 2 mm compared with high-fidelity numerical simulations. In the meanwhile, the mean accuracy of predicting the retaining wall deformations is 2.62 mm compared with the field monitoring data of an engineering case in Shanghai. The strategy of machine learning techniques with the model can predict the maximum retaining wall deformations induced by excavation with high accuracy.

1 INTRODUCTION

With the continuous promotion of urbanization, urban land resources are increasingly scarce, the demand for underground space development is growing rapidly, and the excavation scale of foundation pits is becoming larger. In urban construction, foundation pits are often adjacent to existing buildings and underground pipelines. Retaining wall deformations caused by excavation will lead to the displacement of the surrounding soil, and eventually affect the adjacent infrastructures, which may even have a huge impact on retaining wall and surrounding environment (Finno and Calvello, 2005). Therefore, controlling the retaining wall deformations caused by excavation is very important, which is based on predicting retaining wall deformations – one of the research highlights for many years.

DOI: 10.1201/9781003299127-138

Traditional methods of predicting retaining wall deformations are: 1) Empirical methods: based on a large amount of data, the parameters strongly related to retaining wall deformations are selected, and the formulas of retaining wall deformations are given by curve fitting (Goldberg et al., 1976; Mana and Clough, 1981; Ou and Tang, 1994; Kung et al., 2007; Goh et al., 2017). Although these methods are convenient and simple, it ignores the influence of construction factors (Finno and Calvello, 2005); 2) Theoretical methods: the retaining wall deformations and soil displacement caused by excavation are calculated based on soil mechanics and structural mechanics (Peck, 1969; Hsieh and Ou, 1998; Xu and Poulos, 2000; Zhang et al., 2011). These methods are more theoretical compared with empirical methods, but still based on some assumptions different from reality, which will affect the calculation accuracy (Cao et al., 2014); 3) Finite element methods (FEM): the relationship between key parameters and deformation characteristics of retaining wall can be directly analyzed (Clough and Duncan, 1971; Borja and Ronaldo, 1990; Li et al., 2021), overcoming the limitations of empirical methods. However, the theories of numerical simulation are complex, and the calculation workload is large, which needs a lot of time and is difficult for engineers to use (Mu et al., 2020).

For excavation with strong randomness, fuzziness and nonlinearity, the above methods can not comprehensively consider the influence of relevant factors on retaining wall deformations (Jamali et al., 2013), and is difficult for dynamic prediction during construction. As the requirement of foundation pit deformation control is increasing, a more intelligent method is needed to achieve the rapid and dynamic prediction of retaining wall deformations. Artificial neural networks (ANN) perform excellent in solving nonlinear multivariable problems such as geotechnical engineering. Compared with the traditional methods mentioned above, ANN can calculate faster and achieve dynamic update (Goh et al., 1995). BP neural network (BPNN), with good self-organization and generalization, can use the original monitoring data for learning and training, and predict the later deformations of retaining wall (Hu et al., 2013). Goh et al. (1995) used BPNN to learn the FEM results, and obtained reasonable prediction results of retaining wall deformations in clay. However, the input parameters (especially soil parameters) of the ANN in this study were too few, which was not conducive to establishing the mapping relationship under different soil layers and construction conditions (Gao et al., 2002). The prediction accuracy of BPNN increases with the abundance of training data. Therefore, in order to ensure the accuracy of prediction, a large amount of engineering data must be provided (Yuan et al., 2000; Hu et al., 2013). However, the monitoring data is often poorly collected in engineering for various reasons, such as equipment damage and operation errors, and it is a long and cumbersome process to collect and sort out the engineering data. In order to solve this problem, many scholars have combined other intelligent algorithms to improve BPNN (Ma et al., 2008; Cao et al., 2014; Wang et al., 2019; Zhang et al., 2020; Cui et al., 2021). Most of these enhanced prediction models focus on improving the algorithms by reducing the scale of training set and calculation time, but the mapping relationships ignore the influences of soil conditions, retaining structure parameters and construction conditions on retaining wall deformations.

Considering the advantages of ANN in solving geotechnical problems and the shortcomings of BPNN in predicting retaining wall deformations, this paper presents a new method. Soil parameters considering small-strain properties, foundation pit geometries and retaining structure parameters are taken as the input parameters of the BPNN model. In this way, the new method can effectively consider the effects of each soil layer properties, the positions and mechanics of each support, and the excavation conditions on the maximum retaining wall deformations. The finite element (FE) samples is generated by PLAXIS, and the engineering data samples are obtained from the monitoring data of 18 foundation pit projects in Shanghai. Then a mixed sample database is generated by combining the FE samples and engineering case data samples, which reduces the influence of lacking engineering data on the training effect of BPNN. Based on the mixed sample database, the BPNN is trained to generate a prediction model of the maximum retaining wall deformations. The prediction results of the model for 50 FE examples verify the rationality of the input parameters after comparing with the corresponding FEM results. Then the model is applied in an engineering case in Shanghai to estimate the accuracy.

2 BPNN MODEL

2.1 *BPNN structure*

A BPNN model generally has a structure consisting of input layer, hidden layers, and output layer. As shown in Figure 1, the input layers of our BPNN model consist of key parameters that affect retaining wall deformations, while the output layer is the maximum retaining wall deformation.

As shown in Table 1, the input parameters can be categorized into three groups: soil parameters considering small-strain properties, foundation pit geometries and retaining structure parameters.

HSS model (Benz, 2007) takes into account the mechanical properties of soil in small-strain stage, which has been proved to be suitable for simulating deep excavation (Burland, 1989; Whittle et al., 1994; Kung et al., 2007; Clayton, 2011). Therefore, 5 HSS model parameters(reference secant modulus E_{50}^{ref} and reference loading-unloading modulus E_{ur}^{ref} in triaxial drained shear test, reference tangent modulus E_{oed}^{ref} in consolidation test, initial shear modulus G_0^{ref}, and shear strain $\gamma_{0.7}$) are selected to describe soil mechanic properties, which add the unit weight γ, thickness h, effective cohesion c', and effective friction angle φ' up to 9 parameters for each soil layer. However, the number of input parameters is usually fixed, which makes it difficult to apply the same model to cases with different soil conditions. To solve this problem, the soil within the retaining wall into 9 layers, which means that there are 81 soil parameters in the input layer.

In order to cover most of engineering situations, the number of supports is set to 4. As shown in Table 1, 3 parameters are selected for each support, which means that there are 12 support parameters in the input layer.

Therefore, the constructed BPNN, connected to an output layer of maximum retaining wall deformation by 5 hidden layers (98-86-52-39-32), has an input layer of 98 parameters including the other 5 parameters.

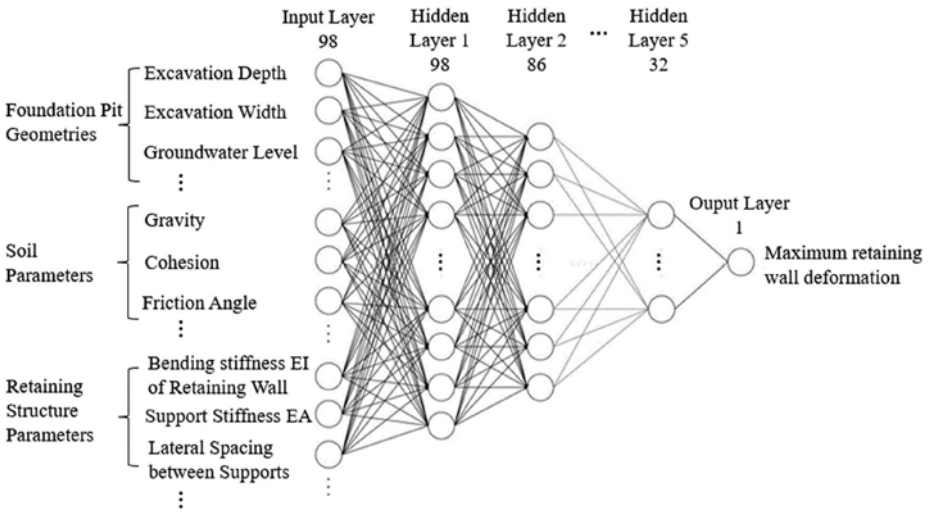

Figure 1. Structure of the BPNN.

2.2 *Sample database*

The lack of engineering data leads to poor training effect of BPNN. Therefore, this paper combines FE samples with engineering data to generate a mixed sample database, which is used to train the BPNN model. The construction process of the mixed sample database is as follows.

Table 1. The input parameters of the model.

Category		Parameters
Soil parameters		Thickness, unit weight, c', φ', E_{ur}^{ref}, E_{oed}^{ref}, E_{50}^{ref}, G_0^{ref}, $\gamma_{0.7}$
Foundation pit geometries		Excavation depth, excavation width, groundwater depth
Retaining structure parameters	Support parameters	Stiffness EA
		Lateral spacing between supports
		Distance from supports to top surface
	Retaining wall parameters	Bending stiffness EI
		Longitudinal length

Step 1: the FE sample database is established based on a large amount of FE samples. In order to ensure that the parameter values and excavation conditions of each calculation sample are independent, an automatic modeling program is prepared based on the Python interface in PLAXIS. The program can perform batch automatic modeling and calculation of foundation pits, and automatically write the maximum retaining wall deformations and the corresponding material parameters in each calculation example into the database. Each sample in the database has 98 input parameters and 1 output parameter. The output parameter - maximum retaining wall deformation is shown in Figure 2. The values of all input parameters in FE samples are based on the fluctuation ranges encountered in the engineering cases collected in this research (e.g., lateral spacing between supports varies from 6 m to 10 m, excavation width varies from 50 m to 336 m). To comprehensively consider the construction conditions such as different number of supports and different parameter values of each support, different input parameters can be taken. For example, for the working conditions not involved in the excavation (such as some supports have not been set), it is considered by taking the parameters of the corresponding supports as 0. Parameters and PLAXIS calculation results of 87368 calculation examples are recorded to build the FE sample database.

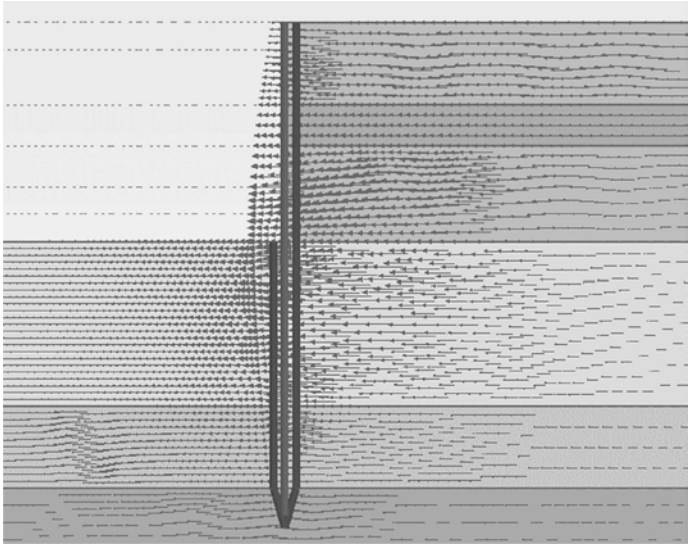

Figure 2. Schematic diagram of maximum retaining wall deformation.

Step 2: 3005 engineering samples from 18 excavation projects in Shanghai are collected for the engineering sample database. The materials required to be provided about the projects are: geotechnical investigation report, foundation pit design and construction drawings, monitoring data (monitoring report of deep horizontal displacement of retaining wall, etc.). Since some HSS model parameters cannot be directly obtained from the engineering data, the empirical method given by Gu et al. (2021) is used, which is obtained by converting pore ratio e and compression modulus Es. The conversion relationship is shown in Table 2.

Step 3: The FE sample database and the engineering sample database are combined into the mixed sample database, having 90373 samples totally. Examples of the samples are shown in Table 3 (*parameters of soils and supports are excluded due to space limitations).

Table 2. The suggested values of HSS model parameters for Shanghai soils.

Parameter	Empirical method
E_{oed}^{ref}	Clay: E_{oed}^{ref}= -4.34ln(e)+3.51 MPa (Based on laboratory test) E_{oed}^{ref} = 0.81$E_{s1\text{-}2}$ (Both clay and sandy soil)
E_{50}^{ref}	Clay: E_{50}^{ref} = -5.33ln(e)+3.95 MPa (Based on laboratory test) E_{50}^{ref} = 1.02$E_{s1\text{-}2}$ (According to this formula if there is no test data for sandy soil)
E_{ur}^{ref}	Clay: E_{ur}^{ref} = -28.8ln(e)+24.5 MPa (Based on laboratory test) E_{ur}^{ref} = 4.2$E_{s1\text{-}2}$+7.24 (According to this formula if there is no test data for sandy soil)
G_0^{ref}	Clay (Clayey silt): G_0^{ref} = 67.5$e^{-1.57}$ MPa (Based on on-site wave velocity test data) Sandy soil (Sandy silt): G_0^{ref} = 98.9$e^{-0.45}$ MPa (Based on on-site wave velocity test data)
$\gamma_{0.7}$	Clay (Clayey silt): $\gamma_{0.7}$ = 2.4~4.4×10^{-4}, the mean value is 3.2×10^{-4} (Based on laboratory test) Sandy soil (Sandy silt): $\gamma_{0.7}$ = 2.9~5.2×10^{-4}, the mean value is 3.9×10^{-4} (Based on laboratory test)

* e is pore ratio; I_p is plasticity index.

Table 3. Examples of the samples in the mixed database.

Foundation pit geometries			Retaining wall parameters		Wall deformation
Depth	Width	Groundwater depth	Longitudinal length	EI	
m	m	m	m	GPa·m^4	mm
18.38	58.14	2.81	55.61	3.49	29.69
17.66	103.46	1.86	59.77	0.71	77.27
11.41	74.66	3.32	24.45	0.55	13.32

2.3 *Model training*

The proposed model is trained by BP algorithm coded in PyTorch module. The activation function for BPNN nodes is rectified linear unit (ReLU), the loss function is mean sum-of-squares error (MSE), and the optimization function is Adam. Among the mixed database, 89834 samples are used to train the model.

3 PREDICTION FOR FE CASES

This paper has calculated 40 examples in total from the proposed model and FEM. Figure 3 (a) to (d) respectively show the prediction of maximum retaining wall deformations when the number of supports is 1, 2, 3, 4. In the FE calculation examples randomly generated, the general trend is that the greater the excavation depth, the more supports are set and the larger maximum retaining wall deformations are. However, the absolute error of the model barely

change with the increase of the corresponding retaining wall deformation, almost within 2mm. The mean absolute error and relative are only 0.81 mm and 4.6%, which shows that the model maintains a high accuracy under different excavation conditions generated by FE. Therefore, the selected parameters of the model are rational.

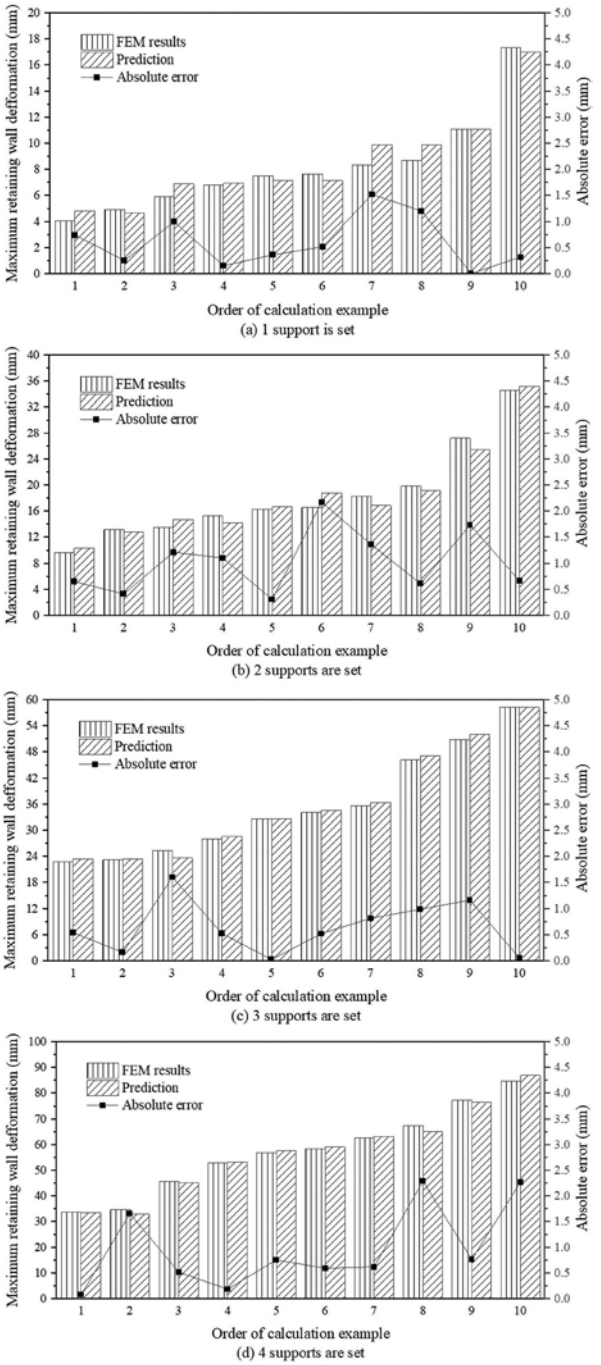

Figure 3. Comparison between prediction and FEM results.

4 PREDICTION FOR AN ENGINEERING CASE

In order to estimate the practical accuracy of the proposed model, it is used to predict the maximum retaining wall deformations in the following engineering case.

Baoshan River-side Business Center Project is located in Baoshan District, Shanghai. Layout and support profile of the foundation pit are shown in Figure 4-5, and the soil parameters and retaining structure parameters are shown in Table 4-6. The proposed model is used to predict the maximum retaining wall deformations when excavating to the bottom. In order to estimate the prediction accuracy of the model more comprehensively, the data of different monitoring points (CX30, CX31, CX32, CX33) are collected for comparision.

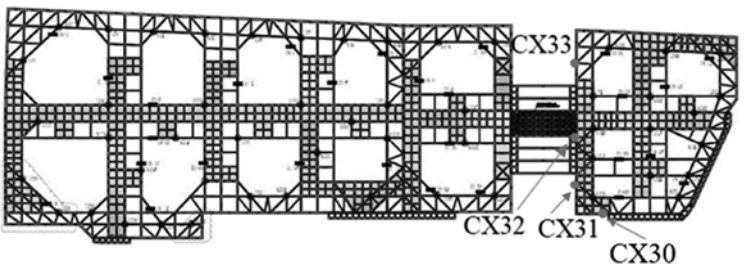

Figure 4. Layout of the foundation pit (Baoshan River-side Business Center Project).

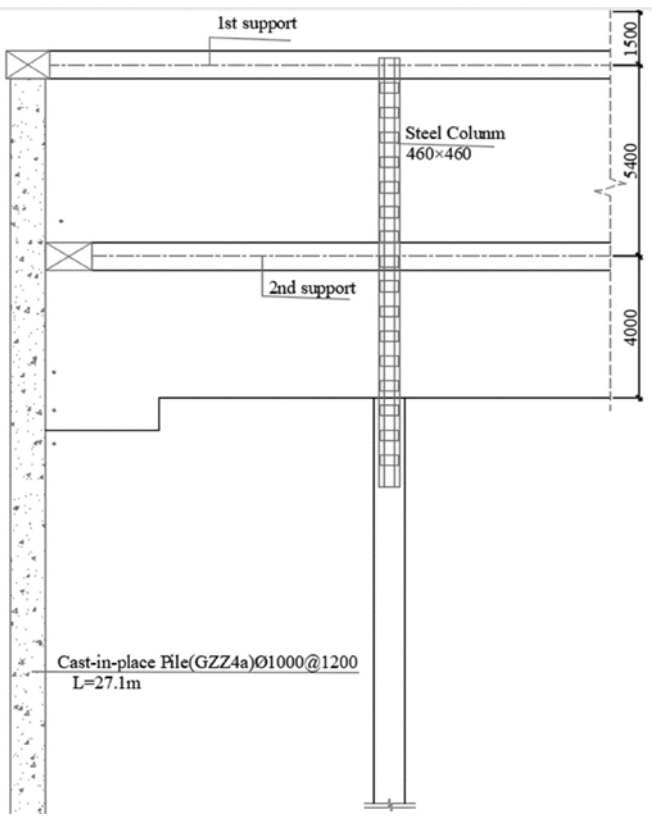

Figure 5. Layout of the foundation pit (Baoshan River-side Business Center Project).

The results in Figure 6 show that the prediction results fluctuate to a certain degree, but the mean absolute error and relative error are only 2.62 mm and 11.9%, meeting the accuracy requirements of actual projects. Therefore, the model can practically predict the maximum retaining wall deformations in satisfactory accuracy.

Table 4. Soil parameters (Baoshan River-side Business Center Project).

Soil layer	h m	γ kN/m^3	c' kPa	φ' °	E_{50}^{ref} MPa	E_{oed}^{ref} MPa	E_{ur}^{ref} MPa	$\gamma_{0.7}$ 10^{-4}	G_0^{ref} MPa
1	5.3	18.7	0	33.0	12.38	9.28	55.37	4.05	129.40
2	1.1	18.1	11	23.5	5.65	4.24	29.20	4.05	99.30
3	3.3	18.5	18	19.0	4.33	3.25	24.10	3.40	77.20
4	5.4	18.8	7	30.0	9.80	7.35	45.40	3.40	129.50
5	3.6	17.6	11	22.0	3.75	2.81	21.80	3.40	56.90
6	9.2	17.0	14	13.5	2.76	2.07	18.00	3.40	43.10
7	5.6	17.5	17	14.0	3.35	2.51	20.26	3.40	53.50
8	20.0	18.3	10	26.5	7.02	5.63	34.54	3.40	75.00
9	20.0	18.3	17	22.5	5.86	4.40	30.00	3.40	75.13

Table 5. Retaining wall parameters (Baoshan River-side Business Center Project).

Monitoring point	Depth m	Width m	Groundwater depth m	*EI* GPa·m^4	Longitudinal length m
CX30	10.42	97.5	2.52	0.32	27.6
CX31		64.7	2.06		
CX32		76.5	2.34	0.37	27.1
CX33		84.9	2.45		

Table 6. Support parameters (Baoshan River-side Business Center Project).

Monitoring point	Order of supports	*EA* GN	Lateral spacing m	Distance from support to top m
CX30-CX33	1st	20.16	8.5	1.5
	2nd			6.9

5 CONCLUSIONS

By collecting a large amount of monitoring data and FE calculation results, this paper generates a mixed sample database of maximum retaining wall deformations, trains the BPNN, and obtains a prediction model of maximum retaining wall deformations. Then an engineering case is used to verify the model. The following conclusions are obtained:

1) The proposed model can maintain a high accuracy for the prediction of FE examples, and the absolute errors are mostly less than 2mm, showing that the selected parameters of the model are rational.
2) The mean absolute error and relative error of the model for the case prediction are 2.62 mm and 11.9%, meeting the engineering requirements.
3) The accuracy of the model for the case is volatile but still within a reasonable range acceptable to engineering, not as good as that for the FE cases. Therefore, the diversity of

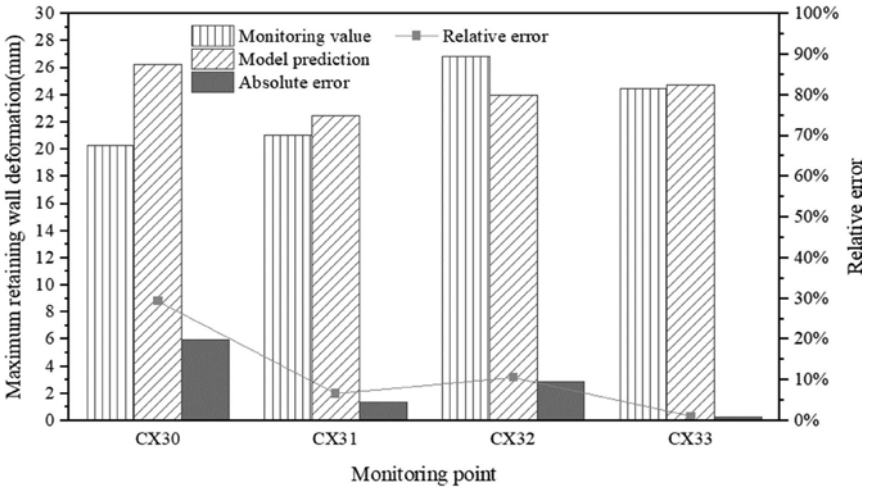

Figure 6. Comparison between prediction and the case (Baoshan River-side Business Center Project).

database can be improved through long-term statistics of more engineering data, so as to improve the prediction accuracy.

REFERENCES

Benz, T., 2007. Small-strain stiffness of soils and its numerical consequences. University of Stuttgart, Stuttgart.

Borja, Ronaldo, I., 1990. Analysis of Incremental Excavation Based on Critical State Theory. *Journal of Geotechnical Engineering* 116(6): 964–985.

Burland, J.B., 1989. Small is beautiful-The stiffness of soils at small strains. *Revue Canadienne De Géotechnique* 26(4): 499–516.

Cao, J., Ding, W.Y., Zhao, D.S., Liu, H.M., 2014. Time Series Forecast of Foundation Pit Deformation Based on BP Neural Network. *Applied Mechanics and Materials* 556–562:5979–5983.

Clayton, C.R.I., 2011. Stiffness at small strain: research and practice. *Géotechnique* 61(1): 5–37.

Clough, G.W., Duncan, J.M., 1971. Finite element analyses of retaining wall behavior. *Journal of Soil Mechanics & Foundation Engineering* 97(12): 1657–1673.

Cui, D., Zhu, C., Li, Q., Huang, Q., Luo, Q., 2021. Research on Deformation Prediction of Foundation Pit Based on PSO-GM-BP Model. *Advances in Civil Engineering* 2021(1): 1–17.

Finno, R.J., Calvello, M., 2005. Supported Excavations: Observational Method and Inverse Modeling. *Journal of Geotechnical & Geoenvironmental Engineering* 131(7): 826–836.

Gao, G.Y., Huang, C., Sun, Y.M., 2002. Application of GA-BP Neural Network in Excavation Monitoring of Deep Foundation Pit. *UNDERGROUND SPACE* 22(4):290-293+370.

Goh, A.T.C., Wong, K.S., Broms, B.B., 1995. Estimation of lateral wall movements in braced excavations using neural networks. *Canadian Geotechnical Journal* 32(6): 1059–1064.

Goh, A.T.C., Zhang, F., Zhang, W., Zhang, Y., Liu, H., 2017. A simple estimation model for 3D braced excavation wall deflection. *Computers and Geotechnics* 83: 106–113.

Goldberg, D., Jaworski, W., Gordon, M., 1976. Lateral Support Systems And Underpinning. Volume I: Design And Construction. *Construction Management*.

Hsieh, P.G., Ou, C.Y., 1998. Shape of ground surface settlement profiles caused by excavation. *Canadian Geotechnical Journal* 35(6): 1004–1017.

Hu, Q.C., Hu, B., Jiang, H.F., 2013. Application of BP Artificial Neural Network to the Displacement Prediction of Deep Foundation Pile. *Safety and Environmental Engineering* 20(3): 154–158.

Jamali, A., Ghamati, M., Ahmadi, B., Nariman-Zadeh, N., 2013. Probability of failure for uncertain control systems using neural networks and multi-objective uniform-diversity genetic algorithms (MUGA). *Engineering Applications of Artificial Intelligence* 26(2): 714–723.

Kung, G.T., Juang, C.H., Hsiao, E.C., Hashash, Y.M., 2007. Simplified Model for Wall Deflection and Ground-Surface Settlement Caused by Braced Excavation in Clays. *Journal of Geotechnical and Geoenvironmental Engineering* 133(6): 731–747.

Li, H., Wei, R., Zhu, H., Jia, C., Shi, G., 2021. Numerical analysis of excavation stability of transfer station of Jinan Metro. *IOP Conference Series Earth and Environmental Science* 632: 022019.

Ma, F. H., Yan, Z., Fan, Y., 2008. Research on deformation prediction method of soft soil deep foundation pit. *Journal of Coalence and Engineering* 14(4): 637–639.

Mana, A.I., Clough, G.W., 1981. Prediction of movements for braced cuts in clay. *Geotechnical Special Publication* 107(118): 1840–1858.

Mu, L., Chen, W., Huang, M., Lu, Q., 2020. Hybrid Method for Predicting the Response of a Pile-Raft Foundation to Adjacent Braced Excavation. *International Journal of Geomechanics* 20(4): 04020026.

Ou, C., Tang, Y., 1994. Soil parameter determination for deep excavation analysis by optimization. *Journal of the Chinese Institute of Engineers* 17(5): 671–688.

Peck, R.B., 1969. Deep Excavations and Tunneling in Soft Ground. *Proc. of 7th ICSMFE*, Mexico.

Wang, J.B., Niu, F.Y., Zhao, J., Peng, L.B., Management, S.O., University, Q.T., 2019. Construction Of metro Pit-Based risk assessment DEA-AHP-BP neural networks. *Architecture Technology*.

Whittle, A.J., Hashash, Y., Whitman, R.V., 1994. Analysis of Deep Excavation in Boston. *Journal of Geotechnical Engineering* 119(1): 69–90.

Xi, X., Li, A., Ban, J., Lu, W., 2010. A neural network model for deformation prediction of deep foundation pit based on multivariate phase space reconstruction. *Sixth International Conference on Natural Computation*.

Xu, K.J., Poulos, H.G., 2000. Theoretical Study of Pile Behaviour Induced by a Soil Cut. *International Society for Rock Mechanics*.

Yuan, J.R., Chi, Y.W., Liu, X.Z., 2000. Dynamic Prediction on Displacement of Diaphragm Wall in Deep Foundation Excavation Engineering Using Artificial Neural Networks. *Journal of Tongji University* 28(3): 282–286.

Zhang, J.Q., Qin, Y.J., Xie, L.F., 2020. Predicting the settlement of Urumqi subway based on wavelet denoising and BP neural network. *IOP Conference Series: Earth and Environmental Science* 570(5), 052019 (11pp).

Zhang, R., Zheng, J., Pu, H., Zhang, L., 2011. Analysis of excavation-induced responses of loaded pile foundations considering unloading effect. *Tunnelling and Underground Space Technology* 26 (2),320–335.

Smart Geotechnics for Smart Societies – Zhussupbekov, Sarsembayeva & Kaliakin (Eds)
© 2023 The Author(s), ISBN 978-1-003-29912-7
Open Access: www.taylorfrancis.com, CC BY-NC-ND 4.0 license

Seismic analysis and design of braced secant pile walls for excavations in Manila, Philippines

P.A.Y. Selda, M.P.V. Follosco, R.A.C. Luna & J.M.I. Tanap
AMH Philippines, Inc., Quezon City, Philippines

ABSTRACT: Typical design of temporary retaining wall systems mainly deals with the lateral pressure induced by both the retained material and the additional surcharge loads. However, earthquakes can also induce considerable destabilizing forces while permanently degrading the effective strength of the subsurface. Seismic analysis is essential when evaluating stability and deformation of deep excavations and high/steep slopes, especially in seismically-active regions like the Philippines. This paper discusses the design criteria, approach and methodology adopted for deformation analyses of a secant pile wall system braced with reinforced concrete struts for an excavation project in the Philippines. Emphasis is placed in the approach adopted when considering the seismic demand for temporary structures. Displacements were estimated and reported to be excessive. Recommendations were, however, ignored, and observed damages to the adjacent structures were later on reported during the excavation stage.

1 INTRODUCTION

With the implementation of the "*Build Build Build*" program of the current Philippine government underway, numerous investors come into the country to capitalize on the vast multitude of opportunities. The rapid economic growth of the country resulted in the upsurge in demand of many high-rise buildings. One particular condominium in Pasay City (Metro Manila), Philippines, was proposed to have a 12.77-meter deep basement. The study area is located just across reclaimed land. As such, a temporary secant pile wall system braced with struts was designed to support the walls of the excavation pit in consideration of the shallow groundwater table and the loose/soft subsurface. Although just a temporary system, consideration of seismic loads is still paramount and should not be overlooked especially since the site is only about 6.5 km away from the West Valley Fault (Mw7.2). This purpose of this study is to provide the developer with technical support services by way of reviewing the design of the proposed system and evaluate its stability.

2 SECANT PILE WALL

A secant pile wall is a type of retaining wall typically used for excavation protection. In this case, it is designed to be a system of bored piles that intersect each other at a uniform interval. Although not necessarily required, secant pile walls can be composed of two piles with different strengths: (1) the primary pile, which is typically weaker, often unreinforced, and whose embedment length can be relatively shorter; and (2) the stronger, reinforced secondary pile, which serves as the main lateral force resisting system. For the proposed system, the Designer opted for jet grout primary piles with an approximate 28-Day Compressive Strength (f'_c) of 5 MPa. On the other hand, the f'_c of the secondary piles is 35 MPa. Figure 1 shows a section of the proposed secant pile wall system. As can be seen, the centerlines of the primary and secondary piles are staggered by 200 mm, and the piles have a center-to-center spacing of 1.20 meters. It should also be noted that two levels of reinforced concrete (RC) struts are used to support the secant pile wall.

DOI: 10.1201/9781003299127-139

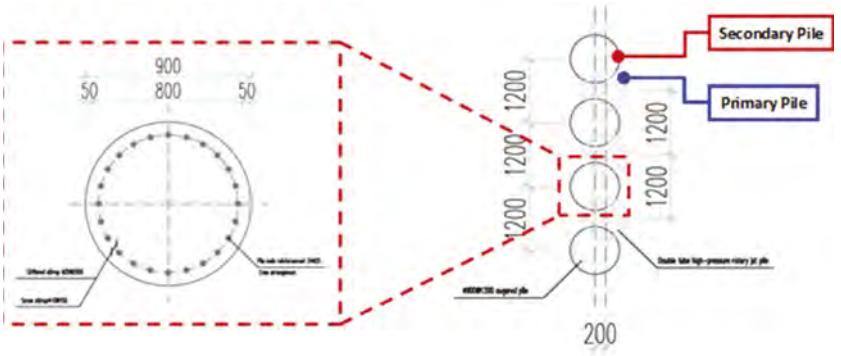

Figure 1. Blow-up section of secondary pile.

3 SUBSURFACE CONDITIONS

3.1 *Geotechnical investigation*

The geotechnical investigation (GI) program for this study consists of seven (7) drilled boreholes where Standard Penetration Tests (SPT) and several lab tests were conducted. The results of the GI program reveal that loose to medium dense sands and silts were encountered up to around 6.0 meters of depth from the surface. The succeeding layers have SPT N-values that are generally indicative of dense to very dense relative condition, with lenses of very dense and/or hard soils interspersed within the upper layers of the subsurface. In addition, the groundwater table was found to be as shallow as 0.65 to 0.80 meters below the existing grade level.

Table 1. Idealized subsurface profile.

Depth (m)	USCS	SPT N-Value	Relative Condition/Consistency
0 - 6.0	SP/SP-SM/SM	7 - 16	Loose to Medium Dense
6.0-12.0	SM/SP-SM	'*refusal*'	Very Dense
12.0 - 16.5	SM/ML/MH	28 - 38	Medium Dense to Dense
16.5 - 22.5	SM/ML	'*refusal*'	Very Dense
22.5 - 25.5	SM/MH	31 - 38	Dense
25.5 - 60.0	CH/SM/ML/MH	'*refusal*'	Very Dense/Hard

3.2 *Site class*

Site class is an indicator of how stiff the subsurface is. Among the different dynamic properties, the average shear wave velocity of the top 30 meters (V_{s30}) is generally accepted as an appropriate measure of an area's site class. Due to the lack of geophysical data, the site class

Table 2. Site class or soil profile types (Source: NSCP 2015 Table 208-2).

		Average Soil Properties for Top 30 m of Soil Profile		
Soil Profile Type	Generic Description	Shear Wave Velocity, V_{s30} (m/s)	N-value	Und. Shear Strength, S_u (kPa)
S_A	Hard Rock	> 1,500		
S_B	Rock	760 to 1,500		
S_C	Very Dense Soil and Soft Rock	360 to 760	> 50	> 100
S_D	Stiff Soil	180 to 360	15 to 50	50 to 100
S_E	Soft Soil	< 180	< 15	< 50
S_F	*Soil Requiring Site-Specific Evaluation*			

will be determined from the harmonic mean of measured SPT N-values with respect to depth, as referenced from the National Structural Code of the Philippines (NSCP) 2015 Table 208-2.

The distribution of in-situ SPT N-values correspond to a value of 30. This value lies within the 15 to 50 range, which suggests that the subsurface underlying the study area can be classified under the S_D (stiff soil) site class.

4 DESIGN CRITERIA

4.1 *Surcharge loads*

Existing structures found within the vicinity of the study area will induce additional surcharge loading to the proposed excavation protection system in the form of lateral earth pressure based on Boussinesq's theory. Figure 2 shows the layout of the adjacent buildings, as well as the sections used in analysis. Given surcharge loadings generally range from 15 kPa (roadway) to 45 kPa. The 7-storey building, however, is assigned a surcharge load of 105 kPa (15 kPa per storey).

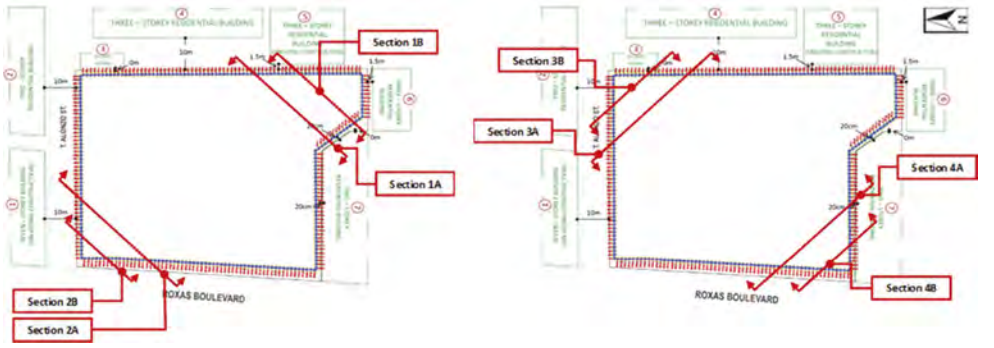

Figure 2. Layout of adjacent buildings.

4.2 *Seismic loading*

Aside from the static lateral earth pressure due to the surrounding structures, earthquakes can also induce considerable destabilizing inertial forces. Seismic loads permanently degrade the shear strength of the soil mass due to the stress and fatigue resulting from the prolonged exposure to cyclic loading. Seismic analysis is therefore essential when evaluating the stability and deformation, especially in seismically-active regions/countries like the Philippines.

In 2017, the Philippine Institute of Volcanology and Seismology (PHIVOLCS) published an atlas called the "Philippine Earthquake Model" (PEM), which comprises of maps containing isolines of equal acceleration, based on the regional probabilistic seismic hazard analysis study conducted by Peñarubia et al. (2017). According to the PEM PGA map of Metro Manila (Figure 3), the 475-year surface PGA on-site is 0.40g.

The secant pile wall system is said to be a temporary retaining structure only. For temporary structures, although oftentimes not required, it is still prudent to at least consider seismic loading associated to an earthquake with a lower hazard level (i.e. return period) than that of the 475-year design level earthquake. In the absence of site-specific studies or regional hazard maps for lower-hazard seismic demand, return period conversion factors (such as in New Zealand Standard 1170 Part 5 Table 3.5, 2004) can be used to convert the reference 475-year PGA to the target/warranted return period.

In lieu of the aforementioned technique, the seismic demand shall be taken as 70% of the 475-year PGA in this study, as agreed upon by all concerned parties or proponents. The resulting seismic demand is close to what would be a 225-year hazard. As such, the design PGA for the temporary structure will be 0.28g. Correspondingly, the horizontal (k_h) seismic coefficient (k_v) for pseudo-static analysis shall be taken as one-half of the design PGA, in accordance with the approaches developed by Hynes-Griffin & Franklin (1984) and Kavazanjian et al. (1997).

Figure 3. 475-Year Stiff Soil PGA map of Metro Manila (Source: PHIVOLCS, 2017).

4.3 *Deformation limits*

The primary criterion for designing excavation protection systems is the serviceability performance in terms of both vertical displacement (e.g. settlement, heaving) and lateral deflection. In the Philippines, it is common practice to set a vertical displacement limit of 25.0 mm for foundation design. Under seismic loading, the vertical deformation limits will be increased to 34.0 mm (approx. one-third increase from its static counterpart).

Moreover, the Philippines has no standard criterion for allowable lateral deflection of excavations. Nevertheless, data from many case studies have been collated over the years, and these provide a relative estimate of the expected lateral deflection of braced cuts. Most data points are said to fall within the range of 0.2% to 0.6% of the exposed height (H_e) for a combination of soil types. Given that the sections in consideration are for a two-level braced excavation pit, the lateral deflection is not expected to reach the upper bound of the aforementioned range. Otherwise, internal forces in the struts will be quite large. As such, stringent limits of $0.2\%H_e$ and $0.3\%H_e$ are adopted in this study for static and pseudo-static conditions, respectively.

5 NUMERICAL ANALYSIS

5.1 *Finite element method*

In order to establish the displacements during and after excavation, deformation analysis will be carried out by way of Finite Element Method (FEM) using the numerical analysis tool, PLAXIS 2D 2018. FEM is a numerical technique used for finding approximate solutions by continuum-based methods wherein the governing equations describing the flow of water and deformation of the body are derived on the principles of conservation of mass, momentum, and energy. These equations, together with the prescribed boundary conditions, result in a nonlinear boundary value problem. The main advantage of FEM is its ability to estimate the deformations leading up to the failure or time point of interest. These deformations correspond to the movement of the soil mass showing how it will behave upon application of loads.

5.2 *Constitutive model*

The constitutive model adopted in this study is the Hardening Soil Small-strain (HSS) model (Schanz et al., 1999; Benz, 2007). The HSS model has the ability to vary stiffness depending on the stress state of the soil elements, even when at small strain levels. This is an ideal constitutive model for excavation projects because certain regions of the soil mass may possibly experience different stress state and conditions than those adjacent to them.

It should be noted that the HSS model utilizes the Mohr-Coulomb (MC) yield criterion and the model's corresponding shear strength parameters. Due to the lack of advanced lab testing, the

HSS parameters were correlated from reported/published values of soil samples with similar relative conditions and/or consistencies to the soil samples obtained from the study area. As it is not the objective of this study to focus on the parameters, the adopted MC and HSS parameters will no longer be presented.

6 RESULTS

6.1 *Displacements*

From the numerical analyses of the sections at static conditions, the maximum calculated deflection, settlement, and heave are 25.0 mm, 27.5 mm, and 27.5 mm, respectively. Although deflection is within the tolerable limit, settlement, and heave both exceed the allowable value by a small margin. As pseudo-static conditions, the maximum calculated deflection, settlement, and heave are 45.0 mm, 45.0 mm, and 40.0 mm, respectively, which all exceed the allowable limits. Table 3 summarizes the maximum calculated displacements for both conditions. In addition, Figures 4-5 show the exaggerated deformed mesh and deformation contour plot of Section 4A for both conditions, as reference and for visualization of the results.

Table 3. Summary of maximum calculated displacements.

	Static		Pseudo-static	
Deformation	Allowable	Calculated	Allowable	Calculated
Deflection (mm)	25.5	25.0	38.3	45.0
Settlement (mm)	25.0	27.5	34.0	45.0
Heave (mm)	25.0	27.5	34.0	45.0

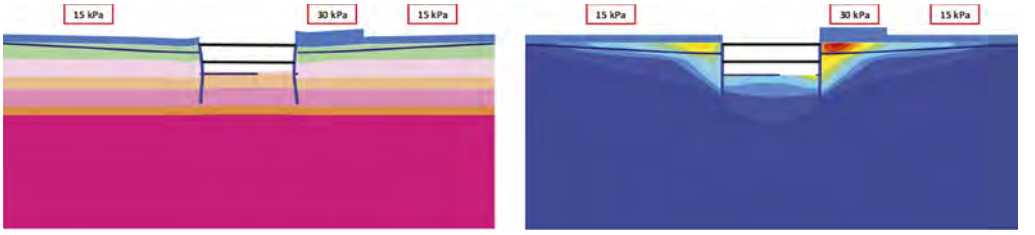

Figure 4. Section 4a Static: (a) exaggerated deformed mesh & (b) deformation contour plot.

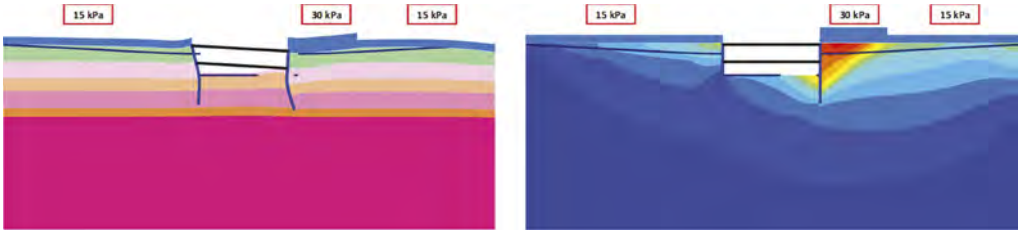

Figure 5. Section 4a Pseudo-static: (a) exaggerated deformed mesh & (b) deformation contour plot.

6.2 *Internal forces*

Aside from estimated displacements, the internal forces of the secant pile wall can also be extracted from the numerical analyses. Table 4 summarizes the maximum unfactored internal axial force, shear force, and bending moment of the secant pile wall elements for both static and pseudo-static conditions.

Table 4. Summary of maximum calculated secant pile wall internal forces.

Scenario	Axial (kN)	Shear (kN)	Bending Moment (kN-m)	
Static	487.18	675.43	(+) 899.83	(-) 1013.67
Pseudo-static	595.78	960.44	(+) 1464.77	(-) 1421.51

7 FINDINGS

Based on the foregoing numerical analyses using the available and inferred/correlated information, results show that estimated displacements are slightly excessive even at static conditions. The tolerable limits are further exceeded for pseudo-static conditions, despite not even considering the full seismic demand brought about by a 475-year earthquake. The developer was informed of this that some protective measures must be undertaken prior to construction, such as replacing the RC struts with steel sections, decreasing the spacing between struts, and even increasing the f'_c of the primary piles. Unfortunately, construction was pushed through, and observed damages to the adjacent structures were later on reported. Figure 6 shows some of the reported damages.

Figure 6. Reported damages: (a) damaged floor tiles & (b) lateral displacement of perimeter wall.

8 CONCLUSIONS

For slopes and cuts, the standard practice in the Philippines is simply to perform a pseudo-static idealization of the seismic demand to check for stability. Full non-linear dynamic analyses are only done in the design of large dams and/or high-rise buildings. In this study, the temporary secant pile wall system was subjected to a lower-level earthquake level, estimated to be 70% of 475-year seismic hazard. Although no earthquakes have occurred yet near the study area, the approach is surmised to be sufficient, and is in agreement with actual conditions given the reported damages.

Moreover, the displacement acceptance criteria used in this study are somewhat arbitrary, selection of the adopted limits are based on actual observations taken from numerous case studies, and thus, have merit. As such, these should not be ignored despite not having been standardized in local codes. In any case, the reported damages shown above validate how significant empirical data is, and how crucial the role of monitoring is in any engineering work.

REFERENCES

Benz, T. 2007. *Small-Strain Stiffness of Soils and its Numerical Consequences* [Doctoral dissertation, University of Stuttgart]. University of Stuttgart Institute of Geotechnical Engineering.

Hynes-Griffin, M.E. & Franklin, A.G. 1984. *Rationalizing the Seismic Coefficient Method. Miscellaneous Paper GL-84-13*, US Army Engineering Waterways Experiment Station, Vicksburg, Mississippi, USA.

Kavazanjian, E., Matasovic, N., Hadj-Hamou, T. & Sabatini, P.J. 1997. "Design Guidance: Geotechnical Earthquake Engineering for Highways, Design Principles." *Geotechnical Engineering Circular 3*. Federal Highway Administration, Washington DC, USA.

Matasovic, N. 1991. "Selection of Method for Seismic Slope Stability Analysis." *2nd International Conference on Recent Advances in Geotechnical Earthquake Engineering and Soil Dynamics*, St. Louis, Missouri, 11–15 March 1991.

Peñarubia, H.C., Deocampo, J.B., Grutas, R.N. 2017. "Probabilistic Seismic Hazard Analysis of the Philippines" *Proceedings of the 18th Association of Structural Engineers of the Philippines International Convention*., Quezon City, Philippines.

Schanz, T., Vermeer, P.A. & Bonnier P.G. 1999. The hardening soil model: Formulation and verification. In Brinkgreve, R.B.J. (Eds.), *Beyond 2000 in Computational Geotechnics: 10 Years of PLAXIS* (pp. 281–296). A. A. Balkema. ISBN 90 5809 040 X.

Smart Geotechnics for Smart Societies – Zhussupbekov, Sarsembayeva & Kaliakin (Eds)
© 2023 The Author(s), ISBN 978-1-003-29912-7
Open Access: www.taylorfrancis.com, CC BY-NC-ND 4.0 license

Geotechnics in creating a new image of the old theater. A case history

V.A. Ilyichev
The Russian Society for Soil Mechanics, Geotechnics and Foundation Engineering, President, Moscow, Russia
The Russian Academy of Architecture and Construction Sciences (RAACS), Vice-President for Innovations, Moscow, Russia

V.V. Semkin
Baltiy CEO, Research Center of Construction - Gersevanov Research Institute of Bases and Underground Structures (NIIOSP), Moscow, Russia

A.V. Shaposhnikov
The Russian Society for Soil Mechanics, Geotechnics and Foundation Engineering, general manager
Research Center of Construction - Gersevanov Research Institute of Bases and Underground Structures (NIIOSP), Moscow, Russia

ABSTRACT: The paper describes some geotechnical aspects of the reconstruction of the Russian State Academic Bolshoi Theatre, which was undertaken in the period of 2005-2008 with direct authors' involvement. The reconstruction of the underground section of the Theatre was carried out under the preserved superstructure. A 20 meters deep excavation was constructed in close proximity of other buildings. An observational method for strengthening foundation was applied. The method involved constantly performed monitoring and settlements management on the base of the monitoring results. The paper discusses design problems of supporting structures with regard to changes in their stress-strain state during reconstruction. A case history of the application of the observational method throughout the entire reconstruction period is considered.

1 INTRODUCTION

It is common knowledge that UNESCO designates the Russian Bolshoi Theatre as the world cultural Heritage site. Architect Albert Kavos and sculptor Peter Klodt designed the Theater building in 1857, and it still preserved its original architectural features. It was not reconstructed or repaired until 2005, by which time some supporting structures were in breakdown condition and many structural members were 50% worn out. It was evident, that further building operation should envisage the complete modification of the stage equipment and auditorium facilities, restoration of already lost décor members or maintenance of those still survived, as well as modification of installations.

All those factors confirmed the inevitability of the reconstruction of the Bolshoi Theatre. It took more than a dozen years to develop a reconstruction project. The project had undergone many alterations made before or within the reconstruction. The paper discusses technical aspects of the reconstruction process, emphasizing design features of the underground section of the UNESCO Heritage Site.

DOI: 10.1201/9781003299127-140

Figure 1. The Bolshoi Theatre before the reconstruction, in the mid-20th century.

2 GEOTECHNICAL ASPECTS OF THE BUILDING BEFORE THE RECONSTRUCTION

The building comprised brick supporting walls with singular pillars inside and outside the building (portico), arched and slab ceilings made of brick or concrete. Foundation consisted of rubble footing, brick strip footing, and independent footings of various cross-sections, whose bottom depth varied from 3.5 m to 6.0 m. There had never been serviceable underground space. The auditorium rested on a concrete slab designed by I. Rекberg. The slab was laid in the 20's of the nineteenth century, following a dangerous settlement of semicircular auditorium walls. When it happened, during a performance, the doors of the auditorium jammed and spectators were evacuated through side boxes.

It is important to note, that all supporting structures of the Theatre rested on three different footings, which carried three superstructures sequentially erected at different times: the wooden Peter's Theatre, the wooden Imperial Theatre, and the brick theater building erected in 1856. Thereby, the footings' depth and cross-section dimensions varied depending on stiffness of the structures they supported (concrete or wooden) and on the corresponding load, they carried. Due to the differential settlement, the portico pillar had deviated from the vertical up to 30 cm since the footing settlement was first recorded in the nineteenth century.

In the beginning of the 2000th, the load-bearing structural members, as well as underground supports were found in a partially functional state and some of them were even out of function.

In the second half of the twentieth century, some supporting structures were strengthened with respect to safety requirements to the building operation, actual for that time. For strengthening the foundation, a grouting method was applied with using materials modern in those days. However, from the technical condition viewpoint, the building required some conservative measures to be applied for ensuring its safe operation for the following operational period (more than a hundred years for structures of KS-3 class designed for mass presence of people, GOST 27751).

In the authors' opinion, adverse impacts responsible for the poor technical conditions of the supporting structures were as follows:

- Design features of the building that rested on mixed foundation carrying different structures and loads.
- Timber piles and beds exposed to rotting and uneven decay across the entire building became the reason for the partial or complete loss of bearing capacity of supports and supporting structures.
- In-service wear and tear of the structures' material caused a significant decrease in bearing capacity of structural members and individual structures, and, finally, of the whole building.
- Changes in geotechnical environment triggered changes in hydrogeological conditions and in soil properties, which in turn led to uneven settlement of footings.

Among the above factors that affected the building, the last one deserves a particular attention. It is a matter of discussion in this paper.

It is obviously worth beginning with the fact that the building was located on the Neglinka river flood plain, close to the dead arm of the river and a sewer built in the period of 1887-1889. In those days, the river was enclosed in a pipe and lowered beneath its original bed then. As a result, a water table lowered and hence intensified the decay of timber piles, thereby triggering uneven settlement of footings.

Geological cross-section of the site comprised Upper Quaternary deposit represented by silty to gravel alluvial sand, with thickness varying from 3,0 to 16,0 meters, underlain by Jurassic clay of varying thickness and consistency. All soil unites of Upper Quaternary deposit were uncertain, varied in plane and with depth, and wedged out in places. There were some areas of erosion indicated by Carbonic limestone overlaid with Upper Quaternary deposit.

An Aquifer was represented by alluvial sand. A water table level varied from 6.0 to 10.0 meters below the day surface. Such magnitude of the water table level was caused not only by the seasonal water flooding or by leakage through underground water supplying pipelines, but also by dewatering of the underground subway structures. The water of Upper Jurassic Aquifer was non-aggressive towards W4-concrete. The second Aquifer was associated with limestone and did not affect the underground structure of the building.

Talking about dangerous geological processes, the site was affected by karst, which occurred in the upper roof of the limestone deposit overlaid by thin Upper Quaternary or Jurassic clay. The karst phenomena at the site could be explained either by shallow occurrence of limestone deposit or by man-made effect. The thin clay layer did not protect the site from the karstic impact. For instance, due to karst occurrence in the neighboring area of the Maly Theatre and Metropole Hotel, jet-grouting technology was used for strengthening foundations at the site.

Originally, the building could be classified as a KS-3 class building designed for mass presence of people (more than a hundred, according to GOST 27751), and without any design features.

Therefore, from the geotechnical viewpoint, the building was a unique KS-3 class structure, with longitudinal and transverse supporting walls made of bricks of different configuration in plane. The supporting structures rested on strip foundations made of rubble, bricks and limestone, and on timber bed and piles. The soil foundation comprised different types of soil, the hydrogeological conditions of which varied causing uneven foundation settlement.

3 SOME GEOTECHNICAL ASPECTS OF THE RECONSTRUCTION PROCESS

The reconstruction design provided strengthening of the basic supporting structures with installation of additional elements necessary for the building operation. The geotechnical aspect was that the design envisaged installation of the underground structure slated to provide mechanical safety of the superstructure, accounting for the following factors: hydrogeological conditions, dangerous geological processes or man-made impact, and the influence of surrounding buildings. The design also had to meet requirements to the installation of the modern stage equipment.

Actually, six floors were designed below the day surface almost under the entire theater building, except for the auditorium. Several underground floors were additionally designed in front of the building and behind it, in Kopyevskiy Lane. Underground work was carried out in strict compliance with requirements to limiting deformations of a base under the preserved superstructure (less than 0.0007 - the relative difference in settlement with regard to emergency strengthening of the superstructure).

The design of the underground structure included an excavation enclosed with a “diaphragm wall”, which would serve as both supporting structure and groundwater protection. Since the underground structure was constructed under the retained superstructure, a “top-down” construction technique was selected, according to which the excavation at each level alternated with subsequent installation of supporting walls and floors at that level. In that case, the word “excavation” denoted the soil volume encompassing the installed underground supporting structures.

The new image of the theater with its newly arranged underground space should have looked as shown in Figure 2.

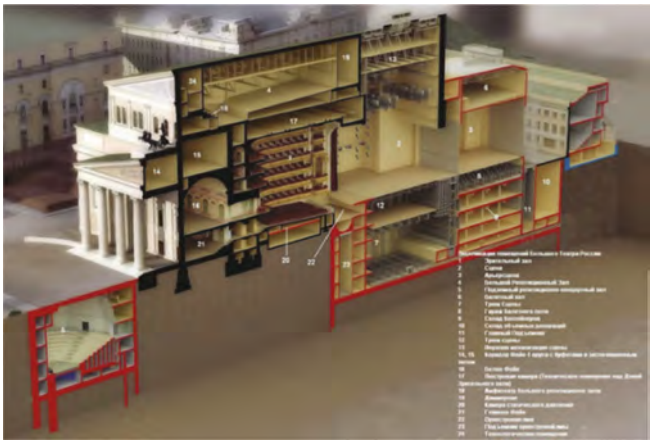

Figure 2. The concept of underground space of the Theatre Building, following the architect guru view.

The following measures were developed to meet the reconstruction design solution:

- Retained load-bearing structural members were temporarily or permanently strengthened for installation of temporary or permanent underground supports.
- Load-bearing concrete pile caps reinforced with rolled elements were arranged under the retained supporting structures (walls, columns).
- Temporary supports (jacked piles inside and end bearing piles outside the building) were installed under the retained supporting members (walls and columns).
- Temporary supports of retained superstructure were put into action, and old footings were taken out of service.
- Enclosing structures were installed outside and inside the building. The outside enclosure was executed as a diaphragm wall. The inside enclosure was installed along the contour of the auditorium, and it comprised secant wall made of small-diameter piles (300 – 350 mm) with a soil lock made using deep mixing technology.
- A pile cap mat executed as a rigid frame disk was arranged for putting caps installed under walls and columns into action, and for excluding horizontal movements.
- Excavation of the first subsoil level and dismantling of the old foundations.
- Temporary supports were braced and combined, thereby making a spatial frame structure that provided the stability of each member (piles, braces) and temporary structures in general. To protect the enclosure, struts bearing lateral soil pressure were arranged.
- Installation of the underground permanent supporting walls and floor of the second level.
- Excavation was performed in-stages. On finishing each excavation stage, temporary spatial frame structure comprising temporary supports (piles) and bracing members was arranged.
- Additional load was applied to piles for improving their capability to bear a load from permanent supporting structures (floor walls) and from elements of the enclosure strut system, as well as from permanent walls and ceilings subsequently constructed at each floor.
- Installation of the foundation slab at the design level.
- Permanent supporting structures and supports (walls, ceilings and foundation slab) were put into operation at minimum deformation, thus ensuring ultimate limit settlement and disabling temporary pile supports together with bracing members.
- Dismantling of temporary supports (piles, bracing members).

Figure 3 shows the general scheme of temporary structures location.

Structurally, both temporary and permanent underground members possess the following basic characteristics:

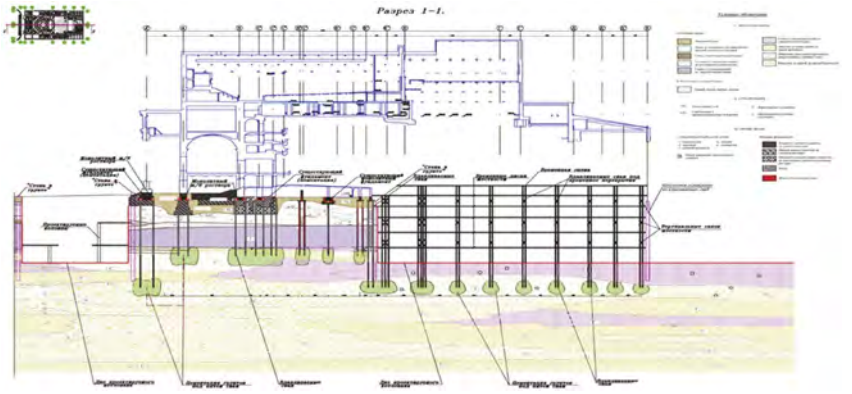

Figure 3. A layout of the underground permanent and temporary structures.

- The total load transferred from the preserved superstructure to temporary supporting frame structure, which included jacked piles and bracing members, was 170 thousand tf, and 230 tf with regard to newly erected underground structures.
- The traditionally installed "diaphragm wall" was 30-35 meters high and 800 mm thick.
- Temporarily supporting jacked pile originally carried the designed load of 80.0 tf and up to 100.00 tf when worked in the framed system then. Piles were 219 mm in diameter, made of weldless hot-formed pipes joined together in a section-by-section manner. The length of each section was 1-2 m, the total pile length was 16.0-26.0m.
- Temporary end bearing supports with a diameter of 630-820 mm and length 25.0-30.0 m carried the design load of 250-300 tf.
- 700 mm thick pile cap mat made of B30 concrete was rigidly reinforced under walls and columns. In spans, the pile cap mat was reinforced with frame made of individual metal rods of A500C class.
- 1500 mm thick foundation slab made of B30 or W12 concrete was reinforced with individual metal rods of A500C class.
- The "Triade Holding" specific non-shrink mortars for putting permanent load-bearing structures into operation was injected into gaps between walls and ceilings, formed while grouting in sequence ceiling-wall.

The geotechnical design of the underground structure was performed by Podzemproekt" LLC and "Baltiy" LLC. The "Podzemproekt" designed installation of the "diaphragm wall" and foundation slab. The "Baltiy" Company designed installation of pile caps under the retained structures, temporary supporting piles, and the installation of the underground structures. It also designed reinforcing piles installed outside the new underground structure, and excavation enclosures installed inside the building area. It should be noted, that a constant geotechnical monitoring performed by LLC "IC"Kreal" had accompanied the construction of the new underground structure for the whole construction period. Authors together with designers provided scientific and technical support to the construction process.

Constantly performed monitoring gave the possibility to make necessary adjustments during the construction without changing the fundamental design solutions. That was exactly what defined as an observational design method, in the regulatory documents. Thus, for example, the constant monitoring of the stress-strain state of the temporary support (jacked piles) was performed when the load was increasing due to newly erected underground structures, or when the stress was changing due to the installation of braces that provided piles stability in the excavated area. Jacking load was regulated for each pile individually on the base of the monitoring results, thereby demonstrating the technical support during the construction.

The monitoring and technical support had accompanied the whole process of the underground construction. This enabled engineers:

– To promptly elicit changes in the technical condition of the retained supporting structures by monitoring settlements and observing existed cracks or newly formed.
– To set up measures necessary to ensure the mechanical safety of individual load-bearing elements (already in place or newly constructed).
– To avoid deformations, which could dramatically reduce the capacity of the structural members and the whole building.
– To complete the construction of the new underground facility under the preserved building of cultural heritage in accordance with the adopted schedule.

The Theater building acquired a new "geotechnical appearance" including the underground part comparable in volume to the superstructure, and at the same time retained its historical appearance, visible to all of us.

4 CONCLUSIONS

The performed reconstruction involved pioneer geotechnical methods and structures installed. They comprised:

– Construction of the deep excavation under the retained structure. The 20 meters deep excavation was enclosed with "diaphragm wall" installed along the outer perimeter of the entire building to the depth of 32 m. Inside the building, along the contour of the auditorium, a 22 m deep enclosing secant wall made of small-diameter piles (300 – 350 mm) was arranged with a soil lock made using deep mixing technology.
– A stepwise installation of the capping raft. The procedure included installation of the caps under the retained walls, combined into a single capping raft after temporary supporting piles were constructed.
– Different types of the temporary supporting piles: small-diameter piles of 219 mm in the diameter and with the length of 21-22 m, cast-in-place end bearing piles of 600-280 mm in the diameter, 28-30 meters long piles reinforced with pipes of 420 mm in the diameter.
– The installation of small-diameter piles took place in confined space inside the building, using the combination of different technologies: drilling through the fill, which included members of the existed foundations and communication lines, pile jacking with soil displacement and thereby producing the preliminary design load that considered only the retained members of the superstructure and the new capping raft, increase in design load by applying additional load to the piles for improving their bearing capacity when the newly erected underground supports, namely, floors and vertical supporting structures were put into operation. Thus, the load applied before excavating was 80 tf, and it was 110 tf when the excavation was finished.
– Temporary cast-in-situ supporting piles were installed in casings outside the building and they carried the design load of 250-300 tf.
– Single piles were combined into a spatial structure, while excavating.
– A stepwise excavation was performed to the depth of a level. After excavation, permanent vertical and longitudinal supporting structures were installed. The structures served as struts resting on temporary pile supports.
– Installation of the foundation slab was followed by putting permanent underground supports into operation. Concurrently, temporary supports were taken out of operation.

REFERENCES

Anshin, L.Z., Semkin V.V., Shaposhnikov A.V. 2015. Designing buildings.
Mangushev R.A. 2010. Modern piling technologies. Association of the Construction Universities (ASU).
Mangushev R.A. & Nikiforova N.S. 2017. Building settlements affected by neighboring underground construction. Association of the Construction Universities (ASU).
Ponomarev A.B. & Vintikov Yu.L. 2006. Underground construction. Perm National Research Polytechnic University.

Smart Geotechnics for Smart Societies – Zhussupbekov, Sarsembayeva & Kaliakin (Eds)
© 2023 The Author(s), ISBN 978-1-003-29912-7
Open Access: www.taylorfrancis.com, CC BY-NC-ND 4.0 license

Analytical methods for calculating passive ground pressure in the construction of ground berms

I.B. Bashmakov
Saint-Petersburg State University of Architecture and Civil Engineering, Saint-Petersburg, Russia

ABSTRACT: This article reveals various methods of accounting for retaining berm in the calculations of the slurry wall construction. For one calculation case, the calculation results were compared using the basic approximate methods for estimating passive pressure when installing ground berms. To validate the existing approximate methods, method of characteristics in limit equilibrium method (*LEM*) was developed, allowing us to obtain a mathematically rigorous solution. The result of the work is a graph of the distribution of passive pressure along the slurry wall construction. The proposed rigorous mathematical method showed high convergence with the CPM method. The suggested approach allows us to obtain characteristic zones of the structure where the passive pressure formed by the soil berm works.

Keywords: passive ground pressure, ground berms

1 INTRODUCTION

In construction practice, to reduce the deformations of the diaphragm wall structures of the pit and increase their stability, various methods of bracing are used, such as the device of a strut system, anchors and soil berms [4]. The simplest and most economical method is the last option, due to the lack of need for additional materials, but at the same time difficulties arise from the point of view of engineering calculations. Classical methods for determining passive pressure, such as Coulomb theory or Rankin theory, associate natural stresses σ_z with passive pressure through the passive pressure coefficient K_p [7].

In modern engineering practice, the Poncelet formula for the passive pressure coefficient (1) has become widely used:

$$K_p = \left(\frac{\cos(\varphi - \alpha)}{\cos(\alpha) \times \left(1 - \sqrt{\frac{\sin(\varphi+\delta)\ \sin(\varphi+\beta)}{\cos(\alpha+\delta)\ \cos(\alpha+\beta)}}\right)} \right)^2 \quad (1)$$

where φ – the angle of internal friction of the soil, degrees, α – the angle of inclination of the wall structure's surface to the vertical, degrees, β – the angle of inclination of the soil surface to the horizontal, degrees, δ – the angle of friction at the contact "wall structure – soil".

This formula allows us to take into account in the calculation the inclined surface of the slurry wall construction and the friction between the wall structure and the soil but does not allow us to take into account the complex layout of the soil mass, which has a significant impact on the stress-strain state of the system. [8]

Therefore, the use of more useful calculation techniques is necessary to estimate the passive pressure during the construction of ground berms. [9, 10]

DOI: 10.1201/9781003299127-141

So that, in this work, a comparative analysis of different approximate methods for calculating passive pressure of ground berms was performed. A high spread of results was obtained.

Because it is difficult to estimate the actual values of passive pressures in field and laboratory conditions, the estimation of the applicability of the approximate methods was performed on the basis of a mathematically rigorous calculation method of soil mechanics.

2 LITERATURE REVIEW

In modern practice, there are the following approximate methods for calculating the passive pressure of the soil when installing ground berms occurred:

1. Additional equivalent load method (*AELM*) [1,6];
2. Method of increasing the level of the pit bottom (*ILPBM*) [1, 5, 6];
3. Modified method of increasing the level of the pit bottom (*Modified ILPBM*) [1, 6];
4. The Coulomb Prism Multiple Method (*CPMM*) [1, 5, 6].

The main condition of these methods are presented below.

The method of additional equivalent load (*AELM*). In this method, the weight of berm (W) is substituted by an equivalent uniformly distributed load (S), which is applied at the bottom level of the pit (Z). The load value (S) is determined by the formula (2):

$$S = \frac{W \ tan(\theta)}{d} \tag{2}$$

where W – the weight of berm, θ - the sliding surface's angle (except for soil-wall friction as calculated by $(45° - \varphi / 2)$, d – the amount of wall embedded in the ground.

The calculation scheme for this method is shown in Figure 1b.

The method of increasing the level pit bottom (*ILPBM*). The essence of the method is that the real berm is substituted by a berm with the same width of the lower base B_{bottom} which equal to real berm, but having a slope of 1:3, then the maximum height of the berm becomes equal to B/3. The calculated berm is taken into account by raising the level of the bottom of the pit by a value of B/6.

The berm area extending beyond the new geometry (the shaded part in Figure 1c) can be taken into account in the calculation as an additional equivalent load. It is worth noting that the method of increasing the level of the pit bottom, in contrast to the method of additional equivalent load, takes into account both the vertical pressure from the berm and partially the lateral pressure that the berm apply on the wall.

Modified method of increasing the level of the bottom of the pit (Modified *ILPBM*). This method is a combination of assumptions accepted in the *AELM* and *ILPBM*.

In contrast to the previous method, this method takes into account not only the geometry of the berm, but also its weight (W). The level of the layout increases by the value y, calculated by the formula (3):

$$y = \frac{W \ tan(\theta)}{\gamma d} \tag{3}$$

where W – berm weight, θ - angle of the sliding surface, γ – specific gravity of the berm soil, d – the amount of wall embedding in the ground.

The calculation scheme for this method is shown in Figure 1d.

The Coulomb Prism Multiple Method (CPMM). This method is based on the equilibrium equations of the Coulomb prism, which is constructed on the basis of the assumption of rectilinear sliding surfaces in the soil mass.

The forces acting in this prism is shown in Figure 2. By decomposing the forces into vertical and horizontal components, we obtain formulas (4) and (5).

$$F = (N + c`l\cot(\varphi))\tan(\varphi)\sin(\theta) + (N + U_R)\cos(\theta) - \ U_W \tag{4}$$

where N – normal reaction to the collapse surface, $\boldsymbol{c`}$ и $\boldsymbol{l}$ – adhesion along the surface and collapse surface length, respectively, $\boldsymbol{\varphi}$ – the angle of internal friction of the soil, $\boldsymbol{\theta}$ - angle of the sliding surface, $\boldsymbol{U_R}$ – pore pressure of water acting on the surface of a theoretical collapse, $\boldsymbol{U_W}$ – pore pressure acting on the wall.

$$N = \frac{c`l(\cos(\beta) + \sin(\beta)\tan(\delta)) + U_R(\cos(\beta)\tan(\delta) - \sin(\beta)) + W - U_W\tan(\delta) + cl_w}{\sin(\beta) - \tan(\varphi)\cos(\beta) - \tan(\varphi)\sin(\beta)\tan(\delta) - \cos(\beta)\tan(\delta)} \tag{5}$$

where $c`l$ – resultant adhesion along the collapse surface, β – angle equal to 90°- θ, δ – the friction angle of the soil against the wall, U_R – pore pressure of water acting on the surface of a theoretical collapse, W – weight of the collapse prism, U_W – pore pressure acting on the wall, cl_w – resultant coupling along the ground/wall surface (where l_w – the depth of the collapse prism under consideration with an abutment to the wall, $\boldsymbol{c}$ – specific gravity of the soil with a wall).

The calculation procedure suggest splitting the surface of the wall into equal sections in depth, after which a search is performed for the angle of inclination of the collapse prism β for each split point, at which the minimum passive resistance of the soil mass is provided. Following the completion of the calculation of the distribution of total passive pressure along depth, a plot of the passive ground pressure is constructed using the differentiation method.

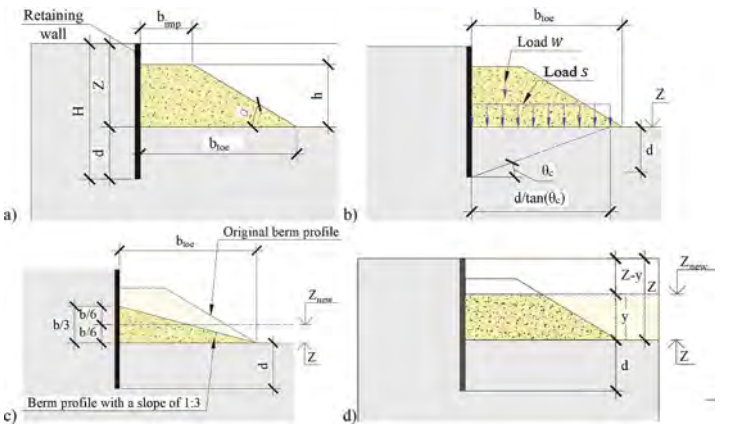

Figure 1. Soil berm calculation schemes: a) geometry of the soil berm; b) additional equivalent load method; c) increasing the level of the pit bottom method; d) modified ILPBM.

3 MATERIALS AND METHODS

3.1 *Mathematically rigorous solution*

Due to the significant differences between the calculation assumptions and the results of calculations according to the above approximate methods, their verification is necessary for their application in practical engineering. For this purpose, it is advisable to compare the results of calculations using existing methods with a mathematically rigorous solution.

In this case it is accepted to use the method of characteristics within the theory of the limit equilibrium method (*LEM*), developed by V.V. Sokolovski [3]. This method is based on the joint solution of the differential equilibrium equation of the plane-strain problem and the Coulomb-Mohr condition (6).

Based on this system of equations, as well as the relationship between the direction of the main stress σ_1 and the direction of the sliding surfaces of the first and second families, a system of four differential equations containing four unknowns can be obtained. This system of equations can be solved by the finite difference method by sequentially solving a number of boundary value problems [2].

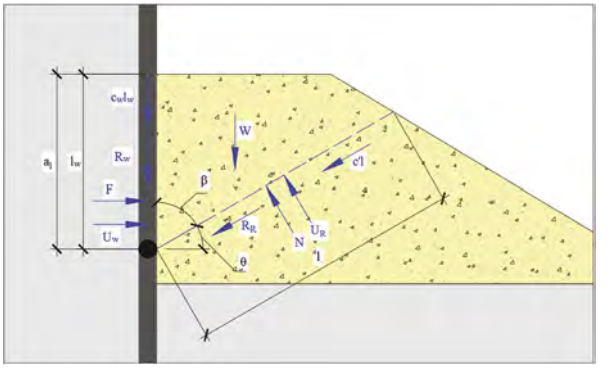

Figure 2. Calculation scheme of the method of multiple prisms.

$$\begin{cases} \dfrac{\partial \sigma_x}{\partial x} + \dfrac{\partial \tau_{xz}}{\partial z} = 0 \\ \dfrac{\partial \tau_{xz}}{\partial x} + \dfrac{\partial \sigma_y}{\partial z} = \gamma \\ \dfrac{\sigma_1 - \sigma_3}{\sigma_1 + \sigma_3 + 2\,c` \cot(\varphi)} = \sin(\varphi) \end{cases} \tag{6}$$

The proposed calculation scheme for assessing the passive pressure of the soil when installing a soil berm is shown in the Figure 3. In this diagram, the numbers indicate the order of solving boundary value problems, yellow – the first boundary value problems, blue – the second, green – the third and pink – the second boundary value problems with a special fan point.

4 RESULTS AND DISCUSSIONS

The main assumption of this research was the patten that the work of the soil berm is quite complex and approaches to its description with an equivalent load or an increase in the level of the pit bottom leads to an incorrect solution to the definition of passive pressure.

From the point of view of practical application, a significant disadvantage of the method of characteristics in LEM is complicated in application in case of nonlinear stratification of the foundation soils.

To compare the calculation results by the proposed method with the calculation results by approximate methods, Figure 4 shows a summary graph of the distribution of passive ground pressure by depth.

As can be seen from Figure 4, the characteristics method and the Coulomb prism multiple method show a fundamentally different nature of the passive pressure distribution over the depth than the other calculation methods. This is because the method of characteristics and the method of Coulomb prisms multiple allow us to take into account the actual complex geometry of the ground surface, while the other methods assume simplifying the design scheme to the horizontal layout of the bottom of the pit. This can also explain the high values of passive pressures that are obtained by the method of characteristics: unlike CPMM and ILPBM, this method takes into account the actual geometry of the soil berm, and does not simplify it as raising the level of the bottom of the pit below the base of the soil berm.

Analyzing the results of calculations, it is important to note that when taking into account the actual geometry of the soil berm, the character of its work corresponds to the case of horizontal layout only on the upper part of the plot, in particular, at a depth of 0 to 2 m.

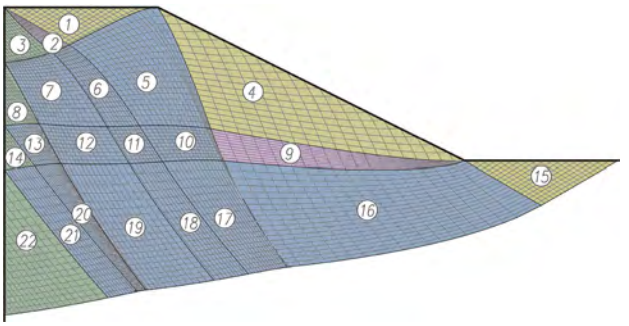

Figure 3. Calculation scheme and sliding surfaces in the soil mass when calculating the passive pressure during the installation of the soil berm by the characteristics method.

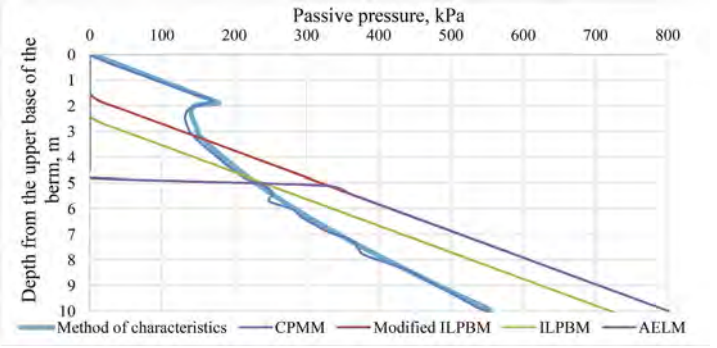

Figure 4. A summary graph of the results of calculating the passive ground pressure by the depth of the wall using various approximate methods and the method of characteristics (*LEM*).

The analysis of the plots of the distribution of passive soil pressure in depth with different geometric parameters of the soil berm allowed us to identify 3 main sections, shown in Figure 5.

The nature of the passive pressure plot in the first zone corresponds to the case of the vertical day level to the mark of the apex of the berm.

For the second zone, the distribution of passive pressure corresponds to the case of an inclined ground surface at an angle equal to the angle of the soil berm and can be determined by the formula (1).

For the third zone, the distribution of passive pressure in depth corresponds to the method of additional equivalent load, but taking into account the nonlinear determination of the value of the additional load.

Testing in a laboratory or in the field is required to validate the theoretical solutions presented in this article.

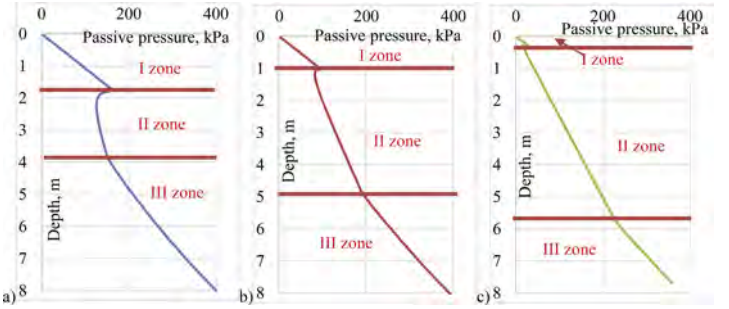

Figure 5. Plots of the distribution of passive soil pressure along the depth of the wall for a soil berm with an upper base of a) 5m, b) 3m, c) 1m, a lower base of 15m and a height of 5m.

5 CONCLUSIONS

1. A calculation scheme is proposed for determining the passive pressure of the soil by the method of characteristics within the theory of limit equilibrium method (LEM).
2. According to the results of the comparative analysis, a high convergence was obtained between the results of the calculation of the passive pressure of the soil during the installation of soil berms by the method of multiple prisms and the method of characteristics (*LEM*). The use of this approximate technique can be recommended for practical calculations, because this approximate method allows us to estimate the passive pressure corresponding to the fundamental laws of soil mechanics.
3. The selected characteristic areas on the obtained plots can be used as the basis for a new simplified method for calculating the passive pressure of the soil when installing ground berms.

REFERENCES

1. Dolgov, P.G. (2014). Calculation methods for earth retaining berms. Proceedings of the conference of Saint-Petersburg State University of Architecture and Civil Engineering. 2014, 465–473.
2. Karaulov, A., & Korolev, K. (2017). A Static Solution for the Problem of the Stability of a Smooth Freestanding Sheet Pile Wall. Soil Mechanics and Foundation Engineering, 54, 211–215.
3. Sokolovski, V. V. (1960). Statics of Soil Media. Butterworths Scientific Publications.
4. Mangushev R.A, Ilichev V.A. (2016). Handbook of geotechnics. Bases, foundations and underground structures. Associations of Construction Universities.
5. Gaba, A. R., Simpson, B., Beadman, D. R., & Powrie, W. (2003). Embedded retaining walls: guidance for economic design. Proceedings of the Institution of Civil Engineers, 156(1),13–15. https://doi.org/10.1680/geng.156.1.13.37294
6. Tavares, T. G. (2017). The efficiency of earth berms in supporting retaining walls [Thesis to obtain the Master of Science Degree in Civil Engineering]. Instituto Superior Técnico - Lisboa.
7. Verruijt, A., & Van Baars, S. (2007). Soil mechanics (pp. 19–25). Delft, the Netherlands: VSSD.
8. Mirsayapov, I., Khasanov, R., & Safin, D. (2021). Ensuring the stability of the deep pit enclosure and foundation bases in the conditions of reconstruction of the architectural monument in the city of Kazan. E3S Web of Conferences, 274, 03022. https://doi.org/10.1051/e3sconf/202127403022
9. Zhou, Y., & Chen, Y. (2022). Active and Passive Earth Pressure Calculation Method for Double-Row Piles considering the Nonlinear Pile Deformation. Geofluids, 2022, 1–17. https://doi.org/10.1155/2022/4061624
10. El-Sherbiny, M. M., El-Sherbiny, R., & Elmamlouk, H. H. (2017). Three Dimensional Effect of Grouted Discontinuous Berms for Passive Support of Diaphragm Walls. Grouting 2017. https://doi.org/10.1061/9780784480809.054

Smart Geotechnics for Smart Societies – Zhussupbekov, Sarsembayeva & Kaliakin (Eds)
© 2023 The Author(s), ISBN 978-1-003-29912-7
Open Access: www.taylorfrancis.com, CC BY-NC-ND 4.0 license

Calculation method of determining the earth pressure on the diaphragm wall considering the undrained soil behavior

R.A. Mangushev, I.P. Diakonov, I.B. Bashmakov & D.A. Paskacheva
Saint Petersburg State University of Architecture and Civil Engineering, Saint Petersburg, Russian Federation

ABSTRACT: In this article is shown a method of analytical calculation of soil pressure on the diaphragm wall of the pit, considering the of excessive pore pressures in the soil. Consideration of the undrained behavior of the soil is performed using the parameters of the Skempton. An analytical solution is obtained for active and passive earth pressures in view the possibility of formation of excess pore pressure. Recommendations are given for calculating the stability of pits in weak clay soils, taking into account with state of excessive pore pressures.

Keywords: passive earth pressure, active earth pressure, excess pore pressure, undrained behavior, Skempton's coefficients

1 INTRODUCTION

Developing of the underground space, the main object of study is the retaining wall structure. A correct assessment of the stress-strain state in the structures helps to avoid failure, as well as excessive reserves of capacity.

To a greater extent, this is relevant for underground construction with a significant thickness of weak soils characteristic in the St. Petersburg region [1], [2]. In relation to the geological conditions of St. Petersburg it is rational to consider time dependence pressure on the diaphragm wall caused by filtration processes in water-saturated weak clay soils.

The purpose of this research is to develop computational method for determining the pressure on the diaphragm wall, taking into account the undrained behavior of the soil. Taking into account the above objective and relevance of the research, the following tasks were set:

- analysis of existing methods of calculating soil pressure on retaining wall;
- derivation of active and passive pressure formulas according the parameters of the undrained behavior in the soil;
- comparison of the results of drained and non-drained calculation of soil pressure on the diaphragm wall.

2 LITERATURE REVIEW

2.1 *Undrained behaviour*

To analysis and control the results of numerical calculations, it is necessary to develop a methodology for approximate analytical calculation, which allows us to estimate the quantitative and qualitative impact of the parameters of undrained strength (coefficients of Skempton) on the stress-strain state in the soil.

DOI: 10.1201/9781003299127-142

The influence of undrained strength parameters on the results of triaxial consolidated-undrained tests (CIUC) within the ideal elastic-plastic model [3] and for hardening models [4], [5] was considered. It is well-known that the results of undrained calculations are largely influenced by the chosen model for describing of the soils strain [6]. A model correctly selected for the calculated situation allows us to obtain high convergence of the calculated data with the results of geotechnical monitoring [7].

2.2 *The concept of active and passive ground pressure*

The problem of determining the limiting pressure of the soil on the enclosing structure is attributed to the problems of the theory of limit equilibrium method (*LEM*) [8].

Studies of the pressure of the soil mass on the diaphragm wall structure were started by W. Rankine [9], he also derived the coefficients of active and passive pressures for ideally loose soils:

$$K_a = \frac{1-\sin\varphi'}{1+\sin\varphi'} = \tan\left(\frac{\pi}{4}-\frac{\varphi'}{2}\right)^2; K_p = \frac{1+\sin\varphi'}{1-\sin\varphi'} = \tan\left(\frac{\pi}{4}+\frac{\varphi'}{2}\right)^2 \quad (1)$$

where φ' – is effective angle of internal friction.

Additions for connected soils were made by A. Bell [10]. For analysis in full stresses under undrained conditions, the ground pressure on the retaining wall can be determined as follows:

$$\sigma_a = \sigma_z - 2\cdot c_u; \sigma_p = \sigma_z + 2\cdot c_u \quad (2)$$

where σ_a – is the active ground pressure; σ_p – is the passive ground pressure; σ_z – is the vertical stresses in the ground; c_u – is the resistance to undrained shear.

Considering the friction on the soil-structure contact, the coefficients of passive and active pressure can be determined by the following formulas:

$$K_a = \frac{\cos(\varphi')^2}{[1+\frac{\sqrt{\sin[\varphi'\cdot(1+\gamma_k)]\cdot\sin(\varphi')}}{\cos(\varphi'\cdot\gamma_k)}]^2}; K_p = \frac{\cos(\varphi')^2}{[1-\frac{\sqrt{\sin[\varphi'\cdot(1+\gamma_k)]\cdot\sin(\varphi')}}{\cos(\varphi'\cdot\gamma_k)}]^2} \quad (3)$$

where γ_k – is a coefficient that takes into account the decrease in strength characteristics at the "soil-structure" contact.

The coefficients of active and passive pressure can be represented as a determining value in the ratio between the contact pressure at the "soil-retaining structure" boundary and the displacement of the wall [11]. Decisions on the implementation of passive and active ground pressure, considering the displacement of the wall structure, are obtained by numerical methods.

3 METHODOLOGY

3.1 *Analysis of undrained behavior in case of active ground pressure*

Considering the undrained behavior in the case of active pressure, we assume that there is no effect of soil friction on the retaining wall or vertical stresses in the soil. Then, in the case of active pressure, there is no change in the total vertical stresses in the ground. We will describe the change in total vertical stresses in the ground through K. Terzaghi's law, expressing effective stresses:

$$\Delta\sigma_z = u_d + \Delta\sigma'_z \rightarrow \Delta\sigma'_z = -u_d \quad (4)$$

where $\Delta\sigma'_z$ – is the change in effective vertical stresses in the soil mass; Δu_d – change in excess pore pressure during deviatory loading.

The change in excess pore pressure under deviatory loading, based on A. Skempton's additions to Terzaghi's law [3], is defined as:

$$u_d = A_f \cdot B \cdot \Delta q \tag{5}$$

where A_f, B – are the Skempton's coefficients; Δq – change of the stress deviator in the soil mass.

The change in horizontal stresses considering expression (4) can be represented as follows:

$$\Delta\sigma'_x = \sigma'_{z0} \cdot (K_a - K_0) - u_d \cdot K_a - 2 \cdot c' \cdot \sqrt{K_a} \tag{6}$$

where σ'_{x0} – is the effective horizontal stresses in the soil mass before excavation; K_0 – coefficient of lateral ground pressure at rest; σ'_{z0} – effective vertical stresses in the soil mass before excavation of the pit.

Then expression (5) will take the form:

$$u_d = \frac{\sigma'_{z0} \cdot (K_0 - K_a) - 2 \cdot c' \cdot \sqrt{K_a}}{\frac{1}{A_f \cdot B} - K_a + 1} \tag{7}$$

Let's write down the formula for determining the active pressure on the wall structure, taking into account the excess pore pressure:

$$\sigma_{xa} = \sigma'_z \cdot K_a - 2 \cdot c' \cdot \sqrt{K_a} + u_d + u_0 = (\sigma'_{z0} - u_d)K_a - 2 \cdot c' \cdot \sqrt{K_a} + u_d + u_0 \tag{8}$$

where u_0 – is the hydrostatic pressure in the soil mass.

Let's present formula (8) in the form of a standard formula for determining the active pressure for a trained calculation, considering the coefficients that take into account the influence of the formation of excess pore pressure:

$$\sigma_{xa} = C_1 \cdot \sigma'_{z0} \cdot K_a - 2 \cdot C_2 \cdot c' \cdot \sqrt{K_a} + u_0 \tag{9}$$

where $C_1 = 1 + [K_0/K_a - K_0 - 1 + K_a]/\left[1 - K_a + 1/(A_f \cdot B)\right]$;
$C_2 = 1 + \left[A_f \cdot B \cdot (1 - K_a)\right]/[1 + A_f \cdot B \cdot (1 - K_a)]$.

3.2 *Analysis of untrained behaviour in the case of passive ground pressure*

In the case of passive soil pressure, the occurrence of excessive pore pressure is due to two reasons:

- anisotropic unloading of the soil mass caused by the excavation;
- deviatory loading of the soil mass caused by the transfer of horizontal loads from the enclosing structure.

Consider the first component of excessive pore pressure. In the case of undrained behavior, the volumetric deformation of the soil (elastic unloading of the bottom of the pit) is due only to the compressibility of the pore water. Volumetric deformations of the soil are determined based on changes in the average effective stress in the soil mass according to R. Hooke's law:

$$\varepsilon_v = \varepsilon_v^e = C_s \cdot \Delta p' \approx 0 \tag{10}$$

where ε_v – are the relative volumetric deformations of the soil; C_s– relative elastic volumetric deformations of the soil; ε_v^e– elastic component of soil compressibility; $\Delta p'$– change in the average effective stresses in the soil mass.

Then, taking into consideration the expression (10), we conclude that there is no change in the effective average stress during excavating. We will reveal the average effective stress through effective Cartesian stress:

$$\Delta p' = \frac{\Delta\sigma'_z + \Delta\sigma'_x + \Delta\sigma'_y}{3} \tag{11}$$

$\Delta\sigma'_z, \Delta\sigma'_x, \Delta\sigma'_y$ – change of Cartesian effective stresses in the soil.

Using the assumption of the absence of overcompaction in the soil and the equality of horizontal stresses, we obtained:

$$\Delta\sigma'_x = \Delta\sigma'_y = K_0\Delta\sigma'_z \tag{12}$$

Then, taking into account (12), expression (11) will take the form:

$$\Delta p' = \frac{\Delta\sigma'_z \cdot (1 + 2 \cdot K_0)}{3} = 0 \tag{13}$$

The change in the vertical effective voltage, taking into account the conclusion that there is no change in the average effective stress, will be zero.

Using K. Terzaghi's law, we obtain a change in excess pore pressure with comprehensive compression:

$$u_a = \Delta\sigma'^{dr}_z - \Delta\sigma'_z = \sigma'^{dr}_z - \sigma'_{z0} \tag{14}$$

where u_a – is the pore pressure caused by the unloading of the base during the development of the pit. In this case, the pore pressure will "inhibit" the change in effective stresses, preventing the soil from elastically decompressing.

Consider the second component of excessive pore pressure. When the resting pressure changes to passive pressure, the stress deviator and, accordingly, the excess pore pressure change in accordance with expression (5).

The change in the effective vertical stress and the change in the effective horizontal stress are determined similarly to clause 2.1.

Let's express the excess pore pressure under deviatory loading:

$$u_d = \frac{\sigma'_{z0} \cdot (K_p - K_0) + 2 \cdot c' \cdot \sqrt{K_p}}{K_p - 1 + \frac{1}{A \cdot B}} \tag{15}$$

Let's write down the formula for determining the passive pressure on the diaphragm wall, taking into account the excess pore pressure:

$$\sigma_{xp} = (\sigma'_{z0} - u_d) \cdot K_p + 2 \cdot c' \cdot \sqrt{K_p} + u_a + u_d + u_0 \tag{16}$$

Let us present formula (16) in the form of a standard formula for determining passive pressure for a drained calculation taking into account coefficients that consider the influence of the formation of excess pore pressure:

$$\sigma_{xp} = C_1 \cdot \sigma'_{z0} \cdot K_p + 2 \cdot C_2 \cdot c' \cdot \sqrt{K_a} + C_3 \cdot \gamma_{sb} \cdot d + u_0 \tag{17}$$

where $C_1 = 1 - [A_f \cdot B \cdot (K_p - 1) \cdot (1 - K_0/K_p)]/[A_f \cdot B \cdot (K_p - 1) + 1]$;
$C_2 = 1 - \left[A_f \cdot B \cdot (K_p - 1)\right]/\left[1 + A_f \cdot B \cdot (K_p - 1)\right]$;
$C_3 = 1 - K_p + \left[A_f \cdot B \cdot (K_p - 1) \cdot (K_p - K_0)\right]/\left[1 + A_f \cdot B \cdot (K_p - 1)\right]$; γ_{sb} – specific gravity of the soil in suspended state; d – excavation depth.

4 RESULTS AND DISCUSSION

The authors have obtained formulas for determining the magnitude of active and passive ground pressures on the diaphragm wall, taking into account the possibility of excessive pore pressures in the soil.

The Skempton's coefficients A_f and B are parameters of undrained behavior. The coefficient B depends on the degree of soil consolidation and allows you to take into account the time dependence excess pore pressure change. So, for the moment of time "0" (the beginning of the calculation), it will be equal to 1, and for the moment of time "∞" – 0 (drained statement).

The Skempton's coefficient A_f – is a particular value of the Skempton's coefficient A in case of collapse. It depends on the type of soil and is determined by the results of field or laboratory tests. For some soils, the coefficient was determined by Skempton based on the results of consolidated-untrained tests [3].

Table 1. Values of the Skempton coefficient A_f for different types of soils [3].

Type of clay soil	Coefficient value A_f
Clays with high sensitivity	0,75 to 1,5
Normally consolidated clay soils	0,5 to 1
Consolidated sandy clay soils	0,25 to 0,75
Slightly overconsolidated clay soils	0 to 0,5
consolidated gravelly clay soils	-0,25 to 0,25
Highly overconsolidated clay soils	-0,5 to 0

According to the formulas (9) and (17) obtained by the authors, it is possible to represent the pressure of the soil on the diaphragm wall as a function of several defining parameters:

$$\sigma_x = f(\varphi', c', A_f, B, z) \tag{18}$$

According to the graphs shown in Figure 1, it can be seen that the active pressure slightly depends on the excess pore pressure, while the passive pressure varies within 100% at different values of the Skempton parameter A_f.

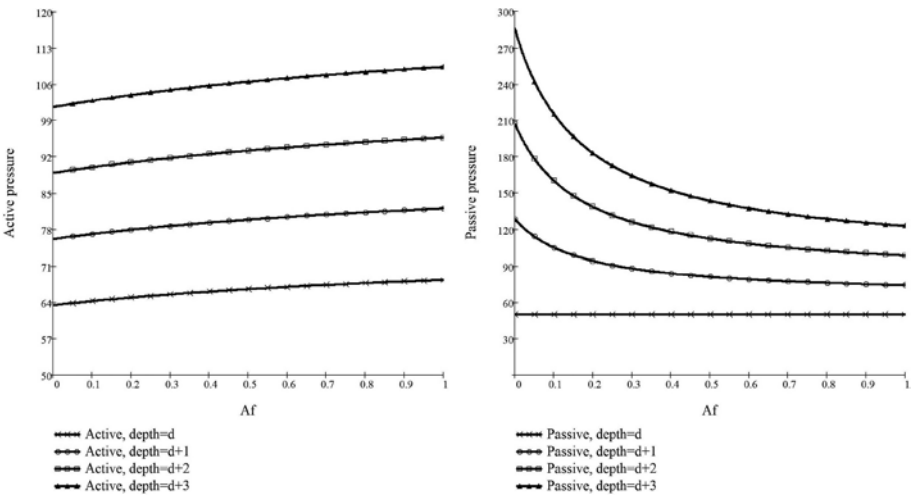

Figure 1. Dependence of the change in the total active pressure on the Skempton's coefficient A_f.

Let's compare the results of the drained and undrained calculation for different soils. The calculation parameters are presented in Table 2.

If soft soils are considered as clay with a high angle of internal friction, it is possible to obtain a passive pressure on the diaphragm structure in an undrained calculation less than the pressure in a drained type. In this case, the results of the drained calculation may be overly optimistic.

Table 2. Comparison of the results of undrained and drained calculations at a depth of 4 m below the bottom of the pit.

Effective friction angle φ`, °	Effective cohesion c`, kPa	The Skempton's coefficient A_f	P_{ae}/P_{ad}*	P_{pe}/P_{pd}**
30	5	0,33	0,981	0,655
		0,5	1,038	0,533
		1	1,060	0,444
20	5	0,33	0,968	1,159
		0,5	1,028	0,982
		1	1,046	0,878
10	5	0,33	1,006	1,360
		0,5	1,009	1,334
		1	1,016	1,279

*The ratio of active pressure in an undrained setting to a drained one.
**The ratio of passive pressure in an undrained setting to a drained one.

According to the results of field tests and numerical calculations for soft soils in deep pits, there are dependences of changes in passive pressure on the displacement of the retaining wall structure during the time [12], which also indicates a lower value of passive pressure at the initial time.

It is worth noting that in the classical consideration, the results of the drained calculation for pits are considered more conservative when estimating capacity of the soil by the failure method [13], [14].

A significant influence on the pressure on the diaphragm wall is exist by excessive pore pressure u_a, which forms a jump in effective stresses in the level of the bottom of the pit [15]. Such a "suction" effect can be noticed by the results of monitoring [16], however, further research is needed to determine the duration and accuracy of this effect.

To justify the applicability of the obtained formulas further verification of the convergence of the solution with experimental data is required.

5 CONCLUSION

This article analysis the influence of the formation of excessive pore pressure in the soils of the base on the example of the task of excavating the soil under the protection of the diaphragm wall.

Analytical solutions have been obtained for determining the active and passive pressure on the retaining wall structure, taking into account the formation of excessive pore pressure.

The results of comparison of calculation schemes with different soil parameters show that for normally compacted clays and high sensitivity soils, the passive pressure in the undrained calculation is significantly less than in the drained one. This suggests the need for an undrained stability analysis when calculating pits in the presence of certain types of soils.

For further analysis of the undrained behavior in the calculation of pits, it is necessary to study in detail the phenomenon of "suction" forming a jump in effective stresses in the bottom of the pit due to negative pore pressure u_a, and also take into account the impact of the implementation of pressure on the diaphragm wall from its displacement.

REFERENCES

1. Mangushev, R., & Osokin, A. (2020). THE EXPERIENCE OF THE UNDERGROUND CONSTRUCTION FOR THE COMPLEX OF BUILDINGS ON A SOFT SOIL IN THE CENTER OF ST. PETERSBURG. International Journal for Computational Civil and Structural Engineering, 16 (3), 47–53. https://doi.org/10.22337/2587-9618-2020-16-3-47-53

2. Mangushev, R., Rybnov, E., Lashkova, E. G., & Osokin, A. (2016). Examples of the Construction of Deep Excavation Ditches in Weak Soils. Procedia Engineering. https://doi.org/10.1016/j.proeng.2016.11.765
3. Skempton, A. W. (1954a). The Pore-Pressure Coefficients A and B. Geotechnique, 4(4), 143–147. https://doi.org/10.1680/geot.1954.4.4.143
4. Mayne, P. W., Coop, M. R., Springman, S. M., Huang, A., & Han, J. (2009). Geomaterial behavior and testing. Proceedings of the 17th International Conference on Soil Mechanics and Geotechnical Engineering. Volume 4, 2777–2872. https://doi.org/10.3233/978-1-60750-031-5-2777
5. Wroth, C. P. (1984). The interpretation of in situ soil tests. Geotechnique, 34(4), 449–489. https://doi.org/10.1680/geot.1984.34.4.449
6. Schweiger, H., & Tschuchnigg, F. (2021). A numerical study on undrained passive earth pressure. Computers and Geotechnics, 140, 104441. https://doi.org/10.1016/j.compgeo.2021.104441
7. Langford, J., Karlsrud, K., Bengtsson, E., Hof, C., & Oscarsson, R. (2021b). Comparison between predicted and measured performance of a deep excavation in soft clay in Gothenburg, Sweden. CRC Press EBooks, 83–90. https://doi.org/10.1201/9780429321559-11
8. Korolev K.V., Karaulov A.M. (2022). Soil mechanics: in 2 t. T. 2., Educational and Methodological Center for Education in Railway Transport, 488.
9. Rankine, W. J. M. (1857b). II. On the stability of loose earth. Philosophical Transactions of the Royal Society of London, 147, 9–27. https://doi.org/10.1098/rstl.1857.0003
10. Bell, A. L. (1915). THE LATERAL PRESSURE AND RESISTANCE OF CLAY AND THE SUPPORTING POWER OF CLAY FOUNDATIONS. Minutes of Proceedings, 199(1915), 233–272. https://doi.org/10.1680/imotp.1915.16217
11. Mei, G. X., Song, L. H., & Zai, J. M. (2009). Mechanical Analysis of Retaining Structure Considering Deformation and Validation. In Slope Stability, Retaining Walls, and Foundations: Selected Papers from the 2009 GeoHunan International Conference (pp. 220–225).
12. Tamano, T., Nguyen, H. Q., Kanaoka, M., Matsuzawa, H., & Mizutani, S. (2006). Passive resistance of soft clay in deep excavations. In Geotechnical aspects of underground construction in soft ground. Proceedings of the 5th international conference of TC 28 of the ISSMGE, the Netherlands, 15– june 2005 (pp. 673–679).
13. Vermeer, P. A. (1999). Column Vermeer. Plaxis Bulletin, 7.
14. Kolybin, I. V. (2008). Lessons of emergency situations in the construction of pits in urban conditions. Razvitie gorodov i geotekhnicheskoe stroitelstvo, (12), 90–124.
15. Xu-chao, S. H. I., & Yun-de, S. U. N. (2020). Analysis of the evolution of excess pore water pressure in soft soil under linear unloading. Rock and Soil Mechanics, 41(4), 1333.
16. Bolton, M. D., & Powrie, W. (1988). Behaviour of diaphragm walls in clay prior to collapse. Geotechnique, 38(2), 167–189. https://doi.org/10.1680/geot.1988.38.2.167

Smart Geotechnics for Smart Societies – Zhussupbekov, Sarsembayeva & Kaliakin (Eds)
© 2023 The Author(s), ISBN 978-1-003-29912-7
Open Access: www.taylorfrancis.com, CC BY-NC-ND 4.0 license

Reverse analysis of geotechnical monitoring results for the estimation of the diaphragm walls stress-strain

I.P. Dyakonov, I.B. Bashmakov, M.B. Zavodchikova & A.P. Cheremhina
Saint Petersburg State University of Architecture and Civil Engineering, Saint Petersburg, Russian Federation

ABSTRACT: The article considers low level convergence problem of bending moments in diaphragm wall is considered in this article. The article presents the main calculation methods that have become widespread in modern design practice. A comparative analysis of stress-strain state calculating results of a trench diaphragm wall for deep pit in the conditions of soil in St. Petersburg. To estimate the accuracy of the calculation methods, the calculation results were compared with the data of inclinometric monitoring in the trench diaphragm wall. At the same time, in order to be able to verify the obtained calculation results not only by the values of deformations, but also by the values of the calculated forces, a method for estimating bending moments in a trench diaphragm walls in the ground via inclinometric monitoring data is suggested. Comparative analysis of geotechnical monitoring data and various calculations showed high convergence with the results of the calculation, taking into consideration the possibility of excess pore pressure, nonlinear soil behavior and nonlinear rigidity of reinforced concrete.

Keywords: geotechnical monitoring, diaphragm wall

1 INTRODUCTION

In modern practice, the construction of deep pits in the engineering and geological conditions of St. Petersburg, a common solution is used to create a trench diaphragm wall in the ground as an retaining structure. One of the most significant parameters is the maximum bending moment that occurs in the wall structure [1, 2, 8, 9].

The existing standards for the design of flexible retaining walls do not provide specific guidance on the definition of bending moments arising in structures. As a consequence, when calculating the same structures by different organizations, the values obtained may differ several times.

In order to assess the applicability of certain calculation methods within the framework of geotechnical monitoring, it is necessary to assess the actual bending moments that occur in structures during the development of the pit [3]. In the modern practice of geotechnical monitoring, estimation of the internal stresses performed using special stress gauge [4]. However, for a full analysis of the nature of the bending operation of the structure, it is necessary to install a significant number of sensors. Since the location of the most loaded section in the height of the structure does not always correspond to the calculated one, it is necessary to install a number of height sensors. In addition, taking into account the stage of work, it is necessary to perform several rows of sensors in the plan. As a consequence, such an approach to monitoring efforts in the wall in the ground requires significant financial supply.

Thus, there is shortage data of stress-strain conditions of diaphragm walls along the ground excavation, which leads to the impossibility of verifying existing calculation methods [5].

DOI: 10.1201/9781003299127-143

2 SITE STUDY

This construction site considering a deep excavation with 6.2 m and 9.0 m depth under the protection of a trench diaphragm walls in the ground with a thickness of 600 mm and a depth of 19 m.

The stage construction of this pit assumed the create the slurry wall with the protection of a soil berm, and then under the protection of struts. During the work at the new construction site, the technology of work production was disrupted, and therefore the actual geometry of the ground berms significantly different from the project. The actual sequence of work on the development of the pit for the section of the pit with a depth of 9 m is shown in Figure 1a, for the section with a depth of 6.2 m in Figure 1b.

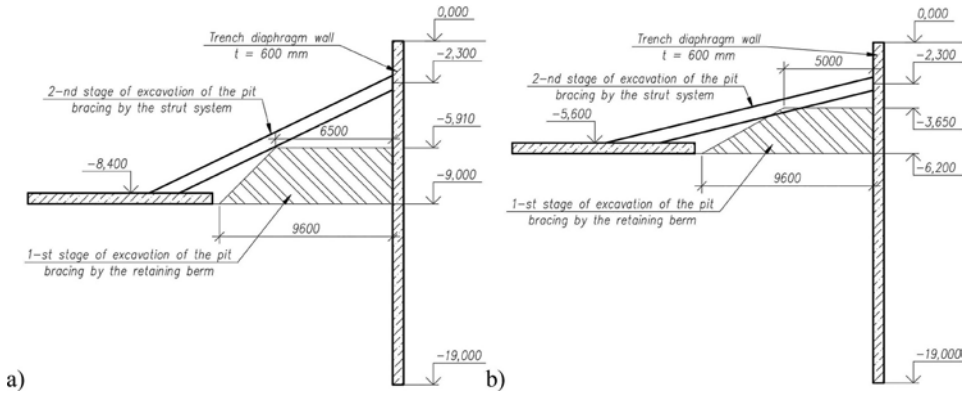

Figure 1. The actual sequence of work on the development of a pit.

The engineering and geological conditions of the construction site under consideration are represented by the occurrence of loams of fluid-plastic and fluid consistency to a depth of up to 20 m. A diagram of the results of testing the foundation soils by static sounding in the considered sections of the pit is shown in Figure 3.

When performing engineering and geological surveys, the strength parameters of the soil were determined by means of a direct shear box test (*DSB*), and the deformation parameters were determined on odometrical tests (*Oed*).This method of assessing the mechanical parameters of the foundation soils is widespread in the conditions of St. Petersburg, although it does not allow to fully estimate the strength and deformation characteristics of soils. In this case, the results of these tests were used to estimate the applicability of the existing methods.

As part of geotechnical monitoring, inclinometric tubes were installed in the ground directly in the panels of the trench diaphragm walls to monitor the deformations of the pit fence.

3 METHODS

3.1 *Calculation methods*

In the modern practice of designing pit fences, calculation methods using software systems based on the finite difference method and the finite element method (*FEM*) have become the most widespread.

The computational analysis based on the finite difference method is based on the equation of an elastic beam on an elastic base [6]:

$$EIw''''(z) + k(z)w(z) = P(z) \tag{1}$$

where, $\boldsymbol{E}$ – is the elastic modulus of the material of the structure in question, kPa; I – is the moment of inertia of the section of the structure in question (one linear meter of the structure for a trench diaphragm walls in the ground), taking into account the direction of movement, m^4;

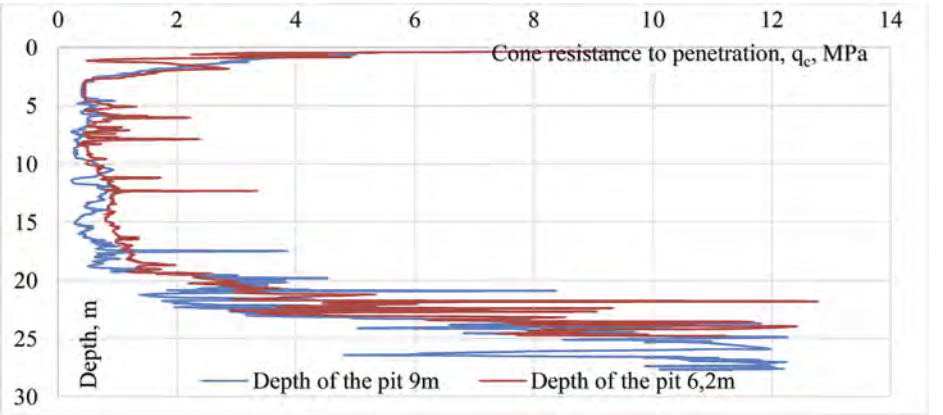

Figure 2. The actual sequence of work on the development of a pit with a depth of 6.2 m.

$\boldsymbol{w}(\boldsymbol{z})$ – is a mathematical function describing the movement of the axis of the curved beam in the direction normal to the initial position of the axis, m; $\boldsymbol{k}(\boldsymbol{z})$ – is the coefficient of the bed, determined depending on the type of soil and the depth of the point under consideration, kN/m^3; $\boldsymbol{P}(\boldsymbol{z})$ – is the initial pressure on the enclosing structure, defined as the sum of the ground rest pressures from the side of the excavation and from the outside of the excavation, kPa.

In this case, the value of the product $k(z)w(z)$ is limited by the values of active and passive ground pressure. The calculation scheme of this calculation method is shown in Figure 3.

When calculating the wall of pit by the finite element method, the most widespread use was of the Hardening Soil model (*HSM*), which implements the hardening mechanism both during compaction of soils and during deviatory loading [10].

When performing comparative calculations, several options for setting the parameters of the Hardening soil model were considered:

1) setting the calculation model in a drained formulation with the setting of strength parameters according to the results of testing soil samples by the method of single-plane rapid cut.
2) setting a computational model in an untrained formulation using an Undrained B behavior model. At the same time, the determination of strength parameters was carried out according to the data of static sounding of the soil of the base on the surface:

$$s_u = q_c/19 \tag{2}$$

where $\boldsymbol{q_c}$ – cone resistance to penetration, MPa.

3.2 *Back-analysis of monitoring results*

It is well-known from the theory of elasticity, the displacements of a loaded structure and the bending moments arising in it are connected by an integral dependence. This dependence can be described by the differential equation of the axis of a curved beam [7]:

$$EIw''(z) = -M(z) \tag{3}$$

where $\boldsymbol{M}(\boldsymbol{z})$ – is a mathematical function describing the values of the bending moment causing the displacement of the axis of the structure, kNm.

Thus, having data on full-scale observations of horizontal displacements and knowing the rigidity of the structure, it is possible to evaluate the bending moments arising in it.

To be able to apply expression (3), it is necessary to bring the full-scale data to a mathematical function. The least squares method is well suited for this purpose, but first of all it is necessary to choose a general form of the function describing the dependence of the horizontal displacement of the trench diaphragm walls in the ground on the depth. Given the assumption that the

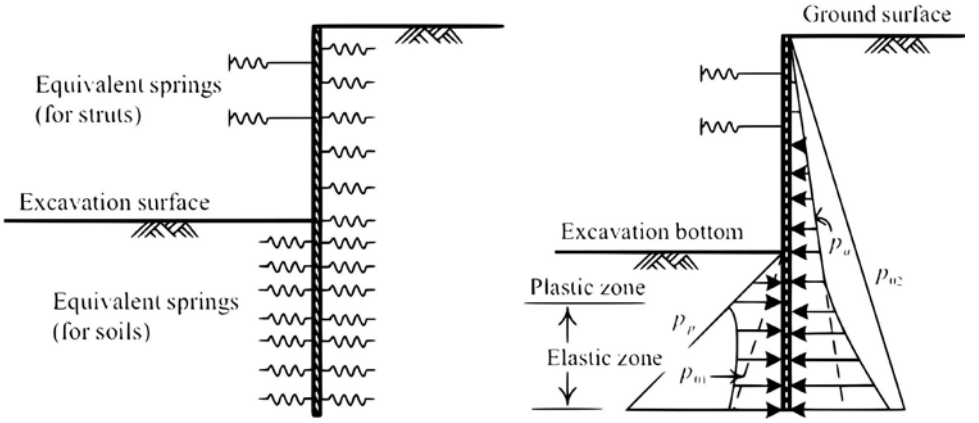

Figure 3. The design scheme of the pit enclosure when calculated by the finite difference method.

dependence of the pressure on the enclosing structure on the depth can be described by a linear function, it is rational to use a fifth-degree polynomial to describe the function of horizontal displacements of the trench diaphragm walls in the ground. In this case, the problem of conducting full-scale data to a mathematical function is reduced to solving the equation:

$$P(A,B,C,D,E,F) = \sum_{i=1}^{n} \left(S_i - Az_i^5 - Bz_i^4 - Cz_i^3 - Dz_i^2 - Ez_i - F\right)^2 \rightarrow min \tag{4}$$

where $\boldsymbol{P}(\boldsymbol{A},\boldsymbol{B},\boldsymbol{C},\boldsymbol{D},\boldsymbol{E},\boldsymbol{F})$ – is a function of the dependence of the sum of the quadratic deviations of the values of the desired function from the field data on the coefficients of the desired dependence; $\boldsymbol{S_i}$ - is the full-scale value of the horizontal displacement according to the results of inclinometric observation, for the i-th point in height, m; $\boldsymbol{z_i}$ – is the height coordinate of the i–th point, m; $\boldsymbol{n}$ – is the number of points at which the inclinometer readings were taken.

And the desired function will take the form:

$$S(z) = A \times z^5 + B \times z^4 + C \times z^3 + D \times z^2 + E \times z + F \tag{5}$$

The results of conducting field data to the function are shown in Figure 4.

When applying expression (3), the second important aspect is the correct assessment of the bending stiffness of the structure in question. As is known, reinforced concrete structures when working on bending have the properties of nonlinearity, and therefore the bending stiffness of the trench diaphragm walls in the ground must also be considered in a non-linear formulation.

To construct a nonlinear relationship between the bending moment and the bending stiffness of the structure, it is advisable to apply a numerical method. In this work, a LIRA-CAD was used to build this dependence. At the same time, the nonlinear diagram of concrete deformation under tension and compression, the actual scheme of reinforcement of the structure and the location of the longitudinal reinforcement in the section of the structure were taken into account. The dependence of the bending stiffness of the structure on the effective bending moment obtained by the calculation results is shown in Figure 5.

4 RESULTS AND DISCUSSIONS

The diagrams of bending moments in the diaphragm wall were obtained from the result of calculation and reverse analysis are shown in Figure 6.

In case of design the construction by the finite element method (*FEM*), a calculation scheme with nonlinear rigidity of the trench diaphragm wall was additionally considered. The nonlinearity parameters were assigned according to Figure 5.

According to the results of comparing the maximum values of bending moments, a high convergence of the results of reverse analysis of monitoring data with the results of calculation

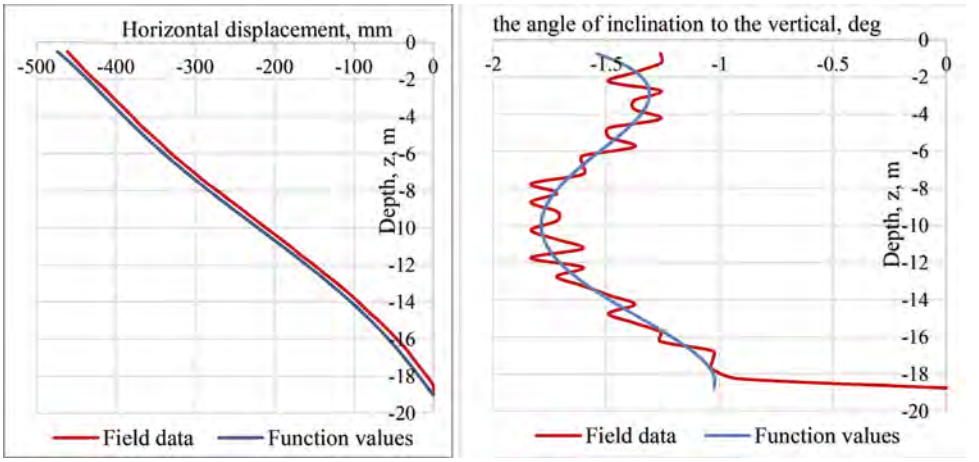

Figure 4. Results of reduction of natural data to a mathematical function.

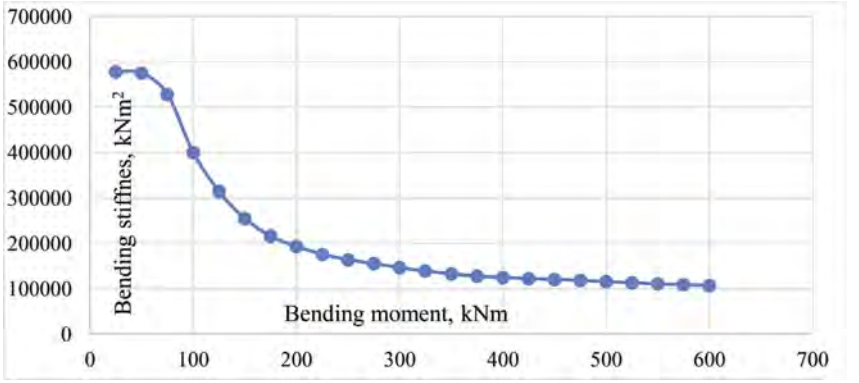

Figure 5. The obtained relationship between the bending moment and the bending stiffness of the structure.

in an undrained state, taking into account the nonlinear operation of reinforced concrete, was obtained. The convergence of the results was 90%.

Comparing the results obtained for the section of the pit with a depth of 9 m and a depth of 6.2 m, it is important to note that with an increase in the depth of the pit by 1.5 times, the variation in the calculated bending moments obtained by various methods increases from 60% to 200%.

The greatest influence on the calculation results is provided by taking or not taking into account the undrained behavior of the soil. For a section of the pit with a depth of 9 m, growing in a drained setting leads to an increase in the maximum bending moment by 80% in relation to the undrained setting. Therefore, it is reasonable to consider the calculation method taking into account the undrained behavior of the soil as a more correct calculation method for analyzing the stress-strain state of the wall in the ground during the phased development of the pit.

5 CONCLUSIONS

1. A method is proposed for estimating the actual bending moments in a trench wall in the ground using reverse analysis of inclinometric monitoring data for horizontal displacements of the structure.
2. Based on the analysis of the results obtained, it was found that when calculating the justification of the fences of deep pits in conditions of weak clay soils, it is advisable to perform calculations in an undrained post, taking into account the nonlinear operation of reinforced concrete.

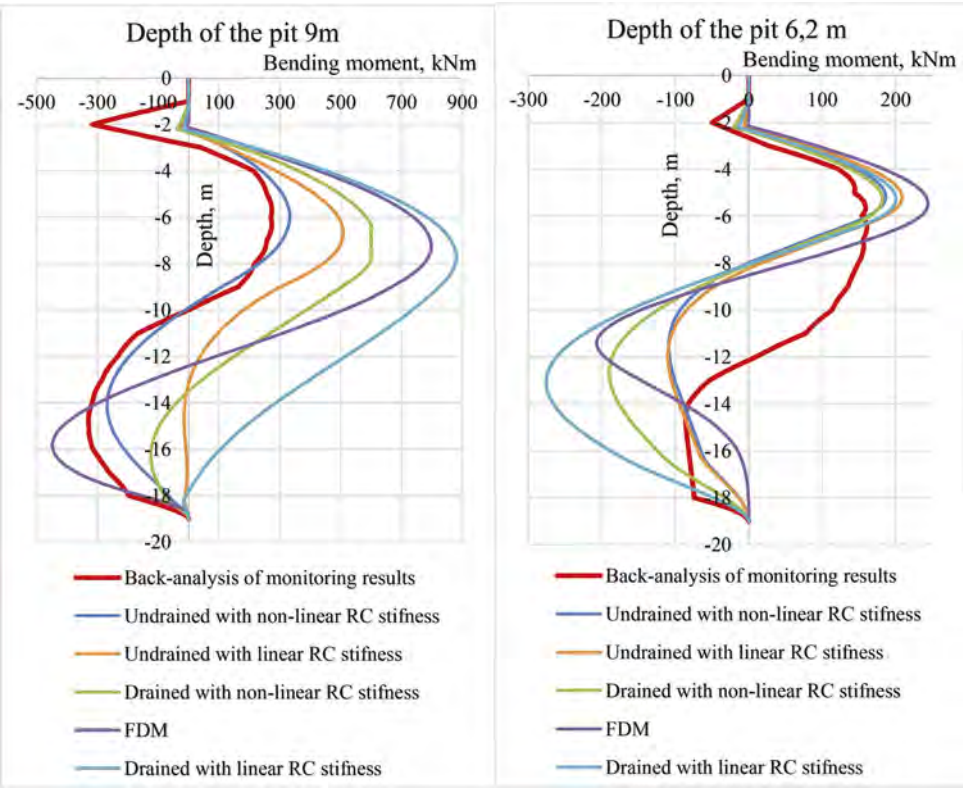

Figure 6. Resulting graphs of reverse monitoring analysis data and calculation results using various methods.

3. The results obtained for the calculation by the finite difference method showed low convergence with geotechnical monitoring data. In this regard, it is necessary to modify this calculation method for conditions of weak clay soils.

REFERENCES

1 Salmin I.A. (2017). Monitoring of the retaining wall structure of a deep pit. Housing construction. 2017. 29–33.
2 Back-analysis of an anchored retaining structure of a deep excavation. (2015). H. Popa, A. Ene, & D. Marcu, XVI European Conference on Soil Mechanics and Geotechnical Engineering. 3995–4000.
3 Osokin A.I., Tatarinov S.V., Denisova O.O., Makarova E.V. (2014). Geotechnical monitoring system as a means of ensuring the safety of construction. Housing construction. 2014. 9–18.
4 Mirsayapov I.T., Koroleva I.V. (2013). Features of geotechnical monitoring of unique buildings and structures. News of KGASU, 4(26), 147–154.
5 Gaba, A. R., Simpson, B., Beadman, D. R., & Powrie, W. (2003). Embedded retaining walls: guidance for economic design. Proceedings of the Institution of Civil Engineers, 156(1), 13–15. https://doi.org/10.1680/geng.156.1.13.37294
6 Verruijt, A., & Van Baars, S. (2007). Soil mechanics (pp. 19–25). Delft, the Netherlands: VSSD.
7 Levchenko N.B., Kagan-Rosenzweig L.M., Kupriyanov I.A., Khaletskaya O.B. (2001). Resistance of materials. Saint-Petersburg State University of Architecture and Civil Engineering.
8 Mangushev, R., & Osokin, A. (2020). The experience of the underground construction for the complex of buildings on a soft soil in the center of St. Petersburg. International Journal for Computational Civil and Structural Engineering, 16(3), 47–53. https://doi.org/10.22337/2587-9618-2020-16-3-47-53.
9 Mangushev, R., Rybnov, E., Lashkova, E. G., & Osokin, A. (2016). Examples of the Construction of Deep Excavation Ditches in Weak Soils. Procedia Engineering. https://doi.org/10.1016/j.proeng.2016.11.765.
10 Schanz, T., Vermeer, P. A., & Bonnier, P. G. (2019). The hardening soil model: Formulation and verification. Routledge EBooks, 281–296. https://doi.org/10.1201/9781315138206-27.

Smart Geotechnics for Smart Societies – Zhussupbekov, Sarsembayeva & Kaliakin (Eds)
© 2023 The Author(s), ISBN 978-1-003-29912-7
Open Access: www.taylorfrancis.com, CC BY-NC-ND 4.0 license

Experimental study on the stress-strain behavior of underground structures affected by adjacent excavation in a carbon rod geometry

Munkyeong Baek
Graduate Student, Department of Civil Systems Engineering, Ajou University, South Korea

Ilhan Chang*
Associate Professor, Department of Civil Systems Engineering, Ajou University, South Korea

ABSTRACT: In this study, the stress and strain variations of an existing tunnel according to adjacent tunnel excavation have been evaluated via laboratory model testing. Since the tunnel has been a typical structure under the plain strain condition, the laboratory model tests were conducted using carbon rods which represents a weathered rock geometry. The stress and strain (deformation and rotation) variations of an existing tunnel model due to adjacent ground relaxation have been assessed with embedded load transducers and particle image velocimetry (PIV) analysis. Different vertical and horizontal spacing conditions between the ground relaxation (tunneling) point and the existing tunnel location were considered. The simultaneous load and PIV analyses data clearly verifies the acceptable construction guide for adjacent tunneling in weathered rock stratum.

1 INTRODUCTION

Underground tunneling construction has been recently increased to relieve urban traffic problems. A new tunnel excavation generally affects to deformation of surrounding ground and existing tunnels. Previous studies have been performed by the similarity to empirical equations and numerical analysis to investigate the effect of tunnel excavation on surrounding ground and existing tunnels. Alejano et al. (2012) studied the longitudinal deformation of the existing tunnel and the ground relaxation around the new tunnel excavation. The presence of adjacent tunnels within the plastic zone caused by ground relaxation will be affected. Because of ground relaxation after tunnel excavation, the load acting on the adjacent tunnel and the surrounding ground relaxation area changes. Recent studies have assessed the effect of ground relaxation through physical model experiments (Kumar and Kumar Shrivastava, 2022), numerical analysis (Baziar and Dehghani, 2021), field observations (Fargnoli et al., 2015), empirical/analytical methods (Franza and Marshall, 2019) and finite element method (FEM) (Zárate et al., 2018; Zakhem and El Naggar, 2020; Zhou et al., 2020).

In this study, stress-strain behavior of underground structure and surrounding ground under adjacent tunnel excavation was assessed through a carbon rod experiment. The effect of a new tunnel location to an existing tunnel was investigated. While a parallel alignment was assessed as a control group, effect of a diagonal alignment was evaluated (Figure 1b).

The tunnels of parallel lines must be taken into consideration in this analysis despite the fact that the floors are different as the underground area is enlarged and numerous tunnels, including water and sewage, electric power, subway, and road tunnels, are built. As shown in Figure 1(a), it is necessary to investigate the feasibility of constructing a new tunnel that is constructed lower than the existing tunnels constructed near the ground and parallel as shown in Figure 1(b).

*Corresponding author: ilhanchang@ajou.ac.kr

DOI: 10.1201/9781003299127-144

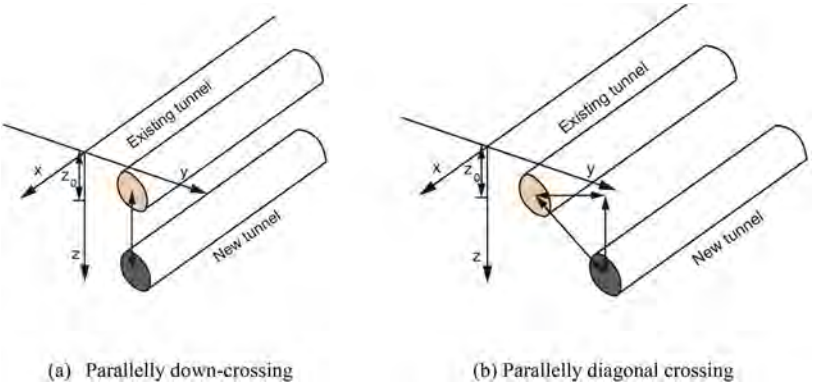

(a) Parallelly down-crossing (b) Parallelly diagonal crossing

Figure 1. Relative position between new tunnel and existing tunnel (Liang et al., 2016). (a) Parallelly down-crossing (b) Parallelly diagonal crossing.

2 EXPERIMENTAL PROGRAM

2.1 *Test geometry*

The test bed was designed to have a dimension of 1500 mm × 1500 mm. The test bed reflected soil made of carbon rods with a groud unit weight of 1.43 kN/m^3, an internal friction angle of 35 °, and a clearance ratio of 0.39. Carbon rods were used to comprise the test bed. The carbon rods were 55 mm long and have different diameters of 3 mm, 5 mm, and 7 mm (Figure 2). The carbon rod amount ratio to compose the test bed was 4: 2: 1.

2.2 *Tunnel modeling*

The new tunnel made of steel, was set at the bottom of the experimental frame, and endure the load as shown in Figure 2a. The new tunnel is divided into three parts a top segment and two side segments. The cross section of the new tunnel was deformed to simulate the ground deformation after excavation. It was initially set to a diameter of 260 mm, but finally adjusted to 250 mm in cross-sectional diameter by vertical rearranging of inner support bars.

The existing tunnel was located at the diagonal direction as shown in Figure 2a. The exact location was set to be a symmetric ratio of vertical 1D: horizontal 1D. The existing tunnel was 250 mm in diameter and the central portion were connected to a load transducer to guarantee that each component of the existing tunnel behaves as a single unit.

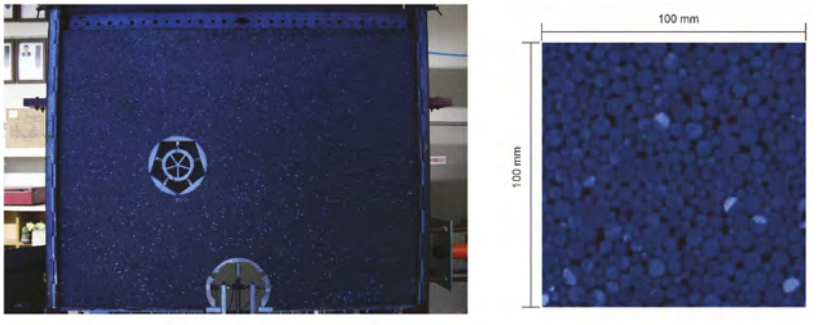

(a) (b)

Figure 2. Test view. (a) Test view (Vertical 1D, Horizontal 1D); (b) Test geometry.

3 RESULTS

To proceed with the analysis, particle image velocimetry (PIV) analysis, which can measure displacement using pixel changes, was conducted using tow images. Experimental photos were used to perform PIV analysis. In PIV, the pixels from the first picture were used to create a grid of a certain size, and the progressing images tracked throughout the experiment to monitor the differences between the initial picture and the target picture in terms of displacement and deformation. The tunnel deformation picture was used as the final image to track and analyze the movement of the carbon rod representing the ground particles. The PIV analysis showed the relaxed area to the top of the new tunnel after tunnel excavation in the absence of an existing tunnel. When the existing tunnel was located in the vertical direction, a relaxation load was generated on the upper part of the new tunnel. In a diagonal alignment (1D:1D configuration,), the ground deformed gradually as the tunnel deformed. As a result, there was a load shift that causes compressive stress in the next segment of the existing tunnel. However, as the ground deformation progressed, the entire tunnel moved to the submerged stage, and a relaxation load was applied to the part facing the new tunnel.

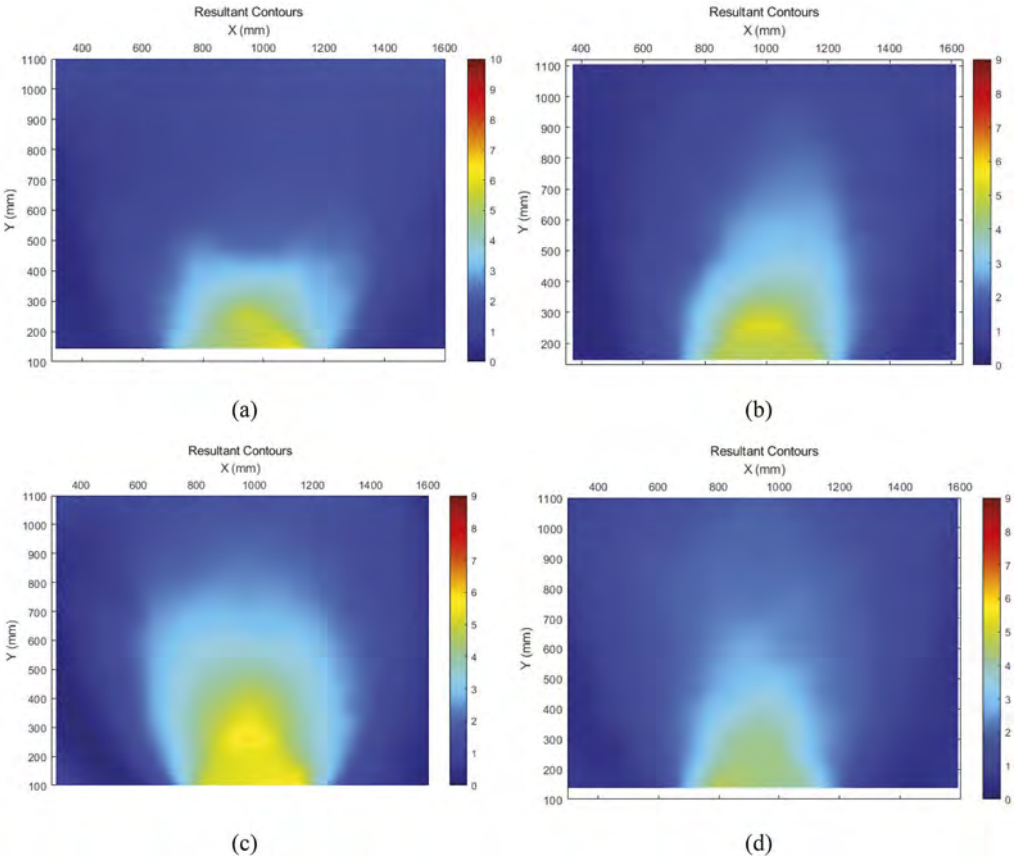

Figure 3. Contours as a result of final displacement (PIV). (a) Location of the existing tunnel (Vertical 1D: Horizontal 0); (b) Location of the existing tunnel (V 1D: H 1D) (c) Location of the existing tunnel (V 1D: H 2D) (d) Location of the existing tunnel (V 2D: H 0).

4 CONCLUSIONS

The PIV basis research indicates that the tension and relaxation of the subsurface are caused by tunnel excavation. There is less distortion due to ground relaxation when there is an adjacent

existing tunnel. As the ground relaxed, the measured load values in the existing tunnel segment changed. The new tunnel direction experienced tensile force, and the adjacent section experienced compressive load, when the existing tunnel was in the diagonal direction. The research's findings indicate that the stress placed on the present tunnel segment varies depending on how far the existing and new tunnels are apart. In this study, it was confirmed that the effect was small when the distance was more than twice the diameter of the tunnel to the left. The consequences of compressive and tensile loads, if any, must be taken into account when excavating a new tunnel.

ACKNOWLEDGEMENT

This work was supported by the National Research Foundation of Korea (NRF) grant funded by the Korea government (MSIT) (No. 2022R1A2C2091517).

REFERENCES

Alejano, L. R., Rodríguez-Dono, A. & Veiga, M. (2012). Plastic radii and longitudinal deformation profiles of tunnels excavated in strain-softening rock masses. *Tunnelling and Underground Space Technology*, *30*, 169–182.

Baziar, M.H. & Dehghani, R., (2021). Evaluation of seismic mechanical response of tunnel linings using shaking table tests and numerical analyses. Soil Dynamics and Earthquake Engineering 147, 106793.

Fargnoli, V., Boldini, D. & Amorosi, A., (2015). Twin tunnel excavation in coarse grained soils: Observations and numerical back-predictions under free field conditions and in presence of a surface structure. Tunnelling and Underground Space Technology 49, 454–469.

Franza, A. & Marshall, A. M. (2019). Empirical and semi-analytical methods for evaluating tunnelling-induced ground movements in sands. *Tunnelling and Underground Space Technology*, *88*, 47–62.

Jin, D., Yuan, D., Li, X. & Zheng, H. (2018). Analysis of the settlement of an existing tunnel induced by shield tunneling underneath. *Tunnelling and Underground Space Technology*, *81*, 209–220.

Kumar, P. & Kumar Shrivastava, A. (2022). Experimental and numerical analysis of deformation behaviour of tunnels under static loading conditions. *Sustainable Energy Technologies and Assessments*, *52*, 102057.

Liang, R., Xia, T., Hong, Y. & Yu, F. (2016). Effects of above-crossing tunnelling on the existing shield tunnels. *Tunnelling and Underground Space Technology*, *58*, 159–176.

Zárate, F., Gonzalez, J. M., Miquel, J., Löhner, R. & Oñate, E. (2018). A coupled fluid FEM-DEM technique for predicting blasting operations in tunnels. *Underground Space*, *3*(4), 310–316.

Zakhem, A. M. & El Naggar, H. (2020). Three-dimensional investigation of how newly constructed buildings supported on raft foundations affect pre-existing tunnels. *Transportation Geotechnics*, *22*, 100324.

Zhou, Z., Chen, Y., Liu, Z. & Miao, L. (2020). Theoretical prediction model for deformations caused by construction of new tunnels undercrossing existing tunnels based on the equivalent layered method. *Computers and Geotechnics*, *123*, 103565.

Smart Geotechnics for Smart Societies – Zhussupbekov, Sarsembayeva & Kaliakin (Eds)
© 2023 The Author(s), ISBN 978-1-003-29912-7
Open Access: www.taylorfrancis.com, CC BY-NC-ND 4.0 license

Numerical study of grouting injectivity according to rock joint characteristics using UDEC

J.Y. Kim
MS.C Student, Department of Civil & Environmental Engineering, Pusan National University (PNU), Busan, Korea

J.H. Weon
Undergraduate Student, Department of Civil & Environmental Engineering, Pusan National University (PNU), Busan, Korea

T.M. Oh
Associate Professor, Department of Civil & Environmental Engineering, Pusan National University (PNU), Busan, Korea

ABSTRACT: Underground space such as undersea tunnels and high-level nuclear waste disposals are constructed in bedrock due to the stability and safety. When the bedrock has unexpected joints and cracks, groundwater inflow and nuclide outflow through joint can occur in underground structures. Grouting in joints is essential for reinforcement and waterproof. Grouting injection performance is affected by parameters (e.g., injection time, injected pressure, viscosity of grouting material or joint aperture size.) Thus, it is difficult to predict for grouting injection performance. In this study, the grouting injectivity was analyzed according to the rock joint characteristics under a single rock joint condition using Universal Distinct Element Code (UDEC) numerical program. This study is helpful to evaluate the rock grouting performance for underground structures.

1 INTRODUCTION

Deep-depth rocks are independent of the external environment, they are advantageous for installing tunnel-like structures compared to ground conditions that are greatly affected by mountainous areas and marine conditions (Kim et al., 2017; Li et al., 2016). When a tunnel is constructed in such a deep-depth rock, it is necessary to verify the characteristics of the deep-depth rock in order to achieve a reasonable design and construction. The bedrock contains various forms of discontinuities (e.g., joint, stratified, fault, or gap). Since the discontinuous surfaces are more affected by the properties of discontinuous surfaces than by the mechanical properties of the rock itself, it is important to consider discontinuities when simulating the behavior of the rock (Choi et al., 1999).

In particular, when a plurality of irregular joints is connected to each other, the joint may be a flow path of surrounding groundwater (Moon, 2013). When the surrounding groundwater flows into the underground space through such a joint, the utilization of the underground space is degraded due to the flooding of the tunnel. This poses a risk of major economic damage (Panhi and Nilsen, 2005; Joo et al., 2010). Therefore, for underground space development, it is essential to improve the watertightness of rock joint (such as using rock grouting) (Jeong et al., 2021).

In this study, the variables required in the grouting injection design are determined to be injected pressure and aperture size. In addition, the injection pattern (injected distance) and performance (injection time) of the grouting with a single joint are estimated using UDEC (a discontinuous flow analysis program).

DOI: 10.1201/9781003299127-145

2 A THEORETICAL SOLUTION OF A ONE-DIMENSIONAL LINEAR FLOW

The flow of grouting injection fluid can be represented by Newtonian fluid characteristics and non-Newtonian fluid characteristics (Warner, 2004). In the case of a Newtonian fluid, when shear stress is applied for flow generation, shear rate is generated regardless of yield strength (Figure 1). On the contrary, in the case of a Bingham fluid, when shear stress exceeding yield strength is applied, shear deformation occurs, that is, a flow of fluid occurs. Representative Newtonian fluids include water or chemical solution type grouting materials, and Bingham fluid includes cement suspension. Bingham fluid model for quantity of flow is shown as Equation (1).

$$Q = \frac{\Delta p}{I}\frac{b^3}{12\mu_g} \tag{1}$$

Where Q = quantity of flow; I = penetration length; Δp = injected pressure; μ_g = viscosity; b = aperture size.

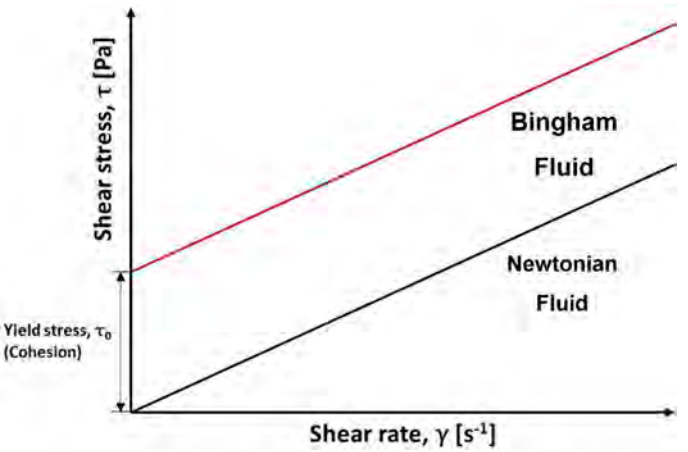

Figure 1. The characteristics of Bingham fluid (after Alfred et al., 2000).

The penetration distance of the injection material is proportional to the square root of the injection time, proportional to the square root of the injected pressure, linear proportional to the initial joint gap, and inversely proportional to the square root of the injection viscosity (Lee et al., 2017).

3 NUMERICAL MODEL

3.1 *Rock model with a single joint*

In this study, the injection behavior of the rock grouting injection material was simulated in a single type of joint (refer to Figure 2). The rock block was assumed to be in a rectangular shape with a length of 50 m and a height of 1 m, and the joint was simulated with a straight line with a length of 0.1 mm in the length direction of the rock block. The input properties of the rock block were set to the density of 3,000 kg/m^3, the volume coefficient of 10 GPa, and the pre-stage number of 3 GPa. As the material of the grout, micro-cement that can be injected into a fine joint. For the physical properties of the injection material (micro-cement), the water/cement mixing ratio is 1.0 in which viscosity is 0.0056 Pa · s in 20°C (Refer to table 1, obtained in Lee at el., 2017). The input properties of the grout material were set to the density of 1,290 kg/m^3, the bulk modulus of 2 GPa and the yield stress of 0.296 Pa.

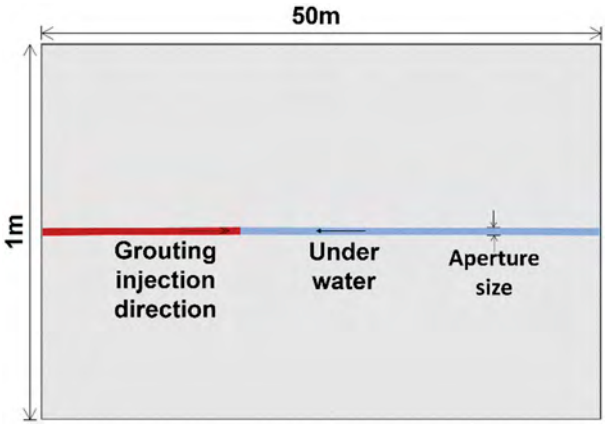

Figure 2. The single joint rock model for numerical simulation.

3.2 *Injection parameters*

The deep-depth rock is located greater than 40 m from the surface. As the depth increases, the pore pressure of groundwater increases. When the rock grouting is performed, it is necessary to inject it with a pressure stronger than that of groundwater pressure. Therefore, in this study, a simulation analysis was considered to inject grouting at a depth of 50 m, 150 m, and 200 m with setting the grouting pump pressure to 2.5 MPa. When the target depths are 50 m, 150 m, and 200 m, the pore-pressure would be 0.5 MPa, 1.0 MPa, and 2.0 MPa, respectively. Therefore, the injected pressure was calculated as the value obtained by subtracting the pore-pressure from the grouting pump pressure so that injected pressure was determined to be 2.0 MPa, 1.0 MPa, and 0.5 MPa, respectively. A decrease in injected pressure means that the depth of the rock deepens.

In the previous study, the aperture size in the large depth bedrock considers 0.138 mm (Yoon et al., 2021). Based on the literature review, the aperture size was set to 0.05 mm, 0.1 mm, 0.2 mm, and 0.4 mm with the joint roughness of JRC 0-2. In this model, friction of joints was not considered. And, total amount grouting material is no limit. The injection performance of the analyzed grouting material was evaluated by the injected distance and injection time.

4 RESULT AND ANALYSIS

4.1 *Injected distance*

Micro-cement grouting material was injected with pressure for 600 seconds. It was confirmed that as the depth increase, the injected pressure decreases due to an increase in pore-pressure. In addition, as the injection time increases, the viscosity of the cement grouting injection material increases, so the injected distance per unit time decreases. The form of increase is a non-linear exponential function (Figure 3(a)-(c)).

When the aperture size is 0.4 mm at the depth of 50 m (injected pressure: 2.0 MPa) injected distance is the longest. The result shows that the injected distance is 47.5 m. It is 41.6 m larger distance than the smallest aperture size of 0.05 mm at the same injected pressure. The injected distance is 23.8m at the aperture size of 0.4mm and 0.5MPa. Accordingly, the injected distance is proportional to the aperture size and injected pressure.

4.2 *Result of parameters*

Given results, the time (required to reach 1 m) with aperture size was analyzed (Figure 4). When the injected pressure is 1.0 MPa at the aperture size of 0.05 mm, the time is estimated to be 30 seconds. When the injected pressure increases to 2.0 MPa, the arrival time is decreased by 62%. When the injected pressure decreases to 0.5 MPa, the arrival time is increased by 39%. As the

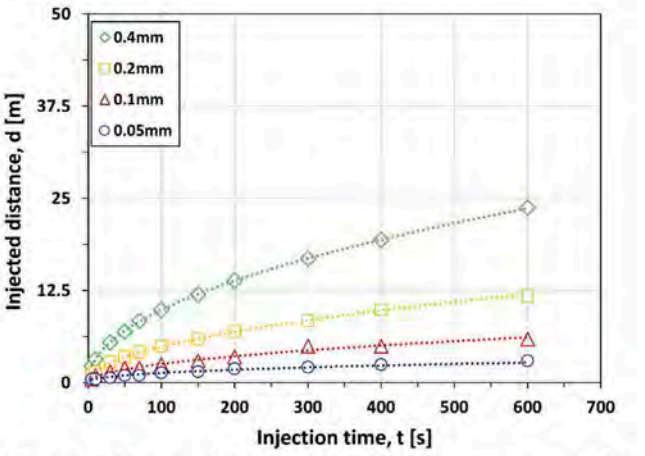

(a) Result of injected distance for injected pressure 0.5 MPa

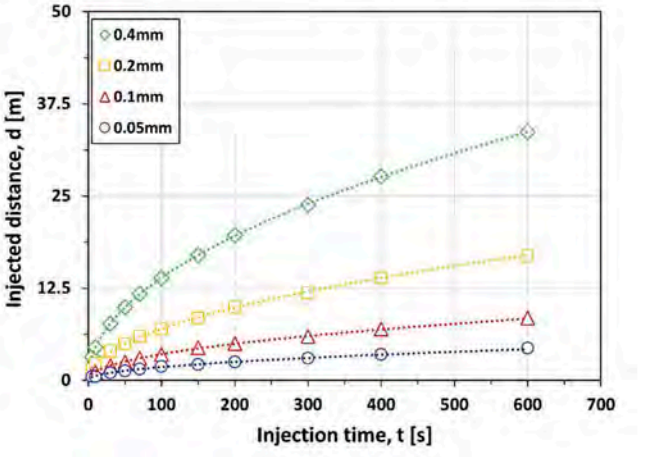

(b) Result of injected distance for injected pressure 1.0 MPa

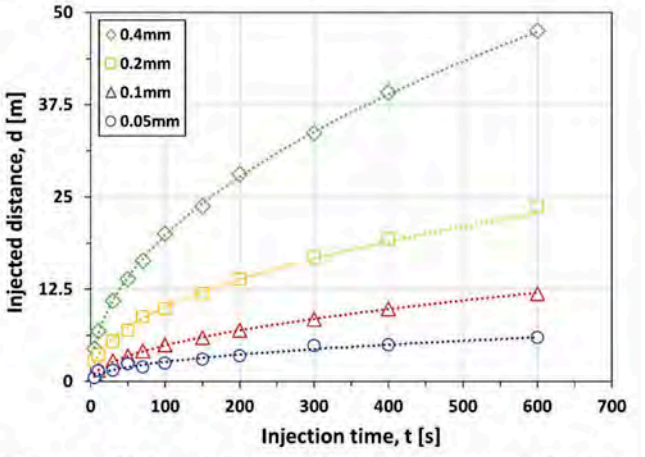

(c) Result of injected distance for injected pressure 2.0 MPa

Figure 3. Result of injected distance according to change of injected pressure.

aperture size is the wider at the same injected pressure, the time is the shorter. The relationship between injection time and aperture size shows a nonlinear exponential curve.

The reach according to the aperture size within the same injected pressure based on the injection time of 300 seconds was also analyzed. When the injected pressure is 1.0 MPa with the aperture size of 0.4 mm, the arrival distance at 300 seconds is 23.8 m. When the injected pressure is increased to 2.0 MPa, the reach at 300 seconds is increased by 29.3%. When the injected pressure is decreased to 0.5 MPa, it is decreased by 29.4%. This increment showed a linear relationship (Figure 5).

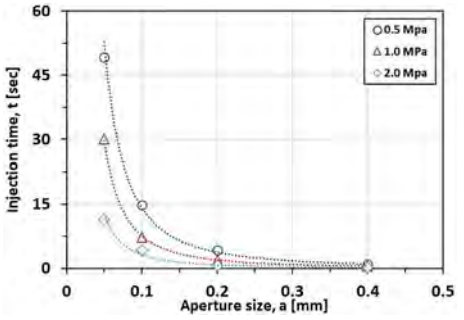

Figure 4. Injection time with aperture size at the injected distance of 1 m.

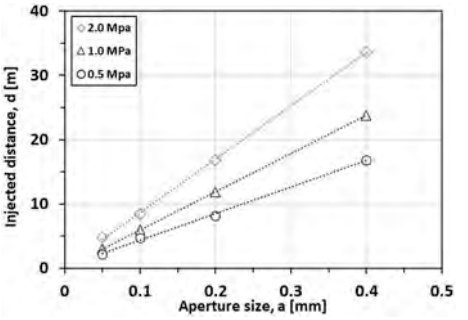

Figure 5. Injected distance with aperture size at injection time of 300 seconds.

5 CONCLUSION

In this study, the performance analysis was conducted by micro-cement grouting injection with the fine single joint in deep depth bedrock using UDEC. The main findings are follows:

- The grouting injection material has a nonlinear increase pattern in which the injected distance per unit time is shortened due to the increase in viscosity over time.
- At the constant injected pressure, the injection time to reach the target distance is decreased by increasing the aperture size.
- With the injected pressure, the injected distance of the grouting filler linearly increases as the aperture size increases at the same injection time.
- In this study, there are limitations that do not consider changes in viscosity of cement grout over time, resistance due to friction of joints, JRC, and deformation of joints due to applied stress. For further studies, effective parameters will be considered to perform experiments for better understanding of the rock grouting characteristics.

ACKNOWLEDGEMENT

This research was supported by Basic Science Research Program through the National Research Foundation of Korea (NRF) (No. NRF-2022R1I1A3065299) and by the Brain Korea 21 FOUR Project in the Education & Research Center for Infrastructure of Smart Ocean City (i-SOC Center).

REFERENCES

Alfred, I.Y., Tok, Freddy, Y.C., Boey, Y.C., Lam. (2000), Non-Newtonian fluid flow model for ceramic tape casting, Materials Science and Engineering, Vol. 280, No. 2, pp. 282–288.

Choi, S., Chung, S. (1999), Stability analysis of a jointed rock slope with the Barton-Bandis Joint Constitutive Model using UDEC, Journal of Korean Society for Rock Mechanics, Vol. 9, No. 2, pp. 141–148.

Jeong, J.H., Kim, K.H., Song, M.K., Shin, J.H. (2021), Groundwater control measures for deep urban tunnels, Journal of Korean Tunnelling and Underground Space Association, Vol. 23, No. 6, pp. 403–421.

Joo, E.J., Kim, Y.K., Shin, J.H., Kwon, O.Y. (2010), Numerical study of the optimum grouting design of subsea tunnels, Journal of Korean Tunnelling and Underground Space Association, Vol. 12, No. 5, pp. 349–358.

Kim, N.Y., Park, G.T., Baek, S.C., Lee, K.H., Choi, J.W., Her, Y. (2017), Analysis of displacement behavior in fractured fault and groundwater flow under tunnel excavation", Journal of Korean Tunnelling and Underground Space Association, Vol. 19, No. 1, pp. 71–82.

Lee, J.W., Kim, H.M., Mahmoud, Y., Park, E.S. (2017) Influence of Design Parameters of Grout Injection in Rock Mass using Numerical Analysis, Korean Society for Rock Mechanics, Vol. 27, No. 5, pp. 324–332

Li, S., Liu. R., Zhang, Q., Zhang, X. (2016), Protection against water or mud inrush in tunnels by grouting: A review, Journal of Rock Mechanics and Geotechnical Engineering, Vol. 8, No. 5, pp. 753–766.

Moon, J.S. (2013), Groundwater inflow rate estimation considering excavation-induced permeability reduction in the vicinity of a tunnel, Journal of Korean Tunnelling and Underground Space Association, Vol. 15, No. 3, pp. 333–344.

Panthi, K.K., Nilsen, B. (2005), Significance of grouting for controlling leakage in water tunnels: A case from Nepal, Proceedings of the ITA-AITES 2005 world tunnelling congress and 31st ITA General Assembly, Istanbul, Turkey, pp. 931–937.

Warner, J. (2004), Practical hand of grouting: soil, rock, and structures, John Wiley & Sons, Hoboken, pp. 40–44.

Yoon, I.K., Moon, J.H., Lee, J.S., Kim, Y.U. (2021) Characteristics of High-viscosity Grouting Materials for Rock Joint Reinforcement of Deep Tunnel, Journal of the Korean Geo-Environmental Society, Vol. 22, No. 12, pp. 59–63.

Smart Geotechnics for Smart Societies – Zhussupbekov, Sarsembayeva & Kaliakin (Eds)
© 2023 The Author(s), ISBN 978-1-003-29912-7
Open Access: www.taylorfrancis.com, CC BY-NC-ND 4.0 license

Investigation of excavation stability with buttress and cross wall

Ari Surya Abdi & Chang-Yu Ou
Department of Civil and Construction Engineering, National Taiwan University of Science and Technology

ABSTRACT: The buttress and cross wall is an excavation support system that has been widely used for the protection of the adjacent building during excavation. However, their mechanism in resisting the basal heave stability has not yet been fully understood. In this study, a series of three-dimensional finite element analyses were conducted to assess the influence of buttress and cross walls on basal heave stability in deep excavations. The results showed that the frictional resistance acting on the contact surface area between the wall (including buttress and cross wall) and the surrounding soil plays an important role in resisting the basal heave failure. Hence, increasing the dimension of the buttress and cross walls could enlarge the frictional area, which resulted in enhancing the factor of safety. Furthermore, a new simplified method considering the buttress and cross wall properties was proposed, which was validated by the finite element method.

Keywords: basal heave stability, buttress wall, cross wall, deep excavation, factor of safety

1 INTRODUCTION

Deep excavation in undrained clay usually cause the large soil movement. In such a case, the implementation of a buttress wall (BW) and cross wall (CW) could be used as a measure to prevent damage to the adjacent building induced by deep excavation. Many researchers have studied the mechanism and characteristics of BW and CW in restraining excessive wall displacement (Hsieh and Ou 2018; Lim et al. 2016; Ou et al. 2006). However, no study has conducted the excavation stability with BW and CW.

In this study, a series of three-dimensional finite element methods (3D FEM) was conducted to investigate the excavation stability with BW and CW. The strength reduction method was adopted in the stability analysis to determine the factor of safety against basal heave at the final excavation stage (Abdi and Ou 2022; Goh et al. 2019). Moreover, a new simplified method was proposed to calculate the factor of safety, which was validated by the 3D FEM results.

2 FINITE ELEMENT MODELING

The commercial geotechnical software PLAXIS 3D v.21 was used to perform the three-dimensional (3D) finite element analysis. The diaphragm wall (DW), floor slab (FS), BW, and CW, were modeled as plate elements with linear-elastic structural behavior. The compressive strength (f_c') of the DW and FS was assumed to be 21 MPa, while the BW and CW were 14 MPa. The nominal value of Young's modulus for all concrete materials was estimated by using $E = 4700\sqrt{f_c'}$ (MPa). The thickness of the DW, BW, CW, is set to be 0.7 m, while the FS is simply assumed to be 0.4 m, following the typical properties of the retaining system in deep excavations.

Furthermore, the Mohr-Coulomb with the total stress undrained analysis was adopted to simulate the undrained behavior of the clay. The normalized undrained shear strength (s_u/σ_v')

DOI: 10.1201/9781003299127-146

and soil modulus ratio (E_u/s_u) were assumed to be 0.30 and 500, followed by the typical properties of Taipei clay. The slippage behavior between the wall (including DW, BW, and CW) and soil was modeled by the interface element, which is controlled by the frictional resistance ratio between the wall adhesion and soil cohesion ($\alpha = c_w/s_u$).

The wished-in-place (WIP) method is adopted for modeling the DW, BW, and CW in the analyses. The excavation depth (H_e) was assumed to be 15 m, while the upper part of BWs was demolished along with the excavation, as presented in Figure 1. The BW length, penetration depth, and spacing were denoted as L_{bw}, D_{bw}, and s_{bw} respectively. On the other hand, the CW penetration depth and spacing were referred as D_{cw} and s_{cw}, respectively.

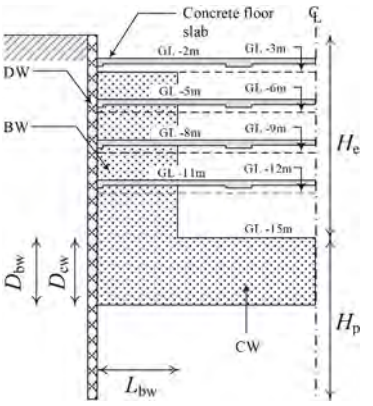

Figure 1. Excavation profile and construction sequence.

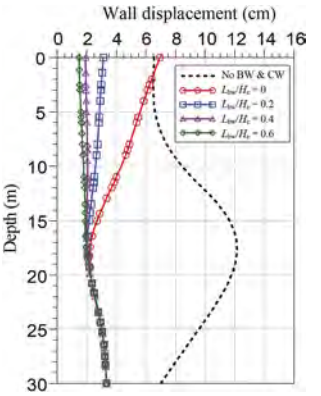

Figure 2. Computed wall displacement at the final excavation stage ($D_{bw} = D_{cw} = 6$ m; $s_{bw} = s_{cw} = 12$ m; $H_p/H_e = 1.0$; $B = 30$ m).

3 DEFORMATION CHARACTERISTIC OF BW AND CW

As shown in Figure 2, the largest wall displacement was found near the final excavation level ($\delta_{h,m} = 12.18$ cm) for the case without BW and CW. When only CW was implemented below the excavation level ($L_{bw}/H_e = 0$), the wall displacement below the excavation level was reduced significantly. However, an excessive wall displacement still occurred above the excavation level due to lower stiffness. Hence, the CW was further combined with BW at the upper part ($L_{bw}/H_e > 0$), which is found to be a useful method in reducing the wall displacement along the depth. The reduction rate of wall displacement begins to slow as the BW length increases (indicated by $L_{bw}/H_e = 0.4$ - 0.6).

4 EXCAVATION STABILITY WITH BW AND CW

4.1 *Basal heave mechanism of excavation with BW and CW*

The factor of safety (FS_{fem}) for the case without BW or CW was 2.717. For the case with rigid friction on BW and CW ($\alpha_{bw} = \alpha_{cw} = 1.0$), the FS_{fem} values were 2.852 and 2.816, respectively. In comparison, the FS_{fem} values for the case without friction on BW and CW ($\alpha_{bw} = \alpha_{cw} = 0.1$) were 2.680 and 2.707, respectively, which is similar to those without BW and CW.

The deformed mesh of soil at divergence conditions was further observed to clarify the above findings (Figure 3a–d). The basal heave could be resisted for the BW and CW with the rigid surface ($\alpha_{bw} = 1.0$). In contrast, for the case of BW and CW without friction ($\alpha_{bw} = \alpha_{cw} = 0.1$), the BW and CW could not resist the heave inside the excavation. This implies that the basal heave resistance was highly governed by the frictional resistance on the interface between the wall (BW and CW) and surrounding soil.

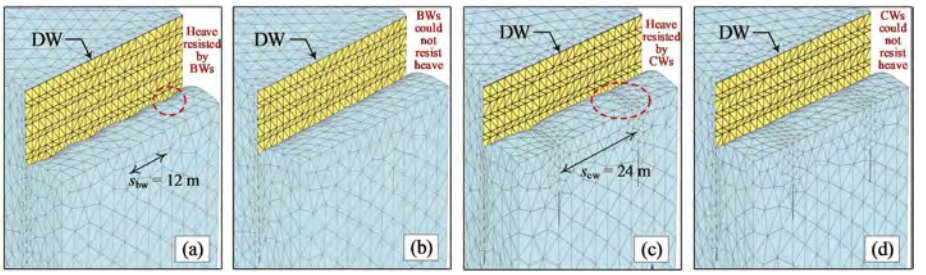

Figure 3. Deformed mesh of soil at divergence condition with H_p/H_e = 1.0; B = 30 m (L_{bw}/H_e = 0.6, D_{bw}/H_p = 1.0, s_{bw} = 12 m for BW only; D_{cw}/H_p = 0.4; s_{cw} = 24 m for CW only): (a) α_{bw} = 1.0; (b) α_{bw} = 0.1; (c) α_{cw} = 1.0; (d) α_{cw} = 0.1.

4.2 *Effect of BW and CW dimension*

Figure 4 plots the variation of factor of safety (FS_{fem}) for different BW and CW dimension. The results showed that the FS_{fem} values increased significantly as the CW depth increased (below abscissa). Similarly, increasing the BW length could enhance the FS_{fem} values (above abscissa). However, the FS_{fem} values for BW case were increased non-linearly as compared to that of CW case, in which the short BW length (e.g., L_{bw}/H_e = 0.2) has an insignificant effect on the basal heave resistance. It is due to a larger heave occurred in the middle of the excavation than that near the diaphragm wall (indicated in Figure 3a-d). Hence, the closer the BW to the middle of the excavation, the higher the basal heave resistance, and vice versa. In such a case, implementing CW has a better effect than that of BW in enhancing the basal heave resistance for the same frictional area, particularly for a small frictional area (L_{cw}/H_p < 0.8 or L_{bw}/H_e < 0.8).

In addition, the effect of L_{bw}/H_e and D_{cw}/H_p in enhancing the FS_{fem} value became more pronounced for larger BW or CW spacing (s_{bw} or s_{cw}). Finally, these findings exhibit that enlarging the BW and CW dimension inside the excavation could enhance the frictional area, which could contribute to the basal heave resistance. This also implies that, for the same required FS values, a reduction of wall penetration depth (H_p) could be considered when implementing BW or CW inside the excavation, which is good for economical manner.

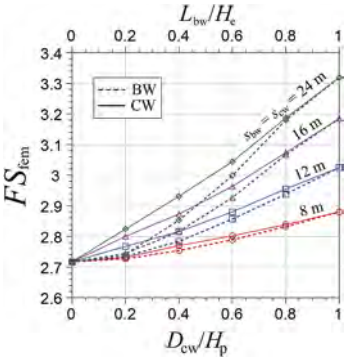

Figure 4. Variation of factor of safety for different BW and CW dimensions (α = 1.0; D_{bw}/H_p = 1.0; H_p/H_e = 1.0; B = 30 m).

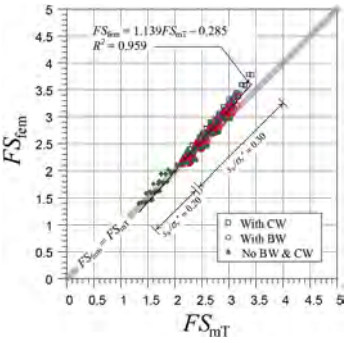

Figure 5. Comparison of FEM results and modified Terzaghi's method.

5 PROPOSED SIMPLIFIED METHOD

A simplified method was proposed to calculate the factor of safety against basal heave in excavations with BW and CW, which was derived based on Terzaghi's bearing capacity theory (Terzaghi, 1943). Some modification is made by extending the center point from the final

excavation level to the wall toe so that the frictional resistance acting along the H_p level is taken into account (α_{dw}) in the formula. Additionally, the frictional resistance acting on the two sides of BWs ($2\alpha_{bw}$) and CWs ($2\alpha_{cw}$) could also be considered by adding the BWs properties (β_{bw}) and CWs properties (β_{cw}) into the formula. Thus, the factor of safety for the proposed modified Terzaghi's method (FS_{mT}) can be expressed as:

$$FS_{mT} = \frac{5.7s_{u,3}B' + s_{u,2}H_p(1+\alpha_{dw}) + s_{u,bw}\beta_{bw} + s_{u,cw}\beta_{cw}}{\gamma H_e B' - s_{u,1}H_e} \quad (1)$$

$$\beta_{bw} = \frac{2\alpha_{bw}L_{bw}D_{bw}}{s_{bw}};\ \beta_{cw} = \frac{2\alpha_{cw}D_{cw}0.5B}{s_{cw}} = \frac{\alpha_{cw}D_{cw}B}{s_{cw}} \quad (2)$$

where γ is the unit weight of the soil, B is the excavation width, $B' = B/\sqrt{2}$ is the radius of the failure surface; $s_{u,1}$, $s_{u,2}$, and $s_{u,3}$ are the average undrained shear strength at the ground surface to the final excavation level, at the final excavation level to the wall toe, and at the wall toe to the radius of failure surface ($B' = B/\sqrt{2}$), respectively. $s_{u,bw}$ and $s_{u,cw}$ are the average undrained shear strength at the level of BW and CW penetration depth.

Figure 5 shows the comparison of the factor of safety between the FEM results and modified Terzaghi's method. A total of 304 different cases were analyzed, involving the case without BW and CW (s_u/σ_v' = 0.2 – 0.3; α_{dw} = 0.5 – 1.0; H_p/H_e = 0.6 – 1.2; B = 30 – 40 m) and with BW or CW (s_u/σ_v' = 0.3; $\alpha_{bw} = \alpha_{cw}$ = 1.0; L_{bw}/H_e = 0.2 – 0.6; D_{cw}/H_p = 0.2 – 1.0; $s_{cw} = s_{bw}$ = 12 – 48 m; H_p/H_e = 0.6 – 1.2; B = 30 – 40 m). As shown in Figure 5, all comparisons were generally close to each other, even for a lower normalized undrained shear strength (s_u/σ_v' = 0.2). Linear regression was adopted, in which the relationship between the FEM results and modified Terzaghi's method can be expressed as $FS_{fem} = 1.139FS_{mT} - 0.285$ with the coefficient of determination (R^2) being 0.959. These imply that the results from the modified Terzaghi's method are similar and consistent for the case with and without BW or CW.

6 CONCLUSION

A series of three-dimensional finite element methods (3D FEM) was conducted to investigate the performance of the buttress wall (BW) and cross wall (CW) in resisting the basal heave induced by deep excavation. The results showed that the basal heave mechanism of excavation with BW and CW is highly influenced by the frictional resistance acting on the contact surface area between the wall (BW and CW) and surrounding soil. Furthermore, the following conclusion can also be drawn:

1. Enlarging the BW or CW dimension inside the excavation could enhance the frictional area, resulting in a higher basal heave resistance
2. The effect of BW in resisting the basal heave failure is insignificant for a short BW length (e.g., L_{bw} = 3 m). Hence, an appropriate BW length should be considered to enhance the basal heave resistance effectively.
3. A new simplified method was proposed to calculate the factor of safety against basal heave, namely the modified Terzaghi's method. It is found that the results from the modified Terzaghi's method are similar and consistent with the FEM results for the case with and without BW or CW, implying that the proposed method could be reasonably adopted.

REFERENCES

Abdi, A. S., and Ou, C. Y. (2022). "A Study of the Failure Mechanism of Braced Excavations Using 3D Finite-Element Analysis." *International Journal of Geomechanics*, 22(7), 1–14.

Goh, A. T. C., Zhang, W. G., and Wong, K. S. (2019). "Deterministic and reliability analysis of basal heave stability for excavation in spatial variable soils." *Computers and Geotechnics*, Elsevier, 108 (July 2018), 152–160.

Hsieh, P. G., and Ou, C. Y. (2018). "Mechanism of buttress walls in restraining the wall deflection caused by deep excavation." *Tunnelling and Underground Space Technology*, Elsevier, 82(October 2017), 542–553.

Lim, A., Hsieh, P. G., and Ou, C. Y. (2016). "Evaluation of buttress wall shapes to limit movements induced by deep excavation." *Computers and Geotechnics*, Elsevier Ltd, 78, 155–170.

Ou, C. Y., Lin, Y. L., and Hsieh, P. G. (2006). "Case record of an excavation with cross walls and buttress walls." *Journal of GeoEngineering*, 1(2), 79–87.

Terzaghi, K. (1943). "Theoretical soil mechanics." Wiley, New York.

Smart Geotechnics for Smart Societies – Zhussupbekov, Sarsembayeva & Kaliakin (Eds)
© 2023 The Author(s), ISBN 978-1-003-29912-7
Open Access: www.taylorfrancis.com, CC BY-NC-ND 4.0 license

A study of the ground volume loss modeling technique influence the soil displacement in course of shield tunneling

R.F. Sharafutdinov, O.N. Isaev & D.S. Zakatov
Research Center of Construction - Gersevanov Research Institute of Bases and Underground Structures (NIIOSP), Moscow, Russia

ABSTRACT: The paper presents results of the study dealing with the influence of various techniques for modeling volume loss on soil deformation. From the surrounding soil deformation viewpoint, the contraction method the effect of weight loss CMW produces the most correct results. It was shown that the application of Hardening soil models (HS, HSS) realized in PLAXIS software does not always give adequate results. These models do not consider the position of yield surface changing, which affects the deformation behavior of soil in the process of unloading/reloading or non-linear stress paths (as in the case of tunneling). In this regard, the ground surface settlement is overestimated by 1.5……2 times for normally consolidated soil (OCR=1), and underestimated for over consolidated soil (OCR>1). Recommendations for prediction of settlement associated with tunneling were stated.

1 INTRODUCTION

Tunneling is an essential part of underground development. Like any other type of geotechnical work, tunneling is associated with changes in stress-strain state of the soil (Figure 1). An importance of the reliable settlement prediction increases when constructing tunnels in close proximity to other structures, water and gas supply conduits.

Methods for prediction tunneling settlement were categorized into empirical, analytical and numerical. Presently, numerical methods based on FEM and realized in geotechnical software (PLAXIS, MIDAS GTS, Z-SOIL) are the most advanced displacement prediction tools which can accommodate non-linear behavior of soil (close to realistic).

Considering unloaded ground surface, the settlement trough can be well described by an error function curve (Attewell et al., 1986; Mair, 1996; Peck, 1969; Pushilin et al., 2007):

$$S_i = S_{\max} \exp\left(-\frac{{x_i}^2}{2i^2}\right) \tag{1}$$

where S_i is a surface settlement at a transverse distance x_i from the tunnel center; $S_{\max}$ is a maximum settlement (at x = 0); i is the horizontal distance from the tunnel axes to the point of inflection of the settlement trough.

Maximum settlement $S_{\max}$ is derived from the ratio:

$$S_{\max} = \frac{V_L \pi \left(\frac{D}{2}\right)^2}{2.5i}, \tag{2}$$

where V_L is a volume loss at tunneling (hereinafter volume loss), D is a tunnel outer diameter.

The volume loss V_L is an integral characteristic, which reflects influence of tunneling on surrounding ground (Il'ichev et al., 2011; Isaev & Sharafutdinov, 2012, 2015; Mair, 1996; Mair & Taylor, 1997; O'Reilly & New, 1982; Strokova, 2008; Ter-Martirosian et al., 2021). Generally, V_L takes into account soil deformations associated with original stress relief, soil softening and soil sampling in a tunnel face (1) and shield lateral plowing (2); ground movement into

DOI: 10.1201/9781003299127-147

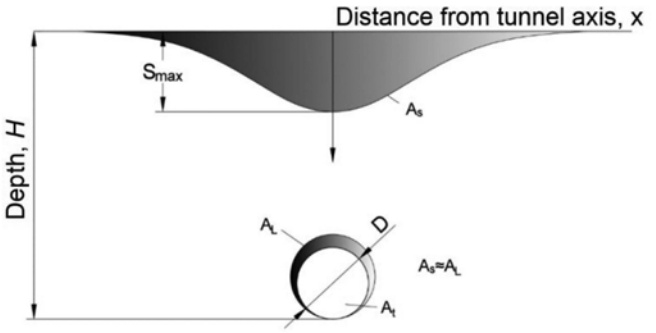

Figure 1. Shield tunneling induced ground surface settlement.

the gap between shield and lining (3); deformation of the lining (4); ground movement due to the shield and tunnel subsidence and consolidation (5) (Figure 2):

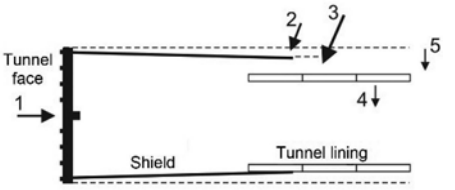

Figure 2. Reasons for ground deformations associated with shield tunneling (Mair & Taylor, 1997; Möller, 2006).

The volume loss is obtained from results of the settlement trough measurement performed during tunneling, using the following equation (Figure 1):

$$V_L = \frac{A_S}{A_t} 100\%, \tag{3}$$

where A_S is an area between horizon and the curve describing settlement of the unloaded ground surface, A_t is a tunnel cross-section area.

V_L values may vary with a considerable scatter. Thus, according to (Mair, 1996; Möller, 2006), in sands V_L can only be 0.5%, whereas in clays it can achieve 2.0%. In the layered ground V_L can range from 2.0 to 4.0% (Mair, 1996; Möller, 2006). Technical manual of U.S. Department of Transportation (Hung et al., 2009) specifies V_L as a soil stiffness and construction experience dependent value, which can range from 0.5 to 4.0% and wider. Thus, depending on soil composition and method for pumping grout into a ground-lining gap, average V_L values range from 1.5 to 5.5% in utility tunnels (Isaev & Sharafutdinov, 2012; Petrukhin et al., 2015). In micro tunnels, the V_L value depends on soil content in the gap between a pipeline and a tunnel wall and falls into a range of 0.4...3.6 % (Isaev & Sharafutdinov, 2015).

Numerical analyses of the tunneling-induced deformations of the surrounding soil may be carried out using two principally different approaches: (I) 3D-modeling of the tunneling working stages, (II) 2D\3D-modeling with considering the determined V_L. The former recently found its application for construction of the most critical tunnel sections. The latter solves a larger number of problems and envisages utilization of various computational methods for modeling. Methods applied can have an influence on the results obtained.

When conducting 2D-modeling of the tunneling influence, the following methods for volume loss modeling tend to be common.

The Contraction method (*CM*) developed by (Vermeer & Brinkgreve, 1993) includes two calculation phases. In the first phase, tunnel excavation is simulated by removing ground elements inside the tunnel while at the same time lining is activated. As the weight of the removed ground is larger than the weight of the lining, the lining will move upwards. In the second

phase, tunnel lining is uniformly contracted until the prescribed contraction ratio c_p, is reached, as Figure 3 shows.

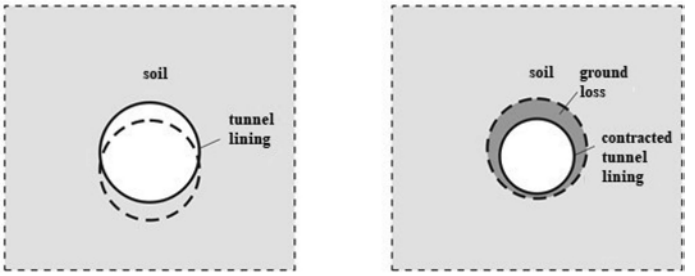

Figure 3. A scheme of the ground loss modeling using contraction method *CM* (Möller & Vermeer, 2005).

The *CM* possesses some peculiarities. Thus, when removing ground elements inside the tunnel, elastic or elastoplastic continuum modeling soil mass unloads. Ordinarily, volume loss and effect of ground removal are not considered separately because these processes occur simultaneously and most researches are focused on volume loss. Zang et al proposed a *contraction method without considering weight loss* (*CMW*) (Zang et al., 2019). In this method, a distinction between the weight loss and volume loss, authors showed that unloading had an effect on calculation results.

The *stress reduction method* (*SRM*) initially was developed for modeling open-face tunneling. In the first phase, the soil elements inside the tunnel are deactivated and equivalent pressure $\beta \cdot p_0$ is activated. Therein, p_0 is initial ground pressure; β is a load reduction factor satisfying the equation $0 < \beta < 1$ and often taken around 0.5. In the second phase, the lining is installed and the ground pressure $\beta \cdot p_0$ is transmitted to the lining. In the case of small β-factor, ground deformations will be relatively large whilst structural forces in the lining will be relatively low. A larger β-factor leads to smaller ground deformations and larger structural forces in lining (Möller, 2006).

The *SRM* has also been proposed to simulate installation of close-face shield tunneling (Addenbrooke et al., 1997; Möller, 2006). Firstly, the stresses inside the tunnel are reduced with concurrent volume loss control. As soon as the prescribed V_L at a corresponding pressure p_A is reached (point A in Figure 4b), the lining is activated. Hence, the β-factor is chosen so that it matches a given volume loss V_L.

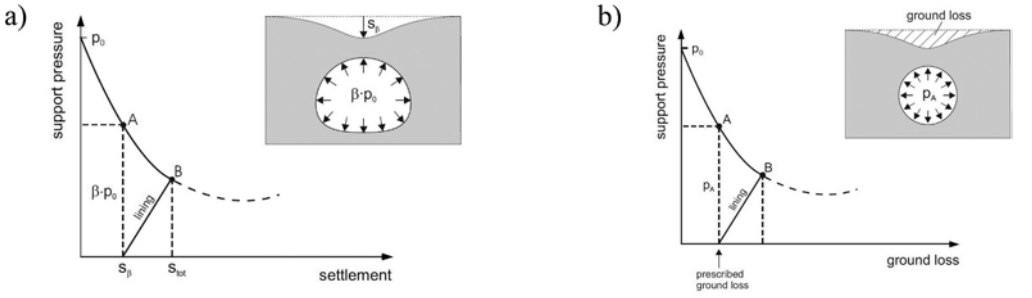

Figure 4. Scheme of the Stress reduction method (Möller, 2006): a – original; b – modified (Addenbrooke et al., 1997).

The *grout pressure method* (*GPM*) proposed in (Möller, 2006) postulates limitation of the ground deformation by the thickness of the ground-lining gap and by grout pressure distribution, while filling the gap. When modeling tunnel installation, ground elements inside the tunnel are deactivated and grout radial pressure is applied to the ground (considering a hydrostatical increase with depth) (Figure 5).

The simulation procedure affects not only predictable deformation of the surrounding soil, but also V_L values received from back analyses of the calculation results. Traditionally, V_L

was evaluated on the basis of the measurement results by describing a settlement trough with Equation (1) (O'Reilly & New, 1982; Peck, 1969). Significant development and advance of numerical methods has given the opportunity to assess V_L by back analysis in geotechnical software complexes (Aldiamar et al., 2021; Elarabi & Mohamed, 2017; Likitlersuang et al., 2014; Möller & Vermeer, 2005; Ter-Martirosyan et al., 2020). For this purpose, both simplified and more comprehensive non-linear soil models have been used at the moment.

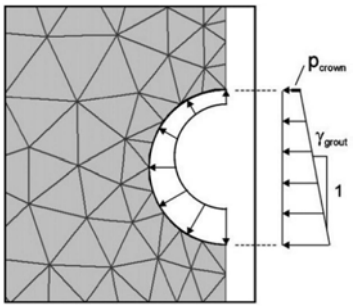

Figure 5. Display of the grout pressure method (Möller & Vermeer, 2008), where p_{crown} is a grout pressure in the upper tunnel arch, γ_{grout} is a grout unit weight.

However, application of comprehensive models often produces uncertain results. Thus, for instance, (Aldiamar et al., 2021; Çelik, 2017; Petrukhin et al., 2014b, 2014a) show that the Hardening soil model (hereinafter HS) and Hardening soil with small strain stiffness (hereinafter HSS) overestimate the settlement value by 1.3. . .2.3 times. This indicates that such tunneling problems should be solved using verified models and approaches. As pointed out in (Elarabi & Mohamed, 2017; Petrukhin et al., 2015), the ideal elastoplastic Mohr-Coulomb model (hereinafter MC) gives more adequate surface settlement than HS.

There is a mutual effect of method for modeling volume loss and applied geomechanical model on soil deformation. Therefore, the paper provides the results of the effect of various plain-strain volume loss models and geomechanical models on settlements associated with shield tunneling. Recommendations for prediction reliable calculated results of the settlement induced by closed tunneling are stated.

2 METHODS

Numerical analyses were performed in PLAXIS 2D. A round-shaped tunnel of 6.0 m in diameter rested at a depth of 24.0 m. Tunnel lining was assumed to be 0.3 m thick and with elastic modulus of 30 GPa. There were no aquifers in the scheme. The calculation was made for drained conditions. The following three soil models were considered in this study: MC, HS and HSS. The study comprised two phases.

In the first phase, various methods of volume loss modeling were analyzed. In consideration were taken *CM*, *CMW*, *SRM* and *GPM* methods described above. Volume loss V_L was assumed to be 2%. For *CM* and *CMW* methods, V_L was directly prescribed using c_p. For the *SRM* method, β-factor was selected so that the volume of the moved soil matched the designed V_L value. For the *GPM* method, radial grout pressure was selected in correspondence with the prescribed V_L value. The V_L was monitored over the ground movement around the tunnel. Medium dense sand was taken into consideration. Soil parameters are listed in Table 1.

HS and HSS soil models take into account the relationship between stiffness and levels of both volume and shear strain. In the shield tunneling, the strain levels depend on V_L when modeling.

In the second phase, numerical analyses of the volume loss influence on ground surface deformation were performed. *CM* and *CMW* methods were taken for the study. V_L was assumed to be 0.5, 1 and 2 % for dispersive soil, such as: sand of various density, normally consolidated and overconsolidated clay (Table 1).

Ground surface movement and the ratio of the trough area to the excavation area n were analyzed. The ratio n is based on the assumption that trough area and excavation area are comparable, and $A_S \approx A_L$ (Ahmed & Iskander, 2011; Cording & Hansmire, 1975; Mair & Taylor, 1997; Petrukhin et al., 2014a) (Figure 1), what makes it possible to assess the adequacy of the calculation results. The denoted assumption is true for most types of dispersive soil (except for soil with explicit dilatancy, $A_S < A_L$). Hence, the following ratio was used for assessing the adequacy of the calculation results:

$$n = \frac{A_S}{A_L} \leq 1 \tag{3}$$

Although this criterion is to a great extent conditional, it is an important tool in the analysis of the numerical calculations results. For example, if n is greatly larger than 1, one can draw a conclusion that the chosen method gives inadequate results. On the contrary, proximity of n to 1 indicates the adequacy of the calculation results.

Table 1. Soil parameters of MC, HS and HSS models.

	Soil				
Parameter	Medium dense sand	Dense sand	Loose sand	Normally consolidated clay	Overconsolidated clay
γ, kN/m^3	17.5	21.7	16.5	20.2	21.6
e	0.68	0.5	0.78	0.84	0.5
c, kPa	1	5	0	18	42
φ,°	30	37	27	20	25
ψ, °	0	7	0	0	0
E, MPa	27	43	15	8	45
E_{50}^{ref}, MPa	15.9	21.3	13.9	7.9	32
E_{oed}^{ref}, MPa	15.9	21.3	13.9	7.9	32
E_{ur}^{ref}, MPa	60.3	80.8	52.9	51.4	310.4
m	0.66	0.63	0.83	1	0.68
p^{ref}, kPa	100	100	100	100	300
OCR	1	1	1	1	2
G_0^{ref}, MPa	103.0	134.2	88.9	81.4	218.8
$\gamma_{0,7}$, %	0.014	0.0118	0.0151	0.0203	0.0245

3 NUMERICAL ANALYSES RESULTS

3.1 *Effect of volume loss modeling method*

Figure 6 shows calculation results obtained from various methods of volume loss modeling performed for medium dense sand.

It was found that volume loss modeling technique had a moderate effect on prediction of the ground surface deformation. *CM* and *CMW* methods with MC-model with *n*-factor differing from 1 less than 10% produced most adequate settlement values. Computation with *SRM* and *GPM* methods overestimated ground surface settlement by 13-20% when compared with *CMW*. From the authors' point of view, all described methods are suitable for calculation of the ground surface settlement. (Ahmed & Iskander, 2011) made a similar conclusion, though methods possessed some limitations. Thus, *CM* and *CMW* produced unrealistic lining forces, and the *GPM* method inserted pore pressure inaccuracy.

However, soil models have a significant influence on prediction of the ground surface settlement. Thus, all methods provide minimum settlement value ranging from 17 to 24.8 mm and most adequate *n*-factor value varying from 0.91 to 1.21, when using MC-model. Settlement values computed with HS model are 70...87 % above those computed with MC-model for all other methods, and *n*-ratio ranging from 1.92 to 2.35 indicates both inadequacy of the computation results and overestimation of settlement by 2 times. The HSS model also produces overestimated and

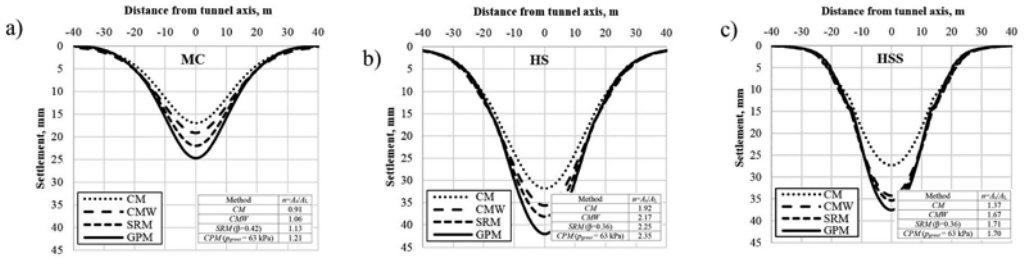

Figure 6. Ground surface settlement profile produced by various modelling methods: a) MC; b) HS; c) HSS.

inadequate settlement values. Thus, settlement values calculated with HSS model were 52. . .61 % above those calculated using MC-model, therefore *n*-ratio varied from 1.31 to 1.71. Considering the above, one can draw a conclusion that the HS and HSS models integrated in PLAXIS software inadequately describe tunneling induced settlement, whatever method of modeling.

Further analyses used *CM* and *CMW* methods.

3.2 *Influence of volume loss on ground surface deformation*

Figure 7 represents ground surface settlement values calculated using various soil models for *CM* and *CMW* methods.

In general, *CM* and *CMW* methods produce similar results (Figure 8). Difference in *n*-ratio does not exceed 10%. Meanwhile, method of modeling has a significant influence on soil models with small deformation modulus when using MC model. Thus, in sand, the difference reaches 117% and in normally consolidated clay, it achieves 525%. Moreover, as Figure 9 shows, the shape of the settlement trough changes indicating the inadequacy of the results. At the same time, when using HS and HSS models, the results of the calculations weakly depend on the method of ~~ground~~ volume loss modeling. Further on, a *CMW* method was used.

Assessment of the V_L influence on the *n*-ratio shows the following. For the MC model, *n* ranges from 0.80 to 0.96 for all considered types of soil and V_L values. This ratio indicates the greatest adequacy of the calculation results. When applying HSS model in normally consolidated soils (*OCR*=1), a significant overestimation of settlement is observed indicating inadequate results.

For the HSS model, when *OCR*=1, *n* ranges from 0.75 to 1.40, and *n*-ratio increases with increasing V_L. For small deformations, when V_L is 0.5%, *n*-ratio lies in an adequate range of 0.75-1.09. It was revealed that the model behavior is more adequate at small strains. This is because a ratio of the stiffness to the shear strain level is in full consideration in the HSS model.

At the same time, in overconsolidated soil with *OCR*=2, HS and HSS models produce *n*-ratio ranging from 0.31 to 0.54, which indicates an underestimation of settlement values. Figure 10 presents areas of elastoplastic deformation of normally consolidated (*OCR*=1) and overconsolidated (*OCR*>1) soil, plotted on the base of comprehensive numerical analyses (with application of HSS model, which provides the qualitative assessment of elastoplastic deformation area).

It can be noted that in normally consolidated soil, zones of plastic failure occur around the tunnel and pass into zones of shear and volume-shear hardening. As V_L increases, the boundaries of these zones shift. Besides, alongside and above the tunnel, at a distance of up to 2D, volumetric hardening zones begin developing. Usually, the development of volumetric hardening zones indicates soil consolidation that occurs when an additional compressive load is transferred. However, in tunneling problems, due to the complex changes in the soil stress-strain-state, unloading accompanied with a change of the yield surface position appears (Fadeev, 1987). The HS and HSS models are isotropic (that is, the yield surface does not change its position) and do not take into account the soil softening, which is typical for tunneling problems. This is associated with significant overestimation of the settlement.

In the case of overconsolidated soils, only shear hardening surfaces are observed around the tunnel at a width of about 1D (with increasing V_L, the width increases). The rest of the soil

tends to have elastic behavior. The shear hardening results in an “arch effect”, which is observed in cohesive soil above the tunnel.

Considering the above stated, when computing deformations associated with tunneling, models with fluctuating yield surface position should be applied. Otherwise, the MC models provide more reliable results, when using *CNW* (Zang et al., 2019) method.

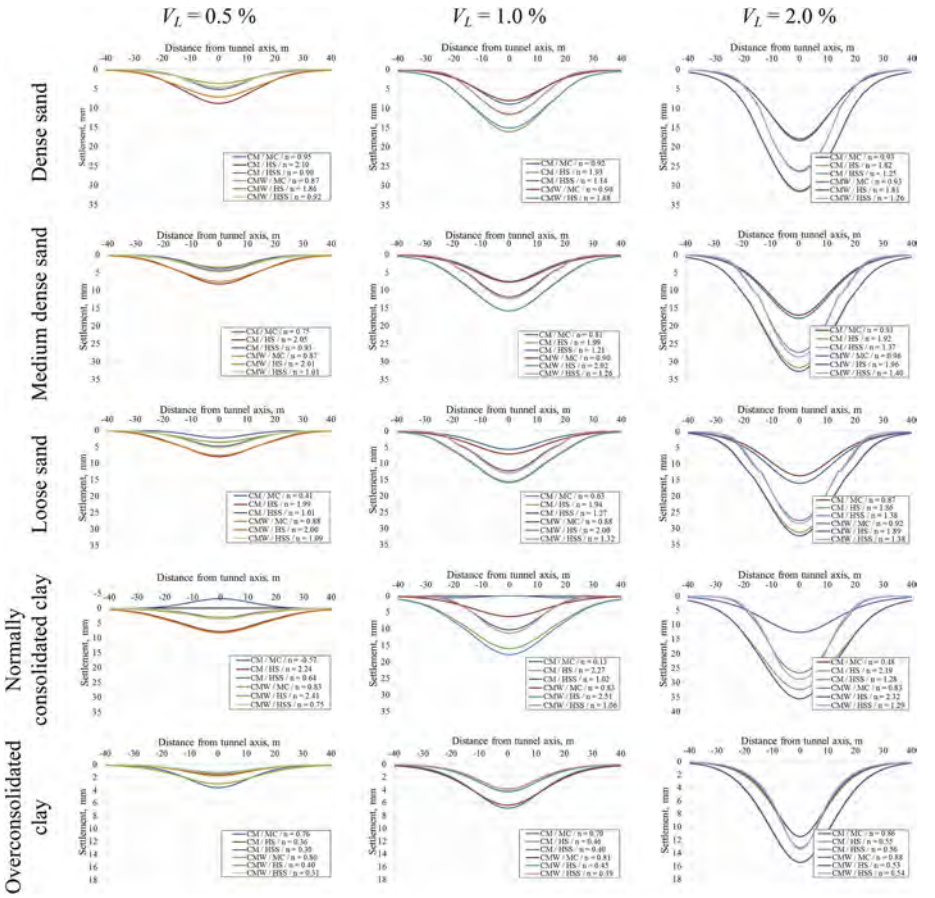

Figure 7. Surface settlement profile produced by different simulation methods for MC, HS and HSS models.

4 DISCUSSION

The performed numerical studies on normally consolidated and overconsolidated soil make it possible to reconsider the applicability of HS and HSS models for predicting tunneling induced settlements. Although a number of authors (Çelik, 2017) conclude that it is necessary to use advanced soil models, their application should be verified. Advanced models, of course, allow researchers to more realistically simulate the soil behavior. However, each model is developed for specific problems and it is necessary to confirm its adequacy to ensure a reliable result. The criterion of truth in geotechnics is monitoring data. However, a lack of coincidence is often attributed to natural, man-made or human factors.

Considering an example of the Double-O-Tube (DOT) tunnel installation in Taiwan, (Chen et al., 2016) performed three-dimensional numerical analysis of tunneling with the use of MC, HS and HSS models. Like this study, they obtained maximum settlement values for HS model, and minimum for MC model. Field data did not completely match the calculated

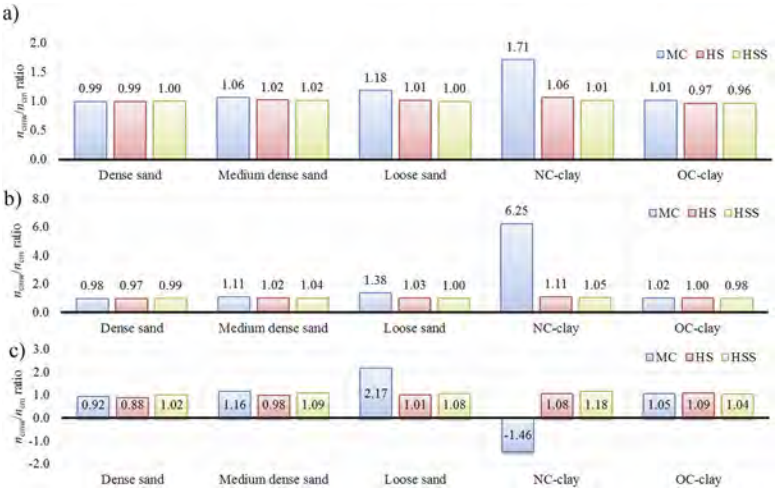

Figure 8. The comparison results of the n_{cmw}/n_{cm} ratio of different soil models at V_L=2 % (a); V_L=1 % (b); V_L=0.5 % (c).

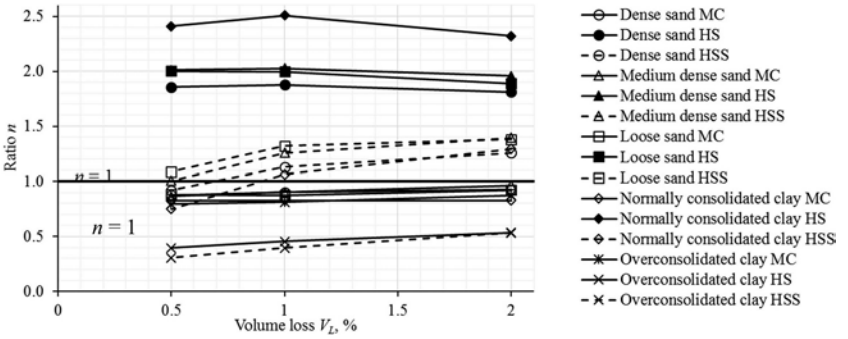

Figure 9. Relationship between *n*-ratio and ground loss in various models and soil types.

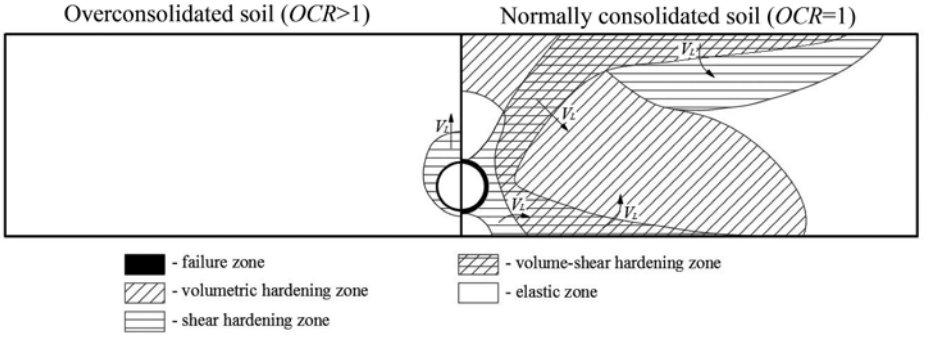

Figure 10. Elastoplastic strain zones for normally and over consolidated soil.

values. Similar comparisons made by (Çelik, 2017) showed that the designed volume loss and the measured settlement differed by 1.39…1.63 times. The considered studies did not analyze the *n*-ratio, and, accordingly, it was impossible to make conclusions about the adequacy of the accepted boundary conditions and models.

The data obtained indicate that tunneling induced settlement predicted for normally consolidated soils with using the HS and HSS models is overestimated. When applying these models, one should use *n*-ratio in order to additionally confirm an adequacy of the calculation results. When the volume loss is estimated by back calculation considering monitoring data, the assessment using *n*-ratio criterion provides adequate V_L value.

The results of the performed study provide a conclusion that if one uses *n*-ratio criteria to assess the adequacy of the tunneling induced settlement values, the MC model should be preferred alongside *CMW* two-dimensional analysis for volume loss modeling.

5 CONCLUSIONS

Tunneling is a part of underground development. Like any other type of geotechnical work, tunneling is associated with a change in the state of stress in the ground and with corresponding strains and displacements. Deformations induced by closed tunneling have been often predicted using numerical analyses integrated in geotechnical software complexes developed on the base of FEM (PLAXIS, MIDAS GTS, Z-SOIL). This tool takes into account complex mechanical soil behavior close to realistic.

Method for modeling ground loss moderately affects strain calculation results. *CM* and *CMW* methods provide the most adequate results. However, as (Ahmed & Iskander, 2011) showed, the methods considered have an influence on the lining forces.

HS and HSS models incorporated in geotechnical software complexes do not provide adequate calculation results. When using the HS model for normally consolidated soil (OCR=1), a significant settlement overestimation (n = 1.81…2.06) is observed. This result is inadequate. For the HSS model, n ranges from 0.75 to 1.40 and increases with increasing V_L. In the case of small strains, when V_L is 0.5 %), *n*-ratio ranges adequately from 0.75 to 1.09. In the HSS model, this phenomenon is associated with a more complete consideration of the stiffness to shear strain level ratio. However, in overconsolidated soil, HSS models provide n ranging from 0.31 to 0.54, indicating a significant underestimation of settlement.

A reason for inadequate results is that applied HS and HSS models with isotropic hardening do not consider the position of yield surface changing which affects on the deformation behavior of soil in the process of unloading/reloading or non-linear stress paths (as in the case of tunneling). Hence, the MC model should be preferred alongside *CMW* two-dimensional analysis for ensuring adequate calculation results.

ACKNOWLEDGEMENTS

The authors wish to thank Raev M.M. for his assistance in performing some calculation and plotting a number of drawings.

REFERENCES

Addenbrooke, T. I., Potts, D. M., & Puzrin, A. M. (1997). The influence of pre-failure soil stiffness on the numerical analysis of tunnel construction. *Géotechnique*, *47*(3), 693–712. doi: 10.1680/geot.1997.47.3.693

Ahmed, M., & Iskander, M. (2011). Analysis of Tunneling-Induced Ground Movements Using Transparent Soil Models. *Journal of Geotechnical and Geoenvironmental Engineering*, *137*(5), 525–535. doi: 10.1061/(ASCE)GT.1943-5606.0000456.

Aldiamar, F., Irsyam, M., Hutapea, B., Susila, E., & Nazir, R. (2021). Evaluation of Lateral and Axial Deformation for Earth Pressure Balance (EPB) Tunnel Construction Using 3 Dimension Finite Element Method. *Journal of Engineering and Technological Sciences*, *53*(5), 210503. doi:10.5614/j.eng.technol.sci.2021.53.5.3.

Attewell, P. B., Yeates, J., & Selby, A. R. (1986). *Soil Movements Inducted by Tunneling and their Effects on Pipelines and Structure*. Glasgow and London Published in the USA by Chapman and Hall.

Çelik, S. (2017). Comparison of Mohr-Coulomb and Hardening Soil Models Numerical Estimation of Ground Surface Settlement Caused by Tunneling. *Journal of the Institute of Science and Technology*, *7* (4), 95–102. doi: 10.21597/jist.2017.202.

Chen, S.-L., Lee, S.-C., & Wei, Y.-S. (2016). Numerical Analysis of Ground Surface Settlement Induced by Double-O Tube Shield Tunneling. *Journal of Performance of Constructed Facilities*, *30*(5). doi:10.1061/(ASCE)CF.1943-5509.0000732.

Cording, E. J., & Hansmire, W. H. (1975). Displacements around soft ground tunnels - general report. *5th Pan American Conference on Soil Mechanics and Foundation Engineering*.

Elarabi, H., & Mohamed, A. A. (2017). The Effect of Installation Procedures and Constitutive Laws for Numerical Simulation of Closed Face Tunneling. *19th International Conference on Soil Mechanics and Geotechnical Engineering*, 725–728.

Fadeev, A. B. (1987). *Fine element method in geomechanics (in Russian)*. Nedra.

Hung, C. J., Monsees, J., Munfah, N., & Wisniewski, J. (2009). *Technical manual for design and construction of road tunnels*.

Il'ichev, V. A., Nikiforova, N. S., & Tupikov, M. M. (2011). Deformation of soil masses during construction of shallow utility tunnels. *Soil Mechanics and Foundation Engineering*, *48*(3), 94–104. doi: 10.1007/s11204-011-9135-7.

Isaev, O. N., & Sharafutdinov, R. F. (2012). Volume loss during the construction of the communication tunnels by the shield method (in Russian). *Mechanization of Construction*, *6*, 2–7.

Isaev, O. N., & Sharafutdinov, R. F. (2015). Experimental study of the ground volume loss in course of microtunneling (in Russian). *Transport Construction*, *7*.

Likitlersuang, S., Surarak, C., Suwansawat, S., Wanatowski, D., Oh, E., & Balasubramaniam, A. (2014). Simplified finite-element modeling for tunneling-induced settlements. *Geotechnical Research*, *1*(4), 133–152. doi: 10.1680/gr.14.00016.

Mair, R. J. (1996). Settlement effects of bored tunnels. *International Symposium on Geotechnical Aspects of Underground Construction in Soft Ground*, 43–53.

Mair, R. J., & Taylor, R. N. (1997). Bored tunneling in the urban environment. *XIV International Conference of Soil Mechanics and Foundation Engineering*, 2353–2386.

Möller, S. C. (2006). *Tunnel induced settlements and structural force in linings*.

Möller, S. C., & Vermeer, P. A. (2005). Prediction of settlements and structural forces in linings due to tunneling. *5th International Symposium on Underground Construction in Soft Ground*.

Möller, S. C., & Vermeer, P. A. (2008). On numerical simulation of tunnel installation. *Tunneling and Underground Space Technology*, *23*(4), 461–475. doi: 10.1016/j.tust.2007.08.004.

O'Reilly, M. P., & New, B. M. (1982). Settlements above tunnels in the United Kingdom – their magnitude and prediction. *Tunneling' 82*, 137–181.

Peck, R. B. (1969). Deep excavation and tunneling in soft ground. State of the art report. *7th International Conference on Soil Mechanics and Foundation Engineering*.

Petrukhin, V. P., Isaev, O. N., & Sharafutdinov, R. F. (2014a). Modeling of deformations of the soil mass during tunneling. Part 1: Studies of the influence of calculated parameters (in Russian). *Transport Construction*, *9*, 7–11.

Petrukhin, V. P., Isaev, O. N., & Sharafutdinov, R. F. (2014b). Modeling of deformations of the soil mass during tunneling. Part 2: Method of selection of numerical simulation parameters (in Russian). *Transport Construction*, *10*, 14–15.

Petrukhin, V. P., Isaev, O. N., & Sharafutdinov, R. F. (2015). Determination of the parameters for numerical modeling of soil deformations when using finite element calculation in course of utility tunneling. In *Geotechnical Engineering for Infrastructure and Development* (Vol.7, pp. 3917–3922). doi: 10.1680/ecsmge.60678.vol7.618.

Pushilin, A. N., Favorov, A. v., & Sheinin, V. I. (2007). Method of calculating forces in buildings subject to bed deformations induced by underground excavations. *Soil Mechanics and Foundation Engineering*, *44*(3), 77–82. doi: 10.1007/s11204-007-0014-1.

Strokova, L. A. (2008). Modeling of the surface settlements during tunneling by the shield method (in Russian). *Bulletin of Tomsk Polytechnic University*, *1*, 45–50.

Ter-Martirosian, A. Z., Kivliuk, V. P., Isaev, I. O., & Shishkina, V. v. (2021). Determination of the actual excess excavation ratio (section "Kosino" - "Yugo-Vostochnaya"). *Construction and Geotechnics*, *12*(2), 5–14. doi: 10.15593/2224-9826/2021.2.01.

Ter-Martirosyan, A. Z., Isaev, I. O., & Almakaeva, A. S. (2020). Identification of the actual excess excavation ratio (Stakhanovskaya street – Nizhegorodskaya street site). *Vestnik MGSU*, *12*, 1644–1653. doi: 10.22227/1997-0935.2020.12.1644-1653.

Vermeer, P. A., & Brinkgreve, R. (1993). *PLAXIS V.5 Manual* (Balkema A.A.).

Zang, Y., Gan, P., Yan, J., Liu, S., & Yan, Z. (2019). Effects of Construction Sequences and Volume Loss on Perpendicularly Crossing Tunnels. *Advances in Civil Engineering*, 2019, 1–12. doi: 10.1155/2019/6017206.

Taylor & Francis
Taylor & Francis Group
http://taylorandfrancis.com

Slope, embankments and dams

Taylor & Francis
Taylor & Francis Group
http://taylorandfrancis.com

Smart Geotechnics for Smart Societies – Zhussupbekov, Sarsembayeva & Kaliakin (Eds)
© 2023 The Author(s), ISBN 978-1-003-29912-7
Open Access: www.taylorfrancis.com, CC BY-NC-ND 4.0 license

Stability assessment of typical Taiwan slopes under steady unsaturated seepage conditions

A.J. Li, J.W. Mburu & Z. Qian
National Taiwan University of Science and Technology, Taipei, Taiwan

ABSTRACT: Rainfall seepage analysis forms an integral part of slope stability studies. Traditionally, seepage flow was only considered in the saturated zone which is not valid for cases where slope failure occurs in the unsaturated zone. Current understanding on the physics of flow in the unsaturated layer has led to development of several analytical solutions which can quantify the negative pore pressure distribution above the water table for use in slope stability analyses. This paper assesses the effectiveness of an analytical framework considering steady unsaturated seepage conditions for typical slopes in Taiwan. Hypothetical slope and infiltration conditions relevant to Taiwan are chosen for slope stability analyses. Parallel numerical seepage and slope stability analyses are conducted and the resultant pore pressure and factor of safety values are compared to the analytical solutions to examine the utility of the proposed framework. Preliminary findings show that the numerical and analytical results are in agreement.

1 INTRODUCTION

Rainwater infiltration is widely understood to be the main trigger of slope failures particularly in tropical and subtropical climatic regions such as Taiwan. The topography in Taiwan consists of high mountain ranges and high level of discontinuity prone to mass movements. Past earthquake events such as the 1999 Chi-Chi earthquake resulted in the loosening of sediments and lowering the threshold of rainfall required to trigger slope failure (Chen et al., 2015).

Research on rainfall-induced slope failure has grown tremendously over the past 3 decades. Several methods ranging from rainfall intensity-duration thresholds, field/laboratory tests, analytical and numerical methods have been adopted to study the failure mechanisms of slopes under rainwater infiltration, develop early warning systems of landslides and effective mitigation measures in landslide-prone areas. Rainfall intensity-duration (I-D) thresholds have been developed for different regions considering meteorological, geotechnical and hydrological conditions which if exceeded may lead to slope failure (Chen et al., 2015) but largely focus on rainfall intensity and duration as the main controlling parameters not much consideration is given to rainfall seepage processes such as evolution of pore water pressure profiles within the unsaturated soil layers (Segoni et al., 2018).

A considerable number of analytical solutions have been proposed to describe the rainfall seepage process in unsaturated soil slopes. These analytical solutions may involve infinite series or integrals that need to be computed numerically. For two-dimensional (2D) slope stability problems, the analytical solutions are derived with various simplifications and assumptions such as homogeneous soil layers and simplified geometries and boundary conditions (Zhang et al., 2018). For verification purposes, the accuracy of the analytical solution could be checked against numerical analyses results.

This study assesses the applicability of Lu and Griffith's (2004) analytical formulation to hypothetical slope cases relevant to Taiwan. The pore water pressures are exported to a 2D finite element software, Optum G2 (2020) for slope stability analysis to calculate the safety

DOI: 10.1201/9781003299127-148

factor, *FoS*. The output results mainly in form of pore water pressure profiles and calculated *FoS* are compared to Finite element (FE) seepage and stability results generated from computer software package Geo-studio, 2012 (SEEP/W, SLOPE/W) (2012a; 2012b).

2 THEORETICAL BACKGROUND

For practical slope stability problems, Lu and Griffiths (2004) proposed a matric suction profile formulation is based on Darcy's governing flow equation (1856) and Gardner's (1958) model, with suitable initial and boundary conditions as shown in equation 1.

$$(u_a - u_w) = \frac{-1}{\alpha}\ln[(1 + q/k_s)e^{-\alpha\gamma_w z} - q/k_s] \tag{1}$$

where, q = flow rate per unit area, negative for downward infiltration and positive for upward infiltration, (u_a - u_w) is the matric suction, α (approximately the inverse of the air-entry value) and n (related to breadth of soil pore size) are fitting parameters used in Van Genuchten's (1980) soil water characteristic curve (SWCC) model, k_s is the saturated hydraulic conductivity (m/s), γ_w = unit weight of water, the boundary condition of (u_a - u_w) = 0 is applied at the water table when z (distance above water table) = 0

The cohesion under variably saturated conditions,C_{app} can be estimated using equations 2 and 3. is the soil friction angle.

$$C_{app} = -\sigma^s \tan\ \phi' \tag{2}$$

$$C_{app} = \tan\ \phi' \frac{(u_a - u_w)}{(1 + [\alpha(u_a - u_w)]^n)^{(n-1)/n}} \tag{3}$$

3 METHODOLOGY

3.1 *Slope model and analysis methods*

To investigate the effectiveness of Lu and Griffiths (2004) analytical solution to slope stability analysis, the software package SEEP/W and SLOPE/W were used to conduct rainfall seepage and stability analysis based on the chosen slope parameters. Since the analytical solution under consideration is based on steady-state conditions, the equilibrated pore pressures from the SEEP/W software are compared to Lu and Griffiths (2004) matric suction profiles. This is followed by slope stability analysis comparison between limit equilibrium software SLOPE/W and finite element limit analysis (FELA) software Optum G2. It is noteworthy that the slope stability analysis in Optum G2 adopts matric suction profiles in the unsaturated zone in form of apparent cohesion whose expression is given in equation 5. Also, the groundwater profile in SEEP/W at steady-state conditions is replicated in Optum G2 to make a reasonable comparison. A 2D plane strain slope model was adopted in this study, similar to Li et al., (2022) as seen in Figure 1. A suction cutoff of 100kPa was set to prevent generation of excessive negative pore water pressures (Sorbino and Nicotera, 2013).

3.2 *Slope and hydrological properties*

This study uses one set of soil mechanical and slope geometry parameters, Effective cohesion, c' = 5 kPa, ϕ' = 25 °, γ = 18 kN/m^3, slope height, H = 5m, slope angle, β = 30°. To capture the hydrological response of different soils to rainfall infiltration, a series of hydraulic and hydrological properties are adopted. The soil types considered range from silty sand to silty clay. The Van Genuchten's (1980) equation is used to describe the soil water and characteristic curve (SWCC) and permeability function (HCF).

The hydrological parameters are drawn from the Taiwan Central Weather Bureau (CWB). Three rainfall scenarios are selected, (1) light rainfall over prolonged period of 15 days and (2)

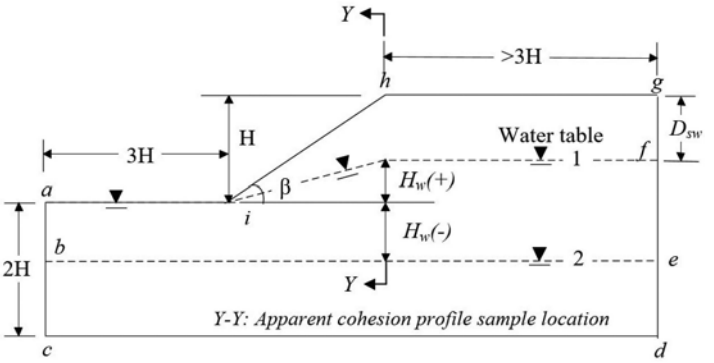

Figure 1. 2D slope model adopted for this study.

heavy rainfall over a 4 day period and (3) torrential rainfall over a period of 2 days. Generally, light rainfall events 0-20mm/day form the majority of rainfall events particularly in Taipei, and may range in duration from 1 to 18 days. Heavy rainfall events (>80mm/day) may range from 1 to 4 days. Torrential rainfall (350 – 500mm/day), normally attributed to typhoons, can last up to 2 days (Taiwan, CWB). For convenience purposes, the soil types are summarized as follows Sandy silt (S-1): $\alpha = 0.1$, n= 4, $k_s = 10^{-4}$ m/s; Silt (M-1, M-2): $\alpha = 0.02$, $n = 2$, $k_s = 10^{-5}$, 10^{-6} m/s and Clayey silt (C-1, C-2): $\alpha = 0.01$, $n = 1.4$, $k_s = 10^{-5}$, 10^{-6} m/s. The parametric study parameters are divided into three main study set categories as shown in Table 1.

The number of analyses for each study set A, B and C is controlled by the hydrological loading limit $q/k_s \leq 1.0$ and the time to reach steady state conditions. For example, soil types M-2 and C-2 could not be assessed using Lu and Griffith's analytical method for heavy and torrential rainfall since $q/k_s > 1.0$. Additionally, the corresponding low k_s may translate to a longer period to reach steady-state conditions. Similarly, slopes with deeper water table, (smaller H_w/H) take longer to reach steady state conditions, beyond the specified rainfall duration. As such, such slope cases are not considered.

Table 1. Parametric study set categories.

Study set	Soil type	Water table (H_w/H)	Rainfall scenario	Hydrological loading (q/k_s)	No. of analyses
A	S-1	0.5, 0.3, 0.0, -0.5	Light Rainfall	0.0017	20
	M-1			0.0170	
	M-2			0.1700	
	C-1			0.0170	
	C-2			0.1700	
B	S-1	0.5, 0.3	Heavy Rainfall	0.0116	6
	M-1			0.1157	
	C-1			0.1157	
C	S-1	0.5, 0.3	Torrential	0.0471	6
	M-1		Rainfall	0.4711	
	C-1			0.4711	

The SLOPE/W stability analysis employs Vanapalli's expression (1996) shown in equation 4 since it captures the non-linear relationship between matric suction and shear strength. The calculated *FoS* is compared to the result drawn from Lu and Griffith's apparent cohesion expression, equation 3, inputted in Optum G2 for stability analysis.

$$\tau = c' + (\sigma - u_a)tan\phi' + [(\theta_w - \theta_r/\theta_s - \theta_r)tan\phi'] \quad (4)$$

4 RESULTS AND DISCUSSION

4.1 *Time to reach steady state conditions*

In this study, the time to reach steady state conditions is based on subjective judgement. The pore water pressure profiles from numerical seepage analyses in SEEP/W are plotted with time. Steady state conditions were assumed when the pore water pressures barely change with time. At least 2 monitoring locations were chosen for each slope case. Slopes with water table above or at the slope toe ($H_w/H \geq 0.0$) had two monitoring locations, vertical profiles from the slope crest and mid-slope to the water table location. Slopes with water table below the slope toe ($H_w/H < 0.0$) had an extra monitoring location at the slope toe.

4.2 *Suction and apparent cohesion profiles*

4.2.1 *Different soil types*

The suction and apparent cohesion profiles presented in Figures 2a - f encompass a wide range of soil slopes (sandy silt to clayey silt) under light rainfall conditions. The initial water table location for the presented cases was 7m below the ground surface. Generally, slopes with soil type M-2 and C-2 undergo loss of suction coupled with a rise in water table leading to critical conditions. As seen in Figure 2c, there is a notable rise in water table location at the steady-state condition. Lu and Griffith's analytical solution yields quite similar pore water pressure and apparent cohesion profiles at initial and steady state conditions to SEEP/W 2D seepage results, with a difference of about 10kPa. It is seen that the difference in pore water pressures and apparent cohesion is most pronounced at the slope crest.

For highly permeable soil slope S-1 subjected to rainfall infiltration, with high water table ($H_w/H = 0.5, 0.3$) water tends to seep out at a faster rate than rainwater accumulating within the soil pores resulting in a lowering of the water table as shown in Figure 2e. Also the pore water pressures generated from the numerical SEEP/W analysis and analytical solution are significantly different at the slope crest, by about 40 kPa, as seen in Figure 2e. For the S-1 soil slope, Lu and Griffith's formulation predicts significantly smaller apparent cohesion values at initial conditions in comparison to SEEP/W results. This trend is observed for all the water table locations and rainfall scenarios analyzed in this study. Interestingly, the apparent cohesion profiles for S-1 soil type at steady-state conditions are quite similar, as shown in Figure 2f.

4.2.2 *Different water table locations*

This study analyzed soil slopes with four water table locations, one above the slope toe ($H_w/H = 0.5$), one at the slope toe, ($H_w/H = 0.0$) and another water table location below the slope toe ($H_w/H = -0.5$). Figures 3a - f present pore water pressure profiles for a typical soil slope, M-1, with moderate permeability and different water table locations under light rainfall conditions. The difference in pore water pressures predicted using the SEEP/W seepage analysis and Lu and Griffith's formulation increases with depth of the water table and is most pronounced at the slope crest. The difference in pore water pressure values ranges from 10 – 15 kPa for shallow water table locations (above slope toe) to about 50 kPa for deep water table locations (below the slope toe) as seen in Figures 3a, e. The difference in apparent cohesion profiles from the two methods is not significantly influenced by the change in water table locations. As shown in Figures 3b, d and f, for slopes with different water locations, the apparent cohesion difference is mostly 3 - 15kPa. Nevertheless, practicing engineers should take caution when using Lu and Griffith's analytical solution to estimate suction profiles for soil slopes with deep water table.

4.2.3 *Different in rainfall scenarios*

The rainfall events considered range from light rainfall over a prolonged period of 15 days, heavy rainfall over a period of 4 days and torrential rainfall over a period of 2 days. The rainfall duration was selected based on typical rainfall periods recorded around Taiwan for the past 10 years (Taiwan Central Weather Bureau). The recorded times to reach steady state conditions are largely within the rainfall durations chosen for this study and applicable to the

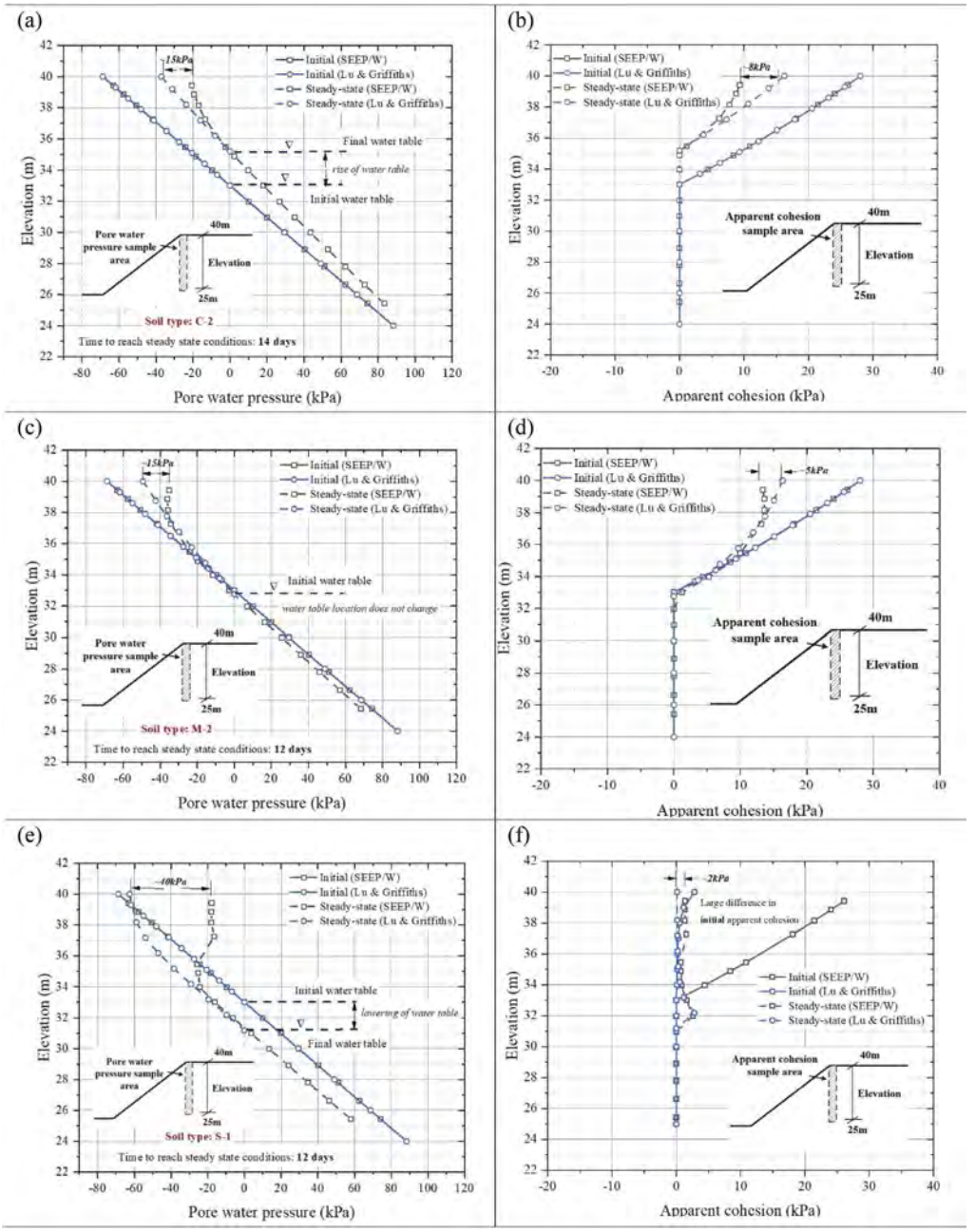

Figure 2. Pore pressure and apparent cohesion profiles for different soil slopes (a) and (b): C-2, (c) and (d): M-2, (e) and (f): S-1.

Taiwan context. It should be noted, however, that a comparison between the numerical seepage method and analytical method for study set C, soil types M-1 and C-1 was not feasible since the slope is fully saturated over the course of the torrential rainfall. Additionally, within study set C, soil type S-1, steady state conditions are reached after 28 hours, beyond the specified rainfall duration of 2 days. Thus, an appropriate comparison of the two seepage analysis methods cannot be made for this case.

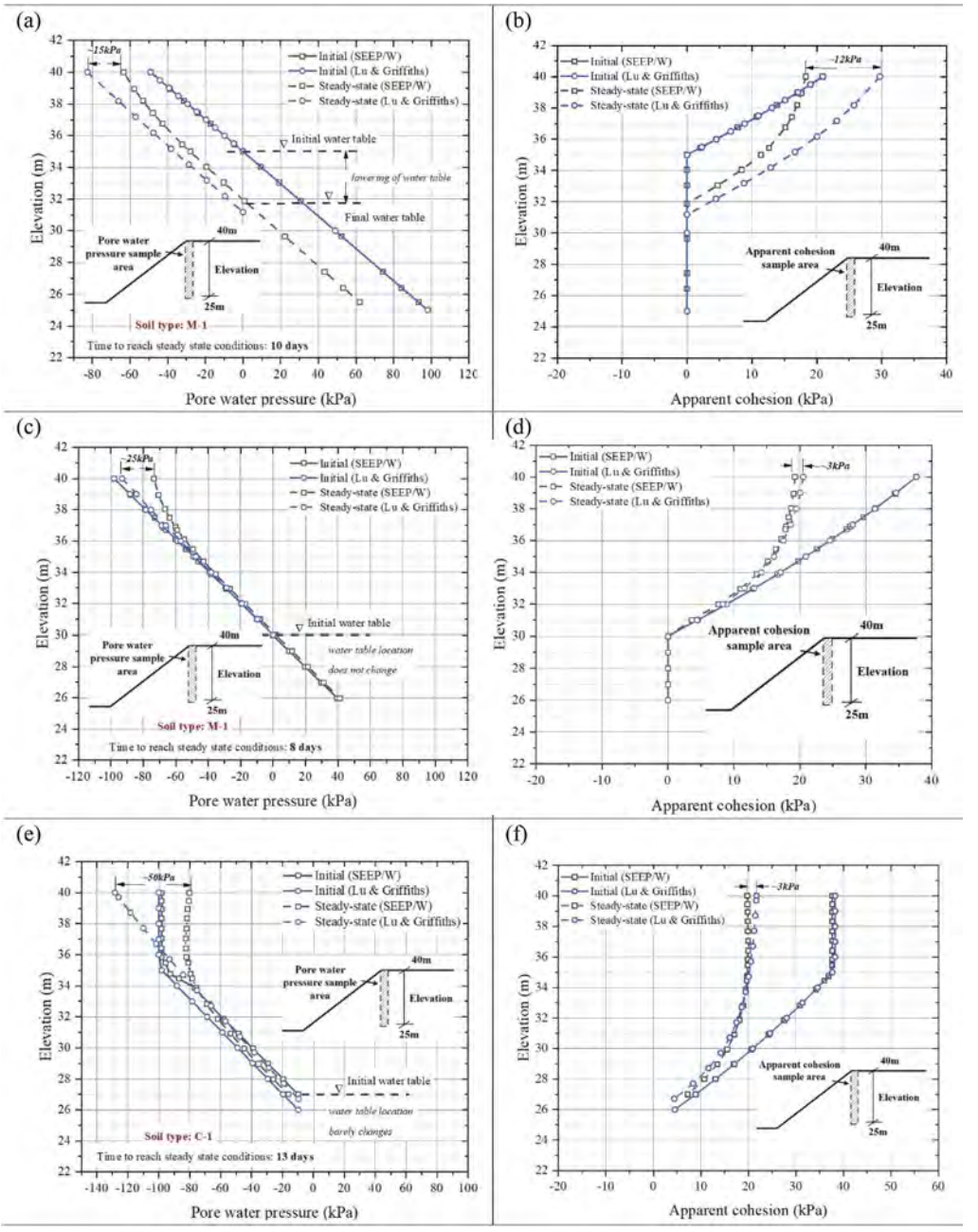

Figure 3. Pore pressure and apparent cohesion profiles for different water table locations (a) and (b): H_w/H = 0.5 (c) and (d): H_w/H = 0.0, (e) and (f): H_w/H = -0.5.

Pore water pressure and apparent cohesion profiles for silty soil slope, M-1, for the two rainfall scenarios in Figures 4a - d demonstrate that the two seepage analysis methods show good agreement with differences of about 10 kPa. Lu and Griffiths formulation is applicable over the range of rainfall intensities chosen for this study.

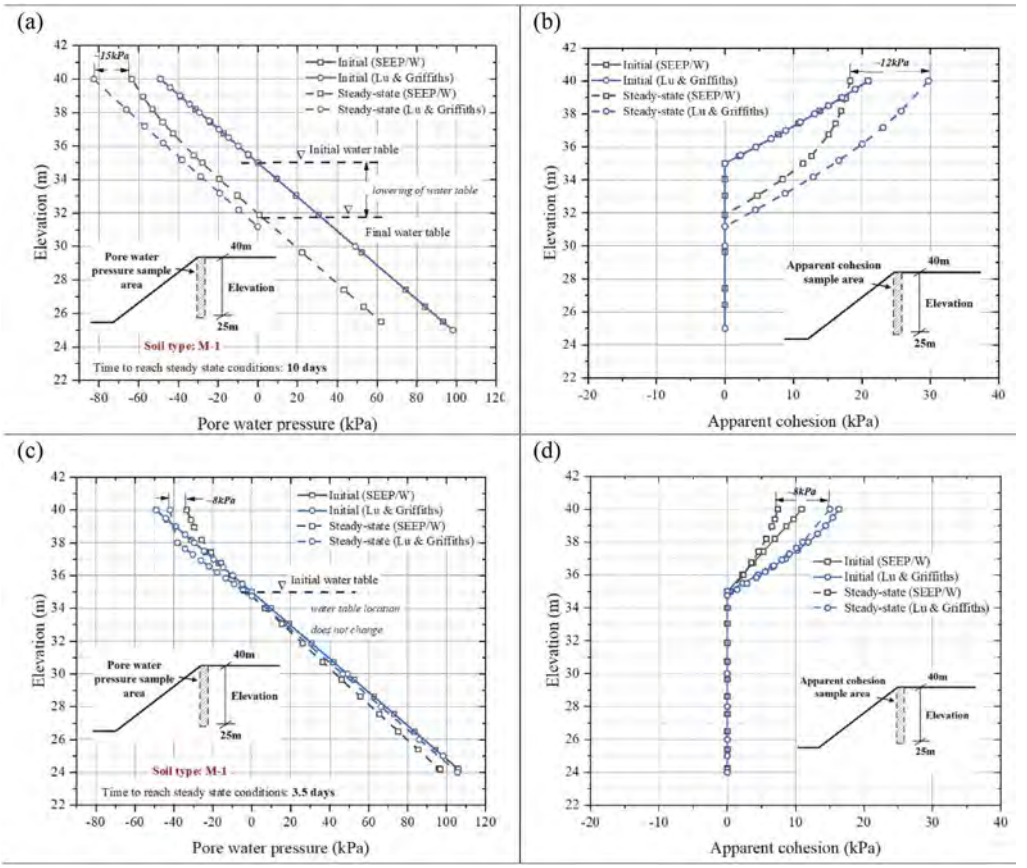

Figure 4. Pore pressure and apparent cohesion profiles for different rainfall events (a) and (b): Light rainfall (15mm/day) (c) and (d): Heavy rainfall (100mm/day).

4.3 *Slope stability analysis comparison*

The slope *FoS* at initial and steady-state conditions from SLOPE/W and Optum G2 are compared. SLOPE/W is a limit equilibrium slope stability program that integrates the calculated pore water pressures from SEEP/W to evaluate the stability of the slope. Pore water pressures estimated from Lu and Griffith's analytical solution are manually inputted in form of cohesion (equation 3) to FELA-based software, Optum G2 for stability analysis. The *FoS* is calculated using the strength reduction method (Krabbenhoft and Lyamin, 2015).

The initial *FoS* calculated using the two approaches is quite similar having a maximum of 10% difference for soil slopes, M-1,2, C-1,2 with water table locations H_w/H = 0.5, 0.0 and -0.5. Notably, the initial *FoS* predicted based on pore water pressures from the analytical approach in soil slope, S-1, is much smaller than SLOPE/W *FoS*. This is due to the large difference in apparent cohesion between the two methods as seen in Figure 2f. In fact, for S-1 slopes with water table location, H_w/H = -0.5, the initial *FoS* % difference was quite large, approximately 46%. Table 2 presents the initial *FoS* values for a section of slope parameters.

The *FoS* comparison at steady state conditions is presented in Tables 3 and 4 for a section of slope and hydrological parameters. The *FoS* % difference between SLOPE/W and Optum ranges from 1 – 24%, showing good agreement.

The failure surfaces shown in Figure 5a-d are for soil slope M-1 with water table location H_w/H = 0.3 at steady state conditions after light or heavy rainfall. The two software programs locate the failure surface by limit equilibrium method (LEM) and by calculation of stresses

Table 2. Initial *FoS* estimated from SLOPE/W and Optum software programs.

Soil type	Water Table H_w/H	Factor of safety, *FoS*		
		SLOPE/W	Optum G2*	% difference
C-1	0.5	1.136	1.129	-1%
	0.0	1.475	1.559	6%
	-0.5	2.323	2.350	1%
M-1	0.5	1.136	1.12	-1%
	0.0	1.549	1.491	-4%
	-0.5	2.322	2.099	-10%
S-1	0.5	1.136	1.066	-6%
	0.0	1.549	1.253	-19%
	-0.5	2.322	1.247	-46%

* *FoS* is the average of upper and lower bounds.

Table 3. Steady-state *FoS* estimated from SLOPE/W and Optum software programs.

Soil type	Rainfall type	Water Table H_w/H	Factor of safety, *FoS*		
			SLOPE/W	Optum G2*	% difference
C-1	Light Rainfall	0.5	1.341	1.428	6%
		0.0	1.482	1.554	5%
		-0.5	2.183	2.217	2%
M-1	Light Rainfall	0.5	1.33	1.416	6%
		0.0	1.505	1.487	-1%
		-0.5	2.230	2.043	-8%
S-1	Light Rainfall	0.5	1.328	1.455	10%
		0.0	1.463	1.250	-15%
		-0.5	1.650	1.251	-24%

* *FoS* is the average of upper and lower bounds.

Table 4. Steady-state *FoS* estimated from SLOPE/W and Optum software programs.

Soil type	Rainfall type	Water Table H_w/H	Factor of safety, *FoS*		
			SLOPE/W	Optum G2*	% difference
C-1	Heavy Rainfall	0.5	1.017	1.034	2%
		0.3	1.088	1.107	2%
M-1	Heavy Rainfall	0.5	1.038	1.040	0%
		0.3	1.157	1.154	0%
S-1	Heavy Rainfall	0.5	1.229	1.154	-6%
		0.3	1.221	1.200	-2%
S-1	Torrential Rainfall	0.5	1.136	1.109	-2%

* *FoS* is the average of upper and lower bounds.

(Optum). The observed failure surfaces from both computer programs are quite similar. The toe failure is the main failure mechanism.

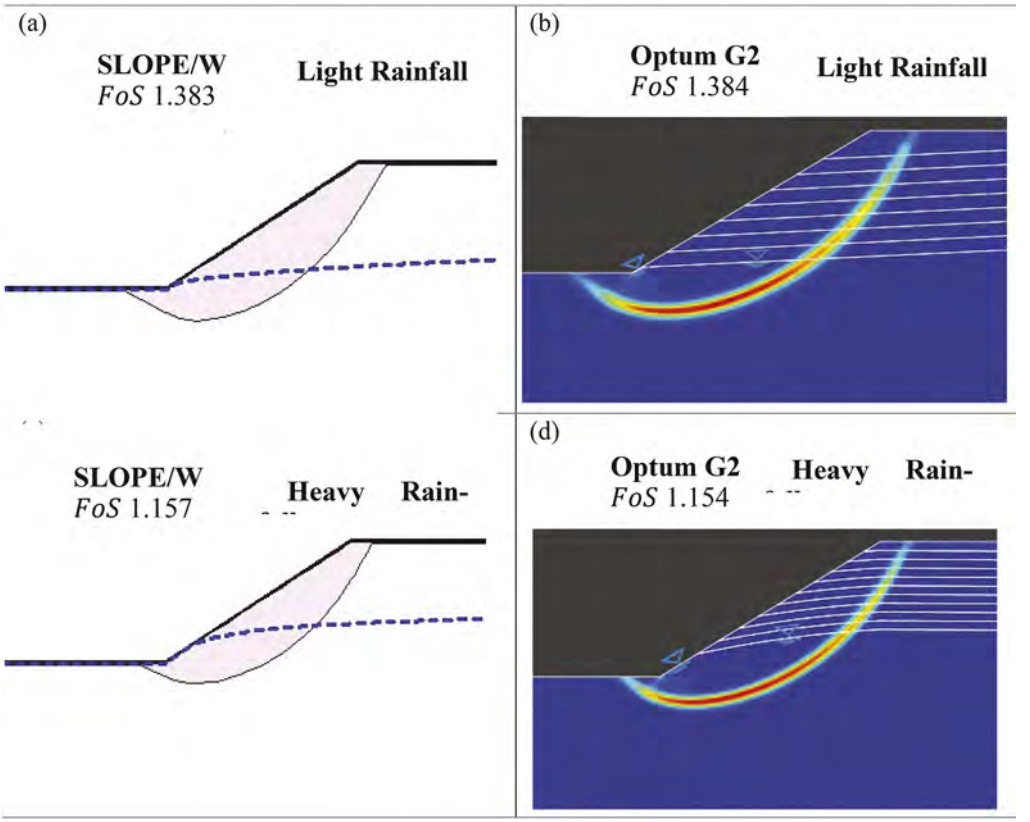

Figure 5. Failure surfaces for M-1 soil slopes at steady state conditions under light rainfall (a) SLOPE/W (b) Optum G2 and heavy rainfall (c) SLOPE/W and (d) Optum G2.

5 CONCLUSION

The utility of a widely used analytical solution is assessed for slope conditions relevant to Taiwan under different rainfall conditions. The results in form of pore water pressure and apparent cohesion profiles and factor of safety are compared to seepage and stability analyses using Geo-studio (SEEP/W and SLOPE/W) software package. The following findings are made:

1. The analytical solution yields reasonable pore water pressures and apparent cohesion profiles for the slope and hydrological parameters considered in this study. There is good agreement with the numerical seepage and stability analysis results.
2. The analytical solution predicts comparatively smaller apparent cohesion values at the initial stage of analysis for highly permeable soil slopes, S-1, leading to very conservative factor of safety values.
3. Notable differences in pore water pressures or apparent cohesion between the analytical and numerical seepage results are most prominent at the slope crest, particularly for slopes with deep water table location (below the slope toe). Engineers may need to take caution when applying the analytical solution to these kind of slopes. Further investigation is still needed for soil slopes with a deeply located water table.
4. The predicted *FoS* at steady state conditions from SLOPE/W and Optum G2 software programs show good agreement for the parameters selected in this study. This can be attributed to the closeness in apparent cohesion profiles obtained from the numerical and analytical solution. The observed failure surfaces, mainly toe failure, are quite similar.

5. The analytical solution assessed in this study assumes steady-state conditions, soil homogeneity and is mostly applicable to simplified slope geometry and boundary conditions. Also, movement of water table due to rainwater infiltration is not accounted for. As such, combining the pore water pressures with the 2D finite element software such as Optum for slope stability analysis should be considered for initial study purposes only. Additionally, engineers could use regional data on water table movement during the rainy season to predict a reasonable water table location when using the analytical solution.

REFERENCES

1. Bishop, A.W. (1959). "The principle of effective stress.:" Teknik Ukeblad, Vol. 39.
2. Chen, C.W., Saito, H. and Oguchi, T. (2015). "Rainfall intensity–duration conditions for mass movements in Taiwan:" Progress in Earth and Planetary Science, Vol. 2, No. 1.
3. Darcy, H. (1856). "Les fontaines publiques de la ville de Dijon:" Recherche.
4. Gardner, W.R. (1958). "Some steady-state solutions of the unsaturated moisture flow equation with application to evaporation from a water table:" Soil Science, Vol. 85, No. 4.
5. Geo-slope International. (2012a). "SEEP/W for finite element seepage analysis (user's guide)":
6. Geo-slope International. (2012b). "SLOPE/W for stability analysis (user's guide)":
7. Krabbenhoft, K. and Lyamin, A. v. (2015). "Strength reduction finite-element limit analysis:" Geotechnique Letters,Thomas Telford Services Ltd Vol. 5, No. 4, pp. 250–253.
8. Li, A.J., Mburu, J.W., Chen, C.W. and Yang, K.H. (2022). "Investigations of Silty Soil Slopes under Unsaturated Conditions Based on Strength Reduction Finite Element and Limit Analysis:" KSCE Journal of Civil Engineering, Vol. 26, No. 3.
9. Lu, N. and Griffiths, D. v. (2004). "Profiles of Steady-State Suction Stress in Unsaturated Soils:" Journal of Geotechnical and Geoenvironmental Engineering, Vol. 130, No. 10.
10. Optum G2 (2020). "Optum G2 2020 (user manual):"
11. Rahardjo, H., Ong, T.H., Rezaur, R.B. and Leong, E.C. (2007). "Factors Controlling Instability of Homogeneous Soil Slopes under Rainfall:" Journal of Geotechnical and Geoenvironmental Engineering, Vol. 133, No. 12.
12. Segoni, S., Piciullo, L. and Gariano, S.L. (2018). "A review of the recent literature on rainfall thresholds for landslide occurrence:" Landslides, Vol. 15, No. 8.
13. Sorbino, G. and Nicotera, M.V. (2013). "Unsaturated soil mechanics in rainfall-induced flow landslides:" Engineering Geology, Vol. 165.
14. Taiwan Central Weather Bureau. Daily Rainfall Data (2009–2022), Available at: https://www.cwb.gov.tw/V8/E/D/DailyPrecipitation.html (Accessed: November 16, 2021).
15. Vanapalli, S.K., Fredlund, D.G., Pufahl, D.E. and Clifton, A.W. (1996). "Model for the prediction of shear strength with respect to soil suction:" Canadian Geotechnical Journal, Vol. 33, No. 3.
16. van Genuchten, M.Th. (1980). "A Closed-form Equation for Predicting the Hydraulic Conductivity of Unsaturated Soils:" Soil Science Society of America Journal, Vol. 44, No. 5.
17. Zhang, L., Li, J., Li, X., Zhang, J., & Zhu, H. (2018). Rainfall-Induced Soil Slope Failure: Stability Analysis and Probabilistic Assessment. (1st ed.), CRC Press. https://doi.org/10.1201/b20116.

Smart Geotechnics for Smart Societies – Zhussupbekov, Sarsembayeva & Kaliakin (Eds)
© 2023 The Author(s), ISBN 978-1-003-29912-7
Open Access: www.taylorfrancis.com, CC BY-NC-ND 4.0 license

Bearing capacity of helix pile on tropical fibrous peat soil under compression loading

Ardy Arsyad
Department of Civil Engineering, Faculty of Engineering, Hasanuddin University, Makasar Indonesia

Pebrinar Riani Sangle
Department of Civil Engineering, Faculty of Engineering, UKI Paulus University, Makassar Indonesia

Andi Baso Firmansyah
Department of Civil Engineering, Faculty of Engineering, Hasanuddin University, Makassar Indonesia

Eko Budianto
Department of Civil Engineering, Faculty of Engineering, Musamus University, Merauke Indonesia

ABSTRACT: Fibrous peat soil is a type of soil which comprises of fibrous organic materials, changed and fossilized to be a soil in wetland. This type of soil is generally deposited in the lowlands of East Sumatera, Central and South Borneo, and West Sulawesi Indonesia. However, due to poor characteristics associated with low shear strength, high compressibility and high-water content, the tropical fibrous peat soil has become problematic for sub-grade embankment of road constructions. The use of helix pile to reinforce the tropical fibrous peat soil for road embankment has been recently investigated. However, load-transfer mechanism of the helix pile in peat soil with more fiber content is not yet fully understood. Therefore, this paper presents laboratory scale experiment and numerical model of helix pile in fibrous peat soil under compression loadings. The effect of helix pile numbers and dimension of helices were investigated through laboratory model tests. In addition, numerical model with back-calculated input parameters from the experimental tests was also undertaken by using ABAQUS in order to examine load-displacement on the helix pile with various number of helices during loading. The results show that bearing capacity of the helix pile much influenced by the number of helices. This is due to the bearing capacity is more contributed from the bearing of helices, at about 60% - 70% of the total capacity, while the shear resistance in between helices just contributes 23% - 35%. The existence of fiber in the peat soil, could increase the shear resistance by factor of 1.30, while the increase of number of helices in the pile would increase the bearing by 5%. Hence, a new formula of predicting bearing capacity of the helix pile in the fibrous peat soil is proposed by modified Mitsch & Clemence Formula (1985) with modified Meyerhof & Adam's (1968) Nq value to accommodate typical fibrous peat soil characteristics, with the accuracy of the prediction of 98% – 99% of the bearing capacity from the experimental tests.

1 INTRODUCTION

Fibrous peat soil is a type of organic soil which has low shear strength with further high secondary, and even continuous tertiary compressibility. In Indonesia, the soil is very dominant in the lowland areas such as those areas in Central and South of Borneo, East of Sumatera, and West of Sulawesi. As a result, the soil become problematic for infrastructure developments throughout the country. A number of studies has been conducted to investigate the mechanical characteristics of peat soil. The primary compressibility of peat soil is 5 to 20 times to the primary compressibility

DOI: 10.1201/9781003299127-149

of soft clay (Mesri and Ajlouni 2007). In addition, the permeability of peat soil is about 1000 times the permeability of soft clay (Mesri and Ajlouni 2007), while its undrained shear strength is just 3 kPa to 15 kPa (Kazemian et al. 2011). Having these characteristics, ground improvement is required such as soil replacement, piled geotextile, and pile-slab to ensure the soil can be used as good foundation for infrastructure. The use of helical piles has been recently investigated for the condition of fibrous peat soil. Several studies focused on the bearing capacity of helix pile in fibrous peat soil (Fatnanta et al 2016; Parlan et al. 2016, Arsyad & Herdiman et al. 2017, Arsyad et al. 2018). The studies performed experimental tests on helix piles drilled to fibrous peat soils, and others undertook numerical analysis of modeling the raft-helix pile. However, detailed study of load transfer mechanism of helix pile to fibrous peat soil is not yet understood, particularly the effect of soil's fiber on the bearing capacity of pile. Therefore, this study aims to investigate the bearing capacity of helix pile in the fibrous peat soil by conducting a lab-scale test of compression loadings, and to examine the stress-strain in each component of the helix pile (helice plates, shaft, and shear failures zones) by numerical modeling with back-calculated parameter to the lab-scale experimental tests. Theoretical analysis was proposed to predict the bearing capacity of the helix pile based on experimental tests and numerical-back calculated model.

2 LABORATORY EXPERIMENTS

2.1 *Properties of fibrous peat soil and dimension of helix pile*

The model test was conducted in a laboratory scale testing apparatus. Figure 1 shows a schematic diagram of the apparatus used in the study. An 800 mm diameter × 1200 mm cylinder steel tank was fabricated for conducting the model tests on helix piled fibrous peat soil. The wall of the tank was made smooth and rigid to create plain strain condition in the tank. A fibrous peat soil bed of 1000 mm depth was prepared in this test tank. Undisturbed samples were taken from the bed for determining the density, moisture content, shear strength of fibrous peat soil bed. The properties of the fibrous peat soil bed are given in Table 1. In general, the properties of fibrous peat soil bed suggested that the soil is a fibric peat soil with fiber content of about 72% of the total soil, with a very high-water content of 151.02%. Its density is 12.9 kN/m^3 while the undrained shear strength is 0.94 kPa and 45^o internal friction angle.

After levelling the fibrous peat soil, helix pile was formed on the top of the soil bed layer by screwing the pile to the soil. The helix pile was made from a pipe with 25.4 mm diameter, and 500 mm height, and the spacing of helices is 100 mm. Three variations of helix pile were created for model test, type A with one helice, type B with two helices, and type C with three helices (Figure 2).

Static load was applied on the helix pile using a hydraulic jack, and the intensity of the load was increased gradually. Loading was done in accordance to the ASTM standards in which

Table 1. Properties of soil.

No	Properties	Results
1	Specific gravity	1.62
2	Water content	151.02%
3	Sieve Analysis	
	4	100.000
	10	96.086
	40	65.166
	200	17.613
4	Direct shear test	
	Cu	0.94 kPa
	ϕ	45^o
5	Fiber content	72%
6	Density	12.90 kN/m3

incremental load applied when deformations reached a steady state value. The load was measured using a proving ring. Dial gauges were place at a certain location at the helix pile to measure vertical and horizontal displacement. Figure 3 shows the profile of fibrous peat soil bed in the tank, and experimental setup for load tests on helix pile, showing the positions of various dial gauges.

Tabel 2. Dimension and spacing of helix pile.

Type of helix pile	Height of helix pile (cm)	Diameter of helix pile (cm)	Diameter of Helices plat (cm)	Helices spacing (cm)	Number of helices (Buah)
A	50	2.54	10	10	1
B	50	2.54	10	10	2
C	50	2.54	10	10	3

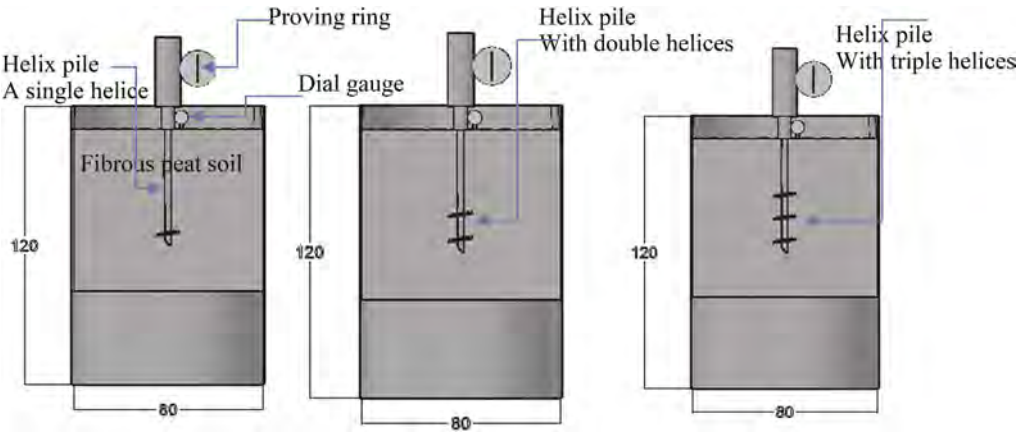

Figure 1. Schematic diagram of lab-scale of helix pile in the tank with fibrous peat soil bed.

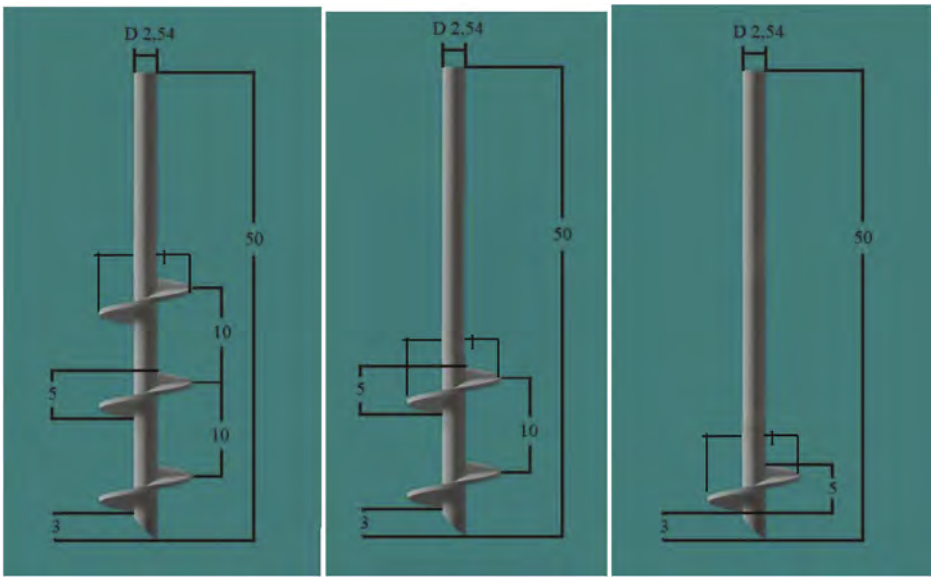

Figure 2. Dimension of helix pile in the experimental test.

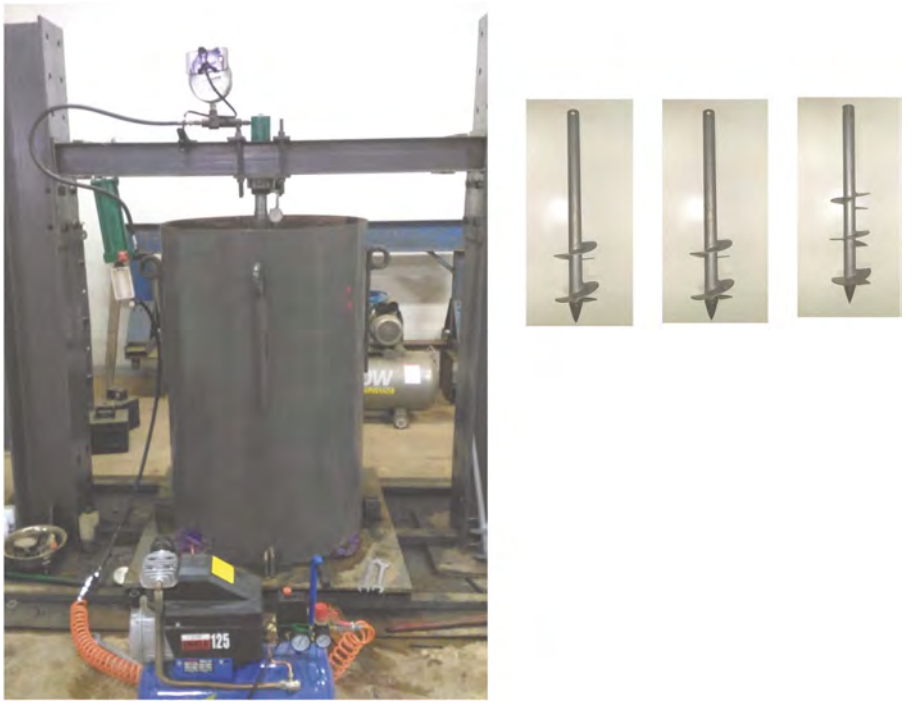

Figure 3. Experimental set up of helix pile under compression loading.

2.2 *Numerical analysis and parametric study*

The performance of the helix pile on the fibrous peat soil bed was investigated. Tests were undertaken on the model testing of helix pile, varying parameters like number of helice plates. In addition, numerical analysis was conducted to investigate the detail stress-strain in each helice plate during loading test. In this way, FEM model ABAQUS was used in which the model is shown in Figure 4. Input parameter of the helix pile is shown in Table 3. The weight volume is 7850 kg/m3, Young Modulus is 1×10^8 kPa, and Poisson ratio is 0.3. On the other hand, input parameter for fibrous peat soil in the FEM model was derived from laboratory tests, except for elastic

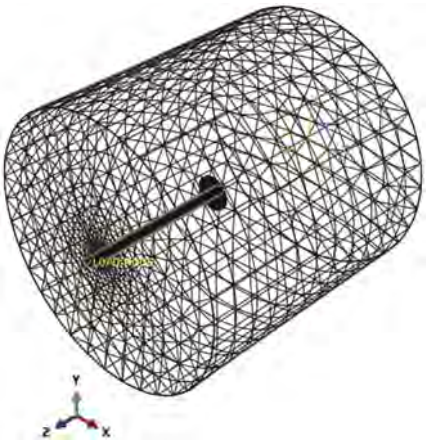

Figure 4. FEM ABAQUS of helix pile in the fibrous peat soil.

modulus which was back analysis determined. Dilatancy angle and interface was determined by assuming typical values for those parameters in the steel pile and peat soil.

Tabel 3. Dimension and spacing of helix pile.

Parameter	Magnitude	Note
Total unit weight, γ (kg/m3)	7850	Assumed value[a]
Young's Modulus, E (kPa)	$2x10^8$	Assumed value[b]
Poisson's ratio, v	0,3	Assumed value[b]

a (*Peraturan Pembebanan Indonesia Untuk Gedung* (PPIUG), 1983)
b (Elsherbiny & Naggar, 2013)

Tabel 4. Dimension and spacing of helix pile.

Parameter	Magnitude	Note
Total unit weight, (kN/m3)	11,48	Density test[c]
Young's Modulus, E (kPa)	125	Back analysis[c]
Poisson's ratio, v	0,15	Assumed value[d]
Cohesion, c' (kPa)	0,94	Direct shear test[c]
Friction angle, ϕ (o)	45	Direct shear test[c]
Dilatancy angle, ψ (o)	15	Assumed value[c]
Interface strength reduction, R_{inter}	0,7	Assumed value[e]
Coefficient of Lateral Earth Pressure at Rest, K_o	0,29	$K_o = 1 - \sin\phi'$

3 RESULTS AND DISCUSSIONS

3.1 *Experimental results*

In all the model tests conducted, during loading tests, failures were the result of the displacement of helix pile which is 10% times diameter of the pile (ISSMFE, 1985). There were three variations of the helix pile: single, double, and triple helices. Each variant was trial within three samples to test its reproducibility. In the single helice of helix pile tests, the ultimate loads were maximum 20 kg for displacements of 10% diameter (Figure 5), while, in the double helice of helix pile tests, the ultimate loads were maximum 29 kg (Figure 6), and in the triple helices, the maximum ultimate loads were 34 kg (Figure 7). It can be observed that helice plates in the helix pile have exhibited higher ultimate capacity. The results reveal that number of helices in the helix pile affect the ultimate bearing capacity. The increase of helice numbers, would increase the ultimate bearing capacity of helix pile (Figure 8). Axial stiffness of the helix pile with increasing helice plates numbers in the fibrous peat soil would increase considerably. The helix pile with a single helice plat have generated a 20 kN/m, while that with double helice plates yielded 29 kN/m, and triple helices generated 34 kN/m.

3.2 *Numerical analysis*

The results of experiments on model tests were back-calculated FEM modeling using a ABAQUS program. The computer program developed for conducting FEM model of helix pile in the fibrous peat soil. Figure 9 show the stress – strain in the FEM model of fibrous peat soil with loading on the helix pile. During the loading in the model of helix pile with a single helice plate, failure zones with stress developed was seen at the soil below the helice plate, reaching at maximum 80 kPa with mean stress of 44.6 kPa. The bearing capacity seems to be contributed from

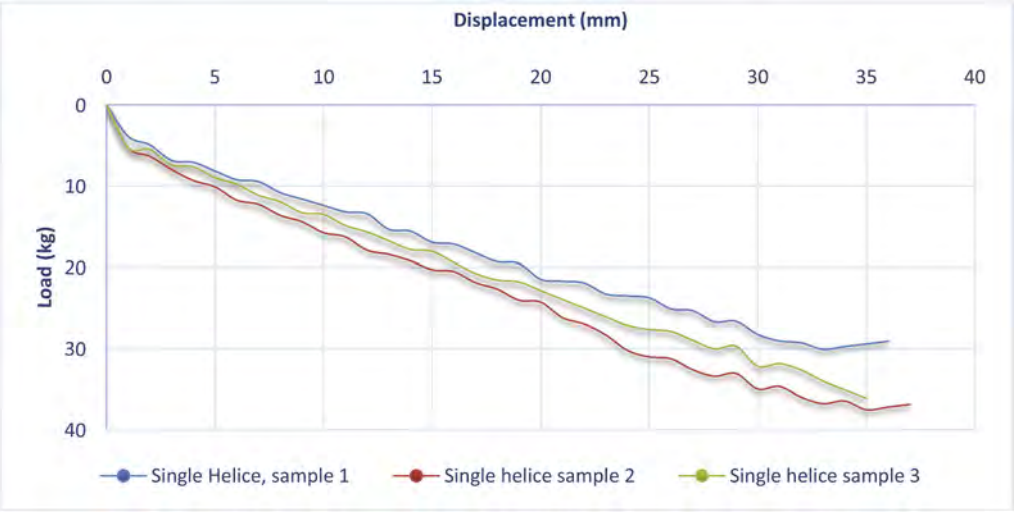

Figure 5. Load – displacement of helix pile with a single helice under compression loading.

Figure 6. Load – displacement of helix pile with double helices under compression loading.

compressive strength of the soil below the helice plate, while the friction between the pile rod and soil just contributed small value of 2.08 kPa. The displacement of the soil below the helice plate was found to be maximum 0.04 m.

On the other hand, the helix pile with a double helice plates (Figure 10) generated a different pattern of failure during the loading. The failure zones were obvious in area below lower helice plates, tip of helix rod, shaft of the rod, and shear failure areas in the area between helice plates. Stress developed at below lower helice plates at maximum 80 kPa, and below the upper helice plates at maximum 44.5 kPa, and shear failure in between helice plates at 30.4 kPa. Maximum displacement was found at the area in between the helice plates, at 0.04 m.

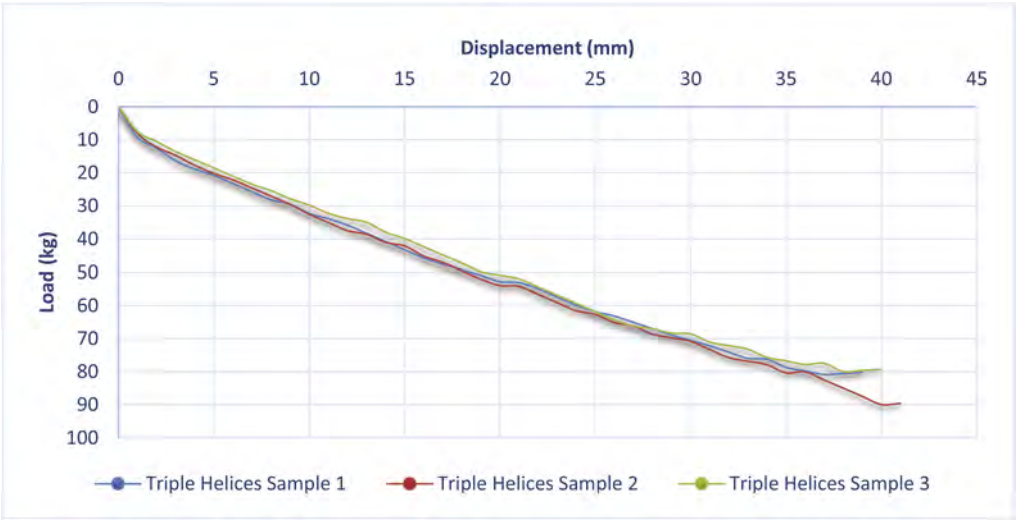

Figure 7. Load – displacement of helix pile with triple helices under compression loading.

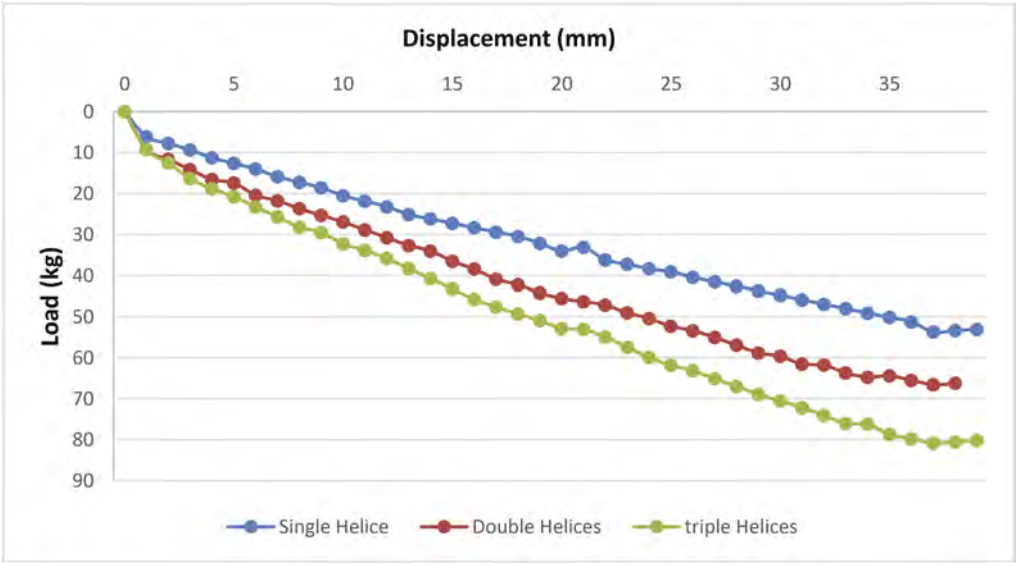

Figure 8. Load – displacement of helix pile with various number of helices under compression loading.

In regards to the helix pile with a triple helice plates (Figure 11), the failure zones were similar to the failure pattern in the double helices pile. However, due to three helices plates, the bearing capacity of the pile derived from the three helice plates with failure zones below, tip of pile rod, and failure shear in between helice plates. The stress developed below the helice plates, was accounted for maximum 80 kPa di lower helice plates, 37.5 kPa at the middle helice plates, and 23.3 kPa at the upper helices plates. Meanwhile, shear failure zones in between helice plates were at 9.16 kPa.

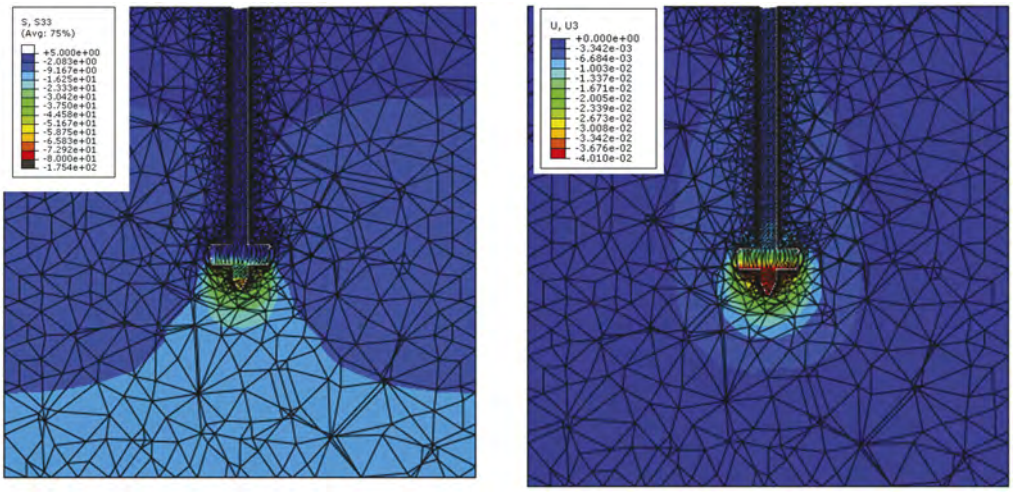

Figure 9. Experimental back-calculated FEM based stress – strain at the helix pile with a single helice.

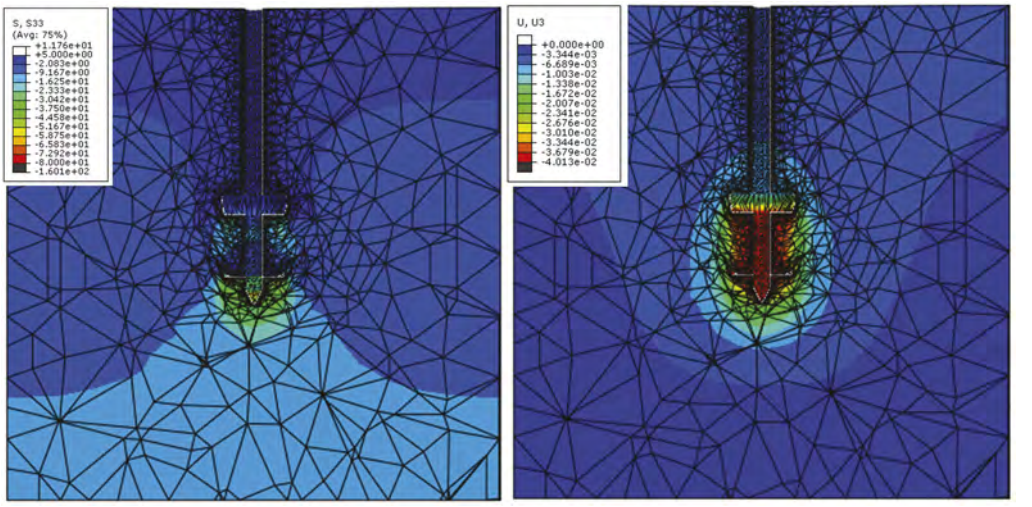

Figure 10. Experimental back-calculated FEM based stress – strain at the helix pile with double helice.

4 THEORITICAL ANALYSIS

Based on both measured and simulated behaviour of the helical piles in fibrous peat soil considered in this study, a method for predicting the axial compressive capacity of the pile is presented. The geometry of the failure area for calculation of the compressive axial capacity of the system can be derived from numerical model with back-calculation of experimental tests. The geometry of the failure area is very important to calculate bearing capacity of the pile. As seen in Figure 11, the failure area between the two lowermost helices is observed to closely follow the profile of the helices. The failure area at the lowermost helices seems to be larger than that in the upper two helices. It can be suggested that the bearing mechanism of the helix pile is contributed by all bearing helice plates, however the lowermost helices comprise more bearing capacity than the others. Above the top of uppermost helices, there is no significant

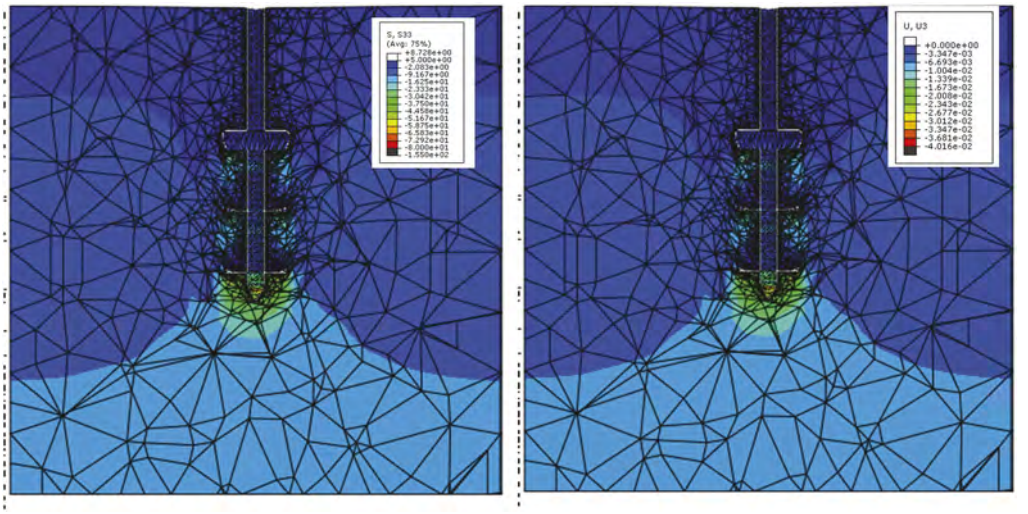

Figure 11. Experimental back-calculated FEM based stress – strain at the helix pile with triple helices.

deformation during the compressive loadings. Considering load transfer mechanism under compressive loading, bearing capacity of the helix pile can be described (Livneh & Naggar, 2008; Mohajerani et al., 2016) as follow: (i) shear resistance derived from a cylindrical failure surface along the interhelical soil profile or Q_{helix}, and (ii) bearing of the bottom helix on the soil below ($Q_{bearing}$) and (iii) friction resistance of the pile shaft along the pile rod to the surrounding soil (Q_{shaft}). As mathematical model, compressive bearing capacity of helix pile in a cohesionless soils was introduced by Mitsch and Clemence (1985) (Mohajerani et al., 2016) as seen in Eq. 1 – 5.

$$Q_c = Q_{helix} + Q_{bearing} + Q_{shaft} \tag{1}$$

$$Q_{helix} = 0.5\pi D_a \gamma' \left(H_b{}^2 - H_t{}^2\right) K_s tan\varphi \tag{2}$$

$$Q_{bearing} = \gamma' H A_H N_q \tag{3}$$

$$Q_{shaft} = 0.5 P_s H_{eff}{}^2 \gamma' K_s tan\varphi \tag{4}$$

$$Q_c = 0.5\pi D_a \gamma' \left(H_b{}^2 - H_t{}^2\right) K_s tan\varphi + \gamma' H A_H N_q{}^* + 0.5 P_s H_{eff}{}^2 \gamma' K_s tan\varphi. \tag{5}$$

where D_a = average helix diameter; H_a = depth to bottom helix; H_t = depth to top helix; K_s = coefficient of lateral earth pressure in compression loading; A_H = area of the bottom helix; P_s = perimeter of the screw pile shaft.

The values of the pile capacity calculated using Eq. 5 are summarized in Table 6 and are compared with numerical back-calculated experimental tests. The calculated capacities are found to be in good agreement with the measured, except for the $Q_{bearing}$ which is far larger than the computed values. The use of Nq in the Eq. 3 is based on internal friction angle (ϕ), as shown in formula of Meyerhof & Adams (1968). The N_q for ϕ' = 45° is 134.87, which is too conservative for fibrous peat soil. The characteristics of the soil is somewhat unique due to very low undrained shear strength, and very high effective internal friction angle. Since the experimental tests show a low $Q_{bearing}$, the N_q must be reduced by factoring 0.4 of ϕ, to accommodate the characteristics of the soil. As result of the N_q becomes 5.15, and the $Q_{bearing}$ values are very good agreement with the experimental tests, as shown in Table 7. It must be noted, that the increasing number of helices also affect the $Q_{bearing}$,

by increase of 5%. The additional 2 helices into the helix pile with a single helice would increase $Q_{bearing}$ by 10%. Besides the $Q_{bearing}$, the computed Q_{helix} also shows a difference, compared to the experimental tested Q_{helix}. Since the Q_{helix} is derived from shear failure zones along the soil between the helice plates, the lateral earth pressure during the compression loading (K_s) and internal friction angle (ϕ) play significant role. However, the effect of fibers in the peat soil must be taken into account. In this experimental study, it was found the fibers effect could increase the Q_{helix} by 30%. Therefore, the factor of 1.30 is used to satisfy this effect. By using the factors considered in the results of the study, the bearing capacity of the helix pile in the fibrous peat soil can be proposed as:

$$Q_c = 1.3.\ 0.5\pi D_a \gamma'^{\left(H_b{}^2 - H_t{}^2\right)K_s} tan\varphi\ + \left(\left(1 + (0.05(n-1))\gamma' H A_H N_q{}^*\right) + 0.5 P_s H_{eff}{}^2 \gamma' K_s tan\varphi \right. \tag{6}$$

$$N_q = \ e^{\pi \tan(0.4\varphi)} tan(45 + (0.4\varphi)/2)^2 \tag{7}$$

Table 5. Bearing capacity of the parts of the helix pile obtained from numerical model with back calculation analysis of experimental model.

Bearing Capacity	Experimental tested forces (kg)		
	Single helice	Double helices	Triple helices
$Q_{bearing}$	19.458	20.352	21.434
Q_{helix}	0	7.817	13.795
Q_{shaft}	1.480	1.654	2.49
Q_c	20.938	29.823	37.719

Table 6. Bearing capacity of the parts of the helix pile based on Mitsch and Clemence Equation (1985) with Nq based on Meyerhof & Adams (1968).

Bearing Capacity	Predicted forces (kg) based on Mitsch & Clemence (1985) and Nq on Meyerhof & Adams (1968)		
	Single helice	Double helices	Triple helices
$Q_{bearing}$	529.38	529.38	529.38
Q_{helix}	0	5.725	10.178
Q_{shaft}	1.450	1.453	2.584
Q_c	530.83	536.558	542.142
Comparison Q predicted/experimented	2535%	1799%	1437%

Table 7. Bearing capacity of the parts of the helix pile with the use of factors as shown in Eq. 6-7.

Parts of Helix Pile	Predicted Forces (kg) based on the use of factors in Eq. 6 – 7.		
	Single helice	Double helices	Triple helices
$Q_{bearing}$	19.625	20.606	21.588
Q_{helix}	0	7.445	13.231
Q_{shaft}	1.450	1.453	2.584
Q_c	21.075	29.504	37.403
Comparison Q predicted/experimented	100.6%	98.93%	99.16%

5 CONCLUSSIONS

A comprehensive investigation was conducted into the axial performance of the helix piles in the fibrous peat soil. The findings of the numerical model are in good agreement with the laboratory- scale load test results, yielding the following noteworthy conclusions:

- The load–displacement curves of the piles tested displayed typical trends, namely an initial linear segment, followed by a non-linear segment.
- Bearing capacity of the helix pile tested show different results, considerably influenced by helices number. The more helice attached to the pile, the higher bearing capacity would be. In this study, the bearing capacity of the helix piles for a displacement of 10% of diameter is 20 kg, 29 kg, and 34 kg for corresponding single, double, and triple helices attached to the piles.
- Numerical model with back-calculated parameter from the experimental tested, show that the bearing capacity from helices contributed major portion of the total bearing capacity of the helix pile, at around 60% - 70%, while the contribution of friction along the pile shaft is around 5% – 7%. The shear failure zone in between the helices contributes the rest, 23% - 35%.
- Due to the existence of large fiber in the fibrous peat soil, the bearing capacity of the helix pile must be corrected. In this way, the Nq values are determined based on 0.4 x ϕ, and shear failure resistance are factored by 1.30, and the effect of helices number on bearing is the increase of 5%. Therefore, new formula of predicted bearing capacity is proposed.

REFERENCES

Arsyad A dan Indra (2017), *Combined Helix Piles Raft Foundation for Supporting Road Construction Peat soil*.

Arsyad A A.B. Muhiddin, Sangle, P., Budianto, E., Firmansyah, A.B. (2018), *Performance of Helix Pile Raft Foundation in Tropical Fibrious Peat Soil Under Traffic Loads*.

Elsherbiny, M, & El Naggar, M. H. (2013), *Dynamic Response of Vertically Loaded Helical and Driven steel Piles*. Canadian Geotechnical Journal.

Fatnanta Ferry (2016) *Karakteristik Daya Dukung Lateral Pondasi Helical Pada Tanah Gambut"*. Jurnal Konferensi Nasional Teknik Sipil 11 Universitas Tarumanegara (in Bahasa Indonesia).

ISSMFE. 1985. Axial pile loading test – Part I: Static loading. Geotechnical Testing Journal, ASTM, 8 (2): 79–80.

Kazemian, S., Huat, B., Prasad, A. and Barghchi, M., (2011). "A State of Art Review of Peat: Geotechnical Engineering Perspective", International Journal of Physical Sciences, Vol. 6 (8),2011, pp. 1974–1981.

Livneh, B., & El Naggar, M. H. 2008. Axial testing and numerical modeling of square shaft helical piles under compressive and tensile loading. Canadian Geotechnical Journal, 45(8),1142–1155.

Mesri G., Ajlouni M. (2007). Engineering properties of fibrous peats. J. Geotech. Geoenv. Eng., 133(7): 851–866.

Meyerhof, G.G., and Adams, J.I. 1968. The ultimate uplift capacity of foundations. Canadian Geotechnical Journal, 5(4): 225–244. doi:10.1139/t68-024.

Mitsch, M.P., and Clemence, S.P. 1985. The uplift capacity of he- lix anchors in sand. In Proceedings of the Uplift Behavior of Anchor Foundations in Soil, Detroit, Mich., 24 October 1985 Edited by S. P. Clemence. American Society of Civil Engineers. pp. 26–47. Mohajerani, A., Bosnjak, D., Bromwich, D. (2016), Analysis and design methods of screw piles: A review, Soils and Foundations, Volume 56, Issue 1, Pages 115-128.

Parlan dkk (2016), *Pengaruh Jumlah Plat Helical Terhadap Daya Dukung Pondasi Tiang Helical Pada Tanah Gambut*. Jurnal Konferensi Nasional Teknik Sipil 11 Universitas Tarumanegara (in Bahasa Indonesia).

Smart Geotechnics for Smart Societies – Zhussupbekov, Sarsembayeva & Kaliakin (Eds)
© 2023 The Author(s), ISBN 978-1-003-29912-7
Open Access: www.taylorfrancis.com, CC BY-NC-ND 4.0 license

A limit equilibrium method for estimating pull-out resistance of flip-type ground anchors in sand grounds

S. Yoshida
Daisho Co., Ltd. Shiga, Japan

X. Xiong
Kanazawa University, Ishikawa, Japan

ABSTRACT: Flip-type ground anchors (hereinafter referred to as "flip anchors") are a kind of ground anchor that does not require grouting to obtain the pull-out resistance. The flip anchors are directly driven into the ground. When pull-out forces act on the anchors, their anchor heads rotate and open in the ground. Unlike ordinary pre-embedded plate anchors, there are few studies on flip anchors. To estimate the pull-out resistance of flip anchors in sand grounds, a calculation method based on 3D ground failure modes by limit equilibrium method is proposed. The calculated values of pull-out resistance agreed with the measured values from pull-out experiments using 5 sizes of actual flip anchors in full-scale model sand grounds.

1 INTRODUCTION

Flip anchors are kind of ground anchors that do not require grouting to obtain pull-out resistance. As shown in Figure 1, flip anchors are driven directly into the ground. After being driven to the designed depth, the anchor head rotates and opens when a tensile force acts on the anchor.

Although the flip anchors have convenient workability, estimating the pull-out resistance depending on ground conditions is more difficult compared to general pre-embedded plate anchors, due to their specific resistance mechanism. A number of previous research on pull-out capacity of the plate anchors were conducted so far, such as Baker & Kondner (1966) and Das & Seeley (1975); however, there are few studies on flip anchors (Niroumand & Kassim, 2013).

In this study, a calculation method of pull-out resistance of flip anchors in sandy ground is proposed. And the calculated values are compared with measured values of field experiments.

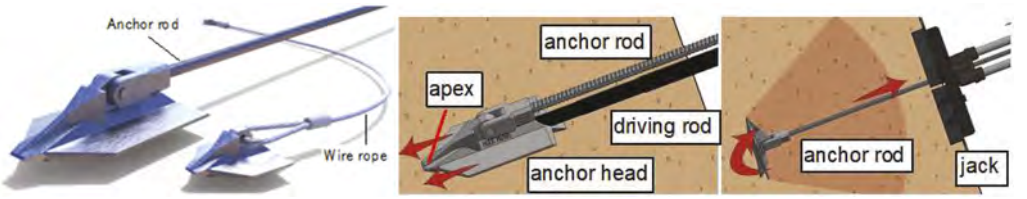

Figure 1. Flip anchors (percussion driven ground anchors).

DOI: 10.1201/9781003299127-150

2 FIELD PULL-OUT EXPERIMENTS OF FLIP ANCHORS EMBEDDED OR DRIVEN IN A SAND GROUND

2.1 *Experimental conditions*

A full-scale model sand ground was prepared in a test pit of 4.0 m in length, 4.0 m in width, and 2.5 m in height in a field. The internal friction angle ϕ' of the sand, which was measured by direct shear tests, was 42 degrees. The ground was compacted using a vibration tamper to have a relative density D_r of around 80% and a dry density ρ_d of around 1.745 t/m^3.

As shown in Figure 2, five sizes of actual flip anchors made of ductile iron were buried in the ground during ground preparation at designated embedment depth H under Opened or Closed head conditions. In driven installation condition, the anchors were driven into the ground from the ground surface. After that, each anchor was pulled out with a hydraulic jack, and pull-out force F and pull-out displacement w were measured.

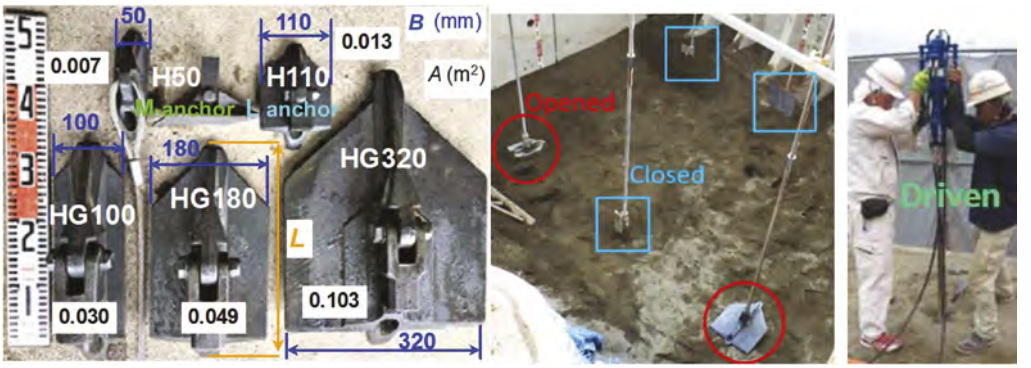

Figure 2. Actual flip anchors and installation conditions in the field pull-out experiment.

2.2 *Experimental results*

Maximum pull-out resistance F_{max} of flip anchors increased as the projected area of the anchors A increased, which will be shown in Section 3 in detail. F_{max} of Driven anchors were equivalent to F_{max} of Closed anchors. F_{max} of Driven anchors, which is corresponding to the practical installation condition of flip anchors, reached about 80% of F_{max} of horizontally embedded plate anchors (Opened anchors). From the results of the field experiment, pull-out displacement w required for the flip anchors to open sufficiently in the dense sand could be the same amount as the length of an anchor plate L or about 1.5 times L.

3 CALCULATION METHODS FOR MAXIMUM PULL-OUT RESISTANCE OF FLIP ANCHORS BY LEM

3.1 *Three-dimensional ground failure model*

Pull-out resistance of pre-embedded plate anchors have been estimated based on the ground failure models (Balla 1961, Majer 1955, Mors 1959). As shown in Figure 3(a), the ground failure models need to be divided into "Shallow anchor" model or "Deep anchor" model according to the embedment ratio H/L (H = embedment depth of anchor head, L = length of anchor plate). It is because the slip lines extend from edges of an anchor plate do not reach the ground surface when the anchor is installed deeper than the critical embedment ratio $(H/L)_{cr}$. If H/L is smaller than the $(H/L)_{cr}$, the failure pattern appears as a "Shallow

anchor" model, and if H/L is equal or greater than $(H/L)_{cr}$, the pattern appears as a "Deep anchor" model.

In this study, to estimate F_{max} of flip anchors, three-dimensional ground failure models are proposed. In Figures 3(b), (c) and 4, γ is the unit weight of the soil, W_r is the weight of the rectangular soil mass, W_{t1} is the weight of the triangular soil mass having a length of L, W_{t2} is the weight of the triangular soil mass having a length of B_c, W_p is the weight of the triangular soil mass at four corners, θ is the angle of slip line from the vertical direction, N is the normal force acting on a failure plane, S_{t1} is the shear force acting along failure plane having a length of L, S_{t2} is the shear force acting along failure plane having a length of B_c, S_p is the shear force acting along failure plane at four corners, σ_n is effective normal stress on a failure plane, $(1 + K_0)\ \sigma_v/2 + (1 - K_0)(\sigma_v/2)\cos 2\omega$, ω is the angle of slip line from the horizontal direction, σ_v is effective vertical earth pressure, K_0 is coefficient of lateral earth pressure at rest. For the calculation, because the flip anchor has a unique shape, the shape is approximated to a rectangle having the same A by adjusting the width of an anchor B as B_c.

F_{max} of flip anchors largely affected by θ. And $(H/L)_{cr}$ needs to be determined to choose the suitable model for calculation. In practice θ can be regarded as a function of the internal friction angle of soil ϕ. According to Meyerhof and Adams (1968), θ ranges from $1/3\phi'$ to $2/3\phi'$. As in Table 1, $(H/L)_{cr}$ also can be set in relation to ϕ'

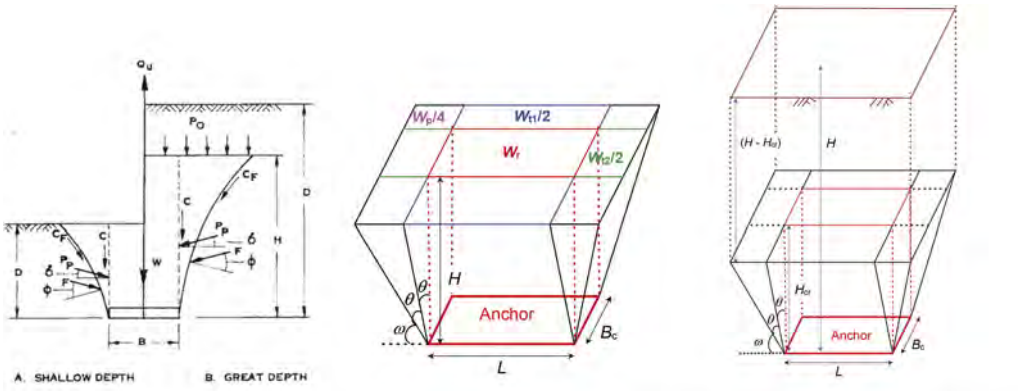

(a) 2D model (Mayerhof & Adams, 1968) (b) 3D Shallow anchor model (c) 3D Deep anchor model

Figure 3. Two-dimensional (a) and Three-dimensional (b & c) ground failure models above a flip (plate) anchor under uplift load.

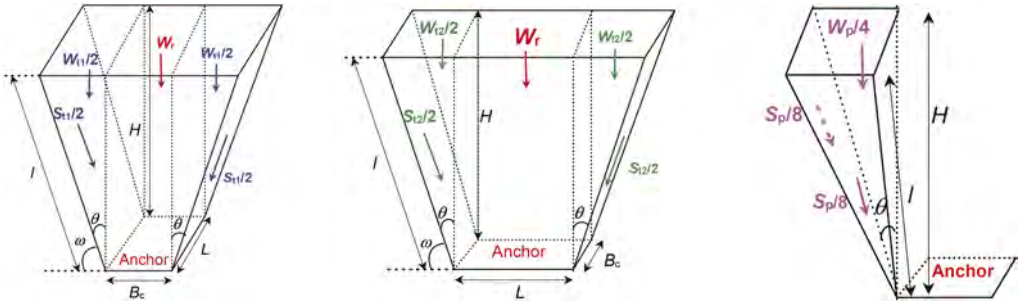

Figure 4. Three-dimensional ground failure models divided into several components for calculation.

Table 1. $(H/L)_{cr}$ depending on ϕ (Meyerhof & Adams, 1968).

ϕ	20°	25°	30°	35°	40°	45°	48°
$(H/L)_{cr}$	2.5	3	4	5	7	9	11

3.2 *Calculation of F_{max} of flip anchors from the 3D ground failure models*

Once θ and $(H/L)_{cr}$ are set, the shape of the 3D ground failure model (Figure 4) is fixed. Now F_{max} of flip anchors can be calculated based on the model. For "shallow anchor", F_{max} of shallow anchors $F_{max(s)}$ can be calculated by Equation 1.

$$F_{max(s)} = \left(W_r + W_{t1} + W_{t2} + W_p\right) + \left(S_{t1}\cos\theta + S_{t2}\cos\theta + S_p\cos\theta\right) \quad (1)$$

For "deep anchor", F_{max} of deep anchor $F_{max(d)}$ can be estimated by Equation 2. $F_{max(d)}$ increases linearly in proportion to the increase of $(H - H_{cr})$.

$$F_{max(d)} = F_{ax(s)} + \left[\{L + 2(H_{cr}\tan\theta)\}\{B + 2(H_{cr}\tan\theta)\}\left(H - H_{cr}\right)\right] \times \gamma \quad (2)$$

where H_{cr} is a critical H at $(H/L)_{cr}$.

Figure 5(a) shows calculated F_{max} based on the 3D models ($\theta = \phi'/2$) vs. measured F_{max} of actual flip anchors (Section 2). The calculated values agreed with measured values. The difference between calculated F_{max} of anchors having same L but different B, is more apparent when θ is larger than $\phi'/2$, such as $\theta = 2/3\phi'$. As shown in Figure 5(b), H for flip anchors should be the depth from the anchor tail to the ground surface after being driven. It is because flip anchors need w at least equivalent to the L to open sufficiently to meet the same installation condition as pre-embedded plate anchors.

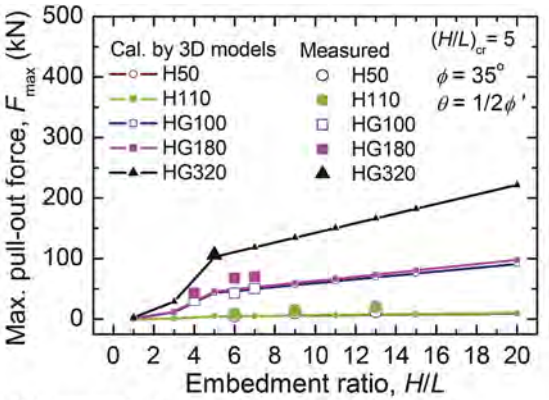

(a) Measured F_{max} vs. calculated F_{max}

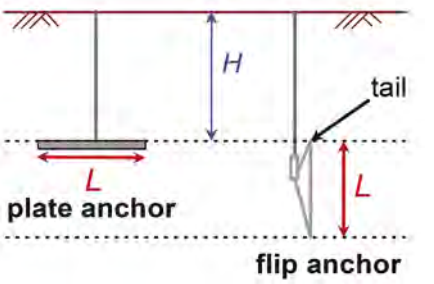

(b) Difference in H between plate anchor and flip anchor in calculation

Figure 5. F_{max} vs. H/L.

4 CONCLUSIONS

In this study, a calculation method of pull-out resistance of flip anchors in sandy ground was proposed. And the calculated values were compared with measured values of field experiments.

Main conclusions in the paper are as follows:

1) F_{max} of flip anchors need to be calculated separately based on "Shallow anchor" model or "Deep anchor" model according to H/L.

2) F_{max} of flip anchors at $(H/L) < (H/L)_{cr}$ increases exponentially; whereas at $(H/L)_{cr} \leq (H/L)$, F_{max} increases linearly.
3) $(H/L)_{cr}$ and θ can be determined according to the empirical values of Meyerhof and Adams (1968).
4) F_{max} of flip anchors can be calculated based on ground failure models similarly to ordinary embedded plate anchors if w until the anchor head sufficiently opens (= L or 1.5 times of L) is taken into consideration besides H.

REFERENCES

Anchoring Rope and Rigging Pty. Ltd. 2022. https://www.arandr.com.au.

Baker, W.H. & Kondner R.L. 1966. Pullout load capacity of a circular earth anchor buried in sand. *Highway Research Record* 108: 1–10.

Balla, A. 1961. The resistance to breaking-out of mushroom foundations for pylons. *Proceedings of the 5th international conference on Soil Mechanics and Foundation Engineering*, 1: 569–576.

Das, B. M. & Seeley, G. R. 1975. Breakout resistance of shallow horizontal anchors. *Journal of the Geotechnical Engineering Division* 101(9): 999–1003.

Majer, J. 1955. Zur berechnung von zugfundamenten. *Osterreichister Bauzeitschift* 10(5): 85–90.

Meyerhof, G.G. & Adams J.I. 1968. The ultimate uplift capacity of foundations. *Canadian Geotechnical Journal* 5(4): 225–244.

Mors, H. 1959. Das Verhalten von Mastgruendungen bei Zugbeanspruchung. *Bautechnik* 39(10): 367–378.

Niroumand, H. & Kassim, K.A. 2013. Pullout capacity of irregular shape anchor in sand. *Measurement* 46(10): 3876–3882.

Smart Geotechnics for Smart Societies – Zhussupbekov, Sarsembayeva & Kaliakin (Eds)
© 2023 The Author(s), ISBN 978-1-003-29912-7
Open Access: www.taylorfrancis.com, CC BY-NC-ND 4.0 license

Application of Sentinel-1 radar image's surface displacement information to the production and transportation of slope debris

K.-L. Wang
Civil Engineering, National Chi Nan University, Taiwan

J.-T. Lin
RST Inc. Taiwan

Y.-H. Lee
Civil Engineering, National Chi Nan University, Taiwan

ABSTRACT: This study uses remote sensing technology and data sharing. It tries to establish the analysis model of slope displacement data, evaluate slope debris production, and multi-sequence debris migration and transition analysis using synthetic aperture radar and other sensing technics. To build a database, this study collects multi-phase SAR images, LiDAR, and aerial photography DEM data. UAV aerial photography modeling is used to collect recent research data. This study uses the SAR intensity interpretation method to analyze the collapse range. Compare the difference with satellite collapse interpretation. Good interpretation results are obtained in both ALOS and Sentinel-1 satellite images. In the analysis of slope displacement information, use 7 DSM, DEM, and 26 satellite images to organize the recent changes in the study area. Combined with SBASInSAR, the slip rate analysis was performed to evaluate the extent of the potential landslide area. Finally, the mechanical model was used to infer the potential slip depth and volume, and the potential of the upstream collapse area was calculated. The sliding volume is about 11 million cubic meters. It is reasonable and feasible to verify the results of DSM analysis as an evaluation method for soil sand production.

1 INTRODUCTION

In Taiwan, the geological phenomenon of broken terrain, high mountains, high currents, and short streams is caused by the extrusion of plates. The geographical location is vulnerable to typhoons and heavy rain. The current trend of climate change has resulted in frequent and more serious sloping land disasters in recent years. Although the sloping land disaster has a wide range of influence and high frequency, it is the most difficult to predict its occurrence and impact. In recent years, due to the advancement of telemetry technology, the above difficulties have the opportunity to be solved. Because telemetry can perform continuous slope monitoring more quickly and at a lower cost, it can help to detect potential hazards earlier.

Slope disasters will bring a lot of soil and sand accumulation to the river. The migration of soil and sand also causes changes in the river course and causes subsequent secondary disasters. Assessing soil and sand volume for sloping land hazards is an important topic before subsequent analysis. Accurate numerical terrain can be obtained by using aerial photography or lidar measurement, but it requires manpower, is limited by weather, and the frequency of data acquisition is also limited. In this study, differential interferometric synthetic aperture radar (DInSAR) is used as a telemetry tool for volume analysis. Synthetic Aperture Radar (SAR) has the advantages of being free from weather interference, large area, and fixed period. SAR

DOI: 10.1201/9781003299127-151

can record information including intensity, polarization, phase, etc. DInSAR technology analyzes the image phase difference of the two repeated orbits and restores it to the surface deformation. Under good conditions, millimeter-level deformation accuracy can be obtained.

This research proposes a plan to establish DInSAR technology to establish an evaluation process for the sloping land disaster areas in Kaohsiung Baolai. Multi-time series collapse volume analysis is carried out, and the failure mechanism of slope sliding is discussed with the slip situation of each time series. Use the high-precision numerical terrain produced by LiDAR and UAV to verify the collapse volume and range. Confirm the accuracy of this assessment, to establish a complete and rapid assessment method of collapse volume.

2 METHODOLOGY

In this study, the NDSI analysis was used to establish a rapid collapse range detection technology, and the collapse range was judged by combining the existing satellites to complete the verification of the analysis results. The NDSI analysis process needs to perform multi-view averaging on the two images and then combine the images. Filtering to remove noise, followed by geographic coordinate projection and radiometric correction to normalize the image. The backscatter normalization index (NDSI) was calculated from the two processed images. Set the NDSI threshold and deduct the more severely affected areas of the terrain effect. To extract the results of mountain changes, it is necessary to set a slope threshold value to remove non-slope areas. The resulting image after completion merges adjacent images into one block.

The NDSI analysis is somewhat noisy due to the characteristics of aboveground vegetation. Filter out using area threshold. Depending on the satellite resolution used, noise filtering needs to be performed. For the ALOS1, ALOS2, and Sentinel satellites used in this study, different filtering thresholds need to be established. Initially, 4 x 4 pixels are used as the minimum filtering standard, and the optimal threshold value is gradually found. Past studies have shown that more than 73% of the collapse range interpreted by ALOS1 SAR can be successfully matched to the real collapse area (Wang et al. 2019).

The preliminarily calculated surface deformation is the surface change (Line of Sight, LOS) in the observation direction, and is projected into the vertical component, which is used as the slip reference. If the brushing depth or sliding phenomenon occurs in the sliding area, theoretically, the vertical change amount will change significantly. By accumulating the analysis results of multiple periods, the sliding volume in the collapsed area can be counted. Regress the

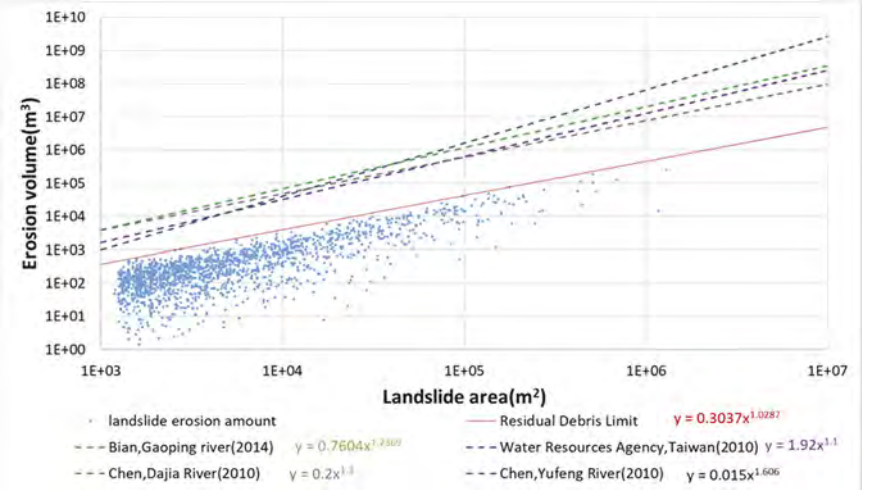

Figure 1. Analysis of residual debris outflow (Wang et al., 2019).

relationship between the collapse area and the volume. Previous studies have shown that the upper limit of the residual volume outflow from the collapse in the Anongxi area is $V= 0.3037A^{1.0287}$ (V is the lost volume and A is the landslide area) (Figure 1, Wang et al., 2019).

3 PROCEDURES AND RESULTS

(1) Analysis of NDSI landslide scope detection and interpretation scope
This study cites the NDSI suggested range of $-1<NDSI<\mu-1.75\sigma$ proposed by Wang et al. (2019). where μ represents the overall image mean and σ represents the image standard deviation. Using this value range, the areas with obvious changes in the NDSI image can be analyzed, and the NDSI values of each period can be separated in this way. After taking it out, the collapse position was compared with the SPOT5 satellite image, and the result is shown in Figure 2. The figure shows the panchromatic images of each SPOT5 satellite before and after each event, and the SPOT5 satellite false-color image of the year that overlaps the NDSI interpretation results. The NDSI interpretation results in each event are quite consistent with the landslide position of the optical image interpretation. The optical image was compared with the NDSI interpretation pixel set to 10m resolution, and the classification results of the statistical classification pixels were removed after the pixels affected by the terrain effect were removed. In the classification results from 2007/8/18 to 2007/10/3, the accuracy rate of pixel interpretation as landslide is 21%, the overall interpretation accuracy rate is 88.7%, and the kappa value is 15.2%. In the classification results from 2008/7/5 to 2008/8/20, the accuracy rate of pixel interpretation as landslide is 38.2%, the overall interpretation accuracy rate is 91.4%, and the kappa value is 21.9%. In

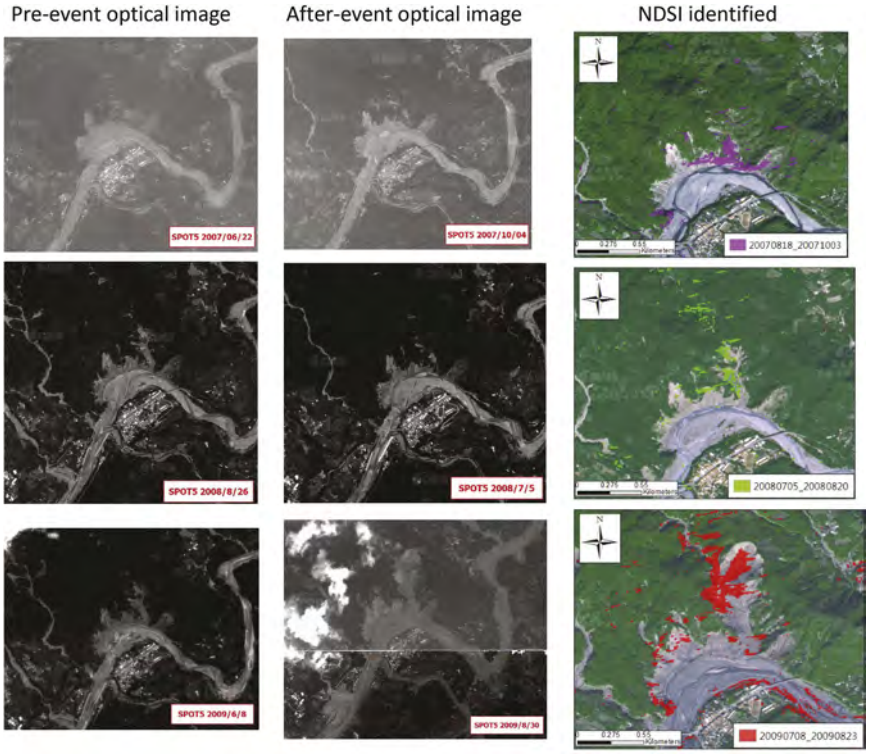

Figure 2. Comparison of NDSI and SPOT5 optical satellites.

the classification results from 2009/7/8 to 2009/8/23, the accuracy rate of pixel interpretation as landslide is 52.4%, the overall interpretation accuracy rate is 84.73%, and the kappa value is 33%. Although the NDSI technology of SAR is not as accurate in interpreting the collapse range as the optical image is. There is still enough reference for judging the area where the collapse occurred, and it is not limited by weather. Application during a disaster can provide another benchmark for quick judgment.

The results of the four main event analyses are overlaid on the orthophoto in 2017, and the results are shown in Figure 3. The brown area in the picture is the collapse catalog in 2007. Since August 2007, the collapsed area has further expanded and has been developing upward year by year. This trend is also clearly shown in the previous NDSI judgment results, ranging from purple (2007/8/18~2007/10/03), green (2008/7/5~2008/8/20), blue (2008/8/20~2009/7/8), red (2009/7/8~2009/8/23), representing 4 events respectively. The most impactful event was the Morakot cyclone in 2009. From the figure, it can be found that the collapse range determined by each event is quite consistent with the final collapse range after fitting.

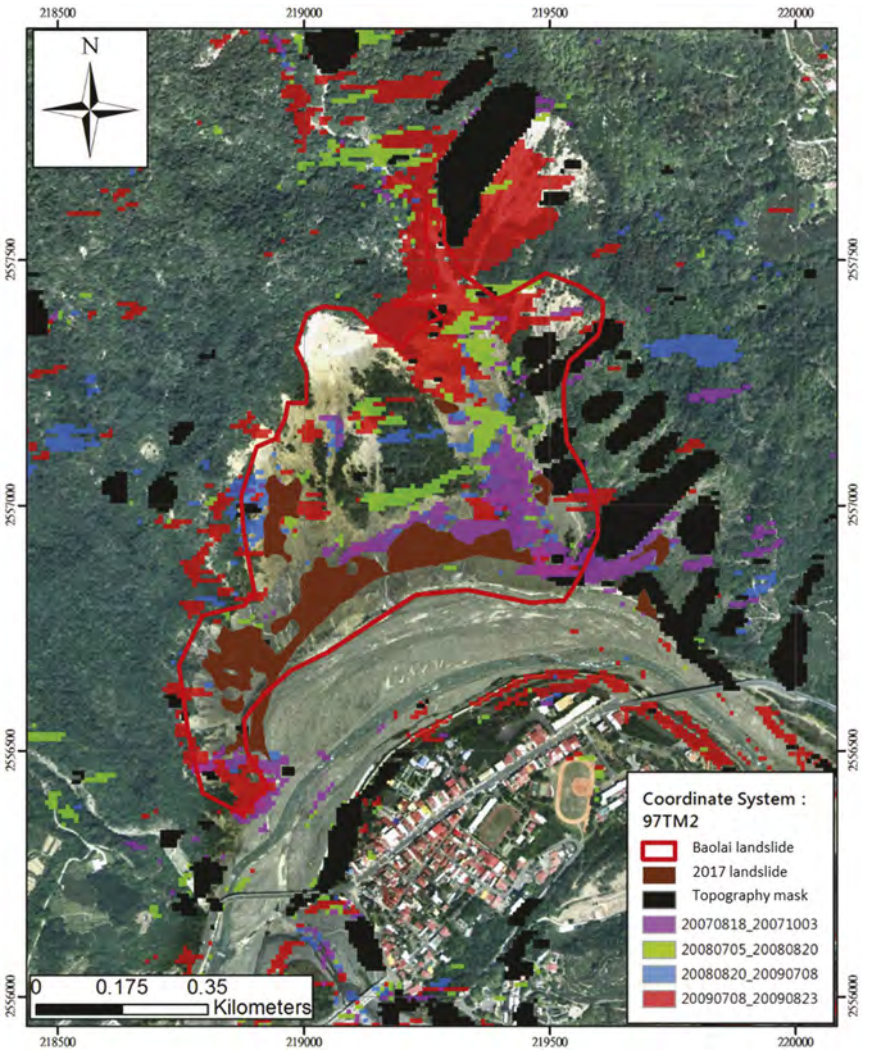

Figure 3. ALOS1 NDSI nesting results for each event from 2007 to 2009.

(2) Landslide slip volume analysis

The landslide area of Baolai is different due to the different product ranges of satellite data. Therefore, it is divided into two periods. In the early period of 2006/12/31~2011/02/26, ALOS1 SAR was used. Sentinel-1 SAR was used from 2016/12/22 to 2020/06/28. After analyzing the displacement of the collapsed land in each period with SBASInSAR technology, the total change is counted.

Changes from satellite imagery are shown in Figure 4. The collapsed site of Baolai began to develop in 2005, expanded significantly in 2006, and further developed in 2009 due to the impact of the Morakot typhoon. In 2017, it collapsed and extended upwards. Therefore, it is speculated that the potential collapse range will continue to the ridgeline. The potential range of the main collapse area with the red dotted line circled in the 2011 LiDAR scan image. In this study, the collapse volume statistics were carried out in this potential range.

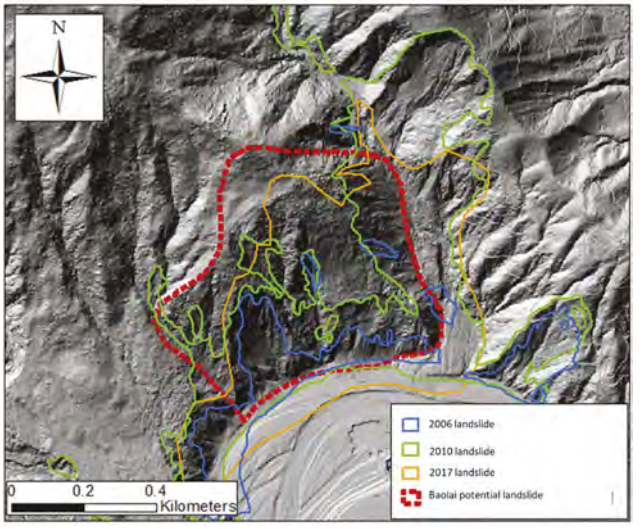

Figure 4. The evolution of the landslide and statistical area.

Twenty ALOS-1 SAR images and 103 sentinel-1 SAR images were collected in this study. After the SBAS point cloud is generated through the SBASInSAR process. The average change of the point cloud in each period in the statistical range is multiplied by the area. Statistics of the collapse volume in each period.

The point clouds of the two periods are calculated after the amount of change in each period. Figure 5 shows the cumulative change in the slope potential area between time series. Figure 5 shows the cumulative changes in the ALOS-1 analysis from 2006 to 2011. From 2006/12/31 to 2007/08/18, the volume change showed an upward trend. It is speculated that the reason may be the accumulation caused by some of the potential sliding ranges located on the edge of the channel. At the same time, after the slope instability before 2006, the phenomenon of sagging and other phenomena began to appear near the sloping site. After that, the slope began to slide continuously until the statistical sliding amount reached -7803 cubic meters on February 26, 2011. The statistical period includes three rainfall events marked by red arrows, including the 2009 Morakot cyclone. There should be a large amount of soil and sand flowing out, but because the sliding body has exceeded the L-band detection range. After the phase saturation is reached, the phase cannot be recovered correctly, and it will become a source of errors in the volume statistics in the analysis.

Figure 5. Cumulative slope deformation volume of each time series analyzed by ALOS-1 SBASInSAR.

During the period from 2016/12/22 to 2020/06/28, 103 sentinel-1SAR images were used to analyze the cumulative change of the slope. The Sentinel-1 satellite has a revisit period of 6 to 12 days, and a shorter time baseline for the analysis can reduce missing correlations. But it uses the shorter wavelength of the C-band, so it is easier to achieve phase saturation.

At the beginning of 2016, there was a clear sliding trend in the collapse of Baolai. Because it is located on the attacked bank of the river, the foot of the slope continues to be washed away, and the scope of the collapse continues to expand to the upper layer. Two rainfall events in 2017 and 2018 are included in Figure 6. From the statistical results, when a large rainfall event (red arrow) triggers the collapse, the speed of the slope slide over a while also increases. stabilized after a while. Statistics up to 2020/6/28, the cumulative slippage is -44635 cubic meters.

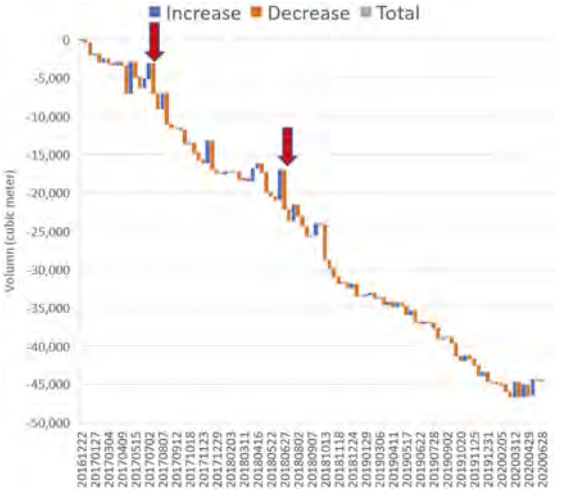

Figure 6. Cumulative slope deformation volume of each time series in Sentinel-1 SBASInSAR analysis.

(3) Landslide Potential Scope Assessment

Combined with the interpretation of lidar images, the results of radar satellite collapse interpretation, and the surface change rate analyzed by SBASInSAR, etc. The collapsed cliff blocks of the Baolai Collapsing Land can be divided into 6 blocks (as shown in Figure 7), of which block 1 has been destabilized in 2005. The destruction of Block 1 in 2008 was further expanded. Block 2 starts to run off at the foot of the slope. The extent of

its damage can be seen in NDSI's analysis. In the analysis of SBASInSAR, it can also be observed that block 4 begins to accumulate deformation. Then in blocks 2, 3, and 4, the destruction begins after the Morakot storm. The NDSI analysis is consistent with the extent of the damage. Blocks 2, 3, and 4 began to destroy and expand in 2015 and developed into the existing collapse area in 2018.

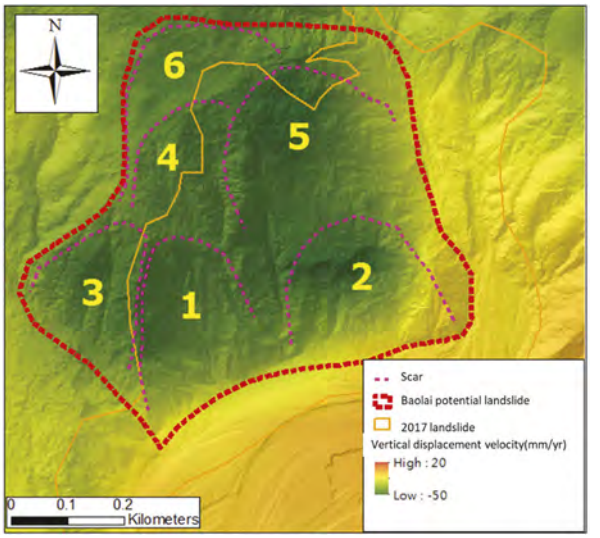

Figure 7. The sliding block inferred by the collapse of Baolai.

4 CONCLUSIONS

This study completed the applicability of DInSAR analysis technology and screened the available analysis interval. Subsequent DInSAR analysis will be performed based on the applicable results, as well as the sliding range and sliding volume. The analysis results of the collapse range were completed by NDSI technology and compared with the optical image interpretation range of each event. The feasibility of this technique for the detection of collapse range is confirmed. Then, according to the analysis results of different bands, suggested analysis parameters are proposed, and a complete collapse range detection technology is established.

In the second stage, the DInSAR technology combined with the numerical analysis mode is used to complete the volume analysis of the previous collapses. Based on the ALOS-1 and Sentinel-1 satellite data, the slope slip statistics in the two periods of 2006-2011 and 2016-2020 were carried out respectively. The potential slips of -7803 and -44635 cubic meters were calculated respectively.

In the third stage, this study combines DInSAR and NDSI analysis techniques to discuss the correlation between collapse and surface deformation between time series.

REFERENCES

Wang, K.-L., Lin, J.-T., Zhang, J.-W., Lin, Y.-H., Hung, J.-S., Hung, J.-Y., Ciou, C.-F., Fu, K.-L. (2019), "A Debris Estimation Method Combining High Accuracy UAV, DInSAR and NDSI Analysis", Journal of Taiwan Agricultural Engineering, 65(4), p 26–39.

Smart Geotechnics for Smart Societies – Zhussupbekov, Sarsembayeva & Kaliakin (Eds)
© 2023 The Author(s), ISBN 978-1-003-29912-7
Open Access: www.taylorfrancis.com, CC BY-NC-ND 4.0 license

Groundwater table of slopes with horizontal drains and effect of pipe inclination

S.O.A.D.Mihira Lakruwan, Akiyoshi Kamura & Motoki Kazama
Tohoku University, Sendai, Miyagi, Japan

ABSTRACT: The complex three-dimensional (3D) geometry of the groundwater table (GWT) profile of a slope with horizontal drains (HDs) demands complex 3D numerical simulations to capture the complete effect of HDs on slope stability enhancement. Alternatively, a novel semi-empirical method is proposed in this study to obtain the steady state GWT profile of a slope with HDs subjected to constant recharge from the top. As HD pipes are generally installed with an inclination to facilitate drain out under gravity, the proposed method was subsequently extended for inclined HDs and verified by a numerical case study. Although a high pipe inclination is favorable for rapid discharge of water, that will reduce the slope stability enhancement. The results of this study showed that the inclination of the HDs should be kept minimum, especially in the presence of slip surfaces with mild inclinations.

1 INTRODUCTION

1.1 *HDs for slope stabilization*

The rise of the GWT can be identified as one of the major causes of slope instabilities in the world. Rainwater infiltration is the main source of the GWT rise. The rise of the GWT increases the porewater pressure (PWP) of a slope reducing the effective stress and finally resulting in a reduction of shear strength and slope stability. Therefore, lowering the GWT is the primary slope stability enhancement method for such slope instabilities. The HDs, which are perforated pipes wrapped with geotextile envelopes, are used as an efficient method for GWT lowering.

1.2 *GWT of a slope with HDs*

The steady state GWT between the HDs takes a semi-elliptical shape (Figure 1b). As the HDs were initially being used in the agricultural lands, the deterministic methods of obtaining GWT of HDs are developed focused on agricultural drains. Those methods assume long, parallel, and horizontally installed HD pipes, which results in uniform distribution of the GWT along the HD pipes. Therefore, a two-dimensional (2D) semi-elliptical distribution of GWT between HD pipes was considered. Among several such methods (Hooghoudt 1940, Ernst 1954, Kirkham 1958), Hooghoudt (1940) method is widely used.

However, unlike in agricultural lands, HDs in slope stabilizations are short in length and installed with an inclination to facilitate water discharge under gravity. Therefore, GWT between HDs varies along the pipe and takes complex 3D geometry. Although some have suggested using the Hooghoudt (1940) method (Greg et al 2013), its applicability for HDs in slopes is limited. Moreover, the GWT behind the HD field, which is critically important in slopes, is not considered in the above methods. Therefore, Crenshaw & Santi (2004) proposed an empirical method to obtain the GWT of short HDs in slopes (Cook et al 2012). However, this method also has several limitations such as the requirement of GWT height at 20ft (6.1 m) behind the HD field and does not sufficiently describe the GWT behind the HDs. Also, the inclination of HDs is not considered.

DOI: 10.1201/9781003299127-152

1.3 *Objective and methodology*

To address the mentioned knowledge gap, the objectives of this study were established as follows;

- To develop a semi-empirical method to determine the steady state GWT profile of a slope, which is subjected to contact recharge from the top, with short and inclined HDs.
- To evaluate the effect of the pipe inclination based on the porewater force (PWF) on the slip surface.

A series of finite element (FE) flow analyses was performed to develop the novel semi-empirical method. Then the PWF acting on a predefined slip surface was calculated by linear integration between the GWT and slip surface profiles and subsequently evaluated the HD inclination effect.

2 NOVEL METHOD TO OBTAIN GWT OF A SLOPE WITH HDS

2.1 *Semi-empirical method to obtain GWT of HDs*

A typical steady-state GWT profile at the mid-section between parallel HDs obtained from a series of PLAXIS 3D (CONNECT Edition V20) (PLAXIS 2020) FE flow analysis is presented in Figure 1a. The GWT was arbitrarily divided into three zones. Then, empirical relationships were established to the GWT heights at the boundaries between Zone 1 & 2 (h_c) and Zone 2 & 3 (h_e) (Figure 1a). Linear distributions were established for the GWT in Zone 1 and 2. The GWT of Zone 3 was established based on Dracy's law and Dupuit-Forchheimer assumption. This profile is the maximum GWT at the mid-section between the HDs. Finally, an average GWT profile (Figure 1b) was established for the semi-elliptical distribution between HDs as,

$$Z_w = \begin{cases} \frac{\pi}{4}\frac{h_c}{L-S}X + D; & if\ X \le L - S\ (Zone\ 1) \\ \frac{\pi}{4}\frac{h_e - h_c}{S}(X - L + S) + h_c + D; & if\ L - S \le X \le L\ (Zone\ 2) \\ H_e^2 + \left[\frac{H_i^2 - H_e^2}{(B-L)} + n(B-L)\right](X-L) - n(X-L)^2; & if\ L \le X\ (Zone\ 3) \end{cases} \quad (1)$$

where Z_w= average GWT; $H_c = h_c + D$; $H_e = h_e + D$; and other parameters as in Figure 1a.

Figure 2 Presents the corrections introduced for the inclined HDs. First, the value of the h_i at the head at the back of the slope is to be corrected with reference to the elevations of the HD at the boundary of Zone 1 and 2, and HDs end. Then the corrected GWT heights are to be obtained from the empirical relationships presented in Figure 1a and pipe elevation is added (Figure 2).

2.2 *Verification of the proposed method*

A numerical case study was performed on the slope section shown in Figure 3 to validate the proposed method. The GWTs at the mid-section between the HDs, with different lengths and inclinations, obtained from the FE flow analysis and the proposed method are compared in Figure 3. The compatibility of the GWTs verifies the accuracy of the proposed method to obtain GWT.

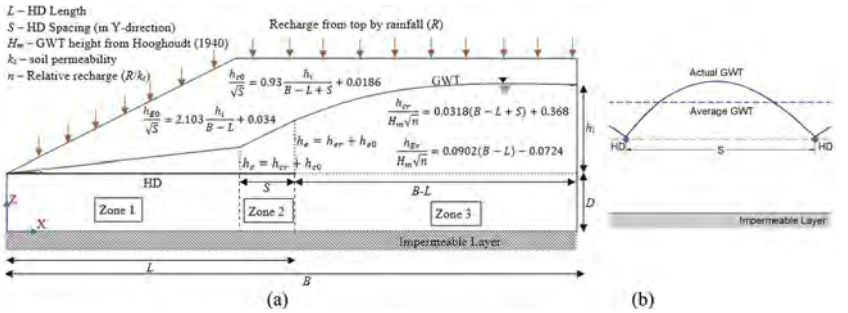

Figure 1. GWT of a slope with HDs; (a) along the HDs; and (b) between HDs (cross-section).

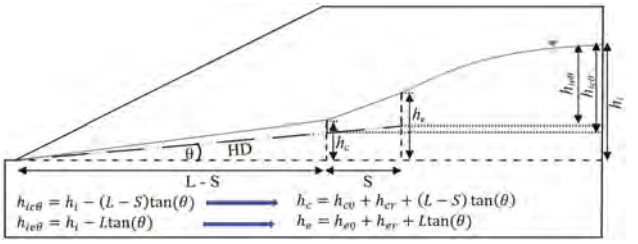

Figure 2. Correction for inclined HDs.

3 EFFECT OF DRAIN INCLINATION ON THE PWF ON SLIP SURFACE

3.1 *Obtaining PWF on predefined slip surface*

As suggested in several studies (Conte & Troncone 2012, Conte & Troncone 2018, and Tsao et al. 2005), the effectiveness of HDs on slope stability enhancement can be evaluated using the PWF acting on a slip surface. Therefore, the PWF acting on a predefined slip surface was obtained by linear integration between the GWT profile (Zw) and slip surface profile (Zs) (Figure 4) as,

$$PWF = \int_0^{X_0} (Z_w - Z_s)(\rho_w g)(sec\alpha)dX \tag{2}$$

3.2 *Effect of HD inclination*

The design parameters of HDs (length, spacing, elevation, and inclination) can be evaluated by the PWF acting on the slip surface. However, this study is limited to the evaluation of HD inclination. Figure 5a presents the variation of PWF acting on the slip surface with inclinations (α) of 10°, 15°, 20°, 25°, 30°, and 35° for HD inclinations (θ) from 0 to 10° (for c = 6m, d = 4m, h_i = 6m, and n = 0.1 (refer to Figures 1 and 4 for notations of the parameters)).

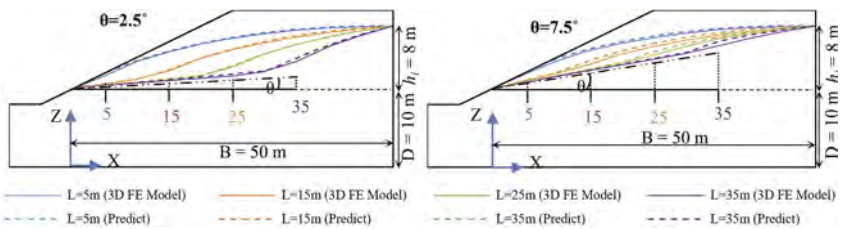

Figure 3. Comparison of GWTs at mid-section between HDs from the proposed method and 3D FE model.

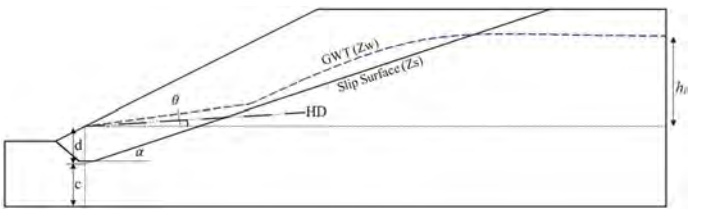

Figure 4. Predefined slip surface and GWT.

The PWF generally increases with the increment of the θ. The PWF increment is significant in small α values but not in higher α values. The variation of the PWF value with $\alpha - \theta$ illustrated in

Figure 5b confirms that. Therefore, it is important to use small inclinations in HDs to ensure low PWF on a slip surface, particularly in small α values. However, the HD pipe should be inclined enough to ensure water drain out under gravity. Therefore, a tradeoff exists in the selection of the drain inclination. The inclination of the HDs can be limited to 5° to 10° as suggested in previous studies (Cook et al. 2012) and should not use higher inclinations, particularly in mild slip surface angles (α) unless there is a special requirement.

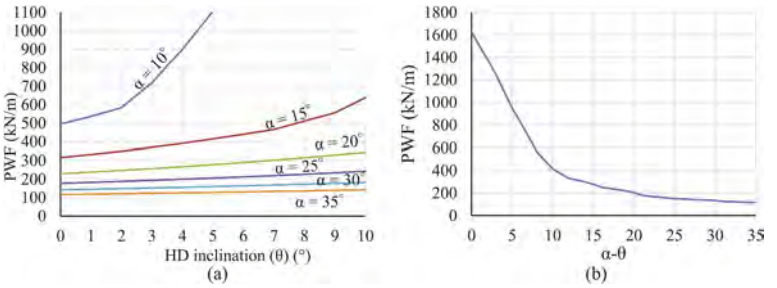

Figure 5. (a) Increment of PWF with θ; (b) Reduction of PWF with α-θ.

4 CONCLUSIONS

A novel semi empirical method was introduced in this study to obtain a steady-state average GWT profile for a slope with HDs. The proposed method was verified by a numerical case study. Subsequently, it was extended to obtain the PWF acting on a predefined slip surface, and an evaluation of design parameters can be done based on that. This study is focused on evaluation of HD inclination and the results showed that the HDs inclination should be minimum to ensure low PWF on a slip surface, particularly in small α values.

REFERENCES

Conte, E. & Troncone, A. 2012. Stability analysis of infinite clayey slopes subjected to pore pressure changes. Géotechnique, 62(1), pp. 87–91.

Conte, E. & Troncone, A. 2018. A performance-based method for the design of drainage trenches used to stabilize slopes. Engineering Geology, Volume 239, pp. 158–166.

Cook, D. I., Santi, P. M., & Higgins, J. D. 2012. Prediction of piezometric surfaces and drain spacing for horizontal drain design. Landslides, 9(4), pp. 547–556.

Crenshaw, B. A. & Santi, P. M. 2004. Water table profiles in the vicinity of horizontal drains. Environmental Engineering Geoscience, 10(3), pp. 191–201.

Ernst, L. 1954. Het berekenen van stationaries groundwater storming walked in verticals flak afgebeeld kunen worden (The computation of steady state groundwater flows, which can be projected in the vertical plane). Groningen, Netherlands: Institute of T.N.O.

Greg, M. P., Rosemary, W. H., Carroll, Donald, M. R., Rishi, P., Balasingam, M., Sutharsan, T., Tom, B., Steve, L., and Kim, A. W. 2013. Design guidelines for horizontal drains used for slope stabilization, Washington: Washington State Department of Transportation.

Hooghoudt, S. 1940. Bjidrage tot de kennis van enige natuurkundige grootheden van der grond. Verslag bouwk Onderzoek, pp. 515–707.

Kirkham, D. 1958. Seepage of steady rainfall through soil into drains. Transactions American Geophysical Union, 39(5), pp. 892–908.

PLAXIS, 2020. PLAXIS 3D Reference Manual CONNECT Edition V20, Bentley.

Tsao, T. M., Wang, M. K., Chen, M. C., Takeuchi, Y., Matsuura, S., and Ochiai, H. et al. 2005. A case study of the pore water pressure fluctuation on the slip surface using horizontal borehole works on drainage well. Engineering Geology, 78(1), pp.105–118.

Smart Geotechnics for Smart Societies – Zhussupbekov, Sarsembayeva & Kaliakin (Eds)
© 2023 The Author(s), ISBN 978-1-003-29912-7
Open Access: www.taylorfrancis.com, CC BY-NC-ND 4.0 license

Numerical analysis on failure mechanism of unsaturated slope due to rain

T. Yoshikawa & T. Noda
Nagoya University, Nagoya, Japan

ABSTRACT: Slope failures have occurred frequently due to heavy rains. Causes of the failures are considered as reduction of strength due to rise in pore pressure and increase in the degree of saturation, and increase of self-weight due to water absorption. However, the detailed failure mechanism has not been elucidated. To elucidate the mechanism, this study conducted deformation and failure simulations of unsaturated slopes in rainfall model tests using a soil-water-air coupled elastoplastic finite deformation analysis code considering inertia force. As a result, we succeed in reproducing the deformation-to-failure behavior of the model slope due to rainfall infiltration. The soil element on the slip surface exhibits "softening behavior with plastic volume expansion" above the critical state line in $p' - q$ skeleton stress space. In addition, we reproduce deformation and failure patterns according to rainfall intensity.

1 INTRODUCTION

In recent years, rainfall-induced slope failures have occurred frequently, such as Heavy Rain of July 2018 and Typhoon Hagibis 2019 in Japan. Causes of the failures are considered as reduction of strength due to rise in pore pressure and increase in the degree of saturation, and increase of self-weight due to water absorption. However, the detailed failure mechanism has not been fully elucidated. Normally, a combination of seepage and stability analysis has been used to predict slope failure due to rainfall. However, the stability analysis, which determines failure based on whether the safety factor exceeds 1 or not using the stress state obtained from seepage analysis, is not sufficient to elucidate the failure mechanism. It is necessary to analyze the behavior from deformation to failure caused by seepage. In addition, since failure is accompanied by accelerated motion, inertial forces must be taken into account even if the external force is rainfall. Furthermore, to numerically simulate large deformation behavior from deformation to failure, it is essential to use an analytical method based on finite deformation theory that takes into account geometric nonlinearity.

Based on the above insight, this study conducted deformation and failure simulations of unsaturated slopes in rainfall model tests (Chueasamat et al. 2018) using a soil-water-air coupled elastoplastic finite deformation analysis code considering inertia force (Noda & Yoshikawa 2015, Yoshikawa & Noda 2020, Yoshikawa & Noda 2022). The results showed that, as in the model tests, the unsaturated slope deformed and failed due to rainfall infiltration, and that the slip failure was caused by the soil elements which exhibited "softening behavior with plastic volume expansion" above the critical state line in $p' - q$ skeleton stress space.

2 OVERVIEW OF REFERENCE EXPERIMENTS AND ANALYSIS CONDITIONS

We referred to rainfall model tests of Chueasamat et al. (2018) because soil water characteristics of the soil materials are clearly shown. Figure 1a shows an overview of the experimental

DOI: 10.1201/9781003299127-153

model. The surface layer composed of Kasumigaura sand was constructed on the foundation of DL clay in a 1G gravity field, and water was sprayed from above. The experiments were conducted under three conditions of 0, 25, and 50 % relative density of Kasumigaura sand (the degree of saturation: about 29-34%) and three conditions of 25, 50, and 100 mm/h rainfall intensity, for a total of nine cases. The degree of compaction of the DL clay foundation is 100 % (the degree of saturation: about 61%). Water pressure was measured at points P1-18 in Figure 1. This paper describes the analytical results of three cases with different rainfall intensities. The experimental results are presented together with the analytical results in the next section.

Figure 1b shows the analytical cross section. The analysis was performed under the 2-D plane strain condition and the dimensions of the analytical cross section were set the same as in the experiment. The analytical cross section was created by adding finite elements of soil layers to reproduce the stress history in the experiment. The left and bottom edges were set to undrained and unexhausted conditions, the right edge to seepage face boundary and unexhausted conditions, and the ground surface to seepage face boundary (during construction)/rainfall boundary (during watering) and exhausted conditions. Horizontal and vertical displacement were fixed at the lower end, and horizontal displacement was fixed at the left and right ends.

The constitutive model of the soil skeleton is the elastoplastic constitutive equation SYS Cam-clay model (Asaoka et al. 2002) considering the unsaturated effect (Yoshikawa & Noda 2020). The skeleton stress equation (Jommi 2000) was used for the stress equation. The material constants of DL clay were given from the previous study by the authors (Yoshikawa & Noda 2020) and the same initial void ratio was given as in the experiment. The mechanical test results for Kasumigaura sand were not obtained, so the same material constants as for DL clay were used here, and a loose condition (the degree of compaction of about 80%) was set as the initial value. The van Genuchten (1980) and Mualem (1976) models were used as the unsaturated seepage characteristic model. The material constants were set to reproduce the soil water retention test results of the water absorption process of each material (Chueasamat et al. 2018), and the same initial degrees of saturation were given as in the experiment.

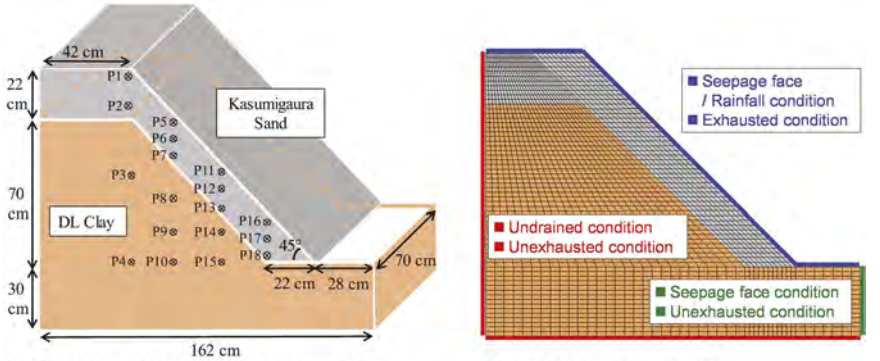

Figure 1. Experimental and analytical conditions.

3 ANALYSIS RESULTS

Figure 2a shows the experimental and analytical results of pore water pressure distribution for a rainfall intensity of 100 mm/h. Only the slope portion is shown enlarged. The comparison between the two shows that the analysis was able to reproduce the infiltration process of rainfall from the ground surface. Figure 2b shows the slip failure behavior at a rainfall intensity of 100 mm/h. The analysis reproduced the slip failure behavior over the entire slope from toe to top of the slope.

Figure 3 shows the mechanical behavior of the soil element at toe of the slope located on the slip line shown in Figure 2b. In Figure 3, ● indicates the state immediately before rainfall, and time passes in the order of ●→▲→■→○. First, from ● to ▲, the increase in the degree of saturation and the rise in pore pressure due to rainfall infiltration caused plastic deformation and it caused the loss of overconsolidation and structure (increase in R and R^*) described by SYS Cam-clay model (Asaoka et al. 2002). Next, from ▲ to ■, overconsolidation and structure were lost further, and softening behavior with plastic volume compression due to the loss of structure occurred. Finally, from ■ to ○, softening with plastic volume expansion above the critical state line q=Mp', which is a characteristic of Cam-clay model, occurred, leading to a large deformation.

Figure 4 shows the difference in slip failure behavior and pore pressure distribution for rainfall intensities of 50 mm/h and 25 mm/h. Together with Figure 2 for a rainfall intensity of 100 mm/h, it can be seen that the analysis reproduced the slip line up to the mid-slope when the rainfall intensity was 25 mm/h, while the analysis reproduced the slip line over the entire slope when the rainfall intensity was 50 mm/h and 100 mm/h. This is because the higher the rainfall intensity, the higher the pore water pressure to the top of the slope.

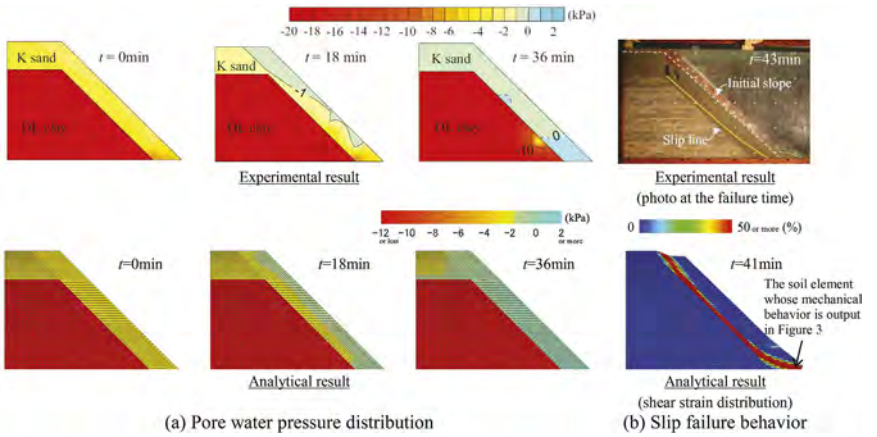

Figure 2. Experimental and analytical results for a rainfall intensity of 100 mm/h.

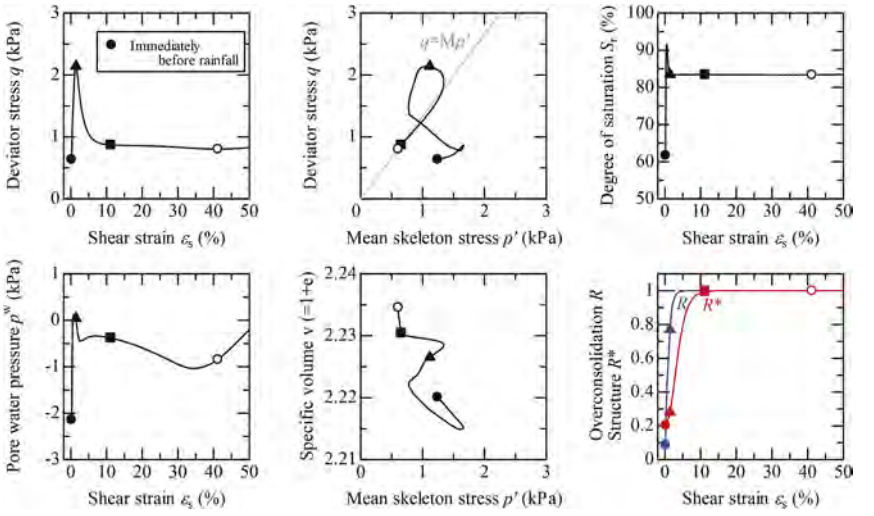

Figure 3. Mechanical behavior of the soil element located on the slip line shown in Figure 2b.

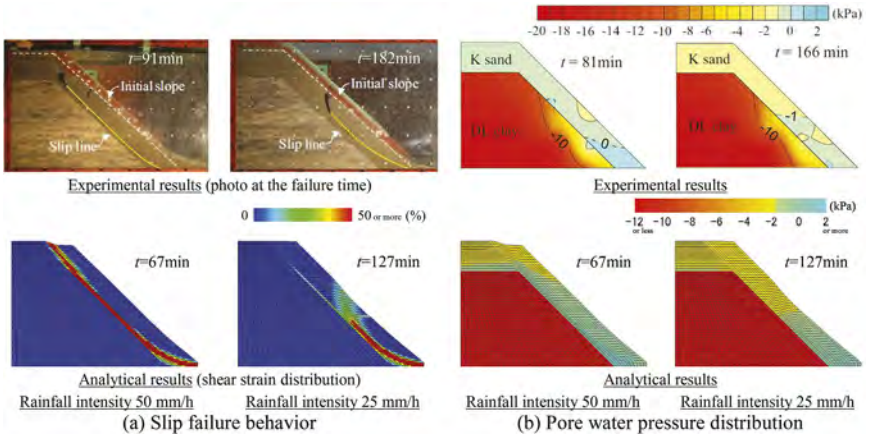

Figure 4. Experimental and analytical results for rainfall intensities of 25 and 50 mm/h.

4 CONCLUSIONS

We have succeeded in reproducing the behavior of unsaturated slope from deformation to failure in rainfall model tests (Chueasamat et al. 2018) using the soil-water-air coupled elastoplastic finite deformation analysis code considering inertia force (Noda & Yoshikawa 2015, Yoshikawa & Noda 2020, Yoshikawa & Noda 2022). It has been found that the soil element on the slip surface exhibits "softening behavior with plastic volume expansion" above the critical state line q=Mp', which leads to slip failure of the slope. In addition, differences in deformation and failure behavior have been reproduced for three different rainfall intensities of 25, 50, and 100 mm/h. Furthermore, it has been shown that large accelerations of 1 G or more occurs at the time of slip failure, though the results were omitted here because of space limitation.

In the future, we will reexamine the material constants and initial values of the failure layer. In addition, we will apply this analysis code to real problems, such as elucidating the failure mechanism of Atami Embankment that occurred in July 2021.

REFERENCES

Asaoka, A., Noda, T., Yamada, E., Kaneda, K. & Nakano, M. 2002. An elasto-plastic description of two distinct volume change mechanisms of soils. *Soils and Foundations* 42(5): 47–57.

Chueasamat, A., Hori, T., Saito, H., Sato, T. & Kohgo, Y. 2018. Experimental tests of slope failure due to rainfalls using 1g physical slope models. *Soils and Foundations* 58(2): 290–305.

Jommi, C. 2000. Remarks on the constitutive modelling of unsaturated soils, *Experimental Evidence and Theoretical Approaches in Unsaturated Soils*. Tarantino, A. & Mancuso, C. (eds): 139–153, Balkema

Mualem, Y. 1976. A new model for predicting the hydraulic conductivity of unsaturated porous media. *Water Resources Research* 12: 513–522.

Noda, T. & Yoshikawa, T. 2015. Soil-water-air coupled finite deformation analysis based on a rate-type equation of motion incorporating the SYS Cam-clay model. *Soils and Foundations* 55(1): 45–62.

van Genuchten, M. T. 1980. A closed-form equation for predicting the hydraulic conductivity of unsaturated soils. *Soil Science Society of America Journal* 44: 892–898.

Yoshikawa, T. & Noda, T. 2020. Triaxial test on water absorption compression of unsaturated soil and its soil-water-air-coupled elastoplastic finite deformation analysis. *Soils and Foundations* 60(5): 1151–1170.

Yoshikawa, T. & Noda, T. 2022. Development and validation of deformation analysis method for unsaturated soil based on new effective saturation degree considering trapped air. *Proceedings of 20th International Conference on Soil Mechanics and Geotechnical Engineering*.

Smart Geotechnics for Smart Societies – Zhussupbekov, Sarsembayeva & Kaliakin (Eds)
© 2023 The Author(s), ISBN 978-1-003-29912-7
Open Access: www.taylorfrancis.com, CC BY-NC-ND 4.0 license

Centrifuge modeling of sand-clay slopes subject to rainfall

Fan Luo, Sujia Liu & Ga Zhang
State Key Laboratory of Hydroscience and Engineering, Tsinghua University, China

ABSTRACT: Rainfall is one of the main causes to slope failure. In this study, centrifuge model tests are conducted to observe the response of the sand-clay layered slopes subject to rainfall. The rainfall induces significant deformation and failure of the sand-clay layered slope that is affected by the rainfall infiltration characteristics of the dual structure. The slope failure is progressive and caused by a few local failure cycles one by one as the rainfall increases. The wetting front moves from the slope surface to the interior as the rainfall increases and the move rate is significant greater in the sand than in the clay. The water accumulates on the top surface of the clay layer and becomes the main sources of the water infiltration of the clay layer. The sand layer has an obvious effect on the deformation of neighboring clay layer of the slope during the rainfall.

1 INTRODUCTION

Rainfall is one of the main causes to slope failure. More than 90% of the landslides are related to rainfall. Previous studies on the behaviors of slopes subject to rainfall put their focus on the homogeneous slopes (Lim et al., 1996, Adrin et al.2007, Zhang et al. 2011, Ma et al.2021). It should be concerned that practical slopes often consist of various soil layers such as sand layer and clay layer. The sand-clay layered slope may exhibit different seepage, deformation and failure behaviors from the homogeneous slope. However, few studies have been conducted on the sand-clay layered slopes under rainfall condition yet.

Centrifuge model tests have been widely employed to investigate the behavior of soil slopes under various conditions (Zhang et al. 2011, Luo et al. 2018, Liu et al. 2020). In this study, centrifuge model tests are conducted to observe the response of the sand-clay layered slopes subject to rainfall. The fundamental rules on the infiltration and deformation behavior of the sand-clay layered slopes are investigated on the basis of the full field measurement of slope displacement under rainfall conditions. The progressive slope failure due to rainfall is analyzed on the basis of test observations and displacement measurement results.

2 TEST

2.1 *Equipment*

The centrifuge model tests were conducted with the geotechnical centrifuge of Tsinghua University, of which the centrifugal acceleration can reach 250 g. The model box, which is 600 mm long, 200 mm wide and 500 mm high, is made of aluminum alloy to install the slope model and rainfall simulation system. It is equipped with a 40mm-thick transparent plexiglass on one long side. A camera is fixed in front of the glass to observe and record the deformation and failure of the slope during the centrifuge model test.

The rainfall simulation system consists of the water tank and a few nozzles. During the test, the water is transported through the pipes from the water tank to the nozzles. Then under the air pressure, the nozzles release the water into the model in forms of spray, thus simulating the natural rainfall. The rainfall intensity can be adjusted by changing the air pressure.

DOI: 10.1201/9781003299127-154

2.2 *Model*

The slope model, 24-cm-high and 15-cm-wide, is 0.75:1 in gradient and consists of two layers with a horizontal boundary in the middle (Figure 1). Both the sand layer and clay layer are 12 cm in height. The top layer is made of the Fujian standard sand with a dry density of 1.55 g/cm^3. The bottom one is made of a silty clay with a dry density of 1.55 g/cm^3 and a moisture content of 18%. Besides, a 50-mm-deep foundation is made with the same silty clay at the bottom to reduce the effect of the model box on the soil slope. Silicon oil is smeared on the both contact sides between the model box and slope model to reduce the friction.

An orthogonal coordinate system is set up with the toe of the slope as the origin, and the positive directions of x-axis and y-axis are defined as rightward and upward respectively (Figure 1(b)).

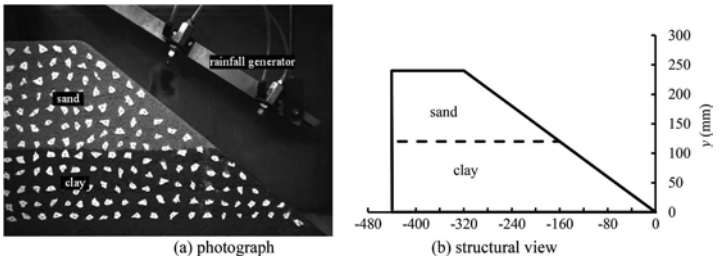

Figure 1. Schematic view of the slope model.

2.3 *Procedure*

At the beginning of the test, the slope model was installed in the centrifuge and accelerated to 50 g gradually, then maintained at a level of 50 g. After the slope settlement stabilized, the rainfall began at an intensity of 3 mm/min using the rainfall simulation system throughout the test. When the deformation and failure of the soil slope could be obviously observed, the rainfall stopped at a final magnitude of 20 mm.

2.4 *Measurement*

During the rainfall, the deformation and failure of the slope were recorded by the camera constantly. The acquired images can be sued to determine the displacement at an arbitrary point of the slope by using correlation-based analysis algorithm (Zhang et al. 2009).

According to the similarity law of the centrifuge model test, the displacement and rainfall of the prototype is 50 times that of the model. The measurement results are presented in the model dimension in this paper.

3 SLOPE FAILURE

The rainfall caused the slope failure (Figure 2 (a)). Figure 2 (b) shows the slip surface of the slope according to the observations on the images of the slope at failure. The slip surface is a continuous curve and extends from the sand layer to the clay layer. The slope is divided into base body and sliding body based on the slip surface.

The slip surface was observed to be caused by the rainfall through a few local failure cycles. Figure 3 exhibits the first local failure cycle that consists of three stages. To analyze the failure process of the cycle, four points were selected at different failure bodies to measure their histories of the vertical displacements (Figure 4). It can be seen from Figure 4 that the vertical displacements of the points increase relatively slowly at the beginning of the rainfall, and then exhibit a rapid increase at some certain rainfalls. It can be inferred that a slope local failure

occurs at the surrounding area of the point at the inflection point on the history curve of vertical displacement. According to the histories of the four inflection points, a local failure cycle can be described with three stages as follows:

(1) The displacement history curves of points A and B, which are located in the top of clay layer, exhibit an inflection point at first. It can be inferred that the local failure first occurs in the top of the clay layer as the rainfall increases. This result implies that sand-clay interface has obvious effect on the failure of the slope.
(2) The displacement history curve of point C, which is located at the bottom of the sand layer, exhibit an inflection point after that of points A and B. It can be inferred that the local failure in the top of the clay layer expands upwards to the bottom of the sand layer across the boundary of sand and clay.
(3) The displacement history curve of point D, which is located in the sand layer, exhibit an inflection point after that of point C. It can be speculated that the local failure at the bottom of the sand layer continues to expand upwards in the sand layer during the rainfall.

The local failure cycles occur one by one as the rainfall increases and induce the final slip surface (Figure 2).

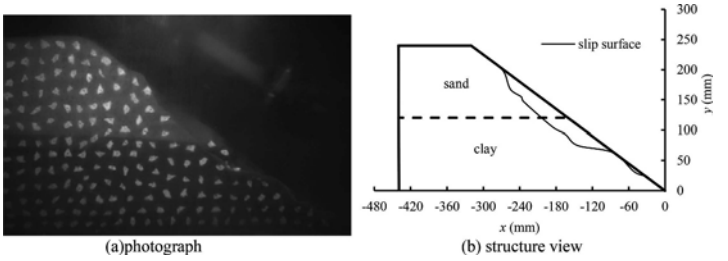

Figure 2. Slip surface after the rainfall.

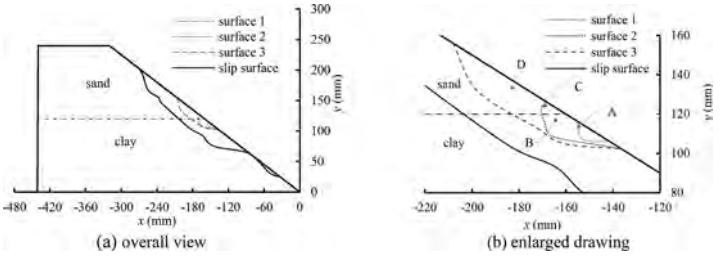

Figure 3. The first cycle during the process of slope failure.

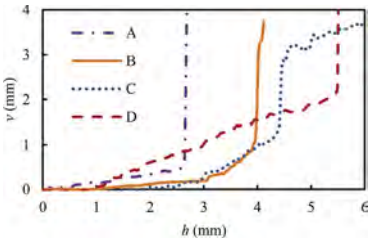

Figure 4. Histories of vertical displacements of typical points (point locations are indicated in Figure 3 (b)). *h*, rainfall; *v*, vertical displacement.

4 SLOPE DISPLACEMENT BEHAVIOR

Several points are selected in different soil layers on both sides of the slip surface to explore the displacement behavior of the slope. Figure 5 shows the histories of vertical displacements of those points during rainfall. It can be seen that the displacements of the points in the base body (points E and G) are fairly small and become nearly invariable when the rainfall increases to a value. On the other hand, the displacements of the points in the sliding body (points F and H) increase slowly at the beginning of the rainfall, and exhibit a rapid growth at a certain rainfall due to the slope failure. The vertical displacement of the sliding body in the clay layer exhibits the rapid growth a bit earlier than that of the sliding body in the sand layer. Therefore, it can be concluded that the slope displacement exhibits different characteristics in different zones during rainfall.

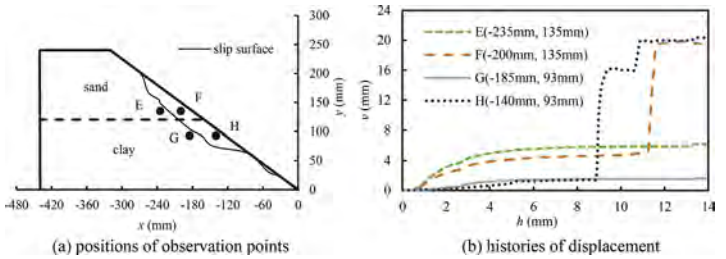

Figure 5. Histories of displacement of points of the slope during rainfall. *h*, rainfall; *v*, vertical displacement.

Figure 6 shows the displacement vectors of the slope at different rainfalls. It can be seen that the slope displacement distributes nearly homogenously when the displacement is fairly small at a rainfall of 2 mm. When the rainfall increases to 14 mm, the displacement distribution tends to be unevenly. The displacement in the sliding body becomes significant and different from the displacement in the base body. Moreover, the displacement of the clay layer seems more synchronous with that of the sand layer when it is closer to the sand layer.

For a closer examination on the displacement behavior, Figure 7 show the horizontal distribution of vertical displacement in the base body at different rainfalls. It can be seen that the vertical displacements of both the sand and clay layers have an inflection point, and the inflection point is farther from the surface of the slope as the elevation decreases. And compared with the rainfall of 2 mm, the vertical displacement at the rainfall of 14mm distributes more evenly on the inner side of the inflection point. In other words, when it is closer to the sand layer, the displacement of the clay layer is more synchronous with that of the sand layer. It indicates that there is a significant interaction between the sand layer and the clay layer during the rainfall.

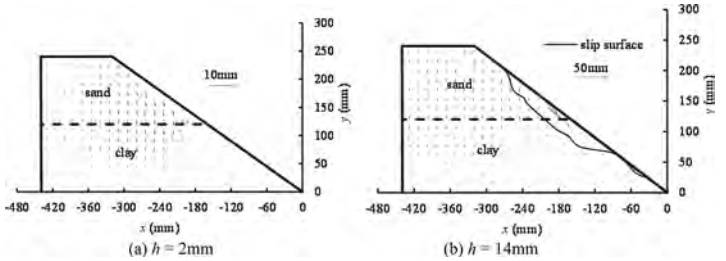

Figure 6. Displacement vectors of the slope.

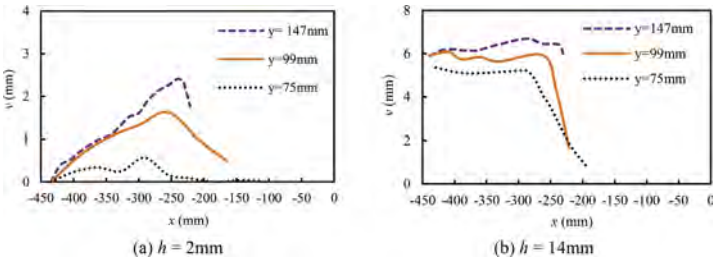

Figure 7. Horizontal distribution of vertical displacement at various elevations and rainfalls. *h*, rainfall.

5 SLOPE DEFORMATION AND INFILTRATION RULE

The vertical strain of the slope was determined on the basis of displacement measurement results to analyze the slope deformation and infiltration rule. Figure 8 shows the histories of vertical strain of typical points at different horizontal lines of the slope during the rainfall. It can be seen that the vertical strain is nearly zero at the beginning of rainfall and starts to increase from zero at a rainfall. It can be deduced that the inflection point can be used to determine the time when the water infiltrates there as the variation of the water content is the main cause to the soil deformation.

In the sand layer, the rainfalls at the water infiltration are close for different positions (Figure 8 (a)). This result indicates that the rain water infiltrates in the sand layer fairly quickly. On the other hand, the rainfalls at the water infiltration are significantly dependent on the positions due to low permeability of the clay (Figure 8 (b)). The closer to the slope surface, the water infiltration is earlier. Closer comparison on the vertical strains between the sand and clay layer shows that the rainfall induced deformation of the clay layer is greater than that of the sand layer at the same vertical line.

The wetting front of the slope can be determined according to measured water infiltration time. Figure 9 shows the wetting front at different rainfalls. It can be seen that the wetting front moves from the slope surface to the interior as the rainfall increases. It is worth noting that the wetting front moves rapidly in the sand layer and thus the water accumulates on the top surface of the clay layer. The sand layer has been totally soaked at the rainfall of 2 mm and then the wetting front is entirely located in the clay layer and becomes mostly horizontal line. Therefore, it can be inferred that most of the rainfall concentrates on the top surface of the clay layer, and the sand layer becomes the main sources of the water infiltration of the clay layer. That rainfall infiltration characteristic significantly affects the deformation behavior of the slope with sand-clay layer.

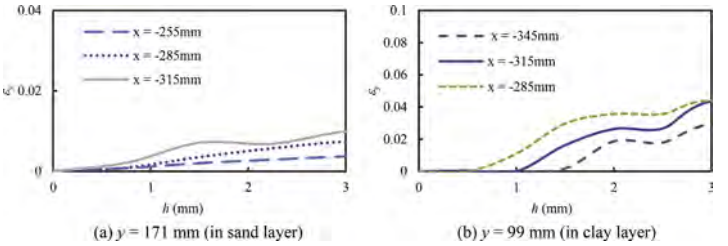

Figure 8. Horizontal distribution of vertical strain of the slope at different layers. ε_y, vertical strain; *h*, rainfall.

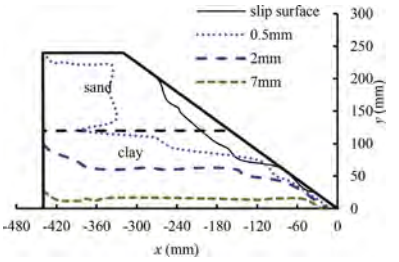

Figure 9. Wetting fronts of the slope during the rainfall.

6 CONCLUSION

The infiltration, deformation and failure behavior of the soil slope with dual structure of sand-clay layers were investigated on the basis of centrifuge modeling under rainfall condition. The main conclusions are as follows:

(1) The rainfall induces significant deformation and failure of the sand-clay layered slope that is affected by the rainfall infiltration characteristics of the dual structure.
(2) The final slip surface is continuous from the sand layer to the clay layer. The slope failure is progressive and caused by a few local failure cycles one by one as the rainfall increases. In a local failure cycle, the local failure first occurs in the top of the clay layer and expands upwards to the of the sand layer across the boundary of sand and clay.
(3) The wetting front moves from the slope surface to the interior as the rainfall increases and the move rate is significant greater in the sand than in the clay. The water accumulates on the top surface of the clay layer and becomes the main sources of the water infiltration of the clay layer.
(4) The sand layer has an obvious effect on the deformation of neighboring clay layer of the slope during the rainfall.

ACKNOWLEDGEMENTS

The study is funded by Tsinghua University Initiative Scientific Research Program and National Natural Science Foundation of China (52039005).

REFERENCES

Adrin T, Makoto N, Mitsuru K (2007) Laboratory rainfall-induced slope failure with moisture content measurement. *Journal of Geotechnical and Geoenvironmental Engineering*, 133(5): 575–587.

Lim TT, Rahardjo H, Chang MF, Fredlund DG (1996) Effect of rainfall on matric suction in a residual soil slopes. *Canadian Geotechnical Journal*, 33(2): 618–628.

Liu SJ, Luo FY, Zhang G (2020) Centrifuge model tests on pile-reinforced slopes subjected to drawdown. *Journal of Rock Mechanics and Geotechnical Engineering*, 12 (6): 1290–1300.

Luo FY, Zhang G, Liu Y, Ma CH (2018) Centrifuge modeling of the geotextile reinforced slope subject to drawdown. *Geotextiles and Geomembranes*, 46(1): 11–21.

Ma BQ, Du YP, Wang HX, Yang AQ, Wang XD, Tian KL (2021) Experimental study on stability of loess slope stability under continuous rainfall. *Journal of Soil and Water Conservation*, 35(5): 50–56.

Zhang G, Hu Y, Zhang JM (2009) New image-analysis-based displacement-measurement system for geotechnical centrifuge modeling tests. *Measurement* 42(1): 87–96.

Zhang G, Qian JY, Wang R, Zhang JM. Centrifuge model test study of rainfall-induced deformation of cohesive soil slopes. *Soils and Foundations*, 51 (2): 297–305.

Smart Geotechnics for Smart Societies – Zhussupbekov, Sarsembayeva & Kaliakin (Eds)
© 2023 The Author(s), ISBN 978-1-003-29912-7
Open Access: www.taylorfrancis.com, CC BY-NC-ND 4.0 license

Stages of developing a prototype landslide forecasting framework using geotechnical monitoring: A case study from India

Neelima Satyam
Department of Civil Engineering, Indian Institute of Technology, Indore, India

ABSTRACT: Landslides have become a major problem in the Darjeeling Himalayas region of India and authorities are seeking ways to reduce the risk of these events through the development of an early warning system. A forecasting framework is the critical part of early warning system, where the occurrence of landslides is predicted using field or remotely based observation. One strategy for predicting landslides is to use rainfall thresholds, but this approach can result in a high number of false alarms. To address this limitation, it is necessary to monitor unstable slopes in real-time using cost-effective methods. In this study, MicroElectroMechanical Systems (MEMS) sensors were used to monitor slopes in the Chibo village of Darjeeling Himalayas and integrated the data with rainfall thresholds to develop a prototype landslide forecasting framework. The results showed that the combination of MEMS sensors and rainfall thresholds is a promising approach which overcomes the limitations of both methods when used separately.

1 INTRODUCTION

Landslides are natural processes that can cause significant damage to human environments, and the increasing population and urbanization of hilly areas is increasing the risk of these events (Dowling and Santi, 2014; Petley, 2012). It is important for authorities to implement risk reduction strategies, such as the development of a Landslide Early Warning System (LEWS). An LEWS should be able to predict the likelihood of landslides in a specific area and provide sufficient time for intervention. One commonly used method for forecasting landslides is the use of rainfall thresholds, which define specific precipitation conditions that may lead to slope failures (Baum and Godt, 2010; Devoli et al., 2018). The threshold defines specific rainfall conditions when exceeded, may trigger slope failures in the region (Segoni et al., 2018). These conditions be derived using physics-based approaches or data-driven approaches. Physics based or process based approaches are generally preferred for site specific studies (De Vita et al., 2017; Fusco et al., 2019; Napolitano et al., 2016; Segoni et al., 2018), and statistical approaches are applied for regional and global scales (Aleotti, 2004; Bordoni et al., 2019; Caine, 1980; Guzzetti et al., 2007). The thresholds are characterized by three rainfall parameters, the event (E), duration (D) and intensity (I). Event rainfall is the total quantity of precipitation, duration is the time period, and intensity is the ratio of event to duration. The thresholds are defined using two of these parameters, I or E on the y axis and D on x axis. Mathematically, the thresholds follow a power law and can be represented as a straight line on logarithmic scale. Sistema Integrato Gestione Monitoraggion Allerta (SIGMA) is an advanced statistical model which uses the standard deviation of rainfall data for landslide forecasting, first developed for Italy (Martelloni et al., 2012). This study uses both these rainfall thresholds for the study area.

Considering the rainfall threshold based approach, the method is simple and can be easily reconstructed (Abraham et al., 2021b, 2021a; Segoni et al., 2021). However, the lower boundary thresholds often results in higher number of false alarms (Bulzinetti et al., 2021). Also, statistical

DOI: 10.1201/9781003299127-155

thresholds which considers both short term and long term rainfall performs even better than the conventional approaches (Lagomarsino et al., 2015). To overcome these limitations, this study proposes the use of geotechnical field monitoring instruments along with rainfall thresholds for landslide forecasting (Abraham et al., 2021a). MicroElectroMechanical Systems (MEMS) based tilt sensors are established to be a cost effective and reliable approach for slope monitoring (Towhata et al., 2015; Uchimura et al., 2011). To be effective, tilt meters should be installed in strategic locations where they can provide early warning of landslides. They can be easily installed on slopes or other areas prone to landslides, and they do not require a lot of maintenance. In addition, they are resistant to extreme weather conditions, making them well-suited for use in the hilly region of Kalimpong, where landslides are often triggered by heavy rainfall. This study involves the use of sensors to monitor unstable slopes in the Kalimpong region of West Bengal, beginning in July 2017. The goal of the study is to determine the effectiveness of tilt sensors in predicting slope failures and how they can improve the performance of conventional rainfall thresholds. The two methods are combined using a decisional algorithm that can be used to forecast slope failures in the region.

2 DETAILS OF STUDY AREA

Kalimpong is a hilly town located in the Darjeeling Himalayas with steep, unstable slopes on the western side, composed of loose debris and prone to erosion during heavy rains (Figure 1). The town's bedrock is made up of golden to silver colored quartz mica shist, which is highly jointed and weathered and prone to stability issues. The increased human activity and resulting land use changes have increased the likelihood and risk of landslides in the region, which are often influenced by slope cuts and untrained mountain streams (jhoras). The most vulnerable locations for landslides are near these jhoras, and the sensors in this study have been installed on a slope near such a stream, called the Pyarieni jhora, in the Chibo village of Kalimpong (Figure 1).

The data for this study was collected from daily rainfall records maintained by Save The Hills and a landslide catalog compiled from various sources, including the Geological Survey of India, media reports, and communication with local residents (Dikshit and Satyam, 2018).

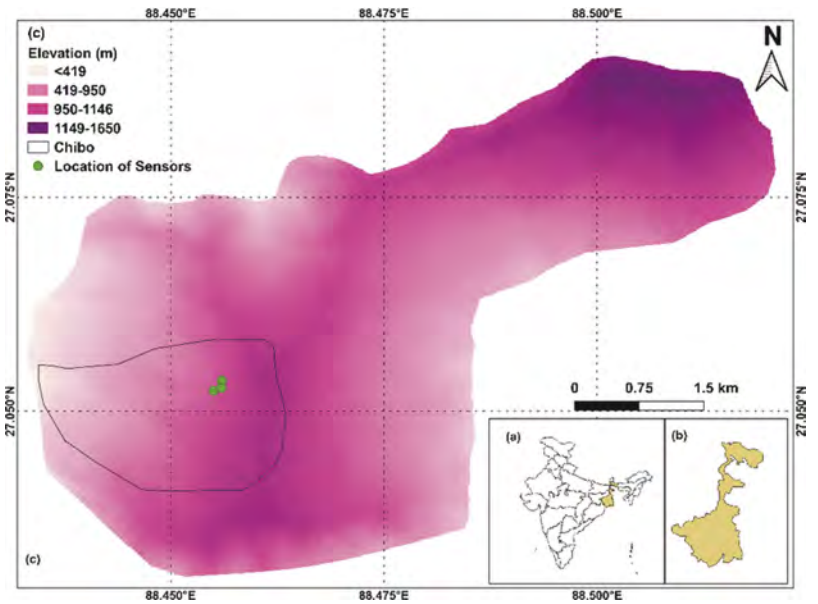

Figure 1. Details of study area and location of sensors, a) India, b) West Bengal and c) Kalimpong.

3 METHODLOGY

3.1 *Conventional rainfall thresholds*

This study evaluates the effectiveness of conventional rainfall thresholds and tilt meters when used individually and in combination. Previous researches (Dikshit and Satyam, 2018; Teja et al., 2019) has determined empirical thresholds for the study area on the ED plane as:

$$E = 4.2\ D^{0.56} \tag{1}$$

3.2 *SIGMA model*

SIGMA model defines different rainfall threshold lines, based on the statistical distribution of precipitation data. As the name indicates, the standard deviation of the data plays a key role in the definition of rainfall threshold. Each threshold curve is defined as a function of the standard deviation, 'σ' ($y = a\sigma$).

The first step is the calculation of cumulative rainfall for 'n' days, where n varies from 1 to 365. The rainfall is cumulated (z) at n days shifts at daily timesteps with the same width. The cumulative distribution function ($CDF(z)$) for each timestep was then calculated, and compared with standard distributions as target function (Martelloni et al., 2012). With cumulative rainfall data of Kalimpong was following asymmetric distributions, for lesser value of n, the distribution is similar to log normal distribution and for larger values of n, it is similar to normal distribution. To calculate the probability of exceeding a certain threshold, gaussian distribution was selected as the target function. Different threshold curves or σ curves can be plotted for each value of n, which are the input for SIGMA algorithm. The cumulated rainfall value for any duration is compared with the corresponding value in the σ curves, to issue the warning. The duration to be considered for each warning and the multiple of σ to be used, are determined by a trial-and-error process. For Kalimpong, the customised algorithm derived in a previous study has been used as the starting algorithm for this work (Figure 2).

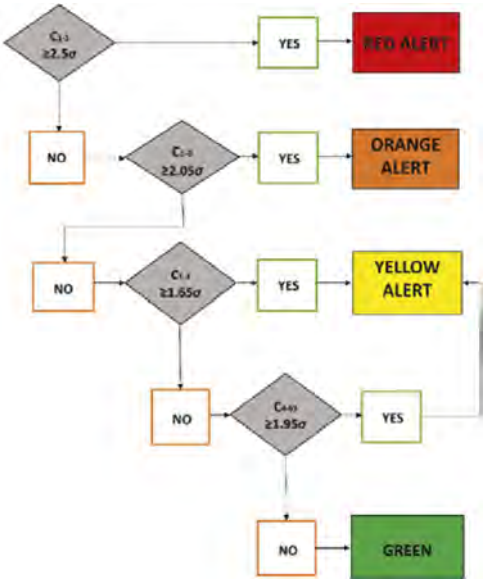

Figure 2. Decisional algorithm used for SIGMA model of Kalimpong (Abraham et al., 2021a).

3.3 *Tilt meter*

In July 2017, three sensor units (S1, S2 and S3) consisting of a volumetric water content sensor, a tilt sensor, and a control unit were installed on unstable slopes near the Pyarieni jhora in the Chibo village of Kalimpong. (Figure 1). The positions of the sensors were carefully selected following field surveys, consultation with the Geological Survey of India, and input from local residents.

The sensor readings were related with observations from the field, to assess the dependability of the recorded data (Abraham et al., 2020b; Dikshit et al., 2018). The records acquired from the tilt meters for the duration of monitoring period implies that large displacements are always associated with heavy rainfall.

3.4 *Combined approach*

The combined approach uses both historical rainfall data and tilt sensor readings. When testing the rainfall thresholds for Kalimpong, it was found that the model also issued false alarms on days when there were no observed displacements. These false alarms can decrease the credibility of the Landslide Early Warning System (LEWS) and reduce the public's response to the warnings. It is important to minimize the number of false alarms to increase the effectiveness of the LEWS.

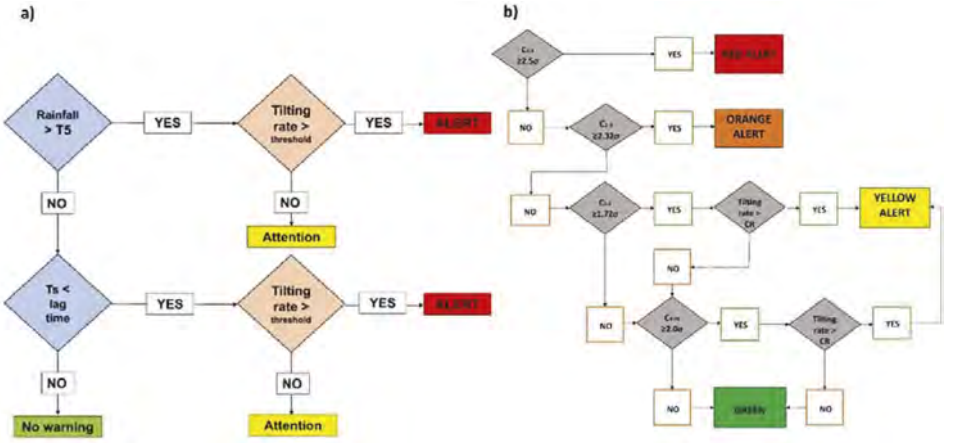

Figure 3. Decisional algorithm used for combined approach a) ED+tilt (Abraham et al., 2020a) and b) SIGMA+tilt (Abraham et al., 2021a).

The algorithm in Figure 3 uses the critical tilting rate (CR), which can be customized for each region through trial and error. For Kalimpong, the CR value has been calibrated at 0.03 degrees per hour. The algorithm first checks if the threshold condition is crossed as per the thresholds. After crossing the threshold, it then checks the maximum tilting rate from the previous day. If that rate is also above the CR value, an alert is issued. The term T_5 in Figure 3 indicates the threshold line with 5 % exceedance probability.

4 RESULTS

The performance of different models was evaluated using slope failure and rainfall data from July 2017 to September 2020. During the years 2017-2019, no major landslides were recorded near the sensors, and the slope failures were in the form of displacements and minor cracks in

roads near the sensors. All of these events were of minor criticality, requiring observation by authorities for any emergencies. In 2020, multiple landslides occurred in Kalimpong along with major cracks in roads near sensor 2, with events near the sensor locations ranging from minor to moderate criticality, resulting in the disruption of a main road to Chibo village and isolation from the rest of the town. The performance of the different models was compared using a confusion matrix, in which the model's predictions were compared to the occurrence or non-occurrence of slope failures. A true positive (TP) was recorded when the model predicted a slope failure and one occurred, and a true negative (TN) was recorded when the model predicted no slope failure, and none occurred. False predictions were divided into false positives (FP), when a slope failure was predicted but none occurred, and false negatives (FN), when no slope failure was predicted but one occurred. The sensitivity and specificity of the model can be calculated using the attributes from the confusion matrix, and the performance of different models can be compared using a Receiver Operating Characteristic (ROC) curve, which plots sensitivity against 1-specificity. Sensitivity is the ratio of is the fraction of TPs among all the landslides considered for validation, and specificity is the fraction of TNs among all the non-landslide das considered. The point (0,1) on the plot represents a perfect model with a sensitivity and specificity of 1 and an area under the curve (AUC) of unity. The higher the AUC, the better the model.

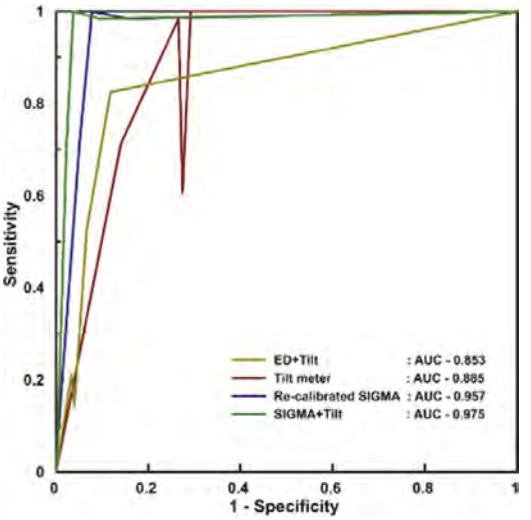

Figure 4. ROCs plotted for different methods considered in the study.

The combined approach using SIGMA and tilt sensors had the highest AUC value of 0.975 and was the best performing model (Figure 4). The curve for the combined approach was closer to the y-axis, indicating that it was more specific and issued fewer false alarms compared to the other models. The points for the tilt meter were farther from the y-axis, indicating a higher number of false alarms. Th recalibrated SIGMA model also has better performance than both ED+tilt and tilt meter alone. The SIGMA model and combined approach had points closer to the perfect point and relatively consistent performance over the years, while the performance of the tilt meter varied significantly each year. The majority of missed alarms with the tilt meter occurred in 2018, when the field displacements were minor and not associated with heavy rainfall. The combined approach is an attempt to improve the prediction performance of the SIGMA model and determine its potential as an operational LEWS for Kalimpong. The results show that the proposed method can significantly reduce the number of false alarms, but do not address alarms missed by the SIGMA model. When comparing the different threshold models

for Kalimpong, the new approach proposed in this study, which enhances the conventional SIGMA model, performed better than previously derived thresholds. However, the model has certain limitations that must be addressed to turn it into an operational LEWS.

5 CONCLUSIONS

This study explains the process of developing a prototype to forecast the occurrence of slope failures in Kalimpong, a town in the Darjeeling Himalayas. The first method relied solely on the rainfall threshold, which assumes that extreme rainfall triggers landslides and that the historical relationship will hold true in the future. The second approach used real-time field monitoring data from three MEMS tilt sensors installed on the western slopes of Kalimpong to understand the field conditions and issue warnings. The third method was a combination of the first two approaches, using a complex algorithm to issue different levels of warnings based on the severity of rainfall and tilt rates recorded in the field. The results showed that both the thresholds and the tilt meters, when used separately, issued numerous false alarms, making them unsuitable for use in a LEWS. The combined approach performed better than either approach when used individually, as verified using a ROC analysis, which showed that the area under the curve values for the ED+tilt, tilt meters, SIGMA model, and SIGMA+tilt were 0.853, 0.885, 0.957, and 0.975, respectively. The combined approach was also compared to other rainfall thresholds developed for the region and was found to be the best-performing threshold for Kalimpong to date. Its minor shortcomings will be addressed and the model will be refined for use as a potential tool in developing an LEWS for the region.

REFERENCES

Abraham, M.T., Satyam, N., Bulzinetti, M.A., Pradhan, B., Pham, B.T., Segoni, S., 2020a. Using Field-Based Monitoring to Enhance the Performance of Rainfall Thresholds for Landslide Warning. Water 12, 3453. https://doi.org/10.3390/w12123453

Abraham, M.T., Satyam, N., Pradhan, B., Alamri, A.M., 2020b. IoT-Based Geotechnical Monitoring of Unstable Slopes for Landslide Early Warning in the Darjeeling Himalayas. Sensors 20, 2611. https://doi.org/10.3390/s20092611

Abraham, M.T., Satyam, N., Pradhan, B., Segoni, S., Alamri, A., 2021a. Developing a prototype landslide early warning system for Darjeeling Himalayas using SIGMA model and real-time field monitoring. Geosci. J. https://doi.org/10.1007/s12303-021-0026-2

Abraham, M.T., Satyam, N., Rosi, A., Pradhan, B., Segoni, S., 2021b. Usage of antecedent soil moisture for improving the performance of rainfall thresholds for landslide early warning. Catena 200, 105147. https://doi.org/10.1016/j.catena.2021.105147

Aleotti, P., 2004. A warning system for rainfall-induced shallow failures. Eng. Geol. 73, 247–265. https://doi.org/10.1016/j.enggeo.2004.01.007

Baum, R.L., Godt, J.W., 2010. Early warning of rainfall-induced shallow landslides and debris flows in the USA. Landslides 7, 259–272. https://doi.org/10.1007/s10346-009-0177-0

Bordoni, M., Corradini, B., Lucchelli, L., Valentino, R., Bittelli, M., Vivaldi, V., Meisina, C., 2019. Empirical and Physically Based Thresholds for the Occurrence of Shallow Landslides in a Prone Area of Northern Italian Apennines. Water 11, 2653. https://doi.org/10.3390/w11122653

Bulzinetti, M.A., Abraham, M.T., Satyam, N., Pradhan, B., Segoni, S., 2021. Combining rainfall thresholds and field monitoring data for development of LEWS ., in: EGU General Assembly 2021. Online, p. 20172. https://doi.org/10.5194/egusphere-egu21-2072

Caine, N., 1980. The rainfall intensity-duration control of shallow landslides and debris flows: An update. Geogr. Ann. Ser. A, Phys. Geogr. 62, 23–27.

De Vita, P., Fusco, F., Napolitano, E., Tufano, R., 2017. Physically-Based Models for Estimating Rainfall Triggering Debris Flows in Campania (Southern Italy), in: Advancing Culture of Living with Landslides. Springer International Publishing, Cham, Switzerland, pp. 289–297. https://doi.org/10.1007/978-3-319-53485-5_33

Devoli, G., Tiranti, D., Cremonini, R., Sund, M., Boje, S., 2018. Comparison of landslide forecasting services in Piedmont (Italy) and Norway, illustrated by events in late spring 2013. Nat. Hazards 19, 1351–1372.

Dikshit, A., Satyam, D.N., 2018. Estimation of rainfall thresholds for landslide occurrences in Kalimpong, India. Innov. Infrastruct. Solut. 3. https://doi.org/10.1007/s41062-018-0132-9

Dikshit, A., Satyam, D.N., Towhata, I., 2018. Early warning system using tilt sensors in Chibo, Kalimpong, Darjeeling Himalayas, India. Nat. Hazards 94, 727–741. https://doi.org/10.1007/s11069-018-3417-6

Dowling, C.A., Santi, P.M., 2014. Debris flows and their toll on human life: A global analysis of debris-flow fatalities from 1950 to 2011. Nat. Hazards 71, 203–227. https://doi.org/10.1007/s11069-013-0907-4

Fusco, F., De Vita, P., Mirus, B.B., Baum, R.L., Allocca, V., Tufano, R., Clemente, E. Di, Calcaterra, D., 2019. Physically based estimation of rainfall thresholds triggering shallow landslides in volcanic slopes of Southern Italy. Water 11, 1–24. https://doi.org/10.3390/w11091915

Guzzetti, F., Peruccacci, S., Rossi, M., Stark, C.P., 2007. Rainfall thresholds for the initiation of landslides in central and southern Europe. Meteorol. Atmos. Phys. 98, 239–267. https://doi.org/10.1007/s00703-007-0262-7

Lagomarsino, D., Segoni, S., Rosi, A., Rossi, G., Battistini, A., Catani, F., Casagli, N., 2015. Quantitative comparison between two different methodologies to define rainfall thresholds for landslide forecasting. Nat. Hazards Earth Syst. Sci. 15, 2413–2423. https://doi.org/10.5194/nhess-15-2413-2015

Martelloni, G., Segoni, S., Fanti, R., Catani, F., 2012. Rainfall thresholds for the forecasting of landslide occurrence at regional scale. Landslides 9, 485–495. https://doi.org/10.1007/s10346-011-0308-2

Napolitano, E., Fusco, F., Baum, R.L., Godt, J.W., De Vita, P., 2016. Effect of antecedent-hydrological conditions on rainfall triggering of debris flows in ash-fall pyroclastic mantled slopes of Campania (southern Italy). Landslides 13, 967–983. https://doi.org/10.1007/s10346-015-0647-5

Petley, D., 2012. Global patterns of loss of life from landslides. Geology 40, 927–930. https://doi.org/10.1130/G33217.1

Segoni, S., Abraham, M.T., Satyam, N., Rosi, A., Pradhan, B., 2021. Application of SIGMA model for landslide forecasting in Darjeeling Himalayas, in: EGU General Assembly 2021. Online, p. 669. https://doi.org/10.5194/egusphere-egu21-669

Segoni, S., Piciullo, L., Gariano, S.L., 2018. A review of the recent literature on rainfall thresholds for landslide occurrence. Landslides 15, 1483–1501. https://doi.org/10.1007/s10346-018-0966-4

Teja, T.S., Dikshit, A., Satyam, N., 2019. Determination of Rainfall Thresholds for Landslide Prediction Using an Algorithm-Based Approach: Case Study in the Darjeeling Himalayas, India. Geosciences 9, 302. https://doi.org/10.3390/geosciences9070302

Towhata, I., Uchimura, T., Seko, I., Wang, L., 2015. Monitoring of unstable slopes by MEMS tilting sensors and its application to early warning. IOP Conf. Ser. Earth Environ. Sci. 26. https://doi.org/10.1088/1755-1315/26/1/012049

Uchimura, T., Towhata, I., Wang, L., Qiao, J.P., 2011. Miniature ground inclinometer for slope monitoring, in: 14th Asian Regional Conference on Soil Mechanics and Geotechnical Engineering.

Smart Geotechnics for Smart Societies – Zhussupbekov, Sarsembayeva & Kaliakin (Eds)
© 2023 The Author(s), ISBN 978-1-003-29912-7
Open Access: www.taylorfrancis.com, CC BY-NC-ND 4.0 license

Centrifuge model test study on the micro pile reinforcement of soil slopes under drawdown condition

Ziang Wang, Sujia Liu & Ga Zhang
State Key Laboratory of Hydroscience and Engineering, Tsinghua University, China

ABSTRACT: Micro anti-slide piles are an effective reinforcement approach for slopes. Centrifuge model tests were carried out to explore the deformation and failure behavior of micro pile reinforced slopes under drawdown condition. The slip surface is discontinuous and divided into two parts by the micro pile group. The slip surface occurs at the top of the slope after the instability of micro piles and develops to the bottom and as the water level decreases. There is a significant coupling effect between slope deformation localization and local failure. The micro piles restrict the deformation localization and greatly improves the stability of the slope structure. The reduction of pile spacing can cause deformation distribution of the slope more uniform and increase the stability of the micro anti-slide pile group.

1 INSTRUCTIONS

Landslide is one of the most serious geological disasters in the world. The variation of water level is an important cause of slope failure. For example, many landslides were induced by step-like annual fluctuation in the water level of the Three Gorges reservoir (Li et al. 2019). Piles have proved to be an effective reinforcement method for soil slope under various conditions (Anbarasu et al. 2010; Liu et al. 2021). There have been some studies on the reinforcement mechanism of anti-slide piles (Zhang et al. 2017).

The micro anti-slide piles have been shown as an effective reinforcement tool for soil slopes (Dong et al. 2018). Compared with traditional piles, the micro anti-slide piles have many advantages such as small construction equipment, economy and flexible layout. Therefore, it is very important to study the reinforcement behavior and mechanism of micro anti-slide pile to promote its application.

Centrifuge model tests have been widely used to study the deformation and failure behavior of slopes. The bearing capacity and influence factors of pile-reinforced slopes were investigated using centrifuge model tests under loading conditions (Yu et al. 2010; Wang and Zhang 2015). Whereas, few centrifuge model test researches have been performed on the micro pile reinforcement under drawdown conditions. This paper conducted centrifuge model tests to investigate the deformation and failure behavior of the slope with micro anti-slide piles, and clarify the reinforcement mechanism of micro anti-slide pile under drawdown conditions.

2 TEST

2.1 *Device*

The 50g-ton geotechnical centrifuge of Tsinghua University is used in the centrifugal model test. The centrifuge can achieve ultimate centrifugal acceleration of 250 g. The slope model is designed to be 500 mm long, 200 mm wide and 290 mm high (Figure 1). The slope model is placed in an aluminum alloy model container. An organic transparent glass with a thickness of 40 mm is installed on one side of the model container along the length direction. A camera is placed in front of the glass to observe the deformation of the slope and the movement of micro anti-slide piles during the tests.

DOI: 10.1201/9781003299127-156

2.2 *Test scheme*

The main research purpose of this paper is to explore the deformation and failure of micro anti-slide pile reinforced slope under drawdown conditions considering the influence of the pile spacing. Therefore, two micro anti-slide pile reinforced slopes with various pile spacings are simulated in the tests. Two pile spacings, 6.3 and 4.7 times the pile diameter, are used to consider sparse and dense pile layouts that are often adopted in practical cases. The slope reinforced with dense and sparse pile group are abbreviated DP slope and SP slope, respectively. The two tests ensure that other factors are completely the same except the pile spacing.

2.3 *Model*

The soil of the slope model is a kind of silty clay with a height of 24 cm (Figure 1). Three rows of micro anti-slide piles are continuously inserted in the slope. The piles are inserted at the bottom 24 cm away from the top of the slope, and the horizontal spacing between the outermost row of anti-slide piles and the foot of the slope is 9.5 cm. The gradient of the slope is 1:1. The pile spacings in the SP slope and DP slope are 55.1 mm and 41.3 mm, and the other parameters are the same for the two slopes. Some small white particles are evenly embedded on the sides of the slope model provides a significant grayscale difference, enabling more accurate observation of soil changes and measurement of soil displacement.

According to the unified soil classification system (USCS), the cohesive soil in the tests can be classified as CL-ML. The soil is compacted layer by layer and the thickness of each layer is 40 mm. The dry density of the soil is 1.6 g/cm^3 and the initial water content of the soil is 18%. The permeability coefficient, cohesion and internal friction angle of cohesive soil are 10^{-5} cm/s, 27 kPa and 25°, respectively, according to the permeability and triaxial compression tests.

The micro anti-slide pile is simulated with an aluminum solid tube with a square section with a side length of 8.7 mm.

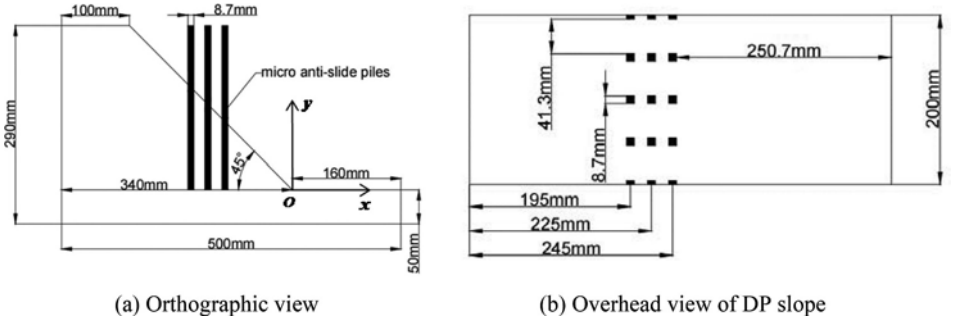

Figure 1. Schematic view of the slope model.

2.4 *Procedure*

The centrifuge model tests are mainly completed in three steps.

First, the centrifugal acceleration is raised from 1 g to 50 g. The g level do not increase until the slope settlement stabilized when the centrifugal acceleration increase to the integer multiple of 10 g.

Second, the water level is gradually increased from 0 to 160 mm after the centrifugal acceleration reach 50 g and the slope deformation became stable. The next impoundment is carried out until the deformation of the slope became stable when the water level increase to the integer multiple of 40 mm.

Finally, the water level decrease from 160 mm to 0 at a rate of 0.7 mm/s in one step.

2.5 *Measurement*

The whole process of the two tests is recorded by the camera in front of the model container. The images are imported into the software and analyzed by relevant algorithms to determine

the displacement at any point of soil and micro anti-slide piles at any time (Zhang et al. 2009). A Cartesian coordinate is established with the foot of slope as the origin and the positive directions of x-axis and y-axis are rightwards and upwards, respectively (Figure 1a). According to the similarity ratio of the centrifuge model test, the water level and displacement of the prototype are both 50 times that of the model.

3 ORSERVATION

Figure 2 shows an obvious slip surface in the slope reinforced with sparse piles. The slip surface is curved, discontinuous and can be divided into two parts by the micro pile group. On the inner side of the micro pile group, the slip surface runs from the top of the slope to the lower middle part of the micro anti-slide pile. And on the outer side of the micro pile group, the slip surface runs from the bottom of the piles to the toe of the slope. In addition, there is no obvious slip surface in the slope reinforced with dense piles. Therefore, the reduction of pile spacing can improve the reinforcement effect of pile group.

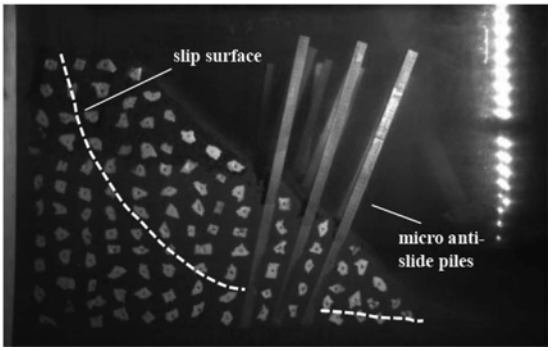

Figure 2. Photograph of the slope reinforced with sparse piles after failure.

Figure 3 shows the history of rotation angle of the middle micro anti-slide pile. The pile is considered as a rigid body and found to rotate around the tip from the captured images. The rotation angle of the pile is small at the beginning of drawdown and then increases rapidly after an inflection point for the slope reinforced with sparse piles, which can be regarded as the occurrence of pile instability. On the contrary, the rotation angle of the piles in the slope reinforced with dense piles is very small during drawdown and there is no inflection point in the history curve. This result indicates that the reduction of pile spacing can increase the stability of the micro anti-slide pile.

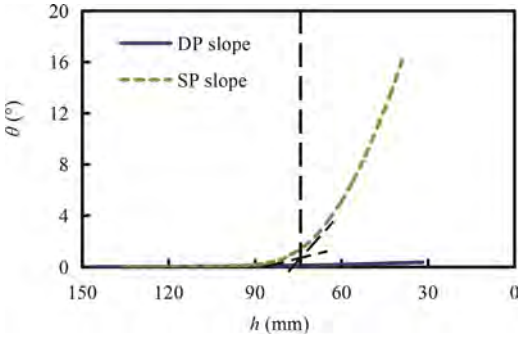

Figure 3. History of rotation angle of the middle micro pile in different tests. h, water level; θ, rotation angle.

The point couple method is used to determine the failure moment of slope during the tests. The point couple consists of a pair of adjacent points on both sides of the slip surface. The relative displacement of the point pair couple is decomposed into tangential and normal directions of the slip surface. The positions of the four point couples selected on the slope reinforced with sparse piles are shown in Figure 4.

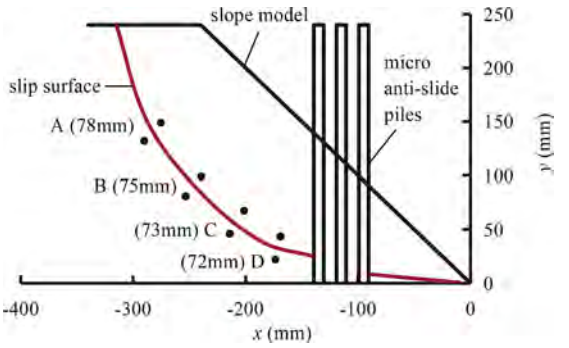

Figure 4. Failure process of the slip surface of the slope reinforced with sparse piles. The water levels corresponding to local failure are included in the round brackets.

Figure 5 shows the relative displacement histories of the selected point couples. It can be seen that the tangential relative displacements of point couples all increase slowly but with small values at the initial stage of water level decrease, and then increase rapidly at a certain inflection points. The inflection point can be regarded as the local failure moment of the slope. The normal relative displacement of the point couple is relatively small. This result indicates that shear failure occurs on the slip surface. The slip surface develops from the top of the slope to the bottom. The water levels at the local failure are shown in round brackets in Figure 4. Compared with Figure 3, the instability of micro anti-slide piles occurs before the failure of slope on the inner side of the pile group.

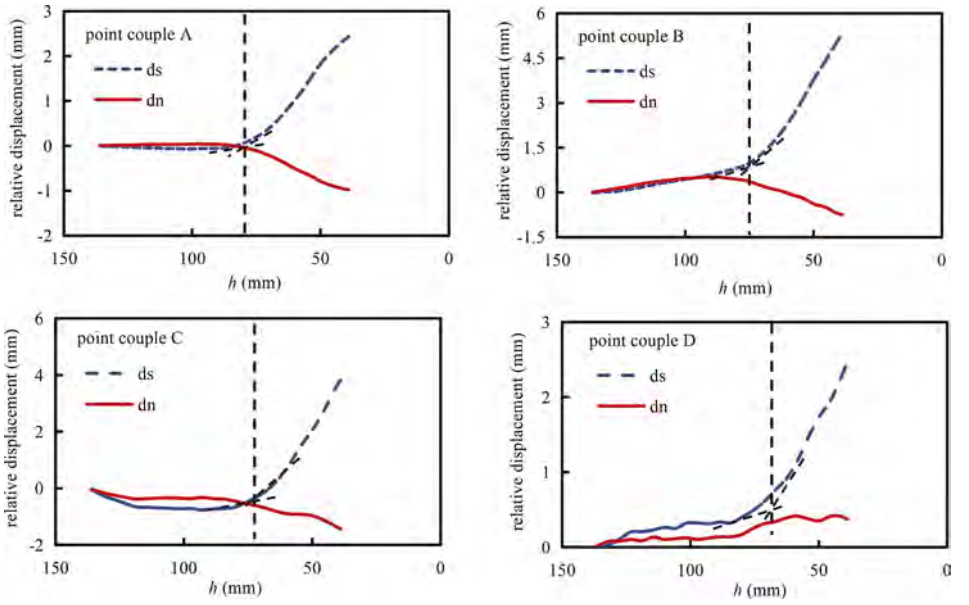

Figure 5. Relative displacement histories of point couples (locations shown in Figure 4). *ds*, the tangential relative displacement; *dn*, the normal relative displacement; *h*, the water level.

Figure 6 shows the slope displacement vectors of the slope. The displacement distributes nonuniformly and decreases from the exterior to the interior of the slopes. The sliding body and base body can be clearly distinguished according to displacement vector distribution. The displacement of the slope reinforced with dense micro anti-slide piles is much smaller than that of the sparse micro anti-slide pile. And the displacement distribution of the slope reinforced with dense micro anti-slide pile is more uniform. Therefore, it can be concluded that the decrease of pile spacing makes the soil deformation distribution more uniform, thus playing a better reinforcement effect.

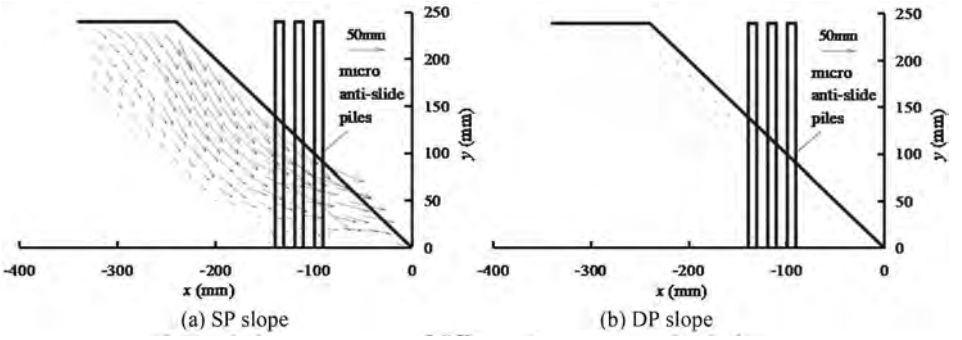

Figure 6. Displacement vectors of different slopes at a water level of 50mm.

Figure 7 shows the vertical distributions of the horizontal displacements of the soil in SP slope on the inner side of the piles (x = -219mm) and on the outer side of the piles (x = -81mm) under drawdown condition. On both sides of the pile, the horizontal displacement shows a trend of increase as the elevation increases. There is an obvious inflection point on the distribution curve near the inner side of the piles with the same location of the slip surface. The displacement of the soil inside the piles is small near the bottom of slope and increases rapidly at the inflection point. However, the vertical distributions of displacement of the soil outside the piles is approximately linear with the elevation and the slip surface outside the piles is close to the bottom. This confirms that the slope deformation behavior on both sides of piles is different. It can be inferred that the deformation of the soil outside the piles is affected by the compaction of the unstable piles during drawdown.

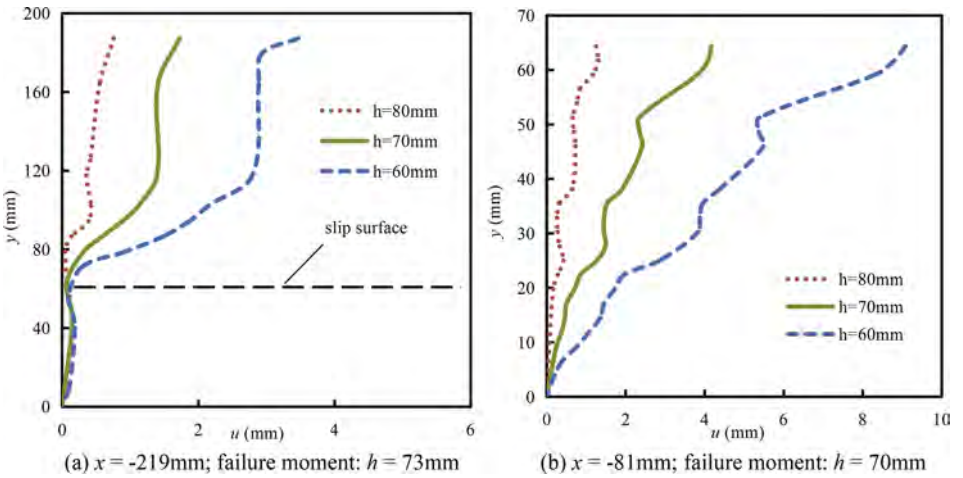

Figure 7. Vertical distributions of horizontal displacement of the soil on the both sides of piles in SP slope. u, horizontal displacement; h, water level.

4 REINFORCEMENT MECHANISM

Figure 8 shows the horizontal distributions of horizontal displacement at different elevations before and after failure of the slope reinforced with sparse piles. It can be seen that the displacement exhibits a uniform distribution. As approaching the foot of slope, the horizontal displacement of soil appears inflection point, which indicates that there is obvious deformation concentration. The displacement of slope increases gradually with decreasing water level. Therefore, the horizontal distributions of the gradient of the horizontal displacements are analyzed to explore the failure mechanism of the slope.

Figure 9 shows the horizontal distributions of the gradient of the horizontal displacements at different elevations. The slope deformation is obvious and its distribution is unevenly. The deformation increases as the water level decreases and there is an obvious peak near the slip surface. The deformation localization is confined within a region and the slip surface occur in this area. This indicates that the deformation localization of the slope leads to the local failure of the slope and the local failure of the slope strengthens the deformation localization of the slope. Therefore, there is a significant coupling effect between slope deformation localization and local failure.

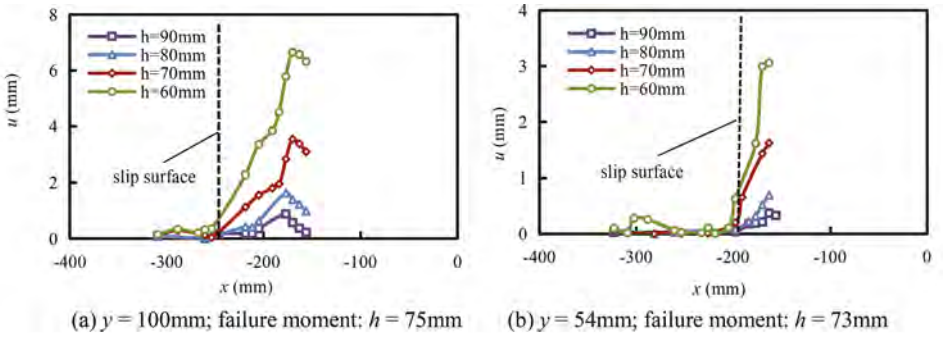

Figure 8. Horizontal distributions of the horizontal displacements of SP slope. *h*, water level; *u*, horizontal displacements.

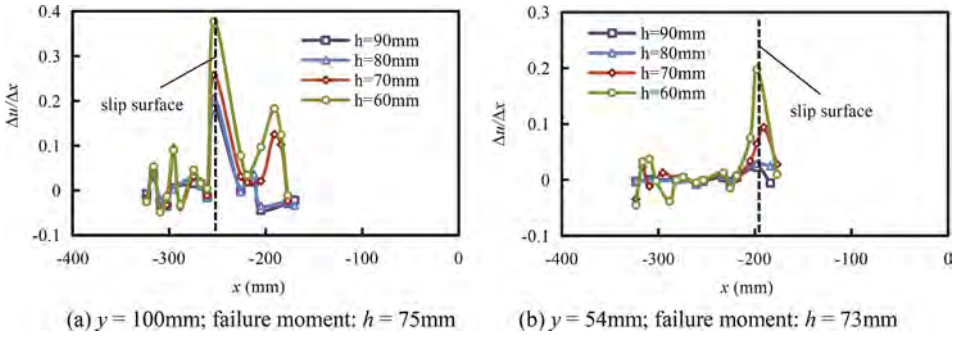

Figure 9. Horizontal distributions of the gradient of the horizontal displacements of SP slope. *h*, water level; *u*, horizontal displacement.

Figure 10 shows the horizontal distributions of the horizontal displacement gradient at the elevation of 100 mm in the two tests. The horizontal displacement gradient of the slope reinforced with sparse piles is larger than that of the slope reinforced with dense piles. There is no obvious peak of the horizontal displacement gradient in the slope reinforced with dense piles. This indicates that the decrease of pile spacing will make the horizontal displacement gradient smaller and the deformation more uniform. It can be deduced that the micro anti-slide piles restrict the deformation localization and thus increase the slope stability level.

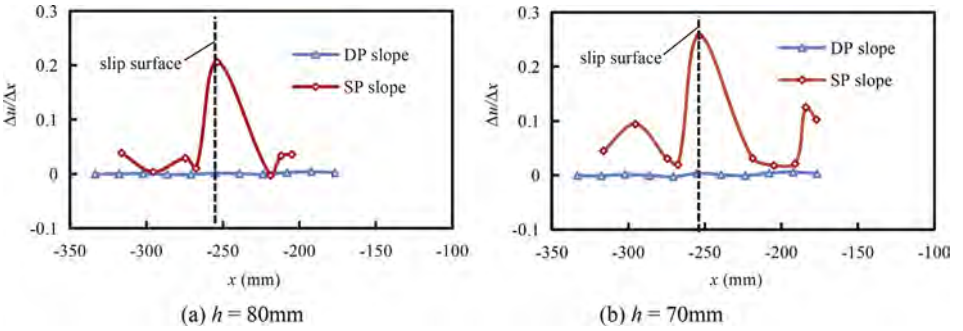

Figure 10. Horizontal distributions of gradient of horizontal displacements of slopes (y = 100mm; failure moment: h = 75mm). h, water level; u, horizontal displacements.

5 CONCLUSION

(1) The slip surface is discontinuous and is divided into two parts by the micro anti-slide pile group under drawdown conditions.
(2) The slip surface develops from the top of the slope to the bottom. The instability of micro anti-slide piles occurs before the slip surface appears on the inner side of the pile group.
(3) As the water level decreases, the slope deformation gradually increases, and the deformation localization appears. The slope deformation localization promotes the local failure of slope, and the local failure intensifies the slope deformation localization. There is a significant coupling effect between slope deformation localization and local failure during drawdown.
(4) The micro piles restrict the deformation localization and greatly improves the stability of the slope structure. The reduction of pile spacing can cause deformation distribution of the slope more uniform and increase the stability of the micro anti-slide pile group.

ACKNOWLEDGEMENTS

The study is funded by Tsinghua University Initiative Scientific Research Program and National Natural Science Foundation of China (52039005).

REFERENCES

Anbarasu K, Sengupta A, Gupta S (2010) Mechanism of activation of the lanta khola landslide in sikkim himalayas. *Landslides* 7(200):135–147.
Dong J, Wu Z, Li X, Chen H (2018) Dynamic response and pile-soil interaction of a heavy-haul railway embankment slope reinforced by micro-piles. *Computers and Geotechnics*, 100, 144–157.
Li CD, Fu ZY, Wang Y (2019) Susceptibility of reservoir-induced landslides and strategies for increasing the slope stability in the Three Gorges Reservoir Area: Zigui Basin as an example. *Engineering Geology* 261:105279.
Liu S, Luo F, Zhang G (2021) Pile reinforcement behavior and mechanism in a soil slope under drawdown conditions. *Bulletin of Engineering Geology and the Environment*, 80(5): 4097–4109.
Wang LP, Zhang G (2015) In flight simulation of pile installation in slopes in centrifuge model tests. *Geotechnical Testing Journal* 38(1): 50–60.
Yu YZ, Deng LJ, Sun X, Lu H (2010) Centrifuge modeling of dynamic behavior of pile-reinforced slopes during earthquakes. *Journal of Central South Universityof Technology* 17(5): 1070–1078.
Zhang G, Hu Y, Zhang JM (2009). New image analysis-based displacement-measurement system for geotechnical centrifuge modeling tests. *Measurement* 42(1): 87–96.
Zhang G, Wang LP, Wang YL. (2017). Pile reinforcement mechanism of soil slopes. *Acta Geotechnica* 12 (5): 1035–1046.

Smart Geotechnics for Smart Societies – Zhussupbekov, Sarsembayeva & Kaliakin (Eds)
© 2023 The Author(s), ISBN 978-1-003-29912-7
Open Access: www.taylorfrancis.com, CC BY-NC-ND 4.0 license

Effects of vertical ground motions on the fragility of slopes

D.T.P. Tran
Graduate Research Assistant, Department of Urban and Environmental Engineering, UNIST, South Korea

Y. Cho
Research Assistant Professor, Department of Urban and Environmental Engineering, UNIST, South Korea

B. Kim*
Associate Professor, Department of Urban and Environmental Engineering, UNIST, South Korea

ABSTRACT: Seismic fragility of slopes has been commonly assessed without the input ground motions in a vertical direction. This study addresses the influence of the vertical component of the input ground motions on the seismic fragility using finite element simulations. We consider 9 slope geometries comprising a combination of three slope heights (10 m, 20 m, and 30 m) and three slope angles (20°, 30°, and 40°). A total of 450 earthquake recordings are collected from NGA-West2 database that contain two horizontal (300=2×150) and one vertical (150) components. Each horizontal component is coupled with the vertical component, resulting in two sets of the input ground motions that produce 300 permanent slope displacements for one slope model. We compute the seismic fragility curves of slopes for three damage states based on a probabilistic seismic demand model. Results show that the probabilities of the slope damage subjected to the vertical-horizontal components of the input ground motions are greater than those subjected to the solely horizontal component. It turns out that the vertical component of the input ground motion affects the seismic fragility curves of the slopes.

1 INTRODUCTION

Seismic fragility of slopes has been mostly assessed through numerical modeling where slope models are subjected to input ground motion in an only horizontal direction. Recent research demonstrated the influence of the input ground motion in a vertical direction along with the horizontal component on the seismic responses of a slope (Zhang et al., 2016) and a bridge (Bhanu, 2018). In this study, we investigate the impact of the input ground motion in the vertical direction on the seismic fragility of slopes using finite element (PLAXIS 2D) simulations. 9 slope geometries (i.e., a combination of 3 slope heights and 3 slope angles) were created that were subjected to two groups of the input ground motions one of which are only with the horizontal components and the other of which are with both the horizontal and vertical components. With permanent slope displacements computed from the simulations, the seismic fragility curves of the slopes were generated based on the probabilistic seismic demand model (PSDM) for the two groups of the input ground motions, which were compared across the slope heights and angles.

2 FINITE ELEMENT SIMULATIONS

2.1 *Geometry and material properties of slope model*

Figure 1 shows a slope geometry generated in the PLAXIS 2D that consists of five geometric parameters (i.e., H_{slope} = a slope height, β = a slope angle, D = a depth below the slope height, L = a horizontal length of the slope model, and h = a thickness of sublayer of the slope model). We only considered a variation in the H_{slope} and β, resulting in 9 slope geometries

*Corresponding author: byungmin.kim@unist.ac.kr

DOI: 10.1201/9781003299127-157

derived from a combination of 3 slope heights (i.e., H_{slope} = 10 m, 20 m, and 30 m) and 3 slope angles (β = 20°, 30°, and 40°). The L, D, and h across the 3 slope angles were input as L = 108 m, D = 10 m, h = 5 m for the H_{slope} = 10 m, L = 215 m, D = 20 m, h = 10 m for the H_{slope} = 20 m, and L = 322 m, D = 30 m, h = 15 m for the H_{slope} = 30 m across 3 slope angles. The equally divided sublayers of the slope model were intended to account for the dependence of the normalized shear modulus reduction curves on the confining pressure. A nonlinear constitutive relationship for the slope material was described by the HSsmall model implemented in PLAXIS 2D. The strength and stiffness parameters required for the HSsmall model are a cohesion (c), friction angle (ϕ), and the initial shear modulus (G_{max}). We input the c = 10 kPa and ϕ = 30° for the strength parameters and four different values of the G_{max}.

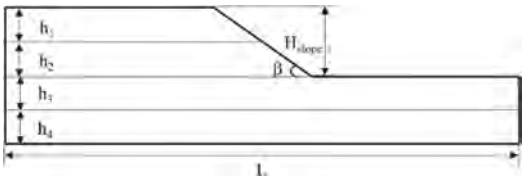

Figure 1. Considered slope geometry in PLAXIS 2D.

2.2 *Input motions and boundary conditions*

A suite of earthquake records was collected from the Next Generation Attenuation West 2 (NGA-West2) database that are 450 for two horizontal (H1 and H2) and one vertical (V) components (i.e., 150 for each component). Figure 2 shows 5% damped response spectra of the collected input ground motions for each component, accounting for a broad range of intensity and frequency contents of the input ground motions. The first group of the input ground motions contains only two horizontal components (i.e., the H1 and H2, 300 motions), and the second group is composed of each horizontal component coupled with the vertical component (i.e., the H1 with V and the H2 with V, 300 motions). They were applied to the 9 slope models, producing 2,700 maximum slope displacements on the slope surface for each group of the input ground motions.

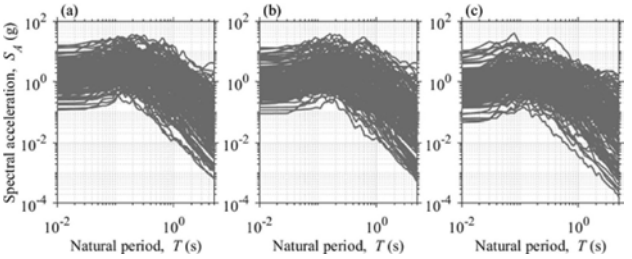

Figure 2. 5% damped response spectra of the 150 ground motions: (a) the first horizontal components; (b) second horizontal components; and (c) the vertical components.

Two conditions for the slope model boundaries are needed for the dynamic analysis, which are free-field condition for the slope model's left and right sides and compliant base condition for the slope model's bottom. Each condition was intended to simulate the semi-infinite boundaries analogous to a realistic ground condition by minimizing the reflected waves at the lateral and bottom boundaries.

3 FRAGILITY ANALYSIS

3.1 *Probabilistic Seismic Demand Model (PSDM)*

The multiple finite element simulations produced the maximum slope displacements (D) on the slope surface of which scatter plots against a peak ground acceleration in the horizontal

direction (PGA_H) are shown in Figure 3 for the slope models with the H_{slope} = 10 m across the three β = 20°, 30°, and 40°. The displacements at the low levels of PGA_H (i.e., $PGA_H \leq 0.05$ g for the slope with slope angle of 20°, and $PGA_H \leq 0.07$ g for the slope with slope angle of 30° and 40°) for the horizontal motions coupled with the vertical motions are mostly greater than those for the solely horizontal motions, however, the difference between the two groups of the input motions becomes negligible at the larger levels of PGA_H.

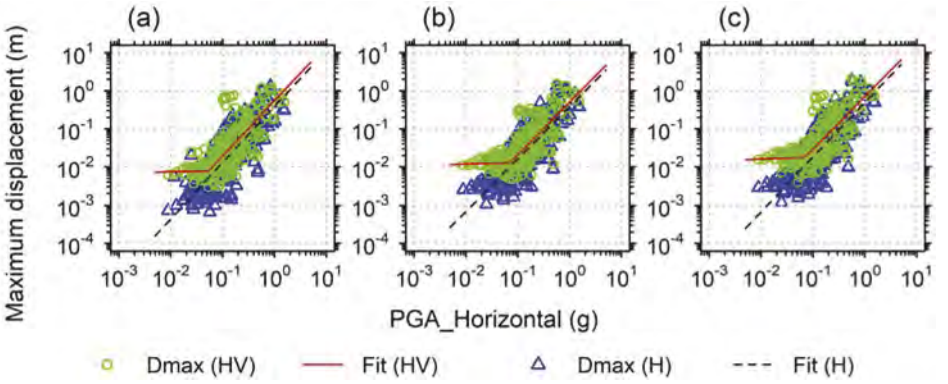

Figure 3. Relative permanent displacement against the PGA of horizontal motion for a slope height (H_{slope}) of 10 m and three slope angles (β) of (a) 20°; (b) 30°; and (c) 40°.

We adopted a probabilistic seismic demand model (PSDM), which describes a relationship between the PGA_H and slope displacement, to compute a probability of slope damage as follows:

$$\ln(D) = \ln(a) + b \cdot \ln(PGA_H) \tag{1}$$

where D is a median prediction of the maximum slope displacement, and a and b are coefficients of the linear regression analysis in natural log of the D and PGA_H.

3.2 *Seismic fragility assessment of slopes*

The fragility curve of the slopes is computed by a conditional probability of exceeding a certain slope displacement value for a given intensity measure (IM) level of the input ground motion as follows (Padgett et al., 2008):

$$P\left[Dd|IM\right] = \phi\left(\frac{\ln(D) - \ln(d)}{\sqrt{\beta_{D|IM}^2 + \beta_C^2 + \beta_M^2}}\right) \tag{2}$$

where $P\left[Dd|IM\right]$ is a probability of the demand exceedance, D is a seismic demand, $d$is values of the limit state, $\beta_{D|IM}$ is a logarithmic standard deviation of the seismic demand, β_C is a logarithmic standard deviation accounting for the uncertainty in the limit state that is assumed 0.3 based on Wen et al. (2004), and β_M = logarithmic standard deviation describing the modeling uncertainty that is assumed 0.3 based on HAZUS-MH (2003).

The $\beta_{D|IM}$ is calculated as below:

$$\beta_{\mathrm{D|IM}} = \sqrt{\frac{\sum\left(\ln(d_i) - (\ln(a) + b \times \ln(IM_i))\right)^2}{\mathrm{N} - 2}} \tag{3}$$

where d_i is the slope displacement computed from the finite element simulations, N is the number of the input ground motions that is 300 for only H1 and H2 component and 300 for the H1 and H2 coupled with V components.

Calculation on the fragility curves requires to specify limit states associated with certain threshold values. We selected three threshold values of slope displacement (i.e., 5 cm, 15 cm, and 30 cm) based on California Geological Survey (CGS) (Perez et al., 2012) which define limit states of the slope represented by the slope displacement exceeding the certain threshold values. Three limit states of the seismic slope displacement were considered that are minor (D < 5 cm), moderate (5 cm < D < 15 cm), and extensive (15 cm < D < 30 cm). The PGA_H was selected for the IM in this fragility analysis.

Figure 4 presents the calculated seismic fragility curves for the slopes with the three slope heights across the three slope angles. The probabilities of exceeding limit states for the motion group of the H1 and H2 combined with V are greater than those for the only H1 and H2 components, indicating that considering both vertical and horizontal components of the input ground motions make slopes more vulnerable than only horizontal components of the input ground motions for all slope models. In addition, the damage probabilities increase with slope angles as well as slope heights, which conforms to the fact that the factor of safety for slope stability analysis decreases with the slope angle and height.

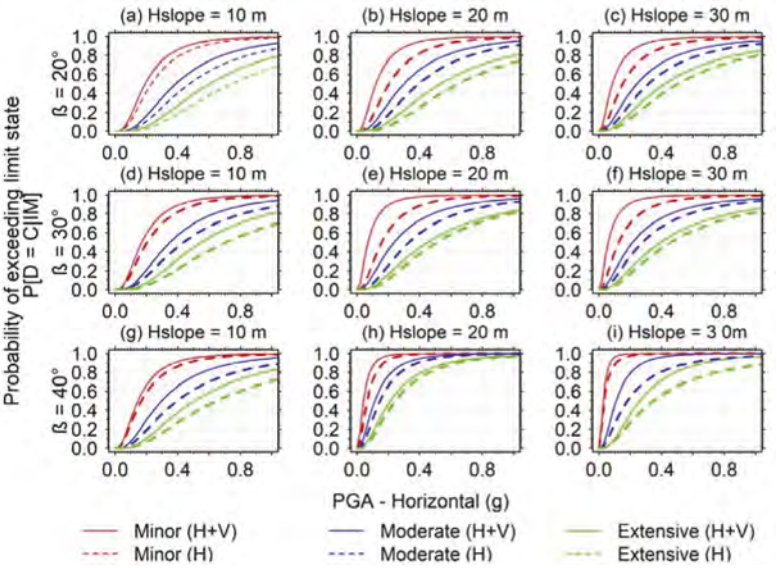

Figure 4. Seismic fragility curves for slope with three slope angles (β), as well as various slope heights (H_{slope}) under the two ground motion characteristics: (a) 20°, 10 m; (b) 30°, 10 m; (c) 40°, 10 m; (d) 20°, 20 m; (e) 30° 20 m; (f) 40°, 20 m; (g) 20°, 30 m; (h) 30° 30 m; and (i) 40°, 30 m.

4 CONCLUSIONS

This study investigated the effect of the ground motions' vertical component along with the ground motions' horizontal component on the seismic fragility curves of the slopes. The parametric finite element simulations were performed to calculate suites of the 5,400 maximum slope displacements for the two groups of the input ground motion that consist of the only horizontal component and the horizontal component together with the vertical component. The probabilities of exceeding limit states for the slopes were computed based on the PSDM for the two groups of the input motion. It was observed that the fragility curves for the motion group with vertical component were generally larger than those for the motion group containing only horizontal component across all the slope heights and angles, implying that the vertical component of the input ground motion had influence on the seismic fragility analysis of the slopes.

REFERENCES

Bhanu 2018. A Study on Vertical Component of Earthquake Ground Motion and its Effects on a Bridge. *Conference paper*.

Hazus-MH 2003. Federal Emergency Management Agency (FEMA). HAZUS-MH MR4 Technical Manual. Natl Inst Build Sci Fed Emerg Manag Agency (NIBS FEMA) 2003.

Padgett, J. E. & DESROCHES, R. 2008. Methodology for the development of analytical fragility curves for retrofitted bridges. *Earthquake Engineering & Structural Dynamics*, 37, 1157–1174.

Perez, Haydon & Wiegers 2012. California Geological Survey Zones of Required Investigation for Earthquake-Induced Landslides – Livermore Valley, California. *Digital Mapping Techniques 10-workshop proceedings U.S. Geological Survey Open-File Report 2012-1171*.

Wen, Ellingwood & Bracci 2004. Vulnerability Function FrameworkforConsequence-based Engineering.

Zhang, F., Gao, Y., Wu, Y., Zhang, N. & Qiu, Y. 2016. Effects of vertical seismic acceleration on 3D slope stability. *Earthquake Engineering and Engineering Vibration*, 15, 487–494.

Smart Geotechnics for Smart Societies – Zhussupbekov, Sarsembayeva & Kaliakin (Eds)
© 2023 The Author(s), ISBN 978-1-003-29912-7
Open Access: www.taylorfrancis.com, CC BY-NC-ND 4.0 license

Influence of pore pressure parameter on seismic stability analysis of geosynthetic reinforced soil slope

P.K. Meena
PhD Research Scholar, Department of Civil Engineering, IIT Roorkee, Roorkee, Uttarakand, India

K. Chatterjee
Assistant Professor, Department of Civil Engineering, IIT Roorkee, Roorkee, Uttarakand, India

ABSTRACT: An accurate seismic external stability analysis of geosynthetic reinforced soil slopes under pseudo-static conditions using limit equilibrium method is presented. The effect of variation of different parameters, such as slope angle, soil friction angle, seismic acceleration coefficients (k_h & k_v), surcharge, cohesion and water forces on required length of reinforcement (L) is presented. The combined effect of parameters like surcharge loading (q), pore pressure ratio (r_u), cohesion (c), hydrostatic & hydrodynamic pressure (p_{st} and p_{dy}) and formation of tension cracks Z_c are also considered in the analysis and their effect on L are discussed. All the computations have been carried out by writing a computer coded program in MATLAB. The present study shows that with the increase in c values, the magnitude of L decreases, while it increases with an increase in q and k_h to resist failure. Further as the pore pressure ratio increases, the length of reinforcement also increases to resist failure.

1 INTRODUCTION

Steep soil slopes are more susceptible to failure. To prevent failure, additional support should be provided to the soil to improve its shear strength. There are several methods to enhance the shear strength of soil, the reinforcement technique is one of them and is also worldwide popular nowadays because of its easy installation and better performance while in service. Analysis of these reinforced soil structures was done by Ling et al. (1997); Baker (1981). As per the available literature, most of the previous studies was done for cohesionless soil, considering dry backfill [Jewell (1990); Leshchinsky and Bodecker (1989)], few of them also considered the effect of water on both sides, but effect of vertical seismic acceleration coefficient was ignored Annapareddy and Pain (2019). Similarly, Agarwal and Pain (2021) considered the effect of k_v, but the effects of submergence were ignored.

In this present study, all the possible forces that cause failure and create the most critical condition for the reinforced soil slope are considered. The combined effect of cohesion, surcharge, hydrostatic, and hydrodynamic pressure is presented in this paper. Based on the previous literature, reinforced soil structures rarely fail in overturning. Therefore, although the primary focus is on direct sliding failure, but the analysis is done for both failure modes. As soil is weak in tension and when tensile forces generated in the soil exceed the tensile strength of soil, then cracks are formed on top surface of the slope. The soil in this tension crack zone already fails due to the formation of cracks; therefore, this soil is not contributing to shear strength but acts as a surcharge over the remaining slopes. In the stability analysis of reinforced soil slope, the effect of tension cracks should not be ignored [Abd and Utili (2017), Utili (2013)].

2 PROPOSED METHDOLOGY

A two-part wedge mechanism is used to analyze the external stability of geosynthetic reinforced soil slope against direct sliding and overturning modes of failure. A similar mechanism which was

DOI: 10.1201/9781003299127-158

used by Ling and Leshchinsky (1998) in their analysis, has been modified in the present study. This entire slope is divided into two wedges wedge A (abdf) is the quadrilateral shape, and wedge B (def) is the triangular shape. For better understanding, analysis is done separately for both wedges. For equilibrium of forces between two wedges, an inter-wedge force P is introduced (P_a and P_b). For the case $K_h = 0$ and $K_v = 0$, hydrodynamic pressure is zero and only hydrostatic pressure is generated, but for all other cases (K_v & $K_h \neq 0$), both hydrostatic and hydrodynamic pressures are considered. Due to the submergence of the soil, instead of using unit weight (γ), equivalent unit weight (γ_{eq}) is used [Ebeling and Morrison (1993)], which is formulated as:

$$\gamma_{eq} = \left(\frac{h_{wd}}{H}\right)^2 \gamma_{sat} + \left[1 - \left(\frac{h_{wd}}{H}\right)^2\right] \gamma_d \tag{1}$$

$$\gamma_{we} = \gamma_w + \left(\gamma_{eq} - \gamma_w\right) r_u \tag{2}$$

where r_u= pore pressure ratio; h_{wd}= height of water on downstream side; γ_{eq}= equivalent unit weight of soil γ_{we} = equivalent unit weight of water.

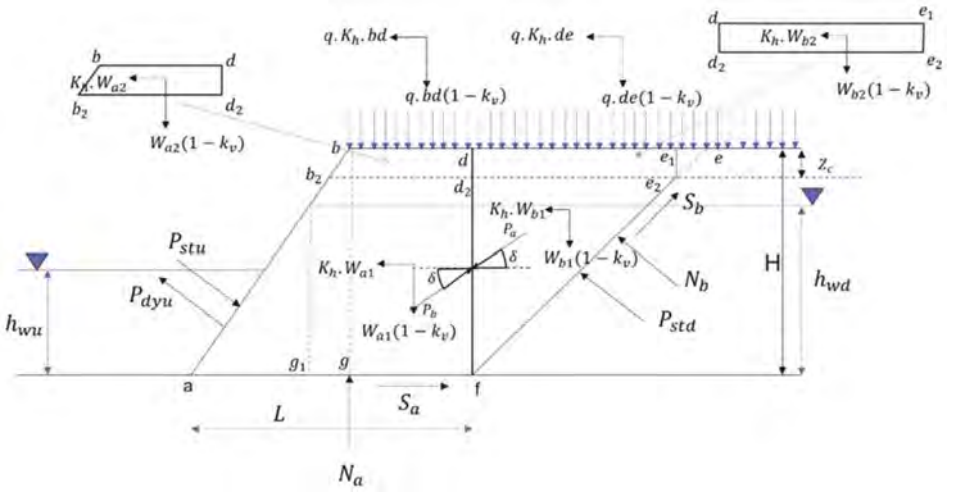

Figure 1. Free body diagram of soil slope for wedge A and B.

2.1 *Force equilibrium of wedge B*

The free body diagram is shown in Figure 1. To evaluate the inter-wedge force P_b equilibrium of forces in horizontal and vertical direction is done ($\Sigma F_y = 0$, $\Sigma F_x = 0$) for the case when formation of tension cracks is considered.

$$\sum F_y = -W_{b1}(1-k_v) - W_{b2}(1-k_v) - q(1-k_v)de_1 + S_b \sin\theta + (N_b + P_{std})\cos\theta + P_b \sin\delta \tag{3}$$

$$\sum F_x = -W_{b1}k_h - W_{b2}k_h - k_h de_1 q - (N_b + P_{std})\sin\theta + S_b \cos\theta + P_b \cos\delta \tag{4}$$

And therefore, expression for inter-wedge force (P_b) is obtained as:

$$P_b = \frac{\sin\theta(N_b + P_{std}) - k_h(W_{b1} + W_{b2} + q\cot\theta) - S_b\cos\theta}{\cos\delta} \tag{5}$$

where $P_{stu} = \frac{1}{2}\gamma_w h_{wu}^2$ and $P_{dyu} = \frac{7}{12}\gamma_w k_h h_{wu}^2$; P_{stu}, P_{dyu} are the hydrostatic and hydrodynamic pressure on upstream side; P_{std} is hydrostatic pressure on downstream side $= \frac{1}{2}\gamma_{we} h_{wd}^2$; k_h and k_v are seismic acceleration coefficients in horizontal and vertical directions.

2.2 *Force equilibrium of wedge A*

The force diagram is exemplified in Figure 1. Present study considered wedge A as rigid for analysis and hydrostatic and hydrodynamic thrust (P_{stu} and P_{dyu}) acting on upstream side is calculated by replacing γ_{we} with the γ_w. The minimum required length of geosynthetic reinforcement L becomes L_s for direct sliding and L_o for overturning conditions, respectively.

2.3 *Depth of tension crack*

In the present analysis, vertical cracks are considered and depth of tension crack which is a part of failure is evaluated by the expression $Z_c = \frac{2c}{\gamma_{eq}\sqrt{K_a}}$, where K_a is the coefficient of lateral earth pressure [Mononobe and Okabe (1926, 1929), Kramer (1996)].

2.4 *Minimum length of reinforcement against direct sliding and overturning*

Minimum required length of geosynthetic reinforcement against direct sliding is evaluated by using driving forces and resisting forces.

$$F_r = N_a C_{ds} \tan\phi + P_{stu} \sin\beta \tag{6}$$

where N_a is calculated by $\Sigma F_y = 0$ and C_{ds} is interaction coefficient between soil and particles.

$$F_d = (qbd + W_{a1} + W_{a2})k_h + P\cos\delta + P_{dyu}\sin\beta \tag{7}$$

where $P = P_a = P_b$, and $P_{dyu} = \frac{7}{12}k_h\gamma_w h_{wu}^2$. Hence, minimum length of reinforcement is calculated corresponding to FS=1.

$$FS = \frac{F_r}{F_d} \tag{8}$$

where weight of tension crack zone is W_{a1} and remaining soil of slope is W_{a2}.

Similarly, minimum required length of geosynthetic reinforcement against overturning is evaluated by using driving and resisting moment about toe.

$$M_d = P\cos\delta\frac{H}{3} + W_{a1}k_h CG_{y1} + W_{a2}k_h((H - Z_c) + CG_{y2}) + P_{dyu}0.4\frac{h_{wu}}{\sin\beta} + k_h qHbd \tag{9}$$

$$M_r = P\sin\delta L + q(1 - k_v)bd\left(ag + \frac{bd}{2}\right) + W_{a1}(1 - k_v)CG_{x1} + P_{stu}\frac{h_{wu}}{3\sin\beta} \tag{10}$$

$$FS = \frac{M_r}{M_d} \tag{11}$$

where, $ag = H\cot\beta$; $bd = L - ag$; $Z_c = \frac{2c}{\gamma_{eq}\sqrt{K_a}}$

3 RESULT AND DISSCUSSION

Analysis for input parameters mentioned in Table 1 are carried out and results have been discussed in this section. All the computation part is done using a computer coded program in

MATLAB for evaluating the required minimum length of the reinforcement against sliding and overturning modes of failure. The optimum value of inter-wedge force P is calculated with respect to assumed failure plane which is inclined at an angle θ with the horizontal. The value of k_h varying between 0.0 - 0.2 with an interval of 0.05. Instead of direct using cohesion (c) and surcharge (q) values, normalized values $c_n = c/\gamma_{eq} H$, $q_n = q/ \gamma_{eq} H^2$ are used in the analysis.

Table 1. Input parameters used in the present analysis.

Soil Properties	Values
H	5 m
β	60˚
ϕ	30˚
$c/\gamma_{eq} H$	0.02, 0.04, 0.06, 0.08, 0.1
$q/\gamma_{eq} H^2$	0.05, 0.1, 0.15, 0.2, 0.25
k_h	0.05, 0.1, 0.15, 0.2
k_v	$k_h/2$
h_{wd}/H	0.75
h_{wu}/h_{wd}	0.75
δ/ϕ	1

Results for varying parameters with different combination to evaluate the required minimum length of the reinforcement against sliding ($L_s = l_{ds}/ H$) and overturning ($L_o = l_{ot} / H$) is obtained. The possible critical conditions are presented and compared with the previous study of Choudhury and Ahmad (2009). When c_n and q_n values are considered, the obtained results are lower than the results of Choudhury and Ahmad (2009) as shown in Figure 2.

3.1 *Effect of k_h on length of reinforcement for sliding and overturning*

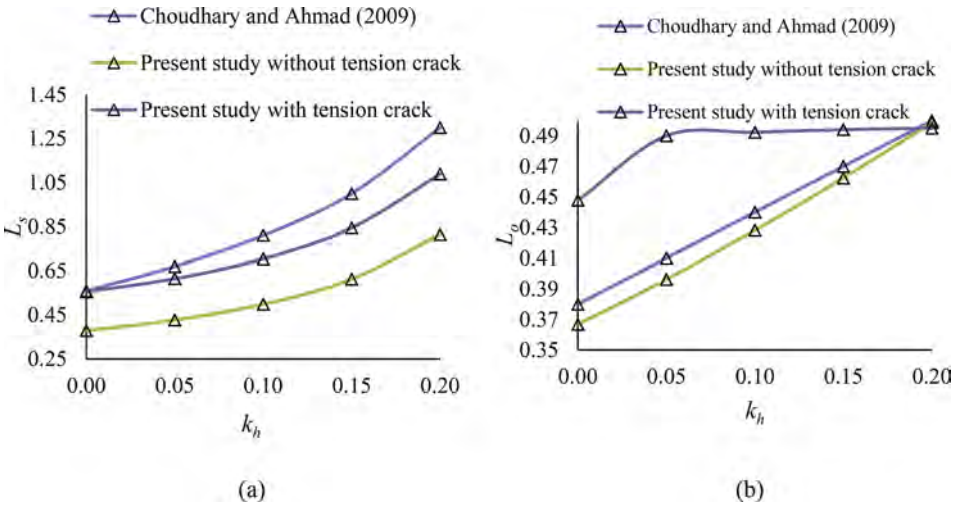

Figure 2. Variation of required minimum length of geosynthetic against (a) sliding, L_s (b) and overturning, L_o for c_n=0.06, q_n=0.15, k_v=k_h/2, β=60˚, ϕ=30˚, H=5 m, h_{wd}=0.75H, h_{wu}=0.75h_{wd}.

It can be seen from the Figures 2(a) and (b) that with increase in k_h from 0 to 0.2, the percentage increase in L_s and L_o are 53.36% and 26.48% (without tension crack), and 48.96% and 9.55% (with tension crack) respectively, for c_n=0.06 and q_n=0.15.

The value of L_s and L_o increases with the formation of tension crack due to reduce in the resisting forces. However, the percentage increase in L_s with the formation of tension crack is less as compared to the condition when there is no tension crack. Hence, for k_h value 0.2, the percentage decreases in L_s compared to Choudhury and Ahmad (2009) are 59.84% and 19.44% respectively for the conditions without tension crack and with tension crack.

3.2 *Effect of c_n and q_n on length of reinforcement for sliding and overturning*

It is observed from the Figure 3(a) and (b) that as the value of c_n and q_n increases, the length of reinforcement in sliding and overturning decreases respectively. It can be seen from Figure 3(b) for higher values of cohesion and surcharge, with increase in k_h there is negligible change in L_o.

With increases in k_h from 0 to 0.2 the percentage decreases in L_s are 55.94% and 92.32% respectively, when c_n increases from 0.02 to 0.1 for q_n is 0.05, and 34.64% and 60.59% respectively for q_n is 0.25.

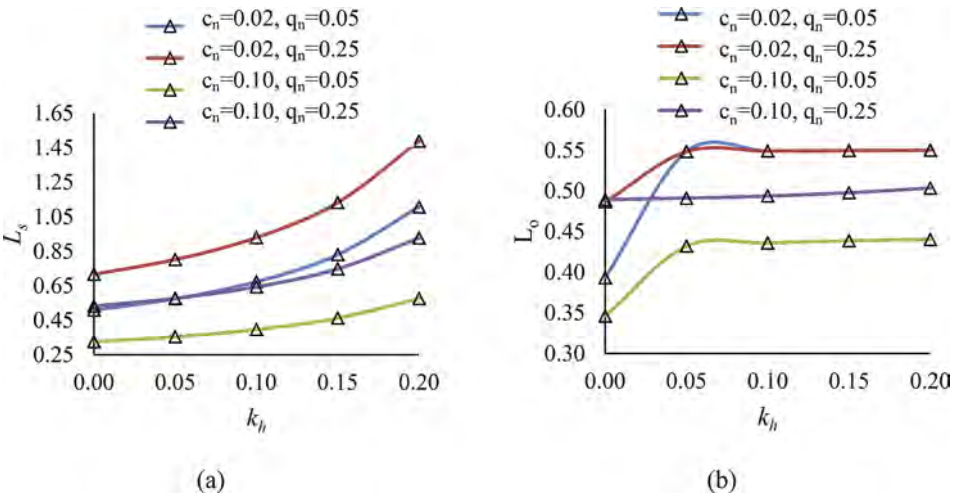

Figure 3. Variation of required length of reinforcement (a) against sliding, L_s (b) against overturning, L_o for different values of cohesion (c_n) and surcharge (q_n).

3.3 *Effect of pore water ratio on L_s*

It is observed the from results that with an increase in pore water ratio, the required length of the reinforcement against sliding and overturning modes of failure increases. However, increase in L_s with the formation of tension crack is higher than the condition when there is no tension crack. It can be observed from Table 2 that as the r_u changes from 0 to 0.4, L_s increased by 3.64% and 11.11% with tension crack, and 4.71% and 10.38% without tension crack corresponding to k_h = 0 and 0.2 respectively. An increase in k_h from 0.0 to 0.2,

Table 2. Variation of r_u over L_s for different k_h values.

	with tension crack		without tension crack	
k_h	r_u=0.0	r_u=0.4	r_u=0.0	r_u=0.4
0.0	0.55	0.57	0.36	0.40
0.05	0.60	0.63	0.41	0.45
0.10	0.69	0.72	0.48	0.52
0.15	0.83	0.86	0.58	0.64
0.20	1.06	1.11	0.77	0.85

percentage increases in L_o are 26.87%, 26.48% and 26.13% for different values of r_u, 0, 0.2 and 0.4 respectively corresponding to k_h vary from 0 to 0.2 for the condition when Z_c is zero.

4 CONCLUSION

The major conclusions that can be made from the present study are as follows:

- The required length of reinforcement against sliding and overturning depends upon the cohesion, surcharge, pore water ratio and k_h.
- As the k_h increases, the length of the reinforcement increases for given value of cohesion and surcharge. For the condition when tension crack is considered the increase in L_s is comparatively less than that of without tension crack condition.
- L_s decreased by 62.27% with increase in cohesion from 0.02 to 0.1, corresponding to k_h value is 0.05.
- for higher values of cohesion and surcharge, with increase in k_h there is negligible change in L_o.
- As the pore water ratio increases, the length of reinforcement against sliding increases for both the situations with and without formation of tension crack.

REFERENCES

Abd, A.H. and Utili, S., 2017. Design of geosynthetic-reinforced slopes in cohesive backfills. *Geotextiles and Geomembranes* 45(6): 627–641.

Agarwal, E. and Pain, A., 2021. Probabilistic stability analysis of geosynthetic-reinforced slopes under pseudo-static and modified pseudo-dynamic conditions. *Geotextiles and Geomembranes* 49(6): 1565–1584.

Annapareddy, V.R. and Pain, A., 2019. Effect of strain-dependent dynamic properties of backfill and foundation soil on the external stability of geosynthetic reinforced waterfront retaining structure subjected to harmonic motion. *Applied Ocean Research*, 91: 101899_1-9.

Choudhury, D. and Ahmad, S.M., 2009. External stability of waterfront reinforced soil structures under seismic conditions using a pseudo-static approach. *Geosynthetics International* 16(1): 1–10.

Ebeling, R.M. and Morrison Jr, E.E., 1993. The seismic design of waterfront retaining structures. *Army Engineer Waterways Experiment Station Vicksburg MS Information Technology Lab*.

Kramer, S.L., 1996. *Geotechnical earthquake engineering*. Pearson Education India.

Leshchinsky, D. and Boedeker, R.H., 1989. Geosynthetic reinforced soil structures. *Journal of Geotechnical Engineering* 115(10): 1459–1478.

Leshchinsky, D., Ebrahimi, S., Vahedifard, F. and Zhu, F., 2012. Extension of Mononobe–Okabe approach to unstable slopes. *Soils and Foundations* 52(2): 239–256.

Ling, H.I. and Leshchinsky, D., 1998. Effects of vertical acceleration on seismic design of geosynthetic-reinforced soil structures. *Geotechnique* 48(3): 347–373.

Ling, H.I., Leshchinsky, D. and Perry, E.B., 1997. Seismic design and performance of geosynthetic-reinforced soil structures. *Geotechnique* 47(5): 933–952.

Mononobe, N and Matsuo, H., 1929. On determination of earth pressure during earthquake. *In Proc. World Engineering Congress* Vol. 9: 177–185.

Okabe, S., 1926. General theory of earth pressure. *Journal of the Japanese Society of Civil Engineers* 12(1).

Senior, R.B., 1981. Tensile strength, tension cracks, and stability of slopes. *Soils and Foundations* 21(2): 1–17.

Utili, S., 2013. Investigation by limit analysis on the stability of slopes with cracks. *Geotechnique* 63(2): 140–154.

Woods, R.I. and Jewell, R.A., 1990. A computer design method for reinforced soil structures. *Geotextiles and Geomembranes* 9(3): 233–259.

Smart Geotechnics for Smart Societies – Zhussupbekov, Sarsembayeva & Kaliakin (Eds)
© 2023 The Author(s), ISBN 978-1-003-29912-7
Open Access: www.taylorfrancis.com, CC BY-NC-ND 4.0 license

Influence of aspect ratio and gully width on the run-out distance and velocity profile of dry granular debris flow

A. Ujjwal
P.G. Scholar, Indian Institute of Technology Guwahati, Assam

S. Sureka
Research Scholar, Indian Institute of Technology Guwahati, Assam

M. Mukherjee
Assistant Professor, Indian Institute of Technology Mandi, Himachal Pradesh

A. Dey
Associate Professor, Indian Institute of Technology Guwahati, Assam

ABSTRACT: Modeling of debris flow is very challenging due to the presence of multiphase heterogeneous materials and their complex interactions. For debris flows occurring in a hilly terrain, the width of the flow channel (or gully) and the aspect ratio of the dislodged mass significantly influences the final run-out distance and velocity profile of the flowing debris. In this regard, granular column collapse studies present a simplistic approach to comprehend the intricacies of such flows. In the present study, a 3-D Discrete Element Method (DEM) based simulation of dry granular column collapse has been carried out emphasizing the effect of initial aspect ratio of collapsing mass and channel width. Additionally, the influence of side wall friction of the channel on the depositional morphology of the flowing mass has been investigated.

1 INTRODUCTION

Understanding the behavior of geophysical flows such as debris flow is vital as its occurrence leads to catastrophic influences on life and property (Iverson 2014). These flows involve complex inter-particle interactions that govern the mass movement (Lajeunesse et al. 2004). It is therefore important to model such phenomena in order to understand the flow characteristics and the associated potential extent of damage. In this regard, several attempts have been made in the past by implementing physical models and different numerical methods; however, each of these approaches have its own merits and shortcomings (Iverson 2014, Kavinkumar et al. 2021). Discrete Element Method (DEM) is an effective numerical technique used for modelling such granular flows owing to its unique feature of capturing particle-particle interactions at every time step (Utili et al. 2015; Kavinkumar et al. 2021). Moreover, granular column collapse aids in creating dry granular debris flow in a simplistic manner, which could be conducted both experimentally (Lajeunesse et al. 2004) and numerically using DEM (Utili et al. 2015).

In hilly regions, the widths of the flow channel (or gully) and the aspect ratio of the dislodged mass appreciably affects the flow behavior and the depositional morphology. Hence, it is prudent to understand the effects of these parameters on the dry granular debris flow emanating from granular column collapse. In this study, granular columns of different aspect ratios have been allowed to collapse freely under gravity on a horizontal rigid bed within the gullies

DOI: 10.1201/9781003299127-159

of different widths. Very recently, an attempt has been made by Zhang et al. (2021) to study the effect of the uniform column thickness on such granular column collapse phenomenon. Keeping parity with the practical scenarios, the present work focuses on the channel geometries in which only the gully width is varied. Further, the influence of side wall friction on the run-out distance of the flowing mass has also been explored.

2 METHODOLOGY

2.1 *Defining run-out distance and validation study*

In DEM simulations of granular column collapse, measuring the run-out distance of dry granular flows is challenging as many particles that are leading the flow, roll to very large distances and, thus, cannot be accommodated in the measurement of run-out. Attempts to define the run-out distance based on certain parameters, such as number of particles (Utili et al. 2015) and coordination number (Kavinkumar et al. 2021), are available in the literature. However, these definitions of run-out distance could not suffice for different conditions of channel bed and granular column modelled using DEM. Considering the fact that run-out is directly related to the velocity of the flowing mass, a definition for the same has been chosen in this study based on the average particle flow velocity. Run-out distance has been defined by considering the flow length within which particles have velocity lesser than 1% of maximum average particle velocity attained during the flow. Such an estimation of run-out distance has been done at a significantly larger time scale so as to incorporate majority of the flowing particles within the run-out distance.

For performing the 3-D DEM simulations, an open-source software, LIGGGHTS (DCS Computing GmbH, Linz, Austria) has been used. The results of the computations have been visualized through a post-processing software called Paraview (Kitware Inc., New York, USA). Using the chosen definition of run-out distance for DEM simulations, granular column collapse simulations over a horizontal bed has been simulated and validated against the experimental results of Shi et al. (2018). The associated model geometry details and the employed model parameters are given in Table 1. Figure 1 shows the results of the validation study. It could be observed that the run-out distance predicted from the DEM simulations agrees well with the experimental results of Shi et al. (2018).

Table 1. Micro-mechanical properties and granular column geometry details considered while validating with the results of Shi et al. (2018).

Parameters/Properties used in validation study	Values
Micro-mechanical properties:	
Particle diameter (d) (m)	0.0021
Particle density (ρ) (kg/m^3)	2700
Modulus of Elasticity of particles (E) (N/m^2)	5×10^6
Coefficient of friction for interaction between column particles (μ)	0.7
Coefficient of friction for particle-wall and particle-gate interactions (μ')	0.424
Coefficient of rolling friction (μ_r)	1.25
Poisson's Ratio (v)	0.31
Coefficient of Restitution (e)	0.7
Packing porosity of the column (n)	0.43
Contact Model used	Hertz tangential history (H – MD) with rolling friction constant directional torque (CDT)
Granular column geometry details:	
Column width (m)	0.05
Column height (m)	0.05
Column thickness (m)	0.09

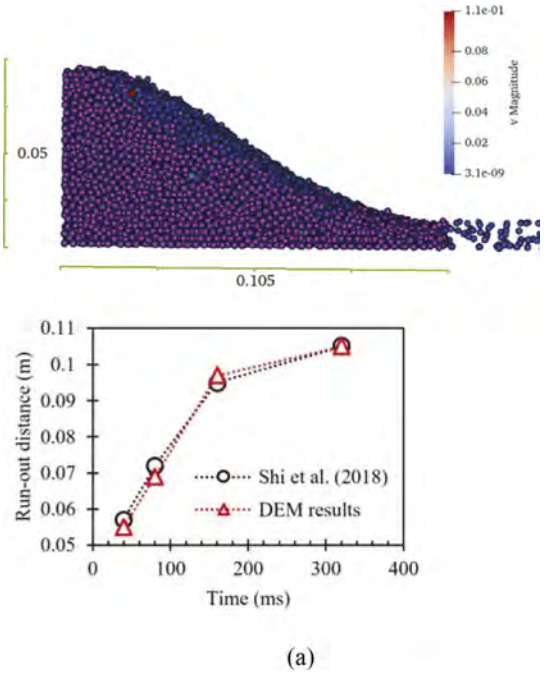

Figure 1. Validation of the experimental results of Shi et al. (2018) using DEM.

2.2 *Model geometry for flow path configuration*

For understanding the effects of gully width on the debris flow behavior using DEM, the particles in the granular column are allowed to flow through a trapezoidal (hopper shaped) channel (Figure 2) before entering the main constricted gully (of uniform width) so as to direct the entire granular mass within the gully. Such a flow path is generally encountered in hilly terrain by the dislodged mass and the same scenario has been mimicked though the chosen geometry condition. The micro-mechanical parameters and other relevant geometry configurations used in this set of DEM simulations are given in Table 2.

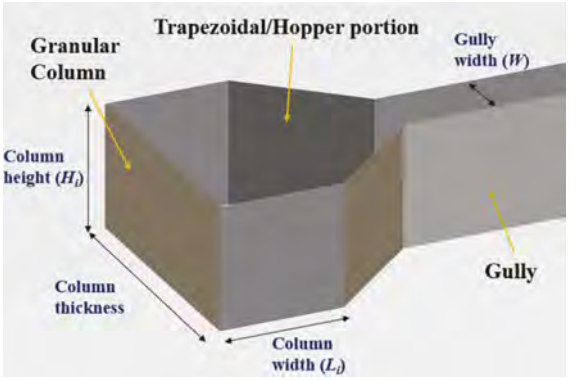

Figure 2. The hopper/trapezoidal channel configuration employed for conveying the initial granular column into the constricted gully.

2.3 *Simulation of flow process*

In this study, four different aspect ratios (a) of the granular column have been taken, i.e., 1, 2.8, 4.6 and 6.4. The particles have been first inserted within the column (rectangular) and then the confining gate has been removed instantaneously to initiate the flow. The granular particles of the collapsing column have been allowed to flow over a frictional planar horizontal bed. In order to carry out effective comparisons, the simulation output parameters have been normalized as per Eq. 1. The width of the gully (W) has been normalized with respect to the particle diameter (d) as given in Table 1.

$$[L] = L_f - L_i/L_i \tag{1a}$$

$$[H] = H_f/L_i \tag{1b}$$

$$[V] = V/\sqrt{gH_i} \tag{1c}$$

$$[T] = T_f/\sqrt{H_i/g} \tag{1d}$$

where L_f is the final run-out distance; L_i is the initial column width; $[L]$ is normalized run-out distance; H_f is the residual column height, i.e., the height of the particles of the column in the final deposited state after the collapse; H_i is the initial column height; $[H]$ is the normalized residual column height; V is the flow velocity; $[V]$ is the normalized flow velocity; T_f is the duration of flow; and $[T]$ is the normalized duration of flow.

Table 2. Micro-mechanical properties and specifications of model geometry considered for DEM simulations of granular column collapse and flow through gully.

Parameters/Properties	Values
Micro-mechanical properties:	
Particle diameter (d) (m)	0.006
Particle density (ρ) (kg/m^3)	2700
Modulus of Elasticity of particles (E) (N/m^2)	5×10^7
Coefficient of friction for interaction between column particles (μ)	0.6 (same for the side walls and gate)
Poisson's Ratio (v)	0.3
Coefficient of Restitution (e)	0.7
Packing porosity in the column (n)	0.43
Contact Model used	Hertz tangential history (H – MD)
Specifications for granular column collapse model:	
Column width (L_i) (m)	0.06
Column thickness (m)	0.12
Aspect ratio ($a = H_i/L_i$)	1, 2.8, 4.6, 6.4
Specifications for trapezoidal channel and gully:	
Length of the trapezoidal/hopper region (m)	0.05
Channel/gully width (W) (m)	0.09, 0.06, 0.03
Normalization of the channel/gully width with respect to particle diameter:	
Normalized channel/gully width (W/d)	5, 10, 15

3 RESULTS AND DISCUSSION

3.1 *Variation in run-out distance with gully width and aspect ratio*

Dry granular debris flow behavior has been studied for different gully widths (W/d) using granular columns of different aspect ratios (a). Particle configuration in the final deposited state of the collapsed granular column is shown in Figure 3. For the sake of brevity, the depositional configurations are depicted only for a = 2.8. Similar particle configurations have

been obtained for other aspect ratios as well. Figure 4 represents the variation in run-out distance with respect to W/d and a. It can be observed that as the gully width increases, the run-out distance increases for all values of a. This indicates that a wider gully increases the reach of disastrous geophysical flows. Moreover, the run-out distance of the flow increases with the increase in the value of a. Hence, the aspect ratio of dislodged mass can significantly influence its flowing distance and reach. Interestingly, it could be observed that the influence of gully width on run-out distance is more prominent for larger aspect ratios.

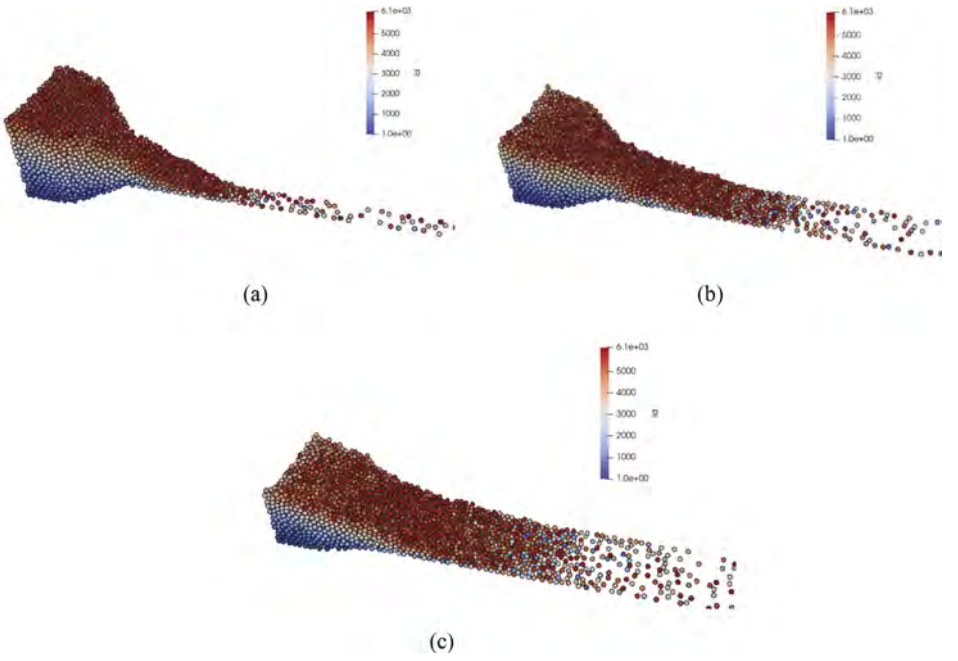

Figure 3. Particle configuration in the final deposit of the collapsed granular column for (a) W/d = 5, (b) W/d = 10 and (c) W/d = 15 for a = 2.8 (color contour shows the particle number).

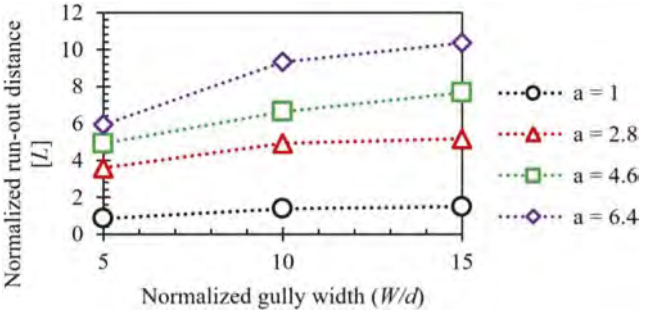

Figure 4. Variation of the normalized runout length [L] with normalized gully width (W/d) for different aspect ratios (a) of the column.

Figure 5 shows the variation in residual column height with W/d and a. It could be inferred that as the gully width increases, the residual column height decreases due to increase in the free movement of the particles. Moreover, residual column height increases with the increase in the value of a, indicating that higher aspect ratios could yield thicker deposits. Similar to the previous observation on run-out distance, residual column height for larger aspect ratios is more affected by gully width variation.

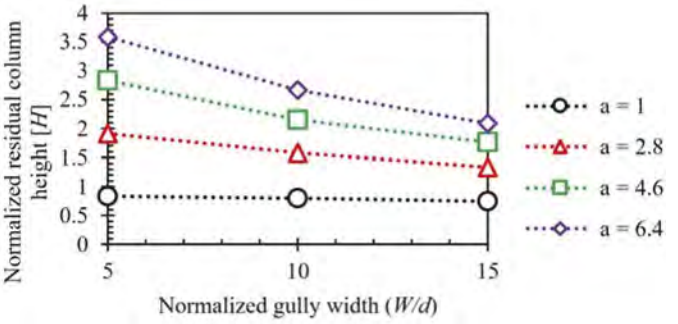

Figure 5. Variation of the normalized residual column height [H] with normalized gully width (W/d) for different aspect ratios (a) of the column.

3.2 *Variation in velocity profile with gully width and aspect ratio*

Figure 6 shows the velocity profiles of flow for different values of W/d and a. These velocity profiles are the plots of average particle velocity (V) with respect to the flow duration (T). Average particle velocity has been obtained by averaging the velocity magnitudes of all the particles at each time step. It could be observed from Figure 6 that as the gully becomes wider, the average velocity of the particles increases for each of the aspect ratios. A direct implication of this behavior is reflected by an increased run-out distance in wider gullies. To investigate the effect of aspect ratio on flow velocity, the variation in maximum of average particle velocity (V_{max}) has been plotted with respect to a for different values of W/d as shown in Figure 7. It could be noticed that as the value of a increases, V_{max} also increases for all gully widths. This implies that

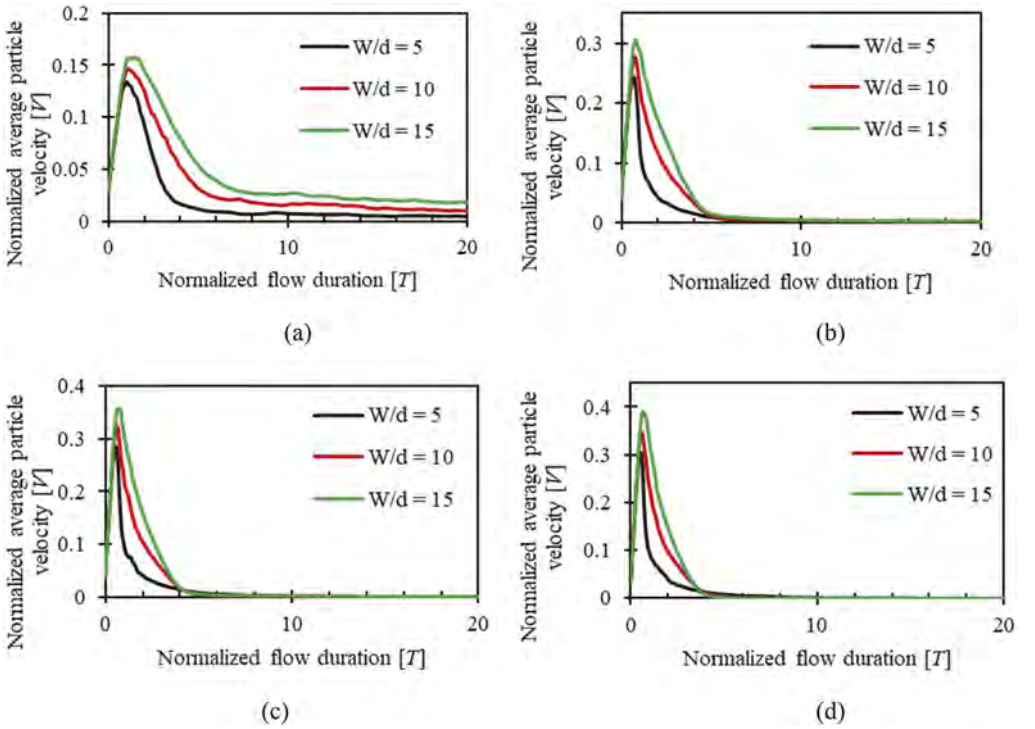

Figure 6. Velocity profiles of the dry granular debris flow represented as variation of normalized average particle velocity [V] with normalized flow duration [T] for (a) a = 1, (b) a = 2.8, (c) a = 4.6 and (d) a = 6.4 at different values of W/d.

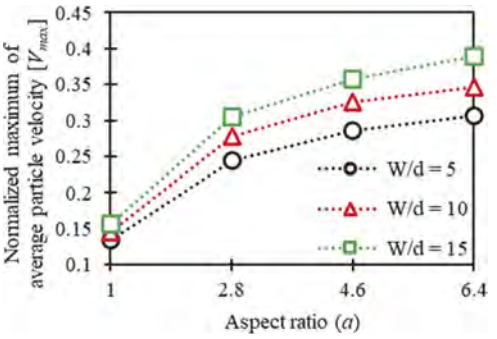

Figure 7. Variation of normalized maximum of average particle velocity [V_{max}] with aspect ratio (a) of the column for different normalized gully widths (W/d).

with the increase in the aspect ratio of the granular column, its initial total energy increases which causes higher kinetic energy and leads to higher velocity as the flow progresses.

Figure 8 depicts the variation of bulk (average) coordination number ($\bar{C}$) of the particles with respect to flow duration (T). $\bar{C}$ represents the average number of particles which are in contact with any specific particle within the flowing mass. It could be observed that as the gully width increases, the bulk coordination number decreases for each of the aspect ratios. This means that as the gully becomes wider, each of the particles have lesser number of neighboring particles in contact and, hence, such particles are more disconnected, thereby leading to an enhanced free movement. The initial sharp reduction in the values of bulk coordination number reaching a trough is related to the attaining of maximum particle velocity (and/or maximum kinetic energy). Therefore, a decrease in the bulk coordination number with the increase in gully width indicates a simultaneous increase in the value of the velocity of the particles, as apparent from Figure 7. On the other hand, for a particular aspect ratio, lesser residual values of the bulk coordination number for higher values of W/d qualitatively indicates larger run-out distances.

Additionally, with the increase in the value of a, the minimum bulk coordination number attained decreases, thereby indicating large particle velocities for higher aspect ratios. Similar observations regarding the effect of aspect ratio on bulk coordination number have been reported by Kavinkumar et al. (2021). However, the bulk coordination number is greatly affected by the initial mass or initial number of particles in the granular column. This is apparent from the fact that the residual values are getting closer for different gully widths as the magnitude of a increases (i.e. initial number of particles in the column increases). Contrary to this behavior of residual values of bulk coordination number which represent the reach of the flow, larger aspect ratios have shown prominent variation in the values of run-out distance based on different gully widths (Figure 4). Hence, it is not wise to correlate the variation in the bulk coordination number quantitatively with the variation in the velocity or run-out distance, especially, when the comparison is done for different aspect ratios having different initial number of particles within the column. Furthermore, the observations made by Zhang et al. (2021), showcasing the relation between particle velocity and bulk coordination number for different thicknesses of the granular column, are not in parity with the findings of this study for different gully widths. This is attributed to the reason that for a particular aspect ratio, the initial number of particles in the column remains the same for each of the gully width considered in the present study; whereas, this is not the case with the increase in column thickness as reported by Zhang et al. (2021).

Figure 9 Shows the plots of total dissipated energy (E_{diss}) with respect to a for different values of W/d. E_{diss} is calculated according to Utili et al. (2015) as mentioned in Eq. 2.

$$E_{diss}=E_0-E_p-E_k \tag{2a}$$

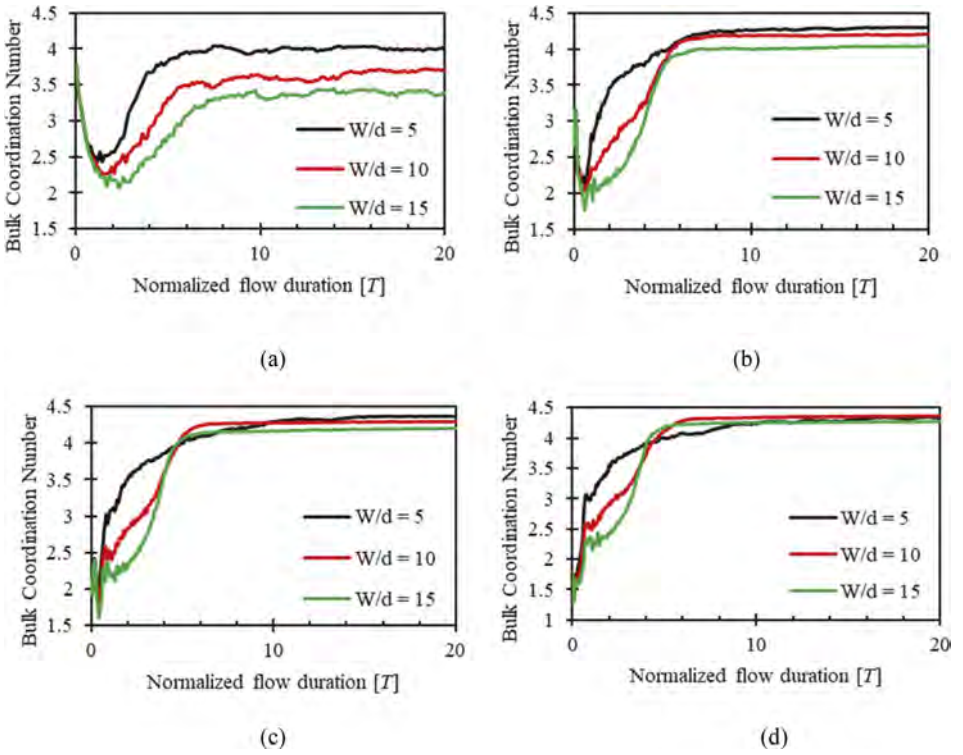

Figure 8. Plots of bulk coordination number ($\bar{C}$) with respect to normalized flow duration [T] for (a) $a = 1$, (b) $a = 2.8$, (c) $a = 4.6$ and (d) $a = 6.4$ at different values of W/d.

$$E_0 = mgH_i/2 \tag{2b}$$

where E_0 is the initial total energy of the column calculated as per Eq. 2b; m is the total mass of particles inside the column; E_p and E_k are the total potential energy and the total kinetic energy, respectively, at the end of the flow. It could be observed that the total dissipated energy (E_{diss}) increases with an increase in the gully width. This is due to the reason that as the gully becomes wider, owing to enhanced free movement of particles, there is a significant increase in particle-particle collisions along with their interactions with the bed and the side walls. This leads to larger energy dissipation. The same is true for the increase in the value of a as well.

3.3 *Effects of side wall friction, coefficient of restitution and rolling friction on the run-out distance*

The depositional morphology of the dry granular debris flow is also governed by the friction of side walls of the gully in hilly terrain. In order to investigate the effect of side wall friction on the depositional behavior of flow emanating from granular column collapse using DEM, four different values of friction coefficient have been chosen, i.e., 0, 0.2, 0.4 and 0.6. The same has been visualized for all the considered gully widths. However, for brevity, only two extreme aspect ratios, i.e., $a = 1$ and $a = 6.4$ are considered in this study. Figure 10 shows the variation in run-out distance and residual column height with respect to the side wall friction coefficient for the chosen cases.

It could be observed from Figure 10 that, for all the gully widths, as the coefficient of side wall friction increases, there is a reduction in the run-out distance with an augmentation in the residual column height. However, such a variation is noted to be more pronounced for $a = 6.4$ than that observed for $a = 1$. This indicates that the effect of side wall friction of the gully on the

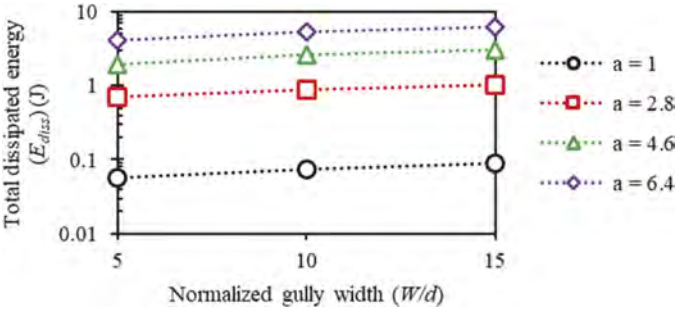

Figure 9. Variation of total dissipated energy (E_{diss}) with normalized gully width (W/d) for different aspect ratios (a) of the column.

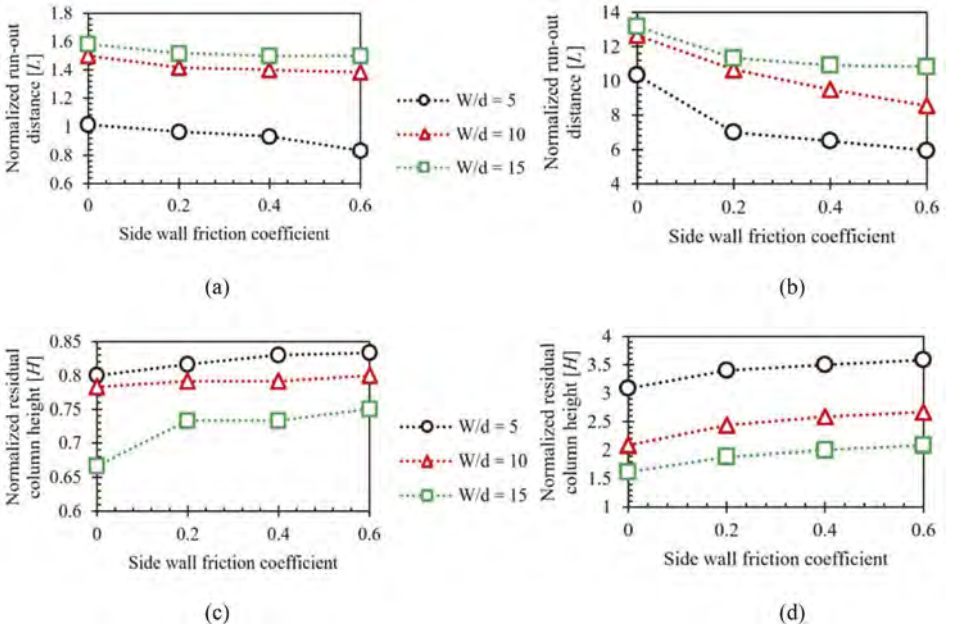

Figure 10. Variation in the values of normalized run-out distance [L] and normalized residual column height [H] for (a, c) a = 1 and (b, d) a = 6.4, respectively with side wall friction coefficient for different values of W/d.

depositional morphology of the collapsing mass is significantly influenced by its initial aspect ratio. Moreover, it is apparent that as the gully becomes wider, the effect of side wall friction on the run-out distance becomes lesser for both the aspect ratios considered in the present study.

4 CONCLUSIONS

Dry granular debris flows in hilly terrains are expected to propagate through gullies of constricted widths which can in turn affect their flowing behavior and depositional morphology. In this study, the influence of gully width has been studied for the flows emanating from dry granular column collapse using DEM. Additionally, the effects of initial aspect ratio of the column on the velocity profile and deposition characteristics of such flows have also been examined. It has been found that as the gully becomes wider, the run-out distance of the flow increases and the residual column height reduces. The obtained velocity profiles show that the

particle flow velocity increases for wider gullies and for larger aspect ratios of the granular column. Similar inferences could also be made on the basis of the variations in bulk coordination number. Moreover, the total dissipated energy during the flow increased with the increase in gully width and aspect ratio of the column. Hence, it could be concluded that larger is the aspect ratio of the dislodged mass and more is the width of the flow channel or gully, larger would be the reach of the flowing particles. Side wall friction of the gully also influences the deposition behavior of the dry granular debris flows, especially those originating from columns of larger aspect ratios. Apparently, wider gullies have lesser effect of side wall friction on the run-out distance.

REFERENCES

Iverson, R. M. 2014. Debris flows: behaviour and hazard assessment. *Geology today* 30(1): 15–20.

Kavinkumar, C., Sureka, S., & Rakesh, J. P. 2021. Influence of erodible layer on granular column collapse using discrete element analysis. *Geomechanics and Geoengineering* 2021: 1–13.

Lajeunesse, E., Mangeney-Castelnau, A., & Vilotte, J. P. 2004. Spreading of a granular mass on a horizontal plane. *Physics of fluids* 16(7): 2371–2381.

LIGGGHTS, DCS Computing GmbH, Linz, Austria. https://www.cfdem.com/liggghts-open-source-discrete-element-method-particle-simulation-code. Last accessed 11/07/22.

Paraview, Kitware Inc., New York, USA. https://www.paraview.org/. Last accessed 11/07/22.

Shi, B., Zhang, Y., & Zhang, W. 2018. Analysis of the entire failure process of the rotational slide using the material point method. *International Journal of Geomechanics* 18(8): 04018092.

Utili, S., Zhao, T., & Houlsby, G. T. 2015. 3D DEM investigation of granular column collapse: evaluation of debris motion and its destructive power. *Engineering geology* 186: 3–16.

Zhang, R., Su, D., Lei, G., & Chen, X. 2021. Three-dimensional granular column collapse: Impact of column thickness. *Powder Technology* 389: 328–338.

Smart Geotechnics for Smart Societies – Zhussupbekov, Sarsembayeva & Kaliakin (Eds)
© 2023 The Author(s), ISBN 978-1-003-29912-7
Open Access: www.taylorfrancis.com, CC BY-NC-ND 4.0 license

Classification of zero-order basins on the basis of valley development and risk assessment of sediment runoff

N. Nakajima
Chiken Co., Ltd, Kochi City, Kochi Prefecture, Japan

T. Hara
Kochi University Kochi City, Kochi Prefecture, Japan

ABSTRACT: In Japan, sediment runoff at zero-order basins has become a serious issue from the viewpoint of disaster prevention and mitigation. Our urgent task is establishing an effective and integrated method of assessing its risk. This study analyzes topographical characteristics of zero-order basins in the actually affected three areas. We show sediment runoff is closely related to valley development and figure out the possibility of assessing the risk at differently featured zero-order basins by categorizing them into four classes; Youth, Adolescent, Mature and Old, and only by measuring their total length.

1 INTRODUCTION

With recent worldwide climate changes progressing, Japan has experienced frequent intensive heavy rains and has been affected by increasing number of sediment disasters annually. To combat these disasters, various countermeasures are now being applied both tangibly (such as debris barriers) and intangibly (such as designating warning zones and informing the residents of them). Of late, sediment runoff from small basins at steep slopes are emerging as new problems. Such sediment disasters cause damages to buildings or cut off roads although they are local and of small scales. Extracting these risky basins is an urgent issue in discussing the countermeasures for them. These small basins are defined as zero-order basins, smaller by one order then first-order basins by Horton-Strahler scales (Tsukamoto et al., 1973). By the Basic Guideline about debris flows (Ministry of Land, Infrastructure, Transport and Tourism, 2016) zero-order basins are defined as a place which has a concave contour line with the ratio of valley frontage width to depth, one to less than one.

Some experts have suggested the methods for extracting dangerous spots at steep slopes including zero-order basins. Kanai et al. (2016) suggested the method for extracting dangerous spots by studying the gradient of slopes and the depth of loose sediment layers. Shirasawa et al. (2018), by using DEM. Kinoshita et al. (2019), by focusing on the number of basins at a specific slope. Murakami (2016) in his site investigation estimated the volume of sediment flows at dangerous basins including zero-order basins and presented the method to extract dangerous basins that would cause damage to high-ways. Their studies are about assessing the possibility of slope failure and the resulting damage but not about assessing the danger of sediment runoff and the volume of its damage in a simple and integrated way.

We organized the data of the topography geological features and the scale of damage at the zero-order basins affected in the incident of Heavy Rain, July 2018 and discussed the extracting methods of dangerous basins. (Nakajima et al., 2019) In this study we tried to categorize zero-order basins focusing on the relation between the topography of the basins and the volume of sediment runoff. We tried to get the rough risk assessment method at zero-order basins by combining this result with the volume of damage.

DOI: 10.1201/9781003299127-160

2 SAMPLE LOCATIONS AND ANALYSIS METHOD

Three locations studied in this study are shown in Figure 1. These locations are situated in Chugoku and Shikoku and affected by the Heavy Rain in July 2018. Tachibanaura, Otsuki-cho, Hata-gun, Kochi is 36km northwest from Ashizuri Cape at the east end of Kochi and has a 530m-wide slope facing east with 6 zero-order basins. Shiraura, Yoshida-cho, Uwajima-City, Ehime is situated 55km north from above mentioned Tachibanaura, and has 370m-wide slope facing north with 14 zero-order basins. Yasuura, Kure-City, Hiroshima is situated 165km north from Tachibanaura and has 520m-wide slope with 8 zero-order basins. Sediment disasters occurred at three basins in Tachibanaura, four in Shiraura and three in Yasuura. In all three locations, the roads were temporarily blocked and building damage was confirmed in Tachibanaura.

We adopted topographical analysis in analyzing, figuring out the average slope gradient adding to total valley length and b/a as in Figure 2. Valley total length is the range with contour lines situated above flat place with houses. The ratio b/a is measured in every specific from 5 to 10m height. The average slope angle is measured using the total valley length and the difference in elevation between the two ends. For topographical analysis we used Sabo Fundamental Geospatial Data prepared before the disaster and a topographical map based on Aerial laser data. We conducted a field survey, checking visually the valley slopes and the source head in the zero-order basins. Three years had passed before our field survey but still evident were the failure and erosion in the zero-order basins. We recognized the damage situation through interviews with the local people and by the aerial photomaps taken just after the disaster. In this study, we defined the surface failure on the source head as failure, the sediment flow reaching the road or the houses at the foot of the slope as sediment runoff, the sediment accumulating at the end of the slope as runoff sediment.

3 CLASSIFICATION OF ZERO-ORDER-BASINS ON THE BASIS OF THE STATE OF DEVELOPMENT

The data of topographical features were gathered from 28 zero-order basins distributed in these three areas. The narrow slopes, even under the same condition of rainfall showed different damage situation, different total valley length and different b/a. Total valley length and estimated amount of runoff sediment are shown in Figure 3. Although our analysis is limited, we found out the estimated runoff sediment increases as the total valley length become longer. In the case of the zero-order basin longer than 80m, sediment runoff begins to be seen, and runoff sediment amount show a sudden big increase when it becomes longer than 200m. It isn't always the case, but the amount of runoff sediment and total valley length are related to some extent. The total valley length is one of the factors influencing the amount of runoff sediment. We classified the development process of zero-order basins according to the total valley length. Table 1 shows a relation between the classified topographical features and the estimated amount of runoff sediment. Zero-order basins are classified into four, in length order, Youth, Adolescent, Maturity and Old. The zero-order basin classified as Old has a low average slope angle of 22 degrees and has no sediment runoff though it has the biggest length of 451m.

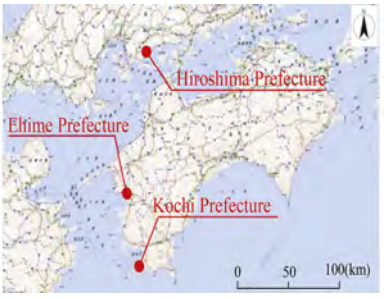

Figure 1. Survey position.

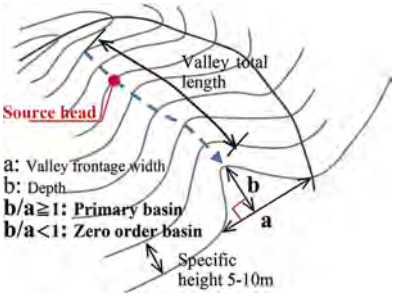

Figure 2. Topography and interpretation schematic of the zero-order basin.

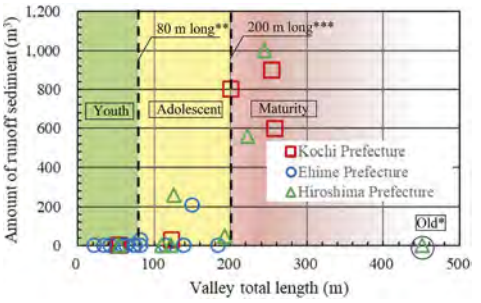

Figure 3. Total length of the valley and amount of runoff sediment.

*Average valley slope is 22 degrees. **Line where sediment outflow begins. ***Line where the amount of runoff sediment increases.

Table 1. Development classification and topographical features of the zero-order basin.

Development classification	Valley total length (m)	Maximum b/a	Valley slope (°)	Amount of runoff sediment* (m^3)
Youth	~ 80	~0.2	35~	0
Adolescent	80 ~ 200	0.2 ~0.4	30~34	0 ~ 500
Maturity	200 ~ 450	0.4 ~	25~29	500 ~ 1000
Old	450 ~		~24	0

* It was calculated by measuring the sedimentary layer thickness and range from field surveys and aerial photographs.

4 DETAILED CLASSIFICATION AND RISK ASSESSMENT

Sediment runoff at zero-order basins occurred by collapse triggered by heavy rain. Collapse of zero-order basins are caused when rainwater from above flow into a valley and the slope becomes unstable. Zero-order basins at steep slopes are narrow and can hold limited amount of water. On the other hand, the valleys at gentle and stable slopes don't collapse. Zero-order basin situated at such a gentle slope with almost no factor of slope failure is classified as Old.

Table 2 is about the relation between the total valley length and estimated amount of runoff sediment and about the possibility of damage to the social infrastructure. Youth is a zero-order basin with the length of under 80m and has no sediment runoff. It is a steep slope with small maximum b/a and in the stage of birth. The valley is slightly lower than the land at both sides. The slope and the trace of streams around here are scattered with protruding bedrocks. Bedrocks are hard to erode, and long time is needed before such places grow to the condition of causing sediment runoff. Adolescent is a zero-order basin with the length of from 80 to 200m and has a possibility of sediment runoff. They are visible valleys from 1 to 2m-wide. Maturity is a zero-order basin with the total length of longer than 200m and has high possibility of sediment runoff, possibly with much amount of runoff sediment. They are over 2m wide. Both sides are fiercely eroded, which is the evidence of a large amount of sediment runoff.

Table 2. Development classification and disaster risk.

Development classification	Valley total length (m)	Amount of runoff sediment (m^3)	Possibility of damage*
Youth	~ 80	0	Low
Adolescent	80 ~ 200	0 ~ 500	High
Maturity	200 ~ 450	500 ~ 1000	Very high
Old	450 ~	0	Low

* Damage means disruption of roads or damage to houses.

Adolescent disaster cases and Maturity disaster cases and the situation of Old are shown in Figure 4. In Adolescent, there was a case of practical road damage and debris flow on the protection net. In Maturity, cases of road disruption and building damage. To summarize Table 2, the possibility of damage is high in Adolescent and higher in Maturity.

Figure 4. Situation of the zeroth basin. a: Adolescent disaster cases. b: Maturity disaster cases. c: Old situation.

5 CONCLUSIONS

As a result of our survey on the slopes affected by Heavy rain in July 2018, we obtained the knowledge below about the risk assessment of zero-order basins. i) Total valley length is a very important factor about the risk assessment of zero-order basins. Sediment runoff is seen in zero-order basins with the total length of over 80m and the volume of sediment greatly increases in zero-order basins with the total length of over 200m. ii) Zero-order basins are classified into four classes on the basis of the total valley length. Adolescent and Maturity have a high risk of sediment runoff damage with the houses damaged and the roads cut off. iii) The factor crucial for risk assessment is total valley length, which is easily computed on the desk. Sabo Fundamental Data and Aerial Survey Data, which are necessary for computing, are now being organized nationwide. Speedy risk assessment is thus possible for wider areas.

The risk assessment we suggested this time is a rough method conducted in limited three areas. To brush up extracting methods, further site investigation and analysis is essential.

REFERENCES

Kanai, T., Asai, K., & Sasaki, Y. 2016. Evaluation of Slope Stability Based on the Soil Strength Probe. *Proceedings of the 2016 Research Presentation of the Japan Society of Engineering Geology*: 169–170. in Japanese

Kinoshita, H., Hasegawa, S., Nonomura, A., & Yamanaka. M. 2019. Drainage Density as Slope Failure Susceptibility Index in Small Catchment Area. *Journal of Japan Society of Engineering Geology*. 59 (6): 19–27. in Japanese

Murakami, T., Shimono, M., & Nakata, Y. 2016. Evaluation method of Debris Flow Hazard Affecting Expressways Based on Documents Investigation. *Japanese Geotechnical Society Chugoku Chapter Paper Report Collection jibantokensetsu*. 34 (1): 19–27. in Japanese

Nakajima, N., Yoshioka, M., Nakane, H., Miyaji, S., & Hara, T. 2019. Topographical and geological characteristics of Zero-order basins where debris flow occurred by heavy rain in July, Heisei 30. *JSCE Proceedings B1 (Hydraulic Engineering)* 75 (1): 184–190. in Japanese

National Institute for Land and Infrastructure Management, Ministry of Land, Infrastructure, Transport and Tourism. 2016. *Sabokihonkeikakusakuteishishin kaisetsu*: 17. in Japanese

Shirasawa, H., Saito, H., Toda, K., Tada, Y., & Daimaru, H. 2018. Shallow landslide hazard assessment using high-resolution DEM for application to road alignment design. *Journal of Forest Utilization Society*. 33 (2): 123–131. in Japanese

Tsukamoto, R., Hiramatsu, S., & Shinohara, S. 1973. Study on the growth of stream channel (III) - Relationship between 0 (zero) order channels and landslides-. *Journal of Japan Society of Erosion Control*. 26 (2).: 14–20. in Japanese

Smart Geotechnics for Smart Societies – Zhussupbekov, Sarsembayeva & Kaliakin (Eds)
© 2023 The Author(s), ISBN 978-1-003-29912-7
Open Access: www.taylorfrancis.com, CC BY-NC-ND 4.0 license

An IoT-based sustainable early warning system for rainfall induced landslides

Y. Liu
Graduate School of Engineering, Kyushu University, Fukuoka, Japan
School of Civil Engineering and Architecture, Wuyi University, Jiangmen, China
Jiangmen Transportation Bureau, Jiangmen, China

H. Hazarika
Graduate School of Engineering, Kyushu University, Fukuoka, Japan

M. Murai
Shimizu Corporation, Tokyo, Japan

Y. Kochi
K's Lab Inc, Yamaguchi, Japan

ABSTRACT: Traditional methods to mitigate landslide disasters often have the shortcomings of high cost or high energy consumption, therefore Early Warning System (EWS) is considered a practical approach in a cost-effective manner. This research proposes an EWS with various sensors and a wireless operating platform for data collection, transmission, and analysis based on Internet of Things (IoT). The EWS setup is supported by an off-grid solar photovoltaic system that can ensure one week of operating without any sunshine. The study presents the design, and development of EWS and conducts a case analysis of typical sandy slopes to confirm the feasibility of the system. Experimental validations prove that the EWS could effectively predict the risk and send warning notifications. Research guarantees the accuracy of the EWS while operating in a low-cost and sustainable manner. Therefore, the newly developed EWS can be put into use in both developed and developing countries.

1 INTRODUCTION

All over the world, the risk of landslide disasters due to frequent rainfall is increasing in mountainous regions. Various methods are continuously being studied and implemented to mitigate rainfall-induced disasters (Hazarika et al. 2016). There are four typical methods as follows: (1) hard type measures by piles or reinforcement material; (2) numerical simulation methods such as *FEM* or *SPH*, (3) statistical or probabilistic method*s*; (4) large-scale monitoring system like *InSAR* and *GNSS*. Soft type approaches such as IoT-based early warning systems (EWS) are also becoming increasingly popular. The evaluation of different methods mainly considers the following points: (1) a good reinforcement effect; (2) a good predictability to carry out evacuations before disasters; (3) easy to operate even without professional skills; (4) good economics to reduce development costs; (5) sustainable enough to reduce energy dependence and environmental damage. Figure 1 shows the effectiveness evaluation results of various methods, in which a larger evaluation value represents a better effect. It can be found that different methods have different advantages. For example, hard type measures can protect slopes, but sometimes may not be economical. The statistical method and the numerical method are very cost-effective, but they are less predictable. After comparing various methods, this study found that the IoT-based EWS with some portable sensors is a practical approach, which can be cost-effective and sustainable (Kanaya et al. 2016; Liu et al. 2021).

DOI: 10.1201/9781003299127-161

Although many researchers are trying to develop EWS, those systems still suffer from cost-benefit, sustainability, and predictive accuracy. To address the shortcomings of the current EWS, the proposed IoT-based EWS will provide an operational platform for comprehensive data storage and analysis. To accurately capture the movement of the soil, the computer vision–based device is also incorporated into the EWS. Additionally, the entire system will be powered by an off-grid solar photovoltaic system to make the operation sustainable. A model test was conducted to check the feasibility of the proposed EWS. This research will be able to provide a cost-effective and sustainable EWS, which can be implemented in all countries of the world.

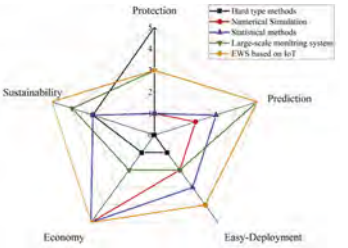

Figure 1. Effectiveness evaluation of various disaster reduction methods.

2 PROPOSED EARLY WARNING SYSTEM

2.1 *Schematic of EWS*

As shown in Figure 2, the proposed IoT-based EWS intends to provide an operational platform for comprehensive data storage and quantitative analysis. Data collected from embedded sensors such as soil moisture sensors and pore water pressure sensors are used to determine the degree of rainwater infiltration and change in the groundwater table, and data from 3D accelerometers are utilized to measure the deflection angle. Real-time images from Raspberry Pi with digital cameras are used to determine landslide time and track the displacement of the monitoring points by motion analysis. A sustainable solar panel is used to power the entire system. All the data can be stored in the cloud and operators can monitor the system remotely. Furthermore, once the monitoring parameters reach predetermined threshold limits, the system sends warning signals.

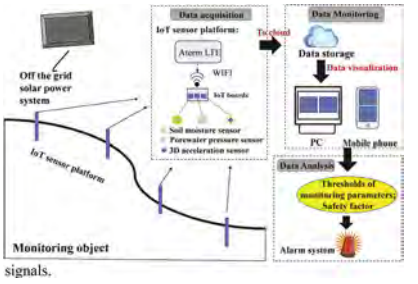

Figure 2. Schematic diagram of EWS.

2.2 *The determination method of threshold*

In this research, these threshold limits depict the transition of slope in each state: Monitoring state, Alert state and Triggering state (Liu et al. 2021). The threshold limits are based on four key soil indices: soil moisture content, pore-water pressure, slope deflection angle, and factor of safety (F_s). Initially, the threshold limits of warning indices are set into the system, which is determined by the type of soil and the terrain of the slope. The current research uses the following thresholds: 1. Soil moisture thresholds M_{c_t1} and M_{c_t2}, which represent the critical stable value of sandy slope before saturation and saturated volumetric moisture content respectively; 2. Pore-water pressure thresholds: P_{w_t1} and P_{w_t2}, P_{w_t1} is the state when the

pore-water pressure is first captured, which is generally 0-0.1 kPa, P_{w_t2} is the critical value before landslide; 3. Small deflection angle thresholds D_{t1} and big deflection angle thresholds D_{t2} before landslide; 4. The threshold of F_s is usually 1, and the slope is in danger state when F_s <1. F_s was obtained from the improved equation based on (Lu et al. 2012). These thresholds help the system in sending warning signals to residents and the concerned authorities for evacuation much ahead of the actual triggering of the landslide.

3 MODEL TEST SETUP AND SENSOR LAYOUT

A laboratory-scale slope model is prepared in a transparent, lucite box to evaluate the performance of the EWS under varying rainfall intensity conditions (Figure 3). The base layer height of the model is 100 mm, while the height of the sloped section is 350 mm. An artificial rainfall simulator is built using pipes with sprinkler nozzles along with a flowmeter to control rainfall intensities. To obtain the soil moisture distribution, 6 soil moisture sensors (S1-S6) are distributed in different parts of the slope, 3 porewater pressure sensors (P1-P3) are located at the bottom to map the movement of the groundwater table and 4 acceleration sensors (M1-M4) are arranged along the slope surface to capture the shallow deflection angles of the slope while movement. Two cameras are placed on the front and side of the model to monitor particle movement.

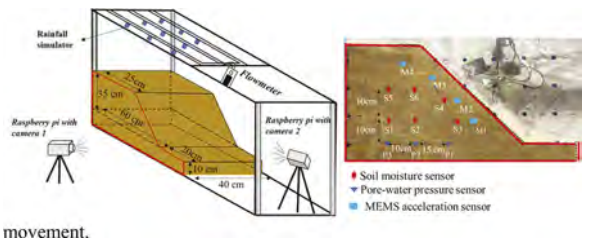

Figure 3. Model test set-up and sensor layout.

4 RESULT AND DISCUSSION

Based on the observations, it can be ascertained that before the rection of the porewater pressure sensor, the soil moisture increases to M_{C_t1}, then keeps stable. After this stage, the slope will gradually become a saturated state (M_{C_t2}) due to the rise of the groundwater table, and the deflection angle will be monitored by 3D acceleration sensors before the landslide. Thresholds generally appear in the following order: M_{C_t1}, P_{w_t1}, M_{C_t2}, P_{w_t2}, D_{t1}, F_{s_t} and D_{t2}. The test result is consistent with the threshold setting principle proposed in this study.

The responses of the pore water pressure sensor, the soil moisture sensor, the acceleration sensors are recorded and plotted against the time and compared simultaneously with the factor of safety (F_s) to evaluate the performance of the system under a rainfall intensity of 70 mm/h. It can be seen in Figure 4 that after the initial landslide, the displacement will accumulate rapidly, and multiple landslides will occur in a short period to the final deep landslide. It only takes 7 mins from the 3rd signal to landslide for rainfall intensity of 70 mm/h. Therefore, it is necessary to start the evacuation in dangerous areas after the first signal is issued, and the transfer work of personnel and assets is completed when the second signal is issued. Using particle tracking technology, the position of the points in any time period can be obtained easily and displacement can be calculated by the distance from the initial position point. The time of each shallow landslide is 82min, 91min and 98min. The motion velocity of the particle at three different landslides is shown in Figure 5 from the analysis of Particle Image Velocimetry. It can be seen clearly that at the time of the three landslides, the motion velocity of the particles is mainly concentrated near the sliding surface, which is also consistent with the observed sliding area of the slope. The maximum velocity of the monitoring point in the slope is 0.188mm/s and the displacement of the monitoring point reached 240 mm.

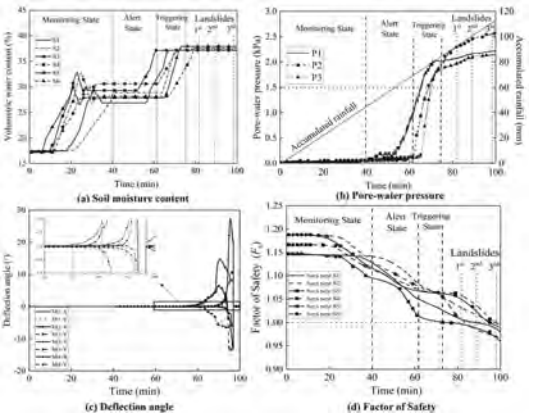

Figure 4. Monitoring results under rainfall intensity 70 mm/h.

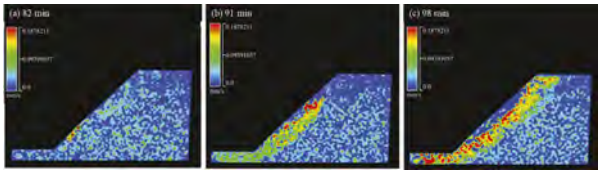

Figure 5. Result of PIV analysis under rainfall intensity 70 mm/h.

5 CONCLUSIONS

The architecture, operation and validation of the newly developed EWS are discussed in this paper. This EWS can monitor the soil moisture content and pore water pressure, track the ground deformation and provide real-time F_s during the rainfall. The application of IoT and solar battery systems enables the proposed EWS to operate cost-effectively and sustainably. Experimental validations prove that the EWS could effectively predict the risk and send warning notifications. The system can robustly predict the triggering of the landslide and provide warnings in advance at monitoring and alert state before the triggering state, thereby helping in saving numerous lives from rainfall-induced landslides disaster. This study also presents how IoT-based EWS can forge new paths for interdisciplinary study and generate a positive impact on disaster mitigation work.

REFERENCES

Hazarika, H. Kazama, M. & Lee, W. F (eds) 2016, Geotechnical Hazards from Large Earthquakes and Heavy Rainfalls. Springer.

Kanaya, H. Mansour, M. M. Hatanaka, S. Nakashima, A. & Takiguchi, O. 2021. Battery-Less Infrastructure Monitoring Sensor Platform. In H. Hazarika, G.S.P Madabhushi, K Yasuhara & D.T Bergado (eds). Advances in Sustainable Construction and Resource Management. Singapore: Springer.

Liu, Y. Hazarika, H. Takiguchi, O. & Kanaya, H. 2021. Developing a Sustainable System for Early Warning Against Landslides During Rainfall. In H. Hazarika, G.S.P Madabhushi, K Yasuhara & D.T Bergado (eds). Advances in Sustainable Construction and Resource Management. Singapore: Springer.

Lu, N. Şener-Kaya, B. Wayllace, A. & Godt, J. W. 2012. Analysis of rainfall-induced slope instability using a field of local factor of safety. Water Resources Research: 48(9).

Smart Geotechnics for Smart Societies – Zhussupbekov, Sarsembayeva & Kaliakin (Eds)
© 2023 The Author(s), ISBN 978-1-003-29912-7
Open Access: www.taylorfrancis.com, CC BY-NC-ND 4.0 license

Centrifuge modeling of failure of structured soil slope under water level fluctuation

Zhuona Ma & Ga Zhang
State Key Laboratory of Hydroscience and Engineering, Tsinghua University, China

ABSTRACT: Natural soil slopes have been caused to failure by water-level fluctuation. The structure of natural soil has a significant effect on the failure behavior of the slope. Therefore, centrifuge model tests were conducted to investigate the deformation and failure of structured soil slope under water-level fluctuation. The artificially structured soil is produced by adding cement into the silty clay and its strength behavior is determined by direct shear tests. The centrifuge model test results show that water-level fluctuation induces a shear failure in the structured soil slope with two deep slip surfaces that develops from the top to the bottom. The failure mechanism is revealed via the deformation localization analysis based on the measurement of full-field displacement of the slope. The water-level fluctuation is discovered to induce significant deformation localization and the localization develops into a local failure there.

1 INTRODUCTION

Natural soil slopes near reservoirs have always been caused to failure by water-level fluctuation. Most natural soils have structure in microscopic view, which refers to the arrangement and bonding of soil particles. Such a structure has a significant effect on the behavior of the natural soil and leads to deformation and failure of natural soil slopes different from remolded soil slopes. Reasonable safety assessment of natural soil slopes under water-level fluctuation is of great value.

Adding cement into silty clay to produce artificially structured soils is a common used method to simulate natural soils at present (Liu et al. 2018). Centrifuge model tests have been widely used to simulate the deformation and failure behavior of the slopes considering different conditions. (Zhang et al. 2011; Chen et al. 2018). Li et al.(2008) used centrifuge tests to analyze slope instability induced by water rise and fall, demonstrating that such water conditions gradually leads to strength reduction and therein induces large slope deformation. The centrifuge model test results revealed that the rise of the outside water level causes obvious collapse deformation inside the slope, and the drawdown of outside water level results in shallow multi-landslide(Yang et al. 2013). Miao et al.(2018) discovered through centrifuge model tests that the deformation and failure of the slope are mainly caused by the dynamic water pressure effect.

Most of centrifuge model tests were conducted on the remolded soil slopes under water-level fluctuation. However, natural slopes are often made of structured soil that exhibits different behavior from the remolded soil. Thus, in this paper, centrifuge model tests were conducted to observe the deformation and failure of the structured soil slope under water-level fluctuation. The deformation behavior and failure mechanism of the slope are investigated based on the full-field displacement measurement results.

2 TEST

2.1 *Devices*

The centrifuge model tests are carried out on the centrifuge at Tsinghua University with a maximum capacity of 50g-ton and acceleration of 250 g. The model container with

DOI: 10.1201/9781003299127-162

a length of 500 mm, a width of 200 mm, and a height of 350 mm is used in the test. It is equipped with transparent organic glass on the lateral side to observe the deformation and failure of the slope during the test.

A water simulator device is used to simulate water-level fluctuation during the centrifuge test (Luo and Zhang 2018). The device can be used to control water inflow and outflow and monitor water level change through pore water pressure sensors at the bottom of the container. In this way, the water level can be controlled and maintained during the test.

2.2 *Model*

A type of artificially structured soil with 1% cement content is used in the test. A type of silty clay, with a plastic limit of 18.5% and a liquid limit of 25%, is used for structured soil preparation. The specific gravity of the soil is 2.7.

The preparation process is to mix silty clay and cement after fully crushed and add water according to certain moisture content. The cement mass and water content account for 1% and 18% of the silty clay mass, respectively. The principle is that use the hydration reaction of cement and water to form the cementation between particles, so as to form a certain structural strength. According to the direct shear test results, the artificially structured soil shows strain-softening and strength due to the structure. The cohesion of the soil is 17 kPa and the friction angle is 17°.

In the model preparation, the structured soil is compacted to a dry density of 1.55g/cm^3 layer with an initial water content of 18% in the container. Each soil layer is 50 mm thick and 4 layers in total. After compaction, surplus soil is removed to achieve the predetermined dimensions of the slope with a height of 200 mm, a width of 100 mm, and a gradient of 1.5:1. White particles are embedded at random on one side of the slope model to reach higher grey differences for the convenience of image-based measurement (Figure 1).

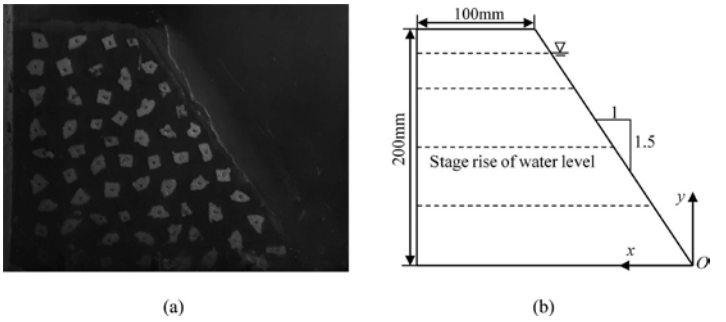

Figure 1. Photograph and schematic of test model. (a) photograph; (b) schematic view.

2.3 *Procedure*

The test process mainly includes three phases: (1) centrifugal acceleration: the acceleration level is raised from 1 g to 50 g with a 5g-step and pauses for 1 min every step, waiting for gravity-induced deformation of the slope to stabilize. (2) water level rising: the water level is raised from 0 mm to 50 mm, 100 mm, 150 mm, and 180 mm. Each level is maintained for 10 mins after the deformation induced by water inflow stabilizes. (3) water level falling: the water level decreases from 180 mm to 0 mm at one time. The process lasts for 79.8 s.

2.4 *Measurements*

Pictures and videos are captured using an image-capture and displacement-measurement system during the tests (Zhang et al 2009). These pictures and videos consist of image series that are used to determine full-field displacements of the slope.

To meet the needs of quantitative analysis, a Cartesian coordinate is set up with the origin at the toe of the model slope. The positive direction of the x-axis and y-axis is leftwards and upwards, respectively. All the dimensions referred to in this paper are in the dimension of the model. The prototype dimension is acquired by amplifying the dimension of the model with the g level, 50.

3 FAILURE PHENOMENON

3.1 *Slip surface*

Figure 3 shows the photograph and diagram of the structured soil slope at the end of the test. The structured soil slope exhibits two slip surfaces with a crack and the integral surface cuts deep into the slope body, dividing the slope into the base body and sliding body.

It can be observed from the test that the slope is stable during the water level rising while the failure happens and forms slip surfaces during the water level falling.

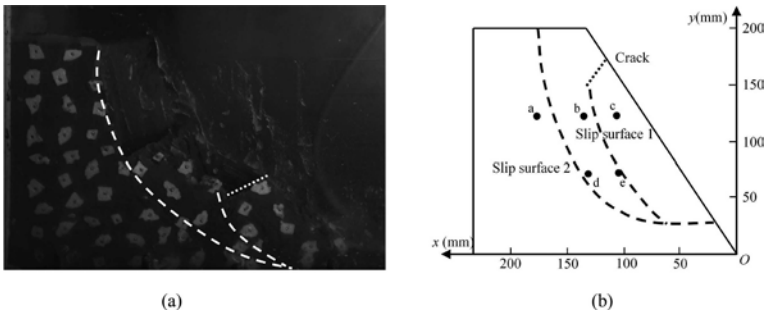

Figure 2. Photograph and schematic of the structured soil slope failure. (a) photograph; (b) schematic.

3.2 *Displacement distribution*

The displacement of the slope induced by the impoundment is so small that be neglected. Figure 3 shows the displacement distribution under water level falling to 70 mm. It can be seen from Figure 3(a) that each distribution curve of horizontal displacements has a significant displacement increase area and slip surfaces are in the area. This is also illustrated by Figure 3(b) and the remarkable displacements appear in a limited zone, which constitutes the sliding part. Meanwhile, the displacements of the base body are still about 1 mm and can be seen as a rigid body. This result indicates that water level fluctuation, especially drawdown, leads to more significant deformations of the slope.

Figure 4 shows histories of displacements of representative points during water level falling. Point a is on the base body, point c is on the sliding body 1 upon the slip surface 1 and point b, point d, point e is on the sliding body 2 upon the slip surface 2. By comparing the displacements of point a, point c and point e, it can be seen that the displacements of the structured soil slope are small before the failure while increasing a lot in a few seconds after the failure. Moreover, the displacements of the sliding body 1 are larger than the sliding body 2. This is due to that the sliding body 2 is affected by both the formation of the slip surface 1 and the slip surface 2 and produces new deformation after preliminary deformation. The horizontal and vertical displacements of both Point b and Point e were greater than those of Point d. This indicates that the deformation is more dramatic on the upper and exterior part of the slope.

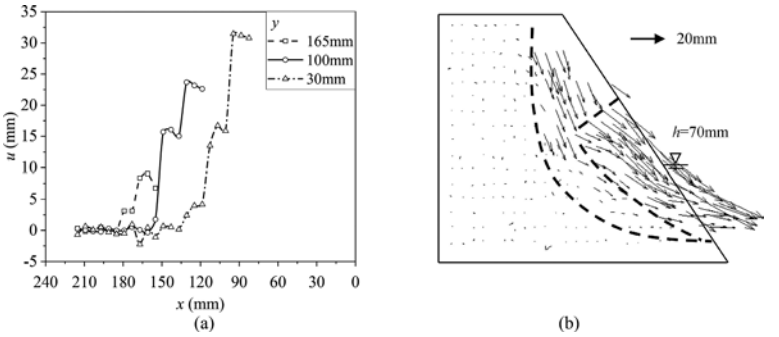

Figure 3. Displacement distribution under water level falling to 70 mm. (a) distributions of horizontal displacements; (b)distributions of displacement vectors. *u*, horizontal displacement; *h*, water level.

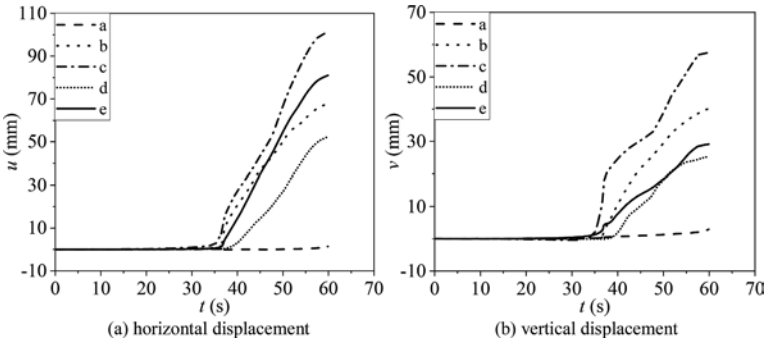

Figure 4. Histories of displacements of representative points during water level falling. (locations shown in Figure 2.) *u*, horizontal displacement; *v*, vertical displacement; *t*, time.

4 FAILURE PROCESS

The failure process of the slope under water-level fluctuation is analyzed using point couple analysis. The point couple is defined as two adjacent points with one on the base body and the other on the sliding body. The relative displacements of the point couple are decomposed to the tangential direction and the normal direction of the slip surface. Based on the observation and analysis of the slope failure, it can be determined that the main failure process happens during the period of water level falling from 150 mm to 50 mm. The process of water level falling from 150 mm to 50 mm lasts for 32.2 s, which is long enough to observe the failure.

Figure 6 shows histories of relative displacements of the point couple near the crack and can determine the property of the crack. The normal relative displacement increases slowly at first and then grows rapidly to 23.5mm at a certain moment. The turning point can be considered as the moment when a local failure occurs between the couple point. When the crack appears, the normal relative displacement is far more than the tangential relative displacement, so it could be concluded as a tension crack. As the water level falls, the slip surface 1 appears and the slope settles rapidly, and the tangential relative displacement is gradually greater than the normal relative displacement. It can be concluded that the generation and development of the crack are a combination of tension and shear.

Figure 7 shows histories of relative displacements of point couples (Point couple C and Point couple F) near slip surface 1 and slip surface 2. The tangential relative displacement is greater than the normal relative displacement for all the point couples near both slip surfaces during water level falling. This result means that the shear failure occurs in the slope. It also can be seen that the relative displacements increase rapidly at a certain moment and appear as a turning

point, which can be used as the moment when the slip surface develops here. The failure process of structured soil slope is sudden and fast, showing characteristics of brittle failure.

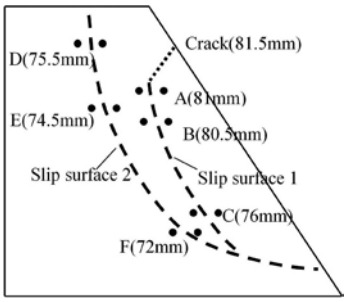

Figure 5. Locations of point couples and failure process.

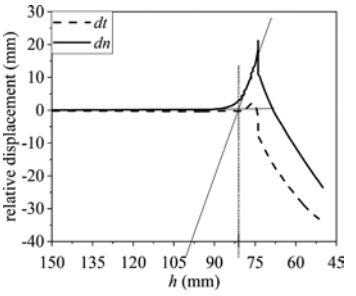

Figure 6. Histories of relative displacements of the point couple near the crack. *dt*, tangential relative displacement; *dn*, normal relative displacement; *h*, water level.

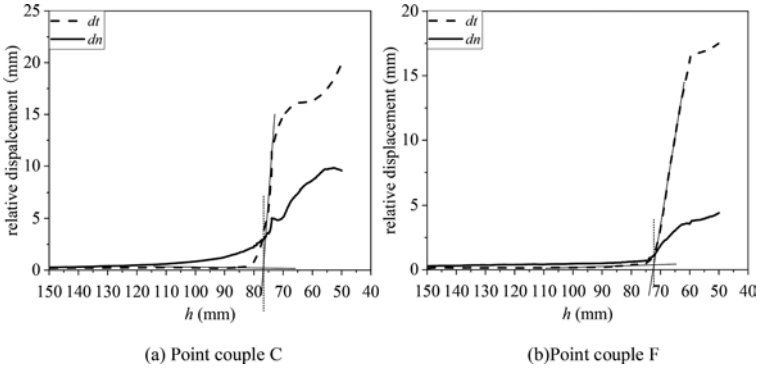

Figure 7. Histories of relative displacements of point couples. (locations shown in Figure 9). *dt*, tangential relative displacement; *dn*, normal relative displacement; *h*, water level.

Figure 5 marks the water levels at failure moments in brackets according to the turning points of histories of relative displacements of each point couple. It can be seen that the local failure in the structured soil slope induced by water fluctuation develops from the top to the bottom. The tension crack first occurs on the upper part of the slope and extends inward. The slip surface 1 starts at the crack extension and develops from top to bottom. The slip surface 2 appears after the formation of the slip surface 1 and develops from top to bottom and forms the integral slip surface with the slip surface 1 at the slope toe. Two slip surfaces are formed independently and the formation time difference is caused by the sequence of water levels falling in the slope.

A point couple can be seen as a soil unit in the shear test. According to the direct shear test results, the shear displacement is small before the shear failure. The shear stress decreases rapidly after the shear failure while the shear displacement starts to grow consistently. The reason why the structured soil slope failure is brittle is that the soil structure enhances the ability to resist external load damage. Once the structure is damaged, the strength will suddenly decrease, resulting in a rapid slip without signs of preliminary deformation.

5 FAILURE MECHANISM

Figure 8 shows the horizontal distributions of the horizontal strain at heights of 100 mm and 80 mm under four representative water levels, corresponding to the four moments before and after the slip surfaces formation. It also marks the locations of slip surfaces at different heights in the figure.

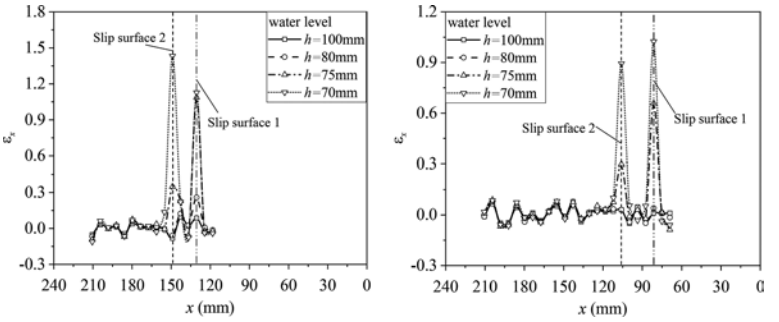

Figure 8. Distributions of horizontal strain at 100 mm and 50 mm height under four different water levels. ε_x, horizontal strain; x, x-coordinate; h, water level.

It can be seen that at the initial stage of water level falling (h=100mm), the horizontal strain is small at different heights. This result means the deformation in the slope is small and distributes evenly. As the water falls (h=80mm), there is a maximum value point on the distribution curve at the height of 100 mm, while the horizontal strain is still small and uniform on the other distribution curve. With the water level falling to 75 mm, there are two maximum value points on each curve. It can be noticed that the locations of two maximum points are near the slip surfaces and the maximum value near the slip surface 1 is much larger than the maximum value near the slip surface 2 and both maximum values on the curve at 100 mm height are larger than those at 50 mm height. This is because that the slip surface 1 is forms at both heights while the slip surface 2 develops to the height of 50 mm instead of 100 mm under the water level. When the water level falls to 70 mm, the maximum values has a significant increase and the slip surfaces are formed at both heights. Based on the analysis above, the slope occurs to progressive failure.

The horizontal strain values around maximum value points are much larger while in other areas horizontal strain is still maintained around zero. This implies deformation location occurs in the area. The locations of slip surfaces are around two maximum values and local failure occurs around here. This finding illustrates that the deformation localization occurs under water level fluctuation and induces local failure ultimately. It can be concluded that the integrated development of deformation localization and local failure under water level fluctuation causes the ultimate slope failure.

Furthermore, the changing patterns of two maximum values on the distribution curve of horizontal strain are different (Figure 8), which are related to the development of slip surfaces. Figure 9 shows the histories of the horizontal strain of two maximum values at the height of 100 mm during water level falling. There is a turning point on each curve and represents the moment that a local failure occurs. The turning point of the first maximum value point near slip surface 1 appears at 35 s, corresponding to the moment that slip surface 1 occurs at the height of 100 mm. After rapid growth, the horizontal strain stabilizes, and then after a fluctuation affected by the formation of the slip surface 2 stabilizes again. The turning point of the second maximum value point near slip surface 2 appears at 36.8 s and stabilizes after experiencing significant growth. This also illustrates that two slip surfaces occurs independently and the parts upon the earlier slip surface will be affected by the later slip surface and produce new deformation.

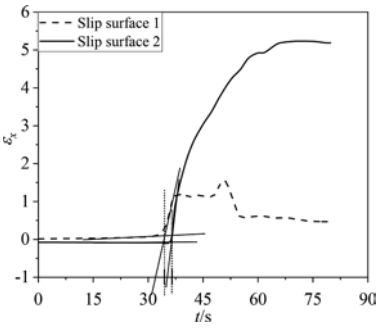

Figure 9. Histories of the horizontal strain of two maximum values during the water level falling. ε_x, horizontal strain.

6 CONCLUSION

The deformation and failure of the structured soil slope under water level fluctuation were investigated using centrifuge model tests. The failure mechanism was revealed via the deformation localization analysis based on the measurement of full-field displacement of the slope. The main conclusions are as follows:

1. The water level fluctuation causes two slip surfaces independently in the slope and the soil upon the earlier sliding body is caused new deformation by the later slip surface.
2. The structured soil slope exhibits progressive failure. The tension crack appears on the upper part of the slope at first, and the slip surface due to shear failure develops gradually from the top to the bottom of the slope.
3. Water level fluctuation leads to uneven deformation and is concentrated at a certain area in the soil slopes, indicating deformation localization there. The accumulation of deformation localization leads to local failure while local failure results in new deformation and enhancement of deformation localization. The coupling development of deformation localization and local failure leads to the ultimate slip surface.

REFERENCES

Liu, E., Wang, S., Zhou, C., & Nie, Q. 2018. Mechanical properties of artificial structured soils under a conventional drained loading–unloading–reloading stress path. *International Journal of Civil Engineering*, 16(4), 383–393.

Zhang, G., Qian, J., Wang, R., & Zhang, J. M. 2011. Centrifuge model test study of rainfall-induced deformation of cohesive soil slopes. *Soils and foundations*, 51(2), 297–305.

Chen T, Zhou C, Wang G, et al. 2018. Centrifuge model test on unsaturated expansive soil slopes with cyclic wetting-drying and inundation at the slope toe. *International Journal of Civil Engineering*, 16 (10): 1341–1360.

Li S J, Knappett J A, Feng X T. 2008. Centrifugal test on slope instability influenced by rise and fall of reservoir water level. *Chinese Journal of Rock Mechanics and Engineering*, 27(8): 1586–1593

Yang C B, Zhu B, Kong L G, et al. 2013. Centrifugal model tests on failure of silty slopes induced by change of water level. *Chinese Journal of Geotechnical Engineering*. 35(7): 1261–1271.

Miao F S, Wu Y P, Xie Y H et al. 2018. Centrifugal test on retrogressive landslide influenced by rising and falling reservoir water level. *Rock and Soil Mechanics*, 39(2): 605–613.

Luo F, Zhang G. 2016. Progressive failure behavior of cohesive soil slopes under water drawdown conditions. *Environmental Earth Sciences*, 75 (11): 973.

Zhang G, Hu Y, Zhang J M. 2009. New image-analysis-based displacement-measurement system for geotechnical centrifuge modeling tests. *Measurement*, 42(1): 87–96.

Smart Geotechnics for Smart Societies – Zhussupbekov, Sarsembayeva & Kaliakin (Eds)
© 2023 The Author(s), ISBN 978-1-003-29912-7
Open Access: www.taylorfrancis.com, CC BY-NC-ND 4.0 license

Effect of cement modification on expansive soil slope

Bin Huang
School of Architecture and Civil Engineering, Huizhou University, China

Yuting Zhang
Discipline of Civil, Surveying & Environmental Engineering, The University of Newcastle, Australia

Jian Shen
Shenzhen Government Investment Project Evaluation Center, China

Jingjing Li & Jianming Xu
Huizhou University, China

ABSTRACT: The swelling characteristic is most important for expansive soil, and it is one of the main factors that cause the disaster of expansive soil slope. After mixing with cement, the engineering behaviours of the expansive soil get improved and, in particular, the swelling characteristic basically disappears. In this paper, Nanyang middle expansive soil, which is encountered in the Middle Route of South-North Water Transfer Project, was studied on the long-term effects. The optimum amount of cement content is determined according to the free swelling ratio. The long-term improvement of swelling potential, strength and modulus are studied by laboratory tests. Based on test results, numerical modelling was used to evaluate the plastic zone development and safety of the expansive soil slope. In addition, a method to determine the thickness of cement treatment was proposed.

1 INTRODUCTION

Expansive soil is a kind of clay which swells, collapses and softens when encountering water, and shrinks, cracks and hardens when losing water. There are two kinds of expansive soil slope instabilities, one happens under the swelling effect, and the other happens due to low fissure strength (Cheng et al., 2011). For the case of shallow instability the water content control method such as geomembrane treatment, or load method such as using unexpansive soil, cement modified, geogrid reinforced or lime modified expansive soil can be adopted to deal with the instability. The Middle Route of South-North Water Transfer Project is an important project in China. The canal passes through about 387 km of expansive soil in total. In order to avoid the problems such as water pollution, farmland destruction caused by soil replacement, and expansive soil disposal (Li et al., 2009), various treatments were compared in the field; at last, the cement modification method was selected to make sure the shallow stability.

This study carried out the laboratory swelling and triaxial tests of expansive soil and cement modified soil. The samples collected from Nanyang expansive soil field were used to demonstrate the long-term modification effect. The effect of treatments with different thicknesses was validated and a method of determining the treatment thickness of expansive soil slope was proposed.

DOI: 10.1201/9781003299127-163

2 THE OPTIMUM AMOUNT OF CEMENT FOR EXPANSIVE SOIL MODIFICATION

The free swelling ratio of Nanyang expansive soil is 77% and its colloidal particles content was 29.5%, which is mid-expansive clay and of high liquid limit. The modification to the mid-expansive soil was done with the composite Portland cement P.C 32.5.

The free swelling ratio test was conducted on cement modified mid-expansive soil (Huang et al., 2009). The modified soil samples were made of clay and cement, which were mixed together and compacted to a compaction degree of 93%, then ground down artificially after the curing time period. The relationship between the free swelling ratio and cement content for modified soil of 28 days old is shown in Figure 1.

It can be seen that the free swelling ratio reduced with the increase of cement content. When the cement content is less than 6%, the free swelling ratio varied greatly with the increase of cement content, and when the cement content was greater than 6%, the modification effect was much lower and the swelling ratio was close to the unexpansive limit of 40%. Therefore, 6% of cement content was recomended for Nanyang mid-expansive soil.

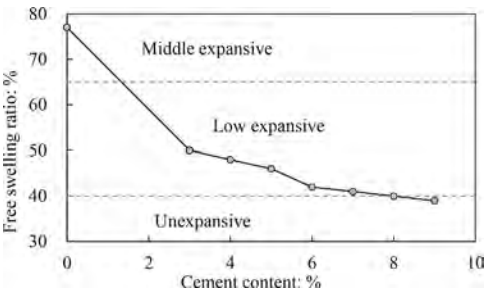

Figure 1. The relationship between the free swelling ratio and cement content for modified soil.

3 THE IMPACT OF CEMENT MODIFICATION ON SWELLING CHARACTERISTIC

Three kinds of soil samples were used in swelling ratio tests under load. One kind of samples were compacted virgin soil; the second kind of samples were modified soil mixing with expansive soil and cement in laboratory; The third kind of samples were field cement modified soil. All samples were of natural water content of 21.0% for virgin soil and compaction degree of 93%. The field sampling is shown in Figure 2. The swelling ratio results of the three kinds of soil samples are shown in Figure 3.

Figure 2. Field sampling of cement modified soil.

It can be seen from the Figure 3 that the swelling ratio of the virgin expansive soil has a steep drop when the vertical stress is between 0 and 12.5kPa, which indicates that the load method can be used to inhibit the swelling deformation of the expansive soil.

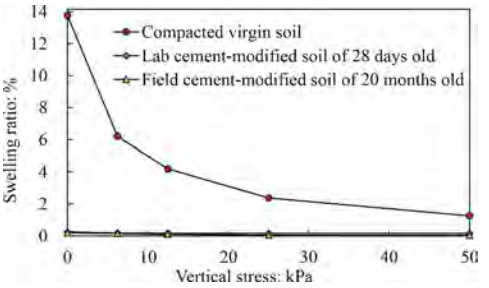

Figure 3. The relationship between swelling ratio and vertical stress.

The swelling ratio without load of the compacted virgin soil is 13.6%, and the swelling ratio of the intact soil is 9.9%. The swelling ratio of laboratory and field modified soils is less than 0.1%. The modification effect on swelling is remarkable when cement content is more than 6%.

4 THE IMPACT OF CEMENT MODIFICATION ON MECHANICAL PROPERTY

The triaxial test results of expansive and modified soil are shown in Table 1. The strength is increased obviously after cement modification. The strength of field modified soil is greater than that of laboratory modified soil. The reason for that, on one hand, is the impact of the age, and on the other hand, is the field modified soil containing more gravel which improve the fabric of the soil particles while it was removed from laboratory modified soil.

For the field modified soil, its strength and modulus are both high. The field modified soil had existed for 20 months, and had experienced water storage and recession process in the canal slope, thus, the cement modification is ideal for inhibiting the strength and modulus softening.

Table 1. Triaxial test results of expansive soil and cement modified soil.

Sample	Cement content: %	Compaction degree: %	Age	c: kPa	φ: °
Intact virgin soil	-	-	-	18.1	21.1
Lab modified soil	6	93	28 days	40.8	23.2
Field modified soil	6	93	20 months	91.2	35.9

5 THE IMPACT OF CEMENT MODIFICATION ON EXPANSIVE SOIL SLOPE

5.1 *The finite element method considering swelling effect*

The ideal elastic-plastic constitute model and Mohr-Coulomb failure criterion are adopted to calculate the swelling deformation of expansive soil after sufficient moisture absorption by taking the swelling strain as the initial strain, and the final stress and strain of the slope are calculated using the initial strain method (Xu et al., 2014).

The swelling strain of expansive soil in triaxial stress state can be expressed by the Equation (1) (Huang et al., 2015):

$$\varepsilon_v = a + b\ln(1 + \frac{\sigma_m}{p_a}) \tag{1}$$

Where ε_v is the swelling volume strain caused by sufficient moisture absorption in expansive soil (%); σ_m is the average principal stress; a and b are the parameters which are related to the

expansion class, initial water content and compaction degree. For Nanyang mid-expansive soil with the initial water content of 21%, a=22.7, b=-4.73.

5.2 *Calculation model*

The effect of cement modification on inhibiting swelling deformation was analysed with slope height of 9 m and slope gradient of 1:1.5, treatment thickness of 0, 1, 2, and 3 m. Based on practical experiences, it is assumed that the water content in slope surface varies from initial water content to saturated state within 2 m. The schematic diagram of calculation model is shown in Figure 4, and the geotechnical parameters obtained from triaxial test are shown in Table 2.

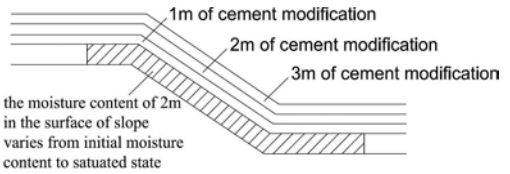

Figure 4. Schematic diagram of cement modification treatment with different thicknesses.

Table 2. Strength and deformation parameters.

Soil type	Density: g/cm^3	c: kPa	φ: °	E: MPa	μ
Cement modified soil	1.85	91.2	35.9	36	0.3
Virgin expansive soil	2.00	18.1	21.1	10	0.4

5.3 *Calculation result*

(1) Plastic zone development

Figure 5 is the distribution of the plastic zone when the water content of expansive soil in slope surface increasing to saturation. It indicates that, for the mid-expansive soil slope, there is no plastic zone for 2 m or more thickness of cement modification.

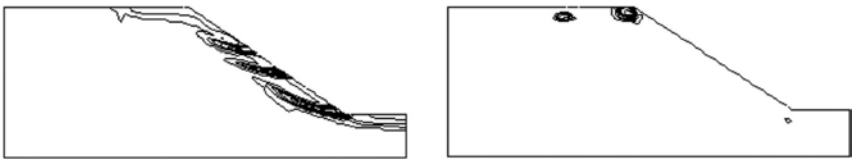

Figure 5. The plastic zones of expansive soil slope with different treatment thicknesses.

(2) Slope stability

For the treatment with different thicknesses, the finite element method considering expansion is used to analyse the stability. The slope safety factors of each treatment are shown in Table 3.

Table 3. Safety factors of slope stability with different treatment thickness.

		Treatment thickness		
Soil	Non-treatment	1m	2m	3m
Middle expansive soil	0.88	1.20	1.70	1.83

The stability of cement modified slope is obviously enhanced when the water content of expansive soil within 2 m changes from initial water content to saturated state. When the expansive soil slope is not treated, the safety factor is 0.88, and the safety factor of 1 m treatment reaches 1.20, which is less than the required value 1.35; the safety factor of 2 m treatment is up to 1.70, which meets the design requirement.

The cement modification treatment with thickness of 2 m was widely used in mid-expansive soil slope in the Middle Route of South-North Water Transfer Project.

6 CONCLUSION

(1) The swelling and mechanical properties of expansive soil can be remarkably improved by cement modification, which is a feasible method for shallow stability of expansive soil slope.
(2) According to the relationship between free swelling ratio and cement content, the optimum amount of cement can be determined.
(3) Using finite element method considering swelling effect, the sensitivity analysis can be conducted to determine the treatment thickness of expansive soil slope.

REFERENCES

CHENG, Z.-L., LI, Q.-Y., GUO, X.-L. & GONG, B.-W. 2011. Study on the stability of expansive soil slope. *Journal of Yangtze River Scientific Research Institute*, 28, 102–111.

HUANG, B., CHENG, Z.-L., ZHANG, W., FU, X.-D. & XU, H. 2015. Expansion Model Test of Expansive Soil in Different Stress State. *Soil Mechanics and Foundation Engineering*, 52, 57–67.

HUANG, B., NIE, Q., XU, Y.-Y. & LUO, J. 2009. Experimental Research on Cement-modification of Expansive Soil. *Journal of Yangtze River Scientific Research Institute*, 11, 27–30.

LI, Q.-Y., CHENG, Z.-L., GONG, B.-W., GUO, X.-L. & BAO, C.-G. 2009. Failure mechanism and treatment technology of expansive soil slope of middle route project. *Journal of Yangtze River Scientific Research Institute*, 26, 1–9.

XU, H., CHENG, Z.-L., HUANG, B. & PAN, J.-J. 2014. The mechanism of inhibiting swelling deformation and slope instability of expansive soils by replacement method. *Tehnički vjesnik*, 21, 1057–1063.

Smart Geotechnics for Smart Societies – Zhussupbekov, Sarsembayeva & Kaliakin (Eds)
© 2023 The Author(s), ISBN 978-1-003-29912-7
Open Access: www.taylorfrancis.com, CC BY-NC-ND 4.0 license

Comparison of soil water characteristic curves estimated using data assimilation and water retention tests

S. Ito, K. Sako & T. Morita
Kagoshima University, Kagoshima, Japan

ABSTRACT: The soil water characteristic curve (SWCC) is an important property for simulating infiltration behavior, and several methods exist for its estimation. This study aimed to investigate the relationship between the SWCC estimated by data assimilation based on field measurement data and that estimated using the pressure plate method (a water retention test). Simulations using the SWCC estimated by data assimilation reproduced 5 days of trained field measurement data and predicted 50 days of unlearned test data with sufficient accuracy. The SWCC estimated by data assimilation had a different shape than that of the SWCC estimated using the pressure plate method.

1 INTRODUCTION

Because soil moisture conditions affect the onset of slope failure during heavy rain, it is important to accurately evaluate the infiltration behavior of the soil. To simulate the infiltration behavior, we need to estimate the unsaturated soil hydraulic properties: the soil water characteristic curve (SWCC) and unsaturated hydraulic conductivity. The SWCC is an important property that indicates the relationship between water content and pore water pressure; it is generally estimated by conducting water retention tests. We studied the data assimilation of unsaturated soil hydraulic properties based on the field measurement data of volumetric water content (VWC) and found that numerical simulations using the parameters estimated by data assimilation could reproduce the field measurement data at various slopes with different types of soils (Ito et al., 2019). There are several methods for estimating the SWCC. The relationship between the SWCCs estimated using different methods has not yet been fully investigated. This study aimed to elucidate the relationship between the SWCC estimated by data assimilation based on field measurement data and that estimated using the pressure plate method (a water retention test). First, unsaturated soil hydraulic properties were estimated based on the field measurement data of the VWC at a site comprising pyroclastic flow deposits. We used the merging particle filter (MPF) (Nakano et al., 2007) as the data assimilation method. Next, the generalization performance of the estimated model was evaluated by conducting Monte Carlo simulations on 50 days of unlearned test data. Finally, herein, the relationship between the two SWCCs estimated using different methods (data assimilation and the pressure plate method) is discussed.

2 METHODS

2.1 *Unsaturated–saturated seepage analysis*

In this study, unsaturated–saturated seepage finite element analysis was used to reproduce soil moisture conditions. The Richards equation (Richards, 1931) was applied for numerical analysis, as follows:

DOI: 10.1201/9781003299127-164

$$C \cdot \frac{\partial \psi}{\partial t} = \frac{\partial}{\partial z}\left\{k(\psi)\left(\frac{\partial \psi}{\partial z} + 1\right)\right\} \tag{1}$$

where C (= $\partial\theta/\partial\psi$) is the hydraulic capacity function, θ is the VWC, ψ is the pressure head, and $k(\psi)$ is the unsaturated hydraulic conductivity. The van Genuchten model (van Genuchten, 1980) was adopted to express the SWCC, and the Mualem model (Mualem, 1976) was used to estimate the unsaturated hydraulic conductivity. The different models are calculated as follows:

$$S_e = \frac{\theta - \theta_r}{\theta_s - \theta_r} = \left\{\frac{1}{1 + (-\alpha \cdot \psi)^n}\right\}^{1-\frac{1}{n}} \tag{2-1}$$

$$k(\psi) = k_s \cdot S_e^{0.5}\left\{1 - \left(1 - S_e^{\frac{n}{n-1}}\right)^{1-\frac{1}{n}}\right\}^2 \tag{2-2}$$

where S_e is the effective soil water saturation, θ_r is the residual VWC, θ_s is the saturated VWC, α and n are material parameters, and k_s is the saturated hydraulic conductivity.

2.2 *Merging particle filter*

The MPF is a sequential data assimilation method wherein the probability distribution of a physical quantity is approximated using its realizations. Each realization is called a particle, and each set of particles is called an ensemble. The MPF evaluates particles at a discrete time using Bayes' theorem. Figure 1 illustrates the computational procedure for the MPF. First, several numerical simulations, wherein different sets of unknown parameters were applied to each particle, were conducted ((a) prediction in Figure 1). If the number of particles is N, then N Monte Carlo simulations are performed. Second, the likelihood was evaluated for each particle by comparing the measurement data and simulated results ((b) filtering in Figure 1). The particles were then resampled into samples (Figure 1(c)). If the number of particles is N, $l \times N$ samples are drawn based on the likelihood. The particles with a high likelihood were resampled more than l, and the samples of the particles with a low likelihood were decreased in number. Finally, the samples merged into new particles (Figure 1 (d)). By performing an iteration of these four steps (prediction, filtering, resampling, and merging) at each discrete time, the MPF modified the unsaturated soil hydraulic properties (θ_r, θ_s, α, n, and k_s) based on the measurement data.

2.3 *Pressure plate method*

Figure 2 shows the test setup for the pressure plate method. Air pressure was applied to the cell pressure chamber, where the soil specimen was installed, and the back pressure chamber, where the electronic balance was installed, to measure the amount of water drainage. The pressure difference causes soil water to drain. In this study, the SWCC of the wetting process was calculated from the relationship between the suction and water content under equilibrium conditions.

The soil specimen was prepared by compacting the disturbed soil sampled at the field measurement site and controlling the void ratio (e = 1.3) and the initial water content (w = 33%). The soils were pyroclastic flow deposits sampled at a site in Kagoshima City, Japan, and the density of the soil particles was ρ_s = 2.51 Mg/m^3. The specimen mold had an inner diameter of 60 mm and a height of 20 mm.

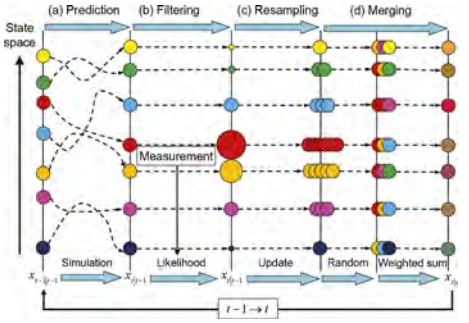

Figure 1. Computational procedure for the MPF.

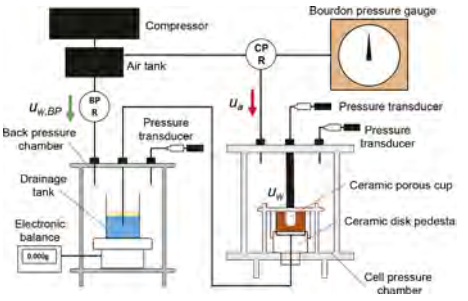

Figure 2. Test setup of the pressure plate method.

3 ESTIMATION OF THE SWCC BASED ON FIELD MEASUREMENT

3.1 *Field measurement data*

We installed a rain gauge and profile soil moisture sensor for the field measurement of precipitation and VWC. The profile soil moisture sensor measured the VWC at 10 cm intervals from a depth of 10 to 40 cm. The measurement intervals of precipitation and VWC were 10 min, and field measurements were performed from June 3 to July 28, 2021. Figure 3 shows the field measurement data. The VWC measured at a 40 cm depth was significantly lower than that measured at other depths and showed little variation in precipitation. It can be presumed that these data were measured because the profile soil moisture sensor was not in contact with the soil at a depth of approximately 40 cm. This study used the time variation of the VWC measured at depths of 10, 20, and 30 cm for data assimilation.

3.2 *Analytical results*

Figure 4 shows the one-dimensional seepage analysis model used to simulate the infiltration behavior. The model was divided into three layers (upper, middle, and bottom) corresponding to the depth of the soil profile moisture sensor. The model introduced a variable flux boundary at the top surface and a free drainage boundary at the bottom of the model. For data assimilation, 500 particles with different sets of unknown parameters were used. All particles were randomly generated within a certain range. The observation noise followed a three-dimensional normal distribution. Data assimilation was performed using 5 days of field measurement data from June 3 to June 8 as the training data to estimate unsaturated soil hydraulic properties. The remaining 50 days of data were used as test data to evaluate the general performance of the estimated model, and Monte Carlo simulations considering only precipitation were performed.

The analytical results are shown in Figure 5. The data assimilation and Monte Carlo simulation conducted 500 simulations such that the mean value, μ, and standard deviation, σ, of the simulations could be calculated. The solid lines indicate field measurement data, dashed lines indicate the mean value, μ, of the posterior distribution of VWC, and dotted lines show the range of $\pm\sigma$ from the mean value. The simulations reproduced 5 days of trained field measurement data used for data assimilation and also predicted 50 days of unlearned test data with sufficient accuracy. Thus, we concluded that data assimilation by the MPF could estimate unsaturated soil hydraulic properties that adequately represent the in-situ infiltration behavior.

4 DISCUSSION

The SWCCs estimated by data assimilation were compared with those estimated using the pressure plate method (a water retention test). Figure 6 shows the results of the comparison; clearly, the SWCCs estimated using the different methods have different shapes at all depths.

The interpretation of these differences is that the methods for the estimation of the SWCCs differed, and data assimilation was applied to undisturbed soils, while the soil specimen in the water retention test was disturbed. However, because this study was conducted at a single site, similar studies need to be conducted in future for other sites, in addition to investigating the effects of the differences in the SWCC on the results of seepage analysis.

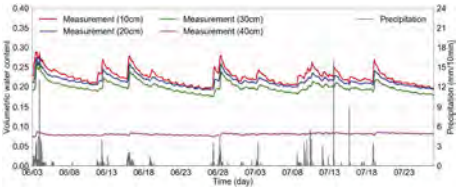

Figure 3. Field measurement data.

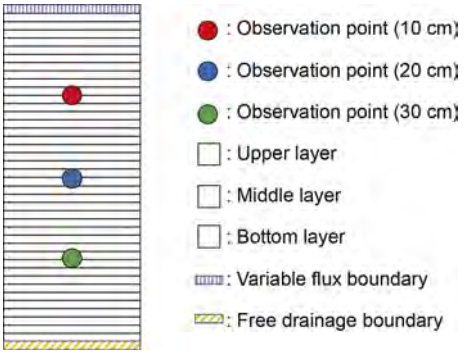

Figure 4. One-dimensional model.

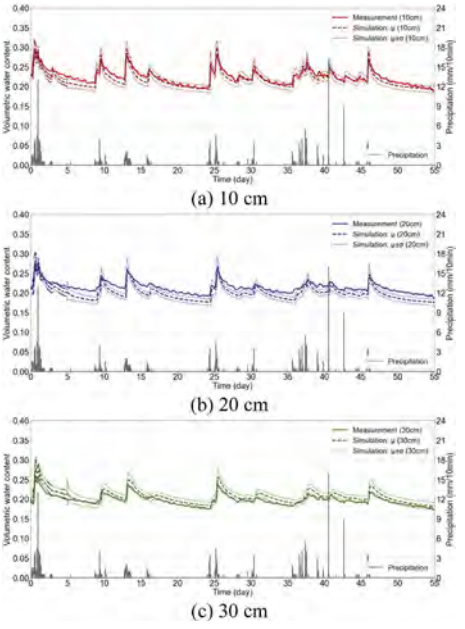

Figure 5. Analytical results.

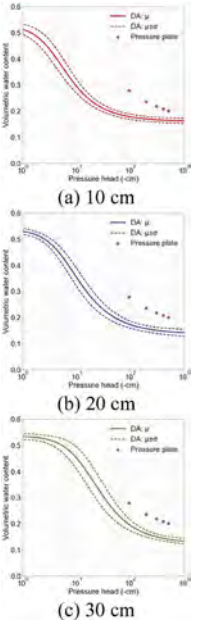

Figure 6. Comparison results of SWCCs.

5 CONCLUSIONS

This study aimed to investigate the relationship between the SWCC estimated by data assimilation and that estimated using the pressure plate method. The main conclusions of this study are as follows.

1. The simulation results reproduced 5 days of trained field measurement data used for data assimilation and predicted 50 days of unlearned test data with sufficient accuracy. This indicated that data assimilation by the MPF could estimate unsaturated soil hydraulic properties that adequately represent the in-situ infiltration behavior.
2. The SWCC estimated by data assimilation was compared with that estimated using the pressure plate method (a water retention test). The comparison showed that the SWCCs estimated using the different methods have different shapes at all depths. The interpretation of these differences is that the method for estimating the SWCCs differed. Data assimilation was applied to undisturbed soil, whereas the soil specimen in the water retention test was disturbed.

REFERENCES

Ito, S., Oda, K., & Koizumi, K. 2019. Availability of the particle filter methods on identification of soil hydraulic parameters based on field measurement, *Proceedings of the 16th Asian Regional Conference on Soil Mechanics and Geotechnical Engineering*: JGS–013.

Mualem, Y. 1976. A new model for predicting the hydraulic conductivity of unsaturated porous media, *Water Resources Research* 12: 513–522.

Nakano, S., Ueno, G., & Higuchi, T. 2007. Merging particle filter for sequential data assimilation, *Nonlinear Processes in Geophysics* 14: 395–408.

Richards, L. A. 1931. Capillary conduction of liquids through porous mediums, *Physics* 1: 318–333.

van Genuchten, M. 1980. A closed-form equation for predicting the hydraulic conductivity of unsaturated soils, *Soil Science Society of America Journal* 44(5): 892–898.

Smart Geotechnics for Smart Societies – Zhussupbekov, Sarsembayeva & Kaliakin (Eds)
© 2023 The Author(s), ISBN 978-1-003-29912-7
Open Access: www.taylorfrancis.com, CC BY-NC-ND 4.0 license

Suffusion experiments under condition of constant or fluctuating hydraulic gradient with focus on concentration-turbidity relationship of drainage

T. Ishimaru, M. Suzuki, S. Takano & A. Komori
Yamaguchi University, Ube, Yamaguchi, Japan

ABSTRACT: The phenomenon whereby only the fine soil particles flow out, while the skeleton of the coarse soil particles remains, is called "suffusion". It has been pointed out that the suffusion occurs in embankment structures affected by long-term seepage, such as river levees and reservoir dams, increasing the risk of collapse. However, the suffusion mechanisms in cases where the seepage force changes with time are often unclear. In this study, water-passing experiments with the suffusion were performed to clarify how the amount and the particle size of eroded soil change with changes in the seepage force. As a result, it was seen that the small soil particles with easy flowability had already eroded when the specimen was subjected to seepage force for the first time, and that the soil particles that flowed out due to changes in the hydraulic gradient were relatively large in diameter.

1 INTRODUCTION

In embankment structures affected by long-term seepage, such as river levees and reservoir dams, turbid water sometimes leaks from the ground surface. Embankment structures with leaking turbid water are at high risk of collapse. The phenomenon in which soil particles move inside open spaces in the ground, and eventually flow out of embankment structures along with water, is called "internal erosion". In particular, the phenomenon whereby only the fine soil particles flow out, while the skeleton of the coarse soil particles remains, is called "suffusion". It has been pointed out that suffusion progresses over a long period of time with repeated episodes of fines migration, pore clogging, and the removal of clogged pores (Luo et al., 2013). Although it has been noted that changes in seepage forces affect the progression of suffusion, the number of suffusion experiments that reproduce changes in the seepage force is still few.

In this study, water-passing experiments were performed assuming the case where the seepage force changes with time, such as river embankments and reservoir embankments, under the condition of constant or fluctuating water levels, to clarify how the amount and the particle size of eroded soil change with changes in the seepage force.

2 OVERVIEW OF WATER-PASSING EXPERIMENTS

2.1 *Outline of experimental apparatus*

Figure 1 shows a schematic diagram of the experimental column apparatus for the water-passing experiments. The specimens were cylindrical with a diameter of 10 cm and a height of 20 cm. At the bottom, where each specimen was located, an acrylic plate with 100 holes, each having a diameter of 5 mm, and mesh with a diameter of 425 μm, were installed. These parts allowed only fine particles, smaller than the size of the sieve, to flow out of the specimen under the application of downward seepage flow. The overburden load was applied by applying air

DOI: 10.1201/9781003299127-165

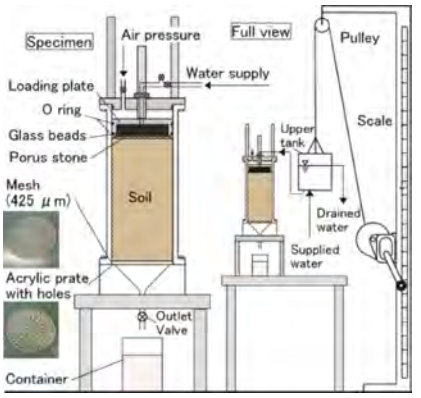

Figure 1. Schematic diagram of water-passing experiments apparatus.

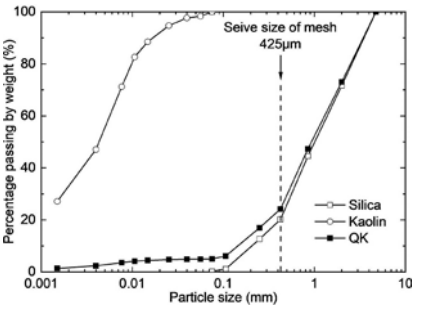

Figure 2. Particle size distribution of soil used in this study.

Table 1. Physical properties of soil used in this study.

Soil	Fines content %	Specific gravity G_s	Optimum water content w_{opt} %	Maximum dry density ρ_{dmax} g/cm^3
QK	5.0	2.651	11.5	1.935

pressure to the space above the loading plate. The hydraulic gradient was adjusted by changing the height of the upper tank, thereby subjecting the specimen to downward seepage flow. The hydraulic gradient is defined as the ratio of the water head difference (the height from the bottom of the specimen to the water surface of the upper tank) to the height of the specimen.

2.2 *Experimental samples used in this study*

Figure 2 and Table 1 show the particle size distribution and physical properties, respectively, of the soil samples used in this study. These soil samples comprise a mixture of sand and kaolin, and are named "QK". The samples were blended to have a particle size distribution resembling that of the decomposed granite soil collected in Ube, Yamaguchi Prefecture, Japan, which is often used as reservoir embankment soil.

2.3 *Experimental procedure*

The soil samples, adjusted to the optimum water content, were divided into five layers and compacted one layer at a time to achieve the pre-determined dry density. The interior of the specimens was replaced with carbon dioxide and infiltrated with de-aired water for 24 hours to achieve a saturation level of 95% or higher. After adjusting the hydraulic gradient to a pre-determined value, the outlet valve was opened to start the seepage process.

Table 2 shows the experimental conditions. In this study, water-passing experiments were performed under the condition of constant or fluctuating hydraulic gradients. C1.0 and C0.5 are the experimental cases performed under a constant hydraulic gradient. After the start of the seepage process, 20 containers were prepared, each with 100 ml of drainage, and the amount of drained water and eroded soil, and the turbidity of the drainage were measured. Cases 1 ~ 3 are the experimental cases performed under a fluctuating hydraulic gradient. In these cases, the hydraulic gradient was increased and decreased six or seven times. The containers for collecting the drainage were changed immediately before the hydraulic gradient was changed. Preliminary experiments showed that the discharge of soil particles almost stopped after about 1500 ml of water flow under the constant hydraulic gradient condition, so the hydraulic gradient was changed every 1500 ml of water flow. In all three cases, the range

in the variation of the hydraulic gradient was 0.5. The measurement items were the waterflow rate, water collecting time, amount of eroded soil, and turbidity of the drainage for each container. The turbidity of the drainage was measured by the transmitted and scattered light method, which has high sensitivity in the wide range of concentration. The polystyrene latex was used for calibration of the sensor.

Table 2. Experimental conditions.

ID	Void ratio	Initial hydraulic gradient	Fluctuating patten of hydraulic gradient	
C1.0	0.58	1.0	Constant	
C0.5	0.58	0.5	Constant	
Case 1	0.58	1.0	Fluctuating	(1.0 ⇔ 1.5)
Case 2	0.58	1.0	Fluctuating	(1.0 ⇔ 0.5)
Case 3	0.58	0.5	Fluctuating	(0.5 ⇔ 1.0)

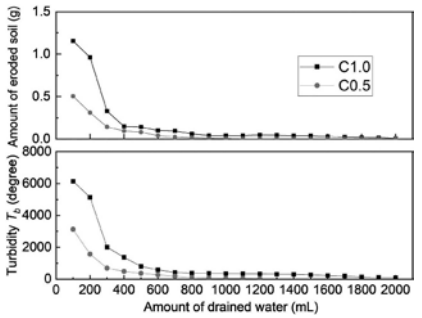

Figure 3. Changes in amount of eroded soil and turbidity.

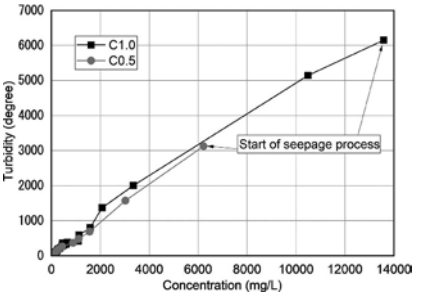

Figure 4. Relationship between concentration before dilution and converted turbidity.

3 RESULTS OF WATER-PASSING EXPERIMENTS

3.1 *Suffusion behavior under condition of constant hydraulic gradient*

Figure 3 shows the changes in the amount of eroded soil and the turbidity in C1.0 and C0.5. The amount of eroded soil gradually decreased when the amount of drained water increased. The larger the hydraulic gradient, the greater the amount of eroded soil and turbidity of the drainage. Figure 4 shows the relationship between the concentration and the turbidity for each container. After starting the seepage process, the concentration–turbidity behavior followed the pathway from the upper right to the origin. In the case of C1.0, the pathway was an upward convex arched pathway. In the case of C0.5, on the other hand, the pathway was nearly straight. It has been found that the turbidity is higher when the particle size of the suspended soil in the drainage is smaller, even when the concentration is the same (Ishimaru et al., 2022). Therefore, the upward convex arched pathway of C1.0 implies that the particle size of the eroded soil changed during the seepage process.

3.2 *Suffusion behavior under condition of fluctuating hydraulic gradient*

3.2.1 *Changes in flow rate*

Figure 5 shows the changes in the hydraulic gradient, the amount of drained water, and the flow rate during the water-passing experiments under the condition of the fluctuating hydraulic gradient. The flow rate was calculated for each section from the time the hydraulic gradient was raised or lowered until just before the next change in the hydraulic gradient. The flow rate fluctuated in conjunction with the change in the hydraulic gradient. As the hydraulic gradient was repeatedly changed, the flow rate became slightly lower at the same hydraulic gradient. The rearrangement of the soil particles may have reduced the hydraulic conductivity.

3.2.2 *Suffusion behavior*

Figure 6 shows the amount of eroded soil in each container of collected drainage. After the hydraulic gradient began to be changed, the amount of eroded soil was only slightly less than 0.5 g. However, as the hydraulic gradient was increased, the amount of eroded soil tended to increase. Figure 7 shows the relationship between the concentration and turbidity of the drainage. This figure also shows the relationship between the concentration and turbidity for suspensions made of kao-lin and the erodible components of QK (soil particles smaller than 425 μm). It can be inferred that many very small soil particles in the specimen were eroded since the data were plotted above the concentration-turbidity relationship of kaolin at the beginning of the seepage process. After the hydraulic gradient began to be changed, on the other hand, the data were plotted closer to the concentration-turbidity relationship of the erodible components of QK. This suggests that when a specimen was subjected to seepage force for the first time, the small soil particles with easy flowability had already eroded, and that the soil particles that flowed out due to the changes in the hydraulic gradient were relatively large in diameter.

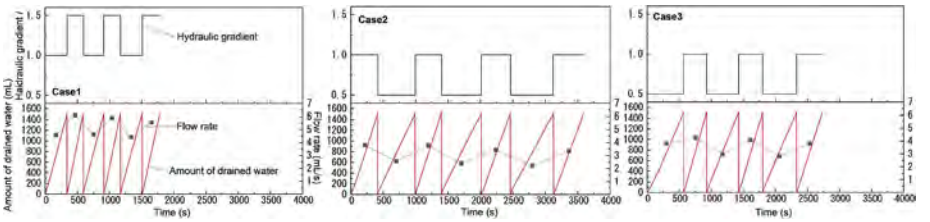

Figure 5. Changes in hydraulic gradient, amount of drained, water and flow rate.

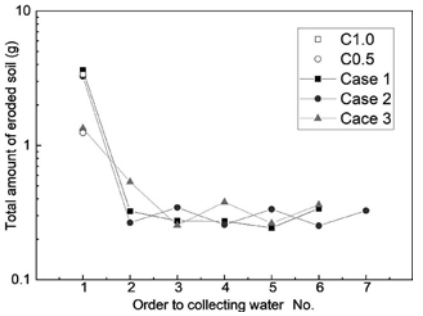

Figure 6. Amount of eroded soil in each collecting container.

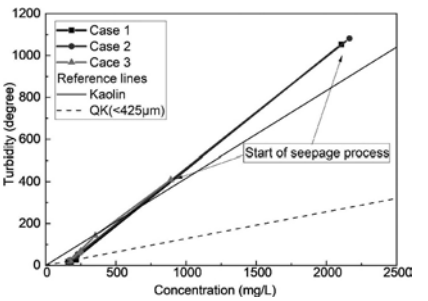

Figure 7. Relationship between concentration and turbidity of drainage.

4 CONCLUSION

Water-passing experiments were conducted to investigate the progression of suffusion under varying hydraulic gradients. The results showed that the discharge of fines continued to increase and decrease as the hydraulic gradient fluctuated repeatedly. The cases in which the soil particles were being discharged under the condition of a fluctuating hydraulic gradient were estimated to be relatively large in diameter among the erodible components.

ACKNOWLEDGEMENTS

This study was financially supported by JSPS KAKENHI Grant Number JP21J14582. We wish to offer our sincere gratitude.

REFERENCES

Ishimaru, T., Suzuki, M., Takano, S. 2022. Particle size composition of migrating soil particles and the time change in water-passing experiments for reproducing suffusion using turbidity, Journal of JSCE, 17 (1), pp. 47–60. (in Japanese)

Luo, Y., Qiao, L., Liu, X., Zhan, M., Sheng, J. 2013. Hydro-mechanical experiments on suffusion under long-term large hydraulic heads. Natural Hazards, 65 (3), pp. 1361–1377.

Smart Geotechnics for Smart Societies – Zhussupbekov, Sarsembayeva & Kaliakin (Eds)
© 2023 The Author(s), ISBN 978-1-003-29912-7
Open Access: www.taylorfrancis.com, CC BY-NC-ND 4.0 license

Impact of internal erosion on soil fabric and mechanical behavior

C. Dong, A. Mehdizadeh & M.M. Disfani
The University of Melbourne, Australia

ABSTRACT: Internal erosion is responsible for an overwhelming proportion of dam failures. The microstructure of soil and its mechanical properties can be affected by particle migration, resulting in a decrease in soil stability. Using a modified erosion testing apparatus, this research examines the impact of internal erosion on the small strain shear modulus (G_0) of gap-graded granular soils. The moist tamping technique was used to prepare internally unstable gap-graded soils with varying fines content and relative densities. The specimens were subjected to a downward seepage flow, while the induced pore pressure and erosion progress both monitored continuously. Three sets of bender elements were mounted on the cell to track the variation in shear wave velocity throughout the sample height during erosion. The results indicate the negative correlation between fine particle content and G_0, while suggesting that the increment of soil compaction would potentially accelerate G_0 at transitionally unstable zone.

Keywords: soil fabric, mechanical property, fine particle content, relative density

1 INTRODUCTION

Subgrade filling materials are often composed of gap-graded soils from mountainous regions (Zhang et al., 2020). In an internally stable soil with a coarse-dominant structure, the coarse fraction acts as the matrix of soil structure to prevent non-plastic fine particles from migration under seepage force. In such a soil structure, fine particles may either provide lateral supports for coarse particles or may contribute directly to force chains within the soil fabric. According to Ke and Takahashi (2012), suffusion, a typical form of internal erosion, significantly decreases soil porosity, thereby reducing soil strength. It is consistent with the findings of (Mehdizadeh et al., 2018) and Tian et al., (2020) that the microstructure and shear strength of soils change with internal erosion. However, few research studies manage to monitor the decrease of shear strength due to soil migration (Kelly et al., 2012). This study investigates the impact of suffusion on the soil fabric and mechanical behaviour of an internally unstable soil through a series of permeameter erosion tests. During the erosion process, the bender element system was employed to monitor the shear wave velocity and G_0 in real-time and the erosion rate was correlated with G_0. A diagram of the shear waves of studied soils was summarised and compared to confirm the impact of fine particle content and relative density on soil structure and G_0.

2 EXPERIMENTAL SETUP AND MATERIAL PROPERTY

2.1 *Apparatus modification*

A rigid-wall permeameter, with dimensions of 211mm (H) x 90mm (D), was modified for erosion testing in this study. A pressure transducer installation hole was fabricated at the bottom

DOI: 10.1201/9781003299127-166

of the cell and three pairs of holes were drilled with a uniform spacing of 33mm to reduce the impact of electromagnetic interference between bender element transmitters. The permeameter pedestal was replaced with a funnel to facilitate the collecting of eroded fine particles. The overviews of the erosion and bender element systems shown in Figure 1(a) and (b) depict the side view of the Plexiglas cell with three pairs of holes along the side wall for modular anchoring of bender elements.

2.2 *Sample preparation*

The under-compaction moist tamping method was used to prepare the binary packing for this study (Frost and Park, 2003; Ladd, 1978). The soil mixture with the initial water content of 6% was evenly segmented into ten layers. Under compaction was intended for lower soil layers since compaction energy applied to upper layers would further compact underlying soil layers.

2.3 *Material property*

Bimodal mixtures of gap-graded cohesionless soils were sized as coarse fraction (1.18 - 2.36 mm) and a fine fraction (0.075 - 0.3 mm). This study applied the gap ratio of 5.2 with the addition of fine particle content (15, 25 and 35% by weight), which represented three fine particle activity states - inactive, semi-active and active (Shire et al., 2014). This research changed the relative density from 30, 60 to 90% to achieve a variety of specimen compactions. Figure 2 presents the particle size distribution diagram of tested soils.

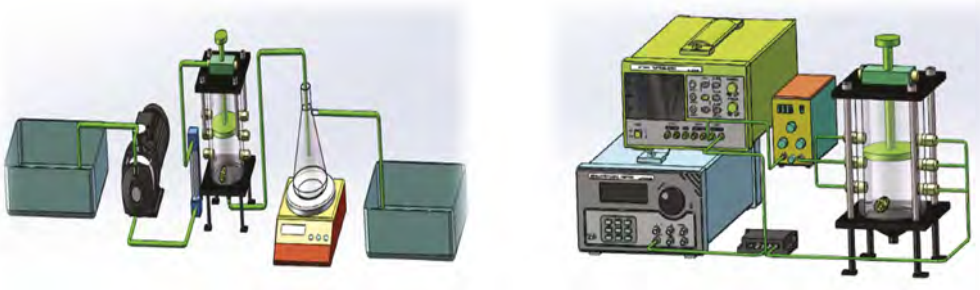

Figure 1. The overview schematics of (a) erosion test system and (b) bender element system.

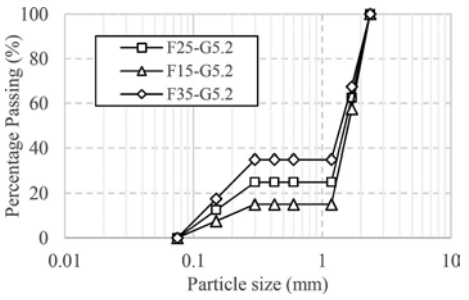

Figure 2. Particle size distribution of tested soils.

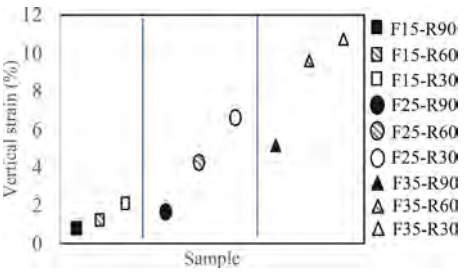

Figure 3. Post-erosion vertical strain of tested soils.

2.4 *Testing regime*

A 2-hour erosion test was conducted under the seepage velocity of 600 ml/min until no further erosion took place. A fixed vertical load of 27.56 kPa was applied to the top of the loading bar. Sine wave signals in a single waveform were generated at 5 kHz and transmitted across the soil

specimens. The transmitting signal amplitude was amplified ten times by a power amplifier, while the signal amplifier contributed 100 times to the receiving signal for signal accuracy improvement.

3 RESULTS AND ANALYSIS

3.1 *Impact of suffusion on soil matrix and G_0*

Vertical strain, the mass of fine particles eroded in real-time, and shear wave velocity of different soil layers were monitored. In this study, the internal soil erosion reduced specimen volume due to the re-adjusting of soil fabric and migration of fine particles. This is called suffusion, which is characterized by a decrease in soil volume due to the removal of fine particles (Richards and Reddy, 2007). It is consistent with the findings of Ke and Takahashi (2012) that with a constant relative density, the post-erosion vertical strain increases with the augment of fine particle content (Figure 3). The vertical strain, however, is negatively impacted by relative density, as higher compaction increases the contact force between particles in force chains, hence the soil skeleton remains unchanged despite the migration of fine particles, which loosely sit within the voids of coarse particles under seepage force (Figure 3).

Table 1. Geotechnical properties and geometrical parameters of studied soils.

Specimen Code	γ_{max} (KN/m^3)	γ_{min} (KN/m^3)	G_s	D_{15}/d_{85}	Sample Height (mm)	Duration (hr)
F15	18.44	15.60	2.65	5.2	137	2
F25	19.48	15.86	2.65	5.2	137	2
F35	19.22	16.40	2.65	5.2	137	2

As an example of how suffusion impacts the small strain shear modulus of soils, Figure 4 illustrates the erosion process of F25-R30 in real time. Particles were rapidly eroded from the cell within 40 minutes, followed by a steady plateau, indicating the end of erosion. The G_0 was measured at almost the same time at the top, middle and bottom of the sample at the beginning of the test. However, the corresponding G_0 measurements along the erosion path showed variations with the erosion progress, especially for the top layer of soil mixture with fine particles continuously migrating to layers below. It can be understood that almost for the first 40 mins, the G_0 increased by erosion of fine particles regardless of the location of measurement. The bender elements recorded minimal changes in G_0 for the middle sections, while a drop was recorded for the bottom section. It seems that the erosion of the middle layer was terminated after 40 mins and the soil structure finds a new stable status. However, the drop in G_0 for the bottom section might have been due to the accumulation of eroded particles from the upper layer at the bottom due to clogging.

3.2 *Impact of relative density and fines content*

Figure 5 presents the pre-erosion shear wave travel time results for the soils reported here. It suggests that the travel time decreased as relative density increased, i.e., denser compaction. The increase of G_0 can be explained by the fact that coarse particles and fine particles that actively take effective stress within the denser soil matrix provide higher resistance to seepage force. The reduced fine particle content (35% to 15%) negatively correlates with G_0. The results are consistent with the findings of Salgado et al. (2000), which suggest that fine particles lost during erosion probably cause soil fabric to be re-adjusted, thereby intensifying the soil structure.

4 CONCLUSION

This study investigated the effects of suffusion on the small strain shear modulus in internally unstable soils with various fine particle content and relative density using a modified rigid-

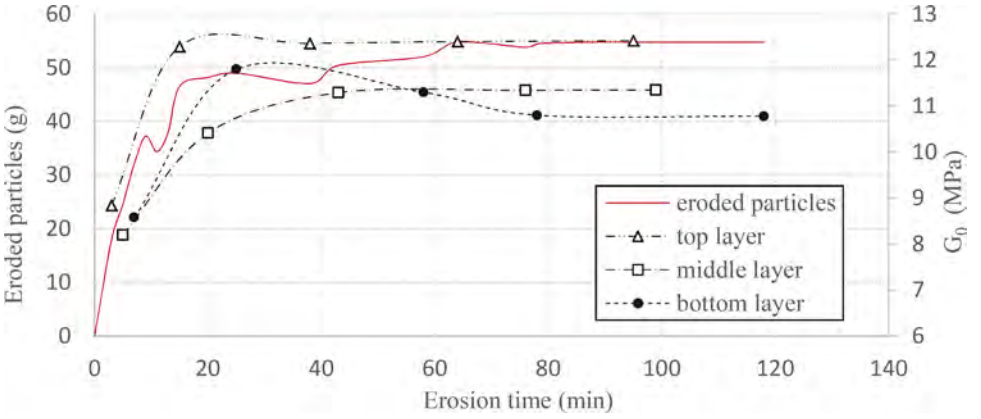

Figure 4. The erosion process and G_0 measurement for different layers of F25-R30.

wall permeameter and bender element technique. The results of erosion tests in this study suggest the following findings:

- Relative density is positively proportional to the small strain shear modulus for fine particle content at 15% to 35%. As a result of erosion of fine particle content at constant relative density, G_0 value is expected to increase.
- The bender element technique coupled with a rigid-wall permeameter has been confirmed as an efficient real-time method for monitoring small strain shear modulus.
- With the loss of fine particles through the voids of a soil skeleton, G_0 slightly increases with the progress of erosion, which probably puts the coarse particles in better contact.
- In contrast with the top and middle layers, G_0 value at the bottom layer is more prone to drop down, following the corresponding erosion progress due to the accumulation of eroded fine particles from the top layers.

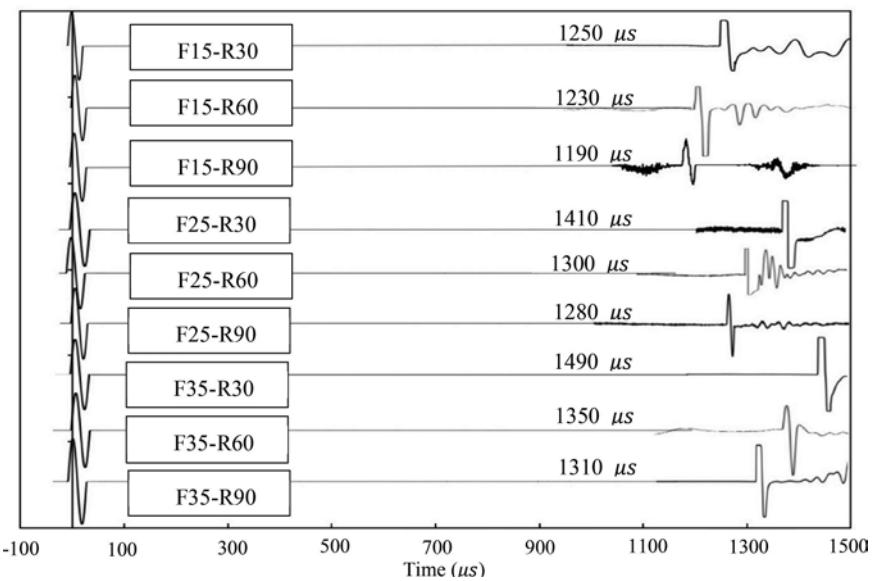

Figure 5. Shear wave forms and travel time measurement for the top layer of studied soils at initial phase.

REFERENCES

Frost, J.D., Park, J.Y., 2003. A critical assessment of the moist tamping technique. Geotech. Test. J. 26, 57–70.

Ke, L., Takahashi, A., 2012. Strength reduction of cohesionless soil due to internal erosion induced by one-dimensional upward seepage flow. Soils Found. 52, 698–711.

Kelly, D., McDougall, J., Barreto, D., 2012. Effect of particle loss on soil behavior, in: Proc., 6th Int. Conf. on Scour and Erosion, Publications SHF, Paris. pp. 639–646.

Ladd, R.S., 1978. Preparing test specimens using undercompaction. Geotech. Test. J. 1, 16–23.

MEHDIZADEH, A., DISFANI, M. M., EVANS, R. & ARULRAJAH, A. 2018. Progressive internal erosion in a gap-graded internally unstable soil: mechanical and geometrical effects. *International Journal of Geomechanics*, 18, 04017160.

Richards, K.S., Reddy, K.R., 2007. Critical appraisal of piping phenomena in earth dams. Bull. Eng. Geol. Environ. 66, 381–402.

Salgado, R., Bandini, P., Karim, A., 2000. Shear strength and stiffness of silty sand. J. Geotech. Geoenvironmental Eng. 126, 451–462.

Shire, T., O'Sullivan, C., Hanley, K.J., Fannin, R.J., 2014. Fabric and Effective Stress Distribution in Internally Unstable Soils. J. Geotech. Geoenvironmental Eng. 140, 04014072.

Tian, D., Xie, Q., Fu, X., Zhang, J., 2020. Experimental study on the effect of fine contents on internal erosion in natural soil deposits. Bull. Eng. Geol. Environ. 79, 4135–4150.

Zhang, F., Zhang, L., Li, Y., 2020. Investigation of gap-graded soils' seepage internal stability with the concept of void filling ratio. PLOS ONE 15, e0229559.

Smart Geotechnics for Smart Societies – Zhussupbekov, Sarsembayeva & Kaliakin (Eds)
© 2023 The Author(s), ISBN 978-1-003-29912-7
Open Access: www.taylorfrancis.com, CC BY-NC-ND 4.0 license

Seepage and stability analysis of a boulder barrage strengthened with geosynthetic sandbags and sheet pile walls

P. Kiruthika
Research scholar, Department of Civil and Environmental Engineering, Indian Institute of Technology Tirupati

A. Boominathan
Former Professor, Department of Civil Engineering, Indian Institute of Technology Madras

A. Murali Krishna
Professor, Department of Civil and Environmental Engineering, Indian Institute of Technology Tirupati

ABSTRACT: Breaching of regulators results in potential threats like scouring, piping, and overtopping of the structures. An attempt has been made to assess the performance of a temporary barrage using boulders constructed on the breached portion of the brick masonry barrage during a heavy flood. The stability analysis was carried out on the temporary barrage using finite element code Plaxis 2D. It is revealed from the analysis that temporary barrage is inept to retain the water. Therefore, it is decided to strengthen the temporary barrage incorporating a row of geosynthetic sandbags concealing the temporary structure and providing sheet piles at upstream and/or downstream of the river to withstand the flood. The stability analysis performed for the strengthened barrage revealed that providing rows of geosynthetic sandbags in front of the temporary barrage and sheet piles both at upstream and downstream is effective in reducing uplift pressure and exit gradient, and thereby prevent any future scouring.

1 INTRODUCTION

Inundation risks can be alleviated by the construction of flood defense structures such as dams, embankments, levees and by creating flow diversions channels. But the durability and long-term performance of these structures depend on the magnitude and rate of recurrence of the flood as well as on the aging of the structure. Therefore, additional measures need to be adopted to improve the strength and reliability of the existing structure to overcome future floods. Numerous solutions for complex flow problems were studied by previous researchers to cut-off seepage and to reduce hydraulic uplift (Bligh 1915; Khosla et al. 1936; Terzhaghi & Peck.1967). The steady-state groundwater flow under the permeable foundation of earthen dam was studied for different permeability ratios and penetration depths (Kalkani et al. 1984). Sand- filled geosynthetic bags can be deployed successfully for the flood protection and stability improvement of dams (Saathoff et al. 2007). The possible failure mode and remedial measure to improve the factor of safety was evaluated by finite element method by Agustawijaya et al. 2015. Sheet pile wall behavior in seepage cut-off and stability improvement was studied by varying the length and position (Tung 2016). An iterative finite element procedure was adapted to various cases of groundwater flow in the short period of time compared to the conventional methods (Neuman & Paul 1970).

In the present study, the performance of a temporary barrage using boulders constructed in the breached portion of the brick masonry barrage during a heavy flood in the river of Cauvery in the Southern region of India was presented. Strengthening the temporary boulder

DOI: 10.1201/9781003299127-167

made barrage by providing rows of geosynthetic sandbags in front of the temporary barrage and sheet piles both at upstream and downstream was also presented. A 2D finite element analysis using Plaxis has been conducted to evaluate optimum number of rows of sandbags, length, and location of sheet pile to minimize the uplift pressure and exit gradient. The improvement of the stability of barrage with geosynthetic sandbag and sheet piles has also been studied.

2 BREACHING OF THE EXISTING MASONRY BARAGE AND CONSTRUCTION OF TEMPORARY BOULDER BARRAGE

The 182-year-old Upper Anicut, remains among the most important regulatory structures for irrigation in the delta region of the Cauvery River in India. During the heavy rain on August 24, 2018, 108 meters of the 685-metre-long brick masonry structure, had been washed away into the river as depicted in Figure 1. After the breach, about 90% (of about 38,262 cusecs) of the flow occurred through the breached section. The concentrated flow resulted in a deep scour. An emergency measure was taken to restore the supply immediately within a few hours by closing the breach to an appropriate height with available resources like sandbags and boulders. Additional casuarina and MS steel pipe piles have been driven and they were tied together to form a grid, to support the bags at a closer interval when the current was high. The effectiveness of the casuarina and MS pipe piles grid and the sandbag cofferdam system to perform its function in the years to come under heavy floods was being uncertain. Thus, it was decided further to strengthen the temporary barrage constructed on the breached portion on the brick masonry barrage.

A field investigation was carried out by drilling boreholes up to a depth of about 25 m. The soil profile obtained from the bore logs shows that the foundation soil comprises of a sand layer up to a depth of 10.5 m with SPT N value in the range of 10-40. Further below, a 2 m thick weathered rock followed by Granitic Gneiss lies up to borehole termination depth. The unconfined compressive strength of the rock layer varies from 40-110 kPa. The phreatic head in the upstream side was observed at a height of 5 m above the ground level.

Figure 1. Breached portion of the regulator at Upper Anicut (Image courtesy: The Hindu, 2018).

3 STRENGTHENING OF THE TEMPORARY BOULDER BARRAGE

An exemplary and cost-effective solution for the critical case of hydraulic failure was to erect sheet piles to divert the flow path and reduce the exit gradient. Further, the upstream apron was proposed to be sealed with geosynthetic sandbags to minimize seepage and subsequent piping failure due to scour. Influence of different lengths of sheet piles includes no socketing into the hard stratum - 8 m and 0.5 m above the hard stratum- 10 m are studied to control the seepage & uplift failures. Five different cases of study as shown in the Table 1 are considered. For all the cases, flow analysis is performed to study the seepage effects. The cross-section of the temporary boulder wall (case I) and sheet piles are installed at both U/s and D/s side with geosynthetic sandbags (case V) is presented in Figure 2 & 3 respectively.

– Case I: Temporary barrage without any strengthening measures
– Case II: Temporary barrage with geosynthetic sandbags as a cover
– Case III: Temporary barrage with geosynthetic sandbags and sheet pile wall on the U/s side
– Case IV: Temporary barrage with geosynthetic sandbags and sheet pile wall on the D/s side
– Case V: Temporary barrage with geosynthetic sandbags and sheet piles on the U/s & D/s side

Table 1. Different cases of study considered in the Breached portion of the barrage.

Cases	Geosynthetic sang bags	Sheet pile location		Sheet pile length (m)	
		U/S	D/S	U/S	D/S
I		Without sheet pile& Geosynthetic sandbags			
II	✓	Without sheet pile			
III	✓	✓	-	8, 10	-
IV	✓	-	✓	-	8, 10
V	✓	✓	✓	8, 10	8, 10

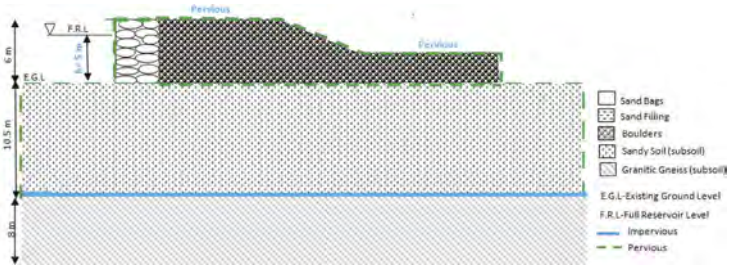

Figure 2. Cross-section of the temporary boulder wall in the breached portion.

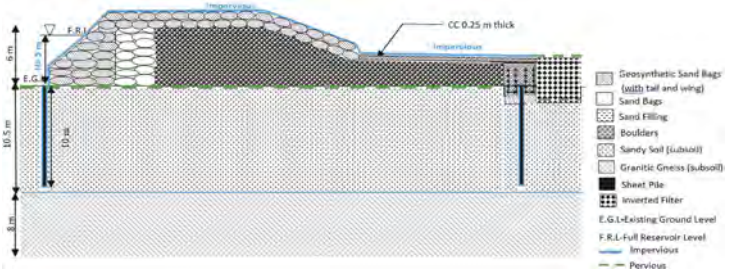

Figure 3. Cross-section of the temporary boulder wall with sheet piles and geosynthetic sandbags.

4 NUMERICAL ANALYSIS

An idealized 2D plane strain model of the temporary barrage constructed on the breached potion of the brick masonry barrage with its dimensions is presented in Figure 4a. 15-noded triangular elements chosen to generate mesh and the meshed model is presented in Figure 4b. A Mohr-Coulomb constitutive relationship has been used for defining the elasto-plastic stress-strain behavior of different materials and the properties are provided in Table 2. The sheet pile is modelled as a plate element and the section details are given in Table 3. The sheet pile section chosen was JFESP-4 with intact interlock pattern which doesn't permit water or soil particles to pass through. A constant hydraulic head of 5 m is maintained throughout the analysis. Translations in all directions along the bottom boundary and translation in the

horizontal direction along the vertical boundaries are constrained in the analysis. Model boundaries are located away from the threshold boundary to avoid the boundary effect on the chosen area of interest.

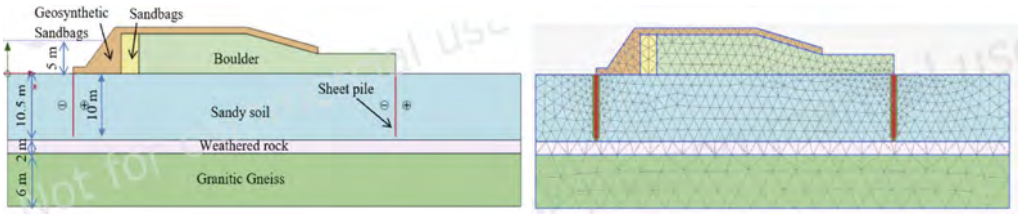

Figure 4. (a) Idealized barrage section and (b) Meshed model.

Table 2. Properties of the sub-soil and embankment materials.

Parameters	Sandy Soil	Granitic Gneiss	Sandbags	Boulders	Geosynthetic sandbags
Υ_{unsat}, (kN/m^2)	17	20	17	20	16.5
Υ_{sat}, (kN/m^2)	18	21	18	21	-
K_x, (m/day)	10	0.3	0.6	0.6	-
K_y, (m/day)	10	0.3	0.6	0.6	-
R_{inter}	0.6	0.6	0.6	0.6	0.6
E (kPa)	5000	100000	50000	50000	18000
c' (kPa)	5	70	5	40	5
φ' (degrees)	32	36	32	34	32
Ψ (degrees)	2	6	2	4	2
Poisson's ratio	0.3	0.35	0.3	0.35	0.25

Table 3. Properties of sheet pile.

Properties	Values
Normal stiffness (EA) (kN/m)	4.85 x 10^6
Flexural rigidity (EI) (kN/m)	7.72 x 10^4
Poison's ratio	0.26
Weight of the sheet pile, (kN)	1.9

5 RESULTS AND DISCUSSION

Because of high flood discharge, hydraulic failures such as piping, and uplift may arise and therefore it is essential to check for the satisfactory safety and stability of the structure. To predict the groundwater flow with the installation of a sheet pile wall, flow analysis has been carried out. Further separate safety analysis has been run to validate the adequate safety factor of the barrage against the piping failure.

5.1 *Seepage analysis*

The sheet pile wall is taken as an impermeable material in the analysis. The flow arrows signify the magnitude and direction of the water flow under the barrage. A steady-state two-dimensional groundwater flow vectors for case I without any strengthening measure is presented in Figure 5. This signifies that in the temporary barrage, a large quantity of flow is taking place through the barrage structure itself. On long-term, it may lead to a progressive increase in the scouring and internal erosion under the barrage. The groundwater flow vector for case II with geosynthetic sandbags is presented in Figure 6 represents that although the geosynthetic sandbags cannot completely mitigate the water seepage under the barrage, it can

protect the periphery to a great extent where the distress is high. The flow vectors presented in the Figure 7 for the case 5 of strengthened barrage with geosynthetic sandbag and sheet pile wall system evidently portray that the performance of combined sheet pile walls and geosynthetic sandbag system has a beneficial effect on seepage control.

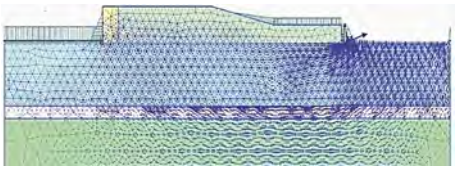

Figure 5. Groundwater flow vectors temporary boulder wall for the breached portion.

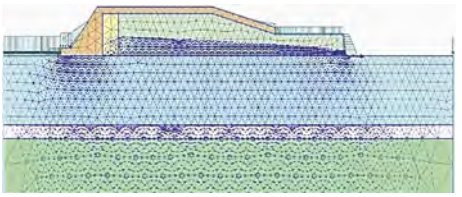

Figure 6. Groundwater flow vectors for strengthened barrage with geo-synthetic bags.

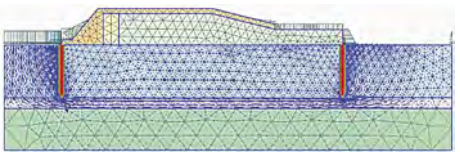

Figure 7. roundwater flow vectors for strengthened barrage with geo-synthetic bags and sheet pile walls installed at U/s and D/s side.

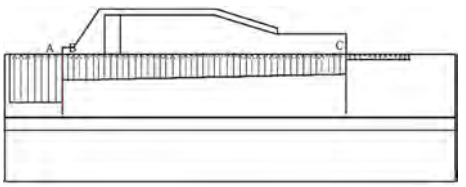

Figure 8. Typical sketch showing uplift pressure variation at the base of the footing.

5.2 *Effect of sheet pile on base heave*

The uplift pressure is measured at three locations, at a point before the sheet pile wall (A), after the U/s sheet pile wall (beginning of the barrage) (B) and before the D/s wall (toe of the barrage) (C) and for a typical case is presented in Figure 8. The base of the barrage structure must sustain the total pressure exerted by the hydraulic seepage beneath the structure. In other terms, if the structural weight is not sufficient to withstand the increased pressure exerted by the seeping water hydraulic heave may potentially occur. It shows that the uplift is reduced to a great extent by providing a sheet pile on the upstream side of the barrage. About 50% reduction in the uplift pressure is attained by providing a sheet pile at the upstream face of the barrage. Table 4 represents the reduction of the uplift pressure at the base of the structure with the installation of sheet pile wall at different locations and length. Nevertheless, the variation in the length of the sheet pile has minor influence in reducing the uplift pressure.

Table 4. Variation of pressure with length and location of sheet pile.

Different cases	Length of the sheet pile	Uplift pressure at the base of the footing (kPa)		
		A	B	C
III	8	50	25	6.5
	10	50	23	5
IV	8	50	45	30
	10	50	48	26
V	8	50	25	18
	10	50	23	17

5.3 *Effect of sheet pile on exit gradient*

One way to ensure the stability of a dam during the flood is to control the exit gradient. If the exit gradient exceeds the critical hydraulic gradient, it can lead to a failure mechanism called

piping. Since the exit gradient is inversely proportional to the path length, installation of sheet pile prominently increases the flow length and reduces hydraulic gradient therefore diminishes the piping failure especially at the toe. This can be seen in the results of a numerical analysis as shown in Figure 9, which illustrates the variation of exit gradient with location and length of sheet pile wall. It was observed that the exit gradient of the temporary boulder barrage was 1.05, but after the installation of sheet piles, it was reduced to 0.2. Additionally, it was found that the sheet pile wall installed at the downstream side was more effective in reducing the exit gradient than if it was only installed at the upstream side. Further with increase in the length of the sheet pile, exit gradient gradually decreases.

5.4 *Effect of sheet pile on factor of safety*

The overall safety factor of the barrage structure strengthened by geobags and sheet piles is calculated in Plaxis. As shown in Figure 10, the safety factor increased for all cases when sheet piles were installed. The safety factor of the temporary boulder barrage was only 1.05, which indicates that it was just safe. However, with the implementation of strengthening measure with sheet piles and geosynthetic sandbags, the FOS is increased to about 2.5. The undamaged section of the barrage has relatively higher FOS of about 1.9 but the long-term seepage may lead to reduce safety factor due to the piping action.

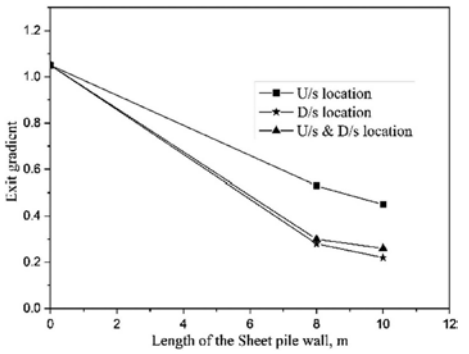

Figure 9. Variation of exit gradient.

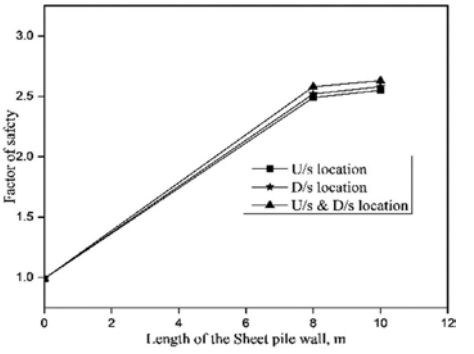

Figure 10. Variation of FOS.

6 CONCLUSIONS

Numerical analyses have been performed on the temporary boulder barrage strengthened with the different combinations of rows geosynthetic sandbags in front of the temporary boulder barrage and sheet pile wall in upstream and downstream of the river. The following are the conclusions drawn from the present study

- The installation of geosynthetic sandbags acts as a protective cover to control seepage and further the introduction of sheet piles acts as a seepage cutoff which improves the stability of the barrage structure.
- The inflowing water generates high porewater pressure that exerts great uplift force on the structure. The erection of the sheet pile wall at the upstream side tends to reduce the hydraulic heave of about 50% at the base of the structure.
- Increasing the sheet pile length favors the reduction of hydraulic exit gradient up to 70%. Thus, the exit gradient reduces with the sheet pile installed at the downstream side
- Along with geosynthetic sandbags provided in front of the temporary boulder barrage, sheet piles installed at both upstream and downstream side of the barrage, effectively arrests the heaving and piping respectively, and provides adequate stability to the hydraulic structure.

REFERENCES

Bligh, W.G. 1910. Dams, barrages, and weirs on porous foundations. *Eng.News* 64 (26): 708–710.

Clayton, C.R.I., Woods. R.I., Bond, A.J., & Milititsky, J. 2013. Earth pressure and Earth-retaining structures. *CRC Press, Taylor & Francis Group*.

Hamed, F., Vermer, P. & Moormann Ch. 2010. Geotextile-soil modeling using material point method (MPM). DGGT 10ICG, Berlin, Germany.

Heerten, G. 1984. Geotextiles in coastal engineering-25 years experience. *Geotextiles & Geomembranes* 1 (2): 119–141.

Jaishankar, C. 2018. Mukkombu regulator dam collapse: Barrage over troubled waters, *The Hindu*, https://www.thehindu.com/news/national/tamil-nadu/barrage-over-troubled-waters/article61537128.ece.

Khosla, A.N., Bose, N.K., & Taylor, E. M. 1954. Design of weirs on permeable foundations. *Central Board of Irrigation*, New Delhi.

Lee, T., & Benson, C.H. 2000. Flow past bench-scale vertical ground-water cutoff walls. *Journal of geotechnical and geoenvironmental engineering* 126(6): 511–520.

Neuman, S. P., & Witherspoon, P. A. 1970. Finite Element Method of Analysing Steady State Seepage with a Free Surface. *Water Resource Research* 6 (3).

Saathoff, F., Oumeraci, H. & Restall, S. 2007. Australian and German experiences on the use of Geotextile containers. *Geotextiles and Geomembranes* 25: 251–263.

Terzaghi, K., & Peck R. B. 1967. Soil mechanics in engineering practice. *Wiley*, New York.

Tung, S., Bhandari, G., & Mukherjee, S. 2016. Behaviour of Sheet Pile as seepage cutoff below earthen dam. *International Journal of Geotechnical Engineering* 10(2): 162–173.

Smart Geotechnics for Smart Societies – Zhussupbekov, Sarsembayeva & Kaliakin (Eds)
© 2023 The Author(s), ISBN 978-1-003-29912-7
Open Access: www.taylorfrancis.com, CC BY-NC-ND 4.0 license

An extended mesh deformation algorithm for solving free surface problems

F.X. Liu & G.H. Lei
Key Laboratory of Geomechanics and Embankment Engineering of the Ministry of Education, Geotechnical Research Institute, Hohai University, Nanjing, China

H. Lin
School of Infrastructure Engineering, Nanchang University, Nanchang, China

ABSTRACT: The finite-element mesh deformation technique is one of the iterative solution methods used to locate the free surfaces in unconfined seepage flows through dams or levees. This technique involves adjusting the element heights and, hence, moving the top boundary of the mesh to the computed free surface as the iterations proceed. Smith et al. (2014) proposed an algorithm and program to adjust the element heights. In order to alleviate element distortion and improve numerical stability, Fenton & Griffiths (1997) proposed an additional algorithm and program to adjust the element widths. Nevertheless, these algorithms and programs have been specialized to the elements above the downstream water level. In this paper, the two algorithms are extended to the elements below the downstream water level. The validity of the extended algorithm is demonstrated by comparisons with results of an analytical solution, a closed-form approximate solution, and a numerical study with a commercial software.

1 INTRODUCTION

Deformed mesh, fixed mesh, and particle tracking techniques have been developed to locate the free surface. The mesh deformation technique was devised by Taylor & Brown (1967), Finn (1967), and Neuman & Witherspoon (1970). The free surface is located by iteratively adjusting the position of elements until the computed potentials along the top surface equal the elevation heads. It can be easily implemented in numerical computations because the hydraulic properties are held constant during the iteration process. Smith et al. (2014) provided a textbook algorithm and program to adjust the element heights and ultimately approach the free surface.

Excessive mesh deformation in the vertical direction can result in severe element distortion. Some elements may achieve an aspect ratio exceeding 5 and interior angles close to 180° as the free surface drops towards the downstream water level. This would lead to numerical instability or slow convergence (Cividini & Gioda, 1989). To overcome this drawback, Fenton & Griffiths (1997) proposed an additional algorithm and program to geometrically decrease the element widths in the downstream direction. Nevertheless, these algorithms and programs were specialized to the elements above the downstream water level. The heights and number of the elements below the downstream water level were not adjusted, as illustrated by Figures 7.14 and 7.19 of Smith et al. (2014). Distortions may occur in these elements. To prevent this from happening, this paper extends the two algorithms to the elements below the downstream water level.

2 INITIAL MESH

Only the lower part of a sloped earth dam or levee that is below the upstream water level is considered, as shown in Figure 1a. A Cartesian coordinate system xoy is defined with the origin at the downstream toe, the y axis positive upward, and the x axis coincident with the dam base. The reference datum for measuring the elevation head is placed at the x axis.

DOI: 10.1201/9781003299127-168

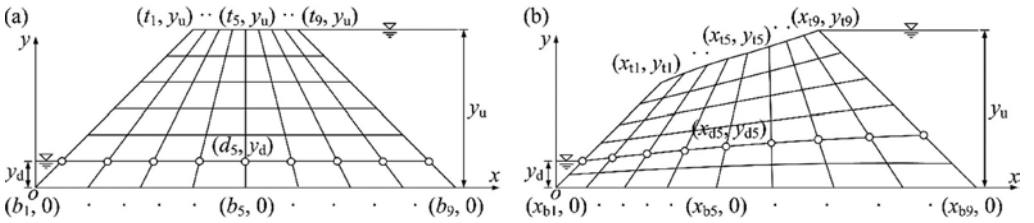

Figure 1. Mesh deformation by adjusting the heights and widths of the elements both above and below the downstream water level: (a) initial mesh; and (b) deformed mesh during the iterations.

The upstream and downstream water levels are denoted by y_u and y_d, respectively. The mesh below the upstream water level consisting of n_{xe} columns and n_{ye} rows of elements is initially generated as follows. The element nodes are evenly distributed along the top and bottom boundaries of the mesh. The x coordinates of the top and bottom nodes are denoted by t_i and b_i, respectively, where $i = 1, 2, \ldots, (n_{xe} + 1)$, increasing in the upstream direction. Each pair of the top and bottom nodes having coordinates (t_i, y_u) and $(b_i, 0)$ respectively is connected to form a straight line segment. These line segments are used to create the columns of the mesh.

A horizontal line at the downstream water level is used to divide the mesh into the upper and lower parts. The points of intersection between this division line and the straight line segments connecting (t_i, y_u) and $(b_i, 0)$ give the nodes on the division line, as shown by the open circles in Figure 1a. The coordinates of these nodes are denoted by (d_i, y_d), where $d_i = b_i + (t_i - b_i)y_d/y_u$.

A proportionality factor is defined to describe the proportion of the downstream water level y_d to the y coordinate of the topmost node on the downstream face, as given by

$$\lambda = \frac{y_d}{surf(1)} \tag{1}$$

where $surf(i)$ = a one-dimensional real array of length $(n_{xe} + 1)$, which is used to store the y coordinates of the nodes on the top boundary of the mesh. This proportionality factor is used to determine the numbers of rows of the elements below and above the division line as follows:

$$n_{ye\_d} = \mathrm{NINT}(\lambda n_{ye}) \text{ and } n_{ye\_s} = (n_{ye} - n_{ye\_d}) \tag{2}$$

where NINT = a function in FORTRAN, which returns the nearest integer to an argument.

The element nodes are evenly distributed along each straight line segment connecting (d_i, y_d) and $(b_i, 0)$ and each straight line segment connecting (t_i, y_u) and (d_i, y_d) according to the allocated numbers of rows of the elements below and above the division line, respectively. The coordinates of these nodes can be readily derived using analytic geometry formulas.

3 EXTENDED MESH DEFORMATION ALGORITHM

In each iterative computation, the free surface is assumed to be at the deformed top boundary of the mesh. The finite element computation is performed using program 7.3 of Smith et al. (2014). The hydraulic heads of the nodes on the top boundary of the mesh computed in the previous iteration are used to deform the mesh. Smith et al. (2014) proposed an algorithm and subroutine geom_freesurf (http://inside.mines.edu/~vgriffit/5th_ed/) to adjust the element heights. Fenton & Griffiths (1997) proposed a geometric spacing algorithm and subroutine mvmesh.f (http://random.engmath.dal.ca/rfem/) to adjust the element widths. By using these algorithms (for details, refer to the source references), the coordinates of the nodes on the top and bottom boundaries of the mesh are shifted to (x_{ti}, y_{ti}) and $(x_{bi}, 0)$, respectively, as shown in Figure 1b.

The array $surf(i)$ is updated using the values of y_{ti}, namely $surf(i) = y_{ti}$. The proportionality factor λ and the numbers of rows of the elements below and above the division line are recalculated using Equations 1 and 2, respectively. During the iteration process, the value of λ increases as the y coordinate of the topmost node on the downstream face, i.e., $surf(1)$,

decreases. This would possibly result in an increase and a decrease in the numbers of the elements below and above the division line, respectively, as illustrated in Figure 1.

The nodes constituting the deformed division line can be generated from the straight line segments connecting the top and bottom nodes, i.e., (x_{ti}, y_{ti}) and $(x_{bi}, 0)$. The y and x coordinates of these nodes are determined by $y_{di} = \lambda \times surf(i)$ and $x_{di} = x_{bi} + (x_{ti} - x_{bi})y_{di}/y_{ti}$, respectively.

The element nodes are evenly distributed along each straight line segment connecting (x_{di}, y_{di}) and (x_{bi}, y_{bi}) and each straight line segment connecting (x_{ti}, y_{ti}) and (x_{di}, y_{di}) according to the reallocated numbers of rows of the elements below and above the division line, respectively. The coordinates of these nodes can be readily derived using analytic geometry formulas.

The above procedure ensures that the total numbers of the elements and nodes are kept unchanged and the downstream water level intersects the downstream face at a node.

4 VALIDATION

To verify the validity of the extended mesh deformation algorithm, the free surfaces in steady-state seepage flows through a rectangular dam and an isosceles-trapezoidal dam were analyzed, as shown in Figures 2a-d and Figure 2e, respectively.

The rectangular dam has a width of 16 m. The upstream and downstream water levels are 24 m and 12 m, respectively. The saturated hydraulic conductivity (k_{sat}) was deliberately specified as 1 m/s because the free surface in a homogeneous isotropic dam is independent of k_{sat}. The initial mesh consisted of 16 columns and 24 rows of 1 m × 1 m square elements. The extended algorithm converged in 20 iterations. Figures 2a, b show the deformed mesh. The total number of the elements was kept unchanged. The elements both above and below the downstream water level were deformed. The elements widths were adjusted to be commensurate with their heights. The maximum aspect ratio of the elements is 1.55. Consider the elements along the downstream face. The numbers of the elements above and below the downstream water level were decreased from 12 to 4 and increased from 12 to 20, respectively. The common node of the elements adjacent to the downstream water level was exactly positioned at the water level. It is evident that the extended algorithm is effective in handling mesh deformation. The top boundary of the mesh represents the free surface obtained from the extended algorithm. The free surface in the rectangular dam was also computed by Liu et al. (2022) using Polubarinova-Kochina (1977)'s solution, as shown by the grey curve in Figure 2a. There is no discernible difference between the free surfaces obtained from the extended algorithm and the analytical solution. However, as shown by Figures 2c, d, the tail ends of the free surfaces obtained from the algorithms of Fenton & Griffiths (1997) and Smith et al. (2014) descend unevenly and exit somewhere below the free-surface exit points obtained from the extended algorithm and the analytical solution.

The trapezoidal dam has a bottom width of 150 m and a width of 30 m at the upstream water level. The upstream and downstream water levels are 37.5 m and 7.5 m, respectively. The k_{sat} value was assumed to be 10^{-7} m/s. The initial mesh consisted of 30 columns and 6 rows of trapezoidal elements. The extended algorithm converged in 11 iterations. Figure 2e shows the deformed mesh and the free surface. The maximum aspect ratio of the elements is 1.09. The free surface in the dam was also analyzed using SEEP/W (GEO-SLOPE International Ltd, 2015). In this analysis, the global element size was set as 2.0 m. The dam was discretized into 2625 four-node quadrilateral elements. The saturated–unsaturated soil model (Papagianakis & Fredlund, 1984) and the built-in volumetric water content function typical for clay were adopted. The saturated volumetric water content and the maximum matric suction were assumed to be 0.5 and 10 kPa, respectively. The Van Genuchten (1980) method was adopted to estimate the hydraulic conductivity function. The saturated hydraulic conductivity, the residual volumetric water content, and the maximum matric suction were set as 10^{-7} m/s, 0, and 10 kPa, respectively. These values made the hydraulic conductivity function steep enough to minimize water flow in the unsaturated zone and ensured that the resulting phreatic surface is close to the free surface (Lam et al., 1987). The free surface obtained from the analysis with SEEP/W is shown by the grey curve in Figure 2e. Additionally, the free surface in the trapezoidal dam was computed using Pavlovsky's method of fragments (Harr, 1962), as shown by the dotted curve in Figure 2e. These free surfaces are in good agreement with the free surface obtained from the extended algorithm.

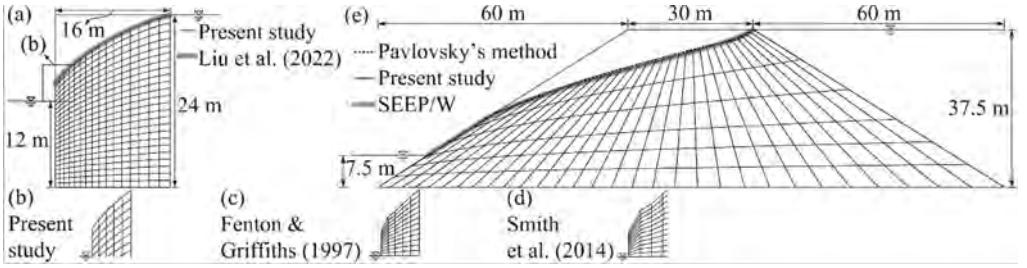

Figure 2. Deformed meshes and free-surface profiles in (a) a rectangular dam (insets b, c, and d: blow-up of the tail ends of the free surfaces obtained from different algorithms); and (e) a trapezoidal dam.

5 CONCLUSIONS

This paper extends the mesh deformation algorithms proposed by Smith et al. (2014) and Fenton & Griffiths (1997) to the elements below the downstream water level of a sloped dam or levee. The numbers of the elements above and below the downstream water level can be reallocated as the computed free surface drops towards the downstream water level. The heights and widths of all the elements are concurrently adjusted. The extended algorithm is shown to be effective in reducing element distortion and ensures that the downstream water level intersects the downstream face at a node throughout the iterations. The computed free surfaces from the extended algorithm are shown to be in good agreement with those from an exact analytical solution, a closed-form approximate solution and a finite-element analysis with SEEP/W.

ACKNOWLEDGEMENTS

The authors gratefully appreciate the financial support of the National Natural Science Foundation of China (grant number 52178326).

REFERENCES

Cividini, A. & Gioda, G. 1989. On the variable mesh finite element analysis of unconfined seepage problems. *Géotechnique* 39(2): 251–267. (discussion and reply, 1990. 40 (3): 523-526)

Fenton, G.A. & Griffiths, D.V. 1997. A mesh deformation algorithm for free surface problems. *International Journal for Numerical and Analytical Methods in Geomechanics* 21(12): 817–824.

Finn, W.D.L. 1967. Finite-element analysis of seepage through dams. *Journal of the Soil Mechanics and Foundations Division* 93(6): 41–48.

GEO-SLOPE International Ltd. 2015. *Seepage modeling with SEEP/W: An engineering methodology*.

Harr, M.E. 1962. *Groundwater and seepage*. New York: Dover.

Lam, L., Fredlund D.G. & Barbour, S.L. 1987. Transient seepage model for saturated-unsaturated soil systems: A geotechnical engineering approach. *Canadian Geotechnical Journal* 24(4): 565–580.

Liu, F.X., Lei, G.H., Wang, W.Y. & Li, Z. 2022. Charts for free surfaces in steady-state seepage flow through homogeneous isotropic rectangular dams. *Journal of Hydrology* 612(A): 128082.

Neuman, S.P. & Witherspoon, P.A. 1970. Finite element method of analyzing steady seepage with a free surface. *Water Resources Research* 6(3): 889–897.

Papagianakis, A.T. & Fredlund D.G. 1984. A steady state model for flow in saturated-unsaturated soils. *Canadian Geotechnical Journal* 21(3): 419–430.

Polubarinova-Kochina, P.Ya. 1977. *Theory of ground water movement*, *2nd edition*. Moscow: Nauka Publishers. (in Russian)

Smith, I.M., Griffiths, D.V. & Margetts, L. 2014. *Programming the finite element method, 5th edition*. Chichester: Wiley.

Taylor, R.L. & Brown, C.B. 1967. Darcy flow solutions with a free surface. *Journal of the Hydraulics Division* 93(2): 25–33.

Van Genuchten, M.Th. 1980. A closed-form equation for predicting the hydraulic conductivity of unsaturated soils. *Soil Science Society of America Journal* 44(5): 892–898.

Smart Geotechnics for Smart Societies – Zhussupbekov, Sarsembayeva & Kaliakin (Eds)
© 2023 The Author(s), ISBN 978-1-003-29912-7
Open Access: www.taylorfrancis.com, CC BY-NC-ND 4.0 license

Computed and observed deformations of fill-type dams by strong earthquake

Tadatsugu Tanaka
The University of Tokyo, Japan

Hiroshi Mori
Faculty of Agriculture and Life Sciences, Hirosaki University, Japan

Kenji Okajima
Department of Environmental Science and Technology, Mie University, Japan

Askar Zh. Zhussupbekov
The Geotechnical Institute, L. N. Gumilyov Eurasian National University, Kazakhstan

ABSTRACT: An earthquake measuring 6.6 Mw struck southern Hokkaido, Japan, September 2018. Mizuho Dam and Azuma Dam were located near the epicenter of this earthquake and strongly shaken. The recorded base peak accelerations of Mizuho Dam in upstream and downstream directions was 491 gal and 937gal was recorded at dam crest. Maximum settlement of crest at upstream slope side was about 12cm and cracks attained about 2.0 m depth were observed around the crest. Azuma Dam's spillway was blocked by debris from landslides. Recorded base peak acceleration was 297 gal and 1293 gal was recorded at dam crest. A simple strain softening elasto-plastic constitutive model is applied to both dams with the features of non-associated flow characteristics, post-peak strain softening, and strain-localization into a shear band with a specific width. The dynamic response analyses of both dams and the computed settlements are compared to observed one.

1 INTRODUCTION

Mizuho Dam is a gravel-fill dam with central clay core zone shown in Figure 1 completed 1998. It is 25.9 m high and 427.05 m long, impounding up to 4,300,000 m^3 of water. Two seismometers were installed at the crest and the base ground as shown in Figure 1. An earthquake measuring 6.7 Mw on the moment magnitude scale struck Iburi Subprefecture in southern Hokkaido, Japan, on 6 September 2018. The earthquake's epicenter was near Azuma Town and occurred at a depth of around 33.0 km. Mizuho Dam located near the epicenter of this earthquake and strongly shaken. The recorded base peak acceleration of Mizuho Dam obtained by the seismometer in upstream and downstream direction was 491 Gal, and 937 Gal was recorded at the dam crest (Figure 2). Maximum settlement of the crest surface was about 8.0 cm (Figure 3), and main three cracks attained about 2.0 - 3.0 m depth were observed around the top edge of downstream slope (Figure 4).

Azuma Dam is a fill-type dam with mudstone and central clay core zone shown in Figure 11 completed 1971. It is 38.2 m high and 222.0 m long, impounding up to 10,080,000 m^3 of water. Two seismometers were installed at the crest and the base ground as shown in Figure 11. Azuma Dam also located around the epicenter of this earthquake and the recorded base peak acceleration obtained by the seismometer in upstream and downstream direction was 297 Gal, and 1293 Gal was recorded at the dam crest (Figure 12). The recorded

DOI: 10.1201/9781003299127-169

acceleration lasted only 30 seconds because the power supply was lost due to the slope failure on the right side downstream of the dam embankment. Maximum settlement of the crest surface was about 14.9 cm (Figure 13).

A simple strain softening elasto-plastic constitutive model is rather robust for application to a dynamic response analysis of fill-type dams. This strain softening material model was applied to Mizuho Dam and Azuma Dam with the features of non-associated flow characteristics, post-peak strain softening and strain-localization into a shear band with a specific width. In order to avoid the numerical instability due to the singularity of non-associated Mohr-Coulomb model, the constitutive model based on the yield function of Mohr-Coulomb type and the plastic potential function of Drucker-Prager type were used.

2 MATERIAL MODEL FOR BEHAXIOR OF GEOMATERIALS

The material model will be briefly described in this section (Tanaka 2002, 2015). The yield function (f) and the plastic potential function (Φ) are given by:

$$f = \alpha I_1 + \frac{\bar{\sigma}}{g(\theta_L)} - K = 0 \tag{1}$$

$$\Phi = \alpha' I_1 + \bar{\sigma} - K = 0 \tag{2}$$

where

$$\alpha = \frac{2\sin\phi}{\sqrt{3}(3-\sin\phi)} \tag{3}$$

$$K = \frac{6c\cos\phi}{\sqrt{3}(3-\sin\phi)} \tag{4}$$

$$\alpha' = \frac{2sin\psi}{\sqrt{3}(3-sin\psi)} \tag{5}$$

$$\sin\psi = \frac{\sin\phi - \sin\phi'_R}{1-\sin\phi\sin\phi'_R} \tag{6}$$

where I_1 is the first invariant (positive in tension) of deviatoric stresses and $\bar{\sigma}$ is the second invariant of deviatoric stress. With the Mohr-Coulomb model, $g(\theta_L)$ takes the following form;

$$g(\theta_L) = \frac{3-\sin\phi}{2\sqrt{3}\cos\theta_L - 2\sin\theta_L\sin\phi} \tag{7}$$

ϕ is the mobilized friction angle, c is the cohesion, ψ is the dilatancy angle and θ_L is the Lode angle.

In case of simple strain softening constitutive model, the frictional softening is given by next function.

$$\alpha(\kappa) = \alpha_p + \alpha_1\kappa/(B+\kappa) \;\; \alpha_1 = -(\alpha_p - \alpha_R) \tag{8}$$

and cohesion softening function is by next function.

$$\gamma(\kappa) = \gamma_p + \gamma_1\kappa/(C+\kappa) \;\; \gamma_1 = -(\gamma_p - \gamma_R) \tag{9}$$

The dilatancy is reduced by next function.

$$\alpha'(\kappa) = \alpha'_p(1 - \kappa/(C + \kappa)) \tag{10}$$

where κ is plastic parameter, B, C, D are constants for softening function. The suffices P, R represent the peak and residual state. Where γ is shear strain, γ_R is reference shear strain.

A more realistic frictional softening functions expressed as follows;

$$\alpha(\kappa) = \alpha_r + (\alpha_p - \alpha_r)\exp\left\{-\left(\frac{\kappa - \varepsilon_f}{\varepsilon_r}\right)^2\right\} \quad (\kappa \geq \varepsilon_f) \tag{11}$$

where ε_f and ε_r are the material constants and α_p and α_r are the values of α at the peak and residual states.

The residual friction angle (ϕ_r) and Poison's ratio (ν) were chosen based on the data from the triaxial compression test.

$$G_0 = G_E \frac{(2.17 - e)^2}{1 + e}\sigma_m^{0.4} \tag{12}$$

The elastic moduli are estimated using the following equations.

$$K = \frac{2(1 + \nu)}{3(1 - 2\nu)}G \tag{13}$$

The peak friction angle is a function of confining pressure, initial void ratio e and G_E is empirical constant.. The dilatancy angle (ψ) was estimated from Rowe's stress-dilatancy relation. The introduction of shear banding in the numerical analysis was achieved by introducing a strain localization parameter s in the following additive decomposition of total strain increment as follows.

$$d\varepsilon_{ij} = d\varepsilon^e_{ij} + sd\varepsilon^p_{ij} \quad s = F_b/F_e \tag{14}$$

where F_b is the area of a single shear band in each element and F_e is the area of the element.

An one-point integration method and an hourglass control scheme are used with 4-noded two-dimensional isoparametric element (Flanagan & Belytschko 1979). This element is effective and suited for collapse analysis of frictional material with shear banding. The most fully integrated continuum elements tend to lock especially for geomaterials, so the selection of element type is important for the collapse analyses of embankment dams. Simple shear strength is appropriate for earthquake response analysis of a fill-type dam and triaxial compression test results of layered soil sample are approximately equivalent to shear strength of horizontally anisotropic fill materials. We employed the triaxial compression test results for the two-dimentional dynamic analyses of fill-type dams.

3 DYNAMIC RESPONSE ANALYSIS OF MIZUHO DAM

The simple strain softening elasto-plastic constitutive equation was applied to the impounded Mizuho Dam. Figure 5 showed the finite element mesh used for dynamic response analysis. Before dynamic response analysis, build-up analysis was carried out.

Table 1 showed the material parameters for the dynamic analysis. The core materials (①, ②) were assumed undrained condition during the earthquake and elasto-plastic constitutive

model was applied. The strengths of core materials were obtained by isotropically consolidated undrained triaxial compression test. The internal friction angle was 25.3°. The cohesion was 32.3 kN/m^2. The constant (G_E) for elastic moduli was 40,000 kN/m^2. The assumed shear band thickness (*S.B.*) was 0.5 cm, taking into consideration that the thickness of shear band is 15~20 times of mean diameter of fill materials.

The strengths of semi-permeable materials were obtained by isotropically consolidated undrained triaxial compression test combined with cyclic loading and succeeding monotonic loading. The material constants of these zones used for the analyses were as follows: φ_{peak} = 32.0°, φ_{res} = 24.6°, c_{peak} = 53.0 kN/m^2, c_{res} = 38.8 kN/m^2, B = 0.5, C = 0.3, D = 0.7, G_E = 80,000 kN/m^2, *S.B.* = 3.0 cm (Case 1).

For semi-permeable zones (④, ⑥, ⑩) mainly at downstream slope side, drained condition were assumed. The strengths of semi-permeable materials were obtained by isotropically consolidated drained triaxial compression tests. The material constants of these zones were as follows: φ_{peak} = 39.2°, φ_{res} = 36.1°, c_{peak} = 22.0 kN/m^2, c_{res} = 19.0 kN/m^2, B = 0.5, C = 0.3, D = 0.7, G_E = 80,000 kN/m^2, *S.B.* = 3.0 cm (Case 2).

The filter zone (⑦) was assumed drained condition and the material constants of this zone are as follows: φ_{peak} = 42.9°, φ_{res} = 33.0°, c_{peak} = c_{res} = 0.0 kN/m^2, B = 0.5, C = 0.3, G_E = 100,000 kN/m^2, *S.B.* = 5.0 cm. The riprap (⑧, ⑨) zones were assumed drained conditions and the material constants of these zone were as follows: φ_{peak} = 44.0°, φ_{res} = 33.0°, c_{peak} = c_{res} = 0.0 kN/m^2, B = 0.5, C = 0.3, G_E = 120,000 kN/m^2, *S.B.* = 14.0 cm.

The Rayleigh damping was assumed 5.0%. The input acceleration was measured one at the base of dam as shown in Figure 2.

In Case 1, Figure 6 showed the computed response acceleration at the crest centre. Although the computed maximum response acceleration was larger than measured maximum response acceleration (937 Gal), the time of computed maximum response acceleration agreed at the time (12 second) of measured maximum response acceleration. Figure 7 showed the computed vertical displacements around crest. Maximum vertical displacements of No.2812 at the crest center and No.2785 around the top edge of upstream slope were about 5.0 cm, and maximum vertical displacements of No.2823 around the top edge of downstream slope was about 7.0 cm. As the measured crest settlements of this dam were within ranging from 5.3cm to 8.0cm, we could say that the comparable results were obtained.

In Case 2, Figure 8 showed the computed response acceleration at the crest center. The computed maximum response acceleration of Case 2 was smaller than that of Case 1, and the time of maximum acceleration agreed well as Case 1. Figure 9 showed the computed vertical displacement around crest. Although results of Case 2 tended to be larger than those of Case 1, the comparable result was obtained in Case 2, too.

Figure 10 showed the computed maximum shear strain distributions after 40 sec. by Case 1 and Case 2. The computed maximum shear strain (Case 1), was about 13% and concentrated around the top edge of downstream slope as shown in Figure 10, so we could say that the comparable results as observed were obtained.

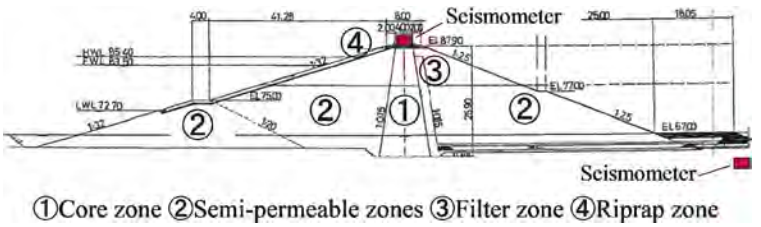

Figure 1. Cross section of Mizuho Dam.

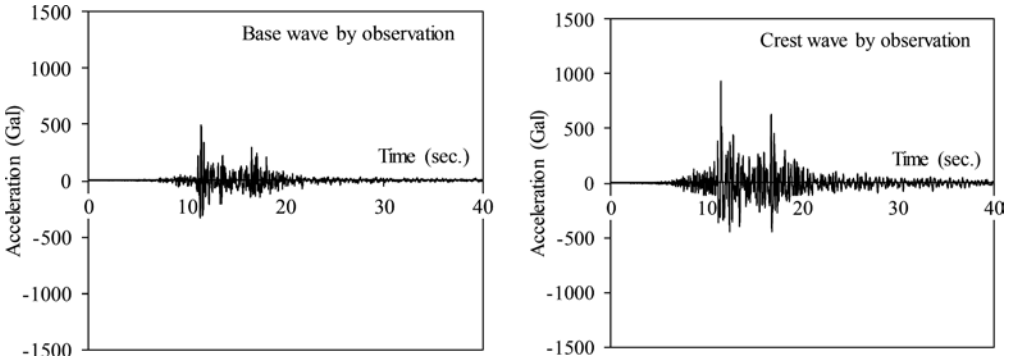

Figure 2. Measured acceleration at the base and crest of Mizuho Dam.

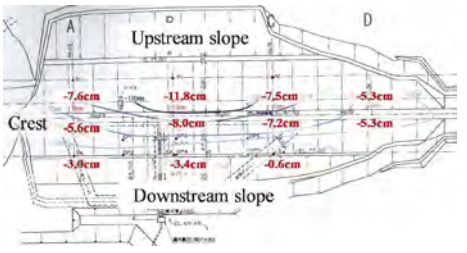

Figure 3. Settlements of crest surface in Mizuho Dam.

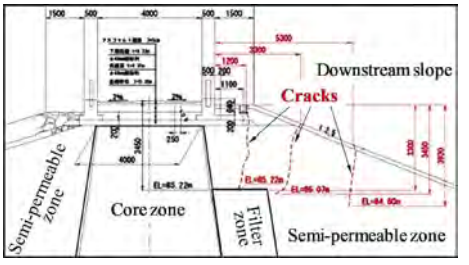

Figure 4. Three major cracks at down stream slope in Mizuho Dam.

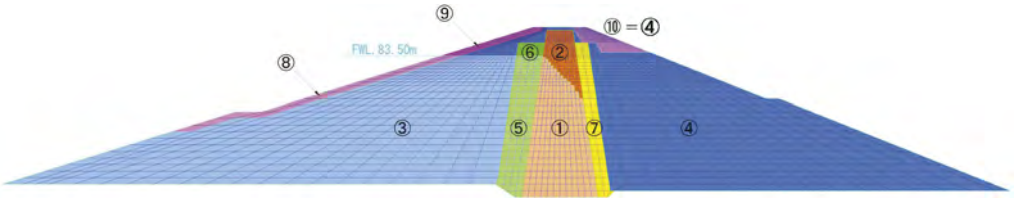

Figure 5. Finite element mesh of Mizuho Dam.
(Total number f elements:2727, Total number of nodes:2835)

Table 1. Material parameters for simple strain softening elasto-plastic analysis.

Material No.	Material name	γ (kN/m3)	φ_{peak} (degree)	φ_{res} (degree)	C_{peak} (kN/m2)	C_{res} (kN/m2)	G_E (kN/m2)	*S.B.* (cm)
①	Core (Saturation)	19.2	25.3	25.3	32.3	32.3	40,000	0.5
②	Core (Un-saturation)	18.7	25.3	25.3	32.3	32.3	40,000	0.5
③=⑤	Semi-permeable (Saturation)	21.4	32.0	24.6	53.0	38.8	80,000	3.0
④=⑤ =⑩	Semi-permeable (Un-saturation)	18.7	32.0 (39.2)	24.6 (36.1)	53.0 (22.0)	38.8 (19.0)	80,000	3.0
⑦	Filter (Un-saturation)	22.7	42.9	33.0	0.0	0.0	100,000	5.0
⑧	Riprap (Saturation)	22.7	44.0	33.0	0.0	0.0	100,000	14.0
⑨	Riprap (Un-saturation)	22.7	44.0	33.0	0.0	0.0	120,000	14.0

The figures in parentheses are obtained by consolidated drained test (CD-test)

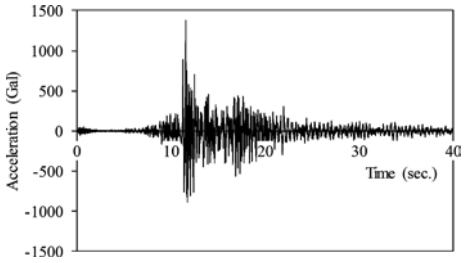

Figure 6. Computed response acceleration at the center crest (Case 1).

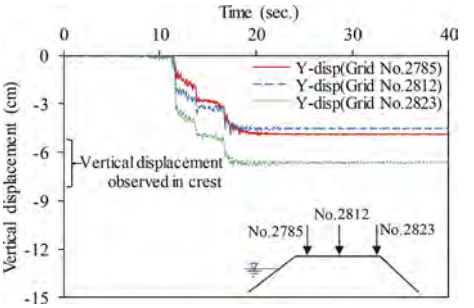

Figure 7. Computed displacements around crest (Case 1).

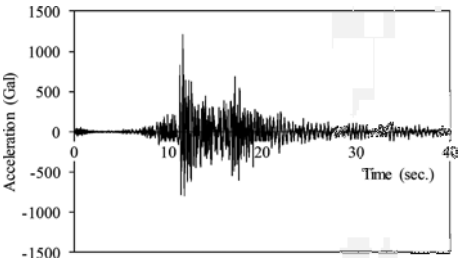

Figure 8. Computed response acceleration at the center of crest (Case 2).

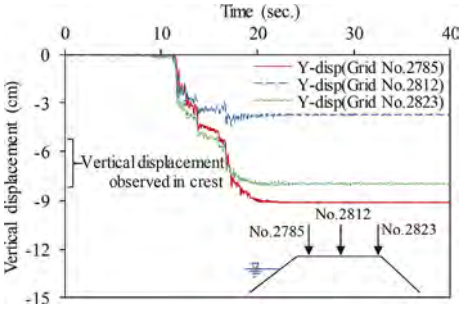

Figure 9. Computed displacement around crest (Case 2).

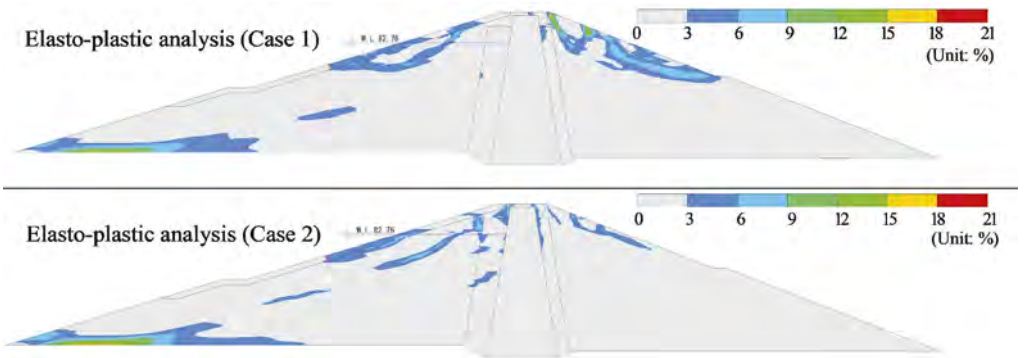

Figure 10. Computed maximum shear strain distributions in 40 second.

4 DYNAMIC RESPONSE ANALYSIS OF AZUMA DAM

The simple strain softening elasto-plastic constitutive equation was also applied to the impounded Azuma Dam. Figure 14 showed the finite element mesh used for dynamic response analysis. Before dynamic response analysis, build-up analysis was carried out.

Table 2 shows material parameters for the dynamic analysis. The Core1 (①, ②) and Core2 (③) materials were assumed undrained condition during the earthquake. The total stress

strengths of core materials were obtained by isotropically consolidated undrained triaxial compression test. The Core1 internal friction angle was 15.0° and cohesion was 37 kN/m^2. The Core2 internal friction angle was 13.0° and cohesion was 51 kN/m^2. The elastic moduli (G_E) were 40,000 kN/m^2. The assumed shear band thickness (S.B.) was 0.2 cm.

The semi-permeable zones (④, ⑥) were assumed undrained condition during the earthquake. The total stress strengths of semi-permeable materials were obtained by isotropically consolidated undrained triaxial compression test. The material constants of saturated semi-permeable zones (④, ⑥) used for strain softening model were as follows: φ_{peak} = 15.0°, φ_{res} = 15.0°, c_{peak} = 81.5 kN/m^2, c_{res} = 81.5 kN/m^2, B = 0.5, C = 0.3, D = 0.7, G_E = 80,000 kN/m^2, S.B. = 4.0 cm. For unsaturated semi-permeable zones (⑤) at downstream slope side, the strengths of the material was obtained by isotropically consolidated undrained triaxial test on the in-situ density (density of 100% D-value). The material constants of this zone were as follows: φ_{peak} = 27.2°, φ_{res} = 27.2°, c_{peak} = 7.4 kN/m^2, c_{res} = 7.4 kN/m^2, B = 0.5, C = 0.3, D = 0.7, G_E = 80,000 kN/m^2, S.B. = 4.0 cm.

The filter zone (⑦, ⑧) was assumed drained condition and the material constants of this zone as follows: φ_{peak} = 40°, φ_{res} = 40°, c_{peak} = c_{res} = 0.0 kN/m^2, B = 0.5, C = 0.3, G_E = 100,000 kN/m^2, S.B. = 1.8 cm. The riprap (⑨, ⑩) zone was assumed drained condition and the material constants of this zone were as follows: φ_{peak} = 30°, φ_{res} = 30°, c_{peak} = c_{res} = 0.0 kN/m^2, B = 0.5, C = 0.3, G_E = 120,000 kN/m^2, S.B. = 20 cm.

The Rayleigh damping was assumed 5.0%. The input acceleration was measured one at the base of dam as shown in Figure 12. Figure 15 showed the computed response acceleration at the crest centre by simple strain softening elasto-plastic analysis. Although the computed maximum response acceleration (1090 Gal) was smaller than measured maximum response acceleration (1293 Gal), the time of computed maximum response acceleration agreed with the time (15.6 second) of measured maximum response acceleration. Figure 16 showed the computed vertical displacements the around crest by simple strain softening elasto-plastic analysis. The maximum vertical displacements of No.1809 at the crest center and No.1814 around the top edge of downstream slope were about 5.4 cm and 8.6 cm. Maximum vertical displacements of No.1805 around the top edge of upstream slope was about 18.1 cm. As the maximum measured crest settlement of this dam was within ranging from 14.9 cm, we could say that the comparable results were obtained.

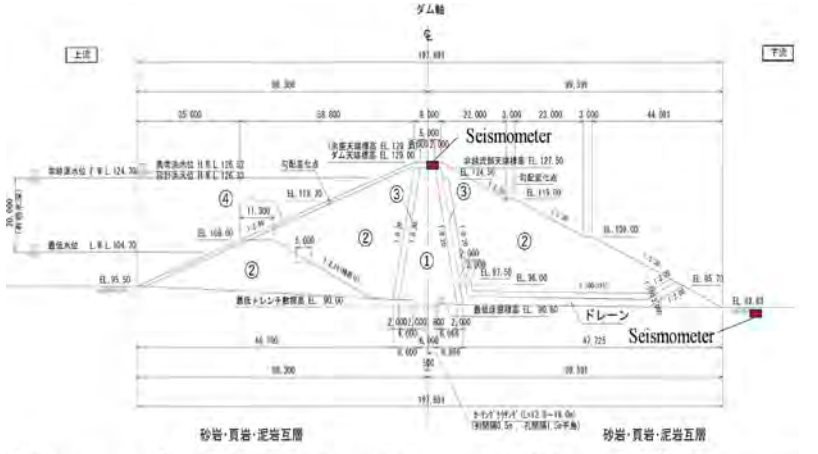

Figure 11. Cross section of Azuma Dam.

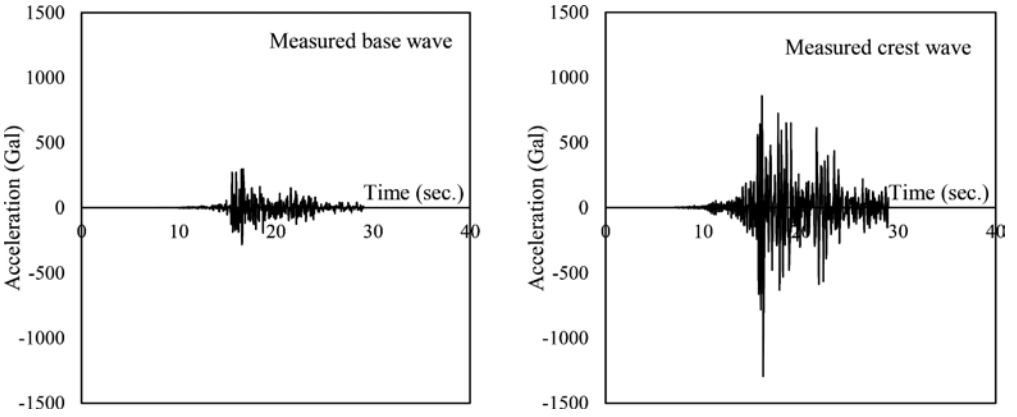

Figure 12. Measured acceleration at the base and the crest of Azuma Dam.

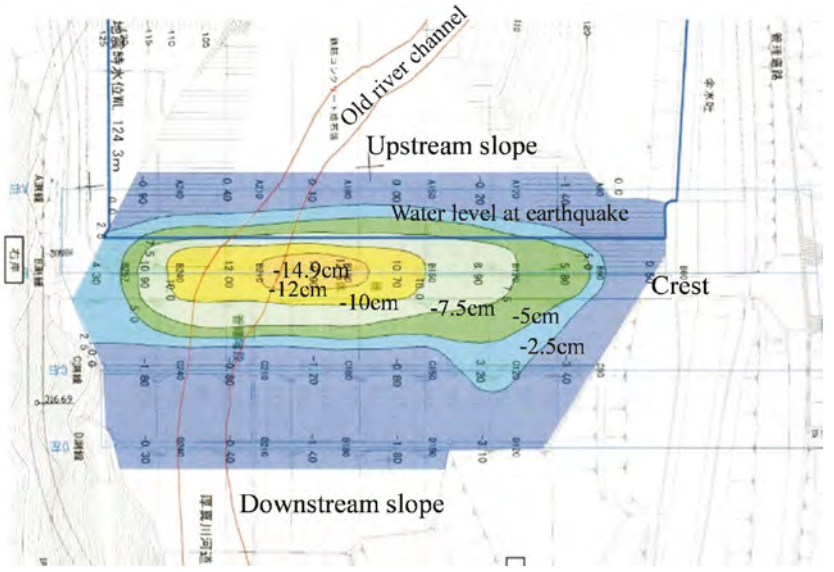

Figure 13. Measured surface settlements of Azuma Dam.

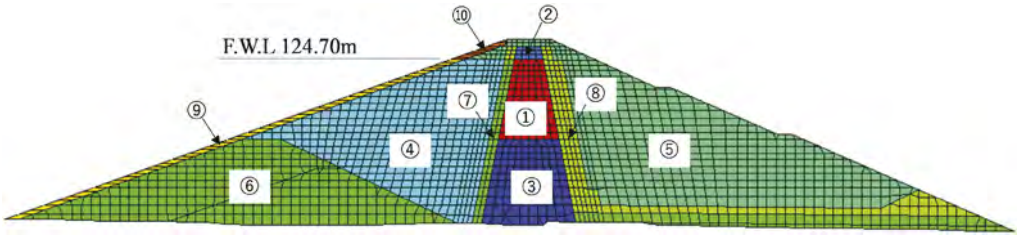

Figure 14. Finite element mesh of Azuma Dam.
(Total number of elements:1761, Total number of nodes:1814).

Table 2. Material parameters for simple strain softening elasto-plastic analysis.

Material No.	Material name	γ kN/m3	φ_{peak} degree	φ_{res} degree	C_{peak} kN/m2	C_{res} kN/m2	G_E kN/m2	S.B. cm
①	Core1 (Saturation)	20.6	15	15	37	37	40,000	0.2
②	Core1 (Un-saturation)	20.3	15	15	37	37	40,000	0.2
③	Core2 (Saturation)	20.7	13	13	51	51	40,000	0.2
④=⑥	Semi-permeable (Saturation)	21.4	15	15	81.5	81.5	80,000	4
⑤	Semi-permeable (Saturation)	20.3	27.2	27.2	7.4	7.4	80,000	4
⑦	Filter (Saturation)	21.1	40	40	0	0	100,000	1.8
⑧	Filter (Saturation)	21	40	40	0	0	100,000	1.8
⑨	Riprap (Saturation)	19.6	30	30	0	0	120,000	20
⑩	Riprap (Saturation)	17.3	30	30	0	0	120,000	20

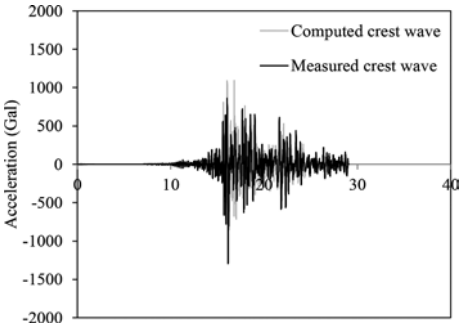

Figure 15. Computed response acceleration at the center of crest.

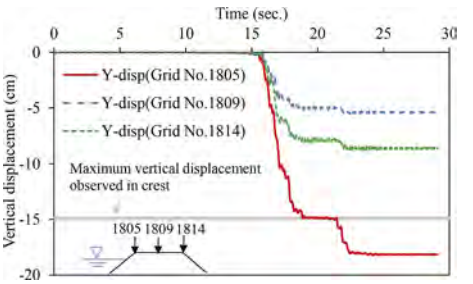

Figure 16. Computed displacements around crest.

5 CONCLUSIONS

A simple strain softening material model for geomaterial is used with the features of post-peak strain softening, and strain-localization into a shear band with a specific width. This material model is applied to the computation of real rock-fill dams. We obtained earthquake induced accelerations and displacements of Mizuho Dam which is 25.9 m high and Azuma Dam which is 38.2 m high. The computed accelerations at the crest of dams are compared to the observed ones and the computed displacements are also verified by the observed displacements. The simple strain softening constitutive model is applicable to the computation of a real fill-type dam.

REFERENCES

Flanagan, D.P. & Belytschko, T. 1979. A uniform strain hexahedron and quadrilateral with orthgonal hourglass control, *Int. J. Numer. Methods Eng.*, Vol.14, 679–706.

Tanaka, T. 2002. Elasto-plastic strain hardening-softening soil model with shear banding. *Proc. 15th ASCE Engineering Mechanics Conf.*, New York, p.8 (CD-ROM).

Tanaka, T. 2015. Cyclic behavior of soils and numerical analyses in cold regions and seismic zones. *Sciences in Cold and Arid Regions*, Vol.7 Issue 5, 492–502.

Smart Geotechnics for Smart Societies – Zhussupbekov, Sarsembayeva & Kaliakin (Eds)
© 2023 The Author(s), ISBN 978-1-003-29912-7
Open Access: www.taylorfrancis.com, CC BY-NC-ND 4.0 license

Safety assessment and disposal advice of post-earthquake working status of road subgrade structure

Zhiqiang Li & Wenwen Feng
China Academy of Transportation Sciences, Beijing, China

Jinbei Li
Sinohydro Corporation Limited, Beijing, China

Jian Tian & Yizhou Jiang
China Academy of Transportation Sciences, Beijing, China

ABSTRACT: The subgrade is an important part of the transportation system. Once it damaged in the earthquake, not only could create huge direct ecnomic loss, but also create difficulties to the rescue work. On 12 May 2008, a magnitude 8.0 earthquake occurred in WenChuan of Sichuan province, caused the destroy of many subgrade existed or in buliding such as overturn, remove and crack. Therefore, the research on emergency assessment of the subgrade damaged in earthquake has practical significance to the structure seismic performance evaluation and the earthquake emergency. In this paper, the key issues associated with post-earthquake emergency inspections of subgrades are presented, such as the forms of subgrade damage, the damage features under earthquake and the influence factors. Safety criteria are established and correlations of such criteria with various damage states are given. This paper presents the methods followed in the evaluation process, highlights the items for evaluation and intends to provide technical references for the post-earthquake disease prevention, diagnosis and disease treatment.

Keywords: subgrade, characteristics of seismic damage, safety assessment

1 INSTRUCTION

The safety of subgrade structure under earthquake action is one of the important problems in geotechnical seismic engineering and highway engineering. In the Wenchuan earthquake, the subgrade project once became the most critical lifeline project to be guaranteed, making the safety evaluation of the subgrade project after the earthquake a key issue to be solved.

In the process of earthquake, it is very common for highway subgrade structure to be damaged. Earthquakes with different intensities may cause subgrade structure deformation, local damage and even collapse. In history, it can be seen from many earthquake cases at home and abroad[1-3]. The damage of highway subgrade caused by earthquake is common, causing great economic losses to the society. Earthquake damage investigation is the most direct and reliable method to understand the working performance of subgrade structure after earthquake, and is also an important basis to verify theoretical analysis, model test methods and results[4]. Under different earthquake action, the earthquake damage characteristics of engineering structures with different site conditions are also different. Previously, the detailed earthquake damage investigation on the embankment was the 2004 Niigata Ken Chuetsu Earthquake[5] in Japan, with magnitude of 6.8. The recorded maximum acceleration exceeded is 1g, which

DOI: 10.1201/9781003299127-170

Figure 1. Direct damage.

Figure 2. Indirect damage.

caused damage to a large range of road embankments. The 2008 Wenchuan earthquake in China, with a magnitude of 8.0, recorded a maximum acceleration of 0.973 g and a duration of more than 80 s [6], was the most powerful earthquake in the western mountainous area of China in modern times. The road embankment in the earthquake area was damaged in various forms and seriously.

China is located in the two most active seismic zones in the world. It is an earthquake prone country. There are numerous highways in the strong earthquake zone. In the Tangshan earthquake in 1976, the highway subgrade structure in the earthquake area was seriously damaged. Among them, at k267 + 374 of Beijing Shanhaiguan railway line, one stone shoulder retaining wall on the side of Shanhaiguan was 3-4m high and 9m long. After the earthquake, the whole retaining wall overturned 20cm outward. In the 2008 Wenchuan earthquake, the highway subgrade was severely damaged. Among them, at k1030 + 400 of Dujiangyan Yingxiu highway of national highway 213, the subgrade subsided, the pavement cracked, the right retaining wall tilted outward and the foundation was empty, and half of the road passed. Therefore, it is of great significance to study the investigation and detection technology of post earthquake highway subgrade structure, conduct rapid evaluation and damage detection on the post earthquake safety of subgrade structure, and provide scientific basis for the seismic reinforcement of subgrade structure.

2 SEISMIC DAMAGE MANIFESTATION OF HIGHWAY SUBGRADE STRUCTURE

2.1 *Two main types of earthquake damage of subgrade structure*

1. Direct damage: the so-called direct damage refers to the rupture or instability of the subgrade structure itself caused by poor filling quality of the subgrade, insufficient retaining capacity of the wall, and excessive seismic load (Figure 1).
2. Indirect damage: refers to the compression deformation of subgrade caused by slope sliding induced by earthquake, which is easy to induce cracking, sliding and even collapse of subgrade, which is the most serious case of all subgrade structural accidents (Figure 2).

2.2 *Specific manifestations of subgrade earthquake damage* [7 ~ 9]

(1) Subgrade settlement, distortion and deformation: This is a common earthquake damage in the earthquake area, which is manifested in two aspects: 1) Subgrade settlement, deformation and damage; 2) The deformation and damage of subgrade surface are caused by the fault dislocation caused by the earthquake or the deformation of underground rock stratum caused by compression, distortion and tension.

(2) Subgrade cracking and sliding damage: it is mainly manifested in the half filled and half excavated subgrade on the slope. Because the compactness of the filled and excavated subgrade is inconsistent, and the base is soft and hard, it is easy to crack along the filling and excavation interface and form a penetrating soft surface with the rock and soil interface or the filling and undisturbed soil interface to cause sliding damage. In addition, when the subgrade filler is gravel soil, loose sliding occurs at the edge of the subgrade during the earthquake.
(3) Subgrade and pavement heave and extrusion damage: affected by seismic surface wave, the surface wave fluctuates, causing the subgrade to fluctuate and deform. In the bulged section, many transverse tensile cracks are generated, and the pavement is squeezed away in serious cases.
(4) Collapses, landslides and mudslides: collapses often occur in high slope sections with developed cracks and loose and broken rock masses. Collapses are mostly related to the presence of soft and broken rocks, groundwater activities, structural weak surfaces, etc., while mudslides often occur in steep valleys due to loose deposits formed by collapses and landslides under the action of rain. In addition, the loose and saturated gravel soil slope often suffers from shallow surface collapse.
(5) Damage of subgrade retaining and protection works: there are many phenomena of subgrade retaining walls in the earthquake area, such as collapse, outward inclination, lateral displacement, wall bulging and foundation void. These phenomena are related to factors such as the reduction of foundation bearing capacity, increase of earth pressure, uneven settlement of foundation, wall material and construction quality during the earthquake. In addition, pebbles are used as raw materials for some retaining walls in the survey area. After the earthquake, these retaining walls basically become loose.
(6) Secondary damage caused by the earthquake to the subgrade: for example, the river is blocked by the collapse, and the water level rises to submerge the highway; The river compression causes the rapid water flow to wash away the subgrade; The subgrade is damaged by collapse and rockfall; Landslide and debris flow buried the subgrade. Not only that, because the rock mass is loosened and the hillside cracks, secondary disasters such as landslides, collapses and mudslides will occur in succession for a long time after the earthquake, causing great harm to the highway.

2.3 *Main characteristics of earthquake damage of subgrade retaining structure*

(1) During the earthquake, the retaining wall will move together with its surrounding media. When the structure has obvious inertia or the stiffness mismatch between the surrounding media and the structure, it will be damaged due to excessive deformation.
(2) The earthquake damage of retaining wall mostly occurs in the area where the stratum conditions are greatly changed. In these areas, the changes of geological conditions or topography cause the stratum vibration and displacement response to be greatly different, thus generating large strain and causing the destruction of retaining wall structure.
(3) The parts with varying wall thickness and height are prone to disease. The corner of the retaining wall is also prone to damage, which is the weak link of anti-seismic.
(4) The retaining wall is easy to be damaged by earthquake when it is located in unfavorable geological conditions such as liquefiable strata and faults.

3 THEORETICAL STUDY ON SIMILARITY RELATION OF SUBGRADE SHAKING TABLE TEST MODEL

3.1 *General requirements for dynamic model tests*

Geometry Condition. Geometric similarity requires that the model and the prototype should remain similar in geometry and corresponding spatial location, so the length L, area A and the volume V should meet the following relationship:

$$A = L^2,\ V = L^3. \tag{1}$$

Movement Condition. The samilarity of the movement condition of the model and the prototype is that the corresponding velocity should in the same directionand proportion to the size, so the displacement, velocity and acceleration should satisfy the following relation equation respectively:

$$[\dot{u}] = \frac{d[u]}{dt},\ [\ddot{u}] = \frac{d[\dot{u}]}{dt} = \frac{d^2[u]}{dt^2},\ [u]^T = [u_x, u_y, u_z] \tag{2}$$

Where: T —— time; $[u]^T$—— soil displacement vector.

Physical Condition. For the physical condition similarity, mechanical properties and responses induced by the load must be similar, Prototype and model should satisfy the following equation:

Soil effective stress principle:

$$\begin{aligned} &[\sigma'] = [\sigma] - [m]p.\ \ [m]^T = (1,1,1,0,0,0) \\ &[\sigma]^T = [\sigma_x, \sigma_y, \sigma_z, \tau_{xy}, \tau_{yz}, \tau_{zx}]. \\ &[\sigma']^T = [\sigma'_x, \sigma'_y, \sigma'_z, \tau'_{xy}, \tau'_{yz}, \tau_{zx'}]. \end{aligned} \tag{3}$$

where $[\sigma]^T$—— total stress vector of soil unit; $[\sigma']$—— effective stress vector of soil unit; P —— pore water pressure.

Soil deformation geometry equations:

$$\begin{aligned} &[d\varepsilon] = [L][du]. \\ &[L]^T = \begin{bmatrix} \frac{\partial}{\partial x} & 0 & 0 & \frac{\partial}{\partial y} & 0 & \frac{\partial}{\partial z} \\ 0 & \frac{\partial}{\partial y} & 0 & \frac{\partial}{\partial y} & \frac{\partial}{\partial z} & 0 \\ 0 & 0 & \frac{\partial}{\partial z} & 0 & \frac{\partial}{\partial y} & \frac{\partial}{\partial z} \end{bmatrix} \\ &[\varepsilon]^T = (\varepsilon_x, \varepsilon_y, \varepsilon_z, \gamma_{xy}, \gamma_{yz}, \gamma_{zx});\ \ [u]^T = (u_x, u_y, u_z). \end{aligned} \tag{4}$$

where $[\varepsilon]^T$—— strain vector of soil element; $[u]^T$—— soil displacement vector.

Constitutive law of soil: expressed by the tangent or secant modulus [D] of the stress-strain relationship and assume particle itself can not compressed, so obtain the following constitutive:

$$[d\sigma']^T = [D][d\varepsilon]. \tag{5}$$

where $[D]$—— tangent or secant modulus decided by the soil stress-strain constitutive;

Dynamic Equilibrium. Dynamic equilibrium equation of soil:

$$[L]^T[\sigma] + \rho[g] = \rho[\ddot{u}].\ \ [g]^T = (0, -g, 0). \tag{6}$$

where ρ—— natural density of soil; $[g]^T$—— acceleration of gravity.

Boundary Condition. The similar transformation of the boundary condition can be obtained by the following to satisfy the similarity.

$$[u]_s = [u]_r \tag{7}$$

where s —— represent the soil;

r —— represent the retaining wall.

The Design of Model Similar Ratio.

Similar Ratio Constant. Prototype and model meet the geometric similarity:

$$C_l = \frac{L_p}{L_m} = \frac{[x]_p}{[x]_m} \tag{8}$$

where p —— represent the prototype; m —— represent the model.

The physical meaning of other symbols is the same as the former.

Similar constant of the soil displacement C_u, the soil velocity $C_{\dot{u}}$, and the soil acceleration $C_{\ddot{u}}$can be expressed by the following equations:

$$C_u = \frac{[u]_p}{[u]_m}, \quad C_{\dot{u}} = \frac{[\dot{u}]_p}{[\dot{u}]_m}, \quad C_{\ddot{u}} = \frac{[\ddot{u}]_p}{[\ddot{u}]_m} \tag{9}$$

Similar constant of the soil stress C_σ, the soil strain C_ε, and the tangent or secant modulus can be expressed by the following equations:

$$C_\sigma = \frac{[\sigma]_p}{[\sigma]_m}, \quad C_\varepsilon = \frac{[\varepsilon]_p}{[\varepsilon]_m}, \quad C_G = \frac{[G]_p}{[G]_m} \tag{10}$$

$$C_D = \frac{[D]_p}{[D]_m}, \quad C_K = \frac{[K]_p}{[K]_m}, \quad C_\mu = \frac{[\mu]_p}{[\mu]_m} \tag{11}$$

Similar constant of the time C_t, the gravity acceleration C_g, and the density $C_{\ddot{u}}$ can be expressed by the following equations:

$$C_t = \frac{t_p}{t_m}, \quad C_g = \frac{[g]_p}{[g]_m}, \quad C_\rho = \frac{\rho_p}{\rho_m} \tag{12}$$

Similar Conditions. Through the similar transformation of the above conditions, we can get the similarity of the prototype and model.

Geometry similar condition: put formula (8) into (1) to conduct similarity transformation, then it comes to the available geometry similar conditions:

$$C_A = C_l^2, \quad C_V = C_l^3 \tag{13}$$

Movement similar condition: put formula (9) into (2) to conduct similarity transformation, we can obtain the movement similar conditions:

$$C_{\dot{u}} = \frac{C_u}{C_t}, \quad C_{\ddot{u}} = \frac{C_{\dot{u}}}{C_t} \tag{14}$$

Physical similar condition: by the similarity transformation of formula (10)~(11) and (3)~(5), it comes to the available physical similar conditions:

$$\begin{aligned} &C_\mu = 1 \\ &C_E = C_G = C_K = C_D \\ &C_u = C_l C_\varepsilon \\ &C_\sigma = C_D C_\varepsilon \end{aligned} \tag{15}$$

Dynamic similar condition: put formula (12) into (6) to conduct similarity transformation, then it comes to the available dynamic similar conditions:

$$C_\sigma C_l^{-1} = C_\rho C_g = C_\rho C_{\ddot{u}} \tag{16}$$

Boundary similar condition: through the similar transformation of the formula (7), we can get:

$$C_{us} = C_{ur} \tag{17}$$

3.2 *Experimental result analysis*

The primary goals of the shaking table model test are to reproduce the mechanical phenomena of the prototype under static and dynamic loading. The similarity relation is to deduce the responses of the prototype based on the monitor of the model responses. On the one hand, the similarity provides the rules of the model results projected to the prototype; the other hand, the similarity provides the similar conditions must be met.

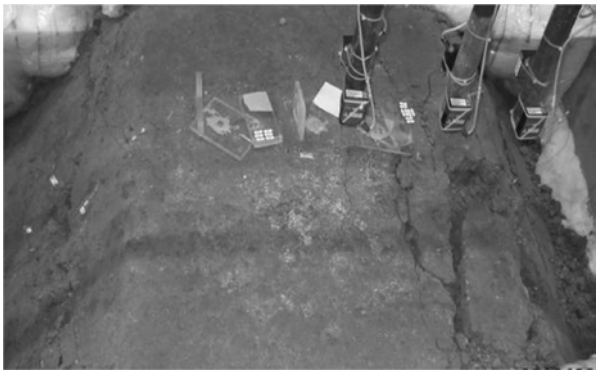

Figure 3. Fracture coalescence on the top of the subgrade model with retaining wall.

The modle test is realized smoothly considering the input earthquake wave type, intensity, frequency and multi-direction input. we use the finite difference program to simulate the shaking table test at the same time, so as to prove the rationality of the numerical analysis model. Based on the shaking table test results and the numerical analysis results, some knowledge of subgrade model dynamic response is achieved which including the acceleration magnification and displacement response and dynamic soil pressure on retaining wall and other aspecets of the analysis.

4 INFLUENCING FACTORS OF SUBGRADE STRUCTURE EARTHQUAKE DAMAGE

4.1 *Affecting factors of subgrade earthquake damage*

(1) The failure of subgrade slope is related to the lithology of rock mass, weathering and fragmentation degree and geological structure.
(2) The degree of subgrade damage is closely related to the distance from the epicenter and the seismogenic fault. According to the investigation, the closer the road subgrade is to the epicenter and the seismogenic fault, the greater the degree of subgrade damage is[10].
(3) The failure of the slope under the subgrade is related to the slope, protection type and height, treatment measures and other factors.

(4) The seismic damage of the upper slope of the subgrade is related to such factors as whether it is protected, whether the protection type is appropriate, the lithology of the rock mass and the degree of weathering and fragmentation.

4.2 *Factors affecting earthquake damage of subgrade retaining structure*

(1) Earthquake intensity. A large number of earthquake damage data show that when the earthquake intensity reaches 7 degrees, the retaining wall may be overturned, slid, cracked or even collapsed.
(2) Geological conditions. The geological conditions directly affect the magnitude and mode of the force exerted by the media around the retaining wall on the retaining wall during the earthquake, and the mode of the force acting on the retaining wall has a decisive effect on the failure mode of the retaining wall.
(3) Structure type of retaining wall. The seismic capacity of masonry retaining wall is weaker than that of reinforced concrete gravity retaining wall, and the seismic capacity of gravity retaining wall is weaker than that of reinforced soil and other flexible retaining walls.

5 SAFETY ASSESSMENT OF SUBGRADE WORKING CONDITION AFTER EARTHQUAKE

5.1 *Safety diagnosis items and evaluation of subgrade structure after earthquake*

After the earthquake, the subgrade shall be specially inspected immediately. The main purpose of the investigation and detection is to confirm the safety of the subgrade, master the status quo of the subgrade after the earthquake, and find out the adverse factors that have an impact on the safety and function of the subgrade structure. Countermeasures shall be taken as soon as possible according to the adverse degree, and timely treatment shall be carried out to ensure the safety of the subgrade and ensure smooth traffic. The inspection items of the subgrade after the earthquake mainly include slope, foundation, pavement, drainage system and retaining structure. Table 1 is the specific inspection contents. According to the inspection results, it is divided into three categories for evaluation.

5.2 *Diagnosis method of subgrade structure after earthquake*

After the earthquake, the main purpose of investigation and detection is to confirm the safety of subgrade structure. Therefore, the investigation and detection methods are required to be fast, convenient and targeted. The diagnostic methods adopted mainly include the following three types:

(1) Visual inspection method. At the construction site, walk for close inspection. In the process of investigation and detection, in addition to careful observation with the naked eye, advanced optical instruments, such as crack observation instrument, total station and digital camera, shall also be combined to provide accurate detection data for judging the safety of subgrade structure.
(2) Non destructive testing methods. According to the visual inspection results, the key inspection parts shall be identified for geological radar inspection to determine the crack development in the subgrade structure.
(3) Special investigation and testing. After the subgrade structure encounters an earthquake, in order to timely grasp the damage of the subgrade structure, judge whether it meets the use function and safety, and provide basis and suggestions for the design of subgrade maintenance and reinforcement, in addition to the above inspection and detection, special investigation and detection shall also be carried out. The main items of special investigation and detection include: surface condition, borehole coring, strength of retaining wall, buried depth of retaining wall toe, etc.

Table 1. Inspection contents of subgrade structure after earthquake.

respondents	Investigation contents
subgrade	Pit (depth, cause and area); Cracks (length, width, spacing, height of staggered sill); Overall settlement; The degree of perfection of drainage facilities and the degree of pavement wetting; Pavement deformation and damage; Deformation and failure of subgrade slope; Deformation of subgrade slope toe and foundation; Water content of slope; Operation of surface drainage system.
retaining wall structure	Apparent integrity; Deformation and movement characteristics (translation and rotation); Rock and soil deformation and failure related to retaining structure; Characteristic indexes of rock and soil mass; Environmental index of rock and soil mass.

Table 2. Evaluation of test results of subgrade structure after earthquake.

Safety grade	Evaluation classification	Damage degree	Damage condition	Traffic measures
No immediate danger	S	No abnormality	Through visual observation, no abnormality is found, the subgrade surface and retaining wall are not damaged obviously, and there is no need to repair after the earthquake.	Normal traffic
		Slight abnormality	Slight cracks on the retaining wall can be observed with the naked eye. There are slight cracks, slight depressions and bulges on the pavement, which do not affect the normal use and traffic. There is no need to repair after the earthquake.	
Danger	B	Abnormal	The subgrade surface is obviously damaged. The pavement is cracked, staggered, uneven and bulging. The crack width is less than 10cm. There is a small-scale collapse phenomenon at the embankment edge. The falling rocks of the cutting slope are peeled off to the pavement, causing inconvenience to the traffic. After simple treatment, the traffic can be smoothly opened; The retaining structure includes wall spalling, pointing dislocation, rebar exposure, expansion joint dislocation, etc., which has an impact on traffic.	Controlled traffic
	A	Significant abnormality	The subgrade surface is damaged obviously, the pavement is cracked obviously, the pavement is staggered seriously, the crack width is more than 10cm, the uneven and bulging of the pavement causes the pavement damage, the embankment collapses and moves sideways, the slope collapses and falling rocks fall on the pavement, the slope landslide buries the pavement, and the driving space is narrow or impassable; The side slope of the retaining wall collapses, the sliding or overturning of the retaining wall, and the foundation of the retaining wall is empty. The traffic can be restored after a certain period of time.	Closed to traffic

6 CONCLUSION

The phenomenon and characteristics of the damage caused by the Wenchuan earthquake to the roads deserve deep consideration, especially the damage to the low-grade roads, which is almost completely destroyed. Through this earthquake, we can see that the seismic capacity of highway engineering is still very weak. When the earthquake intensity reaches 7 degrees, the subgrade structure may crack or even collapse and overturn due to the earthquake damage, interrupt the traffic, and cause huge economic losses. It is very important to study the safety evaluation of the subgrade structure after the earthquake and determine the safety of the subgrade in time so as to take reasonable post earthquake repair measures and ensure the safe operation of the road.

Through earthquake disaster investigation and shaking table test this paper analyzes the general forms of earthquake damage to highway subgrade structures, the main characteristics of earthquake damage and the influencing factors of earthquake damage. On this basis, the contents and evaluation methods of post earthquake safety detection of subgrade structures are given, which can be used as reference for relevant professional and technical personnel in post earthquake investigation and diagnosis of highway subgrade structures.

REFERENCES

[1] Hoe I. Ling et al, Post-earthquake investigation on several geosynthetic-reinfoced soil retaining walls and slopes during the Ji-Ji earthquake of Taiwan, Soil Dynamics and Earthquake Engineering,Vol 21, 2001.

[2] Yang, Y.C.; Chen, T. J, Retaining walls damaged in the Chi-Chi earthquake, Canadian Geotechnical Journal, Vol 40, No. 6, December, 2003.

[3] Sandri, Dean, Performance summary of reinforced soil structures in the Greater Los Angeles area after the Northridge earthquake, Geotextiles and Geomembranes,Vol 15, No.4-6, Aug-Dec, 1997.

[4] Wang Wenshao; Jin chongpan; Wang Kecheng. Seismic calculation, model test and prototype observation of earth rock dam [J] Journal of water conservancy, 1987, (12):1–16.

[5] Tatsuoka F, Tateyama M, Mohri Y, et al. Remedial treatment of soil structures using geosynthetic-reinforcing technology[J].Geotextiles and Geomembranes, 2007, 25(4/5):204–220.

[6] Zhou Chaohui. Observation records of strong motion network of 2008 Wenchuan Ms8.0 earthquake [J] Sichuan earthquake, 2008, (4):25–29.

[7] Li Jianguo; Chu Yuguang; Du Yuzhu. Investigation and analysis of earthquake damage of Railway Subgrade Engineering in Wenchuan earthquake [J]. Journal of railway engineering, 2008, (added):91–95.

[8] Zhu Ying; Wei Yongxing. Earthquake damage characteristics of road engineering in Wenchuan earthquake and consideration of engineering seismic design[J]. Journal of railway engineering, 2008, (added): 86–90.

[9] Xie Heping; Deng Jianhui; Tai Jiajia etal. Wenchuan earthquake disaster and geotechnical engineering problems of reconstruction in disaster areas[J]. Journal of rock mechanics and engineering, 2008, 27(9):1781–1791.

[10] Huang Runqiu; Li Weile. Study on the development and distribution of geological disasters triggered by the "5.12" Wenchuan earthquake[J]. Journal of rock mechanics and engineering, 2008, 27 (12):2586–2592.

Smart Geotechnics for Smart Societies – Zhussupbekov, Sarsembayeva & Kaliakin (Eds)
© 2023 The Author(s), ISBN 978-1-003-29912-7
Open Access: www.taylorfrancis.com, CC BY-NC-ND 4.0 license

Field reconnaissance and InSAR investigation of subsidence-induced damage to electricity dispatch centers – A case study in Tehran

Z. Ghorbani
Ph.D. Student, Faculty of Geodesy and Geomatics Engineering, K. N. Toosi University of Technology, Tehran, Iran

A.G. Darzi
Ph.D. Student, Department of Civil Engineering, Sharif University of Technology, Tehran, Iran

H. Sadeghi
Assistant Professor, Department of Civil Engineering, Sharif University of Technology, Tehran, Iran

A.A. Garakani
Assistant Professor, Niroo Research Institute, Power Industry Structures Research Department, Tehran, Iran

ABSTRACT: Land subsidence, as a gradual settling of the ground surface, has become a threatening hazard to many infrastructures and lifelines. Among them, electricity dispatch centers (EDC) are considered the heart of a typical power transmission system, closely related to both domestic and industrial aspects of society. Therefore, this study aims to systematically explore early warnings and damages imposed on EDCs in Tehran. A combination of field reconnaissance and InSAR time series analyses are adopted to correlate subsidence-induced damages with several triggering mechanisms, such as the dynamic effects of subways and extra groundwater exploitation. Accordingly, spatially- and temporally-distributed deformation time series and velocities are produced between September 2019 to October 2021. To achieve that, the LiCSAR products are derived for all EDC locations using the LiCSBAS processing package. Eventually, the consequences of land subsidence for EDCs in terms of various types of damages and warnings are reported, classified, and discussed.

1 INTRODUCTION

Land subsidence (LS) caused by natural and human factors has become a growing threat infrastructures and a hence a global challenge (Bagheri-Gavkosh et al. 2021). LS occurs mainly in soil strata containing fine-grained plastic particles with evolving microstructures (Sadeghi, 2016; Sadeghi and Ng, 2018). Despite the minor influence of natural factors, human activities such as groundwater over-exploitation and urban infrastructure construction have been recognized as the most important factors affecting the occurrence and development of LS (Roccheggiani et al. 2019). Consequently, human activity mainly causes considerable subsidence-induced damage to many infrastructures and lifelines.

The electricity power distribution system is probably the most influential lifeline affecting a variety of industrial plants and household activities if a network instability and hence a sudden shutdown is enforced. Electricity dispatch centers (EDC) are considered as the central core of a general power transmission system. In other words, any malfunction caused to the electrical facilities installed in an EDC may cause significant property loss and operational delay (Jin et al. 2022). Iran is one of the countries that suffer from a high LS rate in many regions due to a major distribution of problematic soils and prolonged drought (Sadeghi and AliPanahi, 2020). For instance, the maximum cumulative displacements of about 40 cm with an average LS rate of more than 25 cm/yr give a serious warning for Tehran province (Haghighi & Motagh 2019).

DOI: 10.1201/9781003299127-171

Accordingly, several technics have been used to monitor the LS rate and developments. Among them, InSAR is the most well-known technique that can detect vaster spatial deformation of land surfaces and consequently measure the LS rate from small to large scales precisely (Ghorbani et al. 2022). Recently, Fadhillah et al. (2020) used InSAR time series data to detect the LS rate along the subway lines of the Seoul Metropolitan. The LS susceptibility maps were produced using Sentinel-1 data between 2017 and 2020. Similarly, Hu et al. (2019) applied the SBAS-InSAR technique to monitor the LS in downtown Fuzhou after the metro construction process. In addition, Jia et al. (2021) used the InSAR time series to monitor the photovoltaic system in the east of Shanxi province, China. Coal mining activities and the weight of power systems have been recognized as the leading causes of LS in these regions. Despite putting much effort into exploring the LS, there is no research that investigates the subsidence-induced damage to EDCs using InSAR time series analysis and validates with geotechnical reconnaissance.

Therefore, this study's main objective is to systematically explore warning signs and damages imposed on EDCs in Tehran. A mutual methodology of field reconnaissance and InSAR time series analysis is adopted to correlate subsidence-induced damages with several triggering mechanisms, such as the dynamic effects of subways and extra groundwater exploitation. Accordingly, spatially and temporally-distributed deformation time series and velocities during the period of 2019 to 2022 are determined. Then the LiCSAR (an automatic Sentinel-1 interferometric processing system) products using the LiCSBAS processing package are derived for each EDC location. Finally, key findings about the influences of LS on different types of damages are discussed.

2 METHODOLOGY

The LiCSBAS package is used in this study for the displacement time series analysis in Tehran. The LiCSBAS package uses data from the Sentinel-1 InSAR (COMET-LiCS) processor based on a modified small baseline NSBAS approach for the time-series analysis (López et al. 2009; Morishita 2020). In other words, it is possible to reduce gaps error in the sentinel-1 image network by using the NSBAS approach of the LiCSBAS package. This paper utilizes the 57 Sentinel-1 images from September 2019 to October 2021 in a time interval of 12 days. The generated interferograms were processed in a way that covers Tehran well in the ascending data over one frame (ID: 019A_05546_131313). It is worth noting that the GeoTIFF files of unwrapped phase and coherence have been published in a 250 km2 consistent geographic frame basis that is already available in the COMET-LiCS portal. Furthermore, bad interferograms were identified and discarded in the time-series analysis based on the coherence and unwrapped data, checking the loop closure (Morishita, 2020). In the following, to estimate the displacement value of each pixel, the whole interferometric networks were inverted for incremental displacements using the least-squares method. Eventually, using high and low-pass filtering in time and space, respectively, the noise sources from the displacement time series have been separated.

3 RESULTS AND DISCUSSION

Figure 1 shows the displacement map in the line of sight (LOS) direction of the Sentinel-1 satellite, derived from the LiCSBAS time series analysis. Negative and positive values show the ground surface displacement based on the satellite situation. In other words, the negative value reveals the LS, but the positive value indicates the Land uplift (LP). Regarding this figure, it is possible to find the highest LS rate in the southwest of Tehran as 90 mm/yr. This critical region comprises several EDCs, such as Azari and Yakhchi Abad, with an LS rate of 20 mm/yr. However, the other EDCs shown in this figure are in favorable condition from the LiCSBAS time series analysis. Despite the low LS rate (<10 mm/yr) in these regions, several damages have been reported for these EDCs. To find out the source of the damages, other GIS layers, i.e., the Tehran subway line system, have been used, as shown in Figure 1. Considering the distance between the EDCs and subway lines, the main source of EDC damage in the low LS rate region is revealed. Specifically, Khorasan Square EDC is located at the intersection station of subway lines # 6 and # 7, unlike the other EDCs like Railway Town, Shush, Beesat thermal, and Azadegan, which are somehow

far away from the subway lines. Therefore, field reconnaissance has been done in this study to better investigate the critical condition of the Khorasan Square EDC. Based on field monitoring and geotechnical assessments, several damages have been recognized, as shown in Figure 2. These damages can be listed as: 1) vertical cracks in masonry walls, 2) opening of fissure cracks on the ground surface, 3) sinking of the foundation pier into the ground, 4) uneven settling of equipment's foundation, and 5) dislocation of the concrete floor slab.

Considering the low LS rate in this area, the primary motivation for these damages is the tunneling effects. In other words, the settlement caused by the tunneling activities, on the one hand, and the dynamic loading and vibrations made by passaging of the train, on the other hand, have led to the continuous deformation of the ground and the subsequent side effects on the existing vital components of EDCs. It is worth noting that the LS time series drives from the remote sensing technique suffer from various errors. Subways dynamic effect is one of the main sources of errors contributing to the malfunctioning InSAR investigation of LS. Therefore, to better investigate the LS rate in the urban area, care about the source of errors should be considered. Specifically, for the regions exposed to dynamic effects of subways, it is recommended to utilize field monitoring and geotechnical assessments to verify the remote sensing analysis.

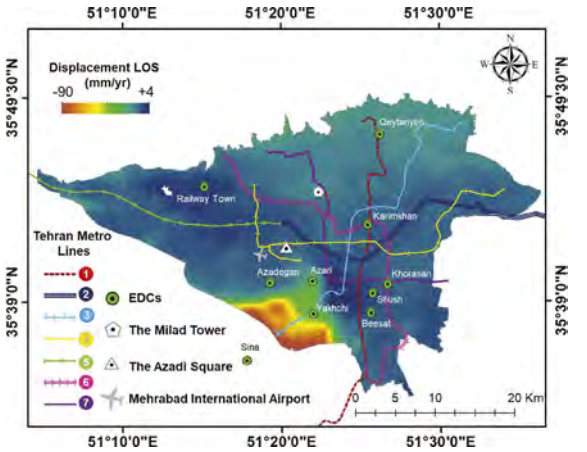

Figure 1. The displacement LOS obtained from the Sentinel-1 images processed by LiCSBAS during the time period of September 2019 to October 2021 for Tehran.

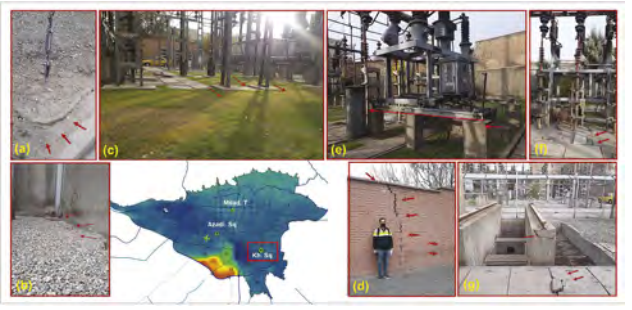

Figure 2. Typical damages observed in the EDC of Khorasan Square due to the interaction between the subway and superstructure: (a, b) opening of fissure cracks on ground surface, (c, e) sinking and the differential settlements of foundation pier, (d) cracking of the masonry walls, and (f, g) dislocation of the concrete floor slab.

4 CONCLUSIONS

In order to assess the EDCs prone to LS hazard, InSAR time series analysis was employed to generate the displacement LOS of Tehran for almost three and half years. The maximum LS rate was revealed as high as 90 mm/yr. Accordingly, the hazard level to EDCs was determined and a pilot EDC located in Khorasan Square was studied in further details. Although a relatively low rate of LS was determined for this area based on remote sensing, field reconnaissance indicated several warnings and damages imposed on the building and electrical facilities. Further investigation of other GIS layers including subway line system revealed the main cause of LS as the occurrence of the intersection station of subway lines # 6 and # 7. Consequently, severe damages were observed including: cracking of the masonry walls, opening of fissure cracks, sinking and the differential settlements of foundation pier. The results confirm that remote sensing can be enriched by complementary methodologies of field monitoring and geotechnical assessments.

ACKNOWLEDGMENT

The financial support provided by TAVANIR Co. for "Mitigation of Land Subsidence Hazard to Power Transmission Network" is gratefully acknowledged. The third author is also grateful to Iran's National Elites Foundation for the financial support through "Dr Kazemi-Ashtiani Award".

REFERENCES

Hu, B., Yang, B., Zhang, X., Chen, X. and Wu, Y., 2019. Time-series displacement of land subsidence in Fuzhou downtown, monitored by SBAS-InSAR technique. *Journal of Sensors*, 2019.

Bagheri-Gavkosh, M., Hosseini, S.M., Ataie-Ashtiani, B., Sohani, Y., Ebrahimian, H., Morovat, F. and Ashrafi, S., 2021. Land subsidence: A global challenge. *Science of The Total Environment*, 778, p.146193.

Fadhillah, M.F., Achmad, A.R. and Lee, C.W., 2020. Integration of insar time-series data and GIS to assess land subsidence along subway lines in the Seoul metropolitan area, South Korea. *Remote Sensing*, 12(21), p.3505.

Ghorbani, Z., Khosravi, A., Maghsoudi, Y., Mojtahedi, F.F., Javadnia, E. and Nazari, A., 2022. Use of InSAR data for measuring land subsidence induced by groundwater withdrawal and climate change in Ardabil Plain, Iran. *Scientific Reports*, 12(1), pp.1–22.

Haghighi, M.H. and Motagh, M., 2019. Ground surface response to continuous compaction of aquifer system in Tehran, Iran: Results from a long-term multi-sensor InSAR analysis. *Remote sensing of environment*, 221, pp.534–550.

Hwang, C., Yang, Y., Kao, R., Han, J., Shum, C.K., Galloway, D.L., Sneed, M., Hung, W.C., Cheng, Y.S. and Li, F., 2016. Time-varying land subsidence detected by radar altimetry: California, Taiwan and north China. *Scientific reports*, 6(1), pp.1–12.

Jia, J., Yang, H., Gong, H., Ke, X., Guo, X., Bie, S. and Wu, N., 2021. Deformation monitoring of photovoltaic power stations and substations in Yangquan using time-series InSAR. In *IOP Conference Series: Earth and Environmental Science* (Vol. 632, No. 3, p. 032036). IOP Publishing.

Jin, B., Yin, K., Li, Q., Gui, L., Yang, T., Zhao, B., Guo, B., Zeng, T. and Ma, Z., 2022. Susceptibility Analysis of Land Subsidence along the Transmission Line in the Salt Lake Area Based on Remote Sensing Interpretation. *Remote Sensing*, 14(13), p.3229.

López-Quiroz, P., Doin, M.P., Tupin, F., Briole, P. and Nicolas, J.M., 2009. Time series analysis of Mexico City subsidence constrained by radar interferometry. *Journal of Applied Geophysics*, 69(1),pp.1–15.

Modoni, G., Darini, G., Spacagna, R.L., Saroli, M., Russo, G. and Croce, P., 2013. Spatial analysis of land subsidence induced by groundwater withdrawal. *Engineering Geology*, 167, pp.59–71.

Morishita, Y., Lazecky, M., Wright, T.J., Weiss, J.R., Elliott, J.R. and Hooper, A., 2020. LiCSBAS: An open-source InSAR time series analysis package integrated with the LiCSAR automated Sentinel-1 InSAR processor. *Remote Sensing*, 12(3), p.424.

Roccheggiani, M., Piacentini, D., Tirincanti, E., Perissin, D. and Menichetti, M., 2019. Detection and monitoring of tunneling induced ground movements using Sentinel-1 SAR interferometry. *Remote Sensing*, 11(6), p.639.

Sadeghi, H., 2016. A micro-structural study on hydro-mechanical behavior of loess (Doctoral dissertation, Hong Kong University of Science and Technology). https://doi.org/10.14711/thesis-b1627816

Sadeghi, H. and AliPanahi, P., 2020. Saturated hydraulic conductivity of problematic soils measured by a newly developed low-compliance triaxial permeameter. *Engineering Geology*, 278, p.105827.

Smart Geotechnics for Smart Societies – Zhussupbekov, Sarsembayeva & Kaliakin (Eds)
© 2023 The Author(s), ISBN 978-1-003-29912-7
Open Access: www.taylorfrancis.com, CC BY-NC-ND 4.0 license

A stratigraphic classification estimation method by Artificial Neural Networks for Geotechnical Information Database

S. Murakami
Fukuoka University, Fukuoka, Japan

ABSTRACT: The purpose of this study is to confirm the applicability of Artificial Neural Networks for stratigraphic classification estimation. The study proposes a machine learning procedure in consideration with ununiformity of spatial density of investigation locations, their depth and different appearance frequency of soils. The proposed method has been applied to Geotechnical Information Database in Fukuoka plain, Japan. The results have shown the proposed method is extremely effective for stratigraphic classification estimation by Artificial Neural Networks.

1 INTRODUCTION

Geotechnical Information Database (Geo-DB) can be used for local vulnerability assessment against geo-disaster. However, almost of geo-information of borehole logs in the Geo-DB have no information on stratigraphic classifications. Therefore, stratigraphic classification must first be performed for all geotechnical information if vulnerability assessment requires stratigraphic classification. So, the availability of a Geo-DB with pre-stratified stratigraphic classification would be extremely useful for the assessment.

The purpose of this study is to confirm the applicability of Artificial Neural Networks (NN) for stratigraphic classification estimation. The study proposes a machine learning procedure in consideration with ununiformity of spatial density of investigation locations, their depth and different appearance frequency of soils. The proposed method has been applied to Geo-DB in Fukuoka plain, Japan. The results have shown the proposed method is extremely effective for stratigraphic classification estimation by NN.

2 NEURAL NETWORKS FOR STRATOGRAPHIC CLASSIFICATION ESTIMATION

Using the geotechnical information (depth, soil type, N-value, etc.) in the BDs, we consider strata classification by Artificial Neural Network (NN). We focus on BD No. p shown in Figure 1. The number of input data corresponding to layer number k is denoted as $N_{p,k}$. This geotechnical information is used as the input value, and the output value is calculated from the input value through an intermediate layer.

In the ordinary NN (ONN), the sum of the error functions for all training data (referred to as the overall error function E in this study) is considered and the NN model that yields good estimation results is determined by minimizing it. E is defined as

$$E = \frac{1}{N} \sum_{p=1}^{P} \sum_{k=1}^{K} \sum_{n=1}^{N_{p,k}} E_{(p,k,n)} \tag{1}$$

The ONN method uses the data equally to make decisions during learning. However, in the case of BD, the survey depth is not uniform, and the number of data tends to become sparser as the depth increases. The engineer recognizes this bias in the data and understands the characteristics of each layer. The stratigraphic classification is then determined by looking at the

DOI: 10.1201/9781003299127-172

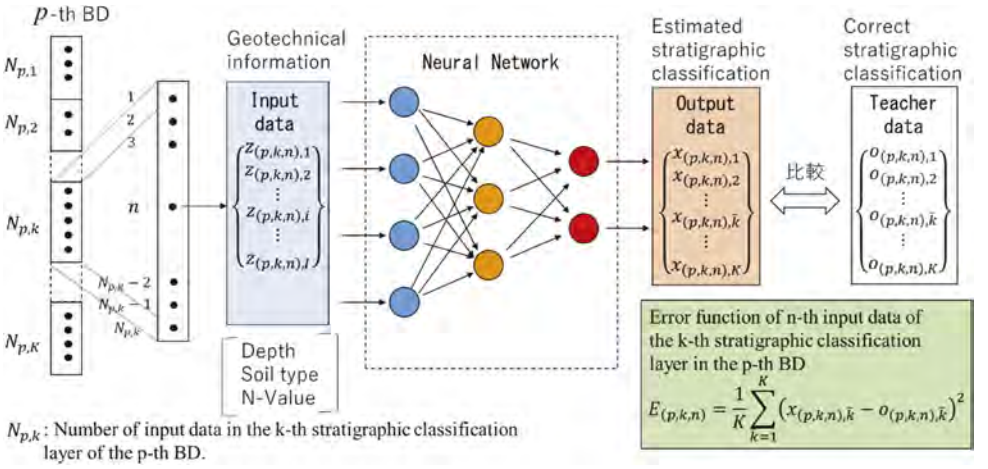

Figure 1. Machine learning of NN for p-th BD and its error function.

surrounding stratigraphic conditions. Therefore, this study considers incorporating the engineer's manner by redefining the overall error function, which is different from the ONN method.

The following overall error function E, which is calculated by averaging to eliminate bias in the data for each stratum in the BD, has been defined by introducing a weight coefficient $r_{p,k}$ with respect to the distance between the locations of BD.

$$E = \frac{1}{K}\sum_{k=1}^{K}\sum_{p=1}^{P}\frac{r_{p,k}}{N_{p,k}}\sum_{n=1}^{N_{p,k}}E_{(p,k,n)} \tag{2}$$

where $\sum_{p=1}^{P} r_{p,k} = 1$.

The method using weight coefficients that depend on the distance is called the Distance-Layer NN method (DLNN method), while the case with equal weight coefficients is called the Simple Layer NN method (SLNN method) (Murakami, 2020).

The SLNN method is a device to eliminate the bias by averaging the teacher data that differ in number per stratum, and the DLNN method further reduces the difference with the teacher data closer to the estimation location. By minimizing the overall error function in this way, we expect the NN model to average the data and reduce the bias, so that the information on BDs closer to the estimated location has smaller errors.

In this study, L2 regularization is applied in machine learning. The training data are first divided into teacher data and test data, and L2 regularization parameter λ is determined by contrasting the estimated value of the test data obtained from the machine learning results using the teacher data with the assumed λ with the measured value of the test data. Next, using the determined λ, the best IDW parameter used in the DLNN method is also selected by comparing the estimated value of the test data obtained from the machine learning results using the teacher data with several assumed IDW parameters and the actual measured value of the test data.

3 OVERVIEW OF THE OBJECTIVE REGION AND PREPARATION OF TRAINING AND VALIDATION DATA

The objective region is the Fukuoka Plain in Japan. The BDs were taken from the Kyushu Geotechnical Information Shared DB (2005, 2012, 2018), and the BDs along the Fukuoka Urban Expressway from Chidoribashi JCT (a) to Tsukiguma JCT (b), where continuous geotechnical information exists as shown in Figure 2.

For the 125 BDs extracted from the DB, stratigraphic classification in the area has been performed using the AIST-Borehole Log Analysis ver. 2.1 provided by the National Institute of Advanced Industrial Science and Technology (AIST) in Japan. The stratigraphic

classification results are shown in Figure-3. The 125 BDs were divided into five parts, four as training data (Dataset A, B, C, and D) and the remaining one as validation data (Dataset X).

The trends of the data for study and validation are shown that there is no difference in the percentage of data occupied by each layer, the Nakasu and Arae layers have a large number of data and account for the majority of the data, while the Kanatake gravel layer tends to be extremely small, about 10 to 15% of the total data (Murakami et. al., 2020).

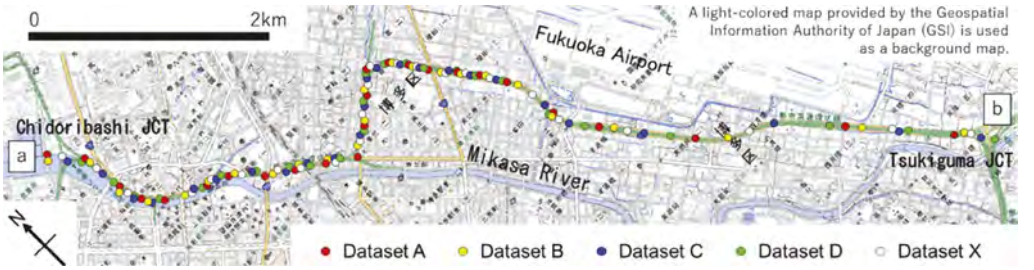

Figure 2. Cross-section line and BD locations in the objective region.

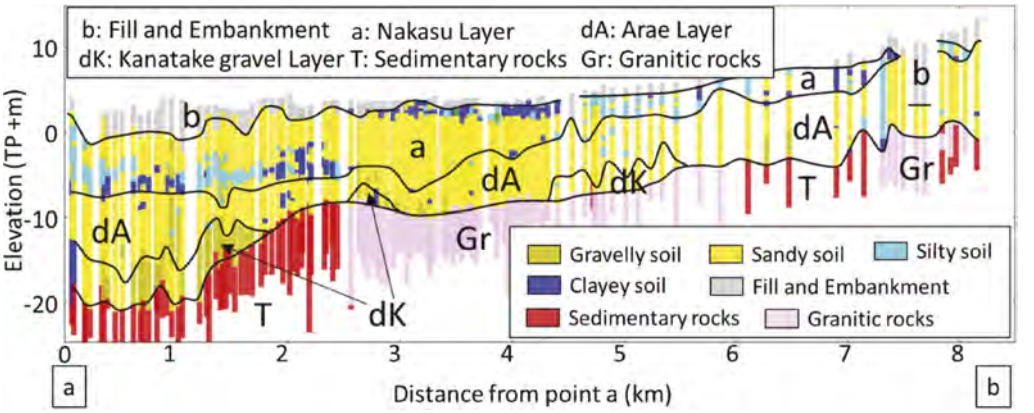

Figure 3. Geological cross section.

4 RESULTS AND DISCUSSIONS

Using four sets of training data (Dataset A, B, C, and D), three sets are used as learning training data and the remaining one set is used as test data for cross-validation, and λ has been determined by the ONN and SLNN methods. Given $\lambda = 10^{-3}$, 10^{-4}, 10^{-5}, and 10^{-6}, λ has been decided on 10^{-6} and 10^{-5}, which had the smallest difference between the percentage correct by the teacher data and the percentage correct by the data for testing, for the ONN and SLNN methods, respectively. Next, the IDW parameter m in the DLNN method has been determined using the results from the SLNN method. In the present study, the search radius R is fixed as 500 m. Based on the results of three comparisons with m=1.0, 2.0, and 4.0, m has been set as 2.0. Using the results of the above studies, the data for validation has been estimated. The number of intermediate layers in the NN model is set to 9, and 50 million machine learning cycles using ADADELTA (Zeiler, 2012) are used for the update calculation.

The results of the distribution of correct and incorrect answers and the percentage of correct answers for the data for validation by the ONN and DLNN methods are shown in Table 1. The table also shows the difference in results with and without the L2 regularization term. The results of the ONN and DLNN methods show that the correct answer rate for the training data slightly decreases with the addition of the L2 regularization term, but the correct answer rate for the verification data increases, confirming the effectiveness of L2 regularization.

The percentage of correct data for the validation of the ONN and DLNN methods is about 10% higher for the DLNN method, indicating that the strata classification estimation by the DLNN method, which attempted to incorporate engineers' methods, is superior to the ONN method.

Table 1. Comparison of ONN and DLNN Results.

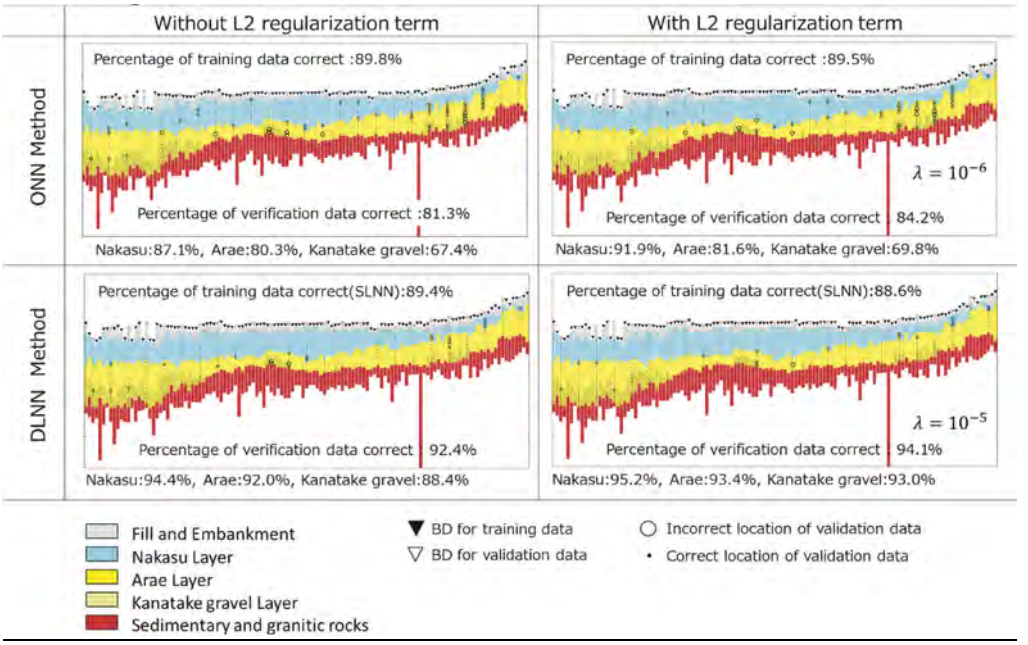

5 CONCLUSION

The purpose of this study is to clarify the applicability of the NN method to stratigraphic classification estimation using BDs, and a cross-section of the Fukuoka Plain has been selected as the objective region. Although the ONN method, which uses all the data equally as a basis for decision making during training, gave a correct estimation rate of more than 80%, the DLNN method, which averages the data to reduce bias and expects the information from BDs closer to the estimated location to have a smaller error rate, gave a higher rate. This suggests that it is necessary to take into account the information bias of the geotechnical information in order to obtain better estimation results.

ACKNOWLEDGMENT

This work was supported by JSPS KAKENHI Grant Number JP20K04691.

REFERENCES

Murakami, S., 2020. The D-Layer Neural Networks Method for Stratigraphic Classification Estimations, *Proc. the 55th Geotechnical Engineering Conference*: DS-2-04 (in Japanese)

Murakami, S., Ryu, S., Miwa, S., 2020. Effectiveness of the D-Layer Neural Networks Method on Stratigraphic Classification Estimations -Case study of a cross section of ground in Fukuoka plain-, *Proc. the 55th Geotechnical Engineering Conference*: 22-12-2-06 (in Japanese)

Zeiler, M. D., 2012. ADADELTA: An Adaptive Learning Rate Method, https://arxiv.org/pdf/1212.5701.pdf.

Smart Geotechnics for Smart Societies – Zhussupbekov, Sarsembayeva & Kaliakin (Eds)
© 2023 The Author(s), ISBN 978-1-003-29912-7
Open Access: www.taylorfrancis.com, CC BY-NC-ND 4.0 license

Model uncertainty in the random finite element analysis for an overall strength of a cement-treated soil column

T. Namikawa
Shibaura Institute of Technology, Tokyo, Japan

ABSTRACT: The finite element method with the random field theory, the Random Finite Element Method (RFEM), has been adopted to evaluate the mechanical behavior of the cement-treated soil ground in which strength varies spatially. The spatial variability of the strength can be appropriately considered in the RFEM analysis. However, the model uncertainty might be included in the analysis result. This paper presents the evaluation of the model uncertainty in the RFEM analysis for an overall strength of a cement-treated soil column. The unconfined compression tests of a full-scale cement-treated soil column are simulated by the RFEM analysis. The statistical parameters of the analyzed overall strength are compared to those obtained from the full-scale test results. The comparison provides model correction factors representing the model uncertainty.

1 INTRODUCTION

The finite element method (FEM) with the random field theory, the random finite element method (RFEM), is a useful tool for evaluating the mechanical behavior of the cement-treated soil ground in which strength varies spatially. RFEM has been used to evaluate the mechanical behavior of cement-treated soil grounds in past studies (e.g. Namikawa & Koseki 2013). The RFEM analysis with a proper constitute model can simulate the ground behavior reasonably. However, it is not possible to correctly describe the ground behavior using the RFEM analysis. The discrepancy arising between the real and simulated behavior can be recognized as a model uncertainty. Such model uncertainty should be evaluated quantitatively in the reliability-based design procedure.

This paper presents the evaluation of the model uncertainty in the RFEM analysis for an overall strength of a cement-treated soil column. The unconfined compression tests of a full-scale cement-treated soil column were conducted in a past study. Those tests are simulated by the RFEM analysis. The statistical parameters of the analyzed overall strength are compared to those obtained from the full-scale test results. The comparison provides model correction factors representing the model uncertainty included in the RFEM analysis.

2 UNCONFINED COMPRESSION TESTS OF A CEMENT-TREATED SOIL COLUMN

The test results of the unconfined compression test conducted in the past study (Building Research Institute and Japan Institute of Country-ology and Engineering 1995) is simulated by the RFEM analysis. In that study, single cement-treated soil columns were constructed by wet method of deep mixing at 4 sites. Sand, silt, sirasu, and loamy layers are improved at these sites. The depth of improvement was around 4 m. The columns were excavated and the lower part of the columns were used for the full-scale column test. The size of the full scale columns used for the unconfined compressive tests was 1.0 m in diameter and 2.2 m in height. Core samples of 50 mm in diameter and 100 mm in height were retrieved from the upper part of the columns. Since it was reported that a loamy layer was to be difficulty mixed with cement homogeneously,

DOI: 10.1201/9781003299127-173

the test results of the columns at the loamy layer are excluded in this study. The test results of 11 columns at the sand, silt and sirusu layers are used for the RFEM simulation.

The unconfined compressive strength Q_u of the full-scale column are listed in Table 1. The unconfined compressive tests were carried out for 4 columns of the sand and silt layers and 3 columns of the sirasu layer. The mean μ_{qu} and standard deviation σ_{qu} of the unconfined compressive strength q_u of the core samples retrieved at each site are also listed in Table 1. When evaluating the model uncertainty, the data obtained at the three sites are handled together. The ratio of Q_u to μ_{qu}, Q_u/μ_{qu}, is adopted when comparing the simulation results to the test results. Q_u/μ_{qu} observed in the full scale tests ranges from 0.3 to 1.1.

Table 1. Full-scale cement-treated soil column test results.

				Core strength	
Soil type	Column No.	Overall strength Q_u	Q_u/μ_{qu}	Mean μ_{qu}	Standard deviation σ_{qu}
Sand	1	2.51 MPa	0.664	3.78 MPa	1.19 MPa
	2	3.60 MPa	0.951		
	3	2.94 MPa	0.778		
	4	4.01 MPa	1.06		
Silt	1	1.32 MPa	0.381	3.47 MPa	1.46 MPa
	2	1.64 MPa	0.472		
	3	1.72 MPa	0.494		
	4	2.24 MPa	0.647		
Sirusu	1	4.44 MPa	0.681	6.52 MPa	1.73 MPa
	2	4.12 MPa	0.631		
	3	6.33 MPa	0.971		

3 RANDOM FINITE ELEMENT ANALYSIS

3.1 *Analysis condition*

q_u of the elements composing the cement-treated soil column is assumed to follow the multivariate normal distribution in the analysis. A stationary random field with an exponential type autocorrelation function is assumed for the spatial variability of q_u. The realizations of the spatial distribution of q_u are generated using the covariance matrix decomposition method (Namikawa 2016). The mean μ_{qu}, standard deviation σ_{qu}, and autocorrelation distance θ_{qu} of q_u are required when generating the realizations. The sample μ_{qu} and σ_{qu} values of the core samples in the full-scale column tests are adopted as the μ_{qu} and σ_{qu} values when generating the realizations. The sample θ_{qu} value of the core samples was not obtained from the full-scale column test results. Assuming θ_{qu} following the log-normal distribution, the θ_{qu} values are generated from the log-normal distribution whose 95% confidence interval ranges from 0.1m to 4.0m. The q_u values of the generated realizations were assigned to elements composing the cement-treated soil column model.

Three dimensional finite element analysis are preformed using the FEM software DIANA. The finite element model of the full-scale column is shown in Figure 1. The full-scale column of 1 m in diameter and 2.2 m in height is modeled in the simulation. A mesh consists of eight-node isoparametric cubic elements with a length of 100 mm. The boundary conditions are smooth at the top and bottom of the model. Uniform vertical displacements are applied at the top boundary on the loading process.

An elasto-plastic model proposed by Namikawa & Mihira (2007) is used to simulate the unconfined compression behavior of the full-scale cement-treated soil column. The material parameters for q_u = 4 MPa are listed in Table 2. These values are determined from the results of the laboratory tests carried out in the past studies (Namikawa & Mihira 2007, Namikawa & Koseki 2006). The elastic modulus E, cohesion c, tensile strength T_f, and fracture energy G_f, are assumed to be stochastic parameters in the RFEM simulation. The stochastic parameters vary proportionally with q_u. Other material parameters, friction angle ϕ, Poisson's ratio v, hardening parameters α and e_y, softening parameter e_r, dilatancy coefficient D_c, localization size t_{s0}, and characteristic length l_c, are assumed to be maintained constant.

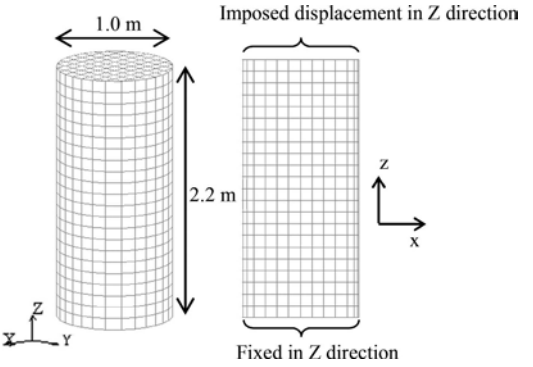

Figure 1. Finite element mesh.

Table 2. Material parameters for cement-treated soil with core strength q_u = 4.0 MPa.

E (MPa)	v	ϕ (degree)	c (MPa)	T_f (MPa)	α
Stoch. 7040	Deter. 0.167	Deter. 30	Stoch. 1.16	Stoch. 0.896	Deter. 1.05
e_y	G_f (N/m)	e_r	D_c	t_{s0} (mm)	l_c (mm)
Deter. 0.0002	Stoch. 21.2	Deter. 0.4	Deter. -0.4	Deter. 0.6	Deter. 100

Note: E = elastic modulus; v = Poisson's ratio; ϕ = friction angle; c = cohesion; T_f = tensile strength; α = hardening parameter; e_y = hardening parameter; G_f = fracture energy; e_r = softening parameter; D_c = dilatancy coefficient; t_{s0} = localization size; l_c = characteristics length; Stoch. = stochastic parameter; Deter. = deterministic parameter

3.2 *Analysis results*

Four hundred realizations are analyzed for the columns in the sand and silt layers and three hundred realizations are analyzed for the columns in the sirasu layers. The calculated Q_u values are shown in Figure 2. The variability of Q_u is large in all the cases. The full-scale test results are superimposed in Figure 2. The test results fall within the range of the values calculated in the RFEM analysis.

Q_u/μ_{qu} calculated in the simulation for the three layers is handled together. The empirical cumulative distribution function (ECDF) for the Q_u/μ_{qu} of 1100 realizations is shown in Figure 3. The cumulative distribution function (CDF) of the normal distribution is also shown in this figure. ECDF of the calculated Q_u/μ_{qu} values agree reasonably with CDF of the normal distribution. The mean and standard deviation of Q_u/μ_{qu} are 0.811 and 0.233.

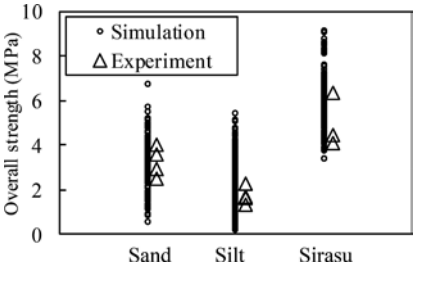

Figure 2. Calculated overall strength.

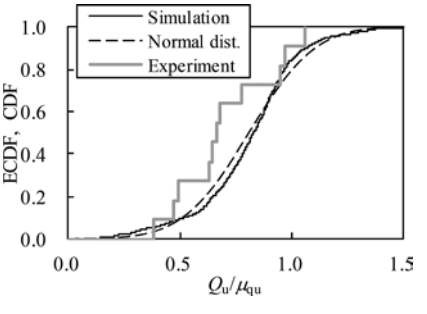

Figure 3. Cumulative distribution function.

4 MODEL UNCERTAINTY

ECDF for the Q_u/μ_{qu} observed in the full scale test is superimposed in Figure 3. The discrepancy in ECDF between the simulation and experimental results indicates the model uncertainty. The model uncertainty involved in the mean of Q_u/μ_{qu} is quantitatively evaluated by comparing the simulation results to the full scale test results. A model correction factor C_{fm} is adopted to represent the model uncertainty for the mean of Q_u/μ_{qu}. The relationship in mean between the full scale test and the simulation result is expressed as

$$M_R = C_{fm} M_S \tag{1}$$

where M_R and M_S are the mean of Q_u/μ_{qu} obtained from the test and simulation results.

The M_R and M_S values are 0.703 and 0.811. The C_{fm} value is 0.867. Since the number of the full scale tests is not large, the statistical uncertainty is involved in the M_R value. Assuming that Q_u/μ_{qu} follows the normal distribution, the expected population mean of Q_u/μ_{qu} follows a Student t distribution. Its standard deviation σ_{MR} can be expressed as

$$\sigma_{MR} = \sigma_{Qu}/\sqrt{n} \tag{2}$$

where σ_{Qu} is the standard deviation of Q_u/μ_{qu} and n is the number of Q_u/μ_{qu}. Assuming that the M_S represents the population mean, the probability distribution of C_{fm} follows the Student t distribution with the mean of M_R/M_S and the standard deviation of σ_{MR}/M_S.

The model uncertainty involved in the coefficient of variation of Q_u/μ_{qu} is examined. A model correction factor C_{fv} is adopted to represent the model uncertainty for the coefficient of variation of Q_u/μ_{qu}. The relationship in coefficient of variation between the full scale test results and the simulation result is expressed as

$$V_{cR} = C_{fs} V_{cS} \tag{3}$$

where V_{cR} is the coefficient of variation of Q_u/μ_{qu} obtained from the test results and V_{cS} is that calculated from the simulation results. The V_{cR} and V_{cS} values are 0.311 and 0.287. The C_{fs} value is 1.08. The evaluated C_{fs} value is not considerable large, indicating that the model uncertainty might be neglected for the coefficient of variation of Q_u.

5 CONCLUSIONS

This paper presented the evaluation of the model uncertainty in the RFEM analysis for an overall strength of a cement-treated soil column. The unconfined compression tests of a full-scale cement-treated soil column were simulated by the RFEM analysis. The mean and coefficient of variation of the analyzed overall strength were compared to those obtained from the full-scale test results. The model correction factors evaluated for the mean of the overall strength was 0.867, indicating that the overall strength is slightly overestimated in the RFEM simulation. The model correction factors evaluated for the coefficient of variation of the overall strength was 1.08. This indicates that there is no need to account for the model uncertainty on the variability of the overall strength in the RFEM analysis.

REFERENCES

Building Research Institute and Japan Institute of Country-ology and Engineering 1995. Development of earthquake disaster prevention technologies for big cities, Report of the subcommittee for the earthquake disaster prevention (architecture) (in Japanese).

Namikawa, T. 2016. Conditional probabilistic analysis of cement-treated soil column strength. *International Journal of Geomechanics* 16(1): 04015021.

Namikawa, T. & Koseki, J. 2006. Experimental determination of softening relations for cement-treated sand. *Soils and Foundations* 46(4): 491–504.

Namikawa, T. & Koseki, J. 2013. Effects of spatial correlation on the compression behavior of a cement-treated column. *Journal of Geotechnical and Geoenvironmental Engineering* 139(8): 1346–1359.

Namikawa, T. & Mihira, S. 2007. Elasto-plastic model for cement-treated sand. *International Journal for Numerical and Analytical Methods in Geomechanics* 31(1): 71–107.

Smart Geotechnics for Smart Societies – Zhussupbekov, Sarsembayeva & Kaliakin (Eds)
© 2023 The Author(s), ISBN 978-1-003-29912-7
Open Access: www.taylorfrancis.com, CC BY-NC-ND 4.0 license

Seismic response analysis of an earth dam by using geostatistical methods and 3-D measurement

S. Nishimura, T. Shibata & T. Shuku
Graduate School of Environmental and Life Science, Okayama University, Okayama, Japan

ABSTRACT: Recently, a three-dimensional (3-D) survey has been developed, using an unmanned aerial vehicle (UAV), which has made the rebuilding of the 3-D topography of structures easier. In this study, for the purpose of incorporating the three-dimensional measurement technique into the design of geo-structures, an earth-fill dam is surveyed three-dimensionally by a drone, and its 3-D finite element model (FEM model) is made based on the measurement results. Finally, the FEM model is applied to a seismic response analysis, in which a search is made for the structurally weak locations inside the dam. The stiffness inside the earth-fill dam is interpolated based on the results of Screw Weight Sounding (SWS) tests. The 3-D kriging method, one of the geostatistical methods, is used as the interpolation method. According to the analytical results, the locations of high acceleration and high shear stress inside the earth-fill dam have been identified.

1 INTRODUCTION

There are many earth-fill dams in Japan, some of which have become old and weak. It is important, therefore, to diagnose the seismic resistance of such dams. The technique of a three-dimensional (3-D) finite element modeling is proposed for such a diagnosis here.

In recent years, due to advances in unmanned aerial vehicle (UAV) technology, the taking of 3-D measurements has become easier. In this study, a 3-D finite element model of an earth dam is created by 3-D measurement by a drone. In order to conduct 3-D FEM, the spatially sufficient information of the underground is required to model the 3-D underground model. In this study, SWS test is used as a method of obtaining 3-D ground stiffness. Because SWS tests can be conducted in narrow spaces or at sites that are difficult to access with large equipment, such as the cone penetration test (CPT) machine, it is advantageous for the earth-fill dam sites. Since these test results are point-estimated values, they need to be spatially interpolated. For this task, kriging, a geostatistical method, is adopted as the 3-D interpolation method.

Finally, to diagnose the seismic resistance, a seismic response analysis is performed on the created 3-D model, and the critical points due to earthquakes are identified. Thus, the novelty of this study is the packaging of the FEM modeling from the 3-D measurement technique, and 3-D underground modeling with the aid of the geostatistical interpolation technique.

2 SOUNDING TESTS AT STUDIED SITE

SWS tests were conducted at Site K, which was studied in this study. The sounding intervals were adjusted so that the parameters necessary for the application of geostatistical methods could be applied. The SWS test is a static test, which is very efficient and suitable for obtaining spatial information on geo-structures. In addition, since it is a very compact test, it can be applied to sites located in narrow spaces, such as the target site in this study.

DOI: 10.1201/9781003299127-174

Equation (1) is a regression equation between the N value, obtained from the standard penetration test for sandy soil, and the results of Swedish weight sounding (SWS) tests, presented by Inada (1960), from which the converted N value (N_{SWS}) is obtained.

$$N_{SWS} = 0.002 W_{SW} + 0.067 N_{SW} \quad (1)$$

where N_{SW} is the number of half rotations and W_{SW} (N) is the total weight of the loads. Figure 1 shows the locations (16 points) where the SWS tests were conducted along the x'-axis parallel to the embankment axis.

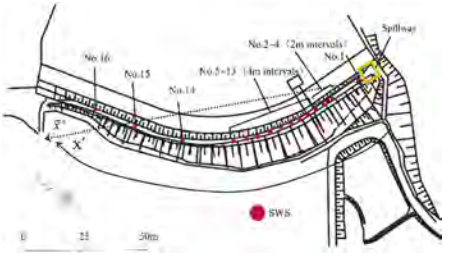

Figure 1. Planview of studied site and SWS test points.

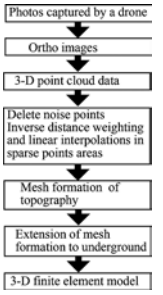

Figure 2. Algorithm of 3-D modeling.

3 THREE-DIMENSIONAL FINITE ELEMENT MODEL

A 3-D finite element model is created from aerial photographs taken by a drone. The procedure for the 3-D measurement by the drone is the same as that given in the authors' previous study (Kaneshige et al. 2021). The outline of the 3-D modeling is presented in Figure 2. LIQCA3D (Development Group of Liquefaction Analysis Code LIQCA, 2020) is used as the seismic response analysis program. The nodal coordinates of the finite elements are set to the x-axis for the east-west direction and to the y-axis for the north-south direction. Figure 3 presents an overall view of the model, and Figure 4 presents the cross section of the central part of the model. Nodes and elements were added to the sides of the model, and the analysis domain is extended to a square 50 times the width of the embankment to reduce the influence of the boundaries.

The boundary conditions are as follows: the bottom is a viscous boundary, the sides along the x-axis direction are fixed to y, the sides along the y-axis direction are fixed to x, and the nodes at the four corners are fixed to x-y and vertical rollers. The bottom and all the sides are set as undrained boundaries. The input seismic waveforms are selected from the Nankai Trough seismic waveform data published by the Cabinet Office. A linear elastic analysis is performed for all of the analyses in this study. In setting the elastic constants, Young's modulus E is set to 2800 N, which provides an empirical relationship (Japan Road Association 2012).

4 INTERPOLATION OF PARAMETERS BY GEOSTATISTICAL METHODS

A statistical model is used to represent the spatial distribution of the N values. Since the measured values obtained by the sounding tests is point-estimated values, it is necessary to interpolate the spatial information between the points by the statistical model. The statistical model allows for the estimation of the data for the points for which no data are available as a probability field. In this study, the procedure presented in Nishimura et al. (2016) is followed to determine the statistical model by MAICE. When the correlation length cannot be properly identified by MAICE, semi-variograms are adopted. The use of semi-variograms is one of the geostatistical methods for identifying the spatial correlation structure in each direction. The specific procedure is shown in Imaide et al. (2019).

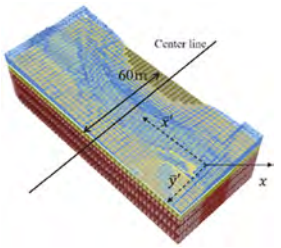

Figure 3. 3-D model of embankment area.

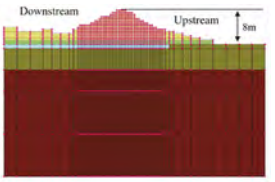

Figure 4. Cross section of center line of 3-D model.

For the estimation of the spatial distribution of $\log N_{SWS}$, the x' axis, which is set along the embankment with the origin at No. 1 (0 m) of the test site (see Figure 1), is converted into a linear $\bar{x}'$axis for simplicity. In the vertical direction, the z' axis is set in the depth direction with the origin at the ground surface. The mean function, and the covariance function determined by the method mentioned above, are shown in Equations (2) and (3), respectively. For simplicity, the correlation structure in the horizontal plane is assumed to be isotropic, namely, the horizontal correlation length of 15.7m in Equation (3), is same for the any horizontal directions.

$$m = 0.987 - 5.97 \times 10^{-3}\bar{x}' + 1.45 \times 10^{-3}z' + 3.91 \times 10^{-5}\bar{x}'^2 + 6.31 \times 10^{-3}z'^2 + 2.48 \times 10^{-3}\bar{x}'z' \tag{2}$$

$$C_{ij} = N_e \cdot 0.383^2 \exp\left(-\frac{\left|\bar{x}'_i - \bar{x}'_j\right|}{15.7} - \frac{\left|z'_i - z'_j\right|}{1.24}\right) \ (i \neq j) \tag{3}$$

$N_e = 0.409 \ \left(\left|\bar{x}'_i - \bar{x}'_j\right| \neq 0, \ \left|z'_i - z'_j\right| \neq 0\right)$ $\quad N_e = 0.593 \ \left(\left|\bar{x}'_i - \bar{x}'_j\right| \neq 0, \ \left|z'_i - z'_j\right| = 0\right)$
$N_e = 0.690 \ \left(\left|\bar{x}'_i - \bar{x}'_j\right| = 0, \ \left|z'_i - z'_j\right| \neq 0\right)$ $\quad N_e = 1.0 \ (i = j)$ $(i,j = 1, 2, 3, \ldots, M)$
N_e: Nugget effect parameter. $\quad M$: number of SWS test points.

In order to interpolate the stiffness values, 3-D kriging, which is one of the geostatistical methods, is employed. Figure 5 shows the inhomogeneous N value distribution of Site K obtained by the kriging.

5 SEISMIC RESPONSE ANALYSIS

A time series of the horizontal acceleration of the transversal direction to the embankment axis on the top of the embankment of the center cross section, is presented in Figure 6. The peak appears at 25 seconds after the start of the earthquake due to the input earthquake motion. A contour plot of the maximum acceleration at 25 seconds is shown in Figure 7. The figure presents a larger concentration of acceleration at the left side of the embankment near the spillway (see Figure 1). The reasons are that the embankment is divided by the spillway, and the stiffness of the ground around the spillway is relatively small (see Figure 5).

In addition, to evaluate the shear behavior, the $\sqrt{2J_2}$ distribution diagram obtained from the second invariant of the deviatoric stress (J_2) is given. The distribution of $\sqrt{2J_2}$ in the cross section, where the acceleration is concentrated (Figure 8), shows that the large $\sqrt{2J_2}$ is presented in the shape of an arc from the top of the embankment. On the other hand, in the central section of the embankment, there is no large $\sqrt{2J_2}$, according to the analytical result. This means that the weak point of the embankment against the shear behavior is assumed to be the left side of the embankment near the spillway. Although large value of $\sqrt{2J_2}$ is also depicted at the foundation ground, this is due to large initial stress.

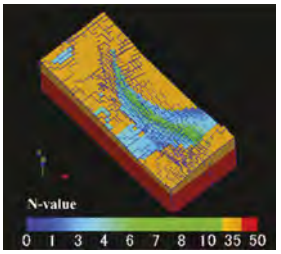

Figure 5. *N* value distribution.

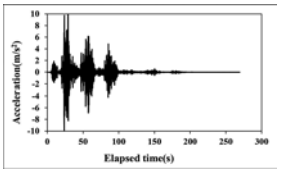

Figure 6. Acceleration of transversal direction at center point of embankment.

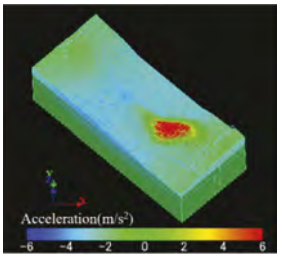

Figure 7. Distribution of acceleration.

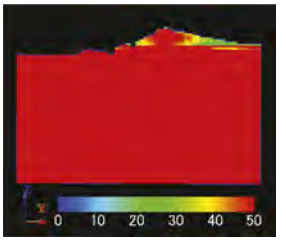

Figure 8. Distribution of deviatoric stress second invariant on concentration of acceleration.

6 CONCLUSIONS

(1) A three-dimensional finite element model has been created by extending the topographic measurement results to the underground using the 3-D measurement results obtained by a drone.
(2) The spatial distributions of the stiffness inside the embankment and the underground have been estimated. As a 3-D interpolation technique, kriging has been selected and it has been performed based on the statistical model derived from the SWS results.
(3) The seismic response analysis has been conducted for the created 3-D FEM model. The findings of the analysis are as follows.

    1) A concentration of local acceleration at the embankment of the earth-fill dam has been found, suggesting that spatial heterogeneity affects the seismic response.
    2) The distribution maps of $\sqrt{2J_2}$ has revealed the possible weak points of the embankment. In addition, detailed ground modeling identifies the location where the acceleration and shear forces of the embankment are concentrated (near the left bank spillway). In the vicinity of this location, the point where $\sqrt{2J_2}$ becomes large, appears in the form of a circular arc, which can be considered to be a structural weak point.

REFERENCES

Development Group of Liquefaction Analysis Code LIQCA 2020. *Data of LIQCA3D20*. (in Japanese).
Imaide, K., Nishimura, S., Shibata, T. and Shuku, T. 2019. Evaluation of Spatial Distribution of Soil Strength inside Earth-fill Dams with Use of Geostatistical Method. *Transactions of the Japanese Society of Irrigation, Drainage and Rural Engineering*, *IDRE Journal*, 308 (87-1): II_29-II_38. (in Japanese)
Inada, M. 1960. Usage of Swedish Weight Sounding Results. *Tsuchi-to-Kiso, Journal of JSSMGE* 8(1): 13–18. (in Japanese)
Japan Road Association. 2012. *Specifications for Highway Bridges*, I and IV. (in Japanese)
Kaneshige, M., Nishimura, S., Shibata, T., and Shuku, T. 2021. Finite Element Modeling of an Earth-fill Dam Based on 3-dimensional Measurement and Seismic Response Analysis. *Transactions of the Japanese Society of Irrigation, Drainage and Rural Engineering*, 89 (1):I_181-I_189. (in Japanese)
Nishimura, S., Shibata, T. and Shuku, T. 2016. Diagnosis of earth-fill dams by synthesized approach of sounding and surface wave method, *Georisk*, 10(4),:312–319.

Smart Geotechnics for Smart Societies – Zhussupbekov, Sarsembayeva & Kaliakin (Eds)
© 2023 The Author(s), ISBN 978-1-003-29912-7
Open Access: www.taylorfrancis.com, CC BY-NC-ND 4.0 license

Changes in the stress-strain state of soils with changes in humidity

A.S. Zhakulin
Doctor of Technical Sciences, Professor, Karaganda Technical University, Karaganda, Kazakhstan

A.A. Zhakulina
Ph.D., Associate Professor, Karaganda Technical University, Karaganda, Kazakhstan

A.U. Yessentayev
L.N. Gumilyov Eurasian National University, Astana, Kazakhstan

E.N. Abdygaliyev & E.K. Imanov
Karaganda Technical University, Karaganda, Kazakhstan

ABSTRACT: The article presents the results of investigation of soils in the base and reasons for the collapse of a reinforced concrete chimney. Based on the materials of the conducted studies, it was concluded that the main reason for the collapse of the reinforced concrete shaft of the chimney of coke oven batteries no. 5 and no. 6 of arcelormittal temirtau jsc (formerly karaganda metallurgical plant) is a decrease in the strength characteristics of concrete due to many years of constant moisture, freezing and thawing in the autumn winter-spring periods of time, and indirectly due to the lack of proper control over the technical condition of building structures of all areas of reinforcement of the reinforced concrete chimney shaft and assessment of their strength characteristics. The design of the reinforcement instead of its original purpose contributed to the development of negative consequences and the safe operation of the facility.

1 INTRODUCTION

As a result of an instrumental examination of slopes and retaining walls made of monolithic reinforced concrete and drainage systems, numerous defects were identified that were made during the design and construction process, which pose a threat to the safe operation of roads. Monolithic reinforced concrete retaining walls lined with natural stone with a height of 4.0-20.0 m, a width of 0.6 m rest on slabs measuring 1.2 x 2.40 m and do not have hard pinching.

Figure 1. Defective retaining wall design.

DOI: 10.1201/9781003299127-175

The slope of the slope is exposed to atmospheric and flood waters during the year. The identified defects indicate unacceptable cracks and inclination of retaining walls along the road (Figure 1).

The slope slopes along the highway are composed of loess subsidence soils. In subsiding loess soils, collapses of the slope slope massif occur with complete or partial water saturation of the soils due to a significant deterioration in the value of the design parameters (cohesion, angle of internal friction and deformation modulus). The relevance lies in the fact that it is necessary to analyze the stress-strain state of the slope of the slope with folded subsidence soils and evaluate the stability and strength of the retaining wall structure to ensure safety during the operation of the highway.

2 FEATURES OF THE CALCULATION OF RETAINING WALLS

According to the study of physical and geological phenomena in the foothill areas of the south of Kazakhstan, they are subject to planar washout, ravine formation, subsidence of slope soils. On the site, the slopes are composed of loamy soils of a brownish -gray color, from hard to hard- plastic consistency, carbonatize, to a depth of 15.5-21.0 m - subsidence. Physical and mechanical properties of loess-like loams: density - 1.50-1.60 g/cm^3**;** porosity coefficient - 0.84–1.1; degree of water saturation - 0.55-0.91; adhesion - 21-35 kPa; angle of internal friction - 16-22 degrees**;** total deformation modulus - 4.9 -15 MPa.

At the same time, the characteristics for loams according to the results of laboratory tests are: density - 15-16 kN/m^3; coefficient porosity - e > 0.9 with low values of mechanical properties. The pressure exerted by the backfill soil on the back face of the wall can be realized in different forms and values, depending on the design features of the wall, on the strength characteristics of the backfill soil and the base, on the magnitude and direction of wall movement.

In the absence of wall movement away from the backfill, the pressure is realized in the form of a rest pressure E_0 (in this case, the backfill soil is in a compressive stress state). The active soil pressure E_a (thrust) is realized when the wall moves away from the backfill and corresponds to the minimum value of the soil pressure. Passive pressure E_p (resistance of the wall) is realized when the wall moves towards the backfill and corresponds to the maximum value of the soil pressure.

The change in soil pressure depending on the displacement of the wall U is shown in Figure 2.

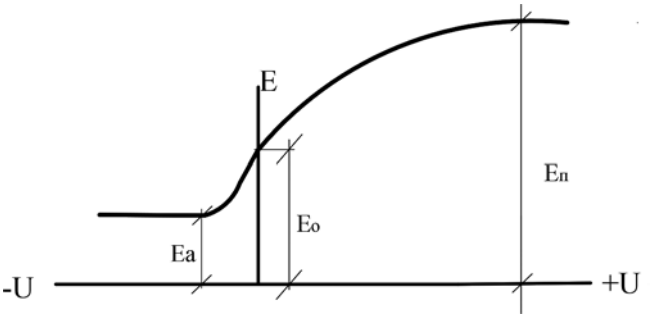

Figure 2. Change in backfill soil pressure E on a retaining wall depending on its displacement U.

Usually, in engineering calculations, the value of the active pressure E_a is used, which is realized at sufficiently small wall displacements. In this case, the wall structure is more economical than in calculations using the rest pressure E_0. Under the influence of active pressure E_a, the wall usually receives a small amount of displacement from the backfill, which, as a rule, cannot realize the full value of the rebuff E_p. To realize the full value of E_p, a displacement value will be required (due to soil compaction), which does not satisfy the conditions for normal operation of the wall. Therefore, when designing retaining walls, it is allowed to enter into the calculations

only a third of the realized resistance. Friction force Tacts on the wall sole. ε and for the angle of inclination of the backfill α, depending on the required calculation. The theoretical basis for calculating retaining walls is the Coulomb hypothesis, based on the following provisions:

1) in the soil of the backfill, upon the onset of the limit state, a collapse prism of the HPT is formed, limited from the rest of the soil, which is in the limit state, by a flat sliding (collapse) surface of the HP (Figure 3);

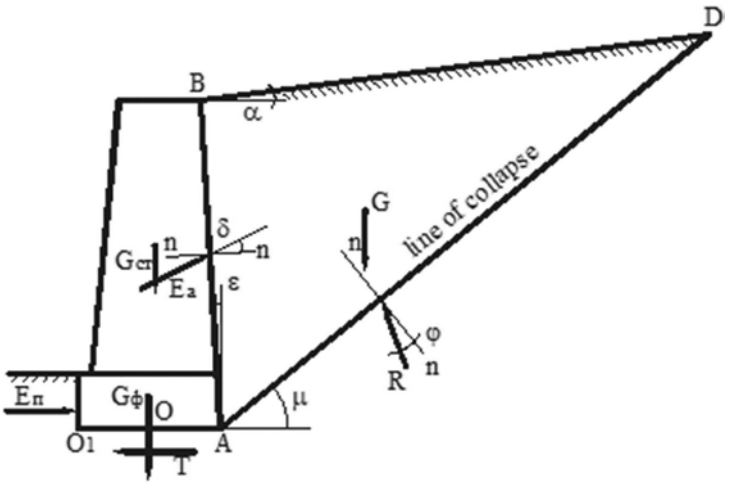

Figure 3. Scheme of the action of forces on the wall (Coulomb's Assumptions).

2) the angle of inclination of the collapse plane A D must be such that the value of the active pressure E a is maximum;
3) the reaction of the calculated resistance of the soil - R, which is in the limit state, is deviated from the normal to the collapse plane A, D by the angle of internal friction φ in the direction opposite to the movement of the collapse prism;
4) the active pressure force E_a (the active pressure reaction), acting on the back face of the wall AB, deviates from the normal to it by an angle δ. The angle δ is the angle of friction between the backfill soil and the wall material.

The collapse prism is in equilibrium under the action of forces G (dead weight) R and E_a

Determination of active and passive pressures acting on a retaining wall . Let us replace the uniformly distributed load - *q,* kPa with a layer of soil of reduced height/1 /:

$$h_{\pi p} = \frac{q}{\gamma_{3ac}}; \tag{1}$$

Calculate the active pressure coefficient:

$$\xi_a = \frac{1}{\left(1+\sqrt{Z_a}\right)^2} \cdot \frac{\cos^2(\varphi-\varepsilon)}{\cos^2\varepsilon \cdot \cos(\varepsilon+\delta)}; \tag{2}$$

$$z_a = \frac{\sin(\varphi+\delta)\cdot\sin(\varphi-\alpha)}{\cos(\varepsilon+\delta)\cdot\cos(\varepsilon-\alpha)}; \tag{3}$$

and ξ_a, special attention should be paid z_a to the signs α and ε.

Let's find the ordinates of the active pressure intensity diagram:

- at the top of the wall

$$e_{a1} = \gamma_{zas} \cdot h_{pr} \cdot \xi_a; \tag{4}$$

- at the level of the sole

$$e_{a2} = \gamma_{zas} \cdot (h_{pr} + H); \tag{5}$$

Then the active pressure

$$E_a = \frac{e_{a1} + e_{a2}}{2} \cdot H; \tag{6}$$

The horizontal and vertical components of the active pressure intensity are as follows:

$$e_{ag1} = e_{a1} \cdot \cos(\varepsilon + \delta); \tag{7}$$

$$e_{ag2} = e_{a2} \cdot \cos(\varepsilon + \delta); \tag{8}$$

$$e_{av1} = e_{a1} \cdot \sin(\varepsilon + \delta); \tag{9}$$

$$e_{av2} = e_{a2} \cdot \sin(\varepsilon + \delta); \tag{10}$$

Accordingly, the vertical and horizontal components of the active pressure

$$E_{ag} = \frac{e_{ar1} + e_{ar2}}{2} \cdot H; \tag{11}$$

$$E_{av} = \frac{e_{aB1} + e_{aB2}}{2} \cdot H; \tag{12}$$

The intensity of passive pressure at the level of the base of the foundation

$$E_p = \gamma_{zas} \cdot d \cdot tg^2(45 + \frac{\varphi}{2}); \tag{13}$$

Passive pressure acting on the front face of the wall,

$$E_p = \frac{\gamma_{3ac} \cdot d^2}{2} \cdot tg^2(45 + \frac{\varphi}{2}); \tag{14}$$

3 CALCULATION OF A RETAINING WALL USING NUMERICAL METHOD

We will calculate the retaining wall using the solutions of the theory of the limit state of a granular medium (numerical methods). When using the numerical method - the finite element method and using the Plaxis application program . When evaluating the stress-strain state of the slope during interactions on retaining walls, the behavior of subsiding soils was considered. At the same time, the subsidence soils of the slope are characterized by: a change in the stress state due to their redistribution after soaking; a change in the components of the strain tensor due to the development of elastic-plastic and viscoplastic deformations /2/. When water is saturated in subsiding soils, the desired stress state arises, which differs significantly from the initial one. A plane problem is considered in an elastic-plastic formulation using the Coulomb-Prandtl model for the medium, which assumes the elastic behavior of the medium at stresses below the yield strength and equal-volume (with zero dilatancy) plastic flow at stresses at the yield strength. The stresses at the yield point are described by the equation:

$$\sigma_{max} = S + \lambda \sigma_{min}; \tag{15}$$

where λ = ctg ^{2} $(\pi/4 - \phi/2)$ - coefficient of passive soil pressure; $S = 2C$ ctg $(\pi/4 - \phi/2)$ - ultimate strength in uniaxial compression; σ_{max}, σ_{min} - maximum and minimum principal stresses.

In the tensile region, the yield (rupture) criterion has the form:

$$\sigma\mu\tau v = -T; \tag{16}$$

where T is the tensile strength, taken in the Plaxis program, equal to C /5. After a rupture occurs at a voltage σ = - $C/5$ in the further analysis, the tensile strength of the element is assumed to be zero (T =*0*). The elastic-plastic solution is implemented by the finite element method and is achieved by the known method of "initial stresses" using the iterative Newton-Raphson procedure with a constant stiffness matrix, but with a variable load vector, replenished during the iterative process by "initial forces" in plastic elements. The error in the calculation of the FEM consisted of the discretization error due to the replacement of a body with an infinite number of degrees of freedom, a model with a finite number of degrees of freedom, and the rounding error of numbers when performing computational operations on a computer /4,5,6,7/. As a result of the numerical analysis of the tasks set and (Figure 4: Design scheme), the following were obtained: finite element mesh distortion (Figure 5), horizontal and general slope deformations when the calculated characteristics of subsidence soils change (Figure 6 and 7), as well as the isolines of the maximum horizontal (shear) stresses and general (full) stresses when changing the stress-strain state of the slope to the retaining wall.

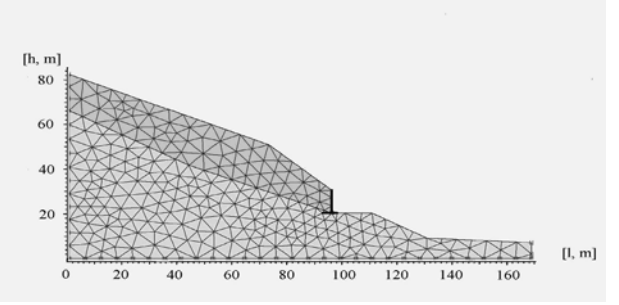

Figure 4. Calculation scheme.

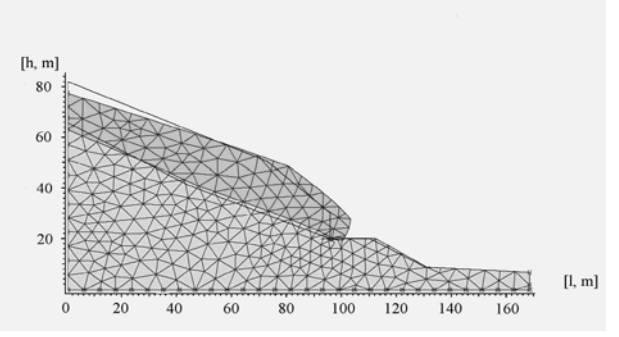

Figure 5. Mechanism deformation (extreme total displacement 162.42* 10^{-3} m).

An analysis of the results of a numerical solution when modeling the interaction of a slope and a retaining wall shows that the most dangerous are the development of maximum horizontal deformations near the retaining walls, due to shear deformations. The shear deformation propagation zone covers a large volume of slope soils. drawdown soils sagging from their own weight on a slope with water saturation worsens the initial value of adhesion, the angle of internal friction, the deformation modulus, completely changing the initial stress-strain state. Trajectories of movement of particles of subsidence soils when the stress-strain state of the slope changes to the retaining wall show that the movement of soil particles occurs at the boundary of subsidence and non- subsidence loams. Calculations for the numerical solution show that the retaining wall on the slope of the slope, composed of subsiding soils, is unstable and soil sliding occurs only in the volume subsiding soils of an elephant slope.

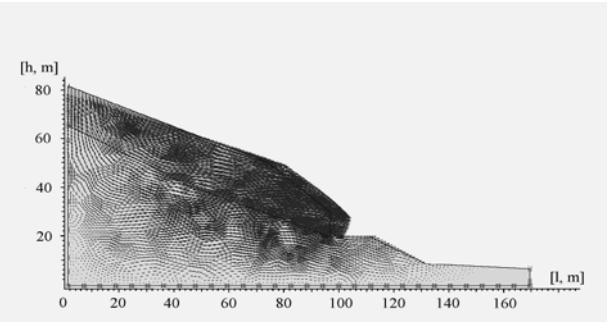

Figure 6. Total deformation (U_{tot}) (Extreme U_{tot} = 0.165m).

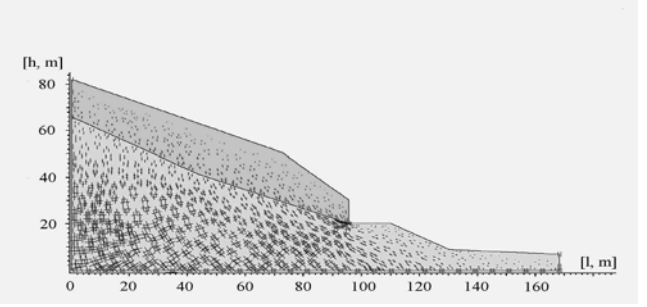

Figure 7. General stresses 483.25 * 10^3 Pa).

4 CONCLUSIONS

In the geological and lithological structure of the slope of the mountains, Lower Quaternary eolian deposits, represented by subsidence loess-like loams, take part.

As a result of instrumental inspection of slopes and measurements of protective retaining walls made of monolithic reinforced concrete and drainage systems, numerous defects and damages were identified during the design and construction process, which pose a threat to the safe operation of the road and the structure.

According to the results of compression tests, loams lying to a depth of 15.5-21.0 m exhibit subsidence properties when soaked. The initial settling pressure varies from 0.028 to 0.361 MPa (0.112). Calculations show that the total subsidence of soils with increasing humidity is 8.8-73.51 cm. Calculations of the stability of retaining walls along the highway located at the slope of the slope, carried out by numerical methods, showed that in the water- saturated state the slope is a landslide. An analysis of the results of a numerical solution when modeling the interaction of a slope and a retaining wall shows that the most dangerous are the development of maximum horizontal deformations near the retaining walls, due to shear deformations of the slope.

REFERENCES

Kovalev I.V. Retaining wall calculation, St. Petersburg, 2012.

Malyshev M.V. Strength and stability of the foundation of structures. Moscow. 1994.

Morgenstern, NR & Price, VE 1967. A numerical method for soving the equations of stability of general slip surfaices. *computer Jornal*, 9, p.388–393.

Fadeev A. B. 1987. Finite element method in geomechanics. Moscow.

Zhakulin. A.S. 2015. Deformability of soils of water- saturated bases. *LAP Lambert academic Publishing*. Saarbrucken.

Brinkgreve RBJ et al. 1997. PLAXIS, *Version 8*. Balkema.

Paramonov B. N .2012. Finite element method for solving non-linear problems of geomechanics. St. Petersburg.

Smart Geotechnics for Smart Societies – Zhussupbekov, Sarsembayeva & Kaliakin (Eds)
© 2023 The Author(s), ISBN 978-1-003-29912-7
Open Access: www.taylorfrancis.com, CC BY-NC-ND 4.0 license

Features of the combined method of development of upland deposits of Kyrgyzstan

K.T. Tajibaev
Institute of Geomechanics and Development of Subsoil of the National Academy of Sciences of the Kyrgyz Republic, Bishkek, Kyrgyzstan

Ch.K. Sulaimanov
Kumtor Gold Company, Issykkul, Kyrgyzstan

ABSTRACT: Today, the mining industry is one of the priority sectors of the development of the Kyrgyzstan economy, of which the gold mining industry currently occupies a leading place. To date, more than 2,500 indigenous gold deposits have been explored on the territory of Kyrgyzstan, of which deposits with ore reserves of more than 30 tons have been identified according to gold reserves. As a rule, the gold deposits of Kyrgyzstan are mountainous, located in zones of tectonic disturbances and ore bodies, some of which come to the sur-face, and the lower part goes deep into the earth's crust, which predisposes a combined method of development. The combined method of field development is complicated by the tense state of the rock mass of the sub-quarry mine workings.

Kyrgyzstan is rich in minerals, has large deposits of gold, coal, antimony, mercury, uranium, zinc, rare earth metals and nepheline syenites, and the mining industry is one of the priority sectors of economic development.

The mining industry is one of the priority sectors of the development of the Kyrgyz economy. The gold mining industry currently occupies a leading position in the industry. Gold deposits, as a rule, are upland and are developed in a combined way. At the first stage, the work is carried out in an open way. (Table 1)

Both primary and placer deposits were developed on the territory of Kyrgyzstan. Traces of ancient developments are observed among the primary indigenous gold deposits such as Boz-Emchek, Kichi-Sandyk, Kuru-Tegerek, Ak-Tash, Kum-Bel, Kuran-Jailoo. To date, about 2,500 indigenous gold deposits have been explored on the territory of Kyrgyzstan. Of these, deposits with ore reserves of more than 30 tons have been allocated for industrial development according to gold reserves (Nikonorov V.V., Karaev Yu.V., Borisov F.I., 2004).

The largest, unique deposit on the territory of Kyrgyzstan is Kumtor, ore reserves exceed 400 tons. 70 tons of ore and more are contained in such deposits as Jeruy, Taldybulak Levoberezhny, Chaarat. At the Makmal, Bozymchak, Uncurtash, Ishtamberdy, Altyn-Zhylga, Nichkesu, Tokhtozan deposits, reserves range from 30 to 70 tons.

Gold deposits, as a rule, are upland and are developed in a combined way. Mining operations in upland quarries are complicated by the relief of the surface and are characterized by complex mining-geological, tectonic and hydrogeological conditions. The host rocks are, as a rule, intrusive and effusive rocks subjected to hydrothermal-metasomatic changes. Rocks are strongly fractured, and the intensity of fracturing increases at the contacts of rock varieties and tectonic disturbances. (Figure 1)

In the coal industry of the country, despite the significant resources and proven reserves of coal of all grades on the territory of Kyrgyzstan, the volume of their production remains insignificant,

DOI: 10.1201/9781003299127-176

Table 1. Licenses for prospecting and exploration of mineral resources of Kyrgyzstan.

Type of mineral	Search	Geological exploration	Total
Oil and gas	33	4	37
Coal		37	37
Metals	20	36	16
Gold is indigenous	58	38	96
Placer gold	20	3	23
Nonmetals	-	105	105
Underground water	-	-	109
Total	131	203	443

with a downward trend. As a result, Kyrgyzstan is forced to import coal from abroad, which, in turn, leads to a deterioration in the financial and economic condition of the republic.

At the same time, the prospects for an increase in energy prices and an increase in demand for them determine the need to revive domestic coal production by involving a large Kara-Keche deposit in the development.

The high-altitude Kumtor gold deposit

The high-altitude Jeruy gold deposit

Figure 1. The highest mountain gold deposits of Kyrgyzstan.

The main reasons for the decline in coal production can be attributed to the general decline in production in the republic and the deterioration of the financial condition of enterprises, which led to a decrease in coal consumption in the real sector of the economy. The transfer of a number of consumers to other types of energy carriers, the reduction of sales markets in the Central Asian region, high transportation costs reaching up to 300% of the cost of production, as well as large physical and moral wear of technological equipment at mining enterprises had a significant impact.

Having its own gas fields, Kyrgyzstan still remains practically a net consumer of imported gas. At the same time, the main role in the structure of natural gas consumption in the republic is played by the municipal and household sector, which accounted for 61.5% of the total volume in 2001. It should be noted that, as before, significant volumes of energy resources are supplied to the republic on a barter basis or are paid in freely convertible currency, which reduces the economic potential of the sector.

At the same time, the self-sufficiency of the republic with petroleum products is only 30%, while the data from the analysis of the possibilities of developing new oil and gas fields say that the use of modern technologies and methods of exploration and development will significantly increase production volumes.

The safety of the operation of upland quarries is determined by the properties of the geological environment. The geological environment is considered as a complex self-organizing nonlinear system in which physical processes in the Earth's crust are of decisive importance. The geological environment includes elements such as terrain, rock mass, rocks and their properties, groundwater, permafrost, natural gravitational processes, and during technogenic activity it experiences an impact that significantly changes the properties of its individual elements, the speed and direction of the processes occurring in it (Nikolskaya, O.V., Kadyralieva, G.A., 2013).

The main factors of the geological environment that significantly affect the stable condition of the sides of the quarry, the stability of the instrument array and the safety of mining operations include:

- Type of rocks, soils and soils, their structure, texture, physico-mechanical and geochemical properties;
- Tectonic disturbance and heterogeneity of the rock mass;
- Parameters of hydrogeological properties and processes;
- Endogenous and exogenous processes, thermal field;
- Features of geological structures;
- Relief of the Earth's surface;
- Geodynamic activity, seismicity;
- Geophysical fields.

Active structure-forming elements of the geological environment are tectonic faults and cracks, which represent a zone of disruption of the continuity of the Earth's crust, dividing the rock mass into two blocks and expressed in a complex and diverse deformation of the Earth's crust. Tectonic faults and cracks are present in any mountain range and in any territory (Sergeev, E.M., 1987).

As a result of discharges and large thrusts, rocks are subjected to prolonged displacement, overlapping of rocks of various origins and their structure, composition and physico-mechanical properties, which have a special effect on the geological environment, are thoroughly changed.

The modern needs of society for mineral raw materials require the development of mineral deposits located in climatically difficult, inaccessible conditions of the highlands. For states whose main territory is occupied by mountain ranges, the development of high-altitude deposits is an economic necessity. Such states, first of all, should include Kyrgyzstan, Tajikistan, Chile, Georgia, Armenia, Colombia and a number of others.

At the same time, the subsoil of the high-mountain countries is rich in mineral resources, the extraction of which makes it possible to effectively develop its own economy. The technology of open-pit mining of high-altitude deposits differs from the technology of lowland quarries in many ways. According to the definition of Russian scientists I.Z. Lysenko and S.A. Ilyin, "a mountain quarry is a quarry that develops a mineral deposit in a mountainous area.

Mining operations in upland quarries are complicated by the sloping terrain of the surface, the high-altitude location relative to sea level, the reduced partial pressure of oxygen in the atmosphere, increased solar radiation and wind activity, fogs, snow drifts and avalanche danger" (Nifadyev, V.I., Usmanov, S.F.).

As the surface mineral reserves are being worked out, many deposits in Kyrgyzstan are moving to the underground method of development.

A combined development system is, as is known, the development of a part of a mineral deposit prepared for excavation using various development systems or their elements. With the underground method, it is used on powerful ore deposits of various strengths, in cases when their effective development cannot be ensured using a single system. At the same time, the floor is divided into regularly alternating chambers close in width. (Figure 2)

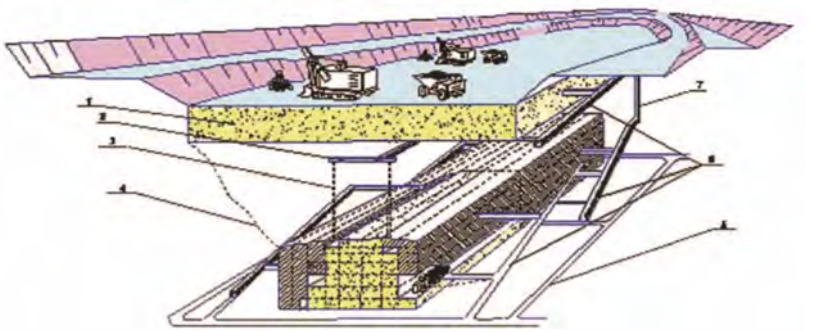

Figure 2. Combined development with horizontal layers with laying in the transition zone and an underground mine: 1 — artificial ceiling; 2 — ventilation-laying horizon; 3 — laying wells; 4 — contour of the ore body; 5 — pumping horizon; 6 — inclined exit.

The characteristic features of the complex open-underground method, which must be taken into account in the design justification of the parameters of the development of steep-falling deposits, are: the presence of a single worked-out space that ensures the placement of overburden rocks in internal dumps; working out the transition zone from open-pit to underground mining operations with one high-altitude ledge using quarry and underground drilling and transport equipment; rational interconnection technological schemes of open and underground mining methods in the process of field development.

Due to the specific conditions of the high-altitude deposits of Kyrgyzstan, with their combined development system, safety, equipment and labor productivity are usually 10-20% lower than at conventional deposits. Combined development of high-altitude deposits has a number of features that significantly complicate mining operations and lead to an increase in the cost of minerals:

- the difficult terrain complicates the location of transport communications, the placement of technological productions, leads to a limitation of the area of the mining enterprise and requires the concentration of all technological sites on a small territory;
- difficult climatic conditions imply low temperatures, high atmospheric pressure, lack of oxygen, which adversely affects the health of personnel and reduced productivity;
- the extremely heterogeneous geological structure of rocks, the presence of tectonic disturbances and structural weakening surfaces reduce the stability of the sides of quarries and underground mine workings
- large water inflow during the melting of glaciers, the presence of groundwater lead to the need for drainage of the quarry field;
- most of the high-altitude quarries are located in regions with high seismic activity, which requires taking into account the impact of natural earthquakes on the stability of mining structures;

– the costs of energy supply of the main technological processes are increasing, the use of mining equipment on diesel fuel is increasing;
– the influence of mass explosions on the stability of mining facilities is increasing;
– the irreversibility of combining combined geotechnology with a sequential transition to underground mining.

The peculiarities of the highlands have a significant impact on both the technology of field development and the safety of mining operations. An important point in the development of high-altitude deposits is to ensure the stability of the sides, ledges, underground mine workings and other geotechnical structures of the deposit.

The main factors contributing to the development of slope deformations in high–altitude and upland quarries are:

- the presence of weakening surfaces - tectonic disturbances, sliding surfaces of ancient landslides, weak contacts between layers;
- waterlogged rocks and their poor drainability due to melting glaciers;
- intense fracturing of individual sections;
- the presence of interlayers of weak clay rocks.

The conditions of such deposits impose their own characteristics on the methods of assessing stability, the choice of geomechanical models, the identification of the primary factors affecting the deformation of the mountain range. Most high-altitude quarries have a complex geological structure, tectonic disturbances, layers of weakened rocks, a significant flow of groundwater and groundwater.

Thus, the peculiarities of the highlands impose additional requirements for the application of new innovative methods for assessing the stability of the sides of quarries, underground mining workings and mining structures. The main condition for effective forecasting of the stability of rock slopes is the use of various techniques in a complex. A complex course will allow you to get a complete and adequate picture of deformation.

REFERENCES

Nifadyev, V.I., Usmanov, S.F. 2009. Features of the development of high-altitude deposits Journal, *"Bulletin of KRSU"*, Volume 9, No. 4, pp. 175–179.

Nikolskaya, O.V., Kadyralieva, G.A. 2013. Features of rock properties in the zones of influence of tectonic disturbances, *Modern problems of continuum mechanics*; *" Issue seventeen, Bishkek*, 136–143

Nikonorov V.V., Karaev Yu.V., Borisov F.I. 2004. Gold of Kyrgyzstan Book 2. *Description of deposits" B. "Nasi", 2004.*

Sergeev, E.M. 1987 Problems of engineering geology in connection with the protection and rational use of the geological environment. *Bulletin of Moscow State University. Ser. 4. Geology*. No.5.77-86.

Smart Geotechnics for Smart Societies – Zhussupbekov, Sarsembayeva & Kaliakin (Eds)
© 2023 The Author(s), ISBN 978-1-003-29912-7
Open Access: www.taylorfrancis.com, CC BY-NC-ND 4.0 license

Synthesis of quality control procedures in the conduct of precision testing of standard soil mixes

J.A.R. Manaloto*, A.P.A. Acacio & M.A.H. Zarco
The University of the Philippines, Diliman, Quezon City, Philippines

ABSTRACT: Geotechnical index property test inputs are very important in foundation design in terms of soil classification and settlement calculations. It is therefore crucial to have accurate and reliable parameters for more reliable and safer foundation design.

In this research, Six Sigma and House of Quality were utilized and incorporated in the inter laboratory study (ILS) precision testing of standard soil mixes of Ottawa sand, Bentonite and manufactured sand. Specific Gravity tests, Sieve Analysis, Liquid Limit Test and Plastic Limit Test were conducted by Six (6) participating laboratories, including the Department of Public Works and Highways (DPWH), Bureau of Research and Standards laboratory.

The conduct of the ILS shows that for the soil tests, only sieve analysis produced good repeatability and reproducibility values. Both Specific Gravity Test and Liquid Limit and Plastic Limit Tests showed high r and R values. To rectify this, the observed probable sources of errors during the conduct of the ILS were identified and quality control measures were employed for a retest conducted in a single laboratory.

Retest results fell within the acceptable range of two results specifications of ASTM. Therefore, the quality control measures and procedures employed in the retest and ASTM precision statements were recommended to be followed for the proposed diagnostic testing for the DPWH Private Laboratory Accreditation and for the proposed accreditation of laboratory technicians.

1 INTRODUCTION

1.1 *Background of the study*

Geotechnical test parameters such as Specific Gravity, percentage passing different Sieve sizes, Liquid Limit and Plastic Limit are important inputs in geotechnical calculations and in determining the factors of safeties for slope or foundation design. A logical approach in determining the appropriate factor of safety for a given case is to consider the uncertainties in the quantities that would enter the calculations (Duncan, 2000).

Bias refers to various statistical issues that are classified as measurement, sampling and estimation. Measurement or sampling bias refers to "the difference between a population mean of the measurements or test results and an accepted reference or true value." Hence, bias causes an underestimation or overestimation of the reference/true value. Measurement bias is usually the result of defective measuring devices or procedures while sampling bias is caused by having an unrepresentative sampling of the target population. Both biases cannot be resolved by increasing sampling effort or the sampling size.

Precision, on the other hand, refers to the absence of random error or variability which is also described as the measure of the statistical variance of an estimation procedure. In contrast to bias, the magnitude of precision is dependent only on the estimated/observed values/measurements regardless of the true value. Thus, it can be described as the spread of the data which can be attributed to the statistical variability existing in the sample gathered. In measurements, precision can be determined from the variance caused by the measuring device or

*Corresponding author: jrmanaloto@up.edu.ph

DOI: 10.1201/9781003299127-177

methodology. This variability produced by the measurement error plus the sample variation and estimation variance contributes to the total variance.

1.2 *Significance of the study*

In the Philippines, there is no available data regarding the precision and reliability of sieve analysis, liquid limit, plastic limit and specific gravity data. These parameters are very important since they are used in the analysis and design of foundations and other earth structures. Therefore, it is very important to adopt a standard procedure in determining the precision statements of soil tests to be able to assess the reliability of soil laboratory tests in the Philippines.

1.3 *Statement of the problem*

There is no existing quality control program or standard/procedure to measure, control and improve precision and bias in soil classification laboratory tests in the geotechnical/soil testing facilities in the Philippines. The lack of such standard procedures puts into question the reliability and acceptability of the soil tests which includes specific gravity tests, sieve analysis, Liquid Limit test and Plastic Limit test which are conducted by the laboratories and also the foundation calculations and designs where these parameters were used.

1.4 *Objectives*

This study aims to establish a quality control procedure to measure, control and recommend improvements in the precision and reliability of geotechnical soil laboratory tests such as specific gravity test, sieve analysis, Liquid Limit test and Plastic Limit test in the Philippine testing laboratories for more accurate geotechnical parameter inputs that would lead to more reliable and safer foundation design.

1.5 *Scope and limitations*

Standard Testing Procedures. All of the tests that will be conducted in this research shall all be based and comply with the American Society for Testing and Materials (ASTM) international provisions. All variations from the ASTM procedures shall be recorded and explained. Moreover, for the purposes of this research, only the specific gravity test (ASTM D854), sieve analysis (ASTM D6913), Liquid Limit test and Plastic Limit test (ASTM D4318) shall be conducted as part of the soil classification routine laboratory tests. Other tests shall not be included and therefore not included in the analysis.

2 REVIEW OF RELATED LITERATURE

2.1 *Inter-Laboratory Study (ILS) to determine precision and bias*

ILS is composed of three basics steps which include planning the ILS, guiding the testing phase of the study and finally analyzing the test results as shown in Figure 1.

The final phase of the ILS is the analysis of test result data wherein "the ILS test results have three purposes, to determine whether the collected data are adequately consistent to form the basis for a test method precision statement, to investigate and act on any data considered to be inconsistent, and to obtain the precision statistics on which the precision statement can be based."

For the cell statistics, the cell average and cell standard deviation for each laboratory are given by Equations 1 and 2, respectively.

$$\overline{x} = \sum_1^n x/n \tag{1}$$

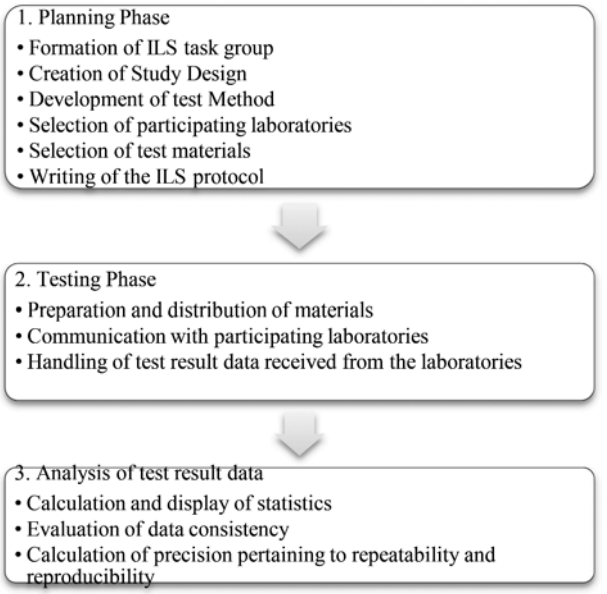

Figure 1. Flowchart of Inter-laboratory Study (ILS) Procedure based on ASTM E691.

where $\bar{x}$ = the average of the test results in one cell; x = the individual test results in once cell; n = the number of test results in one cell.

$$s = \sqrt{\sum_1^n (x - \bar{x})^2/(n-1)} \tag{2}$$

where s = the cell standard deviation.

For the intermediate statistical calculations, the average of the cell averages for each material and the cell deviation for each laboratory can be calculated using Equations 3 and 4, respectively. Furthermore, the standard deviation of the cell averages is given by Equation 5.

$$\bar{\bar{x}} = \sum_1^p \bar{x}/p \tag{3}$$

where $\bar{\bar{x}}$ = the average of the cell averages for one material; $\bar{x}$ = the individual cell averages; p = the number of laboratories in the ILS.

$$d = \bar{x} - \bar{\bar{x}} \tag{4}$$

where d = the cell deviation.

$$s_{\bar{x}} = \sqrt{\sum_1^p d^2/(p-1)} \tag{5}$$

where $s_{\bar{x}}$ = the standard deviation of the cell averages

The fundamental precision statistics for the ILS are the repeatability standard deviation and the reproducibility standard deviation. Equation 6 gives the repeatability standard deviation.

$$s_r = \sqrt{\sum_1^p s^2/p} \tag{6}$$

where s_r = the repeatability standard deviation; s = the cell standard deviation (p of them from Equation 2); p = the number of laboratories

Moreover, the between laboratory variance and between laboratory standard deviation can be calculated using Equations 7 and 8, respectively.

$$s_L^2 = s_{\bar{x}}^2 - s_r^2/n \tag{7}$$

where s_L^2 = the between laboratory variance.

$$s_L = \sqrt{s_L^2} \tag{8}$$

where s_L = the between laboratory standard deviation.

The reproducibility standard deviation, on the other hand, can be calculated using Equation 9.

$$s_R = \sqrt{s_L^2 + s_r^2} \tag{9}$$

where s_L = the between laboratory standard deviation.

For the consistency statistics, the between-laboratory consistency statistic and the within-laboratory consistency statistic can be calculated using Equations 10 and 11. Both computed statistic values should have two decimal places.

$$h = d/s_{\bar{x}} \tag{10}$$

where h = the between-laboratory consistency statistic.

$$k = s/s_r \tag{11}$$

where k = the within-laboratory consistency statistic.

For the precision statement information and using the corrected statistics, the 95% repeatability and reproducibility limits are calculated using Equations 12 and 13, respectively.

$$r = 2.8\ s_r \tag{12}$$

where r = the 95% repeatability limit

$$R = 2.8\ s_R \tag{13}$$

where R = the 95% reproducibility limit

2.2 *Quality management*

2.2.1 *Six Sigma principles*

Six Sigma is a methodology for improvement of processes and also a statistical concept to identify and define the inherent variation in any process. The principal premise of Six Sigma is that any variation in a process gives chances for errors that would then lead to risks for product defects, whether in a tangible process of a service. The yield, which can be used to determine the sigma level via a sigma table, can be calculated using Equation 13. The higher the sigma level, the more "perfect" the process is.

$$Yield = \left(\frac{No.\ of\ opportunities - No.\ of\ defects}{No.\ of\ opportunities}\right) \times 100 \tag{13}$$

2.2.2 *House of quality*
House of Quality (HOQ), which is a set of interrelated matrices, is the heart of QFD and is illustrated in Figure 2 (Goetsch & Davis, 2013).

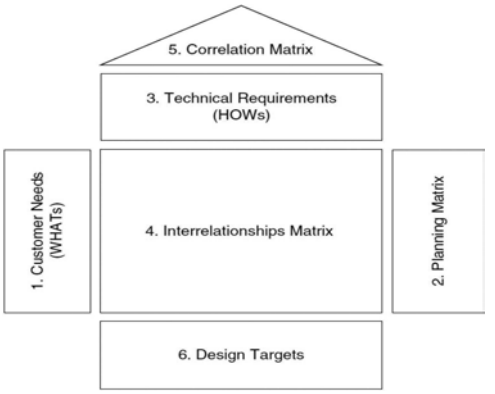

Figure 2. House of quality diagram.

As seen in Figure 2, the HOQ is composed of six sub-matrices. The goal of HOQ is to take input requirements from the customers and then translate them into a set of customer needs (VOC). Based on the VOC, bench-marking with competing shall be done prior the determination of prioritized features of a new or improved product/service that will best respond to the VOC.

3 METHODOLOGY

This chapter describes in detail the conduct of the Inter-laboratory Study (ILS) from the planning, testing, and data analysis phases for the soil classification test methods while applying quality control concepts and procedures all throughout the process.

3.1 *Planning phase*

3.1.1 *Formation of ILS task group*
For this ILS, the researcher shall be the overall ILS coordinator and laboratory supervisor. The statistical and data analyses shall also be done by the researcher with the assistance of the person in charge of the ILS of the Department of Public Works and Highways (DPWH), Bureau of Research and Standards (BRS).

3.2 *Analysis of test result data*

3.2.1 *Calculation and display of statistics*
For the basic statistics, Equations 1–8 shall be used to calculate the cell average, cell standard deviation, average of cell averages, cell deviation, standard deviation of the cell averages, repeatability standard deviation, between laboratory variance and between laboratory standard deviation.

3.2.2 *Calculation of precision pertaining to repeatability and reproducibility*
For the precision statement information and using the corrected statistics, the 95% repeatability and reproducibility limits are calculated using Equations 12 and 13, respectively.

3.3 *House of quality*

Based on the results of the ILS conducted, the House of Quality as discussed in Section 2.2.2 shall be established. This shall determine the needs, technical requirements and design targets of a high-precision proficiency testing system.

3.4 *The use of Six Sigma and house of quality in the soil testing interlaboratory study*

Generally, six sigma concepts and house of quality are used as quality control tools in the business sector wherein the processes are optimized to reduce errors in the procedures and reduce defects in the end products while at the same time increasing customer satisfaction. This research has explored the application of six sigma concepts and house of quality in the laboratory testing setting wherein the end products are the test results and the customers are the geotechnical engineers who require high precision with less errors for satisfaction. In order to fit this setting, some adjustments and simplifications were done in the six sigma processes and house of quality concept.

Table 1 shows the quality control concepts from six sigma and house of quality that were integrated in the conduct of the ILS.

Table 1. Quality concepts integrated within the ILS.

ILS Process	Quality Concept	Taken from
Planning phase	Define: Identify the business case, project scope, stakeholders, team member roles, milestones/timeline for the phases.	Six Sigma
	Measure: Using Failure Modes and Effects Analysis (FMEA), identify risks and errors within all steps of the tests	Six Sigma
Testing phase	Measure: Record/document all measurements and variations in time/measurements in each step process for all tests	Researcher
Data Analysis	Analyze: Using a Pareto Charts, identify the root causes of the variances of results	Six Sigma
	Analyze: Using Spearman Rho non-parametric Correlation, determine if there are relationships between the recorded data test variations and the ILS test results	Researcher
	Analyze: Create House of Quality diagram to serve as a guide to facilitate the design of other ILS tests for the same purpose and future studies.	House of Quality
	Improve: Recommend improvements in the conduct of ILS	Six Sigma
	Improve: Create a criteria for proficiency testing and DPWH accreditation	Researcher

4 RESULTS AND DISCUSSION

4.1 *Laboratory testing records*

The ILS coordinator required the participating laboratories to record testing data/details that may be used for analysis in identifying deviations and possible causes of errors in the tests.

4.2 *ILS test results*

Figures 3, Tables 2 and 3 show the ILS test results conducted on the three (3) soil mix proportions done by the six (6) participating laboratories for three (3) trials each of Sieve Analysis, Liquid Limit and Plastic Limit tests, and Specific Gravity Test, respectively.

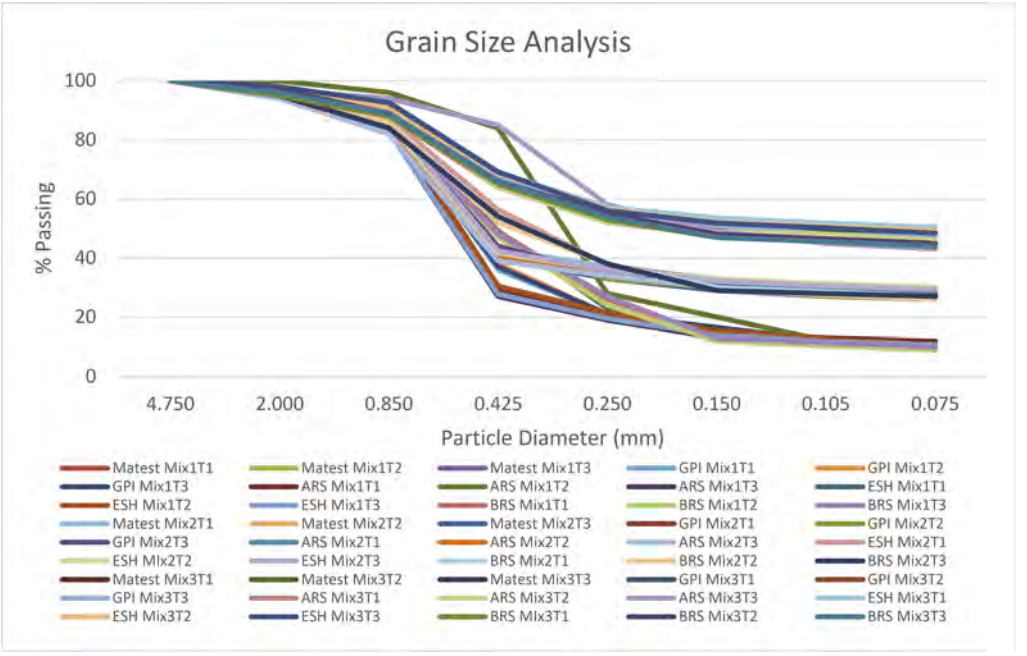

Figure 3. Sieve analysis ILS results.

Table 2. Liquid limit and plastic limit ILS results.

Soil Mix Proportions	Mixture 1			Mixture2			Mixture3		
Matest	LL	PL	PI	LL	PL	PI	LL	PL	PI
Trial 1	70	17	53	166	44	122	191	40	151
Trial 2	64	17	47	165	42	123	196	44	152
Trial 3	63	18	45	181	43	138	196	43	153
GPI	LL	PL	PI	LL	PL	PI	LL	PL	PI
Trial 1	62	19	43	160	20	140	227	22	205
Trial 2	62	19	43	159	20	139	221	22	199
Trial 3	63	19	44	161	20	141	224	21	203
ARS	LL	PL	PI	LL	PL	PI	LL	PL	PI
Trial 1	78	23	55	216	33	183	254	33	221
Trial 2	84	30	54	227	33	194	270	32	238
Trial 3	104	22	82	227	33	194	270	32	238
ESH	LL	PL	PI	LL	PL	PI	LL	PL	PI
Trial 1	99	15	85	193	16	177	210	14	195
Trial 2	83	15	69	220	19	200	216	15	201
Trial 3	77	17	60	223	14	209	199	17	182
Megatesting	LL	PL	PI	LL	PL	PI	LL	PL	PI
Trial 1	56	14	42	164	13	151	222	17	205
Trial 2	71	19	51	178	20	158	134	14	120
Trial 3	70	25	45	188	24	163	210	43	167
DPWH-BRS	LL	PL	PI	LL	PL	PI	LL	PL	PI
Trial 1	97	29	68	236	53	183	141	50	91
Trial 2	98	31	67	237	46	191	213	49	164
Trial 3	97	27	71	230	45	184	244	66	178

Table 3. Specific Gravity ILS results.

Soil Mix Proportions	Mixture 1	Mixture2	Mixture3
Matest			
Trial 1	2.640	2.630	2.480
Trial 2	2.670	2.740	2.530
Trial 3	2.670	2.650	2.530
GPI			
Trial 1	2.700	2.690	2.630
Trial 2	2.720	2.620	2.530
Trial 3	2.680	2.600	2.510
ARS			
Trial 1	2.530	3.020	2.680
Trial 2	2.610	2.850	2.680
Trial 3	2.390	2.930	2.620
ESH			
Trial 1	2.650	2.780	2.540
Trial 2	2.620	2.760	2.520
Trial 3	2.590	2.710	2.570
Megatesting			
Trial 1	2.720	3.006	2.816
Trial 2	2.651	2.422	2.720
Trial 3	2.873	2.479	2.687
DPWH-BRS			
Trial 1	2.650	2.630	2.570
Trial 2	2.520	2.580	2.499
Trial 3	2.660	2.569	2.600

4.3 *Data analysis*

4.3.1 *Comparison of precision statements with ASTM examples*

Table 4 shows the Comparison of ILS Precision Statements with Examples from ASTM.

It can be seen from Table 4 that only percent passing Sieve No. 10 for mixtures 2 and 3 have reproducibility limits less than the precision statement examples of ASTM. All the other repeatability and reproducibility values exceeds the said limits and are very much high in the liquid limit and plastic limit tests. Though the soil samples from ASTM and this ILS are different types, the precision statements in this ILS are very much higher than that of the ASTM examples.

4.3.2 *Retest*

Tables 5–7 show the results of the precision calculations for corresponding mixture.

From Tables 5–7, the acceptable range of two results (2ds) refers to the maximum difference any 2 trials for a given test in a laboratory can have and is determined by multiplying 1.960 $\sqrt{2}$ to the standard deviation. It can be seen that in this retest, all standard deviations and acceptable range of two results values fall within the ASTM specifications. This means that the correction/control of the probable sources of errors found during the ILS was effective.

4.3.3 *Precision testing criteria and checklists for quality control and procedures*

Since it was proven that the ASTM precision statements are achievable, then it shall be adopted as the precision testing criteria as shown in Table 8.

Table 4. Comparison of ILS precision statements with examples from ASTM.

	ASTM		ILS Results						ASTM						ILS Results					
			Mixture1		Mixture2		Mixture3								Mixture1		Mixture2		Mixture3	
Soil type	SP		SW-SM		SC		SC		CH		CL		ML		SW-SM		SC		SC	
Presicion Statement	r	R	r	R	r	R	r	R	r	R	r	R	r	R	r	R	r	R	r	R
Passing Sieve #4	-	-	-	-	-	-	-	-	-	-	-	-	-	-						
Passing Sieve #10	1.1	3.4	4.07	4.07	1.32	1.95	1.84	2.25	-	-	-	-	-	-						
Passing Sieve #20	1.1	3.6	10.22	10.22	2.54	4.43	4.11	4.63	-	-	-	-	-	-						
Passing Sieve #40	1.5	4.3	43.12	43.12	10.69	16.85	15.24	15.24	-	-	-	-	-	-						
Passing Sieve #60	1.2	4.0	6.78	8.24	3.15	5.32	4.69	5.36	-	-	-	-	-	-						
Passing Sieve #100	0.4	2.0	5.23	5.76	3.37	4.58	1.87	6.35	-	-	-	-	-	-						
Passing Sieve #140	0.1	1.1	0.97	0.97	3.66	4.49	2.93	5.64	-	-	-	-	-	-						
Passing Sieve #200	0.1	1.1	1.05	1.99	2.85	4.19	3.69	6.28	-	-	-	-	-	-						
Specific Gravity	0.02	0.02							0.03	0.08	0.02	0.06	0.02	0.06	0.21	0.29	0.39	0.47	0.14	0.27
Liquid Limit	-	-							2	4	1	3	2	4	22.92	45.78	26.65	89.13	82.74	104.00
Plastic Limit	-	-							1	6	1	3	1	3	8.73	16.04	8.41	38.14	21.73	44.84

Table 5. Precision calculations for Mixture 1.

Mixture 1				ASTM*		Difference	
Laboratory	x	s	Acceptable range of two results	s	Acceptable range of two results	Δs	Acceptable range of two results difference
SG	2.6860	0.01	0.02	0.01	0.03	0.00	0.01
LL	29.5000	0.55	1.52	0.70	2	0.15	0.48
PL	20.0000	0.00	0.00	0.50	1	0.50	1.00
Passing Sieve #4	100.0000	0.00	0.00	0.00	0.00	0.00	0.00
Passing Sieve #10	100.0000	0.00	0.00	0.39	1.10	0.39	1.10
Passing Sieve #20	93.0000	0.00	0.00	0.41	1.10	0.41	1.10
Passing Sieve #40	66.6667	0.52	1.43	0.53	1.50	0.02	0.07
Passing Sieve #60	39.8333	0.41	1.13	0.45	1.20	0.04	0.07
Passing Sieve #100	31.0000	0.00	0.00	0.15	0.40	0.15	0.40
Passing Sieve #140	30.0000	0.00	0.00	0.02	0.10	0.02	0.10
Passing Sieve #200	30.0000	0.00	0.00	0.02	0.10	0.02	0.10

5 CONCLUSIONS

In this research, quality control concepts from Six Sigma and House of Quality (HOQ) were used to identify the risk and sources of errors. From these analyzing tools and direct observations, deviations and possible sources of errors in the conduct of the soil laboratory tests were identified. Though the precision statements of the Inter-laboratory Study vary greatly from the ASTM requirements, it was found out that the control/corrective measures that were employed in the retest to rectify the errors as observed in the conduct of the inter-laboratory study were effective in bringing the precision statements to within the requirements of ASTM. In sieve analysis, thorough cleaning prior and after use of all sieves using standard sieve brush and giving after mechanical shaking of an average of 3-4 minutes for pure Ottawa and

Table 6. Precision calculations for Mixture 2.

Mixture 2				ASTM*		Difference	
Laboratory	x	s	Acceptable range of two results	s	Acceptable range of two results		Acceptable range of two results difference
SG	2.6969	0.01	0.02	0.01	0.03	0.00	0.01
LL	96.8333	0.41	1.13	0.70	2	0.29	0.87
PL	27.0000	0.00	0.00	0.50	1	0.50	1.00
Passing Sieve #4	100.0000	0.00	0.00	0.00	0.00	0.00	0.00
Passing Sieve #10	100.0000	0.00	0.00	0.39	1.10	0.39	1.10
Passing Sieve #20	93.0000	0.00	0.00	0.41	1.10	0.41	1.10
Passing Sieve #40	72.1667	0.41	1.13	0.53	1.50	0.12	0.37
Passing Sieve #60	50.8333	0.41	1.13	0.45	1.20	0.04	0.07
Passing Sieve #100	47.0000	0.00	0.00	0.15	0.40	0.15	0.40
Passing Sieve #140	45.0000	0.00	0.00	0.02	0.10	0.02	0.10
Passing Sieve #200	44.0000	0.00	0.00	0.02	0.10	0.02	0.10

Table 7. Precision calculations for Mixture 3.

Mixture 3				ASTM*		Difference	
Laboratory	x	s	Acceptable range of two results	s	Acceptable range of two results		Acceptable range of two results difference
SG	2.6907	0.01	0.02	0.01	0.03	0.00	0.01
LL	167.500	0.55	1.52	0.70	2	0.15	0.48
PL	27.0000	0.00	0.00	0.50	1	0.50	1.00
Passing Sieve #4	100.000	0.00	0.00	0.00	0.00	0.00	0.00
Passing Sieve #10	100.000	0.00	0.00	0.39	1.10	0.39	1.10
Passing Sieve #20	95.000	0.00	0.00	0.41	1.10	0.41	1.10
Passing Sieve #40	84.8333	0.41	1.13	0.53	1.50	0.12	0.37
Passing Sieve #60	67.1667	0.41	1.13	0.45	1.20	0.04	0.07
Passing Sieve #100	63.0000	0.00	0.00	0.15	0.40	0.15	0.40
Passing Sieve #140	61.0000	0.00	0.00	0.02	0.10	0.02	0.10
Passing Sieve #200	60.0000	0.00	0.00	0.02	0.10	0.02	0.10

Table 8. Precision limits and ranges of acceptable values for precision testing.

Soil Parameter	r	R	s	Acceptable Range of Two Values
Sieve Analysis				
% Passing Sieve №4	0.0	0.0	0.0	0
% Passing Sieve №10	1.1	3.4	0.4	1.1000
% Passing Sieve №20	1.1	3.6	0.4	1.1000
% Passing Sieve №40	1.5	4.3	0.5	1.5000
% Passing Sieve №60	1.2	4.0	0.4	1.2000
% Passing Sieve №100	0.4	2.0	0.1	0.4000
% Passing Sieve №140	0.1	1.1	0.0	0.1000
% Passing Sieve №200	0.1	1.1	0.0	0.1000
Atterberg Limits				
Liquid Limit	2	4	0.70	2
Plastic Limit	1	6	0.50	1
Specific Gravity	0.02	0.02	0.01	0.03

Construction sands as well as an average of 6-7 minutes for Mixtures 1, 2 & 3 of manual shaking were effective measures in achieving the ASTM precision statements. Moreover, in the specific gravity test, the drying time shall be given more importance thus in the process of decantation the samples containing water in the pan must be immediately placed in a preheated oven to ensure that the weight of the samples will not be diminished during the taring. The transfer of soil slurry and use of dropper to remove/add water in the pycnometer were effective measures in achieving the ASTM precision statements. In the liquid limit test, using a motorized and level liquid limit device to ensure standard drop rate and ensuring that the technicians refrained from holding the base of the liquid limit device during the blowing procedure were effective measures in achieving the ASTM precision statements. Also, in the plastic limit test, use of a standard 3.2 mm diameter stick during the plastic limit test and placing the analytical balance on a level and permanent station were effective measures in achieving the ASTM precision statements. Further, the precision criteria and checklists that were established shall be useful in the accreditation criteria of Laboratories and also to geotechnical engineers to ensure reliable soil parameters for safe geotechnical design.

It is recommended to conduct another ILS employing the retest control measures and corrections to check whether it would be effective in another ILS setting. It is also recommended that since the primary sources of errors is the laboratory technicians' performance which is directly related to their training and experience in these soil tests, there must be an accreditation of laboratory technicians as well. Moreover, to improve this research, proficiency testing with an established reference laboratory is recommended. For future studies, the specific implications and quantified effects of the errors in the soil parameters and soil classification to the geotechnical design, calculations and decision-making must be explored and discussed.

REFERENCES

Bastidas, A. M. P. 2016. *Ottawa F-65 Sand Characterization*.

Das, B. N. 2014. *Fundamentals of Geotechnical Engineering*. Cengage Learning.

Day, R. W. 2010. *Foundation Engineering Handbook*, *2nd Edition*. McGraw Hill Professional.

Duncan, J. M. 2000. Factor of safety and reliability in geotechnical engineering, *Journal of Geotechnical and Geoenvironmental Engineering*, 126 (4), 307–316.

Goetsch, D. L. & Davis, S. B. 2013. *Quality Management for Organizational Excellence: Introduction to Total Quality*, 7th Edition. Pearson Education

Hackley, V. A. & Stefaniak, A. B. 2013. "Real-world" precision, bias, and between-laboratory variation for surface area measurement of a titanium dioxide nanomaterial in powder form. *Springer link*. doi:10.1007/s11051-013-1742-y

Md. Abdullah Asad *et al*. 2016. *Suitability of Bentonite Clay: An Analytical Approach*.

Mines and Geosciences Bureau 2005. *Mineral Resource Information Series No. 8 "Industrial Minerals and Manufacturing Materials."*

Ojuri, O. O. & Fijabi, D. O. 2012. Standard sand for geotechnical engineering and geoenvironmental research in Nigeria: Igbokoda sand, *Advances in Environmental Research*, Vol. 1, No. 4, 305–321.

Rajapakse, R. 2016. *Pile Design and Construction Rules of Thumb*. Elsevier Inc.

Spiegel, M. R & Stephens, L. J. 2018. Schaum's Outline of Statistics, Sixth Edition. McGraw-Hill Education.

Srikanth V. & Mishra, A. K. 2016. *A Laboratory Study on the Geotechnical Characteristics of Sand–Bentonite Mixtures and the Role of Particle Size of Sand*.

The Council for Six Sigma Certification 2018. *Six Sigma: A Complete Step-by-Step Guide*. Harmony Living, WY.

Walther, B. A. & Moore, J. L. 2005. The concepts of bias, precision and accuracy, and their use in testing the performance of species richness estimators, with a literature review of estimator performance, *Ecography*, 28, 815–829.

Waugh, C. & Clark, G. 2021. *Rev. Sci. Tech. Off. Int. Epiz*., 40 (1).

Smart Geotechnics for Smart Societies – Zhussupbekov, Sarsembayeva & Kaliakin (Eds)
© 2023 The Author(s), ISBN 978-1-003-29912-7
Open Access: www.taylorfrancis.com, CC BY-NC-ND 4.0 license

Geotechnical risk assessment for construction of underground structures

Dmitry Chunyuk* & Serafima Selviyan*
National Research Moscow State University of Civil Engineering (NRU MGSU), Moscow, Russia

ABSTRACT: In underground construction, there is a high risk of emergency situations and accidents that can lead to death of people. Therefore, the article has developed methodology for calculating risks in underground construction, which provides for the allocation of individual components of the total damage (consequences) from risks and the determination of the price of each component from various causes. The proposed approach allows targeted implementation of risk mitigation measures. For example, protective actions are applicable to a specific, most significant consequence, while not addressing causes and events whose risk cost, except for the mitigated consequence, remains acceptable or negligible. The above methodology will later help to create a risk register for typical facilities, which will make it possible to determine the most appropriate protective measures necessary for the construction and operation of underground structures.

Keywords: risk analysis, geotechnical risks, source of risk, underground construction, monitoring

1 INTRODUCTION

The purpose of the study is to identify risks that can lead to an emergency event. The main reasons for the manifestation of risks are related to the engineering and geological conditions of construction. To minimize the risk, it is necessary at the initial stage to identify possible risk factors, analyze the possible impacts and the degree of danger from their manifestation.

Risks and manifestations of non-standard situations in underground construction in large metropolitan areas, primarily due to specific, complex engineering-geological, hydrogeological and urban planning conditions for laying objects, which include:

- the presence of a thick layer of technogenic soils, karst soils, high activity of groundwater and flooding of underground construction sites, etc.;
- significant technogenic loads on the engineering and geological environment of the city, which, by provoking negative fast-flowing geological processes, worsen the conditions for the construction and operation of underground facilities;
- the presence of dense urban development and the need to conduct underground construction work in cramped conditions, where, in addition to those under construction, many other buildings, structures and communications fall into the zone of influence.

2 MATERIALS AND METHODS

The listed risk factors and the possibility of their action in an unfavorable combination determine the need for their identification and accounting throughout the life cycle of the underground structure (during surveys, design, construction, operation and reconstruction), which is designed to optimize the choice of the location of the object (for example, the route

*Corresponding authors: Chunyuk@mail.ru and SelviyanSM@yandex.ru

DOI: 10.1201/9781003299127-178

of the tunnel) and the corresponding protective measures, the cost of which largely depends on the degree of danger for various conditions of laying the mine.

In the modern practice of construction and operation of critical underground facilities in large megacities, many tasks of prevention of non-standard situations, and in case of their manifestation – elimination of consequences, are solved by organizing scientific and technical support of works at all stages of the life cycle of the structure.

At the same time, the main importance is attached to solving geotechnical issues, for example, such as assessing the possible negative impact of new construction on the natural and urban environment, changing the conditions for the static operation of structures under construction over time, and determining the category of geotechnical complexity of construction. For such calculations, software systems PLAXIS, Z_Soil, MIDAS, etc. are used. The PC data are used to calculate the stress-strain state of the "soil mass-structure" system. Based on the results of these works, adjustments are made to design and technological solutions, to methods for ensuring the operational reliability of facilities under construction and in operation. However, the effectiveness of taking into account the peculiarities onto one or another geotechnical situation for risk assessment is still largely determined by the qualifications and experience of organizations performing the design, construction or operation of the facility. The regulatory and methodological framework available on this issue, including the Guidelines of the International Tunneling Association, is mostly of a general nature.

In the modern practice of designing complex and hazardous production processes, mainly a comprehensive assessment of the cumulative probability of the causes, risks and consequences of a possible non-standard situations (event) is used. In this case, the resulting damage (consequences) is not divided into components depending on the causes that caused them. Such an assessment does not allow optimizing the choice and evaluating the effectiveness of measures to reduce the risk from each of the possible types of danger.

The methodology proposed in this article, developed in the development of existing methods, provides for the allocation of individual components of the total damage (consequences) from risks and the determination of the price of each component from various reasons (dangerous engineering and geological processes, deviations from the project, technological failures, etc.). This approach allows you to "point" to carry out risk reduction measures. For example, protective actions are applicable to a specific, most significant consequence, while not addressing causes and events for which the cost of risk, with the exception of the mitigated consequence, remains acceptable or negligible.

3 RESULTS

3.1 *Risk assessment algorithm*

In the practice of underground construction, the implementation of such "point" measures is most relevant due to the ratio of the size of the zone of potential danger of the construction object and the zone of distribution of dangerous engineering and geological processes.

A risk in the described Methodology is an event that has its own cause and adverse consequences. Each event can be caused by several causes, and each effect can be the result of several events.

All objects have their own unique range of risks, which depends, among other things, on the parameters of the object (geometric, structural, functional, etc.) and its location. The cost of risks can be expressed both in shares (%) of the value, and in monetary or conventional units.

At the stage of substantiating investments in the construction of an object, the authors recommend the use of a point-based method for assessing risks, which allows determining the main risk factors and assessing them in an enlarged manner. The point-based method can also be used to narrow the list of considered risks, discarding insignificant risks (risks with low probability and/or magnitude of damage from the consequences).

Risk assessment in underground construction is presented as a process in which certain actions are performed according to the algorithm presented in the flowchart in Figure 1.

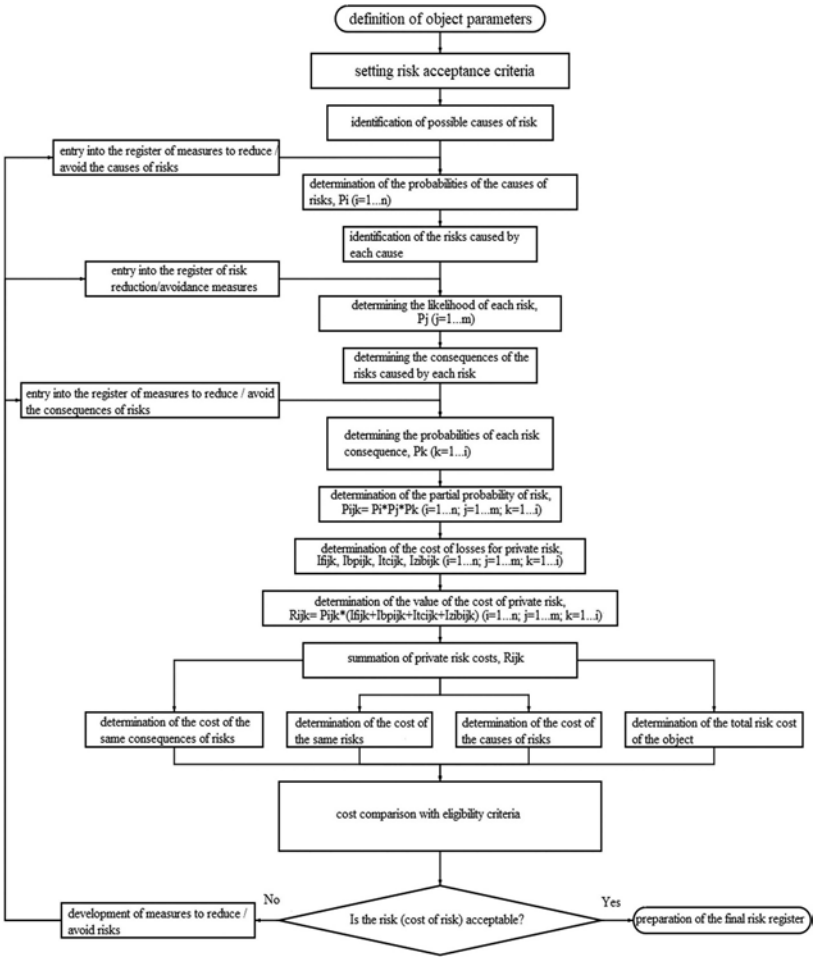

Figure 1. Algorithm of the risk assessment process during underground construction.

3.2 *Relationship between risks and their causes*

Guided by the proposed algorithm, it is possible to estimate the cost of risk (the cost of consequences, taking into account the probability of an non-standard from each of the possible causes) both for individual consequences and for individual events.

The interrelation between the final probability of the occurrence of the consequence with the probabilities of the presence of the cause of the risk and the manifestation of the event is schematically shown in Table 1.

The risk assessment process is a step-by-step process, with each step specifying what actions and by what methods they should be carried out. The risk assessment process (see the flow chart of the risk assessment algorithm in Figure 1.) is recommended to begin with the identification of the risk acceptability category for each object, bearing in mind the following definitions:

- negligible risk - a risk where the possible cost of losses has little effect on the cost of building an object;
- acceptable risk - a risk at which the possible cost of losses can be assumed by an investor, customer or designer;
- conditionally acceptable risk - the risk at which the possible cost of losses can be allowed by the investor if it is more expensive to prevent an non-standard situation;
- unacceptable risk - is a risk, the prevention of which is necessary regardless of the cost.

Table 1. The interrelation of risks with their causes and consequences.

Object parameters																	
Cause 1									Cause n								
$P_i=p_1$									$P_i=p_n$								
Risk 1.1			Risk 1.2			Risk 1.*m*			Risk *n*.1			Risk *n*.2			Risk *n.m*		
$P_j = p_{1.1}$			$P_j = p_{1.2}$			$P_j = p_{1.m}$			$P_j = p_{n.1}$			$P_j = p_{n.2}$			$P_j = p_{n.m}$		
Consequence 1.1.1	*Consequence 1.1.2*	*Consequence 1.1.1*	*Consequence 1.2.1*	*Consequence 1.2.2*	*Consequence 1.2.1*	*Consequence 1.m.1*	*Consequence 1.m.2*	*Consequence 1.m.1*	*Consequence n.1.1*	*Consequence n.1.2*	*Consequence n.1.1*	*Consequence n.2.1*	*Consequence n.2.2*	*Consequence n.2.1*	*Consequence n.m.1*	*Consequence n.m.2*	*Consequence n.m.1*
$P_k = p_{1.1.1}$	$P_k = p_{1.1.2}$	$P_k = p_{1.1.1}$	$P_k = p_{1.2.1}$	$P_k = p_{1.2.2}$	$P_k = p_{1.2.1}$	$P_k = p_{1.m.1}$	$P_k = p_{1.m.2}$	$P_k = p_{1.m.1}$	$P_k = p_{n.1.1}$	$P_k = p_{n.1.2}$	$P_k = p_{n.1.1}$	$P_k = p_{n.2.1}$	$P_k = p_{n.2.2}$	$P_k = p_{n.2.1}$	$P_k = p_{n.m.1}$	$P_k = p_{n.m.2}$	$P_k = p_{n.m.1}$
$P_{ijk} = p_i * p_{1.1} * p_{1.1.1}$	$P_{ijk} = p_i * p_{1.1} * p_{1.1.2}$	$P_{ijk} = p_i * p_{1.1} * p_{1.1.1}$	$P_{ijk} = p_i * p_{1.2} * p_{1.2.1}$	$P_{ijk} = p_i * p_{1.2} * p_{1.2.2}$	$P_{ijk} = p_i * p_{1.2} * p_{1.2.1}$	$P_{ijk} = p_i * p_{1.m} * p_{1.m.1}$	$P_{ijk} = p_i * p_{1.m} * p_{1.m.2}$	$P_{ijk} = p_i * p_{1.m} * p_{1.m.1}$	$P_{ijk} = p_n * p_{n.1} * p_{n.1.1}$	$P_{ijk} = p_n * p_{n.1} * p_{n.1.2}$	$P_{ijk} = p_n * p_{n.1} * p_{n.1.1}$	$P_{ijk} = p_n * p_{n.2} * p_{n.2.1}$	$P_{ijk} = p_n * p_{n.2} * p_{n.2.2}$	$P_{ijk} = p_n * p_{n.2} * p_{n.2.1}$	$P_{ijk} = p_n * p_{n.m} * p_{n.m.1}$	$P_{ijk} = p_n * p_{n.m} * p_{n.m.2}$	$P_{ijk} = p_n * p_{n.m} * p_{n.m.1}$

Based on the results of the research and based on the principal design decisions, a list of potential causes of risks is compiled, which are entered in the risk register. The reasons for the risks may be due to engineering and geological conditions, adopted constructive decisions, construction methods, sequence of work, etc.

- Checklists;
- Scenario analysis;
- Structured analysis "What if?" (SWIFT), etc.

After identifying the causes of risks, the events themselves (risks, non-standard situations) and their consequences caused by the identified causes of risks are determined. At this stage, the following methods are recommended:

- checklists;
- analysis of the event tree;
- fault tree analysis;
- analysis of cause-and-effect relationships.

After compiling a list of considered causes, events and consequences, the probabilities of occurrence of each of the causes, events and consequences are determined. At the same time, for each risk (event), the probability of its manifestation is determined provided that the cause of the risk is present (the probability of the cause of the risk is 100%), and the probability of the manifestation of the consequences of the risk is determined, provided that the event has occurred (the probability of the event is 100%). The main methods for determining these probabilities are:

- Monte-Carlo simulation;
- method of expert assessments;
- statistical method;
- Bayesian analysis;
- Bayesian networks.

For each consequence, the probability of its manifestation is determined (let's call it the partial probability of risk) is determined by multiplying the probabilities of this consequence and

the probabilities of the cause and event that led to this particular consequence. Partial probabilities of risks from other causes or events are evaluated separately:

$$P_{ijk}=p_i \times p_j \times p_k \quad (1)$$

where P_{ijk} is the probability of a particular risk, taking into account the probability of the cause and the risk causing this consequence;

p_i is the probability of occurrence of the risk cause (event);

p_j is the probability of occurrence of a risk (event), while different causes of risk can be a source of the same risks;

p_k is the probability of occurrence of the consequences of a risk (event), while different risks (events) may have the same consequences.

Next, it is necessary to determine the cost of losses from a particular risk, i.e. the cost of eliminating the consequences or damage from the consequences of the risk in the event of its (consequence) occurrence. In most cases, losses can be divided into the following categories:

- financial losses for the facility, expressed in the cost of work to restore the destroyed part of the structure and additional work within the facility;
- increase in construction time, estimated in terms of the cost of downtime (can be expressed in terms of the cost of an object or a stage of an object and the refinancing rate of the Central Bank of the Russian Federation for each day of downtime);
- damage to a third party, expressed through the cost of restoration work on the structures of the surrounding buildings or material losses of vehicles, etc.;
- damage to health and safety (can be expressed in terms of compensation amounts).

The following methods are applicable to determine the cost of losses:

- expert method;
- statistical method;
- special methods for assessing damage from accidents.

At the next stage, the cost of private risk is determined by multiplying the private probability of risk by the cost of losses from private risk:

$$R_{ijk} = P_{ijk}\left(I_f + I_{bp} + I_{tc} + I_{zib}\right)_{ijk} \quad (2)$$

where R_{ijk} is the cost of private risk caused by certain causes and events (risks);

I_f - the amount of financial losses, expressed in monetary units or in shares (%) of the cost of construction;

I_{bp} - the amount of losses due to downtime in construction, expressed in monetary units or in shares (%) of the construction cost;

I_{tc} - the amount of damage to a third party, expressed in monetary units or in shares (%) of the cost of construction;

I_{zib} - the amount of damage to the health and safety of people, expressed in monetary units or in shares (%) of the cost of construction.

After determining the cost of losses from a private risk, the cost of private risks is summed up to obtain the following values:

- The cost of one consequence. In this methodology, it is defined as the sum of all private risk costs from the same consequences (and different causes of risks and/or risks).
- Cost of one risk. In this methodology, it is defined as the sum of all the costs of private risks from the same risks (and different causes).
- Cost of risk causes. In this methodology, it is defined as the sum of all the costs of private risks from one risk cause.
- The total risk cost of the facility. In this methodology, it is defined as the sum of all the costs of private risks.

The next step is to evaluate the acceptability of the risk, i.e. compare the cost of private risks and general risk with the categories of risks accepted for the object. To do this, it is convenient to use the ALARP or SFAIRP methods. These methods are used as criteria for determining the following indicators:

✓ ALARP - shows how much it is possible to reduce the risk to a minimum level;
✓ SFAIRP - serves to define security, showing the extent to which it is possible.

ALARP and SFAIRP are abbreviations for "As Low as Reasonable Practicable" and "So Far as Reasonable Practicable", which embody the principle of "reasonable execution". They are principles in which the condition for risk acceptability or tolerance for risk is how appropriate the costs are for risk reduction: ALARP is the principle of risk reduction to the lowest possible level; SFAIRP the principle of ensuring safety up to practically possible.

The SFAIRP and ALARP criteria are intended to achieve the same result, with ALARP providing security by making the risk as low as practicable and SFAIRP not referring to the level of risk. SFAIRP is usually interpreted as a criterion for evaluating risk management controls.

The ALARP model can be used to classify risks into one of three categories as follows (see diagram in Figure 2):

- unacceptable risk category, when the activity must be stopped in order to reduce it to an acceptable level;
- a broadly acceptable risk category, where the risk is so low that no further reduction needs to be considered (but it can be done if it is practicable and reasonable);
- the area between these boundaries (ALARP) where further risk mitigation should be implemented, if practicable.

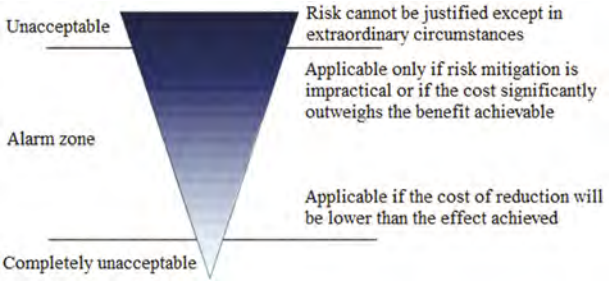

Figure 2. ALARP risk grading diagram.

The input data is information about the source of risk and the risk associated with it; on site controls and other possible control measures; about potential consequences; the likelihood that these consequences will occur; about the cost of possible measures to reduce the level of risk (risk treatment).

The result is a decision about whether risk treatment is necessary and how it should be performed.

After assessing the acceptability of risks, measures are developed and selected to reduce avoid risks defined as unacceptable and conditionally acceptable. In the process of searching for activities, the causes of risks caused by changes in design decisions (implementation of activities) are identified.

For each event, its effectiveness is evaluated by comparing the total risk cost of the object without the activity and with the activity, re-performing the assessment taking into account the implementation of the relevant activities. At the same time, it should be taken into account that risk reduction/prevention measures may lead to the emergence of new risks [6]. The impact (maximum 100%) of a reduction measure of a certain category (cause, event, consequence) is calculated by the formula

$$p_n = \frac{p_{st}}{100\%} \times \left(1 - \frac{p_m}{100\%}\right) \times 100\%, \quad (3)$$

where p_n is the probability of the realization (appearance) of the cause, event (risk) or consequences after the application of the measure,%;

p_{st} - the probability of the realization (appearance) of the cause, event (risk) or consequences before the event,%;

p_m is the effectiveness of risk reduction/avoidance measures, %.

4 DISCUSSIONS

The article presents a new methodology for calculating risks. This technique is a comprehensive risk assessment, which, if correctly identified, will reduce the risk of emergencies at various stages of the structure's life cycle. Subsequently, it is necessary to create a register of risks for the construction of underground structures in an open and closed way. Such a register will allow even before the design and construction stage to identify the most likely risks and their manifestations. It will allow even at the pre-project stage to minimize the possibility of their manifestation and select the necessary measures for further safe construction.

5 CONCLUSIONS

Based on the obtained cost of risks without and with measures, as well as the cost of carrying out the measure, the measures are finally selected according to their technical and financial efficiency.

Based on the results of the study, the following consequences and manifestations of risk were analyzed:a brief description of the risk (name, consequences and sequence of events);

- a statement about the likelihood of occurrence of consequences;
- sources or causes of risk;
- information on what is currently being done to manage the risk.

For the convenience of analyzing the risk register, it is recommended to include in it a list of causes, events and consequences, as well as a description of measures to reduce the likelihood of the corresponding risk occurring.

The initial data for compiling the risk register are the results of the risk assessment process described earlier, and the output is complete information about possible risks.

REFERENCES

M. Yu. Abelev, D. Yu. Chunyuk, D. L. Karalli, and R. R. Bakhronov, "Specifics of constructing the compacted sand bases of buildings with replacement of gas-generating soils," Prom. Grazhd. Stroit., No. 5, 34–40 (2021).

D. Yu. Chunyuk, "Classification specifics and components of geotechnical risk in construction," Prom. Grazhd. Stroit., No. 9, 42–44 (2013).

D. Yu. Chunyuk and A. V. Krasnova, "Geological component of geotechnical risk in the design, construction, and operation of buildings having a developed substructure," Estestv. Tekhn. Nauki, No. 3 (81), 207–209 (2015).

S. N. Bogachev, A. A. Shkol'nikov, R. A. Rozentul, and N. A. Klimova, "Construction risks and ways to minimize them," Academia. Arkhitekt. Stroit., No.1. 88–92 (2015).

M. Yu. Abelev, D. Yu. Chunyuk, I.V. Averin, A.P. Levchenko "Accounting for geotechnical risks in field studies of building foundation soils". Editor V.V. Kosmin. Publisher: Russia, Moscow, LLC "ASV". p. 224. (2021)

V.E. Merkin, K.O. Pudov, M.G. Zertsalov, E.N. Petrova, D. Yu. Chunyuk, V.L. Belyaev and etc. "Reference manual for assessing and accounting for risks in the development of underground space in the city of Moscow". Publisher: Infra-Engineering. p. 305 (2021).

Smart Geotechnics for Smart Societies – Zhussupbekov, Sarsembayeva & Kaliakin (Eds)
© 2023 The Author(s), ISBN 978-1-003-29912-7
Open Access: www.taylorfrancis.com, CC BY-NC-ND 4.0 license

Application of standardized subsurface conditions based on preprocessing of borehole data in Seoul, South Korea

T.K. Chung
Department of Civil and Environmental Engineering, Seoul National University, Seoul, South Korea

H.S. Kim
Korea Institute of Geoscience and Mineral Resources, Daejeon, South Korea

M.G. Kim
Seoul Institute of Technology, Seoul, South Korea

C.K. Chung
Department of Civil and Environmental Engineering, Seoul National University, Seoul, South Korea

ABSTRACT: Local characterization of the geo-layer over a wide area is influenced by spatial uncertainties/differences in borehole data. In this study, the elevation and geo-layer thickness of borehole data in Seoul were standardized using outlier analysis with a 3-sigma model and cross-validation with the leave-one-out method. The borehole data, with or without elevation information, were categorized based on the accuracy of elevation by comparison with the digital elevation model (DEM). According to the errors with DEM, 3-sigma-based outliers were removed from the borehole data. Cross-validation-based mean errors resulting from the 3-sigma model were compared. The boundary elevation of the geo-layer in Seoul was applied based on the average ground conditions using optimum borehole data. The average ground condition method was applied to the boundary elevation of the geo-layer using optimum borehole data and compared with an ordinary kriging to evaluate for accuracy. As a result of comparing the two methodologies, the error tends to increase toward the lower layer. However, the average ground condition could not be applied to the entire area owing to the lack of current borehole data. Thus, additional geophysical data is required in addition to borehole data.

1 INTRODUCTION

As the demand for three-dimensional subsurface maps from the perspective of digital twins has grown, efforts have been made to improve the reliability of geotechnical information data. It is particularly necessary to improve reliability by defining and removing outliers in geotechnical information before applying the geospatial interpolation method.

Boring logs are frequently used to ascertain characteristics such as engineering strata, density, and resistance of the subsurface, by archiving samples and performing in-situ and laboratory tests. However, even borehole data have uncertainties owing to inherent soil variability and uncertainties in measurement and transformation. A reliable assessment of geomaterials requires the appropriate management of outliers (i.e., erratic information) of borehole data. Lee et al. (2017) proposed an improved method of verifying the precision of borehole data by removing outliers of errors in elevation.

In this study, borehole data were categorized and restored using principal attributes such as project location. After the detection of outliers and elimination using a statistical procedure, the borehole data were input into the database. The predicted area according to the distribution of

DOI: 10.1201/9781003299127-179

borehole data was identified for the entire city of Seoul, and the standardized subsurface condition was applied to the boundary elevation of the geo-layer based on the preprocessing of borehole data. The spatial interpolation accuracy according to the borehole density of the cell (250×250 m) was confirmed by comparing the standardized subsurface conditions with ordinary kriging results.

2 PREPROCESSING OF BOREHOLE DATA

2.1 *Classification of borehole data by attribute*

The public data portal (https://www.data.go.kr/) and geotechnical information portal system (https://www.geoinfo.or.kr/) provided data on 33,867 boreholes completed in Seoul (Figure 1). The data consisted of general boring, stratum, and standard penetration test information. Because the borehole data were mainly collected for urban development areas, there were borehole data from mountainous terrains. Consequently, the geo-knowledge-based data (e.g., location of the rock outcrop and shallow geo-layer from cut-slope) were supplemented and reviewed (Kim et al., 2019; Sun & Chung, 2006). The digital elevation model (DEM) was provided by the National Geographic Information Service in South Korea, and the cell size was 10×10 m. Since the surface elevation of the borehole was not provided in 14.27% of the borehole data, the general boring properties were categorized based on whether or not the surface elevation of the borehole was presented.

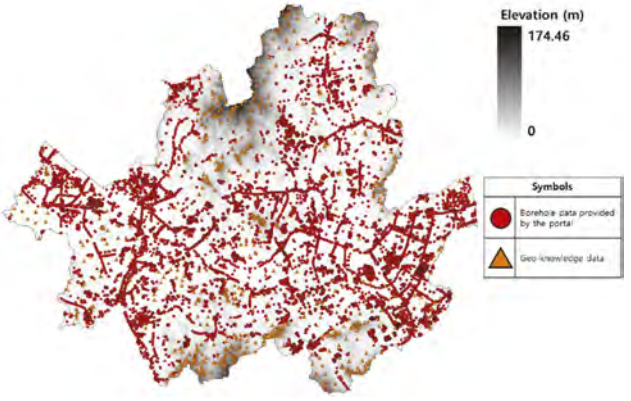

Figure 1. Distribution of borehole data and DEM.

When comparing the surface elevation of the borehole data and the DEM, the difference was mostly concentrated in the 100 m elevation zone. The purpose of the boring investigation was classified to configure the characteristics of the zone where the difference was biased. Borehole data for the railway project had an error of at least 100 m. In the case of the railroad project, the established standard for railroad design states, "the standard elevation is the value obtained by adding 100 m to the elevation announced by the national geographic information service." Conversely, surface elevation was restored by removing 100 m from the recorded surface elevation. As a result of the restoration as shown in Table 1, the mean absolute error (MAE) of the borehole data was 5.09 m, which was 65% lower than before the restoration. MAE is expressed as Eq. (1) by taking the average absolute error. This study used surface elevations from the DEM as observed values and surface elevations from borehole data as true values.

$$MAE = \frac{1}{n}\sum_{i=1}^{n}\left|\hat{Y}_i - Y_i\right| \tag{1}$$

where $\hat{Y}$ = observed value, Y_i = true value, and n = number of data points.

Table 1. Change of error as a result of classifying and restoring borehole.

State of the process	MAE (m)	Standard deviation (m)
Before restoration of borehole data	14.90	32.11
After restoration of borehole data	5.09	11.27

2.2 *Reliability verification through statistical processing techniques and outlier analysis*

The root mean square error (RMSE) was compared for reliability assessment using the cross-validation of the leave-one-out method. The RMSE is expressed by Eq. (2) by taking the square root of the squared errors.

$$RMSE = \sqrt{\frac{1}{n}\sum_{i=1}^{n}\left(\hat{Y}_i - Y_i\right)^2} \tag{2}$$

where $\hat{Y}$ = observed value, Y_i = true value, and n = number of data points.

RMSE and standard deviation are similar concepts. The standard deviation is used to describe the variance of deviation for the population, whereas the RMSE is used to describe the variance of error for two or more unknowns.

The borehole data were restored, but a significant error remained. As shown in Figure 2, the 3-sigma rule (Bakar et al., 2006; Daw et al., 1972; Moivre, 2013) was used to calculate the standard deviation of the surface elevation at the boring location. Outliers were removed using an interval between 68.26% (±1 σ), 95.45% (±2 σ), and 99.73% (±3 σ).

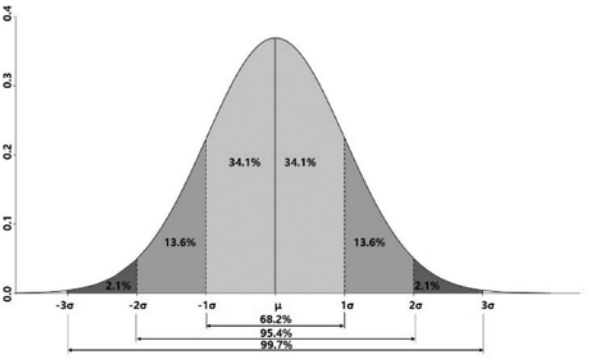

Figure 2. 3-sigma rule (Daw et al., 1972; Moivre, 2013).

Table 2. Attributes of borehole data for a total of 34,506 holes in Seoul.

State of the process	Data classification	Number of boreholes	Outlier removal rate (%)	MAE (m)	Standard deviation (m)	RMSE (m)
Before outlier removal	Data with surface elevation	25,201	0	5.09	11.27	8.75
	Railway project data	3,818				
	Geo-knowledge data	639				
	Data without surface elevation	4,848	–	–	–	
After outlier removal	68.26% (±1 σ	26,600	10.31	2.38	3.38	5.82
	95.45% (±2 σ)	28,075	5.34	3.09	4.97	6.16
	99.73% (±3 σ)	28,855	2.71	3.78	6.76	6.60

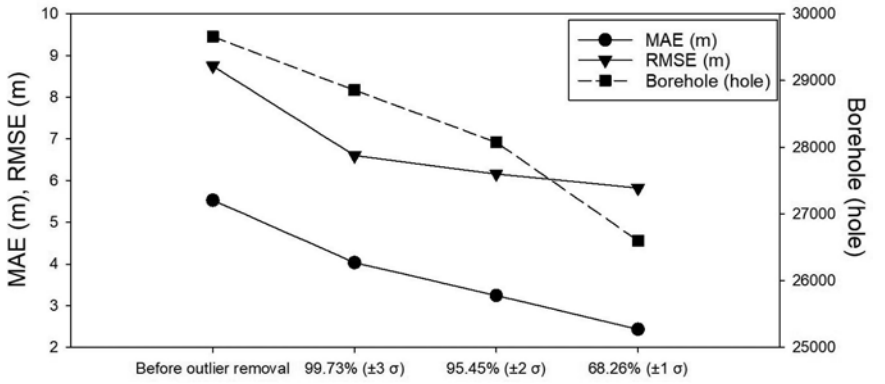

Figure 3. Rate of outlier removal and degree of error reduction.

A 68.26% (±1 σ) interval was used to preprocess the bore data in this study, as shown in Table 2 and Figure 3, taking into account the rate of outlier removal and the degree of error reduction, to increase the reliability of the estimated surface elevation for each borehole.

3 DISTRIBUTION OF GEOTECHNICAL CLASSIFICATION IN SEOUL THROUGH AVERAGE GROUND CONDITONS

3.1 *Distribution of borehole data in seoul*

The distribution of preprocessed borehole data for Seoul is shown in Figure 4. It depicts the distribution of borehole data in the soil and rock layers with and without the addition of geo-knowledge-based data. As the soil depth was directly measured using a hand auger during boring, it was impossible to investigate the rock layers due to equipment limitations. The target locations for the geo-knowledge-based data were concentrated on mountainous terrains (i.e., outside Seoul).

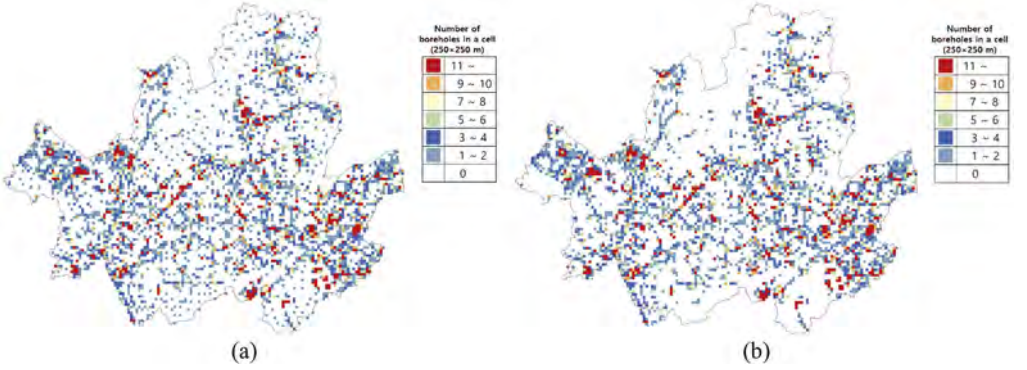

Figure 4. Borehole distribution in Seoul, South Korea: (a) soil layer (with geo-knowledge-based data) (b) rock layer (without geo-knowledge-based data).

3.2 *Application of standardized subsurface conditions*

According to Todo et al. (2013), the uneven distribution of borehole data can be overcome by using the average value within a cell size of 250×250 m considering the surrounding ground conditions in Japan's nationwide electronic geotechnical database systems (NEGDS). This facilitates a quick and intuitive understanding of the characteristic value of the borehole data

within the relevant area. In this study, the average ground condition was used to determine the boundary elevation of the geo-layer (i.e., fill, sedimentary, and weathered soils, and weathered, soft, moderate, and hard rocks), as shown in Figures 5–10, according to the distribution of the geotechnical stratum classification in Seoul. In the case of the soil layer with geo-knowledge-based data and the rock layer without geo-knowledge-based data, the average ground condition method was likewise possible for 38% of Seoul. The interpolated boundary elevation of geo-layers was compared with the results of ordinary kriging to validate the accuracy of the average ground condition. The cell resolution of ordinary kriging was set to 250×250 m, which corresponds to the size of an average ground condition cell.

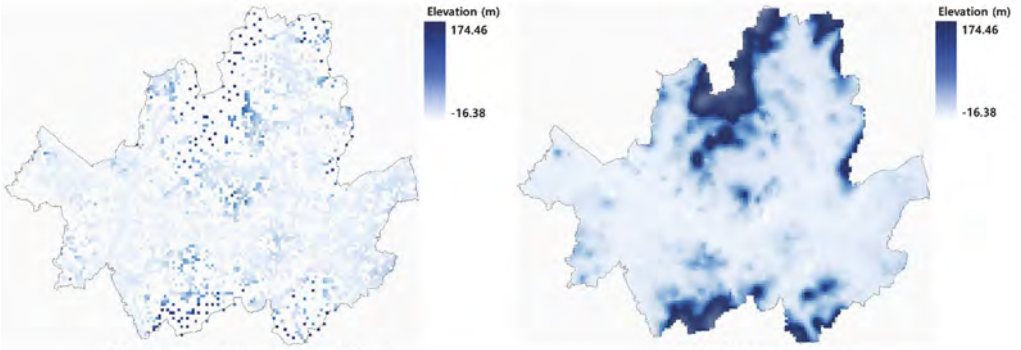

Figure 5. Spatial interpolation at the boundary elevation from the fill soil layer to the sedimentary soil layer.

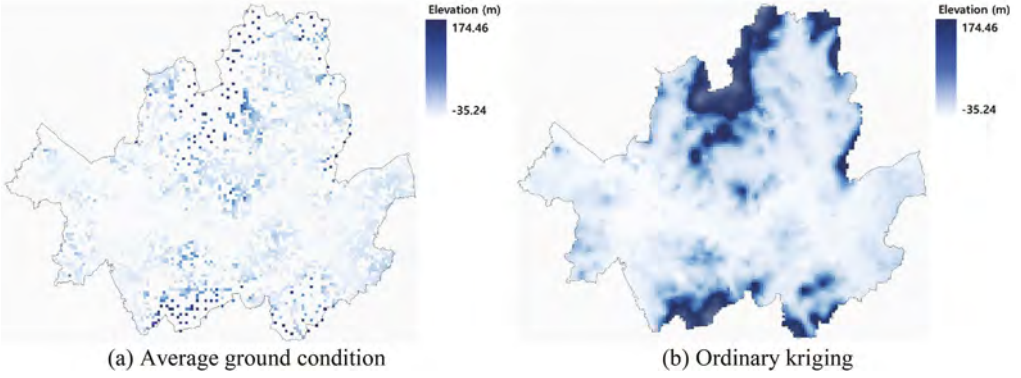

Figure 6. Spatial interpolation at the boundary elevation from the sedimentary soil layer to the weathered soil layer.

Table 3 shows a similar trend between the MAE and RMSE, and the RMSE was larger than the MAE. The average error increased as the elevation boundary of the geo-layer decreased. Geological uncertainty had a much greater influence in the lower layer, and errors in the upper layer accumulated in the lower layer. Moreover, the borehole data for the lower layer were smaller than those for the upper layer. Figure 11 shows substantial inaccuracy when there were primarily one or two boreholes in a cell (250×250 m). In addition, it was observed that the inaccuracy decreased if one cell had three or more boreholes.

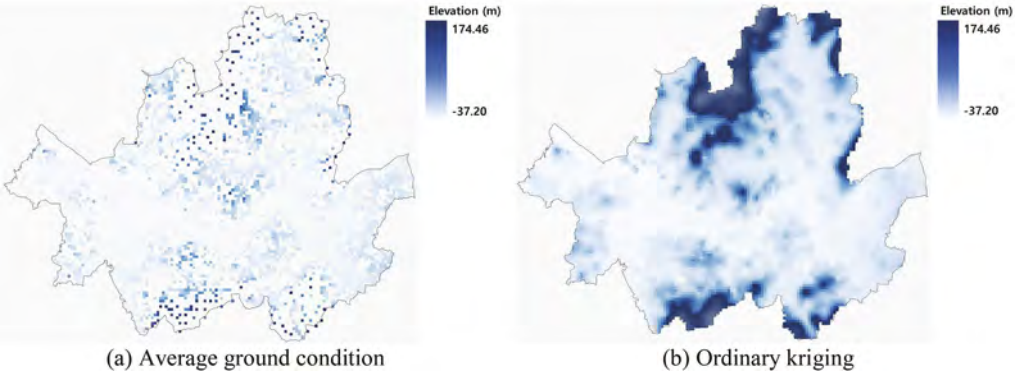

Figure 7. Spatial interpolation at the boundary elevation from the weathered soil layer to the weathered rock layer.

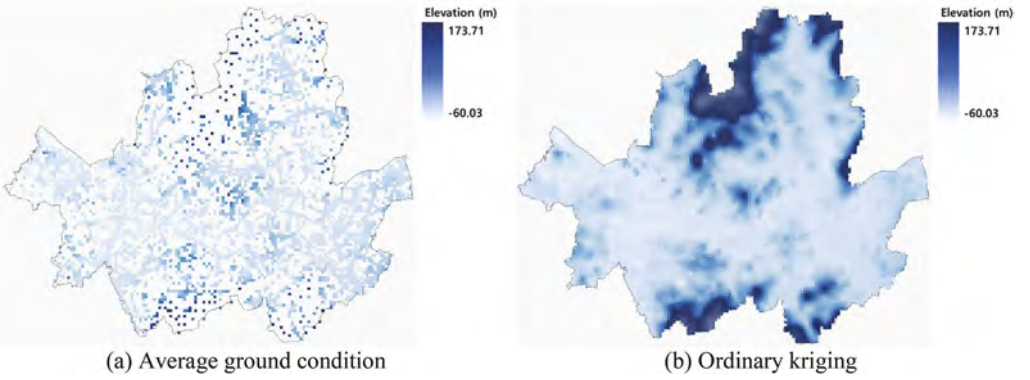

Figure 8. Spatial interpolation at the boundary elevation from the weathered rock layer to the soft rock layer.

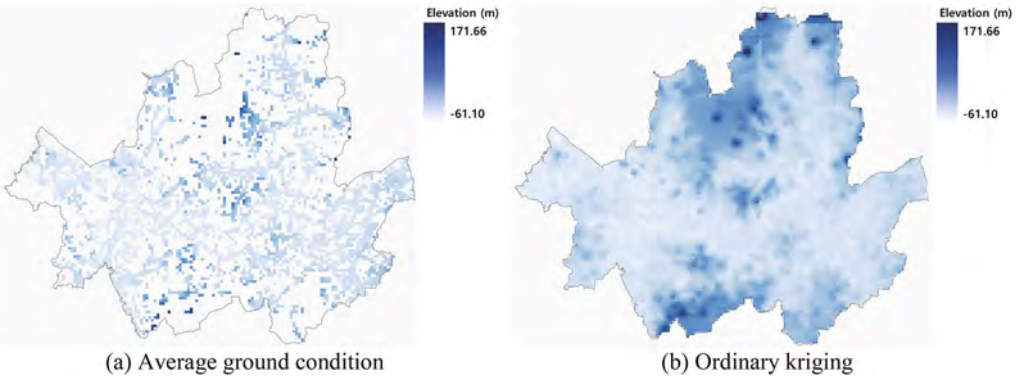

Figure 9. Spatial interpolation at the boundary elevation from the soft rock layer to the moderate rock layer.

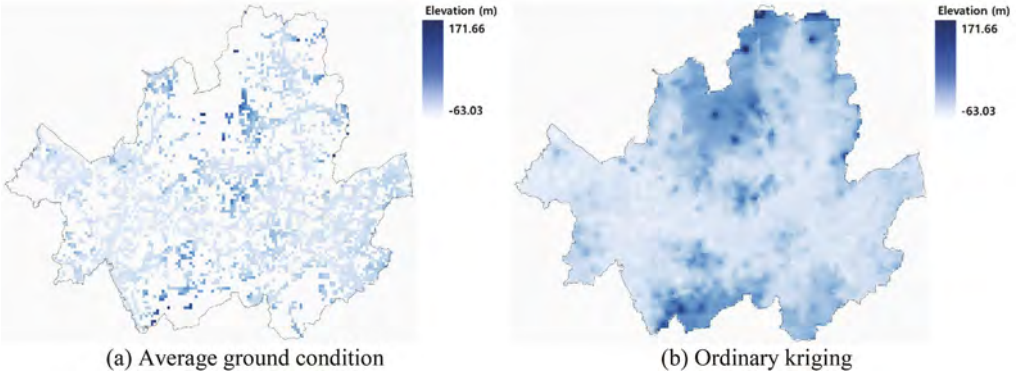

(a) Average ground condition (b) Ordinary kriging

Figure 10. Spatial interpolation at the boundary elevation from the moderate rock layer to the hard rock layer.

Table 3. Errors of boundary elevation of geo-layers by comparing methods of average ground condition and ordinary kriging.

Geo-layer boundary	MAE (m)	RMSE (m)
Fill soil-Sedimentary soil	3.80	6.70
Sedimentary soil-Weathered soil	4.23	7.07
Weathered soil-Weathered rock	4.57	7.53
Weathered rock-Soft rock	5.14	8.18
Soft rock-Moderate rock	5.37	8.89
Moderate rock-Hard rock	5.42	8.96

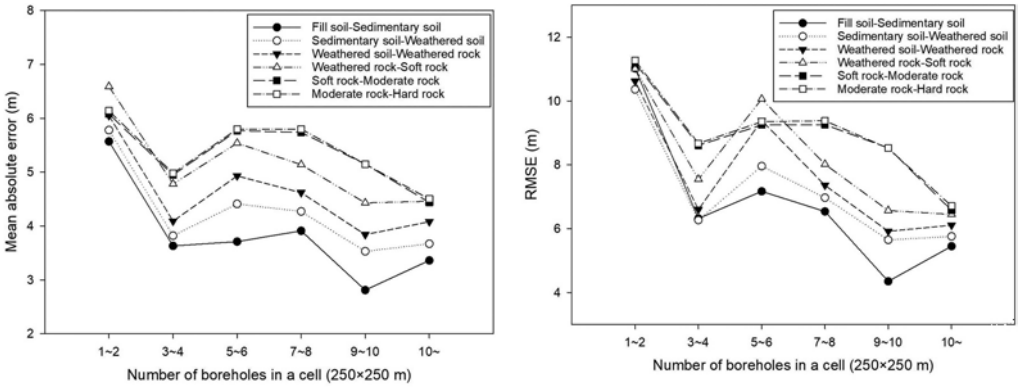

(a) MAE (b) RMSE

Figure 11. Errors according to borehole density in a cell.

4 CONCLUSIONS

Borehole data in Seoul were preprocessed using a statistical method to perform highly reliable spatial interpolation using the boundary elevation of the geo-layer. The borehole data were classified according to attributes and restored based on relevant project criteria. The reliability was then improved by removing outliers in the borehole data using a statistical method, and the database was standardized as a result. The distribution of the subsurface layered structure was obtained by applying spatial interpolation to the entire city of Seoul. Because the average

ground condition method cannot be evaluated for accuracy, it was compared with ordinary kriging. As a result of comparing the two methodologies, the error tends to increase toward the lower layer. Furthermore, the error was lower when the cell had more than three boreholes.

The average ground condition could not be applied to the entire area owing to the lack of current borehole data. Interpolation over a broader area is possible if additional geophysical data are used in addition to borehole data. As a result, further studies will apply the average ground condition to integrated analysis using geophysical data.

ACKNOWLEDGEMENTS

This study was supported by the project titled "Local Assessment on Earthquake Induced Multi-Geohazard in Urban Area based on Site-specific Geotechnical Characterization" funded by the Daelim Suam Scholarship and Cultural Foundation of Korea.

REFERENCES

Bakar, Z. A., Mohemad, R., Ahmad, A., & Deris, M. M. 2006. A comparative study for outlier detection techniques in data mining. *2006 IEEE Conference on Cybernetics and Intelligent Systems*. doi: 10.1109/ICCIS.2006.252287.

Daw, R. H., Watson, R., & Pearson, E. S. 1972. Miscellanea studies in the history of probability and statistics. XXX. Abraham De Moivre'a 1733 derivation of the normal curve: A bibliographical note. *Philosophy* 59 (3). https://academic.oup.com/biomet/article/59/3/677/484894.

Kim, H. S., Sun, C. G., & Cho, H. I. 2019. Site-specific zonation of seismic site effects by optimization of the expert GIS-based geotechnical information system for western coastal urban areas in South Korea. *International Journal of Disaster Risk Science* 10(1): 117–133. https://doi.org/10.1007/s13753-018-0208-3.

Lee, B. Y., Hwang, B. S. and Cho, W. J. 2017. Reliability evaluation methodology of boring investigation DB for the 3D integrated underground space map. *Journal of the Korean Geotechnical Society* 33(9): 35–47.

Ministry of Land Transport and Transportation. 2015. Railway Design Standard: Roadbed. *Ministry of Land Transport and Transportation*: 3–6.

Moivre, A. 2013. The Doctrine of Chances or, A Method of Calculating the Probability of Events in Play. *Cambridge University Press*. doi: 10.1017/CBO9781139833783.

Sun, C. G., & Chung, C.K. (2006). Development and Application of a Methodology to Build Geotechnical Information System Based on Geo-Knowledge Using GIS Technology. Journal of the Korean Society of Civil Engineers, 22(2), 55–68.

Todo, H., Yamamoto, K., Mimura, M., & Yasuda, S. 2013. Japan's nation-wide electronic geotechnical database systems by the Japanese geotechnical society. *Geotechnical and Geological Engineering* 31(3): 941–963. doi: 10.1007/s10706-012-9562-x.

Smart Geotechnics for Smart Societies – Zhussupbekov, Sarsembayeva & Kaliakin (Eds)
© 2023 The Author(s), ISBN 978-1-003-29912-7
Open Access: www.taylorfrancis.com, CC BY-NC-ND 4.0 license

A study for correlation analysis between the density of under-ground utility structures and ground subsidence in urban areas

C. Choi*, J-Y. Kim, J.M. Kang & M. Chung
Korea Institute of Civil Engineering & Building Technology, Goyang-Si, South Korea

ABSTRACT: As many underground structures have been installed in urban areas, various types of ground subsidence have occurred around the world. In this paper, the correlation between the recorded ground subsidence and the density of underground structures in Seoul was studied. The relationship between the density of buried structures using GIS spatial digital data for 6 types of underground utilities (water, sewer, power, heat, communication, natural gas) and ground subsidence was optimized based on the concept of normalized line density. The effect of each buried utility on the recorded ground subsidence was optimized using weight factors generated from a random function. An algorithm was developed that can optimize the line density of buried utilities along with the 6 weight factors and the correlation between the normalized line density and the recorded ground subsidence. As a result of analyzing the normalized line density, it was found that more than 80% of recorded ground subsidence occurred in areas with higher normalized line density when the optimization algorithm was applied. It is concluded that the proposed optimization algorithm can be usefully applied to the analysis of the risk of ground subsidence using GIS digital data of buried utility structures.

1 INTRODUCTION

Various ground subsidence accidents have occurred in urban areas of S. Korea over the past several years, which has increased public anxiety about the safety. Federal and local government established the special Act for underground safety and comprehensive underground safety management system was carried out. Nevertheless, ground subsidence accidents continue to occur in urban areas, and it has been reported that a number of accidents have occurred, especially in areas where underground utilities are complexly buried (Kim 2022).

To prevent ground subsidence accidents, various studies have been conducted to predict the risk of ground subsidence and to use it for maintenance of buried utilities. Representatively, Choi et al. (2016) and Park et al. (2017) suggested a method to analyze the risk of ground subsidence by sensing the structural integrity of water and sewage pipelines and defects such as leakage. Choi et al. (2021) classified the spatial information on underground structures for certain urban areas, and analyzed the correlation between the line density of utilities and the occurrence of recorded ground subsidence. Through this, an optimization model that can predict the ground subsidence risk was presented.

In this paper, GIS-based spatial information data of 6 types of underground utilities (water, sewer, power, gas, heat and network) in an urban area is correlated to the recorded ground subsidence by evolving an optimization algorithm proposed by Choi et al. (2021). The risk prediction through optimizing the correlation conducted by Choi et al. (2021) are summarized and presented. The line density of underground utilities installed in the study area was analyzed, and the correlation of recorded ground subsidences that occurred between 2010 and 2015 were analyzed. Line density is a method used in spatial analysis, and defines the length

*Corresponding author: chchoi@kict.re.kr

DOI: 10.1201/9781003299127-180

of underground structures installed within an arbitrary radius around the cells of the interested region as the quantity per unit area (ArcGIS 2021). This paper presents an algorithm that calculates the line density of buried objects in the cell of interest and optimizes the correlation between the line density and the location of recorded ground subsidence. The accuracy of risk analysis by applying the proposed algorithm at 1km × 1km urban area of Seoul, Korea is verified and presented.

2 LINE DENSITY AND NORMALIZED LINE DENSITY FOR BURIED UTILITIES

The line density of the underground structures was analyzed using the spatial analysis function provided by ArcGIS (2021). Choi et al. (2021) introduced the concepts of line density and normalized line density. Line density indicates the density characteristics of structures installed around unit cells in space, and is an index that can indicate the spatial density of lines included in the area, and is calculated as the length per unit area. Figure 1 shows the concept of calculating the line density (ρ) for each grid cell. Conceptually, the sum of the lengths of lines located in a circle is calculated and the line density (ρ) is calculated by dividing this by the area of the circle. *L1* and *L2* represent the spatial lengths of two structures installed in a circle, and weight factors ω_1 and ω_2 can be assumed according to the characteristics of each structure.

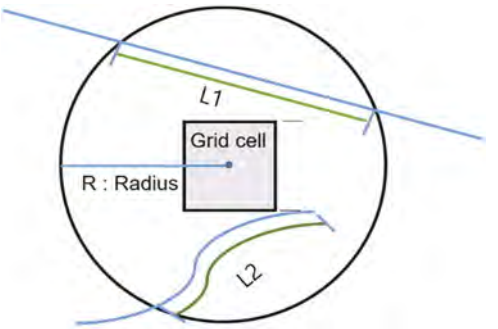

Figure 1. A raster cell and the circular neighborhood used to determine the length for the line density redrawn from ArcGIS(2021) (Choi et al.(2021)).

At this time, the line density (ρ) can be calculated through Equation (1).

$$\rho = \frac{\omega_1 L_1 + \omega_2 L_2}{A_R} \tag{1}$$

Here, A_R is the area of the circle obtained from the radius of the circle affecting the cell. Line density is calculated by determining the size of the grid cell, the radius R, and the weight factors ω_1 and ω_2 from Figure 1 and Equation (1). Choi et al. (2021) proposed the concept of normalized line density (ρ_n) of the interested area as shown in Equation (2).

$$\rho_n = \frac{\omega_1 L_1 + \omega_2 L_2 \ldots + \omega_n L_n}{n \cdot A_R} \tag{2}$$

where, $\omega_1 + \omega_2 \ldots + \omega_n$: weight factors
$L_1 + L_2 \ldots + L_n$: length of each buried structures
n: number of buried structure types
R: radius of affecting zone

$$\sum_{i=1}^{n} w_i = 1.0 \tag{3}$$

In Equation (2), ρ_n (normalized line density) can be defined as a line density normalized by the number of types of underground structures and the sum of the weight factors limited to 1.0 as shown in Equation (3).

3 OPTIMIZED NORMNILZIED LINE DENSITY ANALYSIS ALGORITHM WITH RECODED GROUND SUBSIDENCE

In this study, an optimization algorithm is proposed under the assumption that the normalized line density is largely distributed at the location where the ground subsidence occurs. Six weight factors $\omega_1, \omega_2, \ldots \omega_6$ of underground utilities (water, sewer, power, natural gas, heat, and network) were randomly generated to satisfy Equation (3) and to produce the higher the normalized line density at subsidence locations. Therefore, the core concept of the optimization algorithm is to calculate the weight factor set $(\omega_1, \omega_2, \ldots \omega_6)$ with the highest normalized line density at the location of the recorded ground subsidence by applying randomly generated weight factor sets (ω_i). Table 1 shows the pseudo-code of the algorithm proposed by Choi (2021) to optimize the correlation between the recorded ground subsidence and the normalized line density of underground structures.

Table 1. Pseudo-code to obtain optimal $\omega_i - set$ for finding higher correlation between normalized line density and ground subsidence.

Line No.	Pseudo-code	Description
1	for k=1: 100,000	
2	$\rho_n^k = \rho_{raw} \cdot \ \omega_i^k$	% ρ_n^k : normalized line density with $k^{th}\omega_i - set$ % ρ_{raw} : line density obtained from ArcGIS % ω_i^k : $k^{th}\omega_i - set$
3	$\rho_{n_{max}}^k = \max(\rho_n^k)$	% $\rho_{n_{max}}^k$: maximum scalar value of ρ_n^k
4	$\rho_{ns}^k = \rho_{sh} \cdot \ \omega_i^k$	% ρ_{ns}^k : normalized line density at the locations of ground subsidence % ρ_{sh} : line density at the locations of ground subsidence
5	$N_{ps}^k = \rho_{ns}^k / \rho_{n_{max}}^k$	% N_{ps}^k : normalized ρ_{ns}^k with respect to $\rho_{n_{max}}^k$
6	$Err^k = norm\left(1 - N_{ps}^k\right)$	% Err^k : error norm with $k^{th}\omega_i - set$
7	end	
8	$k_{opt} = find(Min(Err))$	
9	$\omega_{opt} = \omega_i^{k_{opt}}$	% ω_{opt}: $\omega_i - set$ at the index of k_{opt}

Line 6 in Table 1 shows the Error function for implementing the optimization algorithm. The Error function was proposed under the assumption that ρ_n where the subsidence occurred has a relatively higher value in interested area for analysis. Equation (4) is the Error function of the normalized linear density at the location of the recorded ground subsidence among random $\omega_i - set$.

$$Err^k = \left\| 1 - N_{ps}^k \right\| \tag{4}$$

$$\text{Where, } N_{ps}^k = \frac{\rho_{ns}^k}{Max(\rho_n^k)}$$

In Equation (4), Err^k represents the Norm of the error value at the location of the ground subsidence when the k^{th} random ω_i is applied. ρ_{ns}^k is the normalized line density when ω_i^k is applied at the location of the ground subsidence and ρ_n^k is the normalized linear density when ω_i^k is applied to the analysis area. The maximum value of is ρ_n^k defined as $\text{Max}(\rho_n^k)$. In other words, N_{ps}^k is defined as the scaled ratio (0~1.0) of normalized line density when applying ω_i^k at the location where the ground subsidence occurred.

4 NORMNILZIED LINE DENSITY AND CORRELATION ANALYSIS WITH RECORDED GROUND SUBSIDENCE

Figure 2 shows the map of the study area (1km × 1km), and the red circles on the map show the locations of 29 ground subsidence that occurred in the area during 2010-2015. The optimal set of 6 weight factors was obtained by applying the algorithm (Table 1) to the 29 recorded ground subsidences presented in Figure 1. In this study, R (100m) and cell size (10m) were applied to Equation (2) to calculate the normalized line density (ρ_n) of 6 types of underground utilities.

Figure 2. The 1km × 1km Map of analysis area and 29 ground subsidence locations with magenta circle symbol (Choi et al. 2021).

4.1 *Correlation analysis result between normalized line density and recorded ground subsidence with* $\omega_1, \omega_2, \ldots \omega_6 = 1/6$

Figure 3(a) is the normalized line density (ρ_n) of 6 underground utilities subjected to $\omega_1, \omega_2, \ldots \omega_6 = 1/6$. In the figure, the red circle symbol indicates the location where 29 ground subsidence occurred. From visual observation, it can be seen that the ground subsidence occurred relatively frequently in the area with higher normalized line density.

4.2 *Correlation analysis result between normalized line density and recorded ground subsidence when* ω_{opt} *applied*

Randomly generated 100,000 $\omega_i - set$ were applied to the optimization algorithm in Table 1 to analyze the values that minimize Error Norm at 29 ground subsidence locations. Figure 3(b) shows the normalized line density (ρ_n) of 6 underground utilities by applying Equation (2) to minimize Error Norm of the line 6 in Table 1. In the figure, the red circle is the location where 29 ground subsidence occurred. Comparing with the analysis results for $\omega_1, \omega_2, \ldots \omega_6 = 1/6$ case, it can be seen that the normalized line density where the ground subsidence occurs is relatively higher in the analysis area.

4.3 *Analysis of recorded ground subsidence classified with 5 grades*

Based on the maximum normalized linear density, the density was classified into 5 grades. The 5 grades are divided into G1 (lowest), G2, G3, G4, and G5 (highest). The higher the grade, the higher the line density of underground utilities and the higher the risk of ground subsidence.

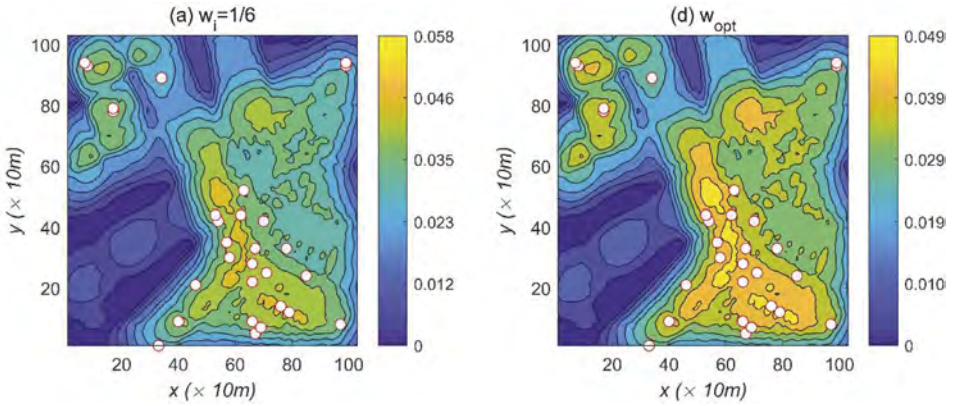

Figure 3. Comparison of ρ_n (normalized line density, m/m^2) analysis results subjected to (a) $\omega_1, \omega_2, \ldots \omega_6 = 1/6$ and (b) ω_{opt} (color bar in right represents 5 degrees of normalized line density).

Figure 4 shows the grades of normalized line density at 29 ground subsidence locations. Figure 4(a) and (b) show the results of $\omega_i = 1/6$ and ω_{opt}, respectively. From the comparison, it can be seen that the grade of normalized line density rises at the location where the ground subsidence occurred when ω_{opt} is applied to the analysis. That is, it means that the relative ground subsidence risk is high at the location where the recorded ground subsidence occurs.

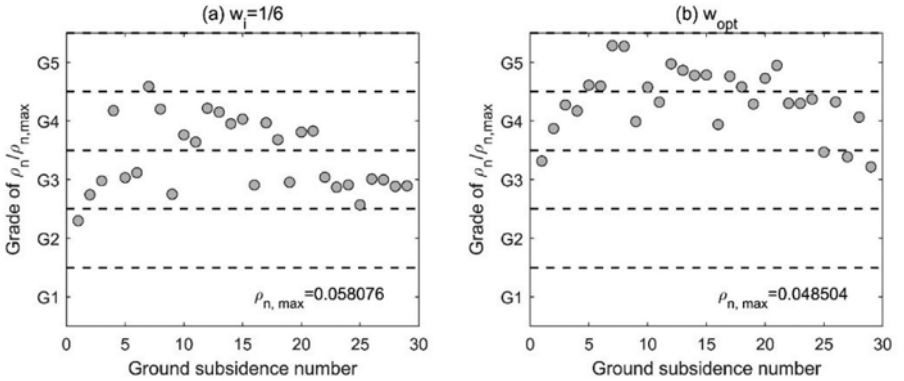

Figure 4. Comparison of 5 grades for $\rho_n/\rho_{n,\,max}$ at 29 sinkhole locations: (a)$\omega_i = 1/6$ and (b)ω_{opt}.

Table 2 summarizes the number of subsidence included in each of the five grades by analyzing the normalized line density at 29 recorded ground subsidence locations. When analyzing

Table 2. Number of ground subsidences corresponding to 5 grades at 29 sinkhole locations with $\omega_i = 1/6$ and ω_{opt}.

Grade	$\omega_i = 1/6$	ω_{opt}
G1	0	0
G2	1	0
G3	15	4
G4	12	12
G5	1	13
% (≥G4)	45	86

the normalized line density by applying ω_{opt}, it was found that 29 ground subsidences occurred at grade 3 (G3) or higher area. In case of applying $\omega_i = 1/6$, the most of ground subsidence occurred even in grade 2 & 3 (G3&G4).

From Table 2, it is denoted that if ω_{opt} obtained by applying the optimization algorithm is applied to the line density analysis of underground utilities in the area of interest, the risk of ground subsidence can be analyzed more accurately.

5 CONCLUSION

In this paper, a method for optimizing the correlation between the line density of underground structures and recorded ground subsidence was presented. A study was conducted to link the density of underground utilities and the risk of ground subsidence. The optimization algorithm was applied to analyze the normalized line density for 1km × 1km area, and the spatial correlation analysis with the 29 recorded ground subsidence data previously occurred in the area (the location data was obtained from the infrastructure management Dept. of Seoul). It was verified that the risk grades of ground subsidence correspond to the normalized line density. The main finding and conclusion for this study are as below.

(1) A study was conducted to maximize the correlation between recorded ground subsidence and the line density of 6 types of underground utilities. When the optimization algorithm using the normalized line density was applied, the case where the normalized line density was grade 4 (G4) or higher at the recorded ground subsidence location was about 80% or more, and the applicability of the algorithm was verified.
(2) If the analysis result is expanded and verified to a wider area, it is thought that the proposed optimization algorithm can be used for basic decision-making analysis tool for facility maintenance and constructing a ground subsidence risk map in urban areas.

ACKNOWLEDGMENT

This study was financially supported by grants from "Underground Utilities Diagnosis and Assessment Technology (KICT 2022-0078-001)," a project of the Korea Institute of Civil Engineering and Building Technology.

REFERENCES

ArcGIS 2022, https://desktop.arcgis.com/en/arcmap/10.3/tools/spatial-analyst-toolbox/how-line–density-works.htm.

Choi, C., Kim, J., Kang, J., Park, Y. 2016, Ground Subsidence Risk Analysis with Intensity and Duration of Rainfall, *Proc. of 3rd International Conference on Geotechnics for Sustainable Infrastructure Development*, GEOTEC HANOI 2016 in Hanoi, Vietnam.

Choi, C., Kim, J., Baek, S-H, Kang, J. 2021, A Study on the Optimization Algorithm for Correlation Analysis of the Underground Utility Structure Density in Urban Areas and Recorded Ground Subsidence, *Journal of the Korean Geotechnical Society*, Vol. 37, No. 10, pp. 77–87.

Kim, J. S. 2022, The Causes and Countermeasures of Urban Ground Subsidence, *National Assembly Research Service, current issues and analysis*, No. 240, Jan. 13, 2022.

Park, S., Kwak, P., Lee, H., Choi, C. 2017, Development of leakage test facility for leak signal characteristic analysis in water pipeline, *Journal of Korean Society of Water and Wastewater*, Vol. 31, No. 5, Oct. 2017.

Smart Geotechnics for Smart Societies – Zhussupbekov, Sarsembayeva & Kaliakin (Eds)
© 2023 The Author(s), ISBN 978-1-003-29912-7
Open Access: www.taylorfrancis.com, CC BY-NC-ND 4.0 license

Vertical scale of fluctuation for spatially varying soil: A case study in Taiwan Using iPDC Data

Ying Zheng, Yu-Syuan Jhuo & Louis Ge
Department of Civil Engineering, National Taiwan University, Taipei, ROC

ABSTRACT: Data collected from soil investigation techniques, including standard penetration test, cone penetration test, and shear wave velocity measurement, are often used for liquefaction potential assessment. The spatial variation of soil properties is challenging to be quantified through limited data collected from standard penetration test. The data collected from a newly developed in-situ investigation technique, namely intelligent piezo drive cone, was adopted to determine their scale of fluctuation in this study. They were calculated by the method of moments and the Bayesian method with various autocorrelation models. The results show that the Bayesian method with the Whittle-Matérn model can effectively reduce the uncertainty of soil spatial variability. It also improves the accuracy of the scale of fluctuation to reflect the actual state of the data.

1 INTRODUCTION

Soil properties are influenced by the geological formation process, which changes with area and depth, and causes spatial variability. The scale of fluctuation (SOF) is a parameter for describing spatial variability. SOF can be used to illustrate the vertical and horizontal variety of soil layers, presenting by probability. Blow count (N) value is an index reflecting soil strength and an vital parameter for soil liquefaction potential analysis, which usually obtain by standard penetration test (SPT). The SPT-N value is recorded every 1.5 m and soil samples are taken. It is possible to misjudge the actual soil layer distribution and the spatial variability at a site when analyzing the SOF using the SPT-N value. The intelligent Piezo Drive Cone (iPDC) developed by OYO Corporation in Japan provides continuous depth-dependent data for site investigation, which is used for evaluating the soil liquefaction potential without sampling (Yoshizawa et al., 2016; Sawada et al., 2019). IPDC is a device whose concept is similar to SPT (Figure 1). On the tip of the rod, a transducer and load cell are mounted, allowing the excess pore water pressure and the loading to be recorded at every penetration. It is possible to determine the fines content and the transmission loss of energy. IPDC displays the calculated N value that is similar to SPT-N at the same depth. The continuous depth-dependent N value would be obtained by every penetration. This study attempts to utilize iPDC data to analyze the SOF, and figure out a proper method to process the unequal-spacing data.

2 SOF AND ACFM

In the past decades, it is necessary to consider spatial variability into practical engineering design (Ching and Phoon, 2017), which is described by scale of fluctuation (SOF, θ). The analysis of spatial variability can be traced back to the time series method of statistics. Similarly, it can be expressed as the spatial properties of soil particles at a given location under the

DOI: 10.1201/9781003299127-181

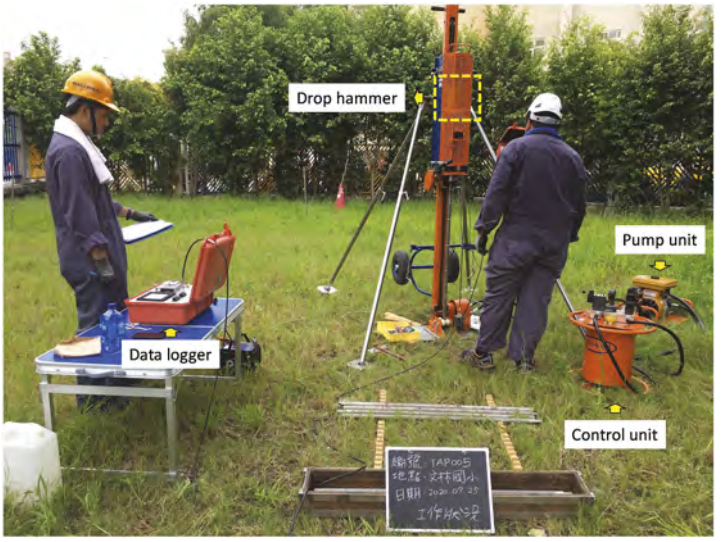

Figure 1. Device set-up of iPDC.

background as the sum of the trend function t(z) and the residual ε(z) in the geotechnical application (Vanmarcke, 1977).

$$X_i = t(z) + \varepsilon(z) \tag{1}$$

where X_i = value of soil property at location i; z = soil vertical depth, unit is meter (m); and i = vertical depth below the ground surface; i.e. takes the total measure data points i =1,2,. . .,k.

It is the SOF that depicts the relationship between a simulated random field and a geotechnical site, which uses the known variety of ACFM as an input. The SOF of soil refers to the continuous relationship or correlation of the parameters within a certain distance (which is lag, τ). In the soil profile, adjacent soil properties usually have the similar SOF, and as the distance between them increases, the correlation decreases. That is, SOF is the integral of the area under the empirical formula of ACFM.

$$\theta = 2\int_0^{\infty} \rho(\tau)d\tau \tag{2}$$

Where ρ = the autocorrelation coefficient of variables.

From the Equation (2), ρ also can be indicated as the formula below:

$$\rho(\Delta z) = \rho[\varepsilon(z), \varepsilon(z+\Delta z)] = \frac{CV[\varepsilon(z), \varepsilon(z+\Delta z)]}{\sqrt{Var[\varepsilon(z)]}\sqrt{Var[\varepsilon(z+\Delta z)]}} \tag{3}$$

Where CV[.] = the covariance, i.e. the covariance between two points; Var[.] = the covariance, i.e. the idle variance between two points; Δz = the soil data interval, i.e. τ.

Recent studies have identified some typical ACFMs frequently used in geotechnical applications. There are two kinds of ACFM. One is the single-parameter model, known as classical ACFMs, and the other is the double-parameter model. Among the single-parameter models, the Markovian (single exponential, M1) model, the second-order Markov (M2) model, the third-order Markov (M3) model, the Gaussian model, and the Cosine exponential model were used in this study. The empirical functions about θ are shown as follows Equations (4)–(8). The Whittle-Matérn model (WM) is selected for the double-parameter model in this study.

Also, Equation (9) shows its empirical function about θ, where the smoothness parameter, the scale parameter, the Gamma function, and the modified Bessel function of the second kind with order v are denoted by v, s, $\Gamma(.)$ and K_v respectively (Cami et al., 2020).

$$\rho(\tau) = \exp\left(\frac{-2|\tau|}{\theta}\right) \tag{4}$$

$$\rho(\tau) = \left(1 + \frac{4|\tau|}{\theta}\right)\exp\left(\frac{-4|\tau|}{\theta}\right) \tag{5}$$

$$\rho(\tau) = \left[1 + \frac{16}{3}\left(\frac{|\tau|}{\theta}\right) + \frac{256}{27}\left(\frac{|\tau|}{\theta}\right)\right]^2 \exp\left[\frac{-16}{3}\left(\frac{|\tau|}{\theta}\right)\right] \tag{6}$$

$$\rho(\tau) = \exp\left(\pi\frac{|\tau|^2}{\theta}\right) \tag{7}$$

$$\rho(\tau) = \exp\left(\frac{-|\tau|}{\theta}\right)\cos\left(\frac{-|\tau|}{\theta}\right) \tag{8}$$

$$\rho(\tau)^* = \frac{2^{1-\nu}}{\Gamma(\nu)}\left(\frac{|\tau|\sqrt{2\nu}}{s}\right)^2 K_\nu\left(\frac{|\tau|\sqrt{2\nu}}{s}\right) \tag{9}$$

3 METHODS OF CASE STUDYAND RESULTS

3.1 *Database*

The iPDC database is from Chen (2021) in Taiwan. The location of the iPDC boreholes was determined by referring to the previous SPT report. They should be within 10 m of the SPT boreholes to reduce spatial variability. Total 25 sites, including 17 in Taipei and 4 each in Changhua and Kaohsiung. The target penetration depth was 20 m on each site. This study illustrated the methodology using the site TAP007 in northern Taiwan as a case study, where the range of vertical depth is 0.901 m - 20.000 m. The SPT report indicates that the technique was applied at TAP031 (depths of 1.05m-37.05m). The soil distribution is as follows: CL from 1.05m-4.29m, SM from 4.3m-25.24m, CL from 25.25m-34.19m, and SM from 34.2m-37.05m. The following SOF analysis will be carried out at a soil depth of 4.3m-20m, considering the depth of application of the iPDC and the fact that it is mostly backfilled before 4.3m. The comparison of the SPT and iPDC reports is shown in Figure 2.

3.2 *Method of moments (MM)*

Statistics use the MM to estimate parameters. By applying the MM, the empirical moments are set equal to the theoretical moments, and the parameters of interest are solved to minimize the error between them. The depth corresponding to each iPDC data is unequally spaced, which is related to the soil strength at the time of penetration, roughly in the range of 0.01 m-0.2 m. Hence, Δz could be set at 0.05 m, 0.1 m, 0.5 m, and 1.0 m before detrending data to determine the appropriate sampling interval required to run a steady random field.

It is noted that the lag term should be considered during MM analysis. The maximum lags were suggested by Box-Jenkins (1970) and adopted as D = n/4 for estimation. The coefficient of determination (R^2) is used to determine the best fitting ACFM with SOF values. With the SOF of the different ACFMs and their R^2 at the interval 0.05 m, the best single parameter ACFM is M3, where the SOF is smallest and R^2 is largest, the values are 0.4497 and 0.8864 respectively. The SOF and R^2 of WM model are 0.4456 and 0.9859.

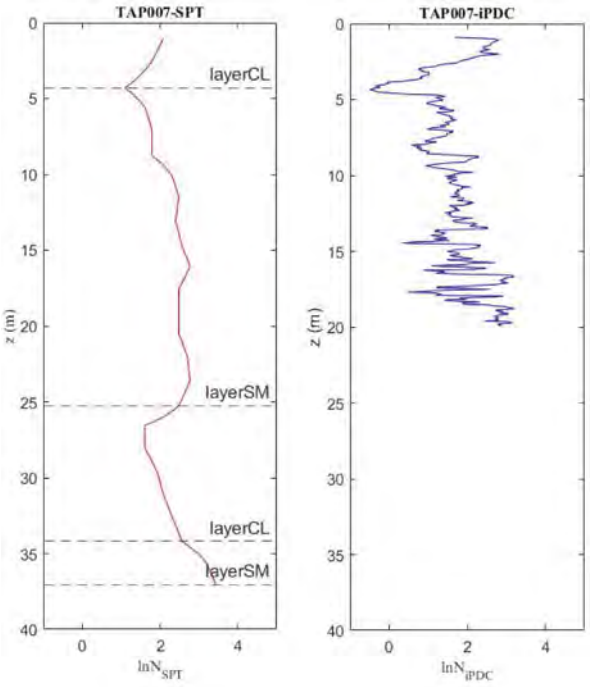

Figure 2. The relationship between N value and depth for SPT data and iPDC data.

When using the method of moment, the reason why the SOFs analyzed by different models are very similar is that the theoretical autocorrelation model is set equal to the sample auto-correlation function. Furthermore, the characteristic of the approach is using a fitting method such as least squares, which reduce the sum of squares of the relevant errors and make the fitting curve close to the sample trace, as Figure 3. It indicates that no matter which ACFMs

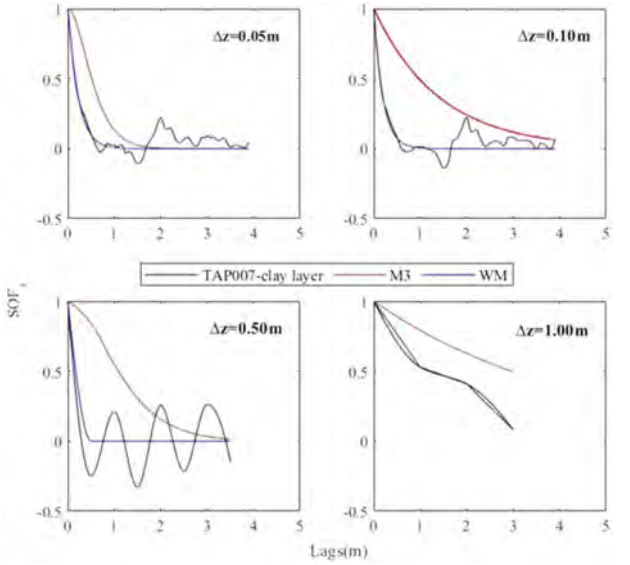

Figure 3. SOF_v of selected ACFMs at different Δz (MM).

is chosen, the SOFs are usually the same. In this study, the large amount of data and the more parameters controlled by the WM model resulted in an increase in the certainty of SOF when using Δz = 0.05 m as the measurement interval.

3.3 *Bayesian method (BM)*

Method of moments follows frequentist analysis methods which means using the known data to calculate the SOF. Bayesian method requires the parameters of probabilistic model for the location (e.g. the mean, the variance, coefficient of variation, and the weights under each parameter). Bayesian method uses these parameters to express the 95% confidence interval of the sample. That is, the defined prior distribution can be defined first then the posterior distribution is determined and updated according to its analytical rules, which benefits geotechnical applications for considering inherent statistical uncertainty.

Using the WM model and sparse Bayesian learning framework (SBL), then sampling randomly under the transitional Markov chain monte Carlo method (TMCMC) around 1000 times can obtain a more accurate value of the SOF (Ching and Phoon, 2017). Take TAP007 as an example. Using the BM to all unknown parameters, such as the trend, the SOF, and standard deviation, gives excellent and reliable results. That is, soil parameters samples are all in their 95 % confidence interval, as shown in Figure 4(a)-(c), respectively: the red line trend sample is in its 95 % confidence interval; the blue fork marker, estimated SOF, with value 0.3727, is also in its 95 % confidence interval; the blue hist, standard deviation of TMCMC sampling, is identical to the above results.

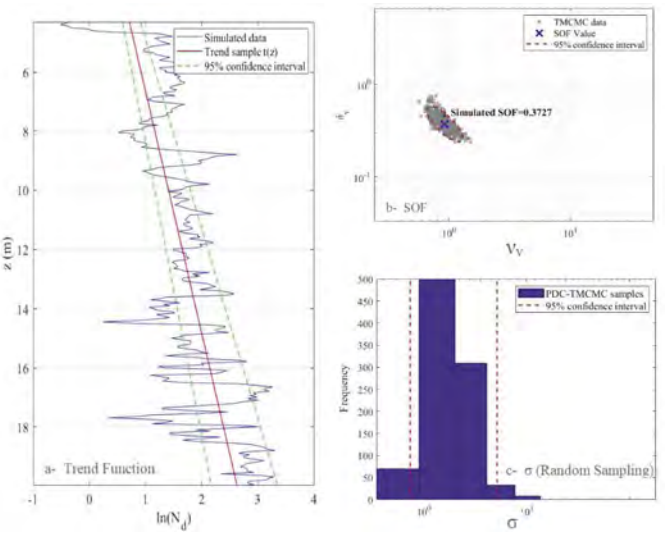

Figure 4. Results of the BM: (a) trend function; (b) SOF; (c) σ (site: TAP007).

4 DISSCATION AND CONCLUSION

This study compares two different approaches to handling in situ borehole data. One is the classical statistical analysis method, the method of moments (MM), and the other is the bayesian method (BM). The result of this study shows that the SOF = 0.3727 for the BM and 0.4456 for the MM. The BM gets a smaller SOF than the MM, which indicates the BM can more fully show the spatial variability of soil properties.

In terms of methodology, the use of MM requires the construction of a smooth random field to comply with the time series analysis method; therefore, the data is interpolated,

diluting the actual soil's spatial variability to some extent. The use of the SBL objectively characterizes the trend function, thus eliminating the need to process the data itself and allowing an objective representation of the spatial variability of the soil (Ching et al., 2017). Consequently, the BM with the WM model is recommended for the analysis of non-equally spaced data such as iPDC to reflect the actual situation of the soil better.

REFERENCES

Cami, B., Javankhoshdel, S., Phoon, K.K., & Ching, J. 2020. Scale of fluctuation for spatially varying soils: estimation methods and values[J]. *ASCE-ASME Journal of Risk and Uncertainty in Engineering Systems, Part A: Civil Engineering*, 6(4): 03120002.

Chen, Guan-Yu. 2021. Use of Piezo Drive Cone for In-situ Site Investigation in Taiwan. *Master's thesis*, Institute of Civil Engineering, National Taiwan University.

Ching, J. & Phoon, K.K. 2017. Characterizing uncertain site-specific trend function by sparse Bayesian learning. *Journal of Engineering Mechanics*, 143(7): 04017028.

Ching, J., Phoon, K.K, Beck, J. L., & Huang, Y. 2017. On the identification of geotechnical sitespecific trend function. *ASCE-ASME Journal of Risk and Uncertainty in Engineering Systems, Part A: Civil Engineering*, 3(4): 04017021.

Sawada, S., Wang, C.W., & Hiruma, N. 2019. A few examples of liquefaction assessment of ground during earthquake using Piezo Drive Cone in Taiwan. *International Conference in Commemoration of 20th Anniversary of the 1999 Chi-Chi Earthquake*, Taipei, Taiwan.

Vanmarcke, E.H. 1977. Probabilistic modeling of soil profiles. *Journal of the geotechnical engineering division*, 103(11): 1227–1246.

Yoshizawa, D., Uemura, K., Fujii, N., & Nobumoto, M. 2016. Development of Piezo Drive Cone with Load Measurement. *Oyo technical report*, (35): 75–82.

Smart Geotechnics for Smart Societies – Zhussupbekov, Sarsembayeva & Kaliakin (Eds)
© 2023 The Author(s), ISBN 978-1-003-29912-7
Open Access: www.taylorfrancis.com, CC BY-NC-ND 4.0 license

Developing geodatabases in data-scarce regions: A case study of the Kathmandu Valley, Nepal

P.J. Vardanega, C.E.L. Gilder*, R. De Risi, F. De Luca & M.J. Werner
University of Bristol, Bristol, UK

R.M. Pokhrel*
Earth Investigation and Solution Nepal Pvt Ltd, Kathmandu, Nepal
[*]formerly, University of Bristol, Bristol, UK

ABSTRACT: The Seismic Safety and Resilience of Schools (SAFER) project aimed to improve seismic hazard assessments in the Kathmandu Valley, Nepal. There remains scarce geotechnical data in this region. Therefore, the SAFER project team collected and sourced new geotechnical and geophysical data to allow for the development of improved maps showing the distribution of shear wave velocity measurements in the study region. This paper summarises geotechnical and geophysical investigations conducted in the valley and outlines the building of SAFER/GEO-591, which contains data from different sources such as previously drilled boreholes in the Kathmandu Valley. A methodology is proposed for geotechnical engineers and engineering geologists wishing to develop geodatabases in data-scarce regions.

1 INTRODUCTION

1.1 *Background*

In 2015, the M_w 7.8 Gorkha earthquake struck the Himalayan region affecting many communities, including the highly populated Kathmandu Valley in Nepal (Goda *et al.* 2015). Significant ground motion and many instances of damage were observed (e.g. Ohsumi *et al.* 2016). There was considerable investment in new seismic engineering research efforts from various agencies and organisations post-earthquake. This paper reports on some key outputs from the Engineering and Physical Sciences Research Council (EPSRC) funded project 'Seismic Safety and Resilience of Schools in Nepal' (EP/P028926/1), hereafter referred to as the 'SAFER project' (https://www.safernepal.net/). This paper primarily focuses on outputs related to geotechnical earthquake engineering from the 'New generation seismic hazard for Nepal' work package, hereafter referred to as 'WP1'.

1.2 *Study aims*

The SAFER project was comprised of five work packages (https://www.safernepal.net/) and ran from 2017 to 2021. A major focus of WP1 was on the compilation and curation of new geo-data sets for use in the development of new tools, such as new and updated maps for seismic hazard assessments in the Kathmandu Valley. This paper has two objectives: (i) it summarises the key deliverables from WP1 elaborating on how the outputs have contributed to improving seismic hazard assessments; and (ii) it offers a general methodology for geodatabase building for geotechnical engineers and engineering geologists working in data-scarce regions.

DOI: 10.1201/9781003299127-182

2 PROJECT OUTPUTS

This section focuses on the first objective of the paper. Sections 2.1 to 2.3 summarise the main deliverables from WP1 across three broad themes: (i) New geotechnical field testing in the Kathmandu Valley; (ii) Development of an open-source geodatabase for Kathmandu Valley soils and (iii) Updated maps for hazard assessments for the Kathmandu Valley.

2.1 *New geotechnical field testing in the Kathmandu Valley*

The field investigation included two new boreholes (progressed with rotary open hole drilling and sample recovery using the Standard Penetration Test (SPT) split spoon sampler), referred to as BH-1 and BH-2 (Gilder *et al.* 2019a). BH-1 was located at Dillibazar on the Padmakanya school premises at a ground elevation of 1309m. BH-2 was located on a site in Bijeshowari at a ground elevation of 1286m (see Gilder *et al.* 2019a for details on the testing). Seismic downhole testing was used to determine shear wave velocities at BH-1 (Gilder *et al.* 2019a), and Horizontal to Vertical Spectral Ratio (HVSR) testing was used for the same purpose at BH-2 (Pokhrel *et al.* 2019).

On a separate trip, Cone Penetration Testing (CPT) (to the authors' knowledge the first undertaken in the area) was carried out on seven sites to obtain measurements of shear wave velocity (*Vs*) using the seismic cone and also acquire continuous ground profile records with depth for the soils in the study region (see Gilder *et al.* 2021a and Gilder 2022 for further details on the CPT work). Figure 1 shows the locations of the new CPT readings (along with the location of the SPT readings from the SAFER/GEO-591 database) in the Kathmandu Valley.

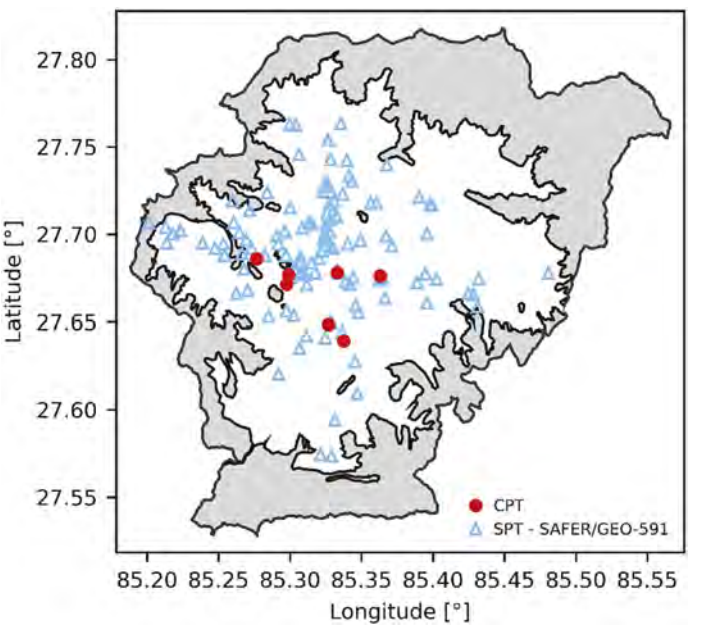

Figure 1. Location of the CPT sites outlined in Gilder *et al.* (2021a) compared with SPT locations from SAFER/GEO-591 (data from Gilder *et al.* 2019b) (figure adapted from Gilder *et al.* 2021a under the terms of the CC BY 4.0 license).

2.2 *Development of an open-source geodatabase for Kathmandu Valley soils*

The construction and data files of the SAFER/GEO-591 database is described in detail in Gilder *et al.* (2020) and the accompanying data record (Gilder *et al.* 2019b). SAFER/GEO-591 is available open-access from the University of Bristol Research Data Repository. While the database

contains almost 600 borehole records collected by the project team from the literature, published reports and industry files, an extensive 'data-cleaning' process was necessary in order for the data to be sensibly put into the database structure (Gilder *et al.* 2021b gives an example of this process). As explained in Section 3, adopting a standard format for a geodatabase is essential for effective data transfer but requires considerable time investment and prior geotechnical knowledge. Figure 2 shows an example borehole log from SAFER/GEO-591 (Gilder *et al.* 2019b, 2020). The log shown in Figure 2 is for a site in the Gokarna formation.

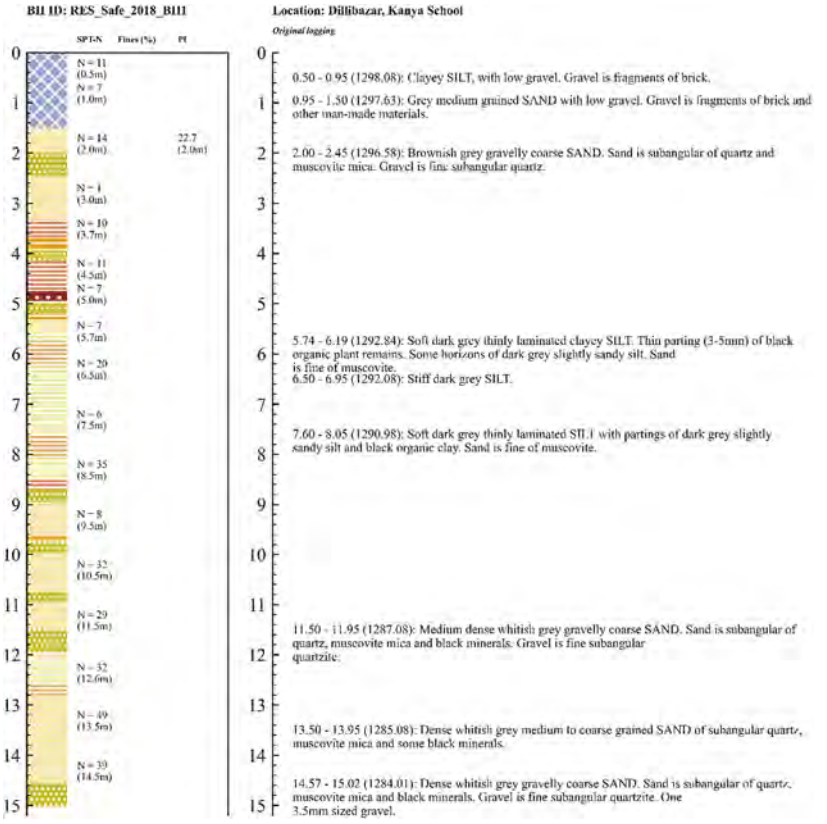

Figure 2. Example SAFER/GEO-591 borehole log from the Gokarna formation: upper 15m of the log shown (data from Gilder *et al.* 2019b).

2.3 *Updated maps for hazard assessments for the Kathmandu Valley*

Shrestha *et al.* (1998) produced a key engineering and environmental geological map for the Kathmandu Valley. During the SAFER project, data digitised from this map was often used as a base for the presentation of new analysis results and as a source of comparison for further findings. An important proxy for site amplification studies is the soil *Vs* averaged across the top 30m depth of ground ($V_{S,30}$), (e.g. Stewart *et al.* 2003). Kriging analysis is often used to estimate $V_{S,30}$ across geographical regions. De Risi *et al.* (2021) presented the results of a newly developed Bayesian-Kriging study making use of the V_{s30} measurements available (not including the new CPT data from Gilder *et al.* 2021a). Then the new V_{s30} measurements from the CPT work as well as those from the original database, were combined and analysed using the further enhanced multi-Gaussian Bayesian updating framework, showing how different kinds of V_{s30} proxies can be used to supplement local data and capture key geological features of the basin (see Gilder 2022 and Gilder *et al.* 2022).

3 DATA COLLECTION & CURATION IN DATA-SCARCE REGIONS

Geodatabases are vital for geotechnical engineers to benchmark results and make a-priori predictions of key design parameters. Thompson (2016) presented a case for public databases and described examples of such databases from various jurisdictions around the world. Open geodatabases allow the technical community to add new data to existing datasets and avoid duplicating digitisation and curation work. Phoon (2019, p.187) explained the 'MUSIC' concept i.e. that geotechnical data is often 'Multivariate, Uncertain and Unique, Sparse, Incomplete, and potentially Corrupted (MUSIC)'.

While the case for open geodatabases can be easily made in the authors' view, there are barriers to their creation and curation. Gilder *et al.* (2021c) presented a detailed review of the current barriers to geotechnical and geological data-sharing, with time and resources often cited as key constraints (as well as incentive) (see also the discussion in Thompson 2016). Based on the learnings from the SAFER project, a general methodology is proposed for those professionals starting work in data-scarce regions (see also Shepheard *et al.* (2019), where similar efforts have been made to develop new databases using a similar methodology, as well as efforts to build a pile load test database for the UK (Vardanega *et al.* 2021) and Thompson (2016) who also articulated many pertinent issues with developing public geodatabases). Phoon (2018) outlines some key challenges and important aspects of 'probablisitic site characterization' an activity for which geodatabases are useful (cf. Phoon 2018).

3.1 *Assess the geo-data landscape*

As with desk studies during site investigation projects, historical soil maps, hazard maps, and other geo-resources should be sourced by the project team. These resources (if available) can serve as useful benchmarks against future analyses (see Section 3.5). During this phase, the literature should be consulted to see if other databases have been compiled for the region of study.

3.2 *Local knowledge*

Liaise with local practitioners to determine who the main 'data owners' are. If they easily identifiable, approach these individuals/entities to determine if contributions to the new database are possible. Discuss at the outset how data records may need to be anonymised, e.g. exact locations removed, project names redacted etc. During this phase, agree the license and terms of use for the compiled database and ensure that those donating data aware of these conditions related to future data release.

3.3 *Local practice*

Unless the project team is familiar with site investigation practices in the area and, if budget permits, arrange to visit local projects or laboratories to determine which testing standards are used and which testing equipment is commonly utilised for laboratory and field studies conducted in the study region.

3.4 *Data harmonization and cleaning*

If data from multiple laboratories or site investigation companies will comprise the database, ensure that a 'data harmonisation' and 'cleaning' process is carried out by an experienced project team member. During this time, determine the data format to be used (see the discussions in Thompson (2016) and Gilder *et al.* (2021c) regarding file formats and workflow) and prepare a database manual with the data sources and notes from the cleaning and harmonisation process.

3.5 *Benchmarking analysis*

The new database should be checked against existing resources (if available), e.g. soil maps, local 'transformation models' (cf. Phoon & Kulhawy 1999a, b) or previously published parameter distributions, to determine if the new database is sufficiently representative of the study area. Also ascertain if the database contains sufficient data for meaningful statistical analyses. Some engineering judgement will be needed to determine if this is the case and during this step, potential outliers may be identified and noted in the database manual. It may be that the database will need further expansion as new data becomes available after the initial data release. This stage is also where major gaps in the database can be identified (cf. Phoon 2019: MUSIC) and these should be noted in the database manual.

3.6 *Data release*

While there are barriers to this stage (e.g. commercial interests), if possible, the database should be released open-access with appropriate disclaimers. Later corrections and clarifications may be needed as practitioners and researchers start using the database, which can be incorporated in future versions. 'Living databases' may, become a useful technical resource for the local and international geotechnical communities, allowing for improved design and model calibration efforts.

4 SUMMARY AND CONCLUSIONS

This paper has presented some of the key outputs from WP1 from the SAFER project. The outputs discussed covered three broad themes: (i) New geotechnical field testing in the Kathmandu Valley; (ii) Development of an open-source geodatabase for Kathmandu Valley soils and (iii) Updated maps for hazard assessments for the Kathmandu Valley. The focus of the SAFER project was on improving the safety and resilience of school buildings in Nepal; however, many of the project findings should be useful for other infrastructure classes. The paper proposed a 'step-by-step' methodology for those developing open-access databases in data-scarce regions.

In conclusion, the lessons from WP1 of the SAFER project have revealed many challenges in building and releasing open-access geodatabases, however such resources are essential for regional statistical analyses (e.g. using Kriging-based methodologies), to produce new maps and information for improved hazard assessments.

ACKNOWLEDGEMENTS

The second author acknowledges the support of EPSRC (EP/R51245X/1). The authors acknowledge the support of: the EPSRC project SAFER (EP/P028926/1), the UoB Faculty of Engineering; IN SITU Site Investigation and Professor Anastasios Sextos for leading the SAFER project.

DATA AVAILABILITY STATEMENT

This study has not generated new experimental data.

REFERENCES

De Risi, R., De Luca, F., Gilder, C.E.L., Pokhrel, R.M. & Vardanega, P.J. 2021. The SAFER geodatabase for the Kathmandu valley: Bayesian kriging for data-scarce regions. *Earthquake Spectra* 37(2): 1108–1126.

Gilder, C.E.L. 2022. Geotechnical data curation and a geostatistical multivariate framework for V_S prediction in data scarce contexts. *Ph.D. thesis*, Bristol, UK: University of Bristol.

Gilder, C.E.L., Pokhrel, R.M. & Vardanega, P.J. 2019a. A ground investigation to inform earthquake hazard assessment in the Kathmandu Valley, Nepal. In H. Sigursteinsson *et al.* (eds.), *Proc. XVII*

European Conf. on Soil Mechanics and Geotechnical Engineering - Reykjavík, Iceland, 1–6 of September 2019. Reykjavík, Iceland: The Icelandic Geotechnical Society (IGS).

Gilder, C.E.L., Pokhrel, R.M. & Vardanega, P.J. 2019b. The SAFER Borehole Database (SAFER/GEO-591_v1.1). Bristol: University of Bristol. https://doi.org/10.5523/bris.3gjcvx51lnpuv269xsa1yrb0rw

Gilder, C.E.L., Pokhrel, R.M., Vardanega, P.J., De Luca, F., De Risi, R., Werner, M.J., Asimaki, D. Maskey, P.N. & Sextos, A. 2020. The SAFER Geodatabase for the Kathmandu Valley: Geotechnical and geological variability. *Earthquake Spectra* 36(3): 1549–1569.

Gilder, C.E.L., Pokhrel, R.M., De Luca, F., & Vardanega, P.J. 2021a. Insights from CPTu and Seismic Cone Penetration Testing in the Kathmandu Valley, Nepal. *Frontiers in Built Environment* 7: [646009].

Gilder, C.E.L., Vardanega, P.J., Pokhrel, R.M., De Risi, R. & De Luca, F. 2021b. Assessing Transformation Models Using a Geo-Database of Site Investigation Data for the Kathmandu Valley, Nepal. *Lecture Notes in Civil Engineering* 125: 331–338.

Gilder, C.E.L., Geach, M., Vardanega, P.J., Holcombe, E.A. & Nowak, P. 2021c. Capturing the views of geoscientists on data sharing: a focus on the geotechnical community. *Quarterly Journal of Engineering Geology and Hydrogeology* 54 (2):[qjegh2019-138].

Gilder, C.E.L., De Risi, R., De Luca, F., Pokhrel, R.M. & Vardanega, P.J. 2022. Geostatistical framework for estimation of V_{S30} in data-scarce regions. *Bulletin of the Seismological Society of America* 112 (6): 2981–3000.

Goda, K., Kiyota, T., Pokhrel, R.M., Chiaro, G., Katagiri, T., Sharma, K. & Wilkinson, S. 2015. The 2015 Gorkha Nepal earthquake: Insights from earthquake damage survey. *Frontiers in Built Environment* 1: [8].

Ohsumi, T., Mukai, Y., & Fujitani, H. 2016. Investigation of Damage in and Around Kathmandu Valley Related to the 2015 Gorkha, Nepal Earthquake and Beyond. *Geotechnical and Geological Engineering* 34(4): 1223–1245.

Phoon, K-K. 2018. Special Collection Announcement: Probabilisitc Site Characterisation. *ASCE-ASME Journal of Risk and Uncertainty Engineering Systems, Part A: Civil Engineering* 4 (4):[02018002].

Phoon, K-K. 2019. Editorial: Flow and transport in porous media in the face of uncertainty, part I. *Environmental Geotechnics* 6(4): 186–187.

Phoon, K-K. & Kulhawy, F.H. 1999a. Characterization of geotechnical variability. *Canadian Geotechnical Journal* 36(4): 612–624.

Phoon, K-K. & Kulhawy, F.H. 1999b. Evaluation of geotechnical property variability. *Canadian Geotechnical Journal* 36(4): 625–639.

Pokhrel, R.M., Gilder, C.E.L., Vardanega, P.J., De Luca, F., Werner, M.J. & Maskey, P.N. 2019. Estimation of V_{S30} by the HVSR Method at a Site in the Kathmandu Valley, Nepal. In *2nd Int. Conf. on Earthquake Engineering and Post Disaster Reconstruction Planning*, *25-27 April*, *2019*: 52–60.

Shepheard, C.J., Vardanega, P.J., Holcombe, E.A., Hen-Jones, R. & De Luca, F. 2019. Minding the geotechnical data gap: appraisal of the variability of key soil parameters for slope stability modelling in Saint Lucia. *Bulletin of Engineering Geology and the Environment* 78(7): 4851–4864.

Shrestha, O.M., Koirala, A., Karmacharya, S.L., Pradhananga, U.B., Pradhan, R. & Karmacharya, R. 1998. *Engineering and environmental geological map of the Kathmandu Valley, Scale 1: 50 000*. Kathmandu, Nepal: Department of Mines and Geology, Lainchaur.

Stewart, J.P., Liu, A.H. & Choi, Y. 2003. Amplification factors for spectral acceleration in tectonically active regions. *Bulletin of the Seismological Society of America* 93(1): 332–352.

Thompson, T. 2016. A 2016 case for public geotechnical databases. In: *Proc. of the 5th Int. Conf. on Geotechnical and Geophysical Site Characterisation (ISC'5) Gold Coast, Queensland Australia. September 2016*. Available from: < https://www.issmge.org/uploads/publications/25/26/ISC5_154.pdf> (20 January 2023).

Vardanega, P.J., Crispin, J.J., Gilder, C.E.L., Voyagaki, E. & Ntassiou, K. 2021. DINGO: A Pile Load Test Database. In K.G. Higgins ***et al***. (eds). *Piling 2020: Proceedings of the Piling 2020 Conference*: 229–234. London, UK: ICE Publishing.

Shallow and deep foundations

Taylor & Francis
Taylor & Francis Group
http://taylorandfrancis.com

Smart Geotechnics for Smart Societies – Zhussupbekov, Sarsembayeva & Kaliakin (Eds)
© 2023 The Author(s), ISBN 978-1-003-29912-7
Open Access: www.taylorfrancis.com, CC BY-NC-ND 4.0 license

Study on prediction method for settlement of multi-belled cast-in-place pile

K. Hama, T. Watanabe, Y. Horii & T. Nagao
Taisei Corporation, Yokohama, Japan

Y. Nakanishi
System Measure Co., Ltd., Tokyo, Japan

Y. Mukai
Kobe University, Kobe, Japan

ABSTRACT: The 'hybrid method', a simplified prediction technique for foundation settlement in which piles are modeled using finite elements, springs representing the non-linear properties of the soil around the piles are attached to the nodes, and elastic interactions through the soil between each element are considered, has been used to predict the settlement of several large-scale buildings with bell piles or diaphragm walls. However, the accuracy of settlement behavior predictions for multi-belled cast-in-place piles has not been sufficiently clarified. In this paper, a soil spring is proposed for an intermediate bell as a modification of the spring recommended for a pile tip. The results of simulating three full-scale load tests using the modified spring, which closely match the actual measurements, demonstrate the validity of the proposed spring.

1 INTRODUCTION

The multi-belled cast-in-place piling method has been developed to meet the high demand for supporting a large load of high-rise or long-span structures in Japan. These are piles that have enlargements (called 'bells') at some intermediate point as well as at the pile tip (Hama et al. 2019; see Figure 1). It is significant for the construction plan and structural design of such piles to understand settlement behavior under vertical loading, but this has not been sufficiently clarified for multi-belled piles. The finite element method (FEM) with solid elements is useful for analyzing behavior, including settlement behavior, in detail, but modeling and calculation are time-consuming. On the other hand, the 'hybrid method' (Clancy & Randolph 1993 and Nagao et al. 1998) is often used in practical design, offering the advantage of flexibility in modeling as design requirements change. There are several examples of this method being used for large-scale buildings with bell piles or diaphragm walls (Sugimura et al. 2017). In this paper, as a basic study on evaluating the settlement behavior of multi-belled piles by the hybrid method, a modified spring is assumed for the intermediate bell, obtained by correcting the equation recommended by the Architectural Institute of Japan (AIJ 2019) for a pile tip according to logical consideration related to the shape of the bell. The validity of the new spring is discussed by simulating full-scale load tests reported in the published literature (Muramatsu et al. 2020, Watanabe et al. 2012 and Sano et al. 2013).

2 SETTLEMENT PREDICTION METHOD

2.1 *Analysis method*

The hybrid method is a means for predicting the settlement of building foundations in which elastic theories and FEM are combined and integrated with non-linear springs for the soil

DOI: 10.1201/9781003299127-183

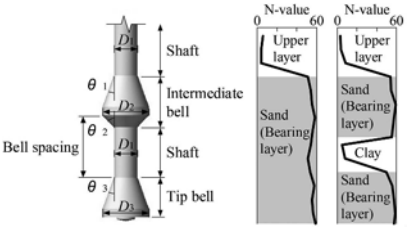

Figure 1. Multi-belled pile and applicable ground conditions.

around the piles (see Figure 2a). It is capable of evaluating complex settlement behavior of piles in a group by modeling interactions between different piles and with the soil. The outline of the hybrid method is summarized as follows. a) Piles and foundation structures are modeled with three-dimensional (3-D) finite beam elements. b) Soil stratums are assumed to be horizontally separated semi-infinite elastic bodies and modeled by equivalent linear springs, of which the deformation moduli are determined in consideration of the non-linear properties of soils. c) Elastic interactions through the soil between each element are computed using Steinbrenner's solution and from the integral of the first Mindlin's solution. d) Springs representing the non-linear properties of the soil around the piles are connected at the piles' nodes. A 3-D hybrid model based on the method outlined in a) – d) is integrally analyzed with building loads. In this paper, since the targets of analysis are single piles, the analysis method is almost equivalent to load transfer analysis (Coyle & Reese 1966).

2.2 *Non-linear spring of intermediate bell*

In this study, non-linear springs for the soil around a pile were defined as the following functions: a hyperbolic function for shaft friction and an exponential function for pile base stress (AIJ 2019; see Figure 2a). The initial stiffnesses K_0 of the hyperbolic springs were set according to Mindlin's solution using the soil deformation moduli, while the ultimate values were defined as ultimate shaft frictional unit stress τ_{max}. The exponential springs were evaluated using Equation 1 (AIJ 2019), in which the coefficients, α and n, were set according to soil type:

$$\frac{S_p/d_p}{0.1} = \alpha \frac{R_p/A_p}{(R_p/A_p)_u} + (1-\alpha)\left\{\frac{R_p/A_p}{(R_p/A_p)_u}\right\}^n \tag{1}$$

where S_p = settlement of pile tip; d_p = diameter of pile tip; R_p/A_p = base unit stress; $(R_p/A_p)_u$ = ultimate base unit stress; α = initial tangential gradient of curve; and n = degree on curve shape.

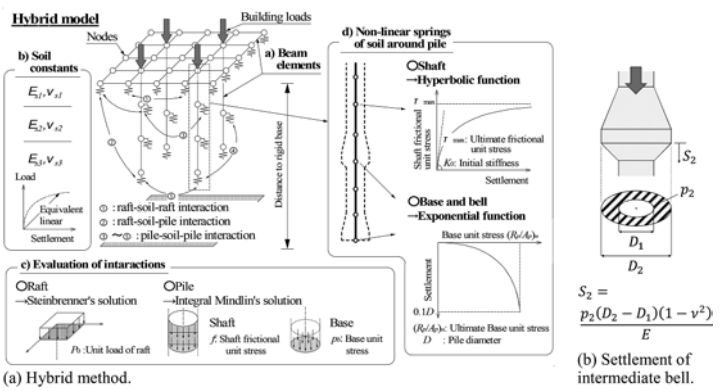

Figure 2. Overview of hybrid method and assumption of intermediate bell settlement.

For an intermediate bell, the non-linear spring was modified as follows (and see Figure 2b). First, the settlement of an intermediate bell was assumed as the settlement of a semi-infinite elastic body with the shape of a projected area of the bell under uniform loading (p_2). This projected shape should be a ring due to the presence of the shaft below the bell. Thus, the bell's settlement S_2 can be calculated using the equation in Figure 2b (AIJ 2019), while settlement stiffness should be $D_2/(D_2 - D_1)$ times as much as the case without a shaft under the bell. Based on this consideration, a modification of Equation 1 was defined as the evaluation equation for the spring of an intermediate bell, in which α is multiplied by the ratio $(D_2 - D_1)/D_2$. It was confirmed that the shape of the curve of this modified spring corresponded to the load versus settlement relation of the intermediate bell in full-scale load test A (described in the next section).

3 SIMULATION OF FULL-SCALE LOAD TESTS

Here, simulation analyses of three full-scale load tests are conducted using the hybrid method and the validity of the modified springs is discussed. In preparation for the analyses, the piles were modeled by the plurality of beam elements and then non-linear springs including the modified springs for intermediate bells were connected at their nodes. The other requirements were set as described below. Figure 3 and 4 outlines the configuration and the results for each test pile, allowing the results of the simulation to be compared. The simulation of each pile is outlined below.

(A) Pile with an intermediate bell in sand stratum and without tip bell (Muramatsu et al. 2020). For the spring of the bell, coefficients α and n in the modified Equation 1 were set to 0.23 and 2.7, respectively (further multiplying α by the ratio $(D_2 - D_1)/D_2 = 0.5$); these are values proposed as the properties of sandy soil (AIJ 2019). The value of $(R_p/A_p)_u$ was calculated as $120*\bar{N}$ (AIJ 2019), where $\bar{N}$ denotes the average N-value near the pile tip as obtained by the standard penetration test (SPT). Soil constants were determined from the results of PS logging. Although load levels in the simulated load–settlement relation of the bell are slightly lower than those in the actual load test, the shape of the curve matches that of the test quite well. The analysis could simulate well the test results in the depth distributions of axial force as the bearing forces at the bell were larger than elsewhere on the pile.

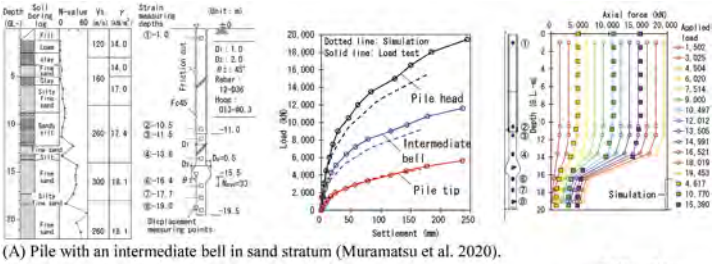

(A) Pile with an intermediate bell in sand stratum (Muramatsu et al. 2020).

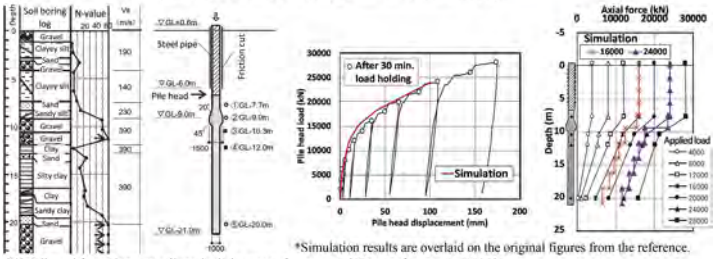

*Simulation results are overlaid on the original figures from the reference.

(B) Pile with an intermediate bell in gravel stratum (Watanabe et al. 2012).

Figure 3. Results of simulations of full-scale load tests (part 1).

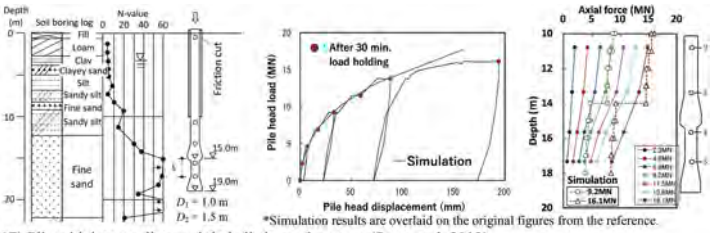

*Simulation results are overlaid on the original figures from the reference.

(C) Pile with intermediate and tip bells in sand stratum (Sano et al. 2013).

Figure 4. Results of simulations of full-scale load tests (part 2).

(B) Pile with an intermediate bell in gravel stratum and without tip bell (Watanabe et al. 2012). Coefficients α and n were set to 0.12 and 3.3, respectively (applied the ratio $(D_2 - D_1)/D_2$ = 0.33 as above), to simulate the properties of gravel (AIJ 2019). The values of $(R_p/A_p)_u$ and the soil constants were set as described above. The simulated load–settlement relation at the pile head and the depth distributions of axial force correspond well to the results of the actual test.

(C) Pile with intermediate and pile-tip bells in sand stratum (Sano et al. 2013). Coefficients α and n were set to 0.23 and 2.7 as above, and $(R_p/A_p)_u$ was calculated as $120^*\bar{N}$. Soil constants were determined from the results of SPT. The simulated load–settlement relation at the pile head corresponds well to the results of the actual test.

Considering that the simulated values approximately corresponded to the test results, the assumption of the modified spring for intermediate bells was regarded as valid.

4 CONCLUSIONS

The following conclusions were obtained from evaluating settlement of multi-belled piles by the hybrid method.

- A suitable non-linear spring for the settlement behavior of an intermediate bell can be defined by modifying the initial stiffness of the non-linear spring proposed to model the behavior of the pile tip while taking into consideration of the bell's shape.
- The results of simulating actual full-scale load tests indicate that the application of the modified spring to intermediate bells is valid.

REFERENCES

Architectural Institute of Japan (AIJ) 2019. *Recommendation for Design of Building Foundations*. Tokyo: AIJ (in Japanese).

Clancy, P. and Randolph, M. F. 1993. An approximate analysis procedure for piled raft foundations. *International Journal for Numerical and Analytical Methods in Geomechanics* 17: 849–869.

Coyle, H. M. and Reese, L. C. 1966. Load transfer for axially loaded piles in clay. *Journal of the Soil Mechanics and Foundations Division* 92 (2): 1–26.

Hama, K., Horii, Y., Nakanishi, Y. and Watanabe, T. 2019. Field trials of large-diameter multi-belled piling method. *Proceedings of 4th GEOTEC HANOI 2019*: 161–168.

Muramatsu, A., Watanabe, T., Horii, Y., Hama, K., Nakanishi, Y. and Fujita, S. 2020. Loading test and simulation of middle-belled and bored piles Part 1. *Annual Meeting of AIJ*: 407–408 (in Japanese).

Nagao, T., Shinozaki, Y., Watanabe, T. and Kuwabara, F. 1998. Study on the settlement behavior of piled raft foundations. *Annual Meeting of AIJ* B-1: 809–810 (in Japanese).

Sano, D., Kaneko, O. and Taguchi, T. 2013. Vertical load tests for bearing capacity of piles with enlarged base and intermediate node. *Toda technical research report* 39: 10-1–10-10 (in Japanese).

Sugimura, M., Tomita, N., Horii, Y., Watanabe, T. and Toyama, J. 2017. Design of piled raft foundation for JR gate tower. *Report of Taisei Technology Center* 50: 25 (in Japanese).

Watanabe, K., Ishii, Y., Sudo, T. and Nishimura, K. 2012. In-situ full scale load test of nodular cast-in-place concrete pile. *Journal of Japanese Geotechnical Society* 60 (8-655): 6–9 (in Japanese).

Smart Geotechnics for Smart Societies – Zhussupbekov, Sarsembayeva & Kaliakin (Eds)
© 2023 The Author(s), ISBN 978-1-003-29912-7
Open Access: www.taylorfrancis.com, CC BY-NC-ND 4.0 license

Centrifuge tests on piled raft foundations in sand subjected to vertical load

N. Elayni & F. Szymkiewicz
Université Gustave Eiffel, Champs sur Marne, France

M. Blanc
Université Gustave Eiffel, Bouguenais, France

P. Reiffsteck, A. Le Kouby & C. Minatchy
Université Gustave Eiffel, Champs sur Marne, France

ABSTRACT: Static centrifuge tests of piled rafts subjected to vertical load were performed in order to examine the interaction of piles-ground-raft. Piles were instrumented with continuous Rayleigh-based optical fiber sensors to measure deformation occurring in the piles. Optical fiber was also set up in the soil to measure deformation of the ground around the foundation. Two types of piled rafts foundation were tested: a rigid raft (1.5cm thick) and a flexible raft (0.2cm thick). A pile group (without raft touching the ground) was also tested in centrifuge to compare the performance. The optical fiber in the soil showed the extent of the deformation resulting from the loading in the container.

1 INTRODUCTION

As high-rise buildings are becoming more common and the concept of environmental cost is now central to the construction sector, piled raft foundations combining deep and shallow foundations will be used more and more frequently. Piled raft foundations consist of a surface foundation that is in contact with the ground and a group of piles connected to the shallow foundation. There are two possible design strategies for mixed foundations:

- reducing settlements by adding piles when the bearing capacity is provided by the shallow foundation but settlements are excessive for the proposed structure (Burland et al. 1977),
- increasing the bearing capacity of the deep foundations by taking into account the additional bearing capacity provided by the surface foundation, with a view to limiting costs and the use of raw materials. Up to now, various studies have been reported on the application of settlement-reducer piles (Hansbo, 1984, Hirokoshi and Randolph, 1998, Viggiani, 2001, Poulos, 2001, Mandolini 2003). In both cases, the combination of these two types of foundations implies that the behavior of the piled raft foundation is different from the foundations taken separately. Indeed, the addition of a footing in contact with the ground on a pile group implies additional interactions.

Experimentation on this type of foundation at real scale is not very common due to their size and cost. 1g models in the laboratory can provide qualitative results whereas centrifuge models can represent the reality with a small scale model. In this study, a series of vertical loading tests was conducted for three type of foundation model. These three types of foundations have 9 piles respectively embedded in rigid raft, flexible raft and free headed.

Many researchers have reported the results of piled raft loading using centrifuge modeling. Among them, Fioravante and Giretti (2010), studied the load transition mechanism in piled raft systems. They studied the effect on the stiffness of the foundation in dense dry sand. The

DOI: 10.1201/9781003299127-184

results showed that the load distribution mechanism in the piled raft foundation depend on the relative stiffness of the pile and soil.

Nguyen et al. (2013), studied the settlement controlling of piled raft foundation in high-rise building by using a centrifuge model. They made two types of foundation with concentrated piles and uniformly distributed piles. The results showed that a foundation with concentrated pile can effectively decrease the total and differential settlements in comparison with a foundation having uniform pile arrangement.

The following study enables us to understand the effect on total load of different rafts.

2 MODEL FOUNDATION AND TEST PROCEDURES

2.1 *Loading devices and instrumentation*

The centrifugal acceleration chosen in the present study was 50g. Figure 1 shows a schematic illustration of the model setup for this study. The model container used for the test is a rigid box with inner dimensions of 120cm in length, 80cm in width and 72cm in depth. Vertical loading test is carried out by displacement control with constant loading rates of 0.01mm/s. The hydraulic jack is used to apply the vertical load respectively for the installation and loading phases. A force sensor with a range of 2200daN (550MN at 50g) was used and four displacement potentiometers were placed at the four corners of the raft. All foundations models were placed as shown in Figure 2 in the same container.

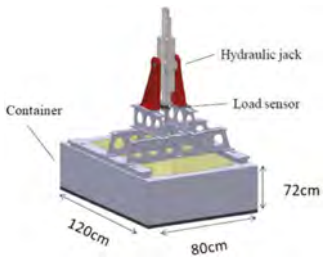

Figure 1. Model setup.

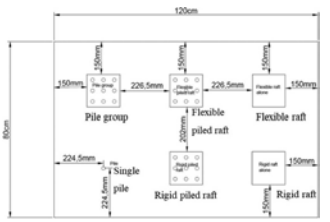

Figure 2. Model foundation position in container.

2.2 *Model foundations*

In the present study static vertical loading tests were conducted on the pile group and two piled rafts. Figure 3 shows the raft and the pile models used in the centrifuge tests.

The model pile was a treaded rod made from brass with an 17mm outer diameter and a 0.72mm thickness. A plastic cap was inserted at the pile base to close the pile. An optical fiber was glued on both sides of the pile to measure the strain. The optical fiber forms a loop at the base of the pile to measure the pile base resistance. To attach the optical fiber to the side of the pile, a very narrow and shallow groove was machine in the pile. After this, a two-component adhesive was used to implement the fiber inside the groove. The glue creates a relatively smooth and uniform pile surface. In the present paper, the results of the optical fiber located in pile will not be shown because of lack of place in this paper.

The piles were rigidly fixed to a steel raft with 150 x 150mm. There is two types of raft model. A flexible raft model with a thickness of 2mm and a rigid raft model with a 15mm thickness. The raft was composed of 9 holes allow the 9 piles heads to fit through, with pile spacing of 3 diameters as shown in Figure 3.

The raft model and the piles were used for the test of piled raft, pile group, raft alone and single pile. For the pile group, the rigid raft was used and a gap between the ground surface and the raft base was maintained. The piles in the pile group were embedded into the ground at 24cm and

were the same in every tests. Table 1 summarize the specifications of the pile and raft both in model scales.

The soil was instrumented with an optical fiber to measure the strain of the ground under the raft base and between the piles. The optical fiber was set up just before the end of the sand pouring with different spaces between each line of the fiber. It was placed taken into account the position of each foundationso as not to damage the optical fiber during the installation of the foundations as shown in Figure 4.

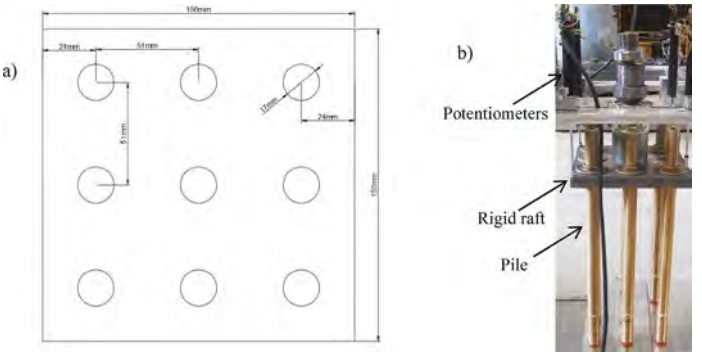

Figure 3. a) Raft model; b) Piled raft model.

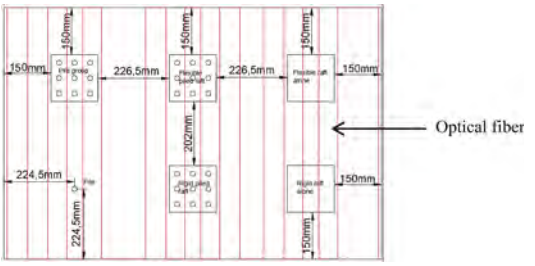

Figure 4. Optical fiber implementation plan.

Table 1. Specification of models foundations.

Properties	Flexible raft	Rigid raft	Pile
Thickness (cm)	0.2	1.5	
Length (cm)	15	15	
Width (cm)	15	15	
Diameter (cm)			0.17
Embedment depth (cm)			24
Materials	steel	steel	brass
Young modulus (GPa)	210	210	105

2.3 *Soil and model preparation*

The reference sand Hostun (HN31) was used during these experiments. The characteristics of the sand and the grain size are presented in Table 2. The sand mass was reconstituted at the required density using dry pluviation. This method produces homogeneous samples and reproduces the natural deposition process of sands (Le Kouby, 2003).

Table 2. Physical properties of Hostun (HN31) sand.

Properties	
Mean particle diameter, D_{50} (μm)	341
Maximum void ratio, e_{max}	0.961
Minimum void ratio, e_{min}	0.624
Solid particle density, ρ_s (g/cm^3)	2.65
Maximum particle density, ρ_{min} (g/cm^3)	1.59
Minimum particle density, ρ_{max} (g/cm^3)	1.32

Densification by sand pouring is effective for drop heights between 0 and 50cm (Vaid and Negussey (1984), Levacher et al. (1994)). For the sand used during these tests, a logbook of the different heights and rates allowed the determination of the parameters required to obtain a relative density of 80%. After the sand pouring of the model ground, the piled raft foundation was jacked in the soil at 1g with a rate of 0.1mm/s. The piles attached to the raft were penetrating into the ground vertically. During the process of jacking, the force and the displacement were monitored to determine the contact of the raft base with the ground surface for each piled raft model. After the installation phase of the foundation, potentiometers were set up to measure the settlements and then the centrifuge acceleration was increased up to 50g.

3 RESULTS AND DISCUSSIONS

3.1 *Load-displacement*

The foundations were jacked in the soil at 1g as explained in section 2.3. Figure 5 shows the load-displacement curve of different foundations during the installation. The load-displacement curve of the pile group is continuous and stopped when the embedded depth of the pile reach 24cm. The load-displacement curve show a displacement of 21cm because of the pile group weight when it was placed on the ground and the piles settle a few centimeters. The rigid piled raft and the flexible piled raft present a slope discontinuity at the end of the loading. As the base of the raft reaches the surface of the ground, the load increases substantially, but the displacement increases slightly. This variation of the load is caused by the raft base pressure. When the contact between the raft and the soil is made, the rotation of the centrifuge starts to reach 50g.

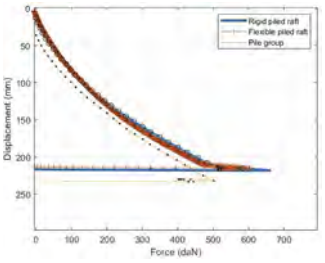

Figure 5. Load displacement curve of a jacked piles group, rigid piled raft and flexible piled raft.

The test experiment could only reach small displacement because of the force sensor capacity (2200daN). The load of the pile group, rigid piled raft and flexible piled raft is shown in the same figure. Figure 6 shows that the total load taken by the flexible piled raft is higher than rigid piled raft. The pile group is less resistant than the others. The flexible piled raft had settled by 1mm for 2200daN, 1.5mm for rigid piled raft and 1.95mm for pile group. However, the Figure 7 shows the displacement of the piled raft and group with the displacement sensor of the hydraulic jack. The flexible piled raft had settled more than the other foundation, with

a settlement of 9mm. The difference between the Figures 6 and 7 is that the rafts are loaded at the center of the raft. This creates a stress concentration on the flexible raft resulting in a bending of the foundation. The potentiometers placed at the corner of the raft are therefore not moving during the test. The piles have undergone a bending moment and were no longer taking the vertical load. The entire load was concentrated on the center of the raft.

The Figure 8 shows the load-displacement between the rigid piled raft and the pile group. The variation of the resistance is due to the contact of the raft on the ground. The higher the load, the bigger the gap between pile group and piled raft. The raft is an immediate asset and transfers a small part of the load to the ground. This variation is linear for the most part of the reloading until 1500daN and reached a level of 2.25mm for the rest of the loading process. This level of settlement means that the raft is providing the same resistance between 1500 and 2200daN. To better understand the behavior of the raft, further tests are required. The tests carried out did not reach a high load value. The tests carried out by Nguyen et al. (2013), showed that if higher loading values are reached, the loading gradient of the load curve is higher. The Figure 7 shows that the piled raft and the pile group curves are very close. This indicates that the piled raft works as a pile group. It may be assumed that 50g creates a loose of contact of the raft by a compaction of the soil. This piled raft model act like a group of piles.

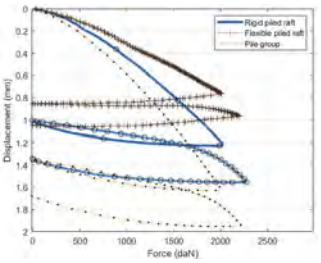

Figure 6. Load displacement curve at 50G (average of four displacement sensor).

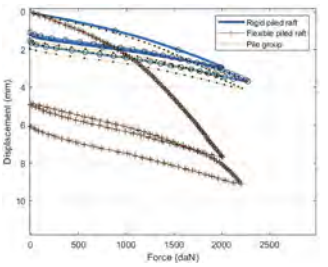

Figure 7. Load displacement curve at 50G (hydraulic jack displacement sensor).

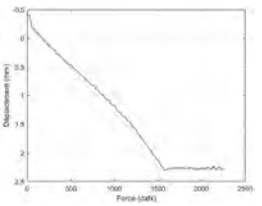

Figure 8. Difference of settlement between pile group and rigid piled raft.

3.2 *Strain in ground*

In this section, the results of the strain measured in the ground with the optical fiber will be discussed for the rigid piled raft at 2200daN. The variation of the strain in the ground between the piles for a load at 2200daN is shown in Figure 9. The strain is increasing at the center of the raft and decreases as you get closer to the ends of the raft. For the optical fiber, positive strain means an extension deformation. Figure 10 shows the extent of the deformation in the container at 2200daN. The deformation decreases with a nonlinear curve and tends toward zero closer to the edge of the container. It means that settlement of sand mass at 50g is observed by optical fiber on all container surfaces. The strain stabilizes from 2B, that means, there is no border effect.

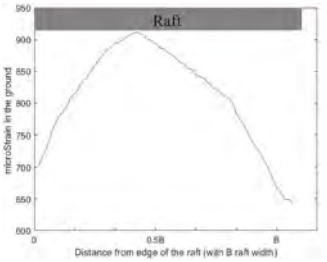

Figure 9. Deformation measured under the raft base.

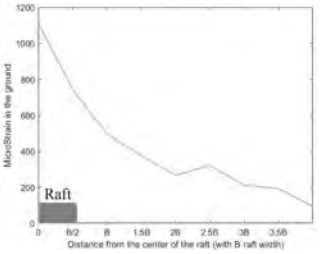

Figure 10. Development of the deformation between the center raft and the wall of container.

4 CONCLUSION AND PERSPECTIVES

To conclude, models of three type of foundation were tested in centrifuge at 50g. Rigid piled raft foundation, flexible piled raft foundation and pile group were loaded vertically. The results shows that the flexible piled raft has a very low stiffness and bended in the center of the raft. The rigid piled raft shows higher stiffness and resistance than the pile group. The results validate our testing procedure as a difference was shown between the pile group and the rigid piled raft foundation. The system will be adapted to allow either higher maximum load or smaller centrifuge acceleration g values or reducing the number of piles. Furthermore increasing the g value creates a compaction of the soil that can provoke a settlement of the soil higher than the rigid piled raft therefore a loose of the contact of the raft from the soil. The results of the optical fiber in the ground has made possible to observe the development of the strain in the soil mass. Using optical fiber made possible to evaluate the effect of loading a foundation on the soil mass.

REFERENCES

Burland, J. B., Broms, B.B., De Mello, V.F.B. 1977. Behaviour of foundations and structures. In Proceedings of the 9th International Conference on Soil Mechanics and Foundation Engineering, Tokio, Japan, Vol. 2, pp. 495–546

Fioravante V, Giretti D. 2010. Contact versus noncontact piled raft foundations. Canadian Geotechnical Journal, No. 11, Vol. 47, pp. 1271–1287.

Hansbo S. 1984. Foundations on friction creep piles in soft clays. International Conference on Case Histories in Geotechnical Engineering, St. Louis, Prakash, 011–922.

Horikoshi K, Randolph M. 1998. A contribution to optimum design of piled rafts, Geotechnique. No. 3, Vol. 48, pp. 301–317.

Le Kouby, A. 2003. Etude du comportement mécanique de micropieux sous chargements monotones et cycliques verticaux. Application aux effets de groupe. Ph.D. thesis. Ecole Nationale des Ponts et Chaussées.

Levacher, D., Garnier, J., Chambon, P. 1994. Reconstitution d'éprouvettes de sable. Appareil de pluviation. Revue française de géotechnique. NO. 68, 49–56.

Mandolini A. 2003. Design of piled raft foundations: practice and development, Proceedings of Deep Foundations on Bored and Auger Piles–BAP IV. Ghent, Belgium, pp. 2–4.

Nguyen, D.D.C., Kim, D.S., and Jo, S.B. 2013. Settlement of piled rafts with different pile arrangement schemes via centrifuge tests. Journal of Geotechnical and Geoenvironmental Engineering 139(10), 1690–1698.

Poulos H. 2001. Piled raft foundations: design and applications. Geotechnique. No. 2, Vol. 51, pp. 95–113.

Vaid, YP., Negussey, D. 1984. Relative density of pluviated sand samples. Soils Found 24(2):101–105.

Viggiani C. 2001. Analysis and design of piled foundations, 1st Arrigo Croce Lecture, Rivista Italiana di Geotecnica. No. 1, Vol. 35, pp. 47–75.

Smart Geotechnics for Smart Societies – Zhussupbekov, Sarsembayeva & Kaliakin (Eds)
© 2023 The Author(s), ISBN 978-1-003-29912-7
Open Access: www.taylorfrancis.com, CC BY-NC-ND 4.0 license

Challenges executing deep foundations in metros and hydro power projects

B. Vidyaranya & A.K. Mishra
Bauer Engineering India Pvt. Ltd., India

O. Eswar Reddy
Sree Vidyanikethan Engineering College, India

ABSTRACT: The construction requirements of the deep foundations for the Urban Infrastructure and Hydro power projects in terms of the equipment, manpower and other resources planning are similar in nature. However, the construction and sequencing are the challenging issues for each activity. The paper tries to bring all the construction challenges in executing the deep foundations starting from the equipment planning, logistics, execution, geographical constrains, work front availability and uncertainties in the geological conditions. Maneuvering of the key construction equipment's like the trench cutters, hydraulic piling rigs and cranes movement in the metros is limited by the working space while on the contrary its limited spaces within the mountains. In terms of the geological constrains metros have the utility diversions and underground debris to be cleared before start of the works, while the fresh and completely weathered rock with shear zones and cavities pose challenges during the construction. In this paper, authors tries to bring in case studies of the projects executed in metros and hydro power project with the same equipment highlighting the insights for better planning and scheduling of the activities.

1 INTRODUCTION

This paper discusses deep foundation works of wtypical projects executed in the urban and hilly terrain for the construction of Metro and Hydro power projects. The challenges encountered during the execution of foundation works for Cairo Metro, Mangdechhu Hydroelectric Project and Jannah Dam projects are described in detail in this paper. This paper makes an effort to detail the equipment's used for construction and other challenges encountered during the execution. The equipment used for the both the projects are the same whose details are shared in below section.

2 MAIN EQUIPMENT FOR DIAPHRAGM WALL (D-WALL) OR CUT-OFF WALL (COW)

For the execution of the Diaphragm Wall or Cut-Off Wall trench cutter systems are used. The trench cutters have cross-sectional area of 2.80 m x 1.20 m. These trench cutters are mounted on base carriers equipped with Hose Drum System (HDS) or Hose Tension System (HTS). To ensure the high-quality standards. During cutting operation bentonite slurry circulation ensures the continuous working process of the D-wall construction by stabilizing the trench and removal of the excavated spoil. The polluted slurry from the trench are sent to the centralized desanding units/ slurry treatment plant to separating the excavated material from the slurry fluid. After the

DOI: 10.1201/9781003299127-185

separation the slurry is available for reuse within the system. Up to 1000 m3 of working slurry is processed every hour by the installed Bauer BE500 and BE550 desanding plants.

3 MANGDECHHU HYDROELECTRIC PROJECT, BHUTAN

Concrete Cut-off Wall in place of permeation grouting was executed in the upstream coffer Dam of Mangdechhu Project (Mishra et al. 2019). The work was carried out by the Bauer, Germany. The induction of Concrete Cut-off Wall was done primarily because the River Borne Material (RBM) had the silt content more than 18%. As per the research carried out worldwide, it is established that the permeation grouting is effective only when the silt content in the RBM is less than 18%. Henceforth, profession Engineers on ground shall appreciate that Concrete Cut-off Wall is the best solution for controlling the river side seepage in the RBM as the same has been seen on ground in Mangdechhu Project, Bhutan. As far as the cost per sq meter of the cross-sectional area of the river is concerned, the Concrete Cut-off Wall is slightly costlier than permeation grouting but 100% effective in controlling the seepage.

Underground Powerhouse (UGPH) of Mangdechhu HE Project had the low dipping shear zones on both the long walls of the UGPH and the consultant advised for shifting the Underground Powerhouse as above along the longitudinal axis by 40m. However, the UGPH as above was not shifted by the MHPA and the 3 DEC software was used for Numerical Modelling by the NIRM to find out the deformations in the Crown and the Sides of the UGPH. Based on the results of the analysis as above, the rock supports were modified, and intensive grouting was carried out by deploying Mahi Pumps. With the above, MHPA saved one year construction time for the Project.

4 CAIRO METRO

Cairo, the capital of Egypt, is the biggest city of the Islamic hemisphere, with approximately 21 million inhabitants in Greater Cairo. The first tram opened in 1896 and this tram system formed an important part of public transportation. But sharing the streets, additionally with busses transporting approximately two billion passengers per year, called for the establishment of an underground infrastructure as being the efficient solution. Consequently, the Cairo Metro has become the most important public transport system. Two lines with a total length of 61.5 km are in operation and transporting approximately 950 million passengers a year by 2004. The National Authority for Tunnels (NAT), a department of the Ministry of Transport, Arab Republic of Egypt, is the owner and in charge of all constructions. When Metro Line 1 was opened in 1987, it consisted of 4.7km long tunnel section. In 1990's, the first tunnel under the river Nile was constructed for Metro Line 2. The works for Line 3 started in 2008. The total lengths are divided into four phases of which phases 2 & 3 with a length of 12 km are already in operation. The works executed by Bauer shown in Figure 1.

4.1 *Geotechnical works for metro line 3*

Bauer commissioned the specialist civil engineering works i.e. 18 of the 22 underground stations on Line 3 and constructed approximately 600,000m² of diaphragm walls and 58,000m² of silicate gel grout plugs (Mostafa et al. 2022) . BAUER executed open excavation pits, for the start shaft of TBM, several Metro stations and ventilation shafts. Excavation and foundation levels for stations planned up to 32m below ground water level requiring retaining walls (Diaphragm walls) with connection to deep-lying silicate gel grout plugs down to a maximum depth of 86m, allowing for the excavation of the construction pit in dry conditions controlled by dewatering of limited seepage. Mostly, the stations are located under existing roads. Depending on traffic, the concerning road was closed partly or completely by temporary traffic diversions. After the completion of D-Walls and silicate gel grout plug, the main contractor shall start excavation and construction using the top-down method with temporary struts.

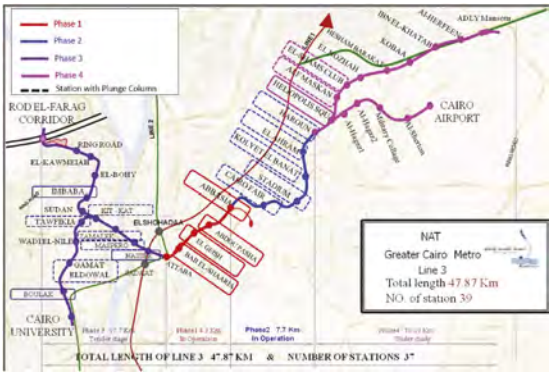

Figure 1. Cairo Metro, Line 3 - Stations awarded to Bauer are surrounded by a rectangle with the same color as the phase. Plunge columns were used in station where the boxes are dotted.

The execution was based on the following general construction sequence:

- Construction of the vertical retaining walls by means of diaphragm wall technique
- Installation of Plunge Columns
- Construction of cut-off walls to divide a station box into smaller boxes
- Construction of the sealing base as a silicate gel grout plug

The general soil profile at awarded sites are investigated had cultural fill, clay, silt, and sand profile. There was no presence of natural impervious soil layer within acceptable depth in typical Cairo soil conditions for Line 3, construction pits usually also needed cut-off from ground water at the bottom by a horizontal grout plug in form of soft gel. The grouting activities for the horizontal sealing of the excavation pits started after completion of the reinforced diaphragm walls in two main phases. Preparation of actual permeation grouting by drilling vertical holes in a defined grid and installation of grouting tubes into the holes supported by a self-hardening bentonite-cement-slurry. When this slurry gained sufficient strength, the actual grouting with soft silicate gel was commenced valve by valve and layer by layer. The silicate gel grout plugs for Cairo Metro Line 3 had thicknesses varying from 4.5-12 m, complying with the individual specifications of site. To allow for grouting up to five layers, the same number of tubes with one valve each per hole were installed at the various layer's elevations accordingly. For mixing the silicate gel, sodium silicate and reactant are required so that the water becomes a gel. Grout by Silicate gel is highly sustainable, as it requires less transportation produce silicate gel on site with less material consumption thus reducing carbon footprint. Before excavation, the water level is lowered inside by internal wells. By means of residual dewatering, the water level is kept at the required level below the bottom of the excavation pit.

4.2 *Diaphragm wall*

The underground retaining structure/ wall is constructed by means of the diaphragm wall technique formed of individual panels, each of panel length varying between 2.80 m to 6.80 m having nominal thickness of 1.20 m. To create a structural and watertight bond between the respective adjacent panels, primary panels are overcut during the excavation of the secondary panels depending on the required depth. Static calculation of the walls require reinforcement in all panels, so prefabricated reinforcement cages are installed in the primary panels in an exact position, to avoid any subsequent contact between the cutter and the reinforcement during the trenching of the secondary panels. The construction sequence is shown in Figure 2.

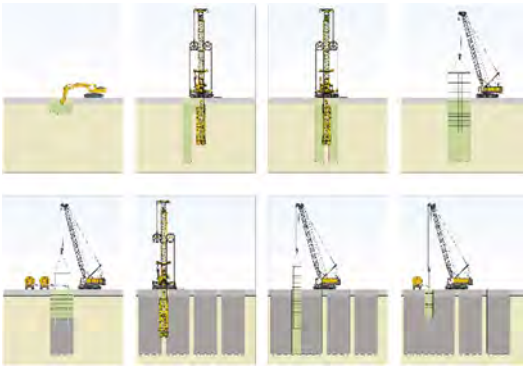

Figure. 2. Schematic Construction sequence of Diaphragm wall using cutter.

4.3 *Trench stability*

Technically and economically appropriate option for the construction of diaphragm wall is the use of supporting bentonite slurry to stabilize the open trench. However, considering the conditions (e.g., the price & availability of bentonite, properties of the subsoil, storage, disposal, etc.) there may be reasons to consider alternatives. Polymers are used in diaphragm wall construction sites.

4.4 *Permeation grouting*

Permeation grouting by means of silicate gel is used in the excavation pits at Cairo Metro project in appropriate depth regarding safety against uplift, and because the subsoils in these depth mostly consists of sand. Grouted horizontal cut-offs for which the safety against hydraulic uplift is to be verified are assumed to be totally impervious with an imaginary membrane located at the proposed underside of the horizontal cut-off. In the analysis the uplift pressure acting on the underside of the grouted horizontal cut-off is balanced against the total weight of all soil layers above the imaginary membrane. Bauer BG 28 piling rigs with extended mast along with grout or soft gel containers with grout pumps are used on site along with several mixing plants.

4.5 *Jet grouting*

The objective of the jet grouting between the existing Sewer and the CML3 tunnel is to allow the TBM to bore the tunnel in a safe way that there is no filling of the sewer with the slurry. In addition, the settlement and the differential settlements of the sewer tunnel should be limited to the minimum possible while the TBM is crossing below the Sewer. The jet grouting soil treatment zone is extended to 20 m along the sewer on each side of the crossing. As per the geometry and design of the treatment zone, a network of Jet Grouting points had to be installed with different inclinations in both directions and different depths. The design Jet Grout column was 2 m. In reality the actual diameters reached up to 2.20m to 2.30 m. The main advantage of Jet grouting is that large solidified elements can be executed in the ground using a relatively small drill rod of approximately 150mm and the method is applicable within limited working space. Bauer BG 28 piling rig, Jet grouting pump and a complete mixing plant for the Jet Grouting Works.

4.6 *Soil freezing*

During the tunnel boring works for Cairo underground metro line 3, a collapse caused by one of the segmental liners having failed during tunnel construction. Inflow of water and soil flooded the tunnel boring machine (TBM) resulting in a sink hole at the ground surface. The TBM was buried at a depth of about 30m under the street level. After evaluation of different

options considering jet grouting, ground freezing and mixed solutions using both techniques, finally the construction of a shaft directly in front of the TBM and horizontal ground freezing was chosen to rescue the TBM. Two rings of bore holes, with the holes tapering towards each other, were necessary for this. These holes were drilled from a previously constructed rescue shaft. The frozen soil body to be produced to act as sealing and structural member. In general, ground freezing technology was used for temporary groundwater control and excavation support in shaft construction and tunnelling projects. The main application is, however, the creation of a water cut off (groundwater control) with a certain aspect of ground stabilization. Therefore, the methodology depends in general on soil material in conjunction with adequate volumes of natural water. The technology is environmentally friendly as it takes temporarily advantage of the physical properties of the soil and water without changing their quality and natural condition permanently. There are two principal artificial ground freezing procedures that are used to convert groundwater to ice, creating a strong watertight soil body in the ground: ground freezing with brine or with liquid nitrogen (Figure 3).

This method utilizes large portable freezing /refrigeration plants where the refrigerant solution is passing through the following circular process. The basic principle involves:

- Compression of gaseous ammonia; this increases the temperature of the gas to approximately 70°C and a pressure of 12 bar.
- Cooling down of the gas to 35°C with the pressure remaining at 12 bar, thereby liquefaction.
- Decompression of the liquid ammonia (evaporation), thereby lowering of the temperature to approximately -35°C.

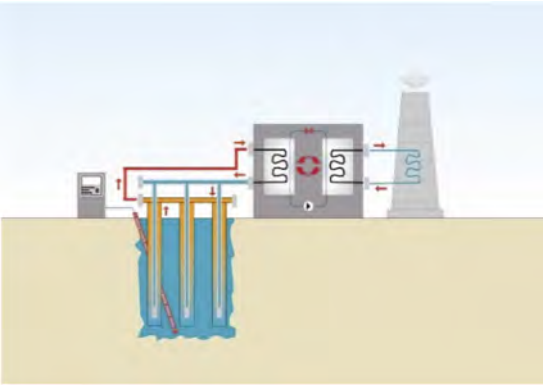

Figure 3. Soil freezing with brine (schematically only).

5 JANNAH DAM, LEBANON

The water shortage in the Mount Lebanon and Greater Beirut area in the year 2035 is estimated by the World Bank at more than 350 million cubic meters. Jannah Dam, with a design capacity of up to 38 million cubic meters, along with other envisaged dams, is expected to help alleviate the problem of water scarcity. The planning study, as well as the dam design, was carried out by the engineering firm Khatib & Alami and Artelia Group respectively. The construction was entrusted to Andrade Gutierrez Group, as the main contractor. The project site extends over a length of 500 m in a relatively narrow, steep and rocky section of the Jannah Valley. The soil conditions are characterized by Quaternary alluvial deposits with a thickness of up to 53 m and underlying limestone and dolomite. Several tectonic folds do exist adjacent to or across the project area.

The alluvial deposits consist mainly of the following:

- Gravels, cobbles and blocks of limestone and dolomite in fine- to coarse-grained sandy-clayey matrix

- Medium-dense to dense, slightly loamy to clayey sand, partly with gravel inclusions. Intermittent areas of loosely bedded sand were also recorded
- Soft to very stiff clay with intercalated bands of sand

5.1 *Main works*

The major deep foundation works executed on this project included:

- Cut-off wall at Upstream cofferdam
- Cut-off wall at Downstream cofferdam
- Diaphragm walls to create a bulkhead
- Consolidation and curtain grouting
- Ground improvement by means of piles

A major challenge of the project was the required deep excavation below the river level. Special concepts to control the water ingress and ensure the stability of the excavation and the footing had to be implemented (Adnan et al. 2022).

5.2 *Cut-off walls at cofferdam*

The cut-off wall at the upstream cofferdam extended to a depth of 42 m and stretched to about 128 m. The excavation was predominantly in alluvial deposits. On the slopes, the cut-off walls are keying into the bedrock. The cut-off wall at the downstream cofferdam extended over 161 m, and the maximum depth reached 50 m. Bauer proposed the utilization of the cutter technique. In addition to the reliable verticality control and higher performance, this technology mitigates the so-called hydraulic windows at the connection to the bedrock.

5.3 *Bullhead – as a block of diaphragm walls*

One of the remarkable challenges on this project was the execution of the bulkhead required for the excavation down to the foundation depth of the dam main body in the non-rocky soil. The relatively limited dimensions of the stretch available for the construction and the related hydraulic conditions prohibited an open excavation. The arch-shaped bulkhead was designed with a thickness of 4 m, supported in the bottom part with tie-back rods. The compressive strength of the bulkhead was specified with 7 MPa, a fully realistic strength magnitude for jet grouting columns executed in non-cohesive soil layers. The consideration of a different version of the jet grouting technique, besides the much longer retrieval rate, associated with almost total replacement of eroded soil by a viscous and solid-rich grout filling, results in much higher quantities of back-flow sludge. The construction of the diaphragm walls had to be associated with preliminary grouting measures. Some zones, with boulders and bedrock fragments adjacent to the trenches, had to be pre-treated to prevent them from falling onto the cutter during the excavation. The statically required use of structural concrete presupposed that the cutting of the already concreted panels was carried out as symmetrically as possible. For this reason, the two outer diaphragm wall rows were constructed first, followed by the middle row of the bulkhead structure. The coarse-grained soil between the two outer diaphragm wall rows therefore had to be pre-treated as well. Otherwise, during the construction of the second external row, the slurry would penetrate into this zone and lean against the previously produced first external row. The supporting effect would be lost, and the entire soil package located between the external rows could fall into the open trench. Apart from the acute risk for the cutter in the open panel, such a situation would require full-scale concrete cutting, together with the associated considerable wear and loss of performance.

5.4 *Grouting*

The grouting works on the project consisted of consolidation grouting under the footprint of the dam and three rows of grouting curtains extended into the abutments through several

layers of galleries, with the related QA/QC measures, such as coring and water pressure tests. The maximum depth reached some 80m in the foundation section and extended down to 100 m at the abutments. The co-existence of cavities on one side and relatively tight joints in the rock stratum on the other side impaired the suitability of the GIN method on the given project. Possibly, the rock properties in the sense of the pattern of the discontinuities at the dam location, have been particularly affected by the tectonic movements manifested by the encountered faults.

6 CONCLUDING REMARKS

The paper makes an attempt to highlight the challenges in executing the Deep foundations in Metro and Hydro Power Projects. Risks due to subsoil profile and working conditions. At Mangdechhu HEP in addition to the challenging mountainous terrain for the execution of works with fractured rock profiles, the reassessment of the shear zone has saved the construction schedule of the project by nearly 1 year. The successful implementation of the single-valve method for the execution of silicate gel grout plugs, and completion of several excavation pits for Metro Line 3, increased the confidence of client and contracted Bauer for six more stations for new Line 4 in Cairo Metro. The conditions at Jannah Dam required a flexible adaptation of the design and execution. The thickness of the clay layers, the diversity of the ground properties and the high static and hydraulic demands on the bulkhead imposed the use of a soil replacement method instead of a soil improvement method for its construction. The frequent and extensive fault zones in the rock called for a flexible adaptation of the originally specified GIN injection method. The case histories of projects executed in metros and hydro power at Mangdechhu HEP, Cairo Metro and Jannah Dam project with the same equipment mandate extensive planning, review of ground profiles and scheduling of the activities for successful completion of projects.

ACKNOWLEDGEMENT

We thank Mr. Mishra and his colleagues (Mishra et al. 2019) for their support in understanding the identification of the shear zone and mitigation measures in Dam structures in Himalayan mountains. We thank our colleagues Mostafa and team (Mostafa et al. 2022) for sharing the learning from the Cairo Metro operating in middle of Urban Infrastructure. Use of soil freezing in retrieving TBM is highly commendable. We thank Adan and other colleagues (Adnan et al. 2022) for the information on the construction of Bulkhead and Grouting works at Jannah Dam.

REFERENCES

Adnan M., Baltruschat M., Abdo G. and Daher K. Jannah Dam in Lebanon – A remarkably broad range of applied geotechnical works. Proceedings of Indian Geotechnical Conference (2022), paper ID T H–10–018.

Flora, A. et al: The diameter of single, double and triple fluid jet grouting columns: prediction method and field trial results. In: Géotechnique Volume 63 Issue11 (2013).

Mishra A.K., Chaudhary R.K., Punetha P., Lahkar K. and Ahmed I. Cut-off wall a boon for deep foundation Pits: A case study of Mangdechhu Hydro-Electric Project, Bhutan. Journal of Engineering Geology (2019), Volume XLIV, No.s 1 & 2.

Mostafa M., Wahby A., Beckhaus K. and Baltruschat M. Special Geotechnical Works for Metro Cairo (Egypt). Proceedings of 11th Annual Conference, DFI India (2022), paper ID DFII2263.

SATCOM: Geotechnical Investigations Jannah Dam Project (Feb 2015).

The National Authority for Tunnels (NAT) (2004) Tender Documents – Cairo.

Smart Geotechnics for Smart Societies – Zhussupbekov, Sarsembayeva & Kaliakin (Eds)
© 2023 The Author(s), ISBN 978-1-003-29912-7
Open Access: www.taylorfrancis.com, CC BY-NC-ND 4.0 license

Performance evaluation of Composite Caisson-Pile Foundation (CCPF) in sand using finite element model

K.C. Rajan
Department of Civil Engineering, Pulchowk Campus, Lalitpur, Nepal
Indian Institute of Technology Kanpur, Kanpur, India

Keshab Sharma
BGC Engineering Inc., Fredericton, Canada

Monu Lal Burnwal & Prishati Raychowdhury
Indian Institute of Technology Kanpur, Kanpur, India

Indra Prasad Acharya
Department of Civil Engineering, Pulchowk Campus, Lalitpur, Nepal

Jibendra Misra
Bridge Branch, Department of Roads, Government of Nepal, Kathmandu, Nepal

ABSTRACT: Caisson (Well) foundation has been widely used in South Asian countries like Nepal, India for construction of bridge piers and abutments. Generally, the caisson is cast in the ground and slowly sunk to the desired depth by gravity. But, due to sinking difficulties, designers are discarding it despite its several advantages. To overcome such a peculiar situation by taking advantage of caisson foundation, a composite caisson-pile foundation (CCPF) has been recently proposed and used to construct a bridge foundation in Nepal. This study aims to investigate the load-settlement behaviour of CCPFs resting on sand subjected to vertical load using three-dimensional finite element analyses. Through other numerical and experimental studies, the accuracy of the finite element analysis was proven to be correct and valid. A detailed parametric study is conducted, which includes the influence of pile length, number of piles and friction angle on the performance of CCPF embedded in sand.

Keywords: Load settlement, Pile foundation, Caisson foundation, Composite foundation, CCPF, FEM

1 INTRODUCTION

Caissons and piles are the two most popular deep-water foundation types for bridges spanning rivers and seas. For long-span bridges (Chowdhury et al. 2017; Bag et al. 2021) and in rivers where the depth of alluvial deposits and scour at the base of pier foundations might be rather significant (Kothyari 2007; Mukherjee et al. 2015), a caisson foundation—also known as a well foundation—is acceptable to meet the criteria for stability and serviceability. Caissons work well in liquefiable soils but are susceptible to strong seismic motion, as shown by recent incidents like the 1995 Kobe Earthquake (Liang et al. 2018). However, its construction has been plagued by recurrent obstacles due to difficulties in sinking to the desired depth. For instance, it took more than 10 years to finish the caisson foundations for a five-span, 175 m long bridge in Lumbini, Nepal's strategic road network because there were unanticipated hard strata within the foundation's design depth. Numerous bridge projects in Nepal, India, and China had similar issues (Bag et al. 2021; Tu et al. 2021; Misra et al. 2022).

DOI: 10.1201/9781003299127-186

Contrarily, pile foundations are more adaptable and favoured in situations when the ground's hard strata are significantly deeper and have a much lower bearing capacity than caissons. However, due to its limited ability to withstand vessel impact and difficulty in construction as a result of its extensive length and reduced rigidity, it might not be the best option to use in deep water. To address these issues, the caisson and piles may be combined to create the cutting-edge Composite Caisson-Pile Foundation (CCPF), a hybrid foundation that utilizes the best aspects of both types of foundations while minimising their drawbacks. Figure 1a and 1b show the schematic diagram of section and plan view of CCPF system.

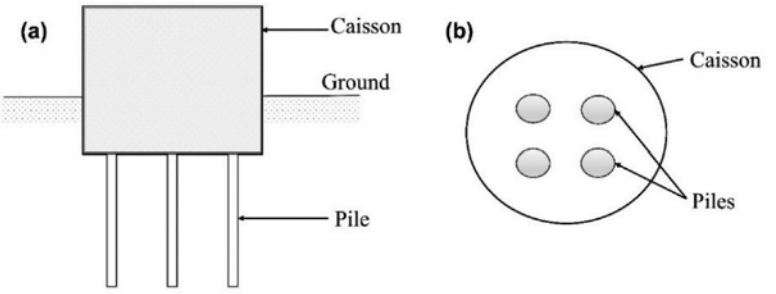

Figure 1. Composite Caisson-Pile Foundation (CCPF): a schematic diagram.

CCPF provides innovative solutions to complex site conditions in deep-water and reduces construction time and cost. Compared to conventional foundations, the CCPF may effectively minimize the length and embedment depth of the caisson and pile foundation, reducing construction complexity and risk (Huang et al. 2018). However, the research on CCPF is still scanty (Tu et al. 2020). Moreover, performance evaluation study of CCPF is still lacking. Due to which, the application of CCPF has been minimal. More research and development initiatives are desperately needed to give designers more confidence in adopting such innovative foundation systems. Thus, in this study, a 3-D finite element model (FEM) of CCPF is developed and parametric study has been conducted based on vertical load-settlement response of the foundation.

2 FEM AND ITS VALIDATION

Plaxis 3D was used to develop 3-D model of the CCPF (Figure 2). The PLAXIS 3D library's 10-node tetrahedral components are used to simulate the soil volume with medium meshing. A linear elastic-perfectly plastic Mohr-Coulomb failure criteria is used to represent the behaviour of sand. Modeling of the caisson and piles is done using plate and embedded beam element with a special interface. The soil and structural elements are assumed to have a smooth interfacial contact by setting 'R_{int}' to 0.67.

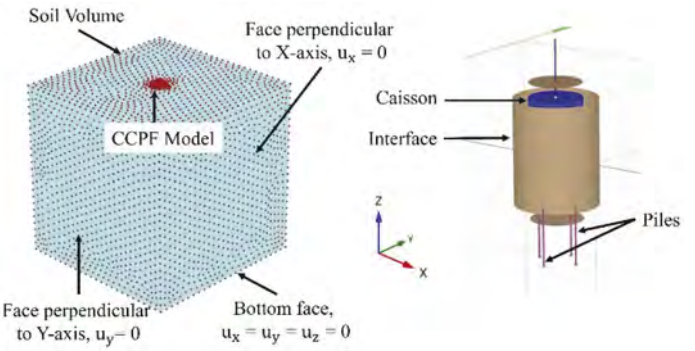

Figure 2. Meshing and boundary conditions of Finite element model of CCPF.

The validation of the model was done with the static CCPF load test conducted in the field by Wang et al. (2015) in China. Two tests are chosen for validation. The first test was performed on a caisson of size 0.6 x 0.6 x 0.8 m and thickness of 20 mm without considering any pile. The second test was performed on a same-size caisson with 3 x 3 piles of 40 mm diameter and 2 mm thickness located under the caisson with 15 mm in thickness. Each pile was 0.5 m in length. Pile and caisson were simulated by steel plate of elastic shear modulus of 216 GPa. The subsoil comprised dry sand. The results of the vertical field test and finite element analyses are presented in the form of load-settlement curves in Figure 3 for caisson alone case and caisson with 3 × 3 piles. Overall, it can be noted that the calculated load-settlement responses of the foundations show a close match with the field test results in terms of both trend and magnitude.

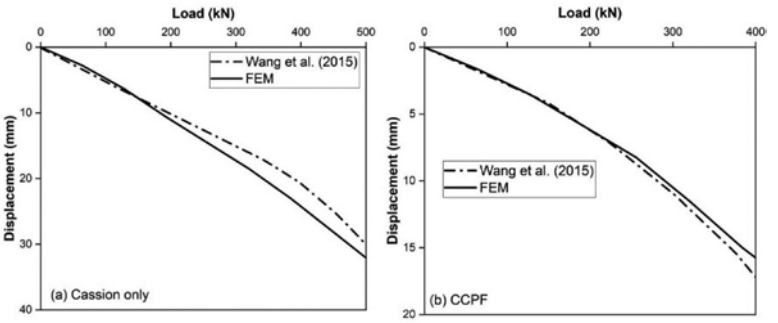

Figure 3. Validation of the finite element model with the vertical load test results of Wang et al. (2015): (a) caisson only (b) CCPF with 50cm long 3 × 3 piles.

3 RESULT AND DISCUSSION

3.1 *Effect of length of piles*

Four pile lengths (10m, 12m, 14m and 16m) were considered for the study to assess the effects of pile length on performance of CCPF. Figure 4 shows the load-settlement response of CCPF for these pile lengths. It can be seen that the settlement has been significantly reduced with increase of pile length from 10m to 14m. However, after reaching 14m, the settlement for 16m long piles found to be increased again. At any settlement level, it is found that the increase in CCPF's load-carrying capability increases with the length of the pile. For instance, load improvement ratios (LIR) for pile lengths 10, 12, 14, and 16 m are calculated as 1.13, 1.32, 1.53, and 1.54 accordingly at 0.1 m settlement level. Another significant finding is that lower settlement levels have a bigger boost in CCPF capacity. For instance, the estimated LIRs for 0.1m to 0.5m settlements at a 14m pile length are determined to be 1.53, 1.41, 1.29, 1.26, and 1.24, respectively. Such a situation can be explained by the fact that the CCPF's rigidity reduces as load level, or greater settlements, increases. In comparison to situations where pile length increases from 14m to higher values at any settlement level, the increment rate of LIR is higher when the pile length goes from 10m to 14m.

3.2 *Effect of pile number*

To assess the effects of number of piles in performance of CCPF, various numbers (0, 1, 2, 4 and 5) of piles were utilized in the 3D model. Figure 5 shows the load settlement response of CCPF for various number of piles. It is worth mentioning that the settlement is reduced with increase in number of piles from 0 to 4, however, it has been found increased in 5 piles condition; which indicates that the sole increase in number of piles beyond a limit cannot decrease the settlement of CCPF.

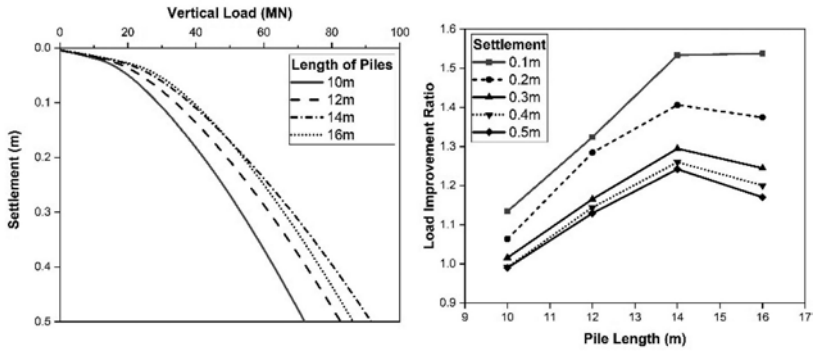

Figure 4. Load-settlement response and LIR ratios of CCPF for various pile lengths.

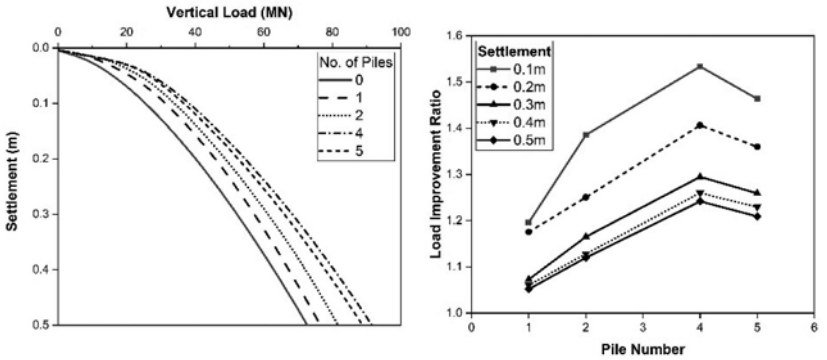

Figure 5. Load-settlement response and LIR ratios of CCPF for various pile number.

3.3 *Effect of friction angle*

In this series, tests were conducted on CCPF foundations in soils having angle of internal friction (ϕ) of 20°, 25°, 30°, and 35°. The remaining parameters and geometry remained the same as described in the previous section. Figure 6 presents the results of this series in the form of load-settlement curves for different angles of internal friction (ϕ). It can be noted that the settlement decreased rapidly with an increase in the angle of shearing resistance from 20 to 35°.

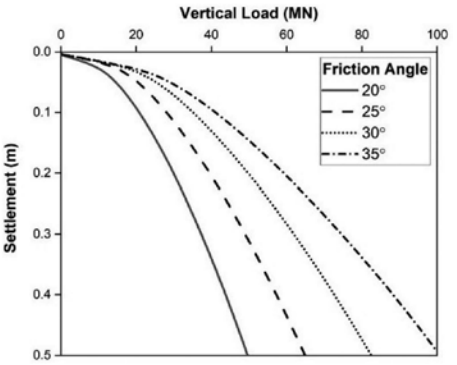

Figure 6. Load-settlement response of CCPF for various angle of friction of sand.

4 CONCLUSIONS

Following are the conclusions of the numerical study on CCPF:

- The CCPF maximizes the vertical load carrying capacity of the soil while successfully controlling the settlement. Generally, the caisson could support the top weight and be utilized as a platform for bridge construction. After bridges are erected, the piles beneath the caisson may be used to regulate the settlement.
- It can be seen that the settlement has been significantly reduced with an increase in pile length from 10m to 14m. However, after reaching 14m, the settlement for 16m long piles was found to be increased again.
- At any settlement level, it is discovered that the increase in CCPF's loadcarrying capability increases with the length of the pile. Another significant finding is that lower settlement levels have a bigger boost in CCPF capacity.
- In comparison to situations where pile length increases from 14m to higher values at any settlement level, the increment rate of LIR is higher when the pile length goes from 10m to 14m. The settlement is reduced with an increase in the number of piles from 0 to 4, however, it has been found to increase in 5 piles condition; which indicates that the sole increase in the number of piles beyond a limit cannot decrease the settlement of CCPF.
- It can be noted that the settlement decreased rapidly with an increase in the angle of shearing resistance from 20 to 35°.

REFERENCES

Bag R, Mandal M, Singhal V. 2021. Rectification of the Tilt and Shift of Well Foundation: A Numerical and Analytical Solution. Indian Geotech J [Internet]. 51(5):1011–1025. https://doi.org/10.1007/s40098-020-00477-5

Chowdhury I, Tarafdar R, Ghosh A, Dasgupta SP. 2017. Dynamic soil structure interaction of bridge piers supported on well foundation. Soil Dyn Earthq Eng. 97:251–265.

Huang M, Tu W, Gu X. 2018. Time domain nonlinear lateral response of dynamically loaded composite caisson-piles foundations in layered cohesive soils. Soil Dyn Earthq Eng [Internet]. 106(December 2016):113–130. https://doi.org/10.1016/j.soildyn.2017.12.015

Kothyari UC. 2007. Indian practice on estimation of scour around bridge piers - A comment. Sadhana - Acad Proc Eng Sci. 32(3):187–197.

Liang F, Jia Y, Zhang H, Chen H, Huang M. 2018. Centrifuge shaking table tests on composite caisson-piles foundation. Phys Model Geotech.:909–914.

Misra J, Subedi M, Sharma K. 2022. Design of composite well-pile foundation (CWPF): A case study of bridge foundation in Nepal. In: Proc 20th Int Conf Soil Mech Geotech Eng Sydney 2021. [place unknown].

Mukherjee A, Saha D, Harvey CF, Taylor RG, Ahmed KM, Bhanja SN. 2015. Groundwater systems of the Indian Sub-Continent. J Hydrol Reg Stud. 4:1–14.

Tu W, Deng Q, Zhang P, Chen HP, Liu Z. 2021. Evaluation of the lateral bearing characteristics of composite caisson-pile foundation considering the scour-hole dimensions. Mar Georesources Geotechnol [Internet]. 0(0):1–25. https://doi.org/10.1080/1064119X.2021.1914247

Tu W, Huang M, Gu X, Chen HP. 2020. Nonlinear dynamic behavior of laterally loaded composite caisson-piles foundation under scour conditions. Mar Georesources Geotechnol [Internet]. 38 (10):1265–1280. https://doi.org/10.1080/1064119X.2020.1724217

Wang L, Mu B, Gong W, Xia A. 2015. Experimental research on vertical bearing behavior of composite foundation constructed by caisson and piles. Comput Methods Recent Adv Geomech - Proc 14th Int Conf Int Assoc Comput Methods Recent Adv Geomech IACMAG 2014 .:991–996.

Smart Geotechnics for Smart Societies – Zhussupbekov, Sarsembayeva & Kaliakin (Eds)
© 2023 The Author(s), ISBN 978-1-003-29912-7
Open Access: www.taylorfrancis.com, CC BY-NC-ND 4.0 license

Negative skin friction effect on pile group due to an adjacent excavation

Paromeeta Bandyopadhyay & Fuchen Teng
Department of Civil and Construction Engineering, National Taiwan University of Science and Technology, Taipei, Taiwan

ABSTRACT: Due to rapid infrastructure development in urban areas, is a common practice to excavate near an existing pile foundation which changes the state of stress of the existing surrounding soil. The unloading due to excavation, changes the behavior of pile as compared to pile subjected to only vertical loading. If the excavation is near to a group pile, the group effect also tends to change the behavior of each pile in the group along with the unloading effect due to excavation. In this study, numerical simulation is done using commercially available software PLAXIS 3D to analyze the change in behavior of group pile due to adjacent excavation in commonly occurring multi-layered soil along the pile shaft. The analysis is done with Hardening soil constitutive model to simulate the naturally existing soil strata. The results from this study can be used for similar type of soil to predict the change in behavior of group pile subjected to deep excavations.

1 INTRODUCTION

Underground construction is often a necessity to improve the infrastructure in urban areas. Such underground constructions lead to deep excavations and tunnel construction which invariably affect the surrounding existing structures. Mostly the existing structures like buildings, bridge piers, and metro corridors are supported by pile foundation. As compared to a single pile, a pile group connected by a pile cap is more common as a foundation system. Hence, how an excavation affects a nearby pile group is a topic of interest for engineers to ensure the safety and serviceability of the existing structures. Most of the previous studies consider only one type of soil, either clay or sand to analyze the change in behavior of an existing pile foundation when it is subjected to a nearby excavation.

Liyanapathirana and Nishanthan (2016) and Ong et al. (2009) numerically analyzed the additional deflection and bending due to excavation caused in a single pile and pile group respectively in clay. Ong et al. (2006) used centrifuge test to predict the post-excavation soil settlement, wall deflection and pile movement for a single pile in clay. Korff et al. (2016) proposed analytical method to determine the vertical movement of pile in soft soil with the assumption that horizontal stress remains same during the excavation. Shi et al. (2019) performed three dimensional numerical analyses to predict the settlement and stress transfer mechanism due to excavation in dry sand.

It is most unlikely that any naturally occurring soil profile will consist of only clay or only sand. Generally, a soil profile is a combination of multiple layers of sand and clay with different properties for every layer of soil. This study tries to focus on the behavior of a pile group with three piles connected by a pile cap placed near to an excavation in the naturally occurring multi-layered soil. The soil excavation analyzed here is part of a metro railway project in Taipei city in Taiwan. Hardening soil model is used to simulate the behavior of soil in Plaxis 3D for this analysis. A typical naturally occurring soil profile in Taipei and the calibrated soil parameters for the Hardening soil model used in the analysis are shown in Table 1.

DOI: 10.1201/9781003299127-187

Table 1. Soil profile and parameters for Hardening Soil model.

Depth(m)	Soil type	γ(kN/m^3)	E_{ur}^{ref} (kPa)	E_{50}^{ref} (kPa)	E_{oed}^{ref} (kPa)
0~2.5	SF	18.84	27887	9296	13944
2.5~7.8	CL	17.66	30130	4184	2929
7.8~10.0	SM	18.76	50809	16936	25404
10.0~12.6	SM	18.76	59081	19694	29541
12.6~17.5	CL	18.02	16290	3694	2586
17.5~22.5	CL	17.81	17560	3263	2284
22.5~25.0	CL	17.81	22180	4456	3119
25.0~27.0	CL	17.81	15600	3469	2428
27.0~29.5	CL	18.41	12070	4060	2842
29.5~32.0	CL	18.41	21460	6061	4243
32.0~35.3	CL	18.41	13560	5767	4037
35.3~36.8	SM	19.33	33607	11202	16804
36.8~42.7	CL	19.16	18760	5681	3977
42.7~46.5	ML/SM	18.92	38233	12744	19116
46.5~70.0	GW	19.00	61980	20660	30990

2 NUMERICAL ANALYSIS

The group pile is located 5 m away from the face of the excavation. The final depth of excavation is 24 m with a 1.2 m thick diaphragm wall. To keep the excavation stable, buttress walls are used at 7.5 m spacing and struts are positioned 5 m center to center distance horizontally. Commercially available finite element software Plaxis 3D is applied for the numerical analysis. Bottom up method of excavation is adopted a struts are placed 70 cm above the excavation level in each phase. The excavation geometry along with the pile group is shown in Figure 1, with the three piles in the group marked as PG1, PG2 and PG3.

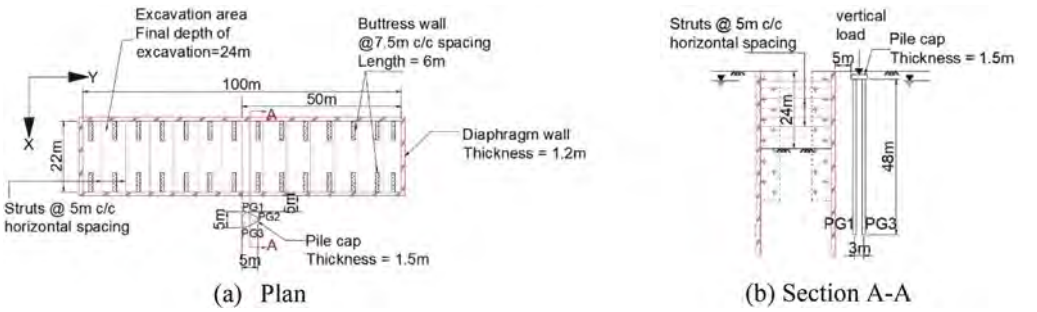

Figure 1. Excavation geometry with pile group.

To study the difference in effect on a single pile as compared to a group pile in the same soil profile, a single pile P1 of same dimension is placed at the location of PG1. The excavation geometry with the single pile P1 is shown in Figure 2. The geometry remains the same; only change is the group of three piles is replaced by a single pile P1 in the position of PG1. The intensity of load is kept same in both the cases.

2.1 *Pile properties*

The piles are 1 m in diameter, 48 m in length and connected by a pile cap of 1.5 m thickness placed 1 m below the ground surface. Embedded beam element is used in Plaxis 3D to simulate the pile. The connection between the pile and the pile cap is considered to be rigid. The pile properties as shown in Table 2.

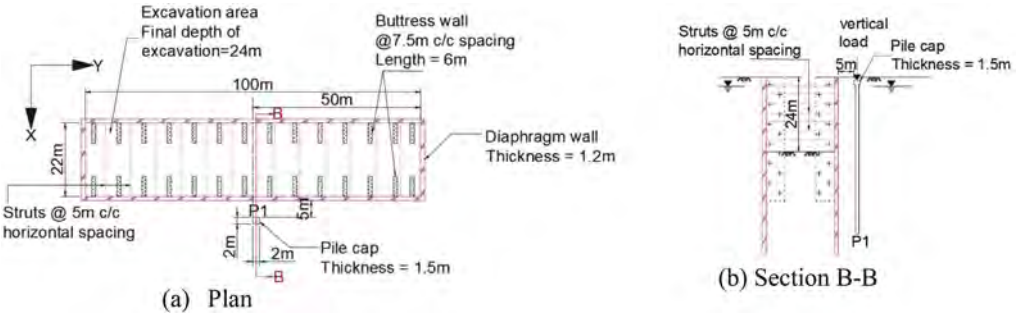

Figure 2. Excavation geometry with single pile.

Table 2. Pile parameters used in Plaxis 3D analysis.

Parameter	Value
Unit weight, ɣ (kN/m^3)	25
Young's modulus, E (kPa)	13*10^6
Pile diameter, d_p (m)	1
Pile length, L_p (m)	48
Maximum skin resistance, T_{max} (kN/m)	1*10^{12}
Maximum base resistance, B_{max} (kN)	1000

2.2 *Boundary conditions*

The vertical sides are fixed normally, base is fully fixed and the top is free to move in any direction. Hydraulically, there is no flow through bottom surface. All the vertical sides and top are open to allow flow of water.

2.3 *Phases in numerical modelling*

"Wished-in-place" piles are activated followed by the working load. The diaphragm wall along with the buttress wall are activated. Excavation is done up to -3.7 m first and first level of strut is installed 70 cm above the excavation level in each phase. This process is continued until the final formation level of 24 m is reached.

3 RESULTS AND CONCLUSION

3.1 *Interpretation of obtained results*

Figure 3 shows the lateral deflection of pile PG1 and P1. The lateral deflection towards the excavation is considered to be positive. The comparison shows that due to the same excavation dimension located at same distance away from the pile, there is no difference in lateral deflection between the pile in the group (PG1) and the single pile (P1). Figure 4 shows the comparison of bending moment between pile PG1 and P1 prior to excavation with only working load on pile (marked as 'WL only' in graphs) and at the completion of excavation (marked as 'final excavation' in graphs). The magnitude of maximum bending moment of PG1 and P1 is almost the same. The lateral behavior of the pile thus remains same for both group pile and single pile provided it is in same position with respect to the excavation.

The vertical settlement of piles PG1 and P1 are shown in Figure 5. Under the same intensity of load prior to excavation, the pile top for PG1 settles by 14.48 mm whereas for P1 it is 9.66 mm. Thus, PG1 settles more than P1 by 49.85%. But when excavation reaches the formation level. The pile top settlement of PG1 is 42.24 mm and that of P1 is 40.79 mm; PG1 settles only 3.54% more than P1. The axial forces of PG1 and P1 prior to and on completion of

excavation are compared in Figure 6. Due to the excavation, a drag down generates in the upper part of both PG1 and P1. The absolute maximum axial force in P1 is 3833 kN and that in PG1 is 3257 kN. Thus the axial force generated in single pile is more than that in the group.

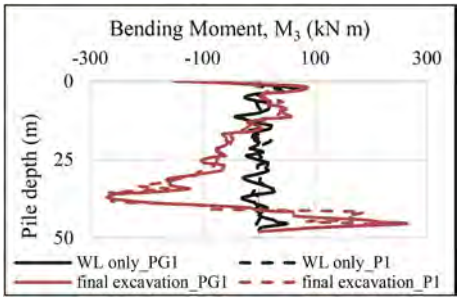

Figure 3. Lateral displacement of pile with depth.

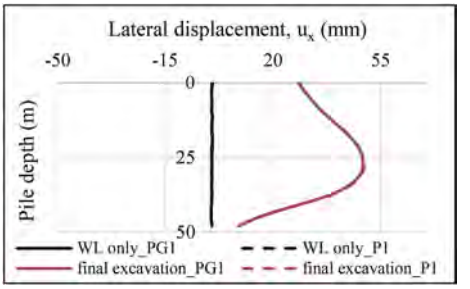

Figure 4. Bending moment of pile with depth.

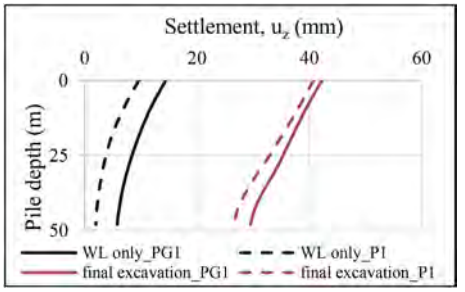

Figure 5. Settlement of pile with depth.

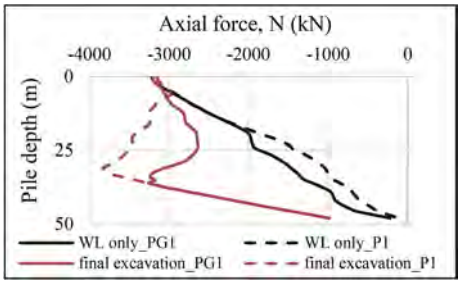

Figure 6. Axial force in pile with depth.

3.2 *Conclusion*

The study analyzed two piles of same dimension located in same position with respect to an excavation in a naturally occurring multi-layered soil. The lateral behavior of the pile, whether placed in a group or single remains same. The axial settlement of the group pile is more as compared to single pile. The axial force after the final phase of excavation, is more for the single pile. This behavior can be attributed to the pile group effect.

REFERENCES

Korff, Mandy, Robert J. Mair, and Frits A. F. Van Tol. 2016. Pile-Soil Interaction and Settlement Effects Induced by Deep Excavations. *Journal of Geotechnical and Geoenvironmental Engineering* 142(8): 1–14.

Leung, C. F., D. E. Ong, and Y. K. Chow. 2006. Pile Behavior Due to Excavation-Induced Soil Movement in Clay. II: Collapsed Wall. *Journal of Geotechnical and Geoenvironmental Engineering* 132(1): 45–53.

Liyanapathirana, D. S., and R. Nishanthan. 2016. Influence of Deep Excavation Induced Ground Movements on Adjacent Piles. *Tunnelling and Underground Space Technology* 52: 168–81.

Ong, D. E. L., C. F. Leung, and Y. K. Chow. 2009. Behavior of Pile Groups Subject to Excavation-Induced Soil Movement in Very Soft Clay. *Journal of Geotechnical and Geoenvironmental Engineering* 135(10): 1462–74.

Shi, Jiangwei, J. Wei, Charles W.W. Ng, and Hu Lu. 2019. Stress Transfer Mechanisms and Settlement of a Floating Pile Due to Adjacent Multi-Propped Deep Excavation in Dry Sand. *Computers and Geotechnics* 116(April).

Zheng, Gang, Si Yuan Peng, Charles W.W. Ng, and Yu Diao. 2012. Excavation Effects on Pile Behaviour and Capacity. *Canadian Geotechnical Journal* 49(12): 1347–56.

Smart Geotechnics for Smart Societies – Zhussupbekov, Sarsembayeva & Kaliakin (Eds)
© 2023 The Author(s), ISBN 978-1-003-29912-7
Open Access: www.taylorfrancis.com, CC BY-NC-ND 4.0 license

P-Y curves from the SPT test for laterally loaded single piles in sand

A. Laouedj
National Marine Science and Coastal Planning School University, Algeria

A. Bouafia
University Saâd Dahleb of Blida, Algeria

ABSTRACT: P-Y curves-based design methods offer a powerful framework of analysis of laterally loaded piles. This paper aims at presenting a practical method of direct construction of the P-Y curves for piles in sand on the basis of the number of blows N_{SPT} measured during the SPT test. This method was developed from a detailed interpretation of full-scale lateral loading tests on single piles carried out in sandy soils. The two main parameters of the P-Y curve, namely the lateral reaction modulus and the lateral soil resistance, were directly correlated to N_{SPT}. The methodology of construction of the P-Y curve from the SPT data is presented and the validation of the proposed method by testing it in a small sized database of full-scale loading tests showed a very good predictive capability.

1 INTRODUCTION

The non-linear subgrade reaction method also called P-Y curve is widely used for the design of laterally-loaded piles. As shown in Figure 1, the P-Y curve has a non-linear shape and is characterized by an initial slope denoted E_{ti} and called the lateral reaction modulus, and a horizontal asymptote P_u corresponding to the lateral soil resistance (Bouafia 2013-2017).

In spite of the large number of applications of the Standard Penetration Test (SPT) in foundation engineering and the important case histories of full-scale lateral load tests of single piles, it has not yet been published an original work dealing with a direct derivation of the lateral reaction P-Y curves on the basis of the Standard Penetration Test (SPT) (Laouedj & Bouafia 2017).

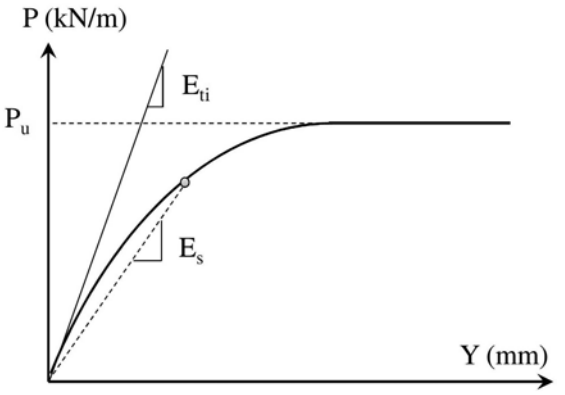

Figure 1. Schematic shape of the P-Y curve (Bouafia 2013-2017).

DOI: 10.1201/9781003299127-188

This paper is aimed at presenting a practical method of constructing the P-Y curves on the basis of a direct correlation of the two main parameters of the P-Y curve with the blow counts N_{spt} of the SPT test, derived from an extensive analysis of several full-scale lateral loading tests on fully instrumented single piles carried out in sandy soils. Subsequent validation of the proposed P-Y curves method was undertaken by predicting the behavior of many test piles reported in the literature.

2 METHODOLOGY TO CONSTRUCT P-Y CURVES

Hereafter is presented a step-by-step procedure to compute the parameters of the P-Y curves:

1. Along the pile, subdivide the soil into N horizontal slides thin so that the N_{spt} value may be considered varying linearly within any slide.
2. Assume the "*effective embedded length of the pile*" D_e equal the pile embedded length D.
3. Along the pile, compute the "*characteristic soil modulus*" E_C along the effective embedded length of the pile D_e as follows:

$$E_C = \frac{1}{D_e}\int_0^{D_e} N_{SPT}(z)\sigma_{v0}(z)dz \tag{1}$$

For practical purposes, the calculation of the integral can be replaced by the summation of the trapezes method.

4. Compute the "*lateral pile/soil stiffness ratio*" K_R defined as follows:

$$K_R = \frac{E_p I_p}{E_c D^4} \tag{2}$$

5. Determine the "*modulus number*" K_E^i of each slide i, from Table 1, depending on the position of the slide with respect to GWT (Ground Water Level) level, and compute the "*characteristic initial lateral modulus*" E_{ti}^C by the following equation:

$$E_{ti}^C = \frac{1}{D_e}\int_0^{D_e} E_{ti}(z)dz = \frac{1}{D_e}\int_0^{D_e} K_E N_{SPT}\sigma_{v0}(z)dz \tag{3}$$

6. Compute the "*elastic pile length*" (or the "*transfer length*") L_0 defined by:

$$L_0 = \sqrt[4]{\frac{4E_p I_p}{E_{ti}^c}} \tag{4}$$

Where E_pI_p is the pile flexural stiffness.

7. Compute the effective embedded length D_e of the pile defined as the smaller of the two following quantities:

$$D_e = min\ \{D, 3L_0\} \tag{5}$$

If $D > 3L_0$ (flexible pile), then repeat steps 3 to 7 according to an iterative process and introducing at each iteration step the value of D_e until the convergence. Otherwise, $D < 3L_0$ the pile is rather semi-rigid or rigid and the method is not applicable.

8. Compute the initial lateral reaction modulus E_{ti} and the lateral soil resistance P_u, K_N being the *"lateral resistance factor"*, for each slide as follows

$$E_{ti} = K_E N_{SPT}\sigma_v' \tag{6}$$

$$P_u = K_N \sigma_v' B \tag{7}$$

It was found that the modulus number K_E and the lateral resistance factor K_N depend on the position of the pile slide with respect to the groundwater table level as summarized in Table 1.

9. Construct the P-Y curve for each segment along the pile by using the hyperbolic function as follows:

$$P(z) = \frac{Y(z)}{\frac{1}{E_{ti}(z)} + \frac{|Y(z)|}{P_u(z)}} \tag{8}$$

10. To analyze the load-deflection response of a single pile under lateral forces, input the P-Y curves constructed according to this step-by-step procedure into any software based on the P-Y curves method, like SPULL (Single Pile Under Lateral Loads) developed at the University of Blida.

Table 1. Values of K_E and K_N for flexible piles.

Above water table	Below water table
$K_E = 207$	$K_E = 156$
$K_N = 21$	$K_N = 17$

3 VALIDATION OF THE PROPOSED METHOD

In order to demonstrate the predictive capability of the proposed method, the lateral load-deflection response of single piles was predicted. 21 full-scale lateral loading tests in 7 sandy soils were collected from the case studies reported in geotechnical literature, and studied according to the proposed method.

The seven test sites are: Chaiyi County, Taiwan (2 tests – Site 1), City of Natal, Brazil (6 tests – Site 2), Algiers Mosque, Algeria (3 tests – Site 3), Calgary, Canada (5 tests – Site 4), Opelika, Alabama, U.S.A. (1 test – Site 5), North Carolina, U.S.A. (2 tests – Site 6), and Solar farm projects (2 tests – Site 7).

The P-Y curves parameters were computed in correlation with the N_{spt} values, and the pile geometry, boundary conditions and P-Y curves were input into SPULL software. For each test pile, the P-Y curves parameters were defined according to the methodology described above. The load-deflection curve was simulated by computation using SPULL. The top lateral deflections calculated for each test pile were compared to measured top lateral deflections.

As shown by the Figure 2, very good agreement between the predicted pile deflections on the basis of the proposed method of P-Y curves and the measured ones is to be noticed. It can also be seen that the best prediction is for small and medium pile deflections.

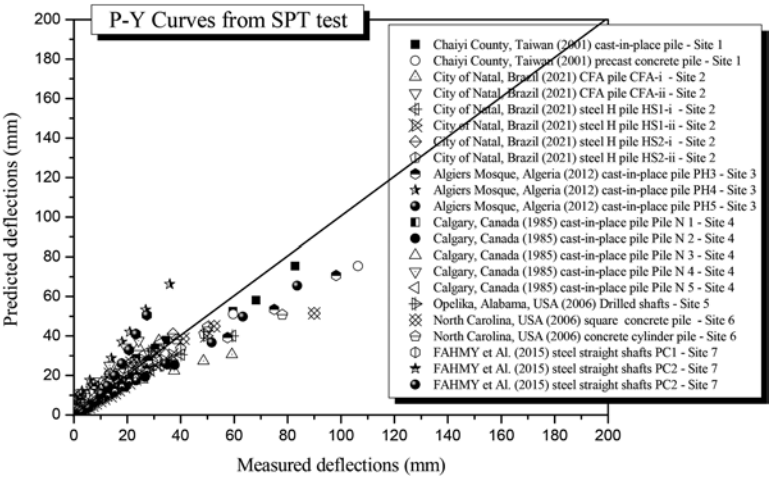

Figure 2. Comparison of predicted to measured pile deflections.

4 CONCLUSION

This paper presents a practical method of construction of the P-Y curves whose parameters, namely the initial reaction modulus and the lateral soil resistance, are directly correlated to the N_{SPT} value of the standard penetration test SPT.

A step-by-step procedure to define the parameters of P-Y curves for a single pile under lateral loads in sandy soils was suggested.

A small sized database of 21 full-scale horizontal pile loading tests carried out in 7 sandy sites worldwide are used to validate the proposed method. The comparison of the predicted pile deflections to the measured ones showed very good predictive capability. This finding is encouraging seeing the multitude of uncertainties affecting the data analysis during the process of development of this empirical method.

REFERENCES

Anderson, J. B., Townsend, F. C. & Grajales, B. 2003. Case history evaluation of laterally loaded piles. *Journal of geotechnical and geoenvironmental engineering*, 129(3): 187–196.

API (American Petroleum Institute). 2014. Petroleum and natural gas industries-specific requirements for offshore structures, Part 4: Geotechnical and foundation design considerations, ISO 19901-4:2003 (Modified), 138 p.

Bouafia A. 1998. Experimental analysis of large lateral displacements of piles in centrifuge. *In: Proc. of the 4th International Conference on Case Histories in Geotechnical* Engineering, *March 8–15 1998*. 1–12 St-Louis, Missouri USA.

Bouafia, A. 2007. Single piles under horizontal loads in sand: determination of P–Y curves from the prebored pressuremeter test. *Geotechnical and Geological Engineering*, 25(3): 283–301.

Bouafia, A. 2013. P-Y curves from the prebored pressuremeter test for laterally loaded single piles. *In Proceedings of the 18th International Conference on Soil Mechanics and Geotechnical Engineering*, 2695–2698. Paris.

Bouafia, A. 2014. P-Y curves from the CPT test for laterally loaded single piles in sand. *In Proceedings of The 3rd International Symposium on Cone Penetration Testing (CPT'14)*, 881–887. Las Vegas, Nevada, USA.

Bouafia, A. 2017. Laterally loaded single piles-Construction of P-Y curves from the cone penetration test. *In 19th International Conference on Soil Mechanics and Geotechnical Engineering*. 2957–2960. Seoul, Korea.

Bouafia, A. & Lachenani, A. 2005. Analysis of P-Y curves for single piles from the prebored pressuremeter test. *In Proceedings of the 16th International Conference on Soil Mechanics and Geotechnical Engineering*, 1955–1958. IOS Press.

Clark, J. I., McKeown, S., Lester, W. B. & Eibner, L. J. 1985. The lateral load capacity of large diameter concrete piles. *In 38th Canadian Geotechnical Conference*, Theory and Practice in Foundation Engineering.

Cosentino, P. J., Kalajian, E., Stansifer, R., Anderson, J. B., Kattamuri, K., Sundaram, S. & Cottingham, M. A. 2006. Standardizing the pressuremeter test for determining p-y curves for laterally loaded piles. Final Report FDOT-BD658, *Florida Department of Transportation*, Tallahassee, Melbourne, Florida.

Fahmy, A. & El Naggar, M. H. 2015. Lateral performance of helical tapered piles in sand. *In Proceedings of the Canadian geotechnical conference* GEOQuebec.

Georgiadis, M., Anagnastopoulos, C. & Saflekou, S. 1992. Centrifugal testing of laterally loaded piles. *Canadian Geotechnical Journal*, 29(2): 208–216.

Huang, A. B., Hsueh, C. K., O'Neill, M. W., Chern, S. & Chen, C. 2001. Effects of construction on laterally loaded pile groups. *Journal of geotechnical and geoenvironmental engineering*, 127(5): 385–397.

Laouedj, A. & Bouafia, A. 2017. Design and analysis of single piles under lateral loads in cohesionless soils based on the standard penetration test (SPT). *In MATEC Web of Conferences*. EDP Sciences. Vol. 120, p. 06001.

Laouedj, A. & Bouafia, A. 2017. Pieux isolés sous charges latérales–Construction des courbes P-Y à partir de l'essai SPT(in French). *Revue Francaise De Geotechnique*, (152), 4.

Laouedj, A. & Bouafia, A. 2021. P-Y curves for single piles in sand from the standard penetration test (SPT). *Journal of Materials and Engineering Structures «JMES»*, 8(1): 159–172.

Sousa, A. M. D. D., Costa, Y. D. J., Araujo, A. G. D. D. & Costa, C. M. L. 2021. Behavior of CFA and H-section steel piles in lateral loading: experimental and numerical analysis. Revista IBRACON de Estruturas e Materiais, e14313: 14(3).

Smart Geotechnics for Smart Societies – Zhussupbekov, Sarsembayeva & Kaliakin (Eds)
© 2023 The Author(s), ISBN 978-1-003-29912-7
Open Access: www.taylorfrancis.com, CC BY-NC-ND 4.0 license

Estimation of stiffness of disconnected piled raft foundation system with pile contribution factors

B. Yoon & W. Lee
Korea University, Seoul, South Korea

H. Choo
Hanyang University, Seoul, South Korea

C. Lee
Chonnam National University, Gwangju, South Korea

ABSTRACT: Behavioral analysis of the disconnected piled raft foundation (DPRF) is more complicated than the conventional piled raft foundation owing to the complex interactions between piles, subsoil, and load transfer platform (LTP). The effect of pile-related parameters and LTP-related parameters on load-settlement behavior of DPRF has been compared by 3-dimentional numerical work. The result of this study shows that both pile-related factors and LTP-related factors affect the load-settlement of DPRF. The simple equation to estimate the load-settlement behavior of DPRF system has been suggested in terms of pile-contribution factors. The results of previous studies were also analyzed to verify the validity of suggested equation. A good agreement between the measured and estimated values were obtained, indicating the potential to apply in practical field.

1 INTRODUCTION

For several years, piled raft foundation (PRF) has been adopted for intermediate situations where shallow foundation is not acceptable for large settlements while the pile foundation is overdesigned (Burland, 1995). However, the structural connection between piles and raft in PRF produces high bending moments in raft and concentrated stress in the pile heads which causes cracking in the raft. To overcome these limitations, disconnected piled raft foundation (DPRF) has been suggested as an alternative. Load transfer platform (LTP) layer, generally composed of granular soils are imposed between the raft and piles to produce physical disconnection between the piles and raft (Wong et al., 2000, Mali and Singh, 2018).

Many researchers studied the mechanical behavior of DPRF by numerical simulations (Zheng et al., 2008, Eslami and Malekshah, 2011, Azizkandi et al., 2019) and physical modeling test (Fioravante and Giretti, 2010, Malekkhani and Bazaz, 2021), however, the analysis and the interpretation method of mechanical behavior of DPRF is still under discussion owing to the complex interaction between piles, raft and subsoil.

This study aims to suggest a simple equation to estimate the stiffness of DPRF within the serviceability range of the raft settlement (i.e., $w_r/B_r < 0.5\%$, where w_r = raft settlement and B_r = width of the raft) (O'Neil, 1996) by 3-dimentional numerical work by ABAQUS. Both the pile design parameters and LTP design parameters were considered as variables.

DOI: 10.1201/9781003299127-189

2 FINITE ELEMENT MODELING

2.1 *Material modeling*

Piles and raft were modeled as a linear elastic material, while subsoil and LTP layers were modeled as a linear elastic-perfect plasticity material using the Mohr-Coulomb yield criterion. The subsoil was modeled to have a linear depth-variation of elastic modulus to simulate the soil stiffening with increment of confinement with depth (Tradigo et al., 2015) (Equation 1). Furthermore, to observe the effect of E_{LTP} (elastic modulus of LTP layer) on DPRF behavior, E_{LTP} was varied to have 30-125 MPa. Table 1 summarizes the mechanical properties applied in this study.

$$E_{sub}(z) = E_0 + E_{inc} \cdot z \tag{1}$$

where E_{sub}=elastic modulus of subsoil, E_0=elastic modulus at the ground level, and E_{inc} = gradient of the elastic modulus

Table 1. Material properties used in FE analysis.

Parameters	Subsoil	LTP layer	Pile	Raft
Unit weight, γ (kN/m^3)	15.3	15.3	24	24
Elastic modulus, E (MPa)	10+2z	30-125	30,000	120,000
Poisson ratio, ν	0.25	0.25	0.15	0.15
Friction angle, φ (°)	35	35	-	-
Cohesion, c (kPa)	<1	<1	-	-
Dilatancy angle, ψ (°)	5	5	-	-

2.2 *Geometrical configuration*

This study modeled a quarter of a whole model as symmetric boundary condition is satisfied (Zheng et al., 2008). The pile was designed to have diameter (D) 0.5m and varied length ratio (L/B_r, where L=pile length and B_r=width of raft) 0.18−0.91, less than 1 to satisfy large piled raft criteria (Sanctis and Mandolini, 2006). Different arrangements of piles were modeled with pile number (N) = 0, 4−64, and spacing ratio (S/D, where S=pile spacing) =2−8. DPRF with N=64 and S/D=8 was excluded owing to the limited geometrical configuration. The LTP layer was designed to have thickness ratio (H_{LTP}/D, H_{LTP}=thickness of LTP layer) =0−3. The rigid raft width was designed to have constant value 22m. The total width and depth of the whole model was 110m and 95m, respectively, to satisfy the wide boundary conditions where they do not affect the results (Azizkandi et al., 2019).

After geostatic condition is satisfied at soil deposit, the weight of structural elements were activated (Richter et al., 2011, Tradigo et al., 2015). Then, a uniform stress (q_0) =500kPa was applied on top of the raft.

3 RESULTS

The stiffness of the foundation (k) was defined as the load applied on the raft divided by the raft settlement at w_r/B_r=0.5%.

3.1 *Stiffness of raft foundation with LTP layer (RL foundation, N=0)*

The effect of E_{LTP} on the stiffness of RL foundation (k_{RL}) shows different trends according to H_{LTP}/D as shown in Figure 1 (a). Behaviors of RL foundation shows very similar to that of shallow foundation on layered soil, where the behavior of shallow foundation is determined by the relative difference in the bearing capacity of layered soils (Das, 2016). In other words, when LTP layer categorized to be 'stronger' than subsoil, increment of H_{LTP}/D increases k_{RL}. On the contrary, increment of H_{LTP}/D decreases k_{RL} when LTP layer is categorized to

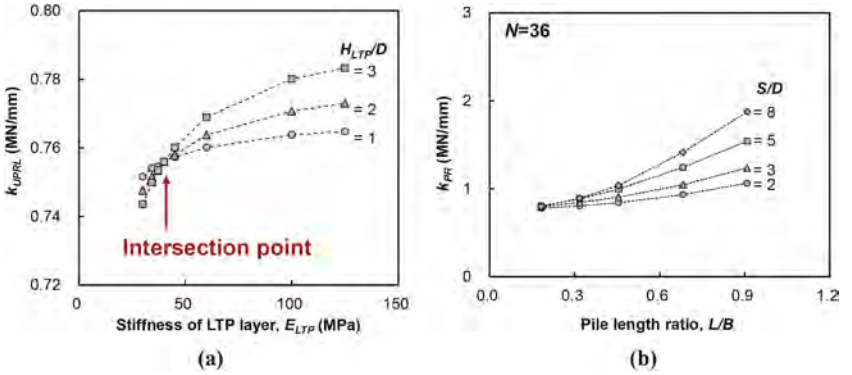

Figure 1. (a) Variation of k_{RL} with E_{LTP} according to H_{LTP}/D and (b) Variation of k_{PR} with L/B according to S/D (PRF with N=36 is only shown).

'weaker' than subsoil. At state where subsoil and LTP layer have similar bearing capacity, k_{RL} will not be affected by H_{LTP}/D. The intersection point at Figure 1(a) may indicate the mentioned situation, where similar bearing capacity of LTP layer and subsoil is satisfied.

3.2 *Stiffness of piled raft foundation (PRF, H_{LTP}=0)*

As identical effect of L/B and S/D was observed at various N, only case of PRF with N=36 is shown in Figure 1 (b). Consistent to previous research, as increment of L/B increases the pile capacity along pile length (Nguyen et al., 2014) and increment of S/D decreases the interaction between the piles (Cao et al., 2004, Rasouli et al., 2015), the stiffness of piled raft foundation (k_{PR}) increased with increment of L/B and S/D.

3.3 *Stiffness of disconnected piled raft foundation (DRPF)*

The effect of LTP-related and pile-related parameters on k_{DPR} showed similar effects on k_{DPR}, that includes the concept of layered soil having LTP layer above and bottom layer with pile reinforced subsoil where the pile reinforcement increases with increment of N, L/B and S/D (Cao et al., 2004, Nguyen et al., 2014, Rasouli et al., 2015). Consequently, the effect of LTP thickness on k_{DPR} varied according to the relative stiffness between LTP layer and pile reinforced subsoil (=E_{LTP}/E_{sub}^*, E_{sub}^* = Equivalent elastic modulus of pile reinforced subsoil) that can be summarized in Figure 2 (a). Since E_{sub}^* varies at given pile configurations, the variation trends of k_{DPR} with H_{LTP} showed inconsistent trends that may depends on pile configurations as shown in Figure 2 (b) and (c), at constant E_{LTP}=125MPa and N=36 for instance.

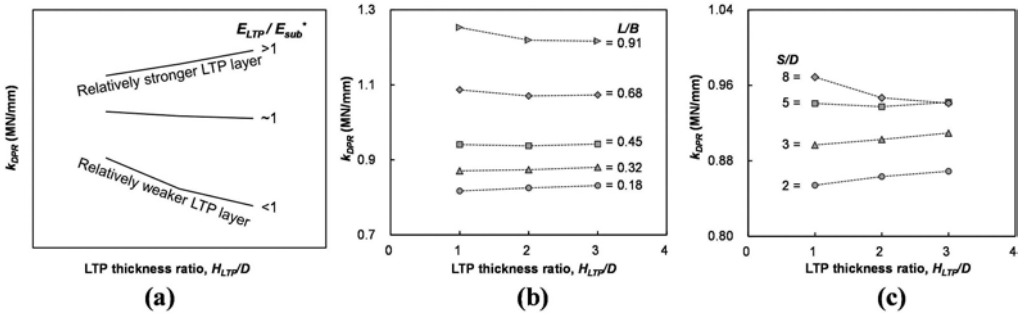

Figure 2. (a) Variation of k_{DPR} with H_{LTP}/D at various E_{LTP}/E_{sub}^*, and inconsistent effect of H_{LTP}/D on k_{DPR} at constant E_{LTP}=125MPa and N=36, shown for instance, according to (b) L/B and (c) S/D.

4 ANALYSIS AND DISCUSSION

4.1 k_{DPR} estimation formula

As both pile-related and LTP-related parameters affect k_{DPR}. To estimate the k_{DPR} simply, this study attempted to represent k_{DPR} with k_{RL} and k_{PR} since they include the effect of LTP-related and pile-related parameters, respectively. While this process, some cases of DPRF were also excluded for further verification process. The overall relationship between k_{DPR}/k_{RL}-k_{PR}/k_{RL} can be summarized as power function with fitting parameters of A and b (Equation 2).

$$\frac{k_{DPR}}{k_{RL}} = A\left(\frac{k_{PR}}{k_{RL}}\right)^{b} \tag{2a}$$

$$k_{DPR} = A \times (k_{PR})^{b} \times (k_{RL})^{1-b} \tag{2b}$$

In this study, the fitting parameter b was defined as 'contribution' factor and it represents the contribution of pile-reinforcement effect to mechanical behavior of DPRF, with ranged values of 0 – no contribution to foundation system, indicating RL foundation; and 1 – full contribution to foundation system where $k_{DPR} \approx k_{PR}$.

4.2 *Contribution factor, b*

Contribution factor b was first calculated at DPRF with constant k_{RL} and k_{PR}. Figure 3 compares the measured b at constant N=36 according to pile-related parameters of H_{LTP}/D and E_{LTP}, at various S/D. As expected, increment of E_{LTP}, and decrement of H_{LTP}/D increased b. The negative effect of S/D on b indicates that the summation of each single pile effect on DPRF is larger than that of group pile.

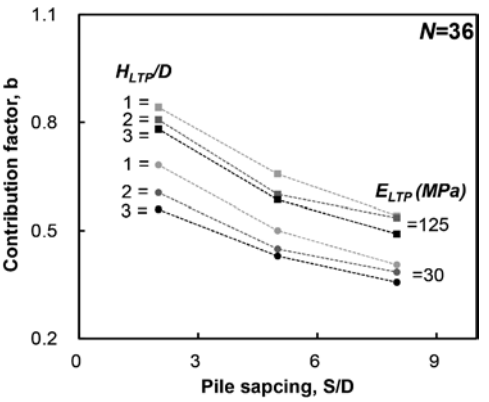

Figure 3. Variation of b according to LTP-related parameters (H_{LTP}/D and E_{LTP}) according to S/D.

Multiple regressions analysis was progressed with the measured b at constant N through statistical software SPSS, and linear correlation of design parameters were obtained (Equation 3). Since there exist upper limit of N, beyond which insignificant effects were expected (Poulos, 2001), the regression factors of a', α, β, and λ were estimated by hyperbolic model (Duncan and Chang, 1970) (Equation 4). Table 2 summarizes the hyperbolic parameters of c_1 and c_2 calculated at each N. Note that E_{LTP} was replaced by $E_{ratio} = E_{LTP}/E_{sub}$ to make the dimensionless factor, where E_{sub}=elastic modulus of subsoil layer.

$$b = a' + \alpha(S/D) + \beta E_{ratio} + \lambda(H_{LTP}/D) \tag{3}$$

$$Regression\ Factor = \frac{N}{c_1 + c_2 N} \tag{4}$$

Where c_1, c_2 = hyperbolic parameters determined as the intercept and slope of linear relationship between N/regression factor – N.

Table 2. Calculated hyperbolic parameters of regression factors.

Hyperbolic parameters	Constant, a'	α	β	λ
c_1	7.32	-278.88	3.50	67.39
c_2	1.12	-14.88	14.74	-30.48

4.3 *Constant factor, A*

Based on Equation 2a, the constant factor A represents k_{DPR}/k_{RL} at k_{PR}/k_{RL}=1 or k_{DPR}/k_{RL} at zero-pile contribution to DPRF. For the former case, the constant factor A was calculated in case of DPRF where $k_{DPR} \approx k_{RL} \approx k_{PR}$ is satisfied. It was calculated to have values of A ranged 1.01–1.03. In the latter case, A has value of 1 since zero-pile contribution implies RL foundation. Finally, the averaged value of A=1.02 was applied.

4.4 *Validation*

Figure 4 compares the measured k_{DPR} and estimated k_{DPR} via Equation 2-4. Good agreement between the measured and estimated values of k_{DPR} was obtained for both cases of included and excluded cases of DPRF while simple formula development process.

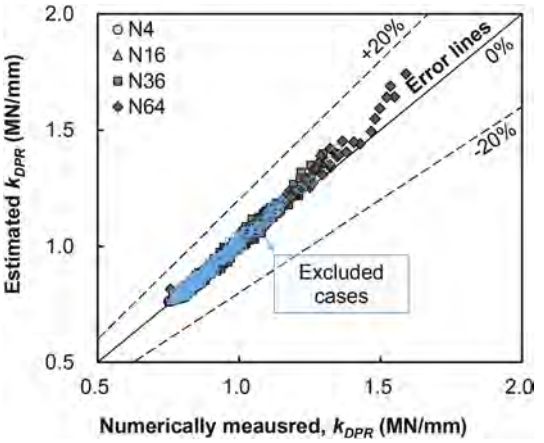

Figure 4. Comparison between the measured and estimated k_{DPR}.

Furthermore, centrifugal testing data of Fioravante and Giretti (2010) and Rasouli et al. (2015) was applied to Equation 2-4 to evaluate the validity of suggested equation in practical field. Since neither of these studies provide the information of E_{ratio} (=i.e., E_{LTP} and E_{sub}), reasonable assumption of this value was made based on the typical correlation of relative density and normalized elastic modulus (E/P_a, where P_a=atmospheric pressure) suggested by Kulhawy and Mayne (1990). As Table 3, it can be concluded that the simple k_{DPR} estimation formula in this study provides reasonable value of k_{DPR} when sufficient information is given.

5 CONCLUSIONS

This study analyzed the effect of both pile-related parameters and load transfer platform (LTP) related parameters on the mechanical behavior of disconnected piled raft foundation (DPRF). Consistent to conventional piled raft foundation, increment of pile length, pile spacing and pile number increased stiffness of DPRF. Increment of stiffness of LTP layer increased stiffness of DPRF while increment of thickness of LTP layer decreased stiffness of DPRF. Furthermore, this study suggests a simple formula to estimate the stiffness of DPRF by considering contribution of piles to the behavior of DPRF that depends on given design parameters. The validity of

Table 3. Validation process of suggested formula with physical testing data.

Centrifugal testing	Design parameters						Given stiffness			Estimated	Error
	N	H_{LTP}/D	S/D		Assumed E_{ratio}		k_{RL}	k_{PR}	k_{DPR}	k_{DPR}	(%)
64g*	4	2	9.63		1-2.5		0.129	0.613	0.178	0.153-0.177	0.8-14.5
	9	2	4.81		1-2.5				0.230	0.263-0.314	14.3-36.2
100g**			4	2.68	4.9	1-5	100.1	74.8	100.9	99.78-92.65	1.1-8.2

* Fioravante and Giretti (2010)
** Rasolui et al. (2015)

the suggested formula was verified by comparing the estimated values with numerically measured data in this study and physical testing data given by previous research.

ACKNOWLDEGEMENTS

This research was supported by research funds from the Korean Society of Civil Engineers, and by the National Research Foundation of Korea (NRF) (2021R1A2C1010281).(Kulhawy and Mayne, 1990)

REFERENCES

Azizkandi, A. S., Rasouli, H. & Baziar, M. H. 2019. Load Sharing and Carrying Mechanism of Piles in Non-connected Pile Rafts Using a Numerical Approach. *International Journal of Civil Engineering*, 17, 793–808.

Burland, J. 1995. Piles as settlement reducers. *Invited Lecture XIX Convegno Italiano di Geotecnica*.

Cao, X. D., Wong, I. H. & Chang, M.-F. 2004. Behavior of model rafts resting on pile-reinforced sand. *Journal of Geotechnical and Geoenvironmental engineering*, 130, 129–138.

Das, B. 2016. *Principles of Foundation Engineering 8th Ed*.

Duncan, J. M. & Chang, C.-Y. 1970. Nonlinear analysis of stress and strain in soils. *Journal of soil mechanics and foundations division*, 96, 1629–1653.

Eslami, A. & Malekshah, S. S. 2011. Analysis of non-connected piled raft foundations (NCPRF) with cushion by finite element method. *Computational Methods in Civil Engineering*, 2, 153–168.

Fioravante, V. & Giretti, D. 2010. Contact versus noncontact piled raft foundations. *Canadian Geotechnical Journal*, 47, 1271–1287.

Kulhawy, F. H. & Mayne, P. W. 1990. Manual on estimating soil properties for foundation design. Ithaca, NY, USA: Electric Power Research Inst., Palo Alto, CA (USA); Cornell University.

Malekkhani, M. J. & Bazaz, J. B. 2021. An Analytical Model to Study the Behavior of Non-connected Piled Rafts with Granular Cushion Subjected to Vertical Load. *International Journal of Civil Engineering*, 1–16.

Mali, S. & Singh, B. 2018. Behavior of large piled-raft foundation on clay soil. *Ocean Engineering*, 149, 205–216.

Nguyen, D. D. C., Kim, D.-S. & Jo, S.-B. 2014. Parametric study for optimal design of large piled raft foundations on sand. *Computers and Geotechnics*, 55, 14–26.

O'neil, M. 1996. Case histories of pile-supported rafts. *Report for ISSMFE, Technical Committee TCl8*. University of Houston.

Poulos, H. 2001. Piled raft foundations: design and applications. *Geotechnique*, 51, 95–113.

Rasouli, H., Saeedi Azizkandi, A., Baziar, M. H., Modarresi, M. & Shahnazari, H. 2015. Centrifuge modeling of non-connected piled raft system. *International Journal of Civil Engineering*, 13, 114–123.

Richter, S., Cudmani, R. O. & Slominski, C. 2011. The behavior of a spread footing over reinforced ground with gravel interface during a strong earthquake. *geotechnik*, 34, 193–204.

Sanctis, L. D. & Mandolini, A. 2006. Bearing capacity of piled rafts on soft clay soils. *Journal of Geotechnical and Geoenvironmental Engineering*, 132, 1600–1610.

Tradigo, F., Pisanô, F., Di prisco, C. & Mussi, A. 2015. Non-linear soil–structure interaction in disconnected piled raft foundations. *Computers and Geotechnics*, 63, 121–134.

Wong, I. H., Chang, M. F. & Cao, X. D. 2000. Raft foundations with disconnected settlement-reducing piles. *In:* Hemsley, J. A. (ed.) *Design applications of raft foundations*. Thomas Telford.

Zheng, J.-J., Abusharar, S. W. & Wang, X.-Z. 2008. Three-dimensional nonlinear finite element modeling of composite foundation formed by CFG–lime piles. *Computers and Geotechnics*, 35, 637–643.

Smart Geotechnics for Smart Societies – Zhussupbekov, Sarsembayeva & Kaliakin (Eds)
© 2023 The Author(s), ISBN 978-1-003-29912-7
Open Access: www.taylorfrancis.com, CC BY-NC-ND 4.0 license

Comprehensive study of the basses and foundations of furnaces No. 61, 63 of the melting shop No. 6 of the Aksu Ferroalloy Plant in connection with the renovation

Zh.S. Nuguzhinov
KazMIRR Institute of the NJC "KarTU named after Abylkas Saginov", Karaganda, Kazakhstan

A.T. Mukhamejanova
Eurasian National University, Nur-Sultan, Kazakhstan

D.T. Tokanov, Zh. Koishybay & N.Zh. Zhumadilova
KazMIRR Institute of the NJC "KarTU named after Abylkas Saginov", Karaganda, Kazakhstan

M.S. Beketova
NJC "KarTU named after Abylkas Saginov", Karaganda, Kazakhstan

ABSTRACT: The work is devoted to a comprehensive study of the bases and foundations of electric furnaces No. 61 and 63 of the melting shop of the Aksu ferroalloy plant. Engineering-geological and hydrogeological surveys of souls, geophysical work, as well as studies of the technical condition of existing foundations were carried out.

Based on the conducted comprehensive scientific and technical studies of the mechanism of interaction of the foundation with the ground foundation, a fundamentally new calculation model has been developed that allows calculating the precipitation of buildings taking into account the long-term water saturation of the foundation soils and an assessment of the reliability of the existing foundations of electric furnaces No. 61 and 63 of smelting shop No. 6 with the possibility of their reconstruction in connection with the upcoming renovation.

1 INTRODUCTION

Aksu Ferroalloy Plant is located on the territory of Pavlodar region, 20 km southwest of Pavlodar and 2.5 km north of Aksu, on the left bank of the Irtysh river. The production infrastructure of the city is represented by two city-forming enterprises: the Aksu Ferroalloy Plant and the electric station of JSC "EEC". The object is connected by asphalt and railways with the cities of Nur-Sultan, Pavlodar, Ekibastuz, Semipalatinsk. Aksu Ferroalloy Plant is a ferrous metallurgy enterprise for the production of high-carbon ferrochrome, manganese and siliceous alloys.

The smelting building of shop No. 6 of the Aksu Ferroalloy Plant is designed for the production of high-carbon ferrochrome. Aksu Ferroalloy Plant is a two-span industrial building of complex shape in plan. This object has overall dimensions in plan in the axes "1-24, A-B" – 276x24 m, in the axes "1-20, B-C" – 228x24 m and one deformation seam in the axes "21, A-B". Gas treatment facilities are adjacent to the building of the smelting building in the axes "1-4, A". The rigidity of the building is ensured jointly by the work of foundations, metal frame elements, vertical and horizontal stiffness connections, coating and floor slabs.

Engineering and geological surveys revealed that clay serves as the bearing base for the foundations of electric furnaces No. 61 and No. 63 (CLAY N1 1-2 ar is opened everywhere at depths of 0.1–4.8 m). The exposed thickness of the clay thickness varies from 3.2 m to 26.7 m . With a relative swelling value of 0.005, the calculated swelling pressure is 3.0 kgf/cm2. The exposed

DOI: 10.1201/9781003299127-190

thickness of the Neogene clays of the Aral formation is considered to be strongly swelling, according to the complexity of engineering and geological conditions according to the Joint Venture of the Republic of Kazakhstan 1.02-102-2014 the survey site belongs to the III category.

According to the field description, the clays are greenish-gray, light gray, dark gray, with the inclusion of gypsum, dense, having the following characteristics:

γ = 18, 1 kN/m^3; γ_s = 25,2 kN/m^3; γ_d = 13,9 kN/m^3; $\varphi_{II} = 7^0$; c_{II} = 10,8 kPa; E_0 = 10 MPa; S_r = 0,95; e = 0,816.

The foundation of Fo-37 for the electric furnace RKZ-63-I1 No. 61 is monolithic reinforced concrete, filled in the form of a disk with a diameter of 12.00 m and a depth of laying – 3.0 m from the level of the clean floor of the first floor of the melting shop No. 6. The foundation of Fo-1 for the electric furnace RKZ-63-I1 No. 63 is monolithic reinforced concrete, made in the form of a disk with a diameter of 14.26 m with rectangular protrusions, a depth of laying -2.30 m from the level of the clean floor of the first floor of the melting shop No. 6.

Based on the field visual description of engineering and geological workings, confirmed by the results of laboratory tests of soils, it was found that up to a depth of 8.0-30.0 m in the geological structure of the survey site, the following take part (up-down): • quaternary deposits, represented by large sands and coarse sands; Neogene clays Pavlodar suite. From the surface, these formations are covered with a layer of bulk soils.

Control calculations of the soil sediment of the foundations were carried out in accordance with the requirements of the current building regulations - SP RK 5.01-102-2013 The basis of buildings and structures [1, 2].

According to the requirements of the norms, the calculation of the sediment of the flooded bases is carried out taking into account the decrease in the modulus of deformation of the soils during their soaking and the change in the stress state of the compressible zone of the foundation base following hydrostatic and hydrodynamic weighing. At the same time, the main reason for the decrease in the modulus of deformation of soils subject to flooding is mainly due to the weakening of their structure due to water saturation. In this regard, when geotechnical design of buildings and structures in conditions of flooded soil bases, it will be advisable to adhere to the basic principles applied to subsidence soils based on the use of the results of compression tests [3, 4].

Construction practice shows that the operational reliability and durability of buildings and structures under construction mainly depend on the reliability of the results of engineering and geological surveys used as input data in geotechnical design. In particular, the calculation of foundation bases according to the second limit state imposes high requirements on the accuracy of determining the values of the soil deformation modulus, on which the risk of accidents of constructed objects directly depends. However, there is still uncertainty in the choice of this important characteristic of soil compressibility, which is due to a significant discrepancy between its values determined by laboratory (compression) and field (stamp) methods.

As is known, compression tests have found wide application in the practice of engineering and geological surveys as one of the main methods for determining the deformation characteristics of the soils of the bases of the projected foundations (GOST 12248-2010). Such tests are characterized by simplicity, low labor intensity and cost.

The compression dependence reflects one of the laws of porosity of dispersed bodies – the law of compaction and is used to solve the main problem of soil mechanics, determining the precipitation of the soil layer under continuous load.

However, at present, according to the current norms (SP 22.13330, 2016), the results of compression experiments are used in the design of foundations on structurally unstable soils and are not directly used in the calculations of deformations of foundations composed of ordinary soils. In accordance with the requirements of standards for buildings and structures of geotechnical category 2 and 3, the value of E according to compression tests for each soil layer should be adjusted based on their comparison with the results of parallel stamp, pressiometric tests, which have a high cost and high labor intensity.

To determine the precipitation of the flooded foundations of newly erected and existing buildings, it is necessary to have the actual dimensions of local sections of water-saturated soil within the active area of the foundation of the foundation under construction and inhomogeneously compacted zones of the foundation of existing foundations. However, the methods of

the current norms based on the theory of linearly deformable bodies, the object of study of which, according to its basic prerequisites, is a conditional, idealized foundation soil as an isotropic solid, are not acceptable for solving such a complex geotech problem. Because this theory does not allow us to predict the actual dimensions of the parameters of the deformed zone of the base, allowing errors of more than 100%, but, as experiments show, its application to calculate stresses in real soils gives quite satisfactory results with an accuracy of 20% [5, 6].

2 METHODOLOGY

Calculation of the sediment of the existing foundations of furnaces No. 61 and No. 63 of the Aksu Ferroalloy Plant, taking into account the flooding of the foundation soils in the operational period by the modulless method.

The forecast of the development of foundation precipitation caused by flooding of previously compacted soils of its base during the operational period is an insufficiently studied complex task. To solve it, we will make assumptions, according to which we will assume that "the precipitation of the base from the prolonged action of loads is stabilized, and the soils are compacted inhomogeneously within the compressed zone in accordance with its stressed state, therefore, additional precipitation of the existing foundation in the process of flooding its base occurs by analogy with the phenomenon of subsidence due to weakening soil structures in the process of soaking".

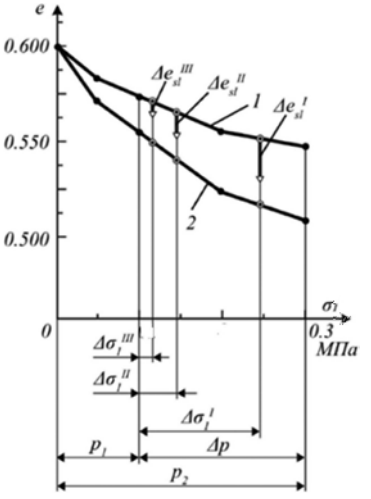

Figure 1. Compression curves of the soil of the foundation base: 1 и 2 – experimental soil compression curves with natural humidity and in a water-saturated state; ● - experimental points; ⊙ - points on the experimental curves used in the calculation of precipitation by the non-modular method; ▽ - prospective test points obtained as a result of soaking of long-compacted soils of the base of the existing foundation.

The following formula is used to determine precipitation without a modular method:

$$S = \frac{1}{A_\Phi} \cdot \sum_{i=1}^{i=n} \left[V_{i3} \cdot \left(1 - \frac{1 + e_2^{i3}}{1 + e_1} \right) \right], \quad (1)$$

where i and n – number and number of dedicated compacted base zones;

$A_ф$ – the area of the sole of the foundation;

Viз – volume of the i – th compacted zone of the base;

e_1 – the porosity coefficient of the soil of natural composition;

$e_2^{iз}$ - porosity coefficient of soil compacted under compressive stress $\Delta\sigma_1^{iз}$, arising in the i – th zone from an external load.

3 RESULTS

The proposed model-free method can also be used to calculate the sediment of foundations having the shape of a sole in the form of a circle, a square and a straight square.

As a result of modeling the behavior of the existing foundation during flooding of its base by conducting three parallel compression tests with soil samples pre-compacted under loads $\Delta\sigma_1^{I}$, $\Delta\sigma_1^{II}$ and $\Delta\sigma_1^{III}$ and subjected to soaking under the same loads, the corresponding values of reducing the porosity coefficient of the soil were obtained $\Delta e_{sl}^{I} = 0{,}024$; $\Delta e_{sl}^{II} = 0{,}018$; $\Delta e_{sl}^{III} = 0{,}012$.

At the same time, additional precipitation of the foundation of the existing building, taking into account the factors of soil compaction and subsequent flooding, amounted to: for position 2 (WL_1) $s_{sat.ex} = 1{,}40$ cm; for position 3 (WL_2) $s_{sat.ex} = 4{,}6$ cm; for position 4 (WL_3) $s_{sat.ex} = 7{,}5$ cm.

Thus, the proposed method, in comparison with the recommendations of the norms, makes it possible to more accurately and reliably predict the nature of the development of additional sediments of the flooded foundations of existing buildings, establish the permissible amount of groundwater level rise and determine the optimal depth of water reduction.

4 DISCUSSIONS

According to engineering and geological surveys, an uneven increase in the groundwater level was noted at the site, which indicates that water saturation of the foundation soils, including swelling clay, occurred for a long time, which usually leads to the development of unacceptable deformations of the foundation and reduces its operational reliability. In addition, with the continuous annual seasonal flooding of the territory (min to the level of 127.30 and max. up to the level of 128.00), the compressibility characteristics (modulus of deformation E_0) and strength (c, φ) of the soils of the base layers undergo significant changes, as a rule, a decrease of 2 or more times, and these changes in space are also uneven in the supporting area of the foundation and in the depth of the base.

Thus, loading of the flooded foundation, composed of swelling soils, in conditions of poor drainability can lead to a dangerous unstable condition of the foundations. In such a situation, as a result of the lag of the "water filtration process" from the "soil compaction process (pore reduction)", the excess pressure in the pore water sharply increases, which leads the foundation to an unstable state or is the cause of the development of excessive plastic deformations of the soil.

5 CONCLUSIONS

The periodically recurring (cyclically) process of flooding of the foundation soils does not favorably affect the nature of the development of foundation sediments, namely, it causes their unevenness, which can be seen from the following analysis of the results of control calculations:

a) when calculating by the method of layer-by-layer summation, an increase in foundation sediment due to the influence of the weighing action of ground water, as can be seen from the following comparison: 5.85 cm < 6.84 cm;
b) when calculating by the non-modular method, the additional precipitation of the foundation of the existing building, taking into account the factors of soil compaction and subsequent flooding, amounted to: 1.40 cm<4.6 cm<7.5 cm. What shows the real values of the precipitation of foundations caused by the flooding of the foundation soils, taking into account the additional change in the compressibility of soils: an increase during watering or a decrease during drying.

REFERENCES

1. SP 5.01 – 102 – 2013 Foundations of buildings and structures. – Astana, 2015.
2. SP 22. 13330 Foundations of buildings and structures. – M., 2016.

3. Utenov, Y.S., Zhusupbekov, A.Z., Abildin, S.K., Mukhamedzhanova, A.T., Abdrakhmanova, B.G. Calculation of Building Settlement on Flood-Prone Foundations by Using the Modulus-Free Method// Soil Mechanics and Foundation Engineering, 2022, 59(1). Scopus - сведения о документе - Calculation of Building Settlement on Flood-Prone Foundations by Using the Modulus-Free Method.
4. Nuguzhinov, Z.S., Bakirov, Z.B., Bakirov, M.Z., Khabidolda, O., Zhilkybayev, D. Methodology of Assessing Strength of Metal Structure Elements with Cracks // IOP Conference Series: Materials Science and Engineering. 2020, 953(1). Scopus - сведения о документе - Methodology of Assessing Strength of Metal Structure Elements with Cracks.
5. Nuguzhinov, Z.S., Bakirov Z.B., Vatin N.I., Bakirov M.Z., Kurokhtina I.A., Tokanov D.T., Khabidolda O. Stress intensity factor of reinforced concrete beams in bending// Buildings, 2021, 287 (7).
6. Nuguzhinov, Z.S., Khabidolda O., Bakirov Zh, Zholmagambetov, S., Kurokhtin A., Tokanov D. Regression dependences in bending reinforced concrete beam whit cracks //Curved and Layered Structures, 2022, 9(1).

Smart Geotechnics for Smart Societies – Zhussupbekov, Sarsembayeva & Kaliakin (Eds)
© 2023 The Author(s), ISBN 978-1-003-29912-7
Open Access: www.taylorfrancis.com, CC BY-NC-ND 4.0 license

Performance of sheet piles subjected to vertical loadings in saturated clay ground

X. Xiong
Kanazawa University, Ishikawa, Japan

L.T. Hoang
Thuyloi University, Hanoi, Vietnam

ABSTRACT: Recently, with the development of new piling methods, steel sheet piles can be penetrated into various grounds with high quality and precision. Though the piles for deep foundations are usually pipe piles, sheet piles could become an alternative. However, the bearing capacities of sheet piles have not been clarified fully yet. In this research, a series of monotonic and quasi-static cyclic load tests on model steel sheet piles in a saturated clay ground have been conducted. The test results show that excess pore water pressures generated during the pile installation and loading, as well as cyclic loading significantly influenced the bearing capacities. Moreover, compared with pile tip resistance, shaft resistance was more influenced by the excess pore water pressures generated and the effect of consolidation. Therefore, the bearing capacity of sheet piles immediately after pile penetration could be used as an index for conservative design.

1 INTRODUCTION

Generally, the piles for deep foundations are concrete piles or steel pipe piles. In recent years, piling methods, such as the Silent Piler and Gyro Piler, have been developed. Using these technologies, steel sheet piles, structures with sheet sections and interlocking edges, can be penetrated into grounds with high quality and precision under various geological conditions (Otani, 2021). Considering that the construction time and cost of sheet piles could be lower than those of pipe piles, therefore, sheet piles could become an alternative to pipe piles for deep foundations.

Considering the space constraints of construction in urban areas, Koda et al. (2003) first proposed a sheet pile foundation by installing sheet pile walls around an existing footing. Recently, a few studies have been conducted to investigate the bearing capacity of sheet piles as foundations to support superstructure. Guo et al. (2021) conducted a series of static load tests on various model pile foundations to investigate the performances of different pile types on dry sand and found that sheet pile foundations would be a promising alternative to conventional pipe pile foundations. However, the performance of sheet piles in clay ground, with high degree of saturation, has not been clarified fully yet.

Therefore, in this paper, a series of monotonic and quasi-static cyclic load tests on model sheet piles in a saturated clay ground have been conducted. Excessive pore water pressures (EPWPs) around the model piles were carefully measured during the load tests to investigate the interaction between the piles and the ground.

2 EXPERIMENTAL DESCRIPTION

2.1 *Model grounds*

Clay ground was prepared in a cylindrical chamber of height 420 mm and diameter 420 mm. The soil used for the model ground was a mixture of Kasaoka clay and Silica sand #6. The model ground was prepared following the procedure reported by Hoang & Matsumoto (2020).

DOI: 10.1201/9781003299127-191

Dry Kasaoka clay powder and Silica sand #6 were mixed at a mass ratio of 1:1 (called K50S50), and water was then added to the mixture to obtain a soil slurry with a water content of 1.3 *LL* (*LL*: liquid limit). This soil slurry was poured into the soil chamber and a vertical load was applied to the soil to consolidate the soil one-dimensionally in several steps up to vertical stress of 100 kPa. Table 1 shows the properties of the model grounds.

2.2 *Model piles*

The model pile used in experiments is shown in Figure 1. Two acrylic plates were used to represent sheet pile walls, which have a width of 40 mm, a length of 195 mm and a thickness of 2 mm. The Young's modulus of the model pile is 3.57 GPa, and the Poisson's ratio is 0.35. To obtain the axial force in the pile, twelve strain gauges were attached on opposite sides of each model pile.

2.3 *Test instrumentation and procedure*

Figure 2 shows test devices and instrumentation used in model tests. During the load tests, the vertical load was applied by a screw jack and was measured utilizing a load cell. Pore water pressure sensors were set 20 mm below the ground surface, and their locations are shown in Figure 3. During the experiments, pile penetration tests (PPTs) were first conducted, and the two model piles (SP1 and SP2) were penetrated into the model ground one by one (Figure 3). Then, monotonic vertical load test (VLT) was conducted on SP1 immediately and on SP2 24 hrs after the installation process to investigate the consolidation effect on the pile capacity. After the dissipation of EPWPs, quasi-static cyclic load tests (CLTs) were conducted on the two piles. And again, VLT was conducted on SP1 immediately and on SP2 24 hrs after CLT to investigate the influence of earthquake.

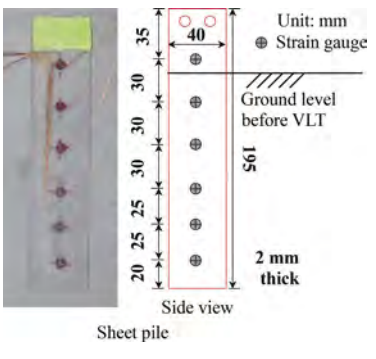

Figure 1. Model sheet pile.

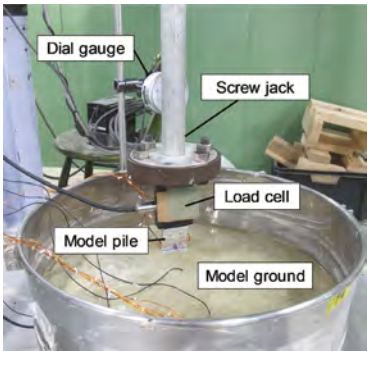

Figure 2. Test devices and instrumentation.

3 EXPERIMENT RESULTS

3.1 *Results of PPTs*

Figures 4 and 5 show the results of PPT on SP1 and SP2. It can be found from Figure 4 that the vertical load applied to the pile head, P_v, increased with the increase in settlement, w. Notably, there was no significant difference in the load-settlement behaviors of the two model piles. EPWPs were generated around the piles during PPTs, as shown in Figure 5. Except EPWP at PWP3, EPWP at other locations increased sharply at first and then turned to decrease gradually. The peak EPWP occurred at w reaching around 25 mm when the pile heads just passed through the level of pore water pressure sensors. This means that the largest EPWP occurred around the pile heads during PPTs. Furthermore, it is clear that EPWP still remained at the end of PPT.

3.2 *Results of VLTs*

The monotonic VLT was conducted on SP1 immediately and on SP2 24 hrs after PPTs. According to Hoang & Matsumoto (2020), the period of 24 hrs is the necessary for the EPWP generated

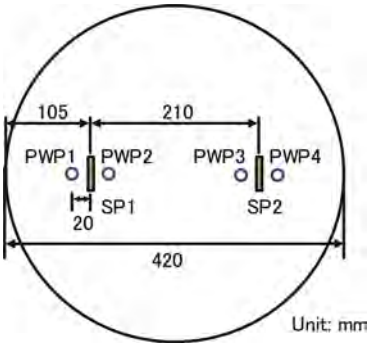

Figure 3. Locations of model sheet piles and pore water pressure sensors.

Table 1. Properties of model ground (K50S50).

Item	Value
Density of soil particle ρ_s	2653 kg/m^3
Effective size, D_{60}	0.15 mm
Effective size, D_{30}	0.006 mm
Effective size, D_{10}	0.001 mm
Plastic limit PL	13.6 %
Liquid limit LL	33.9 %
Initial void ratio e_0	0.703
Permeability k	6.33×10^{-9} m/s

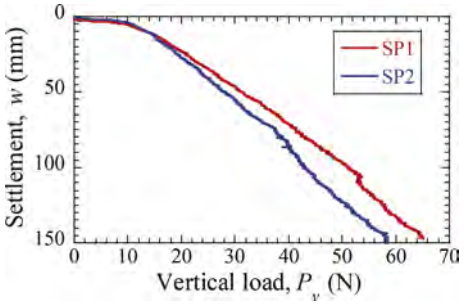

Figure 4. Load-settlement behavior during PPT.

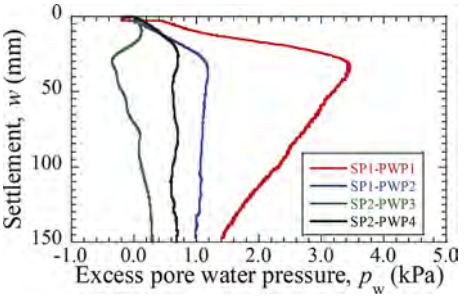

Figure 5. EPWP-settlement behavior during PPT.

during the installation process to completely dissipate. As shown in Figure 6, after 24 hrs of consolidation, the yield P_v of SP increased significantly from 93 N to 139 N (increased around 50%). Comparing with PPTs, the measured EPWP during VLTs was very small (Figure 7). It seems reasonable to assume that lager EPWP was also generated around the pile head at a depth of about 150 mm, which is quite far from the locations of PWP sensors, during VLTs.

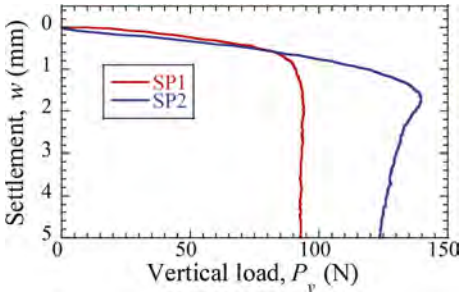

Figure 6. Load-settlement behavior during VLT.

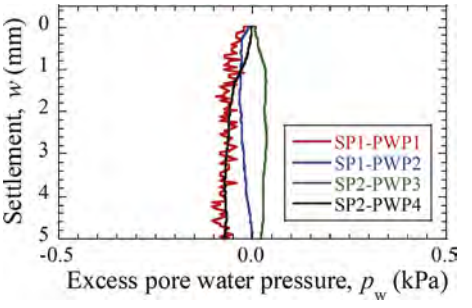

Figure 7. EPWP-settlement behavior during VLT.

3.3 *Results of CLTs*

CLTs were conducted on the two model piles 24 hrs after VLTs. During CLTs, the screw jack pushed and pulled the model piles within 1 mm penetration at a speed of 0.2 mm/s for a total of 50 times to simulate the vertical component of external load from an earthquake. Figure 8 shows the EPWPs generated during CLTs. It can be found that EPWPs accumulated with the increase in cyclic loading times. The signs of EPWPs on both sides of the pile were opposite, indicating that the pile was bent during the CLTs.

Figures 9 and 10 show the results of VLTs conducted on SP1 immediately and on SP2 24 hrs after CLTs. Pile tip resistance, P_t, was calculated from the axial strain near the pile tip, and pile shaft resistance, P_f, was obtained by subtracting P_t from P_v. Regarding P_v, the bearing capacity of SP significantly reduced subjected to cyclic loading. Though the yield P_v recovered a lot 24 hrs after CLT (Figure10), it was much smaller than the yield P_v before CLT (Figure 6, SP2). Moreover, though P_f carried almost the same load with P_t in the case of SP1, it carried a much greater load than P_t in the case of SP2. Compared with P_t, P_f was more influenced by the EPWPs generated during CLTs and the effect of consolidation.

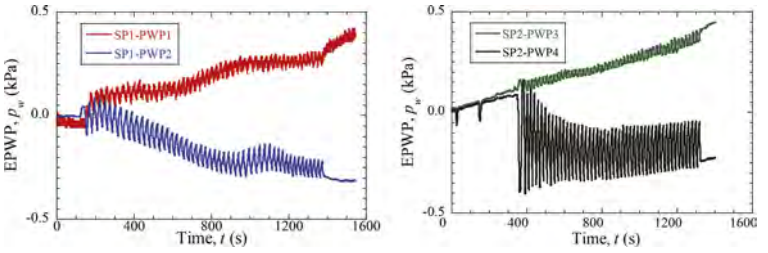

Figure 8. Time-EPWP behavior during CLT.

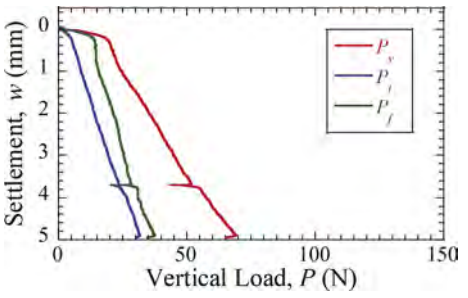

Figure 9. Load-settlement behaviour of SP1.

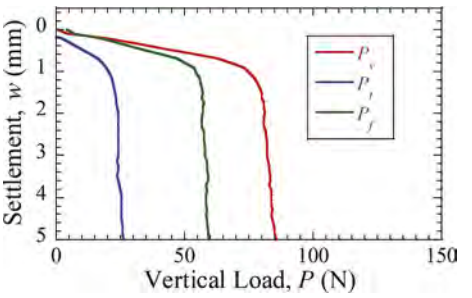

Figure 10. Load-settlement behaviour of SP2.

4 CONCLUSIONS

To investigate the performance of sheet piles in saturated clay ground, a series of monotonic and quasi-static cyclic load tests on model sheet piles have been conducted in this paper. The experimental results show that EPWPs generated during the pile installation and cyclic loading significantly influenced the pile bearing capacities. Moreover, compared with P_t, P_f was more influenced by the EPWPs and the effect of consolidation. Therefore, the bearing capacities of sheet piles immediately after pile penetration could be used as an index for conservative design.

REFERENCES

Guo, W.T., Honda, Y., Xiong, X., Matsumoto, T. & Ishihara, Y. 2021. Behaviour of three types of model pile foundation under vertical and horizontal loading. In T. Matsumoto et al. (ed.), *Proceedings of the Second International Conference on Press-in Engineering 2021*, Kochi, Japan. Boca Raton: CRC Press.

Hoang, L. T. & Matsumoto, T. 2020. Long-term behavior of piled raft foundation models supported by jacked-in piles on saturated clay. *Soils and Foundations* 60(1): 198–217.

Koda, M., Murata, O., Nishioka, H., Punrattanasin, P. & Kusakabe, O. 2003. A proposal for sheet-pile foundation combining footing with sheet piles. *Soil Mechanics and Foundation Engineering* 51(11): 8–10 (in Japanese).

Otani, J. 2021. State of the art report on steel sheet pile method in geotechnical engineering-development of PFS method. In T. Matsumoto et al. (ed.), *Proceedings of the Second International Conference on Press-in Engineering 2021*, Kochi, Japan. Boca Raton: CRC Press.

Smart Geotechnics for Smart Societies – Zhussupbekov, Sarsembayeva & Kaliakin (Eds)
© 2023 The Author(s), ISBN 978-1-003-29912-7
Open Access: www.taylorfrancis.com, CC BY-NC-ND 4.0 license

Examination of the ultimate bearing capacity formula regarding size effect and relative density for sandy soils

T. Iqbal, S. Ohtsuka & Y. Fukumoto
Nagaoka University of Technology, Nagaoka, Japan

K. Isobe
Hokkaido University, Hokkaido, Japan

ABSTRACT: It is proven that the sandy soils exhibit the non-linear trend in the shear stress-normal stress space. This study discusses the assessment of the UBC of surface strip footing on sandy soils concerning size effect and relative density subjected to centric vertical and uniform surcharge loads. The RPFEM, based on the shear strength property of Toyoura sand, is employed in analyses. The findings are consonant with the centrifuge tests in the published references. The results are compared with the existing guidelines, and the modified UBC formula is proposed.

1 INTRODUCTION

The ultimate bearing capacity (UBC) formulas being widely used in Japan are those recommended by the Architectural Institute of Japan's guidelines (AIJ 1988, 2001, 2019) and the Japan Road Association's specifications (JRA 2017). The simplified JRA bearing capacity formula for sandy soils is expressed as Equation 1 in the case of surface strip footing, while the AIJ guidelines do not consider the modification factor for the surcharge term.

$$q_u = \frac{1}{2}\gamma B N_\gamma S_\gamma + q N_q S_q \quad \text{where} \quad S_\gamma = (B)^{\frac{-1}{3}} \;\&\; S_q = \left(\frac{q}{q_o}\right)^{\frac{-1}{3}}, 1 \le \frac{q}{q_o} \le 10 \tag{1}$$

In the above equation, N_γ and N_q depict the well-known bearing capacity factors, γ denotes the soil unit weight underneath the footing, B accounts for the footing size, S_γ and S_q symbolize the size effect modification factors for N_γ and N_q, respectively, and q describes the surcharge load. Besides, q_o=10 kPa is taken as a reference value in the surcharge load.

In both AIJ and JRA formulas, the size effect factor for N_γ only considers the effect of footing size. However, notable experimental studies have underscored the importance of soil unit weight (γ) in estimating the stress level effect on UBC through the term γB (Okahara et al. 1988). Likewise, the effect of relative density (D_r) on UBC through internal friction angle ϕ has been highlighted through numerous experimental investigations (Tatsuoka et al. 1986). Therefore, this study estimates the size effect of footing on UBC under centric vertical and uniform surcharge loads in case of total and effective stress analysis conditions. The rigid plastic finite element method (RPFEM), by using the non-linear yielding characteristics of Toyoura sand, is used in numerical computations. A modified UBC formula is proposed, and its performance is assessed in the case of various relative densities of Toyoura sand.

2 RIGID PLASTIC FINITE ELEMENT ANALYSIS FOR SANDY SOILS

2.1 *Yield function*

The non-linear yield function employed in this study is expressed through Equation 2:

DOI: 10.1201/9781003299127-192

$$f(\boldsymbol{\sigma}) = aI_1 + (J_2)^n = b \tag{2}$$

In the above equation, a and b account for the material shear strength characteristics, i.e. internal friction and cohesion, respectively, while n denotes the non-linearity of the failure envelope in relation to the first stress invariant, I_1, and the second invariant of deviator stress, J_2. The non-linear rigid plastic constitutive equation is used for the numerical analysis (Nguyen et al. 2016).

2.2 *Non-linear shear strength property of sandy soil*

Physical properties of Toyoura sand were utilized, having specific gravity; G_s=2.64, maximum and minimum void ratios; e_{max}=0.977 and e_{min}=0.605, respectively (Tatsuoka et al. 1986). The experimental data of Tatsuoka et al. (1986) are extrapolated to estimate the y-intercept, i.e. initial internal friction angle (ϕ_0) against each void ratio (e) as depicted in Figure 1, to develop a normalized relationship of internal friction angle corresponding to various stress levels (Figure 2). In Figure 2, the relationships are drawn for each void ratio as well as the mean trendline by using the least squares method. Based on relationships pertaining to the various void ratios and mean trendline, the non-linear shear strength parameters are set in Tables 1 & 2, respectively.

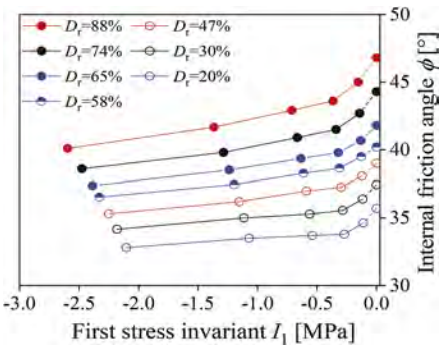

Figure 1. Relationship between ϕ and I_1 for Toyoura sand (after Tatsuoka et al. (1986)).

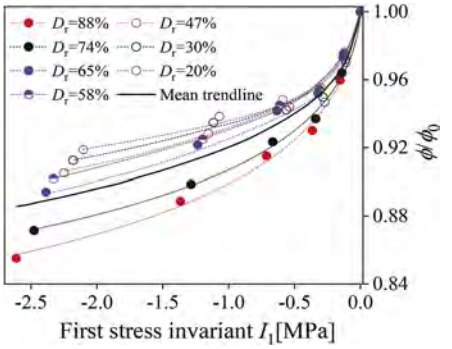

Figure 2. Normalized relationship between ϕ/ϕ_0 and I_1 for Toyoura sand.

Table 1. Shear strength parameters for Toyoura sand.

D_r	ϕ_0	γ	a	b	n
%	°	kN/m^3			
20	35.7	13.6	0.217		0.522
65	41.8	15.0	0.262	1	0.526
88	46.8	15.7	0.280		0.528

Table 2. Parameters based on the mean property.

ϕ_0	a	b	n
°			
30	0.175		
35	0.216	1	0.526
40	0.257		

3 EXAMINATION OF UBC FORMULA FOR SANDY SOILS

3.1 *Ultimate bearing capacity analysis under centric vertical load*

The analysis method is validated against the centrifuge experiments in the published references (Figure 3). Figure 4 indicates good agreement of analysis results by RPFEM with those from the AIJ and JRA formulas in the case of γ=18 kN/m^3 for centric vertical load without surcharge. Figure 5 investigates the normalized UBC against $\gamma B/p_a$ for varying γ and B. The term γB is normalized with respect to normalization factor p_a, i.e. standard atmospheric pressure, p_a=101.325 kPa. The trendline evinces diminution in normalized UBC with increased stress

levels by stepping up both γ and B (Figure 5). Apropos, modification factor η_γ is inevitable, as the effect of γ is not well conceived in the AIJ and JRA formulas (Figure 5). The size effect modification coefficientη_γ is described as ($2q_u/\gamma BN_\gamma$) and graphically illustrated in Figure 6. The data plotted in Figure 6 is fitted with the mean trendline using the least squares method. The mean relationship for η_γ can be closely approximated as given in Equation 3.

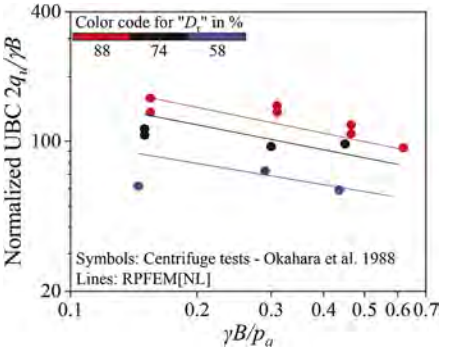

Figure 3. Validation of the analysis method in comparison with the centrifuge tests on Toyoura sand.

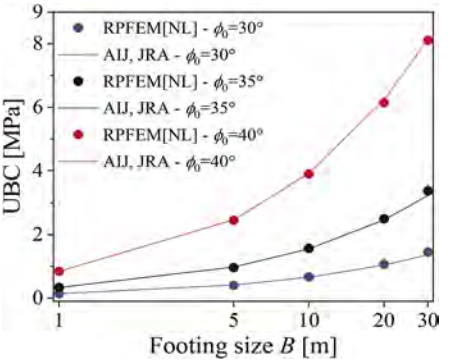

Figure 4. Comparison of ultimate bearing capacity results in case of γ=18 kN/m^3.

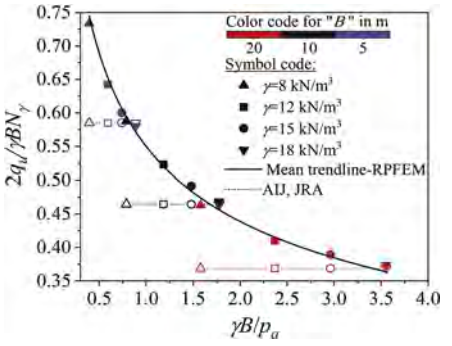

Figure 5. Effect of γ on normalized UBC ($2q_u/\gamma BN_\gamma$) in case of ϕ_0=35°.

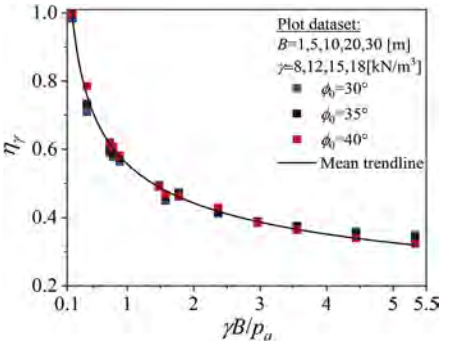

Figure 6. Relationship between modification coefficient η_γ and $\gamma B/p_a$ in case of Toyoura sand.

Hence, the modified UBC formula for the sandy soils, based on the analysis results, is as follows:

$$q_u = \frac{1}{2}\gamma BN_\gamma\eta_\gamma \quad \text{where} \quad \eta_\gamma = 0.55\left(\frac{\gamma B}{p_a}\right)^{\frac{-1}{3}} \; 0 \le \eta_\gamma \le 1 \tag{3}$$

3.2 *Discussion on UBC formula for surcharge loading*

Figure 7 elucidates the trend in UBC against surcharge load amidst RPFEM and other guidelines under the effective stress condition, i.e. γ=8 kN/m^3. The numerical outcomes in Figure 7 exhibit a substantial difference from the AIJ and JRA formulas, therefore, a modification coefficient η_q is necessary to be proposed for N_q. η_q is equal to $\{(q_u\text{-}0.5\gamma BN_\gamma\eta_\gamma)/qN_q\}$ and plotted in Figure 8 against q/p_a for various footing sizes and shear strength characteristics. Here, q denotes the uniform surcharge load. The decrementing trend in η_q is primarily associated with the reduced peak friction angle due to the augmented stress at higher surcharges. The best fit relationship of η_q based on Figure 8, and the modified UBC formula, are proposed as Equation 4. Here, N_γ and N_q

correspond to the Meyerhof bearing capacity factors. Like AIJ recommendations, this study also recommends cutting off the bearing capacity factors at and beyond ϕ=40°. The performance of the proposed formula is surveyed against RPFEM results for various D_r in the case of Toyoura sand (Figure 9). In comparison to the other prevailing guidelines, the proposed UBC formula (Eq. 4) well estimates the size effect concerning γ, B and q (Figure 10).

$$q_u = \left(\frac{1}{2}\gamma B N_\gamma \eta_\gamma\right) + \left(qN_q\eta_q\right) \quad \text{where} \quad \eta_q = 0.55\left(\frac{q}{p_a}\right)^{\frac{-1}{8}} \quad 0 \le \eta_q \le 1 \tag{4}$$

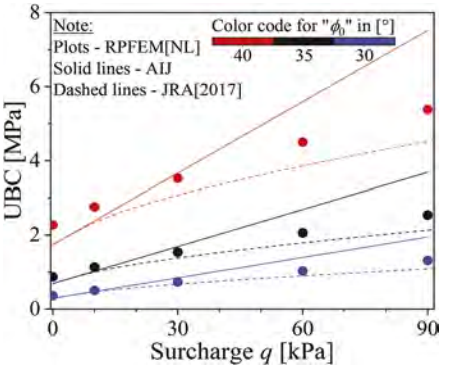

Figure 7. Comparison of ultimate bearing capacity in case of B=10 m and γ=8 kN/m^3.

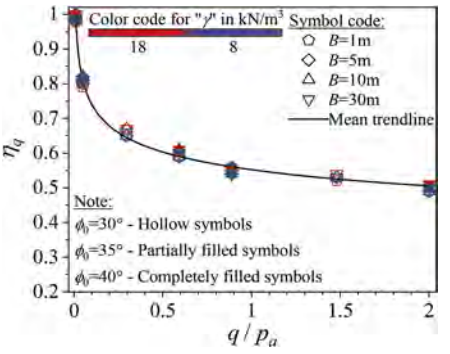

Figure 8. Relationship between modification factor η_q and (q/p_a).

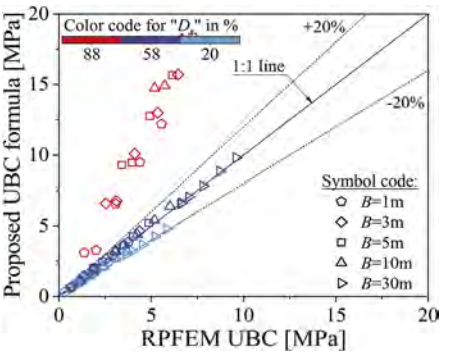

Figure 9. Performance of proposed UBC formula in case of Toyoura sand (q=0-90 kPa).

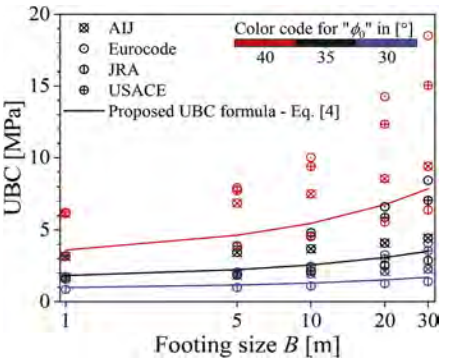

Figure 10. Performance of proposed UBC formula in case of γ=8 kN/m^3, q=90 kPa.

4 CONCLUSIONS

A UBC formula was examined and improved based on the mechanical property of Toyoura sand. The numerical method was validated through centrifuge tests in the published references. The effect of γ was clarified to be well indicated by normalized variable ($\gamma B/p_a$) regarding size effect and the correction factor for N_γ was newly proposed. Furthermore, a correction factor for N_q was proposed, owing to the contradiction amid AIJ and JRA formulas regarding size effect due to the surcharge load. The proposed formula estimates the size effect within ≈±20% for loose to medium dense Toyoura sand. However, the proposed UBC formula can be widely used for UBC estimation by cutting off the bearing capacity factors at and beyond ϕ=40°. Moreover, the international guidelines such as U.S. Army Corps of Engineers (USACE) and Eurocode are also found to have limited applicability concerning the size effect. The aptness of JRA specifications was found to be applicable from an engineering viewpoint.

REFERENCES

AIJ (1988, 2001, 2019). *Recommendations for design of building foundations*. Tokyo: Architectural Institute of Japan.

JRA 2017. *Specifications for highway bridges part iv* (*substructures*). Tokyo: Japan Road Association.

Nguyen, D. L., Ohtsuka, S., Hoshina, T. & Isobe, K. 2016. Discussion on size effect of footing in ultimate bearing capacity using rigid plastic finite element method. *Soils Found* 56 (1): 93–103.

Okahara, M., Takagi, S., Obata, H., Mori, K. & Tatsuta, M. 1988. Centrifuge tests on scale effect of bearing capacity. *In: Proc. 42nd Japan Annual Conf. of Civil Engineers Vol. III*: 250–251 (in Japanese).

Tatsuoka, F., Sakamoto, M., Kawamura, T. & Fukushima, S. 1986. Strength and deformation characteristics of sand in plane strain compression at extremely low pressures. *Soils Found* 26(1): 65–84.

Smart Geotechnics for Smart Societies – Zhussupbekov, Sarsembayeva & Kaliakin (Eds)
© 2023 The Author(s), ISBN 978-1-003-29912-7
Open Access: www.taylorfrancis.com, CC BY-NC-ND 4.0 license

Ultimate bearing capacity of a shallow foundation on unsaturated sandy soil with cavity

E.L. Keba
Hokkaido University, Graduate School of Engineering, Sapporo, Japan

K. Isobe
Hokkaido University, Faculty of Engineering, Sapporo, Japan

ABSTRACT: A series of model footings tests were conducted on unsaturated sand with cavity. The cavity was created using an easily found commercial balloon, placed, and expanded within the model soil. The unsaturated soil was vertically loaded using a circular model footing of diameter $B = 30$ mm after the balloon was deflated. The load versus displacement curves reveal the increase of the ultimate bearing capacity of footing on sand with cavities in deeper layers. The Rigid Plastic Finite Element analysis results are introduced to apprehend the variation of bearing capacity of a footing resting on ground with cavity and confirm the experimental results. As a result, the trade-off relationship between matric suction and effective stress, from the fact that giving higher values of ultimate bearing capacity in deeper cavity cases and lower ultimate bearing capacity in shallower cavity cases, comparing to the cases without consideration of the ground water table.

1 INTRODUCTION

Underground cavity can occur in the ground due to both natural causes (karst dissolution), and manmade causes (tunneling, mining, quarry, defective sewage pipes, etc.). The karst environment occurs in over 20% of the earth's ice-free continental area and 25% of the global population depends on the karst water supply (Ford & Williams, 2007). On the other hand, as the demand for land grows and humans increasingly modify their environment, more and more people might be exposed to the instabilities caused by underground cavities (Holzer, 2009). Researchers analyzed the behavior of ground with cavity and the bearing capacity of the shallow foundation above the ground with cavity (Baus & Wang, 1983; Augarde C.E. et al, 2003). Progress in unsaturated soil mechanics revealed the contribution of the matric suction toward the increase of the shear strength of unsaturated soils (Fredlund & Rahardjo, 1993; Costa, 2003). Oh & Vanapalli (2013) modified the total stress approach and the effective stress approach for the saturated soils to unsaturated soils considering the influence of matric suction.

Previous conventional saturated soil mechanics applications to unsaturated soil might lead to underestimate the ultimate bearing capacity in the design and construction processes. In the semi-arid area, shallow foundations are found in an unsaturated state during their life cycle. Thus, no investigation addressing the issue of ground with a cavity under unsaturated conditions has been found in the literature. This paper introduces an experimental analysis of the ultimate bearing capacity of a footing above an unsaturated sandy soil with a cavity. Results are compared with numerical analysis conducted with the Rigid Plastic Finite Element Method (RPFEM), whose detail is referred in the literature (Du, N.L. et al., 2016), to obtain the influence zone of a cavity within the ground against the bearing capacity. The sandy soil (silica sand No.7) in the model tests was prepared in layers at a relative density of $D_r = 70\%$. The results and different observations are summarized and presented in the following lines.

DOI: 10.1201/9781003299127-193

2 TEST EQUIPMENT AND PROCEDURES

Several model footing tests were conducted considering the different depths of the cavity and saturation degrees. Figure 1 illustrates the equipment used in this study.

The acrylic experimental soil tank has an inner diameter of 300 mm. Valves are connected at the bottom for water supply and soil saturation is realized from the lower part of the model soil to the surface. Air pressure can be supplied from valves on the top metallic plate. A loading device is installed on the top plate of the model soil tank and can be actuated by a motor at a speed of 0.5 mm per minute. The loading device uses a load cell to measure the resistance load received by the footing. The soil (silica sand No.7) sample is dropped into the tank from a certain height and prepared in 10 layers of 30 mm thick each. Table 1 summarizes the soil properties.

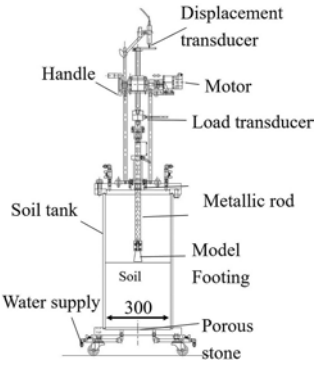

Figure 1. Schematic view of the equipment.

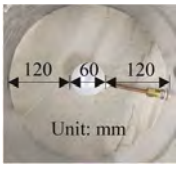

Figure 2. Balloon inserted within the tank.

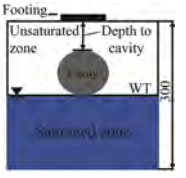

Figure 3. Illustration of unsaturated soil model with cavity.

Table 1. Soil properties.

Soil type	Dry unit weight γ_d (kN/m^3)	Relative density D_r (%)
Silica sand No. 7	14.8	70

After saturation, the water is drained by applying air pressure on the top of the soil out to the desired depth (preferably below the cavity as illustrated in Figure 3 where we assume that the water table is at the limit of the lower part of the cavity). The load and displacement transducers are connected to the computer for recording. The technique used to create the cavity consists of a balloon attached to a tube within the tank, expanded with air, and, its size adjusted to the desired size of the cavity (Figures 2 and 3). This creates a cavity with unsupported walls within the model soil, which is stable enough before the loading process is started. The horizontal and vertical dimensions of the cavity were kept constant (60 mm) before the loading test.

3 RESULTS AND DISCUSSION

The test results on the ground with cavity are presented in form of load-displacement curves under dry and unsaturated conditions (Figure 4). The ultimate bearing capacity for the unsaturated condition cases is summarized in Table 2. Note that their curves for the cases with the cavity depth H = 60 mm in unsaturated and 90 mm in dry conditions clearly reach a peak load considered as the ultimate load. On the other hand, the displacement curves at the cavity depth H = 100, 120, and 150 mm in unsaturated conditions show a linear increase with the load applied. Thus, observe that the ultimate load was defined as the applied load at the displacement corresponding to 10% of the footing diameter B for the cases with the cavity depth H = 100, 120 and 150 mm in unsaturated conditions.

The ultimate load for the cavity at depth H = 150 mm is the largest among all cases. As the cavity (water table) is deeper, the saturation degree is lower. It is, therefore, because matric suction increases the shear strength of the unsaturated sand.

Figure 5 shows RPFEM results that the bearing capacity normalized by the bearing capacity of ground without cavity (BC/BC_{NC}) varies with the normalized horizontal distance from the centerline of the footing (r/D). The ultimate bearing capacity variation in Table 2 can be quantitatively confirmed comparing with the cases beneath the footing at r/D = 0 in Figure 5. The BC/BC_{NC} of the deeper cavity cases tends to be higher along r/D and reach the constant value within a small value of r/D.

For the reference, Table 3 shows a comparison of the ultimate bearing capacity (UBC) obtained in dry conditions and saturated conditions for soil without a cavity. A noticeable decrease in the UBC from dry conditions to saturated conditions is observed.

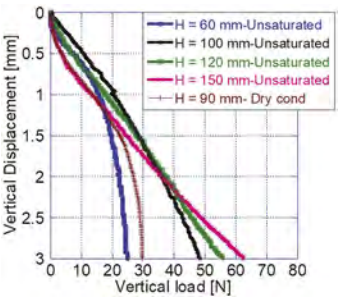

Figure 4. Vertical load vs vertical displacement.

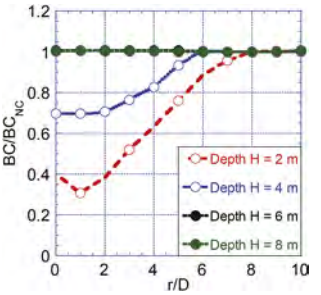

Figure 5. RPFEM results of bearing capacity variation with normalized horizontal distance by cavity diameter r/D.

Table 2. Ultimate bearing capacity obtained in unsaturated conditions.

Depth of cavity H (mm)	Ultimate bearing capacity (kN /m^2)	BC/BC_{NC}	Saturation degree Sr (%)
60	31.2	0.309	47.9
100	65.2	0.645	Unmeasured
120	76.5	0.757	32.3
150	87.7	0.868	29.8

Table 3. Ultimate bearing capacity obtained in dry and saturated conditions without cavity.

Relatively Density Dr (%)	UBC in Dry conditions (kN /m^2)	UBC in Saturated conditions (kN /m^2)
60.0	32.55	3.53
70.0	72.27	2.24

The tables above show an increase in the UBC under unsaturated conditions. The increase of the UBC is even greater for some cases in unsaturated conditions with cavities compared to the cases without cavities in dry and saturated conditions.

Furthermore, the distribution of the porewater pressure in the ground obtained with the RPFEM in Figure 6 shows a zone of negative porewater pressure above the cavity. This confirms the assumption in Figure 3 although the difference in water table shapes around the cavity. The influence of matric suction is revealed by the strain rates distribution around cavities under unsaturated conditions in Figure 7 with the shear bands reaching the cavity. Under the unsaturated condition, the failure mode reveals that the strain rates are concentrated on the edges of the cavity. However, under dry conditions, it should, considering the cavity depth, tend to a general failure mode despite the influence of the cavity. In fact, in the unsaturated cases, the bottom of the cavity is at the boundary of the water table i.e., in the capillary zone where water fills most of the pores and consequently,

a decrease in effective stress occurs. On the contrary, in the upper layers, the generated matric suction increases the soil shear strength as Equation (1) by Karube et al. (1996).

$$C = Se\,(\theta)\tan\phi^{'}.s \tag{1}$$

where C: cohesion under unsaturated condition; $Se\ (\theta)$: effective saturation degree, the function of moisture θ; s: suction; ϕ': effective shear resistance angle.

This study has the merit to embrace a neglected approach up to now regarding the behavior of the shallow foundation above the ground with a cavity. Although the matric suction increases the shear strength of the soil, we need to think about the 'apparent stability' provided by the unsaturated condition in the long term. The collapse of underground cavities is usually sudden, and the water table fluctuates during the life cycle of the foundation. This approach with the revealed trade-off relationship of matric suction and effective stress might be a key to solving the problem.

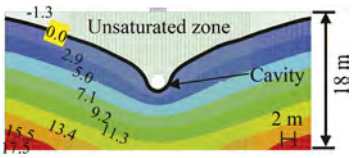

Figure 6. Pore water pressure (kPa) distribution within a ground with a cavity at Depth H = 8 m.

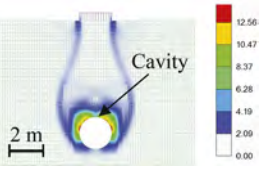

Figure 7. Norm distribution of the strain rate within the ground under unsaturated conditions.

4 CONCLUSION

Several model tests, introducing an easy and cost-effective technique to simulate the cavity in the ground with easily found commercial balloons, were conducted on the ground with a cavity under unsaturated conditions. The trade-off relationship was observed between matric suction and effective stress; giving higher values of ultimate bearing capacity in deeper layers and lower ultimate bearing capacity at a shallow depth of the cavity, compared to the cases without consideration of the groundwater table. The RPFEM results in the cases with the cavity beneath the footing (r/D = 0) qualitatively reproduced the trend of ultimate bearing capacity observed in the model tests. The results can help in understanding the sudden collapse of cavities in the long term as the water table fluctuates within the ground as well as the expansion of the influence zone of a cavity under the observed conditions. Although the measurement of matric suction and saturation degree was not done directly in the present experiments (planned in the future), the designed process proved to be reliable in modeling the ground with a cavity.

REFERENCES

Augarde, C.E., Lyamin, A.V. and Sloan, S.W., 2003. Prediction of undrained sinkhole collapse. *Journal of Geotechnical and Geoenvironmental Engineering*, 129(3), 197–205.

Baus, R.L. and Wang, M.C. 1983. Bearing capacity of strip footing above void. *Journal of Geotechnical Engineering*, 109(1), 1–14.

Costa, Y.C., 2003. Influence of matric suction on the results of the plate load performed on the lateritic soil deposit. *Geotech. Test. J.*, 26(2), 219–227.

Du, N.L., Ohtsuka, S., Hoshina, T. and Isobe, K., 2016. Discussion on size effect of footing in ultimate bearing capacity of sandy soil using rigid plastic finite element method. *Soils and Foundations*, 56(1), 93–103.

Ford, D. and Williams, P., 2007. Karst Hydrogeology and Geomorphology. West Sussex, UK: John Wiley & Sons.

Fredlund, D., G, Rahardjo, H., 1993. Soil Mechanics for Unsaturated Soils. New York: John Wiley & Sons.

Holzer, T.L., 2009. Living with unstable ground. Alexandria, VA: *American Geological Institute, environmental awareness series* 11.

Karube, D., Kato, S., Hamada, K. and Honda, M., 1996. The relationship between the mechanical behavior and the stage of porewater in unsaturated soil. *Proceedings of JSCE*, 535, 83–92 [In Japanese].

Oh, W. and Vanapalli, S., 2013. Interpretation of the bearing capacity of unsaturated fine-grained soil using the modified effective and the modified total stress approaches. *Int. J. Geomech.* 13 (6), 769–778.

Smart Geotechnics for Smart Societies – Zhussupbekov, Sarsembayeva & Kaliakin (Eds)
© 2023 The Author(s), ISBN 978-1-003-29912-7
Open Access: www.taylorfrancis.com, CC BY-NC-ND 4.0 license

Numerical study of lateral resistance of rectangular piles with various pile widths

M. Odagiri, T. Kiriyama & Y. Asaka
Institute of Technology, Shimizu Corporation, Tokyo, Japan

ABSTRACT: The coefficient of lateral subgrade reaction is smaller for piles with wide width. However, applicability for wide piles of reduction factor for lateral reaction with respect to the pile width in pile structural design is unclear. In this study, a 3D FEM model is used to replicate previously reported lateral loading tests on rectangular piles with different widths. A good correspondence between experiment and analysis is achieved. The size of the soil displacement zone during lateral loading of the piles is examined. Pile width is found to affect the lateral subgrade reaction and the extent of the soil deformation area in all three dimensions.

1 INTRODUCTION

It is generally known that the larger the pile width, the smaller the lateral subgrade reaction per width. The design guidelines provide a reduction factor for the coefficient of lateral subgrade reaction with respect to the pile width. However, its applicability to wide piles such as wall-type piles is unclear, and the lateral resistance mechanism of piles is needed to ascertain. In this study, 3D FEM analysis is used to simulate published lateral loading tests of rectangular piles with different pile widths in a centrifuge (Mano et al. 2021) and discuss the effect of pile width on pile lateral resistance based on the size of the soil deformation zone.

2 METHODOLOGY OF 3D-FEM ANALYSIS

2.1 *Outline of experiments and analysis*

The experiments were performed at a centrifugal acceleration of 40g. The model ground was dry Toyoura sand and the relative density *Dr* of the experimental layer exceeded 90%. The rectangular cross-section piles were made of stainless steel. In this study, experimental specimens with equal pile thickness (160mm in prototype scale) and different pile widths (seven cases ranging from 0.4m to 20.4m (the width of the container)) were subject to simulation.

Analyses were implemented using the software SoilPlus. As shown in Table 1, each analysis case (B0.4-B20.4) corresponded to one experimental specimen. Analyses were first performed for initial stress in the gravity field, and then horizontal displacement was applied to the pile head elements (at 0.8 m from the ground surface).

Table 1. Analysis case list.

Case identifier	B0.4	B0.8	B1.2	B2.0	B4.0	B8.0	B20.4
Pile width (m)	0.4	0.8	1.2	2.0	4.0	8.0	20.4
Pile thickness (mm)	160	160	160	160	160	160	160

DOI: 10.1201/9781003299127-194

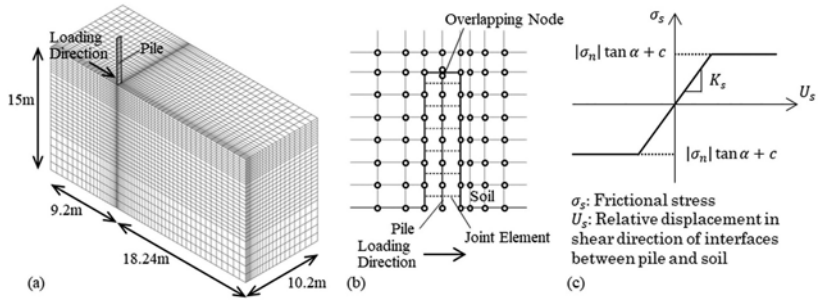

Figure 1. 3D FEM model: (a) entire model (B1.2); (b) plan view of pile region; (c) frictional stress characteristic of joint element.

2.2 *Finite element meshing and material properties*

The finite element mesh for case B1.2 is shown in Figure 1(a). As seen in this figure, half of the domain was modeled by taking advantage of the symmetry in the loading direction. The ground volume is the size of the experimental soil container and is constant regardless of pile width. Soil was modeled with solid elements, while the pile itself was modeled using two-dimensional shell elements. As shown in Figure 1(b), the space representing pile in the soil was void and the interfaces between pile and soil were connected by joint elements. Pile and soil did not have common nodes. The bottom boundary was fixed in all directions. The sides was free to move vertically. In cases B8.0 and B20.4 only, the side parallel to the loading direction was free to move vertically and in the loading direction, because the side walls of the soil container used in experiments were lined with Teflon sheet to remove the effect of friction at the walls.

The material properties are summarized in Table 2. The pile was modeled as a linear elastic perfectly plastic material with a von Mises yield condition. The yield stress was assumed to be 255MN/m^2. The sand was modeled as a linear elastic perfectly plastic material with a Mohr-Coulomb yield condition. The internal friction angle φ of the sand was assumed to be 43° with reference to Hatanaka 1977. Dilatancy angle ψ was 13° ($\psi = \varphi$-30). Cohesion c was 0kPa. The soil was divided into five layers of 3m thickness each in the vertical direction. Shear modulus G was calculated from shear wave velocity Vs obtained in experiments at the center depth of each layer as $0.2 \cdot \rho \cdot Vs^2$ (ρ: density). Taking G as $\rho \cdot Vs^2$ would give a large value, when the constitutive equation of soil is a linear elastic perfectly plastic.

Table 2. Material parameters used in analysis.

Material	Shear modulus G (MPa)	Poisson's ratio ν	Unit weight γ (kN/m^3)	Friction angle φ (deg)	Dilatancy angle ψ (deg)
Pile	7.4×10^4	0.3	77.7	-	-
Soil	$0.2 \cdot \rho \cdot Vs^2$	0.3	16.3	43	13

Joint elements were inserted to model the frictional force, and exfoliation between pile and soil. As shown in Figure 1(c), the frictional stress modeled as a linear elastic perfectly plastic. The maximum frictional force σ_{s_max} was determined by the following equation.

$$\sigma_{s\_max} = |\sigma_n| \tan \alpha + c \tag{1}$$

Where σ_n: normal stresses acting on joint elements; frictional angle α = 26° (coefficient of friction was 0.5); and cohesion c = 0.001 kPa. Shear stiffness K_s was calculated using the following equation.

$$K_s = \tau_{max}/0.02 \tag{2}$$

$$\tau_{max} = K_p \sigma_v \tan \alpha \tag{3}$$

$$K_p = \tan^2\left(45 + \frac{\phi}{2}\right) \tag{4}$$

where σ_v: confining pressure; α: friction angle between pile and soil (26°); and φ: internal friction angle of soil (43°). It is difficult to model the circumferential frictional resistance of a pile under lateral loading correctly. Therefore, in this study, the maximum frictional force acting on the pile is assumed from the Rankine's passive earth pressure, and stiffness K_s was calculated assuming that the frictional force increases linearly until the relative displacement reaches 20 mm.

3 LATERAL SOIL REACTION BY FEM SIMULATION

Figure 2(a)-(c) show the analytical and experimental relationships between load per unit width and horizontal displacement at the loading point for all cases. The experimental and analytical results correspond well, with the load decreasing as the pile width increases. The loads in the analysis are slightly larger than the experimental results. Figure 2(d)-(e) show the distribution of bending moment per unit width in the depth direction when the lateral load per unit width applied to the pile was about 250kN/m (for cases B0.4 and B20.4, respectively). Here, the analysis reproduces the phenomenon by which maximum bending moment value increases as the pile width increases and the depth at which it develops increases.

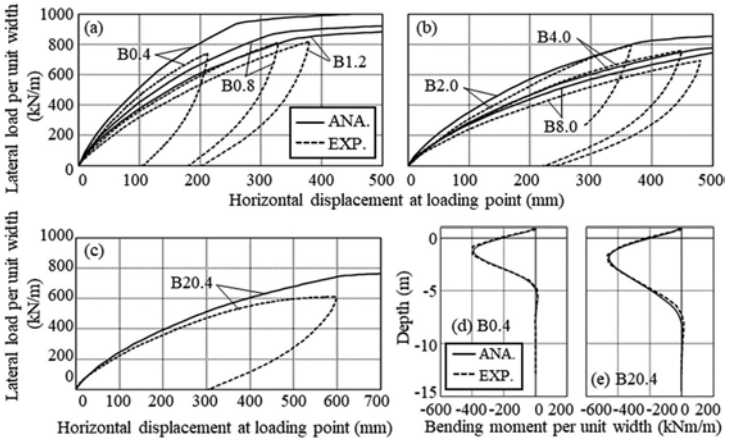

Figure 2. Analytical results vs experimental results: (a)-(c) load per unit width vs displacement; (d), (e) bending moment distribution of piles (B0.4 and B20.4).

The following discuss the results of the analyses. Figure 3 shows lateral subgrade reaction at a depth of 1.5m. Lateral subgrade reaction was calculated by differentiating the shear force of the pile in the direction of depth. Figure 3(a) shows pile displacement versus lateral subgrade reaction (for cases B0.4, B1.2, B8.0, B20.4). The larger the pile width, the smaller the lateral subgrade reaction per unit width. Figure 3(b) shows the relationship between pile width and ratio of lateral subgrade reaction based on case B0.4. Here, lateral subgrade reaction means the value when the pile displacement at 1.5m depth was 10mm. Also plotted on the figure are lines indicating where the lateral subgrade reaction is proportional to the -3/4 to -1/4 power of pile width B. The calculated lateral subgrade reaction is approximately proportional to the -1/2 power of pile width.

Figure 4(a) shows the total displacement contour at the ground surface and for the vertical section through the center of the pile for case B1.2 when pile head displacement was 100 mm. Here, W_x is the extent in the loading direction of the area of soil with a displacement of 20 mm or more. Then, the extent of the deformation area in the direction orthogonal to loading is W_y, and the extent in the depth direction is W_z. The displacement contour at the ground surface shows that W_y exceeds the width of the pile. Figure 4(b)-(d) show the relationships between the extent of the

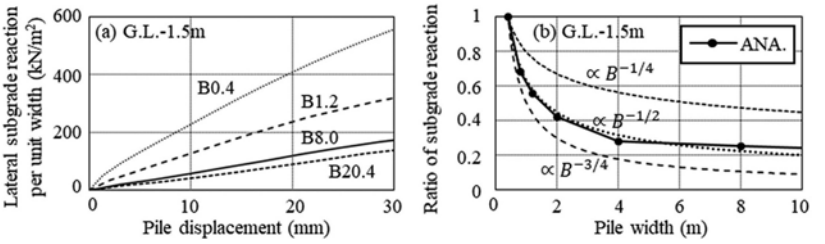

Figure 3. Relationships between pile width and lateral subgrade reaction: (a) pile displacement vs lateral subgrade reaction; (b) pile width vs ratio of subgrade reaction (pile displacement was 10mm).

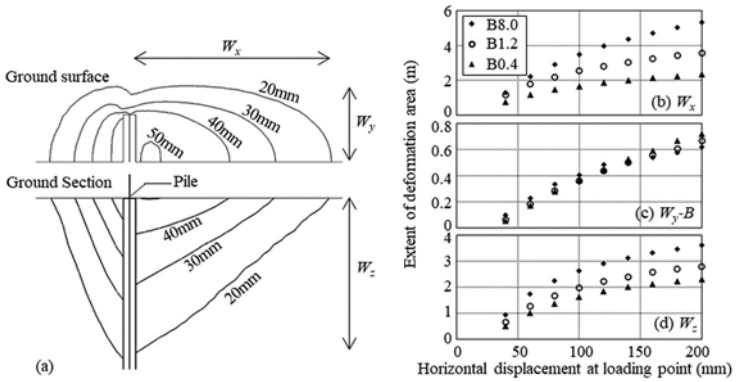

Figure 4. Size of the soil deformation area: (a) contours of total displacement (for case B1.2 when pile head displacement was 100 mm); (b)-(d) horizontal displacement vs extent of deformation area.

deformation area in each direction and pile head displacement for cases B0.4, B1.2, and B8.0. In the direction orthogonal to loading, the value is given as W_y-B to take into account the pile width.

Figure 4(c), the amount by which the deformation area extends beyond the pile was almost constant regardless of pile width. That is, the size of the soil resistance zone beyond the pile does not change with pile width, and the lateral subgrade reaction decreases with increasing pile width. As the lateral subgrade reaction decreases, stresses are transmitted to deeper parts of the pile. Therefore, W_z increase as pile width increases. Since passive soil is pushed up by the pile, deformation at greater depths will result in deformation at locations farther from the pile in the loading direction. This is why W_x was seen to increase with pile width B and W_z.

4 CONCLUSIONS

In this study, lateral loading tests on rectangular piles with various widths in a centrifuge were replicated using a 3D FEM model. The analytical results corresponded well with the experimental observations, confirming the validity of the analytical model. The analytical results showed that the lateral subgrade reaction per unit width was proportional to approximately -1/2 power of the pile width. The extent of the soil deformation area outside the pile caused by a lateral loaded pile almost constant regardless of the pile width. Therefore, it is considered that the resistance zone beyond the pile does not change with pile width, and the lateral subgrade reaction decreases with increasing pile width.

REFERENCES

Hatanaka, M. 1977. Fundamental studies on undisturbed sampling of saturated sands by freezing. Doctoral dissertation. Tokyo Institute of Technology.

Mano, H., Zhou, S. & Yoshinari, K. 2021. Influence of Pile Width and Pile Stiffness on Lateral Subgrade Reaction. *Journal of Japan Association for Earthquake Engineering*. Vol.21. No.6: 1–12.

Smart Geotechnics for Smart Societies – Zhussupbekov, Sarsembayeva & Kaliakin (Eds)
© 2023 The Author(s), ISBN 978-1-003-29912-7
Open Access: www.taylorfrancis.com, CC BY-NC-ND 4.0 license

Bearing pressure of granular bed overlying desiccated normally consolidated ground

J.Y.V. Shiva Bhushan, G.V. Narasimha Reddy & M.R. Madhav
JNT University, Hyderabad, India

ABSTRACT: Bearing capacity of footings, the most important design aspect for structures, is calculated most commonly considering the soil as homogenous and semi-infinite. Naturally deposited clay exhibits a complex variation of undrained shear strength with depth, depending upon the stress history, climatic and environmental exposure, etc. Many studies assume the soil as rigid plastic but in practice soft soil shows non-linear response. In the present study, footings resting on a two-layered soil consisting of dense granular fill over desiccated normally consolidated deposit (DNC) are analyzed considering the non-homogeneity and compressibility of the soils. The analysis is performed for circular footing using PLAXIS software. Bearing pressure – settlement responses are obtained for different thicknesses of sand bed. Effect of depth of footing on the bearing pressure – settlement response of granular bed overlying DNC is also studied.

1 INTRODUCTION

Most of the bearing capacity theories consider the soil to be homogeneous and incompressible. Ultimate bearing capacity of circular footing resting on homogeneous clays was estimated by considering the average undrained strength till 0.67 times the diameter of the footing (Skempton 1951) and average shear strength over depth of soil (Meyerhof 1951). Ultimate bearing capacity, q_u, of shallow footings on homogeneous compressible soils is obtained by Vesic (1973) using cavity expansion theory as

$$q_u = c_u N_c F_{cc} \tag{1}$$

where N_c (= 5.14) is bearing capacity factor, c_u- undrained strength of soil, and F_{cc} - compressibility factor as a function of rigidity index, I_r (= G/c_u) and G is shear modulus of soil. Shiva Bhushan *et al*. (2022) studied the effect of compressibility on undrained bearing pressure of homogeneous soft ground and bearing pressure factors are proposed as functions of rigidity index for specific settlements.

Normally consolidated soil (*NC*) have strength increasing with depth and with a desiccated layer near the top due to diurnal variations of temperature and weathering effects (Day 1996). Top layer of NC soils may loses its moisture due to atmospheric evaporation and lowering of water table which results in desiccation. Desiccated soft deposits with decrease in strength in top portion of NC soil were reported by several researchers (Bozozuk 1972; Almeida and Ferreira 1993; Bergado et al. 2002; Balasubramaniam et al. 2005). Shear strength profiles of DNC soils from various locations are shown in Figure 1. Variability in these soil profiles are evident in the thickness of the desiccated layer which varies from 1.5 to 3.5 m, the rate of increase of undrained strength in NC layer from 1.0 to 4.5 kPa/m, the rate of decrease of undrained strength in the desiccated zone varies from 25 to 0 (crust), and the undrained strength at the interface of desiccated and NC layer from 8 to 20 kPa.

DOI: 10.1201/9781003299127-195

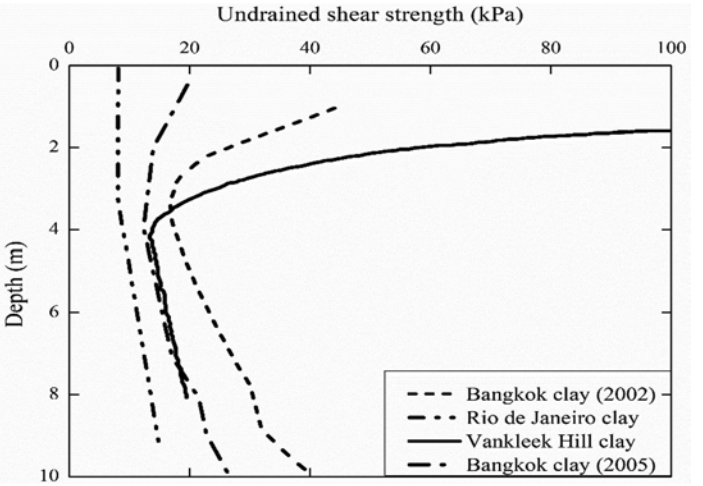

Figure 1. Shear strength profiles of desiccated normally consolidated soil. (Bozozuk 1972; Almeida and Ferreira 1973; Bergado et al. 2002; Balasubramaniam et al. 2007).

Many sites have nonhomogeneous, layered or stratified soils. Few studies (Button 1953; Siva Reddy and Srinivasan 1971; Michalowski 1992; Tani and Craig 1995; Merifield and Nguyen 2006) consider the effect of layering of soils on the bearing capacity of footings. Davis and Booker (1973) based on plasticity theory gave solution for the bearing capacity of strip footing on non-homogenous soil considering the roughness of the footing.

Dense granular bed is placed over the existing desiccated normally consolidated deposits as a part of ground improvement technique. This bed provides a good platform to dissipate the load transferred from foundations. Meyerhof and Hanna (1974) considered the punching mechanism of strong top layer over weak bottom layer and proposed bearing capacity equation. The ultimate bearing capacity of circular footing on dense sand overlying soft soil is given in Equation (2), with a maximum of $q_u = q_{top\ layer} = 0.3\gamma D_f N_\gamma + \gamma D N_q$, where N_γ and N_q are the bearing capacity factors, γ is the unit weight of soil, D and D_f are the diameter and depth of circular footing.

$$q_u = 1.2\,cN_c + 2\gamma H^2\left(1 + \frac{2D}{H}\right)\frac{s}{B}k_s tan\,\phi + \gamma D \tag{2}$$

where s is the shape factor for circular footing, k_s is the coefficient of punching shear resistance, and δ is the angle of mobilized interface friction and its variation with bearing capacity ratio (q_2/q_1) is given in Figure 2(a). It was shown to be dependent on the ratio of bearing capacities of individual layers of sand, q_2 and clay layers, q_1. Variation of coefficient of punching shear resistance, k_s and its variation with angle of shearing resistance, ϕ is given in Figure 2(b) (Meyerhof and Hanna 1978).

Michalowski (2002) considered the rigid block mechanism of failure for semi-infinite soils (depth is very large) and reported that bearing capacity of footings on two-layered clay is unaffected by shear strength of second layer. Load spread mechanism for sand overlying clay is another method of computing ultimate bearing capacity of footings on sand over clays (Terzaghi and Peck 1948; Jacobsen 1977). Rajyalakshmi *et al.* (2015) quantified the effect of non-homogeneity on ultimate bearing capacity of footings on granular bed over soft ground.

The present numerical study accounts for the non-homogeneity of both the desiccation and NC layers of strength profiles over the bearing pressure of dense granular bed overlying DNC

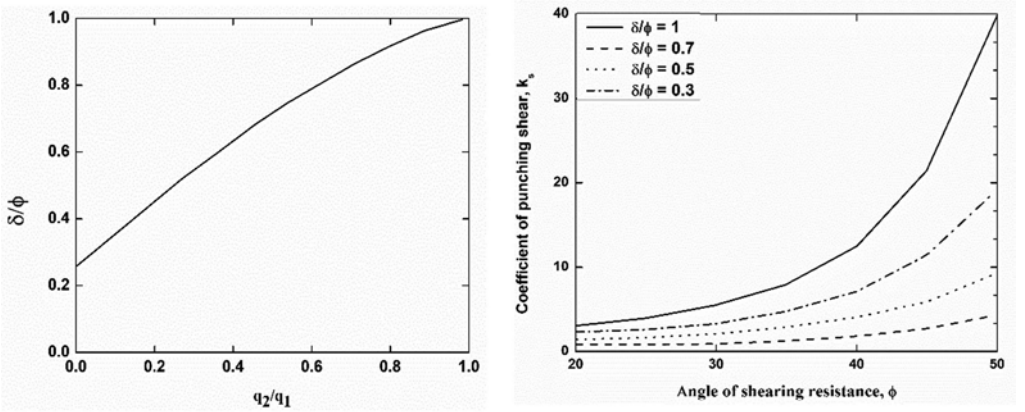

Figure 2. Variation of (a) δ/φ with q_2/q_1 (b) k_s with φ for different δ/ϕ (Meyerhof and Hanna 1978).

ground. This parametric study also quantifies the individual effects of compressibility of NC soil, non-homogeneity of desiccation zone, thickness of granular bed and embedment depth of footing on bearing pressure-settlement responses.

2 PROBLEM DESCRIPTION

Rigid circular footing (diameter, D) located in a dense granular bed overlying desiccated normally consolidated soil is considered (Figure 3). Desiccated normally consolidated (DNC) ground is considered as a two-layer soil whose undrained shear strength varies linearly with depth. The rate of decreasing and increasing of shear strength with depth is denoted by κ and ρ in the top desiccated layer and bottom NC soil respectively. The shear strength of the soil at the interface of the desiccation zone and NC soil is c_{u0}. Desiccation strength ratio, μ ($=c_{uT}/c_{u0}$) is defined as the ratio of undrained strength at the top, c_{uT}, to that at the bottom, c_{u0}, of the weathered soil of thickness, z_0.

Two-meter thick desiccated layer with undrained strength of 30 kPa at the top of desiccated surface and 10 kPa at the interface with NC soil is considered. Poisson's ratio of desiccated normally consolidated ground is taken as 0.495 to simulate the undrained behavior. Unit weight of DNC is taken as 15 kN/m^3 whereas that of granular layer is 20 kN/m^3. Rigidity indices of NC and desiccated layers are assumed as 200 with the strengths of the former increasing and that of the latter decreasing with depth. The angle of shearing resistance of sand, ϕ is taken as 35°. This study considers granular fill over *DNC* soil as a two-layered system that includes the non-homogeneity and compressibility of the ground, in addition to the effect of desiccation on the strength profile.

3 METHODOLOGY

Axisymmetric finite element analysis was carried out using PLAXIS 2D software to simulate the two-layered soil system. A prescribed vertical displacement was applied and stress – settlement responses were analyzed. 15-noded triangular elements were used to discretize the geometry. Mesh convergence was checked and the mesh size was fixed as very fine. The bottom boundary was fixed in both radial and vertical directions, while the side boundaries were fixed in the radial direction and the top boundary was free. The boundaries were fixed at 6 times the diameter in vertical and horizontal directions.

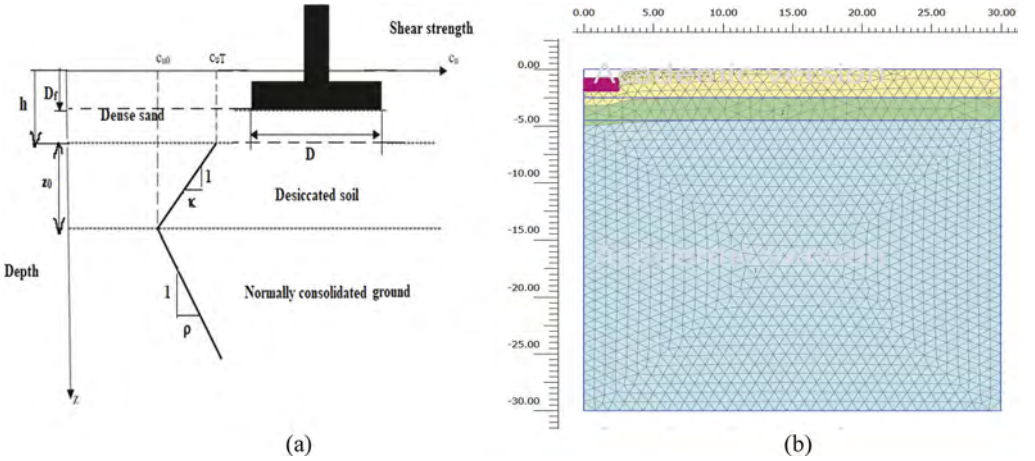

Figure 3. Problem statement showing (a) Strength profile with parameters (b) Deformed finite element mesh of sand overlying DNC (h = 2.5 m).

The analysis is carried out in two stages – initially, the effect of desiccation on NC soil is studied considering the compressibility and heterogeneity of the ground without the granular layer on top. Subsequently, a dense granular bed of thickness, h, laid over the two-layered DNC soil is considered (Figure 3(a)). Figure 3(b) shows the deformed finite element mesh for thickness of sand bed of 2.5 m. The study is limited to a vertical displacement of 10 cm. Numerical model is validated with available literature for incompressible homogeneous ground. Parametric study is carried out and the results obtained based on numerical modeling.

4 RESULTS AND DISCUSSION

A circular footing of 5 m diameter resting in granular bed overlying DNC soil is assumed for the analysis. The non-homogeneity (strength variation with depth) of DNC soil is considered alongside the desiccation effect in the top portion of the clay (Figure 3). Obtained bearing pressure for various prescribed settlements is normalized by unit weight of sand times the diameter of the footing as N_{cf} (= $q/\gamma D$).

a. *Effect of compressibility on bearing pressure*

A dense granular layer 2 m thick and of unit weight, γ of 20 kN/m^3 is considered on top of desiccated NC ground. Rigidity index of desiccated zone, I_r' is taken as 200. Desiccation strength ratio, μ value is 3 and unit weight of DNC is 15 kN/m^3. The cohesion and angle of shearing resistance of sand are taken as 1 kPa and 35° respectively. Rigidity index, I_r of NC soil, is varied from 50 to 1000.

Variations of normalized bearing pressure of granular bed overlying DNC ground for different rigidity indices of NC ground with settlement ratio are presented in Figure 4(a). N_{cf} increases with rigidity of NC ground. N_{cf} increases by 60% as I_r increases 20 fold from 50 to 1000, at SR = 2%. Figure 4(b) shows the effect of compressibility of *NC* soil on normalized bearing pressure for different settlement ratios. For SR = 1%, N_{cf} value increases from 0.9 to 1.72 for I_r increasing by 20 times. Increments in bearing pressure are higher at smaller settlements i.e. for SR = 0.5% and 2%, N_{cf} increased by 1.46 and 0.61 times respectively when I_r increases from 50 to 1000.

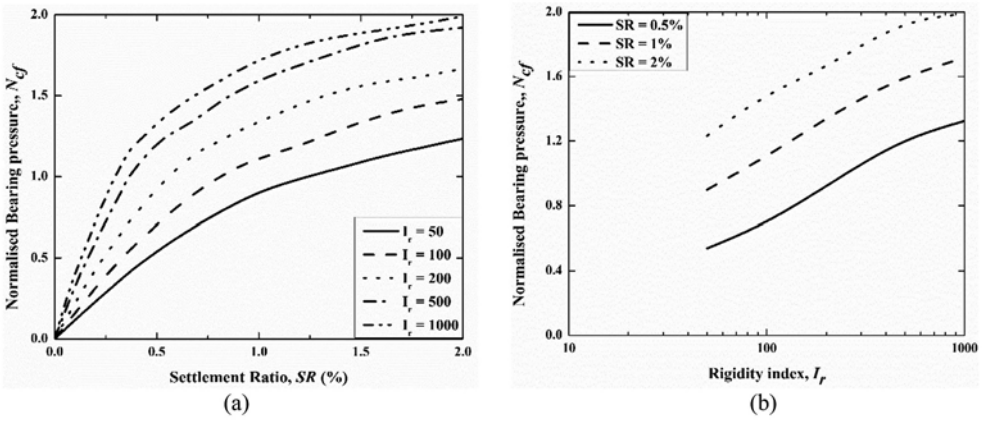

Figure 4. Effect of compressibility of NC soil a) N_{cf} versus SR (%) b) N_{cf} versus I_r at different SR.

b. *Effect of non-homogeneity of desiccation*

Bearing pressure-settlement responses of circular footing resting on sand overlying DNC ground for varying degree of non-homogeneity in desiccation layer is studied in this section. Two meter dense granular bed of unit weight of 20 kN/m^3 and angle of shearing resistance of 35° is considered over DNC ground. Degree of non-homogeneity of NC ground, $\rho D/c_{u0}$ was kept constant at 2.5. Thickness of desiccation layer, z_0 was taken as 2 m. The rate of decrease in strength, κ in the desiccated layer is varied from 2 through 10 kPa/m. Rigidity indices of desiccation and normally consolidated layers are 200. Strength and stiffness decrease gradually with a rate of κ till the interface of desiccated and NC layers.

Figure 5(a) show the normalized bearing pressure - settlement ratio curve obtained for granular bed overlying DNC ground for various degree of non-homogeneity of desiccation for z_0 = 2.0 m. Higher rates of decrease in strength in the desiccation zone results in higher bearing magnitude. N_{cf} increases by 21% for 5 fold increase in rate of decrease of strength in the desiccated zone, κ at SR = 2%.

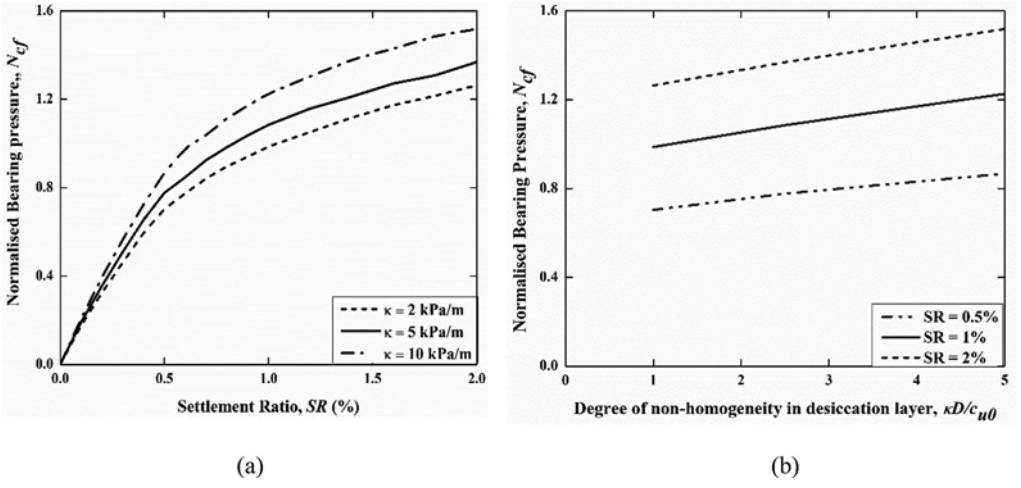

Figure 5. Effect of non-homogeneity of desiccation a) N_{cf} versus SR curves b) N_{cf} versus $\kappa D/c_{u0}$ at different SR.

Normalized bearing pressure of footing, N_{cf} (=$q/\gamma D$) on granular layer overlying DNC ground is plotted against the degree of non-homogeneity of desiccation layer, $\kappa D/c_{u0}$ for different settlement ratios and is depicted in Figure 5(b). As since the degree of non-homogeneity of the desiccated layer correspond to the layer's strength in magnitude, N_{cf} increases linearly with increase in $\kappa D/c_{u0}$ for a given foundation settlement. At SR =1 and 2%, N_{cf} increases by 24% and 20% respectively for 5 times increment in degree of non-homogeneity of desiccation layer.

c. *Effect of thickness of granular layer (Surface footing)*

Bearing pressure-settlement responses of footing resting on sand of varying thickness overlying DNC ground is studied in this section. Desiccation strength ratio, μ value is 3 and DNC soil has ρ and κ values of 5 kPa/m and –10 kPa/m respectively. The thickness of granular bed, H is increased from 1.25 m through 5 m and bearing pressure versus settlement responses are obtained. Figure 6(a) gives variations of N_{cf} of footing on granular layer overlying DNC with SR for different thicknesses of granular bed. N_{cf} increases by 85% at a settlement of 10 cm for four fold increase in thickness of granular bed.

Variations of normalized bearing pressure of two-layered soil with the thickness of granular bed for different settlement ratios are shown in Figure 6(b). N_{cf} increases with thickness ratio, H/D for a specific settlement. For SR = 1%, N_{cf} value increases from 1.07 to 1.98 for H/D increasing by 4 times. Increments in bearing pressure are higher at higher settlements i.e. for SR = 0.5% and 2%, N_{cf} increased by 0.60 and 1.06 times respectively when thickness of sand bed increased from 1.25 to 5.0 m.

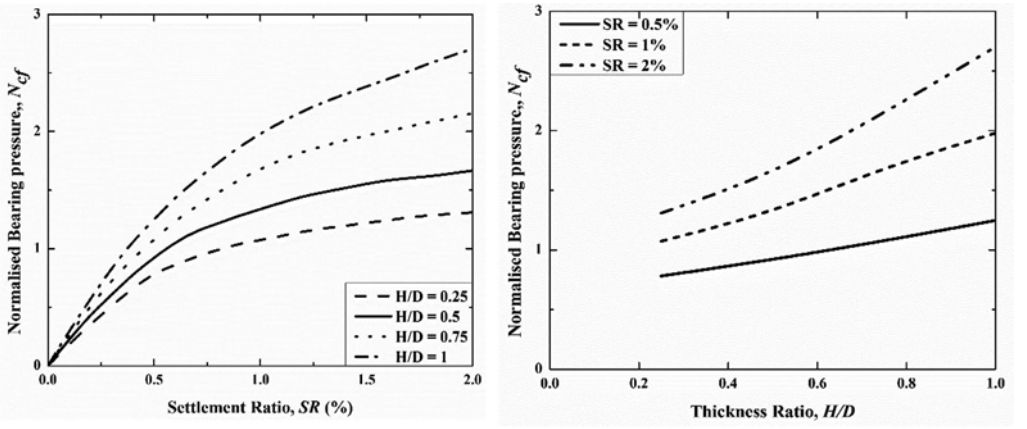

Figure 6. Effect of thickness of granular bed (a) N_{cf} versus SR curves b) N_{cf} versus Thickness ratio (H/D) curves at different SR.

d. *Effect of depth of embedment of footings in the granular layer*

Footing placed at the middle of dense granular layer, i.e. $D_f = 0.5H$ for granular beds of different thicknesses, H, (= 1.25, 2.5, 3.75 and 5 m) are analyzed. All the parameters of DNC and granular bed are the same as those of the previous case. Figure 7(a) gives variations of N_{cf} of footing in granular bed overlying DNC with SR for varying thicknesses of the dense granular bed. N_{cf} increases by 70% at a settlement of 5 cm for four fold increase in the thickness of granular bed.

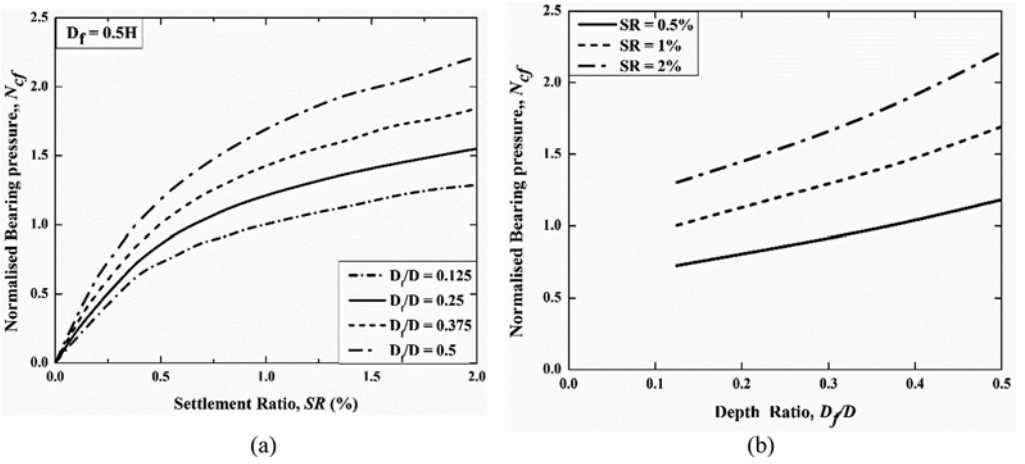

Figure 7. Effect of depth of embedment a) N_{cf} versus SR (%) b) N_{cf} versus Depth ratio (D_f/D) for D_f = 0.5H.

Figure 7(b) illustrates the effect of embedment depth of circular footing on bearing pressure for different sand bed thicknesses. For SR = 1%, N_{cf} value increases from 1.0 to 1.7 for depth ratio, D_f/D increasing by 4 times. Similar to the previous case, increments in normalized bearing pressure are larger at higher settlement ratios i.e. for SR = 0.5% and 2%, N_{cf} increased by 0.63 and 0.70 times respectively when the embedded depth ratio increased from 0.125 to 0.5. N_{cf} values for embedded footing are less than those for surface footing since the contribution of the granular bed gets reduced by half.

5 CONCLUSIONS

The present study analyzed the footing on dense granular bed over soft normally consolidated soil incorporating desiccation into consideration. Variation of undrained shear strength with depth in desiccated layer over an increase in strength in non-homogeneous soil is considered. Bearing pressure-settlement responses obtained from this numerical study are analyzed for various parameters of layered soil. Individual effects of compressibility of NC soil, strength variation in the desiccated layer, thickness of granular bed and embedded depth of footing on bearing pressure are quantified as a function of settlement. Bearing pressure of two-layered sand overlying DNC ground increases with the rigidity index of NC soil and with degree of non-homogeneity parameter in desiccation layer for a specific settlement. The effect of thickness of granular bed and embedment depth on bearing pressure is significant at higher settlements.

REFERENCES

Balasubramaniam, A.S., Oh, E.Y.N., Bolton, M.W., Bergado, D.T., and Phienwej, N. 2005. Deep-well pumping in the Bangkok Plain and its influence on ground improvement development with surcharge and vertical drains. *Ground Improvement*, 9(4): 149–162. doi:10.1680/grim.2005.9.4.149.

Bergado, D.T., Lorenzo, G.A., and Long, P.V. 2002. Limit Equilibrium Method Back Analyses of Geotextile-Reinforced Embankments on Soft Bangkok Clay - A Case Study. *Geosynthetics International*, 9(3): 217–245.

Bozozuk, M. 1972. Foundation Failure of the Vanleek Hill Tower Silo. *Performance of Earth and Earth-Supported Structures*, 2(2): 885–902.

Button, S.J. 1953. The Bearing Capacity of Footings on a two-layer Cohesive Subsoil. In *Proc. 3rd International Conference in Soil Mechanics Foundation* Engineering. *Switzerland*, *16–27 August 1953*. pp. 332–335.

Davis, E.H., and Booker, J.R. 1973. The effect of increasing strength with depth on the bearing capacity of clays. *Geotechnique*, 23(4): 551–563. doi:10.1680/geot.1973.23.4.551.

Day, R.W. 1996. Desiccation Theory for Soft Cohesive Soils. *Journal of Geotechnical Engineering*, 122 (11): 943–947. doi:10.1017/CBO9781107415324.004.

Hanna, A.M., and Meyerhof, G.G. 1980. Design Charts for Ultimate Bearing Capacity of Foundations on Sand Overlying Soft Clay. *Canadian geotechnical journal*, 17(2): 300–303. doi:10.1139/t80-030.

Jacobson, H.M. 1977. Stress-relationship of preconsolidated clay. In *9th International Conference on Soil Mechanics. Tokyo*. pp. 131–134.

Merifield, R.S., and Nguyen, V.Q. 2006. Two- and three-dimensional bearing-capacity solutions for footin`gs on two-layered clays. *Geomechanics and Geoengineering*, 1(2): 151–162. doi:10.1080/17486020600632637.

Meyerhof, G.G. 1951. The ultimate bearing capacity of foundations. *Geotechnique*, 2(4): 301–332. doi:10.1680/geot.1951.2.4.301.

Meyerhof, G.G. 1974. Ultimate Bearing Capacity of Footings on Sand Layer Overlying Clay. *Canadian Geotechnical Journal*, 11(2).

Meyerhof, G.G., and Hanna, A.M. 1978. Ultimate Bearing Capacity of Foundations on Layered Soils Under Inclined Load. *Canadian Geotechnical Journal*, 15(4): 565–572. doi:10.1139/t78-060.

Michalowski, R.L. 1992. Bearing capacity of nonhomogeneous cohesive soils under embankments. *Journal of Geotechnical Engineering*, 118(7): 1098–1118. doi:10.1061/(ASCE)0733-9410(1992)118:7(1098).

Rajyalakshmi, K., Venkata Abhishek, S., and Madhav, M.R. 2015. Effect of shape on bearing capacity of embedded footings on reinforced foundation beds over soft non-homogeneous ground. *Japanese Geotechnical Society Special Publication*, 2(64): 2174–2179. doi:10.3208/jgssp.IND-13.

Shiva Bhushan, J.Y.V., Madhav, M., and Narasimha Reddy, G.V. 2022. Effect of Compressibility on Bearing Pressure of Soft Ground. In K. Muthukummaran et al. (eds.) 2022. Foundation and Forensic Geotechnical Engineering, Lecture Notes in Civil Engineering, Vol. 295, pp. 75–80, Singapore, Springer. doi: 10.1007/978-981-19-6359-9_8

Siva Reddy, A., and Srinivasan, R.J. 1971. Bearing Capacity of Footings on Clays. *Soils and Foundations*, 7(3): 51–64. doi:10.3208/sandf1960.11.3_51

Skempton, A.W. 1951. The Bearing Capacity of Clays. In *Building Research Congress, London*. pp. 180–189.

Tani, K., and Craig, W.H. 1995. Bearing capacity of circular foundations on soft clay of strength increasing with depth. *Soils and Foundations*, 35(4): 21–35. doi:10.3208/sandf.35.4_21.

Terzaghi, K., and Peck, R.B. 1948. Soil Mechanics in Engineering Practice. John Wiley.

Vesic, A.S. 1973. Analysis of Ultimate Loads of Shallow Foundations. *Journal of soil Mechanics and Foundation Division*, 99(1): 45–73. doi:10.1061/JSFEAQ.0001846.

Smart Geotechnics for Smart Societies – Zhussupbekov, Sarsembayeva & Kaliakin (Eds)
© 2023 The Author(s), ISBN 978-1-003-29912-7
Open Access: www.taylorfrancis.com, CC BY-NC-ND 4.0 license

Use of geophysical investigation in assessing the differential settlement of shallow foundations

A.K. Dey & A. Saha
National Institute of Technology Silchar, Assam, India

ABSTRACT: Consolidation settlement is a major concern in designing foundations resting on clayey soil. Under a given load its value may vary from place to place depending on different parameters like loading history, in-situ water content, clay content, plasticity, etc. Again for the same site if the depth of compressible layer below the foundation is different, the expected settlement will also be different. In such a situation, geophysical tests are proven to be more reliable, easy and quick than the conventional borelog survey. The bore log survey at one site at Silchar showed possibility of differential settlement if the depth of foundation is kept constant for all the footings. The MASW test clearly supported the apprehension

1 INTRODUCTION

Settlement calculation is an integral part for obtaining the allowable bearing capacity of soil in a subsoil investigation. In the usual practice, a requisite number of boreholes upto a specified depth is made, and the soil samples are collected at regular intervals. Settlement is then calculated from the relevant soil properties. For clayey soil, the total settlement is not immediate but time-dependent. The time-dependent settlement is called consolidation settlement, and the procedure to obtain the consolidation settlement is prescribed in relevant geotechnical codes. However, it is not sure how much accurate will be the prediction of settlement because of compromise in sample preparation, personal errors and restriction in number of boreholes. The spatial variability of a plot cannot be incorporated in the borelog survey. As a result, the possibility of differential settlement cannot be overlooked. The problem is more acute if a small pocket of very poor soil exists within two boreholes. Geophysical methods of soil survey can be adopted to overcome the limitations of the borelog survey. Geophysical methods give a continuous record of subsurface soil stratification. Geophysical methods are non-invasive, rapid, and mostly accurate depending on the expertise of the investigator (Pazzi et.al.2019).Over the years, researchers have tried to investigate soil's continuous and spatially varying physical and chemical properties through different geophysical testing methods (Ullah and Prado, 2017) which include seismic (Donohue et. al., 2013, Hugenschimdt, 2000), electromagnetic (Atef et. al. 2016, Chambers et al 2011), electrical (Saad et al., 2012), gravitational (Loz & Porzucek, 2019), etc. Each method has its own advantages and disadvantages. In the present work, the seismic survey is adopted considering the potential of shear wave data for predicting static deformation, subsoil conditions and soil stiffness. Different seismic survey methods like Spectral Analysis of Surface Waves (SASW), Continuous Analysis of Surface Waves (CASW), and Multichannel Analysis of Surface Waves (MASW) are in practice. Out of these, MASW is considered to be the most suitable and reliable method for predicting soil stiffness in the urban areas (Donohue et. al., 2011). Shear wave velocity has been rigorously used for site characterization and assessment of soil properties.

DOI: 10.1201/9781003299127-196

In the present study, a city, namely Silchar is chosen for prediction of consolidation settlement using MASW. Silchar is the second-largest city in Assam, a northeastern state in India with a population of around 4,00,000 covering an area of 26.88 km^2. A significant part of the city contains clayey soil upto a considerable depth where consolidation settlement is of prime concern. The usual practice of subsoil investigation is to obtain the allowable bearing capacity for different shapes and sizes of footings founded at different depths based on the borelog survey. The possibility of differential settlement due to spatial variability has never been considered. The secondary stresses developed in the column beam joints due to this differential settlement are totally overlooked. These secondary stresses may govern the failure criteria of a building during seismic vibrations. In the present study it is tried to show the effectiveness of an MASW survey to represent the spatial variation of soil strata and also to obtain settlement of columns along the survey line through correlation ship between shear wave velocity and the geotechnical properties.

2 SITE LOCATION AND GEOMORPHOLOGY OF THE STUDY AREA

Silchar is the second-largest city in Assam, India and is situated between longitudes and latitudes 92°24′ E & 93°15′ E and 24°22′N & 25°8′N respectively in Cachar district.The town area of Silchar is located in an alluvial flat plain, spotted with swamps and bisected by stream and surrounded by isolated small hills (*tillas*).The area experiences a very high rainfall, almost seven to eight months in a year and about 379 cm in average in the monsoon month of July with a moderate climate and an annual temperature variation of 10° to 35° C. The groundwater table is located within 1 m from the ground level in most of the part of the city. So the top soil, which is predominantly clay, is in saturated form in most of the time. The Barak river, which runs through three sides of the city, is the main river in this region. The region also falls in zone V, the highest seismic zone in the seismicity map of India. Earthquakes of magnitude 5 to 5.5 are very common due to presence of an active Indo-Myanmer subduction zone, around 350 km on the eastern side of the city.

Geomorphologically, the area of Cachar district forms a part of north – south trending compressed thrust fold belt of Assam - Arakan basin. The structural style of the sedimentary cover in this area is depicted by a series of NNE – SSW trending, doubly plunging, elongated narrow, and highly faulted anticlines. These anticlines are en-echelon to each other. The anticlines are asymmetrical & are separated by the synclines. A very thick sedimentary cover consisting of alternate layers of shale, claystone, sandstone and siltstone with age from Eocene to Recent exists in this area[28].

Before the birth of the city in 1832 (https://en.wikipedia.org› wiki › Silchar), the area was mainly marshy which was subsequently filled up to promote human habitation. As a result, the major part of the city is prone to consolidation settlement. For construction of multistoreyed structures, people conduct one or two boreholes in a plot and obtain the safe bearing capacity which is considered to be constant for the entire plot. Except a few cases, differential settlement has not yet posed any major problem in the city. However, with rise in population and increase in housing demand, the city may face a threat due to occurrence of differential settlement in the coming days.

3 BORELOG SURVEY

Two boreholes of 15.0 m depth were dug in the proposed site, the locations and the soil profile are shown in Figure 1. It is observed that the site consists of five layers of clayey soil of different consistencies upto 15.0 m depth. Properties of the soil were obtained in the laboratory from undisturbed soil samples and are shown in the figure. From the general observation of the soil profile it is understood that there will be a differential settlement in case the footings

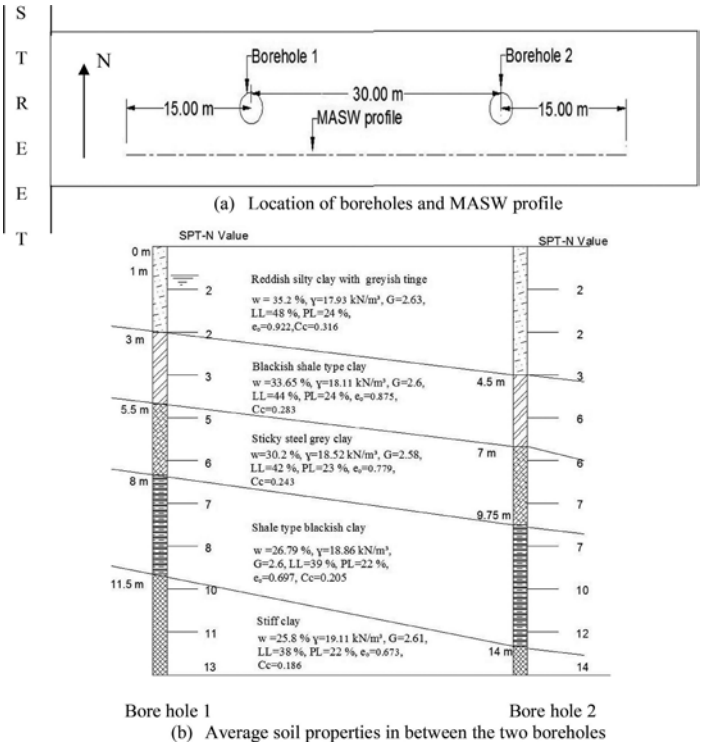

Figure 1. Borehole locations and average soil profile in Plot A (refer Figure 3).

are constructed at the same depth with the same pressure intensity. The probable consolidation settlement near the two bore holes is obtained as follows.

3.1 *Settlement calculation*

The primary settlement due to external loading is calculated using the following equation

$$S = \sum_{i=1}^{n} \left(\frac{(C_c)}{1+e_0} H \log\left(\frac{\sigma' + \Delta\sigma}{\sigma'}\right)\right)_i \quad (1)$$

Where
S=the amount of settlement caused by the load applied
H = thickness of the soil layer within the influence zone
e_0= the soil layer initial void ratio.
σ' = initial effective vertical stress at the mid-height of each soil layer
Δσ= the change in vertical stress caused by loading.
n = number of layers upto the influence zone, taken to be two times the width of footing
i = layer under consideration varying from 1 to n

Considering a square footing of size 2.5 m x 2.5 m founded at a depth of 2.5 m and bearing a loading intensity of 100 kPa, the primary consolidation settlement using Equation 1 is obtained as 164.23 mm near bore hole 1 and 172.8 mm near bore hole 2 with influence zone extending upto two times the width of the foundation i.e. 5.0 m. The soil profile upto the influence zone below the footings near the boreholes is shown in Figure 2. This figure is drawn to show the number of layers fall within the compressible zone i.e. two times the width of the footing.

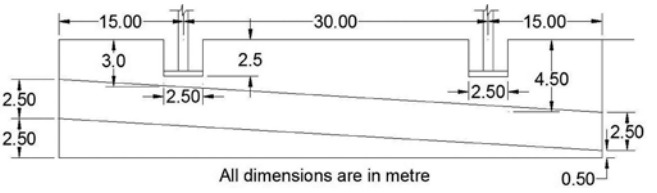

Figure 2. Soil profile upto the influence zone below the depth of footing.

4 GEOPHYSICAL TEST – MULTICHANNEL ANALYSIS OF SURFACE WAVES (MASW)

Multichannel Analysis of Surface Waves (MASW) is a non-invasive method that utilizes the dispersive nature of the surface waves to obtain the subsurface stratification through variation of shear waves with depth. The overall procedure consists of three steps, data acquisition, dispersion analysis, and inversion of dispersion curve. The maximum depth of investigation in an MASW survey varies depending on the length of the site, measurement profile configuration, natural receiver frequency, and type of seismic source employed (Park et al., 2002). In the present study, an 8 kg sledge hammer was used. For data collection, field measurements were undertaken with 24 numbers 4.5 Hz frequency geophones spaced at 2.0 m interval. Total 25 shot points were undertaken, one in the middle of two consecutive geophones and two at the ends. To eliminate the uncertainty/error associated with the actual energy provided in the test sample, 10 shots were applied one after the other sequentially to build a mean shot collect file.

The dispersive nature of the soil is used to obtain a relationship between wavelength and phase velocity. Longer wavelengths reflect properties of soil at larger depth and shorter wavelengths reflect properties at shallower depth. Dispersion curves are derived from this recorded surface wave data as a plot between phase velocity and frequency. Obtaining a high quality dispersion curve is essential for obtaining accurate shear wave velocity (V_s), which is one of the most critical steps encountered during surface wave data processing. The variation of shear wave velocity in a layered medium is obtained by inversion of the dispersion curve. Number of layers is assumed and density, Vs and Poisson ratio of each layer are to be added to software. The software then iterates the data so that the root-mean-square (RMS) error between the theoretical and experimental dispersion curves is reduced to a tolerance limit. 1-Dimensional V_s profile (V_s versus depth) is then obtained. Finally the software gives a 2-dimensional result combining all the shot point results. In the present study 10 layers of soil were assumed and SeisImager/SW software consisting of three individual programmes: PickWin95, WaveEq, and GeoPlot were used. The MASW test was carried out in 24 locations at Silchar city as shown in Figure 3. The plot A is also shown in the drawing where the two bore holes were made. The variation of V_s with depth from all these sites are shown in Figure 4. The bore log data of these 23 sites were collected and correlations between e_0, γ and C_c with V_s are obtained as shown in Figure 5. The best fit curves show the following relations

$$e_0 = 23.982\ V_s^{-0.659} \tag{2}$$

$$\gamma = 9.3322\ V_s^{0.1325} \tag{3}$$

$$C_c = 29.05\ V_s^{-0.928} \tag{4}$$

The MASW test result from plot A is shown in Figure 6. Using the above correlations, the expected settlement is obtained along the length of the plot considering the column spacing at 5.0 m and the pressure intensity as 100 kPa and depth of foundation 2.5 m (Figure 7). The theoretical values from the standard settlement Equation (1) are also shown. The MASW results give a lower value.

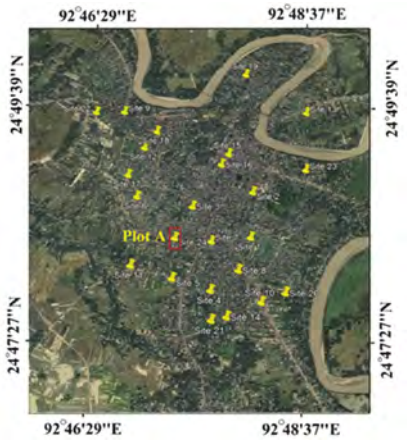

Figure 3. Locations of MASW test at Silchar.

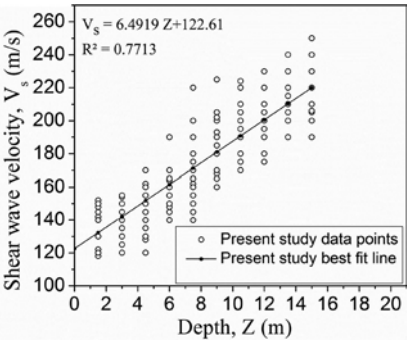

Figure 4. Variation of V_s in Silchar city.

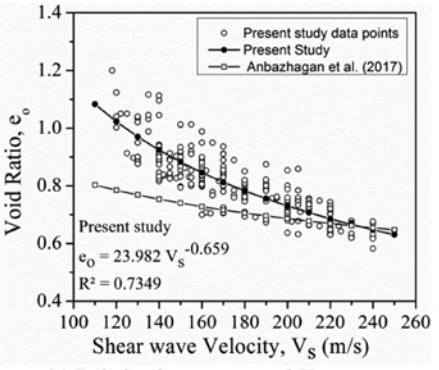

(a) Relation between e_0 and V_s

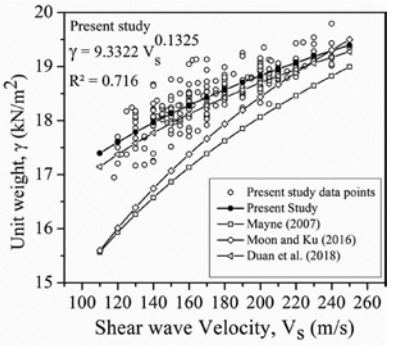

(b) Relation between γ and V_s

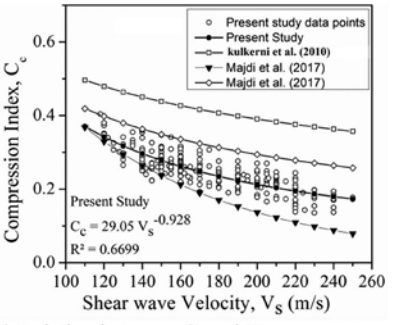

(c) Relation between C_c and V_s

Figure 5. Relations between geotechnical properties and V_s.

5 CONCLUSIONS

Following conclusions are drawn from the present study:

1. Geophysical methods give a continuous prediction of settlement
2. Any soft pocket within a plot can be easily identified with the geophysical method

3. The correlations obtained between geotechnical properties and V_s for the Silchar soil hold good
4. It is possible to fix the depth of foundation for a constant settlement.
5. The long procedure for calculation of C_c can be avoided without compromising the settlement value.
6. The tedious method of collection of undisturbed samples can be avoided

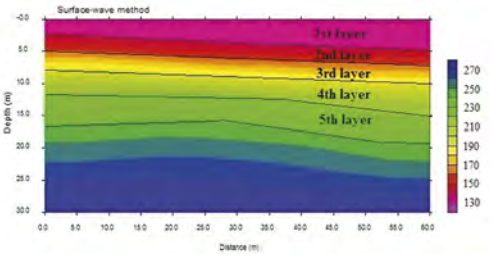

Figure 6. MASW result along the length of plot A.

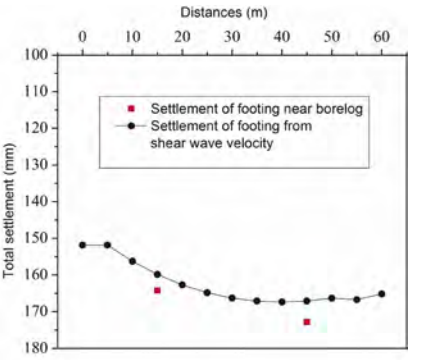

Figure 7. Settlement from MASW and from Consolidation theory.

REFERENCES

Anbazhagan P, Uday Anjali, Moustafa SSR & Al-arifi NSN. 2017. Soil Void Ratio Correlation with Shear Wave Velocities and SPT N Values for Indo-Gangetic Basin. 89:398–406

Atef A, Zayed T & Hawari A. 2016. Multi-tier method using infrared photography and GPR to detect and locate water leaks. Autom Constr 61:162–170. https://doi.org/10.1016/j.autcon.2015.10.006

Chambers JE, Wilkinson PB & Kuras O. 2011. Three-dimensional geophysical anatomy of an active landslide in Lias Group mudrocks, Cleveland Basin, UK. *Geomorphology* 125: 472–484. https://doi.org/10.1016/j.geomorph.2010.09.017

Donohue S, Forristal D, Donohue LA. 2013. Detection of soil compaction using seismic surface waves. *Soil Tillage* Res 128:54–60. https://doi.org/10.1016/j.still.2012.11.001

Donohue S, Gavin K & Tolooiyan A. 2011. Geophysical and geotechnical assessment of a railway embankment failure. Near Surf Geophys 9:33–44. https://doi.org/10.3997/1873-0604.2010040

Hugenschmidt J. 2000 Railway track inspection using GPR. *J Appl Geophys* 43:147–155. https://doi.org/10.1016/S0926-9851(99)00054-3.

Kulkarni MP, Patel A & Singh DN 2010. Application of Shear Wave Velocity for Characterizing Clays from Coastal Regions. 14:307–321. https://doi.org/10.1007/s12205-010-0307-1

Loj M & Porzucek S. 2019. Detailed analysis of the gravitational effects caused by the buildings in microgravity survey. Acta Geophys 67:1799–1807. https://doi.org/10.1007/s11600-019-00336-9.

Park CB, Miller RD& Miura H. 2002. Optimum field parameters of an MASW survey. *Proc Soc Explor Geophys* Japan Tokyo 22–23

Mayne PW. 2007. Cone penetration testing. National Cooperative Highway Research Program Report 368

Moon, S. W., & Ku T. 2016. Development of global correlation models between in-situ stress-normalized shear wave velocity and soil unit weight for plastic soils. *Can Geotech J* 53(10):1600–1611

Pazzi V, Morelli S & Fanti R. 2019. A Review of the Advantages and Limitations of Geophysical Investigations in Landslide Studies. *Int J Geophys*:. https://doi.org/10.1155/2019/2983087.

Saad R, Nawawi MNM & Mohamad ET. 2012. Groundwater Detection in Alluvium Using 2-D Electrical Resistivity Tomography (ERT). *Electron J Geotech Eng* 17:369–376

Ullah I & Prado RL 2017. Soft sediment thickness and shear-wave velocity estimation from the H/V technique up to the bedrock at meteorite impact crater site, Sao Paulo city, Brazil. *Soil Dyn Earthq Eng* 94:215–222. https://doi.org/10.1016/j.soildyn.2017.01.015

Smart Geotechnics for Smart Societies – Zhussupbekov, Sarsembayeva & Kaliakin (Eds)
© 2023 The Author(s), ISBN 978-1-003-29912-7
Open Access: www.taylorfrancis.com, CC BY-NC-ND 4.0 license

Bearing capacity and settlement of foundations on clayey soils under regime block cyclic loading

I.T. Mirsayapov & H.M.A. Sharaf
Kazan State of Architecture and Engineering University, Kazan, Russia

ABSTRACT: In modern conditions the soils base of buildings and structures are exposed to various types of regime cyclic loading. Existing calculation methods for foundations bearing capacity and deformations are developed mainly for the case of short-term single static load or cyclic loading with constant parameters during the whole period of exploitation. Buildings and structures for various purposes and their soil bases, along with cyclic loading with constant parameters, are subjected to cyclic loading of non-stationary regimes which are usually reduced to block loading for calculations and in some cases these loads are the main ones determining the safety of buildings and structures as a whole. Influence of cyclic loading of non-stationary regimes on the behavior of soil foundations is practically unstudied. In this connection researches have been conducted and methods of calculation of bearing capacity and settlement of foundations on clayey soils at regime block cyclic loading have been developed.

Keywords: bearing capacity, settlement, block cyclic loading, clay soil, stress-strain state

1 INTRODUCTION

In fact, most structures are exposed to cyclical loads due to changes in the intensity of the amount of applied load over time, such as wind load, tractor-driven load or load caused by operation. The phenomenon is that small load fluctuations affecting structures can be ignored. However, in some cases, it is impossible to neglect the presence of cyclic loading, in particular, wave load on offshore structures, wind load on structures with high flexibility, transport loads on roads and vibrations on the foundations of heavy machinery [4]. The impact of cyclic loading on structural elements can lead to cyclic loading on soils. To solve the above problems, engineers must offer the best solution in a safe, efficient and cost-effective way. Static analysis may be suitable for cases with very low applied load rates. When changes in the magnitude of stress or strain and the frequency of loading are not ignored, static analysis may give underestimated forecasts, which will lead to unsafe and inefficient designations due to their inaccurate results [6]. Consequently, in geotechnical projects, an extremely important role is played by taking into account the effects of the block cyclic loading regime and its influences, in which the behavior of the soil under cyclic loading should be considered as the root of the problem [7].

2 LABORATORY TESTING OF CLAY SOIL UNDER LOADING MODE

To determine the effect of loading mode and stress state on the strength and deformability of clayey soil, experimental studies of clayey soils under three-axis mode block cyclic loading using 2 types of devices, namely prismatic shape with dimensions 100×100×200 mm and cubic shape with dimensions 100×100×100 mm were given Figure 2a. Characteristic signs of destruction of the samples were obtained. The observed soil sampling zones of different

DOI: 10.1201/9781003299127-197

densities differ from the initial values. This fact indicates a difference in the level of soil damage in these zones. Thus, under mode block cyclic loading Figure 1, the clayey soil density in the upper zones increased by 6-10%, in the middle zones by 1-3% and in the lower zones by 3-5 It was found that the average density of the sample after the tests increased by 3-6% compared with the initial. In addition, it was found that the moisture content under the mode block cyclic loading decreased to 7% Figure 2b.

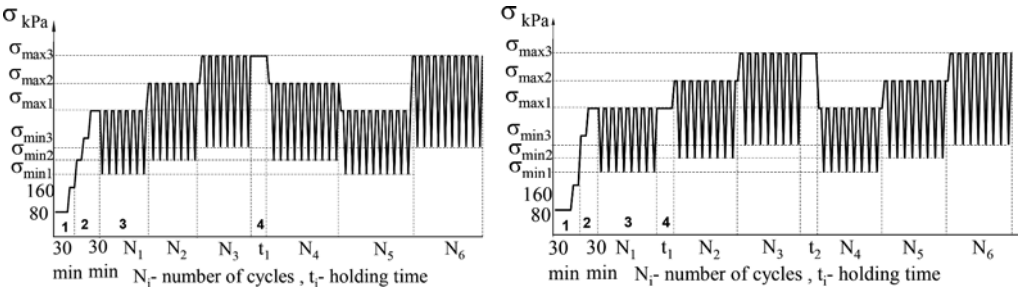

Figure 1. Loading modes under block cyclic loading; 1 – stage of comprehensive compression; 2 – stage of deviatory loading; 3 – stage of cyclic loading; 4 – holding time under static loading.

To determine the change in the values of specific cohesion *C* and the angle of internal friction *φ*, soil samples were taken from characteristic hardened and softened zones and examined using a single-plane slice device. It was found that the specific cohesion in the upper zone increased by 24-50%, and in the middle zone decreased by (30-50%) and in the lower zone increased by (15-30%). The angle of internal friction φ of the soil in the upper zone from the initial values increased by (5-8%), and in the middle zone decreased by 20-30 and in the lower zone increased by (3-4,3%) [3]. With increasing and decreasing the load value, increasing the number of loading cycles and holding time, densified pyramid-shaped zones are formed: in the upper, in the lower part of the sample and on its side surfaces Figure 2b. The geometrical dimensions of these compacted pyramids may be different and depend on the loading mode. Since these pyramids are displaced as solids, the specimen is deformed. The pyramids of solids form the ground with a denser structure; in the areas between the pyramids, shear and tearing occurs, which is accompanied by the appearance of small cracks. At the same time, it should be noted that deterioration of physical and mechanical properties of clayey soils in three-axial compression is fixed in the zone of loosening 2. This is due to the existence of two mutually compensating processes of cracking (destruction) and self-repair in the mode of block cyclic loading Figure 2c. What happens in these zones was described in more detail in the work of Mirsayapov I.T. and Koroleva I.V. [2].

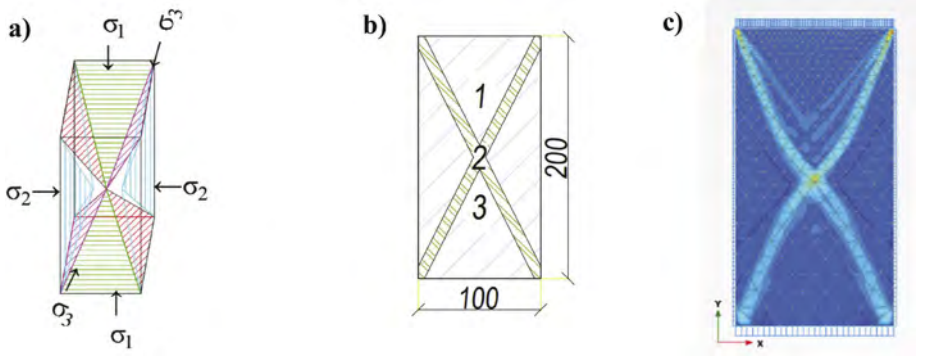

Figure 2. Appearance and fracture diagrams of a clay soil sample in triaxial compression devices. a-diagram of soil loading, b-diagram of local zones in the sample, c-diagram of sample fracture in the program Plaxis.

When describing the deformation of cyclic creep and soil strength under regime cyclic loading, it is necessary to take into account the influence of the vertical pressure of the previous block (σ1) on strength, deformation modulus, shear modulus and relative vertical deformations during subsequent loading after transition to another mode Figure 3.

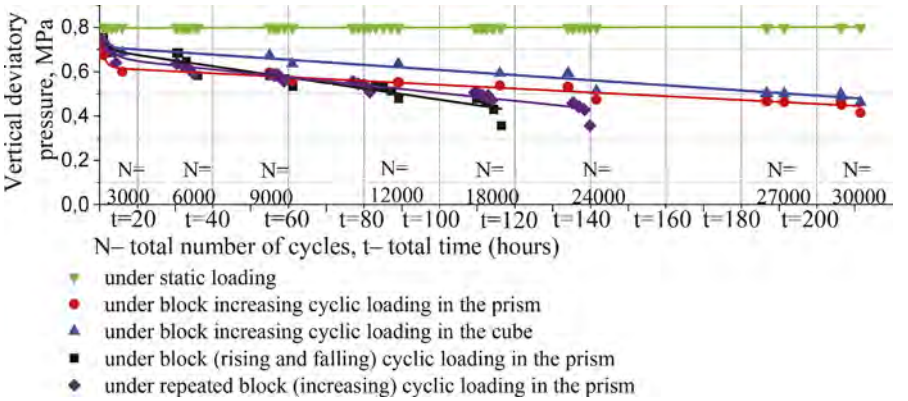

Figure 3. Change in the maximum permissible vertical deviatory pressure of the soil under regime block cyclic loading.

3 BEARING CAPACITY OF CLAY SOIL UNDER BLOCK CYCLIC LOADING

In accordance with the standards of the design of foundations when assessing the bearing capacity of the foundation, the calculated resistance of the soil under the sole of the foundation is determined SP 22.13330.2016 by the equation [1]:

$$N_u = b' \cdot l' \cdot \left(N_\gamma \xi_\gamma b' \gamma_1 + N_q \xi_q \gamma'_1 + N_c \xi_c C_1\right) \tag{1}$$

Where b', l' = Length and width of foundation; $N\gamma$, Nq and Nc = dimensionless coefficients of soil bearing capacity under the base of the foundation depending on the angle of internal friction φi; γ_1, γ'_1 = Specific weight of soil above and below the base of the foundation; ξ_γ, ξ_q, ξ_c = depending on the angle of internal friction φi. When determined analytically, the strength characteristics $C\ (N,\ t,\ \tau)$ and $\varphi\ (N,\ t,\ \tau)$ = determined by equations 2 and 3 for stationary and non-stationary cyclic loading. The specific cohesion under regime block cyclic loading is represented in the following form:

$$C(N, t, \tau) = C_0 + \sum_{i=1}^{n} \Delta C_{dpl}(t, \tau) - \sum_{i=1}^{n} \Delta C(N, t) \tag{2}$$

where C_0 = the initial value of the specific cohesion of the soil; $\Delta C_{dpl}\ (t,\ \tau)$ = the change in specific adhesion in the stages of comprehensive and deviatory loading; $\Delta C\ (N,\ t)$ = the change in specific cohesion during exposure under the action of block cyclic loading.

Then the specific cohesion equation under mode block cyclic loading is presented in the following form:

$$\begin{aligned} \mathrm{C}(N,\ t,\ \tau) = C_0 + \textstyle\sum_{i=1}^{n} \Delta C_{dpl}(t,\ \tau) - \sum_{j=1}^{m} \Delta C(N, t) = \Bigg[\Bigg(C_0 + \Bigg[C_0 . \textstyle\sum_{i=1}^{n} (2. \\ \cdot \left(\Delta \varepsilon_{ij}^{pl}(t, \tau) - \tfrac{1}{3} \Delta \varepsilon_{vi}^{pl}(t, \tau) \cdot \delta_{ij}\right) \cdot \Delta \varepsilon_{vi}^{pl}(t, \tau)\Big)^{1/2}\Bigg]\Bigg) - \textstyle\sum_{j=1}^{m} \left(K_{\varepsilon pli}^{v}(N,\ t,\ t_0) \cdot \right. \\ \left. \Delta \varepsilon_{pli}^{v}(N,\ t,\ t_0) + + K_{\gamma pli}^{v}(N,\ t,\ t_0) \cdot \Delta \gamma_{pli}^{v}(N,\ t,\ t_0)\right)\Bigg] \end{aligned} \tag{3}$$

where $\Delta\varepsilon^{pli}{}_{v}$ (N, t, t_o) and $\Delta\gamma^{pli}{}_{v}$ (N, t, t_o) = increments of vertical and shear strain of cyclic creep in increasing and decreasing blocks of cyclic loading; $K_{\varepsilon pli}{}^{v}$ (N, t, $_{to}$) and $K_{\gamma pli}{}^{v}$ (N, t, t_o) - parameters of proportional relationship between ΔC (N, t, t_o) and $\Delta\varepsilon_{pli}{}^{v}$ (N, t, t_o) and $\Delta\gamma_{pli}{}^{v}$ (N, t, to) determined from experimental studies; $\Delta\varepsilon_{ij}^{pl}(t,\tau)$ = the creep strain tensor increment in the considered loading stages; $\Delta\varepsilon_{vi}^{pl}(t,\tau)$ = the volume creep strain increment in the considered loading stages; δij = Kronecker delta.

The change in the angle of internal friction φ of the soil is determined by the following equation:

$$\varphi(N,t,\tau) = tan^{-1}\left(\frac{\tau_{ultgrt}(N,t) - C(N,t,\tau)}{\sigma(N,t)}\right) \tag{4}$$

where τ_{ultgrt} (N, t) =σ (N, t) tgφ (N, t, τ) +C (N, t, τ) = strength condition by Coulomb-More equation under mode block cyclic loading; φ (N, t, τ) and C (N, t, τ)- strength characteristics of soil under mode block cyclic loading; σ (N, t) = normal maximum stress.

The equation of the ultimate bearing capacity of the base after the transformation is written as following:

$$\begin{gathered} N_u = b'\cdot l'\cdot\left[\left(N_\gamma\xi_\gamma b'\gamma_1 + N_q\xi_q\gamma'_1 + \right.\right. \\ +N_c\xi_c\cdot\left(\left[C_0 + C_0\cdot\sum_{i=1}^{n}\left(2\cdot\left(\Delta\varepsilon_{ij}^{pl}(t,\tau) - \tfrac{1}{3}\Delta\varepsilon_{vi}^{pl}(t,\tau)\cdot\delta_{ij}\right)\cdot\Delta\varepsilon_{vi}^{pl}(t,\tau)\right)^{1/2}\right] - \\ \left.\left.\sum_{j=1}^{m}K_{\varepsilon pli}^{v}(N,\ t,\ t_0)\ .\ \Delta\varepsilon_{pli}^{v}(N,\ t,\ t_0) + K_{\gamma pli}^{v}(N,\ t,\ t_0)\cdot\Delta\gamma_{pli}^{v}(N,\ t,\ t_0)\right)\right) \end{gathered} \tag{5}$$

The functions of the bearing capacity of the soil under stationary and non-stationary cyclic loading after the transformation take the form:

$$N_\gamma = (N_q - 1)\cdot\left(arc\left(\frac{\tau_{ultgrt}(N,t) - C(N,t,\tau)}{\sigma(N,t)}\right)\right); \tag{6}$$

$$N_q = tg^2\left(45^0 + \frac{\varphi_1}{2}\right)\cdot e^{\pi\cdot arctan\left(\frac{\tau_{ultgrt}(N,\,t)-C(N,\,t,\,\tau)}{\sigma(N,\,t)}\right)};\ N_c = \frac{N_q - 1}{arctan\left(\frac{\tau_{ultgrt}(N,\,t)-C(N,\,t,\,\tau)}{\sigma(N,\,t)}\right)} \tag{7}$$

4 SETELLMENT CAPACITY OF CLAY SOIL UNDER BLOCK CYCLIC LOADING

To calculate the settlement of the bases under real regime loading, a calculation method is proposed, which is based on the method of layer-by-layer summation, taking into account the spatial stress state of the soil mass and changes in the mechanical state of soils during regime loading. The volumetric stress is taken, the state of the soil of the base foundation compressible thickness of the base into layers, for each layer, based on the stress deviator, we determine the deformations corresponding to the vertical pressure value, and then the deformation values, within the compressible thickness, the increment of the axial deformation of the i–th layer is summed up at the time of loading is determined by the equation [1, 2]:

$$\Delta_{zi} = \frac{\Delta\sigma_z}{G_v} - \Delta G\cdot\frac{3k_v - G_v}{3k_v\cdot G_v} \tag{8}$$

where $\Delta\sigma z$ = the vertical stress at the moment of loading; Gv = the shear modulus at the moment of loading; kv = the volumetric modulus at the moment of loading.

The increment of axial strain under cyclic loading is determined by the equation:

$$\varepsilon_{pli}^{v}(N,t,t_0) = \sum_{i=1}^{n}\left[\sigma_i^{max}(N,t,t_0)\cdot k_R\left\{\left[\frac{f_{UP}(N)}{\sigma(N,t,t_0)}\right]\cdot f_{UP}(N)\cdot\rho_{cyc}\cdot+\left[\frac{f_{dow}(N)}{\sigma(N,t,t_0)}\right]\cdot f_{dow}(N)\cdot\rho_{cyc}\cdot+\left[\frac{f(t)}{\sigma(N,t,t_0)}\right]\cdot f(t)+\left[\frac{f_{UP}(t_0)}{\sigma(N,t,t_0)}\right]\cdot f_{UP}(t_0)+\left[\frac{f_{dow}(t_0)}{\sigma(N,t,t_0)}\right]\cdot f_{dow}(t_0)\right\}\cdot\right] \quad (9)$$

where σ_i^{max} (N, t, t_0) is the maximum vertical stress in step-down loading blocks, dwell block and at the moment of load change; σ (N, t)- allowable vertical stress in block cyclic loading; k_R - coefficient depending on correlation of parameters of creep and cyclic creep of soil, strength of soil and vertical stress in the considered block of loading; ρ_{cyc} - asymmetry of vertical stress cycle of soil; f_{UP} (N), f_{dow} (N), f(t), f_{UP} (t_0), f_{dow} (t_0) - cyclic creep deformation growth functions of soil in increasing and decreasing blocks of cyclic loading, holding time and at the moment of load change.

Then the foundation settlement under mode block cyclic loading according to the following equation:

$$S(N,t,t_o) = \sum_{i}^{n}\left[\Delta\varepsilon_{zi} + \varepsilon_{pli}^{v}(N,t,t_o)\right]\cdot h_i \quad (10)$$

where ε_{pli}^{v} (N, t, t_0) = the increment of axial deformation under cyclic loading; $\Delta\varepsilon_{zi}$- is the increment of axial deformation of the i–th layer at the time of load application; $\Delta\,\varepsilon_{pli}^{v}$ (N, t, $t_{o)}$ = the increment of axial deformation of the i-th layer under cyclic loading; *hi* = the thickness i-th layer; n – the number of layers.

To test the obtained equations for calculating the settlement of foundation, stamp tests (models of the slab foundation in tray) of clayey soil were carried out Figure4. The results of experimental studies in a volumetric tray Figure 4. show that the development of the base settlement occurs in three stages. At the first stage, the settlement of the base develops with an increase in maximum loads and the number of cyclic loadings, while the settlement values were 50-54% of the maximum settlement value. At the second stage, from the second to the penultimate block, it is seen that the rate of development of the base settlement decreases or their complete stabilization occurs with increasing block cyclic loading, and a decrease in the base settlement with decreasing block cyclic loading. At the third stage (the penultimate and last block), there is an increase in the development of the base settlement as the number of loading cycles increases compared to the previous loading stages. The rate of settlement development increases without stabilization until the limit value for the slab foundation model is reached Figure 4.

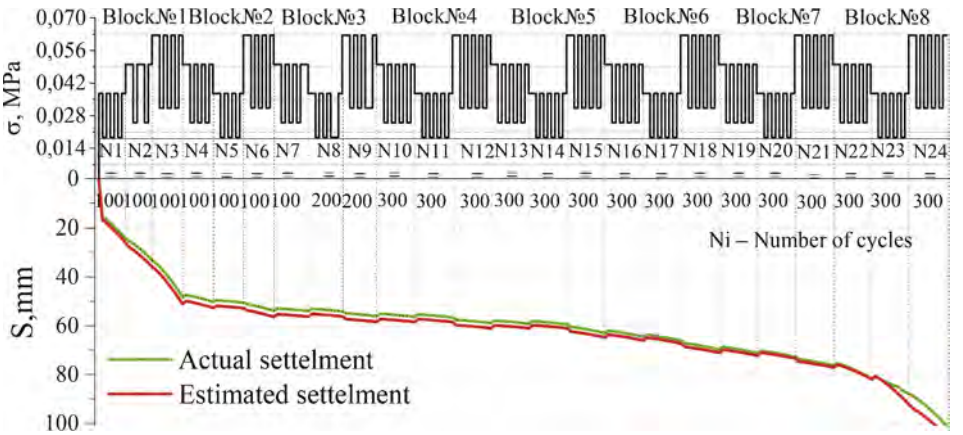

Figure 4. Comparison graph of slab foundation settlement under regime block cyclic loading.

5 CONCLUSION

1) The equation of the ultimate bearing capacity of the soil base under regime block cyclic loading has been developed, taking into account the simultaneous change in rheological and strength characteristics of soils, hardening processes, as well as loading mode;
2) An engineering method for calculating the settlement of the bases has been developed, which is based on the method of layer-by-layer summation, taking into account the simultaneous change in the spatial stress-strain state and mechanical characteristics of soils in the process of regime block cyclic loading.
3) A comparison of the measurement results on the development of the settlement of the slab foundation model in tray under mode block cyclic loading indicates that the obtained dependence of the change in the amount of settlement with a mode block cyclic loading coincides fairly well with the results of tray laboratory tests. The discrepancies between the calculated and experimental values are in the range of 10-20%.

REFERENCES

SP 22.13330.2016 "Foundations of buildings and structures" M. 2011.

Mirsayapov I.T & Koroleva I. V. 2016. Bearing capacity of foundations under regime cyclic loading. *Japanese Geotechnical Society Special Publication 2(33):*1214–1217. doi:10.3208/jgssp.KAZ-18.

Mirsayapov I.T.& Sharaf Hani M.A. 2017. Strength and deformation of clay soils in the conditions of the triaxial compression under block regime cyclic loading. *Izvestiya KGASU. 2017. №4(42) P.*221–227.

Mirsayapov I.T. & Sharaf Hani M.A. Experimental studies of bearing capacity and settlement of foundations of clay soils under block regime cyclic loading. *Izvestiya KGASU.* 2019. *№1(47) P.*175–182.

Mirsayapov I.T & Sharaf Hani M.A. 2020. Experimental studies of bearing capacity and settlement of foundations of clay soils under block regime cyclic loading. *IOP Conf. Series: Materials Science and Engineering 890 (2020) 012134 IOP Publishing* doi:*10.1088/1757-899X/890/1/012134*.

Mirsayapov I.T & Sharaf H.M.A. 2021. Features of clay soil deformation under triaxial block regime cyclic loading, taking into account the formation of micro and macro-cracks. *Deep Foundations and geotechnical problems of territories (DFGC 2021) Journal of Physics: Conference Series 1928 (2021) 012038 IOP Publishing* doi:*10.1088/1742-6596/1928/1/012038*.

Fu, Z.; Wang, G.; Song, W.; Yu, Y.; Wei, P. & Wu, T. Deformation behavior of saturated soft clay under cyclic loading with principal stress rotation. *Appl. Sci.* 2021, 11, 8987. https://doi.org/10.3390/*app11198987*.

Mirsayapov I.T. Method of Calculating the Strength of Clay Soils Under Triaxial Regime Loading. *Izvestiya KGASU. 2021. P.150-159.Mirsayapov I.T. 2021. IOP Conf. Series: Materials Science and Engineering (*2021*) IOP Publishing* doi:10.1007/978-3-030-80103-816.

Smart Geotechnics for Smart Societies – Zhussupbekov, Sarsembayeva & Kaliakin (Eds)
© 2023 The Author(s), ISBN 978-1-003-29912-7
Open Access: www.taylorfrancis.com, CC BY-NC-ND 4.0 license

Ultimate bearing capacity of a raft-pile foundation under cyclic loading

I.T. Mirsayapov
Kazan State of Architecture and Engineering university, Kazan, Russia

ABSTRACT: The bearing capacity of a raft-pile foundation under cyclic loading depends on the conditions of joint deformation of the soil, piles and pile cap, their strength and deformation properties and corresponds to the maximum cycle load that a raft-pile foundation can perceive with a given number of loading cycles and a predetermined maximum settlement. The maximum bearing capacity under cyclic loading is determined for the stage when tangential stresses along the lateral surface are absent in the upper and middle parts of the piles due to the achievement of the maximum shear resistance. It is assumed that a spatial stress-stain state is realized in the soil under the raft and under the pile toe. The bearing capacity of the raft-pile foundation is reached when the stresses under the pile toe and under the raft exceed the fatigue strength and the ultimate deformations of the soil under triaxial cyclic compression. The objective of study is to determine ultimate bearing capacity of the raft-pile foundation under cyclic loading. Theoretical studies have been carried out, the redistribution of efforts between the main elements of the raft-pile foundation has been considered. The change in the stress-strain state of the base of the raft-pile foundation under cyclic loading is considered. The significance of the obtained results for the construction industry lies in the fact that the proposed method for the first time allows us to evaluate the bearing capacity of a raft-pile foundation. Comparison of the calculation results for the proposed model with experimental studies showed good convergence.

Keywords: Deep foundations, Piles, Raft-pile foundation, Cyclic loading, Bearing capacity

1 INTRODUCTION

The limit value of the cyclic load (ultimate bearing capacity) taken by the raft-pile foundation depends on the conditions of joint deformation of the soil, piles and plate grate, and their strength and deformation properties and corresponds to the maximum cycle load that the raft-pile foundation can take at a given number of load cycles and a predetermined ultimate settlement (Indraratna. et al. 2015). The ultimate bearing capacity of the raft-pile foundation under cyclic loading is calculated at design values (γ_f>1) for the first group of the load limiting states and design values of strength and strain characteristics of soil, taking into account the decrease of fatigue strength and increase of cyclic creep deformation by the value of the ultimate resistance of soil base under the condition of limitation of development of vertical deformations in it according to predetermined conditions. In determining the ultimate bearing capacity of the raft-pile foundation under cyclic loading, we consider the ultimate stress-strain state of the system "raft-pile-pile-space-soil below the pile toe" under the bottom end of the pile and under the raft. When the pile is rigidly connected to the raft pile, all elements of the system are deformed together during cyclic loading and forces are redistributed between them (Katzenbach, R. & Leppla, S. 2011, Bokov, I.A & Fedorovski, V.G. 2018, 2019).

The behavior of the components of a raft-pile foundation with the surrounding soil mass in determining the stress-strain state of a raft-pile foundation has been considered by many

DOI: 10.1201/9781003299127-198

authors (Harichkin, A.I. et al. 2018, Shulyatev Q.A. 2016). So, for example, when determining the settlement of a raft-pile foundation, various factors and features are taken into account, one of such features is the additional settlement of a raft-pile foundation due to deformation of the pile shaft (Ter-Martirosyan Z.G. & Chin T.V. 2012).

Gotman, A.L. et al. (2021) describes a method for finding the bearing capacity of the soil under the pile foot as part of a group of piles. The method for determining the stress-strain state is based on the results of tests carried out for a pile as part of a group of piles and for one pile.

2 MATERIALS AND METHODS

The ultimate bearing capacity under cyclic loading of the raft-pile foundation is determined for the stage when tangential stresses along the lateral surface are absent in the upper and middle parts of the piles due to reaching the ultimate shear resistance (Mirsayapov, I.T. & Koroleva, I.V. 2016).

It is assumed that the spatial stress state is realized in the soil at the bottom of the raft cage and under the pile toe. The bearing capacity of the raft-pile foundation is reached when the stresses under the pile toe and under the raft exceed the fatigue strength and ultimate strain of the soil in three-axial cyclic compression. A model consisting of a raft rigidly connected to piles and a soil mass surrounding was taken as a design scheme. The bearing capacity of the raft-pile foundation was determined based on the conditions that the stresses under the pile toe and the stresses at the level of the pile head do not exceed the limiting stresses in the soil.

Calculation of ultimate bearing capacity is performed according to the value of stresses under the pile toe $P_3(N)^{max}$ and stresses under the raft superstructure $P_1(N)^{max}$ which value is determined for any considered loading cycle from solution of equation system (1) considering redistribution of forces between the system elements and their change in the process of cyclic loading.

$$\begin{cases} p \cdot AB = p_2(N) \cdot ab + p_1(N)(AB - ab) \\ p_2(N) \cdot ab = p_3(N) \cdot ab - 4(a+b) \cdot l \cdot \frac{\tau_0(N)}{\alpha} \cdot e^{-\alpha l} + (a+b) \cdot l \cdot \frac{\tau_0(N)}{\alpha} \\ \frac{p_1(N) \cdot \beta_{gr} \cdot L}{E_{gr}(N)} \left(1 - \frac{1}{L}\right) + \frac{k_1 \cdot \tau_0(N) \cdot (A-a)}{3G_{gr}(N)} + \frac{k_2 \cdot \tau_0(N) \cdot (B-b)}{3G_{gr}(N)} = \frac{\omega \cdot a \cdot p_3(N) \cdot (1-v_{gr}) \cdot k(l)}{G_{gr}(N)} \\ \frac{p_1(N) \cdot \beta_{gr} \cdot L}{E_{gr}(N)} + \frac{k_1 \cdot \tau_0(N) \cdot e^{-\alpha l}(A-a)}{3G_{gr}(N)} + \frac{k_2 \cdot \tau_0(N) \cdot e^{-\alpha l}(B-b)}{3G_{gr}(N)} = \frac{\tau_0(N)(a+b)l}{ab\alpha \cdot E_p} + \frac{\tau_0(N)(a+b)e^{-\alpha l}}{ab\alpha^2 \cdot E_p} + \\ + \frac{p_3(N) \cdot l}{E_p} + \frac{\omega \cdot a \cdot p_3(N) \cdot (1-v_{gr}) \cdot k(l)}{G_{gr}(N)} - \frac{\tau_0(N)(a+b)}{ab\alpha^2 \cdot E_p} \end{cases} \quad (1)$$

After definite number of loading cycles, the stresses in the soil reach the endurance limit in some of the elements:

under the raft, and then after a given number of cycles under the pile toe;

under the pile toe;

the simultaneous achievement under the raft and under the pile toe, i.e., in the soil under the raft $P_1(N)^{max} \le \sigma_{1v}(N)$, in the soil under the pile toe $P_3(N)^{max} \le \sigma_{1v}(N)$. Then a thin layer of soil under the pile toe and under the raft is pressed through and, consequently, an increase in displacement (settlement) of the raft pile foundation occurs and this process is periodically repeated until the total cumulative settlement of the pile foundation reaches the limit value for a particular building or structure (Figure 1).

3 RESULTS

The bearing capacity of the slab pile foundation soil under cyclic loading at the calculated moment of time (t = N) depending on the ratio $\tau_0(N) \le \tau^*(N)$ is estimated for two zones (Figure 2) based on the conditions:

In the soil under the raft:

$$p_1^{max}(N) = \sigma_{gr1}^{\max(N)_{gr}(N)} \le \sigma_{1u}(N) \quad (2)$$

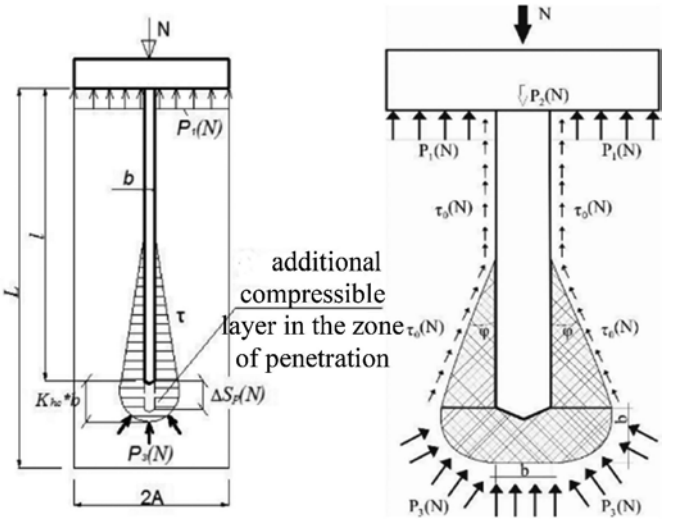

Figure 1. Scheme of the stressed state of the element of a raft-pile foundation according to the ultimate bearing capacity assessment.

In the soil under the bottom end of the pile:

$$p_3^{max}(N) = \sigma_{gr3}^{\max(N)_{gr}(N)} \leq \sigma_{1u}(N) \tag{3}$$

where $\sigma_{1u}(N)$ is the ultimate compression stress in of the soil under triaxial cyclic loading.

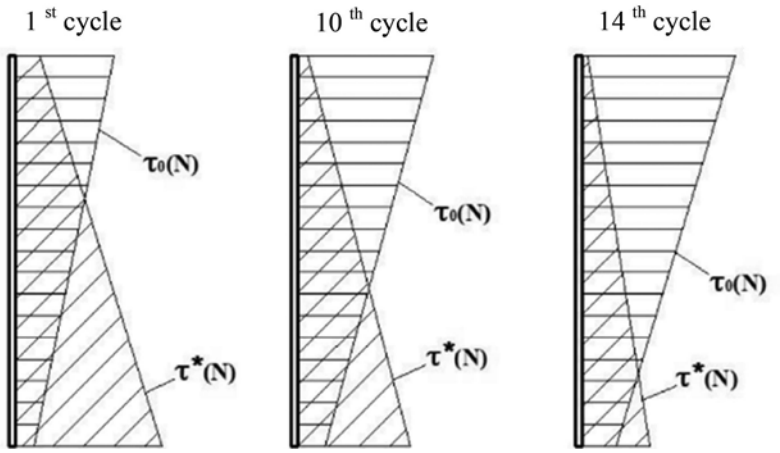

Figure 2. Diagrams of mobilized shear stress and ultimate shear stress by experimental study.

The ultimate stresses in the soil under the raft-pile foundation under triaxial cyclic loading are determined from the calculation model of soil under spatial mode loading developed by Ilizar T. Mirsayapov & I.V. Koroleva (2019) and are represented in the form:

$$\sigma_{1u}(N) = \frac{4}{A_1} \cdot [\sigma_v(t, t_1, N) \cdot A_{sh} \cdot \cos\alpha_1(t, t_1, N) + \tau_V(t, t_1, N) \cdot A_{sh} \cdot \sin\alpha_1(t, t_1, N)] \tag{4}$$

Normal stress to the surface of limiting equilibrium:

$$\sigma_v(t,t_1,N) = \sigma_1 \cdot l(t,t_1,N) \cdot l'(t,t_1,N) + \sigma_2 \cdot m(t,t_1,N) \cdot m'(t,t_1,N) + \sigma_3 \cdot (t,t_1,N) \cdot n(t,t_1,N) \cdot n'(t,t_1,N) + \sigma_d(t,t_1,N) \quad (5)$$

Dilatant stresses:

$$\sigma_d(t,t_1,N) = \frac{E \cdot \Delta\delta d}{(1+v) \cdot r} \quad (6)$$

where E – soil deformation modulus.

Shear stresses at the limiting equilibrium surface:

$$\tau_v(t,t_1,N) = \sigma_v(t,t_1,N) \cdot tg(t,t_1,N) + c(t,t_1,N) \quad (7)$$

where, σ_v (t,t_1,N) – normal stress to the surface of limiting equilibrium;φ (t,t_1,N) - angle of internal friction of soil under cyclic loading;

c (t,t_1,N) – specific cohesion of soil particles under cyclic loading.

Parametres of calculating model for bearing capacity taken according to work of I.T. Mirsayapov & M.A. Sharaf Hani (2020, 2021).

4 DISCUSSION

The bearing capacity of a slab-pile foundation under cyclic loading is determined at the design values of the load, strength and deformation characteristics of the soil, taking into account the decrease in fatigue strength and the increase in cyclic creep deformation by the value of the ultimate resistance of the soil base under the condition of limiting the development of vertical deformations in it. If conditions (2) and (3) are simultaneously fulfilled, the bearing capacity of the raft-pile foundation is ensured.

If the conditions are not fulfilled, the bearing capacity of the foundation is not ensured and there are three possible ways of reaching the bearing capacity ultimate condition of the raft-pile foundation:

1. Condition (2) is not fulfilled, i.e., the stress in the soil under the raft becomes greater than the ultimate stress in the soil. In this case, the part of the load absorbed by the soil is transferred to the pile by loading the pile. The raft-pile foundation absorbs the load as long as the condition (3) is fulfilled. When condition (3) is violated, the soil beneath the bottom end of the pile will be pressed through, and the raft-pile foundation will sink;
2. Condition (3) is violated first, but there is no sharp movement of the foundation, because the pile rests on the raft-suspended buttress, which loads the soil under the raft-suspended buttress.
3. The foundation takes the load until the first condition (2) is violated. At this point, rapid settlement of the raft-pile foundation occurs. Both first and second conditions are not fulfilled at the same time, and rapid subsidence of the raft-pile foundation occurs. This process is periodically repeated in the process of cyclic loading until the foundation's settlement becomes greater than the maximum allowable settlement.

5 CONCLUSION

Equations for the bearing capacity of a raft-pile foundation under cyclic loading have been developed. The resulting equation of the mechanical state of the raft-pile foundation describes the main patterns of behavior of such foundations, observed in experiments at various stages

of loading, make it possible to reliably assess the bearing capacity of raft-pile foundations under cyclic loading. Thus, the limiting value of the bearing capacity of a raft-pile foundation under cyclic loading corresponds to the maximum value of the cycle load, at which the ultimate given value of foundation settlement is achieved for the number of load cycles established by the operating conditions of a particular building or structure at the value of the loads, strength and strain properties of soils accepted. Comparison of the calculation results with the data of experimental studies of pile foundations showed good convergence between the calculated and experimental values (deviation no more than 15%).

REFERENCES

Bokov I.A & Fedorovski V.G. 2018. On the Calculation of Groups of Piles Using Mutual Influence Coefficients in the Elastic Half-Space Model. *Soil Mechanics and Foundation Engineering* 54: 363–370. DOI: 10.1007/s11204-018-9482-8.

Bokov I.A & Fedorovski V.G. 2019. On the Applicability of the Influence Function Obtained from Single-Pile Calculations for the Calculation of Pile Groups, Soil Mechanics and Foundation Engineering 55, 359–365 (2019). DOI: 10.1007/s11204-019-09549-y.

Gotman A.L. & Gavrikov M. D. 2021. Calculation of a large-size bored pile on a vertical load. *Construction and Geotechnics* 12(3): 72–83. DOI: 10.15593/2224-9826/2021.3.08

Indraratna J., Geng X.Y., Carter J.P & Chen Y.L. 2015. Model of soft soils under cyclic loading. *Int. J. Geomech* 15, 212 (2015). DOI: 10.1061/(ASCE)GM.1943-5622.0000411.

Katzenbach, R. & Leppla, S. 2011. Environment-friendly and economically optimized foundation systems for sustainable high-rise buildings, *19th International Conference on Soil Mechanics and Geotechnical Engineering*.

Harichkin, A.I., Shulyatev, O.A., Kurillo, S.V. & Fedorovsky, V.G. 2018. Features of interaction of piles with each other and with the ground as part of groups. *Issues of design and construction of aboveground and underground structures of buildings and structures* 56–67.

Mirsayapov, I.T & Koroleva, I. V. 2016. Bearing capacity of foundations under regime cyclic loading. *Japanese Geotechnical Society Special Publication* 2(33):1214–1217. doi:10.3208/jgssp.KAZ-18.

Mirsayapov I.T & Shakirov M.I. 2016. Bearing capacity and settlement of raft-pile foundations under cyclic loading. *Energy Geotechnics – Proceedings of the 1st International Conference on Energy Geotechnics*, 423–428.

Mirsayapov, I.T & Sharaf, H.M.A. 2020. Experimental studies of bearing capacity and settlement of foundations on clays under regime block cyclic loading. *IOP Conf. Series: Materials Science and Engineering* 890: 012134 IOP Publishing. Doi:10.1088/1757-899X/890/1/012134.

Mirsayapov, I.T & Shakirov, M.I. 2020. Combined Plate-Pile Foundations Settlement Calculation under Cyclic Loading. *IOP Conference Series: Materials Science and Engineering* 890, 012069. DOI: 10.1088/1757-899X/890/1/012069.

Mirsayapov I.T. & Minzianov R. 2020. Rebar movement in seals under static loading. *IOP Conference Series: Materials Science and Engineering, Volume 890, International Scientific Conference on Socio-Technical Construction and Civil Engineering (STCCE - 2020) 29 April - 15 May 2020*, Kazan. DOI: 10.1088/1757-899X/890/1/012073.

Mirsayapov, I.T & Sharaf, H.M.A. 2021. Features of clay soil deformation under triaxial block regime cyclic loading, taking into account the formation of micro and macro-cracks. *Deep Foundations and geotechnical problems of territories (DFGC 2021) Journal of Physics: Conference Series* 1928: 012038 IOP Publishing. Doi:10.1088/1742-6596/1928/1/012038.

Mirsayapov, I.T., Khorkov, E., Minzianov. R. 2021. Research of the stress-strain state of a reinforced concrete beamless floor. *2nd International Scientific Conference on Socio-Technical Construction and Civil Engineering (STCCE – 2021); E3S Web Conf. V. 274*. DOI: 10.1051/e3sconf/202127403031.

Shulyatev O. A. 2016. New set of rules for designing foundations and foundations of high-rise buildings, *Subgrades, foundations, and soil mechanics* 6: 37–40.

Ter-Martirosyan, Z.G. & Chin, T.V. 2015. Interaction of a single long pile with a two-layer base, taking into account the compressibility of the pile shaft. *Vestnik MGSU* 7(4): 28–34.

Travush V. I., Shulyatev O. A., Shulyatev S. O., Shakhramanyan A.M & Katovich Yu. A. 2019. Analysis of the results of geotechnical monitoring of the Lakhta center tower. *Subgrades, foundations and soil mechanics* 2: 15–21.

Smart Geotechnics for Smart Societies – Zhussupbekov, Sarsembayeva & Kaliakin (Eds)
© 2023 The Author(s), ISBN 978-1-003-29912-7
Open Access: www.taylorfrancis.com, CC BY-NC-ND 4.0 license

Case study on CHSL carried out for the design of pile foundation for the longest river bridge in India

Diptesh Chanda
Institute Post-Doctoral Fellow, Department of Civil Engineering, Indian Institute of Technology Bombay, Powai, Mumbai, India

Vansittee Dilli Rao
Former Ph.D. Research Scholar, Department of Civil Engineering, Indian Institute of Technology Bombay, Powai, Mumbai, India

Jaykumar Shukla
Principal Engineer and Senior Consultant, Geo Dynamics, Vadodara, Gujarat, India

Deepankar Choudhury
Prof. T.Kant Chair Professor and Head, Department of Civil Engineering, Indian Institute of Technology Bombay, Powai, Mumbai, India

ABSTRACT: India's longest river bridge (Dhubri-Phulbari Bridge) will be constructed over the river Brahmaputra in the state of Assam/Meghalaya in northeast India. Based on the geotechnical investigations at the site, the entire bridge is proposed to be constructed on pile foundations. The integrity of the piles was verified through the assessment of Cross Hole Sonic Logging (CHSL) tests at the site. The arrival time and signal energy of the stress pulses were used to inspect the pile integrity, and the position and extent of defects, if any. The tests were conducted while maintaining pulse wave speed (>4000 m/s) and recommended signal strengths. Usually, a pile is classified as acceptable if the first arrival time increases up to 20% and the energy reduction is <9 dB. The interpretation of CHSL test data identified a few defective piles attributing cross-sectional changes, honeycombing, and poor concrete quality. This paper presents a detailed case study to handle such an important mega project showing the effective use of the CHSL test.

Keywords: Bridge, CHSL, North-East India, Pile Integrity, Pile Foundation

1 INTRODUCTION

The Dhubri-Phulbari 4-lane road bridge will be constructed over the river Brahmaputra and will connect Dhubri (in North Bank) with Phulbari (in South Bank) in the state of Assam/Meghalaya on National Highway (NH-127B). The total length of the bridge from Dhubri to Phulbari end is approximately 18.36 km. Out of the total length, 12.625 km is navigational span, and the remaining portion is the approach viaduct. This will culminate in establishing the shortest access to Meghalaya from Assam and will serve as a main commercial and strategic link route. The construction of this bridge will reduce the travel time to twenty-three minutes from Dhubri to Phulbari, which presently takes more than eight hours by land route and about two and a half hours by ferry.

The bridge will further provide a stable flood-free route and become an effective alternative to the existing ferry route during monsoon season. Figure 1 (a) presents the geographical location of this proposed bridge on the world map. Based on the geotechnical investigation and subsoil condition, the entire bridge is proposed to be constructed on pile foundations. Quality Assessment

DOI: 10.1201/9781003299127-199

(QA) of these piles is a prime concern as this may eventually affect the pile capacity and ability to resist the desired lateral and vertical loads. For example, Camp et al. (2007) performed pile integrity tests on different projects in southern California and found that 70% of the projects had at least one defective pile. Non-Destructive Testing (NDT) methods are commonly used for quality assessment integrity tests of cast in-drilled-hole piles, bored piles, or other concrete structures, such as the drilled pier, caissons, diaphragm slurry walls, dams, etc. Several methods such as Cross Hole Sonic Logging (CHSL), High Strain Dynamic Pile Test (HSDPT), Pile integrity test (PIT), etc., are presently utilized to perform NDT of pile foundations.

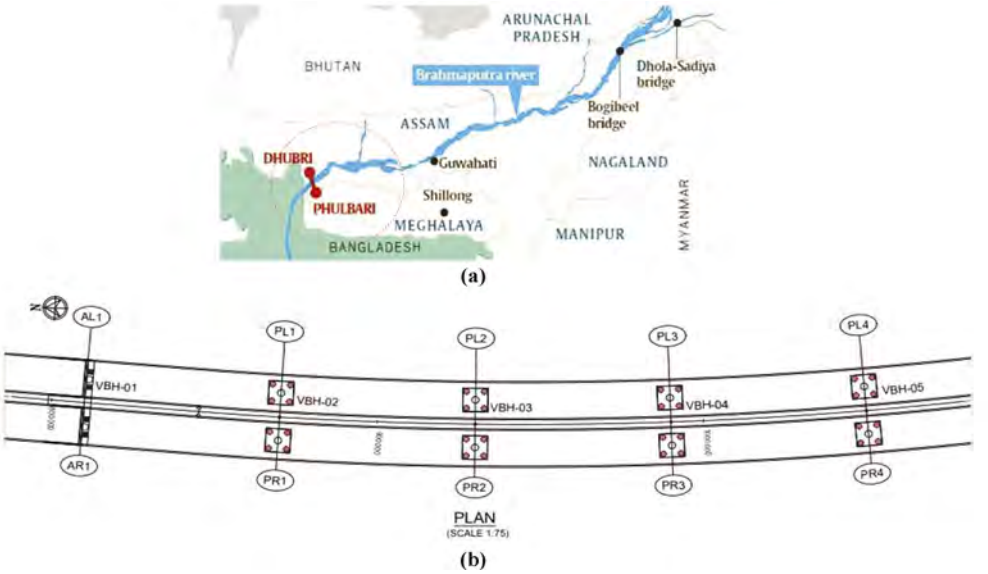

Figure 1. (a) Geographical location of Dhubri-Phulbari Bridge, and (b) Plan view of a small section of the proposed bridge indicating the location of the piers and the piles.

Among these, CHSL is a well-established technique to inspect the soundness of concrete for deep piles and recognizes the defect/flaw position based on the velocity of ultrasonic pulses (Bagui et al., 2020). The test offers several advantages such as (a) precise determination of soil incursion or other irregularities throughout the shaft inside the rebar cage, (b) defects at various depths of the pile can be recognized with high accuracy, (c) uncured concrete in chemically retarded mixes can be identified, and (d) exceptional care in handling is not necessary at the time of the use of radioactive sources. The present study, therefore, preferred to undergo CHSL tests to determine the soundness of concrete for piles at the Dhubri-Phulbari project location and discusses the effectiveness of this test in handling such an important mega project. The discussion is limited to the CHSL test results of four defective bored piles identified as PR1-C1, PL2-C2, PR3-C1, and PR5-C1 under different piers P01, P02, P03, and P05, respectively, as designed for this project. This limitation is for the sake of the brevity of the paper. Figure 1(b) presents a plan view of a small section of the proposed bridge indicating the location of the piers and the piles.

2 METHODOLOGY ADOPTED FOR CHSL TEST

The Cross Hole Sonic Logging tests were performed following ASTM D6760 (2014). The test initially applied drill shafts and six mild steel tubes were installed in a drilled shaft before pouring the concrete. Figure 2 (a) presents a schematic representation of the tubes installed in PR1-C1. A similar arrangement of tubes was followed for the other piles. The installation of tubes was followed by the pouring of water into the tubes and the top and bottom of the tubes were sealed before concreting. The reason behind pouring water into the tubes was to control the differential

temperature during concreting and curing. The CHSL test was conducted after a week of concreting the pile. At first, the ultrasonic transmitter and receiver probes were dropped down to the base of the access tubes. These probes were then pulled off concurrently at the same time to maintain near-horizontal ray paths between them (i.e., zero offset logging). Both transmitter and receiver probes were connected by cables to the Cross Hole Analyzer (CHA) and high-frequency stress pulses were sent from one tube to the other at 50 mm vertical intervals. The CHA recorded the arrival time as well as the signal energy of the pulse at the receiver tube. Figure 2 (b) presents a schematic representation of the CHSL test setup. These recorded data were used to interpret the quality and integrity of the concrete between the tubes. The entire shaft length was scanned in this fashion by repeating the test across diagonals & adjacent perimeters as presented in Figure 2 (a). The tube corridor considered for each pile is represented as 1-2, 2-3, 3-4, 4-5, 5-6, 6-1, 1-4, 2-5 (refer to Figure 2 (a)).

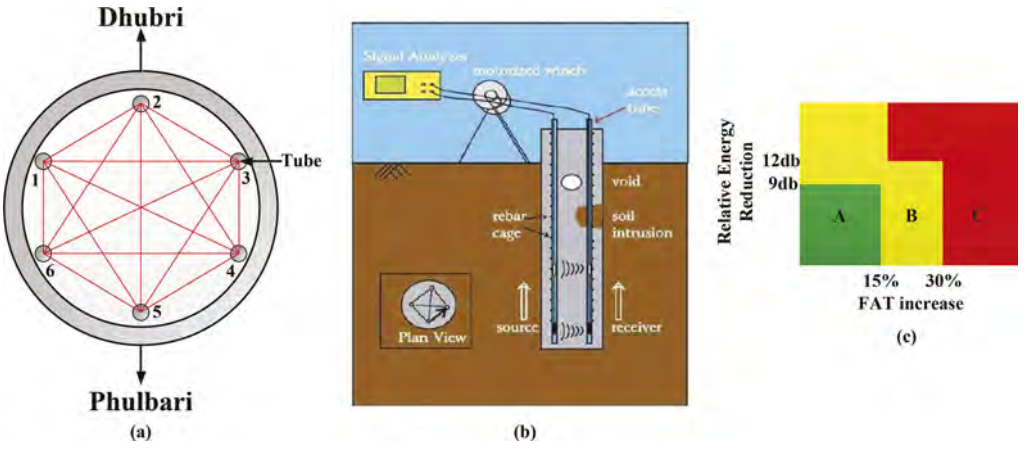

Figure 2. Schematic representation of (a) the tubes used in the CHSL test for PR1-C1, (b) CHSL test setup, and (c) Graphical interpretation of proposed CSHL rating criteria by DFI (2019).

2.1 *Interpretation of the CHSL test results*

The arrival time and signal energy of the stress pulses recorded using CHA were used to inspect drilled shaft's integrity, and the position and extent of defects in the piles. Uniform concrete will result in a near-continuous vertical profile of the waterfall-displayed data and yield consistent first arrival times (FAT) with reasonable pulse wave speed and signal strengths. Non-uniformities in concrete such as honeycombing, formation of voids in concrete, contaminated concrete, or soft concrete exhibit delayed FAT with lower signal amplitudes. The wave speed is affected if the tubes installed are not perfectly straight and parallel and depend on the age of the concrete. DFI (2019) recommended that CHSL results for each profile should be categorized into either of the following three classes based on FAT and signal energy received at the receiver tube relative to FAT and signal energy received in a nearby zone of good concrete: Class A: It represents acceptable test results where percentage increase in FAT value and the reduction in relative energy value is not more than 15% and 9 dB of their local average values, respectively. Class B: It represents conditionally acceptable CSHL test results where the percentage increase in FAT value lies within a range of 15% to 30% of the local average FAT value, and relative energy reduction is less than 12 dB. Further, Class B can be also represented as the percentage increase in FAT value less than 15 % and the reduction in relative energy value higher than 9 dB of their local average values, respectively. Class C: It represents highly abnormal CSHL test results with FAT increasing more than 30% of the local average values. Further, it may also be represented as the percentage increase in FAT value and the reduction in relative energy value greater than 15% and 12 dB of their local average values, respectively. Figure 2 (c) presents a graphical interpretation of the proposed CSHL rating criteria by DFI (2019). The present study followed the classification system

Table 1. Interpretation of defects in the pile shaft based on FAT and signal energy.

S. No.	Pile Classification	% Increase in FAT relative to good concrete	Energy reduction relative to good concrete	DFI (2019) classification guideline
1.	Satisfactory/good	0-10	< 6 dB	Class A
2.	Minor/flaw	11-15	<9dB	
3.	Poor/flaw	15-30 or < 15	9 dB to 12 dB	Class B
4.	Poor/defect	> 30	> 12 dB	Class C

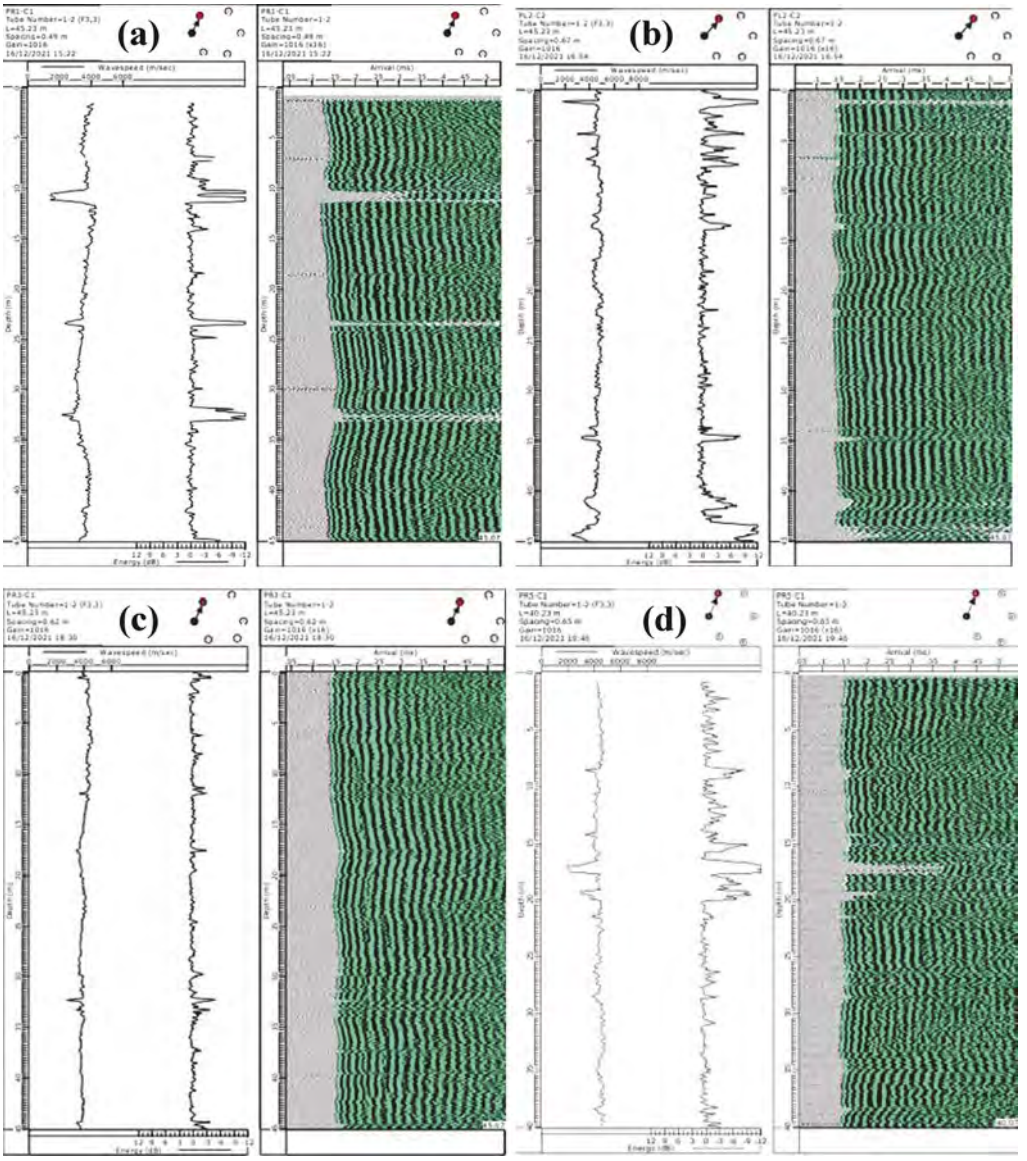

Figure 3. CHSL result of tube corridor 1-2 for (a) PR1-C1, (b) PL2-C2, (c) PR3-C1, and (d) PR5-C1, respectively.

proposed by DFI (2019) to predict the defects and flaws in the pile shaft at the project location. Table 1 typically presents the classification details for the interpretation of defects in the pile shaft.

3 OBSERVATIONS FROM CHSL TEST RESULTS

This section is focused to comment on the critical observations made from the CHSL test results.

Figure 3 presents a sample result for the tube corridor 1-2 (refer to Figure 2 (a)) for PR1-C1, PL2-C2, PR3-C1, and PR5-C1, respectively. The curves indicate the average wave speed, energy reduction values, and FAT values which are used to identify the defects and flaws at different pile locations. Similar types of curves were also generated for all other tube corridors (i.e., 1-2, 2-3, 3-4, 4-5, 5-6, 6-1, 1-4, 2-5) across diagonals & adjacent perimeters for all piles. Further, DFI (2019) guideline is used to categorize the defects in the piles in different classes (i.e., Class A, B, and C). It may be observed from Figure 3 (a) that the energy reduction and percentage increase in the FAT value are greater than 12 and 30, respectively, for PR1-C1 and as a result, indicated poor/defect and can be classified in the Class C category as per DFI (2019) guideline.

Further, it is noticed that PL2-C2 shows poor/defects and poor/flaws (i.e., Class C and B) at around 1 m to 5 m, 6 m to 7 m, and 41 m to 44 m depths, respectively. Apart from these, PR3-C1 test results indicate a uniform pile shaft throughout the depth with minor/flaws (i.e., Class A) at a few locations. Lastly, PR5-C1 shows poor/defect (i.e., Class C) between 16.5 m to 17.5 m depth and poor/flaw (i.e., Class B) at a depth between 19 m to 19.5 m. Further, the detailed review of the defects and flaws for the four piles considering all the tube corridors and attributing the location of defects in the piles are summarized in Table 2.

Table 2. Poor defects and flaws observed at different pile locations.

S. No.	Pile Number	Pile Length (m)	Pile Diameter (m)	Comments
1.	PR1-C1	45.07	1.65	Poor/ defect at • 8.8 m to 11.5 m • 22.3 m to 23.5 m • 31.7 m to 33.1 m
2.	PL2-C2	45.07	1.65	Poor/ defect and Poor /Flaw at • 0.8 m to 1.8 m • 3.0 m to 4.8 m • 6.7 m to 7.7 m • 40.7 m to 45.07m
3.	PR3-C1	45.07	1.65	Poor/ defect at • 29.3 m to 33.3 m
4.	PR5-C1	45.07	1.65	Poor/ defect at • 16.4 to 20 m

Note: Minor defects and flaws are not mentioned in this table.

4 SUMMARY AND CONCLUSIONS

The present study discusses the outcome of the Cross Hole Sonic Logging (CHSL) test results conducted on test piles at the Dhubri-Phulbari Bridge site in Assam, India. The discussion of this study is limited to the CHSL test results of four defective RC bored piles identified as PR1-C1, PL2-C2, PR3-C1, and PR5-C1. The test results are presented across diagonals & adjacent perimeters for each pile and interpretation of the defects in the piles is made based on energy reduction value, FAT, and average wave speed of the signal, respectively. Poor defects and flaws (i.e., Class C and B) are noticed at several pile depths. Apart from this, minor/flaws

are also observed. The details of the defects and flaws observed in this test for all the piles considered are summarized in Table 2. Further, it may be concluded that the CHSL test may be considered appropriate for the initial inspection of the defects/flaws at different pile locations. However, a single CHSL test may not be sufficient to accurately evaluate the integrity of the pile for potential problems like cross-sectional changes, honeycombing, etc. Hence, other low-cost NDT tests such as HSDT and PIT may help in ensuring the discrepancies occurred in the pile. These tests were performed at the Dhubri-Phulbari project site for a re-assurance of the defects in the piles identified in the present study, however, not presented here for the sake of brevity.

REFERENCES

ASTM D6760. 2014. Standard Test Method for Integrity Testing of Concrete Deep Foundations by Ultrasonic Crosshole Testing. DOI: 10.1520/D6760-16.

Bagui, S.K., Puri, S.K., Subbiah, K. 2020. Cross-hole sonic test results for analysis of pile load test. *Advances in Bridge Engineering*. 1:15. https://doi.org/10.1186/s43251-020-00017-4.

Camp, W.M. III, Holley, D.W., Canivan, G.J. 2007. Cross-hole Sonic Logging (CSL) of South Carolina drilled shafts: a five-year summary. *GeoDenver 2007 New Peaks in Geotechnica*, Denver (CD Rom).

Sellountou, E.A., Amir, J., Canivan, G., Chernauskas, L., Hertlein, B., Kandaris, P., Kovacs, T., and Likins, G. 2019. Terminology and Evaluation Criteria of Crosshole Sonic Logging (CSL) as applied to Deep Foundations. DFI, pp. 1–17.

Smart Geotechnics for Smart Societies – Zhussupbekov, Sarsembayeva & Kaliakin (Eds)
© 2023 The Author(s), ISBN 978-1-003-29912-7
Open Access: www.taylorfrancis.com, CC BY-NC-ND 4.0 license

Analysis of the interaction of the massive shell with the ground

N.A. Perminov
Emperor Alexander I St. Petersburg State Transport University, St. Petersburg, Russia

ABSTRACT: Analysis of interaction regularities of large-size reinforced concrete shells at the erection stages in heterogeneous soil mediums allowed to significantly expand the field of their rational use in underground construction parameters and indicators. Strength and deforativeness of a large-size massive structure, its geometrical variability should be calculated not only for the final stage of construction but also for a whole history of driving considering a history of caisson-soil bulk interaction at driving, and, consequently the effect of gradual inheritance of stress-strain state. The methodological approach proposed in the paper allows transferring from the earlier accepted methods of calculation of underground caisson structures to the concept of simulation and prediction of defectless lifecycle at the stage of construction. Modeling and calculative substantiation of schemes and parameters of preventive protection of an underground structure at the stage of its construction using geotechnical methods provides its safety and resistance against technically generated impacts.

1 FEATURES OF INTERACTION OF A LARGE SHELL WITH HETEROGENEOUS SOIL MILIEU AT THE STAGE OF ITS LOWERING

In order to provide stable and safe operation of large caisson structures there is a need to ensure internal integrity of fencing structures with high degree of waterproofness at all stages of their life cycle.

The existing standards (Ilichev & Mangushev. 2016) and regulations (The set of regulations. 2012) envisage checking calculations of underground structures to be lowered for the stages of their construction and operation. However, based on the experience one can say that in case of large caisson structures it is not enough due to specific conditions of their interaction with a soil bulk and inclusion the effect (factor) of a large scale: hyper sizes of an area of lateral surface of the shell, which interacts with heterogeneous soil, and its super large weight, which creates a powerful kinetic impulse during instant, often sudden subsidence, cause a beyond-design situation for a caisson structure. Joint actions of these factors stipulate specific non-linear behavior of the structure at lowering as well as the host soil bulk. Due to strength and deformability of the large massive structure, its geometric changeability it is necessary to calculate not only the final stage of construction but also the whole history of lowering taking into account a history of the process of shell-soil bulk interaction during caisson lowering and, consequently, the effect of gradual inheritance of stress-strain behavior. These problems could be solved only by tackling non-linear problems, non-linear models and computer non-linear simulation (Perminov, Zencov & Perminov. 2013), (Barabash. 2012), (Ilichev. 2008).

The analysis of the results of in situ and calculation-experimental works and the data of the comprehensive system of geotechnical monitoring (Figure 1) of lowering large shells showed the features of their interaction with heterogeneous soil milieu (Perelmuter & Kazantsev. 2015). The geotechnical profile for the monitored facilities is characterized as follows: the upper layer is represented by Quaternary strata down to the depth of 14.0–25.0 m. (Table 1).

The monitoring identified a very important phenomenon: the peak values of horizontal stresses exceed the calculation values 2.3–2.5 times, and it is observed at deviation of the shell from the vertical axis and changes of its geometry (Figure 1). It can be the reason of

DOI: 10.1201/9781003299127-200

Table 1. Characteristics of the geotechnical profile of the monitoring object.

Layer	Deformation model (E)	Specific coupling (C)	Internal friction angle (φ)
Saturated silty sands of medium density	11 MPa	0 MPa	30°
Plastic silty clayey sands	4 MPa	0.01 MPa	15°
Liquid-plastic silty sandy clays	9 MPa	0.025 MPa	16°
Semi-solid silty sandy clays with gravel and pebbles	14 MPa	0.028 MPa	28°
Dislocated solid Proterozoic clays	19 MPa	0.04. . .0.06 MPa	18. . .21°

suspension of the process of lowering the massive shell with a subsequent sudden, conditionally instant drop. Based on the analysis of the graph of lowering (Figure 2a) it can be seen that a value of drop reaches 1.5 m and more. The shell structure takes impact beyond-design loads by creating a powerful kinetic impulse by its drop to the soil bulk of a pit bottom (Perminov. 1997), that can cause occurrence of microcracks in concrete of the structure and inevitably leads to violation of the structural hydro insolation. This phenomenon has been identified after 10–15-year-long operation of the gas and pumping station complex of the water treatment facilities of St. Petersburg (Perminov & Perminov. 2014).

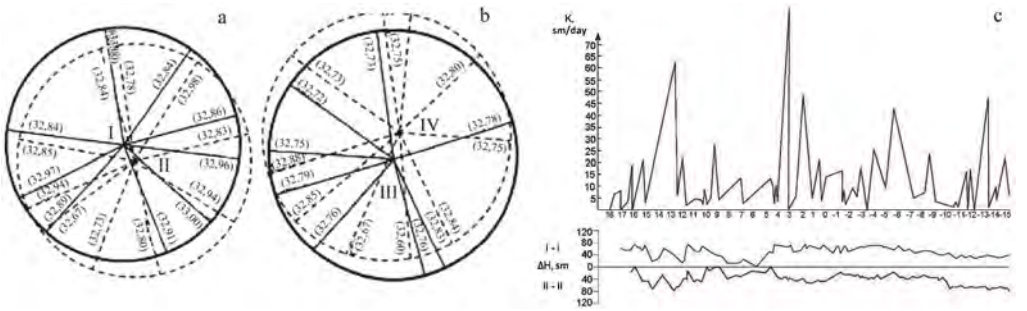

Figure 1. Displacement of the center of circle O during its lowering to a depth: a, b, c– H = 17 m; H =29 m; H = 25m; H = 29m.

Geomonitoring showed unsteadiness of the processes of interaction of the external contour of the massive structure (Perelmuter & Slivker. 2011). Complex and, as a rule, uncontrolled character of the processes during conditionally instant embedment of the shell into the host heterogeneous milieu as well as the environment, that has physical and genetic non-linearity (The set of regulations. 2016), demonstrate that the study of stain-stress behavior of the shell and soil bulk can be carried out only on the basis of computer modeling of this process using geotechnical and structural software complexes.

2 THE SIMULATION OF CONTROLLED REGIMES OF LOWERING THE MASSIVE SHELL INTO A SOIL OF DIFFERENT STRENGTHS USING THE METHODS OF GEOTECHNOLOGY

The analysis of behavior of the caisson structure during its sudden uncontrolled sliding (drop) to the bottom of an open soil cavern from the height 1.3 – 1.5 m with the angles of deviation from the vertical axis 0.5°-5°C was conducted with a help of the software complex Autodesk Robot Structural Analysis Professional (Carmody & Sterling. 1993).

While developing the calculation model (Figure 2) it was considered that the shell structure consists of two cylinders, one stands on the other: the upper cylinder: the external radius R = 36 m, the internal radius R = 30.5 m, the height H1 = 46 m; the lower cylinder: the external radius R = 36 m, the internal radius R = 30 m, the height

H2 = 25 m. Therefore, the external diameter of the shell was D = 72 m, the height of the shell was H = 71 m. Concrete grade - B30.

In order to simulate a value of impact force at dropping the shell in the model the cylinder fell from the height H = 150-250 cm under the action of its own weight with the tilt angle 0.5°-5° to a flexible soil (green-gray clay: φ = 21°, C = 0.04 MPa, E = 19 MPa). A spatial calculation scheme of the shell was modelled: the weight G = 210000 tons; the amount of nodes 16944; the amount of volumetric finite elements 12496; the amount of static degrees of freedom 50828; the amount of loadings 27; the acceleration of gravity g = 9.81 m/kV.s; the time of drop $t=\sqrt{(2*H/g)}$; Δt=0.30-0.54 s. Due to the tilt angle friction forces were applied in the upper part of the caisson from one side and in the lower part – from the opposite one.

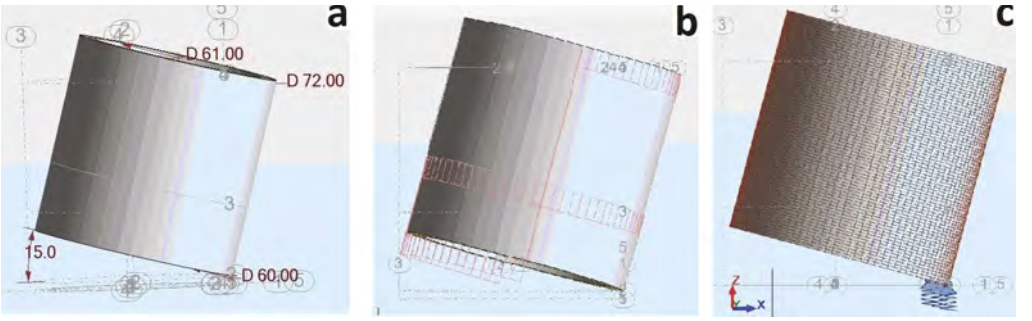

Figure 2. The schemes of calculation models of the lowered shell at different angles of its deviation from the vertical axis: a- static support at tilt; b,c — drop and sliding at tilt (deviation from the vertical axis).

As the simulation of the processes of drop at different angles of deviation of the shell from the axis -α and falling heights –ΔH was made in quite a large range, Figure 3 gives only the most typical results, which were taken for the analysis. The total calculation table of the results of integration of motion equation for the shell during the drop (falling) at speeds VZ, VX, VY (cm/s), acceleration AZ, AX, AY(cm/s^2) and displacements UZ, UX, UY (cm) included 186385 lines.

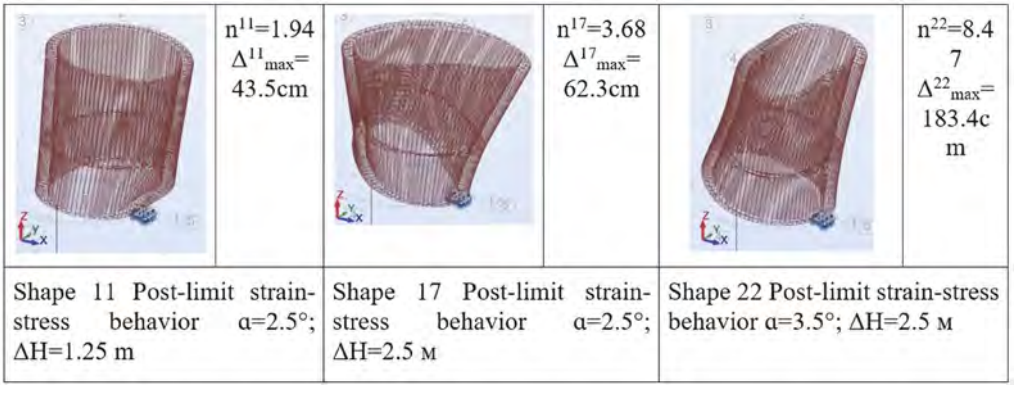

Figure 3. The simulation results.

Based on the simulation results (Figure 4) there were set admissible parameters of spatial location of the shell and the ranges of its conditionally instant drops, which provide pre-limit strain-stress behavior of the shell.

The simulation results show that for the large shell the recommendations of regulatory documents (Ponomaryov, Kaloshina, Zakharov, Bezgodov, Shenkman & Zolotozubov. 2015) have limited application and are needed to be confirmed via calculative modeling.

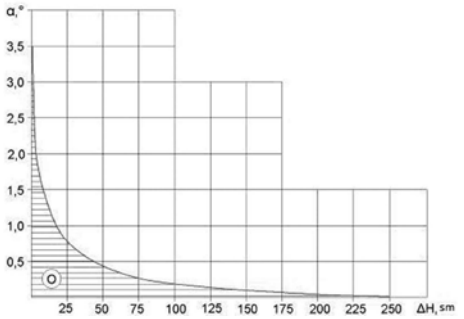

Figure 4. The area of limit admissible values of conditionally instant drops ΔH of the shell, D=61m, height H=71m, weight G=210000 tons, at different angles of deviation of the structure from the vertical axis α°(Concrete B30; φ = 21°, C = 0.04 MPa, E = 19 MPa).

Taking into account the results of the previous steps of modeling, at this stage the problem of geotechnical simulation of the process of lowering the shell into the soil bulk in a controlled mode was solved. The geotechnical methods (Nikiforova, Konnov, Nguyen Van Hoa, Prostotina. 2019) served as external impacts on the "shell-soil bulk" system.

An incremental model of deformation type was used as the calculation soil model for solving the non-linear problem. A stress-strain connection in the model was taken separately for volumetric and shear components of a stress tensor

$$\left.\begin{aligned} dS_{ij} &= 2G^T \cdot de_{ij} \\ d\delta_{cp} &= 3K^T \cdot d\xi_{cp} \end{aligned}\right\} \tag{1}$$

where: dS_{ij} and de_{ij} are increments of deviatoric components of stress and strain tensors, respectively; $d\delta_{ij}$ and $d\xi_{ij}$ are increments of average stress and strain; G^T and K^T- tangent moduli of deformation of shape and volume.

Tangent moduli of deformation G^T and K^T were approximated according to linear polynomial of the second degree with one variable:

$$\left.\begin{aligned} G^T &= G(S_{ij};\delta_{ij}) = A_0 + A_1\delta_{cp} + AS_{ij} \\ K^T &= K(\delta_{cp}) = B_0 + B_1\delta_{cp} + B_2\delta_{cp}^2 \end{aligned}\right\} \tag{2}$$

Approximating dependencies (2) are experimentally substantiated on the example of stabilometer triaxial tests (STT).

The parameters of the calculation model A0; A1; A2; Kp; B0; B1; B2 were defined based of the data of STT. The medium-grained sandy soil of the density Pd=1.65g/cm^3 and water content W=10% was used as the tested soil. All calculations were made using the numerical method of finite elements with a help of geotechnical software. The procedure of solving the non-linear problem was reduced to the well-known method of variable rigidity (Nguyen Van Hoa & Nikiforova. 2018), (Nikiforova & Nguyen Van Hoa. 2020), (Bulychev & Fotieva. 2017), according to which the matrix of rigidity was transformed at each step of the solution in accordance with the current level of stress-strain behavior and orientation of the vector of additional loading.

Figure 5a shows a characteristic graph of the shell contour displacement to the design position with inclusion of a geotechnical impact on strain-stress behavior of the surrounding soil bulk into the calculation. The results of simulation show (Figure 5b) that rectification of the shell contour displacement almost to the design position (from 32.8 cm to 9.01 cm) allows decreasing an area of distribution and a value of settlement of the soil bulk around the shell

several times (the area of distribution reduces from 45 m to 9 m; the value of settlement, respectively, from 150 cm to 8 cm).

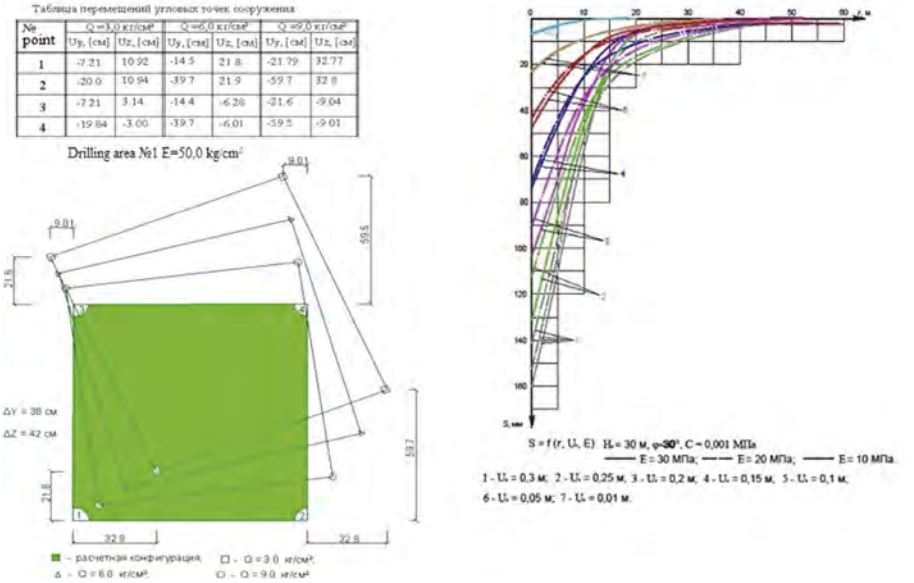

Figure 5. The displacement of the shell contour in continuous milieu: a - at correction of tilt under the conditions of action of a lateral additional load Q = 0.3- 0.9 MPa; b – the influence of a value of the shell contour displacement Ux on settlements of the soil surface at correction of tilt.

3 CONCLUSIONS

Simulation of the interaction of an unstable structure with the ground environment during immersion and the analysis of behavior fencing shell during its gradual increasing and lowering into the heterogeneous soil milieu allowed identifying a number of factors, which characterize its non-linear behavior in the conditions of joint interaction.

Physical non-linearity is caused by behavior in the elasto-plastic area of the soil bulk, which contacts with the lateral surface, during deviation of the structure from the vertical axis. Geometric non-linearity manifests itself when its geometry changes asymmetrically during instant-stepwise drops of the massive shell.

Unsteadiness of the processes of interaction of the massive structure with the soil milieu as well as itself causes the necessity of creating methods of adaptive control of the stress-strain behavior of the system "gravitational large body – heterogeneous host milieu".

Due to joint step-by-step making geotechnical and structural calculations a history of the processes of shell-soil milieu interaction is simulated, the parameters of the adaptive control of the system of strain-stress behavior, which are implemented with a help of external geotechnical impacts at the stage of construction of the structure, are predicted.

REFERENCES

Barabash, M. 2012. Simulation of beyond-design impacts at studying the lifecycle of buildings and structures. *International Journal for Computational Civil and Structural Engineering*, 12 (3): 15–25.

Bulychev, N.S. & Fotieva, N.N. 2017. Theory and practice of tunnel lining design. *Modern tunneling science and technology*: 445–450.

Carmody, Y. & Sterling, R.L. 1993. Underground space design. *A guide to subsurface utilization and design for people in underground spaces (New York: VNR)*: 328.
Ilichev, V.A. 2008. A flat problem of a plate on elastic subsoil with account of a technology of its construction. *Soils, foundations and soil mechanics 3*: 12–16.
Ilichev, V.A. & Mangushev, R. 2016. The reference book of a geotechnical engineer. Soils, foundations and underground structures. *The publishing house of the Association of Construction Universities*: 1034.
Nguyen, Van Hoa & Nikiforova, N.S. 2018. The choice of soil models in design of deep excavation in soft soils of Viet Nam. *MATEC Web of Conferences. Vol. 251. No 04033*.
Nikiforova, N.S., Konnov, A.V., Nguyen, Van Hoa, Prostotina, L.A. 2019. The influence of the device of cut-off screens made using jet technology on the sediment of the surrounding buildings. *Housing construction. №7*: 3–8.
Nikiforova, N.S. & Nguyen, Van Hoa. 2020. Calculating the maximum pressure on the diaphragm wall subjected to seismic loading accounting for geotechnical conditions of Vietnam. *IOP Conference Series: Materials Science and Engineering. № 869*. 072032.
Perelmuter, A.V. & Slivker, V.I. 2011. Calculation models of structures and a possibility of their analysis. *M. The Publishing House of SKAD SOFT*: 710.
Perelmuter, A.V. & Kazantsev, O.V. 2015. The analysis of structures with a changing calculation scheme. *M., AS Publishing House*: 148.
Perminov, N.A. 1997. Comprehensive geotechnical support for the construction of large edifices as a part of St. Petersburg. *Geotechnical Engineering for the Preservation of Monuments and Historic Sites (Viggiani (ed.) Balkema, Rotterdam, ISBN 9054108711)*: 1074–1081.
Perminov, N.A., Zencov, V.N. & Perminov, A. N. 2013. A comprehensive geotechnical support system for underground space development. *Proceedings of the 13th World Conference of ACUUS: Advances in Underground Space Developmen*: 276–286.
Perminov, N.A. & Perminov A.N. 2014. Geothermal aspects of providing safety of long-operating facilities of engineering infrastructure of large cities in difficult soil conditions. *The Journal of Perm Research University 4*: 111–128.
Ponomaryov, A.B., Kaloshina, S.V., Zakharov, A.V., Bezgodov, M.A., Shenkman, R.I. & Zolotozubov, D.G. 2015. Results of geotechnical modeling of the influence of construction of the large foundation ditch on the existing historical building Japanese. *Geotechnical Society Special Publication: the 15th Asian Regional Conf. on Soil Mechanics and Geotechnical Engineering: Geotechnical Heritage. Part 2 (TC 301/ATC 19 Session) Vol№ 78*: 2676–267919.
The set of regulations. 2012. Structures of industrial enterprises SR 43.13330.2012. *An updated version. Construction Code* 2. 09.03-85.M.: 101.
The set of regulations. 2016. Foundations of buildings and structures SR 22.13330.2016. *An updated version. Construction Code* 2. 02.01-83.M.: 172.

Smart Geotechnics for Smart Societies – Zhussupbekov, Sarsembayeva & Kaliakin (Eds)
© 2023 The Author(s), ISBN 978-1-003-29912-7
Open Access: www.taylorfrancis.com, CC BY-NC-ND 4.0 license

Cantilever steel tubular pile wall embedded in soft rock subjected to various loadings

S.M. Shafi & J. Takemura
Tokyo Institute of Technology, Tokyo, Japan

ABSTRACT: Mechanical behavior of large stiffness cantilever steel tubular pile wall embedded in soft rock was investigated by centrifuge model tests under 50g. Two models were prepared with common wall height H=12m and pile diameter Φ=2m, and two embedment depths in soft rock (qu=1.4MPa) dr =2.5m and 3.0m in a prototype scale. Dynamic loadings were first applied to the wall retaining dry sand, and then static loading was simulated by rising water level in the sand. Second series of dynamic loadings were further applied to the wall with the wet sand. It was found that the dr increment of 0.5m could significantly reduce the wall displacement, but increase the moment load and thrust force to the wall, which suggesting the wall structural failure could be a critical condition even for the small dr of about 1.5Φ, especially during the dynamic loading.

1 INTRODUCTION

Embedded (un-propped) retaining walls (known as cantilever-type retaining walls) are commonly used for temporary and permanent structures depending on the site condition. In recent years, one of the popular forms of this retaining structure is cantilever-type steel tubular pile (CSTP) walls. Advanced technology like the rotary cutting press-in method allows applying this CSTP wall for various purposes (Kitamura and Kitamura, 2018). However, like other civil engineering structures, this retaining wall should satisfy the required performance under the design condition. Traditionally, cantilever-type retaining walls are designed considering relatively flexible retaining walls embedded in soft grounds for small retain height (H) (≤4m) (JTASP-PACTC. 2007). As shown in Figure 1(a), the application of CSTP walls might exceed the traditional retaining height. Also, different kinds of temporal load could be expected during the service period, like earthquakes or an increase of the groundwater level in the retained soil, as shown in Figure 1 (b).

This external loading might produce a significant moment load leading to large wall deflection for large retain height. However, if high stiffness (EI) wall, for example, a large pile diameter (Φ) steel tubular pile wall, is embedded in moderately stiff ground (like a soft rock), this large deflection could be untangled. Based on the design guideline by JTASP-PACTC (2007), the minimum required embedment depth ($d_r=L_o\geq 3/\beta$: where β is the characteristics value) could be very conservative for walls embedded in the hard ground (Takemura 2021). Kunasegaram and Takemura (2021) conducted centrifuge tests on simplified plate-type cantilever retaining walls with (d_r)<40% of the required d_r by guidelines. They observed no catastrophic failure with this small embedment depth against static loading by water rise. In this study, two centrifuge models were made following the test conditions of Kunasegaram and Takemura (2021). Sequential dynamic loadings and static loadings (by water rise) were applied to investigate the mechanical behavior of the wall and discuss the critical conditions which should be considered in the rational design of this type of wall.

DOI: 10.1201/9781003299127-201

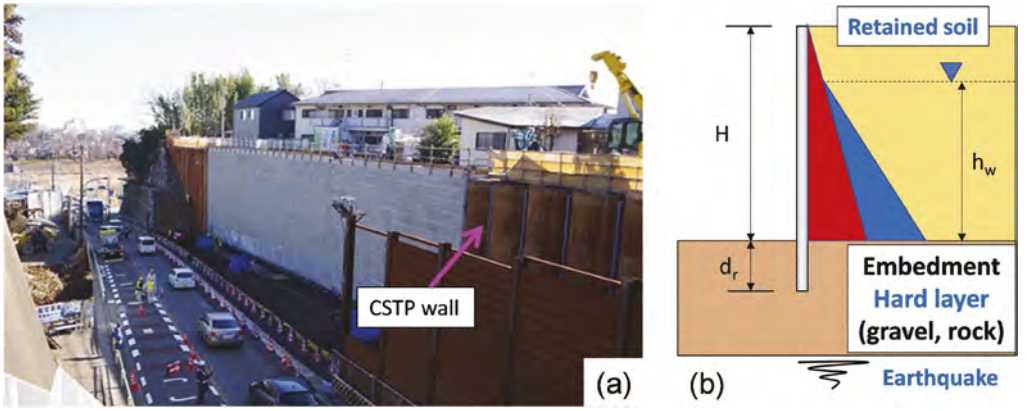

Figure 1. (a) Cantilever type large diameter steel tubular pile (CSTP) wall (Kitamura and Kitamura. 2018) and (b) various loading expected during design life.

2 CENTRIFUGE TEST

The side view of the model is illustrated in Figure 2. This model was made under 50g centrifugal acceleration, as shown in Figure 2 (a). A rigid frame container (shown in Figure 2 (c)) with inner dimensions of 600mm x 400mm x 250mm was used to prepare the model. A 33mm acrylic plate was attached to the back of the container to reduce the width. The model wall consisted of five steel tubular piles (SUS304, shown in Figure 2 (b)) firmly fixed at the top and spanned the width maintaining the plane strain condition. By air pluviation technique, Toyoura sand (maintaining Dr=85%) was poured into the rubber bag placed at the back of the wall. This rubber bag was used to define the boundary condition clearly and make a water-tight environment. Different sensors were used to measure different responses during shaking. More details about the model preparation can be found in Shafi et al. (2021). An artificially prepared soft rock with unconfined compressive strength (q_u) of 1.4MPa (on the 14th day of curing) was used as supporting ground. This soft rock was prepared with sand-

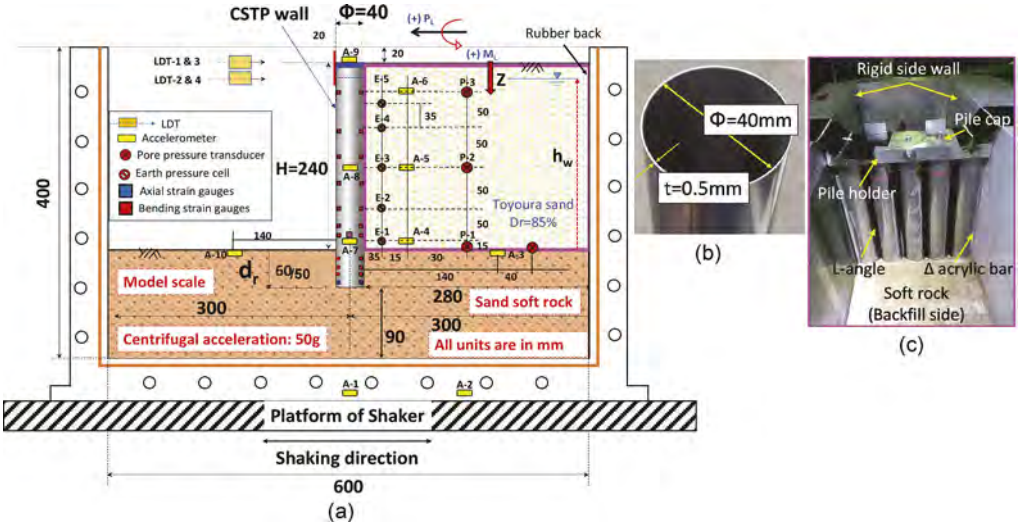

Figure 2. (a) 2D view of model (b) model pile used (c) modeled CSTP wall embedded in solidified soft rock before backfilling.

Table 1. Test conditions, material properties, loading sequences followed in each case.

Test code	Properties of soft rock and sand	Wall height: h_w	Rock embedded depth: d_r ()$^{\$}$, [$\beta d_r$]	Pile Properties Φ, t, EI, M_y	Loading sequences
Case 1 **(C1)**	Toyoura sand (Dr=85%): γ_d=15.8kN/m^3 ϕ'=42° Soft rock: γ_r =20.1kN/m^3 q-$_u$=1.4MPa E_S=660MPa	12m (240mm) $^{\$}$	3.0m (60 mm) **[1.2]**	Φ=2 m (40 mm) $^{\$}$ t = 25 mm (0.5mm) $^{\$}$ Spacing: 2.15m (43mm) $^{\$}$ EI= 6.8 GNm^2/m (5.4x10^{-5}GNm^2/m) $^{\$}$ M_y= 9.0 MNm/m (3.6x10^{-3} MNm/m) $^{\$}$ $M_{y(actual)}$= 65%M_y (Vijay and Takemura, 2022)	Dynamic loading at h_w=0m: 5 shakings **S(a_i){n_c}[A_i]**:S1 (0.14){20}[2], S2(.33){20}[5.3], S3(.4){20}[9.5], S4(.52){20}[13.5], S5(.52){20}[13.5] Static loading by water rise, **WR1**: h_w:0 – 9.6m Dynamic loading at h_w=9.6m: 5 shakings S6(.14){20}[2], S7(.22){18}[5.4], S8(.35){19}[9], S9(.45){18}[11.4], S10(.55){15}[12.5] Static loading by water rise, **WR2**: h_w:9.6– 10.9m Dynamic loading at h_w =10.9m: 1 shaking S11(.6){18}[15]
Case 3 **(C3)**			2.5m (50 mm) **[1.0]**		Dynamic loading at h_w=0m: 1 shaking S1(.6){6}[5.3] Static loading by water rise, **WR1**: h_w:0 – 8.4m Dynamic loading at h_w=8.4m: 1 shaking S2(.62){6}[4.9] Static loading by water rise, **WR2**: h_w:8.4 -9.4 m Dynamic loading at h_w=9.4m: 2 shakings S3(.63){6}[5.2], S4(.6){7}[5.6]

$^{\$}$:(model scale); βd_R: normalized depth of model CSTP wall; a_i=amplitude of input motion (g); n_c= number of cycles; A_i: Arias intensity (m/sec)

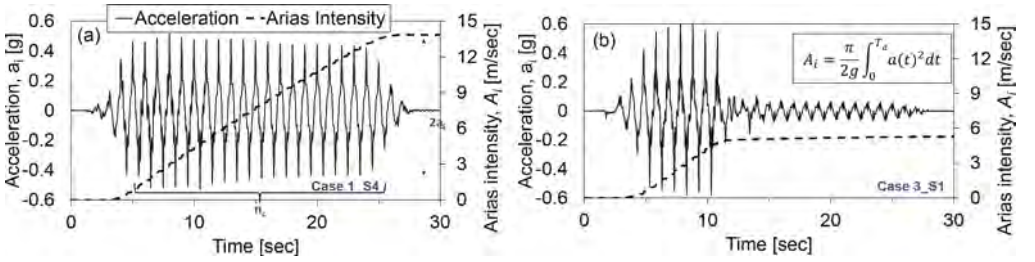

Figure 3. Typical shape of dynamic loading.

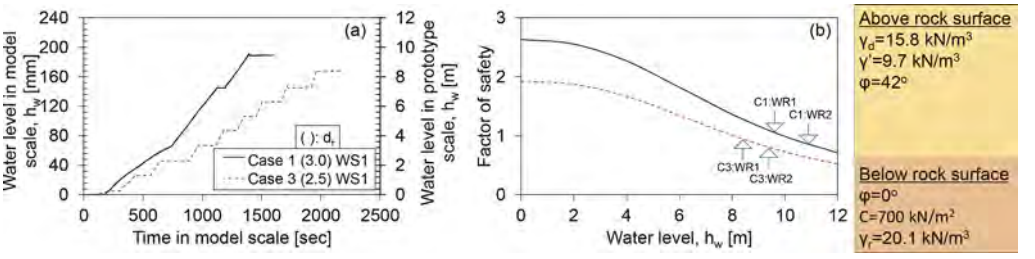

Figure 4. (a) Static loading by water rise (WR1) (b) Variation of factor of safety with h_w.

clay-cement and mixed with the appropriate amount of water. More details about the preparation of the artificial soft rock can be found in Kunasegaram & Takemura (2021).

The stability of the model CSTP wall was checked using the pressure distribution given by Padfield and Mair (1984). In this paper, the factor of safety (FS) is defined by rotational stability computed using the moment minimization technique (Madabhushi et al., 2005), assuming $\phi=0^o$ below the dredge level. The calculated FS for different water levels (h_w) is also shown in Figure 4 (b). In dry conditions, FS of about 2.3 and 1.9 can be ensured for cases 1 and 3, respecttively.

Also, the FS for model water levels is indicated in Figure 4 (b).

The details of the test conditions and loading sequence are given in Table 1. The properties of the wall were identical in all the tests, except for the rock embedded depth (d_r). Case 1 had d_r =3.0m, and case 3 had d_r=2.5m, smaller than the JTASP-PACTC (2007) recommendation calculated based on model conditions given in Table 1. A sinusoidal wave of a predominant frequency of 1Hz was used for dynamic loading, as shown in Figure 3 (a) and (b). The amplitude of the input motion (a_i) is defined by the absolute maximum magnitude measured by the accelerometer. The effective number of cycles (almost the same negative magnitude) is termed 'n_c' in this paper. Due to the variation in number of cycles, Arias intensity (A_i) (defined in Figure 3 (b)) is used as a reference value. The (a_i), (n_c) and (A_i) of each loading are given in Table 1. Static loading was applied by supplying water in the back, as shown in Figure 4 (a) (WR1). In total, water level (h_w) over 3H/4 was achieved by two times the water supply, as shown in Table 1. Both cases have similar loading sequences but different loading histories.

3 RESULT AND DISCUSSIONS

Unless stated otherwise, all the discussion in this paper will be based on the prototype scale. The increment in measured wall top displacement (δ_t), lateral pressure (σ_h) at different depths, and bending moment (M) during dynamic loading is shown in Figure 5 for case 1 shake 4. The solid black line shows residual/static components accumulation during shaking. During the dynamic loading, the residual (δ_t) increased after dynamic loading. Although the residual (δ_t) increased, there was a gradual increase in (σ_h) during shaking. This gradual increase in (σ_h) increased the total force acting on the wall, confirmed by the bending moment increase. Due to elastic resilience and good fixity in the rock part, this gradual increase in (σ_h) is observed with the increase in (δ_t). This phenomenon is termed 'resilience effect' in this paper. The increment in wall top displacement with water level (h_w) is shown in Figure 6. For identical h_w, the wall top displacement observed for d_r=3.0m is smaller than d_r=2.5m. The difference in wall top displacement becomes more visible as the h_w>.33H. However, small wall top displacement (<0.03%H) can be observed for cases 1 and 3 at h_w<0.33H.

Lateral pressure and bending moment distribution with depths are shown in Figure 7. The reference active (σ_{ha}) and at-rest (σ_{ho}) pressure are also shown for (σ_h) distribution. Similarly, the corresponding active moment (M_a) and at-rest moment (M_o) are shown for the bending moment. Based on the lateral pressure distribution (Figure 7a), the initial condition for cases 1 and 3 is observed to be greater than the active pressure. In the bending moment distribution, a similar observation can be made for case 1. However, in case 3, the measurement of the bending moment appears to be underestimated initially.

In Figure 7 (b) and (c), the (σ_h) distribution is drawn for before shake (before), after shake (residual), and maximum (Measured max.) value observed at each depth for cases 1 and 3, respectively. This measured max. value could be considered as an envelope of the maximum (σ_h) experienced by the wall during shaking. Similarly, bending moment distributions are drawn for before shake (before), after shake (residual), and Max. (the time when the max value is observed at Z=10.75m, as shown in Figure 5 (d)). Figures 7 (e) and (f) depict the bending moment distribution. Case 1 shows the stress concentration near the vicinity of the rock surface. For thin tubes, the 3D wall effect, such as stress concentration near the rock surface, can be expected, which cannot be demonstrated by the simplified plate wall model. In this paper, moment load (M_L) is calculated by linearly extrapolating the bending moment distribution up to the rock surface. Overall, the (σ_h) and (M) distribution diagrams show that the measured values increase after the dynamic loading. Especially, the increase in (σ_h) by shaking before water rise might cause the small displacement observed in Figure 6 at shallow water level (h_w<0.33H).

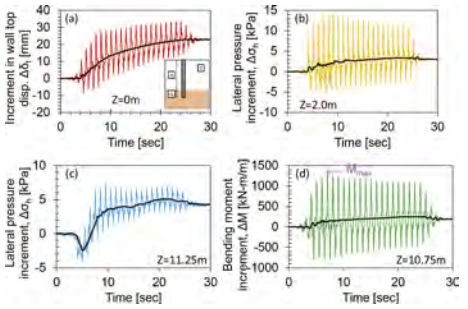

Figure 5. Example of time history of measured data (C1 shake 4).

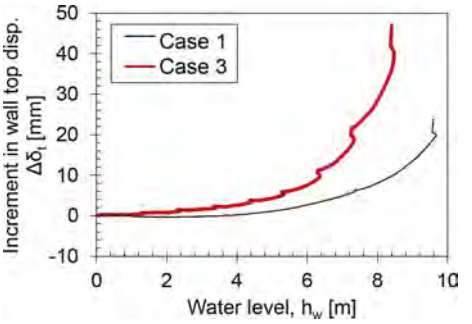

Figure 6. Increment in wall top displacement with water level (WR1).

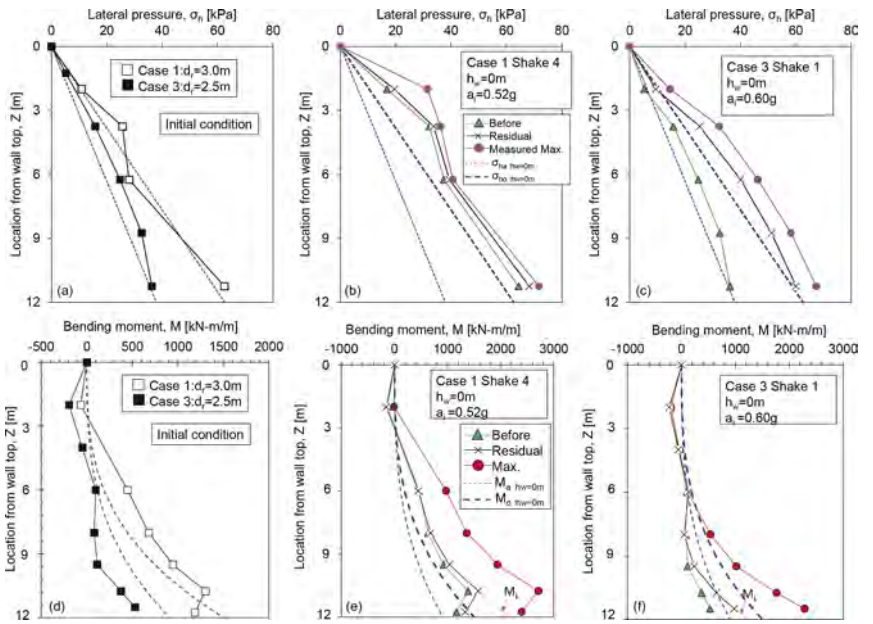

Figure 7. Lateral pressure and bending moment distribution with depths.

The variation of (δ_t) with the (A_i) is shown in Figure 8 (a). For similar (A_i), the (δ_t) observed for d_r=3.0m is smaller than the d_r=2.5m. Although case 1 has severe loading history yet, the overall displacement is almost half of case 3. So, reducing the (d_r) by 0.5m could significantly influence the (δ_t) behavior. Based on the wall and ground condition after the test, as shown in Figures 8 (b) and (c), no catastrophic failure can be confirmed.

The variation of the calculated ($P_{(residual)}$) and extrapolated ($M_{L(residual)}$) immediately after loading with the residual (δ_t) is shown in Figure 9. From the (σ_h) distribution diagram, the resultant thrust force (P) is back calculated. Figure 9 depicts an increase in ($P_{(residual)}$) and ($M_{L(residual)}$) with the increase in residual (δ_t) for both cases. However, for similar (δ_t), the observed ($P_{(residual)}$) and ($M_{L(residual)}$) is higher for d_r=3.0m than the d_r=2.5m. After the final loading, with a small increase in ($P_{(residual)}$) and ($M_{L(residual)}$), the (δ_t) increased significantly, especially for d_r=2.5m indicating the deterioration of the rock confinement. However, for d_r=2.5m, ($P_{(residual)}$) and ($M_{L(residual)}$) is still increasing, although the (δ_t) is >4%H, ensuring secured rock-wall confinement. The effective thrust force (P′) is normalized by the effective vertical force (Pv′) and plotted against the normalized wall top displacement in Figure 9 (b). The

active earth pressure coefficient (k_a) and a-rest earth pressure coefficient (k_o) are also shown in Figure 9 (b). Based on Figure 9 (b), the observed ratio after final loading is about 2 times the at-rest condition for both cases.

($P_{(max)}$) and ($M_{L(max)}$) calculated for the maximum condition are plotted against the (a_i) in Figure 10. Two reference lines are drawn for moment load and thrust force using Mononobe Okabe (1929) equation for dry condition. Based on Figure 10, during dynamic loading, the observed ($P_{(max)}$) and ($M_{L(max)}$) in wet conditions is larger than in dry conditions. For a large magnitude of the earthquake (a_i>0.5g), ($M_{L(max)}$) could be equal to or more than the actual yielding moment (0.65M_y observed by Kunasegaram and Takemura (2022) from single pile loading test) for d_r=3.0m. Therefore, structural (flexural) failure becomes more critical than the wall top displacement for large (d_r). For a_i>0.5g, in dry conditions, the observed ($P_{(max)}$) and ($M_{L(max)}$) becomes about 1.25 times the reference value.

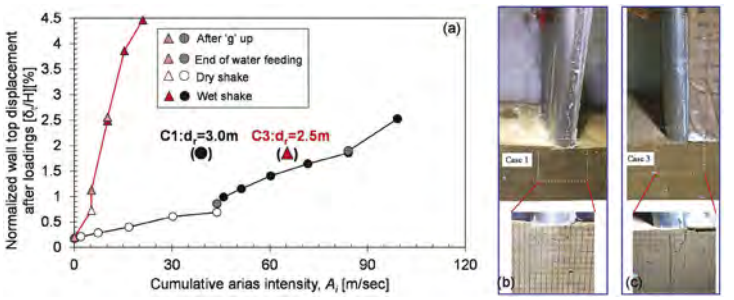

Figure 8. Variation of residual wall top displacement with arias intensity.

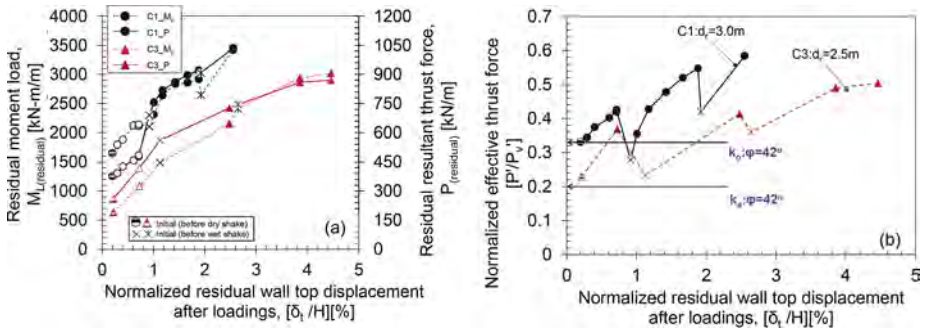

Figure 9. Variation with residual wall top displacement (a) Residual moment load and resultant thrust force (b) Ratio of effective thrust force (P´) and effective vertical thrust force (P_v´).

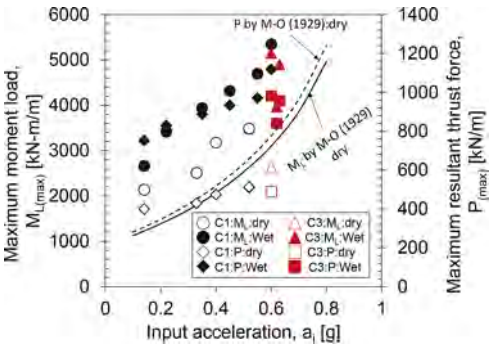

Figure 10. Variation of Maximum moment load and resultant thrust force with input acceleration.

4 CONCLUSIONS

From the centrifuge model tests on cantilever steel tubular pile wall embedded in soft rock, the following conclusions were drawn:

1. Although the applied loading conditions were more severer for the wall with embedment depth d_r=3.0m (1.5times pile diameter) than d_r=2.5m, this half meter d_r increment could significantly reduce the wall top displacement, 2.5%H for the former and 4.5%H for the latter. However, even for the large wall displacement with the small d_r, the wall-rock confinement could be ensured, not causing a catastrophic failure even after dynamic loading.
2. The observed moment load acting on the wall is greater for the large d_r than that of the small d_r. By the dynamic sequential loadings, the moment load (M_L) and thrust force (P) to the wall increased up to about 2 times those of at-rest conditions. Against the dynamic loadings in dry conditions with input acceleration over 0.5g, the maximum M_L and P became 1.25 times the corresponding value calculated from Mononobe Okabe (1929) equation.
3. The loads increasing with the increase of d_r could cause the wall bending moment to be larger than the yielding moment at a relatively small wall movement, suggesting that for the wall with large d_r, the structural (flexural) failure could be the most critical ultimate condition than the excessive wall displacement by the failure of soft rock.

ACKNOWLEDGEMENT

The authors gratefully acknowledge the individual advice and guidance provided by the members and advisers of the International Press-in Association TC1.

REFERENCES

Gopal Madabhushi, S.P. and Chandrasekaran, V.S., 2005. Rotation of cantilever sheet pile walls. *Journal of geotechnical and geoenvironmental engineering*, *131*(2): 202–212.

Japanese Technical Association for Steel Pipe Piles and Advanced Construction Technology Center (JTASP-PACTC) 2007. *Cantilever Steel Piles Retaining Wall-Design Manual:* 138p. (in Japanese).

Kitamura, M. and Kitamura, S., 2018. Cantilevered Road Retaining Wall Constructed of 2,000 mm Diameter Steel Tubular Piles Installed by the Gyro Press Method with the GRB System. *First International Conference on Press-in Engineering*, pp. 437–444.

Kunasegaram, V. and Takemura, J., 2021. Deflection and failure of high-stiffness cantilever retaining wall embedded in soft rock. *International Journal of Physical Modelling in Geotechnics*, *21*(3): 114–134.

Kunasegaram, V. and Takemura, J., 2022. Mechanical Behaviour of Laterally Loaded Large-Diameter Steel Tubular Piles Embedded in Soft Rock. *Geotechnical and Geological Engineering*, pp.1–39.

Mononobe, N. & Matsuo, H. (1929). On the determination of earth pressure during earthquake. *Proc. 2nd World Engng Corm*. (9):177–185.

Padfield, C.J. and Mair, R.J., 1984. Design of retaining walls embedded in stiff clay, CIRIA Report R104. *London, UK: Construction Industry Research and Information Association*.

Shafi, S.M., Takemura, J., Kunasegaram, V., Ishihama, Y., Toda, K. and Ishihara, Y., 2021, June. Dynamic behavior of cantilever tubular steel pile retaining wall socketed in soft rock. *Proceedings of the Second International Conference on Press-in Engineering 2021*, *Kochi*, *Japan*, pp. 324-333. CRC Press.

Takemura, J., 2021, June. State of the art report on application of cantilever type steel tubular pile wall embedded to stiff grounds. *Proceedings of the Second International Conference on Press-in Engineering 2021*, *Kochi*, *Japan*, pp. 27–41. CRC Press.

Smart Geotechnics for Smart Societies – Zhussupbekov, Sarsembayeva & Kaliakin (Eds)
© 2023 The Author(s), ISBN 978-1-003-29912-7
Open Access: www.taylorfrancis.com, CC BY-NC-ND 4.0 license

Accuracy of determining pile capacity by static and dynamic methods in difficult ground conditions in Astana

A.R Omarov, A.Zh. Zhussupbekov, S.T. Mussakhanova & A.B. Issakulov
L.N. Gumilyov Eurasian National University, Astana, Kazakhstan

ABSTRACT: The article presents the results of the dynamic (DLT), static (SLT) and a new method of Pile Dynamic Analyze (PDA) tests of the reinforced concrete piles with rectangular section 30 x 30 cm and length 12m driven piles for problematic soil conditions of the "New Mosque" in Astana city. Field test are carry out in accordance with requirements GOST 5686, for definitions of bearing capacity of the piles in accordance with requirements SP RK 5.01-03-2013 and ASTM D4945. The test method is similar to that used on driven piles with the monitoring of hammer blows and subsequently analyzing the pile response to the stress wave propagation. A separate hammer or drop weight is usually brought to site to allow the dynamic load to be applied to driven pile. According to the results of tests were determined the possible depth of penetration and bearing capacity of driven piles. This geotechnical investigation is important for understanding the soil-pile interaction on difficult and problematical soil ground conditions related to the construction site.

1 INSTRUCTIONS

The congregation was built on a land plot of 10 hectares. The total area of the premises is 68,062 m². The total capacity of the mosque is 235 000 people, of which: 30 thousand men and 5 thousand women can pray simultaneously in the halls; 200 000 people can pray in the open air: 170 000 in the mosque yard and 30 000 in the area of the podium and stage. The mosque has four minarets 130 m high (see Figure 1).

Figure 1. Construction site "New Mosque" in new Capital of Kazakhstan.

DOI: 10.1201/9781003299127-202

Each minaret consists of five parts symbolizing the five pillars of Islam: shahada, namaz, fasting in the month of Ramadan, zakat and hajj. One of the minarets in the left wing is open to visitors and tourists can take an elevator up to the observation deck. The height of the big dome is 83.2 m and the diameter is 62 m. The entrance door of the mosque is 12.4 m high and weighs 1.5 tons and is handmade of hardwood. On the wall on the qiblah side are carved the 99 names of Allah, illuminated with golden light. The mosaic wall is 100 m long and 22.4 m high. The mosaic consists of 25 million glasses of different colors. The total area of the carpet is 15.525m^2, the thickness of the carpet is 15 mm. In the center of the main hall under the dome hangs a crystal chandelier, 27 m in diameter and weighing 20 tons.

The chandelier is made of 1,360,890 crystal fragments. Also in the four corners of the hall hang four chandeliers, each 8m in diameter. The first and second floors of the mosque have classrooms, a conference hall, a wedding hall, a Quranic reading hall, a TV studio, offices, staff rooms, stores, a museum and technical premises in addition to prayer rooms. The underground floor has a banquet hall with 440 seats, a closed parking lot with 405 seats, a lobby, a restroom, technical and ritual services area, sacrificial offering area and other rooms. In terms of mosque capacity, the Republican Chief Mosque in Astana is one of the 10 largest mosques in the world.

2 THE RESULTS OF ENGINEERING AND GEOLOGICAL RESEARCHES OF THE SITE

On the basis of field visual description, confirmed by the results of static sounding and laboratory tests of soils, it was found that to a depth of 17.0-27.0m in the geological structure of the site take part alluvial Quaternary deposits, represented by loam, sand, gravel and gravel soils, as well as eluvial soils of the Lower Carboniferous, represented by loam sands, sands, gravel and rubble soils. According to the drilling data, the groundwater on the survey area is at a depth of 3.00 - 3.60m. Under the conditions of the natural regime, the groundwater level is subject to seasonal fluctuations: the minimum standing is observed in March, the maximum standing is at the beginning of May. The amplitude of level fluctuations in the studied area was 1.0-1.5 m. It is recommended to take the level at 1.3 m higher than the established one for the period of surveying as the predicted one. Groundwater is fed mainly by infiltration of atmospheric precipitation, meltwater and floodwater. The area of aquifer spreading serves as the feeding area.

According to the results of chemical analyses, groundwater is characterized as sodium chloride, very hard, neutral, slightly alkaline, slightly acidic, slightly mineralized, brackish. In relation to steel structures ground water is corrosive. The degree of aggressiveness of ground water in relation to the cable lead sheathing is medium and high, in relation to the cable aluminum sheathing - high.

In relation to concrete of W4 grade, ground water is non-aggressive and slightly aggressive, in well 306-18 highly aggressive on Portland cement, in relation to reinforced concrete structures - moderately aggressive.

3 METHODOLOGY FOR LOAD TESTING OF PILES

3.1 *Static load tests by GOST*

Static load tests carried out for four piles on the construction site (see Figure 2). The measured relationships between the pile head load, L, and the head settlement, S, of the test piles are shown in Figure 3. It is seen from Figure 4 that the load-settlement curves of piles No.4, 9, 13 and No.14 are almost identical, having an ultimate shaft capacity of 1400 kN (Zhussupbekov *et, al* 2015 and Zhussupbekov *et, al* 2017 and Zhussupbekov *et, al* 2019).

In Kazakhstan, a safety factor of SLT is 1.2. Therefore, the design value of the allowable piles capacity, Q_d, was estimated to be Q_d= 1400/1.2=1167kN.

Figure 2. Test piles static loading method SLT by GOST.

According to SLT result, the load-settlement diagrams were drawing (see Figure 3) and compared with PDA results (see Figure 5).

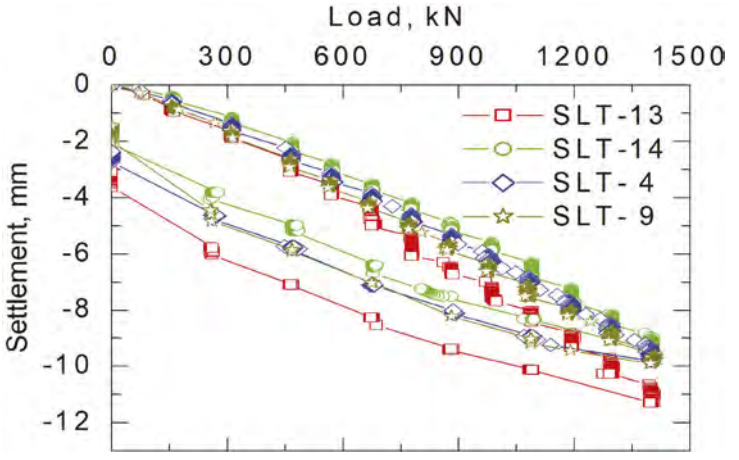

Figure 3. Results of Static load tests by GOST.

3.2 *Dynamic load test by ASTM (DLT - PDA)*

In Kazakhstan carry out dynamic test with using many types of pile driving machine hammers. Before beginning test pile driving on its surface painted whole length of piles through 1 m, but with last meter through each 0.1 m shown.

Pile driving was performed using the piling installation «Junttan PM-25" with hydraulic hammer HHK-7A with a mass of 7000 kg of the hammer and headband weight equal to 990 kg.

Figure 4 presents the monitoring results of PDA test showing pile dynamic compression and tension stresses, static pile capacity and blow counts versus pile penetration depth. CAPWAP analysis results (Figure 4) that include plots of measured pile head data obtained under the hammer blows from the end of driving and associated simulated pile head and toe static load-movement relationships are presented in the Figure 5.

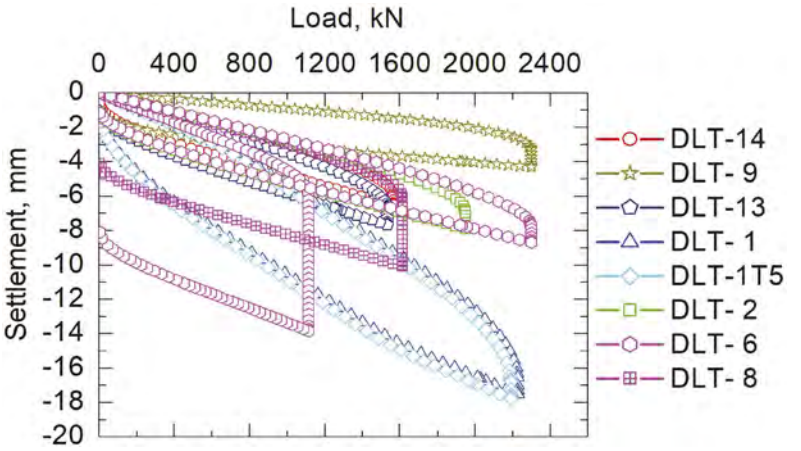

Figure 4. Results of Dynamic load tests by ASTM.

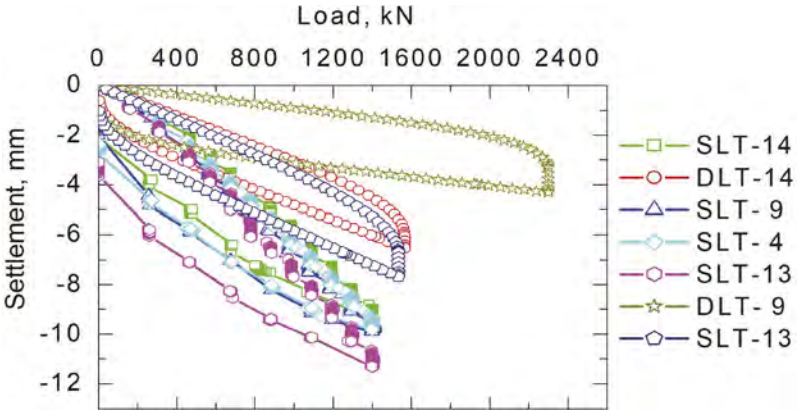

Figure 5. Results of DLT and SLT.

4 CONCLUSIONS

On the construction site of the main mosque hall of the facility "The main mosque for 30,000 places in Astana" static and dynamic tests of driven piles in the amount of 8 pieces were carried out.

The carrying capacity of the piles sunk to a depth of 7.5 m, according to the results of dynamic tests was 1600 kN.

The bearing capacity of the piles sunk to a depth of 7.5 m, according to the results of static tests was 1400 kN.

Allowed load on the pile, taking into account the coefficient of reliability $\gamma_k = 1.2$ in accordance with paragraph 3.10. SNiP RK 5.01.-03-2002 "Pile foundations", should be taken equal to 1176 kN.

DLT (PDA-ASTM) dynamic test shown more coincide with SLT result than traditional DLT test (GOST).

FUNDING

This research was funded by the Science Committee of the Ministry of Science and Higher Education of the Republic of Kazakhstan. (Grant No. AP13268718).

REFERENCES

GOST 5686–94 (1994) "Methods for field testing by piles".
SNIP RK 5.01-03-2002 (2002) "Pile foundations".
SNIP RK 5.01-01-2002 (2002) "Soil grounds of the buildings".
Zhussupbekov A.Zh., Syrlybaev M.K., Lukpanov R.E., Omarov A.R. (2015) The applications of dynamic and static piling tests of Astana. 15th Asian Regional Conference on Soil Mechanics and Geotechnical Engineering, pp. 2726–2729.
Zhussupbekov A., Omarov A., Morev I., Ashkey E., Borgekova K., Popov V. (2017) Analysis results of static and dynamic loads tests of pile foundations in constructions site of Expo-2017, Astana, Kazakhstan. ICSMGE 2017-19th International Conference on Soil Mechanics and Geotechnical Engineering, pp. 3079–3082.
Zhussupbekov A., Chang D.-W., Utepov Y., Borgekova K., Omarov A. (2019) Estimating the Driven Pile Capacities for COF Project in West Kazakhstan. Soil Mechanics and Foundation Engineering, 56 (2), pp. 121–127.
ASTM D4945–89 (1989) Standard Test Method for High-Strain Dynamic Testing of Piles.

Smart Geotechnics for Smart Societies – Zhussupbekov, Sarsembayeva & Kaliakin (Eds)
© 2023 The Author(s), ISBN 978-1-003-29912-7
Open Access: www.taylorfrancis.com, CC BY-NC-ND 4.0 license

Analysis of interaction of boring CFA micro piles with problematic soil conditions Aksai, Kazakhstan

A.Zh. Zhussupbekov, A.R. Omarov, S.T. Mussakhanova & A.B. Issakulov
L.N. Gumilyov Eurasian National University, Astana, Kazakhstan

ABSTRACT: This paper presents the complex analysis of diverse field loading tests of four with diameter 600 mm CFA bored piles. Four static compression pile (by ASTM D1143) loading tests were carried out on the construction site. Static loading tests applied load to a deep-foundation element gradually for measuring foundation settlement. This test is used to measure the axial deflection of a vertical deep foundation when loaded in static axial compression. This vertical compression pile maintained load test is usually carried out to ensure the structural and geotechnical soundness of the pile and also to predict settlement of other piles. Applied load and head movement are measured for static axial compression load tests. The load-settlement and the load-displacement curves were obtained from field tests. Comparison of bearing capacity of bored piles with different length in problematic soil conditions of West Kazakhstan were discussed in this paper. The analysis showed that the bearing capacity of bored piles with different lengths corresponds to the design requirements. These investigations are important for understanding of soil-pile interaction on problematical soft soils ground of Aksai, Kazakhstan.

1 INTRODUCTION

The Karachaganak field is one of the world's largest oil and gas condensate fields located in northwest Kazakhstan and covering an area of more than two hundred eighty square kilometers. The Karachaganak field is located in a remote and challenging working environment with the ambient temperature ranging from minus forty degrees Celsius in winter to plus forty degrees in summer. The field, the top of which is located at a depth of around three thousand five hundred meters, is some one thousand six hundred meter thick and very complex and unique. Karachaganak Field is a gas condensate field in Kazakhstan. It is located about twenty three kilometers east of Aksai (Aksai) in the northwest of Kazakhstan. The field was once a massive Permian and Carboniferous reef complex covering an area thirty by fifteen square kilometers. Karachaganak field was discovered in northwestern Kazakhstan by Uralskneftegas-geologia in 1979 and first produced by Karachaganak in 1984. The shareholder group of ENI-Agip, BG Group, Texaco, and Lukoil operates the field under a 40-yr production-sharing agreement that was signed with the Republic of Kazakhstan in November 1997 to optimize technical and economic recovery. In the field, 252 wells have been drilled, with 163 available for production. An ongoing workover program has restored previously declining production to historic maximum levels.

The current work aims at investigating the ability for the enhancement of clay using CFA piles. The development in bearing capacity has been determined based on field tests carried out including top down static loading tests and pull out load tests. Moreover, the current work com-peres the cost between using normal piles in site project and use improvement of soil by use CFA piles. The paper suggests a method to validate the enhancement in bearing capacity of clay improved with CFA piles.

DOI: 10.1201/9781003299127-203

2 ENGINEERING-GEOLOGICAL CONDITIONS OF THE CONSTRUCTION SITE

In geological structures of a site of researches, take part (GOST 20276–99, 1999):

EGE-1: Loam-heavy, dusty, yellowish-brown, brown color, lumpy, weakly wet, from solid to semisolid consistence, setting;

EGE-2: Clay-light, brownish black, yellowish-brown and brown color, lumpy, weakly wet, from solid to semisolid plastic consistence, setting;

EGE-4: Clay-light, dusty, brown and light brown color, lumpy, weakly wet, from solid to tough plastic consistence;

EGE-5: Clay reddish-brown, dark brown color with black free deigns, solid weakly wet, from solid to tough plastic consistence;

EGE-6: Clay-light, dusty, greyish-brown, dun color with free designs of grey color, average density, weakly wet, wet, from semisolid to tough plastic;

EGE-7: Clay-light, dusty, dun, grey, dark grey color, average density, wet, tough plastic.

Results of physic-mechanical properties of soil the bases of construction site are resulted from top to down in Table 1 (Zhussupbekov *et.al* 2019).

Table 1. Standard and design values of physical and mechanical characteristics of soils.

	Soil Consistency g/cm^3	Specific cohsion MPa	Angle of internal friction, deg.	Modulus of deformation	De sign resistance, kPa
N EGE	ρ	c	ϕ	E	R_0
1	1.73	–	–	9.34	400
	1.96	0.006	20	4.4	200
2	1.77	–	–	7.39	400
	1.97	0.008	19	4.78	200
4	1.92	–	–	8.08	400
	2.03	0.015	19	7.10	250
5	1.94	0.029	17	7.59	250
	2.01	–	–	–	–
6	1.96	0.026	18	8.09	250
	2.01	–	–	–	–
7	1.98	0.020	19	8.33	250
	2.03	–	–	–	–

3 SOIL FIELD TEST BY PLATE LOAD TESTING

Plate Load Test is a field test for determining the ultimate bearing capacity of soil and the likely settlement under a given load. The Plate Load Test basically consists of loading a steel plate placed at the foundation level and recording the settlements corresponding to each load increment. The test load is gradually increased till the plate starts to sink at a rapid rate. The total value of load on the plate in such a stage divided by the area of the steel plate gives the value of the ultimate bearing capacity of soil. The ultimate bearing capacity of soil is divided by suitable factor of safety to arrive at the value of safe bearing capacity of soil. PLT tests by loading a plate with a diameter of 300 mm are made in accordance with requirement GOST20276 (1999) or ASTM D1194. The plate loading test (further PLT) was carried out in the workings at a depth of 1.2 m while maintaining the natural addition of soil, with a flat die 300 mm in diameter, to determine the elastic modulus of deformation (see Figure 1).

Testing with a flat PLT consisted in the fact that the stamp was placed on the bottom of the pit, on the previously cleaned and leveled surface of the ground, after which a step-by-step loading was performed on the stamp. The subsequent stage of loading was carried out after the decay of the deposit from the previous loading. As a support, beams fixed on both sides on the

anchor piles were used. Totally three tests one test in Plate Load Test 1 (further PLT–1), second test in Plate Load Test 2 (further PLT–2) a depth of 1.2 m had been made. The load intensity and settlement observation of the plate load test are plotted. The figure shown below shows a set of typical load settlement curves. Figure 1 shown the results the pressure-settlement diagrams of Plate load tests of PLT–1, PLT–2 and PLT–3.

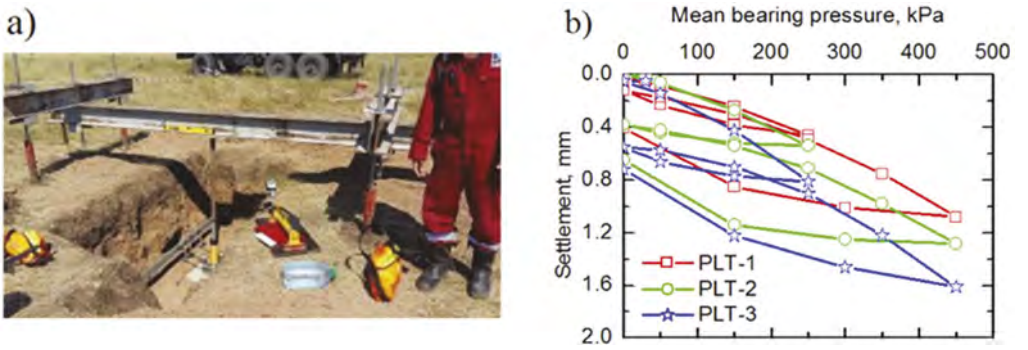

Figure 1. Plate load test: (a) Field test for determining the bearing capacity of the soil; (b) load-settlement curve (PLT–1, PLT–2 and PLT–3).

Modulus of deformation of soils in PLT–1 – 108,8MPa, PLT–2 – 86,1 MPa and PLT–3 – 61,7 MPa depth of 1.2 m.

4 STATIC LOADING PILE TEST (SLT BY ASTM D1143)

The CFA construction sequence is comprised of five stages in Figure 2:

- Stage 1. The digging tip of the auger is fitted with an expendable ca);
- Stage 2. The auger is drilled into the ground to the required depth;
- Stage 3. Concrete is pumped through the hollow stem, blowing off the expendable cap under pressure;
- Stage 4. Maintaining positive concrete pressure, the auger is withdrawn all the way to the surface;
- Stage 5. Reinforcement is placed into the pile up to the required depth.

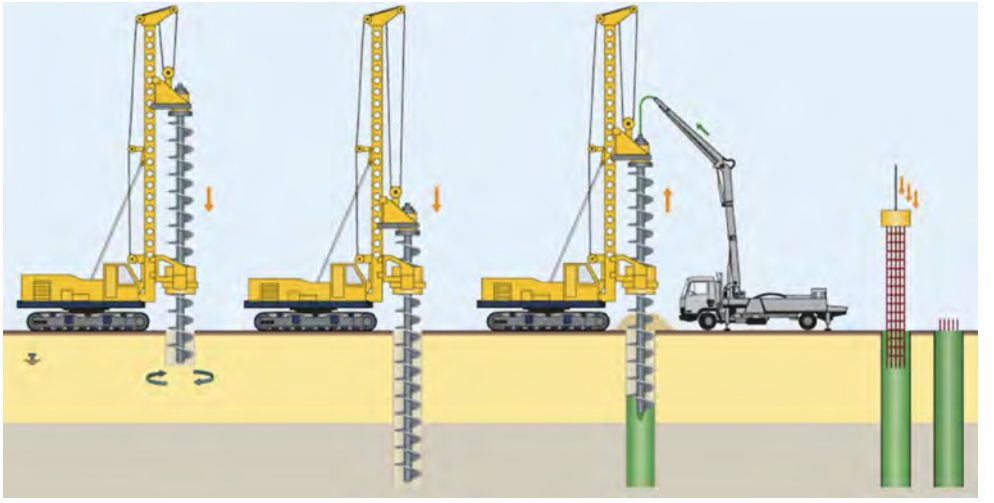

Figure 2. Technological process of CFA piles.

Bored piles, which have diameter of 600 mm and from depths 15.53 to 21.85 m have been executed at the Caspian Sea for more shipments platforms construction site (Zhussupbekov *et.al* 2016).

Static Loading Pile Test (further SLT) one of the more reliable field tests in analyzing pile bearing capacity. SLTs carried out for four piles on the construction site.

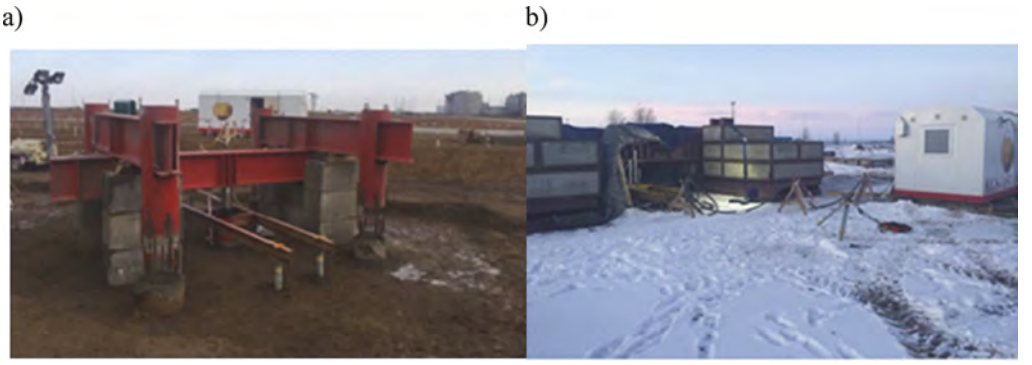

Figure 3. Field pile test by SLT (ASTM): (a) anchors pile system and (b) loading platform system.

It is seen from Figure 4 that the load-settlement curves of four piles SLT-1, SLT-2, SLT-3 and SLT-4 are almost identical, having an ultimate shaft capacity of 1050 kN for SLT-3 and SLT-4, and pile number SLT-2 to loading - 1310 kN and pile number SLT-1 to loading - 1975kN (Zhussupbekov & Omarov, 2016).

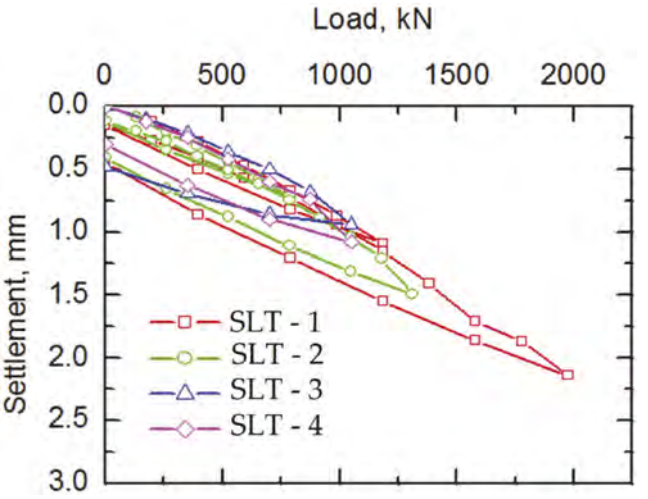

Figure 4. Load-settlement curves of four piles.

Pile static loading tests (top down) were performed on bored piles numbers: SLT-1, SLT-2, SLT-3 and SLT-4, which are with depth from 15.53 and 21.85. In SLT testing, the test load on the pile is specified for one and two cycles (one 1050 kN (for SLT-3,-4) and two cycles from 786 kN to 1310 kN (for SLT-2) and from 1185kN to1975kN (for SLT-1), respectively). Loading and unloading was carried out in the following sequence (for SLT-1): 0, 25, 50, 75, 100, 125, 150, 100, 50, 0, 25, 50, 100, 125, 150, 175, 200, 225, 250, 200, 150, 100, 50 and 0% of design. In the first cycle, the experimental pile was loaded to 150% of the design value (to 1185 kN); during

the second cycle, to 200% (maximal to 1975 kN). The hold time while loading was 60 min; while unloading −15 min. It took 300 min, respectively, to attain peak load (ASTM D1143/D1143M – 07, 2013). Table 2 presents a comparative analysis of the bearing capacity of piles, obtained by different method in this research (Zhussupbekov *et.al* 2016).

Table 2. Results of field piling static loading tests (top down load).

№	Pile numbers	Pile length, m	pile Diameter, mm	Overpressure loads on the pile, kN	Settlement at maximum pile load, mm
1	SLT-1	20.50	600	1975	2.14
2	SLT-2	15.53	600	1310	1.48
3	SLT-3	21.85	600	1050	0.94
4	SLT-4	21.72	600	1050	1.08

5 CONCLUSION

The results of the axial compression loading tests performed in soft to firm or stiff clays demonstrated the suitability of CFA bored pile foundations. The results of the loading testing program confirmed that the CFA bored pile is a viable deep pile foundation option for construction site Oil and Gas in remote areas Kazakhstan and demonstrated their advantages.

The results of the full-scale load tests are also used to validate the theoretical model used for CFA technology bored pile design installed in soft and problematical soils of Kazakhstan.

The bearing capacity of CFA technology boring piles according to the results of shown Table 2 amounted to be maximal load to (top down load, L) 1975kN, settlement (S) from 0.94 mm to 2.14 mm. These investigations are important for understanding of behavior of piles on problematical soil ground of Kazakhstan.

6 FUNDING

This research was funded by the Science Committee of the Ministry of Science and Higher Education of the Republic of Kazakhstan. (Grant No. AP13268718).

REFERENCES

GOST 20276-99 (1999) Soils. Field methods for determining the strength and strain characteristics.

ASTM D 1194. Standard Test Method for Bearing Capacity of Soil for Static Load and Spread Footings.

Zhussupbekov A, Iwasaki Y, Omarov A, Tanyrbergenova G, and Akhazhanov S. (2019). Complex of static loading tests of bored piles. *International Journal of GEOMATE*, 16(58), 8–13.

ASTM D1194 (1994) Standard Test Method for Bearing Capacity of Soil for Static Load and Spread Footings (Withdrawn 2003).

Zhussupbekov A.Zh., Lukpanov R.E., Omarov A.R. (2016) Experience in Applying Pile Static Testing Methods at the Expo 2017 Construction Site. *Journal of Soil Mechanics and Foundation Engineering*. Vol. 53, (4), pp. 251–256.

ASTM D1143/D1143M – 07 (2013) Standard Test Methods for Deep Foundations Under Static Axial Compressive Load.

Zhussupbekov A., Omarov A. (2016). Modern Advances in the Field Geotechnical Testing Investigations of Pile Foundations. *Procedia Engineering*, Vol. 165, pp. 88–95.

Zhussupbekov, A.Z., Lukpanov, R.E., Omarov, A.R. (2016) Bi-directional Static Load testing. *Fourth Geo-China International Conference (Geotechnical Special Publication)*. Shandong, China. pp. 35–42.

Smart Geotechnics for Smart Societies – Zhussupbekov, Sarsembayeva & Kaliakin (Eds)
© 2023 The Author(s), ISBN 978-1-003-29912-7
Open Access: www.taylorfrancis.com, CC BY-NC-ND 4.0 license

Analysis of interaction of precast concrete joint piles with problematic soil conditions Prorva

A.R. Omarov, A.Zh. Zhussupbekov, S.T. Mussakhanova & A.B. Issakulov
L.N. Gumilyov Eurasian National University, Astana, Kazakhstan

ABSTRACT: The Cargo Offloading Facility is an essential strategic project for the expansion of oil fields. The Cargo Offloading Facility is located along the quay and represents a special reinforced concrete surface supporting large cranes needed to unload both bulky and general cargo. According to the design drawings, the Cargo Offloading Facility construction site was planned by installing precast concrete joint piles. Investigation of the interaction of precast concrete joint piles used for the first time on construction site in Kazakhstan with complex soil conditions. In this paper the joint piles with the cross section of 400x400 mm and with pin-joined connection were considered and their interaction with the soil of Western Kazakhstan will be analyzed. Evaluation of bearing capacity of PCJP by interpretation methods of field test data, computational methods using the APILE analysis computer program and the Kazakhstan stand-ard, as well as a dynamic PDA (pile driving analyzer) method while piles driving.

1 INTRODUCTION

Kazakhstan is the world's ninth biggest country by size and the largest landlocked country, and it is the essential transportation hub between Russia, Central Asia, China and Europe. Cargo offloading facility (hereinafter – COF) has been built in the north-eastern part of the Caspian Sea in Western Kazakhstan for the development of transport infrastructure. This facility was started as a part of the Future Growth Project, which will enable the expansion of the large Tengiz oil field, where more than 23 thousand piles were installed. In 2017, a new cargo transportation route has been constructed from the Northeast Caspian Sea to Tengiz for creating access channel to the new facility on the port of Prorva, which designed for offloading the heavy vessels and barges delivered by marine transport. The construction of a cargo offloading facility is considered unique and is an important strategic project to expand oil fields in West Kazakhstan (see Figure 1).

The expediency of using pile foundations is explained by the need to ensure a high bearing capacity of structures. Their effectiveness essentially depends on the accuracy of determining the bearing capacity of the pile and the design load on it. Standards for the design of pile foundations are intended to determine their bearing capacity by an analytical method using reference generalized tables or according to field test data of a loaded pile by static or dynamic load. Before applying these methods, engineering and geological surveys are required to determine the indicators of the properties of each engineering-geological element in contact with the pile. The survey also allows the designer to assign the parameters of the piles and calculate their bearing capacity, which is traditionally considered to consist of the soil resistance under the tip and along the lateral surface of the pile (Zhussupbekov et. Al 2015).

According to the design drawings, COF construction site was planned to be installed by PCJP. This was the first experience of installing such type of piles in Kazakhstan. Applying PCJPs for the first time demanded a comprehensive approach. Therefore, it was decided to

DOI: 10.1201/9781003299127-204

Figure 1. Location of cargo offloading facility.

first conduct their tests in a pilot site. In this study, the pilot site and COF site are marked as A and B (see Figure 2).

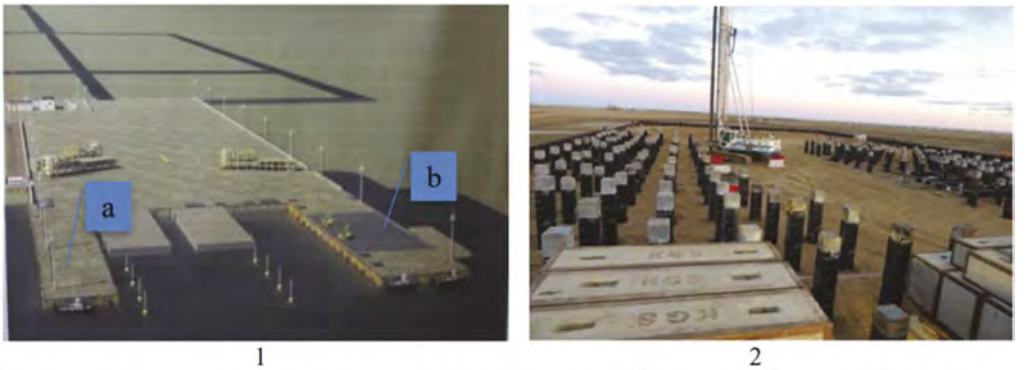

1 2

1 – scheme of COF in the future: a – pilot site; b – COF; 2 – construction site of COF

Figure 2. Cargo offloading facility.

In this paper, the work of precast concrete joint piles with soil of West Kazakhstan was investigated. This type of pile is one of the first products of Kazakhstani production that uses connecting material, and undoubtedly is of practical interest for modern construction of Kazakhstan. However, the application of dynamic tests by Pile Driving Analyzer (hereinafter – PDA) during the driving of precast concrete joint piles is of scientific interest .

2 ENGINEERING-GEOLOGICAL STRUCTURE OF THE CONSTRUCTION AREA

The project area is located along the east coast of the North East Caspian Sea, both onshore and offshore, near the Prorva oilfield, Kazakhstan. The project area is situated on the Northern Caspian Shelf. At present the North Caspian Sea has a limited water depth (maximum 5 to 8 m). The water level in the Caspian Sea depends on a balance between the inflow of river water and evaporation (Zhussupbekov & Omarov 2016).

This has resulted in large variations in sea level in the past. In the sedimentary succession within the planned construction site and with regard to lithology, depositional setting, structure, compositional petrology, state and physical and mechanical properties of sediments and with regard to the State Standard (GOST) 25100-95 the following geotechnical elements (GE) were specified. The physical and mechanical characteristics of soils at construction site A and B shown in the Tables 1 and 2 (Zhussupbekov & Omarov 2016).

Table 1. Physical and mechanical characteristics of soils at construction site A.

Layer thick ness, m	Geological formation	Soil type	General Consistency	γ_{sat}, kN/m^3	φ, deg	Su, kPa	E
0.5	new Caspian	Silt, slightly organic, calcareous	soft to firm	19.3	29.4	-	2.750
4	new Caspian	Sand, silty, calcareous	Medium dense to dense	20.2	31.5	-	30.000
4	Late Khvalynian	Clay, silty, calcareous	stiff	19.1	24.7	80	2.000
19	early Khvalynian	Clay, silty, calcareous	very stiff	20.2	24.7	150	2.000

Table 2. Physical and mechanical characteristics of soils at construction site B.

Layer thick ness, m	Geological formation	Soil type	General Consistency	γ_{sat}, kN/m^3	φ, deg	Su, kPa	E
4	new Caspian	Sand, silty, calcareous	Medium dense to dense	20.2	31.5	-	2.750
4	Late Khvalynian	Clay, silty, calcareous	stiff	19.1	24.7	80	30.000
4	inter Khvalynian	Sand, silty, calcareous	very dense	20	31.8	-	40.000
5	early Khvalynian	Clay, silty, calcareous	very stiff	20.6	23.8	150	4.000
10	early Khvalynian	Clay, silty, calcareous	very stiff	20.2	24.7	150	2000

Soils building up a geological environment at a depth down to 10 m from ground surface are salinized; salinity level is high; at sulfate nature of salinity they contain increased amount of carbonates, gypsum and insignificant amount of organic matters (humus). Loamy silt relates to slightly saturated clayey soil group; it possesses thixotropic properties Light silty clay possesses slight degree of swelling. The ground waters relate to the weak brine group in upgraded version. Water-and-soil environment possesses a medium degree of aggressivity in reference to W8 graded concrete. Soils possess high aggressivity to low-allowed and carbon steel.

3 INSTALLATION OF PRECAST CONCRETE JOINT PILES

The leader boreholes were made before installation of piles. The leader well is a well created for the subsequent immersion of a precast concrete pile. Leader wells are guide holes in the ground, greatly facilitating the process of sinking of the piles. The leader drilling allows piles to sink in vertical direction to a certain depth to reduce the noises occurred during the pile driving [111]. The boreholes were made with preaugering and pre-drilling methods. The pre-augering was

executed by clockwise rotating auger insertion up to designated depth and by removing rotating auger in counterclockwise direction. With this method, a few amount of soil was removed from borehole by a fully hydraulic, self-erecting drilling rig Soilmec CM-70 (see Figure 3a). In the pre-drilling method removing was performed without rotation by Rotary Drilling Rig Bauer-28 (see Figure 3b) (Zhussupbekov & Omarov 2017).

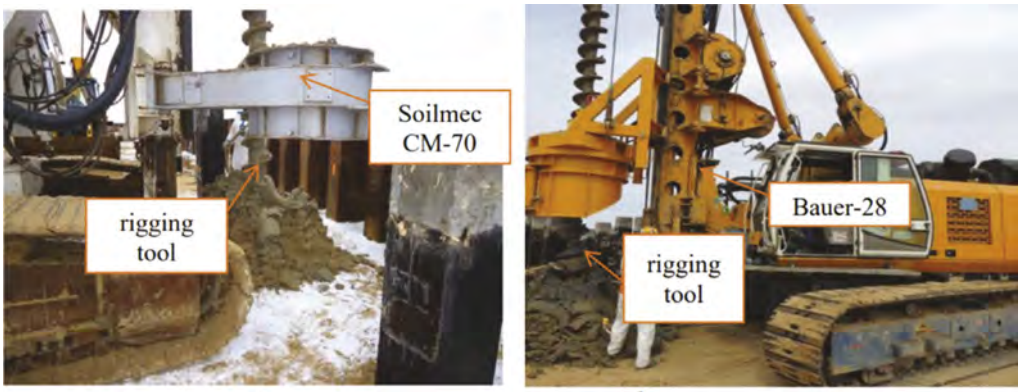

a – pre-auger by Soilmec CM-70; b – pre-drilling by Bauer-28

Figure 3. Pre-auger and pre-drilling processes.

The Junttan PM 25HD is a medium weight piling rig designed for pile driving steel and concrete piles. The rig has excellent stability and wide leader inclination angles. The recommended hammer weight is from 5000 to 9000 kg and the maximum pile length is 24 meters. The rig has proven productivity. The telescopic leader ensures easy and fast handling of piles. Top pile driving performance is guaranteed with Junttan hydraulic hammers. Piles were coated by corrosion protection material (bituminous) and marked by cross-lines every 0.25 m. (see Figure 4).

a – coated PCJP; b – installation of marked coated piles in boreholes

Figure 4. PCJP pile with protective coating and marked every 250 mm.

The head of bottom segment and the bottom of upper segment had steel plates "Emeca 3-Minute Splice", which had jointing and locking mechanisms. Two female (socket) and two male (stud) locking mechanisms are welded on opposite sides of each base plate (see Figure 5).

Figure 5. Two female (socket) and two male (stud) locking mechanisms.

Locking mechanisms are welded to long pieces of reinforcing bar. Two segments of PCJPs were gathered by the four locking pins (see Figure 6) (Zhussupbekov et.al 2018).

Figure 6. Installation of two segments of PCJP.

To ensure the integrity of precast concrete joint piles from destruction in the process of driving parts, a type of equipment was calculated with an effective impact energy according to the formula recommended in the SNiP and in the one-dimensional Wave Equation Analysis program. According to the results of calculations in this construction site, it was decided to use driving equipment with a hammer 9 ton for driving 27.5 m of precast concrete joint piles, for installation of 25.5 m piles – was used 7 ton equipment.

The leader drilling technology with pre-augering and pre-drilling methods for time saving, preserving of pile head was applied before the installation of precast concrete joint piles.

Protected from corrosion precast concrete joint piles were composed of upper segment with the length of 16.0 m and upper segment with the length of 11.5 m and 9.5 m on test area. During the driving piles nylon and wooden plates were used for protection pile head from

structural failure. The locking and jointing mechanism of two segments of pile were connected by the four pins (Zhussupbekov et.al 2019).

Dynamic tests were carried out on two parts of joint reinforced concrete piles separately, and the results of the bearing capacity were determined automatically by the program as an average value. After driving the first part of the joint pile, a pair of accelerometers and strain transducers were attached to the second part of the pile at 8 meters, the data of the piles were entered into the program, and the PDA dynamic tests were continued. After the execution of field part of dynamic test, selected blow data (often one of the last blows) are analyzed in the computer program Case Method &iCAP® in the software PDIPLOT2, Ver 2016.1.56.3.

CAPWAP (Case Pile Wave Analysis Program), which is based on wave equation. Pile model and soil model is initiated with measured value of pile velocity (Vmeasured(t)). The result of CAPWAP analysis is calculated response (Fcalculated(t)), which in the case of perfectly accurate pile and soil model data should be completely identical with the measured force curve.

Static loading tests of PCJPs were carried out according to the requirements of ASTM D1143 – Standard Test Methods for Deep Foundations Under Static Axial Compressive Load. Testing platform (see Figure 7) presented itself system from steel, which consists of metallic beam and 2 load platforms located on equidistant distances from the center main beams. For platforms used concrete blocks, which pack on one platform by total weight 200-205 (250) tons.

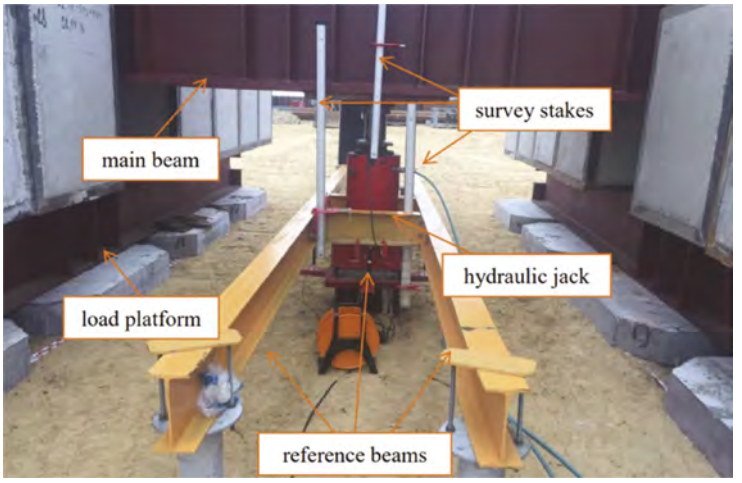

Figure 7. Testing platform for static compression load test.

As reference frame, two H-beams with h = 20cm and length 5.3 m were used which bolted with clamp to screw piles BAU 114*4*2000 drilled in soil with depth 1.5 m. (which were placed on either side of the pile on steel support brackets bolted on piles). The two beams acted as reference for the displacements sensors (see Figure 8a). The reference frames, was regularly checked with an optical level instrument to detect any movements and cross reference the movement of the pile (see Figure 8b).

The load and deflection readings are collected by a data logger, which simultaneously downloads data to a PC. Data is simultaneously displayed and stored for printing. With the concern of limit load, three SLTs were conducted with maximum load of 3278 kN at construction site A. For working load concern, four tests were conducted with maximum load of 1638 kN at construction site B (Zhussupbekov et.al 2019).

Tables 3 and 4 list the pile load test information at these construction sites respectively.

Three SLTs were conducted with maximum load of 3278 kN at construction site A. Figure 9a shows the load-settlement curves obtained from these tests. Four tests were conducted with maximum load of 1638 kN at construction site B. Figure 9b shows the results respectively.

a - reference frame; b – checking the pile settlement with an optical level instrument

Figure 8. During the static compression load test.

Table 3. Pile load test information at construction site A.

Pile ID	A1	A2	A3
Length, m	25.5	27.5	25.5
Cross-section, cm	40x40	40x40	40x40
Penetration length, m	24.25	26.25	22.5
Type of boreholes	Pre-augering diam.330mm, l=12 m	Pre-augering diam.330mm, l=12 m	Pre-augering diam.330mm, l=9 m
Maximum load	3278 kN	3278 kN	3278 kN
Maximum Settl., mm	20.0	34.04	31.53

Table 4. Pile load test information at construction site B.

Pile ID	B1	B2	B3	B4
Length, m	27.5	27.5	27.5	27.5
Cross-section, cm	40x40	40x40	40x40	40x40
Penetration length, m	25.63	25.4	25.86	25.78
Type of boreholes	Pre-augering diam.330mm, l=12 m	Pre-augering diam.330mm, l=12 m	Pre-augering diam.330mm, l=12 m	Pre-drilling diam.440mm, l=15.6 m
Maximum load	1639 kN	1639 kN	1639 kN	1639 kN
Maximum Settl., mm	16.22	7.38	4.43	6.89

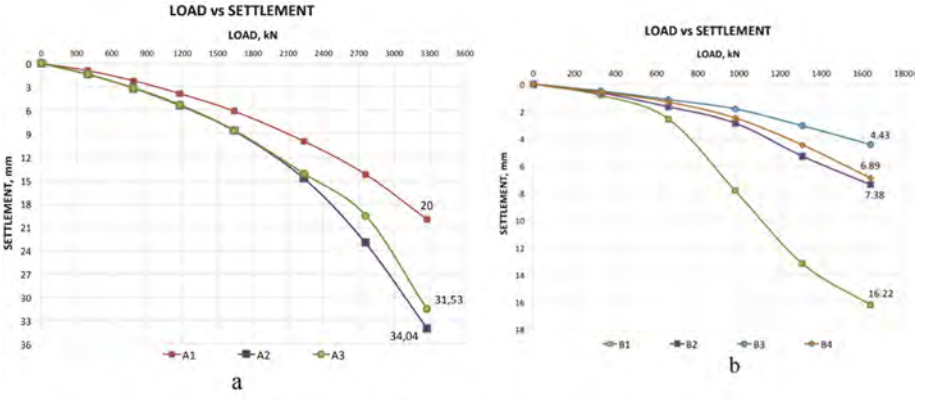

a – load-settlement curves from site A; в – load-settlement curves from site A

Figure 9. Pile loading test results at construction sites.

4 DISCUSSIONS

Estimates of bearing capacity of the PCJPs tested at construction site A (where the maximum applied load was 3278 kN) by a variety of interpretation methods showed that the Chin and Decourt methods gave the highest values. The remaining interpretation methods provided results more or less similar (2000~3000 kN) to those obtained from the APILE analyses, PDA, and manual calculations.

Meanwhile, the bearing capacities of PCJPs at construction site B (where the maximum working load was 1639 kN) obtained using the De Beer, Fuller and Hoy, and Butler and Hoy methods, were considerably lower than those obtained from the APILE analyses, PDA, and manual

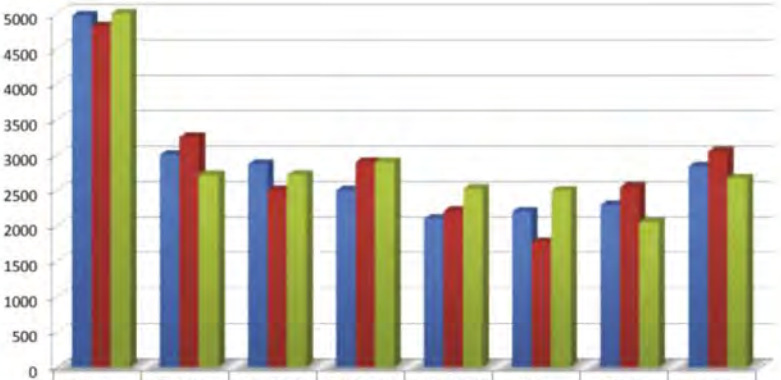

	Chin, Decourt, average	De Beer	Davidson	Fuller and Hoy	Butler and Hoy	PDA	APILE, average	Hand calculation
A1	4966	3000	2870	2500	2100	2202	2291	2836
A2	4812	3250	2500	2900	2208	1768	2544	3043
A3	4994	2714	2717	2900	2520	2497	2045	2670

a

a – for construction site A

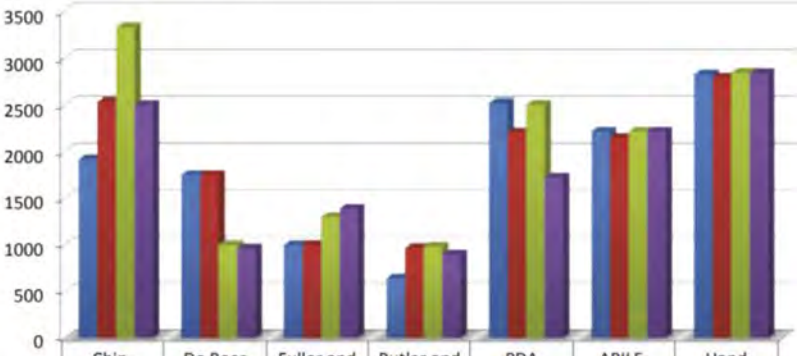

	Chin, Decourt, average	De Beer	Fuller and Hoy	Butler and Hoy	PDA	APILE, average	Hand calculation
B1	1918	1750	1000	643	2518	2217	2828
B2	2528	1750	1000	967	2203	2148	2794
B3	3326	1000	1300	980	2502	2217	2846
B4	2498	963	1391	900	1722	2217	2840

b

b – for construction site B

Figure 10. Comparison of pile capacities at construction sites A and B.

calculations (Table 5, illustrated in Figures 10a and b). This seems to be obvious, since the APILE, PDA, and manual calculations are only appropriate for prediction of ultimate bearing capacity. For the working load tested piles at construction site B, the interpretation methods only predicted yield capacities that were about 1/2 to 1/3 of the ultimate capacities. In general, despite the different approaches used, the results were found to be rational, and consistent with Kazakhstan construction requirements.

Table 5. Comparison of pile capacities at construction sites A and B (units of kN).

Methods / Pile ID	Chin, Decourt, average	De Beer	Davisson	Fuller and Hoy	Butler and Hoy	PDA	APILE, average	SNiP RK
A1	4966	3000	2870	2500	2100	2202	2291	2836
A2	4812	3250	2500	2900	2208	1768	2544	3043
A3	4994	2714	2717	2900	2520	2497	2045	2670
B1	1918	1750	1223	1000	643	2518	2217	2828
B2	2528	1750	-	1000	967	2203	2148	2794
B3	3326	1000	-	1300	980	2502	2217	2846
B4	2498	963	-	1391	900	1722	2217	2840

5 CONCLUSIONS

The interaction of precast concrete joint piles with the square section of 400*400 mm and with the length of 27.5 m with the surrounding soil ground during the construction of a port for offloading bulky goods were considered in this thesis. When assessing the reliability of a pile foundation, one of the determining ones is the question of the bearing capacity of the pile by soil. The greatest attention is paid to the bearing capacity of piles by static and dynamic load in classical and numerical and normative methods for identification of this parameter. The determination of the bearing capacity of precast concrete joint piles by interpretation methods, in the APILE software and by the SNiP formula presents particular interest to practicing engineers and scientists.

The use of precast concrete joint piles during the construction of a cargo offloading facility in Western Kazakhstan in the Prorva field present of particular interest to designers. The identification of an effective method for calculating the bearing capacity of precast concrete joint piles with a length of 27.5 m is determined by the first experience of using these piles at a construction site in Kazakhstan.

Based on the results of this study the following recommendations are made.

1. According to the results obtained from the seven field tests of piles by dynamic and static loads at the construction site of Cargo offloading facilities and the pilot site, it is considered the dynamic tests by PDA for application of identification of bearing capacity of precast concrete joint pile. Because the results of PDA show the similarity with static loading test, analytical methods as APILE analysis and calculation by equation from Kazakhstani standard. Dynamic test by PDA is economical and time saving. Although SLT is reliable but this test is very expensive and time consuming, hence researchers have been trying to come up with other efficient approaches.
2. The bearing capacity of precast concrete joint pile from static loading test data can be determined by conventional methods as Davisson, Chin, De Beer, Fuller and Hoy, Butler and Hoy. However, they are more appropriate for interpretation of high static loading test data, where settlements are bigger.
3. Estimation of bearing capacity of precast concrete joint pile can be made by APILE analysis program and equation from Kazakhstani standard.

FUNDING

This research was funded by the Science Committee of the Ministry of Science and Higher Education of the Republic of Kazakhstan. (Grant No. AP13268718).

REFERENCES

Zhussupbekov A.Zh., Syrlybaev M.K., Lukpanov R.E. (2015) The applications of dynamic and static piling tests of Astana. *Proceed. of the 15th Asian Regional conf. on Soil Mechanics and Geotechnical Engineering, ARC 2015: New Innovations and Sustainability*. pp. 2726–2729.

Zhussupbekov A.Zh, Omarov A.R. (2016) Geotechnical and construction considerations of pile foundations in problematical soils. *Proceed. of the 8th Asian Young Geotechnical Engineers Conf*. pp. 27–32.

Zhussupbekov A., Omarov A. (2016) Modern Advances in the Field Geotechnical Testing Investigations of Pile Foundation. Procedia Engineering. 165. pp. 88–95.

Zhussupbekov A., Omarov A. (2017) The Analysis of field tests of soils by joint piles on the construction site of the Caspian Sea area in Kazakhstan. *Proceed. of the internat. conf. on "Advancement of pile technologies and case histories*. pp. A7-1-A7-7.

Zhussupbekov A., Morev I., Omarov A., Borgekova K., Zhukenova G. (2018) Geotechnical considerations of piling testing in problematical soils of West Kazakhstan. International Journal of GEOMATE. Vol. 15, (47). pp. 111–117.

Zhussupbekov A., Chang D-W., Utepov Y., Borgekova K., Omarov A. (2019) Estimating the Driven Pile Capacities for COF Project in West Kazakhstan. *Soil Mechanics and Foundation Engineering* Vol. 56, (2). pp. 121–127.

Smart Geotechnics for Smart Societies – Zhussupbekov, Sarsembayeva & Kaliakin (Eds)
© 2023 The Author(s), ISBN 978-1-003-29912-7
Open Access: www.taylorfrancis.com, CC BY-NC-ND 4.0 license

Field applications of fiber optic strain sensing systems in geotechnical and structural engineering

S.C. Lee
Smart Sensing Technology Sdn Bhd, Malaysia

M.F. Chong
Dynamic Pile Testing Sdn Bhd, Malaysia

B.P. Tee
Smart Sensing Technology Sdn Bhd, Malaysia

Mohamad Hisham
Civil & Environmental Engineering Department, University Teknologi PETRONAS, Malaysia

ABSTRACT: The fiber optic sensing technologies such as Distributed Fiber Optic system and Fiber Bragg Grating system have received increasing demands in the geotechnical and structural engineering applications. This paper outlines the benefits of the fiber optic sensing systems compared to the conventional sensing systems. The applications, installation and monitoring approaches, and the results of several case studies are also presented in this paper. This paper gives an overview over several industrial applications of the fiber optic strain sensing systems, such as deep foundation testing, tunnel monitoring, and bridge health assessment.

1 INTRODUCTION

The development in construction technology and the growing populations have resulted in more mega structures and underground infrastructures built, especially in the urban areas. Therefore, geotechnical tests and structural health monitoring are very crucial to ensure the safe use of these civil structures during the long design service period.

The fiber optic sensing systems have been extensively applied in geotechnical and structural engineering in recent decades [1-5]. There are various types of fiber optic-based sensing systems such as Distributed Fiber Optic System (DFOS), Fiber Bragg Grating (FBG) system, etc. These systems have proven merits compared to the conventional sensors, such as (1) distributed measurement, (2) real-time static or dynamic measurements, (3) high stability and reliability, (4) immune to chemical and electromagnetic interference, (5) suitable for large scale engineering structures, (6) ease in installation, and (7) higher durability, survival rate and life span [6-12].

This paper showcases the industrial applications of two fiber optic strain sensing systems (i.e., DFOS and FBG) in the monitoring of deep foundation, tunnel, bridge and building. The authors aim to share their experience and challenges to improve the awareness and applications of fiber optic sensing systems in the civil industry.

2 FIBER OPTIC SENSING SYSTEMS

Strain is one of the most critical parameters used in most of the civil engineering designs. In this paper, the strain measurements are carried out using two fibre optic systems, i.e., the Distributed Fiber Optic Strain (DFOS) System and Fiber Bragg Grating (FBG) System.

DOI: 10.1201/9781003299127-205

The Brillouin Optical Time Domain Analyzer (BOTDA) is used measure the changes in frequency of backscattered light along the DFOS cables [3]. The change in frequency will then be changed into strain values by multiplying the coefficients. DFOS system is superior in static measurement however yet to be able to measure dynamic data.

The FBG system able to measure discrete strain data based on the principle of ultraviolet radiation reflection, which can measure both dynamic (thousand measurements per second) and static readings [13,14]. A change in the detected reflected wavelength indicates that strain is induced on the grating and thus, the strain of the structural element can be measured [14]. In a single fibre optic cable, a multitude of sensors can be fitted for many discrete data collection points with high resolution, accuracy, and monitoring frequency [13,14].

3 APPLICATIONS

3.1 *Deep foundation tests*

DFOS has several advantages over conventional discrete strain gauges in the application of foundation tests, i.e., ease of installation and doesn't require predetermined sensor location. DFOS is able to measure continuous strain along the pile (Figure 1), making it unnecessarily to predetermine the strain gauge level based on the different subgrade layers. The continuous strain profile provides better insight of the overall load distribution and stiffness difference between subgrade layers, making it easier for engineers to categorize the subgrade layers and friction mobilized.

The use of DFOS in deep foundation are included but not limited to bored pile, driven piles, steel piles, etc. The challenges are included the selection of proper fibre optic cables, installation approaches and higher entry cost (expensive logger) for the testing specialist.

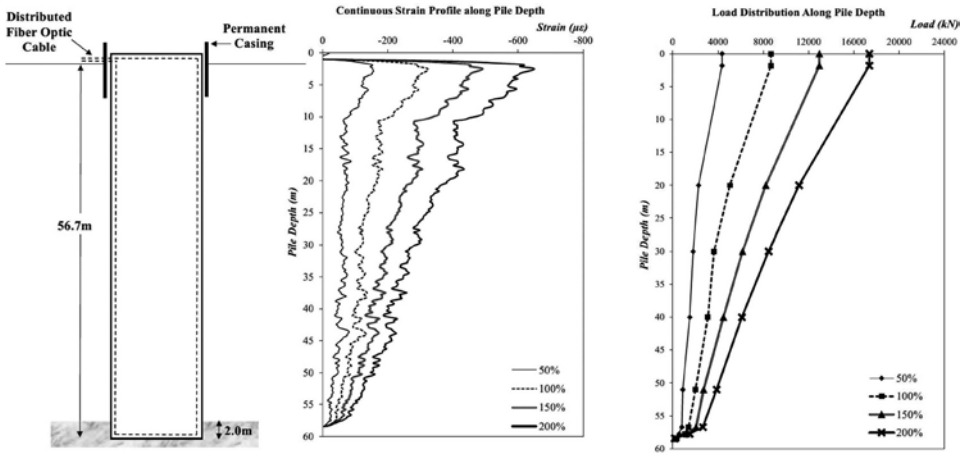

Figure 1. Application of DFOS for deep foundation static load test.

3.2 *Tunnel monitoring*

Maintenance and rehabilitation of an old aqueduct tunnel were carried out by strengthening approximately 25m tunnel section which experienced some collapsed. The collapsed section was approximately 2km from entrance, and was fully grouted prior to excavation, installation and steel ribs and shotcrete. In order to ensure the safety of workers during the work (from further collapse), forepole was installed prior to any excavation of the grouted section. Distributed fibre optic cables were installed inside forepoles to detect any unusual strain which can indicate the sign of further collapse.

After the installation of instrumented forepoles (with DFOS), excavation was done and steel ribs are installed. The distributed strain and temperature cables are then installed on the

steel ribs (as shown in Figure 2) prior to the shotcrete works. These strain and temperature cables on the steel ribs are used to assess the rehabilitated tunnel section's integrity after the completion of the maintenance and repair works.

In a nutshell, the DFOS was utilized in this aqueduct tunnel rehabilitation work for three main reasons (1) to ensure safety during excavation works, (2) to have long-term assessment after completion of work, and (3) this cannot be achieved using the conventional sensors (especially inside water transfer tunnel and the distance to entrance or monitoring station is too far).

The main challenge of the application of DFOS in a tunnel is the coordination of work. The instrumentation can be damaged during the construction work especially if the construction team are of different parties and do not understand the importance of instrumentation protection. The schedule for the instrumentation installation is also very critical as tunnelling work are normally be carried out 24 hours, delay in installation will causes delay in the tunnel construction work.

Figure 2. Application of DFOS for deep foundation static load test.

3.3 *Bridge health monitoring*

DFOS and FBG strain and temperature sensors were used during a load test on a old steel bridge. In order to assess the actual behaviour or condition of a 100-year-old bridge, static (resting locomotive) and dynamic (moving locomotive) load tests were carried out. After the assessment of steel bridge using Finite Element Analysis, several critical locations were identified and the FBG sensors were installed on these locations to measure the strain during the dynamic load test. While the DFOS cable was install along the bottom of the bridge to measure the response of the steel bridge under static load test. Biggest challenge of the application of FBG and DFOS in such an application is the temperature change. The difference in temperature on a steel bridge can be very significant and require a proper temperature compensation to be included during the analysis.

Figure 3. Application of DFOS and FBG sensors for 100-year-old bridge's static and dynamic assessment.

3.4 *Building slab monitoring*

In a project where the basement slab experienced cracks and underground water intrusion issue, DFOS system is one of the best options to monitor the condition of basement slab after all rehabilitation works are completed. The advantage of DFOS, in this case, fixed point DFOS, is that the range of strain is high (not easily break) and yet is capable of measuring cracks as small as 0.3mm. Installation of such cable in a basement slab is significantly easy as the whole cable functions as sensor. Installation of a 4km long fixed point DFOS cables inside a basement slab allows long term monitoring of the slab condition. The biggest challenge of such application is that the cable locations must be properly documented to avoid damaging the cable during the monitoring period.

4 CONCLUSIONS

The applications and merits of DFOS and FBG in geotechnical and structural engineering have been well demonstrated through 4 projects in this paper. Although the installation work of fiber optic sensing system is simple, the applicants must have knowledge in sensor selection, proper installation approach, design of the monitoring scheme, data collection and data interpretation. One limitation of fiber optic sensing system is the higher cost for the interrogator. However, with more experience and knowledge sharing, it will help in increasing the usage of these systems and therefore reduce the cost of the interrogator and sensors.

REFERENCES

Lee, S.C., et al., 2018. *Application of Distributed Fibre Optic Sensor (DFOS) in Bi-Directional Static Pile Load Tests*. Geotechnical Engineering Journal of the SEAGC, 55, pp.48–54.

Mohamad, H., et al., 2016. *Characterizing Anomalies in Distributed Strain Measurements of Cast-in-situ Bored Piles*. Jurnal Teknologi, 78 (8-5).

Tee, B.P., et al., 2017. *Instrumented Pile Load Tests on Rock Socketed Piles with Distributed Fibre Optic Sensor*. Proceeding of PILE 2017, ISNB 978-979-15020-4-7.

Tee, B.P., et al., 2017. *Underground Structure Behaviour and Deformation Monitoring with Distributed Fibre Optic Sensor*. Southeast Asian Conference and Exhibition in Tunnelling and Underground Space.

Tee, B.P., et al., 2019. *Assessment of Long Reinforced Concrete Piles Response under Axial Load Test using Distributed Fibre Optic Strain Sensor*. 1st MGS and GeoSS Conference 2019.

Tee, B.P., et al., 2017. *Application of Distributed Fibre Optic Sensor in Instrumented Pile Load Test*.

Mohamad, H., et al., 2011. *Performance Monitoring of A Secant-piled Wall using Distributed Fiber Optic Strain Sensing*. Journal of Geotechnical and Geoenvironmental Engineering, 137(12),pp.1236–1243.

Mohamad, H., et al.m 2014. *Thermal Strain Sensing of Concrete Piles using Brillouin Optical Time Domain Reflectometry*. ASTM International.

Soga, K., et al., 2008. *Distributed Fiber Optics Strain Measurements for Monitoring Geotechnical Structures*. 6th International Conference on Case Histories in Geotechnical Engineering, pp. 11–16.

Tee, B.P., et al., 2017. *Underground Structure Behaviour and Deformation Monitoring with Distributed Fibre Optic Sensor*. Southeast Asian Conference and Exhibition in Tunnelling and Underground Space.

Mohamad H., et al., 2009. *Fibre Optic Installation Techniques for Pile Instrumentation*. Proceeding of the 17th International Conference on Soil Mechanics and Geotechnical Engineering, IOS Press, Vol. 3, pp. 1873–1876.

Tee, B.P., et al., 2017. *Underground Structure Behaviour and Deformation Monitoring with Distributed Fibre Optic Sensor*. Southeast Asian Conference and Exhibition in Tunnelling and Underground Space.

Lee, S.C., et al., 2019. *Structural Assessment for an Old Steel Railway Bridge under Static and Dynamic Loads using Fibre Optic Sensors*. International Conference on Smart Infrastructure and Construction 2019 (ICSIC) Driving data-informed decision-making (pp. 729–736).

Majumder, M., et al., 2008. *Fibre Bragg Gratings in Structural Health Monitoring - Present Status and Applications*. Sensors and Actuators A: Physical, 147(1), pp.150–164.

Smart Geotechnics for Smart Societies – Zhussupbekov, Sarsembayeva & Kaliakin (Eds)
© 2023 The Author(s), ISBN 978-1-003-29912-7
Open Access: www.taylorfrancis.com, CC BY-NC-ND 4.0 license

Application of electromagnetic waves for evaluating the integrity of model pile

Dongsoo Lee, Seokgyu Jeong, WooJin Han, Jinwook Kim & Jong-Sub Lee
Korea University, Seoul, Republic of korea

Jung-Doung Yu
Joongbu University, Goyang, Republic of korea

ABSTRACT: This study presents a pile-integrity testing method using electromagnetic waves. An experimental study is conducted using small-scale defective piles. Two types of defects are simulated in the middle of the model pile. One is a poorly mixed concrete section and the other is a void. A waveguide system for transmitting electromagnetic waves is configured by installing electrical wires alongside a rebar in the model pile. The electromagnetic waves are generated and detected using a time domain reflectometer. Consequently, the results revealed that poor-quality concrete decreases the amplitude and velocity of the electromagnetic waves. The void increases the amplitude and velocity of the electromagnetic waves. This study suggests that electromagnetic waves can be an effective tool for evaluating pile integrity.

1 INTRODUCTION

Pile foundations are important structural components as they transfer upper loads underground. Thus, defects in piles can adversely affect the stability of structures. Non-destructive methods, such as the sonic echo method and cross-hole sonic logging (CSL), are generally used to evaluate pile integrity. However, detecting the locations of defects in piles with a large diameter is challenging owing to the energy leakage to the soils. The CSL can assess only the concrete between access tubes. Therefore, a new method is required.

Recently, electromagnetic waves have been widely used to evaluate infrastructure integrity. Yu et al. (2020) suggested a smart monitoring system using electromagnetic waves to detect defects in rock bolts. Lee and Yu (2019) investigated variations in the velocity of electromagnetic waves in defective soil nails. The objective of this study was to investigate the suitability of electromagnetic waves for evaluating the integrity of piles. Laboratory experiments were conducted on two defective model piles. One had a poor-quality concrete section and the other had a void in the concrete. A transmission line was configured in the pile to transmit electromagnetic waves, and a time domain reflectometer (TDR) was used for the generation and detection of the electromagnetic waves. Analyses were performed based the reflection coefficient and velocity of the measured electromagnetic waves.

2 EXPERIMENTAL SETUP

2.1 *Model pile*

Two defective model piles were prepared for the experiments, as shown in Figure 1. The model piles were concrete columns with a water-cement ratio (w/c) of 35 %, and a single rebar

DOI: 10.1201/9781003299127-206

was installed at the center along the length of the column. The dimensions of each column were 3.0 m × 0.2 m × 0.2 m. The rebar was a deformed reinforcing bar with a diameter and length of 16.0 mm and 3.2 m, respectively. A two-conductor electrical wire was installed alongside the rebar to configure the transmission line. Two different types of defects with lengths of 1.0 m were introduced at the centers of the model piles. One was poor-quality concrete, and the other was a void, as shown in Figure 1(a) and 1(b), respectively. The poor-quality concrete was a mixture of water and cement with a w/c ratio of 55 %.

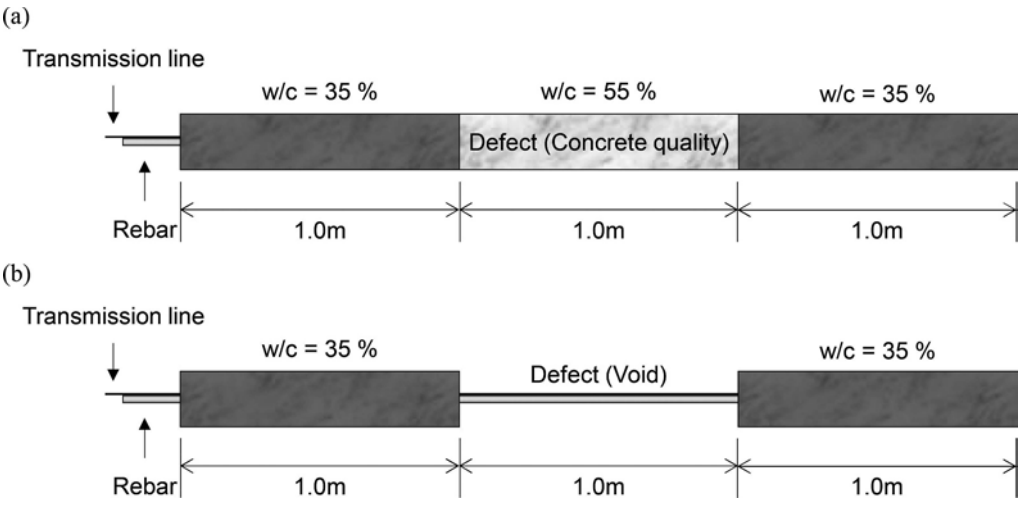

Figure 1. Defective model piles with: (a) poor-quality concrete; (b) void.

2.2 *Measurement system*

The measurement system was configured based on time domain reflectometry as illustrated in Figure 2. The measurement system included a computer, TDR, coaxial cable, and model pile, with the transmission line configured in the model pile. The TDR generated a step pulse with an amplitude of 150 mV. The rising time of the step pulse was 65 ps and the repetition rate was 2 MHz. The transmission line was connected to the TDR using a coaxial cable. Ten signals were stacked to improve the signal-to-noise ratio. The number of data points was set to 8192.

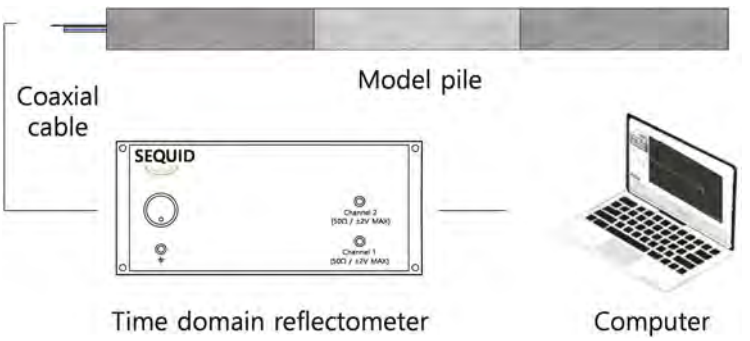

Figure 2. Measurement system.

3 EXPERIMENTAL RESULTS

3.1 *Defective model pile with poor-quality concrete section*

The measured signals are plotted in Figure 3. Reflection coefficient is defined as ratio of input output and input voltages. Also, it is a function of the electrical impedance difference between two media. Note that the impedance is inversely proportional to the dielectric constant. Thus, the reflection coefficient increases as the dielectric constant decreases. Electromagnetic waves reflected at the two ends of the pile were observed. The round-trip time (RTT) of the electromagnetic waves traveling along the length of the pile was 42.0 ns. The velocity of electromagnetic waves was calculated as the ratio of twice the travel length to the RTT. Velocity was calculated as approximately 1.43×10^8 m/s. In addition, the amplitude of the electromagnetic waves was reduced in the section with poor-quality concrete. This poor-quality concrete section can be represented using a reflection coefficient. The dielectric constant of the poor-quality concrete is greater than that of sound concrete. Thus, the reflection coefficient decreases in the poor-quality concrete section. The reflection coefficients for the sound sections exceeded 0.2. The reflection coefficients for the poor-quality concrete section ranged from 0.16 to 0.2. The reflection coefficients for the poor-quality concrete section were less than those for the sound sections.

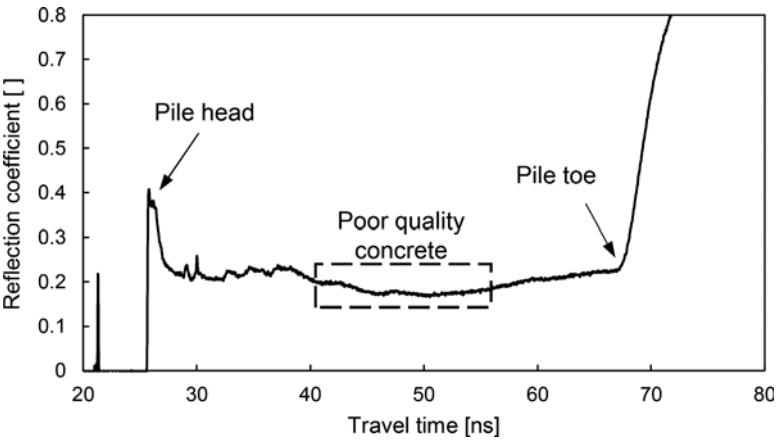

Figure 3. Measured signal for the defective model pile with poor-quality concrete section.

3.2 *Defective model pile with void*

The measured signals are shown in Figure 4. As in the defective model pile, where the poor-quality concrete is present, reflections of the electromagnetic waves occurred at both ends of the pile. The RTT was approximately 36.7 ns and the velocity was 1.63×10^8 m/s. Furthermore, the reflection of the electromagnetic waves owing to voids was clearly detected. The reflection coefficient increases in the void section because the dielectric constant of the void containing air is lower than that of the sound concrete. The reflection coefficients for the sound sections were calculated as approximately 0.2, whereas the reflection coefficient for the void section ranged from 0.25 to 0.37. The reflection coefficient for the void section was larger than that for the sound section.

4 CONCLUSIONS

Experimental studies were conducted to evaluate the local integrity of model piles. Two defective model piles each with a length of 3.0 m were manufactured for the experiments. A defect with a length of 1.0 m was introduced at the center of each model pile. One of the

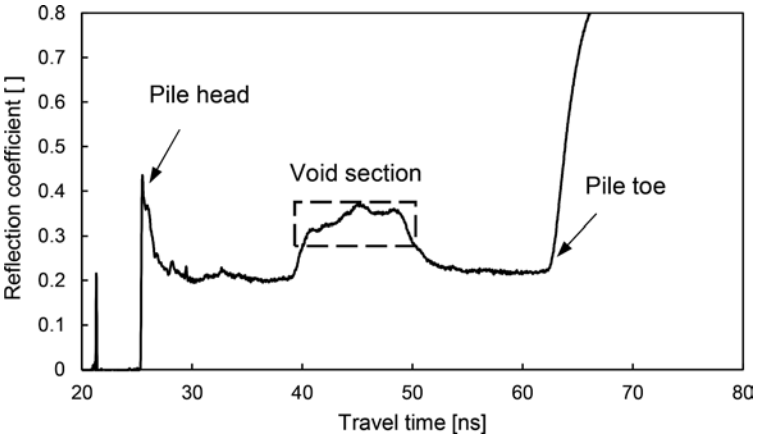

Figure 4. Measured signal for the defective model pile with void.

defects comprised poor-quality concrete, whereas the other was a void. Time domain reflectometry was used to measure the electromagnetic waves propagating on a transmission line in the model piles. The electromagnetic wave velocities were calculated, and the defective sections were evaluated using the reflection coefficient.

The conclusions of study are as follows.

- The experimental results revealed that the wave reflections at both ends of the piles were well-observed. The electromagnetic wave velocity of a defective pile with poor-quality concrete was lower than that of a defective pile with a void.
- For the reflection coefficient, the void section had a higher value than the sound concrete, and the poor-quality concrete section had a lower value than the sound concrete. The local integrity of a pile can be evaluated using the reflection coefficient of the time domain reflectometry signals.
- This study demonstrates that time domain reflectometry may be an effective tool for evaluating the integrity of pile foundations.

ACKNOWLEDGEMENTS

This work was supported by the National Research Foundation of Korea (NRF) grant funded by the Korea government (MSIT) (No. NRF-2021R1A5A1032433).

REFERENCES

Lee, J. S., & Yu, J. D. 2019. Non-destructive method for evaluating grouted ratio of soil nail using electromagnetic wave. *Journal of Nondestructive Evaluation*, 38(2),1–15.

Yu, J. D., & Lee, J. S. 2020. Smart sensing using electromagnetic waves for inspection of defects in rock bolts. *Sensors*, 20(10), 2821.

Smart Geotechnics for Smart Societies – Zhussupbekov, Sarsembayeva & Kaliakin (Eds)
© 2023 The Author(s), ISBN 978-1-003-29912-7
Open Access: www.taylorfrancis.com, CC BY-NC-ND 4.0 license

Lateral load test on bored cast in-situ pile instrumented with distributed fiber optic strain sensors

Y.P. Oh
Advanced Rapid Geotech Services Pte Ltd, Singapore

P.H. Ooi
A-Terra Consultants Pte Ltd, Singapore

Y.K. Lee, H.H.W. Oscar & K.W. Wong
Advanced Rapid Geotech Services Pte Ltd, Singapore

ABSTRACT: To obtain pile-soil response under lateral loading, the test pile shall be instrumented. Common pile instrumentation comprises of pairs of strain gauges fixed onto the reinforcement cages. However, this traditional instrumentation method is limited by the quantity of test points and installation quality is always questionable. Additional instrument like inclinometer casing with tip embedded in competent soil layer is also part of the requirement to measure the lateral pile deflection with pile top measurement as reference. With recent advancement in technology, distributed fiber optic sensing technique (BOTDA) is gaining its popularity especially in pile load test. By using distributed fiber optic sensing technique, it allows continuous strain measurement along the pile. This paper describes the method to compute the deflection profile from the fiber optic strain data. Comparative results show that the computed deflection profile is in good agreement with the traditional inclinometer readings. Additionally, the computed pile deflection is also compared to the pile head deflection measured by displacement transducers.

1 INTRODUCTION

Piled foundation typically are designed to resist axial loading. However, some elevated structures or marine structures are subjected to substantial lateral forces. It is essential that the design assumptions on pile lateral behaviour to be validated by physical test results. Typically, a lateral pile load test is instrumented with inclinometer, pairs of traditional strain gauges and displacement transducer at pile head. Traditional strain gauges have disadvantaged of limited strain measurement points that need to be pre-determined before the construction of pile, which occasionally lead to insufficient data at critical deflection point.

Brillouin distributed fiber optic sensing are widely applied in pile load test to obtain the strain distribution along the pile (De Battista et al., 2016). The full profile of strain distribution allows Engineer to assess the shaft friction at specific pile section as well as the concrete quality along the shaft. Further application of this technique includes the retaining structures monitoring (Mohammed et al., 2011, Xu et al., 2018, Wang et al., 2021), urban tunnel monitoring (Li et al., 2019) and soil slope monitoring (Minardo et al., 2015).

This paper presents the lateral load test on bored pile, instrumented with an innovative technique based on the optical fiber sensing that allows continuous strain measurement known as Brillouin Optical Time Domain Analysis (BOTDA). BOTDA is based on the analysis of back-scattered signals through two counter-propagating beams. The system has higher

DOI: 10.1201/9781003299127-207

accuracy, resist corrosion, anti-electromagnetic interference and it is suitable for long distance monitoring with high spatial resolution. In addition, duration of field works for the installation and preparation of instruments can be shortened by at least 80% which increases the overall construction productivity.

2 PILE INSTRUMENTATION AND TEST SETUP

2.1 *Test pile information and embedded instruments*

The 1200 mm diameter sacrificial bored pile with total length of 35.6 m was casted with concrete grade 50. The main reinforcement bar consists of 28 numbers of H40 with H16 circular links at 150mm center to center. Sub-surface geological condition is reported to consist of very soft sandy clay and hard sandy silt underlain by moderately weathered Siltstone, S(III). Concrete embedment type vibrating wire strain gauges were installed at specific elevation as shown in Figure 1 below. Two loops of distributed fiber optic strain sensors (DFOS) were installed in the pile. Loop A is installed in the loading direction while loop B is perpendicular to the loading direction. Two sets of traditional inclinometer casings were also installed to obtain the deflection profile under load.

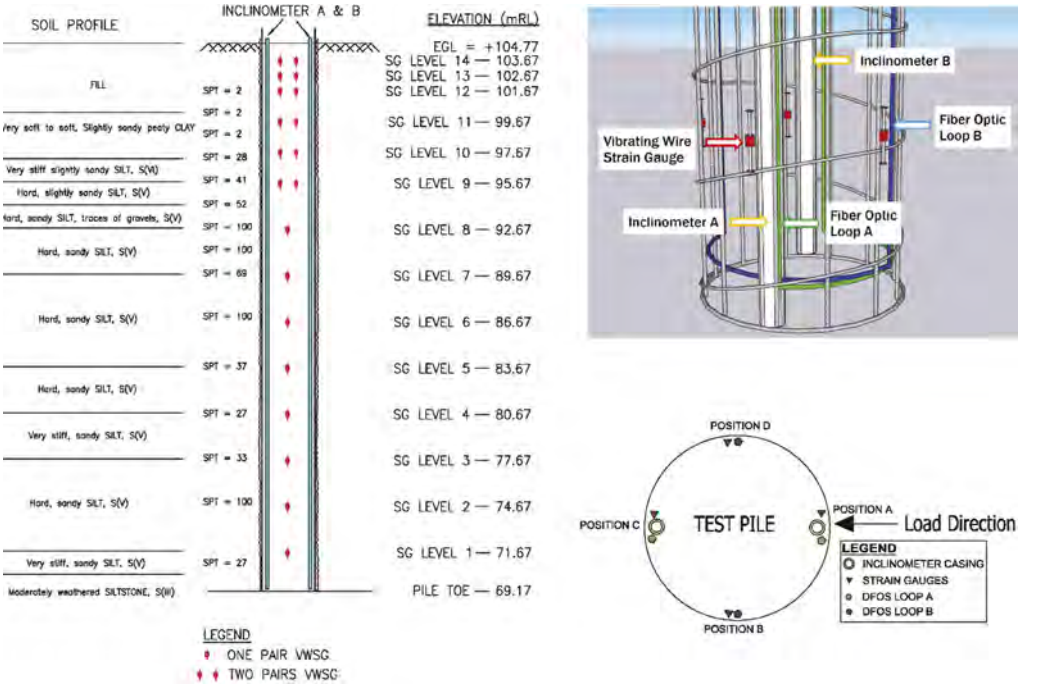

Figure 1. Schematic of strain gauges, 3-D illustration, and plan view of the test pile.

2.2 *Test setup*

Wide variety of arrangement for lateral load test are possible. For this particular test pile, a nearby sacrificial static load tested pile was used as reaction system. Pile head displacemet is monitored by using two numbers of linear vibrating wire displacement transducers (LVWDT) that attached on the pile and set to the reference beam. The reference beam is monitored by using a total station with reading taken for every load increments. The pile is loaded by using a 200T hydraulic jack with 200 mm stroke. Applied load is monitored directly by using load

cell, crosschecked with pressure transducer in the hydraulic system and pressure gauge on hydraulic pump. The site lateral load test setup is shown in Figure 2 below.

Figure 2. Lateral load test setup.

3 RESULT DISCUSSION

3.1 *DFOS data analysis*

Comparison of DFOS continuous readings and VWSG point readings are presented in Figure 3. At position C, that is compression zone under lateral loading, the vibrating wire strain gauges shows good agreement with the distributed fiber optic strain sensors. However, data captured at position A (tension zone) has shown significant variation which is mainly due to the measurement range of the vibrating wire strain gauges.

The compressive strain and tensile strain measured from distributed fiber optic strain sensing sensors can be used to compute the lateral deflection of the pile. By using equation 1 below, the measured strain profile is converted to curvature profile.

$$k(z) = \frac{1}{D}[\varepsilon 1(z) - \varepsilon 2(z)] \tag{1}$$

where D is the horizontal distance between two sensors, ε1 and ε2 is the tensile and compressive strain measurement. By integrating the curvature once and twice as per equation 2 and 3,

the gradient and deflection of the pile can be obtained. The toe of the pile is assumed not to move or rotate during the test; thus, the constant A and B is assumed as zero.

$$\emptyset(z) = \int k(z)\,dz + A \tag{2}$$

$$y(z) = \int \varphi(z)\,dz + B \tag{3}$$

where Ø is the gradient and y is the deflection. The curvature, gradient and deflection profiles are presented in Figure 4 below.

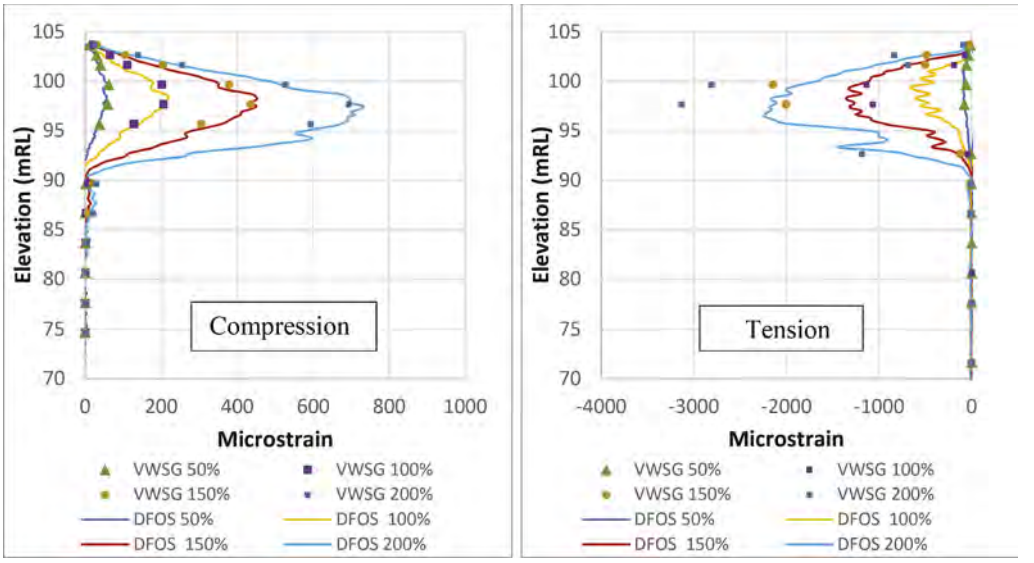

Figure 3. VWSG and DFOS comparison.

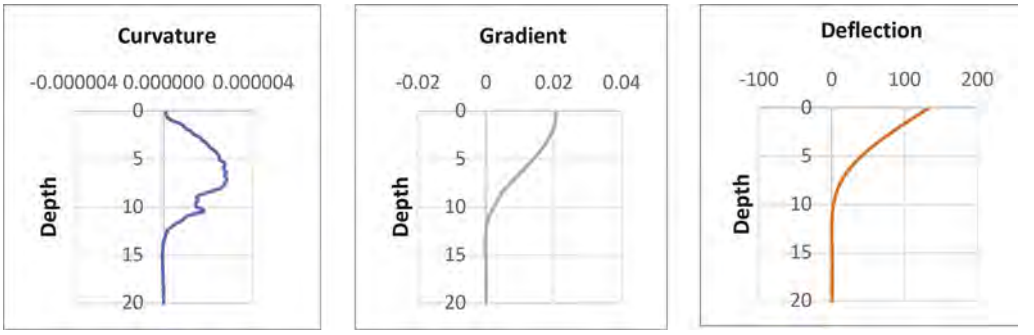

Figure 4. Curvature profile, gradient profile and deflection profile derived from DFOS data.

Figure 5 presents the comparison between measurement by pile top LVWDT, inclinometers and DFOS. It shows very close reading from the beginning of the test until the end of the test. For comparison between DFOS and inclinometer, the DFOS data is selected based on end time of the inclinometer manual readings. Thus, DFOS shows very good agreement with the inclinometer readngs. Refer to Figure 6 for the pile deflection profile comparison between DFOS and inclinometer.

Pile deflection profile computed by using VWSG point readings are presented in Figure 7. It is cleary seen that the computed profile is not identical to the other two profiles constructed by using DFOS continuos readings and inclinometer readings especially at 7-18m depth . Hence, the results indicate that continuos strain reading along the pile is important to obtain a higher accuracy deflection profile.

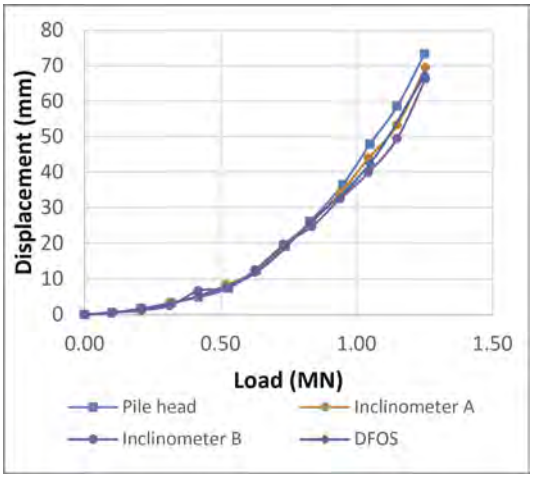

Figure 5. Comparison of pile top displacement and pile deflection profile.

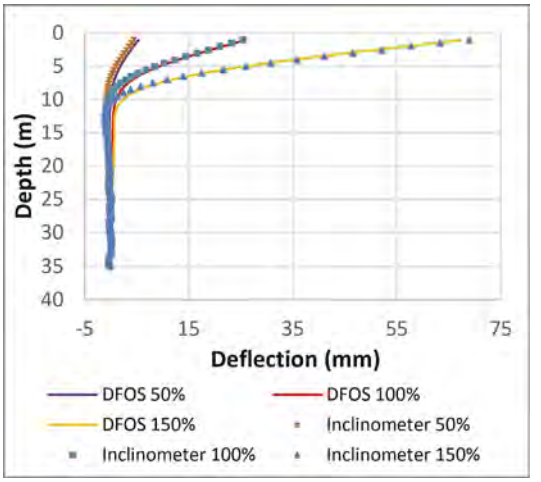

Figure 6. Comparison of pile deflection profiles between VWSG, DFOS and inclinometer.

4 CONCLUSION

A relatively new approach to pile test instrumentation by using distributed fiber optic sensing technology has been successfully carried out in Singapore. Based on the field test data, it shows that DFOS is suitable to be used as alternative instrument to replace inclinometer to measure the structure deflection. With continuous strain reading, the location where the maximum tensile and compressive strain occurred along the pile is accurately identified. Typical

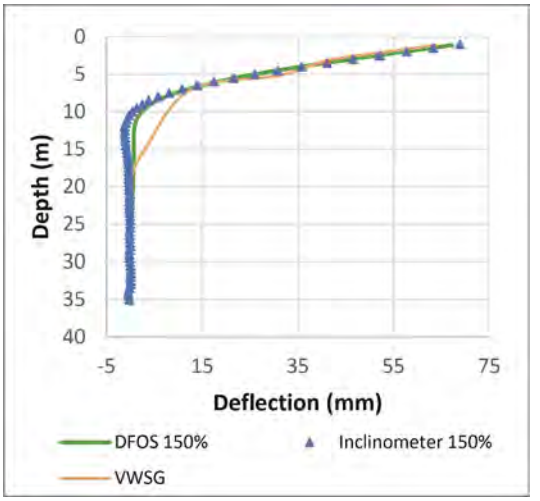

Figure 7. Comparison of pile deflection profiles between VWSG, DFOS and inclinometer.

vibrating wire strain gauge instrumentation work takes one to two days. By contrast, DFOS field instrumentation duration is shortened by at least 80% which increases the overall construction productivity.

REFERENCES

De Battista, N., Kechavarzia C., Soga, K. 2016. Distributed fiber optic sensors for monitoring reinforced concrete piles using Brillouin scattering, Proceedings of the European Workshop on Optical Fibre Sensors.

Li, H., Liu. Y., Cao, J. X., Shu, P. Y. 2019. Investigation of the BOTDA technology for structural condition monitoring of urban tunnel. Proceedings of IOP Conference Series: Material Science and Engineering. Vo. 603

Minardo, A., Damiano, E., Olivares, L., Picarelli, L., Zeni, L., Avolio, B., Coscetta, A. 2015. Soil slope monitoring by use of a Brillouin distributed sensor. Proceedings of Fotonica AEIT Italian Conference on Photonics Technologies. Pp 1–4

Mohamad, H., Soga, K., Pellew, A., Bennett, P. J. 2011. Performance monitoring of a secant piled wall using distributed fiber optic strain sensing", Journal of Geotechnical and Geoenvironmental Engineering, Vol. 137, No. 12, 1236–1243.

Wang, X., Luo, X. H., Long, W. X., Jiang, B. 2021. Back analysis of pile and anchor retaining structure based on BOTDA distributed optical fiber sensing technology. E3S Web of Conference 248 (1–2)

Xu, D.S., Yin, J.H., Liu, H.B. 2018. A new measurement approach for deflection monitoring of large-scale bored piles using distributed fiber sensing technology. Journal of the International Measurement Confederation, Vol. 117, Pp 444–454.

Smart Geotechnics for Smart Societies – Zhussupbekov, Sarsembayeva & Kaliakin (Eds)
© 2023 The Author(s), ISBN 978-1-003-29912-7
Open Access: www.taylorfrancis.com, CC BY-NC-ND 4.0 license

Experimental study on the load transfer behavior of a deep foundation member induced by the settlement in sand

Suhyuk Park
Graduate Student, Department of Civil Systems Engineering, Ajou University, South Korea

Ilhan Chang
Associate Professor, Department of Civil Systems Engineering, Ajou University, South Korea

ABSTRACT: An experimental test was conducted to assess the bearing capacity and load transfer mechanism of a pile model considering progressive settlement in this study. Dry natural sand (Jumunjin sand) was used to compose a model ground, where the cylindrical soil tank has a dimension of 380 mm in diameter and 900 mm in height. 28 load transducers were embedded at the lower bottom of soil tank to measure the load variation due to pile penetration. A pile model was fabricated with acryl which has a diameter of 80 mm and length of 800 mm. The pile model was fabricated to measure both tip bearing and skin friction without interfering with other measurements. Test variables are the distance between the tip of the pile model and the bottom of the soil container. The experimental setup was available to analyze the bearing capacity and load transfer mechanism at different penetration depths which represents the settlement behavior of pile model.

1 INTRODUCTION

Foundation is a basis geotechnical engineering structure which transfers the overlying load to the ground. Generally, foundation structures can be classified into shallow and deep foundation types. Shallow foundation is used when the size and load amount of the overlying structure is relatively low and the ground has a high load carrying capacity, while deep foundations are used when the external load is large and the ground condition is insufficient. The deep foundation serves to transmit the load of the structure to the lower ground by installing an elongated member (e.g. pile) into the ground.

Despite several theoretical and empirical formulas (Terzaghi, 1943, Meyerhof, 1951, Vesic, 1967) are provided to assess the load carrying capacity of pile foundations, there are lack of experimental verifications on the load transfer and support mechanism of pile structures. Thus, this study attempts to perform an experimental study to analyze the vertical stress distribution around a pile structure considering different settlement levels.

2 MATERIALS AND METHODS

2.1 *Experimental apparatus and soil properties*

A cylindrical soil tank was used to assess the vertical stress distribution of the ground according to pile settlement and to indicate the load-displacement curve of the pile. The soil tank was fabricated with acryl having a diameter of 380 mm and height of 900 mm (Figure 1a). Wire mesh was attached to the inner perimeter of the soil tank to simulate an infinite frictional boundary condition.

A series of 7 load ring-shape plates were installed below the soil tank to measure the vertical stress increment at different distances from the center of the pile model during pile penetration

DOI: 10.1201/9781003299127-208

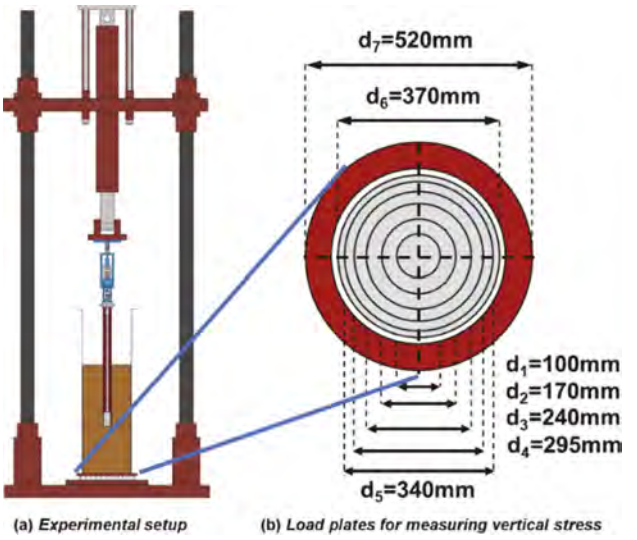

Figure 1. Experimental apparatus for pile driving.

(Figure 1b). 28 load transducers (4 for each ring-shape plate) were attached under the ring-shape load plates, to measure the average load transferred to each circumference individually.

The pile model was fabricated with PVC having a diameter of 80 mm and length of 800 mm. Surface skin friction was presented by attaching sand paper along the outer surface of the pile model. The pile measuring system was used to measure the tip load of the pile and the skin friction without mutual interference.

Dry jumunjin sand (D_{10} = 0.15 mm, D_{30} = 0.28 mm, D_{60} = 0.41 mm, C_u = 2.73, C_c = 1.23, USCS = SP) was used in this study. The unit weight of the model ground set to be 15.77 kN/m^3 (D_r = 21.56%) which is a loose sand deposit. The interparticle cohesion and friction angle were assessed as 0 kPa and 37° from a direct shear test (ASTM D3080-03).

2.2 *Test cases and experiment methods*

The distance from the tip of the pile model to the bottom of the soil tank was set as the main variable for this study. Three tip-to-bottom distances were considered as 20 cm (L20), 30 cm (L30), and 40 cm (L40).

Sand was poured into the tank by maintaining the pluviation height at 50 cm, to form a homogeneous ground condition. . The initial embedded depth of the pile model was set as 400 mm. After model ground formation with a pile embedded, the pile model was penetrated into the ground with a penetration rate of 1 mm/min using a hydraulic cylinder. The penetration was continued for 40 mm (time duration = 40 min).

3 RESULTS AND DISCUSSIONS

3.1 *Bearing capacity of pile*

The load-displacement curves obtained from laboratory tests are displayed in Figure 2. The tip bearing (Figure 2a) gradually increases with pile penetration, while skin friction (Figure 2b) increase up to 10 mm of pile penetration but then converges to a constant level (20 kPa) when the pile penetrated further (> 10 mm).

The bearing capacity of the pile model (Figure 2c) can be expressed by summating the tip bearing (Figure 2a) and skin friction (Figure 2b), where the inflection point in Figure 2c is regarded to be the total bearing capacity (qu) of the pile model. For instance, the inflection point appears at 15.45 mm of pile displacement and stress level of 47.6 kPa (q_u = 47.6 kPa for the L40 case).

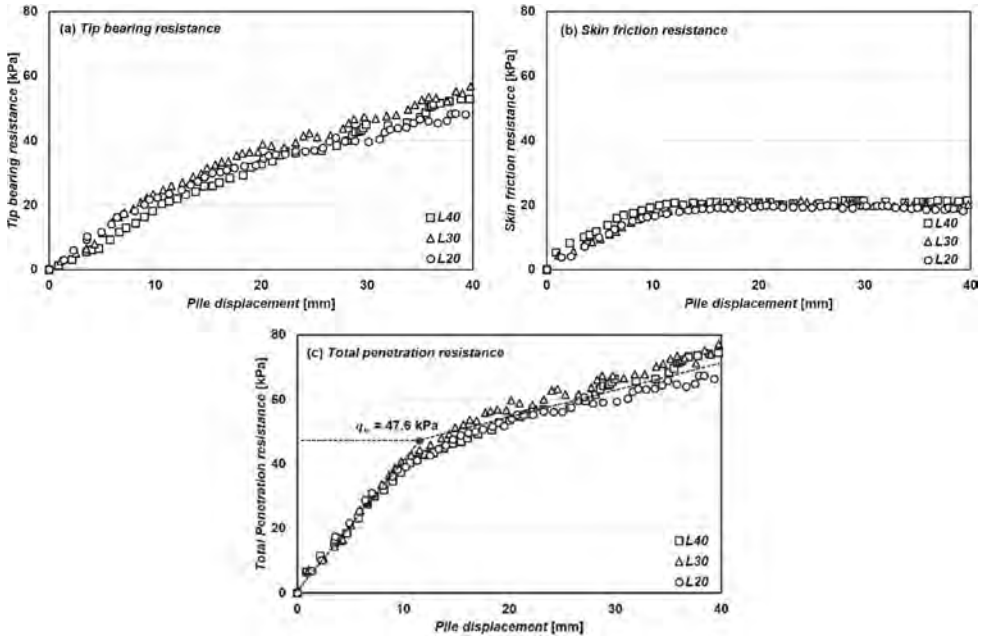

Figure 2. Penetration resistances induced by pile settlement.

3.2 *Stress distribution induced by settlement of pile*

Load transducers were used under the soil container to analyze the distribution of vertical stress induced by pile penetration. The forces measured on each load transducer were divided by the area and expressed as stresses. Figure 3 shows the figure for each stress. As shown in Figure 3, the x-axis represents the normalized distance from the pile center. Normalization was expressed by dividing the distance r from the pile center by the radius R of the soil

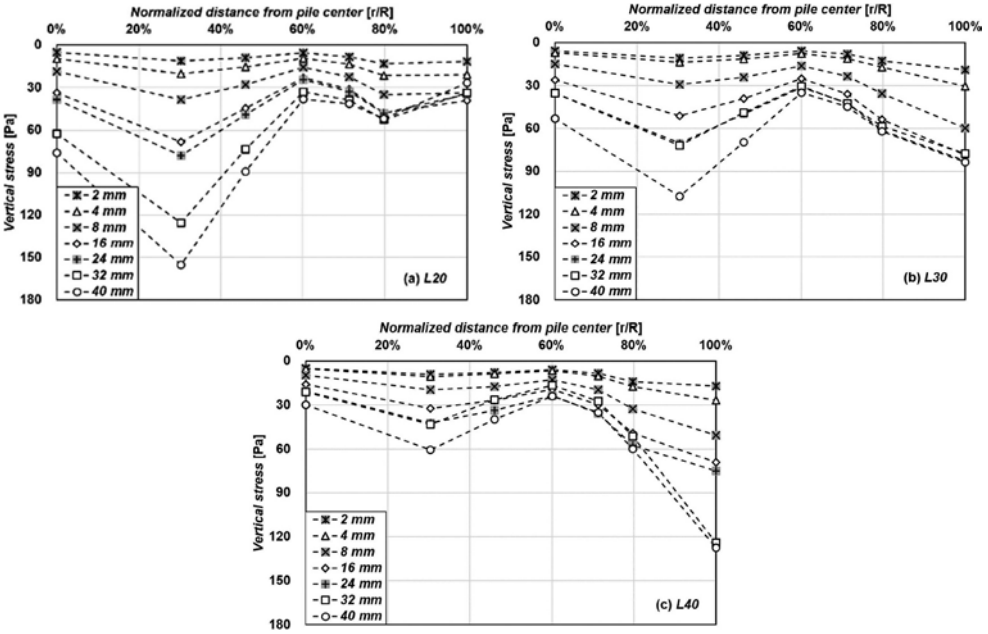

Figure 3. Stress distributions under pile.

container. In Figure 3, the y-axis represents the vertical stress inside the ground according to the pile displacement. As shown in Figure 3, legends represent pile displacement at each stage.

As shown in Figure 3a and b, the largest vertical stress occurred at r/R=30% point. As the pile settlement increased, the stress at the point within 60% close to the pile continued to increase. On the other hand, it was found that the stress at a point more than 60% away from the pile did not increase any more after a certain amount of pile displacement. This point is the point where the bearing capacity of the pile occurs, and it is 16mm. On the other hand, in Figure 3c, the largest vertical stress occurred where the r/R was 100%. Even when the pile displacement was 16mm or more, the vertical stress increased.

When the distance between the tip of the pile and the load plate was small, the vertical stress occurred at a place close to r/R. Whereas, when the distance between the tip of the pile and the load plate increased, the vertical stress was greatly generated in the place where r/R was far. This is because vertical stress near the deep foundation appeared large, and vertical stress far from the deep foundation appeared small (Grillo, 1948). However, in the case of L40, the vertical stress was larger where r/R was larger. This was analyzed to be due to the arching effect (Vesic, 1967) occurring at the interface of the soil container.

4 CONCLUSIONS

The purpose of this paper is to analyze tip resistance and skin friction induced by pile driving and to confirm the stress distribution under the pile. The following conclusions were obtained through model tests.

In all three cases, the load-displacement curves showed the same trends because the penetration depth of the pile was the same. Tip bearing according to pile displacement increased proportionally, but not the skin friction.

The bearing capacity of the pile was calculated using the sum of tip resistance and skin friction. Bearing capacity was calculated as the load where the extension line of the initial linear part and the extension line of the late linear part meet, and the bearing capacity of the pile is 47.6 kPa.

The stress distribution induced by pile settlement showed a different tendency for each case. When it was close to the tip of the pile, the stress was greater where r/R was close. In the case of a place far from the tip of the pile, the stress was larger at a place where r/R was far away. In addition, it was found that the stress did not change even if the pile displacement was 16 mm or more where the stress was small.

In this paper, the bearing capacity of the pile and the resulting stress distribution of the ground were analyzed. However, various factors affect the ground stress distribution induced by pile driving. Additional studies on the diameter of various piles and surface friction conditions are needed.

ACKNOWLEDGEMENT

This work was supported by the National Research Foundation of Korea (NRF) grant funded by the Korea government (MSIT) (No. 2022R1A2C2091517).

REFERENCES

ASTM D3080–03. ASTM D3080-03. *Standard Test Method for Direct Shear Test of Soils Under Consolidated Drained Conditions*.

Grillo, O. 1948. Influence scale and influence chart for the computation of stresses due respectively to surface point load and pile load. *Proc. II ICSMFE*, 6, 70–72.

Meyerhof, G. G. 1951. The Ultimate Bearing Capacity of Foudations. *Géotechnique*, 2, 301–332.

Terzaghi, K. 1943. *Theoretical Soil Mechanics*, Wiley.

Vesic, A. S. 1967. A study of the bearing capacity of deep foundations.

Smart Geotechnics for Smart Societies – Zhussupbekov, Sarsembayeva & Kaliakin (Eds)
© 2023 The Author(s), ISBN 978-1-003-29912-7
Open Access: www.taylorfrancis.com, CC BY-NC-ND 4.0 license

Measured axial capacities of driven pile in Metro Manila reclamation area using high strain dynamic load tests

R.T. Gonzales, R.A.C. Luna & G.P.D. Reyes
AMH Philippines, Inc., Quezon City, Metro Manila, Philippines

ABSTRACT: With the ever-growing population and continuous development of economy in the Philippines, more reclamation projects are being proposed and constructed to expand the land that would cater the spatial needs in the Metro Manila, the country's urban capital. As these various reclamation projects add constructible land areas along the coastlines of Metro Manila, several infrastructures spanning from government, business, commercial, and residential developments are being built as well. Majority of these structures are anticipated to be founded on pile foundations, signifying the importance of pile design and capacity verification. Design of piles are carried out using semi-empirical theoretical approaches and equations developed based on existing soil and rock mechanics concepts. In more recent years, the science and technology of pile testing have been evolving which provides an important tool in the monitoring, verification, and evaluation of integrity and pile capacity as well as optimization of theoretical capacities by yielding cost-effective engineering solutions.

1 INTRODUCTION

In the Philippines, the demand to reclaim land has increased very rapidly in the past decades not because of the scarcity of land but because of the need for valuable space that will be optimized by constructing vital and essential developments and infrastructure near the country's urban capital, Metro Manila.

The simplest method of land reclamation involves directly filling the area with large amounts of rock, clays, and sand fills, followed by compaction of these layers until the desired height is reached. Considering the highly compressible and weak soil layers in landfill areas, pile foundation is almost all the time warranted to carry the structures on top of the reclaimed embankment. Pile foundation transmits loads to underlying dense and hard soil and even bedrock, through frictional and end-bearing resistance. Also, if the expansive and collapsible soils are present in the site, piles may extend beyond the active zone/stable soils.

In order to verify and validate the calculated theoretical capacities of deep foundations, high strain dynamic load testing—a non-destructive load test that measures the mobilized soil resistance forces along the shaft and bearing capacity at the toe using reflection of the compressive stress waves that travel up and down the pile shaft—is carried out. Details are discussed in the following sections.

This paper presents both the theoretical and measured axial capacities of driven piles in Metro Manila reclaimed areas using high-strain dynamic load tests, with the objective of providing a process of verifying and optimizing of theoretical pile capacities and assessing the measured capacities relative to its geologic location.

2 SITE SUBSOIL CONDITION

Manila Bay is built on an extensive flood plain with very small variation in elevation. According to the Metropolitan Manila Development Authority (MMDA), Manila is "relatively flat of

DOI: 10.1201/9781003299127-209

about 0.81% to very gently sloping at 3.17%". The geology of the vicinity is underlain by recent deposits and residual soil deposits of variable thickness, consisting of clays, silts, and sand.

Several sites were explored by drilling boreholes, collecting and testing soil samples. Disturbed soil samples were obtained from Standard Penetration Test (SPT) American Society for Testing and Materials (ASTM D1586). SPT N-values taken from the boreholes within the reclaimed areas are generally indicative of very loose to medium dense relative condition within the upper layers, underlain by hard silt and very dense sand. Also, the recorded water levels during field investigations in most of the sites were relatively shallow given that mostly are located near offshore.

Figure 1 represents the recorded SPT N-values of drilled boreholes, with at least 15.0-meter depth, at several sites in Metro Manila reclaimed areas. Based on the plotted scatter diagram, most of the sites have relatively strong subsoil on the 1st meter depth, presumably the compacted layer of the landfill. The SPT N-values on the succeeding depth indicate very loose to loose sands and very soft to soft clay layers, i.e. SPT-N values < 10. These layers are underlain by the competent strata mostly attributed to the regional bedrock of Metro Manila, Guadalupe Tuff Formation (GTF) consisting of sandstones and siltstones, except on projects 6 and 7 where loose and soft soils persist until termination of boreholes.

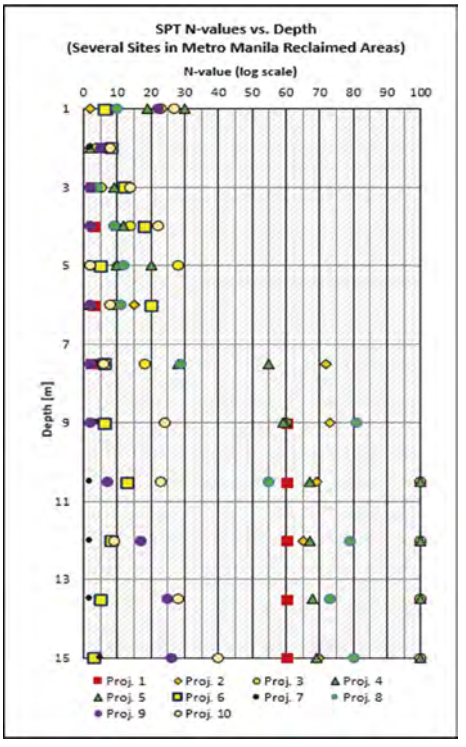

Figure 1. SPT N-Values vs. Depth.

Figure 2. Design allowable capacity per project location.

3 THEORETICAL PILE CAPACITY

Given that the subsurface conditions on a typical reclamation area in Manila consists of very loose to loose sands in the upper layers, driven piles are normally selected to prevent collapse of soil and adjacent existing structures during construction and installation.

Figure 2 presents the location of project sites where pile tests were conducted, as well as their respective design allowable axial capacities. These sites will be developed into various infrastructures such as office, commercial, and residential buildings as well as elevated parking

spaces. The piles were designed by calculating axial capacities based on the well-known methods of Meyerhof, Coyle & Castello, Reese & O'neil etc.

Most of the construction sites within these areas are surrounded by occupied or existing infrastructures already. Given the constraints for construction and the anticipated structural loads from the proposed developments, driven piles are deemed to be the appropriate pile type to be utilized. Driven piles are installed with the use of static pile driver and hammer weights. The pile driver pushes the piles by giving compressive pressure or by simply pushing it to the ground to reach its 'refusal' point based on design capacity.

The factor of safety generally ranges from 2.5 to 4.0. Table 1 presents the summary of test piles with their design allowable capacities, design pile size and actual pile embedment as per pile driving log.

Table 1. Summary of Pile Design Capacity, Size, and Length.

Design Pile Size	Design Allowable Capacity	Actual Pile Penetration in Meters					Total Pile per Capacity	Color Code
		< 10	10 to 15	15 to 20	20 to 25	> 25		
mm x mm	kN	pcs	pcs	pcs	pcs	pcs	pcs	
400 x 400	1000	2	4	5	5	0	16	
400 x 400	1050	0	0	0	1	9	10	
450 x 450	1100	7	7	10	0	0	24	
450 x 450	1200	2	0	2	0	0	4	
400 x 400	1350	0	0	0	10	9	19	
450 x 450	1500	0	0	0	6	6	12	
Total Piles per Size and Length		11	11	17	22	24	85	

As shown in the table, the areas where piles are embedded at relatively shallower depths (yellow areas) attained higher capacities even at smaller pile size (400mm) (See Figure 2 and Table 1 for color coding). For the areas with relatively deeper depths of hard strata (red areas), piles are required to be embedded at deeper depths and have larger pile size (450mm) to attain similar higher capacities as with the piles in the yellow areas.

4 MEASURED CAPACITIES USING PDA

Dynamic Load Testing (DLT) using a Pile Driving Analyzer® (PDA) is performed for all the project sites. The purpose of the DLT is to assess pile structural integrity, calculate pile driving stresses, and evaluate bearing capacity with test methodology and equipment in accordance with ASTM D4945-00. In this test, set/s of strain transducers and accelerometers are bolted at opposite faces of the pile to measure strain (force) and acceleration. An axial force is then applied on top of the pile with a pile driving hammer or large drop weight that will cause high strain at the top as well as generate waves that will travel through the length of the pile. After field testing, the results are further evaluated using the Case Method approach. This method is carried out and a more accurate estimate of the pile capacity is established by using CAPWAP (Case Pile Wave Analysis Program). CAPWAP is an iterative signal-matching technique that determines the most appropriate soil and pile resistance model that would result to a good match between the computed and measured force/velocity data.

Based on the results of the field testing and data post-processing, the measured allowable capacities per size and length are presented in Figure 3. These piles were tested at least seven (7) calendar days after driving.

The usual cross-sectional area of piles tested range from 1,600 cm^2 to 2,025 cm^2 with pile penetration that ranges from 8.0 meters to 28.0 meters in reference to the existing ground. All test piles attained their target capacities, which are twice the allowable capacity or safety

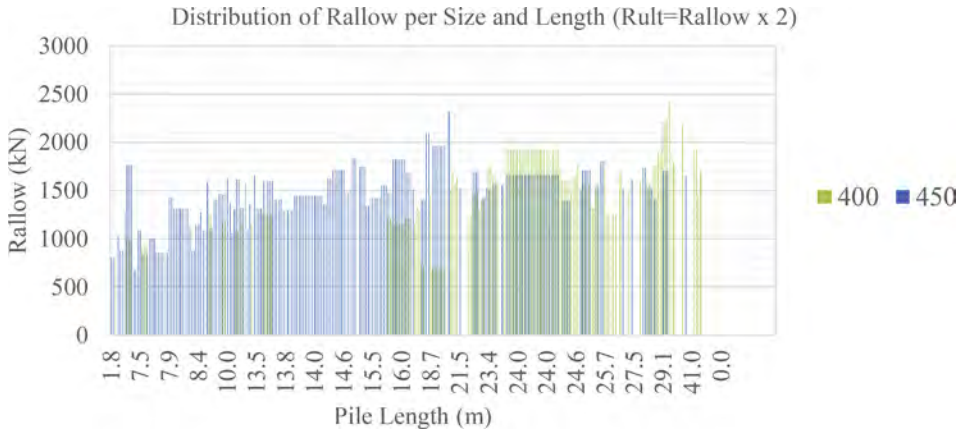

Figure 3. Distribution of Allowable Capacity per Size and Length.

factors equal to 2.0. In the exercise of attaining the target capacity, pile size and pile penetration can significantly affect the result.

Given the subsurface conditions at the reclamation areas as described in the previous section, 400 cm by 400 cm piles with less than 10 m penetration attained allowable bearing capacities of less than 1500 kN, while the 450 cm by 450 cm piles driven with less than 10 m mobilize allowable bearing capacities of about 2000 kN.

Most of the piles with 1600 cm^2 cross-sectional area and embedded at least 25.0 meters provide allowable bearing capacities greater than 2000 kN, while the larger pile, 2025 cm^2, provide allowable bearing capacities greater than 2000 kN with at least 15 m penetration. This shows that a larger pile size has a significant effect in the measured pile capacities.

As shown in Figure 4, 76% of the 400mm x 400mm piles are embedded > 20m, while only 30% of the 450mm x 450mm piles are embedded > 20m. Again, this shows that a slightly larger pile diameter can achieve higher capacities at shallower depths. The pile capacity pie charts also indicate that majority of the measured capacities of piles range from 1250kN to 1750kN for both pile sizes, with 450mm piles having a greater number of piles achieving those capacities (80%).

Table 2. Tabulation of Piles per Size, Capacity, and Length.

Pile Size	Pile Penetration	Number of piles based on measured allowable capacity in kN					Total Piles per Length
		< 1250	1250-1500	1500-1750	1750-2000	>2000	
m x mm	m	pcs	pcs	pcs	pcs	pcs	pcs
400 x 400	< 10	1	1	0	0	0	2
400 x 400	10 to 15	4	0	0	0	0	4
400 x 400	15 to 20	4	1	0	0	0	5
400 x 400	20 to 25	2	5	8	1	0	16
400 x 400	> 25	0	1	6	5	6	18
450 x 450	< 10	1	4	3	1	0	9
400 x 400	10 to 15	0	3	3	0	1	7
400 x 400	15 to 20	0	5	4	2	1	12
400 x 400	20 to 25	0	0	6	0	0	6
400 x 400	> 25	0	0	4	2	0	6
Total Piles per Capacity		12	20	34	11	8	85

Given the theoretical pile capacities discussed in the previous section, pile testing should be able to mobilize at least twice the allowable capacity, i.e. a safety factor of 2.0. In PDA testing practice, a minimum proven safety factor of 2.0 is considered acceptable. The measured ultimate capacities of all test piles range from 2.0 to 4.64 times the allowable capacities.

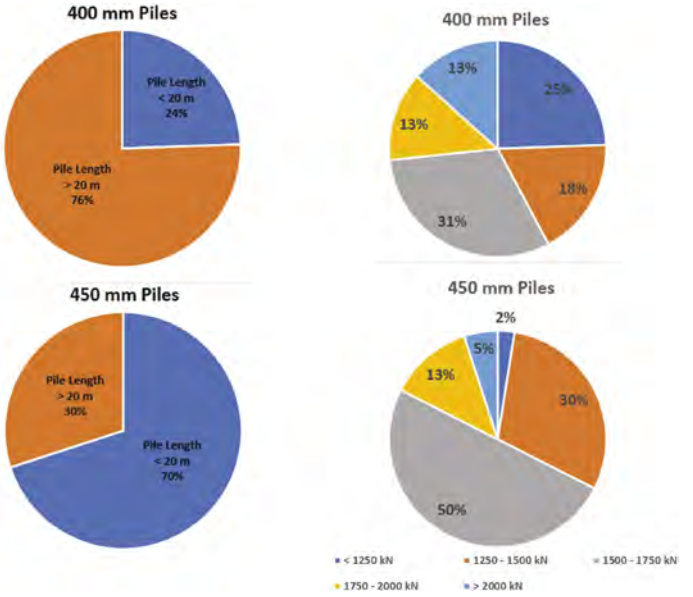

Figure 4. Distribution of pile embedment and pile capacities.

From Figure 5 and Table 3, it can be observed that to achieve similar values of pile capacities (1250 kN to 1750 kN) in the area, most of the 450mm size piles are embedded at relatively shallower depths, e.g. 18m or less, while 400mm size piles are embedded at depths until 30m, about 40% reduction in pile length. Moreover, majority of the 450mm piles attain relatively high safety factors, i.e. greater than 2.5, with FS ranging from 2.00 to 3.91. Factors of safety for the 400mm piles range from 2.03 to 2.96, except for those embedded at 28 to 30m where FS range from 3.42 to 4.64.

Table 3. Tabulation of calculated factors of safety and measured capacities.

Project	Pile Size	Pile Penetration	Theoretical Capacity	Rtoe*	Rskin*	Rtotal*	Safety Factor
	mm x mm	m	kN	kN	kN	kN	
A	450 x 450	11.71	1100	1216.86	1938.57	3155.43	2.87
B	450 x 450	13.90	1100	894.90	2230.10	3125.00	2.84
C	450 x 450	15.97	1200	590.00	2864.00	3454.00	2.88
D	400 x 400	16.49	1000	722.13	1722.13	2444.25	2.44
E	400 x 400	25.21	1350	1624.20	1673.60	3297.58	2.44
F	450 x 450	25.33	1500	981.42	2273.17	3254.58	2.17
G	400 x 400	25.63	1350	1351.89	1843.89	3195.78	2.37
H	400 x 400	28.73	1050	608.50	3535.30	4143.80	3.95

* Rtoe – Toe Resistance; Rskin – Skin Resistance; Rtotal – Total mobilized resistance.

Also presented are the proportion of the skin and tip resistance to the total measured pile capacities:

- Projects A, B, & C: Sites with 450m x 450m piles with measured axial capacities ranging from 2550 kN to 4643 kN. Pile embedment in these projects are relatively shallow, ranging from 7.0m to 19.9m. Calculated factors of safety are 2.32 to 3.91. 72% of the total pile bearing capacity is from shaft resistance.

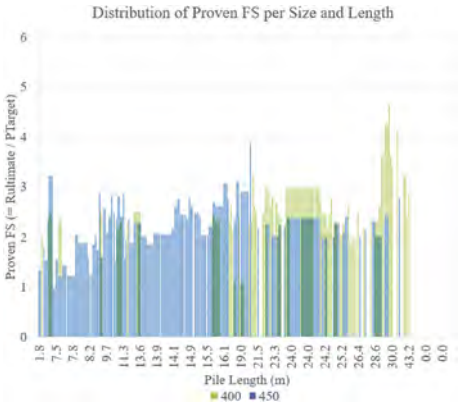

Figure 5. Calculated factor of safety per dimension.

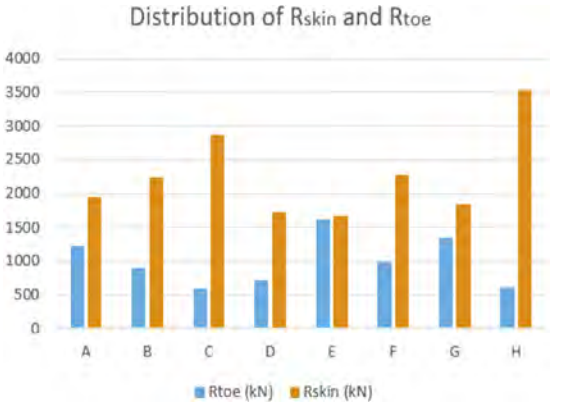

Figure 6. Distribution of rskin and rtoe.

- Project D: Site with 400m x 400m piles with allowable design capacities of 1000 kN and measured axial capacities ranging from 2030 kN to 2962 kN. Pile embedment range from 9.0m to 23.0m. Calculated factors of safety are 2.03 to 2.96. 70% of the total pile bearing capacity is from shaft resistance.
- Projects E, F, & G: Sites with 400m x 400m and 450mm x 450mm piles with measured axial capacities ranging from 2929 kN to 3765 kN. Pile embedment range from 22.8m to 28.8m, as expected for sites located farther from the original land mass. Calculated factors of safety are 2.00 to 2.79. 64% of the total pile bearing capacity is from shaft resistance.
- Project H: Site with 400m x 400m piles with measured axial capacities ranging from 3384 kN to 4870 kN. Pile embedment range from 20.4m to 33.3m, longest pile penetration tested within Manila Bay. Also, all of the calculated factors of safety in this project are relatively high, ranging from 3.22 to 4.64. 85% of the total pile bearing capacity is from shaft resistance, as expected for deep piles.

In summary, the results of the pile capacity analysis, each project is grouped according to depth of embedment, measured pile capacity, and percentage of skin resistance. Projects A, B, & D are sites located inside the original coastline of Manila Bay while Projects C, E, F, G, & H are sites located outside of the original coastline. Driven piles located inside the original coastline are designed to be embedded at relatively shallower depths (mean pile length of 11.7m to 16.5m) compared to the ones driven outside which are embedded at deeper depths (mean pile length of 25.2m to 28.7m) as thickness of the soil cover tends to increase to the direction of Manila Bay itself. Moreover, Projects A, B, & D have measured capacities ranging from 2030 kN to 4300 kN with 72% coming from the skin friction. Projects C, E, F, G, & H have measured capacities ranging from 2802 kN to 4870 kN with 65% derived from shaft resistance. The values indicate that as pile embedment increases, the contribution of toe resistance also slightly increases as compacted soil and/or competent layers are reached by the tip of the pile.

5 CONCLUSIONS

1. In designing piles located within a reclaimed area like Manila Bay, the study of the geology of the site is as important as the calculations of pile capacities. Depending on the subsurface conditions and the proximity to the bay area, pile design may be optimized by either using larger pile sizes with shorter lengths or smaller piles with deeper embedment depth.
2. As expected, larger pile sizes and deeper pile embedment yield higher pile capacities and factors of safety. For most of the project sites in Manila Bay, a larger pile cross section yields higher capacities even at shallower pile embedment when compared to the longer but

smaller piles. On the other hand, at very deep embedment, about 28m to 30m, resulting factors of safety are very high (FS=2.6 to 4.6) as the hard-competent strata is reached.

3. In the Manila Bay area, using smaller piles such as 400m x 400m piles require embedment depths at around 25m to attain typical mid-rise structure design capacities of 1,500 kN to 2,000 kN.
4. From the results of the pile capacity analysis (CAPWAP), about 70% of the total pile bearing capacity is carried by the shaft resistance. This is mainly due to the presence of very thick uppermost cohesionless soil layers and the absence of competent strata which are found at deeper layers.

REFERENCES

Das, B. M. 2011 Principles of Foundation Engineering 7th Edition
Phettplace, B., Hyatt, T., & Alvarez, C. 2019 Dynamic and Static Load Testing: A Cost Saving Approach
Simons, N. & Menzeis, B. 2000 A Short Course in Foundation Engineering 2nd Edition

Smart Geotechnics for Smart Societies – Zhussupbekov, Sarsembayeva & Kaliakin (Eds)
© 2023 The Author(s), ISBN 978-1-003-29912-7
Open Access: www.taylorfrancis.com, CC BY-NC-ND 4.0 license

Hybridnamic rapid load testing with an extended interpretation method of dynamic signals

S. Kamei, S. Lin & I. Yamamoto
Jibanshikenjo Co., Ltd., Tokyo, Japan

T. Matsumoto
Kanazawa University & Jibanshikenjo Co., Ltd., Tokyo, Japan

ABSTRACT: The Hybridnamic testing is a kind of falling-mass type rapid load test (RLT), by which several blows on a pile can be conducted easily and quickly. Hence, static load-displacement curve is constructed by connecting UnLoading Point (ULP) loads. This procedure is called UnLoading Point Connection (ULPC) method. ULP method or ULPC method is employed for cases of the relative loading duration $T_r = t_L/(2L/c)$ greater than 5, where t_L is loading duration, L is pile length and c is bar wave velocity. Segmental ULPC (SULPC) is proposed so that RLT can be employed even in cases of T_r less than 5. A case study was carried out to demonstrate the applicability of SULPC. Load-displacement curve from RLT with the SULPC method was comparable to that from the conventional static load tests.

1 INTRODUCTION

Twenty years have passed since the rapid loading test (RLT) of piles were newly added to the Japan Geotechnical Society (JGS) standard (JGS1815-2002). Until 2002, most of RLTs were conducted using the mass-launching method such as the Statnamic test developed by Middendorp et al. (1992). After 2002, most of RLTs in Japan are conducted using the falling-mass method with a soft-cushion placed on the pile head. The Hybridnamic device (Figure 1) developed by Jibanshikenjo Co. is a typical falling-mass method. In line with this, the number of loading cycles has also changed from one loading of the maximum planned load to multiple loading

Figure 1. Hybridnamic test device.

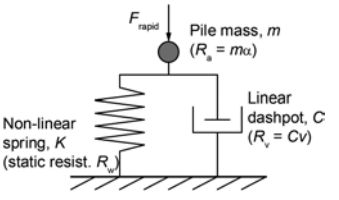

Figure 2. Modeling of pile and soil during RLT (after Middendorp et al, 1992, and Kusakabe and Matsumoto, 1995).

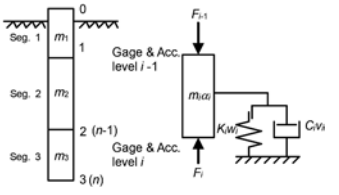

Figure 3. Segmental Unloading Point Connection (SULPC) method.

DOI: 10.1201/9781003299127-210

with the hammer drop height being raised in stages. Therefore, the interpretation method has shifted from the UnLoading Point (ULP) method to the UnLoading Point Connection (ULPC) method (Kamei et al. 2022), which provides a static load-displacement relationship simply by connecting ULPs without the need to obtain the damping constant C required in the ULP method.

As a result of the widespread use of the ULPC method as an interpretation method for RLT signals, some cases have emerged that pose challenges for the analysis of single mass model method in which the entire pile length is considered as a rigid body.

In this paper, as a new interpretation method to address these issues, the Segmental UnLoading Point Connection method (SULPC method) which is an extension of the Segmental UnLoading Point (SULP) method is proposed. The load-displacement relation of a pile from RLT is compared with the result of static load test (SLT).

2 SEGMENTAL UNLOADING POINT CONNECTION METHOD (SULPC METHOD)

Middendorp et al. (1992) treated the pile as a rigid mass during RLT assuming that the effects of wave propagation phenomena in the pile body are negligible. When a dynamic load F_{rapid} is applied to the pile, the static soil resistance R_{w} and dynamic soil resistance R_{v} act on the pile. These relationships are expressed in Equations 1 and 2, and Figure 2.

$$F_{\text{rapid}} = R_{\text{a}} + R_{\text{v}} + R_{\text{w}} = m\,\alpha + C\,v + R_{\text{w}} \tag{1}$$

$$R_{\text{soil}} = F_{\text{rapid}} - m\alpha \tag{2}$$

$$R_{\text{w}} = R_{\text{soil}} - \ C\,v \tag{3}$$

$$R_{\text{soil at ULP}} = R_{\text{ULP}} = R_{\text{w}} \tag{4}$$

where, F_{rapid} = Rapid load, R_{a} = Inertial force of pile, R_{v} = Dynamic soil resistance, R_{w} = Static soil resistance, m = Pile mass, α = Pile acceleration, C = Damping constant, v = Pile velocity, R_{ULP} = ULP resistance (static soil resistance).

Since the ULP method supposes that F_{rapid} equivalent to the ultimate pile bearing capacity is applied once, the damping constant C must be determined to estimate R_{w} (Eq. 3). However, the value of C may vary depending on the displacement and velocity of the pile.

At the maximum displacement w_{max} (called UnLoading Point, ULP) the pile velocity v is 0, hence R_{soil} is equal to R_{w} (R_{ULP}) as Equation 4.

In the Hybridnamic RLT, the hammer drop height h is increased in stages, and several blows are applied to the pile. In each blow, ULP load and the corresponding displacement are obtained. Therefore, by simply connecting the ULPs, the $R_{\text{w}} - w$ relationship can be easily obtained without the estimation of C. This interpretation is called UnLoading Point Connection (ULPC) method (Kamei et al. 2022).

Mullins et al. (2002) proposed the Segmental UnLoading Point (SULP) method for a pile instrumented at several pile sections. In the SULP method, force and acceleration are measured at the pile head whereas only force is measured at other pile sections. The velocity and acceleration at a particular measurement point other than the pile head are estimated using the measured force at that point, and the force and displacement at the pile head. Note that only the total static soil resistance is estimated in the SULP method by summing up the static soil resistance of each segment.

In the proposed Segmental UnLoading Point Connection (SULPC) method, forces and accelerations are measured at several sections of the pile (Figure 3). Soil resistance $R_{\text{soil}i}$ vs displacement w_i of segment i is estimated using the relation of Equation 5 (Step 2 in Table 1).

Table 1. Flow of SULPC.

Step 1 : Multi cycle rapid load test
Step 2 : Calculate relationship of soil resistance R_{soil} - displacement w and ULP load for each segment
Step 3 : Constuct static resistance R_w - displacement w relationship for each pile segment by connecting ULPs (SULPC)
Step 4 : Analize responses of elastic pile subjected to static loading using a load transfer method

Table 2. Specifications of test pile.

Item	Value
Length, L (m)	24.8
Outer diameter, D_o (mm)	800
Inner diameter, D_i (mm)	772
Wall thickness, t_w (mm)	14
Cross-sectional area, A (m^2)	0.0346
Cross-sectional area, A (m^2)†	0.0376
Young's modulus, E (kPa)	2.00×10^8
Density, ρ (ton/m^3)	7.85
Mass, m (ton)	7.032
Bar wave velocity, c (m/s)	5048

† : including steel protection cover for strain gages.

$$R_{soil_i}(t) = F_{rapid_i}(t) - m_i \cdot \alpha_i(t) = F_{i-1}(t) - F_i(t) - m_i \cdot \alpha_i(t) \quad (5)$$

As several blows are applied to the pile in the Hybridnamic test as mentioned earlier (Step 1), static soil resistance R_{wi} vs w_i of segment i is constructed by connecting ULPs (Step 3).

The responses of the whole pile subjected to static pile head load are then calculated using a load transfer method (Step 4). In this calculation stage, the pile is treated as elastic, and non-linear soil resistance behavior estimated in Step 3 is considered at each pile node.

3 CASE STUDY

3.1 *Test description*

The test site was in Okayama Prefecture, Japan. The profiles of soil layers and SPT-N values are shown in Figure 4, together with pile embedment. The test pile was a steel pipe pile (SPP) having the specifications listed in Table 2. The pile was constructed using the down-the-hole hammer method. To increase plugging effect, concrete was filled inside the pile along a section of 1 D_o from the pile tip.

Two strain gages and two accelerometers were attached near the pile head (L1), and strain gages were instrumented at L2, L3 and L4. Furthermore, accelerometers were instrumented at L3 and L4. The acceleration α at L2 was obtained as the weighted mean value of α measured at L1 and L3. The outer surface of the pile section in the weathered rock between L3 and L4 was coated by a friction reduction material to ensure that the load on the pile head was sufficiently transferred to the pile tip.

Static load test (SLT) was carried out 29 days after the pile construction. In the SLT, 6-step load maintenance test was conducted followed by a continuous load test. RLTs using the Hybridnamic test device with a hammer mass of 44 ton was carried out 90 days after the SLT.

3.2 *Test results*

A total of 7 blows were conducted in the RLTs, increasing the hammer falling height h from 0.25 m to 3.0 m.

Figure 5 shows the measured dynamic signals in the RLT with h = 3.0 m. The relative loading duration T_r was 7.1, which satisfied the criterion of RLT ($T_r \geq 5$) specified in the JGS standard. Nevertheless, α at different levels were largely different showing that rigid body modeling of the pile was not adequate. It can be seen from the local pile displacements w that

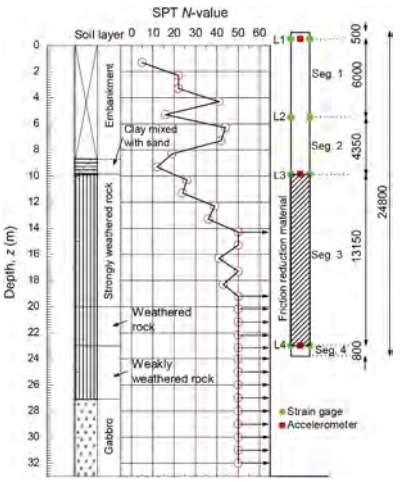

Figure 4. Profiles of soil layers and SPT-N values, together with pile embedment.

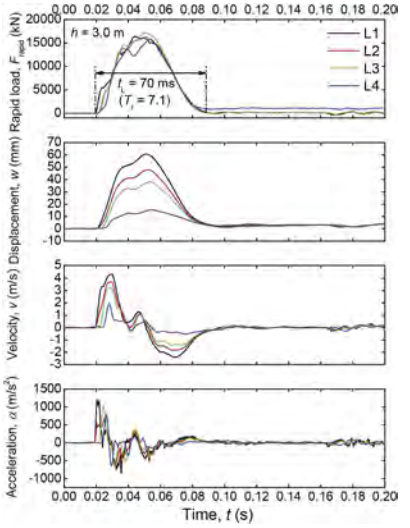

Figure 5. Measured dynamic signals (h = 3.0 m).

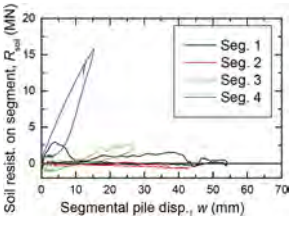

Figure 6. R_{soil} vs w of each pile segment (h = 3.0 m).

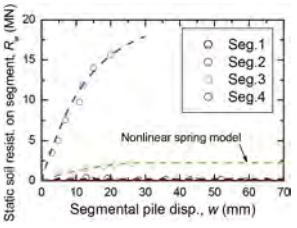

Figure 7. R_w vs w of each pile segment from multiple blows.

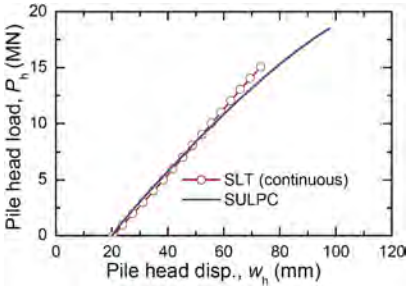

Figure 8. Static load-displacement curves from SULPC and SLT.

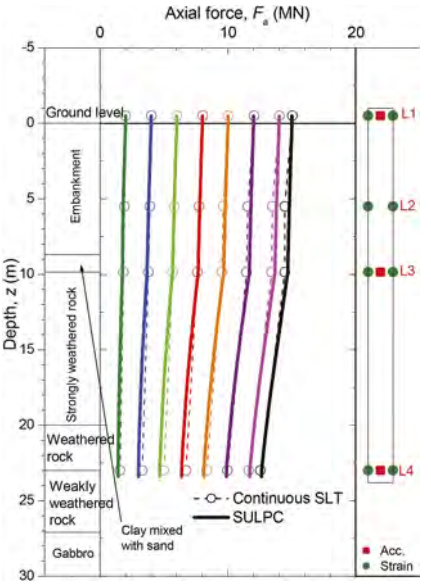

Figure 9. Axial pile force distributions from SULPC and SLT.

relatively large deformation of the pile was caused. Hence, the proposed SULPC interpretation was adopted.

Figure 6 shows the R_{soil} vs w in each segment estimated from the RLT with h = 3.0 m.

By connecting ULPs of each segment from all the 7 blows, the static soil resistance R_w vs w of each segment was obtained as shown in Figure 7. For the load transfer calculation, thus obtained R_w vs w was modeled by the dashed line for each segment.

Figure 8 shows the pile head load P_h vs pile head displacement w_h from the SULPC and the continuous SLT. The result from the SULPC is comparable with the SLT result.

Figure 9 shows the axial pile force F_a distributions from the SULPC interpretation and the continuous SLT. The results from the SULPC are again comparable with the SLT results.

4 CONCLUSIONS

A new interpretation method, SULPC, of RLT signals was proposed in this paper. The behaviors of a steel pipe pile from RLTs with the SULPC interpretation were comparable with those from SLT. The loading in this test was within the range of reloading. In future, similar comparison until ultimate load will be needed.

The authors would like to thank Mr. Tomohiro Fujita, Public Works Research Institute, for his supports in this research.

REFERENCES

Japanese Geotechnical Society. 2002. Method for Rapid Load Test of Single Piles, JGS 1815-2002, Standards of Japanese Geotechnical Society for Vertical Load Tests of Piles.

Kamei, S., Takano, K. & Fujita, T. 2022. Comparison of static load test and rapid load test on steel pipe piles in two sites. *Proc. the 11th intern. conf. on Stress Wave Theory and Design and Testing Methods for Deep Foundations, Rotterdam* (to be presented).

Kusakabe, O. & Matsumoto, T. 1995. Statnamic tests of Shonan test program with review of signal interpretation. *Proc. the 1st intern. Statnamic seminar, Vancouver*: 113–122.

Middendorp, P., Bermingham, P. & Kuiper, B. 1992. Statnamic load testing of foundation pile. *Proc. the 4th intern. conf. on Appl. of Stress-Wave Theory to Piles, The Hague*: 581–588.

Mullins, G., Lewis, L.C. & Justason, M.D. 2002. Advancements in Statnamic data regression techniques. *Proc. intern. Deep Foundations Congress, Orlando*: 1–16.

Smart Geotechnics for Smart Societies – Zhussupbekov, Sarsembayeva & Kaliakin (Eds)
© 2023 The Author(s), ISBN 978-1-003-29912-7
Open Access: www.taylorfrancis.com, CC BY-NC-ND 4.0 license

Hybridnamic rapid load testing with UnLoading Point Connection method invoking Case method

S. Lin, S. Kamei & I. Yamamoto
Jibanshikenjo Co., Ltd., Tokyo, Japan

T. Matsumoto
Kanazawa University & Jibanshikenjo Co., Ltd., Tokyo, Japan

ABSTRACT: The Hybridnamic testing is a kind of falling-mass type rapid load test (RLT), by which several blows on a pile can be conducted easily and quickly. Hence, static load-displacement curve is constructed by connecting UnLoading Point (ULP) loads. This procedure is called UnLoading Point Connection (ULPC) method. ULP method or ULPC method is employed for cases of the relative loading duration $T_r = t_L/(2L/c)$ greater than 5, where t_L is loading duration, L is pile length and c is bar wave velocity. ULPC with Case method (ULPC_CM) is proposed in this paper so that RLT can be employed even in cases of T_r less than 5. A case study was carried out to demonstrate the applicability of ULPC_CM. Load-displacement curves from the ULPC_CM interpretation of RLT signals having smaller T_r less than 5 were comparable to the conventional static load test result.

1 INTRODUCTION

Twenty years have passed since the rapid loading test (RLT) of piles were newly added to the Japan Geotechnical Society (JGS) standard (JGS1815-2002). After 2002, most of the RLTs in Japan are conducted using the falling-mass method with a soft-cushion placed on the pile head. In line with this, the number of loading cycles has also changed from one loading of the maximum planned load to multiple loading with the hammer drop height being raised in stages. Therefore, the interpretation method has shifted from the UnLoading Point (ULP) method to the UnLoading Point Connection (ULPC) method (Kamei et al. 2022), which provides a static load-displacement relationship simply by connecting the ULPs without the need to obtain the damping constant C required in the ULP method.

As a result of the widespread use of the ULPC method as an interpretation method for rapid loading tests, some cases have emerged that pose challenges for the analysis of single mass model method in which the entire pile length is considered as a rigid body.

In this paper, as a new interpretation method to address these issues, the ULPC method invoking the Case method (ULPC_CM) is proposed.

2 HYBRIDNAMIC RAPID LOAD TEST DEVICES

Jibanshikenjo Co. Ltd. has developed several Hybridnamic test devices since 2003. The Hybridnamic test devices are "falling-mass type", in which a hammer mass in the steel frame is lifted using a hydraulic jack and free-dropped to apply rapid load to the pile head via a specially designed cushion on the pile head. By changing combination of stiffness of the cushion system K_{cushon}, hammer mass m_h and falling height of hammer h, loading duration t_L

DOI: 10.1201/9781003299127-211

and the maximum rapid load $F_{rapid(max)}$ can be easily controlled. In the current JGS standards, load test with the relative loading duration $T_r = t_L/(2L/c) \geq 5$, where L is the pile length and c is the bar wave velocity in the pile, is regarded as RLT.

3 UNLOADING POINT CONNECTION METHOD WITH CASE METHOD (ULPC_CM)

Middendorp et al. (1992) treated the pile as a rigid mass during RLT assuming that the effects of wave propagation phenomena in the pile body are negligible. When a dynamic load F_{rapid} is applied to the pile, the static soil resistance R_w and dynamic soil resistance R_v act on the pile. These relationships are expressed in Equations 1 and 2, and Figures 1 and 2.

$$F_{rapid} = R_a + R_v + R_w = m\ \alpha + C\ v + R_w \tag{1}$$

$$R_{soil} = F_{rapid} - m\ \alpha \tag{2}$$

$$R_w = R_{soil} - \ C\ v \tag{3}$$

$$R_{soil\ at\ ULP} = R_{ULP} = R_w \tag{4}$$

where, F_{rapid} = Rapid load, R_a = Inertial force of pile, R_v = Dynamic soil resistance, R_w = Static soil resistance, m = Pile mass, α = Pile acceleration, C = Damping constant, v = Pile velocity, R_{ULP} = ULP resistance (static soil resistance).

At the maximum displacement w_{max} (called UnLoading Point, ULP) the pile velocity v is 0, hence R_{soil} is equal to R_w (R_{ULP}) as Equation 4.

In the Hybridnamic RLT, the hammer drop height h is increased in stages, and the pile is loaded multiple times. In each blow, ULP load and the corresponding displacement are obtained. Therefore, by simply connecting the ULPs, the R_w - w relationship can be easily obtained without the estimation of C.

Kamei et al. (2022) point out that even if $T_r \geq 5$, there are cases where assumption of rigid mass modeling of a pile may not be adequate. To overcome this situation, Kamei et al. (2023, in press) proposes Segmental UnLoading Point Connection (SULPC) method. The SULPC method can be employed in case that the pile is instrumented with strain gages and accelerometers at several levels of the pile.

In many cases, however, dynamic signals are measured only near the pile head. Hence, a new interpretation method is proposed, in which the ULPC method (Kamei et al. 2022) and the Case method (Raushe et al. 1985) are combined as described below.

The Case method is a method based on one-dimensional stress-wave theory, in which the soil resistance R_t (= R_{soil}) of a pile during driving, and the static soil resistance R_s (= R_w) are obtained using an empirical coefficient called the J_c-factor.

First, the downward traveling wave F_d and the upward traveling wave F_u are calculated from the measured dynamic signals (axial force F and pile velocity v) (Equations 5 and 6). Then, using Equation 7, the time variation of the penetration resistance R_t of the pile is obtained (Figure 3).

$$F_d(x_m, t) = \frac{F(x_m, t) + Z \bullet v(x_m, t)}{2} \tag{5}$$

$$F_u(x_m, t) = \frac{F(x_m, t) - Z \bullet v(x_m, t)}{2} \tag{6}$$

$$R_t(x_m, t) = F_d\left(x_m, t - \frac{L_m}{c}\right) + F_u\left(x_m, t + \frac{L_m}{c}\right) \tag{7}$$

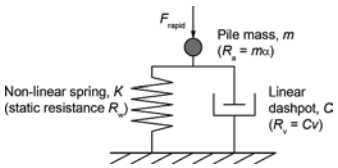

Figure 1. Modeling of pile and soil during RLT (after Middendorp et al. 1992, and Kusakabe and Matsumoto, 1995).

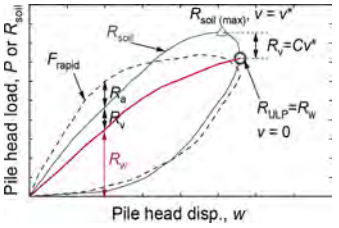

Figure 2. Relationship between load-displacement curve and soil resistance and ULP resistance.

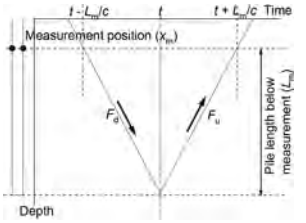

Figure 3. Case method (Raushe et al. 1985).

where, x: Coordinate along the pile axis (pile head = 0), x_m: Measurement position, v: Pile velocity, L_m: Pile length from measurement position to pile tip, Z: Impedance ($=EA/c$), F: Axial force, F_d: Downward force wave, F_u: Upward force wave, c: Bar wave velocity, E: Young's modulus of pile material, A: Cross sectional area of pile

The Case method evaluates the penetration resistance of the pile during driving, but the load-displacement relationship of the pile cannot be obtained by this method alone. Since the Case method is based on the one-dimensional wave theory, the penetration resistance of the pile can be evaluated correctly regardless of the pile length.

In the proposed ULPC_CM method, multiple blows (rapid load tests) are applied to a pile. The time variation of soil resistance R_{soil} is obtained from the Case method, and the time variation of pile displacement w is directly measured. Hence, $R_{soil} - w$ relation is easily obtained. R_{soil} at the maximum pile displacement (ULP) can be regarded as the static resistance R_w. Static load-displacement curve is constructed by connecting ULPs from the multiple blows.

As the ULPC_CM method is based on the one-dimensional stress-wave theory, it has the advantage of not requiring correction for pile inertia. Hence, the ULPC_CM method would be applied to RLTs on piles with $T_r < 5$.

4 CASE STUDY

4.1 *Test description*

The test site was in Ibaraki Prefecture, Japan. The profile of SPT-N values is shown in Figure 4, together with pile embedment. The test pile was a steel pipe pile (SPP) having the specifications listed in Table 1. The pile was constructed using the inner excavation method. Two strain gages and two accelerometers were attached near the pile head.

Static load test (SLT) with 5-step maintained load was carried out 29 days after the pile construction. RLTs using the Hybridnamic test device with a hammer mass of 23 ton was carried out 112 days after the SLT.

4.2 *Test results*

Figure 5 shows the measured dynamic signals in the RLT with $T_r = 3$. In the figure, soil resistance $R_{soil\ (ULP)}$ from the ULP method and $R_{soil\ (Case)}$ from the Case method are also shown. $R_{soil\ (ULP)}$ and $R_{soil\ (Case)}$ at the time of maximum displacement are the static soil resistance R_w from both methods.

By connecting R_w from the all blows, pile head load P_h vs pile head displacement w_h are obtained as shown in Figure 6. P_h vs w_h from both ULPC and ULPC_CM are comparable with the SLT result when $T_r = 5$. However, as T_r decreases, the results from ULPC overestimate the SLT result, while the results from the ULPC_CM are still comparable with the SLT result.

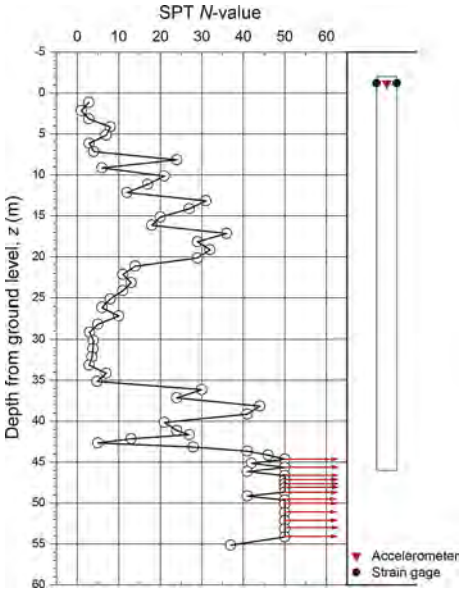

Figure 4. Profile of SPT-N values, together with pile seating.

Table 1. Specifications of the test pile.

Item	Value
Length, L (m)	48.0
Outer diameter, D_o (mm)	800
Inner diameter, D_i (mm)	750
Wall thickness, t_w (mm)	25
Cross-sectional area, A (m^2)	0.0609
Young's modulus, E (kPa)	2.00×10^8
Density, ρ (ton/m^3)	7.85
Mass, m (ton)	22.314
Bar wave velocity, c (m/s)	5133

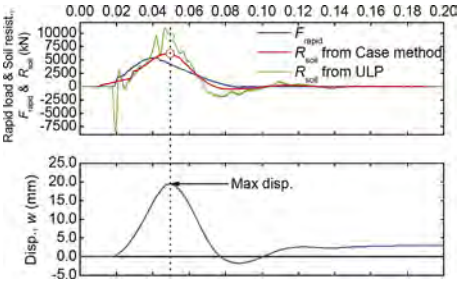

Figure 5. RLT signals (T_r = 3, h = 1.0 m).

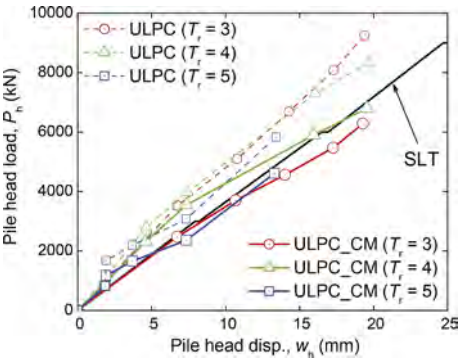

Figure 6. Comparison of load-displacement curves from SLT, RLTs with ULPC and ULPC_CM.

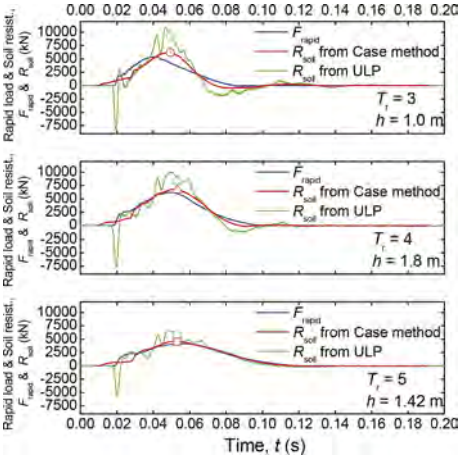

Figure 7. RLT signals (T_r = 3~5).

As shown in Figure 7, for T_r = 5, there is no significant difference between $R_{soil\ (Case)}$ and $R_{soil\ (ULP)}$; as T_r decreases to 4 and 3, the difference between $R_{soil\ (Case)}$ and $R_{soil\ (ULP)}$ increases. The results in Figures 6 and 7 indicate that the ULPC_CM method has a potential applicability to RLTs with T_r < 3.

5 CONCLUSIONS

A new interpretation method, ULPC_CM, of RLT signals was proposed in this paper. The load-displacement relations of an SPP from RLTs with the ULPC_CM interpretation were comparable with the SLT result until T_r was decreased to 3.

The loading in this test was within the range of reloading. In future, similar comparison between RLTs and SLT will be needed to examine the applicability of the ULPC_CM to obtain the load-displacement relation of a pile to the ultimate load. Furthermore, conduction of RLTs with $T_r < 3$ will be needed to discuss the application limit of ULPC_CM method for RLTs with smaller T_r.

REFERENCES

Japanese Geotechnical Society. 2002. Method for Rapid Load Test of Single Piles, JGS 1815-2002, Standards of Japanese Geotechnical Society for Vertical Load Tests of Piles.

Kamei, S., Lin, S., Yamamoto, I. & Matsumoto, T. 2023. Hybridnamic rapid load testing with an extended interpretation method of dynamic signals. *Proc. the 17th Asian Regional Conference on Soil Mechanics and Geotechnical Engineering 2023*, *Nur-Sultan* (to be submitted).

Kamei, S., Takano, K. & Fujita, T. 2022. Comparison of static load test and rapid load test on steel pipe piles in two sites. *Proc. the 11th Intern. Conf. on Stress Wave Theory and Design and Testing Methods for Deep Foundations, Rotterdam* (to be presented).

Kusakabe, O. & Matsumoto, T. 1995. Statnamic tests of Shonan test program with review of signal interpretation. *Proc. the 1st Intern. Statnamic Seminar, Vancouver*: 13–122.

Middendorp P., Bermingham P. & Kuiper B. 1992. Statnamic load testing of foundation pile. *Proc. the 4th Intern. Conf. on Appl. of Stress-Wave Theory to Piles, The Hague*: 581–588.

Raushe, F., Goble, G. & Likins, G.E. Jr. 1985. Dynamic determination of pile capacity. *ASCE Jour. Geotech. Div.*, 111(3): 367–383.

Smart Geotechnics for Smart Societies – Zhussupbekov, Sarsembayeva & Kaliakin (Eds)
© 2023 The Author(s), ISBN 978-1-003-29912-7
Open Access: www.taylorfrancis.com, CC BY-NC-ND 4.0 license

Reliability-based assessment of drilled displacement (DDS) piles bearing capacity using field tests and FEM

A.B Issakulov, A.Zh Zhussupbekov & A.R Omarov
L.N. Gumilyov Eurasian National University

B.R. Issakulov
Baishev University

R.Ye. Lukpanov, A.S. Tulebekova & S.T. Mussakhanova
L.N. Gumilyov Eurasian National University

ABSTRACT: The article deals with geotechnical design of pile foundations, especially by static load tests and by calculation using numerical models. The results of comparison analysis of bearing capacities drilling displacement system (DDS) boring piles obtained by static load tests and by standard are presented in article, as well as results of compression test of surrounding soil after DDS pile installation. Drilled Displacement System (DDS) piles are an innovative technology for pile foundations. These DDS piles are created by rotary drilling with a simultaneous full displacement of the soil in a horizontal direction. The optimal design of DDS piles can be obtained in soils that allow for a horizontal displacement, which causes an increase in the shaft's resistance. Significant differences between experimental (Static Load Test by GOST) and design (by Kazakhstan Standards) values of bearing capacity of DDS pile show us incomplete usage of DDS technology resourced. The results of numerical analysis of DDS and traditional boring pile modeling by FEM (Plaxis 2D) are also presented in the paper. The numerical results have been presented with equivalent static load-settlement curve. By results of numerical analysis coefficient of surrounding work is defined. These investigations are important for un-derstanding of soil-pile interaction on problematical soft soils ground of Astana, Kazakhstan.

Keywords: DDS, bored piles, FEM, bearing capacity

1 INTRODUCTION

Pile foundations are one of the most popular types of foundations on construction sites in Kazakhstan, the expediency of using which is explained by the need to provide a large load-bearing capacity of high-rise buildings and structures. Due to the emergence of new technologies and equipment for the construction of pile foundations, designers have a need to improve the current regulatory documents, which, unfortunately, do not have recommendations for the design of piles arranged according to modern technologies [1]. In this article, the work of a bored pile arranged by the DDS method without excavation was investigated. This technology is one of the latest products of German manufacturers and is undoubtedly of practical interest for modern construction in Kazakhstan. The main advantages of this technology are: high productivity of pile production; high economic efficiency; low noise and no vibration when installing piles; and most importantly, high load-bearing capacity of the pile [2,3]. Large differences between experimental (static tests) and calculated (normative) values of the bearing

DOI: 10.1201/9781003299127-212

capacity of bored piles arranged by the rolling method indicate that the resources of this technology are not fully used. The large values of the bearing capacity of the piles are explained by the fact that when the pile is installed, the excavation does not occur, the soil is radially displaced by the rolling of the drilling tool, thereby, as a result of compaction, there is a change in the strength and deformation characteristics of the soil around the pile. Thus, it becomes obvious that the work of displacement piles is different from the work of a traditional pile, and there are still many unresolved issues concerning this technology: the impact of displacement technology on the bearing capacity of piles; the effect of radial compaction of the surrounding array on the work of piles; the impact of displacement piles on the foundations of adjacent buildings and structures, etc.

2 FEATURES OF DDS TECHNOLOGY

The sequence of work on the installation of drilling piles manufactured using DDS technology includes the following operations (Figure 1): installation of drilling equipment at the drilling site; immersion of the drilling tool with a sealing system to the design mark; connection of the concrete pump followed by filling the well with concrete mixture and one-time extraction of the drilling tool; immersion in the well with concrete reinforcement frame to the design mark.

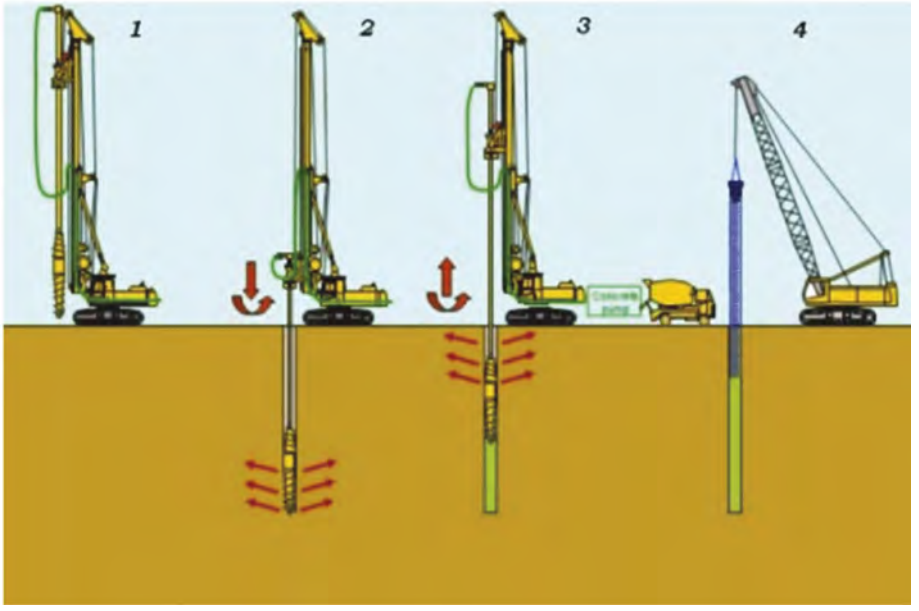

Figure 1. DDS pile devices.

A distinctive feature of the DDS technology is the drilling tool (Figure 2). When drilling the drilling tool down, simultaneously with drilling, the well is rolled out, as a result of which the radial compaction of the soil occurs without its excavation, when drilling up, the walls are compacted.

This technology allows you to arrange piles with a diameter of up to 0.6 m to a depth of up to 30 m. When calculating the productivity, the following parameters should be taken into account: the diameter of the pile, the amount of applied torque and pressing force, density (strength of the soil, compaction of the soil, power of the concrete pump [4].

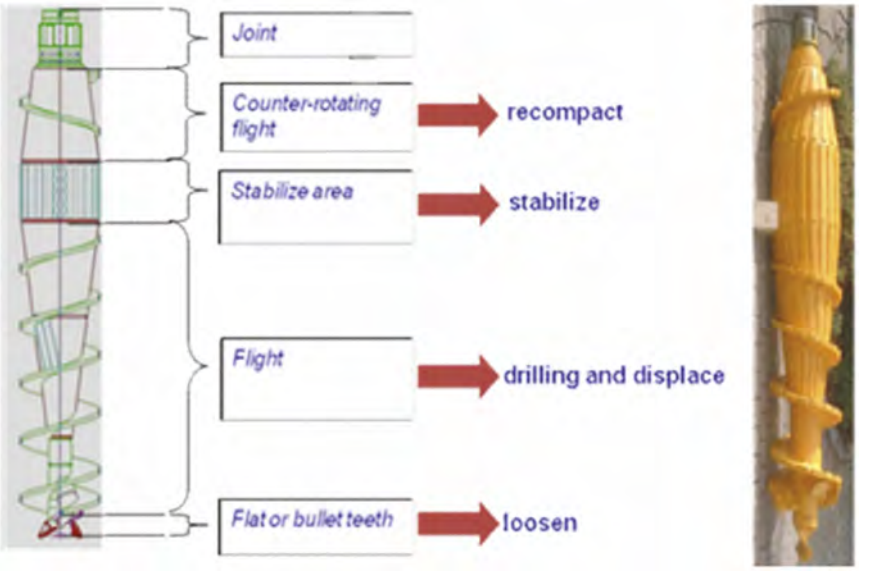

Figure 2. DDS pile drilling Auger.

3 STATIC TESTING OF DDS PILES

In order to clearly demonstrate the differences between the actual and design values of the bearing capacity, static tests of DDS piles were carried out. In total, 14 DDS piles were tested at two construction sites. At the first construction site "Khan Shatyry Shopping and Entertainment Center" 11 piles were tested, 8 of which with a diameter of 410mm, 18m long, 2 piles with a diameter of 500mm, 10m long and 1 pile with a diameter of 600m, 18m long. At the second construction site

"Production base of "KGS" LLP" three piles with a diameter of 500 mm and a length of 2.5m were tested. According to engineering and geological surveys, the geological structure of the survey site is attended by: IGE2 - alluvial medium-odd-quaternary deposits, presented in the form of alternating layers of clay, IGE3 - loamy and loamy–sandy soils, as well as IGE4 - medium-quaternary deposits, presented in the form of clay and loamy deposits [5].

The load on the pile was applied in steps of 400kN and 200kN to the limit of 2800kN with a CM- 158 hydraulic jack. The hydraulic jack force is regulated by the fluid supply from the pumping station and is fixed by a technical pressure gauge. The movement of the pile is measured by deflection meters with an accuracy class 0.01 mm, which are fixed on a reference system fixed to the ground. The reference system is independent of the movement of the system of beams and piles. Unloading was carried out in steps of 800kN and 400kN. For the criterion of the maximum permissible precipitation, the instructions regulated in the SNIP of the Republic of Kazakhstan were adopted 5.01-03-2002 - Pile foundations [6]. For the particular value of the maximum resistance of the pile Fu to the pressing load, the load should be taken, under the influence of which the tested pile will receive a draft equal to S and determined by Formula 1:

$$S_{\max.\text{Sett.}} = \zeta S_{u,mt} \tag{1}$$

$S_{u,mt}$ - the limit value of the average precipitation of the foundation of the projected building or structure, for industrial and civil single-storey and multi-storey buildings with a full frame is assumed to be 8 cm (for reinforced concrete structures) according to the instructions SNiP RK 5.01-01-2002 [7];

ζ- conversion coefficient from the limiting value of the average foundation settlement of the building or structure $S_{u,mt}$ to the pile settlement obtained during static tests with conditional stabilization (attenuation) of settlement is taken equal to 0.2 according to guidelines.

4 COMPARISON OF EXPERIMENTAL AND CALCULATED VALUES OF BEARING CAPACITIES OF DDS PILES

The experimental and calculated (according to the standards) values of the bearing capacities of DDS piles are presented in Table 1. It can be seen from the table that there is a significant difference between the experimental and calculated values of bearing capacities.

Table 1. Comparison of partial values of load-bearing capacities.

№	Geometric dimensions of the pile	Number of piles	Bearing capacity, kN		k = F_u/F_d coefficients
			Experimene al F_u	Calculated F_d	
	L = 17 m d = 410 mm	№1	2280	1545	1,48
		№2	2150	1545	1,39
		№3	2325	1545	1,50
		№4	2475	1545	1,60
		№5	2200	1545	1,42
		№6	2080	1545	1,35
		№7	2190	1545	1,42
	L = 17 m d = 600 mm		2700	2110	1,28
	L = 2 m d = 500 mm	№1	470	272	1,73
		№2	490	272	1,80
		№3	460	272	1,69

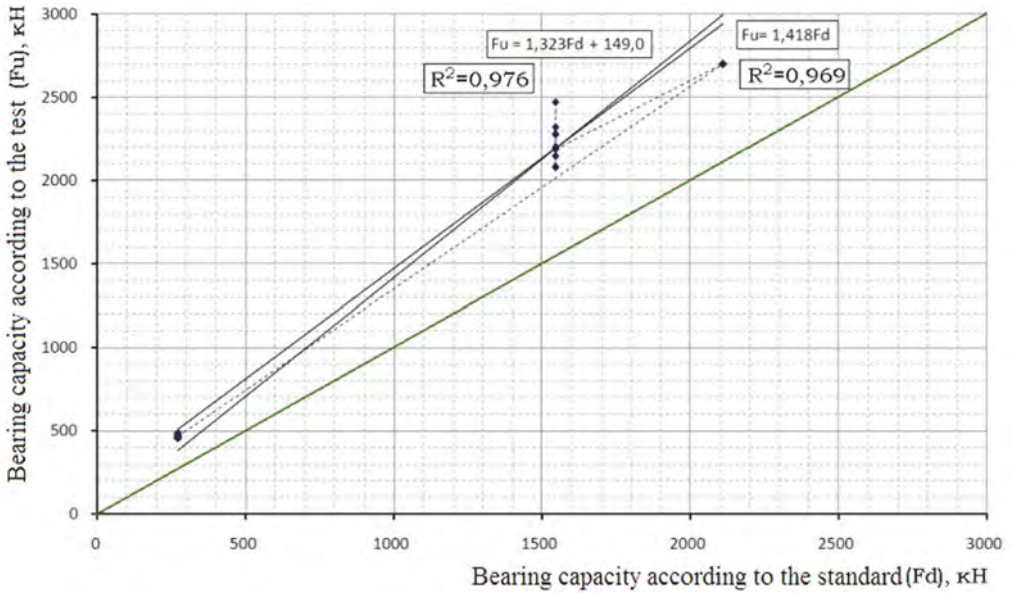

Figure 3. Comparative diagram of experimental F_u and calculated F_d bearing capacities of DDS piles [8].

A comparative diagram of experimental F_uu and calculated $F_d$bearing capacities of DDS piles is shown in Figure 3. As can be seen from the comparative diagram, all points are located above the diagonal, which indicates that all values of experimental bearing capacities are greater than the values of bearing capacities defined by standards.

5 LABORATORY TESTS OF SOIL COMPACTED AROUND THE PILE

The purpose of the laboratory study of the soil mass near the pile is to determine the effect of radial compaction on the physical and mechanical properties of the soil. To study the physical and mechanical properties, soil samples were taken before and after the installation of DDS piles at the construction site of the Khan-Shatyry Shopping and Entertainment Complex in Astana, where DDS piles of various diameters were used (previously mentioned). Soil samples for laboratory studies were selected after static tests of DDS piles at a distance of up to 0.1, 0.2, 0.4, 0.6, 08 and 1 m from the edge of the pile, in order to determine the soil compaction zone along the lateral surface of the pile. More than 30 test wells were drilled with a depth of up to 10 m with an interval of 0.5 m in depth. The distances between the wells were 0.2--1.2 m depending on the distance from the pile. Laboratory tests were carried out in accordance with GOST 12248-96 [9].

The test results were subjected to statistical processing, the purpose of which was to determine the zone of radial compaction, as well as to identify elements of randomness (random values), the cause of which may be the difficulty of extracting soil in an undisturbed state or the error of measuring instruments.

According to the test results, the radial sealing zone for IGE2 was 0.6-0.8 m, for IGE3 and IGE4 0.4-0.6 m. The obtained values of the modulus of deformation, the angle of internal friction and adhesion are displayed graphically in Figures 4-6. With the help of nomograms, it is possible to adjust the deformation modulus, the angle of internal friction and adhesion depending on the diameter of the DDS pile at the design stage [10-12].

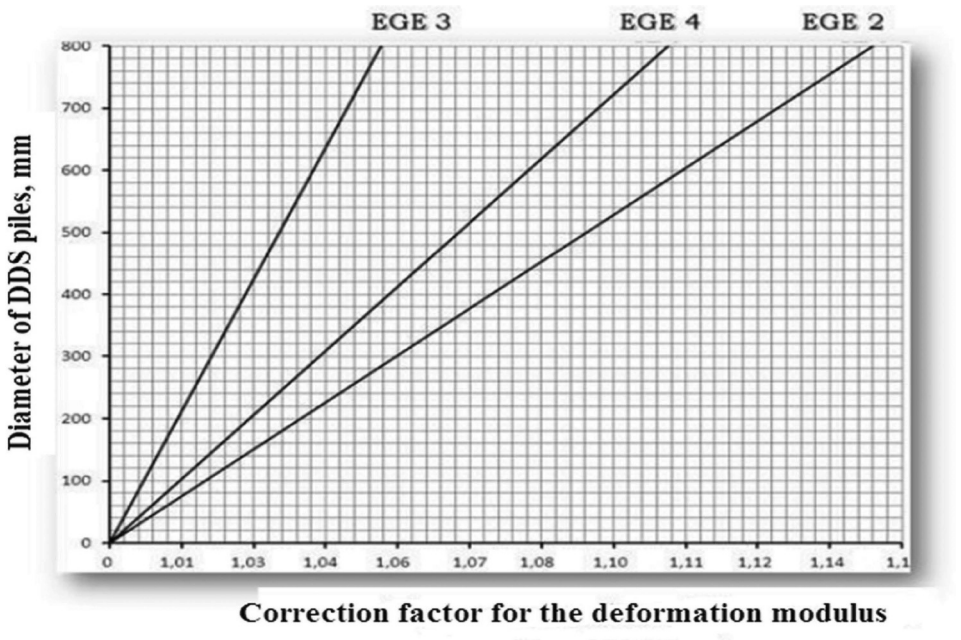

Figure 4. Nomogram for correction of the deformation modulus.

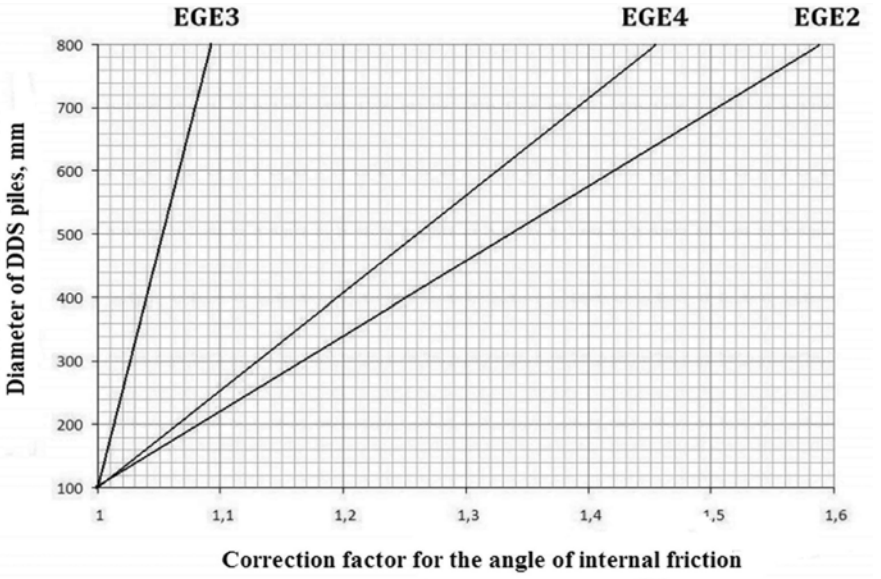

Figure 5. Nomogram for adjusting the angle of internal friction.

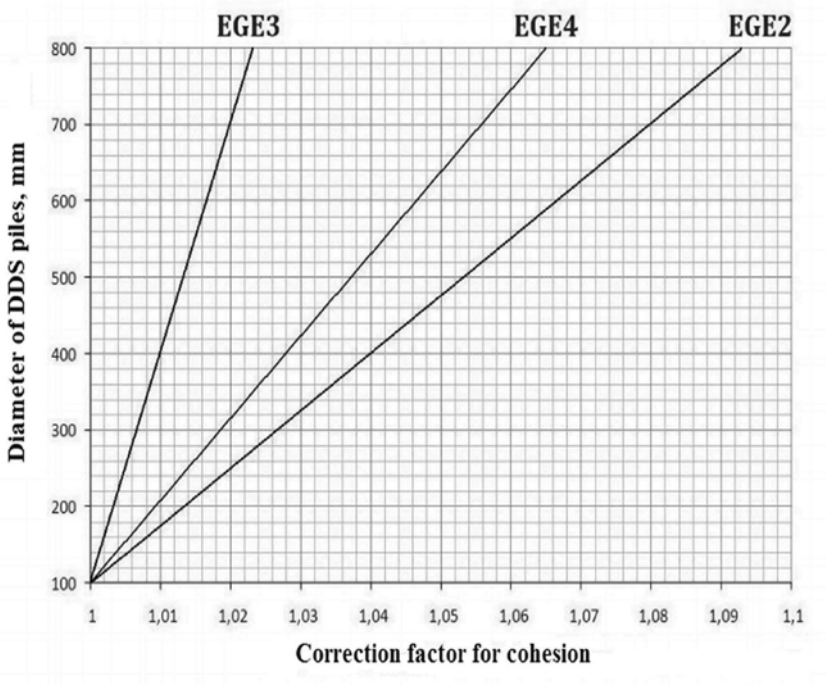

Figure 6. Nomogram for clutch adjustment.

6 NUMERICAL SIMULATION OF DDS PILES

The aim of the study is to determine the effect of soil compaction as a result of its displacement on the bearing capacity of the DDS pile.

Modeling of a bored pile is carried out in an axisymmetric formulation of a two-dimensional model of hardening soil. The dimensions of the geometric model are assumed from the condition that the stress distribution will be negligibly small within a given zone.

Figure 7 shows a geometric model of a bored pile, including the separation of soil within a separately considered engineering-geological element, the pile element and a uniformly distributed load on the pile. The separation of the soil within one IGE implies that the compaction of the soil under the lower end of the pile does not occur, therefore, the cluster located under the lower end of the pile is assigned the parameters obtained from the results of field and laboratory studies of soils before their compaction.

When modeling a DDS pile, the soil cluster located above the end of the pile is given soil parameters determined experimentally after the DDS pile is installed, taking into account the radial compaction zone. Presumably, the bearing capacity of the DDS pile is greater than the bearing capacity of a traditional pile. We introduce the coefficient k, which shows the numerical value of the differences in bearing capacity between DDS piles and traditional piles.

$$k = \frac{F_{d\,(PLX)}^{DDS}}{F_{d(PLX)}^{tr}}\ ,\quad \mathrm{k} \geq 1 \tag{2}$$

where: $F_{d\,(PLX)}^{DDS}$ - calculated soil resistance based on the results of numerical modeling of the DDS pile, kN;

$F_{d(PLX)}^{tr}$ - calculated soil resistance based on the results of numerical modeling of a traditional pile, kN.

Коэффициент условия работы сваи DDS,

it will be determined by formula 4, taking into account the coefficient k.

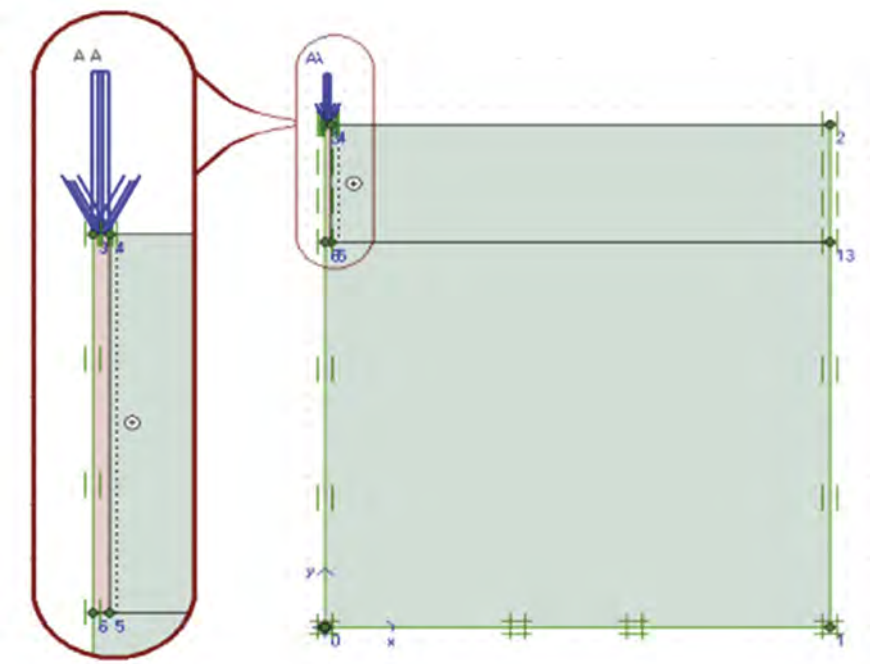

Figure 7. Geometrical model of DDS pile [13].

$$\gamma_{cf}^{DDS} = \frac{kF_a^{tr} - \gamma_c \gamma_{cr} RA}{u\gamma_c \sum f_i h_i} \quad (3)$$

where: γ_{cf}^{DDS} - coefficient of soil working conditions on the side surface of the pile DDS;
F_a^{tr} - estimated bearing capacity of a traditional pile;
$\gamma_c \gamma_{cr}$ - the same as Formula 2.

To determine the dependence of the bearing capacity of DDS piles and traditional piles, we will construct comparative diagrams showing the ratios of the values of the bearing capacity of traditional piles obtained by numerical modeling to the bearing capacity of DDS piles (Figure 8).

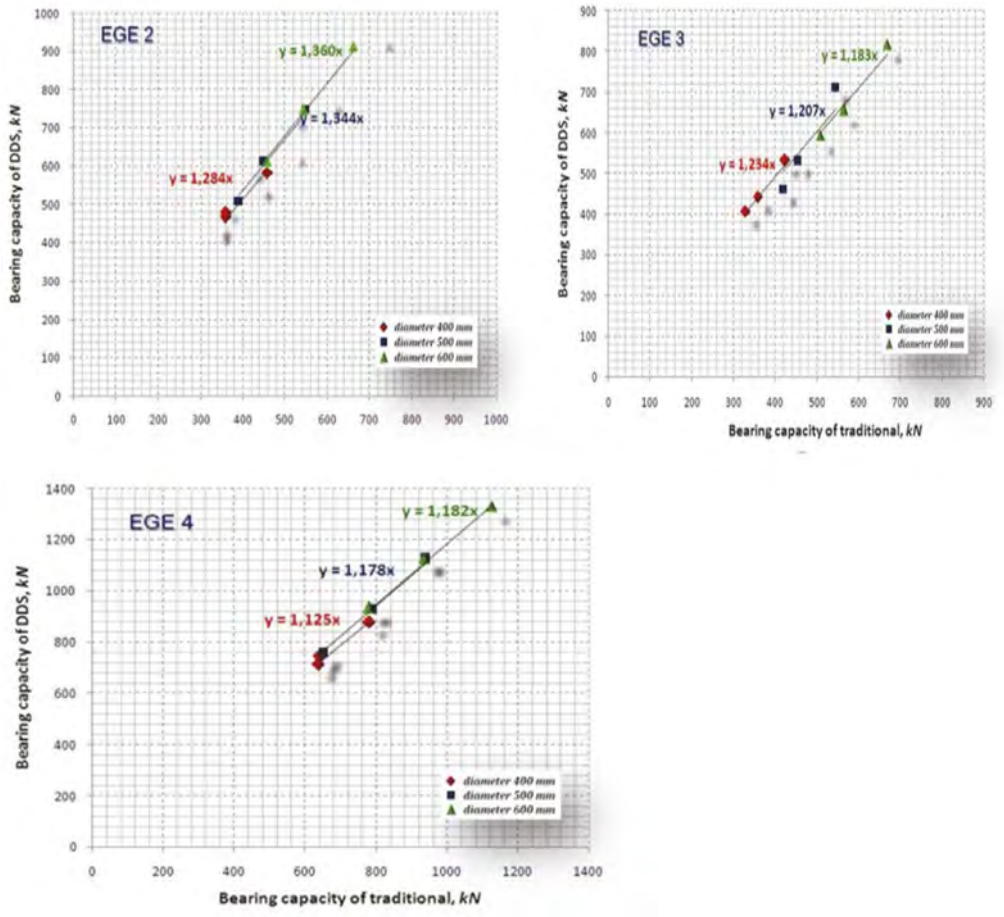

Figure 8. Simulation results.

It can be seen from the diagrams that the values of the coefficients of the soil working conditions on the side surface of the DDS pile are: for IGE2 – 1.38, IGE3 – 1.26, IGE4 – 1.2.

7 CONCLUSION

1. Static tests of DDS piles of various diameters were carried out, according to the results of which a comparative analysis of experimental bearing capacities of piles with normative

ones was carried out. The experimental values of the bearing capacity of DDS piles, on average, are 1.5 times higher than the calculated ones, which in turn indicates that the resources of DDS technology are not fully used.

2. Nomograms describing the dependence of the modulus of deformation, adhesion and the angle of internal friction on the diameter of the DDS piles were obtained. The adjustment of parameters can be used in the design of DDS piles with a diameter from 410 to 600 mm in engineering geological conditions similar to the conditions of the studied construction sites. The obtained dimensions of the radial seal were used in numerical modeling.
3. Based on the results of numerical modeling, an experimental-theoretical coefficient of the soil working conditions on the side surface of the pile DDS was obtained, equal to 1.28. At the same time, the difference between the experimental and calculated values of bearing capacities decreases from 1.51 to 1.14.

REFERENCES

Zhusupbekov, A., Bazarbayer, D., Matsumoto, T. Analysis of the Static Test of Boring Piles Through FDP (Full Displacement Pile) Technology // L. Gumilev atyndagy Euraziya ylttyk universitetinin HABARSHYSY. – Astana, Kazakstan, 2013. – B. 4. – URL: http://dspace.enu.kz/handle/data/9762. (application date 14.06.2013).

Basu P., Prezzi M., Basu D. Drilled Displacement Piles – Current Practice and Design // DFI Journal The Journal of the Deep Foundations Institute. Hawthorne, USA, 2010. – P. 3–20.

Rad S.H., Ghareh S., Eslami A. Experimental and feld studies on the behavior of drilled displacement piles // Innovative Infrastructure Solutions 6, №188 – Springer Nature Switzerland, 2021. – P. 1–-11.10.1007/s41062-021-00557-2.

Sultanov G.A., ZHusupbekov A.ZH., Lukpanov R.E., Enkebaev S.B. Sravnenie raboty tradicionnoj buronabivnoj svai s rabotoj svai ustraivaemoj metodom raskatki po rezul'tatam chislennogo modelirovaniya // Materialy respublikanskoj nauchno-prakticheskoj konferencii ENU im. L.N.Gumileva. - Astana, Kazahstan, 2010. – C. 219–226.

Alibekova, N., Bukenbayeva D. About the engineering-geological conditions of Astana // Proc. 6th Asian Young Geotechnical Engineers Conf. - Bangalore, India, 2008. P. 188–192.

SNiP RK 5.01-03-2002 Svajnye fundamenty. M.: KAZGOR. 2003

SN RK 5.01.-01-2013 Osnovanie i fundamenty. M.: Paragraf. S. 23, 2021.

Sultanov G.A., ZHusupbekov A.ZH., Lukpanov R.E., Enkebaev S.B. Laboratornye issledovaniya modulya deformacii grunta vokrugsvai ustraivaemoj metodom raskatki // Materialy respublikanskoj nauchno-prakticheskoj konferencii ENU im. L.N.Gumileva. - Astana, Kazahstan, 2010. – S. 214–219.

GOST 12248-96 Metody laboratornogo opredeleniya harakteristik prochnosti i deformiruemosti. M.: IPK Izdatel'stvo standartov. S.5, 2005.

Sultanov G.A., ZHusupbekov A.ZH., Lukpanov R.E., Enkebaev S.B. Opredelenie zavisimosti mezhdu eksperimental'nymi i raschetnymi znacheniyami nesushchih sposobnostej svaj vytesneniya // Materialy respublikanskoj nauchno-prakticheskoj konferencii ENU im. L.N.Gumileva. - Astana, Kazahstan, 2010. S. 226–232.

Zhusupbekov A.ZH., Lukpanov R.E., Isina A.Z., Aldungarova A.K. Issledovanie vzaimodejstviya gruntovogo massiva so svayami vytesneniya // Geomekhanika zhane zharatylystanu panderin okytu problemalary atty halykaralyk gylymi-tazhiribelik konferenciya materialdary. S. 223–228.

Zhussupbekov A., Iwasaki, Y., Omarov, A., Tanyrbergenova, G., Akhazhanov, S. (2019). Complex of static loading tests of bored piles. International Journal of GEOMATE, 2019, 16(58), pp.8–13.

Zhussupbekov A., Hoe Ling, Lukpanov R.Ye., Tulebekova A. Investigation of the interaction of a soil massif with displacement piles// BULLETIN of the L.N. Gumilyov ENU University (2012). – URL - http://dspace.enu.kz/handle/data/2144.

Smart Geotechnics for Smart Societies – Zhussupbekov, Sarsembayeva & Kaliakin (Eds)
© 2023 The Author(s), ISBN 978-1-003-29912-7
Open Access: www.taylorfrancis.com, CC BY-NC-ND 4.0 license

Investigation of soils on the base of a reinforced concrete chimney

A.V. Filatov & A.S. Zhakulin
Doctor of Technical Sciences, Professor, Karaganda Technical University, Karaganda, Kazakhstan

A.A. Zhakulina & P.A. Kropachev
Ph.D., Associate Professor, Karaganda Technical University, Karaganda, Kazakhstan

S.S. Kuzmichev
Karaganda Technical University, Karaganda, Kazakhstan

A.U. Yessentayev
L.N. Gumilyov Eurasian National University, Astana, Kazakhstan

ABSTRACT: The article presents the results of investigation of soils in the base and reasons for the collapse of a reinforced concrete chimney. Based on the materials of the conducted studies, it was concluded that the main reason for the collapse of the reinforced concrete shaft of the chimney of coke oven batteries no. 5 and no. 6 of arcelormittal temirtau jsc (formerly karaganda metallurgical plant) is a decrease in the strength characteristics of concrete due to many years of constant moisture, freezing and thawing in the autumn winter-spring periods of time, and indirectly due to the lack of proper control over the technical condition of building structures of all areas of reinforcement of the reinforced concrete chimney shaft and assessment of their strength characteristics. The design of the reinforcement instead of its original purpose contributed to the development of negative consequences and the safe operation of the facility.

1 INTRODUCTION

Coke oven battery No. 5 with a capacity of 690 thousand tons of coke per year was put into operation on June 22, 1969 and is intended for processing coal charge to produce coke and coke oven gas.

The chimney of coke oven batteries No. 5 and No. 6 is designed to remove coke oven gas combustion products, built in 1965. Technical characteristics of the chimney: height H=100 m, diameter of the lower part of the pipe 8.0 m, upper part 4.0 m, thickness walls: bottom 320 mm, top 160 mm.

The material of the shaft is made in the form of a monolithic reinforced concrete structure made of concrete grade 300, the lining is made of ceramic brick grade 125, thermal insulation is made of diatomaceous bricks.

The last geodetic survey was carried out in April 2013. According to the results of the geodetic survey, the vertical deviation of the shaft to the south was 149 mm, to the west 208 mm, the magnitude of the deviations is within the allowable building codes for such structures.

On June 26, 2013, the reinforced concrete chimney of coke oven batteries No. 5 and No. 6 collapsed. When the upper part of the chimney fell, the direct coke oven gas pipeline with a diameter of 2600 mm, the charge conveyor gallery and the associated pipelines for steam, process water, electrical cable products were destroyed, followed by coke oven gas burnout in the damaged section of the direct coke oven gas pipeline.

DOI: 10.1201/9781003299127-213

2 TECHNICAL INSPECTION OF THE CHIMNEY

The chimney was subjected to an annual technical inspection. In 2005, a major overhaul was carried out with the replacement of metal structures, the restoration of a lightning rod, light signaling. In 2008, the blind area around the perimeter of the chimney was repaired.

A detailed instrumental examination of the chimney in order to determine the technical condition and assess the bearing capacity of the reinforced concrete structure and the remaining service life was not carried out.

Under such circumstances, the decrease in the strength characteristics of the material of the reinforced concrete structure was left without due attention and was not under the necessary technical control of the facility's operation services, which led to a complete loss of the bearing capacity of the chimney.

During the construction of the chimney of coke oven battery No. 5, deviations from the project were allowed. For this reason, from e.g. ± 0.0 m to elevation + 15.0 m, the walls of the reinforced concrete shaft were reinforced with a monolithic reinforced concrete belt made of M-300 concrete along the entire outer perimeter of the pipe.

When reinforcing the reinforced concrete pipe shaft, the design, construction and operating organizations ignored the technical design of all interfaces between the existing and new chimney structures, which led to the collapse of the reinforced concrete pipe after 50 years of its operation. Such circumstances required increased control over the technical condition of all sections of the reinforcement of the reinforced concrete shaft up to the level. +15.0 m (elevation of the upper part of the reinforced concrete reinforcement cage).

The scheme of reinforcing the reinforced concrete pipe shaft is shown in fig. one Specialists involved in the investigation of the cause of the collapse of a reinforced concrete chimney with a height of H \u003d 100m at elevation. +15m, conclusions were drawn about the possible cause of the emergency due to the constant leakage of water from the water supply systems of

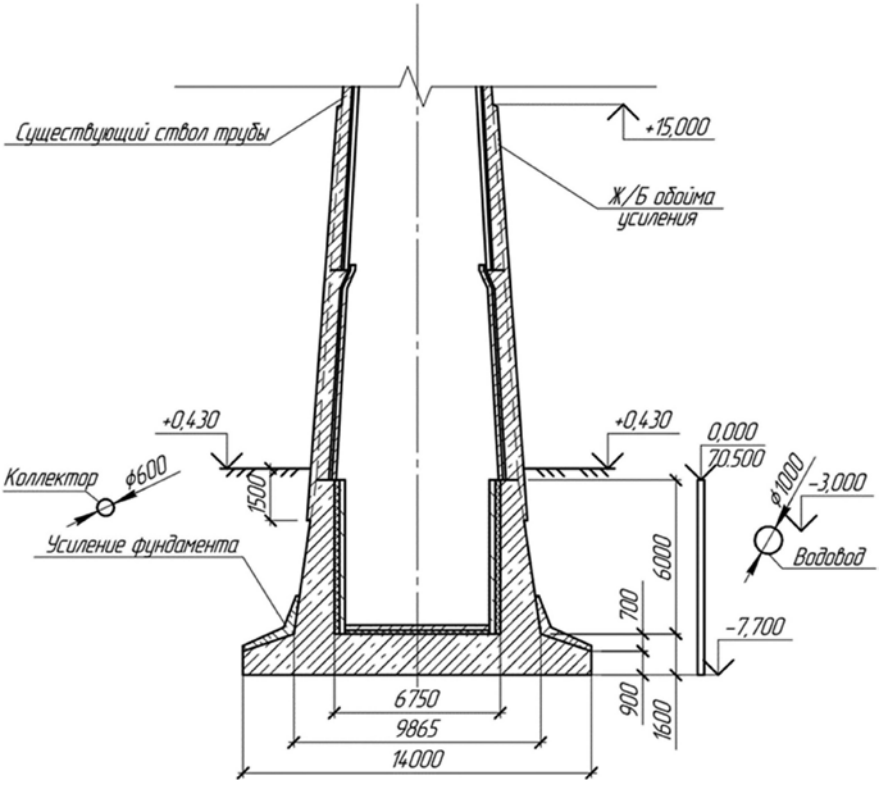

Figure 1. Monolithic reinforced concrete casing reinforcing the chimney shaft of coke oven battery No. 5.

underground utilities (a water conduit with a diameter of 1000.0 mm and a storm collector with a diameter of 600.0 mm) located at a short distance from the object (see Figure 1). For this reason, the need for additional engineering and geological studies of soils located below the sole of the monolithic foundation of the pipe, made in the form of a solid reinforced concrete slab, was determined.

Initial assumptions about the possible cause of the collapse of the chimney due to a decrease in the strength characteristics of soils located under the base of the foundation slab at el. -7.7 m and below were not confirmed.

Incorrect (incorrect) conclusions about the causes of the chimney accident were made on the basis of a technical report based on the results of engineering and geological surveys for the preparation of project documentation for the restoration of a 100.0 m high chimney of coke oven battery No. 5, 6.

3 ENGINEERING GEOLOGICAL SURVEYS

Table 1 shows the obtained values of the soil deformation modulus E (MPa), soil cohesion C (kPa), internal friction angle φ (deg.) obtained by a group of prospectors in April-May 2020 only in two test areas.

Table 1. Values of the soil deformation modulus E (MPa), soil cohesion C (kPa), internal friction angle φ (deg.) obtained in 2020.

		Plot №1			Plot №2		
Depth, m	Soil type	φ, deg	C, kPa	E, MPa	φ, deg	C, kPa	E, MPa
6.0	clay	14	25.0	3.5	14	25.0	3.5
6.5	clay	14	25.0	3.5	14	25.0	3.5
7.0	clay	14	25.0	3.5	14	25.0	3.5
7.5	clay	14	25.0	3.5	14	25.0	3.5
8.0	clay	14	25.0	3.5	14	25.0	3.5
8.5	clay	14	25.0	3.5	14	25.0	3.5
9.0	clay	14	25.0	3.5	14	25.0	3.5

Such uniformity of the physical and mechanical characteristics of clay soils, and even more so their location in depth (modulus of deformation, angle of internal friction, cohesion) called into question their reliability.

Long-term studies of the authors, previously published in the sources of technical information [1,2,3] given in Table 2, show their significant difference in the magnitude of the deformation moduli of clay soils, the main indicator of the strength and deformation properties of the material.

Table 2. Physical and mechanical properties of the soil.

Indicators	one	2	3
Soil specific weight γ, kN/m³	21.0	20.0	19.0
Specific weight of soil particles γ_s, kN/m³	27.5	26.5	25.8
Humidity ω, %	1.2	26.6	27.4
Plasticity I_p, %	28.0	19.5	13.5
Flow I_L	0	0.1-0.3	0.4-0.6
Porosity coefficient e	0.52	0.65	0.73
Angle of internal friction φ, deg	32	23	21
Adhesion coefficient C, MPa	0.05	0.02	0.01
Deformation modulus E, MPa	21.2	14.0	9.0

Note 1-3 numbers of landfills in the construction site of coke oven batteries No. 1-No. 7 of the Karmetkombinat (today ArcelorMittal Temirtau JSC).

These circumstances required additional studies of the physical and mechanical characteristics of clay soils located under the sole of the monolithic foundation of the chimney of coke oven battery No. 5.

Soil tests in the field with a stamp, conducted by Karaganda GIIZ LLP in July 2020, in accordance with GOST 20276-2012, were carried out in order to study the deformation properties of soils lying at a depth below the level of laying the sole of the chimney foundation. The experiments were carried out at a depth of 7.5 m, with round-shaped stamps with an area of 600 cm². Stamp No. 1 obtained a deformation modulus of 6.3 MPa, stamp No. 2 obtained a deformation modulus of 16.2 MPa (Figure 2).

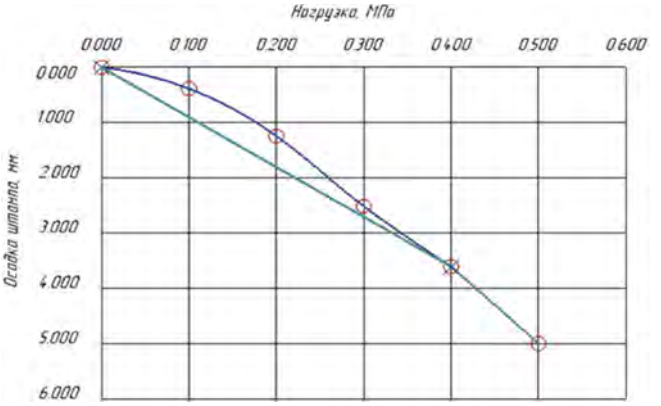

Figure 2. Soil testing with a stamp according to GOST 20276-2012. Graph of the dependence of the draft of the stamp on the load.

From the graph of the dependence of the stamp settlement on the load shown in Figure 2, it can be seen that the modulus of soil deformation at Poisson's ratio v=0.27 is equal to E=16.20 MPa.

4 CONCLUSION

Based on the materials of the conducted studies, it was concluded that the main reason for the collapse of the reinforced concrete shaft of the chimney of coke oven batteries No. 5 and No. 6 of ArcelorMittal Temirtau JSC (formerly Karaganda Metallurgical Plant) is a decrease in the strength characteristics of concrete due to many years of constant moisture, freezing and thawing in the autumn winter-spring periods of time, and indirectly due to the lack of proper control over the technical condition of building structures of all areas of reinforcement of the reinforced concrete chimney shaft and assessment of their strength characteristics. The design of the reinforcement instead of its original purpose contributed to the development of negative consequences and the safe operation of the facility.

REFERENCES

1. Filatov, A.V. "Reconstruction and strengthening of the foundations of buildings and structures of metallurgical enterprises"/A.V. Filatov // Foundations, foundations and soil mechanics. – 1990 - No. 6.
2. Filatov, A.V. "Reconstruction and construction of foundations and underground structures"/A.V. Filatov. - Alma-Ata: " Gylym ", 1991. - 112 p.
3. Filatov, A.V. "Pile-columns in industrial construction"/A.V. Filatov, I.N. Soloviev, V.F. Shepherd // Industrial construction. – 1976 - Number 3.
4. Malyshev M.V. Strength and stability of the foundation of structures. Moscow. 1994.
5. Zhakulin A.S. 2015. Deformability of soils of water- saturated bases. LAP Lambert Academic Publishing. Saarbrucken.
6. Zhakulin A.S., Zhakulina A.A., Kropachev 2021. Research and testing of geotechnical properties of soils. Karaganda technical university. Karaganda, 172 p.

Smart Geotechnics for Smart Societies – Zhussupbekov, Sarsembayeva & Kaliakin (Eds)
© 2023 The Author(s), ISBN 978-1-003-29912-7
Open Access: www.taylorfrancis.com, CC BY-NC-ND 4.0 license

Shaft and base responses of large diameter piles based on cyclic pile load tests results

Vijay Kiran Kota
Research Scholar, Indian Institute of Technology Bombay, Mumbai, India

Madhav Madhira
Professor Emeritus, JNT University Hyderabad
Visiting Professor, Indian Institute of Technology Hyderabad, Hyderabad, India

ABSTRACT: The selection of proper design parameters for assessing pile's axial capacity involves a significant degree of uncertainty as design concepts aren't necessarily consistent with the methods or procedures involved in installation of piles. To obviate this lacuna and to develop a rational design procedure, a new technique for back-analyzing a cyclic pile load test is presented to estimate ultimate base and shaft resistances, as well as initial stiffnesses of the shaft and base of the pile. The novel method facilitates 'a priori' estimation of required pile design parameters based on geotechnical characteristics, geometry (shape, length, and diameter), construction methodologies, and other uncertainties present on the site during pile installation. The method was applied to the results of cyclic pile load tests for subsurface strata of typical Yamuna Sand overlying weathered rock at certain locations.

1 INTRODUCTION

The most efficient and cost-effective method for transferring heavy vertical, uplift, and lateral loads to deeper levels is a pile foundation. The pile's surrounding soil mass acts as support for the imposed loads. The interaction between piles and soil is three-dimensional and non-linear. Finding a closed form solution to such a case is extremely challenging if not impossible. Several approaches were developed to analyse and forecast the response of the composite pile–soil system. Faruque and Desai (1982) incorporated both numerical and geometric non-linearities in their three-dimensional finite element model. Rajashree and Sitharam (2001) developed a nonlinear finite element model for batter piles under lateral loading utilising a hyperbolic relation for static load and a modified hyperbolic relation incorporating degradation and gap for cyclic load conditions.

The ultimate capacity of the pile is evaluated using the strengths and unit weights of soil layers along depth, overburden pressure and other pertinent parameters. The initial maintained load test is always be performed to verify the predicted capacity. Since the values of strength, stiffness, interface resistance between the pile and the soil, lateral earth pressure coefficient with depth, soil stratification, etc., taken into account for estimating the ultimate capacity of the pile may differ from the actual in site values, the estimated capacity may not match in most situation with the actual at the site. Thus, the assessment of a pile's axial capacity entails a great deal of uncertainty in choosing the right design parameters, and the design guidelines aren't always in line with the processes/procedures involved in installation.

Predictions of the composite pile-soil system's reaction are made using a variety of techniques. The load-settlement curve/plot until failure load might be predicted a priori using the techniques by Whitaker and Cooke (1966), Burland et al. (1966), and Poulos (1972).

DOI: 10.1201/9781003299127-214

Brinch-Hansen (1963), Chin (1971a&b) and Chin and Vail, 1973), Davisson (1972), Fellenius (1989), etc. Kondner (1963) and Davisson (1972) have suggested techniques for determining the ultimate pile capacity based on a pile load tested to failure. These techniques relate to several concepts, such as restricting the maximum pile settlement and the settlement to load ratio. The form of the load-settlement curve is identified somewhat similar or close to hyperbolic by Chin (1971) and Brinch-Hansen (1973).

Seed and Reese (1957) and Coyle and Reese (1966) proposed the first axial load transfer curves. Different curve types, based on theory, experience, or both, were described in the literature depending on varying complexity levels and the number of soil characteristics. They are often created for certain ground and pile types (Randolph and Wroth 1978; Wang et al. 2012; Cecilia et al. 2017). Either an empirical relationship or a measurable soil deformation value is used to determine the stiffness of the load transfer curves. Based on correlations with observed soil resistance characteristics, Randolph and Wroth (1978) and Fleming (1992) employed an equivalent deformation modulus or oedometer modulus for the reaction of pile tip. If stiffness is inferred from the linear component of the curve using the standard correlations, the Randolph linear curves correspond to elastic estimate. To simulate side and base load transfer relevant for drilled piles in sands and clays, Hirayama (1990) used hyperbolic functions. The standard in-situ and laboratory test findings served as the basis for the parameters utilised to define these functions. By doing a back-analysis on pile load test data, Fleming (1992) proposed a technique to identify interaction parameters.

2 PROBLEM DEFINITION

Estimation of ultimate resistances, initial shaft and base stiffnesses based on load - displacement from pile load tests is crucial because it enables validation of *a priori* predictions based on geotechnical characteristics, geometry (shape, length, and diameter), construction methodology, and other uncertainties prevalent at the pile installation site. The purpose of this paper is to estimate ultimate shaft and base resistances as well as initial shaft and base stiffnesses using initial pile load tests. Single pile with a diameter of d, and length of L, subjected to an axial load, P, is considered, (Figure 1a). For this investigation, the total pile response and the pile shaft-soil, P_S, and base, P_B, resistances of the pile soil system are analysed using a Winkler type model with non-linear responses (Figure 1b).

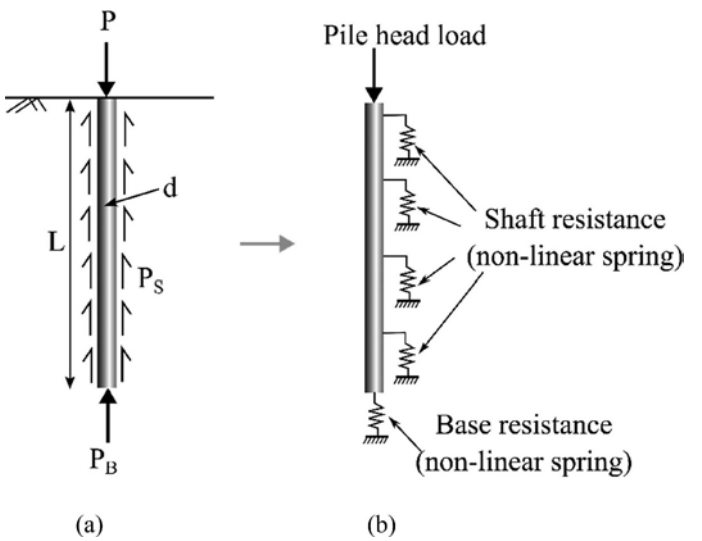

Figure 1. Definition sketch for a single rigid pile – soil system.

3 FORMULATION AND COMPUTATION OF PILE RESPONSE

A rigid pile subjected to axial loading derives its resistance from shaft and base of the pile. Figures 2a, b and c represent idealized representations (assumed to be hyperbolic) of load test results of a rigid pile, shaft (pile-soil) and base resistances respectively. The slopes of the curves 'A', 'B', and 'C' represent the stiffness modulus, k_p, of the rigid pile, k_τ of shaft and k_b base stiffness's respectively. P_u, τ_{max} and q_u are the ultimate load on pile, ultimate shaft and base resistances, respectively.

The load, P, in the pile at a displacement, δ, in the linear part of the load, and displacement curve is expressed as the sum of the resistances mobilized along the shaft and the base as

$$\begin{aligned} P &= k_p.\delta \\ &= \pi.d.L.\tau + \frac{\pi d^2}{4}.q \\ &= \pi.d.L.k_\tau.\delta + \frac{\pi d^2}{4}.k_b.\delta \end{aligned} \tag{1}$$

Where τ and q_b are the shaft and base resistances respectively.

Simplifying the stiffness, k_p, of the pile response, is expressed in terms of shaft and base stiffnesses as

$$k_p = \pi.d.L.k_\tau + \frac{\pi.d^2}{4}.k_b \tag{2}$$

Normalizing Equation (2) with respect to the pile's cross-sectional area ($\pi d^2/4$)

$$k_p{}^* = \frac{4.L}{d}k_\tau + .k_b \tag{3}$$

where $k_p{}^* = k_p/(\pi.d^2/4)$- normalized stiffness of the pile, k_τ and k_b are shaft and base stiffnesses respectively, Ultimate load capacity, P_{ult}, of the pile is the sum of ultimate shaft and base resistances as

$$P_u = P_s + P_b \tag{4}$$

$$P_u = \pi.d.L.\tau_{\max} + \frac{\pi d^2}{4}.q_u \tag{5}$$

where P_u, is ultimate pile load, P_s & P_b are the ultimate shaft and base resistances of pile respectively. Normalizing Equation (5) with $\pi d^2/4$

$$P_u{}^* = \frac{4.L}{d}\tau_{\max} + q_u \tag{6}$$

where $P^*{}_u = P_u/(\pi d^2/4)$.

The shaft resistance, τ, corresponding to a displacement, δ, can be expressed using hyperbolic relation as

$$\tau = \frac{k_\tau.\delta}{1 + \frac{k_{\tau,\delta}}{\tau_{\max}}} \tag{7}$$

Similarly, the base resistance, q_b, corresponding to a displacement, δ, can be expressed using hyperbolic relation as

$$q_b = \frac{k_b.\delta}{1 + \frac{k_{b,\delta}}{q_u}} \tag{8}$$

The load, P_1, corresponding to displacement, δ_1, is expressed in terms of the parameters defined already as

$$P_1 = \pi.d.L.\frac{k_\tau.\delta_1}{1 + \frac{k_\tau.\delta_1}{\tau_{\max}}} + \frac{\pi.d^2}{4}.\frac{k_b.\delta_1}{1 + \frac{k_b.\delta_1}{q_u}} \tag{9}$$

Normalizing Equation (9) by $\pi d^2/4$, and simplifying one gets

$$\frac{P_1{}^*}{\delta_1} = \frac{4.L}{d}\frac{k_\tau.\tau_{\max}}{\tau_{\max} + k_\tau.\delta_1} + \frac{k_b.q_u}{qu + k_b.\delta_1} \tag{10}$$

Substituting for k_b and q_u from Equations (3) and (6), Equation 8 is modified to

$$\frac{P_1{}^*}{\delta_1} = \frac{4.L}{d}\frac{k_\tau.\tau_{\max}}{\tau_{\max} + k_\tau.\delta_1} + \frac{1}{A_1}\left\{\left(k_p{}^* - \frac{4.L}{d}k_\tau\right).\left(P_u{}^* - \frac{4.L}{d}\tau_{\max}\right)\right\} \tag{11}$$

where $A_1 = \left(P_u{}^* - \frac{4.L}{d}\tau_{\max}\right) + \left(k_p{}^* - \frac{4.L}{d}k_\tau\right).\delta_1$ or

$$\frac{P_1{}^*}{\delta_1} - \frac{k_p{}^*.P_u{}^*}{A_1} = \left\{\frac{4.L}{d}\frac{.\tau_{\max}}{\tau_{\max} + k_\tau.\delta_1} - \frac{4.L}{d.A_1}.P_u{}^* + 16\left(\frac{.L}{d}\right)^2\frac{\tau_{\max}}{A_1}\right\}.k_\tau - \frac{4.L}{d.A_1}\tau_{\max}.k_p{}^* \tag{12}$$

Equation (12) in simple terms becomes

$$\mathrm{d_1} = \mathrm{C_1.k_\tau} + \mathrm{C_2}.\tau_{\max} \tag{13}$$

where $d_1 = \frac{P_1{}^*}{\delta_1} - \frac{k_p{}^*.P_u{}^*}{A_1}$, $C_1 = \frac{4.L}{d}.\left\{\frac{\tau_{\max}}{\tau_{\max}+k_\tau.\delta_1} - \frac{P_u{}^*}{A_1}.\frac{4.L}{d}\frac{\tau_{\max}}{A_1}\right\}$ &$C_2 = \frac{4.L}{d.A_1}.k_p{}^*$

Similarly $\mathrm{P_2}$ is evaluated for displacement δ_2 as

$$\frac{P_2{}^*}{\delta_2} = \frac{4.L}{d}\frac{k_\tau.\tau_{\max}}{\tau_{\max} + k_\tau.\delta_2} + \frac{k_b.q_u}{q_u + k_b.\delta_2} \tag{14}$$

$$d_2 = C_3.k_\tau + C_4.\tau_{\max} \tag{15}$$

where $d_2 = \frac{P_2{}^*}{\delta_2} - \frac{k_p{}^*.P_u{}^*}{A_2}$, $A_2 = \left(p_u{}^* - \frac{4.L}{d}\tau_{\max}\right) + \left(k_p{}^* - \frac{4.L}{d}k_\tau\right).\delta_2$,
$C_3 = \frac{4.L}{d}.\left\{\frac{\tau_{\max}}{\tau_{\max}+k_\tau.\delta_2} - \frac{P_u{}^*}{A_2}. + \frac{4.L}{d}\frac{\tau_{\max}}{A_2}\right\}$ &$C_4 = -\frac{4.L}{d.A_2}.k_p{}^*$

Equations (13) and (15) are solved to get $\mathrm{k_\tau}$ as

$$k_\tau = \frac{C_4 d_1 - C_2 d_2}{C_1 C_4 - C_2 C_3} \tag{16}$$

Since the ultimate shaft resistance, P_s, is often mobilized at relatively smaller displacement than δ_2, Equation (15) is simplified considering full mobilization of ultimate shaft resistance as

$$P_2{}^* = \frac{4.L}{d}.\tau_{\max} + \frac{k_b.q_u.\delta_2}{q_u + k_b.\delta_2} \tag{17}$$

Substituting for the values of q_u and k_b in Equation (17), τ_{max} is obtained as

$$\tau_{\max} = \frac{\left\{P_2{}^*.A_2 - \left(\frac{k_p{}^*}{k_\tau} - \frac{4L}{d}\right).P_u{}^*.k_\tau.\delta_2\right\}}{\left\{\frac{4L}{d}\left(A_2 - k_p{}^*.\delta_2 + \frac{4L}{d}.k_\tau.\delta_2\right)\right\}} \tag{18}$$

Equations (13) and (18) are solved iteratively for k_τ, k_b, τ_{max} and q_u.

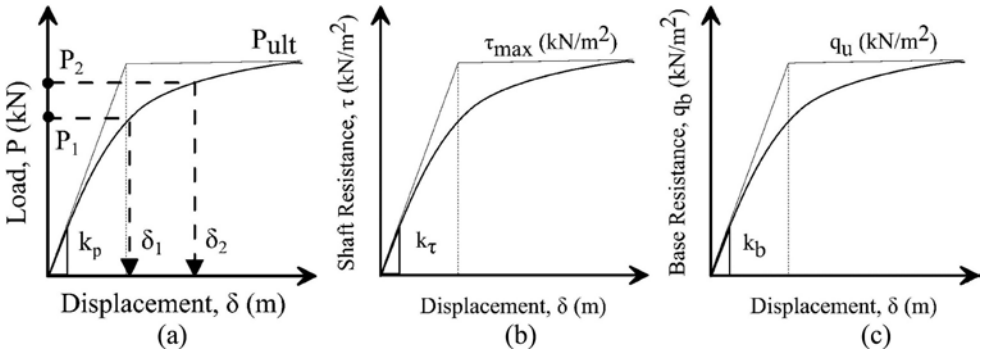

Figure 2. Modelling of (a) Typical pile load vs. Displacement; Assumed (b) Shaft vs. Displacement and (c) Base Resistance vs. Displacement curves.

3.1 *Estimation of P_U and k_P based on Chin (1971)*

The two essential factors needed to estimate the four unknown parameters (k_τ, k_b, τ_{max}, and q_u) of interest are the ultimate pile load capacity, P_u, and pile stiffness modulus, k_p. Chin's technique (Chin 1970 & 1971), which considers the relationship between load, P, and settlement, S, of a pile as hyperbolic, is used in the current analysis from among the methods available in the literature to determine ultimate capacity and initial stiffness of the pile. In Chin's (1971) approach, the ratio of S/Q is plotted versus S and a straight line fitting to the points. The initial pile – soil stiffness, k_p, and the final or ultimate pile load, P_u, are given by the inverses of the intercept, C_2, and slope, C_1, of the fitted line.

$$\frac{S}{Q} = C_1.S + C_2 \tag{19}$$

$$\mathrm{Qu} = \frac{1}{\mathrm{C_1}} \tag{20}$$

$$\mathrm{kp} = \frac{1}{\mathrm{C_2}} \tag{21}$$

where S is settlement of pile at load Q, C_1 and C_2 - slope and intercept of the straight line, respectively.

3.2 *SPT-N based methods for computing Axial Pile capacity*

The shaft and tip resistances for bored piles in sandy soils can be computed using SPT based correlations available in the literature. Many researchers (Aoki & Veloso, 1975, Decourt, 1982), Meyerhof 1976 and Reese & O'Neill, 1989) proposed empirical methods derived from back-analysis of databases of pile loading tests in correlation with N. The end bearing capacity is assumed to be proportional to a representative N_e value around the pile base:

$$\mathrm{qu} = \beta.\mathrm{Ne} \tag{22}$$

The limit skin friction stress at a given depth is proportional to the N value at this depth:

$$\tau_{max} = \eta.\mathrm{N} \tag{23}$$

β and η have the unit of stress and are respectively called tip resistance factor and skin friction factor. SPT-N based correlations from IS 2911 Part-1 were utilized in the current investigation to estimate the shaft and tip resistances for comparison.

3.3 *IS 2911 Part 4 method for the estimation of shaft and base resistances*

The analysis assumes the pile to be incompressible in the first instance and iteratively obtains approximate values of point resistance and skin friction. The method involves creating estimates of point resistance and skin friction by drawing a straight line parallel to the straight segment of curve I. (IS 2911 Part-4). The elastic compression of the pile, D, corresponding to these loads is calculated using the following formula using an estimate of skin friction and information of the loads on top of the pile:

$$D = \frac{\left(T - \frac{F}{2}\right)L}{AE} \tag{24}$$

where D = elastic compression of pile in cm, T - load on pile top in kgf, F - frictional resistance in kgf, L - length of the pile in cm, A - cross-sectional area of the pile in cm^2 and E – modulus of elasticity of the pile material in kgf/cm^2

The elastic compression of the subgrade values is then calculated by deducting the pile's elastic compression from its overall elastic recovery. These new values are then shown on a graph together with the corresponding loads on the top of the pile. If elastic compression of the subgrade results in a negative value, the value is to be ignored until it is positive. The steps are repeated to acquire new values for skin friction. Although successive approximation might go on incessantly, for the purposes of our study, the third iteration often gave accurate enough data for skin friction.

4 APPLICATION OF THE PROPOSED METHOD

The proposed method is applied to load-displacement plots of cyclic pile load test results obtained from initial load tests carried out Delhi – Gurgaon NH8 Access controlled Expressway Project. All the crossings necessitated flyovers with their foundations subjected to cyclic loads (both axial and lateral). The characteristic Yamuna Sand was reported in all the areas, followed by weathered rock, according to the site-specific soil investigation. For flyovers, the sandy substrata required the use of pile foundations. The design pile depth ranged from 12 m to 26 m at various places because of variation of the depth of the sandy layers. The diameter of each pile was 1.2 m. Piles were designed based on subsurface data as per IS 2911 for 435 T load. The formation of bored cast in situ piles involved the use of a rotating rig and M35 Grade concrete. In all the cases, test setup with 1000 T Kentledge was used.

The detailed properties of the soil strata in the test sites are reported in Table 1. The pile capacity is estimated using the procedure described in IS 2911 Part 1 Section 2 for piles installed in non-cohesive soils. The estimated shaft and end bearing resistance for the dimensions of the pile are presented in Table 2. The Initial Cyclic Pile load tests were conducted on test piles to validate the estimated safe axial capacities. The load-displacement data available is used to estimate initial stiffness modulus, k_p, and the ultimate load P_u, on pile. The data is analyzed based on the proposed method to estimate normalized shaft and base stiffness, k_τ and k_b, and corresponding ultimate shaft, τ_{max}, and base resistances, q_u, respectively. Equations (1) to (18) are used to perform the regression analysis. The detailed explanations for each test pile are given briefly.

Table 1. Geotechnical characteristics of the cyclic pile load test sites.

Sl. No	Site Location	Depth (m)	Stratum description	N	φ
1.	Rajokri Junction	0-12	Top layer of 0.5 m to 1.35 m of filled up material, followed by soft to hard yellowish brown/ brown/reddish brown sandy silt of low plasticity.	19	26
		12-20	Hard yellowish brown/brown/reddish brown sandy silt.	26	36
2.	IFFCO junction	0-4.5	Top 1 m of filled material followed by sandy silt with gravels extending up to 30.3 m.	12	28
		4.5-20	Sandy silt with gravels	30	37
3.	Rajiv junction	0-12	Homogeneous strata, with non-plastic sandy silt with gravels. The bulk density was assessed as 1.69 g/cc.	10	28
		12-20	Non-plastic sandy silt with traces of gravel. Bulk density of about 1.75 g/cc.	50	41
4.	Shankar junction	0-12	Non-plastic sandy silt with traces of gravel. Bulk density is 1.89 g/cc.	17-43	33
		12-20	Non-plastic sandy silt with traces of gravel. Bulk density of about 2.1 g/cc.	48	40

4.1 *Test Location – 1*

Figure 3 Shows the load - displacement plot for the initial cyclic pile load test (CPLT-1). The length and diameter of the pile installed are 20.25 m and 1.2 m respectively. The shaft and end bearing resistance for the pile are estimated to be 43.6 kPa and 5.7 MPa, respectively based on the empirical equations from IS 2911 Part 1 Section 2 for piles installed in non-cohesive soils. The shaft and base resistances using IS 2911-Part 4 are 65.49 kPa and 1.32 MPa respectively. The ultimate pile capacity, P_{ult}, from Chin's method is 6865 kN and the initial stiffness, k_p, 2500 MN/m (the intercept C_2 = 4e-7). According to the proposed approach, the predicted values k_τ, k_b, τ_{max}, and q_b, for the shaft and base resistances, are 16.4 MN/m3, 1099.1 MN/m3, 40.88 kPa, and 3.31 MPa, respectively. The load-settlement curve predicted using the estimated parameters corresponds very well with the actual load - settlement one.

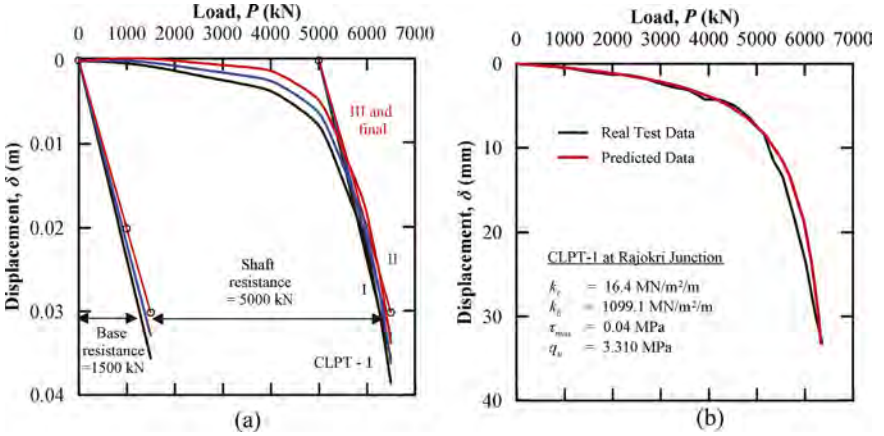

Figure 3. (a) Shaft and base resistances based on IS-2911 for CLPT-1 (b) Comparison of measured and predicted load-displacement curves for CPLT-1.

4.2 *Test Location – 2*

Figure 4 presents similar analysis, results and comparison of measured and predicted load-settlement curve for initial pile load test (CPLT-2). The length and diameter of the pile installed are 20.25m and 1.2m respectively. The ultimate load and initial stiffness modulus, k_p,

of the pile are computed as 10196 kN and 2500 MN/m based on which the corresponding values of the parameters k_r, k_b, τ_{max} and q_u contributing to the pile response are 11.9 MN/m^3; 1402.3 MN/m^3; 28.8 kPa, and 7.07 MPa respectively. Based on empirical formulae from Section 2 of IS 2911 Part 1 for piles constructed in non-cohesive soils, the shaft and end bearing resistance for the pile are predicted to be 51.9 kPa and 6.5 MPa, respectively. According to IS 2911-Part 4, the base resistance is 1.76 MPa, while the shaft resistance is 85.14 kPa.

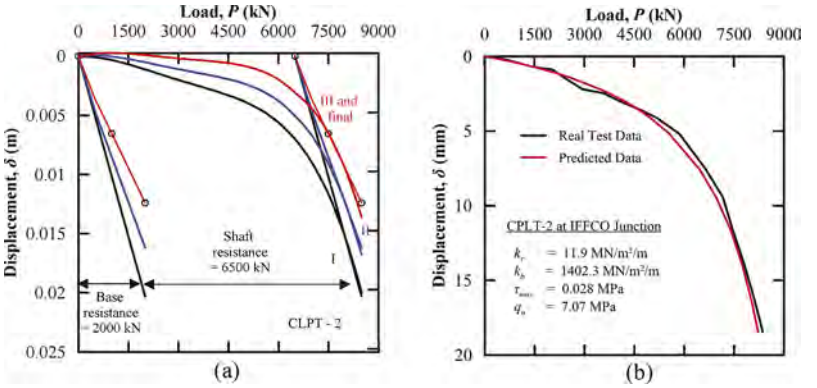

Figure. 4. (a) Shaft and base resistances based on IS-2911 for CLPT-2 (b) Comparison of measured and predicted load-displacement curves for CPLT-2.

4.3 *Test Location – 3*

Similar results as the above two case studies are presented in Figure 5 comparing measured and predicted load-settlement curves for cyclic pile load test (CPLT-3). The length and diameter of the pile installed are 20.25m and 1.2m respectively. The ultimate load and initial stiffness modulus, k_p are computed as 9859 kN and 2782 MN/m. The parameters k_r, k_b, τ_{max} and q_u contributing to the pile response in resisting loads are 11.25 MN/m^3; 1700.6 MN/m^3; 42.25 kPa, and 5.86 MPa respectively. The load-displacement plot from PLT is compared with estimated data, and matches well with the actual. The shaft and end bearing resistance of the pile are anticipated to be 52 kPa and 10.96 MPa, respectively, based on empirical formulas from Section 2 of IS 2911 Part 1 for piles built in non-cohesive soils. The base resistance is 1.76 MPa and the shaft resistance is 85.14 kPa, respectively, according to IS 2911-Part 4 graphical approach.

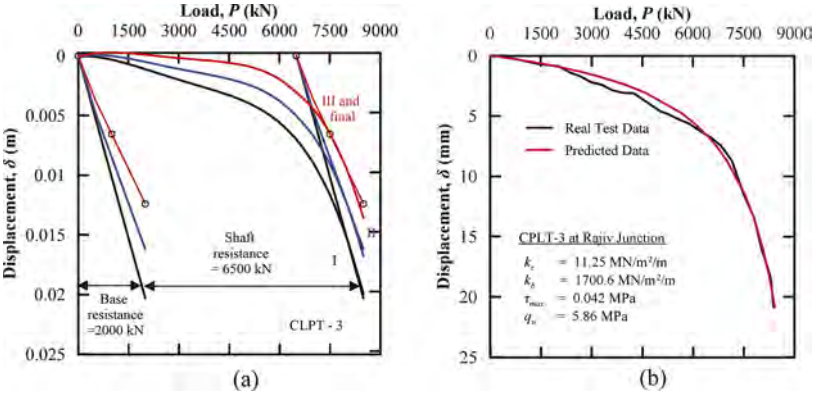

Figure. 5. (a) Shaft and base resistances based on IS-2911 for CLPT-3 (b) Comparison of measured and predicted load-displacement curves for CPLT-3.

4.4 *Test Location - 4*

Figure 6 Compares measured and estimated load-settlement curves for pile load tests (CPLT-4). The length and diameter of the pile installed are 18m and 1.2m respectively. The ultimate load and initial stiffness modulus, k_p are computed as 9322 kN and 3180 MN/m. The parameters k_r, k_b, τ_{max} and q_u contributing to the pile response in resisting loads are 46.2 MN/m^3; 40.39 MN/m^3; 91.59 kPa, and 2.74 MPa respectively. The load-displacement plot from CPLT is compared with estimated data, and matches well with the actual. Based on empirical calculations from Section 2 of IS 2911 Part 1 for piles installed in non-cohesive soils, the shaft and end bearing resistance of the pile are estimated to be 74.4 kPa and 9.3 MPa, respectively. According to the IS 2911-Part 4 graphical method, the base resistance is 2.21 MPa, while the shaft resistance is 88.41 kPa.

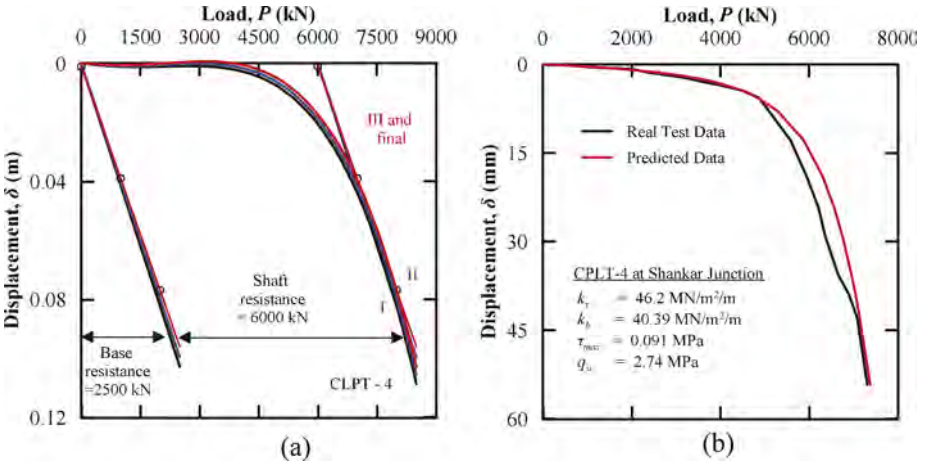

Figure. 6. (a) Shaft and base resistances based on IS-2911 for CLPT-4 (b) Comparison of measured and predicted load-displacement curves for CPLT-4.

5 RESULTS AND DISCUSSION

The predicted and actual load-displacement curves are compared in Figures 3 through 6. A close match in all four of them is obtained in the present study. These comparisons show that the non-linear load transfer functions used in the proposed method are appropriate and effective in characterizing the in situ load-displacement behaviour. Table 2 compiles the information for the four test sites and compares the predicted values with the estimated shaft and base resistances derived using various empirical correlations. The results are very consistent with the correlations in IS 2911 (Part 1 Section 2) that were based on SPT-N. However it should be noted that the empirical equations often underestimate the shaft and base resistances (ratio < 1). The results also match fairly the graphical approach provided in IS 2911 Part-4 in terms of results. Notably, this approach (IS 2911 Part 4) often overestimates (ratio > 1) base and underestimates (ratio < 1) shaft resistances.

6 CONCLUSION

A simple method to estimate the initial shaft-soil and base stiffnesses and the ultimate shaft and base resistances of a pile from the results of initial pile load test data is proposed. The predicted load – displacement plots based on the computed results compare well with the measured load - settlement curves. It is now possible to estimate the average shaft and base stiffnesses and resistances of the pile as installed from initial load test and compare the predictions with assumed values. A large data base can be built for all such cases which may help in revising the Code.

Table 2. Summary of predicted results based on the proposed method and empirical correlations.

Method	CLPT-1		CLPT-2		CLPT-3		CLPT-4		CLPT-1		CLPT-2		CLPT-3		CLPT-4	
Method	τ_{max} (kPa)	q_b (MPa)	τ_{max} (kPa)	q_b (MPa)	τ_{max} (kPa)	q_b (MPa)	τ_{max} (kPa)	q_b (MPa)	$\frac{\tau_{max,est}}{\tau_{max,m}}$	$\frac{q_{b,est}}{q_{b,m}}$	$\frac{\tau_{max,est}}{\tau_{max,m}}$	$\frac{q_{b,est}}{q_{b,m}}$	$\frac{\tau_{max,est}}{\tau_{max,m}}$	$\frac{q_{b,est}}{q_{b,m}}$	$\frac{\tau_{max,est}}{\tau_{max,m}}$	$\frac{q_{b,est}}{q_{b,m}}$
Proposed method	40.88	3.31	28.8	7.07	42.25	5.86	91.59	2.74	1.00	1.00	1.00	1.00	1.00	1.00	1.00	1.00
IS - 2911 Empirical equations	43.6	5.7	51.9	6.5	52	10.96	74.4	9.3	0.94	0.58	0.55	1.09	0.81	0.53	1.23	0.29
IS - 2911 Graphical approach	65.49	1.32	85.14	1.76	85.14	1.76	88.41	2.21	0.62	2.51	0.34	4.02	0.50	3.33	1.04	1.24

ACKNOWLEDGEMENTS

Authors wish to express their appreciation to Sri Kamat, Sr. Vice President Jaiprakash Associates Limited, and Ms Mahuli, Project Coordinator Noble Geo Structs, for providing load test results and geotechnical profile of test site.

REFERENCES

Aoki, N & Veloso, D. (1975). An approximate method to estimate the bearing capacity of piles. Proceedings of the 5th Pan-American Conference on soil Mechanics and Foundation engineering, Vol. 1, pp 367–376, Buenos-Aires.

Bohn, C., Lopes dos Santos, A., & Frank, R. (2017). Development of axial pile load transfer curves based on instrumented load tests. *Journal of Geotechnical and Geoenvironmental Engineering*, *143*(1), 04016081. https://doi.org/10.1061/(asce)gt.1943-5606.0001579

Burland, J. B., Butler, F. G. & Dunican, P. (1966). 2 The behaviour and design of large diameter bored piles in stiff clay. In *Large bored piles* (pp. 51–71). Thomas Telford Publishing. https://www.researchgate.net/publication/274072775

Chin, F. K. (1970). Estimation of the ultimate load of piles from tests not carried to failure. In *Proc. 2nd Southeast Asian Conference on Soil Engineering*, *Singapore, 1970*.

Chin, F. K. (1971). Pile Tests—Arkansas River Project. *Journal of the Soil Mechanics and Foundations Division*, *97*(6), 930–932. https://doi.org/10.1061/JSFEAQ.0001455

Chin, F. K. & Vail, A. J. (1973, July). Behavior of piles in alluvium. In *Proc., 8th Int. Conf. on Soil Mechanics and Foundation Engineering* (Vol. 2, No. Part 1, pp. 47–52).

Coyle, H. M. & Reese, L. C. (1966). Load transfer for axially loaded piles in clay. *Journal of the soil mechanics and foundations division*, *92*(2), 1–26. https://doi.org/10.1061/JSFEAQ.0000850

Davisson, M.T. (1972) High Capacity Piles. *Proceedings of Soil Mechanics Lecture Series on Innovations in Foundation Construction*, ASCE, Illinois Section, Chicago, pp. 81–112.

De Beer, E. E. (1968). Proefondervindlijke bijdrage tot de studie van het grensdraagvermogen van zand onder funderingen op staal. Tijdshift der Openbar Verken van Belgie, No. 6, 1967 and No. 4, 5, and 6.

Decourt, L. (1982). Prediction of the bearing capacity of piles based exclusively on N-Value of the SPT. Proceedings of 2nd European Symposium on penetration testing, Vol. 1, pp: 29–34, Amsterdam.

Decourt, L. (1999). Behavior of foundations under working load conditions. *Proceedings of the 11th Pan-American Conference on Soil Mechanics and Geotechnical Engineering*, Foz Do Iguassu, Brazil, August 1999, Vol. 4, pp. 453–488.

Faruque, M. O. & Desai, C. S. (1982) 3-D material and geometric non-linear analysis of piles. *Proceedings of 2nd International. Conference on Numerical Methods for Offshore Piling*, Austin, TX.

Fellenius, B. H. (2001). What capacity value to choose from the results a static loading test. We have determined the capacity, then what? *Two articles reprinted from Deep Foundation Institute, Fulcrum*, Winter 2001, pp. 19–22 and Fall 2001, pp. 23–26.

Fleming, W. G. K. (1992). A new method for single pile settlement prediction and analysis. Geotechnique, 42(3), 411–425. https://doi.org/10.1680/geot.1992.42.3.411

Hirayama, H. (1990). Load-settlement analysis for bored piles using hyperbolic transfer functions. *Soils and Found*., 30(1), 55–64. https://doi.org/10.3208/sandf1972.30.55

IS: 2911 Part-1 (1979) Code of practice for design and construction of pile foundations, Part 1 concrete piles section 2 bored cast in-situ piles, BIS, New Delhi

IS: 2911 Part-4 (1985) Reaffirmed 2010. Code of practice for design and construction of pile foundations, Part 4 load test on piles, BIS, New Delhi

Kondner, R. (1963) "Hyperbolic Stress-Strain Response: Cohesive Soils". Discussion, *Journal of Soil Mechanics & Foundation Div*., ASCE, Vol. 89, No. SM4, pp. 241–242. https://doi.org/10.1061/JSFEAQ.0000479.

Meyerhof, G. G. (1976). Bearing capacity and settlement of pile foundations. Journal of Geotech. Engg. ASCE, Vol.102, No.3, pp:1–19.

Poulos, H. G. (1972). Load-settlement prediction for piles and piers. *Journal of the Soil Mechanics and Foundations Division*, *98*(9), 879–897. https://doi.org/10.1061/JSFEAQ.0001779

Poulos, H. G. & Davids, A. J. (2005). Foundation design for the emirates twin towers, Dubai. *Canadian Geotechnical Journal*, *42*(3), 716–730. https://doi.org/10.1139/t05-004

Rajashree, S. S. & Sitharam, T. G. (2001) Nonlinear finite element modeling of batter piles under lateral load. *Journal of Geotechnical and Geo-environmental Engineering*, ASCE, 127(7), 604–612. https://doi.org/10.1061/(ASCE)1090-0241(2001)127:7(604)

Randolph, M. F., & Wroth, C. P. (1978). Analysis of deformation of vertically loaded piles. *Journal of the geotechnical engineering division*, 104(12), 1465–1488. https://ascelibrary.org/doi/10.1061/AJGEB6.0000729

Reese, L.C & O'Neill, M. W. (1989). New design method for drilled shafts from common soil and rock tests. Proceedings of Congress foundation engineering-Current principles and practices, ASCE, Vol 2, pp: 1026–1039.

Seed, H. B. & Reese, L. C. (1957). The action of soft clay along friction piles. *Transactions of the American Society of Civil Engineers*, 122(1), 731–754.https://doi.org/10.1061/TACEAT.0007501

Vijayvergiya, V. N. (1977). Load-movement characteristics of piles. Ports '77: 4th*Annual Symp. of the Waterway, Port, Coastal, and Ocean Division*, ASCE, Los Angeles, 269–284.

Wang, Z., Xie, X. & Wang, J. (2012). A new nonlinear method for vertical settlement prediction of a single pile and pile groups in layered soils. *Computers and geotechnics*, 45, 118–126. https://doi.org/10.1016/j.compgeo.2012.05.011

Zhang, Q.-Q., Zhang, Z.-M. and He, J.-Y. (2010). A simplified approach for settlement analysis of single pile and pile groups considering interaction between identical piles in multilayered soils. *Computers and geotechnics*, 37(7–8), 969–976. https://doi.org/10.1016/j.compgeo.2010.08.003\

Smart Geotechnics for Smart Societies – Zhussupbekov, Sarsembayeva & Kaliakin (Eds)
© 2023 The Author(s), ISBN 978-1-003-29912-7
Open Access: www.taylorfrancis.com, CC BY-NC-ND 4.0 license

Efficient reduction of piles frost jacking with special coating

A.G. Alekseev, E.S. Grechishcheva, O.V. Kozlova & R.V. Makhota
N.M. Gersevanov Research Institute of Bases and Underground Structures, Russia

ABSTRACT: Air temperature in the Northern Hemisphere has been progressively warming in the recent decades, and the ground temperatures have increased correspondingly. The air temperature increasing due to the climate change induces degradation of permafrost and frost heaving activation. The frost heaving forces cause unevenly distributed damaging displacement of foundations and thus poses problems to the development of Arctic regions. Frost jacking can be reduced by protecting piles with an OSPT Reline (or Reline) polymer heat-shrinkable jacket. The interaction of heaving soil with a pile covered with the Reline jacket is modeled in laboratory to estimate the uplift force and the related shear strength of frozen soil along the soil-pile adfreeze surface at temperatures from −6 to −1 °C. The data are obtained for silty sand and silty clay soils and mortar (1:5 cement-sand mixture). The experiments show that frost-heave uplift forces on Reline-protected piles are 52% to 85% lower than on uncovered steel piles (steel grade 09G2S—analog to European steel grade S355JR), depending on soil type and temperature.

1 INTRODUCTION

The degrading permafrost loses its bearing capacity, which leads to damaging displacements of buildings and engineering structures [1,2]. Field observations from 1995 to 2007 revealed progressive active layer thickening [3], which continues to increase at 5 cm per year [4]. The mean annual temperature of the active layer was predicted to keep increasing in the future [5]. As the thaw depth increases, the surface area of the contact between the freezing ground and the foundations becomes larger, and the related processes in susceptible soils become ever more hazardous for the infrastructure. The frost heaving of freezing soils is one of such dangerous processes, which can lead to significant deformations of buildings and constructions. Currently, this process is widely studied by various specialists, and one of its directions is focused on the pile foundation stability to the effects of frost heaving forces.

Formation of ice lenses in the ground, or frost heaving, produces uplift forces that can act in tangential (shear) or normal planes, i.e., along the lateral surface or orthogonally to the foundation, respectively [6]. Pile foundations are commonly subject to shear forces that can reach considerable magnitudes and cause major damage to the infrastructure. These forces are caused by soil-pile adfreeze. In 2013–2014, frost heaving caused accidents to two new tanks of liquid natural gas, 20,000 m3 each, in the Zapolariye–Port Pur Pe pipeline system, as 10–15 cm cracks appeared in the cap of piles along the whole perimeter. The ground was stabilized by thermosyphons to −15 °C, till depths of 13–16 m, but the design took no account of the frost-heave uplift forces [7]. Another accident was reported in the same year [8] from the Urengoi area, where a pipeline segment rose 1.5 m above the ground for one year. In general, up to 1 billion USD is spent yearly for maintenance of pipeline structures and mitigation of damage associated with permafrost degradation [9]. One more example of deformation, other than in pipelines, comes from the Norilsk area where about 250 buildings and structures have been deformed for the recent decade out of which 40 houses had to be demolished [8,10].

DOI: 10.1201/9781003299127-215

The frost heave hazard has been currently prevented by placing piles to greater or by layer-by-layer ground freezing [11]. The other method for frost jacking prevention is based on using specially designed piles: screw piles [12] and belled piles [13] of different configurations. An alternative approach is to coat the pile surface with various protective compounds (epoxy or polyurethane resin, zinc, etc.), which can reduce frost-heave uplift forces. An advantageous solution that differs from the existing coating methods is to protect piles with a heat-shrinkable ready-made jacket OSPT Reline designed at the Ural Plant for Polymer Technologies "MAYAK" (Ozyorsk, Chelyabinsk region, Russia).

2 MATERIALS AND METHODS

2.1 *Materials*

Piles were modeled by plates made of 09G2S steel (analog to European steel grade S355JR), which is used for piles in industry. The samples were cut in the form of square parallelepipeds 80 × 50 × 20 (length, height, and width, respectively, in mm) and trimmed to surface roughness similar to that of hot-rolled pipe material. A half of samples was covered by Reline jacket (heat-shrinkable jacket made of a complexly-modified polyolefin polymer composite) 90 mm in diameter, in accordance with the size of the steel piles, and 2.1 mm thick on average.

The soil samples were selected among soil types which are widespread in the Russian Arctic regions. They were silty sand, known to be frost-susceptible [6], and soft high-plasticity silty clay collected, respectively, from the Zapolyariye–Pur-Pe pipeline area and the East Messoyakha oil-gas-condensate field. The investigated samples had a moisture content corresponding to 80% of the water saturation. Unlike the overdriven piles, bored precast piles are embedded into drilled holes of a larger diameter, and the space between the pile and the natural ground is backfilled with mortar (cement−sand mixture in a ratio 1:5). Thus, the precast piles contact the mortar rather than soil. Mortar was prepared by mixing carefully pre-dried silty sand with cement 500. The required amounts of sand–cement mixture were wetted successively. The mixture was compacted by rodding using a steel rod.

2.2 *Samples preparation*

The shearing tests were performed on a system designed by V. Ermakov, which allows estimating adfreeze strength [15], and is especially convenient for coated piles. The design permits coating the tested model and increasing its size correspondingly without changing other units of the system. Furthermore, the larger surface area of the sample (70 cm^2 instead of the 40 cm^2 standard size) ensures better accuracy of adfreeze estimates in the region of low values. The system consists of a steel casing and a covered or uncovered pile model.

Air-dried natural soil samples were saturated with water till specified moisture contents, and the obtained paste was compacted layer-by-layer in a sleeve. Density and moisture content were monitored while compacting and after the tests, respectively. The prepared samples were frozen to −15 °C, and then exposed to the specified run temperatures. We prepared 6 samples for each soil an each temperature (72 samples at all).

2.3 *Shearing tests*

In Russia, methods for estimating uplift forces associated with frost heaving in soils were developed long ago [6,15,16]. The forces of this kind are equivalent to shear strength and arise when the pile walls adfreeze to the ambient soil or mortar. The frost-heave uplift forces mainly consist of adfreeze force (70−80%) and friction (20−30%) [6]. Thus, the tests focused on estimating adfreezing by a well-known method. The testing was performed by incremental stepwise loading to determine shear strength along the adfreezing surface (Raf). The magnitude of load at the first and subsequent steps was chosen to provide at least four loading steps before fracture. Each step lasted till displacement stabilization, which was assumed to

correspond to displacement increment of 0.01 mm for 12 h. The shear strength along the adfreeze surface was determined as the highest shear stress at which displacement stabilized.

3 RESULTS AND DISCUSSION

The efficiency of coating was tested at negative temperatures of −1, −2, and −6 °C corresponding to the temperature range of natural soils (current values to temperatures). The tests provided estimates of shear strength along the adfreeze surface for covered (with Reline) and uncovered steel piles. The results (are applicable to estimate the bearing capacity of soil for permafrost foundation designs, as well as the reduction of frost-heave uplift forces due to Reline jacket. For comparison, a series of tests was performed on uncovered plates. The obtained shear strength values were considered as reference for further testing. Another series of tests was with samples in the Reline jacket. We provide results after statistical processing (Figures 1-3). Every point on a graph is designed value calculated on 6 values by statistical methods.

The testing results (Figures 1–3) show that the soil-pile adfreeze strength becomes lower at higher temperatures, for all materials (soils and mortar), in both covered and uncovered samples. However, the difference is much smaller for the piles in the Reline jacket. The effect of Reline was estimated (in %) by comparing the results for covered and uncovered samples. The result for uncoated steel was taken as 100%. Then the relation of coated (in the Reline) and uncoated steel in % was calculated. The difference between them is the reduction of adfreeze strength. The obtained estimates were applicable to calculate the reduction of frost-heave uplift forces due to Reline, since they are mostly associated with adfreezing. This approach can provide relative estimates despite large ranges of shear strength values for natural soils varying as a function of moisture content, density, mineralogy, and particle size of soils.

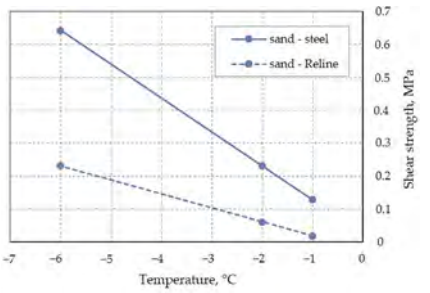

Figure 1. Temperature dependence of shear strength: sand-steel and sand-Reline.

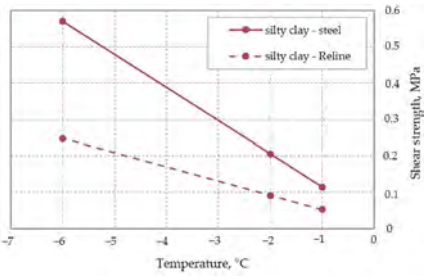

Figure 2. Temperature dependence of shear strength: silty clay-steel and silty clay-Reline.

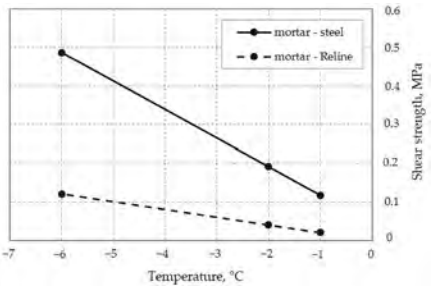

Figure 3. Temperature dependence of shear strength: mortar-steel and mortar-Reline.

Adfreeze strength (uplift forces) for soil and foundation material are usually determined during geotechnical surveys. However, in practice, the decision about frost jacking prevention measures are usually made at the stage of construction designing, when engineering surveys are completed. The calculated reduction of frost heave uplift forces at various temperatures can be used for forecasting of pile foundation stability of real building or engineering construction based on adfreeze strength values (or frost-heave uplift forces) obtained earlier (for example, during geotechnical surveys).

Thus, the use of Reline provides significant reduction of adfreeze strength and related uplift forces (and frost jacking as a result): 62–85% for silty sand, 52–55% for silty clay, and 80–85% for mortar (1:5 cement-sand mixture). The poorer effect of Reline in the case of silty clay at the same roughness reduction (~93%) may be due to smaller particle sizes: on a rough surface, it is easier to displace fine-grained clayey soil than coarser sand. Since the size of sand particles is commensurate with the roughness height of uncovered piles, the roughness reduction causes a greater adfreezing effect on sand than on clay. Furthermore, the effect of coating in the case of sand soil varies with temperature: it increases from 62% to 85% upon warming from −6 to −1 °C, possibly, due to greater amounts of unfrozen pore water and related moisture increase (from 0.2 to 2%, or ten times). The water content increase in silty clay at the same warming conditions is much smaller: 3 to 6%, i.e., two times [17]. The reduction of uplift forces is the greatest in mortar (80–85%), irrespective of temperature. The reason is that mortar develops additional strong structural bonds (compared with fine-grained soil) and lacks unfrozen pore water, due to mineralogy (99% is quartz) and particle sizes of the sand (predominate fraction is 0.2–0.3 mm), since all unfrozen pore water is spent for cement hydration.

4 CONCLUSION

The use of Reline jacket reduces significantly (52 to 85%) the adfreeze strength and related frost-heave uplift forces on piles (and frost jacking too). The jacket is the most efficient for mortar (80–85%) and least efficient for silty clay (52–63%). In general, the reduction of uplift forces and its temperature dependence have several causes: changes in the roughness of protected pile surfaces; soil particle sizes; presence or absence of unfrozen pore water; temperature dependence of total moisture content at the account of unfrozen pore water.

Reline can successfully combat frost jacking of foundations, for both overdriven and bored precast piles. This effect is especially important in the context of ongoing permafrost degradation. Design solutions with due regard for the global change are indispensable for new construction projects in permafrost, in order to minimize deformation of foundations and structures associated with frost jacking and the ensuing accidents. The use of the Reline jacket can be an ideal solution for bored precast piles with grouting.

ACKNOWLEDGMENTS

The authors are grateful to the Ural Plant for Polymer Technologies “MAYAK” for research support: D.V. Alyavdin, V.M. Belyakov, A.D. Levin.

REFERENCES

1. Yurov, F.D.; Grebenets, V.I. Modern dynamics of engineering and geological conditions at Vankor and Zapolyarny oil and gas fields. In Prospects of Engineering Survey Development for Construction in Russia; Geomarketing, Moscow, Russia, 2017; pp. 239–246. (In Russian)
2. Harris, S.; Brouchkov, A.; Cheng, G. Geocryology: Characteristics and Use of Frozen Ground and Permafrost Landforms; CRC Press: London, UK, 2018; 765 p.
3. Wu, Q.; Zhang, T. Changes in active layer thickness over the Qinghai Tibetan Plateau from 1995 to 2007. J. Geophys. Res. Atmosphere 2010, 115, 1–12. doi: 10.1029/2009JD012974.
4. Solovyov, S.A.; Sushev, L.A.; Kochkin, A.A.; Solovyova, A.A. The problem of stability analysis for permafrost soils: Criterion of stability. Stroilestvo Rekonstr. 2021, 4, 3–15. (In Russian)
5. Osipov, V.; Aksyutin, O.; Sergeev, D.; Tipenko, G.; Ishkov, A. Using the Data of geocryological monitoring and geocryological forecast for risk assessment and adaptation to climate change. Energies 2022, 15, 879. doi: 10.3390/en15030879.
6. Orlov, V.O.; Elgin, B.B.; Kim, V.K.H.; Filippov, V.D. Methods for estimation of tangent and normal forces of frost heaving in the field. In Transactions of N.M. Gersevanov NIIOSP; Production Experimental Workshops of VNIIIS Gosstroy of the USSR: Moscow, Russia, 1985; pp. 69–76. (In Russian)
7. Kronik, Y.A. Analysis of accidents and safety of geotechnical systems in permafrost regions. In Proceedings of the 5th Conference of Geocryologists of Russia, Moscow, June 14–17, 2016; Plenary Presentations. Part 1. Engineering Geocryology. Part 2. Pipelines in Permafrost. Part 3. Seasonal and Cooling Systems in Permafrost. Part 4. Geophysical Studies of Permafrost during Construction; Universitetskaya Kniga, Lomonosov Moscow State University: Moscow, Russia, 2016; pp. 104–113. (In Russian)
8. Anisimov, O.A. The main natural and socio-economic consequences of climate change in the areas of distribution of permafrost rocks: A forecast based on the synthesis of observations and modeling. Greenpeace 2010, 1, 14–15.
9. Melnikov, V.P.; Osipov, V.I.; Brouchkov, A.V.; Falaleeva, A.A.; Badina, S.V.; Zheleznyak, M.N.; Sadurtdinov, M.R.; Ostrakov, N.A.; Drozdov, D.S.; Osokin, A.B.; et al. Climate warming and permafrost thaw in the Russian Arctic: Potential economic impacts on public infrastructure by 2050. Nat. Hazards 2022, 112, 231–251. doi: 10.1007/s11069-021-05179-6.
10. Anisimov, O.A.; Lavrov, S.A. Global warming and melting of permafrost: Risk assessment for production facilities of the fuel and energy complex. Tekhnologii v Toplivno-Energeticheskom Komplekse 2004, 3, 78–83. (In Russian)
11. Zhou, J.; Zhou, G.; Ma, W.; Wang, J.; Zhou, Y.; Ji, S.H. Experimental research on controlling frost heave of artificial frozen soil with intermission freezing method. J. China Univ. Min. Technol. 2006, 35, 708.
12. Wang, T.; Liu, J.; Tian, Y.; Lv, P. Frost jacking characteristics of screw piles by model testing. Cold Reg. Sci. Technol. 2017, 138, 98–107. doi: 10.1016/j.coldregions.2017.03.008.
13. Huang, X.; Sheng, Y.; Huang, L.; Peng, E.; Cao, W.; Zhang, X.; He, B. Experimental study on the anti-frost jacking ability of belled pile under unidirectional freezing condition. Adv. Eng. Sci. 2021, 53, 122–131. doi:10.15961/j.jsuese.201901193.
14. Pchelintsev A.M., Levkovich E.A. Recommendations for Reducing Uplift Forces of Frost Heave of Foundations Using Plastic Lubricants and Organic-Silicon Enamels; NIIOSP: Moscow, Russia; 1980; 36p. (In Russian)
15. Pchelintsev, A.M. Laboratory studies of soil application to various surfaces. In NIIOSP Transactions; NIIOSP, Moscow, Russia, 1974; pp. 136–145. (In Russian)
16. Dalmatov, B.I. Effect of Frost Heaving on Foundations; Gosstroiizdat: Leningrad-Moscow, Russia, 1957; p. 60. (In Russian)
17. Chuvilin, E.M.; Bukhanov, B.A.; Mukhametdinova, A.Z.; Grechishcheva, E.S.; Sokolova, N.S.; Alekseev, A.G.; Istomin, V.A. Freezing point and unfrozen water contents of permafrost soils: Estimation by the water potential method. Cold Regions Sci. Technol. 2022.

Smart Geotechnics for Smart Societies – Zhussupbekov, Sarsembayeva & Kaliakin (Eds)
© 2023 The Author(s), ISBN 978-1-003-29912-7
Open Access: www.taylorfrancis.com, CC BY-NC-ND 4.0 license

Determination of the helical pile bearing capacity by its installation torque

A.G. Alekseev, S.G. Bezvolev & S.A. Vinogradova
N.M. Gersevanov Research Institute of Bases and Underground Structures, Russia

ABSTRACT: The paper characterizes the state of the issue of designing effective structures of helical piles, testifying to the relevance of this scientific and technical problem in conditions of insufficient development of the existing norms. The technique of determining load-carrying capacity of a pile by the moment of screwing fixed during its immersion is considered. The correlation coefficient formula and the technique of determining the ultimate soil contact friction on the side surface of several types of helical piles developed as part of the advancement in solving the research problem are presented.

1 INTRODUCTION

At the present time, large construction companies (A.B.Chance Co., etc.) which use helical piles (HP) have the practice of controlling the bearing capacity of HP F_u by the value of the screwing resistance torque T_k fixed during their immersion at the construction site due to the generalization of data on the objects. Even in the absence of normative expressions for the transient dependence $Fu = f(T_k)$, the method of measuring T_k and the determination of this dependence on a particular site allows to reduce the number of control piles at expensive field static tests. For this purpose, in the Russian practice, according to [Town Planning Code of 29.12.2004], individual special technical specifications (STS) are developed for design of foundations made of HP at individual construction sites. In order to develop normative dependences for $f(T_k)$ allowed for use in designing or to develop a corporate standard of the organization (STO), it is necessary to develop a justification for specific types of HPs and soil conditions.

The analysis of the state of the issue is performed on the basis of the research data [Alekseev, Beszvolev et al 2018a. 2018b. 2020], thematic review articles [Halturin 2012] and capital monographs [Zhelezkov 2004, Perko 2019]. According to the current Russian regulatory document [SP 24.13330.2021] for helical piles is allowed to determine the bearing capacity of soils based on the results of static testing of natural piles and using the recommended in [SP 24.13330.2021] for certain types of HP algorithms for calculating the strength characteristics of soil found during the survey.

The most reliable method for determining the bearing capacity of piles is the method of field static tests, at the same time it is the most costly both financially and in terms of time. When applying the calculation methods, there is a question of applicability of the existing calculation algorithms to helical piles of different types (Figure 1), because its size (configuration, number of propeller blades, distance between them, etc.) largely determines the mechanism of the propeller pile. However, analytical methods of calculation [SP 24.13330.2021] are actually developed on the basis of researches only of single helical wide-bladed HP (Figure 1.1a). In addition, in these methods there are inevitable errors associated with the definition of soil characteristics, as well as their averaging over a large volume of heterogeneous soil mass.

The general disadvantage of the recommended methods [SP 24.13330.2021] is the lack of control over the bearing capacity of each pile being installed, which is especially relevant for the building area with heterogeneous engineering and geological conditions. One of the

DOI: 10.1201/9781003299127-216

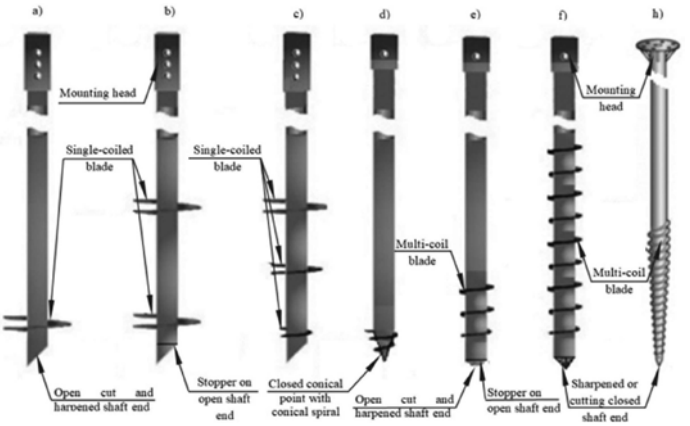

Figure 1. Main types of helical piles produced in Russia and features of their design.

a) single-blade with one working blade, formed by a coil spiral, wide-blade (d/D<0,6); b) multi-blade (two-blade example) cylindrical (with the same blade diameter) wide-blade; c) multi-blade (three-blade example) cone (with different blade diameters); d) single-blade with a solid conical tip with a cone spiral; e) multi-coiled narrow-bladed (d/D>0,6) with open sharpened or cutting shaft end; f) also with closed end; h) also with elongated conic point with conic spiral.

peculiarities of HP foundations arrangement is the possibility to measure the T_k required for pile driving. The presence of correlation between helical pile`s F_u at static compressive and pulling loads and the T_k applied during its immersion has been identified since the 1960s by developers in various countries on a significant number of sites.

The formula [Hoyt et al. 1989] is usually used for the experimental estimation of the calculated helical pile`s F_u by T_k, necessary for its immersion:

$$F_u = K_t T_k \tag{1}$$

where K_t = coefficient of proportionality.

In works [Hoyt et al. 1989, Ghaly 1995, Zhelezkov 2004, Livneh et al. 2008, Tsuha et al. 2010, Perko 2019] the values of K_t, as well as the factors determining it, were studied for different types of HP in different soil conditions. In work [Hoyt et al. 1989] the results of full-scale tests on static pulling loads of 91 piles with the number of turns from 2 to 14 and blade diameters from 152 to 508 mm, performed at 24 different sites were considered. Based on the data obtained in work [Hoyt et al. 1989], it was assumed that the K_t coefficient depends mainly on the diameter of the pile shaft.

In work [Perko 2019] an analysis of the results of more than 300 tests of the HP in different engineering-geological conditions was carried out. Within the framework of testing the hypothesis [Hoyt et al. 1989] that the K_t coefficient depends mainly on the diameter of the pile shaft, a correlation formula was obtained:

$$K_t = \lambda_k / d_{ef}^m \tag{2}$$

where d_{ef} = effective diameter of the pile shaft (for a circular cross-section equals the diameter, for a square cross-section equals the length of the diagonal); m = power factor equal to 0.92; λ_k = coefficient equal to 1433 mm^m/m.

It turned out that dependence (2) has a very low coefficient of determination (R^2) equal to 0.64, therefore, the coefficient K_t depends significantly on other parameters besides the diameter of the pile shaft.

To analyze the parameters influencing the K_t coefficient, in work [Perko 2019] the dependence:

$$K_t = H / d_{ef} \tag{3}$$

in which the parameter H turned out to depend mainly on the diameter of the HP barrel, the diameter, pitch and thickness of its propeller blade, the type of ground and, insignificantly, on the number of coils of the propeller blade, as well as the values of the axial load and torque.

In work [Livneh et al. 2008] the results of full-scale tests of 19 HP on one site with sandy soil and on two sites with dusty-clayey soils are presented. Were tested HP with a square cross-section shaft with a diagonal of 45 mm and three welded blades with diameters of 200, 250 and 300 mm, spaced along the length of the trunk. In work [Livneh et al. 2008] it was concluded that the value of K_t coefficient largely depends on the direction of the force on the pile and on the type of soil.

The article [Tsuha et al. 2010] presents laboratory tests of model HP on pulling out in a centrifuge in sands of different density. The results showed that the value of K_t coefficient depends on relative density of sand, size of barrel and blades of HP and does not depend on their number. The authors developed a formula:

$$K_t = 2/(d_c \tan(\delta_r + \theta)) \tag{4}$$

where δ_r = angle of metal-sand friction; d_c and θ = parameters depending on the diameter of the pile barrel, diameter and pitch of the propeller blade.

A comparison of formulas (2) - (4) shows their common empirical basis. In particular, (2) and (4) can be reduced to the more general form (3).

In Russian practice, the connection between the load-carrying capacity of the HP and the torque was considered by Zhelezkov V.N. in his monograph [Zhelezkov 2004]. The dependence of the K_t coefficient on the load direction and on the physical and mechanical characteristics of the soil was revealed. Dependence on HP configuration was not obtained due to insignificant difference in geometric dimensions of blades and barrels of tested HP.

The above analysis of the articles testifies about the sufficient validity of the determining method of helical piles carrying capacity by the amount of installation torque required for pile`s screwing. The corresponding dependence (1) with the proportionality coefficient K_t has been qualitatively confirmed by numerous experimental and theoretical researches. Quantitative match between the calculated and experimental results is determined by the reliability of the coefficients used for calculations, linking the bearing capacity of the pile and the amount of the installation torque. In order to develop normative dependences allowed for use in designing for calculating the K_t coefficients, it is necessary to conduct experimental studies for each type of helical piles used in various soil conditions.

An essential weak point of published data [Hoyt et al. 1989, Ghaly 1995, Zhelezkov 2004, Livneh et al. 2008, Tsuha et al. 2010, Perko 2019] is a different and sometimes indefinite approach to the evaluation of an amount (criteria) of helical pile`s carrying capacity according to the F_u test results and the differences in their methods (continuous immersion, staggered, accelerated, long-term). At the moment, dozens of different criteria for the experimental value F_u are used during the practice of the geotechnical science. Significant uncertainty is also created by the effect of differences in the designs of the tested helical piles and the immersion techniques (rotation speed, axial load size, etc.), that also includes impact on the value of the torque of screw resistance T_k.

For these reasons, the use of published [Hoyt et al. 1989, Ghaly 1995, Zhelezkov 2004, Livneh et al. 2008, Tsuha et al. 2010, Perko 2019] data on the values of T_k and the correlation between T_k and F_u in order to check the theoretical dependence of T_k and to calibrate the correlation dependence T_k - F_u seems to be difficult due to the practical impossibility of selecting results that meet the requirements of criteria and methods listed in the regulatory documents of the Russian Federation. It also seems problematic because of the inaccessibility of materials related to the characteristics of the tested soils.

2 THEORETICAL BASE OF THE IMPLEMENTED RESEARCH

This article is limited by constructions which are close to cylinder-shaped ones (Figure1d–h). We are going to call it “ground-screw pile” (GSP).

GSP is made of a metal pipe with a spiral-ply and a closed cutting tip with a sharpening angle of 60°. This kind of pile is immersed in the soil by rotation in combination with indentation, it has found application in domestic practice as a bearing element of foundation or hoarding [Moscow Government 1997]. Simple national equipment makes it possible to successfully immerse such constructions with a pipe diameter of 600 mm and length up to 12 m even in very dense and durable soils [Moscow Government 1997].

Recently, foreign cone-spiral screw piles (CSSP) «BAU» [Altai region national expertise 2011], which are close to GSP have appeared in Russia. Spiral winding of these piles is performed on an elongated conical part. With a length up to 3-3.5 m and a tubular shaft diameter up to 108-133 mm CSSPs are immersed with a small torque using a low-power rotator. In addition to transport construction, the driving of such micropiles is very popular in the sphere of small entrepreneurship for the rapid construction of small buildings and constructions, for example, agricultural facilities or residential cottages.

The theoretical analysis of screw pile immersion mechanism which was provided by Gersevanov Research Institute of Bases and Underground Structures shows that T_k (installation torque) is determined mostly by contact friction of the soil and the surface of cylindrical-shaped shaft τ_s, round blade τ_{fi} and soil core τ_{fl} that is located near shaft edge. We should ignore less significant factors such as soil resistance in order to achieve in particular, friction on the surfaces of the edges τ_{ti} and soil resistance to cutting by the edge of the frontal (lower) blade σ_{t1}, the inclination of the helix of the blades and the cone of the tip, as well as the value τ_{fi} that is typical for narrowed (d/D> 0.8) blades (helix) of the GSP. Very complex, actually unsuitable for practical application and, in our opinion, controversial expressions for taking into account these factors are given in [Zhelezkov 2004]. We also note that at the end of the immersion, the friction at the tip of the shaft τ_{fl} along the frontal surface is obviously less than the lateral friction τ_{sl} on the shaft inner surface against the soil "plug" formed during screwing inside the shaft near the edge.

According to the mechanism of immersing GSP, we`ve got a formula for T_k as follows:

$$T_t = 2\pi r^2 \int_0^l \tau_s(z)dz + 2/3\pi r^3 \tau_f(l) \tag{5}$$

where r = radius of tubular shaft (pipe) considering a GSP spiral; l = work length (immersed in the soil) of GSP.

The degeneracy of the second component(5) while pulling out the GSP means a direct proportionality between the corresponding ultimate soil resistance F_u and the installation torque $F_u=T_k/r$. Thus, in this case, the coefficient K_t of dependence (1) is theoretically determined by the formula $K_t = 1/r$, and for dependencies (2) and (3) we obtain $\lambda_k = H=2$, $d_{ef}=2r$ and $m=1$.

According to the presented analysis, it is expedient to process the data of static tests of the GSP to determine the correlation dependence of the helical piles carrying capacity on the installation torque based on the formula:

$$F_{u,n} = K_f T_{k,n}/r \tag{6}$$

where

$F_{u,n}$ = partial value of immersed GSP bearing capacity on the ground for the vertical load; $T_{k,n}$ = installation torque fixed when a helical piles is immersed to the designed mark; K_f = dimensionless correlation parameter.

The absence of dimension demonstrates the obvious advantage of the parameter K_f in comparison with the dimensional proportionality coefficient K_t discussed in detail above (formulas (3) and (4) over (1) and (2)). Thus, the developed equation allowed us to theoretically confirm the feasibility of using the empirical formula (3), which coincides with (4) for $d_{ef} = 2r$ and $H = 2K_f$. By highlighting the main influence of the shaft cross-section (3) and (4), the dimensionless correlation parameter makes it possible to better reflect the influence of other factors.

For FM24 model of CSSP with a shaft diameter d=76.2 mm, there is a set of studies presented in work [Noskov et al. 2019], including experimental immersion and static tests of the CSSP on an experimental site composed of loess-like solid sandy loam. Tested on 2 piles with a length l of 1.5; 2, 2.5, 3 and 3.5 m with a lower conical part 55 cm high. In the last 50 cm of the pile insertion, the average value of the torque T_k was recorded.

The tests were carried out according to the method of the standard [GOST 5686-2012], taking into account the instructions of the standards [SP 24.13330.2021]. The static load was brought to a value at which the draft was at least 40 mm. With this settlement, in all experiments, the pile bursting was achieved, and the particular value of the ultimate pile resistance F_d was taken equal to the previous load value, at which the stabilized pile settlement ranged from 4 to 13 mm. A summary of measured T_k and set F_d is given in the Table 1.

Table 1. Cone-spiral helical piles test results [Noskov et al. 2019].

№	1	2	3	4	5	6	7	8	9	10
l, mm	1500	1500	2000	2000	2500	2500	3000	3000	3500	3500
F_d, kN	20,0	22,5	28,0	28,0	40,0	35,0	42,0	36,0	52,5	52,5
T_k, kN m	0,8	0,91	1,21	1,08	1,65	1,42	1,61	1,5	2,25	2,15

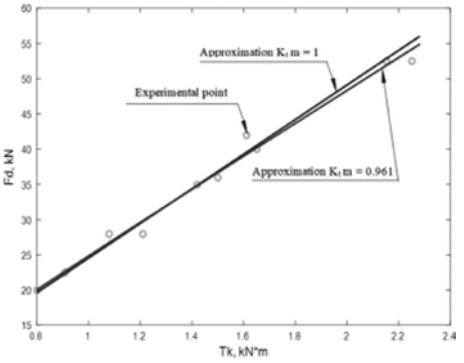

Figure 2. Matching of approximations listed in [TKP 45-5.01-254-2012] experimental data.

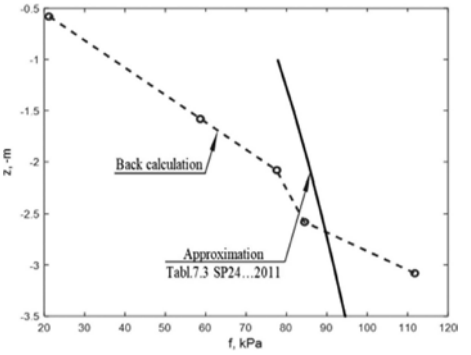

Figure 3. Using the results back calculation method τ_s with f tabl.7.3 [SP 24.13330.2021].

Statistical processing [Noskov et al. 2019] of the obtained data series $F_d - T_k$ using a power model of paired (one-factor) regression led to a two-parameter dependence $F_d = 24{,}845\ T_k^{0{,}961}$ with coefficients of determination $R^2 = 0.986$ and variation $v = 0.040$. The proximity to 1 of the power exponent $m = 0.961$ of this dependence confirms the assumption made above about the direct linear correlation of $F_u - M_u$ for GSP. Thus, our alternative statistical processing with the choice of $m = 1$ led to a one-parameter dependence $F_d = 24{,}552 T_k$ with determination coefficients $R^2 = 0.983$ and variation $v = 0.042$. Thus, both dependencies have excellent and practically equivalent indicators (Figure 2). A certain deviation in the direct one-parameter dependence of the coefficient $K_t = 24.552\ m^{-1}$ from the theoretical value $K_t = 2/d = 26.247\ m^{-1}$ is apparently caused by the frontal work of the cone part of the CSSP when it is pressed in.

For example, the one-parameter dependence $F_d = 24{,}552 T_k$ obtained above for GSP in loess-like sandy loam is converted to $F_d = 0{,}935 T_k/r$, which shows that the influence of other factors is 6.5%.

Tracking the measured values of the screwing torque $M_{u,n}$ as the GSP is immersed and comparing them with the M_u values calculated by (5) is an effective way to assess the strength properties of soils in their natural occurrence [2].

In the simplest case of GSP (see Figure 1d–h), by inverse calculation from formula (5) it is possible to determine the distribution along the length of the pile (the depth of the soil base) of the specific contact friction of the soil on the side surface of the steel shaft of the pile τ_s. In particular, neglecting a slight change with depth τ_f, sequentially determining $\tau_{s,i}$ for each segment of the depth dz_i by $dM_{u,i}$

$$\tau_{s,i} = dM_{u,i}/A/dz_i \tag{7}$$

where $A = 2\pi r^2$; $dM_{u,i} = M_{u,i} - A\sum_{k=1}^{i-1} \tau_{s,k} dz_k$,

Such a definition of τ_s is of great practical importance, since the use of the tabular values τ_s for helical piles established for the side surface of reinforced concrete driven piles (*f* Table 7.3) allowed [SP 24.13330.2021] is theoretically incorrect. In this regard, we note that in the modern standards of the Republic of Belarus [TKP 45-5.01-254-2012], when calculating the helical piles, the values of f are established according to the processing of the results of testing soils with steel piles.

Using the data of [Noskov et al. 2019] (table) and formula (5), the graph of the change in $\tau_s(f)$ along the length of the CSSP immersed in the loess-like solid sandy loam presented in Figure 3 was obtained.

Comparison of the obtained τ_s with the values of *f*, obtained according to the data of Table 7.3 [SP 24.13330.2021], confirms the adequacy of the developed back calculation method. Thus, the average values of τ_s and f in the general depth interval are close to each other. In this case, the growth of τ_s with depth is much more intense than that of *f*, which is consistent with the generalized experimental data [Glotov et al. 1975].

3 CONCLUSION

The theoretical analysis carried out showed the feasibility of using the obtained dependence (6) to determine the bearing capacity of a screw pile $F_{u,n}$ by the value of the torque $M_{u,n}$ required for its twisting. By highlighting the main influence of the shaft radius, the dimensionless correlation parameter K_f makes it possible to better reflect the influence of other factors. The difference between the value of K_f and 1 shows the degree of influence of other factors, in particular, the role of the operation of the blades and the tip in the bearing capacity of the helical pile.

In the simplest case of a helical pile recursive calculation using formula (7) can determine the distribution along the length of the pile (depth of the soil base) of the specific contact friction of the soil on the side surface of the steel shaft of the pile τ_s. Such a definition of s is of great practical importance, since the values of τ_s used by the norms [SP 24.13330.2021] for helical piles established for the side surface of reinforced concrete driven piles (*f* Table 7.3 [SP 24.13330.2021]) are theoretically incorrect. Based on the results of processing the results of soil tests by means of the GSP, reliable and rational standard values of *f* for the lateral surface of steel helical piles can be established.

REFERENCES

Alekseev, A. G., Beszvolev, S. G., Sazonov, P. M., Zvezdov, A.A. 2018a. About necessity of providing researches on helical piles work and actualization of helical piles foundation design standards. *Industrial and civil construction* (1): 43–47.

Alekseev, A.G, Bezvolev, S.G., Sazonov, P.M. 2018b. The experience of applying multi-blade helical piles in silt and clay soil foundation. *Foundations and soil mechanic science* (5): 8–15.

Alekseev, A.G & Bezvolev, S.G. 2020. Adaption to the requirements of helical piles calculation methods engineering practice with using of PLAXIS. *Foundations and soil mechanic science* (1): 23–28.

Altai region national expertise. 2011. *Recommendations on design of helical piles «BAU» for civil, industrial and engineering constructions: P. BAU.01.09.11*. Novosibirsk.

Construction and Architecture Department of Belarus Republic. 2012. *Constructions standards of design work: TKP 45-5.01-254-2012 Foundations of buildings and constructions. Guidelines*. Minsk.

GOST 5686-2012 *Soils. Field test methods by piles*. Moscow.

Ghaly, A. 1995. Drivability and pullout resistance of helical units in saturated sands. *Soils and Foundations* 35 (2): 61–66.

Glotov, N.M. et al. 1975. *Pile foundations*. Moscow: Transport.

Halturin, A.Y. 2012. The determination of helical piles bearing capacity by installation torque. *Polzunov Bulletin* 1(2): 118–121.

Hoyt, R.M. & Clemence, S.P. 1989. Uplift Capacity of Helical Anchors in Soil. *Proceedings of the 12th International Conference on Soil Mechanics and Foundation Engineering, Rio de Janeiro* 2: 1019–1022.
Livneh, B & Naggar, M.H. 2008. Axial testing and numerical modeling of square shaft helical piles under compressive and tensile loading. *Canadian Geotechnical Journal* 45 (8): 1142–1155.
Moscow Government. 1997. *Recommendations about calculations, design and driving piles of new types in Moscow*. Moscow: Committee on Architecture and Town Planning.
N.M. Gersevanov Research Institute of Bases and Underground Structures. 2021. *SP 24.13330.2021. Pile foundations*. Moscow: Russian Federation construction Department.
Noskov, I.V. et al. 2019. Determining of cone-spiral helical piles bearing capacity by theirs installation torque. *Bulletion of SBIU* 49 (2): 66–75.
Perko, H. A. 2019. *Helical Piles: A practical guide to design and installation*. New Jersey: John Wiley and Sons.
Town Planning Code of 29.12.2004. Federal Law №190 with amendments; Technical regulation of Russian Federation about constructions security of 30.12. 2009. Federal Law № 384.
Tsuha, C.H.C. & Aoki, N. 2010. Relationship between installation torque and uplift capacity of deep helical piles in sand. *Canadian Geotechnical Journal* 47 (6): 635–647.
Zhelezkov, V.N. 2004. *Helical piles in energetic and other construction industries*. Saint-Petersburg: Pragma.

Smart Geotechnics for Smart Societies – Zhussupbekov, Sarsembayeva & Kaliakin (Eds)
© 2023 The Author(s), ISBN 978-1-003-29912-7
Open Access: www.taylorfrancis.com, CC BY-NC-ND 4.0 license

On the use of seismic energy in deep compaction of loess subsidence soils by hydraulic explosions

F.G. Habibov
Azerbaijan Research Institute of Construction and Architecture, Baku, Azerbaijan

E.M. Shokbarov
Kazakh Research Institute of Construction and Architecture, Almaty, Kazakhstan

L.F. Habibova
HALLIBURTON Company, Houston, USA

ABSTRACT: The authors have developed a method of deep compaction of loess subsidence loams, which uses the energy of an earthquake (or earthquakes). The energy of earthquakes is commensurate with the energy of explosions, therefore, pre-humidification of the compacted subsidence layer during the seismically active period will improve the quality of soil compaction. Initially, the seismic activity of the territory is recorded. When the locking through drainage wells to a state of fluid consistency stops, deep explosions are produced in the wells. Under the conditions of seismic activity of the territory, physico-chemical processes in the soils are intensified due to the activation of geoelectromagnetic and geoacoustic fields. Under these conditions, capillary and mass transfer processes in soils are intensified. Therefore, during this period, it is most effective to carry out locks and explosions in the ground mass. Post-explosive consolidation of the main part of the deformation of the compacted subsidence array lasts at least 5-8 months. Such a long period is sufficient for the realization of a natural earthquake. Seismic activity during the consolidation of the subsidence array contributes to the consolidation of the subsidence array and accelerates the process. Any tangible earthquake is effective for the process of doubling the subsidence array. The efficiency of the use of earthquake energy in compaction of subsidence soils by hydraulic explosions is theoretically justified.

Keywords: subsidence, earthquakes, energy, territory, explosion, well, compaction, consolidation, seismic activity

1 INTRODUCTION

The works of V.T. Trofimov [1], N.I. Krieger [2], H.M. Rendell [3], S.Z. Rozycki [4], M. Pecsi [5], J. Sajgalik [6], Wei Lanying, Gui Jiuxi, Lu Yanchon [7] are devoted to the study of the properties of loess subsidence soils, M.Zarate, A. Blasi [8] and others.

The works of Yu.M. Abelov and M.Yu. Abelov [9], I.M. Litvinov [10], S.N. Klepikov, A.S.Tregub and I.V. Matveev [11], A.A. Mustafayev [12], S.K. Aliyev [13], V.I. are devoted to the development of effective methods of construction on subsident loess soils. Krutova, A.S. Kovaleva and V.A. Kovaleva [14] and others.

As is known, a significant part of the areas of subsidence of loam falls on areas with high seismic activity. In this regard, the issue of using earthquake energy during deep compaction of subsident loamy massifs with a capacity of more than 10 m, in combination with other methods of deep compaction of subsident soils, in particular with hydraulic explosions, becomes very relevant.

DOI: 10.1201/9781003299127-217

Studies of I.M.Litvinov [10], A.M.Ryzhov [15], F.G.Gabibov [16] and others are devoted to the hydro-explosive method of compaction of subsidence arrays.

2 THEORETICAL FOUNDATIONS OF THE POSSIBILITY OF USING EARTHQUAKE ENERGY IN DEEP COMPACTION OF SUBSIDENCE SOILS

For the first time, the idea of using earthquake energy for deep compaction of subsident loams was put forward by F.G.Gabibov [17] in the early 90s of the last century. The energy of earthquakes is commensurate with the energy of high-power explosions, therefore, pre-humidification of the compacted subsidence layer during the seismically active period will significantly improve the quality of soil compaction.

If, according to the project, the work on deep compaction of subsident loess soils coincides with the seismic activity of the territory, then this factor can practically be used from an engineering point of view.

Modern scientific and engineering achievements allow us to use proven methods of recording seismic activity of the territory. Among them, we can mention seismogeodynamic, electromagnetic and biological methods, described in detail in the monographs of M.Ikea [18], K.Mogi [19], T.Rikitake [20] and others.

Among the seismogeodynamic methods of earthquake prediction, it is interesting to use a seismic harbinger discovered by Soviet scientists. Many months before an earthquake, rock cracking reduces the velocity of longitudinal waves. Based on the algorithms of long-term forecasting developed under the guidance of V.I. Keylis-Borok, the accuracy of the forecast increases several times. The most informative geochemical harbingers are the appearance of components of deep origin in the composition of groundwater and gases: inert gases (primarily helium and radon), hydrogen, nitrogen, as well as mercury vapor. Their variations provide material for various stages of medium- and short-term forecasting (days, months).

Electromagnetic phenomena are short-term harbingers. During compression and destruction of rocks, various mechanoelectric and electrokinetic effects occur, which generate alternating electric fields underground and in the atmosphere. The most effective, although not frequent, electromagnetic harbinger is light phenomena.

Biological methods of earthquake prediction are associated with the abnormal behavior of animals (mammals, birds, reptiles, fish) manifested before an earthquake.

3 DEVELOPMENT OF AN ENGINEERING METHOD FOR DEEP COMPACTION OF SUBSIDENCE SOILS USING EARTHQUAKE ENERGY

The authors have developed a method of deep compaction of loess subsidence loams by hydraulic explosions, which uses the energy of an earthquake (or earthquakes).

Using one of the methods of earthquake prediction, or a set of these methods, the seismic activity of the territory is first recorded.

The compacted section 1 (see Figure 1) is separated from the non-compacted section 2 by digging contour trenches 3. Drainage and blast wells 4 are drilled, into which blast pipes 5 are installed. Explosive charges (explosives) are installed at the bottom of the pipes 6. After that, drainage wells 4 are filled with drainage material 7. The sealed area is locked in a limited zone with boundaries 8, which on the sides coincide with the bottom of contour trenches, and from below reaching the boundary between the subsidence array 9 and the underlying non-subsidence soil 10.

After the seismic activity of the territory is recorded along the boundaries of the compacted area 1, contour trenches 3 are dug using, for example, a deep trencher, to a depth of 5-7 m. Then, within the compacted sections 1, drainage and explosive wells 4 are drilled to a depth of 2/3 of the subsidence array 9. Explosive pipes 5 made of metal or plastic are installed in these wells, at the bottom of which explosive charges 6 are installed. After that, the space between the walls of the well 4 and the blast pipes 5 is filled with drainage material 7,

for example coarse sand or gravel. The compacted section 1 is soaked through drainage wells 4 with water to a state of fluid consistency (see Figure 1). The boundaries of moisture 8 should coincide with the bottom of contour trenches 3, and from below reach the upper boundary of the underlying non-sedimentary soil 10.

When the lock stops, explosives 6 explode in wells 4. Under the influence of these deep explosions, artificial seismic vibrations are created in the compacted subsidence area 1, which contribute to accelerated deep compaction of the subsidence array (see Figure 2).

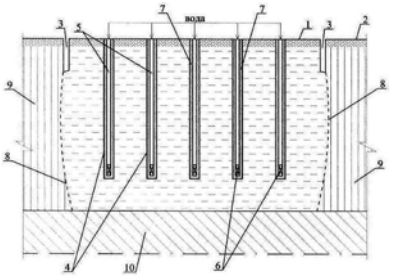

Figure 1. Scheme of deep compaction of loess subsidence loamy massif during soil moistening in the seismically active period before an earthquake.

Under the conditions of seismic activity of the territory, physico-chemical processes in the soils are intensified due to the activation of geoelectromagnetic and geoacoustic fields. Under these conditions, capillary and mass transfer processes in porous media are intensified. Therefore, it is during this period that it is most effective to carry out locks and explosions in the ground mass. After explosions of explosive charges 6, explosive pipes 5 are removed from the well by vibration pulling, which also contributes to additional compaction of the subsidence array. It should be noted that soaking of the compacted area and deep explosions are carried out in the seismically active period before an earthquake.

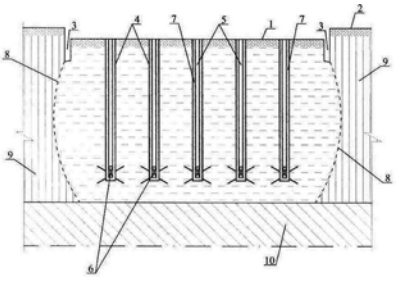

Figure 2. Scheme of deep compaction of loess subsidence loamy massif during the impact of deep explosions on the soil massif in the seismically active period before the earthquake.

The post-explosive consolidation of the main part of the deformation of the compacted subsidence massif lasts at least 5-8 months (see Figure 3). Such a long period is sufficient for the realization of a natural earthquake predicted by the seismic activity of the territory. Thus, an earthquake (or earthquakes) occurred during the consolidation of the subsidence array (see Figure 4) contributes to the consolidation of the drawdown array and accelerates the consolidation process. It should be noted that any tangible earthquake (intensity of at least 3 points) is effective for the process before compaction of the subsidence array. Even if an earthquake does not occur during the period after explosive consolidation in the seismically active period, the activity of geomagnetic and geoacoustic fields, which are an integral part of seismic energy, leads to activation of the consolidation deformation process.

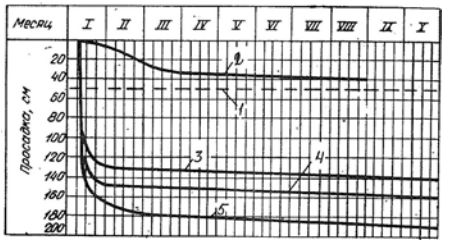

Figure 3. Graphs of consolidation of surface subsidence arrays: 1-calculated drawdown according to the SNiP; 2 - actual drawdown during normal soaking; 3, 4, 5 - actual drawdowns and precipitation during hydro-explosive compaction (according to those characteristic sites).

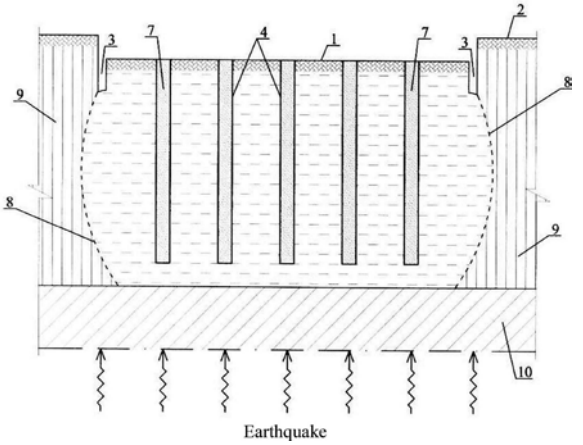

Figure 4. Scheme of deep compaction of loess subsidence loamy massif in the process of compaction of the soil mass by the energy of a natural earthquake.

Seismic waves passing through the ground during the period after explosive consolidation are practically elastic waves, of which transverse waves are of the greatest importance from an engineering point of view. With transverse waves, elastic soil particles oscillate in a direction perpendicular to the motion of the wave front. Let's denote the direction of motion of the wave x, and the direction of vibration of the particles y (see Figure 5). Under the action of a passing wave, the ABCD element moves and takes the form of an element. If the movement of the AB side is assumed to be equal to and, and the sides, then

$$du = \frac{\partial u}{\partial x} dx, \tag{1}$$

where $\partial u/\partial x$ characterizes the shear deformation.

Similarly, if the direction along AB is τ, and along CD $\tau + d\tau$, then

$$d\tau = \frac{\partial \tau}{\partial x} dx. \tag{2}$$

Since the element $ABCD$ experiences acceleration determined by the difference of forces on the sides AB and CD, the equation of motion takes the form

$$d\tau = \frac{\partial^2 u}{\partial t^2} \rho dx, \tag{3}$$

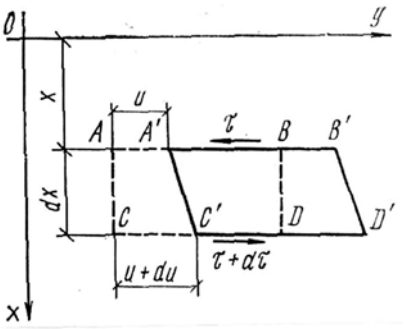

Figure 5. Diagram of the movement of the soil element when the wave is found.

where $\rho-$ the density of the element of the compacted subsidence soil. From here

$$\rho = \frac{\partial^2 u}{\partial t^2} = \frac{\partial \tau}{\partial x}. \tag{4}$$

In an elastic soil environment, stresses are proportional to deformations

$$\tau = G\frac{\partial u}{\partial x} \tag{5}$$

and therefore:

$$\rho = \frac{\partial^2 u}{\partial t^2} - G\frac{\partial^2 u}{\partial x^2} = 0. \tag{6}$$

Taking now

$$c = \sqrt{\frac{G}{\rho}}, \tag{7}$$

we get

$$\frac{\partial^2 u}{\partial t^2} - c^2\frac{\partial^2 u}{\partial x^2} = 0. \tag{8}$$

The resulting equation is a differential equation of shear oscillations. If the appropriate function $F_1(z)$ argument $z = t - \frac{x}{c}$ substitute in (8) instead of and and consider it to be twice differentiable, then any function of the accepted class will satisfy this condition. Therefore:

$$u = F_1\left(1 - \frac{x}{c}\right). \tag{9}$$

With such a fluctuation in the case of constancy $t - \frac{x}{c}$ the displacement in the compacted soil will be the same. Thus, moving in a place with the x coordinate at time t will be the same as moving through time Δt at a point $x + c\Delta t$. This means that a certain set point in the process of oscillation moves in a positive direction with a constant velocity of C. This phenomenon is called wave motion, and c is the propagation velocity. By analogy with the expression (9), another suitable function $F_2(z)$ argument $z = t + \frac{x}{c}$:

$$u = F_2\left(t + \frac{x}{c}\right) \tag{10}$$

it will also satisfy equation (8) and characterizes the wave motion in the negative x direction. The sum of expressions (9) and (10) is also a solution of equation (8).

In an elastic ground environment with propagating waves, deformation occurs at a certain moment t at a distance of x

$$\gamma = \frac{\partial u}{\partial x} = \frac{1}{c} F_1^{'}(z), \tag{11}$$

where the stroke means differentiation F_1 by z. Hence the energy of deformations in a single volume

$$W_s = \frac{G}{2}\gamma^2 = \frac{G}{2c^2}\left\{F_1^{'}(z)\right\}^2 = \frac{\rho}{2}\left\{F_1^{'}(z)\right\}^2. \tag{12}$$

The velocity of the soil particle in this place is equal to:

$$\upsilon = \frac{\partial u}{\partial t} = F_1^{'}(z) \tag{13}$$

and kinetic energy in a single volume

$$W_k = \frac{\rho}{2}\upsilon^2 = \frac{\rho}{2}\left\{F_1^{'}(z)\right\}^2. \tag{14}$$

If we now denote the total energy in a unit volume by W, then as the sum of the deformation energy and kinetic energy, it is equal to

$$W = W_s + W_k = \rho\left\{F_1^{'}(z)\right\}^2. \tag{15}$$

Since this energy is associated with the movement of waves at a speed of c, the energy per unit area per unit of time (the intensity of the energy flow) is equal to:

$$Q = c\rho\left\{F_1^{'}(z)\right\}^2. \tag{16}$$

Usually, waves moving forward and waves moving backward exist simultaneously, and the energy in a single volume is equal to the sum of the corresponding energies of incident and reflected waves in the same volume.

The rising wave, reaching the surface of the earth, is reflected and goes back. In Figure 6, the abscissa axis along the ground surface shows an incident (suitable from below) wave:

$$u_1 = U\left(t + \frac{x}{c}\right) \tag{17}$$

and the wave reflected from the surface (going down)

$$u_2 = D\left(t - \frac{x}{c}\right). \tag{18}$$

In this case, the displacement of the soil is equal to:

$$u = D\left(t - \frac{x}{c}\right) + U\left(t - \frac{x}{c}\right), \tag{19}$$

and the resulting deformations

$$\gamma = \frac{\partial u}{\partial x} = -\frac{1}{c} D'\left(t - \frac{x}{c}\right) + \frac{1}{c} U'\left(t + \frac{x}{c}\right), \tag{20}$$

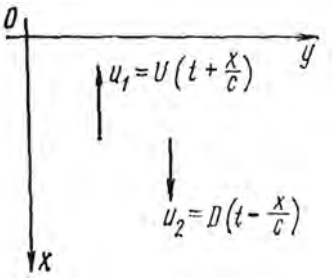

Figure 6. Scheme of incident and reflected waves.

where D' – derivative from D by $t - \frac{x}{c}$, but U' – derivative from U by $t + \frac{x}{c}$.

Shear stress on the ground surface $(x = 0)$ equal to zero. Consequently, the shear strain is equal to zero, i.e.

$$D'(t) - U'(t) = 0. \tag{21}$$

Therefore

$$D(t) = U(t) \tag{22}$$

and

$$D\left(t - \frac{x}{c}\right) = U\left(t - \frac{x}{c}\right). \tag{23}$$

This equation determines the shape of the reflected wave, i.e. the shape and amplitude characteristics of the reflected wave are the same as the parameters of the incident wave. Hence the equation of wave motion in elastic soil.

$$u = U\left(t - \frac{x}{c}\right) + U\left(t + \frac{x}{c}\right). \tag{24}$$

On the surface when $x = 0$ we get

$$u = 2U(t), \tag{25}$$

that is, the amplitude of the surface vibrations is equal to twice the amplitude of the incident wave.

The above relations are valid for the case of reflected waves S moving perpendicular to the surface. When the waves S of the input action approach the ground surface at an angle, the reflected waves, in addition to the waves S, will contain waves P. Similarly, when the waves P approach perpendicular to the surface, the reflected waves will be only P waves, and when falling obliquely, in addition to the waves P, there will be transverse waves in the reflected waves.

When a wave approaches a flat boundary between two layers with different characteristics (in our case, we mean the boundary between the compacted subsidence layer and the lower stable substrate), part of the waves is reflected, and the other passes through the boundary. In

the case of the wave approach perpendicular to the boundary of the layers, the reflected and passing parts of the waves are determined as follows. The fluctuations of the two layers are determined by the expressions:

$$u_1(t,x) = U_1\left(t + \frac{x}{c_1}\right) + D_1\left(t - \frac{x}{c_1}\right), \tag{26}$$

$$u_2(t,x) = U_2\left(t + \frac{x}{c_2}\right) + D_2\left(t - \frac{x}{c_2}\right). \tag{27}$$

Because on the border $(x = 0)$ at any given time, the conditions of continuity of displacements and stresses must be observed, we obtain:

$$u_1(t,o) = u_2(t,o) \tag{28}$$

and

$$\left(G_1 \frac{\partial u_1}{\partial x}\right)_{x=0} = \left(G_2 \frac{\partial u_2}{\partial x}\right)_{x=0}, \tag{29}$$

where from

$$U_1(t) + D_1(t) = U_2(t) + D_2(t) \tag{30}$$

and

$$\frac{G_1}{c_1}\left\{U_1^{'}(t) - D_1^{'}(t)\right\} = \frac{G_2}{c_2}\left\{U_2^{'}(t) - D_2^{'}(t)\right\}. \tag{31}$$

Integrating this equation, we get:

$$U_1(t) - D_1(t) = \frac{G_2 c_1}{G_2 c_2}\{U_2(t) - D_2(t)\} \tag{32}$$

and assuming that

$$\frac{G_1 c_2}{G_2 c_1} = \frac{\rho_1 c_1}{\rho_2 c_2} = k, \tag{33}$$

then

$$U_1(t) - D_1(t) = \frac{1}{k}\{U_2(t) - D_2(t)\}. \tag{34}$$

From the joint solution (30) and (34)

$$U_1(t) = \beta_o U_2(t) + \alpha^{'} D_1(t); \tag{35}$$

$$D_2(t) = \alpha_o U_2(t) + \beta^{'} D_1(t), \tag{36}$$

Where

$$\alpha_o = \frac{1-k}{1+k},\ \beta_o = 1+\alpha_o,\ \alpha^{'} = -\alpha_o,\ \beta^{'} = 1-\alpha_o. \tag{37}$$

Then

$$U_1\left(t+\frac{x}{c_1}\right) = \beta_o U_2\left(t+\frac{x}{c_1}\right) + \alpha' D_1\left(t+\frac{x}{c_1}\right), \tag{38}$$

$$D_2\left(t-\frac{x}{c_2}\right) = \alpha_o U_2\left(t-\frac{x}{c_2}\right) + \beta' D_1\left(t-\frac{x}{c_2}\right). \tag{39}$$

To clarify the physical meaning of dependencies (38) and (39), it is convenient to give the following definitions: α_o– reflection coefficient from the lower boundary of the interface plane; β_o– transmission coefficient from the lower layer to the upper layer along the interface plane; α'– reflection coefficient from the upper boundary of the interface plane; β'– the transmission coefficient from the upper layer to the lower layer along the interface plane.

In the case of the transition of waves from hard substrate soil to soft subsidence soil: 1) the amplitude of the passing wave is greater than the amplitude of the incident wave, and the maximum gain is two; 2) the reflected wave has the same phase as the incident one, and the amplitude of the reflected wave is less than the amplitude of the incident wave.

In the case of the transition of waves from soft subsidence soil and hard underlying soil: 1) the amplitude of the passing wave is less than the amplitude of the incident wave; 2) the reflected wave is opposite in phase to the incident wave, and the amplitude of the reflected wave is less than the amplitude of the incident wave.

Although the reflected waves have reduced amplitudes compared to the incident waves, the shape of the waves and their propagation velocities do not change. Therefore, the ratio of energy fluxes of reflected and incident waves is equal to α_o^2. If the ratio of energy flows of passing and incident waves (energy transfer coefficient), denote λ_o, then

$$\lambda_o = 1-\alpha_o^2. \tag{40}$$

Because $|\alpha_o| = |\alpha^{'}|$, the energy transfer coefficient is the same for the cases of waves approaching the interface plane from below and from above.

As can be seen, even in the theoretical interpretation, made in the first approximation (i.e. idealized), the efficiency of using the energy of an earthquake or earthquakes (taking into account aftershocks) with the hydro-explosive method of compaction of the subsidence of the ground layer is beyond doubt.

The technical and economic effect of the proposed engineering development is that an increase in the period of dynamic impact on the compacted mass of subsidence soil and an increase in the quality of soil compaction due to the energy of natural seismics of the territory is achieved.

4 CONCLUSIONS

1. A significant part of the territories of the distribution of subsidence soils falls on areas with high seismic activity, therefore, the issue of using earthquake energy during deep compaction of subsidence massifs becomes very relevant;
2. Modern scientific and engineering achievements allow us to use proven methods of recording seismic activity of the territory. Among them are seismogeodynamic, electromagnetic and biological methods;
3. A method of deep compaction of loess subsidence loams by hydraulic explosions has been developed, in which the energy of an earthquake (or earthquakes) is used. Under the

conditions of seismic activity of the territory, physico-chemical processes in the soils are intensified due to the activation of geoelectromagnetic and geoacoustic fields. Under these conditions, capillary and mass transfer processes in porous media are intensified. Therefore, it is during this period that it is most effective to carry out locks and explosions in the ground mass;

4. Even if an earthquake does not occur during the post-explosive consolidation in the seismically active period, the activity of geomagnetic and geoacoustic fields, which are an integral part of seismic energy, leads to activation of the consolidation deformation process.
5. Theoretical studies have shown the effective effect of seismic waves on the intensification of deep compaction of soaked subsidence arrays.

REFERENCES

1. Trofimov V.T. Teorija formirovanija prosadochnyh lessovyh porod. Moskva: GEOS, 2003, p. 275.
2. Kriger N.I. Less. Formirovanie prosadochnyh svojstv. Moskva: Nauka, 1986, p. 132.
3. Rendell H.M. Loess deposition during the Late Pleistocence. Geomorpholohy. N.F.76. 1989, p. 247–255
4. Rozycki S.Z. Loess and loess-like deposits. Wroclaw. Polish Academy of Science, 1991.
5. Pecsi M. Nedyedkor es loszkutatas. Budapest. Akademiai Kiado, 1993.
6. Sajgalik J. Geotechnical Properties of the Danubian Lowland Loess soils in the Slovak Carpathians. GeoJournal. vol.24. B.2, 1991, p. 165–174
7. Wei Lanying, Gui Jiuxi & Lu Yanchou. A preliminary study of the physico-mechanic properties of loesses and paleosols of defferent age at Weibei Yuan, Shaanxi province. Loess, environment and global change. Science Press, Beijing, 1991, p. 245–259
8. Zarate M. & Blasi A. Late Pleistocene and Holocene Loess Deposits of the South-estern Buenos Aires province, Argentina. GeoJurnal. Vol.24. №2, 1991, p. 41–47
9. Abelev Ju.M., Abelev M.Ju. Osnovy proektirovanie i stroitel'stva na prosadochnyh makroporistyh gruntah. Moskva: Strojizdat, 1979, p. 271.
10. Litvinov I.M. Ukreplenie i uplotnenie prosadochnyh gruntov v zhilishhnom i promyshlennom stroitel'stve. Kiev: Budivel'nik, 1977, p. 288
11. Klepikov S.N., Tregub A.S., Matveev I.V. Raschet zdanij i sooruzhenij na prosadochnyh gruntah. Kiev: Budivel'nik, 1987, p. 200.
12. Mustafaev A.A. Fundamenty prosadochnyh i nabuhajushhih gruntah. Moskva: Vysshaja shkola, 1989, p. 590.
13. Aliev S.K. Zemljanoe polotno avtomobil'nyh dorog na lessovyh prosadochnyh gruntah. Baku: Jelm, 2005, p. 633.
14. Krutov V.I., Kovalev A.S., Kovalev V.A. Proektirovanie i ustrojstvo osnovanij i fundamentov na prosadochnyh gruntah. Moskva: Izdatel'stvo ASV, 2013, p. 544.
15. Ryzhov A.M. Vvedenie v nelinejnuju mehaniku gruntov i fizicheskoe modelirovanie osnovanij. Zaporozh'e: RIP «Vidavec'», 1995, p. 446.
16. Gabibov F.G. Teorija i praktika uluchshenija svojstv strukturno-neustojchivyh glinistyh gruntov pri reshenii geotehnicheskih i inzhenerno-geojekologicheskih problem. Baku: Jelm, 2011, p. 422.
17. Gabibov F.G. 1990, K voprosu ob ispol'zovanii jenergii zemletrjasenij pri glubinnom uplotnenii lessovyh prosadochnyh gruntov. V kn.: «Lessovye prosadochnye grunty kak osnovanija zdanij i sooruzhenij». Tezisy dokladov Vsesojuznoj nauchno-prakticheskoj konferencii, kniga 3, Barnaul, 1990, p. 154–156.
18. Ikeja M. Zemletrjasenija i zhivotnye. Ot narodnyh primet k nauke. M., Nauchnyj mir, 2008, p. 320.
19. Mogi K. Predskazanie zemletrjasenij. M.: MIR, 1988, p. 384.
20. Rikitake T. Predskazanie zemletrjasenij. M.: MIR, 1979, p. 360.

Smart Geotechnics for Smart Societies – Zhussupbekov, Sarsembayeva & Kaliakin (Eds)
© 2023 The Author(s), ISBN 978-1-003-29912-7
Open Access: www.taylorfrancis.com, CC BY-NC-ND 4.0 license

Study on evaluation of vertical bearing capacity for soil-cement composite pile

K. Watanabe
Department of Civil Engineering, Aichi Institute of Technology, Japan

S. Koga
Construction Robotics Division, Obayashi Corporation, Japan

ABSTRACT: In recent years, works to improve existing structures and strengthen their seismic resistance have increased. Pile construction in narrow spaces is constrained by the site and process. Therefore, a construction method of H-section steel pile construction with soil-cement ground improvement using a mechanical agitator was developed. This construction method which is called as soil-cement composite pile is characterized by having no need to drill up to a fixed depth as in the pre-boring pile construction method. Instead, soil is agitated along with the cement milk at the original position. In this study, static compression load tests on the soil-cement composite pile that were constructed with the actual construction method were carried out to evaluate the vertical bearing capacity. Furthermore, it was evaluated the performance of vertical bearing capacity on the soil-cement composite piles based on the evaluation method as described in the design specifications in Japan.

1 INTRODUCTION

There are several pile construction methods with relatively small construction machinery that are suitable for construction in narrow urban spaces and areas with low overhead clearance. The Top drive Boring Hole (TBH) method, which has a machine height of 4.5m, is often used. However, there are many cases where even these construction machines are interfered with by architectural limitations and existing structures. The Boring Hole (BH) pile method can handle narrow spaces and low overhead clearances better than the TBH method. However, because the BH pile method is a direct circulation method, mud cakes easily form on the hole walls, and slime tends to accumulate at the pile tip.

Pile construction in narrow urban spaces and for existing structures to strengthen the seismic resistance is subjected to constraints on the construction site and process. Especially, this pile is subjected to the lack of bearing capacity due to the increase of superstructure weight by strengthening the superstructure. Therefore, a method for H-section steel pile construction with soil-cement ground improvement (called as the soil-cement composite pile) was developed that uses a compact mechanical agitator. The construction machine is a mechanical agitator with an attached vibrating mechanism and improved drilling capacity. However, there are some problems to be solved on the vertical bearing capacity of the developed soil-cement composite pile.

The purpose of this study is to evaluate the performance of vertical bearing capacity on the soil-cement composite pile that were constructed by the developed construction method. Static compression load tests for the soil-cement composite pile were carried out. Furthermore, it was evaluated the vertical bearing capacity on the soil-cement composite pile based on the evaluation method as described in the design specification in Japan.

DOI: 10.1201/9781003299127-218

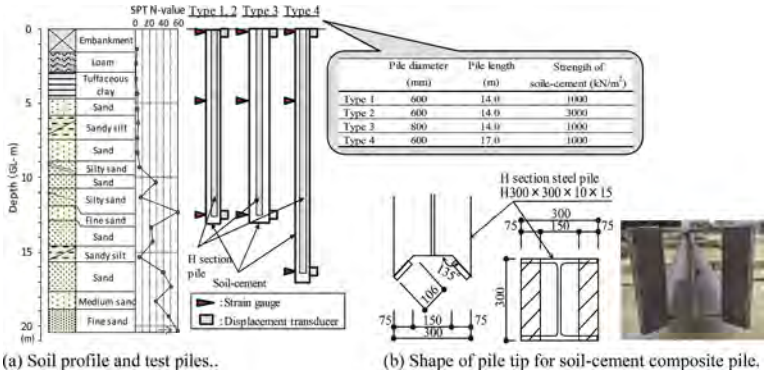

Figure 1. Summary of compression load tests.

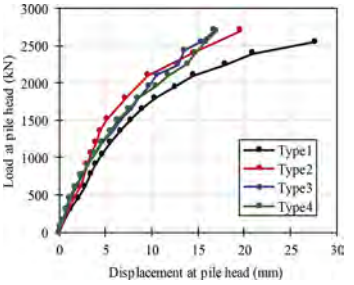

Figure 2. Relationships between load and displacement at pile head.

2 FULL SCALE LOAD TESTS

2.1 *Summary of compression load tests*

The summary of compression load tests indicates in Figure 1. Four piles were constructed for the static load test with varying the soil-cement diameter, pile length, and soil-cement strength as parameters. The specifications of the test piles is also presented in Figure 1. The bearing stratum was adopted to be N=20 and 40 from the results of ground investigation; the test piles were embedded in the bearing stratum. The test piles were pre-drilling soil-cement column diameter of 600mm and 800mm, H-section steel shape of H-300×300×10×15. It was examined that the average strength of soil-cement for all of the test piles was larger than the target strength when the unconfined compression tests for the core specimen of four test piles were carried out after the compression load test.

The static load tests were carried out based on the standards of the Japanese Geotechnical Society (Japanese Geotechnical Society, (2001)). A stepwise multi cycle loading system was employed with a new load holding period of 30min and hysteretic load holding duration of 2min. The measured parameters were the pile head load, pile head and pile tip displacements, and strain of the H-section steel. In order to evaluate the shaft friction of each stratums and the end bearing capacity, the strain was measured at the tip of pile and the boundary of each stratums and pile top.

2.2 *Results of compression load tests*

Figure 2 shows the relationships between the load and displacement at the pile head. The maximum loads were 2500kN for Type 1 and 2700kN for Type 2~Type 4. For all of the piles, the curve was steep from the initial of loading, and all of the piles possessed a large initial stiffness. The gradient of the curve then changed with the loading and reached the maximum load.

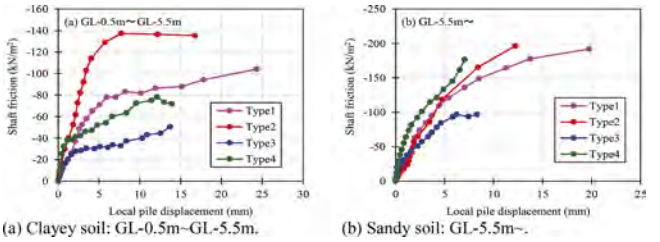

(a) Clayey soil: GL-0.5m~GL-5.5m. (b) Sandy soil: GL-5.5m~.

Figure 3. Relationships between shaft friction and local pile displacement.

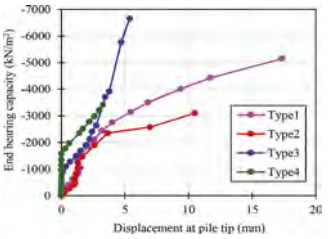

Figure 4. Relationships between end bearing capacity and displacement at pile tip.

The axial force was calculated by considering only the H-section steel such as the measured strain of the H-section steel, the Young's modulus and the cross-sectional area of the H-section steel. The relationships between the shaft friction and local pile displacement which was obtained by dividing this axial force difference by the circumferential area are shown in Figure 3. Figure 3(a) shows that the maximum shaft friction of 50~140kN/m^2 was mobilized in the clayey soil stratum. The average value of the unconfined compressive strength at the corresponding section of the ground was 57kN/m^2. Thus, it can be concluded that the shaft friction was more than the undrained shear strength of the ground (=28kN/m^2). In the sandy ground stratum, it is observed that the maximum shaft friction is 100~200kN/m^2.

The end bearing capacity was calculated by dividing the axial force reaching the pile tip by the envelope area of the H-section steel (BxH). The relationships between the end bearing capacity and displacement at pile tip indicates in Figure 4. The maximum displacement at pile tip is not mobilized the reference displacement which is equal to 10% displacement of the pile diameter when the end bearing capacity is evaluated in these load tests. Thus, the end bearing capacity is evaluated by the value at the maximum displacement at pile tip. The end capacity of 3000~6600kN/m^2 is examined in these load tests. The trend indicates that the end bearing capacity is gradually increasing because the displacement at pile tip is small and does not mobilize the reference displacement to evaluate the end bearing capacity. In addition, the end bearing capacity of the test pile Type 3 indicates the largest value of four test piles.

3 COMPARISON OF DESIGN SPECIFICATION

The vertical bearing capacity which was obtained from the load tests for the developed soil-cement composite pile is compared to the calculated bearing capacity as shown in the design specification in Japan. In this study, the calculated value is estimated by the Design Standards for Railway Structures and Commentary (Railway Technical Research Institute, 2012) because the developed soil-cement composite pile is applied to the railway structure.

The relationships between shaft friction and SPT N value for a clayey soil and a sandy soil indicate in Figure 5. The estimated values are also plotted in Figure 5. According to Figure 5, the shaft friction which was obtained from the load tests is larger than the estimated value from the design specification. Therefore, it is said that the shaft friction of the developed soil-cement composite pile has the enough performance.

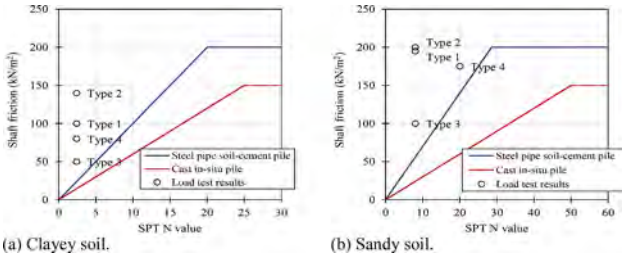

Figure 5. Relationships between shaft friction and SPT N value.

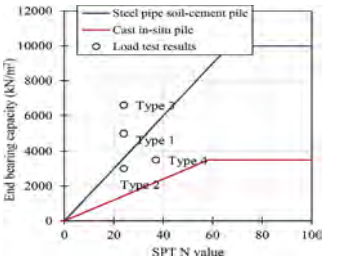

Figure 6. Relationships between end bearing capacity and SPT N value.

The relationships between end bearing capacity and SPT N value for sandy soil are presented in Figure 6. The estimated values are also plotted in Figure 6. It is seen that the end bearing capacity of Type 1 and Type 3 is larger than that of the estimated value. However, the end bearing capacity of Type 2 and Type 4 is lower than the estimated value for a steel pipe soil-cement pile although the end bearing capacity of load test shows the large value for the cast in-situ pile. This means that the end bearing capacity does not mobilize because the displacement at the pile tip is too small and does not mobilize the reference displacement.

4 CONCLUSIONS

The static compression load tests on the soil-cement composite pile were carried out to evaluate the vertical bearing capacity in this study. The following findings were obtained from this study.

1) According to the compression load tests, both the shaft friction and the end bearing capacity has the enough performance on the vertical bearing capacity.
2) It is concluded that the shaft friction of the load test is larger than the estimated shaft friction which is calculated by the design specification in Japan.
3) Compared to the end bearing capacity of the load test and that of estimated value from the design specification, the end bearing capacity of the load test shows the large value. However, the partial results is lower than the estimated value. This means that the end bearing capacity is gradually increasing because the displacement at the pile tip is too small.

REFERENCES

Japanese Geotechnical Society 2001. *Standards of the Japanese Geotechnical Society (Method for Vertical Load Test of Piles*, Japanese Geotechnical Society (in Japanese).

Railway Technical research Institute 2012. *Design Standard for Railway Structures and Commentary (Foundation Structures)*, Railway Technical research Institute (in Japanese).

Smart Geotechnics for Smart Societies – Zhussupbekov, Sarsembayeva & Kaliakin (Eds)
© 2023 The Author(s), ISBN 978-1-003-29912-7
Open Access: www.taylorfrancis.com, CC BY-NC-ND 4.0 license

Load-bearing capacity of a single barette (case study for the Hanoi soil condition)

N.S. Nikitina & Le Trung Hieu
Moscow State University of Civil Engineering (National Research University) (MGSU), Moscow, Russian Federation

D.M. Mukhanov
Eurasian National University, Astana, Kazakhstan

ABSTRACT: The article presents the results of analytical analysis of the bearing capacity of a single baretta in hard geological conditions in the city of Hanoi and compares it with the field test results. The methods provided in the regulatory documents SP 24.13330.2011 "Pile Foundations" [1] have been adopted when determining the bearing capacity of piles and barrettes. As well as the results of field tests with piles (static load method) were used. A new method has been proposed which accounts the mutual arrangement of piles in the ground, their length, pitch, etc. Appendix E of the specified regulatory document provides this method. The investigation shown that the test bearing capacity of a single barrette with a limiting settlement of up to 40 mm is in a good agreement with the results of analytical analysis by proposed method, which accounts unloading on soft soils in deep pits.

1 INTRODUCTION

Since the 21st century, there has been an increase in the loads transferred to the base, and the settlement of structures due to the rapid grow in the construction of high-rise buildings. These circumstance determines the wider use of pile foundations (even if there are sufficiently strong

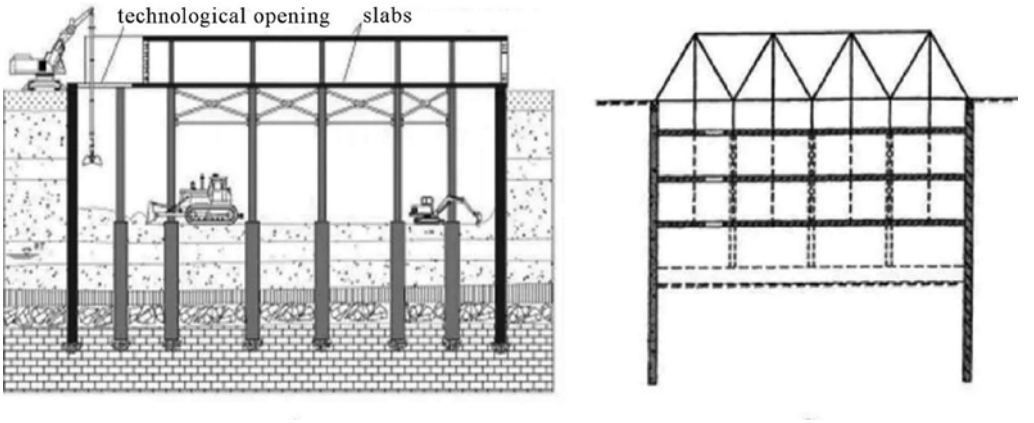

Figure 1. Technological scheme by the "top-down" method.

DOI: 10.1201/9781003299127-219

soils near the surface). The technology of developing deep pits by the "top-down" method is most common approach in the construction of underground structures in such densely populated urban areas (Figure 1) [4].

Barrettes are effective foundation designs for the construction of underground structures by this method and for the work using underground space in soft soils, with a high level of groundwater and in cramped urban conditions. The technological sequence of the installation of a single barrette is the same as in the case of the installation of a "wall in the ground" (Figure 2).

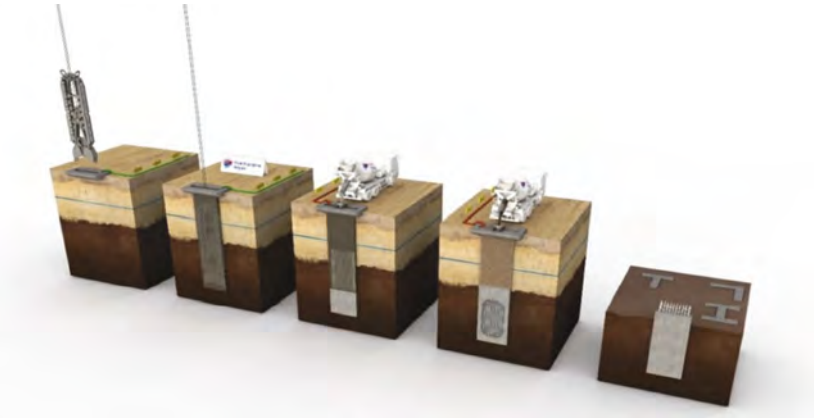

Figure 2. Technological sequence of the barrette installation.

A number of Russian and foreign scientists [6–9] studied the applicability of piles and barrettes in practice, considering the peculiarities of the interaction of piles and barrettes with each other and with the soil. The use of barrettes in these conditions leads to the search for new ways to improve the efficiency of pile foundations. In particular, a possible important condition is the refinement of calculation methods. A new method has been proposed that accounts the mutual arrangement of piles in the soil base, their length, pitch, etc. (Appendix D to SP 24.13330.2011) [1]. The article discusses the existing methods for assessment the bearing capacity of barrettes and compares the results obtained with full-scale field static tests.

2 MATERIALS AND METHODS

In world practice, field tests for assessing the bearing capacity of barrettes allows verification and confirmation the accuracy of the analysis and the quality of the entire construction process [10]. In the problem under consideration, vertical static load testing of a single barrette was carried out using hydraulic jacks up to a maximum load of 30 MN that simulates the 'Top-Down' method. The test procedure met to GOST 20276-2012 [2]. During the field static tests, vertical displacement of the pile under test load had been determined by sensors located on the pile head according to the requirements of 8.2.2 [3].

Since the bearing capacity of a pile depends on the physical and mechanical properties of soil base, the most common analytical method for its determining is the calculation according to tables of standard soil resistances [11]. Let us calculate the bearing capacity of the barrettes, immersed with excavation and filling with concrete. In accordance with 2.7.6. [1], it can be determined from the formula.

$$F_{d,1} = \gamma_c \left(\gamma_{cR} \cdot R \cdot A + u \sum \gamma_{cf} \cdot f_i \cdot h_i \right), \quad (1)$$

where γ_{cR}, γ_{cf} – are the partial factors for condition of soil base resistance under the pile tip and side surface respectively; γ_c – is the partial factor for pile behavior in the soil base, which is adopted as 1; A – is the pile area for supporting on the soil base, m^2, which adopted as cross-sectional area brutto or cross-section of the camouflage widening by its largest diameter, or by the area of the shell pile and the net hollow pile; u – is the external perimeter of the pile cross-section, m; R – is the design strength of the soil under the pile tip, kPa; f_i – is the design strength of the soil layer through the pile surface, kPa; h_i – the depth of the *i-th* soil layer, contacting with the pile surface, m.

We adopted table values of f, R and liquidity index I_L in formula (1) to evaluate the bearing capacity of a structural member (pile, barrett) through the side surface. In this problem, the design strength R of the soil under the lower end of the piles is determined in the case of coarse and sandy soils by the formula.

$$R = 0,75\alpha_4(\alpha_1\gamma_1^{'}d + \alpha_2\alpha_3\gamma_1 h), \quad (2)$$

where $\alpha_1,\alpha_2,\alpha_3,\alpha_4$ – are dimensionless coefficients determined from the table depending on design value of the internal friction angle for the soil; $\gamma_1^{'}$ – is the design value of the specific soil weight, kN/m^3 under the pile lower end (taking into account the weighing effect of water for water-saturarted soils); γ_1 – is the average through the layers design value of specific weight of the soils, kN/m^3, above the pile tip (taking into account the weighing effect of water for water-saturarted soils); d – is the diameter of the pile, m; h – is the depth from the natural relief or from the level of planning in case of cutting to the pile tip, m.

It is necessary to take into account the unloading process, when constructing deep pits. In the soil next to the pit, horizontal stresses decrease during excavation, vertical stresses do not change. At the same time, in the soil at the bottom of the pit, the horizontal stress does not change, the vertical stress decreases when the soil is excavated. At depths of more than 5 m, the effect of "unloading - reloading" becomes most pronounced for a certain thickness of the base as a result of excavation. The phenomenon of "unloading - reloading" is especially manifested in the foundations, composed of weak soils with a small modulus of deformation. Taking into account the significant thickness of soft soils with such a modulus of deformation, deformations under load will play a significant role within the barrett shaft. Applicability limits have also been introduced - the settlements of a small group ($n \leq 25$) and a large pile field are determined considering mutual influence. Therefore, the method for determining the settlement of a single pile depending on the average value of the soil shear modulus G within the pile and under its lower end is also described by the following formula according to 7.4.2–7.4.3 [1]:

$$s = \beta \frac{N}{G_1 l}, \quad (3)$$

where N – is the vertical load on the pile, MN; β – is the dimension factor; G – is the shear modulus, MPa; l – is the pile length, m.

In theoretical soil mechanics, as in continuum mechanics, several deformation moduli are also used. What they have in common is that they are parameters of Hooke's law [5]:

$$\varepsilon = \frac{1}{E}\sigma, \quad (4)$$

where ε – is the strain; σ –is the stress, kPa; E – is the deformation modulus, kPa.

The modulus of deformation is the same coefficient of proportionality in dependence (4) and at a higher level of deformation, when residual deformation occurs during unloading.

It is necessary to determine two moduli of deformation – on the branches of primary (E) and secondary (E_e) loading (Figure 3) in order to calculate the settlement of foundations. Deformation moduli are determined by testing soil samples under uniaxial compression and axisymmetric (triaxial) compression.

In order to find the deformation modulus E_e, it is necessary to know the values of the unloading stresses, upon reaching which the soil sample should be unloaded, and then loaded again (carry out secondary loading). In accordance with the paper [1] soil unloading should be taken into account if the depth of the pit is more than 5 m.

A new method has been developed for the analysis of piles in deep pits. This method based on approach described in Appendix E [1]. The proposed modification of the analytical method for calculation the settlement of a single pile in order to take into account the unloading of the foundation during the development of a deep pit allows describing the behavior of the barrette under load with sufficient accuracy. Therefore, to calculate the settlement of barrettes in deep pits, we proposed to determine the shear modulus accounting the unloading of the soil base and the average value of the soil shear modulus. Within the unloading thickness H_{ur} for soils, the shear modulus G_{ur} of elastic deformations is defined as

$$G_{ur} = \frac{1}{2(1+\nu_{ur})} E_{ur}, \tag{5}$$

where E_{ur} – the soil deformation modulus during unloading/reloading; the lateral to longitudinal deformation ratio of the soil under unloading/reloading.

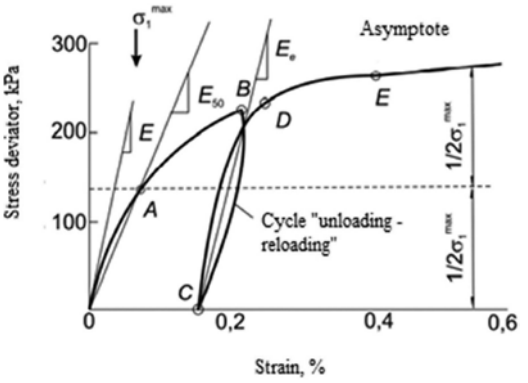

Figure 3. Stress – strain curve to determine deformation modulus in triaxial compression.

As Figure 3 shows, the modulus of soil deformation during unloading and reloading E_{ur} shall be determined from triaxial tests at a compression value equal to the modulus of soil deformation during initial loading. In fact, the soil deformation modulus E_{ur} takes values 2 ... 7 times greater than the secant deformation modulus at 50% of the ultimate stress deviator under conditions of unloading and reloading. Then you can apply the following formula to calculate the approximate values

$$E_{ur} = 5E_{50}. \tag{6}$$

3 RESULTS

According to GOST 5686-2012 "Soils. Field test methods by piles" [3], testing of the barrette should be provide a vertical settlement of 40 mm, which is achieved under the action of a vertical load $F_{d,\text{исп}..}$ = 27500 kN (Figure 4).

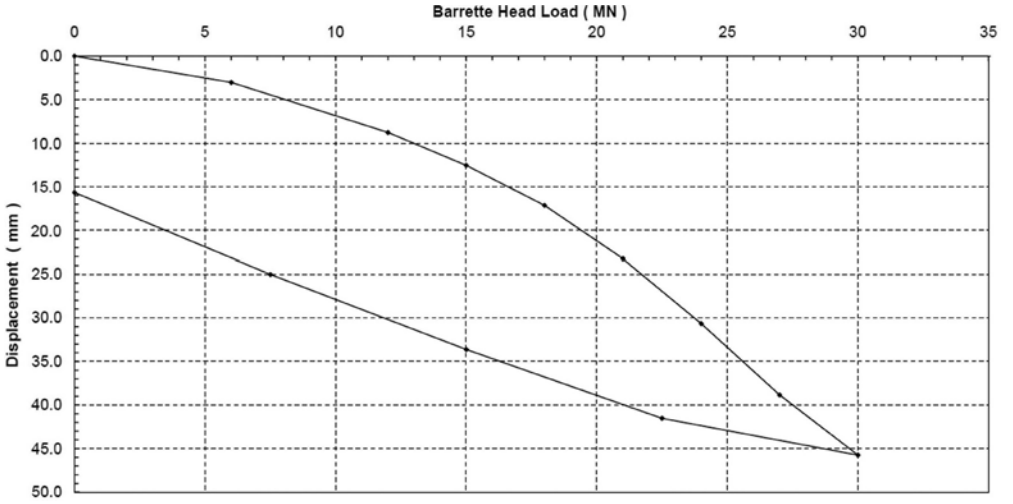

Figure 4. Settlement vs. load relation from field tests of barrettes.

To compare the bearing capacity of single barrettes according to the indicated formulas, let's consider an example for hard geological conditions at the construction site in Hanoi. Experimental single barrettes with a cross section of 800 × 2800 mm and a length of 37 m had been tested in the framework of this study. The dimensions of the baretta are typical for Hanoi. The barrettes located on a site with layers of soft soils near the surface and at a high level of groundwater at a mark from a relative mark of -0.60 m.

According to the results of engineering and geological surveys, it was established that the geological zone under the well has a depth of 61 m and consists of 9 soil layers: compacted embankment (EGE 1), fluid clay, brownish-gray, mixed with organic inclusions (EGE 2), loose sand, ash gray, medium brown, medium density, low moisture (EGE 3), fluid-plastic clay, brownish gray,

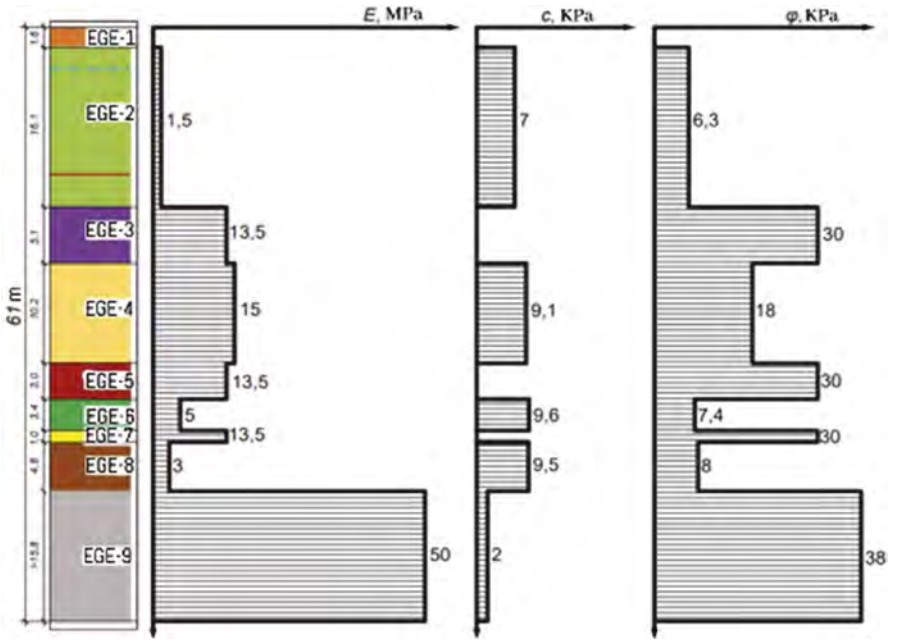

Figure 5. Geotechnical cross-section of the test site with soil characteristics under triaxial compression.

mixed with organic inclusions (EGE 4), sand fine, gray, yellowish gray, medium density, low moisture (IGE 5), soft-plastic loam, brownish-gray (IGE 6), fine, medium-sized, low-moisture sand (IGE 7), fluid-plastic loam, brown-gray, dark gray, mixed organic (IGE 8), gravel-pebble soil (IGE 9). Figure 5 shows an engineering-geological section with the characteristics of the site soils.

Thus, classic analytical calculation allows obtaining the value of the total bearing capacity of this barrette F_d = 27285 kN. According to the results of the calculation, it was found that 77% falls on the tip and only 23% on the lateral surface.

In this problem, the depth of the projected excavation is almost 15 m. After excavation of the pit, we determined the depth of the soil massif of the unloading zone within the unloading thickness for soils in the problem under consideration: H_{ur} = 10 m and the width of the pit b = 61 m. the condition for limiting the draft to 40 mm was $F_{d,2}$ = 24600 kN.

Table 1 presents the calculation and test results for bearing capacity of the barrette in the soil.

Table 1. Calculation and test results for bearing capacity of the barette in the soil.

Methods for calculating the bearing capacity of a pile	bearing capacity F_d, kN
Field test results	27500
Analytical classical method [1]	27285
Analytical method according to the criterion of settlement [1] (consider unloading)	24600
Analytical method according to the criterion of settlement [1] (do not consider unloading)	18450

Thus, it is clearly seen that the bearing capacity of the pile according to the results of field tests:

- 1.0% higher than the bearing capacity of the barette, calculated from the results of analytical solutions using tabular values of soil resistance;
- 10% higher than the bearing capacity of the barette, calculated from the results of analytical solutions for the criterion of settlement (modified) taking into account unloading;
- 33% higher than the bearing capacity of the barette, calculated from the results of analytical solutions based on the criterion of settlement without unloading.

Figure 6 shows the combined load vs. settlement graph for various considered analytical methods and full-scale tests.

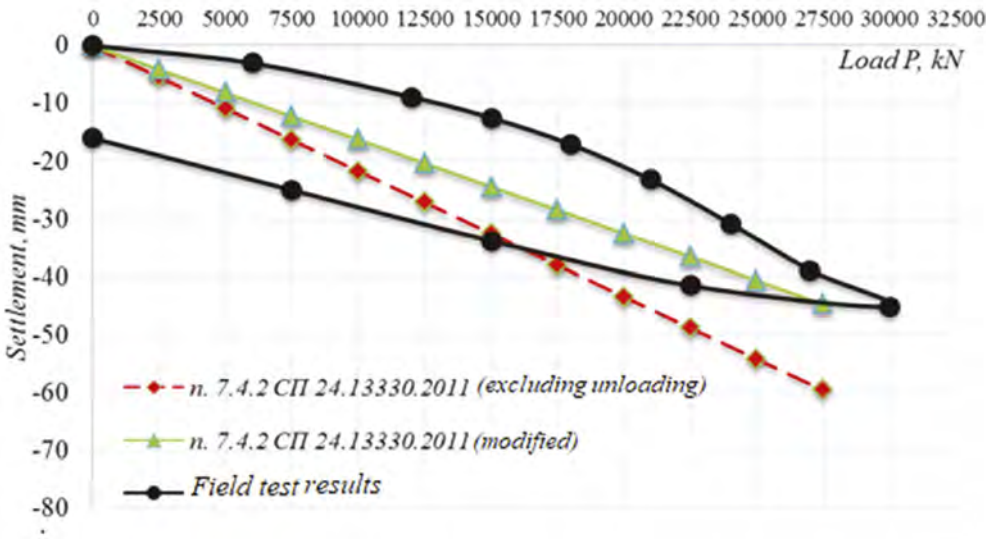

Figure 6. Combined load vs. settlement graph for analytical calculations and field tests.

As we can see from Figure 5, field tests showed a slightly higher indicator than the analytical method without taking into account unloading or modified. The soil around deep pits are always in a complex stress state and considering of the process of unloading is very important in this case. Thus, the results of conventional tests of simple models without unloading describe approximate characteristics of the stress-strain state of soils.

Methods for determining the settlement of a single pile according to the Russian standard, where the soil is considered as a linearly deformed half-space, characterized by a shear modulus and Poisson's ratio, are in good agreement with each other. The bearing capacity values differ by about 10% as Table 1 shows. However, the solutions according to these methods do not meet well with the results of field tests and cannot be applied for practical purposes in conditions of soft soils in deep pits.

4 CONCLUSION AND DISCUSSION

The analysis of the obtained results shows the convergence of the value of the calculated and test bearing capacity of the barette in the soil. In the analytical solution, the reduced shear modulus G is determined taking into account the unloading thickness of the base, for which the soil deformation modulus E_{ur} under unloading/reloading is applied.

The authors recommend further research and use of this method for preliminary calculations of settlement and bearing capacity of piles.

REFERENCES

1. SP 24.13330.2011. Pile foundations. Updated edition of SNiP 2. 02.03-85.
2. GOST 20276-2012. Soils. Field methods for determining the strength and strain characteristics.
3. GOST 5686-2012. Soils. Field test methods by piles.
4. Design and arrangement of underground structures in open pits: a tutorial/R. A. Mangushev, N. S. Nikiforova, V. V. Konyushkov and etc. – Moscow, St. Petersburg: ASV Publishing House, (2013). – 256 p.
5. Ter-Martirosyan Z.G. Soil Mechanics. - Moscow: MGSU, ASV Publishing House, (2009) - 256 p.
6. Mangushev R.A., Nikitina N.S. Bearing capacity of deep pile foundation for high-rise facility on weak soils: comparing of analysis results and experimental data // International Journal for Computational Civil and Structural Engineering (IJCCSE journal). – (2019). – Volume 15 No. 1. - P. 90–97.
7. Shulyatiev O. A. Basic principles of analysis and design of slab and pile foundations for high-rise buildings: specialty 05. 23.02"Soil bases and foundations, underground structures": diss. . . . Dr. tech. Sciences/ Oleg Aleksandrovich Shulyatiev; NIIOSP named after N.M. Gersevanov. - Moscow, (2019). – 352 p.
8. Chang D. W. Three-dimensional Finite Element Analyzes of Barrette Piles under Compression and Uplift Loads with Field Data Assessments/D. W. Chang, D. W. Huang, Y. K. Lin, F. C. Lu, C. J. Kuo. Text: electronic // Geotechnical Engineering. - (2019). - Vol. 50, no. 3. – C. 58–73.
9. Manoj S. Value engineering using load-cell test data of barrette foundations – a case study/Sujatha Manoj, Deepankar Choudhury and Marwan Alzaylaie. Text: electronic // ICE Proceedings Geotechnical Engineering. - (2020). - 89 p.
10. Tran V. T. Studying and calculating the bearing capacity of barrette piles based on comparison with O-cell test/Van Than Tran // Tạp chí Xây dựng Việt Nam 59 (625). - (2020). - C. 232–236.
11. Le V. Ch. Bearing capacity of piles made in the soil, according to the results of static field tests: specialty 05. 23.02"Soil bases and foundations, underground structures": diss. cand. tech. Sciences/ V. Ch. Le; St. Petersburg State University of Architecture and Civil Engineering (SPbGASU) – St. Petersburg, (2021). – 145 p.

Smart Geotechnics for Smart Societies – Zhussupbekov, Sarsembayeva & Kaliakin (Eds)
© 2023 The Author(s), ISBN 978-1-003-29912-7
Open Access: www.taylorfrancis.com, CC BY-NC-ND 4.0 license

Preliminary study of ultimate load prediction using the DINGO database

M.M. Othman, E. Voyagaki, F. De Luca, G. Mylonakis & P.J. Vardanega
University of Bristol, Bristol, UK

J.J. Crispin
University of Oxford, Oxford, UK

ABSTRACT: Chin's analysis method can be employed to interpret the ultimate capacity of pile load tests. Using maintained pile load test data from the DINGO database, consisting of axial compressive loading, the performance of Chin's method was investigated for piles in various UK soil deposits. It is shown that Chin's method tends to be unconservative when predicting ultimate pile capacity regardless of how 'failure' is defined (e.g. head settlement over 10% of pile diameter). The results are compared with test data from Ireland where similar trends were observed.

1 INTRODUCTION

Chin's method is a procedure for predicting the ultimate load a pile can carry without reaching 'failure' during testing (Chin 1970, 1972). In this method, the recorded settlements from load/settlement data are divided by the corresponding load for the same set of data and then plotted against only the settlements from the same load/settlement dataset, and a linear regression in the form of Equation (1) fitted. The ultimate load of the pile is then calculated as the inverse of the slope of the fitted line (Equation 1):

$$\Delta/P = M\Delta + B \tag{1}$$

where Δ = pile head settlement; P = applied load at the pile head; $1/M$ = ultimate pile head load; and B = constant. Chin's method is essentially an extrapolation method (cf. Galbraith et al. 2014).

Other methods have been developed based on forms of Equation (1) (e.g. Fleming 1992, Fellenius 1980, Comodromos *et al*. 2003, Topacio *et al*. 2022) with various modifications proposed. Fleming (1992) suggested that Chin's method may overestimate the ultimate load. In this study, Equation (1) is employed to analyse data extracted from the DINGO database (see Vardanega *et al*. 2021a, 2021b, Voyagaki *et al.* 2022). The DINGO database contains pile load-settlement data (alongside ground investigation data) for 551 piles of various types constructed in different soil deposits in the United Kingdom. The DINGO database data were obtained from various resources in which some of the data were hand digitised from figures and tables.

This study assesses the reliability of Equation (1) for predicting the ultimate load of a pile when a load-test does not reach 'failure' compared to measured ultimate loads in testing based on pile head settlement exceeding 10% of the pile diameter (BSI 2004, Frank *et al*. 2004). Although Equation (1) can be used for different pile loading methods (Chin 1972), this study focusses on compression Maintained Load (ML) tests.

DOI: 10.1201/9781003299127-220

2 DATA SELECTION & FILTERING

It was determined that for 378 piles from the DINGO database a compression ML test had been carried out. Load-settlement tables for each pile were constructed and datapoints from any unloading phases (if present) were excluded. All piles reported with less than 3 load-settlement datapoints were not considered in this analysis (40 piles). The remaining 338 piles were analysed using Equation (1) as shown in the example illustrated in Figure 1. Figure 2 presents the load-settlement datapoints distribution in DINGO database. Confidence interval (CI) analyses were performed on the resulting R^2 values of the Equation (1) fittings to the test data combined with the number of load-settlement datapoints (e.g. Paradine & Rivett 1953, Johnson 1978). The pile tests were then divided into three categories based on the aforementioned analyses. The first category (CI 98%) contains all the piles that have R^2 values equal or higher than for 98% confidence interval for the same number of load-settlement datapoints (degrees of freedom). The number of piles in this category was 296 piles. The second category (CI 90%) presents all the piles with R^2 values equal or higher than that found for the 90% confidence interval but less than for the 98% confidence interval for the same degrees of freedom (17 piles). The third category presents piles with R^2 less than for 90% confidence interval for the same degrees of freedom (25 piles). This analysis indicates that Equation (1) generally provides a robust statistical fit to the pile load test data.

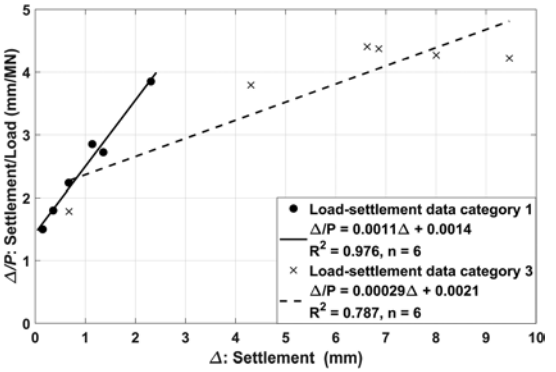

Figure 1. Example of fitting data using Equation (1); for a pile with R^2 higher than that for 98% confidence interval and for a pile from the group with R^2 less than that for 90% confidence interval.

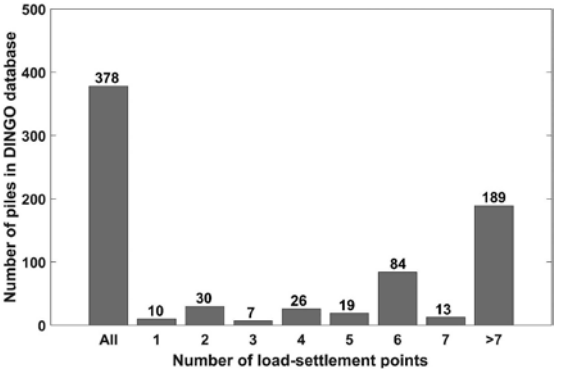

Figure 2. Load-settlement data point distribution for ML piles in the DINGO database.

3 DATA ANALYSIS

Piles from the first category (CI 98%) were used, as the low number of piles in the other categories did not (in the view of the authors) justify lowering the confidence level. The mean (μ) and standard deviation (σ) for the M and B parameters in Equation (1) were calculated and categorised based on the load-settlement datapoints available (Table 1). The values of μ and the σ of the fitting parameters for all the piles are mainly affected by that of piles with more than 7 datapoints (highest number of piles), with no obvious trend observed for μ of M and B with the increasing number of points. In Figure 3, a box plot is shown for coefficient of determination (R^2) values obtained from fitting the piles within CI 98%. Figure 4 shows the pile diameter distribution used in this study with the percent of piles in each diameter range reaching a settlement equal or greater than 10% of the diameter.

Table 1. Descriptive statistics for M and B from Equation (1) applied to pile tests from the CI 98% category.

		All	3	4	5	6	7	>7
Slope (M)	μ	0.86	0.70	1.30	0.78	0.91	1.30	0.75
[MN^{-1}]	σ	0.93	0.64	1.20	0.59	0.86	1.40	0.90
Intercept (B)	μ	3.50	1.50	3.50	1.70	1.50	2.40	4.80
[mm/MN]	σ	6.40	1.50	4.90	1.50	1.90	1.40	8.10

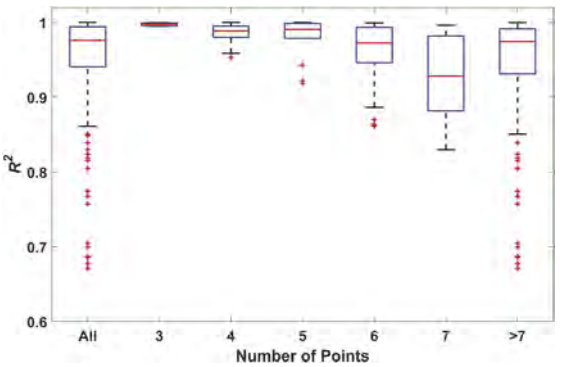

Figure 3. Boxplot of R^2 categorized based on the number of load-settlement data points for piles in CI 98%.

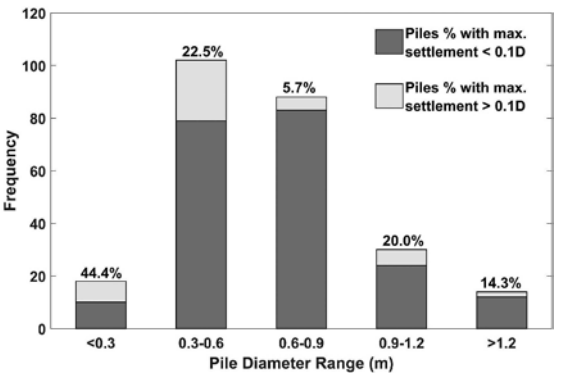

Figure 4. Pile diameter distribution of CI 98% presenting the percentage of piles in each range group with a maximum settlement equal or higher than 10% of the pile diameter.

Initially, piles with maximum test settlement reaching or exceeding 10% of the base diameter were selected (44 piles) and the load corresponding to 10% diameter settlement ($P_{ult,10\%}$) was recorded as the measured ultimate load for each test. This criterion was also used in Galbraith (2011) and Galbraith *et al.* (2014). Figure 5(a, b) shows that most of the predictions fall within the ± 50% bounds shown. However, Equation (1) tends to systematically overestimate the ultimate load. These trends were also observed for 10 pile load tests with recorded settlements greater than 10% of pile diameter hand digitised from Galbraith (2011). Then using the maximum recorded load from the pile testing ($P_{ult,max}$), the number of piles available for analysis increased from 44 to 252 tests. However, the maximum test settlement to diameter ratio, Δ_{max}/D, for this approach ranges from 0.1% to 108%.

To analyse the data using this approach, the piles were divided into three classes based on settlement diameter ratio: (i) Class 1: $\Delta_{max}/D \geq 10\%$ (44 tests); (ii) Class 2: $2\% \geq \Delta_{max}/D > 10\%$ (98 tests) and (iii) Class 3: $\Delta_{max}/D < 2\%$ (110 tests). Figure 6(a, b) shows the measured vs. calculated ultimate load plot with these three sub-groups highlighted. Similar results to those shown in Figures 5(a, b) are shown however, increasing Δ_{max}/D appears to improve the accuracy of Equation (1) to some extent.

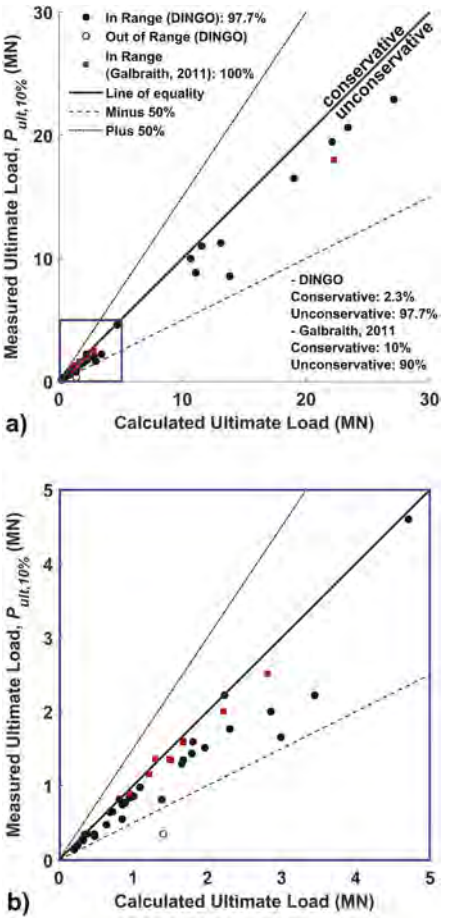

Figure 5. Measured $P_{ult,10\%}$ vs. calculated ultimate load using Equation (1): (a) all data (average over-prediction is about 19.2%), (b) plot for load range 0 to 5MN.

For those tests with recorded settlements equal or greater than 10% of the pile diameter, $P_{ult,10\%}$ and $P_{ult,max}$ have similar values (not shown here for the sake of brevity), which is likely as reaching this settlement threshold was the objective of the original testing. This may

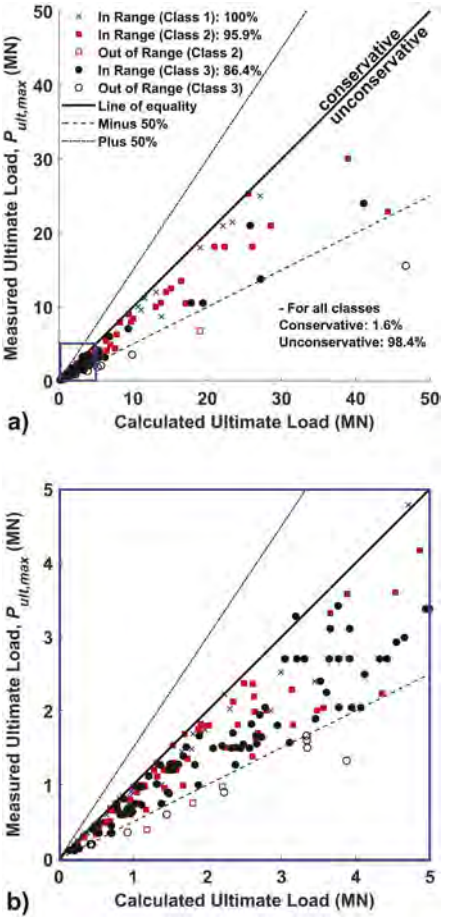

Figure 6. Measured $P_{ult,max}$ vs. calculated ultimate load using Equation (1): (a) all data plot (average overprediction is about 24.8%), (b) plot for load range 0 to 5MN.

explain why the trends observed comparing Figure 5(a, b) with Figure 6(a, b) are similar. In addition, it results in a slightly larger overprediction of $P_{ult,max}$ (24.8%) compared to $P_{ult,10\%}$ (19.2%) as, on average, the former is lower. These trends may not be the case for other data-sets of pile-load tests.

4 SUMMARY & CONCLUSIONS

ML compression pile load tests from the DINGO database (along with data from Galbraith 2011) were analysed using Chin's method (Equation 1). The applicability of Equation (1) for prediction of ultimate pile capacity was assessed by comparing predicted ultimate load values against $P_{ult,10\%}$ and $P_{ult,max}$. For the unconservative predictions across the DINGO database (which equate to around 98% of the analysed pile tests) the Chin method tends to overpredict $P_{ult,10\%}$ by around 19.2% and $P_{ult,max}$ by around 24.8% on average.

ACKNOWLEDGEMENTS

The first author acknowledges the support of AL-Zaytoonah University of Jordan. The DINGO database can be downloaded from the University of Bristol Research Data Repository via the following link: https://doi.org/10.5523/bris.89r3npvewel2ea8ttb67ku4d

REFERENCES

British Standards Institution (BSI) 2004. *BS EN 1997-1: 2004. Eurocode 7: Geotechnical design Part 1: General rules*. London, UK: BSI.

Chin, F.K. 1970. Estimation of the ultimate load of piles from tests not carried to failure. In: *Proceedings of 2nd SE Asian Conference on Soil Engineering*, Singapore, 81–92.

Chin, F.K. 1972. The inverse slope as a prediction of ultimate bearing capacity of piles. In: *Proceedings of 3rd SE Asian Conference on Soil Engineering*, Hong Kong, 83–91.

Comodromos, E.M., Anagnostopoulos, C.T. & Georgiadis, M.K. 2003. Numerical assessment of axial pile group response based on load test. *Computers and Geotechnics* 30(6): 505–515.

Fellenius, B.H. 1980. The analysis of results from routine pile load tests. *Ground Engineering* 13(6): 19–24 and 27-31.

Fleming, W.G.K., 1992. A new method for single pile settlement prediction and analysis. *Géotechnique* 42(3): 411–425.

Frank, R., Bauduin, C., Driscoll, R. & Kavvadas, M. 2004. *Designers' guide to EN 1997-1 Eurocode 7: Geotechnical design - General rules*, vol. 17, London, UK: Thomas Telford.

Galbraith, A.P., 2011. Design & Performance of Deep Foundations in Ireland, *Ph.D. thesis*, Trinity College Dublin The University of Dublin, Ireland.

Galbraith, A.P., Farrell, E.R. & Byrne, J.J. 2014. Uncertainty in pile resistance from static load tests database. *Proceedings of the Institution of Civil Engineers - Geotechnical Engineering* 167(5): 431–446.

Johnson, N.J. 1978. Modified t tests and confidence intervals for asymmetrical populations. *Journal of the American Statistical Association* 73(363): 536–544.

Paradine, C.G. & Rivett, B.H. 1953. *Statistics for Technologists*. London, UK: English Universities Press Ltd.

Topacio, A., Chen, Y-J., Phoon, K-K. & Tang, C. 2022. Evaluation of Compression Interpretation Criteria for Drilled Shafts Socketed into Rocks. *Proceedings of the Institution of Civil Engineers - Geotechnical Engineering*, https://doi.org/10.1680/jgeen.21.00120

Vardanega, P.J., Crispin, J.J., Gilder, C.E.L., Voyagaki, E. & Ntassiou, K. 2021a. DINGO: A Pile Load Test Database. In: K.G. Higgins, Y. Ainsworth, D.G. Toll & A.S. Osman (eds) *Piling 2020: Proceedings of the Piling 2020 Conference*: 229–234. London, UK: ICE Publishing.

Vardanega P.J., Voyagaki E., Crispin J.J., Gilder C.E.L. & Ntassiou K. 2021b. *The DINGO Database, v1.1*. University of Bristol, Bristol, UK, https://doi.org/10.5523/bris.89r3npvewel2ea8ttb67ku4d

Voyagaki, E., Crispin, J., Gilder, C.E.L., Ntassiou, K., O'Riordan, N., Nowak, P., Sadek, T., Patel, D., Mylonakis, G. & Vardanega, P.J. 2022. The DINGO database of axial pile load tests for the UK: settlement prediction in fine-grained soils. *Georisk: Assessment and Management of Risk for Engineered Systems and Geohazards* 16(4): 640–661.

Smart Geotechnics for Smart Societies – Zhussupbekov, Sarsembayeva & Kaliakin (Eds)
© 2023 The Author(s), ISBN 978-1-003-29912-7
Open Access: www.taylorfrancis.com, CC BY-NC-ND 4.0 license

Discrete computational models and stress-strain state of a high-class mechanism taking into account friction forces in kinematic pairs under dynamic loading

A. Yeleussinova, B. Nukhayeva, G. Abdukalikova & L. Utepbergenova
Architecture and Construction Faculty, L.N Gumilyov Eurasian National University, Astana, Kazakhstan

Sh. Toleubayeva
Architecture and Construction Faculty, Karaganda State Technical University, Karaganda, Kazakhstan

ABSTRACT: Quasi-static problems with respect to the stress-strain state and a class of problems with respect to forced vibrations acting in plain and spatial nodes of a high-class mechanism with elastic links are considered, taking into account the model of friction forces in kinematic pairs under the action of vertical and horizontal concentrated forces in kinematic pairs. The developed algorithms of solving quasi-static problems by the finite element method for the entire system of the elastic mechanism with the friction force in kinematic pairs are presented; the basic resolving equilibrium equations for the entire system are drawn up without and taking into account friction forces. The basic relations of the finite element method for plain and spatial nodes of high-class elastic mechanisms with the friction force in kinematic pairs under dynamic loading are presented.

1 INTRODUCTION

The finite element method is better than other methods provided with numerical procedures for studying the mathematical model of an object. Its most important advantage is the presence of implicit unconditionally stable methods of the numerical integration of systems of differential equations of motion that describe the motion of mechanisms and are compiled taking into account the links elasticity.

2 RESEARCH METHOD

For the finite element method in the variant of the displacement method when solving problems of structural mechanics and the theory of elasticity, internal small displacements, velocities, and accelerations are used as unknown values. From the point of view of convergence, when solving this class of problems, there are imposed certain requirements (Zenkevich O. 1975) on the functions of the finite element shape, the most important of which in the case under consideration is the following: it has realized and has not accumulated the energy of elastic deformations.

Modeling the kinematic pairs of a plain and spatial elastic high-class mechanism (HCM) with allowance for Coulomb friction is shown in Figure 1 (Volmir A.S. et al. 1989).

$$\bar{F}_{mp} = -\bar{R}_{jX}, F_{mp} = fN_{Д}\ signR_{jX}, N_{Д} = R_{jY} \tag{1}$$

If a translational pair in a flat mechanism (Figure 1) moves along a fixed guide, then the sliding friction $\bar{F}_{mp}$ force will be directed oppositely to the horizontal component $\bar{R}_{jx}$ of the complete reaction.

DOI: 10.1201/9781003299127-221

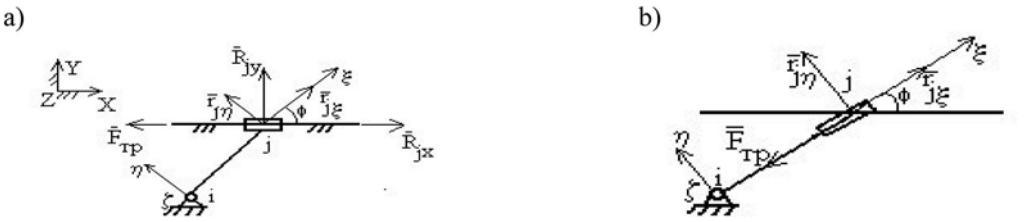

Figure 1. The friction forces in the translational kinematic pair of the plain mechanism.

The R_{jx}, R_{jy} nodes of the complete reaction are determined through the reactions in the $r_{j\xi}, r_{j\eta}$ local coordinate system (LCS):

$$\begin{bmatrix} R_{jX} \\ R_{jY} \\ M_{jZ} \end{bmatrix} = \begin{bmatrix} \cos\phi & \sin\phi & 0 \\ -\sin\phi & \cos\phi & 0 \\ 0 & 0 & 1 \end{bmatrix} \cdot \begin{bmatrix} r_{j\xi} \\ r_{j\eta} \\ m_{j\zeta} \end{bmatrix} \tag{2}$$

In turn, reactions in the LCS are expressed through the unknown internal forces N, Q_η, M_ζ at the nodes in such a way:

$$\begin{bmatrix} r_{i\xi} \\ r_{i\eta} \\ r_{i\zeta} \\ r_{j\xi} \\ r_{j\eta} \\ r_{j\zeta} \end{bmatrix} = \begin{bmatrix} -1 & 0 & 0 \\ 0 & 1 & 0 \\ 0 & l & -1 \\ 1 & 0 & 0 \\ 0 & -1 & 0 \\ 0 & 0 & 1 \end{bmatrix} \cdot \begin{bmatrix} N \\ Q_\eta \\ M_\zeta \end{bmatrix} \tag{3}$$

When studying the dynamics of hinge mechanisms taking into account the friction forces, the reaction $\bar{r}_{j\eta}$ is considered passing through the center of the pivot; in kinematic pairs, the frictional moment is also taken $m_{j\zeta}^{mp}$ into account. In the presence of a rotational $m_{j\zeta}$ pair in a plain mechanism (Figure 2), the frictional moment is directed opposite to the internal moment. It is $\bar{F}_{mp}$ assumed that the normal pressure forces are concentrated at point A and the friction force is applied at the same point. Then:

$$m_{j\zeta}^{mp} = -m_{j\zeta} = -F_{mp} \cdot r = -frN_{Д} = -fr\sqrt{r_{j\zeta}^2 + r_{j\eta}^2} \;\; N_{Д} = \sqrt{r_{j\zeta}^2 + r_{j\eta}^2} \tag{4}$$

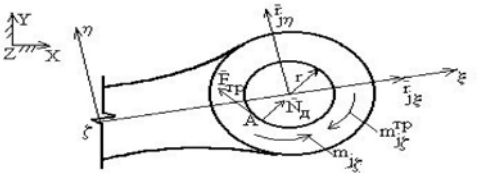

Figure 2. The rotational kinematic pair with the friction force in the plain mechanism.

Figure 3 conventionally shows the slider of the spatial translational pair of the fifth class, which can move along the axis. In such a kinematic pair, it is assumed that the contacts of the links occur in two planes.

Sliding friction forces arise in these planes. The friction force F_{mp1} is proportional to the second component of the reaction in the LCS, and the friction force F_{mp2} in the side face is proportional to the third component of the reaction in the LCS:

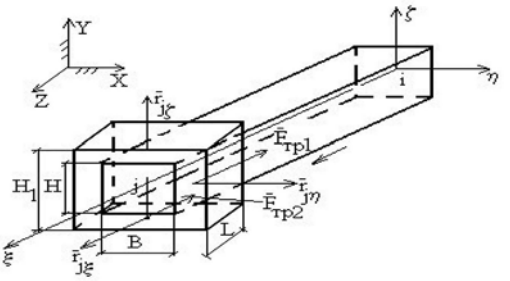

Figure 3. Translational kinematic pair with a frictional force in the spatial mechanism.
B – the slider contact width, L – its length, H1 – its height, H – is the slider contact height

$$F_{mp1} = fr_{j\eta} \cdot signr_{j\eta}, \overline{F}_{mp2} = -\bar{r}_{j\xi}, F_{mp2} = fr_{j\zeta} \cdot signr_{j\zeta}, F_{mp} = F_{mp1} + F_{mp2}. \quad (5)$$

In turn, reactions in the LCS are expressed through the unknown internal forces $N_j, Q_{j\eta}, Q_{j\zeta}, M_j, M_{j\eta}, M_{j\zeta}$ are the nodes and are presented in the form:

$$\{\bar{r}\} = \left[d_{r,s}\right] \cdot \{N\} \quad (6)$$

Where $\{\bar{r}\}^T = \left(r_{i\xi}, r_{i\eta}, r_{i\zeta}, \ldots, m_{j\zeta}\right)$, $\{\bar{N}\}^T = \left\{N_j, Q_{yj}, Q_{zj}, \ldots, M_{z\zeta}\right\}$ $a_{kk} = -a_{k+6,k} = -1$; $a_{5,3} = a_{6,2} = l$; the rest elements are equal to zero.

In the spatial model of a rotational kinematic pair, it is assumed (Figure 4) that contacts occur in the end planes of the hinge at two different points A and B.

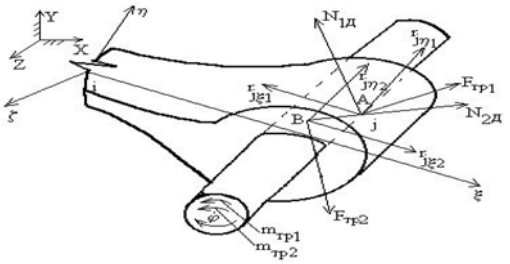

Figure 4. Rotational kinematic pair with a frictional force in a spatial mechanism.

Reactions in the LCS are $r_{j\xi 1}, r_{j\xi 2}, r_{j\eta 1}, r_{j\eta 2}$ determined through the internal forces by formula (6). The friction forces moments are determined by the following formulas:

$$m_{mp1} = -F_{mp1} \cdot r = -fr|N_{1Д}| = -fr\sqrt{r_{j\xi_1}^2 + r_{j\eta_1}^2}, \quad (7)$$

$$m_{mp2} = -F_{mp2} \cdot r = -fr|N_{2Д}| = -fr\sqrt{r_{j\xi 2}^2 + r_{j\eta 2}^2}, \quad (8)$$

$N_{1Д}, N_{2Д}$ where are the normal pressure forces; r is the pivot radius. Reactions *are* determined $r_{j\xi 1}, r_{j\xi 2}, r_{j\eta 1}, r_{j\eta 2}$ by formula (6).

Based on the finite element method and analysis of the stress-strain state of plain and spatial structures based on the HCM with elastic links and friction forces in kinematic pairs, elastic displacements, internal forces in the elements of the rods are determined with and without regard to friction forces.

The relationship equations between the vectors of nodal forces $\{f_\Lambda^e\}$ and displacements are $\{\delta_\Lambda^e\}$ represented in the form:

$$\{f_\Lambda^e\} = [K_\Lambda^e] \cdot \{\delta_\Lambda^e\} \tag{9}$$

where $[K_\Lambda^e]$ is the symmetrical square matrix of rigidity of the 12x12 FRE (finite rod element) order. It is called the matrix of rigidity of a spatial rod element:

$$[K_\Lambda^e] = [K_{ij}],\ (i,j = 1,2,\ \ldots,12) \tag{10}$$

The elements of the matrix of rigidity of the FRE (finite rod element) connecting the force and kinematic parameters at the nodes of a given FRE are determined through its geometric parameters of the cross section, elastic characteristics and length (Postnov et al., 1979, Archer 1965).

If there is a hinge at nodes *i* and *j* of the design element "e", bending moments M_i or M_j in them are equal to zero. In this case, the equations for linking the forces at the nodes with the displacements of the nodes are transformed accordingly. If the node *i* has a hinge, then the corresponding row of the element matrix of rigidity is excluded in the usual way.

If the spatial structure consists of *m* rod elements, then the basic system of equilibrium equations is written as follows:

$$\{F_k\}^T = (F_1, \ldots, F_m), \tag{11}$$

where $\{F_k\}^T = (F_k, F_{yk}, F_{zk}, M_{xk}, M_{yk}, M_{zk})$, $k = 1,2,\ldots,m$ is the vector of external forces applied to the k-th node in the global coordinate system (GCS) OXYZ, m is the total number of nodes.

To determine displacements, angles of rotation and forces in the system of *m* rod elements that make up the structure, it is necessary to satisfy the deformation compatibility conditions and equilibrium equations.

The kinematic characteristics at the nodes of each element automatically satisfy the first condition. Therefore, it is enough to satisfy the equilibrium conditions at the nodes of the structures. Essentially, satisfying these conditions at all nodal *m* points, we construct the main resolving system of linear algebraic equations for the components of the nodes displacements and angles of rotation in the form:

$$\{F\} = [K]\{U\}, \tag{12}$$

where $[K] = [K_{rs}]$, $(r,s = 1,2,\ldots,6m)$ is the square matrix of the 6m*6m order; it is called the system matrix of rigidity (SMR);

$$\{U\}^T = \left(u_1, \vartheta_1, w_1, \phi_{x1}, \phi_{y1}, \phi_{z1}, \ldots, u_m, \vartheta_m, \ldots, \phi_{zm}\right),\ \{F\}^T = \left(N, Q_y, Q_z, M_x, M_y, M_z\right)$$

Thus, the SMR (the system matrix rigidity) is formed from the rigidity matrices of all m rod elements of the mechanism defined in the GCS. Taking into account the boundary conditions, the components of displacements and deformations of the nodes of the mechanism are found by solving system of equations (17) by the iterative Gauss-Seidel method. This method is easy to program, each equation is iterated, and the determined value is refined. The process is repeated as many times as needed to obtain the acceptable solution accuracy.

Accounting for the boundary conditions in the GCS in the presence of friction forces in kinematic pairs is carried out by excluding the corresponding degrees of freedom. This is done using the procedure of calculating the number of zeros in the given matrix ID, the degree of freedom of nodes IID, the boundary condition of internal force factors, and replacing them with the ordinal numbers of the corresponding degrees of freedom, and replacing units with

zeros. When frictional forces act on a structure, corresponding bending moments are generated in rotational kinematic pairs. To study the impact of forces and moments of friction forces of translational and rotational pairs at a certain quasi-static position of the structure, the values of forces and moments of friction are calculated using the determined internal forces at the nodes according to the corresponding formulas [4].

Solutions by the finite element method for plain and spatial dynamic problems on the stress-strain state of structures based on the HCM with elastic links and friction forces in kinematic pairs at their different positions and subject to external dynamic loads.

Methods of accounting for friction forces in various kinematic pairs of plain and spatial elastic HCMs are considered when obtaining the basic systems of differential equations of motion relative to the kinematic parameters of all the structural units for the development of computational algorithms and quantitative analysis of their state at different fixed positions, taking into account the corresponding boundary, initial conditions and specified external variable forces.

The system of equations for the dynamic equilibrium of a set of finite rod elements, with the help of which the considered structure is discretized at the t moment with the mechanism position under study has the form:

$$[M]\{\ddot{U}\} + [C] \cdot \{\dot{U}\} + [K] \cdot \{U\} = \{F(t)\} \tag{13}$$

where $[M], [C], [K]$ are respectively the matrices of the system mass, damping, and rigidity that are obtained by summing up the corresponding matrices of all the computed rod elements; $\{\ddot{U}\}, \{\dot{U}\}, \{U\}$ are vectors of accelerations, velocities and displacements of the nodes with the use of which the computed rood structures are divided into finite two-node rod elements; $\{F(t)\}$ is the given vector of the external variable forces acting at the nodes.

In the calculations of the dynamic stress state of plain and spatial elastic HCMs taking into account the friction forces in kinematic pairs, the matrix of the system damping $[C]$ according to Rayleigh is taken in the form of the combination of the mass matrix $[M]$ and system rigidity $[K]$, i.e. $[C] = \alpha[M] + \beta[K]$; the α and β constants are determined from the values of the damping coefficients related to the two lowest frequencies.

When studying and analyzing the stress state of plain and spatial elastic HCMs taking into account the friction forces in kinematic pairs from the action of external variable forces, system of differential equations (18) was solved by the convenient absolutely stable stepwise method of direct integration according to the Newmark scheme with the step $\Delta t = 0,01$ (Hack & Becker 1999, Harlecki Andrzej. 1999).

3 CONCLUSION

In accordance with the theoretical solution of the quantitative and qualitative analysis of the dynamic stress state of plain elastic HCMs of II, IV classes and the spatial mechanism of VShD-8, taking into account the friction forces in kinematic pairs, algorithms have been developed and object-oriented software packages have been compiled in the Fortran high-level algorithmic language.

In the numerical calculations of the forced vibrations and the dynamic stress state, when the concentrated variable force $F = F_0 \sin \omega t$ acts on them, the dynamic analysis of the stress state of plane elastic HCMs of II, IV class was first carried out taking into account the friction forces in kinematic pairs at different static positions (Chernousko 2000, Massanov, et al. 1994). The elastic physical and geometric characteristics of the link materials are the same as when considering the static problems.

REFERENCES

Zenkevich O. 1975. *The finite element method in technology*. M.: Mir. 541 p.

Volmir A.S. et al. 1989. *Statics and dynamics of complex structures: Applied multilevel research methods*. M.: Mashinostroenie, 248 p.

Postnov, V.A., Dmitriyev, S.A., Yeltyshev, B.K. et al., 1979. *The method of super elements in the calculations of engineering structures*. A.: Sudostroenie. 288 p.
Archer. 1965. Formulation of matrices for analysis of structures using the finite element method. *Rocket technology and cosmonautics*. M.: Mir, No. 10, p. 155.
Hack R.S. & Becker A.A. 1999. Analysis of contact with friction under the action of a tangential load by the finite element method in local axes. Jnt. J. Mech. Sci. 41, No. 4-5, pp. 419–436.
Harlecki Andrzej. 1999. Jumping motion of an open manipulator with flexible drives and dry friction in kinematic pairs. *J. Theor. and Appl. Mech*. 37, N4, p. 873–892. 27.
Harlecki Andrzej. 1999. Newton's method of solving spatial problems of fretting. *Jnt. J. Mech. Sci*. 41, No. 4-5, pages 19–36. Engl.
Velex P.& Cahouet V. Experimental and numerical study of the effect of tooth friction on the dynamics of spur and helical gears. Trans. ASME. J. Mech. Des. 2000.-122, N4, p. 515–522.
Chernousko F.L. 2000. Wavelike movements of many links along the horizontal plane. *Prikl. mat. and fur mat*. 64, No. 4, M., p. 518–531.
Massanov Zh.K., Temirbekov E.S., Birtanov E.A. 1994. Dynamic modeling of HCMs by the finite element method. In the book. *Internatinal Conference spatical mechanisms and high-class mechanisms*. Almaty.
Moldabekov M.M., Tuleshov A.K., Ualiev G.U. 1998. Mathematical modeling of the dynamics of mechanisms and machines. Almaty: Kazak University, p.139–146.

Smart Geotechnics for Smart Societies – Zhussupbekov, Sarsembayeva & Kaliakin (Eds)
© 2023 The Author(s), ISBN 978-1-003-29912-7
Open Access: www.taylorfrancis.com, CC BY-NC-ND 4.0 license

Logistic regression models to predict the probability of high pile rebound using SPT or CPT data

Fauzi Jarushi
Associate Professor, University of Tripoli, Libya

Paul J. Cosentino1
Professor of Civil Engineering, College of Engineering, Florida Institute of Technology, Melbourne, FL

Omran Kenshel
Assistant Professor, University of Tripoli, Libya

ABSTRACT: At certain depths during driving of large diameter displacement piles, rebound greater than 0.25 inches (6.35 mm) occurs followed by a small permanent-set after each hammer blow. High pile rebound (HPR) soils may stop the pile driving and result in a limited pile capacity. The overburden depth at which HPR occurred is typically greater than 50 ft (15.3m). In some cases, rebound leads to pile damage, delaying of the construction project, and the requiring foundations redesign. A simple models for evaluating probability of HPR using Cone Penetration Test (CPT) and Standard Penetration Test (SPT) data are developed based on logistic regression analyses of 18 case histories. The proposed model uses the pore water pressure and sleeve friction and/or SPT blow count with fines content (pass #200 sieve) as input parameters. Comparisons of the proposed probability model with actual pile-driving analyzer (PDA) rebound data are performed to demonstrate the improvements. As a result, the models showed that the probabilities of HPR (percentage) increased as either the pore water pressure or sleeve friction or SPT N-values with fines content. The statistical logistic regression modeling and developed equations showed promise in predicting rebound. This methodology may lead to a simpler evaluation process which allows for the prediction of HPR during the design phase.

1 INTRODUCTION

Contractors and engineers have experienced pile installation problems while driving high displacement piles with single-acting diesel hammers at Florida Department of Transportation (FDOT) construction sites located in the Central and Panhandle regions of Florida. Problems occur during pile driving, when a large initial penetration per hammer blow is followed by a large elastic rebound (termed High Pile Rebound or HPR) resulting in a small or negligible permanent-set per blow. Figure 1 illustrates a typical HPR pile-top displacement versus time record for a single hammer blow obtained from Pile Driving Analyzer (PDA) strain gages and accelerometers. The maximum initial downward motion "DMX," is the sum of elastic and plastic deformations of the pile and soil system. The final displacement is the pile penetration per blow, or "set." Rebound is the difference between the pile maximum displacement and final set.

HPR may prevent the required driving resistance from being achieved and or stop the pile driving process, placing the foundation performance at risk or requiring redesign. HPR problems generally occurred in soils that did not display any unusual geotechnical properties during routine soil investigations 0.

FDOT road and bridge construction specification 455-5.10.3 defines refusal as 20 blows per inch (25 mm) with the hammer operating at its highest fuel setting or at a setting determined

DOI: 10.1201/9781003299127-222

by the engineer with a limit of 0.25 inch (6.35 mm) rebound per blow (Cosentino et al. 2010). For this research, HPR was defined as any rebound exceeding the specified 0.25-inch (6.35 mm) limit.

The objective of this research was to develop a geotechnical engineering protocol that would help engineers anticipate HPR.

2 HISTORY OF HPR

Murrell et al. 2008 presented a case history of HPR which occurred during the construction of a new ferry terminal in coastal North Carolina. Prestressed concrete piles (PCP), 20-inch (508 mm) square and 70 ft (21 m) long, were designed to support an over water structure. The authors describe the high rebound using the term "Bounce". Pile bounce was observed at an overburden depth of 53 ft (16 m) (elevation -43ft, -13m) when the piles penetrated into saturated, firm to stiff, fine-grained marine soils along the southeastern coast of the United States.

During the geotechnical investigation at this site, excess pore water pressures u_2 greater than 20 tsf (1915 kPa) were measured during CPTu testing at the depth where bouncing occurred .When the blow counts during pile driving were at 303 blows per foot (bpf,) (blows per 0.3m), the pile displacement became zero. The driving process was then stopped for two hours and restrike was carried out. However, an additional 2.5 ft (0.76 m) (of pile length was driven with blow counts of 73 bpf, 112 bpf, and 87 blows/6 in (blows/152mm). Again the driving was halted when a large rebound resulted in near zero set. In order to achieve the pile capacity and overcome pile rebound, the pile was driven after four days using a hammer with a larger ram and a shorter stroke.

Hussein et al. 2006 presented a case study related to HPR during driving of PCP for the State Road 528 Bridge over the Indian River in Florida. A group of 30-inch (762 mm) square, hollow core PCP with a length of 115 ft (35m) were used to support the bridge. The piles rebounded when they penetrated into hard soils consisting of saturated medium dense sand with silt (SP-SM) to fine silty sand (SM) to clayey sands and sandy clays (SC). The authors believe that the incompressible water in the soil near and below the pile tip produced excess pore pressure during the driving process which created an upward force on the pile, thereby causing rebound. However, no analytical proof of this conclusion is available.

Likins 1983 analyzed three sites with high pile rebound between 0.4 and 1 inch (10 mm and 25 mm). He determined that the only common geotechnical parameter observed at each site was the fully saturated soils. Preliminary analysis using the basic wave equation was conducted for each site. The author then modified the results to match field data acquired by CAPWAP (Case Pile Wave Analysis Program). He proposed that the only reasonable cause of the HPR was the buildup of excess pore pressure beneath the pile tip. It was also clear through testing, that pile capacities decreased when high quake/rebound occurred. Findings from the work indicated that high quake lowers the pile capacity by a factor of 3. Field observations often led to a false interpretation that the hammer is not large enough for the pile. In these cases where the hammer size is increased, the pile could be damaged. Likins (1983) concludes that alternative pile designs, such as hollow piles, should be considered as an effective way to avoid high soil quake.

Studied by Jarushi et al. 2013 on the effect of fines content (material that pass # 200 sieve) and uncorrected standard blow count (N_{SPT}) on HPR at the presented sites. The study showed that permanent-set and rebound were a direct function of N_{SPT} and fines content of the soil at the pile tip. The authors reported that when the NSPT was less than 15 blows/ft (blows/0.3m) and a fines content of less than 25 percent, the rebound was less than 0.25 inches (6.35mm), yielding an acceptable permanent-set of up to 3 inches (76mm). For N_{SPT} values between 15 and 40 blows/ft (blows/0.3m) and a fines content of 25 to 40 percent, the pile rebound varied between 0.25 and 0.6 inches (6.25 mm and 15mm), yielding acceptable permanent-set values. For cases where the N_{SPT} exceeded 40 blows/ft with a fines content greater than 40 percent, pile rebound was greater than 0.6 inches (15mm) and was accompanied by an unacceptable permanent-set.

3 METHODOLOGY AND TESTING PROGRAM

3.1 *Dynamic PDA testing*

During FDOT construction at seven sites, pile driving was monitored with PDA equipment. Figure 1.Typical PDA pile top displacement versus time diagram from one hammer blow for FDOT HPR site shows typical HPR PDA data from one pile blow at a FDOT site. The plot, with displacement in inches on the vertical axis and time in milliseconds on the horizontal axis, shows a maximum displacement (DMX) of 1 inch (25mm), an inspector permanent-set (iSet) of 0.11 inches (2.8mm) and a digital set (DFN or dSet) of 0.27 inches (6.85mm). The dSet is not used for this study because it is recorded in a short time of 200 milliseconds. The number of hammer blows per foot is used to produce an average inspector set per blow. The maximum displacement and iSet were subtracted to determine the rebound per hammer blow (i.e., DMX-iSet =Rebound), yielding a rebound of 0.89 inches (23 mm). Plots for each of the case studies were developed relating elevations to iSet and rebound. The elevation associated with the start of the PDA data corresponded to the depth at which pile driving commenced. This elevation was below the ground surface because piles at these sites were set into predrilled holes.

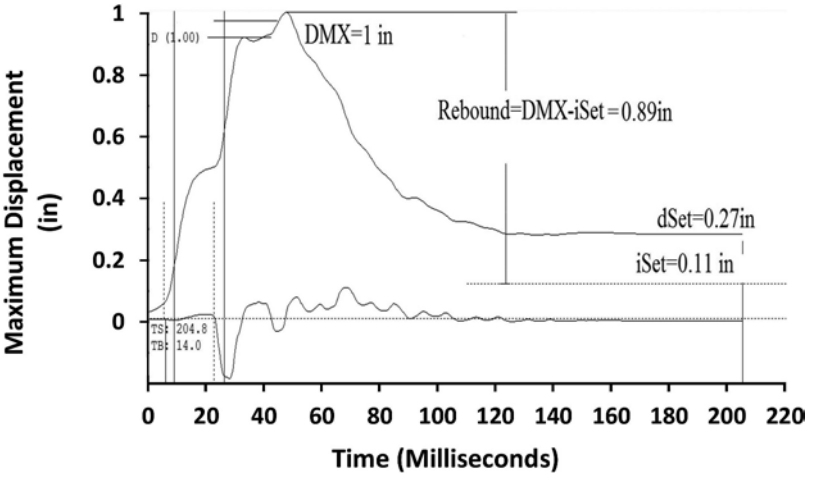

Figure 1. Typical PDA pile top displacement versus time diagram from one hammer blow for FDOT HPR site.

3.2 *CPTu and SPT testing*

An extensive field included SPT, CPTu and laboratory-testing program was carried out the FDOT sites where rebound was encounter. The SPT test procedure followed ASTM D1586 "Standard Test Method for Penetration Test and Split-Barrel Sampling of Soils".

CPTu testing with pore water measurement was performed in soundings and signals were digitally recorded using the Hogentogler standard recording system. The CPTu test procedure followed ASTM D3441-05 "Electronic Friction Cone and Piezocone Penetration Testing." During testing, data was collected digitally to record the cone resistance q_c, sleeve friction f_s, inclination, and designated pore water pressure u_2 at every 2 inches of penetration.

3.3 *Logistic regression models to predict HPR*

The objective of the statistical investigations was to establish relationships that make it possible to predict one variable, rebound or non-rebound in terms of the other variables. SPSS (Statistical Package for the Social Sciences) software was used for this investigation.

In this study, the regression method was used to determine whether these variables are significantly related, and also, the direction and strength of their relationship. The rebound or

non-rebound was represented as a dependent variable (P variable) in the statistical analyses and the remaining variables (N_{SPT} , fine content f_s, q_c, PWP u_2) were represented as the independent variables or the explanatory variables (the X's in the equation). The probability that an event will occur can be predicted using the following equation described by Cox (2010).

$$P = \frac{e^{B_0+B_1X_1+B_2X_2+\ldots\ldots\ldots B_n}}{1+e^{B_0+B_1X_1+B_2X_2+\ldots\ldots\ldots B_n}} \quad (1)$$

Where P= Probability; e= the base of the natural logarithm;
$\beta_0 \ldots \beta_n$ = regression coefficients

Once the model has been fitted to the data, it is a good practice to investigate the adequacy of the fit. This analysis helps to determine how well the model actually correlates with the observed data and which parameters do have significant relationships.

4 RESULTS AND DISCUSSION

Findings from the testing program indicated that the most critical parameters associated with HPR werepercent fines and uncorrected SPT blow counts N_{SPT} or corrected blow counts N_{60}. The fines content defined as the percent passing the No. 200 sieve. CPT Pore water pressure was also an indicator of HPR.

Probabilities between HPR and N_{SPT} and fines content, and between HPR and CPTu data (i.e., f_s, q_c and pore pressure) were developed and resulting trends were examined. After several computational iterations, the N_{SPT}, fines content, pore pressure, and f_s were used, while q_c was eliminated because of its low statistical coefficients (i.e., Significant or p-value >0.05).

4.1 *Model 1: Probability of HPR using N_{SPT} and fines content (%)*

The relationship between the rebound or non-rebound and the other variables, N_{SPT} and fines content was determined. A total of 79 cases or data points were used. The probability of HPR from model 1 predicted by shows a summary of the model 1 classification results (see Table 1). This model allows for correctly classifying the data for 20/29 or 69% of the subjects where the predicted event (Rebound) occurs, and correctly classifies 45/50 or 90% of the subjects where no rebound occurs. Overall 65 predictions were correct out of 79 cases and results in the overall success rate of 83%. The probability of HPR from Model 1 can be predicted using the following equation:

$$P = \frac{e^{(-5.714+0.071NSPT+0.127FC)}}{1+e^{(-5.714+0.071NSPT+0.127FC)}} \quad (2)$$

Table 1. Model 1 prediction accuracy classification.

Field Observed data		Model Prediction		Model Accuracy (%)
Non-rebound	Rebound	Non-rebound	Rebound	
50	NA	45	5	90
NA[a]	29	9	20	69
Overall Prediction				83

[a]not applicable

Where P= Probability of rebound (percent); N_{SPT}= SPT blows count (blows/ft); FC= percent fines content

Table 2 shows the significance test for each of the coefficients in the logistic regression model. Both N_{SPT} and fines content are significant as "sig" is less than 0.05.

Table 2. Variables in the equation.

V Variables	B[d]	S.E.[e]	df[f]	Sig.[c]
FC[a]	0.127	0.031	1	0.000
N[b]	0.071	0.024	1	0.003
Constant	-5.714	1.269	1	0.000

[a]fines content; [b]SPT blows count; [c]significance of model; [d]regression coefficient; [e]standard error around the coefficient; [f]degrees of freedom.

Figure 2 shows the probabilities of HPR using equation (2) increased as either the fines content or N_{SPT} increased and the regression coefficient R^2 approached 1.0. The probability of the HPR was greater than 50 percent when the N_{SPT} exceeded 30 blows/ft (blows/0.3m) and the fines content exceeded 35 percent.

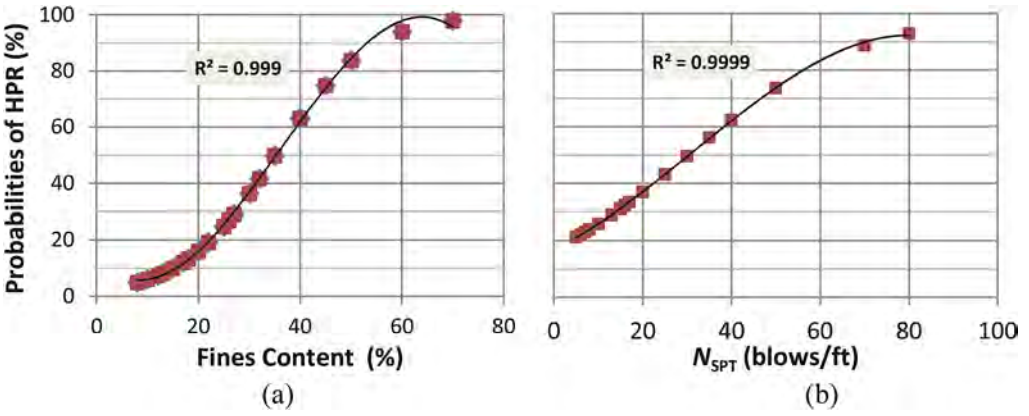

Figure 2. Probability of HPR versus (a) Percent fines content and (b) N_{SPT} based on equation (2).

The probability of rebound (percentage) using equation (2) was also examined using actual PDA rebound data from four of the HPR sites. As shown in Figure 3, probabilities of HPR reached 100 percent at same elevation where rebound increased to over 1 inch. Test piles at these sites, as presented in Figure 3 experienced excessive rebound followed by minimal set.

Similarly using equation (2), the probabilities of HPR was very low and less than 50 percent for the data at three sites which did not experience any driving problem (i.e., rebound < 0.50 with acceptable set) as shown in Figure 4.

It can be concluded that model 1 using N_{SPT} and fines content showed promise in predicting rebound, this methodology may lead to a simpler evaluation process allows for the prediction of HPR during the design phase.

4.2 *Model 2: Probability of HPR using CPTu pore water pressure*

The probability of predicting HPR using CPT pore pressure was also developed and examined using 32 data points. The probability equation is presented in equation (3) shows this model's accuracy in that it correctly classifies 7/8 or 88 % of the subjects for the "rebound" predicted event while 23/24 or 94% of the subjects where the predicted non-rebound was not observed. Overall, model predictions were correct 30 out of 32 cases, for an overall success rate of 94%.

$$P = \frac{e^{B_0 + B_1 X_1 + B_{2X_2 +} \ldots\ldots\ldots\ldots B_n}}{1 + e^{B_0 + B_1 X_1 + B_{2X_2 +} \ldots\ldots\ldots\ldots B_n}} \quad (3)$$

Where P= Probability of rebound (percent); PWP = CPTu pore water pressure (tsf)

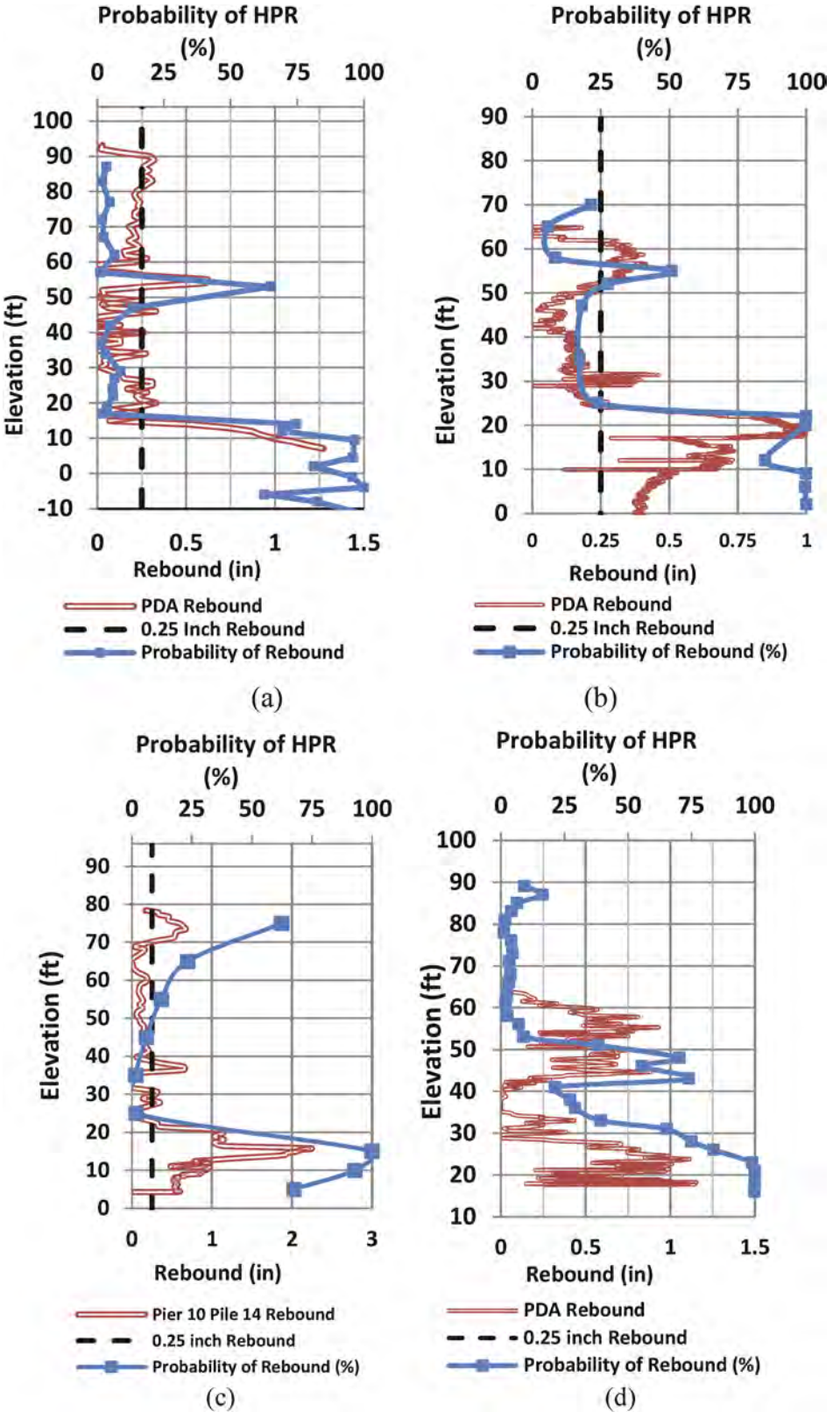

Figure 3. Probabilities of HPR using equation (2) for HPR sites with a minimal set (a) Anderson Street Overpass, (b) I-4/US192 Ramp D and (c) I-4/John Young Parkway and (d) SR50/SR436.

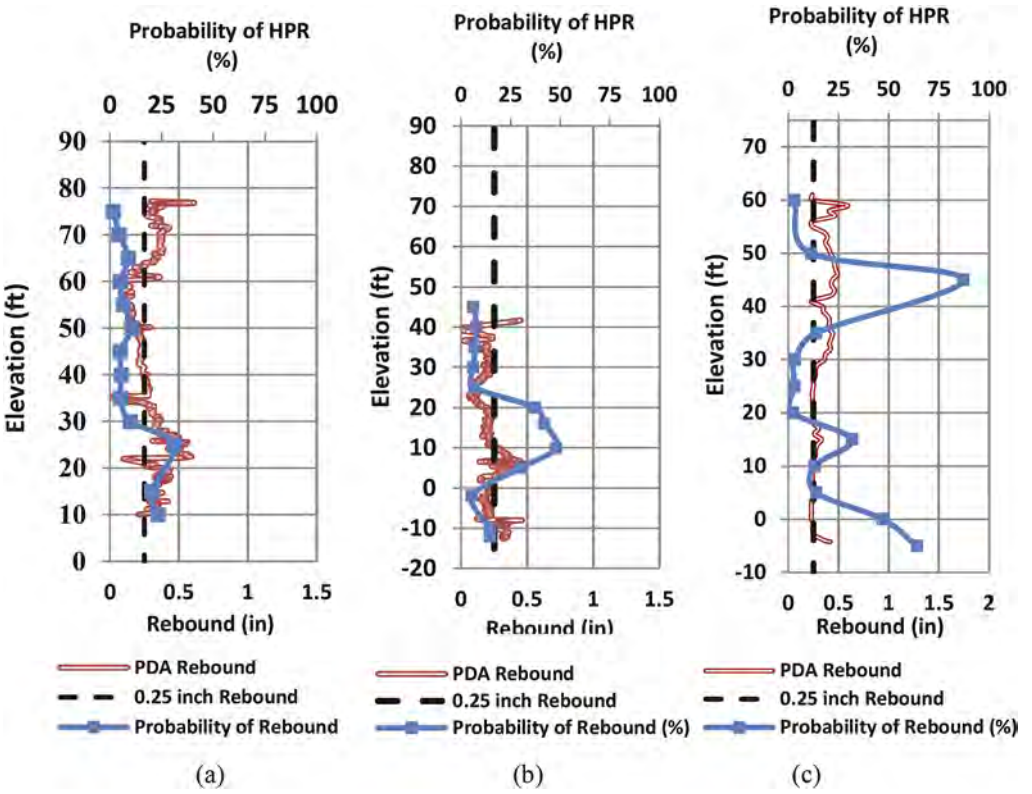

Figure 4. Probabilities of HPR using equation (2) for HPR sites with Acceptable Set (a) I-4/ US192 West Bound, (b) I-4/US192 East Bound and (c) SR417/International Parkway.

The applicability of equation (3) and PDA actual rebound were plotted versus elevation for more than 5000 data points (i.e., CPT record measurements from each 2 inches). It can be seen in Figure 5, that the probability of HPR reached 100 percent at two sites, which experienced excessive HPR with minimal set (i.e. Anderson Street Overpass and I-4/US192). It is also reached 75 percent at the third site but CPT data is not to end of PDA elevation. The probability of HPR was very low (i.e., 2 percent or less) at sites, which experienced low CPTu pore pressure where rebound was less than the FDOT limit of 0.25 inches (6.35mm) as shown in Figure 6. It can be summarize CPT PWP is statistically related to rebound. The overall accuracy of model 2 is higher than model 1.

4.3 *Model 3: Probabilities of HPR using sleeve friction and pore water pressure*

Probability of predicting HPR using CPT pore pressure and sleeve friction was also developed using 51 data points. The probability equation is presented in equation (4).

$$P = \frac{e^{B_0+B_1X_1+B_{2X_2+\ldots\ldots\ldots\ldots}\ B_n}}{1+e^{B_0+B_1X_1+B_{2X_2+\ldots\ldots\ldots\ldots}\ B_n}} \tag{4}$$

Where

P= Probability of rebound (percent); PWP= CPTu pore water pressure in (tsf); f_s =CPT sleeve Friction in (tsf)

The the probability accuracy of HPR using model 3 equation (4) and PDA actual rebound were plotted versus elevation. It can be noted in Figure 7 that the probability of HPR increased to 100 percent at the same elevation where rebound occurred with a minimal set.

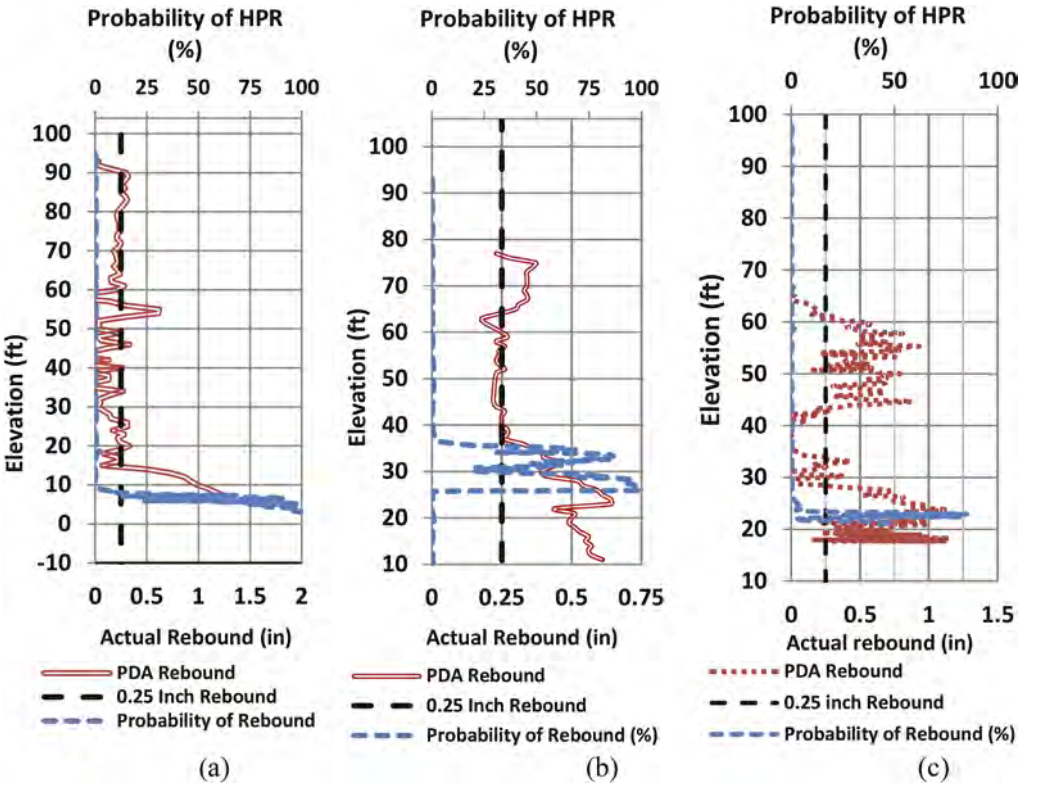

Figure 5. Probabilities of HPR using equation (3) for HPR sites with minimal Set (a) Anderson Street Overpass, (b) I-4/US192 Ramp CA and (c) SR50/SR436.

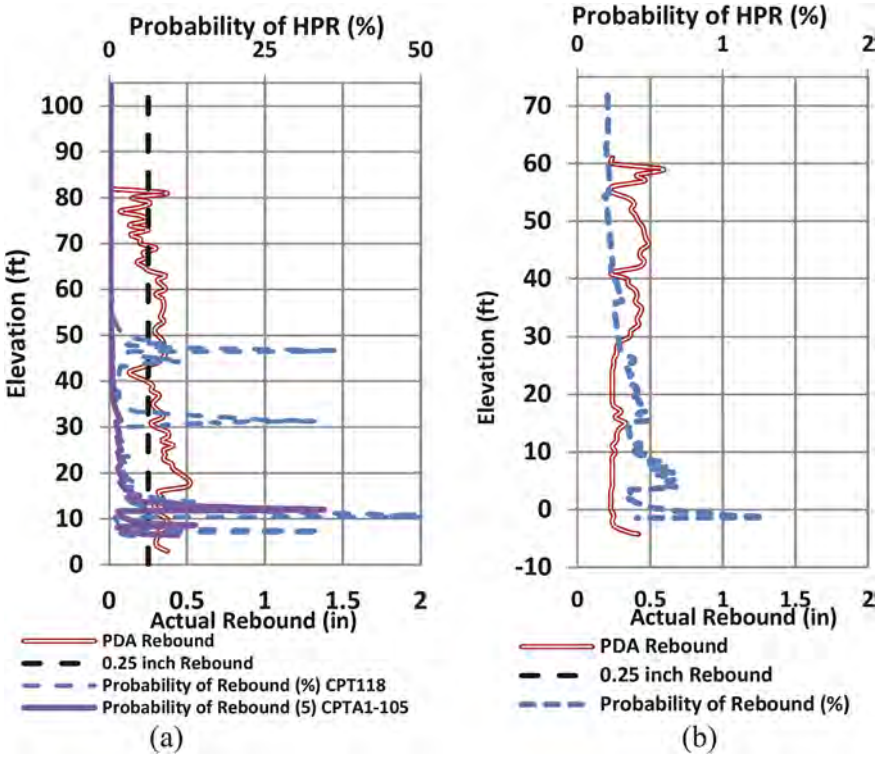

Figure 6. Probabilities of HPR using equation (3) for HPR sites with acceptable set (a) Ramp B and (b) SR 417/International Parkway (minimal Rebound).

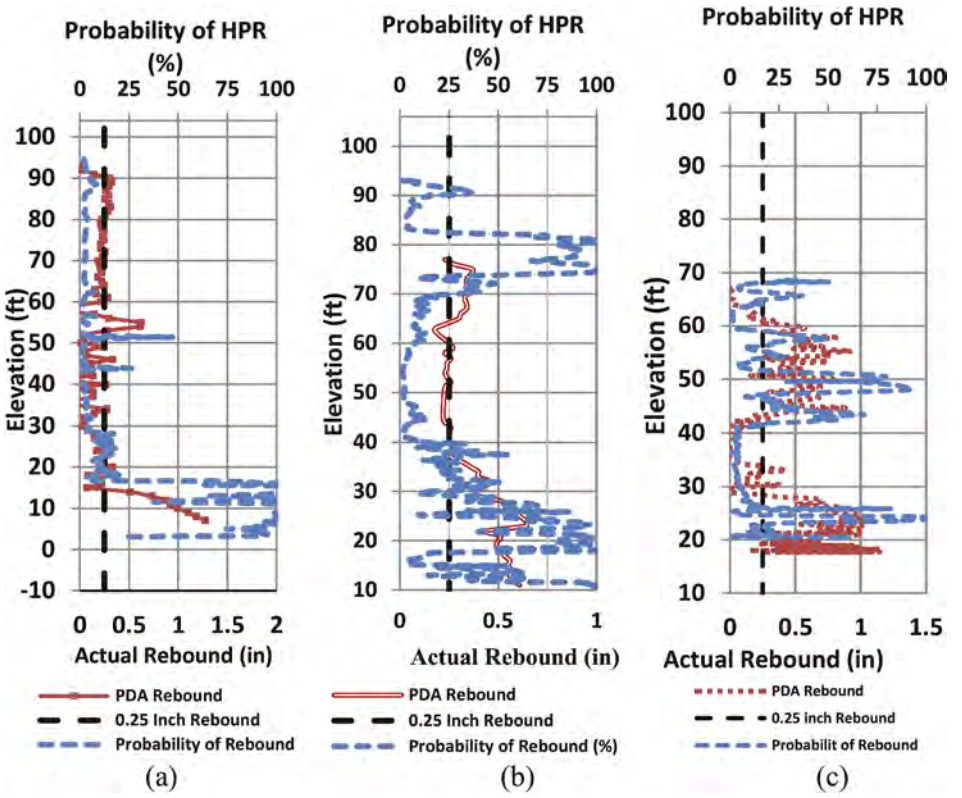

Figure 7. Probabilities of HPR using equation (4) for HPR sites with minmal Set (a) Anderson Street Overpass, (b) I-4/US192 Ramp CA and (c) SR50/SR436.

These sites experienced excessive HPR with minimal set (i.e. Anderson Street Overpass and I-4/US192). The probability of HPR was very low (i.e., < 20 percent) at SR417/International Parkway (see Figure 8). This site experienced rebound of less than 0.25 inches (6.25mm). The probability of HPR was 75 percent at the site where a maximum rebound of 0.50 inches (12mm) followed by an acceptable set (i.e., Ramp B).

5 CONCLUSION AND RECOMMENDATIONS

In summary, probability equations, which relate pile rebound to geotechnical parameters including N_{SPT} and fines content and CPTu pore pressure and sleeve friction were developed. These equations indicated that probability of rebound occurring was a direct function of these parameters. Therefore, this methodology can be used to predict HPR problem during design phase.

Probabilities equations to predict HPR based on fine content, N_{SPT}, CPTu PWP, and f_s, showed that probabilities of rebound were a direct function of these parameters. They showed promise in predicting rebound as the models developed fitted the data and the adequacy of the fit was excellent with R^2 approaching 1.0. This methodology may lead to a simpler evaluation process, which allows for the prediction of HPR during the design phase.

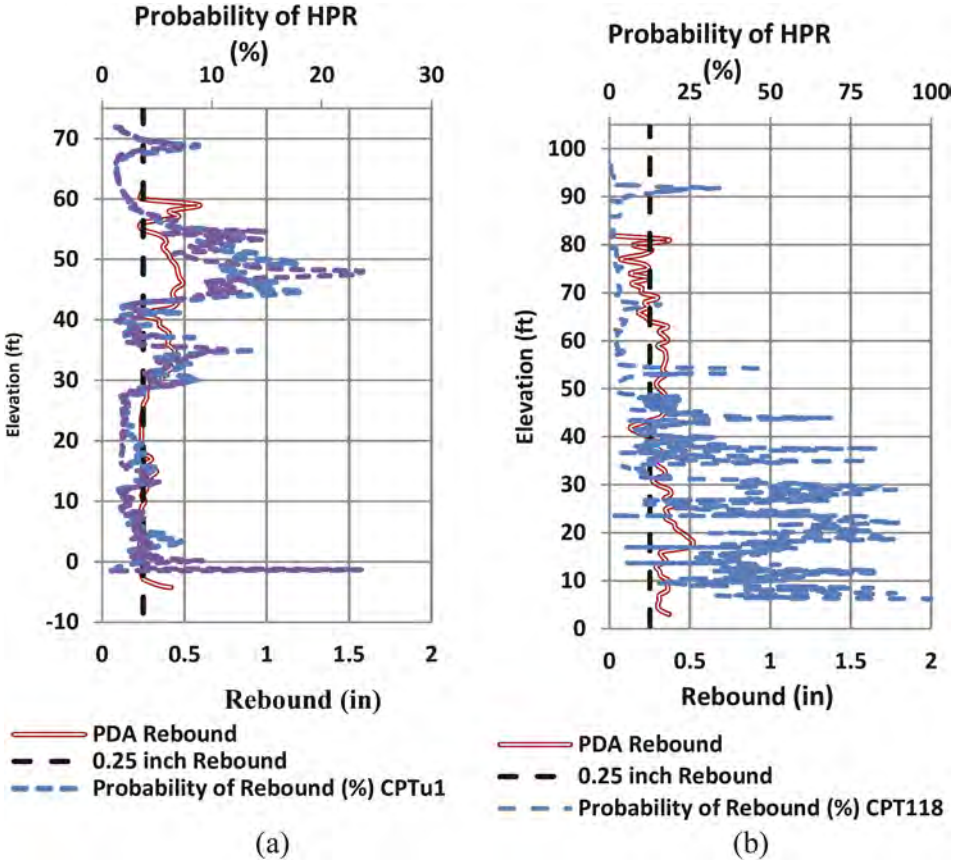

Figure 8. Probabilities of HPR using equation (3) for HPR sites (a) SR 417/International Parkway (minimal Rebound) and (b) I-4/SR408 Ramp B (Rebound with acceptable set).

REFERENCES

ASTM D1586. Standard test method for penetration test and split-barrel sampling of soils.

ASTM D3441-05. standard test method for mechanical cone penetration tests of soil.

Bingjian Z. Study of the pore water pressure variation rule in saturated soft soil caused by prestressed concrete pile penetration. 2013. *Electric Technology and Civil Engineering Conference*. April; Taizhou, China:756–759.

Cosentino P J, Kalajian E H, Jarushi F and Krajcik, Ryan. 2013. Identifying High Pile Rebound Soils Using CPT Pore Water Pressure Measurements: Case Studies in Florida. Transportation *Research Board 92nd Annual MeetingTransportation Research Board 92nd Annual Meeting Compendium of Papers*. Paper No: 13–2871

Cosentino P, Kalajian E, Misilo T, Chin-Fong Y, Davis K, Jarushi F, Bleakley A, Hussein M H, and Bates Z. 2010. Design Phase Identification of High Pile Rebound Soils. *Florida Department of Transportation Technical report*., Contract BDK81 Work Order 977–01.

Cox D R and Snell E J. analysis of binary data, Second Edition. Chapman and Hall/CRC. 1989; London.

FDOT. 2010. Standard Specification for Road and Bridges Section455.

Hussein M H, Woerner W A, Sharp M and Hwang C. 2006. Pile driveability and bearing capacity in high-rebound soils. A*merican Society of Civil Engineers GEO Congress CD-ROM*. Atlanta, GA.

Jarushi F, Cosentino P J and Kalajian E H and Hadeel Dekhn. CPT pore water pressure correlations with PDA to identify pile drivability problem. *International Journal of Environmental, Chemical, Ecological, Geological and Geophysical Engineering*. 9(2):55–61.

Jarushi F, Cosentino P J and Kalajian E H. 2013. Piezocone Penetration Testing In Florida High Pile Rebound Soils. *The Journal of the Deep Foundations Institute*. 7(2):28–45.
Jarushi F, Cosentino P J and Kalajian E H. 2013. Prediction of High Pile Rebound with Fines Content and Uncorrected Blow Counts from Standard Penetration Test. *Journal of the Transportation Research Board*. 2363(1):47–55.
Jarushi F. 2013. Evaluating geotechnical engineering properties associated with high pile rebound. Ph.D. Dissertation, *Florida Institute of Technology, Melbourne Florida*.
Likins G E. Pile installation difficulties in soils with large quakes. In G.G. Globe, editors, *Proceedings of Symposium 6 at the 1983 ASCE Convention, Philadelphia.. ASCE Geotechnical Engineering Division*. 1983 May.
Murrell K L, Canivan G J, Camp W M. 2010.. High and low strain testing of bouncing piles. *Proceedings of the 33rd Annual and 11th International Conference on Deep Foundations.article*. #1603; publication #85.
SPSS Inc. SPSS Statistics for Windows, Version 17.0. 2008; Chicago.

Smart Geotechnics for Smart Societies – Zhussupbekov, Sarsembayeva & Kaliakin (Eds)
© 2023 The Author(s), ISBN 978-1-003-29912-7
Open Access: www.taylorfrancis.com, CC BY-NC-ND 4.0 license

Calculation method for determining the effect of vertical load on the horizontal bearing capacity of a pile

S. Nyamdorj
Institute of Engineering and Technology, Mongolia

R.A. Mangushev
St. Petersburg State University of Architecture and Civil Engineering, Russia

V.V. Znamenskii
Moscow State University of Architecture and Civil Engineering, Russia

A. Batsaikhan
Postgraduate student of Mongolian University of Science and Technology, Mongolia

ABSTRACT: This article discusses some issues on the development of a calculation scheme, a method for calculating a pile in subsiding soil conditions and determining the numerical values of the coefficient of influence of a vertical load on the horizontal bearing capacity of a pile. Developing the methodology for determining the coefficient of influence of the vertical load on the horizontal bearing capacity of the pile, developed by Professor V.V. Znamensky for calculating the cluster pile foundation, a calculation scheme and a calculation method have been proposed for determining the value of the influence coefficient with an increase in the vertical load and wetting of the subsiding soil of a single pile. According to the proposed method of calculation, the numerical values of the coefficients of the influence of vertical loads on the horizontal bearing capacity of bored piles were determined (Table 1). As a result of the latest compared results without taking into account the coefficients, the horizontal bearing capacity is increased at a natural humidity of 181.5. . . . .217 kN and in a water-saturated state of 193.5. . . . .238.5 kN.

1 INTRODUCTION

The basic concept of the operation of a pile in saturated soil under the action of a special combination of loads, including the seismic ones, is that the pile rotates around a certain point 0 located at a depth Z_0 from the ground surface, i.e. a short pile(a length of up to 12.0 m) works according to a rigid scheme. At the same time, an important, somewhat understudied problem arises that the action of a vertical load affects the horizontal bearing capacity of piles. This article discusses some issues on the development of a calculation scheme, a calculation method in accordance with the abovementioned operating conditions of a pile and determining the numerical values of the coefficient of influence of the vertical load on the horizontal bearing capacity of the pile (Mangushev, R.A. et al. 2018; Ishihara, K. 2006; Ilyichev, V.A. et al. 2010; Finn, W.D.L. et al. 2002; Ter-Martirosyan, A.Z. et al. 2020).

2 METHODS AND MATERIALS

Developing the methodology for determining the coefficient (U_{Γ}^{b}) of influence of the vertical load on the horizontal bearing capacity of the pile, developed by professor Znamensky V.V.

DOI: 10.1201/9781003299127-223

(Znamensky, V.V. 2002) for the calculation of a cluster pile foundation, a calculation scheme and a method for calculating the value of the coefficient (U_{Γ}^{b}) with an increase and wetting of the subsiding soil of a single pile have been proposed (Nyamdorj, S. 2023).

For the purpose of a comparative analysis of the patterns of pile operation using the proposed calculation scheme and method, the authors carried out analytical calculations and numerical simulation using the numerical values of the horizontal bearing capacity (150kN) established by the results of field experiments.

3 DESIGN SITUATION

Calculated situation: the territory of the city of Darkhan, soil conditions: subsiding silty sandy loam with preliminary soaking, the calculated indicators of the soil are given in accordance with the natural humidity and water saturation. Piles: single bored reinforced concrete, with the diameter of 0.6 m and the length of 8.0 m, design vertical bearing capacity: 630 kH according to the standard (BNbD 50.01-16), conditional design vertical loads: 300kH, 450kH and 600kH, seismic condition: 7 points (for micro-zoning of the territory the city of Darkhan).

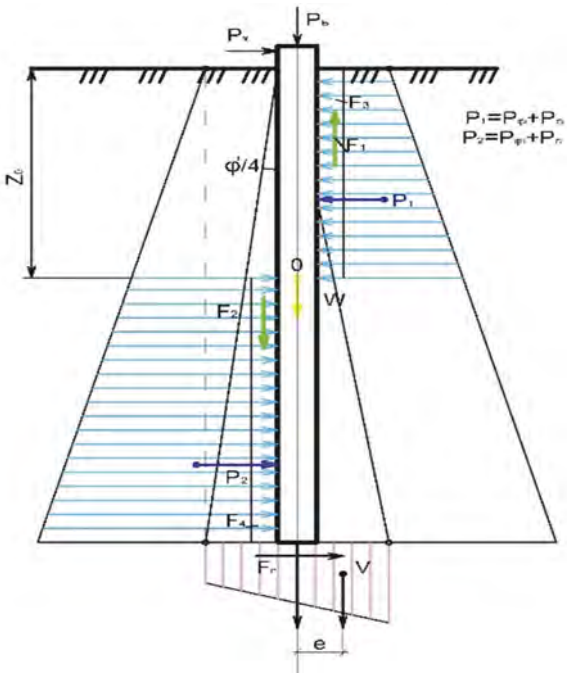

Figure 1. Calculation diagram of a pile to determine the coefficient of influence of the vertical load on the horizontal bearing capacity. Pg-horizontal load; Pv-vertical load; W-weight of the conditional foundation; P1 and P2- soil resistance force on the front and back sides of the pile; F1 and F2 - horizontal force of soil resistance on the front and back sides of the pile; F3 and F4 - resistance force of the lateral surface; Fn - friction force on the plane of the tip of pile; V - total pressure of the tip of pile.

In this calculation scheme it is not possible to fully reflect the mechanisms of various phenomena and processes occurring in the soil near the pile, but it is also possible to reflect the relationship between the main factors influencing the vertical load on the bearing capacity of the pile with a horizontal load, such as a value of the vertical load, which can be determined experimentally, soil conditions of the foundation and the depth of piling.

4 RESULTS OF ANALITICAL CALCULATIONS

The calculation of U_{Γ}^{b} coefficient value for evaluation of influence of the vertical load on the change of the limit horizontal load of the drilled cast-iron pile in the silty sandy loam soil of the given settlement is analytical and numerical in order to evaluate the effect of the vertical load on the value of the limit horizontal load determined by the results tested in the conditions of the silty sandy loam soil of Darkhan city. The tests were carried out under natural and water-saturated wet conditions as well as earthquake intensity of 7 points.

The parameters of the silty sandy loam soil of the test site are taken from Table 3.4 (Nyamdorj, 2023). The purpose of the calculations was to determine the effect of vertical loads Pv = 300kH, 450kH and 600kH on the experimentally determined maximum horizontal load of a single pile and to establish the dependence of the value of a coefficient U_{Γ}^{b} calculated by formula (1) for subsiding clayey sandy soil, taking into account soaking and seismics.

$$U = 1 + \frac{N_1 P_B}{\{n\, D^2[\gamma \cdot n \cdot D(N_3 + N_4)] + C\, N_5\}'} \tag{1}$$

where n = L/D = 8.0/0.6 = 13.338; c - cohesion of the soil, D - diameter of the pile, γ - dead weight of the soil Annex V Table E-1; m' = H/L; n' = L/D; $\alpha = Z_0'/H$, where H, L, D-3 - see the calculation scheme. Z_0' - reduced location depth O of the turning point of the pile, is determined depending on the reduced depth $(\bar{l})$:

$$\bar{l} = \alpha_{\varepsilon}' \cdot \ell; \tag{2}$$

where α_{ε}' – a deformation coefficient, determined by formula (3), l - pile length, m;

$$\alpha_{\varepsilon}' = \sqrt[5]{\frac{K \cdot Bp}{\gamma \cdot EJ}}; \tag{3}$$

where K is a coefficient of the proportional, $\ell_k = 3.5D + 1.5 = 3.5 \cdot 0.6 + 1.5 = 3.6\,m$ within the depth (SP 24.13330.2011. Pile foudndations) is determined according to tables B1, ℓ_k is the depth of the subsiding soil with natural moisture and it is equal to $\ell_k = 0.62$; $\varphi' = 25°$, $c = 10.8$kPa, J_2<0 (solid consistency). K'is determined according to table B1 at J2<0 K'=12000 kN/M4. Bp - a conditional pile width determined according to the following dependence: at D ≥ 0.8 m Bp = (D+1); at D < 0.8m Bp = (1.5D + 0.5);

According to our calculation conditions, D = 0.6 m, therefore, Vr = (1.5 · 0.6 + 0.5) = 1.4 m; γ- γ = 3.0 per 1 pile, EJ- stiffness of pile, concrete B15, E=24·106 kN/m2; J is the moment of inertia of the cross section. $J = \pi r^4/4 = 0.003066$ м^4; EJ=2410^{6}0.003066=73584kH.m^2; $\alpha_{\epsilon}' = \sqrt[5]{\frac{12000 \cdot 1.4}{3.73584}} = 0.612\text{м}^{-1}$, n = 0.8/0.6 = 13.33, m= 7.7/8.0 = 0.963

where $\bar{l}$ = 0.583 ·8.0=4.664, Z-value at $\bar{l} \le 2.5$ $Z_0 = \bar{l}/3$ and $Z_0 = \bar{l}$ along these deep 2 sections, at $\bar{l} > 2.5$ $Z_0 = 0.85/\alpha_{\epsilon}$ are calculated according to the depth section. For our condition z'=0.85/0.583=1.46.

A. The value of the angle of internal friction of soil with natural moisture (W) is assumed to be φ=23°- 2°=21° due to a 7-point earthquake in Darkhan under the condition φ = 25°, V = 0.25; α=0.612. At m=0.963 it is determined according to Table. 5 and provided that α=0.612, m=0.963, according to Table 7, the values of coefficients N_1', N_2', N_3', N_5'.

   a) α=0,6; m=0.5=> 20°=0,347; 25°=0,360; according to φ =21°

$$N_1^{0.5} = \frac{0.360 - 0.347}{5} 1 + 0.347 = 0.350$$

α=0.6; m=1.0=> 20°=0.395; 25°=0.419, according to φ =21°

$$N_1^{1.0} = \frac{(0.419 - 0.395)}{5} 1 + 0.395 = 0.400$$

m=0.963; φ =21˚ value $N_1^{'}$ of silty sandy loamy soil with natural humidity:

$$N_1^{'} = \frac{0.400 - 0.350}{0,5} 0.463 + 0.350 = 0,426$$

b) α=0,6; m=0.5=> 20˚=0,065; 25˚=0,093 according to φ =21˚

$$N_2^{0.5} = \frac{0.093 - 0.065}{5} 1 + 0.065 = 0.071$$

α=0.6; m=1.0=> 20˚=0.353; 25˚=0.494 according to φ =21˚

$$N_2^{1.0} = \frac{(0.494 - 0.353)}{5} 1 + 0.353 = 0.381$$

m=0.963; φ =21˚ value $N_2^{'}$ of silty sandy loamy soil with natural humidity:

$$N_2^{'} = \frac{0.381 - 0.071}{0,5} 0.463 + 0.071 = 0,358$$

c) α=0,6; m=0.5=> 20˚=0,068; 25˚=0,095 according to φ =21˚

$$N_3^{0.5} = \frac{0.095 - 0.068}{5} 1 + 0.068 = 0.073$$

α=0.6; m=1.0=> 20˚=0.392; 25˚=0.529 according to φ =21˚

$$N_3^{1.0} = \frac{(0.529 - 0.392)}{5} 1 + 0.392 = 0.419$$

m=0.963 φ =21˚ value $N_3^{'}$ of silty sandy loamy soil with natural humidity:

$$N_3^{'} = \frac{0.419 - 0.073}{0,5} * 0.463 + 0.073 = 0,393$$

d) α=0,6; m=0.5=> 20˚=0,298; 25˚=0,306 according to φ =21˚

$$N_4^{0.5} = \frac{0.306 - 0.298}{5} * 1 + 0.298 = 0.300$$

α=0.6; m=1.0=> 20˚=0.653; 25˚=0.683 according to φ =21˚

$$N_4^{1.0} = \frac{(0.683 - 0.653)}{5} * 1 + 0.653 = 0.659$$

m=0.963 φ =21˚ value $N_4^{'}$ of silty sandy loamy soil with natural humidity:

$$N_4^{'} = \frac{0.659 - 0.300}{0,5} * 0.463 + 0.300 = 0,63$$

e) α=0,6; m=0.5=> 20˚=0,317; 25˚=0,385 according to φ =21˚

$$N_5^{0.5} = \frac{0.385 - 0.317}{5} * 1 + 0.317 = 0331$$

α=0.6; m=1.0=> 20˚=0.994; 25˚=1.156 according to φ =21˚

$$N_5^{1.0} = \frac{(1.156 - 0.994)}{5} * 1 + 0.994 = 1.026$$

m=0.963 φ =21˚ value $N_5^{'}$ of silty sandy loamy soil with natural humidity:

$$N_5^{'} = \frac{1.026 - 0.331}{0,5} * 0.463 + 0.331 = 0,794$$

There have been defined coefficients $U_{300}^{'}$, $U_{450}^{'}$ and $U_{600}^{'}$ of influence of the vertical load of 300kH, 450 kH and 600 kH on the bearing capacity of the pile with the maximum horizontal load of 150kH at natural (W) humidity in silty sandy loamy soil and the dynamics of the effect is analyzed (Nyamdorj, S. 2023):

1. At the ultimate horizontal load Q=150 kH and vertical load P^b=300 kH, then the value of $U_{300}^{'}$:

$$U'_{300} = 1 + N'_1 P_B / \{n.B^2[\gamma \cdot n\, D(N'_3 + N'_4)] + c\, N'_5 = 1 + 0.426 \cdot 300\kappa H / \{13.33 \cdot 0.6^2[15.5 \cdot 13.33 \cdot 0.6(0.393 + 0.632)] + 10.8 \cdot 0,794\} = 1 + 0,355 * \frac{300}{618,51} = 1.21 \quad (4)$$

2. At the ultimate horizontal load Q=15.0 tons and vertical load P^b=450kH the value of $U_{450}^{'}$:

$$U_{450}^{'} = 1 + 0,426 * \frac{450}{618,51} = 1.31$$

3. At the ultimate horizontal load Q=15.0 tons and vertical load P^b=600kH the value of $U_{600}^{'}$:

$$U_{600}^{'} = 1 + 0,462 * \frac{600}{618,51} = 1.45$$

B. The value of the coefficient U of influence of the vertical load on the horizontal bearing capacity of a pile operating in silty-sandy soil with water-saturated moisture (Wsat) is determined by formula (1). The calculated values of $N_1^{"}$, $N_2^{"}$, $N_3^{"}$, $N_4^{"}$, $N_5^{"}$ are determined by the same method as for soil with moisture content W with parameters φ"=17° and C"=0.68 kPa corresponding to humidity W_{sat}. The earthquake of the region is 7 points, then φ "=17 ° - 2°=15° is taken into account.

a) α=0.6, m=0.5 => at $\varphi^{"}$=15° then $N_1^{0.5} = 0.335$
α=0.6, m=1.0 => at $\varphi^{"}$=15° then $N_1^{1.0} = 0.370$
m=0.963; $\varphi^{"}$=15° => with soil humidity W_{sat} from the value of N_1^{II}:
$N_1^{''} = \frac{0.370-0.335}{0,5} \cdot 0.463 + 0.335 = 0.367$

b) α=0.6, m=0.5 => at $\varphi^{"}$=15° then $N_2^{0.5} = 0.044$
α=0.6, m=1.0 => at $\varphi^{"}$=15° then $N_2^{1.0} = 0.244$
m=0.963; $\varphi^{"}$=15° => with soil humidity W_{sat} from the value of N_2^{II}:
$N^{"}{}_2 = \frac{0.241-0.044}{5}$ 0.463+0.44 = 0.469

c) α=0.6, m=0.5 => at $\varphi^{"}$=15° then $N_3^{0.5} = 0.048$
α=0.6, m=1.0 => at $\varphi^{"}$=15° то $N_3^{1.0} = 0.290$
m=0.963; $\varphi^{"}$=15° => with soil humidity W_{sat} from the value of N_3^{II}:
$N_3^{"} = \frac{0.290-0.048}{0,5}$ 0.463+0.048=0.272

d) α=0.6, m=0.5 => at then $N_4^{0.5} = 0.291$
α=0.6, m=1.0 => at $\varphi^{"}$=15° then $N_4^{1.0} = 0.624$
m=0.963; $\varphi^{"}$=15° => with soil humidity W_{sat} from the value of N_4^{II}:
$N_4^{"} = \frac{0.624-0.291}{0,5}$ 0.463+0.291=0.356

e) α=0.6, m=0.5 => at $\varphi^{"}$=15° then $N_5^{0.5} = 0.259$
α=0.6, m=1.0 => at $\varphi^{"}$=15° then $N_5^{1.0} = 0.821$

m=0.963; $\varphi^{"}$=15° => with soil humidity W_{sat} from the value of N_5^{II}:
$N_5^{"} = \frac{0.821-0.259}{0,5}$ 0463 + 0.259 = 0.779

When determining the value of the coefficient $U^{"}_{300}$; $U^{"}_{450}$; $U^{"}_{600}$ according to formula of (Znamensky, V.V. 2002) for piles embedded in saturated (W_{sat}) silty sandy loamy soil with the same design parameters as in part A, the adhesion force of saturated subsiding soil $C^{"}$ = 0.68 kPa is very small, i.e. it can be considered as non-cohesive soil, therefore, the results of a comparative assessment of the coefficients of influence of the vertical load according to formula (5) for non-cohesive soil and according to formula (6) for cohesive soil show the following:

I. According to formula (5) for non-cohesive soils: the value of $U^{"}_{300}$ at the maximum horizontal load on the pile determined by full-scale tests Q=150 kN and the vertical load P_B = 300 kN:

$$U''_{300} = 1 + N''_1 P^B/\gamma \cdot n^2 \cdot D^3(N''_2 + N''_4) = 1 + 0.338 \cdot \frac{300}{15.5} \cdot 13.33^2 \cdot 0.6^3(0.062 + 0.033) = \\ = 1.57. \quad (5)$$

II. According to formula (6) for cohesive clay soil: $U^{"}_{300}$ value at horizontal load Q=150 kN and vertical load P_B = 300 kN:

$$U''_{300} = 1 + N''_1 P^{30}_B/\left\{n.D^2\left[\gamma \cdot n\left(N''_3 + N''_4\right)\right] + c\,N''_5\right\} = 1 + 0.367 \cdot 300/\{13.33 \cdot \\ 0.6^2[15.5 \cdot 13.33 \cdot 0.6(0.272 + 0.356)] + 0.68 \cdot 0.794\} = 1 + 110,1/376,24 = 1.39 \quad (6)$$

6 DISCUSSION OF THE RESULTS

According to the calculations, the values of the coefficient $U^{"}_{300}$ of the water-saturated silty sandy loamy soil (W_{sat}) calculated by the formula (4) and the values of $U^{"}_{300}$ = 1.57 and by the formula (5) the value of $U^{"}_{300}$ = 1.39, the compatibility of the values of these coefficients is 91%. As a result of the latter, we can conclude that these formulas work with high accuracy and show a high degree of reliability of analytical calculations and field experiments. For further calculation, formula (5) has been chosen for saturated silty sand ($C^{"}$=0.68 kPa).

The value of $U^{"}_{450}$ with horizontal ultimate load Q=150 kN and vertical load P^b = 450 kN:

$$U''_{450} = 1 + 0.367 \cdot 450/376,24 = 1,43$$

The value of $U^{"}_{600}$ with horizontal ultimate load Q = 150 kN and vertical load P^b = 600 kN:

$$U''_{600} = 1 + 0.367 \cdot 600/376,24 = 1.59$$

The pattern of increasing the limit value of the horizontal load on the pile, depending on the effect of the vertical load, is calculated using formula (7) and given in Table 1.

$$P^B_h = U \cdot P_h \quad (7)$$

where U is a coefficient of influence, P_h is the ultimate horizontal load, kN

The growth pattern of the influence coefficient and horizontal bearing capacity is shown in the diagram.

Graphs of the dependence of the coefficient of influence of the vertical load on the horizontal bearing capacity of piles immersed in subsiding soils of the city of Darkhan with natural and water-saturated humidity $U^I = f(P^\sigma)$; $U^{II} = f(P^\sigma)$; $P^I_n = f(U^I)$; $P^{II}_n = f(U^{II})$; $U^I = f(Q/Q^I_n)$; $U^{II} = f(Q/Q^{II}_n)$ are shown in the following figures.

Table 1. The coefficient of influence of the vertical load on the horizontal bearing capacity of piles and its increase.

Ultimat load P_h, kN	Vertic. load, P_v, kN	At natural humidity (W)		At water saturation,(W_{sat})			
		Coeff. influence U^I	P_h^{vI}, кН	Coeff. Influence U^{II}	P_h^{vII} кН	Provided W, P_h/P_h^{vI}	xProvided W_{sat}, P_h/P_h^{vII}
150	300	U^I_{300} =1.21	P^I_{300}=181	U^{II}_{30} =1.29	P^{II}_{300} =193	0.83	0.76
150	450	U^I_{450} =1.31	P^I_{450} =196	U^{II}_{45}= 1,43	P^{II}_{450}=214.5	0,76	0.70
150	600	U^I_{600} =1.45	P^I_{600} =217	U^{II}_{60}= 1,59	P^{II}_{600} =238	0.69	0.63

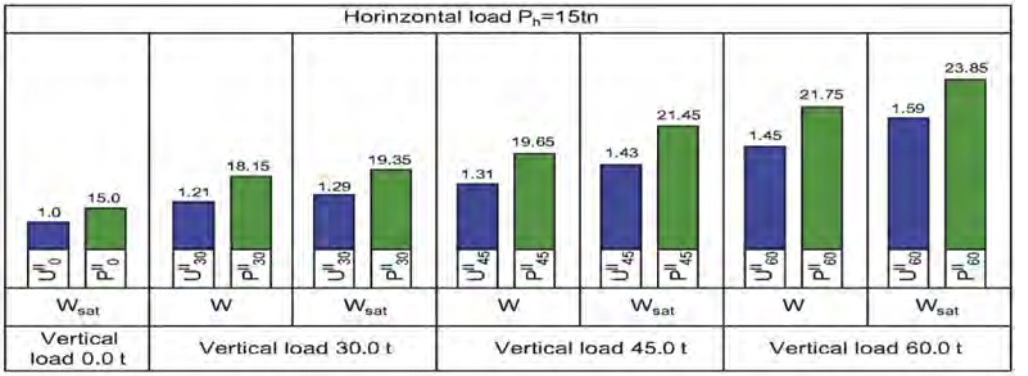

Figure 2. Diagram of the pattern of increasing the horizontal bearing capacity of piles depending on the magnitude of the vertical load.

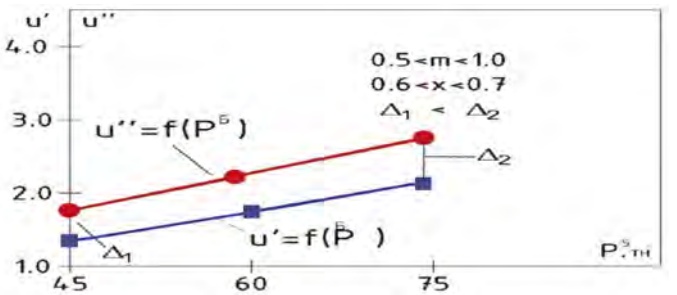

Figure 3. Graph of influence of the vertical load on the horizontal bearing capacity of the pile $U^I f = (P^\sigma)$ and $U^{II} = f\ (P^\sigma)$.

7 CONCLUSIONS

Based on the analysis of the results of calculations to determine the values of the coefficients of influence, the following regularities have been established:

- depending on a moisture content of the subsiding soil and the values of the vertical load, the horizontal bearing capacity of the pile increases;
- compared with the result without taking into account the coefficients of 150.0 kN, the horizontal bearing capacity is increased depending on the intensity of the vertical load at natural humidity 181.5. . .217 kN, and in the water-saturated state 193.5. . .238.5 kN.
- indicators of inequality $\Delta_1 < \Delta_2$ grow with increasing value of the vertical load, and the effect of vertical load decreases with increasing pile length or driving depth. In this case,

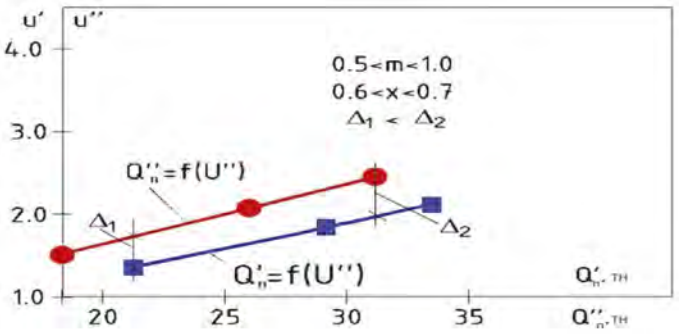

Figure 4. Graph of influence of the vertical load on the horizontal bearing capacity of the pile. $Q_n^I = f(U^I)$ and $Q_n^I = f(U^{II})$.

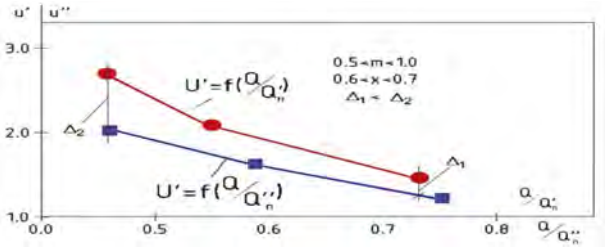

Figure 5. Graph of the influence of the vertical load on the horizontal bearing capacity of the pile $Q^I = f(Q/Q_n^I)$ and $Q^{II} = f(Q/Q_n^{II})$.

a length of pile or a depth of immersion is the main factor of influence, and it can be adjusted by increasing a diameter of pile and an immersion depth;

- with an increase in the intensity of earthquakes, the angle of internal friction decreases (by 2 . . . 7°);
- for subsiding soil with natural and water-saturated moisture, the area of subsoil of the conditional pile foundation decreases inversely and the value of the coefficients U' and U'' increases;
- these processes of increase and decrease are linearly proprotional and their intensity depends on the depth of pile, the coefficients n and m, the angle of internal friction φ and the cohesive force C of soil, the nature of change in physical and mechanical properties of the subsiding soil of pile subsoil when moistened, as well as the I and II type of soil conditions as per subsidence.

REFERENCES

Finn, W.D. L., Fujita, N. 2002. Piles in liquefiable soils: seismic analysis and design issues. *Soil Dinamics and Earthquake Engineering*. Vol.22, 9–12. Oct-Dec.2002.

Ilyichev, V.A., Mongolov, Yu.V., Shaevich, V.M. 2010. *Pile foundations in seismic regions*. Moscow.

Ishihara, K. 2006. *Behavior of soils during earthquakes. Achievements of modern geotechnics*. Translated from English by V.M. Ulitsky, A.G. Shashkin, M.B. Lisyuk. St. Petersburg.

Mangushev, R.A. 2018. Piles and pile foundations. Design, design and technology. R.A.Mangushev, V. V.Znamensky, A.L.Gotman, A.B.Ponomarev. Moscow: DIA publishing house.

Nyamdorj, S. 2023. *Scientific substantiation of the development of rational solutions for buildings and structures foundations built on subsidence soils of Mongolia*. Abstract of the diss. . ..dokt. tenkh. Sciences (Sc. D). Ulaanbaatar.

Ter-Martirosyan, A.Z., Le Duc Anh, Manukyan, A.V. 2020. Influence of soil liquefaction on the design bearing capacity of a single pile. *Vestnik MGSU [Monthly Journal on Construction and Architecture]*. 15 (5) DOI: 10.22227/1997-0935.2020.5. (rus.).

Znamensky, V.V. 2002. *Experimental study of work and engineering methods for calculating pile groups of driven piles*. Abstract of the diss. . ..dokt. tenkh. Sciences (Sc.D). Moscow.

Smart Geotechnics for Smart Societies – Zhussupbekov, Sarsembayeva & Kaliakin (Eds)
© 2023 The Author(s), ISBN 978-1-003-29912-7
Open Access: www.taylorfrancis.com, CC BY-NC-ND 4.0 license

Smart cell: Tip postgrouting and premobilization of resistance of drilled shafts

M.A. Terceros & M. Terceros
Incotec S.A., Santacruz, Bolivia

A. Marinucci
V2C Strategists LLC, New York, USA

ABSTRACT: A Smart Cell is a closed-type grout distribution system that is attached to the bottom of a reinforcement cage for drilled shaft foundations and acts in a similar manner to a hydraulic jack in bi-directional static load testing. Control of the grout is maintained within the device during grouting and a uniform stress is imparted across entire base area simultaneously. The goals of tip post-grouting are to improve the stiffness of the in-situ soil, improve the shaft's nominal axial resistance, and better align the load transfer curves to the project requirements. This paper will present an overview, basic principles, and the design methodology of tip post-grouting using this technique. The construction, tip post-grouting, select results, and general observations from the grouting performed on more than 40 total drilled shafts for the Urubó vehicular bridge structure crossing the Piraí River in Bolivia will also be presented and discussed below. The general subsurface conditions for the sedimentary deposits at the two bridge sites consist of highly variable soil deposits, bedding, composition, and engineering characteristics. The diameter of the temporarily cased drilled shafts was either 1200 mm and the length ranged from nearly 22 m to nearly 28 m Most of the drilled shaft foundations for these bridge structures were installed with a Smart Cell at the bottom of its reinforcement cage to enhance performance and to reduce uncertainty. Using the measurements of the grouting operation, the premobilization of axial resistance and induced load imparted into the drilled shaft and to the soil beneath the base will be discussed.

1 INTRODUCTION

The generalized load transfer behaviors of a conventional (i.e., ungrouted) drilled shaft in cohesionless and cohesive soils loaded in axial compression are presented in Figure 1. The side resistance of a drilled shaft will mobilize its peak strength after a normalized vertical displacement, ΔD_{vn}, (i.e., vertical displacement, δ_v, divided by the diameter of the drilled shaft, D_p) of about 0.2% to 0.4%, regardless of soil type. Chen and Kulhawy (2002) presented that, at a normalized displacement of about 0.4%, approximately 50% of the failure threshold axial resistance is mobilized, about 90% of which is from side resistance and 10% is from end resistance.

The end or tip resistance does not fully mobilize until much larger normalized displacements have been realized: about 4% to 5% in cohesive soils and about 10% (practical limit) in cohesionless soils. At a normalized displacement of about 4%, Chen and Kulhawy (2002) reported that 100% of the failure threshold axial resistance is mobilized (i.e., ultimate state for cohesive soils and serviceability state for cohesionless soils), where about 76% of which is from side resistance and 24% is from end resistance. For cohesive soils, this is the maximum axial resistance that can be achieved. For cohesionless soils, however, the maximum axial resistance is achieved at much larger normalized displacements (governed by bearing capacity), thereby mobilizing 159% of the failure threshold axial resistance, where 76% of the axial resistance is from side resistance and 83% is from end resistance. For practical design purposes, however, the end resistance is typically capped at a normalized displacement of about 10%. Due to this strain incompatibility in

DOI: 10.1201/9781003299127-224

achieving the peak strength, utilizing the full side and end resistance in design is not realistic and designers have typically neglected one component or reduced the relative contributions of side and/or end resistance. Design is clearly and fundamentally essential; however, long-term performance of a drilled shaft is mainly governed by the construction technique(s) utilized and the quality of the craftsmanship applied to install the foundation element.

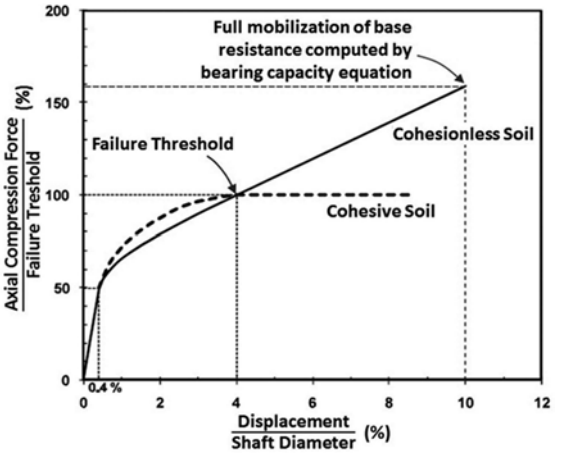

Figure 1. Normalized load-displacement curves of drilled shafts in axial compression in cohesive and cohesionless soils (mod. after Brown et al., 2018).

Holding the concerns of strain incompatibility aside, other issues may manifest as a result of the construction process, even with high quality craftsmanship, which include the accumulation of sediment (i.e., soft bottom condition) and the change in the state of stress (i.e., stress relief) at the bottom of the shaft. As described above, vertical settlement of the shaft is required to mobilize resistance; with an excess of accumulation of sediment and/or stress relief of the in-situ conditions, a greater amount of vertical settlement would be required to mobilize the axial resistance required for the design and proper long-term performance of the constructed shaft.

Tip post-grouting is a technique used to pre-mobilize the axial end resistance of the shaft as well as to mitigate against a soft bottom condition and stress relief due to installation. This technique is used to inject a neat cement grout, under pressure, beneath the base of a drilled shaft to improve its performance when subjected to compressive axial loads. (Note: tip post-grouting should not be used in lieu of proper execution and good quality workmanship in the construction of a drilled shaft.) It is accomplished using an open- or closed-type grout distribution device that is incorporated into the bottom of the steel reinforcement cage. For open-type systems (i.e., sleeve-port or tube-á-manchette systems), the grout is injected out of the supply tubes and into the surrounding ground around the tip of the shaft; conversely, for closed-type systems (e.g., Smart-Cells), the grout is contained within the expanding device and does not contact the ground directly. The key objectives of this technique are to improve the stiffness of the soil, improve the nominal resistance (i.e., load-displacement performance) of the shaft to axial compressive loading, and better align the load transfer curves via mobilization (preloading) of end resistance (Figure 2).

2 OVERVIEW AND BASIC PRINCIPLES

A Smart Cell (SC) is a closed-type tip post-grouting device that is attached to the bottom of the steel reinforcement cage of drilled shafts (Figure 3a) and acts as a hydraulic jack to mobilize the end resistance of the drilled shaft irrespective of the type of ground condition. The device itself comprises top and bottom steel plates, cell walls, and internal connections and appurtenances. As grout is injected under pressure into the device, the cell expands thereby pushing upward against the drilled shaft and downward against the in-situ soil below the base of the shaft and device.

During this process, a bi-directional force is induced into the drilled shaft above and to the soil below, resulting in a pre-mobilization (i.e., preloading) of the side and end resistances. The injection pressure is typically measured at the grout pump as it is being pumped and at a short distance above the top of the drilled shaft. Vertical movements of the top and bottom steel plate during the grouting operation are typically measured using tell tales, and the uplift displacements at the top of the shaft are typically measured using optical survey methods and using displacement transducers.

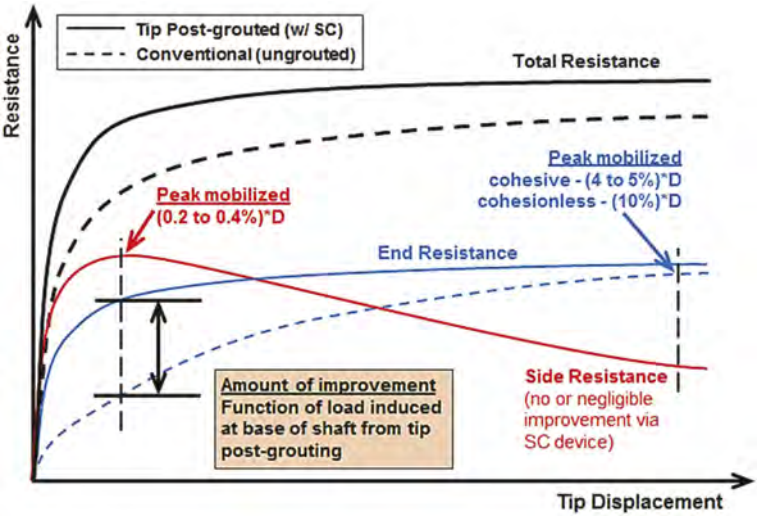

Figure 2. Generalized load transfer behavior of conventional (ungrouted) and tip post-grouted drilled shafts (mod. after Brown et al., 2010).

Since the grout is contained (Figure 3b), the bi-directional load that is induced (P_{SC}) during the grouting process can be computed by multiplying the injection pressure (p) by the cross-sectional area of the device (A_{SC}). The induced load is a function of the in-situ stress state of the soil, self-weight of shaft, and available side resistance between the shaft and the surrounding soil. With this technique, the pressure acts across the entire base of the device simultaneously. In general, the greater amount of load that can be induced from the grout injection process, the greater the pre-mobilization (pre-loading), the greater the increase in soil stiffness, and the greater the improvement in performance that can be achieved (Loehr et al, 2017). Successful and reliable implementation of tip post-grouting will allow designers to optimize the design of a tip post-grouted pile by stiffening its end-bearing response and by allowing the maximum tip resistance at a downward displacement that is consistent with the maximum side resistance (i.e., optimizing of load transfer curves). Other benefits of tip post-grouting with a Smart Cell include stiffening the load-deformation response under working loads, reducing settlement of the pile under applied loading, shortened constructed length of the shaft, ability to be performed in a range of ground conditions, utilizing usable tip resistance in design computations, verifying a lower bound of axial resistance, and improving the ground beneath the base of the shaft.

3 TIP POST-GROUTING – IMPLEMENTATION AND RESPONSE

The general sequence of operations when tip post-grouting is performed along with the ensuing response is described hereinafter. After the borehole is drilled (i.e., dry method, wet method, and/or casing method), the steel reinforcement cage along with the required embedded appurtenances (e.g., NDT access tubes, instrumentation, SC device, and components) is installed in the borehole, which is then filled with concrete and allowed to cure (Figure 4a). A neat cement grout with a water-to-cement ratio (w/c) between 0.45 and 0.55 is typically used with this tip post-grouting technique. The injection of pressurized grout induces a bi-directional load (P_{SC})

Figure 3a. Photograph of a smart cell attached to the bottom of a steel reinforcement cage.

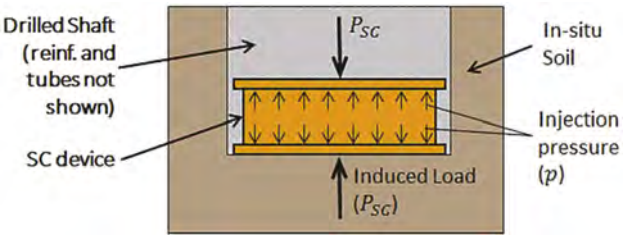

Figure 3b. Graphical depiction of grouting and induced loading.

within the device, which simultaneously mobilizes negative side resistance to resist the upward loading and positive tip resistance to resist the downward loading (Figure 4b–4d). During the grouting process, the side resistance is mobilized first, which along with the self-weight of the shaft, reacts against the upward force and facilitates the pre-mobilization or pre-loading of the in-situ soil below the device. Pre-mobilization or pre-loading of the in-situ soil does not result in an increase in the ultimate axial resistance of the shaft but should reduce the magnitude of displacement that will occur up to the induced load (P_{SC}).

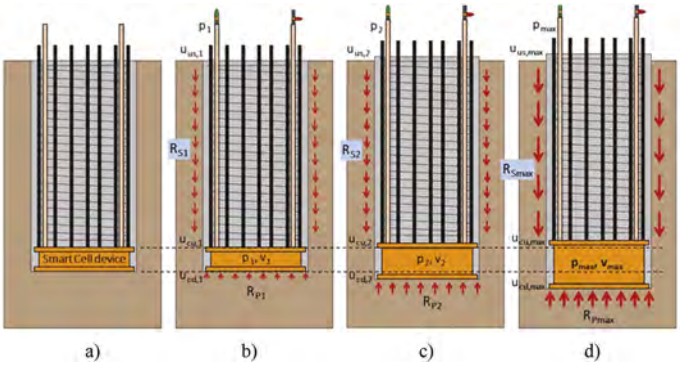

Figure 4. Generalized sequence: (a) installation into borehole and concrete placement, (b) early during grouting process, (c) intermediate grouting stages, and (d) grouting completed.

Since the elastic axial behavior of the drilled shaft is dissimilar to that of the in-situ soil surrounding the shaft, the resulting differential strains induced during tip post-grouting and then later during axial top-down loading cause debonding at the weakest interface, which tends to be along the soil-shaft interface. As a unit length of the shaft (within soil layer i) approaches the geotechnical strength limit state (i.e., ultimate soil- shaft resistance), a highly non-linear profile of bond stress results, whereby this progressive debonding generally results in an inefficient use of the in-situ soil-shaft bond strength. As the shaft is displaced during grouting or axial loading, the available side resistance increases to a peak state; however, once the peak soil-shaft bond strength has been exceeded, the available resistance reduces to a softened strength state and then to a residual strength state with continued deformation. For this reason, quality control measures are employed to mitigate against the negative effects to and reduction in side resistance. Hence, uplift displacement measured at the top of the drilled shaft is typically limited to less than about 0.013 m. Ideally, at the completion of grouting, the end resistance will have been fully mobilized while the side resistance would not have been degraded to a strain-softened state.

The grouting is performed using a controlled process to ensure proper performance of the system as well as to ensure minimal-to-no excess pore water pressures are generated. To ensure control of the grout and its effect on the load response behavior of the drilled shaft, multiple parameters are measured as a function of time, recorded, and analyzed throughout the grouting

operation as part of termination criteria and the overall QA program. The injection pressure, volume and flow of grout, and movements at the top of the shaft and at the SC device are measured and recorded throughout the grouting operation. The grouting operation is continued until the prescribed grouting termination criteria is achieved. The termination criteria for tip post-grouting includes target grout pressure, net grout volume in excess of the amount to fill the delivery system and supply tubes, and maximum uplift displacement of the pile during grouting, and expansion limit of the SC device. During grouting, real-time or near real-time plots of grout pressure vs. injected volume, grout pressure vs. shaft uplift, grout volume vs. expansion of the SC, and grout volume vs. shaft uplift are monitored for conformance with the termination criteria.

The relationship between the induced load (P_{SC}) and the measured vertical displacement provides valuable insight into the behavior during grouting and for estimating the stiffness (or modulus) and unit end resistance of the soil at the completion of grouting. After the net volume has been injected, the injection pressure (or induced load) required to initiate the expansion of the cell is equal to the lesser of the reaction from the self-weight of the shaft along with the side resistance above the cell or the bearing end resistance below the cell. Measurements of vertical displacement and computed induced load from a completed project (Figure 5) will be used to highlight the behaviors and characteristics observed during the grouting operation:

- At about 45 tons of induced load – the load required to initiate the expansion of the cell (downward into the soil below the device) was reached.
- From about 45 to 65 tons of induced load - the disturbed or loose soil was recompressed about 0.018 m, resulting in an average stiffness (k_1) of about 1.1 tons/mm.
- From 65 to 170 tons of induced load - as additional grout was injected, the device continued to expand and compressed the in-situ soil, which resulted in an additional 0.022 m of vertical displacement along with a corresponding increase in the average stiffness ($k_2 \approx 4\ k_1$) from about 1.1 to 4.4 tons/mm.
- Uplift movement of the shaft was first noticed at induced load of about 150 tons, which was close to the second inflection point of the induced load-displacement response. That is, no uplift movement was realized until after the soft bottom was fully restored and the soil compressed. It is fair to say that the induced loads corresponding to the initiation of uplift movement and to the second inflection point would have been in closer agreement had displacement transducers been used to continuously measure/record the displacements instead of discrete optical survey methods.
- From 170 to 380 tons of induced load - higher levels of injection pressure were required to inject the grout, whereby only an additional 0.009 m of vertical displacement occurred resulting in a considerable increase in the average stiffness ($k_3 \approx 7.9\ k_2 \approx 31.8\ k_1$) from about 4.4 to 35.0 tons/mm and a corresponding premobilization of the load into the soil and shaft. For this project, the unfactored design load for each drilled shaft was about 540 tons. The resulting induced load of about 380 tons was about 70% of the design axial load.

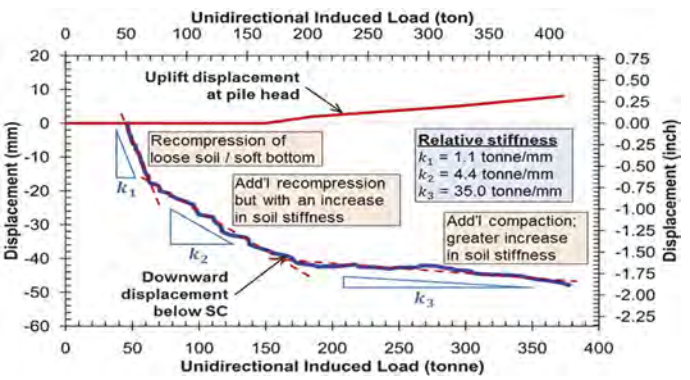

Figure 5. Representative example of induced load vs. vertical displacement during grouting.

4 TIP POST-GROUTING DESIGN – TARGET PRESSURE

An engineer designs a drilled shaft (i.e., diameter, depth, and reinforcement) to resist the anticipated imposed loading while satisfying the applicable limit state conditions. Once the diameter and depth of the drilled shaft have been established using the appropriate axial end and side resistances afforded by the in-situ ground conditions (for strength limit state conditions), the target injection pressure (p_t) can be estimated (for service limit state conditions). Even with the best modeling and the highest quality of construction utilized, the estimated value of p_t is not guaranteed. p_t is dependent upon various factors, including soil type, in-situ stress state, shear strength of the soils, and available reaction force (i.e., self-weight of the drilled shaft plus side resistance).

As discussed by Loehr et al (2017), for tip post-grouting applications, contractors and service firms have reported maximum achieved p_t as high as about 15 MPa in sands and about 8 MPa in clays/silts. Based on experience, the general trend of an injection pressure-vs.-grout volume curve resembles in nature one of the normalized load-displacement curves shown in Figure 1 (Marinucci et al, 2020). That is, if the trend indicated a relatively low maximum grouting pressure that had flattened, this would be indicative of tip post-grouting in cohesive soils, whereby the end resistance fully mobilized. Conversely, if the trend indicated a continued increase in injection pressure with continued grouting, this would be indicative of tip post-grouting in cohesionless soils, whereby the end resistance may not have fully mobilized.

For tip post-grouting with a SC device in Bolivia, the load-displacement curves presented by Chen and Kulhawy (2002) and described by Brown et al (2018) are used to compute the target injection pressure based on the prescribed tolerable displacement of the drilled shaft. The target volume of grout to be injected is dependent upon the dimensions of the drilled shaft and the expanded limits of the SC. The induced load (P_{SC}) is computed by multiplying the measured injection pressure (field) by the internal bearing area of the cell (A_{SC}). As defined in AASHTO §10.8.3.5 (2012), the nominal axial compression resistance of a single drilled shaft (R_n) is computed using Equation (1). The amount of allowable vertical displacement due to axial compression loading indirectly establishes the amount of axial resistance that can be mobilized for that given displacement (i.e., service conditions). If the allowable displacement is less than that required to fully mobilize the axial resistance, tip post-grouting can be used to achieve and induce a bi-directional force to pre-mobilize the required axial resistance.

$$R_n = R_S + R_p = \sum_{i=1}^{n} (q_{si} A_{si}) + q_p A_p \quad (1)$$

where: R_n = nominal axial compression resistance of a single drilled shaft; R_S = nominal side resistance of a single drilled shaft; R_P = nominal end resistance of a single drilled shaft; q_{si} = nominal unit side resistance for soil layer i; A_{si} = nominal surface area of the soil-shaft interface for soil layer i; n = number of soil layer; q_p = nominal unit end resistance; A_p = nominal cross-sectional area of the tip of the drilled shaft.

Recalling, the side resistance is fully mobilized at a normalized displacement (ΔD_{vn}) of about 0.2% to 0.4%, whereas the end resistance is mobilized at ΔD_{vn} of about 4% to 5% for cohesive soils and about 10% for cohesionless soils (Figure 1). The vertical axis on the figure represents the ratio of the axial compression load to the failure threshold (i.e., nominal axial compression resistance, R_n). As shown on Figure 1, 100% of the failure threshold typically occurs at ΔD_{vn} of about 4% for both cohesionless and cohesive soils.

5 CASE HISTORY -URUBÓ BRIDGE PROJECT

The new Urubó Bridge is being constructed adjacent to the existing bridge, which connects the municipalities of Porongo (west) and Santa Cruz de la Sierra (east) in Bolivia. The new bridge will be about 12 m wide and about 420 m in length. The 5-span bridge (Figure 6) will be supported by four pier structures, located about 100 m apart and each with seven drilled shafts (arranged in two rows), located in the Piraí River and two abutments supported by 3 drilled shafts each (arranged in one row), which are located beyond the extents of the river's

edges. Based on the project drawings, each of the bored piles is 1.2 m in diameter with an embedment depth of about 25 m at the abutments and about 30 m for each of the piers.

5.1 *Subsurface conditions*

As shown in Figure 6, one soil boring was performed at each of the four pier locations to a depth of about 40 m along with Standard Penetration Testing (SPT). At the time the soil borings were performed, the elevation of the ground surface at the borings was approximately El. +399.4 m, and the ground water was located just below the ground surface. The soil deposit is classified as quaternary sedimentary silty-clayey sands of alluvial and flood plain origin. In general, the subsurface consists of highly variable soil deposits, bedding, composition, and characteristics, which are the results of a dynamic river environment. The general subsurface profile (Figure 7) contains an upper layer of granular fill underlain by highly heterogeneous and interbedded layers consisting of clay, silt, and sand. For the west and east abutments, the bored piles were tipped into silty sands and lean clay with silt, respectively. The bored piles for the piers were tipped into lean clay soils: lean clay with sand for piers 1 and 2 and lean clay with silt for piers 3 and 4.

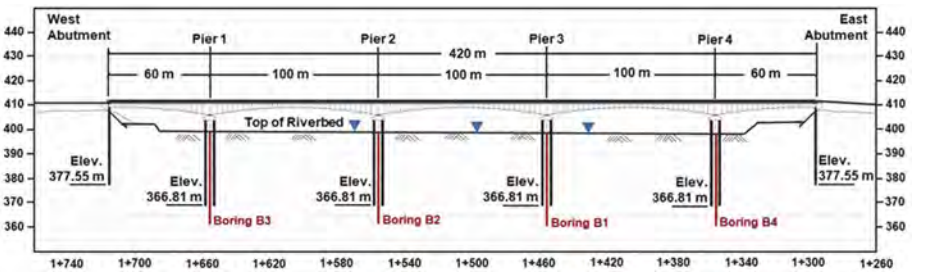

Figure 6. Elevation profile of the bridge super- and substructure and approximate boring locations.

5.2 *Pile installation and Tip Post-grouting*

The bored piles were constructed using temporary segmental casing with the use of a drilling support fluid (water) to prevent instability at the bottom of the borehole. A SC device and attachments were incorporated into the bottom of the steel reinforcement cages and lowered into the borehole, after which the concrete was placed the using tremie method. After the concrete achieved the required minimum unconfined compressive strength and when the water level within the river permitted work to proceed, the tip post-grouting was performed individually for each bored pile.

The target pressure for the tip post-grouting was computed for its worst-case condition. The upper 1.5 m of side resistance was neglected for the computations. For the pier structures, the unfactored axial compression design load per pile ($P_{d,serv}$) was 400 tons with a maximum allowable post-construction vertical settlement ($\delta_{v,allow}$) of 30 mm, resulting in a normalized post-construction displacement (ΔD_{vn}) of 2.5. For the worst-case scenario, the minimum required target pressure was estimated to be about 1025 kPa. Monitoring and recording of the injection pressure, grout volume injected, and grout flow rate were performed in real time using transducers connected to a data acquisition system and observed on a laptop computer. The uplift and downward movements of the bored pile and the SC were measured using manual readings obtained via visual survey and telltale extensometers, respectively.

The target pressure for the tip post-grouting was computed for its worst-case condition. The upper 1.5 m of side resistance was neglected for the computations. For the pier structures, the unfactored axial compression design load per pile ($P_{d,serv}$) was 400 tons with a maximum allowable post-construction vertical settlement ($\delta_{v,allow}$) of 0.03 m, resulting in a normalized post-construction displacement (ΔD_{vn}) of 2.5. For the worst-case scenario, the minimum required target pressure was estimated to be about 1025 kPa. Monitoring and recording of the injection pressure, grout volume injected, and grout flow rate were performed in real time using transducers connected to a data acquisition system and observed on a laptop computer.

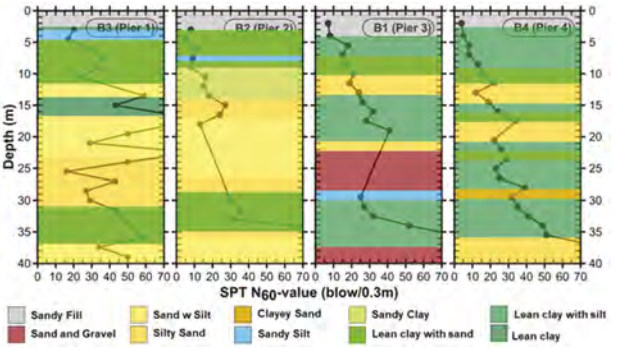

Figure 7. Subsurface profile and SPT N60-values at each soil boring.

The uplift and downward movements of the bored pile and the SC were measured using manual readings obtained via visual survey and telltale extensometers, respectively.

5.3 *Results from injection of production piles*

A summary of the results of the tip post-grouting performed at the abutments and the pier structures is provided in Table 1. As listed, there was considerable variability in the injection pressures achieved and with the observed behavior, even within short distances from each other. The achieved pressures, on average, were notably higher for the piles at the pier structures than for those at the abutments, possibly due to the additional side resistance available for the deeper shafts and due to the increased relative strength at the greater depths. In addition, some of the differences can be attributed to the different soil type present at the base of piles – ranging from silty sand to lean clay.

At the abutments, the unidirectional induced loads ranged from 1538 to 4534 kN, which were about 39% to 116% of the unfactored design load ($P_{d,serv}$). The induced load resulted in a normalized downward displacement ranging from about 1.4% to 4.0%, which corresponds to an average mobilized total axial resistance of about 75% to 100%. For the piles at the pier structures, the unidirectional induced loads ranged from 2239 to 4526 kN, which were about 57% to 115% of the unfactored design load ($P_{d,serv}$). The induced load resulted in a normalized downward displacement ranging from about 0.3% to 4.9%, which corresponds to an average mobilized total axial resistance of about 40% to 109%. As a result of the tip post-grouting and resulting displacement via preloading, increased stiffness of the soil beneath the base of each pile and smaller post-construction vertical displacements would be anticipated.

The maximum achieved injection pressures reported in literature and by firms performing tip post-grouting (not limited to a particular country or region) has been about 15 MPa in sands and about 8 MPa in clays/silts (Loehr et al, 2017). The injection pressures achieved at the west abutment (in silty sand) were on the low range of what has been reported in the literature and is even on the low expected range based on experience in the Santa Cruz region. The injection pressures achieved at the pier structures and east abutment (lean clay with sand or silt) were in the middle to higher end of what has been reported and is in line with what has been achieved on past projects in this soil type in the Santa Cruz region.

The (computed) induced load-displacement relationships from the tip post-grouting performed at piles 2, 3, 5, and 6 at Pier 3 (tipped in lean clay with silt) and Pier 4 (tipped in lean clay with silt) are shown in Figure 8. As shown in Equation (1), the induced load is correlated to the injection pressure: $P_{SC}=p \cdot Asc$, and the downward displacement is measured using telltale extensometers (and can be deduced using the grout volume and the internal dimensions of the cell). The differences in the grouting pressures that were achieved varied appreciably over short distances across each pier (Table 1). In addition, the measured downward displacements varied considerably when compared with the neighboring pier as well as at each pier though the displacements were more similar at Pier 4 than at Pier 3, as did the trend or the development of the load-displacement relationships. Static loading tests were performed in those piers. See results in Figure 9.

Tabla 1. Results of tip post-grouting performed at the Urubó Bridge.

Location	Desc.	Max. Pressure Archieved (MPa)	Max. Download Displacement (mm)	(Norm.)	$\frac{P_{max}}{P_t}$	Undirectional Induced Load (kN)	$\frac{P_{SC}}{P_{d,serv}}$
West Aburment	Range	2.2 – 5.92	65.0 – 98.2	5.4% - 8.2%	214% - 575%	1977 – 4534	50% - 116%
	Average	4.06	81.6	6.8%	394%	3255	83%
	Std Dev	2.63	23.5	2.0%	256%	1808	46%
Pile 1	Range	2.93 – 5.73	8.0 – 58.2	0.9% - 3.0%	284% - 556%	2383 – 4478	61% - 114%
	Average	4.86	24.2	2.1%	472%	3814	97%
	Std Dev	0.99	18.1	1.5%	96%	737	19%
Pile 2	Range	3.51 – 5.8	9.0 – 26.4	1.3% - 2.2%	341% - 563%	2907 – 4526	74% - 115%
	Average	4.65	15.9	1.8%	451%	3674	94%
	Std Dev	0.79	5.9	0.5%	77%	570	15%
Pile 3	Range	3.17 – 5.23	3.0 – 40.9	0.2% - 2.1%	308% - 508%	2552 – 4123	65% - 105%
	Average	4.26	17.0	1.0%	414%	3390	86%
	Std Dev	0.6	12.6	1.1%	58.4%	463	12%
Pile 4	Range	2.37 – 4.48	16.3 – 32.0	1.4% - 2.3%	265% - 435%	2239 – 3595	57% - 92%
	Average	3.48	22.8	1.8%	338%	2834	72%
	Std Dev	0.68	5.9	0.5%	66%	501	13%
East Abutment	Range	1.68 – 3.48	17.3 – 34.0	1.4% - 2.8%	163% - 338%	1538 – 2774	39% - 71%
	Average	2.72	24.0	2.1%	264%	2247	57%
	Std Dev	0.93	8.5	0.7%	91%	638	16%

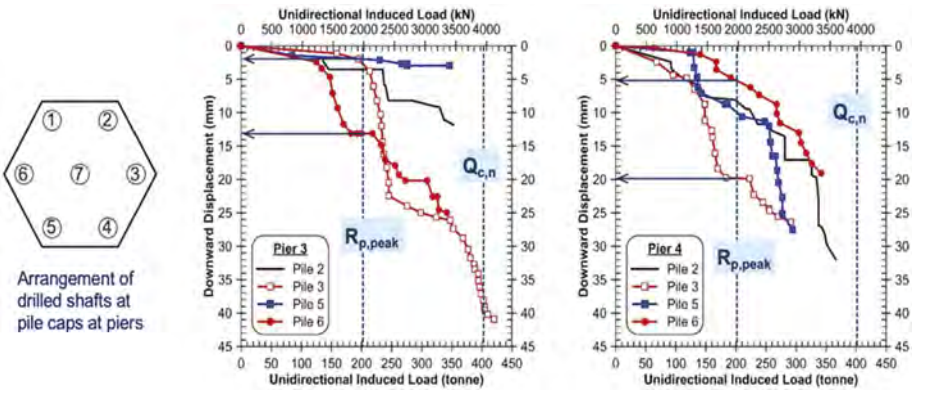

Figure 8. Select results of induced load vs. displacement from tip post-grouting (a) at Pier 3 and (b) at Pier 4.

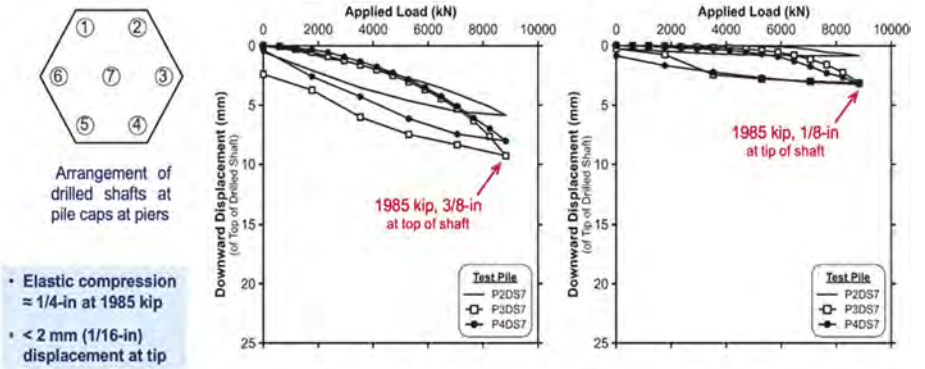

Figure 9. Loading test results from tip post-grouted piles (a) at Pier 3 and (b) at Pier 4.

The differences in the load-displacement behavior reflect the local differences present at the base of the pile and within the soil below. A stiffer soil response would be reflected by a gradual slope in the curve, whereas the curve for a softer soil would be represented by a steep slope. As each of the responses does not reflect a constant slope (i.e., instances of gradual and steep slopes at each pile), the tip post-grouting is influenced not only by the soil conditions immediately below the base of the pile but also by the soil within the influence zone of the loading. In addition, the influence zone may be changing during the grouting process as a compacted soil plug is being formed, which is then facilitating the distribution of the injection pressure into the soil.

6 CONCLUSIONS

During grouting, loose soil or debris (i.e., soft bottom condition) is first compacted, and then, as the injection pressure increases, the in-situ soil is compressed, resulting in a pre-mobilization of the end resistance. Although there was considerable variability in the injection pressures achieved and trends observed in the measured pressure-volume and inferred induced load-displacement responses, even within short distances at the same support structure. Overall, the unidirectional induced load ranged from 1642 to 3931 kN in Las Marotas bridge and from 1538 to 4534 kN in Urubó bridge, which equated to about 91% to 252% (Las Marotas) and from 39% to 116% (Urubó) of the design service load. Although the difference in the responses of a pile under load is typically attributed to the effects of the construction technique and process employed, many of the differences can be explained by the depositional environment and highly variable soil characteristics. The key benefit of using this tip post-grouting technique at each bored pile was the reduction of risk and uncertainty of performance due to the highly variable soil conditions. As a result of the tip post-grouting and resulting displacement via preloading, increased stiffness of the soil beneath the base of each pile and smaller post-construction vertical displacements would be anticipated.

REFERENCES

AASHTO. (2012). AASHTO LRFD Bridge Design Specifications, 6th edition. *American Association of State Highway and Transportation Officials*. Washington, D.C., 1661 pp.

Brown, D.A., Turner, J.P., Castelli, R.J., and Loehr, J.E. (2018). "Drilled Shafts: Construction Procedures and Design Methods." *Geotechnical Engineering Circular No. 10. Report No. FHWA-NHI-18-024. Federal Highway Administration.* March. 758 *pp*.

Chen, Y-J and Kulhawy, F.H. (2002). "Evaluation of Drained Axial Capacity for Drilled Shafts." Geotechnical Special Publication No. 116, Deep Foundations 2002, M.W. O'Neill and F.C. Townsend, eds., *ASCE, Reston, VA, pp.* 1200–1214.

Insepe Ingeniería y Servicios. (2016). "Estudio Geotécnico – Proyecto: Construcción de Puente Vehicular - Fernández Alonzo."

Loehr, J.E., Marinucci, A., Hagerty Duffy, P., Gómez, J., Robinson, H., Day, T.J., Boeckmann, A.Z., and Cadden, A.W. (2017). Evaluation and Guidance Development for Post-Grouted Drilled Shafts for Highways, *Report No. FHWA-HIF–17-024, Federal Highway Administration.* March. 158 *pp*.

Marinucci, A. and Nichols, S.C. (2016). "Optimized Drilled Shaft Design through Post-Grouting," *ASCE/Geo-Institute GeoStrata Magazine.* May/June.

Marinucci, A., Nichols, S.C., and Large, M.E.B. (2018). "Ensuring Performance of Tip Post-grouted Bored Piles (Drilled Shafts) through a Comprehensive Quality Assurance Program." *Proceedings of the DFI 43rd Annual Conference on Deep Foundations*.

Marinucci, A., Terceros Herrera, M., and Terceros Arce, M. (2020). "Improvement of Toe Resistance of Drilled Shaft Foundations in Highly Variable Sedimentary Soils using Smart Cells." *DFI Annual Conference*. *National Harbor, MD*. Accepted for publication.

Mullins, G. (2015). "Grouting Effectiveness – Construction QA/QC of Post-grouted Shafts." *Presentation delivered at FHWA/Caltrans Workshop on Quality Assurance for Post-grouted Drilled Shafts.* April 15- 16. Oakland, CA.

Smart Geotechnics for Smart Societies – Zhussupbekov, Sarsembayeva & Kaliakin (Eds)
© 2023 The Author(s), ISBN 978-1-003-29912-7
Open Access: www.taylorfrancis.com, CC BY-NC-ND 4.0 license

Studies on applications of precast pile planting method

Yan Zhang, Zhigao Li, Youtian Mao & Weihua Zhao
Jianhua Construction Materials Group, Zhenjiang, The People's Republic of China

ABSTRACT: In this paper, engineering applications of precast pile planting under different geological conditions have been carried out, which solved the engineering application problem of precast pile under complex geological conditions such as dense sand layers, aged clays, and shallow buried bedrocks, and greatly expanded engineering application ranges of precast pile. At the same time, through the test analysis of bearing capacity performance, the design method of controlling the bearing capacity of single pile by strength of precast pile body with precast pile planting method is proposed.

1 INTRODUCTION

Many methods have been successfully used to install precast piles, and new techniques and methods are constantly being developed. These methods differ according to the type of precast pile being installed, the purpose to be served by the pile, the forces to be resisted, the soils into which the piles are installed, the structure to be supported, and the pile orientation (vertical or battered)[1]. The most common method of installing precast piles is pile driving hammers. But driven pile is not suitable for some geological conditions such as dense sand layer, aged clays, and shallow buried bedrocks, etc. The construction unit should limit or exclude the use of that installation method that would be harmful. In order to expand engineering application range of precast pile, the precast pile planting has been developed.

The precast pile planting technology is to use a drilling rig or other hole-forming equipment to form a hole in the pile position in advance and fill the filling material or use the stirring and rotary spraying process to form an outer pile, and then use the pile driving equipment to drive, press or insert the precast pile as a core pile. The construction process is shown in Figure 1. The construction ways of drilling mainly include bored pile method, continuous flight auger pile method, cement-soil mixing pile method, high pressure rotary jet pile method, etc. According to the hole-forming way, precast pile planting technology can be divided into soil-taking pile planting and non-soil-taking pile planting. Soil-taking pile planting generally includes rotary drilling hole-forming pile planting, rotary digging pile planting, mid-digging bottom expansion pile planting, continuous flight auger pile planting, etc. Non-soil-taking pile planting includes cement-soil mixing pile planting and high pressure rotary jet pile planting, etc.

The composite piles formed by precast pile planting technology include core piles and outer piles (as shown in Figure 2.). The core piles could be precast piles such as ordinary precast prestressed spun-cast concrete cylinder piles (known as PHC pile) and super high-strength precast prestressed spun-cast concrete cylinder piles (known as UHC pile). And the outer piles could be cast by concrete, cement mortar or soil cement. Composite piles could give full advantages of two types of piles: for example, rotary digging pile planting, which combine the characteristics of two different pile-forming techniques of cast-in-situ piles and precast piles, solve the problem of precast piles that are difficult to pass through thick sand layers and shallow buried bedrocks. This kind of technology has been gradually used in Guangxi, Sichuan, Jiangxi, Hunan, Anhui and other regions of China in recent years. Another example is cement-soil mixing pile planting,

DOI: 10.1201/9781003299127-225

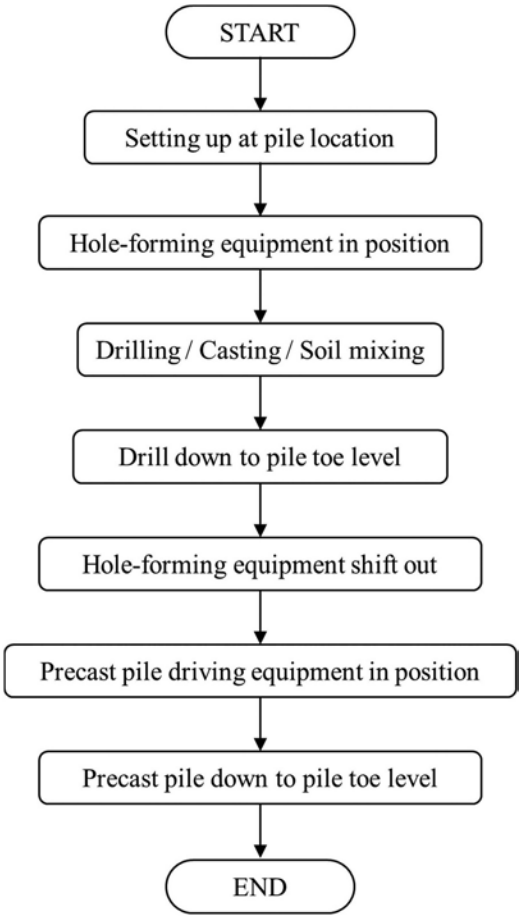

Figure 1. Construction process of precast pile planting.

which not only solves the problem of limited load transmission depth of soil-cement piles, but also solves the problem of the limited application in special geology such as deep and saturated soft soils, they have been widely used in Eastern China in recent years[2].

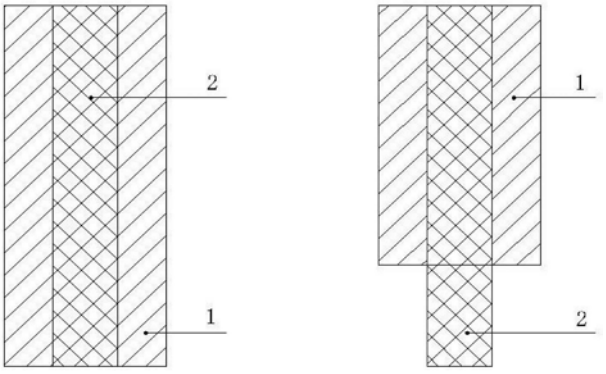

Figure 2. Layout of Precast Pile Planting. 1 – Outer pile (Concrete, cement mortar or soil cement); 2 – Core pile (Precast concrete pile).

2 EXPERIMENTAL RESEARCH ON PRECAST PILE PLANTING

In order to find out the bearing characteristics of precast pile planting technology and expand the application ranges of precast piles, engineering application research on pile planting technology under different geological conditions have been carried out.

2.1 *Soil-taking pile planting technology*

2.1.1 *Railway bridge's pile foundation project (rotary digging pile planting)*

Project overview: Rotary digging pile planting's test were carried out between the S191# and S192# pier of an intercity railway bridge's project. The soil boring's site belongs to the first-order terrace landform of the Huai River. The upper layer of the subsurface is silty clay and silty sand, the lower layer is silt, and the bearing layer is clay.

3-1 layers of the project's site soil are 10 meters thick silty sand. The research on the rotary digging pile planting technology of this project is mainly to solve the problem of the difficulty of sinking precast piles in thick sand layer.

According to the soil conditions of the test site, precast piles are driven by the pile planting method of the rotary drilling pile planting. First, the holes are formed by the rotary drilling equipment with a diameter of 1 meter. The depth of the holes is same as the designed pile length with 34 meters. After the fine stone concrete is poured underwater, the precast piles are sunk by a vibratory hammer.

Design parameters of rotary digging pile planting design parameters: outer pile is fine stone concrete pile which diameter is 1 meter, and pile length is 34 meters. Core pile is UHC800AB130 (UHC pile in diameter of 800 millimeters, wall thicknesses of 130 millimeters), and pile length is 34 meters too. The soil profile is shown in Figure 3.

Figure 3. Soil profile on site.

Results of static load testing: Results of the static load testing are shown in Figure 4, and the vertical ultimate bearing capacities of the rotary digging pile planting piles are higher than 15000 kN. For the core pile of UHC800 pile, the ultimate bearing capacity of the pile concrete strength is 12855 kN, and the bearing capacity estimated by the soil resistance is 12133 kN.

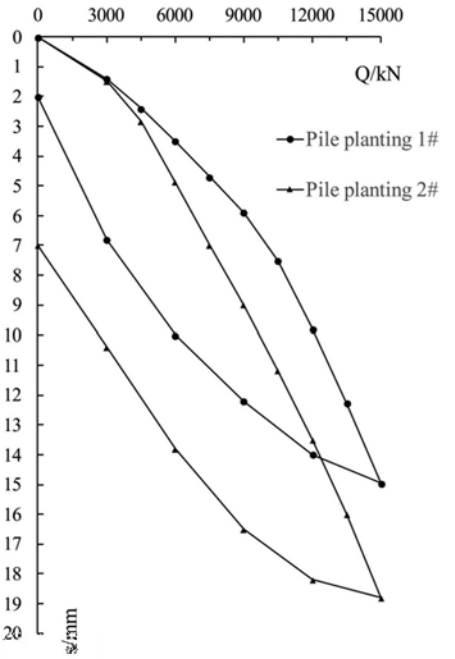

Figure 4. Results of static load testing.

2.1.2 *Residential's pile foundation project (rotary digging pile planting)*
Project overview: A residential project in Xuancheng, Anhui Province, which main buildings include 19 residential buildings with 4, 11 and 17 floors. The subsurface soil layers on the site are embankment fills and clay. The middle layer is coarse sand, and the lower part is bedrock. The research on pile planting technology is mainly to solve the problem that the bedrock of the bearing layer is buried shallowly, and the pile length is difficult to control.

Design parameters of rotary digging pile planting design parameters: outer pile is fine stone concrete pile which diameter is 1 meter, and pile length is 11 meters. Core pile is PHC600A110 pile (PHC pile in diameter of 600 millimeters, wall thicknesses of 110 millimeters), and pile length is 11 meters too. The soil profile is shown in Figure 5.

Results of static load testing: The static load testing results are shown in Figure 6, the vertical ultimate bearing capacity of the rotary digging pile planting piles are higher than 5000 kN. For the core pile of PHC600AB110 pile, the ultimate bearing capacity of the pile concrete strength is 7654 kN, and the bearing capacity estimated by the soil resistance is 4700 kN.

2.1.3 *Commercial complex's pile foundation project (continuous flight auger pile planting)*
Project overview: Continuous flight auger pile planting was carried out at a large-scale commercial complex project in Zhengzhou, Henan Province. The test site is an alluvial plain, the subsurface soil layers on the site is mainly silt and silty sand, the middle soil layer is mainly silt sand and fine sand, the bottom soil layer is mainly dense fine sand or silty clay. The sand layer is buried deeper than 12m.

According to the site conditions, the piles is sunk by continuous flight auger pile planting. The pile site holes are pre-formed by a continuous flight auger which diameter is 900 millimeters. After reaching the design depth of 14 meters, the cement-mixed mortar or fine stone concrete is sent to the bottom of the hole by pressure through the core pipe of the drilled pipe, and the drill lifted to the top of the pile hole. In the end, precast piles are impacted by hammer to reach the bottom of pile hole in concentrically.

Design parameters of continuous flight auger pile planting: outer pile is cement mortar mixture pile which diameter is 900 millimeters, and pile length is 14 meters. Core pile is PHC600AB110

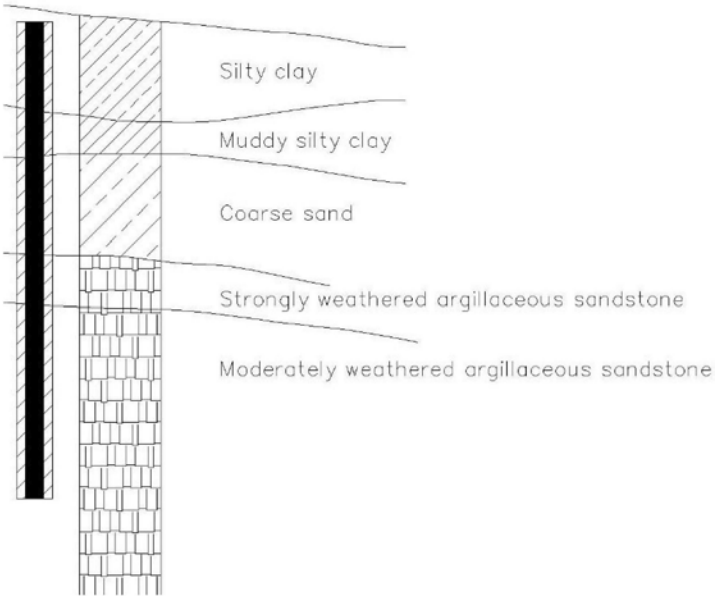

Figure 5. Soil profile on site.

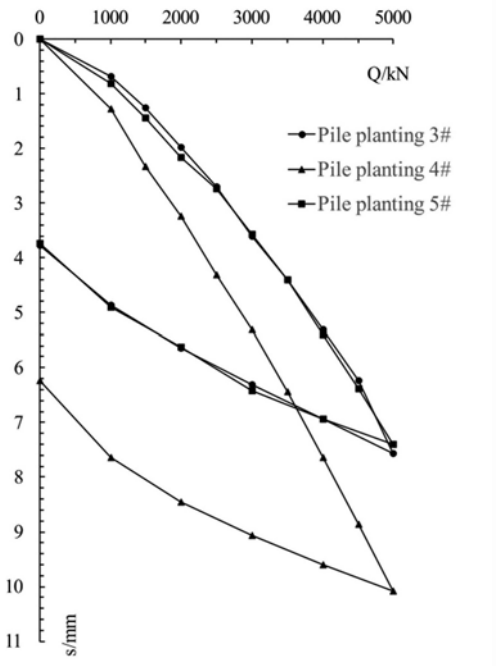

Figure 6. Results of static load testing.

pile (PHC pile in diameter of 600 millimeters, wall thicknesses of 110 millimeters) which pile length is 14 meters too. The soil profile is shown in Figure 7.

Results of static load testing: The static load testing results are shown in Figure 8, the ultimate bearing capacity of the continuous flight auger pile planting piles are higher than 6480 kN.

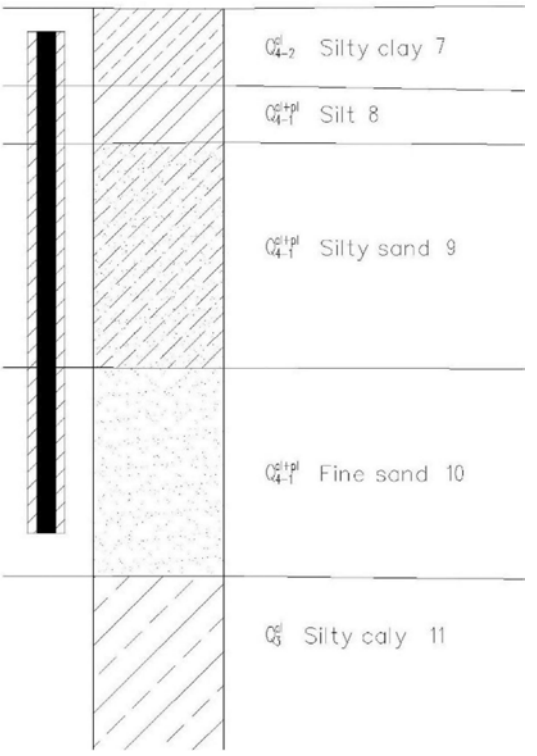

Figure 7. Soil profile on site.

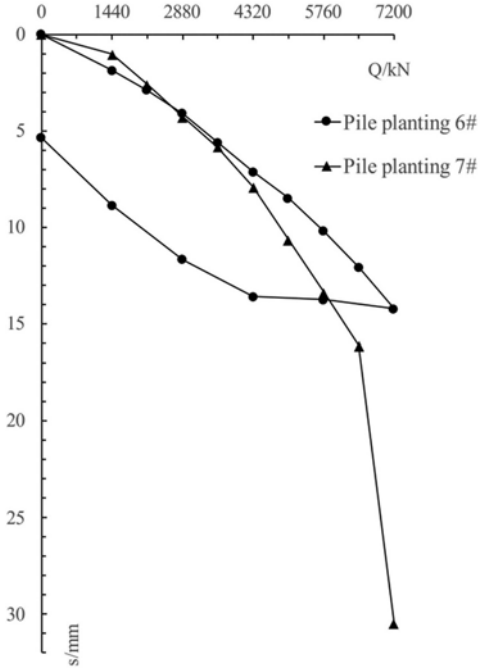

Figure 8. Results of static load testing.

For the core PHC pile, the ultimate bearing capacity of the pile concrete strength is 7654 kN, and the bearing capacity estimated by the soil resistance is 6380 kN.

2.2 *Non-Soil-taking pile planting technology*

2.2.1 *Residential's pile foundation project (cement-soil mixing pile planting)*

Project overview: A residential project in Fuyang, Anhui province, including 14 high-rise residential buildings with 25-34 floors and several commercial and public centers with 3-7 floors. The project site belongs to Quaternary Alluvium which composed by clay, silty clay, medium sand, and coarse sand. This research on the cement-soil mixing pile planting technology of this project is mainly to solve the application problem of precast piles in aged clay area.

Design parameters of cement-soil mixing pile planting: outer pile is cement-soil mixing pile which diameter is 800 millimeters, pile length is 22 meters. Core pile is PHC500AB125 pile (PHC pile in diameter of 500 millimeters, wall thicknesses of 120 millimeters), pile length is 22 meters too. The soil profile is shown in Figure 9.

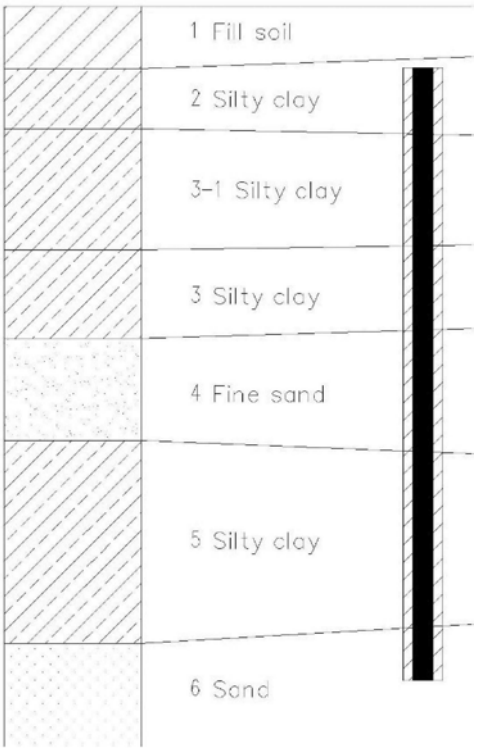

Figure 9. Soil profile on site.

Results of static load testing: The static load testing results are shown in Figure 10. The concrete at the pile head was destroyed at the maximum load of the test, and the vertical ultimate bearing capacity of the cement-soil mixing pile planting piles are 5400 kN. The ultimate bearing capacity of the core PHC pile concrete strength is 5480 kN, and the bearing capacity estimated by the soil resistance is 5300 kN.

2.2.2 *Industrial plant's Pile Foundation Project (high pressure rotary jet pile planting)*

Project overview: A food industrial plant in Yuci, Shanxi province, which's in mountain front alluvial sloping plain. The main soil layers are embankment, silt and sand. Except for the surface silt, which is slightly dense, the other layers are medium dense. And sand layers are

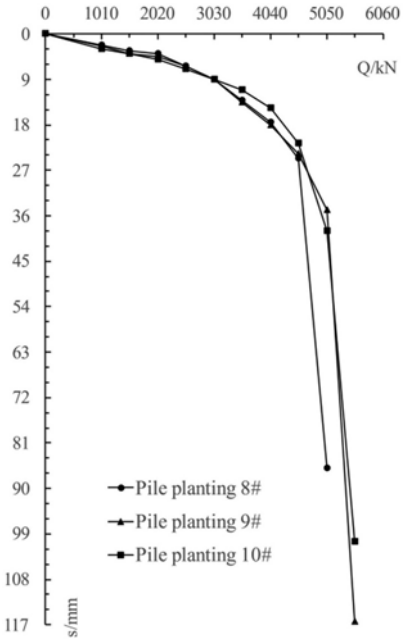

Figure 10. Results of static load testing.

slightly dense. The research on the high pressure rotary jet pile planting technology of this project is mainly to solve the application problem of precast piles in thick sand geology.

Design parameters of high pressure rotary jet pile planting: outer pile is high pressure rotary jet pile which diameter is 850 millimeters, and pile length is 26 meters. Core pile is UHC400AB95 pile (UHC pile in diameter of 850 millimeters, wall thicknesses of 95 millimeters), and pile length is 26 meters too. The soil profile is shown in Figure 11.

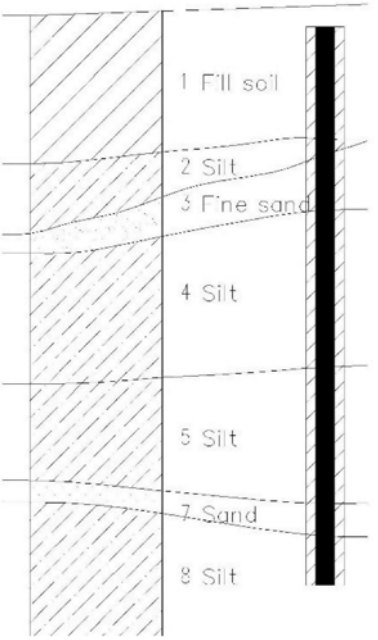

Figure 11. Soil profile on site.

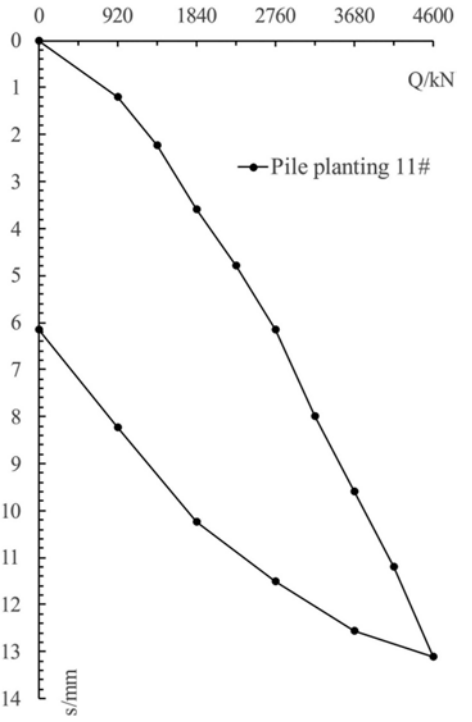

Figure 12. Results of static load testing.

Results of static load testing: Results of the static load testing are shown in Figure 12, and the vertical ultimate bearing capacity of the high pressure rotary jet pile planting pile is 4600 kN. For the core UHC400 pile, the ultimate bearing capacity of pile concrete strength is 4275 kN, and the bearing capacity estimated by the soil resistance is 4500 kN.

3 DESIGN METHOD OF PRECAST PILE PLANTING TECHNOLOGY

The bearing capacity of piles in above engineering applications are estimated based on the design method of precast pile concrete strength. Pile planting's shaft resistance is obtained by outer pile's shaft resistance, and the toe resistance is obtained by core pile's toe resistance. Both are the nominal resistance of the pile planning pile. The comparison of theoretical estimation results and experimental results shows that two are basically consistent, and this design method has greater reliability. The specific calculation method is as follows:

The vertical ultimate bearing capacity of single pile by pile planting method can be estimated by the following formula:

$$Q = u_D \Sigma q_{sik} l_i + q_{pk} A$$

where Q = Vertical ultimate bearing capacity of single pile by pile planting method (kN); u_D = Perimeter of the outer pile (m); l_i = Thickness of soil layer i (m); A = Total cross-sectional area of the core pile toe (m^2); q_{sik} = Unit shaft resistance over the pile surface area (kPa); q_{pk} = Unit toe resistance over the pile toe area (kPa).

The vertical ultimate bearing capacity of single pile can be estimated by the following formula:

$$N = \psi_c f_c A_p$$

where N = Vertical ultimate bearing capacity of single pile (kN); Ψ_c = Working factor, =0.85; f_c = Concrete strength (kN/m^2); A_p = Cross-sectional area of the pile (m^2).

The results of a large number of engineering cases show that in preliminary design, it is feasible to use the above formula to estimate the vertical ultimate bearing capacity of single pile planting pile, and the results have a high degree of agreement with the measured values (Figure 13).

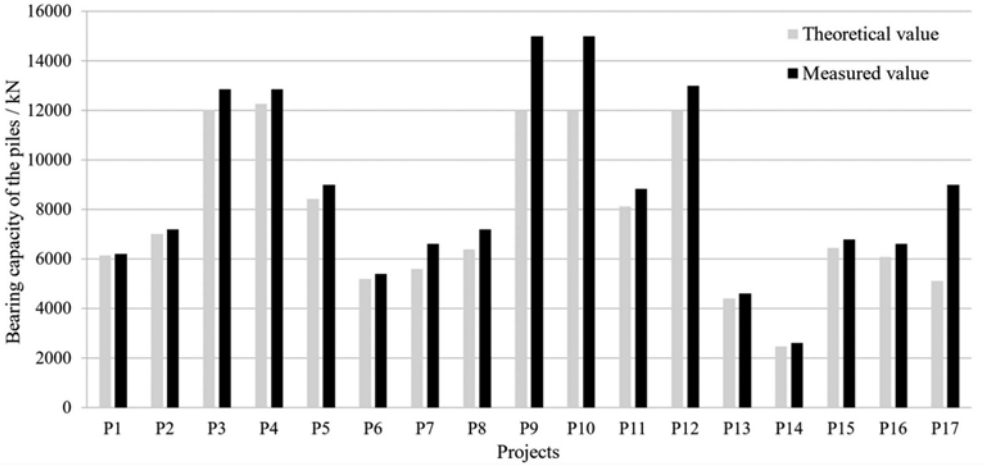

Figure 13. Comparison between theoretical values and measured values of bearing capacity in 11 projects.

4 EPILOGUE

Relevant data show that in Japan, South Korea and other countries, the application of precast pile planting technology has accounted for more than 80% of the total pile foundation projects [3]. The application of precast pile planting technology in Japan is relatively mature. In order to control noise and environmental pollution in cities, Japan introduced the *Noise Regulation Law and Vibration Regulation Law* in 1968 and 1976 respectively, which limited the driven piles. The application in urban areas, on the other hand, also promotes the continuous development of pile planting technology, so that precast pile planting technology has become the mainstream in pile foundation engineering.

Compared with traditional concrete cast-in-site piles, pile planting technology can take advantage of the cast-in-place piles and precast piles, give full play to the bearing capacity of precast piles, and have good economic benefits. At present, in the domestic pile foundation market, the application range of precast pile planting technology is constantly expanding.

Following conclusions are drawn by using precast pile planting technology to test engineering piles under different complex geological conditions:

(1) The precast pile planting technology can give full play to the characteristics of cast-in-situ piles and precast piles, solve engineering application problems such as precast pile construction under complex geological conditions, also obtain better economics, greatly broadening the application of prefabricated piles scope.
(2) Through the comparative analysis of the theoretical value and the measured value, it is verified that the design method of controlling the bearing capacity of a single pile based on the strength of the precast pile body has greater reliability.

REFERENCES

American Concrete Institute. 2021. Guide to Design, Manufacture, and Installation of Concrete Piles. Farmington Hills: ACI.

Wang, WD. & Xu, ZH. & Wu, JB. & Li, Q. 2021. New Technique Development in Deep Excavation Engineering and Pile Engineering. *Jiangsu Architecture* 03: 1–10.

Zhang, RH. 2013. New precast pile products and construction methods. *Special collection of concrete pile production technology innovation* 2013: 12–18.

Smart Geotechnics for Smart Societies – Zhussupbekov, Sarsembayeva & Kaliakin (Eds)
© 2023 The Author(s), ISBN 978-1-003-29912-7
Open Access: www.taylorfrancis.com, CC BY-NC-ND 4.0 license

Features of the application of pile technologies in restrained urban conditions in the historical downtown of Saint-Petersburg on the soft soils

A.I. Osokin
Saint-Petersburg State Architectural and Civil Engineering University, Saint-Petersburg, Russia

ABSTRACT: The geotechnical practice of the construction and restoration in historical downtown of Saint-Petersburg in among old residential and revenue houses, mansion-houses, architectural monuments show, that the main issue is safety of technological processes in relation to the soil massive and foundation of neighboring buildings. The proposed evaluation approach is based on the analysis of the technological features of pile technologies and the determination of the safest. Examples of technical solutions that illustrate the effectiveness of this approach are given. The use of a geotechnical barrier, compensation grouting, reinforcement of the foundations of neighboring buildings with micropiles is considered as preventive measures of protection against the construction impact.

1 INTRODUCTION

The importance of pile foundations on soft soils cannot be overestimated. Today, this is practically the most common method of foundation in conditions of dense urban development in terms of minimizing the impact on the neighboring buildings. Due to the technological nature and definitely ensuring a high degree of reliability, they have become widely used both in domestic and foreign practice of foundation construction. Pile foundations are the only way to erect the foundation of a structure for many construction situations in difficult construction and engineering-geological conditions. The main advantages of pile foundations are optimization of construction time, high manufacturability, reduction of labor intensity of work and volume reduction of excavation work.

The experience of construction and reconstruction in recent years in conditions of dense urban development in the cities of Moscow and St. Petersburg shows that during zero-cycle work, the neighboring buildings often receive greater deformations that impact of deformation from the static loaded foundations of new buildings or overloaded the reconstructed buildings.

2 MODERN PRACTICE OF PILE FOUNDATION CONSTRUCTION IN DENSE URBAN DEVELOPMENT

All applied pile technologies used in dense urban development can be divided into three groups: pile excavation with soil extraction, without soil extraction and with partial soil extraction.

Drilling and piling technologies are widely used in the construction of buildings in dense urban areas. In case with small loads on the piles of a building under construction and to strengthening the foundations of old buildings and monuments during reconstruction and renovation we use micropiles.

In modern conditions of inner-city construction, the following technologies are used for the manufacture and installation of piles (data obtained from the analysis of the experience of geotechnical construction at 64 sites in the central part of St. Petersburg):

DOI: 10.1201/9781003299127-226

– jacked piles - 35%;
– displacement piles – 50%;
– micropiles – 10%;
– drilling piles with excavation - 5% (under the protection of bentonite mortar, under the protection of the casing pipe, continuous through auger (short through auger).

The need to carry out work in cramped conditions of dense development, including in the historical part of the city, led to the fact that since the mid-1980s in St. Petersburg they began to use a self-propelled machine USV-80 (USV-120, USV-160) for jacking prismatic precast piles. Since 2008, pile jacking machines has been carried out on construction sites using hydraulic system which manufactured by the Chinese companies "Strarke" and "Sunward", designed for jacking of precast piles, metal profiles, steel pipes and sheet piling. This modifications of machines presented on the St. Petersburg market have a maximum pressing force of 3600 kN using a additional loads.

For this technology, the following possible geotechnical quality risks can be specified:

– piles don't reach to the design mark;
– possible deviation or displacement from the design location both in terms of already depressed piles and in height due to the removal of piles due to subsequent impact during mass jacking of piles or excavation of the pit;
– non-compliance with verticality;
– in soils with a ribbon texture, the sinking of piles can lead to additional deformations of the foundations and foundations of buildings located at a distance of up to 3 m and the removal of soil with the lifting of previously made piles.

When assigning a method for reducing soil resistance to pile jacking (drilling of lead wells, preliminary loosening with a screw, washing), a possible reduction in the bearing capacity of piles is taken into account due to the use of reducing coefficients in calculations.

Among the replacement piles we distinguish the several types that are actively used today in the construction of foundations in dense urban buildings in weak soils.

Drilling piles arranged under the protection of bentonite mud have been known in Russian construction practice since the mid-50s of the last century.

Rotary drilling machines are used for the manufacture of piles under the protection of bentonite mud. The process of soil destruction during drilling occurs due to mechanical or physico-mechanical impact on it with the help of a drilling tool. At the same time, a field of mechanical stresses is formed that is sufficient to break the continuity in a certain volume of the soil mass, transform it into a solution by feeding the washing liquid into the well, and then removing the loosened soil to the surface.

In unstable and water-saturated soils, an internal overpressure exceeding the external pressure is created in wells to keep the walls from collapsing. To do this, the well is filled with a flushing drilling fluid in the form of process water, water with additives of surfactants (surfactants), polymer or bentonite solution. It should be noted that in order to create excessive pressure on the walls of the well, the drilling bentonite mud level had to be several meters above the groundwater level.

The advantage of the technology of manufacturing drilling piles under the protection of bentonite mud is its safety in relation to neighboring buildings, which allows it to be actively used in reconstruction and engineering restoration, including in operating conditions in buildings when installing reinforcement piles.

Structurally and technologically, the following risks should be noted that affect the quality and reliability of the pile structure manufactured in the ground under the protection of bentonite mud: deviation of the pile from the vertical during drilling; ensuring the stability of the walls of the well when drilling in weak water-saturated soils; formation of "necks", caverns, areas with mixed bentonite mud and concrete is possible; sticking of pieces bentonite mud on the reinforcement frame.

This technology, in compliance with the basic regulatory and technological parameters, allows for the installation of piles in close proximity to existing buildings, without significantly

affecting the condition of the soil mass at the base of the foundations. When installing geotechnical barriers and pit fences when using drilling technology under the protection of clay mortar, the sequence of pile production and their step by grappling, as well as the period of standing during the subsequent manufacture of piles, are additionally regulated.

In the manufacture of piles in water-saturated weak soils, the most reliable protection of soil massive from technological impacts of drilling of the well is the use of casing method. In geotechnical practice bored piles have been used in wells drilled by the Kelly system under the protection of a casing pipes. The Kelly system involves the process of drilling of soil with a drilling tool (a short auger, bucket or core drill) fixed at the end of a telescopic bar (Kelly system).

The technology of arranging piles under the protection of the casing pipe using the Kelly system has a number of advantages, main of them are: direct control is carried out over the compliance of the actual characteristics of the soil laid down in the project during the drilling process, the absence of dynamic and vibration effects on the ground allows you to perform piles near existing buildings and structures.

The disadvantage of the technology is low productivity, so design solutions should ensure full use of the bearing capacity of piles on the ground. In addition, when passing water-saturated soils, in order to avoid their discharge into the well, it is necessary to create a high-altitude ground plug (by calculation) or excessive pressure in the well with water or bentonite solution.

In geotechnical construction, the technology is known like "Double Rotary" in which the production of piles according to this technology is carried out by drilling a well under the protection of an inventory casing pipe with simultaneous right rotation of a continuous through screw located inside the casing pipe and left rotation of the pipe.

The advantages of this technology are: the technology is applicable for all types of dispersed soils (loose dense soils, silts, hard clays); absence of noise and significant vibration effects (this allows you to arrange piles near existing buildings); high productivity due to the extraction of soil by a continuous auger; high quality of filling the well with concrete, due to the supply of concrete mixture under pressure.

Drilling control, regulation of the rotation speed of the drilling body, the supply of concrete and its pressure at the bottom is carried out using a computer installed in the operator's cabin.

The history of the appearance of piles arranged by the method of continuous flight auger piles CFA using modern equipment in St. Petersburg was dramatic. For the first time this technology was applied to the device of bored piles in 1995.

In 1998, during the construction of the transport and commercial complex, the using technology CFA for the installation of drilling piles with a diameter of 600 mm and a depth of 25 m had got catastrophic deformations of the existing houses had occurred with the formation of cracks with an opening of up to 50 mm. The buildings have fallen into disrepair. This required their dismantling. When performing piles using continuous fly auger technology on a construction site stacked with weak soils, it was noted that with the sequential manufacture of these piles, the volume of concrete absorption per well increases several times.

The underestimation of thixotropic decompression of water-saturated clay soils in a near-pile soil array when using this technology with continuous production of a pile field leads to a significant overspending of the concrete mixture (twice or more). The increased consumption of the concrete mixture, as a rule, occurs when there are significant layers of fluid, fluid plastic loams and sandy loams with low strength and deformation characteristics at the base of the site [Dalmatov, 1999].

Let us identify the main geotechnical risks of manufacturing piles arranged according to the technology CFA:

- active mechanical impact on soils;
- in the presence of dense layers of soil, due to a change in the rate of penetration of the well, the removal of excessive soil volume is possible;
- there is a negative impact on the foundations of neighboring buildings;
- overspending of concrete relative to the physical volume of the well (up to 40%).

A significant part of the total volume of pile foundations in urban conditions is made up of displacement piles. Displacement piles are concreted in wells formed as a result of forced

displacement of soil. Wells can be made by punching, rolling, static or vibrational punching of the soil. During construction in dense urban development in conditions of weak soils, methods of static and rotational impact on soils with the exception of vibration and dynamic loads are considered acceptable for use in terms of safety conditions for buildings of neighboring buildings.

The screw-pushing of the well is performed by screwing a spiral projectile or pipe into the ground, the lower end of which is closed by a screw tip left in the ground.

The possibility of using one or another method of well formation for packed piles should be established at the stage of engineering and geological surveys. Table 1 shows the scope of application of various methods of well formation for packed piles, depending on ground conditions (Table 1).

Table 1. Methods of borehole-making for displacement piles depending on soil conditions.

	Soil conditions	
Borehole-making method	Clay soils with index of liquidity I_L	Sand
Static displacement	$I_L > 0,3$	–
Reaming	$I_L > 0,2$	Silty soft water-saturated
Vibration displacement	$I_L > 0,6$	Soft water-saturated
Percussion	$I_L > 0,3$	Fine- and medium-grade

If there are thixotropic soils in the engineering-geological section of the site in depth, their sensitivity to the violation of structural bonds should be determined, i.e. the degree of reduction in the mechanical (strength and deformation) characteristics of soils and the bearing capacity of piles as a result of well penetration. The time of restoration of structural bonds and the degree of increase in soil strength should also be determined.

The technology of the device of displacement piles with a lost tip "Fundex" it was first used in St. Petersburg in 2001. Wells for piles are performed without soil extraction by displacing the soil with a screw-in inventory steel pipe with a tip mounted at the lower end. The spiral tip is a drilling working tool that ensures the process of creating a well and, at the same time, the tightness of the coupling of the casing pipe and the tip through the sealing gasket. When the design mark is reached, the screw tip is separated from the casing (lost tip). A reinforcing frame is lowered into the dry inventory pipe through the open upper end. The drill pipe is removed from the ground by return rotation with simultaneous pulling.

Displacement piles DDS (FDP), manufactured using spiral tool. Wells for such piles are performed without extraction of soil, due to its displacement to the sides-up by a rollout-tool, which is a cone or cylinder of variable cross-section with a screw blade.

When the helical tool is submerged, the soil is displaced to the sides and upwards, a compacted zone is formed around the well, the size of which depends on the properties of the soil, the rate of immersion and the design of the projectile.

A feature of the use of DDS technology is in the implementation of the formation of a well with the stratification of dense interlayers or layers of soil, as well as a condition that ensures the achievement of design marks in the bedrock soils is the possibility of combining a sealing drilling body with a mechanical ripper installed in its lower part, which provides the possibility of preliminary loosening of the stiff soil lays and minimizes the impact on the soils of the base.

3 ANALYSIS OF FACTORS OF TECHNOLOGICAL IMPACTS ON EXISTING BUILDINGS WHEN USING PILE TECHNOLOGIES IN CONDITIONS OF SOFT SOILS

It is recommended to evaluate the technological impact on buildings and structures falling into the zone of influence when installing piles in conditions of dense urban development on weak soils when dividing them into two main groups: arranged with soil extraction and performed without soil extraction.

The degree of technological influence on buildings and structures of the surrounding development from the manufacture of piles arranged using various technologies is assessed in building conditions by observing the deformations of buildings of the surrounding development and measuring deformations on the ground surface.

Conducted field studies of the zone of influence in the manufacture of stuffed piles of displacement of DDS at the construction site in the central part of St. Petersburg [Mangushev R. A., Oshurkov N.V., Osokin A.I., Sbitnev A.V., 2005] using a mobile RIG204 static sensing installation showed that the zone of influence ranged from 2.0 to 2.5 m from the faces of the manufactured pile with a diameter of 520mm. Graphs of the soil resistance to the probe immersion were plotted along the tip and along the lateral surface at depth from the day surface, compared with the sounding data before the pile device, as well as among themselves. This made it possible to estimate the zone of influence from the device of the packed pile of DDS displacement 2 hours after its manufacture.

If we consider the manufacture of a group of piles, there is a mutual influence of the compacted array during the manufacture of earlier piles (as a rule, a technological gap is assumed between the piles in the bush for 3 days) and the soil, which is compacted during the subsequent manufacture of the pile foundation. In the mass production of piles with compaction and displacement of soil, the effect of active impact on the surrounding buildings is observed. This is determined by the principle of superposition of fields that occurs during the sequential manufacture of printed piles. At the same time, it should be noted that observations of deformations of buildings of the surrounding development show the rise of buildings with the concentration of manufactured piles near the existing building. In this regard, the direction of production of piles without excavation (made with displacement of soil) should be determined from the existing development to the center of the site. In this case, the piles made earlier are a screen when the wave of discharge from the devices propagates.

Let's consider the results of observing the deformations of buildings of the surrounding buildings during the manufacture of piles using various technologies (Table 2):

Table 2. Deformations of structures of surrounding buildings in the manufacture of piles using various technologies.

Type of pile technology	Characteristics of the effect on the soil near-pile array	The degree of influence on the soil mass in weak soils	The degree of influence on the neighboring buildings	Manufacturability	Risk of poor quality of pile
Drilling with casing	Mechanical destruction of the soil during drilling	Low or medium. (4,0)	Low (4)	Medium (3)	Low (4)
Drilling under protection the bentonite mud	Mechanical destruction of the soil during drilling, moistening of the soil in the drilling zone	Low (5)	Low (5)	Low (2)	High (2)
CFA -piles	Mechanical destruction of the soil and its continuous transportation along the edges of the auger to the surface	High (1)	High (1)	High (5)	Medium (3,0)
FUNDEX – piles	Compaction and displacement of soil from the volume of the well down-side-up	Medium and high (3,0)	Medium (3,0)	High (5)	Medium (3,5)
Displacement piles DDS	Crushing and compaction with displacement of soil from the volume of the well down-side–up, crushing during compression with a concrete mixture	Medium and high (3,5)	Medium (3,5)	High (5)	Low (4,5)

4 CONCLUSIONS

The result of the presented study allows us to form an understanding of the technological factors for the additional draft of the S_{tech} (1) building located in the zone of influence of geotechnical construction (pile foundation device):

$$S_{tech} = f\ (G,\ M_{dp},\ T_{cb}), \tag{1}$$

$$G = f\ (\gamma,\ \varphi,\ c,\ E,\ W,\ I_L,\ WL), \tag{2}$$

$$M_{dp} = f\left(M_{rot}, N_p, C_{dst}, P_{con}\right) \tag{3}$$

где, *G –a parameter that evaluates the impact of engineering and geological conditions of the construction site (2):* γ – specific gravity of the soil, кN/m^3; φ – the angle of internal friction of the soil, deg.; c – specific cohesion, KPa; E – modulus of general soil deformation MPa; W – natural soil moisture; I_L – consistency indicator; WL – groundwater level; M_{dp} – a parameter that evaluates the impact of drilling technology and the formation of a drilling or packed pile *(3):* M_{rot} – the amount of torque kN*m, N_p – feed force of the working tool, kN, C_{dst} – construction of the working tool, P_{con} – the method of feeding the concrete into the well

REFERENCES

Dalmatov, B.I. 1999. Experience of construction in soft soil (by example of construction of Transportation and Commercial Center in Saint Petersburg) *Urban reconstruction and geotechnical construction. – Saint Petersburg,* 1999. No. 1: 4–7.

Mangushev, R.A., Gotman, A.L., Znamensky, V.V. & Ponomarev, A.B. 2015. Piles and pile foundations. Constructions, design and technologies./ edited by corresponding Member of the RAASN Dr. Tech.of Sciences, Professor R.A. Mangushev- Moscow: Publishing House of Association of Construction Higher Education Institutions.

Mangushev, R.A., Osokin, A.I. & Sotnikov, S.N. 2018. Geotechnics of St. Petersburg. Experience of construction on the soft soils. - Moscow: Publishing House of Association of Construction Higher Education Institutions.

Paramonov, V.N. & Shashkin, A.G. 1997. Modeling of technological processes of drilling piles are installed in weak clay soils. *Problems of foundation construction in the ground conditions of the new capital; Proc. I-th Kazakhstan National Geotech. Conf., Akmola, 1997*.t.II: 462–466.

Ulitsky, V.M., Shashkin, A.G. & Shashkin, K.G. 2010. Geotechnical support for the development of cities. St. Petersburg: Stroyizdat North-West Publisher, Group of companies "Georeconstruction"

Mangushev, R.A., Osokin, A.I., Tatarinov, S.V., Sbitnev, A.V. & Lebedev, M.V., 2006. Determination of the zone of influence during arrangement of bored cast-in-site piles in soft soils. *Tagungsband der XIII. Donau-europäische konferenz für geotechnik, Ljubljana*, *29-31 Mai 2006*. Ljubljana, Slovenien: 637–640.

Mangushev, R.A., Yershov, A. V. & Osokin, A. I. 2010. Modern Pile Construction Technology: Manual. 2nd Edition, revised and updated, Moscow, Publishing House of Association of Construction Higher Education Institutions.

Mangushev, R.A., Fadeev, A.B. Osokin, A.I., Sbitnev, A.V. & Tatarinov, S.V. 2007. Experimental Assessment of DDS Technology-based Bored Pile Effects on Soil Foundation. *Geotecnical Engineering for disaster prevention & reduction. Proc. of the Int. Geotech. Symp. (IGSS,2007), Yuzhno-Sakhalinsk, Russia, Kazakhstan Geotechnical Society, 24-26th July, 2007*., Seoul:Publisher of Korean Publishing Company: 301–304.

Mangushev, R.A. & Diakonov, I.P., 2017. Limits of Practical Application of «Fundex» Piles under Conditions of Weak Soils. *Zhilishchnoe Stroitel'stvo [Housing Construction]*. 2017. No. 9: 1–6.

Taylor & Francis
Taylor & Francis Group
http://taylorandfrancis.com

Soil dynamics and geotechnical earthquake engineering

Taylor & Francis
Taylor & Francis Group
http://taylorandfrancis.com

Smart Geotechnics for Smart Societies – Zhussupbekov, Sarsembayeva & Kaliakin (Eds)
© 2023 The Author(s), ISBN 978-1-003-29912-7
Open Access: www.taylorfrancis.com, CC BY-NC-ND 4.0 license

Dynamic soil structure interaction of beams on multilayered continua

H. Elhuni & D. Basu
University of Waterloo, Waterloo, Ontario, Canada

ABSTRACT: A new method for dynamic analysis of Euler-Bernoulli beams resting on multi-layered viscoelastic continua (soil) is presented. The governing differential equations of beam and soil displacements are obtained using the extended Hamilton's principle, and these equations are solved analytically and numerically. An iterative solution algorithm is used in conjunction with an implicit time integration scheme to obtain the beam and foundation (soil) responses as functions of time. The developed model resembles the traditional two-parameter spring foundation model, but the analysis shows that the traditional foundation spring parameters cannot be prescribed a priori, but determined as part of the solution. The model produces accurate beam responses as illustrated by comparisons with equivalent two-dimensional finite element analysis results. A few problems are analyzed that illustrate the novel features of the dynamic foundation model.

1 INTRODUCTION

In geotechnical engineering, the concept of beams on elastic or viscoelastic foundations is widely used to analyze the behavior of flexible footings and structural elements such as strip footings, grade beams, and concrete pavements. These structural elements are idealized as beams resting on the underlying soil, which is often termed as the foundation (Morfidis and Avramidis 2005). Different models with different degrees of idealization have been proposed to simulate the behavior of the foundation (soil). The simplest and oldest idealization is to represent the soil as a bed of closely spaced linear springs (Winkler 1867). The Winkler model (also often termed as the one-parameter model) is characterized by the spring constant k_s, which represents the compressive resistance of soil against applied vertical loads and can be related to the modulus of subgrade reaction of soil. The main drawback of the Winkler model is that the vertical springs are assumed to work in isolation with respect to each other because of which the resistance of soil obtained through shear stresses are neglected. An improvement over the Winkler model was proposed by several researchers like Hetenyi (1946), Filonenko-Borodich (1945), Pasternak (1954), and Terzaghi (1955) by introducing a second parameter t_s, which essentially captures the shear interaction between adjacent Winkler springs (this model is often referred to as the two-parameter model). The two-parameter model has been widely adapted by researchers to analyze beam on elastic foundations problems under static and dynamic loads (Basu and Rao 2013).

The difficulty in using the Winkler or two-parameter models is that the two foundation parameters k_s and t_s cannot be reliably obtained from measurable soil properties and are often inaccurately determined from ad hoc, empirical equations (Bowles 1996). Further, for dynamic analysis, geometric damping cannot be explicitly considered using the one- or two-parameter models (Elhuni and Basu 2019).

Improvements to the one- or two-parameter models have been proposed by some researchers in which the soil is idealized as an elastic continuum with simplified assumptions regarding its stress or displacement fields, and applied the simplified continuum approach to beam on foundation problems (Biot 1937, Reissner 1936, 1958, Kerr 1964, Protsenko and Rvachev 1976, Vlasov and Leont'ev 1966). However, these simplified continuum approaches mostly depend on specifically assumed contact pressure distributions that may not be true for

DOI: 10.1201/9781003299127-227

all possible cases of contact, are often mathematically complex, are applicable to linear elastic materials only, and do not take into account material damping in the system (Haldar and Basu 2016, Tvrdá 2017, Sitharam 2018).

Out of the simplified continuum approaches, the one by Vlasov and Leont'ev (1966) is distinct because it leads to the same simple differential equation as that of the two-parameter model (mentioned earlier) but has the additional advantage that the parameters k_s and t_s in this model are rigorously related to the elastic constants of the soil without any empiricism involved. Vallabhan and Das (1989) improved the model of Vlasov and Leont'ev (1966) for static beam problems, and Liang and Zhu (1995) analyzed using the model the steady-state (time-independent) response of beams. All these studies considered a single-layer soil (foundation) beneath the beam. There is no systematic time-dependent, dynamic study performed on beams resting on multi-layered elastic foundations following the modified simplified continuum approach by Vallabhan and Das (1989).

In this paper, a dynamic soil-structure interaction model is developed for the steady-state and transient vibrations of beams resting on multi-layered viscoelastic soil and subjected to oscillatory and moving loads. A layered soil continuum under the beam is considered. The differential equations describing the beam motion and soil displacement are obtained using Hamilton's principle and calculus of variations, and are solved following an iterative algorithm. The resulting differential equation for beam motion resembles that of a beam interacting dynamically with a two-parameter foundation with parameters k_s and t_s. These two parameters are mechanistically related to the soil Young's modulus and Poisson's ratio, and, interestingly, change with time even though the soil elastic constants remain constant – this is a novel development of the new model. The accuracy of the analysis is verified by comparing the results of the analysis with those of equivalent two-dimensional (2-D) finite element (FE) analysis performed using Plaxis. Examples illustrate the application of the method for different oscillatory and moving loads.

2 ANALYSIS

2.1 *Problem definition*

A uniform Euler-Bernoulli beam of length L, width b, depth (thickness) d, mass density ρ_b, and Young's modulus E_b is assumed to be resting on a layered elastic soil (continuum), as shown in Figure 1. A dynamic vertical load $P(x, t)$ is assumed to act on the beam which either moves from left to right in the positive x direction with a velocity v or oscillates in magnitude (with time t) but remains stationary in space. In fact, the load P can both oscillate in magnitude and move with time. The continuum (soil) beneath the beam is split into n layers with the bottom nth layer resting on a rigid base. The total thickness of the continuum is H_{Total}, and the i^{th} layer spans over $H_{i-1} \leq z \leq H_i$ with a thickness $T_i = H_i - H_{i-1}$. The soil is assumed to be isotropic, linear elastic, and homogeneous within any layer i with Young's modulus E_{si}, Poisson's ratio υ_{si}, and mass density ρ_{si}. The details of the soil geometry and Cartesian (x-z) coordinate system are illustrated in Figure 1.

2.2 *Soil displacement, strain, and stress fields*

For the plane-strain problem described above, it is assumed that the horizontal soil displacement u_x caused by the vertical forces are negligible (i.e., $u_x = 0$) and that the vertical soil displacement u_z (Figure 1) can be expressed as a product of separable functions:

$$u_z = w(x, t)\phi(z) \tag{1}$$

where $w(x, t)$ is the beam deflection (considered positive in the positive z direction), which is the same as the displacement of the top surface of the continuum, and $\phi(z)$ is a dimensionless soil displacement function varying with depth z. It is assumed in the analysis that $\phi(0) = 1$, which ensures perfect contact (with no separation) between the beam and the underlying continuum, and that $\phi(H_{\text{total}}) = 0$, which ensures that the vertical displacement in the continuum decreases with depth. Thus, the function ϕ takes into account the geometric damping of the beam-foundation system in the vertical direction.

For the assumed displacements in equation (1), the soil stresses and strains at any point in the continuum is given by

$$\begin{Bmatrix}\sigma_{xx}\\ \sigma_{zz}\\ \sigma_{xz}\end{Bmatrix}=\frac{E_s}{(1+\upsilon_s)(1-2\upsilon_s)}\begin{bmatrix}1-\upsilon_s & \upsilon_s & 0\\ \upsilon_s & 1-\upsilon_s & 0\\ 0 & 0 & 0.5-\upsilon_s\end{bmatrix}\begin{Bmatrix}\varepsilon_{xx}\\ \varepsilon_{zz}\\ \varepsilon_{xz}\end{Bmatrix}=\frac{E_s}{(1+\upsilon_s)(1-2\upsilon_s)}\begin{bmatrix}1-\upsilon_s & \upsilon_s & 0\\ \upsilon_s & 1-\upsilon_s & 0\\ 0 & 0 & 0.5-\upsilon_s\end{bmatrix}\begin{Bmatrix}0\\ -w(x,t)\frac{d\phi(z)}{dz}\\ -0.5\frac{\partial w(x,t)}{\partial x}\phi(z)\end{Bmatrix} \tag{2}$$

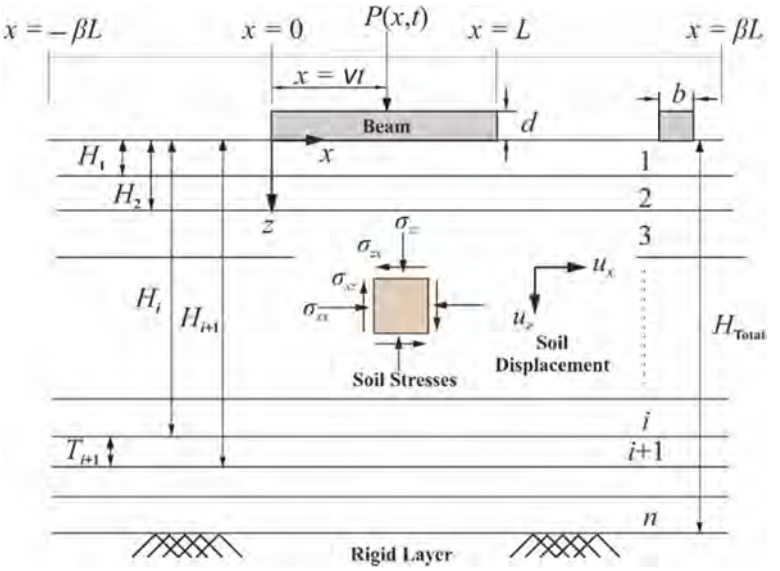

Figure 1. Soil profiles considered in this study.

where $\{\sigma_{xx}, \sigma_{zz}, \sigma_{xz}\}^{\mathrm{T}}$ and $\{\varepsilon_{xx}, \varepsilon_{zz}, \varepsilon_{xz}\}^{\mathrm{T}}$ represent the soil stress and strain tensors, respectively (compressive stresses and contractive strains are considered positive).

2.3 *System energy and extended Hamilton principle*

The extended Hamilton principle of least actions is used to obtain the differential equations of motion of the beam and continuum under dynamic equilibrium:

$$\delta\int_{t_1}^{t_2}(T-U+W_{nc})dt=0 \tag{3}$$

where T and U are the kinetic and potential energies of the beam-soil system participating in the vibration, W_{nc} is the work done by the non-conservative forces acting on the system, t_1 and t_2 are any arbitrary times at which the equilibrium configuration of the beam-soil system is known, and δ is the variational operator. Using equation (2), equation (3) can be rewritten for the present beam-continuum system as

$$\delta\int_{t_1}^{t_2}\left[\int_0^L\frac{\rho_b A_b}{2}\left(\frac{\partial w}{\partial t}\right)^2dx+\sum_{i=1}^{n}\int_{-\beta L}^{\beta L}\int_{H_{i-1}}^{H_i}\frac{\rho_{si}b}{2}\left(\frac{\partial w}{\partial t}\right)^2\phi_i{}^2dzdx\right]dt-\delta\int_{t_1}^{t_2}\left[\int_0^L\frac{E_bI_b}{2}\left(\frac{\partial^2 w}{\partial x^2}\right)^2dx\right.$$
$$\left.+\sum_{i=1}^{n}\frac{1}{2}\int_{-\beta L}^{\beta L}\int_{H_{i-1}}^{H_i}\left(\bar{E}_{si}w^2\left(\frac{d\phi_i}{dz}\right)^2+2G_{si}\phi_i{}^2\left(\frac{\partial w}{\partial x}\right)^2\right)dzdx-\int_0^L P\delta_d(x_0-vt)wdxdt\right]+\delta\int_{t_1}^{t_2}\left[-\frac{1}{2}c\left(\frac{\partial w}{\partial t}\right)^2\right]dt=0 \tag{4}$$

where δ_d is the Dirac delta function, x_0 is the initial position of the applied load P, c is the coefficient of viscous damping of the system, and $\bar{E}_{si}$ (constrained modulus) and G_{si} (shear modulus) are given by:

$$\bar{E}_{si} = [E_{si}(1 - \upsilon_{si})]/[(1 + \upsilon_{si})(1 - 2\upsilon_{si})] \tag{5a}$$

$$G_{si} = E_{si}/[2(1 + \upsilon_{si})] \tag{5b}$$

2.4 *Differential equations for beam and soil displacements*

Considering the variations of functions w and ϕ in equation (4), the differential equations for the beam and soil surface displacements, and for the soil displacement function can be respectively obtained as:

$$E_b I_b \frac{\partial^4 w}{\partial x^4} - 2t_s \frac{\partial^2 w}{\partial x^2} + k_s w + c\frac{\partial w}{\partial t} + (\eta_s + \rho_b A_b)\frac{\partial^2 w}{\partial t^2} = P(x,t) \text{ for } (0 \le x \le L) \tag{6a}$$

$$-2t_s \frac{\partial^2 w}{\partial x^2} + k_s w + c\frac{\partial w}{\partial t} + \eta_s \frac{\partial^2 w}{\partial t^2} = 0 \quad \text{for } (-\beta L \le x \le 0)\ \&\ (L \le x \le \beta L) \tag{6b}$$

$$\frac{d^2\phi_i}{dz^2} - \left(\frac{\zeta_{si} - n_{si}}{m_{si}}\right)\phi_i = 0 \qquad (\text{for } H_{i-1} \le H_i) \tag{7}$$

The parameters in the above equations are given by:

$$\eta_s = \sum_{i=1}^{n} \rho_{si} b \int_{H_{i-1}}^{H_i} {\phi_i}^2 dz \tag{8a}$$

$$k_s = \sum_{i=1}^{n} b \int_{H_{i-1}}^{H_i} \bar{E}_{si}\left(\frac{d\phi_i}{dz}\right)^2 dz \tag{8b}$$

$$t_s = \sum_{i=1}^{n} \frac{b}{2} \int_{H_{i-1}}^{H_i} G_{si}{\phi_i}^2 dz \tag{8c}$$

$$m_{si} = b \int_{-\beta L}^{\beta L} \bar{E}_{si} w^2 dx \tag{9a}$$

$$n_{si} = b \int_{-\beta L}^{\beta L} G_{si}\left(\frac{\partial w}{\partial x}\right)^2 dx \tag{9b}$$

$$\zeta_{si} = b \int_{-\beta L}^{\beta L} \rho_{si}\left(\frac{\partial w}{\partial t}\right)^2 dx \tag{9c}$$

The domains $-\beta L \le x \le 0$ and $L \le x \le \beta L$ for equation (6b) are chosen by trial and error after eliminating the boundary effects (β is a fraction or multiple of L).

The initial conditions required to solve the set of differential equations (6a) and (6b) are that $w = 0$ and $\partial w/\partial t = 0$ at $t = 0$. However, the boundary conditions depend on the end conditions of the beam. For free end beams, the soil domains on both sides of the beam are required in the analysis, and equation (6b) is required to be solved in conjunction with equation (6a) in order to ensure continuity of displacement on both sides of the beam. For such free end beams, the displacements w at $x = \pm\beta L$ are assumed to be zero and continuity of displacement

w at $x = 0$ and $x = L$ is maintained. Further, the beam bending moment $E_bI_b\partial^2 w/\partial x^2$ and shear force $E_bI_b\partial^3 w/\partial x^3$ are assumed to be zero at $x = 0$ and $x = L$. For simply supported or fixed beams, only equation (6a) is solved with the domain spanning $0 \le x \le L$, and the beam deflection w and bending moment $E_bI_b\partial^2 w/\partial x^2$ are assumed to be zero at $x = 0$ and $x = L$ for simply supported beams, while beam deflection w and slope $\partial w/\partial x$ are assumed to be zero at $x = 0$ and $x = L$ for fixed beams. For solving equation (7), the boundary conditions required are $\phi = 1$ at $z = 0$, $\phi_i = \phi_{i+1}$ at $z = H_i$, and $\phi = 0$ at $z = H_{\text{total}}$.

It is important to note that the parameter η_s represents the mass of soil per unit beam length participating in the vibration, the parameter k_s is analogous to the Winkler spring constant of soil and represents the compressive resistance of soil, and the parameter t_s represents the shear resistance of soil and can be interpreted as the shear force acting between adjacent soil springs that are compressed differently because of the applied load.

2.5 *Solution of differential equations*

Solution of the differential equations (6a)-(6b) of w is obtained by using the FE method. Two-noded rod (bar) elements with linear Lagrangian shape functions are used to discretize the domains $-\beta L \le x \le 0$ and $L \le x \le \beta L$ (i.e., the domains in x direction with no beam) and two-noded beam elements with cubic Hermitian shape functions are used to discretize the domain $0 \le x \le L$ (i.e., the domain in x direction in which the beam is present) to obtain a set of algebraic equations of the form:

$$\sum_e [m]^e\{\ddot{w}\} + \sum_e [c]^e\{\dot{w}\} + \sum_e [k]^e\{w\} = \sum_e \{f\}^e \tag{10}$$

where $[m]^e$, $[c]^e$ and $[k]^e$ are the elemental mass, damping, and stiffness matrices, respectively, $\{f\}^e$ is the elemental force vector, $\{w\}$ is the global degrees of freedom vector (consisting of the unknown nodal displacements w for the entire domain and nodal slope $\partial w/\partial x$ for the portion of the domain within the beam), $\{\ddot{w}\}$ is the global acceleration vector, $\{\dot{w}\}$ is the global velocity vector, and $\sum$ represents assembly. The time integration to obtain solutions is performed following the Wilson-θ method (Bathe 1996).

Solution of the differential equation (7) for ϕ is obtained analytically, which for a single soil layer (of thickness T_1) can be expressed as

$$\phi_1(z) = \left\{\sinh\left[\left(\frac{T_1^2(\zeta_{s1} - n_{s1})}{m_{s1}}\right)^{0.5}\left(1 - \frac{z}{T_1}\right)\right]\right\} \Big/ \left\{\sinh\left(\frac{T_1^2(\zeta_{s1} - n_{s1})}{m_{s1}}\right)^{0.5}\right\} \tag{11}$$

2.6 *Solution algorithm*

The parameters k_s, t_s, and η_s must be known in order to solve the differential equations for w (equations (6a) and (6b)) and these parameters depend on ϕ. At the same time, the parameters m_{si}, n_{si} and ζ_{si} must be known in order to obtain ϕ (from Eqs. (7) or (11)) and these parameters depend on w. Therefore, the equations of w and ϕ are coupled, and are solved simultaneously following an iterative scheme.

A guess for the spatial distribution of ϕ is made by assuming a linear distribution of ϕ. With this assumed distribution, k_s and t_s are calculated (note that η_s is not considered in the initial calculation) using equations (8b) and (8c), and these parameters are then used to calculate the displacement w and its spatial derivative $\partial w/\partial x$. Using the calculated w and $\partial w/\partial x$, parameters m_{si} and n_{si} are calculated from equations (9a) and (9b) (note that ζ_{si} is ignored). The parameters m_{si} and n_{si} are then used to obtain a new $\phi(z)$. The newly calculated $\phi(z)$ is compared with the assumed $\phi(z)$ and, if the difference is greater than a prescribed tolerance, the calculations are repeated with the calculated ϕ as the new guess. The iterative calculations are continued until the assumed and calculated ϕ values fall within a tolerance limit. The tolerance limit set on ϕ for the iterations is 10^{-5}.

The distribution of ϕ obtained from the above calculations is given as input to the dynamic analysis (following the Wilson-θ method), and iterations similar to those described in the previous paragraph are performed within each time increment Δt. For the first time step, the initial position

x_0 of the applied load, geometry, material properties, and $\phi(z)$ are given as inputs, and the parameters k_s, t_s, and η_s are calculated. These calculated parameters are used to obtain the beam and soil displacement w, spatial derivative $\partial w/\partial x$ (which is the slope for the beam), velocity $\partial w/\partial t$, and acceleration $\partial^2 w/\partial t^2$. These quantities are used to calculate m_{si}, n_{si} and ζ_{si}, which are used to calculate the distribution $\phi(z)$. The newly obtained ϕ (dynamic) is checked against the previous ϕ (which is the ϕ for the first iteration of the first time increment), and iterations are continued until the difference between two consecutive distributions of $\phi(z)$ fall within the tolerable limit of 10^{-5}. At this point, the calculated w, $\partial w/\partial x$, $\partial w/\partial t$, and $\partial^2 w/\partial t^2$ are the final values for the given time step, and the next increment of time is then applied and the whole iterative process is repeated for each subsequent time steps until the final time increment is completed to reach the final time.

3 RESULTS

3.1 *Verification*

In order to verify the accuracy of the present analysis, comparisons of beam responses obtained from the present analysis are made with those obtained from equivalent two-dimensional (2-D) FE analysis (using Plaxis) in which the linear viscoelastic constitutive relationship is used. The nature and type of load, geometry of the problem, end conditions of the beam, and the material constants are selected differently in the multiple verification problems to ensure that the present analysis works for all possible cases. The boundaries of the FE domain were chosen sufficiently far from the beam (by trial and error) to avoid any boundary effects. Additional boundary conditions are prescribed at the end points of the beams to simulate different types of beam-end conditions (i.e., fixed, free, and hinged supports).

Figure 2 shows the free-end displacement time-history response $w(L, t)$ of a cantilever beam subjected to a concentrated ramp load at the free end with a maximum value of 20 kN and acting over a duration of 1 sec. The figure also shows the corresponding beam response obtained from 2-D FE analysis. The beam is considered to be free to displace and rotate at the right end and completely restrained against translation and rotation at the left end. The details of the beam and soil inputs are given in the figure. From the comparisons it is apparent that the results from both the analyses are in good agreement, with the maximum difference between the results of the present analysis and 2-D FE analysis being 6.2%.

A comparison of beam displacement profiles obtained from the present analysis and 2-D FE analysis for a free-free beam subjected to a point step load of magnitude 60 kN and duration 1 sec acting at the mid-span of the beam is shown in Figure 3 (other inputs for the problem are shown in the figure). The beam rests on a three-layer soil deposit and is free to displace and rotate at both the ends. The maximum difference between the beam displacements obtained from the present analysis and 2-D FE analysis is 3.8%, which further proves that the present analysis framework produces accurate beam response.

3.2 *Dynamic characteristics of the foundation*

The characteristics of the dynamic two-parameter foundation model and its advantage over the conventional beam-foundation models are illustrated by studying the time histories of the soil resistance parameters k_s and t_s obtained using the present analysis for a 10 m-long free beam vibrating on a 10 m thick single soil layer and subjected to different dynamic loads. The time history responses of k_s and t_s for are shown in Figures 4(a)-(c). The details of the beam-soil inputs are given in the figures. In Figure 4(a), the beam is subjected to a 30 kN point load moving with a constant velocity v = 10 m/sec, while a sinusoidal load with 20 kN amplitude, 15 HZ frequency, and 5 sec duration acts at the mid-span of the beam in Figure 4(b). A step load of 25 kN magnitude and 4 sec duration acts at the mid-span of the beam in Figure 4(c).

Interestingly, the two soil parameters change with time even though the soil elastic constants remain constants. The effect of different types of load on k_s and t_s is clear in Figures 4 (a)-(c). Thus, k_s and t_s cannot be given as input a priori, as is conventionally done. These parameters depend on the elastic constants of the soil, on the relative stiffnesses of the beam and soil, and on the loading characteristics.

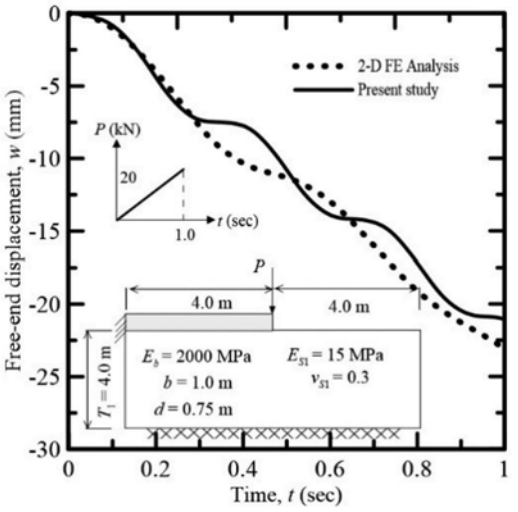

Figure 2. Time history response of free-end displacement of a 4 m long cantilever beam resting on a 4 m thick homogeneous soil deposit and subjected to a ramp load with a maximum value of 20 kN.

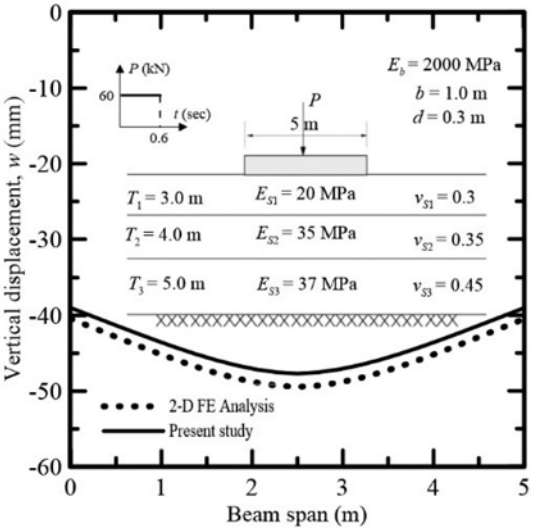

Figure 3. Beam displacement profiles corresponding to time t = 0.6 sec of a 5 m long free-free beam resting on a three-layer soil deposit and subjected to a point step load of magnitude 60 kN acting for 0.6 sec.

The characteristics of the foundation system is further investigated for a free beam resting on a three-layer soil deposit, as shown in Figures 5(a)-(b). The details of the beam-soil inputs are given in the figure. The beam is considered to be free to displace and rotate at both ends (free ends). A concentrated ramp load with a maximum amplitude of 25 KN and duration of 1 sec is assumed to act at the mid-span of the beam. The time histories of the parameters k_s and t_s, and of the vibrating soil mass η_s are plotted in Figures 5(a)-(b). The parameters k_s and t_s tend to be constant at the beginning of the dynamic analysis when the contribution of the vibrating soil mass η_s is small. As η_s starts contributing to the vibrating system over time, the parameters k_s and t_s start to vary as functions of time. In fact, η_s also varies with time initially and becomes constant over time. This is in stark contrast to the discrete two parameter model in which k_s and t_s are kept constants and η_s is usually neglected.

3.3 *Effect of variable speed on the dynamic beam response*

A 20 m long simply-supported beam is considered for investigating the effect of variable velocity of moving load. The beam is assumed to rest on a 4 m thick single-soil layer. The details of the beam-soil system are given in Figure 6. To investigate the effect of variable velocity, four cases are considered. In Case 1, a 5 kN point load starts moving from the left end at x = 0 m with a constant speed of 5 m/sec and exits the beam at x = 20 m with the same speed. In Case 2, the same 5 kN load starts moving from x = 0 m with an initial speed of 5 m/sec and with uniform deceleration of –0.625 m/sec^2 such that the load stops at the right end of the beam corresponding to x = 20 m. In Case 3, the same 5 kN load starts to move from x = 0 with zero initial velocity and uniform acceleration of 0.625 m/sec^2 such that the load attains a speed of 5 m/sec at the right end corresponding to x = 20. In Case 4, a 5 kN point load enters the left end of the beam at point x = 0 with an initial velocity of 5 m/sec and uniformly decelerates at –1.25 m/sec^2 so that the load stops at the mid-span of the beam (corresponding to x = 10 m).

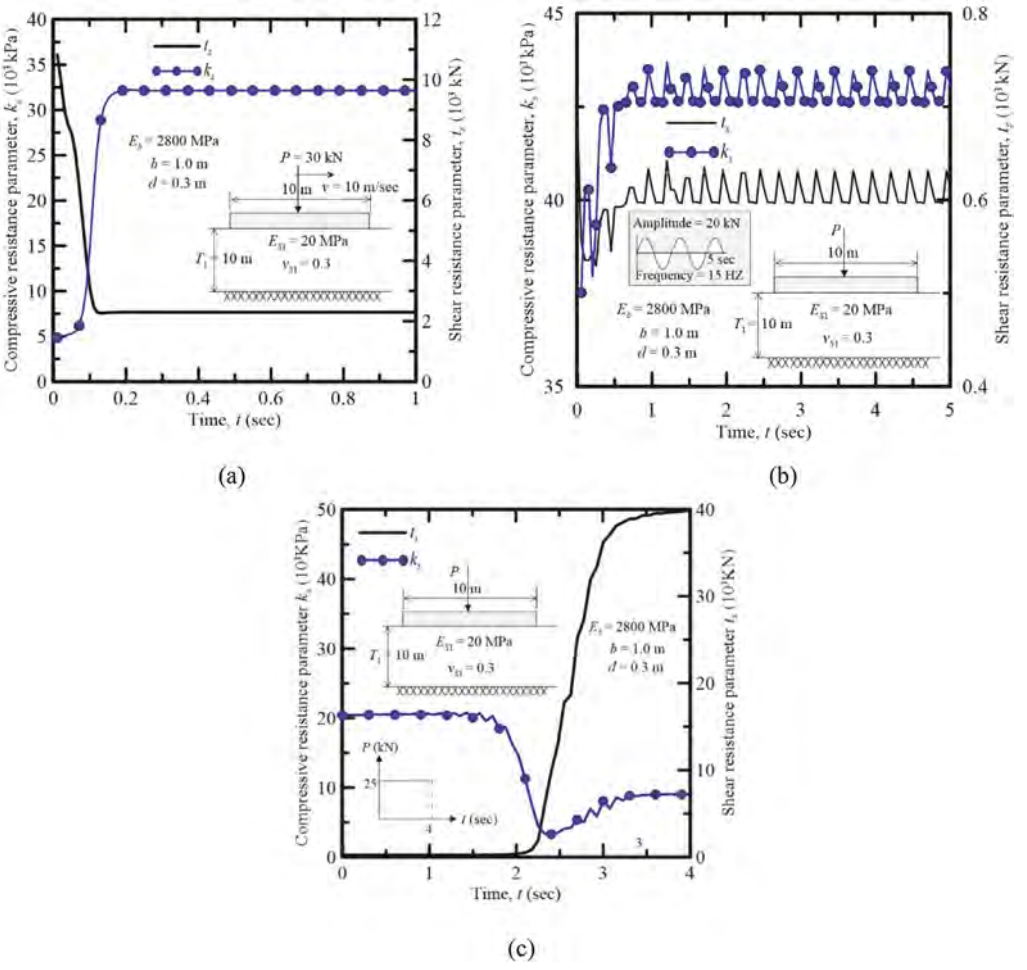

Figure 4. Time history responses of the soil resistance parameters k_s and t_s for a 10 m long free beam resting on a single-layer soil deposit and subjected to (a) a 30 kN point load moving with a constant velocity of 10 m/sec, (b) a sinusoidal point load with a maximum amplitude of 20 kN acting at the mid-span of the beam, and (c) a step point load of 25 kN magnitude acting at the mid-span of the beam.

Figure 6 shows the dynamic amplification factor ψ_D versus the normalized load position vt/L for Cases 1-4. The dynamic amplification factor ψ_D is calculated as the ratio of the mid-span dynamic

displacement $w(0.5L, t)$ to the maximum mid-span static displacement $w(0.5L)$. The beam response is different for loads moving with constant and variable velocities. Accelerating and decelerating loads tend to produce greater dynamic displacements compared with those corresponding to loads moving with a constant velocity.

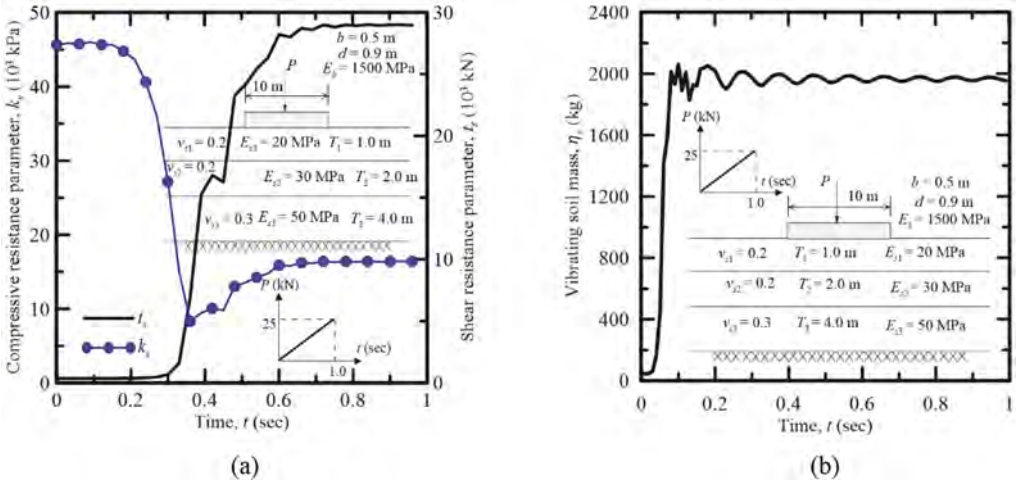

Figure 5. Time dependent response of a 10 m long beam resting on a three-layer soil deposit and subjected to a ramp point load with maximum amplitude of 25 KN: time histories of (a) k_s and t_s, and (b) η_s.

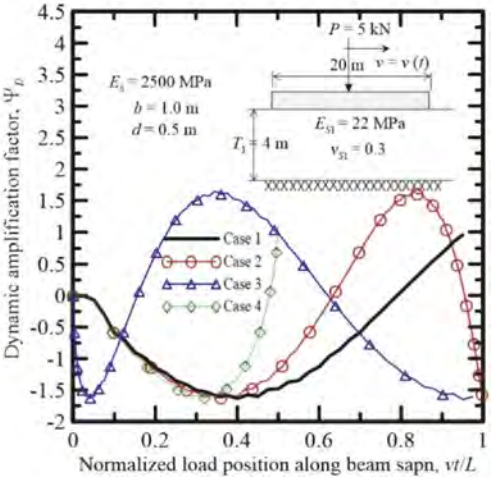

Figure 6. Beam response under loads moving with variable speeds.

4 CONCLUSIONS

A new model for dynamic soil structure interaction is developed using the variational principles of mechanics. The model is applied to the analysis of beams resting on multi-layered viscoelastic soil subjected to oscillatory and moving loads. A continuum approach is adopted in which assumptions regarding the displacement field in the multi-layered soil are made. The extended Hamilton's principle is applied to obtain the Euler-Lagrange equations of motion describing the dynamic equilibrium of the beam-soil system. Solutions are obtained analytically and numerically using an iterative algorithm along with a numerical time integration

scheme. Accuracy of the model in producing reliable beam response is verified through comparisons with equivalent 2-D finite element analysis. Appropriate equivalent elastic constants of soil have to be used to obtain accurate beam response in practice.

The developed model leads to equations similar to beams resting on bed of springs (i.e., the soil is represented by springs, which is commonly termed as the foundation on which the beam rests) characterized by two parameters k_s and t_s representing the compressive and shear resistances of the foundation. However, unlike the traditional approach, k_s and t_s are not foundation constants but depend on the beam-foundation interaction and, therefore, are functions of time – this is a novel finding and a significantly different approach for problems related to dynamic interaction of beams with underlying foundations. These parameters are determined as part of the solution and no empirical estimations are necessary. The inertial resistance of soil (i.e., the foundation) is explicitly taken into account by a parameter η_s, which is also a function of time (inertia of foundations are not taken into account for traditional spring-based foundation models). Thus, the parameters k_s, t_s and η_s are interaction parameters and change with load frequency and velocity. Geometric damping is explicitly taken into account in this model through a function ϕ, which is typically not available in traditional spring-based soil-structure interaction models.

REFERENCES

Basu, D. & Kameswara Rao, N. S. V. (2013). Analytical solutions for Euler–Bernoulli beam on viscoelastic foundation subjected to moving load. International Journal for Numerical and Analytical Methods in Geomechanics, 37(8), 945–960.

Biot, M. A. (1937). Bending of an infinite beam on an elastic foundation.

Bowles, J. E. (1988). Foundation analysis and design.

Elhuni, H. & Basu, D. (2019). Dynamic soil structure interaction model for beams on viscoelastic foundations subjected to oscillatory and moving loads. Computers and Geotechnics, 115, 103157.

Filonenko-Borodich MM. (1945) A very simple model of an elastic foundation capable of spreading the load. Sb. Tr. Mosk. Elektro. Inst. Inzh. Trans 53.

Hetényi, M., & Hetbenyi, M. I. (1946). Beams on elastic foundation: theory with applications in the fields of civil and mechanical engineering (Vol. 16). Ann Arbor, MI: University of Michigan press.

Haldar, S., & Basu, D. (2016). Analysis of beams on heterogeneous and nonlinear soil. International Journal of Geomechanics, 16(4), 04016004.

Kerr, A. D. (1964). Elastic and viscoelastic foundation models.

Liang, R. Y., & Zhu, J. X. (1995). Dynamic analysis of infinite beam on modified Vlasov subgrade. Journal of transportation engineering, 121(5), 434–442.

Morfidis, K., & Avramidis, I. E. (2005). Generalized beam-column finite element on two-parameter elastic foundation. Structural engineering and mechanics: An international journal, 21(5), 519–537.

Pasternak PL, PL. (1954). On a new method of analysis of an elastic foundation by means of two foundation constants. Gosudarstvennoe Izdatelstvo Literaturi po Stroitelstvu I Arkhitekture, Moscow.

Protsenko, V. S., & Rvachev, V. L. (1976). Plate in the form of an infinite strip on an elastic half-space: PMM vol. 40, n□ 2, 1976, pp. 298–305. Journal of Applied Mathematics and Mechanics, 40(2), 273–280.

Reissner, E. (1958). Symmetric bending of shallow shells of revolution. Journal of Mathematics and Mechanics, 7(2), 121–140.

Reissner, E. (1936). Stationary, axially symmetric vibrations of a homogeneous elastic halfspace excited by a vibrating mass. Arch Appl Mech, 7(6), 381–96.

Sitharam, T. G. (2018). Advanced foundation engineering. Taylor & Francis, a CRC title, part of the Taylor & Francis imprint, a member of the Taylor & Francis Group, the academic division of T & F Informa, plc.

Terzaghi, K. (1955). Evalution of conefficients of subgrade reaction. Geotechnique, 5(4), 297–326.

Weaver Jr, W., Timoshenko, S. P., & Young, D. H. (1974). Vibration problems in engineering. John Wiley & Sons.

Tvrdá, K. (2017). Foundation plate on the elastic half-space, deterministic and probabilistic approach. In MATEC web of conferences (Vol. 107, p. 00058). EDP Sciences.

Vallabhan, C. V. & Das, Y. C. (1989). Beams on elastic foundations: a new approach. In Foundation Engineering: Current Principles and Practices (pp. 613–624). ASCE.

Vlasov, V. Z. (1966). Beams, plates and shells on elastic foundation. Israel Program for Scientific Translation.

Winkler, E. (1867). Theory of elasticity and strength. Dominicus Prague.

Smart Geotechnics for Smart Societies – Zhussupbekov, Sarsembayeva & Kaliakin (Eds)
© 2023 The Author(s), ISBN 978-1-003-29912-7
Open Access: www.taylorfrancis.com, CC BY-NC-ND 4.0 license

Shaking analysis of masonry wall in large deformation range using coupled MPM-DDA

S. Kawano & R. Hashimoto
Hiroshima University, Higashi-Hiroshima, Hiroshima, Japan

ABSTRACT: For the investigations on the effective seismic reinforcement method of the masonry walls, a stability evaluation method to reveal the collapse mechanisms of the masonry walls is strongly demanded. This study focused on a coupled Material Point Method and Discontinuous Deformation Analysis (MPM- DDA) that can treat the mechanical interaction among the materials such as the stones and the backfill soil within a large deformation range. A shaking table experiment of a masonry wall model was simulated using the MPM-DDA to check the validation of the method for seismic response analysis of masonry walls. The simulated results agreed quantitatively well with the experiment using the material properties obtained in the experiment, and the validity of the MPM-DDA was successfully confirmed.

1 INTRODUCTION

There exists a lot of castle masonry walls all over Japan, and the conservation of them becomes an important task from the viewpoint of their historical and cultural values. However, in recent years, the masonry walls frequently suffered collapse due to strong earthquakes such as the 2016 Kumamoto Earthquake (Figure 1), and investigations on the mechanical characteristics and the effective reinforcement method of the masonry walls have become an urgent task. The masonry has various structural variables such as the stone size, slope, and height. Therefore, it is required to investigate their dynamic behaviors by parametric analysis of the structural variables using a numerical method. In addition, the analytical method used must be able to consider the nonlinear deformation characteristics of the ground behind the stone wall and discontinuities such as displacement and separation between stones and between stones and ground.

Figure 1. Collapsed masonry wall of Kumamoto Castle during the 2016 Kumamoto Earthquake (Kamiya et al., 2018).

At present, the seismic response of masonry walls is often simulated by Discrete Element Method (DEM) using granular elements. Fukumoto et al. (2014) investigated the stone shape effect on the seismic behavior of masonry walls using particle DEM. A series of centrifugal shaking table experiment was reproduced the deformation even after the large deformation. However,

DOI: 10.1201/9781003299127-228

calibration of the mixing ratio of the particles with different shapes was needed to reproduce the experimental results. Meanwhile, Hashimoto et al. (2017) developed a coupled Numerical Manifold Method and Discontinuous Deformation Analysis (NMM-DDA), a combined continuum-discontinuum method, to achieve a strong coupling analysis of a soil-masonry structure system. In the NMM-DDA, the deformation of continuum is modeled with the NMM (Shi, 1991) is a mesh-based similar to the Finite Element Method, and the discrete behaviors of the masonry stones are modeled with the DDA (Shi and Goodman, 1989)considering the contact between the materials defining. Therefore, the NMM-DDA can simulate the interactive behaviors between the masonry stones and backfill soil. Sueoka et al. (2020) applied the NMM-DDA to a simulation of a shaking table experiment of a masonry wall model, and the failure initiation time and failure mode such as the location of the slip line in the backfill were reproduced. However, since the NMM is a mesh-based method, a complete collapse of the soil could not be reproduced. Hence, to reveal a total failure process of the masonry wall, a method that can simulate soil behavior in a large deformation range is required.

To overcome the above problem, this study focus on a coupled Material Point Method and Discontinuous Deformation Analysis (MPM-DDA) proposed by Hashimoto et al. (2022), a new combined continuum-discontinuum method. Combining the DDA and the MPM which is a numerical method for large deformation of continua, the collapse of stones, large deformation of soil, and interaction between them can be analyzed simultaneously. In this study, the MPM-DDA is applied to the simulation of the shaking table experiment of a masonry wall model by Sueoka et al. (2020), and the validation of the method for seismic response analysis of masonry walls is discussed.

2 A COUPLED MPM-DDA

This section provides an outline of the MPM-DDA (Hashimoto et al., 2022). As mentioned above, the MPM-DDA is a combined continuum-discontinuum method based on the MPM and DDA (Figure 2). The MPM (Suslky et al., 1994) is a hybrid particle-grid based numerical method fo large deformation of continua. A continuum is divided into subdomains and represented as particles, called material points, that have mass, volume, stress, strain, and other state variables. The mass, momentum, and internal force of the material points are projected to nodes of a background finite element mesh prepared over the physical domain, and then, the equation of motion is solved on the mesh. Since the material points can move across the elements, large deformation of the objects can be analyzed without mesh tangling problems in the finite element method.

In the MPM-DDA, a target system that consists of multiple objects is divided into the continuum (e.g., soil) and the discrete objects (e.g., masonry stone), and the former part is modeled with the MPM and the latter ones are modeled with the DDA. Then, the contact between the material points and the polygonal blocks of the DDA is formulated by the penalty method (see Figure 2). An implicit time discretization scheme using the Newmark's β method is employed for the MPM (Iaconeta et al., 2017) as same as for the DDA that originally employs the Newmark's β method. Based on the above formulation, the deformation and motion of the material points and the DDA blocks are solved monolithically including their interactions.

3 SHAKING TABLE EXPERIMENT OF A MASONRY WALL MODEL

To investigate the applicability of MPM-DDA to the seismic response analysis of stone walls, a simulation of a shaking table experiment of a masonry wall model by the second author (Sueoka et al., 2020) is conducted in this study. The outlines of the experiment are explained in this section.

Figure 3 is the schematic figure of the masonry wall model used in the experiment. The model consists of the backfill soil, and the masonry wall that retains the backfill. The masonry wall consists of five stones, named stone 1~5 from bottom to top, stacked with uniform overlapped width. The bottom stone is fixed in contact with the soil container wall. Sydney sand with a moisture content of w_s = 4.31 %, specific gravity G_s = 2.65, and mean grain size D_{50} = 0.31mm was used for making the backfill soil, and hollow concrete blocks (average density: 0.876 g/cm^3, mass: 12.33 kg) were used as the wall material. The strength parameters of the Sydney sand

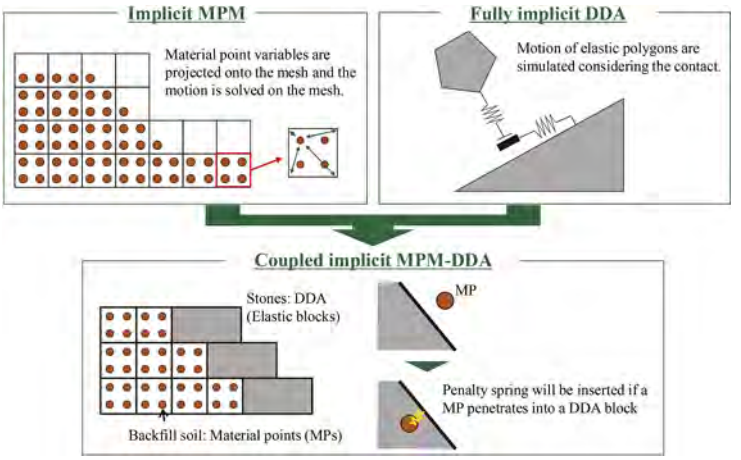

Figure 2. Outlines of the implicit MPM-DDA.

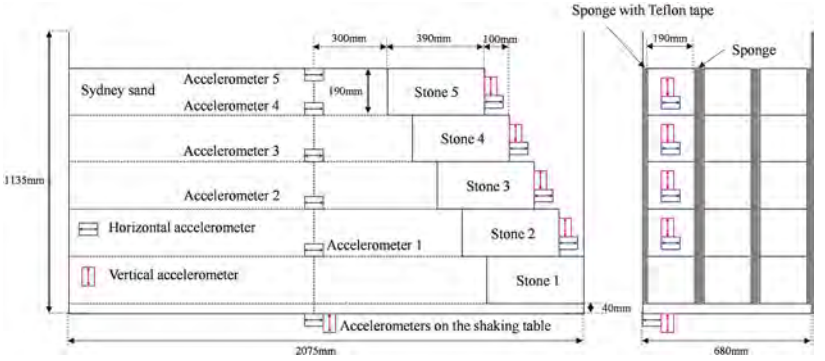

Figure 3. Masonry wall model.

were determined by the direct shear test. The cohesion was 4.09 kPa, and the internal friction angle was ϕ = 33.7 °. The static friction angle ϕ_s and dynamic friction angles ϕ_d between the stones were measured by a shaking table experiment conducted on a pair of stacked concrete blocks. As a result, ϕ_s = 37.0 ° and ϕ_d = 27.5 ° were obtained. The friction properties between the stones and the backfill soil were obtained by a friction test, and both ϕ_s and ϕ_d were 31.0 °.

Figure 4 shows the input acceleration used in the experiment (waveforms measured by an accelerometer installed on the shaking table). The frequency was 4 Hz in the horizontal direction only, and the amplitude was tapered to 706.3 gals from 0 to 20 seconds, followed by 20 seconds of maximum acceleration. Though only the horizontal wave was input, large vertical acceleration was observed due to the collision between the stone and the soil container. To observe the behavior of the stones and the ground behind them, five horizontal accelerometers were attached to the ground behind them, and horizontal and vertical accelerometers were attached to the stones 2~5 and to the shaking table. The displacement of each stone was calculated by analyzing the video taken during the experiment.

4 ANALYSIS USING THE MPM-DDA

4.1 *Analytical conditions*

Simulation of the shaking table experiment explained in the last section is conducted here using the implicit MPM-DDA. Figure 5 is the analytical domain of the masonry wall modeled

with the MPM-DDA. The stones and the soil container are modeled with the DDA and the backfill soil is discretized to the material points. Here, the inner width of the container is slightly different from Figure 3 due to the particle representation of the soil, but the size and shape of the wall are the same as those of the experimental model.

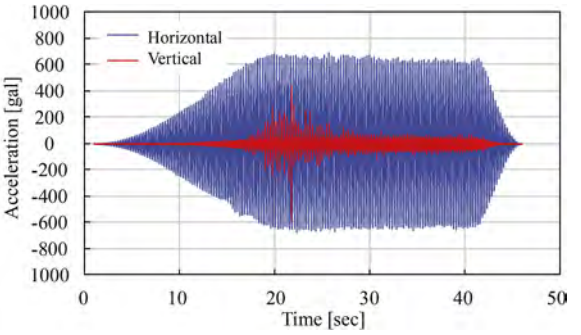

Figure 4. Input acceleration of the shaking table experiment.

The material properties are summarized in Table 1. The stone was modeled as elastic, and the Drucker-Prager model with strain-softening was applied to the backfill soil. The internal friction angle and initial cohesion were set based on the direct shear test, and the initial dilatancy angle was matched to the internal friction angle. Cohesion and dilatancy angle were reduced linearly to zero as the accumulated plastic deviator strain approached 0.1. Table 2 shows the parameters for the material interfaces, and the friction angles were set based on the experiment. The penalty values were determined so that a large penetration between the objects does not occur. It is noted that the B-bar method was used to avoid volumetric locking. Time increment was 0.00005 sec.

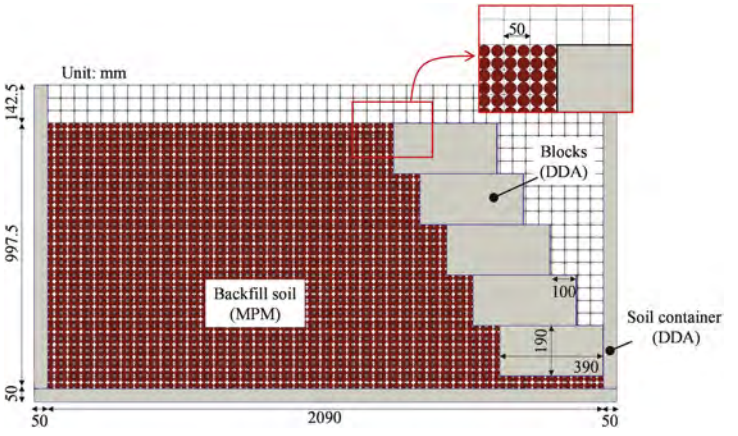

Figure 5. Analytical domain of the masonry wall model.

After giving the initial stress under gravity, the input acceleration in Figure 4 was applied to the soil container. Since the deformation of the wall converged after around 17 seconds from the start of the shaking in the experiment, the simulation was performed for the first 20 seconds.

4.2 *Results*

Figure 6 is the time history of the horizontal displacement of the stone 2 relatives to the soil container. Here, rightward in Figure 3 is the positive direction. In the experiment (black line), the stone started to move rightward around 14 seconds, and then, the velocity increased as the deformation progressed. Finally, the stone stopped at the displacement of 45 mm because

Table 1. Material properties.

		Stone (Elastic)	Backfill soil (Drucker Prager)
Unit weight	[kN/m^3]	8.6	14.8
Young's modulus	[MPa]	1.0×10^4	10.0
Poisson's ratio		0.2	0.3
Internal friction angle	[deg.]	-	33.7
Initial cohesion	[kPa]	-	4.09
Residual cohesion	[kPa]	-	0.0
Initial dilatancy angle	[deg.]	-	33.7
Residual dilatancy angle	[deg.]	-	0.0
Accumulated plastic deviator strain at the residual state		-	0.1

Table 2. Parameters of the contact interfaces.

		Stone-Stone	Stone-Soil
Normal penalty coefficient	[kN/m]	1.0×10^6	1.0×10^6
Shear penalty coefficient	[kN/m]	1.0×10^5	1.0×10^5
Static friction angle	[deg.]	37.0	31.0
Residual friction angle	[deg.]	27.5	31.0

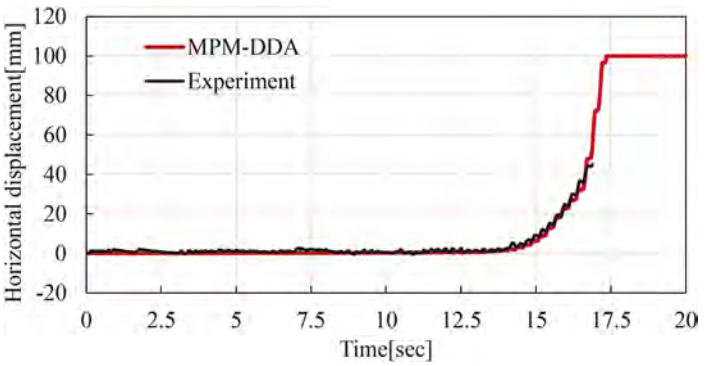

Figure 6. Time history of the relative horizontal displacement of the stone 2.

the accelerometer attached to the stone contacted with the container wall. On the other hand, the simulated result with the MPM-DDA (red line) showed almost identical curve to the experimental result. Since the shape of the accelerometer was not considered in the simulation, the displacement increased up to 100 mm which is the initial clearance between the stone 2 and the container wall.

Figure 7(a) is the snapshot of the model configuration at the moment that the stone 2 reached the soil container wall (17 seconds from the start of shaking) in the experiment, and Figure 7(b) is the simulated deviator strain contour at the same moment with Figure 7(a). According to Figure 7(a), the masonry wall slid rightward and the backfill soil collapsed. Since there was a stepped surface due to a tensile crack on the top of the backfill soil, the location of the slip line in the backfill was presumed to be the white line in the figure that connects the crack and the initial toe of the backfill.

In Figure 7(b), the backfill soil deformed largely showing a clear shear band mainly owing to the strain softening of the soil, and a stepped surface was generated on the top of the backfill as observed in the experiment. In addition, the location of the shear band was almost identical to the presumed slip line in the experiment. Considering these results, therefore, the MPM-DDA could reproduce the experimental results quantitatively even in the large deformation range.

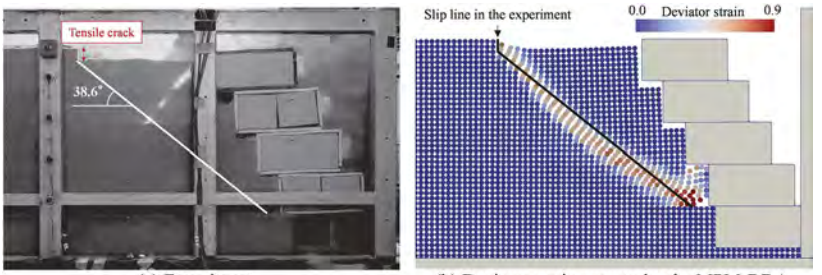

Figure 7. Deformation of the masonry wall when the stone 2 reached the container wall.

5 CONCLUSION

In this study, to establish a numerical method for castle masonry walls in a large deformation range, the applicability of the MPM-DDA, a novel combined continuum-discontinuum method, was examined through the simulation of the shaking table experiment of a masonry wall model. By using the material properties obtained in the experiments, the simulated results agreed quantitatively well with the experimental results from the viewpoint of the stone displacement and failure mode in the backfill soil. As a result, the validation of the MPM-DDA for the seismic response analysis of the masonry walls was confirmed successfully. For further study, the MPM-DDA will be applied to a parametric study on the structural characteristics of the masonry walls.

REFERENCES

Fukumoto, Y., Yoshida, J., Sakaguchi, H. and Murakami, A.: The effects of block shape on the seismic behavior of dry-stone masonry retaining walls: a numerical investigation by discrete element modeling, *Soils. Found.*, Vol. 54, No. 6, pp. 1117–1126, 2014.

Hashimoto, R., Bodhinanda, C. and Soga, K.: A coupled implicit MPM-DDA for soil-structure interaction problems, *Proc. of WCCM-APCOM 2022*, Paper No. 2714, 2022.

Hashimoto, R., Kikumoto, M., Koyama, T. and Mimura, M.: Method of deformation analysis for composite structures of soils and masonry stones, *Comput. Geotech.*, Vol. 82, pp. 67–84, 2017.

Iaconeta, I., Larese, A., Rossi, R. and Guo, Z.: Comparison of a material point method and galerkin mesh-free method for the simulation of cohesive-frictional materials, *materials*, Vol. 10, Paper ID 1150, 2017.

Kamiya, K., Kikumoto, M., Hashimoto, R., Kuwajima, R. and Koyama, T.: Damage analysis of stone walls of Kumamoto castle due to the 2016 Kumamoto earthquake, *J. JSNDS*, Vol. 37, Special issue, pp. 1–16, 2018 (in Japanese).

Shi, G. H.: Manifold method of material analysis, *Trans. 9th Army Conference on Appl. Math. Comput.*, U.S. Army Research Office, Report No. 92-1, 1991.

Shi, G. H. and Goodman, R. E.: Generalization of discontinuous deformation analysis for forward modeling, *Int. J. Numer. Anal. Meth. Geomech.*, Vol. 13, pp. 359–380, 1989.

Sueoka, T., Hashimoto, R., Kikumoto, M., Kamiya, K. and Russell, A.: Simulation of shaking table test of masonry wall by NMM-DDA, *Proc. of the 47th Japanese Symposium on Rock Mechanics*, pp. 165–172, 2020 (in Japanese).

Sulsky, D., Chen, Z. and Schreyer, H. L.: A particle method for history-dependent materials, *Comput. Methods Appl. Mech. Engrg.*, Vol. 118, pp. 179–196, 1994.

Smart Geotechnics for Smart Societies – Zhussupbekov, Sarsembayeva & Kaliakin (Eds)
© 2023 The Author(s), ISBN 978-1-003-29912-7
Open Access: www.taylorfrancis.com, CC BY-NC-ND 4.0 license

Methods of setting stiffness of horizontal joints of large-panel buildings at soil-structure interaction calculation

V.V. Bakrysheva & K.G. Shahskin
Institute "Georeconstruction", Saint-Petersburg, Russian Federation

ABSTRACT: The literature does not pay any attention to stiffness of a horizontal connection of floor slabs between each other in a platform joint. The objective of this paper is to analyze the level of development of calculation methods for stiffness of joints of panel buildings, compare the analytical calculation and numerical solution. There have been analyzed formulae for calculation of compliance of platform joints of panels given in the regulations. There are given results of calculations using numerical methods for defining compliance of a platform joint and comparison with the analytical solution. As the result it is concluded that for the vertical direction the numerical solution is almost equal to the analytical one (the difference is less than 5%), at shear along the wall the discrepancy is a bit bigger, the largest discrepancy with the analytical solution occurs at shear across the wall.

1 INTRODUCTION

Calculation methods for defining forces and deformations in elements of panel buildings and joints of elements at design began to develop at construction of the first large-panel buildings. However, before development of computers the most relevant problems included definition of a total stiffness of a building and evaluation of summarized forces in large-panel buildings; generally, analytical methods were used. Due to decreasing interest to large-panel construction in the post-Soviet period, contrary to the general principles of numerical methods for calculating structures of a building, methods of calculation of large-panel structures were almost not updated.

There are several variants that can be used to calculate stiffness of horizontal joints of large-panel buildings. But it is not clear which of them is more adequate for practical use.

"The textbook for calculation of large-panel buildings. Issue 1. Characteristics of stiffness of walls. Elements and joints of large-panel buildings" issued by V.A.Kucherenko Central Research Institute of Building Structures and Moscow Research and Design Institute of Typology and Experimental Design (1974), Industry specific construction standards 32-77 "Guidelines for design of structures of panel residential buildings" of Gosgrazhdanstroy (1978), "Textbook for design of residential buildings. Issue 3. Structures of residential buildings (to Construction Code 2.08.01-85)" issued by Central Research and Design Institute of Residential and Public Construction, Goskomarchitecture (1989) were the main documents, which regulate design and calculations of large-panel structures in the Soviet period throughout Russia.

In 2017 the new set of construction rules "Set of Rules 335.1325800.2017. Large-panel structural systems. Rules of design" replaced the existing Soviet regulations. At the same time some enterprises involved in panel construction developed standards of organizations which contain guidelines on methods of calculations and design of panel buildings. The main types of calculations and formulae stated in these documents repeat the content of the Soviet regulatory documents.

When calculating structures of panel buildings it is important to consider forces in elements and nodes of structures generated by soil strains. According to Set of Rules 335.1325800.2017

DOI: 10.1201/9781003299127-229

calculations of the structural system of large-panel buildings should be made "in spatial domain with account of joint behavior of underground and above-ground parts of a building as well as the foundation and subsoil".

Joints of panels and floor slabs are the most understudied but the most interesting in terms of strains and strength of structures of a large-panel building in general.

In each joint there are possible displacements and turns of each panel/slab relative to each other in three directions. That means that in a general case each joint of slabs and panels has 12 translational and 12 rotational degrees of freedom. As a rule, at ignoring small values of rotational stiffness due to a possibility of turning of slabs and wall panels and at equal stiffness of both slabs of floors and both wall panels (in case of the same floor slabs and wall panels of the upper and lower floors) each joint still has 6 independent stiffness and strength properties.

In Central Research and Design Institute of Residential and Public Construction, Goskomarchitecture (1989) and Set of Rules 335.1325800.2017 there are given formulae to define strength and stiffness of panels and slabs only at application of a vertical load, at action of horizontal forces the calculation of a joint of wall panels for a shear of the upper wall panel is made. However, for example, at differential strains of subsoil of a building or application of horizontal loads horizontal forces also occur in discs of floors, they "pull out" slabs of floors or compress a joint, their value is compatible with a strength of joints for action of horizontal forces, moreover, a rotation of wall panels and floor slabs etc. occurs.

Strength and stiffness of joints at action of horizontal forces in discs of floors and shear of panels are not defined according to the existing methods of calculations. We consider in detail obtaining values of stiffness of platform joints required for calculation of a large-panel building.

The following types of horizontal joints are used in bearing structures of large-panel buildings: platform, contact and combined ones. Platform joints are the most wide-spread.

According to formula (A.9) of Set of Rules 335.1325800.2017, which was earlier given in Central Research and Design Institute of Residential and Public Construction, Goskomarchitecture (1989), a coefficient of compliance at compression for a platform horizontal joint, where a load is transferred via support sections of floor slabs and two mortar joints between connected elements, is computed as per the formula:

$$\lambda_{c,pl} = (\lambda_m^{'} + \lambda_m^{''} + \frac{h_{pl}}{E_{pl}})\frac{A}{A_{pl}} \tag{1}$$

where $\lambda_m^{'}$, $\lambda_m^{''}$ - coefficients of compliance at compression of the upper and lower mortar joints, respectively; h_{pl} – a thickness of a support part of a floor slab; E_{pl} – an initial elastic modulus of concrete of a support part of a floor slab; A_{pl} – an area of platform sections of a joint through which a compressive load is transferred.

According to formulae (A.4)-(A.5) of Construction Codes 335.1325800.2017 a coefficient of compliance of a mortar joint λ_m (mm^3/N) at a short-term compression of the mortar joint, with the compressive strength of mortar 1 MPa and more and the joint thickness 10-20 mm is recommended to be defined according to formulae:

$$\text{at } \sigma_m \le 1,15R_m^{2/3} \quad \lambda_m = 1,5 \cdot 10^{-3} R_m^{-2/3} t_m \tag{2}$$

$$\text{at } \sigma_m > 1,15R_m^{2/3}, \text{ but more than } 2R_m^{2/3} \quad \lambda_m = 5 \cdot 10^{-3} R_m^{-2/3} t_m \tag{3}$$

where σ_m – an average value of compressive stresses in a mortar joint, MPa; R_m – a cubic strength of mortar, MPa; t_m – a thickness of a mortar joint, mm.

If a long-term compressive load is applied to a joint a coefficient of compliance of a horizontal mortar joint is defined according to formula (A.6), Set of Rules 335.1325800.2017 as per formula:

$$\lambda_{m,t} = \lambda_m(1 + \varphi_t), \tag{4}$$

where φ_t – the characteristics of joint creeping taken as equal 1. That means that a long-term compliance of a mortar joint is accepted twice as high as the short-term.

These dependencies of deformability of mortar joints have been evidently obtained empirically. It is also witnessed by dimensionality of multipliers used in formulae and a desired coefficient to compliance (meanwhile formulae are not in a form which depends on dimensionality of values). There is no information on the origin of the given formulae.

Formulae (2), (3) show the dependency of a joint compliance on a strength and stiffness of a joint mortar if reflected through a parameter of cubic strength of joint mortar R_m. In order to compute a value of a joint stiffness not only in the vertical direction there is a need to know an elastic modulus and a shear modulus of cement mortar used in panel joints. However, there is no single method for defining these moduli – different values and options of calculation of these properties are stated in different sources.

The analysis of formulae (2), (3) and evaluation of a value of deformability of a mortar joint are given in Danel (Danel 2010). It is noted the adequacy of definition of a value of a mortar elastic modulus from expressions (2), (3) according to the formula $E_r = \frac{h_r}{\lambda_r}$ and getting a value of a mortar shear modulus from the well-known ratio $E_r = 2G_r(1 + \mu)$, where μ - Poisson ratio of mortar.

Contrary to vertical joints, which are highly influenced by non-linear behavior of embedded parts, as for horizontal joints, Set of Rules 335.1325800.2017 considers linear behavior of mortar joints and concrete of floor slabs. In this connection behavior of horizontal joints can be quite accurately simulated using the finite element method in linear domain.

2 DEFINITION OF STIFFNESS OF HORIZONTAL JOINTS OF WALL PANELS

In order to evaluate stiffness of a platform joint in the software FEMmodels (IEEcloud) there has been created a parametric finite element model using finite elements of the second order. Properties and parameters used in the calculation are presented in the Table 1. Displacement of the upper wall in a joint in three directions was set as an action. Consequently, joint stiffness is computed according to results of solving the problem by division of the obtained force by the set displacement. The calculation results for 200-mm-thick walls of concrete B30 and 160-mm-thick floor panels of concrete B22.5 are given below in Figures 1-4.

Calculation of stiffness of a platform joint

Table 1. Properties and parameters used in the calculation.

Geometrical parameters (m)	
Wall thickness	b=0.2
Floor slab thickness	h=0.16
Supporting width	b_1=0.09
Mortar thickness	t=0.02
Material parameters	
Strain modulus of concrete of slabs (kPa)	$E_{b,p}$=28750000
Strain modulus of concrete of walls (kPa)	$E_{b,w}$=32500000
Calculated resistance of mortar (MPa)	R=20
Value of stresses in a joint (κPa)	$\sigma_m = 5000$
Poisson's ratio of mortar	$\mu = 0.2$

Strain modulus in different stress ranges, kPa:

$$E_{m,1} = \frac{1}{1.5 \cdot 10^{-3} \cdot R^{\frac{-2}{3}}} \cdot 1000 = 4912042.0 \text{ while } \sigma_{m,1} = 1.15 \cdot R^{\frac{2}{3}} \cdot 1000 = 8473.3$$

$$E_{m,2} = \frac{1}{5 \cdot 10^{-3} \cdot R^{\frac{-2}{3}}} \cdot 1000 = 1473612.6 \text{ while } \sigma_{m,1} = 2 \cdot R^{\frac{2}{3}} \cdot 1000 = 14736.1$$

Account of duration of load application:

$$\phi = 1 \qquad E_{m,t} = \frac{E_m}{1+\phi} = 2456021 \qquad E_{b,p,t} = \frac{E_{b,p}}{1+\phi} = 14375000 \qquad E_{b,w,t} = \frac{E_{b,w}}{1+\phi} = 16250000$$

Mortar shear modulus, kPa $\qquad G_{m,t} = \frac{E_{m,t}}{2\cdot(1+\mu)} = 1023342.1$

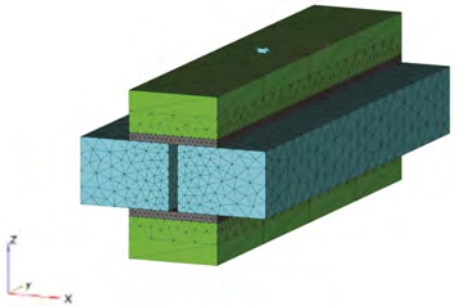

Figure 1. Calculation model.

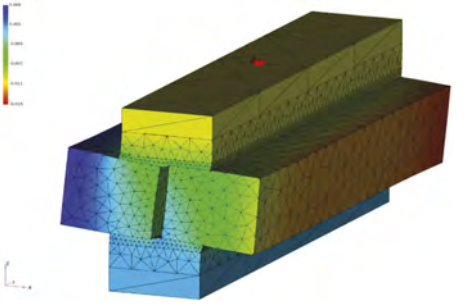

Figure 2. Calculation results. Displacement along axis Z.

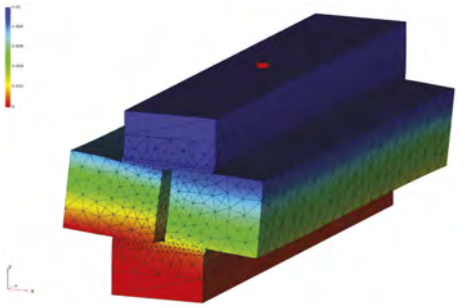

Figure 3. Calculation results. Displacement along axis X.

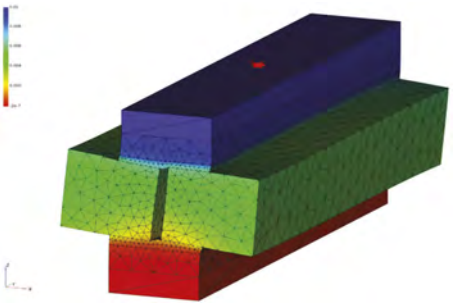

Figure 4. Calculation results. Displacement along axis Y.

Forces from the set displacements

$$N = -63035.7 \qquad Q_z = 7546.8 \qquad Q_y = 23845.0$$

Comparison with analytical solutions

Compliance of the joint according to the numerical calculation (m^3/κN):

$$\lambda_{w,z} = \frac{-\delta \cdot b \cdot s_y}{N} \cdot 10^8 = 3.17 \qquad \lambda_{w,x} = \frac{\delta \cdot b \cdot s_y}{Q_z} \cdot 10^8 = 26.50 \qquad \lambda_{w,y} = \frac{\delta \cdot b \cdot s_y}{Q_y} \cdot 10^8 = 8.39$$

Analytical solution for vertical compliance (m^3/κN):

$$\lambda_m = \begin{cases} 1.5 \cdot 10^{-3} \cdot R^{\frac{-2}{3}} \cdot t \cdot 1000, & \text{if } \sigma_m < 1.15 \cdot R^{\frac{2}{3}} \cdot 1000 = 0.00407 \\ 5 \cdot 10^{-3} \cdot R^{\frac{-2}{3}} \cdot t \cdot 1000, & \text{otherwise} \end{cases}$$

$$\lambda_m = \lambda_m . \frac{0.001^3}{0.001} \left[\mathrm{M}^3/\mathrm{kH}\right] \qquad \lambda_{m,t} = \lambda_m \, . \, (1+\phi)$$

$$\lambda_{c,pl} = \left(2 \cdot \lambda_{m,t} + \frac{h}{E_{b,p,t}}\right) \cdot \frac{b}{b_1 \cdot 2} = 0.00000003 \qquad \lambda_{c,pl} \cdot 10^8 = 3.046$$

Comparison of compliances along z as per the numerical and analytical calculations:

$$\frac{\left|\lambda_{c,pl} - \lambda_{w,z}\right|}{\lambda_{c,pl}} \cdot 100 = 4.15187828$$

Analytical solution for shear compliance (Danel 2012):

$$G_{b,t} = \frac{E_{b,p,t}}{2 \cdot (1+\mu)} = 5989583.3 \quad \lambda_r = \left(\frac{2 \cdot t}{G_{m,t}} + \frac{h}{G_{b,t}}\right) \cdot \frac{b}{2 \cdot b_1} \cdot 10^8 = 7.311$$

Comparison of compliances along y as per the numerical and analytical calculations:

$$\frac{|\lambda_r - \lambda_{w,y}|}{\lambda_r} \cdot 100 = 14.721$$

Compliance along x as per the numerical calculation is considerably higher than as per the analytical calculation:

$$\frac{\lambda_{w,x}}{\lambda_r} = 3.625$$

For the vertical direction the numerical solution is almost equal to the analytical one (the difference is less than 5%). At shear along the wall the discrepancy is a bit bigger. However, the largest discrepancy with the analytical solution occurs at shear across the wall. It is connected with the fact that the analytical solution does not consider a possibility of floor slab rotation. Meanwhile bending stiffness of slabs is quite small and resistance to such a rotation is insignificant, it can be ignored in calculations. Therefore, the value of stiffness across the slab is more adequate as per the numerical solution.

The literature does not pay any attention to stiffness of a horizontal connection of floor slabs between each other in a platform joint. Meanwhile this very stiffness defines a behavior of a floor disc at total bend of a building. This bend manifests itself at any soil-structure interaction calculation. The calculation of stiffness of floor slab fixation in a platform joint for the same parameters is given below in Figures 5-8.

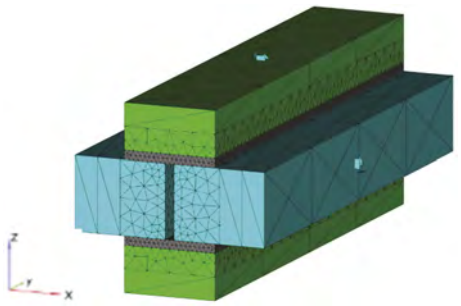

Figure 5. Calculation model.

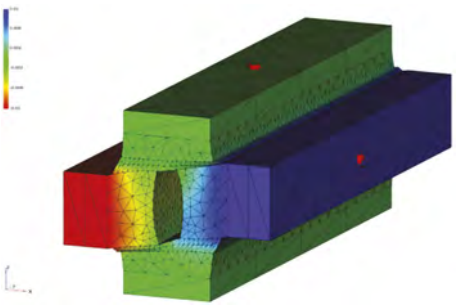

Figure 6. Calculation results. Displacement along axis Z.

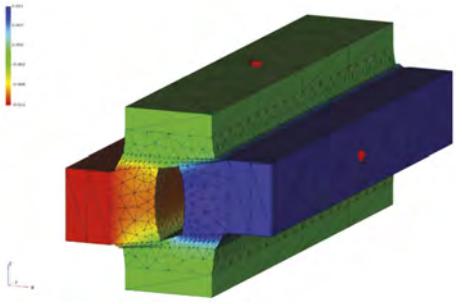

Figure 7. Calculation results. Displacement along axis X.

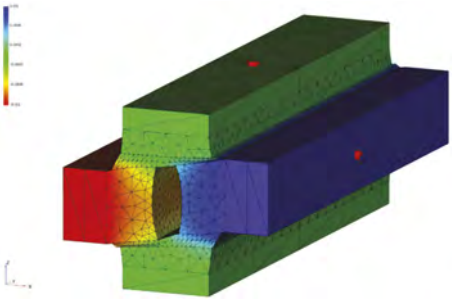

Figure 8. Calculation results. Displacement along axis Y.

Forces from the set displacements

N = 74177.7 Q_z = 101533.9 Q_y = -58653.3

Comparison with analytical solutions

Compliances of the joint according to the numerical calculation (there have been computed linear compliances, not as per an area) (m^2/кN):

$$\lambda_{p,x} = \frac{\delta \cdot s_y}{N} \cdot 10^8 = 13.5 \qquad \lambda_{p,y} = \frac{\delta \cdot s_y}{-Q_y} \cdot 10^8 = 17.0 \qquad \lambda_{p,z} = \frac{\delta \cdot s_y}{Q_z} \cdot 10^8 = 9.8$$

Analytical solution for vertical compliance (m^3/кN):

$$\lambda_{p,x,t} = \frac{t}{2 \cdot G_{m,t} \cdot b_1 \cdot s_y} \cdot 10^8 = 10.9 \quad \lambda_{p,y,t} = \lambda_{p,x,t} \quad \lambda_{p,z,t} = \frac{t}{2 \cdot E_{m,t} \cdot b_1 \cdot s_y} \cdot 10^8 = 4.5$$

One should mention that at differential strains of subsoil and considerable displacement of floor slabs in a platform joint their bearing capacity can reduce. This feature has been considered in Bakrysheva et al. (Bakrysheva 2017). In order to analyze a joint behavior there has also been addressed the modeling using the final element method but with account of nonlinear behavior of concrete and steel. As a result, there has been obtained the nature of joint failure in the form of shear fracture of an angle of wall panels. For the platform joint of 160-mm-thick panels (walls and floor slabs have the same thickness) it has been calculated the limit load applied to horizontal floor slabs – about 200 кN/m.

The calculation results of bearing capacity of platform joints at floor thickness 14 cm and panel thicknesses 14, 18 and 22 cm for different horizontal loads are given in Shapiro (Shapiro 2008).

3 CONCLUSION

The level of development of the existing standards and methods of calculation of joint stiffness for large-panel buildings does not correspond to the existing level of development of construction calculations and methods of numerical calculation.

Empirical formulae (2) и (3) are used for analytical calculation of stiffness of horizontal joints at making soil-structure interaction calculations for a large-panel building. As for the vertical direction, the numerical solution is almost equal to the analytical one (the difference is less than 5%). At shear along the wall the discrepancy is a bit bigger. However, the largest discrepancy with the analytical solution occurs at shear across the wall. It is connected with the fact that the analytical solution does not consider a possibility of floor slab rotation.

REFERENCES

Bakrysheva, V.V., Shashkin, K.G., Sakharov, I.I. 2017. Calculation analysis of behavior of a horizontal joint element of large-panel buildings at differential strains of subsoil using numerical methods. *The proceedings of the All-Russian research-technical conference Engineering-geotechnical investigations, design and construction of subsoils, foundations and underground structures*: 22–28.

Central Research and Design Institute of Residential and Public Construction, Goskomarchitecture. 1989. *Textbook for design of residential buildings. Issue 3. Structures of residential buildings (to Construction Code 2.08.01-85)*. Moscow: Stroyizdat.

Danel, V.V. 2010. Analysis of formulae for definition of compressive stiffness of platform joints of large-panel buildings. *Construction mechanics and calculation of structures* (1): 25–29.

Danel, V.V. 2012. Definition of stiffness of platform joints. *Residential construction*: 32–35.

Gosgrazhdanstroy. 1978. *Industry specific construction standards 32-77. Guidelines for design of structures of panel residential buildings*. Moscow: Stroyizdat.

V.A. Kucherenko Central Research Institute of Building Structures and Moscow Research and Design Institute of Typology and Experimental Design, 1974. *The textbook for calculation of large-panel buildings. Issue 1. Characteristics of stiffness of walls. Elements and joints of large-panel buildings*. Moscow: Stroyizdat.

Recommendation for design of steel embedded parts for RC structures. 1984. Moscow: Stroyizdat.

Shapiro, G.I., Shapiro, A.G. 2008. Calculation of strength of platform joints of panel buildings. *Industrial and civil engineering* (1): 55–57.

Smart Geotechnics for Smart Societies – Zhussupbekov, Sarsembayeva & Kaliakin (Eds)
© 2023 The Author(s), ISBN 978-1-003-29912-7
Open Access: www.taylorfrancis.com, CC BY-NC-ND 4.0 license

Soil-structure interaction with account of non-linear behavior of soils and structural materials

K.G. Shashkin, N.A. Evseev & V.V. Babanov
Institute "Georeconstruction", St. Petersburg, Russia

ABSTRACT: Linear-elastic finite elements are used at making soil-structure interaction calculations to describe models of reinforced concrete (RC) structures. This approach (effective stiffness method) is regarded as applicable in line with recommendations of numerous standards. The account of physically non-linear behavior of reinforced concrete is facilitated by reducing stiffness of elastic elements by conditional effective stiffness coefficients, which values largely differ in literature. The paper analyses relative differential settlements of the building at calculation of a physical non-linear RC model of a building and linear-elastic models with different effective stiffness ratios. Different approaches to assigning effective stiffness of RC lead to considerable differences in calculation results, especially considering soil-structure interaction The objective of the research is to develop a method of soil-structure interaction calculation using linear-elastic model of RC structures, so that its result were in good agreement with the calculations using a non-linear RC strain model. The paper proposes dependencies for estimating effective stiffness reduction ratios. Obtained dependencies allow considering non-linear material behavior without detailed modeling of non-linear behavior itself. It is demonstrated that a correct account of physical non-linearity of structural material is very important for soil-structure interaction calculations.

1 INTRODUCTION

The necessity to consider soil-structure interaction in order to limit differential settlements of structures in the conditions of soft soils constitutes an important feature of designing in St. Petersburg (Shashkin 2006, Ulitsky 2014). When computing settlement difference of a building it is crucial to model both non-linear flexibility of subsoil and stiffness of superstructures with account of their non-linear behavior. Incorrect setting of stiffness of elements in a model of a building due to underestimation of non-linear behavior of structures leads to its excessive stiffness and, consequently, underestimation of differential settlements. The account of physical non-linearity of RC structures, as RC structures almost do not exist without cracking, is especially relevant for calculations (Bondarenko 2004, Karpenko 1996).

In design practice due to complexity of non-linear calculations physical non-linearity of RC structures is facilitated by reducing an elastic modulus of structures in an elastic model with a help of factors, which consider non-linear behavior of reinforced concrete (Zalesov 2005, Zalesov 2007), their values are given in the regulatory documents (SP 430.1325800 and SP 63.13330). This approach is generally accepted in international design practice (Evseev 2018, Das 2019, Das 2020, Das 2021, Ngoc 2014, Zhongwen 2018). In a number of cases using standard values of stiffness reduction factors leads to overestimating stiffness of RC structures (Evseev 2018, Evseev 2017, Vasenin 2019). The objective of the research is developing a method of estimating of the linear-elastic effective stiffness of RC constructions for the finite element method of soil-structure interaction calculations, so that the results of linear-elastic calculations were consistent with physically non-linear calculations.

DOI: 10.1201/9781003299127-230

2 METHODS TO ASSESS BENDING STIFFNESS OF A BUILDING

Sagging of a building results in occurrence of longitudinal tensile forces at lower levels of a building and the compressive ones at upper levels. Meanwhile the stiffness of floor sections in cracking areas is considerably reduced due to compression and tension. After decreasing bending stiffness of a section due to cracking a stiffness of a structure remains almost permanent until the moment of failure. It explains the possibility of using reduction factors in calculations instead of a precise solution according to a non-linear deformation model.

Based on the calculation using a non-linear deformation model for the main types of sections of RC slabs with symmetrical reinforcement, there has been made a dependency for a coefficient of reducing bending stiffness k_1 of a section after cracking at a long-term action of a load from a complex parameter $E_s \cdot I_s / E_b \cdot I_b$ (Figure 1a). There has been also built a dependency of a coefficient of reducing bending stiffness of a section for a longitudinal force k_2 on a percentage of section reinforcement μ (Figure 1b). The diagrams show linear dependencies k_1 and k_2 on parameters $E_s \cdot I_s / E_b \cdot I_b$ and μ, respectively, which are approximated by functions shown in Figure 1 with a sufficient degree of accuracy:

$$k_1 = 1,25 \cdot \frac{E_s \cdot I_s}{E_b \cdot I_b} + 0,03 \tag{1}$$

where I_b, I_s are inertia moments for a concrete section and reinforcement, respectively, relative to a center of gravity of an element cross-section; E_s, E_b – an elastic modulus of reinforcement and an initial elastic modulus of concrete, respectively.

$$k_2 = 9,46 \cdot \mu + 0,07 \tag{2}$$

where μ is a percentage of section reinforcement, unit fraction.

The calculation was made for slabs of the following parameters: section height - 0.15…0.60 m; percentage of section reinforcement - 0.5 … 1.5%; thickness of a protective layer - 10…40 mm; grade of strength of concrete - B25…B50; reinforcement A400 at relative air humidity of the environment 75 %. As at design relative settlement differences of the model are considerably limited, compressive and tensile strains are also very negligible. In this case stiffness reduction factors for longitudinal compression and tension of the section after cracking are almost equal.

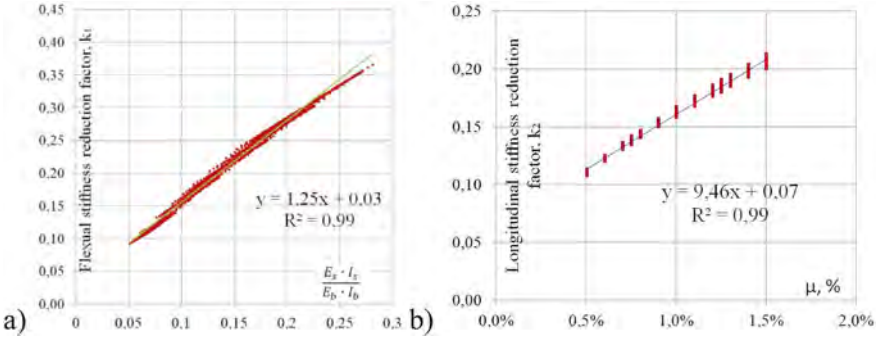

Figure 1. Reduction factors of section stiffness after cracking: a) – graph "k_1 - $E_s \cdot I_s / E_b \cdot I_b$", b) graph "$k_2$ – μ".

Stiffness of horizontal bearing structures in possible cracking areas – a span and an above-span area of floors - is taken with account of factors k_1 and k_2. There is no cracking in walls at bending of a building, their stiffness can be defined with a reduction factor of creeping for concrete.

3 USING THE PROPOSED METHODS TO ASSESS STIFFNESS OF A BUILDING AND CALCULATE DIFFERENTIAL SETTLEMENTS OF A BUILDING

There has been made a cycle of calculations of soil-structure system using elastic and non-linear deformation models for reinforced concrete. There have been considered 4 groups of schemes (Figure 2, 3): slab on elastic 600 and 400 mm – thick subsoil (without considering stiffness of superstructures, that is admissible, for example, for a flexible frame building); buildings of the wall structural scheme: "rigid" scheme (6-floor building) and more "flexible" scheme (1- floor building. Subsoil of the building was modeled with linear-elastic spatial 8-node finite elements. The building structure was modeled with 1*1 quadrangular shell finite elements. Piles were modeled as spatial road finite elements.

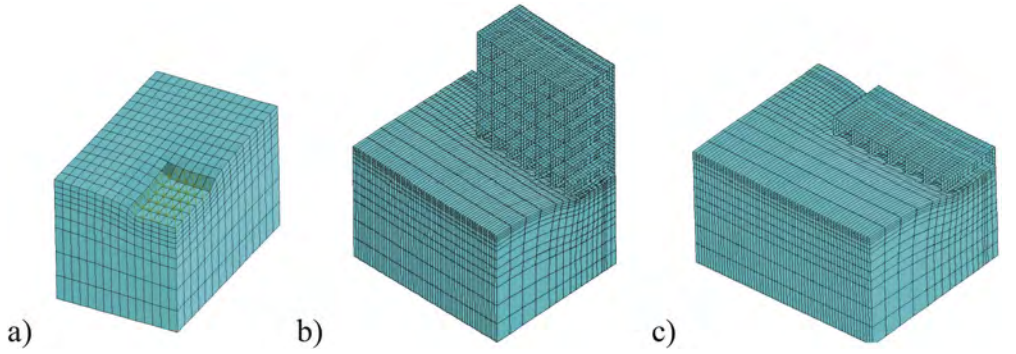

Figure 2. Deformation calculation models: a) – slab, b) – 6-floor building, c) – 1- floor building.

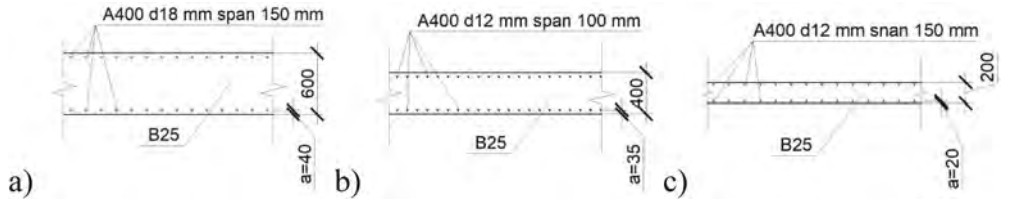

Figure 3. Structure of foundation and floor slabs in calculation models: a) – foundation slab 600 mm: k_1 = 0,127; b) – foundation slab 400 mm: k_1 = 0,141; c) – floor slab 200 mm, k_1 = 0,163, k_2 = 0,144, E_{eq} = 4056461 kPa, h_{eq} = 0,212 m.

Calculations have been made in the verified finite element method software "LIRA-SAPR" for four models of RC behavior:

a) Linear-elastic model. Reduction factors according to SP 430.1325800 relative to an initial elastic modulus of concrete: 0,6 – for walls; 0,2– for slabs.
b) Elastic model. The same reduction factor for all structures relative to an initial elastic modulus of concrete: k= $1/(1+\varphi_{b,cr})$, where $\varphi_{b,cr}$ – a factor of creeping of concrete as per SP 63.13330
c) Account of physical non-linearity of materials using deforming diagrams according to SP 63.13330: a trilinear one considering long-term action of a load at relative air humidity of the environment 75% and a bilinear one for reinforcement.
d) Account of quasi-elastic behavior of structures according to the developed methods.

The general view of the calculation model representing a one fourth of the building with soil is shown in Figure 2. Subsoil was modeled with elastic spatial 8-node finite elements. The building structures were modeled with 1*1 quadrangular shell finite elements. Piles were

modeled as spatial road finite elements. As regards soil models, there are used boundary conditions in the form of fixation at lower and lateral planes of the calculation model, that are standard for solving geotechnical problems.

Figure 4 shows graphs of dependencies of relative differences of settlements of a building on a value of maximum settlement. There has been considered a range of absolute settlements of a building which does not exceed limit values as per SP 22.13330. It was found out that a calculated difference of settlements considerably depends on methods of modeling of RC structures. A smaller difference of settlements corresponds to the calculations according to regulatory recommendations compared to the calculation according to a non-linear strain model of reinforced concrete. The difference increases together with a growth of flexibility of subsoil and reaches 30% and 50% using recommendations as per SP 430.1325800 and SP 63.13330, respectively. These differences can be rather considerable and they can influence on design solutions, for example, require increasing a length of piles for reducing a building settlement. When using the developed methods, a calculated difference of settlements is close to the values obtained by the non-linear calculation. The gap has not exceeded 5%.

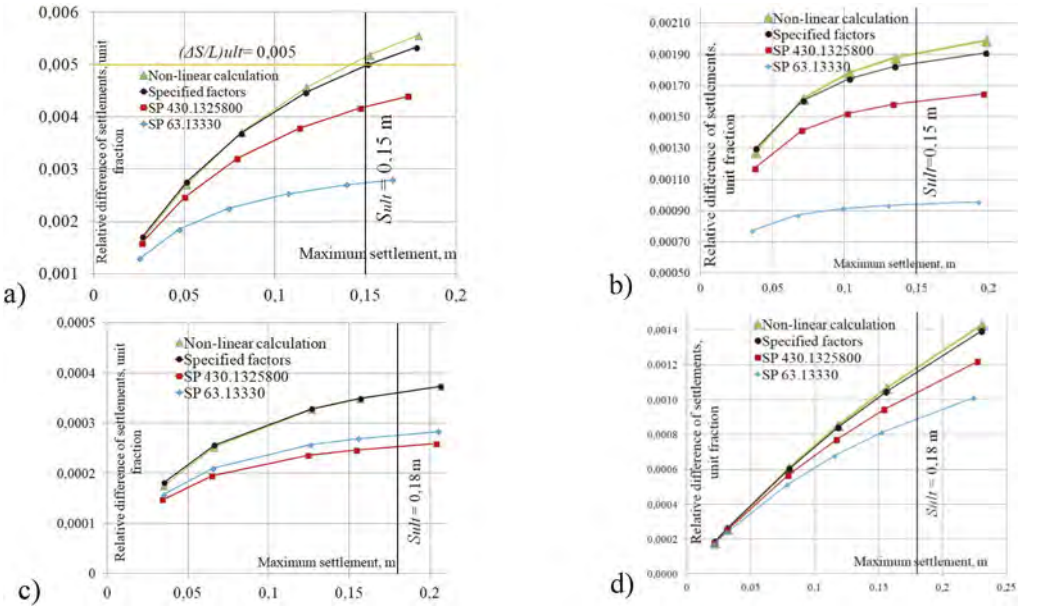

Figure 4. Dependencies of relative differences of settlements on a maximum settlement (m): a) – slab 400 mm, b) – slab 600 mm, c) – 6-floor building, d) – 1- floor building.

4 CONCLUSION

The calculation analysis has demonstrated that physical non-linear behavior of RC structures of a building exerts a considerable influence of the calculation results of the "soil-structure" system and it can affect design solutions on a construction of foundations and superstructures of a building. When computing differential settlements of a building the developed methods of facilitated estimation of reducing stiffness of RC structures of a building at the expense of physically non-linear behavior of RC structures allow reaching close consistence with the results of non-linear calculation. Facilitated approaches using standard values of stiffness reduction factors lead to overestimation of bending stiffness of a building and, consequently, underestimation of differential settlements of a building.

REFERENCES

Bondarenko, V.M., Kolchunov, V. I. 2004. *Raschetnye modeli silovogo so-protivleniya zhelezobetona*. Moscow: ASV.

Das, S. & Choudhury, S. 2019. Influence of effective stiffness on the performance of RC frame buildings designed using displacement-based method and evaluation of column effective stiffness using ANN. *Engineering Structures*: 197.

Das, S. & Choudhury, S. 2020. Evaluation of effective stiffness of RC column sections by support vector regression approach. *Neural Comput & Applic* 32: 6997–7007.

Das, S & Mansouri, I, Choudhury, S, Gandomi, AH, Hu, JW. 2021. A Prediction Model for the Calculation of Effective Stiffness Ratios of Reinforced Concrete Columns. *Materials (Basel). Apr. 5* 2021 14 (7):1792</pg>.

Evseev, N.A. 2017. Account of physical non-linearity of reinforced concrete structures at computation of structural systems. *Vestnik grazhdanskikh inzhenerov [Journal of Civil Engineers]* 5: 66–70.

Evseev, N.A. 2018. The features of reinforced concrete non-linear behavior account in soil-structure interaction calculations. *Geotekhnika [Geotechnics]* 4: 58–69.

Zalesov, A.S. & Mukhamediev, T.A., Chistykov, E.A. 2005. The account of physical non-linearity at calculation of RC monolith structures of high-rise buildings. *Stroitel'naya mekhanika i raschet sooruzhenii [Structural Mechanics and Calculation of Structures]* 1: 4–8.

Zalesov, A.S. & Ivanov, A. 2007. Elaboration of proposals on static calculation of flat RC elements with account of physical non-linearity. *Stroitel'naya mekhanika i raschet sooruzhenii [Structural Mechanics and Calculation of Structures]* 5: 57–60.

Karpenko, N. I. 1996. *General models of reinforced concrete mechanics*. Moscow: Stroyizdat Publ.

Ngoc S.V. & Li, B. & Beyer, K. 2014. Effective Stiffness of Reinforced Concrete Coupling Beams. *Engineering Structures* 76: 371–382.

Shashkin, A.G. & Shashkin, K.G. 2006. The basic regularities of interaction of soils and superstructures of buildings. *Rekonstruktsiya gorodov i geotekhnicheskoe stroitel'stvo [Urban Reconstruction and Geotechnical Engineering]* 10: 63–92.

Ulitsky, V.M. & Shashkin, A.G., Shashkin, K.G, Shashkin, V.A. 2014. *The basics of soil-structure interaction calculations*. Saint-Petersburg: Publishing house of the "Georeconstruction" Institute.

Vasenin, V.A. & Evseev, N.A. Effective stiffness for modeling reinforced concrete structures in soil-structure interaction calculation. 2019. *Geotechnics Fundamentals and Applications in Construction: New Materials, Structures, Technologies and Calculations. Proceedings of the International Conference on Geotechnics Fundamentals and Applications in Construction: New Materials, Structures, Technologies and Calculations "GFAC 2019"* 2: 369–401.

Zhongwen, Z. & Bing, L. 2018. Effective Stiffness of Non-Rectangular Reinforced Concrete Structural Walls. *Journal of Earthquake Engineering*. 22(3):382–403.

Smart Geotechnics for Smart Societies – Zhussupbekov, Sarsembayeva & Kaliakin (Eds)
© 2023 The Author(s), ISBN 978-1-003-29912-7
Open Access: www.taylorfrancis.com, CC BY-NC-ND 4.0 license

Optimal earthquake intensity measures for probabilistic seismic demand models of rectangular tunnels

Van-Quang Nguyen
Department of Civil and Environmental Engineering, Hanyang University, Seoul, Korea
Department of Civil Engineering, Vinh University, Vietnam

Hyeondong Roh & Duhee Park
Department of Civil and Environmental Engineering, Hanyang University, Seoul, Korea

ABSTRACT: This study aims to identify optimal intensity measures (*IMs*) for use in probabilistic seismic demand models (PSDMs) for rectangular tunnels in three soil deposits. To this end, we performed an extended numerical parametricstudy involving two-dimensional time history analyses of selected soil-tunnel configurations to evaluate the response of the selected tunnels under transverse seismic shaking. A series of 23 *IMs* were selected and tested from motions at tunnel level deoth. The selected *IMs* were tested on several metrics, such as correlation, efficiency, practicality, and proficiency, based on an extended number of regression analyses between the IMs and the damage measure (*DM*), for the studied tunnels. The results indicate that the velocity spectrum intensity (VSI) at the ground tunnel level depth can be considered as the optimal *IM*, whereas the peak ground displacement (PGD) has the less efficient.

1 INTRODUCTION

Underground facilities are a crucial component of contemporary urban infrastructure. In the past, seismic design of tunnel structures received less attention than above-ground structures and most of them were designed and built without considering seismic effects. However, strong earthquakes have shown that even underground structures can be damaged significantly under severe seismic excitation (Hashash et al., 2001). An accurate evaluation of the seismic performance of underground structures is inevitable.

So far, several studies have investigated the correlation between *IMs* and the seismic response of the rectangular tunnel. Zhang et al. (2022) explore the optimum *IMs* for probabilistic seismic demand model (PSDM) of a three-story three-span subway station with different burial depths. Zhang et al. (2021) investigate optimum *IMs* for the performance assessment of a two-storey three-span subway station considering the effects of near-fault seismic excitations with velocity pulses, and then establish the fragility curves of subway stations using the optimum *IMs*. However, neither of the numerical models were validated against recordings. The literature review demonstrated that a study using a validated or verified numerical model to calculate the response of the rectangular tunnel has not yet been performed. Also, the more *IMs* is needed to deeply investigate the optimum *IMs* for PSDM.

The aim of this paper was to develop PSDMs for the rectangular tunnel. For that, 23 earthquake IMs are considered in developing PSDMs. The nonlinear numerical modeling of soil-tunnel configurations is constructed using FLAC^{2D} program (Itasca Consulting Group, 2011). A set of 85 ground motion records, which contain a wide range of amplitudes, magnitudes, epicentral distances, significant durations, and predominant periods, are utilized to perform nonlinear time-history analyses. Three different soil deposits are used in this study. Optimal *IMs* are recognized based on statistical indicators of PSDMs, which are the coefficient of determination, dispersion, practicality, and proficiency.

DOI: 10.1201/9781003299127-231

2 NUMERICAL MODEL AND ANALYSES

2.1 *Tunnel model*

The cross-section size is 12 m × 6 m (center-to-center width and height) and located 6 m below the ground. The thickness of side wall, top, and bottom slabs is 1 m. The center column with the cross-section of 0.4 m × 1.0 m is placed at every 3 m.

The tunnel structure was modeled using beam elements with an element size of 0.25 m. Table 1 and Figure 1 presents the properties and cross-section of the tunnel.

Table 1. Properties of the tunnel structure.

Parameters	Value
Density (kg/m^3)	2400
Young's modulus (Pa)	2.5×10^7
Poission's ratio	0.2

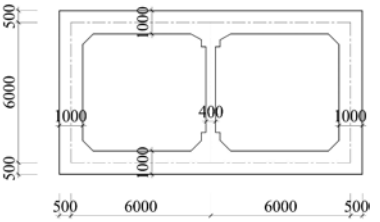

Figure 1. Cross-section of rectangular tunnels (unit: mm).

2.2 *Soil model*

The dimension of the computational model was set to 120 × 30 m (width × height) as presented in Figure 2. Three soil profiles P1, P2, and P3 corresponding to soil classes B, C, and D, according to Eurocode 8 (CEN, 2005). The density and Poisson's ratio of the soil were 1800 kg/m^3 and 0.3, respectively. The shear wave velocity profile of soil is presented in Figure 3. The soil medium was modeled using plane-strain quadrilateral elements. The element size, $\Delta l = 0.5$ m, was selected based on the following recommendation of Kuhlemeyer and Lysmer (1973). The *Sig3* model, which is available in FLAC^{2D} program, was employed to simulate the nonlinear behavior of soil.

2.3 *Soil-tunnel interface and boundary conditions*

The soil-structure interaction was simulated using the interface elements. The interface option *UNBONED* in the FLAC^{2D} program was used in this study. This contact interface can model a realistic partial-slip condition considering the gapping and the slipping phenomena between soil and tunnel under loading.

The free-field boundary was applied for lateral boundaries to absorb reflected waves. The bottom boundary was fixed to simulate the rigid boundary. The acceleration time history of the input motion was defined at the base of the numerical model.

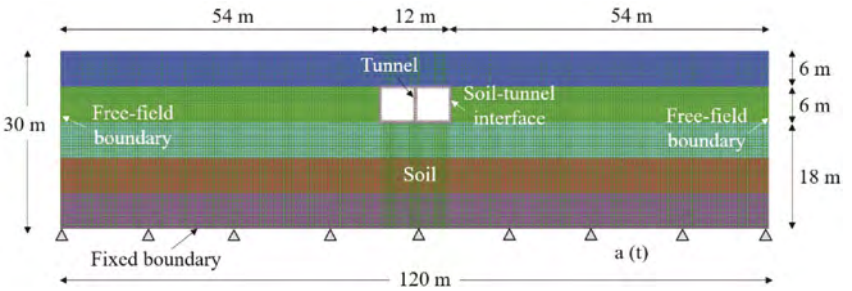

Figure 2. Soil-tunnel numerical configuration in FLAC^{2D}.

2.4 *Ground motions*

A set of 85 ground motion records are selected from historical earthquakes, which are available in the PEER center database (https://ngawest2.berkeley.edu). A wide range of earthquake amplitudes, magnitudes, epicentral distances, significant durations, and predominant periods is considered in used ground motions whose response spectra are shown in Figure 4.

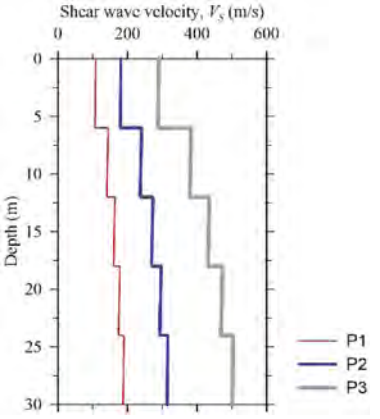

Figure 3. Shear wave velocity profiles.

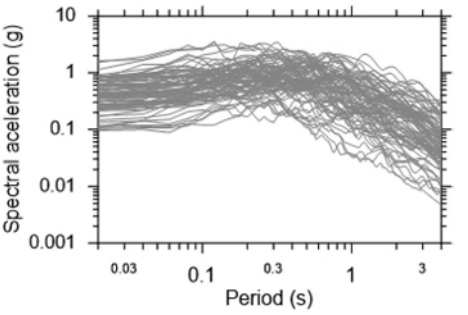

Figure 4. Input ground motions.

2.5 *The numerical validation*

The numerical model in this study was validated against the centrifuge test by (Gillis, 2015). Detail of the centrifuge test and comparison between numerical and experimental results were reported in Nguyen et al. (2022b). The compared results demonstrate that the numerical model was reliable for carrying out parametric research.

3 SELECTION OF OPTIMAL INTENSITY MEASURES

3.1 *Representative numerical results*

This study adopts the results proposed by Nguyen et al. (2022a). The representative numerical result is bending moment at the base of the center column, which is a critical section.

3.2 *Selection of examined seismic intensity measures*

This study accounts for 23 common ground motion *IMs*and these parameters are calculated for every motion record using SeismoSignal (Seismosoft, 2012). The used *IMs* are described in Nguyen et al. (2022b).

3.3 *Overview of PSDM*

PSDM, which contains the relationship between structural demand and an earthquake *IM*, needs to be appropriately established in the probabilistic performance-based seismic design. The most common expression of the relationship between seismic demand and earthquake *IMs* is the power form in Eq. (1) (Nguyen et al., 2021, Cornell et al., 2002):

$$S_D = a \times (IM)^b \tag{1}$$

where S_D is the median value of structural demand; a and b are the regression coefficients; IM is the earthquake intensity measure considered. This equation can be rewritten in forms of linear regression as follows:

$$ln(S_D) = \ln(a) + b \times ln(IM) \tag{2}$$

The conditional failure probability that the structural demand (D) exceeds its capacity for a given *IM* in the fragility analysis can be expressed as:

$$P_f = P[D \geq d|IM] \tag{3}$$

where d is the specified value, normally it is based on the structural capacity. Assuming that the structural demand and capacity follow lognormal distributions, Eq. (3) can be rewritten as:

$$P[D \geq d|IM] = 1 - \Phi\left[\frac{\ln(d) - \ln(S_D)}{\sigma_{D|IM}}\right] \tag{4}$$

The uncertainty in the seismic demand $\sigma_{D|IM}$ is approximated as the dispersion of the simulated demand with respect to the regression fit for the calculated damage data obtained from the non-linear time history analyses, as shown in Eq. (5):

$$\sigma_{D|IM} = \sqrt{\frac{\sum (\ln(d_i) - \ln(a \times IM^b))^2}{n-2}}$$

3.4 *Results of PSDM study*

3.4.1 *Correlation testing*

Figure 5 presents the regression analyses between four representative seismic *IMs* and *DM*. Notably, the *IMs* is determined from the motions at tunnel level depth. It can be observed that VSI has the strongest correlation with the *DM*, followed by PGV and HI. The correlation coefficients R^2 for the three most correlated *IMs* are 0.762, 0.754, and 0.747, respectively. Furthermore, the weakest correlation between *IMs* and *DM* is T_p with a correlation coefficient of 0.118, followed by CAV and PGV/PGA (i.e. correlation coefficients of 0.315 and 0.380, respectively).

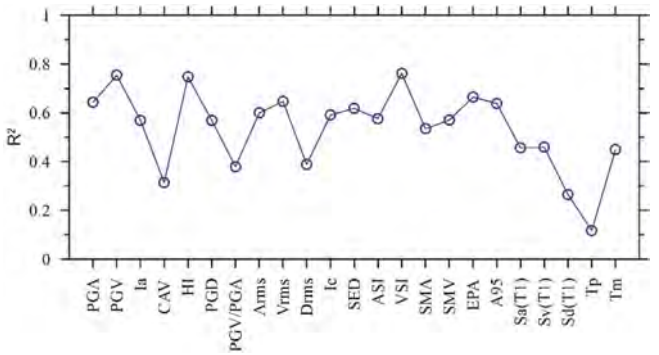

Figure 5. Regression parameter R^2 between four representative seismic *IMs* and *DM*.

3.4.2 *Efficiency testing*

The results of the efficiency analyses are depicted in Figure 6. VSI, PGV, and HI are considered more efficient measures since they have smaller standard deviations $\sigma_{D|IM}$. Among them, VSI is the most efficient *IMs* with the lowest standard deviation $\sigma_{D|IM}$, i.e. 0.194. The corresponding $\sigma_{D|IM}$ for the next two most efficient *IMs* are 0.195 and 0.197, respectively, which are slightly higher than that for VSI. The maximum standard deviation $\sigma_{D|IM}$ is observed for A_{rms}, i.e. 0.714, indicating that this measure is the least efficient. This is followed by PGA and S_d(T1). Their corresponding standard deviations $\sigma_{D|IM}$ are 0.426 and 0.404, respectively, which are lower than that for A_{rms}.

3.4.3 *Practicality testing*

Figure 7. summarises the *b* values calculated from the regression models for each *IM-DM* pair. The comparisons in Figure 7 suggest that T_m is the most practical *IMs* among others, because it has the maximum slope *b* of 0.859. ASI and EPA proved to be the second and third most practical *IMs*, with the corresponding slope *b* equal to 0.841 and 0.798, respectively. In contrast, SED is found to be the least practical *IM* among the other tested *IMs*, as it exhibits the minimum slope *b* of 0.233 for the examined cases. D_{rms} and PGD prove to be the other two least practical *IMs*, with slightly higher slope values b, i.e. 0.282 and 0.343, respectively.

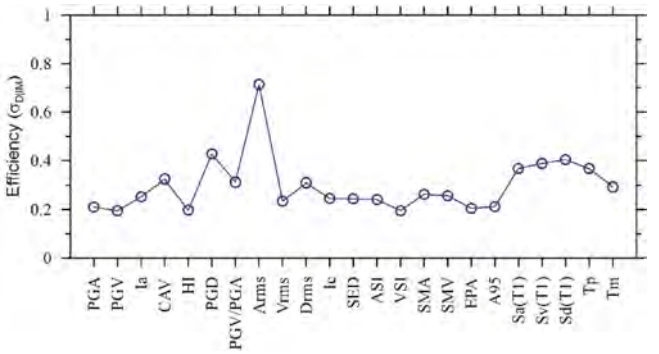

Figure 6. Regression parameter $\sigma_{D|IM}$ between four representative seismic *IMs* and *DM*.

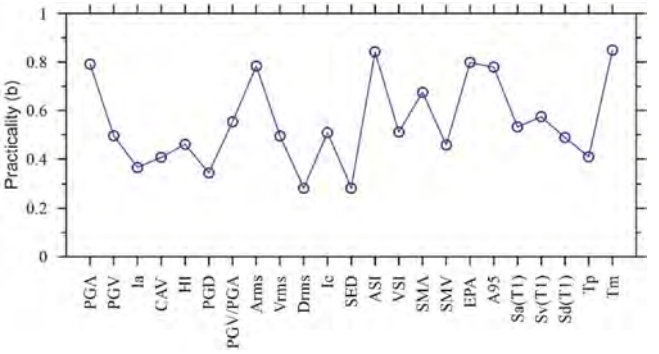

Figure 7. Regression parameter *b* between four representative seismic *IMs* and *DM*.

3.4.4 *Proficiency testing*

Padgett et al. (2008) proposed an indicator, namely proficiency, which can balance the selections between efficiency and practicality. The proficiency is defined by the ratio of dispersion ($\sigma_{D|IM}$) to the practicality (*b*), as shown in Eq. (6). The smaller value of ξ is, the more proficient is.

$$\xi = \frac{\sigma_{D|IM}}{b} \tag{6}$$

Figure 8 compares the computed ξ for the considered *DM* with regard to the 23 tested *IMs*. EPA is the most proficient *IM* due to the corresponding smallest ξ of 0.256, followed by PGA and A_{95}, which have ξ values of 0.266 and 0.273, respectively, which are quite close to the value for EPA. PGD is the less proficient measure, as it has the maximum ξ, i.e. 1.243. The next two least proficient *IMs* are D_{rms} and A_{rms}. Their corresponding values of ξ are 1.095 and 0.911, respectively, which are considerably lower than the value for PGD.

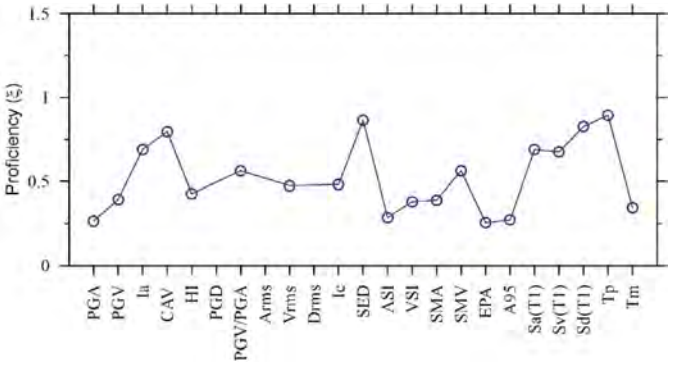

Figure 8. Regression parameter between four representative seismic *IMs* and *DM*.

4 CONCLUSIONS

This study developed PSDMs for various *IMs* and identified optimal *IMs* for the seismic performance of the rectangular tunnel structure embedded in three soil deposits. A group of 85 ground motion records and 23 different *IMs* were used in nonlinear time-history analyses. The selected *IMs* were tested using the correlation, efficiency, practicality, and proficiency metrics, with the aim of identifying the optimal *IMs* from the selected ones for the examined soil-tunnel systems. The following conclusions are drawn.

The optimal *IMs* for PSDMs of the rectangular tunnel structure are VSI followed by PGV and HI. The PSDMs with respect to these *IMs* contain higher values of R^2, lower standard deviations and proficiency values, and larger practicalities than those of others.

The less efficient *IMs* for PSDMs of the rectangular tunnel structure are PGD, D_{rms}, and A_{rms}. These *IMs* are displacement- and acceleration-based parameters.

REFERENCES

Cen 2005. Eurocode 8: Design of structures for earthquake resistance-part 1: general rules, seismic actions and rules for buildings. *Brussels: European Committee for Standardization*.

Cornell, C. A., Jalayer, F., Hamburger, R. O. & Foutch, D. A. 2002. Probabilistic basis for 2000 SAC federal emergency management agency steel moment frame guidelines. *Journal of structural engineering*, 128, 526–533.

Gillis, K. M. 2015. *Seismic Response of Shallow Underground Structures in Dense Urban Environments*. Ph.-D. dissertation, University of Colorado at Boulder.

Hashash, Y. M., Hook, J. J., Schmidt, B., John, I. & Yao, C. 2001. Seismic design and analysis of underground structures. *Tunnelling and underground space technology*, 16, 247–293.

Itasca Consulting Group 2011. *FLAC - Fast Lagrange Analysis of Continua; Version7.0. In: User Manual*.

Kuhlemeyer, R. L. & Lysmer, J. 1973. Finite element method accuracy for wave propagation problems. *Journal of Soil Mechanics & Foundations Div*, 99.

Nguyen, D.-D., Thusa, B., Azad, M. S., Tran, V.-L. & Lee, T.-H. 2021. Optimal earthquake intensity measures for probabilistic seismic demand models of ARP1400 reactor containment building. *Nuclear Engineering and Technology*, 53, 4179–4188.

Nguyen, V.-Q., Lee, Y.-G. & Park, D. 2022a. Seismic damage evaluation of double box metro tunnel using three-dimensional finite element analysis. *Structures (submitted for publication)*.

Nguyen, V.-Q., Tran, V.-L., Nguyen, D.-D., Sadiq, S. & Park, D. 2022b. Novel hybrid MFO-XGBoost model for predicting the racking ratio of the rectangular tunnels subjected to seismic loading. *Transportation Geotechnics*, 100878.

Padgett, J. E., Nielson, B. G. & Desroches, R. 2008. Selection of optimal intensity measures in probabilistic seismic demand models of highway bridge portfolios. *Earthquake engineering & structural dynamics*, 37, 711–725.

Seismosoft, L. 2012. Seismosignal. *Pavia*, Italy.

Zhang, C., Zhao, M., Zhong, Z. & Du, X. 2021. Seismic Intensity Measures and Fragility Analysis for Subway Stations Subjected to Near-fault Ground Motions with Velocity Pulses. *Journal of Earthquake Engineering*, 1–27.

Zhang, C., Zhao, M., Zhong, Z. & Du, X. 2022. Optimum intensity measures for probabilistic seismic demand model of subway stations with different burial depths. *Soil Dynamics and Earthquake Engineering*, 154, 107138.

Smart Geotechnics for Smart Societies – Zhussupbekov, Sarsembayeva & Kaliakin (Eds)
© 2023 The Author(s), ISBN 978-1-003-29912-7
Open Access: www.taylorfrancis.com, CC BY-NC-ND 4.0 license

A study on the mobilization of negative skin friction along end bearing piles installed through layered soils

F.S.A. Ansar & L.I.N. De Silva
University of Moratuwa, Colombo, Sri Lanka

ABSTRACT: This paper presents a study on the mobilization of negative skin friction (NSF) through end-bearing piles for a soil profile containing soft soils sandwiched between stiff residual soil layers. A commercially available finite element package PLAXIS 2D has been used for the analysis. The model has been validated using case study results available in the literature. The position of the neutral plane and magnitude of drag load is analyzed with the change of soil layer thickness for different pile diameters and axial loads. All results were compared with an analytical method suggested in Sri Lankan guidelines and the variation among results was less than 20%. Pile settlement and axial shortening significantly affect the mobilization of NSF whereas the magnitude of the axial load has no significant effect. It can be concluded that finite element analysis can reasonably predict the mobilization of NSF on piles installed through layered soil profiles.

1 INTRODUCTION

Negative Skin Friction (NSF) is induced whenever the soil settles more than the pile (Fellenius, 1984, Wong & Teh, 1996). Negative skin friction has two effects on the pile; The drag load which is the additional compressive axial force and the down drag which is the additional settlement (Chen et al., 2009). Drag load reduces the bearing capacity since it becomes an additional load to the pile. The drag load caused by NSF depends on the location of the neutral plane and the distribution of NSF throughout the pile. Therefore, to estimate the NSF location of the neutral plane and the distribution of NSF throughout the pile should be analysed (Liu et al., 2012, Matyas & Santamarina, 1994). The neutral plane (NP) is the place where the relative settlement is zero. Above the neutral plane, the skin friction is negative. NSF is a complex phenomenon that depends on several factors. Since NSF directly relates to soil settlement all the factors affecting consolidation affect NSF.

According to past researchers, it has been found that the relative settlement of even a few millimetres (2-5 mm) between soil and the pile would mobilize NSF (Chen et al., 2009, Kim & Mission, 2011, Matyas & Santamarina, 1994, Wong & Teh, 1996). Research had been done to evaluate the NSF of different soil types and on layered soil. Drag force and down drag would vary with soil profile (Comodromos & Bareka,2005). Thus, it is important to investigate different types of soil profiles.

Terzaghi consolidation theory overestimates the drag load and down drag since it considers the NSF is fully mobilized in the pile(Chen et al., 2009, Comodromos & Bareka, 2005). Analytical, empirical, and numerical methods have been used to evaluate the mobilization of NSF. The Finite Element Method (FEM) and Finite Difference Method (FDM) have improved the understanding of the mobilization of NSF for various soil and pile conditions (Liu et al., 2012).

When the soft soil layer is at the top of the soil profile, the depth to the neutral plane increases when the thickness of soft soil layer increases and the increase is significant for the higher thickness of the soft soil layer (Hanna & Hoque, 2008). Though there are several research conducted for a case of a soft soil layer at the top of the soil profile, a profile that is

DOI: 10.1201/9781003299127-232

sandwiched is not available in the literature. Also, the analytical and empirical methods are difficult to use in practice when the number of soil layers increases. In this research, the mobilization of NSF with the change of soft soil layer thickness, for a soil profile of soft soil sandwiched between stiff residual soil is conducted using FEM.

2 METHODOLOGY

2.1 *Finite element model*

A numerical model was developed using PLAXIS 2D (version 8.2) software. A single pile was modeled as a volumetric element using the axisymmetric model. First, the model was validated using a known case and the analysis was conducted using the same model. The thickness of the soft soil layer and the bottom stiff residual soil layer was varied to investigate the variation of NSF with the layer thicknesses. The influence of load on the pile was also investigated.

2.2 *Model validation*

The verification of the model was conducted using a known case by Indraratna et al., (1992). This case was conducted for soft Bangkok clay. The subsoil was a thick clay layer overlying a sand layer. Clay layers were categorized into three layers according to soil properties (Tables 1 and 2).

Table 1. Material properties of end bearing layer and the pile (reprinted from (Liu et al., 2012)).

Material	Depth m	Density kN/m^3	Young's modulus MPa	Poisson's ratio	Coefficient of permeability m/day
End bearing	24-28	17	28	0.33	$3.72E^{-05}$
Pile	0-27	15	3000	0.33	$1.00E^{-05}$

Table 2. Mohr-Coulomb parameters used in model validation (reprinted from (Liu et al., 2012)).

Depth m	Density kN/m^3	Young's Modulus MPa	Poisson's ratio	Coefficient of permeability m/day	Cohesion kPa	Friction angle
0-4	17	4900	0.20	$6.76E^{-04}$	3	26°
4-10	17	4900	0.33	$5.50E^{-05}$	5.9	25°
10-20	17	4900	0.33	$2.60E^{-05}$	14.7	25°
20-24	17	6370	0.20	$3.72E^{-05}$	5.9	23°

A circular pile of 400 mm in diameter and 27m long has been used for the test. A 2m high embarkment has been raised as the surcharge. The density of the embarkment material was 16.67 kNm^{-3} with 24×14 m base dimensions and side slopes of 2:1. A UDL of 33.35 kPa, with a radius of 7.4m was used as the surcharge in the model. The Mohr-Coulomb model was selected for validation. A similar procedure was used by Hanna and Sharif, (2006) and Liu et al., (2012). The analysis results are presented in Table 3 and Figure 1.

Table 3. Results of model validation.

Parameter	Actual (Indraratna, B.,1992)	Present study	% Deviation of the model from actual
Max. NSF (kN/m^2)	17.64	-21	19%
Depth at Max. Nsf (m)	13.50	10	26%
Neutral point (m)	17.50	16.9	3.4%

The model results have a good agreement with the actual case. Therefore, the same modelling procedure has been used for the analysis of NSF of a single pile.

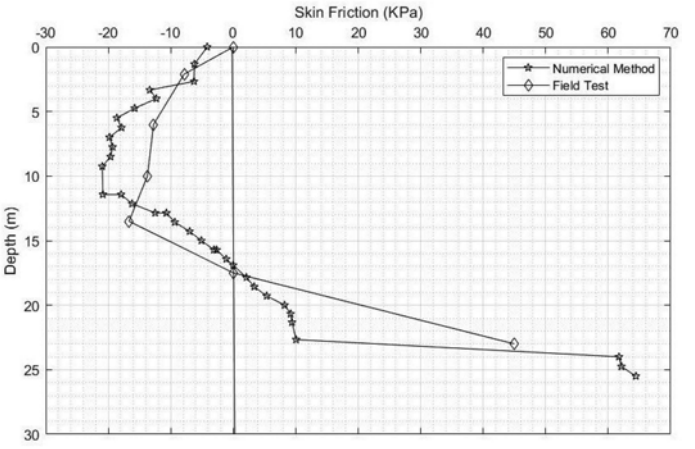

Figure 1. Comparison of model validation.

2.3 *Model details*

A circular pile with diameters 0.4 m,0.6 m, and 1 m and a length of 27 m were modelled. A model radius of 30 m and depth of 27 m was used. The mesh was formed by 15-noded elements with 'medium' global coarseness (Figure 2). The left and right boundaries were vertically free and fixed horizontally. The bottom boundary and the pile were fixed. The groundwater table was placed at the ground level. A 33.5 kPa Surcharge was applied as a uniformly distributed load (UDL).

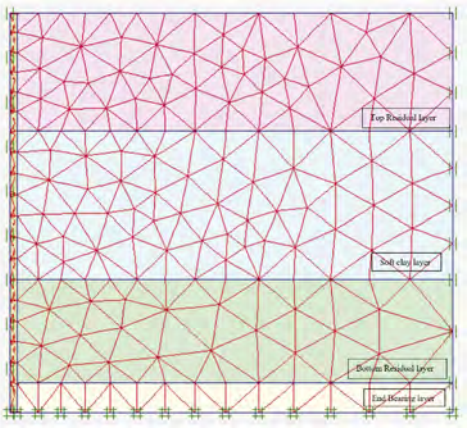

Figure 2. Finite element model with mesh.

The end bearing capacity of the rock was assumed as 5000kPa. The load which could be withstood for this end bearing capacity was applied at the top of the pile (P). An interface reduction factor (R_{inter}) value of 0.67 was used. The initial conditions of the soil are obtained by the K_0 procedure. A consolidation analysis was conducted. In the first stage, the loads and the interface were activated. Analysis results were obtained for the case of minimum excess pore water pressure, $P_{min} < 1$ kPa.

2.4 *Soil profile*

A soft soil layer was sandwiched between two stiff residual soil layers. Drained parameters were used for soil. A residual soil layer of 8m thickness was maintained at the top. The thickness of the soft soil layer and the bottom stiff residual soil layer were varied while a 2m of the

pile socket length was maintained in the end bearing layer. The soft soil layer thickness was varied as 5,7,10,12,15 m and the corresponding bottom residual layer thickness was 12,10,7,5,2 m respectively. Residual soil properties were obtained from Law et al., (2014). Soil and pile properties used for the analysis are listed in Table 4.

Table 4. Material properties used in the model.

Material	Depth m	Model	Density kN/m^3	Young's Modulus kPa	Poisson's ratio	Coefficient of permeability m/s	Cohesion kPa	Friction angle
Top residual	0-8	MC	17	$4.50E^{+04}$	0.25	$1.00E^{-05}$	5	31°
Soft clay	8-t	MC	15	1000	0.35	$1.00E^{-08}$	3	20°
Bot. Residual	t-25	MC	18	$9.00E^{+04}$	0.25	$1.00E^{-05}$	8	33°
End bearing	25-27	LE	22	$1.00E^{+06}$	0.20	$1.00E^{-10}$	-	-
Pile	0-27	LE	15	$3.00E^{+07}$	0.33	$5.04E^{-10}$	-	-

* t is the soft soil layer thickness *MC is Mohr-Coulomb model * LE is Linear Elastic model

2.5 *NSF calculations*

The shear stress along the pile-soil interface was obtained from the software and the drag load was calculated as follows.

$$\text{Total Drag Load} = \sum \Delta\text{NSF} \tag{1}$$

$$\Delta\text{NSF} = 2\pi R^{*}\Delta y^{*}\Delta\tau \tag{2}$$

where Δy = distance between selected points; $\Delta\tau$ = Average pressure between selected points and R= Radius of pile

The values obtained from the model were compared with the method proposed by the ICTAD/DEV/15 guidelines which is mostly used by the practitioners of Sri Lanka. β method is proposed in this guideline.

$$\tau_{neg} = \beta \times p(d) \tag{3}$$

where τ_{neg}= Unit skin friction; β=Negative Skin friction factor (Proposed values are given in the guideline) and p(d)= Vertical effective stress at the mid-depth of the layer that applies negative skin friction

Force due to NSF can be obtained by multiplying τ_{neg} with the associate pile area

3 RESULTS OF FEM ANALYSIS

3.1 *Scenario 01: Axial load on pile top*

First, the load which could be withstood for the end bearing capacity of the pile was applied to the pile and the layer thickness was varied as specified. NP was within the soft soil layer for each layer thickness. The position of NP was not significantly varied with the change in diameter of the pile. A linear relationship can be observed between the graph of NP/L vs T/L where T is the soft soil layer thickness and L is the pile length (Figure 3). The NP varied within 85 to 100% of the soft soil layer.

The Drag load due to the NSF was calculated using Equation 1 and the method proposed in ICTAD. The deviation among the values was less than 20% in each case.

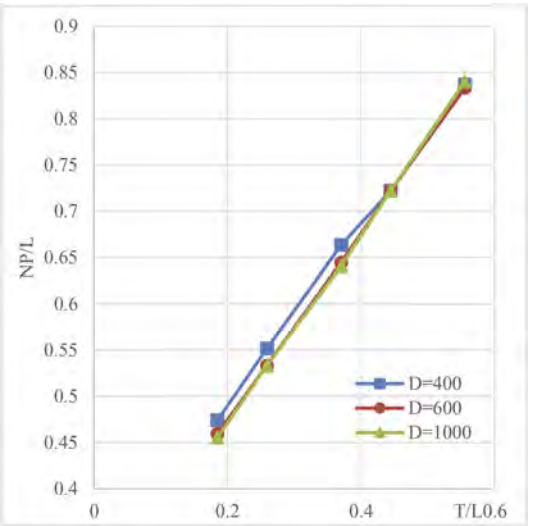

Figure 3. Relationship between soft soil thickness and neutral point (Scenario 01).

3.2 *Scenario 02: Effect of magnitude of axial load on pile*

To investigate the effect of axial load on the top of the pile, the load on the pile was varied for the 400 mm diameter pile. It was observed that the NP and the distribution of NSF don't have a significant effect on the magnitude of the load applied unless P=0. NP is deep when P=0, compared to P≠0. Figure 4 shows the variation of drag load with load applied at the top

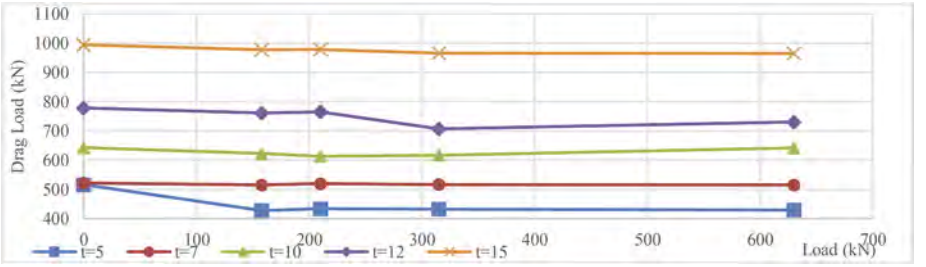

Figure 4. Variation of drag load with load applied (Scenario 02).

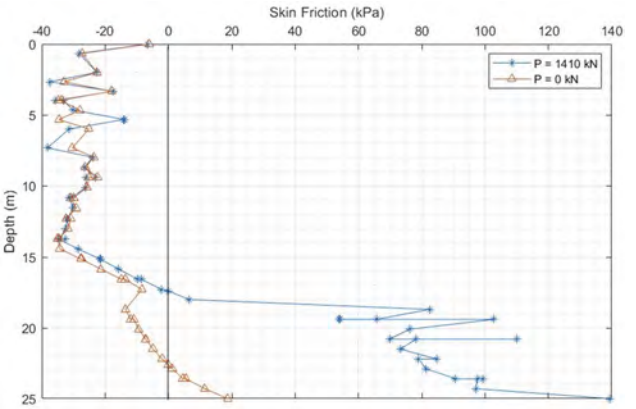

Figure 5. Variation of NSF with and without an axial load on the pile.

of the pile. Figure 5 represents the variation of NSF with depth plotted according to the analysis results for the case of soft soil layer 7 m.

4 CONCLUSION

The mobilization of Negative Skin Friction through soft soils sandwiched between stiff residual soil layers, with the change of soft soil layer thickness was analysed using the finite element software, PLAXIS 2D. The results obtained were compared with the method suggested by ICTAD (now it is called CIDA), which is mostly used by Sri Lankan practitioners.

The research was conducted under 2 scenarios by changing the load applied to the pile at the top. When a load is not applied on the pile NSF is fully mobilized along the soft soil layer while NP lies at the boundary between the soft soil and a bottom residual layer or within the residual soil layer. There is a slight variation of the NP with the change in diameter. When the diameter increases the depth to NP increases. Since the pile is fixed at the bottom the settlement of the pile can be neglected and the axial shortening of the pile is not significant as a load is not applied to the pile. So, the governing factor is the soil settlement.

When a load is applied to the pile the NP lies within the soft soil layer. NP doesn't have a significant variation with the pile diameter. The NSF mobilizes up to 85-98% of the soft soil layer. It was observed that the full mobilization of NSF happens with a small load applied to the pile. The axial shortening comes to play as a load is applied to the pile. Hence, the NP shifts up compared to the previous case. Also, the drag load has a good agreement with the method proposed by ICTAD (now called CIDA). Hence the FEM analysis can be used to predict the variation of NSF in complex cases with reasonable accuracy.

REFERENCES

Chen, R. P., Zhou, W. H., & Chen, Y. M. 2009. Influences of soil consolidation and pile load on the development of negative skin friction of a pile. *Computers and Geotechnics, 36(8)*, 1265–1271. https://doi.org/10.1016/j.compgeo.2009.05.011

Comodromos, E. M., & Bareka, S. V. 2005. Evaluation of negative skin friction effects in pile foundations using 3D nonlinear analysis. *Computers and Geotechnics, 32(3)*, 210–221. http://10.1016/j.compgeo.2005.01.006

Fellenius, B. H. 1984. Negative skin friction and settlement of piles. *Proceedings of the Second International Seminar, Pile Foundations, Nanyang Technological Institute, Singapore, 18*.

Guidelines for interpretation of site investigation data for estimating the carrying capacity of single piles for design of bored and cast in-situ reinforced concrete piles (second edition). (2011). Institute for Construction Training and Development (ICTAD).

Hanna, A., & Hoque, M. A. 2008. Coupled consolidation model for negative skin friction on piles in clay layers.

Hanna, A. M., & Sharif, A. 2006. Drag Force on Single Piles in Clay Subjected to Surcharge Loading. *International Journal of Geomechanics*, 6(2), 89–96. https://doi.org/10.1061/(ASCE)1532-3641(2006)6:2(89)

Indraratna, B., Balasubramaniam, A. S., Phamvan, P., & Wong, Y. K. 1992. Development of negative skin friction on driven piles in soft bangkok clay. *Canadian Geotechnical Journal*.

Kim, H. J., & Mission, J. L. C. 2011. Development of negative skin friction on single piles: Uncoupled analysis based on nonlinear consolidation theory with finite strain and the load-transfer method. *Canadian Geotechnical Journal*. https://doi.org/10.1139/t11-004

Law, K. H., Othman, S. Z., Hashim, R., & Ismail, Z. 2014. Determination of soil stiffness parameters at a deep excavation construction site in Kenny Hill Formation. *Measurement*, *47*, 645–650. https://doi.org/10.1016/j.measurement.2013.09.030

Liu, J., Gao, H., & Liu, H. 2012. Finite element analyses of negative skin friction on a single pile. *Acta Geotechnica, 7(3)*, 239–252. https://doi.org/10.1007/s11440-012-0163-x

Matyas, E. L., & Santamarina, J. C. 1994. Negative skin friction and the neutral plane. *Canadian Geotech nical Journal*. https://doi.org/10.1139/t94-069

Wong, K. S., & Teh, C. I. 1996. Negative skin friction on piles in layered soil deposits. *International Journal of Rock Mechanics and Mining Sciences & Geomechanics Abstracts, 33(3)*, A134–A135. https://10.1016/0148-9062(96)87149–X

Smart Geotechnics for Smart Societies – Zhussupbekov, Sarsembayeva & Kaliakin (Eds)
© 2023 The Author(s), ISBN 978-1-003-29912-7
Open Access: www.taylorfrancis.com, CC BY-NC-ND 4.0 license

Evaluation of soil-structure interaction behaviors in a load test of barrette piles and back-analysis

Fuchen Teng, Xiang Jie Fang & Horn-Da Lin
Department of Civil and Construction Engineering, National Taiwan University of Science and Technology, Taiwan

Fang-Chih Lu, Young-Kuang Lin & Wei-F. Lee
Ground Master Construction Co, Ltd, Taipei, Taiwan

ABSTRACT: The purpose of barrette pile foundations is to transmit heavy loads into the ground and are becoming the preferred underground foundation system. In general, the static pile load tests are commonly conducted to estimate the pile bearing capacity and determine the in-situ soil parameters. In this study, a three-dimensional finite element model was used to simulate the behavior of barrette piles to determine in-situ soil parameters using the load-settlement relationship, and evaluating the pile behavior simulated by the structural elements-embedded beams.

Keywords: barrette pile, underground foundation system, static pile load test, retaining structure

1 INTRODUCTION

In general, the use of piles can effectively suppress soil liquefaction, which is important for area that has frequent earthquakes, such as Taiwan. In recent years, barrette piles have become more widely used in various types of building foundations, including barrette piles and barrette piles combined with buttress walls. Besides, rectangular-shaped piles have a larger pile shaft area than round-shaped piles. Therefore, barrette piles can contribute more skin friction and support higher superstructure load, which is a favorable foundation for urban areas.

The static load test is commonly used for determining the load-bearing capacity of the pile. In this study, the three-dimensional (3D) numerical analysis was used to simulate the static axial load test of the barrette pile, which is the most basic test and involves the application of vertical load directly to the pile head. Simulation of the pile load test is conducted to provide back analysis from the load-settlement results and determine the correct soil parameters of the site. Furthermore, the pile skin friction from the results of the pile loading test on-site was also used for the structure element: embedded beam. The soil parameters and numerical method are thus used in the following simulation stages and components. The simulation of barrette piles with embedded beam can reduce the difficulty during the model configuration (compared to solid element method) and provide more accurate prediction on soil-pile interaction behaviors.

2 SITE CONDITION AND NUMERICAL MODEL

2.1 *Details of excavation site condition*

The project was located near Gong-Guan MRT station, Taipei City, Taiwan. Figure 1 shows the plan view of the site. It consists of three main buildings, which are 12, 10, and 10-story

DOI: 10.1201/9781003299127-233

buildings. Each building has a 3-story basement with a construction area of 113,162 m2. The site includes 127 individual barrette piles, 39 barrette piles combined with the buttress wall, and two groups of the barrette piles axial static load test (both in compression and tension). The dimension of barrette piles is 2700×1000 mm, and the load applied is 4050 ton-force. The CP1 (compression pile 1) pile is 46.45 m in length and near borehole no. 1. The CP2 pile is 49.45 m in length and near borehole no. 8. Figure 2 shows the soil properties in the field.

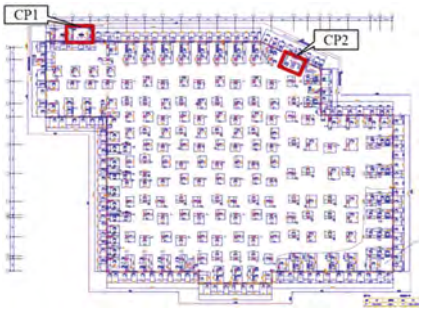

Figure 1. Location of Case Study in Taipei, Taiwan.

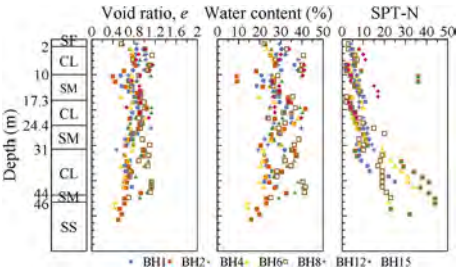

Figure 2. Soil properties at the in-site.

2.2 *Numerical model*

Three-dimensional (3D) finite element analyses were conducted to simulate the barrette piles axial load test with PLAXIS 3D v.22. The dimensions of the finite element model were 208.8 m x 208.8 m x 130.5 m. Figure 3 shows the 3D finite element model of barrette piles and generated mesh. Table 1 summarizes the detail of the PLAXIS 3D models adopted in this study.

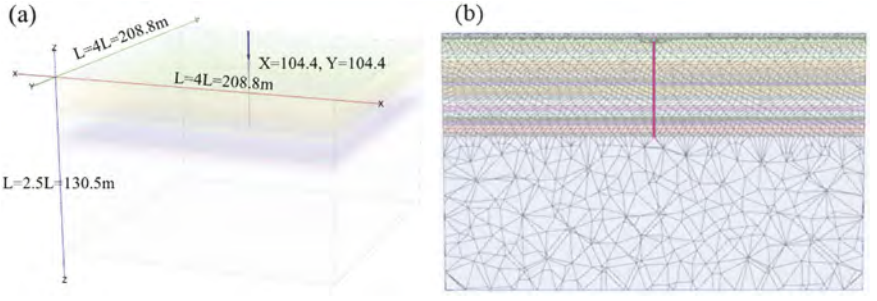

Figure 3. (a) The three-dimensional numerical model for a single barrette pile (b) 3D finite element meshing of 10-node tetrahedrons soil element.

Table 1. Adapted Models description.

Model number	Young's modulus reduction factor of pile, R_E	Model number	Young's modulus reduction factor of pile, R_E	$\gamma_{0.7}$
HS-A	R_E=0.6	HS small-A	R_E=0.6	1×10^{-4}
HS-B	R_E=0.7	HS small-B	R_E=0.7	1×10^{-4}
HS-C	R_E=0.8	HS small-C	R_E=0.8	1×10^{-4}
HS-D	R_E=1.0	HS small-D	R_E=1.0	1×10^{-4}
		HS small-E	R_E=0.7	7.5×10^{-5}

The stabilizer at the top pile was modeled as a beam element, while the barrette pile was modeled by using an embedded beam element to simulate the skin resistance of barrette piles. Hence,

the soil friction from the pile load test could be adopted for the skin friction in the embedded beam model. Table 2 shows the input parameters for structural elements. In these analyses, 21 construction stages were considered to simulate different loading conditions, as listed in Table 3.

Table 2. Input parameters for structural elements.

Structure	Type	A (m^2)	γ (kN/m^2)	I_2 (m^3)	I_3 (m^3)	E (GPa)	Axial skin resistance	Base resistance, F_{max} (kN)
Barrette (no friction)	Beam	2.7	26	1.640	0.225	35.8	-	-
Barrette	Embedded beam	2.7	26	1.640	0.225	35.8	Multi-linear	3000

Table 3. Stage of construction.

Stage	Item
Initial phase	K0-procedure
Phase 1	Excavation to GL.-2.75m
Phase 2	Active the pile.
Phase 3	Apply the axial load to the barrette pile from 225 tons.
Phase 4	Apply the axial load to the barrette pile from 450 tons.
⋮	⋮
Phase 21	Apply the axial load to the barrette pile from 4050 tons.

2.3 *Soil parameters*

The hardening soil model is an advanced elastoplastic constitutive model that is used for simulating both stiff and soft soil behaviors. Moreover, HS small is a modification of the hardening soil model that accounts for the increased stiffness of soils at small strains. Table 4. shows the properties of the soil layers by using HS and HS small soil models.

Table 4. Soil parameters.

Soil	Depth (m)	γ_m (kN/m^3)	e	ϕ'	SPT-N	Su (kPa)	E_{ur}^{ref} (MPa)	E_{50}^{ref} (MPa)	E_{oed}^{ref} (MPa)	G_0^{ref} (MPa)	$\gamma_{0.7}$
SF	0~2	20.6	0.7	30	3		8.2	2.7	2.7	9.6	1×10^{-4}
CL	2~10	18.3	0.9	30	3~4	19~25	65~72	21~23	15~17	76~84	1×10^{-4}
SM	10~17.3	18.94	0.79	30	8		67~74	22~25	22~25	72~86	1×10^{-4}
CL	17.3~24.4	18.40	0.88	31	4~8	25~50	48~86	16~29	11~20	57~101	1×10^{-4}
SM	24.4~31	19.38	0.91	31	15~25		159~277	53~93	53~93	186~323	1×10^{-4}
CL	31~44	18.88	0.91	32	15~23	94~144	129~161	43~54	30~38	150~187	1×10^{-4}
SM	44~46	17.66	0.9	32	35		461	154	154	385	1×10^{-4}
SS	46~52	21.58	0.4	35	40~65		738~1146	246~382	246~382	820~1336	1×10^{-4}

3 ANALYSIS RESULTS AND DISCUSSION

3.1 *Static load-settlement curve*

Figures 4 and 5 show the 3D FEM results and static pile load test for the Load-Settlement relationship by using HS and HS small model. The results showed that the pile settlements from the HS model decreased non-linearly, while the HS model results slightly overestimated the settlement from the monitor data at the initial working loading ($P < 2500$ Ton). It is also found that the HS and HS small model simulation had a close agreement with the monitoring data for $R_E = 0.7$ (30% reduction of pile Young's modulus).

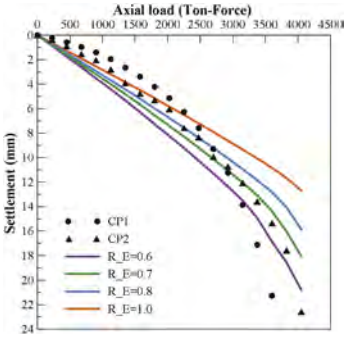

Figure 4. Simulation of Load-Settlement Curve from PLAXIS 3D HS model.

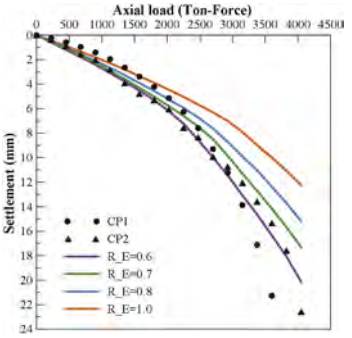

Figure 5. Simulation of Load-Settlement Curve from PLAXIS 3D HS small model.

According to Figure 6, it is found that the HS small model results could fit the monitor data, which was better than that of the HS model results. The reason is that the HS small model is a modification of the HS model, which considers the stiffness dependency of small strains. Based on the study conducted by Li (2022), the $\gamma_{0.7}$ range in Taipei city range is 1×10^{-4} ~ 5×10^{-5}. The difference in the results of changing the $\gamma_{0.7}$ is not significant because the shear strain has not yet reached 70% of $G_{0.}$ Figure 7 shows a simulation of pile behavior using the embedded beam in the HS small model. The results showed that this model could provide accurate skin friction and determine the typical loading behavior of barrette piles.

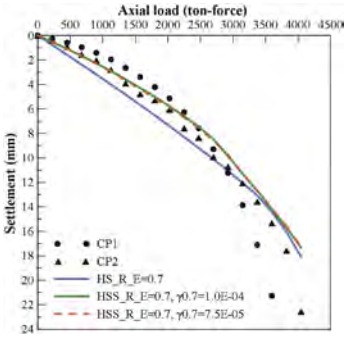

Figure 6. Comparison of load-settlement curve from PLAXIS 3D HS and HS small model.

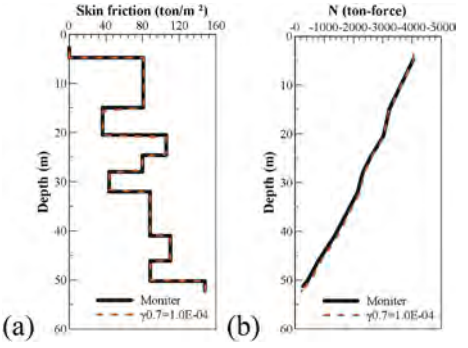

Figure 7. Simulation of pile behavior using embedded beam in HS small model: (a) Unit Shaft Resistance of Curve at CP2 (b) Distribution of Normal Stress of Curve at CP2.

4 CONCLUSION

In this paper, PLAXIS 3D was used to simulate barrette piles, and in-site pile static load tests were used to correct the soil parameters of this case. Following are some of the conclusions from the paper:

1. The pile structure element was modeled as an embedded beam in PLAXIS 3D, which can input soil-averaged pile shaft skin resistance from in-situ pile loading tests and yield more accurate pile behavior.
2. The stiffness dependency of small strain behavior could be considered by using HS small model, which could enhance the soil stiffness under small strain so that the Load-settlement curve is closer to the monitor data.

3. In the barrette pile load test, the displacement of the top pile under the large load is small, indicating that the soil is within the range of small strain. In such a case, the shear strain has not yet reached 70% of G_0, so the change of $\gamma_{0.7}$ is not sensitive to the results.

ACKNOWLEDGMENTS

The authors are grateful for the support from Taipei Water Department and Fortune6446 Construction Co., Ltd. for providing this case and research grants; Diagnostic Engineering Consultants Co., Ltd. for providing pile testing data; and Sanlien Technology Corp. for providing monitoring information.

REFERENCES

Chang, D. W., Huang, D. W., Lin, Y. K., Lu, F. C., Kuo, C. J., & Zhussupbekov, A. (2021). Length Influences on Lateral Performance of Barrette from Three-Dimensional Finite Element Analysis. Journal of Applied Science and Engineering, 25(4),577–591.

Hsu, M. C., Yu, C. H., & Chen, C. H. (2017). Case studies for side resistance of barrette piles using results of ultimate load tests. Journal of GeoEngineering, 12(2),65–79.

Li, Y. X. (2022). "Application of small strain elastic-plastic model in the analysis of deep excavation" M. S. thesis, Dept. Civil and Construction Engineering, National Science and Technology Univ. of Taiwan.

Naveen, B. P., C. R. Parthasarathy, and T. G. Sitharam. (2014). "Numerical modeling of the pile load test." In Proc., 4th China Int. Piling and Deep Foundations Summit, 156–161. Shanghai, China: Shanghai Fangxun Construction Consulting Co., Ltd.

Teshager, D. K. (2019). "Numerical simulation of static pile load test on stratified soil deposits." Ph.D. Thesis, Dept. Geotechnical Engineering, National Science and Technology Univ. of Addis Ababa.

Yi, L. (2005). "Finite element study on static pile load testing." M.S. thesis, Dept. Civil Engineering, National Univ. of Singapore.

Y. H. Chang, J. T. Hsieh, R. T. Ren, and C. H. Shih. (2011). "Construction and load testing of barrette foundations." Sino-Geotechnics, 128, 47–58.

Smart Geotechnics for Smart Societies – Zhussupbekov, Sarsembayeva & Kaliakin (Eds)
© 2023 The Author(s), ISBN 978-1-003-29912-7
Open Access: www.taylorfrancis.com, CC BY-NC-ND 4.0 license

Preliminary assessment of non-conforming *u-p* elements for saturated geomaterials

V.N. Kaliakin & D. Botchway
Department of Civil and Environmental Engineering, University of Delaware, USA

ABSTRACT: To simulate the response of saturated geomaterials requires a numerical approach such as the finite element method that employs a generalized Biot formulation. Under isothermal conditions, the primary dependent variables are displacements (u) and pore pressure (p), which are suitably coupled. The stability of such "*u-p*" elements requires that the displacement approximation be one order higher than the pressure approximation. Typical elements employ quadratic and linear approximation for u and p, respectively. Since, according to Darcy's law, the velocity of flow is proportional to the gradient of the pore pressure, the approximate velocity is thus constant over an element. In slow "consolidation-type" problems the accurate computation of such velocities is not crucial, as they are generally very small. The need to accurately simulate the effects associated with rising sea levels, rapidly rising flood waters, etc., however, now requires that accurate approximate velocities be computed. Consequently, robust and computationally efficient higher-order *u-p* elements need to be used in simulating such problems. The development of such elements that are is not a straightforward undertaking. This paper explains this difficulty and, as a measure to overcome it, describes some non-conforming elements that have been recently developed.

1 INTRODUCTION

Historically, mixed finite elements have been successfully applied to three general classes of problems, namely: 1) problems involving a physical (kinematic) constraint such as incompressibility, inextensibility, etc., 2) certain physical problems involving higher-order derivatives in their governing differential equations and/or boundary conditions and 3) problems having two or more primary dependent variable fields. Formulations based on the generalized Biot theory (Biot 1941) for porous geologic media come under the third category listed above. In addition, since geomaterials exhibit the kinematic constrain of incompressibility under certain conditions, such formulations also qualify for the first category.

Under isothermal conditions, the primary dependent variables used in generalized Biot formulation are displacements (u) and pore pressure (p), which are suitably coupled. The stability of such "*u-p*" elements requires that the displacement approximation be one order higher than the continuous pressure approximation. Traditionally, such elements have employed quadratic and linear approximation for u and p, respectively. Since, according to Darcy's law, the velocity of flow is proportional to the gradient of the pore pressure, the approximate velocity is thus constant over an element.

In slow "consolidation-type" problems the accurate computation of such velocities is not crucial, as they are generally very small. The need to accurately simulate the effects associated with rising sea levels, rapidly rising flood waters, etc., however, now requires that accurate approximate velocities be computed. Consequently, robust and computationally efficient higher-order *u-p* elements need to be used in simulating such problems. Here "higher-order" implies a pressure approximation that is quadratic or higher.

DOI: 10.1201/9781003299127-234

The development of such higher-order *u-p* elements that are is not a straightforward undertaking. This paper explains this difficulty and, as a measure to overcome it, describes some non-conforming elements that have been recently developed.

2 GOVERNING EQUATIONS

This paper is restricted for two-field (*u-p*) generalized Biot formulations (Biot 1941) for a saturated deforming porous medium under isothermal, quasi-static conditions. The deformations and deformation gradients are both assumed to be infinitesimal. To facilitate the presentation, the following variables are defined (Kaliakin 2001): N_{sdim} = spatial dimension of the problem (= 1, 2 or 3), N_{dn} = number of nodes in an element at which displacement degrees of freedom exist, N_{pn} = number of nodes in an element at which pore pressures are unknown, N_{en} = total number of nodes in an element (in general, $N_{en} \neq N_{dn} + N_{pn}$), N_{nddof} = number of displacement degrees of freedom at a given node, N_{eddof} = total number of displacement degrees of freedom for a given element (= N_{dn} * N_{nddof}), N_{epdof} = total number of pressure degrees of freedom for a given element (= N_{pn}), N_{rowb} = number of stress and strain components present in the formulation. For three-dimensiona analyses (N_{sdim} = 2), N_{rowb} = 6. For torsionless axisymmetry N_{sdim} = 2 and N_{rowb} = 4. Finally, for plane strain analyses N_{sdim} = 2 and N_{rowb} = 3.

The governing equations for the aforementioned medium are first re-cast in their weak form. A Galerkin form of the weighted residual equations is next adopted. Time derivatives of displacements and pore pressure are approximated using a one-step family of methods (Hughes 1987) that are characterized by the temporal parameter θ ($0 \leq \theta \leq 1$).

Following a standard discretization process (Kaliakin 2001), the following set of discrete (approximate) element equations, written in incremental vector-matrix form, is obtained:

$$\begin{bmatrix} \tilde{\mathbf{K}}^{(e)} & \mathbf{G}^{(e)} \\ \mathbf{G}^{(e)T} & \left(\mathbf{H}^{(e)} + \mathbf{L}^{(e)}\right) \end{bmatrix} \begin{Bmatrix} \Delta \hat{\mathbf{u}}_n^{(e)} \\ \Delta \hat{\mathbf{p}}_n^{(e)} \end{Bmatrix} = \begin{Bmatrix} \Delta \mathbf{q}_1{}^{(e)} \\ \Delta \mathbf{q}_2{}^{(e)} \end{Bmatrix} \tag{1}$$

where $\Delta \hat{\mathbf{u}}_n^{(e)}$ is an (N_{eddof} * 1) vector of unknown nodal incremental absolute displacements of the porous solid, and $\Delta \hat{\mathbf{p}}_n^{(e)}$ is an (N_{epdof} * 1) vector of unknown nodal incremental values of pressure.

In equation (1) the (N_{eddof} * N_{eddof}) symmetric and positive definite element displacement sub-matrix is defined by

$$\tilde{\mathbf{K}}^{(e)} = \int_{\Omega^e} \left(\mathbf{B}^{(u)T} \mathbf{C}^{(e)} \mathbf{B}^{(u)} \right) d\Omega \tag{2}$$

where Ω^e represents the element domain. In equation (2) $\mathbf{C}^{(e)}$ is an (N_{rowb} * N_{rowb}) matrix of element tangent stiffness coefficients that, depending on the specific constitutive law, can vary with stress, strain or their history. Typically some incremental-iterative nonlinear solution scheme is thus required. In the simplest case, $\mathbf{C}^{(e)}$ is a matrix of elastic material constants.

The (N_{eddof} * N_{epdof}) element "coupling" sub-matrix appearing in equation (1) is defined by

$$\mathbf{G}^{(e)} = -\int_{\Omega^e} \left(\mathbf{B}^{(u)T} \alpha^{(e)} \mathbf{N}^{(p)} \right) d\Omega \tag{3}$$

where $\boldsymbol{\alpha}^{(e)}$ is an (N_{rowb} * 1) vector of generalized "Biot moduli" used in the definition of effective stress (Thompson & Willis 1991), and $\mathbf{N}^{(p)}$ is an (1 * N_{epdof}) matrix of pressure interpolation functions.

Unless stated otherwise, $\boldsymbol{\alpha}^{(e)}$ contains unit entries. More precisely, for three-dimensional idealizations $\boldsymbol{\alpha}^{(e)} = \{ 1 \quad 1 \quad 1 \quad 0 \quad 0 \quad 0 \}^T$, for plane strain idealizations $\boldsymbol{\alpha}^{(e)} = \{ 1 \quad 1 \quad 0 \}^T$, and for torsionless axisymmetry $\boldsymbol{\alpha}^{(e)} = \{ 1 \quad 1 \quad 1 \quad 0 \}^T$.

The (N_{epdof} * N_{epdof}) element "permeability" sub-matrix appearing in equation (1) is defined in the following manner:

$$\mathbf{H}^{(\mathbf{e})} = -\int_{\Omega^e} \left(\frac{1}{\eta^{(e)}} \mathbf{B}^{(\mathbf{p})T} \mathbf{k}^{\mathbf{d}} \mathbf{B}^{(\mathbf{p})} \right) \theta \Delta t_m \, d\Omega \tag{4}$$

where $\eta^{(e)}$ is the dynamic viscosity of the pore fluid (units of FtL^{-2}) associated with the element, $\mathbf{K^d}$ is the intrinsic or geometric permeability tensor (units of L^2), $\Delta t_m = t_{m+1} - t_m$ is a discrete time step, and θ is the aforementioned temporal parameter.

Finally, the (N_{epdof} * N_{epdof}) element "compressibility" sub-matrix $\mathbf{L^{(e)}}$ appearing in equation (1) is defined as follows:

$$\mathbf{L}^{(\mathbf{e})} = -\int_{\Omega^e} \left(\frac{1}{M^{(e)}} \mathbf{N}^{(\mathbf{p})T} \mathbf{N}^{(\mathbf{p})} \right) d\Omega \tag{5}$$

where $M^{(\mathbf{e})}$ is a material constant, commonly referred to as the "Biot modulus" (Detouenay & Cheng 1993), that characterizes the volume compressibility of the soil/fluid mixture. For $M^{(e)} < \infty$ $\mathbf{L^{(e)}}$ is symmetric and negative definite. For infinite values of $M^{(\mathbf{e})}$, $\mathbf{L^{(e)}}$ becomes the zero matrix and, depending on the magnitude of entries in $\mathbf{k^d}$ (and thus in $\mathbf{H^{(e)}}$), can make the entire element matrix *singular*. Whether or not this happens depends on the rank deficiency of $\left(\mathbf{H}^{(\mathbf{e})} + \mathbf{L}^{(\mathbf{e})} \right)$ (Hughes 1987).

The (N_{eddof} * 1) element load vector associated with the displacement degrees of freedom is defined by

$$\Delta \mathbf{q}_1^{(\mathbf{e})} = \int_{\Omega^e} \mathbf{N}^{(\mathbf{u})T} \Delta(\rho \mathbf{g}) \, d\Omega - \int_{\Omega^e} \mathbf{B}^{(\mathbf{u})T} \Delta \boldsymbol{\sigma}^{\mathbf{0}\prime} \, d\Omega + \int_{\Gamma_t} \mathbf{N}^{(\mathbf{u})T} \Delta \bar{\mathbf{t}} \, d\Gamma \tag{6}$$

where $\mathbf{N^{(u)}}$ is an (N_{nddof} * N_{nddof}) matrix of displacement interpolation functions, ρ is the *average* material mass density (i.e., the density of the soil skeleton together with the pore fluid), $\mathbf{g}$ is the gravitational acceleration, $\Delta \boldsymbol{\sigma}^{\mathbf{0}\prime}$ is an (N_{rowb} * 1) vector of initial stresses, and $\Delta \bar{\mathbf{t}}$ is a vector of known applied incremental surface tractions.

Finally, the (N_{epdof} * 1) element load vector associated with the pressure degrees of freedom is defined by

$$\begin{aligned} \Delta \mathbf{q}_2{}^{(\mathbf{e})} = & \int_{\Omega^e} \mathbf{B}^{(\mathbf{p})T} \left[(m) \left(\frac{1}{\eta} \mathbf{k}^{\mathbf{d}} \mathbf{B}^{(\mathbf{p})} \Delta \hat{\mathbf{p}}_{\mathbf{n}}^{(\mathbf{e})} \right) \right] \Delta t_m \, d\Omega \\ & - \int_{\Omega^e} \mathbf{B}^{(\mathbf{p})T} \left\{ \left[(m) \left(\tfrac{1}{\eta} \rho^f \mathbf{k}^{\mathbf{d}} \mathbf{g} \right) (1-\theta) + {}^{(m+1)} \left(\tfrac{1}{\eta} \rho^f \mathbf{k}^{\mathbf{d}} \mathbf{g} \right) \theta \right] \right\} \Delta t_m \, d\Omega \\ & + \int_{\Gamma_Q} \mathbf{N}^{(\mathbf{p})T} \Delta \bar{Q} \, d\Gamma \end{aligned} \tag{7}$$

where $\Delta \bar{Q}$ is the known total hydraulic flux (flow per unit area) normal to the surface.

3 GRAPHICAL CONVENTIONS

In figures contained in this paper, circles depict nodes possessing displacement degrees of freedom. Black circles represent nodes with *constrained* displacement degrees of freedom; white circles represent nodes with unconstrained degrees of freedom. Nodes with pressure degrees of freedom are depicted by triangles. Transparent triangles represent nodes with unconstrained pressure degrees of freedom.

The first one- to three letters describe the type of the element used. These are followed by the number of nodes in the element at which displacement degrees of freedom exist. This number is followed by the letter "P" and the then by the number of nodes in the element at which pore pressures are unknown. The element designation terminates with the letter "c"

which indicates that the pressure approximation is continuous. Thus, the designation T6P3c represents a quadratic triangular element with six displacement nodes and three pressure nodes that are associated with a continuous (linear) pressure approximation, Q9P4c represents a quadrilateral element with nine displacement nodes and four pressure nodes, and so on.

Although interpolation function continuity requirements are somewhat relaxed in mixed formulations, for certain choices of these functions the mixed approximation will not yield meaningful results. As it turns out, this limitation is much more severe than in the irreducible formulation, where continuity and completeness criteria were sufficient to ensure a monotonically convergent form (Kaliakin 2001). In particular, from an assessment of the stability and performance of mixed formulation it is a known that the condition $N_{eddof} > N_{epdof}$ is a necessary but not sufficient condition for stability (Hughes 1987). As a result of this fact, the number of potentially stable elements is rather small.

4 "TAYLOR-HOOD" ELEMENTS

Arguably the most popular subclass of mixed finite elements with continuous pressure approximations consists of two- and three-dimensional elements possessing a displacement interpolation that is one order higher than the pressure interpolation. Such elements are sometimes referred to as "Taylor-Hood" elements, in recognition of the pioneering use of this element class by C. Taylor and P. Hood (Taylor & Hood 1973, Hood & Taylor 1974) for solving incompressible flow problems in field of computational fluid dynamics (CFD). In such elements, a quadratic approximation is assumed for the displacements in conjunction with a linear one for the pore pressure. Since "Taylor-Hood" elements are known to generally yield stable results, they have been used rather extensively in the past.

5 DISCUSSION OF POTENTIAL HIGHER-ORDER ELEMENTS

In this section, some general comments related to the development of higher-order *u-p* elements are presented. As mentioned in the introduction, "higher-order" implies a pressure approximation that is quadratic or higher.

5.1 *Triangular elements*

First consider triangular *u-p* elements. Various forms of such elements have been used in the past to simulate the response of a saturated deforming porous medium.

The first such element is the T4P3c. This conforming element adds a cubic displacement "bubble" function to the linear triangular element. To this is added a continuous linear pressure approximation. The resulting element is shown in Figure 1a. For this element, $N_{dn} = 4$, $N_{pn} = 3$, $N_{en} = 4$, $N_{eddof} = 8$ and $N_{epdof} = 3$. The conjecture behind the T4P3c is that the additional two displacement degrees of freedom associated with the interior node will yield a robust lower-order element (Kaliakin & Jiang 2009). For mesh generation software that is incapable of generating four-node triangles, these degrees of freedom must be "condensed" out of the element equations so as to yield a pseudo-linear three-node element.

The next triangular *u-p* element considered is the T6P3c. This conforming "Taylor-Hood" element combines a quadratic displacement approximation with a linear (continuous) pressure approximation associated with the vertex nodes. The resulting element is shown in Figure 1b. For this element, $N_{dn} = 6$, $N_{pn} = 3$, $N_{en} = 6$, $N_{eddof} = 12$ and $N_{epdof} = 3$.

The third triangular *u-p* element considered herein in the T7P3c. This conforming element is shown in Figure 1c. It adds a cubic "bubble function" to the quadratic T6P3c element; the two additional displacement components of $\hat{\mathbf{u}}^{(\mathbf{e})}$ are globally continuous on the element domain Ω. Similar to the T6P3c, the pressure approximation is linear. For this element, $N_{dn} = 7$, $N_{pn} = 3$, $N_{en} = 7$, $N_{eddof} = 14$ and $N_{epdof} = 3$.

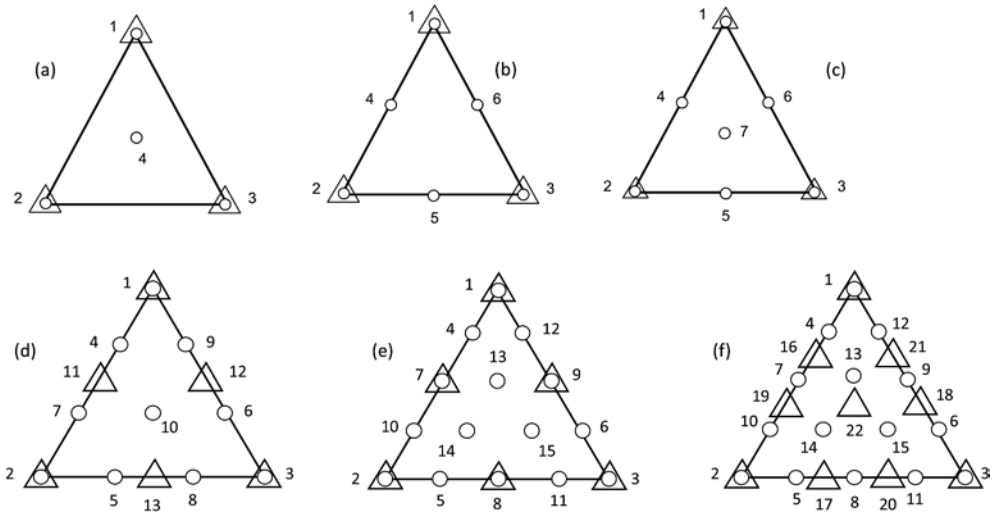

Figure 1. Triangular *u-p* elements: a) T4P3c, b) T6P3c, c) T7P3c, d) T10P6c, e) T15P6c, f) T15P10c.

Although they employ different approximations for the displacements $\hat{\mathbf{u}}^{(e)}$, the T4P3c, T6P3c and T7P3c all use a linear approximation for the pore pressure. Guided by the fact that displacement interpolation should be one order higher than the pressure interpolation (recall the discussion of "Taylor-Hood" elements in Section 4), it follows that to include a higher-order quadratic pressure approximation, the displacement approximation must be at least cubic.

The first potential conforming higher-order triangular *u-p* element is thus the T10P6c, which is shown in Figure 1d. This element combines a standard cubic (10-node) triangular element with a quadratic (6-node) pore pressure approximation. Although the vertex nodes have both displacement and pressure degrees of freedom, the remaining three mid-side nodes associated with the pressure approximation do not coincide with the mid-side displacement nodes. As such, for the T10P6c, $N_{dn} = 10$, $N_{pn} = 6$, $N_{en} = 10+3 = 13$, $N_{eddof} = 20$ and $N_{epdof} = 6$. The presence of mid-side nodes with only pressure degrees of freedom makes this element somewhat impractical. In addition, the presence of such elements would likely require special logic in mesh generation software.

A more practical conforming higher-order triangular *u-p* element is the T15P6c, which is shown in Figure 1e. This element combines a standard quartic (15-node) triangular element with a quadratic (6-node) pore pressure approximation. For the T15P6c, $N_{dn} = 15$, $N_{pn} = 6$, $N_{en} = 15$, $N_{eddof} = 30$ and $N_{epdof} = 6$. This element was used in the CRISP (Britto & Gunn, 1987) and Plaxis (2012) computer programs.

Finally, it is timely to note that another possible conforming higher-order triangular *u-p* element is the T15P10c. This element combines a standard quartic (15-node) triangular element with a cubic (10-node) pore pressure approximation (Figure 1f). Although the vertex nodes have both displacement and pressure degrees of freedom, the remaining six mid-side nodes associated with the pressure approximation do not coincide with the mid-side displacement nodes. In addition, the interior node associated with the pressure approximation does not coincide with the the location of a displacement node. As such, for the T15P10c, $N_{dn} = 15$, $N_{pn} = 10$, $N_{en} = 15+7 = 22$, $N_{eddof} = 30$ and $N_{epdof} = 10$. Similar to the T10P6c element, the presence of mid-side nodes with only pressure degrees of freedom makes this element somewhat impractical. In addition, the presence of such elements would likely require special logic in mesh generation software.

5.2 *Quadrilateral elements*

Next, consider quadrilateral *u-p* elements. Similar to some of the aforementioned triangular elements, various quadrilateral elements have been used in the past to simulate the response of a saturated deforming porous medium.

The first such element is the Q5P4c. This conforming quadrilateral element adds a quadratic "bubble" function to the irreducible bilinear Lagrangian element. The pressure is approximated using a bilinear (continuous) pressure approximation associated with the vertex nodes. The resulting element is shown in Figure 2a. For this element, $N_{dn} = 5$, $N_{pn} = 4$, $N_{en} = 5$, $N_{eddof} = 10$ and $N_{epdof} = 4$. The conjecture behind the Q5P4c is that the additional two displacement degrees of freedom associated with the interior node will yield a robust lower-order element (Kaliakin & Jiang 2009). For mesh generation software that is incapable of generating five-node quadrilaterals these degrees of freedom must be "condensed" out of the element equations so as to yield a pseudo-bilinear four-node element.

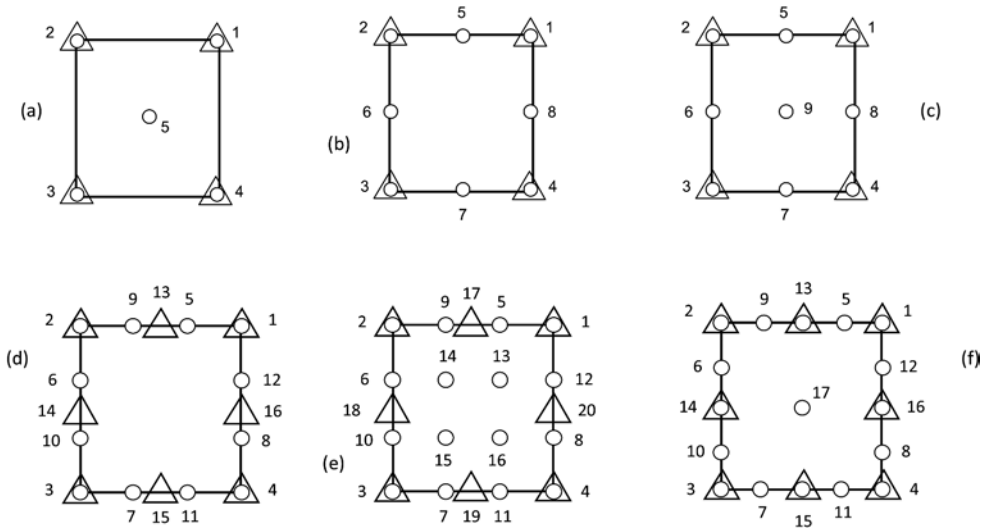

Figure 2. Quadrilateral *u-p* elements: a) Q5P4c, b) Q8P4c, c) Q9P4c, d) Q12P8c, e) Q16P8c, f) Q17P8c.

The next quadrilateral *u-p* element considered is the Q8P4c. This conforming "Taylor-Hood" element combines a bi-quadratic Serendipity displacement approximation with a linear (continuous) pressure approximation associated with the vertex nodes. The resulting element is shown in Figure 2b. For this element, $N_{dn} = 8$, $N_{pn} = 4$, $N_{en} = 8$, $N_{eddof} = 16$ and $N_{epdof} = 4$.

The third quadrilateral *u-p* element considered is the Q9P4c. This conforming "Taylor-Hood" element combines a bi-quadratic Lagrangian displacement approximation with a linear (continuous) pressure approximation associated with the vertex nodes. The resulting element is shown in Figure 2c. For this element, $N_{dn} = 9$, $N_{pn} = 4$, $N_{en} = 9$, $N_{eddof} = 18$ and $N_{epdof} = 4$.

Although they employ different approximations for the displacements $\hat{\mathbf{u}}^{(e)}$, the Q5P4c, Q8P4c and Q9P4c all use a linear approximation for the pore pressure. As in the case of triangular elements, the inclusion of a higher-order quadratic pressure approximation requires the displacement approximation to be at least cubic.

The first potential conforming higher-order quadrilateral *u-p* element is thus the Q12P8c, which is shown in Figure 2d. This element combines a standard cubic (12-node) Serendipity quadrilateral element with a quadratic (8-node) pore pressure approximation. Although the vertex nodes have both displacement and pressure degrees of freedom, the remaining four mid-side nodes associated with the pressure approximation do not coincide with the mid-side displacement nodes. As such, for the Q12P8c, $N_{dn} = 12$, $N_{pn} = 8$, $N_{en} = 12+4 = 16$, $N_{eddof} = 24$ and $N_{epdof} = 8$. Similar to the aforementioned T10P6c element, the presence of mid-side nodes with only pressure degrees of freedom makes this element somewhat impractical. In addition, the presence of such elements would likely require special logic in mesh generation software.

Another possible conforming higher-order quadrilateral *u-p* element is the Q16P8c. This element combines a standard cubic (16-node) Lagrangian quadrilateral element with a quadratic (8-node) pore pressure approximation (Figure 2e). Similar to the Q12P8c element, the vertex nodes have both displacement and pressure degrees of freedom; the remaining four mid-side nodes associated with the pressure approximation do not, however, coincide with the mid-side displacement nodes. For the Q16P8c, $N_{dn} = 16$, $N_{pn} = 8$, $N_{en} = 16 + 4 = 20$, $N_{eddof} = 32$, and $N_{epdof} = 8$. Similar to the Q12P8c element, the presence of mid-side nodes with only pressure degrees of freedom makes this element somewhat impractical. In addition, the presence of such elements would likely require special logic in mesh generation software. In addition, the presence of the four interior displacement nodes makes the Q16P8c even more impractical than the Q12P8c.

A more practical conforming higher-order quadrilateral *u-p* element is the Q17P8c, which is shown in Figure 2f. This element combines a standard quartic (17-node) Serendipity quadrilateral element with a quadratic (8-node) pore pressure approximation. For the Q17P8c, $N_{dn} = 17$, $N_{pn} = 8$, $N_{en} = 17$, $N_{eddof} = 34$ and $N_{epdof} = 8$.

6 OVERVIEW OF NON-CONFORMING QUADRILATERAL ELEMENTS

As evident from the discussion presented in the previous two sections, the robust implementation of a higher-order conforming *u-p* element requires a quartic approximation for the incremental displacement components. Since the computational effort associated with such conforming elements is non-trivial, it is natural to investigate the development of suitable non-conforming *u-p* elements. This section thus gives an overview of two non-conforming quadrilateral *u-p* elements that contain a higher-order pressure approximation. Jiang & Kaliakin (2009) give some preliminary comments regarding such elements.

In these elements, a quadratic approximation for the incremental displacement components identical to that used in either the Q8P4c (Figure 2b) or Q9P4c (Figure 2c) elements is employed; viz.,

$$\Delta\hat{\mathbf{u}}^{(\mathbf{e})} = \mathbf{N}^{(\mathbf{u})}\Delta\hat{\mathbf{u}}_{\mathbf{n}}^{(\mathbf{e})} \tag{8}$$

where $\Delta\widehat{\mathbf{u}}^{(\mathbf{e})}$ is a (2*1) vector of incremental displacement components, $\mathbf{N}^{(\mathbf{u})}$ is a (2 * N_{eddof}) vector of displacement interpolation functions, and $\Delta\widehat{\mathbf{u}}_{\mathbf{n}}^{(\mathbf{e})}$ is again an (N_{eddof} * 1) vector of unknown nodal incremental absolute displacements of the porous solid (recall Eq. 1).

Motivated by the development of irreducible non-conforming quadrilateral elements (Taylor et al. 1976), the pore pressure is approximated as follows:

$$\Delta\hat{\mathbf{p}}^{(\mathbf{e})} = \mathbf{N}^{(\mathbf{p})}\Delta\hat{\mathbf{p}}_{\mathbf{n}}^{(\mathbf{e})} + \mathbf{N}^{(\mathbf{p})*}\Delta\hat{\mathbf{p}}_{\mathbf{n}}^{(\mathbf{e})*} \tag{9}$$

where

$$\mathbf{N}^{(\mathbf{p})} = \left\{ N_1^{(p)} \quad N_2^{(p)} \quad N_3^{(p)} \quad N_4^{(p)} \right\} \tag{10}$$

are standard bi-linear Lagrangian interpolation functions used to approximate the pore pressure, $\Delta\hat{\mathbf{p}}_{\mathbf{n}}^{(\mathbf{e})}$ is an (4*1) vector of unknown nodal incremental values of pressure,

$$\mathbf{N}^{(\mathbf{p})*} = \left\{ \left(1-\xi^2\right) \quad \left(1-\eta^2\right) \right\} \tag{11}$$

is a (1*2) vector of quadratic interpolation functions that cause the element to be non-conforming, and $\Delta\hat{\mathbf{p}}_{\mathbf{n}}^{(\mathbf{e})*}$ is a (2*1) vector of quadratic unknown nodal incremental values of pressure.

Using the above approximations along with their spacial derivatives and following a standard discretization process (Kaliakin 2001), the following set of discrete (approximate) element equations, written in incremental vector-matrix form, is obtained (compare with Eq. 1):

$$\begin{bmatrix} \tilde{\mathbf{K}}^{(\mathbf{e})} & \mathbf{G}^{(\mathbf{e})} & \mathbf{G}^{(\mathbf{e})*} \\ \mathbf{G}^{(\mathbf{e})^T} & \left(\mathbf{H}^{(\mathbf{e})} + \mathbf{L}^{(\mathbf{e})}\right) & \left(\mathbf{H}^{(\mathbf{e})*} + \mathbf{L}^{(\mathbf{e})*}\right) \\ \mathbf{G}^{(\mathbf{e})*^T} & \left(\mathbf{H}^{(\mathbf{e})*^T} + \mathbf{L}^{(\mathbf{e})*^T}\right) & \mathbf{M}^{(\mathbf{e})*} \end{bmatrix} \begin{Bmatrix} \Delta\hat{\mathbf{u}}_{\mathbf{n}}^{(\mathbf{e})} \\ \Delta\hat{\mathbf{p}}_{\mathbf{n}}^{(\mathbf{e})} \\ \Delta\hat{\mathbf{p}}_{\mathbf{n}}^{(\mathbf{e})*} \end{Bmatrix} = \begin{Bmatrix} \Delta\mathbf{q}_1^{(\mathbf{e})} \\ \Delta\mathbf{q}_2^{(\mathbf{e})} \\ \Delta\mathbf{q}_3^{(\mathbf{e})} \end{Bmatrix} \tag{12}$$

where $\tilde{\mathbf{K}}^{(e)}$, $\mathbf{G}^{(\mathbf{e})}$, $\mathbf{H}^{(\mathbf{e})}$, $\mathbf{L}^{(\mathbf{e})}$, and $\Delta\mathbf{q}_1^{(\mathbf{e})}$ are as previously defined.

In equation (12*)*,

$$\mathbf{G}^{(\mathbf{e})*} = -\int_{\Omega^e} \left(\mathbf{B}^{(\mathbf{u})^T} \boldsymbol{\alpha}^{(\mathbf{e})} \mathbf{N}^{(\mathbf{p})*}\right) d\Omega \tag{13}$$

has size (N_{eddof} * 2). The (4*2) augmented element "permeability" sub-matrix appearing in equation (12) is defined in the following manner:

$$\mathbf{H}^{(\mathbf{e})*} = -\int_{\Omega^e} \left(\frac{1}{\eta^{(e)}} \mathbf{B}^{(\mathbf{p})^T} \mathbf{k}^{\mathbf{d}} \mathbf{B}^{(\mathbf{p})*}\right) \theta \Delta t_m \, d\Omega \tag{14}$$

where $\eta^{(e)}$, $\mathbf{k}^{\mathbf{d}}$, Δt_m, and θ are as previously defined.

The (4*2) augmented element "compressibility" sub-matrix $\mathbf{L}^{(\mathbf{e})*}$ appearing in equation (12) is defined as follows:

$$\mathbf{L}^{(\mathbf{e})*} = -\int_{\Omega^e} \left(\frac{1}{M^{(e)}} \mathbf{N}^{(\mathbf{p})^T} \mathbf{N}^{(\mathbf{p})*}\right) d\Omega \tag{15}$$

The (2*2) augmented element sub-matrix $\mathbf{M}^{(\mathbf{e})*}$ is given by

$$\mathbf{M}^{(\mathbf{e})*} = -\int_{\Omega^e} \left(\frac{1}{M^{(e)}} \mathbf{N}^{(\mathbf{p})*^T} \mathbf{N}^{(\mathbf{p})*}\right) d\Omega \tag{16}$$

The second sub-vector appearing in the forcing vector in equation (12*)*, which has size (4*1), is given by

$$\begin{aligned} \Delta\mathbf{q}_2^{(\mathbf{e})} = & \int_{\Gamma_Q} \mathbf{N}^{(\mathbf{p})^T} \Delta\bar{Q} \, d\Gamma + \int_{\Omega^e} \mathbf{B}^{(\mathbf{p})^T} \left[{}^{(m)}\left(\frac{1}{\eta} \mathbf{k}^{\mathbf{d}} \mathbf{B}^{(\mathbf{p})} \Delta\hat{\mathbf{p}}_{\mathbf{n}}^{(\mathbf{e})}\right)\right] \Delta t_m \, d\Omega \\ & + \int_{\Omega^e} \mathbf{B}^{(\mathbf{p})^T} \left[{}^{(m)}\left(\frac{1}{\eta} \mathbf{k}^{\mathbf{d}} \mathbf{B}^{(\mathbf{p})*} \Delta\hat{\mathbf{p}}_{\mathbf{n}}^{(\mathbf{e})*}\right)\right] \Delta t_m \, d\Omega \\ & - \int_{\Omega^e} \mathbf{B}^{(\mathbf{p})^T} \left\{ \left[{}^{(m)}\left(\tfrac{1}{\eta} \rho^f \mathbf{k}^{\mathbf{d}} \mathbf{g}\right)(1-\theta) + {}^{(m+1)}\left(\tfrac{1}{\eta} \rho^f \mathbf{k}^{\mathbf{d}} \mathbf{g}\right)\theta\right] \right\} \Delta t_m \, d\Omega \end{aligned} \tag{17}$$

Finally, the third sub-vector appearing in the forcing vector in equation (12*)*, which has size (2*1), is given by

$$\begin{aligned}\Delta\mathbf{q}_3^{(\mathbf{e})} = &\int_{\Omega^e} \mathbf{B}^{(\mathbf{p})*T}\left[{}^{(m)}\left(\frac{1}{\eta}\mathbf{k}^{\mathbf{d}}\mathbf{B}^{(\mathbf{p})}\Delta\hat{\mathbf{p}}_{\mathbf{n}}^{(\mathbf{e})}\right)\right]\Delta t_m\, d\Omega \\ &+\int_{\Omega^e} \mathbf{B}^{(\mathbf{p})*T}\left[{}^{(m)}\left(\frac{1}{\eta}\mathbf{k}^{\mathbf{d}}\mathbf{B}^{(\mathbf{p})*}\Delta\hat{\mathbf{p}}_{\mathbf{n}}^{(\mathbf{e})*}\right)\right]\Delta t_m\, d\Omega \\ &-\int_{\Omega^e} \mathbf{B}^{(\mathbf{p})*T}\left\{\left[{}^{(m)}\left(\frac{1}{\eta}\rho^f\mathbf{k}^{\mathbf{d}}\mathbf{g}\right)(1-\theta)+\ {}^{(m+1)}\left(\frac{1}{\eta}\rho^f\mathbf{k}^{\mathbf{d}}\mathbf{g}\right)\theta\right]\right\}\Delta t_m\, d\Omega\end{aligned} \tag{18}$$

To eliminate $\Delta\hat{\mathbf{p}}_{\mathbf{n}}^{(\mathbf{e})*}$ from the element equations, the third set of sub-matrices in equation (12) is solved as follows:

$$\Delta\hat{\mathbf{p}}_{\mathbf{n}}^{(\mathbf{e})*} = \left(\mathbf{M}^{(\mathbf{e})*}\right)^{-1}\left[\Delta\mathbf{q}_3^{(\mathbf{e})} - \left(\mathbf{H}^{(\mathbf{e})*T} + \mathbf{L}^{(\mathbf{e})*T}\right)\Delta\hat{\mathbf{p}}_{\mathbf{n}}^{(\mathbf{e})*} - \mathbf{G}^{(\mathbf{e})*T}\Delta\hat{\mathbf{u}}_{\mathbf{n}}^{(\mathbf{e})}\right] \tag{19}$$

Substituting equation (19) into the first set of sub-matrices in equation (12) gives

$$\begin{aligned}&\left[\tilde{\mathbf{K}}^{(e)} - \mathbf{G}^{(\mathbf{e})*}\left(\mathbf{M}^{(\mathbf{e})*}\right)^{-1}\mathbf{G}^{(\mathbf{e})*T}\right]\Delta\hat{\mathbf{u}}_{\mathbf{n}}^{(\mathbf{e})} \\ &\quad+\left[\mathbf{G}^{(\mathbf{e})} - \mathbf{G}^{(\mathbf{e})*}\left(\mathbf{M}^{(\mathbf{e})*}\right)^{-1}\left(\mathbf{H}^{(\mathbf{e})*T} + \mathbf{L}^{(\mathbf{e})*T}\right)\right]\Delta\hat{\mathbf{p}}_{\mathbf{n}}^{(\mathbf{e})} \\ &\quad=\Delta\mathbf{q}_1^{(\mathbf{e})} - \mathbf{G}^{(\mathbf{e})*}\left(\mathbf{M}^{(\mathbf{e})*}\right)^{-1}\Delta\mathbf{q}_3^{(\mathbf{e})}\end{aligned} \tag{20}$$

Substituting equation (19) into the second set of sub-matrices in equation (12) gives

$$\begin{aligned}&\left[\mathbf{G}^{(\mathbf{e})^T} - \left(\mathbf{H}^{(\mathbf{e})*} + \mathbf{L}^{(\mathbf{e})*}\right)\left(\mathbf{M}^{(\mathbf{e})*}\right)^{-1}\mathbf{G}^{(\mathbf{e})*T}\right]\Delta\hat{\mathbf{u}}_{\mathbf{n}}^{(\mathbf{e})} \\ &\quad+\left[\left(\mathbf{H}^{(\mathbf{e})} + \mathbf{L}^{(\mathbf{e})}\right) - \left(\mathbf{H}^{(\mathbf{e})*} + \mathbf{L}^{(\mathbf{e})*}\right)\left(\mathbf{M}^{(\mathbf{e})*}\right)^{-1}\left(\mathbf{H}^{(\mathbf{e})*T} + \mathbf{L}^{(\mathbf{e})*T}\right)\right]\Delta\hat{\mathbf{p}}_{\mathbf{n}}^{(\mathbf{e})} \\ &\quad=\Delta\mathbf{q}_2^{(\mathbf{e})} - \left(\mathbf{H}^{(\mathbf{e})*} + \mathbf{L}^{(\mathbf{e})*}\right)\left(\mathbf{M}^{(\mathbf{e})*}\right)^{-1}\Delta\mathbf{q}_3^{(\mathbf{e})}\end{aligned} \tag{21}$$

The modified element equations thus have a form similar to equation (1*)*; viz.,

$$\begin{bmatrix}\tilde{\mathbf{K}}_{11}^{(\mathbf{e})} & \tilde{\mathbf{K}}_{12}^{(\mathbf{e})} \\ \tilde{\mathbf{K}}_{21}^{(\mathbf{e})} & \tilde{\mathbf{K}}_{22}^{(\mathbf{e})}\end{bmatrix}\begin{Bmatrix}\Delta\hat{\mathbf{u}}_{\mathbf{n}}^{(\mathbf{e})} \\ \Delta\hat{\mathbf{p}}_{\mathbf{n}}^{(\mathbf{e})}\end{Bmatrix} = \begin{Bmatrix}\Delta\tilde{\mathbf{q}}_1^{(\mathbf{e})} \\ \Delta\tilde{\mathbf{q}}_2^{(\mathbf{e})}\end{Bmatrix} \tag{22}$$

where $\Delta\hat{\mathbf{u}}_{\mathbf{n}}^{(\mathbf{e})}$ has size (N_{eddof} * 1) and $\Delta\hat{\mathbf{p}}_{\mathbf{n}}^{(\mathbf{e})}$ has size (4*1).

The sub-matrix $\tilde{\mathbf{K}}_{11}^{(e)}$ appearing in equation (22) has size (N_{eddof} * N_{eddof}) and is defined as follows:

$$\tilde{\mathbf{K}}_{11}^{(\mathbf{e})} = \tilde{\mathbf{K}}^{(\mathbf{e})} - \mathbf{G}^{(\mathbf{e})*}(\mathbf{M}^{(\mathbf{e})*})^{-1}\mathbf{G}^{(\mathbf{e})*T} \tag{23}$$

The sub-matrix $\tilde{\mathbf{K}}_{12}^{(e)}$ has size (N_{eddof} * 4) and is defined as follows:

$$\tilde{\mathbf{K}}_{12}^{(\mathbf{e})} = (\tilde{\mathbf{K}}_{21}^{(\mathbf{e})})^T = \mathbf{G}^{(\mathbf{e})} - \mathbf{G}^{(\mathbf{e})*}\left(\mathbf{M}^{(\mathbf{e})*}\right)^{-1}\left(\mathbf{H}^{(\mathbf{e})*T} + \mathbf{L}^{(\mathbf{e})*T}\right) \tag{24}$$

Finally, the sub-matrix $\tilde{\mathbf{K}}_{22}^{(e)}$ has size (4*4) and is defined as follows:

$$\left[\left(\mathbf{H}^{(\mathbf{e})}+\mathbf{L}^{(\mathbf{e})}\right)-\left(\mathbf{H}^{(\mathbf{e})*}+\mathbf{L}^{(\mathbf{e})*}\right)\left(\mathbf{M}^{(\mathbf{e})*}\right)^{-1}\left(\mathbf{H}^{(\mathbf{e})*T}+\mathbf{L}^{(\mathbf{e})*T}\right)\right] \tag{25}$$

The first sub-vector appearing in equation (22) has size (N_{eddof} * 1) and is defined as follows:

$$\Delta\tilde{\mathbf{q}}_1^{(\mathbf{e})}=\Delta\mathbf{q}_1^{(\mathbf{e})}-\mathbf{G}^{(\mathbf{e})*}\left(\mathbf{M}^{(\mathbf{e})*}\right)^{-1}\Delta\mathbf{q}_3^{(\mathbf{e})} \tag{26}$$

Finally, the second sub-vector has size (4*1) and is defined as follows:

$$\Delta\tilde{\mathbf{q}}_2^{(\mathbf{e})}=\Delta\mathbf{q}_2^{(\mathbf{e})}-\left(\mathbf{H}^{(\mathbf{e})*}+\mathbf{L}^{(\mathbf{e})*}\right)\left(\mathbf{M}^{(\mathbf{e})*}\right)^{-1}\Delta\mathbf{q}_3^{(\mathbf{e})} \tag{27}$$

Once $\Delta\hat{\mathbf{u}}_{\mathbf{n}}^{(\mathbf{e})}$ and $\Delta\hat{\mathbf{p}}_{\mathbf{n}}^{(\mathbf{e})*}$ are known, $\Delta\hat{\mathbf{p}}_{\mathbf{n}}^{(\mathbf{e})*}$ is computed from equation (19).

7 CONCLUSIONS

This paper has presented some general considerations for developing conforming *u-p* elements that possess a higher-order (i.e., quadratic or higher) continuous pore pressure approximation. It was shown that the robust implementation of such a higher-order conforming element requires a quartic approximation for the incremental displacement components.

Since the computational effort associated with such conforming *u-p* elements is non-trivial, an overview of two quadratic (in displacement) *u-p* elements that contain a higher-order non-conforming pore pressure approximation was also presented. The element equations associated with such elements have the same general form as their conforming Q8P4c and Q9P4c counterparts.

REFERENCES

Biot, M. A. 1941. *General Theory of Three-Dimensional Consolidation*. Journal of Applied Physics. 12(2): 155–164.

Britto, A. M. & Gunn, M. J. 1987. *Critical State Soil Mechanics via Finite Elements*. Chichester: Ellis-Horwood.

Detouenay, E. & Cheng, A. H-D. 1993. *Fundamentals of Poroelasticity*. Hudson, J. A. (ed.). Comprehensive Rock Engineering: Principles, Practice and Projects. Oxford: Pergamon Press. 2 (Chapter 5).

Hood, P. & Taylor, C. 1974. *Navier-Stokes Equation using Mixed Interpolation*. Oden, J. T., Zienkiewicz, O. C., Gallagher, R. H. & Taylor, C. (eds.). Finite Elements in Flow Problems. University of Alabama at Huntsville Press: 121–132.

Hughes, T. J. R. 1987. *The Finite Element Method, Linear Static and Dynamic Finite Element Analysis*. Englewood Cliffs: Prentice Hall.

Jiang, P. & Kaliakin, V. N. 2009. *Investigation of Non-Conforming Elements for Geomechanical Applications*. Ling, H.I., Smyth, A. & Betti, R. (eds.). Poromechanics IV, Proceedings of the Fourth Biot Conference on Poromechanics. New York City: DEStech Publications, Inc.: 1047–1052.

Kaliakin, V. N. 2001. *Approximate Solution Techniques, Numerical Modeling and Finite Element Methods*. New York: Marcel Dekker, Inc.

Kaliakin, V. N. & Jiang, P. 2009. *Investigation of Mixed Elements with Continuous Pressure Approximations as Applied to Problems in Geomechanics*. Ling, H.I., Smyth, A. & Betti, R. (eds.). Poromechanics IV, Proceedings of the Fourth Biot Conference on Poromechanics. New York City: DEStech Publications, Inc.: 1041–1046.

Plaxis. 2012. *Reference and Material Models Manual*. Delft, The Netherlands.

Taylor, C. & Hood, P. 1973. *A Numerical Solution of the Navier Stokes Equations using the Finite Element Technique*. Computers and Fluids. 1(1): 73–100.

Taylor, R. L., Beresford, P. J. & Wilson, E. L. 1976. *A Non-Conforming Element for Stress Analysis*. International Journal for Numerical Methods in Engineering. 10(6): 1211–1219.

Thompson, M. & Willis, J. R. 1991. *A Reformation of the Equations of Anisotropic Poroelasticity*. Journal of Applied Mechanics, Transactions of the ASME. 58(3): 612–616.

Smart Geotechnics for Smart Societies – Zhussupbekov, Sarsembayeva & Kaliakin (Eds)
© 2023 The Author(s), ISBN 978-1-003-29912-7
Open Access: www.taylorfrancis.com, CC BY-NC-ND 4.0 license

Recommendation for reducing seismic subsidence deformation of structures

A.U. Tashkhodzhaev & D.N. Galieva
Tashkent Architecture and Civil Engineering University, Republic of Uzbekistan, Tashkent

ABSTRACT: This article gives recommendations for reducing the seismic subsidence deformation of structures. Solutions to ensure the seismic stability of the foundation in the absence of seismic subsidence are presented.

Keywords: seismic subsidence, strength, stability, seismic forces, soils, loads, foundations, soil friction, seismic subsidence threshold

In the Republic of Uzbekistan, most of it is composed of loess and other structurally unstable soils. Their specificity lies in the tendency to subsidence, liquefaction, deformation, curvature, uneven subsidence, etc. which can lead to the destruction of the structure, seismic subsidence threshold a_{lim} and the expected intensity of the earthquake a_c . If, as a result of such a check, it is revealed that the value of the seismic subsidence threshold turns out to be greater than the seismic acceleration, as noted above, then the soils at the base of the structure have sufficient strength and stability, and there is no seismic subsidence deformation. In such cases, existing deformations in buildings will occur as a result of poor construction quality. [1]

However, in a number of cases, we may encounter an inverse ratio of quantities, i.e. $a_{lim} < a_c$. Under such conditions, it is necessary to resort to the use of certain measures aimed at increasing the strength of the soil within the foundations of structures.

As is known, the magnitude of the maximum seismic acceleration a_c is predetermined by natural conditions. All elements of the dynamic mode (amplitude A, frequency f, period T, etc.) under these conditions are outside the sphere of human influence on them. In a completely different aspect, the issue of establishing the threshold of seismic subsidence of the soil $a_{lim\ is\ being\ solved}$.

In accordance with the above experimental studies, the seismic stability of soils at the base of structures can be increased:

– increase in strength characteristics of soils (ϕ *and* c_w)
– reducing the thickness of the core subjected to shaking (compressible thickness).

In the light of this provision, the corresponding "regulation" of the magnitude of the threshold of seismic subsidence a_{lim}, it is possible to significantly reduce the values of the calculated acceleration, thereby reducing (or reducing to zero) the values of the module of seismic subsidence. In this case, by comparing various options for measures that lead to an increase in the seismic subsidence threshold, it is possible to choose the most optimal solution that contributes to an increase in the value of a_{lim}.

The choice of one or another more effective option aimed at increasing the value of a_{lim} should be made in relation to each particular case, taking into account soil conditions and the factors influencing them by comparing and identifying the most appropriate measures. The types and forms of construction measures currently used and which could be suitable for increasing the value of the seismic subsidence threshold are very diverse.

DOI: 10.1201/9781003299127-235

Recall that an increase in the strength characteristics of the soil leads to an increase in the value of the seismic subsidence threshold a_{lim} and thus to increase the seismic resistance of the foundations and reduce the design score of the construction site. Hence, it becomes clear the importance of measures aimed at increasing the parameters of soil strength, which is confirmed by construction practice. Buildings and structures erected in seismic regions without observing the strength of the foundation soils underwent deformations in the form of tilt, curvature, uneven subsidence, and even complete destruction during the very first seismic tremors. [2]

In this regard, the criterion for the threshold of seismic subsidence a_{lim} sets the requirement that any ground conditions and foundations of structures must be stable with respect to the expected seismic force. These requirements can be met in practice by various construction measures aimed at improving the strength characteristics of the foundation soils.

Existing activities can be divided into the following groups:

a) activities carried out with the help of soil compaction with mechanical devices (surface compaction with rollers or rammers, deep compaction with short piles, hydrovibration, electrical, thermal and other methods);
b) measures aimed at reducing the porosity of the soil by introducing various chemical solutions into the pores (cementation, silicification, resinization, etc.)

It should be emphasized that the use of each of the above measures, in some cases, partially or completely, may turn out to be ineffective, especially without taking into account the seismic subsidence deformation of the soil under seismic conditions. At the same time, the cost of any engineering measure regarding soil is very high. [3]

The need for a significant investment of time for fixing and compacting soils, unacceptability in all conditions, insufficient development of technology and the need for special equipment almost completely exclude the possibility of using these measures in the mass construction of buildings of relatively small sizes.

Obviously, as a result of seismic subsidence of large masses of soil under the influence of shaking, the seismic resistance of structures erected on pile foundations cannot be ensured, even with a decrease in the load on them.

According to the definition of the threshold of seismic subsidence a_{lim} the thickness of loess moistened soils leads to a decrease in its value. From these positions, one of the conditions for increasing the seismic resistance of a construction site is to reduce the thickness of weak soils. The most effective measure in this regard is the design of buried structures or the use of pile foundations.

Deep foundations with the justification of structures on stronger rocks are used very often in construction practice. The essence of this measure is fundamentally very simple, however, it is applicable to any structures, including civil structures, bridge supports, hydraulic structures, etc.

These considerations confirm the emerging trend in construction practice to use simpler methods as anti -subsidence measures that are suitable on a wider scale and do not require any special expensive equipment. In particular, it is possible to reduce the forthcoming seismic settlement of buildings by laying their foundations deeper, according to the principle of "suspended foundations", i.e. without cutting through the entire loess layer. [4]

At the same time, the deepening of the foundations of structures, i.e. laying their soles to a certain depth from the surface of the strata will be the simplest and most effective measure to reduce the expected seismic subsidence deformation as a result of the oscillatory movement of the base.

Considering this circumstance, in 2007 we proposed a method of deepening the base of the foundation as an anti- seismic subsidence measure, which showed a fairly good effect when using it in the construction industry (see the act of implementation).

In accordance with the proposed method, the depth of the foundation of any structure (H) erected on cohesive (loess) soils, at which the seismic stability of the foundation is ensured in the absence of seismic subsidence, is determined by the formula:

$$H_0^c = \frac{p_0\,(1 + k_c e^{i\omega t})}{\gamma tg^4(45^0 - \frac{\phi}{2})} + \frac{c}{\gamma tg\phi} \tag{1}$$

For loose soils in the absence of dynamic impact, i.e. when working with non-cohesive soil under static conditions, it takes the form:

$$H_o = \frac{p_0}{\gamma tg^4(45^0 - \frac{\phi}{2})} \quad (2)$$

In expressions (1) and (2): - p_o normal stress in the soil from the weight of the structure; γ– soil density; k_c- seismicity coefficient; ω- circular frequency; t is time; φ - angle of internal friction of the soil; c-cohesion of the soil.

The expression $p_z = 0{,}2p_{np}$ has one very remarkable property. As follows from its consideration, the value h is directly proportional to p_o. In accordance with formula (1), such a dependence also exists between σ_z and p_o.

Consider the practical use of this method in examples.

Initial data: uniformly distributed load transferred to the ground under static conditions p_o \u003d 32 t/m^2, taking into account the inertial force of the seismic effect p_o^c\ u003d \$p_o(1+e^{iwt})$ u003d 45 t/m^2; soil density of natural moisture γ_w = 1.5 t/m^3; angle of internal friction of the soil -22°; soil adhesion - 3.0 t/m^2. It is required to determine the depth of the foundation in terms of ensuring the seismic stability of the foundation. [5]

*Solution***.** Substituting the values of the factors in the formula (1) we get:

H_0^c\u003d 13.5 m. The same value, excluding seismic, according to formula (1), is equal to: H_o \u003d 9.4 m. Thus, to ensure the seismic stability of the foundations under the conditions of given values, the depth of the foundation should be increased by 4.1 m.

REFERENCES

Rasulov R.Kh. 2020 Depth of laying the foundations of structures in seismic regions. Tashkent Publishing house “Tafakkur tomchilari”.

Rasulov H.Z. 1984. Seismic resistance ground grounds. - Tashkent: Publishing house “Uzbekistan”, 192p.

Adilov A.A., Rakhmatullaev H.L. 2012 Changes in the engineering and geological conditions of Tashkent and the prospects for further urban development. // Abstracts of the Republican Scientific and Technical Conference. - Tashkent: SE “NIIMR”, P. 105–108.

Sadikov A.Kh. 2010 Experimental studies of factors influencing the critical acceleration of slope loess soils. // J. Problems of architecture and construction. - Samarkand: SamGASI, No. 1. –S.10–14.

Scientific grant OT-F4–75 2017–2020 “Development of a method for assessing the bearing capacity of loess foundations of structures, taking into account changes in the strength properties of soils during strong earthquakes”.

Smart Geotechnics for Smart Societies – Zhussupbekov, Sarsembayeva & Kaliakin (Eds)
© 2023 The Author(s), ISBN 978-1-003-29912-7
Open Access: www.taylorfrancis.com, CC BY-NC-ND 4.0 license

Evaluating the coefficient of lateral stress at rest (K_0) of granular materials under repetitive loading conditions

Heerym Han, Yeni Seo, Hyojeong Go & Hyunwook Choo
Department of Civil and Environmental Engineering, Hanyang University, Seoul, South Korea

Taeseo Ku
School of Civil and Environmental Engineering, Konkuk University, Seoul, South Korea

ABSTRACT: The coefficient of lateral stress at rest (K_0) is a very important soil parameter determining the in-situ stress states of soils. While the K_0 of soils under static loading conditions have been extensively studied, studies evaluating K_0 under repetitive loading have been very limited. This study aims at investigating the characteristics of K_0 of two granular materials with varying particle shapes during repetitive loading. The modified odeometer tests equipped with bender elements and diaphragm transducer were performed during static loading (-354.0 kPa), repetitive loading ($\Delta\sigma'$ = 176.6 kPa) and extra static loading (-706.9 kPa). The results of this study demonstrate that K_0 of tested materials increases with increasing cyclic loading number (i) though void ratio of tested materials continuously decreases with cyclic loading number. The stiffness anisotropy based on shear wave velocity measurements also confirms the finding of this study. Finally, the results of this study demonstrate that rounded granular material shows greater change in K_0 during repetitive loading compared to angular sand.

1 INTRODUCTION

The coefficient of lateral stress at rest (K_0), expressed as the ratio of effective horizontal stress to effective vertical stress, reflects the characteristics of ground and determines the in-situ stress states of soils. Therefore, K_0 is considered as the most fundamental input parameter in geotechnical analysis and design. Though a number of studies about the K_0 have been performed under the static loading conditions to evaluate the effects of composition, structure (or fabric), stress history, and loading directions on K_0 (Mitchell and Soga, 2005), studies evaluating K_0 under repetitive loading conditions have been very limited (Zhu and Clark, 1994; Mesri and Vardhanabhuti, 2007). Due to the continuous accumulation of plastic strain and the consequent internal fabric change during repetitive loading, the behavior of soils under repetitive loading is totally different from that of soils under static loading (Park and Santamarina, 2019). Therefore, this study aims at evaluating the variations of K_0 of two granular materials with different particle shapes as a function of cyclic loading number.

2 EXPERIMENTAL PROGRAM

2.1 *Tested materials and sample preparation*

Two granular materials (i.e., angular silica sand, K-7 sand and glass beads, GB) with similar median particle sizes (D_{50}) but different particle shapes were selected to determine the values of K_0 during repetitive loading (Figure 1). The index properties and grain size distributions of the tested materials are given in Table 1 and Figure 1, respectively. The dry funnel deposition

DOI: 10.1201/9781003299127-236

method was chosen for the preparation of tested specimens due to its ability to produce a wide range of relative densities. To determine the K_0 under static loading conditions (normally consolidated state), the specimens were prepared with various relative densities ranging from 20% to 80%, and the specimens under repeated loading were tested with the initial relative densities of 30% and 70%.

Table 1. Index properties.

Type	D_{50} (mm)	G_s	e_{max}	e_{min}	R	Particle Shape
K-7 sand	0.20	2.65	1.07	0.68	0.2	Angular
Glass beads	0.12	2.5	0.74	0.61	1.0	Round

Note: D_{50} = median particle size (50% passing); G_s = specific gravity; e_{max} = maximum void ratio; e_{min} = minimum void ratio; R = roundness.

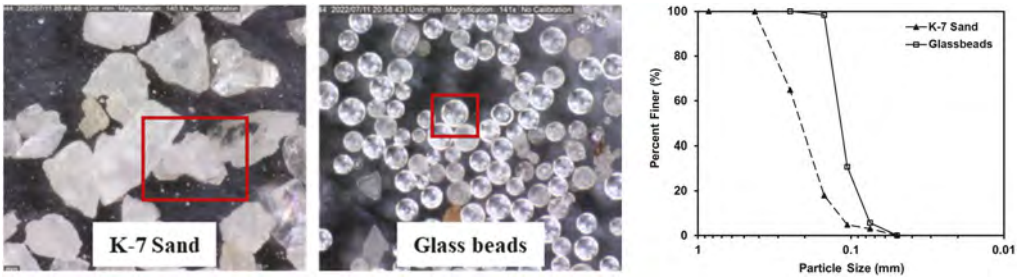

Figure 1. Grain size distributions and optical microscope images of tested materials.

2.2 *Test equipment and measurements*

The modified odeometer cell (sample diameter = 80 mm, sample height = 45mm, wall thickness = 10 mm) made of stainless steel was designed to measure the shear wave velocity and lateral stress under zero-lateral strain conditions. As shown in Figure 2, the diaphragm pressure transducer (Omega PX61V0) installed on the wall of the oedometer cell, was used to measure the lateral stress (Kim et al., 2021), and two pairs of bender elements were fitted in different configurations to measure the vertically propagating and horizontally polarized shear wave velocity, $V_s(VH)$ and horizontally propagating and horizontally polarized shear wave velocity, $V_s(HH)$. A static loading (-354.0 kPa), a repetitive loading ($\Delta\sigma'$ = 176.6 kPa), an extra static loading (-706.9 kPa), and unloading (-6.3 kPa) were applied to the prepared sample under K_0 condition. Total 100 times of repetitive loading with a period of 20 seconds to remove dynamic effects (Chong and Santamarina, 2016) were applied to the tested materials, and the lateral stress, settlement, and shear wave velocity (V_s) were measured according to loading steps and cyclic loading number.

3 RESULTS AND DISSCUSSION

The variations of the measured horizontal effective stress (σ'_h) according to the applied vertical effective stress (σ'_v) of tested two materials with initial relative density = 30% during static loading-repetitive loading-extra static loading-static unloading steps are shown in Figure 3. Glass beads (GB) shows greater σ'_h at a given σ'_v than K-7 sand, reflecting higher K_0 values of rounded GB. During the static loading, the slope between σ'_v and σ'_h remains constant value, reflecting constant K_0 values regardless of stress levels. However, in the case of repetitive loading condition, Figure 3 clearly demonstrates that the measured σ'_h at a given σ'_v continuously increases during repetitive loading. To quantify the results of Figure 3, Figure 4 shows the variations of K_0 according to cyclic loading number. Figure 4 clearly shows a gradual increase in K_0

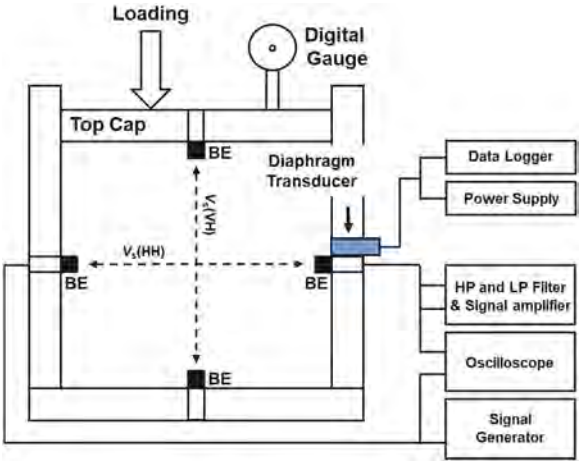

Figure 2. Experimental setup for measuring shear wave velocity and lateral earth stress.

with increasing cyclic loading number. The repetitive loading yields a continuous plastic displacement in the sample; therefore, the void ratio of tested materials continuously decreases with cyclic loading number. Because it is well-known that K_0 decreases with a decrease in void ratio, the results of Figure 4 are surprising and may be attributed to the accumulation of lateral stress locking. There should be no change in overconsolidation ratio of soils under the repetitive loading with constant stress amplitude. However, the repetition of loading-unloading steps may result in the accumulation of locked-in stress, leading to an increase in K_0 according to cyclic loading number; thus it may act as an increase in overconsolidation ratio.

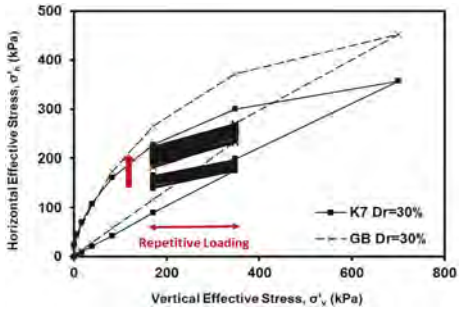

Figure 3. Relation between horizontal effective stress and vertical effective stress.

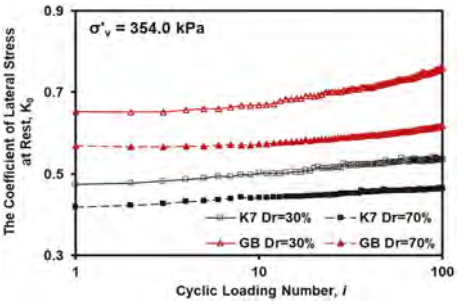

Figure 4. Variation of K_0 according to cyclic loading number.

When the 100 times of repeated loads were applied compared to the static loading conditions, the value of K_0 increased by about 5.9 % for K-7 and about 10.5 % for glass beads at an initial relative density of 30%. The effect of particle shape on the K_0 variation can be identified by directly comparing test results shown in Figure 6. It is observed that the values of K_0 measured in the static loading conditions (cyclic loading number = 0) for K-7 are lower than for glass beads, due to higher degree of angularity and interlocking of sand particles (Lee et al., 2013). Note that the higher interlocking leads to lower degrees of stress transmission in the horizontal direction. The load is more uniformly transferred to the surrounding particles when the particle is closer to a spherical shape.

The shear wave velocity is the power function of mean effective stress. Thus, V_s(VH) and V_s (HH) can be expressed as Equations (1) and (2), respectively. Based on the ratio between V_s (HH) and V_s(VH), the stiffness anisotropy of tested materials can be expressed as Equation (3).

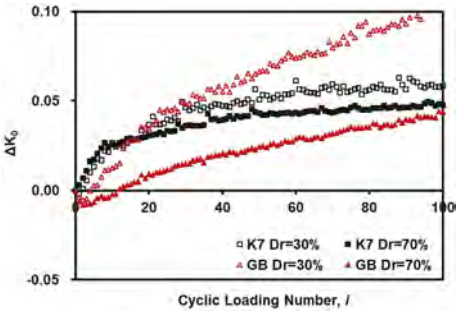

Figure 5. Variation of the coefficient of lateral stress at rest (K_0) of the tested materials.

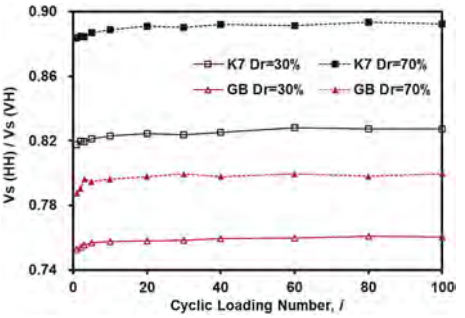

Figure 6. The ratio between V_s(HH) and V_s(VH) according to cyclic loading number (i).

Experimentally determined ratios between V_s(HH) and V_s(VH) of tested materials are shown in Figure 6. Figure 6 indicates the stiffness anisotropy, resulted from stress-induced anisotropy, decreases (or V_s(HH)/V_s(VH) increases) with increasing cyclic loading number. Most notably, Equation (3), which is function of K_0, also demonstrates that V_s(HH)/V_s(VH) should decrease with increasing K_0. Consequently, the wave velocity measurements (Figure 5) also support the finding of this study (Figure 4).

$$V_s(\mathrm{VH}) = \alpha_1 \left(\frac{\sigma_v' + \sigma_h'}{2\mathrm{kPa}} \right)^{\beta_1} = \alpha_1 \left(\frac{1+K_0}{2\mathrm{kPa}} \cdot \sigma_v' \right)^{\beta_1} \quad (1)$$

$$V_s(\mathrm{HH}) = \alpha_2 \left(\frac{\sigma_h' + \sigma_h'}{2\mathrm{kPa}} \right)^{\beta_2} = \alpha_2 \left(\frac{K_0}{1\,\mathrm{kPa}} \cdot \sigma_v' \right)^{\beta_2} \quad (2)$$

$$\frac{V_s(\mathrm{HH})}{V_s(\mathrm{VH})} = \frac{\alpha_2}{\alpha_1} \left(\frac{2K_0}{1+K_0} \right)^{\beta} \quad (3)$$

where, σ'_v = vertical effective stress; σ'_h = horizontal effective stress; α-factor = the V_s at σ'_m = 1 kPa; and β-exponent captures the sensitivity of tested materials on the applied stress.

4 CONCLUSION

This experimental investigation aims to evaluate the K_0 of granular materials under repetitive loading conditions. The results of this study demonstrate that K_0 of tested materials increases with increasing cyclic loading number (i). The stiffness ratio also supports this observation. In addition, rounded material shows greater change in K_0 compared to angular sand.

ACKNOWLEDGEMENTS

This research was supported by Basic Science Research Program through the National Research Foundation of Korea (NRF) funded by the Ministry of Science, ICT (NRF-2019R1C1C1005310).

REFERENCES

Chong, S.H. and Santamarina, J.C. (2016). Sand subjected to repetitive vertical loading under zero lateral strain: accumulation models, terminal densities, and settlement. Canadian Geotech. J., 53: 2039–2046.

Choo, H., Bate, B., Burns, S.E. (2015). Effect of organic matter on stiffness of overconsolidated state and anisotropy of engineered organclays at small strain. Engineering Geology, 184, 19–28.

Kim, J., Seol, Y., Dai, S. (2021). The coefficient of earth pressure at rest in hydrate-bearing sediments. Acta Geotechnica, Vol. 16, pp.2729–2739.
Lee, J., Yun, T.S., Lee, D, Lee, J. (2013). Assessment of K_0 correlation to strength for granular materials. Soil and Foundation, 53(4), 584–595.
Mesri, G., & Vardhanabhuti, B. (2007). Coefficient of earth pressure at rest for sands subjected to vibration. Canadian Geotechnical Journal, 44(10), 1242–1263.
Mitchell, J. K., & Soga, K. (2005). Fundamentals of Soil Behavior.
Park, J. and Santamarina, J.C. (2019). Sand response to a large number of loading cycles under zero-lateral-strain conditions. Géotechnique, Vol. 69, No.6, 501–513.
Santamarina, J.C. and Cho, G.C. (2004). Soil behaviour: The role of particle shape. Skempton Conf.: Advances in Geotechnical Engineering, Vol. 1, Thomas Telford, London, 604–617.
Shin, H. and Santamarina, J.C. (2013). Role of particle angularity on the mechanical behavior of granular mixtures. Journal of geotechnical and geoenvironmental engineering, 139:353–355.
Zhu, F., and Clark, J. I. (1994). The effect of dynamic loading on lateral stress in sand. Canadian Geotech. J., 31(2), 308–311.

Smart Geotechnics for Smart Societies – Zhussupbekov, Sarsembayeva & Kaliakin (Eds)
© 2023 The Author(s), ISBN 978-1-003-29912-7
Open Access: www.taylorfrancis.com, CC BY-NC-ND 4.0 license

Site effect assessment via dynamic analysis – Bukit Timah Granite

S. Abdialim
Nazarbayev University, Nur-Sultan, Kazakhstan

F. Hakimov
RWTH Aachen University, Aachen, Germany
University of Liège, Liège, Belgium

T. Ku
Konkuk University, Seoul, South Korea

J. Kim & S.-W. Moon
Nazarbayev University, Nur-Sultan, Kazakhstan

ABSTRACT: This study aims to assess the site effect of the Bukit Timah Granite area in Singa-pore via 2D dynamic numerical modeling and further comparison with previous geophysical testing results. A 3D geophysical model was created via combining geophysical investigation data with borehole data and geological maps of the region, and then several 2D geological cross-sections were extracted. Those cross-sections were used for dynamic numerical modeling of seismic ground motion and for calculating site amplification using the Universal Distinct Element Code (UDEC). The results show that the fundamental frequency (f_0) is in a good agreement between dynamic numerical modeling and horizontal to vertical spectral ratio (HVSR). Thus, the dynamic numerical models would be used for site effect analysis in the seismic hazard assessment.

1 INTRODUCTION

The local effects that amplify the seismic waves are generally due to the surface topography, the presence of an alluvial/lake, or any other soft deposits, including artificial fills (Wald & Allen, 2007). Therefore, the territory targeted is divided into several microzones to consider seismic amplification effects based on the dynamic soil properties of the site.

Site effect analyses can be conducted using information from geological investigations, borehole drilling, and geophysical surveys (Hakimov et al., 2021). Borehole drilling, an invasive method, is commonly practiced among the listed methods. Drilling will provide data on the thickness of each layer, bedrock depth and layers' stiffness. The latter data can then be empirically used for estimating shear wave velocity (V_S). Despite its popularity, the method contains huge drawbacks, such as being destructive, expensive, and time-consuming. For these reasons, their wide application is not always possible (Zhang et al., 2019, Moon & Ku, 2017), e.g., in Upper Missisipi Embayment, where the bedrock depth can reach up to 1000m (Moon et al., 2017). Geophysical surveys (e.g., multichannel analysis of surface waves (MASW) or horizontal to vertical spectral ratio (HVSR) from microtremor measurements (MM)) are practiced as a fast and cost-effective alternative to deriving dynamic soil properties.

This study aims to evaluate the site effects at the Bukit Timah Granite area in Singapore using 2D dynamic numerical modeling. 2D numerical models are selected from 3D Geomodel in such a way as to contain locations with geophysical and borehole information. The

DOI: 10.1201/9781003299127-237

numerical modeling technique generates a layered digital representation of a Bukit Timah Granite region to improve interpolated data further. The available geophysical survey data with the region's borehole data and geological maps are combined to create a 3D Geomodel. From the resulting numerical model, 2D cross-sections close to available geophysical data are selected for further data validation.

2 STUDY AREA

The Bukit Timah Granite is the most predominant rock formation in Singapore, comprising about 1/3 of the land area, and is one of the five major geological formations. Bukit Timah Granite is considered a base rock formation for the central part of Singapore. In a local context, in accordance with weathering degree, Bukit Timah Granite is graded from G(I) for hard intact rock to G(VI) for fully weathered residual soil. Bedrock depth is considered the depth of G(III), in which gradual stiffness is noticeably increased (Moon & Ku, 2017). The thickness of residual soils in Bukit Timah territory reaches 70 m, with a mean thickness of 30 m (Zhao, 1996).

Previous studies have demonstrated that the MASW test and microtremor measurement (MM) are applicable for bedrock depth estimation in the Bukit Timah Granite (Moon et al., 2019, Ku et al., 2021). Moreover, further works on HVSR inversion in Bukit Timah Granite performed with constrained borehole information resulted in V_S profiles similar to MASW test results (Abdialim et al. (2021). This work compiles the results of all the aforementioned studies for generating and demonstrating a dynamic numerical model in an example of a 2D cross-section. Figure 1 shows test site locations, including MASW results, MM, and borehole data.

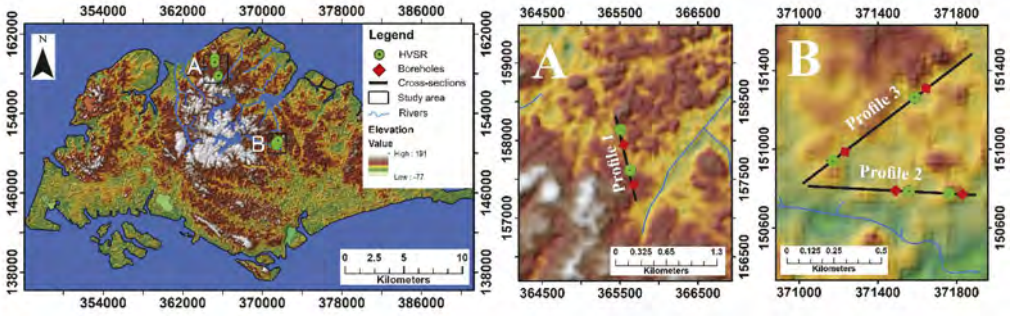

Figure 1. The study area of the Bukit Timah Granite with an indication of three 2D cross-sections (Note: Green circles indicate HVSR points on the profiles, and the red rhomboid shows borehole locations on the profiles).

3 NUMERICAL MODELLING

A 3D geomodel for the Bukit Timah area was generated based on combined MASW, HVSR, and borehole data. This model was obtained using Leapfrog Geo software (version 4.5 from Seequent Limited). The thickness of soil layers (h) susceptible to site amplification was estimated and mapped by the 1-D soil model assumption using the following equation: $h = V_S/4f_0$, where V_S = average shear wave velocity of 30m, f_0 = fundamental frequency. Since the relationship between f_0 and h assumes a high impedance contrast between two underlying layers, only clear peak HVSR curves with high amplitudes were used for Geomodel generation. 3D Geomodel was split into three layers to consider the weathering: soft layer, weathered granite layer, and granite. Thicknesses of soft and weathered layers were introduced following borehole, MASW, and HVSR information. From the 3D geomodel, we extracted three 2D cross sections from the points where HVSR

measurements were taken (Figures 1 and 2). Dynamic numerical simulations of the site effect were performed and compared with HVSR measurements. UDEC software developed by the Itasca Consulting Group was used as the distinct element method-based tool. 2D section consists of a basement, a weathered granite layer, a surface layer, and synthetic receivers. Site effect analysis was performed in an elastic domain for all profiles. Input data were selected from the literature (e.g., stiffness properties of bedrock from Zhao (1996), V_S values from MASW data, densities from Sharma et al. (1999)). Bulk and shear moduli (K and G) data converted from V_P and V_S data. Joint properties of the model, such as joint normal and shear stiffnesses (j_{kn} and j_{ks}) and joint cohesion (j_{coh}), were maximized for the prevention of deformations along the discontinuities (Havenith et al., 2003). Ricker wavelet was used as input signal at the base. Elastic properties of numerical model materials are listed in Table 1.

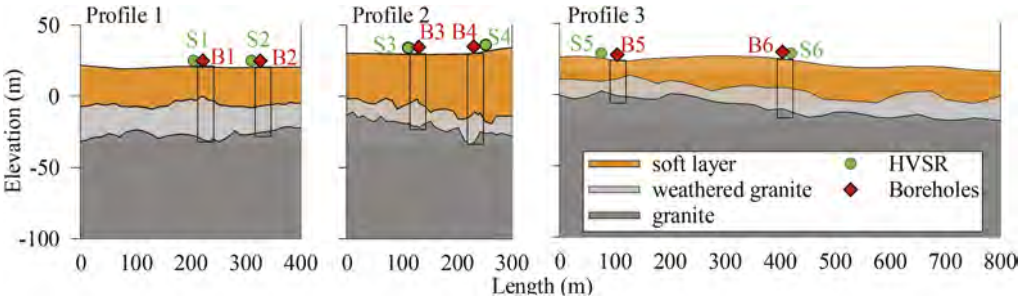

Figure 2. 2D Cross-sectional profiles taken and extracted from 3-D geomodel.

Table 1. Soil engineering properties.

	K (Mpa)	G (Mpa)	ρ (kg/m^3)	H(m)	j_{fric}	j_{tens}
Soft layer	1387	384.75	1900	10-20	–	2e20
Weathered granite	10208	4776	2200	20-30	38	–
Granite	14208	7776	2600	30-50	38	–

4 2D NUMERICAL MODELING PROCESSING

Figure 3a shows the locations of synthetic receivers for dynamic analysis. Standard spectral ratios (SSRs) were obtained for site amplification evaluation at each synthetic surface receiver by the following procedure: The acceleration-time histories generated on the surfaces were compared with those recorded on a synthetic receiver at the model's base. Signals were then multiplied by two to account for the flat surface reflection effect and filtered, respectively (Havenith et al., 2003). By gathering such time histories on the surface, synthetic three-component records were generated. The surface receivers (synthetic receivers) represent the two horizontal components in this set, and base records replace the vertical component. This synthetic data was further processed by following the HVSR analysis procedure. As a result, much like in the HVSR technique, a spectral ratio versus frequency graph would be generated.

5 RESULTS AND DISCUSSION

3D Geomodel construction relies mainly on borehole readings and geophysical test results. Among geophysical tests, HVSR measurements significantly contribute to the modeling because the relationship between f_0 and peak amplitude is directly correlated with the site amplification. For our simulation, we considered the relative changes and shape of the peak rather than the absolute amplitude value. In Figure 3b, we compared the results of simulated

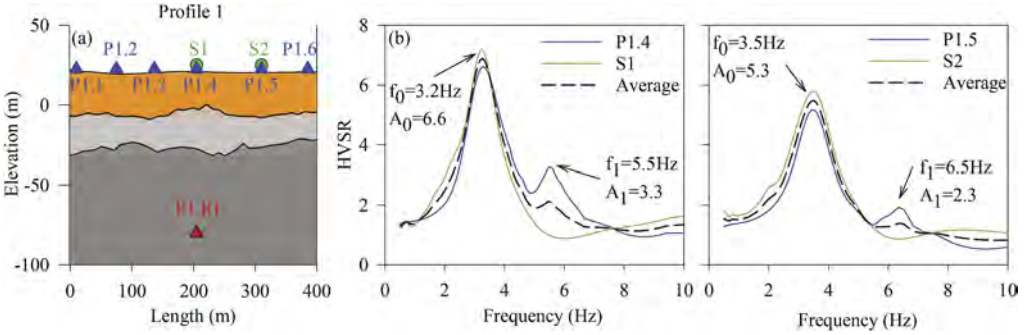

Figure 3. (a) 2D Cross-section with an indication of locations of synthetic receivers and HVSR measurements (green) at Profile 1. The base receiver (red) was a reference for surface receivers (blue). (b) Simulated SSR (P1.4 & P1.5) and HVSR measurements (S1 & S2) in Profile 1.

and real HVSR at profile 1. The comparison shows that both curves have the same trend for low frequencies, especially close to the f_0. At high frequency, simulated SSR had a low amplitude corresponding to a weathered granite layer. A peak frequency match was observed for the frequency range of 2-7 Hz. The extra peak can be because of differences in impedance contrast between weathered granite and soft soil in numerical modeling compared with actual measurements. The numerical model was generated by grouping different granite layers into "soft layer" and "weathered granite" based on weathering degree. Thus, there might be a sudden rise in impedance contrast. In reality, the number of layers will be higher with slowly increasing stiffness, resulting in the absence of an intense surge in impedance contrast between layers. Thus, we believe that this method allows us to detect the resonant frequency of deep deposits and highlight the presence of surface deposits. However, HVSR measurements have clear limitations in application: (1) HVSR data will not be able to estimate soft layer thickness, and other geophysical data, such as V_S., will be needed. (2) the interpretation of peak amplitudes: correlation between site amplification factor and HVSR amplitudes has not been fully proven. These results provide a basis for further research on Geomodel modification and implementation of more geophysical results (e.g., MASW) to minimize the limitations.

6 CONCLUSIONS

To assess the site effects of the Bukit Timah Granite region, 2D cross-sections were generated from 3D Geomodel. Response to the horizontal Ricker wavelet input signal at the base of the model was used to estimate the region's SSR and further comparison with actual HVSR data. In an example of Profile 1, it was demonstrated that both simulated and measured spectral curves had the same shape close to the f_0. It was also mentioned that only the shape of the simulated spectral curve was used for the data analysis of the curve. Moreover, simulated curves contained extra peaks at higher frequencies corresponding to the impedance contrast between the soft and weathered granite layers. A possible reason for such differences at high frequencies was discussed. Known limitations of the method can be minimized in the future by using extra geophysical data, especially when generating 3D Geomodel. The clear trend between synthetic and measured data demonstrates the possibility of using numerical modeling for seismic microzonation works at Bukit Timah Granite formation.

REFERENCES

Abdialim, S., Hakimov, F., Kim, J., Ku, T. & Moon, S.-W. 2021. Seismic site classification from HVSR data using the Rayleigh wave ellipticity inversion: A case study in Singapore. *Earthquakes and Structures*, 21, 231–238.

Hakimov, F., Domej, G., Ischuk, A., Reicherter, K., Cauchie, L. & Havenith, H.-B. 2021. Site Amplification Analysis of Dushanbe City Area, Tajikistan to Support Seismic Microzonation. *Geosciences*, 11, 154.

Havenith, H.-B., Strom, A., Calvetti, F. & Jongmans, D. 2003. Seismic triggering of landslides. Part B: Simulation of dynamic failure processes. *Natural Hazards and Earth System Sciences*, 3, 663–682.

Ku, T., Palanidoss, S., Zhang, Y. H., Moon, S. W., Wei, X., Huang, E. S., Kumarasamy, J. & Goh, K. H. 2021. Practical configured microtremor array measurements (MAMs) for the geological investigation of underground space. *Underground Space*, 6, 240–251.

Moon, S.-W., Hashash, Y. M. A. & Park, D. 2017. USGS hazard map compatible depth-dependent seismic site coefficients for the Upper Mississippi Embayment. *KSCE Journal of Civil Engineering*, 21, 220–231.

Moon, S.-W. & Ku, T. 2017. Estimation of bedrock locations and weathering degree using shear wave velocity-based approach. Proceedings of the 19th International Conference on Soil Mechanics and Geotechnical Engineering (ICSMG), Sept 17- 22, 2017, Seoul, South Korea. Korea Geotechnical Society.

Moon, S.-W., Palanidoss, S., Zhang, Y., Ganapathiraman, V. & Ku, T. 2019. Bedrock depth evaluation using microtremor measurement: empirical guidelines at weathered granite formation in Singapore-NC-ND license (http:// creativecommons.org/licenses/by-nc-nd/4.0/). *Journal of Applied Geophysics*, 171, 103866.

Sharma, J., Chu, J. & Zhao, J. 1999. Geological and geotechnical features of Singapore: an overview. *Tunnelling and Underground Space Technology*, 14, 419–431.

Wald, D. J. & Allen, T. I. 2007. Topographic slope as a proxy for seismic site conditions and amplification. *Bulletin of the Seismological Society of America*, 97, 1379–1395.

Zhang, Y., Li, Y. E., Zhang, H. & Ku, T. 2019. Near-surface site investigation by seismic interferometry using urban traffic noise in Singapore. *Geophysics*, 84, 1–43.

Zhao, J. 1996. Construction and utilization of rock caverns in Singapore .1. The Bukit Timah granite bedrock resource. *Tunnelling and Underground Space Technology*, 11, 65–72.

Smart Geotechnics for Smart Societies – Zhussupbekov, Sarsembayeva & Kaliakin (Eds)
© 2023 The Author(s), ISBN 978-1-003-29912-7
Open Access: www.taylorfrancis.com, CC BY-NC-ND 4.0 license

Comparative analysis of seismic design for shallow foundations adhering to the Kazakhstani and European approaches

A. Zhanabayeva, S.-W. Moon, J. Kim & A. Satyanaga
Nazarbayev University, Nur-Sultan, Kazakhstan

Y. Shokbarov
KazNIISA, Almaty, Kazakhstan

ABSTRACT: Starting in 2015 the transition period from the traditional seismic design to the newly developed system has been initiated in Kazakhstan. The new regulatory system involves the application of the European approach for the design of buildings and structures on the territory of Kazakhstan. This research paper aims to present a comparative analysis of the seismic design code applied in Kazakhstan (SP RK 2.03-30-2017 – Construction in seismic zones) and Eurocode 8 (EC8). One of the key aspects of the research is to understand the difficulties of the integration of the European design standards in Kazakhstan. Moreover, the problems associated with seismic design in Kazakhstan are discussed. The necessity of the application of the European approach considering geotechnical features of the country in the National Annex is defined and proved. The considered codes of practice are also compared in terms of their conservativeness and cost efficiency for seismic design based on the design problem in Almaty city.

1 INTRODUCTION

Seismic, geological, and geographical conditions of Kazakhstan's East, South, and Southwest regions represent a seismic risk for approximately one-fourth of the country's territory (Sajjad et al.). Analytical results of the research work during the Soviet times became the foundation for developing normative documentation for seismic design in Kazakhstan. Since 2006 the SNiP-based regulations have not been modified. The reason referred to the transition to the European standards, which allows the increase in safety of the designed structures under seismic actions (Zhanabayeva et al. 2023). Eurocodes with National Annexes in Kazakhstan were issued in 2016 and were recommended for application in parallel with the existing regulations (Zhanabayeva et al. 2021). For the design and construction of buildings and structures in seismic regions, SP RK EN 1998:2004/2012 identical to Eurocode, was issued. However, due to the complexity of this document, it did not receive a wide application among local specialists (Shaldykova et al. 2020).

Nowadays, the performance of construction works requires integration into a new regulatory system. The Kazakhstani designers and engineers are required to conform to both national and European codes (Zhanabayeva et al. 2022). However, the practice shows that specialists face difficulties due to significant differences between the Kazakhstani and European design approaches for seismic design. The integration issue is explained not only by different design methods but other reasons, considering the lack of the appropriate construction materials, equipment for materials' quality control, standards, technical conditions, methodologies, etc. The considerable differences between design approaches applied in Kazakhstan and European countries refer to (1) seismic magnitude scale, (2) scope of the application, and (3) soil classification.

DOI: 10.1201/9781003299127-238

This research work aims to introduce and evaluate the seismic design procedures adhering to the Kazakhstani and European codes of practice and analyze the sufficiency of the bearing resistance for designing a shallow foundation in Almaty city.

2 SEISMIC DESIGN OF FOUNDATIONS ADHERING TO THE KAZAKHSTANI AND EUROPEAN APPROACHES

Foundation systems ensure load transfer from superstructures to ground without considerable deformation. The design actions on the structures are defined based on the capacity design. This section provides a detailed design procedure for determining the seismic bearing capacity of shallow foundations when adhering to the Kazakhstani (SP RK 2.03-30-2017 2017) and European (EN 1998-1 2005) codes of practice.

2.1 *Kazakhstani approach for the design of foundations constructed in seismic regions*

Seismic design of shallow foundations under seismic actions involves determining (1) bearing capacity for the limit state analysis and (2) sliding capacity. The following condition is required to be performed to determine the sufficiency of seismic bearing capacity of a shallow foundation:

$$N_a \leq \gamma_{c,eq} \frac{N_{u,eq}}{\gamma_n} \tag{1}$$

where N_a = a vertical design eccentric load in a special combination; $\gamma_{c,eq}$ = a seismic operational conditions coefficient; γ_n = a reliability coefficient based on the purpose of the designed structure; $N_{u,eq}$ = a vertical component of the ultimate resistance of the foundation due to seismic action defined in accordance with the ratio between eccentricities e_a and e_u:

$$\text{For } e_a \leq e_u : N_{u,eq} = 0.5bl(p_b + p_0) \tag{2}$$

$$\text{For } e_a > e_u : N_{u,eq} = 0.5bl(p_b + p_o^{'}) = \frac{b1p_b}{(1 + 6e_a/b)} \tag{3}$$

Here eccentricity of the design load e_a and eccentricity of the limiting pressure diagram e_u are defined based on the following equations:

$$e_a = \frac{M_a}{N_a} \tag{4}$$

$$e_u = \frac{b(p_b - p_0)}{6(p_b + p_0)} \tag{5}$$

where N_a = a vertical component of design load acting at the foundation base under a special load combination with the consideration of seismic actions; b = a foundation width; l = a foundation length; d = a foundation depth; M_a = a moment acting at the foundation base under seismic actions; Q_I^s = a horizontal force acting on the foundation base in the design direction under a special load combination; h = a foundation height.

In Equations 2-5 p_o and p_b = the ordinates of the diagram of the ultimate pressure under the edges of the foundation base defined in accordance with the following equations:

$$\begin{aligned} p_0 &= \xi_q F_1 \gamma'_I d + \xi_c (F_1 - 1) \frac{c_I}{tg\varphi_I} \\ p_b &= p_0 + \xi_q \gamma_I b + (F_2 - K_{eq} F_3) \end{aligned} \tag{6}$$

where ξ_q, ξ_γ, ξ_c = shape coefficients; γ'_I and γ_I = design values of the unit weight of soil above and below foundation base; φ_I and c_I = design values of the internal friction angle and cohesion; d = the foundation depth; k_{eq} = a seismicity coefficient; $F_1,\ F_2,\ F_3$ = coefficients defined in accordance with the design internal friction angle φ_I value.

The sliding capacity of a shallow foundation under seismic load is defined in accordance with the following condition:

$$Q_a \leq \frac{\gamma_{c,eq}}{\gamma_n}[N_a tg(\varphi_I - \Delta\varphi_I) + c_I A] \tag{7}$$

where Q_a = a horizontal component of the load at the foundation base level taken as $Q_a = Q_I^s$; A = an area of the foundation base; $\Delta\varphi_I$ = a decrease of the design frictional angle.

2.2 *European approach for the design of foundations constructed in seismic regions*

Eurocode 8 (EC8) represents a part of Eurocodes specializing in seismic and earthquake design. EC8-5 covers a detailed procedure for the design of foundations constructed in seismic regions. Annex F of EC8-5 (EN 1998-5 2004) presents a method for the verification of the seismic bearing capacity of a strip foundation. The general expression for the check of the stability of a strip foundation against seismic bearing capacity failure combines a long-term European experience gained by field, analytical and numerical results. The stability is checked using the following equation related to the soil strength, the design action effects ($N_{Ed},\ V_{Ed},\ M_{Ed}$) at the foundation level, and the inertia forces in soil as follows:

$$\frac{(1+e\bar{F})^{c_T}(\beta\bar{V})^{c_T}}{(\bar{N})^a[(1-m\bar{F}^k)^{k'}-\bar{N}]^b} + \frac{(1-f\bar{F})^{c'M}(\gamma\bar{M})^{c_M}}{(\bar{N})^c[(1-m\bar{F}^k)^{k'}-\bar{N}]^d} 1 \leq 0 \tag{8}$$

where

$$\bar{N} = \frac{\gamma_{Rd}N_{Ed}}{N_{max}};\ \bar{V} = \frac{\gamma_{Rd}V_{Ed}}{N_{max}};\ \bar{M} = \frac{\gamma_{Rd}M_{Ed}}{BN_{max}} \tag{9}$$

N_{max} = an ultimate bearing capacity of the foundation under a vertical centered load; B = a foundation width; $\bar{F}$ = a dimensionless soil inertia force; γ_{Rd} = a model partial factor; $a,\ b,\ c,\ d,\ e,\ f,\ m,\ k,\ k', c_T, c_M, c'_M, \beta, \gamma$ = numerical parameters depending on soil type.

The ultimate bearing capacity under a vertical load N_{max} for purely cohesive soil is defined based on the following equation:

$$N_{max} = (\pi + 2)\frac{\bar{c}}{\gamma_M}B \tag{10}$$

where $\bar{c}$ = an undrained shear strength of soil for cohesive soil; γ_M = a partial factor for material properties.

The dimensionless soil inertia force $\bar{F}$ is defined as follows:

$$\bar{F} = \frac{\rho a_g SB}{\bar{c}} \tag{11}$$

where ρ = a unit mass of soil; a_g = a design ground acceleration on Type A ground ($a_g = \gamma_I a_{gR}$); a_{gR} = a reference peak ground acceleration on Type A ground; γ_I = an importance factor; S = a soil factor.

3 DESIGN PROBLEM IN ALMATY CITY

The seismic design of a shallow foundation is performed based on the design problem provided in Figure 1. The design problem requires checking the seismic design resistance of

a strip foundation with a width of 3 m located at a depth of 1.8 m below ground for Almaty soil properties obtained from (Khomyakov et al. 2013). The soil engineering properties in Almaty, the actions applied on a strip foundation, and the SP RK and EC8 parameters involved in the calculations are provided in Table 1.

Based on the performed design calculations adhering to the Kazakhstani and European design procedures for the determination of seismic bearing resistance of a strip foundation, it was identified that the calculated results of seismic bearing resistance satisfy design requirements. Adhering to the Kazakhstani approach, when substituting the values of soil engineering properties and SP RK parameters into Equation 1, it was obtained that the RHS equals 814 kN. The obtained value is greater than the design vertical load, meaning the seismic bearing resistance satisfies the design condition. EC8 also provides a safe strip foundation design when considering Almaty soil conditions, as the LHS of Equation 11 is equal to –0.08. However, the obtained value is very close to the boundary (i.e., 0). Therefore, it can be concluded that the decided width of the designed strip foundation represents a minimum dimension when adhering to the European approach. Thus, EC8 provides a more conservative seismic design than SP RK.

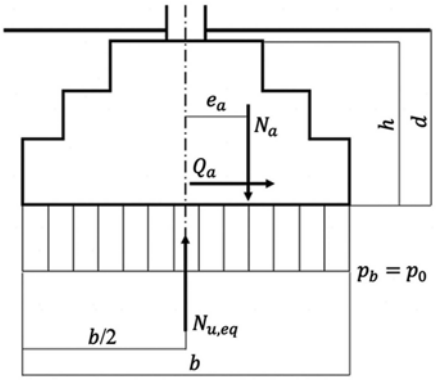

Figure 1. Design problem in Almaty city.

Table 1. Soil engineering properties in Almaty city.

Soil properties	Given data	SP RK parameters	Eurocode parameters
Silty clay:c = 33.00kPa w = 18.80% e = 0.86 E = 12.00MPa $\varphi = 19.00°$ $\gamma = 17.00\text{kN/m3}$ (obtained from (Moon and Ku, 2018))	b = 3m N_I= 700kN Q_I= 66kN M_I= 90kN ∗ m 9-degree intensity	$\gamma_{c,eq}$= 0.8,γ_n= 1.15 ξ_q=ξ_γ=ξ_c= 1 F_1= 5.63,F_2= 2.94 F_3= 9.55	a = 0.7, b = 1.29 c = 2.14, d = 1.81 e = 0.21, f = 0.44 m = 0.21, k = 1.22 $k = 1.00,\ c_T = 2.00$ $c_M = 2.00, c_M = 1.00$ $\beta = 2.57, \gamma = 1.85$ γ_{Rd}= 1.00,γ_M= 1.4

4 CONCLUSION

This research introduces the procedure for seismic design of shallow foundations when applying SP RK and EC8. A significant difference between the Kazakhstani and European approaches for seismic design exists, including the scope of the application of design codes, the application of different seismic magnitude scales and soil classification systems.

Seismic design of a strip foundation in Almaty city is performed adhering to the Kazakhstani and European codes of practice. The design problem is used to analyze the sufficiency of seismic bearing resistance of a strip foundation for the given soil engineering conditions. It is

defined that both regulations provide satisfactory results. However, EC8 provides a more conservative seismic design of a shallow foundation, which means a costlier design than SP RK.

To conclude, the SNiP-based Kazakhstani design code did not experience significant changes for a long time compared to EC8. Therefore, the European approach represents a good alternative for assessing seismic hazards and geotechnical applications in Kazakhstan.

REFERENCES

EN 1998–1 2005. Eurocode 8: Design of structures for earthquake resistance -Part 1: General rules, seismic ac-tions and rules for buildings. Brussels: European Committee for Standardization.

EN 1998–5 2004. Eurocode 8: Design of structures for earthquake resistance –Part 5: Foundations, retaining structures and geotechnical aspects. Brussels: European Committee for Standardization.

Khomyakov, V. A., Iskakov, E. E. & Serdaliev, E. T. 2013. Investigation of gravelly soil during underground construction in Almaty. *Soil Mechanics and Foundation Engineering*, 50(4): 171–177.

Moon, S.-W. & Ku, T. 2018. Undrained shear strength in cohesive soils estimated by directional modes of in-situ shear wave velocity. *Geotechnical and Geological Engineering*, 36(5): 2851–2868. doi:10.1007/s10706-018-0508-9

Shaldykova, A., Moon, S.W., Kim, J., Lee, D., Ku, T. & Zhussupbekov, A. 2020. Comparative Analysis of Kazakhstani and European Approaches for the Design of Shallow Foundations. *Applied Sciences*, 10(8): 2920. https://doi.org/10.3390/app10082920

Sajjad, M., Zhang, D., Moon, S. W., Sarkulova, D., Shokbarov, Y. & Kim, J. (Accepted) Marcro-Seismic Assessment for Residential Building Constructed in the Soviet Union Era in Almaty, Kazakhstan. *Buildings*

SP RK 2.03-30-2017 2017. Construction in seismic zones. Almaty, Kazakhstan: KAZGOR.

Zhanabayeva, A., Abdialim S., Satyanaga A., Kim, J. & Moon, S. W. 2022. Comparative analysis of international codes of practice for pile foundation design considering negative skin friction effect. *International Journal of Geo-Engineering*, 13(1): 1–15. https://doi.org/10.1186/s40703-022-00176-5

Zhanabayeva, A., Moon, S. W., Ocheme, J. I., Shokbarov, Y., Khomyakov, V. A., Kim, J. & Satyanaga, A. 2023. Comparative analysis of seismic design codes adhering to the Kazakhstani and European approaches. *Sustainability*, 15: 615. https://doi.org/10.3390/su15010615

Zhanabayeva, A., Sagidullina N., Kim, J., Satyanaga, A., Lee, D. & Moon, S.W. 2021. Comparative analysis of Kazakhstani and European approaches for the design of raft, pile and piled-raft foundations. *Applied Sciences*, 11(7): 3099. https://doi.org/10.3390/app11073099

Smart Geotechnics for Smart Societies – Zhussupbekov, Sarsembayeva & Kaliakin (Eds)
© 2023 The Author(s), ISBN 978-1-003-29912-7
Open Access: www.taylorfrancis.com, CC BY-NC-ND 4.0 license

Influence of inclined piles in hybrid type steel pile reinforcement used in seismic countermeasure of highway embankment

C.J. Qin & H. Hazarika
Kyushu University, Fukuoka, Japan

N. Ogawa
Giken Ltd, Tokyo, Japan

Y. Kochi
K's Lab Inc, Yamaguchi, Japan

M. Murai
Shimizu Corporation, Tokyo, Japan

G.J. Liu
Changshu Institute of Technology, Suzhou, China

ABSTRACT: A hybrid type reinforcement technique is proposed for application to both existing and new highway embankments for mitigating earthquake induced damages. In the proposed technique, inclined piles are installed at the top of vertical piles, and they are fixed to each other. The inclined piles are assumed to provide an additional restraining force to the vertical piles against lateral loading as well as reduce ground deformation and settlement during earthquake loading. In this study, a series of simulations were performed to determine the optimum inclination angle to achieve the best performance using the proposed technique. The numerical results suggest that a suitable angle (55–60°) between the vertical and inclined pile could effectively reduce deformation of the highway embankment during seismic loading.

1 INTRODUCTION

Sustainable Development Goals 11 (to make cities and human settlements inclusive, safe, resilient, and sustainable) focuses on minimizing the exposure to disasters and enhancing resilience and adaptive capacity. Highways play a crucial role in the connectivity and transportation of critical rescue components and relief materials during disasters. However, numerous highway embankments in Japan, which were constructed on soft soil foundations, are aging and have become susceptible to natural disasters. The highway embankment damage and retaining wall failure in Kyushu Expressway near Mashiki town were observed after the 2016 Kumamoto earthquakes (Hazarika et al. 2017). West Nippon Expressway Company Limited (2017) reported that the key cause of this embankment failure during this earthquake, such as excessive settlement and collapse, is the liquefaction of the loose sand layer underlying the embankment. To protect similar embankments from future earthquakes, an innovative low-cost hybrid type steel pile reinforcement technique was developed, consisting of the vertical and inclined piles, thereby mitigating the effects of liquefaction and reducing excessive deformation in highway embankments. In previous research, the effectiveness of this hybrid type steel pile reinforcement technique was evaluated using 1g shaking table tests (Qin et al. 2021). In this study, the deformations of the highway embankment reinforced by this technique with different configurations are analyzed to determine the optimum angle of the inclined pile using effective stress analysis.

DOI: 10.1201/9781003299127-239

2 NUMERICAL APPROACH

2.1 *Numerical model and boundary conditions*

Finite element modeling was conducted for one configuration of conventional reinforcement and six different configurations of hybrid type reinforcements, as shown in Table 1. Figure 1 illustrated a symmetric embankment 5 m high with a roadway 26 m wide and a slope of 1:2. The foundation comprised a 10 m thick saturated liquefiable sandy layer over a 10 m thick dense sandy layer. A cyclic elasto plastic model was selected as the constitutive law for the soil in the embankment and foundation. The insertion depth of the vertical 1.5 m diameter piles was 15 m, and the length of the inclined 0.2 m diameter piles was 14 m for all the hybrid type reinforcements. The hybrid beam elements for the vertical pile, consisting of conventional beam elements and elastic solid elements, were used to represent the pile volume. Joint elements were along with all the interfaces between the soil elements and piles, which shared identical displacements in the horizontal direction. The bottom of the model was set to be rigid. The drainage boundary was set on the ground surface, with the water table corresponding to the surface level. The ground model was established long enough in the x-direction to minimize the boundary influence.

Table 1. Numerical models with different configurations.

Angle between vertical and inclined piles	
Case 0	Without the inclined pile
Case 1	40°
Case 2	45°
Case 3	50°
Case 4	55°
Case 5	60°
Case 6	70°

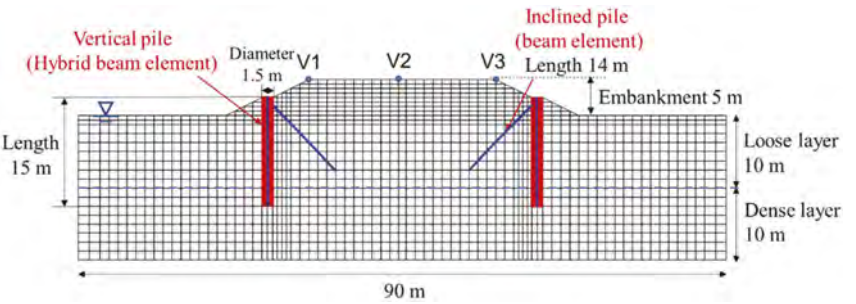

Figure 1. Finite element model for Case 2.

2.2 *Input motion*

The seismic wave from the KMMH16 station, as shown in Figure 2, was applied in the simulation. An incremental time interval of 0.001 s was adopted, while the parameters β and γ in the Newmark integration method are set respectively as 0.3025 and 0.6 to ensure numerical stability.

3 RESULT AND DISCUSSION

Figure 3 depicts the lateral displacements on left and right corners of the embankment side slopes (points A and C) for six different configurations of the hybrid type reinforcements; the locations of points A and C are shown in Figure 1. It can be clearly seen that the most

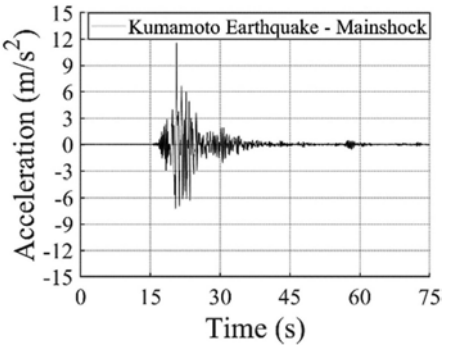

Figure 2. Seismic input motion applied in analysis (Strong-motion Seismograph Networks).

significant reduction in the lateral spreading on left and right corners of the side slopes occurred in Case 6 (angle between the vertical and inclined piles = 70°). In addition, considerable lateral spreading on the sloping sides of the embankment occurred in Case 4 (angle between the vertical and inclined piles = 55°). Figure 4 shows that the vertical displacements on points A and C were improved by the hybrid type reinforcements with six different angles. The large lateral and vertical displacements convincingly demonstrated that the hybrid type reinforcement in Case 1 (angle between the vertical and inclined piles = 40°) could not adequately enhance the embankment stability. A slight decrease in the vertical displacement was detected in Case 3 (angle between the vertical and inclined piles = 50°). Therefore, the installation of the hybrid type reinforcement in the embankment slope, as presented in Figure 1, appeared to provide limited mitigation of the embankment failure on the surface of the embankment.

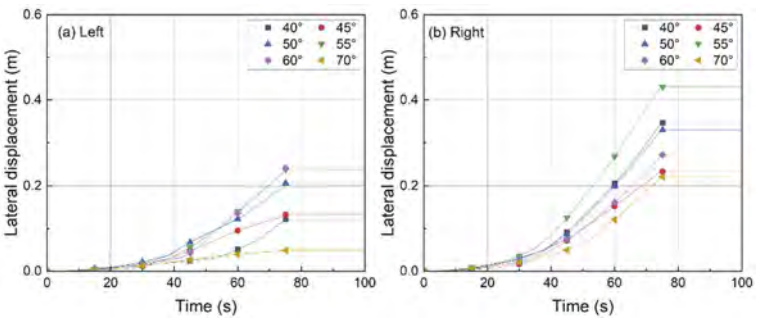

Figure 3. Time histories of lateral displacements on left and right corners of the embankment side slopes (a: point A and b: point C) for six different configurations of hybrid type reinforcements.

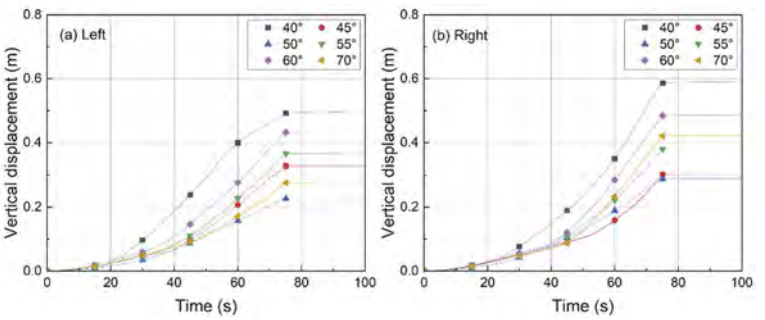

Figure 4. Time histories of vertical displacements on left and right corners of the embankment side slopes (a: point A and b: point C) for six different configurations of hybrid type reinforcements.

Figure 5 (a) shows the recorded time histories of the vertical displacements at the center of the embankment surface. For the conventional reinforcement (Case 0), the vertical displacement increased rapidly during the seismic loading. Figure 5 (b) depicts the final vertical displacements at point B for six different configurations of the hybrid type reinforcements at the end of the numerical simulations. Compared to Case 1, 2, 3 and 6, the settlements for Case 4 (angle between the vertical and inclined piles = 55°) and Case 5 (angle between the vertical and inclined piles = 60°) are less. Case 6, which reduces effectively the lateral spreading on the embankment slopes, has larger settlements than other cases.

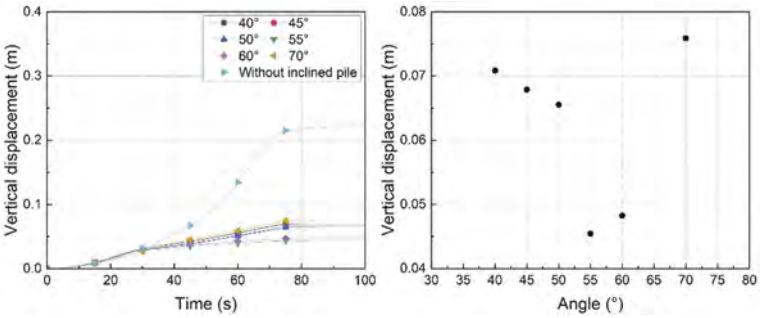

Figure 5. (a) Time histories of vertical displacements at the center of the embankment surface (point B) for six different configurations of hybrid type reinforcements and one configuration of conventional reinforcement, and (b) final vertical displacements at the same point for six different configurations of hybrid type reinforcements at the end of the simulations.

Figure 6 shows the deformed configurations of Case 4 (angle between vertical and inclined piles = 55°) and Case 5 (angle between vertical and inclined piles = 60°) at the end of the mainshock. The blue lines illustrate the locations of the vertical and inclined piles. Both side slopes of the highway embankment show significant deformation in both cases, while the surface is relatively intact after seismic loading.

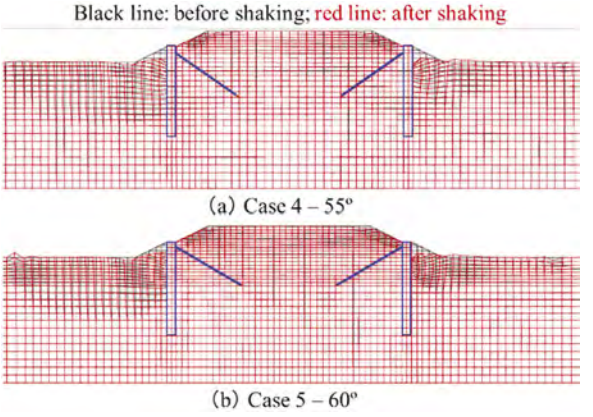

Figure 6. Deformed configurations at the end of the simulation: (a) Case 4 and (b) Case 5 (black line: before shaking; red line: after shaking).

4 CONCLUSIONS

The simulated results have proved that the highway embankment improved by hybrid type steel pile reinforcement has better performance in reducing settlement during seismic loading. In the proposed technique, inclined piles could suppress the deformation on the left and right

corners of the embankment side slopes, especially Case 6 (angle between the vertical and inclined piles = 70°) has the minimum deformation during the seismic wave. In addition, the final settlements at the center of the embankment surface were limited to an acceptable range in Case 4 and Case 5 (angles between the vertical and inclined piles are 55° and 60°). There are two possible reasons for these: (a) the complicated seismic behavior of the loose sandy layer including liquefaction; (b) the hybrid type reinforcement's range of influence. The optimum angle between the vertical and inclined piles should be in the range of 55°–60°. The inclined piles with this optimum angle range could efficiently mitigate earthquake-induced damage to highway embankments.

ACKNOWLEDGMENT

The financial aid for this study was provided by Nippon Expressway Company Limited (NEXCO) and affiliated organizations. A part of this research was also funded by the Kyushu Regional Management Service Association, Fukuoka. The authors wish to express sincere gratitude for the support. The first author would also like to acknowledge the support provided by JST SPRING (JPMJSP2136).

REFERENCES

Hazarika, H., Kokusho, T., Kayen, R.E., Dashti, S., Fukuoka, H., Ishizawa, T., Kochi, Y., Matsumoto, D., Furuichi, H., Hirose, T., Fujishiro, T., Okamoto, K., Tajiri, M., Fukuda, M. 2017. Geotechnical damage due to the 2016 Kumamoto earthquake and future challenges, *Lowland Technology International* 19(3): 189–204.

Qin, C.J., Hazarika, H., Pasha, S.M.K., Furuichi, H., Kochi, Y., Matsumoto, D., Fujishiro, T., Ishibashi, S., Watanabe, N. and Yamamoto, S. 2021. Evaluation of hybrid pile supported system for protecting road embankment under seismic loading, *Advances in Sustainable Construction and Resource Management*: 733–744.

West Nippon Expressway Company Limited. 2017. Kumamoto Earthquake Response Committee WG2Report: About earthquake resistance performance of highway embankment.

Smart Geotechnics for Smart Societies – Zhussupbekov, Sarsembayeva & Kaliakin (Eds)
© 2023 The Author(s), ISBN 978-1-003-29912-7
Open Access: www.taylorfrancis.com, CC BY-NC-ND 4.0 license

Validation of energy-based liquefaction prediction method for rock debris

M. Sawatsubashi & M. Ishimaru
Sustainable System Research Laboratory, Central Research Institute of Electric Power Industry, Abiko, Chiba, Japan

ABSTRACT: Under the new regulatory requirements for nuclear power plants, the evaluation of the liquefaction potential of rock debris, conventionally regarded as non-liquefiable soil, is necessary because the standard ground motion is stronger. Recently, an energy-based method was proposed for rational liquefaction prediction. In this study, to verify the applicability of energy-based liquefaction prediction to rock debris, the predicted results were compared with those of two centrifugal model tests performed on saturated rock debris under a centrifugal acceleration of 50 G. In one case, the entire layer was liquefied, and in another, the deep layer did not liquefy. In the energy-based method, the dissipated energy of each layer was calculated using nonlinear total stress analysis. The liquefaction prediction results of the energy-based method were consistent with experimental results.

1 INTRODUCTION

Liquefaction assessment is necessary to evaluate the seismic stability of ground foundations for Class S facilities, under the new regulatory requirements for nuclear power plants in Japan. The evaluation of the liquefaction potential of rock debris, conventionally regarded as non-liquefiable soil, is necessary because the standard ground motion is stronger.

Recently, an energy-based liquefaction evaluation method was proposed (Millen et al. 2020). In this method, the dissipated energy is calculated using the enclosed area of the hysteresis loop of the stress-strain relationship obtained from an undrained cyclic loading test. The dissipated energy is then compared with the energy produced by an earthquake to evaluate the liquefaction potential (Kokusho et al. 2015). The energy-based method allows a more reasonable evaluation of liquefaction compared with the stress-based method, which is currently the preferred method for evaluating liquefaction. However, most studies have focused on sandy soil, and the applicability of energy-based methods to granular materials, such as rock debris, has not been clarified.

Therefore, in this study, the characteristics of the energy-based method were analyzed to predict the increase in excess pore water pressure using a centrifugal model test on saturated rock debris.

2 TEST CONDITIONS

2.1 *Ground model and measurement items*

Figure 1 shows an illustration of the ground model and arrangement of the measuring instruments. The acceleration, ground surface displacement, and underground water pressure were measured. The ground model had a 1/50 reduction ratio, and a seismic motion was used as the input for a centrifugal force field with a centrifugal acceleration of 50 G. Table 1 lists the specifications of the centrifugal model test according to similarity laws (Kazama & Inatomi 1993).

DOI: 10.1201/9781003299127-240

Table 1. Specifications of the centrifugal model test according to similarity laws.

Parameter	Prototype	Model
Length	1	1/50
Strain	1	1
Stress	1	1
Time	1	1/50
Displacement	1	1/50
Acceleration	1	50

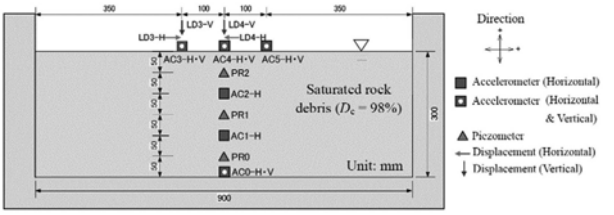

Figure 1. Ground model and arrangement of the measuring instruments (Case 2).

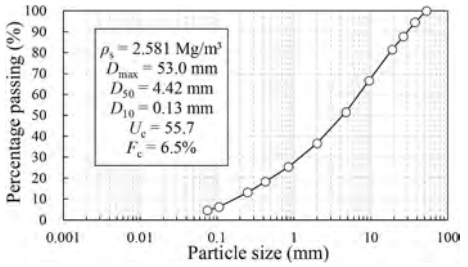

Figure 2. Particle size distribution and basic properties of rock debris.

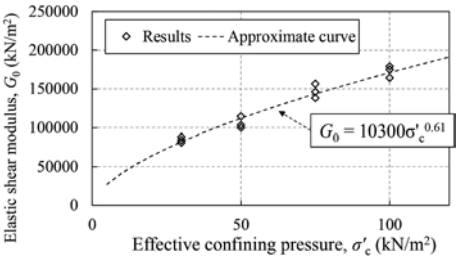

Figure 3. Elastic shear modulus and approximate curve.

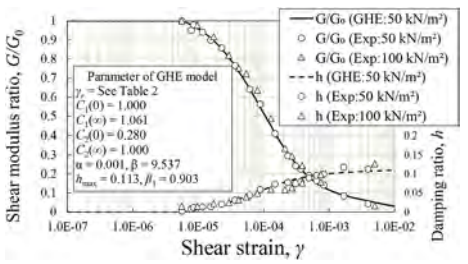

Figure 4. Dynamic deformation characteristics obtained from the cyclic triaxial tests.

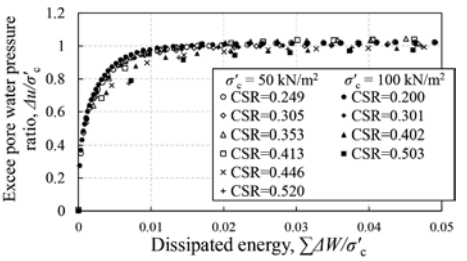

Figure 5. Relationships between the excess pore water pressure ratio and dissipated energy obtained from undrained cyclic loading tests.

The ground model was prepared using rock debris in a rigid-wall box. The ground height was 300 mm (15 m for the prototype scale) and the groundwater was at the same level as the ground surface. The ground model was prepared by compacting each layer at 60 mm intervals to achieve a 98% degree of compaction (D_c). After completion of the ground model, the box was placed in a vacuum container and saturated with deaired silicon oil (viscosity: 50 mN/m^2·s) during deairing.

2.2 *Physical properties of geomaterials*

The basic physical properties of the rock debris are shown in Figure 2. The elastic shear modulus, dynamic deformation characteristics, and liquefaction characteristics were measured via cyclic triaxial tests using specimens (diameter of 300 mm × height of 600 mm) with a D_c of 98%. With respect to the elastic shear modulus (G_0), minute cyclic loadings were performed under various confining pressures, and the relationship between the effective confining pressure (σ_c') and G_0 was obtained. Figure 3 shows the test results and approximate curve.

Figure 4 shows the dynamic deformation characteristics obtained from the cyclic triaxial tests. Cyclic triaxial tests were performed at σ_c' values of 50 and 100 kN/m^2. The test results

were fitted using a general hyperbolic equation (GHE) model (Tatsuoka & Shibuya 1992). The parameters for the GHE model were determined by fitting the experimental results, and the parameter settings are listed in Figure 3.

Figure 5 shows the relationship between the dissipated energy and maximum excess pore water pressure ratio for each cycle obtained in the undrained cyclic loading tests. The dissipated energy, $\Sigma \Delta W/\sigma'_c$, was calculated as

$$\sum \Delta W/\sigma'_c = \oint \tau(\gamma)\mathrm{d}\gamma/\sigma'_c \tag{1}$$

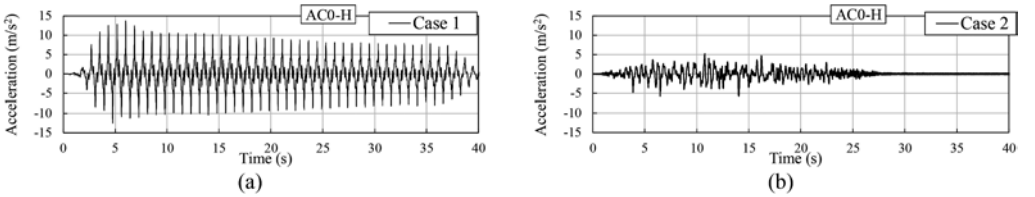

Figure 6. Input seismic motion for (a) Case 1 and (b) Case 2.

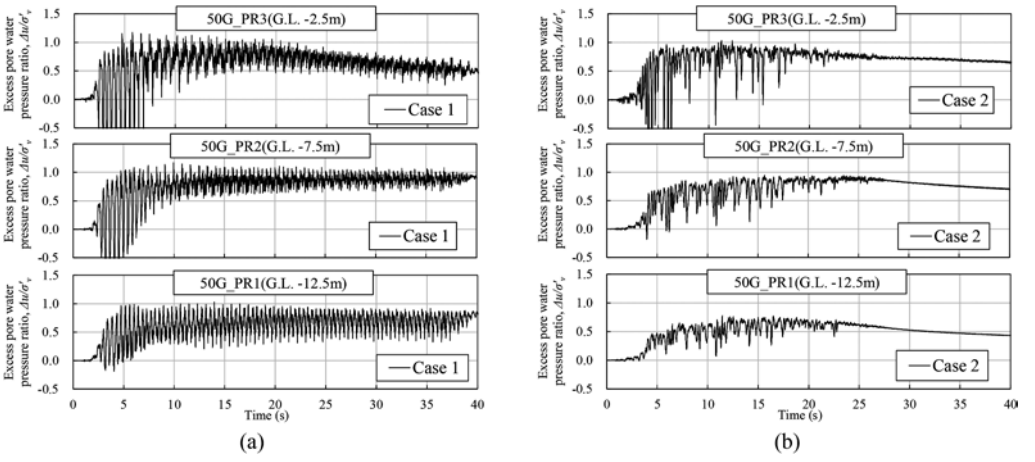

Figure 7. Excess pore water pressure ratio at each depth for (a) Case 1 and (b) Case 2.

where τ is the shear stress (half of the deviator stress), and γ is the shear strain (1.5 times the axial strain, assuming a Poisson's ratio of 0.5). The average $\Sigma \Delta W/\sigma'_c$ required to reach an excess pore pressure ratio of 95% was 0.0168 (standard deviation of 0.0078). The liquefaction resistance of rock debris, defined by an axial strain amplitude of 5% and 20 cyclic loading cycles, was 0.44 (σ_c' = 50 kN/m^2) and 0.39 (σ_c' = 100 kN/m^2).

2.3 *Input seismic motion*

Two centrifugal model tests were conducted. All subsequent data are shown as values converted to the prototype scale, based on Table 1. As shown in Figure 6, the input seismic motion was a 1.2-Hz sine wave with a four-wave taper before and after in Case 1 (PGA:13.7 m/s^2), and a simulated seismic motion in Case 2 (PGA:5.8 m/s^2).

3 TEST RESULTS

Figure 7 shows the excess pore water pressure ratio $\Delta u/\sigma_v'$ (obtained by dividing the excess pore water pressure Δu by the initial vertical effective stress σ_v') at each depth. Except for PR1 in Case 2 (G.L. −12.5 m), the $\Delta u/\sigma_v'$ of all measured layers reached 1.0 and liquefied.

4 APPLICABILITY OF ENERGY-BASED METHOD FOR LIQUEFACTION PREDICTION

4.1 *Nonlinear total stress analysis*

In previous studies, equivalent linear analysis has often been adopted to estimate input seismic wave energies. However, in the preliminary analysis, the shear strain exceeded the range of applicability of equivalent linear analysis (>1%). Therefore, a nonlinear analysis was performed. Table 2 summarizes the physical characteristics of the analysis. The ground was divided into intervals of 1-m layer thickness. The elastic shear modulus (G_0) was set using the equation in Figure 3 by assuming a coefficient of earth pressure at rest (K_0) of 0.5 and calculating the mean effective stress (σ'_c). The dynamic deformation characteristics were modeled using the GHE model, as shown in Figure 4. The values of the reference strain (γ_r) of each layer were calculated based on G_0 and the shear strength of each layer, which was calculated from the internal friction angle (47.9°), cohesion (3.9 kN/m^2), and σ'_c obtained from triaxial compression tests. The input acceleration was the horizontal acceleration measured at the bottom of the rigid-wall box during the centrifuge model experiments (Figure 6). The Newmark–β method (average acceleration method) was used as the numerical integration method. Iterative calculations were conducted to correct for disproportionate forces, and residual forces were applied in the next step.

Table 2. Physical characteristics in the analysis and results of liquefaction prediction.

Layer	Layer center depth (m)	Reference strain (-)	Initial effective mean stress (kN/m^2)	Elastic shear modulus (kN/m^2)	Normalized accumulated dissipated energy in analysis		Maximum excess pore water pressure ratio in experiments	
					Case 1	Case 2	Case 1	Case 2
1	0.5	2.336E-04	3.82	2.332E+04	0.2767*	0.0228*	–	–
2	1.5	2.438E-04	11.45	4.558E+04	0.6342*	0.0766*	–	–
3	2.5	2.695E-04	19.09	6.224E+04	0.6256*	0.0894*	1.17*	1.03*
4	3.5	2.937E-04	26.72	7.642E+04	0.5474*	0.0790*	–	–
5	4.5	3.155E-04	34.36	8.909E+04	0.4424*	0.0628*	–	–
6	5.5	3.354E-04	41.99	1.007E+05	0.3329*	0.0484*	–	–
7	6.5	3.537E-04	49.63	1.115E+05	0.2382*	0.0386*	–	–
8	7.5	3.707E-04	57.26	1.217E+05	0.1744*	0.0316*	1.17*	0.95*
9	8.5	3.866E-04	64.90	1.313E+05	0.1405*	0.0267*	–	–
10	9.5	4.016E-04	72.53	1.405E+05	0.1168*	0.0229*	–	–
11	10.5	4.157E-04	80.17	1.494E+05	0.1071*	0.0199*	–	–
12	11.5	4.292E-04	87.80	1.579E+05	0.1058*	0.0175*	–	–
13	12.5	4.420E-04	95.44	1.661E+05	0.1076*	0.0155	1.03*	0.77
14	13.5	4.542E-04	103.07	1.741E+05	0.1078*	0.0141	–	–
15	14.5	4.660E-04	110.71	1.819E+05	0.1067*	0.0129	–	–

* Judged liquefied.

4.2 *Liquefaction prediction using the energy-based method*

The dissipated energy ($\Sigma \Delta W/\sigma'_c$) obtained from the nonlinear total stress analysis was calculated using Equation 1. In the undrained cyclic loading tests (Figure 5), the excess pore water pressure ratio reached 0.95 when $\Sigma \Delta W/\sigma'_c$ reached an average of 0.0168. Thus, an experimental value of 0.0168 was used as the threshold for liquefaction in the energy-based method. In Case 1, all layers liquefied, whereas in Case 2, the deep layer (G.L. 12.5~14.5 m) did not liquefy. These predicted results were consistent with the test results.

5 CONCLUSIONS

The applicability of an energy-based method to centrifugal model tests with saturated rock debris was investigated. The energy-based method using nonlinear total stress analysis, can predict liquefaction in centrifugal model experiments on rock debris with relatively high accuracy.

REFERENCES

Kazama, M. & Inatomi, T. 1993. Application of centrifuge model testing to dynamic problems. *Proceedings of JSCE* (477): 83–92 (in Japanese).

Kokusho, T., Mimori, Y. & Kaneko, Y. 2015. Energy-based liquefaction potential evaluation and its application to a case history. *6th International Conference on Earthquake Geotechnical Engineering*; *Proc. intern. conf*., *Christchurch, New Zealand, 1-4 November 2015*.

Tatsuoka, F. & Shibuya, S. 1992. Deformation characteristics of soils and rocks from field and laboratory tests. *9th Asian Regional Conference on Soil Mechanics and Foundation Engineering*; *Proc. intern conf* (2)., *Bangkok, Thailand*: 101–170.

M. Millen, S. Rios, J. Quintero, A. Viana da Fonseca. 2020. Prediction of time of liquefaction using kinetic and strain energy, *Soil Dynam Earthq Eng*, Article 105898.

Smart Geotechnics for Smart Societies – Zhussupbekov, Sarsembayeva & Kaliakin (Eds)
© 2023 The Author(s), ISBN 978-1-003-29912-7
Open Access: www.taylorfrancis.com, CC BY-NC-ND 4.0 license

Versatility of u-w-p formulation to instability phenomena of saturated soil

T. Toyoda
Nagoya University, Nagoya, Aichi, Japan

ABSTRACT: Numerical stability of soil-water coupling was evaluated by a spectral radius of simultaneous recursive equations comprised of ***u-p***/***u-w-p*** governing equations with time integration formulas. As a result, the numerical stability of the ***u-w-p*** formulation was confirmed for instability problems as well as highly permeable conditions. Then, the ***u-w-p*** formulation-based soil-water coupled elasto-plastic finite deformation analysis was carried out for the instability problems of saturated soil (i.e. earthquake-induced liquefaction and seepage force-induced boiling problems). Finally, we indicated the versatile applicability of ***u-w-p*** formulation-based analysis without failure of calculation even in the destabilizing stage of analysis which cannot be solved by the ***u-p*** formulation.

1 INTRODUCTION

Most of the soil-water coupled analyses based on the Biot's mixture theory employ ***u-p*** formulation (proposed by Zienkiewicz et al. 1980; hereinafter, referred to as "***u-p***"). The ***u-p*** is a method with an assumption of static pore water permeation neglecting the dynamic motion of pore water (i.e. relative acceleration/convection of pore water viewed from soil skeleton). Although the assumption contributes to reducing the number of unknown variables, the analysis fails when targeting highly-permeable soils due to the negligence of the possible dynamic motion of pore water. Therefore, the "***u-p***"-based elasto-plastic soil-water coupled finite deformation analysis developed in our research group (Noda et al. 2008) was extended to ***u-w-p*** formulation (Noda & Toyoda, 2019; hereinafter, referred to as "***u-w-p***"). The ***u-w-p*** is the scheme for considering relative acceleration/convection of pore water by solving the equation of motion of pore water directly so that the analysis for highly permeable soils exhibiting dynamic motion of pore water can be seamlessly conducted. It can be regarded as a theoretical overcome of the limitation of ***u-p*** formulation. Furthermore, the dynamic pore water motion-induced phenomena solved by ***u-w-p*** were introduced in Toyoda & Noda (2021). Besides, the applicability of the ***u-w-p*** is not limited to solving highly permeable soils with a large coefficient of permeability k, but also to solving instability problems (i.e. failure with strain localization, bifurcation, material softening, liquefaction, boiling, etc.) that requires small time increment Δt for continuing calculations with acceptable accuracy (Noda et al. 2008).

In the first half of this manuscript, the inapplicable range of the ***u-p*** was thoroughly investigated and the potential of the ***u-w-p*** for overcoming the limited applicability of ***u-p*** was empirically indicated. The possibility of the ***u-p***/***u-w-p*** calculation was evaluated using a spectral radius of a simultaneous recursive equation comprised of discretized governing equations and time integration formulas. In the latter half, the ***u-w-p*** elasto-plastic finite deformation analysis was carried out for the instability problems of saturated soil (i.e. earthquake-induced liquefaction of centrifuge model experiment of sandy ground-embankment system and boiling due to an upward local hydraulic gradient). Through these analyses, we confirmed the versatile applicability of the ***u-w-p*** analysis without failure of calculation even in the destabilizing stage of analysis (i.e. decrease of mean effective stress due to softening with pore water absorption) whose stepwise calculation cannot be continued by the ***u-p***.

DOI: 10.1201/9781003299127-241

2 NUMERICAL STABILITY EVALUATION OF SOIL-WATER COUPLING ANALYSIS

2.1 *Governing equation and method for evaluating numerical stability*

The governing equation of the ***u*-*w*-*p*** (Noda & Toyoda, 2019) is indicated as follows:

$$\rho_s \mathrm{D}_s^2 \boldsymbol{v_s} + \rho_f \mathrm{D}_s \mathrm{D}_f \boldsymbol{v_f} + \rho^f (\mathrm{div}\, \boldsymbol{v_s})(\mathrm{D}_s \boldsymbol{v_s} - \boldsymbol{b}) = \mathrm{div}(\mathrm{D}_s S_t) \tag{1a}$$

$$\rho^f \mathrm{D}_f \boldsymbol{v_f} = -\gamma_w \,\mathrm{grad}\, h - (\gamma_w / k)\boldsymbol{w} \tag{1b}$$

$$\mathrm{div}\, \boldsymbol{v_s} + \mathrm{div}\, \boldsymbol{w} = \boldsymbol{0} \tag{1c}$$

where Equations 1a-c represent the equation of motion of mixture, the equation of motion of fluid phase, the soil-water coupling equation, respectively; ρ, ρ_s, ρ_f, ρ^f = densities of mixture, solid phase, fluid phase, pore water, respectively; D_s, D_f = material time derivatives focusing on configurations of solid phase and fluid phase; $\boldsymbol{v_s}$, $\boldsymbol{v_f}$ = solid and fluid velocity; $\boldsymbol{w} = n(\boldsymbol{v_f} - \boldsymbol{v_s})$ = averaged flow rate of pore water; p = pore water pressure; h = hydraulic head; n, k, γ_w, $\boldsymbol{b}$, $\mathrm{D_sS}_t$ = porosity, coefficient of permeability, unit weight of volume, body force per unit mass, rate of nominal stress, respectively. Assuming static pore water permeation ($\mathrm{D}_f\boldsymbol{v}_f - \mathrm{D}_s\boldsymbol{v}_s << \mathrm{D}_s\boldsymbol{v}_s$), Equations 1a-c can be reduced to the governing equation of ***u*-*p***:

$$\rho \mathrm{D}_s^2 \boldsymbol{v_s} + \rho^f (\mathrm{div}\, \boldsymbol{v_s})(\mathrm{D}_s \boldsymbol{v_s} - \boldsymbol{b}) = \mathrm{div}(\mathrm{D}_s S_t) \tag{2a}$$

$$\left(\rho^f k / \gamma_w\right) \mathrm{div}(\mathrm{D}_s \boldsymbol{v_s}) - \mathrm{div}\, \boldsymbol{v_s} + \mathrm{div}(k\, \mathrm{grad}\, h) = 0 \tag{2b}$$

After conducting non-dimensionalization and spatial discretization of Equations 1a-c or 2a-b based on Toyoda & Noda (2019) and coalescing them with the time integration formula of Wilson-θ method, we obtain a pair of algebraic equations:

$$\text{Governing equations and Wilson-}\theta\text{ time integration:} [\mathrm{A}]\{\boldsymbol{u}\}_{n+\theta} = [\mathrm{B}]\{\boldsymbol{u}\}_n \tag{3a}$$

$$\text{Pull-back formulas of Wilson-}\theta : \{\boldsymbol{u}\}_{n+1} = [\mathrm{C}]\{\boldsymbol{u}\}_n + [\mathrm{D}]\{\boldsymbol{u}\}_{n+\theta} \tag{3b}$$

Substituting Equations 3a-b, we obtain the following simultaneous recursive equation:

$$\{\boldsymbol{u}\}_{n+1} = [\mathrm{E}]\{\boldsymbol{u}\}_n \tag{4}$$

where $\{\boldsymbol{u}\}_n$, $\{\boldsymbol{u}\}_{n+1}$, $\{\boldsymbol{u}\}_{n+\theta}$ represent column vectors listing dimensionless unknown variables at time $t = t$, $t+\Delta t$, $t+\theta\Delta t$, respectively; $[\mathrm{E}] = [\mathrm{C}]+[\mathrm{D}][\mathrm{A}]^{-1}[\mathrm{B}]$. Then, investigating the spectral radius $\rho(\mathrm{E})$ of the matrix [E] calculated as a magnitude of the minimum eigenvalues of [E], we can evaluate the numerical stability of Equation 4, i.e., $\rho(\mathrm{E}) \leq 1$ means the numerical stability of the system.

2.2 *Results of numerical stability evaluation*

In this section, the numerical stability of ***u*-*p*/*u*-*w*-*p*** was evaluated assuming the elastic and infinitesimal deformation under one-dimensional condition.

The results of numerical stability analysis changing permeability coefficient k and time increment Δt with typical parameters (θ = 1.4; ground thickness H = 1m; Young's modulus $E = 10^4$ kPa; Poisson's ratio ν = 0.30, specific gravity of soil particles G_s = 2.65; void ratio e = 1.0) are indicated in Figure 1. As for the boundary conditions, undrained fixed and drained free conditions are considered at each end of one-dimensional domain, respectively. The markers ○ and × in the figures denote the numerical stability ($\rho(\mathrm{E}) \leq 1$) and instability ($\rho(\mathrm{E}) > 1$).

In the case of ***u*-*p*** in Figure 1a, the large k/small Δt resulted in the numerical instability of calculations that was able to lead to the failure of calculations. That is, there certainly exists the inapplicable range of ***u*-*p*** formulation. Moreover, the threshold (a blue line on the figure) of the calculation possibility was not indicated as a straight line, but bent around $k = 10^{-2}$~10^{-1} m/s.

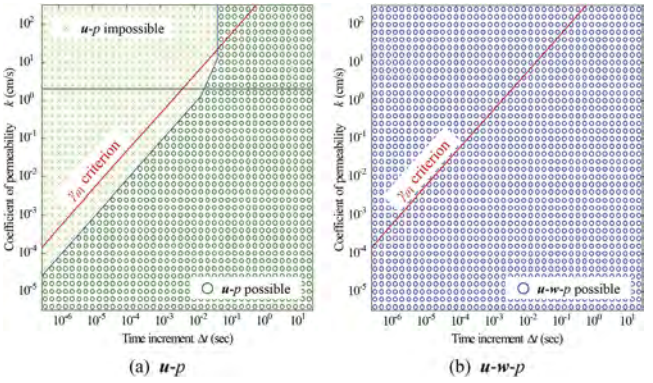

Figure 1. Numerical stability of soil-water coupling analysis evaluated by spectral radius.

Although we omitted the details here, the bending is caused by the change of eigenmodes in the theoretical solution of the one-dimensional governing equation. It could also be confirmed that the $\gamma_{\theta 1}$ criterion for estimating the possibility of ***u-p*** derived by Noda et al. (2008) was more or less valid in the low permeable range (under the horizontal black line on the figure).

In contrast, in the case of ***u-w-p*** in Figure 1b, the numerical stability was ensured even at the inapplicable range of ***u-p***. It means ***u-w-p*** has versatile applicability regardless of the settings of k and Δt. This is a potential of ***u-w-p*** for overcoming the limited applicability of ***u-p***.

It should be noted that the sufficient number of finite elements converged the value of the spectral radius, the threshold in the low permeable range does not depend on the ground height and stiffness, and the above discussion postulates $\theta > 1.37$ ensuring unconditional stability of Wilson-θ method. We've confirmed that the same trends of diagrams in Figure 1 could be obtained through two-dimensional analysis.

3 APPLICATION TO INSTABILITY PROBLEMS

In the former chapter, we confirmed that the ***u-w-p*** has strong applicability not only for highly permeable soil, but also for conditions with small time increment Δt that would usually be required in instability problems of saturated soils. In this chapter, we applied the ***u-w-p***-based elasto-plastic finite deformation analysis of saturated soil to liquefaction and boiling problems for confirming the efficacy of ***u-w-p*** to the instability problems. The targeted problems usually accompany instability caused by a lack of stiffness with a decrease of mean effective stress.

3.1 *Analysis of earthquake-induced liquefaction of sandy soil-embankment system*

Referring the centrifuge model experiment by Japan Institute of Country-ology and Engineering (2002), we prepared one/two-dimensional models in Figure 2a and input irregular wave shown in Figure 2b. The domains are entirely constituted by loosely deposited Edosaki sand whose material parameters and initial states for SYS Cam-clay model were omitted due to the space limitation. Time increment Δt (1.25×10^{-3} sec at the beginning) was changed to the smaller value when the iteration at each step did not converge.

Analysis results for the one-dimensional model with three permeability coefficients (k = 1.95×10^{-4}, 9.75×10^{-4}, 1.95×10^{-3} m/s was indicated in Figure 2c. While the case with $k = 1.95\times10^{-4}$ m/s exhibited perfect correspondence of ***u-p*** and ***u-w-p*** solutions, the case with $k = 9.75\times10^{-4}$ m/s caused a difference in the solutions. As for the case with $k = 1.95\times10^{-3}$ m/s, ***u-p*** failed at the initial stage of calculation whereas the ***u-w-p*** successfully continued the calculation.

The calculation for the two-dimensional model with $k = 1.95\times10^{-3}$ m/s based on ***u-w-p*** was indicated in Figure 2d. The ***u-w-p*** calculations were successfully continued even after the decrease of mean effective stress. Besides, we confirmed in the case of ***u-w-p*** that the occurrence of the substantial magnitude of the relative acceleration of pore water caused dynamic seepage.

3.2 *Analysis of upward seepage force-induced boiling*

Although the detailed information was abbreviated, one/two-dimensional deformation analysis applying hydraulic gradient was conducted with the same parameters of 3.1. As a result of the ***u-w-p*** analysis, we obtained not only the decreasing process of mean effective stress *p'* (softening with pore water absorption) but also the behavior after the state becomes closer to *p'*=0, i.e., surface oscillation with repeated element-wise pore water drainage/absorption in Figure 3a, concentration/disturbance of the streamline in Figures 3b-c. It should be emphasized that ***u-w-p*** calculation could be continued even at an unstable state with a lack of mean effective stress.

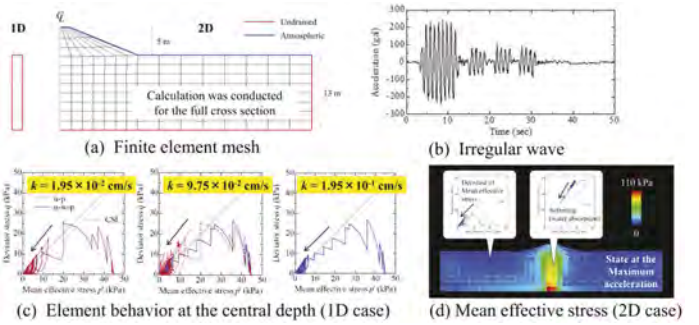

Figure 2. One/two-dimensional liquefaction analysis of sandy ground-embankment system.

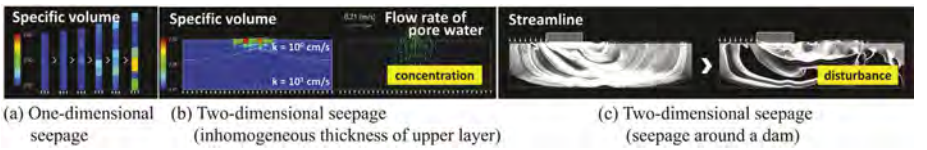

Figure 3. One/two-dimensional boiling analysis of sandy ground.

4 CONCLUSION

A versatile applicability of ***u-w-p*** has been indicated through numerical stability evaluation using a spectral radius of the recursive equations and demonstrated through its application to the liquefaction and boiling problems causing instability with a decrease of effective stress.

ACKNOWLEDGEMENTS

The author is grateful to Prof. Toshihiro Noda in Nagoya University for his valuable advices and Mr. Koyo Satake for assistance with the numerical simulations. This work was supported by JSPS KAKENHI Grant Number 22K14324.

REFERENCES

Japan Institute of Country-ology and Engineering. 2002. Analysis method of deformation amount of river embankment during earthquake (in Japanese), *Document of JSCE* 102001: A1–A2.

Noda, T., Asaoka, A. & Nakano, M. 2008. Soil-water coupled finite deformation analysis based on a rate-type equation of motion incorporating the SYS Cam-clay model. *Soils Found* 48(6): 771–790.

Noda, T. & Toyoda, T. 2019. Development and verification of a soil-water coupled finite deformation analysis based on ***u-w-p*** formulation with fluid convective nonlinearity. *Soils Found* 59(4): 888–904.

Zienkiewicz, O.C., Chang, C.T. & Bettess, P. 1980. Drained, undrained, consolidating and dynamic behaviour assumptions in soils, *Géotechnique* 30(4): 385–395.

Smart Geotechnics for Smart Societies – Zhussupbekov, Sarsembayeva & Kaliakin (Eds)
© 2023 The Author(s), ISBN 978-1-003-29912-7
Open Access: www.taylorfrancis.com, CC BY-NC-ND 4.0 license

Assessment of spectral amplification in city of Lima, Peru

J. Soto
Postgraduate, Faculty of Civil Engineering, National University of Engineering, Lima, Peru

J.E. Alva
Faculty of Civil Engineering, National University of Engineering (UNI), Lima, Peru

C.E. Ortiz
Research Center on Digital Transformation in Engineering (CITDI), Lima, Peru

ABSTRACT: In 1746, the city of Lima was impacted by an earthquake of high magnitude with a seismic intensity of X in the Modified Mercalli scale. Nowadays, a seismic event of similar magnitude has not occurred off the coast of Lima, for that reason is necessary to estimate ground response to verify if design motion of the Peruvian Earthquake-Resistant Code is appropriated. In this sense, the non-linear site response analysis was carried out in the city of Lima, for which synthetic movements in rock were generated and the deep S-wave velocity profiles were characterized. Then, the amplification of ground acceleration and spectral amplification were analyzed, as a result the spectral amplification on average was 3.0, being greater than 2.5 that is the value of the spectral amplification of the Peruvian Code. In addition, a new design spectrum for the city of Lima was proposed.

1 INTRODUCTION

The city of Lima is located in one of the regions with the highest seismic activity. According to seismic history, in the year 1746 off the coast of Lima, a strong movement occurred whose seismic intensity was X on the Modified Mercalli scale (Silgado, 1978).

In the last century, strong earthquakes occurred in 1966, 1970 and 1974 in different regions of the Peruvian coast, where seven seismic records were obtained and analyzed through normalized acceleration Spectra (Sa/PGA) to evaluate the maximum spectral amplification for rigid soil of Lima City, the result obtained was a mean maximum spectral amplification of 2.28 (Meneses & Alva, 1986). From this result and similar maximum spectral amplification values from seismic of other countries a value of 2.5 (maximum amplification) was incorporated in the E030 Peruvian Seismic-Resistant Design Code of 1997.

After several years of absence of analysis and research regarding the evaluation of spectral amplification, Soto (2016) and Soto et al. (2018) compiled the physical and dynamics characteristics of ground to obtain results for deep soil profiles (greater than 200 m). Then evaluated the site spectra by equivalent linear (EL) and non-linear (NL) site analysis, the spectra was normalized to obtain a spectral amplification value of 3.0, which is greater than 2.5, the last value was indicated in E030 Peruvian Code of 2006. In southern of Peru, in Tacna, Ortiz (2019) and Alva et al. (2020) compiled the geotechnical characteristics and conducted an extensive campaign of dynamic characterization through measurements of microtremor arrays specifically at the seismic stations. With this information it was performed the EL and NL site analysis of deep soil. The results obtained for stiff and intermediate soil the acceleration amplification were 1.0 and 1.3, respectively, and the maximum spectral amplification was 3.0 for both types of soil, again these values are higher than 2.5. On the other hand,

DOI: 10.1201/9781003299127-242

Aguilar et al. (2019) performed the NL site analysis of soil profiles with depth of 30 m to estimate the spectral amplification by ratio of soil spectrum over the rock spectrum, as result the amplification values of 3.0 for profiles with Vs30 varying from 200 m/s to 350 m/s.

Recently, Alva (2021) analyzed the acceleration records from the large earthquakes of the years 2001, 2007 and 2019. From these last earthquakes, significant amounts of seismic records were obtained. With these records, the spectral amplification for different types of soil was analyzed, in several stations. It was evidenced that spectral amplification has a maximum value of 3.0, so it is insisted to continue with the evaluation of soil amplification and spectral amplification.

Two types of amplification occur during a seismic event, the first as an increase in ground motion relative to the motion of bedrock (soil amplification factor) and the second as an increase of the motion of structure relative to the ground motion (structural amplification factor) through spectral amplification. These amplification factors could be determined by analysis of seismic records, probabilistic Seismic Hazard, Non-Linear Site Response Analysis and Seismic Design code. Since no strong motion information is available for deep soil deposits, the NL site analysis of the City of Lima was performed in this paper to evaluate the site spectral amplification by means of the normalized acceleration spectra.

2 PERFORMED SITE ANALISIS

2.1 *Analyzed sites*

The analyzed sites were eighteen seismic stations, these stations correspond to the seismic networks CISMID (Peruvian-Japanese Center for Seismic Research and Disaster Mitigation) and UNI-CITDI (Research Center on Digital Transformation in Engineering from National University of Engineering). The stations are located in zones with different seismic geotechnical characteristics, these zones were established in the Seismic Geotechnical Microzonation map (CISMID, 2014). This map was made from the physical characteristics of the ground (soil pits and drilled wells) and the dynamic characterization through the fundamental vibration period (obtained of microtremor HV spectrum). A summarized of four zones are described as follow Zone I has vibration periods less than 0.3 s, Zone II has vibration periods less than 0.4 s, Zone III shows vibration period greater than 0.4 s, and Zone IV as zone of high seismic amplification. The location of the seismic stations on Seismic Geotechnical Microzonation map is shown in Figure 1.

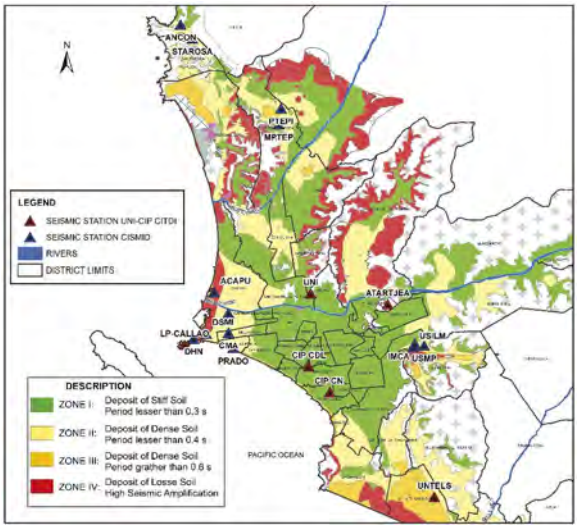

Figure 1. Locations of analyzed seismic stations.

2.2 *Physical characteristics of soil*

The City of Lima is composed of gravel and boulders, which is called Lima Conglomerate (Zone I) in whole depth, as well as the presence of sand, and silts and clays (Zone II, III and IV) superficially. According to drilling wells below 50 m depth in zones II, III and IV, the Lima Conglomerate is present (Soto, 2021).

The average unit weight for clayey and silty soils, is 14.1 kN/m^3, the moisture content is 20.8%, and the Liquid Limit (LL) varies from 1.7 % to 42.0 %. The unit weight for sandy soils is 17.2 kN/m^3, the moisture content is 8.4 %, the compactness varies from dense to very dense, also is presented in an almost dry state and certain degree of natural cementation. The unit weight for the Conglomerate, is 22.0 kN/m^3, the moisture content is 3.6 %, and these values are close to those obtained by Sanchez et al. (2016) who considered the variability of these parameters of the Lima Conglomerate, from the depth of 5 m to 30 m. For rock, it is mostly conformed by igneous and sedimentary rock whose unit weight is about 26 kN/m^3.

2.3 *Dynamics characteristics of soils*

The dynamic characteristic of soils was obtained through of the Fundamental Period (T) and the S-Wave Velocity profile (Vs). The values of T were obtained from HV spectral ratio of seismic records (HV spectrum) and the values of Vs obtained from surface waves measurements tests of the first 30 m depth (Vs_{30}) and the inversion of the HV spectrum, as mentioned by Soto (2021) and Soto & Alva (2022). The values obtained for deep Vs profile are similar to those obtained by Calderon et al (2013).

Due that Lima soil deposit has a thickness varying from 200 m to 400 m in depth, the use of Vs_{30} according to E030 Peruvian Code for site class is not sufficient, so that very thick deposit can influence the behavior during a seismic motion. Therefore, a particular criterion of Class Site (according the Vs_{30}) and Peaks Periods of the HV spectrum was adapted as shown in Table 1, where site type S1 and S2 were subdivided into two subgroups G1 and G2.

Figure 2a shows four HV spectra of the CIP CN, IMCA, LP CALLAO, and UNTELS stations, which according to peak periods T0 and T1, the mentioned stations were characterized as S1-G1, S1-G2, S2-G1, and S2-G2, respectively. From an inversion process of these HV spectra, the corresponding Vs profiles were obtained as shown Figure 2b. These profiles shows that bedrock presents a Vs value of 1500 m/s, with the exception of the IMCA station where the rock has a value almost 1000 m/s and also shows a reduction of Vs at depth of 55 m to 85 m to increase again at greater depth. For others seismic stations according to HV spectra and Vs profile were classified as shown in Table 2.

Table 1. Criterion of class site.

Class	Predominant Period	Condition	Site
S1	0.1 < T0, T1 < 1.0 s	T0<T1	S1, Group 1 (S1-G1)
S1	0.1 < T0, T1 ≤ 1.0 s	T0>T1	S1, Group 2 (S1-G2)
S2	T0≥1.0; 0.1 < T1 < 1.0	T0>T1	S2, Group 1 (S2-G1)
S2	0.1 < T0, T1< 1.0	T0>T1	S2, Group 2 (S2-G2)

T0 is the period of the highest amplitude
T1 is the period of the second highest amplitude

2.4 *Non-linear behavior of soils*

The non-linear behavior of soils was estimated using the empirical equations of normalized shear stiffness curves (G/G_o) and damping ratio curves (D) from available technical literature. For gravelly soils (including the Conglomerate), the empirical relationships of Menq (2003) were used, while for sandy and clayey soils the empirical relationship of Zhang et al. (2005) were used.

Most of empirical equations requires the physical properties such as Coefficient of Uniformity (Cu) and effective isotropic confining pressure (σ'_o) for gravels, while sandy soils and clayey soils depend of the Plastic Index (PI) and mean effective confining stress (σ'_m). For the Lima Conglomerate the Cu value was 70; for sands, the PI was 6 % for UNTELS and CMA stations and PI of 0% for other stations; and for clays, the PI was in range 6% to 21 %.

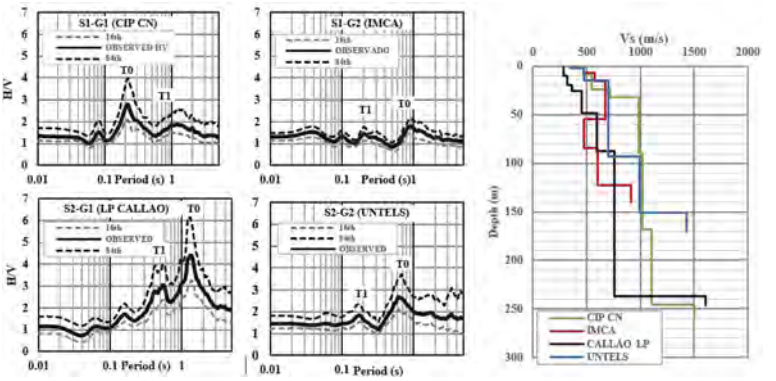

Figure 2. a) HV spectra for determine peak periods, b) Deep vs profiles.

Table 2. Dynamic characteristics for analyzed seismic Stations.

Seismic Station	Lat (°)	Long (°)	Zone	Vs_{30} m/s	Site Class E.030	Site Class ASCE	T0 (s)	T1 (s)	Group
*CIP CDL	-12.091	-77.048	I	664	S1	C	0.30	0.60	S1-G1
*CIP CN	-12.115	-77.029	I	600	S1	C	0.20	0.90	S1-G1
*UNI	-12.023	-77.046	I	713	S1	C	0.25	0.60	S1-G1
STAROSA	-11.787	-77.156	II	780	S1	B	0.15	0.60	S1-G1
IMCA	-12.070	-76.950	II	572	S1	C	0.90	0.18	S1-G2
USMP	-12.072	-76.941	II	515	S1	C	0.80	0.15	S1-G2
*LP CALLAO	-12.071	-77.162	IV	318	S2	D	1.20	0.50	S2-G1
DHN	-12.065	-77.155	IV	352	S2	D	1.20	0.55	S2-G1
DSMI	-12.060	-77.144	IV	323	S2	D	1.25	0.30	S2-G1
ACAPU	-12.022	-77.136	IV	260	S2	D	1.00	0.40	S2-G1
RAMON	-12.042	-77.123	II	327	S2	D	1.00	0.25	S2-G1
CMA	-12.060	-77.123	II	372	S2	C	1.20	0.25	S2-G1
PRADO	-12.074	-77.188	II	359	S2	D	1.20	0.20	S2-G1
*UNTELS	-12.213	-76.932	III	490	S2	C	0.60	0.18	S2-G2
USILM	-12.073	-77.952	II-III	405	S2	D	0.20	0.90	S2-G2
MPIEDRA	-11.867	-77.076	II	293	S2	C	0.50	0.10	S2-G2
PIEDRA	-11.852	-77.074	II	416	S2	C	0.40	0.18	S2-G2
ANCON	-11.774	-77.167	II	402	S2	C	0.40	0.12	S2-G2

* Stations from UNI-CITDI seismic network

2.5 *Input seismic records*

Since there are no rock acceleration records of strong motions in Peru, synthetic accelerograms were generated so that the mean acceleration spectrum is compatible to the rock design spectrum (Kottke & Rathje, 2007). The selected records were from earthquakes of greater magnitude recorded in the Peruvian territory, these correspond to interface and intraplate subduction mechanisms, and Table 3 shows the characteristics of the recorded seismic events.

The rock design spectrum (Vs30=760 m/s) was obtained from uniform hazard analysis with 10% of probability of exceedance in 50 years, same level of seismic risk of E030 Peruvian Code. Resulting in the spectral acceleration at T=0 s of 0.47 g.

The criterion for using these earthquakes was the Arias Intensity (AI) a parameter that reflects the amplitude and frequency by duration of the motion, as well as the structural damage that can be generated by ground motion. Figure 3a shows the AI for each seismic record and Figure 3b shows the compatible spectra where the mean spectrum sufficiently matches the rock spectrum.

These compatible input motions correspond to motion of the outcrop with Vs30=760 m/s, however, it has been observed that bedrock of the deep profiles has a Vs value of 1000 m/s to 1500 m/s for the site analysis. The input motion at bedrock was obtained by deconvolution for the Atarjea station, then at the specific depth where Vs varies from 1000 m/s to 1500 m/s was considered the input motion for site analysis as performed by Soto (2021). The Atarjea station belongs to UNI-CITDI and is located on rock.

Table 3. Characteristics of seismic events.

Station	Mechanism	Date	Time	Long	Lat	R*	Depth	Mw
				(°)	(°)	(km)	(km)	
PQR	Intraplate	1970/05/31	15:23:00	-78.87	-9.36	368.3	64	7.8
PQR	Interfase	1974/10/03	09:21:00	-77.98	-12.50	58.8	13	8.1
MOQ	Interfase	2001/06/23	15:33:00	-73.77	-16.08	325.6	33	8.4
ICA	Interfase	2007/08/07	18:40:58	-76.76	-13.67	117.0	40	7.9
NAZCA	Interfase	2018/01/14	09:18:42	-74.89	-16.07	135.1	48	6.8
MALA	Interfase	2021/06/23	02:54:18	-76.91	-12.77	29.7	32	6.0
UNF	Interfase	2021/07/30	17:10:18	-80.80	-4.89	35.9	36	6.1

* Epicentral distance

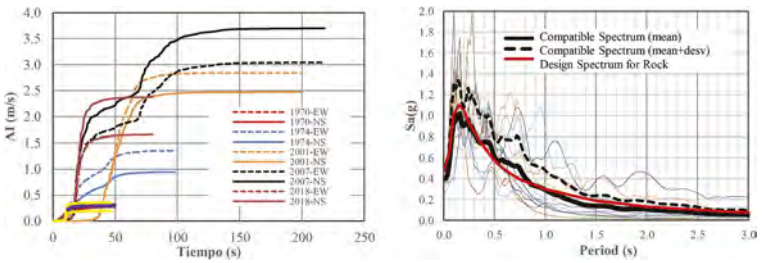

Figure 3. a) Arias intensity of seismic records, b) Compatible design spectrum for rock.

2.6 *Non-linear site analysis*

Non-linear Site Analysis was performed using DeepSoil software (Hashash et al. 2016). For each analysis, profile was discretized in layers such that the maximum vibration frequency is 25 Hz. The constitutive mode and load-unload model of soils were the MRDF pressure-dependent hyperbolic model (Phillips & Hashash, 2009).

3 RESULTS AND DISCUSIONS

3.1 *Acceleration spectra*

After performing the nonlinear analyses, on the surface of each profile, the acceleration spectra with damping ratio of 5% (Sa) were obtained as shown in Figures 4-5 for sites S1-G1, S1-G2, S2-G1 and S2-G2. These figures show the mean values and its variability (mean plus

a standard deviation), due to the high degree of variation of the input motion, however, in the following paragraphs the description and analyses were performed for the mean value of spectra as shown.

For sites S1-G1 (Figure 4a), a maximum average surface acceleration of 0.47 g was obtained, while for S1-G2 (Figure 4b) a maximum acceleration of 0.38 g was obtained. These sites superficially have a similar Vs30 value (Type S1, according E030 Peruvian Code), however the effect of depth and the variation in depth of the Vs profiles influences the seismic response at surface, as shown in acceleration spectra in Figure 4.

For sites S2-G1 (Figure 5a, b) a maximum surface acceleration of 0.40 g was obtained on average, with a notable difference in the shape of spectra, as shown in the LP CALLAO and DSMI stations, this is because the surface layers are more erratic from stations close to ocean (LP CALLAO and DHN). On the other hand, for sites S2-G2 (Figure 5c) the maximum ground acceleration was 0.60 g, this spectrum has a peak spectral acceleration in the period of 0.1 s, this is because the profile is dense in the first 50 m depth.

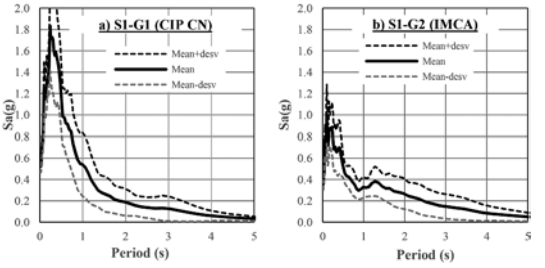

Figure 4. Acceleration spectra at surface for sites S1-G1 and S1-G2.

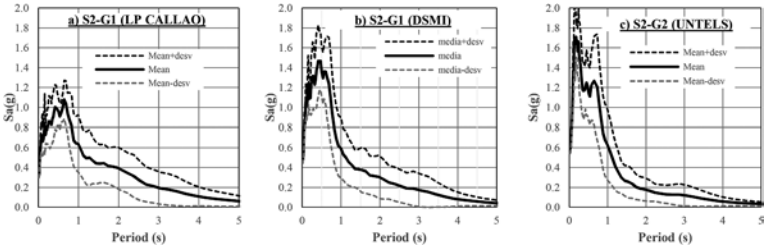

Figure 5. Acceleration spectra at surface for sites S2-G1 and S2-G2.

On the other hand, for sites S1-G1 and S1-G2 the Sa spectra present a peak acceleration in spectral periods less than 0.2 s and 0.3 s, respectively. In the range of periods greater than 1.0 s, the spectral acceleration of S1-G2 are higher than S1-G1, this is due to the behavior of the deep profile and the Vs values of S1-S2. For site S2-G1 as LP CALLAO and DMSI the Sa spectra present a maximum value that apparently are almost flat until periods of 0.9 s and 0.6 s, respectively. In the range of periods greater than 1.0 s the spectral accelerations of LP CALLO are higher than DSMI, this is due to deep Vs profile and shallow layers of both sites (Soto, 2021). For site G2-S2 shows a peak spectral in period 0.1 s, then becomes almost flat up to 0.6 s.

3.2 *Soil amplification*

The ground motion at surface is amplified or de amplified with respect to rock motion, taking into account that the response at the surface is influenced by whole ground profile, it is defined as the soil amplification (S') which is determined as the ratio of maximum acceleration of surface soil to maximum acceleration of outcrop.

From the rock uniform hazard spectrum, the maximum acceleration was 0.47 g, slightly higher than 0.45 g (for Zone 4 of Peru, according E030 code), this last value of rock acceleration is used as a reference for the design of structures in the city of Lima. The amplification was determined considering the rock acceleration of 0.45 g. The S values for sites S1-G1, S1-G2, S2-G1 and S2-G2 are shown in Table 4.

3.3 *Spectral amplification*

The ratio of the spectral acceleration to maximum ground acceleration was defined as the spectral amplification. This ratio is a simplified method that allow identifying the influence on the site over a wide range of periods regardless of maximum ground acceleration level. This ratio allowed identify how deep soil profiles influence the seismic response of the acceleration spectrum.

The spectral amplification has a peak value because the Sa spectrum has a peak value. These values do not necessarily indicate the maximum spectral amplification over the whole spectrum, so therefore a review of the site spectrum and displacement spectrum were necessary to properly define the spectral amplification. A summary of the peak values of spectral amplification (C') are shown in Table 4.

Table 4. Values of aoil amplification (S') and maximum spectral amplification (C').

Group	S'	C'
S1-G1	1.00 – 1.16	2.89 – 3.53
S1-G2	0.80 – 0.95	2.86 – 4.00
S2-G1	0.70 – 0.93	3.33 – 3.59
S2-G1*	0.80 – 1.04	2.76 – 3.09
S2-G2	0.90 – 1.20	2.94 – 3.27

* Stations (DSMI, ACAPU, RAMON, CMA, and PRADO) located in Zone II of Seismic Microzonation

3.4 *Proposed site spectrum and proposed spectral amplification*

To determine the Site Design Spectrum (S_a), in a practical manner, it was established that it is influenced by the maximum ground acceleration and the spectral amplification through the following equations:

$$S_a = ZSC \tag{1}$$

$$T \leq T_P : C = C_o \tag{2}$$

$$T_P < T \leq T_L : C = C_o(T_P/T) \tag{3}$$

$$T > T_L : C = C_o(T_P\, T_L)/T^2 \tag{4}$$

Where Z= maximum horizontal acceleration for rock; S= soil amplification factor; C= spectral amplification; C_o= maximum value of spectral amplification; T= structural period; T_P= limit period to define constant spectral acceleration; and T_L= period that define the beginning the displacement constant spectral.

To define the T_P and T_L periods of Site Design Spectrum, the variability of seismic motions was considered at surface ground, as well as the Displacement Spectrum (S_d) that is influenced at the surface due to seismic motions. The S_d spectrum is defined as $S_a\,(T/2\pi)^2$. To obtain the values of T_P and T_L, the spectra of C, S_a and S_d were analyzed simultaneously, then the same parameters of E030 code were compared.

For each site S1-G1, S1-G2, S2-G1 y S2-G2, a group of S, C_o, T_P y T_L values was proposed as shown in Table 5, where it is observed that sites S2-G1 were subdivided in two groups due to the different behavior of spectral amplification caused by the shallow layers. Then the normalized acceleration spectra was superimposed with spectral amplification (C-proposed), the NL acceleration

spectral (Sa-NL) with the site design spectrum (Sa-proposed) and E030 code acceleration spectrum (Sa-E030), and the NL displacement spectra (Sd-NL) with the site displacement spectrum (Sd-proposed) and E030 code displacement spectrum (Sd-E030) as shown in Figures 6-10.

The proposed spectral amplifications (C-proposed) for all sites (Figures 6a-10a) can be considered as acceptable because it encompassed the normalized spectra of ground motions obtained from NL analyses, with a slightly difference in pointed structural period less than T_P.

The Sa-proposed spectra, for all sites (Figure 6b-10b) encompassed acceptably the Sa-NL spectra with some pointed difference at spectral periods less than T_P, it is similar to the proposed amplifications, however, this does not influence on the displacement generated by seismic motions from the NL analysis. Furthermore, the Sa-proposed spectra are greater than Sa-E030 spectra over the whole range of structural periods.

With respect to the Sd-proposed spectra, for all sites, these are acceptably to cover the Sd-NL spectra over the range of structural periods. In addition, the Sd-proposed spectra are greater than Sd-E030 spectra in all structural periods, satisfactorily covering some upper spectral displacement that may occur due to strong influence of depth at sites. This is evidenced by the deep profile is showed for Sd-NL spectra exceed the Sd-030 spectra, therefore this shows that the C, Sa and Sd parameters of E030 Peruvian Earthquake-Resistant code (Table 5) provides values with deficiencies for deep soil deposits for earthquake design as indicated by this code.

Table 5. Summarized of proposed parameters and peruvian code parameters.

Group	Proposed Parameters				E.030 Parameters			
	(S)	(C_o)	T_P	T_L	(S)	(C)	T_P	T_L
S1-G1	1.05	3.00	0.40	2.50	1.00	2.50	0.40	2.50
S1-G2	0.90	3.00	0.50	2.50	1.00	2.50	0.40	2.50
S2-G1	0.90	3.00	0.90	2.50	1.05	2.50	0.60	2.00
S2-G1*	0.90	3.00	0.65	2.50	1.05	2.50	0.60	2.00
S2-G2	1.10	3.00	0.60	2.00	1.05	2.50	0.60	2.00

* Stations (DSMI, ACAPU, RAMON, CMA, and PRADO) located in Zone II of Seismic Microzonation

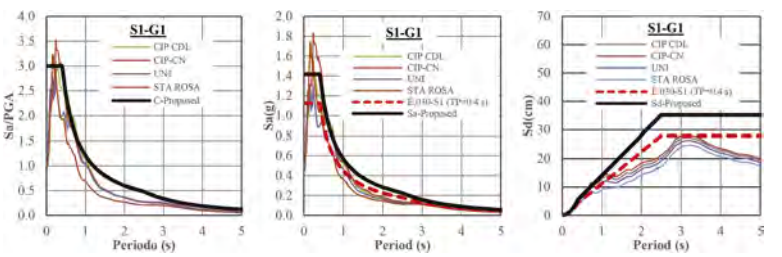

Figure 6. a) Spectral amplification, b) Acceleration spectra, c) Displacement spectra, for site S1-G1.

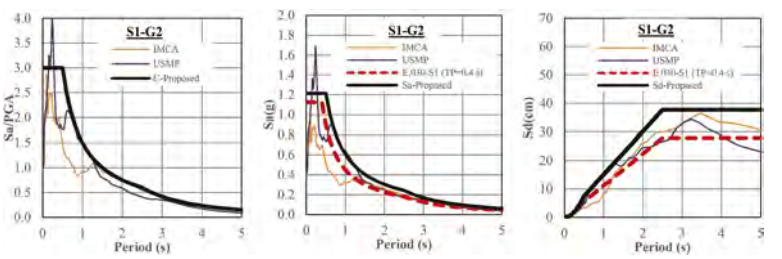

Figure 7. a) Spectral amplification, b) Acceleration spectra, c) displacement spectra, for site S1-G2.

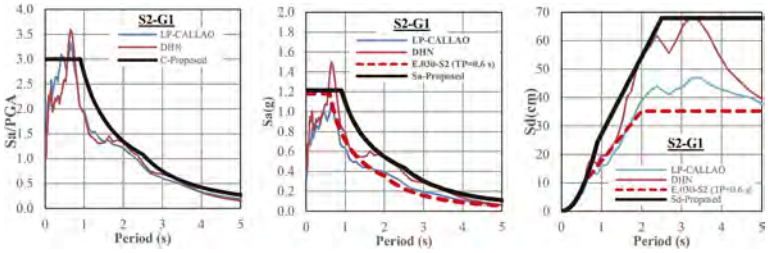

Figure 8. a) Spectral amplification, b) Acceleration spectra, c) displacement spectra, for site S2-G1, first subdivision.

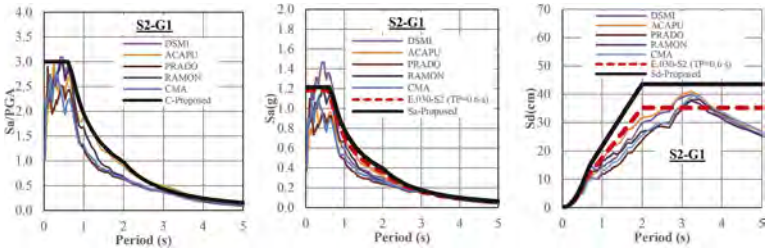

Figure 9. a) Spectral amplification, b) Acceleration spectra, c) Displacement spectra, for site S2-G1, second subdivision.

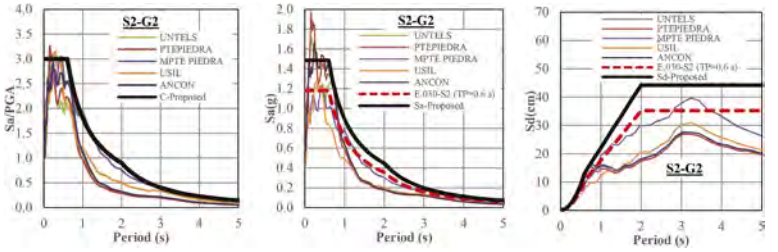

Figure 10. a) Spectral Amplification, b) Acceleration spectra, c) Displacement spectra, for site S2-G2.

4 CONCLUSIONS

The spectral amplification of deep soil deposits in city of Lima was analyzed using the simplified method from obtained surface ground motion of the nonlinear site response analysis.

The results shows that the deep soil deposits characterized by the HV spectrum of earthquakes and deep Vs profile show a notable influence on the shape of the normalized acceleration spectrum, the acceleration spectrum and the displacement spectrum, for which the spectral amplification (C) and Design Spectrum (Sa) were proposed in equations 1-4. A maximum value of spectral amplification (C_o) is 3.0 greater than 2.5 (value stablished by the E030 Peruvian code). On the other hand, for deep deposits the E030 code is deficient in covering the displacement spectral values that may occur for design earthquake.

REFERENCES

Alva, J.E., Ortiz, C.E. & Soto, J. 2020. Seismic Amplification in Tacna-Peru using Seismic Motion Data and Arrangements of Microtremor. In proceeding of 17th World Conference on Earthquake Engineering. Paper 1d–00068.

Alva, J.E. 2021. Contributions of Geotechnical Engineering to E.030 Earthquake-Resistant Code (In Spanish). In proceeding of 34*th National Symposium on Disaster Prevention and the International Symposium on Earthquake-Resistant Engineering*, 20–21 of August. Lima, Peru.

Aguilar, Z., Tarazona, J., Vergaray, L., Barrantes, J. 2019. Site Response Analysis and its Comparison with the Peruvian Seismic Design Spectrum. *Journal TECNIA*. 29: 91–97.

Calderon, D., Aguilar, Z., Lazares, F., Sekiguchi, F., Nakai S. 2013. Estimation of Deep Shear-Wave Velocity Profiles in Lima, Peru, Using Seismometers Arrays. *Journal of Disaster Research*. 8:252–258

CISMID, 2014. Updated Map of Seismic Geotechnical Microzonation, Lima, Peru.

Hashash, Y.M.A., Musgrove, M.I., Harmon, J.A., Groholski, D.R., Phillips, C.A., & Park, D. 2016 DEEPSOIL 6.1, User Manual.

Kottke, A.R., Rathje, E.M. 2007. Semi-automated selection and scaling of earthquake ground motions. In proceeding of *4th International Conference on Earthquake Geotechnical Engineering*, Thessaloniki, Greece.

Meneses, J. & Alva, J.E. 1986. Determination of the Elastic Design Spectrum and the Seismic Coefficient for Lima (In Spanish). In proceeding of *6th National Congress of Civil Engineering*, Cajamarca, Peru.

Menq, F. 2003. Dynamic Properties of Sandy and Gravelly soils. Doctoral thesis. University of Texas, Austin, Texas.

Ortiz, C.E. 2019. Determination of the amplification of seismic waves of soils and seismic coefficient established in the E.030 Peruvian Code, in the city of Tacna (In Spanish). MSc Thesis. National University of Engineering, Lima, Peru.

Phillips, C. & Hashash, Y. 2009. Damping formulation for non-linear 1D-site response analyses. *Soil Dynamics and Earthquake Engineering*. 29, pp 1143–1158.

Sanchez, S., Rodriguez, J.M., López J.D., Laina, C., Jiménez A. 2016. Characterization of Coarse Granular Soils, The case of the Lima Gravel (In Spanish). In Proceeding of*10th National Symposium of Geotechnical Engineering and Spanish Society of Soil Mechanics and Geotechnical Engineering*. pp 305–312.

Silgado, E. 1978. History of the most notable earthquakes in Peru (1513-1974) (In Spanish). *Institute of Geology and Mining*, Bol 3, Serie C. Lima, Peru.

Soto, J. 2016. Assessment of Response Spectra through One-dimensional Site Response Analysis in seven districts of Lima (In Spanish). Graduated Dissertation. National University of Engineering. Lima, Peru.

Soto, J., Alva, J.E. & Ortiz, C.E. 2018. Assessment of Response Spectra through One-Dimensional Site Response in City of Lima (In Spanish). In proceeding of *21th Brazilian Congress of Soil Mechanics and Geotechnical Engineering Geotechnics and Urban Development*. Salvador, Bahia, Brasil. GJ 34877.

Soto, J. 2021. Amplification Factors in City of Lima through Site Response Analysis (In Spanish). MSc Thesis. National University of Engineering. Lima, Peru.

Soto, J. & Alva, J.E. 2022. Estimation of Deep S-Wave Velocity profile using Seismic records Case of Lima, Peru. In Proc. *Third International Conference on Geotechnical Engineering-Iraq*, 17–19 of May 2022. Paper 1035.

Zhang, J., Andrus, R., Juang. H. 2005. Normalized Shear Modulus and material Damping Ratio Relationships. *Journal of Geotechnical and Geoenvironmental Engineering*, Vol. 131, No. 4.

Smart Geotechnics for Smart Societies – Zhussupbekov, Sarsembayeva & Kaliakin (Eds)
© 2023 The Author(s), ISBN 978-1-003-29912-7
Open Access: www.taylorfrancis.com, CC BY-NC-ND 4.0 license

An experimental investigation on ejecta-induced settlement in sand with varying fines contents and densities

M.-C. Chu
Postdoctoral Fellow, Department of Civil Engineering National Chung Hsing University

C.-C. Tsai
Professor, Department of Civil Engineering National Chung Hsing University

ABSTRACT: Ground settlement may occur due to ejecta during soil liquefaction and consequently cause damages to structures and lifelines. To investigate factors that affect the settlement induced by sand boil, an experimental investigation by the special design apparatus is conducted in this study. Sandy deposit is prepared by filling in transparent acrylic cylinder with varying densities and fines contents. An acrylic circular plate, acting as a non-liquefied layer, is placed on the top of sandy deposit (specimen). Then, the cylinder is subjected to torsional shaking to produce soil liquefaction and sand boil. Soil particles are ejected out from the gap between the circular plate and cylinder and the plate starts to sink simultaneously. The thickness of ejecta can be observed from the accumulated sand particles on the plate. The influences of varying densities and fines contents on the ejecta amount as well as the settlement are quantitatively analyzed. It is found that the larger density of clean sand deposit results in smaller ejecta amount and associated settlement. However, the influence of density on the ejecta amount of sand and silt mixture is not as obvious as that of clean sand. Moreover, the ejecta contains more silt than the prepared specimen from the sieve analysis results.

Keywords: Sand Boil, Liquefaction, Settlement, Fines content, Ejecta, Density

1 INTRODUCTION

Liquefaction settlement is an important issue in geotechnical engineering, and many researches have been conducted to evaluate the liquefaction settlement. The mechanism of liquefaction settlement has been discussed by Bray & Dashti (2014) that including three types: ejecta-induced settlement, shear-induced settlement, and consolidation settlement. The ejecta-induced settlement could be more significant compared the other two. However, the ejecta-induced settlement is hard to be captured by continuum analyses (Bray & Macedo 2017). Hence, an experimental investigation by the special design apparatus is used in this study. Effects of non-liquefied thickness, gap size, overburden weight on the amount of ejecta have been investigated in the model experiment by Tsai et al. (2022). In this study, the effects of fines and densities on the ejecta amount is further evaluated.

2 TEST PROGRAM

2.1 *Test system*

The experimental apparatus in this study is presented in Figure 1. The 2500g loading system (Figure 2) is placed on the top of soils. The laser distance transducer is installed on the top to

DOI: 10.1201/9781003299127-243

measure the total settlement. The transparent acrylic cylinder is designed to observe soil response during the test and to measure the pore water pressure changes by pore water pressure transducers installed at different depths on the cylinder. The acrylic cylinder is fixed on the shaking table during tests, and acceleration is measured by accelerometer through the tests. Torsional shaking is applied to induce liquefaction. During liquefaction, soil particles are ejected out from the 2mm gap between the loading system and acrylic cylinder (Figure 2) during the test. The ejecta amount could be observed and recorded by the monitoring camera.

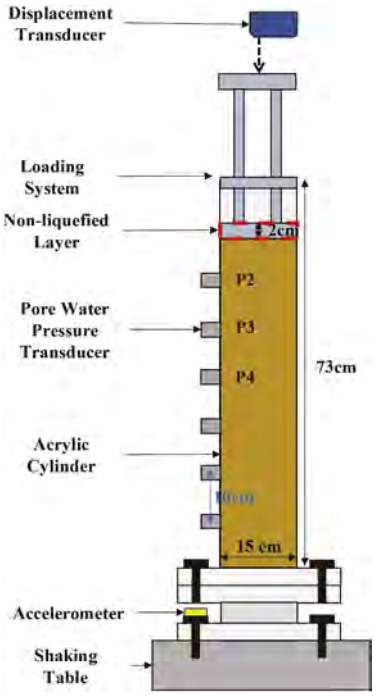

Figure 1. Testing system.

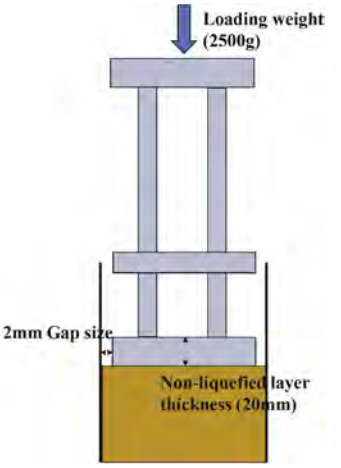

Figure 2. Loading system.

2.2 *Specimen preparation and testing procedure*

The clean sand and non-plastic silt (Figure 3) were used as the test materials in this study (Table 1). The 5% silt is added in pure sand to investigate the effect of fines on sand boils. Clean sand specimens are produced by water pluviation method which has been adopted in previous researches (Ueng et al. 2006, Tsai et al. 2022). However, water pluviation method may lead to severe segregation of coarse and fine particles in the specimens of dirty sand. On the other hand, the dry deposition method and wet tamping method may also cause non-uniformity in specimens. Therefore, a modified deposition method is proposed herein for preparing specimens with fines after Carraro & Monica (2008) with the following steps.

1. The sand is first mixed with fines in the dry condition.
2. An acrylic tube is filled with de-air water to 1/5 height of tube.
3. Mixed soil is slowly filled in tube, and water is added to until it merges the soil.
4. The rubber stoppers are installed on the rube and the tube is placed upside down for allowing air bubbles to move up toward the top of tube.
5. Extra water is added to replace the space occupied by air bubbles. Previous step could be repeated several times until no visible air bubble.

6. Plastic wrap is installed on one side of tube.
7. The tube is suspended in sedimentation apparatus, and plastic wrap is penetrated to let soils flow out the tube and deposit in the transparent acrylic cylinder.

The proposed method effectively reduces the amount of air bubbles, and improve the uniformity. A pre-test small shaking is applied to achieve the desired densities. The settlement and porewater pressure are recorded and measured through the tests.

Table 1. Basic properties of used materials.

Materials	Sand	Silt
Specific gravity of solids	2.65	2.66
Median size D_{50} (mm)	0.193	0.012
Effective size D_{10} (mm)	0.147	0.002
Coefficient of uniformity C_u	1.36	7.58
Coefficient of curvature C_d	1.1	2.07
Hydraulic conductivity k(cm/s)	0.034	0.0056
e_{max}	0.922	2.102
e_{min}	0.598	1.182

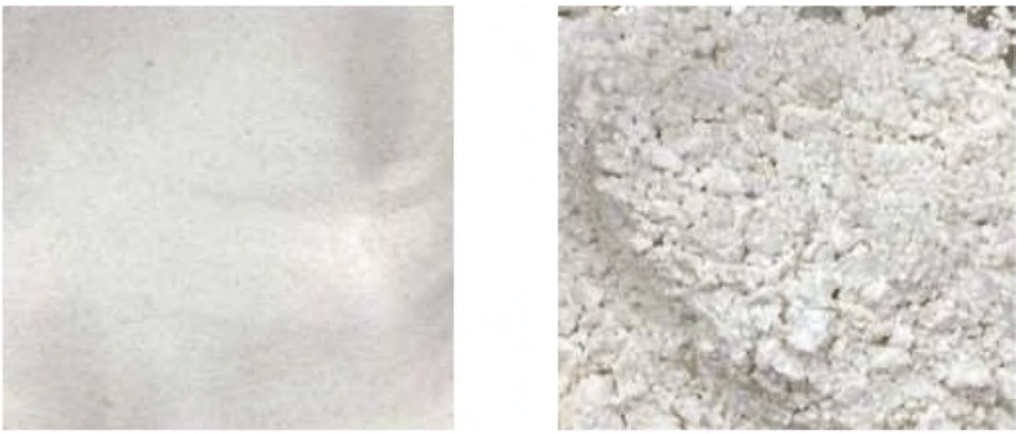

Figure 3. Photos of materials.

3 TEST RESULTS

The measured total settlement is contributed by ejecta-induced and consolidation settlement. The observed thickness of ejecta is considered as the same as the ejecta-induced settlement but is corrected to for the density difference between the ejecta and the specimen. Therefore, the consolidation settlement is estimated by the total settlement subtracting the ejecta-induced settlement.

3.1 *Density effect*

The test results on clean sand of different densities (relative densities, Drs) are collected and shown in Figure 4. As the density increases, the total settlement (Figure 4 (a)), ejecta-induced settlement (Figure 4 (b)), and consolidation settlement (Figure 4 (c)) decrease. Moreover, the total settlement is mainly contributed by the ejecta-induced settlement as the density decreases. The excess pore water pressures in tests are shown in Figure 4 (d). It could be observed that the duration of excess pore water pressure maintaining around 2kPa is longer as densities is lower.

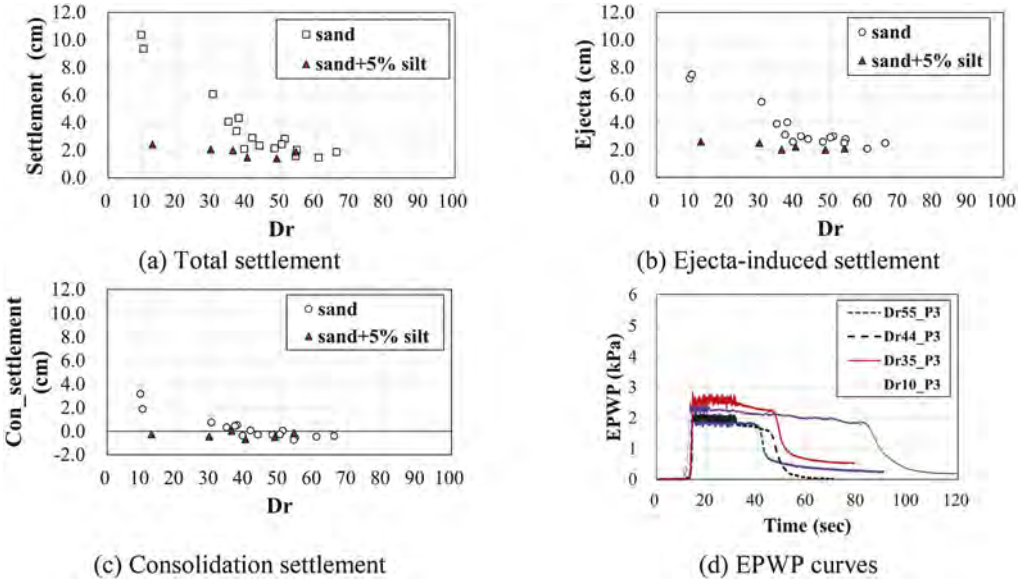

Figure 4. Test results under varying densities for clean sand and dirty sand.

3.2 *Fines effect*

Figure 4 also shows the tests results of adding fines. It could be seen that density have a more obvious influence on liquefaction settlement in clean sand than dirty sand specimens. With the similar relative density, the ejecta (Figure 4 (b)) and consolidation (Figure 4 (c)) settlement of dirty sand specimens are less than clean sand. The excess pore water pressure dissipates right after the shaking stops in the dirty sand specimen as shown in Figure 5(a). With the similar density, pore water pressure maintains (PWP time) in 2kPa is longer in the clean sand than the dirty sand. In Figure 5(b), it could be seen that the PWP time reduces with the increasing relative density. It is also found that the fines contents in ejecta is around 15% to 25%, which is higher than the fines content (5%) in designated specimens. This shows that the fines are easier to be ejected out.

Table 2. Test information.

Test Series	Test No.	e (-)	Dr (%)	Gap size (mm)	Shaking duration (s)
sand	12	0.75	54	2	20
Sand+5% silt	M2	0.71	52	2	20
	M3	0.76	40	2	20
	M5	0.73	49	2	20

4 CONDLUDING REMARKS

Through the series of test results, it is concluded that density is influential on the amount of ejecta on both clean and dirty sand specimens. As density increase, the total settlement, ejecta-induced settlement, and consolidation settlement are reduced. However, the influence is more obvious in clean sand than dirty sand. On the other hand, the excess pore water pressure dissipates right after the shaking stops in the dirty sand specimen. The PWP time reduces as the density increases, which is more profound in the clean sand than the dirty sand specimens.

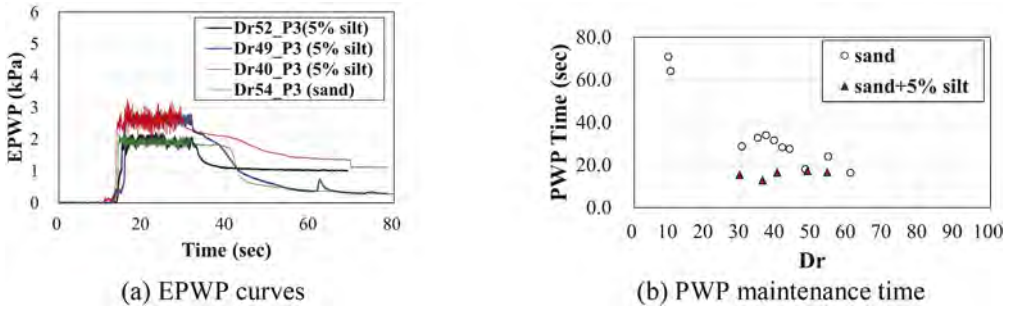

Figure 5. Test result of adding fines specimens.

REFFERENCES

Bray, J. D., & Dashti, S. (2014). Liquefaction-induced building movements. Bulletin of Earthquake Engineering, 12(3), 1129–1156. doi:10.1007/s10518-014-9619-8

Bray, J. D., & Macedo, J. (2017). 6th Ishihara lecture: Simplified procedure for estimating liquefaction-induced building settlement. Soil Dynamics and Earthquake Engineering, 102, 215–231.

Carraro, J. A. H., & Prezzi, M. (2008). A New Slurry-Based Method of Preparation of Specimens of Sand Containing Fines. Geotechnical Testing Journal, 31, 1–11.

Tsai, C.-C., Lin, W.-C., Chu, M.-C., & Chi, C.-C. (2022). Experimental study on the mechanism of sand boils and associated settlements due to soil liquefaction in loose sand. Engineering Geology, 306, 106708.

Ueng, T.-S., Chen, C.-H., Chen, H.-W. & Wu, C.-W. 2006. Large-Scale Shear Box Soil Liquefaction Tests on Shaking Table (III) - Settlement of Saturated Vietnam Sand Specimen in Shaking. National Center for Research on Earthquake Engineering.

Smart Geotechnics for Smart Societies – Zhussupbekov, Sarsembayeva & Kaliakin (Eds)
© 2023 The Author(s), ISBN 978-1-003-29912-7
Open Access: www.taylorfrancis.com, CC BY-NC-ND 4.0 license

Propose of design method about seismic reinforcement of embankment using soil nails and slope protection works

T. Matsumaru & S. Nakajima
Railway Technical Research Institute, Tokyo, Japan

ABSTRACT: In recent years, reinforcements of railway embankments have been conducted for increasing the seismic resistance and reinforcements using soil nails are adopted. At the slope of the embankment, slope protection works are often constructed and can also contribute to the increase of seismic performance by connection with soil nails. However, this effect has not been studied clearly. In this paper, the effects were studied through the series of shaking table tests and the calculation method with consideration of the effect was developed and validated.

1 INTRODUCTION

In recent years, severe earthquakes have often occurred, and a lot of railway earth structures collapsed (Koseki et al. 2012). Therefore, increasing seismic resistance of earth structures is important so the reinforcements of the earth structures have been conducted positively. Furthermore, the new methods of reinforcements have been established (Nakajima et al. 2021). The methods of reinforcements aimed to embankments are selected according to the prediction of their failure modes and calculations of residual settlements. In the case where the reinforcement of the embankment body is required, the reinforcement method of installing soil nails in embankment is often selected. This method has been validated from series of tests and been used in business practices with the establish of its design (Railway Technical Research Institute 2007).

On the other hands, the slope protection works on the surface of slope of embankments are often constructed in Japan for increasing resistance to severe rainfall (Matsumaru and Sato 2018) and realizing economical maintenance of slopes. When the soil nails are constructed at existing embankments with slope protection works, the top of the soil nails are often connected with the works. In this case, the soil nails will work as group and can show larger effect of reinforcement. However, the mechanism about the effect of the soil nails and the slope protection works on seismicity has not been studied and the design method has not been established.

In this paper, the series of shaking table tests of embankments with soil nails were conducted, to clarify the effect of slope protection works for the increase of seismic resistance. Then, the method considering this effect in predicting the residual displacement of embankment was developed. Finally, the validation of the proposed method was examined through the simulation analysis of shaking table tests.

2 SHAKING TABLE TESTS OF EMBANKMENT

2.1 *Test conditions*

Figure 1 Shows the illustrations of the experimental model of embankment and the slope protection works for three cases used in the shaking table tests. The dimension of the embankment was 60 cm in height and 1: 1.2 in gradient of the slope. For all cases, four soil nails with 50 cm in length were used arranged as shown in Figure 1. We conducted three cases of tests under the presence/absence or kind of the slope protection work. In Case 1, any slope protection work was not used, and the top of the soil nails were fixed with the bearing plate. In Case 2, the lattice rigid

DOI: 10.1201/9781003299127-244

frame was adopted. The tops of the nails were connected with the intersections of the frame work. Thought the region surrounded by the frame was opened, the surface of the slope was in contact with the frame. In Case 3, the small frame for keeping the distances between soil nails was used. The frame did not touch the surface of the surface of the slope so there was no effect of the small frame on retaining earth pressure of slope.

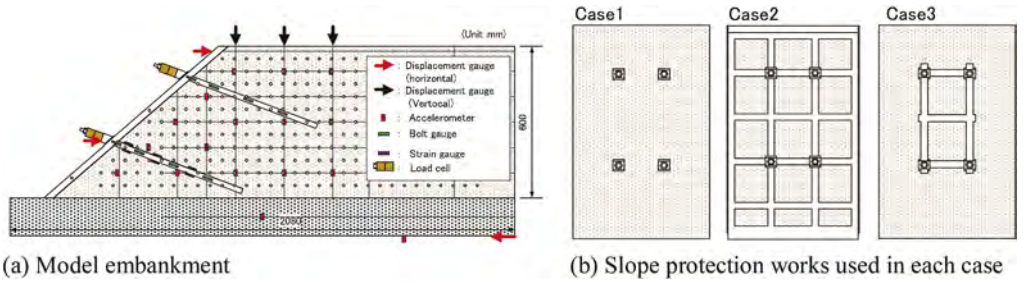

Figure 1. Model embankment and cases about presence/absence or kinds of slope protection works.

The material of the embankment was Inagi sand, whose particle density G_s was 2.723; 50% diameter on the grain size diagram D_{50}, 0.134mm; the uniformity coefficient U_c, 9.29; the fine fraction content F_c, 9.7 %; and the maximum dry density, 1.517 g/cm^3. The embankment was prepared so that the dry density and the water content would be 1.335 g/cm^3 and about 13% respectively. The ground was constructed using crushed stone for mechanical stabilization.

The measurement included acceleration, horizontal and lateral displacement at the top and the surface of the embankment, and the tensile force and the strain of soil nails for making dynamic behavior of the embankment clear. Furthermore, we photographed reference points in the embankment with a high-speed camera and analyzed the obtained data to estimate a deformation mode of the embankment. For the input motion, a sinusoidal wave of 5 Hz was used. For both the cases, the shaking table test was continued with gradual increase of the amplitude of acceleration until the embankment collapsed.

2.2 *Results and discussions*

Figure 2 Shows the relationship between the inputted acceleration and the residual vertical displacement at the shoulder of the embankment. In Case 1, the residual displacement occurred at the shaking of 700 gal and increased rapidly. In Case 3, the displacement occurred at the shaking of 800 gal, which showed similar tendency to Case 1. Even if the distance between soil nails was kept, the seismic resistance of the embankment was not largely improved. Compared to these two cases, the displacement of Case 3 showed smaller gradient of the increment against to the amount of the inputted motion. It is possible to understand that the seismic resistance was improved by soil nails with slope protection work using the lattice frame.

Figure 3 Shows the relationship between the inputted acceleration and the tensile force of the soil nail located at the lower part. In Case 1 and Case 3, the tensile forces gradually increased by increasing the amount of the inputted motion, but the value was still small after the deformation of the embankment occurred. On the other hand, the force showed larger value from the start of the shaking of Case 2. The soil nails became more effective by use with the lattice frame.

In order to clarify the mechanism of the increase of the tensile force of soil nails with the lattice frame, Figure 4 shows the enlarged time histories of the tensile force of the soil nails and displacements of the marked points at the lattice frame and the embankment close to the surface of the embankment in Case 2. When the embankment moved to the anterior direction, the tensile force increased. Focused on the time histories of displacements, it is possible to understand that the amount of displacement at each point is different. The displacements of the embankment were larger than those of the lattice frame. This tendency is remarkable at the points to close to the surface of the slope. This means that the embankment pushed the lattice frame affected by the inputted motion.

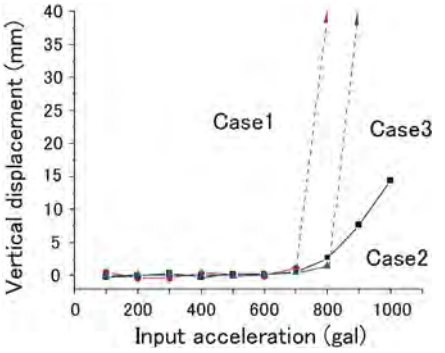

Figure 2. Residual displacement for three cases.

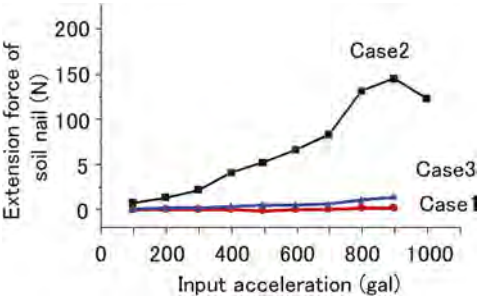

Figure 3. Extension force of soil nail for three cases.

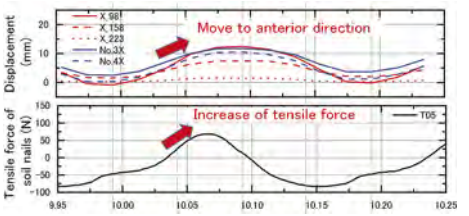

Figure 4. Time histories of extensile force and displacements.

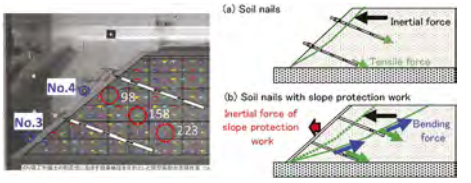

Figure 5. Effect of slope protection work.

Figure 5 Shows the illustration of the mechanism of the increase of seismic resistance by using the lattice frame. In Case 1 and 3, when the inertial force caused by the inputted motion exceeds the resistance force of the embankment at the slip surface, the embankment collapses. On the other hands, in the conditions where the tops of the soil nails are connected and the surface of the slope has contact with the slop protection work as the experiment of Case 2, the slip surface moved to deeper area and the combination of the soil nails and the slope protection work prevents from the occurrence of the severe collapse of the embankment due to the increase of the tensile force. Furthermore, the experimental results from the strain gauges showed that the soil nails were deformed with showing bending mode, so the soil nails demonstrated not only extension resistance but also bending resistance.

3 DESIGN METHOD OF SEISMIC REINFORCEMENT CONSIDERING EFFECT OF SLOPE PROTETION WORKS

3.1 *Proposed method*

For the evaluation of the seismic resistance of the embankment, the Newmark's sliding method (Newmark 1965) is adopted for the calculation of the residual displacement and the calculated displacement is examined by comparing with the limited value. This method is adopted for the design of railway earth structure (Railway Technical Research Institute 2007). In this method, the reinforcement effect of the soil nails is considered as the resistance force. Based on the results of the shaking table tests, the effect of the soil nails with slope protection works will be considered as shown Figure 6. As mentioned in the previous discussion, the bending resistance of soil nails were demonstrated, so this resistance is added in Newmark's method. The total value of bending resistance is considered as the increment of the resistance moment M_{RT} by using the displacement of circular slip and the ground reaction force R_g under the rigid part, as shown in Figure 6 (a), expressed by the following equation.

$$M_{RT} = \Sigma R_g \cdot r \tag{1}$$

Where r is the radius of the circular slip. Therefore, this effect is considered as increase of yield seismic intensity in Figure 6 (b). In the existing Newmark's method, the yield seismic intensity is constant. However, in the proposed method, it is possible that the intensity increases according to the displacement of soil nails, due to the increase of the moment M_{RT}.

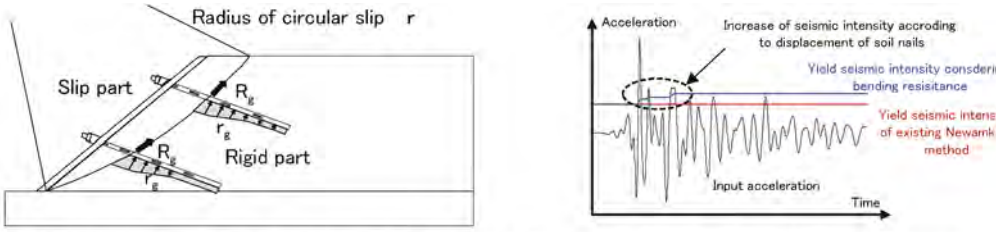

(a) Resistance by soil nails and slope protection works (b) Increase of yield seismic intensity

Figure 6. Calculation method of residual displacement considering effect of slope protection works.

3.2 *Validation of proposed method*

By using the proposed method, the simulation analysis of shaking table was conducted. Figure 7 shows the relationship between the inputted acceleration and the residual displacement obtained by the experiment and the simulations of Case 2. The calculated result using existing Newmark's method overestimated the residual displacement obtained by the experiment. The existing method has difficulty for the case of use of the slope protection work and the tendency is similar to the experimental results for Case 1 and 3 as shown in Figure 2. On the other hands, the calculated result became largely smaller than the existing method and showed good agreement with the experimental result. So, the proposed method was validated.

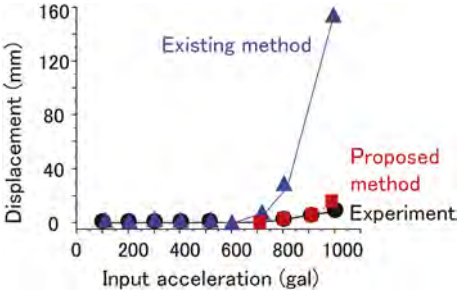

Figure 7. Calculated residual displacement of shaking table test of Case 2.

4 CONCLUSIONS

In this paper, the mechanism of the increase of seismic resistance about embankments reinforced by soil nails with slope protection works were studied. From the series of shaking table tests, it is revealed that connecting the top of soil nails with slope protection works and retaining the slope surface by the slope protection works contribute to the increase of seismicity. Furthermore, the method for calculating the residual settlement of embankments was developed by the modification of Newmark's method. The proposed method showed good agreement with the residual displacements obtained by the shaking table tests so the validation was confirmed.

REFERENCES

Koseki, J., Koda, M., Matsuo, S., Takasaki, H. & Fujiwara, T. 2012. Damage to railway earth structures and foundations caused by the 2011 off the Pacific Coast of Tohoku Earthquake, *Soils and Foundations* 52(5): 872–889.

Matsumaru, T. & Sato, T. 2018. Field measurement about water content in embankment covered by slope protection works, *Japanese Geotechnical Society Special Publication*, 7(2): 501–504.

Nakajima, S., Sanagawa, T., Matsumaru, T. & Koda, M. 2021. Recent research development and their applications on aseismic reinforcement of existing railway earth structures, *Soils and Foundations* 62(1): 1–27.

Newmark, N.M. 1965. Effects of earthquakes on dams and embankments, *Geotechnique* 15(2): 139–159.

Railway Technical Research Institute 2007. *Design Standard of Railway Structure -Earth Structure-*, Maruzen ed. (in Japanese)

Smart Geotechnics for Smart Societies – Zhussupbekov, Sarsembayeva & Kaliakin (Eds)
© 2023 The Author(s), ISBN 978-1-003-29912-7
Open Access: www.taylorfrancis.com, CC BY-NC-ND 4.0 license

Deep neural network based approach for site amplification prediction of shallow bedrock sites

Yonggook Lee, Dongyeon Lee, Jieun Kang & Duhee Park
Department of Civil and Environmental Engineering, Hanyang University, Seoul, Korea

ABSTRACT: Site amplification models have been proposed based on the empirical and simulation results and represented by the functional form with regression analysis. However, these regression models result in large differences between the results. In this study, a new site amplification model is developed by using a deep neural network (DNN) to reduce the uncertainties in site amplification predictions. The results of the linear and nonlinear site response analyses are used to train and test the model. The results of the DNN-based model are compared with those of the regression model. The DNN-based model outperforms the regression model and shows lower residuals throughout spectral periods. The DNN model can replace the regression models and reduce the uncertainties caused by simple prediction models.

1 INTRODUCTION

Predicting the local site amplification is important to design the geotechnical structures during earthquakes. One-dimensional (1D) site response analysis (SRA) has been widely performed to estimate the site amplification factors (Hashash and Park, 2001). Site amplification models have been developed and used to predict ground motion intensity measures with ground motion prediction equations (GMPEs). The 1D SRA results were performed and used to develop the site amplification models with respect to the time-averaged shear wave velocity (V_S) of the top 30 m (V_{S30}), depth to bedrock (H), site period (T_G), and other site proxies (Kamatchi et al. 2010; Derras et al. 2014; Ilhan et al. 2019, Aaqib et al. 2021). Monte Carlo (MC) simulations were also utilized to deal with a large suite of data. The site amplification models were proposed by regression analyses. However, the regression-based amplification models showed significant differences. In this study, both linear and nonlinear 1D SRA were performed and all the simulation results were used to train a deep neural network (DNN) model.

2 SITE AMPLIFICATION PREDICTION MODELS

2.1 *Site response analysis*

Linear and nonlinear analyses were performed in frequency and time domains, respectively, using 1D site response analysis software DEEPSOIL v7 [Hashash et al. 2017]. Because of the insufficient number of V_S profiles, forty baseline V_S profiles were used and twenty randomized profiles were generated by using the model of Toro (1995). The input ground motions were selected from the NGA-West2 database. The magnitude (M_w), rupture distance (R_{rup}), and peak ground acceleration of the rock outcrop motions (PGA_{rock}) range from 5 to 7.5, 0 to 100 km, and 0.01 to 0.5 g. The number of V_S profiles and recorded ground motions are 840 and 51, respectively (Figure 1). The 42,840 cases were performed for linear and nonlinear analyses, respectively. The results were used to train the proposed DNN model.

DOI: 10.1201/9781003299127-245

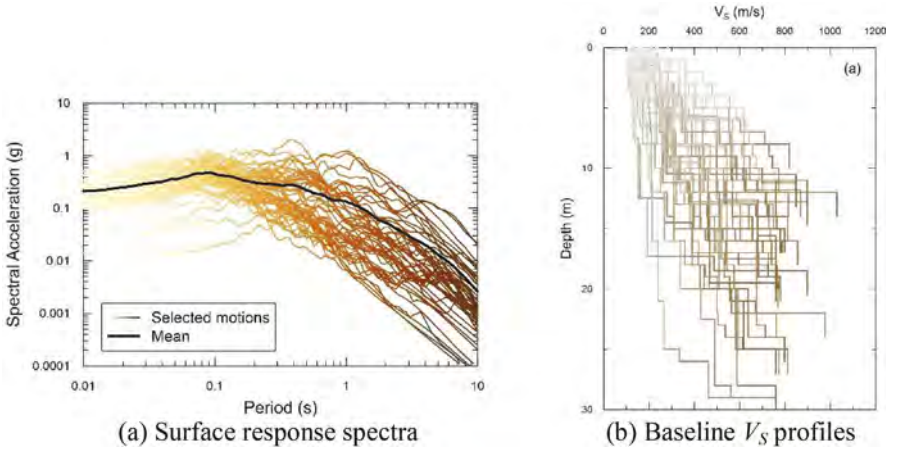

Figure 1. Input surface response spectra and V_S profiles.

2.2 *Proposed deep neural network model*

The response spectra of bedrock were used as the input features of DNN model. The thickness, V_S, unit weight, and damping ratio were also selected as input features to represent soil characteristics (Figure 2). Four hidden layers were used to extract the features of input data for the input ground motions and soil profiles, respectively. The features were concatenated and connected to four fully-connected hidden layers. The surface spectral accelerations of a 113×1 vector were labeled as output data. In all hidden layers, the rectified linear unit (ReLU) was used as an activation function (Nair & Hinton 2010). For the initialization of the model, the weights and biases were initialized by Glorot uniform initializer (Glorot & Bengio 2010) and zero, respectively. The Adam optimizer (Kingma & Adam 2015) was used as an optimization algorithm used in this study. A loss function is defined by a mean squared error (MSE). The batch size was 256 and the learning rate was selected as 0.005. The whole dataset was split into 80% of the dataset as a training set and 20% dataset as a test set.

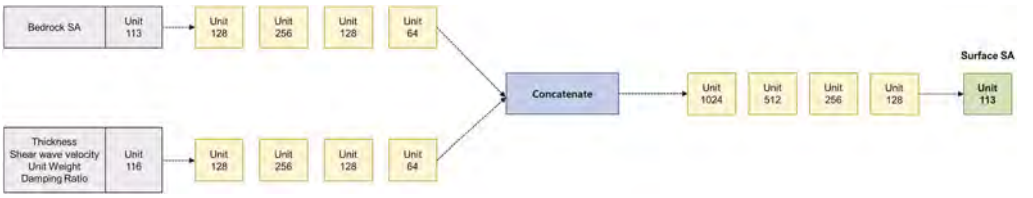

Figure 2. Proposed deep neural network.

3 RESULTS

The calculated MSE and mean absolute error (MAE) are shown in Table 1. The differences in MSE show that the proposed DNN model does not overfit. Figures 3, 4 illustrate the comparison of linear and nonlinear amplification components. The trained DNN model can predict well with the test data. To compare the results of a conventional method, a regression-based site amplification model by Aaqib et al. (2021), AEA21 model, was compared with the proposed DNN model. Because of the use of site proxies, the AEA21 model only can predict the median trends for the spectral periods. The DNN model shows exceptional performance in predicting both linear and nonlinear site amplifications.

Table 1. Comparison of MSE and MAE between train and test dataset.

Analysis	Dataset	MSE	MAE
Linear	Training	0.00056	0.01666
	Test	0.00069	0.01788
Nonlinear	Training	0.00096	0.02135
	Test	0.00131	0.02392

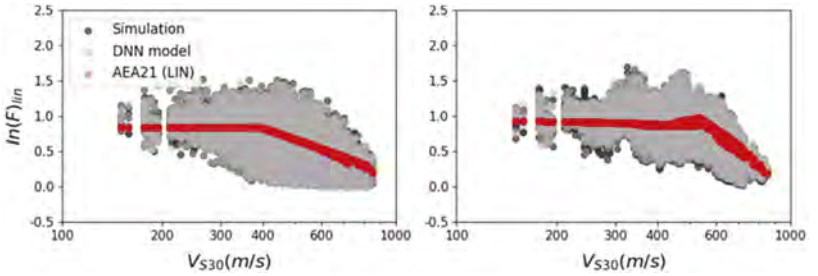

Figure 3. Comparison of linear amplifications for the spectral periods of 0.01 s (left) and 0.1 s (right).

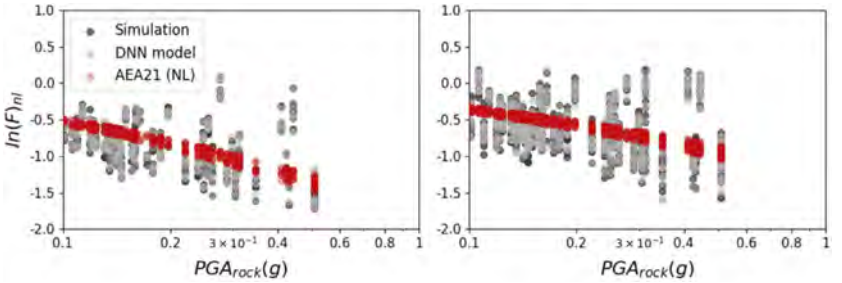

Figure 4. Comparison of nonlinear amplifications for V_S from 200 to 250 m/s (left) and V_S from 300 to 350 m/s (right) at spectral period 0.01 s.

4 CONCLUSION

In this study, site response analyses were performed to predict the site amplifications for the shallow bedrock profiles. The DNN-based model was used to train and test the site response analysis data instead of using the regression-based model. The DNN-based model can use extensive raw data excluding the use of site proxies. The 85,680 pairs of input and result data were used directly. And the database was divided into 80 and 20 % for training and test sets, respectively. As a result, the DNN-based model shows remarkable performance in reproducing the surface response spectra. The proposed DNN-based model can overcome the limitation of the regression-based model, which is caused by the use of site proxies. Future studies will be conducted by using a wide range of site characteristics as well as ground motions.

REFERENCES

Aaqib, M., Park, D., Adeel, M. B., Hashash, Y. M., & Ilhan, O. (2021). Simulation-based site amplification model for shallow bedrock sites in Korea. Earthquake Spectra, 37(3),1900–1930.

Derras, B., Bard, P. Y., & Cotton, F. (2014). Towards fully data driven ground-motion prediction models for Europe. Bulletin of Earthquake Engineering, 12(1), 495–516.
Glorot, X., & Bengio, Y. (2010). Understanding the difficulty of training deep feedforward neural networks. In Proceedings of the thirteenth international conference on artificial intelligence and statistics, 249–256, JMLR Workshop and Conference Proceedings.
Hashash Y, Musgrove M, Harmon J, et al. (2017). DEEPSOIL 7.0, user manual. University of Illinois at Urbana-Champaign.
Hashash, Y. M., & Park, D. (2001). Non-linear one-dimensional seismic ground motion propagation in the Mississippi embayment. Engineering Geology, 62(1-3), 185–206.
Ilhan, O., Harmon, J. A., Numanoglu, O. A., & Hashash, Y. M. (2019). Deep learning-based site amplification models for Central and Eastern North America. In Earthquake Geotechnical Engineering for Protection and Development of Environment and Constructions, 2980–2987, CRC Press.
Kamatchi, P., Rajasankar, J., Ramana, G. V., & Nagpal, A. K. (2010). A neural network based methodology to predict site-specific spectral acceleration values. Earthquake Engineering and Engineering Vibration, 9(4), 459–472.
Kingma D.P., & Adam, J.B. (2014). A method for stochastic optimization. arXiv:1412.6980.
Nair, V., & Hinton, G. E. (2010). Rectified linear units improve restricted boltzmann machines. In Icml.

Smart Geotechnics for Smart Societies – Zhussupbekov, Sarsembayeva & Kaliakin (Eds)
© 2023 The Author(s), ISBN 978-1-003-29912-7
Open Access: www.taylorfrancis.com, CC BY-NC-ND 4.0 license

A comparative study of liquefaction simulations with two cyclic constitutive models

K.T. Yap, F.H. Yeh & Y.S. Jhuo
National Taiwan University, Taiwan

C.C. Tsai
National Chung Hsing University, Taiwan

C.W. Lu
National Taiwan University of Science and Technology, Taiwan

L. Ge
National Taiwan University, Taiwan

ABSTRACT: Taiwan is located at the junction of the Philippine Sea Plate and the Eurasia Plate, where earthquakes occur frequently. Soil liquefaction has often been observed during an earthquake, and the associated settlement and lateral spreading usually lead to structural damage and property loss. In this study, numerical analyses were carried out to mimic a dynamic centrifuge model test and examine liquefaction behavior due to seismic shaking. The numerical simulations were performed using two cyclic constitutive models. The constitutive modes were first calibrated against laboratory element test results. A comparison was made to evaluate the effectiveness of these two models used in the finite element analyses.

1 INTRODUCTION

Numerical simulation is often used in geotechnical engineering analysis and design, including modeling complex soil behaviors due to liquefaction. Liquefaction Experiments and Analysis Projects (LEAP) is an international collaboration on producing a series of reliable experimental data for constitutive model calibration and numerical modeling techniques for analysis and assessment of soil liquefaction. In this study, one dynamic centrifuge model test in the LEAP-2017 project (Kutter, 2017) was chosen for numerical analyses to investigate soil liquefaction under slight sloping surfaces due to seismic shaking, where the specimen model is a 4-meter thick Ottawa F-65 sand with a surface slope of 5 degrees in a rigid box.

The study aims to verify two constitutive models (UBC3D-PLM and PM4Sand) in predicting centrifuge model test results. Firstly, model parameters and constants for both constitutive models were calibrated individually by fitting the experimental data of the cyclic direct shear tests, including shear stress versus shear strain, shear stress versus mean effective stress, mean effective stress versus shear strain, and excess pore pressure ratio versus the number of cycles. The calibrated parameters and constants were then used for numerical analyses in PLAXIS, which were applied to mimic a dynamic centrifuge model test and examine the liquefaction behavior due to seismic shaking.

2 CONSTITUTIVE MODEL

2.1 *Introduction*

There are 13 and 15 parameters (including primary and secondary) in the constitutive models of PM4Sand and UBC3D-PLM, respectively. The material properties with physical meanings

DOI: 10.1201/9781003299127-246

include the critical friction angle and elastic moduli, where the critical friction angle of φ_{cv} is 33° for both models. According to the relationship between elastic moduli, the parameters PM4Sand (G_0) of and UBC3D-PLM (K_G^e & K_B^e) can be determined by

$$G = \frac{E}{2(1+\upsilon)} \tag{1}$$

$$G = K\frac{3(1-2\nu)}{2(1+\upsilon)} \tag{2}$$

where the elastic modulus (Young's modulus E) for granular material (Dr=72.6% of dense sand was considered in this study) is about 70 MPa based on Obrzud & Truty (2012), and the Poisson's ratio (υ) was taken as 0.3. The other parameters for both models are calibrated using the best fits from cyclic direct shear tests. These tests were carried out at an initial confining pressure of 100 kPa with 8 cyclic stress ratios (CSR = 0.075, 0.085, 0.095, 0.105, 0.12, 0.125, 0.13, and 0.15), were taken from the LEAP-2017 Project. The calibrated model parameter sets of the PM4Sand and UBC3D-PLM model are presented in Table 1 and Table 2.

2.2 *PM4Sand model*

PM4Sand model can successfully simulate the behavior of sand under dynamic loading, pore pressure variation, liquefaction, and post-liquefaction phenomena. This model was extended by Dafalias & Manzari (2004), incorporating stress ratio control, critical state compatibility, and bounding surface plasticity. PM4Sand version 3.1, developed by Boulanger & Ziotopoulou (2017), has been implemented in PLAXIS2D. The elastic response is described by the elastic shear moduli as given by:

$$\mathrm{G} = G_0 p_A \sqrt{\frac{p}{p_A}} \tag{3}$$

where G_0 is the shear modulus coefficient, p_A is the atmospheric pressure, and p is the mean effective stress. A detailed description of the default values of the primary and secondary parameters of PM4Sand can be found in Boulanger & Ziotopoulou (2017).

2.3 *UBC3D-PLM model*

The UBC3D-PLM model is developed by Tsegaye (2010) for the liquefaction behavior of sand under seismic loading, which is an improvement on the UBCSAND model. UBCSAND was developed by Puebla et al. (1997) and Beaty & Byrne (1998) and is one of the advanced constitutive models commonly used to evaluate liquefaction problems. The UBC3D-PLM model has been successfully implemented in PLAXIS (Petalas & Galavi 2013).

The UBC3D-PLM model involves two yield surfaces (principal stress pace for primary loading and simplified kinematic hardening rule for secondary loading) using the Mohr-Coulomb yield functions. The elastic response is described by the shear and bulk moduli given by:

$$G = K_G^e p_A \left(\frac{p}{p_A}\right)^{ne} \tag{4}$$

$$K = K_B^e p_A \left(\frac{p}{p_A}\right)^{me} \tag{5}$$

where K_G^e and K_B^e are the factors of elastic shear and bulk moduli, respectively, p_A is the atmospheric pressure, p is the mean effective stress, and me and ne are rates of stress-dependency of elastic modulus. A detailed description of the default values of the primary and secondary parameters of UBC3D-PLM can be found in Petalas & Galavi (2012).

2.4 *Inspection of element tests*

Figure 1 shows the respective numerical simulations for both models compared to the experimental data in different spaces: shear stress vs. shear strain, shear stress vs. mean effective stress, mean effective stress vs. shear strain, and excess pore pressure ratio vs. the number of cycles. The simulations using the same set of parameters for each constitutive model in the simulations of cyclic resistance curves are shown in Figure 2. Both models demonstrate good agreements against laboratory element test results.

Table 1. Calibrated PM4Sand parameters.

D_r (%)	G_0 (-)	h_{p0} (-)	p_A (kPa)	e_{max} (-)	e_{min} (-)	n_b (-)	n_d (-)
72.6	270	0.0022	100	0.7389	0.4915	0.4	0.1
φ_{cv} (°)	υ (-)	Q (-)	R (-)	PostShake (-)			
33	0.3	10	1.5	0			

Table 2. Calibrated UBC3D-PLM parameters.

K_B^e (-)	K_G^e (-)	K_G^p (-)	p_A (kPa)	me (-)	ne (-)	np (-)	φ_{cv} (°)
580	270	310	100	0.5	0.5	0.4	33
φ_p (°)	R_f (-)	f_{dens} (-)	f_{post} (-)	$(N_1)_{60}$ (-)	c (kPa)	σ_t (kPa)	
34	0.9	1	0.3	23.43	0	0	

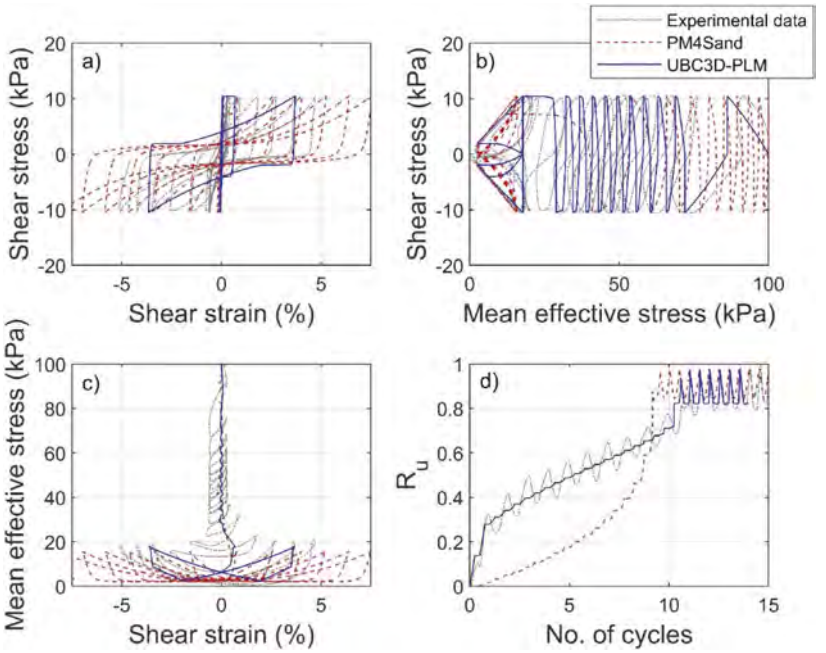

Figure 1. Comparison between cyclic direct simple shear test data and predictions using PM4Sand and UBC3D-PLM with the initial relative density D_r = 72.6%, CSR = 0.105, and σ'_{v0} = 100 kPa: (a) Shear stress versus shear strain; (b) Shear stress versus mean effective stress; (c) Mean effective stress versus shear strain; (d) Pore pressure ratio versus number of cycles.

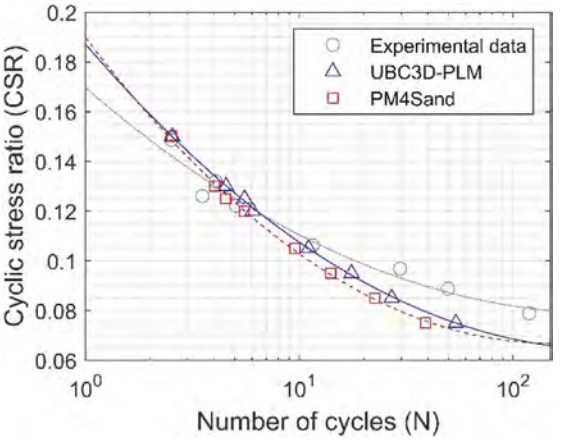

Figure 2. Cyclic liquefaction resistance curves.

3 NUMERICAL ANALYSIS

3.1 *Model mesh and boundary conditions*

Figure 3 shows the configuration of the centrifuge test and the instrumentation layout. The deformation boundary in the static phase was set up to (a) fully fix (in the X and Y direction) at the bottom, and (b) X direction was fixed for both vertical sides. The dynamic boundaries, in Figure 4, were assigned as a compliant base at the bottom of the model. Free-field boundaries were used on both sides of the model to minimize the seismic reflection. According to the study by Vilhar et al. (2018), when the PM4Sand model is used in PLAXIS, it is recommended to add drainage zones with the free-field boundary on both sides, as shown in Figure 4b.

The initial geostatic stress was calculated in the first stage by the gravity loading procedure. In the second stage, the acceleration history was added to the bottom of the model and simulated using dynamic calculations type.

3.2 *Comparison between simulation and experimental result*

According to sections 2.2 and 2.3, two constitutive models are used for the numerical analyses of a dynamic centrifuge test. This study compares horizontal accelerations and pore pressures at the specified positions (i.e. the accelerometers of AH4, AH6, and AH10 and the piezometers of P2, P5, and P7, as shown in Figure 3 and Figure 4). Despite the fact that the position of the measuring points may not be 100% the same between simulations and tests, the differences are negligible.

In Figure 5 and Figure 6, the horizontal acceleration results show that the PM4Sand produced more oscillated acceleration than the UBC3D-PLM in some periods. In addition, in Figure 7, it can be seen that the PM4sand has a better pore water pressure prediction for the experimental results of P2 and P5 compared with the UBC3D-PLM. However, by evaluating the effectiveness of these two models in the results of acceleration and pore water pressures, both models can mimic the dynamic centrifuge test well.

4 CONCLUSION

PM4Sand and UBC3D-PLM are used separately in the finite element simulation of a centrifuge model test. The model parameters of PM4Sand and UBC3D-PLM models are firstly calibrated by cyclic direct shear tests with different CSRs. It can be seen that the PM4Sand model can perform softening behavior much better than the UBC3D-PLM after the number of cycles. It can also been seen that by checking the first few loops in the hysteresis plot, the UBC3D-PLM model always shows a high stiffness before the soil is liquefied. In the

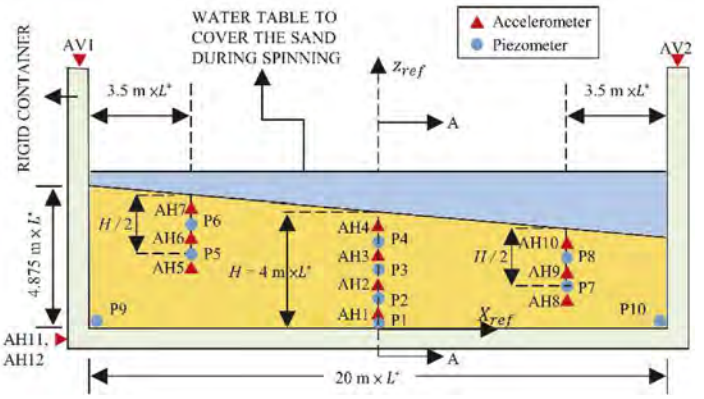

Figure 3. Configuration of centrifuge test and instrumentation layout (redrawn after Kutter et al. 2019).

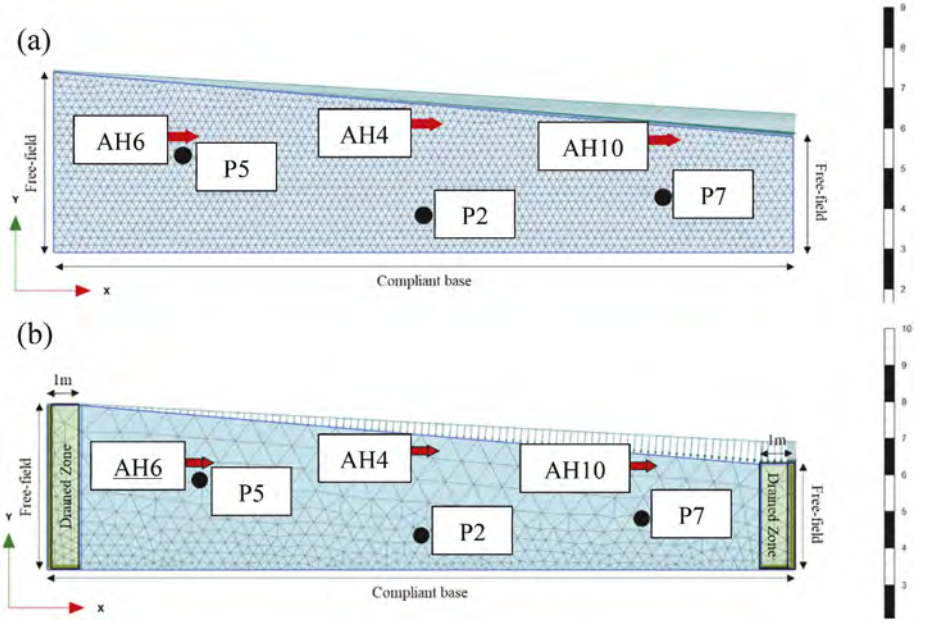

Figure 4. Numerical models in PLAXIS: (a) UBC3D-PLM; (b) PM4Sand.

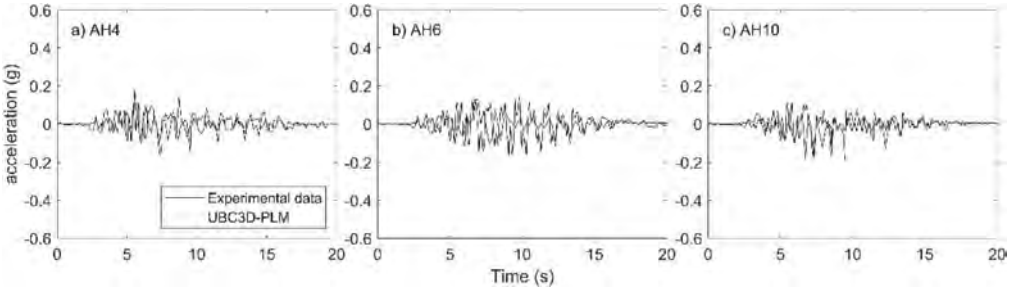

Figure 5. Acceleration versus time for three accelerometers of AH4, AH6, and AH10 (UBC3D-PLM).

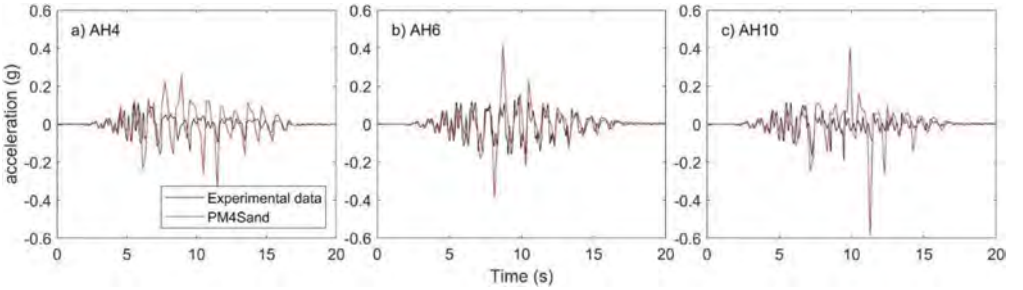

Figure 6. Acceleration versus time for three accelerators of AH4, AH6, and AH10 (PM4Sand).

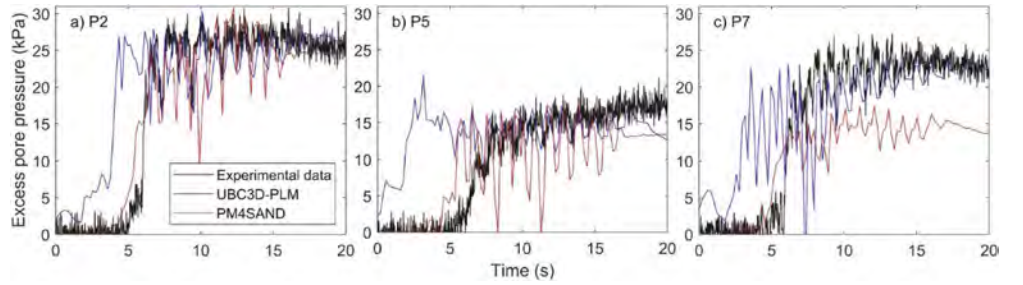

Figure 7. Excess pore pressure versus time for three piezometers of P2, P5, and P7.

simulation of the shear stress-shear strain curve, it was observed that the PM4Sand model simulates the stress-strain curve more effectively than the UBC3D-PLM model.

It is noted that the initial geostatic stress could be inaccurate when using the UBC3D-PLM and PM4Sand models under the gravity turn-on phase in PLAXIS. It is advised to use another soil model (Mohr-Coulomb herein) for the initial geostatic stress calculation. In the inspection of the centrifuge test, both constitutive models can capture the behavior of the centrifuge tests very well and achieve good agreement in the simulation of soil liquefaction. However, it can be observed from the results of pore water pressure that PM4Sand is more suitable for predicting pore water pressure than the UBC3D-PLM model. A comparison of displacement versus time in the centrifuge test is not inspected due to the lack of data from existing laboratory data. To further understand these two constitutive models, future investigation can be focused on predicting displacement and dissipation of pore water pressure for post-liquefaction.

REFRENCES

Boulanger, R.W., Ziotopoulou, K. 2017. PM4Sand (version 3.1 Revised Jully 2018): A sand plasticity model for earthquake engineering applications. *Report No. UCD/CGM-17/01*, Center for Geotechnical Modeling, Department of Civil and Environmental Engineering, University of California, Davis, CA, USA

Kutter, B., Trevor J.C, & Stone, N. 2019. LEAP-UCD-2017 Comparison of Centrifuge Test Results. In B. Kutter et al. (Eds.), Model tests and numerical simulations of liquefaction and lateral spreading: *LEAP-UCD-2017*. New York: Springer.

Dafalias, Y.F., Manzari, M.T. 2004. Simple plasticity sand model accounting for fabric change effects. *Journal of Engineering Mechanics*, 130(6), 622–634.

Beaty, M., Brne, P. 1998. An effective stress model for predicting liquefaction behavior of sand. *Geotechnical Earthquake Engineering and Soil Dynamics III ASCE Geotechnical Special Publication No*.75, 1:766–777.

Beaty, M., Brne, P. 2011. Ubcsan constitutive model version 904ar. *Itasca UDM Web Site*, page 69.

Petalas, A., Galavi, V. 2013. PLAXIS liquefaction model ubc3d-plm. *PLAXIS knowledge base*.

Puebla, H., Byrne, M., & Phillips, P. 1997 Analysis of canlex liquefaction embankments prototype and centrifuge models. *Canadian Geotechnical Journal*, 34:641–657.

Obrzud R., Truty, A. 2012. The hardening soil model – *A practical guidebook soil*. Zace Services.

Tsegaye, A. 2011.PLAXIS liquefaction model. *Report no. 1. PLAXIS knowledge base*.

Vilhar G, Brinkgreve RBJ, Zampich L. 2018. The PM4Sand model 2018. Plaxis BV, Delft, the Netherlands.

Smart Geotechnics for Smart Societies – Zhussupbekov, Sarsembayeva & Kaliakin (Eds)
© 2023 The Author(s), ISBN 978-1-003-29912-7
Open Access: www.taylorfrancis.com, CC BY-NC-ND 4.0 license

Evaluation of DSM-soil interaction effect on the liquefaction remediation of loose soil layers using numerical simulations

S. Shakeri talarposhti
Ph.D. candidate, Iran University of Science and Technology, Tehran, Iran

A.A. Khodaei Ardabili
Ph.D. candidate, K.N. Toosi University of Technology, Tehran, Iran

M. Aghamolaei
Ph.D. candidate, Iran University of Science and Technology, Tehran, Iran

F. Hashemi
Graduate Student, University of Science and Culture, Tehran, Iran

ABSTRACT: Deep soil mixing is an effective mitigation strategy that reduces the devastating impacts of liquefaction hazards. These strong columns decrease the induced damage to the substructures while there are still lots of uncertainties about the design assumptions of DSM configurations in the liquefiable areas. Considering the practical concerns, a series of fully nonlinear numerical simulations are conducted and the effect of interaction of DSM grids and liquefied subsurface layer on the ground shaking motions is evaluated. Effect of DSM pattern and mechanical properties on the response of system were examined and results compared with those analytical methods proposed in the literature. Reduction of excess pore water pressure near the columns was obvious.

1 INTRODUCTION

Liquefaction triggering during seismic events in loose soil strata could induce destructive damage to the superstructure. Correct estimation of liquefaction triggering, the performance of foundations during liquefaction, and hazard mitigation strategies were favorable topics during the last decades.

Improvement procedures using stone columns and pile columns were proposed by Asgari et al. (2013). By employing 1g shaking table tests, Rasouli et al. (2015) proposed a sheet-pile wall as an effective method for reduction of settlements of foundation in a liquefiable soil layer. Rayamajhi et al. (2015) stated soil cement columns after liquefaction remains intact and will support the superstructure. Also, it was reported that columns with floating piles had a negligible effect on the reduction of excess pore water generation.

Hasheminezhad and Bahadori (2019) employed 3D numerical simulation and studied the efficiency of single DSM columns in the reduction of excess pore water pressure during seismic scenarios. Shaking table modeling was employed by Bahrampour et al. (2018) to investigate effect of the DSM column on the remediation of liquefaction. Boulanger et al. (2018) reported the performance of soil-cement walls on improvement of liquefaction for an embankment based on centrifuge and numerical modeling. The installation of soil cement walls reduced potential of ground displacement. Zhang et al. (2021) conducted a series of shaking table tests and reported that the presence of cement columns will have direct effects on acceleration amplification, fundamental periods, and pore water pressure. Tong et al. (2018) used DSM method to a reduction of liquefaction hazard of caisson walls. The findings of Demir and Ozener (2020) revealed that the current design method based on strain compatibility overestimates the seismic shear stresses reduction

Khosravi et al. (2017) performed a series of centrifuge tests modeling and examined the performance of structures found on a soil cement grid. The results of physical modeling showed

DOI: 10.1201/9781003299127-247

that during shaking events, soil-cement grids are useful to control the settlement in a soft clay layer. Nguyen et al. (2013) proposed an analytical procedure for designing a DSM grid for liquefaction reduction. The results were extracted based on some linear elastic finite element models. DSM walls were introduced as shear stress reduction elements and the design method was developed based on an assumption of strain compatibility.

Although some efforts have been conducted to recognize the effectiveness of DSM columns and grids in the reduction of liquefaction risk, there are still practical issues regarding the implementation of proposed methods. In this regard, a series of 3D non-linear FEM models are conducted in the present study, and the effect of both DSM columns and grids on the redistribution of excess pore water pressure is investigated properly.

2 FEM MODELING

The three-dimensional fully non-linear dynamic method is employed for numerical simulation of a liquefiable soil deposit using PLAXIS 3D version 2021 finite element-based software. The centrifuge tests results obtained by Ramirez et al. (2017) were modeled in the prototype scale to match the FEM modeling

2.1 *Geometry*

The centrifuge tests conducted by Ramirez et al. (2017) were used for the calibration of the numerical model. Three soil layers with different dry densities were modeled at the free field condition. The lower soil layer was prepared by a dense Ottawa sand with and thickness of 10 m and D_r of 90%. The same soil material with D_r=40% was placed at the middle layer with a thickness of 6m. Finally, a 2m layer of Monterey sand and D_r=90% were constructed at the top layer. The soil body was modeled with 29-noded triangle elements. A view of the model is depicted in Figure 1.

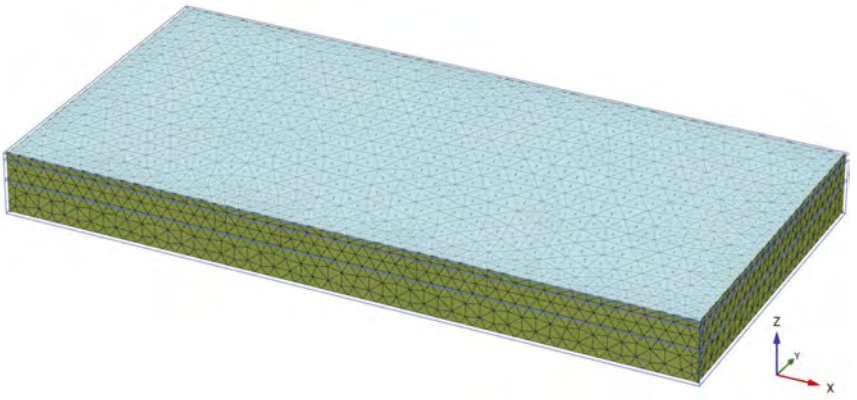

Figure 1. Model mesh view.

2.2 *Constitutive model*

The UBC3D-PLM model which has been developed by Tsegaye (2010) and implemented as a user-defined model in the PLAXIS software was used for modeling the behavior of soil layers. The formulation of the soil model is based on hyperbolic strain hardening and the Duncan-Chang approach. Based on previous contributions this constitutive model predicts the excess pore pressure with a good degree of accuracy while the prediction of settlements is questionable. The calibrated soil parameters are presented at the Table 1.

Table 1. Soil properties.

	me	ne	np	φ_{cv}	φ_p	$(N_1)_{60}$
Monterey sand	0.5	0.5	0.4	38	45.5	35
Ottawa dense	0.5	0.5	0.4	38	45.5	35
Ottawa loose	0.5	0.5	0.4	31.3	32	7

2.3 *Boundary conditions*

A free field boundary condition was introduced at the side walls to absorb reflected waves along the boundary to reduce the radiation damping effect. A compliant base boundary condition was also defined for the bottom of the model.

2.4 *Validation*

Numerical modeling was employed to simulate the outcomes of centrifuge tests. Kobe L seismic motion with peak ground acceleration (PGA) equal to 0.34 g imposed to the base of models in X direction according to Ramirez et al. (2017). Figure 2. Shows the FEM model and experimental outcomes in terms of pore pressure. Based on the results it can be concluded that the proposed FEM model matched the centrifuge outcomes with an acceptable degree of accuracy.

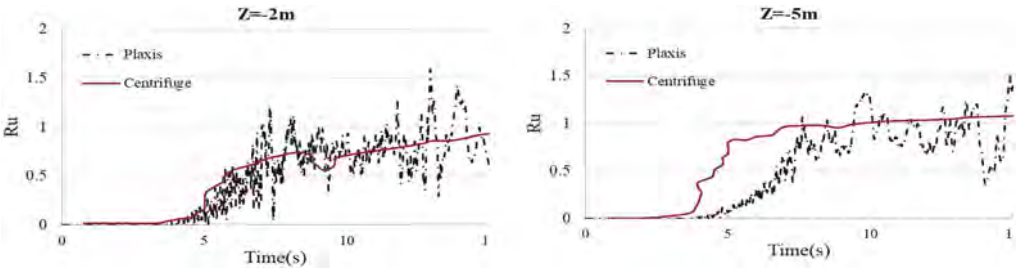

Figure 2. Validation of excess pore water pressure.

3 RESULTS

3.1 *Single column*

First, single columns with a diameter of 1.6m and qu=1,2 and 3MPa were placed and the response of the system was captured. The Ru contours are achieved as illustrated in Figure 3.

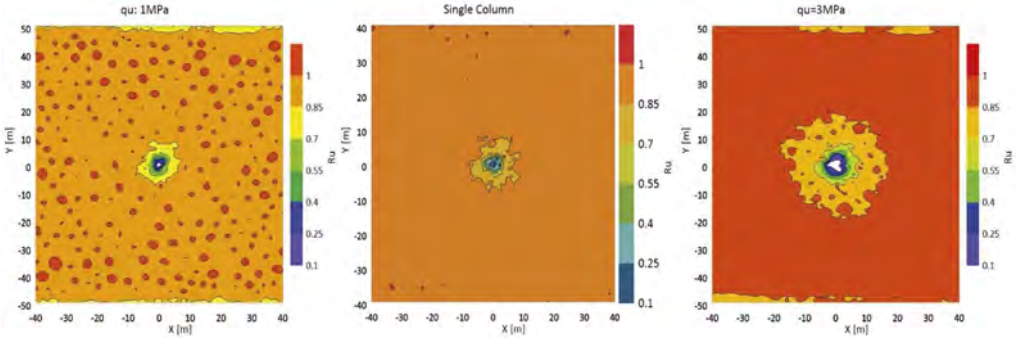

Figure 3. Ru contour for single pile with different USCs at the middle of the liquefiable layer.

It is obvious that the effective radius that reduces the Ru, is increased by enhancing the stiffness of the column. These radiuses are 1.7, 2.7m, and 3.5m for columns that their values of USC are 1MPa, 2MPa, and 3 MPa, respectively.

3.2 *Grids*

For assessing the effect of the DSM grids on liquefaction remediation, the procedure proposed by Nguyen (2013) was employed. Based on that method and the condition of soils used in the model, using a DSM grid with a length of 15 for columns with a diameter of 1.6m will improve factor of safety against liquefaction to the desired state. The procedures are implemented to consider different methods of liquefaction susceptibility based on the available methods in the literature. Some parts of the used in-house app are depicted in Figure 4.

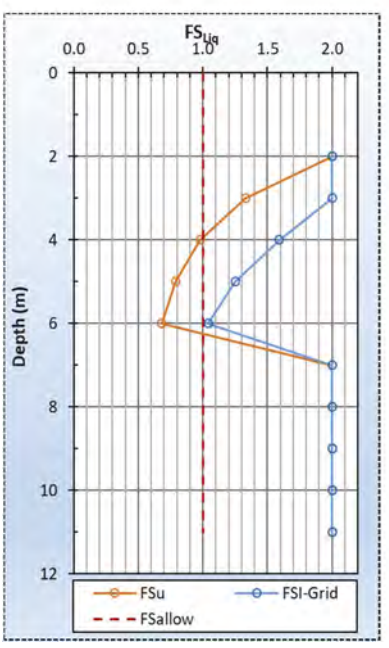

SPT Based Method

SPT Correction parameters

Param.	Precedure	Value
Hammer Type	Safety hammer	
C_N	Idriss, Boulanger (2003)	
C_R	NCEER	
C_E	User Defined	1
C_B	NCEER	
C_S	Standard	
$(N_1)_{60\text{-}cs}$	NCEER	

CSR and CRR calculation parameters

Param.	Precedure	Value
r_d	Boulanger, Idriss (2004)	
$CRR_{Sand\text{-}Like}$	Idriss, Boulanger (2004)	
$CRR_{Clay\text{-}Like}$	Boulanger, Idriss (2004)	
$K_{\alpha\ Sand\text{-}Like}$	Idriss, Boulanger (2003)	
$K_{\alpha\ Clay\text{-}Like}$	Boulanger, Idriss (2004)	
K_σ	Boulanger (2003)	
f	NCEER	
$MSF_{Sand\text{-}Like}$	Idriss (1999)	
$MSF_{Clay\text{-}Like}$	Boulanger, Idriss (2004)	

Figure 4. Calculation of liquefaction susceptibility based on analytical solutions.

The same configurations were modeled in the FEM models. The Ru contours are depicted in the Figure 5. The results of modeling showed that using DSM grids will reduce the Ru both with this dimension still high magnitude of excess pore water pressures were captured in some points. These observations showed that designing only based on simplified methods needs to be verified by numerical models for clarifying the doubts.

Also, the magnitude of acceleration in the middle of the liquefiable layer is recorded at the time 8s. Higher magnitudes of accelerations are captured near the DSM grids. It can be attributed to the fact that large strain due to the liquefaction caused higher damping and resulted in a considerable reduction in the magnitude of acceleration while the stiff column sensed smaller damping.

3.3 *Effect of grid size*

2 different size grids including 5m and 10m with a diameter of 80cm have selected and the effect of DSM grids on the redistribution of pore water pressure was investigated. The results are depicted in Figure 5

It shows that small DSM grids significantly reduced the excess pore water pressure and proper design of DSM grids will be a beneficial option for mitigation of liquefaction. The contour of liquefaction in the model is also depicted in Figure 7.

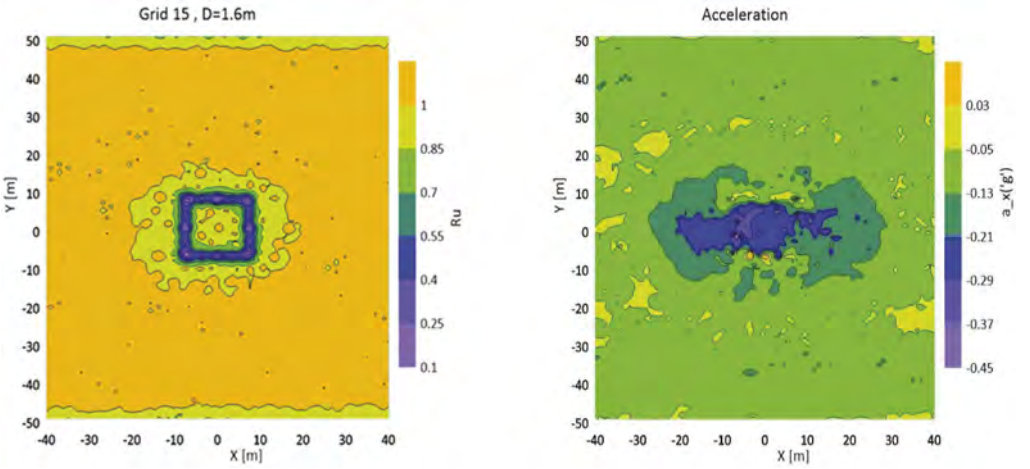

Figure 5. Ru and acceleration contour for the grid of DSM in the middle of the liquefiable layer.

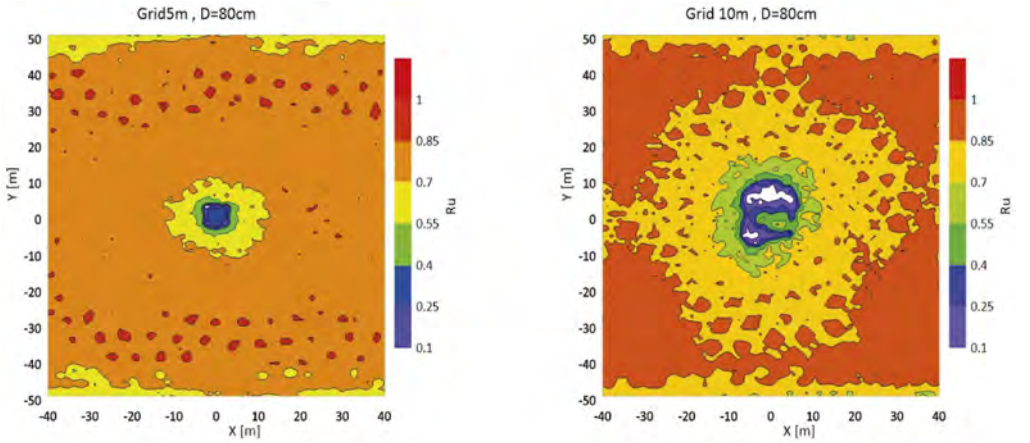

Figure 6. Effect of grid dimensions on the development of pore water pressure.

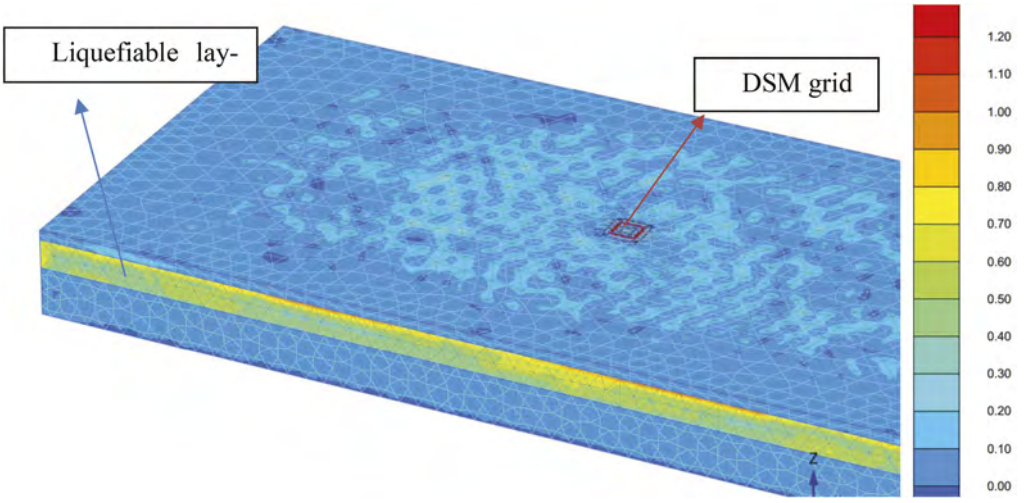

Figure 7. Pore water pressure contours of FEM model.

4 CONCLUSION

A series of FEM models were conducted for the evaluation of the effects of DSM columns and grids on the liquefiable layer. The main findings are summarized as the following:

1. An acceptable prediction of excess pore water generation during earthquakes can be achieved by the UBC3D-PLM model.
2. Depending on the stiffness of the columns, a clear reduction of Ru was observed around the columns.
3. Using DSM grids will reduce the excess pore water pressures but for large grids still, some liquefiable points in the middle of grids were observed.

ACKNOWLEDGMENTS

The manuscript was supported by the Baspar Pey Iranian (BPI)

REFERENCES

Asgari, A., Oliaei, M. and Bagheri, M., 2013. Numerical simulation of improvement of a liquefiable soil layer using stone column and pile-pinning techniques. Soil Dynamics and Earthquake Engineering, 51, pp.77–96.

Bahmanpour, A., Towhata, I., Sakr, M., Mahmoud, M., Yamamoto, Y. and Yamada, S., 2019. The effect of underground columns on the mitigation of liquefaction in shaking table model experiments. Soil Dynamics and Earthquake Engineering, 116, pp.15–30.

Boulanger, R.W., Khosravi, M., Khosravi, A. and Wilson, D.W., 2018. Remediation of liquefaction effects for an embankment using soil-cement walls: Centrifuge and numerical modeling. Soil Dynamics and Earthquake Engineering, 114, pp.38–50.

Demir, S. and Özener, P.T., 2020. Parametric investigation of effectiveness of high modulus columns in liquefaction mitigation. Soil Dynamics and Earthquake Engineering, 139, p.106337.

Hasheminezhad, A. and Bahadori, H., 2019. Seismic response of shallow foundations over liquefiable soils improved by deep soil mixing columns. Computers and Geotechnics, 110, pp.251–273.

Hasheminezhad, A. and Bahadori, H., 2022. On the deep soil mixing method in the mitigation of liquefaction-induced bearing capacity degradation of shallow foundations. Geomechanics and Geoengineering, 17(1), pp.334–346.

Zhang, D., Wang, A. and Ding, X., 2022. Seismic response of pile groups improved with deep cement mixing columns in liquefiable sand: shaking table tests. Canadian Geotechnical Journal, 59(6), pp.994–1006.

Khosravi, M., Boulanger, R.W., Wilson, D.W., Olgun, C.G., Tamura, S. and Wang, Y., 2017. Dynamic centrifuge tests of structures with shallow foundations on soft clay reinforced by soil-cement grids. Soils and foundations, 57(4), pp.501–513.

Nguyen, T.V., Rayamajhi, D., Boulanger, R.W., Ashford, S.A., Lu, J., Elgamal, A. and Shao, L., 2013. Design of DSM grids for liquefaction remediation. Journal of geotechnical and geoenvironmental engineering, 139(11), pp.1923–1933.

Rasouli, R., Towhata, I. and Hayashida, T., 2015. Mitigation of seismic settlement of light surface structures by installation of sheet-pile walls around the foundation. Soil Dynamics and Earthquake Engineering, 72, pp.108–118.

Rayamajhi, D., Tamura, S., Khosravi, M., Boulanger, R.W., Wilson, D.W., Ashford, S.A. and Olgun, C.G., 2015. Dynamic centrifuge tests to evaluate reinforcing mechanisms of soil-cement columns in liquefiable sand. Journal of Geotechnical and Geoenvironmental Engineering, 141(6), p.04015015.

Tong, B., Schaefer, V., Liu, Y. and Han, B., 2018. Optimization of deep mixing design for seismic liquefaction mitigation of Caisson walls. Geomatics, Natural Hazards and Risk.

Smart Geotechnics for Smart Societies – Zhussupbekov, Sarsembayeva & Kaliakin (Eds)
© 2023 The Author(s), ISBN 978-1-003-29912-7
Open Access: www.taylorfrancis.com, CC BY-NC-ND 4.0 license

Seismic risk assessment of USBRL project in Jammu and Kashmir: Implications towards earthquake resilient infrastructure in the Himalaya

Abdullah Ansari, KS. Rao & AK. Jain
Department of Civil Engineering, Indian Institute of Technology Delhi, Hauz Khas, New Delhi, India

ABSTRACT: Jammu and Kashmir in the northwestern part of the Himalayas witnessed many moderate to large magnitude frequent earthquake events. In the last two decades, the progress of infrastructure projects is boomed in this region. Earthquake-resilient design of structural elements of any development project is very challenging, especially in seismic-prone zones. In this paper, an attempt has been done to develop the seismic fragility functions for various tunnels located in three phases of the Udhampur Srinagar Baramulla Rail Link (USBRL) Project. The outcomes of this study reveal that most of the tunnels in Phase 1 of this project are subjected to extensive damage. Near-field active tectonic sources, weathered rock conditions, high seismicity, and landslide vulnerability all contributed to portal damage and significant lining failure at such sites. This study will assist design engineers in advocating for earthquake-resistant tunnels and underground facilities in Jammu and Kashmir. It will pave the way for earthquake-resistant design of infrastructure projects in the Himalayas.

1 INTRODUCTION

The development and progress of any region require a well-established transportation network as a prerequisite for overall economic growth. Tunnels are built as part of infrastructure projects or upgraded transportation networks. Any seismic damage to them might disrupt the overall serviceability of road or railway transit, causing socioeconomic disruption and perhaps disastrous outcomes. Jammu and Kashmir (J&K) is one of India's fastest-growing union territories, with continuing infrastructural developments to support economic development (Ansari et al. 2022). The Indian government proposed a 345 km Udhampur Srinagar Baramulla Rail Link (USBRL) Project connecting the Kashmir Valley with the Indian Railways network to offer J&K an easy way of transportation option.

The alignment of the USBRL project track and neighbouring active tectonic sources are shown in Figure 1. The construction of a new railroad line in the Indian subcontinent has never been more challenging than this one. The young Himalayas that is full of geological surprises and myriad issues are traversed by the terrain. In the present study, an attempt has been done to assess the seismic risk of the USBRL project. The fragility curves provided will serve as a valuable tool for increasing public awareness and directing track operations in the event of a major earthquake that occurs in or near J&K in the future.

2 OVERVIEW OF USBRL PROJECT

The main concept behind the proposal of the USBRL project is to work on the traffic issues in the Jammu and Kashmir. The project has been divided into 4 subsections for execution

DOI: 10.1201/9781003299127-248

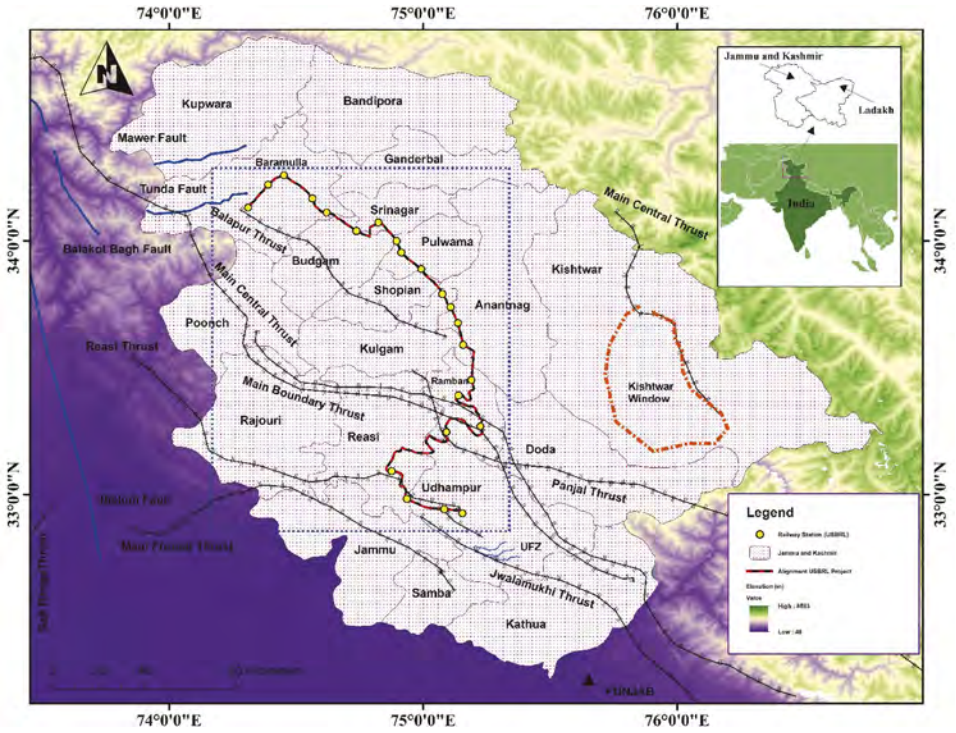

Figure 1. Location of the Udhampur Baramulla Srinagar Rail Link (USBRL) Project.

purposes. The alignment and structural details for each subsection are mentioned in Table 1. The Chenab Bridge and Anji Bridge are located in the Reasi and are the two main bridges under the subsection between Katra to Banihal. The Chenab Bridge is one of the engineering marvel structures in Reasi. The Anji Khad Bridge is the first cable-stayed bridge by the Indian Railways located in Reasi which acts as a connecting chain between Tunnel T2 and Tunnel T3.

Most of the tunnels under this project are located near the major tectonic sources including MBT, MCT, PT, and BT (Ansari et al. 2022b). The Tunnels T2, T49, and T80 are the main tunnels of this route. The total length of Tunnel T49 is 12.75 km which is going to become India's longest tunnel. The Tunnel T80 is known as the Pir Panjal tunnel passing through the Pir Panjal ranges and acts as a gateway to KV. This is the only tunnel in Banihal to Quazigund (BN-QZ) subsection with maximum overburden of 1300 m.

Table 1. Comprehensive detailing of the subsections of the USBRL Project.

	Subsections			
Parameters	Udhampur-to-Katra (UD-KT)	Katra-to-Banihal (KT-BN)	Banihal-to-Quazigund (BN-QZ)	Quazigund-to-Baramulla (QZ-BR)
Total Stations	3	10	1	15
Route length (km)	25	111	18	118
Total Tunnels	10	27	1	0
Length (km)	11	164	11.21	0

3 MAJOR GEOLOGICAL CHALLENGES

The Himalayas have the world's most difficult ground conditions from the standpoint of tunnelling. One of the prime reasons for this is that they are the youngest of the mountain chains. Slope instability issues resembling landslides and debris flows were seen in the vicinity of Tunnel T1, Tunnel T5, and Tunnel T11. The presence of a shear zone offers a particularly favourable environment for cavity formation at the tunnel crown.

The cavity formation observed on the left side that stretched to the crown of Tunnel T40/41 (Wani and Alamgir 2017). During the excavation process of T50 in Ramban, a chimney formed at the collapsed tunnel face (Srivastav et al. 2022). The tunnel T74R consists of Main Tunnel; parallel Escape Tunnel; nineteen cross passages and one Adit (Yusoff and Adhikari 2017). Cracks of 5-8 mm were observed at junctions. Due to weak rock mass condition (RMR less than 40), over the break of strata had been observed at various sections along the tunnel.

4 SEISMIC RISK ASSESSMENT

Seismic fragility functions are important tools since they define the damage probabilities of tunnels in both pre and post-earthquake stages (Hashash et al. 2001; Tsinidis et al. 2020). According to the mid-term theory, the efficiency of the resultant complex is distributed in the form of Lognormal if the structural capacity and seismic demand are two variables with a Normal or Lognormal distribution. As a result, the probability density function indicates the probable distribution described in the fragility curves (Argyroudis and Pitilakis 2012; Wang et al. 2020). As shown in Eq. (1), the fragility functions are represented by fragility curves with a lognormal distribution, assuming that all database uncertainty can be stated just by median uncertainty.

$$\boldsymbol{P[DS \geq DS_i |\ IM] = \emptyset(ln\ IM - ln\ IM_{DS_i}/\beta_{total},\ DS_i)} \tag{1}$$

where $\boldsymbol{DS}$ is the type of damage state in the tunnel lining.
$\boldsymbol{\beta_{total}}$ is estimated using the Eq. (2) considering the cumulative effect of $\boldsymbol{\beta_C}$, $\boldsymbol{\beta_D}$, and, $\boldsymbol{\beta_{DS}}$.

$$\boldsymbol{\beta_{total} = \sqrt{\beta_C{}^2 + \beta_D{}^2 + \beta_{DS}{}^2}} \tag{2}$$

The Probabilistic Seismic Hazard Analysis (PSHA) technique, which considers both spatial and temporal uncertainty, was utilised to define the seismic hazard. The central part of Udhampur, the bedrock level PGA is estimated as 0.34 g (Ansari et al. 2022a). The Reasi and Ramban have shown the maximum PGA of 0.4 g due to the combined seismic influence of Main Boundary Thrust (MBT), Main Central Thrust (MCT), and Reasi Thrust (RT). The probability of experiencing extensive damage to the North Portal of Tunnel T2 is 0.92 for PGA of 0.6 g, as shown in Figure 2a. The highly jointed and weathered dolomite rock mass at the South Portal of Tunnel T5 indicates the 85% risk of extensive damage, which corresponds to 0.8 g as bedrock PGA produced at RT. The near-site shear zone and strong seismicity characteristics of MCT enhance the risk of both portals of the Tunnel T13 suffering moderate damage. For the Tunnel T40/41, the chance of extensive damage gradually increases when PGA > 0.5 g (Figure 2b). Due to landslide-prone zones, the chances of extensive damage ($\boldsymbol{DS_3}$) of tunnel portals is very high for the tunnels in P2 among all three major phases. For the Tunnel T44/45, minor damage is twice as likely to occur for the same level of seismic intensity as moderate damage.

As illustrated in Figure 2c, there is a considerable decline in the damage probability from $\boldsymbol{P[DS \geq DS_1 \mid PGA = 0.7g] = 0.89}$ to $\boldsymbol{P[DS \geq DS \mid PGA = 0.7g] = 0.32}$, respectively at the North Portal of Tunnel T80. The vicinity of Tunnel T78 in Phase 33 is extremely vulnerable to slope failure, and debris flow indicates an equal probability of moderate and extensive damages. The Tunnel T80 is around 22.5 km from MCT and MBT, where PGA is anticipated to be more than

0.7 g. From the perspective of structural safety for T80, the tilting of the hazard scenario towards greater PGA and the proximity of the Himalayan thrusts are not looking good. The damage contribution of Tunnel T77D and Tunnel T78 under Phase P33 increases the likelihood of a portal collapse by 50%. The probability of minor damage ($\boldsymbol{DS_1}$), moderate damage ($\boldsymbol{DS_2}$), and extensive damage ($\boldsymbol{DS_3}$) are propounded in Table 2.

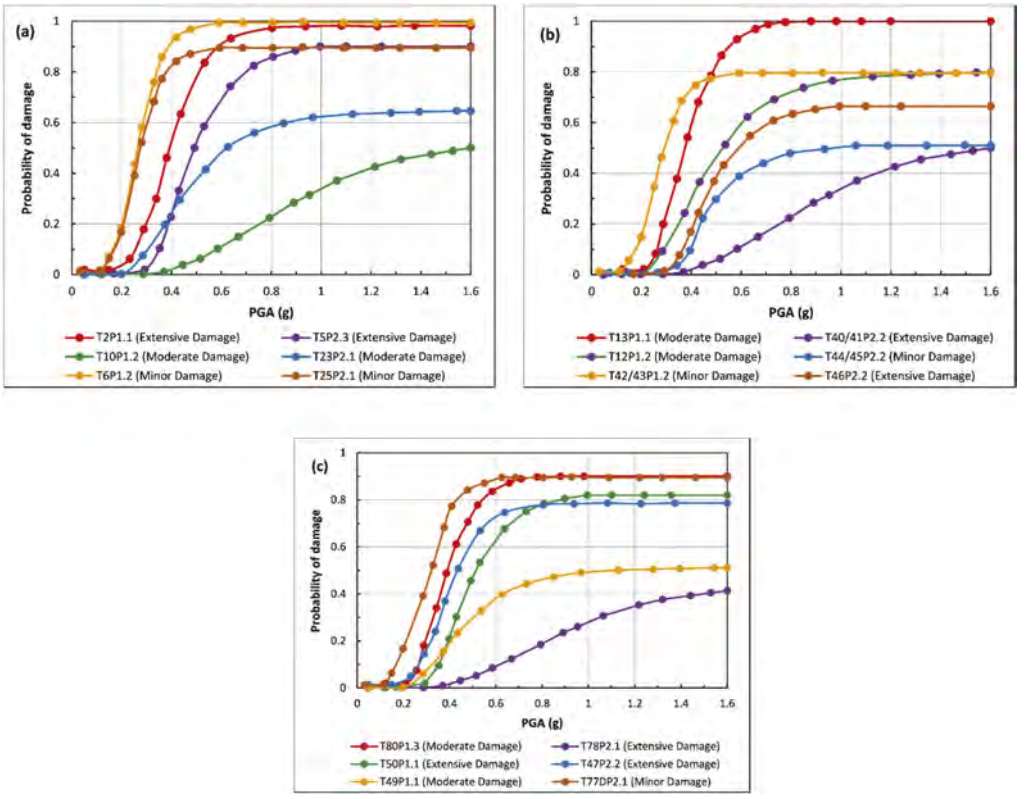

Figure 2. Seismic fragility curves for tunnel sections along the USBRL track located between the railway stations (a) Udhampur to Reasi (b) Reasi to Sangaldan, and (c) Sangaldan to Quazigund.

Table 2. Damage probabilities of USBRL tunnels for post-seismic scenarios.

		Probability of Exceedance		Probability of Damage State		
Phases	Tunnels	DS_2	DS_3	DS_1	DS_2	DS_3
Phase 1	T23	0.56	0.35	0.44	0.21	0.35
	T25	0.88	0.14	0.12	0.74	0.14
	T1	0.72	0.21	0.28	0.51	0.21
	T2	0.94	0.92	0.06	0.02	0.92
	T3	0.82	0.43	0.18	0.39	0.43
	T5	0.74	0.72	0.26	0.02	0.72
	T6	0.92	0.45	0.08	0.47	0.45
	T10	0.16	0.13	0.84	0.03	0.13
	T11	0.18	0.17	0.82	0.01	0.17

(*Continued*)

Table 2. (*Continued*)

Phases	Tunnels	Probability of Exceedance		Probability of Damage State		
		DS_2	DS_3	DS_1	DS_2	DS_3
Phase 2	T12	0.15	0.12	0.85	0.03	0.12
	T13	0.89	0.27	0.11	0.62	0.27
	T14	0.75	0.44	0.25	0.31	0.44
	T15	0.92	0.73	0.08	0.19	0.73
	T40/41	0.81	0.79	0.19	0.02	0.79
	T42/43	0.79	0.78	0.21	0.01	0.78
	T44/45	0.93	0.92	0.07	0.01	0.92
	T46	0.68	0.52	0.32	0.16	0.52
Phase 3	T47	0.83	0.43	0.17	0.4	0.43
	T48	0.76	0.16	0.24	0.6	0.16
	T49	0.77	0.54	0.23	0.23	0.54
	T50	0.65	0.63	0.35	0.02	0.63
	T74R	0.62	0.59	0.38	0.03	0.59
	T77D	0.87	0.77	0.13	0.1	0.77
	T78	0.92	0.78	0.08	0.14	0.78
	T80	0.83	0.71	0.17	0.12	0.71

5 CONCLUSIONS

- The 345 km long route of USBRL Project, which starts in Udhampur and finishes in Baramulla, traverses highly weather and jointed rock masses, folded and faulted tectonic features, shear zones, unstable sloping terrain, and landslide-prone areas. The construction of tunnels and bridges alongside railway tracks is a challenging task that presents significant geological difficulties.
- At Tunnels T2, T5, T40/41, T50, and T74R, excavation-related phenomena including cavity development, face wall deformation, squeezing, chimney formation, and water leakages were noted. Phase P1, Phase 2, and Phase 3 are classified as accessible, accessible with moderate repair, and inaccessible.
- The Tunnels in the Katra-Banihal (KT-BN) subsection of this project have demonstrated a significant propensity for extensive damages. Adverse seismic behaviour of tunnels, Phase 2 is no longer in an accessible state. Due to the effects of a high degree of seismicity, landslide susceptibility, weathered rock mass, and close source characterization, Phase 3 is the riskiest track in terms of post-seismic functionality.
- The seismic performance of Tunnels T48, T74R, and T80 has been triggered by the presence of shear zones, the proximity of the Panjal and Balapur thrusts, and the highly weathered and fractured rock mass beyond the Sangaldan railway station. All associated phases were transferred into an inaccessible category due to the high probability of damage. The tunnel designers, engineers, and risk management authorities may use this study to better understand how different components of the USBRL project will work in post-seismic situations.

REFERENCES

Ansari, A., Rao, K. S., & Jain, A. K. (2022). Seismic Analysis of Shallow Tunnels in Soil Medium. In Stability of Slopes and Underground Excavations (pp. 343–352). Springer, Singapore. https://doi.org/10.1007/978-981-16-5601-9_29

Ansari, A., Rao, K. S., & Jain, A. K. (2022a). Seismic vulnerability of tunnels in Jammu and Kashmir during post-seismic functionality. Geotechnical and Geological Engineering, 40(11),1–26. https://doi.org/10.1007/s10706-022-02341-0

Ansari, A., Rao, K. S., Jain, A. K. & Ansari, A. (2022b). Deep Learning Model for Predicting Tunnel Damages and Track Serviceability under Seismic Environment. Modeling Earth Systems and Environment, 8(4),1–20. https://doi.org/10.1007/s40808-022-01556-7

Argyroudis, S.A., Pitilakis, K.D., 2012. Seismic fragility curves of shallow tunnels in alluvial deposits. Soil Dynamics and Earthquake Engineering, 35, 1–12.https://doi.org/10.1016/j.soildyn.2011.11.004

Hashash, Y.M., Hook, J.J., Schmidt, B., John, I., Yao, C., 2001. Seismic design and analysis of underground structures. Tunnelling and underground space technology, 16 (4), 247–293. https://doi.org/10.1016/S0886-7798(01)00051-7

Srivastav, A., Satyam, N., Rajan, K.S., 2022. Seismic Vulnerability Assessment of Steel Fiber Reinforced Shotcrete Lined (SFRS) Tunnel: A Himalayan Case Study. Journal of the Geological Society of India, 98 (2), 185–192. https://doi.org/10.1007/s12594-022-1957-6

Tsinidis G, de Silva F, Anastasopoulos I, Bilotta E, Bobet A, Hashash YM, He C, Kampas G, Knappett J, Madabhushi G, Nikitas N. Seismic behaviour of tunnels: From experiments to analysis. Tunnelling and underground space technology. 2020, 103334.

Wang, Y.H., Tang, Q., Su, M.N., Tan, J.K., Wang, W.Y., Lan, Y.S., Luo, W., Zhou, Y., 2020. Post-earthquake fire performance of square concrete-filled steel tube columns. Thin-Walled Structures, 154, 106873. https://doi.org/10.1016/j.tws.2020.106873

Wani AR, Alamgir J (2017) Murre formation and geological problems encountered and mitigation thereof. Him Prabhat IX:11–23.

Yusoff R, Adhikari KN (2017) Geological studies for construction of T-74R- problems and solutions. Him Prabhat VIII:28–47

Smart Geotechnics for Smart Societies – Zhussupbekov, Sarsembayeva & Kaliakin (Eds)
© 2023 The Author(s), ISBN 978-1-003-29912-7
Open Access: www.taylorfrancis.com, CC BY-NC-ND 4.0 license

Analysis of the dynamic stability of the base, taking into account the peculiarities of the distribution of the liquefaction potential over the depth of the soil mass

E. Sobolev & G. Anzhelo
Federal State Budget Educational Institution of Higher Education
"National Research Moscow State University of Civil Engineering" (NRU MGSU),
Moscow, Russian Federation

ABSTRACT: The present study was carried out in order to improve the prediction of the stress-strain state of the soil foundations under dynamic influence based on the assessment of the liquefaction potential. The influence of the distribution of the potential of soil liquefaction over the depth of the soil mass is investigated, a hypothesis is put forward about the need to consider the potential of liquefaction with mandatory reference to the depth of the soil and the inadmissibility of using the concept of "average" liquefaction potential for the entire layer, regardless of its capacity, which leads to an unreasonably optimistic assessment of the stability of the soil mass. The tests were carried out for an engineering survey site composed mainly of sandy soils, shallow and dusty, loose and medium density, water-saturated, prone to dynamic instability. The predicted seismic impacts are taken on the basis of direct measurements made at the site of engineering surveys. The research was carried out on the basis of special laboratory studies of soils under conditions of dynamic triaxial compression. Samples of fully water-saturated soil were tested to determine shear stresses at the time of dynamic liquefaction. Then the liquefaction potentials were calculated in the first case on average for the entire soil layer, in the second case taking into account the distribution over the depth of the layer. As a result of the studies performed, the initial hypothesis was confirmed. For the studied sandy soils, the use of the "average" value of the liquefaction potential is not correct, since part of the studied soil is characterized as dynamically stable, while the other part is prone to liquefaction. If only the average value of the liquefaction potential is calculated, a false statement of the stability of the entire layer will be obtained. The conducted research complements and expands the current understanding of the assessment of the dynamic stability of soils under seismic influences and can be used to predict the stress-strain state of buildings and structures in complex engineering and geological conditions.

1 INTRODUCTION

Analysis of the dynamic stability of the foundations of buildings and structures is carried out, as a rule, in seismically hazardous areas. The presence of complex engineering and geological conditions has a significant impact on dynamic stability. From the point of view of dynamic stability, bases are considered weak, which are characterized by the presence of dusty and fine sandy water-saturated soils and sandy-clay soils with high fluidity. The magnitude of the predicted seismic impact also plays an important role, since it is obvious that under equal ground conditions, a stronger impact is more likely to cause a loss of dynamic stability of the soil mass. The main parameter characterizing the dynamic stability of the base is the liquefaction potential. In the physical sense, the liquefaction potential is a coefficient showing the ratio of dynamic strength to the maximum shear stresses arising in the soil mass during seismic action. The liquefaction potential can be determined both on the basis of laboratory tests of soils, and directly at the research site by field methods. None of the possible methods has decisive advantages, so they are all used equally in the global geotechnical practice.

DOI: 10.1201/9781003299127-249

This article deals with the problem of assessing the dynamic stability of the base based on the determination of the liquefaction potential in laboratory conditions. In geotechnical practice, it is often necessary to face the problem of misunderstanding the results of research in this area. The liquefaction potential is a parameter rigidly linked on the one hand to the specific soil for which it is determined, and on the other hand to the sampling depth for which the test was performed. The magnitude of the dynamic strength and the maximum shear stresses at which destruction occurs in the dynamic mode depend on the magnitude of the natural pressure, and, consequently, on the depth of sampling. Thus, it is incorrect to say that for the same engineering-geological element, it is possible to take samples from different depths, conduct dynamic tests to determine the liquefaction potential and determine a certain "average" value of the liquefaction potential for the entire layer as a whole.

At this stage, one may wonder about the statistical reliability of the research. If it is impossible to determine the average value based on tests of the same soil taken from different depths, then how can the reliability of the studies performed be ensured? The answer to this question lies in the need to take several samples of the same soil from the same (or comparable) sampling depth from one or neighboring engineering-geological workings (boreholes). Thus, a series of tests (from three to six) will be performed for each selected sampling depth to ensure the specified statistical reliability of the results.

The purpose of this study is to prove the hypothesis that for the same soil, a situation may arise in which the "average" liquefaction potential will indicate the stability of the soil layer to the predicted dynamic impacts, while the analysis of the liquefaction potential based on the reference to the depths of soil sampling shows that part of the layer will be it is stable, but the other one is not.

It should be mentioned that the construction regulatory documents in force in Russia do not define this issue. A lot of regulatory documents in the field of engineering surveys for construction and geotechnics establish the need to perform a dynamic stability forecast, test methods and processing of the results. However, there is still no full-fledged regulatory document dedicated to the process of analyzing dynamic stability under seismic impacts.

2 MATERIALS AND METHODS

The analysis of the dynamic liquefaction process is carried out by comparing the shear stress caused by the seismic load and the shear stress required to start soil liquefaction, or the level of shear strain amplitude, which is considered unacceptable for design.

To determine the liquefaction potential, the results of special laboratory studies of soils by dynamic triaxial compression were used. The equipment manufactured by Antriebs-, Pruf- und Steuertechnik (APS) GmbH "Wille Geotechnik" (Germany) was used for testing, which is a servo-hydraulic load frame with a maximum axial force of 63 kN, a triaxial compression chamber of type "A", a servo-hydraulic drive control unit, a data processing unit coming from pressure and displacement sensors, air pressure control unit and control computer. The general view of the installation with the assembled camera is shown in Figure 1.

Soil samples were Quaternary deposits of proluvial genesis, represented by silty sands, loose, saturated with water. The thickness of cover sands varies from 0.5 to 2.0 m. The average density of dry soil was 1650 kg/m^3.

The formation of samples from samples of the disturbed structure was carried out by the method of dry layer-by-layer filling into a cylindrical detachable form. Water saturation of the initially dry soil was carried out directly in the chamber of the device. The preparation made it possible to obtain fully water - saturated samples with the Skempton parameter $\beta \geq 0.95$. A comprehensive pressure equal to household pressure was applied to the sample at a given depth and a consolidation stage was carried out in open drainage conditions.

After the consolidation was completed, a vertical dynamic load was applied to the sample. The frequency of dynamic action was assumed to be equal to 0.5 Hz, the number of cycles for each amplitude was 10. The amplitude of dynamic vertical loading increased in increments from 0.10 to 0.25 MPa until the criteria for the destruction of the soil sample.

At the initial stage, the soil sample was compacted under the action of an isotropic pressure σ'_0. The initial compression pressure corresponded to the natural pressure at the depth of soil

sampling. The natural pressure was equal to the product of the specific gravity of the soil and the free fall acceleration. Then the initial static shear stress σ_s was applied to it, in these tests 10 kPa was accepted – the minimum permissible value due to the technical features of the test installation. Then a predetermined number of shear stress cycles were applied sequentially to the sample, while performing several series of homogeneous axial loads under untrained conditions with increasing amplitude. Series of loadings with increasing amplitude were repeated until the criterion for determining the dynamic strength was reached. Dynamic loading was carried out either before destruction (visible destruction of the sample or the achievement of axial deformation of more than 10%).

Figure 1. General view of triaxial compression equipment with dynamic loading.

The magnitude of the cyclic shear stress at any point under the horizontal ground surface during an earthquake when a shear wave passes from below is determined by the formula:

$$\tau_{\max} = \frac{a_{\max}}{g} \cdot r_d \cdot \gamma \cdot z, \tag{1}$$

where $a_{\max}$ is a peak value of horizontal acceleration on the ground surface; g is an acceleration of free fall; γ is specific gravity of the soil; r_d is a stress reduction coefficient; z is a depth of soil sample.

Taking into account the distribution of total σ_z and effective stresses σ'_z in a soil column, the formula (1) takes the following form:

$$\frac{\tau_{\max}}{\sigma'_z} = \frac{a_{\max}}{g} \cdot r_d \cdot \frac{\sigma_z}{\sigma'_z}, \tag{2}$$

where $\sigma_z = \gamma \cdot z$ is a full vertical stress.

Using formula (2), the cyclic stress acting under a given seismic action is calculated, and the strength of the soil under dynamic action is determined by the results of soil tests in dynamic triaxial compression devices.

Having expressed the relative magnitude of the applied stresses in terms of the relative equivalent stress τ_{av}/σ'_z, then the corresponding strength is determined in terms of the relative equivalent stress $\tau_{av,l}/\sigma'_z$. At the same time, τ_{av} is the average amplitude of the cyclic action,

which is 0.65 of the maximum shear stress τ_{max}. Thus, the liquefaction potential k_s of the soil layer is estimated through the expression:

$$\frac{\tau_{max,l}/\sigma'_z}{\tau_{max}/\sigma'_z} = \frac{\tau_{av,l}/\sigma'_z}{\tau_{av}/\sigma'_z} \tag{3}$$

The relative level of shear stresses operating in the soil τ_{av}/σ'_z is called cyclic stress ratio CSR and the value of cyclic strength $\tau_{av,l}/\sigma'_z$ is called the cyclic resistance ratio CRR.

The calculation of CSR is considered as an impact from an earthquake and is determined by the formula:

$$\mathrm{CSR} = 0.65\frac{\sigma_z}{\sigma'_z}a_{max}r_d \tag{4}$$

where 0.65 is a specific factor introduced by Sid to calculate the number of cycles of uniform stresses necessary to create pore pressure, as in the case of uneven displacement of the ground during an earthquake; σ_z is total vertical stresses at the appropriate depth; σ'_z is effective vertical stresses at the appropriate depth; a_{max} is maximum horizontal acceleration in the soil mass, units of measurement g (acceleration of gravity); r_d – the coefficient of stress reduction in depth in accordance with a certain function (NCEER, 1997/1999).

Computational and experimental methods for assessing the possibility of liquefaction are based on comparing CTR and CTR values to determine the liquefaction potential:

$$k_s = \frac{\mathrm{CRR}}{\mathrm{CSR}} \tag{5}$$

Liquefaction is possible if $k_s < 1$. Water-saturated soils are non-liquefied at $k_s > 1.15$. When determining the depth after which dynamic liquefaction is impossible, the normative coefficient of 1.15 was taken into account. That is, the depth of the zone of dynamic soil liquefaction should be determined at values corresponding to $k_s \leq 1.15$.

3 RESULTS

For the analysis of dynamic stability, the following parameters of seismic impact are adopted: the maximum acceleration in the horizontal direction is PGA a_{max}=3.43m/s^2; the moment magnitude of the earthquake is M_s=6.3; the frequency of dynamic impact is 0.5 Hz; the number of cycles for each amplitude of dynamic impact is 20 pcs. The test results of a series of seven soil samples are presented in Table 1.

The analysis of Table 1 shows that the average value of the liquefaction potential for all tests indicates the stability of the studied soil to dynamic liquefaction. At the same time, it should be noted that samples taken from a depth of 0.4 m to 1.0 m have a liquefaction potential of less than 1.15, which indicates their dynamic instability.

The obtained results are presented in the form of a graph of the dependence of the liquefaction potential on the depth of soil sampling (Figure 2).

4 DISCUSSION AND CONCLUSIONS

The analysis of the performed special laboratory studies of the dynamic stability of samples of sandy fully water-saturated soils allowed us to confirm the hypothesis put forward at the beginning of the study. It is a mistake to assume that the average value of the liquefaction potential can be used as a fundamental assessment of the dynamic stability of a particular soil under given parameters of dynamic impact.

For the studied sandy soils, the use of the average value of the liquefaction potential is incorrect, since part of the studied soil is characterized as dynamically stable, while the other

Table 1. Results of dynamic soil tests.

Number in order	Test number	Stratigraphic index	Engineering-geological element	Borehole	Depth from the surface, m	The amplitude of shear stresses, kPa	Maximum shear stresses, kPa	Maximum vertical stress, kPa	Maximum effective stress, kPa	Reduced pore pressure, fractions of a unit	Liquefaction potential	The average value of the liquefaction potential
1	test_1			1645	1,6	173,4	86,7	197,0	200,3	0,21	1,95	
2	test_2			Sh.1192	1,4	208,1	104,0	260,5	273,1	0,17	1,89	
3	test_3			Sh.1247/2	1,2	98,6	49,3	118,8	127,0	0,15	1,38	
4	test_4	pQ_{III}	1	Sh.1628	1,0	77,4	38,7	97,7	99,1	0,25	1,10	1,2
5	test_5			1626	0,8	45,2	22,6	56,2	59,0	0,14	0,91	
6	test_6			1615	0,6	19,8	9,9	31,8	30,3	0,18	0,85	
7	test_7			1644	0,4	63,5	31,7	83,6	83,9	0,34	0,55	

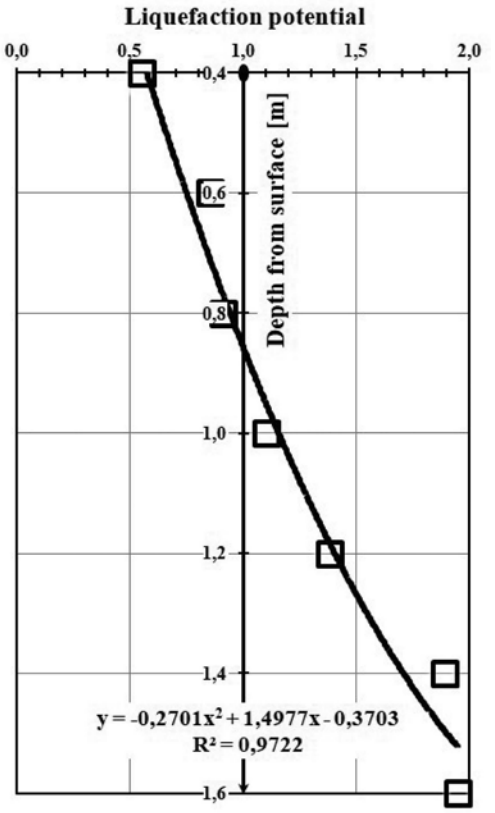

Figure 2. Experimental dependence of the liquefaction potential (fractions of a unit) on the depth of soil sampling (m).

part is prone to liquefaction. If only the average value of the liquefaction potential is calculated, a false statement of the stability of the entire layer will be obtained.

The performed studies clearly show that the layer, generally considered stable, should be divided into two zones in depth. The first zone is at a depth of 0.4 m to 1 m, where this layer is dynamically unstable and is characterized by liquefaction potential values less than 1.15. The second zone is at a depth of 1 m to 1.6 m, where this layer is dynamically stable and is characterized by liquefaction potential values of more than 1.15.

The conducted research complements and expands the current understanding of the assessment of the dynamic stability of soils under seismic influences and can be used in predicting the stress-strain state of buildings and structures in complex engineering and geological conditions.

REFERENCES

Aleksandrovych V.A., Havryliuk O.V. 2020. Investigation of the influence of dynamic loads of industrial equipment on the occurrence of prolonged yielding of their foundation soils. *IOP Conference Series: Materials Science and Engineering*. Volume 1021, Issue 1, 19 January 2021, art. n. 012010, DOI: 10.1088/1757-899X/1021/1/012010

Ding Z., Zhuang J., Wei X., Kong B., Ma S. 2020. Experimental study on critical dynamic stress of coarse-grained soil in railway subgrade. Yanshilixue Yu Gongcheng Xuebao/*Chinese Journal of Rock Mechanics and Engineering*, 39, pp. 3178–3187. DOI: 10.13722/j.cnki.jrme.2019.0976

Faizan A.A., Kırtel O. 2021. Non-linear soil-structure interaction analysis of railway bridge subjected to earthquake ground motions considering different types of soil. *Arabian Journal of Geosciences*, Volume 14, Issue 6, art. n. 509, DOI: 10.1007/s12517-021-06834-9

Fu H., Yuan X. 2018. Study on In-situ Liquefaction Test of Reconstituted Saturated Sand. Yingyong Jichu yu Gongcheng Kexue Xuebao/*Journal of Basic Science and Engineering*, Volume 26, Issue 2, 1 April 2018, pp. 403–412. DOI: 10.16058/j.issn.1005-0930.2018.02.017

Fu H., Yuan X. 2021.Dynamic Properties of Saturated Sand Based on the in-situ Liquefaction Test. *Journal of Earthquake Engineering*. Volume 25, Issue 3, pp. 512–534, DOI: 10.1080/13632469.2018.1523072

Idriss I.M., Boulanger R.W. 2008. Soil Liquefaction during Earth-Quakes. Monograph MNO-12. Earthquake Engineering Research Institute, Oakland, CA

Il'ichev V.A., Golubtsova M.N., Musaélyan A.A. 1989. Changes in seismic properties of loess soils under engineering site preparation. *Soil Mech Found Eng* 26, 98–102. DOI: 10.1007/BF02302817

Ishihara K. 1996. Soil behaviour in earthquake geotechnics. Oxford science publications, Oxford, UK

Ivanov P.L. 1962. Liquefaction of Sandy Soils. Gosenergoizdat, Moscow (in Russian)

Kechidi S., Colaço A., Alves Costa P., Castro J.M., Marques M. 2021. Modelling of soil-structure interaction in OpenSees: A practical approach for performance-based seismic design. *Structures*, Volume 30, pp. 75–88, DOI: 10.1016/j.istruc.2021.01.006

Kundu A., Patra N.R., Bandyopadhyay S., Reddy G.R. 2021. Static and dynamic characterization and response analysis of soils from northern India. *SN Applied Sciences*, Volume 3, Issue 2, art. n. 205, DOI: 10.1007/s42452-021-04196-1

Mangushev R.A., Usmanov R.A. 2019. Experience in compacting weak water-saturated loess soils with vertical sand drains in seismic regions. *Construction and Geotechnics*, 10(2), 26–35 (in Russian)

Mirsayapov I.T., Koroleva I.V., Zaripov G.Z. 2015. Estimation of seismic stability of bases stacked clays and water-saturated sandstones. *Soil Mechanics and Foundation Engineering in Geotechnical Engineering: Materials of the International Scientific Conference, Novocherkassk, 13–15 May 2015 /South-Russian State Technical University (NPI) to Them*, MI Platov, YURGPU (NPI), Novocherkassk, pp. 31–37 (in Russian)

Mousavi S., Ghayoomi M. 2021. Seismic Compression of Unsaturated Silty Sands: A Strain-Based Approach. *Journal of Geotechnical and Geoenvironmental Engineering*, Volume 147, Issue 5, art. n. 04021023. DOI: 10.1061/(ASCE)GT.1943-5606.0002507

Rong W., McCartney J.S. 2020. Drained Seismic Compression of Unsaturated Sand. *Journal of Geotechnical and Geoenvironmental Engineering*, Volume 146, Issue 5, art. n. 04020029. DOI: 10.1061/(ASCE) GT.1943-606.0002251

Rong W., McCartney J.S. 2021. Undrained Seismic Compression of Unsaturated Sand. *Journal of Geotechnical and Geoenvironmental Engineering*, Volume 147, Issue 1, art. n. 04020145. DOI: 10.1061/ (ASCE)GT.1943-5606.0002420

Seed H.B. 1979. Soil liquefaction and cyclic mobility evaluation for level ground during earthquakes, *ASCE J Geotech Eng Div*, vol. 105, no. 2, pp. 201–255.

Seed H.B., Idriss I.M. 1971. Simplified procedure for evaluating soil liquefaction potential, *ASCE J Soil Mech Found Div*, vol. 97, no. SM9, pp. 1249–1273.

Sidorova, A.I., Voznesensky, E.A. 2010. Estimation of additional foundation settlements caused by dynamic loading in urban areas, *Acta Geophysica*, vol. 58, no. 1, pp. 126–142. DOI: 10.2478/s11600-009-0040-7 (in Russian)

Sobolev E., Buslov A. 2018. Dynamic stability analysis and basic action for struggle with dynamic soil liquefaction. *MATEC Web of Conferences* 196, 03021, DOI:10.1051/matecconf/201819603021

Sobolev E., Ter-Martirosyan A. 2018. Interaction of the base and construction under seismic action, with considering various characteristics of soil damping. *MATEC Web of Conferences* 251(6):04011. DOI:10.1051/matecconf/201825104011

Stavnitser L.R. 2010. Seismic Stability of the Foundations. Monograph, Publishing building schools Association, Moscow (in Russian)

Ter-Martirosyan A., Sobolev E. 2020. Dynamic problems of scientific support construction. *IOP Conf. Ser.: Mater. Sci. Eng*. 869 072011, DOI:10.1088/1757-899X/869/7/072011

Ter-Martirosyan A., Sobolev E. 2021.Analysis of the seismic stability of foundations according to laboratory soil tests. *IOP Conf. Ser.: Mater. Sci. Eng*. 1030 012032, DOI: 10.1088/1757-899X/1030/1/012032

Voznesensky E.A., Kushnareva E.S. 2008. Methodological aspects of experimental evaluation of dynamic stability of sands in geotechnical survey, *Saint Petersburg 2008: Geosciences - From New Ideas to New Discoveries*. DOI: 10.3997/2214-4609.20146895 (in Russian)

Voznesensky E.A. 1999. Dynamic Instability of Soils. Moscow: Editorial URSS (In Russian)

Youd T.L. 1999. Physics and mechanics of liquefaction from field records and experience. *Physics and mechanics of soil liquefaction.Proceedings of the international workshop, Baltimore, September 1998*, pp. 325–334.

Yu J., Wang Z.Z. 2021. The dynamic interaction of the soil-tunnel-building system under seismic waves. *Soil Dynamics and Earthquake Engineering*, Volume 144, art. n. 106686, DOI: 10.1016/j.soildyn.2021.106686

Smart Geotechnics for Smart Societies – Zhussupbekov, Sarsembayeva & Kaliakin (Eds)
© 2023 The Author(s), ISBN 978-1-003-29912-7
Open Access: www.taylorfrancis.com, CC BY-NC-ND 4.0 license

The specifics of soil friction against a retaining wall under seismic load

O.P. Minaev
Military Academy of Logistics named Army General A.V. Chrulev, The Russian Federation

ABSTRACT: For the first time ever, the author of the paper has found that the classical quasi-static analysis of a retaining wall for seismic load provides indirect evidence of the wave nature of the impact the sandy backfill soil exerts on the rear surface of the retaining wall. In order to prove this, the paper presents the comparative results of the calculations of a gravity retaining wall with and without consideration of soil friction under operational static and seismic loads. The calculations are based on the given dimensions of the retaining wall and the characteristics of sandy backfill soils laying on weak clay foundation soils. Thus, we obtained the dependence for measuring the angle of soil friction against the rear surface of the retaining wall under seismic load of different intensity. It seems quite convincing that the retaining wall can be designed for a seismic load of 9 points without taking into account the soil friction because soil slips on the surface of the retaining wall in case of such seismic impact. The evidence is given that the calculation results are quite consistent with the research data on the behavior of sandy soils in the base of the plate under dynamic wave loads.

1 INTRODUCTION

It is well-known (Ivanov 1991, Budin 2014) that the soil friction on the rear surface of the retaining wall significantly affects the results of the design carrying capacity and stability under static load of the retaining wall.

According to many researchers, e.g. Prof. A.Ya. Budin (Budin 2014), calculations conventionally assume that the angle at which soil frictions against the retaining wall is equal to the angle φ of internal friction of the backfill soil or to its half $\varphi/2$.

Given the wave character of the dynamic effect on the retaining wall, it seems that such a convention in determining the angle of internal friction of soil against the retaining wall is not likely to be applicable for calculating seismic loads and here is why.

Headed by Prof. P.L. Ivanov (Ivanov 1991) the Soil Mechanics Laboratory of the Department of Underground Structures, Foundations and Bases, Peter the Great St. Petersburg Polytechnic University conducted numerous studies of the effect produced by dynamic wave load on the friction of sandy soil on the surface of a vibrating plate installed on its surface. In the experiments with a vibrating plate for in-plane shear, in addition to the static stresses from the weight of the plate and the vibrator, the mechanical vibrator added dynamic stresses from the rotation of the vibrator cams that acted according to the harmonic law. The vertical mechanical vibrator varied the stresses raging within the values of $\pm\Delta\sigma$**.** The dynamic pressure amplitude was controlled by changing the eccentricity of the vibrator cams while the frequency was adjusted by their rotation speed. The shear resistance considered according to the Coulomb dependence in the form of $\tau = (\sigma\text{-}\Delta\sigma)tg\varphi$ indicates a periodic shear of the plate on the sand surface.

As a result of the tests it has been found that within the range of vibration acceleration up to 1.0 g the angle of internal soil friction does not change while the decreasing shear resistance should be taken into account through changing normal stresses at the plate bottom. Thus, in case of vibration and seismic effects the shear stability of structures has to be tested given the

DOI: 10.1201/9781003299127-250

dynamic component of stresses at a constant value of the angle of internal soil friction, imposed on the static tests.

Therefrom, the author obtained a dependence for determining the angle ω of soil friction against the retaining wall at various values of force E_a^c of active lateral soil pressure at seismic load, in the form

$$\omega = arctg\left(2 - \frac{E_a^s}{E_a}\right) tg\phi \tag{1}$$

where E_a is the force of active lateral soil pressure on the retaining wall under the operational static load, kN; E_a^s is the force of active lateral soil pressure on the retaining wall under seismic pressure, including the force of lateral soil pressure under operational static load; φ is the angle of internal friction of the backfill soil.

In case the expression in brackets has a negative value, the angle ω of soil friction against the retaining wall is taken to be equal to 0. In this case, with wave dynamic impacts occurring at a time when the force of soil pressure is directed away from the rear surface of the wall during soil vibrations from seismic action, the backfill soil can shift (slip) along the wall surface due to the gravity of the soil and payload. We consider this factor as there is no soil friction against the retaining wall during seismic action.

Figure 1 shows a characteristic graph of the dynamic wave action on the retaining wall.

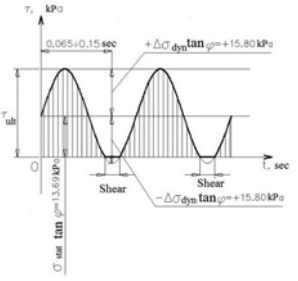

Figure 1. Graph of dynamic wave impact on the retaining wall at seismic intensity of 9 points.

The paper presents the results of comparative calculations of retaining walls with and without regard to the soil friction on the rear surface for seismic load intensity of 9 points. The results confirm the wave nature of the impact on the retaining wall during seismic action.

2 THEORETICAL DEPENDENCIES

The coefficient of active lateral pressure λ_a^s given the angle ω of soil friction against the retaining wall under seismic impact is determined according to Equation 1:

$$\lambda_a^s = \frac{cos^2(\varphi - \varepsilon)}{(1 + \sqrt{z^2}\cos\varepsilon} \tag{1}$$

where in Equation 1:

$$z = \frac{\sin(\varphi - \varepsilon)\sin(\varphi + \omega)}{\cos(\omega + \varepsilon)} \tag{2}$$

According to the standards applicable for a retaining wall calculated for seismic load (Stavnitser 1991, Savinov, Uzdin, Belash 1995), the most hazardous is the horizontal direction of the seismic pressure of soil.

For this case the dependence has the form of Equation 3:

$$\gamma^s = \frac{\gamma_i}{\cos \varepsilon} \tag{3}$$

where $\varepsilon = arctgAK_1$ is the angle of deviation from the vertical of the specific gravity equilibrium γ_i of soil and seismic force $y_i^s AK_1$, A is the coefficient whose values are taken equal to 0.1; 0.2; 0.4 respectively for the seismic intensity of 7, 8 and 9 points, K_1 is the coefficient that considers the admissible damage to buildings and structures, taken equal to 0.25 for hydraulic structures.

In the case the lateral active pressure of water-saturated soil on the retaining wall under seismic effects is determined, the weight of suspended soil y_{sb} should be introduced into the formulas, just as in case of operational load. The seismic force $y_{satur}AK_1$ should be determined according to the density of saturated soil y_{satur}. In this case, the deviation angle of the resultant is determined by the following formula in Equation 4:

$$\varepsilon_{satur} = arctg\frac{\gamma_{satur}}{\gamma_{sb}}AK_1. \tag{4}$$

The well-known dependencies are used to check the stability of the retaining wall for sliding under in-plane shear of the base and for in-depth shear under seismic load.

The theoretical dependences for calculating the retaining wall using this methodology are discussed in more detail in the following publications (Minaev 2019a, Minaev 2019b, Minaev 2019c).

3 INITIAL PARAMETERS AND LOADS

The calculations were carried out for a reinforced concrete retaining wall with a front cantilever. The total height of the retaining wall was 7.4 m, the water depth $h_в$ next to the embankment was 6.1 m and the height of wall elevation h_0 above water level was 1.3 m. Average sand with specific weight γ = 18.4 kN/m^3 and humidity W = 14% was taken as backfill soil. The foundation of the retaining wall is composed of water saturated clayey soils (highly plastic clay-bearing soils) having specific weight γ = 20.0 kN/m^3 and humidity W = 24 %. The humidity of clayey soils at liquid limit W_L = 0.30 and at plastic limit W_p = 0.16. The design angle φ of internal friction of sandy soils was 32°, and that of clayey soils was 17° with cohesion c = 16.67 kPa. The elastic modulus E of sandy soils was 31 MPa and that of clayey soils was 17 MPa.

The value of the useful load q on the surface of the base (on the cordon) was 29 kPa.

Initially, the values of active lateral pressure under operational and seismic load of 7, 8 and 9 points were estimated without considering soil friction and at the angle of soil friction against the rear surface of the retaining wall being equal to the angle φ of internal friction of backfill soil or to its half $\varphi/2$.

For all of these cases, we calculated the width of the retaining wall bottom.

Further comparative calculations on the bearing capacity and stability of the retaining wall for a maximum seismic load of 9 points did not consider soil friction. The angle of soil friction against the rear surface of the retaining wall was equal to the angle φ of internal friction of backfill soil or to its half $\varphi/2$.

We used the results of these calculations for analyzing the behavior of soils under dynamic wave loads.

Tables 1, 2 and 3 show the coefficients of active lateral pressure λ_a^s calculated according to Equations 1 – 4 for seismic intensity of 7, 8 and 9 points, respectively.

The calculations show that the width of the retaining wall bottom under operational load is 7.2 m without considering the friction against the rear surface of the wall. Considering the soil friction against the wall, the width of the retaining wall bottom goes down to 6.8 m for both design cases at the angle of soil friction against the wall $\varphi/2$ and φ.

The calculations for seismic load of 7 and 8 points show that the width of the retaining wall bottom is 8.3 and 8.6 m, respectively without considering the soil friction against the wall.

Table 1. The coefficients of active lateral pressure for seismic intensity of 7 points.

Item No.	Angle of soil; friction against the wall, ω	The coefficient of active lateral pressure of soil on the wall		
		Operational load, λa	Seismic intensity	
			above water, $\lambda^s_{a_1}$	under water, $\lambda^s_{a_2}$
1	**2**	3	**4**	**5**
1	0	0.307	0.321	0.336
2	**φ** /2	0.278	0.293	0.308
3	**φ**	0.277	0.293	0.311

Table 2. The coefficients of active lateral pressure for seismic intensity of 8 points.

Item No.	Angle of soil; friction against the wall, ω	The coefficient of active lateral pressure of soil on the wall		
		Operational load, λa	Seismic intensity	
			above water, $\lambda^s_{a_1}$	under water, $\lambda^s_{a_2}$
1	**2**	3	**4**	**5**
1	0	0.307	0.336	0.365
2	**φ** /2	0.278	0.308	0.340
3	**φ**	0.277	0.311	0.347

Table 3. The coefficients of active lateral pressure for seismic intensity of 9 points.

Item No.	Angle of soil friction against the wall, ω	The coefficient of active lateral pressure of soil on the wall		
		Operational load, λa	Seismic intensity	
			above water, $\lambda^s_{a_1}$	under water, $\lambda^s_{a_2}$
1	**2**	3	**4**	**5**
1	0	0.307	0.365	0.431
2	**φ** /2	0.278	0.340	0.412
3	**φ**	0.277	0.347	0.434

Considering the soil friction against the wall, the width of the retaining wall bottom reduces from 8.3 m down to 7.9 and 8.0 m under seismic load of 7 points and from 8.6 m down to 8.3 m and 8.4 m under seismic load of 8 points, respectively at the angle of soil friction against the wall $\varphi/2$ and φ.

Similar calculations for seismic load of 9 points show that the width of the retaining wall bottom is 9.1 and 9.3 m respectively at the angle of soil friction against the wall $\varphi/2$ and φ. In the latter case it is equal to the width of the retaining wall bottom if the calculation does not consider the soil friction against the wall.

Figure 2 presents a common active pressure diagram drawn for the vertical plane led through the front of the retaining wall, under a seismic load of 9 points.

In further calculations of the retaining wall for bearing capacity and stability, the seismic intensity was assumed to be 9 points.

4 RESULTS OF BEARING CAPACITY AND STABILITY CALCULATIONS

The results of the verified calculations of the base soils resistances show that the construction of a retaining wall of this type directly on natural base soils is possible.

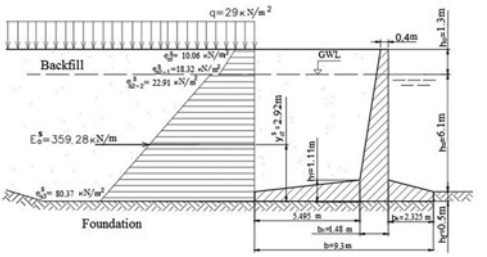

Figure 2. Diagram of active lateral pressure on a reinforced concrete corner retaining wall under seismic load of 9 points.

A diagram of isolines with highlighted areas of plastic deformations was built according to the methodology suggested by Prof. Kirillov, V.M. (Minaev 2019a). It was found out that the deformations spread to a depth of 6.63 and 6.66 m, respectively, while the angle of soil friction against the wall is $\varphi/2$ and φ (and φ=0).

Due to the plastic deformations at the base of the retaining wall, the weak soils of the base had to be substituted for a sand backfill cushion. The soils were compacted with the common vibro-dynamic compacting methods (Minaev 2011, Minaev 2014).

At the right edge of the wall, the the sand cushion width is set equal to 0.7 of the maximum depth y_{max} of the areas to which plastic deformations spread. In terms of design, it is taken as its half at the left edge of the wall, which corresponds to values equal to 4.34 (2.32) m at the angle of soil friction against the wall being $\varphi/2$and 4.66(2.33) m at φ (and φ=0).

We verified the stability of the retaining wall for in-plane shear slip under seismic load. The values of stability coefficient $K^{\text{in-psb}}$ for in-plane shear are 1.08, 1.04 and 1.05, respectively for the angle of soil friction against the wall $\varphi/2$, φ and φ=0.

Thus, the stability of the wall to the in-plane shear in the wall base is not ensured, as the value $K^{\text{in-psb}}$ (the same as K^{deep}) must be equal to 1.15 at least.

The calculations show that with the sand cushion layer being 2.32 (2.33) m thick, the stability coefficient rises to 1.23 for all design cases.

The results of calculations of the retaining wall for in-depth shear, show an even greater decrease in the stability coefficient K^{deep} with values of 1.02, 0.99 and 0.97 respectively at the angle of soil friction against the wall $\varphi/2$, φ and φ=0.

At the same time if a 2.32 and 2.33 m thick sand cushion was built, the stability coefficient could increase from 1.02 to 1.18 and from 0.99(0.97) to 1.15 respectively at the angle of soil friction against the wall $\varphi/2$ and φ (and φ=0).

In the base of the reinforced concrete retaining wall, 81, 87 and 83 piles are required per 10 linear meters of the retaining wall, respectively, at the angle of soil friction against the wall $\varphi/2$, φ and φ=0.

In the case of a pile foundation, the resistance of the wall to deep shear increases a lot up to the values of K_{deep} over 2.

5 ANALYSIS OF CALCULATION RESULTS

Based on the studies of soil behavior under dynamic wave loads in (Ivanov 1991), the author of this paper analyzed the results of the calculations of the retaining wall for seismic load.

According to the calculations, the force E_a^s of lateral active pressure on the retaining wall under seismic impact of 9 points amounts to 341.65, 357.89 and 359. 28 kN/m at the angle of soil friction against the wall $\varphi/2$, φ=0 and φ. The proportionate force E_a of lateral active pressure on the retaining wall under operating static load is 172.52, 190.56 and 171.98 kN/m.

The comparison of the design value shows that the additional force ΔE_a^s of active lateral pressure on the retaining wall on seismic impact is either insignificantly lower than the force E_a of active lateral pressure under operational static load or exceeds it. The verification of the

dependence to Equations 1 indicates that on seismic impact the angle ω of soil friction on the rear surface of the retaining wall is either insignificant or absent at all.

Figure 1 presents a typical graph of dynamic wave action on the retaining wall when the active lateral pressure force under seismic load exceeds the pressure under operational static load.

In support of the above we can refer to the experimental studies of Kazakh scientists (Khomyakov 2015). Their experiments included a table, on top of which was a tray with a retaining wall and sand. The table was subjected to multidirectional horizontal displacements to simulate wave vibrations of soil under seismic load. The wave vibrations of the soil even made the backfill soil separate and slip along the rear surface of the retaining wall.

In addition, at the seismic intensity of 8 point, the lateral active pressure force E_a^s on the retaining wall reduces to 283.49, 304.53 and 289.05 kN/m while at seismic intensity of 7 point it decreases even further down to 257.47, 280.93 and 259. 81 kN/m respectively at the angle of soil friction against the wall $\varphi/2$, $\varphi=0$ and φ. It can be defined from Equation 1 that at seismicity of 7 and 8 points, the angle ω of soil friction against the rear surface of the retaining wall is 0.569 φ and 0.440 φ**.**

6 CONCLUSION

1. For the first time ever the author of the paper used Equations 1 for defining the angle of soil friction on the rear surface of the retaining wall under seismic load of various intensity given the wave character of the dynamic impact on the retaining wall.

2. This research proves that Equations 1 can be practically applied for computational justification of the retaining walls that are designed on natural foundation and pile foundation soils in seismic areas.

REFERENCES

Budin, A.Ya. 2014. City and port embankments. St. Petersburg: Polytechnic.

Ivanov, P.L. 1991. Soils and foundations of hydraulic structures. Soil mechanics. Moscow: Higher School.

Khomyakov, V., Bessimbyev, E. Research of stability of slopes on soil models in the conditions of static and seismic influence.15th Asian Reg. Conf. on Soil Mech. and Geot. Eng., ARC 2015. New Innovations and Sustainability: 924–929.

Minaev, O.P. 2011. Development of vibratory method for soil compaction during construction. Soil Mechanics and Foundation Engineering 48(5): 190–195.

Minaev, O P. 2014. Development of Dynamic Methods for Deep Compaction of Slightly Cohesive Bed Soils. Soil Mechanics and Foundation Engineering 50(6): 251–254.

Minaev, O.P. 2019a. The most important aspects of the calculation and design of the base of the gravity retaining wall for seismic load. Seismic construction. Building Safety 6: 49–56.

Minaev, O.P. 2019b. Features of calculating gravity retaining wall without assumption of base soil liquefaction. R. Mangushev, A. Zhussupbekov, Y. Iwasaki, I. Sakharov (editors), Proc. in Earth and geosc. Geotechnics Fundamentals and Applications in Construction: New materials, structures, technologies and calculations (GFAC 2019), Saint Petersburg, Russia, 6–8 February 2019. Netherlands: Balkema, London: Taylor and Francis Group 2: 182–186.

Minaev, O.P. 2019c. Features of calculating stability of retaining wall with significant horizontal load on base soil. R. Mangushev, A. Zhussupbekov, Y. Iwasaki, I. Sakharov (editors), Proc. in Earth and ge osc. Geotechnics Fundamentals and Applications in Construction: New materials, structures, technologies and calculations (GFAC 2019), Saint Petersburg, Russia, 6–8 February 2019. Netherlands: Balkema, London: Taylor and Francis Group 2: 187–192.

Savinov, O.A., Uzdin, A.M., Belash, T.A., Dolgaya, A.A. 1995. Estimation of features of seismic effect at the selection of parameters of seismoinsulating constructions of foundations. Soil Mechanics and Foundation Engineering 4: 9–13.

Stavnitser, L.R. 1991. Stability of soil bases during earthquakes. Proc. of the Intern. Conf. on Soil Mech. and Found. Eng. 2: 911–912.

Smart Geotechnics for Smart Societies – Zhussupbekov, Sarsembayeva & Kaliakin (Eds)
© 2023 The Author(s), ISBN 978-1-003-29912-7
Open Access: www.taylorfrancis.com, CC BY-NC-ND 4.0 license

Mitigation of liquefaction through induced partial saturation by bio - gas bubbles

Rima Das
Research Scholar, Department of Civil Engineering, National Institute of Technology, Tiruchirappalli, Tamilnadu, India

Kasinathan Muthukkumaran*
Professor, Department of Civil Engineering, National Institute of Technology, Tiruchirappalli, Tamilnadu, India

ABSTRACT: Recent research have shown that the liquefaction potential of saturated sand can be drastically reduced if the sand is made slightly unsaturated. By introducing gas into the saturated sand, one can lessen the degree of saturation. However, injecting gas uniformly into sand is a challenging task. This paper describes the studies conducted to generate gas bubbles by introducing non-pathogenic denitrifying bacteria. The produced bio gas is tiny, chemically inert, less soluble, and has less impact on the environment. Triaxial cyclic tests are conducted on both saturated and partially saturated sand, as well as sand containing nitrogen gas bubbles created by bacteria to evaluate the effectiveness of this method towards liquefaction resistance. When the degree of saturation of the specimens is reduced from 100 to 90%, the excess pore water pressure generation and the liquefaction potential of sand under cyclic loading are found to be significantly reduced.

1 INTRODUCTION

Soil liquefaction is a phenomena that occurs when soil loses its shear strength and acts like a fluid due to an increase in pore water pressure. Liquefaction is commonly accompanied with significant soil deformations and can have catastrophic effects on structures and human life. Granular soils have a high drainage capacity and negligible pore pressure accumulation under static loads. Due to the rapidity of the seismic event, a completely saturated granular deposit may exhibit undrained behavior under dynamic stress. These factors can cause liquefaction of the soil. There are successful conventional soil liquefaction mitigation strategies, such as soil densification, cementation, and groundwater table lowering. However, these methods are typically expensive and inapplicable to existing buildings. Ordinary constructions and buildings cannot afford a suitable remedy for soil liquefaction. Consequently, many older buildings and infrastructure remain vulnerable to soil liquefaction. We require a solution that is economical, eco-friendly, and technically sound. According to particular experimental data, decreasing the degree of saturation can enhance the strength and resistance to liquefaction of sand (Yoshimi et al. 1989; Okamura 2006; Wang et al. 2016; Mele et al. 2019; Tsukamoto 2019). It has been demonstrated that a significant liquefaction resistance effect can achieve if the saturation level of sand reduced up to 5 %. On the basis of this hypothesis, a new mitigation strategy dubbed Induced partial saturation was recently presented. In the Induced partial saturation method, the presence of air or gas bubbles reduces the bulk modulus of the pore fluid, allowing the soil to conserve energy by reducing its volume and limiting the generation of further pore pressure due to cyclic loading. Desaturation can be done by decreasing the groundwater table or injecting gas into the soil pores (Yoshimi et al. 1989). The former is more intrusive and produces a high degree of desaturation; the latter is less invasive and produces a different degree of saturation. Several techniques have been adopted to achieve the purpose, including air injection

*Corresponding author: kmk@nitt.edu

DOI: 10.1201/9781003299127-251

(Ishihara et al. 2003; Yasuhara et al. 2008; Okamura et al. 2009, 2011; Raghunandan et al. 2014; Marasini et al. 2015; Zeybek et al.,2016, 2017; Amanta et al. 2021; Flora et al. 2021), electrolysis and drainage recharge method (Yegain et al., 2007), chemical method (Bayat et al. 2013, 2020; Nababan et al. 2016), biogenic desaturation (Rebata -Landa et al. 2012; He et al., 2016; Pham et al. 2016; Donnell et al. 2017a, 2017b; Mousavi et al.,2019;2021; Peng et al. 2021), inducing microbubbles (May et al. 2010).In recent years, attempts have been made to use microbiology to geotechnical engineering, with an emphasis on either increasing shear strength or decreasing soil permeability by inducing calcite crystallisation through the microbial hydrolysis of urea. The generation of small gas bubbles by a microbial denitrification process is yet another possible use of biotechnology. The primary purpose of this method is to create and evenly disperse gas bubbles. This method has been named as "Microbial induced partial saturation" or MIPS. In this investigation, denitrifying bacteria were injected and examined for their ability to create bio gas bubbles. Later liquefaction resistance is evaluated by conducting cyclic triaxial tests on microbially-treated, nitrogen-bubble-containing soil

2 GAS PHASE DISTRIBUTION IN PARTIALLY SATURATED SOIL

Depending on the arrangement of the gas phase, soil is often classified as fully saturated, partially saturated, or unsaturated zones (Tsukamoto 2018). In fully saturated zones, the interparticle pores of the soil are filled with water and contain no gas phase. A sample of soil subjected to an isotropic increase in total stress, denoted by $\Delta\sigma$. It exhibits a rise in pore pressure under undrained condition, with Δu equal to the total stress increment if the fluid is assumed to be nearly incompressible. This makes the pore pressure coefficient B equal to 1 ($B = \Delta u/\Delta\sigma$). In unsaturated zones, matric suction caused by water surface tension interacts with soil grains to generate additional compressive normal stresses between soil particles, hence enhancing soil shear strength (Tsukamoto2018). Under a rise in total stress, pore air pressure and pore water pressure increase at distinct rates, which may be determined by specializing the pore pressure parameters, which are always less than 1, as $B_a = u_a/\Delta\sigma$ and $B_w = u_w/\Delta\sigma$. Since the gas phase is continuous below 80% saturation, the pore water pressure increases faster than the pore air pressure, resulting in a decrease in matric suction (Tsukamoto et al. 2014). Soils that are partially saturated separate the two forms. While the liquid phase is continuous, air bubbles are blocked in the pore spaces of the grains. There is no air-grain contact because air bubbles are confined in the void of the soil skeleton. Therefore, there is no mobilization of shear strength, matric suction is low, and effective stresses are still utilised to depict mechanical behaviour. Occluded gas bubbles only increase the compressibility of the pore fluid without influencing the interlocking forces between grains. When partially saturated soils are subjected to an increase in confining stress, the gas phase becomes discontinuous and the difference between liquid and air pore pressures becomes negligible, making the two pore pressure parameters equal to $B_a \approx B_w$ (Kamata et al. 2009). Thus, the pore pressure parameter can be unique.

3 MICROBIAL DENITRIFICATION PROCESS

Denitrification, or the dissimilatory reduction of nitrate, was the source of nitrogen gas in the biogas process (Figure 1). The biological denitrification mechanism gradually converts nitrate (NO_3) to nitrogen gas (N_2).In this work, heterotropic denitrification has been considered. The overall equation for the process with ethanol as the electron donor is

$$5C_2H_5OH + 12KNO_3 \rightarrow 10CO_2 + 6N_2 \uparrow + 9H_2O + 12KOH \quad (1)$$

CO_2, H_2, CH_4, and N_2 are the most abundant biogenic gases in near-surface soils. Carbon dioxide (CO_2) is very soluble in water and has a short residence time, but hydrogen (H_2) and methane can burn. One of the numerous benefits relevant to this inquiry is that nitrogen gas (N_2) is neither combustible nor a greenhouse gas. Nitrogen gas is having the property of extremely

low solubility, which is 0.014 l of gas per litre of water at 250°C and atmospheric pressure, is its most notable quality (He and Chu 2014). There are a few constraints to microbial denitrification. According to certain research, a high quantity of nitrate might produce a buildup of nitrite, resulting in incomplete denitrification (Paassen et al. 2010). Other limiting variables include pH, temperature, the presence of oxygen, etc. Previous research demonstrated that a neutral to moderately basic pH environment is optimal for high activity and complete denitrification (Saleh-Lakha et al. 2009). Denitrification by microorganisms is a natural process that is common in soil environments. Conditions for its occurrence in soil are quite simple to satisfy.

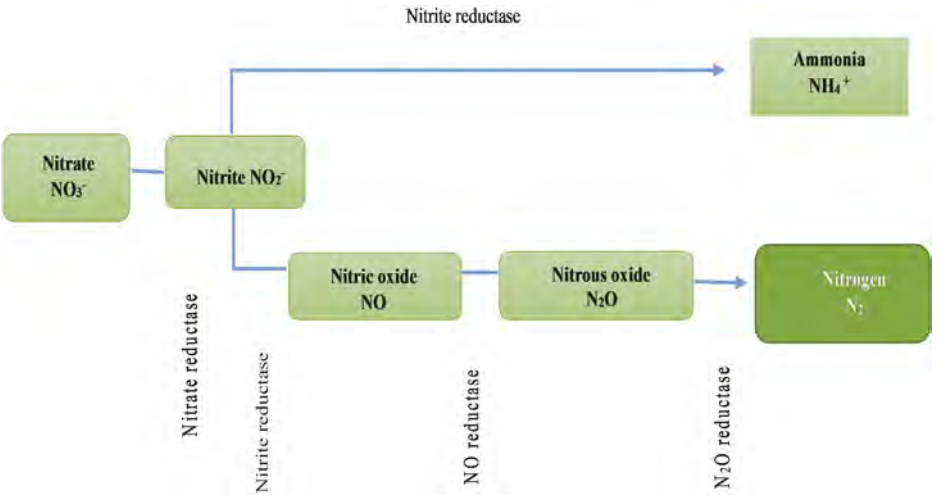

Figure 1. Nitrate dissimilatory reduction, enzymes, and products (Kraft et al., 2011).

4 LABORATORY EXAMINATION

4.1 *Material classification*

The tested soil is a liquefiable silty sand collected from a place in Chidambaram, Tamil Nadu, India. The soil is designated as poorly graded sand (ASTM D2487) and enclosed inside the limits of extremely prone to liquefiable soil (Tsuchida, 1970) (Figure 2). Pseudomonas stutzeri was chosen to conduct the experiment on soil desaturation. Pseudomonas stutzeri (MTCC 863) was obtained and cultivated on nutrient agar-stabilized Petri dishes. It is a mesophilic organism that can grow at temperatures as low as 4°C and as high as 44°C, but grows optimally at temperatures about 35°C. This bacterium doubles in around 53 minutes when cultured in lysogeny broth (LB) medium ($MgSO_4.7H_2O$ 0.2 g, KNO_3 2 g, K_2HPO_4 1 g) at 32 °C.

4.2 *Soil desaturation test*

The bacteria solution has been combined with a broth containing nitrates, which stimulates the metabolism. We must understand the biogas production regulation process in sand in order to obtain the necessary level of saturation for a given concentration. As seen in Figure 3, a basic soil desaturation experiment is conducted using a bacterial solution using a basic setup. A syringe was filled with a sample of sand that had been combined with denitrifying bacteria and nutrients. The syringe was attached to a burette. As a result of the formation of gas bubbles in the sand sample, a part of the sand's water was replaced, causing the water level in the burette to increase. Changes in the water level in the burette reflect the quantity of gas production. The saturation level is

determined by the phase relationship. Four different initial nitrate concentrations, including 146,198.6, 300.7, and 370 mg/L, were utilized during the experiments. As shown in the table, the degree of saturation begins to decrease as nitrate concentration increases. The appropriate level of soil saturation can be achieved by altering the amount of nitrate added to soils. The reaction rate was slowed by five days, while the maximum change was noticed between two and three days. During the course of monitoring, regular bubble production was observed. On the third or fourth day, bubbles form, and their density increases. Regardless of the nitrate concentrations, the gas production rates are comparable across all samples. As indicated in Table 1, the pH values of all three samples increase as well. This increase in pH is consistent with the reaction depicted in Equation 1, which shows that hydroxyl is one of the process byproducts.

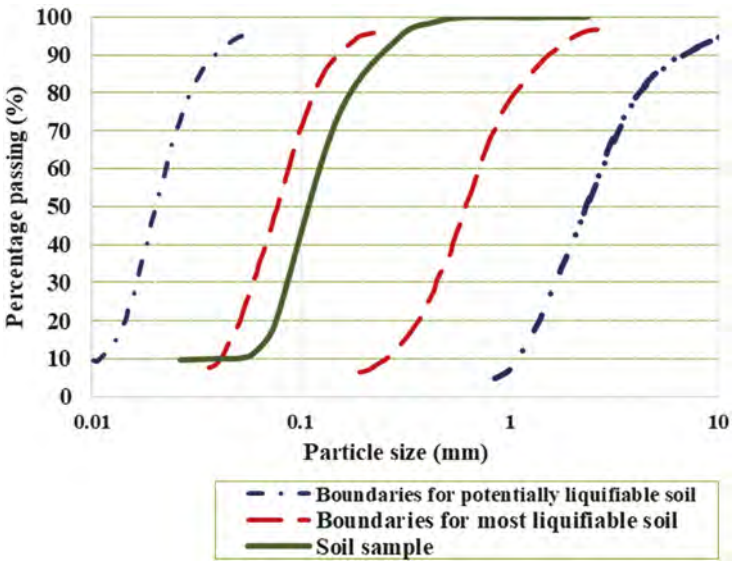

Figure 2. Particle size distribution of sand used in this study.

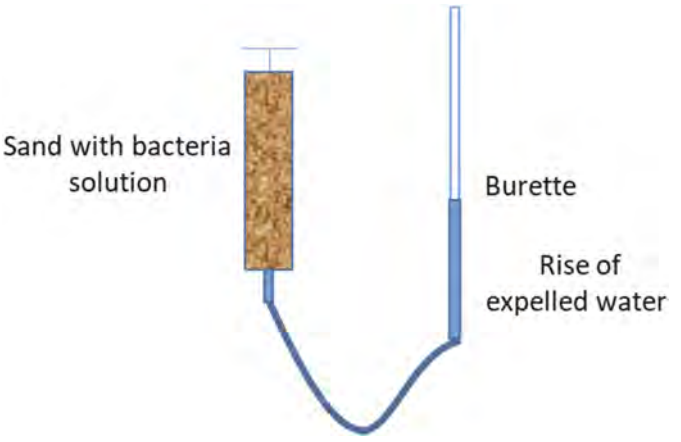

Figure 3. Setup of soil desaturation test.

Table 1. Result of soil desaturation test.

Void ratio (e)	Initial Nitrate concentration mg/L	Degree of saturation (S_r%)	pH
0.702	146.00	92.40	7.65
0.702	198.66	90.12	8.1
0.702	300.75	80.25	8.16
0.702	370.20	75.00	8.2

5 LIQUEFACTION BEHAVIOR OF UNTREATED SAND MICROBIALLY TREATED SAMPLE

5.1 *Testing procedure*

A modified cyclic triaxial setup is used to determine the liquefaction resistance of fully saturated and microbially-induced partially saturated sand during the test. A closed burette linked to the drainage value was added to the standard triaxial arrangement as a volume measuring method. The apparatus for measuring volume can measure the volume of water evacuated. The moist pluviation is produced immediately in the solution of bacteria and nitrates. With a 30% D_r sample of loose relative density and confining pressures of 50, 75, and 100 kPa and cycle stress ratios(CSR) of 0.1, 0.2, 0.3, and 0.4, consolidated undrained tests were conducted.

5.2 *Testing results and discussion*

The variation of deviatoric stress and excess pore pressure (r_u) (EPP) with the number of loading cycles, deviatoric stress with axial strain, and Cyclic stress ratio (CSR) with the number of loading cycles were obtained for fully saturated and partly saturated samples. All samples displayed identical behaviour. The Figure 4 illustrates typical graphs exhibiting the variation at 0.2 CSR and 75 kPa confining pressure. Figure 4 (a) depicts the variation of EPP with loading cycles (N_L). The soil liquefaction failure criteria for EPP ratio is found when r_u equals one. The samples with a greater 'N' value are more resistant to liquefaction. As the number of loading cycles (N_L) increases, so does the r_u, indicating the accumulation of EPP. The saturated sample displayed early liquefaction at a lower number of loading cycles than the partly saturated sample, as seen by the Figure 4a,b. Partially saturated sample look more number of loading cycles to reach maximum pore pressure ratio (r_u) of 0.46 (Figure 4b). Comparing the resistance to liquefaction of both samples in terms of loading cycles, it is obvious that the partially saturated sample displayed greater resistance to liquefaction. In terms of deviatoric stress, the initiation of liquefaction can be defined when the deviatoric stress reaches zero. The soil is completely liquefied and approaching almost zero after seven cycles for the fully saturated sample (Figure 4c). Since the partially saturated sample is not liquefied, the deviatoric stress ranges between about 37 kPa with increasing number of loading cycles. (Figure 4d). As observed in the Figure 4e, the deviatoric stress against axial strain loop becomes flatter as the deviatoric stress decreases continuously with increasing loading cycles (N_L). This clearly indicates the reduction in soil stiffness for the completely saturated sample compared to the partially saturated sample (Figure 4e,f). Figure 4g, h shows the CSR and N_L trends for untreated and MIPS-treated specimens at an effective confining pressure of $\acute{\sigma_c}$ 75kPa. No sample of partly saturated sand exhibited a pore pressure ratio (r_u) of 0.9 or 1. Under all combinations of stress conditions, the r_u is restricted to a maximum of 0.6. As CSR magnitude increases, the number of cycles necessary to achieve liquefaction reduces for both saturated and partially saturated samples.

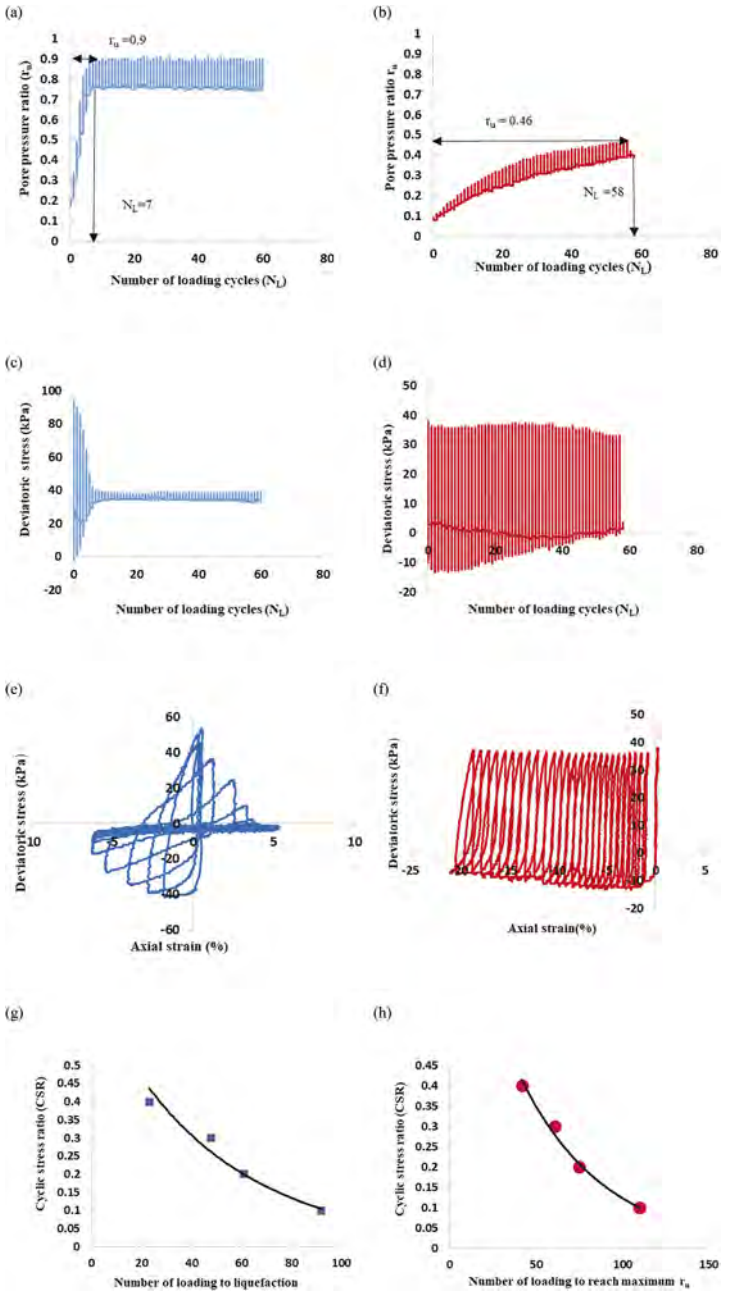

Figure 4. Undraind cyclic response of saturated and desaturated loose sand (D_r 30%) at 0.2CSR, effective confining stress of σ_c' 75kPa(a) Pore pressure ratio with number of loading cycles (N_L) (untreated sample) at degree of saturation (S_r) 99 %. (b) Pore pressure ratio with number of loading cycles (N_L) (treated sample) at degree of saturation (S_r) 93.74 % (c) Deviatoric stress vs. number of loading cycles of untreated sample at S_r 99% (d) Deviatoric stress vs. number of loading cycles of treated sample at S_r 93.74% (e) Deviatoric stress vs. strain of untreated sample at S_r 99% (f) Deviatoric stress vs. strain of treated sample at S_r 93.74% (g) Cyclic resistance curve of untreated sample at S_r 99% (h) Cyclic resistance curve of untreated sample at S_r 93.74%.

6 CONCLUSIONS

In this research, partial saturation generated by denitrifying bacteria metabolism has been evaluated, as well as the liquefaction behaviour of the treated sample. The desaturation test proved that the microbial denitrification process may create nitrogen (N_2) gas in sand, resulting in the sand desaturation. By changing the nitrate content of the soil, a saturation level of less than 80% can be reached. The cyclic triaxial test reveals that reducing the saturation level of sand from 100 % to 90% can greatly reduce its liquefaction potential. Saturated sands lose their stiffness much more rapidly than partially saturated sands when subjected to cyclic loading, as evidenced by the less number of cycles necessary to produce early liquefaction in the saturated samples. After inducing partial saturation with the MIPS approach, the soil's resistance to liquefaction increases rapidly. This suggests that induce partial saturation of sand by this technique can be a highly effective countermeasure against liquefaction.

REFERENCES

Amanta, A. S., & Dasaka, S. M. (2021). Air injection method as a liquefaction countermeasure for saturated granular soils. Transportation Geotechnics, 30(March), 100622. https://doi.org/10.1016/j.trgeo.2021.100622

Eseller-Bayat, E. E., & Gulen, D. B. (2020). Undrained Dynamic Response of Partially Saturated Sands Tested in a DSS-C Device. Journal of Geotechnical and Geoenvironmental Engineering, 146(11), 04020118. https://doi.org/10.1061/(asce)gt.1943-5606.0002361

Eseller-Bayat, E., Yegian, M. K., Alshawabkeh, A., & Gokyer, S. (2013). Liquefaction Response of Partially Saturated Sands. II: Empirical Model. Journal of Geotechnical and Geoenvironmental Engineering, 139(6), 872–879. https://doi.org/10.1061/(asce)gt.1943-5606.0000816

Flora, A., Bilotta, E., Chiaradonna, A., Lirer, S., Mele, L., & Pingue, L. (2021). A field trial to test the efficiency of induced partial saturation and horizontal drains to mitigate the susceptibility of soils to liquefaction. In Bulletin of Earthquake Engineering (Vol. 19, Issue 10). Springer Netherlands. https://doi.org/10.1007/s10518-020-00914-z

He, J., & Chu, J. (2014). Undrained Responses of Microbially Desaturated Sand under Monotonic Loading. *Journal of Geotechnical and Geoenvironmental Engineering*, *140*(5), 04014003. https://doi.org/10.1061/(asce)gt.1943–5606.0001082

He, J., Chu, J., Wu, S. fan, & Peng, J. (2016). Mitigation of soil liquefaction using microbially induced desaturation. *Journal of Zhejiang University: Science A*, *17*(7), 577–588. https://doi.org/10.1631/jzus.A1600241

He, J., Chu, J., Wu, S. fan, & Peng, J. (2016). Mitigation of soil liquefaction using microbially induced desaturation. *Journal of Zhejiang University: Science A*, *17*(7), 577–588. https://doi.org/10.1631/jzus.A1600241

Ishihara, M., Okamura, M., & Oshita, T. (n.d.) (2003). Desaturating sand deposit by air injection for reducing liquefaction potential. 89.

Kamata, T., Tsukamoto, Y., & Ishihara, K. (2009). Undrained shear strength of partially saturated sand in triaxial tests. *Bulletin of the New Zealand Society for Earthquake Engineering*, *42*(1), 57–62. https://doi.org/10.5459/bnzsee.42.1.57-62

Kraft B, Strous M and Tegetmeyer H E (2011) Microbial Nitrate Respiration – Genes, Enzymes and Environmental Distribution. Journal of Biotechnology 155(1): 104–117.

Marasini, N., & Okamura, M. (2019). Air injection to mitigate liquefaction under light structures. August 2015. https://doi.org/10.1680/ijpmg.14.00005

May, M., & Nagao, K. (2010). Applicability Test of Soil Improvement Using Micro-Bubbles Against Soil Liquefaction. 0–12.

Mele, L., Tian, J. T., Lirer, S., Flora, A., & Koseki, J. (2019). Liquefaction resistance of unsaturated sands: Experimental evidence and theoretical interpretation. *Geotechnique*, *69*(6), 541–553. https://doi.org/10.1680/jgeot.18.P.042

Mousavi, S., & Ghayoomi, M. (2021). Liquefaction Mitigation of Sands with Nonplastic Fines via Microbial-Induced Partial Saturation. *Journal of Geotechnical and Geoenvironmental Engineering*, *147*(2), 04020156. https://doi.org/10.1061/(asce)gt.1943-5606.0002444

Mousavi, S., Ghayoomi, M., & Jones, S. H. (2019). Compositional and geoenvironmental factors in microbially induced partial saturation. *Environmental Geotechnics*, *8*(4), 282–294. https://doi.org/10.1680/jenge.18.00087

Nababan, F. R. P. (2016). Development and evaluation of Induced Partial Saturation (IPS), delivery method and its implementation in large laboratory specimens and in the field. November, 234.

O'Donnell, S. T., Rittmann, B. E., & Kavazanjian, E. (2017a). MIDP: Liquefaction Mitigation via Microbial Denitrification as a Two-Stage Process. I: Desaturation. Journal of Geotechnical and Geoenvironmental Engineering, 143(12), 04017094. https://doi.org/10.1061/(asce)gt.1943-5606.0001818

O'Donnell, S.T.; Kavazanjian, E.; Rittmann, B.E. (2017b) MIDP: Liquefaction Mitigation via Microbial Denitrification as a Two-Stage Process. II: MICP. Journal of Geotechnical and Geoenvironmental Engineering 2017, **143**, 04017095, doi:10.1061/(ASCE)GT.1943-5606.0001806.

Okamura, M., and K. Noguchi. 2009. "Liquefaction resistances of unsaturated non-plastic silt." Soils Found. 49 (2): 221–229. https://doi.org/10.3208/sandf.49.221.

Okamura, M., Takebayashi, M., Nishida, K., Fujii, N., Jinguji, M., Imasato, T., Yasuhara, H., & Nakagawa, E. (2011). In-Situ Desaturation Test by Air Injection and Its Evaluation through Field Monitoring and Multiphase Flow Simulation. Journal of Geotechnical and Geoenvironmental Engineering, 137(7), 643–652. https://doi.org/10.1061/(asce)gt.1943-5606.0000483

Okamura, M., Yasumasa, S., 2006.Effects of pore fluid compressibility on liquefaction resistance of partially saturated sand. Soils and foundations, Japanese Geotechnical Society Vol.46, No. 5,695-700

Peng, E., Hou, Z., Sheng, Y., Hu, X., Zhang, D., Song, L., & Chou, Y. (2021). Anti-liquefaction performance of partially saturated sand induced by biogas under high intensity vibration. Journal of Cleaner Production, 319 (December 2020), 128794.https://doi.org/10.1016/j.jclepro.2021.128794

Pham, V.P., Passen Van, L.A., Van der Star, W.R.L., (2016)Quantifying the desaturation effect of biogenic gas formation in sandy soil. International Society for soil mechanics and Geotechnical Engineering

Raghunandan, M. E., & Juneja, A. (2011). A Study on the Liquefaction Resistance and Dynamic Properties of De-Saturated Sand. October 2014.

Rebata-Landa, V., & Santamarina, J. C. (2012). Mechanical Effects of Biogenic Nitrogen Gas Bubbles in Soils. Journal of Geotechnical and Geoenvironmental Engineering, 138(2), 128–137. https://doi.org/10.1061/(asce)gt.1943-5606.0000571

Saleh-Lakha, S., Shannon, K. E., Henderson, S. L., Zebarth, B. J., Burton, D. L., Goyer, C., & Trevors, J. T. (2009). Effect of nitrate and acetylene on nirS, cnorB, and nosZ expression and denitrification activity in Pseudomonas mandelii. *Applied and Environmental Microbiology*, *75*(15), 5082–5087. https://doi.org/10.1128/AEM.00777-09

Tsuchida H (1970) Prediction and counter measure against the liquefaction in sand deposits. Seminar in the Port and Harbour Research Institute, Ministry of Transport, Tokyo, Japan, 1–3

Tsukamoto, Y. (2019). Degree of saturation affecting liquefaction resistance and undrained shear strength of silty sands. *Soil Dynamics and Earthquake Engineering*, *124*(August 2017), 365–373. https://doi.org/10.1016/j.soildyn.2018.04.041

Tsukamoto, Y. 2018. "Degree of saturation affecting liquefaction resistance and undrained shear strength of silty sands." Soil Dyn. Earthquake Eng. 124 (Sep): 365–373. https://doi.org/10.1016/j.soildyn.2018.04.04

Tsukamoto, Y., Kawabe, S., Matsumoto, J., & Hagiwara, S. (2014). Cyclic resistance of two unsaturated silty sands against soil liquefaction. *Soils and Foundations*, *54*(6), 1094–1103. https://doi.org/10.1016/j.sandf.2014.11.005

Wang, H., Koseki, J., Sato, T., Chiaro, G., & Tan Tian, J. (2016). Effect of saturation on liquefaction resistance of iron ore fines and two sandy soils. *Soils and Foundations*, *56*(4), 732–744. https://doi.org/10.1016/j.sandf.2016.07.013

Yasuhara, H., Okamura, M., & Kochi, Y. (2008). Experiments and predictions of soil desaturation by air-injection technique and the implications mediated by multiphase flow simulation. Soils and Foundations, 48(6), 791–804. https://doi.org/10.3208/sandf.48.791

Yegian, M. K., Eseller-Bayat, E., Alshawabkeh, A., & Ali, S. (2007). Induced-Partial Saturation for Liquefaction Mitigation: Experimental Investigation. Journal of Geotechnical and Geoenvironmental Engineering, 133(4), 372–380. https://doi.org/10.1061/(asce)1090-0241(2007)133:4(372)

Yoshimi, Y., Tanaka, K., Tokimatsu, K., 1989. "Liquefaction resistance of a partially saturated sand" Soils and foundations, Japanese Society of Soil Mechanics and Foundation Engineering, Vol, 29 No. 3, 157–162.

Zeybek, A. (2017). Centrifuge testing to evaluate the liquefaction response of air-injected partially saturated soils beneath shallow foundations. 339–356. https://doi.org/10.1007/s10518-016-9968-6

Zeybek, A., & Madabhushi, S. P. G. (2016). Influence of air injection on the liquefaction-induced deformation mechanisms beneath shallow foundations. Soil Dynamics and Earthquake Engineering, 97(October 2015), 266–276.https://doi.org/10.1016/j.soildyn.2017.03.018

Smart Geotechnics for Smart Societies – Zhussupbekov, Sarsembayeva & Kaliakin (Eds)
© 2023 The Author(s), ISBN 978-1-003-29912-7
Open Access: www.taylorfrancis.com, CC BY-NC-ND 4.0 license

Laboratory cyclic shear test to investigate the cyclic response of biopolymer-treated sand

Mintae Kim
Graduate Student, Department of Civil Systems Engineering, Ajou University, South Korea

Dong-Yeup Park
Graduate Student, Department of Civil & Environmental Engineering, Korea Advanced Institute of Science and Technology, South Korea

Gye-Chun Cho
Professor, Department of Civil & Environmental Engineering, Korea Advanced Institute of Science and Technology, South Korea

Jin-Tae Han
Research Fellow, Department of Geotechnical Engineering Research, Korea Institute of Civil Engineering and Building Technology, South Korea

Ilhan Chang*
Associate Professor, Department of Civil Systems Engineering, Ajou University, South Korea

ABSTRACT: The effect of biopolymer-based soil treatment (BPST) on the liquefaction resistance of loose sand was investigated in this study. Cyclic simple shear (CSS) apparatus was used to assess the cyclic responses of untreated (natural) and gel-type biopolymer-treated sand specimens. Laboratory test results show that BPST is effective on improving both cyclic shear stress ratio (CSR) and cyclic shear resistance ratio (CRR) where BPST could be considered as a new ground improvement method for seismic mitigation and anti-liquefaction purposes.

1 INTRODUCTION

Natural disasters such as earthquakes generally accompany geotechnical engineering instability issues including slope failure, retaining wall collapse, ground liquefaction, sink holes, and so on.

Among others, in general, ground liquefaction occurs when saturated loose sand is subjected to repeating cyclic motion where the excess pore water pressure generation induces intergranular effective stress decrease (Akhila et al., 2019). In geotechnical engineering, ground liquefaction is an important concern where it directly affects the ground bearing capacity. Thus, numbers of research have been conducted to improve the liquefaction resistance of sandy soils, including replacement, compaction, or chemical ground improvement with cement or lime (Adalier and Elgamal, 2004, Xiao et al., 2018, Bao et al., 2019, Sharma et al., 2021).

Liquefaction resistance may generally be achieved by repeated direct shear testing and triaxial tests. The cyclic load is normalized to the effective payload (effective normal stress and effective average stress). The cyclic shear stress ratio (CSR) is defined as the normalized cyclic load, and the cyclic stress (Eq. 1), while resistance ratio (CRR) is defined as the CSR in the number of cyclic shear stress loads (N) when liquefaction occurs in the experiment. CRR is defined as the ground's liquefaction resistance (Seed and Idriss, 1971).

$$CSR = \frac{\tau_{cyc}}{\sigma'_{vc}} \tag{1}$$

where τ_{cyc} = shear stress; σ'_{vc} = confinement

*Corresponding author: ilhanchang@ajou.ac.kr

DOI: 10.1201/9781003299127-252

A series of repeated shear experiments were carried out in this study to explore the suitability of biopolymer, an eco-friendly ground reinforcement new material, to replace the present structure installation and ground reinforcement method using cement.

2 MATERIALS AND METHOD

2.1 *Jumunjin sand*

The test sample was constructed using Jumunjin sand, a non-stick standard sand in Korea. The USCS classifies it as SP low-grade sand. The following Figure 1 and Table 1 are the particle size distribution characteristics of Jumunjin sand.

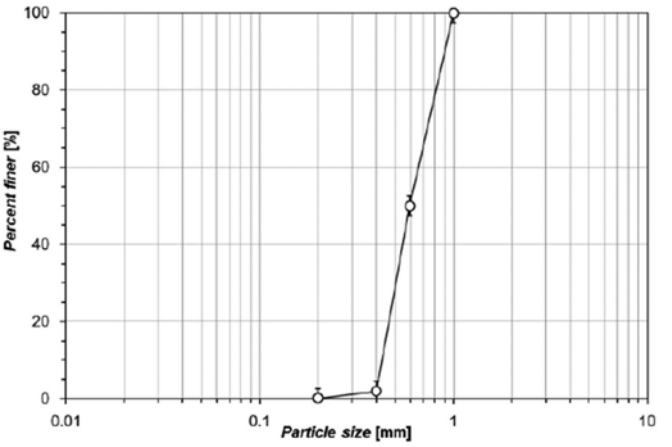

Figure 1. Characteristics of particle size distribution of Jumunjin standard sand.

Table 1. Basic geotechnical engineering properties of Jumunjin standard sand.

C_u	C_c	e_{max}	e_{min}	G_s	USCS
1.94	1.09	0.89	0.64	2.65	SP

2.2 *Biopolymer: gellan gum*

Gellan gum (In this study, gellan gum is referred to as GG), a high molecular weight polysaccharide generated by Sphingomonas elodea bacterium, was employed in this study. Gellan gum is an eco-friendly new material with heat-gelling capabilities that has lately gained notice. It has a limited solubility at low temperatures, but it dissolves evenly when combined with water to create a gellan gum solution at temperatures over 90 degrees (Chang et al., 2016).

Biopolymers have recently been shown to be useful as a geotechnical engineering ground reinforcement material. Biopolymer-based soil treatment (BPST) improves ground shear strength, friction angle, and decreases permeability. It also serves as an environmentally friendly construction material by improving groundwater retention, avoiding desertification, and promoting plant growth (Chang et al., 2015, Qureshi et al., 2017). Laboratory specimens were prepared using research grade gellan gum (Merck; CAS: 71010-52-1) in this study.

2.3 *Sample preparation*

Samples for cyclic simple shear test were prepared by mixing dry sand and heated gellan gum solution at a designated biopolymer-to-soil content and water-to-soil content in mass. The gellan gum-to-soil content in mass was set as 1%, while the water content was set as 20%. Thus a 5% gellan gum solution was prepared by dissolving 5 g of gellan gum into 95 g of

deionized water heated over 90ºC. Sand and gellan gum solution was quickly mixed above a hot plate to maintain the temperature and avoid thermo-gelation before sample molding. Hot and moist gellan gum-sand mixtures were shaped into a disk (63.5 mm in diameter and 20 mm in height) having a relative density (Dr) of 60%. Then samples were cooled down to the room temperature to allow thermo-gelation.

2.4 *Cyclic simple shear test*

A cyclic simple shear test was used in this study to compare the resistance to cyclic stress of samples made of normal sandy soil and biopolymer-treated sandy soil. In the cyclic simple shear test, a shear stress is repeatedly delivered to the sample at a fixed frequency to produce deformation in the presence of a constant overhead load. Geocomp's ShearTrac-II equipment was employed (Figure 2).

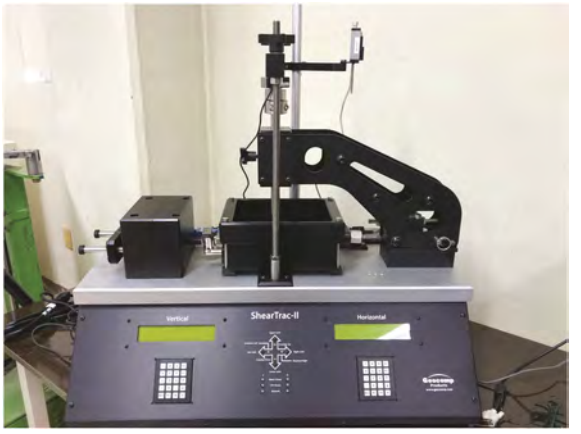

Figure 2. Overview of cyclic simple shear testing machine.

The experiment is carried out in phases. Consolidation is accomplished in the first phase of repeated simple shearing by increasing the restraining pressure on the top of the sample to 100 kPa. Following that, in step 2, shear stress is applied to the sample at a uniform frequency of 1 Hz, and the experiment is repeated until the sample's shear displacement in both directions reaches 7.5% (Vaid and Sivathayalan, 1996).

3 RESULTS AND DISCUSSION

3.1 *Experimental results: CRR (Cyclic Resistance Ratio) Comparison*

The shear strain of the sample is increased uniformly in both directions in the cyclic shear test, and the surplus pore water pressure is increased until the effective vertical stress approaches 0 kPa, causing liquefaction. Seed (Bolton Seed et al., 1985) employed the CSR at the time of 15 repeated loads based on an earthquake magnitude of 7.5 to estimate the CRR in this research. Figure 3 shows the CSR graph for each cycle of each sample collected in the experiment, and the CRR values are summarized in Table 2.

4 CONCLUSION

A cyclic direct shear test was used in this work to evaluate the liquefaction resistance of sandy soil treated with gellan gum. The liquefaction time of the gellan gum treated sample was delayed relative to the untreated sample because of the experiment, and the CRR value of each sample was inferred from the CSR graph generated from the experiment. The gellan gum-treated sample had a CRR of 0.3, which was around 0.2 greater than the untreated

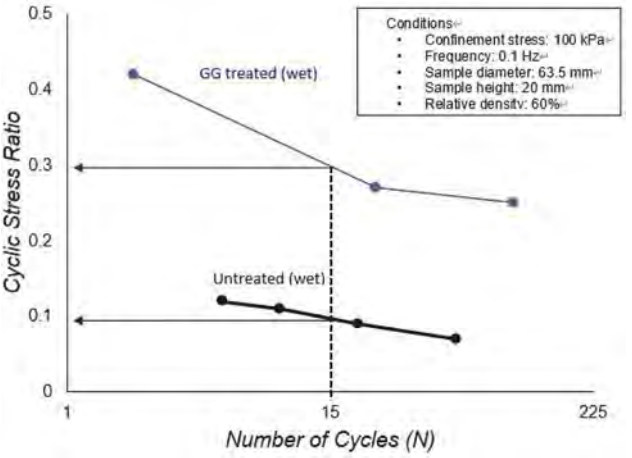

Figure 3. CSR graph according to shear cycle.

Table 2. CRR table for each case.

Case	BP (%)	Condition	10^{th} cycle CSR(CRR)
Untreated	0	Wet	0.1
GG treated	1.0	Wet	0.3

sample's CRR of 0.1, showing that the gellan gum biopolymer helps to increase liquefaction resistance. Experiments on the basic physical properties of biopolymer-treated samples, as well as the correlation between shear modulus and damping ratio, are also required.

ACKNOWLEDGMENT

This work was supported by the National Research Foundation of Korea (NRF) grant funded by the Korea government (MSIT) (No. 2022R1A2C2091517).

REFERENCES

Adalier, K. & Elgamal, A. 2004. Mitigation of liquefaction and associated ground deformations by stone columns. *Engineering Geology*, 72, 275–291.

Akhila, M., Rangaswamy, K. & Sankar, N. 2019. Undrained response and liquefaction resistance of sand–silt mixtures. *Geotechnical and Geological Engineering*, 37, 2729–2745.

Bao, X., Jin, Z., Cui, H., Chen, X. & Xie, X. 2019. Soil liquefaction mitigation in geotechnical engineering: An overview of recently developed methods. *Soil Dynamics and Earthquake Engineering*, 120, 273–291.

Bolton Seed, H., Tokimatsu, K., Harder, L. & Chung, R. M. 1985. Influence of SPT procedures in soil liquefaction resistance evaluations. *Journal of geotechnical engineering*, 111, 1425–1445.

Chang, I., Im, J. & Cho, G.-C. 2016. Geotechnical engineering behaviors of gellan gum biopolymer treated sand. *Canadian Geotechnical Journal*, 53, 1658–1670.

Chang, I., Prasidhi, A. K., Im, J., Shin, H.-D. & Cho, G.-C. 2015. Soil treatment using microbial biopolymers for anti-desertification purposes. *Geoderma*, 253, 39–47.

Qureshi, M. U., Chang, I. & Al-Sadarani, K. 2017. Strength and durability characteristics of biopolymer-treated desert sand. *Geomech. Eng*, 12, 785–801.

Seed, H. B. & Idriss, I. M. 1971. Simplified procedure for evaluating soil liquefaction potential. *Journal of the Soil Mechanics and Foundations division*, 97, 1249–1273.

Sharma, M., Satyam, N. & Reddy, K. R. 2021. State of the art review of emerging and biogeotechnical methods for liquefaction mitigation in sands. *Journal of Hazardous, Toxic, and Radioactive Waste*, 25, 03120002.

Vaid, Y. & Sivathayalan, S. 1996. Static and cyclic liquefaction potential of Fraser Delta sand in simple shear and triaxial tests. *Canadian Geotechnical Journal*, 33, 281–289.

Xiao, P., Liu, H., Xiao, Y., Stuedlein, A. W. & Evans, T. M. 2018. Liquefaction resistance of bio-cemented calcareous sand. *Soil Dynamics and Earthquake Engineering*, 107, 9–19.

Smart Geotechnics for Smart Societies – Zhussupbekov, Sarsembayeva & Kaliakin (Eds)
© 2023 The Author(s), ISBN 978-1-003-29912-7
Open Access: www.taylorfrancis.com, CC BY-NC-ND 4.0 license

Extremely long coseismic flow of sandy slopes and its mathematical modelling

I. Towhata
Kanto Gakuin University, Yokohama, Japan

ABSTRACT: This paper addresses coseismic landslides in gentle sandy slopes wherein the displacement exceeded 500 m and claimed hundreds of deaths in destroyed houses. This extent of displacement was substantially greater than what happened during past earthquakes. Aiming at mathematical reproduction of this extreme event, the study reviews the reconnaissance findings and then refers to field surveys. Accounting for the loss of shear resistance under the surface crust, a mathematical theory was developed on the basis of gravity-induced compression of the crust in the slope direction induced by high ground water pressure underneath and loss of shear resistance. Consequently, the passive failure of the crust was found to have shortened the length of the slopes, thus triggering the extreme downslope displacement as occurred in the field.

1 INTRODUCTION

Liquefaction-induced lateral movement in gentle sandy slopes has been known during past earthquakes. In 2018, a profoundly striking movement was triggered by an earthquake of Mw=7.5 in Palu, Sulawesi Island, Indonesia, in which the lateral displacement exceeded 500 m and was in a clear contrast with those of several meters during the 1964 Niigata, the 1983 Nihonkai-Chubu and the 1994 Northridge earthquakes. Many houses on the moving slopes were transported with the ground movement and were destroyed at the terminus where moving materials deposited and hundreds of residents were killed under debris.

After this disaster, JICA (2021) conducted a comprehensive field study on the details of this slope disaster and published a report. As one of the study team, the author picks up the information on the displacement mechanism from the report and presents its mathematical modelling.

Figure 1. Head scarp of Balaroa site; see spring water in the foreground.

Figure 2. Accumulation of earth and debris at the terminus of Balaroa slope failure.

DOI: 10.1201/9781003299127-253

2 FINDINGS DURING FIELD RECONNAISSANCE

Major slope failure occurred at four sites which are namely Balaroa, Petobo, Jono Oge and Sibalaya, accompanied by a few smaller events. Figure 1 illustrates the head scarp of the Balaroa event, which is a typical example, accompanied by PGA=281 cm/s^2 recorded in the vicinity. Many lateral cracks were found beyond the scarp, implying tensile stress there. In the base of the landslide plane, water springs were still visible six weeks after the disaster. Figure 2 shows the terminus of the lateral movement where house debris and soil got accumulated.

The JICA study inquired the eyewitnesses on what they experienced during the seismic shaking and slope movement (Figure 3). Among many issues, it is interesting that water ejection (possibly liquefaction) started during or immediately after the end of strong shaking. Ground started to move shortly (typically 20 seconds) after the end of shaking and some eyewitnesses felt several meters of depression, followed by uplift. These phenomena had been hardly experienced during past earthquakes.

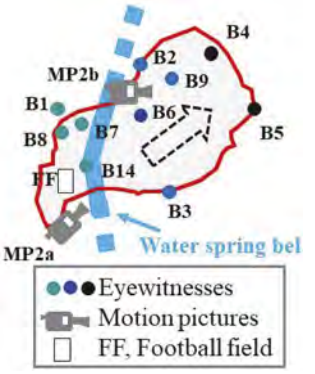

Figure 3. Location of eyewitnesses in Balaroa.

3 DISCUSSION ON BEHAVIOUR OF SUBSOIL UNDERGONG LONG-DISTANCE FLOW

Because the observed flow distance in 2018 was extremely longer than the past experiences, researchers sought for some 'special' conditions in the study areas. The effects of water leakage from the unpaved irrigation channel beyond the head scarp called attention (e.g., Nurdin et al. 2018) but this leakage is not the major cause because the Balaroa site did not have any water channel at its head. Similar to the other three sites of major slope failure, the Balaroa slope rested on a belt of water springs (Figure 3) that are common at the bottom end of alluvial fans; see water spring in Figure 1 as well.

Very loose sand exhibits strain softening during undrained shear, sometimes leading to total loss of shear strength. In the JICA study, this phenomenon was removed from the possible cause of the observed slope movement because the collected undisturbed sand samples did not behave in this manner. Another idea was the formation of water films between the surface soil crust and the underlying liquefied sand, meaning that the overlying crust can move freely along this frictionless 'water film'. This mechanism likely occurs at many places in alluvial planes and is considered not to be sufficiently 'special' to the Sulawesi sites.

The third possibility is the outbreak of underground aquifers triggered by earthquake shaking. This idea comes from the fact that the long-distance slope movements occurred in relatively low gaps between bigger and older fans (Figure 4). The low gap has less overburden and likely allows outbreak of pressurized water. Then, the last possibility is the water ejection from a tectonic origin. This idea stems from the fact that the site is a pull-apart basin formed by the very active

Palu-Koro strike-slip fault (annual displacement = 30-40 mm). It is recalled that the Matsushiro earthquake swarm was triggered by upward flow of tectonic water (Nakamura 1984) and this flow triggered three landslides. To date, no single mechanism has been decided on.

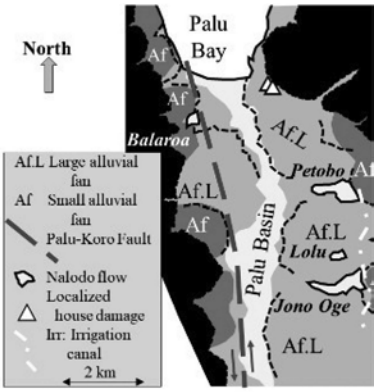

Figure 4. Sites of slope failure (called Nalodo here) between bigger fans (Af.L).

4 MECHANISM OF LONG LATERAL DISPLACEMENT OF SURFACE CRUST

In contrast to the preceding discussion on source of water pressure, the consideration on the surface crust is simple. Figure 5 schematically shows the crust resting on water. It does not matter whether this water stands for water film, outburst of pressurized water aquifer or tectonic water. Without shear stress in the lower face of the crust, the gravity force increases the longitudinal stress, σ_1, with the distance, x, from the head scarp. In case that the slope is long, this longitudinal stress exceeds the passive earth pressure and triggers shear failure as illustrated in this figure.

Figure 6 indicates the idealized stress state in which the principal stresses are given by

$$\sigma_1 = 2\rho_s g x \frac{z}{H} \sin i$$

in the longitudinal direction, and

$$\sigma_3 = \rho_s g z \cos i \tag{1}$$

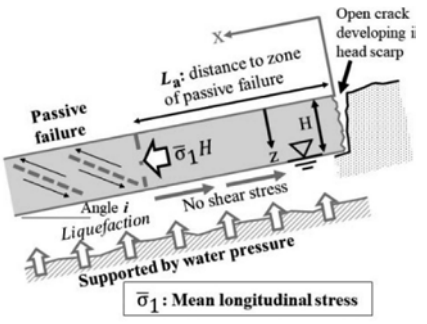

Figure 5. Surface crust subject to gravity-induced longitudinal compression.

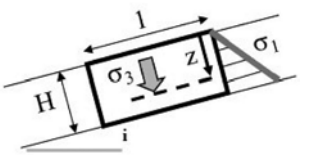

Figure 6. Idealization of stress state in the dry surface crust.

Where $\rho_s g$ stands for the unit weight of soil, and i means the slope angle. Accordingly, the mean longitudinal stress, $\overline{\sigma_1}$, satisfies the force equilibrium without base friction;

$$\overline{\sigma_1} H = \rho_s g H x \sin i \tag{2}$$

At a long distance (x=L_a) from the open crack at the top (Figures 1 and 6), the two principal stresses satisfy the passive failure conditions. Therefore, the distance from the top of the slope to the first passive failure (Figure 5) is given by

$$L_a = \frac{H}{2 \tan i} tan^2 \left(45^\circ + \frac{\phi}{2} \right) \tag{3}$$

Suppose that the soil thickness, H, = 3-5 m, the frictional angle, φ, = 30 degrees in loose sand, and tan$i$=0.02, the distance to the passive failure is L_a= 225-375 m (Figure 5), which is substantially long and accounts for the reason why passive failure and long-distance flow did not occur in shorter slopes during past earthquakes. Figure 7 illustrates the idealized model of surface crust beyond the passive failure point. The upriding of blocks occurs in the direction of 45°-φ/2 and the forces between blocks are the normal force, N, and the shear force, S=Ntanφ, whereas the contact force, N_p, with the floor becomes null at limit equilibrium after upriding. Following geometrical and force equilibrium calculations, the values of a and b are determined;

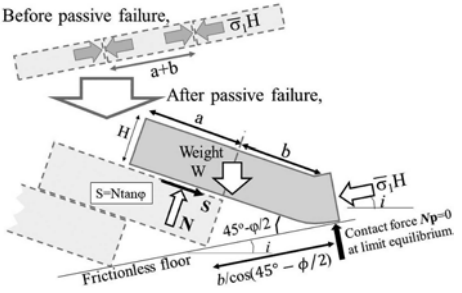

Figure 7. Surface soil blocks riding up on adjacent blocks as a consequence of passive failure.

$$\begin{gathered} a + b = sin\, i \frac{cos(45^\circ + \frac{\phi}{2})}{sin(45^\circ + \frac{\phi}{2} - i)} x \ and \\ b = H / \tan(45^\circ - \phi/2) \end{gathered} \tag{4}$$

This means that a soil block of the slope-parallel length = a+b rides up on an adjacent one (obduction) and the new longitudinal length per block decreases to b/cos(45° - φ/2). This shortening is calculated over the entire zone of passive failure and the slope displacement is worked out. The shortening ratio is defined as 'shortening' / 'original length' which is equivalent with compressional strain in continuum mechanics. Note that a fixed boundary condition is assumed at the foot of the slope as evidenced by the soil accumulation (Figure 2). It attracted attention that this theoretical study revealed negative shortening ratio near the top of the slope, suggesting a formation of big void under the upriding blocks and elongation in this part of the slope. Because formation of a big void is not realistic, the present calculation ignores this negative shortening.

5 EXAMPLE CALCULATION OF LATERAL DISPLACEMENT

Displacement was calculated by considering the shortening ratio to be equivalent with 'strain' and integrating it along the slope length. Figure 8 shows the results in which the realistic combination of H=3m and the slope length, L, =1000-2000 m gives the maximum displacement (see ○ in the

figure) of 100-700 m, which is consistent with reality. Note that the slope has to be longer than 500 m for this parameter combination in order to trigger the passive failure mechanism. This is the chief reason why the long distance flow did not occur in shorter liquefied slopes during past earthquakes. Further, the upriding of blocks and its collapse account for the substantial depression and uplift as mentioned by eyewitnesses. Figure 9 illustrates the effects on the maximum displacement exerted by the slope gradient and the friction angle in the surface crust. Within the range of calculation, the friction angle is less important than the slope gradient.

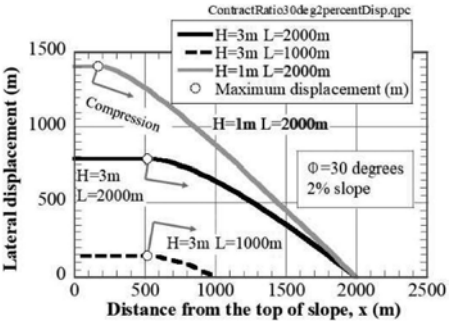

Figure 8. Calculated lateral displacement.

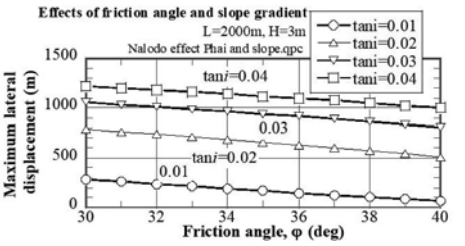

Figure 9. Maximum displacement affected by slope gradient and friction angle in the surface crust.

6 CONCLUSIONS

In response to the 2018 landslide disaster in Sulawesi, Indonesia, a predictive method was developed on the long-distance flow of gentle slopes. The major conclusive points are listed below.

1. As suggested by sand ejecta and water springs inside the landslide area, high ground water pressure presumably promoted the long-distance flow. The present study supposes that this high pressure erased the effective stress under the surface soil crust, and the loss of shear resistance underneath allowed extremely long lateral movement.
2. The gravity of the crust has a component in the slope-parallel direction that increases the longitudinal stress in the crust.
3. When the slope is long enough, the accumulated longitudinal stress becomes high enough to cause passive failure, causing upriding of the blocks in the surface crust.
4. An analytical method was developed that considers the above-mentioned mechanism and gives the displacement which is consistent with the observed displacement.

ACKNOWLEDGEMENT

Deep appreciations are expressed by the author to Mr. H. Furuichi of Yachiyo Engineering Company and the research team of the landslide disaster that was organized by JICA.

REFERENCES

JICA (2021) Technical report on liquefaction and landslides on shore. *Report of the domestic supporting committee* (in Japanese).

Nakamura K (1984) Three different mechanisms for elongate distribution of shallow earthquake epicenters. *Workshop XIX on Active Tectonic and Magmatic Processes beneath Long Valley Caldera, Eastern California*, USGS Vol. I: 482–492.

Nurdin S et al.(2018) Liquefaction disaster mitigation and geohydrology conditions, Lessons from the Palu earthquake magnitude 7.4 *M*w 28 September 2018. *Proc. 23rd Annual National Conference on Geotechnical Engineering*, HATTI, Indonesian Society for Geotechnical Engineering.

Smart Geotechnics for Smart Societies – Zhussupbekov, Sarsembayeva & Kaliakin (Eds)
© 2023 The Author(s), ISBN 978-1-003-29912-7
Open Access: www.taylorfrancis.com, CC BY-NC-ND 4.0 license

Collapse behavior and microstructure of loess soils in middle Asia

C. Boley
Institute for Soil Mechanics and Geotechnical Engineering, Bundeswehr University Munich, Germany

C. Meier
Boley Geotechnik GmbH, Munich, Germany

ABSTRACT: Mazar-e-Sharif is located in northern Afghanistan in a basin with thick alluvial sediment (loess). In its dry state, loess is rock hard, however, with an increase in water content (rainfall events), the dry soil structure collapses and sags. This leads to massive problems for construction projects.

Previous research focusses on collapse-criteria, solely for qualitative estimates on sagging potential due to the increase of water concentration (hydroconsolidation). A new method of prediction, also with a quantitative estimate, is presented by determining the influencing factors on the sagging like clay and lime percentage, pore space and macro-/microstructure of the soil in transition from semi-stable to compact. The results enable the formulation of an empirical-deductive method to predict the collapse-like deformation due to hydroconsolidation.

The intent is a practice-orientated and applicable design method that approximates the behavior of meta-stable soil structures in the event of an earthquake or the effects of weapons-related explosions.

1 INTRODUCTION

Loess and loess-like deposits cover more than 10% of the earth's surface and represent the most widespread deposit of the Quaternary period (Pécsi 1996). As an aeolian or fluvial sediment, loess belongs to a group of soils that have a high degree of strength and load-bearing capacity when they are earth-moist. The increase in water content leads to a loss of the high stability and to a qualitative change in the soil-mechanical behavior (Feda 1966) as a result of rearrangement of the grain structure. The reduction in volume associated with this rearrangement is generally referred to as sagging.

The structure of the examined loess soil, before the subsidence occurs, is described as meta-stable if the following soil characteristics occur simultaneously (Rogers 1995):

- geologically recent or recently altered sediments
- high porosity
- open pore structure
- high sensitivity to changes in water content
- weak interparticle binding forces

The Afghan loess soils of the Hindu Kush region around Mazar-e-Sharif and Kunduz considered here show all the characteristics mentioned above and, according to Rogers 1995, lead to a classification as soil prone to subsidence, i.e. soil prone to collapse.

In addition to geochemical investigations to determine the mineral composition and the water solubility of individual components, the empirical determination of the subsidence, i.e. collapse potential under static load, was the focus of the investigations. The aim was to formulate a new empirical prognosis method for estimating the collapse deformation of a recently formed loess soil (Meier 2011).

DOI: 10.1201/9781003299127-254

2 STRESS-STRAIN BEHAVIOR UNDER STATIC LOAD

The experimental determination of the deformation to be expected as a result of hydroconsolidation is not standardized in Germany. However, international normative regulations such as the Russian standard "GOST 23161-78" or the Chinese set of rules "GBJ 123-88" describe a method for examining the hydroconsolidation behavior. This is a modification of the one-dimensional compression test described in the German standard DIN EN ISO 17892-5. This was carried out using the test setup and procedure described below to determine the deformation behavior under static load.

2.1 *Research methodology*

In order to study the sensitivity of the loess soils in Mazar-e-Sharif to water, collapse tests were performed in laboratory according to Chinese Standard GBJ 123-88 (Boley 2009). For the tests, undisturbed loess samples with natural water content were compressed at first in an oedometer under different vertical pressures p. For the modified, one-dimensional compression tests, undisturbed soil samples, with in-situ water content and density properties, and with a diameter of 71 mm and a height of 14 to 24 mm were used. Since only natural samples were used, the determination of the influence of the examined parameters (clay content, pore content and lime content) was carried out exclusively based on the range of the respective parameter occurring in the naturally grown soil. That means, that the parameters were not varied, for example by adding clay or lime.

Before installing the sample, the top and bottom surfaces of the sample were machined flat and fitted with a filter plate. This filter plate ensures saturation of the sample from above as well as from the underside of the sample (Figure 1).

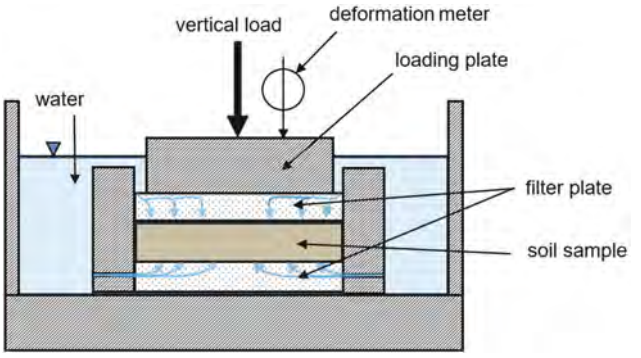

Figure 1. Experimental setup for saturation in consolidation press.

Five specimens with the specified dimensions were obtained from a special specimen. The specimens were gradually loaded in the axial direction via the loading plate. The vertical stresses applied were applied in the following increments: σ_v = 15, 50, 100, 150 and 200 kN/m².

The vertical stresses were only increased once the settlements from the previous load increment had subsided. After the deformation was complete, the samples were saturated, with the level of saturation being different for each of the five samples. The first specimen was saturated after the settlements from the first load increment (σ_v = 15 kN/m²) had subsided. All other samples went through the first load increment without a change in water content. Similarly, the second sample was only saturated after the settlements of the second load increment had subsided. The saturation of the remaining samples followed accordingly. The deformation that takes place as a result of loading and watering can be represented as a function of the effective stress. Figure 2 shows a schematic load-settlement curve for the test setup shown in Figure 1.

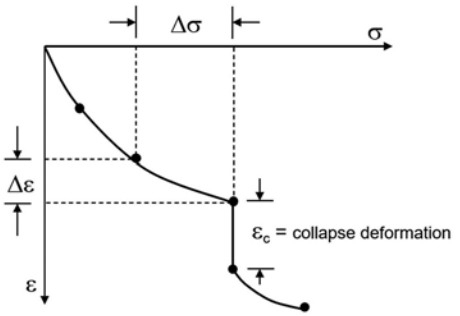

Figure 2. Deformation behavior of a collapsible loess soil.

2.2 *Study of various influencing parameters*

The test setup and procedure described for the modified compression tests was used to investigate the deformation behavior of Afghan loess soils as a result of hydroconsolidation. The study of various parameters and their influence on the average collapse deformation ε_{cav} was the focus of the study. In addition to the influence of the vertical stress (load level) and the soil density (pore content) described below, the influence of the natural clay content and lime content was also examined. The related relevant results can be found in Meier 2011.

The vertical stress σ_v acting on the soil at the time of saturation largely determines the degree of collapse-like deformation that occurs. Figure 3 shows the mean collapse deformation ε_c (index av = average) as a function of the vertical stress. The almost linear progression of the graph results from the connection of the marked points. These in turn characterize the mean collapse deformations for the five load levels σ_v = 15, 50, 100, 150 and 200 kN/m².

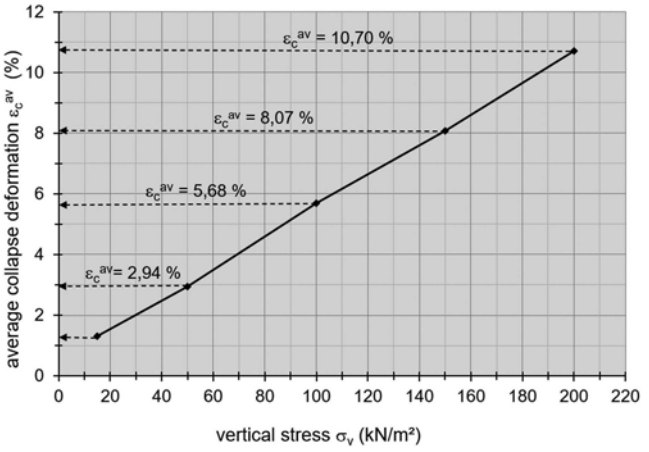

Figure 3. Influence of vertical pressure on collapse deformation.

In addition to the load level, the soil density and thus also the content of the pores in the soil are of particular importance regarding the deformation behavior. Figure 4 shows the influence of the porosity, of the natural soil on the subsidence behavior due to hydroconsolidation at a vertical stress of 200 kN/m². The porosity of the tested sample material was in the range $0.7 < e < 1.0$. As expected, the collapse strain increases with increasing porosity. This increase was shown to be linearly proportional in all tests. The metastable soil structure loses its strength due to the reduction in apparent cohesion due to changes in water content. Due to the collapse of the structure, the soil goes into a denser and therefore more stable structure. This behavior makes the pore content and thus the number of pores e, in addition to the vertical stress σ_v, the decisive parameter in hydroconsolidation.

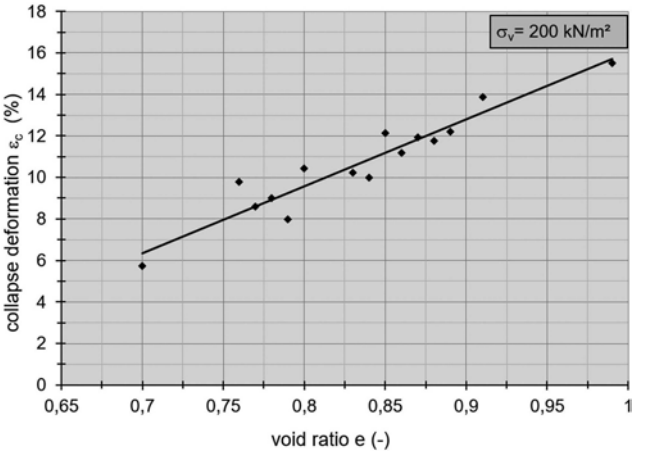

Figure 4. Influence of void ratio on collapse deformation, vertical pressure σ_v = 200 kN/m².

3 CONCLUSIONS

The study used the modified compression tests to determine the influence of various parameters on the collapse deformation ε_c. The results showed that both the clay content and the proportion of lime (calcite CaCO3) have no clear influence on the collapse deformation (Meier 2009 and 2011). Therefore, it does not make sense (for the Afghan loess soil) to use clay or lime content when predicting the expected subsidence due to hydroconsolidation. The influence of the void ratio on the other hand, proved to be a clear indicator in all tests, since the collapse deformation was always linearly proportional to the number of pores. In addition to the void ratio, the vertical load applied when changing the water content also has a major influence. Thus, the subsidence occurring as a result of hydroconsolidation is largely determined by the in-situ prevailing density, i.e. the void ratio, as a function of the applied load.

The verification of the applicability of existing forecasting methods to the Afghan loess soil examined in the work by Meier 2011 makes it clear that, despite the existing approaches, there is a need for a reliable and practice-oriented method for the quantitative determination of hydroconsolidation behavior. Based on the results obtained from the modified, one-dimensional compression tests, a new empirical forecasting method was presented (Meier 2011). This enables a quantitative estimation of the collapse deformation for recently formed fluvial and aeolian loess soils.

REFERENCES

Boley, C., Meier, C., Zou, Y. 2009 Bauen in Erdbebengebieten von Afghanistan: Besondere Herausforderung bei der Gründung auf kollapsgefährdeten Böden, 7. Österreichische Geotechniktagung, Tagungsband, 35–46, Wien, 2009

Feda, J. 1966 Structural stability of subsident loess soils from Praha-Dejvice, Engineering Geology 1, pp. 201–219, Amsterdam, 1966

Meier, C. 2011 Untersuchungen zur Mikrostruktur und zum Setzungsverhalten von Lössböden, Dissertation, Universität der Bundeswehr München, 2011

Meier, C., Boley, C., Zou, Y. 2009 Practical Relevance of collapse behaviour and microstructure of loess soils in Afghanistan, Proceedings of the 17th International Conference on Soil Mechanics and Geotechnical Engineering, pp. 738–741, Alexandria, 2009

Pécsi, M. 1996 Löss – Herkunft, Gliederung, Landschaften, Zeitschrift für Geomorphologie 98, p. 391 1996

Rogers, C.D.F. 1995 Types of distribution of collapsible soils, Genesis and Properties of Collapsible Soils – E. Derbyshire et. al., pp. 1–17, Springer 1995

Smart Geotechnics for Smart Societies – Zhussupbekov, Sarsembayeva & Kaliakin (Eds)
© 2023 The Author(s), ISBN 978-1-003-29912-7
Open Access: www.taylorfrancis.com, CC BY-NC-ND 4.0 license

Characteristics of liquefaction strength for sandy soil

K. Ishii & S. Kamao
Department of Civil Engineering, Nihon University, Japan

ABSTRACT: Liquefaction has also been reported in soils containing fine grains, and studies have been conducted on the liquefaction characteristics of fine-grained sands. Evaluation of liquefaction strength using skeleton void ratio and fine-grained void ratio focusing on the skeletal structure of the soil has been studied. However, it is difficult to evaluate the liquefaction strength of sands containing fine grains with different plasticity index based only on the skeleton void ratio and fine fraction void ratio. In this study, fine-grained Toyoura sand with different plasticity index was mixed with the sand to make specimens, and repeated undrained triaxial tests were conducted. The objective of this study is to understand the characteristics of fine-grained sand on liquefaction strength.

1 INTRODUCTION

Liquefaction has also been reported in soils containing fine grains, and studies have been conducted on the liquefaction characteristics of fine-grained sands. Evaluation of liquefaction strength using skeleton void ratio (Sato 1997, Wen 2021, Ishii 2022) and fine fraction void ratio (Sato 1997, Wen 2021, Ishii 2022) focusing on the skeletal structure of the soil has been studied. Ishii et al. have conducted undrained cyclic triaxial tests using soil mixtures with a constant void ratio e and varying fine-grain content from 0 to 40%. (1) In the region where the skeleton void ratio e_s does not exceed the maximum void ratio e_{max} of sand alone ($e_s < e_{max}$), the liquefaction strength R_{20} is uniquely related to the skeleton void ratio e_s regardless of the type of fine fraction. (2) With a skeleton void ratio e_s above the maximum void ratio e_{max} for sand only ($e_s > e_{max}$), the liquefaction strength R_{20} has a good correlation with the "Fine fraction void ratio e_{ff}" in the region where the fine fraction is predominant. (3) In the region with skeleton void ratio e_s exceeding the maximum void ratio e_{max} of sand alone ($e_s > e_{max}$), liquefaction strength tends to be different depending on the plasticity index I_p of fine fraction. However, it is difficult to evaluate the liquefaction strength of sands containing fine grains with different plasticity index based only on the skeleton void ratio and fine fraction void ratio. In this study, fine-grained Toyoura sand with different plasticity index was mixed with the sand to make specimens, and undrained cyclic triaxial tests were conducted. The objective of this study is to understand the characteristics of fine-grained sand on liquefaction strength.

2 EXPERIMENT OVERVIEW

2.1 *Sample*

The samples used were Toyoura sand as coarse-grained soil and kaolin clay as fine-grained soil. Fujinomori clay and Kasaoka clay, which have a higher plasticity index than kaolin clay, were also used to examine the effects of the different properties of the fine-grained soil. The mixing ratio was determined as a percentage of the dry mass of the fine-grained fraction to the total dry mass, ranging from 0 to 60%. Each mixed soil is referred to as K5 (kaolin-mixed soil

DOI: 10.1201/9781003299127-255

with 5% fine-grain content), F10, or KS20, depending on the initial letter of the name of the fine-grained soil and the mixing ratio. Main soil property values and particle size distributions of each sample are shown in Tables 1 and 2, Figure 1.

Table 1. Main soil property values ofcoarse-grained soil.

	Soil particle dencity	Mean grain size	Clay fraction	Fine fraction	Plasticity index
Coarse-grained soil	P_s (Mg/cm^3)	D_{50} (mm)	CC (%)	FC (%)	I_p
Toyoura sand	2.64	0.161	0	0	NP

Table 2. Main soil property values of fine-grained soil.

	Soil particle dencity	Mean grain size	Clay fraction	Fine fraction	Plasticity index
Coarse-grained soil	P_s (Mg/cm^3)	D_{50} (mm)	CC (%)	FC (%)	I_p
Kaolin clay (K)	2.714	0.003	64	100	13.7
Fujinomori clay (F)	2.535	0.009	37	92	20.4
Kasaoka clay (KS)	2.710	0.006	46	100	30.8

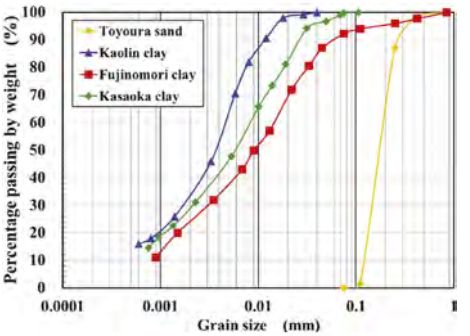

Figure 1. Grain size accumulation curves the sample.

2.2 *Experimental method*

The specimen is a cylindrical sample of 5cm in diameter and 10 cm in height. The specimens were divided into ten equal parts and then divided into ten layers, each layer of which was solidified with a rammer. After the specimens were prepared at a predetermined density, the specimens were first allowed to stand on their own at a constraint pressure of 20 kPa and were saturated by aerating carbon dioxide, passing sufficient degassed water, and then saturated by applying 200 kPa of backpressure, which is about three times the volume of the specimens. Subsequently, consolidation was performed with effective constraint pressure σ_c' = 100 kPa. The consolidation time was set as shown in Table 3 for each sample, considering that the consolidation could be completed sufficiently. After the consolidation was completed, the B-value was measured to confirm the saturation, and the backpressure was further applied to make the B-value more than 0.95. After confirming that the B-value was more than 0.95, the material was repeatedly loaded with a sinusoidal wave of 0.1 Hz frequency at the prescribed cyclic stress ratio R(= $\sigma_d/2\sigma_c$'). The test conditions for each sample are shown in Table 3.

Table 3. Test conditions for cyclic triaxial.

Sample	Density () indicates D_r (%)	Initial void ratio e_0	Consolidation time t (hour)	Cyclic stress ratio $R = (\sigma_d/2\sigma_c')$
Toyoura	Loose (40)	0.828	0.5	0.12, 0.13, 0.15
	Medium (60)	0.757	0.5	0.16, 0.17, 0.18
	Dense (80)	0.687	0.5	0.21, 0.22, 0.24
K5	Loose	0.828	1	0.09, 0.10, 0.14
	Medium	0.757	1	0.12, 0.14, 0.16
	Dense	0.687	1	0.15, 0.17, 0.18
K 10	Loose	0.828	5	0.08, 0.10, 0.12
	Medium	0.757	5	0.08, 0.10, 0.12
	Dense	0.687	5	0.10, 0.11, 0.12
K 15	Loose	0.828	12	0.08, 0.10, 0.12
	Medium	0.757	12	0.08, 0.10
K20	Medium	0.757	24	0.07, 0.08, 0.09
K25	Medium	0.757	24	0.08, 0.09
K30	Medium	0.757	24	0.10, 0.12, 0.15
K35	Loose	0.828	24	0.08, 0.09
	Medium	0.757	24	0.11, 0.13, 0.15
K40	Loose	0.828	24	0.09, 0.13
	Medium	0.757	24	0.11, 0.13, 0.15
K60	Medium	0.757	72	0.14, 0.16
F3	Medium	0.757	0.5	0.2, 0.17, 0.125
F5	Medium	0.757	1	0.16, 0.14, 0.12
F10	Medium	0.757	5	0.12, 0.11
F15	Medium	0.757	15	0.11, 0.09
F20	Medium	0.757	18	0.105, 0.115
F25	Medium	0.757	24	0.11, 0.12
F40	Medium	0.757	48	0.16, 0.17, 0.18
KS5	Medium	0.757	1	0.17, 0.13
KS10	Medium	0.757	5	0.15, 0.12, 0.10
KS20	Medium	0.757	15	0.11, 0.10
KS30	Medium	0.757	48	0.12, 0.13, 0.14
KS40	Medium	0.757	48	0.17, 0.18, 0.19
KS60	Medium	0.757	72	0.22, 0.26, 0.27

In this study, the most densely packed sand is called "Dense", the most loosely packed sand is called "Loose", and the sand with a density in between is called "Medium". When only Toyoura sand was used, to consider the effect of density change, the relative densities were adjusted in three ways: D_r = 40% (Loose), D_r = 60% (Medium), and, D_r = 80% (Dense). When the same test was conducted using mixed soil, the density was controlled so that the initial void ratio e_0 was e_0 = 0.828(Loose), e_0 = 0.757(Medium), and e_0 = 0.684 (Dense), respectively, which was the same value as the initial void ratio e_0 when the density was adjusted using only Toyoura sand.

3 EXPERIMENT RESULTS

3.1 *Relationship between fine fraction content and liquefaction strength*

As an index of liquefaction strength, the cyclic shear stress R at which both amplitude strains DA = 5% after 20 cycles of cyclic loading was used as the "liquefaction strength R_{20}. Figure 2 shows the relationship between the liquefaction strength R_{20} and the fine-grain content FC calculated from the liquefaction strength curves of each sample. Figure 2 shows that the liquefaction strength R_{20} of each soil mixture decreases with increasing fine-grain content, and

then R_{20} begins to increase around FC = 20%. Furthermore, as the fine-grain content increases, the difference in liquefaction strength due to the type of fine-grain content becomes more pronounced.

3.2 *Skeletal structure of mixed soils*

In this study, the effect of the fine fraction on liquefaction properties was considered using "Skeleton void ratio e_s" and "Fine fraction void ratio e_{ff}". The skeleton void ratio e_s is the void ratio when all fine fractions are considered as pores while the skeleton void ratio e_s is the void ratio. The fine fraction void ratio e_{ff} is a void ratio that ignores the volume of coarse-grains and focuses only on the fine fraction content, which is an indicator of how well the fine fraction content is plugged. The void ratio can be calculated by the following Equations (1) and (2). Equations (1) and (2) use the symbols shown in Figure 3.

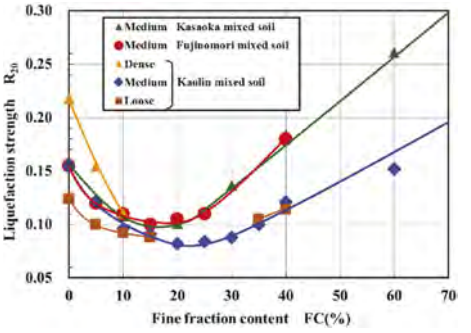

Figure 2. Effect of fine fraction content FC on liquefaction strength R_{20}.

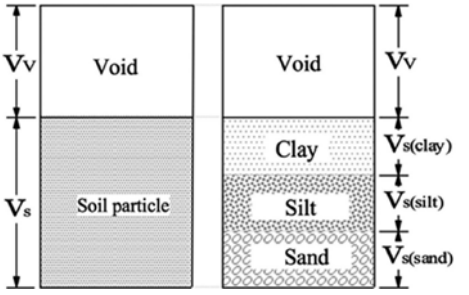

Figure 3. Schematic of mixed samples.

$$\text{Skeleton void ratio } e_s = \frac{V_v + V_{s(silt)} + V_{s(clay)}}{V_{s(sand)}} \tag{1}$$

$$\text{Fine fraction void ratio } e_{ff} = \frac{V_v}{V_{s(clay)} + V_{s(silt)}} \tag{2}$$

3.3 *Relationship between skeleton void ratio and liquefaction strength*

The relationship between the skeleton void ratio e_s and the liquefaction strength R_{20} of each soil mixture is shown in Figure 4. Previous studies have shown that (Ishii 2022) the

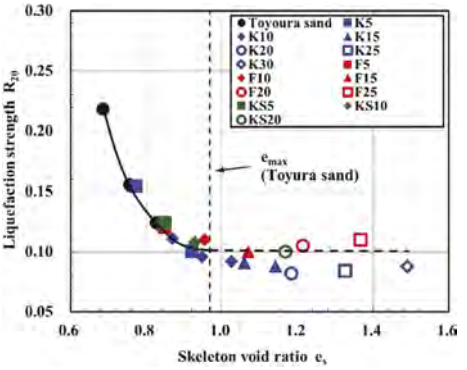

Figure 4. Relationship between Skeleton void ratio e_s and Liquefaction Strength R_{20}.

liquefaction strength increases with the plasticity index of fine-grained soil when the skeleton void ratio e_s is larger than the maximum void ratio of sand, and the liquefaction strength of fine-grained soil increases with the plasticity index of fine-grained soil when the skeleton void ratio e_s is larger than the maximum void ratio of sand. The figure focuses only on the non-plastic mixed soil and plots only the data for the non-plastic mixed soil. For the Toyoura sand only, the skeleton void ratio e_s is on the same curve as R_{20} regardless of the type of fine-grained soil, indicating a good relationship between the skeleton void ratio e_s and R_{20}. This indicates that in the range smaller than the sand-only e_{max}, the skeletal structure of the soil is formed by the sand content, and the fine-grain content has no effect on R_{20}, and R_{20} is determined by the skeleton void ratio e_s. In the range where the skeleton void ratio e_s is larger than the maximum void ratio e_{max} of sand only, the liquefaction strength R_{20} is approximately equal to the liquefaction strength when the skeleton void ratio is equal to the maximum void ratio of sand. In the range where the maximum void ratio of sand only, e_{max}, is larger than the skeleton void ratio, e_s, the sand becomes the sand becomes misalighed and the influence of fine grains gradually increases, but the liquefaction strength does not increase significantly because the soil is a non-plastic mixture.

3.4 *Relationship between fine fraction void ratio, plasticity index and liquefaction strength*

In the range where the skeleton void ratio e_s is larger than the maximum void ratio e_{max} of sand, R_{20} is considered to be influenced by the skeletal structure and soil properties of fine grains, and is considered to be closely related to the fine fraction void ratio e_{ff} and the plasticity index I_p. The relationship between the fine fraction void ratio e_{ff} and liquefaction strength R_{20} is shown in Figure 5. Figure 5 shows that the liquefaction strength increases as the fine fraction void ratio e_{ff} decreases, but the results are divided between kaolin mixed soil (blue dashed line) and other mixed soil (green dashed line) due to the difference in the plasticity index of fine-grained soils. Therefore, the relationship between the plasticity index and liquefaction strength of mixed soils with fine fraction content in the range where the skeleton void ratio e_s is larger than the maximum void ratio e_{max} of sand is examined as shown in Figure 6. The liquefaction strength tends to increase as the plasticity index increases, even at the same fine fraction content. Therefore, it can be said that there is a better relationship between the plasticity index I_p and liquefaction strength R_{20} in the range where the skeleton void ratio e_s is larger than e_{max} than the fine fraction void ratio e_{ff}.

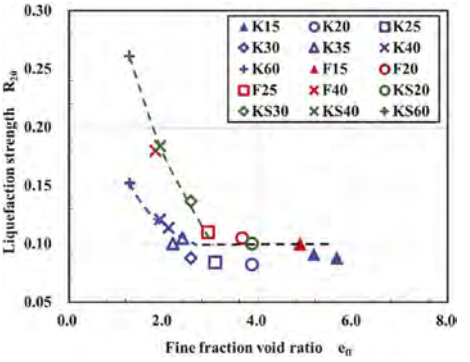

Figure 5. Relationship between Fine fraction void ratio e_{ff} and liquefaction strength R_{20}.

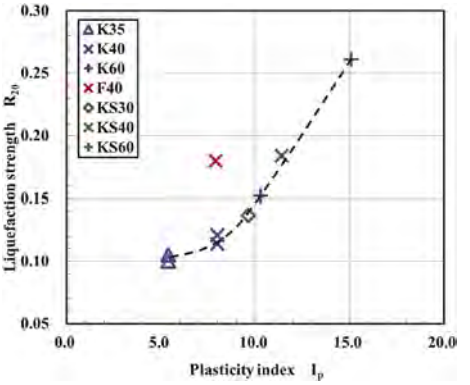

Figure 6. Relationship between plasticity index I_p and liquefaction strength R_{20}.

4 CONCLUSION

(1) The liquefaction strength R_{20} was found to have a good relationship with the skeleton void ratio e_s regardless of the type of fine-grained soil in the range of skeleton void ratio e_s less than the maximum void ratio of sand only ($e_s < e_{max}$).
(2) In the range of skeleton void ratio e_s greater than the maximum void ratio of sand only ($e_s > e_{max}$), the liquefaction strength R_{20} tends to be approximately equal to the liquefaction strength R_{20} when the skeleton void ratio e_s is equal to the maximum void ratio of sand when the mixed soil is unplasticized.
(3) The plasticity index I_p of the mixed soil tends to show a better relationship than the fine fraction void ratio e_{ff} in the range ($e_s > e_{max}$) where the maximum void ratio of sand only is greater than the skeleton void ratio e_s.

REFERENCES

Sato Masayuki et-al, 1997. Fundamental study on the effect of fines on liquefaction strength of the reclaimed ground, Journal of JSCE No.561/III-38: 271–282, 1997. (In Japanese only)

Wen Liu et-al, 2021. Effect of fines content on liquefaction characteristics, International Journal of GEOMATE, June., 2021, Vol.20, Issue 82:40–45

Ishii Kentaro et-al, 2022. Relationship between liquefaction strength ofsand with fine fraction and various void ratios, International Journal Of Geomate, March, 2022, Vol.22, Issue 91:1–7.

Smart Geotechnics for Smart Societies – Zhussupbekov, Sarsembayeva & Kaliakin (Eds)
© 2023 The Author(s), ISBN 978-1-003-29912-7
Open Access: www.taylorfrancis.com, CC BY-NC-ND 4.0 license

Investigation of dynamic response of sand-tire derivatives mix for geotechnical applications

A.S. Amanta
Postdoctoral Fellow, IIT Bombay, Mumbai, India

S.M. Dasaka
Professor, IIT Bombay, Mumbai, India

ABSTRACT: Disposal of used tires is a major global challenge. Used tires are recommended for usage in a variety of sectors due to their durability. The usage of derivatives out of used tire is reported in many recent researches for a variety of civil engineering applications. For potential use in liquefaction countermeasure techniques, the current study examines the dynamic characteristics and liquefaction resistance of sand, sand-tire chips, and sand-tire crumbs mixes. A number of cyclic triaxial tests were conducted in strain controlled condition, considering variables like all round pressures and strain. The present report includes description of the dynamic characteristics and liquefaction resistance for each mix in terms of excess pore pressure ratio. The findings indicated that the mix made with tire crumbs has the best damping behavior and is the most resistant to liquefaction, but it has a lower modulus than the mix with tire chips.

1 INTRODUCTION

Tire disposal is a huge global issue. Due to their longevity, used tires are suggested for use in many industries. A number of recent studies have proposed the use of scrap tire derivatives as light weight filler material in embankments (Tweedie et al. 1998; Shrestha et al. 2016),, drainage materials (Edil et al. 2004; Reddy et al. 2010) and use for vibration mitigation (Tsang 2008, Hazarika et al. 2010).

These tire derivatives are divided into three categories in accordance with ASTM D6270-17. Tire derivatives with sizes less than 12 mm, between 12 mm and 50 mm, and more than 50 mm are referred to as tire crumbs, tire chips, and tire shreds, respectively. Secondly, tire shreds are expected to have both fiber and metal reinforcements of the tires, while tire crumbs are not permitted to have any reinforcements.

The present study investigates the dynamic properties and liquefaction behaviour of sand, sand-tire chips, and sand-tire crumbs mixes for potential application in liquefaction countermeasure approaches.

2 MATERIALS AND EXPERIMENTAL PROGRAM

The present study considered sand and tire derivatives for the investigation. The sand used, had a specific gravity of solids as 2.62. The soil was poorly graded. Tire chips and crumbs are used in the study. The specific gravities of chips and crumbs were 1.14 and 1.02, respectively. The scrap tires that were available locally were shredded into tire chips, whereas the tire crumbs were commercially available. The tire chips had regular dimensions with largest particle size passing through 19 mm sieve and retained in 9.5 mm sieve. The used tire crumbs, however, were well graded, with a mean diameter of 1.87 mm and a maximum particle size of 9.5 mm. list further information about the tire chips, tire crumbs and sand. The maximum and minimum dry density of sand was 1.74 g/cm^3 and 1.44 g/cm^3, tire chips was 0.65 g/cm^3

DOI: 10.1201/9781003299127-256

and 0.51 g/cm^3, and tire crumbs was 0.57 g/cm^3 and 0.38 g/cm^3, respectively. Sand and tire derivatives were uniformly mixed together in a 4:1 weight ratio to uniform mix. M1 stands for sand-tire chips mix, and M2 for the sand-tire crumbs.

Twenty-seven number of strain-controlled, undrained, cyclic triaxial experiments (CTX) were conducted to examine the dynamic properties and liquefaction resistance of the sand-tire derivative mixes. In line with ASTM D3999-91 and D5311-92, the tests were conducted. Additionally, experiments were conducted at confining pressures of 50 kPa, 75 kPa, and 100 kPa; and strain amplitudes of 0.11%, 0.19%, and 0.26% to examine the impact of all round pressure and strain the liquefaction and dynamic response of the mixes. Experiments were done at 1 Hz frequency and 60% relative density. The cylindrical sample used for the CTX testing has dimensions of 100 mm by 200 mm. Dry pluviation was used to prepare the samples for analysis. Various test parameters were continuously recorded as the experiments progressed.

The dynamic parameters discussed in the paper were damping ratio (D) and shear modulus (G). These characteristics were determined using the stress-strain curve from the CTX tests. The excess pore pressure ratio (R_u), which is the ratio of the generated excess pore pressure (EPP) to the initial confining pressure, was used to compare the liquefaction behavior of the mixes. Liquefaction is said to have occurred when this R_u is close to unity.

3 RESULTS

Stress-strain plot is observed for all the CTX tests. For each of the three mixes taken into consideration in the study, a similar hysteresis loop is seen. The stress-strain plot flattens out as the loading cycles proceed, showing a decrease in the stiffness of the material. These hysteresis loops serve as the basis for the dynamic properties presented in this research.

The variation of the G for each of the three mixes is shown in Figure 1. It can be seen that among the three mixes, sand and M2 have the highest and lowest G values. Even though the proportion of tire derivatives in M1 and M2 is the same, the particle sizes vary. Even the M1 mix had tire derivatives with fiber reinforcement which must have contributed to the increase in the total stiffness of the sample.

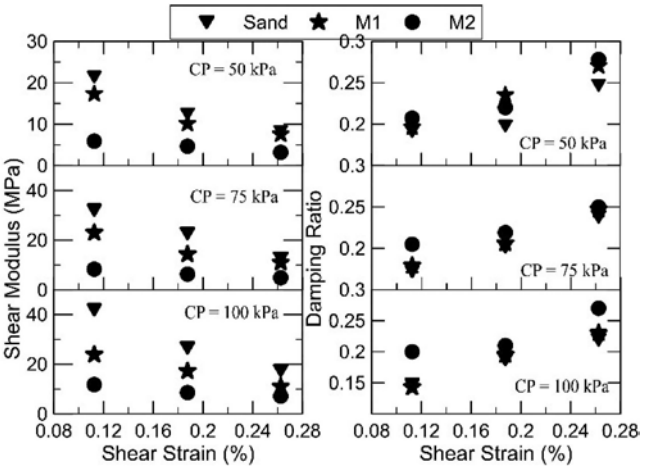

Figure 1. Dynamic properties of different mixes tested under different conditions.

The D values for all the mixes are also shown in Figure 1. It should be observed that even though tire derivatives only make up 20% of the weight of the mixes M1 and M2, the D of the sand was significantly impacted by them. As can be observed, the damping characteristics showed a tendency that was the reverse of G. Comparing the three combinations, the one with

tire crumbs consistently demonstrated the maximum damping. Of the three, the sand displayed the least damping. This damping characteristic of the mixes can be linked to the nature of the tire derivatives to deform easily when compared to the stiffer sand particles. Sand particles have a greater resistance to deformation.

Additionally, it can be seen in Figure 2 that strain amplitudes significantly affect the dynamic properties of all the mixes. The G value fell as the D value rose with increasing strain amplitude.

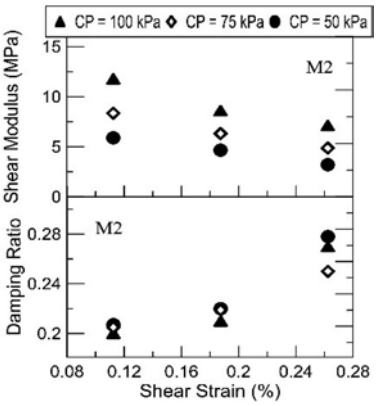

Figure 2. Effect of shear strain on G and D.

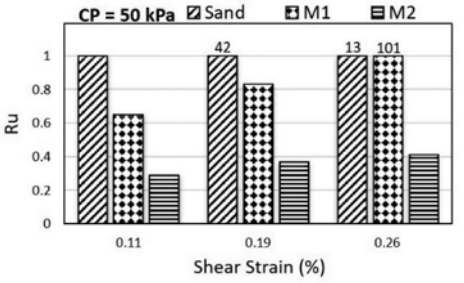

Figure 3. Variation of R_u with shear strain at confining pressure of 50 kPa.

The impact of confining pressures on the dynamic properties of all three mixes can be seen in Figure 2. It is evident that as confining pressure is increased, G increases while D decreases. This may be due to the fact that higher confining pressures would have produced a stronger matrix, increasing the stiffness of the sample and, consequently, its G value. This would have also led to a sample that was more resistant to deformation, which would have decreased the D values at confining pressures.

The liquefaction behavior of each mix in terms of R_u is described in this section. The R_u value after 200 loading cycles for specimen tested with 50 kPa confining pressure is shown in Figure 3. The number of cycles at which the sample reported liquefaction is also noted in the figure for samples that liquefied in less than 200 cycles. Three samples of sand liquefied out of the nine tests depicted in the figure. The three samples got liquefied at 0.19% and 0.26% shear strains for 13 to 101 number of loading cycles.

The figures show that for all mixes, the R_u value increases with increasing shear strain. Additionally, as confining pressures are raised, the R_u value decreases, making the samples more resistant to liquefaction. Similar results were obtained for tests carried out with confining pressures 75 kPa and 100 kPa.

The behavior of pore pressure generation is observed for all mixes. M2 has the lowest R_u value of the three mixes and did not liquefy in any of the circumstances taken into account. Despite having a similar amount of tire derivatives as M2, M1 displayed far higher R_u values than M2, and in every instance, the R_u value for M1 was found to be greater than double that of M2. Even with a confining pressure of 50 kPa and a strain amplitude of 0.26%, M1 achieved liquefaction after 101 cycles. The sand sample, in contrast to the mixes M1 and M2, reached liquefaction in all but two cases.

For the case where the confining pressure was the lowest i.e. 50 kPa and the strain amplitude was maximum i.e. 0.26%, the sand sample reached liquefaction after only 13 loading cycles. M1 mix liquefied at the same conditions at 101 cycles, which is nearly eight times than sand, whereas M2 barely reached a R_u value of 0.41.

4 CONCLUSIONS

The key conclusions from the current investigation are as follows:

- Among the three mixes studied, sand samples had the lowest D and the highest G.
- Sand has a lower G but a higher dampening characteristic when tire derivatives are included.
- Among the two mixes considered, tire chips exhibited higher modulus with sand but tire crumbs displayed stronger damping behavior.
- Liquefaction resistance was enhanced remarkably by the tire derivatives addtion.
- Among the three mixes, those containing tire crumbs demonstrated the greatest resistance to pore pressure generation.
- With increasing strain amplitudes, all of the mixes displayed a decrease in modulus and an increase in damping.
- For all the combinations, the increase in confining pressure increased G and decreased D.

REFERENCES

Amanta, A. S. and Dasaka, S. M. (2021). Evaluation of Engineering Properties of Sand–Tire Chips Mix. *Indian Geotechnical Journal*, 1–11.

Amanta, A. S., & Dasaka, S. M. (2022). Dynamic Characteristics and Liquefaction Behavior of Sand–Tire Chip Mixes. *Journal of Materials in Civil Engineering, ASCE*, *34*(10), 04022269.

ASTM D3999–91 (1996). Standard test methods for the determination of the modulus and damping properties of soils using the cyclic triaxial apparatus.

ASTM D5311–92 (2004). Standard test method for load controlled cyclic triaxial strength of soil.

ASTM D6270–17 (2017). Standard practice for use of scrap tires in civil engineering applications. West Conshohocken, PA.

Edil, T.B., Park, J.K., and Kim, J.Y. (2004). Effectiveness of scrap tire chips as sorptive drainage material. *Journal of Environmental Engineering*, 130(7), 824–831.

Hazarika, H., Yasuhara, K., Kikuchi, Y., Karmokar, A.K., and Mitarai, Y. (2010). Multifaceted potentials of tire-derived three-dimensional geosynthetics in geotechnical applications and their evaluation. *Geotextiles and geomembranes*, 28(3), 303–315.

Reddy, K.R., Stark, T.D., and Marella, A. (2010). Beneficial use of shredded tires as drainage material in cover systems for abandoned landfills. *Practice Periodical of Hazardous, Toxic, and Radioactive Waste Management*, *14*(1), 47–60.

Shrestha, S., Ravichandran, N., Raveendra, M., and Attenhofer, J.A. (2016). Design and analysis of retaining wall backfilled with shredded tire and subjected to earthquake shaking. *Soil Dynamics and Earthquake Engineering*, *90*, 227–239.

Tsang, H.H. (2008). Seismic isolation by rubber–soil mixes for developing countries. *Earthquake engineering and structural dynamics*, 37(2), 283–303.

Tweedie, J.J., Humphrey, D.N., and Sandford, T.C. (1998). Tire shreds as lightweight retaining wall backfill: active conditions. *Journal of geotechnical and geoenvironmental engineering*, 124(11), 1061–1070.

Smart Geotechnics for Smart Societies – Zhussupbekov, Sarsembayeva & Kaliakin (Eds)
© 2023 The Author(s), ISBN 978-1-003-29912-7
Open Access: www.taylorfrancis.com, CC BY-NC-ND 4.0 license

Experimental study of uplift of buried pipe liquefiable soil at different depths

M. Hajialilue-Bonab
Professor of Geotechnical Engineering, Faculty of Civil Engineering, University of Tabriz, Tabriz, Iran

S. Bahram Ghannad
MSc. Student, Faculty of Civil Engineering, University of Tabriz, Tabriz, Iran

ABSTRACT: Many buried structures, including tunnels and lifelines, have been severely damaged in recent earthquakes. It is noteworthy that the phenomenon of soil liquefaction has played a significant role in the occurrence of these damages. Damage caused by the uplift of lifelines has motivated the study of the uplift of buried structures. Therefore, in this study, an attempt has been made to experimental study of the uplift of buried pipes in liquefiable soils by physical modeling at different depths. The soil used in this study is Gum Tape sand and shaking table has been used to simulate seismic load. Buried pipe at three depths: 1.5, 2.5 and 5 times the diameter of the pipe has been subjected to seismic load and the degree of elevation and deformation mechanism have been investigated. The results show that with decreasing the buried depth of the pipe, due to the relatively high pore water pressure in the lower depth of the soil, the overpressure created after dynamic loading tends to be wasted and flows towards the low-pressure points (surface part). And because in the surface areas, the flow is upward, so the uplift continues to some extent. Also, the displacement vectors on the sides of the pipe are in the form of circular rings that try to raise the pipe.

1 INTRODUCTION

Today, the increase in population and, consequently, the increase in demand, has highlighted the role of lifelines in human life.

Natural disasters such as earthquakes can cause damage to these lines. According to statistics, the rise of pipes is one of the obvious failures that the occurrence of which will lead to other damages [1, 2]. Therefore, it is important to find out the cause of uplift.

What makes the conditions more suitable for the occurrence of soil liquefaction is three factors: 1- Loose sand soil 2- High groundwater level 3- Earthquake that aggravate the conditions for its occurrence. It is worth noting that liquefaction is one of the destructive factors of lifelines that has been studied in this study. Loose sand soils have high permeability, but if this type of soil is saturated and subjected to seismicity, despite the high permeability, due to high loading speed and tendency to reduce soil volume, the opportunity for water exit is not provided and undrain condition governs the problem [3]. As a result, with the occurrence of undrain condition, the role of effective stress, as a representative of soil resistance due to increased water pressure will be diminished, and as a result, the soil loses its shear strength and will behave like a liquid. In other words, it can be stated that the soil has become liquefied [4]. By reducing the shear strength, the soil does not tolerate the maintenance of the buried pipe and the conditions for the rise of the pipe are provided [5, 6].

In the 1995 Kobe and 1999 Jiji earthquakes, the failure of water transmission lines due to liquefaction led to the failure of firefighters to contain the fire and caused irreparable damage

DOI: 10.1201/9781003299127-257

[7-9]. Examples of earthquakes that have caused soil liquefaction include the 1995 Kobe Earthquake [10], the 2004 Chuetsu Earthquake [11], the 2010 Chile Earthquake [12], and the 2011 Tokyo Earthquake [13].

In the study of Tokida et al. [14], the effect of liquefiable soil thickness under buried substructure and the width of the structure on the amount of uplift caused by liquefaction has been investigated experimentally and shaking table has been used to simulate the earthquake load. The results show that by stopping the applied load, deformation and uplift also stop and by reducing the thickness of liquefied soil and the thickness of the buried structure, the amount of uplift decreases. Also in this research, a kind of wall around the underground structure has been used to reduce the amount of overhang. Laboratory study of the effect of buried depth and diameter on the elevation of buried structures has been done by Chian et al. [5], the results have been indicated that with increasing the diameter and buried depth of the pipe, its elevation has decreased. The elevation of sewer pipes due to the liquefaction of the embankment behind the pipe has been investigated by Koski et al. [15]. In this research, shaking table has been used to model the seismic load. By considering the relative density of soil as the studied variable, it was concluded that the amount of uplift in the samples with loose sand at the beginning of the experiment was 5 to 15 mm, while there is no significant change in dense samples. However, at the end of seismic loading, the elevation of dense specimens increased significantly (about 100 mm = buried depth). The elevation of subway stations as a result of soil liquefaction was studied as numerical modeling (finite difference-finite element) by Ji-Lei et al. [16] and the results showed that liquefaction because of seismic load can initiate elevation but cannot be main reason. The uplift starts gradually from the first stage of liquefaction and increases with the amount of liquefied area, and finally with the complete liquefaction of the area, the amount of uplift occurs more intensely. It should also be noted that with the seismic stop, the simultaneous ascent does not stop. The seismic behavior of shallow foundations located on liquefiable soil was investigated numerically by Hasheminezhad et al. using flac software. In this study, soil columns have been used to improve the soil properties against liquefaction and the amount of liquefaction has been investigated by changing the geometric characteristics of the foundation and soil columns. With increasing the width of the foundation, the amount of overpressure of the pore water pressure has decreased [17]. In a study conducted by Nourzadeh et al., The vulnerability of Tehran gas facilities to liquefaction was evaluated. In this study, the phenomenon of liquefaction and vulnerability of buried pipes has been investigated by numerical and laboratory modeling. The results indicate that in some areas of Tehran there is a possibility of damage to lifelines that can be reduced by improving the soil characteristic [18]. Reduction of gas pipe vulnerability by Castiglia, et al. Has also been investigated by shaking table. A new method proposed to reduce gas pipe vulnerability in this study is the use of sandbags buried in the lower or upper part of the pipe [19]. Another method to deal with liquefaction and reduce the damage caused by it is the use of geogrids or geocomposites, which by Bahadori et al., Proved that the impact of geocomposites is more than geogrids [20]. In the study of Papadimitriou et al., The behavior of steel pipes buried in the riverbed that are affected by lateral slip has been investigated. In this study, numerical modeling of finite element has been performed with the aim of finding the maximum ground surface motion (PGD). The results showed that by increasing the thickness of the walls of the buried pipe, the allowable movement of the ground surface can be increased [21]. In a numerical study conducted by Sudevan et al., The elevation of structures buried in the soil has been investigated. In finite element software with Mohr Columbus behavioral model combined with Finn model, liquefied soil modeling has been performed[22]. According to Wu et al., The elevation of buried pipes at deep and shallow depths has been investigated. The result of this study is the dependence of the critical depth of buried pipes on the density of sand [23]. In order to reduce the uplift due to liquefaction, numerical modeling of liquefaction in FLAC software was performed by Mahmoud et al. As a result of this study, drainage around the structure and a layer of impermeable material under it is one of the methods to reduce uplift [24]. Huang et al. [25] believed that the rise of the pipe stops when the loading is complete. Therefore, in this research, the stopping time of the uplift will be evaluated in proportion to the loading.

2 MATERIALS AND METHODS

2.1 *Material properties and dimensional analysis*

Due to the presence of relatively large impurities, sifted soil has been used. The type of soil used in the experiments is Gum Tape sand, the properties of which are given in "Table 1".

Table 1. Properties of sand soil.

parameter	value
G_S	2.66
D_{10}	0.21 mm
D_{30}	0.3 mm
D_{60}	0.43 mm
Unified Soil Classification System	SP
C_C	1
C_u	2.05
$\rho^d_{\min}$	1.49 gr/cm^3
$\rho^d_{\max}$	1.72 gr/cm^3

It should also be noted that for physical modeling, it is necessary to perform dimensional analysis in order to maintain the behavior of soil and structure. In this study, Lai modeling law [26] has been used. The dimensional analysis used is similar to the dimensional analysis used in the study of Otsubo et al. [27], in this study, liquefaction and strategies to diminish it, were examined. It is noteworthy that in the modeling of the Otsubo study, the law of Lai modeling has been used for dimensional analysis. In Lai modeling law, dimensional analysis for physical modeling is performed using equilibrium equations and boundary conditions governing the problem. Lai stated that in shaking table models, due to the limited modeling space, it is necessary to scale the model to small dimensions, so by using this scale, other parameters that affect soil behavior can be scaled. In the present study, as in the Otsubo study, a scale of 1 to 5 (laboratory model to the main model) has been used.

According to Lai modeling law, the relative density of the original model (DrP) has been reduced by 15% to obtain the relative density of the laboratory model. Therefore, it can be stated that the relative density scale specified by NDr is equal to DrP-15%. The reason for the decrease in relative density is that in laboratory modeling the limiting pressure is reduced and in order to achieve the same dilatation angle and softening behavior at large strains, it is necessary to reduce the relative density by 15%. "Table 2".

Table 2. Dimensional analysis.

variable	parameter	Shaking table modeling	Value in current study
Geometry	N_G	1/5	(cm)100(length)* (width) 62* (height)64
Relative density	N_{Dr}	Dr_P-15%	30%
frequency	N_f	5	8 Hz
Pipe diameter	N_{dp}	1/5	6 cm

2.2 *Shaking table*

The reason for using shaking table in physical modeling is the need to apply seismic loading to create liquefaction in the soil. For this reason, the shaking table of Tabriz University, which was inaugurated in2016, has been used "Figure 1a".

The University of Tabriz shaking table has up-to-date equipment that allows dynamic simulation of experimental studies. Dynamic excitation like an earthquake is transmitted by the stimuli to the base of the model and simultaneously the seismic response of different points of the model is recorded by sensors and by analyzing and interpreting the records, the dynamic behavior of the real structure can be evaluated. The test platform of the shaking table is a rectangle with dimensions of m2 × m3, which is made of steel sheet and the capacity of the shaking table is up to 6 tons. The shaking table of Tabriz University has 1 degree of freedom and has a displacement range of 100 mm. The frequency designed for seismic operation is 0-20 HZ and the input movement enters the test platform through a horizontal hydraulic actuator. The test box is of rigid type with dimensions of 100 m (length) * m62 (width) * 64 m (height) "Figure 1b".

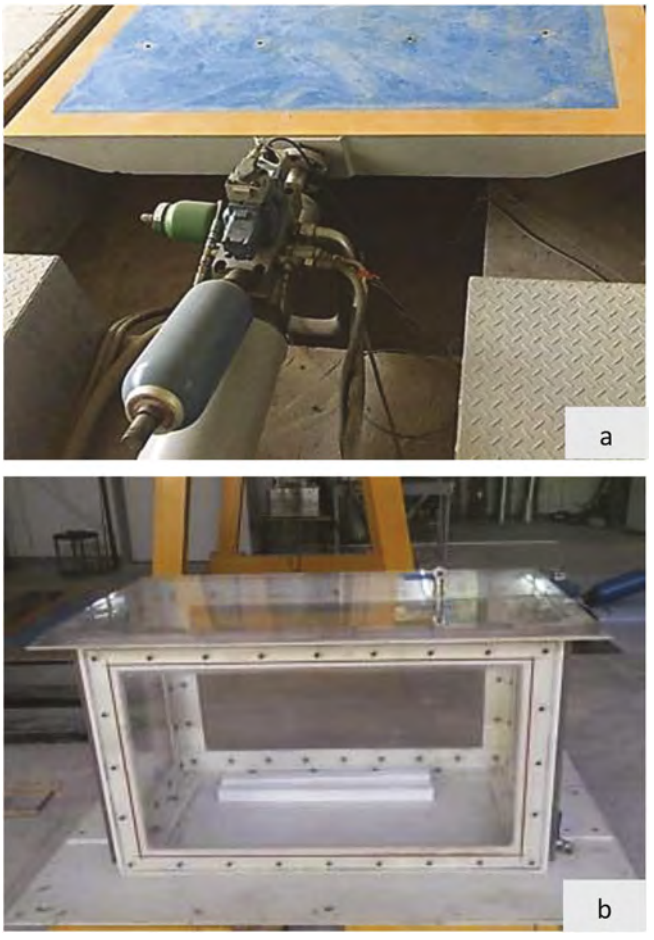

Figure 1. A) Shaking table b) rigid box.

2.3 *Properties of buried pipe, sensors, loading*

In this study, a hollow PVC pipe with an outer diameter of 6 m and a length of 61 cm and a density of 39 gr/cm3 was used to simulate the buried structure. Also, due to the lack of modeling of the water inside the pipe, both sides of the pipe are blocked so that water cannot enter the pipe.

In this study, an accelerometer has been used to control the applied seismic acceleration and a pressure gauge has been used to detect the excess pressure of the pore water during liquefaction. Relevant data can be recorded by connecting the accelerator and pressure gauge to the data logger.

Hatami et al. [28] After numerical study of the seismic response of concrete retaining walls, concluded that the seismic response of the retaining wall under the influence of different characteristics of ground input movements such as: dominant frequency, maximum ground velocity, earthquake intensity, earthquake duration and Also, the applied inputs of the recorded data of the earthquake accelerometer are real or applied in the form of harmonic motions. Also, many experimental studies on simpler physical systems have shown clear evidence of turbulent response with non-uniform correlations for various motion parameters that affect model behavior (such as range of motion and amount of final settlement). However, the most important purpose of model experiments in this study is to obtain information on the behavior of soils under dynamic loading. This goal can also be achieved by applying inputs from the earth's motion that do not reflect real seismic motion [29]. Therefore, in seismic experiments, instead of using the actual data of recorded earthquakes, simplified and harmonic loads can also be used to study the seismic behavior of soil and structures.

2.4 *Sample preparation*

In the case of soil liquefaction, soil saturation is a requirement. To prevent from Obstruction of Side valves, almond-shaped coarse grains are used at the bottom of the box to the top of the valves and a layer of geotextile is used to distribute the water evenly into the soil. The relative density of the tested soil is 30% which sand pluviation method has been used b to achieve this goal "Figure 2".

Figure 2. Sand pluviation device.

It should be noted that the load applied to the seismic is in the form of displacement over time. The sinusoidal load considered in this study is represented in "Figure 3".

Figure 4 is a photo of the model before the test. The cause of the bulge in the middle part is the presence of the pipe and due to the effect of the relative density of the sand precipitation device, there is no manual change in soil height in the middle part. In this study, in order to investigate the effect of buried depth of the pipe, three physical models were performed according to Table 3. In this table, the buried depth of the pipe with parameter H, the diameter of the pipe with parameter D, and the relative density of the sample with parameter Dr are specified.

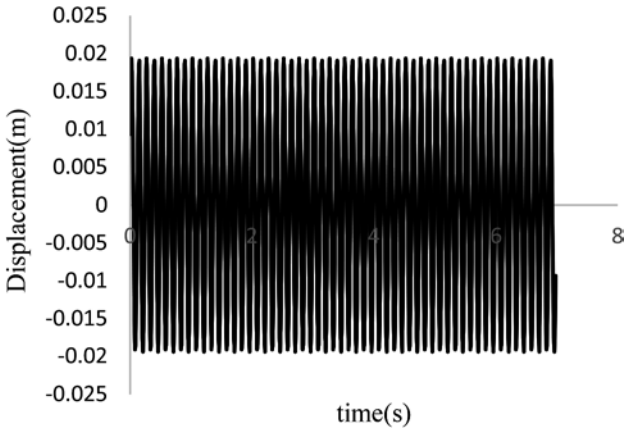

Figure 3. Seismic load.

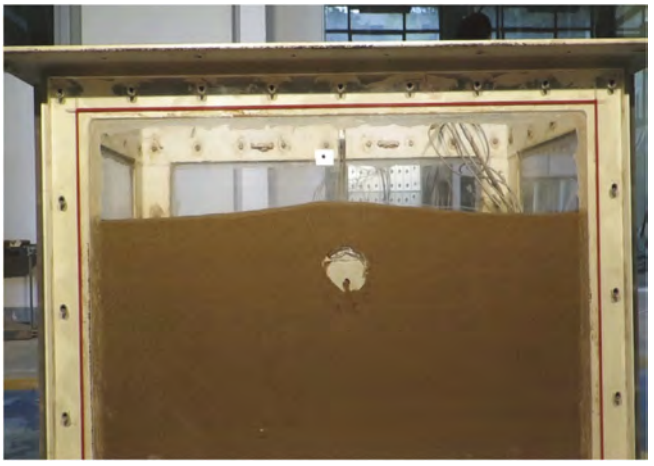

Figure 4. Laboratory physical modeling.

Table 3. Test program.

Modeling	frequency	acceleration	Dr	H/D
Model 1	Hz 8	g 0.5	30 %	1.5
Model 2	Hz 8	g 0.5	30 %	2.5
Model 3	Hz 8	g 0.5	30 %	5

3 RESULTS AND DISCUSSION

Due to the reduction of soil shear strength due to liquefaction and as a result of increasing pore water pressure, the stability of the pipe is difficult. As a result of soil liquefaction, the pipe buried in the soil prone to liquefaction will be transformed, which can be seen in "Figure 5b", the vertical movement of the pipe in an earthquake with a frequency of Hz8 and acceleration of 0.5 g at different buried depths. Also, the relationship between the buried depth of the pipe and the degree of elevation of the pipe is shown in "Figure 5a". It is worth

mentioning that the vertical axis parameter ($\frac{\Delta h}{D}$) represents the ratio of uplift to the pipe diameter and the horizontal axis parameter ($\frac{H}{D}$) represents the ratio of buried pipe depth to pipe diameter. In order to achieve the amount of elevation at different buried depths, a relationship has also been proposed as a correlation between the elevation and the buried depth of the pipe.

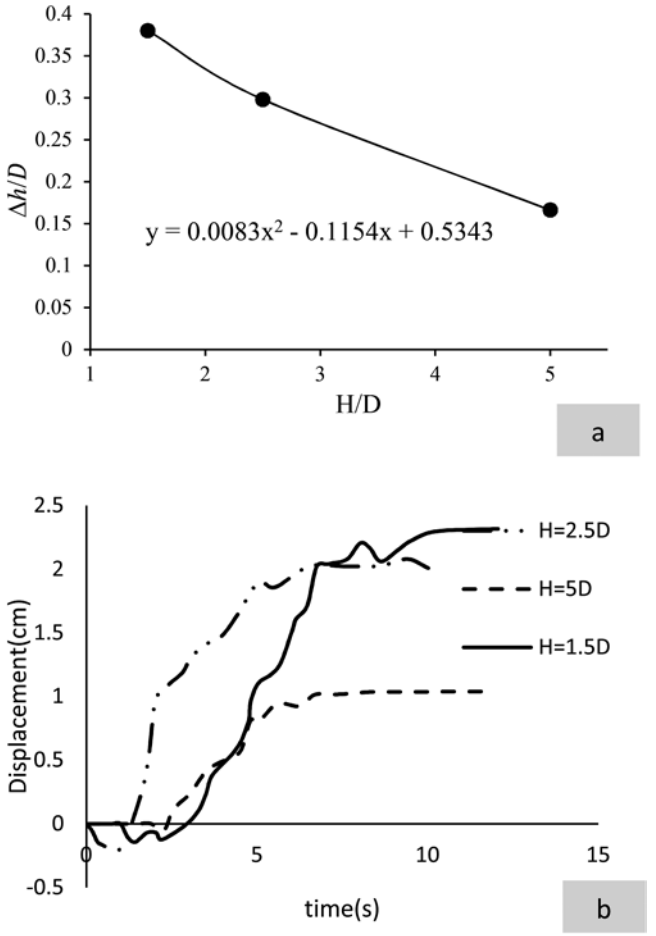

Figure 5. A) Relationship between elevation and buried depth of pipe b) Displacement of buried pipe in liquefiable soil in different buried depths.

As can be seen from the diagram, the amount of uplift decreases with increasing depth, so that when the depth of the pipe becomes 3.33 times, the ratio of the uplift of the pipe to the diameter of the pipe decreases by 56%. The reason for this can be attributed to the increase in resistive force due to the weight of the soil above the pipe. As the buried depth of the pipe increases, the amount of soil mass above the pipe, which acts as an uplifting force, increases, and as a result, the overpressure of the pore water as one of the driving forces will not be able to lift the pipe. Also, in general, first the pipe moves downwards, then, due to the elasticity in the sandy soil, the upward movement occurs and causes the pipe to reach its initial level first and then continue to rise. According to many researchers, the elevation of pipes buried in liquefied soil follows the seismic load. In this way, with the start of loading, the uplift starts

and with its end, the uplift stops [13, 30]. In order to study the beginning and end of the uplift, the diagrams of the input load, the excess of the pore water layer and the uplift are examined in "Figure 6". As can be seen from "Figure 6", the onset of uplift occurs when excess water pressure forms inside the soil. It is also important to note that uplift does not stop with the end of the load, although it continues in small amounts. Therefore, it can be concluded that seismic load is not only the initiator of uplift in buried structures during liquefaction, and the excesses pore water pressure also plays a role in this phenomenon. It is noteworthy that in order to getting Dimensionless axes of the diagram, the excess water pressure is divided into the initial effective stress and is expressed as $\frac{\Delta u}{\sigma}$ that is available at each stage of the experiment with Pressure indicator and indicates the degree of liquefaction. In relation to the pore water pressure diagram, it can be noted that due to the return wave application, the pore water pressure increases with each return wave and some of the water pressure surplus until the return wave is applied to the sample. Excesses pore water pressure disappear and the same process continues in the next wave. Also, "Figure 7" shows the relationship between the buried depth of the pipe and the excesses pore water in order to find out the effect of the buried depth of the pipe on the excesses of the pore water. It is noteworthy that when the buried depth of the pipe increases 3.33 times, the ratio of the excesses pore water pressure to the effective stress is reduced by 75%.

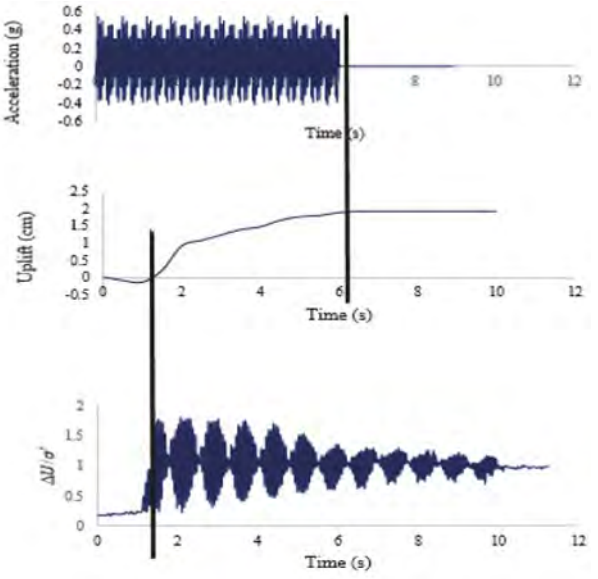

Figure 6. Acceleration, pipe uplift and degree of liquefaction charts in terms of time in the second experiment of the present study.

Figure 6. Demonstrates the time histories of selected measurements during shaking. The uplift of the pipe initiated after the surrounding sand layer had attained liquefaction. Uplift displacement proceeded at nearly constant rate mainly during shaking. Although pore pressure after shaking maintained the value equal to that during shaking uplift displacement rate decreased after shaking. There for, it is suggested that uplift displacement be affected by shaking intensity in addition to pore pressure.

According to this diagram, it can be seen that when the buried depth increases, the pore water pressure around the pipe has decreased. So, in order for the lifelines to be safe from the excesses pore pressure and as a result of the uplift caused by it, it is necessary to place them in the deep depths of the earth.

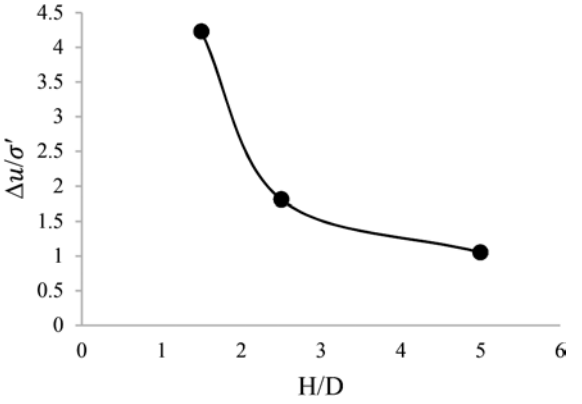

Figure 7. Relationship between excesses pore water pressure and buried depth of pipe.

4 CONCLUSION

The elevation of structures buried in liquefiable soil has been one of the important geotechnical issues due to irreparable damage. Therefore, in this study, through physical modeling, the elevation of the buried pipe has been investigated. Various parameters are effective in the uplift of the pipe, including: applied acceleration, loading frequency, relative soil density, buried depth of the pipe, etc., what is considered as a variable parameter in this study is the buried depth of the pipe. Therefore, an attempt has been made to check the elevation of the pipe by changing the buried depth of the pipe. In order to study this subject, shaking table, rigid Plexiglas box, loose sand, sand pluviation device, pressure gauge and accelerometer, deaired water device and vacuum have been used.

1. In this study, when the buried depth of the pipe increases 3.33 times, the ratio of the excess pore water pressure to the effective stress decreases by 75%. With increasing the buried depth of the pipe, due to the increase in the amount of resistive force caused by the soil mass above the pipe, the amount of uplift of the pipe has decreased. It should be noted that due to the stability of other influential parameters, the reason for the decrease in the elevation of the pipe can be attributed to the increase in the buried depth of the pipe.
2. When the buried depth of the pipe decreases, the rising of the pipe continues even after the loading is completed. Due to the high excesses pore water pressure in the lower depths of the soil, the excesses pressure created after dynamic loading tends to be wasted and flows towards the low pressure points (surface area) and because in the surface areas, the flow is upward, so the uplift It goes on to some extent. It is noteworthy that with 3.33 times the buried depth of the pipe, the ratio of uplift to pipe diameter decreases by 56%.
3. Excesses pore water pressure during seismic loading is one of the most important and effective variables in the elevation of buried pipes. The results show that the prerequisite for uplifting is reaching the excesses pore water pressure to a certain amount.

REFRENCES

[1] N. Taylor, V. Tran, Experimental and theoretical studies in subsea pipeline buckling, Marine Structures, 9(2) (1996) 211–257.
[2] T.C. Maltby, C.R. Calladine, An investigation into upheaval buckling of buried pipelines—II. Theory and analysis of experimental observations, International journal of mechanical sciences, 37 (9) (1995) 965–983.
[3] K. Sugito, T. Okano, R. Fukagawa, LIQUEFACTION ANALYSIS OF VERIFICATION ON THE INFLUENCE OF UNDERGROUND STRUCTURE, INTERNATIONAL JOURNAL OF GEOMATE, 16(58) (2019) 104–109.
[4] M. Jefferies, K. Been, Soil liquefaction: a critical state approach, CRC press, 2015.

[5] S. Chian, S. Madabhushi, Effect of buried depth and diameter on uplift of underground structures in liquefied soils, Soil Dynamics and Earthquake Engineering, 41 (2012) 181–190.
[6] T. Travasarou, J. Chacko, W. Chen, A. Fernandez, Assessment of Liquefaction-Induced Hazards for Immersed Structures, in: Offshore Technology Conference, Offshore Technology Conference, 2012.
[7] K. Horikawa, Y. Sakino, Review of damage in welded joints caused by the Kobe earthquake, Transactions of JWRI, 24(2) (1995) 1–10.
[8] C. Scawthorn, P.I. Yanev, 17 January 1995, Hyogo-ken Nambu, Japanese earthquake, Engineering Structures, 17(3) (1995) 146–157.
[9] W.W. Chen, B.-j. Shih, Y.-C. Chen, J.-H. Hung, H.H. Hwang, Seismic response of natural gas and water pipelines in the Ji-Ji earthquake, Soil Dynamics and Earthquake Engineering, 22(9–12) (2002) 1209–1214.
[10] I. Towhata, Geotechnical earthquake engineering, Springer Science & Business Media, 2008.
[11] M. Ghayamghamian, T. Tobita, S. Iai, G.-C. Kang, Reconnaissance Report of July 16, 2007 Niigata-Ken Chuetsu-Oki, Japan, Earthquake, Journal of Seismology and Earthquake Engineering, 9(1–2) (2007) 73–84.
[12] A.R. Bagherieh, I. Loloi, A. Bagherieh, Numerical Modeling of Tunnels and Lifelines in Liquefiable Grounds Under Seismic Loading, Journal of Ferdowsi Civil Engineering, 27(2) (2016).
[13] S. Chian, K. Tokimatsu, Floatation of underground structures during the M w 9.0 Tōhoku Earthquake of 11th March 2011, in: Proceedings of the 15th World Conference on Earthquake Engineering, Lisbon, Paper ID, 2012.
[14] K. Tokida, Y. Ninomiya, T. Azuma, Liquefaction potential and uplift deformation of underground structure, WIT Transactions on The Built Environment, 3 (1970).
[15] J. Koseki, O. Matsuo, S. Tanaka, Uplift of sewer pipes caused by earthquake-induced liquefaction of surrounding soil, Soils and foundations, 38(3) (1998) 75–87.
[16] J.-L. Hu, H.-B. Liu, The uplift behavior of a subway station during different degree of soil liquefaction, Procedia engineering, 189 (2017) 18–24.
[17] A. Hasheminezhad, H. Bahadori, Seismic response of shallow foundations over liquefiable soils improved by deep soil mixing columns, Computers and Geotechnics, 110 (2019) 251–273.
[18] D.D. Nourzadeh, P. Mortazavi, A. Ghalandarzadeh, S. Takada, M. Ahmadi, Performance assessment of the Greater Tehran Area buried gas distribution pipeline network under liquefaction, Soil Dynamics and Earthquake Engineering, 124 (2019) 16–34.
[19] M. Castiglia, F.S. de Magistris, J. Koseki, Uplift of buried pipelines in liquefiable soils using shaking table apparatus, (2019).
[20] H. Bahadori, H. Motamedi, A. Hasheminezhad, R. Motamed, Shaking table tests on shallow foundations over geocomposite and geogrid-reinforced liquefiable soils, Soil Dynamics and Earthquake Engineering, 128 (2020) 105896.
[21] A.G. Papadimitriou, G.D. Bouckovalas, D.J. Nyman, A.I. Valsamis, Analysis of buried steel pipelines at watercourse crossings under liquefaction-induced lateral spreading, Soil Dynamics and Earthquake Engineering, 126 (2019) 105772.
[22] P.B. Sudevan, A. Boominathan, S. Banerjee, Numerical Study of Liquefaction-Induced Uplift of Underground Structure, International Journal of Geomechanics, 20(2) (2020) 06019020.
[23] J. Wu, G.P. Kouretzis, L.P. Suwal, Y. Ansari, S.W. Sloan, Shallow and deep failure mechanisms during uplift and lateral dragging of buried pipes in sand, Canadian Geotechnical Journal, (ja) (2019).
[24] A.O. Mahmoud, M.N. Hussien, M. Karray, M. Chekired, C. Bessette, L. Jinga, Mitigation of liquefaction-induced uplift of underground structures, Computers and Geotechnics, 125 (2020) 103663.
[25] B. Huang, J. Liu, D. Ling, Y. Zhou, Application of particle image velocimetry (PIV) in the study of uplift mechanisms of pipe buried in medium dense sand, Journal of Civil Structural Health Monitoring, 5(5) (2015) 599–614.
[26] S. Iai, T. Sugano, Shake table testing on seismic performance of gravity quay walls, in: Proceedings of the 12th World Conference on Earthquake Engineering, 2000.
[27] M. Otsubo, I. Towhata, T. Hayashida, M. Shimura, T. Uchimura, B. Liu, D. Taeseri, B. Cauvin, H. Rattez, Shaking table tests on mitigation of liquefaction vulnerability for existing embedded lifelines, Soils and Foundations, 56(3) (2016) 348–364.
[28] K. Hatami, R. Bathurst, P.D. Pietro, Static response of reinforced soil retaining walls with nonuniform reinforcement, International Journal of Geomechanics, 1(4) (2001) 477–506.
[29] A.J. Crewe, The characterisation and optimisation of earthquake shaking table performance, University of Bristol, 1998.
[30] L. Sun, Centrifuge modeling and finite element analysis of pipeline buried in liquefiable soil, (2002).

Smart Geotechnics for Smart Societies – Zhussupbekov, Sarsembayeva & Kaliakin (Eds)
© 2023 The Author(s), ISBN 978-1-003-29912-7
Open Access: www.taylorfrancis.com, CC BY-NC-ND 4.0 license

Study of the effect of wet-dry cycles on the dynamic properties of expansive soils

Juan Liu
Sichuan Metallurgical Geological Survey and Design Group Co. Ltd., Chengdu, China

Maoji Fan
Southwest Jiaotong University, Chengdu, China

Haifeng Li & Lei Zhu*
China 19th Metallurgical Group Co. Ltd., Chengdu, China

Dan Yang, Xin Liao & Zhiming Zhao
Southwest Jiaotong University, Chengdu, China

ABSTRACT: Under the influence of the wet-dry cycles, the dynamic properties of expansive soil in railway subgrade tends to be more complex. In this study, the effects of wet-dry (WD) cycles, dynamic loading and moisture content are investigated by dynamic triaxial tests. The results show that these factors have significant effects on the dynamic properties of expansive soils. In the different deviator stress conditions, soil deformation shows different trends. The expansive soil was stable as the deviator stress was less than the critical dynamic stress. Conversely, the expansive soil was destroyed as the deviator stress exceeded critical dynamic stress. With the increase of wet-dry cycles, the critical dynamic stress decreased and the accumulated strain increased. The cumulative deformation increased rapidly when the wetted time was from 0 to 1, and the increase rate slowed from 2 to 3. The results reveal the cumulative deformation law of expansive soil under the combined action of repeated wetting and dynamic load. It is expected to provide theoretical support for the construction and long-term performance evaluation in the expansive soil area.

1 INTRODUCTION

Expansive soil is characterized by expansibility, fissure and strength attenuation due to its water sensitivity. During the change in moisture content, its volume and microstructure will change significantly. In the seasonal wet and dry environment, clay minerals in the soil will expand and contract repeatedly, leading to soil structure damage and soil strength reduction. However, in the construction of railway, highway and railway projects, it is inevitable to reshape the expansive soil. Therefore, the mechanical characteristics of expansive soil under the action of wet and dry cycles affect all aspects of infrastructure construction (Ajdari et al. 2013; Tripathy et al. 2002; Vilar and Rodrigues 2011; Lu and Godt 2012; Zha et al. 2013; Zhang et al. 2015).

Current research shows that wet-dry (WD) cycle has a significant impact on the static characteristics of expansive soil. The shear strength of expansive soil decreases with the increase of the number of WD cycles, and finally tends to be stable. The stability value of strength and the number of WD cycles required for stability decrease with the increase of the change range of moisture content (AlTaie et al. 2016; Dan et al. 2018; Estabragh et al. 2015; Yarba et al. 2020). The expansion and contraction deformation of the sample in the normal WD cycle

DOI: 10.1201/9781003299127-258

gradually tends to be stable with the increase of the number of cycles. The expansion and contraction characteristics are obviously affected by the drying and shrinking paths, and the expansion rate increases with the increase of the WD cycles. The expansion rate of the sample in the process of WD cycle depends on the moisture absorption capacity to a certain extent (Gaspar et al. 2022; Yazdandoust et al. 2010). The reason why the performance of expansive soil was weakened under the condition of WD cycle is investigated from the microscopic perspective. These results indicate that the cohesion of expansive soil will be seriously lost in the first three WD cycle process, and the total pore volume will increase. Repeated WD cycles will lead to irreversible fatigue damage of microstructure and micro-crack growth (Ajdari et al. 2013; Chittoori et al. 2018; Dao et al. 2020; Liu et al. 2021).

With the development of high-speed and heavy haul traffic construction in expansive soil areas, people gradually pay attention to the dynamic characteristics of expansive soil, such as dynamic elastic modulus, dynamic resilience modulus, critical dynamic stress, cumulative strain characteristics (Yang et al. 2019; Wang et al. 2012; Zhou et al. 2019). But the dynamic characteristics of expansive soil under WD cycles still needs deeper investigation.

Most areas in southern China are in the typical WD environment. Therefore, the moisture content of expansive soil in the railway subgrade changes significantly in different seasons. In order to simulate the wet-dry process of the expansive soil under train road, the influence of dynamic stress amplitude, WD cycle and moisture content on the dynamic characteristics of compacted expansive soil is analyzed through the dynamic triaxial tests. The results reveal the cumulative deformation law of expansive soil under the action of repeated wetting and dynamic load.

2 SAMPLES PREPARATION

2.1 *Samples properties*

Expansive soil samples from Chengdu, Sichuan Province of China were selected as the test objects, which were taken from 1.5-2m below the surface. This sampling depth range was chosen because it is below the depth of maximum impact of superficial weathering. In order to determine the physical parameters of the soil samples, the moisture content, relative density, particle size distribution and related properties are tested. The results are shown in Table 1. The mineral compositions mainly include quartz, feldspar, and some clay minerals, which were obtained by X-ray diffraction (XRD) analysis (in Table 2).

Table 1. Physical properties of expansive soil.

				Atterberg limits			Particle size distribution		
Nature moisture content	Dry density	Specific gravity	Free swelling rate	Liquid limit	Plastic limit	Shrinking limit	Clay	Silt	Sand
22.7%	1.6g/cm3	2.73	82%	30.5%	52.8%	82%	50.26%	40.77%	8.77%

Table 2. Mineral compositions wt. %.

Illite	Chlorite	Quartz	Feldspar	Calcite
0.69	0.38	95.03	2.10	1.80

2.2 *Sample preparation*

All basic geotechnical tests were performed based on American Standard Test Method (ASTM). The dynamic triaxial test and backpressure saturation are carried out on dynamic triaxial instrument (DYN77S) that was made by GDS Instruments of the UK (Figure 1). In

this test, the density of the samples was controlled to be 1.6 g/cm^3. Soil and water were mixed according to the moisture content. The sample is divided into 5 layers of compaction, with a diameter of 50 mm and a height of 100 mm. The moisture content of the soil sample is controlled within 10% ~ 25%. In order to study the effect of WD cycle on dynamic characteristics, dynamic triaxial tests of 0~3 WD cycles were carried out. In each cycle, three moisture content (ω = 10%, 17%, 24%) were selected as control points. Backpressure saturation was obtained by GDS instrument. The temperature was controlled at 40°C to simulate the dehumidification process by the oven. The moisture content of the samples was measured by weighing method at the interval of each 1 hour during the early drying process. The measurement frequency increased when the moisture content was close to the target moisture content. After the moisture content drops to the control point, the sample is sealed and cured for 24h to make the moisture distributed uniformly.

3 DYNAMIC TRIAXIAL TEST SCHEME

The dynamic triaxial test adopts stress-controlled loading mode. A half-sine curve load is set to simulate the traffic load (Figure 2). The lateral pressure of railway subgrade surface was 20 ~ 60 kPa (Han et al., 2002), so the confining pressure was 50 kPa and all samples were consolidated by isobaric pressure. The frequency range of train vibration is usually F≤2.35 Hz (Liu et al. 2009). Considering that frequency is not used as a variable factor in the test, 1Hz is selected as the simulation frequency. The test is ended as the dynamic loading reaches 10000 times or the axial cumulative plastic strain of the sample is greater than 10%. The parameters in the test scheme are shown in Table 3.

Figure 1. DYN77S dynamic triaxial test apparatus.

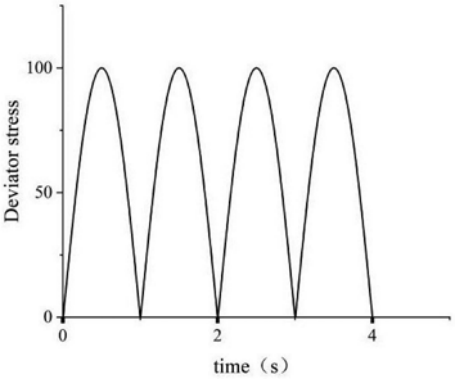

Figure 2. Curve of cyclic loading.

Table 3. Dynamic triaxial test scheme.

Moisture content (%)	Confining Pressure (kPa)	Vibration Frequency (Hz)	Number of wet-dry cycles (n)	Deviator stress (kPa)
15	50	1	0	150
			0	90, 150, 200, 250, 300
17	50	1	1	90, 150
			2	90, 150
			3	90, 150
19	50	1	0	150

4 RESULTS AND DISCUSSION

4.1 *Dynamic deformation characteristics of expansive soils*

The axial strain changes with the number of vibrations (lg N) with a confining pressure of 50 kPa and a moisture content of 17% at different stress amplitudes as shown in Figure 3(a). This curve can generally be divided into three types according to its development mode: plastic stability type, plastic creep type and incremental damage type (Perez et al. 2006; Xiao et al. 2017). For the plastic stability type, as the deviator stress are 90kPa and 150kPa, the cumulative plastic strain under cyclic loading increases rapidly and stabilizes at fewer vibration times. The cumulative plastic strain is 1.11% and 1.05% after 2000 vibrations, respectively. For the plastic creep type, as the deviator stress is 200kPa, the cumulative plastic strain increases rapidly at the initial stage under cyclic load, then slows down but keeps growing. Finally, the cumulative plastic strain reaches 3% at 1000 vibration times and continues to increase slowly. The characteristic of the incremental damage curve is that the cumulative plastic strain increases rapidly under cyclic load, and reaches 10% of the strain of the termination test when the number of vibrations is less than 100 as deviator stress is 250 kPa and 300 kPa. The reason is speculated that the relative slip between the particles in the sample results in the rapid growth of the cumulative plastic strain of the sample at the initial stage of loading. At the same time, the impaction and occlusion between internal particles are relatively enhanced, and the ability of the specimen to resist external loads is enhanced. Therefore, the curve shows that the cumulative strain rises rapidly and then becomes stable. When the deviator stress is 90 kPa or 150 kPa, the dynamic load is less than the strength of specimen, so the state of the sample is characterized by elastic deformation after the internal particles impaction and occlusion. As the deviatoric stress increases to 200 kPa, the specimen changes from elastic state to plastic state, and the cumulative strain increases slowly. When the deviatoric stress increases to 250 kPa, the strength of the specimen is significantly insufficient to resist the effect of the current dynamic load. As a result, the specimen with rapid growth of cumulative plastic strain was destroyed after less than 100 times of vibration.

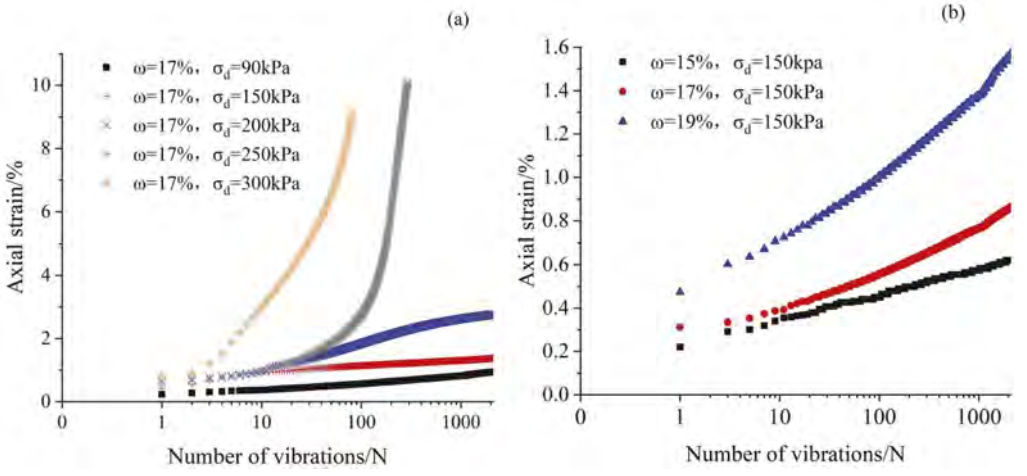

Figure 3. Permanent deformation curve under different deviator stress and moisture content.

The result of permanent deformation of the expansive soil varies with different moisture content as shown in Figure 3(b). The axial strains are 0.58%, 0.85% and 1.4% after 1000 vibrations as the moisture contents are 15%, 17% and 19%, respectively. It is obvious that the permanent deformation of the soil specimens increases with the increase of moisture content. It can be deduced that the critical dynamic stress of the expansive soil would decrease during this process. As a result, if the expansive soil is used as the roadbed filler in the railway construction, it should pay attention to the arrangement of waterproofing and drainage facilities.

4.2 *Impact of the number of wet-dry cycles on the dynamic deformation*

The relationship between cumulative axial strain and vibration number of the expansive soil with the moisture ω=17% at different dynamic stress and WD cycles is shown in Figure 5. It is obvious that the number of WD cycles has a great influence on the expansive soil deformation. After expansive soil experienced at least one time WD cycles, the axial strain was about two times than that of soil samples without WD process. The reason is speculated that the percent of grain size of clay grade increases and that of silt and sand grades decreases, which could cause the soil structure to decompose partially (Rao et al. 2001; Yazdandoust et al. 2010). Nevertheless, the axial strain increases slightly with the increase of WD cycle since the one time WD cycle. Besides, the dynamic stress has a certain influence on the axial strain as well. The axial strain of soil samples at σ_d=150kPa is about 34% higher than that of soil samples at σ_d=90kPa. However, the overall change tendency is almost the same for all samples at different dynamic stress. It is indicated that the WD cycles have a significant influence on the dynamic properties of the expansive. The effect of WD process is essentially caused by the migration of pore water. This effect not only brings additional deformation but also causes changes in physical and mechanical properties of expansive. The mechanism of dynamic strength decreases needs further study in the view of microstructure.

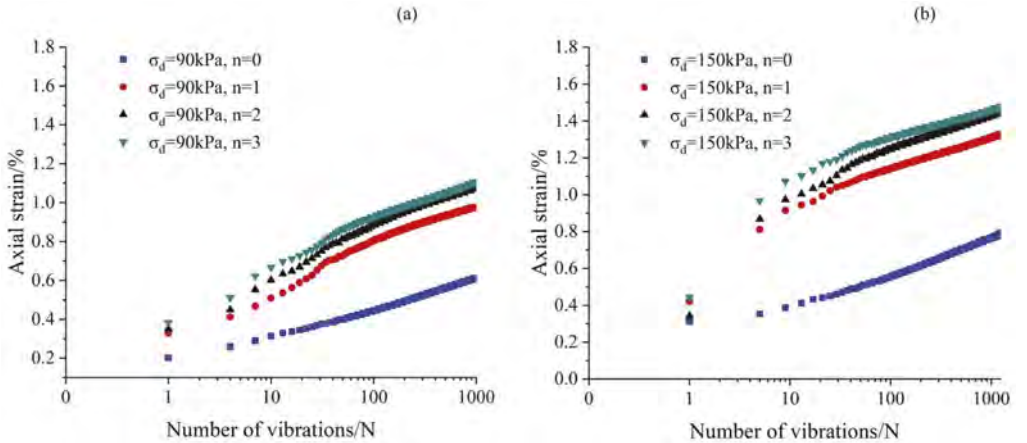

Figure 4. Relationship between axial strain and vibration number under different dynamic stress and WD cycles.

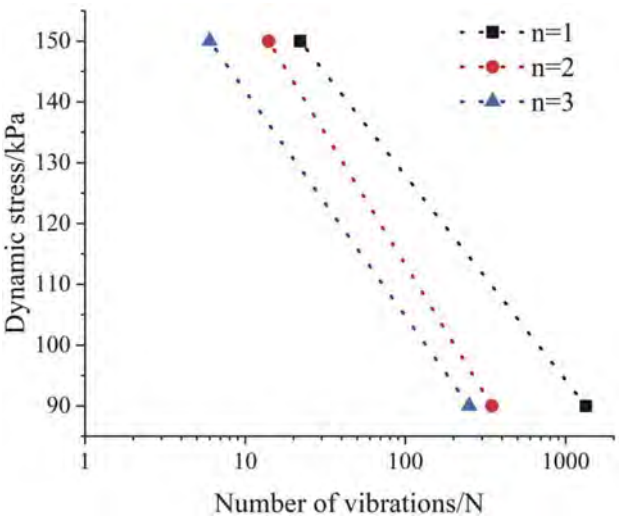

Figure 5. Dynamic strength curve of different WD cycles.

Dynamic strength of soil refers to the dynamic stress of soil under dynamic load vibrations according to the failure criterion. When the axial cumulative plastic strain reaches 1%, the failure criterion is taken into account (Wu et al., 1998). Based on the deformation characteristics of soil in Figure 4, the dynamic strength of expanding soil under different WD cycles is shown in Figure 5. It is indicated that the more WD cycles performed, the fewer times of vibration required to achieve the failure standard under the same stress condition. The numbers of vibrations required to attain the failure standard are 1339 and 346 as the deviator stress is 90kPa but the WD cycle is 1 and 2, respectively. The descending percentage of vibration number is close to 75% after one more time WD cycle. Furthermore, the vibration number decreased from 22 to 14 as the deviator stress is 90 kPa and WD cycle increased from 1 to 2. In this condition, the descending percentage of vibration number is about 36%. It is obvious that the wet-dry process has significant influence on the dynamic strength of expanding soil, especially under the higher deviator stress.

4 CONCLUSION

In this paper, the dynamic properties of the expansive soil in Chengdu city, China were investigated by dynamic triaxial tests. The following conclusions were obtained.

(1) The permanent deformation curve under different deviator stress can generally be divided into three types according to its development mode: plastic stability, plastic creep and incremental damage types. All three types showed a rapid increase in cumulative strain in the first stage. The plastic stability type entered the elastic stability stage after a rapid increase. The plastic creep type entered the plastic slow deformation stage after a rapid increase. The deformation of incremental damage type continues to increase until it is destroyed.
(2) The permanent deformation of the soil specimens increases with the increase of moisture content.
(3) Wet-dry cycles have a greater influence on the dynamic properties of expansive soils. Under the same dynamic stress amplitude, the permanent plastic strain of expansive soil specimens increases significantly with the increase of the number of WD cycles. The dynamic strength of expansive soil specimens decrease with the increase of number of WD cycles under certain confining pressure.

ACKNOWLEDGMENTS

We would like to thank Analytical and Testing Center of Southwest Jiaotong University for dynamic triaxial test. This research was supported by the Degree and Postgraduate Education Teaching Reform Project of Southwest Jiaotong University (YJG5-2022-Y028).

REFERENCES

Abbas, M. F., Shaker, A. A., & Al-Shamrani, M. A. 2022. Hydraulic and volume change behaviors of compacted highly expansive soil under cyclic wetting and drying. *Journal of Rock Mechanics and Geotechnical Engineering*, 28(3): 87–95.

AlTaie, A., Disfani, M. M., Evans, R., Arulrajah, A., & Horpibulsuk, S. 2016. Swell-shrink Cycles of Lime Stabilized Expansive Subgrade. *Procedia Engineering*, 143(5): 615–622.

Ajdari, M., Habibagahi, G., & Masrouri, F. 2013. The role of suction and degree of saturation on the hydro-mechanical response of a dual porosity silt–bentonite mixture. *Applied Clay Science*, 83–90.

Chittoori, B. C. S., Puppala, A. J., & Pedarla, A. 2018. Addressing clay mineralogy effects on performance of chemically stabilized expansive soils subjected to seasonal setting and drying. *Journal of Geotechnical and Geoenvironmental Engineering*, 144(1): 28–35.

Dao, H. M., Nguyen, A. T. T., & Do, T. M. 2020. Effect of wetting-drying cycles on surface cracking and swell-shrink behavior of expansive soil modified with ionic soil stabilizer. *Journal of Mining and Earth Sciences*, 61(6): 1–13.

Estabragh, A. R., Parsaei, B., & Javadi, A. A. 2015. Laboratory investigation of the effect of cyclic wetting and drying on the behaviour of an expansive soil. *Soils and Foundations*, 55(2), 304–314.

Han Z. 2002. Study on countermeasures for increasing speed of subgrade on existing lines. *China Railway Science*, 23 (2): 53–58.

Liu, K., Ye, W., & Jing, H. 2021. Shear strength and damage characteristics of compacted expansive soil subjected to wet–dry cycles: a multi-scale study. *Arabian Journal of Geosciences*, 14(24): 42–52.

Liu, J., Xiao, J., Yang, X., et al.2009. Dynamic stability of silt railway subgrade under the condition of speed increase Qualitative research. *Geotechnical Mechanics*, 30 (2): 399–405.

Rao, S.M., Reddy, B.V.V., Muttharam, M., 2001. The impact of cyclic wetting and drying on the swelling behavior of stabilized expansive soil. *Engineering Geology Journal*, 60, 223–233.

Tripathy, S., Rao, K. S., & Fredlund, D. G. 2002. Water content-void ratio swell-shrink paths of compacted expansive soils. *Canadian geotechnical journal*, 39(4): 938–959.

Vilar, O. M., & Rodrigues, R. A. 2011. Collapse behavior of soil in a Brazilian region affected by a rising water table. *Canadian Geotechnical Journal*, 48(2): 226–233.

Wang, M., Kong, L., Zhao, C., & Zang, M. 2012. Dynamic characteristics of lime-treated expansive soil under cyclic loading. *Journal of Rock Mechanics and Geotechnical Engineering*, 4(4), 352–359.

Wu, S., & Xu, Y. 1998. Present situation and development of soil dynamics. *Journal of Geotechnical Engineering*, 20 (3), 125–131.

Yang, Z., Zhang, L., Ling, X., Li, G., Tu, Z., & Shi, W. 2019. Experimental study on the dynamic behavior of expansive soil in slopes under freeze-thaw cycles. *Cold Regions Science and Technology*, 163(6): 27–33.

Yarba, N., & Kalkan, E. 2020. Investigation of wet-dry cycle effect on swelling behavior of stabilized expansive soils. *International Journal of Science and Engineering Applications*, 9(12): 153–157.

Yazdandoust, F., & Yasrobi, S. S. 2010. Effect of cyclic wetting and drying on swelling behavior of polymer-stabilized expansive clays. *Applied Clay Science*, 50(4): 461–468.

Zha, F., Liu, J.,Xu, L., & Cui, K., 2013. Effect of cyclic drying and wetting on engineering properties of heavy metal contaminated soils solidified/stabilized with fly ash. *Journal of Central South University*, 20(7), 1947–1952.

Zhang, F., Jing, R., Feng, D., & Lin, B. 2015. Mechanical properties and an empirical model of compacted silty clay subjected to freeze-thaw cycles. *In Innovative Materials and Design for Sustainable Transportation Infrastructure*, 12(5): 200–212.

Zhao, G., Han, Z., Zou, W. l., & Wang, X, 2021. Evolution of mechanical behaviours of an expansive soil during drying-wetting, freeze–thaw, and drying-wetting-freeze–thaw cycles. *Bulletin of Engineering Geology and the Environment*, 80(10): 8109–8121.

Smart Geotechnics for Smart Societies – Zhussupbekov, Sarsembayeva & Kaliakin (Eds)
© 2023 The Author(s), ISBN 978-1-003-29912-7
Open Access: www.taylorfrancis.com, CC BY-NC-ND 4.0 license

Assessment of soil liquefaction potential index using probability concept for Baghdad City, Iraq

Hussein H. Karim*
Professor, Civil Engineering Department, University of Technology, Baghdad, Iraq

Zeena W. Samueel
Assistant Professor, Civil Engineering Department, University of Technology, Baghdad, Iraq

Dalia Ali Abdul Hussein
M.Sc. in Geotechnical Engineering, Civil Engineering Department, University of Technology, Baghdad, Iraq

ABSTRACT: Due to the position and the high importance of Baghdad city as the capital of Iraq with its very high population of about 10 million, and its subjection to frequent earthquakes in the last decade. This study tries to assess the factor of safety against liquefaction potential indices (LPI) for the most critical seismic situations under the effect of seismic loading during earthquakes. Huge data were used for 630 boreholes represent 200 site location points for many different types of projects spread all over the city has been chosen and analyzed using special soft wares. Input data of the studied sites represent soil geotechnical properties at different depths such as the total borehole depth, the ground water level, standard penetration number (N), unit weight, and fines content. Six earthquake magnitudes with 0.5 interval (M_L=4, 4.5, 5, 5.5, 6, and 6.5) have been chosen to analyze the data. Only 121 points show susceptibility to liquefaction. Three mathematical equations were proposed for analyzing the studied ten factors. Three equations with their accuracy were proposed for points with high percent of clay, points with high percent of silt, and points with high percent of sand. The probability of ground failure (P_G) and the calculated LPI was considered for assessing liquefaction risk. As the probability of liquefaction (P_L) and the probability of ground failure (P_G) are considered to be better measure of liquefaction potential than the factor of safety, so they were determined using the factor of safety and L.P.I.

Keywords: Earthquakes, Soil liquefaction potential index, probability of ground failure (P_G) and probability of liquefaction (P_L), Baghdad soil

1 INTRODUCTION

In this work, the potential of liquefaction damage will be quantified by an averaged index property, i.e., the liquefaction potential index (LPI), which was originally proposed by Iwasaki et al. (1978 and 1982) has been subsequently used and calibrated by many investigators. Many researchers performed a number of studies on liquefaction and liquefaction-induced ground failures.

Soil liquefaction is a catastrophic occurrence takes place in saturated soils that is generated by seismic events or dynamic shaking. It is considered to be an earthquake-related phenomenon. This phenomenon happens owing to the incapability of soil to dissipate pore water pressure that buildup under abrupt loading. The unexpected increase in pore water pressure in addition to dynamic-induced stresses can carry the soil structure to an unstable condition (Kramer, 1998; Fattah et al. 2002).

*Corresponding author: 40062@uotechnology.edu.iq

DOI: 10.1201/9781003299127-259

The liquefaction potential index (LPI defined by Iwasaki et al. (1978) combines depth, thickness, and factor of safety of liquefiable material inferred from a CPT sounding into a single parameter (Toprak and Holzer, 2003).

The potential for liquefaction to occur at certain depth at a site is quantified in terms of the factors of safety against liquefaction (F.S.) (Dixit et al., 2012). The factor of safety less than 1 at a certain depth indicates that the soil layer at that particular depth is likely to liquefy. The F.S. values for a particular depth can be seen to be decreasing with the increase in the magnitude of earthquake. This shows that the increase in the susceptibility of liquefaction with the increase in intensity of seismic events.

Liquefaction phenomenon has been registered and developed in many parts of the world where ground vibration is repeated and soils consist of loose fine sand under water table. Iraq involving the capital Baghdad is in general an alluvial deposits consisting of fine sand and silt deposits with shallow ground water table in most places. Although the older alluvium is less susceptible to liquefaction, the recent deposits along the river flood plains may liquefy during a severe earthquake. Thus, any structure, if not properly designed for liquefaction, may lead to its failure or sustain excessive cost through conservative design. No study has so far been achieved to show liquefaction possibilities at local levels in Iraq. In the absence of a definite knowledge of liquefaction probabilities at various localities, difficulties arise in accomplishing design of many important structures. This adds to the construction time and cost. It has been, therefore, felt necessary to undertake a study to develop a liquefaction potential map of Baghdad city.

Further related studies concerning Baghdad city is that accomplished by Karim and Schanz (2006) who analyzed the data of 44 sites within the city. This study found that 8 sites only show liquefaction zones mainly occurring in the first 15 m from ground surface, with total settlements $\leq$20 cm. Later, Karim et al. (2010) evaluated some geotechnical properties and liquefaction potential for 14 sites in Iraq from seismic parameters. To investigate the liquefaction potential of soils, two selected sites have been studied using the computer program. The application shows a total settlement for saturated and dry sand of 32 mm for the first site while no settlement has been indicated for the second site. Lastly, Karim and Wadaa (2017a and b) assessed liquefaction potential of Baghdad soil under earthquakes effect with analyzing Baghdad soil geotechnical properties. Data for 630 boreholes were used in both studies representing 200 sites. Only 121 points show susceptibility to liquefaction.

This article is concentrated on the assessment of soil liquefaction potential index using probability concept For Baghdad City, Iraq and to calculate the applicability of the LPI equations in evaluating damage severity in Baghdad city.

Evaluation of the Liquefaction Potential Index (LPI) using probability concept

Determination the probability of ground failure (P_G) and probability of liquefaction (P_L)

Using the factor of safety and L.P.I, another two determinations will be produced, the probability of ground failure (P_G) and the probability of liquefaction (P_L). Those are considered to be better measure of liquefaction potential than the factor of safety.

Based on the Bayes' theorem the relationship between the probability of ground failure (P_G) and the calculated L.P.I. can be established:

$$P_G = \frac{1}{(1 + e^{(4.9 - 0.73 * L.P.I.)})} \tag{1}$$

Table 1. Probability of liquefaction-induced ground failure (Li et al. 2006).

Probability	Description of the risk of liquefaction-induced ground failure
$0.9 < P_G$	extremely high to absolutely certain
$0.7 < P_G \leq 0.9$	high
$0.3 < P_G \leq 0.7$	medium
$0.1 < P_G \leq 0.3$	low
$P_G \leq 0.1$	extremely low to none

Using Bayes' theorem as outlined by Juang et al. (1999 and 2002), the probability of liquefaction (P_L) is calculated as follows:

$$P_L = \frac{1}{\left(1 + \frac{F.S.}{0.85}\right)^{5.54}} \quad (2)$$

Thus P_G and P_L for liquefied points with different earthquake magnitudes can be calculated.

2 RESULTS AND DISCUSSION

In this study, SPT N-values, along with other necessary geotechnical properties adopted for 630 boreholes and are representing 200 site location points (105 in Rusafa and 95 in Karkh) for different kinds of projects of Bahgdad City, were used to assess the liquefaction potential of the geological materials of the city using simplified procedure to determine the factor of safety against liquefaction.

Input data of the studied sites represent soil geotechnical properties at different depths such as the total borehole depth, the ground water level, standard penetration number (N), unit weight, and fines content. Six earthquake magnitudes with 0.5 interval (M_L=4, 4.5, 5, 5.5, 6, and 6.5) have been chosen to analyze the data. Only 121 points show susceptibility to liquefaction.

To assess the liquefaction potential, the LiqIT software was used (GeoLogismiki, 2006), which enables LPI estimation from the combination of observations (i.e.…. In this work, liquefaction hazard is quantified and mapped in terms of an averaged index called the LPI, initially proposed by Iwasaki et al. (1978) and Iwasaki et al. (1982).

The 200 site points are mapped using geographical information system (ArcGIS10.3.). The GIS techniques were used to show the first map, which is spatial locations and distributions of site point's location of Baghdad City as shown in Figure (1).

The depth of the studied boreholes has been adopted to only 30 m, the soil layers were grouped into each 2m, where 15 layers studied. The factor of safety is taken according to Adriss and Seed with F.S. =1.5.

Applying Excel software, six tables evaluated with six different earthquake magnitudes have been constructed using specific the above two equations in order to show the values of P_G and P_L of soil for Baghdad City. Table 1 represents the values of P_G and P_L values for the liquefied points with earthquakes magnitude 4.

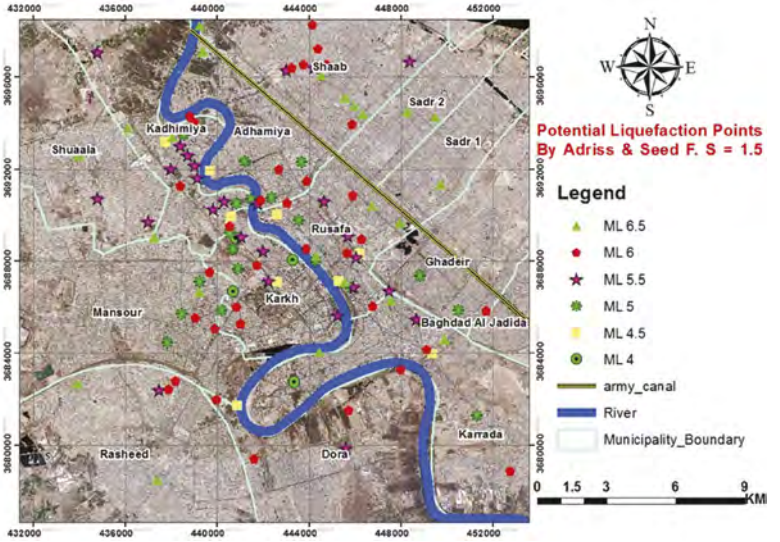

Figure 1. Liquefaction potential site point's location according to the considered option.

The significance of the relationship between the probability of ground failure PG and the calculated LPI relation is for assessing liquefaction risk.

The P_G values for M_L=4 are ranging between 0.012 (extremely low to none) - 0.373 (medium), but most the values are <0.1. P_L values are ranging between 0.272-0.45 (Table 2).

The probability of ground failure (*PG*) and probability of liquefaction (P_L) values have been constructed as digital interpolation maps and as digital combined contour–interpolation maps.

Table 2. P_G and P_L for liquefied points with earthquake magnitude =4.

Point	Name	District	Mag.	F.S.	f	Depth (Z) m	W(Z)	H	W(Z)*H*F	PG	PL
P5	Sheikh Junaid	203	4.0	0.93	0.070	12.0	4.000	7.5	3.360	0.079643549	0.320185523
P101	SheikhMarouf	202	4.0	0.90	0.100	4.0	8.000	4.5	3.200	0.071491565	0.360264849
P107	Karrada	913	4.0	0.97	0.030	6.5	6.750	3.5	0.709	0.012338537	0.272410491
				0.84	0.160	7.0	6.500	3.5	3.640	0.095972334	0.450610666
				0.86	0.140	7.5	6.250	3.5	3.063	0.065108523	0.419105891
				0.88	0.120	8.0	6.000	3.5	2.520	0.044770593	0.388947681
				0.93	0.070	8.5	5.750	3.5	1.409	0.020399939	0.320185523
				0.96	0.040	9.0	5.500	3.5	0.770	0.012895468	0.283747144
P145	Karkh	216	4.0	0.88	0.120	12.5	3.750	1.0	6.000	0.372852234	0.388947681

maps have been constructed for earthquakes magnitudes M_L=4-6.5 and for each P_G and P_L,for digital combined contour–interpolation map for liquefaction potential index (Figures 2) (Figures 3).

The P_G values in the maps for M_L=4-5 are ranging between 0.026-0.244 (Figure 2- a). Higher values are located in the northern part of Baghdad city, besides some parts in the southwestern part. While lower values are located in the southeastern part. According to the risk description of liquefaction-induced ground failure indicated that the probability values of the risk is of very low-none ($P_G \leq 0.1$) to low ($0.1 < P_G \leq 0.3$). Concerning the probability of liquefaction (P_L) for M_L=4-5, their values are ranging between 0.305-0.379 (Figure 3- a). As in the P_G maps, higher values of P_L values (0.38) are located in the northern part and southwestern parts of Baghdad city, with low values (0.3) in its southern and southeastern parts. Comparing P_G and P_L values with that of LPI values, it seems that there is coincidence between the two maps particularly in their northern parts where high values of LPI are found to reach LPI>10.

Regarding the P_G values in the maps for M_L=5.5 are between 0.05-1.283 (Figure 2- b), where high values (>1 reaching 1.2) are located in the NW part with intermediate (0.5) in the SE part to low values (< 0.1) in the middle (NE-SW) parts. Consequently, the risk appears to be extremely high to absolutely certain in the northwestern part, medium in the SE part, with extremely low-none in the in the middle (NE-SW) parts. Regarding P_L values, they are ranging between 0.27-0.50 (Figure 3- b) where high values are assigned to NW and SE parts with 0.5 while lower values (<0.3) are located in the NE-SW parts. In comparison between P_G and P_L values with LPI values for M_L=5.5, it is clearly shown the full coincidence between the three maps, where high values of LPI are found in the north western half (>23) with low values (3-8) in the middle parts to medium (8-13) in the SE part of Baghdad city.

The P_G values for M_L=6 are ranging between 0.01-0.203 (Figure 2- c), where higher values (0.2) are assigned to the center parts surrounded by lower values (~ 0.01). Therefore, the risk description of liquefaction-induced ground failure indicated that the probability values of the risk appears to be medium in the center parts to extremely low to none for the rest areas. The P_L values are ranging between 0.245-0.375 (Figure 3- c) with high values in the northern part reaching >0.3 with lower values for the rest areas. In comparison with LPI map with P_G and P_L, there is similarity between LPI and P_G where both have high values in the north eastern and central parts surrounded by lower values for the rest parts. While, some similarity is found between LPI and P_L maps.

The P_G values for M_L=6.5 are ranging between 0.022-0.756 (Figure 2- d), where higher values (>0.17) are assigned to the third part of northern part, while lower values (<0.17) are assigned to the middle and southern parts of the city. Subsequently, the risk description of liquefaction-induced ground failure is indicated to be medium risk (>0.3) in the upper third part of north to low- none risk (<0.18) for the rest area. For the probability of liquefaction (P_L) for M_L=6.5 (Figure 3-d), their values are between 0.152-2.563 with higher values (>0.4) reaching 2.5 in the western and southern

parts, while lower values (<0.4) for the rest parts of the city of Baghdad. Comparing P_G values with that of LPI values, it looks that there is some coincidence between them, with higher values of LPI (>20) in the NE part associated with high values of P_G while low-intermediate values of LPI (≤ 20) in the NW and southern parts associated with low P_G values. Comparing $P_{L\ values}$ with that of LPI values, it looks that there is also some coincidence between them, with higher values of LPI (>20) and low values (0.15) of P_L in the NE part and lower LPI values (<20) in the NW and southern parts, while high P_L values are indicated in the NW part.

3 CONCLUSIONS

The main conclusion for the aassessment of soil liquefaction Potential index using probability concept For Baghdad city can be summarized in the following remarks:

1. The probability concept can be considered a new encouraging approach can be implemented to develop liquefaction potential evaluation criteria.
2. Three mathematical equations were proposed for analyzing the studied ten factors. The three final equations with their accuracy were proposed for points with high percent of clay, points with high percent of silt, and points with high percent of sand.

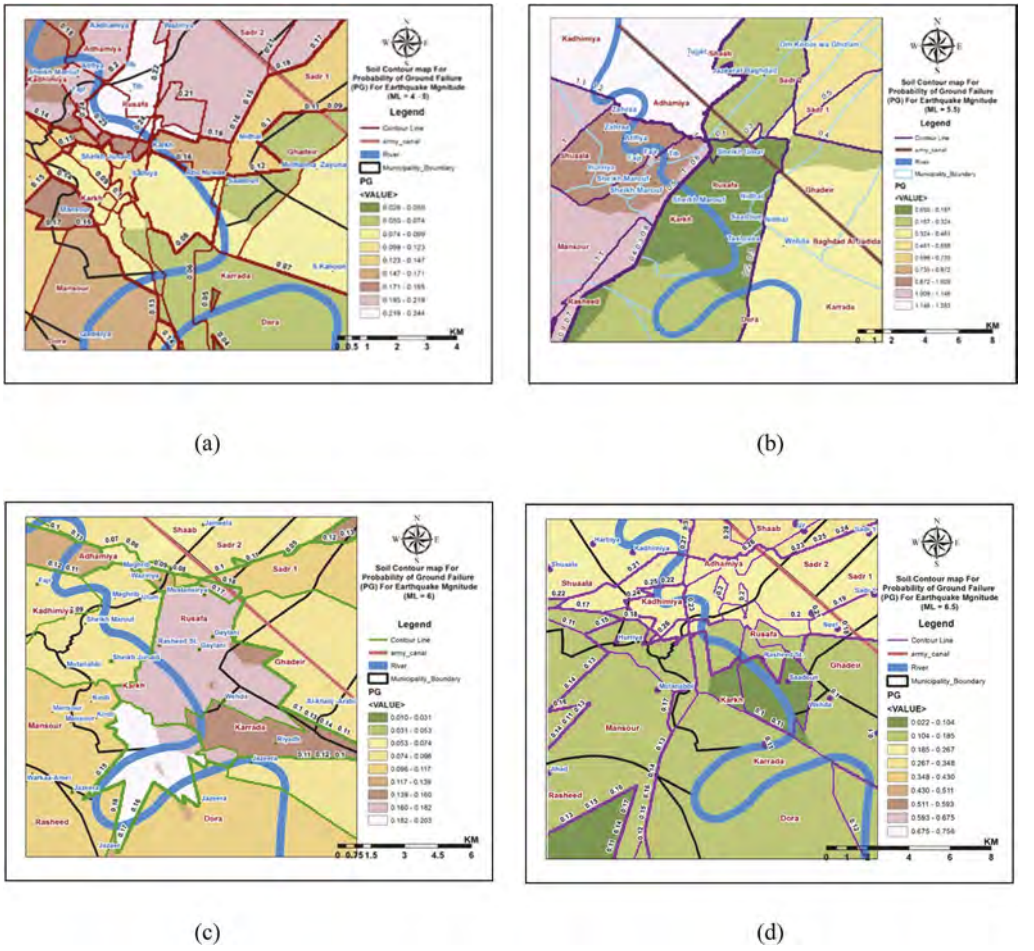

Figure 2. Digital combined contour-interpolation map for the probability of ground failure (*PG*) with different ML values: (a) ML=4-5, (b) ML= 5.5, (c) ML=6, (d) ML=6.5.

3. It was found that LPI is generally effective in predicting moderate-to-severe liquefaction manifestations, but its utility diminishes for predicting less severe manifestations.
4. The probability of ground failure (P_G) and the calculated LPI was calculated for assessing liquefaction risk. As the probability of liquefaction (P_L) and the probability of ground failure (P_G) are considered to be better measure of liquefaction potential than the factor of
5. safety, so they were determined using the factor of safety and L.P.I.

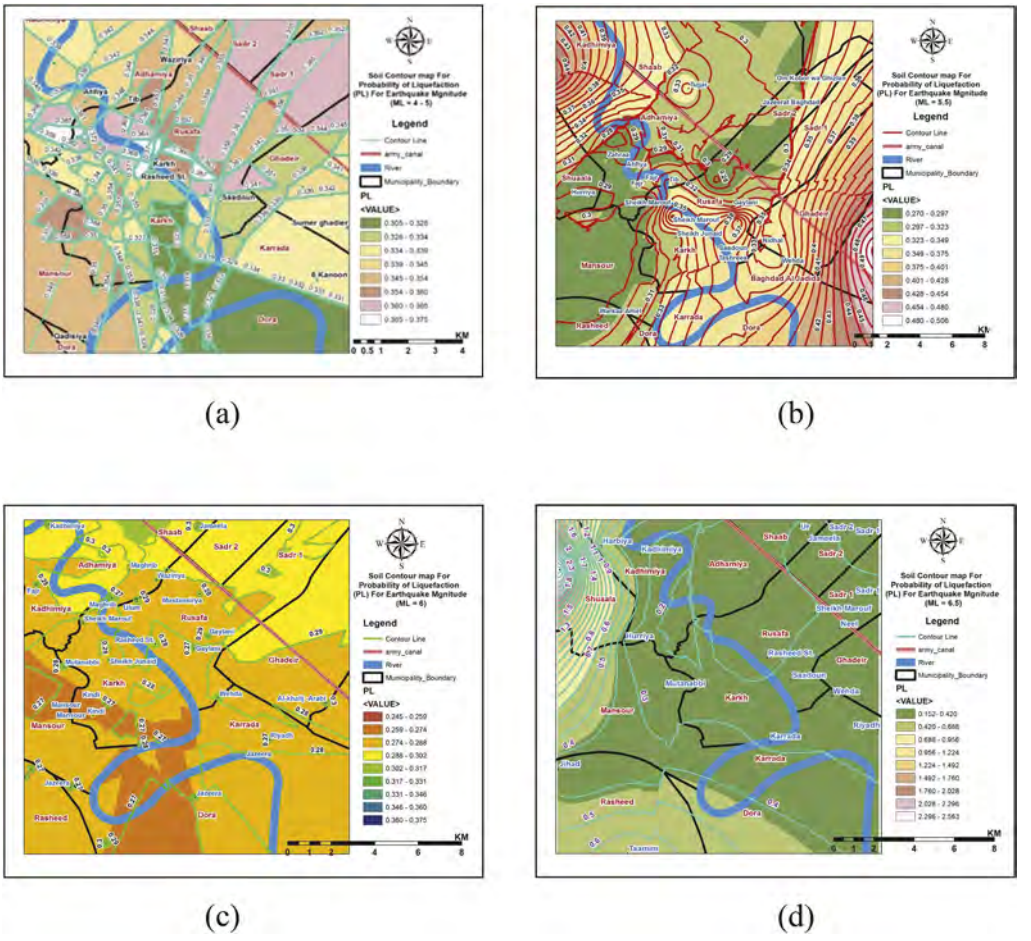

Figure 3. Digital combined contour-interpolation map for the probability of liquefaction (*PL*) with different ML values: (a) ML=4-5, (b) ML= 5.5, (c) ML=6, (d) ML=6.5.

REFERENCES

David, Fattah, A.A., Ali, H.E.A. and Ebid, A.M. (2002). Predicting of soil liquefaction using genetic programming. III Middle East Regional Conference on Civil Engineering Technology & III Int. Symposium on Environmental Hydrology.

Dixit, J., Dewaika, D.M. and Janbid, R.S. (2012). Assessment of liquefaction index for Mombai city. Nat. Hazards Earth Sys. Sci., Vol. 12, pp. 2759–2768.

GeoLogismiki (2006)

Iwasaki,T., Tatsuoka, F. Tokida, K. and yasuda, S. (1978) A practical method for assessing soil liquefaction potential based on case studies at various sites in Japan, Proc. 2nd Int. Conf. on Microzonation, San Francisco, pp. 885–896.

Iwasaki, T., Arakawa, T., and Tokida, K. (1982).simplified procedures for assessing soil liquefaction during Earthquiks. Proc. of the conference on Soil Dynamics and Earthquake Engineering, Southampton, UK, pp. 925–939.

Juang, L.H., Rosowsky, D.V. and Tang, W.H. (1999). Reliability-based method for assessing liquefaction potential of soil. Journal of Geotechnical and Geoenvironmental Engineering. ASCE Vol 127, No. 8, pp. 684–689.

Juang, L.H., Jiang, T. and Andrus, R.D. (2002). Assessing probability-based methods for liquefaction evaluation. Journal of Geotechnical and Geoenvironmental Engineering. ASCE, Vol 128, No. 7, pp. 580–589.

Juang, C.H. Yuan, H., Lee, D.K., Yang, S.F. and Christopher R.A. (2005). Estimating severity of liquefaction – induced damage near foundation. Soil Dynamics and Earthquake Engineering.

Li, D.K., Juang, C.H. and Andrus, R.D. (2006). Liquefaction potential index: A critical assessment using probability concept, J. of GeoEngineering, Vol. 1, No. 1, pp. 11–24.

Luna, R. and Frost, I.D. (1998).Spatial liquefaction analysis system, J. Comput. Civ. Eng., Vol. 12 No. 11, pp. 48–56.

Toprak, S. and Holzer, T.L. (2003). Liquefaction potential index field assessment. J. of Geotechnical and Geoenvironmental Engineering, ASCE, Vol. 129, No. 4, pp. 315–322.

Karim, H.H., Fattah, M.Y. and Hasan, A.M., (2010), "Evaluation of some geotechnical properties and liquefaction potential from seismic parameters", Iraqi Journal of Civil Engineering, Vol. 6, No. 3, P. 30–45.

Karim, H.H. and Schanz, T., (2006), "A study of sediments homogeneity of Baghdad area with evaluating liquefaction potential and settlement", Iraqi Geol. J., Vol. 40, No. 1.

Karim, H.H, and Wadaa, S.J. (2017a). Evaluation of liquefaction potential of Baghdad soil during earthquakes, Global Journal of Engineering Science Research Management (GJESRM), Vol. 4, No. 5, pp. 86–99.

Karim, H.H, and Wadaa, S.J. (2017b). Geotechnical study of Baghdad soil. Global Journal of Engineering Science Research Management (GJESRM), Vol. 4, No. 9, pp. 92–106.

Smart Geotechnics for Smart Societies – Zhussupbekov, Sarsembayeva & Kaliakin (Eds)
© 2023 The Author(s), ISBN 978-1-003-29912-7
Open Access: www.taylorfrancis.com, CC BY-NC-ND 4.0 license

Effects of density and anisotropic confining pressure on liquefaction potential of sandy soil

K. Ishikawa & S. Yasuda
Tokyo Denki University, Saitama, Japan

K. Harada & T. Ideno
Fudo Tetra Corporation, Tokyo, Japan

R. Tsuboi
Graduate School of Tokyo Denki University, Saitama, Japan

ABSTRACT: In this study, cyclic torsional shear tests were conducted under experimental conditions of density, fine-grain fraction, and static earth pressure coefficient in order to quantify the liquefaction countermeasure effect of the compaction improved. Liquefaction properties were evaluated as liquefaction strength ratio and normalized accumulated dissipation energy. We concluded that the static earth pressure coefficient, in addition to density, has a significant effect on liquefaction properties. The denser the specimen, the stronger the mutual effect was. The estimated equations obtained from multivariate analysis using the test condition as parameters showed a high correlation with the experimental data.

1 INTRODUCTION

The 1995 Great Hanshin Earthquake and the 2011 Great East Japan Earthquake caused ground disasters in Japan owing to liquefaction in a wide area of young, reclaimed land. However, Yasuda et al. (1996, 2012) reported less liquefaction damage in areas where the ground was improved by compaction. They thus concluded that compaction was effective as a liquefaction countermeasure. The effect of compaction is hypothesized to be an increase in the coefficient of static earth pressure and density of the original ground. However, reclaimed land is more heterogeneous than alluvial ground. Additionally, the effects of material properties, density, and static earth pressure coefficient on the liquefaction potential have not been quantitatively determined previously. It is expected that quantifying the effects of these parameters will lead to more advanced design of the improved compaction method.

In this study, liquefaction tests were carried out on specimens having variable fine-grain content and densities. Isotropic and anisotropic stress conditions using adjusted specimens that simulate the process of reclamation were tested to evaluate the effects of these parameters on the liquefaction strength ratio and normalized accumulated dissipation energy.

2 TEST PROCEDURE

2.1 *Material properties*

Three types of sandy soil with different fine-grained content were used as soil samples. The sandy soil was collected from Chiba Prefecture, Japan. It was classified by water plunging and remixing in a 2 m high acrylic cylindrical container to simulate reclamation. After 24 h, the sandy soil with low fine-grain content was deposited in the lower layer and fine-grain soil with low sand content was deposited in the upper layer. The material properties of each sample and the grain size distribution curves are shown in Figure 1. The maximum void ratio e_{max}

DOI: 10.1201/9781003299127-260

was obtained using the JGS 0161-2009, a Japanese Geotechnical Society standard. The minimum void ratio e_{min}* was defined as the maximum dry density obtained from the soil compaction test (JGS 0711-2009), as followed by Ishihara et al (2016).

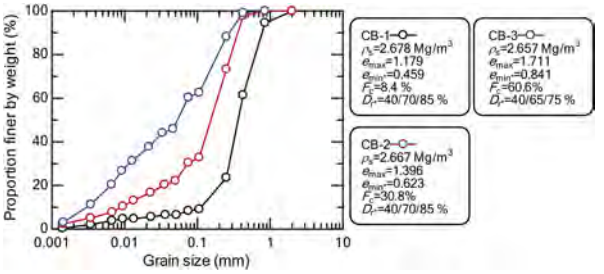

Figure 1. Grain size distribution curves and the material properties.

2.2 *Cyclic torsional shear test method*

The specimen was a hollow cylinder with an outer diameter of 100 mm, inner diameter of 60 mm, and height of 100 mm. The density of the specimens was set as per the relative densities shown in Figure 1. The three types of specimens were defined as loose, medium, and dense. They were prepared using a dry vibration method. The sides of the mold were tapped with a wooden hammer, and the height of each layers was controlled by dividing the specimen height into five sections. Once the specimens were prepared, their saturation was checked based on the pore water pressure coefficient B using CO_2 and de-aerated water. The value of B was confirmed to be greater than 0.95. Consolidation was carried out for 30 min at each confining pressure. Three static earth pressure coefficients K_0 of 0.5, 1.0, 1.5, were used for the confining pressure, based on a mean effective principal stress σ'_m of 130 kN/m^2. In anisotropic stress conditions, cyclic undrained shear tests were performed by correcting the axial displacement of the specimen to reproduce the plane strain conditions, as performed by Tatsuoka et al (1982). The loading method is a shear stress control with a 0.1 Hz sine wave.

3 TEST RESULT

3.1 *Characteristics of number of cycles and shear stress*

In this study, liquefaction is defined the condition when the double amplitude shear strain γ_{DA} = 7.5 % is reached in the soil patch under analysis. Figure 2 shows the relationship between the number of cycles to liquefaction and the cyclic shear stress ratio normalized by the vertical effective stress. In the figure, from left to right, CB-1, CB-2, and CB-3 are divided by their fine-grain content. The plots show difference in the coefficient of static earth pressure. The colors indicate the density of the specimens, where red, green, and blue indicate loose, medium, and dense specimens, respectively. The numbers in the figure are the average relative density of each specimen after consolidation. The liquefaction strength curve of CB-1, with a low fine-grain content, is characterized by an upward shift as the density and static earth pressure coefficient increase under the same confining pressure conditions and density conditions, respectively. The same trend is observed for CB-2, which contains a moderate amount of fine grains, and CB-3, which is highly fine-grained.

Figure 3 shows the relationship between the number of cycles to liquefaction and normalized accumulated dissipation energy. The accumulated dissipated energy can be obtained by calculating the hysteresis area for each cycle from the stress-shear-strain relationship of each specimen and accumulating it over the liquefaction time, as calculated by Kokusho (2013). The accumulated dissipation energy was then divided by the vertical effective stress to obtain the normalized accumulated dissipation energy. The normalized accumulated dissipation energy during liquefaction in the loose conditions for CB-1 and CB-2 is similar. The marginal variation observed is due to the difference in the static earth pressure coefficient. However, when the specimen density moves towards dense form medium, the normalized accumulated

dissipation energy becomes larger than the loose state. It also increases because the static earth pressure coefficient is not as significant under the same density conditions. The cause of these observations is hypothesized to be due to an increase in the shear strain before the excess pore water pressure reaches the effective confining pressure in fine-grained soils. This tendency is characteristic to fine-grained soils, unlike CB-1 and CB-2.

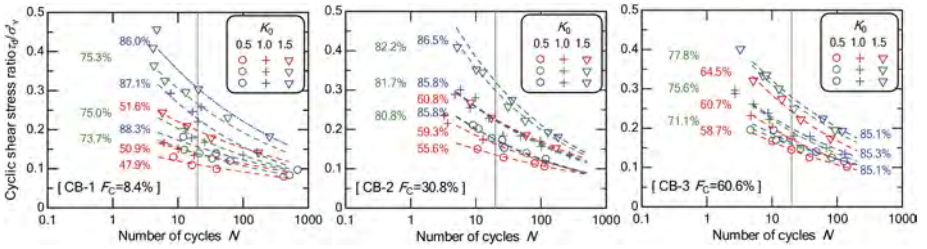

Figure 2. Liquefaction strength curves for each sample.

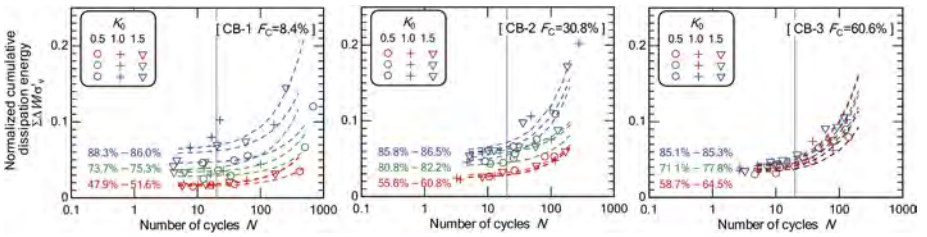

Figure 3. Normalized accumulated dissipation energy vs. number of cycles.

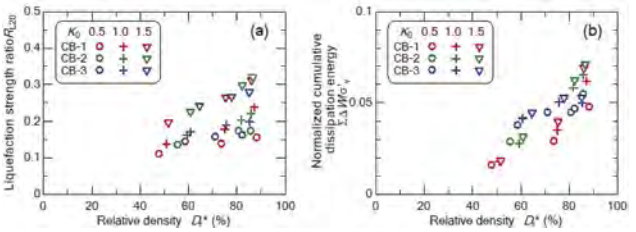

Figure 4. Relative density vs. liquefaction strength ratio (a) or normalized accumulated dissipation energy (b).

3.2 *Characteristics of liquefaction strength ratio and liquefaction potential*

From the liquefaction strength curves for each test condition in Figure 2, the cyclic shear stress ratio over 20 cycles was used to derive the liquefaction strength ratio. Similarly, the normalized accumulated dissipation energy over 20 cycles from Figure 3 was used to derive the liquefaction potential of the specimen in Figure 3. The relationship between the average relative density and the liquefaction strength ratio and normalized accumulated dissipation energy for each test condition is shown in Figure 4 (a) and (b), respectively. The liquefaction strength ratio and static earth pressure coefficient increase with an increase in the relative density. Additionally, the increase in the static earth pressure coefficient under dense conditions is significant. The effect of the fine grains is not as significant as that of the density and static earth pressure coefficient. This may be because the specimens were reconstructed and therefore did not include the effect of aging. Additionally, the normalized cumulative dissipation energy corresponding to its liquefaction strength ratio for a material is shown to be unique and variable for loose and dense relative density conditions, respectively. The normalized cumulative dissipated energy is also found to vary with the amount of fine grain in the soil sample. This suggests that evaluating liquefaction properties with normalized accumulated

dissipation energy may allow for the consideration of more details of the soil such as the effects of material properties, density and static earth pressure coefficient.

The liquefaction strength ratio and the equivalent normalized accumulated dissipation energy are mutually influenced by the relative density, static earth pressure coefficient, and amount of fine-grain. Therefore, a multivariate analysis was performed using the liquefaction strength ratio and the equivalent normalized accumulated dissipation energy as objective variables and the test conditions as explanatory variables. Figure 5 compares the experimental values with the estimates derived from the multivariate analysis. The figure shows that the coefficient of determination R_2 between the experimental and estimated liquefaction strength ration is 0.95, indicating a high correlation. The root mean square error (RMSE) is 0.014. Similarly, the R_2 between the experimental and estimated normalized accumulated dissipation energy is 0.92, and the RMSE is 0.0046. They also show a high degree of correlation. The estimated equation obtained from the multivariate analysis are shown in Figure 5.

Using this correlation equation, liquefaction potentials can be evaluated for different fine-grain content, density, and static earth pressure coefficient. However, since the correlation equation is based on a reconstructed sample, the compatibility with the actual ground conditions needs to be confirmed in the future.

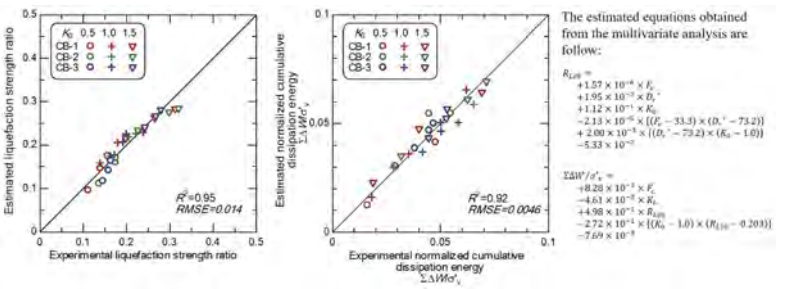

Figure 5. Comparison of experimental and estimated liquefaction strength ratios and normalized cumulative dissipation energies.

4 CONCLUSIONS

In this study, liquefaction strength ratios and normalized accumulated dissipation energy were obtained from cyclic torsional shear tests. The parameters considered during the test were material properties, density, and static earth pressure coefficient of the specimens. We concluded that the static earth pressure coefficient, in addition to density, has a significant effect on liquefaction properties. The denser the specimen, the stronger the mutual effect was. The estimated equations obtained from multivariate analysis using the test conditions as parameters showed a high correlation with the experimental data.

REFERENCES

Ishihara, K., Harada, K., Lee, W.F., Chan, C.C. and Safiullah, A.M.M. 2016. Post-liquefaction settlement analyses based on the volume change characteristics of undisturbed and reconstituted samples, *Soils and Foundations*, 56(3): 533–546.

Kokusho, T. 2013. Liquefaction potential evaluations: energy-based method versus stress-based method, *Canadian Geotechnical Journal*, 50: 1088–1099.

Tatsuoka, F., Muramatsu, M. and Sasaki, T. 1982. Cyclic undrain stress-strain behavior of dense sands by torsional simple shear test, *Soils and Foundations*, 22(2): 55–70.

Yasuda, S., Ishihara, K., Harada, K. and Shinkawa, N. 1996. Effect of soil improvement on ground subsidence due to liquefaction, *Special Issue of Soils and Foundations*: 99–107.

Yasuda, S. Harada, K., Ishikawa, K. and Kanemaru, Y. 2012. Characteristics of liquefaction in Tokyo Bay area by the 2011 Great East Japan Earthquake, *Soils and Foundations*, 52(5): 793–810.

Smart Geotechnics for Smart Societies – Zhussupbekov, Sarsembayeva & Kaliakin (Eds)
© 2023 The Author(s), ISBN 978-1-003-29912-7
Open Access: www.taylorfrancis.com, CC BY-NC-ND 4.0 license

Foundation impedance function from physical model tests by two-way horizontal loading

Fardin Jafarzadeh
Associate Professor, Sharif University of Technology, Tehran, Iran
President of Iranian Geotechnical Society, Tehran, Iran

Jafar Maleki
Geotechnical Engineer, Abgeer Consulting Engineers Company, Tehran, Iran
M.Sc. of Geotechnical Engineering, Sharif University of Technology, Tehran, Iran

ABSTRACT: The dynamic impedance function is presented for massless rigid foundations, which is possible to obtain the dynamic response of foundations for different frequencies. This study investigates the dynamic impedance functions using physical model tests on sandy soil subjected to two-way horizontal harmonic loading. The tests were carried out inside a steel container which was filled with Babolsar sand. A 10 cm thickness sawdust was employed between the container and sand to simulate infinite half-space. Also, concrete slabs of 15 cm thickness were applied to simulate the bedrock beneath the sandy layer. The selected foundations were square and circular and investigated to determine the effects of foundation shape and embedment ratio to impedance function. The results show that dynamic stiffness and damping coefficient increase with increasing embedment ratio. Also, the dynamic response of square and circular foundations is different due to wave propagation, which depends on foundation geometry.

1 INTROUDUCTION

One of the fundamental problems in dynamic soil-structure interaction is the characterization of the dynamic response of surface foundations resting on a soil medium under time-dependent loads. In modern methods of machine foundation analysis, impedance functions are used frequently. Consequently, the most critical step in machine foundations' current dynamic analysis method is to determine dynamic impedance functions. Impedance functions are ratios of applied interfacial force or moment to induced displacement or rotation angle of foundation.

In recent years, a large and growing body of literature has examined numerical methods to predict the response of shallow foundations to harmonic and seismic loadings (Li et al. 2019, Zeolla et al. 2022). Large-scale experiments are performed to assess the impedance function of surface foundations. Typically, the large-scale testing results are the best data for verifying numerical modeling (Cheney et al. 1990, Amendola et al. 2021). However, there are limited studies conducted on small-scale experiments. As the example is Nii (1987) who carried out an extensive investigation on the impedance function of a rigid rectangular surface foundation under viscoelastic homogeneous half-space conditions. By considering a high expenditure of in-situ tests and lack of control over the soil parameters, researchers became interested in physically modeling this issue in the laboratory. A few important studies have been performed in this regard on surface foundations by Erden (1974), Nii (1987), and Pak & Guzina (1995). In these studies, a surface footing was placed in a container box, and a dynamic load was applied to it. However, all of these researches investigated foundation response to vertical vibration. Jafarzadeh & Ghassemi (2011) investigated the shallow foundation response to one-way horizontal direction loading by physical model tests in half-space model conditions.

DOI: 10.1201/9781003299127-261

Keeping above observations, the investigation of impedance functions for a foundation exposed to two perpendicular co-phase horizontal loading has yet to be investigated. So, this study examines the dynamic foundation response to two-way horizontal loading using physical modeling in a rigid base model condition.

2 PREPARATION OF THE MODEL

In the present research, using physical modeling, dynamic response of shallow foundations on homogeneous rigid base model was studied. Soil medium was built in a 1 by1 by 0.8 m^3 steel box whose interior walls were covered by a 0.1 m thick layer of sawdust (a material with high damping). For separation, a wooden frame by a thin plastic layer (0.1 mm) was placed all around the container. Also, a concrete slab with a thickness of 15 cm was placed at the bottom of the container to simulate the bedrock conditions (Figure 1-a).

In this study, "Babolsar" sand obtained from coastal city of Babolsar in the south of Caspian Sea. This soil, according to the USCS standard, is classified as SP. The soil properties are calculated where e_{max}, e_{min} and e_{ave} are the maximum, minimum and average of the void ratio of the model 0.775, 0.547 and 0.51, respectively. Furthermore, G_s that is the specific gravity of the sandy soil determined 2.753. Also, Babolsar sand particle-size distribution curve is displayed in Figure 1-b. Using the sand-raining method, uniform unit weight of the soil was poured into a steel container. In this method, by controlling falling height and sand flux (by using a sieve with proper holes diameter) desired density of sand can be achieved. The soil was prepared in layers and resembled the condition of soil layers in nature. In this study, air pluviation technique was used, and sand was dropped from 70 cm height by a sieve with opening sizes of 6 mm and formed layers with a thickness of 5 cm making a soil with relative density of about 54%.

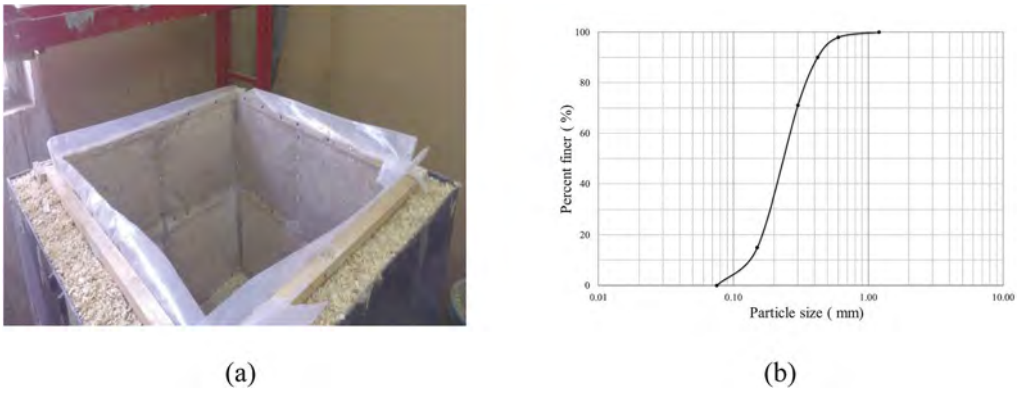

Figure 1. A) Steel box, wood frame and sawdust, and b) Particle size distribution for Babolsar sand.

3 TEST SETUP

Two different footing shapes: square and circle with equal surface area were used in this research. The dimensions were chosen such that the footing was protected against slipping. The foundation was joined to a steel column with a height of 20 cm, and it was connected to the signal generators. After the preparation of the soil-foundation system, the footing and column were placed on the center of the soil surface with an embedment depth of zero and was subjected to the two-way of co-phase horizontal directions of loading vibrations. Next, a loading system consisting of a shaker, metal rod, harmonic signal generator, and an amplifier was connected to the model. Harmonic loading with specified amplitude and frequency was produced by signal analyzer and amplified by power amplifier and was applied using two shakers in the horizontal direction through the column on the footing. The shakers received a horizontal harmonic signal generated by the signal generator from the amplifier. The signal passed through the two metal rods and finally transmitted to the column.

The excitation frequency range was chosen as 50-900 Hz, compatible with frequency range of most industrial machines, for observing the dynamic response of various types of structures. It included the frequency limits of large foundations, e.g. turbines, large silos, as well as large and relatively rigid footings in power plants. The loading duration was 16 seconds consisting of sinusoidal harmonic cycles at a specific frequency. Also, 20 Hz steps were used for tests as uniform intervals.

The force amplitude was recorded via two load cells located between the column and string. The amplitude of the horizontal load was maintained approximately constant by changing the voltage gain of the signal analyzer unit as frequency increased. The foundation displacements in horizontal and vertical directions were recorded via accelerometers mounted on them. These sensors were piezoelectric-type and were connected to a signal analyzer. Two accelerometers were placed on the foundation in the vertical direction. These sensors enabled the measurement of vertical displacement of the footing. These accelerometers were strain gauge type and were connected to a data logger, which transmitted data to a computer for later processing. In addition, using these recorded data, calculating the rotation angle of the footing was possible. The schematic cross section of the model and the loading system are shown in Figure 2.

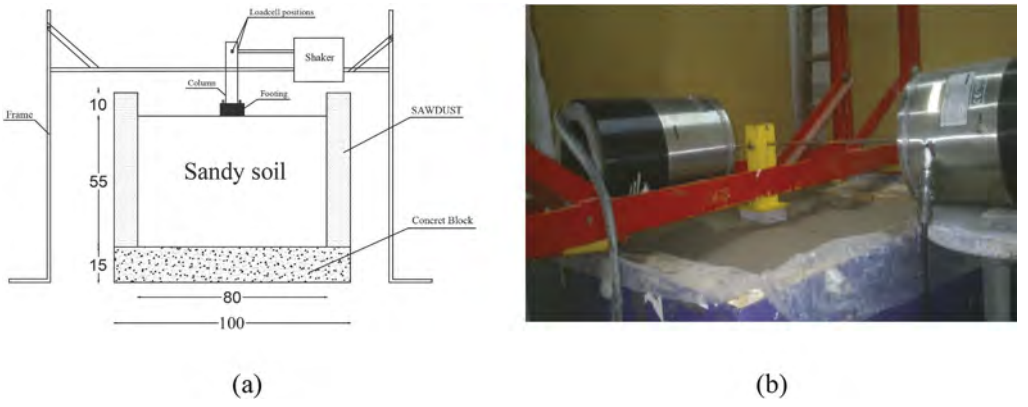

Figure 2. Physical model, (a) Schematic experimental setup (measurements are in centimeters), and (b) Real side view.

4 COMPLEMENTARY TESTS

Travel time tests were conducted in order to measure the compressional and shear wave velocities of the models. Two accelerometers were installed inside soil models 0.4 m apart from each other vertically. One footing was set on the soil model, and body waves were generated using a specific hammer, in the vertical direction. By knowing the distance and delay time, the compressional wave velocity was calculated. Next, by repeating this procedure, and putting accelerometers 0.4 m apart from each other in the horizontal direction, the shear wave velocity of the soil medium was measured. So, the compressional and shear wave velocities being calculated as 116 m/s and 54 m/s; respectively. The minimum and maximum dry unit weight of Babolsar sand are measured as 15.45 (kN/m^3) and 17.8 (kN/m^3); respectively. Using data in Table 1 and formula given by Gazetas (1983) static stiffness is calculated:

$$k_h = \frac{8GR}{2-\upsilon}\cdot\left(1+\frac{R}{2H}\right) \qquad (H/R > 1) \qquad (1)$$

Where: k_h = horizontal static stiffness; G = shear modulus; R = footing radius (or equivalent radius); υ = Poisson's ratio; and H = soil layer thickness.

Table 1. Physical model properties.

Parameter	Unit	Value
Maximum dry density	kN/m^3	17.8
Minimum dry density	kN/m3	15.45
Dry density	kN/m3	16.65
Relatively density (D_r)	%	54
Compressional wave velocity (V_c)	m/s	116
Shear wave velocity (V_s)	m/s	54
Elastic modulus (E)	MPa	13.2
Shear modulus (G)	MPa	4.8
Poisson's ratio (υ)	-	0.36

5 BASIC RELATIONS

The foundation response to the dynamic loading can be obtained by considering a soil-foundation system. In the case of foundation vibration, displacement proportional to vibration will occur in the soil. Impedance functions are defined as ratios of the total interfacial load (force or moment) at the soil-foundation interface to induced displacement or rotation angle of foundation, which are function of frequency. It is common to introduce complex notation and to express each of the impedances in form below:

$$K = K_1(\omega) + K_2(\omega) = K(K_h + \omega C_h i) \tag{2}$$

in which both real component K_1 and imaginary component K_2 are functions of the circular frequency ω. Also, K is typically referred to as the static stiffness, K_h is horizontal dynamic stiffness, and reflects the stiffness and inertia effects of the supporting soil. In imaginary component, C_h is the dashpot coefficient showing the radiation and material damping generated in the system (due to energy carried by waves spreading away from the foundation and energy dissipated in the soil by hysteric action; respectively). Alternatively, a dimensionless frequency number is often introduced:

$$a_0 = (\omega B)/(v_s) \tag{3}$$

where B = half width of the foundation; ω = circular frequency of vibration; and V_S = shear wave velocity in soil medium. Rewriting Equation 2:

$$K = K_1(a_0) + K_2(a_0) = K(K_h + a_0 C_h i) \tag{4}$$

So, in this study, the results are given in the form of figures that include parameters k and c against dimensionless frequency, a_0.

A dynamic horizontal loading to the soil-foundation medium will appear in a horizontal force and rotation on the foundation surface. The two degrees of freedom of motion will result in four impedance equations, i.e. horizontal, rotation, rotation combined with horizontal, and horizontal combined with rotation. This approach is problematic since only two independent responses, i.e. horizontal sliding and rotation, can be measured, while four unknown impedances are to be determined. In this research, to solve the problem, the following method is used (Dunn 2010). By assuming that coupled impedances are negligible, the horizontal impedance can be calculated using Equation 5:

$$S_h = F_s/U_h \tag{5}$$

where, F_s is a function of the applied horizontal force and the inertia of the footing and U_h is the maximum horizontal displacement of the footing bottom interface with the soil. For calculating F_s, it is necessary to consider changes in the sliding force due to the foundation rotation and any structure attached to the foundation. So, it can be computed by Equation 6:

$$F_s = F_T + \omega^2(M_0U_b - M_0b_2\phi_b) + \omega^2[1]^T[M]\{U\} \quad (6)$$

where: F_T = applied horizontal force to the column (or footing); M_0 = footing weight; U_b = the total motion of the instrumentation measuring horizontal motion; b_2 = the distance from the instrumentation to the gravity center of the foundation; φ_b = the maximum rotation of the footing; [1] = the unit matrix; [M] = the matrix of point masses; and {U} = the maximum horizontal displacement corresponding to the matrix of point masses. The first part of Equation 6 describes the horizontal force exerted to the column (F_T), the second part shows the foundation movement, and the third part considers the structural effect on the foundation. When calculating this effect, the structure is separated to individual points, each with mass properties. This separation is done as the column and frame may not be considered rigid. Each point is employed as a point that will move a unique magnitude and impart a force on the foundation. Regarding the column as rigid, the third part of Equation 6 can be assumed zero. Therefore:

$$F_s = F_T + \omega^2(M_0U_b - M_0\ b_2\ \phi_b) \quad (7)$$

On the other hand, Equations 8 and 9 are used to calculate U_h and Φ_b:

$$U_h = U_b - 2b_2\varphi_b \quad (8)$$

$$\varphi_b = (v_1 + v_2)/2B \quad (9)$$

In this study, the contact between the column to footing was considered rigid and attached through bolts together. Thus, Equation 7 was used to calculate the horizontal impedance function.

6 TEST RESULTS

The tests were done in rigid base conditions for square and circular footings. The test program was designed such that minimum disturbance occurred in the soil-foundation system. In these experiments, influential parameters, including footing shape and embedment ratio, were chosen to examine their influence on impedance functions.

According to Figure 3, in square footing, the dynamic stiffness coefficient of the square footing grows with the increase in the embedment ratio (D/h; D, embedment and h, footing thickness). The dynamic stiffness at the embedment ratios 0 and 1 showed almost a similar trend. Also, the dynamic stiffness fluctuations were observed at the dimensionless frequency, $a_0 \leq 4.5$. This fluctuation may be due to the sharp edges of square footing affecting the wave propagation into the soil. Further, upon elevation of the buried ratio, the distance between the bed of the square foundation and the rigid bed decreases. Distance reduction can cause higher level reflection, which significantly affects the results. Both test results show a peak at a_0=3.5. Furthermore, in the square footing, dynamic damping coefficients grow with the rise in the embedment ratio with similar trends.

As illustrated in Figure 4, in the circular footing, upon D/h increase, the dynamic damping at $a_0 \leq 2$ is almost unchanged, while at higher values, it fluctuates. On the other hand, the dynamic damping of the circular footing showed a similar trend, where the embedment ratio of 1 resulted in a higher value than 0. Also, by comparing the circular and square footing results, it is noticed that the results are more regular in the circular footing than the square ones. These results confirmed the general rule that a higher embedment ratio could increase the impedance functions.

Figure 5 indicates that the dynamic stiffness of the square footing has higher values of circular footing. Also, it can be noticed that circular footing has a smooth trend in front of the square footing, which may be from the sharp edges of the square footing. Damping of circular and square footings follows relatively similar trends at the lower frequency range of $a_0 \leq 3$. In higher a_0, the square footing shows higher damping values.

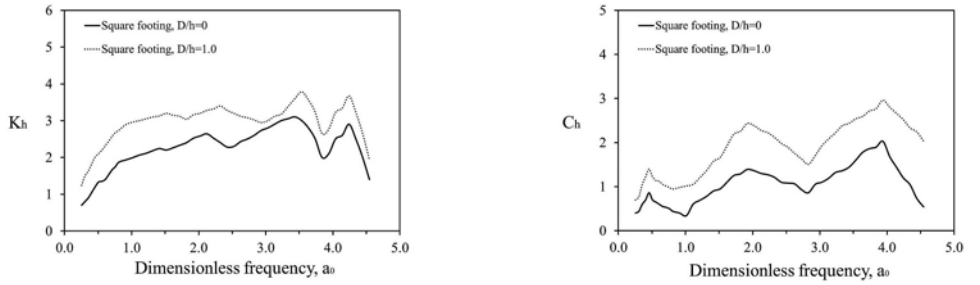

Figure 3. Comparison of the effect of embedded ratio on dynamic stiffness and damping of square footing.

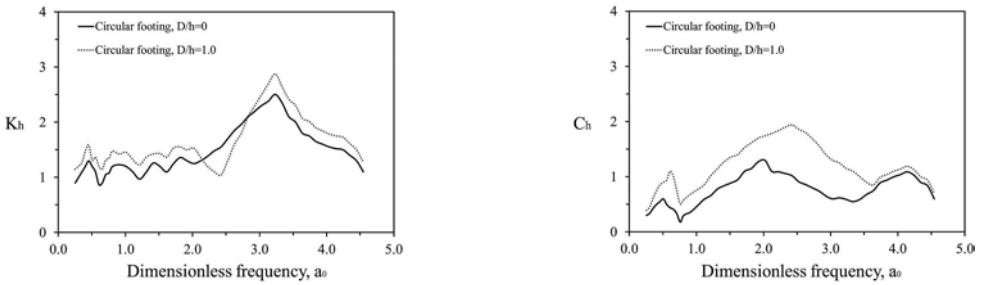

Figure 4. Comparison of the effect of embedded ratio on dynamic stiffness and damping of circular footing.

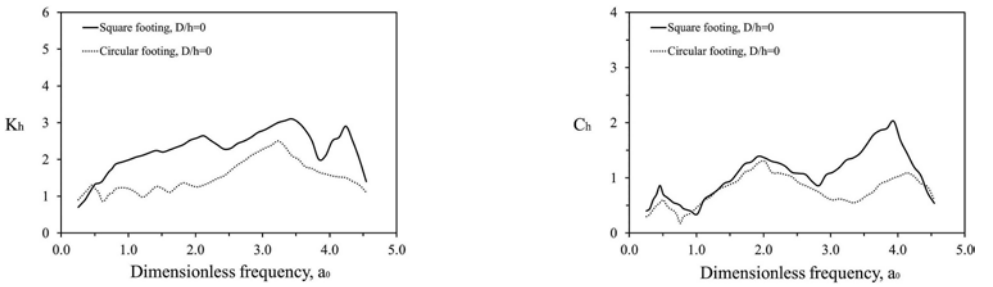

Figure 5. Comparison of the effect of footing shape on dynamic stiffness and damping.

7 CONCLUSION

The main goal of the current research was to determine the dynamic response of surface footings by physical tests to two-way horizontal harmonic loading. For this purpose, a systematic experimental investigation was conducted to obtain the impedance functions in sandy soils. Tests were performed in a rigid base model condition. The relative density of the models was 54%, and the shear wave velocity was 54 m/s. These tests were conducted in dimensionless frequency limits of 0.3 to 4.5 and for two footing shapes: square and circular. From the results, it can be found that complex and unpredictable behaviors were observed in the rigid base model condition due to the propagation and reflection of waves inside the soil. Also, upon elevation of the embedment ratio, dynamic stiffness and damping increased. It was also marked that the circular footing had a smoother response than square foundations.

REFERENCES

Amendola, C., de Silva, F., Vratsikidis, A., Pitilakis, D., Anastasiadis, A., & Silvestri, F. 2021. Foundation impedance functions from full-scale soil-structure interaction tests. *Soil Dynamics and Earthquake Engineering*, 141, 106523.

Cheney, J., Brown, R., Dhat, N. & Hor, O. 1990. Modeling free-field conditions in centrifuge models. *Journal of geotechnical engineering*, 116(9),1347–1367.

Dunn, P. W. 2010. Comparison of cone model and measured dynamic impedance functions of shallow foundations. *PhD Thesis*, University of Florida.

Erden, S. M. 1974. Influence of shape and embedment on dynamic foundation response. University of Massachusetts Amherst.

Gazetas, G. 1983. Analysis of machine foundation vibrations: state of the art. *International Journal of Soil Dynamics and Earthquake Engineering*, 2(1), 2–42.

Jafarzadeh, F., & Ghassemi, R. 2011. Investigation of Dynamic Response of Shallow Foundations to Horizontal Vibrations. *In International Conference on Geotechnics for Sustainable Development (GEOTEC), October, Hanoi, Vietnam*, ISBN (pp. 978–604).

Li, Z.-y, Li, J.-b & Lin, G. 2019. Dynamic Response of Arbitrarily Shaped Foundation Embedded in Multilayered Partially Saturated Half-Space. *International Journal of Geomechanics*, 19(11), 04019121

Nii, Y. 1987. Experimental half-space dynamic stiffness. *Journal of geotechnical engineering*, 113(11), 1359–1373.

Pak, R. Y., & Guzina, B. B. 1995. Dynamic characterization of vertically loaded foundations on granular soils. *Journal of geotechnical engineering*, 121(3), 274–286.

Zeolla, E., Sica, S., & De Silva, F. 2022. Dynamic impedance functions for neighbouring shallow footings. *In Geotechnical Engineering for the Preservation of Monuments and Historic Sites III* (pp. 883–892). CRC Press.

Smart Geotechnics for Smart Societies – Zhussupbekov, Sarsembayeva & Kaliakin (Eds)
© 2023 The Author(s), ISBN 978-1-003-29912-7
Open Access: www.taylorfrancis.com, CC BY-NC-ND 4.0 license

1g shaking table tests for small scale superstructure - pile groups in sandy soil

Sumin Song & Sangseom Jeong
Yonsei University, Seoul, South Korea

ABSTRACT: In this study, 1g shaking table tests were performed with a superstructure supported group pile to investigate the dynamic response of soil-structure interaction with rigid base and deep foundation. The super and sub structure were modeled as a 1/25 scaled 6-story steel-framed building, 2x2 group pile with the end bearing pile, fixed and hinge pile head condition, and embedded in dense SP soil. An experimental program had sweep tests performed to assess the natural period of the structure with different foundation conditions, and the dynamic behavior of the earthquake in Korea was analyzed using the sinusoidal wave. The test results showed that the natural period was longer in the case of pile-supported structures than structure without pile, and it was found that the pile head hinge condition have a longer natural period. The lateral displacement also showed that the hinge condition was larger, and the largest lateral displacement occurred at the frequency near the natural period.

1 INTRODUCTION

The dynamic response of building structures depends on its natural period of vibration and the natural period is widely used in the design codes. Matsumoto et al. (2004) performed the shaking table tests on piled-raft model embedded in dry sand with varying the height of the superstructure structure. J. Roy et al. (2018) described that the natural frequencies of piled-raft foundation with superstructure effect by using numerical analyses.

In this study, the dynamic response of pile-supported superstructure was investigated in dense sand conditions(relative density, D_r = 80) from 1g shaking table tests.

2 1G SHAKING TABLE TESTS

2.1 *Test apparatus*

Dynamic tests on small scaled piles and superstructures were carried out from 1g shaking table tests. The platform width and length of the shaking table are 1,500 mm and, 1,500 mm, respectively.

2.2 *Test soil and small-scaled pile-supported structure*

This study used Jumunjin standard sand according to the Unified Soil Classification System-(USCS) as SP(Poorly graded Sands), with a specific gravity(G_s) is 2.65 for 1g shaking table tests. The properties of the test soil are shown in Table 1.

The prototype piles are assumed to be general steel pipe piles with a diameter of 0.5 m, a thickness of 0.05 m, and a length of 12.5 m. In this study, the small-scale model pile has a hollow circular portion with a 2.0 cm outer diameter as the scale factor, 25, and the 50 cm

DOI: 10.1201/9781003299127-262

embedment depth to consider the long pile condition based on the pile conditions theory. The 1g shaking table test devices are summarized in Figure 1.

Table 1. Physical properties of test soil.

USCS	γ_{max} (kN/m^3)	γ_{min} (kN/m^3)	Gs	D_{10} (mm)	D_{30} (mm)	D_{60} (mm)	C_u	C_C
SP	16.2	13.6	2.65	0.38	0.49	0.49	1.59	0.99

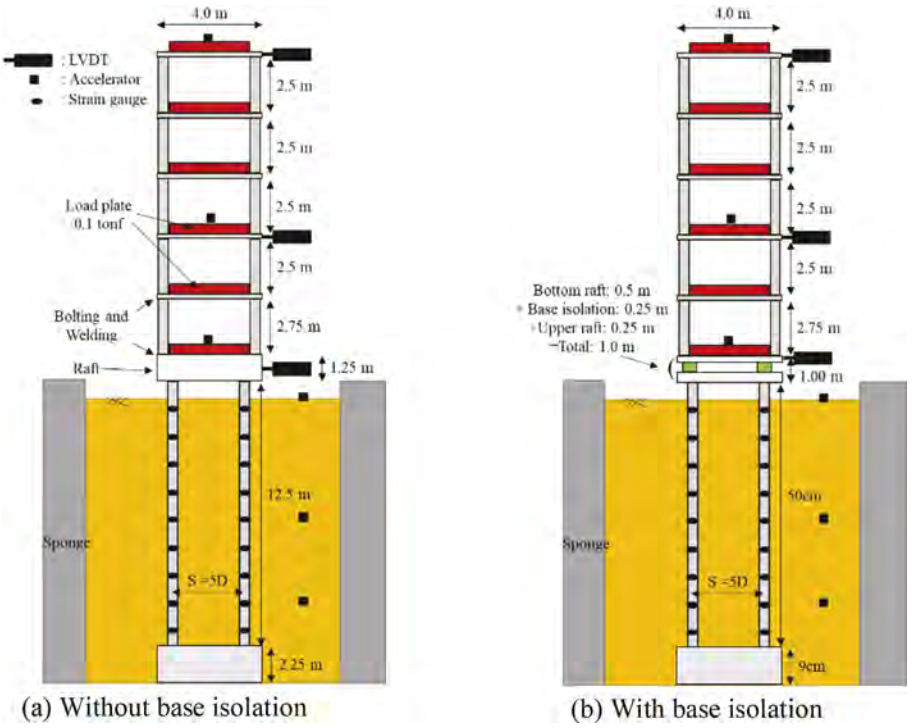

Figure 1. Illustration of the pile-supported structure in this study.

2.3 *Test programs*

In phase 1, this study conducted sweep tests to assess the natural frequency structure systems under various input sinusoidal acceleration. In phase 2, the sinusoidal acceleration test conducted with a specific natural frequency(f_r). The test programs are summarized in Table 2, 3.

Table 2. Sweep tests of Phase 1.

Case	Stories	Foundation	Pile head condition	Input acceleration	
				Peak acc. (g)	Frequency(Hz)
1		Pile	Fixed		Sweep test
2	6		Hinge	0.05	1 – 30 Hz
3		Footing	-		

Table 3. A sinusoidal test case of Phase 2.

Case	Stories	Foundation	Pile head condition	Input acceleration	
				Peak acc. (g)	Frequency(Hz)
4	6	Pile	Fixed	0.1	0.37
				0.2	0.96
5			Hinge	0.3	1.65
				0.4	

3 TEST RESULTS AND ANALYSES

Figure 2 (a) shows test results of the natural period with varying input acceleration. The natural periods were calculated from the 6th-floor acceleration by using FFT(Fourier Fast Transformation). The results show that as increasing of input acceleration, the natural period of pile-supported superstructure increases. Figure 2 (b) shows the natural period of pile-supported superstructure compared to the natural frequency equation for steel-framed buildings in KDS. It is shown that the natural period of the rigid(direct) foundation show almost similar value but increased in the cases of pile-supported case. The hinged pile head condition recorded longer natural period than fixed condition because of increase lateral displacement of superstructure (Figure 3).

Figure 3 shows the lateral displacement of superstructure in varying input acceleration. The largest lateral displacement of superstructure at the Hinged pile head condition. Hinged pile head condition showed more lateral displacement than fixed condition, but fixed condition recorded larger lateral displacement in Figure 3.

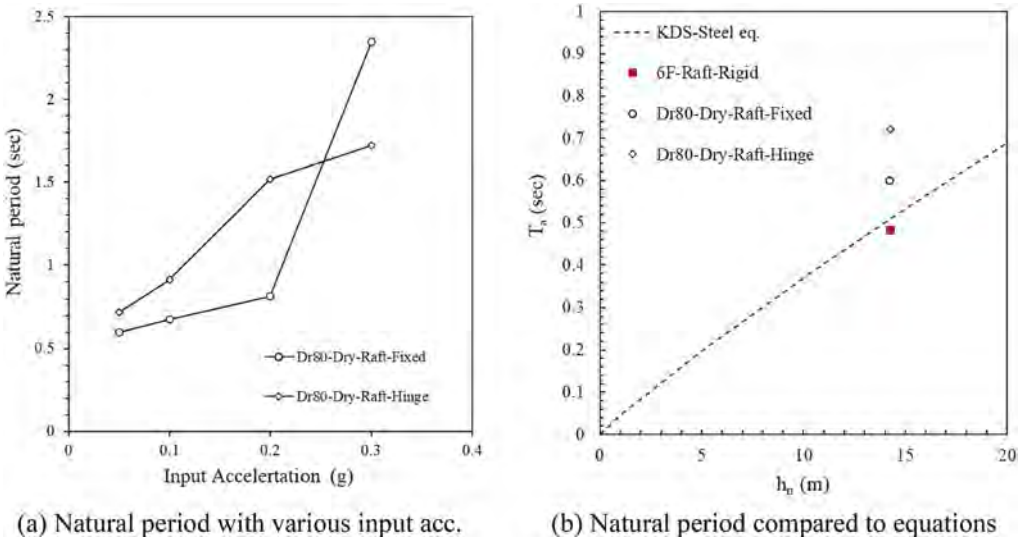

(a) Natural period with various input acc. (b) Natural period compared to equations

Figure 2. Test results of the natural period.

4 CONCLUSIONS

In this study, shaking table tests of pile supported superstructure on cohesionless sand were carried out by considering soil-structures interaction. The key conclusions obtained in this study as follows:

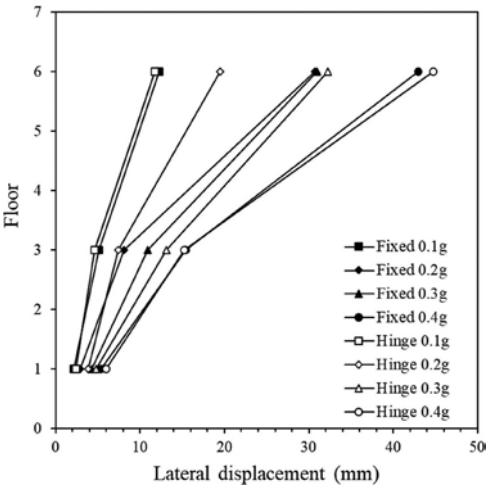

Figure 3. Lateral displacement of superstructure in various input acceleration.

1. All pile-supported superstructures got larger natural periods than without pile conditions. As increase the input acceleration, the natural period of pile-supported superstructure increases.
2. The lateral displacement of superstructure in various input acceleration showed low frequency domain case, and fixed condition showed larger lateral displacement than in 0.96 Hz case.

ACKNOWLEDGMENT

This work was supported by a Basic Science Research Program through the National Research Foundation of Korea (NRF) funded by the Ministry of Education (No. 2018R1A6A1A08025348).

REFERENCES

Jashod Roy, Ashutosh Kumar, Deepankar Choudhury. 2018. Natural frequencies of Piled Raft Foundation including Superstructure Effect. *Soil Dynamics and Earthquake Engineering*. 122: 69–75.

Mastumoto T, Fukumura K, Pastsakorn K, Jorikoshi K, Oki A. 2004. Experimental and Analytical Study on Behaviour of Model Piled Rafts in Sand subjected to Horizontal and Moment Loading. *International Journal of Physical Modelling in Geotechnics*. 4(3):1–19.

Korean Design Standard. 2019. Dynamic Structure Design. KDS 41 17 00.

Smart Geotechnics for Smart Societies – Zhussupbekov, Sarsembayeva & Kaliakin (Eds)
© 2023 The Author(s), ISBN 978-1-003-29912-7
Open Access: www.taylorfrancis.com, CC BY-NC-ND 4.0 license

Ground motion predictions based on soil properties using convolutional neural network

P.T.H. Nguyen, Byongkyu Bae & Jaehun Ahn
Department of Civil and Environmental Engineering, Pusan National University, Republic of South Korea

ABSTRACT: Earthquakes are among the most devastating natural disasters. In the past few decades, neural networks and other machine learning models have had significant success in geotechnical earthquake engineering. This paper studies the Convolutional Neural Network (CNN) model in predicting ground motion based on acceleration history measured in bedrock and soil properties. A CNN model is proposed; then, the model was trained and tested for 500 seismic events obtained from the Kiban Kyoshin Network (KiK-net, NIED 2016). When the predictions were compared with the baselines (actual measurements), the proposed CNN model presented good agreements.

Keywords: Earthquake, Convolutional neural network, Spectral acceleration, Soil properties, Source characteristic

1 INTRODUCTION

When natural disasters such as earthquakes occur, human and huge economic damages are caused (Green et al. 2011; Lee et al. 2012). To reduce the damage caused by earthquakes, models are developed to predict earthquakes and create preventative measures. As a result, earthquake ground response analysis contributes significantly to seismic design reliability (Kramer 1996; Phanikanth et al. 2011). During earthquakes, the waves propagate from the seismic source through rocks eventually to ground surface. This paper proposes a prediction model based on Convolutional Neural Network (CNN) for estimating the acceleration response spectrum of ground motion.

2 DATA IN ANALYSIS

2.1 *Site information and earthquake events*

Detailed information on earthquake sites and events in Japan as well as measured acceleration histories are shown in the seismograph network Kiban Kyoshin Network (KiK-net, NIED 2016). In this study, a total of five sites named FKSH18, FKSH19, IWTH02, IWTH05, and IWTH12 were selected from KiK-net. In order to perform modeling, out of 100 earthquake input and output datasets each site, 80 earthquake events were used for the training, and 20 earthquake events were used for the testing.

2.2 *Soil properties*

In the prediction model, shear wave velocity (Vs) and P-wave velocity (Vp) profiles were used together with input seismic signal. An example of the wave velocity profiles used in the analysis is presented in Figure 1.

DOI: 10.1201/9781003299127-263

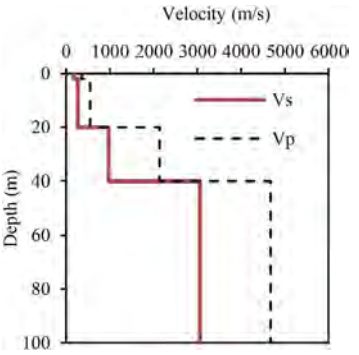

Figure 1. Shear wave and P-wave velocity profiles for the site FKSH19.

3 DEEP LEARNING MODEL

3.1 *Spectrogram*

This paper used the spectrogram representation of acceleration history motion as the input of models. The spectrogram is a three-dimensional representation of changes in the content of a signal over frequency and time. The acceleration was transformed into the FFT spectrogram by using Matplotlib as a Python calculation option.

3.2 *Convolutional neural network*

This study proposed a CNN model to estimate the effect of soil properties based on the acceleration measured at the bedrock for predicting seismic ground responses. Acceleration spectrogram, shear wave velocity (Vs), and P-wave velocity (Vp) are used as input data for the model. The CNN model structure was shown in Figure 2. A CNN has a convolutional layer at the input and a fully connected layer at the output. In the hidden layers, there are a number of convolutional layers and a number of pooling layers. The CNN model applied 20, 40, 80, and 160 filters for each layer respectively with MaxPooling size 2x2 and stride of 2. Figure 3 represented the overview of the proposed procedure based on CNN. Also, the errors are represented as mean squared errors (MSE).

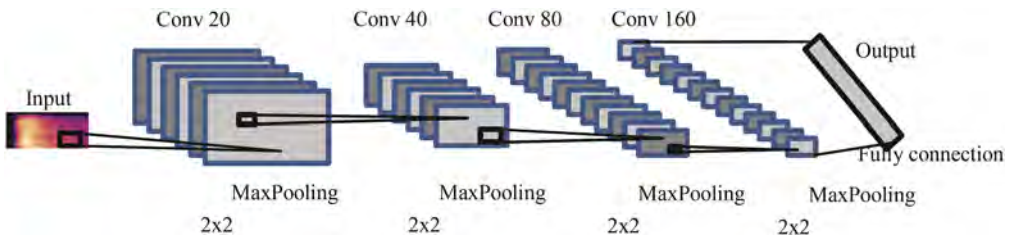

Figure 2. Scheme of the process of Convolutional Neural Network (CNN).

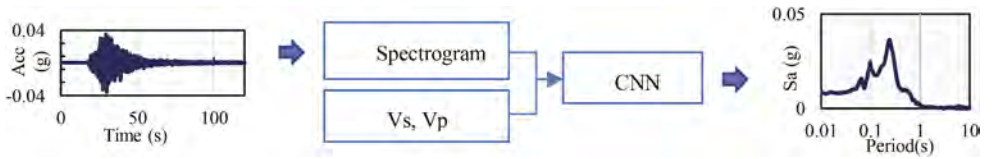

Figure 3. The overview of the proposed procedure is based on CNN.

4 RESULTS

4.1 *Prediction*

In the five-site earthquake dataset, models for the site were trained. Among the results, the response spectra of 4 sample results each site are presented in Figure 4. Most of the predictions show good agreements with the baselines.

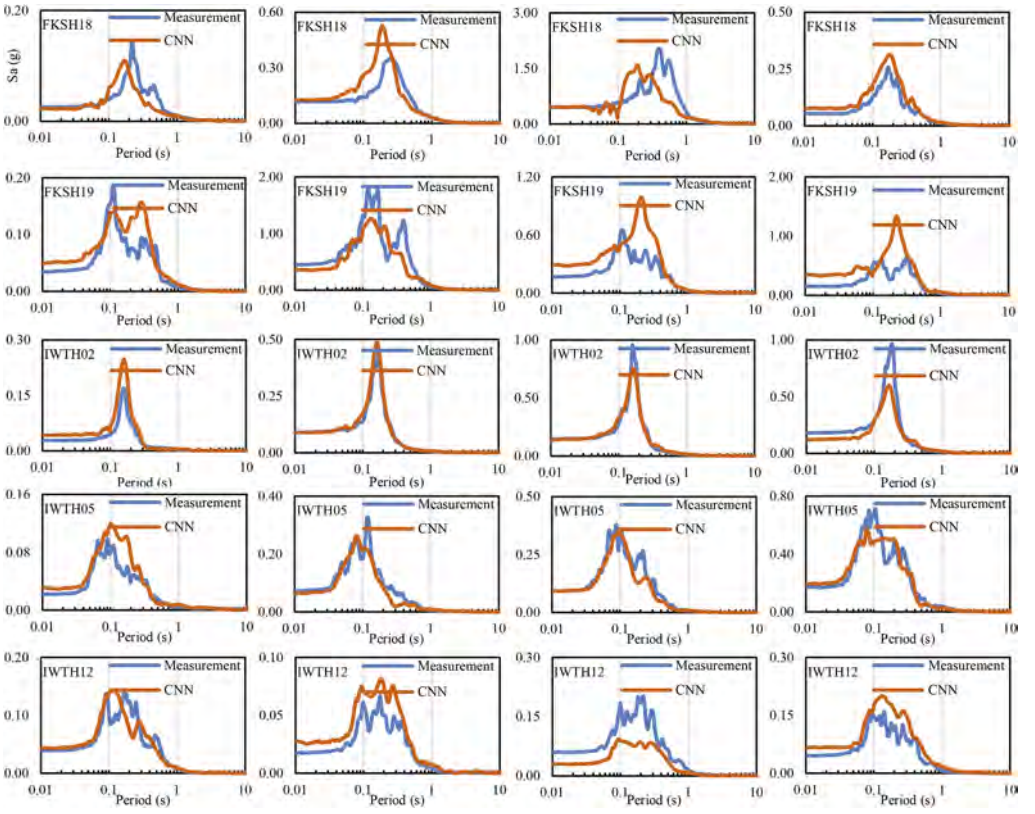

Figure 4. Spectrum acceleration response prediction.

4.2 *Prediction errors*

The errors of the estimation of five sites are calculation by Equation (1) and plotted in Figure 5. The training and testing loss value of the CNN model were calculated based on MSE and shown in Table 1.

$$\text{Error\_each} = \text{Sa\_measured} - \text{Sa\_predicted} \tag{1}$$

where Sa_predicted is the estimation by the CNN model, and Sa_test is the ground motion measurement.

Table 1. Training and testing mean square error loss.

Dataset	MSE
Train	4.3815e-04
Test	0.00498

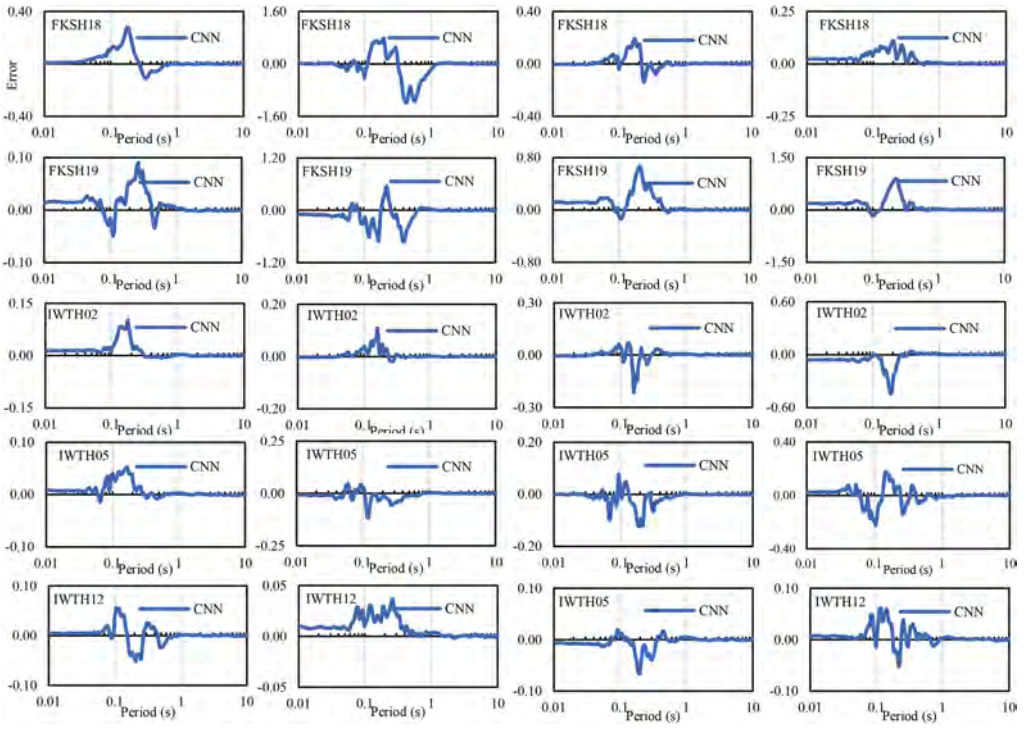

Figure 5. The errors of the ground motion prediction.

5 CONCLUSIONS

The study proposed a model to predict the seismic response spectrum based on CNN. Among the 100 datasets for each site, 80 sets were used for the training, and 20 sets were used for the testing for 5 sites in the KiK-net database. The ground response spectrum prediction result was affected by soil properties. Developing future research results requires to implement the other characteristic of soil used in the deep-learning model for seismic response prediction.

ACKNOWLEDGMENT

This research was supported by the project titled 'Development of Underwater Space Re-source Creation Technologies' (No. 20220364) funded by the Ministry of Oceans and Fisheries, Korea, and by Basic Science Research Program through the National Research Foundation of Korea (NRF) funded by the Ministry of Education (No. 2022R1I1A3069043).

REFERENCES

Green, Russell A. et al. 2011. "Geotechnical Aspects of Failures at Port-Au-Prince Seaport during the 12 January 2010 Haiti Earthquake." *Earthquake Spectra* 27(SUPPL. 1).

Kramer, Steven L. 1996. *Geotechnical Earthquake Engineering*.

Lee, Sei-Hyun, Chang-Guk Sun, Jong-Ku Yoon, and Dong-Soo Kim. 2012. "Development and Verification of a New Site Classification System and Site Coefficients for Regions of Shallow Bedrock in Korea." *Journal of Earthquake Engineering* 16(6): 795–819.

NIED. 2016. "Strong-Motion Seismograph Networks (K-NET, KiK-Net)." http://www.kyoshin.bosai.go.jp/ (August 1, 2016).

Phanikanth, V S, Deepankar Choudhury, and G Rami Reddy. 2011. "Equivalent-Linear Seismic Ground Response Analysis of Some Typical Sites in Mumbai." *Geotechnical and Geological Engineering* 29(6): 1109. https://doi.org/10.1007/s10706-011-9443-8.

Smart Geotechnics for Smart Societies – Zhussupbekov, Sarsembayeva & Kaliakin (Eds)
© 2023 The Author(s), ISBN 978-1-003-29912-7
Open Access: www.taylorfrancis.com, CC BY-NC-ND 4.0 license

Development of liquefaction judgment methods in Japan and future problems

S. Yasuda & K. Ishikawa
Tokyo Denki University, Saitama, Japan

ABSTRACT: Since damage due to liquefaction occurs every year or two in Japan, liquefaction potential is considered in the design of most structures in the country. Simple methods based on the SPT *N*-value and particle size are used to judge liquefaction potential. More than 10 methods are used, depending on the type of structure. A method to judge liquefaction potential was introduced into a design standard in 1970, and since then, the simple judgment methods for each structure have been revised several times based on the results of cyclic triaxial tests and case studies of earthquake damage. Nevertheless, there are still some issues to be noted in the application of current judgement methods and several problems to be studied in the future.

1 INTRODUCTION

Methods using the *N* value of the standard penetration test are widely applied all over the world to estimate the liquefaction potential. However, the SPT *N* values is merely ground parameters, not direct indicators of liquefaction strength. Therefore, it is necessary to indirectly estimate the liquefaction strength by incorporating other indicators, such as particle size. Various simple formulae for this estimation have been proposed, and different simple formulae are used in each country. In Japan, different simple formulae are used for each type of structure design standard (JGS, 1998). As there are more than 10 types, overseas engineers wonder why so many simple formulae are used. In Japan, a method to judge liquefaction potential was introduced in the design standards for port facilities in 1970, and different simple judgment methods have been introduced in other structures. After that, an earthquake that produced liquefaction occurred every year or two, and the validity of the judgment methods was verified based on case studies. Subsequently, based on cyclic triaxial tests on undisturbed samples, each judgment method has been revised.

2 LIQUEFACTION JUDGMENT METHOD AT THE BEGINNING OF DEVELOPMENT

In Japan, the 1964 Niigata Earthquake triggered widespread research on liquefaction. The soil condition in Niigata City was investigated just after the earthquake based on existing and newly conducted boring data. Then, a simple liquefaction prediction method based on critical *N*-value was derived by several researchers. In 1970, liquefaction potential was first taken into consideration in the code for harbor facilities. A consideration of liquefaction was also introduced in the design codes for highway bridges in 1972 and for railways and buildings in 1974. After that, this method was changed to the "F_L value method", described later, for highway bridges, building foundations, and railway structures, but it was revised to make the same judgment as the F_L value method by modifying the critical *N* value method for port structures. The critical *N* value method was also introduced in the design codes for oil tanks and LNG tanks.

After Seed et al. started research on liquefaction potential based on laboratory tests in the United States after the 1964 Alaska Earthquake, similar experiments were started in Japan

DOI: 10.1201/9781003299127-264

around 1970. For example, Ishihara et al. conducted cyclic torsional tests to investigate the influence of seismic load and anisotropic confining pressure. In addition, around 1975, the procedure for taking undisturbed samples from the field and conducting cyclic triaxial tests began. Using the results of cyclic triaxial tests conducted on undisturbed samples and the N values at the depths of the samples, a method to estimate the liquefaction resistance ratio (also called cyclic strength ratio) R_L from the N value and particle size was proposed by Tatsuoka et al. in 1978 as follows:

$$\begin{cases} R_L = 0.0882\sqrt{N/(\sigma'_v+0.7)} + 0.225\log_{10}(0.35/D_{50}) & (0.04 \le D_{50} < 0.6\ \text{mm}) \\ R_L = 0.0882\sqrt{N/(\sigma'_v+0.7)} - 0.05 & (0.6 \le D_{50} \le 1.5\ \text{mm}) \end{cases} \quad (1)$$

However, since this R_L is a liquefaction resistance ratio obtained by cyclic triaxial tests with isotropic confining pressure and sine wave load, it was necessary to convert to the liquefaction strength ratio R (or CRR) when receiving seismic load in the anisotropic confining pressure in the in-situ soil. Then the following correction was made. C_1 and C_2 are correction coefficients for confining pressure and seismic load, respectively.

$$R = C_1 \times C_2 \times C_3 \times C_4 \times C_5 \times R_L \cong R_L \quad (2)$$

Next, they decided to use the simple formula proposed by Seed and Idriss in 1971 as a method for estimating the shear stress ratio L (or CSR) generated in the ground during an earthquake.

$$L = r_d\ (\alpha_{max}/g)(\sigma_v/\sigma'_v) \quad (3)$$

where, r_d is the reduction coefficient in the depth direction, α_{max} is the peak ground acceleration, σ_v is the overburden pressure, and σ'_v is the effective overburden pressure. Seismic response analysis with six input waves was performed on two ground models to obtain the depth distribution of r_d. Then the following formula was proposed as an average relationship.

$$r_d = 1 - 0.015z \quad (4)$$

where, z: depth (m).

In 1980, the F_L value method (determined as liquefaction resistance factor $F_L = R/L$) based on these was introduced in the specification for highway bridges. For railway structures, the F_L value method was introduced in 1986 and was then modified for dense soils and for soils with large amounts of fine particles.

Tokimatsu and Yoshimi (1983) conducted cyclic triaxial tests using samples taken by the freeze sampling method and by the normal sampling method, and obtained a relationship in which the liquefaction strength increased sharply when the relative density was high. Next, using the relationship between the Dr and the N value proposed by Meyerhof, a method for estimating the R_L from the N value and the fines content F_C was derived. In addition, the method in Equation (4) was used for the shear stress ratio in the ground, and the relational expression of 0.1 (M-1) was used to convert to sine wave loading. In 1986, the F_L value method was introduced in the design of building foundations in consideration of the liquefaction data at the time of past earthquakes.

3 BACKGROUND OF REVISION OF JUDGMENT METHOD

After the introduction of different methods to judge liquefaction potential for different design standards, as described above, the applicability of each method has been continuously examined and the judgement method for each design standard has been revised several times.

For highway bridges, cyclic triaxial tests on undisturbed samples were added and revised in 1990 to add the influence of the F_C as the third item in Equation (1). As the 1995 Kobe

Earthquake caused a very strong shaking, it became necessary to judge liquefaction potential under such strong ground motion (called Level 2 seismic motion), and an appropriate revision was made in 1996. Since Level 2 seismic motion may cause liquefaction even in dense ground, cyclic triaxial tests were conducted by sampling ground with an N value of about 20 to 30 by the freeze sampling method. Then, the liquefaction strength was corrected for medium-dense-to-dense ground. A formula for gravel soil has also been added. In addition, since Level 2 seismic motion is divided into Type I (plate boundary type) and Type II (inland type), the correction coefficient C_W (a combination of C_1 to C_5 in Equation (2)) was set for each type. After that, it became necessary to correct R_L for soil with a small N value due to a relatively large amount of fines content. In 2017, R_L was revised based on the results of cyclic triaxial tests conducted on samples with relatively large amounts of fine particles taken using the tube sampling method, as shown in Figure 1.

For the design of building foundations, since there was no contradiction with the liquefaction/non-liquefaction phenomenon during the 1995 Kobe Earthquake, the 1988 version of the method to judge liquefaction potential was retained in the 2001 revision. However, the coefficient of the N value of gravel ground was corrected, and the cone penetration test and cyclic triaxial test for undisturbed samples were recommended for soil with a small N value and a high fine particle content. There was no big change in the 2019 version as shown in Figure 2, but soil layers with small N values, even in diluvium, are now subject to liquefaction potential judgment.

In the design standards for railway structures, the 1999 revision included new judgment methods for Levels 1 and 2 seismic motions. It was recommended to obtain R by a cyclic triaxial test, but if it is difficult to carry out the test at Level 1, a simple formula estimated from the N value and F_C (different from 1986) could be used. For Level 2, it was recommended to conduct a cyclic triaxial test and seismic response analysis.

Initially, in the technical standards for port and harbor facilities, soil was divided into two types according to the grain size distribution curve, and the relationships between maximum acceleration and the critical N value to cause liquefaction for each soil type were set. This was revised in 1990 to judge the susceptibility to liquefaction in four stages.

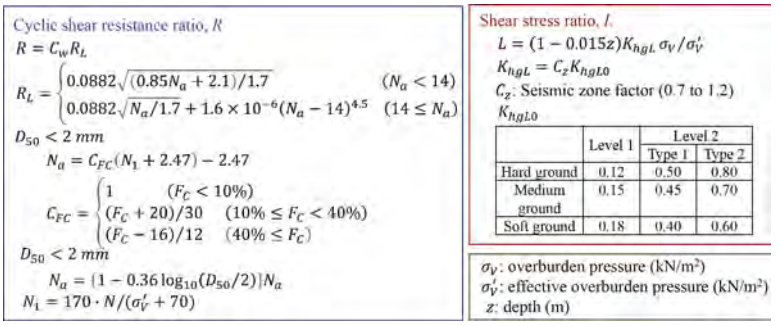

Figure 1. The method used in the specification for highway bridges (2017).

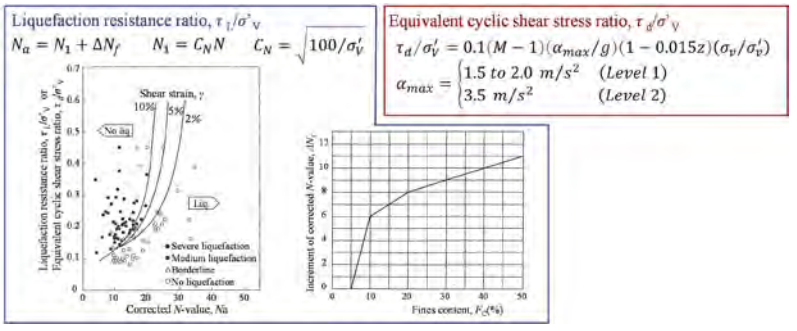

Figure 2. The method used in the recommendation for design of building foundations (2019).

4 POINTS TO NOTE WHEN APPLYING CURRENT METHODS AND FUTURE PROBLEMS

As described above, since the judgment of liquefaction potential began to be incorporated into design standards in 1970, each standard has been revised many times. For example, under certain conditions, the R_L calculated by the highway bridges formula has changed as shown in Figure 3. However, problems remain to be solved. Below, we present the issues and points to note when using the current judgment methods and future studies needed

(1) Since the N value is not directly related to the liquefaction strength, a judgment based on the N value inevitably contains an error. As stated in the standard for railway structures, it is desirable to determine the liquefaction strength by cyclic triaxial tests. These tests must be conducted on samples with little disturbance. In many design standards, Equations (3) and (4) are used to estimate the L and r_d, respectively. However, since the variation in r_d is large, the error is also large in the estimation of L. Half a century before these formulae were proposed, computers were not yet easy to use, but now, seismic response analysis can be performed easily with a personal computer. L should be obtained by seismic response analysis.

(2) When the liquefaction potential of a certain ground is judged by different methods, it is usually not the same. When only the R_L was compared from three judgement methods, the results shown in Figure 4 are obtained. As can be seen in the figure, the shape of the $N - R_L$ relationship from the three methods is similar for soil with a small amount of fine particles, such as Fc = 5%, but differs for soil with large amounts of fine particles.
Since the reclaimed land along Tokyo Bay liquefied extensively during the 2011 Tohoku Earthquake, many institutions estimated the liquefied depth by each method after the earthquake. However, since the reclaimed soil contained a large amount of fine particles, it was difficult to determine the depth where liquefaction occurred (Ishikawa and Yasuda, 2020). There may be considerable error in the estimation of R_L in sandy soil with a large amount of fine particles.
Furthermore, in several cases, the judgment method yielded a result that was opposite the finding that the alluvium soil at the bottom had liquefied without liquefaction in the reclaimed layer. It is known that R_L and N increase with time after soil deposition due to soil aging. However, it is not known whether the R_L of soils with different sedimentary ages can be determined by the same simple formula. Research is needed to consider the aging effect in the simple judgment methods.

(3) When creating a liquefaction hazard map, the characteristics of local soil cannot be reflected simply by applying the nationally uniform judgment methods. For such soil, it is desirable to take undisturbed samples, conduct tests, and propose an appropriate evaluation formula for R_L.

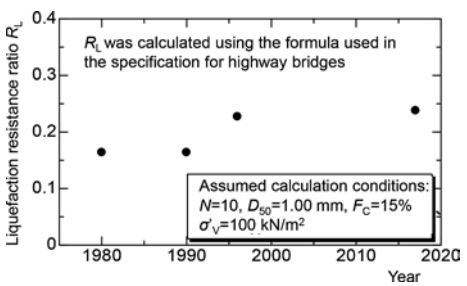

Figure 3. An example of change in R_L calculated by the formula of the highway bridges.

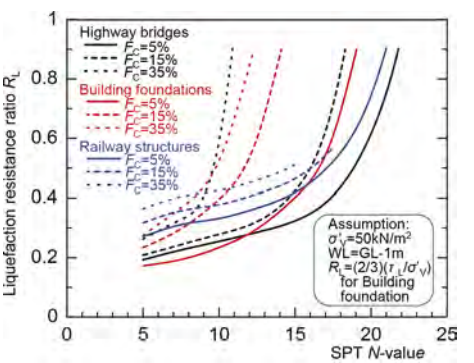

Figure 4. Relationships between N and R_L estimated by three methods.

5 CONCLUSIONS

Methods to judge liquefaction potential using *N*-value differ by country. In Japan, their validity has been tested during past earthquakes, and they have been revised several times. Even so, it is still quite difficult to accurately predict liquefaction because the *N* value does not directly express liquefaction strength. Therefore, judgement methods based on the *N* value contain some errors. It is desirable to conduct cyclic triaxial tests and seismic response analyses.

REFERENCES

Ishikawa, K. and Yasuda, S. 2020. Comparison of various liquefaction predictions based on ground investigation of reclaimed land in Tokyo Bay. *17th WCEE*. 4b-0014.

JGS. 1988. Remedial measures against soil liquefaction. *Balkema*, 443p.

Tatsuoka, F., Iwasaki, T., Tokida, K., Yasuda, S., Hirose, M., Imai, T., and Kon-no, M. 1978. A method for estimating undrained cyclic strength of sandy soils using standard penetration resistances. *Soils and Foundations*. Vol.18. No.3. pp.43–58.

Tokimatsu, K. and Yoshimi, Y. 1983. Empirical correlation of soil liquefaction based on SPT *N*-value and fines content. *Soils and Foundations*. Vol.23. No.4. pp.56–74.

Smart Geotechnics for Smart Societies – Zhussupbekov, Sarsembayeva & Kaliakin (Eds)
© 2023 The Author(s), ISBN 978-1-003-29912-7
Open Access: www.taylorfrancis.com, CC BY-NC-ND 4.0 license

Response of buried pipeline in soil slopes to surface blast loading

T. Lodh & K. Chatterjee
Department of Civil Engineering, IIT Roorkee, Roorkee, Uttarakand, India

ABSTRACT: Precise modelling and simulation of the effects of blast occurrences, especially in or around the slope, is of interest in this study. Applications include minimizing casualties and improving buried pipeline survivability from attacks using improvised explosive tools. In the present study, coupled Eulerian-Lagrangian capability in FEM-based computer program ABAQUS/ Explicit was used to simulate experimental tests in which the structural response to the detonation of a surface charge was characterized. Soil has been modeled as a three-phase porous media to accommodate various degrees of saturation. Lagrangian representation was used for the pipe, while Eulerian representation was used for the soil, explosive, and ambient air.

Detonation products were modeled using the Jones-Wilkins-Lee equation of state. The blast design parameter PPV (peak particle velocity) has been obtained for input parameters. The simulations agree favorably with the test results and produce higher adherence solutions than traditional analytical or empirical blast models.

1 INTRODUCTION

Blasting vibrations may be an activating figure for soil movement developments and avalanches. A quantitive assessment is of need to serve this purpose. Evaluation is generally done in terms of peak particle displacement (PPD), peak particle velocity (PPV), or peak particle acceleration (PPA). But due to the scarcity of PPD and PPA-related established existing papers, analysis is performed referring to PPV only. Lu *et al.* (2005) gave the conceptual overview of the fully-coupled method with a comparative study of the buried structure. An attempt was made by Newmark and Kuesel (2015) for the seismic design of buried pipelines which are likely to be damaged by earthquakes or distant explosions. Malachowski *et al.* (2018) used the ALE method and applied blast load to the pipes with and without a protective cover. A combined Eulerian-Lagrangian method was used by Mokhtari (2015) to study the response of buried steel pipelines to the explosion and generally concerns with finding a safe distance of explosion where the pipeline deformation does not reach to the plastic stage. Adib *et al.* (2017) studied the effects of mass charges pipeline thickness on pipeline deformation using the Drucker-Prager resistance equation for soil. Similarly, other researchers used the finite element method along with the finite-difference method or individually each of them to solve the blast-related problems.

The present study explores the reaction of buried pipelines subjected to impact waves numerically. The numerical modeling technique is one of the alternatives to study the dynamic response of underground structures subjected to blast load because a very high cost is associated with the full-scale field blast test. A self-assertive Lagrangian-Eulerian strategy was embraced to create a full-coupled 3D finite component demonstration. The analysis performed here is in Abaqus/Explicit program for dry soil only. In choosing legitimate fabric models, the speed and push of the pipeline, and the impact of buried depth were examined within the investigation. The outcomes from the study can be utilized for improvement in the defensive plan of steel pipelines.

DOI: 10.1201/9781003299127-265

2 PROPOSED METHODOLOGY

The objective is to implement a fully-coupled demonstration that can handle the impact wave engendering through the air, the impact wave interaction with the structure, and the related primary reaction of the system and would be perfect for showing everything from the ground up.

2.1 *Geometry and material assigning*

Beginning with the geometry as shown in Figure 1 below, a 1m diameter and 0.01m thick embedded pipeline is used in the analysis. The soil slope was maintained at 45°.

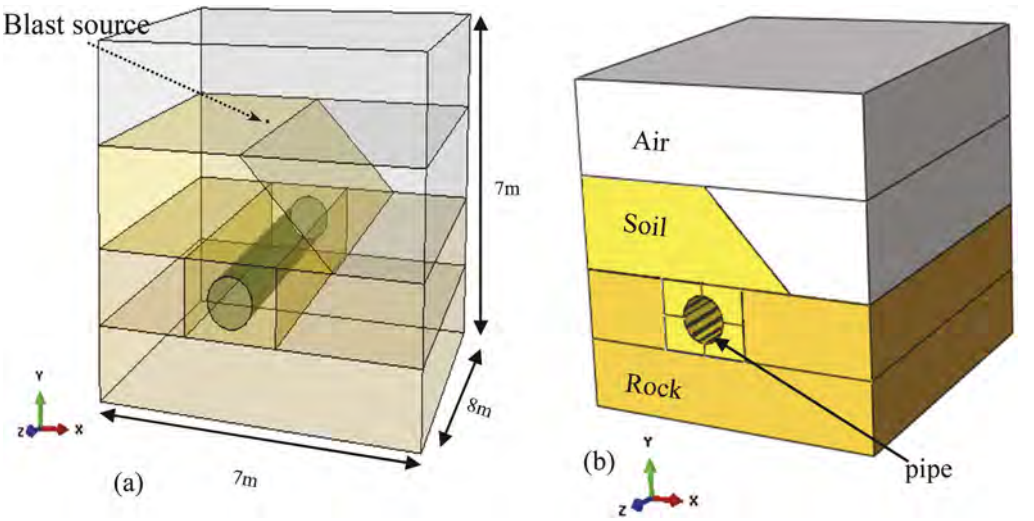

Figure 1. (a) Model geometry (b) Material assigned view of the model.

2.2 *Material properties*

According to the Abaqus/Explicit manual requirements, the material parameters used in the present study are adopted from Tang *et al.* (2021). The Mohr-Column material model was adopted for the soil layer. The model of the sandstone and ductile iron gas pipeline assumes the user input elastic-plastic material model by giving elastic, plastic, and density parameters as tabulated below in Table1.

Table 1. Input parameters used in the present analysis.

	Values		
Properties	Soil	Rock	Pipe
Density (kg/m^3)	1920	2500	7850
Elastic Shear modulus (*GPa*)	3.85	-	-
Elastic modulus(*GPa*)	-	30	150
Yield Strength (*Pa*)	-	2580	3000
Poisson ratio	0.32	0.3	0.3
Cohesion (*Pa*)	5000	-	-
Friction angle (°)	10		

Blast material is modeled by selecting EOS (Equation of State) in the mechanical module in which the JWL type is taken. In the sub-option EOS of Abaqus/Explicit, detonation

coordinates and time are mentioned. The concerning parameters of explosive detonation products are shown in Table 2 below. The relationship between specific volume and pressure in the model is mentioned in equation (1) and the process of explosive by detonation is simulated using the JWL equation of state.

$$P = A\left(1 - \frac{W}{R_1 V}\right)e^{-R_1 V} + B\left(1 - \frac{W}{R_2 V}\right)e^{-R_2 V} + \frac{wE_0}{V} \quad (1)$$

In equation (1), P is pressure; A, B, $R1$, $R2$, and W are material parameters; V is relative volume; E_0 is initial specific internal energy. The material of air is defied by the ideal gas equation of state, which is one of the simplest forms of the equation of state of a gas. The equation of state was used for the gas with uniform initial conditions and can be written as in Equation (2):

$$Ph = (\gamma - 1)\rho e \quad (2)$$

In equation (2), ρ is density, e is specific internal energy, γ is the adiabatic index and P_h is hydrostatic pressure. These are tabulated in Table 3.

Table 2. JWL parameters used in the present study.

Properties Density	Detonation (kg/m^3)	Density Velocity (m/s)	A (MPa)	B (MPa)	Omega	R_1	R_2	Detention Energy Density	Pre-detonation Bulk Modulus
Values	1100	3500	47600	524	0.3	3.5	0.9	6e6	**0**

Table 3. Air parameters used in the analysis.

Properties	Density (kg/m^3)	Specific volume ($J/kg\ k$)	Temperature	Adiabatic Exponent
Values	1.225	0.3	288.2	1.4

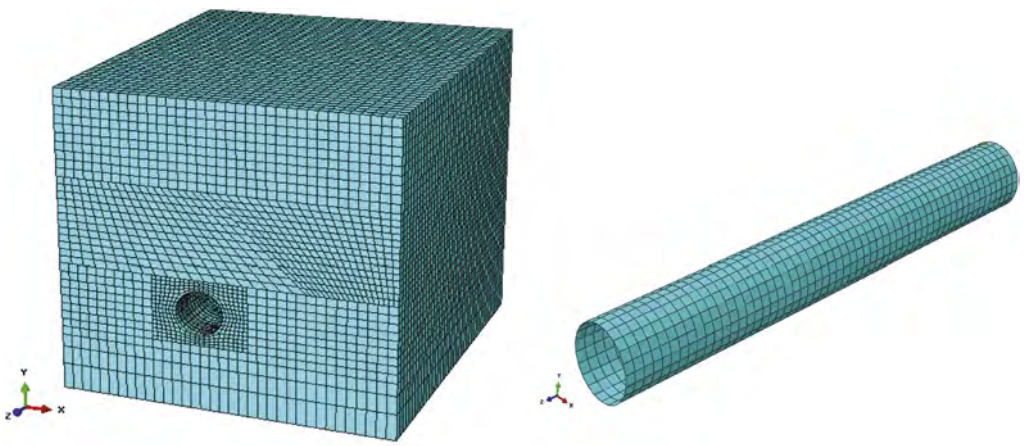

(a) (b)

Figure 2. Meshing view of the (a) full model (b) pipe.

2.3 *Meshing and contact properties*

General contact explicit definition was used in the contact module of Abaqus/Explicit. Eulerian elements were used in soil, air, rock, and blast parts since these will undergo large deformations. Lagrangian elements were used for the pipeline. After performing a variety of convergence studies and doing proper seeding in edges along with that required partitioning and meshing were done effectively. Meshing is liner near the pipe and blast and coarser as one moves far from the pipe and blast source, as indicated in Figure 2.

2.4 *Boundary conditions*

The bottom of the model was fixed and the non-reflecting boundary was applied on all other sides of the model. Acceleration due to gravity of 9.81m/s^2 was applied to all the materials.

3 RESULT AND DISSCUSSION

Analysis for input parameters mentioned in earlier Tables was carried out and results have been discussed in this section. All the computation part is done using Abaqus/Explicit solver for evaluating the influence of surface explosion in different positions such as soil surface, soil slope, and buried pipe. The stress contours on the pipe after the blast indicates that the stress effect of the blast first reached the zone immediately below the pipe. In a short span of time, the stress wave propagated radially along the pipe and total stress dissipation happened in a short span of blast time (almost in 5 milliseconds), as illustrated in Figure 3.

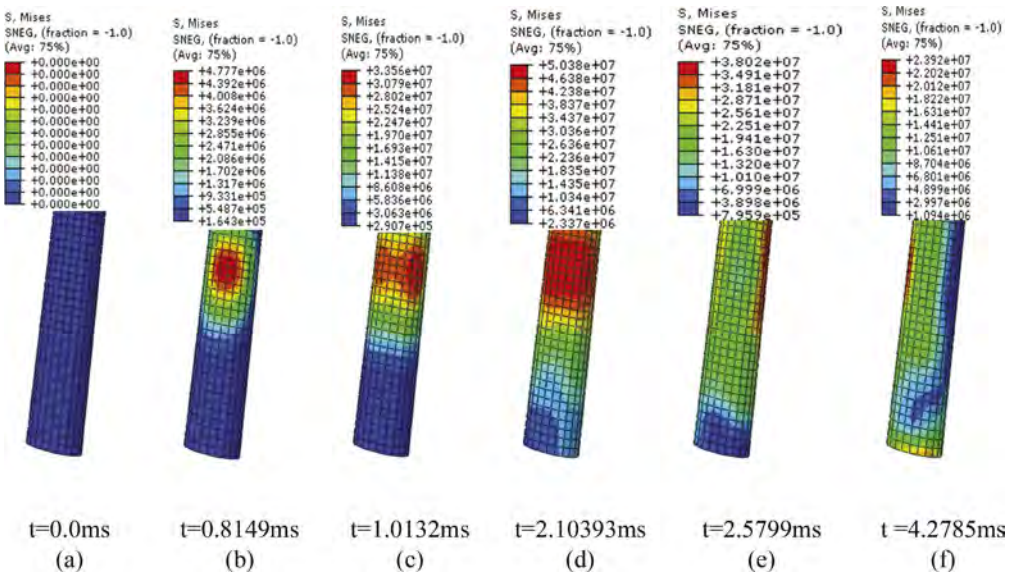

Figure 3. Stress propagation at different time intervals on pipe immediately after the blast (t=0ms-4.27ms).

Tables 4 and 5 show the peak particle velocity at various positions of the soil slope and pipeline for different quantities of blast load. It is observed that with an increase in horizontal distance the peak particle velocity decreases significantly, i.e., for 100g TNT, when the observation point changes from G_1 to G_2, PPV changes by almost 67.37%, as illustrated in Figure 4.

3.1 *Effect of slope on PPV*

It was observed that slopes are more vulnerable to blast as PPV values are on the higher side than direction despite the higher distance, as the surface of the slope is free on one side. For 100gm TNT the PPV values initially decrease at a slower rate of 8.36%-15.91% and followed by a higher rate of 38.26%-56.52% at the bottom of the slope. The variation becomes higher if the blast load is increased to 200gm TNT. Moreover, the trend of results in the present study compares well with the field test results of Tang *et al.* (2021) that were carried out at a test site located in Wuhan city and tabulated in Table 4.

Table 4. Comparison of the present numerical results with the field results of Tang *et al.* (2021) for varying weight of explosive charge.

Explosive charge	Position	Field Results (cm/s)	Numerical Results (cm/s)	Error (%)
100g	G_1	8.04	8.72	+8.46
	G_2	4.83	5.21	+7.87
	G_3	1.98	2.09	+5.56
	P_1	2.79	3.10	+11.11
	P_2	1.45	1.64	+11.59
	P_3	0.88	1.02	+15.91
200g	G_1	10.50	11.98	+14.09
	G_2	7.76	7.85	+1.16
	G_3	2.88	3.09	+7.29
	P_1	4.17	4.51	+8.15
	P_2	2.25	2.68	+19.11
	P_3	0.97	1.01	+4.12

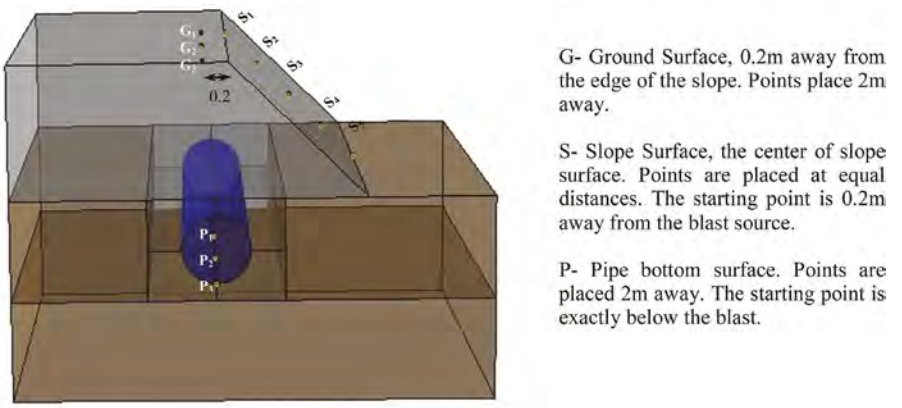

Figure 4. PPV measuring positions on ground (G), pipe bottom (P) and slope (S).

It is seen from Table 4 that there is a variation of 5.56%-15.91% between the field test results and developed numerical model. This may be attributed to various influencing

Table 5. Variation of PPV at different points of the slope for different amounts of explosives.

	100gm TNT					200gm TNT				
Position	P_1	P_2	P_3	P_4	P_5	P_1	P_2	P_3	P_4	P_5
PPV (cm/s)	9.98	9.18	7.92	5.06	3.65	12.58	11.73	9.89	6.46	4.97

parameters acting in the complex modeling which need a separate discussion but are not elaborated in the present study.

Five equally spaced points were taken along the slope, as shown in Figure 4 and the PPV of corresponding points were measured separately for both 100g and 200g TNT. It is seen that the PPV values increase with depth from the top of the slope. In the top portion, the variation is almost 26.05% and, in the bottommost portion the variation is 36.16%.

4 CONCLUSIONS

The major conclusions that can be made from the present study are as follows:

- At starting phase just after the blast (1-2 milliseconds), there is maximum influence on PPV value then gradually it gets reduced to zero in the next few milliseconds, in case of TNT blasting.
- PPV on the ground surface is a lot higher than the PPV in the pipe.
- With increased horizontal distance and burial depth PPV gets reduced significantly.
- Slope is vulnerable to the blast and PPV values are decreasing significantly at the bottom of the slope, which gives a conclusion that special care should be taken in case of a blast around the slope.
- Free surface of slope may be one of the probable reasons for higher PPV in slopes.
- A robust analysis is needed to give absolute judgment regarding slope stability.

ACKNOWLEDGEMENT

The authors are thankful to the Board of Research in Nuclear Sciences, Department of Atomic Energy, Government of India, for providing financial support with Grant Number 52/20/02/2021-BRNS to carry out the research work presented in this paper.

REFERENCES

Adibi, O., Azadi, A., Farhanieh, B. and Afshin, H., 2017. A parametric study on the effects of surface explosions on buried high pressure gas pipelines. Engineering Solid Mechanics, 5(4), pp. 225–244.

An, J., Tuan, C.Y., Cheeseman, B.A. and Gazonas, G.A., 2011. Simulation of soil behavior under blast loading. International Journal of Geomechanics, 11(4), pp. 323–334.

Ji, C., Song, K. and Xu, Q., 2015. Numerical simulation of buried pipeline subjected to blast seismic waves. Vibroengineering Procedia, 5, pp. 411–416.

Jiang, N., Gao, T., Zhou, C. and Luo, X., 2018. Effect of excavation blasting vibration on adjacent buried gas pipeline in a metro tunnel. Tunnelling and Underground Space Technology, 81, pp. 590–601.

Lu, Y., Wang, Z. and Chong, K., 2005. A comparative study of buried structure in soil subjected to blast load using 2D and 3D numerical simulations. Soil Dynamics and Earthquake Engineering, 25(4), pp. 275–288.

Mazurkiewicz, Ł., Małachowski, J., Tomaszewski, M., Baranowski, P. and Yukhymets, P., 2018. Performance of steel pipe reinforced with composite sleave. Composite Structures, 183, pp. 199–211.

Mokhtari, M. and Alavi Nia, A., 2015. A parametric study on the mechanical performance of buried X65 steel pipelines under subsurface detonation. Archives of Civil and Mechanical Engineering, 15(3), pp. 668–679.

Sangroya, R. and Choudhury, D., 2013. Stability analysis of soil slope subjected to blast induced vibrations using FLAC3D. In Geo-Congress 2013: Stability and Performance of Slopes and Embankments III (pp. 472–481).

Tang, Q., Jiang, N., Yao, Y., Zhou, C., Luo, X. and Wu, T., 2021. Safety assessment of buried gas pipeline subject to surface explosion: A case study in Wuhan, China. Engineering failure analysis, 120, pp.105119.

Smart Geotechnics for Smart Societies – Zhussupbekov, Sarsembayeva & Kaliakin (Eds)
© 2023 The Author(s), ISBN 978-1-003-29912-7
Open Access: www.taylorfrancis.com, CC BY-NC-ND 4.0 license

Comparative analysis of dynamic vibration dampers

M.B. Zhumamuratov
JSC Kazakhstan Highway Research Institute, Astana, Kazakhstan

ABSTRACT: This article provides an overview and analysis of methods for calculating the structures of dynamic dampers designed to reduce aeroelastic vibrations of continuous girder bridges. The article also outlines the main provisions for determining the parameters of an alternative design of a hydrodynamic damper, which is used to reduce the vibrations of bridges.

In the "conflict" between external loads and bridges, one of the most important problems is the instability of aerodynamics, which is characterized by the possibility of aeroelastic vibrations in the structural elements of the structure from strong wind currents. Aeroelastic vibrations as a phenomenon, is one of the types of instability of aerodynamics, are largely found on large-span flexible structures: hinged and cable-stayed bridges, pipeline crossings and, as the practice of recent decades has suddenly demonstrated, on continuous girder bridges, as well as so-called "Skyscrapers".

In order to ensure aerodynamic stability in the processes of interaction of structures with wind flows, an intensive study of this topic began in the middle of the twentieth century, in order to determine further branches of the study of aerodynamics with new types of solutions.

At the beginning of the twentieth century in the USSR, and in particular in Kazakhstan, the problems of different types of structures with the interaction of wind flows on them were developed. N. Rynin was the first to study the issues of aerodynamics of building structures and structures, on the basis of his studies of models of buildings and structures, the flow spectra, the acting forces of aerodynamics, as well as the issues of redistribution of wind pressure on the surface of structures were studied [1]. In the study of the physical foundations of the interaction of structures and structures with wind pressure, a significant contribution was made by the Russian teachings of K.A. Bunkin and A.M. Cheremukhin.

Soviet researcher E. Retter invented a special wind tunnel with unique scientific and technical requirements to determine the possible degree of turbulence of the air flow and wind pressure.

In different years, the work of L. Gandin, G. Fomin, M. Barstein, A. Bernstein, A. Zeitlin, N. Popov, K. Fedyaevsky, M. Kazakevich, L. Devnin, G. Savitsky, A. Lugovtsev, V. Mugalev, E. Solovieva, S. Gorlin, G. Khudyakov, V. Samsonov was devoted to the problem of interaction of structures with wind flow, S. Herzenstein, I. Nekrasov, A. Ordanovich, V. Nazarenko, K. Strelkov, M. Berezin and other scientists [2].

Experimental work on the study of air flow around buildings and structures was done by foreign scientists Irminger in 1891 and Stanton in 1903. J. Sermak studied all possible nuances in modeling the interactions of wind flow and pressure with various structural elements [3].

As indicated in the literature review, methods of dynamic vibration damping are used to eliminate aeroelastic vibrations and ensure safe operation of bridge structures. Structurally, this is due to the installation of passive adaptive mass dampers. The calculation of such dampers is based on the use of a spring pendulum - a mechanical analogue of a beam on two supports. The additional mass of the vibration damper is attached to the beam by means of an

DOI: 10.1201/9781003299127-266

elastic coupling (dynamic damper without damping) or an elastic coupling and a viscous component (dynamic damper with damping).

The disadvantage of using dynamic vibration dampers is that each dampener reduces vibration only of a certain frequency.

Vibration dampers are most effective when used to reduce vibration in mechanisms with stable vibration frequencies, such as turbo generators, pumps and power units. Vibration dampers are also very effective for reducing the vibration of chimneys in high-rise buildings (300-400 m). To reduce the vibration of the chimneys caused by the wind load, loads of different weights are suspended on cables inside the chimney to act as vibration absorbers with different natural frequencies [4].

The natural frequency of the vibration damper is selected in accordance with the frequency of the wind load. The high reliability and efficiency of vibration dampers for chimneys is confirmed by many years of experience.

The vibration absorption (vibration damping) method is used to reduce the vibration of the housing and other sheet metal components, such as fences.

The vibration absorption method involves coating the vibrating surface with an elastic body (rubber, plastic or anti-vibration rubber) with high internal friction. By allowing this elastic body to absorb vibration energy, the vibration of the structural component can be reduced. As a result, the vibration energy is converted into heat, and the vibration amplitude is significantly reduced, especially in the resonant mode.

Vibration-absorbing membranes are effective when the length of the absorbing layer corresponds to several wavelengths of bending vibration. If the length of the absorbing membrane is small, the bending vibration force decreases slightly. This should be taken into account when using absorbing membranes on structures with low vibration frequencies, where the wavelength reaches several meters.

Vibration absorption is ineffective for reducing the intensity of longitudinal waves with high frequency and high vibration energy. To reduce such vibrations, it is effective to provide a vibration isolation gap between individual structural elements. These gaps must be filled with a wave-resistant material (for example, rubber bands, air layers, etc.), different from the material of the machine. The material of the vibration-absorbing membrane and its dimensions are selected depending on the vibration range. Vibration-absorbing membranes are used in places with the highest vibration amplitude, determined on the basis of studies of the vibration rate at various points of the structure. The use of vibration-absorbing membranes can significantly reduce production noise, especially in high-frequency ranges. Reduction of the noise level (dB) during vibration of metal surfaces lined with a vibration-absorbing coating can be approximately calculated by formula 1:

$$\Delta L = 20 \lg \left[\frac{n_1 - n_2}{n_2} \right]$$

Formula 1 – determination of approximate noise reduction.

where n_1 is the loss coefficient of the vibration—absorbing surface before applying the vibration-absorbing layer;

n_2 - is the loss coefficient in the presence of a vibration—absorbing layer.

Depending on the dynamic modulus of elasticity, vibration-absorbing coatings are divided into hard (Ed = 109 Pa) and soft (Dc = 107 Pa). Hard coatings are effective for reducing vibrations of low and medium frequencies, soft coatings are used to reduce the intensity of high-frequency vibrations.

Sheet plastic materials (for example, vinyl, foam) are used as soft coatings that are glued to thin metal surfaces, such as casings, fences and ventilation ducts. Special mastics consisting of synthetic resins and fillers are used to cover surfaces of complex shape with vibration-absorbing materials.

Polyacrylic and biponite composite absorbing materials, which consist of a layer of hard plastic or metal and a layer between layers of polymer materials, have high efficiency. The optimal thickness of the vibration-absorbing membrane is 2. 3 thicknesses of the coated structure [5].

To obtain higher efficiency, the damper must have parameters close to optimal by preliminary analysis of the structure on which it will be installed. The correct setting of the pendulum damper is ensured by choosing the length of the pendulum suspension. As a rule, one or more stranded cables are used as a suspension.In the event that the fastening of the cable at the suspension point is rigid, the frequency of oscillation of the pendulum damper, taking into account the action of the tensile force N in the cable, can be determined by the formula 2:

$$\omega^2 = \frac{\beta^3 ch\beta}{\beta ch - sh\beta} \times \left(\frac{EI}{Ml^3}\right)$$

Formula 2 – determination of the oscillation frequency.

where l is the length of the suspension of the damper with a mass of M; EI is the bending stiffness of the cable, $\beta = 1(N/EI)^{1/2}$

The energy absorption coefficient in such a extinguisher can be found by the formula 3:

$$\psi = \frac{\psi_0}{\left[\frac{2(\beta ch\beta - sh\beta)^2}{\beta(sh\beta ch\beta - \beta)}\right]}$$

Formula 3 – determination of the energy absorption coefficient

where ψ0 is the energy absorption coefficient in the cable during bending deformations

The analysis of this equation shows that with an increase in the tensile force of the cable, the attenuation of the extinguisher decreases, and with an increase in the bending stiffness of the cable, the attenuation of the extinguisher increases accordingly. Therefore, to increase the attenuation of the damper, it is necessary to use a cable with high internal friction and design a damper with as little β as possible.

REFERENCES

[1] Zakora, A. L. 1983. Damping of vibrations of bridge structures/A. L. Zakora, M. I. Kazakevich; edited by N. G. Bondar. – M.: *Transport*. 134.

[2] Naumova G. A. 2012. Hydrodynamic method of damping vibrations of bridge spans/G. A.

[3] Naumova, S. A. Ponomarenko // *Bulletin of Civil Engineers*. – № 6 (35). 51–59.

[4] Naumova, G. A. 2013. Solutions to the problem of aerodynamic instability of continuous girder bridges // G. A. Naumova, S. A. Ponomarenko/*Dorozhnaya derzhava*. – No. 50. 22–26.

[5] Ponomarenko, S. A. 2012. Hydrodynamic dampener of bridge vibrations/G.A. Naumova, V. V. Samsonov, S.A. Ponomarenko // *Bulletin of the Volgograd State University*. Series 10, Innovation activity. – Issue 7. 93–98.

[6] Development of project documentation for the overhaul of the first launch complex of the first stage of the bridge crossing over the Volga River in Volgograd. 2011. — Moscow: JSC "Giprotransmost». 688.

Smart Geotechnics for Smart Societies – Zhussupbekov, Sarsembayeva & Kaliakin (Eds)
© 2023 The Author(s), ISBN 978-1-003-29912-7
Open Access: www.taylorfrancis.com, CC BY-NC-ND 4.0 license

State of the art review of seismic hazard approaches in Indian context

Arindam Das
Ph.D. Research Scholar, Department of Civil Engineering, Indian Institute of Technology Bombay, Powai, Mumbai, India

Deepankar Choudhury
Prof. T. Kant Chair Professor and Head, Department of Civil Engineering, Indian Institute of Technology Bombay, Powai, Mumbai, India

ABSTRACT: Numerous researchers have carried out seismic microzonation of India using various criteria. Seismic zonation was conducted at the national and regional levels using the conventional approaches i.e., either a probabilistic or a deterministic approach. Between the computed peak ground acceleration and the real peak ground acceleration observed during the seismic event, significant differences have been detected. Different approaches (conventional and new) have been used in the literature to conduct seismic hazard analysis and site-specific analysis of India in order to address this issue. The goal of the current work is to evaluate critically various researchers' approaches to seismic hazard analysis and compare those to Indian codal provisions already in place with a highlight of need for further research and modifications.

Keywords: Hazard Analysis, Peak Ground Acceleration, Seismic microzonation, India

1 INTRODUCTION

A natural phenomenon that results in the instant loss of life and property is an earthquake which results in the abrupt release of energy. Although deemed to have a low chance, earthquakes pose a significant risk to society. Large earthquakes have caused extremely significant damage and fatalities throughout history worldwide as recorded by USGS such in 1960 Chile (M_w of 9.5), 1964 Southern Alaska (M_w of 9.2), 2004 Sumatra (M_w of 9.1), 2011 Japan (M_w of 9.1), 2010 Chile (M_w of 8.8), 2018 Indonesia (M_w of 7.5), 2020 Turkey-Greece (M_w of 7.0), 2022 Afghanistan-Pakistan (M_w of 6.2) etc.

India is regarded as one of the world's earthquake-prone countries. India has experienced earthquakes since the prehistoric times. Devastating earthquakes in India have resulted in disasters in terms of property destruction and fatalities, including those in 1819 Kutch, 1897 Assam, 1905 Kangra, 1934 Bihar & Nepal, 1950 Assam, 1967 Koyna, 1991 Uttarkashi, 2001 Bhuj, 2005 Kashmir, 2011 Nepal, 2015 Nepal. The majority of reported fatalities are attributed to building and structure collapses brought on by the seismic events.

It is extremely important to study the insight of earth tectonics for the region given the size and severity of the hazard capability of earthquakes. India can be divided into three seismotectonic regions based on its seismic activity: the stable continental region (SCR), subduction zones, and shallow crustal region. The northwest part of the Indian plate i.e., the southern Tibetan Plateau and the Himalayas are examples of shallow crustal regions that are tectonically active. Among the subduction zones are the Indo-Myanmar arc in the northeast, the Andaman-Sumatra seismic belt in the southeast, and the Hindukush-Pamir in the northwest part of India. Due to its intraplate seismicity and low to moderate seismic activity, peninsular India is referred to as the SCR or Stable Continental Region (Nath & Thingbaijam 2012, Sitharam et al. 2014).

DOI: 10.1201/9781003299127-267

2 METHODOLOGY

Seismic Hazard Analysis is generally carried out by the conventional way and a new earthquake hazard technique considering the regional rupture characteristics which is also known as Rupture Based Seismic Hazard Analysis (RBSHA).

In conventional way, Deterministic seismic hazard analysis approach (DSHA) and Probabilistic seismic hazard analysis approach (PSHA) can be used to conduct the seismic hazard assessment. According to DSHA, the greatest possible earthquake happens at the nearest possible location. Whereas, PSHA is based on the integration of all potential earthquake effects anticipated to occur over a certain time period at various sites while taking uncertainty into account. These studies would concentrate on the regional seismic risk over the long term, but they do not account for the impacts of seismic wave attenuation or amplification caused by local, site-specific variables.

For the purpose of designing future infrastructures, the majority of traditional evaluations of seismic hazard take into account historical earthquake location, size, and frequency on the fault or in the area. Large to moderate earthquakes must have enough energy to rupture the faults. The amount of time needed to accumulate the necessary energy to produce moderate to big earthquakes varies by region. As the strain energy accumulated on faults get released during earthquakes, the future earthquakes in a particular area are more certain to occur in places with low or no recent seismic activity (Kramer 1996). The time between two successive earthquakes in the same place is therefore large, yet it is inadequately taken into account by traditional hazard analysis techniques. Additionally, this conventional method does not take into consideration the probability of destructive earthquakes occurring in other places or sources. Anbazhagan et al. (2011) presented a novel seismic hazard analysis approach, known as Rupture Based Seismic Hazard Analysis (RBSHA), to consider the likelihood of earthquake occurrence in the regions different from the locations of previously catastrophic earthquakes. The rupture features of the local faults and lineaments are taken into account in the RBSHA method. This method can be employed to determine the maximum probable earthquake magnitude. This method of M_{max} estimate could simulate the worst-case earthquake in the future. The Ground Motion Prediction Equations (GMPE) chosen in this method will use weights together with the statistical techniques like the Log Likelihood (LLH) approach and Data Support Index (DSI) values. The full methodology or the steps for this rupture-based approach can be found in the study of Anbazhagan et al. (2011).

3 DETERMINISTIC SEISMIC HAZARD ANALYSIS (DSHA) STUDIES

Pervez et al. (2003) provided a nationwide seismic hazard map using a deterministic approach that divided entire India into forty seismic zones. Seismic hazard maps were presented for the Indian territory in terms of D_{max}, V_{max}, and Design Ground Acceleration (DGA) by computing realistic synthetic seismograms. DGA ranged from 0.3g to 0.6g in Assam, Andaman-Nicobar Islands, and the central and western Himalayas. Using the Iyengar & Raghu Kanth (2004) attenuation relationship, Boominathan et al. (2008) assessed the earthquake hazard taking into account local site impacts for microzonation studies of Chennai metropolis. Peak Ground Acceleration value for that area was in the range of 0.004g - 0.106g. Using data from remote sensing to locate lineaments in the Bangalore region, Sitharam et al. (2006) had computed the peak horizontal acceleration (PHA) for Bangalore City. They made use of the attenuation correlation provided for south India. For the city, PHA ranged from 0.005g to 0.13g. Sitharam et al. (2006) performed DSHA for Bangalore city using the empirical equation provided by Wells & Coppersmith in 1994. PHA varied depending on the method from 0.001g - 0.146g. Sitharam & Anbazhagan (2007) evaluated the Peak Ground Acceleration for Bangalore City using the attenuation relationship developed by Iyengar & Raghu Kanth (2004) and the Wells & Coppersmith (1994) by RLD approach for cross validation. The PGA value was observed to be 0.146g & 0.159g when using the DSHA method & RLD approach, respectively. Raghu Kanth et al. (2009) used the enhanced 1-D stochastic simulation model developed by Boore (1983) to simulate ground motion in Imphal city. For the Imphal city, the PGA varied between 0.12g and 0.2g at rock level. PGA value at the surface ranged from 0.14g to 0.24g. Desai & Choudhury (2014) carried out DSHA for the Greater

Mumbai region. They took into account 7 GMPEs in the logic tree analysis to calculate the PHA and S_a values (0.1s and 1s) at the bedrock level. The PHA values varied from 0.076g to 0.328g. Shukla & Choudhury (2012) conducted DSHA for the 5 major cities of Gujrat. For the seismic hazard analysis, 7 ground motion prediction equations were used in the logic tree to calculate the PGA values for each of the cities. PGA values for the five cities were 0.13g (Ahmedabad), 0.15g (Surat), 0.64g (Bhuj), 0.14g (Jamnagar), 0.20g (Junagadh). Kataria et al. (2013) carried out DSHA of the Andaman and Nicobar Islands taking into account seven seismogenic source zones. GMPEs applicable for subduction zones and shallow crustal earthquakes in active tectonic regions, respectively, had been employed. In that study, the PGA value was in between 0.27g – 0.58g. Naik & Choudhury (2014) carried out DSHA for Goa state of India. 7 attenuation equations (GMPEs) were utilized to calculate the PGA value for the state. PGA map developed for Goa shows high hazard values in the central Goa part compared to the other parts of the state. Rao & Choudhury (2021) carried out DSHA for the North-Western part of Haryana. As an important structure like Nuclear Power Plant (NPP) is going to come up very soon, proper seismic hazard analysis was necessary. Seismic hazard maps were developed for the region by taking into account 3 scenarios. PGA values for the 3 scenarios considered were found to be 0.088g, 0.110g and 0.151g respectively. Anbazhagan et al. (2023) carried out seismic hazard analysis of Tripura (NE India) using both conventional and rupture-based approach. Seismic hazard maps obtained by both the approaches for the state of Tripura was provided as the results of the study. The Peak Ground Acceleration value was found to be in the range of 0.05g – 0.58g.

4 PROBABILISTIC SEISMIC HAZARD ANALYSIS (PSHA) STUDIES

Bhatia et al. (1999) generated a seismic hazard map of India and surrounding areas using the probabilistic approach. The key geological characteristics and seismicity trends were used to define 86 possible seismic source zones. This investigation used the Joyner & Boore (1979) attenuation relationship. The projected PGA values for the Tibetan plateau were 0.25g, 0.35g – 0.4g for the North-East and North-West Himalayan regions, 0.1g for the Indian Shield, and 0.2g for the Koyna region. Nath & Thingbaijam (2012) conducted PSHA of India using 16 ground motion prediction equations (GMPE) with equal weights for the hazard computation. Plots of PGA and PSA for several cities were shown at 0.2 and 1 seconds. Based on 104 regional seismic source zones in India, Sitharam & Kolathayar (2013) conducted a seismic hazard study of the nation utilising areal sources. They took into account four attenuation relationships for the analysis. PHA and S_a (Spectral Acceleration) values (for durations of 0.1 and 1 s) were analysed at rock level for the entire country for probabilities of exceeding 10% and 2% in 50 years. Desai & Choudhury (2014) assessed the seismic hazard for the Mumbai region and provided PGA and S_a. Seven attenuation equations for shallow crustal intraplate regions developed for the other parts of the world had been applied. From the hazard map, it was revealed that Panvel, JNPT, Vashi and Belapur of Navi Mumbai were high hazard places compared to the other parts of Mumbai. Das et al. (2016) carried out PSHA for North-East India into 9 seismogenic zones. PGA and S_a values for the region were calculated and seismic hazard maps were presented for the region at the bed rock level. From the maps, it was seen that there was a significant spatial variation locally unlike the constant value of PGA given in IS code. Coefficient of Variation (COV) map had also been provided along with the hazard map for the region. For the city of Bangalore, Sitharam et al. (2006) took into account 52 faults and lineaments, and seismic hazard analysis used the attenuation relationship of Iyengar & Raghu Kanth (2004). For that area, PHA ranged from 0.001g – 0.146g. Shukla & Choudhury (2012) conducted PSHA of two of the most important ports of India located in the state of Gujrat. Uniform Hazard Spectra (UHS) for the two ports (Kandla and Mundra port) was developed by using 7 GMPEs. For the site characterization, soil profiles were obtained from the investigations carried out at the two ports. It was concluded that UHS amplitude depends heavily on local site conditions and cannot be described properly by IS code. Using the Poisson method, Anbazhagan et al. (2008) carried out PSHA for the city of Bangalore. In their analysis, the attenuation relation for a rock site in Peninsular India developed by Raghu Kanth

(2005) was applied. For the city of Bangalore, the PGA value was in the range of 0.17g – 0.25g. Mohanty & Yanger (2008) used a quasi-probabilistic methodology to calculate the seismic hazard for Kolkata city while taking five seismic source zones into account. The attenuation relationship of Toro et al. (1997) was applied in the study. From the south-eastern to the eastern parts of Kolkata, PGA varied from 0.10g – 0.34g. The estimate of the seismic hazard for the Delhi region was done by Agrawal & Chawla (2006). Contour maps of the entire region were used to display the results. The PGA ranged from 0.12g – 0.17g for the study area. Kumar et al. (2013) conducted Lucknow's seismic hazard analysis taking into account nearby and active seismic gaps. PGA ranged for 10% and 2% risk of exceeding in 50 years are 0.04g – 0.07g and 0.07g – 0.13g, respectively. Patil et al. (2014) carried out PSHA for Himachal Pradesh and its surrounding area. Two cases (constant b and varying b value) were considered to find out PGA values at bedrock level. PGA values ranged between 0.14g to 0.37g and 0.07g to 0.24g for the two cases respectively. Rout et al. (2015) conducted PSHA for the North-Western and Central Himalayas by dividing the area into 22 seismogenic source zones. Considering the varying b value case, PGA values at bed rock level was ranging from 0.06g to 0.65g.

5 RUPTURE BASED SEISMIC HAZARD ANALYSIS (RBSHA) STUDIES

The seismic hazard map of Coimbatore was presented by Anbazhagan et al. (2012), who also highlighted 8 likely places called the probable locations where earthquakes might be anticipated soon. They also compared the hazard map developed using the Rupture based approach with the map developed using the conventional DSHA approach. Anbazhagan et al. (2023) conducted the rupture based seismic hazard analysis of Tripura state of North-East India. They have provided the hazard maps of the state developed with this new method. It showed that Tripura state can experience higher PGA values than as mentioned in IS 1893: Part 1 (2016).

6 DISCUSSIONS

The examination of papers mentioned above demonstrates the many methods used to calculate the PGA value at both the national and regional levels.

Agrawal & Chawla (2006) provided PGA values for Delhi that are comparable to Bhatia et al. (1999) and that ranged from 0.12g to 0.17g for 10% risk of exceeding in 50 years, although the IS code zone factor is larger for Delhi than the value provided by Agrawal & Chawla (2006). The PGA values recommended by Boominathan et al. (2008) varied from 0.004g – 0.106g, that is comparable with the zone factor of 0.16g for Chennai specified in IS 1893: Part 1 (2016). Comparing the zone factor for Kolkata in IS 1893: Part 1 (2016) to the regional PGA value provided by Mohanty & Yanger (2008), the zone factor was understated as 0.16g. The IS code zone factor for Lucknow is 0.16g, however the PGA value ranged from 0.07g – 0.13g for 2% likelihood (2475 years) of exceedance in 50 years provided by Kumar et al. (2013). In comparison to Sitharam et al. (2006) & Anbazhagan et al. (2008) for Bangalore region, IS 1893: Part 1 (2016) underestimated the PGA value of zone II as 0.10g. Andaman and Nicobar are classified as being in zone V according to IS 1893: Part 1 (2016), which is an underestimation compared to the PGA value provided by Kataria et al. (2013). Nath & Thingbaijam (2012) for Andaman and Nicobar recommended PGA values between 0.30g and 0.60g while taking the DSHA technique into consideration, which is similar to the PGA values stated in Khattri et al. (1984). The PGA value reported for the same in Bhatia et al. (1999) was 0.15g to 0.30g, which is less than the PGA value stated in Khattri et al. (1984). Anbazhagan et al. (2023) reported PGA value for the state of Tripura in the range of 0.05g – 0.57g which is much higher than 0.36g given in IS code. Both conventional and rupture-based approach was used in the study. PGA map was provided for the state and it was revealed from the study that there was a spatial variation within the small area of the state. Also, the reported values of PGA across the state were deviating from the constant value given in the IS code for the state. Few of these comparisons made above shows a fair deviation from the value given in the IS code. For instance, PGA value for the whole North-East India as given

by IS code is constant (0.36g). But it is not true as observations from the studies of different researchers tells us a different story. These deviations in the hazard values obtained by the different researchers shows the importance of carrying out micro level hazard estimation in which use of different seismic hazard methodologies plays an important role.

7 CONCLUSIONS

India is split into four zones, with zone factors in the range of 0.10g - 0.36g, according to IS: 1893: Part 1 (2016), but the site geology and criteria for identifying these soils are not entirely given. These data have been compared, and it was discovered that the Indian Standard code overpredicts PGA values for hard rock sites, while underpredicting values for soil locations. Therefore, site-specific research is crucial by taking into account the local, geological, geophysical, seismotectonic and rupture characteristics of the area. It has also been seen that most researchers use predictive relationships in hazard analyses without considering if they are valid for the region being studied. Therefore, one of the most crucial factors in the seismic hazard analysis is the right selection or development of a predictive relationship for a location. Some studies have employed a variety of methods to categorize seismically active regions, including the zone-wise approach, the fault-based approach, and the grid-based technique. However, thorough study of these methodologies is crucial for future research. Also, since there are not many studies done using the RBSHA methodology, seismic hazard analysis in the national or regional level can be performed using this approach by formulating new GMPE equations for any region or considering the nation as a whole. IS code needs also be updated considering the scientific approaches and should provide PGA values obtained from microzonation analysis.

ACKNOWLEDGEMENT

Authors would like to express sincere thanks to Dr. Ranjit Das, Assistant Professor, Universidad Catolica del Norte, Chile, for his valuable and constructive suggestions during the planning and development of this review manuscript.

REFERENCES

Agrawal, S. & Chawla, J. 2006. Seismic hazard assessment for Delhi region. 2006. *Current Science* 91 (12): 1717–1724.

Anbazhagan, P., Vinod, J.S. & Sitharam, T.G. 2008. Probabilistic seismic hazard analysis for Bangalore. *Natural Hazards* 48: 145–166.

Anbazhagan, P., Gajawada, P. & Parihar, A. 2012. Seismic hazard map of Coimbatore using subsurface fault rupture. *Natural Hazards* 60: 1325–1345.

Anbazhagan, P., Das, A., Silas Abraham, G. 2023. Regional Rupture-Based Seismic Hazard Analysis of Tripura State—NE India. *Soil Dynamics, Earthquake and Computational Geotechnical Engineering. Lecture Notes in Civil Engineering*, 300. Singapore: Springer.

Bhatia, S.C, Kumar M.R, and Gupta H.K. 1999. A Probabilistic Seismic Hazard Map of India and Adjoining Regions. *Annali Di Geofisica* 42(6).

Boominathan, A., Dodagoudara, G.R., Suganthi, A. & Uma Maheshwari R. 2008. Seismic Hazard Assessment of Chennai City Considering Local Site Effects. *Journal of Earth System Science* 117: 853–863.

Boore, D.M. 1983. Stochastic Simulation of High frequency Ground Motions Based on Seismological Models of the Radiated Spectra. *Bulletin of the Seismological Society of America* 73 (6A): 1865–1894.

BIS (2002) IS 1893 (part 1): 2016—Indian standard criteria for earthquake resistant design of structures, part 1: general provisions and buildings. Bureau of Indian Standards, New Delhi

Das, R., Sharma, M.L. & Wason, H.R. 2016. Probabilistic seismic hazard assessment for northeast India region. *Pure and Applied Geophysics* 173(8): 2653–2670.

Desai, S. & Choudhury, D. 2014. Deterministic seismic hazard analysis for greater Mumbai, India. In *Geo-Congress 2014: Geo-characterization and Modeling for Sustainability, Geotechnical Special Publication No. GSP* 234: 389–398.

Desai, S.S. & Choudhury, D. 2014. Spatial variation of probabilistic seismic hazard for Mumbai and surrounding region. *Natural Hazards* 71(3): 1873–1898.
Gupta, I. D. 2006. Delineation of probable seismic sources in India and neighborhood by a comprehensive analysis of seismotectonic characteristics of the region. *Soil Dynamics and Earthquake Engineering* 26: 766–790.
Iyengar, R.N. & Raghu Kanth, S.T.G. 2004. Attenuation of Strong Ground Motion in Peninsular India. *Seismological Research Letters* 75(4): 530–540.
Iyengar, R.N., Chanda, R.K., Balaji Rao, K. & Raghu Kanth, S.T.G., "Development of Probabilistic Seismic Hazard Map of India. 2010. Technical report of the Working Committee of Experts (WCE), The National Disaster Management Authority, Government of India, New Delhi.
Joyner, W.B. & Boore, D.M. 1981. Peak acceleration and velocity from strong-motion records including records from the 1979 Imperial Valley, California, Earthquake. *Bulletin of the Seismological Society of America* 71: 2011–2038.
Kataria, N.P., Shrikhande, M. & Das, J.D. 2013. Deterministic Seismic Hazard Analysis of Andaman and Nicobar Islands. *Journal of Earthquake and Tsunami*, 7(4).
Khattri, K.N., Rogers, A.M., Perkins, D.M. & Algermissen, S.T. 1984. A Seismic Hazard map of India and adjacent areas. *Tectonophysics* 108(1-2): 93–134.
Kumar, A., Anbazhagan, P. & Sitharam, T.G. 2013. Seismic hazard analysis of Lucknow considering local and active seismic gaps. *Natural Hazards* 69: 327–350.
Mohanty, W.K. & Walling, M.Y. 2008. Seismic hazard in mega city Kolkata, India. *Natural Hazards* 47: (39–54).
Naik, N. & Choudhury, D. 2015. Deterministic seismic hazard analysis considering different seismicity levels for the state of Goa, India. *Natural Hazards*, *75*(1): 557–580.
Nath, S.K. & Thingbaijam, K.K.S. 2012. Probabilistic Seismic Hazard Assessment of India. *Seismological Research Letters* 83(1): 135–149.
Parvez, I.A., Vaccari, F. & Panza, G.F. 2003. A deterministic seismic hazard map of India and adjacent areas. *Geophysics Journal International* 155(2): 489–508.
Patil, N.S., Das, J., Kumar, A., Rout, M.M. & Das, R. 2014. Probabilistic seismic hazard assessment of Himachal Pradesh and adjoining regions. *Journal of earth system science* 123(1): 49–62.
Raghu Kanth, S.T.G., Singh, K.D & Pallav K. 2009. Deterministic Seismic Scenarios for Imphal City. *Pure and Applied Geophysics* 166: 641–672.
Sitharam, T.G., Anbazhagan, P. & Ganesha Raj, K. 2006. Deterministic Seismic Hazard Analysis and Estimation of PHA for Bangalore City. International Conference on Earthquake Engineering, Pakistan: 1–8.
Sitharam, T.G., Anbazhagan, P. & Ganesha Raj, K. 2006. Use of Remote Sensing and Seismotectonic Parameters for Seismic Hazard Analysis of Bangalore. *Natural Hazards and Earth System Sciences* 6: 927–939.
Sitharam, T.G. & Anbazhagan, P. 2007. Seismic Hazard Analysis for the Bangalore Region. *Natural Hazards*, 40: 261–278.
Sitharam, T.G., Ganesha Raj, K., Anbazhagan, P. & Mahesh U.G. 2006. Use of Remote Sensing Data and Past Earthquake Events for Deterministic Seismic Hazard Analysis of Bangalore. Proceedings of the Conference on Advances in Space Science and Technology.
Rao, V.D. & Choudhury, D. 2021. Deterministic seismic hazard analysis for the Northwestern Part of Haryana State, India, considering various seismicity levels. *Pure and Applied Geophysics* 178(2): 449–464.
Rout, M.M., Das, J. & Das, R. 2015. Probabilistic seismic hazard assessment of NW and central Himalayas and the adjoining region. *Journal of Earth System Science* 124(3): 577–586.
Shukla, J. & Choudhury, D. 2012. Estimation of seismic ground motions using deterministic approach for major cities of Gujarat. *Natural Hazards and Earth System Sciences* 12(6): 2019–2037.
Shukla, J. & Choudhury, D. 2012. Seismic hazard and site-specific ground motion for typical ports of Gujarat. *Natural Hazards* 60(2): 541–565.
Sitharam, T.G., Kolathayar, S. & James, N. 2014. Probabilistic assessment of surface level seismic hazard in India using topographic gradient as a proxy for site condition. *Geoscience Frontiers*, 6(6): 847–859.
Sitharam, T.G. & Kolathayar, S. 2013. Seismic hazard analysis of India using areal sources. *Journal of Asian Earth Sciences* 62: 647–653.
Toro, G.R., Abrahamson, N.A. & Schneider J.F. 1997. Model of strong ground motions from earthquakes in central and eastern North America: best estimates and uncertainties. *Seismological Research Letters* 68 (1): 41–57.
Wells, D.L. & Coppersmith, K.J. 1994. New Empirical Relationships among Magnitude, Rupture Length, Rupture Width, Rupture Area and Subsurface Displacement. *Bulletin of the Seismological Society of America* 84 (4): 974–1002.
Yanger, M.W. & Mohanty, W.K. 2008. An overview on the seismic zonation and microzonation studies in India. *Earth-Science Reviews* 96(1–2): 67–91.

Smart Geotechnics for Smart Societies – Zhussupbekov, Sarsembayeva & Kaliakin (Eds)
© 2023 The Author(s), ISBN 978-1-003-29912-7
Open Access: www.taylorfrancis.com, CC BY-NC-ND 4.0 license

Development of sediment foundations of clay soils

A.S. Zhakulin
Doctor of Technical Sciences, Professor, Karaganda Technical University, Karaganda, Kazakhstan

A. Zh. Zhussupbekov
Doctor of Technical Sciences, Professor, L.N. Gumilyov Eurasian National University, Astana, Kazakhstan

A.A. Zhakulina
Ph.D., Associate Professor, Karaganda Technical University, Karaganda, Kazakhstan

M.A. Khan & E.N. Abdygaliyev
Karaganda Technical University, Karaganda, Kazakhstan

A.U. Yessentayev
L.N. Gumilyov Eurasian National University, Astana, Kazakhstan

ABSTRACT: The article presents the results of long-term geodetic observations of deformations of blast furnace bases at the Karaganda Metallurgical Combine and the main provisions of the development of the elastic-plastic clay model for soils of Central Kazakhstan. The results of experimental studies of clay soils and numerical analysis of the forecast of basement sediments are presented.

1 INTRODUCTION

For more than 60 years, geodesic monitoring has been carried out for the precipitation of structures of the Karaganda Metallurgical Plant. During the construction of the foundations of blast furnaces No. 1-4, coke oven batteries No. 1-4 and chimneys with a height of 250 m, reference points were installed (according to the project requirements), which still record deformations of the foundations of structures. It is known that the main precipitation occurs during the construction of the structure and during the first few years of its operation, and in clay soils, precipitation stabilization occurs much later than in sandy soils. In this regard, it is very important to monitor the deformations of the base, starting from the moment of foundation construction, i.e. from the very beginning of load transfer to the base. It should be noted that the ground water level is at a depth of 23.0 meters and the ground at the base of the foundations is wet. In 1982, there was a need for a complete replacement of the blast furnace No. 1, its overhaul after 20 years of operation. During the dismantling period, elastic deformations of the base were recorded, the value of which was 32 mm. After the blast furnace was built and fully loaded, the sludge stabilized in 2 months. A similar pattern was observed during the reconstruction of all blast furnaces.

2 ANALYSIS OF THE RESULTS OF ENGINEERING AND GEOLOGICAL SURVEYS

Analysis of the results of engineering and geological surveys shows that most buildings and structures They are built on soils, mainly of Quaternary age (systems). Soils of the Quaternary system are characterized by the variability of their physical state, complexity, and variety of mechanical properties. Therefore, as part of the object (geotechnical system), the forecast of

DOI: 10.1201/9781003299127-268

precipitation of industrial structures 'foundations on clay soils of Central Kazakhstan was chosen as the subject of research. The main factors that lead to changes in the properties of clay soils of foundations are, first of all, man-made (technical and technological) and climatic (precipitation infiltration). The negativity of the process lies in the fact that the factors that lead to changes in the properties of the base soil are irreversible and are primarily associated with human engineering activities. Therefore, taking into account these factors that directly affect the stress-strain state of soils is necessary for a reliable forecast of foundation precipitation. Figure 1 shows the distribution of the porosity and density coefficients over depth on clay substrates. Analysis of the graphs shows that the porosity coefficients vary in depth from 0.6 (15.0 m) to 1.1 (1.0; 10.0; 25.0 m) and the density values - from 1.75 to 2.1 g/^{cm3}.

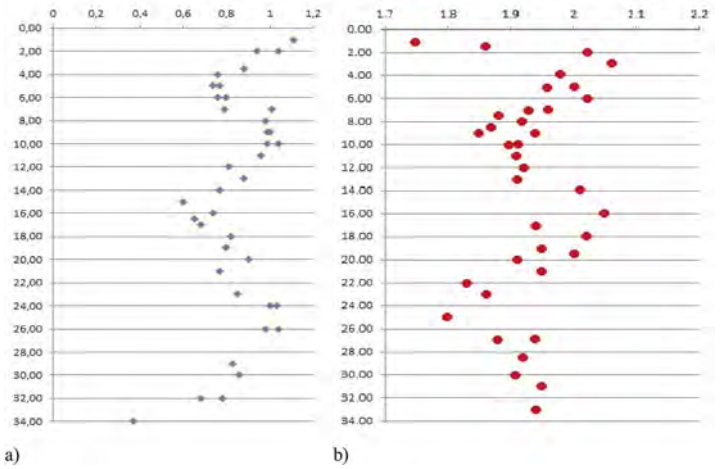

Figure 1. Depth distribution of physical properties of clay soils. (a. porosity coefficient b. density).

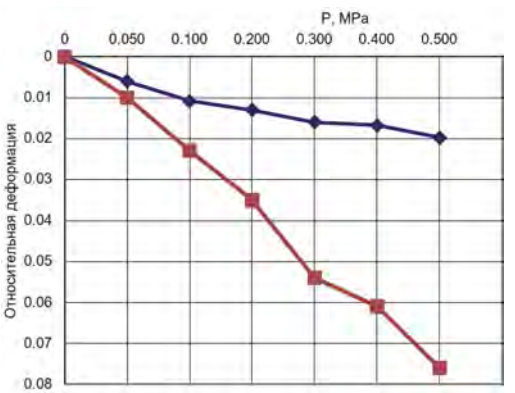

Figure 2. Compression graphs before and after soaking clays.

Figure 2 shows the results of testing clays in a compression device with the initial data: W=14.3, p=1.85 g/^{cm3}, e=0.695, While the results are obtained: natural humidity-m $_0$ = 0.045 MP a, E $_k$=17.8 MP a, E $_{od}$=44.4 MP a and at soaking – m0=0.254 $_{MP}$ a, ek=6.0 MP a, E $_{od}$=7.5 MP a. The analysis shows that the compression module is 2.9 times smaller when soaked than in the natural state, and the odometric module is 5.8 times smaller.

To study the stress-strain state and forecast the sedimentation of foundations of structures, an improved elastic-plastic model of clays based on the tent model of Professor T. Tanaka is

presented [3,7,8]. Tent (deformation) models are the most developed for describing the deformation of clay soil bases [3]. When applying this model for clays, we consider the incremental relationship between stresses and deformations when testing soils on triaxial compression devices. The analysis of the results is carried out in stresses, since clay soils of the base are moist and not fully compacted in their natural state:

$$p = 1/3(\sigma_1 + 2\sigma_2) И\, q = \sigma_1 - \sigma_2, \tag{1}$$

and deformations:

$$_{ei} = {}_{e1+}\, 2e2 \text{ and } \gamma = 2/3\ (_{e1} - e2), \tag{2}$$

where σ_1, σ_2, ε_1, ε_2 - stresses and deformations.

A graphic representation of the tent model is shown in Figure 3.

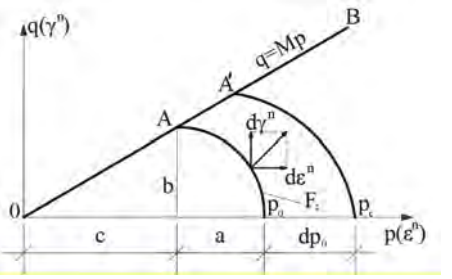

Figure 3. Graphic representation of the elastoplastic model.

Line with the equation:

$$Mp = q, \tag{3}$$

in Figure 3: the line with the equation $q = Mp$ is the limit line of this soil,

where M = constant is a coefficient that varies within 0.7÷1,2, which corresponds to the internal friction angles from 18 ° to 30 °.

When solving the problem, the following model assumptions are made::

- isotropic compression under pressure – P_o forms the elastic zone OAR_0 and within this zone the change in the stress state is accompanied only by small elastic deformations. Beyond the boundary of the yield surface AP_0 is accompanied by the appearance of plastic deformations $d\gamma^n$ and dfe^n;
- the yield surface AP_0, this is the surface of the plastic potential and, in accordance with the associated flow law, the total vector of plastic deformations is normal to the yield surface.

An increase in stresses, accompanied by the accumulation of plastic deformations, will lead to an expansion of the elastic region and the yield surface (tent) will occupy a new position A'P *C*. At the same time, the volume plastic deformation at any point of the new tent will be independently constant and equal to the deformation by which the soil is deformed under isotropic compression from pressure P_0 and P_C. Experimental compression parameters for implementing the model – λ and decompressions – k were obtained from compression curves in semilogarithmic coordinates (Figure 4). In this case, changes in the soil porosity coefficient linearly depend on the logarithm of the external pressure change.

Then the equation of the compression curve has the form:

for the load branch

$$e_i = e_0 - \lambda \ln\left(\frac{P_i}{P_0}\right), \tag{4}$$

for the unloading branch

$$e_i = e_0 - k \ln\left(\frac{P_i}{P_0}\right), \tag{5}$$

where e0 and P0 are the initial porosity and pressure coefficients; *ei and* Pi *are the porosity coefficient and pressure corresponding to the* i*-th* load stage; λ – compression ratio; k – decompression ratio.

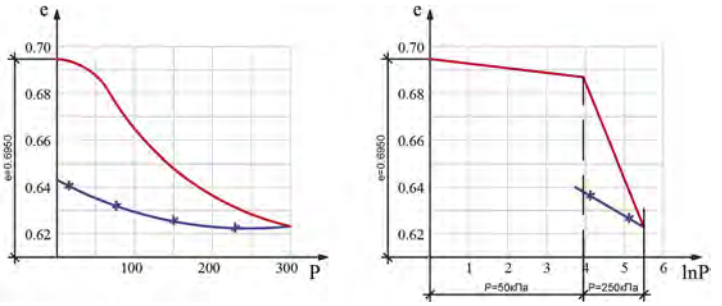

Figure 4. Compression graphs for determining load parameters-λ and unloading – k.

Compression ratios λ and decompression k is the tangent of the angle of inclination of the semi-logarithmic curve to the pressure axis, numerically equal to the difference in the porosity coefficients. If *Pi = e*, this condition should be taken into account in *Pi = e ln pi = 1* [3,4]. These coefficients are dimensionless and characterize the compressibility of soils in a large pressure range [5].

Bearing in mind that the total increase in volume deformation consists of elastic and plastic parts, the total deformation is defined as:

$$d\varepsilon_{ij} = d\varepsilon_v = d\varepsilon_{ij}^v + d\varepsilon_{ij}^n = d\varepsilon_v^v + d\varepsilon_v^n. \tag{6}$$

Increments of the elastic strain component are related by linear relations of the generalized Hooke's law with stress increments:

$$d\varepsilon_{ij}^v = \left[(1+v)d\sigma_{ij} - 3v\delta_{ij}d\sigma_{cp}\right]/E, \tag{7}$$

where δ_{ij} is the Kronecker symbol.

The increment of plastic deformation components that occurs under active loading at a regular point on the loading surface is determined by the ratio:

$$d\varepsilon_{ij}^n = dk\frac{\partial \Phi}{\partial \sigma_{ij}}, \tag{8}$$

the use of which implies the construction of the loading surface *F=const,*
where *dk* is a scalar infinite multiplier; *F is* the loading function.
Loading function in the elastic domain at *F < 0* in matrix form:

$$d\varepsilon = \ d\varepsilon^{y} + s \cdot d\varepsilon^{n} = D^{y-1} d\sigma + s\lambda B, \tag{9}$$

plastic deformations from experimental graphs are determined by:

$$\varepsilon_{ij}^{n} = \ \frac{\lambda - k}{1 + e_0} \frac{1}{2.3} \ln\left(\frac{-3P}{-3P_0}\right), \tag{10}$$

where: *-3P = P_s*
then:

$$\varepsilon_{ij}^{n} = -A \ln(-P_C) + B, \tag{11}$$

$$A = \frac{1}{2.3} \frac{\lambda - k}{1 + e_0} \text{И}\, B = -A \ln(-3P_0), \tag{12}$$

coefficients A and B are constant

$$P_c = \exp\left(\frac{B - \varepsilon_{ij}^{n}}{A}\right), \tag{13}$$

The yield surface equation for an isotropic medium in the stress space is written as:

$$f(\sigma) = 0, ij, \tag{14}$$

where *f is* the yield function in the elastic region *f < 0*.
In the case of an elastic-plastic medium *F = f*, then (8) takes the form:

$$d\varepsilon^{y} = dk \frac{\partial f}{\partial \sigma_{ij}}, \tag{15}$$

It should be noted here that if the guiding cosines of the normal to the loading surface are proportional, then the ratio (8) means the vector of increment of plastic deformation at a regular point directed along the normal to the loading surface-F_2 in any direction of the loading vector. In this case, only the value of the vector depends on the loading vector . The loading surface is used to establish the relationship between stresses and deformations in the pre – limit state of the soil, and the yield surface is used in the limit state.

In general, the yield function is defined as:

$$f = \alpha I_1 + \frac{J_2^{1/2}}{g(\theta)} - K = 0, \tag{16}$$

At: *f (σ, k) = 0; df = 0;*
Then we have

$$\text{a}^{\ t}\ d\sigma - A\lambda = 0, \tag{17}$$

$$A = -\frac{1}{\lambda} \frac{\partial f}{\partial k} dk, \text{a} = \frac{\partial f}{\partial \sigma}, \text{b} = \frac{\partial \Phi}{\partial \sigma}, \tag{18}$$

the final element area coefficient is defined as follows:

$$S = \frac{Fb}{Fe}, \tag{19}$$

where fb is the area of the final element after shear or deformation; $_{F}\, e\, _{is\ the\ area}$ of the final element at the beginning of the calculation.

Formula (9) is an equation for the relationship between strain increments and stresses for the accepted model. And also the proposed model considers the OM line as the limit line of normally compacted soil and defines:

$$\alpha_{cs} I_1 + \frac{I_3^{\frac{1}{2}}}{g(\theta)} = 0 \text{ or } \alpha_{xs} P_0 + \frac{b}{g(\theta)} = 0, \tag{20}$$

where: $b = -\alpha_{cs} P_0 g(\theta)$ and $\alpha = R(-\alpha_{cs} P_0 g(\theta))$,

Then

$$P_c = P_0 - a = P_0[1 + \alpha_{cs} g(\theta) R], \tag{21}$$

where α_{cs} – critical condition coefficient;

In this model, the associated yield surface and plastic potential for normally compacted clays ($F_2 = f$ or AP_c) is a section of an ellipse described by the equation:

$$\frac{(I_1 - P_0)^2}{a^2} + \frac{I_2}{b^2} = 1, \tag{22}$$

where a and b are geometric parameters of the ellipse,$a/b = R = const;$ P0 is the center of the ellipse.

The yield surface is described by the equation:

$$f = F_2 = b^2 (I_1 - P_0)^2 + \frac{a^2 I_2}{(g(\theta))^2} - a^2 b^2 = 0, \tag{23}$$

or

$$f = F_2 = b^2 (P_c P_0)^2 + - a^2 b^2 = 0, \tag{24}$$

Given the Mohr-Coulomb law, we define:

$$g(\theta) = \frac{\cos\frac{\pi}{6} - \frac{1}{\sqrt{3}} \sin\frac{\pi}{6} \sin\varphi}{\cos\theta - \frac{1}{\sqrt{3}} \sin\theta \sin\varphi} = \frac{3 - \sin\varphi}{2\sqrt{3}\left(\cos\theta - \frac{1}{\sqrt{3}} \sin\theta \sin\varphi\right)}, \tag{25}$$

where θ - parameter: e;

$$\sin 3\theta = -\frac{3\sqrt{3} J_3}{2 J_2^{\frac{3}{2}}}, \tag{26}$$

The given invariants are determined by the well-known formulas.

The position of the ellipse is determined by two constants a and b and a function that relates the position of the tent to the bulk plastic deformation-$e\ v^{\,p}$.

$$P_c = F_2(\varepsilon_v^n), \tag{27}$$

It should be noted that the theoretical stress increase is defined as:

$$n\ v\ \varepsilon^{\,Kd} - y\ dp_{=}^{\ dp} \text{ and } dq = dq^{\,y} - 2\ G dq^{\,n}, \tag{28}$$

where dqy and dpy are the elastic stress increment; $K,\ G\ are$ the secant modules of bulk strain and shear.

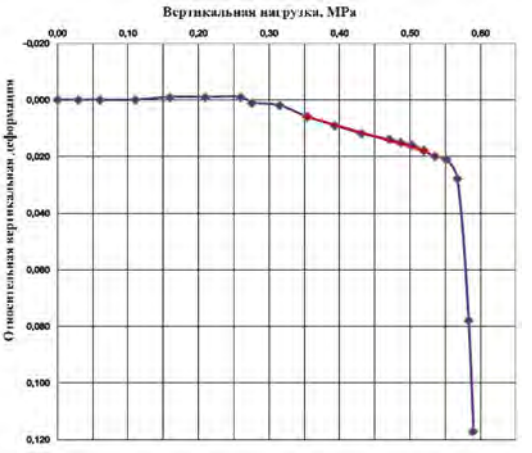

Figure 5. Results of triaxial clay tests.

Thus, to study the stress-strain state in an elastoplastic model, it is necessary to determine the strain modulus, Poisson's ratio, and secant strain modulus. Figure 5 shows that the results of triaxial tests of clays were obtained at the initial clay data-W=14.3%, p=1.85 g/^{cm3}, e=0.695, modulus of deformation-E = 13.8 MPa; Poisson's ratio-v = 0.21; secant modulus of deformation-E =7.2 MPa.

We will make a forecast of basement sediment using the Nonsolan applied geotechnical program (Japan) using the finite element method in the elastic-plastic formulation-application-Soil Creep. To construct a system of finite element equations, we use the condition that the powers of contour forces at displacement velocities and internal stresses at strain velocities are equal. Also, the forecast of basement sediment requires consolidation and creep parameters, which are determined using compression tests of clays (Figure 6).

To determine $_{C}v$ *and Ca* by the logarithmic method, we construct $_{a}$ consolidation curve in the coordinates: relative strain ε (ordinate) - logarithm of time *lg t* (abscissa). The curve should be used to find the strain corresponding to 100% primary compression at a given load. For this purpose, a tangent is drawn to the final section of the curve $\varepsilon = f(lg\ t)$. Then draw a tangent to the steepest part of the curve (Figure 6).

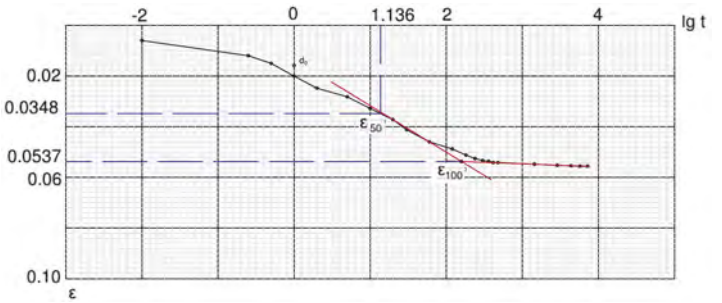

Figure 6. Consolidation charts for determining calculated consolidation parameters and creep.

Filtration consolidation coefficient-C_{v} (^{cm2}/year), calculated by the formula:

$$Cv = T_{50}h^2/t_{50}, \tag{29}$$

where T_{50} is the coefficient (time factor) corresponding to the degree of consolidation of 0.5;

50_t – time corresponding to 50% primary compression, min.

The creep coefficient- C_a (dimensionless value) is determined by the tangent of the angle between a straight line parallel to the abscissa axis and a straight line segment of the curve in the secondary consolidation section using the formula:

$$C_a = tg_a = \varepsilon(t_2) - \varepsilon(t_1)/lg\ (t_2) - lg\ (t_2), \tag{30}$$

where $\varepsilon(t2)$ and $\varepsilon\ (t1)$ are the values of the sample deformation at the secondary consolidation site; *t1* and *t2* are the time corresponding to the deformations $\varepsilon(t2)$ and $\varepsilon\ (t1)$, min.

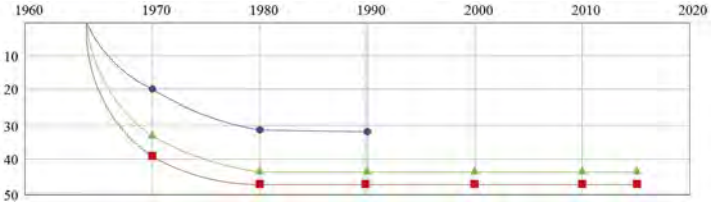

Figure 7. Graphs of basement sediments (experimental "round – elastic", "triangular – full-scale" and theoretical ones using the elastic-plastic model).

3 CONCLUSION

It was found that the total draft for the blast furnace was 43.0 mm. Elastic precipitation due to soil compaction was 32.0 mm and creep precipitation – 12.0 mm.

To compare the calculated foundation precipitation with the actual and maximum permissible values, the foundation precipitation was recalculated. The draft was determined for the design load: for a blast furnace-300 t/^{m2}, with the dimensions of slab foundations: 27.0 m in diameter, with a depth of 3.5 m. Precipitation was calculated using the methods recommended by the regulatory literature. Comparison of calculated, actual, and maximum permissible precipitation showed that the actual precipitation of blast furnace foundations is several times less than the calculated precipitation recommended by the regulatory literature. The actual precipitation of the blast furnace is many times less than the calculated and limit values. Calculations of the forecast of basement precipitation using the Nonsolan applied geotechnical program (Japan) using the finite element method in the elastic-plastic formulation showed that the discrepancy between the actual and theoretical precipitation is no more than 15%.

Comparing the results obtained, we come to the conclusion that it is necessary to conduct additional studies to accumulate and systematize new data and make amendments to the generally accepted formulas for determining basement sediments.

Adjustments and corrections of the main calculation formulas will allow us to approximate the obtained data on the depth of propagation of the main compressive stresses, the amount of precipitation, and the calculated soil resistances under the base of foundations obtained theoretically to the practical values revealed by construction practice and long-term observations of deformations of buildings and structures in operation.

More accurate (real) calculated values will reduce the total cost of construction, since the design of building foundations is carried out with a large margin of safety, which entails unnecessary labor and material costs.

LIST OF LITERATURE

1 Ter-Martirosyan Z. G. Rheological parameters of soils and calculations of the bases of structures. - Moscow: Stroyizdat, 1990. - 200 p.

2 Zaretsky Yu. K. Viscoplasticity of soils and calculations of structures, Moscow: Stroyizdat, 1988, 352 p.

3 Fadeev A. B. Metod konechnykh elementov v geomekhanike [The finite element method in geomechanics], Moscow: Nedra Publ., 1987, 221 p.
4 Tsytovich N. A. et al. Forecast of the sedimentation rate of the foundations of structures, Moscow: Stroyizdat, 1967. -239 p.
5 Ukhov S. B. et al. Mechanics of soils, bases and foundations, Moscow: Vysshaya shkola Publ., 2002, 566 p.
6 Das, M. Braja "Principles Geotechnical Engineering." *Third Edition*. 1993, *PWS Publishing Company*, Boston, p.672.
7 Paramonov V. N. Finite element method for solving nonlinear geomechanics problems. 2012. *Geokonstruktsiya Group of Companies*. Saint-Petersburg.
8 Zhakulin, N. A. S. Deformability of soils of water-saturated bases. 2015. *LAP Lambert Academic Pablishing*. Saarbrucken.
9 Brinkgreve R.B.J et al. PLAXIS, 1997. *Version 8*. Balkema.

Geoenvironmental engineering and frost geotechnics

Taylor & Francis
Taylor & Francis Group
http://taylorandfrancis.com

Smart Geotechnics for Smart Societies – Zhussupbekov, Sarsembayeva & Kaliakin (Eds)
© 2023 The Author(s), ISBN 978-1-003-29912-7
Open Access: www.taylorfrancis.com, CC BY-NC-ND 4.0 license

Freeze-thaw shrinkage potential in fine-grained soils

S. Nishimura & K. Yamaoka
Hokkaido University, Sapporo, Japan

ABSTRACT: Fine-grained soils cause permanent volume reduction when subjected to freeze-thaw cycles, even when obvious ice-lensing and other meso-/macroscopically inhomogeneous structures do not appear. The volume reduction amount is dependent on the stress level. The envelope of the eventual states reached after many freeze-thaw cycles is defined as Freeze-Thaw Residual Line (FTRL), and its characteristics are investigated for fine-grained soils with different plasticity. Possible correlations between FTRL parameters and plasticity index are indicated. Comparison between natural and reconstituted samples is also made, which revealed that natural soil structure was not easily lost after multiple freeze-thaw cycles.

1 INTRODUCTION

The volume reduction seen in fine-grained soils due to freeze-thaw cycles can be an engineering concern in many contexts. The effective stress and hence the shear strength are reduced immediately after thawing and before the pore water pressure dissipation (Nixon & Morgenstern 1973). In longer term, this will lead to thaw consolidation and can result in uneven settlement or ground distress. Both in natural and artificial ground freezing, therefore, an analytical model based on sound understanding of the physical processes behind freeze-thaw-induced volumetric straining is desired. The first author (Nishimura 2021) proposed a Thermo-Hydro-Mechanically (THM) coupled model for describing mesoscopic plastic volumetric strain associated with freezing and thawing processes by upscaling smaller-scale internal water transfer driven by inhomogeneity in water potential at subzero temperature. The model is formulated in a rate form, and can therefore be adopted in incremental, nonlinear numerical analysis based on continuum mechanics, such as finite element analysis.

The first part of this paper provides a summary of the model. It will be shown that the Freeze-Thaw Residual Line, defined as a characteristic line in the volume – effective stress space, and the parameters to represent it are at the core of the model. The second part of this paper presents experimental exploration of these parameters by testing fine-grained soils with different plasticity. The eventual aim is to correlate the degree of plastic straining, or the shrinkage potential, due to freeze-thaw cycles to such indices as plasticity index, I_p.

2 MODEL FOR FREEZE-THAW-INDUCED PLASTIC VOLUMETRIC STRAIN

2.1 *Freeze-Thaw Residual Line (FTRL)*

When normally consolidated fine-grained soils are subjected to one-dimensional, closed-system freeze-thaw cycles under constant stress, the volume reduction accumulates and converges to a limit value. If the soil specimen is small and freezing rate is high such that the internal water transfer to frozen fringe is minimal, this volume change is uniform across the specimen, and can hence be regarded as behaviour of mesoscopically representative element (Nishimura et al. 2020). Figure 1 shows example of the experimental results on high-plasticity Kasaoka clay, involving five cycles of freezing to –20 °C and thawing to +24 °C under the vertical stress of 100, 200, 400 or 800 kPa. By extrapolating the results to an infinite number of cycles, the residual states are defined by a line in the specific volume v – the vertical effective

DOI: 10.1201/9781003299127-269

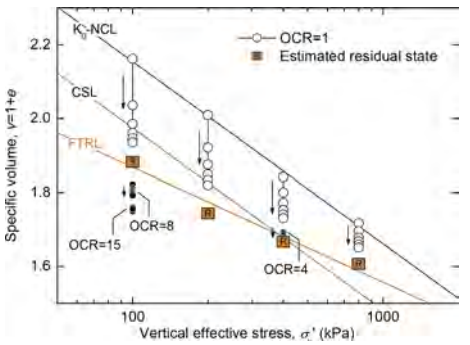

Figure 1. Freeze-thaw-induced volume changes in kasaoka clay (after Nishimura et al., 2020).

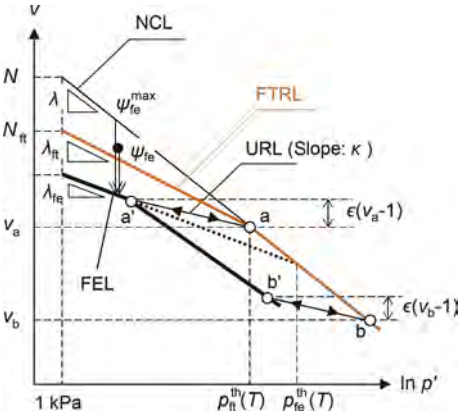

Figure 2. Definitions of FTRL, FEL and ψ_{fe} (after Nishimura, 2021).

stress σ_v' space. This line is defined as the Freeze-Thaw Residual Line (FTRL). It is straightforward to identify this line from experiments, and the two parameters are deduced; λ_{ft} for its slope and p_{ft}^{th} for its intersect with the Normal Compression Line (NCL) for a given freezing temperature T. In addition to such standard material parameters as λ, κ and N, these parameters are used in the proposed model. Here, λ: slope of the NCL, κ: slope of the Unloading-Reloading Line (URL), and N: the intercept of NCL at $\sigma_v' = 1$ kPa. Five freeze-thaw cycles are usually sufficient to estimate the FTRL.

2.2 *Freeze Equilibrium Line (FEL) and shrinkage potential ψ_{fe}*

The FTRL only describes the state after the thawing, and the state during freezing, where the effective stress σ_v' is not clearly defined, remains unclear. The proposed model, following Nishimura & Wang (2019), assumes that the state during freezing is where the URL should have started to bring the post-thaw state onto the FTRL. As Δv during thawing and κ can be measured, the URL can be followed back from the FTRL. The frozen state after many freeze-thaw cycles estimated this way is on the Freeze Equilibrium Line (FEL), as schematically shown in Figure 2. Nishimura (2021) explained the meaning of the FEL based on an idealised micromechanical soil structure consisting of two distinct micro-domains with different water retentivity. It corresponds to a state reached at prolonged freezing, where any internal imbalance of water potential disappears.

It is difficult in reality to directly observe the FEL. However, its geometric relationship with the FTRL allows it to be determined from λ_{ft} and p_{ft}^{th} as:

$$\lambda_{fe} = \frac{(1+\epsilon)k\lambda_{ft}}{k+\lambda_{ft}\epsilon} \tag{1}$$

$$p_{fe}^{th}(T) = p_{fe}^{th}(T)\exp\left\{\frac{\epsilon\lambda_{fe}-\kappa}{\kappa\lambda-\lambda_{fe}}(N-1-\lambda\ln p_{ft}^{th}(T))\right\} \tag{2}$$

where ϵ is the volume expansion factor for undrained freezing, and the other parameters are as defined in Figure 2. The proposed mode uses ψ_{fe}, the excess of v over the FEL at given σ_v', as a potential to cause the plastic volumetric strain arising from the internal water equilibration. By considering Darcian flow in freezing porous media between the micro-domains within the assumed soil structure (see Nishimura 2021, for detail), the plastic volumetric strain rate, $\dot{v}_p$, is expressed as:

$$\dot{v}_p = -\frac{1}{\rho_1 g}\frac{\alpha}{L^2}ks\frac{\langle\psi_{fe}\rangle}{\psi_{fe}^{max}} \qquad (\langle\psi_{fe}\rangle = \psi_{fe} \text{ for } 0 \le \psi_{fe},\ \langle\psi_{fe}\rangle = 0 \text{ for } \psi_{fe} < 0) \tag{3}$$

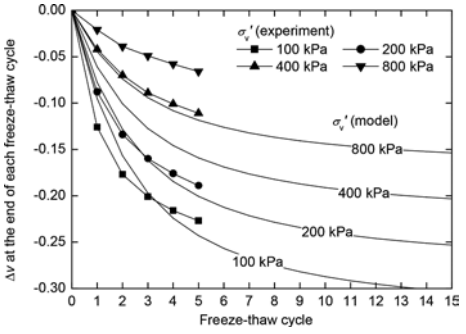

Figure 3. Simulation of freeze-thaw-induced volume changes in Kasaoka clay (after Nishimura, 2021).

Table 1. Tested clays (LL: liquid limit, PL: plastic limit).

Sample	LL (%)	PL (%)	λ
Kasaoka clay	62	28	0.216
Kaolin	46	32	0.087
Kibushi clay	73	38	0.192
Fujinomori clay	44	27	0.093
Higashi-Osaka clay 1	88	33	0.212
Higashi-Osaka clay 2	110	49	0.242
Tuffaceous clay	61	25	0.153
Atsuma clay	48	23	0.101

where $\rho_l g$ is the liquid water unit weight, k is the hydraulic conductivity and s is the cryogenic suction. A parameter α/L^2 is related to the characteristic scale of the problem, to be determined by fitting the model to experimentally observed volume – freeze-thaw cycle number curves. Equation 3 forms the core of the proposed model. Of course, these equations alone are not sufficient to describe the freeze-thaw behaviour. They are meant to be coupled with other THM equations representing, for example, soil-water characteristics curve, soil skeletal constitutive relationship, liquid saturation-dependent hydraulic conductivity, effective stress equation, etc. Examples of these additional equations are given by Nishimura (2021), but other equations may be used. Figure 3 shows examples of modelled volumetric changes due to freeze-thaw cycles, in comparison to the experimental results. The trend is well described by the model.

3 SHRINKAGE POTENTIAL OF FINE-GRAINED SOILS

3.1 *Experimental investigation: Correlation of FTRL parameters with plasticity*

The key model parameters λ_{ft} and p_{ft}^{th} can be determined by experiment in relatively straightforward manners. However, it will be helpful to have guiding knowledge of the parameter values expected for soils within a typical plasticity range. An experimental program has been undertaken in which eight reconstituted soils with different plasticity are tested, as shown in Table 1. They were subjected to five freeze-thaw cycles between +24 °C and –20 °C, following the method by Nishimura et al. (2020). The plasticity index range was 14–61, all tested at σ_v' = 100-800 kPa. In the following, p_{ft}^{th} values cited are all for –20 °C.

Figure 4 shows the observed value of λ_{ft} and p_{ft}^{th} plotted against the soils' plasticity. Here the parameter λ_{ft} is normalised by λ to make the non-parallelism between the FTRL and NCL clearer. There is a weak correlation, with higher I_p leading to lower λ_{ft}/λ. At I_p = 14 (Kaolin), λ_{ft}/λ = 1, meaning that the FTRL and NCL are parallel to each other, and therefore p_{ft}^{th} (their intersection) cannot be defined. Nishimura et al. (2020) discussed this phenomenon observed for low-plasticity soils, and attributed their volume changes to soil skeletal deformation hysteresis, rather than the water potential equilibration – i.e. a mechanism different from that assumed in the model. In any case, the offset of the FTRL from NCL is very small for low-plasticity soils, and the freeze-thaw-induced strain is minor. The correlation between p_{ft}^{th} and I_p seems weaker still, scattering between about 2,000 and 10,000 kPa. Data are not shown where p_{ft}^{th} cannot be defined for the above reason. At low to medium stresses, the NCL-FTRL distance was generally greater for lower I_p.

3.2 *Influence of natural soil structure*

A limited number of natural samples were also tested to understand the influence of natural structure, which is characterised by a curved NCL located outside the reconstituted, 'intrinsic' NCL (Burland, 1990). Both natural and reconstituted samples of Atsuma clay and Higashi-Osaka clay 1 and 2 were tested to make comparison. All the samples of each clay were taken from a single

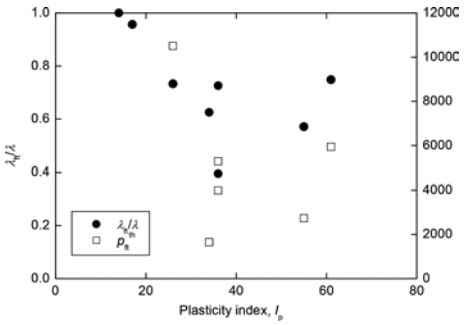

Figure 4. Correlation of FTRL parameters λ_{ft} and p_{ft}^{th} with plasticity index I_p.

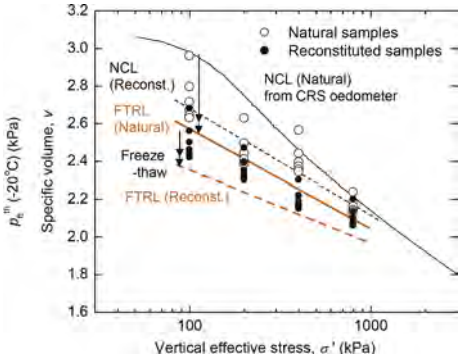

Figure 5. State changes by freeze-thaw cycles in natural and reconstituted Higashi-Osaka clay 2.

borehole core of 100 mm in height and 76 mm in diameter, without re-using. This was possible because the experiment uses very small specimens, with 20 mm in height and 20 mm in diameter. Figure 5 shows the NCLs and FTRLs for both types of samples of Higashi-Osaka clay 2. A continuous compression curve obtained by a constant-rate-of-strain oedometer test on the natural sample is also shown in the same figure, as connecting individual test origins from freeze-thaw cycle tests does not always reveal the compression curve clearly. Despite the significant plastic volume compression, the eventual states of the natural sample after five freeze-thaw cycles do not appear to be asymptotic to the reconstituted FTRL. The natural soil seems as if it has its own FTRL, and the plastic strain due to the freeze-thaw cycles were not sufficient to cause sufficient destructuration that would bring the FTRL of natural sample to that of reconstituted soil. This is despite the fact that the amount of compression after five cycles at, for example, $\sigma_v' = 100$ kPa (from $v = 2.96$ to 2.63, or 11% strain) corresponds to mechanical compression well over the apparent yield stress seen around 100-150 kPa. This investigation is still preliminary, and more tests with a larger number of freeze-thaw cycles may be necessary to reach more definitive conclusions. However, the results hint at relatively robust natural structure against freeze-thaw action.

4 CONCLUSIONS

This paper firstly provided a digest of the model proposed by Nishimura (2021) for describing freeze-thaw-induced plastic volumetric strain. One of the key components is the Freeze-Thaw Residual Line (FTRL) defined in the volume – effective stress space. The two parameters needed to define the FTRL were obtained for reconstituted fine-grained soils with different plasticity. Correlations were recognised between the model parameters and the plasticity index, I_p, which may be useful in estimating soil's shrinkage potential against freeze-thaw cycles in early stages of ground investigation. Natural soils seem to have their own FTRLs that are not easily disturbed and do not coincide with reconstituted FTRLs even after significant compression.

REFERENCES

Burland, J.B. 1990. On the compressibility and shear strength of natural clays. The 30th Rankine Lecture, *Géotechnique* 40(3): 329–378.

Nishimura, S. 2021. A model for freeze-thaw-induced volume changes based on microscopic inhomogeneity in clays. *Soils and Foundations* 61(4): 1054–1070.

Nishimura, S. & Wang, J. 2019. A simple framework for describing strength of saturated frozen soils as multi-phase coupled system. *Géotechnique* 69(8): 659–671.

Nishimura, S., Okajima, S., Joshi, B.R., Higo, Y. & Tokoro, T. 2020. Volumetric behaviour of clays under freeze-thaw cycles. *Géotechnique* 71(12): 1150–1164.

Nixon, J. F. & Morgenstern, N. R. 1973. The residual stress in thawing soils. *Canadian Geotechnical Journal* 10 571–580.

Smart Geotechnics for Smart Societies – Zhussupbekov, Sarsembayeva & Kaliakin (Eds)
© 2023 The Author(s), ISBN 978-1-003-29912-7
Open Access: www.taylorfrancis.com, CC BY-NC-ND 4.0 license

Foamed polyethylene installation to prevent permafrost degradation

V.A. Ilyichev
Russian Academy of Architecture and Construction Sciences, Moscow, Russia

N.S. Nikiforova
National Research Moscow State University of Civil Engineering, Moscow, Russia

A.V. Konnov
Scientific-Research Institute of Building Physics of the Russian Academy of Architecture and Construction Sciences, Moscow, Russia

ABSTRACT: In cryolithozone the problem of buildings and structures adaptation to the increasing climate warming is relevant. Solutions based on thermal insulation of permafrost are being developed. The purpose of this study was to evaluate the effectiveness of a foamed polyethylene (FP) insulation in the base of a building on a pile foundation. For 2022-2092, taking into account the climate warming, a forecast of the temperature in the soil base and piles bearing capacity was carried out in the Frost 3D software. Results shows that FP installation keeps the base in a frozen state and reduce the rate of the seasonally thawed layer increase (in 2052, it's 2.7 m more outside the building). However, the average annual permafrost temperature raises (by 1°C in 2042). The piles bearing capacity increases up to 10% and 50% (improper building maintenance in last case) with FP installed.

1 INTRODUCTION

The Earth's climate is changing and global warming occurs according to the most pessimistic scenario: the intensity and speed of changes are much greater than the previous estimates of the scientific community suggested. In 2010-2019, there was a global increase in surface air temperature by 0.9-1.2 °C. Temperature growth is observed in almost all regions. Warming in the Arctic region is predicted to be twice as strong as the global average (IPCC, 2021).

An urgent issue is the adaptation of buildings and structures located in the cryolithozone to current and predicted climate changes. Solutions based on the use of thermal insulation materials are common. Installation of thermal insulation on permafrost soils is used in railways (Ashpiz et al. 2008) and highways (Bessonov et al. 2022), industrial and civil construction (Ilyichev et al. 2003; Alekseev, Konash, Khrustalev 2018; Nikiforova & Konnov 2022), in mining (Goncharov & Belchenko 1998).

There are solutions for the I principle of construction on permafrost soils (preserving the frozen state) with the use of strip foundations on sand embankment with thermal insulation (Alekseev, Konash, Khrustalev 2018).

The purpose of this study is to evaluate the effectiveness of a foamed polyethylene (FP) insulation in the base of a building on a pile foundation.

Advantages of FP are low average density and thermal conductivity, high elasticity, sufficient strength characteristics, resistance to aggressive media. This material is suitable for use in systems operating at low (up to -60 ° C) and alternating temperatures (Semenov et al.

DOI: 10.1201/9781003299127-270

2018). FP is steam- and moisture-proof (Zhukov, Ter-Zakaryan, Bessonov et al. 2018). A heat-reflecting foil layer can be applied to its surface, increasing its resistance to ultraviolet radiation, protecting it from moisture ingress under the insulation and mechanical damage.

2 RESEARCH METHOD

The forecast of the temperature distribution in the soil base was carried out numerically using the Frost 3D software for thermal calculations of soils (Kovalenko, 2013; Gordiychuk, 2017).

The study used the results of engineering geological investigations and temperature measurements of the soil to a depth of 15 m at construction site in the Oktyabrsky district of Yakutsk. Soil thermal properties are given in Table 1. The soil profile of the model is presented in Figure 1.

Table 1. Soil thermal properties.

Soil type	Volumetric heat capacity, kcal /m^3 °C		Thermal conductivity coefficient, kcal/ h m °C		Freezing point $T_{bf,}$ °C
	unfrozen soil C_{th}	frozen soil C_f	unfrozen soil λ_{th}	frozen soil λ_f	
Anthropogenic soil fine sand, strongly saline	670	510	1.85	2.05	-2.1
Lean and silty clay soft, moderately saline	720	520	1.25	1.35	-1.2
Sand fine and medium, moderately saline	750	560	2.15	2.35	-0.7
Silty clay frozen, weakly saline	800	560	1.55	1.60	-0.7
Sand fine frozen, weakly saline	720	520	1.65	1.85	-0.3
Sand medium frozen, weakly saline	750	560	2.15	2.35	-0.6
Sand fine frozen	660	490	1.65	1.85	-0.2

Zero heat flux (q=0) was set at the lower and lateral boundaries of the calculated area. The dimensions of the calculated area were selected from the condition that the temperature distribution at the lateral boundaries should be similar to the distribution obtained during the calculation without taking into account the thermal effects of the modeled objects. A soil mass with a depth of 15 m (according to Russian standard SP 446.1325800.2019 "Engineering geological investigations for construction. General rules" and results of investigations) and a plan size of 26 x 32 m was modeled.

Modeling was carried out on the basis of the concept developed by TEPOFOL company to protect the pile foundation of a building designed according to I principle of construction on permafrost (preserving its frozen state) with the FP insulation. This concept assumes installation of a horizontal FP layer under a residential building with an open ventilated space and beyond its borders. At some distance from the building along its perimeter to the permafrost at 2,1 m depth, a vertical layer of FP is arranged (Figure 1). The insulation is installed out of rolls, its edges are sealed with a lock joint, which is sticked together with a construction fan. A protective layer of soil is provided above the insulation.

When modeling the FP, the following thermophysical properties were set, provided by TEPOFOL company: thermal conductivity coefficient $\lambda_{th} = \lambda_f$ = 0,039 Вт/(м·°С), ρ = 25 kg/m^3. Volumetric heat capacity was $C_{th} = C_f$ = 33,5 kJ/(m^3·°C).

A time interval of 70 years was modeled, starting from 2022 to 2092. Climatic conditions affecting heat exchange on the ground surface were set for Yakutsk according to long-term

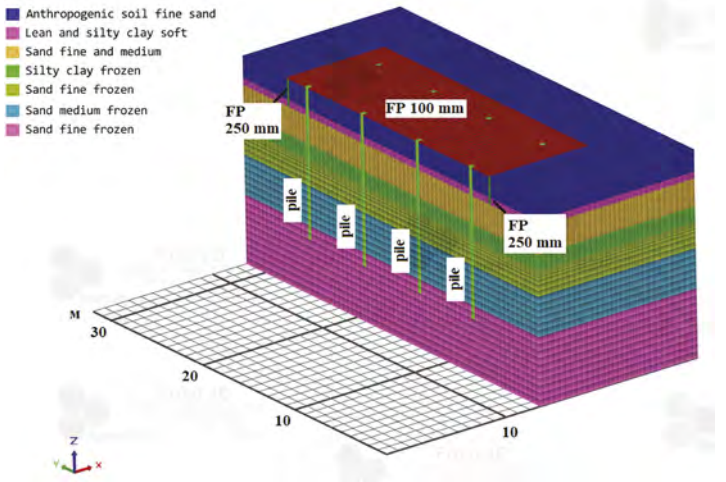

Figure 1. Cross section of the calculated area in the YZ plane.

observations given in SP 131.13330.2020 standard and the Climate of Russia reference book (Razuvaev et al. 2020).

Taking into account the small size of the studied area, a regional climate model of future climate changes in Russia of the Voeikov Main Geophysical Observatory was chosen as the source of the predicted temperature values (Kattsov et al. 2016,2019; Shkolnik & Efimov 2015). This model is characterized by a high spatial resolution (25 km). The trend of increasing surface air temperature for Yakutsk was determined according to the forecast map of anomalies of the Roshydromet Climate Center, based on ensemble calculations using this model, under the scenario of changes in the content of greenhouse gases and aerosols in the atmosphere RCP 8.5.

The prediction of changes in the bearing capacity of piles over time due to climate warming with installation of FP thermal insulation was made by numerical method in the Frost 3D software module called Frost.Pile. In this module the calculation of the bearing capacity of piles is implemented, according to SP 25.13330.2020 and SP 24.13330.2011 (in the case of thawed soils) Russian standards on the basis of the forecast thermal calculation performed in the Frost 3D. Within the problem considered in the article, the technology of pile construction was not taken into account in the thermal calculation. Calculation of the bearing capacity of piles in Frost.Pile is made in accordance with the SP 25.13330.2020 formula:

$$F_u = \gamma_t \gamma_c (RA + \sum_{i=1}^{n} R_{af,i} A_{af,i}) \quad (1)$$

where γ_t – a temperature coefficient that takes into account changes in the temperature of the base soils due to random changes in the outdoor temperature; γ_c – coefficient of working conditions of the base; R – calculated resistance of frozen soil under the lower end of the pile, kPa; A – the cross-sectional area of the pile, m^2; $R_{af,i}$ – calculated shear strength along the lateral freezing surface of the pile within the i-th soil layer, kPa; $A_{af,i}$ – the freezing surface area of the i-th soil layer with the side surface of the pile, m^2; n – the number of layers of permafrost soil selected in the calculation.

In the Frost.Pile module, the load-bearing capacity of a bored precast reinforced concrete pile located under the middle of the building was calculated. The pile is b = 0.35x0.35 m in size with a tip at the depth of 10 m. The load on the pile is 80 tons.

When calculating the bearing capacity of the pile, a constant value of the temperature coefficient γ_t = 0.851 was used, given in the work of Khrustalev L.N., Emelyanova L.V. (2013) for Yakutsk.

3 RESULTS

The installation of the FP layer (horizontal with a thickness of 100 mm and vertical – 250 mm at 2.1 m depth) in an open ventilated space under a building allows to keep its soil base in a frozen state. After 30 years the soil base begins to thaw under the influence of climate warming. In 2052 the thickness of the seasonally thawed layer (STL) outside the building will be 3 m, under the building – 0.3 m (Figure 2).

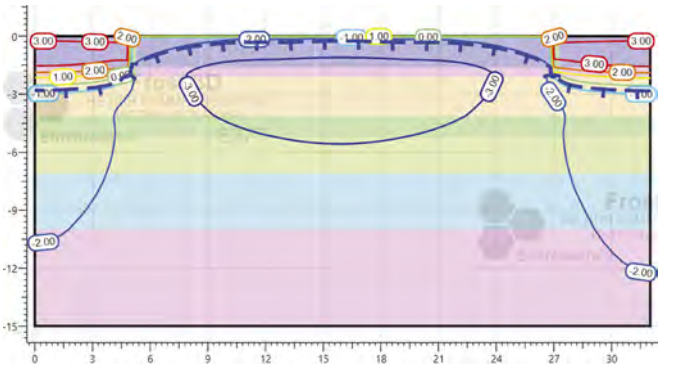

Figure 2. Temperature distribution in the soil mass for 2052 (for a building with an open space under it after 30 years of operation) in the warm season (September) with the FP layer (the thickness of the horizontal layer is 100 mm, the vertical layer is 250 mm to a depth of 2.1 m).

The horizontal layer of the FP reduces the cooling effect of the ventilated space under a building on its soil base in winter. The average annual temperature of permafrost soil is increasing. In 2042 for the base of a building with an open ventilated space, it will be -3.4 °C without the FP installation and -2.4 °C with its installation.

The load-bearing capacity of piles of a building with an open ventilated space under it varies slightly when installing the FP. For a building which has a closed ventilated space with blowouts, the FP usage increases the bearing capacity of piles to 10% (Figure 3).

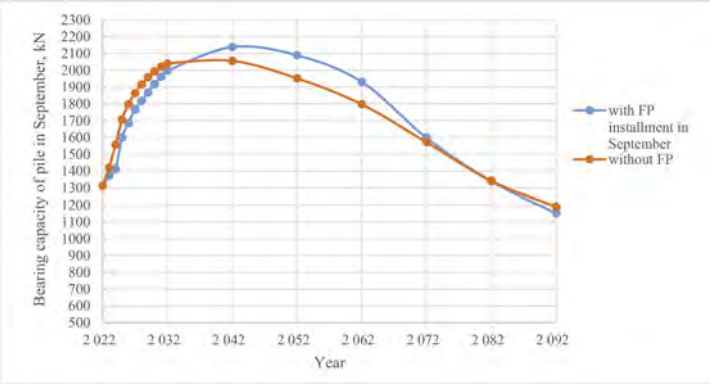

Figure 3. The bearing capacity of the pile in September for 70 years of a building operation (space under a building with blowouts closed for the summer) the thickness of the horizontal FP is 100 mm, the vertical one is 250 mm to a depth of 2.1 m.

The bearing capacity of piles was calculated based on the temperature distribution in the soil mass for the case when there is improper maintenance of a building with an open ventilated space and a snow cover is formed over the insulation. With the FP installed, a significant increase in the bearing capacity of piles (up to 50%) was obtained (Figure 4), which allows

extending the life of a building and reducing the designed number of piles. This increase in load-bearing capacity will be especially evident for existing buildings with the specified improper maintenance. The use of FP for existing buildings is the subject of further research.

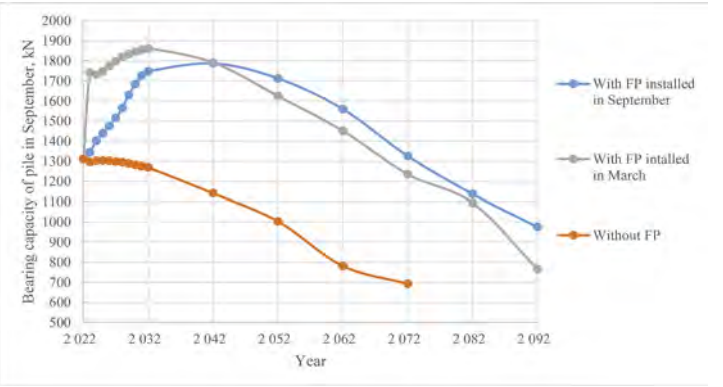

Figure 4. The bearing capacity of the pile in September for 70 years with improper maintenance of a building in winter (snow builds up in open space under it) with a thickness of the horizontal layer of the FP 100 mm, vertical – 250 mm to a depth of 2.1 m.

The installation time of the FP (September or March) in the first 10 years leads to a difference in the bearing capacity of piles from 20 to 10% (larger values are for March). In subsequent years of the building operation, the time of FP installation basically does not affect the temperature distribution in the soil mass and, accordingly, the bearing capacity of piles (the difference is up to 7%).

4 CONCLUSION

Numerical modeling of the soil temperature regime in the Frost 3D software with thermal insulation made of foamed polyethylene (FP) in geological conditions of Yakutsk showed the following:

1. The installation of the FP layer under a building with an open ventilated space allows to keep its soil base in a frozen state. After 30 years the base begins to thaw under the influence of climate warming; in 2052 the thickness of the seasonally thawed layer outside the building will be 3 m, under it - 0.3 m. Horizontal layer of the FP reduces the cooling effect of the ventilated space under a building on its soil base in winter. The average annual temperature of permafrost soil is increasing. In 2042 for the base of a building with an open ventilated space, it will be -3.4 °C without the FP installation and -2.4 °C with it.
2. The load-bearing capacity of piles of a building with an open or closed ventilated space with blowouts varies slightly when installing the FP (up to 10%). For the case when there is improper maintenance of a building (snow builds up in ventilated space) a significant increase in the bearing capacity of piles (up to 50%) is obtained, which allows extending the life of a building and reducing the designed number of piles.
3. The installation time of the FP (September or March) in the first 10 maintenance years of the building leads to a difference in the bearing capacity of piles from 10 to 20% (with larger values in March), but later the difference decreases.

REFERENCES

Alekseev, A.G., Konash, V.E., Khrustalev, L.N. 2018. Use of low-rise building foundations on heat-insulated sand pads in permafrost regions. *Soil Mechanics and Foundation Engineering 55 (2):* 134–138.

Ashpiz, E.S. et al. 2008. Using of synthetical thermal insulators for conservation of frozen soil conditions in the base of railway embankment. *Earth`s Cryosphere* 12(2): 84–89.

Bessonov, I.V. et al.2022. Analysis of design solutions depending on the type of insulating materials in road pavements in permafrost soils. *Transport construction* 1: 14–17.

Goncharov, S.A. & Belchenko, E.L. 1998. Thermal insulation of thawed gold-bearing sands, provided that they are allowed to freeze to a given depth. *Gornyj Informacionno-Analiticheskij Byulleten'* 6: 28–32.

Gordiychuk, V.V. 2017. Computer simulation of permafrost thermal regime under the thermal influence of engineering constructions and cooling units. *XI International Symposium on Permafrost Engineering: Book of abstracts, Magadan,* 5–8 *September 2017*. Magadan: Melnikov Permafrost Institute.

IPCC, 2021: *Climate Change 2021: The Physical Science Basis. Contribution of Working Group I to the Sixth Assessment Report of the Intergovernmental Panel on Climate Change*. Cambridge, United Kingdom and New York, NY, USA: Cambridge University Press.

Ilyichev, V.A. et al. 2003. *Prospects for the development of settlements in the North in modern conditions*. Moscow: Russian academy of architecture and construction sciences.

Kattsov, V.M. et al.2016. Development of the technology of probabilistic forecasting of the regional climate on the territory of Russia and the construction of scenario forecasts of changes in climate impacts on economic sectors on its basis. Part 1: Problem statement and numerical experiments. *Proceedings of Voeikov Main Geophysical Observatory* 583: 7–29.

Kattsov, V.M. et al.2019. Development of the technology of probabilistic forecasting of the regional climate on the territory of Russia and the construction of scenario forecasts of changes in climate impacts on economic sectors on its basis. Part 2: Climate impact assessments. *Proceedings of Voeikov Main Geophysical Observatory* 593: 6–52.

Khrustalev, L.N. & Emel'yanova L.V. 2013. Determination of the temperature coefficient for calculation of the bearing capacity of permafrost beds in a changing climate. *Soil Mechanics and Foundation Engineering* 1: 14–16.

Kovalenko, V. I. 2013. The application of Frost 3D software to modeling of three-dimensional temperature distribution in permafrost soil for its thermal stabilization. *Journal of oil and gas construction*. 3: 14–18.

Nikiforova, N.S. & Konnov A.V. 2022. The effectiveness of the use of foam glass to prevent soil degradation in the cryolithozone. *Soil mechanics in geotechnics and foundation engineering; Proc. intern. conf., Novocherkassk, 28–30 September 2022*. Novocherkassk: Lik.

Razuvaev, V.N. et al.2020. *Climate of Russia*. Obninsk: VNIGMI-MCD.

Semenov, V.S. et al.2018. Features of realization of insulation systems under conditions of the far North. *Stroitel'nye Materialy (Construction Materials*) 4: 65–69.

Shkolnik, I.M. & Efimov, S.V. 2015. A new generation regional climate model for Northern Eurasia. *Proceedings of Voeikov Main Geophysical Observatory*. 576: 201–211.

Zhukov, A.D., Ter-Zakaryan, K.A., Bessonov, I.V. et al.2018. Systems of construction insulation with the use of foam polyethylene. *Stroitel'nye Materialy (Construction Materials*) 9: 58–61.

Smart Geotechnics for Smart Societies – Zhussupbekov, Sarsembayeva & Kaliakin (Eds)
© 2023 The Author(s), ISBN 978-1-003-29912-7
Open Access: www.taylorfrancis.com, CC BY-NC-ND 4.0 license

Composite anti-frost heaving pile

A.V. Boyarintsev, K.M. Astashkevich & S.V. Lanko
Saint Petersburg State University of Architecture and Civil Engineering, Saint Petersburg, Russia

ABSTRACT: Frost heave is a widespread phenomenon for northern countries, especially for Russia. The soil increases its volume and influence the foundation of building during soil freezing. This effect is most dangerous for low weight buildings. The using of anchoring is most effective solution for protection the building foundation against frost heave force impact. In this paper, the new solution for protection of building foundation is shown. This solution is composite anti-frost heaving pile. The main idea is described. The results of researches show effectiveness of using this type of piles.

1 INTRODUCTION

The Far North, Siberia and the Far East are the main development regions of the Russian Federation. The wealth of these regions with natural resources, minerals and the tourism potential, encourage the government of the Russian Federation, as well as the management of large companies to develop these territories. The success of regional development directly depends on the reliability for buildings and structures erected in these territories.

The soil conditions of Russia, as in any other countries, have some features due to the history of the origin of soils, climate and other factors. One of such features that Russian geotechnical engineers must consider is the phenomenon of frost heave, which is widespread throughout the country. Freezing to depths of 0.5 meters in the southern regions, up to 3.5 meters in the Far North and Far East, the soils increase in volume and affect the structures immersed in them. According to studies (Boyarintsev 2019), frost heave in 20% of cases is the cause of accidents of civil buildings located on frozen soils, and in 35% - of infrastructure facilities. According to Russian Railways reports (Tsvigunov 2018), 48% of the pylons of catenary system operated on the Far Eastern railway are in disabled condition, and one of the main reasons is frost heave.

Thus, the development of structures that effectively resist frost heave is one of the key factors to increase the reliability of buildings and constructions, and, as a result, the successful development of these regions.

2 METHODS OF FROST HEAVE PREVENTION

Copy All methods of frost heave prevention can be divided into three main groups: thermal, ameliorative and constructive (Karlov 2007).

The most effective and popular are constructive ones that allow to change the parameters of the foundation structure so that the intensity of shearing heaving stresses decreases, and the efficiency of their acceptance increases. The main types of constructive methods are the reduction of an adfreezing area, sprinkling, reduction of adfreezing strength between the freezing soil and the foundation material, anchoring of underground structures in soil layers that are not subject to freezing and the device of inclined faces.

DOI: 10.1201/9781003299127-271

According to the previously mentioned report (Tsvigunov 2018), 80% of deformed buildings have a post footing, and only 8% are piled foundation. Thus, using piled foundations, a constructive method of protecting the foundation from the impact of shearing heaving stresses is implemented, namely anchoring. In addition, in practice, two or three constructive methods can be implemented simultaneously, and such piles are called anti-frost heaving piles.

Nowadays there are several options for the construction of anti-frost heaving piles. They are concrete pile covered with polymer compound; concrete and steel piles covered anti-frost heaving lube oils BAM-3 and BAM-4 or heat-shrinkable modified polyethylene (Alyavdin et al. 2013) in the area of contact with the active layer.

To upgrade the anchoring properties, any of the known methods of increasing the total bearing capacity of piles can be applied, for example: screw piles with one or more screws, welding of scrap metal (Iospa et al. 2015) or screws (Noskov & Svidersky 2019) for steel piles and transverse ribs with a certain fin pitches for concrete piles. The dimensions of these transverse ribs are larger than pile shaft. The ribs are made when concreting piles by filling cavities on the inner surface of a special formwork with concrete (Naberezhny & Savvina 2016).

Pyramidal concrete double-tapered piles (Figure 1a) are also anti-frost heaving ones. Their peculiarity is the variation of face slope across the length. So, in the zone of the active layer, the pile widens from top to bottom, thereby implementing a constructive method of frost heave prevention, and further, below the active layer, it narrows, which provides an increase in the bearing capacity under the compressive load (Dobrynin et al. 2004, Dobrynin & Yushkov 2013). A similar principle is realized in a steel anti-frost heaving pile (Figure 1b).

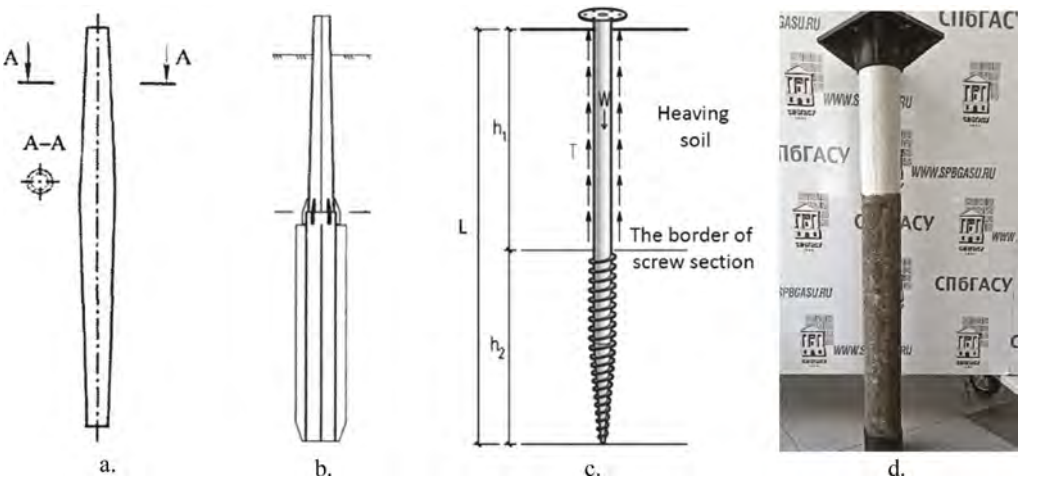

Figure 1. Caption of a typical figure. a. Pyramidal double-tapered pile (Dobrynin & Yushkov 2013) b. Steel anti-frost heaving pile (Romanov & Kasatkin 2018) c. Screw tapered pile (Noskov & Svidersky 2019) d. Composite anti-frost heaving pile (Boyarintsev 2020b).

Despite the effectiveness of countering shearing heaving forces, the described designs have some disadvantages: the lube oils BAM-3 and BAM-4 are difficult to fix on the pile shaft securely; heat-shrinkable anti-frost heaving hoses have insufficient adhesion to the pile material; concrete piles are not always economical, since pyramidal double-tapered and ribbed piles are labour-consuming in manufacturing.

Analyzing the shortcomings of the described solutions, the author proposes a new design of an anti-frost heaving pile which preserves all the principles of present structures and is devoid of their main disadvantages (Boyarintsev 2020b) (Figure 1. d). The main difference of the

proposed pile is that its body is made of composite pipe. As a material, it is proposed to use a pipe made by filament-winding technique or pultrusion (Galinovsky et al. 2019) of a polymer composite material (PCM) such as glass-fiber or basalt-fiber reinforced polymer or a combination of them.

Due to the increased corrosion resistance, the internal space of the pile can remain empty, and all external loads will be supported by the composite pipe. If the pipe's own strength and rigidity are insufficient, the interior space can be filled with concrete or reinforced concrete.

The mechanical properties of a composite pipe are enough to perceive an axial compressive load, as demonstrated by an experiment in which a composite hollow pipe, a concrete cylinder and a composite pipe filled with concrete were tested. The results show that the ultimate compressive stress supported by the composite pipe is 132 MPa, and the use of a composite shell as an external reinforcement of a concrete cylinder contributes to an increase in the ultimate compressive load on a concrete sample from 30 to 62 MPa.

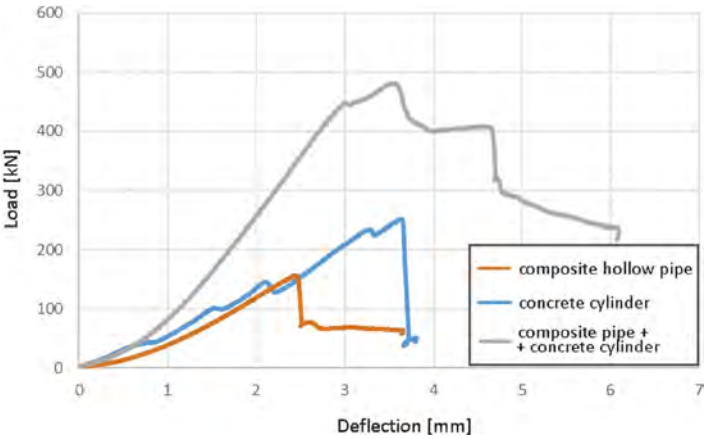

Figure 2. Testing samples for axial compression.

The recommended method of pile driving in permafrost soils is drilling - the most common method of pile placement in in permafrost. It is recommended to fill the spaces between the hole and the pile with sand-cement mortar, or with drilled sludge.

The anti-frost heaving properties of the pile are achieved through the simultaneous application of three methods of countering shearing heaving forces: reduction of the adfreezing strength of the soil and pile in the active layer; anchoring in the soil layers below the active layer; reducing the frost depth.

The decrease in adfreezing strength from the use of polymers is also confirmed by the author's experiments (Boyarintsev & Lanko 2019b). 6 samples of fiberglass, in the form of rings with a diameter of 100 mm and a height of 50 mm, made by pultrusion, and 8 samples of steel hot-rolled seamless tube, were accepted for comparison. The samples were filled with the same clay soil, frozen and then tested according to the method (Boyarintsev 2020a). The experiment was carried out conditionally instantly, with a stem shifting speed of 5 mm per second. The test results show that adfreezing strength of fiberglass samples is 28% lower in relation to steel, and 42% lower in relation to concrete.

The improvement of the anchoring properties of the pile can be achieved by increasing its bearing capacity in the ground by the method (Boyarintsev & Lanko 2019b). In continuation of the experiment described earlier, 6 fiberglass samples were tested, the inner surface of which was covered with sand with a particle size of at least 2 mm. The test results show that adfreezing strength of these samples is 30% higher than adfreezing strength of steel and is comparable

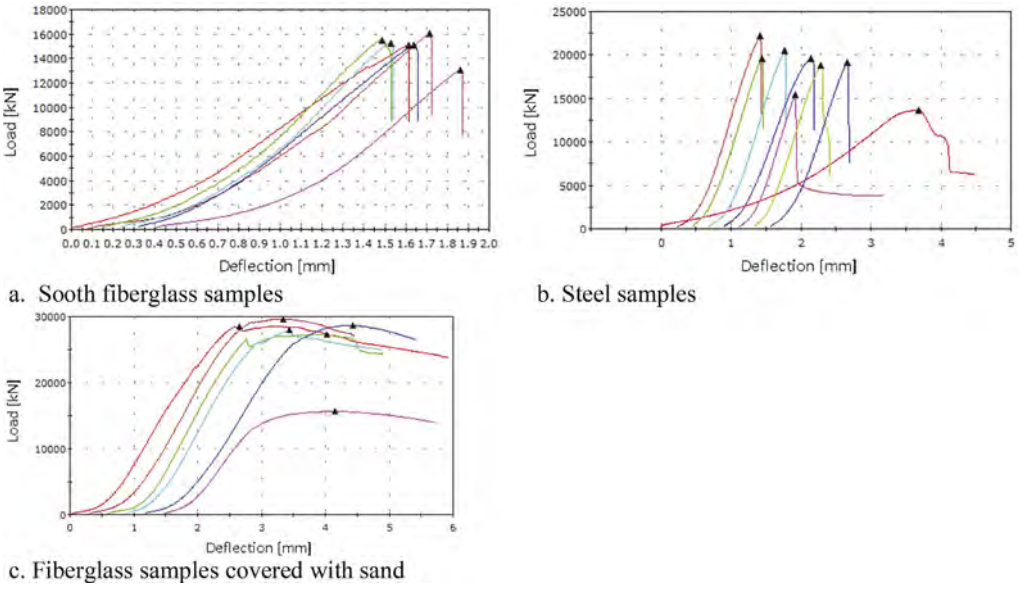

Figure 3. Adfreezing strength results.

to concrete. At the same time, the cut occurred not on the surface of the material-soil, but soil-soil, as evidenced by the nature of the test curve (Figure 3).

3 ADVANTAGES OF ANTI-FROST HEAVING PILES

Numerical simulation of the soil freezing process around single fiberglass and steel piles shows that a funnel of frozen soil is formed around the steel pile, the height of which varies from 20 to 5% of the freezing soil depth over a period of negative temperatures, while this funnel does not form at all around the anti-frost heaving composite pile (Boyarintsev & Zybtseva 2019) (Figure 4). This is because the fiberglass thermal conductivity is less than the soil thermal conductivity, and significantly less than the steel one. Thus, the use of composites helps to reduce the freezing depth, and, accordingly, the shearing heaving stresses. In addition, the curvature of the freezing front towards the pile contributes to the migration of moisture to the material surface, which is confirmed by numerical calculations (Kudryavtsev 2004). Water fills all voids at the pile-ground boundary, which entails an increase in adfreezing strength when it freezes. If the funnel does not form, the described effect is also excluded.

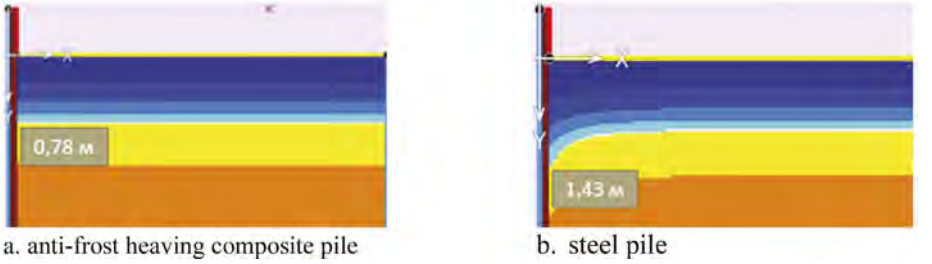

Figure 4. Distribution of soil temperatures around.

Thus, the use of the anti-frost heaving composite pile eliminates the need to apply additional material that reduces adfreezing strength in active layer, since the composite already has the necessary properties; it increases anchoring properties without requiring complex and expensive technological operations and also excludes the occurrence of a funnel from the frozen or thawed soil around the pile, which complicates the process of analytical assessment of heaving.

The advantage of anti-frost heaving composite pile compared to traditional pile materials is their strength–to–unit weight ratio. So, for concrete grade B25, this coefficient is 0.74, for steel 4.37, and for fiberglass 13.17. This ratio can affect the reduction of costs when delivering materials to the construction site, which becomes most relevant when building in hard-to-reach areas of the Far North and the Far East. Corrosion resistance of composite piles will extend the service life of the buildings erected on them and reduce the operating costs for maintaining the structure in a working condition.

4 CONCLUSION

Anti-frost heaving pile is an effective tool in protecting the foundations of buildings from the negative effects of frost susceptible soils. Its effectiveness is realized due to three features of structure and properties of the materials used. The first of them is the low thermal conductivity of the composite which the pile body is made of. This property allows the pile to prevent the intensive advance of cold into the soil mass and reduces the contact area of the pile with the frost susceptible soil. The second one is the hydrophobic properties of polymer which is the basis of the composite used. It allows to reduce adfreezing strength, which is applied to the pile in the active layer zone. And the third feature is a high roughness of the pile surface in the anchor zone, which increases the bearing capacity. In addition to the above, it should be noted such beneficial properties of polymer composites as corrosion resistance, low unit weight and significant strength. Due to these aspects, anti-frost heaving piles are prospective for implementation in geotechnical construction.

REFERENCES

Alyavdin, D.V. 2013. Determination of the effectiveness of the use of radiation-modified polyolefin coatings of foundations to reduce the freezing and the forces of frost heaving soils. *Bulletin of the Technological University*: 136–139.

Alyavdin, D.S. & Kuzmin, A.V. 2017. Pile with anti-buckling shell. Patent of the Russian Federation No. 170032.

Boyarintsev, A.V. 2019. A representative analysis of the experience of building foundations on permafrost soils. *Bulletin of Construction and Architecture*: 57–68.

Boyarintsev, A.V. 2020a. A method for determining the soil freezing strength. Patent of the Russian Federation No. 2749226.

Boyarintsev, A.V. 2020b. Composite anti-frost heaving pile. Patent of the Russian Federation No. 205047.

Boyarintsev, A.V. & Lanko, S.V. 2019a. A method of increasing the bearing capacity of the pile on the ground. Patent of the Russian Federation No. 2720595.

Boyarintsev, A. V. & Lanko, S. V. 2019b. Experimental estimate of instantaneous adfreeze strength of glass-fiber reinforced plastic in frozen soil. *Geotechnics Fundamentals and Applications in Construction* – Mangushev et al. (Eds): 49–53. London: Taylor & Francis Group.

Boyarintsev, A.V. & Zybtseva, A.V. 2019. The influence of the pile foundation material on the soil freezing depth. *Actual problems of modern construction: materials of the 72nd All-Russian Scientific and Practical Conference of Students, Postgraduates and Young Scientists in two parts*: 119–130. Saint Petersburg: St. Petersburg University of Architecture and Civil Engineering.

Galinovsky, A.L. & Bochkarev, S.V. & Nelyub, V.A. 2019. Technologies of production and diagnostics of composite structures of aircraft. *Stary Oskol*: 384.

Dobrynin, A.O. & Yushkov, B.S. 2013. The method of calculating the frost heaving forces and the size of the foundation choice in the form of a two-conical piles bush. *Roads and bridges*: 204–223.

Dobrynin, A.O. & Yushkov, B.S. & Repetsky, D.S. 2004. Piles for freezing soils. *Housing construction* (8): 10–12.
Iospa, A.V. & Aksenov, V. I. & Shmelev, I. V. 2015. Some test results of anti-heaving and anti-corrosion coatings for the protection of steel foundations on permafrost soils. *Basal complexes, foundations and soil mechanics* (5): 27–31.
Karlov, V. D. 2007. Foundations and foundations on seasonally freezing heaving soils: 362. Saint Petersburg: St. Petersburg State University of Architecture and Civil Engineering.
Kudryavtsev, S.A. 2004. Computational and theoretical justification of the design and construction of structures in conditions of freezing heaving soils: 344. Saint Petersburg: St. Petersburg State University of Architecture and Civil Engineering.
Naberezhny, A.D. & Savvina, A. E. 2016. Experimental studies of models of hanging piles in frozen soils and methods of increasing their bearing capacity. *Industrial and Civil Engineering* (8): 70–74.
Noskov, I.V. & Sviderskikh, A.V. 2019. The work of screw cone-spiral piles in conditions of frosty heaving of soils. *Bulletin of Civil Engineers* (1): 67–75.
Romanov, P.I. & Kasatkin, S.P. 2018. Anti-frost heaving pile. Patent of the Russian Federation No. 181501.
Tsvigunov, D. G. 2018. Interaction of seasonally freezing soils with foundations of vertical core elements: 24. Moscow: Russian University of Transport (MIIT).
Zemlyansky, A. A. 2003. A screw-shaped pile and the method of its construction. Patent of the Russian Federation No. 2278211.

Smart Geotechnics for Smart Societies – Zhussupbekov, Sarsembayeva & Kaliakin (Eds)
© 2023 The Author(s), ISBN 978-1-003-29912-7
Open Access: www.taylorfrancis.com, CC BY-NC-ND 4.0 license

Artificial ground-freezing with liquid nitrogen: A field test and numerical simulations

Fuchen Teng & Yong Cheng Sie
Department of Civil and Construction Engineering, National Taiwan University of Science and Technology, Taiwan

Chihping Kuo
Department of Civil and Construction Engineering, National Yunlin University of Science and Technology, Taiwan

Jhih-Yong Jhang
Geotechnical Department of Engineering Division, CTCI Resources Engineering Inc, Taiwan

Jung-Tai Lee
Department of Forestry and Natural Resources, National Chiayi University, Taiwan

Bin-Chen Benson Hsiung
Department of Civil Engineering, National Chung Hsing University, Taiwan

ABSTRACT: Artificial ground-freezing method is an advanced ground improvement technique. It uses artificial freezing to improve soil strength and impermeability. The cold source can be divided into brine and liquid nitrogen (LN_2). However, most studies focus on brine systems, the LN_2 method utility and the frost heave are still not well understood. To explore the applicability and frost heave of LN_2 freezing technology, a field test with LN2 freezing system is conducted. The freezing behavior and frost heave were observed according to the ground settlement and inclinometer deformation. Numerical simulations on soil frost heave were performed by PLAXIS with Frozen and Unfrozen soil model (FUS), the monitoring results are compared with numerical analysis and geophysical explorations. The results show that the LN_2 methods can effectively and quickly form frozen soil walls. The thickness of the frozen soil wall reaches 1.2m in 6 days through PLAXIS FUS model back analysis. Moreover, subsurface temperature and media changes are detected by geophysical exploration, explaining the freezing results.

1 INTRODUCTION

Artificial ground-freezing (AGF) is a particular temporary ground improvement method (Alzoubi et al., 2020). It involves introducing coolant into underground pipes to freeze groundwater in the soil. The frozen soil contacts together to form the frozen walls. The coolant of the AGF is divided into two types, brine and liquid nitrogen (LN_2). The brine freezing method is relatively low cost and long construction period. The circulating system (closed system) is used in this method with brine at -30 to -40°C. The LN2 freezing method uses a much lower temperature coolant, which is -196°C, with a direct expansion system (open system).

Although the AGF technology has been developed for decades, most research still focuses on the brine freezing method. The LN2 method utility and the frost heave displacement prediction are still not well understood. Moreover, the estimated development of underground frozen walls in the past was inferred by the trend of temperature change, which didn't consider

DOI: 10.1201/9781003299127-272

the mechanical behavior of frozen soil. To tackle these problems, the Norwegian University of Science and Technology (NTNU) and Plaxis B.V. cooperative developed a new numerical model, the Frozen and Unfrozen soil (FUS) model. Haxaire et al. 2017 first applied the FUS model to simulate the frost heave phenomenon caused by the chilled pipelines. Korshunov et al. 2020 calibration of the FUS model according to laboratory tests and in-situ monitoring results. Tuohion et al. 2021 modeled the effect of freeze-thaw on low-volume roads.

The main objective of this research is to explore the applicability and frost heave of LN2 freezing technology. Therefore a field test using an LN2 freezing method is conducted. The freezing behavior and frost heave were monitored and recorded according to ground settlement and inclinometer deformation. Numerical simulations on soil frost heave were performed by FUS mode, and the monitoring results were compared with numerical analysis and geophysical explorations.

2 FIELD TEST: LIQUID NITROGEN FREEZING METHOD

The profile of the field test is shown in Figure 1(a). The field test was conducted for a week in Yilin, Taiwan. The test location was next to the pond to ensure the stability of the groundwater level. The LN2 was supplied by a tank car. The white smoke position was the discharge end of the LN2 system. The site soil consisted of a 1.8 m cobbles backfill near the surface and a silty clay layer below 1.8 m. The groundwater level was at a depth of 1.6 m.

In the test, nine vertical freezing pipes were installed in a row. The length of the pipes was 8 m. The four PT100 thermometers, twenty ground settlement points, and three inclinometers were set up around the pipes. The arrangement details are shown in Figure 1(b).

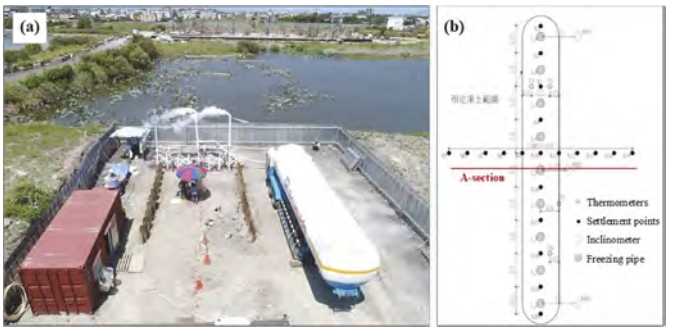

Figure 1. The liquid nitrogen freezing method field test (a) the profile, (b) the instrument arrangement details.

3 NUMERICAL SIMULATION: FUS MODEL

The FUS model is a critical-state elasto-plastic mechanical soil model. It was developed from the Barcelona Basic Model, which changed the idea of the unsaturated soil states to frozen/unfrozen states. The stress behavior is based on the mutual control of the cryogenic suction and the solid phase stress. In the FUS model, there were 28 input parameters. The parameters could be divided into four classifications. There were responsible for general, solid strain, suction strain, and the coupling effects between solid stress and cryogenic suction, respectively.

Because the FUS model was the PLAXIS 2D finite element code, the simulation was performed for the A-section in Figure 1(b). Depending on the results of the geological boring, the simulated soil layers were cobbles backfill and silty clay layer. Since the primary frost heave behavior occurs in the soil layer with sufficient water, the FUS model is used for the particle backfill and silty clay layer below the groundwater level. Most of the backfill layer was simulated using the MC model. The FUS model parameters in Table 1 were used in numerical simulation.

Table 1. The FUS model parameters were used in numerical simulation.

Parameter	Unit	Description	Backfill	Silty clay
G_0	N/m^2	Unfrozen soil shear modulus	1.33E6	2.1E6
κ_0	-	Unfrozen soil elastic compressibility coefficient	5.19E-3	4.7E-2
$E_{f,ref}$	N/m^2	Frozen soils Young's modulus at a reference temperature Tref	36E6	5.68E6
$E_{f,inc}$	$N/m^2/K$	Rate of change in Young's modulus with temperature	54E6	8.2E6
ν_f	-	Frozen soil Poisson's ratio	0.35	0.35
m	-	Yield parameter	1	1
γ	-	Plastic potential parameter	1	1
$(p^*_{y0})_{in}$	N/m^2	Initial pre-consolidation stress for unfrozen condition	120E3	150E3
p^*_c	N/m^2	Reference stress	100E3	100E3
λ_0	-	Elasto-plastic compressibility coefficient for unfrozen state	0.02	0.07
M	-	Slope of the critical state line	0.78	0.78
$(S_{c,seg})_{in}$	N/m^2	Initial segregation threshold	3.38E6	3.38E6
κ_s	-	Elastic compressibility coefficient for cryogenic suction variation	8E-3	8E-3
λ_s	-	Elasto-plastic compressibility coefficient for cryogenic suction variation	0.1	0.8
k_t	-	Rate of change in apparent cohesion with cryogenic suction	0.1	0.1
r	-	Coefficient related to the maximum soil stiffness	0.6	0.6
β	$(N/m^2)^{-1}$	Rate of change in soil stiffness with cryogenic suction	0.8E-6	0.8E-6

4 RESULTS AND DISCUSSION

4.1 *Analysis results*

Comparing the simulation result to monitoring the inclinometer displacement is shown in Figure 2(a). On the first day, the monitoring showed that the frost heave hadn't happened yet. Conversely, the cryogenic suction caused the water flow to slightly move the inclination tube. The FUS model accurately simulated this phenomenon. The output showed the direction of the water flow towards the inclination. The frost heave started occurring on the second day. In the last three days, the simulation value became little more than the monitoring, especially at a depth of 6 m. On day 6, the maximum monitoring value, 62 mm, was observed at a depth of 5.6m, and the maximum displacement of the simulation was 60 mm at 4.2 depth.

Figure 2(b) is shown the frozen soil walls' evolution below the groundwater level during the field test by numerical simulation. On the first day, the frozen walls appeared from the bottom of the freezing pipe, and the thickness was approximately 10 cm. From the second day, the frozen walls were produced on a large scale. The profile shape of the frozen walls was rectangular. The thickness reached 120 cm on the 6th day.

4.2 *Geophysical explorations discussion*

The numerical results showed that the simulation value at a depth of 6m is significantly larger than the monitoring result. The inclinometer monitoring displacement presented a double peak type. The discontinuity phenomenon was difficult to explain by numerical simulations. Thus, the geophysical exploration technique was used to investigate the underground situation. Through geophysical exploration, a large groundwater flow flowed 6m below the surface. Because the groundwater flow was at high speed and temperature, the frozen walls were difficult to produce. It reasonably explained the more significant displacement of the simulation.

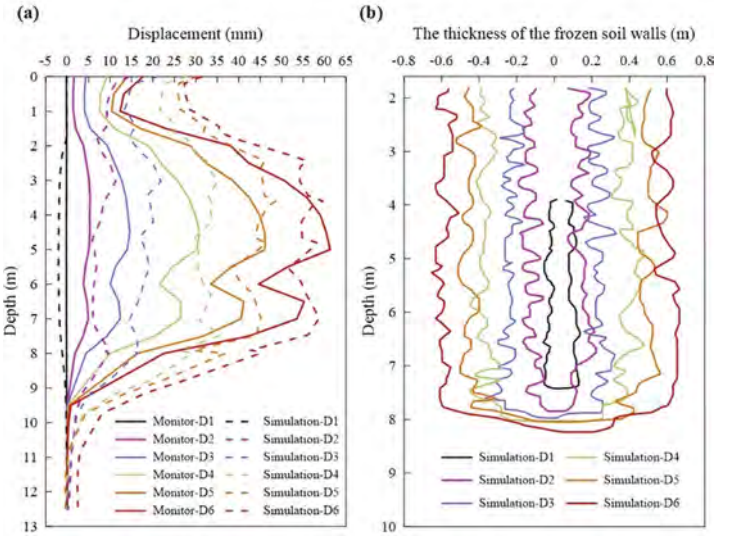

Figure 2. The simulation result (a) comparing the simulation result to monitoring the inclinometer displacement, (b) frozen soil walls' evolution below the groundwater level.

5 CONCLUSION

In this paper, the frozen soil behavior of the liquid nitrogen freezing method was studied using a field test and the FUS model in Plaxis 2D. The results show that the LN2 method can effectively and quickly form frozen soil walls rather than the traditional brine freezing method. The frozen soil walls provided strength and impermeability but also caused frost heave.

The FUS model was proven to be able to model complex multi-physical phenomena. It played a key role in understanding the LN_2 method utility and the frost heave. The thickness of the frozen soil wall reaches 1.2m in 6 days through PLAXIS FUS model back analysis. The inaccurate simulation was also reasonably explained by geophysical exploration. In summary, the utility of the liquid nitrogen method can be anticipated in the future, and reliable behavioral predictions will be obtained through the FUS model.

REFERENCES

Alzoubi, M.A., Xu, M., Hassani, F.P., Poncet, S., Sasmito, A.P., Artificial ground freezing: A review of thermal and hydraulic aspects. Tunnelling and Underground Space Technology. Volume 104.

Haxaire, A., Aukenthaler, M., Brinkgreve, R.B.J., Application of a Thermo-Hydro-Mechanical Model for Freezing and Thawing. Procedia Engineering. Volume 191.

Korshunov, A.A., Churkin, S.V., Nevzorov, A.L., Calibration of PLAXIS Frozen/Unfrozen Soil Model According to Results of Laboratory Tests and In-situ Monitoring. Transportation Soil Engineering in Cold Regions. Volume 2: pages 105–120.

Tuohino, M., Solowski, W., Abed, A., Koivisto, K., Lei, X., Application of the Frozen and Unfrozen Soil model to modelling effects of freeze-thaw on low-volume roads. IOP Conf.

Smart Geotechnics for Smart Societies – Zhussupbekov, Sarsembayeva & Kaliakin (Eds)
© 2023 The Author(s), ISBN 978-1-003-29912-7
Open Access: www.taylorfrancis.com, CC BY-NC-ND 4.0 license

Detailed hydrogeological models to evaluate the risk of reactivating contaminations when re-construction harbor areas in urban environments

T.R. Andersen, A.B. Medhus & S.E. Poulsen
R&D center for Built Environment, Energy, Water and Climate, VIA University College, Horsens, Denmark

ABSTRACT: The increasing population density often leads to the development of areas previously omitted due to construction risks such as e.g., harbours. Typically, the redevelopment includes establishing both green, blue, and grey infrastructure components. However, city planners are faced with multiple challenges as the reconstruction of the harbour areas in conjunction with insufficient knowledge about the geological and hydrological setting introduces significant uncertainties in the groundwater level. They can potentially mobilize existing soil contamination previous considered less critical and immobile due to a location above the groundwater table. The study aims to use borehole data, geophysics, and GIS information to construct high-resolution hydrogeological models. The models serve as the basis for simulating the contamination transport in relation to the new harbour constructions. This paper presents the results of such modelling for the area of Horsens harbour as an example for inspiration.

1 INTRODUCTION

In 2050 UN estimates that more than 65 % of the world's population will live in urban areas. As cities expand, former industrial areas such as harbors are being urbanised due to the social and economic opportunities they present (Andersen et al., 2020; Cen et al., 2020; Loures, 2018; Weng et al., 2019). Horsens, like many other small to medium size coastal cities, are developing the harbor area. Traditionally harbor areas were the key infrastructure and the perfect location for industries depending on external resources. This former use has left many harbors area highly contaminated. As the value of a view to the sea has increased tremendously and a location near city centers is considered attractive the former industrial harbor areas are in many places converted to attractive residential areas. This is also the case for the Horsens harbor area. In this transformation the sins of the past must be assessed in order to make sure the contaminants will not get in contact with the new residents. Prior to construction works, the subsoils are investigated, and the location and concentrations of contaminants are mapped. This mapping provides a picture of the actual situation at the time of construction. In the evaluation, though, it is often forgotten that construction works alter the subsurface situation potentially changing the hydrological situation in the area which may cause contaminants to become mobile and hence affect new areas. In the Horsens Harbor case, due to the new construction, the entire sheet pile made of wood was changed to an impermeable steel sheet pile wall and a canal was excavated inland. The location of the canal is shown in blue in Figure 1.

This paper presents the result of contaminant transport modeling for the contaminated area of Horsens harbor recently transformed from an industrial to a residential area, Figure 1. Calculations were carried out for two scenarios:

- The original situation prior to construction, renovation and remediation works
- The situation after construction, renovation and remediation works

DOI: 10.1201/9781003299127-273

The purpose was to assess the impact of the development of the Horsens harbor area on the location and flow of contamination in the area.

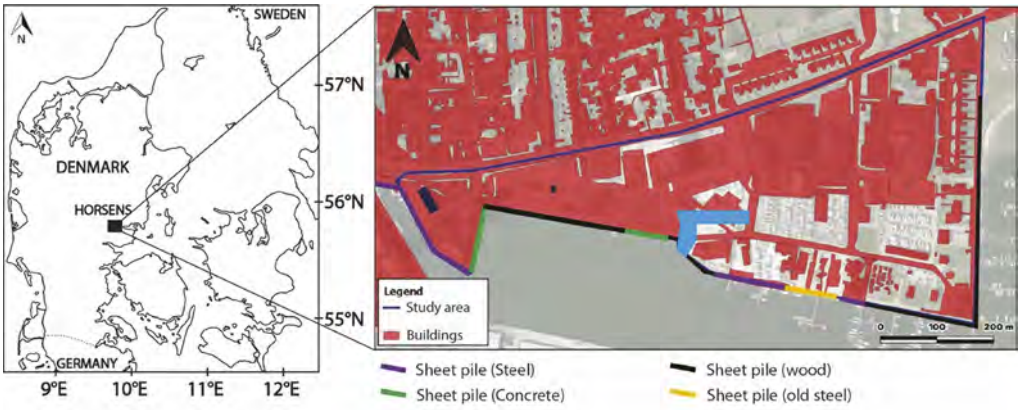

Figure 1. Overview map.

2 DATA AND METHODOLOGY

2.1 *Data*

Data included for interpretation of the hydrogeological model is shown in Figure 2. A detailed elaboration of the data can be found in Andersen et al. 2020.

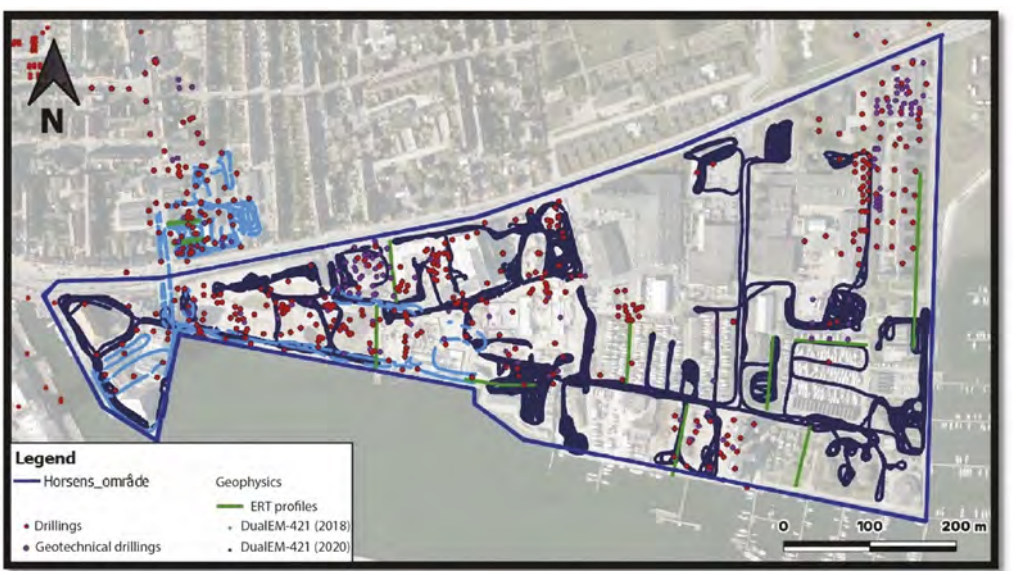

Figure 2. Input data for the hydrogeological model. The blue polygon outlines the area of investigation. dark blue and light blue dots which appears connected as lines shows where Dual-EM data has been collected. Green lines outline ERT profiles collected. Red dots represents borehole information collected from the Jupiterdatabase, while purple dots identifies boreholes from the database belonging to the Central Region of Denmark.

3 RESULTS AND DISCUSSION

3.1 *Hydrogeological model*

Based on lithology information from boreholes and geophysical data a hydrogeological model was created. Initially, the general geological layers of the model were interpreted as a layer model. Then it was converted to a voxel model, with cells sizes of 1x1m along the horizontal axes and 0.5m in the vertical direction, to be able to add more details. Pipes and buildings were added to the voxel model and the model was re-evaluated along gridlines and voxels updated to represent lenses of different lithology within layers as identified from the boreholes. Furthermore, abrupt changes in the fill materials that were difficult to obtain with interpolated layers were updated.

The shallow geology of the Horsens harbor area consists of glacial and postglacial marine layers overlain by fill materials. The hydrological model identifies an uppermost layer in the area consisting of mixed fill materials with abrupt thickness variations typically 0-2m but often thicker towards the harbor front. Underneath the fill material gyttja is present in most of the area, but pinching out to the northwest. The greatest thickness of gyttja is found in the southeastern corner of the harbor area. In one borehole a thickness of 6.1m of gyttja is encountered. Where it has not been removed or remolded by construction processes a relatively thin, typically up to 1m of marine sand is found underneath the gyttja. Below this, to the depth of interest for the modeling, moraine clay with lenses or layers of sand is found in the western part of the area while sand layers with lenses or layers of clay dominate in the southeast.

3.2 *Contaminant transport model*

The transport of various contaminants was modelled using the FEFLOW software based on the hydrogeological model, estimated extents and concentrations of contaminants, available information on groundwater levels, infiltration, and assumptions on hydraulic conductivities.

Information on different contaminants in the area was collected. These included preconstruction reports on accredited analyses for contaminants (soils, groundwater, and pore air). All test location information was georeferenced and added to the same GIS workspace in order to obtain an overview of the entire area including connections between contaminants across the cadasters often representing boundaries of single reports. Contamination in the area is mainly located at depths 0-3 mbgl. From the resulting overview, the mobile compounds that could have a negative impact on humans, animals or recipients were selected. This implies that e.g. heavy metals which are quite immobile have not been included in the mapping, since no change in extent is expected. Furthermore, contaminants entering from areas outside the study area are also excluded from the assessment. Thus, the results of this study show relevant changes related to a different hydraulic situation but cannot be applied for a general assessment of the contamination situation of the area.

For the selected compounds a polygon defining the contaminant extent was interpreted and assigned with a representative concentration based on sample analyses. In cases where only soil sample analyses were available fugacity calculations based on the present soil types were applied for estimating the groundwater concentrations. Diffuse concentrations of cyanide and tar present over a large part of the area are omitted in this study. The presence and concentration of contaminants differ between the pre-and post-construction works because some contaminants were required to be removed/reduced during construction works. Such contaminants have also been removed/reduced in the post-construction transport modelling. In the contaminant transport modelling, the concentrations of contaminants have been held constant. E.g., degradation has not been considered.

The results of the hydrological model can be observed on Figure 3

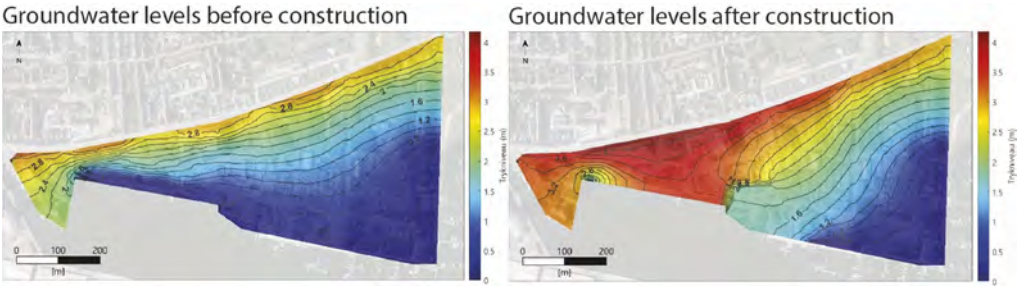

Figure 3. Modelled hydrostatic pressure before and after harbor front renovation and construction works.

In the case area of Horsens harbor addition of impermeable steel sheet walls along the harbor front and along an artificial stream, added to drag in the blue areas for recreational value, determines the flow direction. As expected, the impermeable walls toward the sea significantly alter the flow. Drainage happens at one location in the western part of the area, but it is not enough to account for the reduced outflow along the long stretch. Consequently, groundwater is expected to raise and introduce a risk of flooding from below. The increased amount of infiltration doesn't make the situation any better but has a lower contribution to the problem compared to the hindered outflow. As the eastern part of the area remains permeable the groundwater flow direction change from mainly north to south oriented to become more west to east flowing along the harbor front. The changing flow direction in combination with the higher groundwater level affects the transport of soluble contaminants in the area. The new transport situation causes contaminants to generally extend further east from the current hot spots which leads to unforeseen pollution of new areas and increased washing into the sea.

4 CONCLUSIONS

By carrying out a detailed mapping and contaminant transport modeling it has been possible to foresee the changes in the extent and discharge of contaminants in the Horsens harbor area prior to construction. This potentially allows for remediation measures and assessment of what should be taken care of in the process or as a consequence of the alterations. The modeling clearly shows that the condition of the harbor front is the main parameter affecting the flow pattern. Thus, an impermeable wall will permit contaminants to enter the sea. An impermeable wall will keep in the contaminants in the harbor area, where they may be distributed to new areas. Further, the lack of outflow options increases the risk of flooding from below as groundwater levels are already close to the surface. This may potentially bring contaminants to the surface.

REFERENCES

Burke, H., Hough, E., Morgan, D.J.R., Hughes, L., Lawrence, D.J., 2015. Approaches to inform redevelopment of brownfield sites: An example from the Leeds area of the West Yorkshire coalfield, UK. *Land Use Policy* 47, 321–331.

Weng, X.-H., Zhu, Y.-M., Song, X.-Y., Ahmad, N., 2019. Identification of key success factors for private science parks established from Brownfield regeneration: a case study from China. *Int. J. Environ. Res. Public Health* 16, 1295.

Cen, X, Medhus, A.B., Andersen, T.R., Poulsen, S.E., Mo, X, Mou, Z., Du, F. Hydrogeological modelling to support urban planning in harbour areas: a case study from Horsens, Denmark. *Bulletin of Engineering Geology and the Environment* 80(9), 2021

Andersen, T.R., Poulsen, S.E., Pagola, M.A., Medhus, A.B. Geophysical Mapping and 3D Geological Modelling to Support Urban Planning: A Case Study from Vejle, Denmark. *Journal of Appied Geophysics* 2020, 180

Smart Geotechnics for Smart Societies – Zhussupbekov, Sarsembayeva & Kaliakin (Eds)
© 2023 The Author(s), ISBN 978-1-003-29912-7
Open Access: www.taylorfrancis.com, CC BY-NC-ND 4.0 license

Hydraulic characteristics of granular bentonite amended with hydroxy methyl cellulose under adverse chemo-mechanical loadings

Sharad Dadhich, Himanshu Yadav & Tadikonda Venkata Bharat
Indian Institute of Technology Guwahati, Guwahati, Assam, India

ABSTRACT: Granular bentonite base clay liners are widely used in landfills as hydraulic barrier because of their low hydraulic conductivity and self-sealing ability. Recent studies reported that the hydraulic conductivity of Granular bentonite has significantly increased due to the presence of different inorganic cations (i.e., Na+, K+, and Ca++), which causes the mechanical instability. This subsequently results in ground water contamination due to leachate migration from the liners. To address this problem, a composite mixture of granular bentonite and hydroxy methyl cellulose at different proportions (2-10% HMC) has been tested in the laboratory under extreme chemical (0.50M $CaCl_2$) and mechanical (20-100kPa) loadings. The performance of different mixtures is evaluated in terms of hydraulic conductivity and volume change. It is found that the mixture of granular bentonite and 10% hydroxy methyl cellulose has attained lower hydraulic conductivity (10^{-11}-10^{-9}m/s) than the critical hydraulic conductivity (10^{-9}m/s) under extreme chemical and mechanical loadings.

1 INTRODUCTION

Bentonite has been extensively used in landfills as liner material because of its low hydraulic conductivity, high swelling potentials, self-sealing ability, and higher absorption capacity (Benson, Zhai and Wang, 1994; Bharat, 2014; Chen et al., 2016). It prevents the permeation of various organic and inorganic contaminants into the ground water (Hornsey et al., 2010). Geosynthetic clay liners (GCL) have replaced the conventional thick clay liners due to the ease of handling in production and installation (Bouazza, 2002). GCL consists of 10mm thick bentonite layer sandwiched between geotextile layers. The granular bentonite is commonly used now a days because of its self-sealing ability (Yadav and Tadikonda, 2022). The self-sealing ability plays a vital role in filling the gaps between the blocks in nuclear repositories and healing the puncture after the placement in the field (Parastar et al., 2017a; Rowe and Li, 2020; Das and Bharat, 2021; Rowe and AbdelRazek, 2021). The self-sealing ability refers to the filling of the macro-voids, because of the disintegration of coarser particle into finer particle during the process of hydration (Yu, El-Zein and Rowe, 2020). The disintegration phenomenon can be considered as the results of the double diffuse layer formation and existence of the repulsive inter particles forces, which ultimately lower down the hydraulic conductivity to a limiting value (10^{-9}m/s) (Darde et al., 2021) and retard the process of diffusion (Lee and Shackelford, 2005; Bharat, Sivapullaiah and Allam, 2009). The municipal solid waste disposal landfills generate inorganic leachate consists of sodium, potassium, and calcium ions due to slat laden waste from chemical, electronic industries and demolition waste (Weber et al., 2002; Yeheyis et al., 2013; Turkyilmaz et al., 2019; Colman et al., 2020). Recent studies reported significant decrease in osmotic potential and lack of sealing ability under different chemo-mechanical loading thus, allowing the ease of contamination (Parastar et al., 2017b; Salemi et al., 2018; Wang et al., 2019). Polymeric compound base GB are currently being explored to

DOI: 10.1201/9781003299127-274

enhance the performance of GB under severe chemo-mechanical loadings. Several synthetic polymers either straight or crosslinked has been investigated in the literature (Onikata, Kondo and Kamon, 1996; Fehervari et al., 2016; Tian, Benson and Likos, 2016; Tian, Likos and Benson, 2019). The mechanism of polymeric compound with GB can be understood by long range columbic interaction and short-range ion-dipole interaction, cation bridging and hydrogen bonds(Ashmawy et al., 2002; Deng et al., 2006).

In the present study, hydraulic characteristics of granular bentonite (GB) amended with hydroxy methyl cellulose (HMC) has been investigated. The optimal proportion of HMC amended with GB has been identified for application in place of conventional GB based GCL under adverse mechanical loadings (20-100kPa) and 0.50M potassium chloride and 0.50M calcium chloride solutions.

2 MATERIALS AND METHODS

2.1 *Materials*

Granular bentonite used in this study has been extracted from commercially available GB based geosynthetics clay liner. The material is first characterized in the laboratory. The properties of GB are presented in Table 1. The hydraulic and volume change behavior of GB under different chemical and mechanical loading conditions is discussed in details in the results section.

Table 1. Characterization of granular bentonite.

Property	Method	Value
Specific Gravity	Density Bottle (BIS 1980)	2.78
Liquid Limit	ASTM D4318-17el	658
Plastic Limit		48
Specific Surface Area (in m^2/gm)	Methylene Blue sorption	648
Cation Exchange Capacity (in meq/100gm)		152.67
Na+	Flame Photometer and Atomic Adsorption Spectrometry	86.1
K+		0.87
Ca++		42.2

The hydroxy methyl cellulose is purchased from AKSHAR CHEM company. It is gelatinous compound, extracted from the cellulose, which is hydrophobic in nature. It helps in hydrophilization (Pramono et al., 2019) of Granular bentonite under high ionic salt concentration to accelerate the disintegration of the granule.

The calcium chloride dihydrate ($CaCl_2.2H_2O$, M_w = 147.02gm) and potassium chloride (KCl, Mw = 74.55gm) are purchased from Sisco Research Laboratories, which is minimum 99.50% pure. The solutions of 0.50M concentration are prepared in the laboratory as per the standard procedure.

2.2 *Methods*

To study the hydraulic conductivity and volume change characteristics of composite mixture the oedometer test setup is used with slight modification (Yadav and Tadikonda, 2022). The mould is fabricated from solid acrylic cylinder with an opening at bottom periphery to accommodate a burette for maintaining the hydraulic head upto 60cm. The modified mould has inner and outer diameter of 53 and 60mm, respectively. It can accommodate a 10mm thick compacted sample sandwiched between 5mm thick porous stones. A filter paper (A 42-grade) is placed at top and bottom side of soil specimen to avoid the clogging of the porous stones.

The soil sample is compacted at dry density of 1.20gm/cm^3 as per the density of GB in GCL (Das and Bharat, 2021). The mould is placed on the load assembly and a dial gauge (Least count = 0.002mm) is placed at the top of the mould for measuring the axial strain under chemo-mechanical loading. A burette containing the 0.50M calcium chloride solution is connected at bottom of the mould. The valve of the burette is opened immediately placing the mechanical loading (20kPa, 50kPa, and 100kPa) to simulate the in-situ loading conditions. The permeation rate is estimated using the principle of variable head permeability test and the volume change is recorded in terms of normalized thickness using dial gauge readings (Yadav and Tadikonda, 2022).

3 RESULTS AND DISCUSSION

3.1 *Influence of Polymer proportion*

The fluid permeation rate of 0.50M calcium chloride solution through GB alone and different proportions of HMC amended with GB under 50kPa mechanical loading is presented in Figure 1 (a). The permeation rate of GB alone is found to be much higher than the limiting permeation rate, which confirms the inability of GB in sealing the macro-voids in the presence of 0.50M calcium chloride solution. A decreasing trend in the permeation rate is observed at equilibrium with increase in the proportion of the HMC. The 2HMGB sample completely fails to seal the macro-void at equilibrium. The 5HMGB sample initially seals the macro-void at 480 minutes but it starts leaking around 1000 minutes. However, 10HMGB sample completely seals the macro-void at 240 minutes and the permeation rate continue to fall down till the equilibrium.

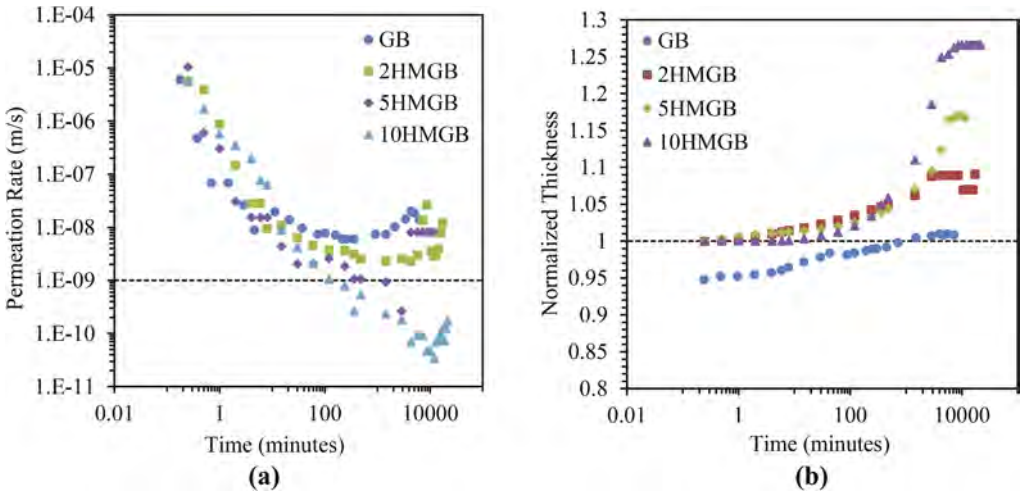

Figure 1. Temporal Variation of (a) Permeation rate and (b) Normalized Thickness for different samples with Calcium Chloride (0.50M) solution under 50kPa mechanical loading.

The volume change behavior of GB alone and different proportions of HMC amended with GB under 50kPa mechanical loading with 0.50M calcium chloride are presented in Figure 1 (b). A significant collapse in GB is observed under the applied chemo-mechanical loading. The collapse is slightly reducing with the time because of the formation of the diffused double layer as the hydration progresses. Initially, the diffused double layer formation is slow, which may be because of the limited presence of water. An insignificant collapse is noted for GB amended with HMC initially, which confirms that the HMC resist the collapse. The normalized thickness shows increasing trend with the proportion of HMC. The maximum normalized thickness is observed for 10HMGB sample (H_N = 1.28), indicating the swelling of the soil specimen.

3.2 *Performance of composite mixture under mechanical loadings*

The fluid permeation rate of 0.50M calcium chloride solution through GB amended with 2% HMC under different mechanical loadings (20-100kPa) is shown in Figure 2 (a). The 2HMGB sample fails to seal the macro-void for each mechanical loading. However, the permeation rate is slightly lower with respect to the GB alone.

The volume change behavior of GB amended with 2% HMC under different mechanical loading (20-100kPa) is shown in Figure 2 (b). A slight collapse is observed initially for 20kPa mechanical loading, which is further vanished with the time as the hydration increase. At equilibrium significant swelling is observed under different mechanical loadings (20-100kPa). It confirms the diffused double layer formation, which is primarily responsible for self-sealing behavior of GB. The maximum swelling (H_N =1.18) is observed under 20kPa.

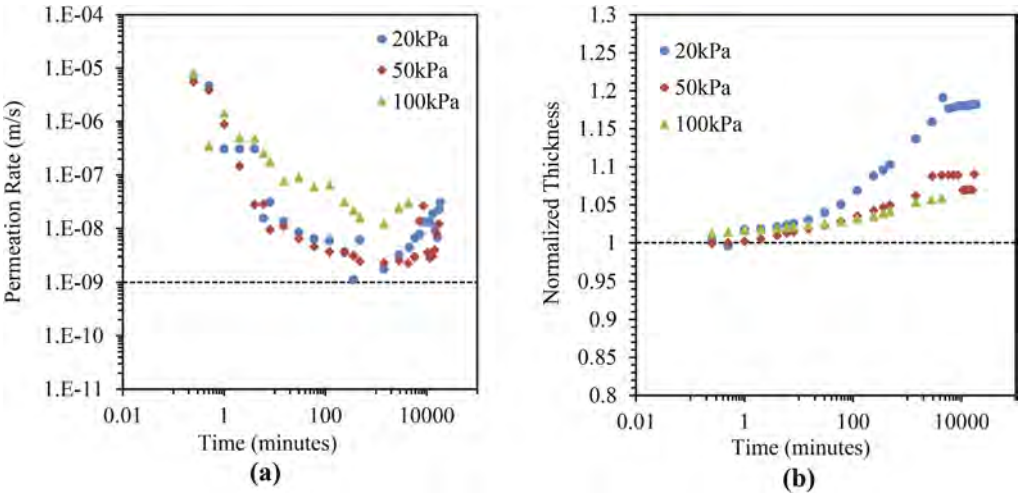

Figure 2. Temporal Variation of (a) Permeation rate and (b) Normalized Thickness for 2HMGB sample with Calcium Chloride (0.50M) solution under different mechanical loading (20-100kPa).

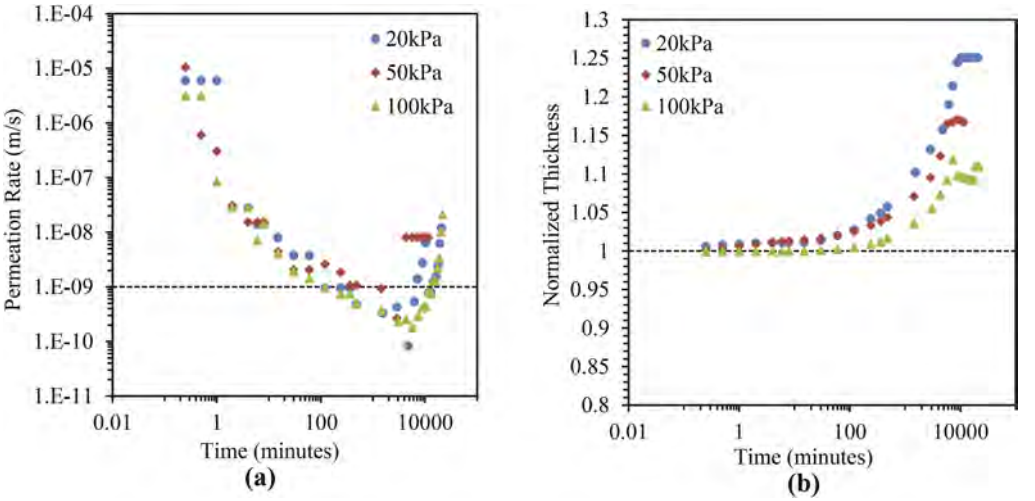

Figure 3. Temporal Variation of (a) Permeation rate and (b) Normalized Thickness for 5HMGB sample with Calcium Chloride (0.50M) solution under different mechanical loading (20-100kPa).

The fluid permeation rate of 0.50M calcium chloride solution through GB amended with 5% HMC under different mechanical loading is drawn in Figure 3 (a). Initially, the 5HMGB seals the macro-void in time intervals 240-360 minutes. As the time progresses the seal-ability goes on increasing up to a certain time and starts decreasing afterwards. Thus, permeation rate starts increasing and 5HMGB sample fails to seal the macro-void for each mechanical loading at equilibrium. However, the permeation rate is still slightly lower with respect to the 2HMGB.

The volume change behavior of GB amended with 5% HMC under different mechanical loadings (20-100kPa) is shown in Figure 3 (b). An insignificant collapse is observed initially for 20kPa mechanical loading, which is further vanished with the time as the hydration increase. At equilibrium significant swelling is observed under different mechanical loading (20-100kPa). It confirms the diffused double layer formation, which is primarily responsible for self-sealing behavior of GB. The maximum swelling (H_N = 1.25) is observed under 20kPa loading.

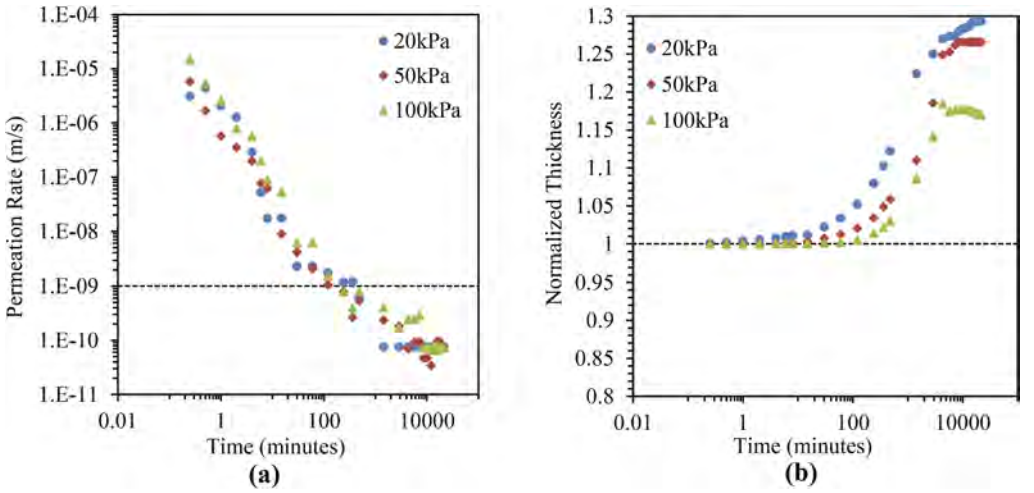

Figure 4. Temporal Variation of (a) Permeation rate and (b) Normalized Thickness for 10HMGB sample with Calcium Chloride (0.50M) solution under different mechanical loading (20-100kPa).

The fluid permeation rate of 0.50M calcium chloride solution through GB amended with 10% HMC under different mechanical loading is drawn in Figure 4 (a). The 10HMGB seals the macro-void in 240-480 minutes and the permeation rate goes on decreasing with the time. The average permeation rate at equilibrium for each load is found to be in order of 10^{-11}m/s which is manifolds lower than the limiting permeation rate (10^{-9}m/s).

The volume change behavior of GB amended with 10% HMC under different mechanical loadings (20-100kPa) is shown in Figure 4 (b). At equilibrium significant swelling is observed under different mechanical loading (20-100kPa), which confirms the diffused double layer formation. The maximum swelling (H_N = 1.30) is observed under 20kPa loading at equilibrium.

3.3 *Influence of cation type*

The fluid permeation rates of 0.50M potassium chloride and 0.50M calcium chloride solutions through GB amended with 10% HMC under 100kPa mechanical loading are drawn in Figure 5 (a).

The 10HMGB seals the macro-void in 240-480 minutes and the permeation rate is slightly higher for $CaCl_2$ solutions. This slight increase is because of the divalent Ca^{++} cation, which limits the formation of diffused double layer (Bharat and Das, 2017). The average permeation rate at equilibrium for each load is found to be in order of 10^{-10}m/s which lower than the limiting permeation rate (10^{-9}m/s).

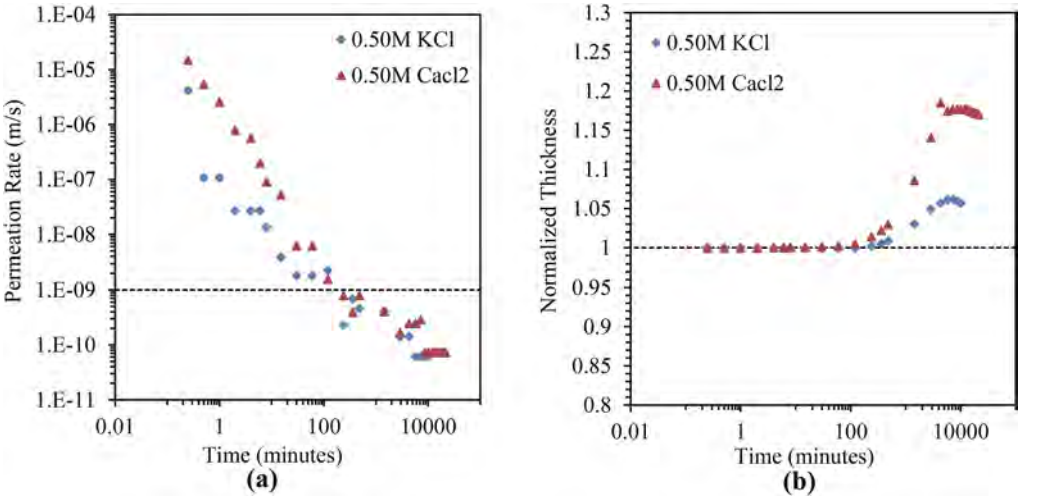

Figure 5. Temporal Variation of (a) Permeation rate and (b) Normalized Thickness for 10HMGB sample with Potassium Chloride and Calcium Chloride (0.50M) solutions under 100kPa mechanical loading.

The volume change behavior of GB amended with 10% HMC under 100kPa mechanical loading under different salt solutions (0.50M KCl and 0.50M $CaCl_2$) is shown in Figure 5 (b). At equilibrium significant swelling is observed under different salt solutions. The swelling is less for KCl solution than the $CaCl_2$ solution which may be result of the thin diffused double layer formation because of low osmotic suction.

4 CONCLUSIONS

In this study, hydraulic and volume change behavior of granular bentonite amended with hydroxy methyl cellulose is studied. The following conclusions are drawn from the study:

- Volumetric collapse was observed in the GB under adverse chemo-mechanical loading and the GB alone was found to be inefficient to seal the macro-voids.
- The inclusion of the HMC minimize the collapse in the GB and allows the formation of the diffused double layer under the high ionic salt concentration, which enables the GB to disintegrate into smaller particles and sealing the macro-voids.
- The optimal proportion of the HMC amended with the studied GB was found to be 10% HMC (w/w) for use in the GCL liners.

REFERENCES

Ashmawy, A.K. et al. (2002) 'Hydraulic performance of untreated and polymer-treated bentonite in inorganic landfill leachates', Clays and Clay Minerals, 50(5), pp. 546–552.

Benson, C.H., Zhai, H. and Wang, X. (1994) 'Estimating hydraulic conductivity of compacted clay liners', Journal of geotechnical engineering, 120(2), pp. 366–387.

Bharat, T.V. (2014) 'Analytical model for 1-D contaminant diffusion through clay barriers', Environmental Geotechnics, 1(4), pp. 210–221.

Bharat, T.V. and Das, D.S. (2017) 'Physicochemical approach for analyzing equilibrium volume of clay sediments in salt solutions', Applied Clay Science, 136, pp. 164–175. https://doi.org/10.1016/j.clay.2016.11.021.

Bharat, T.V., Sivapullaiah, P. v and Allam, M.M. (2009) 'Swarm intelligence-based solver for parameter estimation of laboratory through-diffusion transport of contaminants', Computers and Geotechnics, 36(6), pp. 984–992.

Bouazza, A. (2002) 'Geosynthetic clay liners', Geotextiles and Geomembranes, 20(1), pp. 3–17.
Chen, Y.-G. et al. (2016) 'Effects of solution concentration and vertical stress on the swelling behavior of compacted GMZ01 bentonite', Applied Clay Science, 124, pp. 11–20.
Colman, C. et al. (2020) 'Valorization of fine recycled aggregates contaminated with gypsum residues: Characterization and evaluation of the risk for secondary ettringite formation', Materials, 13(21), p. 4866.
Darde, B. et al. (2021) 'Investigating the hydromechanical behaviour of bentonite pellets by swelling pressure tests and discrete element modelling', Acta Geotechnica, 16(2), pp. 507–524.
Das, P. and Bharat, T.V. (2021) 'Kaolin based protective barrier in municipal landfills against adverse chemo-mechanical loadings', Scientific Reports, 11(1), p. 10354. https://doi.org/10.1038/s41598-021-89787-z.
Deng, Y. et al. (2006) 'Bonding between polyacrylamide and smectite', Colloids and Surfaces A: Physicochemical and Engineering Aspects, 281(1–3), pp. 82–91.
Fehervari, A. et al. (2016) 'Potential hydraulic barrier performance of cyclic organic carbonate modified bentonite complexes against hyper-salinity', Geotextiles and Geomembranes, 44(5), pp. 748–760.
Hornsey, W.P. et al. (2010) 'The impact of mining solutions/liquors on geosynthetics', Geotextiles and Geomembranes, 28(2), pp. 191–198.
Lee, J.-M. and Shackelford, C.D. (2005) 'Impact of bentonite quality on hydraulic conductivity of geosynthetic clay liners', Journal of Geotechnical and Geoenvironmental Engineering, 131(1), pp. 64–77.
Onikata, M., Kondo, M. and Kamon, M. (1996) 'Development and characterization of a multiswellable bentonite', in Environmental geotechnics, pp. 587–590.
Parastar, F. et al. (2017a) 'A parametric study on hydraulic conductivity and self-healing properties of geotextile clay liners used in landfills', Journal of environmental management, 202, pp. 29–37.
Parastar, F. et al. (2017b) 'A parametric study on hydraulic conductivity and self-healing properties of geotextile clay liners used in landfills', Journal of environmental management, 202, pp. 29–37.
Pramono, E. et al. (2019) 'Hydrophilic poly (vinylidene fluoride)/bentonite hybrid membranes for microfiltration of dyes', Materials Research Express, 6(10), p. 105376.
Rowe, R.K. and AbdelRazek, A.Y. (2021) 'Performance of multicomponent GCLs in high salinity impoundment applications', Geotextiles and Geomembranes, 49(2), pp. 358–368.
Rowe, R.K. and Li, T.-K. (2020) 'Self-healing of circular and slit defects in GCLs upon hydration from silty sand under applied stress', Geotextiles and Geomembranes, 48(5), pp. 667–683.
Salemi, N. et al. (2018) 'Geosynthetic clay liners: effect of structural properties and additives on hydraulic performance and durability', Environmental earth sciences, 77(5), pp. 1–13.
Tian, K., Benson, C.H. and Likos, W.J. (2016) 'Hydraulic conductivity of geosynthetic clay liners to low-level radioactive waste leachate', Journal of Geotechnical and Geoenvironmental Engineering, 142(8).
Tian, K., Likos, W.J. and Benson, C.H. (2019) 'Polymer elution and hydraulic conductivity of bentonite–polymer composite geosynthetic clay liners', Journal of Geotechnical and Geoenvironmental Engineering, 145(10), p. 04019071.
Turkyilmaz, A. et al. (2019) 'A comprehensive construction and demolition waste management model using PESTEL and 3R for construction companies operating in Central Asia', Sustainability, 11(6), p. 1593.
Wang, B. et al. (2019) 'Hydraulic conductivity of geosynthetic clay liners to inorganic waste leachate', Applied clay science, 168, pp. 244–248.
Weber, W.J. et al. (2002) 'Leachate from land disposed residential construction waste', Journal of environmental engineering, 128(3), pp. 237–245.
Yadav, H. and Tadikonda, B.V. (2022) 'The Influence of Mechanical Granulation Process and Granular Bentonite Plasticity on Self-Sealing and Volume Change Behavior', Journal of Hazardous, Toxic, and Radioactive Waste, 26(2), p. 04022003.
Yeheyis, M. et al. (2013) 'An overview of construction and demolition waste management in Canada: a lifecycle analysis approach to sustainability', Clean technologies and environmental policy, 15(1), pp. 81–91.
Yu, B., El-Zein, A. and Rowe, R.K. (2020) 'Effect of added polymer on the desiccation and healing of a geosynthetic clay liner subject to thermal gradients', Geotextiles and Geomembranes, 48(6), pp. 928–939.

Smart Geotechnics for Smart Societies – Zhussupbekov, Sarsembayeva & Kaliakin (Eds)
© 2023 The Author(s), ISBN 978-1-003-29912-7
Open Access: www.taylorfrancis.com, CC BY-NC-ND 4.0 license

Soil columns for the investigation of bioremediation and moisture distribution in vadose zone

B. Rahimi
MSc. Student, Department of Civil Engineering, Sharif University of Technology, Tehran, Iran

H. Sadeghi
Assistant Professor, Department of Civil Engineering, Sharif University of Technology, Tehran, Iran

H. Moghimi
Associate Professor, Department of Microbial Biotechnology, School of Biology, College of Science, University of Tehran, Tehran, Iran

P. Samari
MSc. Graduate, Department of Civil Engineering, Sharif University of Technology, Tehran, Iran

ABSTRACT: The development of industries has contaminated the soil both below and above the water table. Although extensive research has been conducted on the contaminant transport through saturated domain, the knowledge about the mechanism of contaminant transport in the vadose zone is rather limited. Therefore, this study aims to introduce an instrumented soil column to study bio-logical methods as an eco-friendly approach to remove soil pollutants. The soil column is equipped with moisture measuring sensors and sampling ports. Therefore, the new apparatus can be used to monitor flow of water and contaminant because soil moisture distribution affects the microbial degradation of hydrocarbons. The performance of new device is explored and dis-cussed via conducting a preliminary bioremediation test on a compacted soil column initially contaminated with 7% (w/w) of diesel. The results in terms of microbial activity are interpreted based on the temporal and spatial variations in the total petroleum hydrocarbon (TPH).

1 INTRODUCTION

Oil pollution is a global problem causing the contamination of soils. Oil spilled during production, transportation and exploitation causes toxic hydrocarbons such as long-chain alkanes and polycyclic aromatic hydrocarbons to pollute the soil. These hydrocarbons change the structure and metabolic activities of soil micro-organisms and they have a negative impact on the soil ecosystem (Liu et al. 2020; Gao et al. 2022). Hydrocarbon pollutants in the leachate of landfills also penetrate the underground water and pollute it (Hedayati-Azar & Sadeghi, 2021; 2022).

Some petroleum products such as diesel are light non-aqueous liquid phase pollutants (LNAPL). These pollutants penetrate the bridges of capillary menisci and hence distributed in the vadose zone. In the unsaturated zone, the fluctuations of underground water and precipitation cause LNAPL migration (Dobson et al. 2007). However, changes in the underground water level cause air to be entrapped as an additional source of oxygen for the microorganisms decomposing the pollutants (Zuo et al. 2021). As a result, changes in water content are effective for bio-logical activities and natural degradation of hydrocarbons. The main goal of this study is hence to develop a bioremediation soil column to explore the microbial activity through measuring the distribution of petroleum hydrocarbons in a polluted soil column at various water contents.

DOI: 10.1201/9781003299127-275

2 METHODS

Soil columns were made of PVC with a height and diameter of 90 cm and 10 cm, respectively. Each column had sampling ports at six different depths first one at 7.5 cm from the top and the others having equal 15 cm intervals (Figure 1). The parameters monitored for the laboratory experiments included moisture content, total petroleum hydrocarbon (TPH), and total heterotrophic count (THC). The flow rate chosen for the test was 54 ml/h, which is considered a high flow rate (Li et al. 2009). The flow rate was maintained by Mariotte bottle (Sadeghi, 2016). In addition, soil sampling was conducted at the initiation of the test and on days 14, 28, 42, and 60 afterward.

It is also mentioned that fertilizers diluted in water were used for sample preparation. These nutrients were added at a ratio of 100:10:1: of carbon, nitrogen, and phosphor (CNP) (Chaineau et al., 2005). The initial average TPH concentration in the soil samples was 7% (w/w). The nitrogen (N) source was supplied from $CO(NH_2)_2$, and the phosphorus (P) source was supplied from KH_2PO_4. The soil samples were collected from a contaminated site in plastic bags and transported to the laboratory. The soil used in the experiment was silty sand (Sadeghi & Nasiri, 2021). The soil samples were left to dry in ambient conditions for approximately three days. The samples were then sieved using a 2-mm sieve mesh to remove any unwanted large aggregates or particles (Sadeghi et al., 2019). After sieving, the samples were placed into storage containers and cooled down to 4 °C before the experiments so that microbial activities be minimized before initiation of the column tests. After the application of each treatment, the soils inside the test columns were sampled using a manual hand-auger set for both TPH and THC. All samples were then refrigerated at 4 °C and transported to the chemical laboratory for further analyses.

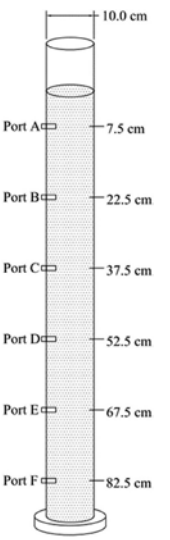

Figure 1. The schematic diagram of soil column.

3 RESULTS

The total petroleum hydrocarbons at the beginning of the experiment was equal to 4250 mg/kg, which at the end of 60 days of the experiment in A and C ports reached 3322 and 2320 mg/kg, respectively. With the increase of depth around Port A and C, the amount of TPH decreases by 21.8% and 45.4%, respectively.

At the beginning of the experiment, the population of different bacteria was equal to 1.5×10^5 CFU/g soil this amount increased during the experiment at all depths, and the

maximum was on the 28th day of the experiment (Figure 2). However, the amount of bacterial population decreased after 28 days until the end of the experiment. The bacterial population was 7.4×10^5 CFU/g soil in Port A on the 28th day of the experiment. These results are consistent with what Chaudhary et al. (2021) and Zhang et al. (2020) reported. The increase in the population of some microbial com-munities against petroleum hydrocarbons has increased the amount of bacteria at the beginning of the experiment (Zhang et al. 2020).

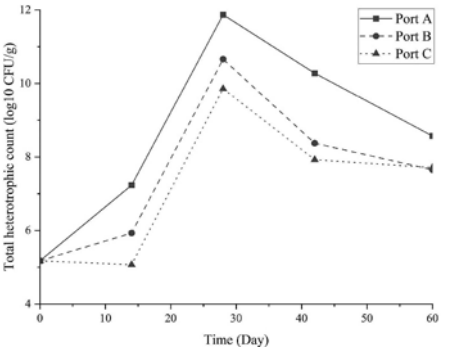

Figure 2. Variations in the bacterial population at different time steps and depths.

Changes in volumetric water content are shown in Figure 3. With the increase in depth, the volumetric water content was increased (Kolahdooz et al., 2020). High moisture caused an increase in the removal of oil pollutant, as also reported in the results of Liu et al. (2020). This phenomena can be attributed to the increase of some oil-degrading bacteria. While in the research of Lee et al. (2018), it was revealed that the increase in moisture causes a decrease in the oxygen diffusion coefficient and, as a result, a decrease in the amount of oil pollutant removal.

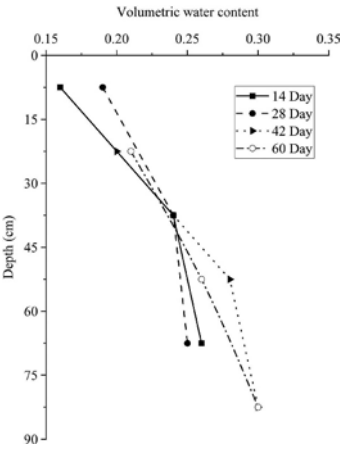

Figure 3. Distribution of the volumetric water content with depth.

4 CONCLUSIONS

The results of bioremediation of soil column systems showed that the decomposition rate of petroleum hydrocarbons changes with depth. The changes in the bacterial population vary according to the changes in moisture and the distribution of the amount of pollutants in the depth. Over time, the bacterial population first increased and then decreased. The maximum bacterial population at a depth of 7.5 cm was 7.4×10^{11} the same on the 28th day.

ACKNOWLEDGEMENTS

The second author is grateful to Iran's National Elites Foundation for the financial support pro-vided to him by way of "Dr Kazemi-Ashtiani Award".

REFERNCES

Ali, N., Dashti, N., Khanafer, M., Al-Awadhi, H., & Radwan, S. 2020. Bioremediation of soils saturated with spilled crude oil. *Scientific Reports*, 10(1), 1–9.

Chaudhary, D. K., Bajagain, R., Jeong, S.-W., & Kim, J. 2021. Insights into the biodegradation of diesel oil and changes in bacterial communities in diesel-contaminated soil as a consequence of various soil amendments. *Chemosphere*, 285 October 2020, 131416.

Chaineau, C.H., Rougeux, G., Yepremian, C., Oudot, J., 2005. Effect of nutrient concentration on the biodegradation of crude oil and associated microbial populations in the soil. Soil. *Soil Biology and Biochemistry*. 37, 1490e1497

Dobson, R., Schroth, M. H., & Zeyer, J. (2007). Effect of water-table fluctuation on dissolution and biodegradation of a multi-component, light nonaqueous-phase liquid. *Journal of Contaminant Hydrology*, 94(3–4), 235–248.

Gao, H., Wu, M., Liu, H., Xu, Y., & Liu, Z. (2022). Effect of petroleum hydrocarbon pollution levels on the soil microecosystem and ecological function. *Environmental Pollution*, 293(August 2021), 118511.

Hedayati-Azar, A., & Sadeghi, H. (2021). A review of research approaches to contaminant transport in saturated deformable clay under coupled hydro-chemico-mechanical processes. Sharif Journal of Mechanical Engineering, 37(2), 97–115.

Hedayati-Azar, A., & Sadeghi, H. (2022). Semi-empirical modelling of hydraulic conductivity of clayey soils exposed to deionized and saline environments. *Journal of Contaminant Hydrology*, 249, 104042.

Kolahdooz, A., Sadeghi, H., & Ahmadi, M. M. (2020). A numerical study on the effect of salinity on stability of an unsaturated railway embankment under rainfall. In E3S Web of Conferences (Vol. 195, p. 01004). EDP Sciences.

Lee, S. H., Ji, W., Kang, D. M., & Kim, M. S. (2018). Effect of soil water content on heavy mineral oil biodegradation in soil. *Journal of Soils and Sediments*, 18(3), 983–991.

Li, X., Zhang, L. M., and Fredlund, D. G. (2009). "Wetting front advancing column test for measuring unsaturated hydraulic conductivity." Can. Geotech. J., 46(12), 1431–1445.

Liu, H., Gao, H., Wu, M., Ma, C., Wu, J., & Ye, X. (2020). Distribution Characteristics of Bacterial Communities and Hydrocarbon Degradation Dynamics during the Remediation of Petroleum-Contaminated Soil by Enhancing Moisture Content. *Microbial Ecology*, 80(1), 202–211.

Sadeghi, H. (2016). A micro-structural study on hydro-mechanical behavior of loess (Doctoral dissertation, Hong Kong University of Science and Technology). doi: 10.14711/thesis-b1627816

Sadeghi, H., Kiani, M., Sadeghi, M., & Jafarzadeh, F. (2019). Geotechnical characterization and collapsibility of a natural dispersive loess. Engineering geology, 250, 89–100.

Sadeghi, H., & Nasiri, H. (2021). Hysteresis of soil water retention and shrinkage behaviour for various salt concentrations. Géotechnique Letters, 11(1), 21–29.

Zhang, R., Jiang, L., Jiang, D., Wang, S., Zhang, D., Zhong, M., Xia, T., & Fu, Q. (2020). Peculiar attenuation of soil toluene at contaminated coking sites. *Chemosphere*, 255(59), 126957.

Zuo, R., Zhao, X., Yang, J., Pan, M., Xue, Z., Gao, X., Wang, J., & Teng, Y. (2021). Analysis of the LNAPL migration process in the vadose zone under two different media conditions. *International Journal of Environmental Research and Public Health*, 18(21).

Smart Geotechnics for Smart Societies – Zhussupbekov, Sarsembayeva & Kaliakin (Eds)
© 2023 The Author(s), ISBN 978-1-003-29912-7
Open Access: www.taylorfrancis.com, CC BY-NC-ND 4.0 license

Wind erosion control using biotechnological methods

S.M. Fattahi
Assistant Professor, Department of Civil and Environmental Engineering, Amirkabir University of Technology, Tehran, Iran

A. Soroush
Professor, Department of Civil and Environmental Engineering, Amirkabir University of Technology, Tehran, Iran

N. Huang & J. Zhang
Professor, Department of Civil Engineering and Mechanics, Lanzhou University, Lanzhou, China

ABSTRACT: Wind erosion is a natural phenomenon that has been widening due to anthropogenic activities. One-third of the global land area suffers from wind erosion and its prevention is a critical issue in many arid regions of the world. Crusts on soil surfaces are well recognized for wind erosion control. In the last two decades, the use of biotechnological methods for crust formation on the soil surface has been developed. This paper presents the results of the wind tunnel experiments and the penetrometer tests conducted on a biocrust created by *Microcoleus vaginatus* cyanobacterium and a biocemented sand crust induced by precipitation of calcium carbonate by *Bacillus megaterium* bacterium. The biocemented sand crust had more resistance than the biocrust against wind erosion; however, both crusts reduced the amount of erosion several thousand times.

1 INTRODUCTION

Wind erosion is a natural phenomenon of soil degradation in which particles of different sizes are detached from the surface, transported, and redeposited by wind (Shao, 2008). In recent decades, anthropogenic activities such as overgrazing, inordinate agricultural practices, drainage of arable land, construction, and mining operations have increased the frequency and intensity of wind erosion even in non-arid areas of the world (Middleton and Kang, 2017; Goudie, 2018). Approximately 30% of the global land area suffers from wind erosion (Gemma et al., 2016). The largest area of wind erosion is located in the northern hemisphere and is known as the 'dust belt' extended from the west coast of North Africa, through the Middle East and Central and South Asia, to China (Gemma et al., 2016). Figure 1 shows the geological map of the 'dust belt' and its 11 main dust sources.

Sand and dust storms (SDS), the primary consequence of wind erosion, are of the most serious environmental issues threatening economic and human health globally (Gemma et al., 2016; Duniway et al., 2019; World Bank, 2019). Of impacts of SDSs are loss of agricultural productivity, damage to infrastructures, pollution of air, and deterioration of water supplies (Duniway et al., 2019). A single SDS event can damage hundreds of millions of dollars; for an instance, in northeast Asia in March 2021, a major SDS event canceled hundreds of flights in China, caused health problems to people in South Korea, killed 200,000 livestock, and destroyed 121 animal shelters in Mongolia (FAO, 2022). Table 1 presents other examples of the economic impacts of SDSs in a number of Asian countries.

DOI: 10.1201/9781003299127-276

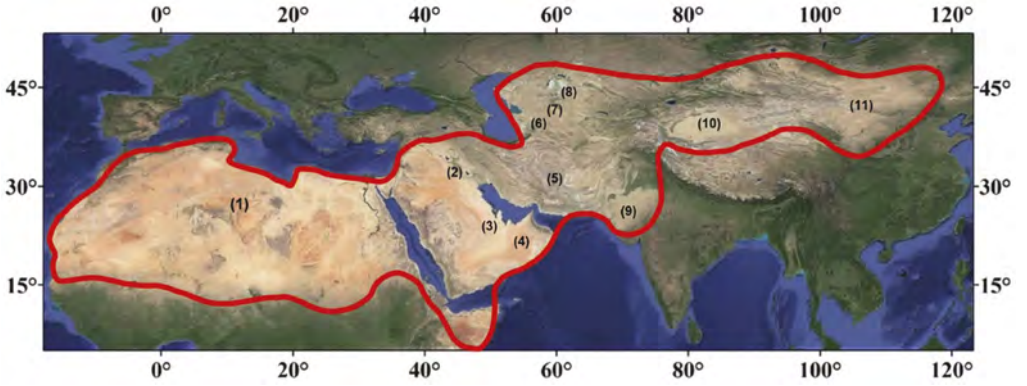

Figure 1. Geographical map of 'dust belt' (specified by the red line) and 12 main dust sources; 1) Sahara desert, 2) Tigris-Euphrates delta, 3) Rub al Khali desert, 4) Oman deserts, 5) Iranian plateau, 6) Karakum desert, 7) Kyzylkum desert, 8) Aralkum desert, 9) Thar desert, 10) Taklimakan desert, 11) Gobi desert.

Table 1. Examples of economic impacts of SDSs in Asian countries.

Country	Year	No. of events	Impact	Cost (M $)	Reference
Kuwait	2001-2014	115	Oil export, air transportation	$0.8 per tanker 0.03 per airline delay	Al-Hemoud et al. (2017)
Iraq	2013	-	Health, transportation, agriculture	1. 4	Meibodi et al. (2015)
	2013	-		1.0	
Iran	2000-2005	335	Health, transportation, Cleaning, irrigation, closure of schools and offices	124.85	Miri et al. (2009)
	Annual			6.82	Ekhtesasi & Sepehr (2009)
South Korea	2002	1	Health, cleaning, air transportation	5600	Jeong (2008)
China	2000	1	Agriculture, construction, manufacturing	485.8	Ai & Polenske (2008)

Multitude conservation methods have been proposed/implemented to control wind erosion. These practices can be divided into two main categories, including methods to reduce wind erosivity by use of diverse elements as windbreaks with a proper arrangement (Xu et al., 2018) and methods to reduce soil erodibility by use of various organic or inorganic compounds to form a crust on the soil surface (Zang et al., 2015).

Recently, biotechnology has made possible the application of microorganisms for soil stabilization. Using this technique, a soil crust is created/developed within a few millimeters of the soil surface by inoculating microorganisms, including heterotrophic bacteria (Stabnikov et al., 2013; Tian et al., 2018; Fattahi et al. 2020a, 2021a,b), phototrophic cyanobacteria (Fattahi et al., 2020b,c), fungi and lichens (Burri et al., 2013), or mosses (Zhao et al., 2016) on the soil surface.

This study aims to examine the erodibility and strength of a desert sand stabilized by inoculation of *Microcoleus vaginatus* cyanobacteria and biocemented by precipitation of calcium carbonate by *Bacillus megaterium* bacteria.

2 MATERIALS AND METHODS

2.1 *Materials*

The sand used in this study was non-plastic and poorly graded (according to USCS) with, D_{50}, of 180 μm, 3% passing the #200 sieve, Cu, of 2.3%, G_S of 2.65, γ_d of 15.7

kN/m^3, and porosity of 0.4. This study used *Microcoleus vaginatus FACHB-1854* cyanobacterium and *Bacillus megaterium* BNCC 336739 heterotrophic bacterium to form *respectively* interparticle polysaccharide bonds and $CaCO_3$ bridges (based on Equation 1) on the sand surface.

$$Ca(C_2H_3O_2)_2 + 4\ O_2 \rightarrow CaCO_3 \downarrow + 3\ CO_2 \uparrow + 3\ H_2O \quad (1)$$

Where $Ca(C_2H_3O_2)_2$ is calcium acetate.

2.2 *Methods*

Table 2 presents concisely the steps involved in the biomasses and samples preparation. The Active culture of *M. vaginatus* and freeze-dried cells of *B. megaterium* were grown respectively in the BG-11 and 0002 liquid media. For the preparation of the required samples, a number of stainless-steel cube boxes (10 cm × 10 cm × 10 cm) filled with the sand was used. Three groups of samples, including samples with untreated sand, samples treated by the biomass of *M. vaginatus*, and samples treated by the biomass of *B. megaterium*, were prepared according to the steps of Table 2. The amount of biomass sprayed on each sample was 40 mL. Figure 2 shows the photographs of the samples.

Table 2. Steps of the microorganisms' culture and sample preparation.

Step	Task	*M. vaginatus*	*B. megaterium*
1	Mass cultivation	Diluting the algal liquid with BG-11 medium and maintaining the biomass in an incubator for 14 days	Adding 5 mm^3 of bacterial biomass from the solid medium to the liquid medium and maintaining liquid biomass in a shaker incubator for 36 h
2	Preparing biomass and spraying it on the soil surface	Resuspending algal liquid, adding 0.05 % xanthan to the algal liquid and spraying the bacterial suspension on the surface of the samples	Adding 0.05 % xanthan to the bacterial suspension, adding 20 g/L calcium-acetate to the bacterial suspension, spraying the bacterial suspension on the surface of the samples
3	Curing samples	Maintaining the sample in a greenhouse in the culture condition, watering the samples 2 mm per day for 21 days	Maintaining the sample in a greenhouse at a temperature of 23 °C until the sample dries

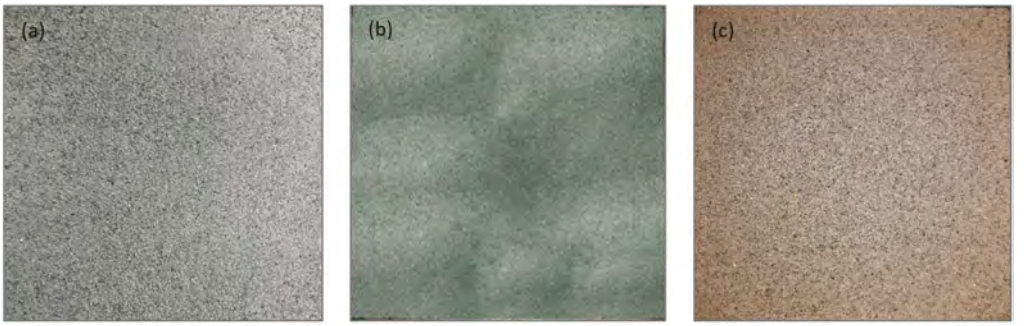

Figure 2. Photographs of the samples; a) untreated sand, b) treated by the *M. vaginatus* biomass, c) treated by the *B. megaterium* biomass.

The wind tunnel experiments were conducted in triplicate on the samples with five different wind velocities of V = 6, 10, 15, 20 and 25 m/s for 5 minutes. In order to measure the strength of the surface of the samples, this study employed the penetrometer test (Fattahi et al., 2020d), in which crusts were penetrated perpendicularly by a flat-tip stainless-steel needle with a diameter of 0.6 mm. The rate and maximum depth of penetration were 158 μm/s and 5 mm, respectively.

All of cultivation processes of the microorganisms, wind tunnel tests were conducted in the Key Laboratory of Mechanics on Disaster and Environment in Western China, Lanzhou University.

3 RESULTS AND DISCUSSION

Figure 3 presents the average force (F_P) – depth (D_P) penetration curves obtained from the penetrometer tests carried out on the samples. F_P of untreated sand did not exceed 0.03 N. For the samples treated by the *M. vaginatus* biomass, F_P showed a moderate climb, but F_P of the samples treated by the *B. megaterium* biomass experienced a sharp increase during penetration.

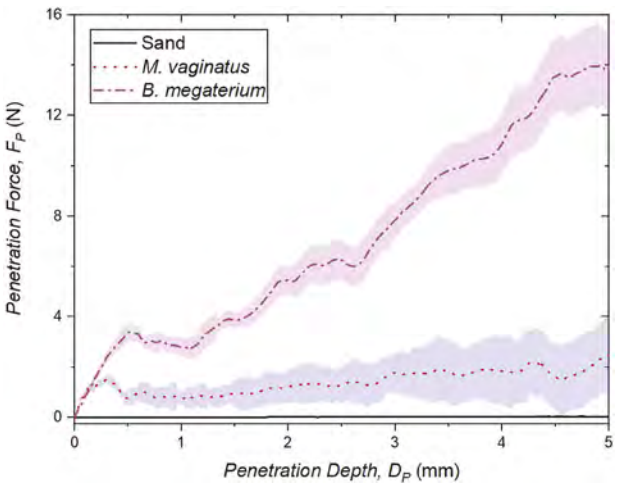

Figure 3. Force (F_P) – depth (D_P) penetration curves of the untreated sand, sand treated by the *M. vaginatus* biomass, and *B. megaterium* biomass.

Figure 4 presents the rate of erosion, E_R, in terms of kg/(m^{2}h) and in the logarithmic scale for the samples. E_R was calculated based on the eroded masses from the surfaces of the specimens in 5 minutes. As expected, E_R of untreated sand was remarkably high at all of the wind velocities and increased with the rise of V. The erosion rates of the samples treated by the *M. vaginatus* and *B. megaterium* biomasses were zero up to V=25 m/s at which the ratio of E_R of these samples over E_R of untreated sand were 7.5 $\times 10^{-5}$ and 5.6×10^{-5}, respectively.

In this study, the erodibility of the samples was obtained by subjecting the samples to different wind velocities for a short time of 5 min; hence, in contrast to the crusts' strength, the erosion rates of the crusts had no remarkable difference. In case of exposure of the crusts to wind flow for a long time, the *M. vaginatus* biocrust may deteriorate faster than *B. megaterium* biocemented sand crust due to its weaker interparticle bonds.

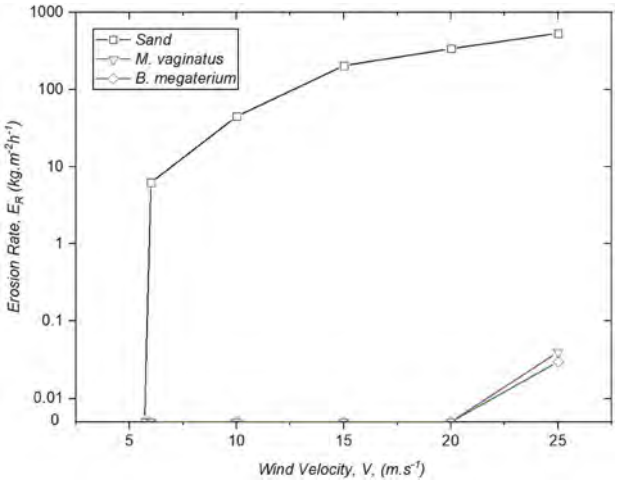

Figure 4. Erosion rates of the untreated sand, sand treated by the *M. vaginatus* biomass, and *B. megaterium* biomass at different wind velocities.

Table 3 compares the advantages and disadvantages of the cyanocrust and biocemented sand crust. The quick biocementation reaction, no water requirements for formation, and high strength are the merits which turn the biocemented sand crust as a favorite choice for quick (even emergency) controlling of wind erosion and dust emission from mine tailings, containing harmful materials, and drylands with highly erodible deposits (e.g., dunes and sand seas). In order to benefit from the advantages of the biocrust (i.e., releasing O_2, enhancing soil fertility and biological conditions, and self-recovery), protecting the biocrust at the time of its early stages of development and finding proper scientific and technical methods to reduce water necessities (especially in areas with dry climates) for the cyanocrust development is vital. The costs of the required raw materials for the biocrust and biocemented sand crust formation are about 1500 and 750 US$/ha, respectively.

Table 3. Comparison of the biocrust created by *M. vaginatus* and biocemented sand crust created by *B. megaterium.*

Crust	Advantages	Disadvantages
Biocrust	- Release of O_2 in the photosynthesis process - Enhancing soil fertility and biological conditions* - Self-treatment	- High water requirement for the formation - Long creation time - Low strength
- Biocemented sand crust	- Quick biocementation reaction - No need to water - High strength	- Release of CO_2 during biocementation process

* Fattahi et al. (2020c)

4 CONCLUSION

In order to assess the efficiency of biotechnological methods for wind erosion control, this study subjected a biocrust formed by *Microcoleus vaginatus* cyanobacterium and a biocemented sand crust created by *Bacillus megaterium* to wind flow with five different velocities. This study also measured the strength of the crust by the penetrometer test. The biocemented sand crust was relatively stronger and showed less erosion than the biocrust; however, both of them provided good protection against wind erosion for the highly erodible sand by diminishing the erosion rate several thousand times.

REFERENCES

Ai, N. and Polenske, K.R., 2008. Socioeconomic impact analysis of yellow-dust storms: An approach and case study for Beijing. *Economic Systems Research*, *20*(2), pp.187–203.

Al-Hemoud, A., Al-Sudairawi, M., Neelamanai, S., Naseeb, A. and Behbehani, W., 2017. Socioeconomic effect of dust storms in Kuwait. *Arabian Journal of Geosciences*, *10*(1), pp.1–9.

Burri, K., Gromke, C. and Graf, F., 2013. Mycorrhizal fungi protect the soil from wind erosion: a wind tunnel study. *Land Degradation & Development*, *24*(4), pp.385–392.

Duniway, M.C., Pfennigwerth, A.A., Fick, S.E., Nauman, T.W., Belnap, J. and Barger, N.N., 2019. Wind erosion and dust from US drylands: a review of causes, consequences, and solutions in a changing world. *Ecosphere*, *10*(3), p.e02650.

Ekhtesasi, M.R. and Sepehr, A., 2009. Investigation of wind erosion process for estimation, prevention, and control of DSS in Yazd–Ardakan plain. *Environmental monitoring and assessment*, *159*(1), pp.267–280.

Fattahi, S.M., Soroush, A. and Huang, N., 2020a. Biocementation control of sand against wind erosion. *Journal of Geotechnical and Geoenvironmental Engineering*, *146*(6), p.04020045.

Fattahi, S.M., Soroush, A. and Huang, N., 2020b. Wind erosion control using inoculation of aeolian sand with cyanobacteria. *Land Degradation & Development*, *31*(15), pp.2104–2116.

Fattahi, S.M., Soroush, A., Huang, N., Zhang, J., Abbasi, S.J. and Yu, Y., 2020c. Laboratory study on biophysicochemical improvement of desert sand. *Catena*, *190*, p.104531.

Fattahi, S. M., Soroush, A., Huang, N., Zhang, J., Abbasi, S. J., and Yu, Y., 2020d. Soil properties affecting erosion induced by saltating particles. *Environmental Geotechnics*, DOI: 10.1680/jenge.19.00230.

Fattahi, S.M., Soroush, A., Huang, N., Zhang, J., Jodari Abbasi, S. and Yu, Y., 2021a. A framework for predicting abrasion rupture of crusts in wind erosion. *Earth Surface Processes and Landforms*, *46*(13), pp.2565–2581.

Fattahi, S. M., Soroush, A., Huang, N., Zhang, J., Abbasi, S. J., and Yu, Y., 2021b. Durability of biotechnologically induced crusts on sand against wind erosion. *Journal of Arid Environments*, 189, 104508.

FAO, 2022. Sand and Dust Storms, https://www.fao.org/land-water/land/sds/en/.

Gemma, S., Terradellas, E., Baklanov, A., Kang, U., Sprigg, W., Nickovic, S., Boloorani, A.D., Al-Dousari, A.B.S., Benedetti, A., Sealy, A. and Tong, D., 2016. Global assessment of Sand and dust storms. *Published by the United Nations Environment Programme (UNEP) Nairobi, Kenya*, *139*.

Goudie, A.S., 2018. *Human impact on the natural environment*. John Wiley & Sons.

Jeong, D.Y., 2008. Socio-economic costs from yellow dust damages in South Korea. *Korean Social Science Journal*, *35*(2), pp.1–29.

Meibodi, A.E., Abdoli, G., Taklif, A. and Morshedi, B., 2015. Economic modeling of the regional polices to combat dust phenomenon by using game theory. *Procedia Economics and Finance*, *24*, pp.409–418.

Miri, A., Ahmadi, H., Ekhtesasi, M.R., Panjehkeh, N. and Ghanbari, A., 2009. Environmental and socio-economic impacts of dust storms in Sistan Region, Iran. *International journal of environmental studies*, *66*(3), pp.343–355.

Middleton, N. and Kang, U., 2017. Sand and dust storms: Impact mitigation. Sustainability 9 (6), 1053.

Shao, Y. ed., 2008. *Physics and modelling of wind erosion*. Dordrecht: Springer Netherlands.

Stabnikov, V., Chu, J., Myo, A.N. and Ivanov, V., 2013. Immobilization of sand dust and associated pollutants using bioaggregation. *Water, Air, & Soil Pollution*, *224*(9), pp.1–9.

World Bank, 2019. Sand and Dust Storms in the Middle East and North Africa Region: Sources, Costs, and Solutions.

Tian, K., Wu, Y., Zhang, H., Li, D., Nie, K. and Zhang, S., 2018. Increasing wind erosion resistance of aeolian sandy soil by microbially induced calcium carbonate precipitation. *Land Degradation & Development*, *29*(12), pp.4271–4281.

Xu, B., Zhang, J., Huang, N., Gong, K. and Liu, Y., 2018. Characteristics of turbulent aeolian sand movement over straw checkerboard barriers and formation mechanisms of their internal erosion form. *Journal of geophysical research: Atmospheres*, *123*(13), pp.6907–6919.

Zang, Y.X., Gong, W., Xie, H., Liu, B.L. and Chen, H.L., 2015. Chemical sand stabilization: a review of material, mechanism, and problems. *Environmental Technology Reviews*, *4*(1), pp.119–132.

Zhao, Y., Bowker, M.A., Zhang, Y. and Zaady, E., 2016. Enhanced recovery of biological soil crusts after disturbance. In *Biological soil crusts: An organizing principle in drylands* (pp. 499–523). Springer, Cham.

Smart Geotechnics for Smart Societies – Zhussupbekov, Sarsembayeva & Kaliakin (Eds)
© 2023 The Author(s), ISBN 978-1-003-29912-7
Open Access: www.taylorfrancis.com, CC BY-NC-ND 4.0 license

Cementation effect on swelling and permeability properties of bentonite considering microscopic structural evaluation

D. Ito & H. Komine
Waseda University, Tokyo, Japan

ABSTRACT: Bentonite buffer material in the geological disposal of high-level radioactive waste would be subjected to high temperatures and pressures for a long period, which may cause alteration through cementation and changes of swelling and permeability characteristics. In this study, bentonite ore was used to simulate the cemented buffer material, and effects of cementation on swelling and permeability properties were evaluated. As results, swelling pressure of undisturbed specimens was about half that of reconstituted specimens, while hydraulic conductivity was almost in the same order. To elucidate mechanism from microstructural viewpoint, SEM and XRD was utilized. SEM observations showed the undisturbed specimens had more complex structure at same dry density. XRD analysis indicated that undisturbed specimens had smaller montmorillonite basal spacing at same water content. Therefore, cementation may reduce permeability by complexity of structure, and inhibit water absorption and swelling of montmorillonite interlayers, resulting in almost no change in hydraulic conductivity.

1 BACKGROUND

In the geological disposal of high-level radioactive waste, bentonite is planned to be used as a buffer material surrounding the waste in many countries (Pusch, 1992; Sellin & Leupin, 2013). Bentonite has high swelling capacity and low permeability, so it can delay contact between radionuclides and groundwater. The properties of bentonite at the initial condition of disposal have been investigated experimentally and theoretically in many countries (Alonso & Gens, 1999; Komine & Ogata, 2004; Garitte et al., 2017), and repository design proposals have been established (Ogata et al., 1999). On the other hand, because of the long half-life of radionuclides, buffer material is required to maintain their integrity for tens of thousands of years. However, because the buffer material may be subjected to high temperatures and pressures and inflow of groundwater containing salts, there is concern that cementation would occur and properties such as swelling and low permeability will deteriorate. It is difficult to reproduce and evaluate such long-term alteration phenomena only by laboratory experiments. In this study, we focused on natural analogues, a geological research method, and used raw ore from bentonite deposits that has undergone diagenesis in the natural ground as a simulated buffer material.

In this paper, to quantitatively evaluate the effect of cementation on swelling and permeability properties of bentonite, measuring swelling pressure, and hydraulic conductivity experiments were conducted, and microscopic structural evaluation was performed using SEM and XRD.

2 SAMPLE USED IN THIS STUDY AND TESTING APPARATUSES

2.1 *Fundamental properties of bentonite ore and specimen preparation*

Na-bentonite ore from the Tsukinuno Mine in Yamagata, Japan (Tsukinuno ore) was used. Fundamental characteristics of the ore are shown in Table 1. The bentonite ore used in this study is shown in Figure 1.

To evaluate the cementation effects on swelling and permeability properties, undisturbed and reconstituted specimens were prepared by the following method. The undisturbed specimens were

DOI: 10.1201/9781003299127-277

formed from ore using cutter rings, trimmers, knives, and were made into specimen sizes (28 mm in diameter × 10 mm in height for swelling pressure test and 28 mm in diameter × 2 mm in height for permeability experiment). The reconstituted specimens were prepared using a crusher with grain sizes of ~0.425 mm, 0.850 to 2 mm, and 2.00 to 4.75 mm, and then compacted to an arbitrary dry density by applying static load. All grain sizes were used in the swelling experiments, while only specimens with grain diameters of ~0.425 mm was used in the permeability experiments.

Table 1. Fundamental characteristics of bentoniteore.

Soil particle density (Mg/m^3)	2.77
Liquid limit (%)	419.1
Plastic limit (%)	29.2
Plasticity index	389.9
Montmorillonite content (%)	44.7
Leached cation (Na^+) (cmol(+)/kg)	43.7
Leached cation (Ca^+) (cmol(+)/kg)	5.6
Leached cation (K^+) (cmol(+)/kg)	Lower than detection limit
Leached cation (Mg^{2+}) (cmol(+)/kg)	0.9
Accessory minerals	Quartz, Plagioclase
Approximate geological age	Ten million years

Figure 1. Appearance of bentonite ore.

2.2 *Testing devices of swelling pressure and hydraulic conductivity test*

Figure 2 shows the experimental apparatus. Lateral deformation of the specimen was restrained by a stainless ring, and vertical deformation was controlled by tightening the clamp knob in the swelling pressure experiment. Evaluation is based on the relationship between the value obtained when the increase in swelling pressure converges after a certain period (maximum swelling pressure) and the dry density at that time.

Figure 3 shows the hydraulic conductivity apparatus. This apparatus is for falling head hydraulic conductivity test, and burettes are connected to both the inlet and outlet sides and air pressure is applied to add hydraulic gradient. Details of the experimental setup and procedures are described in Ito et al., 2022. Tests were conducted under conditions of a hydraulic gradient of 4000- 20000 during the test period, and in this range of hydraulic gradients, proportional relationship between flow flux and hydraulic gradient was observed which follows Darcy's law. Average hydraulic conductivity was taken for each measurement period in a similar way as Ito et al. (2022a).

3 TESTING RESULTS ON SWELLING AND HYDRAULIC PROPERTIES

Figure 4 shows relation between maximum swelling pressure and dry density of specimen. For the reconstituted specimens, maximum swelling pressure tended to be higher with higher dry density, and the effect of grain size before compaction was small. On the other hand, the undisturbed specimens showed a variation in pressure values, but all of them were only about half of those of the reconstituted specimens of similar dry density. These results indicate that swelling pressure of undisturbed specimen is reduced by cementation, although the effect of cementation might be small when the samples are crushed before compaction.

Figure 5 shows the relation between hydraulic conductivity and dry density of specimens, as well as theoretical calculation using equations proposed by Komine (2008). Hydraulic conductivities of the undisturbed and reconstituted specimens were all in the order of 10^{-12} to 10^{-13}, which are similar to the calculation results.

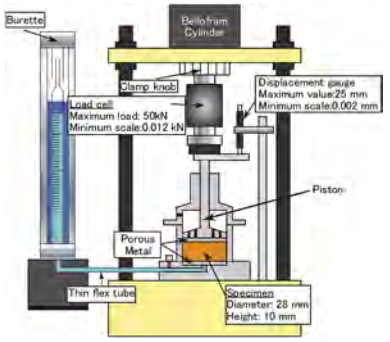

Figure 2. Swelling pressure test apparatus.

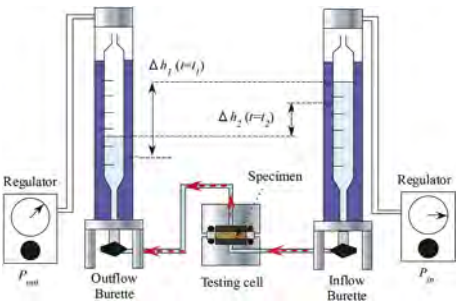

Figure 3. Hydraulic conductivity apparatus.

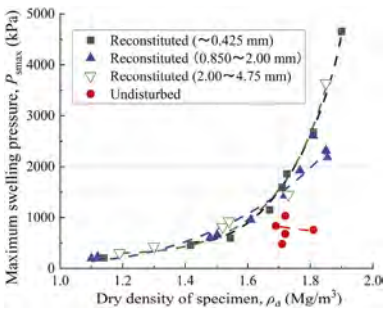

Figure 4. Relation between maximum swelling pressure and dry density.

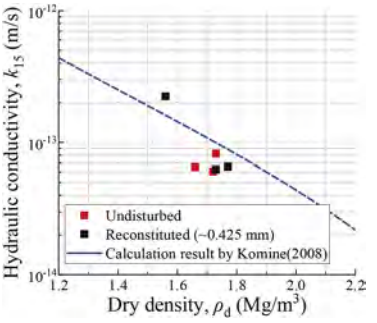

Figure 5. Relation between hydraulic conductivity and dry density.

4 MICROSTRUCTURAL OBSERVATION RESULTS BY SEM AND XRD

The differences in the shape and skeleton of the soil particles in the undisturbed and reconstructed specimens were observed using SEM (S-4500, Hitachi). When making observed sample, undisturbed and reconstituted specimens (∅ = 28 mm × h = 10 mm) of similar dry density (ρ_d = 1.7 Mg/m^3), and then the specimens were broken to expose fresh internal sections and formed to a size of 5 mm × 5 mm. Figure 6 shows appearance of SEM observation sample.

Figures 7 and 8 show observation results of undisturbed and reconstituted samples, respectively. Undisturbed sample had a complex soil particle shape, and reconstituted sample had larger pores that were not seen in undisturbed sample. From these results, the more complex soil skeleton because of cementation in undisturbed specimens might affect lower water permeation.

Also, XRD measurements were performed on the undisturbed and reconstituted specimens after water absorption and swelling pressure measurements. Montmorillonite basal spacing and adsorption state of water molecules were evaluated from the peak shapes obtained by XRD. Details of this measurement and devices are described in Ito et al. (2022b).

Figure 9 shows peak shape comparison of undisturbed and reconstituted specimen at water content of 17.0% and 18.8%. From these results, in reconstituted specimen, peak of water molecule three-layer hydration (2θ=4.7 deg) is dominant, whereas in undisturbed specimen, two-layer hydration peak (2θ=5.8 deg) remains beside the three-layer hydration peak. Undisturbed specimen has fewer water molecules between montmorillonite crystalline layers because of cementation. In undisturbed specimens, pore outside montmorillonite interlayer remains, rather than only between the montmorillonite layers which dominate the low permeability of bentonite. The combination of two factors, which complexity of skeleton and inhibition of swelling of montmorillonite layers, is assumed to be the reason why the permeabilities of the undisturbed and reconstituted specimens were not significantly different.

Figure 6. SEM observation sample.

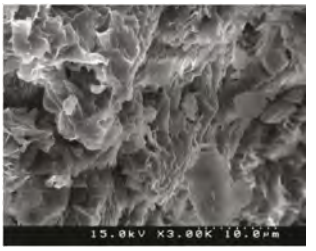

Figure 7. Observation on undisturbed sample (×3000).

Figure 8. Observation on reconstituted sample (×3000).

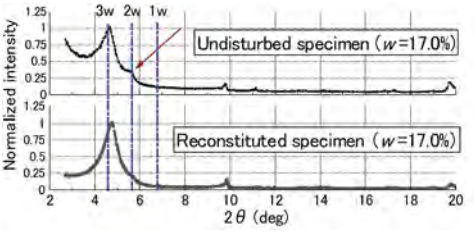

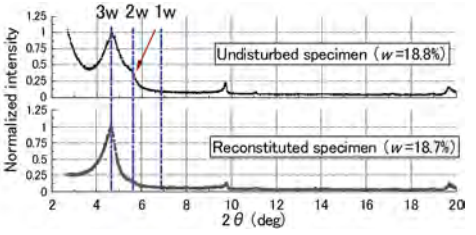

Figure 9. XRD peak shape comparison of undisturbed and reconstituted specimen at water content of 17% and 18.8%.

5 CONCLUSION

1. Because of cementation, swelling pressure of undisturbed specimen was almost half of that of reconstituted specimen, on the other hand, hydraulic conductivity was in the same order.
2. From SEM observation, undisturbed specimen has more complex soil particle structure. From XRD analysis, montmorillonite interlayer in undisturbed specimen is inhibited swelling and has less water molecules. From these factors, while undisturbed specimens decrease in swelling, the hydraulic conductivity remained almost the same.

ACKNOWLEDGEMENTS

This research was supported by the Ministry of Economy, Trade, and Industry of Japan. This study was part of JSPS KAKENHI 21K04260. XRD and SEM tests were conducted at the Materials Characterization Central Laboratory, Waseda University (Izutani et al. 2016).

REFERENCES

Alonso, E. E. & Gens, J. V. A. 1999. Modelling the mechanical behavior of expansive clays. *Engineering Geology* 54: 173–183.

Garitte, B., Shao, H., Wang, X. R., Nguyen, T. S., Li, Z., Rutqvist, J., Birkholzer, J., Wang, W. Q., Kolditz, O., Pan, P. Z., Feng, X. T., Lee, C., Graupner, B. J., Maekawa, K., Manepally, C., Dasgupta, B., Stothoff, S., Ofoegbu, G., Fedors, R., Barnichon, J. D. 2017. Evaluation of the predictive capability of coupled thermos-hydro-mechanical models for a heated bentonite/clay system (HE-E) in the Mont Terri Rock Laboratory. *Environmental Earth Sciences* 76(64): 1–18.

Ito, D., Wang, H., Komine, H. 2022a. Experimental study of aging-induced cementation effect on permeability property of bentonites. *EUROCK2022*. (To be printed)

Ito, D. & Komine, H. 2022b. Experimental study to elucidate cementation effect on swelling pressure and montmorillonite basal spacing of bentonite ore. *Proceedings of 20th International Conference on Soil Mechanics and Geotechnical Engineering* (in Press).

Izutani, C., Fukagawa, D., Miyashita, M., Ito, M., Sugimura, N., Aoyama, R. et al. 2016. The materials characterization central laboratory: an open-ended laboratory program for fourth-year undergraduate and graduate students. *Journal of Chemical Education* 93(9): 1667–1670.

Komine, H. & Ogata, N. 2004. Predicting swelling characteristics of bentonites. *Journal of Geotechnical and Geoenvironmental Engineering* 130(8): 818–829.

Komine, H. 2008. Theoretical equations on hydraulic conductivities of bentonite-based buffer and backfill for underground disposal of radioactive wastes. *Journal of Geotechnical and Geoenvironmental Engineering* 134(4): 497–508.

Ogata, N., Kosaki, A., Ueda, H., Asano, H., Takao, H. 1999. Execution techniques for high level radioactive waste disposal: IV design and manufacturing procedure of engineered barriers. *Journal of Nuclear Fuel Cycle Environment* 5(2): 103–121.

Pusch, R. 1992. Use of bentonite for isolation of radioactive waste products. *Clay Minerals* 27: 353–361.

Sellin, P. & Leupin, O. X. 2013 The use of clay as an engineered barrier in radioactive-waste management – A review. *Clays and Clay Minerals* 61(6): 477–498.

Smart Geotechnics for Smart Societies – Zhussupbekov, Sarsembayeva & Kaliakin (Eds)
© 2023 The Author(s), ISBN 978-1-003-29912-7
Open Access: www.taylorfrancis.com, CC BY-NC-ND 4.0 license

Numerical study on fluid transport with viscosity reduction due to diffusion in porous materials

J. Yang & T. Mukunoki
Kumamoto University, Kumamoto, Japan

ABSTRACT: The purpose of this study is to elucidate the flow phenomena of a highly viscous fluid in sandy soil for the recovery of heavy oil using the vapor extractor (VAPEX) method. In this study, the diffusion of heavy oil into a solvent is investigated. Syrup and distilled water are used as model to simulate the behaviors of heavy oil and organic solvents. The numerical model is validated by coupling the Navier–Stokes equation with the advection–diffusion equation. Subsequently, the concentration distribution of the fluid with a constant diffusion coefficient (D) is compared with that with a variable D, which is due to viscosity reduction in a porous geometry obtained from X-ray computed tomography images.

1 INTRODUCTION

Oilsands refers to sand that contains heavy oil with high viscosity or bitumen components without fluidity at room temperature. The mainstream methods of recovering oilsands are opencast mining and steam-assisted gravity drainage (SAGD). These methods require significant amounts of energy and water during production; in fact, the fuel cost constitutes more than one-half of the production cost. These methods are primarily limited by their high production cost.

Heavy oil can be recovered using organic solvents instead of heat from steam. The vapor extractor (VAPEX) method, which involves viscosity reduction via the diffusion of organic solvents into heavy oil, has garnered significant attention in recent years (Lin *et al.* 2014). To understand flow behavior in a porous structure, it is important to evaluate the pore structure quantitatively. Then, samples of the oilsands core are difficult to obtain, and investigation regarding the pore structure of the core and fluid flows in pores in the undisturbed state are few. In this study, to investigate heavy oil recovery using the VAPEX method, the flow of high viscous fluids in a porous material is analyzed. First, the behaviors of syrup and distilled water as heavy oil and solvent, respectively, are simulated owing to their similar viscosity. Their pore structure geometries can be obtained from X-ray computed tomography (CT) images. Subsequently, their flow and concentration in the pore are analyzed using the finite element method in 2D.

2 RELATION AMONG VISCOSITY, DIFFUSION COEFFICIENT, AND CONCENTRATION

The viscosity of syrup was measured by the viscosity measuring instrument shown in Figure 1. The viscosity measuring range of the experimental device is 0.015–200 Pa·s. The initial viscosity of syrup measured is 34 Pa·s, and the volume is approximately 400 mL. An appropriate amount of water is added to the syrup from the initial concentration state, and after it is completely stirred and mixed, the concentration change is measured using a saccharimeter. Subsequently, the viscosity change is measured after mixing is performed using a viscometer. After the measurement is performed, an appropriate amount of water is added again. After fully mixing and stirring the solution, the measurement is repeated until the viscosity is reduced to the minimum viscosity.

DOI: 10.1201/9781003299127-278

The diffusion coefficient (D) of matter in a liquid varies with the viscosity of the liquid. It is generally believed that D is inversely proportional to the viscosity of liquid. In this study, Wilke–Chang's formula was applied to calculate the D in liquid.

$$\mathrm{D} = 7.4 \times 10^{-8} \times \frac{(xM)^{1/2} T}{\mu V^{0.6}} \tag{1}$$

where x is the association parameter of the pure solvent (when solvent is water, x = 2.6), M the molecular weight of the solvent (g/mol), μ the viscosity (Pa·s), c the concentration, V the molar volume of the solute (cm^3/mol), and T the temperature (°K). The parameters of the syrup (as shown in Table 1) are used in this study. Figure 2 shows the profile of the diffusion coefficient–viscosity obtained using Wilke–Chang's formula and the viscosity measured at different concentrations using the setup shown in Figure 1. When the diffusion coefficient is lower than 1Pa·s, the diffusion coefficient is almost unchanged. Meanwhile, the viscosity remains almost unchanged when the concentration is lower than 65%.

Table 1. Wilke–Chang's parameters.

Molecular weight of the solvent (g/mol)	18	Molar volume of the solute (cm^3/mol)	244.5
Viscosity of the solvent (Pa·s)	0.001	Temperature (K)	293.15

Figure 1. Viscosity measuring instrument.

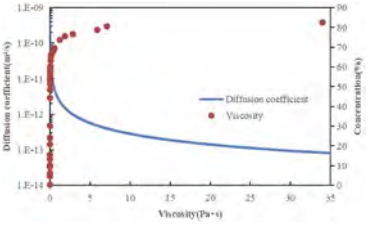

Figure 2. Viscosity–diffusion coefficient-concentration.

3 NUMERICAL ANALYSIS

3.1 *Numerical model*

Authors prepare a container model which is upper is free (i.e. no pressure and no inflow). Therefore, the Navier–Stokes (NS) equation and hydrostatic pressure condition are expressed by only the upper-end open boundary condition.

$$\frac{dV_i}{dt} = \frac{\partial V_i}{\partial t} + u\frac{\partial V_i}{\partial x} + v\frac{\partial V_i}{\partial y} + w\frac{\partial V_i}{\partial z} = -\frac{1}{\rho} gradP + \frac{\mu}{\rho}\nabla^2 V_i + F \tag{2}$$

$$P = \rho g z \tag{3}$$

Here, V_i is the velocity in the pore; $i = x, y;$ t is the time; u and v are the velocities for each dimension; ρ is the fluid density; P is the pressure; μ is the viscosity; F is the body force. The velocity V_i is substituted into the advection term of the advection–diffusion equation. For the analysis, the diffusion of syrup in the pore into water is expressed by the following advective–diffusion (AD) equation:

$$\frac{\partial c}{\partial t} = D \cdot \nabla^2 c - V_i \cdot \nabla c \tag{4}$$

c is the concentration. The parameters as shown in Table 2. To evaluate the variable D, two cases are prepared. One is using a constant D of 5.1 × $10^{-1\circ}$ (m^2/s). And the other case is that in the

analysis, the viscosity can be deduced by Figure 2, and then the deduced viscosity can be used in equation (1) to get diffusion coefficient D and both parameters are use in equation (2) at each time step. The flow of fluid in granular material models with different particle shapes and sizes is only affected by gravity. The calculation time is 2000 s, and the outputs are obtained every 10 s. Figure 3 shows three different meshes in a 4.5 mm × 3.5 mm area obtained from an X-ray CT image. To investigate the relationship between the fluid behavior and pore structure, silica sand 5, glass beads (GB), and crushed glass beads (CGB) are prepared as three different types of particles. Table 3 shows the settings of the meshes. The pore is filled with the syrup, and water is filled in the bottom reservoir. For the initial condition, the concentration at the top is set as c = 82.5%, and the concentration of water at the bottom of the model is set as c = 0%. The hydrostatic pressure condition is used in the Navier–Stokes equation. To elucidate the relationship between the pore structure and the advection–diffusion phenomenon, the authors analyzed the advection–diffusion of three types under the effect of gravity only. All calculations were performed using computational fluid dynamics (CFD) simulation and the surface flow modules in COMSOL 5.3a.

Table 2. Fluid parameters.

Diffusion coefficient (m^2/s)	5.1×10^{-1} ◦
Water density (kg/m^3)	1000
Water viscosity (Pa·s)	0.001
Syrup density (kg/m^3)	1400
Syrup initial concentration (%)	83
Syrup viscosity (Pa·s)	34

Table 3. Numerical setting.

	Silica 5	GB	CGB
Number of nodes	14561	13946	10339
Number of elements	246554	254046	204322
Time step (s)	10	10	10

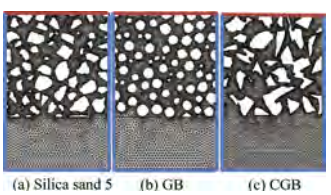

Figure 3. Geometry from numerical analysis.
(Red line: open boundary, without velocity; blue line: without velocity)

3.2 *Analysis results*

Figure 4 shows the pore size distribution curve of the three grains obtained from the method of Mukunoki *et al.* (2016). The average pore diameters of silica sand 5 and GB are similar, i.e., 0.13 mm. In addition, the average pore diameter of CGB is 0.17 mm. Figure 5 (I) and (II) show the concentration distributions calculated using (I) a constant D and (II) various D values at 1000 s for each material, respectively. The concentration obtained using the D from Wilke–Chang's equation shows that the diffusion layer becomes thinner as the concentration gradient increases. As shown in Figure 2, the D at high concentrations is small; therefore, the flow change at high concentrations on the upper region is extremely slow. Figures 6 (I) and (II) show the concentration at 2000 s. The results based on the constant D show that diffusion occurs faster as compared with those based on variable D values, as shown in Figure 6 (I). The change in D with the viscosity confirms almost no progress in dissolution in the upper interstitial region, as shown in Figure 6 (II). When D changes because of the viscosity, the syrup at the top of exhibits high viscosity and less fluidity; therefore, D is less than 10^{-12} m^2/s and water cannot diffuse into the syrup. Comparing between silica sand 5 and GB, although their porosity diameters are the same as that shown in Figure 4, the diffusion of syrup is different. The concentration of syrup in GB is distributed uniformly, but the diffusion on the left region of silica sand is faster than that on the right. The analysis shows in all cases, the syrup is trapped in the yellow circle shown in Figure 6. Figure 7 shows the concentration and velocity profiles at the black

point indicated in Figure 6. Compared among silica sand 5, GB, and CGB, at the initial state of the position where the syrup appears trapped, the liquid flow speed is low, and the transport of syrup is primarily governed by diffusion. Furthermore, the liquid flow velocity in the pores of GB is 10 times faster than those of silica sand 5 and CGB, and the diffusion speed of syrup is relatively fast. When the syrup concentration reaches a certain concentration and the fluidity of syrup increases significantly, the migration speed is expected to be high.

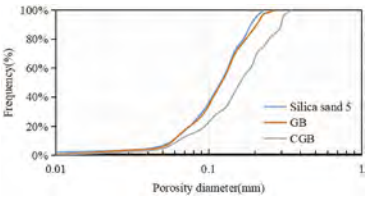

Figure 4. Pore diameter distribution curves of three types of sand.

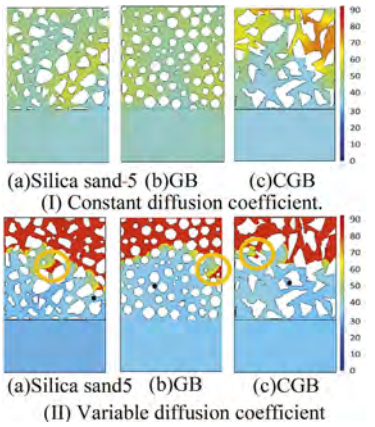

Figure 6. Concentration at 2000s.

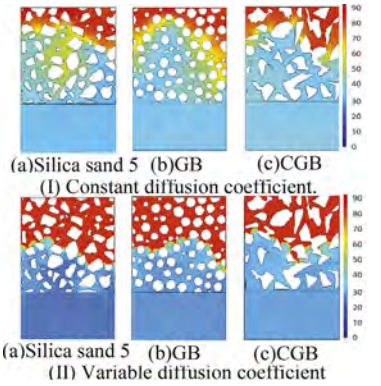

Figure 5. Concentration at 1000 s.

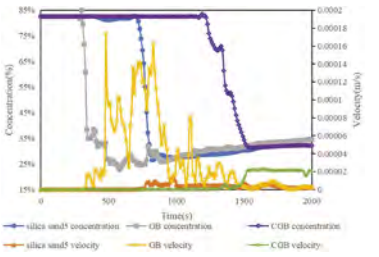

Figure 7. Concentration-velocity relationship.

4 CONCLUSIONS AND ACKNOWLEDEGMENT

In this study, authors focused on the flow and concentration of syrup in granular materials are analyzed using 2D-FEM coupled NS and AD equations with/without change of the diffusion and viscosity coefficients with concentration change of syrup in water. When the syrup concentration reaches a certain concentration, the fluidity of the syrup increases significantly because of increase of diffusion coefficient and reduction of viscosity. The area where water and syrup contacted has concentration change so that the changing speed of diffusion and viscosity coefficient become fast locally. The liquid flow rate in the pores of GB is 10 times that of silica sand5 and CGB under same porosity condition. This indicates that pore structure affects fluid migration.

In the end, authors would like to acknowledge that this research has been supported by Fund for the Promotion of Fostering Joint International Research(B) (19KK0109). We also appreciate China Scholarship Council about financial support for Chinese students.

REFERENCES

Lin, L., Zeng, F. & Gu, Y. 2014: A circular solvent chamber model for simulating the VAPEX heavy oil recovery process, *Journal of Petroleum Science and Engineering*, 118, 27–39.

Mukunoki, T., Miyata, Y., Mikami, K. & Shiota, E. 2016: X-ray CT analysis of pore structure in sand, *Solid Earth* 7(3), 929–942.

Smart Geotechnics for Smart Societies – Zhussupbekov, Sarsembayeva & Kaliakin (Eds)
© 2023 The Author(s), ISBN 978-1-003-29912-7
Open Access: www.taylorfrancis.com, CC BY-NC-ND 4.0 license

Scaling effects on lead release from excavated hydrothermally altered rock

X. Du, T. Inui & S. Ogata
Osaka University, Suita, Osaka, Japan

ABSTRACT: Excavated hydrothermally altered rocks naturally contain hazardous elements. When these rocks are exposed to the environment, they generate leachates containing toxic elements like lead and arsenic exceeding the environmental regulations. In this study, column percolation tests were performed for crushed hydrothermally altered acid rock sample at various particle sizes and column dimensions to assess the leaching of lead. Both the larger particle size and larger thickness lowered the pH values of the effluents and promoted the leaching of Pb, almost proportional to the specific surface area of the samples and the retention time in the column. pH values influenced by the particle size and layer thickness were found to have a significant correlation with Pb concentrations. This finding supports that the scaling effects arising from particle size and column dimensions on Pb leachability can be accounted for by the pH alternation.

1 INTRODUCTION

Hydrothermally altered rocks contain certain amounts of non-anthropogenic toxic metals and metalloids such as lead and arsenic due to their geological histories. Although these toxic elements could remain stable in the rock mass under an anaerobic depositional environment, they become mobile and might contaminate the surrounding soil and groundwater when they are excavated, since an increased specific surface area, exposure to water and air, and wetting-drying processes promote their leachability.

Column percolation test is one of the most common methods used to evaluate the leaching behaviors of toxic elements in geomaterials (e.g. ISO/TS 21268-3 2019). Currently, most column experiments employ a particle size of less than 2 mm or so to prepare the specimens, mainly due to the limitations in dimensions of columns adopted to ensure the sample homogeneity and prohibit the preferential flow (Inui et al. 2017). The scaling effects resulting from particle size and column size on the leaching behavior are apparent but still not fully understood and should be evaluated quantitatively to appropriately interpret the laboratory testing results into the in-situ leaching behavior. To address these issues, column percolation experiments were performed for a hydrothermally altered rock with two different particle size distributions and two column thicknesses. Changes in pH and the evolution of Pb were continuously monitored to evaluate the scaling effects arising from both particle and column sizes.

2 MATERIALS AND METHODS

2.1 *Materials*

The hydrothermally altered rock in this study was collected around a tailing dump of a copper-lead mine in Japan. Rock samples were collected randomly by hand shovels with varying original sizes from 20 to 100 mm. After being transported to the laboratory, these rocks were air-

DOI: 10.1201/9781003299127-279

Table 1. List of column experimental conditions.

Case	Particle size (mm)	Inner diameter (mm)	Thickness (mm)	Dry density (g/cm^3)	Porosity	Flow rate (cm/day)	Specific surface area (cm^2/g)
S	2-9.5	50	280	1.55	42.6%	3.06	2.41
M	2-26.5	150	280	1.55	42.6%	3.06	1.03
L	2-26.5	150	560	1.55	42.6%	3.06	1.03

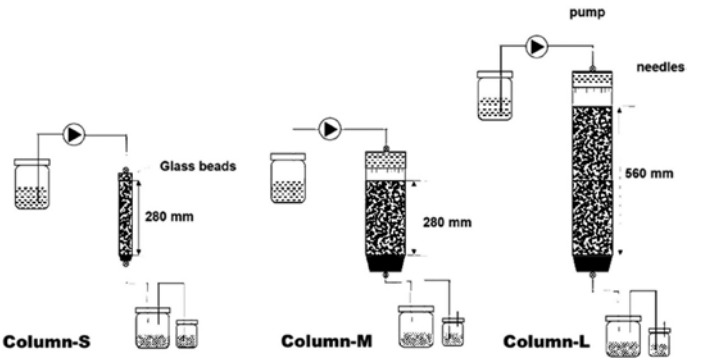

Figure 1. Schematic diagram of the column experimental setup.

dried, manually crushed by a hammer, and sieved into 4 fractions: 2-4.75 mm, 4.75-9.5 mm, 9.5-19.5mm, and 19.5-26 mm. Then these four fractions were remixed to 2-9.5 mm (2--4.75 mm×50 wt.% +4.75-9.5 mm ×50 wt.%) and 2-26.5 mm (2-4.75 mm×12.5 wt.% +4.75-9.5 mm ×12.5 wt.%+ 9-19.5 mm ×25 wt.% + ×19.5-26.5 mm×50 wt.%), both of which were used to pack the columns. The X-ray diffraction (XRD) analysis revealed that the main mineral compositions of the rock were quartz, chlorite, and mica. The bulk chemical composition of the altered rock samples primarily includes SiO_2 (wt. 59.91%), Al_2O_3 (wt. 15.62%), Fe_2O_3 (wt.15.23%), and PbO (wt. 0.05%). Pb concentration obtained from the test method Japanese Environment Agency Notification No.46 in 1991 was 35 μg/L.

2.2 *Column percolation tests*

Table 1 and Figure 1 show the column setup and experimental conditions. Three columns were set up. In Column S, the particle size was 2-9.5 mm while particle size was 2-26.5 mm in Column M and L. Column S and M shared an identical thickness of 280mm, but Column L had as twice the thickness(560mm) as that of Column M. For standardization, rock samples were packed to a dry density of 1.55 g/cm^3 in all three columns. Deionized water was introduced at a flow rate of 3.06 cm/day through three peristaltic pumps and allowed to flow by gravity. Effluents were collected every other day in the sampling bottles at the bottom of each column. The pH of the effluents was measured. Then, effluents were filtrated through 0.45μm filters and the filtrates were acidified and refrigerated. Pb concentration was analyzed by a Microwave Plasma Atomic Emission Spectroscopy (MP-AES) (4210 MP-AES, Agilent Technologies, Inc.).

3 RESULTS

3.1 *Effect of particle size distribution on the leaching of lead*

Figure 2 shows the evolution of Pb concentrations in the effluents from the columns with 2-9.5 mm (Column S) and 2-26.5 mm (Column M) in particle sizes. The ratio of the SSA (specific surface area) of Column S to that of Column M was 2.3. Pb concentrations of Column

S showed a fluctuating pattern during the first 90 days and then stabilized at around 50 μg/L, while Pb concentrations of column M fluctuated at 20 μg/L after a decline during the first 10 days. Leaching concentrations of Pb in both cases exceeded the Japanese standard for groundwater (10 μg/L). Cumulative mass of released Pb with the cumulative flow volume in the liquid to solid ratio (L/S), shown in Figure 3, revealed that the final cumulative Pb leachability in Column S was 2.7 times that in Column M, which is almost equivalent to the ratio of the SSA.

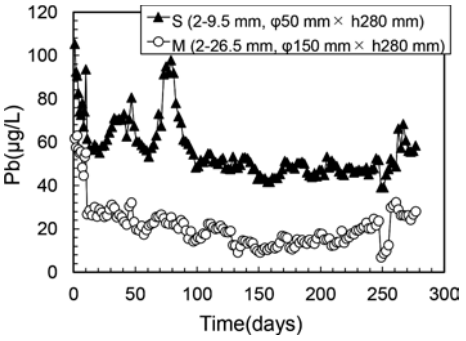

Figure 2. Particle size effect on Pb concentration.

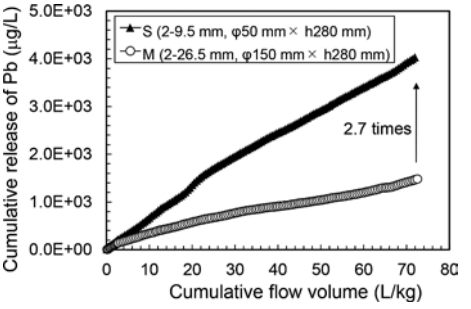

Figure 3. Particle size effect on cumulative Pb release.

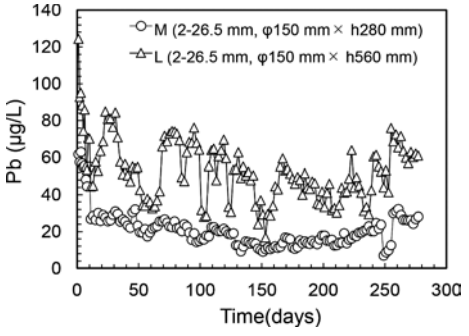

Figure 4. Thickness effect on Pb concentration.

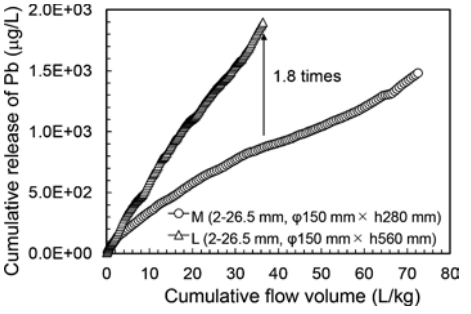

Figure 5. Thickness effect on cumulative Pb release.

3.2 *Effect of column thickness on the leaching of lead*

Figure 4 shows the evolution of Pb concentrations in columns with 280 mm (Column M) and 560 mm (Column L) thicknesses. Pb concentrations of Column L fluctuated strongly at around 50 μg/L after a sharp drop within the first 10 days and were1.5-5 times those of Column M. To compare the leaching under the same L/S ratio, Pb accumulative releases were plotted with the cumulative flow volume in the L/S ratio (Figure 5). The cumulative Pb leachability of the 560 mm thickness column was almost twice (1.8 times) that of the 280mm column except for the initial stage. This increase in Pb leachability proportional to the thickness could be attributed to the lower pH in the 560mm column, which will be further discussed in the section below.

4 DISCUSSION

Figure 6 shows the profiles of effluent pH in the three columns. The lowest pH values among the three columns occurred on the first day and then all pH values increased in the successive 20 days prior to stabilization. After 140 days, all pH values started to rise again and eventually

stabilized around 5.0, 5.4, and 5.2. Except for the initial 20 days, pH values in the fine-sized Column S were about 0.4 pH units lower on average (i.e. 2.5 times in H^+ concentration) than those in coarse-sized Column M and pH values in the thick Column L were about 0.25 pH unit lower in average (i.e. 1.8 times in H^+ concentration) than those in thin Column M over the entire experimental duration, although the fluctuations of pH values in the coarse-sized column, particularly in Column L, were greater than that in fine-sized Column S. This observation support that the pH values also correlated quantitatively to the SSA and the column thickness.

To evaluate the pH effect on Pb leaching in column percolation tests, concentrations of Pb obtained in the three column tests were plotted with respect to the effluent pH values in Figure 7, which indicates that the lower pH values, associated with the higher reactivity of the fine particles and the longer retention time of the leachate in the column, enhanced the Pb leaching. This relatively high correlation between Pb and pH values indicated that pH was the dominant factor in Pb leaching in column experiments regardless of the various particle size and column thicknesses.

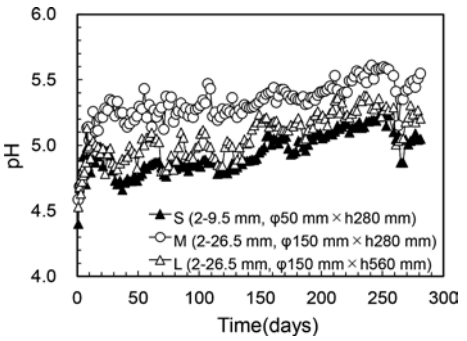

Figure 6. Evolution of pH values with time.

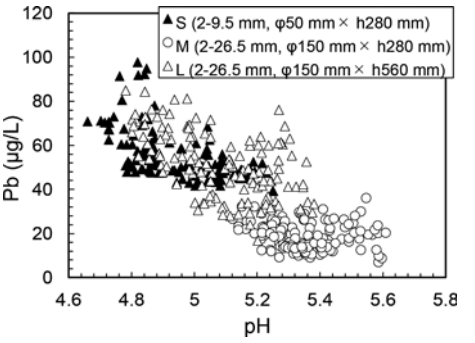

Figure 7. Relations between pH and Pb concentrations.

The accordant fluctuations in pH and Pb concentration, particularly in the 560mm column, also supported this deduction (Figures 4 and 6). The high pH-dependency of Pb leaching may primarily be explained by the adsorption-desorption of Pb onto Fe-oxyhydroxide and the dissolution-precipitation of carbonate minerals cerussite ($PbCO_3$) and hydrocerussite ($Pb_2(CO_3)_2(OH)_2$) (Gadde et al. 1974; Godelitsas et al. 2003; Tabelin et al. 2012). As pH becomes more acidic, Pb-carbonates become more soluble and Fe-oxyhydroxides/oxides become more positively charged, which could release more Pb into the solution.

5 CONCLUSIONS

The scaling effects on non-anthropogenic Pb leaching from the hydrothermally altered rock, triggered by the particle size and layer thickness, were investigated by performing column experiments with two particle size ranges and two thicknesses. The main findings of this study are summarized as follows;

(1) Both the larger SSA of the rock sample and layer thickness led to the lower effluent pH values and the higher Pb release with respect to the cumulative water flow in the L/S. They quantitatively correlated well with each other.
(2) A significant correlation between pH and Pb release demonstrated that pH values could account for the Pb leaching from the acidic hydrothermally altered rock, influenced by the particle size and column dimension. Further research is necessary to evaluate the scaling effects on the leaching of other typical toxic elements such as arsenic.

ACKNOWLEDGEMENT

This research was supported by the Japan Society for the Promotion of Science (JSPS) for scientific research (Project No. 19H02236 and 18H03797).

REFERENCES

Gadde, R. R. & Laitinen, H. A. 1974. Studies of heavy metal adsorption by hydrous iron and manganese oxides. *Analytical Chemistry* 46(13): 2022–2026.

Godelitsas, A., Astilleros, J.M., Hallam, K., Harissopoulos, S. & Putnis, A. 2003. Interaction of calcium carbonates with lead in aqueous solutions. *Environmental Science and Technology* 37(15): 3351–3360.

Inui, T., Satoshi, S., Atsushi, T. & Takeshi, K. 2017. Scaling effects on inorganic constituents leaching from excavated rocks with natural contamination. *Proceedings of the 2nd Symposium on Coupled Phenomena in Environmental* Geotechnics *(CPEG2)*: 7–10. Leeds: UK.

ISO/TS 21268-3. 2019. *Soil quality —leaching procedures for subsequent chemical and ecotoxicological testing of soil and soil materials Part 3: Up-flow percolation test*.

Tabelin, C.B., Igarashi, T., Tamoto, S. & Takahashi, R. 2012. The roles of pyrite and calcite in the mobilization of arsenic and lead from hydrothermally altered rocks excavated in Hokkaido, Japan. *Journal of Geochemical Exploration* 119–120:17–31.

Smart Geotechnics for Smart Societies – Zhussupbekov, Sarsembayeva & Kaliakin (Eds)
© 2023 The Author(s), ISBN 978-1-003-29912-7
Open Access: www.taylorfrancis.com, CC BY-NC-ND 4.0 license

Swelling deformation and unloading curve of compacted bentonite in saline solution

Y. Watanabe & E. Yoshikawa
Central Research Institute of Electric Power Industry, Chiba, Japan

ABSTRACT: The swelling deformation of compacted Na-bentonite using NaCl solution was investigated. A higher concentration resulted in a lower swelling rate. Upon unloading the void ratio increased along the normal consolidation line, however the unloading curves for deionized water (DW) and NaCl solution differed after a threshold void ratio. The unloading curve in DW gradually increased its slope, whereas that in NaCl seemed to reach upper value. It is indicated that the osmotic effect basically dominates the swelling deformation in lower confining stress and the crystalline swelling of montmorillonite controls the limits of volumetric change in saline solution.

1 INTRODUCTION

The design of most geological disposal facilities for radioactive waste is based on the multibarrier concept, which involves natural host rocks and engineered barriers. Owing to the low permeability, compacted bentonite can be used to inhibit the migration of radioactive nuclides. Swelling deformation of the material is important in terms of the self-sealing, which fills the primary space caused by construction difficulties, and the self-healing, which fills the gap generated by material erosion and gas migration after saturation (Pusch, 1992, NUMO, 2013). According to the environmental condition, the saline solution, such as seawater (SW), infiltrates the engineered barrier. The change in swelling property is a key issue on the evaluation of self-sealing and healing.

The swelling pressure and deformation have been discussed on the basis of the void ratio–effective stress, *e*-*p*', relationship (Sridharan et al., 1986, Wang et al., 2012). The osmotic swelling likely characterizes the consolidation-swelling behavior of the compacted bentonite, specifically upon unloading process (Kyokawa et al., 2020). Higher ionic concentration of porewater declines the osmotic effect. It is significant to understand the swelling deformation of the compacted bentonite in saline solution in relation to the ordinal consolidation-swelling test result on *e*-*p*' plane.

This study investigated the swelling deformation of compacted Na-bentonite using NaCl solution. After the equilibrium swelling pressure was measured, the swelling deformation was measured by unloading the confining stress in steps. The unloading curves in deionized water (DW) and saline solution were compared and the difference was discussed.

2 EXPERIMENTAL PROCEDURE

2.1 *Sample preparation and specimen production*

Na-bentonite (Kunigel-V1, Kunimine Industries Co., Ltd.), mined from Yamagata Prefecture in Japan, was used. The physicochemical properties of the bentonite are listed in Table 1. The leachable cations, which approximately correspond to the exchangeable cations, were identified by leaching with a 1-mol/L NH_4Cl solution. Leachable Na ions were dominant in the bentonite. The amount of methylene blue absorbed was measured according to the Japanese Industrial Standard

DOI: 10.1201/9781003299127-280

(JIS Z 2451). Assuming that the methylene blue absorbed on to the pure montmorillonite in the bentonite was 140 mmol/100g, the montmorillonite content was estimated to be 51.4%. According to X-ray diffraction analysis, other than the montmorillonite, the bentonite contained quartz, feldspar, clinoptilolite, calcite, pyrite, and dolomite (Watanabe and Tanaka, 2022).

The compacted bentonite was produced by static compaction. The target dry density of the specimen was 1.6 Mg/m^3. The specimen was 20 mm in height and 60 mm in diameter, including a center hole of 6.0-mm diameter. A noncontact-type displacement gauge of 6.0 mm in diameter was inserted the hole and the small-scale deformation of the specimen was directly measured.

Table 1. Physicochemical properties of the Na-bentonite used in this study.

Particle density of soil (Mg/m^3)		2.674
Methylene blue adsorbed (mmol/100g)		72
Total amount of leachable cation (meq/100g)		106.7
Amount of leachable cation (meq/100g)	Na	57.9
	K	1.9
	Ca	44.1
	Mg	2.8

2.2 *Swelling deformation test*

Figure 1 depicts the swelling deformation test apparatus equipped with controls for the application of a small strain and loading pressure. First, the swelling pressure was measured under constant constraining condition by controlling small strain using the stepping motor during the hydration by DW or NaCl solution (0.5 mol/L and 1.0 mol/L), because the slight deformability of specimen during saturation influences the equilibrium swelling pressure (Watanabe and Tanaka, 2022). The small strain control was turned off after the equilibrium swelling pressure was measured, and a vertical pressure equal to the equilibrium swelling pressure was applied to the specimen. Subsequently, the vertical pressure was unloaded, and the swelling deformation was measured. The vertical pressure was reduced in steps, and the swelling deformation was measured when it approximately converged to a constant value at each stage. The swelling rate was defined as the ratio of the incremental height of the specimen to the initial height of the specimen.

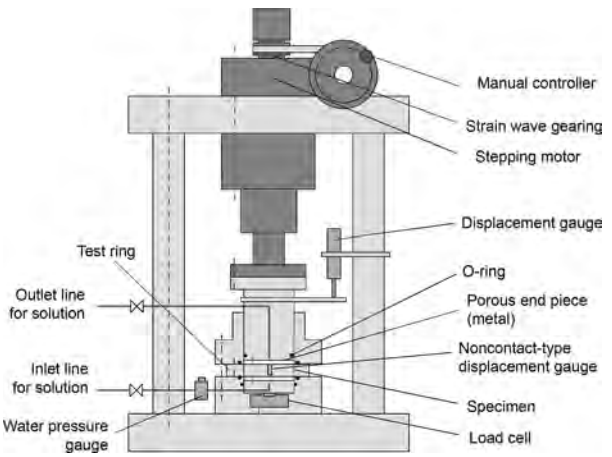

Figure 1. Apparatus for swelling deformation test.

3 RESULT AND DISCUSSION

3.1 *Swelling pressure and swelling deformation*

The relationship between the equilibrium swelling pressure and NaCl concentration is shown in Figure 2. The equilibrium swelling pressure was exponentially decreased along the increase in NaCl concentration. The equilibrium swelling pressure in 1.0 mol/L-NaCl solution was approximately 62% of that in DW.

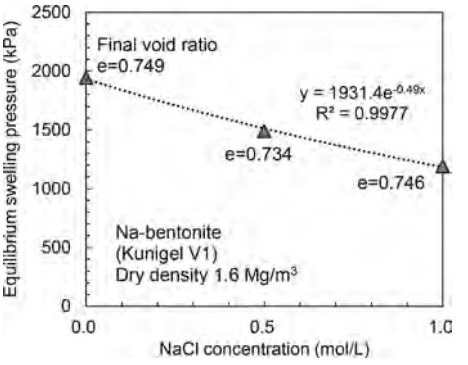

Figure 2. Relationship between equilibrium swelling pressure and NaCl concentration.

The relationship between the vertical pressure and the swelling rate is depicted in Figure 3. A smaller vertical pressure resulted in a larger swelling rate of the compacted bentonite. Furthermore, a higher NaCl concentration showed a lower swelling rate. The swelling rate in NaCl solutions when 26–28 kPa of the vertical pressure was 24–29%, which was consistent with the result in SW, considering the ionic strength of SW.

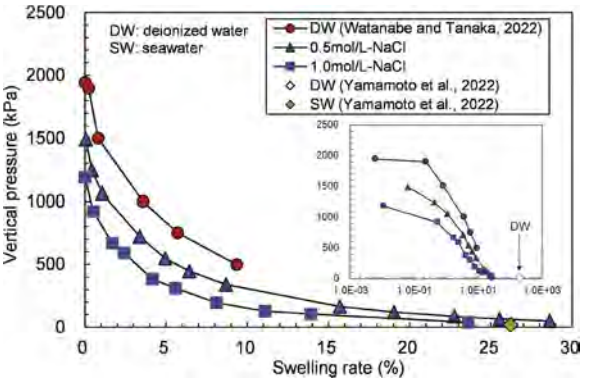

Figure 3. Relationship between vertical pressure and swelling rate.

3.2 *Unloading curves in the swelling deformation for deionized water and saline solution*

The void ratio after swelling deformation in each vertical pressure was compared to the normal consolidation line (NCL) in Figure 4. Upon unloading of the specimen saturated using DW, which had no consolidation history, the specimen swelled, and the void ratio increased along the NCL (Watanabe and Tanaka, 2022). The unloading curves for DW and NaCl solution differed after a threshold void ratio. In lower vertical pressure for DW, afterwards, the void ratio greatly exceeded from the extrapolated values of the NCL in the high-pressure range. It was close to the swelling pressure calculated based on the diffuse double

layer (DDL) theory (Komine and Ogata, 2004). It is suggested that the lower vertical pressure, as a threshold around the void ratio of 1.0, causes a significant non-linearity of the unloading curve through that the electrostatic swelling becomes more dominant. The clay particles would more disperse in the specimen, and the microstructure might be reconstructed.

For NaCl solution, the unloading curve was approximately same as that in DW, although it included a slight nonlinearity. Stepped unloading after constant volume saturation was expected to lead to approximately the same void ratio as when the material was swollen from unsaturated to saturated in saline solution. However, the swelling deformation seemed to be stopped around 1.2 of void ratio in the saline solution. This is because that the diffuse ion layer growth on montmorillonite is curtailed in the saline solutions (Rao et al., 2013), and it was surmised that only crystalline swelling was operative on swelling deformation in that condition. The crystalline swelling would be a key to estimate the swelling rate of compacted bentonite in higher ion concentration condition, that osmotic effect cannot work.

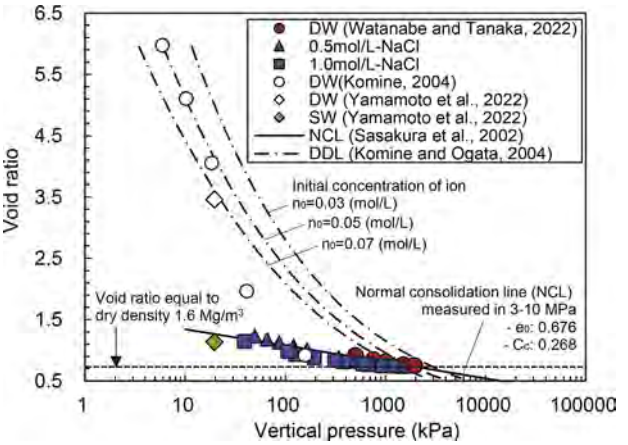

Figure 4. Relationship between void ratio and vertical pressure.

4 CONCLUSIONS

This study investigated the swelling deformation of compacted Na-bentonite (1.6 Mg/m^3) using NaCl solution, comparing some literature values. The void ratio of the compacted bentonite increased along the NCL for a while after unloading. The unloading curve in DW gradually increased its slope after a threshold void ratio, whereas that in NaCl seemed to reach upper value. It should be noted that the limit of swelling rate changes according to the ion concentration. Further study needs to infer the limitation by considering the crystalline swelling of montmorillonite.

REFERENCES

Komine, H. (2004). Simplified evaluation for swelling characteristics of bentonites. Engineering Geology. 71, 265–279

Komine, H. & Ogata, N. (2004). Predicting swelling characteristics of bentonites. J. Geotech. Geoenviron. Engng 130, No. 8, 818–829.

Kyokawa, H., Ohno, S. & Kobayashi, I. (2020). A method for extending a general constitutive model to consider the electro-chemo-mechanical phenomena of mineral crystals in expansive soils. Int. J. Numer. Analyt. Methods Geomech. 44, No. 6, 749–771.

NUMO (2013). Safety of the geological disposal project 2010 – safe geological disposal based on reliable technologies, NUMO technical report NUMO-TR-13-05. Tokyo, Japan: Nuclear Waste Management Organization of Japan (NUMO).

Pusch, R. (1992) Use of bentonite for isolation of radioactive waste products. Clay Minerals. 27, 353–361.

Rao, S.M., Thyagaraj, T. & Rao, P.R. (2013). Crystalline and osmotic swelling of an expansive clay inundated with sodium chloride solutions. Geotech. Geol. Eng. 31, 1399–1404.
Sasakura, T., Kuroyanagi, M. & Okamoto, M. (2002). Studies on mechanical behaviour of bentonite for development of the constitutive model, Report JNC TJ8400-2002-025. Ibaraki, Japan: Japan Nuclear Cycle Development Institute (in Japanese).
Sridharan, A., Rao, A. S. & Sivapullaiah, P. V. (1986). Swelling pressure of clays. Geotech. Test. J. 9, No. 1, 24–33.
Yamamoto, Y., Goto, T., Kitagawa, Y., Watanabe, Y., Yokoyama, S. & Shimbashi, M. (2022). Fundamental engineering properties of compacted Japanese bentonites and bentonite-sand mixtures. NUMO technical report NUMO-TR-21-02. Tokyo, Japan: Nuclear Waste Management Organization of Japan (NUMO). (in Japanese).
Wang, Q., Tang, A. M., Cui, Y. J., Delage, P. & Gatmiri, B. (2012). Experimental study on the swelling behaviour of bentonite/clay stone mixture. Engineering Geology. 124, 59–66.
Watanabe, Y. & Tanaka, Y. (2022). Swelling pressure of compacted bentonite acting on constraining material with deformability. Géotechnique. In press. doi: 10.1680/jgeot.20.P.348.

Smart Geotechnics for Smart Societies – Zhussupbekov, Sarsembayeva & Kaliakin (Eds)
© 2023 The Author(s), ISBN 978-1-003-29912-7
Open Access: www.taylorfrancis.com, CC BY-NC-ND 4.0 license

Elevated temperature on leaching of arsenic and boron from excavated rocks

T. Kato, A. Takai, L.W. Gathuka & T. Katsumi
Graduate School of Global Environmental Studies, Kyoto University, Kyoto, Japan

Y. Xie
Graduate School of Engineering, Kyoto University, Kyoto, Japan

ABSTRACT: This work evaluated the leaching behaviors of geogenic arsenic and boron of two excavated rocks under different temperatures. Excavated rocks with geogenic contamination are expected to be used in embankments with proper countermeasures. Their leaching behaviors might change because of seasonal and daily changes in ground temperature. However, the effect of temperature on leaching behaviors has not been well examined. Column tests at temperatures of 20 and 40°C were performed using rock samples. Elevated temperatures led to the release of greater amounts of arsenic and boron. The largest arsenic concentrations obtained from the column tests were 0.53 mg/L at 40°C, while at 20°C was 0.15 mg/L for one rock sample. The largest concentrations of arsenic and boron obtained at 40°C were at most 3.5 times larger than at 20°C. Boron concentrations decreased as electric conductivity decreased. Electric conductivity can be one index to predict the leaching behavior of boron.

1 INTRODUCTION

Large volumes of excavated soils and rocks were generated from construction projects. As a result, a certain percentage of the soils and rocks contain contaminants derived from geological processes. Geogenic contaminants, such as arsenic (As) or boron (B), are widely distributed in Japan (e.g., Tabelin et al., 2018). Such soils and rocks are expected to be used in embankments as a part of ongoing efforts to achieve sustainable soil management. However, their proper utilization is sometimes a concern, especially because contaminants can be released from the soils and rocks. Given the importance of developing economical and effective utilization methods for geogenically contaminated soils and rocks, evaluating the leaching behaviors is essential.

When excavated materials are utilized in embankments or other shallow geostructures, the effect of ground temperature on the leaching behavior of toxic elements becomes a technical concern. The daily and seasonal temperature changes in the shallow ground can be much more significant than those in the deep ground. Temperature near the ground surface can be elevated because of solar radiation. The ground temperature was often more than 30°C (Menberg et al., 2013). However, laboratory leaching tests are usually conducted at room temperature (approximately 20°C). Since leaching behaviors of geogenic contamination can be affected due to thermo-mechanical-chemical interactions, the effects of elevated temperature on leaching behaviors need to be clarified from a geoenvironmental perspective.

This work evaluated the leaching behaviors of As and B from two excavated rocks with geogenic contamination using column tests under different temperatures. Column tests were less applied to evaluate the leaching behaviors of geogenic contaminants under different temperatures, while several researchers investigated using batch leaching tests (Saito et al., 2016; Takai et al., 2020). Although batch tests have advantages in simple experimental protocol with a short testing time, the applicability of this test may be limited. Since the solute kinetics under the flow conditions can be evaluated, column tests can evaluate closer to the in-field condition than batch tests (Kato et al., 2021).

DOI: 10.1201/9781003299127-281

2 MATERIALS AND METHODOLOGY

2.1 *Materials*

Two types of rocks used in this work were excavated from tunnel construction sites. The rocks were crushed to particles smaller than 2 mm for the experiments. The rock samples were stored in sealed plastic bags to prevent their oxidation by air. Table 1 highlights the fundamental physical properties of the rock samples. In addition, the total amount of As and chemical compositions of the rock samples were measured. The rock samples were air-dried at room temperature and ground into a powder with a diameter smaller than 75 μm. The samples were evaluated by X-ray fluorescence (XRF) analysis using a Shimadzu EDX 720 energy-dispersive X-ray spectrometer.

Table 1. Physical and chemical properties of rock specimens.

Parameter	Rock 1	Rock 2
Particle density, ρ_s	2.686 g/cm^3	2.749 g/cm^3
Water content, w	1.4%	4.7%
Particle size distribution		
Sand fraction [0.075–2 mm]	83%	62%
Fines fraction [<0.075 mm]	17%	38%
Average particle size	0.85 mm	0.25 mm
As content	51 mg/kg	87 mg/kg

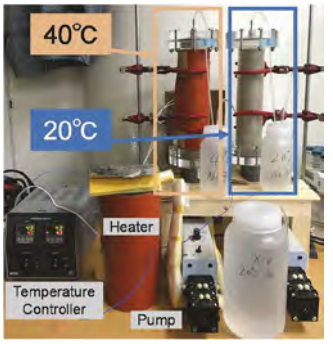

Figure 1. Setup of the column test.

2.2 *Column tests with temperature control system*

Column tests were conducted using acrylic columns (ϕ 5 cm × h 30 cm) as shown in Figure 1. A rock sample was placed in the column. Each specimen was compacted in the acrylic column in five layers with equal heights. A 125-g rammer was dropped freely from a height of 20 cm during compaction. This method was based on the corresponding ISO 21268-3 (2019). The specimen was placed between filter papers to prevent channel clogging due to fine soil particles. The dry density of the specimen for Rocks 1 and 2 were approximately 1.3 and 1.4 g/cm^3, respectively. Then distilled water was percolated in an up-flow direction using a peristaltic pump at a flow rate of approximately 15 mL/h until the specimen reached saturation. Finally, percolation was interrupted for 15 hours to achieve a saturated condition. After 15 hours, distilled water was percolated in an up-flow direction via a peristaltic pump at 15 mL/h. Leachate was collected from the outlet of the column. Column tests were conducted until the liquid-to-solid ratio (a volume of permeated solution to a dry mass of soil ratio) was larger than 10.

Temperatures of 20 and 40°C were applied to account for possible temperature changes (Menberg et al., 2013). Tests under 20°C were conducted in a constant temperature room, while 40°C were conducted by wrapping the column with rubber heaters. The temperature of the rubber heater was controlled using a controller (MTCD, Misumi Corporation). Distilled water was pre-heated to 40°C using a constant temperature bath. Tubes connected to the column were covered by glass wool (DK-089, Yamawaki Sangyo) to prevent heat dissipation. A non-contact thermometer measured the temperature of the column surface to confirm whether 40°C was achieved.

For leachate, centrifugation at 3000 rpm for 10 min and filtration with a 0.45 μm membrane filter was conducted. The filtrate electric conductivity (EC) and pH were measured using a pH/EC meter (Horiba F-54). Arsenic concentration was measured using an atomic absorption spectrophotometer (Shimadzu GFA-7000). Boron concentration was measured using an inductively coupled plasma optical emission spectrometer (Agilent Technologies ICP-OES 710).

3 RESULTS AND DISCUSSION

3.1 *Arsenic concentration and pH*

Figure 2 shows the profiles of As concentrations with pore volumes of flow (PVF) obtained from column tests. Since PVF is calculated as the volume of a permeated solution divided by a void volume, 1 PVF means one pore water is exchanged. As shown in Figure 2(a), the largest As concentration at 40°C was 0.53 mg/L, while at 20°C was 0.15 mg/L. The largest concentration at 40°C was approximately 3.5 times greater than at 20°C. As shown in Figure 2(b), As concentrations also once increased and decreased at both 40 and 20°C. The largest concentration at 40°C was 3.94 mg/L, while at 20°C was 3.19 mg/L. The largest concentration at 40°C was approximately 1.2 times greater than that at 20°C. Results show that leaching As concentration might increase as the temperature raised.

Herein, As concentrations at 1 PVF is discussed. Arsenic concentrations once increased and decreased at both 40 and 20°C. If the leaching concentration drastically decreased before 1 PVF, most contaminants flowed out as one pore water was replaced, and the leaching was considered to diminish immediately. However, even though PVF > 10, As was leached at more than 0.1 mg/L, which was 10 times larger than the regulatory limit in Japan for both rock samples. These results imply that As leching might continue relatively longer. For both Rock 1 and 2, the largest leaching concentrations were obtained after 1 PVF. Shapes of the concentration profile might not be different, but the value of the concentration might be greater at elevated temperatures.

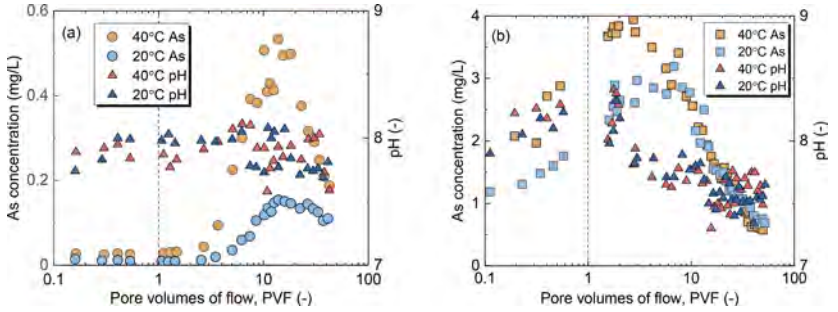

Figure 2. Arsenic concentrations and pH obtained from (a) Rock 1 and (b) Rock 2.

Figure 2 shows the profiles of pH with PVF. Alkaline pH between 7-9 was obtained from both rock samples. As shown in Figure 2(a), similar pH values were obtained regardless of temperatures, while As concentrations differed. The elevated temperature might affect not pH but As leaching behavior. According to XRF analysis, both rock samples contained some amounts of sulfide minerals. More acidic pH values should be obtained if the dissolution of sulfide minerals is promoted under elevated temperatures. However, such trends cannot be observed. Since geogenic As is usually contained in the sulfide minerals such as pyrite, dissolution of sulfide minerals is considered one of the major mechanisms of As leaching (Tabelin et al., 2018). The leaching behavior of As from these rock samples might not be related to the dissolution of sulfide minerals. In future work, the mineral composition of the rock samples and the state of the surface charge should be analyzed to investigate the leaching mechanisms of As affected by elevated temperature.

3.2 *Boron concentration and EC*

Figure 3 shows the profiles of B concentrations with PVF. Boron concentrations generally decreased as PVF increased at both 40 and 20°C. For Rock 2, the largest B concentration at 40°C was 0.14 mg/L, while at 20°C was 0.079 mg/L. The largest concentration at 40°C was approximately 1.8 times greater than at 20°C. Results show that leaching B concentration might increase as the temperature raised. In contrast to As, the largest B concentrations were obtained

before 1 PVF for both rock samples. Boron leaching might diminish more immediately than As. For B contamination, even if column tests are conducted in a short period (e.g., < 1 PVF), enough to evaluate the leaching behavior because the largest concentration can be measured.

Figure 4 shows the profiles of EC vs. B concentrations. Electric conductivity decreased drastically before 1 PVF. Generally, B concentrations decreased as EC decreased. These results mean most ions in the pore water were drained by 1 PVF. Therefore, most B might be leached with other ions as one pore water was replaced. Since measuring EC is much easier than B concentration, the EC value can be helpful indices to predict B leaching behavior approximately.

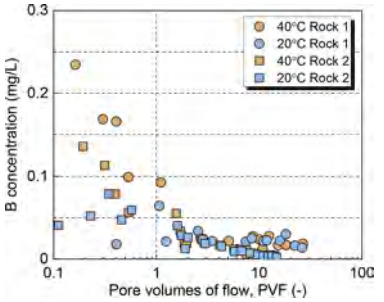

Figure 3. Boron concentrations.

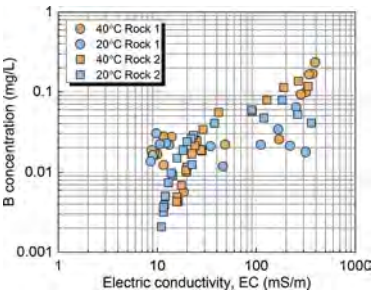

Figure 4. EC vs boron concentration.

3.3 *Geotechnical considerations for leaching behaviors under elevated temperature*

As shown in Figures 2 and 3, the largest concentrations of As and B at 40°C were at most 3.5 times larger than at 20°C. Elevated temperatures led to the release of greater amounts of As and B, but the increase was not drastic. Leaching concentration obtained from column tests is used as the boundary condition when solute transport analysis is conducted to evaluate the contamination. Since the in-situ ground temperature used by excavated materials is not always at 40°C but sometimes below 20°C, column tests conducted at 40°C may be safe side. If the solute transport analysis is performed using the As or B concentration supposed to be several times larger than obtained from the tests at room temperature, a safe prediction may conduct considering the effects of elevated temperature.

4 CONCLUSIONS

The leaching behaviors of As and B from two excavated rocks with geogenic contamination were investigated under elevated temperatures. Herein, column tests were performed at 20 and 40°C. The results support the following conclusions.

Elevated temperatures led to the release of greater amounts of As and B. The largest As concentrations obtained from the column tests were 0.53 mg/L at 40°C, while at 20°C was 0.15 mg/L for one rock sample. The largest concentrations of As and B obtained from the column tests at 40°C were at most 3.5 times larger than at 20°C. Boron concentrations decreased as EC decreased. Since measuring EC is much easier than B concentration, the EC value can be helpful indices to predict the leaching behavior of B.

REFERENCES

ISO 21268-3, 2019. Soil Quality—Leaching Procedures for Subsequent Chemical and Ecotoxicological Testing of Soil and Soil Materials—Part 3: Up-Flow Percolation Test.

Kato, T., Gathuka, L.W., Okada, T., Takai, A., Katsumi, T., Imoto, Y., Morimoto, K., Nishikata, M., and Yasutaka, T. 2021. Sorption-desorption column tests to evaluate the attenuation layer using soil amended with a stabilizing agent. *Soils and Foundations* 61(4), 1112–1122.

Menberg, K., Bayer, P., Zosseder, K., Rumohr, S., and Blum, P. 2013. Subsurface urban heat islands in German cities. *Science of the Total Environment* 442, 123–133.

Saito, T., Hamamoto, S., Ueki, T., Ohkubo, S., Moldrup, P., Kawamoto, K., and Komatsu, T. 2016. Temperature change affected groundwater quality in a confined marine aquifer during long-term heating and cooling. *Water Researches* 94, 120–127.

Tabelin, C.B., Igarashi, T., Villacorte-Tabelin, M., Park, I., Opiso, E.M., Ito, M., and Hiroyoshi, N. 2018. Arsenic, selenium, boron, lead, cadmium, copper, and zinc in naturally contaminated rocks: a review of their sources, modes of enrichment, mechanisms of release, and mitigation strategies. *Science of the Total Environment* 645, 1522–1553.

Takai, A., Iwata, Y., Gathuka, L.W. & Katsumi, T. 2020. Laboratory tests on arsenic leaching from excavated shale rock by elevated temperatures, *E3S Web of Conferences (ICEGT 2020)* 205, 09006.

Smart Geotechnics for Smart Societies – Zhussupbekov, Sarsembayeva & Kaliakin (Eds)
© 2023 The Author(s), ISBN 978-1-003-29912-7
Open Access: www.taylorfrancis.com, CC BY-NC-ND 4.0 license

Observations on deformations and pore pressures of a bentonite-sand mixture caused by heating application

T. Nishimura
Department of Civil Engineering, Ashikaga University, Tochigi, Japan

ABSTRACT: The variation in both dry density and temperature caused by the heating of a compacted, unsaturated bentonite-sand mixture tends to be the most important factor in the engineering of radioactive waste disposal barriers. The thermal effort of the bentonite-sand mixture is a significant trigger fac-tor in the coupling phenomena. Several previous experimental studies using different dry densities have reported that the most affected properties are pore pressure and expansion deformation. However, most reports lack experimental data on determination of deformation and measurement of associated pore pressures owing to a progressive increase in temperature. This study aims to establish the connection between the basic deformation properties and pore pressures produced under heating conditions and the effect on hydro-mechanical properties of a bentonite-sand mixture. This study investigated the shrinkage/expansion behavior for temperatures up to 100°C and considered the occurrence of pore pressure in the void structure for a variety of temperatures.

1 INTRODUCTION

The structural design of deep geological repositories for high-level radioactive waste consist of a barrier system using a material of hard stiffness as the sealing material (Delage et al. 2010). Some couple behavior was recognized as thermo-hydro-mechanical (THM) loadings to bentonite-sand, and THM behavior was widely studied, conducted out on previous works. Prospective designs of geological repositories for high level radioactive waste generally include an engineered berried consisting of bentonite around the waste stiffens canisters (Gens et al. 2010). As one of complex couple phenomena, a number of interacting thermal, hydraulic, mechanical and chemical phenomena produced that have a series of efforts on growing and long-term. The purpose of this study is to establish the connection between the deformation properties and the pore pressures produced under heating conditions for a bentonite-sand mixture. This study applied reliable determination of shrinkage/expansion behavior and considered the occurrence of pore pressure in void structure for a variety of temperatures.

2 TEST PROCEDURE

2.1 *Soil material and specimen*

Kunigel V1, a sodium bentonite, was used in a series of two testing programs to confirm the hydro-mechanical properties of previous experimental laboratory studies. Owing to its high montmorillonite content, the bentonite had a fines content greater than 95 %. In this testing program all of specimens mixed a silica sand, named Iitoyo No.4, into the bentonite, which had a uniformity grain size distribution. The air-dried bentonite and silica sand were humidified by spraying deionized water to reach the desired water content, which was 17.0 % in this test. All specimens had a diameter of 38 mm and a height of either 76 mm or 66 mm. The initial specimens had the following physical properties: a dry density of 1.600 Mg/m^3, void ratio of 0.710, and degree of saturation of 65.61 %. The prepared specimen size was relatively small.

DOI: 10.1201/9781003299127-282

Figure 1. Deformation test in heating.

Figure 2. Mold installed two sensors.

2.2 *Apparatus for this study*

To measure the pore fluid pressures, an improved steel mold was used, as shown in Figure 1, with two pore pressure sensors placed on the upper and lower portions of the lateral surface area. Iso-tropic heating action was supplied indirectly to the specimen through the mold. The sensors had a maximum temperature capacity of over 100°C. A steel mold without sensors was used to measure deformation in the axial direction, as shown in Figure 2. The specimen was contained by the mold, and the height of the specimen was 66 mm, which is smaller than the height of the steel mold at 76 mm.

2.3 *Series of testing program*

In the heating-deformation test, the steel mold and a thermostat chamber were used, as shown in Figure 2, and the dry densities were selected as 1.600 Mg/m^3, 1.400 Mg/m^3 and 1.200 Mg/m^3. The temperatures were 20, 60, 80 and 100°C. Only the dry density of 1.600 Mg/m^3 was used in the unconfined compression test, which was conducted after the specimen reached equilibrium at each temperature. The pressure exerted on the pores is affected by the heating effort. Therefore, to compare the pore pressure behaviors, the pore pressures were measured at both the upper and lower portions.

3 TEST RESULTS

3.1 *Deformation and unconfined compressive strength*

This study investigated the behavior of unsaturated bentonite-sand specimens with three different dry densities under increasing temperatures. Prepared heating control condition had a rage from 20°C to 100°C, and all specimens were free to deform (by shrinking or expanding) in the axial direction. All specimens exhibited expansion deformation, but the specimen with the largest deformation of 1.75 % had a dry density of 1.600 Mg/m^3, as shown in Figure 3. All specimens experienced shrinkage regardless of their dry densities at 60°C. As the temperature was incrementally and progressively increased, the shrinkage became more pronounced. The linear tendencies were verified between 60°C and 100°C, and the incline was approximately 0.01 percent per degree Celsius. Most of the shrinkage deformations occurred for the specimens with a dry density of 1.600 Mg/m^3. Subsequent to the evaluation of deformations, unconfined compression tests were conduct-ed, and the stress strain curves are shown in Figure 4. All specimens achieved peak strengths at small axial strains of less than 2.0 %. The obtained unconfined compressive strengths in order of dry densities are as follows: 563.1 kPa, 1056.9 kPa, 1121.6 kPa, and 1426.0 kPa. This verifies that the unconfined compressive strength clearly increases with increasing temperature. The black narrow symbols in Figure 4 describe the failure phenomena by unconfined compressive strength and axial strain. Considering that the performance in terms of compression stresses is a fundamental mechanical property, four straight lines were established along the data points until peak strength. The incline of the straight line clearly depends on the temperature and the determined unconfined

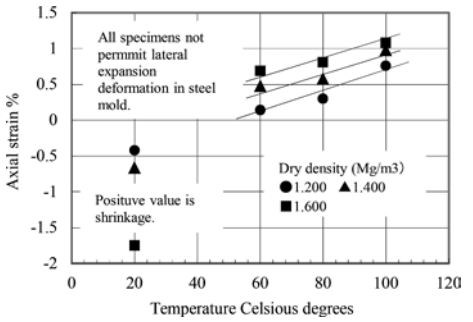

Figure 3. Change of axial strain with temperature.

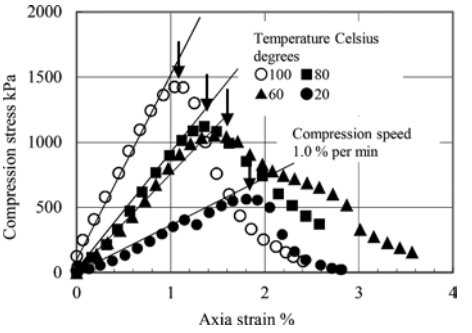

Figure 4. Stress-strain curve for dofferent temerature.

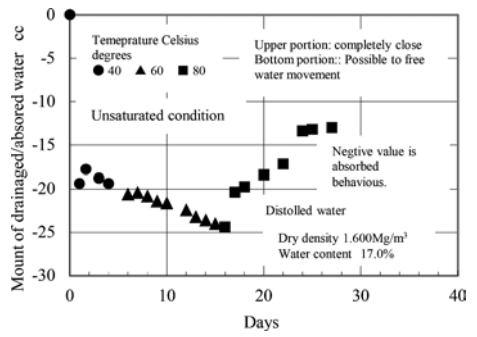

Figure 5. Change of drainaged/absorbed water.

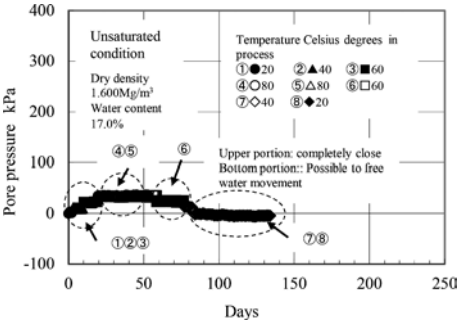

Figure 6. Measured pore pressure at upper portion.

compressive strength. The modulus of rigidity for artificial barrier structures is calculated based on the safety of predicted situations at high level radioactive waste disposal systems as follows: 170 MPa and 32 MPa for specimen temperatures of 100°C and 20°C, respectively. In addition, as the modulus of rigidity has been proven to increase with temperature, it is interesting to establish quantitative solutions.

3.2 *Hydraulic-mechanical properties under heating*

Engineered barriers are exposed to heat transfer from the radioactive waste canisters, and it is reasonable to assume that a complex coupling phenomenon is established. This phenomenon is investigated in this study by observing the change in soil moisture movement in an unsaturated bentonite-sand specimen of a constant volume in a steel mold. The hydration process and the temperature increments are shown in Figure 5. The temperature of the initial condition was 20°C. First, 40°C was applied and increased up to a maximum of 80°C. The soil moisture movement corresponding to the temperature increment was measured successfully. The soil moisture movement investigation of the unsaturated specimen, using the aforementioned heating process, described how the soil moisture movement differs for different temperature magnitudes. Almost all data sets showed the phenomenon of absorption (i.e. increased soil moisture) when the temperature was increased to 60°C. Beyond 60°C, the movement of moisture caused a drainage phenomenon, and the outflow was accurately measured. The accumulation of fluid in the small voids and the increase in pore fluid pressure causes excess soil moisture. It is possible to predict the soil moisture movements in an unsaturated bentonite-sand specimen subjected to variations in temperature.

To further understand the hydration behavior associated with soil moisture movement, pore fluid pressure measurements were also carried out. The pore pressure test was performed using two pressure sensors, which were in-stalled at the upper and lower portions of the lateral surface

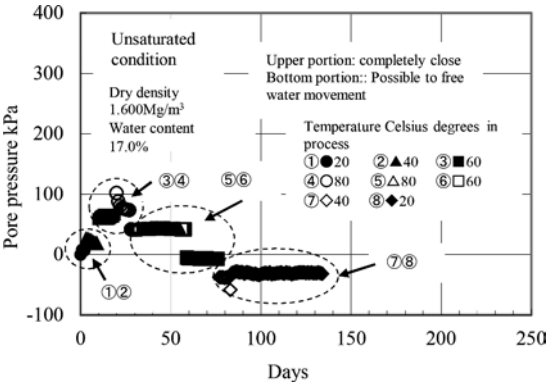

Figure 7. Measured pore pressure at bottom portion.

area of the steel mold. The temperature control process was applied at increments of 20°C with a maximum temperature of 80°C. After the temperature had reached 80°C, cooling was carried out to investigate the influence of heating-cooling hysteresis on pore pressure. At the start when the temperature was under 20°C, the specimens had different drainage conditions, which were maintained up to 80°C. The measured pore pressures of the upper portion, which remained in the completely closed condition, are shown in Figure 6. Figure 7 shows the variation in pore pressure at the lower portion, which remained in a free-draining condition. The pore fluid pressure obviously in-creased due to the temperature exceeding 40°C. The change in pore pressure according to temperature increment further varied with time. In the upper portion, the measured pore pressure reached 35 kPa at 80°C, after which the cooling process commenced. The pore pressure behavior in the cooling process was opposite to that in heating process, which is a decrement to the phenomenon. At end of test, the temperature was 20°C and the pore pressure was zero. It can be verified that the increase in pore pressure is governed by an increase in temperature by heating. The pore pressure behavior measured at the lower portion, as shown in Figure 7, is similar to that shown in Figure 6. The maxi-mum pore pressure was 102 kPa at a temperature of 80°C. In the cooling period, the pore pressure decreased smoothly to minus 30 kPa; however, the negative pore pressures contradict the pore pressure properties defined by the upper portion.

4 CONCLUSIONS

The conclusions are summarized as follows:

(1) Axial strain measurements and unconfined compression tests for different dry densities and temperatures confirm that shrinkage deformation and unconfined compressive strength are completely governed by temperature. Both the coefficient of deformation with temperature and the modulus of rigidity from stress strain properties were established and quantified.
(2) It is further clear that soil moisture movement as a hydraulic property depends on temperature. When the temperature approached 100°C, the pore fluid pressure increased and caused an out-flow of fluid.
(3) It can be verified that the pore pressures were created as a result of the applied heat, and that this pressure obviously decreased with the decrease in temperature through cooling.

REFERENCES

Delage, P., Cui, Y. J. & Tang, A.M. 2010. Clays in radioactive waste disposal, Journal of Rock Mechanics and Geotechnical Engineering, 2(2), 111–123.

Gens, A., Guimaräes, L.N., Olivella, S., Sánchez, M. 2010. Modelling thermo-hydro-mechano-chemical interactions for nuclear waste disposal, J. Rock Mechanics and Geotechnical Engineering, 2(2), 97–102.

Smart Geotechnics for Smart Societies – Zhussupbekov, Sarsembayeva & Kaliakin (Eds)
© 2023 The Author(s), ISBN 978-1-003-29912-7
Open Access: www.taylorfrancis.com, CC BY-NC-ND 4.0 license

Dry density effect on water diffusivity of compacted bentonite

H. Wang
Waseda University, Tokyo, Japan

H. Kyokawa
The University of Tokyo, Tokyo, Japan

ABSTRACT: This paper studied the effect of dry density (ρ_d) on water diffusivity (D) of compacted bentonite based on the distribution of volumetric water content (θ) during wetting. Four ρ_d cases with a range from 1.14 to 1.62 Mg/m^3 were conducted. The θ- D relation was obtained with an updated equation to fit the relation between a time coefficient and θ. With the θ- D relation numerical calculations (finite differential method) were conducted for specimens with different ρ_d. Both experimental and numerical results suggest that ρ_d would have minor effect on the θ- D relation, that is, the time to reach full saturation are very similar for specimens within the tested density range though there are some differences at the beginning of water diffusion.

1 INTRODUCTION

As a candidate material for the geological disposal system proposed to dealing with the high level radioactive waste (HLW), bentonite has been studied extensively in terms of swelling pressure, swelling deformation, hydraulic conductivity etc., however, water diffusivity (D) has not been concerned so much. One possible reason is that in simulations to predict bentonite behaviors, most of the numerical simulations were used hydraulic conductivity data to observe movement of water in bentonite. However, the hydraulic conductivity data for unsaturated bentonite are practically obtained from diffusivity data (i.e. unsteady state method) due to the difficulties, such as controlling high suction, in the steady state method of permeability test (Klute 1972, Masrouri et al. 2008). This paper studied the effect of specimen dry density (ρ_d) from distribution of volumetric water content (θ) of compacted bentonite during wetting. D value was obtained by updating the fitting equation proposed by Wang et al. (2020). Additionally, one dimensional numerical prediction was also conducted using finite differential method to visualizing difference of time histories of the degree of saturation (S_r) induced by the difference of the θ- D relation.

2 TEST PROGRAM AND METHODOLOGY

The commercial bentonite Kunigel V1 (K_V1), a candidate material for use in the Japanese geological disposal project, was used. Its specific gravity is 2.8±0.03, room gravimetric water content (w) is about 6-8% (relative humidity: ~50% and temperature: ~23 °C), montmorillonite content is 53%, liquid limit is 505%, plastic limit is 45%, and cation exchangeable capacity is 71.9 meq/100g with extractable Na+, Ca2+, Mg2+ and K+ of 53.8, 35.5, 1.6, and <1.0 meq/100g, respectively (Wang et al. 2022a, 2022c, Shirakawabe 2021, 2022).

Specimens with a diameter of 28 mm and thickness (h_{sp}) of 10 mm or 20 mm were prepared by means of static compaction using an oil jack. Four ρ_d cases with a range from 1.14-1.62 Mg/m^3 were conducted and two or three specimens were prepared for each case. The ρ_d, initial θ (θ_i) and saturated θ (θ_{sat}) are shown in Table 1; note that these values are average values with slight variations. After specimen preparation, the specimen was installed in the apparatus shown in Figure 1a, where the specimen was sandwiched between two stainless steel plates and fixed by four M5 bolts. Though a pressure transducer with capacity of 7MPa was glued at the center of the top plate, the measured

DOI: 10.1201/9781003299127-283

pressure data were not shown due to space limitation. Water was supplied from the top plate and transported to the specimen through a membrane filter (Wang et al. 2017). Note that porous metal was not installed to simplify apparatus design, however, the apparatus and testing method has been verified by Wang et al. (2022b). After a certain wetting period (t) shown in Table 1, the specimen together with the specimen ring was moved to the push-out device (Figure 1b). The specimen was pushed out and sliced every 1 mm from the wetted end. Note that for some cases with relatively small t, the last 2-3 mm could not be well sliced, for which it was regarded as one slices. Immediately after each slicing, water content (w) was measured using a balance with a solution of 0.1 mg.

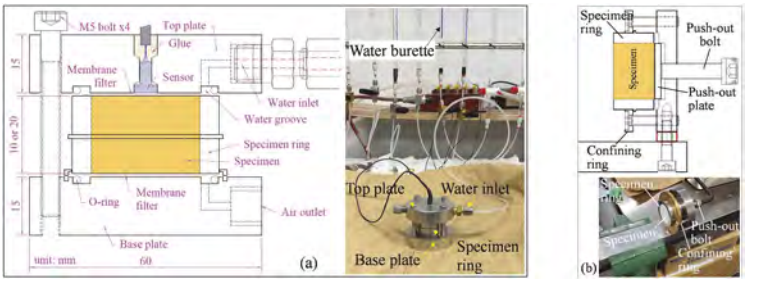

Figure 1. (a) Testing apparatus, (b) push-out device.

Table 1. Testing program and simulation parameters.

ρ_d Mg/m^3	θ_i %	θ_{sat} %	t (h_{sp}) h (mm)	Parameters A	B	C
1.14	7.30	59.3	2.73 (20), 6.13 (10)	4.70	1.12	7.28
1.33	8.67	52.5	1.77 (10), 18.5 (10), 17.3 (20)	4.85	1.25	8.44
1.48	9.94	47.1	2.00 (10), 18.3 (10), 16.9 (20)	5.07	1.36	8.89
1.62	11.2	42.1	2.45 (10), 18.2 (10), 22.6 (20)	5.23	1.45	8.66

3 TEST RESULTS AND DISCUSSIONS

Figure 2 Presents the relation between θ and the distance from water absorption side (z) for tested four cases. The θ_i range and θ_{sat} for each case were indicated by gray bars. Apparently,θ increases as z is smaller and t is longer. In some cases, θ of the slice closest to the water absorption surface exceed θ_{sat}, which is physically not possible. One possible reason is the dry density becomes smaller during to swelling deformation locally, while the pore water density larger than 1 Mg/m^3 is another possible reason (Wang et al. 2022c).

With the θ distribution shown in Figure 2, the movement of water in the specimens can be described in terms of water diffusivity (D) by combining the extended Darcy equation for unsaturated soil and the conservation of mass (Richards 1931, Klute 1972) as shown in Equation 1, where gravity potential was ignored. Bruce and Klute (1956) and Jackson (1964) used the Boltzmann transform to solve Eq. 1, of which D was set as a function of time coefficient $\lambda=z/\sqrt{t}$. With the initial condition: $\theta=\theta_i$ at $z>0$ and $t=0$ and the boundary condition $\theta=\theta_{sat}$ at $z=0$ and $t>0$, they obtained Equation 2. Note that the middle part of right-hand side of Equation 2 is the slope of λ-θ relation at θ, and rightest part is integral of λ from θ_i to θ. Wang et al. (2020) proposed a fitting equation (Equation 3) to describe the λ-θ relation and derived Equation 4 to calculate D, where A and B are fitting parameters. However, the λ-θ relation often could not be well matched if θ_i of tested specimen was assigned to θ_i in Equation 3. Thus, herein, θ_i is changed to C as the third parameter (Equation 5), by which D can be obtained by Equation 6.

$$\frac{\partial\theta}{\partial t}=\frac{\partial}{\partial z}\left(D\frac{\partial\theta}{\partial z}\right) \tag{1}$$

$$D(\theta) = -\frac{1}{2}\left(\frac{d\lambda}{d\theta}\right)_{\theta}\int_{\theta_i}^{\theta}\lambda d\theta \tag{2}$$

$$\lambda = A - B\ln(\theta - \theta_i) \tag{3}$$

$$D(\theta) = \frac{AB}{2} - \frac{B^2}{2}(\ln(\theta - \theta_i) - 1) \tag{4}$$

$$\lambda = A - B\ln(\theta - C) \tag{5}$$

$$D(\theta) = \frac{B(A+B)(\theta-\theta_i)}{2(\theta-C)} - \frac{B^2\ln(\theta-C)}{2} + \frac{B^2(\theta_i - C)}{2(\theta-C)}\ln(\theta_i - C) \tag{6}$$

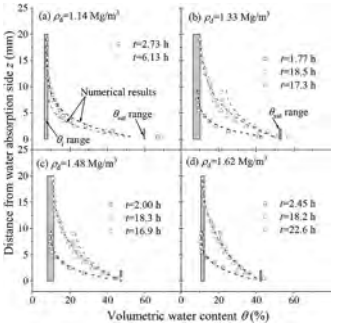

Figure 2. Relation between θ and z.

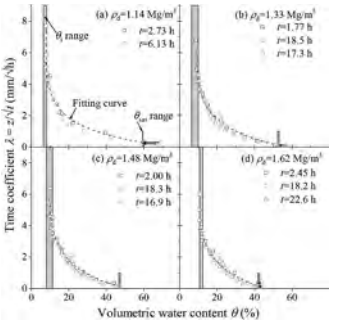

Figure 3. Relation between θ and λ.

Dash lines in Figure 3 are fitting results for each case with Equation 5 and parameters were put in Table 1. Note that some data with values very close to θ_i (pink color) were not considered in fitting since apparently θ at some z positions keeps its initial conditions if z is large enough or t is short enough. Additionally, θ_{sat} was assigned to data that numerically exceed θ_{sat} (horizontal arrows in Figure 3). Then, D as a function of θ was calculated by Equation 6 using parameters A, B and C obtained and shown in Figure 4, in which results obtained by Takeuchi et al. (1995) with ρ_d of 1.6 Mg/m^3 and Wang et al. (2020) (Equation 4) with ρ_d of 1.53 Mg/m^3 were also added. The U shape curve from Takeuchi et al. (1995) seems to be a result of the specific method they used. When θ closes to θ_i or θ_{sat}, denominator (slope of θ, $\partial\theta/\partial z$) of their equations to obtain D would approach zero resulting in unstable values. For Equation 4 used by Wang et al. (2020), D also approaches infinite when θ closes to θ_i, however, it is expected from Equation 2 and by physical sense that D would be 0 when θ equals θ_i (i.e. $\int_{\theta i}^{\theta}\lambda d\theta$=0) or θ_{sat} (i.e. dλ/dθ=0). Equation 6 produces D =0 at θ_i and a small value at θ_{sat} since setting dλ/dθ=0 at θ_{sat} in Equation 5 causes reduction of one parameter. Nevertheless, D values by Equation 6 seems to be very close for specimens with different densities when θ >20%. To visualize this difference, Equation 1 was changed to Equation 7 and numerically solved using finite differential method (Equation 8), where i and j represent space and time steps, and k and h are intervals between space and time steps, respectively.

$$\frac{\partial\theta}{\partial t} = \frac{\partial D}{\partial\theta}\left(\frac{\partial\theta}{\partial z}\right)^2 + D\frac{\partial^2\theta}{\partial z^2} \tag{7}$$

$$\theta_i^{j+1} = \theta_i^j + \frac{k}{4h^2}\frac{dD}{d\theta}\left(\theta_{i+1}^j - \theta_{i-1}^j\right)^2 + \frac{k}{h^2}D\left(\theta_{i+1}^j - 2\theta_i^j + \theta_{i-1}^j\right) \tag{8}$$

Dash lines in Figure 2 show numerically calculated θ distribution with the initial and boundary conditions of θ=θ_i at z >0 and t=0, θ=θ_{sat} at z=0 and t>0, and dθ/dz=0 at z=h_{sp} and t>0. As expected, the results are very close to testing results. Figure 5 shows the predicted average S_r time history for specimens with thickness of 10 mm with the same boundary and

initial conditions. It is shown that the average S_r becomes very close though there is about 10% difference initially, which implies that the time need to reach saturation is very similar regardless specimen density in the tested range.

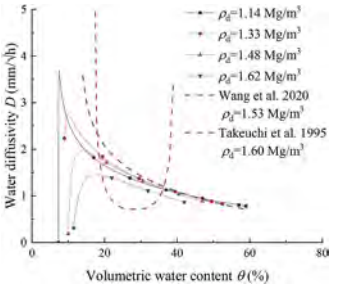

Figure 4. Relation between θ and D.

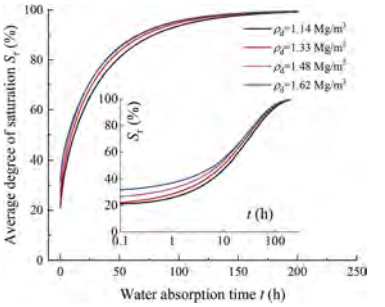

Figure 5. Time history of calculated S_r.

4 CONCLUSIONS

The effect of dry density (ρ_d) on water diffusivity (D) of compacted bentonite was studied. An updated equation to fit the relation between a time coefficient and volumetric water content (θ) was proposed. Results suggest that ρ_d would have minor effect on the θ- D relation.

ACKNOWLEDGEMENTS

This study was performed as a part of the activities of the Research Institute of Sustainable Future Society, Waseda Research Institute for Science and Engineering, Waseda University, and partially supported by the Taisei Foundation

REFERENCES

Bruce, R.R. & Klute, A. 1956. The measurement of soil moisture diffusivity. *Soil Science Society Proc*., 20: 458–462.

Jackson, R.D. 1964. Water vapor diffusion in relatively dry soil: I. theoretical considerations and sorption experiments. *Soil Science Society Proc*., 28:172–176.

Klute, A. 1972. The determination of the hydraulic conductivity and diffusivity of unsaturated soils. *Soil Science*, 113(4): 264–276.

Masrouri, F., Bicalho, K. & Kawai, K. 2008. Laboratory hydraulic testing in unsaturated soils. *Geotechnical and Geological Engineering* 26(6): 691–704.

Richards, L.A. 1931. Capillary conduction of liquids through porous mediums. *Physics* 1(5): 318–333.

Shirakawabe, T., Wang, H., Goto, S., Yamamoto, S. & Komine, H. 2021. Study of thermal history effect on water movement in unsaturated bentonite. *Journal of Japan Society of Civil Engineers* (Geosphere Engineering) 77(2): 103–117.

Shirakawabe, T., Wang, H., Komine, H. & Morodome, S. 2022. On methods to measure cation exchange capacity and leached cations of bentonites. *Japanese Geotechnical Journal* 17(1): 61–71.

Takeuchi, S., Hara, K., & Nakano, M. 1995. Water retention curve, water diffusivity and water movement of compacted bentonite. *Soil and Foundations* 35(3): 129–137. (in Japanese).

Wang, H., Koseki, J., Nishimura, T. & Miyashita, Y. 2017. Membrane filter properties and application of the filter to undrained cyclic triaxial test of unsaturated materials. *Canadian Geotechnical Journal* 54(8): 1196–1202.

Wang, H., Shirakawabe, T., Komine, H., Ito, D., Gotoh, T., Ichikawa, Y. & Chen, Q. 2020. Movement of water in compacted bentonite and its relation with swelling pressure. *Canadian Geotechnical Journal* 57(6): 921–932.

Wang, H., Komine, H. & Gotoh, T. 2022a. A swelling pressure cell for X-ray diffraction test. *Géotechnique* 72(8): 675–686.

Wang, H., Ruan, K., Harasaki, S. & Komine, H. 2022b. Effects of specimen thickness on apparent swelling pressure evolution of compacted bentonite. *Soils and Foundations*, in press. https://doi.org/10.1016/j.sandf.2021.101099.

Wang, H., Ito, D., Shirakawabe, T., Ruan, K. & Komine, H. 2022c. On swelling behaviors of a bentonite under different water contents. *Geotechnique*,online first, https://doi.org/10.1680/jgeot.21.00312.

Smart Geotechnics for Smart Societies – Zhussupbekov, Sarsembayeva & Kaliakin (Eds)
© 2023 The Author(s), ISBN 978-1-003-29912-7
Open Access: www.taylorfrancis.com, CC BY-NC-ND 4.0 license

Actual evaporation reduction rate considering the pore structure of sandy soils

J.G. Hussary, A. Alowaisy, N. Yasufuku & R. Ishikura
Kyushu University, Fukuoka, Japan

ABSTRACT: The falling rate stage of evaporation (Stage 2) is dominant in drylands and responsible for most water loss in the field. Therefore, predicting its evaporation rates is of a great importance. Through an experimental approach and using Fick's law of diffusion, a new determination method of the actual evaporation reduction rate during Stage 2 is proposed in this study. The model indicates that the water flux during Stage 2 is controlled by the receding rate of the vaporization plane, which is in turn dependent on the pore properties of the soil profile.

1 INTRODUCTION

Drylands cover over 41% of the Earth's surface. Alowasiy et al. (in press) mentioned the importance of acquiring new design criteria to avert soil degradation and desertification. Water evaporation from soil profiles is considered the dominant flux in drylands. The literature extensively studied the Actual Evaporation (AE), yet, accurate determination of its rate has been challenging.

Evaporation from fully saturated bare soil profiles is divided into three stages. During Stage 1 (Constant rate stage), water is sufficiently supplied to the surface by capillary liquid flow, maintaining a high AE rate. However, when the drying front, saturated-unsaturated interface, reaches a specific depth, the hydraulic connection with the surface is disrupted (Lehmann et al. 2008). Consequently, a new vaporization plane (VP) is formed below the surface, topped with an air-dry layer announcing Stage 2 (Falling rate stage). During this stage, water transports by capillarity from the drying front to the VP through water-filled pores (film region). Then continues by vapor diffusion through the air-dry layer (Shokri et al. 2009). The AE rate drops instantly and continues receding throughout the stage. Subsequently, the AE rate converges to a low and constant value announcing the diffusion-controlled Stage 3 (Residual rate stage).

Stage 1 is relatively short in drylands due to the arid climate and lack of water availability. Consequently, Stage 2 becomes dominant and responsible for most water loss. Therefore, it is essential to accurately determine its AE rate and investigate its controlling factors. Hussary et al. (2022) confirmed that Stage 2's AE reduction rate is almost linear and is controlled by the VP receding rate following Fick's law of diffusion. Moreover, the paper introduced a new Pore Size Distribution Index (I_{PSD}) that shows a strong correlation with the characteristics of Stage 2. Accordingly, the present study proposes a new determination method of the AE reduction rate during Stage 2 based on Fick's law and the I_{PSD} considering homogeneous sandy soil profiles.

2 MATERIALS AND METHODOLOGY

Homogeneous drying soil column tests were conducted. The columns were initially fully saturated to capture Stage 1 and Stage 2, while testing was stopped at the onset of Stage 3. The column's preparation and saturation were done following Hussary et al. (2022, in press).

DOI: 10.1201/9781003299127-284

A 1-D evaporation flow was allowed from the profile's top, at which the atmospheric conditions were unified at 27±1 °C, relative humidity of 47±3%, and wind speed of 2±0.2 m/s. The columns were mounted on a digital balance to determine the AE rates. Besides, TDRs (moisture sensors) were attached alongside the columns to capture the saturation profiles during drying.

Four textures of sandy soil silica sand were used; K-7, K-6, K-5, and K-4. Their particle size distribution curves are delineated in Figure 1a. The columns were compacted at different relative densities; 70, 80, and 90%. A summary of the tested columns' physical properties is shown in Table 1. Figure 1b delineates the samples' Soil Water Characteristics Curves (SWCCs) determined using the continuous pressurization method (Alowaisy et al. 2020). The Pore Size Distribution curves (PSD), Figure 1c, were inferred from the SWCCs as in Hussary et al. (2022). The scatter plots delineate the calculated pore diameters while the smooth lines show their lognormal distribution fitting. The I_{PSD} (1/μm) was adopted as the main parameter in the proposed AE determination method. Therefore, it was calculated as follows (Hussary et al. 2022):

$$I_{PSD} = \left(\frac{1}{d_1} - \frac{1}{d_2}\right) \times CV \tag{1}$$

where $(1/d_1)$ - $(1/d_2)$ corresponds to the width of the PSD. d_1 and d_2 are the smallest and largest capillaries, corresponding to the residual and air-entry suction values, respectively. CV is the coefficient of variation of the fitted lognormal distribution.

3 ACTUAL EVAPORATION REDUCTION RATE

Hussary et al. (2022) reported that the vapor diffusion transport is dominant during Stage 2, and the VP controls its AE rate. Therefore, the proposed method adopts Fick's law under the following assumptions: (1) water flows upwards under steady-state conditions (the capillary flow in the film region equals the diffusion flow in the air-dry layer); (2) water evaporates by diffusion only at the VP (bottom of the air-dry layer); (3) diffusion occurs in 1-D under isothermal conditions; (4) the change in water vapor density (∂C) is constant under unified atmospheric demand; (5) vapor diffusion coefficient (D) is constant for the homogeneous air-dry layer with constant concentration. Thus, the normalized AE reduction rate during Stage 2 (ΔNAE/Δt) is expressed as follows:

$$\frac{\Delta NAE}{A\Delta t} = \frac{D\partial C\left(\frac{1/\Delta L}{\Delta t}\right)}{AE_i} \tag{2}$$

$\Delta NAE/\Delta t$ ($1/s.m^2$) is the AE reduction rate (ΔAE) over the AE rate in Stage 1 (AE_i). The diffusion area ($A=1\ m^2$) is constant for 1-D flow. $D = D_o\, b\Phi^m$ (m^2/s) by Campbell (1985). D_o is the free air vapor diffusion coefficient, Φ is the soil porosity, while b=0.66 and m=1 are Penman's constants. ∂C (g/m^3) is the difference between the vapor densities at the VP, assumed fully saturated (C_{sat}), and at the soil surface (C_∞). $(1/\Delta L)/\Delta t$ is the inverse of the VP receding rate with time during Stage 2 (1/s.m), where L is the VP depth (diffusion distance), and it is calculated as follows:

$$\frac{1/\Delta L}{\Delta t} = -3.2 \times 10^{-6} I_{PSD} - 0.00013 \tag{3}$$

This formula was found by tracing the VP from the saturation profiles in Figure 2, where each line indicates a TDR location. The VP was assumed to reach a TDR once its reading converges to a constant residual value. Stage 2 duration was found from the AE curves (Figure 4), while the VP depth at a specific time was collected for two points once the saturation converges to residual (Figure 2). The results were plotted with the I_{PSD} in Figure 3 to deduce the formula. The strong correlation confirms that the diffusion distance dynamics highly depend on the soil pore properties.

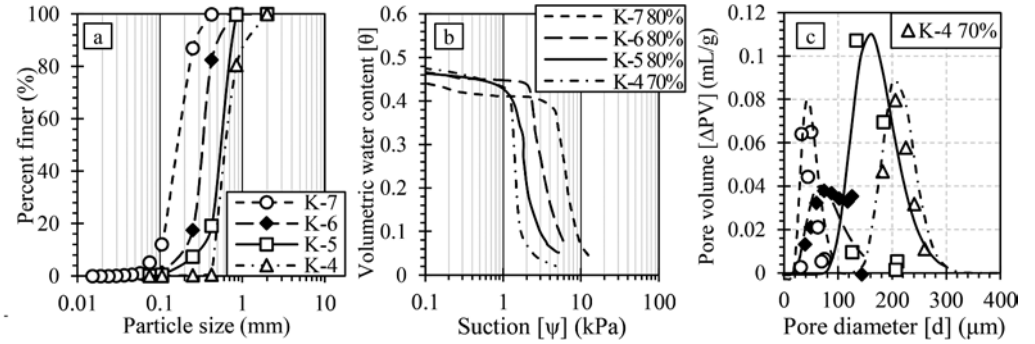

Figure 1. (a) Particle size distribution (b) soil water characteristics curves (c) pore size distribution.

Table 1. Soil columns' physical properties.

Relative Density	Dr	(%)	70		80			90	
			K-5	K-4	K-7	K-6	K-5	K-5	K-4
Specific gravity	Gs		2.65	2.65	2.65	2.64	2.65	2.65	2.65
Effective size	D_{10}	(mm)	0.31	0.47	0.10	0.20	0.31	0.31	0.47
Dry density	ρ_d	(g/cm^3)	1.469	1.475	1.477	1.502	1.501	1.535	1.544
Void ratio	e		0.802	0.794	0.789	0.752	0.763	0.724	0.714
Pore size distribution index	I_{PSD}	(10^{-4}/μm)	1.96	0.37	14.52	7.88	1.29	0.87	0.14

4 RESULTS AND DISCUSSION

The proposed determination method was used to find the ΔNAE/Δt for all the tested profiles. The values were then compared with the experimental ΔNAE/Δt for validation. The latter was found from the normalized AE curves, delineated in Figure 4. Figure 5a depicts the relationship between the I_{PSD} and the determined and experimental ΔNAE/Δt. In addition to the strong correlation, the results showed very close patterns for both values, confirming the method's validity. However, despite the I_{PSD}, the ratio between determined and experimental ΔNAE/Δt was almost constant for all profiles, around 0.015 ±0.005. This discrepancy might be related to the simplicity of the method and the diffusion coefficient. Therefore, the determined values were multiplied by the average ratio ($R_{E/D}$), and the results were delineated in Figure 5b. Accordingly, it can be concluded that the proposed determination method is reliable for determining ΔNAE using $R_{E/D}$.

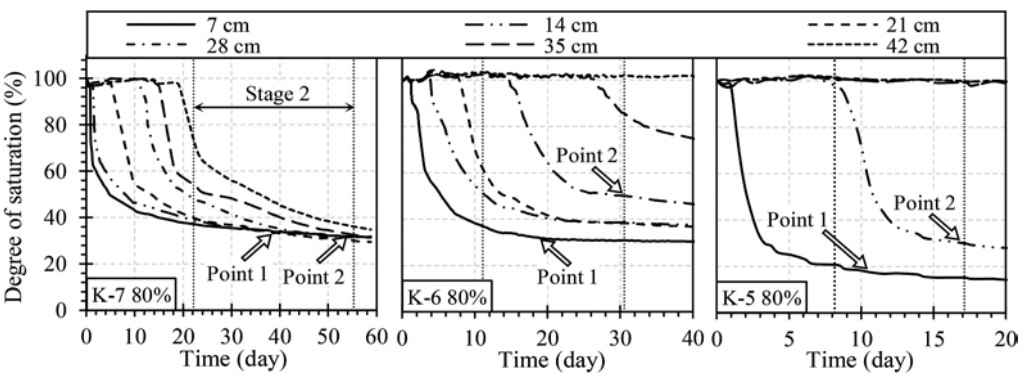

Figure 2. Soil columns' saturation profiles.

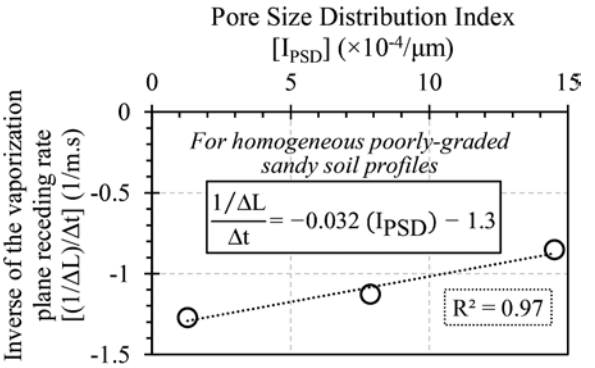

Figure 3. Empirical determination of the (1/ΔL)/Δt based on the I_{PSD}.

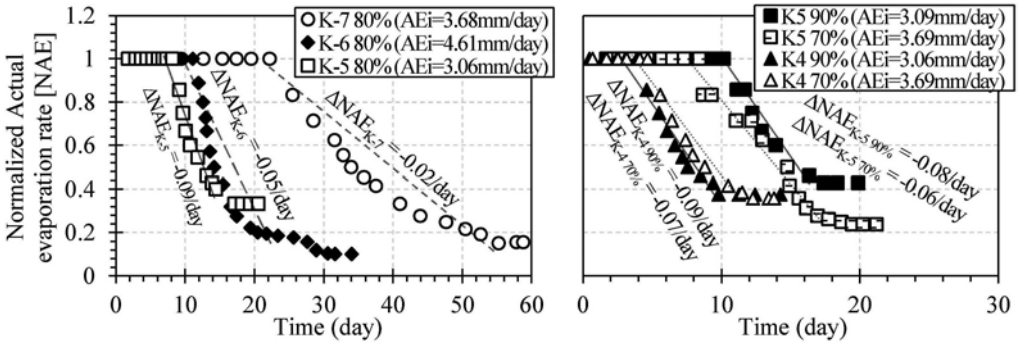

Figure 4. Actual evaporation curves showing the experimental ΔNAE/Δt.

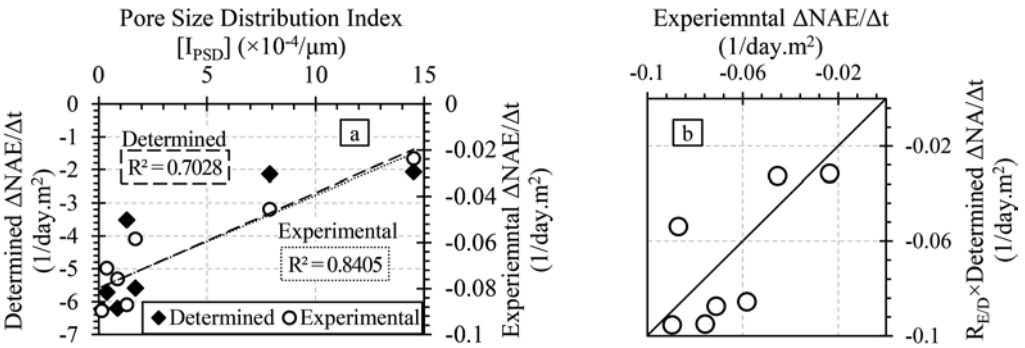

Figure 5. Comparison between the determined and experimental ΔNAE/Δt.

5 CONCLUSIONS

A new determination method of the normalized actual evaporation reduction rate during Stage 2 was proposed for homogeneous poorly-graded sandy soil profiles under unified conditions. The method adopts Fick's law of diffusion and assumes a linear reduction in the actual evaporation rates during Stage 2. Moreover, it was confirmed that the change in the vaporization plane depth depends on the pore properties, and its receding rate can be empirically found

using the Pore Size Distribution Index (I_{PSD}). The findings are believed to improve the evaporation prediction in drylands, thus finding innovations to combat droughts and desertification.

REFERENCES

Alowaisy, A., Yasufuku, N., Ishikura, R., Hatakeyama, M. & Kyono, S. 2020. Continuous pressurization method for a rapid determination of the soil water characteristics curve for remolded and undisturbed cohesionless soils. *Soils and Foundations*. 60(3): 634–647.

Alowaisy, A., Hussary, J., Yasufuku, N., Ishikura, R. & Abdelhadi, M. in press. Analysis of the surface layer properties influence on the actual evaporation and efficiency of the soil cover to combat desertification. *Journal of Arid Land Studies*.

Campbell, G. S. 1985. *Soil physics with BASIC: transport models for soil-plant systems*. Elsevier.

Hussary, J., Alowaisy, A., Yasufuku, N., Ishikura, R. & Abdelhadi, M. 2022. Pore structure and falling rate stage of evaporation in homogeneous sandy soil profiles. *Soils and Foundations*. 62(2): 101108.

Hussary, J., Alowaisy, A., Yasufuku, N., Ishikura, R. & Abdelhadi, M. in press. Drying front dynamics during the falling rate stage of evaporation from homogeneous sandy soil profiles. *Journal of Arid Land Studies*.

Lehmann, P., Assouline, S. & Or, D. 2008. Characteristic lengths affecting evaporative drying of porous media. *Physical Review E*. 77(5):056309.

Shokri, N., Lehmann, P. & Or, D. 2009. Critical evaluation of enhancement factors for vapor transport through unsaturated porous media. *Water resources research*. 45(10).

Smart Geotechnics for Smart Societies – Zhussupbekov, Sarsembayeva & Kaliakin (Eds)
© 2023 The Author(s), ISBN 978-1-003-29912-7
Open Access: www.taylorfrancis.com, CC BY-NC-ND 4.0 license

Application of biomass-added masa soil to ground materials

T. Hyodo, T. Yoshizaki & T. Terasako
Toyama Prefectural University, Imizu, Japan

N. Tatta
University of Toyama, Toyama, Japan

H. Nagai
Hazama Ando corporation, Tokyo, Japan

ABSTRACT: In Toyama Prefecture of Japan, which has abundant nature, the primary industry is thriving, but a lot of waste-based biomass is generated in the manufacturing process, and we are having a hard time disposing of it. Therefore, the authors wondered if these and Masa soil could be mixed and used as a ground material. In this study, compaction test, CBR test, and repeated triaxial compression test were conducted to examine whether biomass mixed soil can be applied to simple pavement. In all the samples conducted in this study, CBR was 3% or more, so it was found that they can be generally used not only for simple pavement and pedestrian pavement but also for roadbed materials. In addition, as a result of repeated non-drainage triaxial tests using biomass-mixed Masa soil, the liquefaction strength increased when 10% of crab and bamboo powder were mixed.

1 INTRODUCTION

One of the goals of the Sustainable Development Goals (SDGs) adopted by the United Nations General Assembly in 2015[1)] is to significantly reduce waste generation by preventing, reducing, recycling and reusing waste. In Toyama Prefecture, heavy snowfall area of Japan, primary and secondary industries are thriving, and a large amount of waste-based biomass is generated in the process of production and processing. This waste-based biomass incurs a large amount of disposal cost and has a strong psychological negative image, so it is difficult to take it out of the prefecture for disposal. Therefore, waste-based biomass is required to be locally produced for local consumption and consumed in large quantities at low cost. In previous studies, it was confirmed that the uniaxial compressive strength was increased by reducing the amount of cement added and mixing fine powder of industrial by-products in the biomass pavement [2)]. As one, it was proposed to prepare mixed soil from soil samples and biomass used as ground materials and use them as construction materials. On the other hand, many damages due to liquefaction have been reported in Japan, which is an earthquake-prone country. In particular, during the Hyogo-ken Nanbu Earthquake (1995, i.e. the 1995 Southern Hyogo Prefecture Earthquake), Masa soil (Decomposed granite soil), which was previously thought to be difficult to liquefy, was liquefied at Kobe Port Island, which was used as a landfill material for artificial islands. Therefore, in order to use biomass as a construction material, it is necessary to understand the dynamic behavior during an earthquake.In this study, arbitrary proportions of biomass were added to the soil, and the compaction characteristics were investigated in order to investigate whether it was suitable for the work to be carried out. In addition, repeated triaxial compression tests were carried out to investigate the dynamic characteristics of the biomass mixed soil.

DOI: 10.1201/9781003299127-285

2 MATERIALS

As the samples used in this test, waste-based biomass samples (hereinafter referred to as biomass) include rice husks from agriculture, rice husk ash incinerated from them, wood ash from forestry, wood ash from incinerated bark, bamboo chips, and thinned wood. Bottom ash, which is the main ash consisting of silica sand and ash, which is generated during biomass power generation using the above, and from the fishery industry, the shells of Benizuwai crab were sufficiently oven-dried at 110°C and crushed into powder. As the soil sample, we selected Masa soil from Hyogo prefecture. For soil-based pavement used for simple pavement and pedestrian pavement, this sample was adopted because it is often used as a pavement material because it has excellent harmony with the landscape and shock absorption. Table 1 shows the physical characteristics of Masa soil.

Table 1. Physical characters of masa soil.

e_{max}	e_{min}	$\rho_s(g/cm^3)$	U_c	Fc(%)
1.019	0.562	2.638	90	13.3

3 COMPACTION CHARACTERISTICS OF BIOMASS MIXED SOIL

3.1 *Testing method*

A soil compaction test (JIS A 1210) was carried out by compacting with Masa soil and mixed soil with a mass ratio of 5% and 10% for each biomass. n addition, a CBR test (JIS A 1211) was conducted to determine the bearing capacity of the mixed soil based on the optimum water content ratio obtained from the compaction test. Seven kinds of samples were selected based on the compaction curve obtained in the compaction test, and the test was carried out with mixed soil having a mass ratio of 5% for each biomass. For those with a CBR value of more than 10%, the mixing ratio was increased to 10% and the test was conducted. This time, assuming the case where the construction was carried out in the densest condition, the sample was compacted at the optimum water content and was not flooded.

3.2 *Test results*

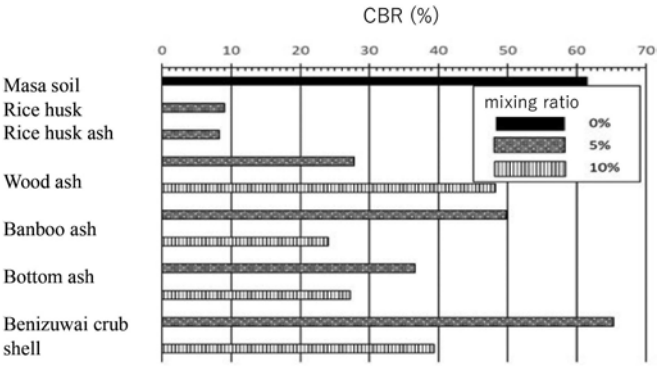

Figure 1. CBR of each sample.

Figure 1 shows the CBR of each mixed soil obtained in the CBR test. The CBR was the highest compared to the soil sample, Masa soil, and the only sample with a larger CBR than Masa soil was Benizuwai crab shell 5%. On the contrary, the CBR of 5% of rice husks and 5% of rice husk ash did not exceed 10%, which were relatively small values. In wood ash, CBR was larger in 10% mixed soil than in 5% mixed soil. Next, the correlation diagram of the relationship between CBR, maximum dry density, optimum water content, and each is shown in Figures 2 and 3.

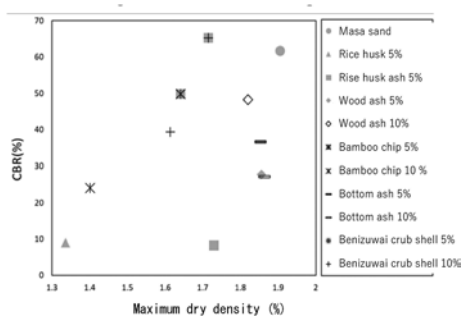

Figure 2. Relationship between CBR and maximum dry density.

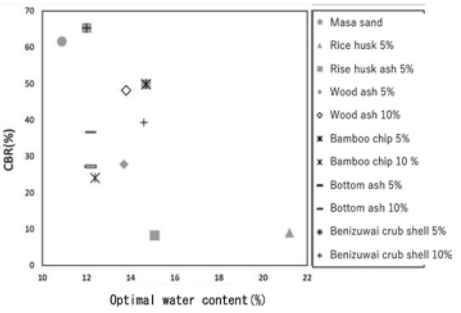

Figure 3. Relationship between CBR and optimal water content.

3.3 *Applicability as a paving material*

According to the design guidelines[4] stipulated by the Hokuriku Regional Development Bureau of the Ministry of Land, Infrastructure, Transport and Tourism, the design CBR was 3% or more as a regulation of bearing capacity for the entire roadbed. In all the samples conducted in this study, CBR was 3% or more, so it was found that they can be generally used not only for simple pavement and pedestrian pavement but also for roadbed materials. However, when actually applying it as a pavement material, it is necessary to investigate the water absorption expansion test assuming the worst water content due to rainfall, the chemical properties, and the long-term durability.

4 DYNAMIC CHARACTERISTICS OF BIOMASS MIXED SOIL

4.1 *Testing method*

In this section, as in the previous section, masa sand was used as the base material. In the repeated non-drainage triaxial test of soil, the amount of Masa soil that passed through a 2 mm sieve was used. In this test, a non-drainage triaxial test was repeatedly conducted using a mixed soil containing only bamboo soil at a mixing ratio of 0% and a mixed soil containing bamboo powder and crab powder at a mass ratio of 10% each. In this test, a non-drainage triaxial test was repeatedly conducted using a mixed soil containing only bamboo soil at a mixing ratio of 0% and a mixed soil containing bamboo powder and crab powder at a mass ratio of 10% each.The dimensions of the specimen were 50 mm in diameter and 100 mm in height. The specimen was prepared by using the aerial drop method so that the initial target relative density Dr = 50%. After preparing the specimen, CO_2 and degassed water were flowed in this order to saturate the specimen, and after confirming that the B value was 0.95 or more, isotropic consolidation was performed. After the completion of isotropic consolidation, a repeated load was applied under non-drainage conditions, and a repeated non-drainage triaxial test was carried out. After the test was completed, the fine particle content Fc (%) of each specimen was examined. As a result, it was 15.6% when the mixing ratio was 0%, 17.2% when the bamboo was mixed, and 19.1% when the crab was mixed.

4.2 *Test result*

Figure 4 shows the liquefaction intensity curve when the excess pore water pressure ratio is 0.95. The liquefaction strength ratio Rl_{20} was used as the repeated stress amplitude ratio at 20 times of repeated loading, and comparison was performed. As a result, when crab and bamboo were mixed, Rl_{20} increased. In the previous study[5], the liquefaction strength ratio increased with the increase in the fine particle content, and the same tendency was seen in this study.

Photo 1 shows the skeleton of crab and bamboo powder taken using SEM. As a result, when observing the particles, it was found that large and small pointed crab shells and rough

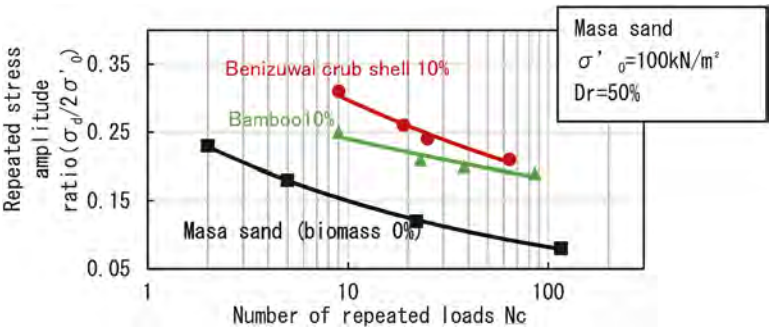

Figure 4. Liquefaction strength curve at excess pore water pressure ratio 0.95.

surface crab shells were mixed. It is considered that the addition of crab powder exerted an interlocking effect due to the engagement of the particles and increased the liquefaction strength. In addition, large and small elongated bamboos were mixed in the bamboo powder. It is considered that they played a role as a staple fiber tensile reinforcement and the resistance to liquefaction increased due to the increased toughness.

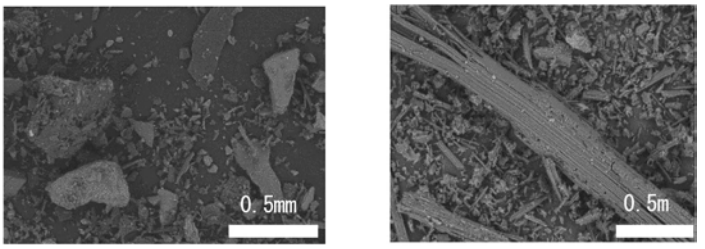

(a)Benizuwai crab powder (b) Bamboo powder

Photo 1. Observation of the skeleton of each biomass by SEM.

5 CONCLUSIONS

In this study, we investigated whether biomass could be used as a ground material by adding it to masa sand. As a result of various laboratory tests, the results are as follows.

1) It was found that mixing 5% of Benizuwai crab shell with masa sand increased CBR, and mixing 5% of rice husk and rice husk ash significantly decreased CBR. In addition, CBR is considered to be more influenced by the mechanical properties and particle size of biomass than the compaction properties and soil particle density. All the samples conducted in this study have a CBR of 3% or more, and it can be said that they can be generally used as road-bed materials.
2) As a result of repeated non-drainage triaxial tests using soil mixed with biomass, it was found that mixing 10% of crab and bamboo powder increases the liquefaction strength and suppresses the sudden occurrence of axial distortion. In addition, the liquefaction strength increased as the fine particle content increased. However, it was found that the liquefaction strength of the biomass-mixed soil is greatly affected by the surface and shape of the skeleton.

REFERENCES

Ministry of Agriculture of Japan, Forestry and Fisheries SDGs goals and targets, https://www.maff.go.jp/j/shokusan/sdgs/sdgs_target.html, (Retrieved January 31, 2022)

Shojima,Y. Akiba,S. Kanou,Y & I,M. 2012. STUDY ON IMPROVED MATERIAL OF SUBGRADE SOIL USING POWDER OF INDUSTRIAL BYPRODUCT: Journal of JSCE. Vol.68, No.3, I_89-I_95 (in Japanese)

Ministry of Land of Japan, Infrastructure, Design standards for road pavement, https://www.mlit.go.jp/sogoseisaku/inter/keizai/gijyutu/pdf/road_design_j2_01.pdf, (Retrieved January 31, 2022)

Hokuriku Regional Development Bureau (2020) Design Guidelines [Road Edition] (in Japanese)

Kawahara, K. Sato,K. Ishida,M & Fujiwara, T. 2007. MECHANICAL PROPERTIES OF PAVING MATERIAL OF PEDESTRIANS-FRIENDLY PAVEMENTS USING COAL FLYASH. Journal of JSCE. Vol.12, 123–129 (in Japanese)

Kanazawa,H. & Harada,K. 2011. REVISION OF RELATIVE DENSITY AND ESTIMATION OF LIQUEFACTION STRENGTH OF SANDY SOIL WITH FINE CONTENT Journal of JSCE. Vol.68, No.4, I282-292 (in Japanese)

Smart Geotechnics for Smart Societies – Zhussupbekov, Sarsembayeva & Kaliakin (Eds)
© 2023 The Author(s), ISBN 978-1-003-29912-7
Open Access: www.taylorfrancis.com, CC BY-NC-ND 4.0 license

Modelling and monitoring behavior of vegetated slopes in variable weather conditions

Slobodan B. Mickovski & Mandy Wallace
Glasgow Caledonian University, Glasgow, Scotland

Jovan Br. Papic
Faculty of Civil Engineering, University Ss. Cyril and Methodius, Skopje, R. N. Macedonia

Igor Simeonovski
Tirrena Scavi S.p.A., Skopje, R. N. Macedonia

ABSTRACT: Soil erosion and shallow landslides are the most common forms of instability encountered during the life cycle of earthworks. It is generally well established that vegetation can contribute towards minimization of the risks associated with instability on earthworks slopes, although holistic consideration of geo-environmental conditions and connection with hydro-meteorological hazards is still lacking. The aim of this study is to investigate the link between the vegetation planted on earthwork slopes and the likelihood of failure of the earthwork in form of erosion or shallow landslide. To achieve this aim, experiments on vegetated and fallow earthwork slopes in contrasting geo-climatic conditions were carried out. These included setting up, monitoring, sampling and testing under simulated rainfall and dry conditions. The results of this study will help designers, engineers, land use planners, and landscape architects in reaching decisions that consider multi-disciplinary approach to earthwork design and construction.

1 INTRODUCTION

Although the contribution of the vegetation in the reduction of erosion and shallow landslides has a long both empirical and scientific documented history, there is still a lack of coupled consideration of geo-environmental conditions and connection with the hydro-meteorological hazards. For that purpose, parallel investigations have been started in Scotland and N. Macedonia, where the influence of planted vegetation on stability of earthwork slopes under different atmospheric conditions has been monitored. These were carried out in-situ and in laboratory, where tests on both vegetated and fallow earthwork slopes for two contrasting geo-climatic regions of Europe were performed. Complex equipment was set up, enabling continuous monitoring within the soil. Unlike the field work, the fluctuating atmosphere conditions in laboratory had to be simulated.

Having in mind the experiences and risks of infrastructure instability and the wide range of associated topics/factors, e.g.: erosion and shallow landslide typology and processes ((aggregate) stability, erodibility, soil strength, slope angle/cover, etc); hazards/risks for earthworks, climate change drivers (environmental and hydro-meteorological); hazard/risk mitigation, the aim of this study was to investigate a limited set of environmental and hydro-meteorological hazards and their effects on earthworks with a view of proposing a mitigation approach that involves vegetation as a stabilisation agent.

DOI: 10.1201/9781003299127-286

2 APPLIED MATERIALS AND MODELS

Within this very limited scope, the objectives of the research were as follows: a) for the case study in Scotland, to set up and monitor the effects of hydro-meteorological hazards on the erosion and shallow landslide risk on a major live linear infrastructure construction site; b) for the case study in N. Macedonia to model variable hydro-meteorological hazards in laboratory environment for the purpose of slope design and monitor development of erosion and/or shallow landslide and parameters in the soil before, during, and after simulated rainfall events.

2.1 *Description of the site in Scotland*

- Motorway cutting (Slope 1; Figure 1) formed in mineral podzols near Luncarty (NO 09252 29729); slope length 445 m; slope angle 1:2; slope height: 6.0 – 8.5 m; aspect: west-facing.
- In situ testing from 12 locations on 5 occasions between July and January: moisture content, shear stress (peak and residual), penetration resistance.
- Bulk samples were collected but not analysed and the monitoring was curtailed as a result of the Covid-19 pandemic (site closed).

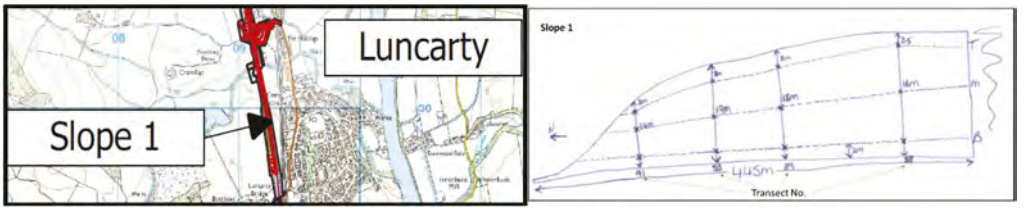

Figure 1. Case study area location in Scotland (left) and the general earthwork arrangement with monitoring point location (right).

2.2 *Description of site and laboratory model in Macedonia*

- Cutting formed in silty (sandy silt, marked as 1) and sandy (silty sand, marked as 2) materials on express road in process of construction; slope length 340 m; slope angle 1:1; slope height: 6.0 - 8.0 m; aspect: south-facing (Figure 2a).
- Two containers were prepared LxWxD=100x50x25 cm, where materials 1 and 2 were separately placed. Drainage is enabled both at the surface and at the bottom end, through a pipe.
- Sensors placed at middle depth of each soil layer, at two positions along model: sensors 1 (at upper part) and 2 (nearby toe) in mat.1, while sensors 3 (upper) and 4 (toe) in mat.2 (Figure 2b).
- Local hydro-meteorological reports were analyzed for modelling rainfalls *via* sprayers.
- Tests were performed for cases of bare soil and vegetated slope, and with dried vegetation when a heater was used to simulate the effect of the sun (Figures 2c–2d), while eroded material, run-off water and filtered water through soil were collected with dishes placed below each container.

3 RESULTS AND ANALYSIS

3.1 *Highway slope (Scotland)*

The shear strength of the exposed cutting did not change significantly with the changes in moisture content near the crest and at mid-slope (Figure 3a). However, the shear strength decreased with the increase in moisture content near the toe of the slope. While the shear

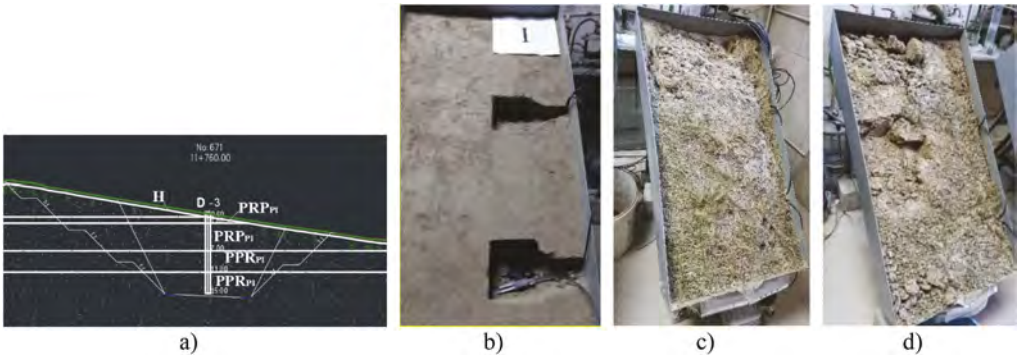

Figure 2. a) Geotechnical profile of case study area in Macedonia (PPR – sandy silt and PRP – silty sand); b) Placing sensors; final lookout of slopes after test with dry vegetation: c) material 2 (sampling nearby the sensor 3); d) material 1 (sampling in the upper part, nearby the sensor 1).

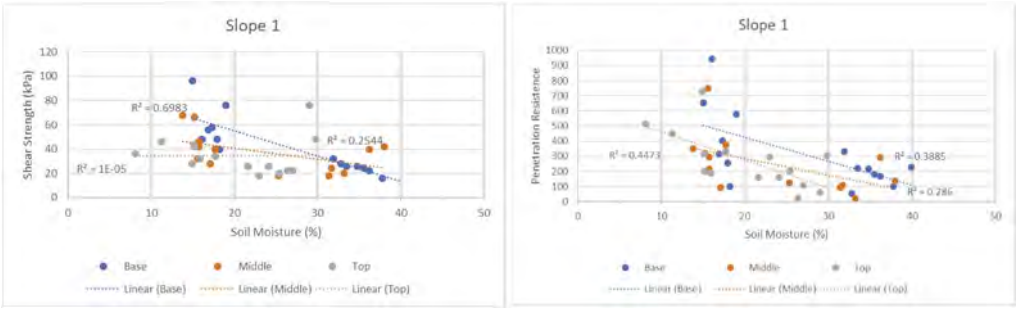

Figure 3. Relationship between the soil moisture (%) and: a) shear strength; b) penetration resistance (N) at different locations on the slope during monitoring.

strength of the exposed slope averaged approximately 40 kPa across the slope, there were a number of readings below 20 kPa during the monitoring period.

The penetration resistance of the exposed cutting showed a decreasing trend with the increase in moisture content of the soil but these trends, although similar across the slope, were not statistically significant. In general, the penetration resistance appeared to be the lowest near the crest and the highest near the toe of the slope (Figure 3b).

3.2 *Laboratory model for slope (Macedonia)*

The testing program in the laboratory considered simulating rainfalls with 30 l/m^2/h. The first test was performed on a bare soil on 30.11.2020. Planting of vegetation begun on 05.12.2020, and rainfalls were simulated on a slope with thriving vegetation on 08.01.2021. In the next period, the grass was left to dry, but for simulating prolonged sunny periods, daily heating of the surface was conducted. The final test was performed on 01.04.2021 on a slope with dry vegetation.

The sensors installed in the model continually registered the soil suction (Figure 4). As could be noticed, the sensors near the toe (No.2 and No.4, respectively) exhibit lower suction. This means that the lower part of the slope, despite the surface runoff and the underground piped drainage, contains more water than the upper part and it is exposed to lower shear strength.

Furthermore, after the initial rainfall on fallow soil, the sensors in both slopes registered sudden reduction in soil suction. Subsequent drainage and drying enabled slight increase in

the suction, with a gradient slightly increased after planting the vegetation - this was probably due to evapotranspiration of the vegetation – after which it appeared that the suction reached a constant value. The rainfall event on green slope did not significantly decrease the suction, which may be a result of both the above- and below-ground vegetation parts, preventing the drops to reach the soil and absorbing the water that has infiltrated the soil. Moreover, as long as the vegetation was green, the suction was constant, forming conditions for long term stability - an effect even more visible in the sandy material. As the vegetation dries out, this positive effect decreases and disappears.

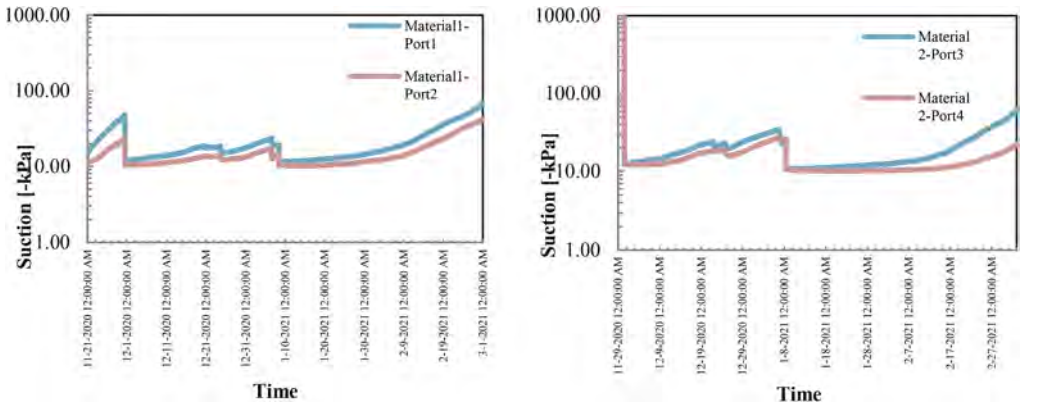

Figure 4. Measured suction during the laboratory experiment.

4 DISCUSSION AND CONCLUSIONS

Natural variability was recorded in soil strength across the slope in Scotland with locations where the strength dropped below 20 kPa due to the hydro-meteorological conditions (rainfall, water retention capacity), or disturbances during earthwork operations. The soil behavior at the toe of the slope appeared to be connected to the drainage (wetter soil at toe) but may pose a risk if the soil is shown to loose strength due to increase in moisture.

Longer-term monitoring is needed to ascertain any significant connection between the penetration resistance and soil moisture content. A decrease in penetration resistance would allow for better conditions for the vegetation to grow and an increase in moisture content would also provide for the physiological needs of the root systems.

The relationship between the shear strength and penetration resistance across the slope gives a rise to a concept of biodiversity employed in the context of slope protection and stability against shallow landslides and erosion: the crest of the slope may be a better environment for grasses and low vegetation to thrive due to low penetration resistance (slope protection from erosion initiation and rill formation due to the surface runoff and sediment entrapment) while the toe of the slope may be better suited for shrubs and trees (providing toe support and arching effect, while their strong structural roots anchoring the slope).

The aim of the laboratory experiment was to model the typical life cycle of a slope in transportation infrastructure: bare soil, slope with vegetation and slope with dry vegetation, at realistic climatic scenarios. These models showed the many very positive influences of the vegetation system, but also suggested that there may be a requirement of a suitable irrigation system during the maintenance and operation stage of a transportation project in regions with extreme conditions such as cyclic change of heat waves and intense rainfall, which are expected to be frequent.

Although these findings highlighted similar trends in contrasting environments, the limitations posed by the pandemic restricted the breadth and depth of the envisaged research. Both experiments, however, demonstrated the importance of relevant monitoring and testing.

While there were complex multi-organizational relationships on site which made getting support for monitoring/testing challenging, the laboratory experiment had challenges related to the reproducibility and applicability which could have been solved only with verification in situ. Additional to demonstrating good practice of carrying thematic laboratory and *in situ* testing in parallel, this study also showed that specific vegetation-related monitoring and testing have to form part of the earthwork design from the onset of a geotechnical project. Future work will see the development of relevant sampling, testing, and monitoring protocols which will incorporate vegetation and its effects on the soil properties and lead to more sustainable and resilient geotechnical design.

ACKNOWLEDGEMENTS

The work of Mandy Wallace was funded by Innovate UK through a Knowledge Transfer Partnership grant.

REFERENCES

Mickovski, B. S. 2018. Risk-based framework accounting for the effects of vegetation in geotechnical engineering. CE/Papers. 2, 2-3, p. 377–382.

Simeonovski, I. 2022. Geomechanical interpretation of the influence of vegetation on prevention of erosion and shallow landslides. Master thesis. University Ss. Cyril and Methodius. (In Macedonian).

Wallace, M., Mickovski, S. B. & Griffin, I. 2019. An innovative framework for selecting sustainable options to reduce the risk of soil erosion and environmental pollution incidents on road construction sites. In: *Proceedings of the XVII ECSMGE-2019*. Reykjavik: IGS. Doi: 10.32075/17ECSMGE-2019-0249

Wallace, M., Meldrum, A., Mickovski, S., McNee, I., Lear, D., Flint, S. 2020. Developing a Methodological Framework for Estimating Temporary Drainage Capacity to Inform Land Requirements for a Highway Construction Project in Scotland. *Sustainability*, 12, 5522.

Smart Geotechnics for Smart Societies – Zhussupbekov, Sarsembayeva & Kaliakin (Eds)
© 2023 The Author(s), ISBN 978-1-003-29912-7
Open Access: www.taylorfrancis.com, CC BY-NC-ND 4.0 license

Numerical modeling in the calculations of tailings dumps based on approaches in soil mechanics

A.K. Bugrov, A.B. Ponomaryov & V.A. Melnikov
Peter the Great St. Petersburg Polytechnic University, Saint Petersburg, Russia

ABSTRACT: The paper discusses the problems of construction and reconstruction of existing tailings and the development of modern computational methods and programs. In order to improve the calculations of tailing dams the authors suggest complex accounting of deformation, strength, filtration properties of soils and probability reliability of structures. Up-to-date methods and programs have been developed. The example of the calculations of the unique tailing dam "Teghout" erected in Armenia is given in the paper.

Keywords: tailing dump, consolidation, basic design model, stability, anisotropy of properties, probabilistic reliability, numerical program

1 INTRODUCTION

Currently, the tailings dumps of large mining and processing enterprises and combines (GOPs, GOKs) have a height of 200 m or more, and the volumes of waste storage ("tailings") transported in the form of pulp reach tens of millions of m3. With the continuous operation of the concentrator, the construction and operational periods of the tailings dump practically coincide in time.

The purpose of the study is the substantiation of the design and construction of the tailings dump with the use of modern apparatus and means of continuum mechanics, soil mechanics and computer technology capabilities. An indispensable condition for ensuring proper reliability of calculations is an experimental study of the physical and mechanical properties of the soils of the tailings dump and its foundation with the determination of statistical characteristics of properties - values of mathematical expectation, standard, coefficient of variation, etc. [20, 21, 22], which is also of great practical importance.

2 BASIC APPROACHES TO SOLVING THE PROBLEM

To solve the problems of the construction of new and reconstruction of existing structures in the NIL "Soil Mechanics and stability of tailing dumps" SPbPU has been actively developing computer programs (TFCOMPL, GRUNTUS, etc.) since the 1980s, allowing for comprehensive calculations of tailing dumps [1]. At the same time, the experience of the operation of the Sever-ZM program (1980) was used - the first program in the USSR to calculate a tailings dump growing in height [2].

The TFCOMPL program is used to calculate and evaluate structures operated in harsh climates and permafrost [27]. However, at present, most of the continuously growing tailings dumps remain in a thawed state even in winter, so now the GRUNTUS program is the most in demand [3].

DOI: 10.1201/9781003299127-287

The GRUNTUS program uses the theory of consolidation developed by prof. V.A. Florin within the framework of the soil model, which he called the "basic calculation model", to assess the stress-strain state (VAT) of water-saturated soils of the tailings dump in time [4]. Based on this model, consolidation equations for plane and spatial problems were obtained, which are partial differential equations of parabolic type. The derivation and analysis of the equations are given in the fundamental works of Florin [4, 5, 26].

Calculations of the consolidation and stability of the tailings dump and its base are carried out, as a rule, according to the scheme of flat deformation in vertical section, since the planned dimensions, the length of the thrust prisms are many times higher than the height of the tailings dump, even at its height of 200 m or more.

For the flat problem of compaction of tailings storage soils under the assumption of complete water saturation (two-component soil), the use of soil characteristics with filtration anisotropy and in the absence of skeleton creep and initial pressure gradient, the consolidation equation has the form [4,5]:

$$\frac{\partial H}{\partial t} = \frac{1}{2\gamma_B} \cdot \frac{\partial \theta^*}{\partial t} + \frac{(1+e)(1+\xi)}{2\gamma_B a} \left[k_{\phi x} \cdot \frac{\partial^2 H}{\partial x^2} + k_{\phi z} \cdot \frac{\partial^2 H}{\partial z^2} \right] \quad (1)$$

where $\theta^* = \sigma_x^* + \sigma_Z^*$ are stabilized stresses, $\gamma_в$ is the specific gravity of water; e, ξ are porosity and lateral pressure coefficients; a, $k_{\phi x}$, $k_{\phi Z}$ are soil compaction and filtration coefficients along the X and Z axes.

3 RESEARCH METHODS

The GRUNTUS program [3] adopted the integro-interpolation method of finite differences when approximating partial derivatives by difference relations according to an explicit scheme. Moreover, the time step is determined automatically from the condition of mathematical stability of the design scheme. With a strongly pronounced nonlinearity of the coefficients of the consolidation equation, additional splitting of time steps is provided to ensure the reliability of the calculation scheme.

Detailed in-situ and laboratory studies of the properties of alluvial deposits of various zones of tailing dumps formed as a result of fractionation of soils during alluviation [8,9] allowed us to establish the most significant properties and characteristics, which are necessary to take into account when calculating tailing dumps. These, first of all, are the nonlinear change in deformability and permeability from the stress state and filtration anisotropy. In particular, experimental graphs $e = e\ (\sigma)$, $k_f = f(\sigma)$ are used, which allow determining the values e, k_f, $a = \partial e / \partial \sigma$ in equation (1) for the moment $t + \Delta t$ based on the results of calculating the stress-strain state for the moment t [10,11].

As a result, the finite difference method makes it quite easy to take into account when calculating consolidation the technology of construction and the design features of the structure (the presence of drainage devices, anti-filtration curtains, etc.), the significant properties of the soils of the zones of heterogeneity of the tailings and its base and change (if necessary) the partition grid in accordance with the deformations of the soil massif. Note that well-known software systems using the finite element method (Plaxis, Cosmos, etc.) do not allow to fully reflect these features of the calculation of tailings. These software complexes, as a rule, carry out calculations of the bases of unchanged geometry without taking into account deepening or vice versa extension [7].

The calculated values of the pore pressure calculated according to the "Consolidation" block were repeatedly compared with the data of field measurements and their coincidence was noted. At the same time, it was shown that neglecting excessive pore pressure when calculating consolidating soil masses (dams, tailings ponds) can lead to their damage and even destruction [1,5,13,24].

The composition and volume of the initial information for the work of the GRUNTUS program on the calculation of consolidation and subsequent determination of stability are presented in [3].

The "Consolidation" block of the program determines overpressure $p = \gamma_w \cdot H$, pressure H, and automatically sends it to the "Stability" block. If necessary, the results of the consolidation calculation are printed out for the characteristic moments of the construction of the structure.

To assess the stability of the tailings dump, the GRUNTUS program implements a calculation under the assumption of a shift along a circular cylindrical sliding surface (CCPS) of radius R in the conditions of a flat problem. The coefficient of stability margin K_3 is determined by the formula of *K*. Terzagi:

$$\kappa_3 = \frac{R}{M_{\text{акт}}}\left[\Sigma(q_i + g_i - p_i)b_i cos\alpha_i \; tg\varphi_i + \Sigma\frac{c_i b_i}{cos\alpha_i}\right], \tag{2}$$

in which: *qi+gi* is the vertical pressure created on the base of the *i-th* element (column) by an external load and the weight of the water-saturated soil;

pi is the boundary pressure in the water along the sliding curve, including hydrostatic pressure and excessive pore pressure of consolidation;

ai is the angle of inclination of the base of the i-th element to the horizontal x axis;

φi,ci - characteristics of the strength of the soil of the base of the *i-ro* element;

M act is the moment of active forces, including seismic forces (for a special combination of loads), which are taken into account as additional horizontal forces.

The program provides an automatic search for the most dangerous sliding surface using the Gauss-Seidel method, which consists in alternately varying the parameters of the shear curve (radius *R*, coordinates of the center of rotation *Xo, Zo*) and determining the shear curve with a minimum coefficient of stability margin K_{3min} [3].

4 THE OBJECT OF THE STUDY AND THE MAIN RESULTS

To illustrate the possibilities of the GRUNTUS program, detailed results of calculations of consolidation and stability of the unique tailings storage facility of the Tehut copper-molybdenum combine are given below. The tailings storage facility is located in the north of Armenia in a seismic zone and is a typical example of a mountain-type storage facility.

Design studies (2014) were performed for the first stage of the tailings dump with a crest mark of 780 m (Figure 1a) and a maximum height of 110 m in cross section *x≈450 m*. Alluvial deposits are represented by loam (zone 1), sandy loam (zone 2) and powdery sand (zone 3).

The primary dam with a height of ~ 50m is made of a stone outline (zone 5) and has a screen along the upper slope (zone 4). The base is composed of blocky-clastic soil (zone 6) and fractured rock (zone 7). The construction of the tailings dam is carried out (according to the project) in 5 years, while the pond is filled up to the crest of the dam ($\nabla 715m$) in 1 year, and the next 4 years the construction is increased to the level of 780m with an intensity of 16m per year. The position of the depression curve in Figure 1a was determined by filtration calculations.

When calculating the consolidation for the soils of zones 1-3, the experimental dependences *e=e(σ), kf=f(σ),* shown in Figure 1b,B. The calculation results are presented in Figure 1g by the pore pressure plot $p = \gamma_w$ H vertically x = 350m (vertical V-V in Figure 1a). The plot is constructed at the time of the tailings ridge exit at the level of 780m. Above the depression curve and at the base (zones 6, 7), excess pressure $p = 0$.

The coefficient of stability margin was determined by the formula (2) under the assumption of a shift in the CCPS. According to the experimental data, the calculated characteristics of soil strength are assigned: zone 1 -φ = *25* °, c = 0.01 *MPa*; zone 2 - φ=29°, c = 0.01 *MPa*; zone 3-φ=30 °, c = 0.01MPa; zones 4, 5 - φ= 34 °, c =0.006MPa; zone 6 - φ=36°, c=0. Calculation

results: for the main combination of loads K_{3min} =2.09, R=265m, Xo=207m, Z_O=293m (shear surface - k.shift. in Figure 1a); for a special combination including seismic impact, K_{3min} =1.75, R=264.7m, X_O=207m, Z_O=294m. The sliding surfaces mostly pass through sandy loam (zone 2), as expected.

According to the above scheme, the calculation of the tailings storage of the Natalkinskoye field (Russia), given in [3], was carried out in a similar way.

5 CONSIDERATION OF SOIL ANISOTROPY IN THE CALCULATION OF TAILINGS

Above, the problems of calculating VAT, consolidation and stability of tailings dumps and their bases were considered, in solving which the characteristics of deformability and strength of soils are used under the assumption of their isotropy [28]. At the same time, equation (1) of the Florin consolidation theory takes into account filtration anisotropy, the manifestation of which in ground structures has been recorded since the XIX century.

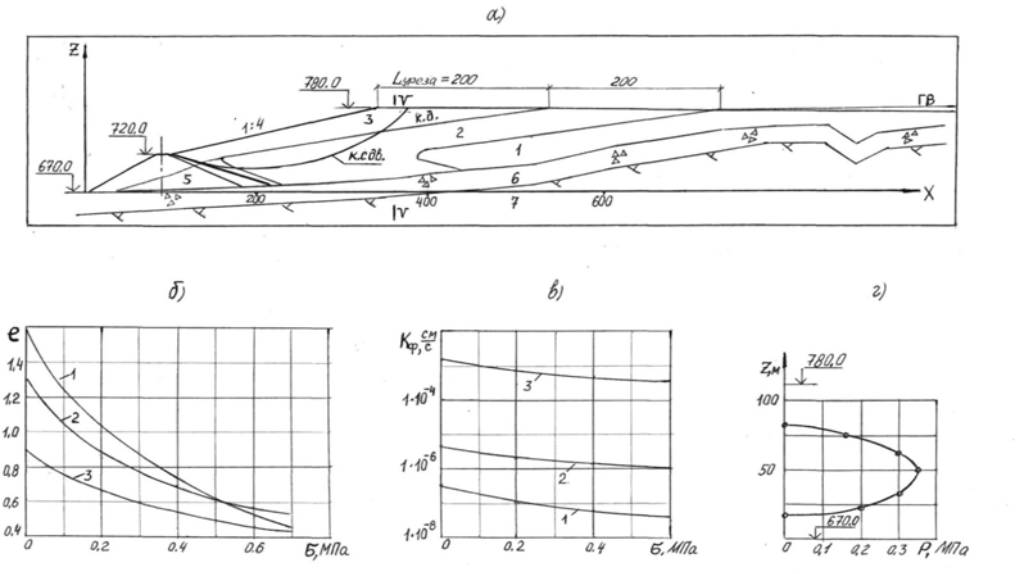

Figure 1. Calculation scheme and results of calculations of consolidation and stability of the Teghutsky MMK tailing dump.

The study of the anisotropy of other properties began later. To date, based on a review of numerous original studies, it has been established that soils - natural and man-made - have, as a rule, anisotropy of all properties at the same time - deformation, strength, filtration, etc. [7, 12, 13, 23].

As part of the improvement of consolidation calculations in the GRUNTUS program, along with filtration ($Kfx \neq Kf_Z$), consideration of deformation anisotropy ($a_x \neq a_z$) is introduced when determining the compaction coefficients a_x, a_z based on the results of compression tests of soil samples horizontally and vertically oriented in the array. The account of deformation anisotropy is easily carried out if in equation (1) the second term of the right part is represented as part of (7):

$$\frac{(1+e)(1+\xi)}{2\gamma_B a}\left[k^*_{\phi x}\cdot\frac{\partial^2 H}{\partial x^2}+k_{\phi z}\cdot\frac{\partial^2 H}{\partial z^2}\right] \tag{3}$$

where $a = a_z, k^*_{\phi x} = k_{\phi x}\cdot\frac{a_z}{a_x} = k_{\phi x}\cdot\frac{a_z}{a_x}$ is a fictitious filtration coefficient in the direction of the x axis, taking into account, along with filtration, deformation anisotropy.

Since the ratios of K_{fh}/K_{fz} and az/ax practically coincide in magnitude for the soils of tailings dumps [12] and, accordingly, we obtain $k*fx=kfz$, then the use of an isotropic model is fully justified in the calculation of consolidation, which was carried out above for the Teghutsky tailings dumps.

The strength anisotropy inherent in the soils of the base and body of the tailings dump in the GRUNTUS program is proposed to be taken into account in the "Stability" block. Detailed data on the strength anisotropy of the natural soils of the bases are given in [6, 7, 12]. It is especially pronounced in layered soils, for example, in ribbon clays, where the shear resistance tz across the layering is 5-10 times greater than t_x along the layering. For alluvial sandy soils and tailings storage materials close to them, according to Filimonov V.A., Nabokov I.M. et al., t_z/t_x =1,2-1,3 [12].

The Casagrande-Carrillo dependence is used in soil mechanics to describe the change in the strength of anisotropic soil to shear over various sites

$$\tau_\alpha = \tau_x + (\tau_z - \tau_x)sin^2\alpha, \tag{4}$$

in which α is the angle of inclination of the shear site to the X axis [12].

Since the Coulomb law $\tau = \sigma\cdot tg\varphi + c$ is laid down in the formula (2) for the stability margin coefficient, it is recommended to take the strength characteristics of $tg\varphi$ and "c" in the form of dependence (4) when taking into account strength anisotropy.

An increase intg φ_α *and* c_α with an increase in the angle α certainly provides higher values of K_3 when taking into account strength anisotropy. For gentle sliding curves (CCPs), this increase will be insignificant, for steeply inclined to the X-axis CCPs, the increase will be very noticeable. For example, for the sliding curve (Figure 1a), the margin coefficient, according to our calculations, will increase from K_3min =2.09 (isotropic soils) to K_3min= 2.25, taking into account the strength anisotropy characterized by the ratio t_z/t_x = 1.2. As a result, taking into account the anisotropy of the strength of the soils of the body of the tailings dumps allows to one way or another to increase the steepness of the slopes and, accordingly, the volume of the tailings dumps while meeting the requirements of the current standards for stability.

6 APPLICATION OF PROBABILISTIC CALCULATION MODELS

Currently, in geotechnics, further improvement of calculations of foundations and ground structures (dams, tailings dumps, waste accumulators) is associated with the use of probabilistic calculation models [14-17].

The most developed version of the theory of reliability of structures and foundations is the so-called parametric theory of reliability (PTN), which represents a probabilistic interpretation of calculations of stability, deformability, etc. [16].

In particular, the stability of the tailing dump according to the PTN is provided if the following condition is fulfilled:

$$Y1 \geq Y2 \; or \; Y1 - Y2 = Y \geq 0 \tag{5}$$

where: $Y1$ is an external factor characterized by a calculated reserve coefficient K_3min when assessing stability; $Y2$ is an internal factor (the potential capabilities of the system) characterized by a normative (permissible) stability reserve coefficient [K_3]; Y is a cumulative factor.

Taking into account the random (probabilistic-statistical) nature of the factors *Y1, Y2, Y,* the probability *P* of not reaching the limit state, determined by the dependence, is taken as a quantitative indicator of reliability

$$P[Y \geq 0] \; = \; 1-Fy(Y), \tag{6}$$

where: *Fy* is the distribution function of the value of *Y*.

There are various methods for determining the probability of R. The most common is the method of statistical tests (Monte Carlo method), especially effective in solving nonlinear problems. In particular, this method was used to assess the reliability (probability) of elastic-plastic foundations of structures based on sediment [14].

With a limited number of random variables characterized by a normal distribution law, an approximate way of representing the function F_y by the Charlier series is proposed in the monograph [18]. Taking into account the first terms of the series, which is quite sufficient when calculating the tailings, we obtain [19] an approximate dependence for probability (reliability) in the form [18]:

$$P \cong \frac{1}{2}\left[1 + \Phi\left(\frac{1}{\upsilon_y}\right)\right], \tag{7}$$

in which: υ_y is the coefficient of variation Y associated with the values m_y and σ_y by the dependence

$$\frac{1}{\upsilon_y} = \frac{m_y}{\sigma_y}, \tag{8}$$

where my is the mathematical expectation of *Y*; at the same time

$$\boldsymbol{m_y} = \boldsymbol{m_{y_1}} - \boldsymbol{m_{y_2}}, \tag{9}$$

σ_y – standard deviation (standard) Y; related to the Y_1 and Y_2 standards by dependency

$$\sigma_y^2 = \sigma_{y_1}^2 + \sigma_{y_2}^2, \tag{10}$$

$\Phi\left(\frac{1}{\upsilon_y}\right)$ is the probability integral for the value $\frac{1}{\upsilon_y}$.

As an example, we give an assessment of the level of reliability (probability) The stability of the Teghutsky tailing dump for the main combination of loads, for which K_3min =2.09 was obtained (Figure 1a.). We accept the standard reserve coefficient [K_3] = 1, 2. We assign the coefficients of variation of soil characteristics according to the recommendations [15, 18].

As a result, the dependencies (4-6) obtained: $\frac{1}{\upsilon_y} = 4,45$, F = 0.9927 and the estimated probability P = 0.9963.

Currently, a systematic assessment of the calculated reliability is carried out, as a rule, for particularly responsible unique structures (nuclear power plants, offshore platforms, etc.) [24]. The maximum permissible value of probability (reliability) according to the limit states for these structures is assumed to be *Rpr* ≥ 0.999. For tailings dumps, even with a height of *H*≥100m, the reliability of *Rpr* =0.99 seems to be sufficient [25].

7 CONCLUSION

1. Modernization of the original computing program GRUNTUS and improvement of the methodology of numerical calculation of tailing dumps have been carried out.

2. Further development of calculations is proposed, taking into account the anisotropy of the properties of the soil of the tailing dump, using probabilistic calculation models to assess its reliability.
3. The use of probabilistic models to assess the reliability of tailing dumps as hydraulic structures of increased responsibility is proved.
4. Considering the extreme complexity of the tasks to be solved, the comments of the forthcoming discussion will be taken into account in the future.

ABOUT THE AUTHORS

Alexsandr K. Bugrov, Doctor of Technical Science, Professor, e-mail:bugrov@cef.spbstu.ru
Viktor A. Melnikov, Ph. D. in Technical Science, Associate Professor E-mail:melvik702@gmail.com
Andrey B. Ponomaryov, Doctor of Technical Science, Professor, e-mail: andreypab@mail.ru

REFERENCES

1. Trunkov G.T. Research laboratory of Soil mechanics and stability of tailing ponds of St. Petersburg State Polytechnic University - 30 years. / Florinsky collection. St. Petersburg, SPbSTU, 1999, pp. 38–52.
2. Technical guidelines for calculating the consolidation of tailing dumps taking into account the temperature regime. G.T. Trunkov, S.B. Zalivako, V.I. Shcherbachev. L., All-Russion Research Institute Mekhanobr, Leningrad Polytechnic Institute named after M.I. Kalinin, 1980, 43p.
3. Recommendations for the numerical calculation of consolidation and sustainability of tailing ponds under the GRUNTUS program. Teaching-methodical manual. - L.G. Zinoviev, D.S. Maslova, edited by A.K. Bugrov. SPbPU, "Soil mechanics and stability of tailing dumps", 2014, 40p.
4. Florin V.A. Theory of compaction of earth masses. Moscow, Stroyizdat, 1948, 284p.
5. Florin V.A. Fundamentals of soil mechanics. Moscow-Leningrad, Stroyizdat, vol.1, 1959, 356c; t.2, 1961, 540p.
6. Ivanov P.L. Soils and foundations of hydraulic structures. Soil mechanics. Moscow, Higher Ed., 1985, 385c; 1991, 447 pp.
7. Bugrov A.K. Soil mechanics. Tutorial. SPbSPU. Priority national project "Education". SPb.,Publishing house of the Polytechnic University, 2011, 307p.
8. Recommendations on the evaluation of physical and mechanical properties of tailings of tailings. / Comp. L.V. Schultz, G.T. Trunkov. L., All-Russion Research Institute Mekhanobr, Leningrad Polytechnic Institute named after M.I. Kalinin, 1979, 31c.
9. Recommendations for calculating the fractionation of the soils of the tailing dumps during reinjection. / Comp. M.L. Kiseleva, G.T. Trunkov. L., VNIPI Mekhanobr, 1982, 44p.
10. Zinovieva L.G. Consolidation of bases taking into account the variability of soil characteristics under conditions of drainage and variable loads. Author's abstract of the thesis ... PhD of Engineering. St. Petersburg, 1989, 16 pp.
11. Zinovieva L.G. Numerical method for solving the consolidation problem using the coordinate transformation. / Florinskysbornik. St. Petersburg, SPbSTU, 1999, p.89–95.
12. Bugrov A.K., Golubev A.I. Anisotropic soils and foundations of structures. - St. Petersburg: Nedra, 1993–245p.
13. Bugrov A.K. Mechanics of deformable solid. Information tools for soil structures and foundations. Tutorial. St. Petersburg. Publishinghouse, SPbSTU, 1999, 86s.
14. Bugrov A.K., Shilin V.G. Calculation of the reliability of the elastic-plastic foundation by the method of statistical tests // Reconstruction of cities and geotechnical construction. 2000, №2, p.79–83.
15. Belendir E.N., Ivashincov D.A., Stefanishin D.V., Finagenov O.M., Shulman S.G. Probabilistic methods for assessing the reliability of groundwater hydraulic structures. Volume 1, St. Petersburg, 2003, 354c; Volume 2, St. Petersburg, 2004, 524p.
16. Solsky S.V., Stefanishin D.V., Finagenov O.M., Shulman S.G. Reliability of industrial and household waste storage. SPb., 2006, 300s.
17. Albert I.U., Shulman S.G. Methods for assessing the reliability of a seismic insulation system for buildings and structures. SPb, 2014, 432p.

18. Ermolaev N.N., Mikheev V.V. Reliability of the foundations of structures. M., Stroiizdat, 1976, 247p.
19. Bugrov A.K., Zinovieva L.G., Kiseleva M.L., Maslova D.S. Improvement of calculations of tailing dumps for the justification of their designs in complex engineering-geological conditions and seismically dangerous territories. - Proceedings of All-Russian Research Institute named after B.E. Vedeneev, volume 274, St. Petersburg, 2014, p.48–59.
20. Ponomaryov A., Zolotozubov D. Several approaches for the design of reinforced bases on karst areas. // Geotextiles and Geomembranes. 2014 №42, p. 48–51. DOI:10.1016/j.geotexmem.2013.12.002
21. Bartolomey A., Ponomaryov. A., Kleveko V. Use of geosynthetic materials for increase bearing capacity of clayish beddings. Geosynthetics: applications, design and construction. Proc. 1st European geosynthetics conference, Maastricht, 1996. pp. 459–461. WOS:A1996BH16G00060
22. Storage of industrial waste Patent for utility model RU 9235 U1, 02/16/1999. / Ponomarev A.B., Ofrichter V.G. Application No. 97120318/20 of 04.12.1997.
23. Ponomaryov A., Sychkina E. Analysis of strain anisotropy and hydroscopic property of clay and claystone. Applied Clay Science. 2015. V. 114. pp. 161–169. DOI 10.1016/j.clay.2015.05.023
24. Melnikov V.A., Zinovieva L.G., Kiseleva M.L., Maslova D.S. Calculation studies of the stability of the tailing dump №1 in the Davasamiregion of the Agarak MMK during its erection to the level of 890.0 m. - St. Petersburg, Report on Research and Development, SPbSPU, 2012, 123p.
25. Utkin, V.S. Calculation of the reliability of the earth foundations of buildings and structures according to the deformation criteria with limited information on the soils and loads (2016) Magazine of Civil Engineering, 61 (1), pp. 4–13. DOI: 10.5862/MCE.61.1
26. Sainov, M.P., Anisimov, O.V. Stress-strain state of seepage-control wall constructed for repairs of earth rock-fill dam (2016) Magazine of Civil Engineering, 68 (8), pp. 3–17. doi=10.5862%2fMCE.68.1
27. Tretiakova, O.V. Normal stresses of frost heaving as function of excess moisture (2017) Magazine of Civil Engineering, 76 (8), pp. 130–139. doi=10.18720%2fMCE.76.12
28. Sirotyuk, V.V., Lunev, A.A. Strength and deformation characteristics of ash and slag mixture (2017) Magazine of Civil Engineering, 74 (6), pp. 1–14. doi=10.18720%2fMCE.74.1

Smart Geotechnics for Smart Societies – Zhussupbekov, Sarsembayeva & Kaliakin (Eds)
© 2023 The Author(s), ISBN 978-1-003-29912-7
Open Access: www.taylorfrancis.com, CC BY-NC-ND 4.0 license

Obtaining light technogenic soil in the process of sulfur-alkali waste disposal

V.G. Ofrikhter, A.S Grishina, A.A. Ketov, Y.A. Ketov, Y.I. Vaisman & E.I. Korolev
Perm National Research Polytechnic University, Perm, Russian Federation

ABSTRACT: The article deals with an innovative light technogenic soil obtained by utilization of sulfur-alkali desulfurization waste. The environmental safety of the lightweight technogenic soil has been proved. The granulometric composition of the product, its density, moisture and compaction ability in comparison with natural soils have been studied. Based on the determination of physical and mechanical characteristics, the conclusion about the possible use of the obtained material as a technogenic soil was made. The most important advantage of the product is its density, which is on average 30% lower than the density of natural disperse soils. Also noteworthy is the increased strength properties of the lightweight soil established in laboratory tests.

Sulfur-alkali wastes are formed during cleaning of pyrolytic gases from hydrogen sulfide and carbon dioxide with sodium hydroxide solution. The effluents are formed in a number of processes: during the purification of liquefied gases, the production of lower olefins, the purification of kerosene and gasoline fractions and some other petrochemical processes. The resulting sulfur-alkali wastes are aqueous solutions of usually yellow-brown color with a pungent bad smell and alkaline reaction of the medium. From the chemical point of view, sulfur-alkali waste contains, in addition to sodium sulfide, a complex mixture of polysulfide, mercaptide and carbonate sodium salts, sodium phenolates, as well as mechanical impurities and various oil products in the dissolved or colloidal form.

Thus, sulfur-alkali wastes pose a dual environmental hazard: they contain toxic sulfur (II) compounds, mainly of the sulfur-organic type, and have a high pH due to the high content of sodium hydroxide in the solution

1 PRODUCTION OF LIGHT TECHNOGENIC SOIL

1.1 *Choosing the sulphur-alkali waste disposal method*

There are various methods for the decontamination of sulfur-alkali waste (Budnik et al 2019, Ksandopulo et al 2009), the most acceptable of which are physical or reagentless, chemical, and integrated treatment methods. As a result, sulfur (+2) compounds are usually concentrated and converted to less toxic compounds. Thus, oxidation of sulfur-containing odorants by ozonation allows us to utilize them, obtaining less dangerous compounds (Neretin et al. 2016).

In some cases, the technical solution involves the utilization of sulfur-alkali wastes as a single material, without sequential conversion into safe products of sulfur compounds and an alkaline component. An example is the production of a mineral additive based on sulfur-alkali waste to improve the properties of concrete (Badikova et al. 2020). The introduction of such a mineral additive from sulfur-alkali waste significantly improves the properties of concrete compositions, as well as reduces the consumption of resources for the production of concrete mixture and structures based on it (Murtazaev et al 2017, Batrakov 2006).

However, the necessity to utilize significant volumes of sulfur-alkali waste requires searching for a form of the obtained stuff that allows for a safe disposal of the resulting multitonnage product in the environment (Vaisman et al. 2018). For this reason, the technology of

DOI: 10.1201/9781003299127-288

waste recycling into anthropogenic soils, which minimizes the migration ability of ecotoxicants while creating an equilibrium and durable structure of the resulting material, has a long-term perspective. It has been proposed to utilize sulfur-alkali wastes using amorphous trepel oxide and obtaining a cellular silicate material (Knat'ko et al. 2015). It was shown that as a result of heat treatment, sulfur (II) from sulfur-organic compounds oxidized to sulfur (IV), and after water detachment, sodium hydroxide was a part of the obtained glassy cellular silicate material. Therefore, the purpose of this work was to study the characteristics of the resulting product as a man-made soil, and to determine the fundamental possibility of applying it for the erection of earthworks in difficult geotechnical conditions, on weak soils. After the first studies of physical and mechanical characteristics, of additional interest was the density of the obtained technogenic dispersed soil, which was on average 30% lower than that of natural soils, and its significant strength properties. The material obtained by the thermal treatment of sulfur-alkali desulfurization solution and trepel was chosen as the object of the study. Earthen structures erected from such a man-made soil will significantly reduce the load on the environment by decreasing the load on the underlying soils and downsizing the geometric dimensions of the structure due to steeper slopes, which will require a smaller area to accommodate such a bulk structure.

1.2 *Selecting the initial product composition and the utilization process parameters*

Industrial sulfur-alkaline effluent was used for the research; according to the chemical analysis, it contains 8.6 wt.% sodium hydroxide and 1.4 wt.% sulfur (II). The density of the solution is 1.094 kg/m^3.

Silica gel KSKG was selected to study the possibility of binding sulfur-alkali effluents into a silicate. Trepel with an average chemical composition (wt.%): SiO_2 - 76.16; Al_2O_3 - 9.33; Fe_2O_3 - 4.10; CaO - 1.05; MgO - 1.01 and SO_3 - 0.31 was used as a natural analog of amorphous silicon oxide.

The toxicity class of water and aqueous extracts was determined according to the "Methodology for determining the toxicity of water and aqueous extracts from soils, sewage sludge and wastes by mortality and changes in the fecundity of daphnia", Federal Register (FR) FR.1 .39.2007.03222 and in accordance with the "Methodology for determining the toxicity of water, water extracts from soils, sediments, sewage and wastes by changes in chlorophyll fluorescence and algae cell number", Federal Register (FR) FR.1.39.2007.03223.

At the first stage, the task was set to determine the conditions for obtaining an environmentally safe product. Samples of pellets heat-treated at different temperatures were subjected to the standard procedure of biotesting. As a result, it was found that heat treatment of pellets at temperatures above 700°C allows obtaining a material with zero toxicity and acidity of the aqueous extract not higher than pH = 8.5. For a preliminary study of the physical and mechanical characteristics of the obtained environmentally safe granules, tests recommended by national and interstate standards for natural and man-made soils were carried out.

Acceptable quantities of the test material were obtained from a pilot plant designed and tested for the disposal of up to 200 liters of the sulfur-alkali solution per shift. The general view of the light technogenic soil is shown in Figure 1.

Granules were prepared by mixing trepel powder and the sulfur-alkali solution, 400 g of the sulfur-alkali solution was added to 1000 g of trepel and the granules were pelletized in a disk granulator. The silicate material obtained from trepel and sulfur-alkali wastes consists of strong granules. A photo of such a pellet, heat-treated at 700°C, is presented in Figure 1.

Some areas with remnants of diatomite microorganisms can be traced in the structure of the material, but in general, it has a high porosity and homogeneity. To analyze the hazard of the initial waste and the resulting product, standard techniques were used.

The proposed technological scheme was implemented as follows. The initial sulfur-alkali solution of waste is mixed with trepel powder in a disk granulator in the ratio of 400 ml of the sulfur-alkali solution per 1000 g of trepel powder (Figure 2).

The obtained raw pellets are fired in a drum furnace at 700°C with a calculated residence time in the firing zone of 25 minutes. The organosulfur compounds in the form of water vapor, carbon

monoxide (IV) and sulfur monoxide (IV) are removed from the raw pellets, and the obtained pellets form a strong glassy silicate material. The proposed technology was implemented in practice on a pilot scale. Figure 2 shows the external view of the firing furnace.

Figure 1. Light technogenic soil: left – general view; right - micrograph of a chipped silicate pellet obtained by utilizing a sulfur-alkali solution through interaction with trepel.

The technology of sulfur-alkali waste recycling makes it possible to receive an environmentally safe material from the alkaline component of sulfur-alkali waste and to transform highly toxic sulfur-organic compounds into sulfur oxide (IV) of a low hazard class. In this connection, the physical and mechanical properties of the material were investigated for the possibility of its application as a technogenic soil.

Figure 2. Production of a technogenic soil: left - production of raw pellets from sulfur-alkali waste and trepel in a pan pelletizer, right – the drum kiln.

2 GEOTECHICAL INVESTIGATIONS OF OBTAINED TECHNOGENIC SOIL

2.1 *Physical properties of light soil*

2.1.1 *Granulometric composition*

The granulometric composition of the material was determined according to GOST 12536-2014 by the sieve method with water washing. Samples weighing 100 g in an air-dry condition were taken. At the first stage, the sample was placed on a sieve with a hole diameter of 0.1 mm

and washed under a stream of water until the water flowing out of the sieve became clear. The particles remaining on the sieve were dried in a desiccator and sifted through 10, 5, 2, 1, 0.5, and 0.25 mm diameter sieves. The results of partial determination of the particle size distribution are shown in Table 1.

Based on the sieve analysis it was concluded that, in accordance with GOST 25100-2020 "Soils. Classification", the obtained material corresponds to the dusty sand by particle size distribution (the content of particles with a diameter of more than 0.1 mm is less than 75%).

Table 1. Particle size distribution.

Size of fractions, mm	Share of total mass, %
>10	0
5-10	0
2-5	0.11
1-2	3.72
0.5-1	14.02
0.25-0.5	11.96
0.1-0.25	14.19
<0.1	56.0

2.1.2 *Density of solids*

Next, an attempt was made to determine the density of solid particles of the material using the pycnometric method according to GOST 5180-2015. The test involves boiling a soil sample with distilled water in a sand bath to remove the absorbed air. When testing the man-made soil, the boiling reaction was very violent, so the water was replaced by a neutral liquid - acetone, which does not contradict GOST. As a result, a preliminary value of the particle density of the technogenic soil was obtained, which was 1.83 g/cm^3. Thus, it can be concluded that the density of the technogenic soil particles is about 30% lower than the density of natural soil.

2.1.3 *Compaction ability*

The next test of the product was a preliminary study of its ability to compact and finding the maximum density by the method of standard compaction according to GOST 22733-2016. The method consists in determining the dependence of the dry soil density on its moisture content during compaction. For the test, we used a device for mechanized compaction of soil by a falling load from a constant height and samples of man-made soil, the moisture content of which was sequentially increased.

The maximum density of the dry soil according to the preliminary tests of standard compaction was ρ_d = 0.98 g/cm^3 at moisture content w = 56%. At these parameters, the natural density of soil is ρ = 1.53 g/cm^3. Thus, one can make a preliminary conclusion that the density of man-made soil is about 25% lower than the density of natural soil, and the optimum humidity, at which maximum density is reached, is higher compared with the optimum humidity of natural sandy and clayey soils approximately by 4.5 and 2.5 times respectively. In this case, the nature of the compaction process is similar to natural soils.

It should be noted that the resulting product does not have the plasticity characteristic of clay soils, that is, the man-made soil does not have the ability to deform under external pressures without disturbing the continuity and does not retain the given shape after the removal of the load.

2.1.4 *Filtration ability*

To assess the ability of man-made soil to pass water, we determined the filtration coefficient k according to GOST 25584-2016. A filtration device for determining the filtration coefficient of sandy soils at a variable head gradient was used for the test. A sample of the material with a density ρ = 1.48 g/cm^3 and moisture content w = 62%, which corresponds to the compaction factor = 0.93, was placed in the device. As a result of the test, the material filtration coefficient

k = 0.013 m/day was obtained. In accordance with GOST 25100-2020 “Soils. Classification”, the technogenic soil can be preliminarily classified as “low permeable”. In terms of the permeability characteristic, the obtained product is close to dense loams and sandy loams.

2.1.5 *Degree of heaving*

To assess the degree of material heaving, tests were carried out to determine the relative deformation of frost heaving on the device UPG-MG4 “Soil” according to GOST 28622-2012. A sample of the material was prepared in the device casing using layer-by-layer tamping. Density was $\rho = 1.38$ g/cm^3 with moisture content w = 62%, which corresponds to the compaction factor = 0.87. As a result of the test, the relative deformation of swelling was $\varepsilon_{fh} = 0.1$, according to which the man-made soil can be tentatively classified according to GOST 25100-2020 “Soils. Classification” as “strongly heaving soil”. By the degree of heaving the obtained product is close to clayey soils.

2.2 *Mechanical properties of light soil*

2.2.1 *Results of compression tests*

The deformability characteristics were obtained from the preliminary compression tests. A sample of the material with density $\rho = 1.51$ g/cm^3 and humidity w = 56%, which corresponds to the compaction factor = 0.99, was placed in the device,. The load on the samples was transferred in stages equal to 25, 50, 100, 200 kPa. Transition to every next stage was realized when the conditional stabilization of soil was achieved, the criterion for which was strain increment not exceeding 0.05 % in 6 hours.

The compression curve shows that the nature of deformation of the technogenic soil is similar to that of the natural soil. The compression tests gave the normative value of the odometric deformation modulus in the interval of construction pressures of 0.1-0.2 MPa $E_{oed} = 5.8$ MPa. In order to switch from the odometric modulus to the strain modulus, which is used in calculating strains of soil masses, according to SP 22.13330.2016 “Foundations of buildings and structures” we need an empirical factor m_{oed}, which depends on the type of soil and is taken, based on the physical state of soils, equal to 1.0-3.0. Since the test material is not a natural soil, further research, including large-scale one, is required for a full assessment of its deformation characteristics. Another deformation characteristic by which the deformability of the material can be estimated is the compressibility factor m_0. In the pressure range of 0.1-0.2 MPa, the average compressibility factor of the tested samples was $m_0 = 0.34$ MPa^{-1}, which allows us to classify the soil as “highly compressible”.

2.2.2 *Strength characteristics of light soil*

The strength characteristics of the technogenic soil were obtained by the method of single-plane unconsolidated shearing, which allows obtaining the values of the angle of internal friction and cohesion in the unstabilized state. Samples for the shear test were prepared with a density $\rho = 1.44$ g/cm^3 at moisture content w=59%, which corresponds to the compaction factor = 0.92.The shear test was conducted in a kinematic mode with a given shear rate of 0.5 mm/min. Samples were tested at normal pressure values of 100, 200 and 300 kPa.

As a result of single-plane shear tests we obtained the normative values of strength characteristics of the material: the angle of internal friction $\varphi = 18°$ and cohesion c = 79 kPa. Thus, we can make a preliminary conclusion that the obtained material has a high shear resistance, and the resulting strength parameters are close to the normative values of semi-solid clays according to SP 22.13330.2016 “Foundations of buildings and structures”.

3 CONCLUSIONS

Based on the preliminary tests, we can conclude that the resulting material has the characteristics of both cohesive and non-cohesive soil. The granulometric composition of the product is close to silty sands. It is also united with the non-cohesive soil by the lack of plasticity. At the

same time, the technogenic soil has high strength and low water permeability, typical for cohesive soils. The material is highly compressible as per the compressibility coefficient, and as per the degree of heaving - highly heaving, which is also close to cohesive soils. The density of the material is about 25% lower than that of natural soil.

When studying the properties of the technogenic soil, attention was also paid to the density of solids, which was on average 30% lower than that of natural soils. It should be noted that the soil is characterized by the properties of both non-cohesive and cohesive soils. The strength characteristics of this soil obtained in conditions of unconsolidated shear tests are of certain interest: the angle of internal friction $\varphi = 18°$ and the cohesion $c_u = 79$ kPa.

The initial void ratio at the compaction coefficient of 0.99 was 0.9, which corresponds to 47% porosity. The optimum moisture content was 56%, which exceeds the average values of this indicator for natural sandy and clayey soils by about 4.5 and 2.5 times, respectively.

Thus, the conducted research has established in principle the possibility of recycling sulfur-alkali wastes of gas purification into a safe silicate material. The obtained material has the characteristics of light technogenic soil and can be placed in the environment without restrictions. According to the preliminary studies, the most important feature of the resulting technogenic soil was found to be its lower density, which was on average 30% less than that of natural soil, thus making it possible to build earth structures on weak soils without additional improving measures and to substantially reduce the impact on the environment. The significant strength characteristics of the obtained product in comparison with natural soils also attract attention. Increased strength properties allow us to construct embankments with steeper slopes from such soil, which in turn reduces the area occupied by the earthworks on the ground surface.

The study was conducted with the financial support of the Ministry of Education and Science of Russia as part of the program of the world-class Scientific and Educational Center "Rational Subsoil Use".

REFERENCES

Badikova, A.D., Sakhibgareev, S.R., Fedina, R.A., Rakhimov, M.N., Tsadkin, M.A. 2020. Effektivnaya mineral'naya dobavka na osnove otkhodov neftekhimicheskikh proizvodstv dlya betonnoi stroitel'noi smesi. *Nanotekhnologii v stroitel'stve: nauchnyi Internet-zhurnal.* 12 (1): 34–40. DOI: 10.15828/2075-8545-2020-12-1-34-40.

Batrakov, V.G. 2006. Modifikatory betona: novye vozmozhnosti i perspektivy. *Stroitel'nye materialy (eISSN: 2658-6991)* 10: 4–7.

Budnik, V.A., Bobrovskii, R.I., Babkin, D.E. 2019. Kompleksnye metody ochistki sernisto-shchelochnykh stochnykh vod neftepererabatyvayushchikh proizvodstv. In *Neftegazovoe delo (eISSN: 1813-503X)* 5: 58–85.

Knat'ko, M., Zhabrikov, S., Podlipskii, I. 2015. Utilizatsii otkhodov toplivno-energeticheskogo kompleksa. *Ekologiya i promyshlennost' Rossii. (ISSN: 2413-6042)* 19 (4): 20–23.

Ksandopulo, S.Yu., Shurai, S.P., Barko, A.V. 2009. Perspektivy ochistki stokov neftepererabatyvayushchikh zavodov v tselyakh sokhraneniya kachestva okruzhayushchei sredy. *Sanitarnyi vrach (ISSN: 2074-8841)* 12: 25–33.

Murtazaev, S.-A.Yu., Bataev, D.K.-S., Ismailova, Z.Kh. 2017. *Melkozernistye betony na osnove napolnitelei iz vtorichnogo syr'ya: nauchnoe izdanie*. M., Komtekhprint. ISBN: 978-5-903511-13-6.

Neretin, D.A., Pimenov, A.A., Vasil'ev, A.V. 2016. Primenenie metodov ozonirovaniya pri utilizatsii otkhodov odoranta. *Ekologiya i promyshlennost' Rossii (ISSN: 2413-6042)* 20 (10): 21–23.

Vaisman, Ya., Glushankova, I., Ketov, Yu., Rudakova, L., Krasnovskikh, M. 2018. Utilizatsiya sernisto-shchelochnykh otkhodov pererabotkoi v yacheistyi silikatnyi material. *Ekologiya i promyshlennost' Rossii*. 22 (10): 24–27. DOI: 10.18412/1816-0395-2018-10-24-27.

Smart Geotechnics for Smart Societies – Zhussupbekov, Sarsembayeva & Kaliakin (Eds)
© 2023 The Author(s), ISBN 978-1-003-29912-7
Open Access: www.taylorfrancis.com, CC BY-NC-ND 4.0 license

Use of the enzyme-induced carbonate precipitation method for containing the sulfate

J. Kim & T.S. Yun
Yonsei University, Seodaemun-gu, Seoul, Republic of Korea

ABSTRACT: The high concentration of sulfate (SO_4^{2-}), involved in wastewater and leachate, damages the environmental condition and human health when it leaks. This study aims to contain SO_4^{2-} into the ground by applying chemical precipitation with calcium ions. The enzyme-induced carbonate precipitation (EICP) was proposed to get Ca^{2+} which remained after the reaction and the effect of SO_4^{2-} was observed in terms of stiffness. The results showed SO_4^{2-} solution decreased the shear wave velocity a little, which means it is negligible, and the SEM image proved SO_4^{2-} was precipitated on the sand particle surface.

1 INTRODUCTION

Sulfate (SO_4^{2-}) is a common contaminant in industrial wastewater like effluent from mining, fertilizer production, and landfill leachate (Tait et al., 2009). Exposure to SO_4^{2-} has little effect since SO_4^{2-} is chemically inert and non-toxic. However, the high concentration of SO_4^{2-} causes many problems, such as damage to the natural sulfur cycle, pipe corrosion, water mineralization, and diarrhea. Among the management of SO_4^{2-} concentration, chemical precipitation is the most widely used method due to its cost-effectiveness and simplicity. The calcium ion (Ca^{2+}) has been used to precipitate SO_4^{2-} as forming gypsum in typical conditions, which is non-toxic and reusable although the solubility is higher than the barium sulfate (Benatti et al., 2009).

In a synthetic solution, the gypsum crystallization reaches equilibrium in 1 ~ 2 hours, while takes more time in wastewater, because of the inhibition of crystal nucleation by impurities (Tait et al., 2009). Geldenhuys et al. (2003) and Tait et al, (2009) demonstrated the increase of crystallization rate and decrease of the SO_4^{2-} concentration by adding the seed crystal to wastewater.

In this study, SO_4^{2-} removal proceeded using Ca^{2+} remained after enzyme-induced carbonate precipitation (EICP) reaction. In order to exist adequate Ca^{2+} to react with SO_4^{2-} in EICP, the concentration of urea, calcium chloride, and urease was calculated, where the raw soybean powder was used as urease in this study because the purified urease is expensive. Also, the effect of the seed gypsum crystal on SO_4^{2-} removal in the EICP solution was investigated because cells and tissue of soybean in the EICP solution, except for urease, can act as an impurity. The effect of SO_4^{2-} on EICP-treated sand was analyzed by measuring the shear wave velocity using the bender element test.

2 MATERIAL AND METHOD

2.1 *Urease activity*

Raw soybean used in this study was stored in a refrigerator at 2°C before experiments and the target amount of powder was added to distilled water. The mixture was mixed until homogeneous and was centrifuged at 3000 rpm for 15 min. After then, clear supernatant including crude urease was used for the urease solution.

DOI: 10.1201/9781003299127-289

The crude urease activity was measured using the electrical conductivity (EC) method. In general, the urease decomposes the urea to ammonium and carbonate, called urea hydrolysis, and the EC increases due to increase ions. In standard conditions (1 M urea at 20℃ and pH = 7), the increasing rate of 1 mS/cm/min of EC means 11 mmol/L/min of urea hydrolyzing rate, which corresponded to activity. The 3 ml of crude urease and 27 ml of urea (1.11 M) were prepared, and the EC proceeded for 15 min. Since only 3 ml of crude urease was used in 30 ml of total volume, the actual activity should consider a 10-times dilution factor.

2.2 *Optimal recipe of EICP for removing* SO_4^{2-}

The molar ratio of urea-calcium chloride ($CaCl_2$) was an important factor to decide the amount of calcium carbonate ($CaCO_3$). Song et al, 2020 measured the amount of $CaCO_3$ by changing the molar ratio of urea-$CaCl_2$ in a certain urease concentration. The result shows the 1.5 molar ratio of urea-$CaCl_2$ had the highest efficiency regardless of the concentration of $CaCl_2$. Also, the maximum concentration of SO_4^{2-} in this study based on the leachate from Korean landfill cooperation was 0.1 M. Therefore, 1.5 M urea and 1 M $CaCl_2$ were used, and the crude urease solutions with 5 – 55 g/L were prepared to calculate the reaction efficiency where reaction efficiency was calculated by dividing the amount of produced $CaCO_3$ by the amount of theoretically producible $CaCO_3$. The reaction was allowed for 3 days, after then, the 3 ml of supernatant was mixed with an equal volume of 0.1 M SO_4^{2-}.

As shown the Figure 1, the reaction efficiency increased as the urease concentration increased and reached 100 % at 50 g/L. 100 % reaction efficiency indicates all Ca^{2+} is so exhausted in the EICP supernatant that the gypsum is not formed when SO_4^{2-} is added. To remain the excessive Ca^{2+} and produce as much $CaCO_3$ as possible, 15 g/L was used, and the reaction with SO_4^{2-} reduced by about 20 ~ 30 % SO_4^{2-}. To increase the SO_4^{2-} reduction, the seed gypsum above mentioned was produced, and more details are provided in the next section.

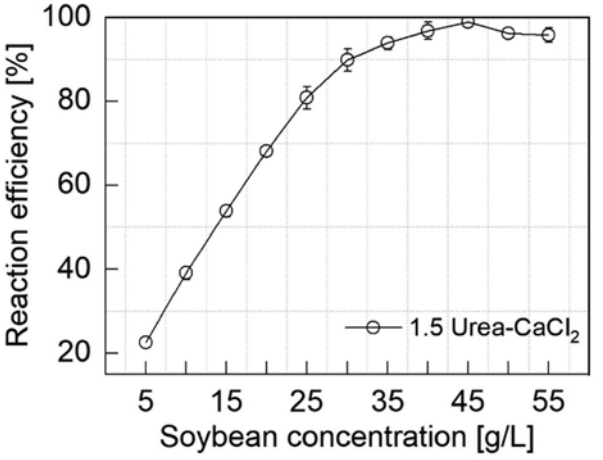

Figure 1. Reaction efficiency as a function of soybean concentration under 1.5 molar ratio of urea-$CaCl_2$.

2.3 *Seed gypsum crystal*

The equimolar concentrations of calcium chloride and sodium sulfate were mixed for preparing the synthetic seed gypsum. Figure 2 (a) shows the reaction was constant after 8 hours of reaction. The mixed solution composed of analytical reagent chemicals was stored at room temperature (25 ± 2℃) for 24 hours. After the reaction, the crystals were filtered and rinsed with distilled water to remove the chloride and sodium ions because the ions may inhibit the reaction SO_4^{2-} with Ca^{2+} in EICP supernatant. And then, the absolute ethanol was added to

the filtered crystals and the filtering process was repeated to get the pure crystal seed. After completing the course, the crystals were dried in the oven for a day at 45℃, and the detailed features of the crystal were shown in Figure 2 (b) through SEM image and EDS analysis.

To observe the change of produced $CaCO_3$ and SO_4^{2-} concentration according to the addition of seed gypsum, EICP samples were made with different amounts from 4 g/L to 10 g/L in increments of 2 g/L. After 3 days of reaction, SO_4^{2-} was mixed with the EICP solution, and SO_4^{2-} concentration was measured at 1-day intervals for 3 days considering the reaction time of gypsum.

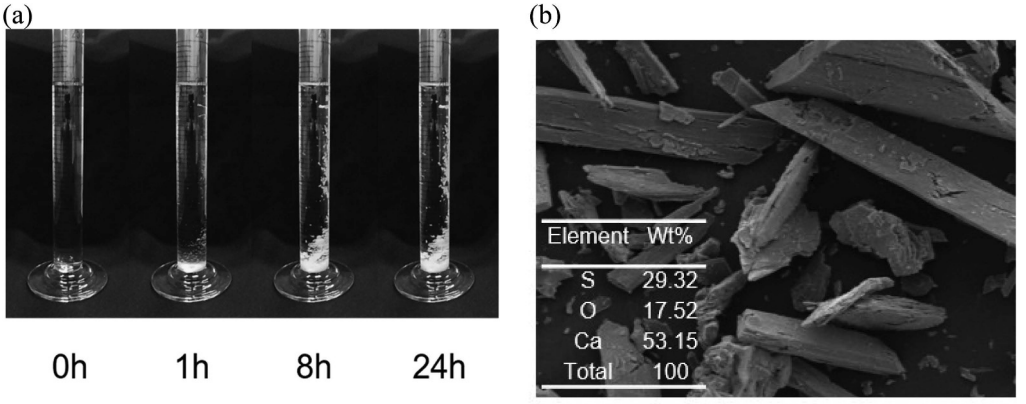

Figure 2. (a) The proceeding of gypsum formation and (b) SEM and EDS of seed gypsum crystal.

2.4 *The shear wave velocity*

The shear wave velocity (V_s) has been utilized to observe the contact level between soil particles, and bender element tests are a method to measure V_s in a laboratory as well as simple and have low cost. This study used this method to confirm the effect of SO_4^{2-} solution on the connection of EICP-treated soil particles. A pair of bender elements were embedded on the top and bottom cap of the oedometric cell and a 50Hz square wave was propagated from bottom to top. The arrival signal was filtered by a filer-amplifier (Krohn-hite 3944, low-pass filter: 1 MHz, high-pass: filter 100 Hz). The 1 pore volume (PV) of EICP was poured on the jumunjin standard sand (D_{50} = 0.542 mm, e_{max} = 0.897, and e_{min} = 0.6) with 70 % of relative density, and the reaction was allowed for 2 days. After finishing the EICP reaction, the 0.1 M sulfate solution made by adding Na_2SO_4 (403008, Sigma Aldrich) into distilled water was circulated using JIHPUMP 253Yx. 12 ml/min of flow rate was applied to minimize the effect of flow on particle arrangement and the circulation proceeded until the sum of circulated solution volume reached 2 PV. After the circulation, V_s was measured at 2-hour intervals for 8 hours.

3 RESULTS

3.1 *Urease activity and optimal recipe*

The activity of crude urease increases linearly as the concentration of soybean powder increases and ranged from 1.02 to 9.26 mM/min (Figure 3). Many researchers have evaluated the activities of bacteria or urease for ground improvement fell in the range of 0.5 to 10 mM/min (Whiffin et al., 2007, Chu et al., 2013, Jiang et al., 2017). These results indicate the soybean powder in this study can be used sufficiently for soil treatment.

Figure 4 (a) shows the SO_4^{2-} removal efficiency according to the added seed gypsum and curing time under 15 g/L urease concentration. The removal efficiency increased from 30 % to 62 % by adding the seed gypsum, and there was no significant difference in the SO_4^{2-} removal on the 2nd and 3rd days of the reaction, although the 2nd day has higher efficiency than the

1st day. Also, the removal efficiency and the reaction efficiency were similar in all seed gypsum. The reaction efficiency was 50 % and may decrease by the change of Ca^{2+} in the EICP solution due to the solubility of gypsum (Figure 4 (b)).

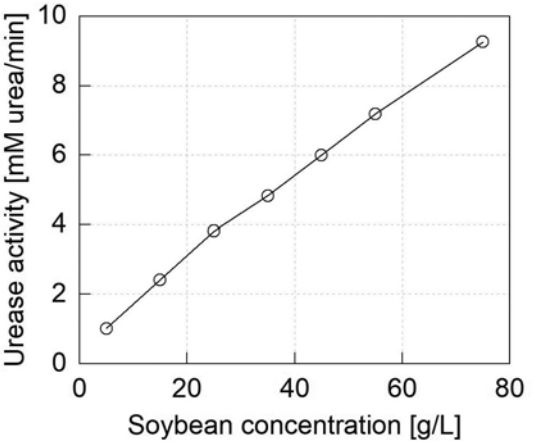

Figure 3. The activity of crude urease as a function of soybean concentration.

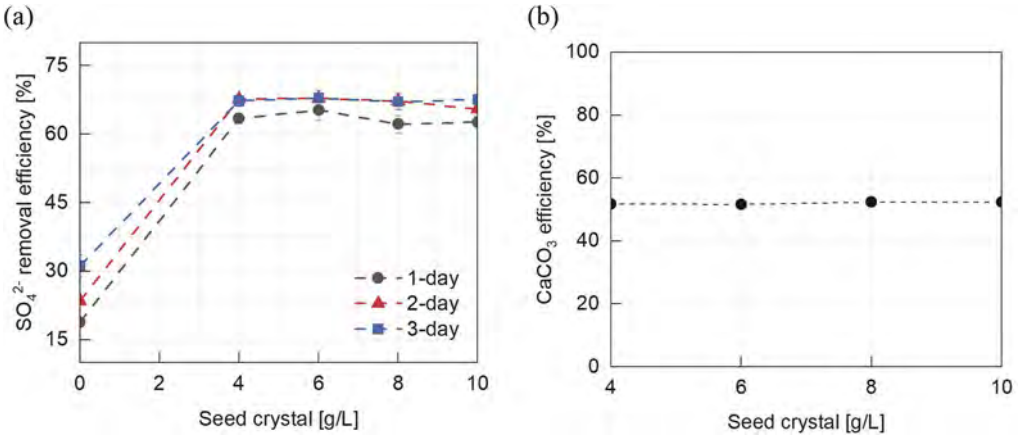

Figure 4. (a) The SO_4^{2-} removal efficiency and (b) $CaCO_3$ efficiency as a function of the added seed gypsum crystal.

3.2 *The effect of SO_4^{2-} in V_s*

V_s during the EICP reaction and SO_4^{2-} circulation is presented in Figure 5. Initial V_s increased sharply from 229 m/s to 858 m/s within 24 hours and 973 m/s at 48 hours, increasing shear stiffness by 18 times. In general, shear stiffness depends on the bonding between particles, and many researchers have studied the improvement of soil stiffness by the EICP treatment using purified urease. Song et al, 2020 showed an almost 31 times increase under 12 kPa sitting pressure, and Nafisi et al., 2019 proved 9 times increase through the triaxial test. Such comparative results mean that the crude urease used in this study has an ability for soil treatment. V_s after 48 hours reaction indicate the effect on SO_4^{2-} in soil structure. After SO_4^{2-} circulation, V_s initially decreased a little from 973 m/s to 951 m/s and increased as time goes by. It may be the result that the precipitated gypsum increased the bonding of particles.

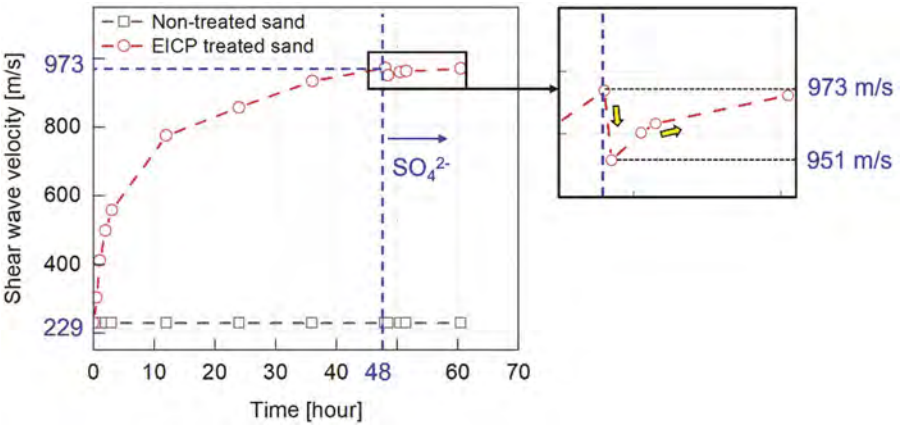

Figure 5. V_s evolution of EICP treated and SO_4^{2-} circulated specimen.

4 CONCLUSIONS

This study evaluated the SO_4^{2-} removal efficiency using remained Ca^{2+} in the EICP solution, and V_s was measured to observe the effect of SO_4^{2-} on the bonding between particles. The crude urease was used in this study to replace the purified enzyme, which had enough activity that can be utilized for ground improvement. To increase the SO_4^{2-} removal from the reaction with the EICP supernatant, the seed gypsum was used, and it increased the removal efficiency from 30 % to 62 %. So, the 1.5 M urea, 1 M $CaCl_2$, 15 g/L crude urease, and 10 g/L seed gypsum were determined as the optimal recipe.

V_s was measured using the bender element test, and the jumunjin sand was treated with 1 pore volume of the optimal solution. 0.1 M SO_4^{2-} solution was circulated to the specimen after 2 days of EICP reaction using a peristaltic pump, and V_s was measured during the gypsum was precipitated. The shear stiffness increased about 18 times by EICP reaction and SO_4^{2-} did not significantly affect the shear stiffness.

ACKNOWLEDGEMENTS

This work was supported by the Land and Housing Institute (LHI) grant funded by the Ko-rea Land and Housing Corporation, and the National Research Foundation of Korea (NRF) Grant funded by the Korea government (MSIT) (Nos. 2020R1A2C1014815, NRF-2021R1A5A1032433).

REFERENCES

Tait, S., Clarke, W. P., Keller, J., & Batstone, D. J. 2009. Removal of sulfate from high-strength wastewater by crystallisation. *Water Research*, 43(3), 762–772.

Benatti, C. T., Tavares, C. R. G., & Lenzi, E. 2009. Sulfate removal from waste chemicals by precipitation. *Journal of Environmental Management*, 90(1), 504–511.

Geldenhuys, A.J., Maree, J.P., de Beer, M., & Hlabela, P., 2003. An integrated limestone/lime process for partial sulfate removal. J. S. Afr. Inst. Min. Metall. 103, 345–353.

Song, J. Y., Sim, Y., Yeom, S., Jang, J., & Yun, T. S. 2020. Stiffness loss in enzyme-induced carbonate precipitated sand with stress scenarios. *Geomechanics and Engineering*, Vol. 20, No. 2(2020), 165–174.

Whiffin, V. S., Van Paassen, L. A., & Harkes, M. P. 2007. Microbial carbonate precipitation as a soil improvement technique. Geomicrobiology Journal, 24(5), 417–423.

Chu, J., Ivanov, V., Stabnikov, V., & Li, B. 2014. Microbial method for construction of an aquaculture pond in sand. In Bio-and Chemo-Mechanical Processes in Geotechnical Engineering: Géotechnique Symposium in Print 2013 (pp. 215–219). ICE Publishing.

Jiang, N. J., Soga, K., & Kuo, M. 2017. Microbially induced carbonate precipitation for seepage-induced internal erosion control in sand–clay mixtures. Journal of Geotechnical and Geoenvironmental Engineering, 143(3), 04016100.
Gao, Y., He, J., Tang, X., & Chu, J. 2019. Calcium carbonate precipitation catalyzed by soybean urease as an improvement method for fine-grained soil. Soils and Foundations, 59(5), 1631–1637.
Almajed, A. A. 2017. Enzyme induced carbonate precipitation (EICP) for soil improvement (Doctoral dissertation, Arizona State University).
Nafisi, A., Safavizadeh, S., & Montoya, B. M. 2019. Influence of microbe and enzyme-induced treatments on cemented sand shear response. *Journal of Geotechnical and Geoenvironmental Engineering*, 145(9), 06019008.

Investigation of foundations of historical structures and monitoring

Taylor & Francis
Taylor & Francis Group
http://taylorandfrancis.com

Smart Geotechnics for Smart Societies – Zhussupbekov, Sarsembayeva & Kaliakin (Eds)
© 2023 The Author(s), ISBN 978-1-003-29912-7
Open Access: www.taylorfrancis.com, CC BY-NC-ND 4.0 license

Non-invasive methods for in-situ analysis of historic structures

K.M. Begimbay
Department of Design and Engineering Graphics, Eurasian National University, Nur-Sultan, Kazakhstan

A.M. Kumisbek*
Master of Science in Urban Systems Engineering, Debrecen University, Debrecen, Hungary

Zh.B. Baizhanova & S.M. Bazarbayeva
Department of Design and Engineering Graphics, Eurasian National University, Nur-Sultan, Kazakhstan

Sh.M. Tusupbekova
Master of Science in Pedagogical Science, Eurasian National University, Nur-Sultan, Kazakhstan

ABSTRACT: Non-destructive techniques (NDT) for on-site analysis of various structures such as historic buildings and monuments are gaining traction due to inherent limitations of conventional invasive methods requiring sample collection for often off-site assessment. This work will investigate current trends in non-invasive assessment of built structures of historic and/or cultural significance, which include methods such as infrared thermography (IRT), ultrasonic pulse tomography (UPT), ground (surface) penetrating radar (GPR), and others. It will also explore whether NDTs available today can replace traditional destructive analysis methods in physical assessment.

1 INTRODUCTION

Preservation of cultural and historic heritage, which includes physical structures such as monuments and buildings as well as construction methods among other things, is essential to society's identity and sense of belonging. Preservation activities may involve exploration, health monitoring, and, if necessary, restoration processes, all of which require appropriate tools for the assessment of the structure's physical conditions (Goncalves, Rodrigues & Gaspar 2018).

The conventional procedure for an assessment of structures with historic and/or cultural significance (often referred to as heritage) consists of several stages. It starts with determining objectives of the investigation, i.e. clarifying if the final goal is conservation of the structure, scientific exploration or some other objective. It is usually followed by preliminary investigation of the structure including steps such as analyzing available information on the structure's building materials and previously performed construction and restoration works (Hughes & Callebaut n.d., Wong 2019). Then, based on the scope of the investigation and the preliminary inspection results, the methods for a further detailed analysis can be selected. Common analytical techniques are invasive in their nature and require sampling for off-site laboratory analyses (Goncalves, Rodrigues & Gaspar 2018).

However, this poses significant challenges in terms of both heritage conservation and validity of the obtained results, as the stakeholders involved in the structure's assessment try to minimize interventions while striving for greater accuracy. The significance of the studied objects accompanied by difficult physical and political circumstances impose restraints on the

*Corresponding author: aiganymkumisbek@gmail.com

DOI: 10.1201/9781003299127-290

assessment process enforcing additional caution during sample extraction and handling stages. Moreover, conservation philosophy encourages minimal alterations to the original form of the structure leading to small or non-representative sample quantities, which can possibly cause doubts in the validity of assessment results (Hughes & Callebaut n.d.).

This work will investigate current trends in non-invasive assessment of built structures of historic and/or cultural significance, which include methods such as infrared thermography (IRT), ultrasonic pulse tomography (UPT), ground (surface) penetrating radar (GPR), and others. It will also explore whether NDTs available today can replace traditional destructive analysis methods in physical assessment.

2 REVIEW OF SELECTED NON-DESTRUCTIVE METHODS FOR HERITAGE ASSESSMENT

The primary difference between destructive and non-destructive testing is the fact that the former destroys the sample during the analysis. Non-destructive testing (NDT), on the other hand, allows repeatable testing as well as preservation of the sample material.

2.1 *Infrared thermography (IRT)*

IRT is a technique based on measured discrepancies in heat flow rate of surfaces due to various features such as subsurface voids, delamination, poor bonding, moisture retention, deteriorated surface, different building materials, materials of varying porosity or thermal heat transmission, and air leakages. The method does not need a direct contact with the structure's elements (Tavukcuoglu 2018) and has been successfully applied to study hidden structural elements, undocumented transformations as well as consequences of restoration activities (Goncalves, Rodrigues & Gaspar 2018).

Since the method relies heavily on thermal conductivity, it can be challenging to apply it in tropical climates due to low temperature variation during the day. This is often negated by performing IRT during sunrise and sunset hours or before and after the rainfall to achieve maximum possible temperature difference. Another workaround involves spraying the analyzed surface with water or heating it (common approach applied in the active IRT method) provided that the structure will not be damaged as a result (Chaban, Deiana & Tornari 2020).

In addition, the IR results are affected by distance and angle and the assessment can be impeded by wind, shade, blockage by trees, and recessed corners. This is why the IRT imaging assessment is often coupled with tactile and supplementary inspection.

2.2 *Ultrasonic pulse tomography (UPT)*

UPT is an acoustic method based on measuring travel time of ultrasonic waves sent through a solid material between the instrument's transmitter and receiver (Tavukcuoglu 2018). Due to this, the method is naturally better at studying structures made of homogeneous materials such as concrete (for detecting cracks) and timber (for studying rot and termite attack), but struggles with masonry due to resultant echo (Wong 2019).

Ultrasonic pulse velocity measured in the structure is correlated with physical and mechanical properties of the materials, state of structure deterioration, moisture content, presence and size of various discontinuities (e.g. invisible cracks). This makes UPT suitable for identifying used materials, their dimensions, and various embedded members, as well as determining the state-of-deterioration of buildings by assessing visible and invisible defects and failures such as deep or surface cracks and detachments (Tavukcuoglu 2018). The analytical technique can also be useful in detecting failures in functional systems of historic structures, such as water supply and drainage systems. Finally, it can be utilized for in-situ monitoring of the existing conditions before and after applied treatments to determine their efficiency.

2.3 *Ground penetrating radar (GPR)*

GPR is an electromagnetic pulse reflection method based on physical principles similar to those of seismic reflection, which emits very short electromagnetic pulses in a specific frequency band and measures their propagation through the studied material (Goncalves, Rodrigues & Gaspar 2018). It is usually used for shallow investigations requiring high resolution and can be performed to achieve three-dimensional visualization. GPR can be utilized for the following purposes: identifying hidden elements, detection of cracks, estimation of wall thickness, detection of moisture in structural elements, detection of reinforcing steel bars, subsoil investigation, and more. Goncalves, Rodrigues & Gaspar (2018) list several cases where GPR was successfully applied, including studies on a medieval church, a stone masonry bridge, and a masonry house.

GPR offers a rapid and relatively simple way to acquire data, but requires direct contact between the instrument's antenna and the analyzed surface, which adds to an already challenging heritage assessment (Chaban, Deiana & Tornari 2020). The selected center frequency affects the resolution, where the standard range is between 200 MHz and 1 GHz, but high frequencies of 1-2 GHz can yield detailed low-depth imaging (Wong 2019). One of the profound challenges of this method is the complexity of result interpretation and the subsequent need for highly-skilled specialists (Goncalves, Rodrigues & Gaspar 2018). In addition, its results have to be often verified using other methods.

2.4 *Concerns related to use of NDTs*

There are numerous concerns with using NDTs in the assessment of historic and cultural heritage. NDTs have considerable limitations in their accuracy and analytical depth, most of them being performed only for surface analyses. They also often require extensive work with interferences such as echoes due to the composite nature of building materials utilized in construction and restoration of the heritage objects (Wong 2019). The inherent difficulty of interpretation and quantification of these methods leads to the need for highly trained personnel (Fais et al. 2018, Tavukcuoglu 2018). Another common limitation of non-destructive methods is an inability to provide data on the chemical composition as well as some physical and mechanical properties (Wong 2019). All of these contribute to the need to conduct destructive analysis to verify the results of and/or fill in the gaps left by NDTs.

Although, NDTs can supply data necessary to reduce the quantity of samples needed for invasive assessment by aiding in selecting strategic sampling points and highlighting areas requiring further investigation (Wong 2019). There are some cases, when a combined use of two or more NDTs enhanced their performance and enabled quantification (Fais et al. 2018, Tavukcuoglu 2018).

3 CONCLUSIONS

Non-destructive testing (NDT) methods today offer a non-invasive way to investigate various physical properties of the object of interest. This is crucial to exploration and conservation of structures with historical and cultural significance, as utilization of NDTs can become a common practice when preservation of the object's materials is imperative. Since the use of NDTs such as infrared thermography (IRT), ultrasonic pulse tomography (UPT), and ground penetrating radar (GPR) entails certain challenges, especially the need in an additional testing to investigate chemistry of the studied materials, it is commonly advised to pair NDTs with conventional invasive methods. NDTs can form the basis of preliminary analyses and become complementary analytical techniques informing strategic invasive assessment as well as aid in monitoring of structures' health and restoration processes.

REFERENCES

Chaban, A., R. Deiana & V. Tornari. (2020). "Wall mosaics: a review of on-site non-invasive methods, application challenges and new frontiers for their study and preservation". Journal of Imaging 6, 108. doi:10.3390/jimaging6100108.

Fais, S., Casula, G., Cuccuru, F., et al. (2018). "An innovative methodology for the non-destructive diagnosis of architectural elements of ancient historical buildings". *Scientific Reports 8*, *4334*. doi:10.1038/s41598-018-22601-5.

Goncalves, L., H. Rodrigues & F. Gaspar. (2018). Nondestructive Techniques for the Assessment and Preservation of Historic Structures. CRC Press Taylor & Francis Group, Boca Raton. Pp. 1–9.

Hughes, J. & K. Callebaut. (n.d.). "In-situ visual analysis and practical sampling of historic mortars". Available online: https://www.rilem.net/images/publis/rep028-002.pdf.

Tavukcuoglu, A. (2018). "Non-Destructive Testing for Building Diagnostics and Monitoring: Experience Achieved with Case Studies". *MATEC Web of Conferences 149*. doi:10.1051/matecconf/201814901015.

Wong, C.W. (2019). "Applications of non-destructive tests for diagnosis of heritage buildings: case studies from Singapore and Malaysia". *Built Heritage 1*. doi:10.1186/BF03545732.pdf.

Smart Geotechnics for Smart Societies – Zhussupbekov, Sarsembayeva & Kaliakin (Eds)
© 2023 The Author(s), ISBN 978-1-003-29912-7
Open Access: www.taylorfrancis.com, CC BY-NC-ND 4.0 license

Surface morphology of stone chamber using less destructive thermoplastic resin impression

Mai Sawada
Tokyo Institute of Technology, Tokyo, Japan

Mamoru Mimura
Kyoto University, Kyoto, Japan

ABSTRACT: The development of less destructive methods for estimating the shear strength of stone joints is necessary to improve the stability assessment of historical monuments. This study proposes a novel impression method using thermoplastic resin to examine the surface morphology of stone joints, which significantly influences the shear strength, and its application in the stone chamber of a burial mound. The three-dimensional coordinates of the impressions were obtained using an optical profiler, and roughness was determined using a statistical coefficient. This case study shows that the proposed impression method can be successfully applied to field surveys and is valuable for quantifying the geometric characteristics of stones. The polished and rough faces were quantitatively distinguished. Furthermore, the roughness of the polished faces of the granite ceiling and tuff sidewalls was slightly different owing to the difference in the ease of processing between the granite and tuff.

1 INTRODUCTION

Accurate stability assessment and the development of countermeasures are critical for conserving historical monuments, such as masonry buildings, petroglyphs, and rock caves. The shear strength of stone joints significantly influences the stability of historical monuments. However, investigations are limited to the application of less invasive techniques, and the shear strength contribution from the surface morphology of stone joints is challenging to estimate. Some noncontact methods such as laser profilers, optical scanners, and photogrammetry have been developed for examining the surface morphology of stone joints. However, the requirements for obtaining highly accurate stone surface morphology using these methods in field surveys are difficult to satisfy.

Thus, the authors developed a less destructive impression method for obtaining the surface morphology of stone joints, which is beneficial for use in historical monuments (Sawada & Mimura, 2022). The method uses a thermoplastic resin solid in the air but becomes soft and clay-like at temperatures higher than 70 °C. Impressions are rapidly stabilized and can be smoothly detached from the stone joints within approximately 10 s. Thermoplastic resins can be applied to floors, walls, and ceilings owing to their low fluidity and short curing times. This impression method has been proven to yield sufficient geometric accuracy while having other advantages. The geometric accuracy of the replicas produced using impressions is comparable to that of the replicas used in previous studies.

The aim of this study was to quantify the surface morphology of the stone chamber of a burial mound using the impression method as a case study for application in field surveys. The acquisition of the surface morphology enables shear strength estimation using empirical models, such as the JRC–JCS model (Burton, 1973), or practical/computational shear tests on the stone joints, which is particularly useful for accurate seismic analysis of burial mounds because the stone joint shear strength is a critical factor influencing seismic damage to burial

DOI: 10.1201/9781003299127-291

mounds (Sawada et al., 2022). Twenty-three impressions were obtained on cut stones from a stone chamber, and the surface geometry was acquired using an optical profiler. The geometric characteristics of the stones were analyzed by quantifying the roughness of the impressions using a statistical coefficient.

2 METHOD

Figure 1 shows the impression process using thermoplastic resin (K-500, Muto Trading Inc.) in a field. The stone surface was wiped with a wet cloth before accurately obtaining the surface morphology. The thermoplastic resin (20 g) was warmed in boiling water for several minutes before being rolled into a ball, as shown in Figure 1(b). The resin ball was carefully placed on the stone surface and pressed slowly using a trowel to prevent air-trapping between the stone surface and the resin (Figure 1(c)). After pressing for 10 s, the impression was detached from the stone and cooled to an ambient temperature of approximately 10 °C for 5 min (Figure 1 (d)). The pressing force was controlled to produce an impression with a diameter of 70 mm and a height of 5 mm. The impression cannot provide representative stone surface morphology when the impression area is tiny. The appropriate representative area can be estimated from the specimen length used for the direct shear tests; a length of at least 10 times the maximum asperity height is recommended (Muralha et al., 2014). Impression height influences surface geometry measurements using an optical profiler. The optical profiler can be applied to semitransparent objects; however, incorrect surface recognition can occur for thin impressions with a high degree of transparency.

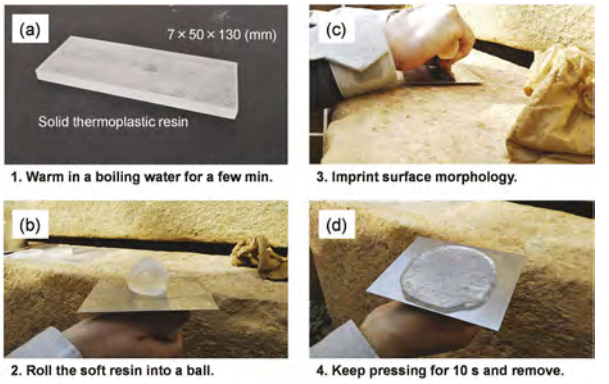

Figure 1. Impression process using thermoplastic resin in field.

The impressions were shaped into disks using a cutter ring with a diameter of 60 mm. The three-dimensional (3D) coordinates of the shaped impressions were measured using an optical profiler (VR-3200; Keyence Co., Ltd.). The measurement accuracy values were ±5 and ±3 μm (the width and height, respectively), and the measurement repeatability values were 1 and 0.5 μm (the width and height, respectively). The apparatus provided 3D coordinates at intervals of approximately 25 μm in the x- and y-axes by default. In this study, the interval was modified to approximately 0.25 mm by extracting every 10 data points from the raw data because roughness coefficients and their correlations with the shear strength of rock joints are mainly established based on the joint surface geometry measured at intervals larger than 0.25 mm (Yu & Vayssade, 1991).

3 CASE STUDY

The impression of the resin was applied to the stone chamber of the Nakaoyama Tumulus in Nara, Japan, which was constructed at the beginning of the eighth century. Figure 2 shows a cross-section of the burial mound and photographs captured in the arrow directions. The

stone chamber with inner dimensions of 90 cm × 90 cm × 90 cm consisted of stone plates hewn out from three different rocks: granite (ceiling), tuff (sidewalls), and granodiorite (floor). The inner faces of the stone chamber were polished, except for the floor, whereas the outside and joint faces were rough. Impressions were obtained at 23 points (A–W) on the ceiling (A–G, 7 points), sidewalls (H–S, 12 points), and floor (T–W, 4 points) in February 2021 when the earth mound was excavated for archeological investigations. Six (H–M) out of 12 points on the sidewalls were placed on the upper and lower joint faces, and the remaining points were placed on the inner faces.

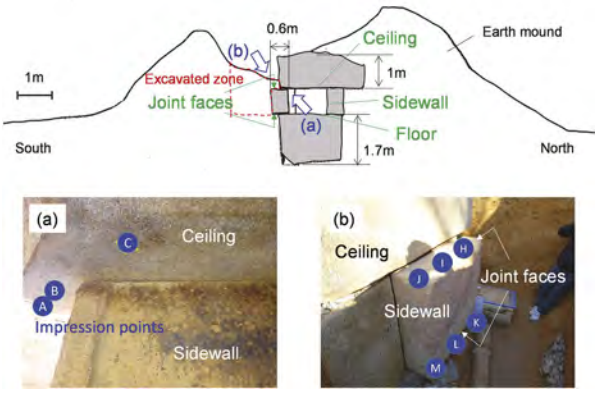

Figure 2. Cross-section of burial mound and impression points.

Figure 3 shows contour maps of the impressions obtained at representative points. The legend shows the distance from the highest point in each impression. The concave and convex portions of the impressions are inverse to those on the original stone surface. The contour maps show that the floor was rough compared to other faces.

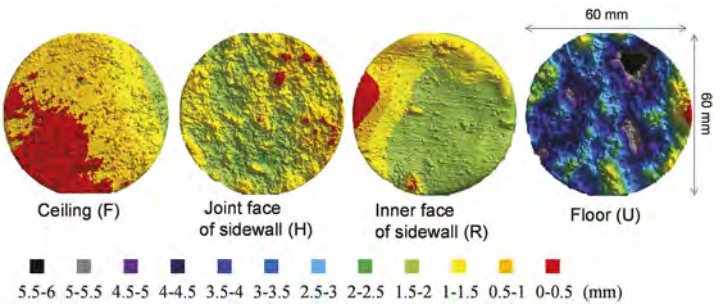

Figure 3. Contour maps at impression point F, H, R, and U.

The scan data of a square area of 40 mm × 40 mm in the center of the impression were extracted from the entire dataset to quantify the roughness. In this study, a statistical roughness coefficient, called the root-mean-square first-derivation, Z_2 (Myers, 1962), was used. Z_2 is widely used for predicting the joint roughness coefficient (JRC) used in Burton's empirical shear-strength estimation model (Burton, 1973) because it significantly correlates with the JRC. Z_2 is defined as follows:

$$Z_2 = \sqrt{\frac{1}{M-1}\sum_{i=1}^{M-1}\left(\frac{\Delta z}{\Delta x}\right)_i^2} \quad (1)$$

where M is the number of data points along the profile line, Δz is the elevation difference between two adjacent data points, and Δx is the interval between data points (0.25 mm). The modified scan data were used to calculate Z_2 to minimize the effect of the slope of the specimen surface. The scan data were modified by rotating the x- and y-axes based on the angle of the regression plane of the surface obtained using Microsoft Excel. Z_2 was calculated for 160 profile lines in the x- and y-axes on the square. The calculated Z_2 values of the impressions are presented in Figure 4. The mean values of Z_2 in the x- and y-axes of each impression on the polished faces are equivalent, whereas the roughness anisotropy on the non-polished joint faces and floor is significant. This indicates that the inner faces of the ceiling and sidewalls were thoroughly polished, but the sidewalls were slightly smoother than the ceiling. This difference in roughness could be attributed to the differences in rock type; that is, the granite used for the ceiling might have been difficult to polish because it was stiffer than the tuff used for the sidewalls.

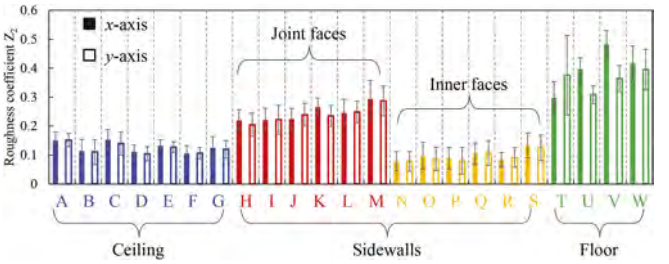

Figure 4. Roughness coefficients at different impression points.

4 CONCLUSIONS

In this study, a less destructive impression method that offers advantages for use in historical monuments was developed and applied to a stone chamber of a burial mound to evaluate the characteristics of stones by quantifying the surface morphology. The results showed that the polished and rough faces were quantitatively distinguished based on the roughness coefficients of the impressions. Furthermore, the roughness of the polished faces of the granite ceiling and tuff sidewalls was slightly different, which can be attributed to the difference in the ease of processing between the granite and the tuff. This case study shows that the proposed impression method can be successfully applied to field surveys and is useful for quantifying the geometric characteristics of stones. Establishing a shear strength estimation of stone joints using geometric data obtained with the impression method is required in future studies.

ACKNOWLEDGMENTS

This study was supported by the Matsui Kakuhei Memorial Foundation.

REFERENCES

Barton, N. 1973. Review of a new shear-strength criterion for rock joints. *Engineering Geology*, 7(4), 287–332.

Muralha, J., Grasselli, G., Tatone, B., Blümel, M., Chryssanthakis, P. & Yujing, J. 2014. ISRM suggested method for laboratory determination of the shear strength of rock joints: revised version. *Rock Mechanics and Rock Engineering*, 47(1), 291–302.

Myers, N. O. 1962. Characterization of surface roughness. *Wear*, 5(3), 182–189.

Sawada, M., Mimura, M. & Udo, T. 2022. Dynamic centrifuge model tests on Tumulus Mounds on cut slopes. *In Geotechnical Engineering for the Preservation of Monuments and Historic Sites III*, 679–689.

Sawada, M. & Mimura, M. 2022. Use of a thermoplastic resin to generate rock surface impressions and geometrically accurate replicas. *EUROCK 2022.* (in press)

Yu, X., & B. Vayssade. 1991. Joint profiles and their roughness parameters. *International Journal of Rock Mechanics and Mining Sciences & Geomechanics Abstracts*, 28(4), 333–336.

Smart Geotechnics for Smart Societies – Zhussupbekov, Sarsembayeva & Kaliakin (Eds)
© 2023 The Author(s), ISBN 978-1-003-29912-7
Open Access: www.taylorfrancis.com, CC BY-NC-ND 4.0 license

Proactive conservation of the foundation of the Main Tower, Bayon, Angkor Thom

Y. Iwasaki
Geo Research Institute, Osaka, Japan

M. Fukuda
Taisei Geotech, Kurume, Japan

M. Ishizuka & R. McCarthy
JASA Conservation Office, Siem Reap, Cambodia

T. Nakagawa
Waseda University, Tokyo, Japan

ABSTRACT: The main tower of Bayon temple, Angkor Thom stands upon a platform foundation of thick manmade sandy fill by a shallow direct sandstone and laterite foundation. The sandfill consists of very densely compacted fill of SPT, N value of 100 to 200 with the special feature of collapsing under a submerged condition. In the projected coming climate change, long and heavy rain is anticipated in Cambodia and every heritage site should be prepared to protect against the change of water conditions. The present situation at Bayon was evaluated by monitoring the change of water contents during rain. In case of squall type rain, heavy but short duration, water does not penetrate deeply in the ground. However, in long and heavy rain conditions, the situation is quite different. This paper discusses how to protect the main tower of Bayon temple based upon the basic principles of conservation based on 1. minimum intervention, 2. incremental approach, and 3. removable measures.

1 FOUNDATION OF BAYON TEMPLE

1.1 *Bayon temple, Angkor Thom*

Bayon, as shown in Figure 1, is the central temple of Angkor Thom constructed around in the late twelfth to early thirteenth century. Figure 2 shows section and plan view of the Bayon temple. Japanese Government Team Safeguarding Angkor (JSA) performed an archaeological trenching study at the northeastern corner as a "long trench" as shown in Figure 2.

1.2 *Trenched foundation*

The result of the long trench has revealed the following facts as shown in Figure 3.

1. The surface of the first terrace was covered with sandstone and laterite blocks, beneath which densely compacted sandy filled layer was identified.
2. Compacted sandy filled layer continued with and additional laterite block layer to the level of the original ground surface.
3. It was identified that the compacted sandy filled layer continues from the original ground level to 2–3 m in thickness.
4. The compacted sandy filled layer below the original surface was found to continue horizontally to about 10 m outside of the outer gallery plinth.

DOI: 10.1201/9781003299127-292

Figure 1. Bayon temple, Angkor Thom.

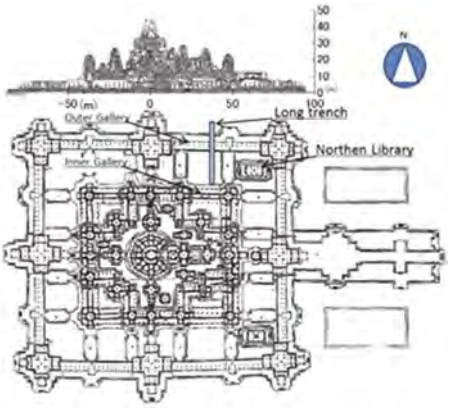

Figure 2. Section and plan view of Bayon Temple.

The archaeological study suggests that the foundation work for the Bayon is "trenched foundation" and was systematically constructed by excavating the original ground 2–3 m vertically as well as about 10 m outside of the temple boundary of the outer gallery as shown in Figure 2. The stone masonry structures were constructed upon terraces with three different levels of 2.95, 6.95, and 12.40 m.

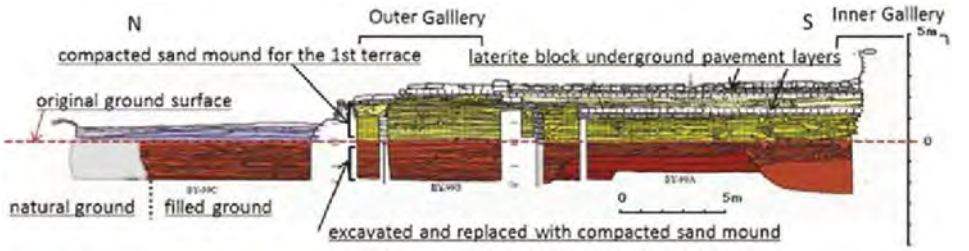

Figure 3. Long trench of archaeological study (Narita).

1.3 *Platform foundation of main tower of Bayon temple in Angkor Thom*

At the center of the base of the main tower of Bayon, a vertical shaft was excavated in 1933 by the French mission as shown in Figure 4. The stone masonry main tower of 31 m in height stands upon the platform of manmade fill of 14 m in thickness by direct shallow base stone as shown in Figure 4. It is amazing that the tower has been standing for 800 years since the late twelfth early thirteenth century upon the manmade fill (Iwasaki).

Several borings were carried out to study the platform foundation. The results of two borings are shown in Figure 5 BYV-2009 at the vertical shaft and BYV-2010 at the edge of the foundation of the tower on the third terrace. Boring BYV-2009 at the vertical shaft shows very loose sand layer of SPT, $N < 4$, which shows no compaction efforts were initiated by the French conservator. Boring BYV-2010 shows laterite block of 6 m in thickness beneath the pavement stone followed by densely compacted sandy fill.

The manmade filled layer showed very large SPT, N-values larger than 100–250 as shown in Figure 5 with water contents.

Based upon several borings, a ring-shaped laterite structure has been identified in the filled mound as shown in Figure 6.

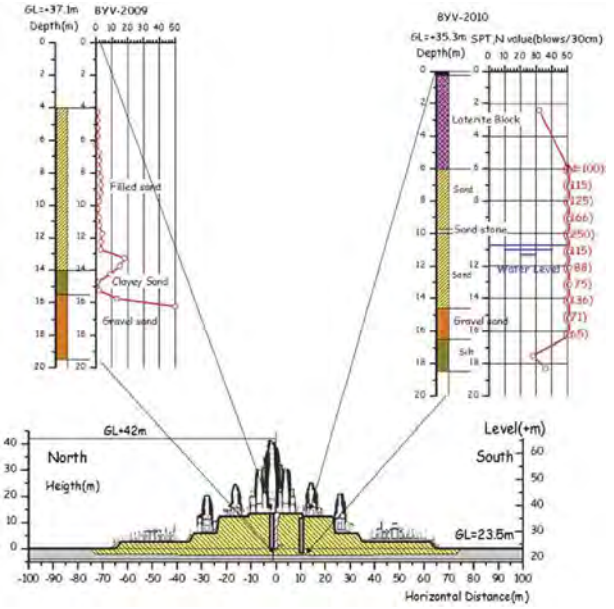

Figure 4. Boring results at the platform foundation.

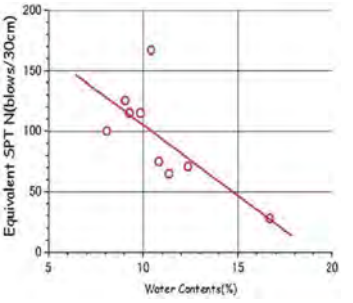

Figure 5. SPT N-value and water contents.

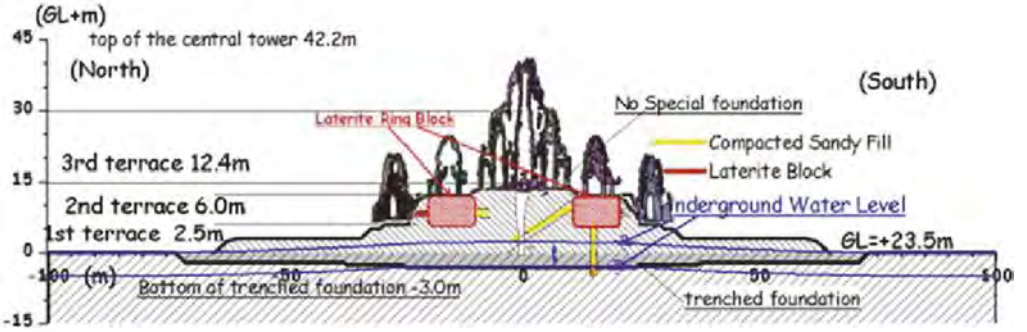

Figure 6. Trenched foundation and ring shaped laterite blocks.

2 CHARACTRISTICS OF FILLED SOILS IN BAYON TEMPLE

2.1 *Response to water*

The sampled soil, when dry, is the equivalent of soft rock rather than sand. A sample of the sandy fill was put into water as shown in Figure 7. The stiff unsupported sandy fill collapsed in the water within 10 min (Iwasaki).

2.2 *Grain size distribution*

Grain size distributions of the samples of filled soil by the vertical boring within the platform foundation are plotted in Figure 8 including additional horizontal boring in the platform, Northern and Southern Libraries, N1 Prasat Suor Prat and Baphuon Temple. Surprisingly, two kinds of clayey and sandy fills are clearly separately grouped with uniformity.

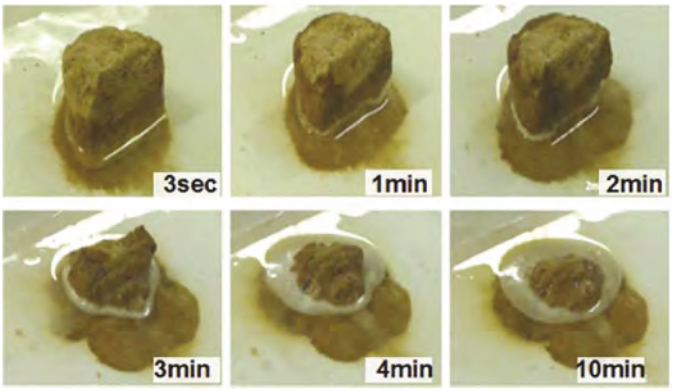

Figure 7. Collapse of stiff sandy filled soil in water.

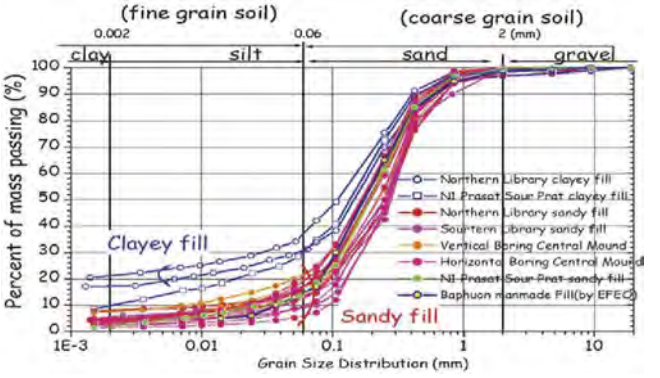

Figure 8. Grain size distribution.

2.3 *X-ray diffraction analysis*

X-ray diffraction analysis was performed to study the mineral components of the filled soil. Figure 9 shows the results of X-ray diffraction analysis. The major mineral is quartz with the clay mineral halloysite of the kaolin group.

The micrograph sample of the sandy fill is also shown in Figure 10. The rounded particles of sand of quartz are gathered filled with kaolin clay.

3 PROACTIVE COUNTERMEASURES AGAINST FAILURE OF THE MAIN TOWER

3.1 *Failure of filled mound by heavy rain*

In the history of Angkor, heavy rains had caused failures of filled mound monuments and embankments. One of the examples of such failure was the failure of northern east slope of Baphuon Temple (Figures 11 and 12), constructed in 1060, near Bayon in the same Angkor Thom site during a heavy rain in June 1943 as shown in Figure 12.

The characteristic of grain size distribution of the mound of Baphuon is shown in Figure 8, which shows the distribution shape is the same as those of Bayon Temple. This implies the original mound of the Baphuon had very high strength and had been stable for 900 years. The stability of high mound of 40 m in height with the steep angle of 45° of the manmade filled structure (shown in Figure 12) is never realized by the present common knowledge of the geo-technical engineering.

In 1960, EFEO (Ecole Francaise d'Extreme-Orient), French governmental organization had tried to reconstruct the failed mound by the compaction of the original soil. However, the fill

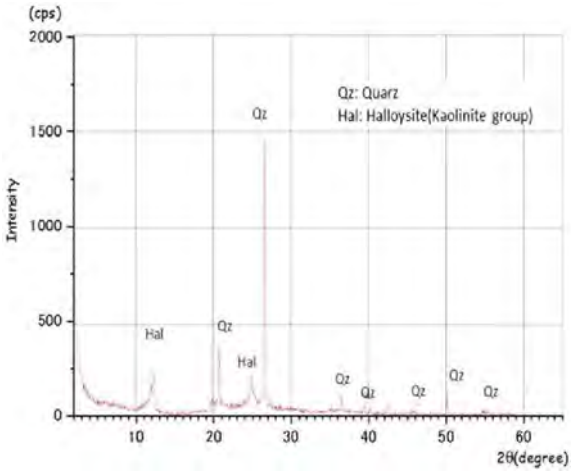

Figure 9. X-ray diffraction analysis.

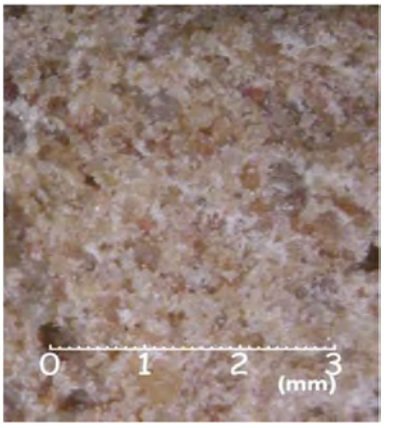

Figure 10. Micrograph of sandy fill.

height reached at 5 m in height, and the filled mound failed three times. The clear mechanism of stability of the high mounds for several hundred years from tenth -thirteenth century to twenty-first century for such high mound structures as the Bayon temple and Angkor Wat in Angkor are not known. The secret was the very large strength of the sandy soil in a dry condition.

Figure 11. Baphuon temple in Angkor Thom.

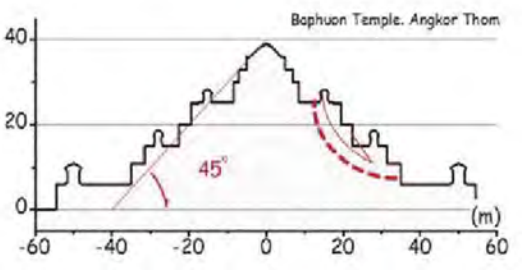

Figure 12. Vertical section of Baphuon (east side).

3.2 *Safety mechanism of filled mound of Bayon for 700 years*

The effects of rainfall to the sandy filled mound were evaluated by monitoring the moisture change within mound. Moisture sensors were installed from the top third terrace to several depths as shown in Figure 13.

An example of monitored results during May 27 to 28 in 2017 is shown in Figure 14. The rainfall intensity was about 10–15 mm/10 min for about one and half hours of 80 mm in total. The rain was a very heavy intensity, but rather in short duration of a few hours with squall conditions in a monsoon area.

As shown in Figure 14, the water content at GL-2.0 m has increased with some delay time, but returned to a dry condition due to stopping the supply of rainwater from the surface.

In the projected coming climate change, the duration time of precipitation is anticipated to become much longer, and the supply of rainwater will result in high water content to cause the damage to the platform foundation leading to the failure of the Main Tower of Bayon.

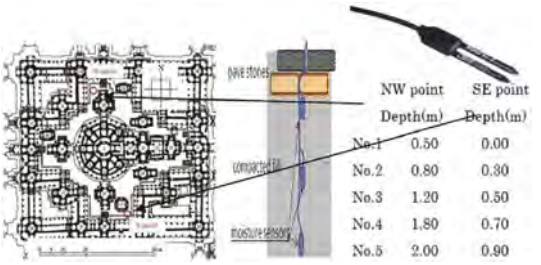

Figure 13. Installation moisture sensors.

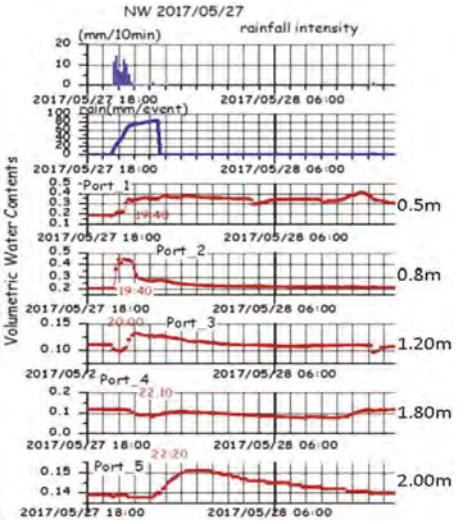

Figure 14. Monitored results of water contents.

3.3 *Proactive countermeasures against projected climate change*

In the projected coming climate change, the present rain of squall type is anticipated to change to a heavy and long duration. To avoid water seepage into foundation soil, the following countermeasures are being prepared based upon the basic three principles of countermeasures for conservation of cultural heritage of 1. minimum intervention, 2. incremental approach, and 3. removable measures.

There are three routes for rainwater to penetrate into the foundation of the main tower of Bayon as follows,

1. Open space at the top of the main and sub towers
2. Gaps between stone pavement on the mound surface
3. Gaps between step stones of the surface of side steps of the platform foundation

As proactive countermeasures for the above objectives, A. To cover the open spaces of the top of the central and sub towers by some cover, and B. To fill the gap between surface and step stones to prevent the rainwater from penetrating into the inside of the towers as well as to seepage into the foundation mound as shown in Figure 15.

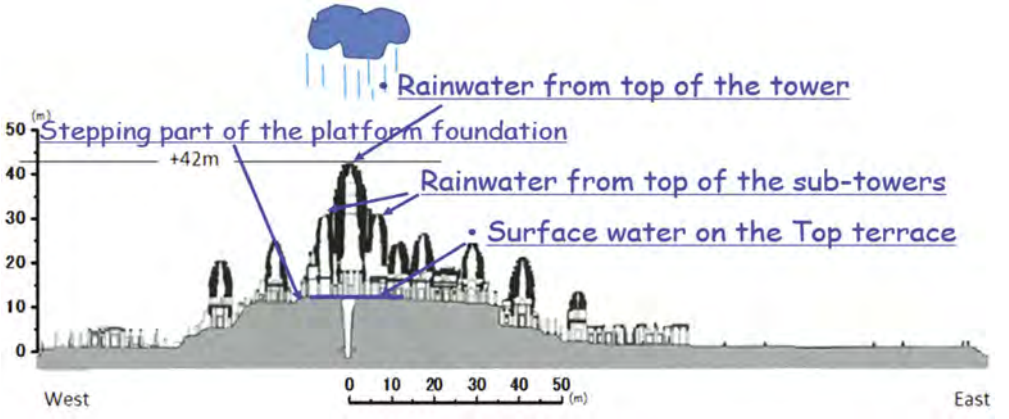

Figure 15. Proactive measures to prevent rainwater into the foundation soil.

It is also being prepared to install sensors under the ground to obtain moisture changes of the ground under the platform surface to confirm the effectiveness of the countermeasures.

4 CONCLUSIONS

The foundation was identified to consist of densely compacted sand fill with large strength in dry, but collapsible in submerged conditions. The projected coming climate change is expected to result in heavy rain for a long duration. To prevent the rainwater from penetrating the foundation, the simple and yet effective counter measures are being prepared to prevent the failure of the Main Tower of Bayon temple in Angkor Thom.

REFERENCES

Iwasaki Y., Fukuda M., Haraguchi T., Kitamura A., Ide Y., Tokuhnaga T., & Mogi K., 2014, Structure of platform mound of central tower based upon boring information, 2014, 93-113, Annual Technical Report on the survey of Angkor Monument 2012-2013, 2014, JASA (Japan-Apsara Safeguarding Angkor), Tokyo.

Koyama T., Yamada S., Iwasaki Y., Fukuda M., Shimoda I., Ishizaki M., Installation of Moisture Sensor, 2015,132-137, Annual Technical Report on the survey of Angkor Monument 2014-2015, 2015, JASA (Japan-Apsara Safeguarding Angkor), Tokyo.

Narita T., Nishimoto S., Shimizu M., Akazawa Y., Outline of excavations and investigation at the outer gallery of Bayon complex, 2000, 3-22, Annual Technical Report 2000, JASA (Japan-Apsara Safeguarding Angkor), Tokyo.

Smart Geotechnics for Smart Societies – Zhussupbekov, Sarsembayeva & Kaliakin (Eds)
© 2023 The Author(s), ISBN 978-1-003-29912-7
Open Access: www.taylorfrancis.com, CC BY-NC-ND 4.0 license

Architectural and design features of the brick buildings of petropavlovsk city XIX-XX centuries

R.U. Chekaeva, M.G. Chekaev, F.M. Chekaev, A.Z. Issina, Ye.N. Khvan & Ye.D. Sarsembayeva
L.N. Gumilyov Eurasian National University, Astana, Kazakhstan

ABSTRACT: This paper discusses the stone, brick architecture of Petropavlovsk at the end of the 19th century and the beginning of the 20th century. The paper analyzes the architectural planning solution and the style of objects. At the end of the XIXth century, in the era of the industrial revolution, it was necessary to create new types of buildings - industrial workshops, railway stations, covered markets, trading houses, gymnasiums, and apartment houses. Turning into the main customer of construction work, the merchants introduced traditions, criteria, and views of their own cultural environment. The meaning of the activities of the merchants in this area is reduced to one thing - to make obvious the cultural and historical roots of the merchants, to show its connection with the folk culture (Voloshinov et al. 2011).

1 INTRODUCTION

Compositional techniques and artistic norms of the classicism style that prevailed before in the architecture were not always able to meet the requirements of the new time, therefore, it became a natural departure from them. Eclectic architectural style appeared in response to the needs of life itself (Ageeva et al. 2011). Well-preserved to our time buildings, the expressiveness of which was built on the brickwork and aesthetic properties of the brick. The red-brick style is called non-plastered eclecticism. Such buildings were relatively inexpensive and more "unpretentious" in the conditions of the harsh Siberian climate, so they quickly gained popularity in the province. One of the most expressive architectural and constructive elements are the crowning eaves of buildings. (Figure 1) Giving the building a finished look, at the same time, they perform an important function of protecting the walls of the house from moisture. Under the brick cornices are often brackets that complement the architectural decor, facilitate the laying, support the cornices and allow them to increase the removal from the wall. Above the windows and doors, too, arrange small cornices topped with gables - sandriks. From the point of view of engineering mechanics, curtain elements reinforce the load-bearing walls, correctly distributing the load.

In the late nineties of the XIX century, a new stage of development of trade and the entire economic life of the city of Petropavlovsk began, which was associated with the completion of the construction of the Siberian Railway. During this period, merchant houses, trading houses, shops, banks, offices with intricate brickwork, transforming the view of the city, are being built (Morozov 1981). A large number of houses and shops of Petropavlovsk merchants were located along Voznesensky Prospekt (Kazakhstan Constitution Street) and many of which are preserved today.

The merchants financed gymnasiums, madrasas, a merchant club, on the basis of which the local drama theater grew. They owned enterprises for processing livestock raw materials, mills, warehouses, factories equipped with the most modern equipment (Makhmutov 2015).

Most of the architectural monuments of Petropavlovsk are merchant houses and shops. Having emerged in 1752 as a military fortress, the city soon lost its military destination,

DOI: 10.1201/9781003299127-293

becoming the center of commerce. The favorable geographical position made Petropavlovsk one of the major trading centers. Archival documents say that "in 1777 in the fortress of Sts. Petra (Petropavlovsk) exchanged steppe goods more than in Ust-Kamenogorsk, Semipalatinsk, Yamyshevsk and Omsk fortresses together." Merchants made a significant contribution to the architectural appearance of Petropavlovsk (Poluyanova 2014).

Houses and shops still adorn the streets of the city, they are located mainly on the streets of the Constitution of Kazakhstan. The surviving merchant houses and buildings gave Petropavlovsk a unique architectural appearance. At the end of the XIXth century, the architects of Russia and Siberia used the techniques of such styles as Baroque and Classicism, and also reproduced forms of ancient Russian architecture - Old Russian romanticism. It was the so-called pseudo-Russian style or red-brick architecture. The expressiveness of the red-brick style is based on the use of shaped brickwork (Ponomarenko 2008).

Well-preserved to our time buildings, the expressiveness of which was built on the brickwork and the aesthetic properties of the brick. The red-brick style is called plastered eclecticism. Such buildings were relatively inexpensive and more "unpretentious" in the conditions of the harsh Siberian climate, so they quickly gained popularity in the province. Thus, the brick style represents the rationalization of eclecticism for mass and utilitarian construction (Gumenyuk 2009).

Beautiful examples of the red-brick style in the architecture of Petropavlovsk are: House and Shop of the Merchant Strelov, House of the Merchant Arkel (Complex of the Museum of Regional History); House and Shop of Merchant Ismailov (Restaurant; private enterprises); House of merchant Shamsutdinov (Shops, private enterprises); The house of the merchant Mukhamedyarov and many others. Architectural and structural elements of historic buildings determine the belonging of a building to a specific architectural style, and also combine in themselves a decorative and functional purpose. One of the most expressive architectural and structural elements is the crowning eaves of buildings (Figure 1).

Figure 1. Crowned cornices with ribbon toothed brick brackets.

Giving the building a finished look, at the same time, they perform an important function of protecting the walls of the house from moisture. Under the brick cornices are often brackets that complement the architectural decor, facilitate the laying, support the cornices and allow them to increase the removal from the wall. Above the windows and doors, too, arrange small cornices topped with gables - sandriks. From the point of view of engineering mechanics, curtain elements reinforce the load-bearing walls, correctly distributing the load. (Figure 2).

Figure 2. Figured Sandrik above the windows.

2 MAIN PART

Constitution Street is a pedestrian street, a kind of local "Arbat". Before the revolution, the street was called Voznesensky Prospekt and had a narrow wooden pavement. In Soviet times, it was called the standard for such streets - Lenin Street.

Figure 3 presents a vivid example of decorative towers, attic and dormer windows, as well as the rich complex red-brick architecture of the facades of the house and merchant Shakirzhan Shafeev's shop.

The eclecticism of these buildings combines elements of red-brick style, baroque and classicism. The facades of many merchant buildings erected in the eclectic style are decorated with embossed masonry and pilasters, which have a considerable amount of brick columns and turrets on the roof. This is the house and shop of the merchant Shafeev. Figured parapet columns and walls connected by an openwork metal fence give buildings special expressiveness and completeness.

Figure 3. Architectural decor of the facade of the House of Merchant Shafeev.

The next object is "Trading house of the merchant of the first guild of Blumenthal" in Petropavlovsk (Figure 4). Before the revolution, a merchant family of Jewish origin, Blumenthal, lived in Petropavlovsk. In 1909, a stationery shop and the printing house of the merchant of

the 1st guild Alexander Lazarevich Blumenthal was in place of the present TSUM. Alexander Blumenthal was a great expert in hides leather. At that time there were three or four such experts in this business as he, to the whole of Russia. Taking the item, Blumenthal sorted it at the same time. He did not enter into any contracts, everything was built on trust, no one was deceiving anyone or cheating. A few years later, the owners sold the building for the construction of the Siberian Trade Bank. In 1915, a rubble foundation was laid for the bank, walls were erected, but the revolution of 1917 prevented the final construction of the bank.

Figure 4. Trading house of the merchant of the first guild A. Blumenthal.

The Bolshevik government seized the unfinished building, and the next mention of it dates back to 1926. In the same year, the building was finally completed and the People's Commissar of the Kazakh SSR was located there, which was later renamed the North Kazakhstan regional executive committee. At present, the building houses the "Tsum" trade house by all recognizable residents of Petropavlovsk (Figure 5).

Figure 5. Modern view of trading house of the merchant A. Blumenthal.

The merchant Blumenthal's family, who lived in Petropavlovsk before the revolution, left a legacy to contemporaries in the form of a series of postcards with views of the city of the publishing house Blumenthal Alexander Lazarevich and Lydia Isaevna. In 1912, Blumenthal and his family left Petropavlovsk forever, where they lived for 12 years.

3 CONCLUSION

For the construction of houses at the end of the XIXth century, burnt bricks were used and they were built in eclectic style in the Petropavlovsk city. We need to preserve these unique architectural monuments, which, being in the center of the city, without detracting from its appearance, still fascinate with their exterior. As each of these houses conceals the history of its roommates and their greatness.

In the process of studying, studying historical and architectural monuments, an understanding of the relationship of the artistic image of each building, its design features, and the mechanics of its parts is taking place. Each element is multifunctional, as it adorns the building, and strengthens it, at the same time, giving it originality.

The buildings are a sample of the historical planning of a provincial merchant city, characteristic of the XIXth - early XXth century, expressed in the planned integrated building of brick buildings of a hotel and shopping destination and are the architectural heritage of the city.

REFERENCES

Voloshinov, A.V. & Losin, D.O. 2011. Merchant architecture and cultural appearance of a modern provincial city. *Bulletin of Saratov State Technical University*, 2 (55), v.1: 207–211.

Ageeva, E.Yu., Akilova, E.V. & Kostina, E.A. 2011. Architectural styles of the late XIX - early XX centuries .: *Tutorial. N.Novgorod: Publishing house of the Nizhny Novgorod State Archit.- Civil Engineering University*.

Morozov, M.A. 1981. On Petropavlovsk: Guide. Alma-Ata, Kazakhstan.

Makhmutov, Z.A. 2015. Trading activity of Tatar merchants of Kazakhstan in the pre-revolutionary time (on the example of Petropavlovsk). *Historical, philosophical, political and legal sciences, cultural studies and art history Journal*. Questions of theory and practice, 11–1 (61). Access mode: http://cyberleninka.ru

Poluyanova, N.A. 2014. Historical architectural monuments of the XVII - XX centuries and their influence on the personality of a person. *Science Forum: Materials of the VI International Scientific Conference*. Access mode: http://www.scienceforum.ru.

Ponomarenko, E.V. 2008. Features of the "red-brick" style in the Southern Urals. *Bulletin of Chelyabinsk State University*, 23: 175–179.

Gumenyuk, A.N. 2009. "Brick style" and "gotizing premodern" in the architecture of Omsk at the beginning of the twentieth century. World of science, culture, education, 1(1): 81–84.

Smart Geotechnics for Smart Societies – Zhussupbekov, Sarsembayeva & Kaliakin (Eds)
© 2023 The Author(s), ISBN 978-1-003-29912-7
Open Access: www.taylorfrancis.com, CC BY-NC-ND 4.0 license

Solution of geotechnical problems in operational basement floors construction process during restoration

M.A. Stepanov & Ya.A. Pronozin
Industrial University of Tyumen, Tyumen, Russia

ABSTRACT: Restoration of cultural heritage sites and their adaptation in the modern urban environment as dominant objects is one of the most important issues in the development of historical cities.This paper presents the results of computational modeling with regard to step-by-step work to increase the volume of restoration building by basement floor construction: arrangement of bored injection piles, step-by-step soil excavation, construction of insitu reinforced concrete caisson and foundation plate. According to monitoring data, this method of basement floors construction excluded critical additional deformation of the structure and can be applied in similar conditions.

1 INTRODUCTION

A restoration of cultural heritage sites and their adaptation in a modern urban environment as dominant objects is one of the most important issues in a development of historical cities.

Appearance of Tyumen, the first Russian city in Siberia, is largely determined by the historical center and individual historical districts, such as, for example, a complex of buildings with a park on Daudelnaya Street.

One of buildings in this complex is the City Hospital ("Tekutievo hospital"), which built in 1902–1904 by A.I. Tekutiev, Tyumen mayor, merchant of the first guild, honorary citizen of Tyumen (Kozlova-Afanasyeva, 2008). A historical value of this building is in the fact that S.I. Karnatsevich, N.I. Russkikh, A.S. Gasilov worked in the "Tekutievo hospital" in first decades of twentieth century. They are well-known famous Tyumen doctors. In the summer of 1914, Grigori Rasputin was treated in the hospital after a severe wound.

Before 2019 the object of cultural heritage of regional significance is not in operation and was closed because of critical conditions (Figure 1).

Figure 1. "Tekutievo hospital" before restoration (2011).

DOI: 10.1201/9781003299127-294

"Tekutievo hospital" is a two-storey building without underground floors, which has a complex configuration in plan and made in a classical red-brick style with elements of eclecticism (Figure 1). The structural layout is frameless with lateral load-bearing walls, which consist of clay brick and lime mortar. External load-bearing walls have a thickness of 640 mm, internal - 570 mm, foundations of the building are shallow, strip type. The bottom of foundations is approximately 1.2 m from the level of ground surface.

As preliminary work, depreciation analysis and inspection of the building load-bearing structures were made. It was established, that the building was out-of-commission and thus, it was necessary to renew roof construction and floor decks, partially to replace brick layout, repair cracks and reconstruct fronts of the building. The foundations being walls' broadening and didn't have waterproof finish, but there were not any other construction defects.

The main engineering issue during restoration work was to increase the volume of the building by constructing a full-functional underground floor and entering it into united space. For this reason, works were done to deepen of the basement below the existing foundation footing.

Geomorphologically, the site of building is confined to the high right-bank terrace above flood-plain of Tura River. The soil of the ground bed was composed of loams of various densities ranging from firm-stiff to soft-firm (consistency index I_c classification, ISO 14688). Physical-mechanical properties of soil base are presented in Table 1.

Table 1. Physical-mechanical properties of the soil base.

№ of engineering-geological element	1	2	3
Unit weight γ, kN/м^3	19.1	19.2	18.5
Water content w, %	20.3	19.5	30.5
Liquidity index I_L	0.29	0.49	0.69
Void ratio e	0.67	0.9	0.87
Angle of internal friction φ, °	17	19	19
Cohesion c, kPa	22	26	24
Elastic modulus E_{oed}, MPa	10	12	6

The groundwater level was found at depth of 2.7 m from the ground level, which is 1.3 m higher than the level of the foundation footing.

Floor loading increasing during basement floor construction below the existing foundation footing was difficult geotechnical task in conditions of high groundwater level and high sandiness of loams. It was necessary to ensure the reliability and stability of the foundations of the building, as well as limiting deformations (technological settlements), during execution of work. Otherwise, the building could have been subjected to structural failure (Mangushev 2015, Mangushev&Osokin 2020, Ilyichev&Mangushev 2016, Shashkin et al. 2019, Ulitskiy et al. 2012).

2 METHODS

During restoration of "Tekutievo hospital", its painterly architectural look, agreeable with the time of construction, was recreated (Figure 2).

Underground floor construction was carried out by using low impact construction technology (Pronozin et al. 2013), embracing:

1. Drilling a perforation at an angle into the brick foundations for the bored-injection piles.
2. Installation of the bored-injection piles of "Atlant" type with a diameter of 200 mm and a length of 5 m (Ibragimov & Semkin 2012, Mangushev 2013, Pronozin et al. 2014, Salnyi et al. 2021, Pronozin & Samokhvalov 2018).
3. Implementation of dewatering measures.
4. Installation of tie girder for the underground floor.

Figure 2. «Tekutievo hospital» design view after restoration.

5. Ground excavation to the depth of the underground floor with the installation of a barrier to ensure there is no soil dumping out of the base of the existing foundation.
6. Laying the base of crushed stone, the base of concrete preparations and an installation of the waterproofing membrane. Installation of the caisson slab with protruding reinforcement.
7. Installation of welded meshes of the caisson wall, fixing them with protruding reinforcements and reinforcement passing through the existing foundation.
8. Concreting of the caisson walls with monolithic underground floor beams.
9. Installation of the underground floor slab.

In the bored injection process, cement mortar displaces drill cuttings and ensures the bearing capacity of piles. It is injected through a chisel located at the bottom of the piles.

The bored-injection piles depth was accepted using the results of calculating the required bearing capacity of piles and the Plaxis program numerical modeling (Pronozin et al. 2013, Strokova 2010, Ulitskiy et al. 2014). Stabilization of the foundation and soil base was considered. Mohr-Coulomb model was accepted by the standard engineering geology prospecting data in spite of the ground unloading modeling disadvantages. Excavation depth was about 3 m.

Pile diameter, pile length and caisson thickness (stiffness of the structure) were designed by computational modeling. Figure 3 presents one of calculation schemes.

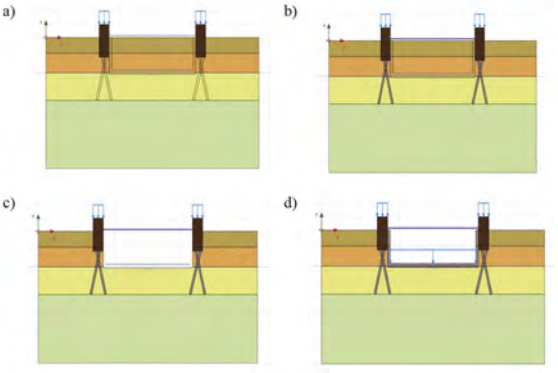

Figure 3. Calculation scheme with taking into account the sequence of work: a - before basement floor construction; b - installation of piles and tie girder; c - soil excavation to the depth of the basement; d - after basement floor construction.

As a result of the numerical simulation it was established:

1. Caisson usage minimizes irregular settlements, because of foundation and walls combined action. Stiffness of the substructure increases. Caisson wall thickness is equal to 200mm, thickness of caisson slab is equal to 400 mm.
2. Minimal pile depth is 5000 mm for the settlement uniformity condition and uncritical advance of plastic strain zone in the basement. Pile diameter is 200 mm (Figure 4).
3. Because of Mohr-Coulomb model disadvantages, soil behavior doesn't correspond to the real situation. According to numerical modeling, soil surface raises in 20 mm after design basement excavation of 2600 mm (assuming that the deformation modules are equal at the stages of loading and unloading (Ulitskiy et al. 2014, Shashkin & Shashkin 2005, Stepanov et al. 2017).
4. Caisson usage balances the settlements of the whole building (Figure 4). Additional design settlement from the application of all operational loads was 20 mm. But there are some areas with more than 20mm settlements under the caisson. It happens because in Mohr-Coulomb model stress-strain relationship develops linearly up to a point of yielding (Ulitskiy et al. 2014, Shashkin & Shashkin 2005, Stepanov et al. 2017).

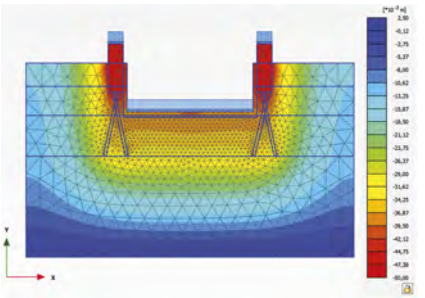

Figure 4. Isolines of vertical displacements.

To clarify the applied bored-injection piles bearing capacity, two test piles were made on the site of the restored object. The tests were carried out with a static load in steps of 1-tonne force (Figure 5). Each step was maintained until the stabilization of soil displacements (velocity of pile settlement at the loading step does not exceed 0.1 mm over the last 2 hours of observations) in accordance with the requirements (GOST 5686-2020). After experimental data processing, the bored-injection piles bearing capacity was 90 kN with a settlement of 12 mm (maximum allowable settlement for this object) and 120 kN with a settlement of 30 mm.

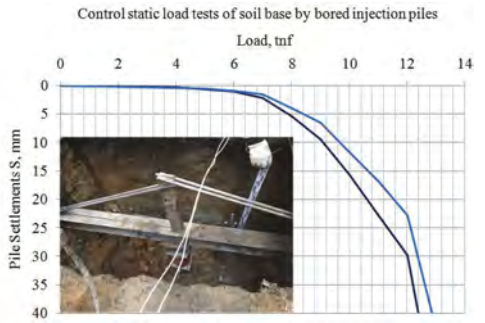

Figure 5. Graph «load – settlements» of test static load tests of piles.

3 RESULTS AND DISCUSSION

In June 2016 restoration work of "Tekutievo hospital" started. The authors monitored construction technology of underground floor building such as injection pile installation, soil excavation, erection of insitu reinforced concrete caisson (Figure 6).

Figure 6. Work process: installation of tie girder for the basement floor; excavation of the soil to the depth of the underground floor.

Geotechnical monitoring showed the following:

- the chosen method of underground floor construction did not cause the development of ultimate stresses and deformations in the building structures;
- the maximum technological settlement was 9 mm, even taking into account gross violations of work rules, widespread soil dumping from beneath the foundations and regular problems with dewatering;
- factual injection pile shape was different from pile shape used in computational modeling; the diameter of the piles along the length is not constant, from 200 to 230mm.

This method of basement floor construction excluded ultimate additional deformation of the structure, cracks in bearing constructions and can be applied in similar conditions. In 2019 restoration work of "Tekutievo hospital" was finished. Figure 7 presents the exterior of "Tekutievo hospital" after restoration.

Figure 7. "Tekutievo hospital" after restoration.

4 CONCLUSION

1. Field tests of bored injection piles ("Atlant" type, 5 m long) confirmed the results of numerical modeling pile bearing capacity, which was 90 kN.
2. According to numerical modeling, the additional calculated settlement from the application of all operational loads was 20mm. The restoration work with increasing the volume of underground space was completed, and according to the results of geotechnical monitoring, the maximum technological settlement was 9mm.
3. The accepted method of the basement floor construction did not cause ultimate additional deformations of the building, overstresses and cracks in the load-bearing structures in conditions of a high level of groundwater, interbedding of sandy and silty-clay weak soils. Thus, the method can be recommended for use in similar conditions.

REFERENCES

Ibragimov, M.N. & Semkin, V.V. 2012. *Strengthening the soil with injections of cement mortars*. Moscow: ASV.

Ilyichev, V.A. & Mangushev, R.A. 2016. Reference book of geotechnical engineering. Bases, foundations and underground structure. Moscow: ASV.

Kozlova-Afanasyeva, E.M. 2008 *Architectural heritage of the Tyumen region*. Tyumen: Isdatelstvo Iskusstvo.

Mangushev, R.A. 2013. Reconstruction of the underground part of the Russian State Academic Bolshoi Drama Theatre (ABDT) named after G.A. Tovstonogov in St. Petersburg. *Proc. Of the All-Russian conference "Geotechnics: theory and practice"*: 9–32.

Mangushev, R.A. 2015. Experience of building underground parking construction in the conditions of weak soils of Saint-Petersburg. *Bulletin of Civil Engineers* 5 (52): 91–100.

Mangushev, R.A. & Osokin, A.I. 2020. Practical restoration-related experience with creation of basement level and underground parking into and near architectural monuments in down-town of Saint-Petersburg. *IOP Conference Series: Materials Science and Engineering* 775 (1): 012070.

Pronozin, Ya.A. et al. 2013. Experience of combined use of injection piles and caisson at arranging the underground floor of historical and cultural heritage building in Tobolsk. *Modern problems of science and education* 3.

Pronozin, Ya.A. et al. 2014. Strengthening of the building foundation at arranging the underground floor of the object of historical and cultural heritage in Tyumen. *Proc. of the Int. scien.-pract. conf. "Urgent problems of construction, ecology and energy saving in the conditions of Western Siberia"*: 69–74.

Pronozin, Ya.A. & Samokhvalov, M.A. 2018. Analysis of the Interaction of Drill-Injection Piles with Soil Foundation. *Soil Mechanics and Foundation Engineering* 55(2): 82–86.

Salnyi, I.S. et al. 2021. Interaction of drill-injection piles with the surrounding soil. *Magazine of Civil Engineering* 4 (104): 10407.

Shashkin A.G. & Shashkin K.G. 2005. Elastic and visco-plastic model of structural and unstable clay soil. *Reconstruction of the cities and geotechnical construction* 9: 221–228.

Shashkin, A.G. et al. 2019. Analysis of causes of deformations in historic buildings on weak clay soils. Geotechnics Fundamentals and Applications in Construction: New Materials, Structures, Technologies and Calculations; Proc. Intern. Conf.: 329–334.

Stepanov, M. et al. 2017. Generation of stress-strain state in combined strip pile foundation beds through pressing of soil. *MATEC Web of Conferences* 106: 02011

Strokova, L.A. 2010. *Application of the finite elements method un soil mechanics*. Tomsk: Tomsk Polytechnic University.

Ulitskiy, V.M. et al. 2012. *The geotechnical guidebook*. St. Petersburg: Geo-Reconstruction Institute.

Ulitskiy, V.M. et al. 2014. *Basics of the modern numerical calculations of buildings and bases*. St. Petersburg: Geo-Reconstruction Institute.

Smart Geotechnics for Smart Societies – Zhussupbekov, Sarsembayeva & Kaliakin (Eds)
© 2023 The Author(s), ISBN 978-1-003-29912-7
Open Access: www.taylorfrancis.com, CC BY-NC-ND 4.0 license

Features of brick architecture of architectural monuments of northern Kazakhstan

R.U. Chekaeva, A.T. Bokachyova, A.A. Toishiyeva, L.A. Zhakhsylykova, E.N. Khvan, Z.S. Bissenova & A.S. Temirova
Department of Architecture of the Faculty of Architecture and Construction, L.N.Gumilyov Eurasian National University, Kazakhstan, Astana

M.B. Hudoyarova
Samarkand State Architectural and Civil Engineering Institute named after M. Ulugbek, Uzbekistan, Samarkand

ABSTRACT: The study of urban wooden, brick and stone-wooden architecture is of undoubted historical and cultural value and is perceived as evidence of an important stage in the history of architecture and urban planning of cities in Kazakhstan. The preserved residential buildings of the XIX and early XX centuries are a valuable representative in the urban structure, which creates an interesting color in combination with other buildings. As a result of studying, for the first time, the development of urban planning and architecture of the cities of Northern Kazakhstan in the XIX-XXI centuries are considered and studied comprehensively and in detail. For the first time, regional specificities of the architecture of residential, public, religious buildings and facilities, their architectural and planning solutions are identified. The stylistic and compositional characteristics of the architectural monuments of the region and objects of modern architecture are considered, the systematization and classification of buildings and structures is carried out, the chronological description of the development of urban planning in Northern Kazakhstan up to the XXI century is restored, the genesis of architectural forms of facilities and the main historical stages of the architecture development of the period under consideration are determined. In this paper we consider brick residential architecture.

Keywords: brick houses, residential buildings, analysis, architectural style

1 INTRODUCTION

From the mid-90-s of the 19th century began intensive resettlement of the population from Russia to Siberia and Kazakhstan. The development of industry and domestic trade was largely contributed by the construction of railway lines connecting Kazakhstan with Siberia and other regions of the Russian Empire [1]. One of the conductors of the agricultural policy of the autocracy was the Siberian Railway Committee. The issue of the construction of Trans-Siberian Railway arose at the end of the 19th century. Projects of its construction were compiled and discussed for many years. Finally, in 1891, a Royal Decree was issued on its construction. For the general management of the construction of the road, on October 10, 1892, the "Special Committee of the Siberian Railway" was established which existed until December 15, 1905, that is, until the end of its construction [2]. The Trans-Siberian Railway, which construction began in 1891, was supposed to pass through Northern Kazakhstan. The "Special Committee of the Siberian Railway" allocated 24489,31 km^2 of land in the three

DOI: 10.1201/9781003299127-295

Aqmola regions for resettlement of 160 thousand of peasants. From the mid-90-s of the 19th century began intensive resettlement of the population to Siberia and Kazakhstan [3].

During the last decade of the 19th century, 514 km of rail lines were built in Kazakhstan [4]. In general, the local industry was predominated by enterprises processing agricultural raw materials: tanneries, fat-making factory, soap-making factory, distilleries, oil mills, and others. Wool and fleece factories, meat cannerie, milling and cereal industry have received its wide development in Semirechensk, Aqmola and Semipalatinsk regions, in which the military department showed their special interest [5].

Intensive migration of the population since the 90s of the 19th century from Russia to Siberia and Kazakhstan served and led to the development of industry and domestic trade. This was facilitated by the construction of railway lines connecting Kazakhstan with Siberia and other parts of the Russian Empire [6]. As a result of implementing «temporary rules» with settlers to Kazakhstan came the traditional wooden and stone architecture. The settlers brought the original architecture of their regions, which has undergone changes in the layout, due to the climatic conditions of Northern Kazakhstan [7]. Urban housing in the 19th and early 20th centuries is a striking feature of the historic city, shaping its environment and preserving its national and regional flavor.

Historic wooden, stone (of burnt bricks) and mixed development of the period studied have until recently retained its urban planning significance as an essential component of architectural ensembles in a number of city districts (mostly in historical centers). However, active urban planning transformations of the last decade in the cities of Northern Kazakhstan (Petropavl, Kostanay, Pavlodar, Kokshetau) has entailed the mass destruction of entire blocks and streets with wooden and stone buildings. In addition, many buildings has changed in the process of repairs or reconstruction.

Due to insufficient scientific substantiation of the value of the wooden, stone, stone-wood architecture of the historic city, this heritage is often negatively assessed for its short lifespan, the lack of modern comfort levels and its poor condition, which requires repair and restoration. Urban planners do not take their significance and value into account when designing master plans of cities.

Based on archival material, historical sources and field surveys, it is safe to say that the architectural shaping, volume-spatial composition, planning features of stone buildings in the cities of Northern Kazakhstan at the end of 19th - beginning of 20th century emphasize consistent approaches to formation of building styles (Art Nouveau, eclectic, brick and wooden architecture), which accentuates the relevance in the study of this issue.

The purpose of this study was to identify understudied buildings and structures that are important for determining the process of evolution in urban architecture in Northern Kazakhstan. The study of the cities of Northern Kazakhstan in the 19th and early 20th centuries contains a comprehensive systematic analysis of features of brick, stone and wooden architecture, which helped to fill the lack of scientific data on historical and architectural, urban planning, artistic and aesthetic significance, and determine the relevance of this work.

As a result, the objectives of the study were defined:

– to analyze the identified factual material;
– to conduct field surveys of the architecture of the cities of Northern Kazakhstan (Petropavl, Kostanay, Pavlodar, Kokshetau) of the 19th and early 20th centuries;
– to systematize and determine the classification of brick buildings and structures.

Work has been carried out to determine architectural planning and compositional solutions of residential buildings (brick buildings and stone-brick, with the first storage being made of stone-wood, and the second of wood); 2-storey, urban multi-bedroom residential buildings in «brick», «Art Nouveau» and «Eclectic» styles.

2 MATERIALS AND METHODS

The method of research is based on a systematic analysis of the objects of study, a compositional and graphic analysis of urban planning, with the use of graphic measurements and scientific generalizations.

The work was built on a holistic coverage of the extensive factual material collected by the authors as a result of the study of the state archive materials, analytical review of the scientific literature, as well as information collected during field research (measurement work) and inspection of historical sites.

3 RESULTS AND DISCUSSION

In the study of general patterns and regional peculiarities of the development of residential buildings architecture during the XIXth and early XXth centuries, the following houses were identified: wooden, brick and stone-and-wooden type. The study of wooden, brick and stone-wood urban architecture is currently of undoubted historical and cultural value and is perceived as evidence of an important stage in the history of architecture and urban development of the cities of Northern Kazakhstan. In order to trace the dynamics of the architecture of residential buildings in a historical retrospective in the stated period, consider examples of residential buildings.

3.1 *One-story brick houses of rectangular or square shape with a corridor system*

For example - house of merchant Kolmogorov, which was built in 1906 in Pavlodar, located on Lenin Street, 155. (Figures 1 and 2).

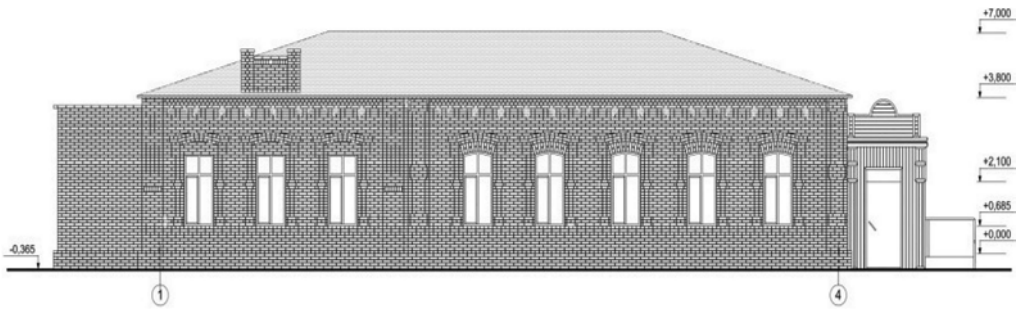

Figure 1. Kolmogorov Merchant's House, graphic work, measurement of the building in 2016.

Figure 2. The house of merchant Kolmogorov, color scheme, measurement of the building in 2016.

The house has wooden entrance part (hallway). Apparently, the original volume was close to a square in plan, had 5 windows on the facade. Subsequently, an additional volume was

added to the northern end. Decorative masonry with high skill applied to all elements of the facade, enriching, emphasizing and artistic expressiveness of the whole. Skillfully drawn plinth, visually ending with a wide part, uniting all the window openings.

Developed plinth, elongated window frames and rich cornice visually increase the height of the building. The floors are wooden with joists. Foundation and walls are made of fired brick. Windows, double doors. Interior finish: plastering with cement mortar, whitewashing. The outer part of the walls has decorative elements [8].

The residential building of the private entrepreneur Turlapov was built in 1900. There was a small sheepskin coat factory in the yard. The building is one-storey, rectangular in plan, measuring 19x10 m, made of brick, with external walls of 710 mm thick, and it's installed on a brick foundation. The overlap and roof structures are wooden. Roofing is made of galvanized roofing steel. The facade of the building is decorated with elements of brickwork. Window openings are completed by the segmental form of masonry. Elements of the uncovered cornice, as well as the platbands on the windows, are executed in the distinctive old Russian style. The shape of the parapet is closer to the baroque style, with elements of the Art Nouveau. The stylistic direction of the monument is characteristic of the eclecticism, which was widespread at the beginning of the 20th century. The building is an example of historical layout of a merchant small-town, typical for the early 20th century and is an architectural heritage of the Pavlodar city.

The next brick house was built in 1907 for the merchant family of the city head I.L.Osipov, who owned salt mines. Located in Pavlodar, Dzerzhinskiy str., 160. One-storey brick-building, with complex masonry on a high basement, built in the traditional style of merchant architecture (Figures 3 and 4).

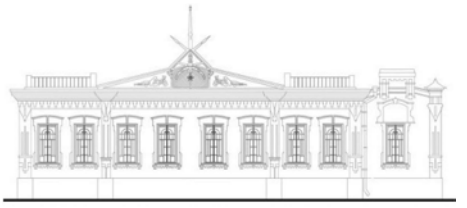

Figure 3. Merchant's house of the city head I.L. Osipov. Graphic work, measurement of the building, 2015.

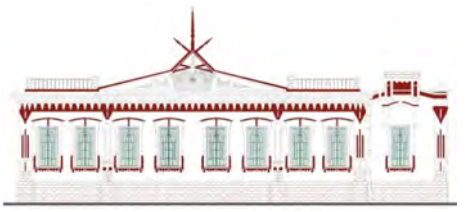

Figure 4. Merchant's house of the mayor I.L. Osipov. Color scheme, measurement of the building, 2015.

The building has a central gable with a spire. The windows are high and elongated, protruding from the plane of the walls due to their design . The corners are finished with semi-column walls with intricate ornamentation. The last ones have drainpipes. The roof of the building is made of iron. The average height of the premises is 3.45m. The total useful space - 316,7 sq.m. Exterior and interior walls are made of brick, double-casement windows, without shutters. The doors are paneled. Finishing: plaster, whitewash. In 1976-77 in the building conducted restoration work (interior repairs, whitewashing the facade). Now it is in private hands, which oversees the state of the house (Figure 5).

3.2 *2-story "brick" style urban multi-room apartment houses*

The merchant Senokosov's house, which was built at the end of the XIX century - beginning of the XX century, is a good example of a "brick" style two-storey city multi-room apartment building (Figures 6 and 7).

The residential building is located on Gogol Street - former Altynsarina, 70, Kostanay [9]. The house belonged to famous Kostanay merchant Turlapov and sold to Senokosov. It is a rectangular building with a brick addition on the north-eastern side of the front yard (Figures 8 and 9).

Figure 5. The house now, a photo taken in 2015.

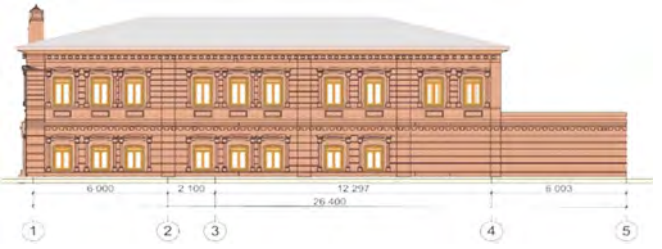

Figure 6. Merchant Senokosov's House, facade in axes 1-5, measurement of the building, 2016.

Figure 7. House of Merchant Senokosov, facade in the D-A axes, color scheme.

The internal structure is a set of rooms, almost not communicating with each other, with two corridors and a hallway with stairs. The building is made of brick, not plastered, is set on a cobble foundation.

The house stands at the intersection of two streets and the solution of its street facades makes it stand out actively compared to surrounding buildings. The brick 2-storey building has a clearly defined integral volume, despite its varied decor solutions (Figure 6).

The main facade is 26.5 meters long and faces Pushkin Street. The facades are decorated with typical Russian folk architecture techniques of the late 19th and early 20th centuries. All

Figure 8. Merchant Senokosov's House. Plan of the 1st floor, measurement of the building, 2016.

Figure 9. Merchant Senokosov's House. Plan of the 2nd floor, measurement of the building, 2016.

kinds of masonry laid on the surface of the wall create a sort of 2nd cladding of the building with a lot of protruding and receding elements. The corner of the building (at the intersection of the streets) is distinguished by a two-story rectangular-shaped tower (belvedere), which is an organic continuation of the shallow risalit.

The lower floor has a doorway flanked by half-columns made of brick and they resemble balusters. The 1st and 2nd floors have slightly different solutions. On the first floor, the wide windows have segmental arches, accentuated by a wedge arch, supported by semi-columns. Between the windows are blades with vertically elongated perspective panels. The blades at the level of the upper boundary of the windows have shallow perspective pediments, above which are capitals-consoles, a ribbon of entablature, lined with masonry, separating the floors (Figures 6 and 7).

2-story multi-bedroom, Art Nouveau residential buildings. The former house of merchant Kiyatkin (1911). The building is located in Kostanay, Tolstoy Street 40, on the corner of 5th April Street, now it's the town planning and construction department of akimat. The building is one of the unique monuments of residential architecture of the early 20th century (Figure 10).

Figure 10. House of merchant Kiyatkin (1911), a photo taken in 2015.

It is one of the few surviving examples of so-called pure Art Nouveau in Kazakhstan. It is a one-storey, angular, two-faced brick house with risalit and an iron, multileveled roof. The towers of the parapet are connected by a decorative metal lattice. The windows are high with double glazing. Apart from pilasters, other decorative elements of the façade are rectangular niches above and below window apertures and in the basement on a strip foundation of natural stone. There is a wooden house adjoining the building on the northeast side. There is a corridor floor planning. Its measurements are 22 m x 17 m. The height of the building is 6 m (Figure 11).

Figure 11. Merchant Kiyatkin's apartment building. Facade in axes 1-5, measurement of the building in 2015.

The fate of the owner of this house - one of the founders and most prominent industrialists of the city, Fyodor Petrovich Kiyatkin - is remarkable. Coming from a family of Mordovian peasants - immigrants, hardworking and enterprising Fyodor Kiyatkin graduated only from a parochial school, but in his youth he decided to become rich. Beginning with the construction of a windmill, he proved himself as a talented financier and entrepreneur. F.P. Kiyatkin owned the largest highly mechanized steam mill in the city. By the way, the Kiyatkin family owned three of the city's five steam mills. Later, F.P. Kiyatkin took part in financing the construction of the first railroad between Troitsk and Kostanay, was chairman of the Kostanay branch of the Russian-Asian commercial and industrial bank, and a member of the city council. In 1916 he sold his businesses, saying he wanted to retire from business but "remain useful to society by lending to industry". After the revolution, Fyodor Petrovich thought it's best for him to leave Kostanay. Until 1928, he had never been a stranger to any kind of work, he used to work modestly as a carpenter. Then he returned to the city and got a job as a janitor and guard at the local Collective Farmers' House, which, by a curious coincidence, used to be the former and long ago nationalized house of F.P. Kiyatkin. The townspeople were firmly convinced that the former rich man was working here for a reason and was probably going to secretly dig up his hidden treasures. But the treasure remained one of the city's legends, and Fyodor Petrovich Kiyatkin, who experienced ups and downs in his life, died peacefully in the summer of 1941, leaving a good memory of himself and his house, which even now remains one of the most interesting monuments of Kostanay architecture.

3.3 *One-storey, mixed - enfilade and corridor - systems of planning are made in the style of eclectic*

The following eclectic buildings are worth attention: Strelov's and Arkel's houses that currently make up a complex of buildings of Regional Museum (1891, Lenin St. 44, 46, 48 and Kirov St. 145). Strelov's house of 1891 consists of 2 volumes with a "passage" between them and is L-shaped. The facade facing Lenin Street on the right side, apears to look like a detached composition, there is an entrance 2-winged panelled door [10].

The remaining three sections claim symmetry - the middle one, is the main one, topped by a 2-stepped attic with a triangular gable at the end. The tympanum of the gable has two semicircular arched niches "covered" by a suspended superimposed arch; the side parts of the attic have a panelled decorative design. Overhead multilobed archeswith "sagging" segments, that are supported by pilasters with shaped imposts in the upper, middle and lower parts of the building, have two rectangular panels. The panels in turn frame the windows of the 2nd floor. The balcony with openwork metal railings uniting all 3 windows of the central part gives the building a distinct splendor and functional singularity. The asymmetry of the facade, with the balcony and the attic, can obviously be explained by the introduction of a section with an entrance opening: in this way the architect consciously "deforms" the usual classic 3-part scheme (Figure 12).

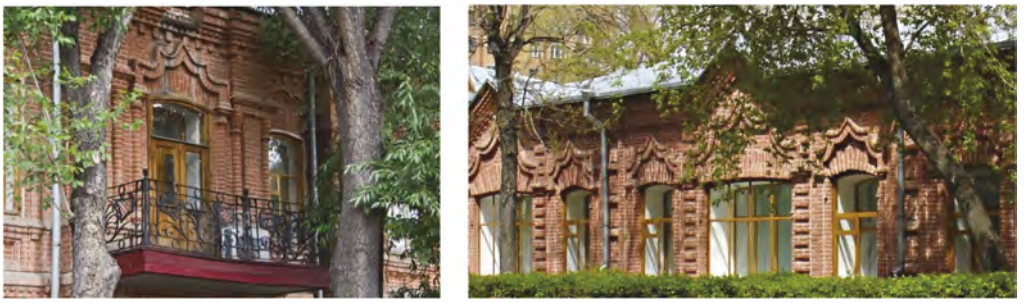

Figure 12. House of the merchant Strelov - was built at the end of the XIX century, 1891.

The structure of the L-shaped plan of the 2-storey house is designed so that only the front rooms face the city street and the secondary rooms face the courtyard part (Figure 13). The mixed - enfilade and corridor - system of layout, widespread at that period, was used. At present, the Strelov House, in a complex with neighboring buildings, the Arkel House, is part of the spatial exhibition of the ancient history of the region and includes part of the administrative premises of the museum.

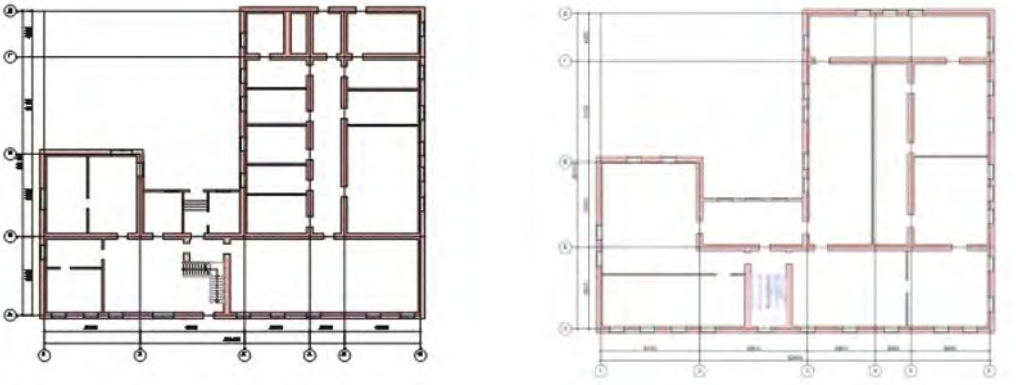

Figure 13. Arkel House, 1891. Plans of the 1st and 2nd floors, measurement of the building in 2016.

Arkel House is one of the largest and most magnificent residential buildings not only in Petropavl, but also in all of Northern Kazakhstan. Its architecture had a noticeable influence on the formation of both the planning structure and the appearance of urban dwellings of the period under consideration. Arkel House, 1891, is located at Constitution Street 48, Kazakhstan (corner of Park Street). Arkel House is a two-storey building, L-shaped in plan (Figure 14).

Built of burnt brick, with external walls710 mmthick. Facade of the building is decorated with decorative elements of masonry. The building has two outward balconies, with openwork wrought iron lattices, located on the main facade . On the first floor, the window openings are completed with segmental form of masonry. On the second floor the window openings are decorated with architectural elements (Figure 15). The architectural appearance of the building is characteristic of the widespread in the late 19th - early 20th century style - eclecticism.

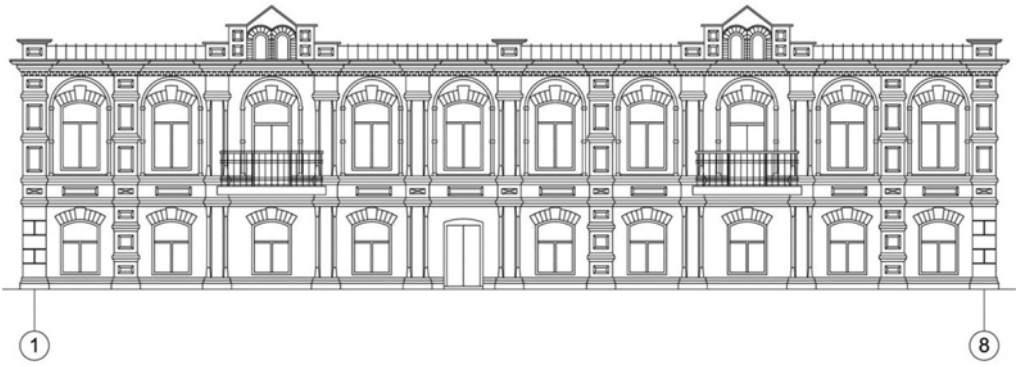

Figure 14. Arkel House, graphic work, measurement 2016. Facade in axes 1-8.

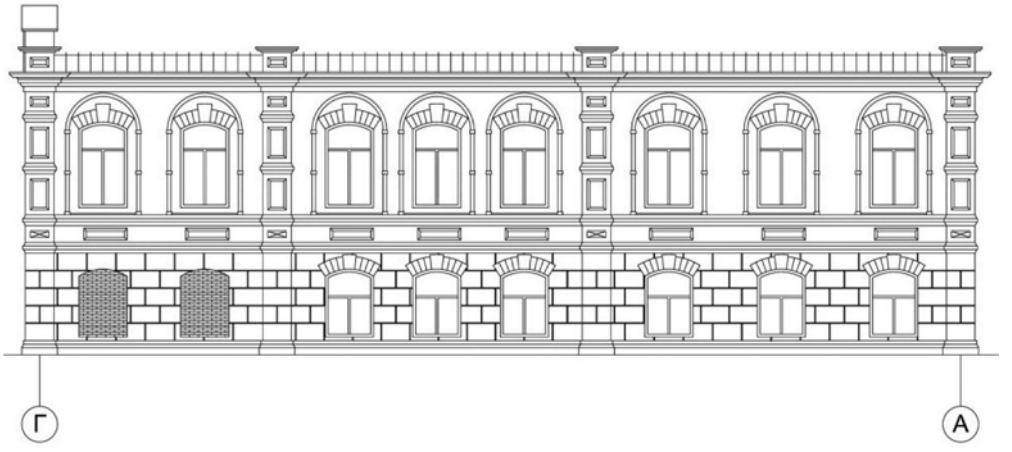

Figure 15. Arkel House, graphic work, measurement 2016. Figure facade in the axes D - A.

4 CONCLUSIONS

On the basis of field research and the study of archival materials, an analysis of the development of the planning structure of stone and stone-wood dwellings was carried out, it allowed to determine the following features:

- In the first half of the 19th century, the predominant type of house was the one, in which the first floor, divided by stone walls into large rooms - kitchen and utility rooms - was used mainly for household. The second floor with living rooms had an enfilade layout. The layout was compact as a rule. The entrance was made through a wooden enclosure attached to the side or courtyard facade.
- The second half of the 19th century saw the development of the stone and stone-wood dwelling house type with separate apartments on each floor. Entrance to the building was made from the street through the half-stone (less often wooden) volume with staircase along the side facade (the second additional ladder was located on the side of the yard in the same or a separate volume); there is the formation of an internal structure with a distribution space in the form of a corridor, an example is the residential house of the merchant Davletkadiev.

In the first half of the 19th century, when classicism and early eclecticism prevailed, the stylistic and morphological unity of the system of brick and wooden decoration parts was achieved due to the fact that the wooden decor largely copied the architecture of stone buildings.

The second half of the 19th century saw the development of mature and late eclecticism and an increase in the range of stylistic currents characteristic of stone architecture. There is a variety of forms of stone decor with the inclusion of stucco elements; as well of forms of wooden decor, corresponding in general to the classicist tradition of shaping, which are often enriched with motifs from folk architecture.

Early 20th century - the final stage of late eclecticism; variations on the theme of art nouveau and neo-Russian style; the "brick style" in stone decor is prominent(The wooden part of the buildings was the most stylistically expressive, the stone floor was often a volume with little or no decoration).

Architectural and planning solution of these buildings, in accordance with the requests and tastes of the customers, imitated the various currents of Russian architecture in the second half of 19th early 20th centuries.:

The survey revealed the main types of volumetric-spatial composition of stone and stone-and-wooden houses, typical for different stages of the 19th - early 20th centuries.

In the first half of the 20th century, the following type of stone buildings was identified:

Type 1 - stone, 1-2-storey house in the form of a horizontally extended parallelepiped;

type 2 - stone, 1-2 storey house of compact parallelepiped with symmetrical-axial main facade.

And mixed type, i.e. wood on stone half-storey houses:

Type 1 - a wooden house on a stone half-storey in the form of a compact parallelepiped with a symmetrical-axial main facade;

type 2 - wooden house on a stone half-storey in the form of a horizontally extended parallelepiped.

At the end of the 19th and beginning of the 20th centuries there were these types of masonry houses influenced by the architecture of late eclectic and art nouveau mansions:

- Type 1 - a stone house in the form of a horizontally extended parallelepiped with a protruding accent element (a bay window with a hipped roof or a tower);
- Type 2 - stone dwelling house with a stone archway.

The analysis of buildings reflects the basic concept of stylistic preferences in architecture during the late 19th - early 20th centuries in the cities of Northern Kazakhstan, with adjustments and adaptations for regional features, which largely depended on socio-economic aspects. This confirms the formation of the typological foundations and characteristics of the buildings and structures that were built in the North Kazakhstan region during the period under study.

Solution of the problem. The problem of preservation and use of buildings and structures can be solved by creating compositional units, grouping in an ensemble of residential, public, religious buildings, shopping malls of the early 20th century, as well as modern buildings, which determine the silhouette and panorama of the city. Allocate architectural accents so as to harmonize the space of the urban environment as much as possible. Speaking of the artistic and aesthetic aspects, it is necessary to use the contrast in form and materials between existing historical and new objects, to accentuate squares and intersections, to form an environment of scale for the perception of the viewer, as it improves the visualization of the city space.

The determining factors in this case are the folk traditions and ornamental art of local peoples - Kazakhs, Russians, Tatars and decorative design style architecture - Art Nouveau, "brick style", eclectic [12].

The above expected results will allow to systematize the educational process, to achieve the training of architects and improve the level of scientific and pedagogical staff, in accordance with the requirements of industrial-innovative development of the country and achieve a world-class quality and performance of scientific research on the basis of updating the material and technical base and the stimulation of research activities.

Thus, the evolutionary path of development of the architecture of Northern Kazakhstan from the end of the 19th to the beginning of the 20th centuries was traced, while the continuity and formation of new properties of architecture were also revealed.

REFERENCES

Artykbaev Zh.O. 1992. Istoriya Kazakhstana v XIX veke. – Karaganda, S. 148. URL: https://rusneb.ru/catalog/000202_000006_456582/.

Bagdat K.A., Chekaeva R.U., Revtova V.V. «Arkhitektura zdanii g. Pavlodar (1889 g.)» Mezhdunarodnaya nauchno-prakticheskaya konferentsiya na temu «Sovremennye problemy arkhitektury i gradostroitel'stva» 6 fevralya 2016 goda – Almaty. S. 27-34. https: //primeminister.kz/ru/documents/gosprograms/stratplan-2025).

Bagdat K.A., Chekaeva R.U., Revtova V.V. «Arkhitektura zdanii g. Pavlodar (1889 g.)» Mezhdunarodnaya nauchno-prakticheskaya konferentsiya na temu «Sovremennye problemy arkhitektury i gradostroitel'stva» 6 fevralya 2016 goda – Almaty. S. 27–34.

Vyatkin M.P. 1941. Ocherki po istorii Kazakhskoi SSR. M., URL: https://libcats.org/book/770828

Zhanysbekov M.A. 2002. Kazakhstan v torgovo-ekonomicheskikh svyazyakh so stranami Zapada v kontse XIX nachale KhKh vv. — Almaty: 23s.

Zhirenchin A. 1996. «Politicheskoe razvitie Kazakhstana v KhIKh- nachale KhKh vekov» - Almaty.

Istoriya Kazakhskoi SSR 1949. S drevneishikh vremen do nashikh dnei. T. 1, izd. 2. A-Ata, 1957. URL: https://www.academia.edu/43174967/Omarov_I_O_Pankratova_A_M_red_Istoriya_Kazakhskoi_SSR_S_drevneishikh_vremen_do_nashikh_dnei_2_e_izd_T_1_Alma_Ata_.

Kereibaeva A.S., Istochniki formirovaniya kuptsov stepnogo kraya vtoroi poloviny XIX – nachala XX veka. Vestnik Surgutskogo gosudarstvennogo pedagogicheskogo universiteta, N. 3 (60) /2019: N. 3 (60), 2019. URL: file:///D:/Stat'i%202021%20goda%20(pishushchie)/Stat'ya%20-%20Skopus/Geotekhnika%20-%20Konferentsiya/istochniki-formirovaniya-kuptsov-stepnogo-kraya-vtoroy-poloviny-xix-nachala-xx-veka%20(1).pdf. DOI 10.26105/SSPU.2019.60.3.006.

Suleimenov R.B., Basin V.Ya. 1981. Kazakhstan v sostave Rossii XVIII - nach. XX vv. Alma-Ata. URL: https://rutracker.org/forum/viewtopic.php?t=2793632.

Chekaeva R.U., Revtova V.V 2015. Uchebnoe posobie. «Etnokul'turnye osnovy sovremennoi arkhitektury» dlya studentov arkhitekturnykh vuzov: TOO Master PO, Astana, 108 s.

Chekaev F.M.,Talipova V.M. «Pamyatniki zhiloi arkhitektury Petropavlovska XV111-nachala KhKh vekov». Mezhdunarodnaya nauchno-prakticheskaya konferentsiya «Arkhitektura i stroitel'stvo Kazakhstana v usloviyakh global'noi integratsii». 29 – 30 maya 2015g. v KazNTU im. K.I. Satpaeva.

Smart Geotechnics for Smart Societies – Zhussupbekov, Sarsembayeva & Kaliakin (Eds)
© 2023 The Author(s), ISBN 978-1-003-29912-7
Open Access: www.taylorfrancis.com, CC BY-NC-ND 4.0 license

Ecology and architecture of Kazakhstan cities in the 21st century

O.N. Semenyuk, B. Ozganbayeva, N. Lutsenko & D. Sadykbekov
Gumilyov Eurasian National University, Kazakhstan

ABSTRACT: On the base of general theory on bio ecological territorial systems, the article analyzed urban planning, resource, infrastructural and environmental problems cities, on the example of development modern Nur-Sultan and other cities of Kazakhstan. It known that the greening of the entire socio-economic system of any state is the basis for successfully solving environmental problems and preventing environmental disasters. Environmental security, as an integral part of national security, is a prerequisite for sustainable development and serves as the basis for preserving natural systems and maintaining the appropriate quality of the environment. The environmental consequences of industrial development of cities are air pollution, chemical contamination of soils, surface fresh water and fish stocks in reservoirs, and an increase in the level of morbidity of the population.

1 INTRODUCTION

For the first time, the term "sustainable development of the city" defined in the report of the UN Commission on Environment and Development in 1992. It implies programs to stabilize the population and industrial production, to develop an economy that does not destroy the nature of the Earth. In the concept of sustainable development, the concept of urban habitat is not limited to the ecological aspects of the interaction between man and nature. The city considered as a holistic anthropogenic complex, where society must provide and preserve for descendants optimal living conditions. Not to the detriment of the environmental component, the attractiveness of the urban environment has strengthened due to the streamlining of economic and economic activities and the expansion of various types of services.

Sustainable urban development defined as a much broader concept than environmental protection. This concept has socio-economic, cultural, and environmental characteristics. The problem of sustainable urban development includes the problems experienced within cities, the problems caused or created by cities, as well as potential solutions that can found and represented by cities.

The influx of population into cities related to their attraction, which is that large settlements are centers of work. Multi-functional cities provide a variety of livelihoods and job choices, while offering a wide range of cultural and social services. The unification of various places of employment and the satisfaction of social and everyday needs are very important for a person of the 21st century. A habitat that fully possesses such properties recognized as optimal, but only if protection provided against the negative effects caused by the concentration of people in small areas.

However, according to the UN, most modern cities have negative properties, the main of which are:

- Intensive pollution of the environment by products of economic activity concentrated in one place;
- Disequilibrium in the use of indigenous labor resources, changes in the properties of the "ecological niche" occupied by Aboriginal people;

DOI: 10.1201/9781003299127-296

– Insufficient housing, health and hygiene services due to overcrowding and overcrowding;
– Expansion of urban areas, which entails the removal of the population from each other's points of attraction and the consequent deterioration of transport services, unless the problems of intensification and organization of traffic are resolved;
– Insufficient water and energy supply, drainage and disposal of solid waste.

2 MATERIALS AND METHODS

Urban design, like architecture, is an exercise in analysis and synthesis enhanced by intuition. But uniting a building with its immediate hinterland, creating a community of buildings, or recreating a part of a city provides greater opportunities for beneficial environmental design and allows us to address the wider aspects of sustainability. Whereas a master plan often ends up as a conceptual model of physical infrastructure buildings and landscape, it is the design of the life support systems that link them that lies at the heart of holistic environmental design. Flows of heat, light and energy, air and water, material and waste and most importantly the movement of people are all issues that need to considered, mapped and modeled.

The study analyses the state of modern cities in Kazakhstan from the standpoint of urban planning ecology. Urban planning, resource, infrastructural and environmental problems of the cities of Kazakhstan and the capital of Nur-Sultan are analyzed based on the general theory of bioecological territorial systems. The purpose of the study is to identify existing problems and form ways to improve the environmental situation in the urbanized environment of cities. Numerous environmental problems of cities, mainly the largest of them, are associated with the excessive concentration of population, transport and industrial enterprises in relatively small areas, with the formation of anthropogenic landscapes, which are very far from the state of ecological balance. On the one hand, urbanization improves the living conditions of the population. On the other hand, it leads to environmental pollution, an increase in the chemical, physical and mental load on the human body.

Kazakhstan has a very vulnerable natural environment. The territory of the republic is mainly composed of steppes, semi-deserts and deserts. There are unique inland seas and lakes, such as the Caspian, Aral, Balkhash, Zaysan, Alakol. As result of anthropogenic loads in almost the entire territory of Kazakhstan, the natural ability of the natural environment to ensure the future economic and social development of the country has violated. In the cities of Kazakhstan, the main contribution to air pollution made by road transport. The poor quality of the fuel used and the lack of filters for cleaning exhaust gases, the poor condition of the rolling stock of motor farms, the increase in the number of cars in cities, leads to the release of huge amounts of carbon monoxide, lead into the atmosphere. Urban air pollution is increasing during the heating season. (Figure 1).

Fifteen cities of the republic have increased the level of atmospheric air pollution by harmful emissions. Among these cities are Zyryanovsk, Aktau, Temirtau, Taraz, Petropavlovsk, Shimkent, and Almaty. The high level of air pollution in cities is the result of outdated production technologies, inefficient treatment facilities, and poor quality of fuel used. The main pollutants are dust, sulfur dioxide, nitrogen dioxide, hydrocarbons, phenol, lead, hydrogen sulfide, hydrogen chloride, ammonia, etc. Each of these substances negatively affects health in its own way.

Dust, for example, causes diseases of respiratory substances, liver, blood. The dustiest cities of Kazakhstan are Aktau, Atyrau, Zhezkazgan, Semipalatinsk, and Ust-Kamenogorsk. Disorders of the nervous system can caused by an increased content of carbon monoxide in the air. At the same time, headaches occur, memory decreases, sleep gets upset. High carbon monoxide content observed in cities such as Almaty, Aktobe, Karaganda, Kostanay, Petropavlovsk, Pavlodar, Semipalatinsk and some others. If there are several types of pollutants in the air, which usually happens, the negative effect even more enhanced. This affects the immune system, which often leads to cancer [1].

Figure 1. Air pollution in Nur-Sultan during the heating season.

Figure 2. General plan of Nur-Sultan by the architect Kisho Kurakawa. Adjustment general plan until 2030.

3 RESULTS

3.1 *Impact of urban planning systems on the environment*

Cities are the largest consumers of all types of natural resources - territorial, energy, food, and are the main source of environmental pollution. The pressure on the natural environment is increasing dramatically not only in the cities themselves, but also beyond their borders. The ecological impact of a large city on the environment is 50 times its own radius. Urban planning ecology deals with the problems of the impact of urban planning systems on the environment. In urban planning ecology, there are three degrees of ecological balance: complete, conditional, relative. Ecological balance in urban planning defined as the state of the natural anthropogenic environment, which ensures its long-term stability.

As in the rest of the world, in large cities of Northern Kazakhstan and in Nur-Sultan, it is also possible to predict a violation of the ecological balance of the environment of urban spaces associated with a sharp increase in the population, if measures not taken to eliminate the negative impact of factors of urban pollution and environmental problems. The rapidly developing capital of Kazakhstan, the city of Nur-Sultan, is at high risk of environmental degradation in the near future. The rate of demographic growth of the population in the capital has surpassed all projected indicators. Back in the first half of 2003, the forecast indicator, which was the basis for the development of the general plan of Nur-Sultan by the architect Kisho Kurakawa, was significantly overlapped, which provided for an increase in the city's population to 800 thousand inhabitants in 2030 (Figure 2).

Currently, there are more than a million people in Nur-Sultan; over the past year, the population of the capital of Kazakhstan has grown significantly. With the current population growth, rate of Nur-Sultan the population of the capital will reach 3-4 million inhabitants in 2030 [2]. A large city changes almost all components of the natural environment - atmosphere, vegetation, soil, relief, hydrographic network, groundwater, soil and even climate.

The fundamental concept is also comfort, defined as the most favorable conditions for the life of people, a set of amenities, livability and environmental safety. The very rapid pace of urban development in the modern world has revealed a number of problems associated with maintaining a stable ecological situation. A number of major environmental problems can identified. These include the following problems: - urban planning; - infrastructural; - resource; - environmental protection. Let is consider these problems in sequence, deciphering each of them. Urban planning problems:

– Unbalanced transport framework of the city, inability to accommodate increased traffic flows, resulting in increased air pollution;
– Excessive building density, because of which there is a violation of urban planning norms for insolation and aeration of territories;
– A significant shortage of green areas, a discrepancy between the area of greenery and the number of residents in cities;
– Lack of a developed recreational infrastructure.

Road transport is one of the main sources of air pollution in cities. This is due to a number of reasons:

– Narrow streets;
– High building density;
– Insufficient level of landscaping.

Ultra-dense residential buildings reduce wind speed, and stagnant air contributes to the concentration of highly toxic traffic pollutants. According to environmental monitoring data in recent years, over large cities, the atmosphere will contain 10 times more aerosols and 25 times more gases. At the same time, 60-70% of gas pollution provided by road transport. The low level of greening of urban areas leads to a lack of fresh air, oxygen, pollution and gas pollution of the air environment. The cities of Northern Kazakhstan have a sharply continental climate with a low amount of natural precipitation, as well as swampy and saline soils, and this does not contribute to the rapid growth of plants. Therefore, there is a problem of greening urban areas. In particular, in the capital Nur-Sultan, trees have to plant several times in the same areas, as they do not take root well. At present, a program for landscaping the territories of Nur-Sultan has developed, which defines the stages of planting new trees in the city. Selected tree species that can survive in harsh climatic conditions [3]. A green ring created around the city to protect the city from strong steppe winds. There is a need to develop program of the following points in order to solve the environmental problems of Nur-Sultan and other large cities:

– Creation of a regional environmental doctrine;
– Determination of the ecological potential of the environment;
– Development of the urban ecological framework of Nur-Sultan (calculation of the area of compensatory zones, calculation of the ecological load on the environment);
– Carrying out urban ecological zoning of the city territory;
– Carrying out a clear normative regulation of urban development of the territory;
– Optimization of the city's transport framework, the introduction of new types of transport, such as the monorail;
– Substantiation and design of the city's recreational system;
– Compliance with the optimal ratio of building and landscaping. The implementation of this program will improve the ecological state of the capital of Kazakhstan, as well as program and control the ecological situation in the city.

It should note that during period there were violations of urban planning norms and rules during the development of the old part of cities in Northern Kazakhstan. The houses are on the red line close to the road, there are no protective green stripes. As a result, residents of older residential areas not protected from noise and pollution. One of the important urban-ecological problems that have a significant negative impact on the existing natural landscape is the lack of a developed recreational infrastructure. For example, in Nur-Sultan, the available 500 meters of sandy beach in the park on the banks of the Esil River do not solve the problem of recreation for the citizens of the millionth city. Therefore, many residents of the capital rush out of the city, using the banks of the river outside the city park for recreation. The consequences of spontaneous rest are the most negative. The coastal zone of the river outside the city limits for kilometers polluted with household waste: broken glass, bottles, plastic bags, food leftovers. Rubbish also dumped into the water, and piles of rubbish block the already narrow riverbed. The solution to this problem lies in the purposeful creation of a scientifically grounded system of recreational areas with organized parking, swimming places. These zones are not concentrated in one place, but distributed along the riverbed to reduce the environmental load on the recreational area. Urban development of the banks of the Esil River in the capital is a complex environmental problem. For many years, construction carried out close to the banks of the river. Esil, flowing through the steppe landscape, receives water replenishment only during the period of snow melting. Slight precipitation does not affect the water level in the river. The construction of multistore buildings along the banks of the river requires the digging of foundation pits for the installation of pile foundations, which leads to artificial drainage and outflow of water from the river.

The southern capital of Kazakhstan, the city of Almaty is located in the southeastern part of Kazakhstan in the north of the mountain spurs of Tien Shan at the foot of the slope of the Zailiysky Alatau at an altitude of 600-900 meters above sea level, in the valleys of the Big and Little Almaty rivers. The territory adjacent to the city and lying at 600 meters above sea level is fertile, abundantly overgrown with forest and shrubs. Like any big city of Almaty, it faces great environmental problems, which will discussed below. Almaty is the largest city in Kazakhstan, on the territory of which there are large enterprises, thermal power plants and the private housing sector, which, along with vehicles, are intensive sources of environmental pollution. The catchment area of the rivers of Almaty flowing into Ili characterized by a high degree of pollution, including heavy metals. The Big Almaty, Little Almaty, Esentai rivers flow through the territory of Almaty, into which sewage pipes of a number of enterprises discharged. The Yesentai River flows into Big Almaty further into the Kaskelen River and into Ili, the Little Almaty River flows into the Kapchagai Reservoir. The multifaceted distribution of contaminated waters, self-treatment and conversion of contaminants in water bodies has led to the fact that the problem of forming water quality in rivers and reservoirs with anthropogenic effects has not solved sufficiently. In addition, unorganized and untreated waters of the private residential sector and numerous car washes, catering points and other small business facilities discharged into the waters of these rivers; these discharges are not actually controlled.

Today, freshwater pollution has become so significant that it takes on the nature of a disaster and is alarming in many countries of the world. The Republic of Kazakhstan is relatively poor in water resources compared to European countries, but richer than other States in the Central Asian region. According to its sources, Kazakhstan's water resources divided into surface, underground, glacial and artificial reservoirs. The southern capital of the Republic of Kazakhstan is unique in its physical, geographical and natural-climatic characteristics. The city of Almaty is located in the north of the mountain spurs of the Tien Shan mountain system, at the northern foot of the Zaili Alatau, on the cones of the Ulken (Big) - Almaty and Kishi (Little) Almaty interfluve. In Almaty, the natural zones of the harsh north and the sultry south are crossed. Complex terrain, climatic features create unfavorable conditions for dispersing impurities from low sources of emissions, as result of which harmful substances accumulate at high concentrations, which then take part in the formation of smog phenomena. Pollution of the city's atmospheric air is one of the serious factors of water and soil pollution, since due to poor storm sewage, pollutants are washed away into water bodies with meltwater and storm water. The most polluted is the atmospheric air of Almaty, according to

the estimates of the Environmental Monitoring Center. The main source of air pollution in Almaty is motor transport. As a result, the atmospheric air of the city has an increased content of formaldehyde, nitrogen dioxide, phenols, carbon monoxide. The most disadvantaged areas of the city are the TETs-1 areas, the highway along Rayimbek Avenue, the area of the Fruit Canning Plant (Figure 3).

Figure 3. Air gas content in Almaty city.

The ecological state of rivers, taking into account the state of the catchment basin, water protection zones, strips and water quality, estimated according to the data of the Research Institute of Environmental Problems as follows: Big Almaty River - more satisfactory; Yesentai River - less satisfactory; Little Almaty River - extremely unsatisfactory; - other watercourses are extremely unsatisfactory.

The vegetation of Almaty performs a certain positive function in normalizing and supporting the ecological situation of Almaty. According to the official statistics of Almaty, green spaces of public use occupy 3% of the city, which in translation per resident is about 7.0 m of green spaces. Parks, squares, green streets are, for various reasons, in unsatisfactory condition. The largest environmental problem for Almaty is the problem of accumulation and storage of solid industrial waste. About 24 hectares of city land contaminated with household waste. Of which the city garbage reloading station and spontaneous landfills in various areas of the city occupies 10 hectares. The ecological state of any region, city, and settlement known to be a factor characterizing their demographic situation. According to the Almaty City Statistical Office, over the past 10 years, almost all indicators of the demographic situation in Almaty have worsened. Thus, the birth rate (per 1000 people) since 1990 has decreased from 15.8 to 10-11 with an average republican value of 14.7. There currently only six posts that monitor atmospheric air. 10-20 points are required for the city, in accordance with regulatory requirements. Being one of the most beautiful cities in the country, Almaty remains one of the most environmentally disadvantaged. To improve the situation, "Rules for the protection of the plant fund of public use in Almaty," a program for the reconstruction and restoration of green spaces in the city, have developed [4].

3.2 *Threats to environmental safety*

Threats to Kazakhstan's environmental security environmental problems, depending on the importance and level of their solution, divided into global, national and local. Global environmental issues included climate change, the state of the ozone layer, and conservation of biodiversity, opus and land degradation. Kazakhstan ratified the UN Framework Convention on

Climate Change in 1995, for the implementation of which it is necessary to achieve stabilization of the concentration of greenhouse gases in the atmosphere at a level that does not allow dangerous anthropogenic impact on the natural climate system. In 1999, Kazakhstan signed the Kyoto Protocol to this Convention, according to which commitments have made to reduce greenhouse gas emissions, which opens up great prospects for our country to attract international investment. Over the next few decades, anthropogenic activity projected to determine the change in the state of the ozone layer, suppressing natural factors, including the impact of solar activity cycles. Observations since 1973 show that the thickness of the ozone layer over Kazakhstan has decreased by 5-7%. The control measures adopted under the Vienna Convention for the Protection of the Ozone Layer and the Montreal Protocol on Substances that Deplete the Ozone Layer have contributed to an 85 per cent reduction in the production of ozone-depleting substances from 1986 levels. Kazakhstan had ratified those instruments in 1998 and had begun implementing commitments to reduce the use of ozone-depleting substances and to remove them from circulation. One of the most important global environmental challenges is the conservation of biodiversity. The ecosystems of Kazakhstan distinguished by the uniqueness of biological diversity in the ecosystems of Central Asia and the continent as a whole. Under the influence of anthropogenic factors in Kazakhstan, the number of many species of animals began to decline and their habitat began to decrease [5].

The main areas of conservation of biological diversity:

- Assessment and inventory of objects of biological diversity at different levels of its structural organization (species, population, landscape and regional);
- Development of a network of specially protected natural areas and the maintenance of natural populations of rare species through their artificial reproduction;
- Restoration of biological diversity in disturbed areas, taking into account modern natural and anthropogenic-stimulated processes.

Desertification and land degradation are a serious problem. In Kazakhstan, significant areas (66% of the territory) are subject to desertification and degradation to varying degrees, which leads to the withdrawal of land from agricultural circulation [6]. This is due to extensive agriculture, pollution of mining areas, hydrocarbon transportation and processing areas, including oil products and radioactive compounds. To prevent these processes, it is necessary:

- Restoration of degraded land and soil fertility;
- Improving public administration of land use;
- Introduction of economic mechanisms for environmentally sustainable land management.

In addition to the listed global environmental problems, the Republic of Kazakhstan has identified national environmental problems. There are zones of environmental disaster (Aral and Semipalatinsk regions). In these zones, due to the unfavorable environmental situation, significant damage to the health of the population and the destruction of natural ecological systems, degradation of flora and fauna occurred.

The main directions of solving problems:

- Comprehensive analysis of the socio-economic and environmental conditions of the population in environmental disaster zones;
- Development of rehabilitation and rehabilitation measures taking into account the environmental assessment of the territories of the Aral Sea region and the Semipalatinsk region;
- The consequences of nuclear explosions and other factors on public health and the environment;
- Development of programmers for internal population migration and economic use of ecological disaster zones.

The widespread development of hydrocarbon resources by the Caspian Sea basin States increases the scale of negative impacts on marine and coastal ecosystems. In accordance with the State Development Program of the Kazakh sector of the Caspian Sea, special studies envisaged to determine the maximum possible level of oil production without damaging marine ecosystems, eliminate orphan wells and other historical pollution and take measures to

stop the burning of associated gas on flares. Work is currently under way at the international level to adopt the draft Framework Convention for the Protection of the Marine Environment of the Caspian Sea. The decision of the regional Strategy of Priority Actions adopted, which identified the main directions for the use of the resources of the Caspian Sea, and measures for the protection of the Caspian ecosystem. The environment also affects public health. It has found that many types of human diseases are associated with negative changes in the environment. However, the issues of determining the causal relationship of the incidence of the population with environmental factors remain insufficiently studied. In this regard, it is necessary to expand work in the field of medical ecology with medical assessment and monitoring of geographical studies in cities. One of the important issues is the impact of the military-space complex landfills. Currently, there are four military test sites and the Baikonur complex in the country. Fragments of rockets, spills of highly toxic fuel and other factors that have a negative impact on the environment pose a particular danger to the environment. In this regard, it is necessary to organize work on monitoring the environmental condition of landfill territories with the development of a set of measures to eliminate the consequences of their activities.

The solution of local environmental problems has an important role in the policy of Kazakhstan. These include:

- Pollution of the air basin (emissions from non-ferrous metallurgy, thermal power engineering, ferrous metallurgy, oil and gas complex);
- Depletion and pollution of water resources (heavy pollution by mining, metallurgical and chemical industries, urban utilities);
- Radioactive contamination (the presence of large uranium-bearing geological provinces, many small deposits and uranium mining, which lead to an increased level of natural radioactivity);
- Accumulation of industrial and domestic waste; natural and fabricated emergencies.

3.3 *Implementation of the concept of sustainable development in the Kazakhstan cities*

The concept of sustainable development on the international agenda emerged in the second half of the 20th century when environmental and societal problems have become an obvious obstacle stable economic development. Social and environmental problems - inequality, poverty, resource depletion, climate change - continued to worsen and began to affect not only the negative impact on the environment and society, but as a result, on economic development in the long term.

Sustainable development takes into account social and environmental factors and aims to achieve economic growth through social well-being and preservation of the environment. That is why the concept often presented in the form of trinity economy, society and nature.

All three aspects are equal and balanced. Environmental dimension addresses status issues environment, resource consumption, air pollution, water and energy use, etc. The social dimension concerns quality of life issues people and their well-being, economic – condition the economy, its opportunities and development.

At present, sustainable development is becoming increasingly relevant.

Kazakhstan's cities take necessary measures to achieve sustainable development based on economic, social and environmental interaction. The State, the financial sector and business are the driving forces of an economy that depends entirely on society and the environment. Society and the environment provide the necessary resources for the development of the economy, which turn into goods and services, private capital, waste and emissions. If resources entering the economy not properly regulated or adversely affected and depleted, the entire process of economic development jeopardized.

Environmentally oriented urban infrastructure should aim to preserve and restore the environment, reduce air pollution and greenhouse gas emissions, minimize and properly manage waste, take into account the development of the territory and preserve biodiversity. It is

resistant to the effects of climate change, for example, emergencies (fires, floods, etc.). Transport infrastructure development enables developing countries to become involved in international trade, and the growing share of rail transport increases transport energy efficiency and reduces emissions to the atmosphere.

Sustainable development is necessary to achieve the goals of the Development Strategy of Kazakhstan until 2030. The principle of sustainable development is also the basis of Kazakhstan's strategy to become one of the fifty most competitive countries in the world [7].

This Concept for the transition of the Republic of Kazakhstan to sustainable development for 2007-2024 defines the vision of principles, goals, objectives and basic mechanisms for achieving sustainability in all spheres of the country's life. To this end, it is necessary that the economic, environmental, social and political factors of development integrated and considered as a single process aimed at improving the quality of life of the population of Kazakhstan.

The Republic of Kazakhstan, as a full member of the world community, has undertaken to fulfil the objectives set out in Agenda 21 (Rio de Janeiro, 1992) and the declarations of the Millennium Summit (New York, 2000) and the World Summit on Sustainable Development (Johannesburg, 2002). Kazakhstan is a member and active participant of the UN Commission on Sustainable Development, the processes "Environment for Europe" and "Environment and Sustainable Development for Asia," the regional Eurasian network of the World Council of Entrepreneurs for Sustainable Development. The Development Strategy of Kazakhstan until 2030 has adopted. The Republic of Kazakhstan plays a special role in ensuring the ecological stability of the Eurasian continent. As a political, cultural and economic bridge between Europe and Asia, Kazakhstan performs a similar connecting function in the development of landscape and ecological systems on the continent. The size of the territory of Kazakhstan, the variety of climatic conditions, the peculiarities of the water balance of the region entail a significant dependence of the ecological situation throughout Eurasia on its stability in Kazakhstan. The goal of the Concept is to achieve a balance of economic, social, environmental and political aspects of the development of the Republic of Kazakhstan as the basis for improving the quality of life and ensuring the competitiveness of the country in the long term.

There is a significant gap in the economic and social situation of the regions of Kazakhstan. Problems remain in the demographic and health situation of the country's population, while there is still an insufficient level of its legal, economic and environmental literacy. Overcoming these barriers should be a major milestone in Kazakhstan's transition to sustainable development.

The main principles of the transition to sustainable development in the Republic of Kazakhstan are:

- The involvement of society as a whole in the achievement of sustainable development;
- creating a policy framework for sustainable development;
- Inter-agency integration, a systematic approach to state management, improving the efficiency of forecasting, planning and regulating key development indicators;
- Economic progress because of the active introduction of high technologies into the country's economy, improving the efficiency of resource use;
- ensuring the competitiveness of science and education;
- Improving the health of the population and demographic situation because of the introduction of the paradigm of a healthy society;
- Improving environmental protection;
- Territorial development based on a trans-regional ecosystem approach.

The priorities for the transition to sustainable development are:
The introduction of sustainable production and consumption patterns;

- The use of new and environmentally sound technologies;
- The development of sustainable transport systems;
- Energy efficiency and energy conservation;
- Regional sustainable development issues;
- Improving the social security of the population;
- Combating poverty from an environmental and gender perspective;

– Further development of science and education for sustainable development;
– Preservation of historical and cultural heritage;
– Prevention and reduction of environmental threats to public health;
– Combating desertification;
– Conservation of biological diversity;
– Reducing emissions, including greenhouse gases and ozone-depleting substances;
– Access to quality drinking water;
– Addressing transboundary environmental problems;
– Radiation and biochemical safety;
– Waste management;
– Formation of environmental status indicator systems;
– Environmental zoning;
– Development of solutions to local environmental problems;
– Creation of new resource-saving, low-waste, environmentally efficient technologies [8].

4 DISCUSSIONS

For the sustainable development of cities, projects in the field of urban planning aimed at:

1) Reconstruction of old residential areas;
2) Revitalization of former industrial sites by creating social infrastructure and residential and commercial real estate facilities on them;
3) Formation of architectural uniqueness of the city (including creation of symbolic structures);
4) Creation of recreational zones, including parks.

Specialized strategies:

1) Development of the tourism industry;
2) Attracting the headquarters of large corporations and developing business tourism [9].

Environmental initiatives can developed with the goals:

1) Environmental policy to improve the environmental situation in the city;
2) Regulation of enterprises from the environmental point of view;
3) Combining environmental and social policies (recreational areas for city residents and tourists).

The management of sustainable development of the modern city based on the following factors [10]:

1) In the field of technology;
   a) Replacement of non-renewable resources with renewable ones;
   b) Phasing out particularly environmentally hazardous technologies;
   c) Reuse of extracted substance and waste disposal;
2) In the demand structure:
   a) Shift towards reduction of material and energy intensity consumption of products;
   b) Development of services;
   c) Emphasis on the production of durable goods;

Abandoning expensive needs;

3) During production:
   a) Orientation to the production of biodegradable products;
   b) Shift towards reduction of material and energy intensity production;
   c) Production of products of improved quality;
   d) Reduction of the quantity of products produced;

4) In the field of production organization:
   a) Zoning of the territory;
   b) Increasing the diversity of natural and cultural landscapes;
   c) Deepening of specialization between regions.

Strategies for the sustainable development of modern agglomerations in Kazakhstan - is an objective process to better utilize the concentration of human, material and financial resources, as well as to obtain synergies from resource management not only territory as a spatial resource, but also production urban infrastructure, engineering and technical support networks, knowledge and technology.

Development of sustainable development strategies for Russian cities opens up new opportunities for rational and efficient use all types of resources, striking a balance of interests between social, environmental and economic factors of development, between the authorities, business and society. Potential targeted design of sustainable cities with a centrally oriented approach to agglomerations in directions corresponding to patterns of spatial development, deployment of productive forces in the territory of cities and their surroundings.

If we build logical relationships between agglomerations and cities, suburbs and other settlements, then we can to count in the medium term on synergistic and multiplicative effects in the country's economy [11].

Indicators and indicators of environmentally sustainable development in the regional context perform a number of functions:

1) Defining goals in the formulation of long-term and medium-term regional development strategies;
2) Forecasting the effect of sustainable environmental management policies;
3) Monitoring the achievement of goals and objectives and evaluation of results;
4) Evaluation of the effectiveness of programs, strategies;
5) Holding interregional comparisons;
6) Attracting investments and forming programs.

5 CONCLUSIONS

In this regard, the key challenges of sustainable urban development can identified. One of them is long-term planning of economic and production and economic activities. There is a need to develop a city-forming base with the creation of various places of employment. This is important for residents, since there are wide opportunities for choosing jobs. When determining the composition of production, one should take into account the stereotypes prevailing among the population. Use human resources in production and agriculture in accordance with their demographics and qualifications.

Another problem of forming an urban planning base related to the ecological safety of the habitat. It is necessary to introduce resource-saving, low-cost and waste-free technologies into all production. It is necessary to improve and build facilities for the treatment and disposal of solid and liquid waste.

Another problem is the rational development of the city's engineering life support infrastructures. The purpose of their development is to meet the needs of the population for resources such as clean water, electricity and other energy.

The systems of engineering infrastructure include transport. It is necessary constantly improve transport services for citizens by reconstructing the existing road network, improving the organization of urban traffic and communication with external transport.

Social policy recommended aimed at increasing the palette of cultural services. It is rational to expand the system of objects of culture, recreation and trade. Due to the need for religious and religious buildings to restore them and build new ones.

In cities, the problem of preserving landscapes is very acute. Land resources should use sparingly to prevent their degradation. It is optimal to combine the development of new

territories with the compaction of existing buildings. Consider that the expansion of cities, among other consequences, entails the problem of long-distance transport.

Sustainable and environmentally optimal urban habitat can created only with a rational combination of economic activities and environmental measures. Therefore, the strategy and tactics of maintaining and developing cities should base on the principles of an integrated approach to the space-planning organization of territories. Such an organization is the subject of urban planning. Therefore, urban planning inextricably linked with the organization of optimal habitat, environmentally friendly and necessarily stable over time.

Sound economic policies play a key role in the area of environmental security of States and sustainable urban development. Moreover, every State today faces environmental problems that it cannot solve alone. There is therefore a need to integrate the efforts of all countries. Sources of ecological disadvantage: accumulations of ash dumps, spontaneous landfills and the absence of citywide treatment facilities; poor condition of sewage networks and filtration fields located near cities; large volumes of dumps of mining enterprises; emissions of pollutants from numerous solid fuel boiler houses. Sustainable development is the ideology of Kazakhstan's development strategy. The future of Kazakhstan connected with unity, balance of all aspects of the development of society. Kazakhstan seen as a country that achieves sustainable urban development, economic growth, well-being, health and a favorable environment for all its citizens. The sustainable development of the country is a set of conditions, factors, tools that ensure the growth of social wealth, natural capital, cultural heritage and the standard of living of society. The countries of the world in the 21st century are in constant interaction, cooperation and competition with each other. In relation to the nature of the Earth, urban entities act as elements of the global environmental system. Due to population growth, globalization processes are increasing, and competition between countries of the world for spheres of influence and resources. Sustainable urban development inextricably linked to a country's competitiveness. The Republic of Kazakhstan plays a special role in ensuring the ecological stability of the Eurasian continent. As a political, cultural and economic bridge between Europe and Asia, Kazakhstan performs a similar connecting function for landscape and ecological systems on the continent. The size of the territory of Kazakhstan, the variety of climatic conditions, the peculiarities of the water balance of the region entail a significant dependence of the situation throughout Eurasia on environmental stability in Kazakhstan.

REFERENCES

[1] Bigaliev, A.B., Khalilov, M.F., Sharipova 2017. Fundamentals of general ecology. Almaty: Қазақ University.

[2] Reports of the Ministry of Environmental Protection of the Republic of Kazakhstan. *On the State of the Environment of the Republic of Kazakhstan. 2000-2007*. // https://www.gov.kz/memleket/entities/ecogeo?lang=en.

[3] Concept of ecological safety of the Republic of Kazakhstan. *Astana. 2012*. // https://helpiks.org/9-38534.html.

[4] Columbaeva, S.Z., Bildebaeva. R.M. 2017. General Ecology. Almaty: Қазақ University.

[5] Shokamanov, Yu., Makazhanova, A. 2016. Human development in Kazakhstan. *Textbook*. Almaty: S-Print.

[6] New Environmental Code in Kazakhstan to Promote Green Technology, Sustainable Development. 2021. // https://astanatimes.com/2021/03/new-environmental-code-in-kazakhstan-to-promote-green-technology-sustainable-development/.

[7] Concept on sustainable development in the Republic of Kazakhstan. //https://www.freepapers.ru/19/koncepciya-po-ustojchivomu-razvitiju-v/290472.1964325.list1.html.

[8] Environmental Code of the Republic of Kazakhstan. // https://adilet.zan.kz/eng/docs/K070000212_.

[9] Sheresheva, M. Yu., 2015. Network forms of organization in the development of regional tourism business. *New economy and regional science*. № 1.

[10] Prokofiev, S. E., Popadyuk, N. K., Semkina, O. S. 2015. New approaches to the development of cities and agglomerations. *Sustainable development management: monograph, edited by A.V. Trachuk*. St. Petersburg: Real Economy Publishing House LLC.

[11] Semenyuk O., Kuc, S., 2019. Development of eco architecture in Kazakhstan is gaining ground. *World Transactions on Engineering and Technology Education*, 17(3): 379–384.

Smart Geotechnics for Smart Societies – Zhussupbekov, Sarsembayeva & Kaliakin (Eds)
© 2023 The Author(s), ISBN 978-1-003-29912-7
Open Access: www.taylorfrancis.com, CC BY-NC-ND 4.0 license

Development of residential architecture in Astana

O.N. Semenyuk & U.D. Dyisebayev
Gumilyov Eurasian National University, Kazakhstan

ABSTRACT: New socio-economic conditions of Kazakhstan in recent years, as well as increased requirements for the most efficient use of the territory of Astana and the cities of Northern Kazakhstan, have led to new design directions, where intensive construction of a large number of new residential buildings has begun. A prestigious home appeared in terms of comfort and location. The capital city develops in its own way, different from other cities of the country. Construction trends and characteristic architectural and typological features of residential buildings of the last decade considered on the example of Astana architecture. In the urban environment, the formation of a new aesthetics of residential buildings traced. Improving the quality level became possible due to competition in the housing construction market, with the beginning of the modernization of industrial technologies and the use of new building materials. Under these conditions, the typology changes. The changes affect both the functional and planning structure of the dwelling and the appearance of residential buildings. Identification and analysis of the process of changing the economic, typological, functional and artistic content of the dwelling allows us to draw certain conclusions and predict further trends in its evolution.

1 INTRODUCTION

The construction of residential buildings is one of the complex problems of architecture, synthesizing the achievements of construction art, modern technology and architectural craftsmanship. The compositional significance of such buildings in the development of the city determines the high requirements for their architecture. It is residential buildings that are designed to create the individual face of the city's districts, to be the most expressive.

The analysis of architectural compositions of residential buildings and their conditioning on functional, hygienic, economic and technical requirements is of practical interest, despite the relatively small amount of their construction.

Leading experts in modern architecture consider residential development as the main task of modern urban planning. With their works and project proposals, they proved that economic and demographic conditions and changes in the way of life of people lead to the emergence of such problems of a large city that cannot solved without the development of residential development.

The modern architectural practice of housing design and construction represents a great variety - this is associated with the formation of a typology in the aspect of time. The process of improving the home in accordance with changing needs is noted. Currently, in Astana, commercial residential buildings for citizens with medium and high-income levels of the sectional type of medium and variable storeys are the most common, while, for the most part, these houses are single piece objects, and individual houses of the cottage type are also common.

The previously developed typology of residential buildings, unified for the whole country, with the nomenclature of apartments intended for an average consumer, in modern conditions does not meet the requirements of the emerging new socio-economic structure of the urban population and does not always correspond to the multivariability of the lifestyle of specific

DOI: 10.1201/9781003299127-297

families. The recommendations of outdated norms and rules do not fully comply with the requirements for modern housing by various categories of the population.

Currently, there are not enough scientific studies analyzing all the factors that collectively affect the formation of housing in the city. A comprehensive study of space planning and composition features and development trends of residential buildings in Astana and North Kazakhstan not carried out. All this, along with the constantly changing requirements of people for the comfort of living, testifies to the relevance of the topic of this study and the need for a theoretical solution to the problem.

2 HISTORY OF URBAN DEVELOPMENT

History of North Kazakhstan's urban development in XX century's 50-60-s have especial importance. The development of virgin lands and strong growth of productive forces between 1954 -1964 in the north regions of Kazakhstan served as a powerful stimulus for the development of the city. Sharply rising of agricultural production in the region was issues of industrial, social and cultural development of the city with particular urgency. Only in the first three years of development of virgin lands between 1954 -1957 made Akmola actively building and developing city. Despite the presence of newly build large buildings, in the beginning of 1950, overwhelming majority of town remained single-story, mainly with wooden and adobe houses. Progress of construction volumes during this period led to the transition to standard projects and a series of residential buildings. One of beginning projects in the republic was residential buildings of the series 207. Town's in 1954 planning terms completely preserved the existing quarterly building and consisted of the city itself and the settlement village, which developed along the railway in the north-west direction. Streets, thoroughfares, squares, which exceeded regulatory requirements by more than 3 times, occupied the predominant part of urban areas (41.3%). Wide streets (40 m.) In the city formed tiny quarters of 0.6 to 2 m.

Construction of housing did not satisfied at all demands of growing urban population. According housing department of the city council's information, whereas needed rate of living area at a rate of nine square meters per city dweller the town has only approximately 3.6 square meters per city dweller. The existing housing stock of the city had a large percentage of depreciation, in the first place were housing municipal public utilities. Statistics represents that 88,000 square meters the living area of the city worn out by 20-40%, 71,000 square meters by 40-60%, 73,000 square meters by 60%. Repairing the housing of the municipal fund was broke systematically from year to year. For example, in 1957 only two houses repaired in the whole city. The Almaty «Gorselstroyproektom» developed first master plan of the city in 1957. Reflecting the building principles of the time, the plan considered formation of a residential area of the city from quarters of 6-10 hectares. In addition, there were trend of growth from one to five storied buildings with the corresponding zoning of the territory by the number of storied in the buildings. It was also planned distinguish a zone of individual building. Town's development and construction under this master plan were until 1961-1962. At this time, there were build 2, 3 and 4 storied buildings in Monina street, half of Mira street and numerous quarters in the eastern part of the city.

By order of the Kazakh Railways Administration, the contractor, construction management in the construction of the Stalin-Magnitogorsk highway, built completed architectural ensemble on Monina Street and a complex of large-panel houses along Mira Street. Rapid growth of urban construction, both in quantitative and in qualitative parameters, occurs in the early 60-ies, about which the witness the following figures. If the input of living space in 1959 was 23 thousand square meters, in 1961 it increased to 62 thousand square meters. In late 1950s, which had about 57 thousand square meters, more than half of the built-up public housing stock were low-rise houses that have poor house-improvements like courtyard. Since 1961, all of housing stock, which gets into exploitation, consists of 4-5-storeyed large-panel and stone houses, in which all the elements of apartment improvements as courtyard were present. Only in one 1962 were built about 200 residential houses and commissioned in the city.

Despite the well develop housing construction; it was not easy to solve the housing problem. In 1962, repairs needed around 70% of the city's residential area consisted of old dilapidated houses. The commission period of objects into exploitation were annually broken. Construction works extremely disorganized, existing mechanisms are often idle, and the quality of work was poor, observed gross violations of technical conditions.

In the construction of the existing part of the town, there were problems. For the reason that mass housing construction carried out by typical 4-5story houses, were created type of different-story buildings, which was difficult to improve with the methods of volumetric-spatial composition. Moreover, the construction of the territory carried out without the presence of project with detailed planning (PDP). The construction carried out according to the projects developed for individual quarters, parts of quarters, and sometimes made the binding of single residential objects to already existing arrays. The planning and composition organization of the building and cultural-consumer services of the population did not correspond to the present achievements of urban planning. Developed in 1953 – 1957 years Akmola's master plan did not meet the prospects of development of the city as the administrative center of Tselinograd region, according to several parameters:

- Forecasts on the population for 1965-1975;
- Changes in the provision of residential area of citizens;
- The location in the city of a number of large administrative and public buildings, which were to become priority, objects of construction;
- Not matching the economy of the current stage of urban development with more than half of the housing stock: 57% were low-rise buildings, 4-story houses – 43%, 2-3-story –31%, single-story – 26%.

Single-story buildings were 52% of the total volume of urban housing commissioned in 1957 – 1960. The desire for "light square meters" led to an irrational expansion of the urban area, an increase in the scope of works for improvement, the extension of communications of engineering equipment, a rise in the cost of housing construction. However, it did not take into account that the cost of one square meter of area in a 4-storey house is 9–10% less than in a one-story house. Akmola Regional Committee subsequently adopted a decision to ban in a single-story building along the state building and transition to a massive 3-4-story building construction based on cooperation means developers.

Starting 1960 until 1980 in the residential part of the Tselinograd based on the availability of living space per one person determined: 1965 –7 sq. m., 1970 9 sq. m., 1980 – 15 square meters. m. New housing construction for the period from 1962 to 1980. Was 5140 thousand square meters. Including in 1962–1965. – 560 thousand square meters. m., in the years 1965–1970. – 1180 thousand square meters, in the 1970–1980's. – 3400 thousand square meters.

The abolition of the Tselinograd region in 1964 and the decline in the status of the city of Tselinograd to the regional administrative center and, as a consequence, the reduction of budget funding, could not affect the city development plans and the volume of construction work. At the same time, the city continued to grow quite dynamically, consistently and systematically improving and developing its planning structure and architectural appearance of the building.

The construction of the city was conducted mainly 4–5 story houses, mainly with the construction of large-panel construction. The houses planned taking into account the best orientation on the sides of the world, in relation to the prevailing winds, taking into account the terrain and the features of the relief. House united in residential groups, made closed courtyard spaces to neutralize constantly blowing winds. Residential houses of a tower type, 9-story houses, as high-storied the buildings, were located in different parts of the districts, on sites with good prospects. They were supposed to bring excitement and flavor to the building [1].

The architecture of residential complexes and individual residential houses of recent years favorably differs from previously erected by professional elaboration and imagery of architectural solutions. Sharply increased the number of stories of residential development. The first five-story houses appeared in the city in 1960, nine-story houses - in 1970, twelve-story - in 1980. By percentage of total number of buildings on 1.01.1989 in the city was 9–12 floors – 4%; 5 floors – 53%; 2 floors –14.5% and one floor – 28.5% [2].

Housing construction 70-80 is different from housing construction in early 1960 with a higher professional study of design solutions, improved layout of apartments and some imaginative expressiveness of the buildings. Changing and silhouette characteristics of the city.

In 1960, the first five-story houses appeared in the city, which occurs the leveling of the building at this level. In the 1970–1980ies built 9-12-story houses, used to highlight urban sites as high-rise dominants [3].

In 1970, the first 9-storey residential building commissioned at the intersection of Monina and Mira streets, according to the typical project 1-447s-41. The dwelling house consisted of one section and had 36 apartments with a total area of 1374 sq. m. The next multi-story residential building commissioned in 1973. Further multi-story housing built every year, therefore the volume of housing construction of small and medium-storied buildings started decrease.

In the 1970s, similar multi-story residential buildings with inexpressive architecture built, but already at this time, architects began to build in and attach various kinds of people serving the population. In those years, it dominated by the type series 9-storey residential buildings 1p-447s-25m. In total, the 70-ies of nine 9-storey residential buildings built.

In the early 1980s built a complex of apartment buildings, located on both sides of the avenue consisted of two pairs of 12-storey and 9-storey single-section residential homes on an individual project. At that time, the complex was differed from the same type of urban development, as the number of floors, and architecture. At mid-1980s put into operation similar houses on the "students" avenue (today Al Farabi Avenue) in the monument district, dedicated to the victims in Afghanistan. It should note that the 80-ies multi-story housing construction is gaining momentum. Fifty-one multi-story apartment house built in the years, mostly 9-storey, in some cases 10-12-storey building. The prevailing model series were 86 and 83 series [4].

3 DEVELOPMENT OF MODERN ARCHITECTURE

With Kazakhstan's independence in 1991, marked the construction of multi-story housing slump, it lasted until the transfer of the capital in 1997 from Almaty to Astana. As a result, there have been dramatic changes in the development of high-rise housing in Astana. The city begins to develop as a capital. Mainly being build individual multi-story residential buildings, the first of them are two 26-storey residential buildings along Bogembai Prospekt, and the people called buildings - "Candles".

In 2000–2001, the development of the planning structure has defined and development of the city in accordance with the General Plan developed by a group of "Saudi Bin Laden" and approved by the Government. The program of this stage included the beginning of work on the formation of a new planning structure of the city, the active demolition of existing dilapidated buildings and the construction of new facilities in their place, corresponding to the metropolitan standards and requirements. Along with domestic construction companies and organizations in the construction of Astana, foreign construction companies began to take an ever more active part.

Significant contribution to the development of Astana, in the formation of its architectural appearance of the building made of Switzerland, Great Britain, the Czech Republic, Turkey and Other De countries. From the beginning Kazakhstan independent, the construction of the new capital of Kazakhstan were active participation of Turkish construction firms: for example, the Turkish construction company «Ahsel Ins. Investment "on-site wetland at the beginning of Republic Avenue in 1999 built a new residential district" Samal "on the 718 apartments.

In order to create a favorable investment climate and attract funds from domestic and foreign companies, in January 2002, the President of the country signed a decree "On Introduction of the Regulations of the Free Economic Zone -" Astana - New City ". As a result, the number of domestic and foreign companies that want to invest in the construction of the new capital of Kazakhstan has sharply increased and take an active part in the construction of modern residential complexes, facilities for maintenance, trade and entertainment. Almost all the construction in Astana, with the exception of social and city facilities, as well as the transport and engineering infrastructure of the city, began financed by private investors. In this regard, it

should be noted these domestic and international investors, property developers, as "Basis-A", "Kuat", "of Bi GROUP», «HIGHVILL», « Ceylan", "Sembol","Okan" and "Axel" that investing considerable funds for the construction of ultra-modern residential complexes and unique buildings and structures, made a great contribution to the formation of an expressive architectural appearance of the new capital of Kazakhstan. However, the President set the task to the designers and builders not just to build a typical, a beautiful city, but the city corresponding to the level of achievements of modern architectural and town-planning ideas, the city XXI century. To the architectural appearance of Astana meet the following requirements - model city XXI century, it was necessary to raise sharply the level of the art-planning solutions to the level of creative search for new directions in the development of architecture. To this end, the outstanding architects of the present began to be involved in the design of the most significant facilities built in Astana on the instructions of the President of the Republic of Kazakhstan. The then President of the International Union of Architects Vasilisa Sgutasa and president of the International Academy of Architecture Georgi Stoilov exerted all possible assistance to the city akimat. Due to their help, a number of world-famous architects took part in international competitions for the development of projects of the most significant facilities in Astana. It has become the practice of the system construction of large projects with urban importance in shaping the architectural appearance of the main streets and squares, only for projects selected in the competition [5].

With the approval of the Government of the Republic of Kazakhstan Astana Master Plan, developed by the research group led by Dr. K. Kurokawa, with the official presentation of the new General Plan as a project embodying the philosophy and theory of urban development postulates XXI century, large-scale work on their active implementation, the formation of a new planning structure and architectural appearance of the city. The main part of construction work was moved to the left side of river Yesil.

In 2004, the Corporation "Basis-A" has commissioned houses "Nurly -Dala" and "Zhan Saya." At the same time, large-scale works developed to reconstruct the old part of the city.

In 2001, commissioned 231 thousand square meters. Meters of housing, and in 2005 – 1 million 67 thousand square meters. The capital housing stock of the capital increased from 4 million 768 thousand square meters in 2000 to 7 million 204 thousand square meters in 2005. In the old part of large-scale demolition of dilapidated housing and construction of modern residential complexes started in the areas of Soldier and Cossack suburb, Central Market, Valikhanov, Potanin Tlendiev and others streets. They began actively build up high-rise residential complexes areas south of the Water-Green Boulevard. Within the framework of the state program "Affordable housing" designed by architects, "Astanagenplan" project organization turned the construction of urban complexes.

In 2006, the corporation "Basis-A" has started construction of a super contemporary multi-functional residential complexes of the original architecture "Emerald Quarter", "Northern Lights" and "Triumph of Astana".

In 2006–2007, there were incompatibility on real of population growth rates and predictions, which led new conditions and opportunities created by the dynamics of the country's economic and social progress. Situation in the city put before the architects and city planners of the capital a number of problematic tasks related to the adjustment of the current master plan and beyond with the corresponding changes in the urban development policy of the city development. Taking into account the analysis of the results of town-planning activities for of the Master Plan, bans made to unreasonably high-density of buildings in of the old part of the city. Due to the growing number of citizens made mandatory as part of the residential complexes and parking buildings including parking at the rate of not less than one parking space per apartment. Also were established strict requirements for compliance with the regulatory density of buildings and insolation of residential apartments and territories.

In order to create conditions that would make buildings mutual and holistic as complex, it was decided to move from the method of "dotted" development of local plots to the method of integrated development of the block or its most part by one investor-developer. An example of such an integrated apartment complexes, "HighVill" and "Grand Astana", erected with all the objects of social and cultural-leisure purpose, necessary for serving the inhabitants of the microdistrict. In 2007, "Astana genplan" in conjunction with the "Kazgor" based on the

study and understanding of international experience developed updated standards of urban planning, designed for the conditions of Astana. In the future, an adjustment of the Master Plan of Astana using urban-regulating documents will carried out only based on these standards, relevant international standards and local conditions.

For the consideration of projects of large objects and the most individual problems, and to develop the most effective strategy was established by President of Kazakhstan urban development of Astana in 2007. The Council, along with well-known architects of Kazakhstan involves the most respected masters of world architecture. All these measures, approaches and principles were the basis for urban development policies pursued by the akimat of the city and the Department of Architecture at the new stage of development of the capital. However, not only the organizational and technical measures and activities influenced architectural appearance of the buildings in this period.

Middle and late of 2010's of XXI century, characterized by the appearance of new factors that raise the architectural appearance of the capital to a new level. Such factor was the active participation of architects around the world to design unique objects of Astana. Currently, the various stages of implementation are objects constructed in a project of outstanding masters of world architecture. Momyshuly prospect were construction it high-rise modern apartment complex. New residential areas with original architecture grows in the southern and western parts of the city.

4 CONCLUSIONS

Capital of Kazakhstan strongly and greatly growing upwards and outwards, causing widespread astonishment and delight. So on based of close cooperation and competition of Kazakh architects with bests of world architecture, powerful innovation, making the necessary adjustments and changes to the adopted programs and plans of construction the Astana – became city of the future, the city of XXI century.

Regional features influence the architecture of residential buildings in the city of Astana and the cities of Northern Kazakhstan: natural and climatic, socio-economic, national, architectural and artistic factors. Recently, much attention has been paid to energy saving and environmental qualities of individual residential buildings.

Housing is an important part of the architectural environment of the city, which reflects the structure of the structure of society, culture and social ties. The global changes of recent decades that have taken place in Kazakhstan require a serious revision of the concept of the formation of an urban, in particular, residential environment.

The option to solve the design problem lies in the field of environmental design of residential buildings. This approach can be justified based on regional features: climatic conditions, local construction conditions and increased use of local materials with a long life. Taking into account all modern trends, a new regional quality should developed based on this principle. Only taking into account regional differences can a cost-effective, individual nature of a residential structure created.

REFERENCES

[1] Akmola: Encyclopedia - Almaty: "Atamura", 1995, 400 p.
[2] Serbinovich P.P. 1985. Architecture of civil and industrial buildings. Civil construction of the building mass. Textbook for building schools. Ed. 2nd Corr and add. M., "Executive. School", 399 p.
[3] Astana Encyclopedia. - Almaty "Atamura", 2008, 576 p.
[4] Kabuldinov Z.E. 2007. History Astana. Tutorial. – Publisher "Arman B". Astana, 130 p.
[5] Olga, S., Aida, S., Elmira, Y., Tatyana, A., Aida, B.Integrated Urban Design. Civil Engineering and Architecturethis, 2022, 10(4), pp. 1631–1640

Smart Geotechnics for Smart Societies – Zhussupbekov, Sarsembayeva & Kaliakin (Eds)
© 2023 The Author(s), ISBN 978-1-003-29912-7
Open Access: www.taylorfrancis.com, CC BY-NC-ND 4.0 license

Vibration characteristics of lightweight embankments converted from bridges on soft ground using polyurethane filling

A. Koyama, D. Suetsugu & Y. Fukubayashi
University of Miyazaki, Miyazaki, Japan

ABSTRACT: A method of filling the lower space of a bridge with rigid polyurethane foam (RPU foam) to reduce the traffic load along with seismic reinforcement is often applied to extend the life of bridges in Japan. The purpose of this study was to evaluate the reinforcement effect and change in the vibration characteristics of a bridge that was converted into a lightweight embankment using RPU foam filling. A truck was driven before and after filling an actual bridge with RPU foam and monitored the embankment behavior. RPU foam was observed to reduce the vibration and strain of the slab at the center of the span. The predominant frequency inside the RPU foam when a traffic load was applied was approximately 5 Hz, and long-period vibration was confirmed compared to the slab.

Enclosed CPI_AR_PDF1.7.joboptions should be used to create the final camera ready copy PDF file. The publisher will reduce camera-ready copies by 75%. For the convenience of the authors, template files for MS Word 6.0 (and higher) are provided. R_PDF1.7.joboptions should be used to create the final camera ready copy PDF file. The publisher will reduce camera-ready copies by 75%. For the convenience of the authors, template files for MS Word 6.0 (and higher) are provided.

1 INTRODUCTION

The maintenance and management of aging bridges has become a worldwide problem in recent years. In Japan, to extend the life of bridges and prevent them from falling, a rare method of filling lightweight embankment materials such as rigid polyurethane foam (RPU foam) and air mortar in the space under the bridge girders is adopted. In this case, as inspecting a bridge is impossible, it is maintained as a lightweight embankment. There is no need for traffic control when compared with seismic reinforcement and the replacement of bridge members. However, the reinforcing effect of bridge members and changes in earthquake resistance owing to the filling of lightweight materials have not been investigated. Among the lightweight materials used in existing construction cases, RPU foam was selected in this study. This is because RPU foam is extremely lightweight (approximately $1/50^{th}$ of the soil weight), and after filling under the girder, it yields a top-heavy structure. Polyurethane foam is a polymer material that is foamable, lightweight, and waterproof (Buzzi et al. 2008). A lightweight embankment method using RPU foam has been independently developed for approximately 30 years in Japan (Koyama et al. 2022). However, in recent years, many unpredictable earthquakes have occurred, including long-period ground and direct earthquake motions. As top-heavy structures are susceptible to long periodic oscillations, it is necessary to elucidate the vibration characteristics of a composite lightweight embankment consisting of bridges and RPU foam. To reduce the earth pressure on the back of the abutment and underground structures, an expanded polystyrene (EPS) geofoam polymer material is installed in the ground (Bartlett et al. 2015). However, the target structure used in this study has bridge members buried in lightweight materials, and the structure itself is very different from that of the previous study.

In this study, to elucidate the structural performance and vibration characteristics of lightweight embankments converted from bridges, trucks were driven before and after filling the

DOI: 10.1201/9781003299127-298

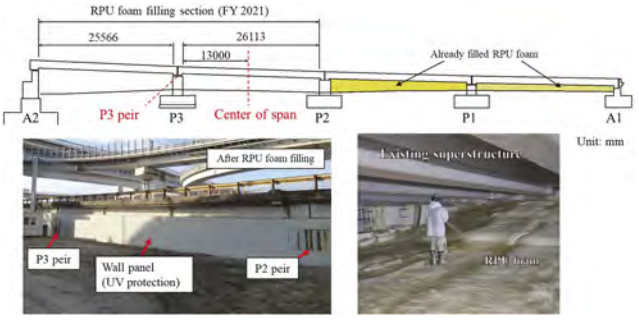

Figure 1. Monitoring target bridges and RPU foam filling process.

bridge on soft ground with RPU foam, and each member was monitored. The load and acceleration generated by slabs, piers, and RPU foam were measured, and the load and vibration reduction effects of the RPU foam were examined.

2 OVERVIEW OF TARGET BRIDGES AND MONITORING METHOD

The bridge to be monitored was an elevated expressway. Figure 1 shows a cross-sectional view of the bridge and the RPU foam filling process. The subdermal space between piers A2 and P2 was filled with RPU foam and reinforced in 2021. We monitored the bridge before and after filling the RPU foam in the section from A2 abutment to P2 pier. Measuring instruments were installed in the center of the span in the section between piers P2 and P3 and near pier P3. This study reports the measurement results at the center of the span. To satisfy the seismic performance of this bridge during a large-scale earthquake, it was necessary to add collapse-prevention devices and seismic reinforcement to large-scale piers. Furthermore, because the foundation ground was soft with a layer thickness of approximately 40 m (N = 4), there was a concern regarding high construction costs. Therefore, despite the reduction in the bearing capacity of the bridge due to disasters or deterioration over time, the substructure was filled with RPU foam to ensure that it could be restored while maintaining traffic capacity. Two-component RPU foam was used in this study. This RPU foam was used in an actual lightweight embankment with a weight of 0.35 kN/m^3. It is assumed that the structural functions of the bridge will be utilized until the superstructure and bearing functions of the existing bridge are lost. Finally, the deadweight is supported only by RPU foam.

Figure 2 shows the installation position of the instrument. The bridge has two lanes on each side, and the driving lane of the down line was monitored. An earth pressure gauge, accelerometer, and strain gauge were installed in series below the slab. To measure the compressive stress at the center of the RPU foam, a steel plate was fixed to the scaffolding at the bottom, and the earth pressure gauge Pu1 was attached to it. The accelerometer Au1 was embedded inside the RPU foam 300 mm above the scaffold. The heat-insulating property of the RPU foam was confirmed using a thermocouple, but the results are omitted in this paper. A 10t truck loaded with iron plates (23.8t in total) was used as the monitoring vehicle. At a speed of 80 km/h, the tire on the right side of the truck passed directly above the instrument. A low-pass filter of 150 Hz was applied for data sampling, and the frequency was set to 1000 Hz.

3 MONITORING RESULTS AND DISCUSSION

This section describes the changes over time of each instrument and the results of the spectral analysis of the acceleration waveform. The change in the sampling data over time is obtained by extracting the data for 5 s before and after the rear wheel of the truck passes through the center of the span, and the running data of the 5th week is shown as a representative.

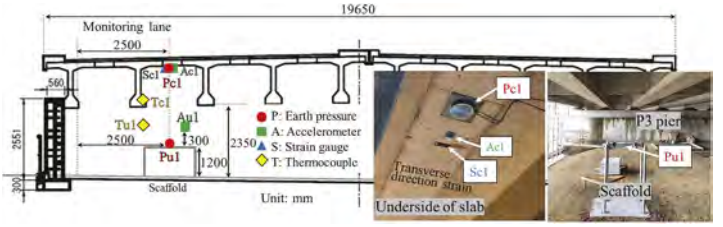

Figure 2. Instrument installation position.

3.1 *Behavior of strain and earth pressure*

Figure 3 shows the changes over time in each strain gauge and earth pressure gauge. From the behavior of the strain gauge in Figure 3 (a), the strain decreased in Sc1 after RPU foam filling. In particular, the strain when the rear wheels passed through the gauge, was reduced by 35%. In addition, Sb1 installed on the slab directly above P3 pier had no change in the strain behavior regardless of the presence or absence of RPU foam because the bearings supported the superstructure. Figure 3 (b) shows the results of the earth pressure gauge. In this study, the earth pressure before running the truck was set to the initial value (zero). It was installed such that a positive value could be obtained when a compressive force acted on the earth pressure gauge. Because an earth pressure of up to 1.2 kPa is generated in Pc1 in the center of the span, the RPU foam supports the superstructure and suppresses deflection. A positive earth pressure of 0.15 kPa was generated in Pu1 when the front wheels passed through Sc1, after which a slight but temporary negative earth pressure was generated when the rear wheels passed through Sc1 and Sb1. Based on this behavior, it is considered that the RPU foam was compressed by the load of the truck in the center of the span, and then deformed to repel when it was unloaded. Moreover, the value of Pu1 was much smaller than that of Pc1, and the load was supported near the surface layer of the RPU foam.

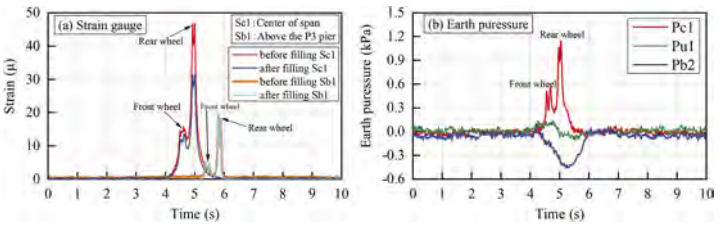

Figure 3. Variation of strain and earth pressure with time.

3.2 *Acceleration waveform and spectrum analysis*

Figure 4 (a) shows the time course of accelerometer Ac1 on the slab in the central part of the span. The accelerometer was installed such that its output were positive and negative values in the vertically upward and downward directions, respectively. The figure shows the time required for a truck to pass through each strain gauge. The positive acceleration shows the maximum value regardless of the presence or absence of RPU foam when the rear wheels pass through Sc1. In addition, the acceleration of Ac1 was reduced to approximately half by the RPU foam in 4 to 6 s, as shown in Figure 4 (a). It is considered that the deflection of the superstructure was reduced and the vibration was suppressed. Figure 4 (b) shows the behavior of Au1 embedded inside the RPU foam. A long-period acceleration waveform was confirmed for Au1. Figure 5 shows the Fourier amplitude spectrum of the acceleration waveform shown in Figure 4, which was subjected to waveform processing by FFT transformation. For Ac1 in Figure 5 (a), multiple dominant frequencies were confirmed between 4 and 35 Hz before filling. After RPU foam filling, the amplitude was particularly reduced to below 5 Hz from–15–20 Hz. The frequency at which the amplitude is the highest before filling is 16.5 Hz, but after filling, it decreases slightly to 14.6 Hz. It is assumed that the flexibility of the RPU foam affects the frequency. In Au1, as shown in Figure 8(b), the components of low-frequency

waves of 1–6 Hz are more prominent than those of Ac1 after filling. These results indicate that the natural frequency of the RPU foam dominates the embankment behavior for vibrations in which long-period components are pre dominates.

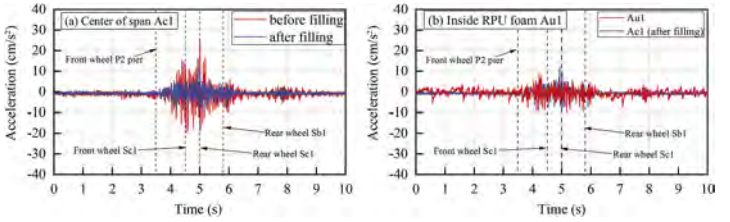

Figure 4. Acceleration waveforms of the slab and inside RPU foam in the center of the span.

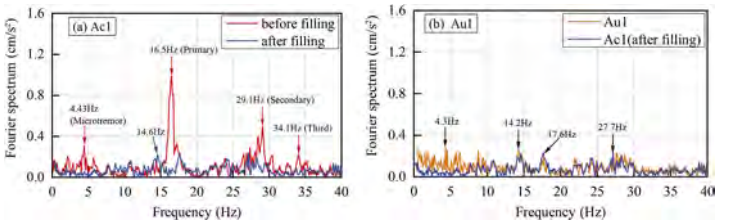

Figure 5. Fourier spectra of Ac1 and Au1.

4 CONCLUSION

The key findings of the present study can be summarized as follows:

1) After filling of RPU foam, the deflection of the slab at the center of the span decreased. However, because the supporting function of the bearing was maintained, the deflection near the bearing did not change regardless of the presence or absence of the RPU foam.
2) The acceleration of the slab after RPU foam filling decreased by approximately half compared with that before filling.
3) Multiple predominant frequencies of the slab were observed at frequencies of 10 Hz and higher. The predominant frequency at the maximum amplitude of the slab decreased slightly because the space under the girder was filled with flexible material. By contrast, low frequencies of 1–6 Hz were predominant inside the RPU foam.

In a future study, we will analyze the monitoring results using FEM analysis and investigate the behavior of the embankment during earthquakes with respect to long-period ground motion.

ACKNOWLEDGEMENTS

This study was financially supported by the NEXCO Group Companies' Support Fund to Disaster Prevention Measures on Expressways. We wish to offer our sincere gratitude.

REFERENCES

Koyama, A., Suetsugu, D., Fukubayashi, Y., Mitabe, H. 2022. Experimental study on the dynamic properties of rigid polyurethane foam in stress-controlled cyclic uniaxial tests. *Construction and Building Materials* 321: 126377.

Bartlett, S. F., Lingwall, B. N and Vaslestad, J. 2015. Methods of protecting buried pipelines and culverts in transportation infrastructure using EPS geofoam. *Geotextiles and Geomembranes* 49: 1380–1392.

Buzzi, O., Fityus, S., Sasaki, Yand Sloan, S. 2008. Structure and properties of expanding polyurethane foam in the context of foundation remediation in expansive soil, *Mechanics of Materials* 40 (12):1012–1021.

Smart Geotechnics for Smart Societies – Zhussupbekov, Sarsembayeva & Kaliakin (Eds)
© 2023 The Author(s), ISBN 978-1-003-29912-7
Open Access: www.taylorfrancis.com, CC BY-NC-ND 4.0 license

Integrity and restoration of soil structures damaged by the 2016 Kumamoto earthquake

D. Suetsugu
University of Miyazaki, Miyazaki, Japan

K. Sahara
Hirose Hokyodo & Co., Ltd., Okinawa, Japan

T. Konami
Okasanlivic Co., Ltd., Tokyo, Japan

N. Fukuda
Shin-nihon Consulting Engineers Co., Ltd., Kagoshima, Japan

F. Hirae
Nippon Chiken Co., Ltd., Fukuoka, Japan

ABSTRACT: During the 2016 Kumamoto earthquake, which caused two seismic intensities of seven for two days, numerous severely damaged infrastructures were constructed in the vicinity of active faults. Most of these structures have now been reconstructed and are currently in service. In such areas, it is necessary to consider the minimization of the damage as much as possible in the event of future seismic motion or ground surface displacement. In addition, if the deformed structure can avoid collapse, it is necessary to evaluate its integrity for its use. In this study, surveys were conducted on two types of structures: a steel strip reinforced soil wall and an expanded polystyrene lightweight embankment located near active faults that was damaged during the Kumamoto earthquake. The methods were used to evaluate the integrity of the structures and the policies and methods of reconstruction.

1 INTRODUCTION

In April 2016, two severe earthquakes occurred in two days, M6.5 and M7.3, with seismic intensities of seven, centered in Kumamoto. The earthquakes caused extensive damage to numerous soil structures in a wide area of Kumamoto Prefecture. The structures near the active faults were subjected to earthquake motion and ground displacement. This study investigated the methods of integrity evaluation and restoration for two types of soil structures: a steel strip reinforced soil wall and an EDO-EPS (by EPS Development Organization, hereinafter referred to as EPS) lightweight embankment located near active faults damaged during the Kumamoto earthquake, as shown in Figure 1.

2 DAMAGE AND RESTORATION OF REINFORCED SOIL WALL

2.1 *Damage of a reinforced soil wall immediately after the earthquake*

The partially collapsed reinforced soil wall with steel strip reinforcements was constructed along the Nigori River on Prefectural Road No. 149, and numerous earthquake-induced damages and

DOI: 10.1201/9781003299127-299

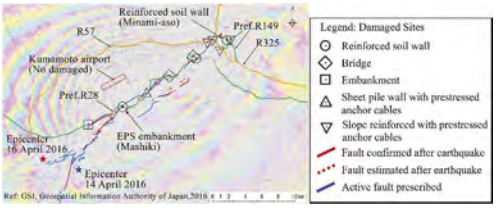

Figure 1. Damaged structures along the active fault shown on an InSAR analyzed map by Geospatial Information Authority of Japan.

ground deformations occurred around the site. As shown in Figure 2, the reinforced soil wall had a mixture of collapsed and remaining sections within the same wall alignment. The characteristics of the wall are as follows: (i) River flows in front of the wall, and gravity concrete trestles are used as the foundation. (ii) The plane alignment of the wall is a folded line and the collapsed wall is at the protraction zone. (iii) The section of the collapsed zone had two overburden layers, whereas the remaining area had one overburden layer. (iv) The adjacent wall of the completely collapsed wall retained an unstable self-supporting condition. Although approximately 20 years have passed since construction, no significant deterioration was observed in the reinforcements and facings.

Figure 2. Condition of remaining and collapsed reinforced soil wall and plane alignment of wall.

2.2 *Evaluation of integrity by close visual inspection*

The visual inspection points of the reinforced soil walls include the road pavement condition, embankment deformation above the wall, wall-facing deformation, embankment material leakage between wall-facings, and foundation ground stability. After close visual inspection of the reinforced soil wall, an emergency damage assessment was performed to evaluate the current condition on a 6-level risk scale. The collapsed and severely deformed sections of the reinforced soil wall in this study correspond to the VI level of damage. However, the remaining sections correspond to sections I (no damage) to II (partial damage). Therefore, it is necessary to verify the difference in the condition of the remaining sections compared to the collapsed and severely deformed sections and to evaluate the integrity of the remaining sections before putting them into service in the future.

2.3 *In situ pull-out test with core extraction*

It is difficult to ascertain the internal conditions of the reinforced soil wall. However, it is possible to confirm the internal stability of the wall by pulling out the reinforcement directly through the concrete facing a drilled hole that is in turn facing the remaining wall, as shown in Photo 2. Because the original design documents could not be found from the field pull-out tests of the two sites, structural stability calculations were performed based on the site conditions to estimate the density and length of the installed reinforcement. The results of the pull-out resisting force at the first site were 60 kN at the site (>54 kN at the design site), and at the second site, 45 kN at the site (>33 kN at the design site) confirmed that the pull-out resistances were greater than the assumed design pull-out load. From the in situ pull-out tests, the steel-strip-reinforced soil wall was confirmed to be internally stable.

2.4 *Measuring wall displacement with a laser rangefinder*

Because each wall facing the reinforcement is stacked without rigid connections, reinforced soil walls are flexible and allow a certain degree of deformation. The degree of deformation was within 3% of the wall height and 30 cm between the top and foot of the wall. To confirm the wall condition, the displacement of the wall was measured using a laser rangefinder.

Figure 3. In situ pull-out test and displacement measurement of wall facings by laser rangefinder.

The measurement locations and results are shown in Figure 3. The maximum difference between the displacement and area near the foundation occurred at a medium wall height and reached more than 3% of the wall height. The integrity of the large deformation area was not secured, and the wall was removed and reconstructed.

2.5 *Status of restoration and future issues*

The reconstructed section, compared with the collapsed and remaining sections, and the completion of the wall are shown in Figure 4. The collapsed section was removed, and the large deformed section was reconstructed by removing staircase-like wall material. In this study, the existence of a fracture zone was revealed by a γ-ray survey (Sahara, K., et al., 2019). Future issues include how to conduct a collapse investigation at the time of planning and how to utilize the results for restoration design.

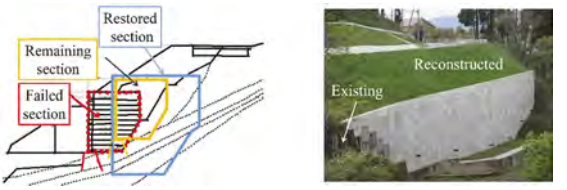

Figure 4. Comparison of sections between collapsed, remained, and reconstruction as a photo.

3 DAMAGE AND RESTORATION OF EPS EMBANKMENT

3.1 *Damage of EPS embankment immediately after the earthquake*

The damaged EPS embankment on the prefectural road along the Kumamoto Takamori line was located directly above an active fault (Futagawa-Hinaku fault zone), as shown in Figure 5 (Taneichi, K., et al., 2018). As shown in the figures, the road surface had an 80 cm wide crack, a 50 cm differential settlement, and a 30 cm horizontal displacement. In addition, the foundation of the EPS embankment subsided locally by approximately 90 cm, and the wall-facings in the heavily subsided section fell off.

An 18 m wide surface slide occurred on the slope just behind the damaged EPS embankment.

Figure 5. Damage of EPS embankment affected by active fault.

3.2 *Methods of reconstruction*

The EPS embankment and the slope behind it collapsed owing to the earthquake and subsequent heavy rainfall. Therefore, countermeasures were taken for the surrounding areas, including the EPS embankments. The slope above the ground anchors was protected by surface protection. The collapsed lightweight embankment was designed in accordance with the "EDO-EPS Method of Design and Construction Standards (Draft)". The EPS embankment had $H/B = 0.76 \leq 0.8$ and $H = 5.8$ m ≤ 6 m. Generally, seismic design can be omitted for embankments; however, because this line has already been severely damaged by an earthquake, seismic design was applied. Based on the ground investigation, stability was examined using the standard value of the design horizontal seismic coefficient for ground type III ($k_{h0} = 0.15$) and the design horizontal seismic coefficient ($k_h = 0.13$) based on the regional correction factor $C_Z = 0.85$.

The stability did not satisfy the bearing capacity under normal conditions and stability against sliding under seismic conditions. Therefore, root piles were used as the foundation to satisfy the bearing capacity under normal conditions, and horizontal force deterrents due to nailings were used to integrate the upper slab with the background to prevent sliding during the earthquakes. Figure 6 shows the designed cross section and front view of the reconstructed EPS embankment.

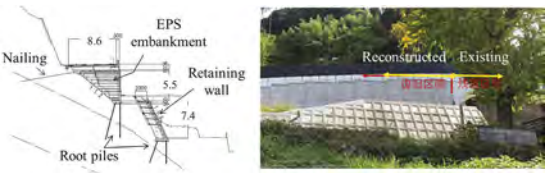

Figure 6. Designed cross section and front view of restoration of EPS embankment.

4 CONCLUSION

This paper introduced a case study on the restoration of two heavily damaged soil structures located near the active faults caused by the Kumamoto earthquake. The integrity of the reinforced soil wall was evaluated based on on-site tests for the remaining wall, and the wall was reconstructed using a seismic design. A new seismic design was applied to an EPS lightweight embankment. It is necessary to verify the earthquake resistance of structures that have been improved and reconstructed when they are subjected to seismic ground motion and ground displacement. Furthermore, we believe that the analysis of reconstruction measures for structures damaged by earthquakes will be useful for quick reconstruction from similar earthquake damage in the future.

ACKNOWLEDGMENTS

This study was part of the research conducted by the Research Committee of JGS-Kyushu. For this research, we received convenience from the Kyushu Regional Bureau of the Ministry of Land, Infrastructure, Transport and Tourism, and Kumamoto Prefectural Government. We also received financial support from the Kyushu Kensetsugijutsu Kanrikyokai. The authors hereby express their sincere gratitude.

REFERENCES

Sahara, K., Suetsugu, D., Fukuda, N., Yoshimura, T., Sato, H. & Hirae, F. 2019. Fracture zones effect for a failed reinforced soil wall induced by severe ground motion during 2016 Kumamoto Earthquake, *Proc*. 16 *ARC, Taipei, Taiwan*: WED-P2-006_JGS-082.

Taneichi, K., Konami, T., Tsukamoto, H., Kubota, T. & Yasuhara, K. 2016. Opening Traffic for a Temporarily Remediated EPS Road After the 2016 Kumamoto Earthquake: A World First, *Proc. EPS* 2018: 351–359.

Smart Geotechnics for Smart Societies – Zhussupbekov, Sarsembayeva & Kaliakin (Eds)
© 2023 The Author(s), ISBN 978-1-003-29912-7
Open Access: www.taylorfrancis.com, CC BY-NC-ND 4.0 license

Case study of slope failure and early warning system of landslides induced by heavy rainfall in Tajikistan, Central Asia

Avzalshoev. Zafar
Ph.D. candidate, Geotechnical and Geosphere Research Group: GREG, Saitama University, Saitama Japan

Taro. Uchimura
Professor, Geotechnical and Geosphere Research Group: GREG, Saitama University, Saitama, Japan

ABSTRACT: In the current paper, the author would like to present the most common annual natural hazard hitting Tajikistan: landslides. Although Tajikistan is landlocked, it is prone to many natural hazards such as earthquakes, liquefaction, rockfall, avalanches, and mudflow. Previous researchers investigated landslides induced by earthquakes. However, in this paper author would like to focus on landslides and mudflow caused by heavy rainfall. Especially now, due to climate change and global warming, glaciers melt, and the intensity of rains eventually increases the frequency of landslides. Per the Tajik Glavgelogy, annually 50, 000 landslides have been reported all over the republic, including both seismic and non-seismic. Thus, this paper analyzes the case study from a geotechnical perspective and suggests early warning systems to prevent such threats in the future.

1 INTRODUCTION

The current paper aims to define the reasons and possible mitigation measurements for the most common natural disaster-landslides occurring annually in Tajikistan. In particular, section 6 of Obigarm – Nurabad road. Tajikistan is prone to many natural hazards, such as earthquakes, liquefaction, rockfall, avalanches, and mudflow. Previous researchers investigated landslides induced by earthquakes. However, in this paper author would like to focus on landslides caused by heavy rainfall.

It has been recorded by Tajik Glavgelogy that annually 50, 000 landslides have been reported all over the republic, including both seismic and non-seismic.

Although landslide hazard analysis has a long history in Central Asia, mainly the earlier publications were in Russian Fedorenko (1988), eventually stuck around, and were either never published or buried. In addition to that, a large amount of data was stored and never shown due to security requirements. Even if it was published somewhere, most figures were presented without identification, making them almost useless for further studies Havenith (2013).

Table 1. List of prominent landslides in the last 50 years technical background of the site.

Date	Disaster type	Total death	Total affected
13.05.1992	Landslide	243	24100
07.05.1993.	Landslide	5	75357
19.11.1997	Landslide	40	not available
13.04.2003	Landslide	1	6000
03.02.2005	Landslide	16	1853
26.01.2006	Landslide	21	728
03.04.2015	Landslide	10	not available

DOI: 10.1201/9781003299127-300

Table 1 shows all types of landslides, seismic and non-seismic, that have occurred in Tajikistan in the last 50 years Emergency and Disaster Reports (2018).

1.1 *Background*

This paper presents attributes of investigated area based on geological and metrological aspects. Due to the new road construction crossing the studied area, it is essential to propose mitigation and early warning systems to prevent landslides after construction.

1.2 *Geological background*

The current section of the road is a landslide-prone massif. The length of the area is about 315 m. There is no precise orientation of the cracks; they are located randomly. The soils are stable in a dry state; they become subsiding and easily eroded when moistened. Landslide processes are strongly developed on the section of the route; during periods of rain, they are activated.

The slope is flooded, as evidenced by small springs. The springs are located on the upper slope of the road.

Figure 1 illustrates the location of the investigated site and its geological condition. In the current area, the predominant type of soil is loam.

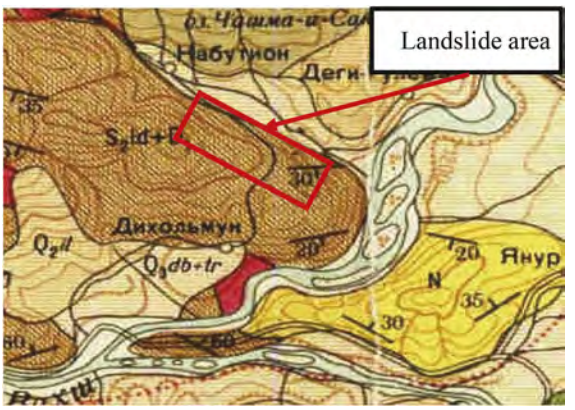

Figure 1. Geological map of the investigated area.

The following rock complexes are distinguished: a. Cover loose deposits of sandy-loamy soils with the inclusion of coarse-grained material, b. rocky soils, limestones, conglomerates, siltstones.

Figure 2(a) demonstrates the field condition and slope failure during the investigation. Figure 2(b) shows water infiltration through the slope induced by rainfall and springs.

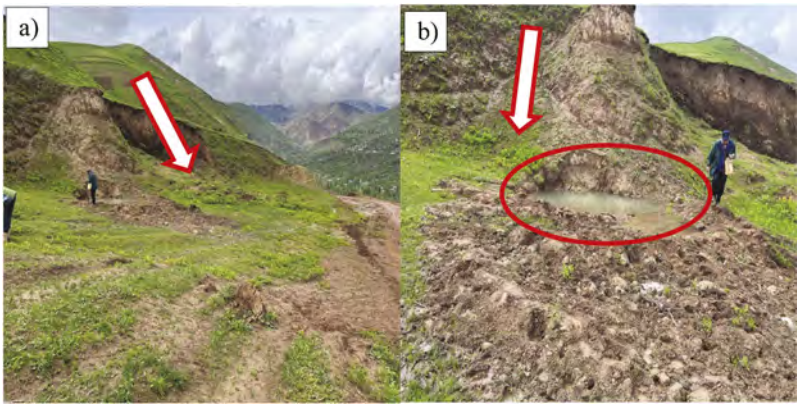

Figure 2. Field photos of the investigated area, a) slope failure, b) infiltration of the water.

1.3 *Hydrological background*

Underground waters are opened at depths from 0.5 m to 6.5 m. Groundwater is of a porous type and occurs sporadically in loose Quaternary formations and comes to the surface in the form of springs of seasonal manifestation.

The rock formations that make up the area are characterized by dip angles of up to 30° and large fractures, which is why no aquifers are sustained over the place. The formation and accumulation of groundwater in this area are associated with precipitation in the form of rain and snow.

2 EARLY WARNING SYSTEM

2.1 *Current condition*

A landslide is a mass of rock, debris, or soil moving down a slope under gravity Cruden, (1991). Not only in Central Asian countries but worldwide, landslides cause significant damage and casualties annually. Brabb (1993) persevered that 90% of landslide damage can be avoided if the risk is recognized before the landslide event. The first successful prediction by Saito (1965) used a model where the time to failure in the tertiary creep phase was inversely proportional to the current strain rate. Further, based on Saito's model, Fukuzono (1985) introduced an extended model expressed as the displacement's inverse velocity.

2.2 *Monitoring system*

Monitoring slope failure is considered one of the best options for predicting slope failure. Monitoring rainfall intensity is widely used as a warning system. There have been proposed lot of applications based on real-time rainfall records. The Japan Meteorological Agency has developed a Soil Moisture Index (SMI) as a more appropriate index to represent the virtual moisture content in slope grounds Uchimura (2015). It is calculated by assuming a three-tank model for the infiltration and drainage process of rainwater Ishihara & Kobatake (1979), Okada (2001). However, monitoring only the rainfall intensity is not enough. Monitoring each slope's characteristics along with the rainfall is more reliable. Displacement or deformation of the slope is the most commonly observed property Uchimura (2015). At the moment, extensometers shown in Figure 3(a) are the most widely used equipment for monitoring the displacement of the slope surface. Although this type of sensor is less costly than the construction of retaining walls or other structures, there are still some disadvantages.

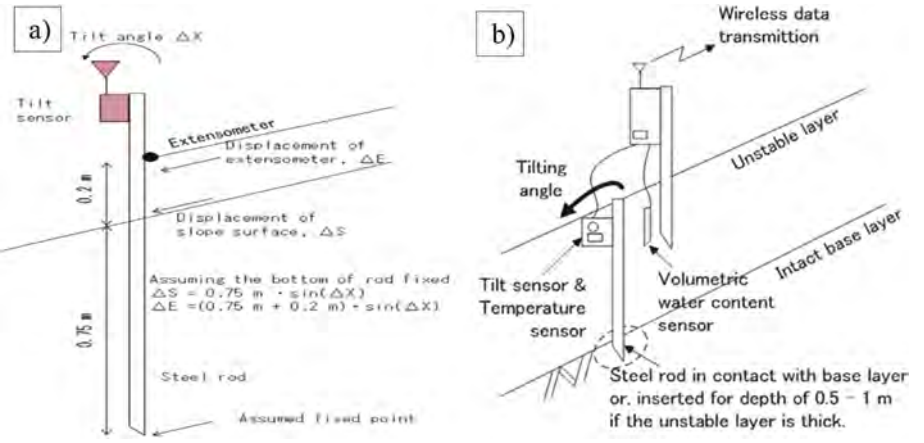

Figure 3. Slope monitoring equipment a) extensometer, b) tilt sensor, Micro Electro Mechanical Systems (MEMS), Uchimura (2015).

Considering new development techniques and previous experiences, Uchimra (2015) proposed a simple monitoring system with Micro Electro Mechanical Systems (MEMS), shown

in Figure 3(b) technology, that can measure the tilt angles (rotations) in the unstable surface layer of slopes. The proposed system is primarily suitable for detecting the pre-failure stages of surface failures with shallow slip surfaces. Based on the obtained results, Uchimura (2015) suggests that a precaution be issued at a tilting rate of 0.011 per hour and that a warning be issued at a tilting rate of 0.11 per hour to be on the conservative side.

3 CONCLUSION

From the case study presented in the current paper author would like to highlight the following findings:

I. The landslide length in a current case study is 300m – 315m. Landslide due to heavy rainfall occurs annually in Tajikistan. In most cases, an unstable layer is affected by the continuous rain that infiltrates through the top layer. On the bottom layer effect of the capillary barrier may occur that triggers the displacement of the unstable layer.
II. It has been recorded that there are springs inside the ground, affecting the slope stability jointly with seasonal rainfall. Consequently, it triggers the failure of the slope, which is the main reason for the collapse in such a hilly area of the country.

In most cases, individual slope failure is not studied well in Tajikistan. Typically, typical stabilization methods are promoted and applied for most slopes; however, from a geotechnical perspective, it is incorrect. Therefore, the author would like to suggest implementing the monitoring system and strengthening activities.

The author would like to focus on a monitoring system of slope displacement that should be implemented through the current case study.

ACKNOWLEDGMENTS

All the field studies were done by GUP "IPTS," to whom the author would like to express his gratitude. In addition, the author would like to thank Professor Taro Uchimura for his continued support and advice.

REFERENCES

1. Emergency and Disaster Reports. ISSN 2340-9932 Vol 5, Num 3, (2018)
2. Fukuzono, T., 1985. A new method for predicting the failure time of a slope. In: Proceedings of the IV International Conference and Field Workshop on Landslides, Tokyo, pp. 145–150.
3. H.B. Havenith. Geomorphology (2013), researchgate. Tien Shan geohazards database: Earthquake and landslides.
4. N.R.Ischuk Natural Hazards in Tajikistan, Dushanbe, Tajikistan, OSCE Technical Report. (2016)
5. Perov. V.F Mudflow studies. Moscow State University, pp. 271, (2012)
6. Taro Uchimura, Ikuo Towhata, Lin Wang, Shunsaku Nishie, Hiroshi Yamaguchi, Ichiro Seko, Jianping Qiao. 2015. Precaution and early warning of the surface failure of slopes using tilt sensors. Soils and Foundations 2015;55(5):1086–1099.
7. Uchimura, T., Towhata, I., Wang, L., Seko, I., 2009. Development of a low-cost early warning system of slope instability for civilian use. In: Proceedings of the 17th ISSMGE, Alexandria, vol. 3, pp. 1897–1900.
8. Uchimura T, Suzuki D, Hongkwan S (2011) Combined moni- toring of water content and displacement for slope instabilty. In: Proceedings of 4th Japan-Korea Geo- technical Engineering Workshop, Japanese Geotechnical Society, Kobe, pp.67–72
9. UNDAC Mission Disaster Response Preparedness in Tajikistan (2006).

Smart Geotechnics for Smart Societies – Zhussupbekov, Sarsembayeva & Kaliakin (Eds)
© 2023 The Author(s), ISBN 978-1-003-29912-7
Open Access: www.taylorfrancis.com, CC BY-NC-ND 4.0 license

Remote, safe and cost-efficient observations and assessment of geohazard subsidence risks for Kazakhstan energy industry (case study: Tengiz oilfield)

E. Bayramov
School of Mining and Geosciences, Nazarbayev University

M. Buchroithner
Institute for Cartography, Dresden University of Technology

M. Kada
Institute of Geodesy and Geoinformation Science, Technical University of Berlin

A. Duisenbiyev
Kazakh-British Technical University, Kazakhstan Maritime Academy

Y. Zhuniskenov
School of Mining and Geosciences, Nazarbayev University

S. Aliyeva
ADA University

ABSTRACT: Tengiz oilfield was selected as a study area for the present research because of its historically reported continuous subsidence and limited studies for this area during recent years. This study focused on the quantitative assessment of the vertical displacement velocities retrieved using Sentinel-1 and Cosmo-SkyMed synthetic aperture radar images for the Tengiz oilfield. The small baseline subset time-series technique was used for the interferometric processing of radar images acquired for the period of 2018–2020. The geospatial and statistical analyses allowed to determine the existing hotspots of the subsidence processes induced by oil extraction in the study area. Ground deformation measurements derived from the Sentinel-1 and COSMO-SkyMed satellite missions showed that the Tengiz oilfield continuously subsided during 2018–2020 with the maximum annual vertical displacement velocity around −77.4 mm/y and −71.5 mm/y, respectively. The vertical displacement velocities derived from the Sentinel-1 and the COSMO-SkyMed images showed a good statistical relationship with $R^2 \geq 0.73$ and RMSE ≤3.68 mm. The cumulative vertical displacement derived from both satellites for the most subsiding location also showed a good statistical relationship with R^2 equal to 0.97 and RMSE = ± 4.69. The observed relative differences of measurements by both satellites were acceptable to determine the ongoing vertical surface displacement processes in the study area. These studies demonstrated a practical novelty for the petroleum industry in terms of the comparative assessment of surface displacement measurements using time-series of medium-resolution Sentinel-1 and high-resolution COSMO-SkyMed radar images.

1 INTRODUCTION

Tengiz oilfield is located at the coast of the Caspian Sea with low-lying wetlands. The recent successful studies by (Bayramov et al. 2021; Grebby et al. 2019 and Orynbassarova 2019) proved that the Tengiz oilfield was under the impact of ground deformation processes induced by the petroleum and gas operational activities.

DOI: 10.1201/9781003299127-301

Nowadays, industry significantly benefits from the ground deformation mapping as one of the important advancements for the surveillance programs of onshore oil and gas reservoirs. It is well known that the interferometric technologies were verified as effective for the measurement of the sensor-to-target line of sight projection of the ground deformation mapping of large onshore reservoirs rather than traditional in-situ measurements using geodetic tools (Zhou et al. 2006; Mirzaii et al. 2019). The studies by Grebby et al. (2019) and Orynbassarova (2019) clearly indicated the vertical displacements caused by oil and gas exploitation in the Tengiz oilfield during 2004-2009 and 2016-2017, by using Envisat and Sentinel-1 radar images, correspondingly. The investigations by Grebby et al. (2019) and Orynbassarova (2019) applied the Intermittent Small Baseline Subset (ISBAS) method from Sowter et al. 2013 which contributed to the determination of the continuously increasing cumulative vertical displacement (maximum of -79.3 mm/year) in the Tengiz oilfield during 2016–2017.

To the extent of our awareness, there have been few publically accessible studies on the multi-satellite monitoring of vertical displacements in the Tengiz oilfield, in particular with the focus on the comparative assessment of vertical displacements derived from multiple Sentinel-1 and Cosmo-SkyMed Synthetic Aperture Radar (SAR) imagery.

Our research specifically focused on the assessment of vertical displacements derived from COSMO-SkyMed and Sentinel-1 SAR imagery using SBAS multi-temporal interferometric technique and geostatistical interpolation techniques followed by the cosine corrections to derive vertical movements from LOS measurements. The primary advantage of the present research is to quantitatively examine the differences in vertical displacement measurements using C-band Sentinel-1 and X-band Cosmo-SkyMed SAR imagery since in-situ geodetic measurements were not accessible for the present research. The detailed goals of the present research are as follows:

1) SBAS-based detection of vertical displacement hotspots using COSMO-SkyMed and Sentinel-1 imagery acquired during 2018–2020
2) Quantitative analyses of the vertical displacement velocities and cumulative vertical displacement derived from Sentinel-1 and COSMO-SkyMed satellite images
3) Determination of spatial relationships between the detected patterns and the hotspots of vertical displacements, wells and faults

2 DATA PROCESSING

2.1 *Research area*

Tengiz oilfield is one of the largest in the world and it is located at the coast of the Caspian Sea with an area of 2,500 km2 (Figure 1a and b). The climate in the study area is semi-arid with temperature range −30 °C - 40° in summer and winter, respectively. The average annual precipitation is in the range of 100–200 mm (Klein et al., 2012). Tengiz field is located in the seismically active region of Kazakhstan. The seismic faults derived from (Anissimov et al. 2000) are indicated in Figure 1. According to (Grebby et al. 2019), the reservoir is estimated to be around 25 billion barrels of oil and is located at the depth of 3885–5117 m. High pressure with large proportion of gas was observed in the oil coming out of wells. The production is estimated to be 720,000 barrels per day. Sour gas injection enhanced oil recovery method is used in the Tengiz oilfield (Bealessio et al. 2020).

2.2 *Quantitative assessment of vertical displacement in the Tengiz Oilfeld using SBAS processing of Sentinel-1 and Cosmo-SkyMed images*

Sentinel-1 A/B TOPS with C-band (5.6 cm wavelength and 5.4 GHz) images from the European Space Agency (ESA) and COSMO-SkyMed (CSK) with X-band (3.1 cm wavelength and 9.6 GHz) from the Italian Space Agency were used for the present study to assess the vertical displacement velocities and cumulative vertical displacement in the Tengiz oilfield. The extents of the Sentinel-1 and COSMO-SkyMed imagery are presented in Figure 1b. 96 Sentinel-1 images were acquired on descending Path 35, Frame 441, Absolute Orbit 30,557 in the TOPSAR Interferometric Wide Swath (IW) mode, with VV + VH Polarization between 1 January 2018 and 31 December 2020

Figure 1. (a) Tengiz oilfield with the representation of wells and faults; (b) Extents, count and acquisition period of Sentinel-1 and COSMO-SkyMed imagery.

(Figure 1b). VV polarization band of Sentinel-1 was used because of a higher coherence (Imamoglu et al. 2019). Sentinel-1images in wide-swath mode provide a wide coverage of about 250 km with a range resolution of 5 m and an azimuth resolution of 20 m (Yang et al. 2019).

87 COSMO-SkyMed images were acquired on descending Frame 2, Absolute Orbit 39,000 in the interferometric StripMap HIMAGE mode with HH polarization between 1 January 2018 and 31 December 2020. HH polarization band of COSMO-SkyMed that was only available had been used for the present research. COSMO-SkyMed images in StripMap Himage mode provide coverage of about 40 km with a range resolution of 3 m and an azimuth resolution of 3 m (Tapete and Cigna 2019) (Figure 1b). Descending tracks of Sentinel-1 and COSMO-SkyMed satellite images provided a complete coverage of the Tengiz oilfield.

SBAS - based interferometric processing technique was used for the assessment of the vertical displacement. SBAS workflow is presented in Figure 2 with the following processing steps: creation of a connection graph, definition of AOI, generation of interferograms, refinement and reflattening, first inversion, second inversion and geocoding (Loesch and Sagan 2018; Sarmap 2021).

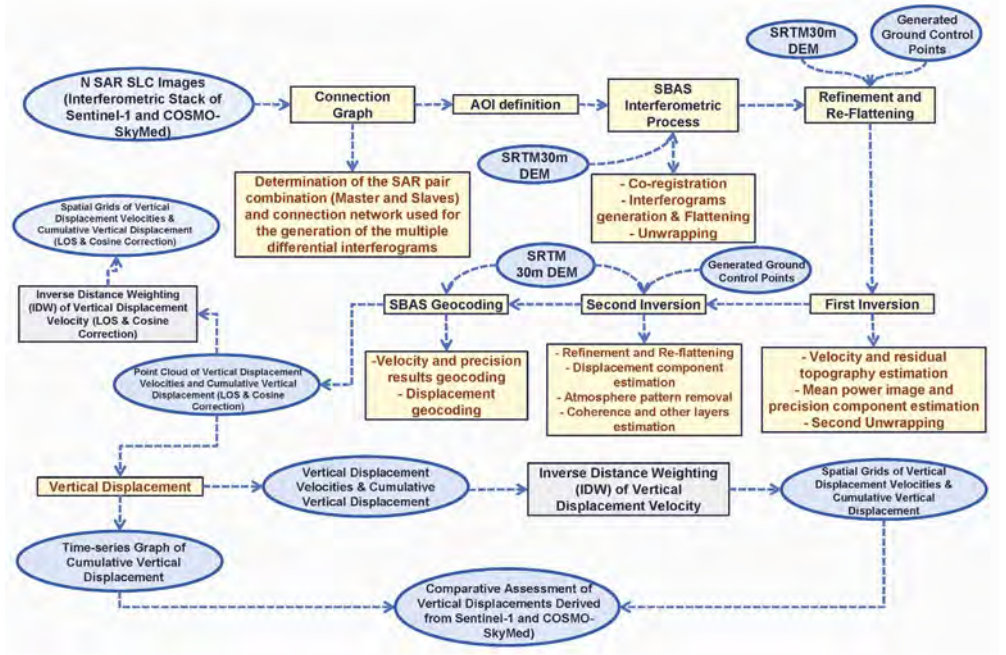

Figure 2. Workflow of SBAS interferometric processing followed by the cosine correction for the assessment of vertical displacements and spatial interpolations.

3 RESULTS

LOS displacement velocity derived from the Sentinel-1 radar satellite images was observed to be in the range of − 58.9 - 22.7 mm/y (Figure 3a). The vertical displacement velocity derived through the division of the LOS displacement rates by the cosine of the radar incidence angle is presented in Figure 3b with the range of −77.4 - 29.4 mm/y. The spatial distribution histogram of the measured LOS and vertical displacement velocities derived from the cosine corrections are presented in Figure 3c. It is possible to clearly observe the prevailing number of pixels with negative values which confirms the ongoing subsidence in the Tengiz oilfield.

The hotspot of significant subsidence can be observed at the crossing of profile lines in Figure 4a. The same location was observed to be as the most subsiding. As it is possible to observe in Figure 4b, the maximum annual subsidence velocity along the profiles reaches about −70 mm/y. The cumulative vertical displacement is shown in Figure 5a with the range of −243.7 - 79.9 mm. The maximum cumulative vertical displacement along the profiles on 23 December 2020 reaches − 235 mm (Figure 5b).

Unfortunately, because of no accessibility to the historical in-situ high-precision geodetic measurements in the present research, it was not possible to validate the reliability and accuracy of the SBAS measurements derived from the Sentinel-1 images. Therefore, it was considered to use the COSMO-SkyMed images for the cross-validation of measurements from both satellites. The processed area of the COSMO-SkyMed images was limited to the subsiding hotspots derived from the processing of the Sentinel-1 images. The spatially interpolated vertical displacement velocity derived from the COSMO-SkyMed images is presented in Figure 6a. Figure 6b presents the spatial distribution of SBAS measured points derived from the COSMO-SkyMed and the Sentinel-1 images. These points with measured vertical velocities were used in the interpolation of spatial grids used in the comparative analysis (Figure 6a). The enhanced view of the vertical displacement velocity derived from the COSMO-SkyMed images and profile lines are presented in Figure 6c. The histogram of negative vertical displacement velocities derived from the COSMO-SkyMed images is presented in Figure 6d. This implies that the SBAS analyses using the COSMO-SkyMed images also showed the subsidence processes in the same hotspot detected by the processing of the Sentinel-1 images.

The profiles of the vertical displacement velocities derived from the Sentinel-1 and the COSMO-SkyMed images are presented in Figure 6c and Figures 7a–d. As it is possible to observe, the vertical displacement velocities derived from the Sentinel-1 and the COSMO-SkyMed images for the Profile 1 showed a good statistical relationship with R^2 equal to 0.93, p-value < 0.05, RMSE equal to ±2.86 (Figures 7a and b). Good statistical relationship was also observed for the Profile 2 with R^2 equal to 0.73, p-value < 0.05, RMSE equal to ±3.68 (Figures 7c and d). The standard deviation of the phase calculated over the profiles 1 and 2 was observed to be 8.9 for profile 1 and 7.9 for the profile 2 (Figures 7a and c).

The location for the maximum subsidence derived from the Sentinel-1 images is presented in Figure 8a. The cumulative vertical displacement derived from the Sentinel-1 and the COSMO-SkyMed images for the most subsiding location are presented in Figure 8b. The cumulative vertical displacement in the most subsiding location reaches around 245 mm on 23 December 2020 (Figure 8b). The regression analysis between the cumulative vertical displacements derived from the Sentinel-1 and COSMO-SkyMed images for the most subsiding location showed a strong statistical relationship with R^2 equal to 0.97. This was also reflected in RMSE = ± 4.69 and p-value < 0.05. This allows to conclude that SBAS produced identical results from the Sentinel-1 and the COSMO-SkyMed images. It is obvious that the ground deformation measurements from the COSMO-SkyMed images are more detailed because of the higher spatial resolution of images.

Since the hotspot of the most subsiding areas is not anyhow spatially related to the concentration of wells, it is possible to assume that the primary factors controlling the vertical displacements in the Tengiz oilfield are the oil and gas extraction industrial processes and natural subsurface tectonics. However, it is possible to observe that a number of wells are located within the detected hotspot of the subsidence in Figure 8a. The oil terminal is located outside of the subsidence hotspot (Figure 1a; Figure 8a) and it is obviously less vulnerable to the potential geohazards.

Besides these areas are crossed by faults which might be subject to the potential reactivation (Figure 8a). Hence, some of the wells located within the detected subsidence hotspot should always be prioritized for the regular geotechnical and geohazard risk assessment.

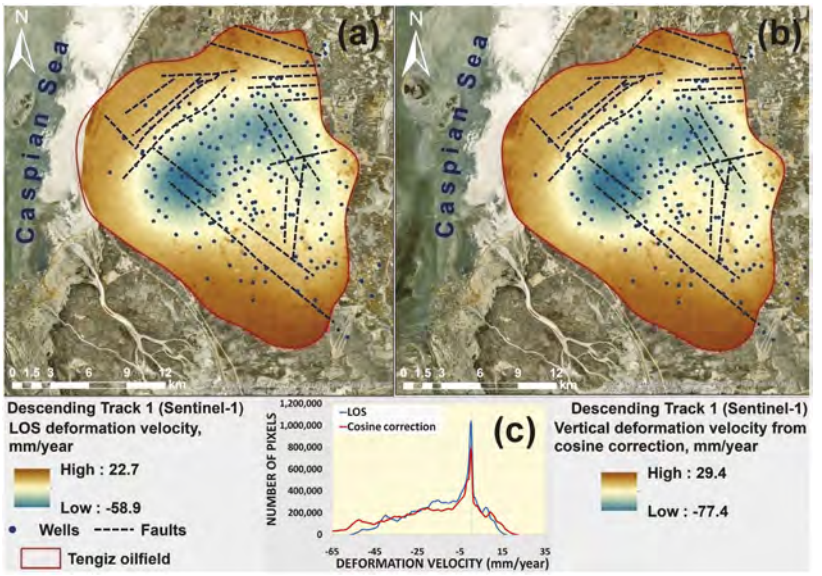

Figure 3. (a) LOS and (b) vertical displacement velocity from cosine correction of the Tengiz oilfield; (c) Histogram of LOS and vertical displacement velocity.

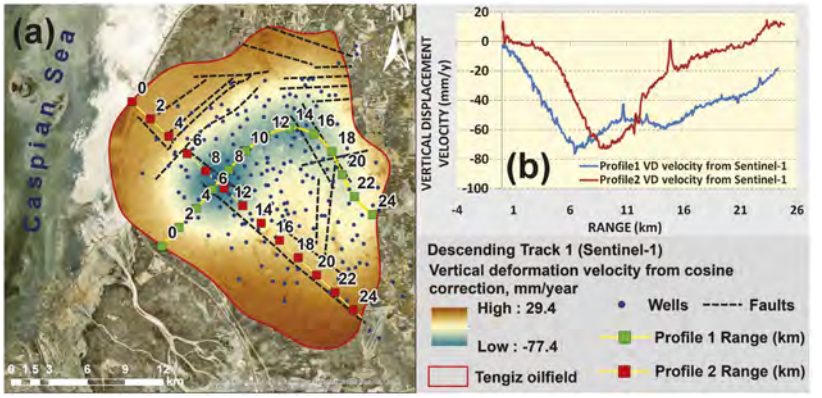

Figure 4. (a) Map of vertical displacement velocity derived from the Sentinel-1 images with the indication of profile lines; (b) profile lines of vertical displacement velocities.

4 DISCUSSION

The assessment of the vertical displacement velocities and cumulative vertical displacement derived from the Sentinel-1 and the COSMO-SkyMed images showed a good statistical relationship. This allows to assume that the measurements by both satellites are reliable. The present research results also exhibit shortcomings related to the non-accessibility to the historical in-situ geodetic measurements to verify the accuracy of the measurements. Therefore this study used both Sentinel-1 and COSMO-SkyMed images to cross-validate the achieved results from both satellites. The qualitative judgment for the verification of the present research

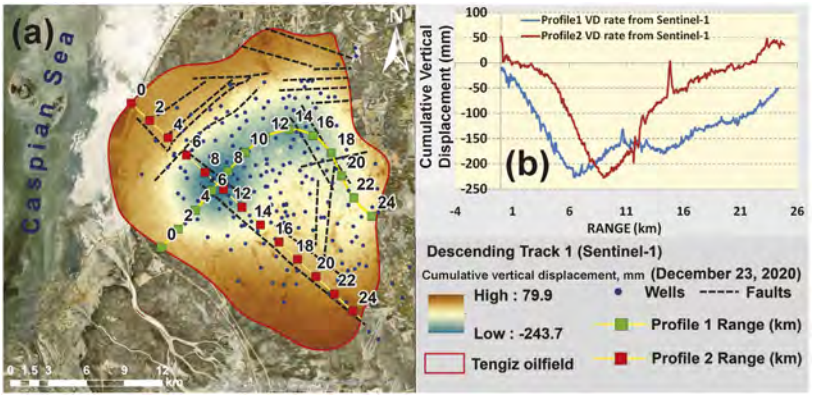

Figure 5. (a) Map of cumulative vertical displacement derived from the Sentinel-1 images with the indication of profile lines; (b) profile lines of cumulative vertical displacement.

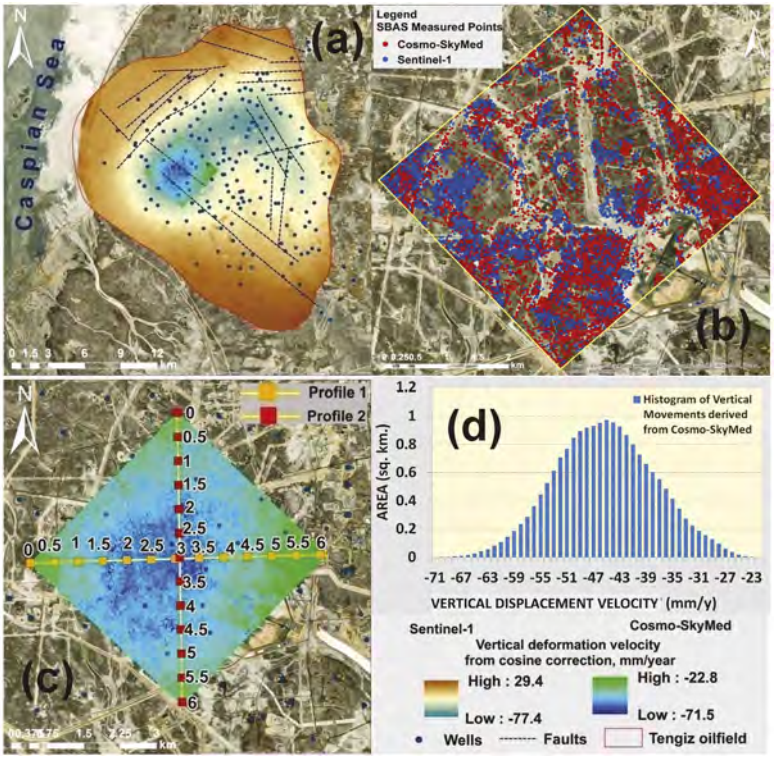

Figure 6. (a) Map of the spatially interpolated vertical displacement velocity derived from the Sentinel-1 and COSMO-SkyMed satellite images; (B) SBAS measured points from the Sentinel-1 and COSMO-SkyMed satellite images used for the spatial interpolation; (C) profile lines of vertical displacement velocity derived from the COSMO-SkyMed images; (D) histogram of vertical displacement velocities derived from the COSMO-SkyMed satellite images.

results was also based on the previously published studies which also observed and detected continuous subsidence processes in the Tengiz oilfield (Del Conte et al. 2013; Comola et al. 2016; Grebby et al. 2019; Orynbassarova 2019; Bayramov et al. 2021). The identical spatial deformation patterns and trends with a maximum subsidence rate rising up-to −79.3 mm/year were observed in the previous studies by Grebby et al. 2019 and Orynbassarova 2019.

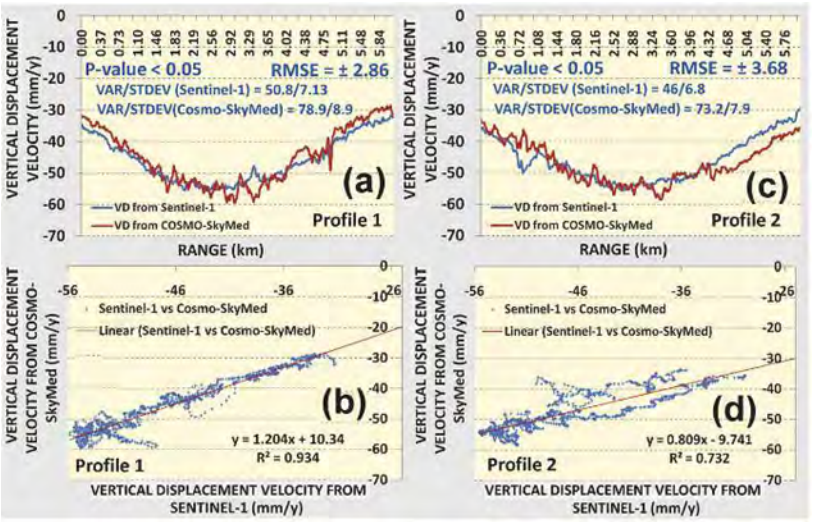

Figure 7. Vertical displacement velocity derived from the Sentinel-1 and COSMO-SkyMed satellite images for: (a) profile 1 VD, (b) regression analysis between vertical displacement velocities derived from the Sentinel-1 and COSMO-SkyMed satellite images for profile 1; (c) profile 2 VD, (d) regression analysis between vertical displacement velocities derived from the Sentinel-1 and COSMO-SkyMed satellite images for profile 2.

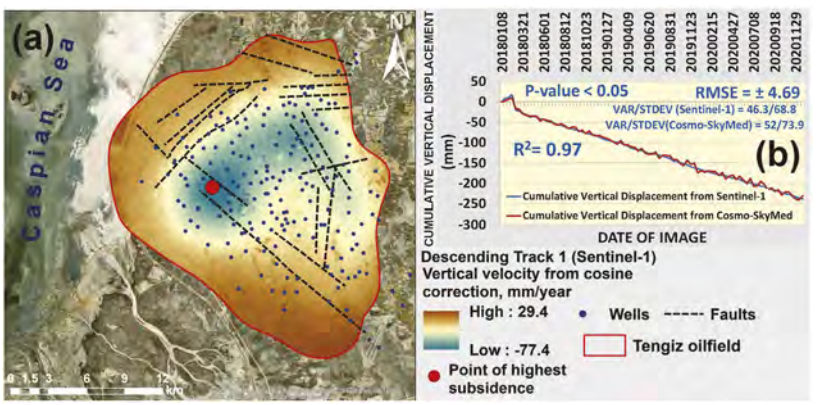

Figure 8. (a) Location of the most subsiding location based on the cumulative vertical displacement derived from the Sentinel-1 images; (b) regression analysis between the cumulative vertical displacements derived from the Sentinel-1 and COSMO-SkyMed satellite images for the most subsiding location.

It is quite difficult to judge about the criticality level of the ongoing and increasing vertical displacement velocities and cumulative vertical displacement of the Tengiz oilfield subsidence in the relationship to the petroleum and gas industry standards for the effective risk management.

However the previous studies by (Mahajan et al. 2018) indicated that the reservoir compaction cases in Oman resulted in the well damages, well integrity, and subsidence damage to the facilities of surface tremors because of fault reactivation. As it was possible to observe in the present studies, around 15 wells of the Tengiz oilfield are located in the detected subsidence hotspot from two satellites. Besides, it is necessary to emphasize the fact of the increasing subsidence velocity that was also well spotted by the present research and previous studies of (Grebby et al. 2019). The application of Sentinel-1 or COSMO-SkyMed images should be selected depending on the scale of analysis, required density and precision of measurements.

5 CONCLUSION

The present research compared the vertical displacements derived from the Sentinel-1 and COSMO-SkyMed radar images collected during 2018-2020 for the Tengiz oilfield.

- The vertical displacement velocities and cumulative vertical displacement derived from the Sentinel-1 and COSMO-SkyMed images showed good agreement. The vertical displacement velocities derived from the Sentinel-1 and COSMO-SkyMed images showed a good statistical relationship with R^2 equal to 0.93, P-value < 0.05 and RMSE equal to ±2.86 for the Profile one and R^2 equal to 0.73, P-value < 0.05 and RMSE equal to ±3.68 for Profile 2. The cumulative vertical displacement derived from the Sentinel-1 and COSMO-SkyMed images for the most subsiding location showed a good statistical relationship with R^2 equal to 0.97, P-value < 0.05 and RMSE = ± 4.69. This allowed to assume that the SBAS measurements from both satellites are reliable and also confirmed the ongoing subsidence processes in the Tengiz oilfield.
- Vertical displacement velocities and cumulative vertical displacement derived from the COSMO-SkyMed images were observed to be more dispersed than from the Sentinel-1 images. This was reflected in the higher sample variance and standard deviation of the vertical displacement values derived from the COSMO-SkyMed mages.
- Ground deformations derived from the Sentinel-1 and COSMO-SkyMed images showed that the Tengiz oilfield subsided during 2018-2020 with the maximum annual vertical displacement velocity around −77.4 mm/y and −71.5 mm/y, respectively. - The detected hotspot of the most subsiding areas was not anyhow spatially related to the concentration of wells. Therefore, it is possible to assume that primary factors controlling the vertical displacements in the Tengiz oilfield are the oil and gas extraction industrial processes and also natural subsurface tectonics.
- The selection among the Sentinel-1 or COSMO-SkyMed images should be decided depending on the scale of analysis, required density and precision of measurements.

FUNDING

This research was funded by the Nazarbayev University through the Social Policy Grant and Faculty-development Competitive Research Grant (FDCRGP) - Funder Project Reference: 080420FD1917.

ACKNOWLEDGMENTS

The authors would like to acknowledge the Italian Space Agency (Agenzia Spaziale Italiana) for the provision of COSMO-SkyMed (CSK) images within the Open Call for Science Project ID 767.

REFERENCES

Bayramov, E., Buchroithner, M., Kada, M., and Zhuniskenov, Y. 2021. Quantitative Assessment of Vertical and Horizontal Deformations Derived by 3D and 2D Decompositions of InSAR Line-Of-Sight Measurements to Supplement Industry Surveillance Programs in the Tengiz Oilfield (Kazakhstan). Remote Sensing 13, 2579. doi:10.3390/rs13132579.

Grebby, S., Orynbassarova, E., Sowter, A., Gee, D., and Athab, A. 2019. Delineating Ground Deformation over the Tengiz Oil Field, Kazakhstan, Using the Intermittent SBAS (ISBAS) DInSAR Algorithm. Int. J. Appl. Earth Observation Geoinformation 81, 37–46. doi:10.1016/j.jag.2019.05.001.

Orynbassarova, E. 2019. Improvement of the Method of Integrated Preparation and Use of Space Images in Tasks of Assessment of Sedimentation of Industrial Surface in the Conditions of Operation of Tengiz Oil and Gas field PhD Dissertation. Satbayev University.

Zhou, W., Chen, G., Li, S., and Ke, J. 2006. InSAR Application in Detection of Oilfield Subsidence on Alaska North Slope, in Proceedings of the 41st US Symposium on Rock Mechanics (USRMS), Golden, CO, USA, 17–21 June 2006.

Mirzaii, Z., Hasanlou, M., Samieie-Esfahany, S., Rojhani, M., and Ajourlou, P. 2019. Land Subsidence Monitoring in Azar Oil Field Based on Time Series Analysis. Proceedings 18 (1), 2. doi:10.3390/ecrs-3-06190.

Klein, I., Gessner, U., and Kuenzer, C. 2012. Regional Land Cover Mapping and Change Detection in Central Asia Using MODIS Time-Series. Appl. Geogr. 35, 219–234. doi:10.1016/j.apgeog.2012.06.016.

Anissimov, L., Postnova, E., and Merkulov, O. 2000. Tengiz Oilfield: Geological Model Based on Hydrodynamic Data. Pet. Geosci. 6, 59–65. doi:10.1144/petgeo.6.1.59.

Bealessio, B. A., Blánquez Alonso, N. A., Mendes, N. J., Sande, A. V., and Hascakir, B. 2020. A Review of Enhanced Oil Recovery (EOR) Methods Applied in Kazakhstan. Petroleum 7 (1), 1–9.

Imamoglu, M., Kahraman, F., Cakir, Z., and Sanli, F. B. 2019. Ground Deformation Analysis of Bolvadin (W. Turkey) by Means of Multi-Temporal InSAR Techniques and Sentinel-1 Data. Remote Sensing 11, 1069. doi:10.3390/rs11091069.

Yang, C., Zhang, D., Zhao, C., Han, B., Sun, R., Du, J., et al. 2019. Ground Deformation Revealed by Sentinel-1 MSBAS-InSAR Time-Series over Karamay Oilfield, China. Remote Sensing 11, 2027. doi:10.3390/rs11172027.

Tapete, D., and Cigna, F. 2019. COSMO-SkyMed SAR for Detection and Monitoring of Archaeological and Cultural Heritage Sites. Remote Sensing 11 (11), 1326. doi:10.3390/rs11111326.

Loesch, E., and Sagan, V. 2018. SBAS Analysis of Induced Ground Surface Deformation from Wastewater Injection in East Central Oklahoma, USA. Remote Sensing 10, 283. doi:10.3390/rs10020283

Sarmap (2021). SBAS Tutorial. Available at: https://www.sarmap.ch/index.php/software/sarscape.

Del Conte, S., Tamburini, A., Cespa, S., Rucci, A., and Ferretti, A. 2013. Advanced InSAR Technology for Reservoir Monitoring and Geomechanical Model Calibration, in SPE Kuwait Oil and Gas Show and Conference. doi:10.2118/167339-ms.

Comola, F., Janna, C., Lovison, A., Minini, M., Tamburini, A., and Teatini, P. 2016. Efficient Global Optimization of Reservoir Geomechanical Parameters Based on Synthetic Aperture Radar-Derived Ground Displacements. Geophysics 81 (3), M23–M33. doi:10.1190/geo2015-0402.1.

Mahajan, S., Hassan, H., Duggan, T., and Dhir, R. 2018. Compaction and Subsidence Assessment to Optimize Field Development Planning for an Oil Field in Sultanate of Oman, in Dhabi International Petroleum Exhibition & Conference, Abu Dhabi, November 2018 (UAE). Paper presented at the Abu. doi:10.2118/192744-MS.

Smart Geotechnics for Smart Societies – Zhussupbekov, Sarsembayeva & Kaliakin (Eds)
© 2023 The Author(s), ISBN 978-1-003-29912-7
Open Access: www.taylorfrancis.com, CC BY-NC-ND 4.0 license

Issues and challenges in geotechnical investigations – Case studies from Cochin, India

Akhil Anil
Junior Engineer, Geostructurals Pvt Ltd, Cochin, India

Anil Joseph
Managing Director, Geostructurals Pvt Ltd, Cochin, India

ABSTRACT: Heightened development activity occurring throughout the world leaves us with more challenging or marginal land for future developments. Soil related issues and challenges, are often poorly or conservatively evaluated thus inviting risk or additional costs to the project. This paper shares the case studies of challenges encountered for value engineering with respect to geotechnical investigation for a 40 Storied Twin towers in Smart City, Cochin and the problems encountered with the bulk movement of very soft clay during the construction of foundation for a Mall at Maradu, Cochin. In terms of controlling the risks of over-expenditure on a project, a good soil investigation can save a client considerable amount in the project foundation cost even up to 100%. It is worthwhile to spent up to 2% of the project cost in geotechnical investigation as a safety against financial risk involved due to inadequate data.

1 INTRODUCTION

Construction in soft soil is a great challenge in the field of geotechnical engineering. Ground engineering issues such as slope instability, bearing capacity failure or excessive settlement could occur either during or after the construction phase due to low shear strength and high compressibility of this soil (Mohamad et al 2015). The most important aspect of every civil engineering project is acquiring reliable information on the ground on which the project will be constructed (Hussain et al 2022). Preliminary geophysical investigation of subsurface strata is important prior to tendering or execution of project and preparation of project plan of any construction which help in proper planning, cost estimation, and time-bound project execution (Anbazhagan 2018). During the planning of subsurface investigation, the Engineer shall always remember majority of the unforeseen costs associated with construction on soft clay are geotechnical. Additional costs are often attributed to inadequate planning of subsurface investigation and improper interpretation of the results of field and laboratory tests (Gue et al 2000). Given the wide range of topics covered by site investigations, the geotechnical consultant should bring the required adjustments for each unique project. The need of "value engineering" should be made clear to those who are procuring site investigations in order to make sure that site investigations are integrated into project planning as early as feasible and not as a last-minute "necessary evil." Along with providing advice on site investigation requirements, a skilled geotechnical consultant should also emphasize the importance of using a staged strategy for practically any size of study. The concept of a single phase ground investigation should be firmly resisted by any geotechnical practitioner, as only once the investigation proceeds can one assess the need or otherwise, for further probing (SAICE, 2010). Geotechnical investigations are an essential component of a successful geotechnical engineering analysis and foundation recommendation report. These investigations allow geotechnical engineers and geologists to characterize subsurface conditions and make engineering judgments about how the earth will behave when subjected to structure and embankment loads (MnDOT Geotechnical Manual, 2017).

DOI: 10.1201/9781003299127-302

2 COCHIN MARINE CLAYS

Port City of Cochin in India has been witnessing large scale construction activities due to the rapid industrialization of the area. Most of the "Greater Cochin" area consists of extremely soft marine clays, posing numerous problems for foundation engineers (Jose et al 1988). Therefore, the need for accurate and reliable geotechnical investigation methods and proper site characterization is becoming vital. The marine clays of Cochin have very low undrained shear strength and possess moderate sensitivity. Pandian et al 1991 indicated the change in the index and engineering properties of Cochin Marine Clay on air drying and that the test results of standard procedures which recommend air drying could be misleading. Physico-chemical and mineralogical studies on Cochin marine clays indicate that these marine soil samples have high water content and high void ratio. The natural moisture contents are very close to the liquid limit. These soils are classified as organic and active in view of their high colloidal activity (Rajasekaran et al 1994). The smear zone radius of Cochin marine clays was estimated to be about 130 to 150mm, which was five to six times the radius of the central drain. The horizontal permeability within the smear zone is about 25 to 30% less than in the undisturbed zone (Anil et al 2015). This paper deals with two case studies of challenges encountered for value engineering with respect to geotechnical investigation for a 40 Storied Twin towers in Smart City, Cochin and the problems encountered with the bulk movement of very soft clay during the construction of foundation for a Mall at Maradu, Cochin.

3 CASE STUDY I: 40 STORIED I.T. TWIN TOWERS PROJECT AT SMART CITY, COCHIN, INDIA

3.1 *About the project*

The project consists of 40 Storied IT Twin Towers with a total plinth area of more than 45 lakh square feet, located in Cochin, India. The project contains a robotic parking garage that can hold roughly 4500 parking spaces. The tender for an end bearing pile foundation sitting on rocks was called after the initial soil research studies and preliminary drawings. The project was referred to the authors for value engineering and peer review. The project's projected cost for piling was 7 Million USD, and the total number of piles anticipated according to the original design was 4500 numbers. Figure 1 displays the site plan and building elevations.

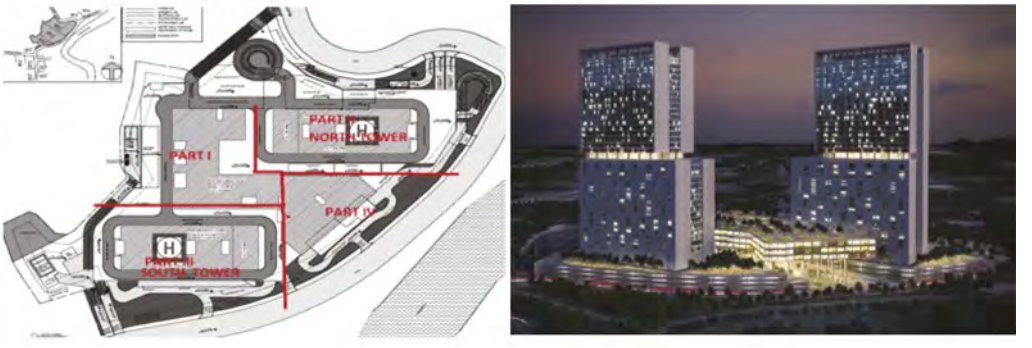

Figure 1. Layout and elevation of the proposed project.

3.2 *Soil profile*

Rotary drilling was used to drill six bore holes a maximum of 17.1m deep. Standard Penetration Tests were carried out at regular vertical intervals, and laboratory testing was done on

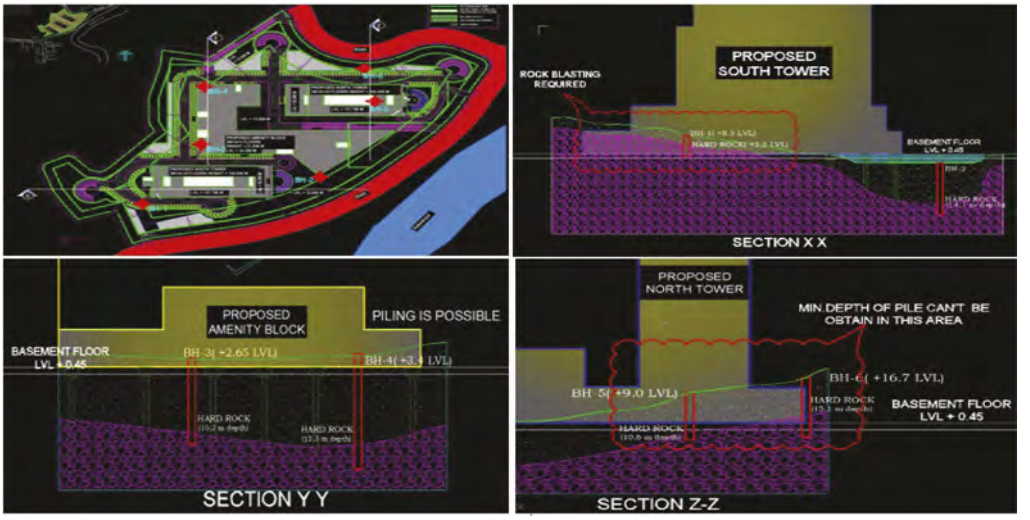

Figure 2. Layout of boreholes and sections through the towers.

the samples collected throughout the study. The analysis of boreholes revealed that the soil profile exhibits unpredictable fluctuation. The plot has a level difference of about 18m, and the founding strata are composed of very hard volcanic rock in some places, hard lateritic formation in others, and thick deposits of very soft organic clay with S.P.T. values ranging from 0 to 1 that extend to a depth of 8m. Figure 2. depicts the location of the boreholes as well as the cross section along the towers.

3.3 *The problem*

According to the drill investigation, some sites would require rock blasting at the foundation level and the first concept of the piling is not feasible throughout the entire region. The minimum pile depth won't be available in some other places, and in some places, deep piles resting on hard rock will need to be provided together with suitable anchorage. For a complete study of the foundation needs and to determine an estimate of cost, the data from the available geotechnical investigation is insufficient. Additional boreholes are therefore necessary.

3.4 *The solution – Value engineering*

Additional 21 bore holes were drilled at the site as part of the decision to conduct a thorough study, as indicated in Figure 3(a). In order to determine the depth of encounter of rock strata and guarantee the minimal length of pile in the piled raft region, bore holes were taken in every 10m grid in the transition zones in the south tower and north tower areas where rock strata suddenly dips and soft weak layer shows up. Additionally, rock bottom profiling was done, and the results are shown in Figure 3(b). Based on the newly acquired geotechnical information, the foundation system was modified to include deep piles end bearing in hard rock with sufficient anchorage for soft clay areas, footings resting on hard rocks or on piles end bearing in hard rock for amenity blocks, rafts for towers beginning from the hard rock layers, and piled raft systems for lateritic areas. The total number of piles on redesign was decreased to 1356, lowering the cost of piling to 1.9 million USD, and resulting in a 5.1 million USD reduction in budget for piling. The case study emphasizes the significance of thorough geotechnical investigation to determine an accurate project estimate. The construction of the foundation work and current stage of the project are displayed in Figure 4(a) and (b).

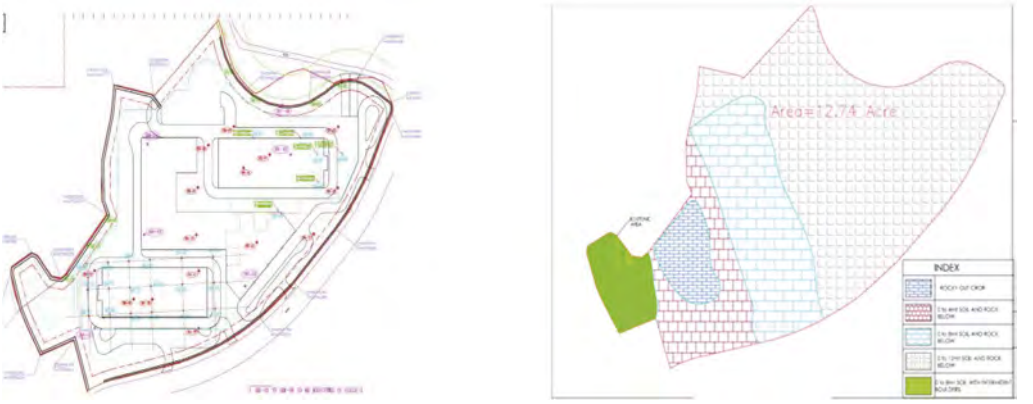

Figure 3. Work of superstructure in progress (a) Layout of additional bore holes (b) Rock bottom profiling.

Figure 4. (a). Foundation work in progress (b). Current status of the project.

4 CASE STUDY II: MALL AND RESIDENTIAL TOWERS AT MARADU, COCHIN

4.1 *About the project*

Project comprises of a Shopping Mall of about 10 lakhs square feet consisting of Hyper market, restaurant, retail shops, multi-level car parking, Multiplexes and swimming pool and two residential towers of 20 floors, having an approximate area of 5 lakh square feet. The site location and 3D view of the project is shown in Figure 5. The soil investigation conducted at site reveals the presence of very soft marine clay extending up to a depth of 24m. The Towers and Mall building is designed as resting on D.M.C. Piles end bearing in the very dense sand strata noted from a depth of about 47 to 56m. The compound wall and the ramp area piles were terminated at a depth of 36 to 40m in the medium dense sand strata.

4.2 *The problem*

Building has two basements catering to car parking and services, and the depth of excavation required from the existing ground level was 7m. As the cost of Diaphragm wall and touch piles was too high, where ever sufficient set back were present the contractors decided to go for stage excavation with ordinary sheet piling. During the progress of excavation, the entire system failed and due to the bulk movement of the soft marine clay, the D.M.C. piles

Figure 5. Site location and 3D View of the project.

Figure 6. Failure of stage excavation.

moved laterally and shearing failure was noted in many piles. Figure 6. shows the failure of stage excavation.

4.3 *The solution - Value engineering*

The project was referred to authors for working out a safe and optimum solution for retaining system. After carrying out detailed investigation of failure, additional data regarding soils were collected at specified intervals. The plan indicating the phases of construction and retaining requirement for excavation is shown in Figure 7. The corrective piles were executed in place of the damaged piles. After carrying out the analysis for different retaining

system it was decided to go for profiled high strength interlocking sheet piles extending up to 12m depth with back anchorage systems where ever sufficient set back is available. Where ever set backs are less it was decided to go for touch piles with propping system to optimize the design. During the course of construction, it was noted that due to the bulk movement of the soil happening the stress formation on the supporting system on the interlock piles was much higher than envisaged, and the system moved to the verge of collapse as shown in Figure 8.

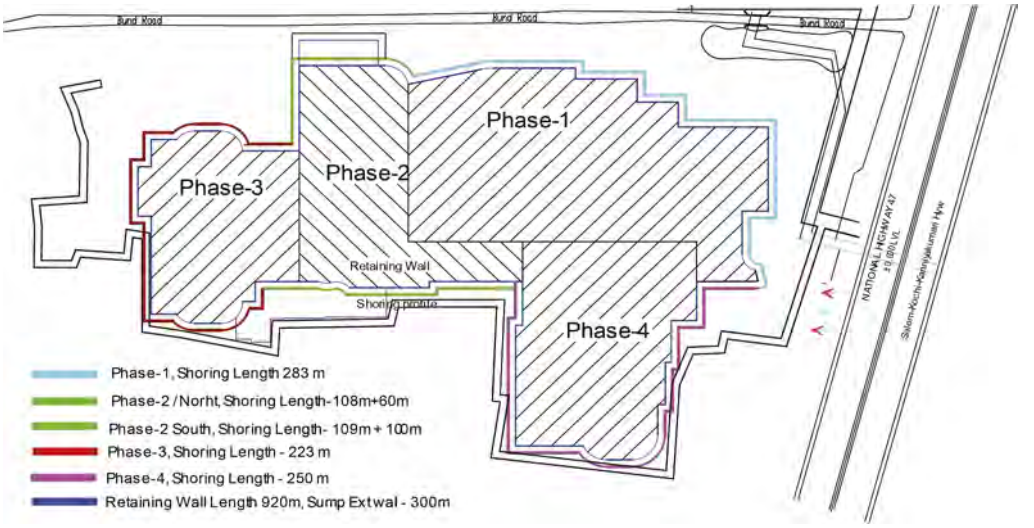

Figure 7. Plan indicating phases of construction and retaining requirement for excavation.

Figure 8. Huge stress on sheet piling system due to block movement of the soft clay.

Additional propping was provided from the bottom to prevent the collapse. In order to prevent the bulk movement of soft marine clays and to have better factor of safety, in the remaining phases for the areas where sufficient set backs are available it was decided to improve the ground by providing a combination of preloaded compacted lime fly ash columnar intrusions and Multiple Driven Fibre Reinforced Columnar intrusion as indicated in Figure 9. Figures 10(a) and (b) shows the photographs of the project during construction and current stage.

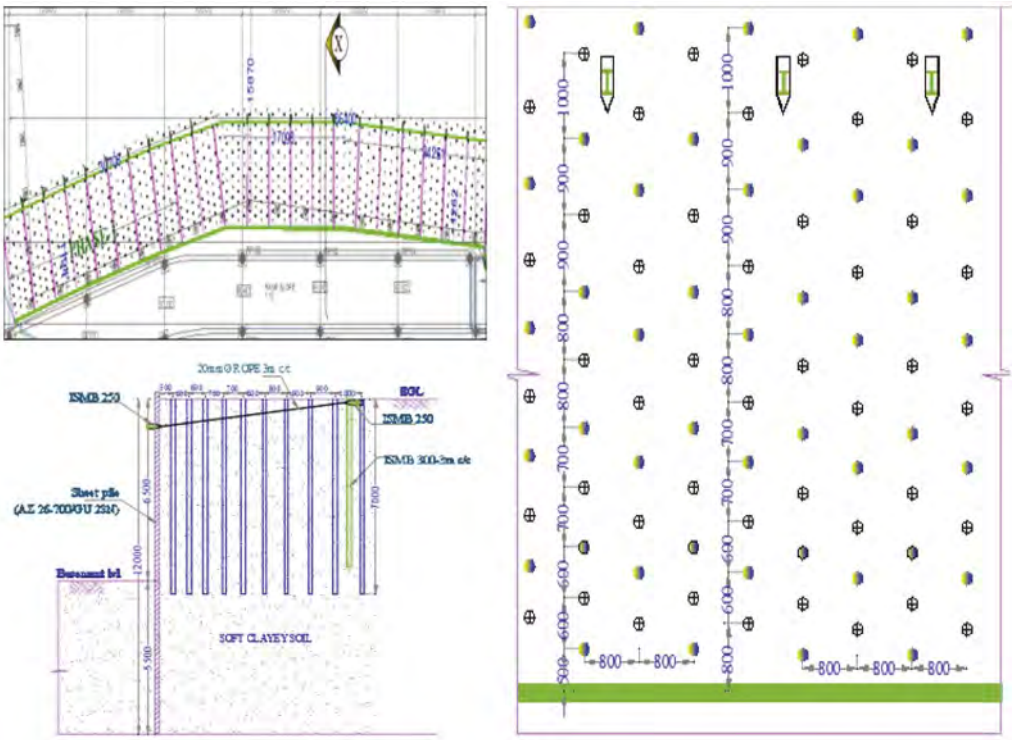

Figure 9. Ground improvement system by providing a combination of preloaded compacted lime fly ash columnar intrusions and Multiple Driven Fibre Reinforced Columnar intrusion for preventing bulk movement.

Figure 10. (a) Project during construction (b) Current status of the project.

5 CONCLUSION

A good geotechnical consultant apart from giving guidance on site investigation requirements has to highlight the phased investigation approach that is essential to almost any size of investigation. The case study for the 40 storied I.T. Twins Towers project emphasizes the significance of thorough geotechnical investigation to determine an accurate project estimate. The total number of piles on redesign was decreased to 1356 from 4500, lowering the cost of piling to 1.9 million USD from 7 million USD, resulting in a 5.1 million USD reduction in budget for piling. From the case study of the mall and residential towers, it is noted that the block movement of soft marine clays can cause catastrophic effects - shearing concrete piles and exerting huge pressure on the sheet pile/ touch pile retaining wall systems. Providing a combination of preloaded compacted lime fly ash columnar intrusions and multiple driven fibre reinforced columnar intrusion for ground improvement in soft marine clays can prevent the bulk movement and thereby leading to optimization of design of retaining walls and improving the safety of the projects. It is worthwhile to spent up to 2% of the project cost in geotechnical investigation as a safety against financial risk involved due to inadequate data.

REFERENCES

Anbazhagan P. 2018. Subsurface Investigation—Integrated and Modern Approach. *Geotechnics for Natural and Engineered Sustainable Technologies*.

Anil Joseph, S Chandrakaran, N. Shankar & Babu T Jose. 2015. Laboratory evaluation of extent of smear zone on columnar intrusion for cochin marine clays. *Proceedings of 50th Indian Geotechnical Conference – Pune*.

Babu T. Jose, A. Sridharan & Benny Mathews Abraham. 1988. A study of geotechnical properties of Cochin Marine Clays. *Marine Geotechnology. Vol 7*: 189–209

Gue S.S & Tan Y C. 2000. Subsurface Investigation and Interpretation of Test Results for Foundation Design in Soft Clay, *Seminar on Ground Improvement – Soft Clay*, Kuala Lumpur, Malaysia.

Hussain, K., Bin, D., Hussain, J., Shah, S.Y.A., Hussain, H., Hussain, A. and Hussain, S. (2022) Engineering Geological and Geotechnical Investigations for Design of Oxygen Plant. *International Journal of Geosciences. Vol 13*: 303–318

MnDOT Geotechnical Manual. 2017. *Geotechnical Engineering Manual Geotechnical Engineering Section*.

N.O, Mohamad, C.E, Razali1, A.A. Hadi, P.P Som, B.C, Eng, M.B, Rusli & F.R Mohamad. 2015. Challenges in Construction Over Soft Soil – Case Studies in Malaysia. *Soft soil engineering international conference, Malaysia.*

Pandian, N. S., T. S. Nagaraj & G. L. Sivakumar Babu. 1991. Effects of Drying on the Engineering Behaviour of Cochin Marine Clays. *Geotechnique* 41 (1): 143–147.

Rajasekaran, G., Essaku, S., & Mathews, P. K. 1994. Physico-chemical and mineralogical studies on cochin marine clays. *Ocean Engineering*. 21(8),771–780.

SAICE. 2010.Site Investigation Code of Practice, 1st Edition, *South African Institution of Civil Engineering - Geotechnical Division*.

Smart Geotechnics for Smart Societies – Zhussupbekov, Sarsembayeva & Kaliakin (Eds)
© 2023 The Author(s), ISBN 978-1-003-29912-7
Open Access: www.taylorfrancis.com, CC BY-NC-ND 4.0 license

Restoration works of dry dock of Sveaborg

K.C. Avellan
KAREG Consulting Engineers, Helsinki, Finland

ABSTRACT: Sveaborg (Suomenlinna) is an UNESCO sea fortress. The dry dock is built under Swedish, Russian and Finnish rule. Most of the concrete structures are made after Finnish independence (1917). The masonry debris of the wall face is concrete covered. The northern corner of the basin is supporting the floating gate. The corner restoration started in 2012 by grouted steel pipes. Anchors were drilled though the existing structure. A drainage system and reinforcement were installed, and concrete was poured. Instability of the damaged structures made the projects challenging and safety precautions had to be implemented at all work stages. By close monitoring, and the ability to resolve problems of the flowing water, the project's first phase was successfully completed. The design water pressure is 95 kN/m². The second phase was undertaken in 2018 by repairing the drainage channels around the dock and repairing the wall faces and the floor.

1 INTRODUCTION

Suomenlinna (Sveaborg) is a sea fortress which was built on a group of islands at the entrance to Helsinki harbor. It was originally built for defending Sweden against Russia (1748-1809). After the Crimean war (1853-1856) the fortress was strongly strengthened structurally and by heavy artillery due the defense problems against English and French fleet. The reason was that time to defend ST. Petersburg. The Russian empire continued to strengthen the fortress until the October revolution (1917). The independent Finland started to use the fortress and deepened the bottom of the yard by blasting and pouring concrete up to WW2.

In 1991, the fortress was added to the UNESCO World Heritage List as a unique monument of military architecture.

Figure 1. Dry dock of Suomenlinna and strengthened corner of the floating door.

DOI: 10.1201/9781003299127-303

2 MANDATE AND SCOPE OF WORKS

The first scope was strengthening of supporting corner of floating door and the old quay wall 2011-2012 (Figures 1–2).

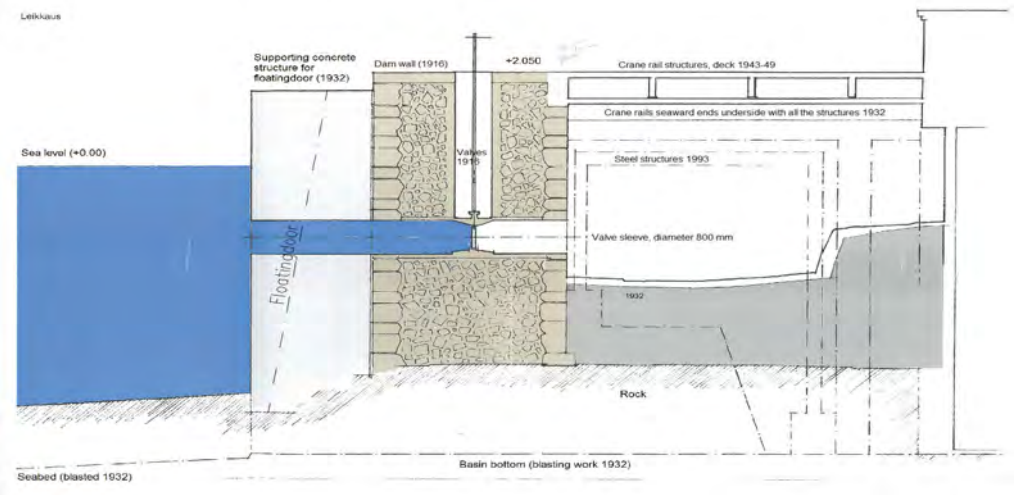

Figure 2. Supporting corner of the floating door. Section. Construction phases and periods.

The second scope was renovation of the bottom slabs (2 x 2 x 0.1 m^3) of concrete and dewatering channels of the bottom. The channels are situated near the rand of the walls having occasionally wipeholes. The environmental problems were based on having the dock after WW2 mainly as repairing dock for ships. The sandblasting of the ships caused environmental problems due to toxic paint.

3 STABILIZATION OF SUPPORTING CORNER OF THE FLOATING DOOR

The supporting corner of the floating door at the dry dock was made in 1932. Over the years, a section of approximately 4 m (width) by 11 m (height) of the corner of the concrete basin wall supporting the floating door had deteriorated from exposure to seawater and frost damage and was in a poor state of repair. Further damage and disintegration of the structure was caused by water leakage through the wall at an increasing rate despite an attempt to recondition it in 2009.

The process of restoration of temporary stabilization of the damaged gravity wall was initiated using two vertical grouting steel pipes (114.3 x 5 mm) with 120 holes per meter, ϕ = 10 mm, driven 2.0 m deep into bedrock, drilled and installed on the level 2.05 m. Having had the old corner stabilized, and water from the basin pumped out, the structure could be then tieback anchored. In order to cease and prevent supplementary water leakage from the structure, the old, traditional method of timber wedges was employed (Figure 3).

The Tieback anchors, Titan 40/16 Combi-coat, were drilled through the existing structure to the depth of 3 m into the bedrock using rock crown drill bit of ϕ =90 mm with centralizing spaces 88 mm. The reason for the large crown drill bit was that the denoted location of the bedrock was based on expert assessment using available data, therefore there was a slight, but potential probability that the anchors could have been as well bonded in the old, underwater structure (Figure 3).

Figure 3. The corner before rebuilding. Timber wedges.

4 REPAIRING THE BOTTOM COCRETE SLAB AND THE WALLS

During the years after WW2 some of the concrete slabs 2 x 2 x 0.10 m^3 were broken to pieces. The slabs were slightly reinforced, and the quality of concrete was poor (Figures 4–5).

A practical but important problem was to make the contract documents so understandable that the builders can estimate the lumpsum. For that reason KAREG took a lot of photos and made an overview drawing with the situations of the photos. The bill of quantities was one part of the contact documents. The contractor could then estimate the workmanship and equipment for the work (Figures 4–5).

The contaminated material paid by weights (tn) had to be lifted by crane to trucks and then delivered first by vessels to Helsinki and then by trucks to waste treatment facility. The wet contaminated material was first packed in big bags with holes for having the material without extra water but still wet (w ≤ 10 %).

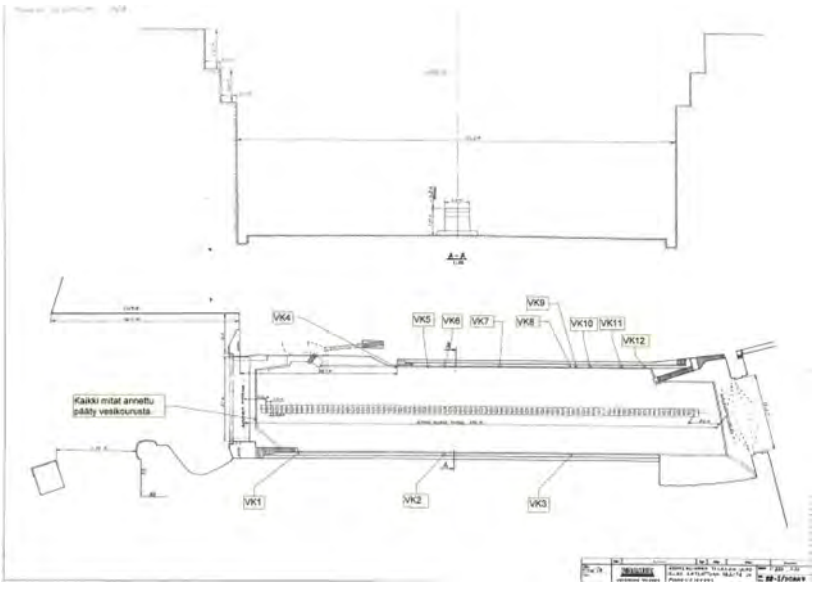

Figure 4. Section and overview. Bottom. Photos for the bill of quantitative.

Figure 5. Bottom. Section. Quantity surveying by photos.

5 CONCLUSSIONS

5.1 *Strengthening the supporting corner of the floating door*

The strengthening scheme presented is an economic and aesthetic solution to the refurbishment, restoration and preservation of understrength and unstable wall of the dry dock of Suomenlinna.

The use of the selected strengthening option and technique for structural intervention of the wall of the dry dock was found to be an appropriate technique to achieve the desired objective and at the same time being minimal invasive, quick and discreet when compared to conventional strengthening techniques. In addition, the selected method has proven effective in keeping the wall in as close to its original condition as possible for many years to come.

5.2 *Repairing the bottom*

The quantity of rebuilt dewatering channels (meters) and wipeholes (pieces) could be surveyed as exactly as possible and to be listed in the bill of quantifies. The amount of broken slabs were predicted for the bill of quantities in a practical and understandable way by photos.

To have the wet contaminated material first packed in big bags with holes and having then the moisture content $w \leq 10\ \%$ saved a lot of money.

REFERENCES

KAREG Consulting Engineers, Helsinki, Finland 2011-12, 2017-18. Internal archive.
Suomenlinna. Suomenlinna Official web site. www.suomenlinna.fi.

Smart Geotechnics for Smart Societies – Zhussupbekov, Sarsembayeva & Kaliakin (Eds)
© 2023 The Author(s), ISBN 978-1-003-29912-7
Open Access: www.taylorfrancis.com, CC BY-NC-ND 4.0 license

Analytical and numerical methods for determining the stress-strain state of a soil massif for solving a planar problem

V.M. Polunin, I.S. Kolyukayev & M.R. Gorkina
SPbGASU, Saint-Petersburg, Russia

ABSTRACT: In this work, an own calculation module, written in Python and based on a numerical method for processing elements, which solves the issues of plane deformation within the framework of a linear elastic soil model. The right-hand side vector and the local stiffness matrix construction algorithms are provided. The Dirichlet and Neumann boundary conditions are taken into account using various methods that are described. The analytical solutions to the elastic problem of the stress-strain half-space and the Plaxis software are compared with the calculation results obtained by solving the problem with the calculation module. The results obtained by the developed numerical solution converge with the analytical solutions and with the results obtained in the Plaxis software package.

Keywords: boundary conditions, finite element method, linear elastic soil model, plane strain, stiffness matrix of elements

1 INTRODUCTION

Finite element method was chosen because it allows for the numerical calculation to take into account the interactions between foundation soil and structures, the interactions between materials with linear and nonlinear properties, and the intricate stratification of soils. A set of soil models that are each applicable for solving the corresponding problem are included in modern computational complexes, as well as an easy-to-use interface for developing a computational scheme and dividing the finite element mesh. However, in such calculation systems, due to their commercial nature, the program code is closed to users, which makes it impossible to add custom or make changes to existing soil models. Regarding view of this, it is necessary to develop open-source numerical calculation module that can be altered to account for unique and non-standard conditions applied to the problems of soil mechanics and geotechnics.

2 LIERATURE REVIEW

The numerical finite element method is the primary method used in geotechnical practice to calculate soil foundations [1, 2, 3, 4, 5]. Despite the popularity of computational computing complexes such as Plaxis, Midas, there are still difficulties in setting certain parameters of soil models that cannot be adjusted. Especially, in order to be able to take into account the specific conditions characteristic of weak soils of St. Petersburg [6, 7] or temperature problems [8].

The plane strain problem, which assumes that there is no deformation along an axis perpendicular to the considered plane, is used to solve an elastic problem in a plane formulation. For more information on the plane strain problem, see [9, 10, 11].

DOI: 10.1201/9781003299127-304

The following dependencies of the theory of elasticity hold true within the context of the elastic problem of plane deformation:

$$\begin{cases} \sigma_x = \frac{E}{(1-2\nu)(1+\nu)} \cdot \left(\varepsilon_x(1-\nu) + \varepsilon_y\nu\right) \\ \sigma_y = \frac{E}{(1-2\nu)(1+\nu)} \cdot \left(\varepsilon_y(1-\nu) + \varepsilon_x\nu\right) \\ \tau_{xy} = \tau_{yx} = \frac{E}{2(1+\nu)} \cdot \gamma_{xy} \end{cases} \quad (1)$$

where σ_x, σ_y = stresses along the *x, y* axes, kN/m^2; τ_{xy} = shear stresses, kN/m^2; ε_x, ε_y = relative strains along the *x, y* axes; γ_{yx} = shear deformations, *rad*; E = deformation modulus, kN/m^2; v = the lateral expansion coefficient.

The strain and stress elements in (1) can be represented as vectors in a matrix [9]:

$$\{\sigma\} = \begin{Bmatrix} \sigma_x \\ \sigma_y \\ \tau_{xy} \end{Bmatrix}, \ \{\varepsilon\} = \begin{Bmatrix} \varepsilon_x \\ \varepsilon_y \\ \gamma_{xy} \end{Bmatrix} \quad (2)$$

After translating the stress vectors (2) from system (1) into matrix form, we arrive at Hooke's law:

$$\{\sigma\} = [D]\{\varepsilon\}$$
$$\downarrow$$
$$\begin{Bmatrix} \sigma_x \\ \sigma_y \\ \tau_{xy} \end{Bmatrix} = \frac{E}{(1-2\nu)(1+\nu)} \cdot \begin{Bmatrix} 1-\nu & \nu & 0 \\ \nu & 1-\nu & 0 \\ 0 & 0 & \frac{1-2\nu}{2} \end{Bmatrix} \cdot \begin{Bmatrix} \varepsilon_x \\ \varepsilon_y \\ \gamma_{xy} \end{Bmatrix} \quad (3)$$

where $[D]$ = element properties matrix:

$$[D] = \frac{E}{(1-2\nu)(1+\nu)} \cdot \begin{Bmatrix} 1-\nu & \nu & 0 \\ \nu & 1-\nu & 0 \\ 0 & 0 & \frac{1-2\nu}{2} \end{Bmatrix} \quad (4)$$

The purpose of the finite element method (FEM) is to find an unknown parameter, which is described by a surface function. The *x, y* coordinates, a fundamental physical principle (in our case, Hooke's law), and boundary conditions (bonds, loads, [12, 13, 14, 15]) all affect how this surface will look.

3 METHODS

In general terms, to solve the problem using the FEM, a system of linear equations is compiled, which contains the desired values of the unknown parameter, the boundary conditions of displacements and loads, body forces and fundamental laws that characterize the linear and nonlinear properties of the material. All of the aforementioned initial data are contained in three main matrices that make up the matrix analogue of such a system [16, 17, 18, 19, 20]:

$$\{s\} = [K]^{-1}\{R\} \quad (5)$$

where $\{s\}$ = the vector of values of the function of the desired parameter in nodes (in our case, the desired parameter is displacement); $[K]^{-1}$ = global stiffness matrix of elements, containing basic functions [9], FE material properties (in our case, elastic properties) and boundary conditions for displacement. Consists of local stiffness matrices determined for each FE; $\{R\}$ = the vector of the right-hand side or the vector of known values, containing the boundary

conditions of loads and displacements, as well as body forces (in our case, the own weight of the soil). Consists of local vectors of the right-hand side determined for each FE.

The displacements u and v along the x, y coordinates, respectively, are needed parameters in the plane strain elasticity problem. The values of the desired parameters within each element are presented as functions of linear polynomials of the first degree after discretizing the computational domain into a three-node FE [9]:

$$\begin{aligned} u(x,y) &= a_1 + a_2 x + a_3 y \\ v(x,y) &= a_4 + a_5 x + a_6 y \end{aligned} \tag{6}$$

where $u(x,y)$, $v(x,y)$ = displacement functions within one FE along the x, y axes, respectively (hereinafter referred to as u, v); $a_1 \ldots a_6$ = constants. Each of the functions (6) has three components for each node. In sum, these components form a local displacement vector $\{\delta\}$, which is part of the global vector (5).

The result of the matrix transformation of functions (6) [9] is the determination of relative deformations:

$$\{\varepsilon\} = [B]\{\delta\} \tag{7}$$

where $[B]$ = matrix of derivatives of shape functions (a detailed derivation of this matrix is presented in [9]).

The matrix of the form's derivative functions takes the following shape:

$$[B] = \begin{bmatrix} y_j - y_k & y_k - y_i & y_i - y_j & 0 & 0 & 0 \\ 0 & 0 & 0 & x_k - x_j & x_i - x_k & x_j - x_i \\ x_k - x_j & x_i - x_k & x_j - x_i & y_j - y_k & y_k - y_i & y_i - y_j \end{bmatrix} \tag{8}$$

According to (5), the global stiffness matrix and the global vector of the right-hand side, which are composed of the corresponding local matrices and vectors, must be known in order to identify the components of the displacement vector.

The local stiffness matrix is determined from the condition of equality of the work of the external force and the work of internal stresses at small displacements and contains a matrix that includes the fundamental law of material behavior under load, as well as a matrix of derivatives of shape functions:

$$[K] = \int_S [B]^T [D][B] dS = \Delta [B]^T [D][B] \tag{9}$$

where S = FE integration area.

Each component of the matrix [K] is an integral over the area of the element according to the area integration sign in equation (18). Integration over the area of the element can be replaced by multiplying the integrand by the area of the FE Δ [9].

The right-hand side's local vector is made up of loads and boundary conditions. It includes internal processes that take place right inside the boundaries of the finite elements; these processes are also referred to as body forces and include the self-weight of the soil. However, in problems solved in a plane setting, the body force is distributed over the area of the structure in the considered plane and along one linear meter in the direction perpendicular to the considered plane.

The body forces must be distributed equally among the nodes in each FE in order to be taken into account in the local vector of the right-hand side for the forces acting uniformly throughout the FE's entire volume. By turning the body force into a concentrated force, multiplying by the FE area, and then dividing the resulting force by the quantity of FE nodes, it is possible to distribute the force over the FE nodes.

The load value applied to the chosen design scheme boundaries is determined by the Neumann boundary conditions. Only the components of the vector on the right-hand side–the nodes of those FE—whose boundary is subject to the Neumann condition are taken into consideration. The load that is dispersed along the FE boundary is recalculated into a concentrated force and distributed evenly among its nodes by multiplying by the length of the FE boundary.

The Dirichlet conditions are taken into account in the elements of the local stiffness matrix and the local vector of the right-hand side, which correspond to the FE nodes that fall on these boundaries according to the following rule: the elements of the main diagonal of the stiffness matrix are assigned one, and the rows corresponding to the main diagonal are reset; for the vector of the right-hand side of the displacement according to the Dirichlet condition is assigned to the corresponding element of the vector according to the boundary condition. As applied to our problem, the displacement along the Dirichlet boundary along the side boundaries of the computational scheme is equal to zero in the direction of the x axis and zero in the direction of both axes along the lower boundary.

The local stiffness matrix and the local vector of the right-hand side take into account stiffness parameters and boundary conditions for each FE separately. However, the calculation of the unknown displacement vector is performed for the entire computational domain, which includes many FEs, so it is necessary to ensure their joint interaction. Since the FEs are connected at the nodes, the neighboring FEs will have nodes with a common number in the global reference frame. Accounting for the interaction of FE with each other is provided by summing the elements of the corresponding blocks of the local stiffness matrix and the local vector of the right-hand side according to the corresponding numbers of nodes in the global system.

The components of the stress and relative strain vectors (2) act over the entire area of the FE. The stress vector for each FE is determined according to Hooke's law (3) through local displacement vectors $\{\delta\}$, determined by the results of finding the general displacement vector (5), the matrix of element properties [D] and the matrix of derivative functions of the form [B]:

$$\{\sigma\} = [D]\{\varepsilon\} = [D][B]\{\delta\} \tag{10}$$

The authors have created a calculation module that implements the definition of the stress-strain state of the soil mass for an elastic problem in a flat formulation in accordance with the aforementioned algorithm. Further, the results of calculations of the stress-strain state of the soil mass from the application of a strip load are given and a comparison is made with analytical solutions and solutions in the Plaxis software package. The design scheme is shown in Figure 1.

Basic formulas for calculating stresses through rigorous analytical solutions [6]:

1. Normal vertical stresses from the application of a strip load σ_{zp}:

$$\sigma_{zp}(x,z) = \frac{-p}{\pi}\left(\operatorname{atan}\left(\frac{0,5b-x}{z}\right) + \operatorname{atan}\left(\frac{0,5b+x}{z}\right)\right) - \frac{-b\cdot p}{\pi}\cdot\frac{z\cdot\left(x^2-z^2-0,25b^2\right)}{\left(x^2+z^2-0,25b^2\right)^2+z^2b^2} \tag{11}$$

where p = band load; b = band load application width; z = depth;

2. The value of relative deformations:

$$\varepsilon = \frac{-\sigma_{zp}(x,z)\cdot\beta}{E(z)} \tag{12}$$

where β = coefficient taking into account the transverse expansion of the soil;

3. Base settlement:

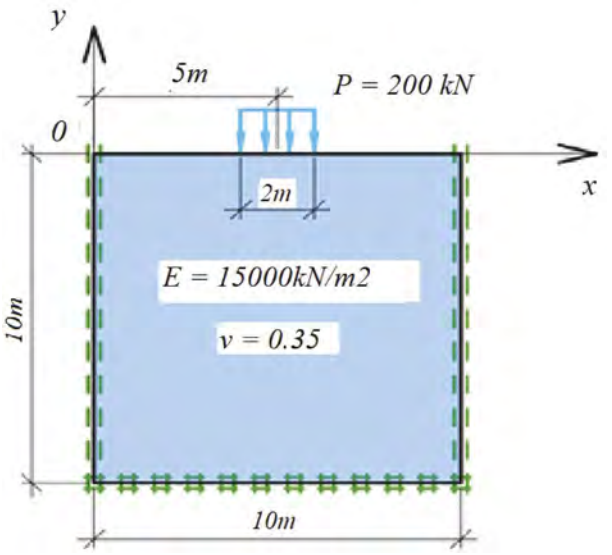

Figure 1. Calculation scheme.

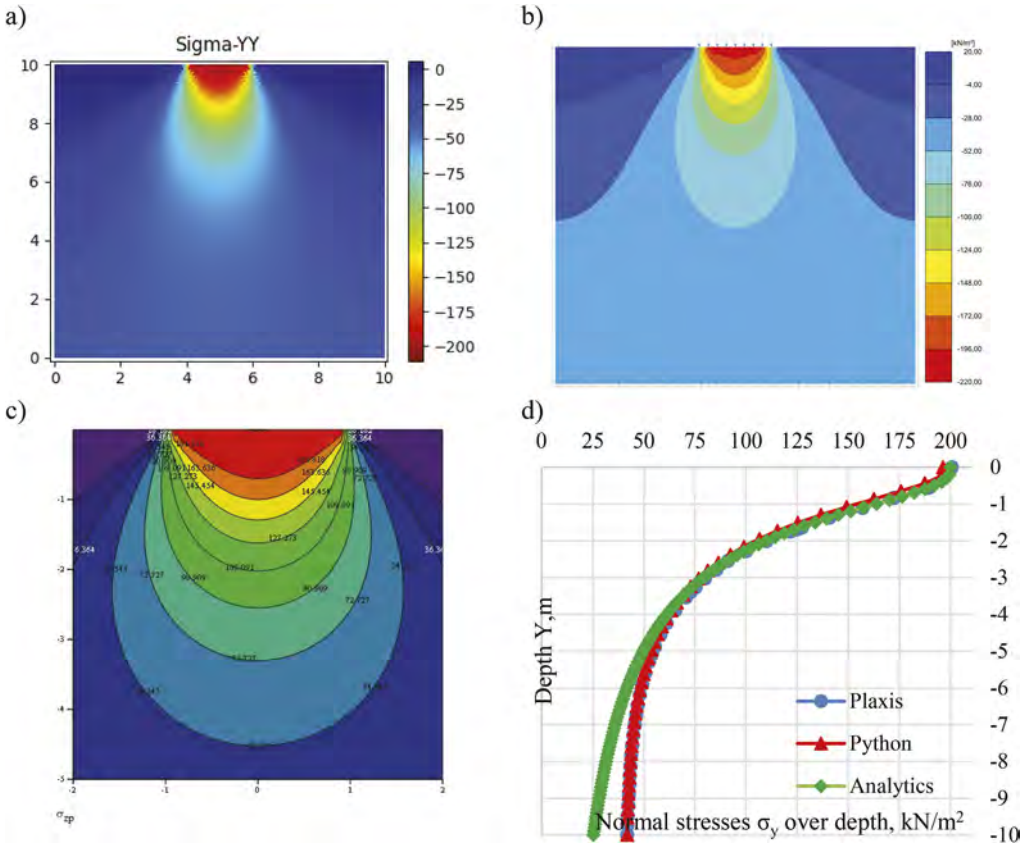

Figure 2. Calculation results of normal stresses σy from the applied strip load.

$$s = \int_0^{Hc} \varepsilon dH \tag{13}$$

where H_c = depth of compressible thickness equal to 10m.

Figure 2 shows calculation results of normal stresses σy from the applied strip load a – stress isofields obtained by means of the calculation module written by the authors; b – stress isofields obtained in the Plaxis software; c – stress iso-fields obtained by rigorous analytical solutions in Mathcad; d – comparative graph of the results obtained in the center of application of the load in depth: blue line - results “a”; red line - results “b”; green line - results “c”.

Figure 3 shows the results of the calculation of vertical displacements from the applied strip load.a – isofields of displacements obtained by means of the calculation module written by the authors; b – displacement isofields obtained in the Plaxis software; c – displacement isofields obtained by rigorous analytical solutions in Mathcad; d – comparative graph of the results obtained in the center of application of the load in depth: blue line - results “a”; red line - results “b”; green line - results “c”.

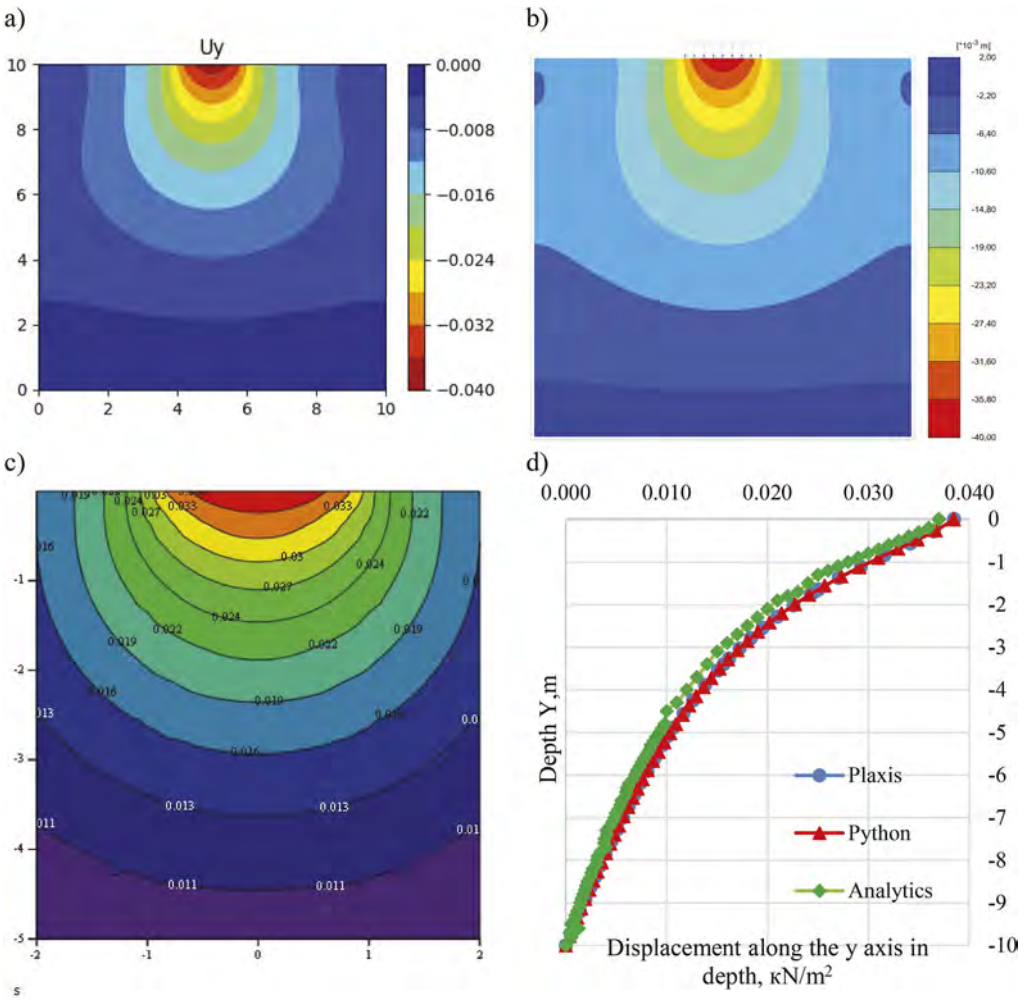

Figure 3. The results of the calculation of vertical displacements from the applied strip load.

Figure 4 shows the results of calculation of relative deformations εy from the applied strip load. a – isofields of relative deformations obtained by means of the calculation module written by the authors; b – isofields of relative deformations obtained in the Plaxis software; c – relative strain isofields obtained by rigorous analytical solutions in Mathcad; d – comparative graph of the results obtained in the center of application of the load in depth: blue line - results "a"; red line - results "b"; green line - results "c".

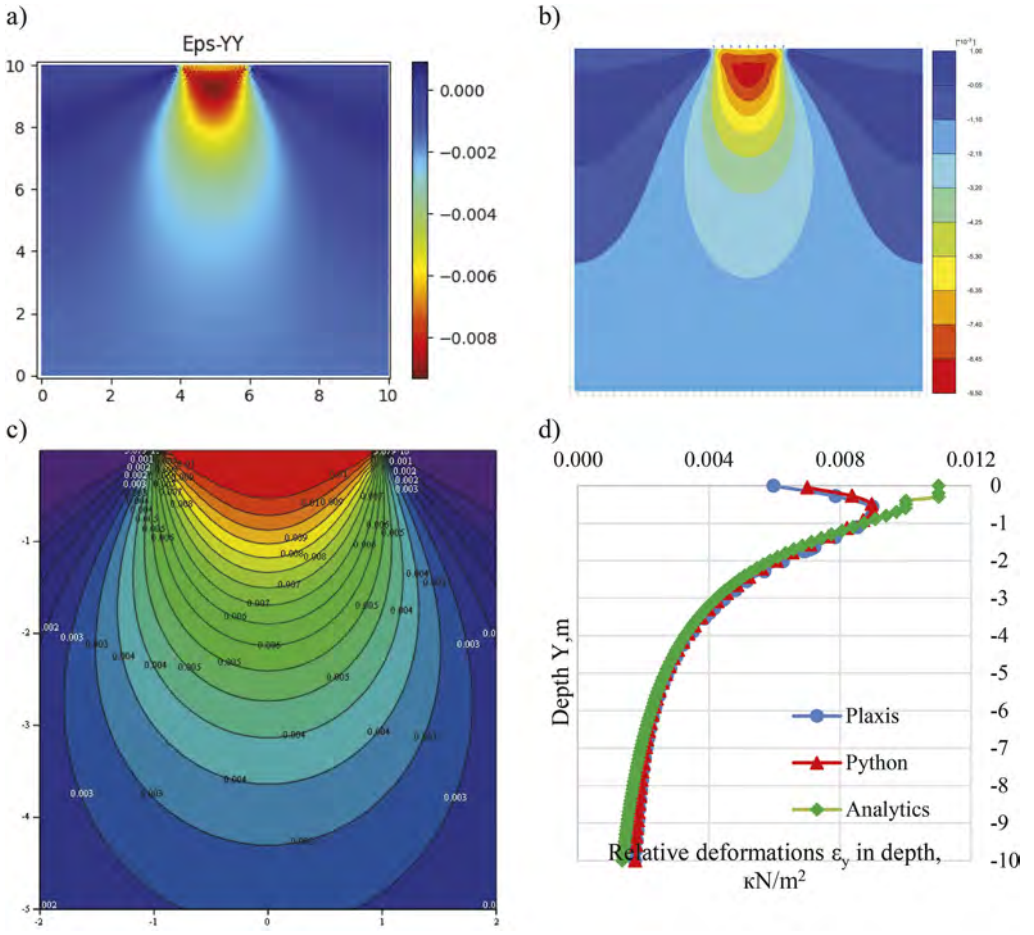

Figure 4. Results of calculation of relative deformations εy from the applied strip load.

4 CONCLUSIONS

1. The stresses and displacement isofields that were calculated using the three methods mentioned above have a general distribution.
2. Plaxis and Python charts built on the basis of the calculation results have the highest convergence compared to the Analytics chart.
3. In contrast to the computational module created by the authors, which uses 3-node FE with first-degree interpolation polynomials and a structured FE mesh, Plaxis software employs 15-node FE with fourth-degree interpolation polynomials and an unstructured FE mesh. The Plaxis program can generate highly accurate calculations thanks to a significant amount of interpolation and an unstructured grid. However, both calculations showed

a convergence of over 95% despite the disparity in how the interpolation accuracy was implemented between Plaxis and the Python calculation module within the context of a flat elastic problem of determining the stress-strain state in a soil mass.

4. The algorithm described can be used as a foundation for calculations of nonlinear problems where the distribution of stresses in finite elements is crucial.

REFERENCES

1. Loseva E., Osokin A., Mironov D., Dyakonov I. (2020). Specific features of the construction and quality control of pile foundations in engineering and geological conditions of saint Petersburg. Architecture and Engineering, 5(2),38–45. https://doi.org/10.23968/2500-0055-2020-5-2-38-45
2. Loseva, E., Lozovsky I., Zhostkov R., Syasko V. (2022). Wavelet Analysis for Evaluating the Length of Precast Spliced Piles Using Low Strain Integrity Testing. Applied Sciences. 12(21). https://doi.org/10.3390/app122110901
3. Shutova O.A., Ponomarev A.B. (2018). Numerical modeling of the vibration impact of vehicles on the foundations of buildings. Bulletin of the Perm National Research Polytechnic University. Construction and architecture. V.9, №1, 93–102. https://doi.org/10.15593/2224-9826/2018.1.09
4. Schanz T. (2006). Aktuelle Entwicklungen bei Standsicherheits- und Verformungsberechnungen in der Geotechnik. Empfehlungen des Arbeitskreises 1.6 «Numerik in der Geotechnik», Abschnitt 4. Geotechnik, №1, 13–28.
5. Polunin V.M., Lobov I.K., Gursky A.V. (2021). Numerical modeling of the process of high-frequency vibroextraction of sheet piles in conditions of water-saturated dusty-sandy and dusty-argillaceous soils. Bulletin of civil engineers. 2(85), 94–101.
6. Mangushev R.A., Penkov D.V. (2021). Comparison of the results of numerical calculations using modern soil models (hardening soil, hardening soil small and generalized hardening soil) with monitoring results. Bulletin of civil engineers, 2(85), 85–93. https://doi.org/10.23968/1999-5571-2021-18-2-85-93
7. Skvortsov K.D., Mangushev R.A. (2022). Accounting for the influence of deformations of sheet pilings of foundation pits on additional settlements of environmental buildings. Bulletin of civil engineers, 5(94),61–68. https://doi.org/10.23968/1999-5571-2022-19-5-61-68
8. Slivets K.V., Kolmogorova S.S., Kovalenko I.A. (2022). Parameters of frozen soils in the numerical simulation of thermophysical problems. Izvestiya of the Petersburg University of Communications, №2, 359–366.
9. Fadeev A.B. (1987). Finite element method in geomechanics, 221.
10. Chandrakant S. Desai Musharraf Z. (2014). Advanced Geotechnical Engineering. Taylor & Francis Group.
11. Paramonov V.M. (2012). Finite element method for solving non-linear geotechnical problems. St. Petersburg: Group of companies "Georeconstruction".
12. Klaus-Jürgen Bathe Edward L. Wilson. (1976). Numerical methods in finite element analysis. Prentice-Hall.
13. Larry J. Segerlind. (1976). Applied finite element analysis. Department of Agricultural Engineering.
14. He Z., Su B., Yu-long L. (2022). Seepage Analysis Based on Weak Galerkin Finite Element Method. Yantu Gongcheng Xuebao. Chinese Journal of Geotechnical Engineering.
15. Gallagher R. (1984). Finite Element Method. Basics, 428.
16. Bin W. Phil V., Hicks M., Zhen C. (2016). Development of an implicit material point method for geotechnical applications. Computers and Geotechnics, 159–167.
17. Sakhno I.G. (2012). Numerical modeling of geomechanical processes taking into account their nonlinearity. Problems of rock pressure. Donetsk National Technical University, №1, 57–67.
18. Nesterov I.V., Merzlyakova A.D. (2021). Features of the formation of adaptive FEM grids for solving geotechnical problems. Mechanics of composite materials and structures, complex and heterogeneous media. M.: Proceedings of the 11th All-Russian Scientific Conference, 356–361.
19. Lade P.V. (2005). Overview and evalution of constitutive models. Soil Constitutive Models: Evaluation, Selection, and Calibration. Ed. J.A. Yamamuro, V.N. Kaliakin. American Society of Civil Engineers. Vol. 128, 69–98.
20. Schanz T. (2006). Aktuelle Entwicklungen bei Standsicherheits - und Verformungsberechnungen in der Geotechnik. Empfehlungen des Arbeitskreises 1.6 «Numerik in der Geotechnik», Abschnitt 4. Geotechnik, №1, 13–28.

Smart Geotechnics for Smart Societies – Zhussupbekov, Sarsembayeva & Kaliakin (Eds)
© 2023 The Author(s), ISBN 978-1-003-29912-7
Open Access: www.taylorfrancis.com, CC BY-NC-ND 4.0 license

An investigation on non-linear behavior of unsaturated soils focusing on Barcelona Basic Model

Alireza Sadeghabadi
Ph.D., Project Manager, Pars Gostareh Consultant Engineering Co, Tehran, Iran

Ali Noorzad*
Dean, Associated Professor, Faculty of Civil, Water & Environmental Engineering, Shahid Beheshti University, Tehran, Iran

Amirali Zad
Assistant Professor, Department of Civil Engineering, Faculty of Civil and Earth Resource Engineering, Central Tehran Branch, Islamic Azad University, Tehran, Iran

ABSTRACT: An anisotropic constitutive model (BBM) has been implemented in a finite difference-based computer program to simulate the geo-mechanical behavior of unsaturated soils subjected to continuous wetting and drying. In this view, the Barcelona Basic Model (BBM) has been implemented into the finite difference-based computer program to clarify the mechanical behavior of fine-grained partially saturated soils during the wetting process. This numerical modeling was verified based on available data in the literature review. The application of the code was investigated for modeling a slope considering the suction-induced process. The research also determined the effect of the over-consolidation ratio in partially saturated or unsaturated soils, especially stress paths, as a modification to yield relation. In this regard, a soil structure system and its capability for checking the instant and consolidated settlements in different stress paths have been evaluated. Based on the results, finite difference methods with BBM and modified BBM efficiently demonstrate the actual behavior of unsaturated or partially saturated fine grained soils. Moreover, OCR criterion has been added to BBM fundamental relations to improve its application in wetting-Induced processes. In this way, more rational results have been gained by this modification.

Keywords: Continuum mechanics, Barcelona Basic Model, unsaturated soil, Bending failure, improvement systems, finite difference analysis, fine grained soils

1 INTRODUCTION

A geo-mechanical constitutive model for considering the elastoplastic behavior of partially saturated soils is known as Barcelona Basic. This model was developed and presented in the earlier 1990s by extending the Modified Cam-Clay (MCC) model for unsaturated soil conditions (Alonso et al. 1990). The model has to describe specific aspects of unsaturated-soil behavior, including wetting-induced swelling or collapse strains, depending on the magnitude of applied stress, as well as the boosting in shear strength and apparent pre-consolidation stress through suction (Gens et al.,2006; Sadeghabadi et al. 2021). A key factor in the design procedures of soil stabilization systems is studying the mechanical behavior of clays in the porous medium, especially expansive soils. An appropriate model for this type of soil is required for numerical simulations. Alonso et al. (1987, 1990) presented the (BBM) describing the low activity stress-strain behavior of partially saturated soils. Figure 1 represents the 3D

*Corresponding author: a_noorzad@sbu.ac.ir

DOI: 10.1201/9781003299127-305

yield surface in $\bar{p} - q - s$ space, where $\bar{p}$ is the net mean stress (i.e., total stress minus air phase pressure), q is the shear stress, and s is matric suction. In this paper, the the BBM into a coupled multiphase fluid flow has been implemented in FLAC.

In Figure 1 the 3-Dimensional yield criteria in $p - q - s$ space has been represented, in which p'q and s are the net mean stress, shear stress and suction, respectively. As shown, both saturated and unsaturated status has been depicted. In two-phase zone, the first variable is air pressure, which is greater than water pressure (vanapalli and Oh 2014). Therefore, for saturated and unsaturated cases, the behavior of soil model is related in these stress variables. The first one is net mean stress and the next is suction, identified in Eq. (1) and (2).

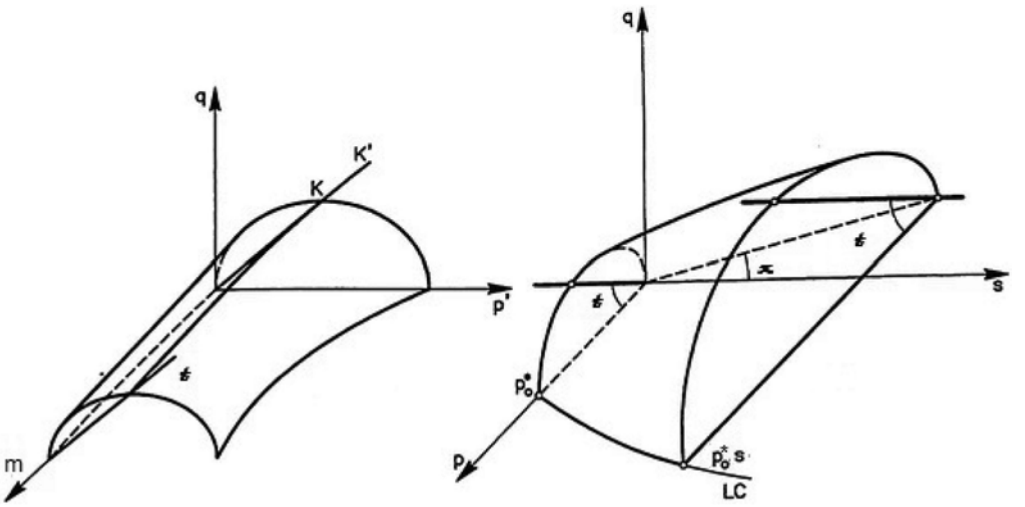

Figure 1. The yield surface in 3-D space for BBM (after Alonso et al. 1990).

A well-known sample for a single stress measured for unsaturated soils refer to Bishop's proposal for a general effective stress σ' to un-saturated states (Bishop, 1959) who identified an averaging parameter χ, being a function of the water pressure u_w:

$$\sigma' = \sigma - (1 + \chi)u_a - \chi u_w \tag{1}$$

Fine-grained soils in earthen structures such as slopes are usually under unsaturated conditions. In this study, an applicable model from Zheng and Lytton (2012) has been considered to demonstrate a compacted soil fill structure's suction response to estimate model displacements. In these structures, the wetting-induced proceedings occur while rising the water table. Volumetric and linear strain change behavior has been investigated in disparate confining stresses toward loading collapse (LC).

Stress paths have been produced for two instances, one for BBM and the other for BBM, considering the over-consolidation ratio, which has been carried out by describing an algorithm in Finite Difference formulation, then comparing them with experimental results of Alonso's research. Finally, immediate and consolidation settlements and vertical displacements of the soils are presented.

2 VERIFYING THE MODEL BY FINITE DIFFERENCE METHOD

FISH is a program with a Finite Difference Method (FDM) base linked with FLAC. This language program provides opportunities for users to introduce new variables and functions. Also, servo-control could be used to simplify numerical modelings (Ho and Hesieh 2018). The

wetting and drying-induced paths due to suction changes have been depicted by decrement from an identified value to the minimum. This analyzing method can simulate the reduction changes in suction relatively simply. Volumetric deformation related to the wetting-induced problem (After Gens et al. 2006) has been depicted in Figure 2, which has produced a stress path in the SI part of the yield surface. In this moving chart, the elastic zone is along with the route ABFH inducing a bit of swelling.

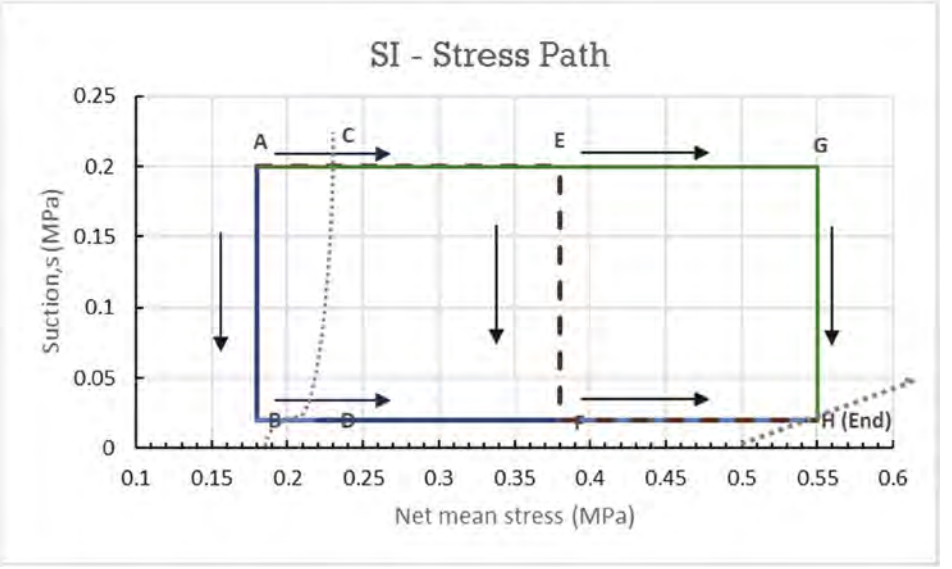

Figure 2. Stress paths in this study (Gens et. al 2006).

In Gens's research, the specimen had been compressed to a specific value for net mean stress in the path AEFH. For smaller stresses, the soil experienced a little swelling. A comparison of the results indicates an acceptable agreement between the experienced (Alonso et al. 1990) and numerical analysis obtained using FDM (Figure 3).

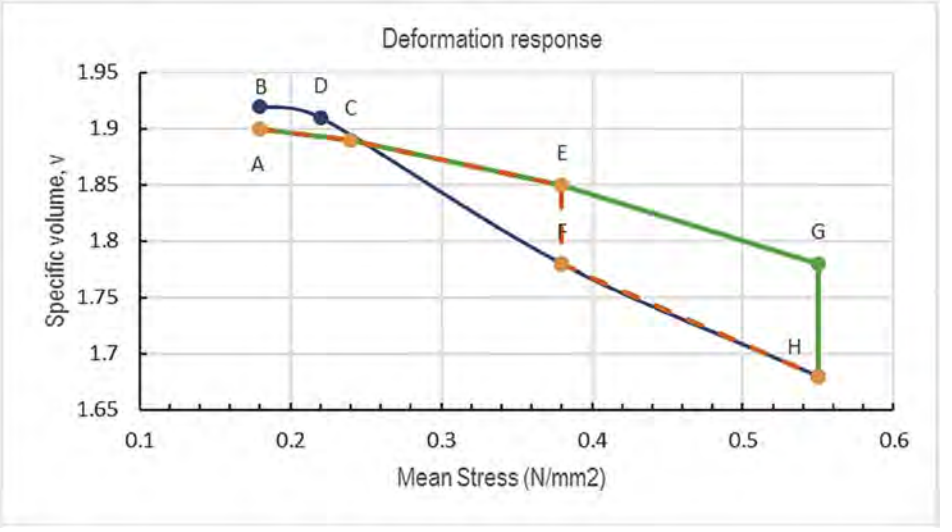

Figure 3. Numerical analysis prediction and experimental model analytical results comparison in the stress paths.

This approach causes wetting process shorten leading to suction reduction.

2.1 *Modeling of a soil structure in an unsaturated approach*

A soil slope structure has been considered to evaluate modeling application in design criteria in different stages of construction and matric suction contents. Table 1. indicates unsaturated soil parameters related to BBM, which have been utilized for the present model. These parameters were reported by Josa et al. in 1987.

Table 1. BBM parameters from Josa et al. (1987).

	Stress Phase				Matric Suction Phase						Reference stress parameters	
Soil type	λo	K	β $(MPa)^{-1}$	r	P^c MPa	λs	κs	G MPa	M	a	Pp_o	S_o MPa
CK	0.14	0.015	16.4	0.20	0.04	0.05	0.001	3.0	1.0	0.8	0.06	0.03

CK Compacted Kaolin

In this part, the Compacted Kaoline (CK) from Josa et al. 1987 with definite unsaturated model parameters have been categorized as the model properties. On the other side, the stress paths are generally utilized to characterize parameters captured from isotopically triaxial tests presented by Alonso et al. (1990). The soil slope structure has been demonstrated by numerical modeling in Figure 4. This centrifuge model was constructed in research executed by Zhang and Lytton (2009a).

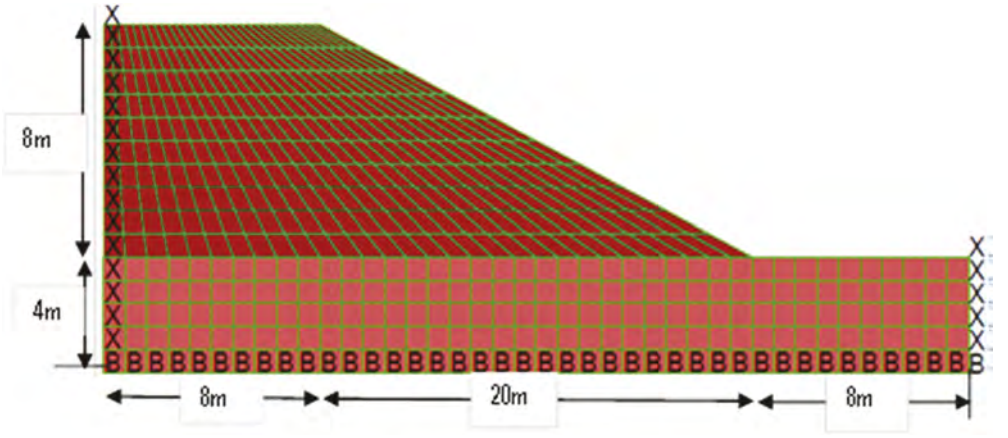

Figure 4. Numerical model of the soil slope structure (after Zheng and Lytton).

The partially saturated zone (Body) and the saturated zone (Foundation) of the slope have been modeled with BBM and Mohr-Coulomb (MC), respectively. Boundaries at the bottom have been fixed in the X and Y directions and lateral sides in the X direction. BBM codes have been implemented for analysis of unsaturated to partially saturated parts with the initial value of 150 kPa for matric suction. In the centrifuge model, the soil structure has been constructed in 8 continuous parts. While the suction value changes from the amount of 150 kPa to zero, the whole slope has been subjected to transient equilibrium.

In this way, natural situation in real construction process could have been better demonstrated.

2.2 *Discussion on implemented model*

The BBM codes programming by FISH were utilized to make analytical solutions and to be compared with those in the same conditions in the experimental research. In the first step, by calculating displacements in the Y-direction, the values of 63 mm and 144 mm have been reached, respectively, which are in good agreement with the same in the literature. Therefore, numerical analyses are applied for evaluating settlements and displacements in the lateral direction in various conditions.

With providing partially saturated to fully saturated zone in numerical modeling, settlements of the slope base in various distance from the centerline are measured. Figure 5 illustrates settlements in comparative charts gained from the current research and former experimental studies. In this figure, by following the fully saturation, the settlement of the slope surface is about two times larger than that at the initial situation. In current study, vertical displacements has reached 205 mm and while the value of 196 mm had been recorded in the literature.

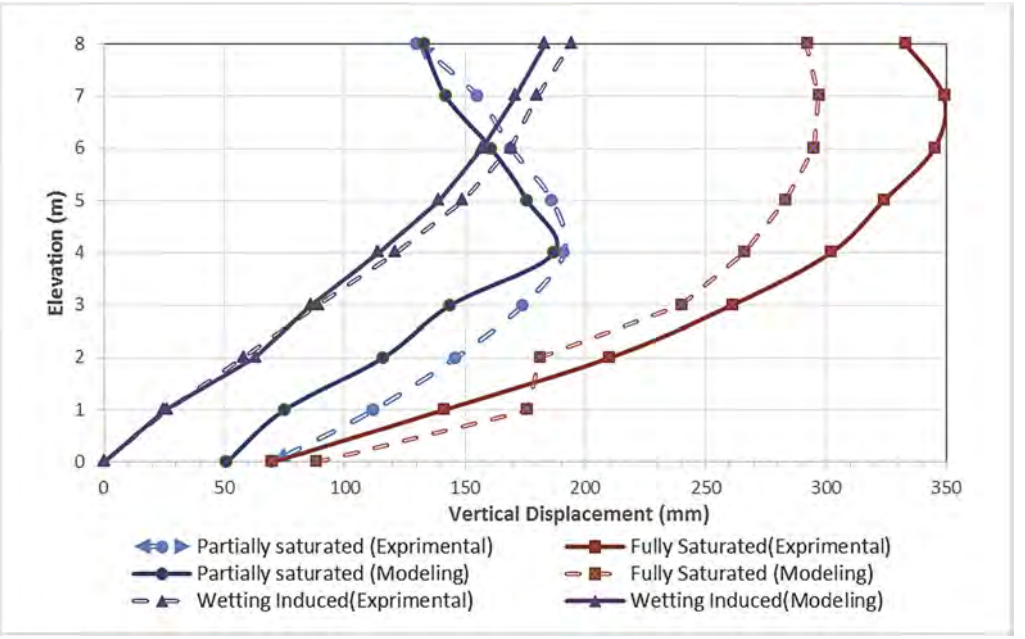

Figure 5. Comparative charts for vertical displacements in partially and fully saturated, and wetting-induced process.

Vertical displacements of the slope at a different elevation have been presented in Figure 6 including he maximum settlement related to Zhang and Lytton experiments and also present study, have taken place at the upper third-height of the soil structure. Cause the slope has been constructed in stages, the accumulative displacements have been resulted since the placement of each level. Also, the modeling results are in fine agreement with the same comparative values extracted from literature.

3 EVALUATION OF WETTING AND OVER CONSOLIDATION IN UNSATURATED MEDIA

According to the previous studies on unsaturated soils the most researchers had focused on studies related on the mechanical behavior of partially saturated soils. Relevant constitutive models have been developed to predict the stress-strain behavior of normally or over-consolidated unsaturated soils (Mojezi et. al 2018; Sadeghabadi et al. 2022).

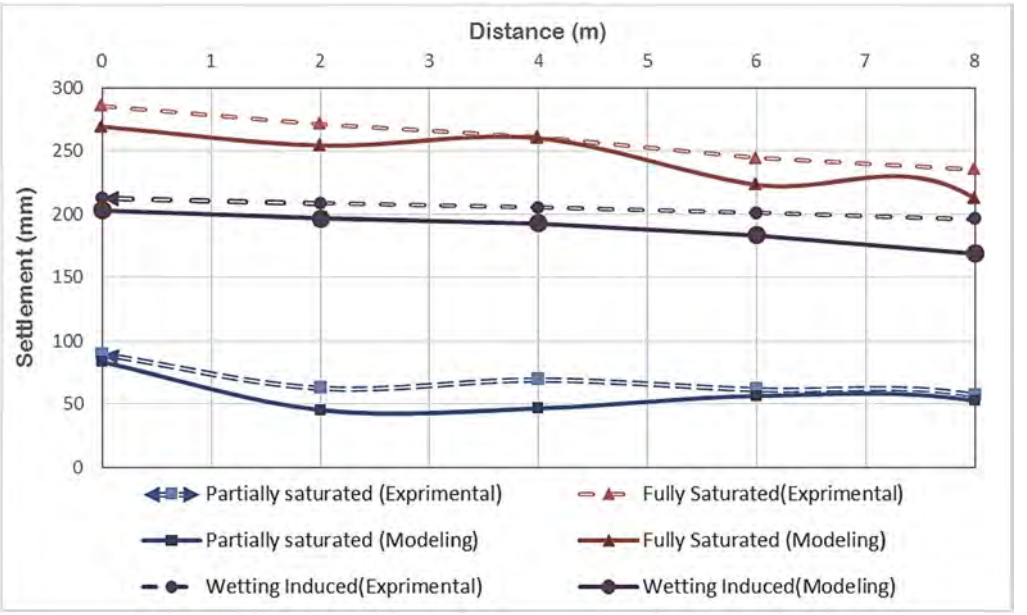

Figure 6. Comparative charts for settlements in different stages in partially and fully saturated, and wetting-induced process.

Since the initial principles of soil mechanics have been from the study on fully saturated soil behavior, some remarkable progresses in comprehension of unsaturated soil behavior have been observed in the last decades, both in experimental and in theoretical analysis (Alonso et al. 1990; Cui and Delage 1996; Fredlund et al. 1996; Wheeler 1996). However, by the recent studies, unsaturated soil mechanics problems are still in an initial stages and involved in a number of unsolved problems.

The critical state in stress spaces and Hvorslev state surfaces have been studied for an over-consolidated unsaturated fine grained soil through a complex of suction -controlled laboratory researches. For silty compacted soils, the history of applied stress can also be reflected by the different densities nearly, and the effect of density on the geo-mechanical behavior of these types of unsaturated soils has been studied.

Figure 7 has demonstrated the volume change behavior in unsaturated specimens in initial matric suction 300 kPa. As can be seen from the figure, in normally consolidated conditions, the curves has been dilated however in over-consolidated ones contractions are observed. (Zhu et al. 2018).

On the other side, as demonstrated in Figure 8. the compression curve decreases while suction value is being increased in a fine grained unsaturated soil. As can be seen, the slope of the unloading curve hasn't been changed (Alonso et al.1990). On the presumption that the values of plastic volume strain at points X and Y are equal, the equation for function of the yield curve (Loading-Collapse) can be gained as following relation:

$$\frac{Po}{p^c} = \left(\frac{p_o^*}{p^c}\right)^{\left(\frac{\lambda(o)-\kappa}{\lambda(s)-\kappa}\right)} \tag{2}$$

In this equation p_0^* and p_0 are pre-consolidation pressures for saturated and unsaturated fine grained soils, κ is the slope of unloading line for unsaturated states; $\lambda(0)$ and λ (s) are the slopes of the compression curves for saturated condition; and p^c is the pre-consolidation stress under saturated conditions ($s = 0$).

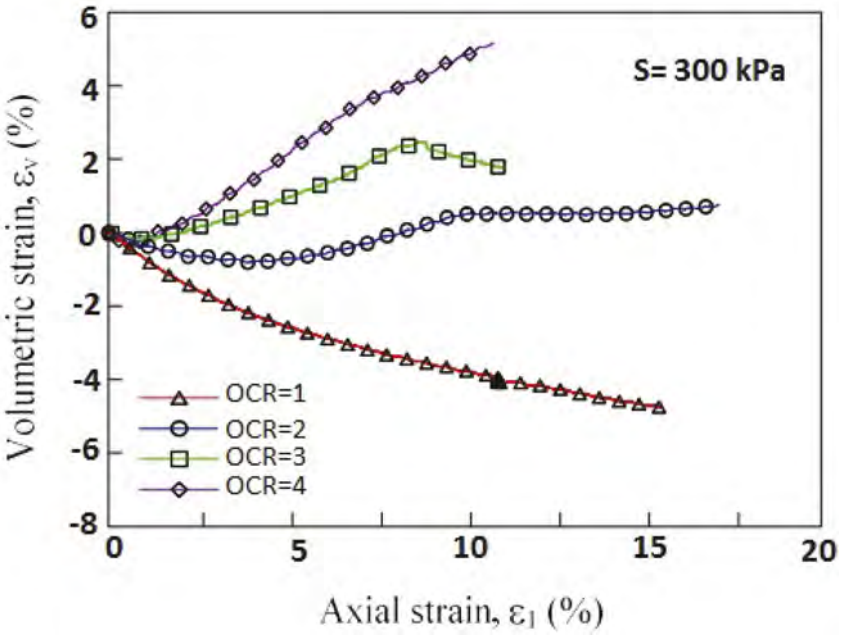

Figure 7. Volumetric strain changes in different over-consolidation ratios for a definite value of matric suction (Zhou et. al 2018).

By Alonso's experimental studies, as categorized in Figure 2 there are stress paths named BDFH, ACEGH, and ACEFH. In the present study, the path BDFH has been investigated using an over-consolidation phenomenon in unsaturated model (BBM). In Figure 9 comparative charts have been identified as the results of Alonso's experimental studies, Numerical Modeling prediction, and BBM with OCR consideration. The curves produced in Figure 9 mention that applying over-consolidation as a modification in (LC) yield relation, causes more acceptable results that match the experiment compared with normally consolidation states.

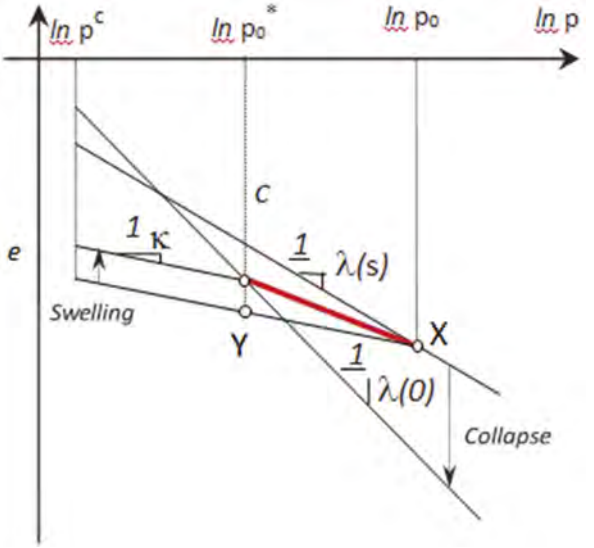

Figure 8. The relationship between p_0^* and p_0 (Alonso et al. 1990).

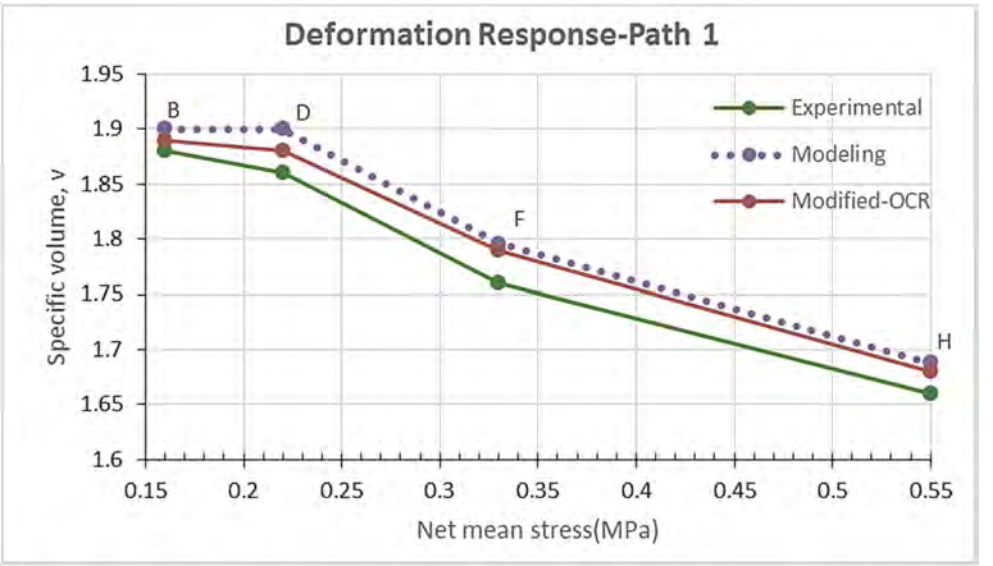

Figure 9. Comparative curves of numerical modeling, Alonso's experimental results, and modeling with OCR modification for stress path BDFH.

By investigation on the current soil structure, it's concluded that considering over-consolidation phenomenon has a positive effect on an optimized design of soil slope in partially saturated or unsaturated media with minimum settlement approach. As demonstrated in Figure 10, three cases of numerical modeling, Alonso's experimental results, and modeling with OCR Modification for stress path BDFH, for calculating vertical displacement of upper crust of the soil structure have been presented in which the path based on the OCR consideration has a better situation compared to the real circumstances.

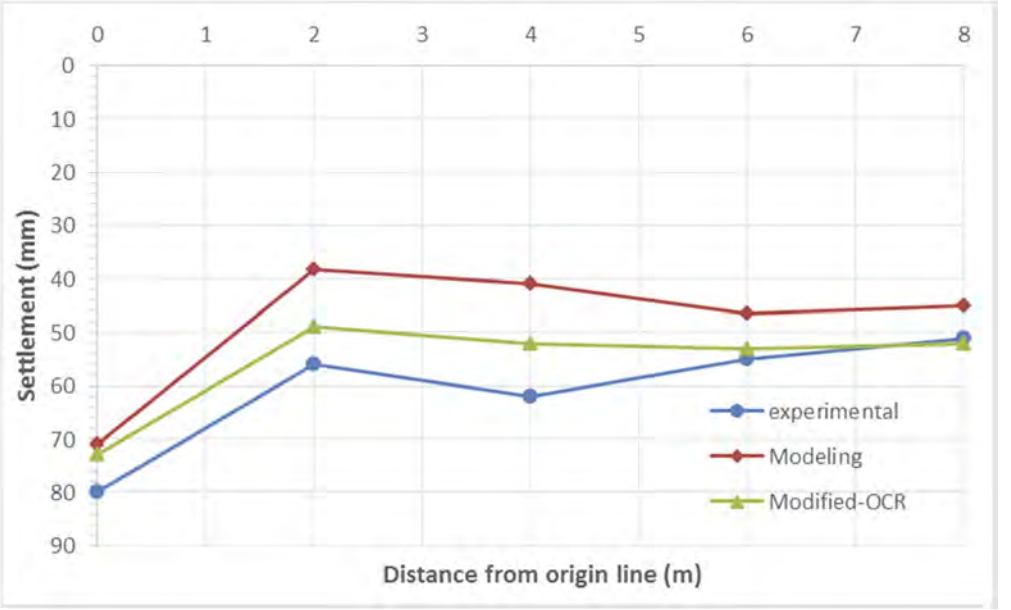

Figure 10. Vertical displacement of crust of the surface at different cases along the path BDFH.

4 CONCLUSIONS

The current study has been directed to achieve innovated methods for slope design and foundations in soil construction subjected to wetting in partially saturated or unsaturated medium. To achieve this subject, numerical modeling in Finite Difference approach was applied to investigate on a definite constitutive model based on the Alonso's former study. The initial target was checking geo-mechanical behavior of unsaturated soils. The current model was examined utilizing different case studies. On the other side, analytical computations were performed to test and optimize the finite difference program (FISH).

The study clarified that considering over-consolidation in an unsaturated constitutive model leads to preferable results comparing with the original model in stress path approach. Moreover, stress paths in BBM yield surfaces (i.e., LC and SI) are the most effective segment to simulate behavior of unsaturated soils, wetting-induced process, and volumetric strain variations. In this way, demonstrations of stress paths in BBM with the Characterized algorithm in FISH program indicate fine agreement with Alonso's experimental research. The checked model depicts a rational compliance to check practical engineering programs such as the response of a slope structure subjected to wetting and drying processes. Moreover, in wetting induced duration, OCR as a modification in BBM matches better with stress paths in the based model. The results indicate that the slope structure has a significant effect on settlements throughout the wetting and drying. The relative vertical displacements can be decreased significantly at higher value of matric suction when role of over-consolidation in LC yield function in BBM, is considered. As an example in S_i=150 kPa, the after fully saturation, the surface settlement in the slope has been approximately 65 mm larger than that for S_i=100 kPa. while, this difference in settlements for the modified model is less than 44 mm. It can be also derived from modified BBM that considering OCR in BBM formulation results a lower value of settlements. Vertical and lateral displacement analysis of the model with this modification have no more difference about 5% from to experimental results. Furthermore, investigation on differential displacements of the slope surface through a definite stress path has come to similar conclusion with unsaturated approach.

In unsaturated media, matric suction variations are in such a close relationship with over-consolidation conditions that considering this parameter into unsaturated models has a remarkable effect on both stress paths and consolidation's displacements. The current study conclusions can be applied for more optimize design of soil structures, slopes, and pavements related to loading-unloading cases on partially saturated or unsaturated over-consolidated soils.

REFERENCES

1. Alonso E. E., Gens A., and Josa A., "A constitutive model for partially saturated soil." Geotechnique, Vol. 40, No. 3 (1990) 405–430.
2. Alonso, E. E.; Gens, A.; and Hight, D.W., "Special Problem Soils, General Report". Proc., 9th Eur. Conf. on Soil Mech. and Found. Engrg., Dublin, Vol. 3, (1987) 1087–1146.
3. Bishop A. W., "The Principle of Effective Stress". Lecture delivered in Oslo, Norway, in 1955, published in: Teknish Ukeblad, Vol.106, No. 39, (1959) 859–863.
4. Cerato, A.B., Miller, G.A., and Hojjat, J., "The influence of cold size and structure on wetting-induced volume change of compacted." J. Geotech. Geoenviron. Eng., 10.1061(ASCE)GT. 1943-5606.000146, (2009) 1620–1628.
5. Fredlund D.G., Rahardjo H., Fredlund M.D., "Unsaturated soil mechanics in engineering practice." JOHN WILEY & SONS INC., (2012).
6. Fredlund D.G., Rahardjo H.,"Soil mechanics for unsaturated soils." Wiley, New York, (1993).
7. Gallipoli D., D'Onza F., and Wheeler S. J., "A sequential method for selecting parameter values in the Barcelona basic model." Can. Geotech. J., Vol. 47, No.11 (2010) 1175–1186.
8. Gens A., Sanchez M., and Sheng D., "On constitutive modeling of unsaturated soils." Acta Geotechnica., Vol.1, No. 3 (2006) 137–147.
9. Hatami A., Tourchi.S.,"A thermomechanical constitutive model for unsaturated clays." Intl Journal of Geotechnical Engineering. Vol. 12, No. 2 (2018).

10. Hatami K., Granados J. E., Esmaili, D., and Miller G. A., "Influence of gravimetric water content on geotextile reinforcement pullout resistance in MSE walls with marginal soils." Transp. Res. Rec., Vol. 13, No. 3836 (2013) 66–74.
11. Ho H. and Hsieh C.C., "Numerical modeling for undrained shear strength of clays subjected to different plasticity indexes." Journal of Geongineering, Vol. 8, No.3 (2018).
12. Josa, A., "Un modelo eslastoplastico para suelos no saturados." PhD. thesis, Univ. of Politencnica de Catalunya, Barcelona, Spain, (1988).
13. Jayanth S., Kannan K. R. I. & Singh D.N., "Continuous determination of drying path SWRC of fine grained soils.", Geomechanics and Geoengineering, An International Journal, (2012), DOI:1001080/17486025.2012.727034.
14. Li L. and Aubetin M., "An analytical solution for the nonlinear distribution of effective and total stresses in vertical backfilled stopes." Geomechanics and Geoengineering, An International Journal, Vol. 5, No. 4, (2010) 237–245.
15. Lyu S., Carol K. H. Hon., Albert P. C. Chan., Francis K. W. Wong and Arshad Ali Javed., "Relationships among Safety Climate, Safety Behavior, and Safety Outcomes for Ethnic Minority Construction Workers." Int'l J. Environmental Reasearch and Public Health, Vol. 15, No. 484 (2018).
16. Mojezi M., Biglari M., Kazem M., Ashayeri J & I. "Determination of shear modulus and damping ratio of normally consolidated unsaturated kaolin." Intl Journal of Geotechnical Engineering. (2018), DOI:10.1080/19386362.2018.1425179.
17. Mun, W., and McCartney, J. S., "Compression mechanisms of unsaturated clay under high stress levels." Can. Geotech. J., 52(12), (2015) 2099–2112.
18. Nishimura T., Hirabayashi,Y., Delwyn G. Fredlund, and Julian K.-M. Gan., "Influence of stress history on the strength parameters of an unsaturated statically compacted soil" Can. Geotech. J., Vol 36, (1999) 251–261.
19. Nuth M., and Laloui L.,"Effective stress concept in unsaturated soils: Clarification and validation of a unified framework." Int. J. Numer. Anal. Methods Geomech., Vol. 32, No. 7 (2008) 771–801.
20. Roscoe, K. H. and Burland, J. B., "On the Generalized Stress-Strain Behavior of Wet Clay". Engineering Plasticity, eds: J. Heyman and F. A. Leckie, Cambridge University Press, (1968) 535–609.
21. Sadeghabadi A, Noorzad A., and Zad A., "Numerical and experimental modeling of geomechanical behavior of partially saturated soils." International Journal of Geo-Engineering 12, No. 1 (2021): 1–22.
22. Sadeghabadi A, Noorzad A., and Zad A., "An extension to barcelona basic model predicting the behavior of unsaturated soils." Transportation Infrastructure Geotechnology 9, No. 2 (2022): 133–154.
23. S. Pakbaz,M., and Alipour,R., "Influence of cement addition on the geotechnical properties of an Iranian clay" Applied clay science., Vol.1, No.4 (2012) 67–68.
24. Sexton B.G., McCabe B.A., "Modeling stone column installation in an elasto visco plastic soil." Intl Journal of Geotechnical Engineering., Vol. 9, No. 5 (2015).
25. Shen D., Oki T., Shingiro K., Hanasaki N., Otsomi N., Kiguchi M., "Projection of future world water resources under SRES scenarios: an integrated assessment." Hydrological Science J., Vol.59, No. 10 (2014) 1775–1793.
26. Sheng D., Sloan S.W., and Gens, A., "A constitutive model forunsaturated soils: Thermomechanical and computational aspects." Comput. Mech., Vol.33, No. 6 (2004) 453–465.
27. Sheng D., Zhou AN., "Coupling hydraulic with mechanical models for unsaturated soils." Can Geotech Journal., Vol.48, No. 5 (2011) 453–465.
28. Vanapalli S. & Oh W., "A model for predicting the modulus of elasticity of unsaturated soils using the soil-water characteristic curve." International Journal of Geotechnical Engineering. Vol. 4, No. 4 (2014).
29. Wheeler S.J., Sharma R.S., Buisson, M.S.R. "Coupling of hydraulic hysteresis and stress strain behavior in unsaturated soils." Géotechnique, Vol. 53, No. 1 (2003) 41–54.
30. Xu Y.S., Shen S.L., Lai Y., and Zhou A.N. "Design of sponge city: Lessons learnt from an ancient drainage system in Ganzhou", China. Journal of Hydrology, Vol. 563 (2018) 900–908.
31. Investigation. "Journal of Geotechnical and Geoenvironmental Engineering," Vol. 133, Issue 4 (2007).
32. Zhang X., and Xiao M., "Using modified state surface approach to select parameter values in the Barcelona basic model." Int. J. Numer. Anal. Methods Geomech., Vol. 37, No. 12 (2013) 1847–1866.11.
33. Zhang X., and Lytton R. L., "A modified state surface approach on unsaturated soil behavior study. I: Basic concept." Can. Geotech. J., Vol. 46, No. 5 (2009a) 536–552.
34. Zheng X., and Lytton, R. L., "A modified state surface approach on unsaturated soil behavior study. III: Modeling of coupled hydraumechanical effect." Can. Geotech. J., Vol. 49, No. 1 (2012) 98–120.

Smart Geotechnics for Smart Societies – Zhussupbekov, Sarsembayeva & Kaliakin (Eds)
© 2023 The Author(s), ISBN 978-1-003-29912-7
Open Access: www.taylorfrancis.com, CC BY-NC-ND 4.0 license

Introduction of geotechnical modelling and seismic disaster prediction in the case of Utsunomiya City, Tochigi Prefecture, Japan

T. Seiki
Utsunomiya University, Utsunomiya, Japan

K. Soramoto
Kanto Regional Development Bureau, MLIT, Mito, Japan

ABSTRACT: The authors have tried to propose the geotechnical model of Utsunomiya City, Tochigi Prefecture, Japan based on borehole data from the local governments of Tochigi prefecture, Japan by the Three-dimensional grid model method. Its grid has 250m in each side. This method includes averaged geological feature around boreholes by geostatistical concept. At first the authors had assembled the borehole data from the local government. Actually, even though it is difficult to get sufficient numbers of borehole data, it has done someway. The authors discussed the geological and topological characteristics in this area. Finally, the authors carried out seismic stability analysis to consider in the area. Based on the results, we considered the seismic intensity of the area on the geotechnical model. As local government also has opened hazard map on the website, we compared those results and discussed the seismic response in this area.

1 INTROUCTION

1.1 *Background*

Geological and geotechnical information on the subsurface structure is a public asset, which can be used not only for earthquake disaster prevention but also for various other fields. In the past, a large number of subsurface structural investigations have been carried out for various purposes in Japan, but these data have not been fully utilised except for limited purposes, and some of them have been in danger of being lost. On the other hand, recently concept of digital transformation is focused on applying and utilising that geotechnical information actively to prevention for natural disaster.

1.2 *Objectivity*

In Utsunomiya City, which is a capital city in Tochigi Prefecture, Japan, a hazard map that assumes damage from floods and landslides that may occur as a result of large-scale natural disasters, and a map that indicates the index of shaking susceptibility, have been prepared. Hazard maps that not only show where buildings will shake in an earthquake, but also take into account building collapse, ground cracks and so on, are required (Utsunomiya City Hall, 2020). It is desirable to identify and visualise the possibility of earthquakes from viewpoints other than floods and landslides, so that citizens can know where exactly they should evacuate to in the case of an earthquake. As a first step towards the disaster prevention, this study analyses geotechnical information models using earthquake ground motions.

2 GEOLOGICAL MODEL FOR UTSUNOMIYA CITY

2.1 *Geotechnical model for Utsunomiya City*

In this study, a three-dimensional grid model (hereafter 3D grid model) was created using its construction programme (Kimura, et. al, 2011), which was created as a means of linking

DOI: 10.1201/9781003299127-306

geotechnical information from a nationwide perspective, as was the objective of the National Geotechnical Information Map Creation Support System. The elevation ranges from about 100 m to 160 m, decreasing from north to south. There is relatively little difference in elevation between the east and west, and the terrain is gentle. In addition, the distribution of the strata is dominated by gravelly soil, with sandy soil, clayey soil and volcanic ash clay. A 3D grid model of Utsunomiya City is created using its construction programme. The number of borehole data used to create the 3D grid model in this study is 953. The borehole data were provided by Tochigi Prefectural Government and Utsunomiya City Hall. Although there are relatively more borehole data in Utsunomiya City than in other cities in Tochigi Prefecture, the distribution range of the data is very uneven. If more accurate modelling is to be aimed at, it is necessary to narrow down the range. Therefore, in this study, it was decided to model the central area of Utsunomiya City, where many borehole data were distributed (blue dots in Figure 1).

2.2 *Example of cross section in 3D grid model*

The starting latitude and longitude of the central section is Lat. 36.56 degree North and Long. 139.83 degree East, and the ending latitude and longitude are Lat. 36.56 degree North and 139.94 degree East. The elevation of the central part of Utsunomiya City is not so high, which is around 110 m to 120 m, but the elevation differs between the east and west sides of the city, with the central part of the model as the boundary. The soil types in this area consist of clay, sandy soil, gravelly soil, Kanto loam and topsoil, with the central part also mostly gravelly soil. The surface layer is mainly Kanto loam in the western part, with topsoil in the other parts. In terms of stratigraphy, the surface has been covered by vegetation and only fragments can be observed, and the strata themselves have been deformed by folding, faulting and other fragmentation, or have been partially lost due to erosion (Yoshikawa et.al, 2010). The terrace deposits, alluvium and terrace deposits are separated from the west, so there is a difference in elevation at the centre of the terrace. The area on the left-hand side or west side of the figure, where the elevation drops sharply, is fed by a river. The borehole data are also reasonably well represented in this area.

3 SEISIMIC STABILITY OF MODELS

3.1 *Seismic response analysis using earthquake ground motions*

In this section, the earthquake records of relatively small magnitude less than M6.0 at each location, which is hereafter referred to as small earthquakes, are the 3.2 magnitude earthquake centred in southern Ibaraki Prefecture on 27 November 2018 and the 2011 off the Pacific coast of Tohoku Earthquake, which is hereafter referred to as 3.11 earthquake and is the largest earthquake that has occurred around Tochigi Prefecture in recent years and caused much damage within the prefecture. In this paper, the authors mentioned the results from small earthquakes. The East-West and North-South components of the acceleration of the seismic wave system were applied to individual grid of the 3D grid model corresponding to each axis. From the observed acceleration data at KiK-net TCG007, sections with relatively large acceleration were extracted, and the seismic waveforms were prepared and input to the analysis model for approximately 120 s, which is the S-wave part of the seismic wave where large changes in acceleration were observed.

3.2 *Seismic analysis of geotechnical models*

In this section, representative geotechnical models were selected from the northern, central and southern cross-sections of Utsunomiya City as section 1, section 2 and section 3(Figure 1) for seismic response analysis by the equivalent linearization method by DYNEQ. In order to make the seismic response analysis more accurate and to reproduce realistic phenomena, and to confirm the differences in seismic response due to differences in geological structure, the geotechnical models were selected on the basis that they contain as much borehole data as possible and have the topographical and geological characteristics of each region. This paper mentioned the results om section 1(Figure 2). The selection assumed that the model should contain as much borehole data as possible and have the geomorphological and geological

characteristics of the regions. The N-value and S-wave velocity models for the regions from section 1 to section 3 created during the construction of the 3D grid model. The N-values show the distribution resulting from quadratic interpolation, and the conversion to the S-wave velocity model uses equations of Ohta and Goto (Ohta, Y. and Goto N., 1978). In consideration of the conversion to S-wave velocity (m/s), the upper limit of the N- value was set to 50. The S-wave velocity model clearly shows a gradual increase in S-wave velocity in the direction of depth, reaching 50 m/s at the top and more than 550 m/s at the deepest part. This S-wave velocity model can be used for seismic response analysis.

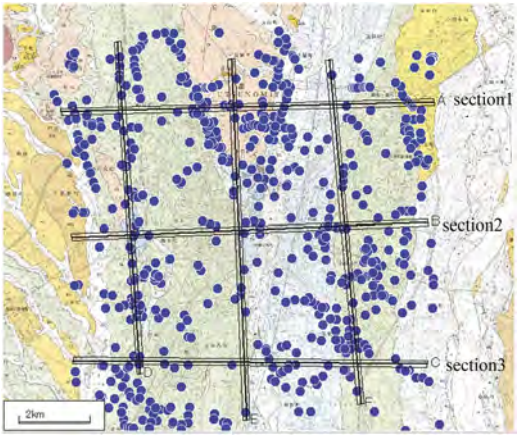

Figure 1. Geology map and borehole data location of Utsunomiya City, blue dots show the borehole location, solid lines are location of cross section.

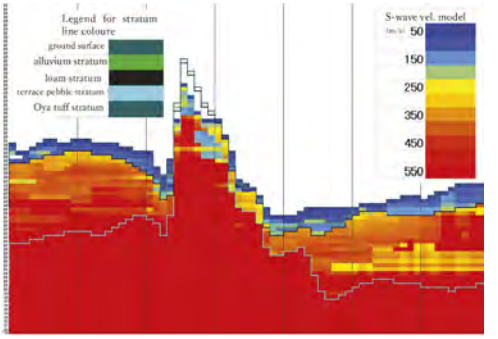

Figure 2. North cross section of S-wave velocity on the 3D grid model (section 1).

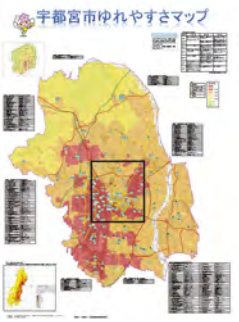

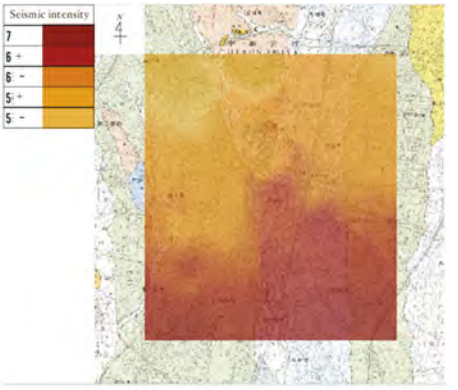

Figure 3. Utsunomiya City Shakeability Map (in Japanese, left hand side) and the seismic intensity distribution on 3D grid model by 3.11 earthquake (right hand side). Solid rectangle on the left figure is the area for 3D grid model on the right figure.

3.3 *Using seismic data for disaster prevention against earthquakes*

The acceleration of the seismic waveform calculated is transformed according to the method specified by Japan Meteorological Agency, JMA, and the measured seismic intensity is calculated. This result is compared with the measured seismic intensity actually observed, and the seismic behaviour of the ground under consideration is discussed. The measured seismic intensities obtained from the seismic data observed in Utsunomiya City at Kik-net TCG007 and those occurring near the ground surface of the analytical model took similar values. Hazard maps in Utsunomiya City provide

information on evacuation and preparation in the event of an increase in the risk of large-scale flooding or landslides due to typhoons, torrential rains or earthquakes, with the aim of predicting the areas where damage may occur and the extent of damage, evacuating citizens to a safe place quickly and minimising the damage. The information on evacuation and preparedness is compiled for the purpose of minimising damage. The shaking susceptibility map shows the location of evacuation centres (left hand side of Figure 3). The seismic intensity-converted values obtained by analysing the input seismic waves of 3.11 earthquake uniformly to the geotechnical model are shown as areal distributions in QGIS software (right hand side of Figure 3). The seismic values obtained from the seismic intensity conversion of the 3D grid model are visualised by the different colours. The conditions are divided into 69 grids in the east-west direction and 81 grids in the north-south direction, and the seismic intensity is converted for each of them. The seismic intensity map shows the distribution of seismic intensity when an earthquake of magnitude 6.9 occurs, with the epicentre as the City Hall (main office). The similarity between these maps is that the southern part of Utsunomiya tends to be more vulnerable to shaking in the flat areas. The Utsunomiya hillside area is at risk of landslides and is subject to evacuation. The difference is that the seismic intensity map of Utsunomiya City has a coarser stepwise distribution of seismic intensity in the southern part of the city. If the grid can be divided more finely, as in this study, detailed information on shaking susceptibility can be obtained.

4 SUMMARY

In this study, an attempt to update and compare the 3D grid model was made in Utsunomiya City, the prefectural capital of Tochigi Prefecture, Japan using borehole data provided by the city hall and prefectural government. The validity of the 3D grid model and the geological characteristics of each area were confirmed and examined for use in disaster prevention through seismic response analysis using one-dimensional seismic response analysis by DYNEQ. The characteristics of the models created were discussed by comparing them with the columnar maps and geological history illustrated for each cross section. The results of seismic response analysis are discussed. Section 1, section 2 and section 3 are divided into three analytical sections. This paper has mentioned section 1 only. The S-wave velocity model clearly shows a stepwise increase in the S-wave velocity model in the direction of depth. The input seismic waves were strong earthquake and a small earthquake. The three patterns in this analysis showed a similar tendency in terms of shaking susceptibility. Finally, the seismic intensity distribution based on the seismic intensity conversion of the 3.11 main shock and small earthquakes is shown for use in disaster prevention against earthquakes. Regarding evacuation centres, it was stated that evacuation centres are expected to be set up in the northwestern part of Utsunomiya City, which is a flat area with low seismic intensity. The seismic analysis in this study differs in some respects from the method of geotechnical modelling and the consideration of seismic models in the government's evaluation of strong ground motions, but the seismic analysis using the 3D grid model was connected to the seismic intensity distribution to create the basis for the hazard map. Comparing the created hazard map with the shaking susceptibility of Utsunomiya City, the similarity is that the southern flat area of Utsunomiya shows a tendency to shake easily and is a dangerous area. In addition, parts of the Utsunomiya hills are at risk of landslides and are subject to evacuation. The difference is that the seismic intensity map of Utsunomiya City has a coarser gradient distribution in the southern part of the city.

REFERENCES

Yoshikawa, T., Geology of the Utsunomiya district, 1. Topography. Quadrangle Series, 1: 50,000, *Geol. Surv. Japan*, AIST, pp.1–4., (in Japanese) 2010.

Utsunomiya City Hall, Utsunomiya City Shakeability Map. HP of Utsunomiya City Hall, https://www.city.utsunomiya.tochigi.jp/kurashi/machi/kenchiku/shidou/1016430.html, (in Japanese), 2020.

Kimura, K., K, Ishihara, Y., Hanashima, Y. and Nemoto, T. (2011) Three-dimensional grid model of the Chuseki-so: a case of the northern Tokyo and the southern Nakagawa Lowlands, no. 539, 29p, 1 CD-ROM, *Geol. Surv. Japan*, AIST, (in Japanese), 2011.

Ohta, Y. and Goto N., Empirical Shear Wave Velocity Equations in Terms of Characteristic Soil Indexes, 6(2),pp.167–187, 1978.

Smart Geotechnics for Smart Societies – Zhussupbekov, Sarsembayeva & Kaliakin (Eds)
© 2023 The Author(s), ISBN 978-1-003-29912-7
Open Access: www.taylorfrancis.com, CC BY-NC-ND 4.0 license

Desiccation crack characterization in clay using deep learning based video instance segmentation method

Xiao-Le Han
Department of Civil and Environmental Engineering, University of Hawaii at Manoa, Honolulu, USA

Ning-Jun Jiang
Institute of Geotechnical Engineering, Southeast University, Nanjing, China

Yi-Jie Wang
Department of Civil and Environmental Engineering, University of Hawaii at Manoa, Honolulu, USA

Ke-Xin Guo
Institute of Geotechnical Engineering, Southeast University, Nanjing, China

ABSTRACT: Clay with different moisture contents has very different mechanical properties, which are vital for the stability of geotechnical structures. When desiccation cracks start to develop, the failure of soil structure might happen. Traditional image processing methods have been extensively applied to analyze the development of desiccation cracks in clay. However, these image analysis methods usually rely on the interval image shooting technique, which lacks continuity and might miss some critical moments during cracking process. This study proposes a deep learning-based video instance segmentation algorithm to locate, identify and segment soil cracks in real-time video stream. The training loss was found less than 0.1. The algorithm could record the cracks' locations and numbers simultaneously. Besides, the crack ratio of clay could be calculated by crack pixels divided by total clay pixels among the entire soil cracking process. The proposed video instance segmentation method monitored the soil crack reached a number of 25 and the crack ration was about 8.5% at the experiment end, which has demonstrated the potential application for crack monitoring of geotechnical infrastructures via surveillance cameras.

1 INTRODUCTION

The generation and propagation of the desiccation crack network within clayey soil is a complex phenomenon controlled by the coupling of soil hydraulic and mechanical characteristics.The propagation of the desiccation crack network could deteriorate the engineering performance of clayey soil, and change the hydraulic properties of soils. Therefore, it is crucial to characterize the patterns of desiccation cracks in clayey soil as they have practical solid implications in geotechnical and geoenvironmental engineering (Lakshmikantha et al., 2009; Taboada et al., 2008).

Traditionally, the inspection and acquisition of soil desiccation crack patterns require in-situ manual measurements (Dasog & Shashidhara, 1993), which take a lot of effort and resources to complete. Also, labor-dependent work lacks automation. Therefore, researchers have sought more intelligent and automated ways to characterize soil cracks. With the rapid developments in computer vision and image processing techniques, many image process techniques (IPTs) have been utilized for crack detection and segmentation in concrete structures, steel structures, and asphalt surfaces (Spencer et al., 2019). To achieve a higher accuracy of

DOI: 10.1201/9781003299127-307

crack segmentation, Otsu's method has been applied in threshold selection to transfer an RGB image into a binary image (Lu et al., 2016; Otsu, 1979). Yamaguchi & Hashimoto, (2010) proposed a percolation-based image processing technique to accelerate the crack detection speed in large-resolution images.

With the development of computer science and information technology, an innovative network was developed by imitating human neuron function, which was named as the artificial neural network (ANN). Inspired by the human visual cortex, a convolutional neural network (CNN) was designed for feature extraction based on ANN (Fukushima & Miyake, 1982; LeCun et al., 1989). He et al., (2017)proposed the mask region conventional neural network (Mask R-CNN) based on Faster R-CNN (Ren et al., 2015)by attaching a binary mask to the detected object, which could help highlight each target from the background with masks in varying colors. Due to its outstanding performance in instance segmentation, the three-fold-function Mask R-CNN soon got the attention of the civil engineering community. So far, Mask R-CNN has been applied for automated crack characterization in various scenarios, such as concrete crack detection (Xu et al., 2022), road crack characterization (Singh & Shekhar, 2018), tunneling crack, and water leakage detection (Zhao et al., 2020), defects detection (concrete crack and spalling) in structure health monitoring (Kim & Cho, 2019), and cable-stayed bridge inspection (Hou et al., 2020). However, few studies have reported video instance segmentation of desiccation cracks in clay.

This study adopted a deep learning approach based on the state-of-the-art Mask R-CNN algorithm for clayey soil desiccation crack characterization. A soil crack dataset consisting of multi-source crack images was prepared and annotated for the Mask R-CNN training, validation, and testing.

2 MATERIALS AND METHODS

2.1 *Soil parameters*

To ensure the repeatability of the experiment, a commercial bentonite was obtained, and a series of soil classification tests were finished. The results of the physical and mechanical properties are listed in Table 1. The soil was oven dried thoroughly before mixing with water and reaching a water content of 120%.

Table 1. The physical and mechanical properties of the bentonite.

Soil parameters	Value
Soil classification (ASTM D2487)	MH
Liquid limit (LL)	95.4%
Plastic limit (PL)	58.2%
Plasticity index (PI)	37.2
Specific gravity (G_s)	2.464
Water content in soil misture(%)	120%

2.2 *Video capture device*

Once the soil mixture was stirred into a uniform paste, it was poured into a transparent petri dish. The petri dish was carefully transferred to a mini photo studio with LED lights. Due to the desiccation process usually taking more than 40 hours, mass storage will be required for the video write-in. An interval image shooting method was obtained using a Nikon D7000 digital camera. The camera will automatically take images of the petri dish every 2 minutes, and later these images can be compressed into a video for further instance segmentation.

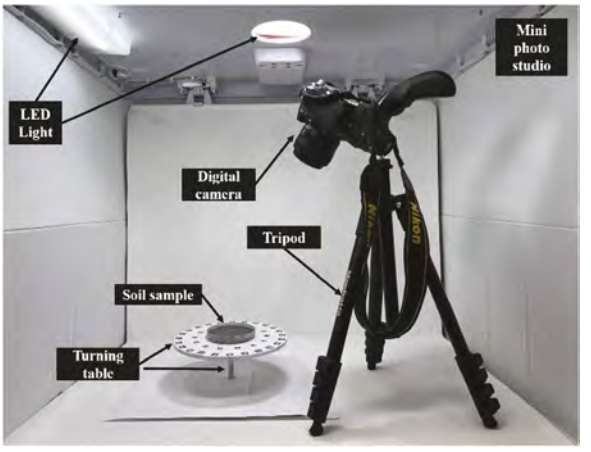

Figure 1. Video recording setup.

2.3 *Mask R-CNN architecture*

Mask R-CNN adopts a two-stage framework to accomplish the detection, locating, and segmentation with sufficient accuracy. Crack images are fed into the backbone network (Resnet-50) and unique feature maps are produced at the first stage. Based on a feature map, a region proposal network (RPN) could generate a series of pre-designed bounding boxes that possibly contain targets (i.e., cracks in this study). These bounding boxes are also known as regions of interest (RoI). Taking Figure 2 as an example, it could be found that more proposed bounding boxes are shown on the right side since the crack appears on the right side of the image. Then, the RoIAlign properly aligns the proposed bounding boxes on the feature map with a more accurate location, which results in a higher detection precision (He et al., 2017). At the second stage, the fully connected (FC) layers passed the fixed feature map to a normalized exponential function (SoftMax) and a bounding box regression layer parallelly, giving the classification and object detection results, respectively. Parallelly, a full convolution network (FCN) is utilized to generate a binary mask, which could segment the detected objects from the background.

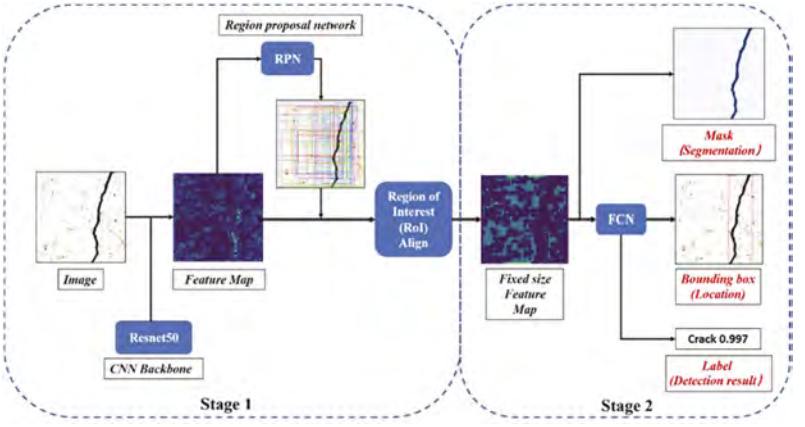

Figure 2. Mask R-CNN algorithm structure diagram.

2.4 *Dataset preparation*

The clayey soil crack images were obtained from Google Images, Instagram, and laboratory-captured images to prepare the dataset. Therefore, the diversity of the dataset could be assured and the high generalization ability of the proposed algorithm could be achieved. After all raw images were downloaded or captured, these images were cut into a series of small patches with a uniform resolution of 256×256 pixels through a Python program (Han et al., 2022). This way, a balance between keeping image details and lowering computational demands can be sustained. In total, 1200 crack images were selected and shuffled randomly to eliminate the bias from the same image. Within these chosen crack images, images originating from Google Images, Instagram and laboratory accounted for 60%, 20%, and 20%, respectively.

In the current study, the images were annotated using the VGG Image Annotator (Dutta & Zisserman, 2019). All cracks in the images were carefully annotated along their boundaries using the polygon region shapes. All annotation information, including file name, category name, coordinates of the polygon, etc., were saved into a json file and ready for the training process. Then the total dataset was further divided into the training set, validation set and test set, as shown in Table 2.

Table 2. Image details in the soil crack dataset.

Dataset name		Amount	Resolution
Calibration set (90%)	Training set (80%)	864	256×256
	Validation set (20%)	216	256×256
Test set (10%)		120	256×256
Total		1200	256×256

3 RESULTS AND DISCUSSIONS

3.1 *Model training and validation*

The online platform Google Colaboratory (Colab) was used for the Mask R-CNN model training and fine-tuning. The platform offers a Tesla P100 GPU (16 GB graphic memory) for online model training.

To balance the calculation efficiency and hardware capacity, the batch size of the training dataset was set as 8, and the synchronous stochastic gradient descent (SGD) was used to train the model with the weight decay and momentum set as 0.0001 and 0.9, respectively. A stage-wise training strategy was adopted here to help the model converge earlier and avoid gradient explosion in the early training phase. To begin with, the head part of the whole network composed of the bounding box generator and mask generator was trained for 10 epochs at an initial learning rate of 0.001. Then, for the subsequent 40 epochs, the learning rate was reduced by 10 times and the first three stages of the Resnet-50 were activated to continue the training process. After that, the learning rate was decreased by 10 times again and all five stages of the Resnet-50 were activated to train another 100 epochs. Finally, the learning rate was decreased by another 10 times until the last 50 epochs were finished. The entire training process took less than 6 hours to complete.

The loss curves during the training and validation process in the current study are shown in Figure 3. The training loss curves demonstrate a sharp decline at the initial 10 epochs, which indicates the algorithm parameters and dataset size were reasonable. Then the loss curve showed a smooth and slow declination from about 0.6 to less than 0.1. Thus no overfitting was observed during the training and validation period (Hou et al., 2020).

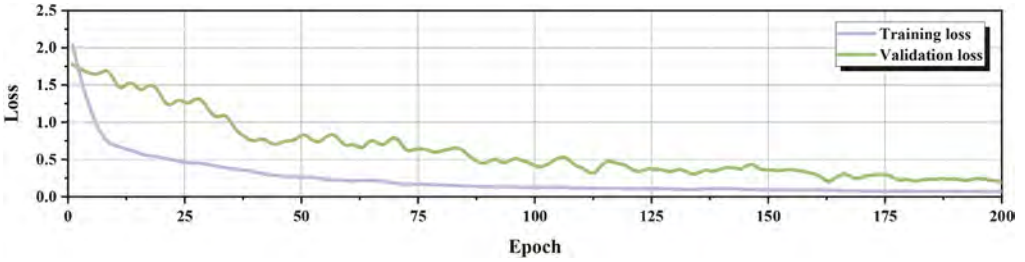

Figure 3. Curves of the loss function during model training and validation process.

3.2 *Soil crack characterization via images*

Before the Mask R-CNN is applied to video instance segmentation, the algorithm is executed on the test dataset. The inference results of the instance segmentation and crack characterization are shown in Figure 4. The raw images containing various crack patterns are shown in Figure 4(a)-(d), and the crack characterization results are exhibited in Figure 4(e)-(h). The green bounding box reveals the crack locations within the image. The crack number, crack pixel area, and crack ratio(total crack area in pixels/total soil area in pixels) are shown on the left corner of each detected crack. For example, three soil cracks are detected, located, and segmented in Figure 4(f). The most significant crack in Figure 4(f) is crack No.2, with a crack area of 894 pixels, which accounts for 1.36% of the total soil area in the image. The test dataset has proved the accuracy and efficiency of the Mask R-CNN algorithm. Xu et al., (2022) achieved soil crack recognition using a semantic segmentation algorithm (U-Net)(Ronneberger et al., 2015). The method could calculate the crack ratio but fail to distinguish every crack. The defects of the semantic segmentation algorithm make it hard to extract useful information like single object dimension and object amount. However, the semantic segmentation algorithm usually requires less dataset and training efforts. A detailed evaluation shall be made before adopting these algorithms with different focuses.

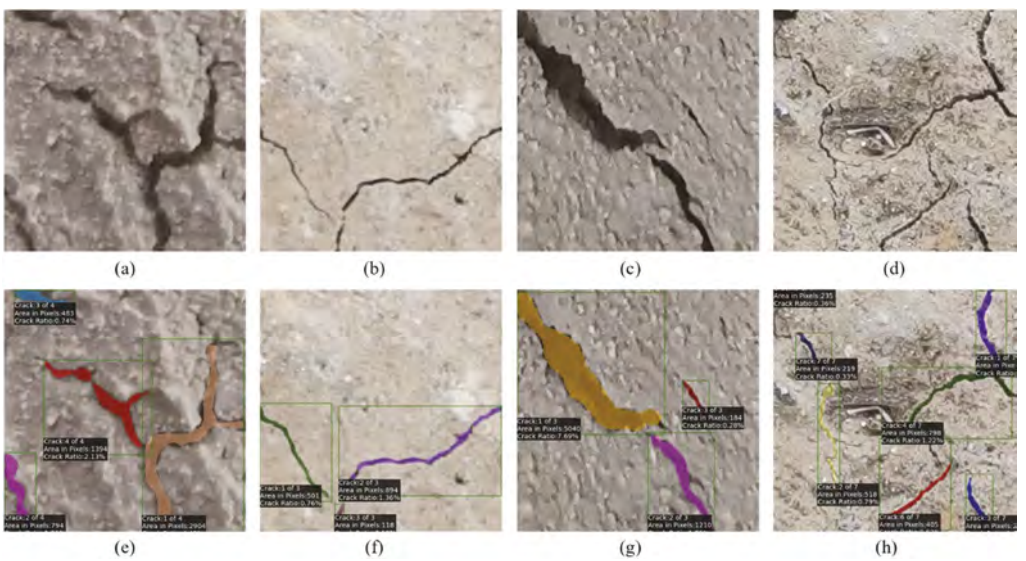

Figure 4. Instance segmentation results of the desiccation crack in clay:(a)-(d) raw images from the test dataset;(e)-(h)characterization results from the Maks R-CNN algorithm.

3.3 *Soil crack characterization via videos*

3.3.1 *Instance segmentation results*

During the whole desiccation process of the clay, 1500 images are captured through the camera at an interval of 2 mins. These images are transferred into a 50 seconds video with a resolution of 3840×2160 pixels. The video has a frame ratio of 30 FPS (frame per second). The video will later be fed into the Mask R-CNN algorithm to implement the instance segmentation and crack characterization tasks.

In order to demonstrate the results from the abovementioned tasks, four sample frames are extracted from the video and displayed in Figure 5. Figure 5(a)-(d) shows the raw images of the desiccation crack. With the speckle pattern, it is not easy to spot the thin cracks at the initial stage of the desiccation process. Besides, the crack pattern and number are more complex and less significant than the cracks shown in Figure 4. However, the algorithm could successfully detect, locate and segment these cracks, as shown in Figure 5(e)-(h), which proves an excellent generalization capability of the model. These cracks have been highlighted with different colors. Thus, the shapes can be observed with less effort.

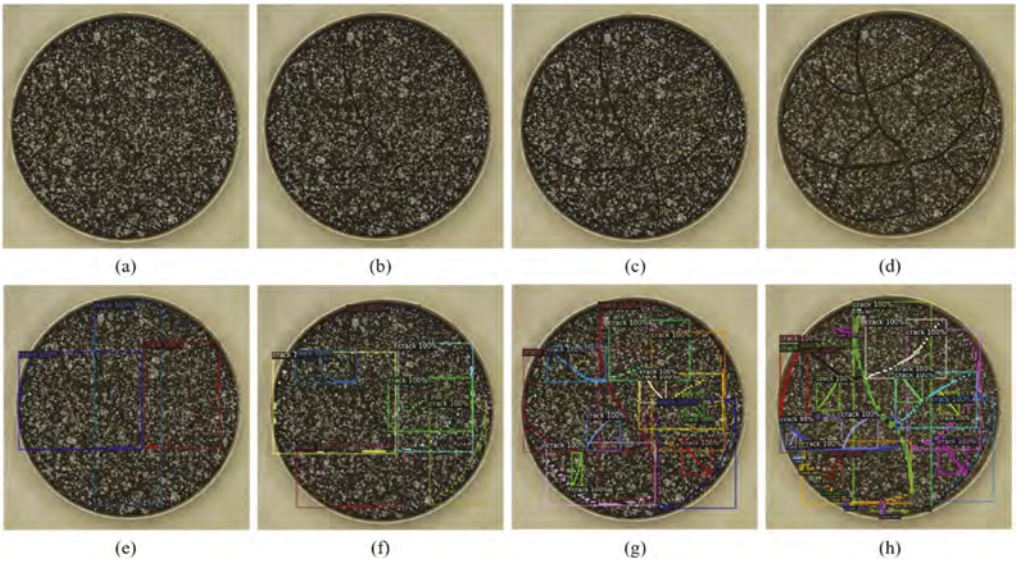

Figure 5. Instance segmentation results of the desiccation crack in the clay.

3.3.2 *Crack characterization results*

During the clay desiccation process, the crack network develops from a single thin crack into a crack backbone structure that covers the top, bottom, left, and right sides of the petri dish. After that, more minor cracks begin to expand along the branches. Finally, these cracks develop into a crack network. There are 3, 7, 13, and 27 cracks detected in Figure 6(a)-(d). The pixel area and the crack ratio of each crack are also listed in the image.

After the algorithm processes the entire video, the crack number and crack ratio of each frame are calculated automatically by the algorithm. The results are demonstrated in Figure 7. It can be seen from Figure 7 that the first crack is generated around 1870 minutes after the experiment starts. When the experiment lasts 2100 minutes, the crack number reaches the first plateau (15 cracks). The plateau phenomenon was also reported by Zeng et al., (2019), where crack segments number reached a plateau at about 3000 minutes. However, only one plateau was reported in their study and the image sampling frequency was not provided.

When it comes to the crack ratio, the crack ratio keeps increasing from 5% to 6.5% until it reaches its plateau at 2190 minutes. The delay of the crack ratio indicates that once 15 cracks are generated, these cracks keep growing longer or thicker to cover more area of the clay. The

same pattern can be seen from 2700 minutes when the crack number peaks at 27. Nevertheless, the crack ratio increased slowly from around 8.2% to 8.5%. Yang et al., (2021) utilized the traditional image processing (IPT) method (binarization method) to monitor the soil crack ratio. The desiccation crack ratio at the end varies from 6% to 11%. The image sampling interval was not reported either.

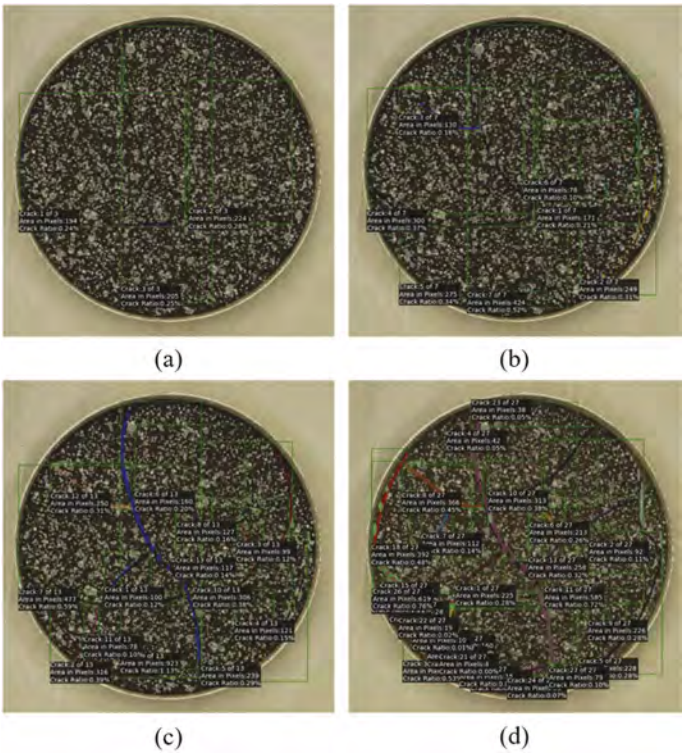

Figure 6. Video instance segmentation results in desiccation cracks in clay.

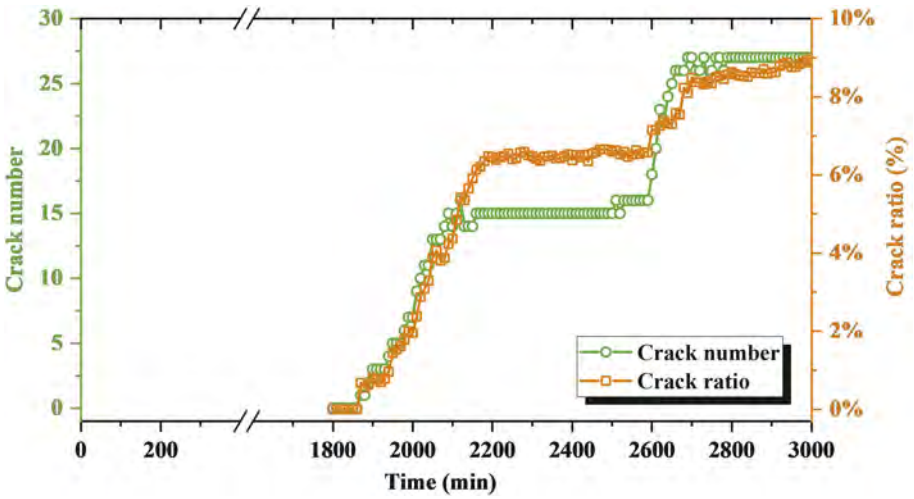

Figure 7. Characterization results of desiccation cracks in clay via video instance segmentation.

4 CONCLUSION

In the current study, a state-of-the-art deep-learning algorithm Mask R-CNN was introduced for clayey soil desiccation crack characterization via video instance segmentation. The Mask R-CNN could automatically detect, locate and segment soil desiccation cracks with sufficient accuracy and efficiency. The following conclusions could be obtained: (1) A mixing dataset containing images from multi-sources can be used for Mask R-CNN algorithm training and validation. The trained model can be applied for desiccation crack characterization in clay. The model has proved the generalization capacity of the algorithm. (2) The algorithm can be applied to the instance segmentation of images and videoes. Essential information like crack location, area, and shape can be displayed. (3) The algorithm captured the final crack number to be 25 and the crack ratio of 8.5%. Besides, the delay phenomenon of the crack ratio and the crack number would be an interesting topic for future research. (4) The algorithm demonstrates its potential to characterize soil desiccation cracks automatically, which can improve crack monitoring accuracy and efficiency.

ACKNOWLEDGEMENTS

This study was financially supported by the Natural Science Foundation of China (No. 42007246) and the Hawaii Department of Transportation (No. 2020-4R-SUPP). We would also like to thank Google Colab for offering online computation resources to all deep learning users.

REFERENCES

Dasog, G. S., & Shashidhara, G. B. (1993). Dimension and volume of cracks in a vertisol under different crop covers. In Soil Science (Vol. 156, Issue 6, pp. 424–428). https://doi.org/10.1097/00010694-199312000-00007

Dutta, A., & Zisserman, A. (2019). The VIA Annotation Software for Images, Audio and Video. *Proceedings of the 27th ACM International Conference on Multimedia*, 2276–2279. https://doi.org/10.1145/3343031.3350535

Fukushima, K., & Miyake, S. (1982). Neocognitron: A self-organizing neural network model for a mechanism of visual pattern recognition. In *Competition and cooperation in neural nets* (pp. 267–285). Springer.

Han, X., Jiang, N., Yang, Y., Choi, J., Singh, D. N., Beta, P., Du, Y., & Wang, Y. (2022). Deep learning based approach for the instance segmentation of clayey soil desiccation cracks. *Computers and Geotechnics*, *146* (March), 104733. https://doi.org/10.1016/j.compgeo.2022.104733

He, K., Gkioxari, G., Dollar, P., & Girshick, R. (2017). Mask R-CNN. *2017 IEEE International Conference on Computer Vision (ICCV)*, 2980–2988. https://doi.org/10.1109/ICCV.2017.322

Hou, S., Dong, B., Wang, H., & Wu, G. (2020a). Automation in Construction Inspection of surface defects on stay cables using a robot and transfer learning. *Automation in Construction*, *119* (October 2019), 103382. https://doi.org/10.1016/j.autcon.2020.103382

Hou, S., Dong, B., Wang, H., & Wu, G. (2020b). Inspection of surface defects on stay cables using a robot and transfer learning. *Automation in Construction*, *119*, 103382. https://doi.org/10.1016/j.autcon.2020.103382

Kim, B., & Cho, S. (2019). Image-based concrete crack assessment using mask and region-based convolutional neural network. *Structural Control and Health Monitoring*, *26*(8), 1–15. https://doi.org/10.1002/stc.2381

Lakshmikantha, M. R., Prat, P. C., & Ledesma, A. (2009). Image analysis for the quantification of a developing crack network on a drying soil. *Geotechnical Testing Journal*, *32*(6), 505–515. https://doi.org/10.1520/GTJ102216

LeCun, Y., Boser, B., Denker, J. S., Henderson, D., Howard, R. E., Hubbard, W., & Jackel, L. D. (1989). Backpropagation Applied to Handwritten Zip Code Recognition. *Neural Computation*, *1*(4), 541–551. https://doi.org/10.1162/neco.1989.1.4.541

Lu, Y., Liu, S., Weng, L., Wang, L., Li, Z., & Xu, L. (2016). Fractal analysis of cracking in a clayey soil under freeze-thaw cycles. *Engineering Geology*, *208*, 93–99. https://doi.org/10.1016/j.enggeo.2016.04.023

Otsu, N. (1979). A Threshold Selection Method from Gray-Level Histograms. *IEEE Transactions on Systems, Man, and Cybernetics*, *9*(1), 62–66. https://doi.org/10.1109/TSMC.1979.4310076

Ren, S., He, K., Girshick, R., & Sun, J. (2015). *Faster R-CNN: Towards Real-Time Object Detection with Region Proposal Networks*. http://arxiv.org/abs/1506.01497

Ronneberger, O., Fischer, P., & Brox, T. (2015). *U-Net: Convolutional Networks for Biomedical Image Segmentation*. http://arxiv.org/abs/1505.04597

Singh, J., & Shekhar, S. (2018). *Road Damage Detection And Classification In Smartphone Captured Images Using Mask R-CNN*. http://arxiv.org/abs/1811.04535

Spencer, B. F., Hoskere, V., & Narazaki, Y. (2019). Advances in Computer Vision-Based Civil Infrastructure Inspection and Monitoring. *Engineering*, *5*(2), 199–222. https://doi.org/10.1016/j.eng.2018.11.030

Taboada, M. A., Barbosa, O. A., & Cosentino, D. J. (2008). Null creation of air-filled structural pores by soil cracking and shrinkage in silty loamy soils. *Soil Science*, *173*(2), 130–142. https://doi.org/10.1097/SS.0b013e31815d8e9d

Xu, J.-J., Zhang, H., Tang, C.-S., Cheng, Q., Liu, B., & Shi, B. (2022). Automatic soil desiccation crack recognition using deep learning. *Géotechnique*, *72*(4), 337–349. https://doi.org/10.1680/jgeot.20.P.091

Yamaguchi, T., & Hashimoto, S. (2010). Fast crack detection method for large-size concrete surface images using percolation-based image processing. *Machine Vision and Applications*, *21*(5), 797–809. https://doi.org/10.1007/s00138-009-0189-8

Yang, B., Li, D., Yuan, S., & Jin, L. (2021). Role of biochar from corn straw in influencing crack propagation and evaporation in sodic soils. *Catena*, *204*(88), 105457. https://doi.org/10.1016/j.catena.2021.105457

Zeng, H., Tang, C. sheng, Cheng, Q., Inyang, H.I., Rong, D. zheng, Lin, L., & Shi, B. (2019). Coupling effects of interfacial friction and layer thickness on soil desiccation cracking behavior. *Engineering Geology*, *260* (June),105220. https://doi.org/10.1016/j.enggeo.2019.105220

Zhao, S., Zhang, D. M., & Huang, H. W. (2020). Deep learning–based image instance segmentation for moisture marks of shield tunnel lining. *Tunnelling and Underground Space Technology*, *95* (February 2019), 103156. https://doi.org/10.1016/j.tust.2019.103156

Smart Geotechnics for Smart Societies – Zhussupbekov, Sarsembayeva & Kaliakin (Eds)
© 2023 The Author(s), ISBN 978-1-003-29912-7
Open Access: www.taylorfrancis.com, CC BY-NC-ND 4.0 license

Challenges associated with the use of earth pressure cells in field tests

Dinesh Bishnoi, Vikas Patil & S.M. Dasaka
Civil Engineering Department, Indian Institute of Technology, Bombay, India

ABSTRACT: Earth pressure cells (EPCs) are the most common part of any geotechnical instrumentation project. These are used on the structures or within the soil to monitor soil pressures or to verify the adopted design methodology. The selection of EPC type varies depending on the project requirement. In present paper, a brief idea is given to the new EPC users about the parameters that needed to be considered while selecting EPC for field studies. The challenges associated with EPC installation, EPC output reliability and other miscellaneous factors are discussed by mentioning the issues faced by authors during field testing. Proper EPC selection, calibration and installation is very essential for obtaining reliable data from the EPCs.

1 INTRODUCTION

In geotechnical engineering, field studies are essential to verify the results obtained by small-scale physical model tests or through numerical simulation. Instrumentation is an important component of field studies and the measurement of earth pressure is a common parameter in various structures such as retaining structures, buried pipelines, tunnels, etc. There are several types of Earth Pressure Cells (EPCs) available for the measurement of earth pressure. Keykhosropour et al. (2018) mentioned briefly the types of EPCs available. Extensive work is carried out by the researchers such as Selig (1980), Weiler & Kulhawy (1982), Hanon & Jackura (1985), Take & Valsangkar (2001), Kootahi & Leung (2022), etc., to understand the parameters that affect the performance of EPCs. It can be found that there are multiple parameters that can affect the response of EPC such as soil properties, properties of contact material, if different from soil, EPC properties, installation methods, temperature, etc.

An understanding of the EPC from literature is necessary before procurement but the aim of the present study is to give an idea to EPC users about the factors that need to be considered when selecting EPCs for field tests, which are seldom mentioned in the literature. The authors of the present study constructed a retaining wall of 6 m height to perform large-scale tests for understanding the behavior of Expanded polystyrene (EPS) as an inclusion material and EPCs were a major part of the instrumentation of the field study. Thus, the challenges faced during the field tests such as EPC selection, EPC installation, and reliability of measurement are mentioned briefly in the present paper.

2 PARAMETERS FOR SELECTION OF SUITABLE EPC

The EPC selection is dependent on several parameters such as expected pressure, measurement type, project type, budget, etc. Some of the parameters are discussed below which were considered before purchasing EPCs for the field project carried out to assess the suitability of EPS as an inclusion material.

DOI: 10.1201/9781003299127-308

2.1 *EPC capacity and accuracy*

The expected pressures in the field are calculated by using the traditional earth pressure theories and the EPC capacity required should be determined accordingly. The EPC capacity should be taken 1.5-2 times the calculated pressure to take into account the uncertainties associated with the field studies such as compaction stresses, environmental changes, temperature effects, etc., and more importantly, the uncertainties associated with the transformation model used to estimate the earth pressures.

The EPCs are available in various ranges such as 200 kPa, 350 kPa, 500 kPa, etc. and generally, there is no difference in cost due to the EPC range for same model types but the accuracy or least count of the EPC is dependent on the range of the EPC. The least pressure that can be measured by the EPC is some percentage of the EPC capacity or Rated Output (RO). For an EPC if it is 0.05% of RO then for 200 kPa, it is 0.1 kPa but for 500 kPa it increases to 0.25 kPa. Thus, the EPC should be selected by considering the expected pressures as well as the accuracy of pressure required for the tests.

2.2 *Type of EPC*

There are numerous types of EPCs available that work on different principles such as strain-gauge based, vibrating-wire based, tactile pressure sensors, null pressure based sensors, etc. The selection of EPC type depends on whether the measurements are static or dynamic and the monitoring period i.e., short-term or long-term monitoring. Strain gauge-based EPCs are able to measure dynamic variations but they undergo drift with time. The vibrating wire EPCs are found to be more suitable for long-term monitoring but for dynamic measurements, the EPC cost increases significantly.

2.3 *Calibration of EPC*

The EPC manufacturer generally provides a calibration chart for each EPC, generated by correlating the EPC response to the applied pressure. Usually, the manufacturer calibration is carried out in a fluid medium due to its simplicity but for soil, the calibration values may be different from the fluid. Thus, it is recommended that the EPC is calibrated for both fluid and soil conditions. The fluid calibration can be carried out in the modified triaxial calibration device suggested by Dave & Dasaka (2013) or the Pneumatic calibration chamber (PCC) by Gade & Dasaka (2018). Set-up similar to the universal calibration chamber developed by Theroux et al. (2001) can be used for soil calibration.

3 CHALLENGES WITH EPC IN THE FIELD

3.1 *EPC Installation*

The EPC sensing surface should be flushed with the interface of the structure during installation to minimize the deviation of measurements from the absolute values (Lazebnik & Tsinker 1998). The EPC can be installed during the construction of the structure or suitable openings should be provided if the EPCs are not available during the construction.

The procedure followed for the installation of dual diaphragm EPC used in the field study is shown in Figure 1. Apart from the flushing of the EPC with the surface, the base prepared for EPC (refer to Figure 1c) should be strong and uniform so that EPC gets a proper reaction. Depending on the type of EPC, the installation process will vary but two key points mentioned above should be taken care of properly.

3.2 *Contact material with EPC*

It is not necessary that the material in contact with the earth pressure cells will always be soil as the use of various materials such as geosynthetics, waste rubber tyres, fly ash, etc. is rapidly

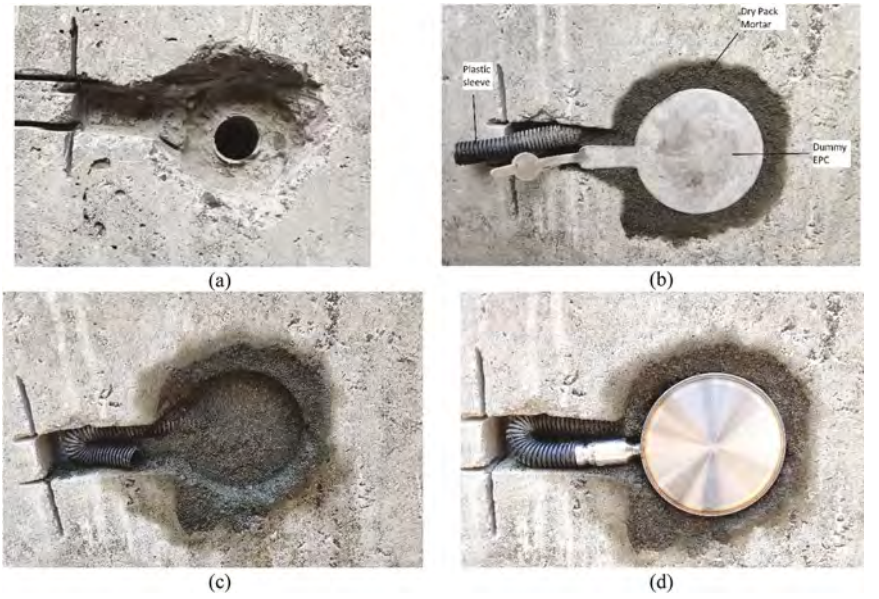

Figure 1. EPC installation process a) the groove made during construction, b) the filling of groove with mortar using a dummy EPC, c) the slot made in the wall for EPC after proper curing and, d) the final installation of EPC.

increasing. Gade & Dasaka (2019) mentioned that the response of EPC changes when the contact material changes. Calibration tests with three different contact materials are performed with diaphragm type EPC and the result is shown in Figure 2. The slope of the equation shown in Figure 2 represents the calibration value for that particular case. Thus, it can be observed that the calibration factor provided by the manufacturer gives higher pressures compared to the actual pressure which can be obtained by using soil calibration factor. It can be seen from Figure 2 that even if the material is sand, there is difference in calibration value. Thus, the EPC should be calibrated with the contact material expected in the field prior to installation and to the likely densities to be achieved during the actual backfilling.

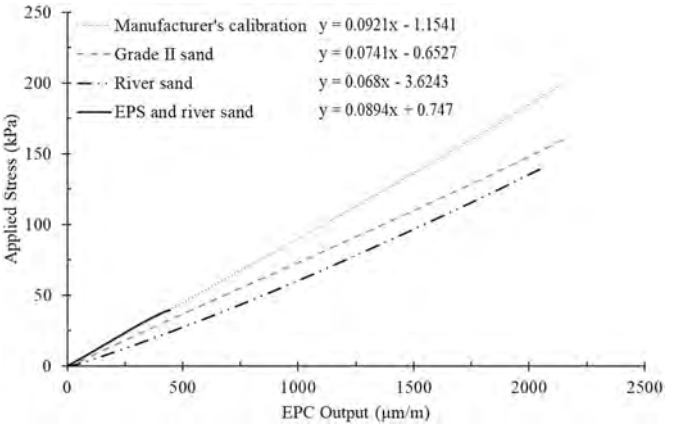

Figure 2. Calibration result of dual diaphragm EPC with Grade II sand, river sand and Expanded polystyrene (EPS) - sand as contact material.

3.3 *Reliability of EPC data*

The EPC calibration along with proper installation are important for field studies but the data obtained by the EPCs should be sensible and user should analyse the data properly. For example, Figure 3 shows the lateral earth pressure measured by 4 nos. of EPCs at same height on a cantilever concrete retaining wall constructed to study suitability of EPS as inclusion material as mentioned earlier.

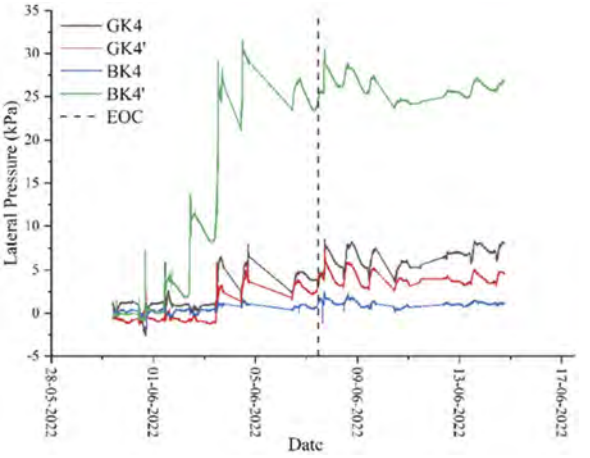

Figure 3. Earth pressure recorded by EPCs in control case (GK4 & GK4') and EPS inclusion case (BK4 & BK4').

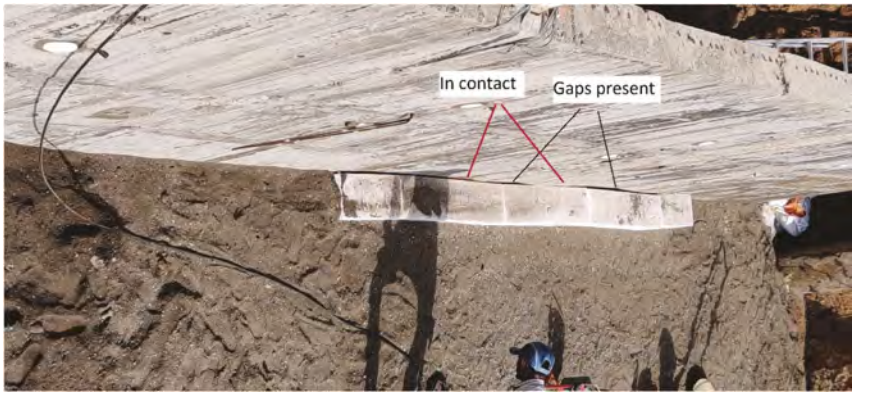

Figure 4. Inadequate contact between EPS and pressure sensor causing earth pressure measurement errors.

Two EPCs are placed on control side (i.e., no EPS inclusion) viz. GK4 & GK4' and two EPCs are placed with EPS as contact material viz. BK4 and BK4' in Figure 3. The EPCs in control case showed sensible results but in EPS inclusion case, the EPCs are giving either extremely high (BK4') or extremely low pressures (BK4) compared to control case. By carrying out some site investigation it was found that at the EPS locations, the EPS blocks are not in contact with the wall uniformly, as shown in Figure 4, which led to error in pressure measurements. Thus, as suggested by Hanon & Jackura (1985), apart from EPCs some other alternatives should also be used to back up the data obtained by EPCs regarding soil stress conditions.

3.4 *Miscellaneous*

There are other miscellaneous factors also which can affect the performance of the EPCs in field studies such as corrosion, water proofing, damage by compaction etc. It is necessary that the EPCs are properly protected against the corrosion before installation and the zone at the cable-sensor connection should be covered by waterproof material. The EPCs may get damaged during compaction by the compaction equipment, thus at least a layer of manually compacted sand should be provided above EPC or the manual of EPC should be referred to avoid damage of the sensors.

4 CONCLUSIONS

The selection of suitable EPC for field tests is important to get reliable results. The capacity of EPC and its type should be determined by calculating the expected earth pressures and project requirement respectively. It is necessary to calibrate these EPCs with the actual contact material expected in the field prior to installation as the calibration factor of EPC changes with contact material. There are numerous unknown factors in the field that can affect the response of EPC output and use of alternative methods along with EPC will provide confidence in EPC measured data.

REFERENCES

Dave, Trudeep N., and S. M. Dasaka. 2013. In-House Calibration of Pressure Transducers and Effect of Material Thickness. *Geomechanics and Engineering* 5(1): 1–15. https://doi.org/10.12989/gae.2013.5.1.001.

Gade, Vinil Kumar, and S. M. Dasaka. 2018. Calibration of Earth Pressure Sensors. *Indian Geotechnical Journal* 48 (1): 142–52. https://doi.org/10.1007/s40098-017-0223-0.

Gade, Vinil Kumar, and S. M. Dasaka. 2019. Influence of Contacting Material on Calibration Response of Diaphragm Earth Pressure Cells. *Indian Geotechnical Journal* 50(1): 133–41. https://doi.org/10.1007/s40098-019-00363-9.

Hannon, Joseph B., and Kenneth A. Jackura. 1985. Measurement of Earth Pressure. *Transportation Research Record*, no. 1004: 6–13. https://doi.org/10.1016/0148-9062(86)91797-3.

Keykhosropour, Lohrasb, Anne Lemnitzer, Lisa Star, Antonio Marinucci, and Steve Keowen. 2018. Implementation of Soil Pressure Sensors in Large-Scale Soil-Structure Interaction Studies. *Geotechnical Testing Journal* 41 (4): 730–46. https://doi.org/10.1520/GTJ20170163.

Kootahi, Karim, and Anthony Kwan Leung. 2022. Effect of Soil Particle Size on the Accuracy of Tactile Pressure Sensors. *Journal of Geotechnical and Geoenvironmental Engineering* 148(10): 1–10. https://doi.org/10.1061/(asce)gt.1943-5606.0002899.

Lazebnik, George E., and Greogory P. Tsinker. 1998. *Monitoring of Soil-Structure Interaction : Instruments for Measuring Soil Pressures*. Springer Science & Business Media Dordrecht.

Selig, E. T. 1980. Soil Stress Gage Calibration. *Geotechnical Testing Journal* 3(4): 153–58. https://doi.org/10.1016/0148-9062(82)91104-4.

Take, W. A., and A. J. Valsangkar. 2001. Earth Pressures on Unyielding Retaining Walls of Narrow Backfill Width. *Canadian Geotechnical Journal* 38(6): 1220–30. https://doi.org/10.1139/cgj-38-6-1220.

Theroux, Brent, Joseph F. Labuz, and Shongtao Dai. 2001. Field Installation of an Earth Pressure Cell. *Transportation Research Record*, no. 1772: 12–19. https://doi.org/10.3141/1772-02.

Weiler, William A. and Fred H. Kulhawy. 1982. Factors Affecting Stress Cell Measurements in Soil. *Journal of Geotechnical and Geoenvironmental Engineering* 108: 1529–1548.

Smart Geotechnics for Smart Societies – Zhussupbekov, Sarsembayeva & Kaliakin (Eds)
© 2023 The Author(s), ISBN 978-1-003-29912-7
Open Access: www.taylorfrancis.com, CC BY-NC-ND 4.0 license

Application of soil moisture sensor with submersion detection to slope

K. Omine
Nagasaki University, Nagasaki, Japan

ABSTRACT: The author developed a cheap and simple sensor for measurement of soil moisture using a voltage control element transistor (MOSFET). The soil moisture sensor consists of multi-MOSFETs, carbon electrodes, plastic rod, PVC pipe, and cloth for cover. The moisture sensor can be installed into a hole made by portable cone rod in arbitrary depth of the slope. Voltage of the sensor is measured and the value is converted to soil moisture. One of MOSFET detects a submerged condition of the soil. The moisture sensor is applied at a site of the slope and its applicability is discussed based on the field observation. From the result, it is indicated that the simple sensor using MOSFET are useful for not only the measurement of soil moisture but also detection of submerged condition of the ground.

1 INTRODUCTION

Due to the effects of torrential rains and typhoons caused by climate change, river floods and sediment-related disasters occur frequently. Many countries are facing the deterioration of social capital, and it is required to control the maintenance cost of soil structures and reduce the damage in the event of a disaster. Therefore, it is expected to develop a low-cost, power-saving, long-distance communication system that can observe, detect, and communicate ground moisture condition in real time .The cause of the collapse of slopes on steep slopes is a rise in groundwater level due to heavy rain. Although it is difficult to identify the location of the slope failure, it is important to grasp the risk of collapse in advance by observing the rise in groundwater level and the submerged ground condition in real time.

This paper introduces a soil moisture sensor with submersion detection that can detect various states of the ground using a voltage control element. In addition, The author will describe the concept of a ground water detection system by combining wireless communication and simple sensors, and discuss on the results by field observation on steep slope.

2 SOIL MOISTURE SENSOR USING VOLTAGE CONTROL ELEMENT

MOSFET is a type of transistor, and there are two types, N-channel type and P-channel type. Basically, a 3-terminal electrode (gate, drain, source) is used, and when a voltage is applied to the gate of the P channel used in this study, the drain is turned off. For the P-ch MOSFET, the voltage of the drain is turned on before the electrodes A and B are submerged in water, and is turned off when the electrodes A and B are submerged in water. In this circuit, the voltage changes according to the magnitude of the resistance attached to the gate of the MOSFET and the amount of soil moisture. Taking advantage of this feature, the author will make a simple soil moisture sensor.

Figure 1 shows the results of investigating the relationship between resistance and voltage by inserting electrodes A and B into sand with different soil moisture content. The larger the resistance, the more sensitive the voltage changes to a slight change in volume moisture content. The smaller the resistance, the larger the volume moisture content at which the voltage drops. Although the voltage does not change with a smaller resistance (10 kΩ), it is possible to measure the difference in the volumetric water content of the soil by changing the resistance

DOI: 10.1201/9781003299127-309

within a certain range. However, this relationship changes depending on the type of soil and the salinity in the soil, it is therefore calibration is required. Using this feature, the author will try to construct a soil moisture sensor and a soil submersion detection sensor.

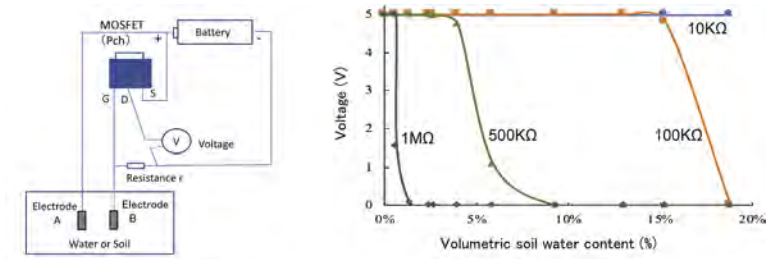

(a) MOSFET circuit diagram (b) Measurement of voltage

Figure 1. Relationship between voltage and volumetric soil moisture content at different resistances.

3 APPLICATION OF THE SOIL MOISTURE SENSOR FOR SLOPE MONITORING

3.1 *Overview of soil moisture sensor with submersion detection*

Figure 2 (a) shows the circuit diagram of the soil moisture sensor. Here, four pieces of MOSFET are used to detect four different water contents. Different resistances ri reacting to each soil moisture are connected from the gate of the MOSFET circuit to the minus (GND). The larger the resistance value, the smaller the soil water content, and the smaller the resistance value, the higher the soil water content. If the resistance R attached to the drain of the MOSFET is connected in parallel, it is possible to know a number of reacting MOSFETs by measuring the voltage value of the resistance R'. In addition, a change of R' enables to arrange by setting resistance Ri to an appropriate value. In this study, R_1 = 100kΩ, R_2 = 150kΩ, R_3 = 180kΩ, and R_4 = 220Ω are used. For example, if the number of responding sensors is 0 (low water content), the voltage of the resistance R' becomes the maximum value, and if all the sensors (high water content) react, the resistance R' becomes 0V. Furthermore, the structure of submersion detection sensor is shown in Figure 2 (b). The submersion detection sensor has a structure of an electrode in 20 mm length, tube, mesh, and non-woven fabric, and the total length is about 30 mm. The submersion detection sensor reacts by wrapping a non-woven fabric and when excess water touches a carbon rod. In addition, since the water attached to the non-woven fabric may not separate from the carbon rod, a mesh is wrapped between the non-woven fabric and the carbon rod. The apparatus consists of three soil moisture sensors and one submersion detection sensor, and when the submersion detection sensor reacts, the voltage becomes 0V. Therefore, from the voltage value of the resistance R', the author can confirm not only the soil moisture level but also whether it has saturated and submerged.

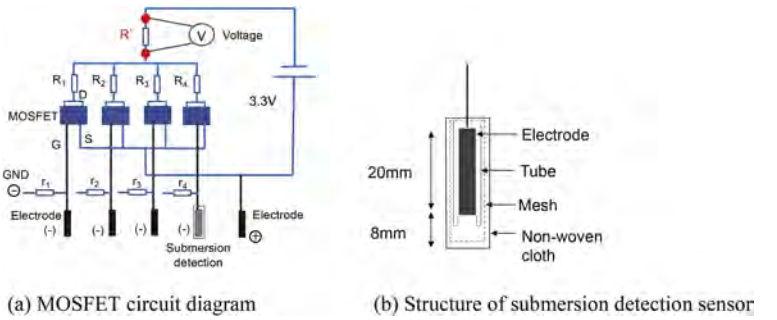

(a) MOSFET circuit diagram (b) Structure of submersion detection sensor

Figure 2. Circuit of soil moisture sensor with submersion detection.

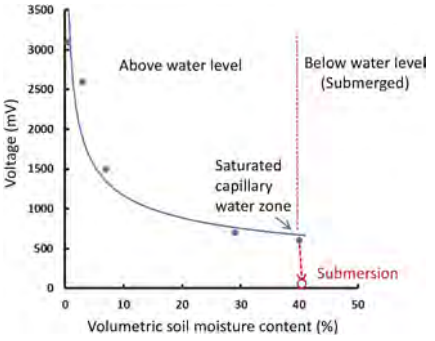

Figure 3. A change of voltage value of the soil moisture sensor with submersion detection.

Figure 3 shows the relationship between the volumetric soil moisture content and the voltage value by the submersion detection sensor. It was confirmed that the voltage was 1000mV or less in the saturated capillary water zone on the groundwater table, all three resistances (r_1, r_2, r_3) of the soil moisture sensor reacted, and the submersion detection sensor did not react. In addition, the voltage became zero below the groundwater level, indicating that the submersion detection sensor can respond correctly to the submerged state.

3.2 *Verification by field observation of slope*

The soil moisture sensor is connected with wireless communication device (TWELITE DIP) and microcomputer (Arduino Mini Pro 3.3V). The wireless communication device can send and receive data between the slave unit and the master unit. Corrosion does not occur even if a voltage is applied to the carbon rod for a long period of time, however it was found that the resistance on the surface of electrode has changed. It is therefore that an instantaneous voltage is applied to the soil moisture sensor using Arduino. As a result, stable measurement can be performed over a long period of time, and an arbitrary time interval can be set. The data from the soil moisture sensor is wirelessly communicated from the slave unit to the master unit, the data is saved in the cloud from the ESP8266 connected to the master unit, and the measurement results can be viewed on an external terminal. The power supply is a dry battery (3.3V) for the soil moisture sensor on the slave unit side, and a solar panel and battery for the ESP8266 on the master unit side. The master unit can always receive radio waves from the slave unit. The soil moisture sensor was installed on the slope in Nagasaki City, Japan. This site is designated as a steep slope in Nagasaki City, and is where sand control dam construction is being carried out. The soil moisture sensor is installed at a depth of 0.2m, 0.4m, and 0.6m from the ground surface. For a detection of the different soil moistures, the resistance values of r_1 = 1MΩ, r_2 = 200KΩ, r_3 = 100KΩ, and r_4 = 1MΩ (submersion) are used. The reason for using high resistance of r_4 is to ensure that the sensor is turned on when water comes into contact with it, regardless of the soil. For comparison, two EC-5 sensors are also installed at 0.2m and 0.4m from the ground surface. Using Arduino, a voltage is applied to the soil moisture sensor and the slave unit at 30-minute intervals, and the voltage value at that time is wirelessly transmitted to the master unit about 100 m away from the slave unit. The slave unit was powered by Arduino using 3.3V battery. The data of the master unit is transmitted to the cloud at 30-minute intervals by ESP. A rain gauge was also installed.

Figure 4 (a) shows the change of the volumetric soil moisture content converted from the voltage value of EC-5 and the hourly precipitation. Figure 4 (b) shows the change of the volumetric soil moisture content converted from the voltage value of the soil moisture sensor which was obtained by the cloud service (Ambient). From this relationship, the volumetric soil moisture content tended to increase after rainfall. After rainfall, the volumetric soil moisture content increases from the side closer to the ground surface, and then the value increases in the depth direction. At a depth of 0.6 m, the volumetric soil moisture content rises to about 40% after rainfall, confirming that the value is close to saturation. Figure 5 shows the volumetric soil moisture contents measured by the soil moisture sensor and EC-5 before and after rainfall.

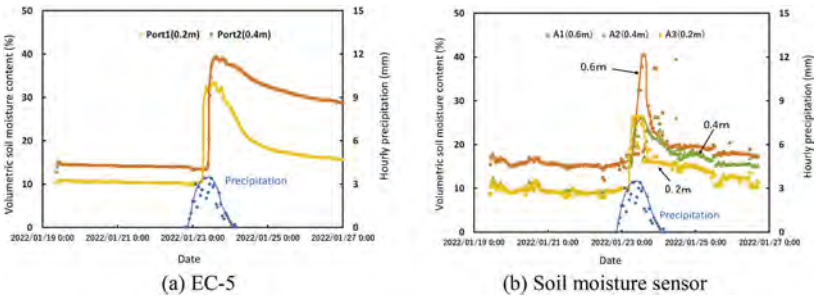

Figure 4. Change of the volumetric soil water content and the hourly precipitation.

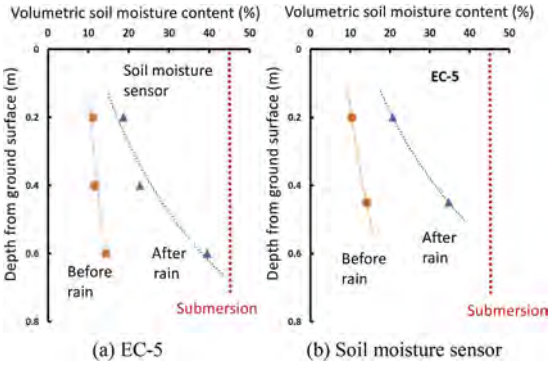

Figure 5. Volumetric soil moisture contents before and after rainfall.

Before rainfall, it can be confirmed that there is no difference in volumetric soil moisture content in both sensors in the depth direction. However, after rainfall, the deeper the ground surface, the larger the volumetric soil moisture content, and it is considered that rainwater has penetrated into the ground. From the measurement results, it is considered that the ground at a depth of 0.6 m was almost saturated after rainfall.

4 CONCLUSIONS

A ground water detection system was made by a simple moisture sensor using wireless communication equipment, a microcomputer, and a voltage control element. It is possible to receive data from the slave unit and the master unit by using a wireless communication device even in forests and slopes where the communication environment is harsh. It was clarified that the soil moisture sensor with submersion detection can measure the submerged state below the groundwater level. The soil moisture sensor was applied at a site of the slope for the field observation. From the monitoring result, after rainfall, it was possible to confirm the change in volumetric soil moisture content by the soil moisture sensor equivalent to that of the conventional soil moisture meter. For disaster prevention and mitigation, it is expected to be used as a low-cost sensor for observing, detecting, and communicating ground moisture condition in real time.

REFERENCES

Kodešová, R., Kodeš V., Mráz, A. 2011. Comparison of Two Sensors ECH2O EC-5 and SM200 for Measuring Soil Water Content. *Soil & Water Res.*, 6(2): 102–110.

Matsunaga, R., Li, C., Omine, K. 2020. A Proposal for Detection System of Ground Transformation using Simple Sensors. *Proceedings of 62nd Symposium on Geotechnical Engineering*: 1–4 (in Japanese).

Smart Geotechnics for Smart Societies – Zhussupbekov, Sarsembayeva & Kaliakin (Eds)
© 2023 The Author(s), ISBN 978-1-003-29912-7
Open Access: www.taylorfrancis.com, CC BY-NC-ND 4.0 license

Long-term monitoring and design of piled raft of a 162 m high isolated residential tower

J. Hamada, K. Yamashita & T. Tanikawa
R. & D. Institute, Takenaka Corporation, Chiba, Japan

M. Yamada
Building Design Department, Nagoya Branch Office, Takenaka Corporation, Nagoya, Japan

ABSTRACT: This paper offers long-term monitoring and design of piled raft foundation supporting a 162 m high isolated residential tower. The average contact pressure over raft is 600 kPa. The foundation consists of thirty-six 50 m long cast-in-place concrete piles which diameter are from 1.5 m to 1.9 m and compression strength is 48 N/mm^2. To confirm the validity of the foundation design, long-term field monitoring was performed in the settlement of the foundation and ground, axial loads and bending moments on the piles, contact earth pressure and pore-water pressure beneath the raft from the beginning of construction to over thirteen years after the end of construction. In addition, the piles' bending moments due to differential settlements between center and corner of the raft can be well measured, however those are sufficiently small comparing to design values during earthquake. These values were almost stable after the end of construction.

1 INTRODUCTION

Recently, piled raft foundations were applied for the foundation of super high-rise buildings, e. g., the world's tallest building of 828 m in height, Burj Khalifa in UAE (Poulos & Bunce, 2008), and the tallest building in Japan with 300 m in height (Hamada et al, 2016).

This paper presents performance and design of a piled raft with end-bearing cast-in-place high strength concrete piles supporting a 162 m high isolated residential tower. To confirm the validity of the foundation design, long-term field monitoring was performed on the foundation settlement, loads of the selected piles and contact pressures between raft and soil as well as pore-water pressure beneath the raft. A part of the measured results from the beginning of construction to seventeen months after the end of construction have been reported (Yamashita et al, 2011). In this paper, the measured data to thirteen years and five months after the end of construction are added and axial/ bending strains on monitored piles also discussed.

2 BUILDING AND SOIL CONDITIONS

The 48-story (47th and 48th floors for machine rooms) residential tower of 162 m in height above the ground surface and measures 50 m by 34 m in plan is located in Nagoya, Japan. Figure 1 shows a schematic view of the building and foundation with soil profile. The building is a reinforced concrete structure with base isolation system of laminated rubber bearings. The soil profile down to a depth of 4 m from the ground surface consists of fill and alluvial silt. Below the depth of 4 m, there lie Pleistocene medium-to-dense sand-and-gravel and sand with SPT N-values of 20 to 30 with some thin layers of silt to a depth of 17 m, underlain by medium silt. Between depths of 27 m to 43 m, there lie dense sand, very dense sand-and-gravel and medium-to-dense sand with SPT N-values 20 to 60 or higher. Below a depth of 43 m, there lies medium silt. Below a depth of 53 m, there lies very dense sand-and-gravel. The groundwater table appears

DOI: 10.1201/9781003299127-310

approximately 2.5 m below the ground surface. The shear wave velocity derived from P-S logging was from 180 m/s at the foundation level and 510 m/s in the sand-and-gravel below a depth of 53 m.

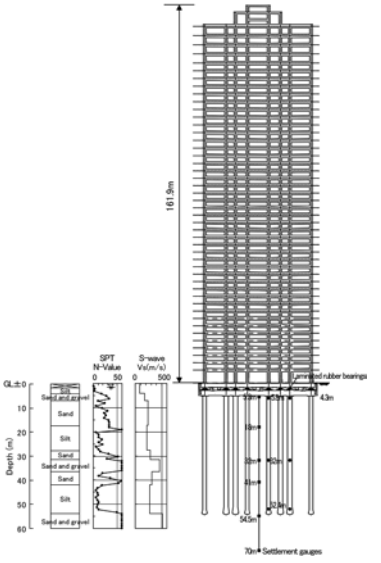

Figure 1. Schematic view of the building and foundation with soil profile.

3 FOUNDATION DESIGN

Because the building has a base isolation system, differential settlement of the foundation is rigorously restricted. The average contact pressure over the raft is 600 kPa. The reinforced concrete raft located 4.3 m below the ground surface is founded on the medium-to-dense sand-and-gravel. In order to reduce the differential settlement, a piled raft foundation consisting of thirty-six 50-m long cast-in-place concrete piles was proposed, where the piles were embedded in the very dense sand-and-gravel layer below a depth of 53 m. The ratio of the load carried by the piles to the total load was assumed to be 0.8 to 0.9 in the design, based on the values of 0.74 to 0.84 derived from the numerical analysis.

The piles have a diameter varying from 1.5 to 1.9 m and a 1.8 to 2.2 m enlarged bell at pile bottom. The nominal compressive strength of concrete is 48 MPa. The lateral loads and incremental axial loads on piles in the seismic design are relatively small due to the use of a base isolation system which can reduce the inertial force and overturning moment of superstructure. Thus piled rafts are compatible foundation system especially for isolated high-rise buildings. If a conventional pile foundation was adopted, the diameters of piles would be larger

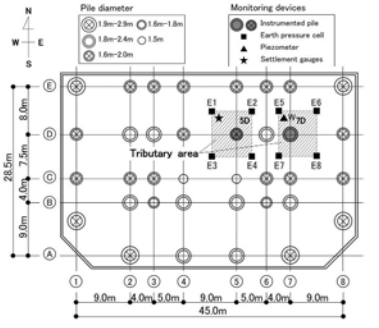

Figure 2. Layout of piles with locations of monitoring devices.

than these values, e.g., 2.0 to 2.5 m at shaft and 2.5 to 3.0 m at bottom. Figure 2 shows the foundation plan with a layout of the piles.

4 INSTRUMENTATION

The locations of the monitoring devices are shown in Figure 2. The two piles, 5D and 7D, were provided with a couple of LVDT-type strain gauges at depths of 5.8 m (at pile head), 32.0 m (at intermediate depth) and 52.4 m (at pile toe). Surrounding the instrumented piles, eight earth pressure cells E1 to E8 and one piezometer were installed beneath the raft. The vertical ground displacements below the raft were measured using differential settlement gauges. LVDT-type transducers were installed below the raft at depths of 5.3, 18.0, 32.0, 41.0 and 54.5 m to measure the relative displacements to the reference point at a depth of 70 m from the ground surface as shown in Figure 1.

The measurements on the strains of the piles, the contact pressures between raft and piles and pore-water pressure beneath the raft started just after casting of the 0.5 m thick foundation slab. The measurement of vertical ground displacements below the raft began just before the beginning of the excavation for the foundation construction in December 2006.

5 OBSERVATIONS

Figure 3 shows the measured vertical ground displacements at depths of 5.3 m, 18.0 m, 32.0 m, 41.0 m and 54.5 m relative to the reference point at a depth of 70 m where the initial values of the displacements were taken right before casting the foundation slab. The broken lines after 2013 January are assumed values no differential displacements have occurred because the settlement gauges at depth of 54.5 m, 32.0 m and 18.0 m had broken. The ground displacement measured at a depth of 5.3 m is approximately equal to the foundation settlement. The measured ground displacement increased with construction progress and reached 23.4 mm at the end of construction. Thereafter the displacement increased very slightly and reached 26.6 mm at thirteen years and five months after the end of construction. The differential settlement of Pleistocene medium silt layer between a depth of 54.5 m and 41.0 m was 12.4 mm at E.O.C. which was relatively larger than other layers.

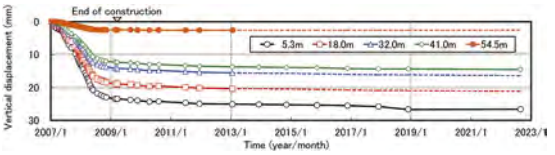

Figure 3. Measured vertical ground displacements.

Figure 4 shows the development of the strains measured on the pile 5D (diameter of 1.6 m). The negative value means compression. The average compression strains reached about -400 m at both pile head and intermediate depth, whereas the strain at pile toe was relatively small. (The strains at a depth of 32 m and 52.4 m have not measured since 2013.) The average strain of -400 m correspond to axial load of 25.5 MN (Axial stiffness, EA = 63700 MN). Figure 5 shows those on the pile 7D (diameter of 1.8 m). The average compression strains were about -350 m at both pile head and intermediate depth, whereas the strain at pile toe was relatively small similar to pile 5D. The average strain of -350 m correspond to axial load of 28.2 MN (axial stiffness, EA = 80600 MN). The measured pile-head loads were almost stable for both piles. Focusing on difference of strains at pile head, the strains at South direction (1S) were considerably larger than those at North direction (1N) for both the piles 5D and 7D. The difference of a couple of strains, 250 and 300 m were shown at piles 5D and 7D, respectively. These values correspond to bending moment of 1.71 and 2.88 MNm (bending stiffness, EI = 9590 and 15400 MNm^2, respectively). The bending moments on the piles may have occurred due to the differential settlements between center and corner of the raft, however those are sufficiently small

comparing to design values during earthquake. Figure 6 shows the settlement profile measured by the optical level of street 7 at the end of construction and sketch of possible deformation of the piles.

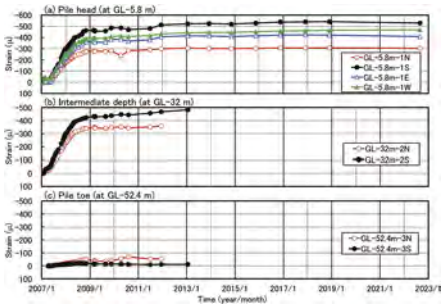

Figure 4. Measured axial loads of the piles 5D.

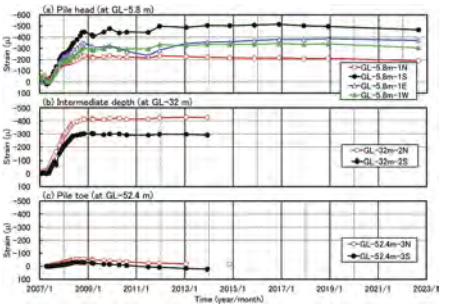

Figure 5. Measured axial loads of the piles 7D.

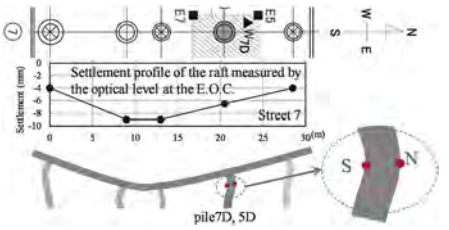

Figure 6. Measured settlement profile and sketch of possible deformation of piles.

Figure 7 shows the development of the measured contact pressures between raft and soil and pore-water pressure beneath the raft. The measured contact pressures differ considerably and the values were 28-98 kPa from the earth pressure cells E1-E4 near the pile 5D and 63-137 kPa from the earth pressure cells E5-E8 near the pile 7D at the end of construction. The measured pore-water pressure was approximately 20 kPa that is consistent with the ground water table from the soil investigation. Thereafter the measured contact pressures were almost stable except E2 and E8. The earth pressure cell of E8 would have been broken since circa 2011.

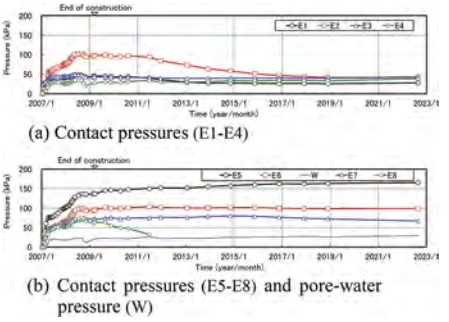

Figure 7. Measured contact pressures and pore-water pressure.

Figure 8 shows the time-dependent load sharing among the piles, soil and the groundwater buoyancy on the tributary areas of the columns 5D and 7D shown in Figure 2. At thirteen years and five months after the end of construction, the sum of the measured pile-head load and raft load on the tributary area is 29.3 MN and 32.4 MN on the columns 5D and 7D, respectively.

The raft load was obtained based on the mean value of the contact pressures near the columns. The design vertical loads of the columns 5D and 7D, which correspond to the sum of dead load and live load, are 26.3 MN and 35.6 MN, respectively. Therefore, the sum of the measured pile-head load and raft load on the tributary area is consistent with the design loads of both columns.

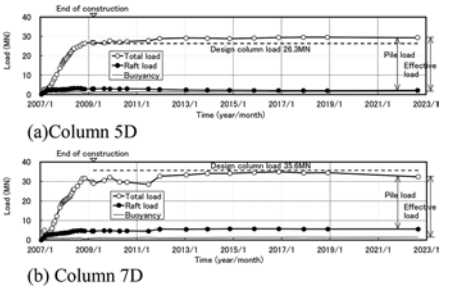

Figure 8. Time-dependent load sharing between raft and piles on the tributary area.

The ratio of the load carried by the pile to the effective loads (total load minus buoyancy) in the tributary area of columns 5D and 7D were estimated to be 0.93 and 0.87, respectively, at the end of the construction and 0.98 and 0.87, respectively, at thirteen years and five months after the end of construction.

The above observations are simulated and validated by three-dimensional finite element analysis. The results will be shown at another chance for want of space.

6 CONCLUSIONS

Performance and Design of piled raft foundation supporting a 162 m high isolated residential tower were described. Long-term monitoring was performed on settlement and load sharing of the piled raft foundation from the beginning of construction. The measured ground displacement was 23.4 mm at the end of construction, thereafter the displacement increased very slightly and reached 26.6 mm at thirteen years and five months after the end of construction. The ratio of the load carried by the pile to the effective loads were also stable from 0.87 to 0.98 at thirteen years and five months after the end of construction.

ACKNOWLEDGEMENTS

The authors are grateful to Messrs. Y. Soga and T. Yokonami of Takenaka Corporation for their contribution to the structural design and field measurements of the piled raft foundation.

REFERENCES

Hamada, J., Yamashita, K. & Hirakawa, K. 2016. Case history of behavior of piled raft foundation supporting the tallest building in Japan constructed by top-down method, *19th Southeast Asian Geotechnical Conference & 2nd AGSSEA Conference* (19SEAGC & 2AGSSEA).

Poulos, H. G. & Bunce, G. 2008. Foundation design for the Burj Dubai – The world's tallest building-, *Proc. of 6th Int. Conf. on case histories in Geotechnical Engineering*, Paper No. 1. 47.

Yamashita, K., Yamada, T. & Hamada, J. 2011. Investigation of settlement and load shearing on piled rafts by monitoring full-scale structures, *Soils and Foundations*, 51(3): 513–532.

Smart Geotechnics for Smart Societies – Zhussupbekov, Sarsembayeva & Kaliakin (Eds)
© 2023 The Author(s), ISBN 978-1-003-29912-7
Open Access: www.taylorfrancis.com, CC BY-NC-ND 4.0 license

Evaluation of the strength parameters of clay loams during freezing–thawing cycles

E.P. Bragar
Department of Constructions, L.N. Gumilyov Eurasian National University, Nur Sultan, Kazakhstan
Department of Construction Operations, Industrial University of Tyumen, Tyumen, Russia

Y.A. Pronozin
Department of Construction Operations, Industrial University of Tyumen, Tyumen, Russia

A.Zh. Zhussupbekov
Department of Constructions, L.N. Gumilyov Eurasian National University, Nur Sultan, Kazakhstan
Department of Geotechnics, Saint Petersburg State University of Architecture and Civil Engineering (SPbGASU), Saint Petersburg, Russia
Department of Soil Mechanics and Geotechnics, Moscow State University of Civil Engineering (MGSU), Moscow, Russia

A.D. Gerber
A.I. Proshlyakov Tyumen Higher Military Engineering Command College, Tyumen, Russia

B. Indraratna
University of Technology Sydney, Sydney, Australia

ABSTRACT: Destructuring settlements due to frost heave during the structures' exploitation are often not taken into account at the designing stage, although they are indirectly related to the bearing capacity of the soils. The objective of this research was analyzing the effect of the number of freezing–thawing cycles on the strength characteristics of soils. Tests of the clay loams with void ratio $e = 0.55$ and with various initial parameters (initial moisture content, and the number of freezing–thawing cycles) was carried out. According to the experimental results, the cohesion largely depends on the above parameters which might lead to its decrease by up to 5 or 6 times. The internal friction angle demonstrated an indefinite behavior during the freeze-thaw cycles, which is confirmed by a literature review. Changes in strength parameters of the soil during freezing–thawing cycles can lead to significantly decreasing of the soil bearing capacity. A program based on the least-squares method was used to calculate the approximation coefficients of the dependence describing the changes in strength characteristics from the abovementioned parameters. Changes in strength characteristics must be taken into account when designing structures, as they can lead to additional settlement or even subsidence of the foundations.

1 INTRODUCTION

Many scientists around the world have observed changes in soil moisture and density during freeze–thaw cycles and, accordingly, a change in bearing capacity, directly related to engineering characteristics (Wang et al. 2010, Sarsembayeva & Zhussupbekov 2021, Qi et al. 2008). Options for addressing these impacts were investigated by (Yarbaşı et al. 2007, Kalkan 2009, Ghazavi & Roustaie 2010). Russian scientists from the Soviet era, including M.N. Goldstein, A.M. Pchelintsev, E.P. Shusherina, and N.A. Tsytovich (Goldstein 1948,

DOI: 10.1201/9781003299127-311

Pchelintsev 1964, Tsytovich 1973, Shusherina et al. 1970), have studied the influence of the number of freezing–thawing cycles on the mechanical properties of soils and contributed to the development of methods for strengthening base soils subject to freezing (Medvedev 2007, Kiselev 1985).

A significant part of the conducted experiment deals with road construction in areas with seasonally frozen soils, as well as problems associated with freezing–thawing of the roadway and its subgrade, such as settlement, frost heaving, and slope sliding (Ling et al., 2009; Li et al., 2016; Tebaldi et al., 2016).

Destructuring settlement and heave settlement during the exploitation of buildings and structures are not taken into account in most construction design standards, although they are indirectly related to the strength characteristics of the soil. According to (Magushev et al. 2011), the vertical deformation of foundations on a natural base is determined as the sum of four components (Equation 1): calculated settlement, elastic settlement, destructuring settlement, and heave settlement.

$$\boldsymbol{S} = \boldsymbol{S_{comp}} + \boldsymbol{S_{elast}} + \boldsymbol{S_{destr}} + \boldsymbol{S_{heave}}, \tag{1}$$

where $\boldsymbol{S_{comp}}$ is the calculated value of the final settlement, according to regulations, which is a consequence of repacking of particles under a load, leading to soil compaction, within the compressible thickness.

$\boldsymbol{S_{elast}}$ is settlement associated with the unloading of the excavation and the subsequent construction of the foundation and backfilling with soil.

$\boldsymbol{S_{destr}}$ is settlement associated with destructuring of soil, for example, under the influence of heavy machinery, frost exposure, water saturation, unfavorable weather conditions, etc.

$\boldsymbol{S_{heave}}$ is heave settlement associated with the accumulation of shear strains in the soil leading to the squeezing out of the soil from under the base of the foundation.

Destructuring settlement S_{destr} and heave settlement S_{heave} are not taken into account by domestic standards (SP 22.13330.2016) and are indirectly related to the strength characteristics of soil. The change to these characteristics caused by freezing–thawing is studied in this paper.

Many geotechnical scientists have paid great attention to studying the changes caused by freezing in the cohesion and the angle of internal friction of the soil as these are the main strength characteristics. It is generally accepted that with an increase in the number of freezing–thawing cycles, cohesion decreases, but the stabilized value of cohesion after several freezing–thawing cycles remains controversial (Chang et al. 2014, Wang et al. 2005, Wang et al. 2018, Yu 2007, Liu et al. 2016, Zhang et al. 2015). However, some results show that cohesion increases or defies the obvious law when exposed to freezing–thawing (Fang et al. 2012). Studies of changes in the angle of internal friction of soil are rather contradictory: according to some studies (Wang et al. 2010, Wang et al. 2005, Yu 2007, Fang 2012), the angle of internal friction increases; according to other studies (Chang et al. 2014), it decreases or remains constant (Zhang 2015, Su et al. 2008, Dong et al. 2010). Some studies note the inconsistent nature of the change in the angle of internal friction during freezing–thawing (Wang et al. 2005, Lui et al. 2016, Wang 2012). One way or another, the obtained scientific results are difficult to apply in engineering practice unambiguously. In 2018, Wang et al. were the first to propose a mathematical equation using correction factors for calculating the shear strength of soil during freezing–thawing, which had never been considered before (Wang et al. 2018). However, the dependence is only for clays with a moisture content of 18.5%.

The purpose of this research is to analyze and to study the mathematical dependence of changes in the strength characteristics of clayey soils with different void ratios and initial moisture content due to freezing–thawing cycles.

2 MATERIALS AND METHODS

The southern area of the Tyumen region of the Russian Federation contains -clayey soils which are considered as frost-susceptible soils, resulting in severe frost heave during the winter time.

Remolded clay loam samples with the particle density 2.70 g/cm3 were compacted in accordance with the Russian State Standard GOST 30416–2012 "Soils. Laboratory testing. General" (GOST 30416-2012). The samples were compacted in four layers, with the required density and moisture content. The specimens were prepared as cylinders in metal rings of 71.5 mm in diameter and 35 mm in height. Physical characteristics of the soils are presented in Table 1.

Table 1. Physical characteristics of the soil.

No.	Designation	Indicator	Unit	Value
1	ρ_s	Density of soil particles	g/cm3	2.70
2	w_P	Plastic limit	-	0.15
3	w_L	Liquid limit	-	0.27
4	I_p	Plasticity index	-	12.1
5	e	Soil void ratio	-	0.55
6	W	Initial moisture content	%	16.5/19.5

In the experiment, two paired samples were considered for testing with varied initial settings (Table 1). Tests were conducted on loam with void ratio e = 0.55 and two different initial moisture contents (W = 16.5% and W =19.5%).

The samples were frozen at a temperature of −20 °C and thawed at 20 °C, with the freezing time and thawing time each being 12 h. The specimens were covered with sleeves during the freeze–thaw cycling to prevent the evaporation of water. The all-round freezing method with constant temperature was applied for the freeze–thaw cycle test in a closed system without a water supply. The samples were placed in metal rings without normal stress. The samples experienced different numbers of freeze-thaw cycles of 0, 1, 3, 5, 10 (Table 2).

The experiment set matrix is presented in Table 2.

Table 2. Experiment set.

Experiment No.	Void ratio, e	Moisture content W, %	Number of freeze-thaw cycles, Nc
1	0.55	16.5	0
2	0.55	16.5	1
3	0.55	16.5	3
4	0.55	16.5	5
5	0.55	16.5	10
6	0.55	19.5	0
7	0.55	19.5	1
8	0.55	19.5	3
9	0.55	19.5	5
10	0.55	19.5	10

The engineering properties of soil samples after freeze–thaw cycles were determined using a direct shear apparatus, according to GOST 12248–2010 "Soils. Laboratory methods for determining the strength and strain characteristics" (GOST 12248-2010). Four shear tests were conducted with normal stresses 100, 150, 200, and 300 kPa. After conducting experiments under each set of conditions and processing the results of the direct shear test, the data were analyzed to determine the influence of each of the studied factors (Lawson & Erjavec 2017).

3 RESULTS AND DISCUSSIONS

The results of the direct shear test for each experimental sample set are presented in Table 3.

Figure 1 shows that the angle of internal friction increases dramatically up to two times during the first freeze-thaw cycle. Further freezing-thawing up to three cycles can lead to a decrease in the angle of internal friction to the initial value or lower. In general, the character of the freeze-thaw curve is not constant. After ten freeze-thaw cycles, the characteristic either remains equal to the initial value (W=16.5%) or exceeds it by 1.5 times (W=19.5%).

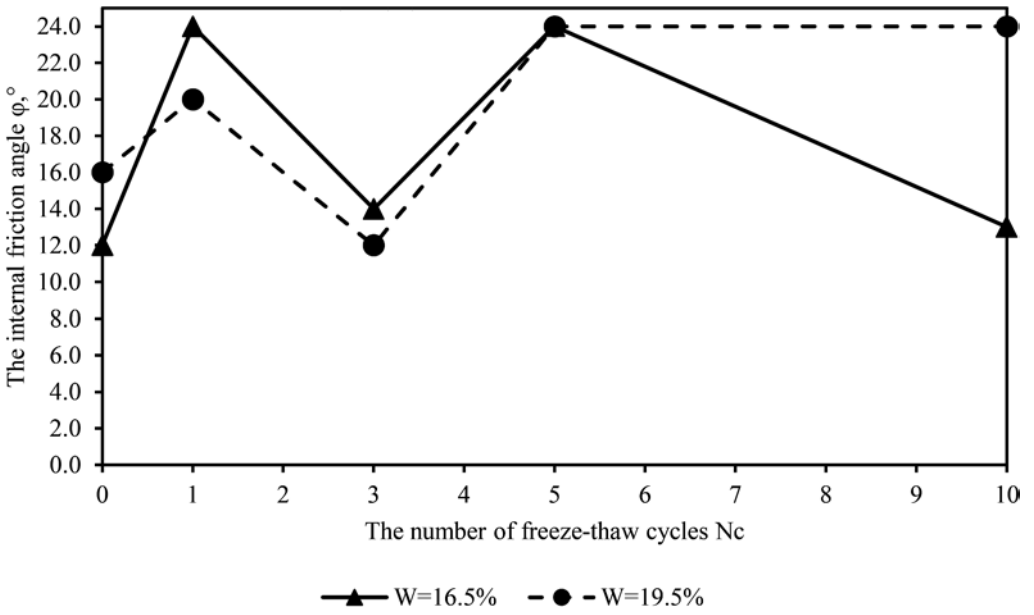

Figure 1. Dependence of the internal friction angle of the soil with e=0.55 from the number of freeze-thaw cycles.

Table 3. Direct shear test results.

Experiment No.	Void ratio, e	Moisture content W, %	Number of freeze-thaw cycles, N_c	Internal friction angle φ,°	Cohesion, kPa
1	0.55	16.5	0	12	39
2	0.55	16.5	1	24	22
3	0.55	16.5	3	14	41
4	0.55	16.5	5	24	6
5	0.55	16.5	10	13	28
6	0.55	19.5	0	12	39
7	0.55	19.5	1	24	22
8	0.55	19.5	3	14	41
9	0.55	19.5	5	24	6
10	0.55	19.5	10	13	28

The study have shown that the first freeze-thaw cycle leads to a decrease in the cohesion up to 44% (Figure 2). Further freezing-thawing leads to restoration of the initial value of the cohesion. However, the cohesion decreases up to 6 times after five or ten cycles of freezing-thawing.

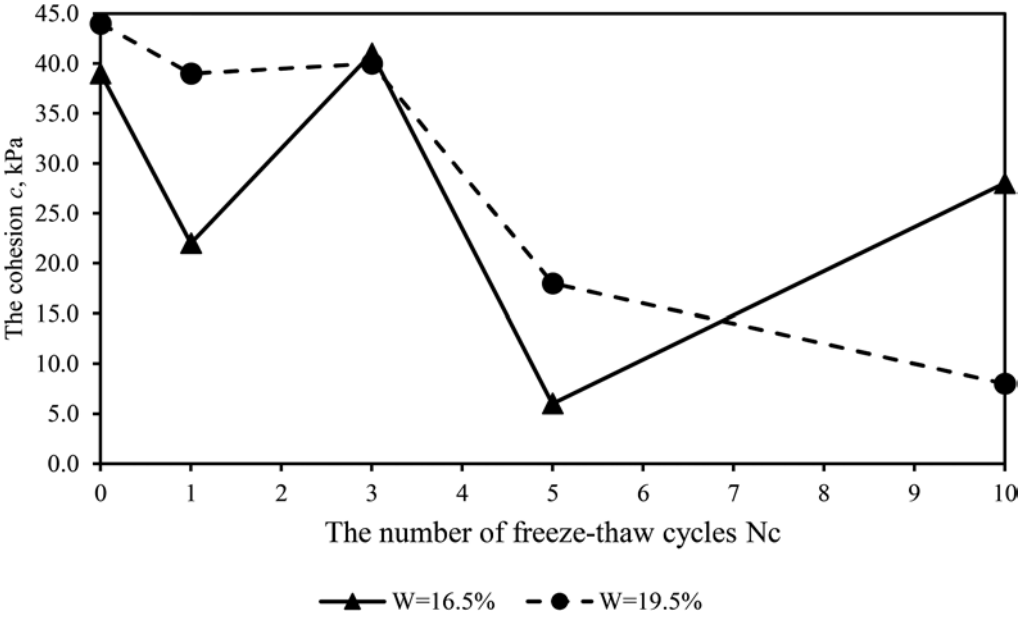

Figure 2. Dependence of the cohesion of the soil with e=0.55 from the number of freeze-thaw cycles.

4 CONCLUSIONS

In this work, a paired experiments were conducted in order to analyze the influence of the number of freezing–thawing cycles on the engineering characteristics of soil, such as angle of internal friction and cohesion. According to the results of the study, the following outcomes were highlighted:

The angle of internal friction increases dramatically up to two times during the first freeze-thaw cycle. Further freezing-thawing up to three cycles can lead to a decrease in the angle of internal friction to the initial value or lower. In general, the character of the freeze-thaw curve is not constant. After ten freeze-thaw cycles, the characteristic either remains equal to the initial value (W=16.5%) or exceeds it by 1.5 times (W=19.5%).

The first freeze-thaw cycle leads to a decrease in the cohesion up to 44%. Further freezing-thawing leads to restoration of the initial value of the cohesion. However, the cohesion decreases up to 6 times after five or ten cycles of freezing-thawing.

REFERENCES

Wang, T.; Luo, S.; Liu, X. Testing Study of Freezing-Thawing Strength of Unsaturated Undisturbed Loess Considering Influence of Moisture Content. *Rock Soil Mech*. 2010, 31, 2378–2382.

Sarsembayeva, A.; Zhussupbekov, A. Experimental study of deicing chemical redistribution and moisture mass transfer in highway subsoils during the unidirectional freezing. *Transp. Geotech*. 2021, 26, 100426.

Qi, J.; Ma, W.; Song, C. Influence of Freeze–Thaw on Engineering Properties of a Silty Soil. *Cold Reg. Sci. Technol*. 2008, 53, 397–404.

Yarbaşı, N.; Kalkan, E.; Akbulut, S. Modification of the geotechnical properties, as influenced by freeze–thaw, of granular soils with waste additives. *Cold Reg. Sci. Technol*. 2007, 48, 44–54. https://doi.org/10.1016/j.coldregions.2006.09.009.

Kalkan, E. Effects of silica fume on the geotechnical properties of fine-grained soils exposed to freeze and thaw. *Cold Reg. Sci. Technol*. 2009, 58, 130–135. https://doi.org/10.1016/j.coldregions.2009.03.011.

Ghazavi, M.; Roustaie, M. The Influence of Freeze–Thaw Cycles on The Unconfined Compressive Strength of Fiber-Reinforced Clay. *Cold Reg. Sci. Technol*. 2010, 61, 125–131.

Goldstein, M.N. Deformation of the Subgrade and Foundations of Structures during Freezing and Thawing; Transzheldorizdat: Moscow, Russia, 1948; 212p.
Pchelintsev, A.M. Structure and Physical and Mechanical Properties of Frozen Soils;Publishing House "Nauka": Moscow, Russia, 1964; 260p.
Tsytovich, N.A. Mechanics of Frozen Soils; Study Guide; Vysshaya Shkola: Moscow, Russia, 1973; 448p.
Tsytovich, N.A. Foundations on Frozen Ground; USSR Academy of Sciences Publishing House: Moscow, Russia, 1958; 168p.
Shusherina, E.P.; Rachevsky, B.S.; Otroshchenko, O.P. Study of temperature deformations of frozen rocks. In Permafrost Research; MSU Publishing House: Moscow, Russia, 1970; pp. 273–283.
Medvedev, S.N. Technology of Construction of Foundations of Buildings on Seasonally Freezing Soils: Author's Abstract of the Dissertation for the Degree of Candidate of Technical Sciences: 05.23.08/ Sergey Nazarovich Medvedev; MGSU: Moscow, Russia, 2007; 22p.
Kiselev, M.F. Prevention of Soil Deformation from Frost Heaving; Leningrad: Stroyizdat, Russia, 1985; 131p.
Ling, X.; Zhang, F.; Zhu, Z. Field Experiment of Subgrade Vibration Induced by Passing Train in a Seasonally Frozen Region of Daqing. *Earthq. Eng. Eng. Vib*. 2009, 8, 149–157.
Li, Q.; Ling, X.; Sheng, D. Elasto-Plastic Behaviour of Frozen Soil Subjected to Long-Term Low-Level Repeated Loading, Part I: Experimental Investigation. *Cold Reg. Sci. Technol*. 2016, 125, 138–151.
Tebaldi, G.; Orazi, M.; Orazi, U.S. Effect of Freeze—Thaw Cycles on Mechanical Behavior of Lime-Stabilized Soil. *J. Mater. Civ. Eng*. 2016, 28, 06016002. https://doi.org/10.1061/(asce)mt.1943-5533.0001509.
Magushev, R.A.; Karlov, V.D.; Sakharov, I.I.; Osokin, A.I. Foundation engineering: Textbook for bachelors of construction; ASV Publishing House: Moscow, Russia; SPbGASU: Saint Petersburg, Russia, 2011; 394p.
Code of Practice SP 22.13330.2016. Soil Bases of Buildings and Structures; Updated Edition of SNiP 2.02.01-83*(2014); Standartinform: Moscow, Russia, 2016; 227p.
Chang, D.; Liu, J.; Li, X.; Yu, Q. Experiment Study of Effects of Freezing-Thawing Cycles on Mechanical Properties of Qinghat-Tibet Silty Sand. Chin. *J. Rock Mech. Eng*. 2014, 33, 1496–1502.
Wang, D.Y.; Ma, W.; Chang, X.X.; Sun, Z.Z.; Feng, W.J.; Zhang, J.W. Physico-Mechanical Properties Changes of Qinghai—Tibet Clay due to Cyclic Freezing and Thawing. Chin. *J. Rock Mech. Eng*. 2005, 24, 4313–4319.
Wang, M.; Meng, S.; Sun, Y.; Fu, H. Shear strength of frozen clay under freezing-thawing cycles using triaxial tests. *Earthq. Eng. Eng. Vib*. 2018, 17, 761–769.
Yu, J. Design of Low Temperature Triaxial Testing Machine and Experimental Study on Cyclic Freeze-Thaw on the Mechanical Properties of Silty Clay. Ph.D. Dissertation, Wuhan Insitute of Rock and Soil Mechanics, The Chinese Academy of Sciences, Wuhan, China, 2007.
Liu, J.; Chang, D.; Yu, Q. Influence of freeze-thaw cycles on mechanical properties of a silty sand. *Eng. Geol*. 2016, 210, 23–32. https://doi.org/10.1016/j.enggeo.2016.05.019.
Zhang, H.; Wang, T.; Luo, Y. Freezing-Thawing Strength of Unsaturated Undisturbed Loess. *J. Northwest AF Univ. (Nat. Sci. Ed.)* 2015, 43, 1–6.
Fang, L.; Qi, J.; Ma, W. Freeze-Thaw Induced Changes in Soil Structure and its Relationship with Variations in Strength. *J. Glaciol. Geocryol*. 2012, 34, 435–440.
Su, Q.; Tang, D.; Liu, S. Test on Physico-Mechanical Properties of Qinghai—Tibet Slope Clay under Freezing-Thawing Cycles. Chin. *J. Rock Mech. Eng*. 2008, 27, 2990–2994.
Dong, X.; Zhang, A.; Lian, J.; Guo, M. Laboratory Study on Shear Strength Deterioration of Loess with Long-Term Freezing-Thawing Cycles. *J. Eng. Geol*. 2010, 18, 887–893.
Wang, J. Research on the Mechanical Properties of Pavement Soil after Several Freeze Thaw Cycles in Seasonally Frozen Soil Region and Microscopic Mechanism Analysis. Ph.D. Dissertation, Jilin University, Chang Chun, China, 2012.
GOST 30416–2012. Soils. Laboratory testing. General. Available online: https://docs.cntd.ru/document/1200096093 (accessed on 12 January 2022).
GOST 12248–2010. Soils. Laboratory Methods for Determining the Strength and Strain Characteristics. Available online: https://docs.cntd.ru/document/1200084869 (accessed on 12 January 2022).
Lawson, J.; Erjavec, J. Basic Experimental Strategies and Data Analysis for Science and Engineering; CRC Press, Taylor & Francis Group: Boca Raton, USA, 2017; 445p.

Smart Geotechnics for Smart Societies – Zhussupbekov, Sarsembayeva & Kaliakin (Eds)
© 2023 The Author(s), ISBN 978-1-003-29912-7
Open Access: www.taylorfrancis.com, CC BY-NC-ND 4.0 license

Moisture sensing technology for assessment of rainfall-induced slope failure

A.N. Amantay, A. Satyanaga, S.-W. Moon & J. Kim
Nazarbayev University, Astana, Kazakhstan

ABSTRACT: The frequency and duration of rainfall are two examples of the climatic conditions that have changed as a result of global warming. According to earlier research, slope failures are more likely to happen after a protracted period of drought followed by a strong rainfall or after a long period of light rains followed by a heavy rainfall. This occurrence demonstrates the significance of slope susceptibility or hazard maps in identifying high-risk areas during periods of excessive precipitation. The stability of high-risk slopes can then be sustained before failures by designing the proper slope preventive actions. This study reviewed various moisture sensing technologies for real-time evaluation of slope collapses brought on by rainfall. A thorough analysis of various literatures revealed that capacitance moisture sensors offer the best compromise for affordable and effective early warning systems, particularly in a tropical environment.

1 INTRODUCTION

As industry and human activity has increased, so have greenhouse gas emissions, which has significantly accelerated global warming. According to the most recent conclusions from the Intergovernmental Panel on Climate Change (IPCC, 2021), any forecasted emission scenarios will result in an inescapable rise in temperature over this century. Temperatures and humidity have risen throughout numerous regions, while rainfall patterns have altered. Numerous geotechnical structural issues involving road building, foundation design, slope stability, municipal waste storage, and nuclear waste disposal are frequently caused by climate variations, and these issues call for a fundamental understanding of unsaturated soil mechanics. Rainfall-induced slope failures are one of the most frequent physical dangers in the globe (Kristo et al., 2017; 2019; Rahardjo et al., 2007). Long and severe episodes of rainfall, which are anticipated to occur more frequently as a result of climate change, are what cause the majority of these slope failures. In example, steep and high slope with deep groundwater table frequently experience rainfall-induced slope failures (Chua et al., 2022; Rahardjo et al., 2007). According to research, shallow slip surfaces are typically involved in rainfall-induced slope failures in Asia, as seen in Kazakhstan (Satyanaga et al., 2022), Hong Kong (Brand, 1993), Singapore (Chan et al., 2020; Rahardjo et al., 2020a), Sri Lanka (Nawagamuwa and Dayarathne, 2014), and Malaysia (Saadatkha et al., 2015).

The main contributing variables to unsaturated soil mechanics have been identified as changes in soil suction and volumetric water contents. In addition, reductions in soil suction and shear strength can result in slope failures brought on by rainfall (Fredlund et al., 2012; McCartney and Khosravi, 2013). Numerous studies on landslides are carried out to promote the development of in-situ real-time monitoring employing field equipment (piezometers, tensiometers, and moisture sensors) to measure the water and suctions contents of the soil (Alonso et al., 2003; Greco et al., 2013; Rahardjo et al., 2014; Leung and Ng, 2016; Kim et al., 2017).

In order to measure soil suction in the slope, conventional water-based tensiometers are frequently employed. However, there were numerous restrictions on soil suction measurements, particularly in relation to concerns with maintenance and durability (Guan and Fredlund, 1997;

DOI: 10.1201/9781003299127-312

Tarantino and Tombolato, 2005; Rahardjo and Satyanaga, 2019; Satyanaga and Rahardjo, 2020). Therefore, considerable work has been put into developing a soil moisture measurement system with increased measurement capacity and reliable performance. The goal of this work was to offer acceptable soil moisture sensors for real-time assessment of rainfall-induced slope failures by analyzing the various types of moisture sensing devices.

2 MOISTURE SENSING TECHNOLOGY

Early Warning Slope Stability Monitoring (EWSSM) systems are becoming more and more popular, but their widespread deployment has been stymied (Oguz et al., 2019) by the expensive sensors, complexity, and lack of automation of the techniques, as well as the need for regular maintenance. To predict rainfall-induced slope failures, scientists from all over the world are searching for an effective EWSSM solution (Pajali et al., 2021). Unpredictable behavior of landslides leads to serious outcomes like human casualties and financial damage. One of the key elements in keeping track of the slope instability brought on by rainfall is the soil-water dynamics. Regular measurements of the soil moisture are required for excellent simulation accuracy (Rodriguez-Iturbe, 2003).

For a variety of purposes, including agriculture, oil and gas, studies of climate change, slope stability evaluation and monitoring, numerous companies and researchers have researched soil moisture sensing systems in the recent years. The system should have appropriate response time for an early warning system built in, be low cost, simple to maintain, and suitable for real-time monitoring before a slope fails.

The many methods for detecting soil moisture that are currently available each have their own benefits and drawbacks. To choose the best one to use, some work is needed. Figure 1 depicts common methods for assessing soil moisture. Typically, two methods can be used to measure soil moisture: Soil Water Potential (SWP) and Volumetric Water Content (VWC). The most popular key parameter for assessing slope stability is SWP. SWP can be measured using tensiometers and resistance blocks (gypsum blocks), which are pricey and require extensive maintenance (WMO, 2018). Additionally, salinity has a significant impact on the readings of Gypsum blocks, and sensors have a limited lifespan in a salty environment.

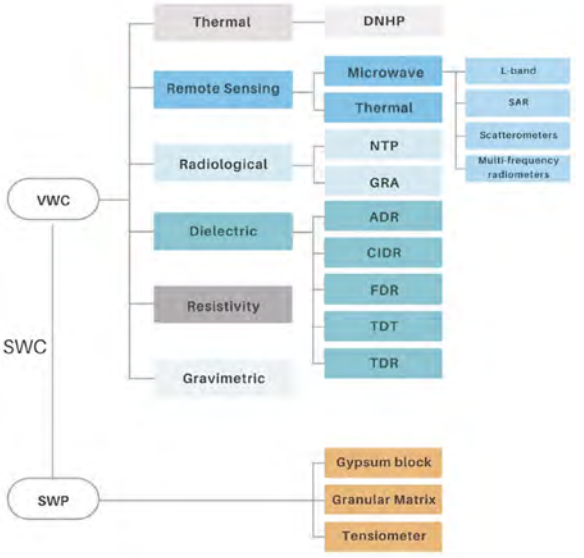

Figure 1. Prevalent soil water content (SWC) measuring techniques.

VWC is a crucial measure to quantify the effect of rainfall on the stability of the slope, according to studies by Greco et al. (2010) and Rahardjo et al. (2020a). Additionally, Greco et al. (2010) determined that VWC should be prioritized over SWP when developing a successful EWSSM system since VWC varies gradually whereas SWP may experience abrupt changes that are challenging to interpret. To increase the precision, accuracy, optimization, and cost effectiveness of moisture sensing technology, a variety of businesses and research institutes have looked at a number of approaches to measure and monitor VWC. Only a few of the widely used VWC approaches that are practical for slope stability monitoring can fulfill specific project needs when taking into account the advantages and disadvantages of each technology. Low cost, which includes the price of the sensor system, installation, and maintenance, was one of the key factors in the decision. Cost-cutting, though, shouldn't come at the expense of accuracy. At the same time, the technology must be reliable, straightforward to use, and energy-efficient. The sensor system should also be able to gather measurements from various depths in one place. This will enable the creation of a hydrological profile of slopes and improve the usability and accuracy of monitoring.

2.1 *Thermogravimetric technique*

The thermogravimetric method measures gravimetric water content (GWC) directly and uses oven drying to ascertain the real water content of soil samples. VWC can be calculated from GWC using the bulk density of the soil. The strategy is not practical for the EWSSM system due to its destructive nature and lack of logging capacity (Little et al., 1998). Before installing them on the actual slopes, it can be used to calibrate some water content sensors (such capacitors) for the soil.

A reliable methodology for carrying out automated VWC measurements with high temporal and spatial precision in the field is the Dual Needle Heat Pulse technique (DNHP) (Oschner et al., 2003). The DNHP sensor consists of two tiny (a few millimeters) needles, one of which acts as a heater and the other of which records temperature changes. Heat capacity is calculated and converted into VWC. Since the probe needles are so sensitive, any physical variation can cause measurements to be inaccurate. The technique precisely measures temperature changes just a few millimeters from the needle. To reduce the fluctuation of the DNHP sensor accuracy, Liu (2011) developed a thermo-Time Domain Reflectometry technique (TDR) sensor based on the combination of two techniques: heat-pulse and time-domain reflectometry. Thermo-TDR sensor might offer precise field estimations of VWC.

2.2 *Remote sensing*

The soil thermal characteristics measured by remote sensing can be used to estimate the moisture of the topsoil (top 5 to 10 cm) on a global scale (Mohanty et al., 2017; Lakhankar et al., 2009). To remotely monitor soil moisture over wide areas, radiometers and radars are fitted to satellites (Muoz-Carpena, 2012). The two main categories of remote sensing technologies are thermal infrared and microwave remote sensing. By analyzing interactions between the ground and electromagnetic (EM) waves, microwave techniques can estimate the soil's dielectric characteristics, allowing for the determination of the landcover's VWC (WMO, 2018). On the basis of the variations in the thermal characteristics of soil and water, thermal infrared remote sensing can be used to determine VWC (WMO, 2018). The strong contrast between the dielectric and thermal characteristics of wet and dry soil is used to determine the soil moisture (Lakhankar et al., 2009). In most cases, space-based remote sensing techniques offer measurements of moisture with time intervals of one to three days (passive radars) (WMO, 2018) or a few months (active radars) (Mohanty et al., 2017).

The Soil Moisture Near Real-Time Processor (SM-NRT-OP) was introduced in a new version of Soil Moisture and Ocean Salinity (SMOS) released by the European Space Agency in May 2021. With the fastest data retrieval possible, it promises to give soil moisture readings based on a neural network approach within three hours of sensing (European Space Agency, 2021). The spatial resolution of the measurements ranges from ten meters (synthetic aperture radar) (Moran et al., 2004) to tens of kilometers (passive radiometer) (Mohanty et al., 2017) depending on the remote sensing technique. Through the application of averaging parameters,

the use of satellite-based technology to retrieve soil moisture data for vast areas appears promising. However, because of the relatively high cost, complexity of implementation, and highly fluctuating soil moisture across both time and location, this technology is not yet ready to be employed for the EWSSM system in small metropolitan islands (such as Singapore). The technique's ability to accurately predict rainfall-induced slope failures is constrained by the fact that it can only determine the soil moisture content within the top 10 cm of the surface and at a time-frequency of 3 hours at best.

2.3 *Radiological technique*

A reliable way for obtaining precise VWC profiles at any depth up to the length of the logging line is radiological technology. Currently, the soil water content (SWC) can be measured using either the neutron thermalization probe (NTP) or the gamma ray attenuation method (GRA). According to Muoz-Carpena (2012) and WMO (2018), the NTP approach is based on the interaction of high-energy (fast) neutrons with hydrogen atom nuclei. A wetter soil is represented by a slower neutron flow. Gamma ray attenuation as it travels through soil pores is measured using the GRA method (Muoz-Carpena, 2012).

2.4 *Resistivity and dielectric technique*

By measuring electrical resistivity between two electrodes, the Resistivity method (Res) is used to determine the relative moisture content. Due to its extremely low precision, the resistance probe is not appropriate for effective warning systems (Fares et al., 2011). Salinity of the soil has a considerable impact on it, necessitating frequent calibration (Tremsin, 2017). Additionally, sensors lose their effectiveness quickly. According to Muoz-Carpena (2012), the soil-probe impedance can be utilized to determine the soil water content using the amplitude domain reflectometry technique (ADR). An electro-magnetic field that is propagating between the rods is created by an oscillator. The measured impedance is a function of the soil dielectric constant. There are numerous more soil factors that affect the VWC as evaluated by the ADR approach (e.g., density, temperature, and salinity). The usefulness and viability of the ADR approach for slope stability monitoring were proven by Shimobe and Ujihira (2009). Rod contact with stones, air spaces, or water channels has a significant negative impact on the accuracy of ADR measurements. The cost of deployment is impacted by how sophisticated the system is set up. Additionally, there aren't enough field studies and publications to draw firm conclusions about its applicability for the larger EWSSM system.

Based on measured dielectric permittivity (real and apparent), the soil moisture is estimated using the Coaxial Impedance Dielectric Reflectometry technique (CIDR). The electromagnetic signal (EM) produced by an oscillator travels through the metal tines and goes into the soil (Ojo et al., 2015). The sensor determines the strength of the incident and reflected signals. After determining impedance, the raw voltage ratio is used to determine dielectric permittivity. Although the CIDR sensor's creators assert that soil-specific calibrations are not necessary, the results of an independent research revealed that doing so improves the accuracy of the sensors (Ojo et al., 2015). In order to minimize ongoing dependencies, it is not recommended to use the sensor for large-scale applications because CIDR is a patented technology.

Based on apparent dielectric permittivity, the Frequency Domain Reflectometry technique (FDR) is used to measure SWC (Ferrarezi et al., 2020). An oscillator creates an electromagnetic signal (EM signal) that travels through metal electrodes. The interference waves that are produced are then monitored at continuous frequencies (Brahma and Goswami, 2017). For reliable results, a soil-specific calibration is needed for the FDR sensor (Muoz-Carpena, 2012). Additionally, the accuracy of sensors is greatly dependent on the probes making excellent contact with the soil, and soil temperature might have an impact (Brahma and Goswami, 2017). However, this sensor is able to produce measurements at various depths at the same spot and can be used in high salinity environments. This method is also thought to be too sophisticated and expensive to be used with the EWSSM system.

The Time Domain Reflectometry (TDR) method is a well-liked method for obtaining precise measurements of VWC (Nobrio, 2001; Ferrarezi et al., 2020; Askarinejad et al., 2018). The usage of TDR technology in the field is supported by a considerable number of publications. The sensors can detect the presence of water in many types of soil, but only at a single depth and one location (Campbell, 2017). The generator transmits an EM pulse through the sensor rods, which is the fundamental idea behind TDR. The pulse moves to the rod's end and reflects there. The soil's dielectric permittivity, which can be translated into water content, determines how long it takes for the pulse to go down and then return up (Topp, 2003).

A more advanced substitute for the TDR is the Time Domain Transmissometry technique (TDT). The TDT method only calculates the length of time needed for an EM pulse to travel to the rod's end. Consequently, the transmission line must have an electrical connection at both ends (Will et al., 2012). It is possible to estimate the water content by using the relationship between the pulse's travel time and the dielectric constant. TDT, like TDR, is a sophisticated and pricey technology that does not meet the specifications of the EWSSM system.

2.5 *Capacitance technique*

The dielectric permittivity of the soil is determined using the capacitance technique (Cap), which is influenced by the soil's water content (Atkins et al., 1998). The ability of a medium to store charges is measured using two electrodes (metal probes). The charge time in the soil is measured using an oscillating voltage, which links the dielectric permittivity to the volumetric water content. Capacitance sensors have undergone a revolution in electronics recently, including their accuracy. Capacitors are out of date due to their inaccuracy and overestimation of moisture in saline environments. The effects of salinity are minimized by using the high-frequency technique (Fares et al., 2011) in the construction of contemporary sensors. Capacitance sensors are a common low-cost option for large sensing networks nowadays since they are very precise (Campbell, 2017). Additionally, this sensor's setup, upkeep, and data administration are the most straightforward of all the soil moisture measurement options. Because cap sensors use less energy and are environmentally beneficial, they could be used for many years (Campbell, 2017). Additionally, Cap sensors that have been modified with a unique circuit architecture may detect incredibly minute changes in VWC. These customized sensors have been used by NASA to investigate whether there is water on Mars (Campbell, 2017). Thus, Cap can be seen as a very alluring technology that may be used in effective and affordable EWSSM systems.

3 CONCLUSION

A thorough analysis of several moisture sensing technologies revealed that capacitance moisture sensors offer the best compromise for affordable and effective early warning systems, particularly in a tropical environment. With less expense, precision, and little maintenance requirements, capacitance sensors enable smooth water content measurement for critical slopes of interest.

REFERENCES

Alonso, E.E., Gens, A., and Delahaye, C.H. 2003. Influence of rainfall on the deformation and stability of a slope in overconsolidated clays: a case study. *Hydrogeology Journal*, Vol. 11, pp. 174–192.

Askarinejad, A., Akca, D., and Springman, S.M. 2018. Precursors of instability in a natural slope due to rainfall: a full-scale experiment. *Landslides*, Vol. 15, pp. 1745–1759.

Atkins R.T., Pangburn, T., Bates, R.E., and Brockett, B.E. 1998. Soil Moisture Determinations Using Capacitance Probe Methodology. US Army Corps of Engineers. *Cold Regions Research & Engineering Laboratory*. Special Report 98–2.

Brand, E.W. 1993. Landslides in Hong Kong caused by the severe rainfall event of 8 May 1992. *Landslide News*, 7: 9–11

Brahma M., and Goswami B. 2017. Electrical Methods of Soil Moisture Measurement: A Review, *ADBU Journal of Electrical and Electronics Engineering*, Vol. 1, No.2. pp. 14–17.
Campbell C. 2017. Soil Moisture Sensors: Why TDR vs. Capacitance May Be Missing the Point, *Environmental Biophysics*, Accessed 21 December 2021, https://www.environmentalbiophysics.org/soil-sensors-tdr-vs-capacitance/
Chan, Y.E.C., Ng, Q.L., Satyanaga, A. and Rahardjo, H. 2020. Regional stability and adaptation measures slope failures due to rainfall in Singapore. *Environmental Geotechnics*. Published online on 04 May 2021, 1–16.
Chua, Y. S., Rahardjo, H., Satyanaga, A. 2022. Structured Soil Mixture for Solving Deformation Issue in GeoBarrier System. *Transportation Geotechnics*, 33: 100727.
European Space Agency. 2021. Read-me-first note for the release of the SMOS Level 2 Soil Moisture Near Real Time Neural Network (L2-SM-NRT-NN) data product version 300. https://earth.esa.int/eogateway/documents/20142/37627/SMOS-level-2-Soil-Moisture-NRT-V300-release-note.pdf
Fares, A., Abbas, F., Maria, D., and Mair, A. 2011. Improved Calibration Functions of Three Capacitance Probes for the Measurement of Soil Moisture in Tropical Soils. *Sensors*, Vol. 11, No. 5, pp. 4858–4874.
Ferrarezi R.S., Nogueira T.A.R., and Zepeda S.G.C. 2020. Performance of Soil Moisture Sensors in Florida Sandy Soils. *Water*, Vol. 12, No. 2, pp. 358.
Fredlund, D.G., Rahardjo, H., and Fredlund M.D. 2012. *Unsaturated Soil Mechanics in Engineering Practice*. John Wiley & Sons, Inc., New York, NY, USA.
Greco R., Guida, A., Damiano, E., and Olivares, L. 2010. Soil water content and suction monitoring in model slopes for shallow flowslides early warning applications. *Physics and Chemistry of the Earth*, Vol. 35, No. 2-5, pp. 127–136.
Greco, R., Giorgio, M., Capparelli, G., and Versace, P. 2013. Early warning of rainfall-induced landslides based on empirical mobility function predictor. *Engineering Geology*, Vol. 153, pp. 68–79.
Guan, Y., and Fredlund, D.G. 1997. Use of the Tensile Strength of Water for the Direct Measurement of High Soil Suction. *Canadian Geotechnical Journal*, Vol. 34, No. 4, pp. 604–614.
Intergovernmental Panel on Climate Change (IPCC). 2021. Summary for Policymakers. In: Climate Change 2021: The Physical Science Basis. Contribution of Working Group I to the Sixth Assessment Report of the Intergovernmental Panel on Climate Change. Cambridge University Press. In Press
Kim, J., Kim, Y., Jeong, S., and Hong, M. 2017. Rainfall-induced landslides by deficit field matric suction in unsaturated soil slopes. *Environmental Earth Sciences*, Vol. 76, No. 808.
Kristo, C., Rahardjo, H., and Satyanaga, A. 2017. Effect of variations in rainfall intensity on slope stability in Singapore, *International Soil and Water Conservation Research*, Vol. 5, pp. 258–264.
Kristo, K., Rahardjo, H., and Satyanaga, A. 2019. Effect of hysteresis on the stability of residual soil slope. *International Soil and Water Conservation Research*, Vol. 7, No. 3, pp. 226–238.
Leung, A. K., and Ng, C. W. W. 2016. Field investigation of deformation characteristics and stress mobilisation of a soil slope. *Landslides*, Vol. 13, pp. 229–240.
Lakhankar, T., Ghedira, H., Temimi, M., Sengupta, M., Khanbilvardi, R., and Blake, R. 2009. Non-parametric Methods for Soil Moisture Retrieval from Satellite Remote Sensing Data. *Remote Sensing*, Vol. 1, No. 1, pp. 3–21.
Little K.M., Metelerkamp, B., and Smith, C.W. 1998. A comparison of three methods of soil water content determination. *South African Journal of Plant and Soil*, Vol. 15, No. 2, pp. 80–89.
Liu, X. 2011. Evaluation of the Heat-Pulse Technique for Measuring Soil Water Content with Thermo-TDR Sensor. *Procedia Environmental Sciences*, Vol. 11, pp. 1234–1239.
McCartney, J.S., and Khosravi, A. 2013. Field-monitoring system for suction and temperature profiles under pavements. *Journal of performance of constructed facilities* Vol. 27, No. 6, pp. 818–825.
Moran M.S., Peters-Lidard, C.D., Watts, J.M., and McElroy, S. 2004. Estimating soil moisture at the watershed scale with satellite-based radar and land surface models. *Canadian Journal of Remote Sensing*, Vol. 30, No. 5, pp. 805–826.
Mohanty, B.P., Cosh, M.H., Lakshmi, V., and Montzka, C. 2017. Soil Moisture Remote Sensing: State-of-the-Science. *Vadose Zone Journal*, Vol. 16, No. 1, pp. 1–9.
Muñoz-Carpena R. 2012. Field Devices for Monitoring Soil Water Content. *Agricultural and Biological Engineering Department*, University of Florida. BUL343. http://edis.ifas.ufl.edu.
Nawagamuwa U.P., and Dayarathne W. H. R. S. 2014. Slope Stability Analysis at Bloemendhal Open Dump Site in Sri Lanka. *Proceedings of the 3rd World Landslide Forum*, Beijing, China, 2-6 June 2014.
Noborio K. 2001. Measurement of soil water content and electrical conductivity by time domain reflectometry: a review. *Computers and Electronics in Agriculture*, Vol. 31, No. 3, pp. 213–237.
Ochsner T.E., Horton, R., and Ren, T. 2003. Use of the Dual-Probe Heat-Pulse Technique to Monitor Soil Water Content in the Vadose Zone. *Vadose Zone Journal*, Vol. 2, No. 4, pp. 572–579.

Oguz E.A., Robinson, K., Depina, I., and Thakur, V. 2019. IoT-Based Strategies for Risk Management of Rainfall-Induced Landslides: A Review. *Proceedings of the 7th International Symposium on Geotechnical Safety and Risk*. Taipei, Taiwan, 11-13 December 2019.

Ojo, E.R., Bullock, P.R., and Fitzmaurice, J. 2015. Field Performance of Five Soil Moisture Instruments in Heavy Clay Soils. *Soil Science Society of America Journal*, Vol. 79, No. 1, pp. 20–29.

Pajalić, S., Peranić, J., Maksimović, S., Čeh, N., Jagodnik, V., and Arbanas, Ž. 2021. Monitoring and Data Analysis in Small-Scale Landslide Physical Model. *Applied Sciences*, Vol. 11, No. 11, 5040.

Rahardjo, H., Satyanaga, A., Leong, E.C., Ng, Y.S., Foo, M.D., Wang, C.L. 2007. Slope Failures in Singapore due to Rainfall. *Proceedings of 10th Australia New Zealand Conference on Geomechanics "Common Ground"*. Brisbane, Australia, 21-24 October, 2, 704–709.

Rahardjo, H., Satyanaga, A., Harnas F.R., and Leong, E.C. 2014. Comprehensive instrumentation for real time monitoring of flux boundary conditions in slope. *Procedia Earth and Planetary Science*, Vol. 9, pp. 23–43.

Rahardjo, H., and Satyanaga, A. 2019. Sensing and monitoring for assessment of rainfall-induced slope failures in residual soil. *Geotechnical Engineering*, Vol. 172, No. 6, pp. 496–506.

Rahardjo, H., Kim, Y., Gofar, N., and Satyanaga, A. 2020a. Analyses and design of steep slope with GeoBarrier System under heavy rainfall. *Geotextiles and Geomembranes*, Vol. 48, No. 2, pp. 157–169.

Rodríguez-Iturbe, I. 2003. Hydrologic dynamics and ecosystem structure. *Water science and technology*, Vol. 47, No. 6, pp. 17–24.

Saadatkhah, N., Kassim, A., and Lee, L.M. 2015. Susceptibility Assessment of Shallow Landslides in Hulu Kelang Area, Kuala Lumpur, Malaysia Using Analytical Hierarchy Process and Frequency Ratio. *Geotechnical and Geological Engineering*, Vol. 33, pp. 43–57.

Satyanaga, A., Ibrahimi, A.B., Mohammad, A.S., Hamdany, A.H., Wijaya, M., Moon, S.-W. and Kim. R.J. (2022) Geotechnical Engineering Journal of the SEAGS & AGSSEA. Accepted in October 2022

Shimobe, S., and Ujihira, N. 2009. Monitoring of model slope failure tests using Amplitude Domain Reflectometry and Tensiometer methods, in *Prediction and Simulation Methods for Geohazard Mitigation* – Oka, Murakami & Kimoto (eds), Taylor & Francis Group, London.

Tarantino, A., and Tombolato, S. 2005. Coupling of hydraulic and mechanical behaviour in unsaturated compacted clay. *Géotechnique*, Vol. 55, No. 4, pp. 307–317.

Tremsin V.A. 2017. Real-Time Three-Dimensional Imaging of Soil Resistivity for Assessment of Moisture Distribution for Intelligent Irrigation. *Hydrology*, Vol. 4, No. 4, pp. 54.

Topp G.C. 2003. State of the art of measuring soil water content. *Hydrological Processes*. Vol. 17, pp. 2993–2996.

Will, B., Gerding, M., Schulz, C., Baer, C., Musch, T., and Rolfes, I. 2012. A time domain transmission measurement system for dielectric characterizations. *International Journal of Microwave and Wireless Technologies*, Vol. 4, No. 3, pp. 349–355.

WMO-No. 8 (WMO). 2018. Guide to Instruments and Methods of Observation Volume I –Measurement of Meteorological Variables

Smart Geotechnics for Smart Societies – Zhussupbekov, Sarsembayeva & Kaliakin (Eds)
© 2023 The Author(s), ISBN 978-1-003-29912-7
Open Access: www.taylorfrancis.com, CC BY-NC-ND 4.0 license

Sensing technology for measurement of thermal properties of frozen soil

Bakytkul Serikbek, Alfrendo Satyanaga, Sung-Woo Moon & Jong Kim
Department of Civil and Environmental Engineering, Nazarbayev University, Kazakhstan

ABSTRACT: Soil is one of the most widely used materials in the civil engineering sphere. Different types of soil can be broadly used in its natural or compacted form in the construction of roads, dams, canals, and railways. Due to the differences in moisture content and temperature, soil can be in various states; saturated and unsaturated, frozen or thawed. Advances in the development of laboratory testing equipment for unsaturated soil properties along with the ability to measure soil suction have prepared the way for the implementation of unsaturated soil mechanics. It is now possible to measure most unsaturated soil properties, and these achievements help for unsaturated soil property characterization that best describe the actual unsaturated soil properties. However, the static and dynamic responses of frozen soils have been found to be distinctly different from those of unfrozen soils. The behavior of frozen soils is expected to depend on the inter-particle friction and particle interlocking, the unfrozen water content, pressure melting, and the ice/water phase change. Therefore, unsaturated frozen soil properties should be measured and investigated separately from unsaturated unfrozen soil. The objective of this study is to investigate the appropriate sensors for the measurement of thermal properties of unsaturated frozen soil.

1 INTRODUCTION

Extreme weather conditions, such as lengthy periods of drought, rain or frost significantly impact building foundations. The level of soil moisture is a critical factor in potential detrimental influence. During rainy seasons, the soil absorbs large amounts of water, combined with freezing and further thawing, threatening urban infrastructure (Azmatch et al., 2012). Such activities can severely damage the foundation and load-bearing structures of houses, buildings, and facilities. During frosts, unfrozen water remains in the soil's pores, and the processes of freezing and thawing strongly influence it. These processes significantly affect the physical and mechanical properties of the soil. Therefore, studying the relationship between the amount of unfrozen water and sub-zero temperatures is an important aspect, and it is defined as the soil freezing characteristic curve (SFCC) (Malaya and Sreedeep, 2012). During the freezing period, the pore model changes, and a water film forms around the ice, which is located between the soil particles (Wang et al., 2017). According to the studied information, soil freezing begins with ice formation in the pore with the largest radius (Watanabe and Mizoguchi, 2002).

The freezing and thawing and drying and moistening cycles have similar characteristics. Water with a low matrix potential remains in the soil during the drying process, and the pores filled with water are gradually filled with air. A similar process occurs during the process of freezing, water takes on a solid form. Adsorption and capillary forces affect changes in the matrix potential of water in the soil. The decrease in the matrix index is considered to be the same for both processes, due to the fact that during freezing, water is absorbed by the soil pores in the form of a thin film and the presence of water or air and considered insignificant

DOI: 10.1201/9781003299127-313

(Spaans and Baker, 1996). For capillary strength, there is a difference in the values of the matrix index, since the surface energy of particles is different for soils in the cycles of freezing and drying (Spaans, 1994).

Figure 1 describes the process of soil freezing. The following conclusions emerge from it. The upper part of the soil undergoes freezing, while the lower layers remain unfrozen. There is a partially unfrozen layer which leads to negative pore pressure, which causes water to move into the frozen ground and ice lenses formation (Ren, 2018). The formation of ice lenses and their uneven distribution leads to the appearance of cracks, which can be a problem for infrastructure system in cold regions.

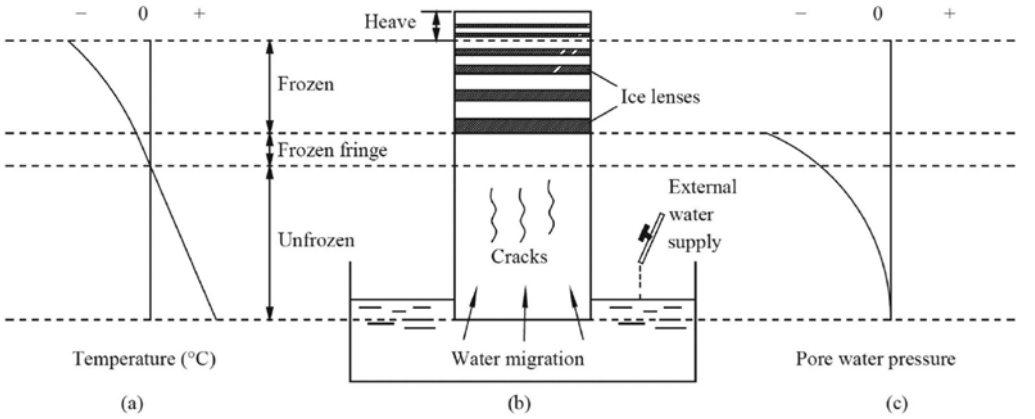

Figure 1. Soil freezing process (Ren et al., 2018).

The inter-particle friction and particle interlocking, the amount of non-frozen water, pressure melting, and the ice/water phase change are all expected to affect the behavior of frozen soils (Xiantiang et al., 2018). These distinctive features are primarily caused by the ice lens and the ice solidifying between soil particles. For instance, the presence of ice in the soil pores for frozen soils result in a decrease in hydraulic conductivity (Fredlund et al., 2012). Due to the distinct behavior of frozen soils, using existing well-established knowledge of mechanical behavior and modeling frameworks for non-frozen soil is not recommended for frozen soils without firstly performing a thorough analysis and examination. Therefore, unsaturated frozen soil properties should be measured and investigated separately from unsaturated non-frozen soil, so that a concept of unsaturated soil properties in frozen soil can be implemented in engineering practice. The objective of this research is to review the sensing technology for the measurement of thermal properties in unsaturated frozen soils.

2 THE HP METHOD FOR MEASUREMENT OF FROZEN SOIL PROPERTIES

Precision measurements of soil thermal and hydraulic parameters are required for environmental sciences and engineering applications and steady-state methods are impractical in determination of these parameters. In lab and field settings, the heat pulse (HP) method is a rapid way to detect soil thermal parameters and a range of other physical features (He et al., 2018).

Single-probe HP (SPHP) and dual-probe HP (DPHP), shown in Figure 2, are the two categories into which HP probes fall. Since SPHP can be either short or long, there are several available sampling volumes. In addition, SPHP is sturdy which provides the reduction in

inaccuracy caused by needle deflection (He et al., 2018). Unfortunately, single-probe HP can only be used to test soil thermal conductivity. In order to improve SPHP to assess other parameters such as heat capacity and soil water content, a deeper understanding of the thermal contact conductance between the soil and the probe is required (He et al., 2018).

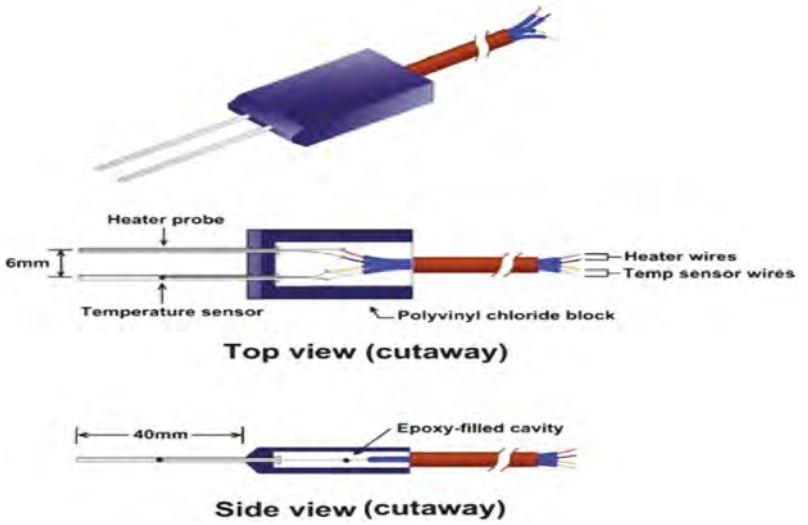

Figure 2. Example picture of dual-probe HP probe (He et al., 2018).

Heat and water flow in non-frozen soils have been measured extensively using the HP technique. However, heat causes soil ice to melt and then refreeze, complicating the use of the HP approach in partially frozen soils (He et al, 2018). When ice melts and subsequently refreezes, a considerable part of the energy in the heat pulse is concentrated on phase shifts rather than conduction heat transfer (He et al, 2018). Thermal properties of the system, such as thermal conductivity and thermal diffusivity, vary in conjunction with phase transitions, such as when water crystallizes or ice melts (Zhang et al., 2015). The measurement of soil thermal properties during such a process can be extremely useful in understanding and forecasting heat transport in such material systems.

Melting ice increases the volumetric heat capacity anticipated by HP and reduces the thermal diffusivity of the soil because partially frozen soils do not fulfill the general assumptions of the HP approach, namely no phase change and temperature invariant thermal characteristics. In accordance to the findings of Ochsner and Baker (2008), dual-probe HP sensors overestimated λ and C values in partially frozen soils (Kojima et al., 2018). Overestimation of λ was most common between 2 °C and 0 °C, whereas Putkonen (2003) discovered that C was overestimated between 10 °C and 0 °C (Kojima et al., 2018). C readings from dual-probe HP sensors were utilized in certain studies to determine the quantity of soil ice. Zhang et al. (2011) observed that the ice content of sand based on C measured with DPHP sensors was incorrect at temperatures ranging from 2 °C to 0 °C (Kojima et al., 2018). Furthermore, in partially frozen soils, as compared to non-frozen soils, C and κ (thermal diffusivity) have a distinct dependence on ambient soil temperature (Ochsner & Baker, 2008). For example, when the soil ambient temperature is very low (below 20 to 2 °C depending on the soil type), the HP melts less ice and the thermal values obtained by the HP are more accurate (He et al, 2018).

The heat conduction Equation (1) shows how heat flows from the heater to the sensors by using the radial coordinate system and refers to the phase shift in partially frozen soils.

$$C_v \frac{\partial T}{\partial t} = \frac{1}{r}\frac{\partial}{\partial r}\left(r\lambda \frac{\partial T}{\partial r}\right) + L_f \rho_I \frac{\partial \theta_I}{\partial t} \quad (1)$$

There is no analytical alternative to equation (1) for practical soil conditions and using HP technology in frozen soils is difficult by the melting and refreezing of ice induced by the heat pulse. There are three ways in the literature for applying the heat pulse to experiments on partially frozen soil (He et al, 2018):

- By utilizing the analytical procedure applied in non-frozen soil and assuming the absence of phase change.
- By limiting ice melting through optimal heat application. Nevertheless, the only temperature range where ice melting induced by HP could be stopped was between -2 and 20 degrees Celsius, and ice melting was substantial at low temperatures, particularly around 0 °C.
- By considering how the melting of the ice changes the thermal parameters that were measured. Ochsner and Baker (2008) included the effects of melting ice into apparent thermal properties to quantify lumped conduction and latent heat components. Once the HP-induced temperature change and the change in λ with temperature are both low, λ can be removed from the partial derivatives in equation (1) and and the equation simplified as in Equation (2).

$$C_{\mathrm{a}} \frac{\partial T}{\partial t} = \lambda_{\mathrm{a}}\left(\frac{\partial^2 T}{\partial r^2} + \frac{1}{\mathrm{r}}\frac{\partial \mathrm{T}}{\partial \mathrm{r}}\right) \quad (2)$$

The apparent heat capacity is defined as the amount of energy required to raise the temperature of a unit volume of partially frozen soil by one degree whereas the phase shift between water and ice occurs as a result of the temperature change caused by the HP. The technique employed by Ochsner and Baker (2008) did not try to monitor ice melting or calculate real thermal soil values. He et al. (2015) evaluated the Time Domain Reflectometry (TDR) method's capacity to quantify ice melting and improve the chance of getting exact thermal properties of frozen soil. For non-frozen liquid water and ice content, they combined Ochsner and Baker's (2008) technique with composite dielectric mixing models (He et al., 2018). C might be determined before to adding HP using the liquid water and ice content observed by TDR using Equation (3). The amount of ice melt may be calculated by comparing the computed C to the Ca estimated using the HP technique, which is influenced by ice melting (He et al., 2018).

$$C_v = \theta_v \rho_I c_I + \rho_g c_g f + (1 - \phi)\rho_{\mathrm{s}} c_{\mathrm{s}} \quad (3)$$

He et al. (2015) applied this approach to a sandy soil and observed that ice melting of 0.5% and 2% had a major influence on the soil thermal characteristics as determined by the heat pulse method. This investigation proved that the HP technique without extra modifications was useless for measuring thermal properties of frozen soil at temperatures ranging from 5 to 0 °C (Putkonen, 2003). The soil freezing characteristics, freezing and thawing curves, and heat capacity estimations from TDR and HP all exhibit hysteretic behavior (He et al., 2018). At temperatures ranging from 5 to 0 ° C., determining both λ and C simultaneously remains problematic.

3 CONCLUSION

This paper described the applications of heat pulse (HP) method and HP sensors to determine the thermal properties of frozen and partially frozen soils. In frozen soils when the ambient temperature is between 20 and 2 ° C, HP sensors gave more accurate thermal values. However,

at 5 to 0 ° C, HP method without developments can not be applied to measure the frozen soils parameters. Therefore, it is needed to conduct further research on modification of HP technique and HP sensors to identify frozen and partially frozen soil properties under variable low temperature conditions.

ACKNOWLEDGEMENT

This research was supported by the Nazarbayev University Research Fund under Grants 11022021CRP1512 and 20122022FD4133. The authors are grateful for this support. Any opinions, findings, and conclusions or recommendations expressed in this material are those of the author(s) and do not necessarily reflect the views of the Nazarbayev University.

REFERENCES

Azmatch, T.F., Sego, D.C., Arenson, L.U. and Biggar, K.W., 2012. Using soil freezing characteristic curve to estimate the hydraulic conductivity function of partially frozen soils. Cold Regions Science and Technology, 83, pp.103–109.

Baker, T. H. W. & Goodrich, L. E. 1984. A probe for measuring both thermal conductivity and water content of soils. In Proceedings Third International Specialty Conference Cold Regions Engineering (2): 835–849. Canada: North Resources Development. Edmonton, Alberta.

Baker, T. H. W., & Goodrich, L. E. 1987. Measurement of soil water content using the combined time-domain reflectometry-thermal con-ductivity probe. Canadian Geotechnical Journal, 24(1): 160–163.

Kojima, Y., Heitman, J. L., Noborio, K., Ren, T. & Horton, R. 2018. Sensitivity analysis of temperature changes for determining thermal properties of partially frozen soil with a dual probe heat pulse sensor. Cold Regions Science and Technology (151): 188–195. https://doi.org/10.1016/j.coldregions.2018.03.022.

Malaya, C. and Sreedeep, S., 2012. Critical review on the parameters influencing soil-water characteristic curve. Journal of Irrigation and Drainage Engineering, 138(1), pp.55–62.

Ochsner, T. E. & Baker, J. M. 2008. In situ monitoring of soil thermal properties and heat flux during freezing and thawing. Soil Science Society of America Journal, 72(4): 1025–1032. https://doi.org/10.2136/sssaj2007.0283

Putkonen, J. 2003. Determination of frozen soil thermal properties by heated needle probe. Permafrost and Periglacial Processes 14(4): 343–347.

Ren, J., Vanapalli, S.K. and Han, Z., 2018. Soil freezing process and different expressions for the soil-freezing characteristic curve. Sciences in Cold and Arid Regions, 9(3), pp.221–228.

Ren, T., Horton, R. & Ochsner, T. E. 2003. Development of thermo-time domain reflectometry for vadose zone measurements. Vadose Zone Journal 2(4): 544–551

Spaan, E.J.A. 1994. The soil freezing characteristic: Its measurement and similarity to the soil moisture characteristic. PhD dissertation university of Minnesota, St Paul.

Spaans, E.J., Baker, J.M., 1996. The Soil Freezing Characteristic: Its Measurement and Similarity to the Soil Moisture Characteristic. Soil Sci. Soc. Am. J. 60 (1), 13–19.

Wang, C., Lai, Y. and Zhang, M., 2017. Estimating soil freezing characteristic curve based on pore-size distribution. Applied Thermal Engineering, 124, pp.1049–1060.

Watanabe, K. and Mizoguchi, M., 2002. Amount of unfrozen water in frozen porous media saturated with solution. Cold Regions Science and Technology, 34(2), pp.103–110.

Zhang, B., Han, C. & Yu, X. 2015. A non-destructive method to measure the thermal properties of frozen soils during phase transition. Journal of Rock Mechanics and Geotechnical Engineering (7): 155–162.

Smart Geotechnics for Smart Societies – Zhussupbekov, Sarsembayeva & Kaliakin (Eds)
© 2023 The Author(s), ISBN 978-1-003-29912-7
Open Access: www.taylorfrancis.com, CC BY-NC-ND 4.0 license

Potential applications of maturity sensors for monitoring geotechnical structures and their setup methods

A. Aniskin
University North, Varaždin, Croatia

Sh. Zharassov
L.N. Gumilyov Eurasian National University, Astana, Kazakhstan

ABSTRACT: Recent years demonstrated the widespread use of maturity sensors for monitoring structural elements of monolithic building frame resulting in the development of many instructions on their application, which does not apply to the monitoring of geotechnical structures. This paper presents potential use cases and setup methods of embedded maturity sensors. Proposed instructions can be used as a method statement for the real-time strength control of concrete foundations and underground walls.

1 INTRODUCTION

Concrete is one of the basic and widely used materials on the construction site. Many processes have to wait for this building material to reach its strength, which can lead to postponement under negative circumstances. For this reason, the goal of timely achievement of strength or design strength after 28 days plays a very important role in reducing the time of construction. It is worth noting that the priority in the accumulation of strength has massive structures, lying below the net floor level of the first floor, taken as 0.000 m. Solid and strip foundations, deep and shallow foundations, retaining walls, crossbeams, etc. are considered massive constructions. The processes inside the concrete and measures such as summer watering and winter heating (concrete care) to maintain favorable conditions are therefore given close attention(Christiaan 2019).

The process of concrete strength gain is a set of physical and chemical processes at the time of hardening. For example, concrete curing is accompanied by an exothermic reaction and its persistence for 1, 3, 7, 14,and 28 days with a rise at the beginning and a subsequent decrease in temperature at the end. The temperature graph arising from the exothermic reaction is the standard, approved by the destructive method of quality control of cubic specimens at the achievement of indicators for 28 days, and any discrepancy suggests a deviation from the mixing technology of concrete or the subsequent care of him(Jung 2009; Rudeli 2015).

In connection with the above, some regularities apply to new methods of monitoring and controlling concrete curing. In turn, the new monitoring methods involve the use of high-precision sensors and sensors that track various indicators during the curing process. In the information environment, such electronic devices are called temperature sensors or sensors of concrete maturity. The second name is rather more scientific than the first because it is derived from a method (ASTM 1998)and describes the nature of the method by reference to the temperature-time factor (TTF). (ASTM 1998)regulates two fundamental formulas in the basis of the method for calculating the temperature-time index known as Nurse-Saul (Formula 1) and Arrhenius (Formula 2). It is worth noting that the maturity method Nurse-Saul is widespread in the market of electronic devices (Jung 2009). The advantage of this method is the obvious relationship between concrete strength and the hydration temperature of the cementitious paste.

DOI: 10.1201/9781003299127-314

$$M(t) = \sum_{0}^{t} (T_a - T_0)\Delta t \tag{1}$$

where M(t)= temperature-time factor, ºC-days or ºC-hours; Δt = time interval, days or hours; T_a = average concrete temperature, ºC, during the time interval, Δt; and T_O = datum temperature, ºC.

$$t_e = \sum e^{\frac{-E_a}{R}\left(\frac{-E_a}{T_a} + \frac{-E_a}{T_s}\right)\Delta t} \tag{2}$$

where t_e= equivalent age at a specified temperature, T_s, days or hours;

E_a= activation energy, J/mol; R = gas constant, 8.31 J/(K*mol);T_a= average temperature of concrete during the time interval, Δ*t*, K; T_s= specified temperature, K; and Δ*t* = time interval, days, or hours.

The current market for electronic devices offers various variants of maturity sensors, both foreign and domestic, and assemblies (Figure 1).

Figure 1. Examples of existing concrete maturity sensors.

Several parametersare considered when choosing a maturity sensor, such as the presence of a wireless or wired network, the measurement of various indicators, the minimum and maximum temperature range, the accuracy of the error and measurement interval, as well as the data transmission range and battery life(Utepov 2022).

During the existence of maturity sensors, the development of the electronic component has gone far beyond the technical regulations and regulatory and technical documentation for their installation and operation. Based on the analysis of existing literature sources, it can be concluded that the works (Christiaan 2019; Jung 2009; Rudeli 2015), where concrete maturity sensors were used, mainly refer to the building framework, that is, columns and floor slabs lying above zero level of the first floor.During the existence of maturity sensors, the development of the electronic component has gone far beyond the technical regulations and regulatory and technical documentation for their installation and operation. Going back to what was said before, the priority in strength gain is given to massive structures lying below the level of the clear floor of the first floor; the problem that emerges in this article is the following. Concrete maturity sensors should be installed in the areas withthe slowest strength gain and the most stressed areas(Nurakov 2020).In this connection, as the main attention is paid to the typical floors above the 0.000 m elevation, the moment of installation of concrete maturity sensors and operation, in the form of instructions, not to mention technological charts has been missed, which forms the purpose of this article. The authors offer effective methods of installation and operation of concrete maturity sensors in the construction of geotechnical structures (foundations, retaining walls, etc.) (Awwad 2019; Zhussupbekov 2019).

2 USE CASES

Long-term durability is very often discussed in the construction of reinforced concrete structures. Various sensors and devices for monitoring the condition of reinforced concrete structures are used for this purpose. Thus, in the example of tunnel construction, the focus is on concrete life-cycle monitoring sensors. Depending on the environment in which the structure is operated,

the installation of sensors plays a very important role. The importance of technology compliance and subsequent monitoring is described in (Feng-Hui 2000), where an example of the collapse of parts of tunnel interior walls is given. The colossal damage to public property and the threat to ordinary citizens is the result of an untimely inspection of the structure. The authors decide to use a robotic automatic tunnel inspection system compatible with sensors in the concrete, but the question of their design when the sensors are immersed in the body of the concrete remains open. The behavior of sensors during construction of the tunnel is considered in (Bursi 2016), where the performance of built-in and externally installed sensors are compared. It is worth noting that the difference in readings was 50%. To give an example of other constructions, we can highlight works related to massive foundations (Utepov 2022).Another important factor deals with the monitoring of deformation and temperature of reinforced concrete pile foundations, namely, the careful installation of sensors for obtaining correct data. Attention is paid to such secondary, but not unimportant factors as the transportation of sensors and the protection of sensors during the process of concreting foundation wells. Some works (Qin 2014) mention the use of several sensors to monitor the condition of reinforced concrete structures. An interesting point when conducting experiments of this type is the compatibility of electronic devices or their location relative to each other. The construction of massive structures or large volumes of concrete has always had its nuances. This problem is discussed in (Chang 2012), where a temperature difference exceeding the permissible limit is considered. This phenomenon is fraught with cracking, which leads to the subsequent penetration of moisture and further corrosion of the reinforcement (Lukpanov 2021; Lukpanov 2021).The prerequisites for determining the location of temperature sensors are given in (Ye Utepov 2019). This method can be applied to temperature sensors (Utepov, Tolkynbayev 2022; Utepov, Tulebekova 2022), which may not be applicable in other cases, but the validity of this methodology can form the basis for instructions or process maps for installation and operation of temperature sensors. Thus, when examining the sources currently available, it can be concluded that the given examples of using sensors to monitor phenomena occurring in concrete contain information for theoretical analysis, while attention to the features of installation in practice, especially on geotechnical structures and structures, is not adequately paid.

3 MATURITY SENSORS SETUP METHODS

The installation process for any sensor on a construction site begins with a secure attachment to the structure. Before installation begins, the depth of the sensor or its components, such as a cable with a sensor at the end, must be determined. Here is an example of fixing a concrete maturity sensor to working rebar (Figure 2).

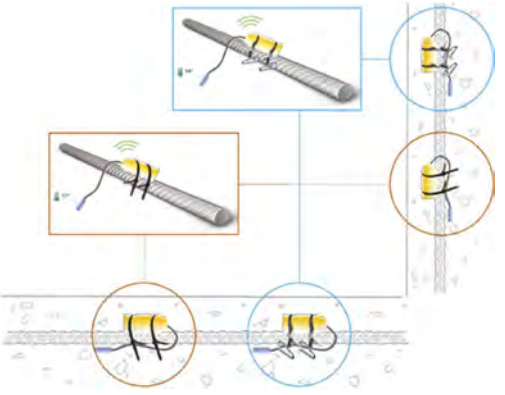

Figure 2. Example of mounting and fixing the concrete maturity sensor on horizontal and vertical reinforcement.

According to the figure above, the sensors are installed according to a certain scheme on the longitudinal (working) and transverse (distribution) fittings. Fixing in the field is done with

a wire or a clamp. Depending on the strength of the signal transmission at the construction site, the sensor is immersed to a greater depth than the protective layer of concrete. This distance from the surface of the housing to the paved mixture must be strictly maintained, as required by the technology of the concrete mix. If the casing is leaking or the signal transmission is poor, only the cable with the sensor at the end is immersed, while the main part of the cable is placed on the surface. The contact of the sensor with other surfaces, except for the concrete mixture, is excluded, as it may lead to distorted data. It is worth noting that when pouring and compacting the concrete mixture, you must be careful because the vibrating machine can damage the sensor. The transmission of measured data goes locally within the range of the sensor and does not apply to the entire structure. In this regard, the pitch and depth of the sensors are very important. The logic of the schematic location of the sensors on the example of a strip foundation on pour piles, a foundation slab, and a retaining wall is given in the sections below.

In the case of a cast-in-place pile, the sensors are installed at the initial stage when the frame is tied in because access to the sensor is restricted after the frame has been sunk into the borehole. Depending on the depth of the pile, the required number of sensors is selected. Due to the location of sensors under the soil layer the signal transmission power can significantly decrease, in this regard it is reasonable to sink only the cable with the sensor into the concrete body and fix the body itself on the armature outlet above the ground (Figure 3). When assembling the strip foundation formwork, the sensor housing can be both in and out of the concrete body. In this case, it is advisable to install the sensors on the transverse reinforcement, so that the cable with the sensor at the end is located in the center of the structure (Figure 3).

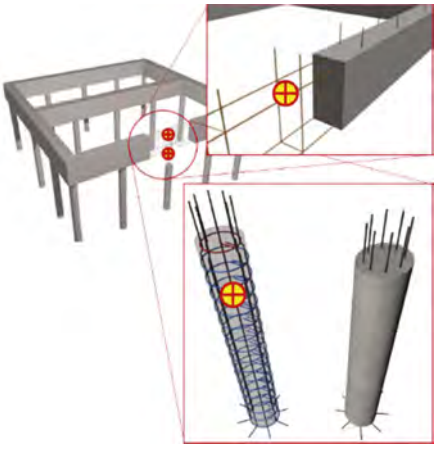

Figure 3. Location of sensors inside the strip foundation on pour piles.

The foundation slab is the most massive structure when installing sensors for monitoring. At this scale, it is necessary to install sensors at several heights (Figure 4).

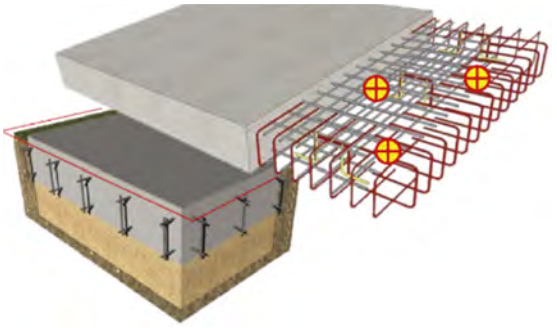

Figure 4. Sensor location inside the foundation plate.

In the case of installation of sensors in structures at height, it is necessary to install scaffolding, decking, and scaffolding with enclosing structures. An obvious example of installing sensors at height is retaining walls, which come in different heights and thicknesses. Alternatively, sensors are installed as in the case of pouring piles at the initial stage of tying the reinforcement cage, and then the finished cage is connected to the outlet of the reinforcement at the bottom of the foundation (Figure 5).

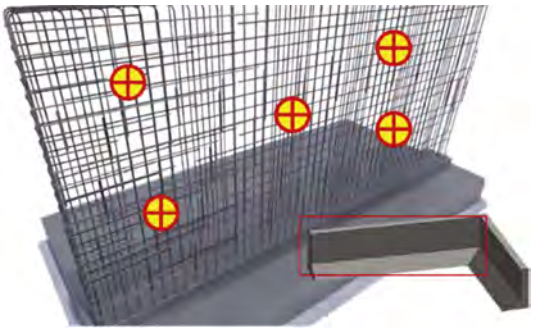

Figure 5. Sensor location inside the retaining wall.

4 CONCLUSIONS AND RECOMMENDATIONS

Based on various examples, based on the existing sensors on the market for concrete monitoring, the following generalized conclusions and recommendations have been formulated, which apply to the installation of any sensor, regardless of its purpose:

1. Subsequent monitoring of the design may be accompanied by the following hazardous and harmful factors:
- increased or decreased temperature of the air in the working area;
- increased air humidity, noise and vibration level;
- location of working place at a considerable height relative to the surface of the ground (floor, overlapping);
- insufficient illumination of the working places;
- physical overloading.

2. To ensure the reliability of the results obtained, you should pay attention to the following points in the operation of the sensors:
- completeness and reliability of attachment of parts;
- serviceability of the sensor components, protective sheathing, and presence of mechanical damages;
- the integrity of insulating parts of the sensor housing;
- serviceability of the sensor activator (free switching on and off before the beginning of work);
- serviceability and connection of the data acquisition station, if any, to the socket with voltage (change of light indicators);
- location of the data collection station in a hard-to-reach and low-traffic location for safety and uninterrupted operation.

The results are reflected in the technological schemes (Figures 2–5), which show the proposed locations for the installation of sensors. The number, pitch, and depth of installation may vary depending on the size, massiveness of the structure, and the peculiarities of the geotechnical construction. It is worth noting that the issue of using different sensors to monitor one structure remains open, which makes it possible to continue the development of technological schemes and maps when several sensors work in one working field.

REFERENCES

Standard Practice for Estimating Concrete Strength by the Maturity Method, 1998.

Awwad, T. 2019. Development of the Computer program of Calculation of concrete bored piles in soil ground of Astana city. *International Journal of GEOMATE*, *17*(60). https://doi.org/10.21660/2019.60.17339.

Bursi, O. S., Tondini, N., Fassin, M., & Bonelli, A. 2016. Structural monitoring for the cyclic behaviour of concrete tunnel lining sections using FBG sensors. *Structural Control and Health Monitoring*, *23*(4), 749–763. https://doi.org/10.1002/stc.1807.

Chang, C.-Y., & Hung, S.-S. 2012. Implementing RFIC and sensor technology to measure temperature and humidity inside concrete structures. *Construction and Building Materials*, *26*(1), 628–637. https://doi.org/10.1016/j.conbuildmat.2011.06.066.

Chen, J., Li, P., Song, G., & Ren, Z. 2016. Piezo-based wireless sensor network for early-age concrete strength monitoring. *Optik*, *127*(5), 2983–2987. https://doi.org/10.1016/j.ijleo.2015.11.170.

Christiaan, E.. 2019. *Investigation of a practical application of the Maturity Method to estimate the early-age strength of concrete*. Stellenbosch: Stellenbosch University.

Feng-Hui Yao, Gui-Feng Shao, Yamada, H., & Kato, K. 2000. Development of an automatic concrete-tunnel inspection system by an autonomous mobile robot. *Proceedings 9th IEEE International Workshop on Robot and Human Interactive Communication. IEEE RO-MAN 2000 (Cat. No.00TH8499)*, 74–79. https://doi.org/10.1109/ROMAN.2000.892473.

Fukuro, A., Torigoe, T., Mizuguchi, H., & Ueda, T. 2006. Application of a new measuring method using an optical fiber strain sensor to an under-ground tunnel. *International Journal of Modern Physics B*, *20* (25n27), 3692–3697. https://doi.org/10.1142/S0217979206040210.

Jung, J., & Cho, Y. 2009. Comparison between Nurse-Saul and Arrhenius equations. *Can. J. Civ. Eng.*, *36*, 514–518.

Lai, J., Qiu, J., Fan, H., Zhang, Q., Hu, Z., Wang, J., & Chen, J. 2016. Fiber Bragg Grating Sensors-Based In Situ Monitoring and Safety Assessment of Loess Tunnel. *Journal of Sensors*, *2016*, 1–10. https://doi.org/10.1155/2016/8658290.

Lukpanov, R., Dyussembinov, D., Bazarbayev, D., Tsygulyov, D., & Yenkebayev, S. 2021. Homogeneous pore distribution in foam concrete by two-stage foaming. *Magazine of Civil Engineering*, *3*(103), 10313. https://doi.org/10.34910/MCE.103.13.

Lukpanov, R., Zharassov, S., Mkilima, T., & Aldungarova, A. 2021. Performance of maturity method for estimation of concrete strength based on cubic specimens. *Technobius*, *1*(4), 0008. https://doi.org/10.54355/tbus/1.4.2021.0008.

Nurakov, S. 2020. Calculation of Soils cutting force by knife type cutting elements of the earthmoving machine. *International Journal of GEOMATE*, *19*(71). https://doi.org/10.21660/2020.71.43612.

Qin, L., Ren, H.-W., Dong, B.-Q., & Xing, F. 2014. Acoustic Emission Behavior of Early Age Concrete Monitored by Embedded Sensors. *Materials*, *7*(10), 6908–6918. https://doi.org/10.3390/ma7106908.

Rudeli, N., Santilli, A., & Arrambide, F. 2015. Striking of vertical concrete elements: An analysis using the maturity method. *Striking of Vertical Concrete Elements: An Analysis Using the Maturity Method*, *95*, 40–48.

Tondini, N., Bursi, O. S., Bonelli, A., & Fassin, M. 2015. Capabilities of a Fiber Bragg Grating Sensor System to Monitor the Inelastic Response of Concrete Sections in New Tunnel Linings Subjected to Earthquake Loading. *Computer-Aided Civil and Infrastructure Engineering*, *30*(8), 636–653. https://doi.org/10.1111/mice.12106.

Utepov, Ye, Aniskin, A., Ibrashov, A., & Tulebekova, A. 2019. Maturity sensors placement based on the temperature transitional boundaries. *Magazine of Civil Engineering*, *90*, 93–103. https://doi.org/10.18720/MCE.90.9.

Utepov, Ye, Tolkynbayev, T., Aniskin, A., Zharassov, S., Tulebekova, A., & Akishev, M. 2022. Assembling a Multisensory device for Monitoring and Assessing concrete curing conditions. *Eurasian Physical Technical Journal*, *19*(39), 90–98. https://doi.org/10.31489/2022No1/90-98.

Utepov, Ye, Tulebekova, A., Aldungarova, A., Zharassov, S., & Sabitov, Y. 2022. Performance of a Wireless Sensor adopted in monitoring of Concrete strength. *GEOMATE Journal*, *23*(95), 73–80. https://doi.org/10.21660/2022.95.3265.

Utepov, Yelbek, & Zharassov, S. 2022. On-site pilot testing of maturity sensors in conjunction with ambient condition monitoring device to get an insight into the concrete strength gain process. *Technobius*, *2*(2), 0019. https://doi.org/10.54355/tbus/2.2.2022.0019.

Zhussupbekov, A., Chang, D.W., Utepov, Y., Borgekova, K., & Omarov, A. 2019. Estimating the Driven Pile Capacities for COF Project in West Kazakhstan. *Soil Mechanics and Foundation Engineering*, *56*(2), 121–127. https://doi.org/10.1007/s11204-019-09579-6.

Smart Geotechnics for Smart Societies – Zhussupbekov, Sarsembayeva & Kaliakin (Eds)
© 2023 The Author(s), ISBN 978-1-003-29912-7
Open Access: www.taylorfrancis.com, CC BY-NC-ND 4.0 license

Swedish weight sounding test: Site investigation for a solar power facility in the Philippines

M.J.P. Armario, M.P.V. Follosco, J.M.B. Gargullo, P.A.R. Lu & R.A.C. Luna
AMH Philippines, Inc.,University of the Philippines, Diliman, Quezon City, Philippines

ABSTRACT: Swedish Weight Sounding Test (SWST) is one of the common in-situ penetration testing techniques. This is often utilized as a part of the geotechnical investigation for foundation, liquefaction, and landslide assessments. In the Philippines, this is typically conducted as a supplement to Standard Penetration Test (SPT), which is the most used in-situ test in the country. Empirical correlations between the SPT N-values and the number of half-turns (N_{SW}) from SWST are developed from the data gathered on several soil exploration sites. Considering the portability of the equipment and the cost of the test, this offers a good supplement and/or alternative to SPT.

A case study of a solar power plant located in the Central Luzon Region is presented. A total of fifty-four (54) test points are located strategically for the subsurface investigation for the expansion of the said solar power plant. The correlation was found to be applicable to fine-grained or clayey soils, with conservative inherence. The verification and development of correlations based on the local/Philippine setting are needed to provide more accurate and consistent results.

1 INTRODUCTION

At the end of the 19th century, the SWST was first used in Scandinavia by the Swedish State Railways as a survey of bad roadbed conditions. The commission was called State Railways Geotechnical Commission, which developed and standardized a penetrometer test, later to become known as the Swedish Weight Sounding Test. The main purpose of the test is to obtain estimates of the shear strength of SPT-Numbers of soil deposits (Tsukamoto et. al., 2004). The SWST has also been used in reconnaissance and surveys of landslides and earthquake-disaster-stricken sites (Towhata et. al., 2004).

The SWST is composed of 1-meter-long steel rods with a 19 mm diameter, with the first rod being 800 mm long with a 200 mm long twisted screw point. It is common in Scandinavian countries but also became popular in Japan for assessing the liquefaction susceptibility of soil and determining its bearing capacity.

It was in 1954 that this testing method was first introduced in Japan for field inspections on river embankments. Since then, it has become a popular technique for soil surveys for the construction of subgrade and base of pavements and port facilities. In 1976, it was standardized by the Japanese Industrial Standards (JIS), and by the International Society for Soil Mechanics and Foundation Engineering (ISSMFE) in 1989.

2 BACKGROUND OF SWST

The Swedish Weight Sounding Test (SWST) was popularized and is widely used in Japan and some European countries. It is an in-situ type of static penetration test commonly used in loose to medium dense sand and silt, clay, peat, and organic soils.

DOI: 10.1201/9781003299127-315

The SWST equipment consists of a 200 mm screw-shaped point, steel plates weighing a total of 100kg (0.98kN), 22mm Ø steel extension rods (standardized by ENV 1997:3-2000), and a handle for rotating the equipment. Measurement of soil resistance can be recorded as N_{SW}, which is the number of half turns the device is rotated for every 1 meter penetration. The typical depth that the SWST can penetrate is 6 meters up to 9 meters, the data gathered from this depth is sufficient for light structures, typicall1 1 to 2-storey residences. The SWST presumes that the project site is on a flat semi-infinite ground, similar to a standard penetration test.

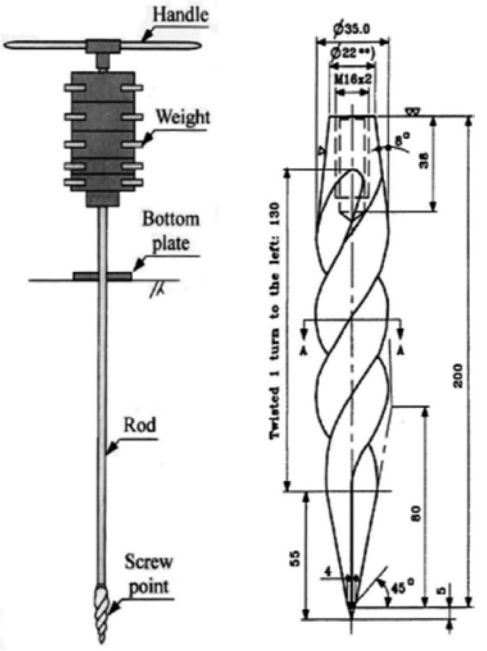

Figure 1. (a) Schematic view of SWST (Tsukamoto et. al., 2004) (b) SWST Screw (ENV 1997:3-2000).

3 METHODOLOGY

The SWST equipment is assembled by connecting the rods, connecting the screw at one end of the rods, and placing the dead weights equal to 100kg (0.98kN), W_{SW}, as shown previously in Figure 1-a. For soft soils, penetration may occur even without rotation, the depth penetrated is then recorded. If there is no more self-penetration, the handle is then rotated. The number of half turns (180 degrees) for every 1 meter is then recorded and is called N_{SW}. The higher the N_{SW}, the harder the soil.

Testing should be terminated when a certain penetration resistance or certain depth is reached. Testing could be terminated if the screw point does not penetrate anymore when rotated or when driven by at least 10 blows of a 3.0 kg sledgehammer. Another criterion is when two adjacent 25 cm thick layers are encountered with increasing penetration resistance exceeding 50 half turns per 25 cm, or penetration is less than 1 cm per blow after 5 blows of the sledgehammer.

4 CORRELATIONS

There are several correlations developed between the SWST and SPT results (e.g., Inada, 1960; JGS, 19995; Tsukamoto et. al., 2004). The great advantage of using Japanese correlations is that it uses a small variation of SPT Energy Ration (ER) in Japanese practice. An average value of 72% can be considered as the average value of ER in Japan (Ishihara, 1993).

The equivalent SPT N-value may be obtained using the empirical formula developed by M. Inada (1960).

For Sandy Soils,

$$N = 0.02 W_{SW} \tag{1}$$

$$N = 2 + 0.067 N_{SW} \tag{2}$$

For Clayey Soils,

$$N = 0.03 W_{SW} \tag{3}$$

$$N = 3 + 0.05 N_{SW} \tag{4}$$

Inada suggests a factor of safety of ±1.5 to 4 for sandy soils and 3 for cohesive materials due to the various types of soil and other factors. The empirical equation for the unconfined compression strength of the soil is as follows:

$$q_u = 0.045 W_{SW} + 0.75 N_{SW} \tag{5}$$

On the other hand, Tsukamoto (2004) proposed an empirical formula to estimate the SPT-N values and the relative density, D_r by using the void ratios and the effective overburden pressure. The empirical equation for the SPT N-value and relative density are as follows:

$$N = \frac{\sqrt{e_{max} - e_{min}}}{10} (N_{SW} + 40) \tag{6}$$

$$D_r = \sqrt{\frac{(N_{SW} + 40)(e_{max} - e_{min})^{2.2}}{90} \sqrt{\frac{98}{\sigma'_v}}} \tag{7}$$

where σ'_v is the effective overburden stress in kPa, and the values of maximum and minimum void ratios, e_{max} and e_{min}, are evaluated based on the testing method by the Japanese Geotechnical Society (2009). This method is usually employed for fine sands containing fines less than 5%, though it is not limited to silty sands.

5 ADVANTAGES AND LIMITATIONS

One of the advantages of the SWST is that it can easily detect weak thin strata, but it is not suitable for soil sampling at a specific depth and for monitoring the groundwater depth accurately.

Like other sounding methods, the primary advantage of SWST is that a nearly continuous profile of penetration resistance is developed for stratigraphic interpretations. It allows detailed definitions of soil layers and detection of thin layers of seams. The manual type of SWST has the optimal performance/accuracy in the soils with rotational resistance between 2 to 40 half turns per 0.20 meter of penetration (Habibi, 2007). SWST, as compared with other soundings is simpler, faster, has lighter reaction weight, and better cost-efficiency. SWST can be classified as a "low-cost in-situ test". However, it has low accuracy on soil classification, and the rod friction included in the test result makes the ability lower.

As mentioned, SWST is optimal for soil resistance of 2 to 40 half-turns for every 0.20 meter. Below this limit, the accuracy of SWST measurements decreases due to the discontinuous measurement of resistance. Also, in high resistances (N_{SW} > 100 half turns/0.20 meter) the repeatability of the results is not clear (Habibi, 2006).

The effect of friction along the rods should be taken into consideration also (ENV 1997:3-2000, JIS A 1221-2002). This effect is considerably high, particularly when there are fill material or peat layers on-site (Broms and Flodin, 1998; Habibi, 2006). Using SWST in these cases should be accompanied with caution.

Other factors considered to have direct impacts on the results of the SWST are the location of maximum rotation diameter from the screw point, screw point abrasion, and different shapes of screw points. The variation in these factors leads to differences in cutting mechanisms. Specifically, this can lead to a considerable impact on self-weight penetration (Fujii et al, 2003).

6 CASE STUDY

6.1 *Project location*

The study area is in Mt. Sta. Rita in Subic, Zambales. It has generally mountainous terrain which makes soil investigation difficult. As such, SWST was performed in conjunction with the SPT to cover as much area as possible.

The study area can be accessed through Binictican Drive, then passes through Pamulaklakin Trail. It is approximately 7.67 kilometers from Subic Bay Freeport Zone and 10.10 kilometers from the City of Olongapo.

6.2 *Results*

The empirical equation proposed by M. Inada gives a very low equivalent N-value. With this, we have come up with a new empirical equation to derive N-values which is closer to the N-value from SPT.

For Sandy Soils,

$$N = 2 + 0.54N_{SW} \tag{8}$$

For Clayey Soils,

$$N = 3 + 0.40N_{SW} \tag{9}$$

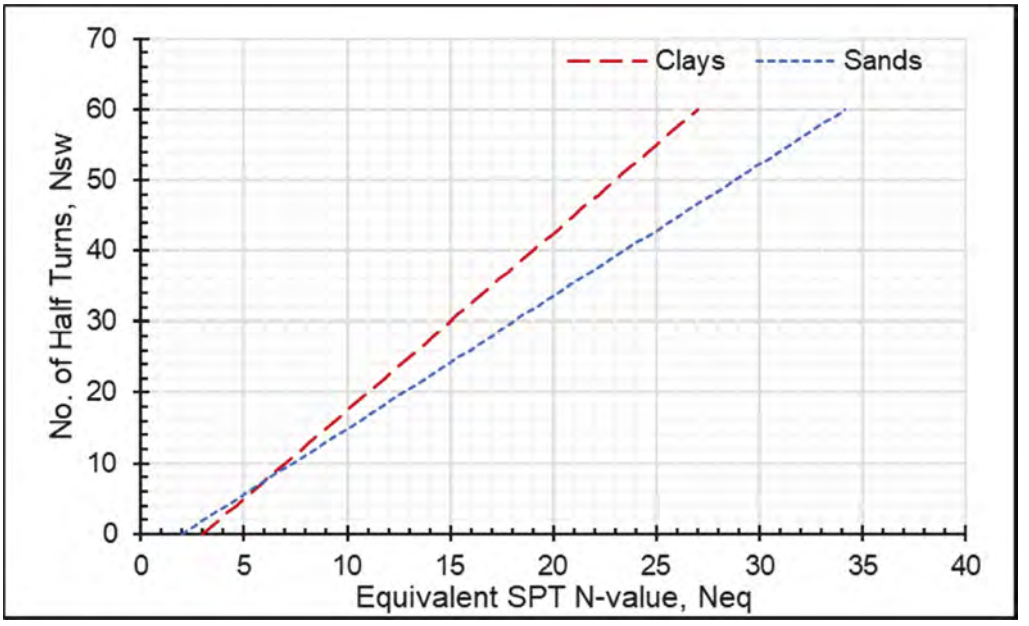

Figure 2. Corresponding N-value from the results of the SWST.

The following chart presents the result of 54 SWS tests conducted in the study area. Due to uncertainties at the test points, the equivalent N-values for sands and clays are presented to give the range of the possible actual N-value.

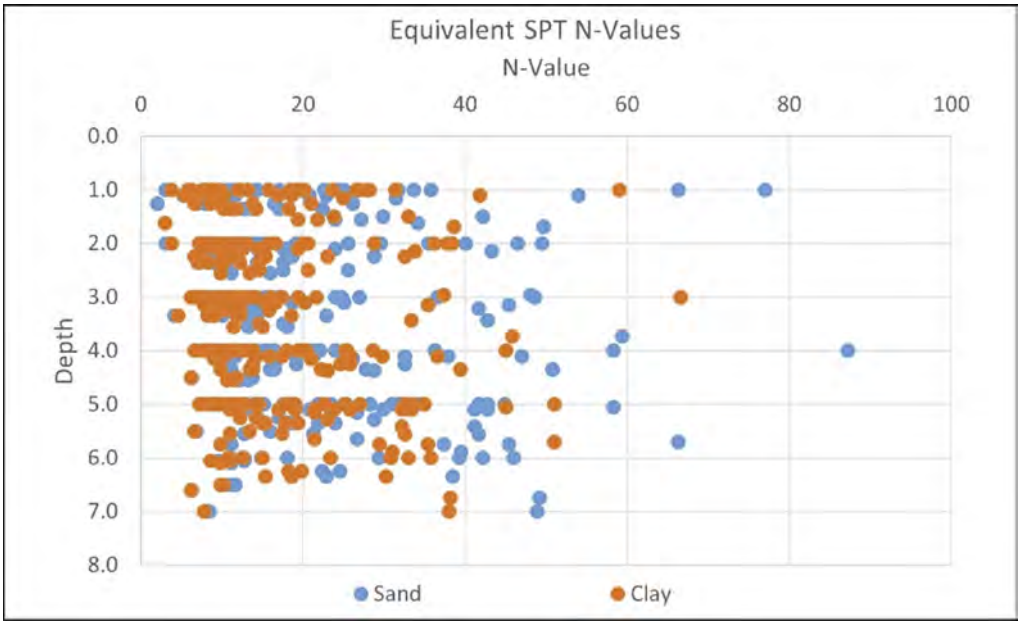

Figure 3. Equivalent SPT N-values from the results of the SWST.

6.3 *Comparison with SPT*

The data obtained from the site with the SWST need to be verified. As such, an SWST was conducted immediately adjacent to one of the SPT (MV-10). Based on the laboratory tests conducted on the soil samples of MV-10, the soil is classified as clay. Thus, Equation (4) proposed by M. Inada will be used.

The following table presents the SPT N-value from the SPT conducted on MV-10 and the equivalent N-value from the SWST conducted immediately adjacent to the SPT using Equations (4) and (9). It could be observed from the table that the N-value from the SWST is generally conservative compared to the values obtained from the SPT.

Table 1. SPT N-Value of MV-10 and Equivalent N-Value from SWST.

Depth	Soil Classification	Soil Penetration Test N-Value	N_{SW}	Equivalent N-Value (Equation 4)	Equivalent N-Value (Equation 9)
0.00 – 1.50	ML	39	30	4	15
1.50 – 3.00	MH	16	39	5	19
3.00 – 4.50	Sandy Clays	13	21	4	11
4.50 – 5.00	Sandy Clays	11	19	4	11
5.00 – 5.50	Sandy Clays	13	15	3	9

6.4 *Findings and recommendations*

The test results of the SWST conducted immediately adjacent to the SPT at MV-10 show that the equivalent N-value from the SWST is generally consistent with the recorded N-values from SPT for fine-grained or clayey soils. The calculated equivalent N-values are also

consistently relatively more conservative, which in turn, results in the use of more conservative soil strength and deformation properties for use in the analysis and design of foundations.

Furthermore, it is recommended to always conduct an additional SWST immediately adjacent to an SPT for correlation purposes since the proposed empirical equation by M. Inada will need further verification for other types of soil. Some modifications to the said correlation equations may be essential to better suit local soil conditions.

The results of the investigation were based on the SWST conducted by AMH on the project site which is composed of 54 SWST points. The investigation aims to provide a practical alternative to the SPT by providing the equivalent N-value of the soil at these test points. The verification is deemed limited at this time and recommended to be supplemented in future opportunities in the potential expansion areas of the project site.

7 CONCLUSIONS AND WAY FORWARD

The SWST was utilized for the subsurface investigation of a study area in Subic, Zambales. The SWST data were correlated using the empirical equations by M. Inada (1960) to an equivalent SPT N-value for the individual subsurface layers. The correlation was found to be applicable to fine-grained or clayey soils, with conservative inherence. The verification and development of correlations based on the local/Philippine setting are needed to provide more accurate and consistent results, which may allow SWST as an alternative to SPT in certain project conditions.

Further use of the SWST adjacent to borehole sites with SPT is highly encouraged to further develop an empirical relationship of SWST data to SPT N-values in the Philippine setting.

REFERENCES

Broms, B.B., & Flodin N. 1988. *History of soil penetration testing; Proc. of 1st International Conference on Penetration Testing, Orlando,* 20-24 March 1988. Rotterdam: Balkema.

Fujii, M., Ijuin, H., Kawamura, M., Edahiro, T., Mizutani, Y., Wakame, Y., & Tamura, M. 2003. *Ground Evaluation by Swedish Weight Sounding for Detached House Construction*.

Habibi, M., Cheshomi, A., & Fakher, A. 2007. *Advantages and Disadvantages of Using Swedish Weight Sounding for Liquefaction Assessment*.

Habibi, M., Cheshomi, A. & Fakher, A. 2006. *A case study of liquefaction assessment using Swedish Weight Sounding: Proc. of 4th International Conference on Earthquake Engineering*, *Taipei,* 12-13 October 2006. Taiwan: NCREE.

Inada, M. 1960. *Use of Swedish weight sounding tests. Tsuchi-to-Kiso, Japanese Geotechnical Society*, 8(1), 11–13.

Ishihara, K., Acacio, A., & Towhata, I. 1993. Soils and Foundations. *Liquefaction-induced ground damage in Dagupan in the July 16, 1990 Luzon earthquake*.

Tsukamoto, Y, Ishihara, K., & Sawada, S. 2004. Soils and Foundations. *Correlation between penetration resistance of Swedish weight sounding tests and SPT blow counts in sandy soils*.

Tsukamoto, Y., Ishihara, K., & Harada, K. 2009. Soils and Foundations. *Evaluation of undrained shear strength of soils from field penetration tests*.

Tsukamoto, Y., Hyodo, T., & Fuki, N. 2015. *Some recent applications of Swedish weight sounding tests to earthquake reconnaissance investigations. 6th International Conference on Earthquake Geotechnical Engineering*. Christchurch, New Zealand.

Towhata, I., Ghalandarzadeh, A., Shahnazari, H., Masoud, M., & Shafiee, A. 2004. *Seismic Behavior of Local Soil and Foundations in Bam City During the 2003 Bam Earthquake in Iran*.

Zarco, M., Pekley Jr., D., & Tan, S. 2010. *Guidelines of the Swedish Weight Sounding Test (SWST) in the Philippine Setting. 3rd AUN-SEED-Net Regional Conference on Geo-Disaster Mitigation*. Kyoto, Japan.

Smart Geotechnics for Smart Societies – Zhussupbekov, Sarsembayeva & Kaliakin (Eds)
© 2023 The Author(s), ISBN 978-1-003-29912-7
Open Access: www.taylorfrancis.com, CC BY-NC-ND 4.0 license

Comprehensive recognition of soil and water conditions in the area of critical infrastructure - case study

P. Popielski, Ł. Kaczmarek, A. Dąbska & B. Bednarz
Faculty of Building Services, Hydro and Environmental Engineering, Warsaw University of Technology, Warsaw, Poland

R. Mieszkowski
Faculty of Geology, University of Warsaw, Warsaw, Poland

ABSTRACT: The article presents selected advantages of a wide range of applied soil testing methods in the field used to evaluate undesirable changes in soil and water conditions at the site of critical infrastructure represented by a drinking water pipeline. The pipeline is located in the flood zone of a large lowland river. Various testing methods were applied due to the diverse geological structure characterised by the high dynamics of geomorphology evolution. Drilling, two penetration methods (Cone Penetration Test with pore water pressure measurement - CPTu, Dynamic Probing Super Heavy - DPSH), piezometric observation, three geophysical methods (Electrical Resistivity Tomography - ERT, Seismic Refraction Tomography - SRT, Multichannel Analysis of Surface Waves - MASW), and laboratory tests were done. Hence, it was possible to identify the exact locations of soils susceptible to deformations inducted by seepage zones. The paper briefly synthesises the selected results of the realized field and laboratory tests.

1 INTRODUCTION

The value of critical infrastructure induces that the soil and water conditions studies program has to be comprehensive and customised to each individual case. Therefore, there is a necessity to face various types of challenges (research, methodological and organisational), such as:

1. The need to determine the full range of boundary conditions to eliminate the slowly progressing unfavourable processes. Here, it is essential to point out the integration of the study's results previously carried out, as well as from neighbouring areas. A large amount of data enables a description of soils with naturally possible large variations through statistical tools. Dealing with such a task is very difficult due to the usually time-limited research schedule. In this context, various geotechnical and geological-engineering databases are invaluable (e.g. Zhussupbekov et al. 2021);
2. The reliability of determining soil parameters (referred to the previously mentioned statistical analysis). Thus, the need to consider the specifics of different testing methods - in some cases, despite obtaining the same parameters, their values are different (e.g. determination of shear strength parameters: field vis laboratory tests). A particular solution is to use a "preserving" approach, no less, it often results in the emergence of very high reinforcement costs;
3. Related to the issue of reliable determination of soil parameter values is the knowledge of the soil characteristics modification (e.g. geomechanical) as a result of various processes (e.g. soil creep phenomenon - Kaczmarek et al. 2021; cyclic freezing and thawing - Bragar et al. 2022);
4. Limited possibilities of conducting invasive testing methods such as repeated drilling of a small study site. It can lead to soil and water conditions degradation. Also, critical infrastructure sites may be legal protection areas limiting further the locations of testing as well

DOI: 10.1201/9781003299127-316

as the range of methods to be employed. Moreover, next to the critical infrastructure, there is often a significantly developed accompanying underground and aboveground infrastructure (e.g. high voltage lines), causing the lack of possibility of entering heavy and high equipment. The described situation can translate into the reliability of the obtained data (it is worth mentioning the need for subsequent application of test results extrapolation);
5. The lack of possibility to turn off such infrastructure for conducting a study, especially *in situ* reference studies in the case of already existing facilities.

The aforementioned exemplary challenges underline the value of practical papers on study programs for critical infrastructure areas, as well as the presentation of their results.

The study was done with the perspective of analysing the development of soil deformation (inducting geomechanically parameters changes) caused by water flowing through the soil (examples of such relations: Chang & Zhang 2013; Ke & Takahashi 2014). Such processes can be crucial for the safety of critical infrastructure in the flood zone of a large lowland river. Deformations due to seepage, like different types of suffusion, can lead to serious failures and disable the water supply (in the case of a water supply line), which can be destructive, especially during hydrological drought. In order to define zones of soil susceptible to suffusion, diversified field and laboratory tests have to be done.

2 RESEARCH AREA

The analysed area is located at the right embankment of the river, situated within a large city. Morphologically, the area is on the floodplain terrace. Nearby areas are mainly green areas; they are not industrially developed. The ground elevations vary (Figure 1), related to river activity and anthropogenic changes. Denivelations within the study area amount to several meters. The dominant slopes in the analysis area range from 5% to 12%.

3 INFRASTRUCTURE

The critical underground infrastructure at the research site states a pipeline supplying drinking water for the city. This pipeline, about 310 m in length and 5 m in height is founded ca. 6 m below ground level before the embankment and about ca. 8.5 m below ground level within the embankment area.

4 METHODS

The following field and laboratory works were carried out in order to recognise the soil and water conditions in the vicinity of the pipeline (a description of the research methods can be found in, i.e. Head 2006 and Tarnawski et al. 2020):

1. Geophysical surveys - Electrical Resistivity Tomography (ERT), Seismic Refraction Tomography (SRT), Multichannel Analysis of Surface Waves (MASW);
2. Exploratory drillings with sampling for further testing;
3. CPTu static penetration tests and DPSH dynamic penetration tests;
4. Laboratory tests covering physical parameters (water content, grain size distribution, minimum and maximum density of the soil skeleton) as well as shear strength properties (where during numerous triaxial compression tests also the liquefaction has been observed);
5. Piezometers installation with groundwater monitoring, including the measurements of the groundwater table, water temperature and electrical conductivity at various depths.

Investigations were performed at two longitudinal cross sections and four cross sections perpendicular to the pipeline (at eight test nodes). The location of the research nodes (boreholes, piezometers, static and dynamic penetration tests) is shown in Figure 1.

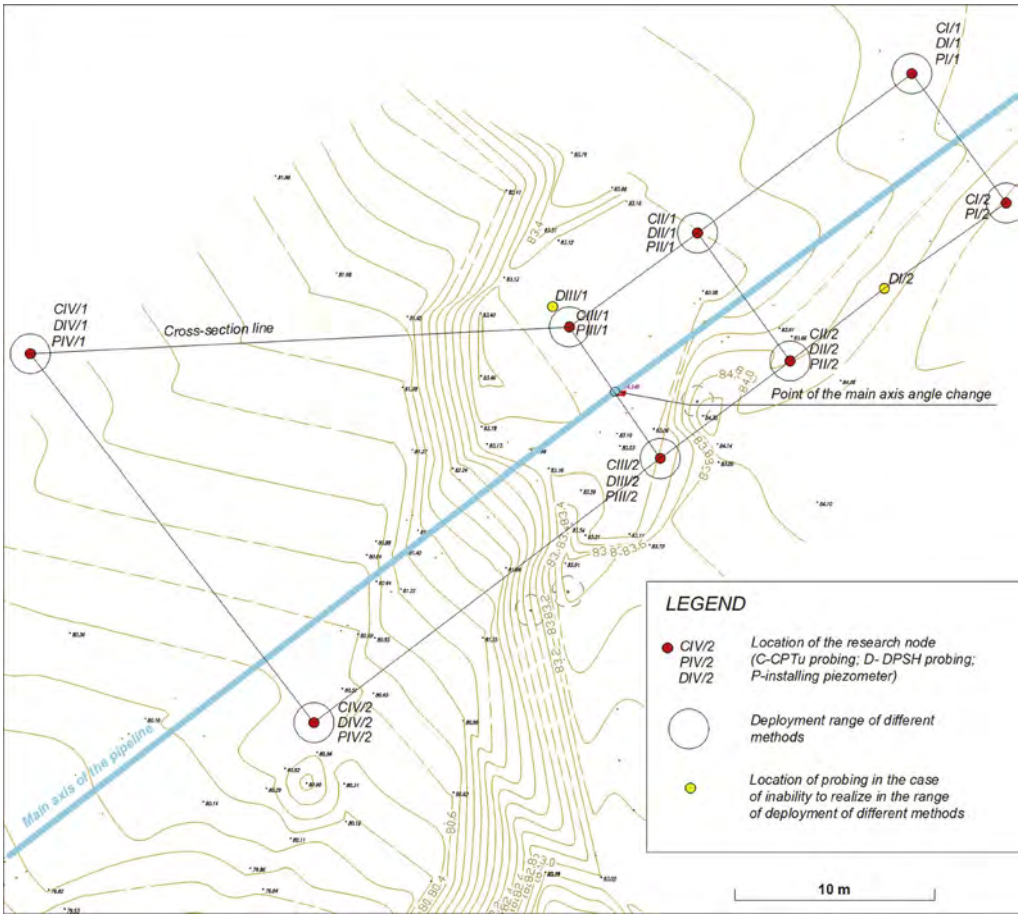

Figure 1. The geomorphology of the research site and the location of individual field tests were realised as part of the filtration deformation analysis.

5 RESULTS

Two types of *in situ* penetration test - dynamic (DPSH) and static (CPTu) - were carried out at all testing nodes to identify loose soil zones. Furthermore, the outcome of the MASW geophysical prospecting, led through the testing nodes, provided the data converted to a generalised density index cross-section (Figure 2). A compilation of the results (there were cases, where different methods suggested various places of loose soils) indicates that there are loose sands at various elevations in most of the research nodes (Figure 3). Loose soils were also found in the contact zones between the underground infrastructure and the soil. Each testing method revealed loose soils in PIII/1 at 74-76 m a.s.l., PIII/1 at 76-78 m a.s.l. and PIII/2 at 78-80 m a.s.l. It confirmed that these soils are especially susceptible to the occurrence of deformations due to seepage. Most probably, local zones of loose soils are already a result of the deformations induced by seepage. In order to obtain clear documentary material, monitoring is continued to cover extreme *boundary conditions*.

One of the elementary factors affecting the subsoil is infiltrating water. The direction of groundwater flow (Figure 4) is related to the piezometric head and the water level in the river (the documented groundwater flow paths corresponding to the direction of flow into the adjacent river). Piezometric observations show varying filtration conditions along the pipeline below the ground surface. Deformation caused by seepage (Dąbska & Popielski 2019) is

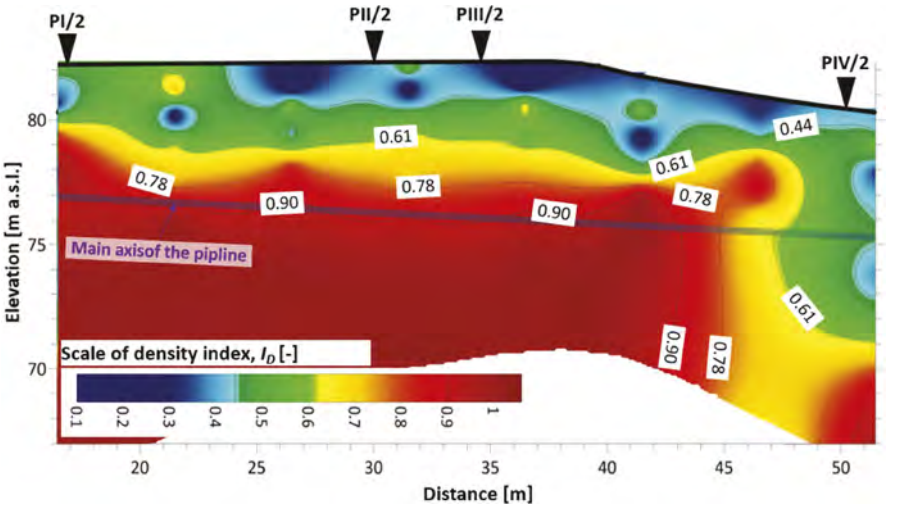

Figure 2. Results of seismic prospecting (converted to a density index) in the cross-section from the PI/2 to PIV/2 testing node.

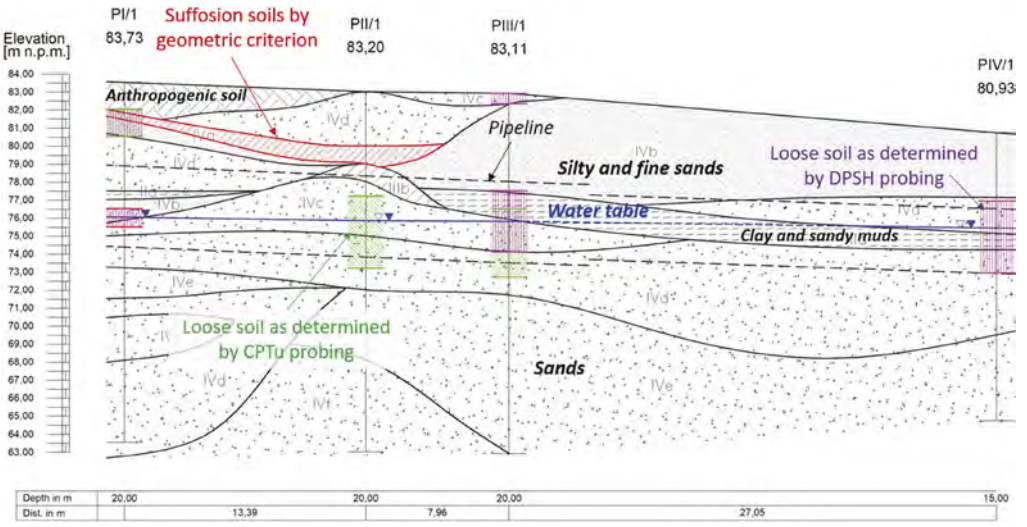

Figure 3. Locations of loos zones against the background of the observed soil and water conditions in cross-section PI/1-PIV/1.

a phenomenon determined by the current value of the hydraulic gradient and the granulometric characteristics of the soil, characterised by high dynamics and variability over time. No critical hydraulic gradient exceedances were registered in the analysed soil and water conditions from 29.04.2022 to 2.09.2022. However, exceedances must have occurred in the past, as evidenced by specific soil loose zones.

The occurrence of intensive filtration (caused by seepage) will lead to further development of deformations. It should be underlined that the lack of an appropriate safety margin of soil bearing capacity was documented during the recognition of the soil and water conditions. Therefore, it is necessary to permanently monitor water levels in the installed piezometers along with river water level monitoring. It will provide a range of filtration directions and flow velocities in relation to critical hydraulic gradients and zones prone to deformation. If the filtration velocity increases or there are unfavourable changes in soil structure at the

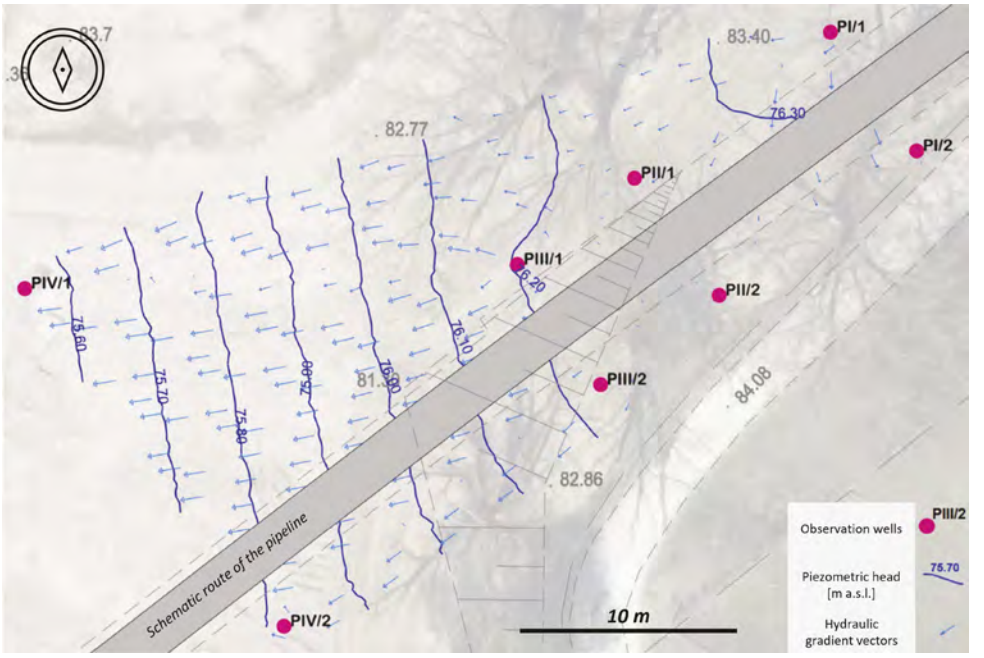

Figure 4. Groundwater flow in the research site on 2.09.2022.

filtration path, soil modification should be performed (low-pressure injections or subsoil compaction).

Comparative geophysical surveys can be applied to monitor the development of deformation caused by seepage in addition to piezometric measurements. Surface geophysical surveys have documented the current subsoil state as the reference point in the research site. It is reasonable to perform analogous cyclic geophysical surveys at the same locations (e.g. every 3 months - in the first survey period and after a cycle of 4 surveys, the frequency can be adjusted).

6 SUMMARY

The comprehensive research program provides a reference overview of soil and water conditions. Effects of deformation induced by seepage have been revealed in the pipeline area at the research site. One of the most crucial elements is the presence of loose zones of non-cohesive soils. The further development of deformations must be monitored, and emergency response needs to be taken in case their increase. Otherwise, large settlements, pipeline damage, and soil liquefaction with loss of embankment equilibrium may happen. Thus, it is particularly essential to monitor the groundwater table and the neighbouring river to cover the extremes. It will enable the identification of places where (permanently or temporarily) an increased hydraulic gradient and intensive filtration is present.

REFERENCES

Chang, D. S., Zhang, L. M. 2013. Critical Hydraulic Gradients of Internal Erosion under Complex Stress States. *Journal of Geotechnical and Geoenvironmental Engineering* 139(9): 1454–1467.

Bragar, E., Pronozin, Y., Zhussupbekov, A., Gerber, A., Sarsembayeva, A., Muzdybayeva, T., Sarabekova, U.Z. 2022. Evaluation of the Strength Characteristics of Silty-Clayey Soils during Freezing-Thawing Cycles. *Applied Sciences* 12 (2), 802: 1–13.

Dąbska, A., Popielski, P. 2019. Filtrational micro-deformations of soils. *Gospodarka Wodna* 79(10): 7–12.

Head, K.H. 2006. Manual of soil laboratory testing. Volume 1: Soil Classification and Compaction Testes. Dunbeath: Whittles Publishing.

Kaczmarek, Ł., Dobak, P., Szczepański, T., Kiełbasiński, K. 2021. Triaxial creep tests of glacitectonically disturbed stiff clay – structural, strength, and slope stability aspects. *Open Geosciences 13*(1): 1118–1138.

Ke, L., Takahashi, A. 2014. Experimental investigations on suffusion characteristics and its mechanical consequences on saturated cohesionless soil. *Soils and Foundations* 54: 713–730.

Tarnawski, M., Frankowski, Z., Godlewski, T., Gwizdała, K., Kłosiński, J., Mieszkowski, R., Nowosad, A., Saloni, J., Słabek, A., Szczepański, T., Ura, M., Wierzbicki, J., Wójcik, M. 2020. *Badania podłoża budowli (Investigations of the construction subsoil)*. Warsaw: PWN.

Zhussupbekov, A., Alibekova, N., Akhazhanov, S., Sarsembayeva, A. 2021. Development of a unified geotechnical database and data processing on the example of Nur-Sultan City. *Applied Sciences* 11 (1) 306: 1–20.

Smart Geotechnics for Smart Societies – Zhussupbekov, Sarsembayeva & Kaliakin (Eds)
© 2023 The Author(s), ISBN 978-1-003-29912-7
Open Access: www.taylorfrancis.com, CC BY-NC-ND 4.0 license

Results of geotechnical monitoring of the high-rise building "Lakhta Center" in St. Petersburg

A.G. Shashkin, V.A. Shashkin & S.G. Bogov
Institute "Georeconstruction", St. Petersburg, Russia

V.M. Ulitsky
Emperor Alexander I St. Petersburg State Transport University, St. Petersburg, Russia

R.E. Dashko
St. Petersburg Mining University, St. Petersburg, Russia

ABSTRACT: Basic results of geotechnical monitoring at construction of skyscraper "Lakhta-Center" are presented. Pit fencing displacements while constructing under-ground part of building are considered, effectiveness of excavating pit of regular shape in plan is shown: operations in open pit. Measurements of building settlements are given based on extensometer system witnessing possibility of minimum settlements of high-rise building at pile driving to Venda deposits which opens prospective of high-rise construction in geotechnical conditions of Saint-Petersburg. Pore pressure gauge measurement results show no excessive pore pressure in subsoil, expectedly, due to solid consistency of pre-quaternary clayey soils. Gauges are reported to record water head within permeable fractured-block structure of Venda clays and overlaying soils. Measurements by system of sensors located in piled raft stated that pressure is not transferred to soil via piled raft base, i.e. pile-raft foundation effect is not manifested in unevenly compressible subsoil – all load it applied to piles.

1 INTRODUCTION

Monitoring of structures at operation is a direct requirement of the existing Russian legislation, which is especially relevant for technically difficult structures including high-rise buildings. It is important not only for providing mechanical safety at operation of a structure but also as a tool of back analysis of actual strain-stress behavior of soil and structures corresponding to a calculation prediction implemented at design, that finally should facilitate development of construction theory and practice (Katzenbach 2005). The purpose of the research work was to make an efficient system of monitoring at construction and operation of the unique high-rise building constructed on a thick soil bulk of sedimentary origin. The methods of organization of the monitoring system as well as the measurement results are significant.

2 THE MAIN REQUIREMENTS TO THE SYSTEM OF MONITORING AT OPERATION

Monitoring systems should be based on the principles of interactive monitoring, i.e. they must include a possibility of comparison of monitoring data and a prediction, back analysis of monitoring results using computer models of an object, an opportunity to adjust the prediction or make necessary managerial decisions based on the conducted analysis.

The main features of an efficient monitoring system include (Shashkin 2018): (1) an ability to respond to possible hazardous processes; (2) adequate assessment of a danger degree, timely

DOI: 10.1201/9781003299127-317

identification of dangerous processes to give experts an opportunity to analyze a situation and take necessary measures; (3) existence of a formalized managerial decision-making subsystem.

The efficient monitoring system should contain at least an intermediate state between the "normal" and "failure" states. The "alarm" signal (like the yellow of the traffic lights) should timely emerge when dangerous trends occur and leave a sufficient time period for a required response – beginning from the analysis of causes of the signal emergence to taking measures on structure reinforcement (if necessary).

In order to create an efficient monitoring system, the criteria of a state of structures should not be set only based on limit states of these elements according to the standards, it is necessary to introduce the notion "a predicted value of a parameter". A significant deviation of measurement results from a predicted parameter is to be considered as an alarming signal.

Contrary to calculations at design which are always conducted with a "safety factor", calculations for defining predicted parameters should reflect the most probable state of a calculated structure, if possible, computer models should completely reflect actual structural behavior.

The system of setting ultimate values of parameters is advisable to be generalized using relative distances to limit values for groups of physically interlinked parameters. In this approach, for a control subsystem a state of groups of any number of parameters is described by a minimum set of two numbers – a relative distance to the limit value and a value of the "alarm" signal.

3 THE THEORETICAL BASIS FOR GETTING CRITERIA OF "ALARM" AND "FAILURE" STATES

For a single measured parameter X the system of criteria should include a limit value (which in most of cases is defined according to the requirements of the existing standards) and a predicted value (or several predicted values as per different combinations of loads) of the parameter. A predicted value is calculated as the most probable value of the parameter in certain conditions (without tolerances towards "a safety factor", with account of actually applied loads etc.) As a result of a series of calculations for different combinations of loads we obtain a suite of possible results of the calculation $X_1 \ldots X_n$. Then one should define the most probable average value$\bar{X}$ based on either general consideration (for example, a calculation without wind impacts), or on the arithmetic mean of the obtained calculation results.

Let a monitoring system observe some value of the parameter X. We indicate a difference between a predicted average value and an observed value as $r = |X - \bar{X}|$ $r_{\lim}$ is a distance to the limit value, we sort out of two limits in the numerical axis, they limit in the same direction, in which X deviates from$\bar{X}$. Mathematically it can be written down as:

$$r_{lim} = |X_{lim} - \bar{X}| \text{ ПрИ } (X - \bar{X})(X_{lim} - \bar{X}) > 0. \tag{1}$$

It is not expedient to overload the system of control representation of the results with difficult values in different measurement units. Therefore, in order to facilitate let introduce the notion of a relative distance to the limit value:

$$\varepsilon = \frac{r}{r_{lim}} \tag{2}$$

In this case the limit state corresponds to $\varepsilon = 1$. A location of the "alarming" boundary is obtained according to the results of a series of prediction calculations $X_1 \ldots X_n$. For each of these calculations we compute a distance from the mean value $r_i = |X_i - \bar{X}|$ and a distance to the limit value in the corresponding direction $r_{\lim i}$. Then the area of admissible values of the parameter can be limited by a relative value:

$$\varepsilon_a = \gamma \cdot max\left(\frac{r_1}{r_{\lim_1}} \ldots \frac{r_n}{r_{\lim_n}}\right) \tag{3}$$

where γ – a factor, which takes into account prediction inaccuracy and it is accepted, for example, as 1.1…1.2.

For the system of interlinked data this approach can be generalized, in this case X represents not a single value, but a suite of values, instead of the limit values of parameters one should consider surfaces, which limit the areas of their admissible values.

Let consider building a system of restrictions for a set of parameters on the example of observation of a column cross-section. A set of strain gauges should be installed in a column cross-section to record not only longitudinal forces but also the moments. According to the log of these gauges least square method defines a longitudinal strain and angles of section rotation (with account of the hypothesis of flat sections which is conventional for frame systems). Based on the obtained values of deformations, with account of the known material properties, forces are defined: a longitudinal force N and a moment in two directions My and Mz. The acting forces can be manifested as a point in the space N, My and Mz. One can depict with a point the predicted values of forces in the same space.

Then, according to the requirements of the standards, for example, as per non-linear strain model of reinforced concrete a limit surface is built in the space of coordinates N, My and Mz. The boundary of admissible values at monitoring is computed according to formula (3) around the area of predicted values of forces.

The described mathematic transformations result in unification of operation with any groups of interlinked data. In any case, for the control system a group state is described by one number – a relative distance to the failure boundary ε. If this value exceeds 1, the "failure" signal sounds. An admissible value ε_a is computed for timely response to development of a process for each group of parameters in the monitoring system. If $\varepsilon > \varepsilon_a$ the system gives the "alarm" signal.

It is noteworthy that as the complex multidimensional system of limitations is actually reduced to one number ε_a, this value is not stationary. When gauge logs change, not only a value, but a direction of black and white vectors shown in Figure 1 change. Therefore, both values ε and ε_a should be recalculated.

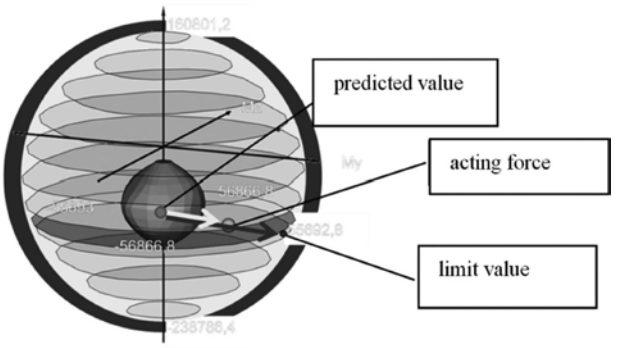

Figure 1. An example of the system of limitations for strain gauges in a column: the white vector shows the distance from the predicted values to the observed ones, the black vector shows the distance to the limit values (the "failure" boundary); the relative distance to the limit values ε equals the ratio of the length of the white and black vectors; the boundary of admissible values (beyond which the "alarm" signal occurs) is shown in the center.

4 THE COMPONENTS OF INTERACTIVE MONITORING

In an efficient monitoring system for a building or a structure, which meets the requirements of mechanical safety, in practice the "failure" system should not emerge at all. The whole operation of the monitoring system is to be made after receiving the "alarm" signal without allowing the system to reach the limit state (the "failure" signal).

An approximate sequence of possible measures on the analysis of work of a structure and fixing possible negative trends after receiving the "alarm" signal can be represented as follows (Figure 2).

In order to provide serviceability of the monitoring system it should include the following main components:

1. The system of gauges in structural elements and subsoil.
2. The system of collecting and archiving the logs from gauges.
3. The system of control observation of logs of groups of gauges, which track emergence of the "alarm" and "failure" signals and generate signals to inform people in charge.
4. The system of managerial decision making.
5. The interactive calculation models for assigning the "alarm" and "failure" criteria with a possibility of recalculation and adjustment of predicted values during monitoring.

Let consider determining the "alarm" and "failure" criteria on the example of a high-rise building in St. Petersburg.

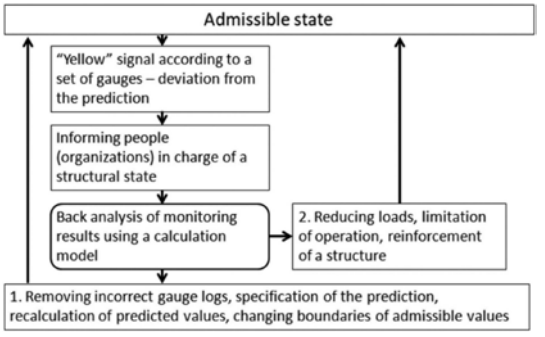

Figure 2. The facilitated algorithm of managerial decision making.

5 A BRIEF CHARACTERISTICS OF THE HIGH-RISE BUILDING

The construction of the tallest building in Europe – "Lakhta center" tower in St. Petersburg was completed in 2019. Considering a high degree of responsibility of the building, a part of information is closed but the authors think that open information is interesting for experts.

The structural section of the design was developed by the companies "Inforsproekt" and "Gorproekt" under the supervision of V.I. Travush and A.I. Shakhvorostov (Travush 2015, 2018), the design solution of the underground part was elaborated under the supervision of O.A.Shulyaev (Shulyaev 2016). The main dominant of the multi-functional complex "Lakhta Center" reaches 462 m, it consists of 86 floors and 3 underground levels (Figure 3a, b).

The high-rise building has a frame-and-stem structural scheme. Its rigidity and stability are provided due to joint operation of the central RC core and 10 streel-reinforced concrete columns along the perimeter interconnected with outriggers, which are located at several levels. To decrease spans in the building there were implemented other 5 streel-reinforced concrete columns up to the level of the 47^{th} floor.

The underground part of the high-rise building has the shape of an equilateral pentagon in plan, the side length is 57.5 m. It forms a box foundation, which consists of a lower 3.6-m-thick slab, located at the depth 17.65 m from the ground surface, an upper 2.0-m-thick slab, the central rigidity core of 28.5 m diameter and 10 vertical rigidity diagram walls. The box footing is supported by 264 piles of 2 m diameter. The piles are 65-m-long (84 m from the surface) within the contour of the high-rise building and 55-m-long (74 m from the surface) beyond it.

The engineering-geological profile of the high-rise building consists of quaternary deposits of different genesis and Upper Proterozoic Kotlin solid clays (Venda deposits; their roof lies at the depths of about 25 m from the ground surface), which serve the subsoil for pile foundations of the structure (Figure 4).

As regards headed aquifers within the area under consideration, Venda aquifer suite is of special importance, it is connected with interlayers of sandstones in the lower part of Venda

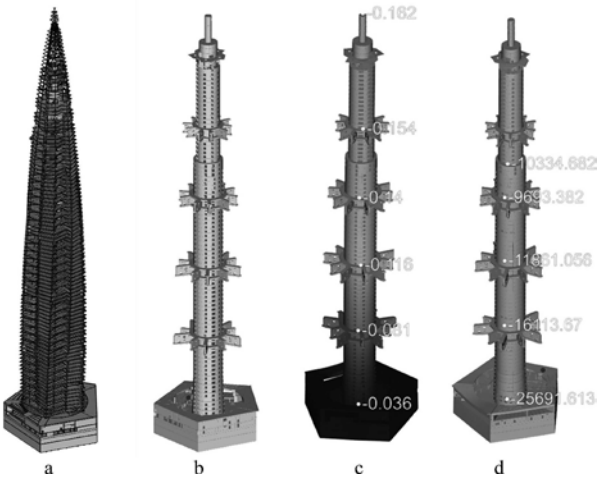

Figure 3. The general view of the calculation model (*a*) and its fragment made of volumetric finite elements for organizing monitoring at operation (b); vertical displacements of the core, m (*c*) and stresses in the core concrete, kPa (*d*).

deposits, with the head at 90 m of the absolute elevation – minus 12 m BS. Moraine deposits underlain by dislocated Venda clays lie directly under the base of the piled raft.

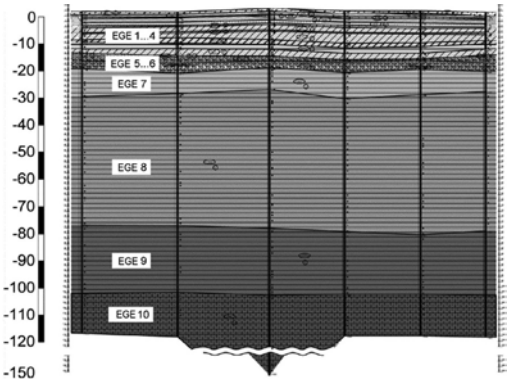

Figure 4. Engineering-geological profile in the area of the high-rise building. Notes: EGE (engineering-geological element) -1. . .4 – Quaternary deposits, EGE-5, 6 – glassier deposits; EGE-7. . .10 – Upper Proterozoic Kotlin deposits.

6 THE CONTROLLED PARAMETERS OF THE MONITORING SYSTEM

The controlled parameters of the monitoring system of technical condition of the building's bearing structures include:

- movements of the upper point of the tower;
- a tilt of the foundation;
- a tilt of the building;
- natural frequencies and maximum amplitudes and fluctuation curves of the walls of the tower core;
- frequencies of mutual fluctuations of parts of the tower;
- strains in RC cross arms;
- strains in RC walls of the superstructure;
- strains in metal columns;
- strains in outrigger beams.

Movements of the upper point of the tower are defined automatically via processing results of measurements by a high-precise GPS-system.

A tilt of the foundation and structures of the building is controlled with a help of automatic inclinometers installed in the foundation and structures of the building.

Frequencies, amplitudes and fluctuation curves are defined via processing the results of measurements of 3D vibro-sensors-accelerometers.

Strains in the tower structures are controlled by strain gauges installed in slabs and walls of the box foundation, walls of the core and columns of the building. Strain gauges were installed to obtain data on a relative longitudinal deformation of the box foundation, a relative longitudinal deformation of composite columns, core walls and outrigger frames during construction of the building and at the stage of its operation.

Reading of gauge logs is implemented with a help of the automated system of data collection.

The sensors of geotechnical monitoring, namely strain gauges controlling deformations in piles, pore pressure gauges, pressure gauges along the base of the piled raft slabs are also connected with the monitoring system.

The monitoring system at operation was developed by the Institute "Georeconstruction" together with "Telros" company. Geotechnical monitoring at construction of the building was implemented by the Institute "Georeconstruction".

7 THE NUMERICAL MODEL AND PREDICTED VALUES OF THE CONTROLLED PARAMETERS

A mathematical model of the building implemented in the software complex FEMmodels-IEECloud, which was developed by the Institute "Georeconstruction" and allows making soil-structure interaction calculations taking into account non-linear properties of structural materials and soils (Ulitsky 2014), is the key element of the monitoring system, it represents a kind of an analytical center. The layout of the geometrical position as well as assigning parameters of the tower structures in the calculation model were made via conversion of an analytical model of a scheme built in "Revit", issued as initial data in the environment of "FEMmodels-IEECloud". The model consists of volumetric, plate and rod finite elements. The mathematical model considers joint behavior of the building structures, piles and subsoil.

The respective standard piecewise linear, bilinear and trilinear diagrams of deformation of steel and concrete were used as deformation curves. The results of the model calculation with account of non-linear strain model of RC structures include not only more adequate consideration of their rigidity but also a possibility of building sought-after strength surfaces, which define "the red boundary" (a surface of the "failure" signal). Therefore, "the red boundary" for each point of strain gauge installation is defined by a strength surface in axes N, My and Mz, obtained according to the results of the numerical calculation of the analytical model of the building for a certain section of an element of the bearing structure where a gauge is installed. Based on this limit strength surface, limit strain surfaces in each point of installing strain gauges and ultimate values for each strain gauge are defined.

The value of the "red level" of strain-stress behavior of the walls of the tower core is suffice to be limited by a standard value of limit strain due to their predominantly compressive operation.

As regards the "yellow level" (surfaces of the "alarm" signal), it is more justified to take an area near the predicted (based on the calculation results) forces (in the case under consideration deviation from the area of the predicted values of more than 10% is accepted as the yellow border). Exceeding the "yellow level" means that a structure operates not in compliance with the prediction, that requires additional examinations and identification of causes of deviation from the assumed strain-stress state.

It is noteworthy that making a calculation model implies multiple simplifications at assigning models of material behavior, boundary conditions, loads, which in line with various violations and drawbacks in the course of construction work implementation often lead to inconsistency of a calculation model with an actual operation of a structure. Therefore, during in situ measurements at the site monitoring initial parameters of a calculation model of the building should be specified, then it is necessary to make recalculation of the changed model. As a result of several

iterations the calculation model of operation of the structural system under consideration will start to be consistent with its actual behavior. It is this iteration method which allowed bringing the mathematical model of the tower of "Lakhta Center" in consistency with the in situ measurement results.

The figures below give the results of building-structure calculation. According to the results of the calculation for each group of installed gauges (ranges), predicted values of changeable parameters have been defined. The predicted values are taken directly from the calculation model as per a coordinate of location of a group of gauges (Figure 3c, d, 5).

Foundations of the tower structure have different tilts from the vertical axis due to applying horizontal forces (wind loads) at different heights in different time moments.

According to the design assessments, deviation of the tower top from the vertical line due to applying wind loads is 301 mm from the average wind load and 161 mm from pulsing loads (the total displacement of the top of the building is 462 mm). According to the results of monitoring, measuring a wind speed, there has been identified a period of time when the wind speed approached to the maximum calculated one.

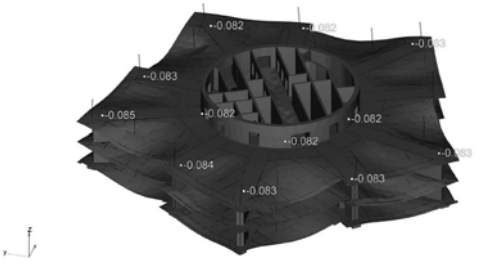

Figure 5. Vertical displacement of outrigger levels L17-L18, m, the scope of strains has been increased 100 times.

According to the analysis, in this case the maximum value of deviation is in a good agreement with the calculated one (Figure 6a). According to the results of the analysis of the maximum angles of tilt there were accepted borders as per inclinometers which change depending on a level of a gauge location (Figure 6b).

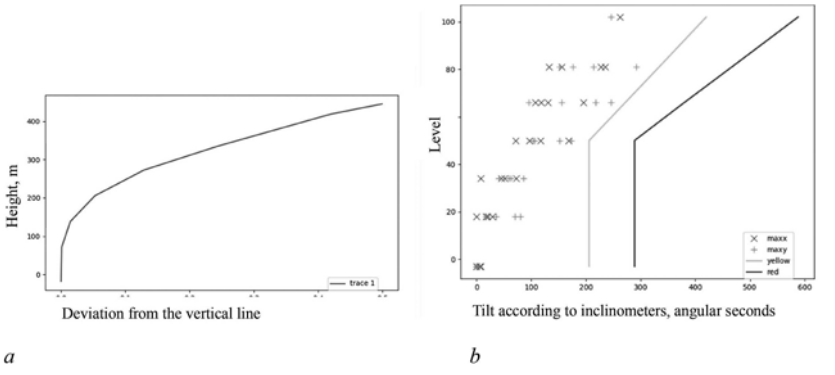

Figure 6. Evaluation of a shape of deviation from the vertical line of the building tower at wind loads, which are close to the maximum calculated ones, m (*a*), maximum values of tilts in directions x and y (*b*) according to the results of measurements at wind loads, which are close to the calculated ones; the location of the "yellow" and "red" boundaries depends on a number of a level relating to the building height.

8 THE CRITERIA FOR DEFINING FREQUENCIES OF SELF-INDUCED OSCILLATIONS

A reduction of a frequency of oscillations witnesses a decrease of the building rigidity or an increase of weights, it characterizes changes in the scheme of operation of bearing structures.

An increase of a frequency of oscillations of the building is highly unlikely, and it does not witness worsening of operation of structures.

According to the calculation results made by the authors of the design, the first self-induced frequency of oscillation was 0.12 Hz. The first actual measured frequency of vibrations after termination of the construction (March 2019) was 0.178 Hz. In the course of constructing floors, partitions in the tower, increasing useful loads and changing glaze ice loads a weight of the building changed along with reduction of the oscillation frequency. In June 2019 the first frequency ranged from 0.161 to 0.167 Hz, the second frequency – from 0.570 to 0.610 Hz; the third frequency – from 0.744 to 0.771 Hz.

It is possible to make an approximate evaluation of the predicted frequency of oscillations depending on a share of loads from floors, partitions, useful and glaze ice loads applied to the building, without account of tolerances for quick creeping, and considering the dynamic RC modulus according to the following formula:

$$\nu = \nu' \cdot \sqrt{\frac{M_1}{M_1 - (M_2 \cdot (1-\kappa))} \cdot \frac{1}{\phi_b} \cdot \frac{1}{\phi_0}} = 0.160 \text{ Hz}, \quad (4)$$

where $\nu' = 0.122$ Hz – the calculated frequency of oscillations, $\phi_b = 0.85$- the factor of quick creeping, $\phi_0 = 0.83$ – the ratio between the initial and dynamic RC modulus (at very small deformations), M_1=509392 t – the designed weight of the building, M_2=134206 t – floors, partitions, useful and glaze ice loads, k = 0.3 – the approximate factor of account of loads of floors, partitions, useful and glaze ice loads.

Therefore, the changed frequencies are quite in a good agreement with the calculated ones.

As the limit values of oscillation frequencies are not regulated by the existing documents, the condition of reduction of the frequency of tower oscillations by 10% of the actual one is taken as the "yellow" boundary of accelerometer logs, the "red" boundary implies reduction of the recorded frequencies of oscillations by 30% of the measured value.

9 THE RESULTS OF THE GEOTECHNICAL MONITORING AT CONSTRUCTION

Creating the efficient monitoring system at operation is possible as continuation of the efficient monitoring system at construction. Therefore, it is important to pay attention to the results of the geotechnical monitoring.

In the framework of geotechnical monitoring before digging the pit a system of inclinometers was installed around the pit fence; pore pressure gauges and extensometers were installed in the subsoil; in the course of constructing the structures of the underground part of the building strain gauges were installed under the base of the piled raft.

The measurement results demonstrate that, opposite to the cylindrical shape of the underground part, the underground structure, which is pentagonal in plan with the fence in the form of diaphragm wall with strut rings, does not allow reaching the same horizontal displacements of the pit fence as expected. In more rigid corner areas displacements are almost twice as small as in the middle of each side of the pentagon (Figure 7). The maximum total displacement was observed at inclinometer I-11 at the depth 14 m, it was 46.4 mm, that did not exceed the maximum calculated values (76 mm). However, the correct shape of the underground structure in plan still allows using the effect of "a barrel with hoops inside", which works for external pressure, and thereby carrying out works in an almost open pit with a minimum working area under cover of contour strut "hoops".

Observations of layer by layer settlements of the subsoil were made according to extensometers down to the depth 97 m (see Figure 8). As the lower elevation of an extensometer is only 12 m lower than the toes of piles of the central part of the high-rise building compound and it can settle itself, location of the upper elevation was controlled using geodetic methods.

The settlements of the high-rise building developed along an increasing curve and came to an end by the moment of termination of the construction in 2018 – 32 mm in the area under the core. In the edge zones the settlements were twice as small. Almost the same settlements were recorded

by geodetic methods connected with foundation benchmarks. Therefore, one can state that quite a limited layer of soil under pile toes has settlements. The compressed bulk below the pile toe is about 15 m. This conclusion is rather expected as the thickness of the bulk of solid Venda clays under the pile toe is 20 m, they are underlain by sandstones, which have higher rigidity and lower flexibility.

The effect of compression of piles and soil in the inter-pile area also made a contribution to the development of settlements (its share is almost 2/3 of the accumulated settlements). Based on the simplest calculations, elastic compression of the shaft of the pile of 2.0 m diameter and 65 m length under the load 3000 t is approximately 2 cm, that is in full agreement with the measured value of settlement due to self-compression of a "default foundation".

The measured values of settlements correlate with the results of the conducted calculation of long-term settlements of the building on non-linear visco-plastic soil (with account of possible development of long-term creeping) (Shashkin 2014). According to the calculation results the maximum long-term settlement of the building will reach 8 cm at a relatively small differential settlement. About 1/3 of settlements occur during construction, i.e. about 3 cm, that is in a good agreement with the observation results.

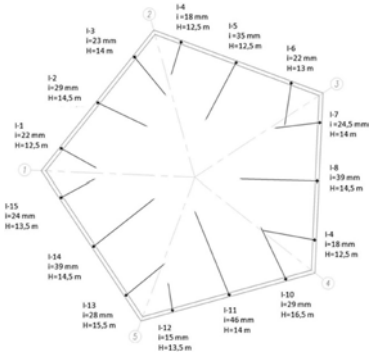

Figure 7. The scheme of layout of inclinometers and vectors of maximum total displacements of inclinometers with indication of a depth of the maximum displacement (28.08.2013 – 05.04.2015).

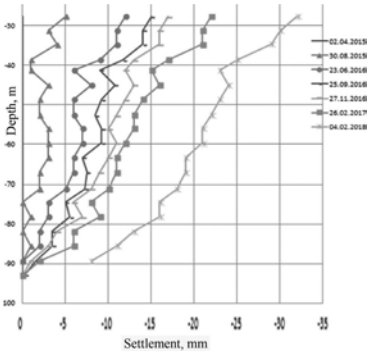

Figure 8. Strain curves of the soil bulk as per extensometer #1.

The gauges installed under the base of the piled raft demonstrated that contact pressures of soil are small (they do not exceed the pressure of the dead load of the slab of the piled raft). Therefore, the slab of the piled raft does not participate in operation of the pile foundation, it witnesses that the idea of a pile-raft foundation works only for a homogenous soil (Ulitsky 2014). If soil under the slab of the piled raft is more flexible than under piles, the raft is excluded from operation. Identical logs, which almost correspond to the water head pressure with zero elevation at rest approximately at the level of the Gulf of Finland, were recorded at all borehole piezometers (Figure 9). In the period of construction of the underground part of the building gauge logs drop (07.08.2013- 07.04.2014) precisely by the value of the water head released at the pit excavation (15–16 m). Then, in the course of building construction there was observed a slow growth of the gauge readings.

The gauge logs demonstrate permeability of Venda clays due to their intrinsic fracturing-block structure (Dashko 2000, 2011), earlier they used to be considered almost impermeable (it is noteworthy that chemical composition of water samples taken at the level of the slab of the piled raft showed their origin from Venda aquifer, i.e. from the depth 90 m). As expected, no excessive pore pressure was observed: it cannot occur in solid clays where pore water is in cohesive state.

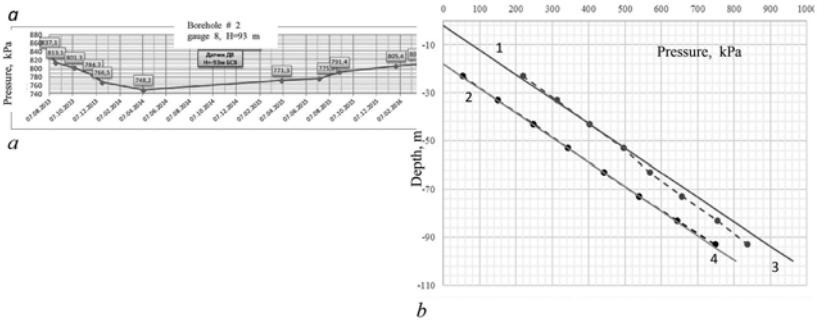

Figure 9. The logs of pore pressure gauges installed in borehole #2: *a* – measurement of pore pressure in time; *b* – graphs of pore pressure development as per the depth (1 – hydrostatic pressure before excavation and 2 – after excavation of an 18-m-deep pit; 3, 4 – logs of pore pressure gauges before and after excavation of the pit, respectively).

10 CONCLUSIONS

The practical implementation of the system of interactive monitoring at the site of "Lakhta Center" has demonstrated efficiency of using the soil-structure interaction calculation model at the analysis of the monitoring results and definition of the boundary values of the parameters for the "alarm" signal.

The calculation model for monitoring purposes which reflects the most probable state of a site without tolerances and safety factor simplifications considerably differs from the calculation models applied at design.

Assigning parameters of the "alarm" signal at the boundary of predicted parameters of the most probable state of the system ensures sensitivity of the system to negative changes, which appear possible to be identified at an early stage of their development, it provides timely analysis of a situation and taking adequate measures.

REFERENCES

Dashko, R.E. 2000. Geotechnical diagnostics of bedrock clays of St. Petersburg region (on the example of Lower Cambrian clay bulk). *Urban development and geotechnical engineering* (1): 95–100.

Dashko, R.E. & Alexandrova, O.Yu., Kotykov, P.V., Shidlovskaya, A.V. 2011 The features of geotechnical conditions of St. Petersburg. *Urban development and geotechnical engineering. St. Petersburg* (13): 25–71.

Katzenbach, R. & Schmitt, A., Ramm, Ch. 2005 The main principles of design and monitoring of high-rise buildings in Frankfurt-on-Maine. Case studies. *Urban development and geotechnical engineering* (9): 80–99.

Travush, V.I. & Shakhvorostov, A.I., Bobkov, A.A., Morozova, E.V., Nikiforov, S.V. 2015. Concreting of the lower slab of the box foundation of the "Lakhta Center" tower. *High-rise construction* (1): 92–101.

Travush, V.I., & Shakhramanyan, A.M., Kolotovichev, Yu.A., Shakhvorostov, A.I., Desyatin, M.A., Shulyatiev, O.A., Shulyatiev, S.O. 2018. "Lakhta Center": automated monitoring of bearing structures and subsoil. *Architecture and construction* (4): 94–108. Academia.

Shashkin, A.G. 2014. Design of buildings and underground structures in difficult geotechnical conditions of St. Petersburg. Moscow: Akademicheskaya nauka — Geomarketing.

Shashkin, K.G. 2018. Theoretical basics of interactive monitoring of complex buildings and underground structures. *Geotechnics* (3): 26–37.

Shulyatiev, O.A. 2016. Soils and foundations of high-rise buildings. Moscow: ASV.

Ulitsky, V.M., & Shashkin, A.G., Shashkin, K.G., Shashkin, V.A. 2014. *The basics of soil-structure interaction calculations*. St. Petersburg: "Georeconstruction".

Smart Geotechnics for Smart Societies – Zhussupbekov, Sarsembayeva & Kaliakin (Eds)
© 2023 The Author(s), ISBN 978-1-003-29912-7
Open Access: www.taylorfrancis.com, CC BY-NC-ND 4.0 license

Assessment of deformation modulus of dispersive soils by multichannel analysis of surface waves

V.G. Ofrikhter & V.V. Antipov
Perm National Research Polytechnic University, Perm, Russian Federation

ABSTRACT: Nondestructive techniques of wave analysis can be applied for the express preliminary geotechnical soil assessment. One of these techniques is Multichannel Analysis of Surface Waves (MASW) which allows obtaining velocities profile of shear waves and the initial shear modulus for the upper section promptly and at minimal labor costs. The soil deformation properties assessment requires the deformation modulus that is obtained by the direct technique of plate load test (PLT). The purpose of the study is to assess the correlation between the PLT deformation modulus and the initial shear modulus determined with MASW.

Plate load tests (PLT) were carried out for various plates and moduli of deformation were calculated. Deformation modulus adjustment factors were applied to bring values of different size plates to the 5000 cm^2 plate one in order to perform a comparative analysis. Wave analysis was carried out by the active method of MASW.

During the comparative analysis a correlation coefficient was evaluated for the deformation modulus determined strictly according to the Russian State Standard (GOST 20276-2012). In this case "correlation coefficient - unit weight" indicative dependence was observed. The regression equation is presented.

Correlation between the two types of tests was established by in-situ tests. The proposed empirical regression equation allows us to obtain the deformation modulus on the basis of MASW data and to perform an express soil foundation geotechnical assessment for the future construction.

Preliminary assessment of the geotechnical situation on the site enables carrying out a technical and economic analysis of the object of reconstruction or new construction. Preliminary geotechnical evaluation includes: determination of the geotechnical category of the object of construction or reconstruction, analysis of nearby structures, assignment of the survey work scope, and determination of arrangement options for the underground part of the object and their economic comparison. To correctly choose the variants of constructive solution of the future construction underground part, it is necessary to know the existing layering of soils on the construction site, their physical and mechanical characteristics, and the presence of anomalous inclusions (mines, pipeline cavity, other underground structures, etc.) that will allow performing the feasibility study as correctly as possible. Modern non-destructive research methods enable rapid and cost-effective construction of ground layer sections and estimation of physical and mechanical characteristics of soils. One of such methods is MASW.

The MASW technique was first introduced in (Park et al. 1999) and continues to develop and improve up to now (Park & Carnevale 2010). The authors of this study also conducted a number of natural and numerical experiments to determine the possibility of using the wave analysis for geotechnical calculations (Ofrikhter & Ofrikhter 2015, Antipov & Ofrikhter 2019). The MASW technique is applied to measure the surface wave velocities in layered soil thicknesses. From the received velocities it is possible to pass to the initial shear modulus at small deformations by the known dependence (Foti et al. 2015). For practical purposes, it is very useful to establish the relationship between the surface wave velocity, the initial shear modulus, and the soil deformation modulus from the plate tests. The purpose of the researches is to establish the correlation between the initial shear modulus determined with MASW and the soil deformation modulus determined with PLTs.

DOI: 10.1201/9781003299127-318

1 MATERIALS AND METHOD (ANTIPOV & OFRIKHTER 2019)

1.1 *Description of the sites*

PLT and MASW surveys were performed at five sites with different soil conditions:

1. Site No. 1. Soil under the foundation slab:

a. Sand fill of fine homogeneous dense low moisture sand;

2. Site No. 2. Highway. Site beside a pillar of bridge crossing:

b. Medium strength loose fractured saturated argillite-like clay with pockets of low and medium strength sand rock;

c. Fine-grained loose fractured saturated sand rock of low and medium strength;

3. Site No. 3. Site of the former factory that is free from construction:

d. Tough and medium-hard clay;

4. Site No. 4. Base of the foundation plate for a residential building:

e. Gray-brown areneceous fluid clayey sand with veins and pockets of 3–5 cm fine gray saturated sand and very soft brown clayey sand;

f. Dark-grey heavy silty very soft sandy clay with up to 15% inclusions of well-decomposed black organic matter;

5. Site No. 5. A test site of the Department of Construction Operations and Geotechnics of PNRPU that is free from construction:

g. Brown fine-grained sand.

Physical properties of the soils determined in the laboratory are presented in Table 1.

Table 1. Physical properties of the soils at testing sites.

Site No	Soil type	w	w_L	w_p	γ, kN/m^3	γ_s, kN/m^3
1	a	0.068	–	–	17.84	25.68
2	b	0.170	0.34	0.14	19.99	25.68
	c	0.170	–	–	20.09	26.07
3	d	0.129	0.33	0.07	20.78	26.46
4	e	0.296	0.24	0.18	19.80	26.46
	f	0.299	0.35	0.19	18.42	25.87
5	g	0.099	–	–	15.97	24.60

w is water content; w_L is liquid limit; w_P is plastic limit; γ is unit weight of soil; γ_s is unit weight of soil particles

1.2 *PLTs*

PLTs were performed in accordance with the standard procedure set out in the Russian State Standard (GOST 20276-2012). The true value of the deformation modulus is assumed as the modulus E5000 obtained for a plate of 5000 cm^2 (Kashirsky 2014, Kalugina et al. 2017). Deformation modulus determined for the 600 cm^2 plate was transformed to the modulus E5000 using formula (1) (Lushnikov 2014):

$$E_{5000} = E_{600} \cdot m \tag{1}$$

where E_{600} is the deformation modulus for the 600 cm^2 plate; m is the conversion factor depending on the void ratio e according to Table 3 of (Lushnikov 2014).

According to (Lushnikov 2014), for the plates of other areas the coefficient m in equation (1) can be calculated by the expression (D.3) from Annex D of (SP 23.13330.2018):

$$m = (A_{5000}/A_i)^{n/2} \tag{2}$$

where A_{5000} is the 5000 cm^2 plate; A_i is the i cm^2 plate area; n is the reduction argument according to Annex D of (SP 23.13330.2018), for silt-loam soil n = 0.15–0.3, for sandy soil n = 0.25–0.5, minimum or maximum value from the conditions $\sigma_{z,p} = 0.5\sigma_{z,g}$ or $\sigma_{z,p} = 0.2\sigma_{z,g}$ respectively (p. 11.6.2 of SP 23.13330.2018).

1.3 *MASW*

MASW is an express inexpensive non-invasive in-situ technique of wave analysis of the low velocity zone in the upper part of the soil profile. The procedure of the in-situ survey and further data processing used by the authors is described in detail in (Park et al. 1999). A telemetric 24-channel seismic exploration system TELSS-3 was applied for the MASW technique. The system consists of: seismic wire interface for communication with a laptop; vibration seismic receivers – 24 vertical 10 Hz geophones; 7 seismic streamers for 4 geophones; telemetric modules for signal transmission from receivers to the interface; a 4.5 kg (10 lbs) sledgehammer with a metal base plate used as a wave source. The trigger was implemented by closing the sledgehammer and the plate. The signal from the trigger at the beginning of recording was transmitted to the interface via a connecting cable. A streamer test and a full seismic station test were made at each shot before recording.

MASW tests were performed with an active flank observation system ZZ with an offset of 10 m. Two layouts of the surveillance system were used: a 46 m receiving line with a 2 m receiver spacing, and a 11.5 m receiving line with a 0.5 m receiver spacing. As an example, Figure 1 shows the scheme of the second layout type on the site No. 4 at the location of the e soil type and it also illustrates the actual in-situ testing. The receiving line length corresponds to the maximum measured wavelength, and the receiver step corresponds to the minimum wavelength. The centers of the receiving lines were located as close to the points of the PLT tests as possible.

Figure 1. Surveying system on the site No. 4 at the location of the e soil type: left – layout of the site; right – image of the site.

Optimum parameters were taken according to (Ofrikhter & Ofrikhter 2015, Ofrikhter et al. 2018). The number of repeats at each point was 3 (two main and one reconnaissance). Noise interference and distortions were eliminated by repeating the record 5–8 times in each measurement at each point. The accepted MASW parameters are shown in Table 2.

Experimental data were processed with RadexPro 2014 Starter software package in a semi-automatic mode. The obtained average values of the S-wave velocities in the tested soil layers were used to calculate initial shear moduli from the expression (Mayne 2001):

$$G_0 = \rho \cdot V_s^2 \tag{3}$$

where ρ is soil density determined in laboratory tests, kg/m^3; V_s is soil layer shear wave velocity, m/s.

It is worth noting that expression (4) proposed in (Mayne 2001) allows calculation of the soil unit weight with values of S-wave velocities and depth:

$$\gamma = 8.32 \cdot \log V_s - 1.61 \cdot \log z \tag{4}$$

where γ is the unit weight of the soil layer, kN/m^3; z is the layer base depth, m.

Table 2. MASW testing parameters.

Site No	Soil type	D,m	X,m	dx,m	dt,ms	tn	N
1	a	11.5	2.5	0.5	0.5	2048	5–8
2	b	46.0	10.0	2.0	0.5	2048	5–8
	c	46.0	10.0	2.0	0.5	2048	5–8
3	d	46.0	10.0	2.0	0.5	2048	5–8
4	e	11.5	2.5	0.5	0.5	2048	5–8
	f	11.5	2.5	0.5	0.5	2048	5–8
5	g	11.5	2.5	0.5	0.5	2048	5–8

D is the receivers line; X is the source offset; dx is the receiver spacing; dt is the sampling interval; tn is the number of samples, i.e. the total recording time; N is the number of stacking data

2 EXPERIMENTAL DATA (ANTIPOV & OFRIKHTER 2019)

As an example, the MASW result for No. 4 site at the location of the e soil type and PLT results for the same soil are given in Figure 2.

The summarized MASW results are presented in Table 3 together with the soil unit weight calculations. Unit weights determined in the laboratory are provided for comparison. Calculated deformation moduli and initial shear moduli according to PLT and wave analysis are given in Table 4. Deformation modulus E was estimated according to the standard procedure recommended by the Russian State Standard (GOST 20276-2012) using the well-known Schleicher's equation for the first four points of the load-settlement curve counting from the initial pressure under plate.

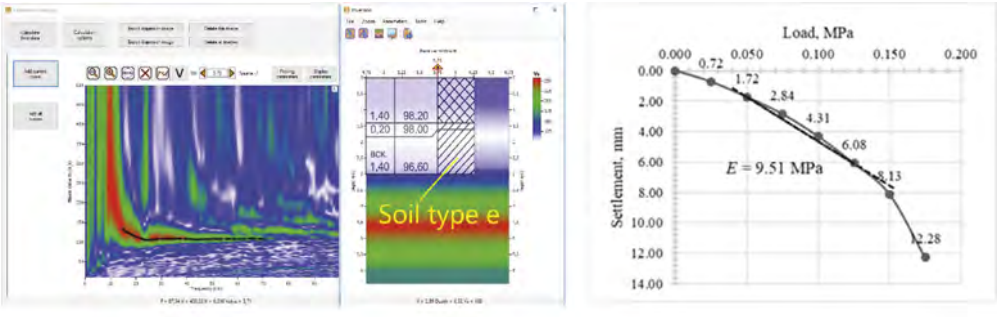

Figure 2. Experimental results for the site No. 4: left – the MASW survey; right – PLT.

Figure 3 and Table 5 present correlation coefficients between the deformation modulus and the initial shear modulus. The correlation coefficient was calculated by the formula: $k = E_{5000} / G_0$, and next the dependency was obtained:

$$k = -0.003321\gamma^3 + 0.206374\gamma^2 - 4.281230\gamma + 29.789383 \quad (5)$$

Table 3. Summary table of the MASW results and data of unit weight calculation.

Site No	Soil type	V_s,m/s	G_0,MPa	z,m	γ_{calc} (4), kN/m^3	γ_{lab}, kN/m^3
1	a	245	109.25	1.5	19.59	17.84
2	b	332	224.86	11.5	19.27	19.99
	c	417	356.47	12.6	20.03	20.09
3	d	151	48.34	0.5	18.61	20.78
4	e	172	59.76	3.0	17.83	19.80
	f	118	26.18	3.1	16.45	18.42
5	g	142	32.87	1.0	17.91	15.97

where γ is the soil unit weight, kN/m^3; k is the correlation coefficient between the MASW initial shear modulus and the soil deformation modulus determined by formula (6):

$$E = k \cdot G_0 \tag{6}$$

Table 4. Evaluation of deformation modulus by (GOST 20276–2012).

Site No.	Soil type (plate area)	h_{pl},m	P_n,MPa (S_n,sm)	P_0,MPa (S_0,sm)	E,MPa	n	m	E_{5000}, MPa
1	a (2500)	0.00	0.250 (0.390)	0.100 (0.139)	24.24	0.25	1.09	26.43
2	b (600)	9.19	0.800 (0.350)	0.200 (0.053)	40.14	0.15	1.17	47.06
	c (600)	11.7	0.800 (0.255)	0.200 (0.044)	53.12	0.15	1.17	62.28
3	d (600)	0.10	0.200 (0.560)	0.05 (0.035)	5.24	0.15	1.17	6.14
4	e (5000)	1.60	0.125 (0.608)	0.05 (0.172)	9.51	0.15	1.00	9.51
	f (5000)	2.40	0.125 (1.326)	0.05 (0.506)	4.84	0.15	1.00	4.84
5	g (600)	0.10	0.200 (0.251)	0.05 (0.026)	13.25	0.25	1.30	17.27

h_{pl} is the plate level from the surface; P_n is the plate pressure corresponding to the fourth point of the linear part of the load-settlement curve; P_0 is the initial pressure corresponding to the vertical intergranular stress from the soil self-weight at the test level; G_0 is the initial shear modulus of small strains; E is the PLT deformation modulus; n is the reduction argument according to Annex D of (SP 23.13330.2018) accepted as the minimum recommended value for the condition $\sigma_{z,p} = 0.5\sigma_{z,g}$; m is the deformation modulus conversion factor; E_{5000} is the calculated deformation modulus of a 5000 cm^2 plate.

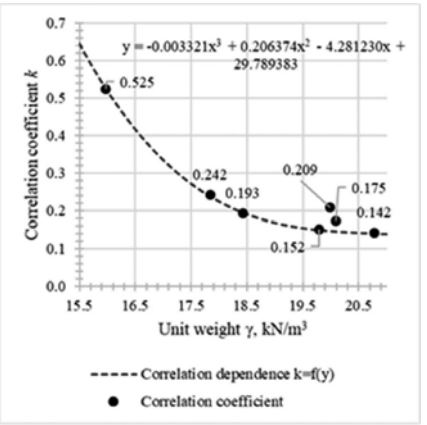

Figure 3. Unit weight – correlation coefficient.

Table 5. Unit weight – correlation coefficient.

No.	Soil type	G_0,MPa	E_{5000},MPa	γ_{lab} kN/m^3	k=E_{5000}/G_0,
1	a	109.25	26.43	17.84	0.242
2	b	224.86	47.06	19.99	0.209
3	c	356.47	62.28	20.09	0.175
4	d	48.34	6.14	20.78	0.142
5	e	59.76	9.51	19.80	0.152
6	f	26.18	4.84	18.42	0.193
7	g	32.87	17.27	15.97	0.525

3 DISCUSSION OF THE RESULTS

In the course of the experiments, a simple mathematical dependence (6) was obtained between the deformation modulus, comparable with the results of the plate test, and the initial shear modulus. The transition coefficient k in the formula depends only on the specific gravity of the soil. Taking into account that the magnitude of the initial shear modulus depends only on the speed of surface waves and the soil specific gravity, and that the specific gravity is directly related to the speed of surface waves in accordance with formula (6), the obtained dependences make it possible to estimate the soil deformation modulus in the shortest time both by the velocity of surface waves and by the soil unit weight. The soil unit weight can be determined by the standard engineering and geological surveys or can be calculated using formula (4) in case of a site without geological survey data. The proposed approach seems to be very convenient for the specialists in assessing the geotechnical situation at the site.

4 CONCLUSION

The article presents the results of soil plate load testing and wave analysis by the MASW method at the sites of Perm and Perm Region, Russian Federation, for different soils and their comparative analysis. Based on field researches, regularity was established and the relationship between the initial shear modulus G_0 according to wave surveys and the soil deformation modulus E according to standard plate load tests was determined. The correlation coefficient k between the soil deformation modulus E and the initial shear modulus G_0 varies within 0.142–0.525 according to the explicit regularity presented in Figure 5, and it decreases as the soil unit weight increases. A simple empirical formula (6) is proposed, which allows one to perform express evaluation of the soil deformation modulus by MASW and make a preliminary geotechnical assessment of the proposed construction site of the future facility.

The authors thank the research support services of Perm National Research Polytechnic University for providing the equipment for field and laboratory testing.

REFERENCES

Antipov, V.V., Ofrikhter, V.G. 2019. Field estimation of deformation modulus of the soils by multichannel analysis of surface waves, *Data in brief* 24. DOI: 10.1016/j.dib.2019.103974.

Foti, S., Lai, C.G., Rix, G.J., Strobbia, C. 2015. *Surface wave methods for near-surface site characterization*. ISBN 9780415678766. London: CRC Press.

GOST 20276-2012. Soils. Field methods for determining the strength and strain characteristics. Moscow: Standartinform. (In Russian).

Kalugina, Yu.A., Kek, D., Pronozin, Ya.A. 2017. Determination of soil deformation moduli after National Building Codes of Russia and Germany. *Magazine of Civil Engineering* 7(75): 139–149. DOI:10.18720/MCE.75.14 (In Russian).

Kashirskiy, V.I. 2014. Comparative analysis of deformation characteristics of the foundations carried out with laboratory and field methods. *Geotechnics* 5–6: 32–44. (In Russian).

Lushnikov, V.V. 2017. Development of pressiometry method for soils in Russia. *Geotechnics* 5–6: 46–61. (In Russian).

Ofrikhter, V.G., & Ofrikhter, I.V. 2015. Investigation of municipal solid waste massif by method of multichannel analysis of surface waves. *Proc. 15th Asian Reg. Conf. on Soil Mechanics and Geotechnical Engineering: Innovations in environmental geotechnics (TC215 Session), JGS Spec. Publ.* 57(2): 1956–1959. http://doi.org/10.3208/jgssp.TC215-01.

Ofrikhter, V.G., Ofrikhter, I.V., Bezgodov, M.A. 2018. Results of field testing of municipal solid waste by combination of CPTU and MASW. *Data in Brief* 19: 883–889. DOI:10.1016/j.dib.2018.05.109.

Mayne, P.W. 2001. Stress-strain-strength-flow parameters from seismic cone tests. *Proc. of Intern. Conf. on In-Situ Measurement of Soil Properties and Case Histories*. Bali, Indonesia: 27–48.

Park, C.B., & Carnevale, M. 2010. Optimum MASW survey – revisit after a decade of use. *GeoFlorida*: 1303–1312. DOI: 10.1061/41095(365)130.

Park, C.B., Miller, R.D., Xia, J. 1999. Multichannel analysis of surface waves. *Geophysics* 64(3): 800–808. DOI: 10.1190/1.1444590.

SP 23.13330.2018. The foundations of hydraulic structures. (In Russian).

Smart Geotechnics for Smart Societies – Zhussupbekov, Sarsembayeva & Kaliakin (Eds)
© 2023 The Author(s), ISBN 978-1-003-29912-7
Open Access: www.taylorfrancis.com, CC BY-NC-ND 4.0 license

Sand-plate interaction experimental investigations

S.O. Shulyat'ev
NIC Stroitelstvo, NIIOSP N.M. Gersevanova

ABSTRACT: The article presents stress distribution analysis in sand soil, loaded with a square reinforced concrete foundation with dimensions 2*2*0,2 m. Vertical and horizontal stresses, as well as layer-by-layer deformations in sand with increasing load, were obtained. Comparison of experimental data with the results of analytical and numerical data made it possible to draw important conclusions regarding bases calculations.

1 INTRODUCTION

Investigations were made in tray with dimensions 5*15 m and depth 4 m (Figure 1). To increase thickness of sand layer, embankment 2 m high was arranged on top of the tray. Medium size sand with density 18,9 kN/m^2 used as tray filler. Load was transferred through two special made reinforced concrete plate with dimensions 2*2*0,2 m, made by B35 and B60 concrete. There were three tests in two stages. At the first stage, two plates were tested at the same time with 6 m distance between edges. At the second stage, one slab was tested, located in central part of the tray (Figure 1). During the experiments, tray was covered with a tent with constant temperature ±5C°.

1 – test plate №1 (stage №1), 2 – test plate №2 (stage №1), 3 – test plate №1 (stage №2), 4 – reflector, 5 – displacement sensor, 6 – pressure sensor, 7 – settlements sensor, 8 – vertical and

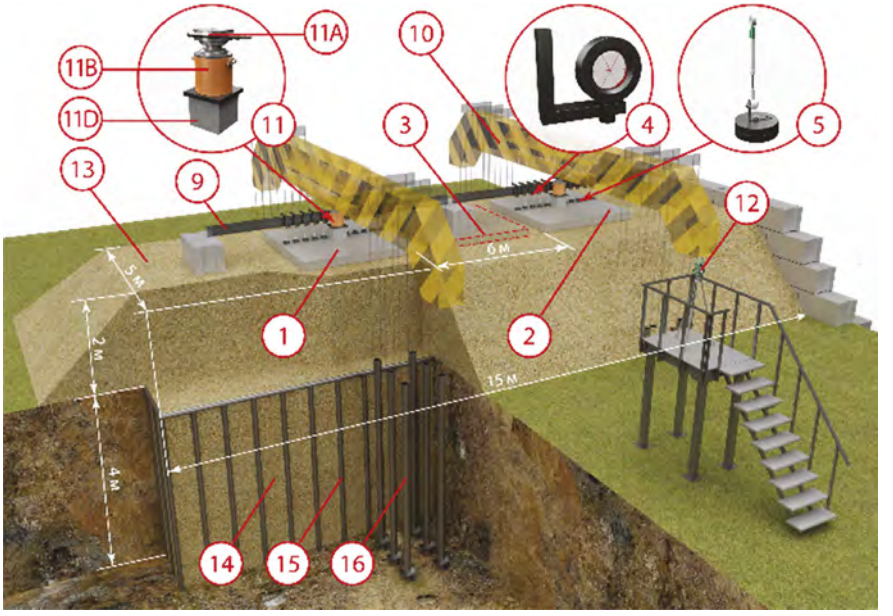

Figure 1. Test layout.

DOI: 10.1201/9781003299127-319

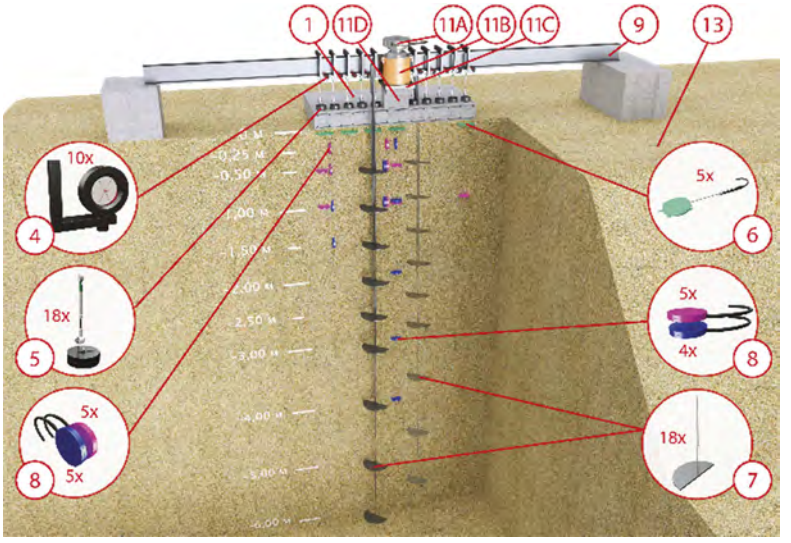

Figure 2. Test plate with equipment.

horizontal stress sensors (blue – plate №1, stage №1, pink – plate №1 stage №2), 9 – reference beam, 10 – force beam, 11 – loading system, 11A – load sensor, 11B – jack, 11D – concrete reinforced cube 0,2 m, 12 – automated level, 13 – sand embankment, 14 – experimental tray 15*5 m, 15 – tray steel pile wall, 16 – anchor pile.

2 EQUIPMENT

Base was equipped with 76 sensors operating simultaneously in automated mode. Displacements of each plate were measured using 10 potentiometric sensors located along one of its sides. Layered deformations were also measured using potentiometric sensors at 10 points, set with step of 0,5 m with base depth for each slab (Figure 2). All vertical movements were fixed relative to reference beam, hinged at one end. Reference beam position was controlled using automated level, position of which was monitored using three reference points (Figures 1 and 2). Horizontal and vertical stresses in soil were measured using strain gauge pressure transducers PMD-70/II (force cell). Force cells were located in depth increments of 0,25, 0,5 and 1 m to depth of 4 m. (Figure 2). More details about tests in (Travush & Shulyat'ev 2022).

3 TEST PROCEDURE

Loading of each plate was made in two stages, at first stage plate loaded up to 0,4 MN, after which controlled unloading was carried out. At second stage plates were loaded up to 1,5 MN, followed by controlled unloading. Loading step was 0,1 MN, unloading was 0,2 MN. Next loading step was applied when settlements velocity were less than 0,1 mm per 1 h. Loading was applied using jack equipped with tow pressure gauges. Load on plate was transferred through reinforced concrete cube with a side of 0,2 m. Measurements were made in automated mode with a frequency once every five minutes.

4 MEASUREMENT ANALYSIS

Lets compare measurement results with stresses obtained by solving problem of stress distribution in elastic half-space base. Solutions prepared by G.V. Kolosov for flat task with

uniformly distributed load (Tshitovich 1963), J. Boussinesq for three-dimensional task for vertical concentrated force applied to elastic half-space bace (Boussinesq 1885), A. Lyav (Lyav 1935) and V.G. Korotkin (Korotkin 1938) for conditions three dimensional stress-state by load distributed over square area.

J. Boussinesq's solution for upper base part isn't considered due to peculiarity that arise when concentrated force is applied to half-space. As depth increases, vertical normal stress most closely match with analytical three dimensional case. Distribution of vertical normal stresses obtained by plane stress solution is significantly higher than real, which indicates limited use of plane stress models. Under the load of 1,5 MN, thickness of base, on which additional stresses are half of natural reaches 3,7 m, which corresponds to the depth of compressible thickness, equal to 4 m and determined according to Russian codes (Figure 3).

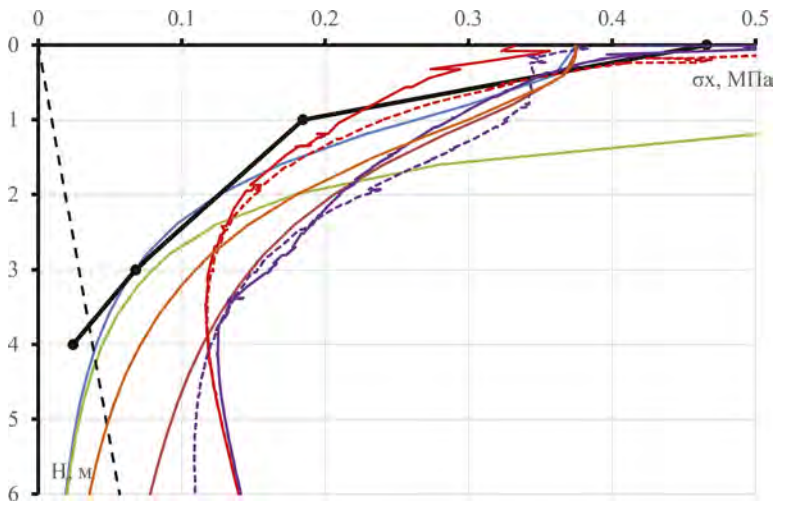

Figure 3. Vertical stress distribution along dept, under 0,375 MPa.

Analytical solutions: Blue – A. Lyav, gray - J. Boussinesq's, orange - G.V. Kolosov, green - V.G. Korotkin, black – monitoring data, dotted black line – half of natural stress, Numerical solutions: Elastic model FE 250 mm (100 mm) – red (dotted red), Mohr-Coulomb (Hardening soil) – violet (dotted violet).

Deformation measurements shows that settlement developed at certain depth linearly depends on average pressure value. Distribution of layer-by-layer deformations with depth correlates with general ideas about deformation of layer and is shown in Figure 4. Limitation of compressible thickness adopted in Russian codes as half of natural stresses for dispersed non-weak soil makes it possible to determine settlement with an accuracy of 10%, which acceptable for engineering purposes. Measurement results and comparison made possibility of using theory of elasticity and continuum space for geotechnical problems.

Lets perform numerical simulation using various soil models, such as elastic model, ideal elastic-plastic model with Mohr-Coulomb strength criterion and Hardening soil model. As can be seen from Figure 3, changing the size of finite element by two times leads to differences in vertical stresses of up to 40% at top of base. Comparing upper parts in different models, results of numerical and analytical calculations are quite close to each other. With increasing depth, vertical stress distribution largely depends on chosen foundation model, however, for any model, stress distribution in general does not coincide with results obtained analytically from monitoring date. This is consequence of influence of artificial stress concentration when boundary conditions are introduced, selection of which should be given special attention. Choice of soil model should be approached taking into account problem under consideration, type of soil and level of stresses.

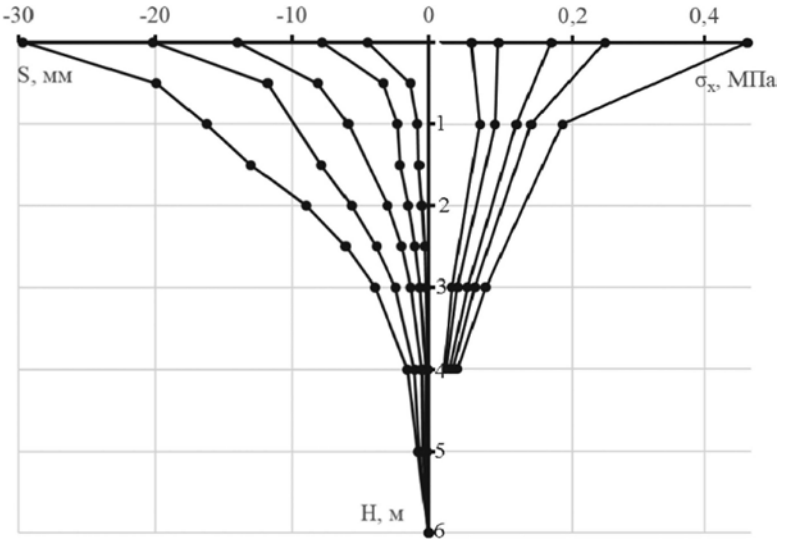

Figure 4. Combined graph of settlements distribution and vertical stresses along depth of foundation at average pressures 0,375 MPa, 0,3 MPa, 0,25 MPa, 0,175 MPa, 0,125 MPa.

5 CONCLUSIONS

Unique investigations of interaction of reinforced concrete slab with sandy soil were carried out, 76 sensors were involved in testing process, measuring stresses under base of slab, vertical and horizontal stress in soil, layer-by-layer settlement of soil. In general, investigations results confirm possibility of using theory of elasticity and continuum space for geotechnical calculations. Present research confirm Russian code approach to determining depth of compressible soil. Contribution of additional settlement from soil under compressible thickness does not exceed 10%. Choice of size of finite element, accepted boundary conditions, as well as soil model significantly depends on magnitude of vertical stresses in soil, as well as their distribution in depth. Investigations of influence of parameters of finite element model should be given special attention and require additional research.

REFERENCES

Travish, V.I. & Shulyat'ev S.O. 2022. Tray research of slab-sand interaction. *Zhilishnoe stroitel'stvo*.9: 3–11

Tsitovich, N.A. 1963. Soil mechanics. 638 p. Moscow: GSI.

Boussinesq, J. 1885. Application des potentiels a l'etude de l'equilibre et du mouvement des solides elastiques.350 p. Paris: Phisics.

Lyav, A. 1935. Mathematical elasticity theory. 674 p. Saint-Petersburg: ONTY.

Korotkin V.G. 1938. Volumetric problem for elastically isotropic half-space. *Gidroproject proceedings*. 1: 52–85

Smart Geotechnics for Smart Societies – Zhussupbekov, Sarsembayeva & Kaliakin (Eds)
© 2023 The Author(s), ISBN 978-1-003-29912-7
Open Access: www.taylorfrancis.com, CC BY-NC-ND 4.0 license

Calculation of shallow foundations with contour reinforcement

M.L. Nuzhdin
Department of Engineering Geology and Foundations, Novosibirsk State University of Architecture and Civil Engineering (Sibstrin), Russia

A.B. Ponomaryov
Department of Industrial and Civil Engineering, Saint Petersburg Mining University, Russia

L.V. Nuzhdin
Department of Engineering Geology and Foundations, Novosibirsk State University of Architecture and Civil Engineering (Sibstrin), Russia
Department of Construction Operations and Geotechnics, Perm National Research Polytechnic University, Russia

ABSTRACT: An effective way to strengthen shallow foundations is contour reinforcement - the execution of vertical elements in the soil base along the edges of the foundation. The introduction of reinforcement elements that perform the function of a "compression wall" leads to a noticeable decrease in deformations and an increase in the bearing capacity of the soil at the base of the reinforced foundations. As reinforcing elements, various structures and materials with strength properties that exceed the corresponding properties of the soil can be used.

To determine the rational parameters of the contour reinforcement with injection bodies, a set of numerical experiments was performed to calculate the stress-strain state of the soil foundation for different reinforcement schemes in the MIDAS GTS NX 2019 software package. The calculations were carried out in a 3D formulation, taking into account the nonlinear nature of the soil operation.

Based on the results of the calculation, the most effective schemes for the location of reinforcement elements were determined when strengthening shallow foundations with contour reinforcement with injection bodies, and the technology for consistent reinforcement work with a gradual increase in the number of reinforcement elements was substantiated.

1 INTRODUCTION

An efficient way of strengthening shallow foundations is contour reinforcement, i.e. applying a number of vertical elements in the soil body along foundation sides. Application of reinforcing elements, functioning as "compression wall", leads to a significant reduction of deformations and increase in the bearing capacity of reinforced foundation base [1-5]. Various structures and materials with strength properties exceeding the corresponding soil properties can be used as reinforcing elements [6–10, 18–20].

A method of forming reinforcing elements by means of high-pressure pack injection grouting has proved itself. The essence of the method consists in simultaneous supply of cement and sand mortar through several pressurized sources, arranged in series and exceeding the structural strength of soil, and further formation of flat grouting bodies of a conditionally rectangular shape in the soil body [11–14]. A major issue in contour reinforcement is defining optimal parameters of injection grouting, i.e. the number and grid of the grouting bodies both in plan and depth, that can lead to an essential reduction of complexity and cost of works of the reinforcement [15, 16].

DOI: 10.1201/9781003299127-320

2 METHODS AND PROBLEM STATEMENT

In order to define rational parameters of contour reinforcement of shallow foundations by grouting bodies a complex of numerical experiments to calculate stress-strain state of the foundation soil with different strengthening schemes was performed. Numerical modeling was realized in software package MIDAS GTS NX 2019. Calculations were performed in 3D with account of nonlinear character of soil behavior.

Shallow foundation of the existing building that had suffered significant deformations was considered as an example. Foundation bottom size in plan – 2.4×2.4 m, bottom pressure P = 210 kPa. Foundation soil to a depth of 10 m consisted of loam that was light, pulverescent, very soft, non-subsiding, nonsaline: $\rho = 1.95$ g/cm^3, $\varphi = 14°$, C = 15 kPa, E = 4.5 MPa. Settlement of foundation during building construction achieved 156 mm that is significantly higher than the limit value of 10 cm recommended by Rules SP 22.13330.2016.

The calculation was performed for the reinforcing elements of a rectangular shape and size of 0.5×0.2 m, height 0.7 m; distance to foundation sides – 25 cm; gap between the elements in depth – 50 mm and 75 mm in plan; stress-strain properties: $\gamma = 20$ kN/m^3, $\nu = 0.2$, E = 100 MPa. Foundation material – heavy concrete.

Options with uninterrupted and interrupted contour reinforcement along the entire perimeter and at the opposite sides of the foundation were considered. For each option cases of 5-, 4-, 3-, 2- and 1-level reinforcement to the depth of 1.5b, 1.2b, 0.9b, 0.6b, 0.3b, respectively, were calculated (Picture 1).

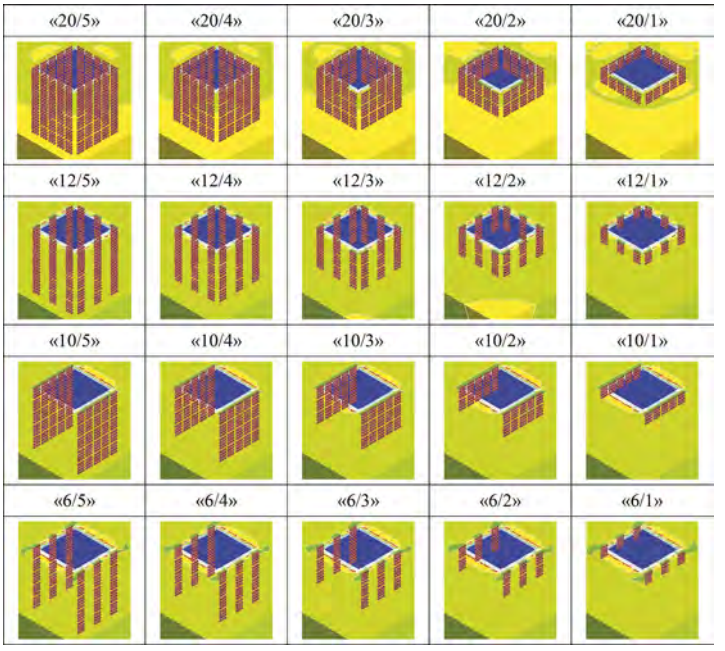

Figure 1. Arrangement schemes of reinforcement elements when strengthening shallow foundation with contour reinforcement.

Note to Picture 1. Symbols in schemes: first figure – number of columns, second figure – number of levels of reinforcing elements in depth.

The structural model in MIDAS consisted of a grid of hexahedral and tetrahedral elements, including 26,070 finite elements and 13,908 nodes with 42,231 degrees of freedom. Overall dimensions of the computational domain were 13.5×13.5×15 m.

The calculations of the foundation reinforced by means of contour reinforcement were performed consecutively in three stages: calculation of stress-strain state of the foundation due to

soil's own weight; after foundation construction and implementation of reinforcing elements; calculation of reinforced foundation after load application.

3 CALCULATIONS RESULTS AND ANALYSIS

The settlement value of foundation with natural (not reinforced) basis calculated in MIDAS, using elastic-plastic Mohr-Coulomb model, comprised 144 mm that is close to the value of real foundation settlement.

The calculation results of the foundation on a reinforced basis are given in Table 1, the contours of vertical movements of foundation soil strengthened according to characteristic schemes are given in Picture 2.

Table 1. Results of Calculating Shallow Foundations Strengthened by Contour Reinforcement With Reinforcing Elements Arrangement According to Different Schemes.

«20/5»	«20/4»	«20/3»	«20/2»	«20/1»
S = 110 мм ΔS = 34 мм V = 7,00 м^3 $К_{ПРМ}$ = 2,06	S = 112 мм ΔS = 32 мм V = 5,60 м^3 $К_{ПРМ}$ = 1,75	S = 114 мм ΔS = 30 мм V = 4,20 м^3 $К_{ПРМ}$ = 1,40	S = 116 мм ΔS = 28 мм V = 2,80 м^3 $К_{ПРМ}$ = 1,00	S = 122 мм ΔS = 22 мм V = 1,40 м^3 $К_{ПРМ}$ = 0,64
«12/5»	«12/4»	«12/3»	«12/2»	«12/1»
S = 121 мм ΔS = 23 мм V = 4,20 м^3 $К_{ПРМ}$ = 1,83	S = 123 мм ΔS = 21 мм V = 3,36 м^3 $К_{ПРМ}$ = 1,60	S = 123 мм ΔS = 21 мм V = 2,52 м^3 $К_{ПРМ}$ = 1,20	S = 124 мм ΔS = 20 мм V = 1,68 м^3 $К_{ПРМ}$ = 0,84	S = 128 мм ΔS = 16 мм V = 0,84 м^3 $К_{ПРМ}$ = 0,53
«10/5»	«10/4»	«10/3»	«10/2»	«10/1»
S = 126 мм ΔS = 18 мм V = 3,50 м^3 $К_{ПРМ}$ = 1,94	S = 127 мм ΔS = 17 мм V = 2,80 м^3 $К_{ПРМ}$ = 1,65	S = 128 мм ΔS = 16 мм V = 2,10 м^3 $К_{ПРМ}$ = 1,31	S = 129 мм ΔS = 15 мм V = 1,40 м^3 $К_{ПРМ}$ = 0,93	S = 132 мм ΔS = 12 мм V = 0,70 м^3 $К_{ПРМ}$ = 0,58
«6/5»	«6/4»	«6/3»	«6/2»	«6/1»
S = 133 мм ΔS = 11 мм V = 2,10 м^3 $К_{ПРМ}$ = 1,91	S = 134 мм ΔS = 10 мм V = 1,68 м^3 $К_{ПРМ}$ = 1,68	S = 134 мм ΔS = 10 мм V = 1,26 м^3 $К_{ПРМ}$ = 1,26	S = 134 мм ΔS = 10 мм V = 0,84 м^3 $К_{ПРМ}$ = 0,84	S = 136 мм ΔS = 8 мм V = 0,42 м^3 $К_{ПРМ}$ = 0,53

Note to Table 1. S – settlement of foundation on a reinforced basis, ΔS – difference between settlements of foundations on natural and reinforced bases, V – volume of reinforcing elements, $К_{ПРМ}$ – coefficient of given material consumption equal to the ratio of volume (V) of reinforcing elements to the difference of settlements (ΔS).

The efficiency of various strengthening schemes is clearly shown by the coefficient of given material consumption $К_{ПРМ}$ (Table 1), equal to the ratio of the reinforcing elements volume to the difference of settlements of foundation on a natural basis and that after reinforcement and numerically identical to the volume of reinforcing elements in m3 necessary for the settlement reduction by 1 cm.

Thus, for instance, as might be expected, the minimum value of foundation settlement is achieved by maximum reinforcement (uninterrupted 5-level to the depth of 20/5) – S = 110 mm that is by 34 mm or 24% lower than the settlement of foundation on a natural basis. However, interrupted reinforcement along two opposite sides of the foundation, one-level to the depth (6/1), allows to reduce the settlement by 8 mm, i.e. by 6%, at the same time the volume of the reinforcing elements used differs 17-fold – 0.42 m^3 against 7.00 m^3 in the first case. When strengthened according to 20/5 scheme the coefficient of given material

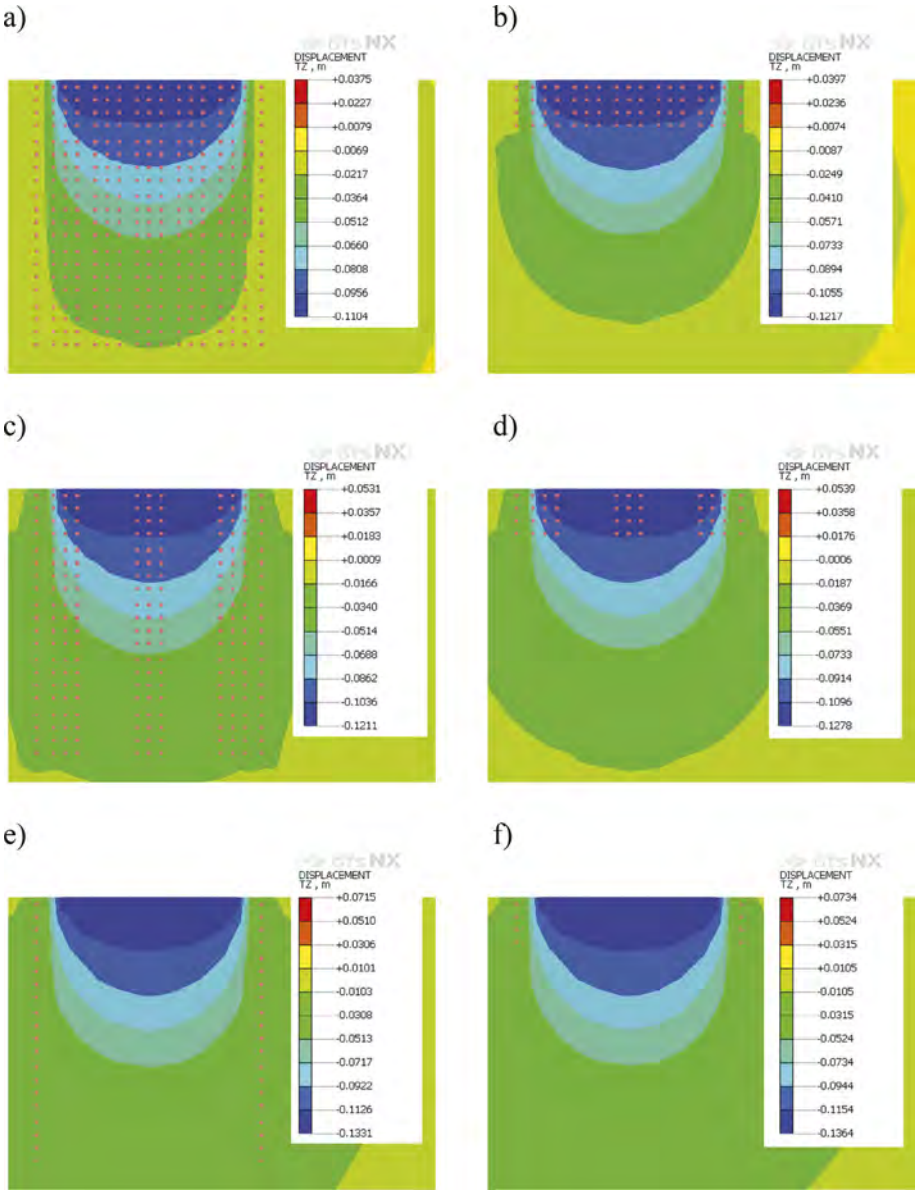

Figure 2. Isolines of vertical displacements of the foundation soil base when reinforced with contour reinforcement: (a, b) – solid 5-level («20/5») and one-level; (c, d) intermittent 5-level («12/5») and one-level («12/1»); discontinuous, along two opposite sides of the foundation: (e, f) – 5-level («6/5») and one-level («6/1»).

consumption $K_{ПРМ}$ = 2.06, when done so according to scheme 6/1 – $K_{ПРМ}$ = 0.53, that is to say specific efficiency of strengthening at maximum reinforcement is 4 times lower.

Interrupted contour reinforcement is more cost effective than uninterrupted one. The coefficient of given material consumption $K_{ПРМ}$ for interrupted 5-level contour reinforcement along the entire foundation perimeter (12/5) comprises 1.83 and for one-level (12/1) – $K_{ПРМ}$ = 0.53. When uninterrupted 5-level reinforcement is applied, the coefficient of given material consumption $K_{ПРМ}$ = 2.06 and when uninterrupted one-level reinforcement is applied, $K_{ПРМ}$ = 0.64. Uninterrupted reinforcement along two opposite sides also has higher specific efficiency

in comparison with uninterrupted reinforcement along the entire perimeter of the foundation – $K_{ПРМ}$ = 1.94 and $K_{ПРМ}$ = 0.58, respectively.

By analyzing the values of coefficient $K_{ПРМ}$, it is fair to say that in all cases the increase in the number of columns of reinforcing elements, as well as in the levels to depth, leads to the reduction of foundation soil deformations, but at the same time the reduction of settlement from minimum to maximum reinforcement schemes is not proportionate to the volume growth of reinforcing elements used, i.e. specific efficiency of strengthening decreases.

The comparison of deformations of soil foundation strengthened by reinforcement according to schemes with similar number of levels allows to make a conclusion about almost direct dependence of the settlement value on the number of reinforcing elements in plan at approximately equal values of $K_{ПРМ}$. For example, when 5-level reinforcement is applied the difference of settlements

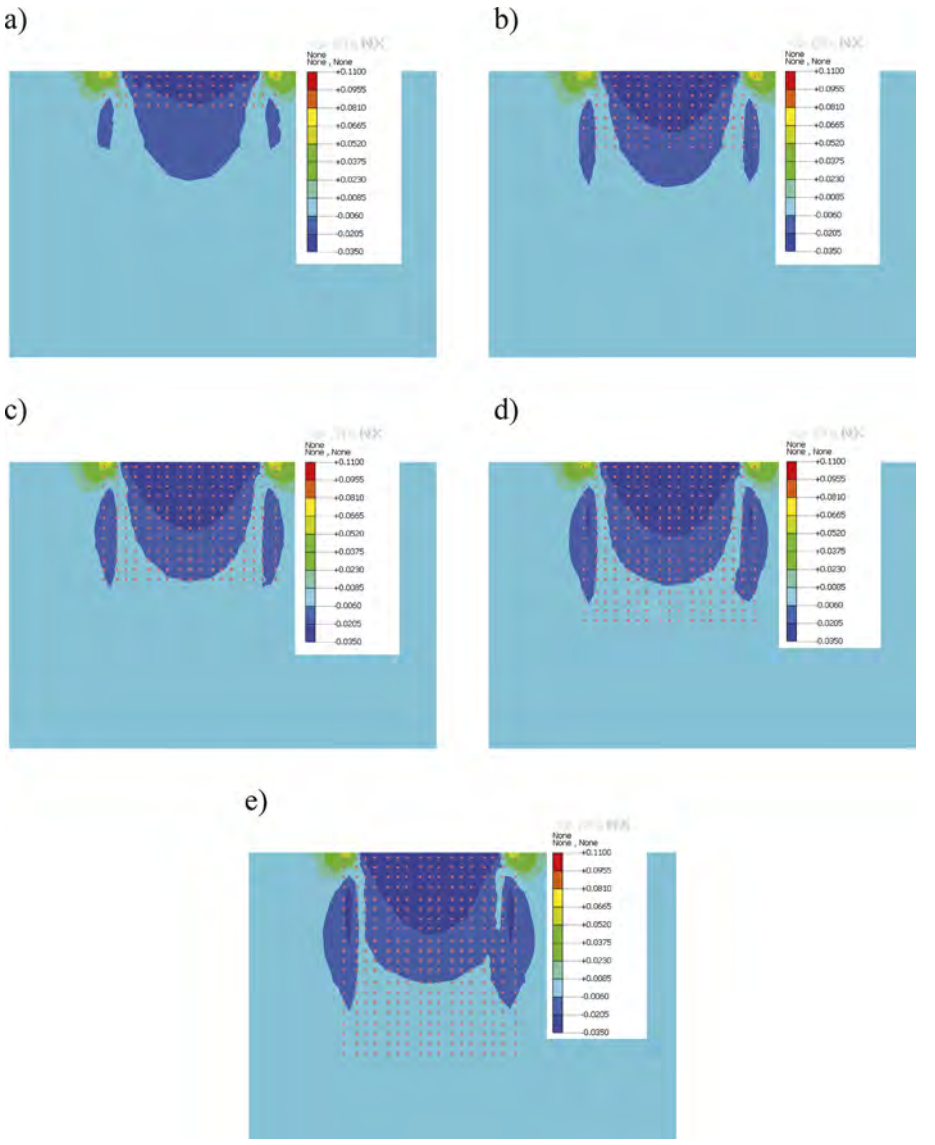

Figure 3. Isolines of differences in soil base deformations before and after reinforcement: (a) – with a single («20/1»), (b) – two («20/2»), (c) – three («20/3»), (d) – four («20/4») and e – five-level («20/5») solid reinforcement.

of foundations on a natural basis and on the basis strengthened by interrupted contour reinforcement at two opposite sides (6/5) is 11 mm, by uninterrupted contour reinforcement at two opposite sides (10/5) – 18 mm, by interrupted reinforcement at four sides (12/5) – 23 mm, and by uninterrupted contour reinforcement at four foundation sides (20/5) – 34 mm. The value of $K_{ПРМ}$ in such a case lies within 1.83 and 2.06, and at that point the minimum value of $K_{ПРМ}$ equal to 1.83 corresponds to the scheme of interrupted contour reinforcement at four foundation sides (12/5). The latter is also true for options with 4-, 3-, 2- and one-level reinforcement.

As the implementation of additional levels of reinforcing elements from the top down is extremely difficult while strengthening real foundations [17], it is necessary to assign the reinforcement depth at the stage of design.

To define effective depth of contour reinforcement the comparison of deformation contours of soil foundation without strengthening and after it was made. The calculation was performed for all schemes. Differences of deformations of soil foundation before and after strengthening by uninterrupted contour reinforcement along the entire perimeter for options with different levels in depth are represented in Picture 3 as an example.

Picture 3 shows that contour reinforcement leads to a substantial change of the strain state of the soil body – the difference area of deformations of the foundation before and after strengthening is wedged-shaped and extends to the depth of 0.81b, 0.86b, 0.90b, 0.91b and 0.97b at 1-, 2-, 3-, 4- and 5-level reinforcement, respectively. When 1- or 2-level reinforcement is applied, the area border is located below (0.3b and 0.60b), with 3-level reinforcement – it practically coincides (0.9b), with 4-level reinforcement – it is above (1.2b), and with 5-level reinforcement – it is significantly higher than the reinforcement depth (1.5b). At 2-, 3- and 4-level reinforcement the reduction of lateral deformations within and beyond the reinforcement contour is clearly observed. Elements of the 5^{th} level provide certain increase mainly in the side areas of a soil body transformed state, however, at the same time, they do not expand below the elements of the 4^{th} level. Therefore, the schemes with 3- and 4-level reinforcement that correspond to the depth of 0.9b…1.2b from the foundation bottom are the most effective. This statement is true for all schemes of reinforcing elements arrangement in plan, when applying contour reinforcement to shallow foundations.

4 CONCLUSION AND DISCUSSION

On the basis of numerical modeling on the forecast of stress-strain state of soil foundation with various strengthening schemes performed by the authors in software package MIDAS GTS NX 2019, the following conclusions can be made:

1. Strengthening of shallow foundations by contour reinforcement, using rigid reinforcing elements, transforms the stress-strain state of the soil body; change of the strengthening scheme together with the increase in the number of reinforcing elements reduces stress and vertical deformations. When interrupted contour reinforcement of shallow foundations is applied, the reduction of the settlement can reach 16% in relation to the settlement of the foundation that is not reinforced, in case of uninterrupted contour reinforcement the settlement can be reduced by 24%.
2. Strengthening by the maximum number of reinforcing elements leads to the maximum reduction of soil foundation deformations. However, any reinforcement scheme reduces the settlement, and in most cases the coefficient of given material consumption $K_{ПРМ}$ grows along with the increase in the volume of the reinforcing elements used.
3. Interrupted contour reinforcement is more cost effective than uninterrupted one, the coefficient of given material consumption $K_{ПРМ}$, when reinforcing the sites of the same length, is lower in the first case. Interrupted contour reinforcement along the entire perimeter of the foundations is more effective than strengthening by uninterrupted reinforcement along two opposite sides – deformations of the basis and the value of the coefficient of given material consumption $K_{ПРМ}$ are higher in the second case.
4. Based on the above, strengthening of shallow foundations by rigid reinforcing elements – grouting bodies – is advisable to be carried out in stages, increasing the number of reinforcing

elements at each stage and changing the reinforcement scheme respectively: from interrupted contour reinforcement along opposite sides to uninterrupted contour reinforcement along the entire foundation perimeter. The necessity of performing further works must be defined on the basis of results of monitoring the development dynamics of soil foundation deformations during and after each stage.

5. Optimal depth of soil foundation reinforcement for shallow foundations is 0.9b…1.2b (where b – width of the foundation bottom).

Further line of research by the authors of the article will be connected with establishing common principles of approach to strengthening foundations by high-pressure pack injection grouting based on the results of mathematical modeling.

ACKNOWLEDGEMENTS

The authors of the article would like to extend their gratitude to the employees of the Department of Geotechnics of Industrial University of Tyumen, Candidate of Technical Sciences, Associate Professor R.V. Melnikov and Candidate of Technical Sciences, Associate Professor D.V. Rachkov, for valuable advice and guidance in carrying out the research.

REFERENCES

1 Spravochnik geotehnika. Osnovanija, fundamenty i podzemnye sooruzhenija: izdanie vtoroe, dopolnennoe i pererabotannoe/Pod obshhej red. V.A. Il'icheva i R.A. Mangusheva. – Moskva, 2016. – 1040 s.
2 Mirsajapov I.T., Sharafutdinov R.A. Naprjazhenno-deformirovannoe sostojanie gruntovogo osnovanija, armirovannogo vertikal'nymi i gorizontal'nymi jelementami [Stress-strain state of a soil base reinforced with vertical and horizontal elements] // Izvestija KGASU, 2017. – № 1 (39). – S. 153–158.
3 Mirsajapov I.T., Popov O.A. Raschet osadki armirovannyh vertikal'nymi sterzhnevymi jelementami gruntovyh osnovanij [Calculation of the settlement of soil foundations reinforced with vertical rod elements] // «Fundamenty glubokogo zalozhenija i problemy osvoenija podzemnogo prostranstva»: trudy mezhdunarodnoj konferencii. – Perm', 2011. – S. 407–413.
4 Bogdanova E.O., Kleveko V.I. Komp'juternoe modelirovanie razvitija osadok zdanija na osnovanii, usilennom vertikal'nym armirovaniem [Computer modeling of the development of the settlement of a building on a foundation reinforced with vertical reinforcement] // Akademicheskij vestnik UralNIIproekt RAASN. 2017. – № 4. – S. 73–77.
5 Mangushev R.A., Nikiforova N.S. Tehnologicheskie osadki zdanij i sooruzhenij v zone vlijanija podzemnogo stroitel'stva. – M.: ASV, 2017. – 168 s.
6 Ibragimov M.N., Semkin V.V., Shaposhnikov A.V. Zakreplenie gruntov v podzemnom stroitel'stve. – M.: ASV, 2022. – 434 s.
7 Malinin A.G. Strujnaja cementacija gruntov. – M.: «Strojizdat», 2010. – 226 s.Ramya M., 11. Jeyapriya S. Behaviourial Study on Geopolymer Column Soil // Ground Improvement Techniques and Geosynthetics. – IGS 2016. – V.2 – Singapore, Springer, 2019. – P. 1–9.
8 Ramya M., Jeyapriya S. Behaviourial Study on Geopolymer Column Soil // Ground Improvement Techniques and Geosynthetics. – IGS 2016. – V.2 – Singapore, Springer, 2019. – P. 1–9.
9 Kumar P. Bearing Capacity of Strip Footing on Clay Soil Reinforced with Metal Strips and with Anchors // Ground Improvement Techniques and Geosynthetics. – IGS 2016. – V.2 – Singapore, Springer, 2019. – P. 77–84.
10 Croce P., Flora A., Modoni G. Jet Grouting. Technology, Design and Control – London: CRC Press, 2014. – P. 284.
11 Nuzhdin M.L. Jeksperimental'nye issledovanija usilenija gruntovogo osnovanija svajnyh fundamentov armirovaniem zhestkimi vkljuchenijami [Experimental studies of strengthening the soil base of pile foundations by reinforcing with rigid inclusions] // Vestnik PNIPU. Stroitel'stvo i arhitektura. – 2019. – T. 10, № 3. – S. 5–15. DOI: 10.15593/2224-9826/2019.3.01
12 Nuzhdin M.L., Nuzhdin L.V., Ponomaryov A.B. Experimental studies on model pile foundations reinforced by hard inclusions // Geotechnics for Sustainable Infrastructure Development: Lecture Notes in Civil Engineering, Vol. 62. – Singapore: Springer, 2019. – P. 193–197. DOI: 10.1007/978-981-15-2184-3_24
13 Nuzhdin M.L., Nuzhdin L.V. Jeksperimental'noe podtverzhdenie vozmozhnosti sozdanija v gruntovom massive inekcionnyh tel ustanovlennoj formy [Experimental confirmation of the

possibility of creating injection bodies of the established shape in the soil mass] // Izvestija vuzov. «Stroitel'stvo». – 2019. – № 10. – S. 101–112. DOI: 10.32683/0536-1052-2019-730-10-101-112
14 Nuzhdin M.L., Nuzhdin L.V. Strengthening of supporting ground of a damaged building by high-pressure injection of a moving cement-sand mixture // Proceedings of the 17th African Regional Conference on Soil Mechanics and Geotechnical Engineering (7-9 October 2019, Cape Town). – University of Pretoria, Pretoria, South Africa, 2019. – P. 785–788.
15 Pronozin Ja.A., Kajgorodo v M.D. Regulirovanie geometricheskogo polozhenija zdanij, v uslovijah sil'noszhimaemyh gruntovyh osnovanij [Regulation of the geometric position of buildings, in conditions of highly compressible soil foundations] // «Mehanika gruntov v geotehnike i fundamentostroenii»: materialy mezhdunarodnoj nauchno-tehnicheskoj konferencii. – Novocherkassk, 2018. – S. 462–467.
16 Mel'nikov R.V., Pronozin Ja.A., Tarasenko A.A. Chislennoe opredelenie oblastej grunta dlja ispravlenija krena zdanija [Numerical determination of ground areas to correct building roll] // Vestnik Sibirskogo gosudarstvennogo universiteta putej soobshhenija. – 2021. – № 4 (59). DOI: 10.52170/1815-9265_2021_59_108
17 Lubjagin A.V., Fedorov V.K. Modifikacija gruntovyh osnovanij metodom kompensacionnogo nagnetanija [Modification of soil bases by the method of compensatory injection] // Osnovanija, fundamenty i mehanika gruntov. – 2015. – № 2. – S. 28–31.
18 Ponomarev A.B., Ofrihter V.G. Analiz i problemy issledovanij geosinteticheskih materialov v Rossii [Analysis and problems of geosynthetic materials research in Russia] // Vestnik Permskogo nacional'nogo issledovatel'skogo politekhnicheskogo universiteta. Stroitel'stvo i arhitektura. – 2013. – № 2. – S. 68–73.
19 Kuznecova A.S., Ofrihter V.G., Ponomarev A.B. Issledovanie prochnostnyh harakteristik peska, armirovannogo diskretnymi voloknami polipropilena [Study of strength characteristics of sand reinforced with discrete polypropylene fibers] // Vestnik Permskogo nacional'nogo issledovatel'skogo politekhnicheskogo universiteta. Stroitel'stvo i arhitektura. – 2012. – № 1. – S. 44–55.
20 Lushnikov V.V., Bogomolov V.A. Vysokonapornaya inekciya gruntov kak sposob sozdaniya geotekhnogennyh sistem v stroitelstve // Inzhenerno-geologicheskie problemy urbanizirovannyh territorij: mat. mezhdunar. simp. – Ekaterinburg: AKVA-PRESS, 2001. – T. 2. – S. 732–740.

Smart Geotechnics for Smart Societies – Zhussupbekov, Sarsembayeva & Kaliakin (Eds)
© 2023 The Author(s), ISBN 978-1-003-29912-7
Open Access: www.taylorfrancis.com, CC BY-NC-ND 4.0 license

Influence of pile foundation technology on the skin friction

O.A. Shulyatyev & S.O. Shulyatyev
NIIOSP named after N.M. Gersevanov of the JSC «Research center of construction», Moscow, Russia

ABSTRACT: The lateral bearing capacity of bored piles is determined by horizontal stresses and soil strength. The paper investigates the influence of piling technology and loading history on horizontal stresses, as well as the effect of polymer solution, which has recently been used in piling, on the strength characteristics of the ground. As a result, it is found that the horizontal stresses can vary many times depending on the bored pile technology. The horizontal stresses increase as the pile is loaded. An additional increase in horizontal stresses occurs as a result of the mutual influence of the piles. The application of polymer solution instead of bentonite increases the resistance along the side surface of the ground up to 30%.

Keywords: bored piles, tests, bearing capacity of soil, lateral surface of pile, polymer solution, mutual influence of piles, pile field

1 INTRODUCTION

Comparison of the results of experimental determination of the resistance of hard clayey soils on the lateral surface of bored piles with calculations in the construction of high-rise buildings showed that the closest results are obtained when applying the dependence based on Coulomb's law, taking into account soil over-compaction (Shulyatyev, 2020):

$$f_i = \sigma\prime_x \mathrm{tg}\varphi + \ c. \tag{1}$$

The value σ'_x depending on the vertical stresses can be determined by the formula

$$\sigma\prime_x = K_o \sigma\prime_z, \tag{2}$$

where $K_o = (1 - \sin\varphi)$;

φ and c are strength properties of the soil.

In the case of over-compacted soil, the K-factor can be determined according to the formula

$$K_o = (1 - sin\varphi)\mathrm{OCR}^{\sin\varphi}. \tag{3}$$

The main parameters influencing the calculation results are the horizontal stresses and the strength properties of the ground. The article deals with the change in horizontal stresses during pile installation and loading and the effect of the borehole drilling stability solution used on the strength properties of the soil.

2 STUDY OF THE STRESS-STRAIN STATE OF THE SOIL MASS DURING BARETTA INSTALLATION

2.1 *Analysis of experimental studies in the construction of Okhta Centre*

Until the beginning of this century, in St. Petersburg it was feared that a monolithic 'wall in soil' of the trench type would be constructed using standard technology due to the possible loss of stability of the walls of the enclosure in the ribbon loam, which has a latent flowing consistency.

DOI: 10.1201/9781003299127-321

In order to investigate this hazard, pilot works were carried out at the Okhta Centre site, which consisted of an investigation of the soil mass composed of strip loam. Five barettes were constructed with a working length of 65 m and a cross-section of 1.5 × 2.8 m (Shulyatyev, 2020). Three of the five tested barettes were subjected to a group test in which they were loaded simultaneously. The arrangement of the test burettes is shown in Figure 1.

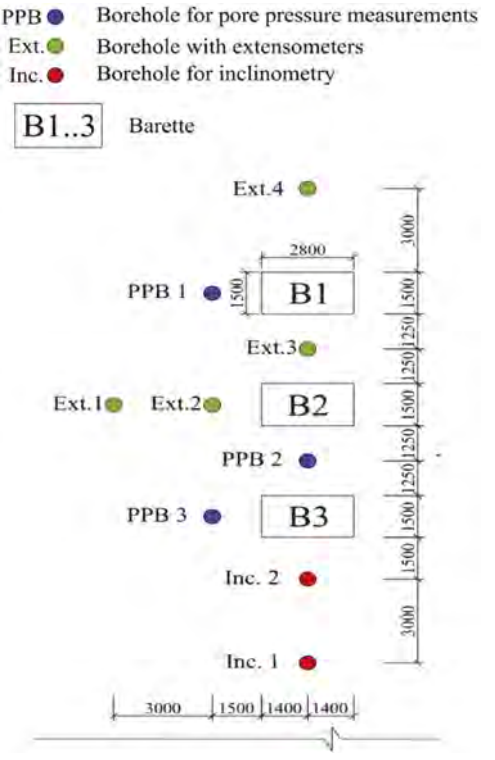

Figure 1. Baretta placement diagram for stress-strain state of the soil mass research during installation of diaphragm wall.

The engineering and geological conditions of the construction site are represented by weak water saturated soils to a depth of 30. . .35 m. Beneath them there is a layer of moraine sediments of small thickness. From 45 to 200 m there are Vendian clays, below – rocky soils. The Vendian clays are relatively firm soils and are classified as hard clay and half-rock soil at the same time.

The adjacent soil mass was equipped with monitoring sensors and instruments. A total of 9 monitoring boreholes were constructed (Figure 1), of which three (PPB 1 - 3) were for pore pressure measurements, four (Ext.1, Ext.2, Ext.3, Ext.4) were for vertical ground deformation layer-by-layer measurements and two (Inc.1, Inc.2) were for inclinometer observations.

Using the example of baretta B2, located 1.5 m away from borehole PPB 2, consider the change in pore pressure during baretta fabrication. Table 1 shows the values of natural pore pressure at various stages of the fabrication process in absolute and percentage terms compared to the natural pore pressure.

When analysing Table 1 it can be noted that the maximum change in pore pressure was observed in soils up to a depth of 20 m. The soils from the surface to this depth are weak water saturated clay soils, the application of load to which immediately causes a jump in pore pressure. The increase in pore pressure during the excavation phase is due to the fact that the clay mud used during drilling creates excessive pressure on the borehole walls from the inside. The same process, but with a greater change in pore pressure, occurs during concreting. The

Table 1. Change in pore pressure with the PPB 2 barretta.

Sensor installation depth, m	Pore water pressure before work P_{w0}*, kPa	Trenching		Installing the frame		Concreting	
		P_w*, kPa	Change, %	P_w,* kPa	Change, %	P_w*, kPa	Change, %
3	45	55	22.2	48	6.7	70	55.6
9	105	130	23.8	108	2.9	140	33.3
16	170	195	14.7	180	5.9	215	26.5
25	259	263	1.5	260	0.4	270	4.2

* P_w – pore water pressure during operation (maximum values).

reason is that the density of the concrete mix is 2.3. . .2.4 times higher than the density of the drilling mud. The maximum change of the pore pressure was fixed at the depth of 3 m and made up 55 % of the initial one. At deeper depths, the change of pore pressure in relation to natural one is not so significant, which is caused by higher density of soil at this depth. In addition, the natural pore pressure increases with depth and therefore the percentage change in pore pressure decreases.

Inclinometer measurements were taken with a Digitilt hand-held inclinometer in boreholes up to 52 m deep. Inc.1 and Inc.2 inclinometer boreholes (see Figure 1) were located 3.0 m and 1.5 m from the B3 barrette wall, respectively. The values of horizontal ground displacement towards the trench measured in Inc.2 borehole reached 29 mm during the development of trench B3 (Figure 2). At depths up to 30 m from the surface, maximum displacement values were observed. The measured horizontal displacement values are up to 5% of the barrette width and are generally in line with the expected values under the ground conditions considered. At these depths are dusty clays and loams of soft plastic and soupy consistency prone to thixotropic softening. From a depth of 30 m to the bottom of the observation well, at the depths of the more resistant semi-solid and solid loams, the movements of the soil mass surrounding the baretta are linearly attenuated with depth. Later in the concreting process, the opposite process was observed - soil movement away from the excavation was 6. . .8 mm (Figure 2).

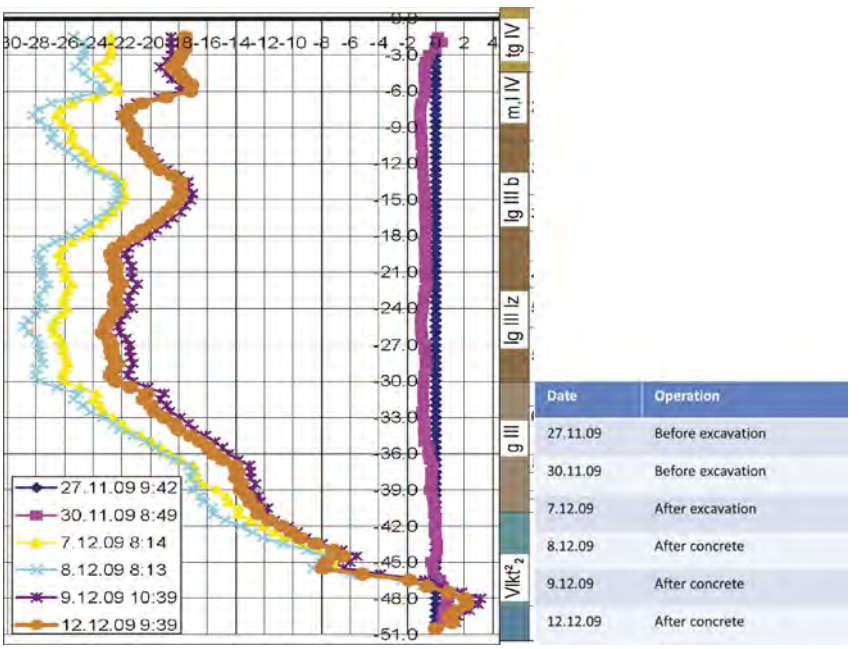

Figure 2. Horizontal movements of Inc.2 inclinometer during installation of baretta B3 for stress-strain state of the soil mass research during installation of diaphragm wall.

2.2 *Experimental studies at the Zagorskaya hydroelectric pumped storage power station*

As a result of experimental studies carried out at the Zagorskaya hydroelectric pumped storage power station construction site (Mamonov 1982, 1989), data were obtained on the actual values of radial pressures σ'_r at the contact of the bored pile with the ground. The σ'_r values were determined using pressure transducers (soil pressure cell) placed on the walls of three boreholes drilled for a 1 m diameter, 16-18 m deep pile. Immediately after placing the concrete mixture in the borehole, a radial pressure distribution σ'_r close to the hydrostatic pressure calculated for a mixture with a specific gravity of 23.3 kN/m^3 was obtained (Figure 3). Subsequently, during setting and hardening of the concrete mixture, a decrease of σ'_r pressures was observed, and after four months they were 6-16 % of the initial value.

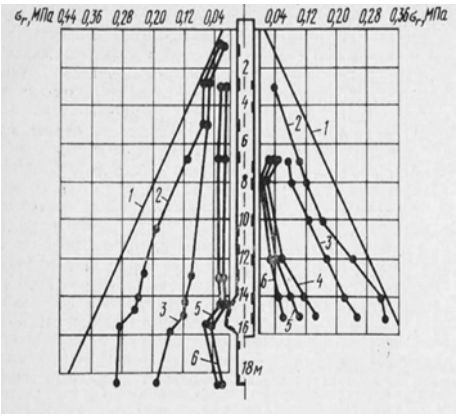

Figure 3. Radial pressure diagrams σ'_r along the length of pile No. 8 (a) and No. 3 (b) after concreting: 1 - hydrostatic pressure; 2 - after concrete filling; 3 - after 2.5 h; 4 - after 12 h; 5 - after 7 days; 6 - after 28 days.

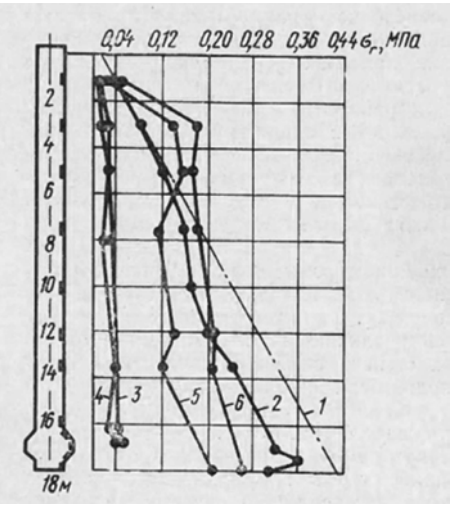

Figure 4. Radial pressure diagrams σ'_r along the length of pile No. 7 after concreting and during pile loading: 1 - hydrostatic pressure of concrete; 2 - after well filling with concrete; 3 - after 7 days; 4 - after 28 days; 5 - at 6500 kN load; 6 - at 7500 kN load.

2.3 *Calculation of concrete pressure*

Experimental data have now been obtained regarding the pressure of concrete on the borehole wall and within the concrete during the fabrication process to a greater extent barrette (Ng, 1999; Delattre, 2002; Lächler, A. 2006, 2007; Uriel, 1977; Gaba, 2017). Having processed the experimental data, Loreck (2007) obtained that the maximum pressure of the concrete mixture on the trench wall when concreting a wall grip in the ground is distributed according to a bilinear law (Figure 5). Up to a certain depth, which is conventionally called the critical depth, the concrete pressure is distributed according to the hydrostatic law. Below this depth, due to the concrete hanging on the trench walls and the onset of setting, it is assumed that the pressure of the concrete mixture on the trench walls continues to increase linearly, but with a lower intensity depending on the density of the clay solution (for each meter of depth the pressure on the trench wall increases by the value γ_{bt}×1 m):

$$\sigma_{bz} = \begin{cases} \gamma_b \times h \; at \; h \le h_{cr} \\ \gamma_{bt} \times h + (\gamma_b - \gamma_{bt}) \times h_{\text{крит}} \; at \; h > h_{cr} \end{cases} \tag{4}$$

where σ_{bz} is the pressure of fresh concrete on trench walls at depth z, kN/m^2;
γ_b is the volume weight of concrete mixture, kN/m^3;

γ_{bt} is the volume weight of the clay solution, kN/m^3;
h is the depth below the top of the wall in the ground, m;
h_{cr} is the critical depth, m.

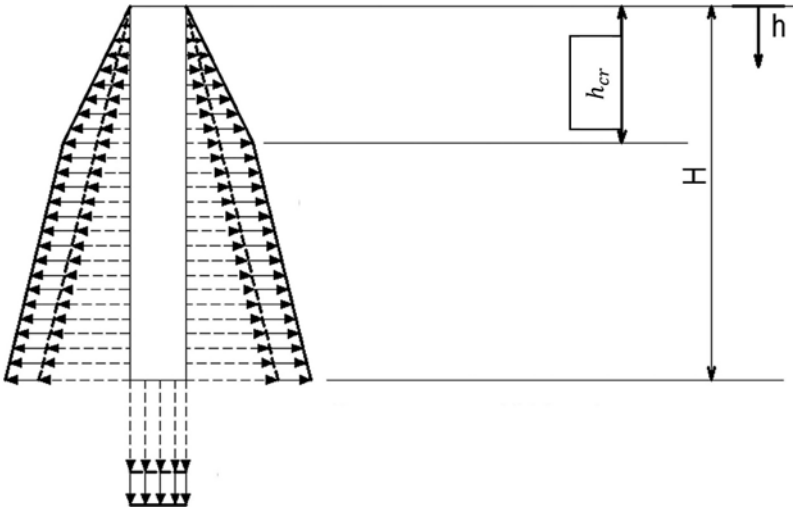

Figure 5. Diagram for determining the pressure on the trench wall during concreting.

In the publications of Lings et al. (Lings, 1991, 1994), the critical height was proposed to be defined as ⅓ of the diaphragm wall height. This approach was based on the analysis of the experimental data available at the time of publication of the paper on the three test work zones. In the publication of O.A. Shulyatyev and D.K. Minakov (Shulyatyev 2017) it was shown that the real values of critical height fluctuate within a wide range, from 0.17 to 0.57H, deviating significantly from the value of 0.33H predicted by Lings et al. (Lings, 1994), and a simple formula (5) was derived by linear approximation to determine the critical height h_{cr} depending on concreting rate:

$$h_{cr} = 0.85Vt + 1.78, \tag{5}$$

where V is the average concreting speed of the diaphragm wall, m/h; t is the time equal to 1 hour.

2.4 *Determination of pressures after stress relaxation*

After concreting is completed, stress relaxation takes place. Based on the analysis of experimental data, it was obtained that in general the value of additional effective pressures occurring in the soil at the interface with the concrete barrette at depth z ($\Delta\sigma_{gz}$) will be

$$\Delta\sigma'_{gz} = \sigma_{bz} - \sigma_w - \sigma'_{rz} = \sigma_{bz} - \sigma_{gwz} \tag{6}$$

$$\text{at } \sigma_{gwz}=\sigma_w+\sigma'_{gz}, \tag{7}$$

where σ_w is pore water pressure;
σ_{gz} is effective horizontal pressure from own weight of soil;
σ_{gwz} is total horizontal stress in the soil mass;

$$\sigma'_{gz} = K_0\gamma' z.$$

For normally compacted soil, K_0 can be determined through the transverse strain factor ν:

$$K_0 = \frac{\nu}{1-\nu}, \tag{8}$$

or by Jaky's empirical formula

$$K_0 = 1 - \sin\varphi. \tag{9}$$

For the case of over-compacted soil

$$K_0 = (1 - \sin\varphi) OCR^{\sin\varphi}. \tag{10}$$

Based on this research, a methodology for calculating the effect of bored piles and barettes on the change in horizontal pressures at the contact between the piles and the barettes and the surrounding soil is proposed (Shulyatyev, 2022).

The use of different bored pile technologies for the same soil conditions can result in a difference in the already mentioned pressures $\Delta\sigma_{gz}$ of up to 70%. The highest pressures occur when the bored piles are protected by bentonite solution and relatively lower pressures when they are protected by casing.

Due to the fact that the soil is a plastic material, the final value of the horizontal stresses is influenced by the loading history depending on the technology and the ground conditions of the site, which it is advisable to consider by applying appropriate ground models.

3 CHANGE OF HORIZONTAL STRESSES DURING LOADING

3.1 *Studies at the Zagorskaya hydroelectric pumped storage power station*

During pile testing at the Zagorskaya hydroelectric pumped storage power station (see Section 1.2, Figure 4) it was found that during loading the horizontal stresses increase to an average of 200 kPa with a pile load of 750 kN. The reason is that the soil resistance forces on the lateral surface cause an increase in the vertical stresses in the soil mass, which in turn increases the horizontal stresses.

3.2 *Study at the Okhta Centre construction site*

At the Okhta Centre construction site (see Section 1.1) three barrettes were tested together: B1, B2 and B3 (Figure 1) measuring 1.5×2.8 m, spaced 1.5 m apart from each other in the clear. The tests were performed by the O-Cell method. The barettes were equipped with sensors to measure the forces in the concrete in height (Figure 6). The tests showed that the ground resistance on the lateral surface of B2, located between B1 and B3, exceeded that of the neighbouring burettes by an average of 30% (Figure 7).

This indicates that, as a result of loading under pile field conditions, there is an additional increase in soil resistance along the lateral surface as a result of the mutual influence of neighbouring barettes.

4 EFFECT OF POLYMER AND BENTONITE SOLUTION ON SOIL RESISTANCE ON THE LATERAL SURFACE OF PILES

The bored piles can be constructed either under or without casing piles ('dry') if the borehole walls remain stable.

Figure 8 shows the results of the baretta and pile tests in the Vendian clays carried out during the construction of Okhta Centre and Lakhta Centre respectively. The burettes were installed with bentonite solution, the piles were installed 'dry'.

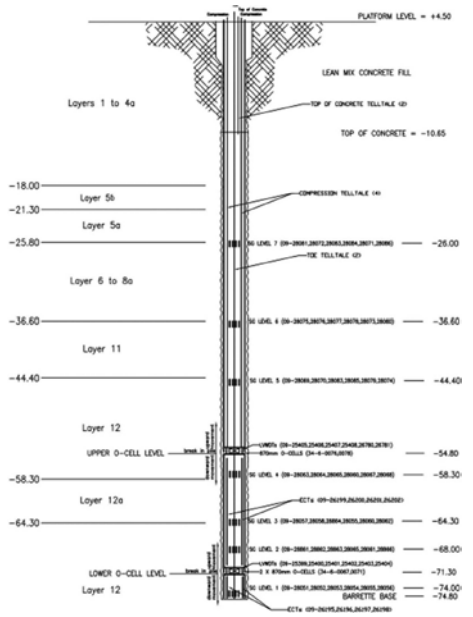

Figure 6. Layout of jacks and sensors in the baretta body.

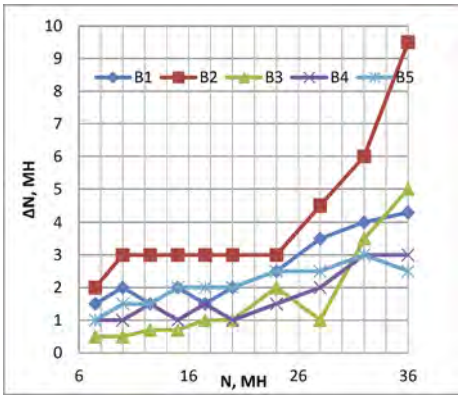

Figure 7. Change of force in the barrette body ΔN during Stage 1 loading, recorded between the Level 2 transducer and the lower O-Cell.

The tests showed that the average resistance of the soil on the lateral surface of the barettes was 240 kPa, the piles were 450 kPa at a displacement of more than 25 mm. The reason is that the burettes were made under polymer solution and the piles were made 'dry'. Thus, the use of bentonite reduces the lateral resistance of the soil by more than 30%!

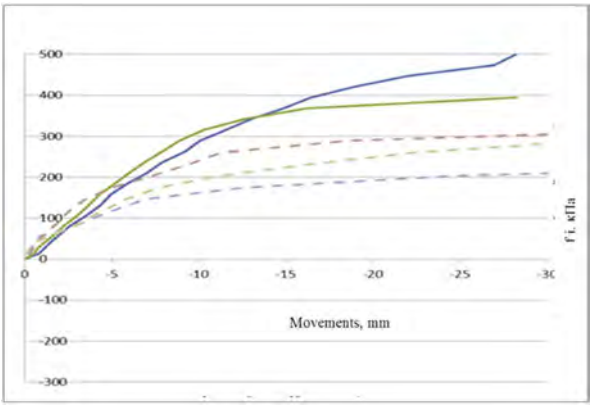

Figure 8. Dependence of skin friction (f_i) on movements: solid lines – bored piles; dashed lines – barrettes.

In recent years, in addition to bentonite solution, polymer solution has also been used for piling. Figure 8 shows the results of pile testing at the site of NIIOSP named after N.M. Gersevanov performed under bentonite and polymer solutions. The tests were carried out in sands of medium grain size, and medium density. Diameter of piles was 270 mm and working length was 1.5 m. Three types of polymer solution were tested: 1520, Bauer 703 and Bauer 709. The test results are shown in Table 2 and Figure 9.

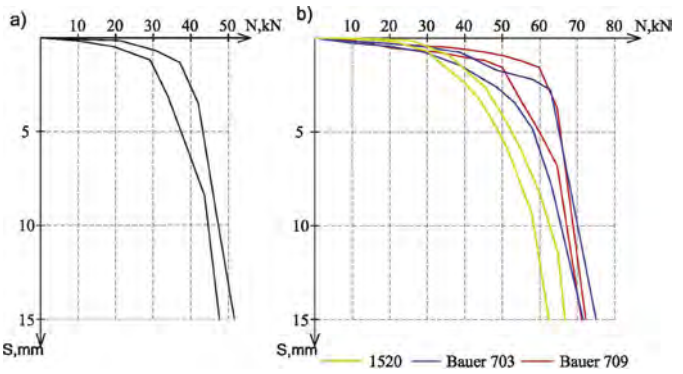

Figure 9. Test results of pilot piles: *a* – piles made under bentonite solution; *b* – piles made under polymer solution.

Table 2. Specific resistance along the side of the piles with different types of retaining solution.

No	Name of solution	Load, kN	Specific lateral resistance, kPa		Deformation value, mm
			on a pile	mean value	
1	Bentonite slurry	46.8	39.8	40.8	15.1
2		48.5	41.8		16.45
3	Polyacrilamide solution SLURRY	69.4	59.3	59.3	11.6
4	LTP 709	69.4	59.3		9.6
5	Polyacrilamide solution SLURRY	58.1	49.7	49.7	8.6
6	LTP 703	58.1	49.7		4.9
7	Polyacrilamide Polyflock 1520	56.5	47.9	48.8	15.96
8		58.1	49.9		11.3

In evaluating the test results, it should be noted that the lateral resistance of piles made under polyacrylamide solution protection is 1.2-1.46 times higher than that of piles made with bentonite solution.

CONCLUSIONS

1. In the process of piling, both pore pressure and horizontal stresses in the soil mass change.
2. Depending on the piling technology, the horizontal stresses can vary by up to 70 %.
3. Horizontal stresses increase during the loading process.
4. Additional horizontal stresses increase as a result of reciprocal influence of the piles.
5. The lateral resistance depends on the method of anchoring the borehole: the highest values occur when the borehole is dry or with casing, the lowest - when bentonite solution is used.

This article presents the results of research work carried out under the assignment of the Federal Scientific and Technical Centre for Certification in Construction of the Ministry of Construction and Housing and Communal Services of the Russian Federation:

1. Development of recommendations on calculation of the influence of the wall in the trench-type ground on the change of the stress-strain state of the surrounding soil mass and on its consideration during the design of newly erected buildings and structures in sandy soils, 2020.
2. Development of a methodology for determining technological settlements during the installation of bored-injection piles and assessment of technological settlements during the installation of the diaphragm wall of the trench type and ground injection anchors, 2015.

REFERENCES

Delattre, L. & Duca V. 2002. Measured pressure exerted by a fine soil on a diaphragm wall under construction. *Proceedings of the international symposium on geotechnical aspects of underground construction in soft ground*, Lyon: 547-552.

Gaba A. et al. 2017. Guidance on embedded retaining wall design. London: CIRIA. 455 p.

Lächler, A. et al. 2006. A comparison between monitoring data and numerical calculation of a diaphragm wall construction in Rotterdam. *Proceedings of the international conference on numerical simulation of construction processes in geotechnical engineering for urban environment*, Bochum, Germany: 83-96.

Lächler, A., Vermeer P.A. & Wehnert M. 2007. Assessment of diaphragm wall stability and deformation. *In XIV European conference on soil mechanics and geotechnical engineering*, Madrid: 1055-1060.

Lings, M. L., C. W. W. Ng, D. F. T. Nash. 1994. The Lateral Pressure of Wet Concrete in Diaphragm Wall Panels Cast under Bentonite. *Proc. of the Institution of Civil Engineers. Geotechnical Engineering*. 107(3): 163–172.

Lings, M.L., et al. 1991. Observed Behavior of a Deep Excavation in Gault Clay. *Proc. of the 10th European Conf. on Soil Mechanics and Foundation Engineering*, Florence: 467–470.

Loreck C. & Triantafyllidis T. 2007. Berücksichtigung des Frischbetondrucks bei der FE-Simulation der Schlitzandherstellung. *Bautechnik* 9: 646–655.

Mamonov, V. M., Dzagov, A. M. &, Ermoshkin, P. M. 1989. Bearing capacity of bored piles made of concrete of different composition. *Soil Mechanics and Foundation Engineering*. 1: 11–14.

Mamonov, V.M. & Ermoshkin, P.M. 1982. Investigation of conditions of formation of bearing capacity and strength of bored piles. *Soil Mechanics and Foundation Engineering*. 1: 10–14.

Ng C.W.W., et al. 1999. Observed performance of a short diaphragm wall panel. *Géotechnique* 49(5): 681–694.

Shulyatiev O.A. 2020. Footings and foundations of high-rise buildings. Ed. 2, revised and supplemented. Moscow: ASV Publishing house.

Shulyatyev O.A. & Minakov D.K. 2017. Pressure of Fresh Concrete on Trench Walls during Construction of a Wall in Soil. *Geotechnica*. 6: 30–38.

Shulyatyev O.A., Dzagov A.M. & Minakov D.K. 2022. Change of Stress and Strain State of Ground Massif as a Result of Drilled Piles and Barretts. *Vestnik SIC "Stroitelstvo"*. 2022; 34(3): 26–44.

Uriel, S. & Oteo C.S. 1977. Stress and strain besides a circular trench wall. *Proceedings of the 9th conference on soil mechanics and foundation engineering*, Tokyo 781–788.

Smart Geotechnics for Smart Societies – Zhussupbekov, Sarsembayeva & Kaliakin (Eds)
© 2023 The Author(s), ISBN 978-1-003-29912-7
Open Access: www.taylorfrancis.com, CC BY-NC-ND 4.0 license

Subgrade assessment of unpaved roads subjected to cyclic wheel loads using dynamic cone penetration and crosshole-type dynamic cone penetrometer

Namsun Kim, Geunwoo Park, Younggeun Yoo & Jong-Sub Lee
Korea University, Seoul, Korea

Won-Taek Hong
Gachon University, Seongnam-si, Korea

ABSTRACT: For the estimation of the behaviors of unpaved roads under cyclic wheel loads, investigation of the mechanical properties with depth is required. In this study, the dynamic cone penetrometer (DCP) and crosshole-type dynamic cone penetrometer (CDP) are applied to an unpaved road to characterize both the strength and stiffness along the depth. The strength and stiffness of the unpaved road subjected to cyclic wheel loads are characterized by the penetration index (DCPI) and shear wave velocity (Vs), respectively. Experimental results clearly show the changes in strength and stiffness increase due to the wheel loads. This study demonstrates that the DCP and CDP may be effectively used for subgrade assessments of unpaved roads with depth.

1 INTRODUCTION

The assessment of the degree and uniformity of compaction according to repetitive dynamic load induced by the traffic is considered one of the most critical steps in the process of unpaved road construction (Arvidsson and Keller, 2007). For the evaluation of compacted subgrade, plate bearing test (PBT), falling weight deflectometer (FWD), and California bearing ratio (CBR) have been widely used (Roy, 2016; Rahim and George, 2003). Using heavy equipment to assess characteristics of the subgrade of unpaved roads, however, has limited by concerns about instrument cost and low accessibility. Therefore, portable devices are required to assess unpaved roads.

Dynamic cone penetration (DCP), introduced by Scala (1956), has been used to estimate THE strength properties of compacted subgrade. The DCP test is conducted by dropping a hammer from a certain height, which penetrates the penetrometer into the target depth. The test results are expressed as the dynamic cone penetration index (DCPI) which is the penetration depth per blow (mm/blow). The DCP test with its small diameter minimizes the ground disturbance and provides reliable strength characteristic profiles of subgrade along depth.

In this study, crosshole-type dynamic cone penetrometer (CDP) is adopted as a method for characterizing stiffness along the depth. The CDP test can be carried using two CDPs and penetrates in a similar way to the DCP. The hammer impact is detected by an accelerometer installed in the source CDP and the shear wave signal passing through the medium is detected by an accelerometer installed in the receiver CDP. Accordingly, the CDP test can characterize in the depth profile of the stiffness by measuring the shear wave velocity. The main objective of this study is to assess strength and stiffness along the depth of the target ground according to cyclic wheel loads using portable devices. This paper shows the experimental setup of the DCP and CDP, and the experimental results from the field tests.

DOI: 10.1201/9781003299127-322

2 DESCRIPTION OF PORTABLE DEVICES

2.1 *Dynamic Cone Penetrometer (DCP)*

The dynamic cone penetrometer (DCP) is a fast and economical method for the characterization of the subgrade strength. The device consists of a 78.5 N hammer that falls from a height of 575 mm, a cone tip with a diameter of 20 mm and a tip angle of 60°, and a driving rod with a length 1,000mm and diameter 16mm (ASTM D6951/D6951M-18, 2018), as shown in Figure 1. During the operation of the DCP, the number of blow and penetration depth are recorded. The dynamic cone penetration index (DCPI) is expressed as follows:

$$DCPI\,(mm/blow) = D_n - D_{n-1} \tag{1}$$

where D_{n+1} and D_n are the penetration depth at the blow counts of n+1 and n, respectively.

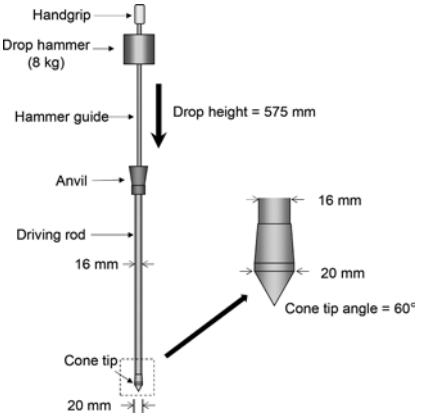

Figure 1. Dynamic cone penetrometer (DCP).

2.2 *Crosshole-type Dynamic cone Penetrometer (CDP)*

The crosshole-type dynamic cone penetrometer (CDP) introduced by Hong et al. (2017) is a portable device that was developed to characterize the strength and stiffness of the track substructure. The components of the CDP are similar to those of the DCP: a 118 N hammer that falls from a height of 575 mm, a cone tip with a diameter of 24 mm and a tip angle of 60°, and a driving rod with a length 1,000 mm and diameter 20 mm. To detect of the shear waves, a uniaxial accelerometer with a measurement range of 0–10,000g is installed on the top of the cone tip, as shown in Figure 2. The shear wave velocity (V_s) measured using an accelerometer is calculated as follows.

$$V_s\,[m/s] = \frac{L}{\Delta t} \tag{2}$$

where L is the distance and Δt is the travel time of the shear wave between the source and receiver CDPs.

3 FIELD TEST

3.1 *Experimental setup*

The DCP and CDP tests were conducted at two locations: Point-1 and Point-2. For the subgrade compaction, the test location was initially filled with 300mm of soil and then compacted to 200mm using roller compactor with a weight of 24 tons. Secondary compaction was conducted on the target ground by using a 15-ton vehicle over 200 times for Point-1 and 400 times for

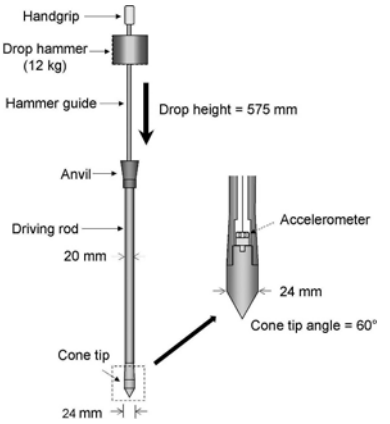

Figure 2. Crosshole type Dynamic Penetrometer (CDP).

Point-2. Note that a rut depth of 100 mm was employed as a failure criterion (AASHITO, 1993). For unifying the target depth, experiments were performed at a ground level of 100 mm.

3.2 *Experimental results*

3.2.1 *Penetration index (DCPI) measured by DCP according to cyclic wheel loads*

The DCPIs obtained from the DCP tests at Point 1-2 are plotted in Figure 3. At Point 1-2, the DCPIs of 0 cycle gradually decrease along the depth within 6–13 mm/blow at depths of 100–600 mm due to the low confining stress near the surface and effective overburden pressure. At Point 1-2, the DCPIs after 200 cycles and 400 cycles show relatively uniform results at depths of 100–400 mm with a DCPIs of 7–9 mm/blow, and show decreased results compared to 0 cycle. The range of stress applied to the subgrade by the wheel load is considered from the ground surface to a depth of 400 mm. For all DCP tests, the DCPIs gradually increase at depths larger than 600 mm.

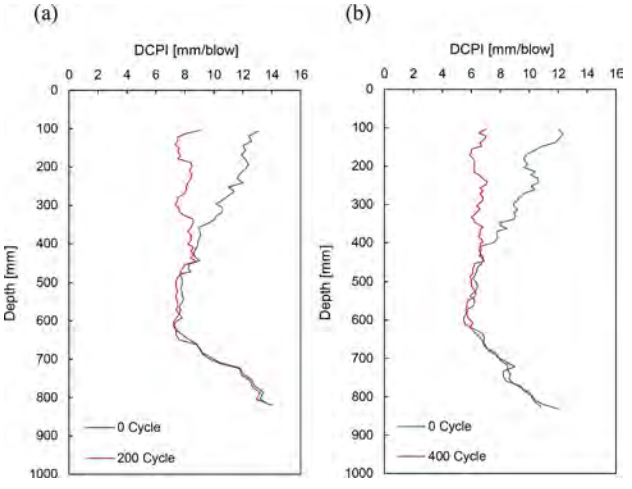

Figure 3. Experimental results of DCP tests: (a) Point-1; (b) Point-2.

3.2.2 *Shear wave velocity (V_S) measured by CDP according to cyclic wheel loads*

The shear wave velocity is obtained at the Receiver-CDP by detecting the vibration generated from the Source-CDP. The V_s values are calculated using the travel time and distance, as described in Eq. (2). The calculated V_s values are profiled at penetration depths ranging from

100 to 820 mm, as shown in Figure 4. For the 0 cycle at Point 1-2, V_s gradually increases along the depth within 110–210 m/s at depths of 180–600 mm. At Point 1-2, the V_s values after 200 and 400 cycles increase to 190 and 210 m/s, respectively, at a depth of 190–610 mm, respectively. At depths of 610–820 mm for all CDP tests, the V_s values show slightly decreased results.

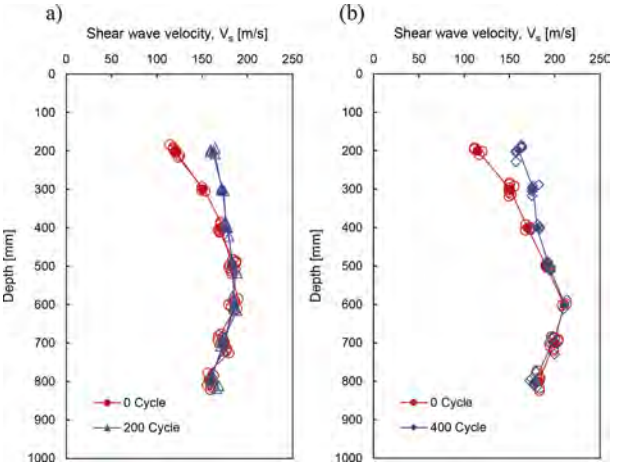

Figure 4. Experimental results of CDP tests: (a) Point-1; (b) Point-2.

4 SUMMARY AND CONCULSIONS

The objective of this study is to estimate the strength and stiffness characteristics of the unpaved roads under cyclic wheel loads using the dynamic cone penetrometer (DCP) and crosshole-type dynamic cone penetrometer (CDP). The DCP and CDP are performed at three different states including 0, 200 and 400 cycles of wheel load for two unpaved road locations named Point-1 and Point-2. Based on the experimental results, the remarkable observations are as follows:

- The dynamic cone penetration index (DCPI) and shear wave velocity (V_S) of subgrade significantly increase with the cyclic wheel loads.
- The changes of DCPI and V_S of the subgrade due to wheel load vary with depth: at the first 400mm depth, the changes are significant, and after 400mm, very little changes are observed.

ACKNOLEDGEMENT

This work was supported by the National Research Foundation of Korea (NRF) grant funded by the Korea government (MSIT) (No. NRF-2021R1A5A1032433).

REFERENCES

Arvidsson, J., & Keller, T. 2007. Soil stress as affected by wheel load and tyre inflation pressure. *Soil and Tillage Research*, *96(1-2)*, *284-291*.

ASTM D6951/D6951M-18. 2018. Standard Test Method for Use of the Dynamic Cone Penetrometer in Shallow Pavement Applications. *The American Society for Testing and Materials*, *West Conshohocken, United States*.

Hong, W. T., Kim, S. Y., Lee, S. J., & Lee, J. S. 2017. Strength and stiffness assessment of railway track substructures using crosshole-type dynamic cone penetrometer. *Soil Dynamics and Earthquake Engineering, 100, 88-97*.

Rahim, A., & George, K. P. 2003. Falling weight deflectometer for estimating subgrade elastic moduli. *Journal of Transportation Engineering*, *129(1)*, *100-107*.

Roy, S. 2016. Assessment of soaked California bearing ratio value using geotechnical properties of soils. *Resources and Environment*, *6(4)*, *80-87*.

Smart Geotechnics for Smart Societies – Zhussupbekov, Sarsembayeva & Kaliakin (Eds)
© 2023 The Author(s), ISBN 978-1-003-29912-7
Open Access: www.taylorfrancis.com, CC BY-NC-ND 4.0 license

Evaluation of strength and volumetric water content using instrumented TDR dynamic cone penetrometer

Geunwoo Park, Namsun Kim, Hyun Seok Kang & Jong-Sub Lee
Korea University, Seoul, Republic of Korea

Sang Yeob Kim
Konkuk University, Chungju, Republic of Korea

Kangil Lee
Daejin University, Gyeonggi, Republic of Korea

ABSTRACT: The objective of this study is to evaluate the strength and volumetric water content of ground using an instrumented TDR dynamic cone penetrometer (ITDP). The ITDP, which is developed to simultaneously measure two parameters on a borehole, is installed by an accelerometer, strain gauges, and electrodes. ITDP tests are carried out for ground up to a depth of 700 mm under rainfall conditions, and the two parameters are measured according to time (0 h, 3 h, and 9 h). Generally, the strength of the ground decreases and its volumetric water content increases after the rainfall. The decrement of the strength and increment of the volumetric water content at 3 h are greater than those at 9 h until a depth of 150 mm, while those at 3 h are smaller than those at 9 h beyond a depth of 150 mm. Thus, ITDP may be effectively used to profile the strength and volumetric water content of ground.

1 INTRODUCTION

For prevent the natural disaster such as slope failure, landslide, and debris flow caused by heavy rainfall, characterization of ground strength and water content is very important. Most of slope grounds, where have a high possibility of failure, are hard to access. Therefore, a portable in-situ penetration testing device with high mobility is required to characterize the properties of such slope grounds.

A dynamic cone penetrometer (DCP) has been widely used to evaluate the strength properties of ground. In the DCP test, the DCP is impacted by a free-fall hammer at a constant potential energy, and penetration depth per a blow is recorded as penetration index of the DCP (DCPI). However, an inconstant potential energy caused by friction and artificial factor reduces the reliability of the DCP results. To compensate for the inconstant energy, an instrumented DCP (IDCP) was developed (Byun and Lee 2013). Transferred energies at rod head and cone tip can be calculated using accelerometers and load cells in IDCP. The strength of a slope ground can be evaluated using IDCP with high reliability.

For evaluation of volumetric water content, time domain reflectometry (TDR), which is an electromagnetic wave survey technique, has been used. A portable penetrometer incorporated with TDR probe (TDRP) was developed to profile the volumetric water content of ground (Lee et al., 2018). The IDCP and TDRP should be used to evaluate the strength and volumetric water content of the ground; however, it is not efficient to use both devices in terms of economy, convenience, and consistency. Accordingly, an instrumented TDR dynamic cone penetrometer (ITDP) was developed to simultaneously estimate the strength and volumetric water content of the ground (Park et al. 2023). The ITDP, which is IDCP incorporated with

DOI: 10.1201/9781003299127-323

TDR, is simultaneously evaluate the transferred energy and volumetric water content using accelerometers, load cells, and TDR sensors.

In this study, the ITDP test was conducted on compacted soils in an embankment for evaluation of ground strength and volumetric water content according to the time in rainfall condition. This paper provides the design and measurement system of the ITDP and calculation method for the transferred energy and dynamic resistance. In addition, the site of field test is described, and experimental results are analyzed and discussed.

2 INSTRUMENTED TDR DYNAMIC CONE PENETROMETER (ITDP)

2.1 *Design of ITDP*

The ITDP was developed by combining the IDCP and TDRP to simultaneously profile the ground strength and volumetric water content. The ITDP is composed of an ITDP probe, driving rod, energy module anvil, and hammer, as shown in Figure 1. The ITDP probe consists of cone tip energy module for evaluation of transferred energy at cone tip and a TDR probe for the estimation of the volumetric water content. Accelerometers and load cells are installed in the energy modules to obtain the dynamic responses. Shock-type accelerometers, which can measure up to 10,000 g, are used to endure the high external shock. The load cell is composed of four strain gauges configured with Wheatstone full-bridge circuit to compensate the effects of temperature and eccentricity. TDR probe is made of three electrodes in body of mono-cast nylon. The three electrodes are connected to a coaxial cable. The driving rod with 1 m length is connected to ITDP probe, and extra driving rods can be connected to estimate the ground properties at deeper depth. The hammer with 117.7 N weight is dropped at a 575 mm of height; thus, potential energy is calculated as 67.77 N·m.

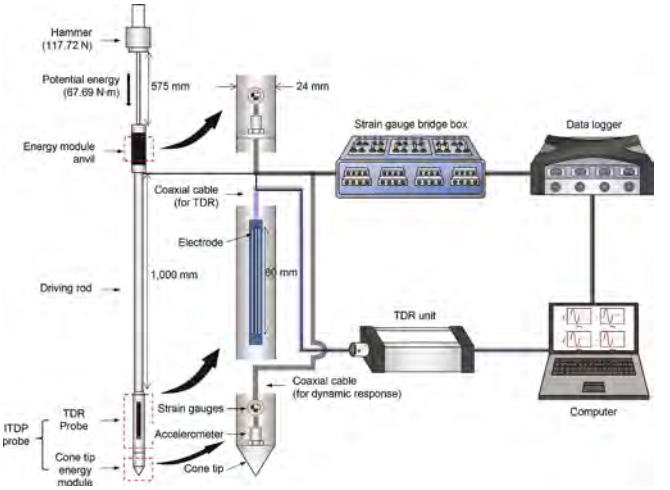

Figure 1. Design of instrumented TDR dynamic cone penetrometer (ITDP).

2.2 *Transferred energy*

The acceleration and force signals are measured using accelerometer and load cell. Velocity can be calculated by integrating the measured acceleration. Using the force measured by load cell (F_s) and velocity calculated by accelerometer (V_a), the transferred (E) can be calculated (ASTM D4633) as follows.

$$E = \int F_s \times V_a dt \tag{1}$$

The transferred energy at rod head, which is measured by energy module anvil, is used to correct the inconsistence potential energy. The transferred energy at cone tip, which is measured by cone tip energy module, considers energy loss caused by friction (Park et al., 2022).

2.3 *Volumetric water content*

In general, the survey using TDR is predominantly used to estimate the volumetric water content of ground. The generated electromagnetic wave travels through the coaxial cable and electrode. The velocity of electromagnetic wave depends on a dielectric constant of soils (Noborio et al. 1996). The travel time of electromagnetic wave is measured to obtain the dielectric constant of soils according to volumetric water content. The travel time can be calculated by apparent length and velocity of electromagnetic wave in vacuum (3×10^8 m/s). Subsequently, the dielectric constant (κ) can be expressed using apparent length (L_a) and electrode length (L) as follows.

$$\kappa = (L_a/L)^2 \tag{2}$$

Generally, dielectric constants of air, dry soils, and water are 1, 3-8, and 81, respectively. The volumetric water content is determined by dielectric constant, and Topp et al. (1980) suggested a cubic polynomial with an empirical coefficient obtained from the calibration test.

3 FIELD TEST

3.1 *Site description*

To characterize the ground strength and volumetric water content in rainfall condition, the ITDP tests were conducted on compacted soils in embankment, as shown in Figure 3. Initial ITDP test was carried out before watering; subsequently, water was sprayed on the embankment to simulate the rainfall condition. After 3 and 9 h of watering, the ITDP tests were conducted at intervals of 1 m from the borehole, where first ITDP test had been carried out. The ITDP tests were performed until a depth of 700 mm.

3.2 *Experimental results*

3.2.1 *Penetration index measured by ITDP according to the time*

The penetration index of ITDP per blow was measured as ITDPI. The ITDPI was averaged in units of 50 mm and was calculated as a representative value for the depth. The representative ITDPI was plotted with time, as shown in Figure 2. At depths of 50–150 mm, the ITDPI are greatest 3 h after watering (Figure 2a), which means that the ground strength is weakest after 3 h. The ITDPI increase as time increases at depths of 200-450 mm (Figure 2b). At depths of 500 and 550 mm, the ITDP only increases after 9 h. There is no significant change at depths of 600-700 mm (Figure 2c). Therefore, the water may be infiltrated until a depth of 450 mm after 3 h, and a depth of 550 mm after 9 h.

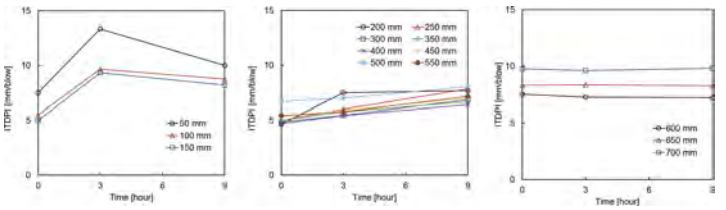

Figure 2. ITDPI with time according to depth: (a) 50-150 mm; (b) 200-550 mm; (c) 600-700 mm.

3.2.2 *Volumetric water content measured by ITDP according to the time*

The volumetric water contents were measured in unit of 50 mm and plotted with time, as shown in Figure 3. At depths of 50-150 mm, the volumetric water contents after 3 h are greater than those after 9 h due to the evaporation near the surface (Figure 3a). The volumetric water contents increase with time increases at 200-450 mm, same as ITDPI (Figure 3b). The volumetric water contents increase at depths of 500 and 550 mm after 9 h. At 600-700 mm, there is no significant change (Figure 3c). Similar to the results of ITDPI, the water may be infiltrated until a depth of 450 mm after 3 h, and a depth of 550 mm after 9 h.

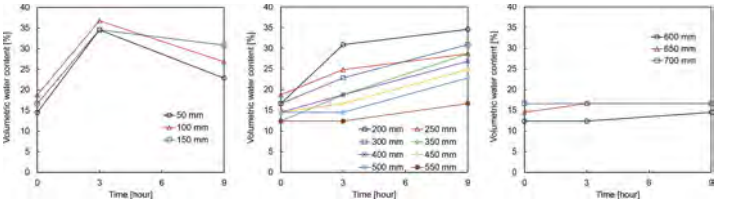

Figure 3. Volumetric water content with time according to depth: (a) 50-150 mm; (b) 200-550 mm; (c) 600-700 mm.

4 SUMMARY AND CONCULSIONS

The developed instrumented TDR dynamic penetrometer (ITDP) was applied to compacted soils in embankment to estimate the ground strength and volumetric water content, in this study. The penetration index measured by ITDP (ITDPI), and volumetric water content are generally increased according to water infiltration. Near the surface, the ITDPI and volumetric water content are greatest after 3 h due to evaporation of water. The main observations of this study are as follows:

- Near the surface, the ground strength is weakest after 3 h as the ITDPI and volumetric water content are greatest. The ground strength is about 1.77 times weaker, and the volumetric water content is more than doubled after 3 h.
- The ground strength generally weakens with time as ITDPI, and volumetric water content increased as time increases at depths of 200-550 mm.
- The characteristic of ground strength and volumetric water content can be estimated using ITDP. Thus, ITDP may be effectively used for evaluation of ground properties in rainfall condition.

ACKNOLEDGEMENT

This work was supported by the National Research Foundation of Korea (NRF) grant funded by the Korea government (MSIT) (No. NRF-2021R1A5A1032433).

REFERENCES

Byun, Y. H., & Lee, J. S. 2013. Instrumented dynamic cone penetrometer corrected with transferred energy into a cone tip: a laboratory study. *Geotechnical Testing Journal*, *36*(4): 533–542.

Lee, J. S., Hong, W. T., Park, K., Hong, S. S., Lee, S. H., & Byun, Y. H. 2018. Evaluation of water content in an active layer using penetration-type time domain reflectometry. *Applied Sciences*, *8*(6): 935.

Noborio, K., McInnes, K. J., & Heilman, J. L. 1996. Measurements of soil water content, heat capacity, and thermal conductivity with a single TDR probe1. *Soil Science*, *161*(1): 22–28.

Park, G., Kim, N., Hong, W.T., & Lee, J.S. 2022. Rod effects on transferred energy into SPT sampler using smart measurement system. *Smart Structures and System*, 30(2): 159–172.

Park, G., Kim, N., Kang, S., Kim, S.Y., Yoo, C., & Lee, J.S. 2013. Instrumented dynamic noce penetrometer incorporated with time domain reflectometry. *Measurement*, 206: 112337.

Topp, G. C., Davis, J. L., & Annan, A. P. 1980. Electromagnetic determination of soil water content: Measurements in coaxial transmission lines. *Water resources research*, 16(3): 574–582.

Smart Geotechnics for Smart Societies – Zhussupbekov, Sarsembayeva & Kaliakin (Eds)
© 2023 The Author(s), ISBN 978-1-003-29912-7
Open Access: www.taylorfrancis.com, CC BY-NC-ND 4.0 license

Practical method for pile construction management using non-contact pile penetration movement measuring device and pile driving formulas: A case study

Seunghwan Seo, Moonkyung Chung, Ju-Hyong Kim & Changho Choi
Department of Geotechnical Engineering Research, Korea Institute of Civil Engineering and Building Technology, Goyang-si, Republic of Korea

ABSTRACT: The pile penetration movement is typically measured manually by field workers during pile driving. Manual measurement method may lead to potential risks to workers' health and safety as well as issues with measurement accuracy dependent on the operators and ground vibration. In this study, in order to address these issues, a non-contact pile penetration movement measuring device was developed and applicability was evaluated. In addition, a method to improve the reliability of the pile driving formulas was reviewed by using the values measured by the development device and the results of the dynamic load test. As a result, it is essential to accurately measure the hammer energy delivered to the pile, as well as the set value and rebound movement of pile in order to increase the reliability of the bearing capacity predicted by the pile driving formulas. Furthermore, the bearing capacity of pile obtained from the dynamic load test can be used to improve the reliability of the bearing capacity calculated by the pile driving formulas.

1 INTRODUCTION

In South Korea, precast piles, such as pretensioned spun high-strength concrete (PHC) piles, have been developed into ultra-high-strength and composite piles with the development of technology, and their utilization is increasing. However, for pile construction management only limited management regulations, such as the number of dynamic load tests or static load tests, are available and there is no clear regulation on the construction and management of all piles. Most precast pile construction sites in Korea examine the bearing capacity of 1–3% of the total number of piles by performing a dynamic load test. The final pile set value is measured and used as the management reference value. The pile set of the remaining 97–99% of the total number of piles is measured immediately after construction and compared with the management reference value. In recent years, with the increasing number of construction projects in urban areas, auger-drilled piles are increasingly being used rather than driven piles owing to noise and vibration problems. In Korea, auger-drilled piles are typically installed using the pile driving method after pre-excavation, and construction using auger-drilled piles is assessed considering the driving penetration in the final stage using a drop hammer (Lee et al. 2000; Hong et al. 1997).

During pile driving, an automatic measurement method using machines is necessary for ensuring worker safety and reliability in penetration measurement. Accordingly, various studies have been conducted to address this issue. Studies have been conducted on non-contact penetration measurement methods using optical displacement meters, laser sensors, or line scan cameras (Ha et al. 1997; Yun et al. 2005; Yeu et al. 2016; Lee et al. 2002). Previous studies focused on the measurement accuracy for driving penetration and rebound. Most methods were not applied in the field owing to inconvenient usage and procedures, such as separately

DOI: 10.1201/9781003299127-324

analyzing the data measured in the field. Methods for measuring the pile set by attaching a label to the hammer or a sensor to the drop hammer have been used recently. However, the accuracy of the pile set and rebound value calculations is limited because they measure the displacement of the hammer and casing rather than directly measuring the displacement of the pile. This study developed a device that can accurately measure the pile set and rebound values by supplementing the limitations of previous studies related to non-contact driving penetration measurement. Furthermore, a method for estimating and managing the bearing capacity of all working piles in addition to field test piles was examined using the measurement results and a dynamic bearing capacity formula.

2 NON-CONTACT DRIVING PENETRATION MEASUREMENT DEVICE

The driving penetration measurement device developed in this study (KPM, KICT Pile driving Monitor) consists of a measuring unit, hardware board, and battery. It can perform measurements without a separate analysis personal computer. The measuring unit uses an infrared light-emitting diode light source (IR-LED transmitter) as a non-contact method for detecting the light signal returned by the reflective tape attached to the observation target using a receiver. The light source concentrates the radiation angle of light as it passes through the optical lens and is designed to perform measurements within a distance of up to 70 m. Therefore, the pile displacement is measured using the speed of the light returned by the reflective tape and the measured distance according to the movement before and after pile driving. The sampling rate is 200 Hz. Figure 1 shows the overall shape of the proposed device. The exterior of the device is made of an aluminum plate and it weighs approximately 1 kg. The position of the reflective tape attached to the pile can be corrected through the device display, and it takes 1–3 min. to prepare for measurement.

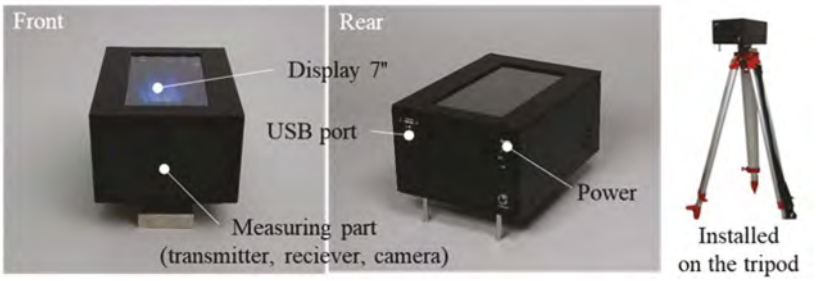

Figure 1. Device configuration and exterior.

3 EXPERIMENTAL METHOD

3.1 *Experiment overview*

The pile displacement was measured using the proposed device while a dynamic load test was performed using a pile driving analyzer (PDA) at an actual site to examine the possibility of estimating the bearing capacity of the pile using the final pile set value (Figure 2). The piles used at the site were 600 mm diameter PHC piles. They were installed through the separated doughnut auger (SDA) pre-excavation method using a 6-ton drop hammer. The piles were expected to be installed primarily in hard weathered soil or weathered rock. The soil investigation results showed that the standard penetration test (SPT) N values and construction depths were 27/30 and 13 m and 50/3 and 17 m for weathered soil and weathered rock, respectively. At the beginning of construction, a dynamic load test and measurement using the proposed device were performed simultaneously on three test piles.

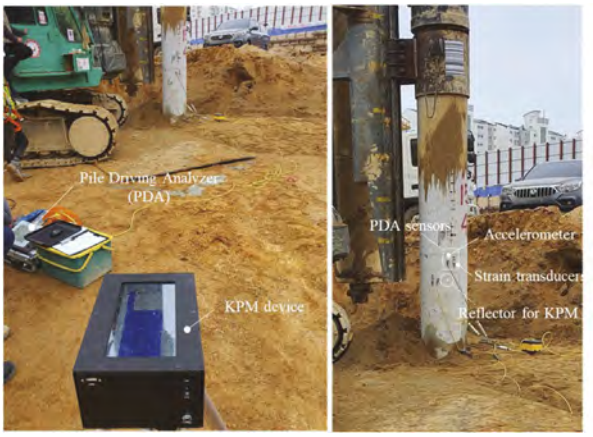

Figure 2. Experimental methods in field test.

3.2 *Dynamic bearing capacity formula*

Among various driving formulas, the Hiley formula is based on the energy balance between the driving energy of the hammer and work required for pile penetration. It is a representative calculation method that considers the pile set and rebound values. The input variables of the Hiley formula can be modified to apply the measured values of the PDA. The existing Hiley formula can be summarized as Equation 1 (Cho and Lee 2001; Denes and Kroenert 2019). In Equation 1, Ru is the total pile resistance, η is the efficiency of the hammer (energy loss allowance), W is the weight of the hammer, g is the gravitational acceleration, and h is the fall height equal to EMX, the hammer energy transmitted to the pile. S is the pile set value, and C is the rebound value, representing the temporary compressive or elastic behavior of the pile.

$$R_u = \frac{\eta Wgh}{S + C/2} = \frac{EMX}{S + C/2} \tag{1}$$

The pile set (S) and rebound (C) values were measured using the proposed penetration measurement device. The hammer weight and fall height were manually recorded. Because hammer efficiency is typically estimated and can cause an error, it must be examined using a dynamic load test equipment. Removing dynamic resistance from the Hiley formula is necessary because it contains dynamic and static resistance components. To remove the dynamic resistance component, Cho and Lee (2001) introduced a damping coefficient. The damping coefficient is related to ground and driving conditions and can be characterized for different sites. This damping coefficient is referred to as the field correction factor or dynamic reduction factor (DRF). This coefficient can be applied to the dynamic bearing capacity formula to estimate the static component from the total resistance during tests (Cho and Lee 2001; Damen and Denes 2017). The DRF is expressed as Equation 2 by comparing the control and provisioning of wireless access points (CAPWAP) static resistance of the test piles and the resistance estimated using the Hiley formula through the dynamic load test.

$$x = \frac{Hiley\ \ Resistance}{CAPWAP\ \ Resistance} \tag{2}$$

The DRF (χ) increases as the set value increases; a high pile set value indicates a high dynamic resistance component in the total resistance (Cho and Lee 2001; Denes and Kroenert 2019). Because dynamic energy is generated by the speed-dependent pile movement, the dynamic effect increases as the pile movement increases, similar to the resistance estimation

method in the dynamic load test. Therefore, the DRF can be expressed as a relationship between the pile set value obtained through the dynamic load test and measured using the proposed device. It may vary at each site and is affected by many factors, such as the hammer system, pile size, end condition, ground condition, and hammer fall height. Equation 3 shows the modified Hiley formula reflecting the field characteristics through the DRF and represents the bearing capacity of the pile at the end of initial driving (EOID).

$$R_u = \frac{EMX}{(S + C/2)x} \tag{3}$$

The long-term bearing capacity can be calculated by considering the set up factor (SUF) in Equation 3. The SUF can be obtained through the EOID and restrike tests on test piles in the field. It is calculated by dividing the restrike bearing capacity by the EOID bearing capacity (Chun and Cho 1999). In this study, the change in pile bearing capacity over time was excluded, and evaluation was performed based on the EOID test results to analyze the possibility of pile construction quality control using the final pile set value.

4 EXPERIMENTAL RESULTS

4.1 *Dynamic bearing capacity formula*

For the test piles, the driving management standard was set based on a fall height of 1.5 m for a 6-ton drop hammer. From the time when the pile began to penetrate the hard layer, the EMX value, the energy transmitted to the pile at each blow, was measured and recorded using the accelerometer and strain gauge attached to the pile. In the PDA test, the energy transmitted to the pile (EMX), maximum pile displacement (DMX), maximum pile speed (VMX), and pile bearing capacity (RMX) can be evaluated at the site for each blow. A highly reliable dynamic load test was performed at the site through rough judgment of the signal characteristics of the strain gauges and accelerometer. The EMX value measured at each blow was recorded (Figure 3). In this study, the EMX value was obtained by excluding the small values measured at the EOID and calculating the average value.

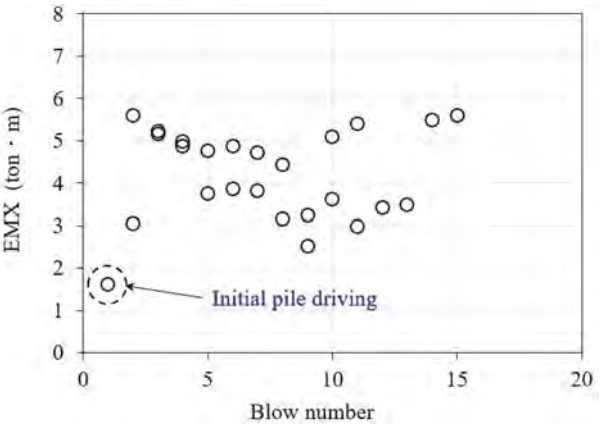

Figure 3. EMX value for each blow measured from dynamic load test.

4.2 *DRF calculation*

As shown in Figure 2, the dynamic load and penetration measurement tests using the proposed device were performed on the test piles simultaneously. The RMX value of the dynamic

load test was used for each blow to calculate the DRF (χ). The CAPWAP protocol is a standard for obtaining more accurate bearing capacity. However, the intuitively calculated RMX value was used for test convenience (Cho 2003). The results indicated that there was no significant difference between the bearing capacity calculated through an actual CAPWAP analysis and the RMX value because the end bearing capacity was primarily developed with low skin friction during the dynamic load test at the test site. The modified Hiley formula shown in Equation 3 was applied for the bearing capacity of the driving formula. The EMX value obtained from the dynamic load test was used as the numerator, and the values measured using the proposed device were used for the pile set and rebound values. Figure 4 shows the relationship between the DRF (χ) for the test piles calculated using the RMX and the pile set value. To calculate the functional relationship for various pile set values, the pile set value was measured using the dynamic load test and proposed device before calculating the final pile set value corresponding to the design bearing capacity.

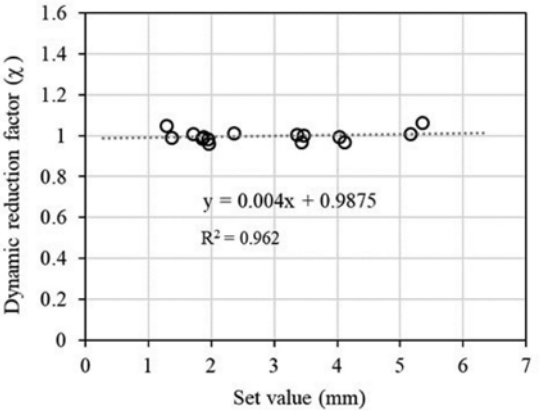

Figure 4. Dynamic reduction factor for pile set values.

4.3 *Estimation of bearing capacity using the developed device*

Based on the DRF (χ) and EMX values obtained from test pile, the bearing capacities of other test piles were estimated using the proposed device. The weight, fall height, and efficiency of the hammer or the EMX value of the PDA can be used for the EMX in Equation 3. The average hammer efficiency calculated from the dynamic load test (0.8) was applied as the hammer efficiency. In addition, the DRF for the measured penetration was applied using relationship between the DRF (χ) and pile set value in Figure 4. Figure 5 compares the bearing capacity derived using the pile set and rebound values measured using the proposed device, with the RMX obtained from the dynamic load test. Figure 11 shows a significant difference (approximately 40%) in the RMX obtained from the dynamic load test despite applying the relatively accurate EMX, pile set, and rebound values before applying the DRF. However, when the bearing capacity was corrected by applying the DRF, it was estimated with a 5–10% difference. This indicates that a highly reliable bearing capacity can be estimated using the driving formula using the EMX, pile set and rebound values by driving, and the DRF (χ) between the bearing capacity measured from the initial dynamic load test and driving formula.

5 DISCUSSIONS

In the case of measuring the set and rebound values of a pile using the non-contact pile penetration measurement device (KPM) developed in this study, there may be issues with the true

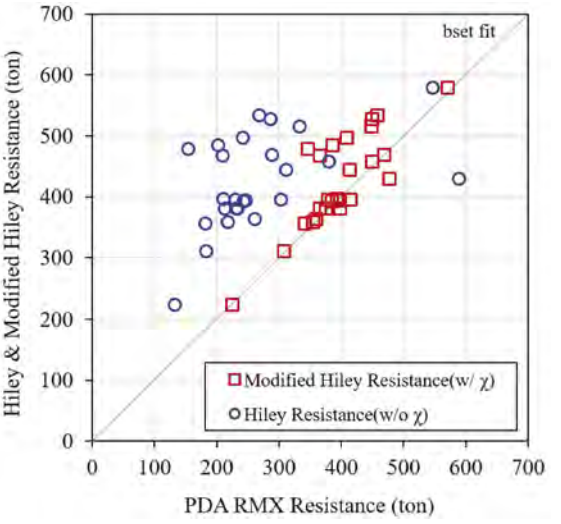

Figure 5. Comparison of the bearing capacity obtained from the dynamic load test and estimated bearing capacity using the KPM.

value in the actual field. In the case of comparing the measured values in the actual field, it will be necessary to use the maximum pile displacement (DMX) in the dynamic load test. DMX is calculated by integrating the measured velocity in dynamic load test, and since the maximum displacement occurs at one point in time, it is a highly reliable value. The theoretical maximum displacement is obtained by adding the set and rebound values measured by the penetration measurement device, so the performance of the measurement device can be checked by comparing this value with DMX. In order to reduce the estimation error for bearing capacity in the field test, it will be necessary to further improve the precision of the development device through comparison with.

In addition, in the case of prebored and precast piles, it will be necessary to calculate the set up factor through the EOID and restrike results of the dynamic load test in order to consider the time effect.

6 CONCLUSIONS

This study developed a non-contact pile penetration measurement device to secure the reliability of driving penetration measurement and work safety during pile driving. The field applicability was examined and the bearing capacity estimation method using the modified Hiley formula was analyzed using the proposed device and dynamic load test results. The primary conclusions of this study are as follows:

(1) Because the conventional manual measurement method is inaccurate and unreliable, the performance of the proposed device was evaluated through comparative measurement with a commercially available high-precision measurement device. The results of the comparative measurement performed at an actual pile construction site showed that the proposed and existing device had similar performances in terms of measurement accuracy. However, the results obtained using the proposed device showed a trend that matched the actual driving profile obtained through data processing considering the secondary recoil and hammer rise. The proposed device also has a higher field applicability owing to its low measurement preparation time requirement of 1–2 min and simplified measurement program.
(2) The proposed penetration measurement device measured the pile set and rebound values accurately. The bearing capacity calculated using the modified Hiley formula and DRF was

more reliable than that obtained from the dynamic load test (RMX). The bearing capacity obtained from the dynamic load test differed significantly with that obtained from the driving formula. Correcting the driving formula by expressing the DRF as a function of the pile penetration improved the reliability of the pile bearing capacity calculation using the driving formula.

(3) Conventionally, only piles subjected to load tests are evaluated for bearing capacity. The design bearing capacity of piles is increasing, and there are cases where pile tips are installed on hard soil rather than bedrock in areas with deep sedimentary layers or weathered soil layers. Thus, it is necessary to establish a management method estimating the bearing capacity of piles used in such conditions in addition to those of test piles. The measurement reliability using the dynamic driving formula is questionable. However, a more reliable bearing capacity estimation is possible using the proposed field correction procedure considering the dynamic load test performed at each site. Applying the corrected dynamic driving formula and proposed bearing capacity estimation procedure enables pile construction management considering the bearing capacity even for piles not subjected to dynamic load tests.

ACKNOWLEDGEMENTS

This research was supported by a grant from the project "Geotechnical research for disaster management and new growth in the future geotechnical industry", which was funded by the Korea Institute of Civil Engineering and Building Technology (KICT).

REFERENCES

Lee, M.W., Hong, H.S., Kim, S.H., and Jun, Y.S. 2000. A new proposal for the appropriate quality control of driven piles by using set values, Proceeding of pile foundation in the Korean Geotechnical Society, Seoul. pp. 53–63.

Hong, H.S., Cho, C.H., Kim, S.H., and Lee, M.H. 1997. A study on the reliability of dynamic pile formulae, Proceeding of '97 National Conference in Korean Geotechnical Society, Seoul. pp. 55–62.

Ha, I.S., Han, S.S., Han, S.G., and Kim, M.M 2003. Measurement of pile rebound and penetration using laser sensor, Proceeding of Korean Society of Civil Engineering, pp. 3257–3262.

Yun, H.S., Seok, J.W., Hwang, D.J., and Kim, M.M. 2005. Quality control of driven piles using DPRMs, Proceeding of Korean Society of Civil Engineering, pp. 3945–3948.

Park, J. 2012. Safety Management Information System in Plants Construction Work, Journal of Korea Safety Management & Science, Vol. 14, No. 4, pp. 23–29.

Park, T., Park, Y., and Kim, T. 2013. An analyzing Safety education contents propriety for Accident type in Construction work, Proceedings of the Korea Institute of Building Construction, Vol. 13, No. 2, pp. 94–95.

Yeu, Y., Kim, Y.S., and Kim, D. 2016. Development of safe and reliable real-time remote pile penetration and rebound measurement system using close-range photogrammetry, International Journal of Civil Engineering, Vol. 14, No. 7, pp. 439–450.

Lee, S.N., You, B.J., Limb M.S., Oh, S.R., Han, S.S., and Lee, S.H. 2002. Visual measurement of pile penetration and rebound movement using a high-speed line-scan camera, Proceeding of 2002 IEEE International Conference on Robotics and Automation, Washington DC, Vol.4, pp. 4307–4312.

Cho, C.W., and Lee, M.W. 2001. The application of new pile driving formulas, J. of the Korean Geotechnical Society, Vol. 17, No. 5, pp. 157–164.

Damen, R., and Denes, D. 2017. Improving site specific modified driving formula using high frequency displacement monitoring, Proceeding of 20th NZGS Geotechnical Symposium, CJ Alexander, pp. 1–7.

Denes, D., and Kroenert, B. 2019. A case study of pile testing and verification. Berth 4 upgrade – port of Townsville, Australasian Coasts & Ports 2019 Conference, Hobart, pp. 1–7.

Chun, B.S., and Cho, C.W. 1999. Consideration of set-up effect in wave equation analysis of pile driving, J. of the Korean Geotechnical Society, Vol. 15, No. 2, pp. 95–101.

Cho, C.W. 2003. Driveability analysis of driven steel tublar piles, J. of the Korean Geotechnical Society, Vol. 19, No. 5, pp. 123–132.

Smart Geotechnics for Smart Societies – Zhussupbekov, Sarsembayeva & Kaliakin (Eds)
© 2023 The Author(s), ISBN 978-1-003-29912-7
Open Access: www.taylorfrancis.com, CC BY-NC-ND 4.0 license

Comparative study of slope displacements using distributed fiber optic sensing technology and inclinometer

Umar Zada
Master Student, Department of Civil Engineering, National Central University, ROC

Chih-Chung Chung
Associate Professor, Department of Civil Engineering, National Central University, ROC

ABSTRACT: In order to minimize losses due to landslides, slope displacement monitoring is a vital early warning system. As a result, the internal deformation of the slope was monitored using distributed fiber optic sensing technology based on Brillouin optical time domain reflectometer (BOTDR) attached on the casing of the in-place inclinometer (IPI). Primarily, laboratory experiment was conducted followed by large scale physical slope model. The strain changes in the large-scale model were measured at regular interval of 10 minutes respectively. The finding demonstrated that the calculated displacements measured by both of the devices were closed to each other as well as a consistency was observed between them. Moreover, it was also found that the offer mentioned application can accurately locate the location of potential sliding surface and provide adequate access to the internal deformation of the slope.

1 INTRODUCTION

One of the main natural disasters is landslides, which causing loss of life and seriously harm infrastructure around the world. Approximately 2600 non-seismically generated landslides caused 30,000 casualties worldwide between 2004 and 2010 (Petley 2012). Significant efforts have been made over the past few decades to understand the underlying mechanics behind landslides (Jibson 2011). Water filtering, excavation, and erosion are among the causes that cause an increase in shear stresses and pore water pressures, which lowers the soil's overall resistance. This mechanism causes an abnormal strain field to form on the failure surface and causes segments of the slope to shift relative to one another. Then, considerable shear strains that are localized close to the failure surface start to occur. At first, they build slowly, but eventually their rate picks up speed and the stability is ultimately jeopardized. As a result, strain and displacement (both above and below ground) are acknowledged as two physical factors that are of utmost significance and more directly related to the occurrence of landslides (Zhu, Shi, and Zhang 2017).

In the past 20 years, a number of distributed fiber-optic sensors, including numerous single-point sensors that imitate conventional equipment, have been presented for the measurement of strain and displacement in landslide monitoring (LLoret et al. 2003). With a spatial resolution of a few meters, a BOTDA interrogator was used to track the St. Moritz landslide in Switzerland using a fiber cable buried in a road that crossed the slide. With enough spatial precision to distinguish the landslide limits, the fiber-equipped road functioned as a long dispersed strain meter (Iten, Puzrin, and Schmid 2008). The soil-embedded "micro-anchor" cable system was subsequently tested at the same location. Tridimensional "micro-anchors" mechanically secured to the cable at predetermined intervals were part of the system, which also included a small metal-free cable. To stop the relative slippage between the strain sensing cable and the surrounding soil, the anchors offered bearing capability in three perpendicular planes. Additionally, the anchors enabled pre-stretching of the cable during installation (Iten and Puzrin 2009). The slow-moving Ripley landslide in Ashcroft, British Columbia, Canada, was also seen by a BOTDR interrogator,

DOI: 10.1201/9781003299127-325

with the sensing cable tied to the lock-block retaining wall. Curiously, the system remained in place for three months before a black bear destroyed it, and the prolonged exposure to below-freezing conditions led the cement (an epoxy resin and caulking mixture) to disintegrate, causing the system to become detached from the retaining wall (Strong et al. 2008).

The distributed fiber optics sensor based on Brillouin scattering has been extensively studied in the field of structural safety and health monitoring (SSHM) for aircraft, bridges, tunnels, highways, and railways due to its high measurement accuracy, high spatial resolution, and real-time fully distributed measurement characteristics (Pang et al. 2021; Dakin 1993; Ding et al. 2018). Brillouin optical time domain reflectometry with coherently probed (BOTDR), A single-ended device with a basic construction that can continue to function even if the fiber breaks uses frequency-shifted local heterodyne sensing to increase signal-to-noise ratio (SNR). Several methods, including the Raman amplification technique, have been developed to enhance the functionality of BOTDR sensing systems (Ding et al. 2018; Li et al. 2018). Additionally, several unique fibers, such as those with a large effective area, photonic crystal fiber, few-mode fiber, and multicore fiber, among others, have been thoroughly explored to solve the issue of temperature and strain cross-sensitivity (Li et al. 2012; Bai et al. 2019).

The OTDR and BOTDR are feasible and affordable alternatives to slope monitoring among the point-based approaches. The fibers used to implement OTDR in slope research are cheap and offer long-term, remote monitoring of slope movement. Measurements only take a few seconds, which is far faster than the traditional, labor-intensive "cable pull" method of inclinometer probing (Sargand, Sargent, and Farrington 2004). The advantages of optical fiber and fiber grating technologies, including their low optical signal loss, 80 km maximum measuring range, and ability to pinpoint defects, have made them very popular in the field of civil and geotechnical engineering. (Zhang et al. 2006; Chai et al. 2004).

2 WORKING PRINCIPLE

BOTDR technique can be employed with Brillouin optical time domain reflectometry; the wavelength of Brillouin scattering depends on the temperature and strain of the optical fiber sensor. The way it functions is by injecting a beam of light with a specified frequency into the fiber, which then interacts with the elastic sound waves to create Brillouin backscattered light. The fiber's changes in temperature and stress have an impact on the wavelength of Brillouin scattering. Brillouin frequency shift can be measured, and its relationship to strain and temperature can be used to determine how external variables affect the fiber (Bai et al. 2019; Lee 2003).

There is a linear relationship between the temperature and strain of the optical fiber and the frequency shift of Brillouin scattered light; the strain and temperature of the object can be measured using BOTDR technology. The relationship between Brillouin frequency shift with strain and temperature is given by equation (1) (Dan, Bin, and Hongzhong 2004; Horiguchi et al. 1995; Hong et al. 2017).

$$\Delta Vb(\Delta T, \Delta \in) = Vb(\in, T) - Vb(0, To) = \mathrm{CT}\ (\mathrm{T} - \mathrm{To}) + \mathrm{C} \in (\in - \in 0) \tag{1}$$

Equation (1) demonstrates that distributed real-time monitoring of the measured object can be used to determine the strain and temperature induced by external forces (Zhang et al. 2018).

3 MATERIALS AND METHODOLOGY

3.1 *Laboratory set-up*

Initially laboratory experiments were performed to check the applicability of the distributed fiber optic sensing technology based on brillouin optical time domain reflectometry. Strain and temperature calibration were executed to find the calibration coefficient for the large-scale application of the DFOS. Moreover, the laboratory experiment was also conducted to investigate the relationship between frequency shift, strain and horizontal displacement of the fiber optic cable. Figure 1 illustrate the laboratory experimental set-up of the DFOS technology.

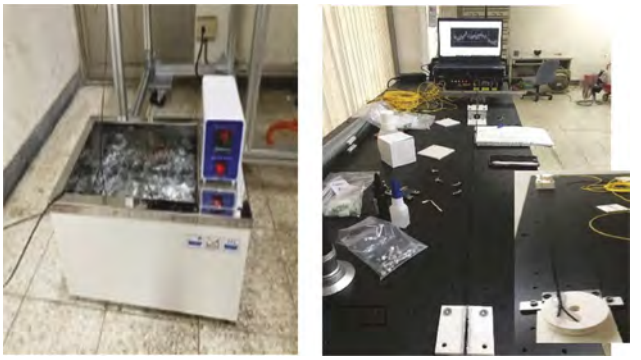

Figure 1. Strain and temperature calibration set-up.

3.2 *Field application*

After the conduction of laboratory experiments, large scale physical model was conducted. Two PVC tubes were installed in the slope model with Fiber optical cable pasted on four sides of the PVC pipe and then connected with the brillouin optical time domain reflectometer. Similarly, Inclinometer was also installed in the same tube. Two experiments were performed at time interval of 10 minutes just to check the applicability and accuracy of the fiber optic sensing technology based on BOTDR with inclinometer.

4 RESULTS

4.1 *Strain and temperature calibration*

The purpose of the calibration is to determine the relationship between Brillouin frequency shift with strain and temperature. The calibration was carried out with a 50 m span fiber cable that was clamped at lengths ranging of 1m. A combination of displacement and temperature influences the fiber at the same time, with the temperature adjusted to 50 degrees Celsius. The results of the calibration is shown in Figure 2.

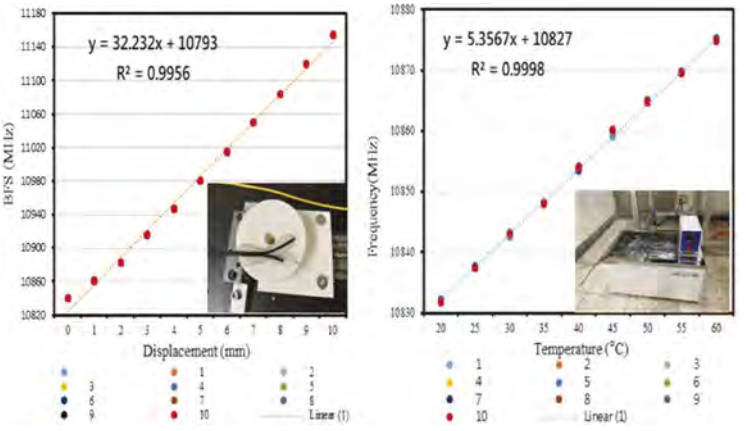

Figure 2. Calibration results.

4.2 *Field displacements measurement*

Displacements were measured by using distributed fiber optic sensing (DFOS) based Brillouin optical time domain reflectometry and in place inclinometer. DFOS recorded Frequency shifts

with the help of BOTDR and then frequency shifts was converted to displacements. The frequency shifts is actually due to the external stresses on the cable which change the internal configuration of the cable due to which the light waves bounced back and the spectrum was analyzed using BOTDR device. Similarly, the displacement was measured using inclinometer at the same time. The results of the displacements is shown in Figure 3. Moreover, the data was recorded at a regular time interval of 10 minutes and at this stage only two values have been reported just to confirm and encourage the implementation of the distributed fiber optic sensing technology for the large scale physical model test.

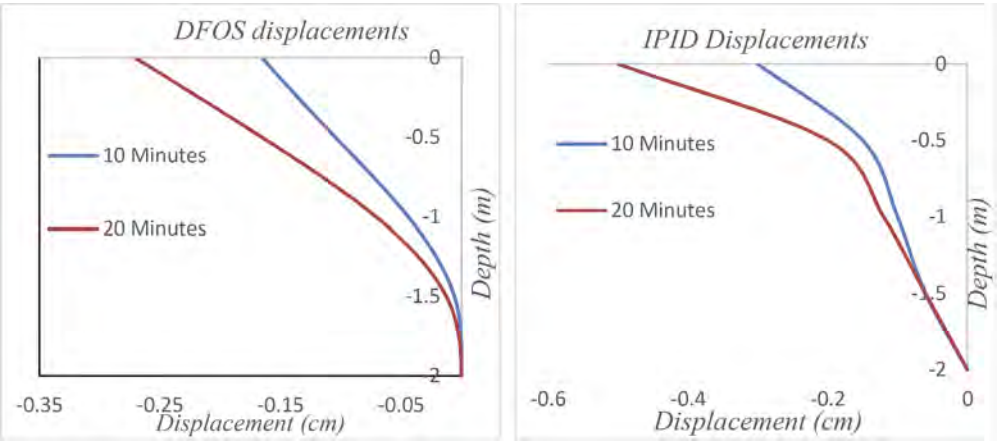

Figure 3. Displacements.

5 CONCLUSION

Based on the laboratory and field experimental observations it was concluded that both of the displacements results were closed and consistent. As a results the distributed fiber optic sensing technology based on BOTDR can be used for the displacement measurement and can be implemented for large scale geo-hazards monitoring.

REFERENCES

Bai, Qing, Qinglin Wang, Dong Wang, Yu Wang, Yan Gao, Hongjuan Zhang, Mingjiang Zhang, and Baoquan Jin. 2019. 'Recent advances in Brillouin optical time domain reflectometry', *sensors*, 19: 1862.

Chai, J, SM Wei, XT Chang, and Y Li. 2004. 'Distributed optical fiber sensor for monitoring rock deformation', *Chinese Journal of Rock Mechanics and Engineering*, 23: 4068–71.

Dakin, John P. 1993. 'Distributed optical fiber sensors', *Distributed and Multiplexed Fiber Optic Sensors II*, 1797: 76–108.

Dan, Zhang, SHI Bin, and Xu Hongzhong. 2004. 'The BOTDR-based strain monitoring for tunnel', *工程地质学报*, 12: 422–26.

Ding, Zhenyang, Chenhuan Wang, Kun Liu, Junfeng Jiang, Di Yang, Guanyi Pan, Zelin Pu, and Tiegen Liu. 2018. 'Distributed optical fiber sensors based on optical frequency domain reflectometry: A review', *sensors*, 18: 1072.

Galindez-Jamioy, Carlos Augusto, and Jose M Lopez-Higuera. 2012. 'Brillouin distributed fiber sensors: an overview and applications', *Journal of Sensors*, 2012.

Habel, Wolfgang R, and Katerina Krebber. 2011. 'Fiber-optic sensor applications in civil and geotechnical engineering', *Photonic sensors*, 1: 268–80.

Hong, Cheng-Yu, Yi-Fan Zhang, Guo-Wei Li, Meng-Xi Zhang, and Zi-Xiong Liu. 2017. 'Recent progress of using Brillouin distributed fiber optic sensors for geotechnical health monitoring', *Sensors and Actuators A: Physical*, 258: 131–45.

Horiguchi, Tsuneo, Kaoru Shimizu, Toshio Kurashima, Mitsuhiro Tateda, and Yahei Koyamada. 1995. 'Development of a distributed sensing technique using Brillouin scattering', *Journal of Lightwave Technology*, 13: 1296–302.

Iten, Michael, and Alexander M Puzrin. 2009. "BOTDA road-embedded strain sensing system for landslide boundary localization." In *Smart Sensor Phenomena, Technology, Networks, and Systems 2009*, 333–44. SPIE.

Iten, Michael, Alexander M Puzrin, and Andreas Schmid. 2008. "Landslide monitoring using a road-embedded optical fiber sensor." In *Smart Sensor Phenomena, Technology, Networks, and Systems 2008*, 328–36. SPIE.

Jibson, Randall W. 2011. 'Methods for assessing the stability of slopes during earthquakes—A retrospective', *Engineering Geology*, 122: 43–50.

Lee, Byoungho. 2003. 'Review of the present status of optical fiber sensors', *Optical fiber technology*, 9: 57–79.

Li, Cunlei, Yuangang Lu, Xuping Zhang, and Feng Wang. 2012. 'SNR enhancement in Brillouin optical time domain reflectometer using multi-wavelength coherent detection', *Electronics letters*, 48: 1139–41.

Li, Yongqian, Lixin Zhang, Hanbai Fan, and Hong Li. 2018. 'Rayleigh Brillouin optical time-domain analysis system using heterodyne detection and wavelength scanning', *Optical engineering*, 57: 056112.

Liehr, Sascha, Philipp Lenke, Mario Wendt, Katerina Krebber, Monika Seeger, Elke Thiele, Heike Metschies, Berhane Gebreselassie, and Johannes Christian Munich. 2009. 'Polymer optical fiber sensors for distributed strain measurement and application in structural health monitoring', *IEEE Sensors Journal*, 9: 1330–38.

LLoret, Sandra, Pramod Kumar Rastogi, Luc Thevenaz, and Daniele Inaudi. 2003. 'Measurement of dynamic deformations using a path-unbalance Michelson-interferometer-based optical fiber sensing device', *Optical engineering*, 42: 662–69.

Pang, Fufei, Lina Xiang, Huanhuan Liu, Liang Zhang, Jianxiang Wen, Xianglong Zeng, and Tingyun Wang. 2021. 'Review on fiber-optic vortices and their sensing applications', *Journal of Lightwave Technology*, 39: 3740–50.

Petley, David. 2012. 'Global patterns of loss of life from landslides', *Geology*, 40: 927–30.

Sargand, Shad M, Lisa Sargent, and Stephen P Farrington. 2004. "Inclinometer-time domain reflectometry comparative study." In.: Ohio Research Institute for Transportation and the Environment.

Song, Zhanpu, Bin Shi, Hsein Juang, Mengfen Shen, and Honghu Zhu. 2017. 'Soil strain-field and stability analysis of cut slope based on optical fiber measurement', *Bulletin of Engineering Geology and the Environment*, 76: 937–46.

Strong, Andrew P, Norman Sanderson, Gareth Lees, Arthur Hartog, Richard Twohig, Kamal Kader, Graeme Hilton, and Artem Khlybov. 2008. "A comprehensive distributed pipeline condition monitoring system and its field trial." In *International Pipeline Conference*, 711–19.

Sun, Yijie, Bin Shi, Dan Zhang, Hengjin Tong, Guangqing Wei, and Hongzhong Xu. 2016. 'Internal deformation monitoring of slope based on BOTDR', *Journal of Sensors*, 2016.

Zhang, Cheng-Cheng, Hong-Hu Zhu, Su-Ping Liu, Bin Shi, and Dan Zhang. 2018. 'A kinematic method for calculating shear displacements of landslides using distributed fiber optic strain measurements', *Engineering Geology*, 234: 83–96.

Zhang, Cheng-Cheng, Hong-Hu Zhu, and Bin Shi. 2016. 'Role of the interface between distributed fibre optic strain sensor and soil in ground deformation measurement', *Scientific Reports*, 6: 1–9.

Zhang, LX, YZ Liu, ZH Ou, ZY Dai, and C Zhou. 2006. 'Research on rock body thrust monitoring system', *Opto-Electronic Engineering*, 33: 52–56.

Zhu, Hong-Hu, Bin Shi, and Cheng-Cheng Zhang. 2017. 'FBG-based monitoring of geohazards: current status and trends', *sensors*, 17: 452.

Smart Geotechnics for Smart Societies – Zhussupbekov, Sarsembayeva & Kaliakin (Eds)
© 2023 The Author(s), ISBN 978-1-003-29912-7
Open Access: www.taylorfrancis.com, CC BY-NC-ND 4.0 license

Geotechnical risks in the construction of reinforced embankment

P. Cernoch
CEZ Energy products, Prague, Czech Republic
INSET, s.r.o., Prague, Czech Republic

J. Kostal
Czech Technical University in Prague Faculty of CE, Prague, Czech Republic
INSET, s.r.o., Prague, Czech Republic

ABSTRACT: Construction of a very steep, 6 m high embankment for the expansion of the capacity of the existing high-voltage transformer station took place nearby nuclear power plant. A complex of geotechnical control monitoring was carried out including hydrostatic levelling gauges, pore pressure gauges, geodetic stabilized points and piezometers. Main geotechnical risk was the presence of low-bearing fully-saturated sediments of the hidden river bed of the former stream, which had passed directly below the embankment. Technology of future construction is very sensitive to uneven settlement. Values obtained via long-term monitoring were continuously being compared with mathematical modelling. Subsequently, measurements were used to determine the construction speed of the embankment.

1 INTRODUCTION – BASIC INFORMATION ABOUT THE CONSTRUCTION

The aim of the project was to expand the current high-voltage transformer station. The old construction was located on the approx. 3 meters high embankment and for its expansion was necessary further land occupation. To minimize annexation of surrounding area which is always very expensive and costly (property transfers can sometimes be time consuming), a very steep embankment slope – almost perpendicular – was designed (see Figure 1).

The new embankment had a projected height of up to 6 meters. The high-voltage transformer station extension included a transformer field, one main brick building and two small service buildings. Together with the embankment a large load of the subsoil was expected. The designed building is very sensitive to uneven settlement.

2 GEOTECHNICAL CONDITIONS

Main geotechnical risk was the presence of low-bearing fully-saturated sediments of the hidden river bed of the former stream, which had passed directly below the new embankment body.

Bedrock is formed by Proterozoic gneiss in the locality of interest covered with tertiary claystone. Quaternary surface is represented by floodplain fine-grained sediments of the former river. In some places there is also peat.

During topsoil overburden and terrain work, local landslides of the old embankment occurred and in the vicinity of the relocated watercourse. Because of the presence of poor sediments of the former stream below the projected embankment a redevelopment of subsoil was designed – special geo-drains were used for subsoil of the upcoming foundation.

Dynamic penetration probes were made as control tests within the redevelopment with geo-drains (see Figure 2). These probes also served as a geological survey and were used as

DOI: 10.1201/9781003299127-326

piezometers (hydrogeological wells) as well. The field work also included installation of hydrostatic leveling gauges in the subsoil of the embankment together with pore pressure gauges installed in boreholes [1].

Figure 1. Construction of the embankment in process (high voltage transformer in the background).

3 MONITORING

The following geotechnical control devices and objects were monitored:

Geotechnical monitoring devices – hydrostatic levelling gauges, pore pressure gauges and geodetic stabilized points. System of hydrostatic leveling in individual profiles of measuring stations (HPG) served for monitoring vertical movements of the subsoil of the embankment body. The results of measurements were be used to check the expected magnitude of settlement and their development in real over time. Pore pressure gauges were used to monitor the development of pore pressures in the subsoil from the weight of the embankment body being built. Geodetic stabilized points were installed for monitoring of deformations of body surface parts.

The basic frequency of periodic control readings was realized in a 14-day interval. The measurement was used for the main geotechnical engineer of the construction, who could allow faster construction of embankments or, on the contrary, extend the intervals between sub-phases of construction. At the same time, the results of the measurements were continuously available for authorized persons on the SAHURE portal of INSET s.r.o. company: *https://inset.sahure.cz/Sahure*.

The heights of the geodetic points were determined by lateral intents from the leveling program measured by the geometric leveling method from the center. The Trimble DiNi instrument was used for measurement.

Coordinates of fixed geodetic points on the wall of the new embankment were determined by total station by measuring oblique lengths, zenith angles and horizontal directions. The

TS60 total station was used for measurement, whose accuracy is characterized by standard deviations of 0.15 mgon for zenith angle and horizontal direction and 0.6 mm and 1 ppm for inclined length.

The measuring apparatus for measuring vertical movements based on hydrostatic leveling consisted of a sensor which measured the pressure on a vibrating conductor, a hose filled with liquid wound on a portable drum, a tank with a sight glass and a signal cable with liquid hose which led from the sensor to the meter. Model 4651 Geokon was used as a measuring device. Standard range is 7 m, sensitivity ± 2 mm, accuracy ± 4 mm and temperature range of use is from -20 ºC to +80 ºC. The GK-403 is a reading unit that enables accurate measurement of vibration sensors (see Figure 3).

Figure 2. Dynamic penetration probes made during the redevelopment of subsoil with geo-drains.

Measurement of pore pressures determines the water stress in the pores in the subsoil under the foundation. The results of the measurements served as a check of the expected magnitude of the stress in the subsoil and its development over time. W9 Vibrating Wire Piezometer manufactured by Soil Instruments was installed with range from 0 to 500 kPa, accuracy classes 0.1%. The sensors were embedded in the boreholes into a pre-prepared bed of fine gravel (1.5 m above gauges), followed by a cement swab CEM 32.5 R (density 1 490 kN/m^3). Two sensors were placed in each borehole, each at a depth of 6.0 m and 1.5 m below the ground. The cables from the sensors were led to the nearest HPG site where they were led into a steel protective measuring box.

Two observation piezometers (DPV) were equipped. Immediately after the probing, a perforated casing (PVC, ø 25 mm) was embedded in the hole. Perforation of the observation piezometer equipment after its insertion into the penetration shaft begun 0.5 m above the bottom of the piezometer and ended 0.5 m below ground level (surface sealed with clay-bentonite). Steel casing with length 1.3 m and diameter 50 mm was put on perforated PVC casing to protect the probe. A standard electro-contact level meter was used to measure the ground water level in hydrogeological wells.

4 COMPARISON OF MEASURED DATA WITH MATHEMATICAL MODELLING

Estimated magnitude of deformations and their development over time were measured. At the same time, the water stress in the pores in the active zone below the foundation was documented after being loaded by the embankment and the building structure. The obtained values were compared with mathematical modelling. Numerical simulations were made in PLAXIS software using finite element method. Subsequently, measurements were used to determine the rate of the build of the embankment.

4.1 *Geodetic stabilized points and piezometers (GWL)*

Most of geodetic stabilized points the situated on the wall of the embankment showed a steady settlement (vertical drop) over the entire measurement period, while there were only small horizontal movements (changes did not exceed a total shift of 20 mm). Point installed on the north wall recorded a steady decline at the base of the wall with a maximum of 33.1 mm. Situation on the south wall was slightly different – maximal subsidence -55.1 mm was measured. The settlement process was quite fast at the first phase (the beginning of construction of the embankment), then the values stabilized.

Figure 3. Hydrostatic levelling – all measured data were continuously available on portal *https://inset.sahure.cz/Sahure*.

Declines in measured points were without significant anomalies, except in March 2019, when there was an unexpected movement at almost all points. Several control measurements were carried out, which recorded a decrease to the original values and a steady slight decrease due to the continuation of settlement of the whole embankment. The anomalous movement was attributed to the release of stress in the embankment body due to spring snow-melting without any negative consequences for the embankment body. No surface deformations or

cracks were noticed. This phenomenon was confirmed by measuring the evolution of groundwater level in hydrogeological wells (piezometers) [1].

In the last six months of monitoring, however, all geodetic points have recorded a steady settlement and their character turned from a small permanent drop into an oscillatory movement.

4.2 *Hydrostatic levelling*

The embankment settlement monitored by hydrostatic leveling did not show any uneven settlement (with the highest value of -277 mm in the HGP1 profile; see Figure 4), except for the HG2 profile.

The average decrease of the HPG2 profile was -82 mm, the maximum decrease was -586 mm (as of October 31, 2018). The measurement of the HPG2 profile was terminated prematurely on November 29, 2018 due to permanent damage of the measuring site (destroyed by construction). The speed of construction had to be slowed down in certain passages in response to the above measurements. As a result the values were stable at the end of the measurement and corresponded to the results obtained from mathematical modeling – settlement prediction [2]. Otherwise the construction would have to be interrupted.

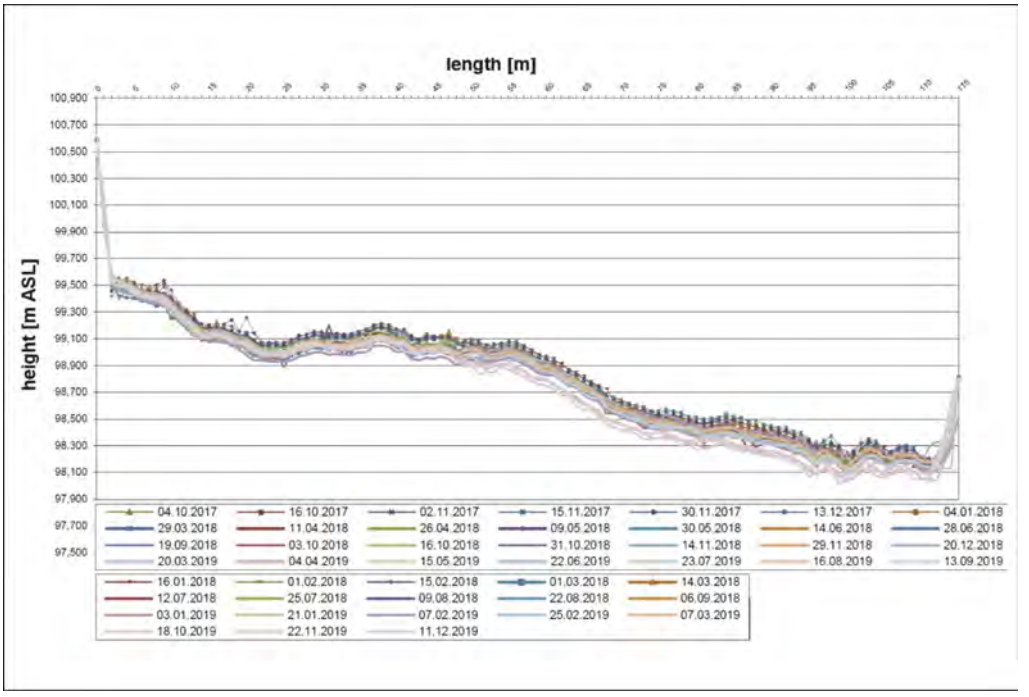

Figure 4. Results from HPG1 profile – even settlement of the embankment.

4.3 *Hydrostatic levelling*

Pore pressure sensors placed at 6 m below the foundation of the embankment body showed higher pore pressure values than gauges located 1.5 m below the surface. However, the trend in pressure development was the same for all sensor pairs.

During the whole follow-up period there was no anomaly fluctuation of the pore pressure values in any MPT, which would indicate a warning increase or decrease of soil stress in the subsoil.

The pore pressure values for sensors at a depth of 1.5 m below the ground ranged from -7 to 20 kPa, gauges at a depth of 6 m below the surface in the range of 25 to 60 kPa.

The measured values were in accordance with the numerical modelling [2].

5 CONCLUSION

A complex monitoring system was built in advance for the 6-meter high embankment to expand the high-voltage transformer station for nearby nuclear power plant.

Deformations and settlement were measured during process of construction. Obtained values were compared with mathematical modelling. The speed of construction had to be slowed down in certain parts in response to negative measurement development. As a result the values were stabilized. Finally the measured values from monitoring corresponded to the settlement prediction acquired from the mathematical modeling after all. After completion of the construction, the measured data recorded a settling of values related to the main consolidation process. The existing geotechnical control system is still functional for subsequent periodic measurements and for assessing potential risks of the monitored body.

REFERENCES

[1] Cernoch P. & Kostal J. & Podojil A. (2019) Extension of transformer station TR110; Geotechnical monitoring SO 311. MS. 12/2019, INSET s.r.o., Prague, Czech Republic

[2] Cernoch P. & Kostal J. (2017) Mathematical model for high-voltage transformer station. MS. 03/2017. INSET s.r.o., Prague, Czech Republic

Smart Geotechnics for Smart Societies – Zhussupbekov, Sarsembayeva & Kaliakin (Eds)
© 2023 The Author(s), ISBN 978-1-003-29912-7
Open Access: www.taylorfrancis.com, CC BY-NC-ND 4.0 license

Development of the Osaka sedimentary basin due to surface geological structure and sea level changes using boring database

N. Kitada, N. Inoue & K. Mizutani
Geo-Research Institute, Osaka, Japan

M. Mimura
Kyoto University, Kyoto, Japan

ABSTRACT: The Osaka Sedimentary Basin is surrounded by mountains and active faults. The tectonic movement causes the surrounding area to rise and the basin to subside. The basin is submerged in the sea due to sea-level changes, and the marine clay deposits. Using the boring database accumulated by KG-NET, we learn the layer thickness, bottom elevation distribution, and distribution limit of the Holocene marine clay layer. Consider the environment at the time of deposition. In particular, the Kawachi Plain on the east side of the Uemachi fault showed the environment of an inner lake, and it was clarified that a sandbank was formed around the strait when it flowed in and out due to the ebb and flow of the tide. In this area of poorly drained seawater and freshwater, sensitive clays rich in organic matter are thought to have accumulated extensively.

1 INTRODUCTION

The Osaka Plain is mainly deposited by the river flooding of the Yodo River. The north-south-trending Uemachi fault (reverse fault: footwall on the west side) and Ikoma fault (same) pass through the center and eastern edge of the plain. Since the Osaka-wan fault (mainly reverse fault: east side is the footwall side) is distributed in the western end of Osaka Bay, the sedimentary basin continues to subside gradually. The Osaka Plain is filled with sediments with a thickness of over 1000m (Figure 1.). The surface layer is alternately composed of a marine clay layer that was formed during the warm period when the sea level was high and a sand-gravel layer that was deposited mainly as river flooding during the cold period when the sea level was low. KG-NET has a database of boring logs in this area, and it is possible to understand the ground characteristics of the area (Figure 2.). About 50,000 borehole data in this area.

In this study, we discuss the potential geological risks obtained by examining using the boring database.

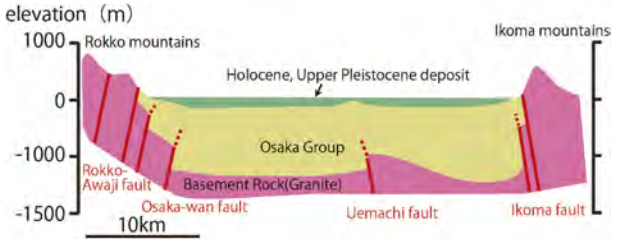

Figure 1. East-West cross section of Osaka plain[1)].

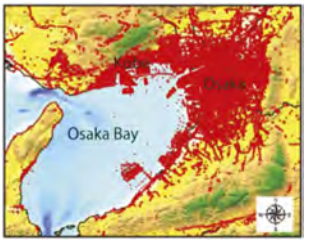

Figure 2. Distribution of boring data red cercle is location of data.

DOI: 10.1201/9781003299127-327

2 LOWER EROSION OF STRATA SEEN IN THE OLD RIVER CHANNEL

In rivers flowing through plains, since the ground level of the riverbed is lower than that of the surrounding area, downward erosion is strong, and riverbed gravel is distributed. Figure 3 shows a cross-sectional view of the former river channel of the former Yodo River. For example, if an old river channel is not assumed during shield excavation in the Ma12 layer, a gravel layer will suddenly be encountered. It is a latent geological risk that causes construction work to stagnate if a preliminary survey or geological factors are not understood.

It is important to note that the marine clay layer deposited in a calm environment has a constant layer thickness in the Osaka Plain, and that the layer thickness has been denuded to less than half by the passage of the river channel. If you don't recognize it, you will suddenly encounter a gravel layer even if you are excavating in the clay layer. Furthermore, even among the river bed gravel, if it is a large river such as the Yodo River, the diameter of the gravel is large, and depending on the location, it is as large as a human head. In addition, since there is also groundwater flow, there is a high possibility that it will become a factor such as flood accidents (Figure 4).

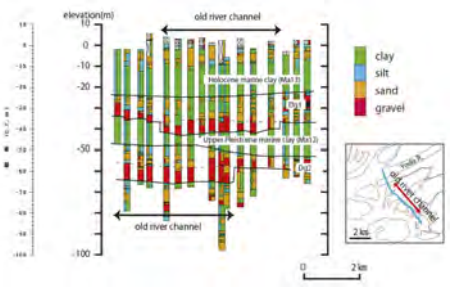

Figure 3. East-West cross section of Osaka plain[1].

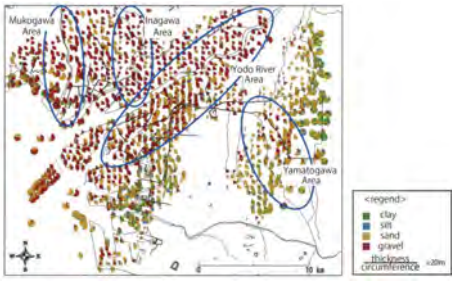

Figure 4. Distribution and grain size composition of the upper Pleistocene gravel layer[2].

3 DISTRIBUTION OF SANDBARS

During the warmest period of the Jomon period (about 6,000yr before), the Osaka Plain was almost submerged in the sea. It has been clarified from previous research that the Uemachi plateau, which is the center of Osaka, was a land at that time because it was a slightly high ground. During this period, a marine clay layer called the Ma13 layer was deposited over most of the Osaka Plain, but sand layers have been confirmed in some areas. After the boring database was completed, we examined the distribution and found that the sand layer is distributed on the

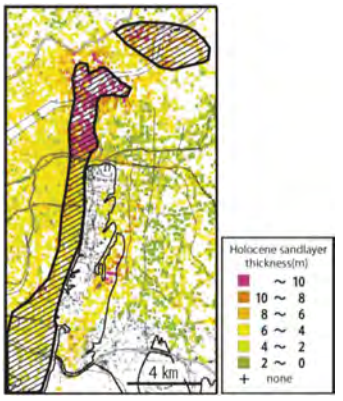

Figure 5. Distribution map of sandbars on the western side of the Uemachi plateau[2].

west side of the Uemachi Plateau and from the north to the east side of the plateau, as shown in Figure 5. A cross-section confirms that the sediments are in a relationship of simultaneous stratification (they are deposited at the same time, but the grain size is different between clay and sand) with the Ma13 layer. In addition, it was confirmed that sandy sediments (sand bank) developed due to tidal current flow due to the ebb and flow of the tide in the connecting part of the inner bay with the Kawachi Plain. Figure 5 traces the thickness of the upper alluvial sand layer distributed over the Ma13 layer. In the black shaded area, the thickness is lower and the Ma13 layer is not distributed. A cross-sectional view of this part is shown in Figure 6.

4 DEFORMED PART OF THE STRATUM ASSOCIATED WITH AN ACTIVE FAULT

It should be noted that the lateral discontinuity of the geological ground due to the passage of active faults causes large changes in groundwater flow and changes in ground strength due to large changes in strata. Furthermore, if displacement (deformation) occurs in the geological ground due to the activity of an active fault, the risk will be very high because structures will also be affected.

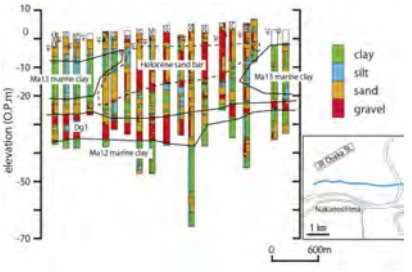

Figure 6. East-west section across the sand bar[1)].

In alluvial plains where urban areas are developed, displacement due to active faults is hidden, and flexural structures may be shown near the ground surface. In the Osaka Plain, the Uemachi fault passes through the western part of the Uemachi plateau, but the western edge of the plateau is not the point where the fault passes (Figure 7). Geomorphologically, the western edge of the plateau was previously thought to be the fault scarp, but boring data reveals that the cliff is different from the fault passage. The east-west cross section shown in Figure 8 is an area that appears particularly conspicuously. The origin of the Uemachi plateau is considered to have been formed with the activity of the Uemachi fault. As mentioned earlier (3.3), the fault scarp is thought to have receded eastward due to wave erosion during the period of high sea level. Therefore, the actual displacement and flexure of the fault are located on the west side of the fault scarp, and because the topography is flat, it is difficult to determine the exact location. In the vicinity of the fault, the stratum changes rapidly and the groundwater flow is complicated, so it is a place that requires attention during construction. In fact, even if the drilling data is used, it is not possible to judge whether the adjacent clay layers are sediments of the same period or not because the marine clay layers are greatly tilted and deformed. However, if there is a boring survey that can determine the information to some extent, it is possible to use adjacent boring data to estimate the deformation of the stratum. It becomes possible to consider bending deformation. Figure 9 is a geological cross-sectional view near the fault passage created by combining the boring data and the boring data for the geological sedimentary environment survey. The Ma12 layer in the figure is a Pleistocene sediment (deposited from about 125,000 years ago[6)]), and since it is a marine clay layer, it was deposited horizontally at the time of deposition. At present, the sediments have been significantly deformed, and the fact that a drop of about 50 m is observed at the base can be judged to be deformation associated with fault movement. Furthermore, since the upper alluvial clay

layer (Ma13 layer) has hardly deformed, the cumulative displacement of older sediments is larger than that of newer sediments (repeated displacement = periodic deformation). Such deformation structures due to active faults are latent in the underground part of the alluvial plain and cannot be fully understood from the topographical shape near the surface. Therefore, lateral contrast of strata must be carefully performed in order to make it apparent as a geological ground risk.

Figure 7. Distribution of the Uemachi fault (Left: active fault database of the geological survey of Japan, AIST[4)], right: urban active fault map published by the Geospatial Information Authority of Japan[5)].

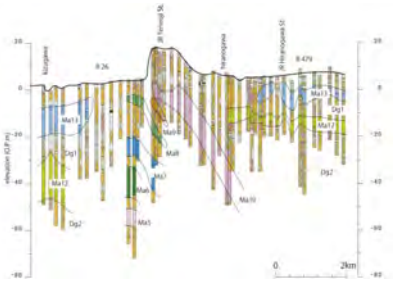

Figure 8. Relationship between the plateau topography and the Uemachi fault in an east-west cross section.

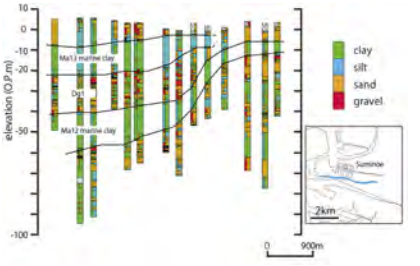

Figure 9. Flexural structure of the Ma12 layer at the suminoe flexure[7)].

5 CONCLUSIONS

When examining geological ground risk using ground information, it is necessary to read the characteristics while fully considering the geological development history of the area. The following five points are important for understanding geological ground risk.

1. It is necessary to fully understand the sedimentary structure and sedimentary environment of strata, and to fully understand the risks that lie hidden therein.

2. Even if it is the same stratum, there is no stratum that increases in the same way on the side.
3. It is necessary to have a good understanding of the geological structure and grasp the geological ground risk.
4. In particular, it is necessary to pay attention to the underlying geological ground risk in plain urban areas, which does not appear in the topography and has latent geological structures.
5. When grasping the geological ground risk, it is effective to use physical geological analysis etc. as necessary.

REFERENCES

1. Kitada Naoko: Geological ground risk assessment using ground information, Journal of Geotechnical Society, 70(5), p10–13.2022.
2. KG-NET/Kansai Area Geotechnical Research Group: New Kansai Geotechnical Field -From Osaka Plain to Osaka Bay-, 354p., 2007.
3. Geotechnical Society Kansai Branch: Report of Research Committee on Ground Characteristics and Countermeasure Techniques Where Trouble Occurs in Underground Construction Work, 99p., 2013.
4. National Institute of Advanced Industrial Science and Technology, Active Fault Database <https://gbank.gsj.jp/activefault/index_gmap.html> (accessed 2022.10.10)
5. Takashi Nakata, Atsumasa Okada, Yasuhiro Suzuki, Mitsuhisa Watanabe, Yasutaka Ikeda: 1:25,000 active fault map of urban area ``Northern Osaka'' and ``Tohoku Osaka'', Geospatial Information Authority of Japan, 1996.
6. Mieko Uchiyama, Muneki Mitamura, Shusaku Yoshikawa: Displacement Velocity and Basement Block Motion of the Uemachi Fault, Central Osaka Plain, Geological Journal, vol.107, 228-236, 2001.
7. Research and Development Bureau, Ministry of Education, Culture, Sports, Science and Technology, Disaster Prevention Research Institute, Kyoto University: 2012 Results Report on Focused Investigation and Observation in the Uemachi Fault Zone, 258p., 2013.

Smart Geotechnics for Smart Societies – Zhussupbekov, Sarsembayeva & Kaliakin (Eds)
© 2023 The Author(s), ISBN 978-1-003-29912-7
Open Access: www.taylorfrancis.com, CC BY-NC-ND 4.0 license

Analysis of existing methods for processing GNSS survey data for deformation monitoring

Zh.M. Aukazhiyeva, A.M. Muratova & Zh.N. Nugmanova
L.N. Gumilyov Eurasian National University, Astana, Kazakhstan

ABSTRACT: The issues of processing GNSS survey data, the results of observations at the points of the state geodetic network, the concepts of the quality of the result of deformation monitoring are considered.

GNSS survey data processing occupies one of the most important places in the methodology. The results of observations at GNSS points carry information both about displacements of the foundations of structures (for example, pit wall landslides) and about periodic (seasonal, annual) deformations of components caused by external factors (uneven solar heating, temperature fluctuations, wind load, snow load, icing, seismic activity, etc.). Periodic observations help to identify negative geological processes in the area where the engineering facility is located.

Changes in the position of Permanent Operating Base Stations (PBSs) installed at dynamic sites can have different values, speeds and nature. In order to determine the most accurate antenna phase centre displacement under certain conditions, different, sometimes non-standard methods of spatial information processing need to be applied. At the same time it is necessary to know exactly the expected accuracy of geodetic observations. The notion of quality of result of deformation monitoring implies high accuracy of coordinates measurement, detailed description of antenna motion, absence of influence of big errors and so on. [1].

It should also be remembered that each object of study has its own unique nature. Data processing methods may be acceptable for one type of object, but for another, seemingly identical object, such methods will not be correct. In order to accurately assess the suitability of a methodology, control or test measurements are usually carried out. This activity is experimental in nature, needed to confirm suitability by testing the same survey results, but carried out using different techniques. The method that gives the most accurate result, corresponding to the actual movement of the object, is deemed optimal and is used for further work on an ongoing basis. Such measures also help identify the influence of various mistakes that occur during surveying. One of the most widespread mistakes is signal over-reflection that occurs as a rule in urban areas with high-rise buildings. Multipathing is the cause of an error ranging from a few centimetres to a metre. Such measurements are to be rejected [2].

Geodetic monitoring of dynamic objects involves measuring the coordinates of the points in the deformation network in order to detect coordinate deviations of the points. In order to describe the coordinate deviation in detail, mathematical processing of the data obtained is necessary. This step is one of the most important, as the choice of mathematical function determines the details of the display of dynamic processes in the terrain. In practice, the most commonly used methods for mathematical processing are the moving average method, the median filter, the window function and the interval composite method. To further select the best method it is necessary to disambiguate them, in particular [3].

The moving average method is often used when it is necessary to smooth time series and remove high frequency components from the radio signal. According to the algorithm, an

DOI: 10.1201/9781003299127-328

interval of a certain length is first taken from the original data set. This is followed by finding the arithmetic mean of all signal values in this interval.

For the example, assume that signal f has N points. For each N-point there is a signal value K. The value of the moving average gi in the interval of point i will be equal to the arithmetic mean of the K previous and subsequent points, including point i. Each new value of gi will be defined as the smoothing factor in the 2K+1 interval (1).

$$g_i = \frac{1}{2K+1}\left(f_{i-k} + f_{i-K+1} + \cdots + f_i + f_{i+k}\right) \tag{1}$$

The calculation results in a new series of smoothed data consisting of arithmetic mean values (Figure 1). This method is good in that it allows fast data processing, but has a disadvantage in the accuracy of the result obtained. This is due to the fact that the averaging takes place where there may be incorrect signal values (noise, radio wave reflections, etc.). Therefore, values from the start and end points of the signal are not taken into account in the smoothing calculation. If a result with an accuracy of 1 cm is required (example: determination of the deformation of a job during operation), this method is not optimal [4].

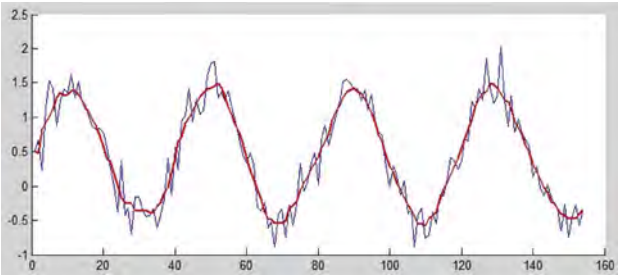

Figure 1. Result of smoothing the signal using the moving average method.

The second method is median signal filtering. This method is widely used in digital processing and can reduce impulse noise. Impulse noise is caused by electromagnetic waves or a technical failure in the signal reception system. The median filter differs from the arithmetic average filter in that it is selective in the signal window (aperture). If the values in the signal window are a monotonous sequence of numbers, the filter will leave them unchanged. With values standing out from neighbouring points, the filter performs averaging, depending on the chosen aperture. As can be seen in Figure 2, median filtering with the correct aperture is able to preserve the sharp variations in the signal while suppressing the interference in the array [5].

The median method has found its application in inertial navigation systems where fast orientation in space with an accuracy of approximately 1 meter is required. However, it is not widely used in engineering geodesy, as two-step processing first of statistical, then of impulse noises is not rational for high-precision measurements [6].

The processing methods discussed above are based on calculating the average value of a section of the signal and then averaging it further. We will now look at a new technique. This method is called the interval superposition method. The main difference from previous methods is that it applies a statistical calculation algorithm inside the signal segment. This method is basic in deformation monitoring for a structure along with the kinematics mode. The great advantage of this method is the millimetre accuracy of coordinate determination, but such a result requires strict consistency in methodology and favourable surveying conditions [7]. In static mode, the resulting data array is divided into time intervals of a certain length. Depending on the company of the equipment used (Leica, Trimble etc.) these intervals are processed in special software. The result of the processing is presented as a diagram,

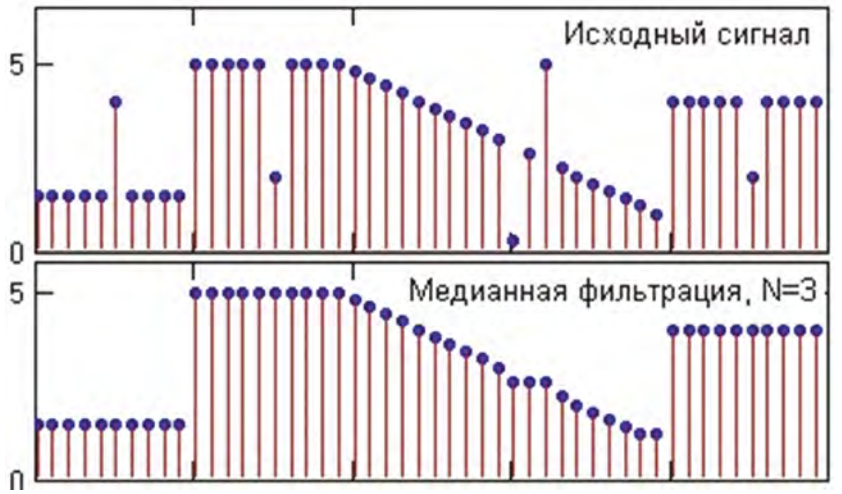

Figure 2. Comparison of signal after median filtering.

where the abscissa axis shows the offset, and the ordinate axis the time interval. Figure 3 shows an example of processing, where 1 hour was taken as the time interval.

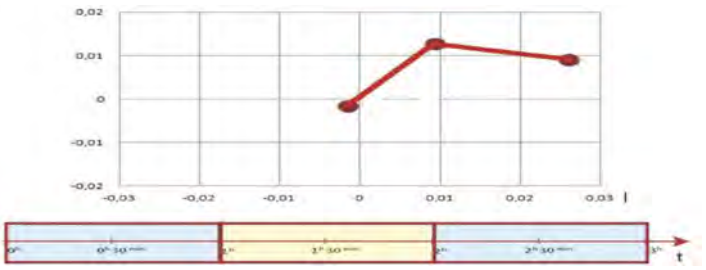

Figure 3. Processing of satellite measurements in static mode at 1-hour intervals.

Static mode requires presetting, as the quality of the result may vary depending on the shooting conditions and the task at hand. The detail can be improved by reducing the time interval, but this may lead to a decrease in the accuracy of the displacement detection. Repeated measurement of coordinates in a short period of time contributes to error accumulation. Studies have shown that 15 to 20 minute intervals are possible if there is no chance of signal re-reflection; the required number of satellites is available; and the geometric arrangement of the receiver stations is correct. But such conditions are rare. For this reason, other survey parameters must be used. The optimum is to have overlapping time slots so that observations are frequent, but not excessive. We now have four time slots of 1 hour and an overlap of 45 minutes. The observation time is three hours. As shown in Figure 4, the overlapping of intervals allows detailed tracking of the GNSS receiver antenna movements on a dynamic object. The appearance of intermediate points helps to study the trend of the object. When monitoring deformation of structures it is possible to track how stable a structure is. For geological monitoring of crustal movement, the data obtained is of great importance if the area is seismically active and suffers from destructive natural phenomena [8].

In the course of the work, the optimum mathematical variant of satellite signal processing for monitoring dynamic objects was established. The static mode proved to be one of the most

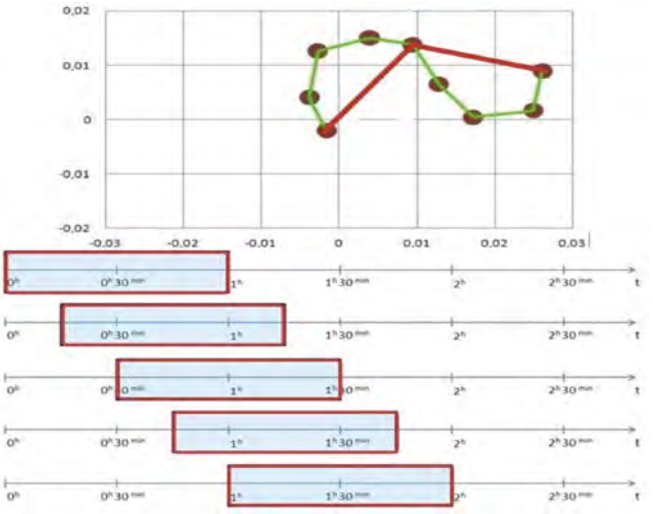

Figure 4. Processing in static mode with overlapping time slots.

feasible, as it meets most of the monitoring requirements. The resulting detail of the displacement trajectory has been realised through repeated measurements under different conditions.

Satellite observation methods have opened up new possibilities for geodetic monitoring of buildings, structures and geological processes. GNSS geodetic monitoring is actively used to study areas of high seismic hazard; for landslide monitoring of quarry sides; for geodetic monitoring of dynamic structures such as towers, bridges, etc. However, it should be noted that the development of the latest technical solutions in the field of geodesy implies the development of modern approaches to geodetic solutions [9]. In other words, when using modern geodetic equipment, it is also necessary to use modern methods of fieldwork and cameral work to replace traditional methods. Therefore, a GNSS overlay survey interval method was developed to address the processing of displacement monitoring data [10].

As is already clear from the name of the interval method, the main role here is played by the duration of those very intervals. The use of one-hour intervals is an acceptable survey parameter, but results in an averaging of the resulting structural displacement. One hour intervals may be used when monitoring targets that are not highly deformable, or when creating an overview model to show the total displacement pattern [11]. If there is a requirement to show more detailed displacement of structures, intervals of 15-20 minutes are used. And following this logic, the shorter the time interval, the more detailed changes to the object will be shown. The reason for this is that more intermediate measurements are taken in a shorter time interval. However, there is always the danger in processing satellite measurements - using short intervals may lead to a poor quality solution. As foreign experience of GNSS application shows, in absence of objects reflecting the signal, sufficient number of satellites and optimum geometric position the use of intervals of 10-15 minutes for processing of observations in static mode allows to receive the solution corresponding to the required level of accuracy of equipment. However, if conditions are different from ideal, the use of 10-minute intervals becomes risky and may affect the accuracy of the final result, so the length of the interval should be chosen, starting from external survey conditions [12]. As can be seen in Figure 5, the interval stacking method is good in that it allows the coordinates of intermediate points to be obtained.

From the above, intermediate points increase the detail of the detected antenna displacements of the receiver and allow for a more accurate representation of the dynamics of the instrument's point of origin. Increasing the detail of the detection of displacements is in fact an increase in the accuracy of the coordinates of the antenna attached to a dynamic object, as a more detailed trajectory at any given time shows a closer approximation to the real position of the antenna [13].

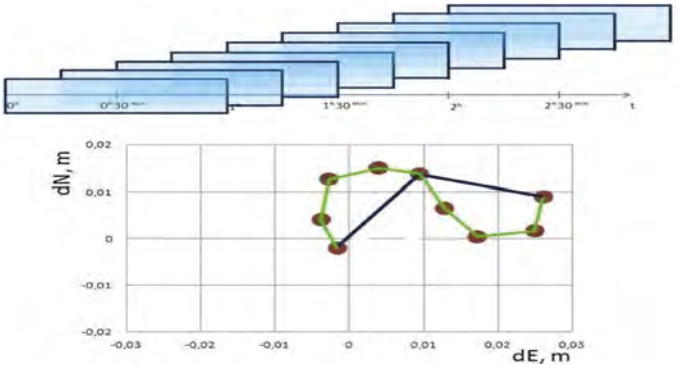

Figure 5. Diagram of displacements using the 1-hour interval treatment.

One of the parameters that characterise the accuracy of a measurement is the RMS value. According to theory, the RMS characterises the internal convergence of measurement results. If a systematic error is taken as a constant value, such as an error for signal over-reflection, this error will have a negligible effect on the RMS value. The RMS value may not be affected by a systematic error which is constant in magnitude, e.g. due to the effect of an over-reflected signal [14]. However, there is the potential for error in short acquisition sessions if the interreflected signal is active for the whole processing interval. One advantage of using the interval overlapping method is that the influence of the signal over-reflections on the measurement result is eliminated. This advantage is due to the fact that there will always be several intervals that include the start or end of an overreflected signal [15].

When selecting the interval length, it is worth paying attention to the drift rate of the permanently installed base station antenna. This value can vary depending on the type of object: for dams and low-rise buildings it can be millimetres, while for radio towers and TV towers the displacement is up to a metre. Accordingly, displacement rates are measured in mm/h to dm/h and, in exceptional cases, in m/h. Logically, when station displacement rates are high, processing using long intervals will produce poor quality results. In theory, the rate of change of position of some structural elements can be calculated from the original data on the parameters of the structure. However, as practice shows, these calculations do not always coincide with reality: this is due to many factors, for example, external conditions, period of operation, etc. [16].

In order to study the dependence of the interval value on the displacement velocity in more detail, test observations using GNSS receivers were carried out. In order to study the dependence of the interval limit value on the displacement rate of the receiver antenna attached to a dynamic object, we carried out observations using GNSS receivers capable of working simultaneously with the signals of most satellite geo-positioning systems.

From the results of the test field surveys, a graph was plotted showing the dependence of the interval value on the receiver antenna displacement rate (Figure 6). It allows determining the limit value of the processing interval depending on the displacement velocity of the structure. If, for a particular velocity, the interval length is greater than the limit values shown in the graph, an incorrect solution is likely [17].

For length intervals between 1 and 5 minutes, it is possible to process measurements even at high displacement rates, up to metres per hour. However, such results require input data with high accuracy and a clear signal. To summarise, the interval stacking method has a number of advantages but, like other methods, requires certain survey conditions. Sufficient number of satellites throughout the measurement period, monitoring network geometry, over-reflection of signals from extraneous objects - all this leads to a decrease in the accuracy of coordinate determination [18].

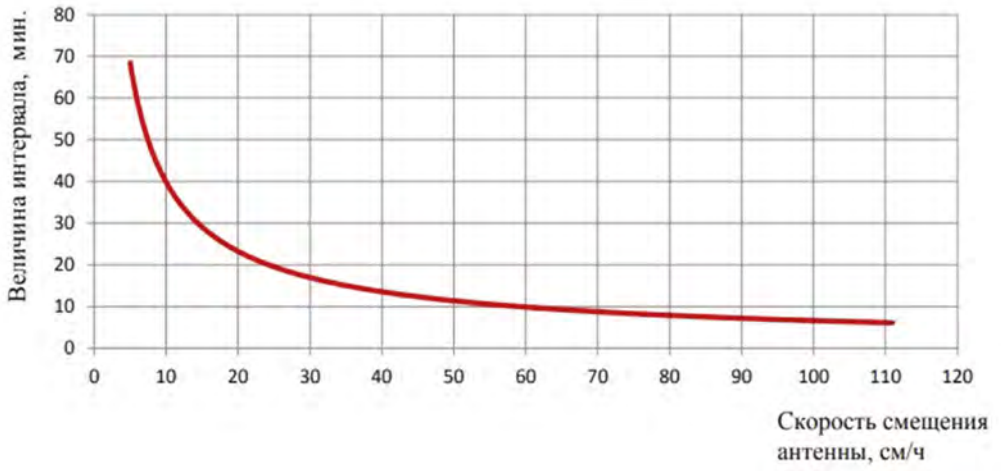

Figure 6. Plot of the interval value versus receiver antenna shift speed.

REFERENCES

1. Markuse Y. I., Golubev V. V. Theory of mathematical processing of geodetic measurements. Moscow: Academician's Prospect, 2010. 247 c.
2. Melnikov N.P., Ishlinskiy A.Y. V.G. Shukhov - an outstanding engineer and scientist. Proceedings of the Joint Scientific Session of the USSR Academy of Sciences dedicated to scientific and engineering works of Honorary Academician V.G.Shukhov. Moscow: Nauka, 1984. 96 c.
3. Mikhailov S. Influence of multi-band radio wave propagation from navigational spacecraft on GPS-receiver coordinate determination accuracy (in Russian) // Wireless Technologies. 2006. №2. C. 60–71.
4. Mishin V. P. Metal Structures of Academician V.G. Shukhov. Moscow: Nauka, 1990. 112 c.
5. Ovcharenko A. V. Complex GNSS monitoring of deformations of high-rise structures of tower type // Ovcharenko A. V., Belikov V. T., Balandin D. V. et al. Engineering Surveys. 2012. №7. C. 38–45.
6. Osipov V. I., Medvedev O. P. Moscow. Geology and the City. Moscow: Moscow Textbooks & Cartography, 1997. 400 c.
7. Rainkin V.Я. Determination of Ostankino TV tower bend by geodetic methods // Izv. of Vuzov: Geodesy and Aerial Survey. 1972. №1. C. 43–51.
8. Weather schedule [electronic resource]. URL: http://rp5.ru/Погода_в_мире (accessed 21.02.2015).
9. Reznik B. E. Continuous geodetic measurements of deformations of building structures of operated structures // Geoprofi. 2008. №4. C. 4–10.
10. Sato Y. Don't panic. Digital signal processing. Translated from Japanese: Dodeka XXI, 2010. 176 c.
11. Sverdlik S. N., Tsutskov S. N. On Possibility of Monitoring of Displacements of Elevation Objects by Single-Frequency Satellite Equipment GLONASS/GPS // Geoprof. 2007. №1. C. 59–61.
12. Serapinas B.B. Global Positioning Systems. Moscow: IKF Katalogue, 2002. 104 C.
13. Sergienko A. B. Digital Signal Processing. SPb: Peter, 2002. 608 c.
14. Serov A., Gavrilov S. G. Creation of a modern geodesic base of the Moscow region // Geoprofi. 2014. № 3. C. 4–7.
15. Skripnikov V. A., Skripnikova M. A. To the question of modernization of the planning network to determine deformations of hydroelectric dams // Geodesy and Cartography. 2012. №1. C. 4–7.
16. Smith S. Digital signal processing. Practical manual for engineers and scientists. Translated from English by Linovich A., Vityazev S. V., Gusinskiy I. S. Moscow: Dodeca-XXI, 2012. 720 c.
17. SNGO of Moscow [electronic resource]. URL: http://sngo.mggt.ru (accessed 05.07.2015).
18. Theory and practice of digital signal processing [electronic resource]. URL: http://www.dsplib.ru (accessed 16.07.2015).

Smart Geotechnics for Smart Societies – Zhussupbekov, Sarsembayeva & Kaliakin (Eds)
© 2023 The Author(s), ISBN 978-1-003-29912-7
Open Access: www.taylorfrancis.com, CC BY-NC-ND 4.0 license

Developing a methodology to improve GNSS monitoring of dynamic objects

Zh.M. Aukazhiyeva, S.S. Sattarov, A.M Muratova & A.S. Sariyeva
L.N. Gumilyov Eurasian National University, Astana, Kazakhstan

ABSTRACT: The issues and examples of remote monitoring, methods of technological improvement on the example of bridge structures are considered. After the analysis of the problems and examples of deformation monitoring was carried out, the next stage of the development of a technique for technological improvement began. As the analysis showed, the big problem of GNSS is the distortion of the signal from satellites. Also, international experience has shown under what conditions it is possible to use satellite coordinate determination. The first step in developing the methodology will be to study the conditions of monitoring and the object of research itself. And only then, starting from the specifics of the bridge structure, the optimal options for the provision of deformation monitoring with the use of satellite technologies will be considered.

1 LOCATION OF DEFORMATION MONITORING

The arch-cable-stayed bridge "Arkhar" is located in the center of the capital Astana and passes through the Ishim River. This object is one of several bridges connecting the left and right banks of the city. A four-lane highway runs along the bridge in two directions. Pedestrian paths are also laid along the edges. Figure 1 shows the bridge "Argali" [1].

Figure 1. "Argali" bridge in Astana.

DOI: 10.1201/9781003299127-329

The basis of the bridge design is two arches running along the bridge. Arches hold the roadbed with the help of a system of cables. This bridge is the first cable-stayed bridge built in the capital.

The width of the bridge is 40 meters with a length of the central part of 150 meters. During the development of the project, it was decided that the bridge would have an arched superstructure with a special configuration. According to the architects' plan, all connected structures and struts passing over the roadway were removed. This decision was made for the sake of a special architectural style. Therefore, special arches were designed for stability, located along the sidewalks on each side. One arched element consists of two interconnected flexible arches. The roadbed was supported by a cable-stayed system developed by the French company Freyssinet. This solution gave the lightness of the design and a positive perception from the point of view of architectural aesthetics. In fact, the bridge structure consists of two parallel arch bridges connected by a roadway with a beam cage.

Today, the bridge "Argali" is one of the main ways to cross the Ishim River. Every day, a relatively large flow of cars passes over the bridge. This is especially noticeable on weekdays, between 8:00-10:00 in the morning and in the evening at 19:00-21:00. These time intervals are considered rush hour, as many residents of the capital go to and from work. Consequently, in the morning and evening there will be fluctuations in the bridge due to the load of the traffic flow.

With regard to weather conditions, a sharply continental climate prevails in the capital. In summer, the temperature can reach up to +35 degrees Celsius. Solar activity exerts uneven heating on the bridge structure, resulting in deformation processes. It is also worth noting that Astana is located on a flat terrain. Therefore, a strong gusty wind is a normal phenomenon both in winter and in summer. The wind load causes fluctuations in the bridge structure. Such fluctuations are noticeable when walking across the bridge [2].

Having studied the features of the Argali Bridge and familiarized ourselves with the climatic conditions, we can begin to develop a methodology for technological improvement. During the development process, we will consider the above sources of error in GNSS surveys, and study ways to correct them. As a result, an up-to-date methodology for conducting deformation monitoring using GNSS technology for the Argali bridge is expected. As mentioned earlier, each object is a unique object, and in developing the methodology it is worth remembering this and starting from the real situation at the object.

Turning directly to the development, it is worth noting that satellite technologies represent a relatively new direction in geodesy. Satellite positioning technologies are becoming more advanced every year. And at the moment, the maximum accuracy of determining the coordinates of a point has reached a sub-centimeter indicator. Achieving such accuracy largely depends on the equipment used, since modern geodetic equipment is able to level the influence of errors to a minimum.

During the analysis of the problems of improving the GNSS monitoring methodology, it was decided to divide the workflow into two stages. The first stage is the technological improvement of field survey using GNSS. At this stage, possible improvements in point-by-point shooting will be considered. The second stage is the technological improvement of in–house processing with the use of up-to-date software. In the improvement plan, special attention will be paid to optimizing the processing of geodetic measurements, their further integration with GIS and final visualization.

2 IMPROVEMENT OF THE FIELD SURVEY METHODOLOGY

Technological improvement of the field GNSS survey technique consists in the selection of the optimal way to eliminate errors. To do this, let's go through each type of errors that occur during the geodetic survey. Figure 2 lists the main types of errors during GNSS shooting [3].

The main sources of satellite measurement errors are:

– desynchronization of satellite onboard clocks, ephemeris errors, unsuccessful geometric arrangement of satellites in the sky;
– errors resulting from signal delay when passing through the troposphere and ionosphere;
– errors related to the receiver (noise, signal re-reflection, etc.).

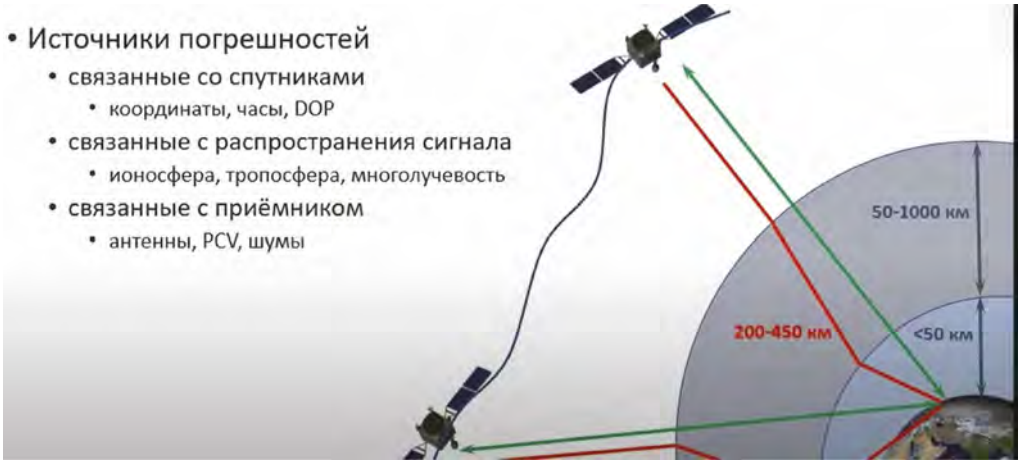

Figure 2. Sources of errors in GNSS shooting.

Let's start with the errors associated with the satellite segment. Ephemeris errors can be eliminated by updating the ephemeris database. Depending on the GNSS equipment used, the selection of current databases is made. Ephemeris data is available on the official websites of GPS, GLONASS, etc. Errors caused by the discrepancy between the clocks of the satellites and the receiver are leveled by calibrating the receiver. Therefore, when using geodetic equipment, it is always necessary to carry out alignment, after which several test measurements should be made at reference points. The error associated with the DOP (dilution of precision) indicator is eliminated by selecting the optimal shooting time. The DOP indicator itself means a concept used in the field of global positioning systems for parametric description of the geometric relative position of satellites relative to the receiver antenna. Figure 3 shows two examples of the location of satellites, where the first option is unsuccessful, since the close location of the satellites and a small angle give an incorrect result. Also, to work with GNSS, it is necessary that at least four satellites are available [4].

Next, in Table 1, we will look at the DOP values, which show us how optimal the spatial location of the satellites is. DOP indicators range from 1 to 50, where 1 is the best value.

Next, we will analyze the errors associated with the GNSS receiver. One of the common mistakes associated with the receiver antenna is the incorrect determination of the antenna phase center. Before installing the receiver in the operating state, it is necessary to determine the location of the phase center. This is usually done in the monitoring project setup menu. By default, the phase center of the antenna is located at the base of the receiver attachment to the vertex [5]. It is recommended to use this option, since when centering above the point, it will be easier to maintain the level of the axis relative to the plane of the device's standing. Also, the appearance of noise during the transmission of a radio signal is inevitable. But this error can be eliminated at the stage of desk work, since such measurements stand out strongly against the background of other correct ones. If the signal quality is poor, an additional antenna can be used [6].

Most of the listed errors can be compensated with the relative method of determining coordinates. Also, modern GNSS receivers coupled with controllers are able to eliminate the impact of gross errors. Most modern receivers operate at several frequencies at once, which helps to avoid the influence of signal delay through the ionosphere.

One of the most dangerous errors is the re-reflection of the signal, since the error greatly affects the accuracy. Multipath occurs as a rule in urban areas where there are many high-rise buildings. This problem is solved by correctly positioning the points in an open space. In our case, on the Argali Bridge, large distortions will occur under arched structures that overlap the horizon and the sky.

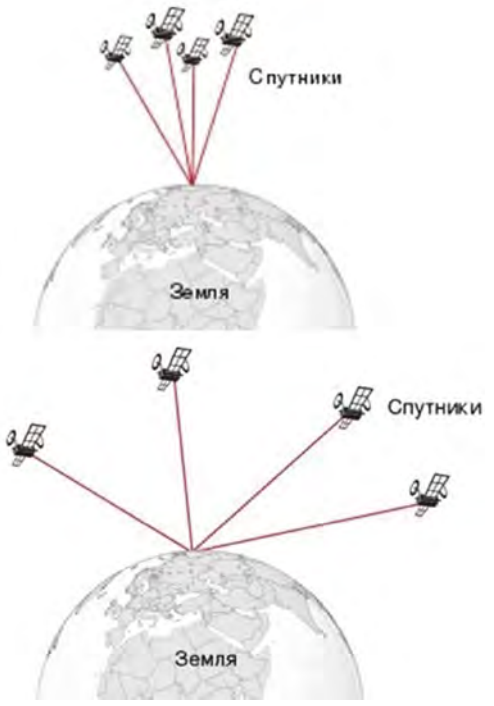

Figure 3. Variations of the spatial location of satellites in the sky.

Table 1. DOP values.

DOP values	Accuracy	Description
1	Ideal	The best indicator, recommended for work requiring maximum accuracy
2-3	Excellent	Sufficient accuracy when working with sensitive equipment
4-6	Good	The minimum allowable value for measurements used in production
7-8	Average	Acceptable results for navigation, it is recommended to try to go to a more open space to improve accuracy
9-20	Below average	The results can be used to determine the approximate location
21-50	Bad	The accuracy of determining the position is equal to half of the football field, the results are subject to rejection

Now let's move on to choosing the shooting mode. In previous chapters, we discussed the advantages of relative methods of satellite observations, namely the static mode. In static mode, the receiver stands still. But since we have the ability to connect the base station, the measurements will be carried out in RTK mode. This method is most suitable for deformation monitoring. After the rover is installed at the facility, we will use a SIM card to connect to the Geokurs base station, located not far within a radius of 5 km from the Arkhar Bridge. As a result, we will succeed, so that our rover in RTK shooting mode will calculate its location for a certain time. The resulting calculations will already go together with the differential corrections and with the postprocessing performed. The expected measurement accuracy should be a few centimeters. After completing the shooting at one station, we will move on to the next. In total, it is planned to make 6 observation stations. This amount will be enough for our research object. As a result, we expect to receive spatial data that displays up-to-date information about the vibrations of the bridge. At the experimental stage, we will determine the method of station placement and the choice of equipment used [7].

REFERENCES

1. Measurements of long lengths, coordinate-time and navigation measurements. Research and development and operation of metrological support of coordinate-time and navigation systems [Electronic resource]. URL: http://www.vniiftri.ru/index.php/ru/struct/nio-8 (accessed 25. 04. 2015).
2. Kalabin E. V., Lokhov V. S. Principles of conducting continuous monitoring on geodynamic objects // Geoprofi. 2012. No. 2. pp. 58–61.
3. Kaftan V. I., Dokukin P. A. Determination of displacements and deformations according to satellite geodetic measurements // Geodesy and cartography. 2007. No.9. pp. 18–22.
4. Kuzmin Yu. O. Modern geodynamics of fault zones: faulting in real time // Geodynamics and tectonophysics. 2014. No. 2. pp. 401–443.
5. Lapshin A. Yu., Staroverov S. V., Fyalkovsky A. L. Investigation of the daily movement of the Shukhov Tower by satellite methods/Ninth All-Russian Conference: "Prospects for the development of engineering surveys in construction in the Russian Federation": collection of materials. 2013. p. 127130.
6. Leggett R. Cities and geology. Moscow: Mir, 1976. 560 p.
7. Lobazov V. Ya., Mayorov A. A., Yambaev H. K. Geodynamic monitoring of architectural monuments of the Moscow Kremlin // Izv. vuzov "Geodesy and aerial photography". 2009. No. 3. pp. 3–12.

Smart Geotechnics for Smart Societies – Zhussupbekov, Sarsembayeva & Kaliakin (Eds)
© 2023 The Author(s), ISBN 978-1-003-29912-7
Open Access: www.taylorfrancis.com, CC BY-NC-ND 4.0 license

Deep learning approach for GPR image classification

Ngoc Quy Hoang, Seonghun Kang, Sang Yeob Kim, Junghee Park & Jong-Sub Lee
Korea University, Seoul, Republic of Korea

Hyung-Koo Yoon
Daejeon University, Daejeon, Republic of Korea

ABSTRACT: The objectives of this study are to classify ground penetrating radar (GPR) images using a deep learning network trained on raw GPR images and to verify the performance of GPR images treated with white noise. The image dataset includes manually labeled images with three classes: background noise, hyperbola, and manholes. In addition, white noise is introduced into the raw GPR images with different coefficients of variation and new images are used to train the deep learning model. The experimental results reveal that the deep learning model performs well on the raw GPR images, with high classification accuracy. Furthermore, the white noise added to the raw images increases the robustness of the deep learning model. The results of the present study demonstrate the application of a deep learning approach and white noise for classifying GPR images.

1 INTRODUCTION

Investigations of underground conditions using electromagnetic waves, such as ground penetrating radar (GPR), have been commonly applied for the detection of buried objects (Ko et al., 2012; Hong et al., 2018). GPRs use reflected electromagnetic signals propagating through media with different electromagnetic properties to investigate underground conditions (Saarenketo et al., 1998; Gutiérrez et al., 2011). As the reflected electromagnetic signals do not provide any visual pictures of the underground and must be manually analyzed to understand their implications, biased man-made decisions are a potential problem. To address this problem, numerous studies have applied learning networks, such as convolutional neural networks (CNNs) (Zhang et al., 2020) and support vector machines (Xie et al., 2013). Thus, the present study adopted a pre-trained CNN and two different methods of data augmentation using white noise. The augmentation using white noise comprises adding white noise to real GPR images.

The objectives of this study were to test the classification CNN on GPR images and to evaluate the data augmented using white noise. First, this study briefly describes the GPR data, augmentation using white noise, and the classification CNN. Next, the experimental results from the training are presented. In the following sections, the results are analyzed using gradient-weighted class activation mapping (Grad-CAM) to validate the decision-making of the CNN.

2 DATA AND METHOD

2.1 *Data*

The detection of buried objects, underground anomalies, or interfaces of different soil layers using electromagnetic waves is based on the electromagnetic response, which represents the reflections of the electromagnetic waves propagating through materials with different electromagnetic properties (Saarenketo et al., 1998; Hong et al., 2018). An electromagnetic wave is generated over

DOI: 10.1201/9781003299127-330

a single pulse and emitted into the ground via a sender antenna, and the reflected electromagnetic wave is detected via a receiver antenna.

In this study, GPR surveys were conducted at several construction sites in South Korea from 2018 to 2020. The GPR surveys conducted in the fields produced 3,000 black and white GPR images (GPR B-scan images) at 400 × 400 pixels (106 mm × 106 mm), which were classified as noisy reflection (NS), hyperbolic reflection (HB), and heavy loss-of-signal reflection (MH), such as reflections of metal covers of manholes. Typical sample images are shown in Figure 1. Figure 1 (a) shows a typical NS image, i.e., a random signal without any typical visual shape reflected from electrical noise in the field caused by electronic devices, vehicles, or nearby base transceiver stations. Figure 1 (b) shows a typical HB image, i.e., a typical hyperbola indicating the change in travel distance of the electromagnetic response as the GPR antenna signals move toward and pass buried objects, such as pipelines. Figure 1 (c) shows a typical MH image exhibiting a very strong reflection beneath the ground surface as the metal manhole cover does not allow radio waves to penetrate through. A stack of hyperbolic reflections follows as the radio waves meet the interface between the ground and air inside the manhole.

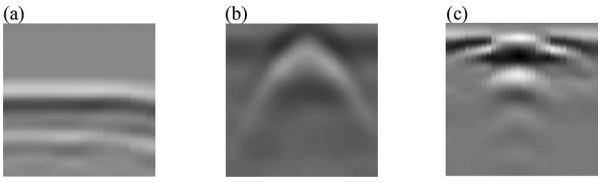

Figure 1. Typical images of 3 classes: (a) NS class; (b) MH class; (c) MH class.

2.2 *Method*

2.2.1 *Image augmentation*

To generate new augmented images, white noise was introduced into the raw GPR images. In particular, white noise with a coefficient of variation (cov) of 0.1 was sequentially introduced into the raw images, as shown in Figure 2. Figure 2 shows the original and augmented MH images. The newly augmented HB images became hazier when the noise was added.

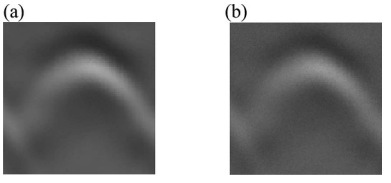

Figure 2. Image augmentation: (a) raw image; (b) augmented image.

2.2.2 *Classification*

A convolutional configuration was employed for the classification of the GPR images, as shown in Figure 2. The configuration includes a feature extractor for extracting deep features from the input images and a classification task for classifying the extracted features into the three designated classes. Herein, a well-known VGG16 network with approximately 138 million weights distributed on 16 layers (introduced by Simonyan & Zisserman (2015)) was adopted to extract the deep features.

For the classification experiment, the raw GRP images were used to train the models with a training and validation ratio of 6:4. In addition, to study the performance of the augmented im-ages, the augmented images were used to train the models with a training and validation ratio of 6:4.

3 EXPERIMENTAL RESULTS

3.1 *Training on raw data*

The results from the training and validation of the raw GPR data are shown in Figure 3. Figure 3 (a) shows the training loss versus epoch for the training and validation of the model on the raw images that the loss quickly decreased until the 20th epoch, and then gradually reached an early stopping point at the 157th epoch; at this point, the training loss continuously decreased, whereas the validation loss increased. Figure 3 (b) shows that the training accuracy quickly increased and approached 0.998 (the highest value) at the early stopping point. The validation accuracy exhibited a similar trend, i.e., quickly increasing in the first few steps and then slowly reaching the highest value of approximately 0.97 at the early stopping point. The validation exhibits an insignificant difference from the training and indicates no overfitting.

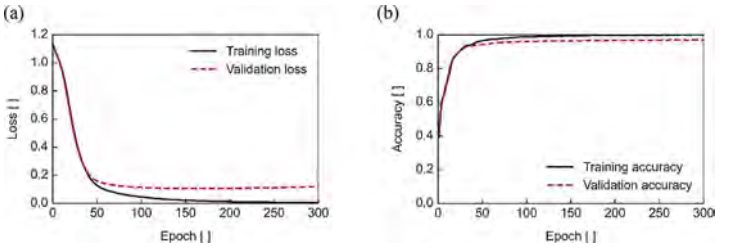

Figure 3. Training results on raw images: (a) Loss; (b) Accuracy.

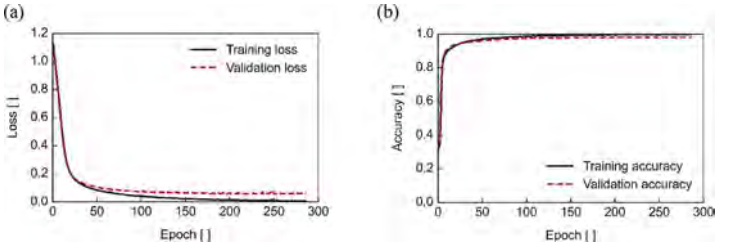

Figure 4. Training results on augmented images: (a) loss; (b) accuracy.

3.2 *Training on augmented data*

The training results for the models for the augmented images are plotted in Figure 4. Figure 4 shows that training on the augmented data exhibited a similar result with that on the raw images, where the training loss quickly decreased in the first few epochs. However, the validation loss quickly decreased, reached its lowest at the early stopping point, and then slightly increases. The training accuracy increased continuously to 1.0, whereas the validation accuracy exhibited a slightly lower value of 0.986 at the early stopping point.

4 ANALYSIS AND DISCUSSION

To analyze the performance, Grad-CAM (Selvaraju et al., 2019) was created by back-propagating from the last convolution layer to the input to indicate the contribution of a pixel to the decision-making of the models, as shown in Figure 5. Figure 5 (a) shows the Grad-CAM for an MH image using the model trained on raw images, whereas Figure 5 (b) shows the Grad-CAM for the same MH image using the model trained on augmented images. Figure 5 (a) shows a localization mostly covering all pixels containing the MH object; however, some parts on the right-hand side show less

of a contribution relative to the left. In contrast, Figure 5 (b) shows a symmetric localization covering the upper part of the MH object. Therefore, the white noise significantly improved the accuracy of the classification of CNN models and localization. This finding agrees with those of previous studies, such as Borji & Lin (2019), Fong et al. (2018), and Deng et al. (2019).

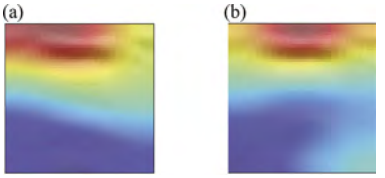

Figure 5. Grad-CAM performance by models trained on: (a) raw images; (b) augmented images.

5 SUMMARY AND CONCLUSIONS

The objectives of this study were (1) to classify GPR images using a deep learning network trained on raw GPR images and (2) to verify the performance of GPR images treated with white noise. Raw GPR images were collected through experiments at construction sites and labeled into three classes: BN, HB, and MH. For the data augmentation, white noise with cov = 0.1 was combined with the raw GPR images. For the classification task, a learning network consisting of a pretrained VGG16 feature extractor and classifier was adopted and used for the training of raw, Method A synthetic, and Method B synthetic data. Grad-CAM was used to evaluate the performance of the learning network. Based on the experimental results, the main observations were as follows:

- The performance on raw images was sufficiently high and avoided overfitting.
- The images augmented by white noise improved the performance of the CNN classification. Grad-CAM indicated that the localization of the model using augmented images is more accurate than that using raw images.

ACKNOWLEDGEMENTS

This work was supported by the National Research Foundation of Korea (NRF) grant funded by the Korea government (MSIT) (No. NRF-2021R1A5A1032433).

REFERENCES

Borji, A., & Lin, S. 2019. White noise analysis of neural networks. arXiv preprint arXiv:1912.12106.

Deng, J., Zhang, W. & Yang, X. 2019. Recognition and Classification of Incipient Cable Failures Based on Variational Mode Decomposition and a Convolutional Neural Network. *Energies* 12(10): 2005.

Hong, W. T., Kang, S., Lee, S. J. & Lee, J. S. 2018. Analyses of GPR signals for characterization of ground conditions in urban areas. *Journal of Applied Geophysics* 152: 65–76.

Saarenketo, T. 1998. Minnesota GPR project, report: TH28, Burtrum, District 3. Minnesota Department of Transportation, Office of Minnesota Road Research.

Simonyan, K. & Zisserman, A. 2015. Very deep convolutional networks for large-scale image recognition. 3rd International Conference on Learning Representations, ICLR 2015 - Conference Track Proceedings, 1–14.

Xie, X., Li, P., Qin, H., Liu, L. & Nobes, D. C. 2013. GPR identification of voids inside concrete based on the support vector machine algorithm. *Journal of Geophysics and Engineering* 10(3): 034002.

Zhang, J., Yang, X., Li, W., Zhang, S. & Jia, Y. 2020. Automatic detection of moisture damages in asphalt pavements from GPR data with deep CNN and IRS method. *Automation in Construction* 113: 103119.

Smart Geotechnics for Smart Societies – Zhussupbekov, Sarsembayeva & Kaliakin (Eds)
© 2023 The Author(s), ISBN 978-1-003-29912-7
Open Access: www.taylorfrancis.com, CC BY-NC-ND 4.0 license

Construction tests of diaphragm wall with enlarged part

M. Kato, T. Watanabe & A. Iwata
Taisei Corporation, Yokohama, Japan

ABSTRACT: The increase in ultra-high rise building column intervals in recent years has meant that the direct bearing load applied to each column has increased. For this reason, the piles need increased bearing capacity and pullout resistance, and continuous underground walls are used in some cases. A diaphragm wall foundation with an enlarged part has been developed in order to achieve even greater bearing capacity and pull-out resistance. Field construction tests confirmed that with proper construction control diaphragm walls with an enlarged part can be constructed in the required shape, dimensions, and quality.

1 INTRODUCTION

It is reported that the increase in ultra-high rise building column intervals in recent years has necessitated the increased direct bearing load applied to each column. For this reason, the piles are now subject to increased bearing capacity and pull-out resistance, and continuous underground walls are used in some cases (Ninomiya et al. (2017)). To achieve even greater bearing capacity and pull-out resistance, a diaphragm wall foundation with an enlarged part has been developed. In order to cope with these problems, we have been studying the trench stability of diaphragm walls with an enlarged part both from numerical simulations and model tests (Iwata et al. (2022)). The purpose of this study is to confirm that with proper construction control diaphragm walls with an enlarged part can be constructed in the required shape, dimensions, and quality.

2 OUTLINE OF CONSTRUCTION METHOD

2.1 *Shape and constructable range*

A schematic view of a diaphragm wall with an enlarged part is shown in Figure 1(a), while representative dimensions and constructable range are summarized in Table 1. Maximum wall-thickness is 1.5m. Enlarged part has a fan-shape in the wall-thickness direction. Maximum constructable width of the enlarged part is 3.16m. Maximum design strength of concrete is set at 60N/mm^2 to make the diaphragm wall highly durable. Image of formed diaphragm wall with enlarged part is shown in Figure 1(b).

2.2 *Excavator for enlarged part*

Mechanism of an excavator for the enlarged part is shown Figure 1(c). The excavator is comprised with three-axis cutters consisting of three rods for excavating the enlarged part and upper and lower stabilizers for keeping them vertical. Enlarged part with a fan-shape in the wall thickness direction is constructed by swinging the three-axis cutters sideways while turning. A clinometer is installed in the upper part of the excavator and in three-axis cutters.

DOI: 10.1201/9781003299127-331

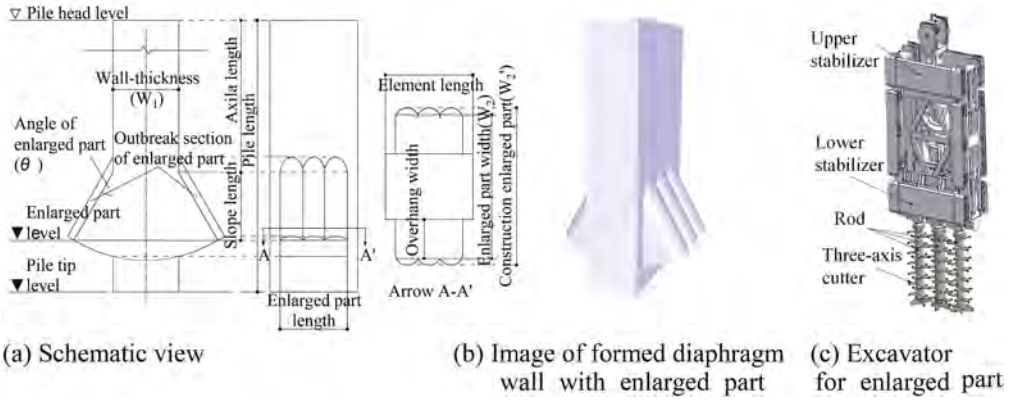

Figure 1. Outline of diaphragm wall with enlarged part.

Table 1. Measurement and constructable range.

Wall – thickness (W_1)	Enlarged part width (W_2)	Construction enlarged part width (W_2)	Maximum angle of Enlarged part (θ)	Pile tip level	Design strength of concrete
[mm]	[mm]	[mm]	[°]	[m]	[N/mm^2]
1200~1500	1300~3160	1615~3730	30.5	80	18~60

2.3 *Excavating procedure*

Main excavating procedure is shown in Figure 2. Axial part of the diaphragm wall is first excavated with the excavator of the reverse type from diaphragm wall top level to predefined tip level. The enlarged part is then excavated. Cut soil drops into the bottom end of the axial part. After excavating the enlarged part is completed, debris on base is removed by the excavator from the bottom of the axial part. Thereafter, resetting the excavator level to the enlarged part, remaining debris is scraped off. This completes the excavation procedure. This excavation process is hereinafter called "process control".

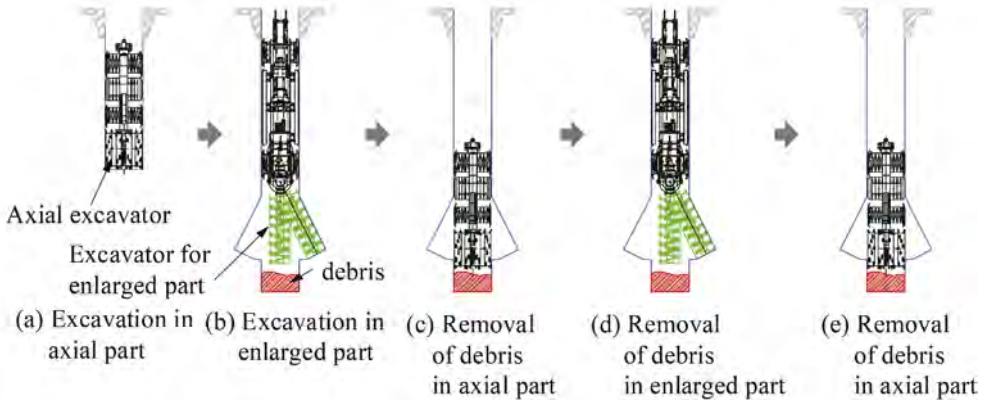

Figure 2. Excavating procedure.

3 SPECIMENS

An outline of field trial construction and main test diaphragm walls is shown in Table 2. Six Diaphragm walls are constructed under various conditions. In this paper, results of two specimens (14-1 and 14-5) which are characteristic in excavation depth and concrete strength are described.

Table 2. Outline of field trial construction and main test piles.

Specimen name	Wall – thickness [m]	Enlarged part width [m]	Angle of enlarged part [°]	Element length [m]	Pile tip level [m]	Enlarged part level [m]	Soil type (N-value)	Concrete strength [N/mm^2]
14-A	1.5	2.66	30.0, 15.0	3.2	5.7	4	*1	-
14-B	1.5	3.16	27.1	7.7	23.6	22	Find sand (about 30)	-
14-1	1.5	3.16	27.1	3.2	13.6	12	Find sand (about 15)	60
14-2	1.5	3.16	27.1	7.7	21.6	17	Find sand (about 50)	-
14-4	1.2	2.57	21.4	3.2	17.5	16	Find sand (about 50)	45
14-5	1.2	2.57	21.4	3.2	74.5	72.5	Silt mingled with sand (about 100)	-

*1. . .Improved ground, Uniaxial compressive strength (285 day material age): 1.43 N/mm^2

4 TEST RESULTS

4.1 *Deep layer excavation test in clayey soil (specimen 14-5)*

To confirm ability of excavator, shape of the enlarged part and verticality of the trench, the enlarged part was excavated to a maximum depth of 72.5m in a clayey soil with an equivalent N-value of about 100.

Shape of specimen 14-5 and its columnar section are shown in Figure 3(a). One gut of the enlarged part was excavated at an angle of 21.4 degrees in a hard silt layer at a depth of G.L.-72.5m.

Results of ultrasonic measurement for the trench are shown in Figures 3(b), (c) and (d). The results show error in the perpendicular direction to the trench is negligible. The ultrasonic measurement result confirms that the proposed excavation method satisfies the design dimensions, and that excavating in the hard clayey soil is possible at great depths.

4.2 *Field construction test for shape and size (specimen 14-1)*

After excavating the enlarged part and placing concrete, diaphragm wall was dug out and shape and dimensions we measured. In this result, validity of "process control" was confirmed. In addition, conducted were the compressive strength tests on core specimens collected from specimen 14-1.

Shape of specimen 14-1 and columnar section are shown in Figure 4(a). One gut of the enlarged part was excavated at an angle of 21.4 degrees in a sandy ground with an N-value of about 15. Results of ultrasonic measurement for the trench are shown in Figure 4(b). The figure also indicates the design dimensions calculated by clinometers and laser measurement results after specimen 14-1 was dug out. From the figure ultrasonic measurement results confirm that the proposed construction method satisfies the design dimensions and that the trench does not fail.14-1

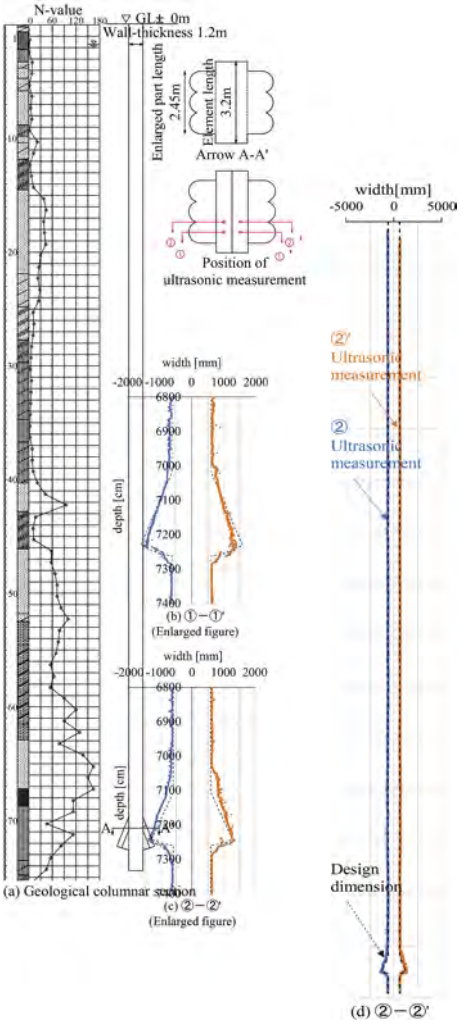

Figure 3. Outline and measurement results of 14-5 specimen.

specimen is dug out to investigate concrete strength, shape and dimensions of enlarged part. The enlarged part was appropriately cut into several pieces so as to retrieve it from underground. The enlarged part of specimen 14-1 is shown in Figure 4(c). It may be seen that the excavated enlarged part is a series of cylindrical holes at different angles. It is because it was produced by turning three-axis cutters of the excavator while swinging the excavator sideways. Changing the angles of the excavator from the vertical, the enlarged part with the groove of arc shape at the bottom is formed. The laser measurement results are generally consistent with the design dimensions. Compressive strength results on concrete cores are shown in Figure 5. Validity of "process control" is confirmed in this result. It was also confirmed that the prescribed compressive strength of concrete was developed.

5 CONCLUSIONS

This study presents workability and development of compressive strength necessary for diaphragm walls with an enlarged part. From the construction test results, the following conclusions are obtained:

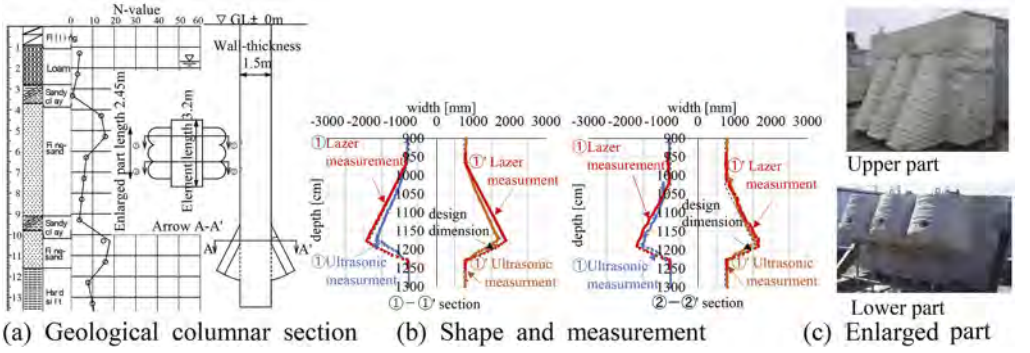

Figure 4. Outline and measurement results of 14-1 specimen.

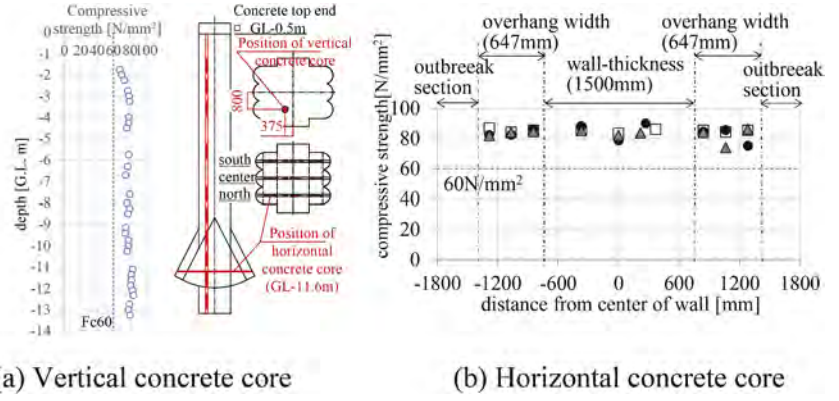

Figure 5. Compressive strength results.

1) The "process control" ensures that diaphragm walls with an enlarged part can be constructed in the required shape and dimensions.
2) It was confirmed that the prescribed compressive strength of concrete was developed.

REFERENCES

Ninomiya, T., et al. 2017. Design of Piled Raft Foundation with Diaphragm Walls for High-rise Building, Part 1~5, *Annual Meeting of AIJ*: 531–540 (in Japanese).

Iwata, A., et al. 2022. Study on Trench Stability of Diaphragm Wall Foundation with Enlarged Part, 10th International Conference on Physical Modelling in Geotechnics (submitted).

Smart Geotechnics for Smart Societies – Zhussupbekov, Sarsembayeva & Kaliakin (Eds)
© 2023 The Author(s), ISBN 978-1-003-29912-7
Open Access: www.taylorfrancis.com, CC BY-NC-ND 4.0 license

Determination of the dynamic characteristics of the building and its base from the accelerograms of weak earthquakes

Vladimir Lapin, Yerken Aldachov, Nurakhmet Makish, Seric Aldachov & Alimzhan Ali
Kazakh Scientific Research and Design Institute of Civil Engineering and Architecture JSC, Almaty, Kazakhstan

ABSTRACT: An interesting local seismic event was registered on the Almaty territory. In terms of intensity, this is a two-point earthquake. The earthquake was recorded only by the stations of the engineering and seismometric service of KazRDICA JSC on October 18, 2017. The station is located in a 4-story frame building. Ground conditions – boulders and pebbles. Using AT 1105 sensors and an RSM-8 recorder, station No. 1 "Institute" recorded instrumental records of accelerations in the basement and on the building roof and plotted the spectral curves β. Period 0.43 sec corresponds to the value of the free oscillation period. It was revealed that even with a low-intensity local seismic impact, the dynamic characteristics of the building are exposed. The active operation of the building as a whole corresponds to the classical Biot spectral theory. The periods of oscillation of the building and soil of the base are quite accurately determined.

1 INTRODUCTION

The entire territory of the Almaty region is prone to earthquakes, which can pose a danger to buildings and structures on the Almaty territory.

The seismic hazard of Almaty is usually associated with the seismogenic zones of the Northern Tien Shan. Strong earthquakes with sources in these zones and magnitudes from 7.5 to 8.5, respectively, are possible, and the earthquake intensity in the city can reach from 8 to 10 points Mikhailova, (2015), Mikhailova, (2018), Sadykova, (2021), Galperin (1985).

The city was destroyed twice by the strongest earthquakes – Vernenskoe in 1887 with a magnitude of 7.2 and Keminskoe in 1911 with a magnitude of 8.2. These are the strongest earthquakes in Central Asia in the last 200 years. The city has repeatedly experienced less severe earthquakes. The Zhalanash-Tüp earthquake of 1978 with a magnitude of 6.9 and the Suusamyr quake of 1992 with a magnitude of 7.3 can be noted. On the city's territory, in different parts of it, they were felt with an intensity of 5 – 6 points Mikhailova, (2015).

For a long time, there was an opinion that there were no earthquake foci on the city's territory. It was believed that faults located on the city's part could enhance or weaken the passing seismic waves of earthquakes with foci in other seismogenic zones outside the city.

In the last 15 years, the appearance of earthquake foci has been noted on the city's territory, the seismic effect of which has so far been pointed out in the range of 2 – 4 points.

In Almaty, there are 10 engineering and seismometric stations on buildings, which also recorded earthquakes with foci in the city. The stations are equipped with digital and analog systems. It is planned to re-equip the stations with new digital systems Deng, (2019), Zhang (2017), Yang, (2018), Qiao (2018).

Every year, several hundred weak earthquakes of varying intensity occur, which are recorded by seismic stations. There is a need to use the accelerograms of such earthquakes to

DOI: 10.1201/9781003299127-332

determine the dynamic characteristics of buildings, to determine the rigidity and dissipative parameters. Determining the dynamic characteristics of buildings is solved using instrumental records of even weak earthquakes registered in the city.

2 MATERIALS AND METHODS

A series of weak earthquakes continue, recorded by the network of stations of the engineering and seismometric service of KazRDICA JSC Yerzhanov, (2017). On October 18, 2017, at 8:18 am, seismic station No. 1 "Institute" recorded a weak seismic event – a local earthquake. Such earthquakes are guaranteed to be recorded infrequently, so it is advisable to consider instrumental records in more detail.

There is no information on the earthquake on October 18, 2017, on the website of the Kazakhstan National Center for Seismic Data. It can be assumed that this is a local earthquake in the Almaty territory. Interestingly, the seismic event was recorded by only one station equipped with a digital instrumentation and measurement system.

Seismic station No. 1 "Institute" is located in a 4-story L-shaped frame building. The frame is reinforced concrete obtained (Figure 1). Now this is the building of the People's Bank of Almaty. Soil conditions – boulders and pebbles. The station was installed in 1968 and modernized in 2008. The devices are installed in the basement on the foundation and the building roof. Currently, the seismic station is equipped with analog sensors OSP and VBP and the instrumentation and measuring system RSM-8.

This station is the first of a network of engineering and seismometric stations on buildings in the Republic of Kazakhstan and, apparently, one of the first in the territory of the former USSR.

In 2016, ADXL sensors at station No. 1 "Institute" were replaced by AT 1105 sensors of Russian production. That made it possible to record even rather weak seismic events.

Thus, as part of solving the problem of determining the building's dynamic characteristics, experimentally obtained earthquake records are used. Spectral analysis methods are used based on the construction of reaction spectra at various registration points.

3 RESULTS

Instrumental records of accelerations – accelerograms were obtained (Figures 2–3). It should be noted that the instrumental records of the earthquake at the basement level have the form of the "white noise" type without areas of an apparent increase in the amplitude of the oscillations. That is due to the small amplitude of the seismic impact.

Of particular interest is the OX accelerogram at the basement level. It looks like a broken "white noise". Nevertheless, the building, even with this impact, makes free vibrations.

Instrumental recordings along the OY and OZ axes at the basement level are very similar to segments of "white noise."

However, at the roof level along the OY and OX axes, instrumental recordings take the form of ordinary accelerograms.

Table 1 shows the maximum acceleration values for each of the instrumental recording components. Lines 1 – 3 correspond to accelerations on the building roof, 4 – 6 – to the building foundation. The maximum values of acceleration along both axes within 1.5 – 1.7 cm/s^2. Spectral coefficients along the OY axis on the foundation and the roof are approximately the same.

Figure 4 shows spectral curves of seismic events on October 18, 2017. Acceleration peaks at the basement level correspond to an oscillation period of 0.03 – 0.10 sec. The building base, made up of boulders and pebbles, makes high-frequency vibrations. On the building roof, the period of the spectrum maximum along the horizontal and vertical axes logically increases. When exposed to the impulse type, the building vibrates freely. Period 0.43 sec corresponds to the value of the free oscillation period.

Figure 1. A frame-brick building with installed engineering and seismometric station.

Table 1. Maximum acceleration values and accelerograms parameters.

Component	Acceleration	Effective duration	Spectral Coefficient	Spectrum maximum period
	cm/s^2	s		s
OX-u1	1.52	37.70	3.11	0.43
OX-u2	1.78	2.54	2.82	0.12
OX-u3	1.28	70.85	3.90	0.07
OX-u6	0.23	70.69	2.93	0.03
OX-u7	0.13	71.69	2.76	0.10
OX-u8	0.20	70.85	3.39	0.03

It should be noted that, despite the low earthquake intensity, the spectrum along the OX axis on the building roof is very saturated and has several maxima. At the basement, the spectral curves have one maximum at high frequencies.

On the OX axis, the value of the maximum period of the spectrum coincides with the period of oscillations of the building in this direction. In Yerzhanov (2017) the values of the period of the spectrum maximum are given under the influence of two remote earthquakes on April 21, 2017, which occurred with an interval of 14 minutes. The value of the period of the maximum of the spectrum is 0.42 s, which is very close to the value of 0.42 s from Table 1.

Thus, it can be considered proven that even with a very weak seismic impact (Figure 3), the value of the oscillation period of the building along the OX axis is determined.

Thus, even based on the results of recording a very weak earthquake, it is possible to determine the main dynamic characteristics of the building and the soil of the base. Therefore, it is advisable to install engineering and seismometric service stations on buildings on standard buildings, high-rise buildings and at unique facilities. Unfortunately, the network of KazR-DICA JSC stations is the only one in the Republic of Kazakhstan. In the future, it is planned to install new seismic stations on buildings in the cities of Shymkent, Taraz, Kapshagai, Ust-Kamenogorsk, Zaisan.

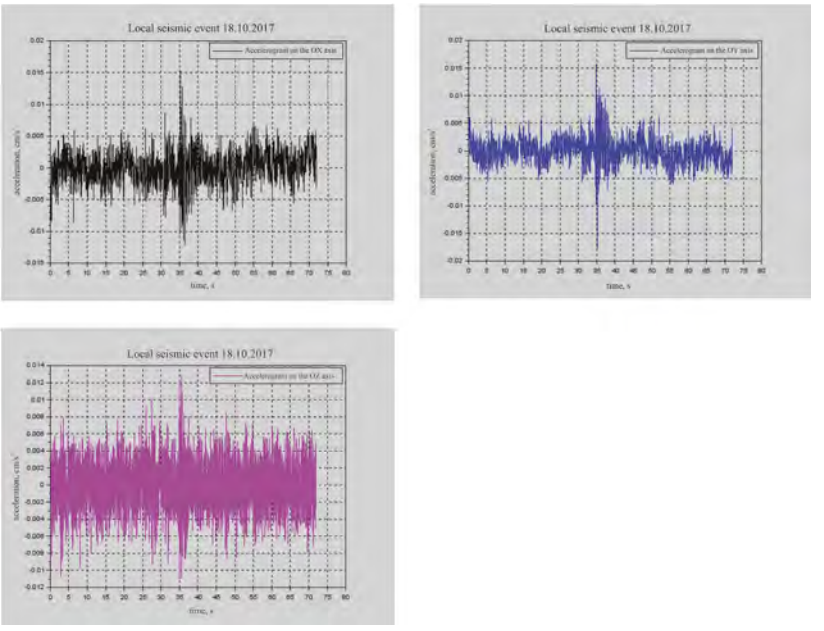

Figure 2. Accelerograms of the seismic event on October 18, 2017 (station № 1 “Institute”, roof).

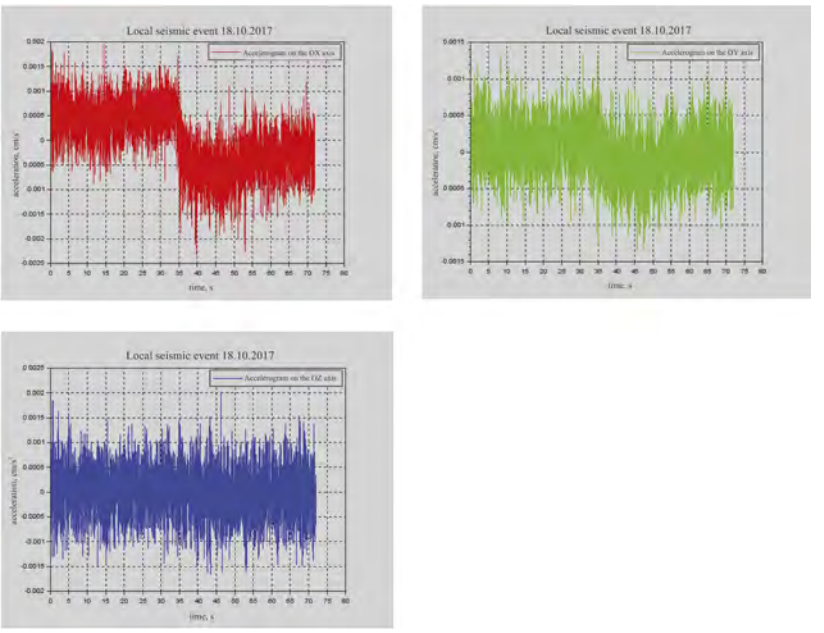

Figure 3. Accelerograms of the seismic event on October 18, 2017 (station № 1 “Institute”, foundation).

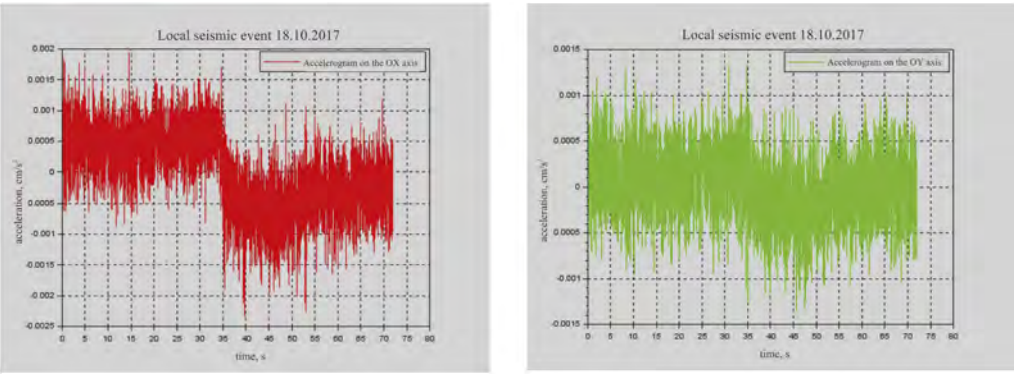

Figure 4. Spectral curves of seismic events on October 18, 2017 (top picture – roof, bottom one – foundation).

4 CONCLUSIONS

1. On October 18, 2017, seismic events are a weak local earthquake with an intensity of no more than 2 points in intensity and frequency composition.
2. Impact not identified by other sources. It is indicated the possibility of earthquakes with foci in the Almaty territory Mikhailova, (2015), Mikhailova, (2018).
3. The operation of the building as a whole corresponds to the classical Bio spectral theory, based on the dynamics of a single-mass oscillator. The structure makes free oscillations with a period along the OX axis equal to 0.43 sec. The period of oscillation of the base soil is within 0.08-0.1 sec.
4. Instrumental records of even very weak earthquakes provide sufficient information to determine the dynamic characteristics of a building. Therefore, to determine the dynamic characteristics of buildings, it is recommended to install temporary engineering seismometric stations that register seismic effects of various intensities, including the weakest.
5. The installation of new engineering and seismometric service stations is recommended to be carried out on buildings with new structural solutions, complex shapes, or built using various seismic isolation systems Bulat (2018), Ahmad (2009), Dyrda,(2019), Bulat (2019), Lapin (2019) . In addition, seismic stations should also be installed on buildings built on sites with difficult ground conditions Zhussupbekov (2015). In connection with intensive high-rise construction, it is advisable to equip high-rise buildings with a height of 20-40 floors with seismic stations. It is planned to install new seismic stations on buildings in the cities of Shymkent, Taraz, Kapshagay, Ust-Kamenogorsk, Zaysan.

REFERENCES

Ahmad, S., Ghani, F. Md. Raghib, A. 2009. Seismic friction base isolation performance using demolished waste in masonry housing. *Construction & Building Materials* 23: 146–152 https://doi.org/10.1016/j.conbuildmat.2008.01.012.

Bulat, A. F., Dyrda, V. I., Lysytsya,M. I., Grebenyuk, S. M. 2018. Numerical Simulation of the Stress-Strain State of Thin-Layer Rubber-Metal Vibration Absorber Elements Under Nonlinear Deformation. *Strength of Materials* 50 (3) 387–395 http://doi.org/10.1007/s11223-018-9982-9.

Bulat, A. F., Dyrda, V I, Grebenyuk, S. N., Klimenko, M. I. 2019. Determination of effective characteristics of the fibrous viscoelastic composite with transversal and isotropic components. *Strength of Materials* 51 (2): 183–192 https://doi.org/10.1007/s11223-019-00064-x.

Deng, M., Wang, M., Jin, S, Zhang, Q, Chen, K. and Cheng, S. A. 2019. A wireless monitoring system for a high-power borehole-ground electromagnetic transmitter. *Geoscientific Instrumentation Methods and Data Systems*, 8 13–19 https://doi.org/10.5194/gi-8-13-2019.

Dyrda, V. I., Kobets, A., Bulat, A.F. et al. 2019.Present problems of vibration isolation in heavy mining machines at long-term cyclic loads. *E3S Web of conference* 168 00042 https://doi.org/10.1051/e3sconf/202016800042.

Galperin, R. M., Nersesov, I. L., Galperin E. I. 1985. Seismic regime of Almaty for 1972 – 1982 years. Moscow: Science.

Lapin, V. 2019. Comparative Analysis of the Effect of Seismic Isolation by Means of Stations of Engineering Seismometric Service on Buildings. *16th World Conference on Seismic Isolation, Energy Dissipation on Active Vibration Conference of Structures* 325–332 http://doi.org/10.13753./2686-7974-2019-16-482-527.

Mikhailova, N. N. & Uzbekov A. N. 2018. Tectonic and technogenic earthquakes in central Kazakhstan. *News of the Republic of Kazakhstan's national academy. Series of geology and technical science* 429 (3) 146–155 ISSN 2518 170X (Online), ISSN 2224 5278 (Print) http://www.geolog-technical.kz/images/pdf/g20183/146-155.pdf

Mikhailova, N. N., Sokolova, I. N., Velikanov, A. E., Sokolov, A. N. 2015. Earthquakes in the city of Almaty. *Bulletin of the National Nuclear Center* 3 87–93.

Qiao, S., Duan, H., Zhang, Q., et al., 2018.Development of high-precision distributed wireless microseismic acquisition stations. *Geoscientific Instrumentation Methods and Data Systems* 7 253–263 https://doi.org/10.5194/gi-7-253-2018.

Sadykova A B, Silacheva N V and Stepanenko N P 2021. Seismic micro zoning of the territory of Almaty on a new methodological basis *News of the national academy of sciences of the Republic of Kazakhstan. Series of geology and technical sciences* 445 (1) 127–134 https://doi.org/10/32014/2021.2518-170X.18

Yang, L., Stehly, L., Paul, A. 2018. Working Group High-resolution surface wave tomography of the European crust and uppermost mantle from ambient seismic noise. *Geophysical Journal International* 214 (2):1136–1150 https://doi.org/10.1093/gji/ggy188

Yerzhanov, S. 2019. On some issues of taking account of the interaction of seismically isolating pile foundations with foundation soil under seismic effects. *16th World Conference on Seismic Isolation, Energy Dissipation on Active Vibration Conference of Structure: s*955–963. http://doi.org/10.13753./2686-7974-2019-16-919-927.

Yerzhanov, S. Y., Lapin, V. A., Daugavet, V P., Devyatykh, A A. 2017. Instrumental registration of 2 earthquakes on 21.04.2017 in Kyrgyzstan by the ISS "Institute station". *Bulletin of KazRDICA JSC* 4 (68): 10–18.

Zhang, X., Zhang, Q., Wang, M., et al. 2017.Development of a full-waveform voltage and current recording device for multichannel and current recording device for multichannel transient electromagnetic transmitters. *Geoscientific Instrumentation Methods and Data Systems* 6: 495–503 https://doi.org/10.5194/gi-6-495-2017.

Zhussupbekov, A. Zh., Frankovská, J., Stacho, J., Al-Mhaidib, A. I., Doubrovsky, M., Uranhayev, N., Yerzhanov, S., Morev I. 2015. Geotechnical and construction considerations of pile foundations in problematical soils. *15th Asian Regional Conference on Soil Mechanics and Geotechnical Engineering, ARC 2015: New Innovations and Sustainability:* 2704–2709 https://doi.org/10.3208/jgssp.TC305-05.

Smart Geotechnics for Smart Societies – Zhussupbekov, Sarsembayeva & Kaliakin (Eds)
© 2023 The Author(s), ISBN 978-1-003-29912-7
Open Access: www.taylorfrancis.com, CC BY-NC-ND 4.0 license

Recent RE Wall failures - Lessons learned

S.M. Dasaka
Professor, Department of Civil Engineering, Indian Institute of Technology Bombay, India

Ammavajjala Sesha Sai Raghuram
Postdoctoral Fellow, Department of Civil Engineering, Indian Institute of Technology Bombay, India

ABSTRACT: The distress in the RE walls is attributed to either one multiple reasons, such as insufficient ground investigations, poor interpretations, inadequate designs, improper construction, and human errors. The current study examines failures of two recent Reinforced Earth wall in India, and identifies the likely causes of failure, through a systematic study of all stages of construction. Measures to avert such failures are also discussed. The investigation of the three case studies revealed that the drainage of RE Wall must be properly considered in RE walls, and highest quality control measures must be exercised in its construction. In view of the changes in the rainfall pattern, and increased probability of occurrence of high intensity of rainfall over several parts of India, it is suggested to cover the backfill material in order to avoid the water infiltration, if any, during the construction phase.

1 INTRODUCTION

Reinforced earth (RE) walls are common earth retaining structures. Space and economic constraints have made RE walls popular worldwide, notably in India. It is easy to place the reinforcement in the soil at the desired depths and compact a RE wall, making its construction cost-effective and straightforward. Road embankments and cuttings, and buildings used RE wall technology. Internal and external stability must be taken into consideration while designing RE walls.

RE walls provide many advantages over other earth-retaining structures. Insufficient drainage and compaction have led to certain RE wall failures. Koerner et al. (2005) highlighted the need of drainage control in RE walls and proposed the drainage behind the reinforcement zone when impermeable soils are utilized as the backfill material. Koerner & Koerner (2018) examined 302 case studies of RE wall failures and reported that insufficient compaction and the use of impermeable backfill materials led to 245 and 232 RE wall failures, respectively. Miszkowska et al. (2018) observed that clogging and retention have a substantial effect on the permeability of geotextiles. After 22 years of installation, the permeability of geotextile in an earthen dam had decreased by 2.6 times. Recently, Raghuram & Dasaka (2022) highlighted the importance of backfill compaction in the construction of RE wall.

The aforementioned studies demonstrate that drainage and compaction characteristics of reinforced fill material, as well as clogging and retention capacity of the geotextile filter, play a significant role on the stability of RE walls and should be taken into account. This study presents two case studies of a recently failed RE walls. The present study identified and discussed the most crucial factors behind failure of these RE walls.

2 CASE STUDY - 1

2.1 *Project details*

The Maharashtra government chose to expand and build a rail over bridge (ROB) in the city of Mumbai. The focus of the current study is on the two RE walls, RE wall-1 and RE wall-2,

DOI: 10.1201/9781003299127-333

which witnessed problems after construction. No geotechnical examination was performed on the foundation soil of the RE walls. An adjacent borehole shows clay in the upper 4 m to 5 m. RE wall-1 is 6.04 m high and RE wall-2 is 4.47 m high.

2.2 *Problem description*

After RE wall work began, the initial design was changed. Once the RE wall started, the public insisted on constructing a box culvert in the narrow zone. This caused an accessibility concern, because of which soil underlying the RE wall was unable to be compacted adequately once the box culvert was built. Before excavating the box culvert, sheet pile walls were erected on three sides to reach required depth for construction of box culvert. Moreover, water mains that bring water to Mumbai run beneath the surface of the ground near the RE wall. RE wall backfill and already compacted soil were excavated to create an excavation ramp for the box culvert. After installing the box culvert, the excavation was backfilled and compacted. Narrow area adjacent to the box culvert hindered proper compaction of the underground part and the refilled material. It resulted in the soil settlement at the culvert zone which in turn caused the settlement of RE wall facia and backfill, and pavement cracks.

The ROB was about to open to traffic. According to the Indian Meteorological Department, the area experienced 117 mm of rain immediately after the ROB was completed. A 5 mm crack and depressions were noted on the rigid pavement on 13 June 2021. Figure 1 shows that RE wall-1 fascia (modular blocks) settled 25 mm. Figure 2 shows that RE wall-2 fascia settled 65 mm.

Figure 1. Fascia settlement of RE wall-1 by 25 mm.

Figure 2. Fascia settlement of RE wall-2 by 65 mm.

Traditional boring from the rigid pavement could not be used due to the site constraints. One side of RE wall has large-diameter Mumbai water pipelines. On the opposite side of the RE wall, existing traffic lanes are present. In addition, a geogrid with very small aperture sizes (2 cm x 2 cm) was employed to reinforce the RE Wall backfill. Therefore, geophysical investigations, such as multichannel analysis of surface waves (MASW) and ground penetrating radar (GPR), were conducted at various locations to assess backfill and foundation soil and thereby to recognize the probable source of RE wall distress and cracks on the rigid pavement.

2.3 *Remedial measures*

Pressure grouting was considered the most effective preventive measure for this project due to the aforementioned site constraints. At the excavated ramp the inadequately compacted fill was pressure grouted. After grouting, galvanized iron grout pipes were left in the soil and filled with cement mortar. This could serve as additional reinforcement. The MASW test was

repeated post grouting, to assess the performance of improved ground. It was noted that shear wave velocities improved at the box culvert zone.

Moreover, pressure grouting is done to fill the PQC-DLC gap. As a precaution, a load test was performed on the treated pavement with a concrete block of size 1 m x 1 m. A vertical compressible load of 24 kPa, equivalent to typical traffic load (IRC:6 (2016), was given on the DLC layer to witness any further settlement of the DLC layer. The pavement was loaded in 10 kPa increments for 12 hours. Under the ultimate load, a 2 mm settling was recorded, which was deemed acceptable. The PQC was then reconstructed using M50 grade concrete. Additionally, a 10-cm test plate was also laid on DLC layer and a MS rod was mounted to test plate placed. This was done to observe DLC layer settlement under real traffic loads. After sixty days of traffic, there was no evidence of settling., demonstrating the good performance of the grouted ground and pavement.

3 CASE STUDY – 2

3.1 *Project details*

In the state of Maharashtra (near Nagpur), the public works department intended to construct a Road Over Bridge (ROB) as part of a state highway across a busy railroad line. Two RE walls were intended for the approaches on either side of the ROB for this reason. This study focuses on these RE walls and the flexible pavement that was constructed on top of the embankment.

The geotechnical investigation indicated the presence of clayey soil for 3 m below the surface of the ground. A ground improvement technique was implemented due to the existence of highly compressible clayey soil in the top layers in order to increase the strength of foundation soil. In addition, the groundwater table is located at 10 m below ground level.

3.2 *Problem description*

The maximum height of RE walls is 14.3 m and the approach length is approximately 1 km. As mentioned in the earlier sections, basal reinforcement and partial soil replacement was adopted as a ground improvement technique. The perforated drainpipe was encased in a non-woven geotextile. In addition, a geotextile layer was placed between the inverted filter and the RE wall's fascia. The backfill material was designed in accordance with IRC:SP:102 (2014) requirements. The RE wall was designed considering a backfill with unit weight of 20 kN/m^3 and an internal friction angle of 32°. The backfill cohesion is zero. Nonetheless, the proposed backfill material was not utilized during the actual construction of the RE wall. As a thermal power station is located in the close vicinity of the RE wall site, fly ash was used as backfill. It is acceptable to utilize any material in the reinforced zone, provided it is readily available near the construction site and meets the requirements indicated in IRC:SP:58 (2014). It was observed that 76% of the fly ash is composed of fines (silt and clay). However, the RE wall design and stability calculations were not modified when fly ash was employed as backfill. As the RE wall design and stability were not checked after considering the fly ash as backfill material, the same non-woven geotextile that was designed for the originally planned backfill was also used for fly ash. Therefore, the apparent aperture size of the geotextile was larger than the corresponding particle size of fly ash.

Due to time restrictions, work continued. This area received 174.8 mm of rainfall in August 2019 as per IMD records. Unfortunately, during the rains the backfill was not covered. Hence, the backfill was exposed to rainfall before the pavement was laid on the RE wall. A flexible pavement was laid over the RE wall without draining the pore water from the backfill. In September 2019, the project site received another heavy rain of 297 mm. In fact, perforated PVC pipes at a slope of 1 in 300 must be installed along the wall as per the design. During construction, horizontal drainage pipes with no slope were placed. Due to a faulty drainage system, rainwater and fly ash fines leaked through the fascia of the RE wall. As

illustrated in Figure 3, the fines were able to escape via the pore of the geotextile from the fascia of the RE wall, as the pore size of the geotextile is bigger than the size of the fines in the fly ash. As a result of the formation of loose soil pockets beneath the flexible pavement, a number of potholes appeared in various locations. The reinforcement was exposed at multiple locations, as shown in Figure 4.

Figure 3. Escape of the fly ash fines from the fascia of the RE wall.

Figure 4. Large potholes at various locations on the flexible pavement.

3.3 *Remedial measures*

All potholes on the flexible pavement were detected, loose soil pockets were eliminated, and gravity grouting was used as a preventative technique. By grouting the potholes, the stiffness of the ground would improve, reducing future settlements. In 2021, the pavement was exposed to rain fall throughout the months of July, August, and September. Now that the roadway is open to traffic, its performance is good and there are no signs of distress.

4 CONCLUSIONS

This study examined the potential causes of the failure of two RE walls in India. The key conclusions that can be drawn from this study are as follows.

➢ Case Study – 1
- Prior to the start of traffic on this freshly constructed ROB, localized depressions and surface cracks were observed in the pavement. In addition, the fascia of the RE walls 1 and 2 settled approximately 25 mm and 65 mm, respectively.
- At the edge of the box culvert, a wide gap was noticed between the PQC and DLC layers. Similar gaps were found in the subsequent two PQC panels.
- Evidence from visual damage and post-distress geotechnical investigations, indicates that the probable cause of the rigid pavement and RE wall collapse was inappropriate compaction of the re-fill underlying the RE wall adjacent to the box culvert.
- Pressure grouting was used as a preventive measure.
- Finally, a MS rod was mounted to the test plate and is placed on top of the DLC layer to monitor the DLC layer settlement, if any. No settlement was seen for 60 days of opening the highway for traffic.

➢ Case Study – 2
- A forensic analysis found that the drainage system was not properly installed as per design. Hence, excess pore water could not flow through the longitudinal drainage pipes placed along the facing.

- The design of the RE wall did not change when fly ash substituted granular backfill. Therefore, the apparent opening size of the geotextiles was greater than that of the fly ash particles.
- Due to heavy rainfall in August and September 2019, percolated water and fly ash fines escaped through the RE wall fascia joints.
- At several locations, loose pockets were observed under flexible pavement which caused severe potholes on the surface of the pavement.
- Grouting the potholes was chosen as a remedial measure.

Every site is distinct and requires a comprehensive site investigation before construction can commence. The above two case studies provide three important lessons. To begin, prior to construction of any structure, the geotechnical characteristics of the natural ground must be thoroughly examined. Second, the design and analysis must be updated to reflect any modifications in the type and quality of planned materials. Third, and perhaps most crucially, the backfill should be covered daily at the end of work to prevent the entry of rainwater. This protects the backfill material against any unanticipated rainfall infiltration. In order to enable periodic maintenance, it is recommended that the sub-surface drainage pipe within the filter/drainage layer be situated outside of the RE wall (i.e., in front of the fascia).

REFERENCES

IMD (Indian Meteorological Department). Regional meteorological center, Nagpur, India. http://www.imdnagpur.gov.in/eindex.asp.

IRC:6 (Indian Road Congress). 2016. Standard specifications and code of practice for road bridges, section: II, Loads and load combinations. No: 6, New Delhi, India.

IRC:SP:102 (Indian Road Congress: Special Publication). 2014. Guidelines for design and construction of reinforced soil walls. No: 102, New Delhi, India.

IRC:SP:58 (Indian Road Congress: Special Publication). 2014. Guidelines for use of fly ash in road embankments. No: 58, New Delhi, India.

Koerner, R.M., & Koerner, G.R. 2018. An extended data base and recommendations regarding 320 failed geosynthetic reinforced mechanically stabilized earth (MSE) walls. *Geotextile and Geomembranes* 46(6): 904–912.

Koerner, R.M., Soong, T.Y. & Koerner, G.R. 2005. Back drainage design and geocomposite drainage materials. *Proc. GRI-19 Conference, Las Vegas*, GII Publication, Folsom, PA, 51–86.

Miszkowska, A., E. Koda, A. Sieczka, & P. Osiński. 2018. Laboratory tests of the influence of clogging on the hydraulic properties of nonwoven geotextiles. *Proc. Intern. Congr. Environ. Geotech.*, *Springer*, Singapore, pp. 686–691.

Raghuram, A. S. S., & Dasaka, S. M. (2022). Forensic analysis of a distressed re wall and rigid pavement in a newly constructed highway approach. *International Journal of Geosynthetics and Ground Engineering*, 8(3),1–14.

Offshore, harbor geotechnics and GeoEnergy

Taylor & Francis
Taylor & Francis Group
http://taylorandfrancis.com

Smart Geotechnics for Smart Societies – Zhussupbekov, Sarsembayeva & Kaliakin (Eds)
© 2023 The Author(s), ISBN 978-1-003-29912-7
Open Access: www.taylorfrancis.com, CC BY-NC-ND 4.0 license

Hybrid monopile supported offshore wind turbine subjected to static and dynamic loads: A state-of-the-art review

Haroon Rashid
PhD PMRF Scholar, Department of Civil Engineering, Indian Institute of Technology Bombay, Mumbai, India

Deepankar Choudhury
Professor T. Kant Chair Professor and Head, Department of Civil Engineering, Indian Institute of Technology Bombay, Mumbai, India

ABSTRACT: Currently, majority of OWT around the globe have monopiles as their foundation system. However, with increase in water depth, diameter of monopile required for such cases increases to a greater extent. To address this issue, a new cost-effective foundation system is needed. In this paper, hybrid monopile foundation has been reviewed that is a combination of monopile and gravity foundation. This new foundation structure fared exceptionally well in a number of centrifuge tests under both static and dynamic loading conditions. Hybrid monopiles have been found to be effective for reducing lateral deflection and improving bearing capacity. Hybrid monopiles have also been proven to minimize the susceptibility to liquefaction. In the paper various parametric studies have been reviewed pertaining to hybrid monopile foundation for both static and dynamic loads. The aim of this paper is to critically review and discuss the hybrid monopile foundation and identify its future scope.

Keywords: Centrifuge Modelling, Hybrid Monopile, Numerical Modelling, Offshore Wind Turbine

1 INTRODUCTION

Interest in the offshore wind energy has increased recently as people have shifted to renewable sources of energy because conventional fossil fuel cannot keep up with the expansion of the global economy. Offshore wind turbines (OWT) are lightweight structures that experience intense lateral loads caused by wind, ice, waves, etc. (Zhao *et al.* 2017). Offshore wind energy is preferred over onshore due to higher wind speed at sea, lesser disruption to human lives and more available area (Bhattacharya 2019). World's offshore wind capacity has reached 32.5GW reducing carbon emissions by 62.5 million tons (GWEC 2021). United Kingdom currently has the largest capacity of offshore farms followed by Germany and China. Typically, 20% to 40% of the overall capital expenditure goes for the design, transportation, and installation of the foundation (Mathern *et al.* 2021). Various foundation types currently exist for offshore wind turbines like monopile, jacket, tripod, floating foundation, gravity type etc. The most typical foundation for OWTs is a monopile due to various advantages (O'Kelly and Arshad 2016). Monopile is a very large diameter pile about 5-6 meters having slenderness ratio of about 6-7. For offshore conditions this diameter further increases compared to onshore as additional loads come into play due to wave loads. These wave loads depend primarily on water depths and also monopile diameter. Hence for deeper waters higher wave loads are expected. To reduce the wave loads in deeper waters monopile of lesser diameter has to be used while still satisfying design requirements but it is not possible using conventional

DOI: 10.1201/9781003299127-334

monopile. Hence majority of monopiles are constructed in waters upto 25 meters (Kuo *et al.* 2012). It has been found that if offshore wind farms with monopiles are installed in deeper waters, cost of energy will increase (Schwanitz & Wierling 2016). Hence an alternative cost effective foundation is required that can serve the purpose for using monopile of lesser diameter in deeper waters. The hybrid monopile foundation is a novel idea composed of gravity footing known as "wheel" and an embedded pile. Hybrid monopile is better suited to withstand the combined lateral and vertical loads brought on by the OWT while preserving the design's simplicity. In seismically active regions, several offshore wind farms are being constructed (Bhattacharya *et al.* 2021). In India, first offshore wind farm has been proposed in Gujarat that's a seismically active zone (Rashid and Sarkar 2022). Liquefaction is yet another problem that occurs in seismically active regions. Hybrid monopile foundation is known to reduce the liquefaction susceptibility and tilt caused due to earthquake (Wang *et al.* 2019b).

2 HYBRID MONOPILE FOUNDATION

Hybrid monopole foundation consists of conventional monopile and gravity wheel foundation added at the mudline. This friction wheel can be a frame filled with gravels or a solidly built circular foundation. The hybrid monopile is known to increase the lateral capacity of conventional monopile. Addition of wheel generates shear stress which resist lateral load and generate additional restoring moments. This addition of moments eventually adds to reduced pile rotations. It was asserted that hybrid footing was more beneficial if vertical translations were permitted between the wheel and the pile since the two components were working separately (Arshi 2016). When used with a wheel, the monopile is identical to a retaining wall with a stabilizing base. The base creates a bearing pressure that generates a resisting lateral load as well as moment (Carder *et al.* 1999). Hybrid monopile foundation is comparable to a pile having pile caps, and the benefits of pile caps have been extensively researched (Mokwa & Duncan 2001, Rollins & Cole 2006). Merits of pile cap has been attributed to significant contribution of passive resistance on the pile cap (Rollins & Cole 2006). Hence analogous to retaining wall and pile cap, hybrid monopile foundation is effective in resisting lateral loads. In general, two different arrangements have been proposed for hybrid monopile foundation i.e., coupled and decoupled.

2.1 *Coupled hybrid monopile foundation system*

In coupled hybrid monopile foundation system, the gravity circular footing is firmly connected to monopile. The pile and wheel in the coupled system share all vertical loading, and to achieve a contact pre-stress between the wheel and the soil, the loads applied must exceed the pile's axial capacity. This will prevent settlement and maintain the plate's contact with the underlying soil. This solution is fundamentally similar to a pile raft with a one pile and would give considerable savings in depth and diameter of monopile.

2.2 *Decoupled hybrid monopile foundation system*

In decoupled hybrid monopile foundation system, the gravity circular footing is not rigidly connected to monopile and is free to slide. The vertical loads applied are taken individually by the wheel and pile. The vertical load transfer occurs only due to frictional force at wheel-monopile connection. The wheel can resist significant vertical loads e.g., the loads coming from weight of wind turbine tower and small additional loads. Hence decoupled system can be used with little or no additional loads coming on pile.

2.3 *Various limit states for design of hybrid monopile*

The state beyond which the structure-foundation assembly will no longer meet the required performance standards is known as a limit state. For hybrid monopile foundation, four limit states are generally considered for design. These limit states are Ultimate limit state (ULS), Serviceability limit

State (SLS), Fatigue Limit state (FLS) and Accidental limit state (ALS). ULS is the maximum load-carrying capacity of a structure. It can be reached owing to various reasons like extreme buckling, loss in equilibrium of structure, extreme yielding and failure of component. For ULS load factors are taken as 1.35 and 1.0 for environmental loads and permanent loads respectively (DNV.GL 2016, Ma & Yang 2020). However, for cyclic loading condition ULS is not commonly experienced (Byrne & Houlsby 2003). Hence for cyclic conditions worst expected transient load is taken, which is calculated by dividing ultimate bearing capacity by 1.35. SLS is in accordance with tolerance requirements related to the usual and typical use of the wind turbine. The serviceability is generally lost due to very high deflections, excessive vibrations and differential settlements causing excessive tilt. Generally maximum allowable rotation is 0.25°. The Fatigue limit state (FLS) pertains to the cumulative effect brought on by repeated loads. To estimate fatigue, estimation of stiffness of foundation is necessary. The FLS depicts the likelihood of failure brought on by the accumulation of cyclic loadings, which may happen at 10^7 cycles. (Wang et al. 2019a). ALS takes into account potential unanticipated or inadvertent loads that could result in a loss of regional or local structural integrity.

In addition to the above mentioned states, there are various design considerations affecting limit states like scour, marine growth and corrosion. A significant design factor is scour, which can alter the structural integrity of foundations. With increase in scour depth, lateral capacity of hybrid monopoles can be reduced by around 15-20% for both SLS and ULS (Li *et al.* 2022).

3 STATIC RESPONSE OF HYBRID MONOPILE SUPPORTED OFFSHORE WIND TURBINE

Offshore wind turbines are slender structures that are subjected to lateral loads due to wind, wave and earthquakes. In this section, review of static response of hybrid monopile supported offshore wind turbine is presented.

Arshi (2016) performed experimental and numerical tests for hybrid monopile supported wind turbine. The effect of addition of wheel was examined for lateral loading conditions. Various parameters were varied and the effect on lateral bearing capacity was examined. Wang *et al.* (2018) performed various centrifuge tests for hybrid monopile foundations and increase in lateral capacity was noted more for loose sand than dense sand. Yang *et al.* (2019) studied lateral-moment loading using centrifuge and numerical modelling for saturated sand. Increase in lateral resistance of pile is found to be due to increase in bearing pressure in front part of the wheel. Wang & Li (2020) performed series of centrifuge tests for parametric studies of hybrid monopile and analytical method was proposed. Wang *et al.* (2022) performed centrifuge tests as well as developed numerical models to study the lateral response. Two different pile connection modes i.e., perfectly rough & perfectly smooth were studied. Different intensities of vertical loadings were also studied. The review of various studies pertaining to parametric variations is given below.

3.1 *The effect of vertical load*

The addition of vertical load enhances the bearing capacity of hybrid monopile considerably. However, this effect has been found to be dependent on position, intensity of vertical load as well as pile-wheel connection. For vertical load applied on wheel, the capacity increases to a greater extent. The enhancement in bearing capacity is because of better connection between wheel and soil due to applying loads directly on wheel (Arshi 2016). This effect of increase in bearing capacity when load applied directly on wheel is more pronounced in case of smooth connection between wheel and pile. It has been found with increase in vertical load, the stiffness decreases while as bearing capacity increases (Wang *et al.* 2022). Slight increase in capacity is also found when load is applied directly on pile. The increased stress in front of the pile is the cause of this increment. Moreover, it has been found that vertical bearing mechanism of hybrid rigidly joined monopile is similar initially to that of wheel only foundation implying more dominance of wheel during initial stages. Also vertical bearing capacity of hybrid monopile is smaller than that of pile and wheel individually. This decrease is due to overlapping stress zones (Brown *et al.* 1988, Ashour *et al.* 2004).

3.2 *The effect of connection type*

Three different connection types are possible between wheel and pile i.e., perfectly smooth, perfectly rough and frictional. Frictional coefficient has very less effect on lateral response of hybrid monopile (Wang *et al.* 2022). Hence perfectly rough and frictional connection are similar as far as lateral load response is considered. No increase in bearing capacity has been found for smooth connection type when vertical loads are applied directly on pile as there is no contact between wheel and pile. This increase is more pronounced in case of rough connection (Arshi 2016). This rigid connection eliminates the effect of position of vertical load. Further for higher loads the bearing capacity is high when loads are applied directly on wheel for smooth connection.

3.3 *The effect of wheel diameter*

Bearing capacity is found to be increased with increase in diameter of wheel. Centrifuge tests conducted have revealed that wheel rotates into the soil in addition to translation that results in soil heave right in front of wheel. Soil behind the wheel is found to be separated on application of lateral load (Yang *et al.* 2019). This embedment of wheel is found to be the reason of increase in lateral resistance (Pedram 2015). Hence with increase in diameter of wheel, the embedment will occur over large area resulting in increase in bearing capacity. The relationship between wheel diameter and ultimate bearing capacity was fitted by series of power curves (Wang & Li 2020)

3.4 *The effect of wheel thickness*

It has been established that as wheel thickness increase, so does lateral bearing capability (Yang *et al.* 2019). However, especially for wheels with very little thickness, the increase in stiffness is not as considerable as wheel diameter. The hybrid foundation system's lateral bearing capability increases linearly with wheel thickness (Wang & Li 2020).

4 DYNAMIC RESPONSE OF HYBRID MONOPILE SUPPORTED OFFSHORE WIND TURBINE

A few offshore wind turbines have already been built in seismically active areas, and some more are also planned (Bhattacharya *et al.* 2021). The soil becomes softer due to dynamic loads, which lowers the soil's bearing capacity. As a result, during the strong earthquake, significant structural settlements and tilts are observed (Liu & Dobry 1997). The soil liquefaction that occurs during an earthquake in an offshore area, in addition to the vibrations brought on by interactions with dynamic loadings and the vibrations of the blades, may seriously harm the entire structural system made up of the upper structure as well as foundation system.

4.1 *Liquefaction*

Liquefaction is one of biggest challenges in regions having high seismicity. Liquefaction of soil can cause serious damage to wind turbine. With highly seismic regions like Taiwan, India etc having plans of building wind turbine farms, the problem of liquefaction is inevitable (Kaynia 2019). Liquefaction could happen in the shallow deposits, which could cause the foundation structure to severely overturn and settle (Li *et al.* 2021). Few studies have been carried out to study liquefaction performance of OWT on monopile foundations (Esfeh & Kaynia 2020, Patra & Haldar 2021). Loss of support along monopile's depth occurs during liquefaction, significantly reducing the system's stiffness. Decrease of the fundamental frequency is observed and may cause resonance with high energy wave loads (Demirci *et al.* 2022). Hybrid monopiles have been found to reduce liquefaction both at the foundation edges and beneath the foundation close to the pile (Wang *et al.* 2020). Pore water pressure ratios near the pile where found to be reduced than free field response and hence chances of liquefaction were reduced. Review of various parametric studies are given below.

4.2 *The effect of wheel diameter*

For saturated as well as dry sand with increase in wheel diameter steep decrease in lateral displacement is seen. However, with increase in wheel diameter the settlements are increased due to dissipation of excess pore pressure requiring a longer pathway. Furthermore, for same weight, the hybrid settles with increase in diameter. Hence for settlement criteria, influence of wheel diameter has to been seen in conjugation with wheel weight. The large diameter pile is likely to attain lesser pore water pressure ratios though rate of dissipation has been found to be reduced. Hence with increase in wheel diameter, soil is found to be less susceptible to liquefaction (Wang *et al.* 2019b).

4.3 *The effect of wheel thickness*

Wheel thickness has considerable effect on response of OWT for both dry and saturated conditions. The lateral displacement tends to diminish as wheel thickness increases. However, the settlement increases with increase in diameter. Nonetheless, the rate of change is less severe than the lateral displacement. Also with increase in wheel thickness similar to wheel diameter, pore water pressure ratio is found to be reduced and hence chances of liquefaction are diminished by use of hybrid monopiles (Wang *et al.* 2019b)

5 CONCLUSIONS

This paper presents a comprehensive review of a novel hybrid monopile-supported offshore wind turbine. Sufficient experimental centrifuge studies and few numerical studies have been reviewed pertaining to hybrid monopile supported offshore wind turbine. Overall review of hybrid monopile along with its types have been presented in the paper. The review of numerous parameters for both static and dynamic conditions is also presented. Following important conclusions can be drawn.

1. It has been confirmed by various studies that hybrid monopiles are very effective for reducing lateral deflections, improving bearing capacity and also reduce liquefaction susceptibility.
2. With increase in wheel thickness and diameter, lateral deflections have been reduced for both static and dynamic tests. Lateral bearing capacity has been found to be increased.
3. Vertical load has improved the lateral bearing capacity as well as reduced lateral deflections and its effect is dependent on connection type as well as position of load.
4. Liquefaction susceptibility has also reduced by hybrid monopile. With increase in wheel thickness and diameter, susceptibility has been found to be reduced.
5. With many advantages in comparison to conventional monopile. There are few disadvantages of hybrid monopile. It has been found that hybrid monopile increases settlement in comparison to traditional monopile.
6. Though experimental and few numerical studies have been conducted in recent years for hybrid monopile still there are many aspects which have not been studied yet. In order to determine the foundation system's versatility, its performance should be examined for a variety of soil types. Wind turbine experience combined loading conditions. VMH failure envelopes can be developed for hybrid monopile foundation. All the experimental liquefaction studies conducted were not fully undrained tests, hence fully undrained centrifuge tests need to be conducted along with numerical studies to give a better picture of liquefaction of sand.

REFERENCES

Arshi, H. 2016. Physical & numerical modelling of hybrid monopiled-footing foundation systems. PhD Thesis. University of Brighton, Brighton, UK.

Ashour, M., Pilling, P., & Norris, G. 2004. Lateral behavior of pile groups in layered soils. *Journal of Geotechnical and Geoenvironmental Engineering*, 130 (6), 580–592.

Bhattacharya, S. 2019. *Design of Foundations for Offshore Wind Turbines*. John Wiley & Sons.

Bhattacharya, S., Biswal, S., Aleem, M., Amani, S., Prabhakaran, A., Prakhya, G., Lombardi, D., & Mistry, H. K. 2021. Seismic Design of Offshore Wind Turbines: Good, Bad and Unknowns. *Energies*, 14 (12), 3496.

Brown, D.A., Morrison, C., & Reese, L.C. 1988. Lateral load behavior of pile group in sand. *Journal of Geotechnical Engineering*, 114 (11), 1261–1276.
Byrne, B.W. & Houlsby, G.T. 2003. Foundations for offshore wind turbines. *Philosophical Transactions of the Royal Society of London. Series A: Mathematical, Physical and Engineering Sciences*, 361 (1813), 2909–2930.
Carder, D.R., Watson, G.V.R., Chandler, R.J., & Powrie, W. 1999. Long-term performance of an embedded retaining wall with a stabilizing base slab. *Proceedings of the Institution of Civil Engineers-Geotechnical Engineering*, 137 (2), 63–74.
Demirci, H.E., Jalbi, S., & Bhattacharya, S. 2022. Liquefaction effects on the fundamental frequency of monopile supported offshore wind turbines (OWTs). *Bulletin of Earthquake Engineering*, 20 (7), 3359–3384.
DNV.GL. 2016. DNVGL-ST-0437: Loads and Site Conditions for Wind Turbines. Det Norske Veritas, Oslo, Norway.
Esfeh, P.K. & Kaynia, A.M. 2020. Earthquake response of monopiles and caissons for Offshore Wind Turbines founded in liquefiable soil. *Soil Dynamics and Earthquake Engineering*, 136, 106213.
GWEC, 2021. GWEC global wind report. *Global Wind Energy Council (GWEC): Brussels, Belgium*.
Kaynia, A.M. 2019. Seismic considerations in design of offshore wind turbines. *Soil Dynamics and Earthquake Engineering*, 124, 399–407.
Kuo, Y.S., Achmus, M., & Abdel-Rahman, K. 2012. Minimum embedded length of cyclic horizontally loaded monopiles. *Journal of Geotechnical and Geoenvironmental Engineering*, 138 (3), 357–363.
Li, B., Wang, Y., Qi, W., Wang, S., & Gao, F. 2022. Lateral Bearing Capacity of a Hybrid Monopile: Combined Effects of Wing Configuration and Local Scour. *Journal of Marine Science and Engineering*, 10 (12), 1799.
Li, X., Zeng, X., Yu, X., & Wang, X. 2021. Seismic response of a novel hybrid foundation for offshore wind turbine by geotechnical centrifuge modeling. *Renewable Energy*, 172, 1404–1416.
Liu, L. & Dobry, R. 1997. Seismic response of shallow foundation on liquefiable sand. *Journal of Geotechnical and Geoenvironmental engineering*, 123 (6), 557–567.
Ma, H. & Yang, J. 2020. A novel hybrid monopile foundation for offshore wind turbines. *Ocean Engineering*, 198, 106963.
Mathern, A., von der Haar, C., & Marx, S. 2021. Concrete support structures for offshore wind turbines: Current status, challenges, and future trends. *Energies*, 14 (7), 1995.
Mokwa, R.L. & Duncan, J.M. 2001. Experimental evaluation of lateral-load resistance of pile caps. *Journal of Geotechnical and Geoenvironmental Engineering*, 127 (2), 185–192.
O'Kelly, B.C. & Arshad, M. 2016. Offshore wind turbine foundations–analysis and design. *In*: *Offshore Wind Farms*. Elsevier, 589–610.
Patra, S.K. & Haldar, S. 2021. Seismic response of monopile supported offshore wind turbine in liquefiable soil. *Structures*, 31, 248–265.
Pedram, B. 2015. A numerical study into the behaviour of monopiled footings in sand for offshore wind turbines. PhD Thesis. University of Western Australia.
Rashid, H. & Sarkar, R. 2022. Site-specific response of a 5 MW offshore wind turbine for Gujarat Coast of India. *Marine Georesources & Geotechnology*, 40 (9), 1119–1138.
Rollins, K.M. & Cole, R.T., 2006. Cyclic lateral load behavior of a pile cap and backfill. *Journal of Geotechnical and Geoenvironmental Engineering*, 132 (9), 1143–1153.
Schwanitz, V.J. & Wierling, A. 2016. Offshore wind investments–realism about cost developments is necessary. *Energy*, 106, 170–181.
Wang, X. & Li, J. 2020. Parametric study of hybrid monopile foundation for offshore wind turbines in cohesionless soil. *Ocean Engineering*, 218, 108172.
Wang, X., Li, S., & Li, J. 2022. Lateral response and installation recommendation of hybrid monopile foundation for offshore wind turbines under combined loadings. *Ocean Engineering*, 257, 111637.
Wang, X., Zeng, X., Li, J., & Yang, X. 2018. Lateral bearing capacity of hybrid monopile-friction wheel foundation for offshore wind turbines by centrifuge modelling. *Ocean Engineering*, 148, 182–192.
Wang, X., Zeng, X., Li, X., & Li, J. 2019a. Investigation on offshore wind turbine with an innovative hybrid monopile foundation: An experimental based study. *Renewable Energy*, 132, 129–141.
Wang, X., Zeng, X., Yang, X., & Li, J. 2019b. Seismic response of offshore wind turbine with hybrid monopile foundation based on centrifuge modelling. *Applied energy*, 235, 1335–1350.
Wang, X., Zeng, X., Li, X., & Li, J. 2020. Liquefaction characteristics of offshore wind turbine with hybrid monopile foundation via centrifuge modelling. *Renewable Energy*, 145, 2358–2372.
Yang, X., Zeng, X., Wang, X., Berrila, J., & Li, X. 2019. Performance and bearing behavior of monopile-friction wheel foundations under lateral-moment loading for offshore wind turbines. *Ocean Engineering*, 184, 159–172.
Zhao, H.Y., Jeng, D.-S., Liao, C.C., & Zhu, J.F. 2017. Three-dimensional modeling of wave-induced residual seabed response around a mono-pile foundation. *Coastal Engineering*, 128, 1–21.

Smart Geotechnics for Smart Societies – Zhussupbekov, Sarsembayeva & Kaliakin (Eds)
© 2023 The Author(s), ISBN 978-1-003-29912-7
Open Access: www.taylorfrancis.com, CC BY-NC-ND 4.0 license

Difference in cyclic lateral loading behavior of a monopile on sandy and clayey grounds

K. Nakai
Nagoya University, Nagoya, Aichi, Japan

M. Ito & S. Sato
Obayashi corporation, Tokyo, Japan

ABSTRACT: As the market for renewable energy continues to expand, expectations for offshore wind power are growing. Monopiles, the most common type of offshore wind turbines foundation, are subjected to cyclic lateral loading due to wind and ocean waves during their service life. Therefore, it is desirable to accurately understand the cyclic loading characteristics of monopiles for design purposes. In this paper, we attempted to understand the difference in cyclic loading behavior of a monopile on sandy and clayey grounds through both model experiments and finite element analysis. As a result, it was confirmed that the lateral displacement of the sandy ground was gradually suppressed by the densification in front of the pile during cyclic loading. On the other hand, the clayey grounds showed rapid increase of displacement if the soil was disturbed by large cyclic loading.

1 INTRODUCTION

As the market for renewable energy continues to expand, expectations for wind power are growing. In Japan, there are few suitable sites for wind power generation on land, so offshore wind power generation is expected to become more popular. Monopiles, the most common type of offshore wind turbines foundation, are subjected to cyclic lateral loading from wind and ocean waves during their service life. Therefore, it is desirable to accurately understand the cyclic loading characteristics of monopiles for design purposes. Large-scale wind farms have been already constructed in Europe, and many studies have been accumulated. However, most of the studies on the behavior of monopiles subjected to cyclic loading have been conducted on sandy grounds (Long et al. 1994, Liao et al. 1999), and few studies have been conducted on soft clayey grounds which frequently exist around Japan. The purpose of this paper is to understand and compare the cyclic lateral loading behavior of a monopile on sandy and clayey grounds through model experiments and FEM analysis.

2 OUTLINE OF MODEL EXPERIMENTS AND NUMERICAL ANALYSIS

Schematic diagrams of the model experiment are shown in Figures 1a, b. The model pile was made of aluminum with an outer diameter of 130mm, a wall thickness of 3.0mm, and a length of 1,600mm, about 1/50th the scale of the real pile. The sandy ground was made of Nikko silica sand No. 6 in a rigid soil tank to achieve a relative density of 60%. The clayey ground was excavated from the surface soil at the outdoor test site to expose clay with N-values of 2 to 4. In both cases, a model pile was installed into the ground with a penetration depth of 800mm. Lateral loading was conducted by an electric jack 720mm above the ground surface.

DOI: 10.1201/9781003299127-335

The analysis code used was a soil-water coupled finite deformation analysis (Noda et al. 2008) employing elasto-plastic constitutive model; SYS Cam-Clay model (Asaoka et al. 2002), that can describe the mechanical behavior of various soils from sand to clay within a same theoretical framework. FEM mesh is shown in Figure 1c. The mesh was prepared with reference to the rigid soil tanks used in the model experiments, and a half-section model was used considering the symmetricity. The same mesh was used even for clayey ground. Here, the distance from the monopile to the boundary of the analysis domain is more than 3φ for a pile diameter of φ130mm, so the difference in boundary conditions was considered to have less effect. The material constants and initial conditions were determined from the results of laboratory tests (standard consolidation and triaxial compression tests) conducted under the same conditions as the model experiments. The monopile was assumed to be a linear elastic body using solid elements, and the elastic constants of aluminum were used to obtain the same conditions as in the model experiment.

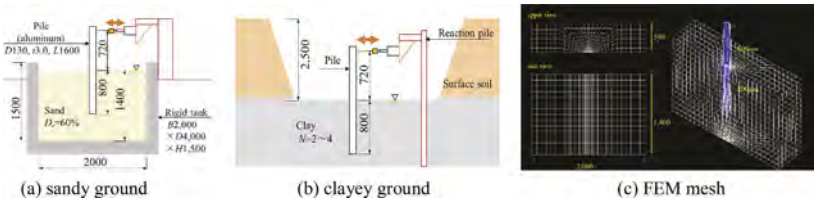

Figure 1. Schematic diagram of model experiments and FEM analysis.

3 MONOTONIC LATERAL LOADING BEHAVIOR

Figure 2 shows the reaction force-displacement relationship at the loading point for the monotonic lateral loading test conducted on sandy and clayey grounds. The analytical results for both grounds reproduce the experimental results well. Comparing the two grounds, the clayey ground had a clear ultimate bearing capacity *Pu*, while the sandy ground continued to increase lateral load. Based on the experimental results, *Pu* = 0.82kN for the sandy ground and *Pu* = 5.9kN for the clayey ground were determined.

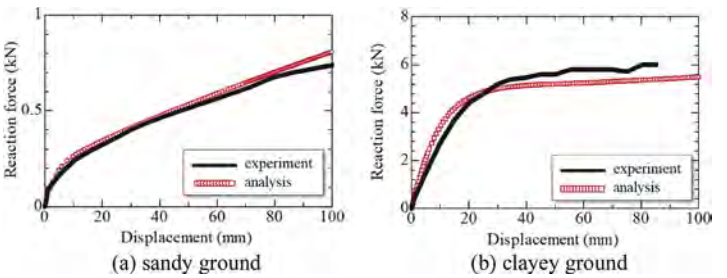

Figure 2. Monotonic loading behavior by model experiment and FEM analysis.

4 CYCLIC LATERAL LOADING BEHAVIOR

Cyclic lateral loading tests were conducted at amplitudes of 0.1*Pu*, 0.3*Pu* and 0.5*Pu* based on the ultimate load *Pu* obtained from the monotonic loading tests. The 0.1*Pu* assumes ocean waves at ordinary conditions, while the 0.3*Pu* and 0.5*Pu*, storm waves. The loading was given in the form of a one-sided triangular wave, and the periods are assumed to be 6, 11 and 16 seconds for 0.1*Pu*, 0.3*Pu* and 0.5*Pu*, respectively, as average values of the assumed external forces.

Figure 3 shows the relationship between the displacement increase rate at ground surface $\delta N/\delta N_1$ and the number of cycles N in the model experiments (where δN and δN_1 are the displacement at the Nth and 1st cycles, respectively). The lateral displacement increased with the

number of cycles for both grounds. For the sandy ground, the displacement tended to converge showing linear relation on the one-logarithmic graph. Moreover, the increase rate did not change significantly regardless of the amplitude. On the other hand, for clayey ground, the increase rate became large with the amplitude, and the lateral displacement increased rapidly during the cycles. In addition, the larger the amplitude, the more rapidly the displacement increased after a smaller number of cycles. The analytical results are shown in Figure 4. Although the number of cycles at which the displacement began to increase is slightly smaller for clay, the analytical results captured the trend of the experimental results well, as the increase rate was linear for the sandy ground and the displacement increased rapidly for the clayey ground.

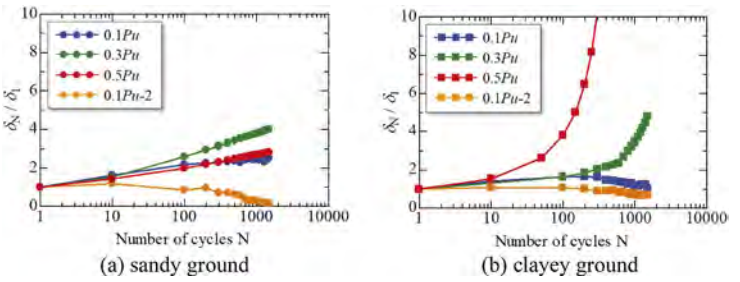

Figure 3. Relationship between displacement increase rate and number of cycles (model experiments).

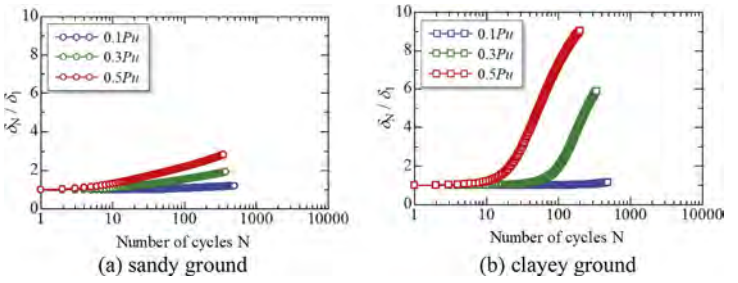

Figure 4. Relationship between displacement increase rate and number of cycles (FEM analysis).

The difference in cyclic loading characteristic between sandy and clayey grounds are discussed in detail. Figures 5 and 6 show the distribution of void ratio change, degree of structure and shear strain after 40 cycles at an amplitude of $0.5Pu$ in sandy and clayey ground, respectively. Here, structure stands for the bulkiness of the soil, which is widely observed in soft soils, and the higher the degree of structure, the more sensitive the behavior. Lowering/collapse of the structure can be regarded as soil disturbance, which causes volumetric compression and decrease in strength. The void ratio change shows that the sandy ground became denser in front of the monopile during cyclic loading. On the other hand, clay with low permeability showed little density change. This indicates that the displacement of the monopile in the sandy ground was gradually suppressed by the density increase during cyclic loading. The distribution of the structure indicates that clayey ground possessed higher degree compared with sandy ground at initial condition. In addition to that, the clayey ground was strongly disturbed during cyclic loading, and the structure around the monopile was lowered over a wide area. Especially in the case of large amplitude, the clay ground was significantly disturbed, and the displacement of the monopile increased rapidly during loading. The shear strain shows that the strain in the sandy ground was concentrated around the pile, whereas that in the clayey ground was spread over a wide area. This tendency was the same as the experimental results, although the details are omitted due to the limited pages.

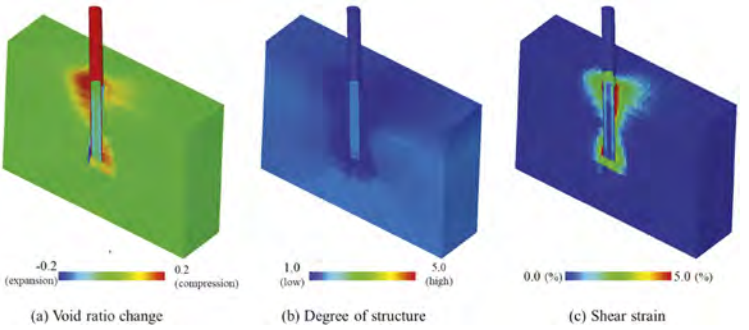

Figure 5. Contour distributions of sandy ground subjected to 40 cycles of cyclic loading with 0.5*Pu*.

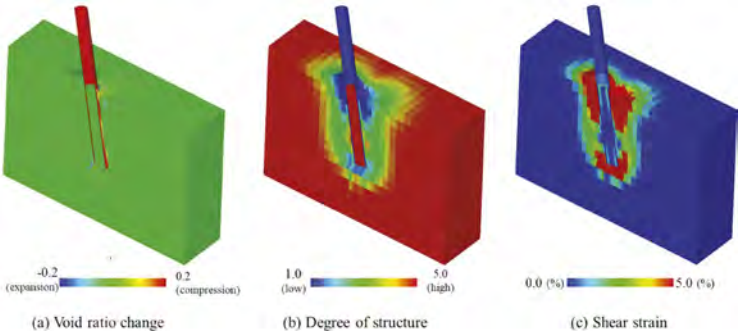

Figure 6. Contour distributions of clayey ground subjected to 40 cycles of cyclic loading with 0.5*Pu*.

5 CONCLUSIONS

We compared the cyclic lateral loading behavior of a monopile on sandy and clayey grounds through both model experiments and FEM analysis. In sandy ground, lateral displacement was gradually suppressed by density increase during cyclic loading. On the other hand, the clayey ground showed rapid increase of displacement if the soil was disturbed by large cyclic loading. In addition, the 0.1*Pu*-2 in Figure 3 was the result of cyclic loading at 0.1*Pu* after a cyclic history of 0.3*Pu*. This result also confirms experimentally that, if the load history is large beforehand, displacement hardly propagates under small amplitude loading.

Comparison between model experiments and FEM analysis has confirmed the validity of the analytical code. Therefore, in the future, this analysis code will be used to study complex stratification alternating clay and sand layers that cannot be reproduced by model experiments, as well as for full-scale studies.

Finally, we would like to thank Prof. Toshihiro Noda (Nagoya University) and Mr. Taku Kurimoto (Obayashi corporation) for valuable advice in the course of this research.

REFERRENCES

Long J. H. and Vanneste Geert. 1994. Effects of cyclic lateral loads on piles in sand, *Journal of Geotechnical Engineering* 120(1): 225–244.

Lin San-Shyan and Liao Jen-Cheng. 1999. Permanents strains of piles in sand due to cyclic lateral loads, *Journal of Geotechnical and Geoenvironmental Engineering* 125(9): 798–802.

Asaoka, A., Noda, T., Yamada, E., Kaneda, K. & Nakano, M. 2002. An elastoplastic description of two distinct volume change mechanisms of soils, *Soils and Foundations* 42(5): 47–57.

Noda, T., Asaoka, A. & Nakano, M. 2008. Soil-water coupled finite deformation analysis based on a rate-type equation of motion incorporating the SYS Cam-clay model. *Soils and Foundations* 45(6): 771–790.

Smart Geotechnics for Smart Societies – Zhussupbekov, Sarsembayeva & Kaliakin (Eds)
© 2023 The Author(s), ISBN 978-1-003-29912-7
Open Access: www.taylorfrancis.com, CC BY-NC-ND 4.0 license

Enhancing load carrying performance of helical anchor with changes in load application point

J. Lee, Q. Abbas, J. Yoon, D. Nam & J. Lee
Yonsei University, Seoul, Korea

ABSTRACT: Helical anchor is effective to support offshore structures as the installation is relatively fast and simple. The installation requires mooring lines, which need to be introduced to carry floating upper structures. The mooring configuration for helical anchor usually shows an inclined loading condition. In this study, the effect of load application point (z_p/L) and inclined loading condition on the load carrying mechanism of helical anchor is presented. The pullout capacity of helical anchor for different load inclination conditions is described considering changes in load application point. Optimal load application point, which leads to the largest load carrying capacity, is shown for various helical-anchor configurations. The pullout load carrying capacity of helical anchor became different depending on the position of load application point, which was similar to the case of suction anchors. The location of optimal load application point that maximized the pullout load capacity was presented.

1 INTRODUCTION

For the past few decades, helical anchors have been used frequently for offshore foundation system. Helical anchors have various advantages including immediate mobilization of the load carrying capacity, fast installation, and flexibility in changing configurations. The helical anchor consists of a shaft and helically shaped plates welded along the shaft. Owing to the constitution of different structural components, helical anchors indicate a variety of configurations and can be effective to resist against both compressive and tensile loads. Furthermore, helical anchors can carry loads in various directions including axial, lateral, and inclined direction as the mooring system is introduced.

The load-carrying behavior of helical anchors has been widely studied (Rao et al. 1991,1993, Merifield 2011, Wang et al. 2013, Schiavon et al. 2016, Harnish & El Naggar 2017, Kwon et al. 2019). Merifield (2011) presented a design method for tensile load-carrying capacity of helical anchor installed with multiple plates for various anchor configurations. Wang et al. (2013) performed a large-deformation finite element (FE) analysis to characterize the tensile load-carrying capacity of helical anchors.

When helical anchors are installed for supporting an offshore floating structure, a mooring system with load-carrying lines is necessary to deliver loads from floating structure to the anchors. Cortes-Garcia et al. (2019) and Kwon et al. (2019) studied the load-carrying behavior of helical anchor subjected to inclined loading conditions and, and that for cyclic loading condition was investigated by Lee et al. (2019).

As the mooring system is introduced, the location of the load application point, given by pad-eye, also needs to be considered as a component that affects the load carrying behavior of the anchors. As reported in the literature (Aubeny et al. 2003, Tian et al. 2015, Kim & Hossain 2016), the location of the load application point on the shaft indicates certain effect on the load-carrying behavior of embedded types of anchor systems. The effect of the load application points for helical anchors was also investigated by Lee & Lee (2022).

DOI: 10.1201/9781003299127-336

In this study, the effect of the load application point on the load-carrying mechanism of helical anchors is presented. For this purpose, the results given by Lee & Lee (2022) were introduced and analyzed. 4 types of helical anchor with different failure types and number of plates were considered and the mooring location inducing the largest load-carrying capacity was proposed.

2 DESCREPTION OF ANALYSIS MODEL

2.1 *Model description*

The configuration of a helical anchor is illustrated in Figure 1. L, H, D, S, and d in the figure represent the depth of lowermost plate, the depth of uppermost plate, diameter of plates, spacing between plates, and the diameter of shaft, respectively. In this study, four different configurations of helical anchors were considered, and specifications are given in Table 1.

For the analyzing the effect of load application point on load-carrying capacity of helical anchors, the coupled Eulerian-Lagrangian (CEL) finite element (FE) analysis was adopted. Five load application points (z_p) of 0.0L, 0.25L, 0.5L, 0.625L, and 0.75L and four load inclination angles (θ) of 0°, 30°, 60°, and 90° were considered.

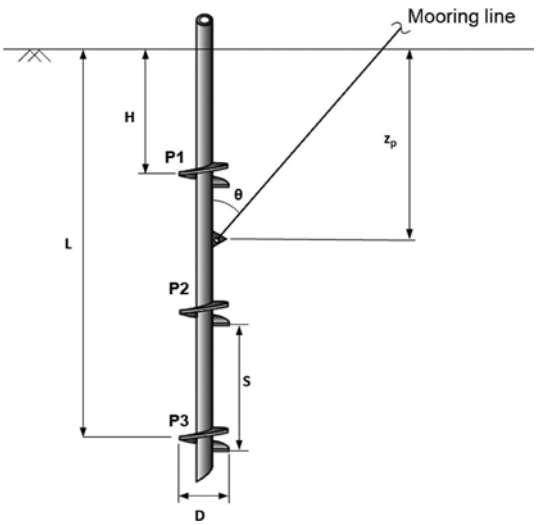

Figure 1. Configuration of helical anchor and mooring condition.

Table 1. Configurations of helical anchors.

Name	d (mm)	Plates	D (mm)	H (m)	L (m)	S (mm)	S/D
S2	160	P2, P3	300, 400	1.6	2.2	600	1.2
S3	160	P1, P2, P3	300, 400, 500	1.0	2.2	600	1.2
L2	160	P2, P3	300, 400	5.5	8.0	2,500	5
L3	160	P1, P2, P3	300, 400, 500	3.0	8.0	2,500	5

3 ANALYSIS RESULT

3.1 *Effect of load application point*

The value of load-carrying of helical anchor with each z_p (Q_u) obtained from the FE analyses were normalized with the value of the maximum load-carrying capacity of each θ condition

($Q_{u,max}$) in Figure 2. The normalized value ($Q_u/Q_{u,max}$) in the figure has showed similar shapes of changes. $Q_u/Q_{u,max}$ increased as z_p became greater, around to 0.5L or 0.625L. It decreased as z_p further increased. The case of $\theta = 90°$ in Figure 2(c) showed a consistent depth-profile shape with normalized load application point depth (z_p/L) for conditions.

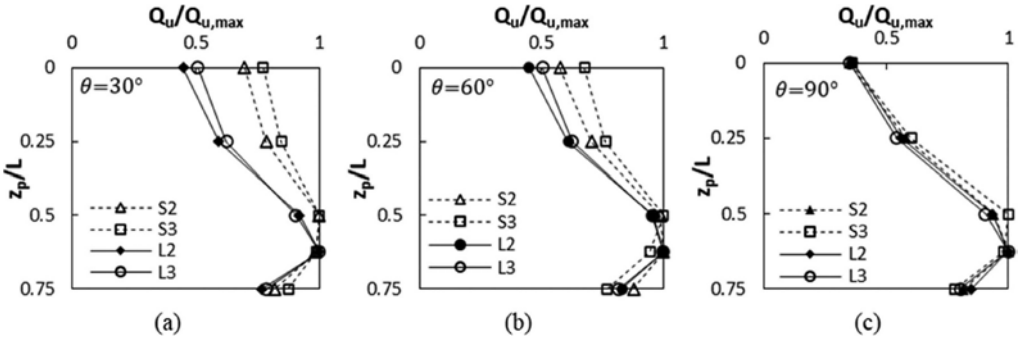

Figure 2. Values of $Q_u/Q_{u,max}$ for (a) $\theta = 30°$; (b) $\theta = 60°$; and (c) $\theta = 90°$.

3.2 *Design implication and optimum location of load application point*

It was shown that the load application point (z_p) affects the load-carrying capacity of helical anchors, and there is an optimal location of the load application point. The horizontal load-carrying mechanism indicated key role in the overall load capacity for helical anchors. For the optimum load application point, the vertical and horizontal load capacity components, given by Q_H and Q_V, were normalized with the maximum vertical and horizontal load capacity components of $Q_{H,M}$, and $Q_{V,M}$. These were plotted in Figure 3. For $Q_H/Q_{H,M}$, the results were unique while those for $Q_V/Q_{V,M}$ depended on the inclination angle as shown in Figure 3(a).

The correlation of $Q_V/Q_{V,M}$ to z_p/L and $Q_H/Q_{H,M}$ to z_p/L given in Figure 4 were:

$$Q_V/Q_{V,M} = 1 - 0.56(\theta \cdot z_p/L) \qquad (z_p/L \leq 0.625) \tag{1}$$

$$Q_H/Q_{H,M} = 1.1(z_p/L - 0.625) + 1 \qquad (for\ z_p/L \leq 0.625) \tag{2}$$

For Equation (1) and (2), the installation effect was considered for which the strength reduction factor of 0.6 was applied within the surrounding soil. Note that Equation 1 is valid for the condition $30° \leq \theta \leq 60°$.

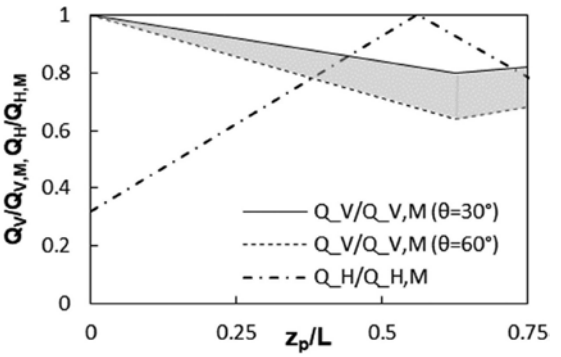

Figure 3. Normalized vertical and horizontal load capacities with z_p/L: (a) $Q_V/Q_{V,M}$; (b) $Q_H/Q_{H,M}$.

4 CONCLUSION

In this study, the effect load application point (z_p) on the load-carrying capacity of helical anchors under inclined loading condition was presented. Four configurations of helical anchors with different z_p and load inclined angles (θ) were considered. Unlike the conventional loading condition for helical anchor with loads applied at the top of the anchor, it was shown that adjusting z_p can further enhance the pullout load-carrying capacity of helical anchors. The load capacity of helical anchor increased for depths to the optimal load application point ($z_{p,opt}$), and decreased as z_p further increased to depths deeper than $z_{p,opt}$. The value of $z_{p,opt}$ equals to 0.625. Design equations for different loading conditions to quantify load-carrying capacity of helical anchor was presented.

REFERENCE

Aubeny, C.P. & Han, S.W. & Murff, J. D. Murff., 2003. 'Inclined load capacity of suction caissons', *International Journal for Numerical and Analytical Methods in Geomechanics*, vol. 27, no. 14, pp. 1235–1254, <https://doi.org/10.1002/nag.319>.

Harnish, J. & El naggar, M. H., 2017. 'Large-diameter helical pile capacity–torque correlations', vol. 54, no. 7, pp. 968–986, <https://doi.org/10.1139/cgj-2016-0156>.

Kim, Y. H. & Hossain, M. S. 2016. 'Numerical study on pull-out capacity of torpedo anchors in clay', *Géotechnique Letters*, vol. 6, no. 4, pp. 275–282, <https://doi.org/10.1680/jgele.16.00106>.

Kwon, O., Lee, J., Kim, G., Kim, I. & Lee, J., 2019. 'Investigation of pullout load capacity for helical anchors subjected to inclined loading conditions using coupled Eulerian-Lagrangian analyses', *Computers and Geotechnics*, vol. 111, no. 5, pp. 66–75, <https://doi.org/10.1016/j.compgeo.2019.03.007>.

Lee, J., Kwon,O., Kim, I., Kim, G. & Lee, J., 2019. 'Cyclic pullout behavior of helical anchors for offshore floating structures under inclined loading condition', *Applied Ocean Research*, vol. 92, no. 56, pp. 101937. <https://doi.org/10.1016/j.apor.2019.101937>.

Lee, J. & Lee, J., 2022. 'Enhancing Pullout Load Capacity of Helical Anchor in Clay with Adjusted Load Application Point under Inclined Loading Condition', *Journal of Geotechnical and Geoenvironmental Engineering*, vol. 148, no. 10, pp. 04022075.

Merifield, R. S., 2011. 'Ultimate uplift capacity of multiplate helical type anchors in clay', *Journal of Geotechnical and Geoenvironmental Engineering*, vol. 137, no. 7, pp. 704–716, <https://doi.org/10.1061/(ASCE)GT.1943-5606.0000478>.

Rao, S. N., Prasad, Y. V. S. N. & Shetty, M. D., 1991. 'The behaviour of model screw piles in cohesive soils', *Soils and Foundation*, vol. 31, no. 2, pp. 35–50, <https://doi.org/10.3208/sandf1972.31.2_35>.

Rao, S. N., Prasad, Y. V. S. N., & Veeresh, C., 1993. 'Behaviour of embedded model screw anchors in soft clays';, *Geotechnique*, vol. 43, no. 4, pp. 605–614, <https://doi.org/10.1680/geot.1993.43.4.605>.

Schiavon, J. A., Tsuha, C. D. H. C., & Thorel, L., 2016. 'Scale effect in centrifuge tests of helical anchors in sand', *International Journal of Physical Modelling in Geotechnics*, vol. 16, no. 4, pp. 185–196, <https://doi.org/10.1680/jphmg.15.00047>.

Tian, Y., Gaudin, C., Randolph, M. F., & Cassidy, M. J., 2015. 'Influence of padeye offset on bearing capacity of three-dimensional plate anchors', *Canadian Geotechnical Journal*, vol. 52, no. 6, pp. 682–693, <https://doi.org/10.1139/cgj-2014-0120>.

Wang, D., Merifield, R. S. & Gaudin, C., 2013. Uplift behaviour of helical anchors in clay', *Canadian Geotechnical Journal*, vol. 50, no. 6, pp. 575–584, <https://doi.org/10.1139/cgj-2012-0350>.

Smart Geotechnics for Smart Societies – Zhussupbekov, Sarsembayeva & Kaliakin (Eds)
© 2023 The Author(s), ISBN 978-1-003-29912-7
Open Access: www.taylorfrancis.com, CC BY-NC-ND 4.0 license

Commentary on the art and science of hydraulic filling

O. Boumendjel-Game
University of Bristol, Bristol, UK
Arcadis Consulting, UK & Ireland

A. Diambra & P.J. Vardanega
University of Bristol, Bristol, UK

ABSTRACT: Hydraulic filling remains arguably a relatively new geotechnical engineering process, despite having been used for decades to construct mega projects around the globe. The publication of the Hydraulic Fill Manual has been an important initiative to standardize some key aspects of the hydraulic filling process. However, there are key aspects such as consideration of contractual arrangements that are aligned with current industry trends, characterization of the 'at source' and 'after deposition' properties of the hydraulic fill, and performance criteria of the fill mass for which further/revised guidance may be needed. This paper reviews the current state of hydraulic filling guidance documents and offers some suggestions for future developments.

1 INTRODUCTION

Hydraulic Filling (HF) is the process followed for excavation, transportation and deposition of fill, using a stream of water, to create new land and/or raise the elevation of existing low-lying land. HF has become synonymous with dredging and reclamation works, in particular for major infrastructure, civil and marine projects. This association is expected to continue, based on observed trends of reclamation contract volumes and the forecast for the demand for dredging services in the coming years (van 't Hoff & van Der Kolff 2012, Fmi 2022). Until the publication of the Hydraulic Fill Manual (HFM) (van 't Hoff & van Der Kolff 2012), guidance for reclamation projects using hydraulic fill was limited. Therefore, the HFM is considered a milestone in recognizing the complexity associated with the initiation, planning and construction of HF projects. This paper aims to highlight some areas that would benefit from further enhancement and future development of applicable codes of practice and standards specific to HF, while taking into consideration established local practices for reclamation works (e.g. Shen & Lee 1995, Shen et al. 1997, CEO 2002).

2 THE HYDRAULIC FILLING PROCESS

HF is the method/technique used to reclaim land and/or raise the elevation of low-lying land using a soil and water mixture to dredge, transport and deposit the hydraulic fill material in the designated development area (e.g. Kolman & van 't Hoff 2013) (see Figure 1 for a flowchart that depicts the key elements of the process).

3 PRACTICAL ENGINEERING CONSIDERATIONS

3.1 *Contractual aspects*

The HFM was developed around the interfacing among three contractual partners, namely Client-Consultant-Contractor (see HFM Sn. 1.3 & Fig. 1.3, p. 4). This suggests that HF project are planned, designed and constructed using a 'traditional contract' arrangement. However, as

DOI: 10.1201/9781003299127-337

'traditional contracts' have sometimes become the exception rather than the norm and considering the claims and disputes noted in recent years due to the use of other types of contracts (e.g. 'Design and Build' or 'Engineering Procurement and Construction'), it would be beneficial to adapt the manual to include other contractual arrangements. Such types of contracts are already apparent in the recommended example specification clauses in Chapter 12 of the HFM. In 2016, FIDIC published the FIDIC Blue Book, which is the second edition of the Form of Contract for Dredging and Reclamation Works (FIDIC 2016, Maddock & Vanderburghe 2016), was another milestone in recognizing the need of the marine industry for specialized guidance on contractual arrangements for HF projects.

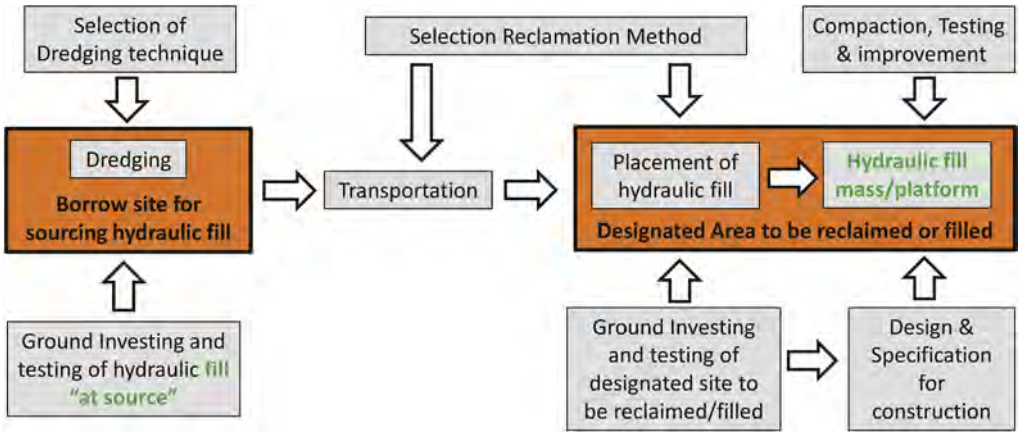

Figure 1. Key aspects of the HF process (based on van 't Hoff & van Der Kolff 2012, Kolman & van 't Hoff 2013).

3.2 *Ground investigation/Data collection*

For a HF project, there are two distinct areas/sites of interest, namely: (i) the borrow for sourcing the fill and (ii) the site receiving the hydraulic fill (see Figure 1). The borrow is usually located offshore up to several km away from the designated areas to be reclaimed and/or filled. The objectives and scope of ground investigation for each site are different, despite some elements of investigation and testing being similar for performance assessment. There is also the influence of the contractual arrangements discussed in Section 3.1 of this paper, regarding the scope and the stage of the project when gathering information for each area is required. To enable adequate interpretation of the hydraulic fill characteristics 'at source' and 'after deposition', the ground investigations for these two distinct sites/areas should be covered separately because of the influence of the latter on the design and construction of the intended development (e.g. Cao 2003, Lee et al. 1999, Mengé 2021).

3.3 *Design standards*

In this paper, the authors have endeavored to cite the most recent version of a British Standard Institution (BSI) standard when mentioned in this paper while noting that other cited publications may refer to earlier versions of these standards. Several standards are referred to in the HFM, notably the *Code of practice for earthworks* (BSI 2010a). Whilst it is accepted that the process involves earth moving activities, there are still several aspects that are distinctly different from a typical earthworks project. This has been recognized in the publication of the dedicated HF part (part 6) of BS EN 16907 (BSI 2018b). This could be applied to updates to other codes of practice such as *Eurocode 7: Geotechnical design* (BSI 2010b, 2014) to include specific guidance for characterization and testing of hydraulic fill, design of the hydraulic fill mass, and consideration of the serviceability of the intended constructions.

3.4 *Gradation of hydraulic fill*

The nature and characteristics of the in-situ soils forming the hydraulic fill 'at source' are not all equal due to varying local and regional geological settings and structures. As a result, change in gradation of the fill 'after deposition' is anticipated for some fill types (see Figure 1). The level of change is influenced by the composition of the in-situ sand fill, potential degradation during dredging, deposition and compaction at the designated site (e.g. van 't Hoff & van der Kolff 2012, Kolman & van 't Hoff 2013). Concentration of fines may also occur due to material segregation during transportation and compaction, which in turn, may lead to ponding of remnant water within the fill mass, all of which would affect the fill mass geotechnical characteristics and performance (e.g. Lee et al. 1999, Gens 2019, van Ginkel & Olsthoorn 2019). However, testing and modelling of the in-situ fill to mimic anticipated gradation and, therefore, potential properties 'after deposition' is generally not carried out, with reliance often being placed on investigation and testing of the fill mass 'after deposition' and compaction (e.g. Cao 2003, Mengé 2021). This is recognized in the manual (see HFM Sn. 5.2.1 p. 104 and Sn. 9.2.5.1 p. 357), subsequently recommending testing of fill samples having a range of different gradings (this is echoed in BSI 2018b).

3.5 *Drainage*

An overview has been provided in the HFM (see HFM, Sn 10.2 pp. 388–394) for the drainage aspects of the hydraulic fill mass. One of the highlighted issues relates to the formation of a fine-grained crust at the top of the fill mass during hydraulic placement (see HFM, Sn. 10.2.1, p. 390), thus, affecting permeability of the fill. Localized soft spots/bands can develop at any depth and extent of the fill mass during HF. There is also the issue of the remnant sea water after construction, which will affect both the dissipation rate of this remnant water within the fill mass and drainage of surface stormwater run-off during service (cf. van Ginkel & Olsthoorn 2019). The latter is usually addressed through design of appropriate surface storm water drainage systems (cf. van Ginkel & Olsthoorn 2019). The former, however, is influenced by the hydraulic conductivity of the newly formed fill mass, which in turn is governed by the gradation of the fill after deposition and compaction, vertical and lateral drainage paths within the fill mass, location and lateral distance of the ponded area from the discharge point of the same fill mass and the drainage system adopted to control phreatic levels (cf. van Ginkel & Olsthoorn 2019).

3.6 *Construction specifications*

One of the objectives of the manual is help avoid problems associated with stringent and conflicting specifications. As indicated in Section 3.1 of this paper, Chapter 12 of the HFM provides examples of typical specification clauses. As further enhancement, it is recommended that this overview is developed to include preparation of standard specifications for HF, thus, reduce uncertainties and potential mis-interpretations, and then, discontinue reliance on adapting technical specifications that were developed for previous dredging and reclamation projects or use of standard specifications that were developed for different earth moving practices (e.g. NH 2022). Such initiatives would complement the FIDIC Blue Book (FIDIC 2016) that was developed specifically for dredging and reclamation works, as discussed in Section 3.1 of this paper.

4 SUMMARY AND CONCLUSIONS

HF is commonly used in land reclamation and filling works. The publication of the HFM in 2012 (van't Hoff & van der Kolff 2012) and *Earthworks – Part 1: Principles and general rules* (BSI 2018a) and *Earthworks – Part 6: Land reclamation earthworks using dredged hydraulic fill* (BSI 2018b), are fundamental advances in specifications and guidelines for HF. This paper has highlighted some key aspects which would benefit from further consideration if updates of the manuals and/or preparation of new guidelines are considered. It is suggested that improvement of the practice in this manner combined with adopting the FIDIC Blue Book (FIDIC 2016) as a form of contract would reduce contractual disputes, claims and/or litigations through shared risks.

ACKNOWLEDGEMENT

The first author acknowledges the support from Dr. Jeff Keaton and Arcadis Consulting UK support for her pursuing this research.

REFERENCES

British Standards Institution (BSI). 2010a. *BS 6031: 2009 Code of practice for earthworks*. London, UK: BSI.

BSI. 2010b. *BS EN 1997-2:2007 Eurocode 7 — Geotechnical design — Part 2: Ground investigation and testing*. London, UK: BSI.

BSI. 2014. *BS EN 1997-1:2004+A1:2013 Eurocode 7: Geotechnical design — Part 1: General rules*. London, UK: BSI Standards Limited.

BSI 2018a. *BS EN 16907-1:2018 Earthworks - Part 1: Principles and general rules*. London, UK: BSI Standards Limited.

BSI 2018b. *BS EN 16907-6:2018 Earthworks - Part 6: Land reclamation earthworks using dredged hydraulic fill*. London, UK: BSI Standards Limited.

Cao, L.F. 2003. Soil Investigation in Land Reclamation. *GEO-WCS 2003, Shanghai, China*. https://doi.org/10.13140/2.1.2068.7365

Civil Engineering Office (CEO). 2002. *Port Works Design Manual Part 3: Guide to Design of Reclamation*. Hong Kong: Civil Engineering Office, The Government of the Hong Kong Special Administrative Region.

Fédération Internationale des Ingénieurs-Conseils (FIDIC). 2016. *Form of Contract for Dredging and Reclamation Works 2nd Edition* (Blue Book). Geneva: Fédération Internationale des Ingénieurs-Conseils.

Future Market Insight (Fmi). 2022. Dredging Market Outlook (2022-2032). Available from: < https://www.futuremarketinsights.com/reports/dredging-market > (16 January 2023).

Gens, A. 2019. Hydraulic fills with special focus on liquefaction. In H. Sigursteinsson, S. Erlingsson & B. Bessason (eds), *Proc. XVII European Conference on Soil Mechanics and Geotechnical Engineering – Reykjavík, Iceland, 1 – 6 of September 2019: Geotechnical Engineering, foundation of the future*, Reykjavík, Iceland: The Icelandic Geotechnical Society (IGS). https://doi.org/10.32075/17ECSMGE-2019-1108.

Kolman, R. & van 't Hoff, J. 2013. Port Expansion through land reclamation. *Port Technology International* 58: 26–28.

Lee, K.M., Shen, C.K., Leung, D.H.K & Mitchell, J.K. 1999. Effects of Placement Method and Geotechnical Behavior of Hydraulic Fill Sands. *Journal of Geotechnical and Geoenvironmental Engineering (ASCE)* 124(10): 832–846.

Maddock, T. & Vandenburghe, M. 2016. A review of the FIDIC Blue Book (Second Edition). *Terra et Aqua* Number 145, December 2016: 15–22.

Mengé, P. 2021. Compaction Control of Offshore Land Reclamation by In situ Tests. In T. Huszák, A. Mahler & E. Koch (eds.), *Proc. of the 6th International Conference on Geotechnical and Geophysical Site Characterization, Budapest, Hungary*, *26-29* September *2021*. https://doi.org/10.53243/ISC2020-512.

National Highways (NH). 2022. *Manual of Contract Documents for Highway Works: Vol. 1 – Specification for Highway Works*. Birmingham, UK: National Highways. Available from: < https://www.standardsforhighways.co.uk/ha/standards/mchw/vol1/index.htm > (16 January 2023).

Shen, C.K. & Lee, K.M. 1995. *Hydraulic Fill Performance in Hong Kong. GEO Report No. 40*. Hong Kong: Geotechnical Engineering Office, Hong Kong Government.

Shen, C.K., Lee, K.M. & Li, X.S. 1997. *A Study of Hydraulic Fill Performance in Hong Kong. Phase 2. GEO Report No. 64*. Hong Kong: Geotechnical Engineering Office, The Government of the Hong Kong Special Administrative Region.

van Ginkel, M. & Olsthoorn, T.N. 2019. Distribution of grain size and resulting hydraulic conductivity in land reclamations constructed by bottom dumping, rainbowing and pipeline discharge. *Water Resources Management* 33(3): 993–1012.

van 't Hoff, J. & van der Kolff, A.N. (eds) 2012. *Hydraulic Fill Manual: For Dredging and Reclamation Works*. Leiden, The Netherlands: CRC Press/Balkema.

Smart Geotechnics for Smart Societies – Zhussupbekov, Sarsembayeva & Kaliakin (Eds)
© 2023 The Author(s), ISBN 978-1-003-29912-7
Open Access: www.taylorfrancis.com, CC BY-NC-ND 4.0 license

Increase in injection efficiency using surfactant for the geological carbon sequestration

Seok-Gu Gang, Jae-Eun Ryou & Jongwon Jung
Chungbuk National University, Cheong-ju, South Korea

ABSTRACT: Carbon dioxide is a greenhouse gas which cause the global warming. The geological carbon sequestration is one of ways to reduce the amount of atmospheric carbon dioxide. Among various sites such as hydrate-bearing sediments, coal seam etc., saline aquifer is one the possible sites for the geological carbon sequestration because saline aquifer has the larger volume capacity than others. Thus, it is important to store as much carbon dioxide as possible in aquifers with the limited volume space. In this study, we conducted micromodel experiments and PNM (pore network model) numerical analysis to increase the carbon dioxide injection efficiency using surfactants. Finally, the technique to enhance the carbon dioxide injection efficiency through surfactants was developed for the geological carbon sequestration

1 INTRODUCTION

1.1 *Global warming induced by carbon emission increasing*

With the development of mankind, carbon dioxide emissions are steadily increasing. Carbon dioxide emitted into the atmosphere induces global warming, and global warming threatens human living areas in the form of rising sea levels, floods, and explosions. Table 1 shows the main effects of global warming (1.5°C, 2°C). As a book to deal with such a climate crisis, the international community, through the IPCC (Intergovernmental Panel on Climate Change) and the Paris Climate Treaty, has derived scientific evidence and draft agreements for reducing carbon emissions by country (IPCC, 2018).

Table 1. Main effects of global temperature rise on 1.5°C vs 2°C (Government of Korea. 2020. 2050 Carbon...).

Impacts on earth & humans	1.5°C	2°C
Ecosystems and Humans	High risk	Very high risk
Mid-latitude heatwave temperature	3°C increase	4°C increase
High latitude cold wave temperature	4.5°C increase	6°C increase
Coral extinction	70~90%	≤99%
Population vulnerable to climate impact and poverty	Up to hundreds of millions more by 2050 at 2°C	
Water scarce population	Up to 50% increase at 2°C	
Risk of large-scale extreme events	Medium risk	Medium to high risk
Sea level rise	0.26~0.77m	0.3~0.93m
Frequency of complete extinction of arctic sea ice	Once in 100years	Once in 10 years

DOI: 10.1201/9781003299127-338

1.2 *Carbon neutral using geological carbon sequestration*

Countries around the world have established and implemented carbon neutral policies to reduce carbon emissions. Measures to achieve carbon neutrality are roughly divided into two categories, namely emission reduction and carbon dioxide capture and utilization storage in the fields of industry, construction and transportation. Carbon dioxide is stored in aquifers, dielectric waste gases, etc. In this study, experiments and numerical analyzes were performed with the aim of improving the injection efficiency of reservoirs using surfactants.

2 MATERIAL AND METHOD

2.1 *Material*

Surfactants are divided into positive, negative, non-ionic and amphipathic surfactants according to their hydrophilic charge state. Such a hydrophilic group charge state varies in characteristics depending on the ground soil particle surface charge. For example, the charge compatibility between the surfactant hydrophilic groups and the ground particle surface causes adsorption of the surfactant to the particle surface by attractive forces. This adsorption reduces surfactant loss and injection efficiency. Considering adsorption on particle surface, in this study use anionic surfactants. Because pore surface which use in this study consist of silica (represent anionic charge). So, two anionic sodium dodecyl sulfate (SDS) and sodium dodecylbenzene sulfonate (SDBS) surfactants were used in this study. Table 2 shows the properties and mechanisms of different types of surfactants in geotechnical applications The surfactant solution was diluted to wt% with deionized water (DI).

Table 2. Advantages and mechanism on surfactants ionic characteristic (Negin et al., 2017. most common. . .).

	Cationic	Anionic	Non-ionic	Amphoteric
Advantages*	Cationic and nonionic surfactants mixture is most effective agent for EOR (carbonate reservoir)	Effective for sandstone reservoir	Effective for surfactant flooding in high salinity water or hard water	Strong electrolyte tolerance, temperature resistance, thermos stability, better wetting and foaming
Electrical interaction of reservoir pore surface**	Carbonate surfaces have both cation and anion exchange sites	Sandstone surfaces have anion sites	Not effected by reservoir surface charge	-
Mechanism*	Reducing IFT and wettability alteration	Reducing IFT	Reducing IFT	Reducing IFT and wettability alteration

* Negin et al., 2017. Most common. . .
** Brady, P.V & Thyne, G. 2016. Functional wettability . . .

2.2 *Method*

The Micromodel (Micronit Micro Technologies, Netherlands) used a uniform network model with uniform voids, a pore-volume of 2.3μL, and a porosity of 0.58. Micromodel internal surfactant and carbon dioxide injections were injected via low pressure (New Era Pump Systems, NE-1010) and high pressure (Teledyne, Syriux 500x) syringe pumps, respectively. All injection processes were filmed with a micro lens camera.

2.3 *Experimental procedure*

Figure 1 shows a schematic of this experiment. The main equipment in conducting the experiment consists of a two-dimensional micromodel, low and high-pressure Teflon pumps, and

a micro lens for imaging the injection process. A micromodel connected to low- and high-pressure syringe pumps via high-pressure peak tubing is placed on the imaging bed. The surfactant solution is injected at a constant rate (0.5 ml/min) through a low-pressure syringe pump into the cavity until the air bubbles are completely removed. After 1 hour for Micromodel internal surfactant equilibration, inject carbon dioxide via a high-pressure syringe pump. All injection processes were recorded through a micro lens camera, and calculation of the replacement rate from the captured images utilized image j.

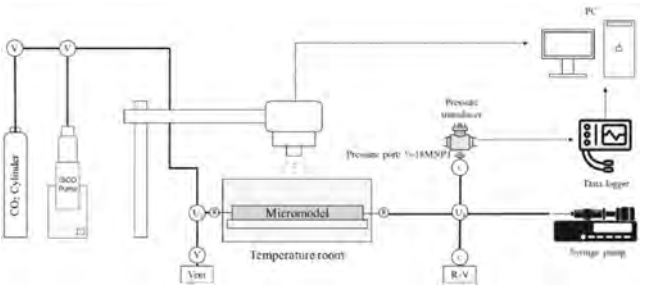

Figure 1. Experiment schematic and equipment.

2.4 *Pore network modeling (PNM)*

Through numerical analysis using MATLAB, we aim to develop micro model experimental verification and evaluation technology. For model validation, water or surfactant-carbon dioxide injection simulations were performed under normal temperature (20–25 °C) and low pressure (500 KPa) conditions. Interfacial tension, contact angle and viscosity in atmospheric condition are used as the fluid physical properties necessary for injection analysis by model, and the physical properties of water, carbon dioxide, SDS and SDBS are shown in Table 3.

Table 3. Physical properties of water, CO_2 and surfactant.

Property Material	Interfacial tension [mN/m]	Contact angle [°]	Viscosity [Pa·s]
Water	72	67.5	$1.002\ 10^{-3}$
Carbon dioxide (CO_2)	68.5*	29**	$1.3 \cdot 10^{-5}$
SDS (0.01 wt%)	55.57	33.3	0.9
SDS (0.02 wt%)	53.08	37.55	0.93
SDBS (0.01 wt%)	51.47	36.2	0.9

* D. Nicolas Espinoza and J. Carlos Santamarina. 2010. Water-CO_2. . .
** X. LI and X. Fan. 2015. Effect of. . .

3 RESULT

3.1 *2D micromodel experiment*

Figure 2 shows the injection pattern over time and the results of image processing using image j. As a result of image processing, black areas indicate injected carbon dioxide, and similarity to images taken with a micro lens can be confirmed. In Figure 3, when the pore water was saturated with water, the replacement rate showed a tendency to converge after increasing with the carbon dioxide injection rate, and SDS did not show a tendency with concentration (0.01, 0.02 wt%) and injection rate. SDBS was 0.01 wt% and showed a slight increasing trend with increasing injection rate. The displacement ratio by the number of voids and the injection speed is shown in Table 4.

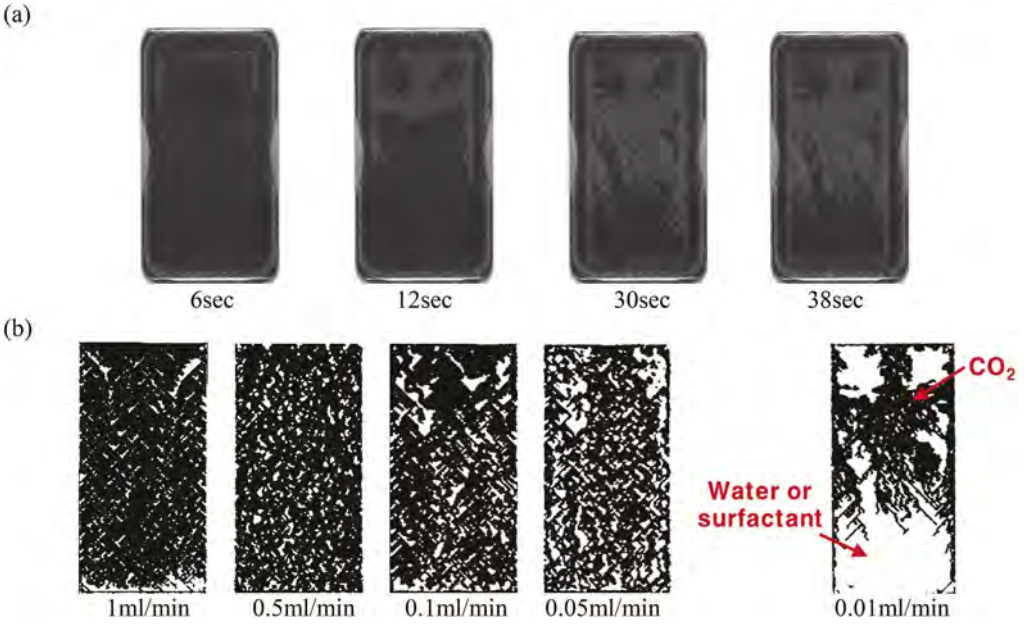

Figure 2. Result of water-CO2 displacement (a) displacement on time (b) image processing result.

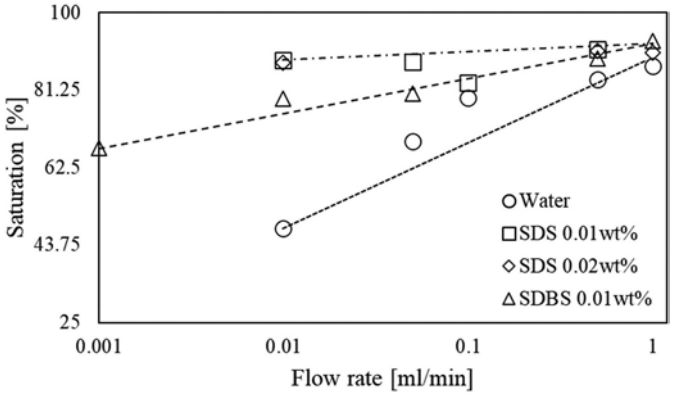

Figure 3. Displacement ratio of carbon dioxide on surfactant and flow rate.

Table 4. Displacement ratio of CO_2 on pore fluid.

Displacement ratio [%] Flow rate [ml/min]	Water	SDS [0.01wt%]	SDBS[0.01wt%]	SDS[0.02wt%]
1	87.035	-	93.204	90.408
0.5	83.815	91.053	88.854	90.694
0.1	79.475	83.06	-	-
0.05	68.948	88.097	80.485	-
0.01	47.723	88.578	79.12	87.912
0.001(1μl/min)	-	-	67.312	-

3.2 *2D pore network modeling*

Figure 4 shows the pnm simulation results with carbon dioxide injection into the water- and surfactant-saturated void under room temperature and low-pressure conditions. The carbon dioxide injection pressure was 500 KPa, and the distribution ratio according to the type of saturated pore fluid is shown in Table 5. Figure 5 shows the substitution rate according to concentration. Using a surfactant increased the distribution ratio. SDS also increased the displacement ratio as the concentration increased from 0.01wt% to 0.02wt%. At 0.01wt%, SDBS showed a higher displacement rate than SDS. These results showed the same trend as the results of the injection experiments using the micromodel.

Table 5. Displacement ratio of CO_2 on pore fluid using pnm.

Pore fluid Pressure [KPa]	Water	SDS [0.01wt%]	SDBS[0.01wt%]	SDS[0.02wt%]
500	37%	60.25%	66.45%	72.34%

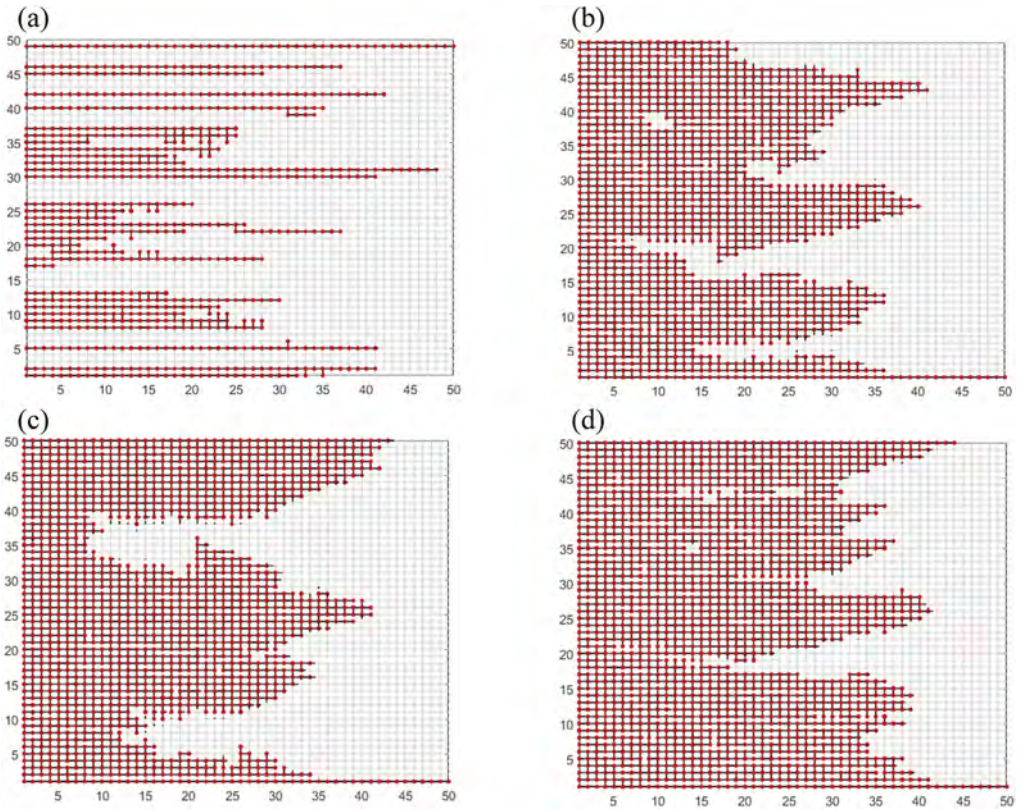

Figure 4. Displacement of carbon dioxide using pnm (a) water (b) SDS 0.01wt% (c) SDS 0.02 wt% (d) SDBS 0.01 wt%.

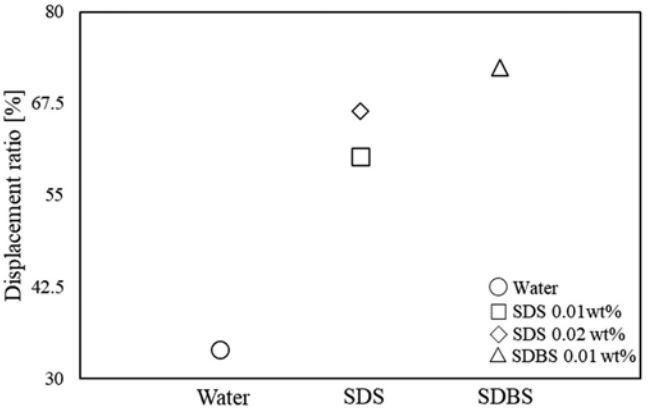

Figure 5. Displacement of carbon dioxide on concentration and surfactant.

4 CONCLUSION

In this study, injection experiments and pnm using a two-dimensional micromodel were performed. Water-carbon dioxide replacement results in a trend of increasing replacement rate with increasing injection rate. As a result of surfactant-carbon dioxide substitution, SDS showed no change in substitution rate with increasing injection rate and concentration, while SDBS showed a slight increasing trend of substitution rate with increasing injection rate. The results of water or surfactant-carbon dioxide injection simulations using PNM were confirmed to be like micromodel experiments. The construction of additional surfactant rheological property data and validation by pnm simulations is deemed necessary.

REFERENCES

Brady, P.V & Thyne, G. 2016. Functional wettability in carbonate reservoirs. American chemical Society, 30, 11, 9217–9225.

Espinoza, D.N & Santamarina, J.C. 2010. Water-CO2-mineral systems: Interfacial tension, con tact angle and diffusion-Implications to CO2 geological storage. Water resources research, Vol. 46, W07537.

IPCC, 2018: Global Warming of 1.5°C.An IPCC Special Report on the impacts of global warming of 1.5°C above pre-industrial levels and related global greenhouse gas emission pathways, in the context of strengthening the global response to the threat of climate change, sustainable development, and efforts to eradicate poverty [Masson-Delmotte, V., P. Zhai, H.-O. Pörtner, D. Roberts, J. Skea, P. R. Shukla, A. Pirani, W. Moufouma-Okia, C. Péan, R. Pidcock, S. Connors, J.B.R. Matthews, Y. Chen, X. Zhou, M.I. Gomis, E. Lonnoy, T. Maycock, M. Tignor, and T. Waterfield (eds.)]. Cambridge University Press, Cambridge, UK and New York, NY, USA, 616 pp.

Li, X & Fan, X. 2015. Effect of CO2 phase on contact angle in oil-wet and water-wet pores. International journal of greenhouse gas control, Vol. 36: 106–113.

Negin, C. Ali, S. Xie, Q. 2017. Most common surfactants employed in chemical enhanced oil recovery. Petroleum, Vol. 3: 197.211.

The Government of the Republic of Korea. 2020. 2050 Carbon neutral strategy: toward a sustainable and green society. pp: 17–18.

Smart Geotechnics for Smart Societies – Zhussupbekov, Sarsembayeva & Kaliakin (Eds)
© 2023 The Author(s), ISBN 978-1-003-29912-7
Open Access: www.taylorfrancis.com, CC BY-NC-ND 4.0 license

Unsymmetrical thermal loading effects on a 2×2 pile-group: 1g physical modeling approach

Fardin Jafarzadeh
Associate Professor, Sharif University of Technology & President of Iranian Geotechnical Society, Tehran, Iran

Sina Afzalsoltani
Ph. D. Candidate, Sharif University of Technology, Tehran, Iran

ABSTRACT: A 2×2 pile group with one of its piles acting as an energy pile is modeled using a 1g test setup. The model piles are closed-end aluminum pipes with 2cm diameter and 60cm length. The energy pile goes under several heating and cooling cycles which in return induces unsymmetrical loading on the pile group. A single steel U-tube through which water with a desired temperature is to be circulated is placed inside the initially water-filled energy pile to control its temperature during thermal cycling. A plastic tilt of the pile cap is observed with each thermal cycle having a gradually decreasing rate as the number of cycles increased. Readings from the horizontally oriented total pressure cells underneath the pile tips indicated changes in soil pressure during thermal cycling. Each of the heating and cooling phases had additive and subtractive effect on the soil pressure readings underneath the energy pile, respectively. Results showed that the use of unsymmetrical energy pile arrangement in a group should be approached with caution.

1 INTRODUCTION

The use of ground heat exchangers is not a new phenomenon. The concept was developed by Lord Kelvin in 1852 (Lund et al. 2004). The practice of fitting heat exchanger pipes inside the structural elements began from Austria and Switzerland: First inside base slabs (early in the 1980s), inside piles in 1984, inside diaphragm walls in 1996 and thermo-active tunnels in early 2000 (Brandl, 2006; Markiewicz and Adam, 2009; Katzenbach, 2015 and Sani et al. 2019).

During recent years many scholars have studied thermal efficiency and thermo-mechanical behavior of geothermal energy piles through field and laboratory scale experiments. Ng et al. (2015) studied effect of temperature on bearing capacity of energy pile in medium dense saturated sand using centrifuge tests. They concluded that piles at 37°C and 52°C have bearing capacities 13% and 30% greater than that at room temperature (22°C), respectively. Goode et al. (2015) carried out centrifuge tests on energy piles in medium dense dry sand and reported that bearing capacity of the pile is insensitive to temperature changes. McCartney et al. (2011) reported that bearing capacity of single energy piles in unsaturated silt increase by about 60% with 35°C increase in temperature. Senejani et al (2020) investigated thermo-mechanical behavior of a single energy pile using a small-scale physical model setup. They reported a reduction in elastic response of the soil during longer thermal cycles. Ng et al. (2021a) studied the Performance of elevated energy pile groups with different pile spacing in clay subjected to cyclic non-symmetrical thermal loading. They conducted a centrifuge modeling of pile spacing effects on thermo-mechanical interactions between piles within energy pile groups. Ng et al. (2021b) compared the behavior of non-symmetrical thermally loaded 2×2 elevated pile group with a piled raft. They stipulated that piled rafts undergo smaller tilts under unsymmetrical thermal loads.

The present study investigates the behavior of a 2×2 pile group behavior when on of its piles undergoes cyclic temperature changes with an amplitude of ±6°C. The results are briefly presented and discussed in the following sections.

DOI: 10.1201/9781003299127-339

2 TEST SETUP

The model contains a 2×2 pile group (each pile with outer diameter of D=2 cm) placed at a center-to-center distance of 6cm (3D). The soil container is a 100×100×80 cm (width × length × height) rigid steel box. The model ground is dry silty sand with relative density of 74%, placed in the container using dry tamping technique. Figure 1 shows the schematic of the model configuration and Figure 2 depicts the constructed model.

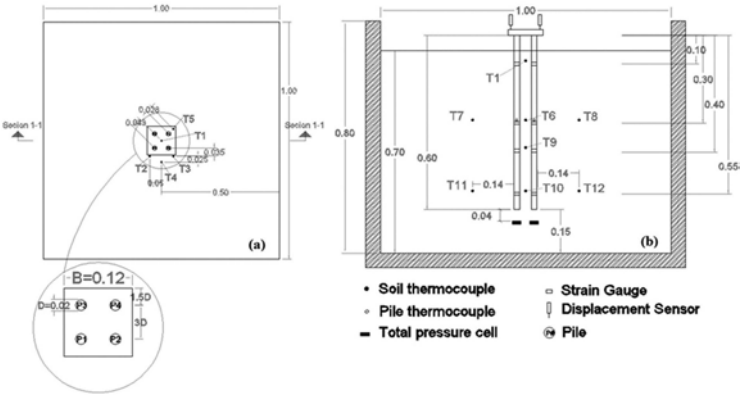

Figure 1. Schematic views of the model configuration; a) plan view and b) section 1-1.

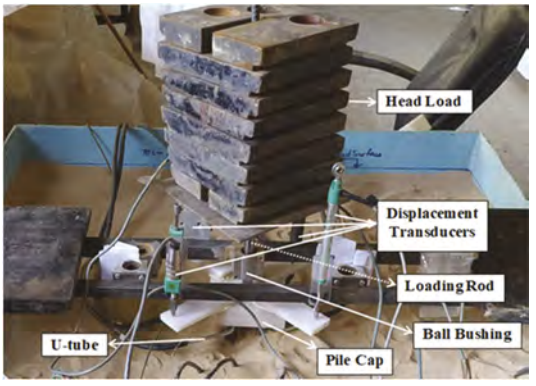

Figure 2. Pile cap and loading mechanism.

Pile temperature is controlled by circulating temperature-controlled water through steel U-tubes placed inside the piles. In order to provide sufficient thermal interaction between pile and U-tube, each pile is initially filled with water. The pile group was first mechanically loaded in 8 steps up to 400 N with resting time of 5 minutes for each step. Under constant mechanical surcharge, the energy pile has gone through 10 consecutive heating-cooling cycles with temperature amplitude of ±6˚C. Three tests were conducted. In test "Group1", Pile1 was energy pile and the other piles were non-energy piles. In test "Group2", Pile1 and Pile2 were energy piles and finally in test "Group3", Pile1, Pile2 and Pile3 were energy piles. After each test the whole model was reconstructed. Particle size distribution of the model ground is depicted in Figure 3. As can be seen the model ground is comprised of fine sand and 40% passing from #200 sieve. Results of Atterberg tests showed the part finer than #200 sieve is non-plastic silt. Hence the soil based on the Unified Soil Classification System is SM.

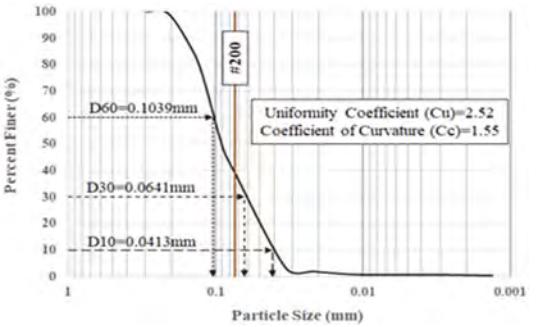

Figure 3. Particle size distribution analysis of the model ground.

3 RESULTS

Time histories of total pile head displacements during the test are presented in Figure 4. It can be seen that the energy pile has larger settlements than conventional piles of the group. During the first few heating phases, no upward displacement occurs in the energy pile until the third heating phase in day five of the test. In fact, during first and second heating phases, the upward thermal forces generated by the tendency of the energy pile for expansion, cannot overcome the downward reaction forces from the conventional piles of the group. As thermal cycling continues, settlement of the energy pile and the consequent redistribution of forces acting on the pile contribute to help the energy pile to slightly push the pile cap upwards which is recorded as small heaves during heating phases in Figure 4. The magnitude of total settlement of each pile remains smaller than the maximum allowable settlement, which is conventionally taken as 10% of the pile diameter (2mm). Figure 5 shows time histories tilt/rotation of the pile cap. The tilt can be calculated by dividing the relative vertical displacements of any two points on the cap, by the horizontal distance between them in the tilting direction. As can be seen, except for the first and second heating phase, the heating caused a decrease while cooling caused an increase in the tilt of the cap. The amplitude of oscillations in the tilt of the cap becomes smaller with an asymptotic trend. As indicated in Figure 5, tilt of the cap exceeds the allowable limit of 1/500 (0.2%) suggested by EN 1997-1 (2004) in the second cooling phase. Time histories of vertical soil pressure at depth of 4cm below the pile tip for different piles are recorded by four total pressure cells (for sensor locations refer to

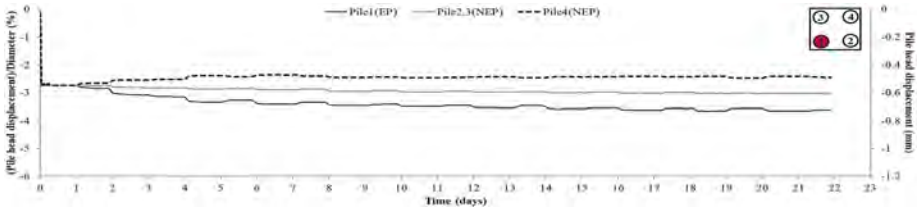

Figure 4. Time histories of pile head displacements presented as absolute values and also normalized with respect to pile diameter (positive values show heave and negative values show settlement).

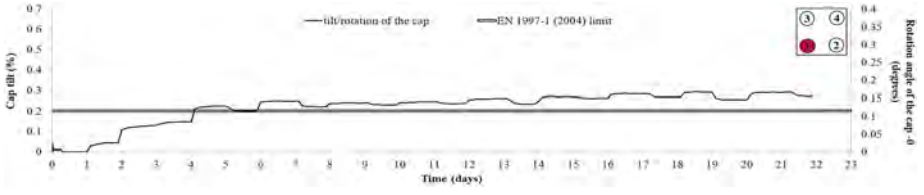

Figure 5. Tilt and rotation angle of pile group cap.

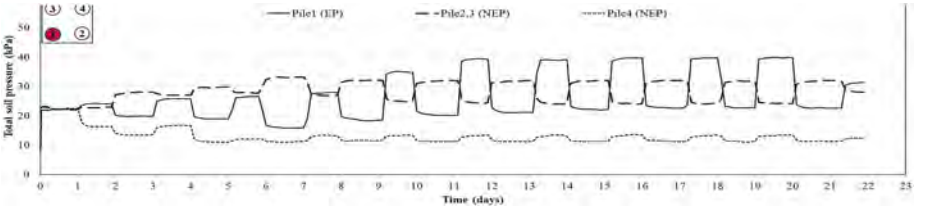

Figure 6. Time histories of total soil pressure under different piles.

Figure 1) and are plotted in Figure 6. It was observed that, with each heating/cooling phase the soil pressure under the energy pile has increased/decreased; respectively. The amplitude of soil pressure oscillations has increased gradually during the first few cycles until it remained almost constant after the fifth cycle.

4 CONCLUSION

A 1g physical modeling setup was developed to study the thermo-mechanical behavior of a 2×2 pile group when one energy pile is included. Results showed that even though displacements of each pile remain below the allowable limit of 2mm, the presence of energy pile may cause unallowable rotations of the pile cap. Results from the total pressure cells under the pile tip where also presented. It was observed that, with each heating/cooling phase the soil pressure under the energy pile has increased/decreased; respectively.

REFERENCES

Brandl H, Adam D, Markiewicz R. Ground-sourced energy wells for heating and cooling of buildings. Acta Geotech Slov 2006;1:5–27.

BSI, BS EN 1997–1: 2004. Eurocode 7. Geotechnical design. General rules. 2004, BSI London, UK.

Goode Iii, J. C., & McCartney, J. S. (2015). Centrifuge modeling of end-restraint effects in energy foundations. Journal of Geotechnical and Geoenvironmental Engineering, 141(8), 04015034.

Katzenbach R. New technologies and applications: materials and equipment in near surface geothermal systems 2015; doi: 10.1179/1937525514Y.0000000012.

Lund, J., Sanner, B., Rybach, L., Curtis, R., & Hellström, G. (2004). Geothermal (ground-source) heat pumps: a world overview. Geo-Heat Center Quarterly Bulletin, 25(3).

Markiewicz R, Adam D. Energy from earth-coupled structures, foundations, tunnels and sewers. Géotechnique 2009;59:229–36. https://doi.org/10.1680/geot.2009.59.3.229.

McCartney, J. S., Rosenberg, J. E., & Sultanova, A. (2011). Engineering performance of thermo-active foundations. In GeoTrends: The Progress of Geological and Geotechnical Engineering in Colorado at the Cusp of a New Decade (pp. 27–42).

Ng, C. W. W., Farivar, A., Gomaa, S. M. M. H., Shakeel, M., & Jafarzadeh, F. (2021a). Performance of elevated energy pile groups with different pile spacing in clay subjected to cyclic non-symmetrical thermal loading. Re-newable Energy, 172, 998–1012.

Ng, C. W., Farivar, A., Gomaa, S. M., & Jafarzadeh, F. (2021b). Centrifuge Modeling of Cyclic Non-symmetrical Thermally Loaded Energy Pile Groups in Clay. Journal of Geotechnical and Geoenvironmental Engineering, 147(12), 04021146.

Sani, A. K., Singh, R. M., Amis, T., & Cavarretta, I. (2019). A review on the performance of geothermal energy pile foundation, its design process and applications. Renewable and Sustainable Energy Reviews, 106, 54–78. doi:10.1016/j.rser.2019.02.008

Senejani, H. H., Ghasemi-Fare, O., Cherati, D. Y., & Jafarzadeh, F. (2020). Investigation of thermo-mechanical response of a geothermal pile through a small-scale physical modelling. In E3S Web of Conferences (Vol. 205, p. 05016). EDP Sciences.

Smart Geotechnics for Smart Societies – Zhussupbekov, Sarsembayeva & Kaliakin (Eds)
© 2023 The Author(s), ISBN 978-1-003-29912-7
Open Access: www.taylorfrancis.com, CC BY-NC-ND 4.0 license

Application of hydraulic-thermal conductivity of steel slag based CLSM on the performance evaluation of horizontal GSHPs

Young-Sang Kim & Ba Huu Dinh
Chonnam National University, Gwangju, Republic of Korea

Gyeong-O Kang
Gwangju University, Gwangju, Republic of Korea

ABSTRACT: This study evaluated the feasibility of steel-making slag-based controlled low-strength materials (CLSM) as a heat transfer medium for horizontal ground source heat pump systems. Engineering properties of CLSM mixtures with different steel-making slag contents and steel-making slag types were evaluated. The in-door thermal response test was conducted to validate the numerical model and access the heat exchange rate of spiral-coil GHE backfilled with CLSM and natural sand. Finally, to access the beneficial use of the CLSM over the sand, economic analysis of 50 case studies for the horizontal GHE was performed. The results indicate that the ground type steel-making slag-based CLSM not only can replace the sand in the CLSM mixture but also can enhance the thermal conductivity up to 2.35 W/(mK). Another advantage of CLSM is a high air-entry value, which can limit the influence of the GWT drop. As expected, the GHE backfilled with the CLSM shows a better economic performance compared to that of the GHE backfilled with an ordinary soil owing to its high heat transfer performance.

1 INTRODUCTION

The ground-source heat pump (GSHP) system is a well-known environmentally clean and energy-efficient technology for the cooling and heating of buildings with ground energy sources. Among GSHPs, the horizontal GSHP system is expected to widely use in Korea since it is easy to install and has low construction cost compared to that of vertical GSHP system; however, its low heat transfer efficiency requires the larger installation area.

By-product-based controlled low-strength material (CLSM), with a relatively high thermal conductivity and good workability, is expected to utilize in the horizontal GSHP in order to increase the heat transfer efficiency of the system (Kim et al., 2020).

It should be noted that horizontal GHE is generally embedded at a shallow depth above the GWT, where unsaturated soil exists (Dinh et al., 2021). The change in the GWT strongly affects the thermal properties of the soil and therefore influences the heat transfer efficiency of the HGHEs. Thus, thermal conductivity of the proposed CLSM should be evaluated over the entire degree of saturation and effect of the GWT level drop on the heat transfer performances of HGHEs should be considered.

Besides increasing the thermal conductivity of backfill materials, another solution to increase the heat transfer performance of the horizontal GSHP system is using the new ground heat exchanger type to increase heat exchanger length (i.e., slinky, spiral coil types). Yoon et al. (2015) found that using spiral-coil and slinky-type pipes increased the total heat exchange nearly twice that of the conventional GHEs (U-type).

The results presented that suggested CLSM with spiral-coil type heat exchanger is a potential solution to enhance the performance of the horizontal GSHP system; however, it

DOI: 10.1201/9781003299127-340

may cause an increase in the initial investment cost (Kim et al., 2020; Yoon et al., 2015). The economic analysis is, therefore, necessary to answer the question: "Whether the high heat transfer performance of the spiral-coil GHE and CLSM can offset its high installation cost?".

2 EXPERIMENTAL PROGRAMS

2.1 *Evaluation of characteristics of controlled low-strength material*

The CLSM mixture in this study used different steel slag sizes (raw steel slag and ground steel-making slag) and content (10 %, 20 %, and 30 %) to replace the natural sand in the conventional control low strength material. The engineering properties of mixtures, such as flowability, unconfined compressive strength (UCS), and thermal conductivity, were tested in accordance with applicable ASTM Standards (2004): D 6103, D 4832, and D 5334, respectively.

2.2 *Numerical analysis for evaluating performance of horizontal GSHP system considering hydraulic-thermal characteristics of backfill material and groundwater table level drop*

The soil-water characteristic curves and unsaturated thermal properties of backfill materials (natural sand (NS), weathered granite soil (WGS), and controlled low-strength materials (CLSM)) were evaluated using modified 150-SWCC devices and a high-pressure membrane extractor, coupled with a thermal conductivity measurement system as shown in Figure 1. Subsequently, the influence of the GWT level change on the moisture content of the backfill materials was investigated using a seepage analysis (SEEP/W) (Dinh et al., 2021). Furthermore, the thermal performance analysis of the HGHEs with different backfill materials was conducted using a commercial finite element code program (COMSOL Multiphysics) (Figure 3).

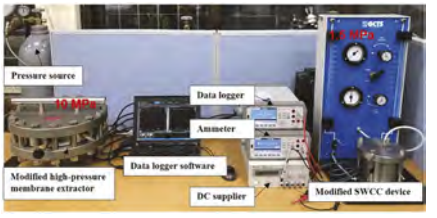

Figure 1. Modified SWCC device and modified high-pressure membrane extractor.

2.3 *In-door thermal response test and economic analysis*

The TRT test set-up is shown in Figure 2. A spiral-coil type heat exchanger was buried in a steel box (5 × 1 × 1 m) and backfilled with CLSM and sand. The inlet and outlet fluid temperature were measured by resistance temperature detector (RTD) sensors connected with a data logger program. Then, a finite element model using COMSOL Multiphysics was created and compared to validate the experiment model (Figure 3) (Dinh et al., 2022a, b).

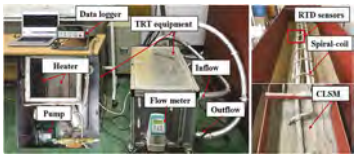

Figure 2. Thermal response test set-up.

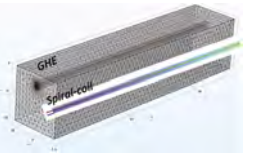

Figure 3. Full-size numerical model.

3 RESULTS AND DISCUSSION

3.1 *Thermal conductivities of proposed CLSMs*

The thermal conductivities of proposed CLSM mixtures are evaluated and compared with other grouts. Depending on the degree of saturation, the thermal conductivities of the CLSM mixtures in this study range from 1.21(dry) to 2.35(saturated) W/mK. The thermal conductivity of the CLSM proposed in this study is significantly higher than those of conventional grout materials as shown in Figure 4 (Kim et al., 2020).

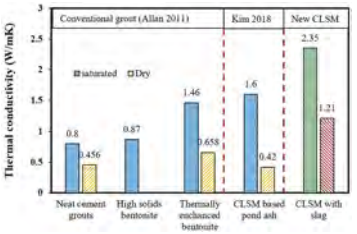

Figure 4. Comparison of thermal conductivity of different backfill materials.

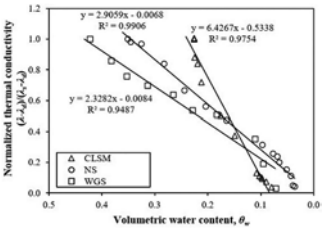

Figure 5. Normalized thermal conductivity and volumetric water content relationship.

3.2 *Water retention characteristics and thermal conductivity-water content relationship*

The water retention curves the backfill materials are measured using modified 150-SWCC devices and a high-pressure membrane extractor, coupled with a thermal conductivity measurement system (Dinh et al., 2022b). The air-entry value (AEV) of the proposed CLSM mixture, which represents the water retention ability, was significantly greater than that of the natural sand and weathered granite soil. The AEV of the CLSM was 1000 kPa, whereas the AEVs of natural sand and WGS were 4 kPa and 16 kPa, respectively. The relationships between the normalized thermal conductivity and volumetric water content of the backfill materials are shown in Figure 5. The thermal conductivity significantly decreases with the decrease in the volumetric water content. A linear relationship is observed for all backfill materials.

3.3 *TRT and economic analysis*

A very well agreement in the experimental (TRT) and numerical results (COMSOL) (Figure 6 (a) outlet fluid temperature, (b) soil temperature) demonstrated that the model proposed in Figure 3 and the parameters used for analysis are suitable to simulate the heat transfer in the horizontal GSHP system. With the same installation depth, the total construction cost of the Spiral-CLSM type is about 22 % higher than that of the Spiral-Soil (Figure 6(c)) since the CLSM costs about 40 USD/ m^3 while the soil is free to use (Kim et al., 2020). However, above the groundwater table level, where the horizontal GSHP system is located, the unsaturated thermal conductivity of CLSM is 1.68 W/(mK), which is about 52 % higher than that of the unsaturated soil (1.16 W/(mK)). As a result, the annual heat exchange rate of the Spiral-CLSM is significantly higher than that of the Spiral-Soil (39 % higher); thus, the net cash inflow of the Spiral-CLSM is considerably higher than the Spiral-Soil one. Consequently, the Spiral-CLSM has a lower simple payback period and higher IRR, compared to that of the Spiral-Soil one. Note that the annual heat exchange increases with an increase in the installation depth and fluid velocity (Figure 7(a)); however, it causes a significant increase in the total construction cost (Figure 6(c)) (i.e., excavation cost) and operation cost (i.e., the electrical power consumption of the pump). The Spiral-CLSM type with a buried depth of 2.5 m and a fluid velocity of 10 *l*/min has the lowest SPP and highest IRR (case 44); thus, it is the most beneficial use case from the standpoint of the economic analysis.

4 SUMMARY AND CONCULSIONS

This study comprehensively evaluated the feasibility of steel-making slag-based CLSM as a heat transfer medium for horizontal GSHP systems. The advantages of CLSM were found as follows: (1) CLSM has a high flowability; thus, it can fill the GHE without compaction; it is especially appropriate for spiral-coil GHE. (2) CLSM has a high thermal conductivity at both saturated and unsaturated conditions; thus, it can improve the heat transfer performance of the horizontal GHE. (3) CLSM has a UCS of 2.0 MPa (or higher); thus, it can protect the coil pipe from broken and shaped deformation. (4) The GWT level drop can give a negative effect on heat transfer performance of horizontal GHE, especially where the soil has a weak water storage ability (low AEV) (e.g., sand and sandy soil). However, CLSM with a strong water retention ability (AEV = 1000 kPa) can limit the influence of GWT level drop. (5) CLSM can incorporate many kinds of waste materials and by-products (i.e., pond ash, bottom ash, steel-making slag); therefore, the use of CLSM is not only economically beneficial but also has a good impact on waste treatment and environmental protection.

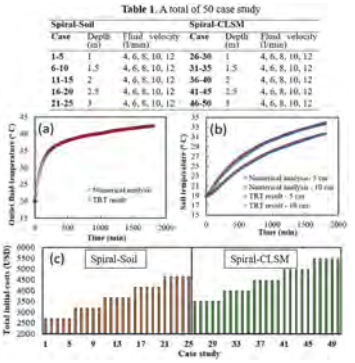

Figure 6. (a) Outlet fluid temperature, (b) soil temperature, (c) total initial costs.

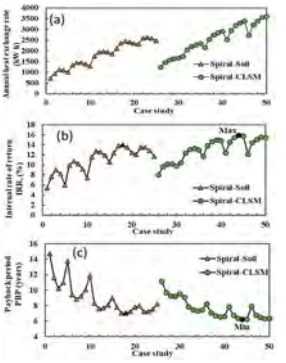

Figure 7. (a) Annual heat exchange rate, (b) Internal rate of return, (c) Payback period.

ACKNOWLEDGEMENT

This work was supported by a National Research Foundation of Korea (NRF) grant funded by the Korean government (NRF-2022R1A4A1033838 and NRF-2021R1A2B5B01002809).

REFERENCES

Kim, Y.S., Dinh, B.H., Do, T.M., Kang, G. O. 2020. Development of thermally enhanced controlled low-strength material incorporating different types of steel-making slag for ground-source heat pump system, *Renewable Energy*. 150: 116–127.

Dinh, B.H., Go, G.H., Kim, Y.S. 2021. Performance of a horizontal heat exchanger for ground heat pump system: Effects of groundwater level drop with soil – water thermal characteristics, *Applied Thermal Engineering*. 195: 117203.

Dinh, B.H., Kim, Y.S., Yoon, S. 2022a. Experimental and numerical studies on the performance of horizontal U-type and spiral-coil-type ground heat exchangers considering economic aspects, *Renewable Energy*. 186: 505–516.

Dinh, B.H., Kim, Y.S., Kang, G.O. 2022b. Thermal conductivity of steel-making slag-based controlled low-strength materials over entire range of degree of saturation: A study for ground source heat pump systems, *Geothermics*. 88: 101910.

Yoon, S.; Lee, S.; Go, G. 2015. Evaluation of Thermal Efficiency in Different Types of Horizontal Ground Heat Exchangers. *Energy & Buildings*. 105: 100–105.

Smart Geotechnics for Smart Societies – Zhussupbekov, Sarsembayeva & Kaliakin (Eds)
© 2023 The Author(s), ISBN 978-1-003-29912-7
Open Access: www.taylorfrancis.com, CC BY-NC-ND 4.0 license

Compression behavior and crushable properties of calcareous sand in South China sea

J.C. Che
School of Civil Engineering, Tianjin University, Tianjin, China

M.J. Jiang
School of Civil Engineering, Tianjin University, Tianjin, China
School of Civil Engineering, Suzhou University of Science and Technology, Suzhou, Jiangsu, China
College of Civil Engineering, Tongji University, Shanghai, China

P.M. Jiang
School of Civil Engineering, Suzhou University of Science and Technology, Suzhou, Jiangsu, China

Z.J. Ding
School of Environment and Architecture, University of Shanghai for Science and Technology, Shanghai, China

ABSTRACT: Understanding the geotechnical properties of Calcareous sand is essential to develop ocean engineering construction in South China sea. Therefore, a series of one-dimension compression tests were carried out on calcareous sand obtained from the South China sea to investigate its compressive property and particle breakage during compression. The results show that calcareous sand has normal consolidation line (NCL). Sample with relatively uniform gradation has smaller compressibility. The single particle strength plays an important role in compression properties, sample with larger particle size has smaller yield stress. Hardin's relative crushing theory was applied to quantitate the particle breakage during testing. It can be seen that particle breakage occurred at low stress region, and continues to occur to high pressure region with a nearly linear trend. The particle breakage is corresponding to particle size distribution. Under the same vertical stress, sample with uniform distribution and small particle size has less particle breakage.

1 INTRODUCTION

The Calcareous sand is widely distributed in the South China sea (Liu & Wang, 1998). In recent year, within the growing requirement of resource extraction and military construction on the South China sea, lots of large-scale engineering has been constructed, such as oil platform, military base, and so on. Due to the special component with biological debris and existence in the marine environment, calcareous sand is different from terrigenous soil. Therefore, it is essential to investigate the mechanical properties of calcareous sand.

Coop (1990) analyzed properties of calcareous sand of Dog's Bay, the results show that calcareous sand has a similar property to normal clay on compressibility. However, the influence of particle breakage dominates the calcareous sand compressive property gradually with stress increase to a high level. Catano & Pando (2010) investigated the differences between the uncemented calcareous sand and silica sand, results show that calcareous sand exhibits higher

DOI: 10.1201/9781003299127-341

tenacity, shrinkage, and peak friction angle, and yield axial stain, but lower shear modulus than silica sand. Salem et al. (2013) investigated the influence of relative density and confining pressure of calcareous sand by undrained triaxial tests. Shaqour (2007) conducted a series of CPT tests to detect penetration mechanism of calcareous sand. Sharma & Ismail (2006) found that the stress-strain relationship of calcareous sand in different location has a similar trend, although it shows great difference quantitatively. Also, some scholars have conducted many tests to research the effects of cementing materials and cementing content on the mechanical properties of calcareous sand (Ismail et al., 2002, Chai et al., 2021). Different from common sand, particle breakage plays an important part in mechanical properties of calcareous sand. Hence, many research on particle breakage had been carried on. Lee & Farhoomand (1967) indicated that the particle size distribution, particle size, particle shape, single particle strength may have effect on particle breakage. Hall and Gordon (1963) observed that particle size distribution has a significant influence on particle breakage, the more uniform the gradation, the less particle breakage. Luzzani & MR (2002) found that particle breakage of calcareous sand would appear until the strain come to a high level. Donohue et al. (2009) conducted a series of drained cyclic triaxial tests on Dog's Bay Sand, which showed that the increase of the number of cycles would aggravate particle breakage. Coop et al. (2004) found that particle breakage of calcareous sand would reach a limit under shear tests when the strain is large, and the final result of particle breakage correspond to the initial particle size distribution and normal stress. Shahnazari & Rezvani (2013) researched the influence of different parameters of calcareous sand on particle size with triaxial tests and revealed that axial strain has a significant influence on particle breakage. Zhang et al. (2005) conducted a series of compression tests on calcareous sands under lateral confinement, the results show that the particle breakage is considered the primary factor to explain the sample yield during compressing. Dehnavi et al. (2010) studied the mechanical properties of calcareous sands with isotropic compression tests and undrained triaxial compression tests, and found that peak deviator stress and particle breakage could be influenced with the change of confining pressure and compaction. Although many research has been conducted to study the mechanical properties of calcareous sand, the comprehensive analysis of calcareous sand on the aspect of microstructure and particle breakage is still elusive.

In this paper, a series of one-dimensional compression tests for calcareous sand in the South China sea with different particle size were carried out. Based on the analysis of the results of compression behavior and particle breakage on these tests, we studied the compression and crushable properties of calcareous sands obtained in the South China sea with the combination of single particle strength properties.

2 TEST MATERIALS AND TEST METHOD

2.1 *Test materials*

The calcareous sand used in this study was taken from island and reefs in the South China Sea. It is a loose and uncemented granular material. and is mainly composed of coral debris and some skeleton of marine debris. The X-ray diffraction (XRD) tests were conducted to determine the specific mineral composition of calcareous sample. It can be observed from the result of X-ray diffraction that the main composition of calcareous sand is aragonite ($CaCO_3$), calcium aluminate ($Ca_3Al_2O_6$) and magnesite ($MgCO_3$ $FeCO_3$).

The original particle size distribution of calcareous sand was measured by sieve method, and its curve is shown in Figure 1, while the indexes of original particle size distribution are shown in Table 1. It can be seen that the calcareous sand in this research has many coarse grains. It can be inferred that calcareous sand which is used in the tests has non-uniform grading. Figure 2 shows the scanning electron microscopic (SEM) image of calcareous sand particle (Jiang et al., 2017), it shows that the calcareous sand particles can be well divided into three inhomogeneous types: block, flake and strip, and it also shows that the surface of calcareous sand is dominated by tiny pore.

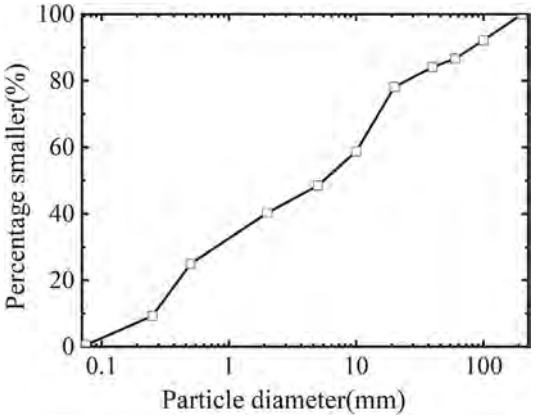

Figure 1. Particle size distribution of original calcareous sand.

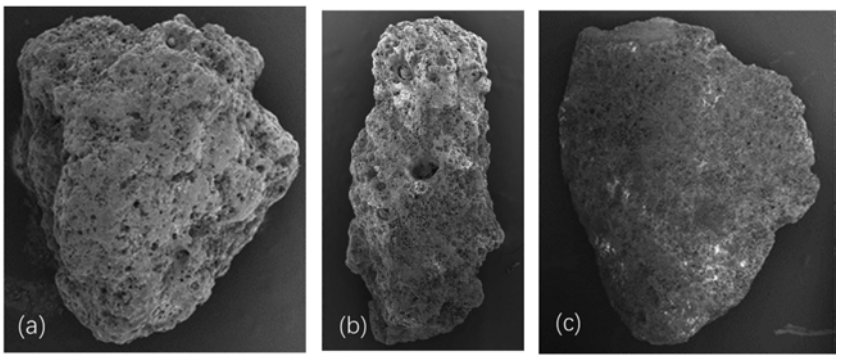

Figure 2. SEM photos of different shapes: (a) block, (b) strip, (c) flake.

Table 1. Basic parameters of original calcareous sand.

Sample	d_{10}(mm)	d_{30}(mm)	d_{60}(mm)	C_u	C_c
Original sand	0.26	0.79	11	42.31	0.22

2.2 *Test apparatus and method*

One-dimensional compression test, which is an uniaxial compression test under lateral restraint, was performed to investigate the geomechanical behavior of calcareous sand. Three types of gradation were selected, their curve is shown in the Figure 3. Samples with different particle size were prepared by sieve method, they include an overall gradation with maximum particle size of 2mm and single gradation of 1-2mm and 0.5-1mm respectively.

In the tests, loading was conducted by step, each step of compressive stress was 0.05, 0.1, 0.2, 0.4, 0.8, 1.6, 3.2, 6.4, 10, 15, 20, 25, 30 MPa respectively. The apparatus of test is shown on the Figure 4, the internal diameter and internal height of apparatus are 61.8 mm and 35 mm respectively. The calcareous sand samples were compressed to the default compaction degree by vibrating the compression tool. In each step of loading, the deformation data was recorded with an interval of an hour. The condition of sample could be seen as stable when the deformation data recorded in an interval is no bigger than 0.005mm. Test termination pressure was set to be 6.4, 10, 15, 20, 25, 30 MPa respectively, and the particle breakage of each termination can be researched by the change of grain gradation with sieve method.

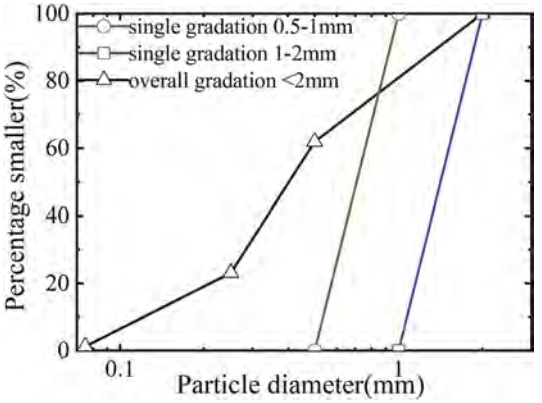

Figure 3. Particle size distribution of calcareous sand used in the one-dimensional compression tests.

Figure 4. Schematic diagram of compression test apparatus.

3 RESULTS AND ANALYSIS

3.1 *Compression behavior*

The results of the compression tests were shown in Figure 5, it is an e-lg P graph of sample with different particle size distribution. It described the relationship between pressure and compress deformation of calcareous sand. It can be seen that the curvature of e-lg P graph is increasing gradually with the increase of pressure under one-dimensional compression test. And then the e-lg P graph gets to be a straight line when the press increases to a higher level. This phenomenon shows that calcareous sand has a familiar one-dimension compression property with normal consolidated clay, which means that it exists normal consolidation line (NCL). It can be illustrated that rearrangement of particles make sample to reach a dense state with the increasing pressure and the particle breakage, which substitute the rearrangement of particles, take in charge of the procedure of compression gradually when the pressure continues to increase.

According to the e-lg P curves of different particle size distribution, it can be observed that the sample with particle size of 1-2mm has biggest void ratio and sample with particle size of <2mm has smallest void ratio. The sample with different gradation and void ratio has different compressive curve. However, compression curve of each sample has a trend to converge into a same line, it shows that the effect of initial void ratio on compressive property of calcareous sand will disappear with the increase of vertical pressure. Therefore, the compression of

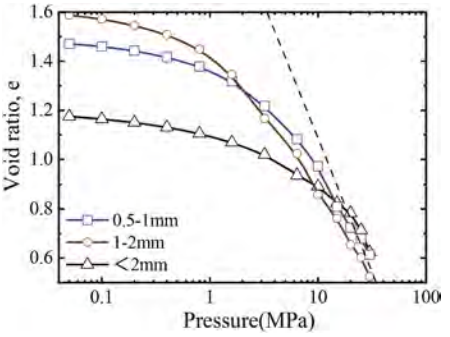

Figure 5. Compression curves of calcareous sand with different particle size distribution.

calcareous sand sample is stable in the final limiting condition, regardless of the initial conditions. It also can be observed that the sample with particle size of 1-2mm and 0.5-1mm have a relatively similar strain under compression, which is obviously larger than sample with particle size of not more than 2mm. The crushed particles in the sample with single gradation will fill the pore between particles, it induces the void ratio of sample decrease sharply. However, due to a more uniform distribution, the pore caused by larger particle in the sample with overall gradation has been filled by small particle, it makes the overall gradation sample has a relatively small change on void ratio when compressing. It shows that calcareous sand with relatively uniform particle size distribution has a better performance on compression property.

Generally, point with the maximum curvature is seen as the compression yield point of the sample. It can be seen that the overall gradation sample has higher yield strength than single gradation sample, it is because the relatively uniform particle size distribution lead to a uniform distribution of stress in the sample, and make it relatively hard to reach the yield point. For single gradation sample, it can be clearly observed that the sample with larger particle size has smaller yield strength.

Usually, we also describe the compression behavior by a bilinear model:

$$e = e_0 - \lambda \ln P \tag{1}$$

where e is void ratio, e_0 is initial void ratio, P is vertical pressure, λ is compression index. According to this model, we can get a relationship between compression index and pressure, and it is shown in the Figure 6. It can be found that compression index increases with the increase of pressure, while the λ of normal sand is a constant value under compression, it also shows a similar characteristics to clay and soil with component of calcium carbonate. The nonlinear curve of e-lg P and λ-lg P all shows that unique compression behavior caused by particle breakage is conspicuous.

3.2 *Relationship between compression behavior and single particle strength*

Generally, we believed that calcareous sand is elastic when the vertical stress is lower than yield point, the deformation of calcareous sand is mainly caused by compression and the rearrangement of particle. However, when the vertical stress reaches the yield point, calcareous sand starts to yield, it shows that a big scale of particle breakage starts to occur and the particle breakage has become the main reason to induce compression deformation, hence a parameter corresponding to the particle strength is supposed to use on the analyze of compression properties in aspect of micro-mechanical properties. Strength of single particle is believed to have a significant influence on the macroscopic mechanical properties (Jiang et al., 2018, Jiang et al., 2019). In order to research the relationship between particle strength and

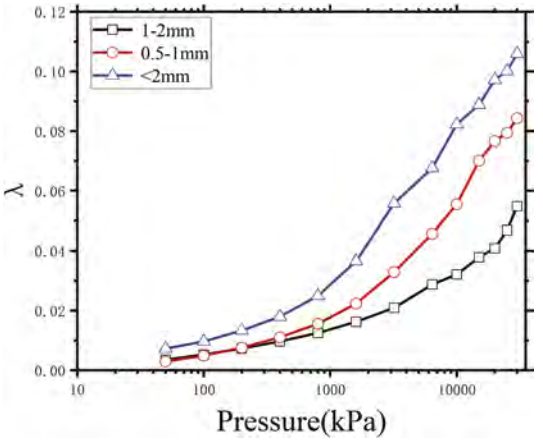

Figure 6. Compression curves of calcareous sand with different particle size distribution.

yield strength of compression, 320 groups single particle compression tests had been made to research the property of single particle strength on different size of calcareous sand particle used in this article before one-dimension compression tests (Jiang et al., 2018). The results are shown in Figure 7, it can be seen that the distribution of single particle strength with different particle size is discrete, and the strength of single calcareous sand decreases with the increasing particle size. Compare with single particle strength with different particle shape, we observed that block particles have a higher strength than flake particles when the particle size is same. Weibull distribution function is cited to make a further analysis statistically on the measured data, it shows that single particle strength follows Weibull distribution.

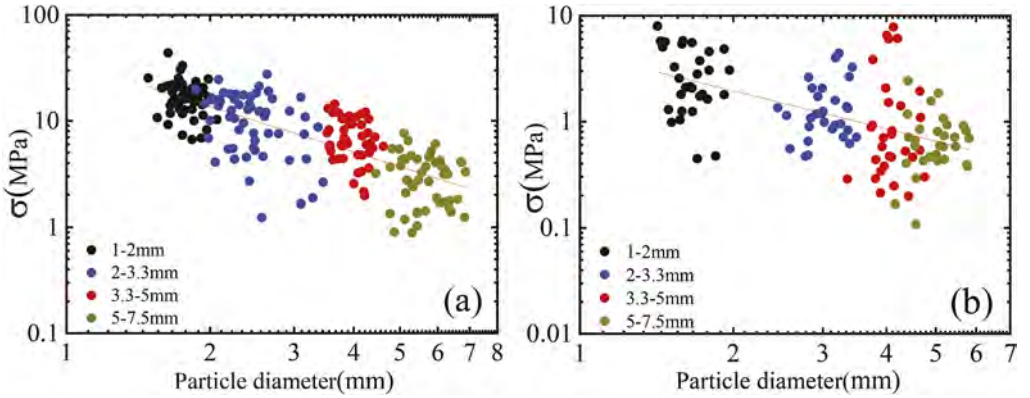

Figure 7. Strength distribution of single particle with different particle sizes: (a) Block particle, (b) Flake particle.

Based on the Weibull distribution function, we get the characteristic stress of each particle with different particle size when the probability of survival is 37%, each characteristic stress for the block particle is 19.4 MPa (1.5mm), 13.8 MPa (2.65mm), 7.7 MPa (4.15mm), 3.7 MPa (6.25mm) respectively and each characteristic stress for the flake particle is 3.1 MPa (1.5mm), 1.3 MPa (2.65mm), 0.9 MPa (4.15mm), 0.7 MPa (6.25mm) respectively. The results of characteristic stress are corresponding to the conclusion obtained in the above. After that, we use the characteristic stress of different particle to normalize the corresponded compression curves.

Figure 8 shows the normalized compression curves of calcareous sand, the characteristic stress chosen for sample with particle size of 0.5-1 mm is 19.4 MPa (block particle) and 3.1 MPa (flake particle), and the characteristic stress chosen for sample with particle size of 1-2 mm is 13.8 MPa (block particle) and 1.3 MPa (flake particle). It can be seen that normalized curves that corresponding to different particle size have extremely close yield points with each other, it shows that the single particle strength is a main reason to influence the yield point and the particle breakage of calcareous sand under compression. If the particle in the sample have a relatively higher single particle strength, it may have a relatively high yield point and more difficult to crush.

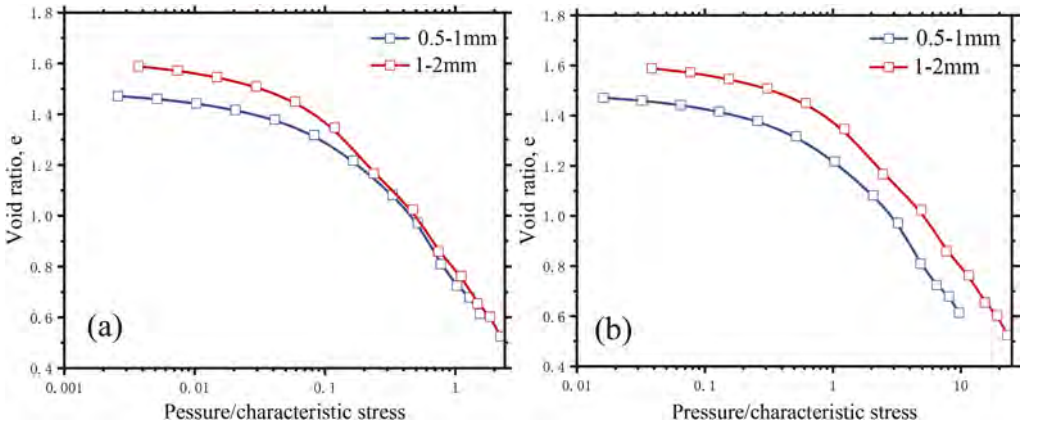

Figure 8. Normalized compression curves of calcareous sand with different particle size distribution: (a) Compression curves normalized by characteristic stress of block particle, (b) Compression curves normalized by characteristic stress of flake particle.

3.3 *Particle breakage*

The one-dimensional compression curves of calcareous sand show that particle breakage plays an important role in the compression process. The results of particle breakage of each sample on different termination of pressure are shown in Figure 9. It demonstrates that almost all part of particles has different level of particle breakage in the compression, and the particle size distribution become more uniform with the increase of pressure. The deduction of particle size on sample with single gradation (0.5-1mm and 1-2mm) is clearly larger than that on sample with overall gradation (<2mm). It shows that that the sample with relatively uniform particle size distribution has a minor particle breakage.

In order to analyze the results of particle breakage quantitatively, Hardin's relative crushing theory was applied (Hardin, 1985), Hardin believed that particle has a larger possibility to crush with the increase of its particle size, and the particle will not crush until its particle size is smaller than 0.074mm. According to this, Hardin define the potential of breakage and relative breakage.

In Hardin's relative crushing theory, the potential of breakage of a certain particle size (bp) was defined as:

$$b_p = \lg\left(\frac{d}{0.074}\right) \tag{2}$$

where d is particle diameter. According to the potential of breakage of a certain particle size (b_p), the potential of breakage (B_p) and total breakage (B_t) was given as:

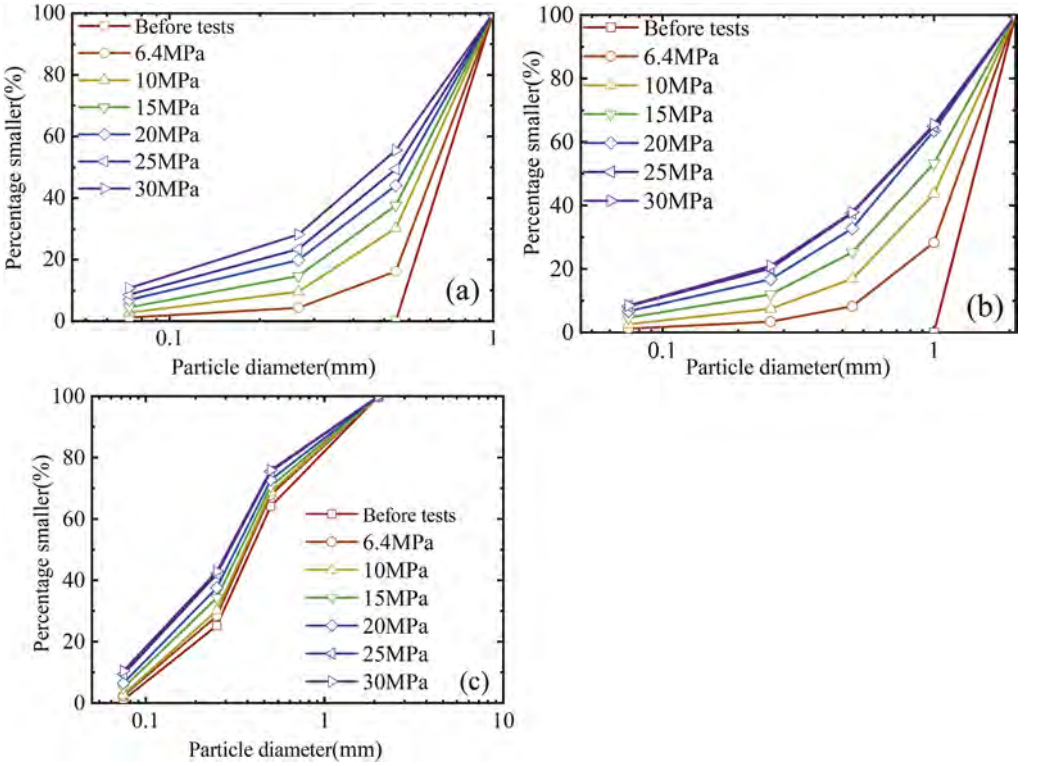

Figure 9. Particle size distribution of sand with different particle size distribution before and after compression tests: (a) 0.5-1mm, (b) 1-2mm, (c) <2mm.

$$B_p = \int_0^1 b_p df \tag{3}$$

$$B_t = \int_0^1 (b_{p0} - b_{p1}) df \tag{4}$$

where df is screening pass rates corresponding to the b_p, and b_{p0} and b_{p1} are the breakage potential of each grain gradation before and after tests respectively. Relative breakage (B_r) was calculated by B_r and B_t using the following equation:

$$B_r = \frac{B_t}{B_{p0}} \tag{5}$$

According to Hardin's relative crushing theory, relative breakage (B_r) is a value with a range from 0 to 1, it presents that particle have not any breakage when its value is 0 and all the particle size become smaller than 0.074mm through crush when its value is 1.

The relationship between pressure and relative breakage B_r on different particle size distribution is shown in Figure 10. From the graph, it can be found that relative particle breakage of calcareous sand is nearly lineal, it shows that particle breakage happens when stress is small and the particle breakage will continue to happen when stress reach a high level. It can be observed that the amount of particle breakage in single gradation sample (0.5-1mm and 1-2mm) is larger than overall gradation sample (<2mm) under the condition of same vertical pressure, it is because the filling of small grain size in the overall gradation sample reduces the

contact force of each grain. In the single gradation sample, the relative breakage of sample with larger particle size is larger than sample with smaller particle size, and the change of relative breakage on the sample with larger particle size is relatively faster than the sample with smaller particle size with the increase of pressure. It shows that sample with larger particle size has more amount of particle breakage, and the velocity of production of particle breakage of sample with larger particle size is faster than sample with smaller particle size. It can also be observed that the change of relative breakage decreases gradually for sample with particle size distribution of 1-2 mm and sample with particle size distribution of no more than 2mm. It might illustrate that particle breakage of sample will reach a limit if compression pressure reaches to a high value.

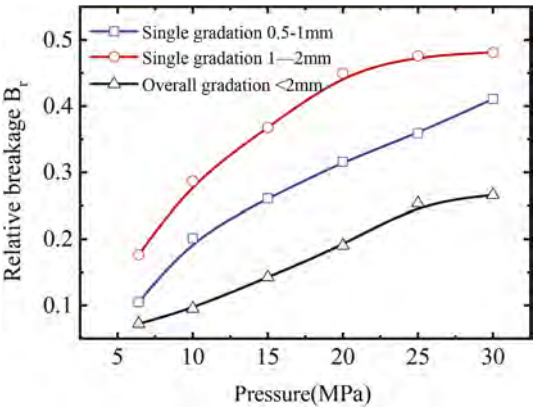

Figure 10. Relative breakage of calcareous sand sample with different particle size distribution.

4 CONCLUSION

In this paper, a series of one-dimensional compression tests were carried out to research the compression properties and particle breakage properties of calcareous sand obtained in the South China sea under compression. The main conclusions are summarized as follows:

(1) Calcareous sand has normal consolidation line (NCL). For samples with different initial condition, their differences on compression curves diminish with the increase of pressure, it can be seen as the particle breakage take in charge of procedure of compression when pressure level is high.
(2) Compare to the single gradation sample, overall gradation sample has a conspicuously better performance on compression properties because of its relatively uniform particle size distribution. For single gradation sample, sample with smaller particle size has a relatively better performance than sample with larger particle size because it has a relatively smaller initial void ratio.
(3) The vertical stress means an initial stress that a big scale of particle breakage starts to occur. The yield stress decreases with the increase of particle size, and the normalized results of one-dimension compression curves show that the divergence of yield stress is caused by difference of single particle strength of different particle size.
(4) Each sample of calcareous sand exhibit an obvious level of particle breakage, the sample with relatively uniform particle size distribution have less particle breakage. Relative breakage (B_r) was used to quantify the particle breakage, it can be found that the amount of particle breakage increases with increasing pressure, and particle breakage occurs from a small level of stress to a high level of stress. It can also be found that the larger the particle size, the larger the amount of particle breakage.

ACKNOWLEDGMENTS

The National Natural Science Foundation of China (Grant No. 51979128, 51890911 and 51639008), National Key Research and Development Program of China (Grant No. 2019YFC032130).

REFERENCES

Catano, J. & Pando, M. A. 2010. Static and dynamic properties of a calcareous sand from southwest Puerto Rico. *GeoFlorida 2010: Advances in Analysis, Modeling & Design*.

Chai, Y., Jiang, D.-P., Wang, F.-J. & Lyu, H.-B. 2021. Investigation of engineering properties of cement-stabilized calcareous sand foundation. *Advances in Materials Science and Engineering*, 2021, 1–14.

Coop, M. 1990. The mechanics of uncemented carbonate sands. *Géotechnique*, 40, 607–626.

Coop, M., Sorensen, K., Bodas Freitas, T. & Georgoutsos, G. 2004. Particle breakage during shearing of a carbonate sand. *Géotechnique*, 54, 157–163.

Dehnavi, Y., Shahnazari, H., Salehzadeh, H. & Rezvani, R. 2010. Compressibility and undrained behavior of Hormuz calcareous sand. *Electronic Journal of Geotechnical Engineering*, 15, 1684–1702.

Donohue, S., O'sullivan, C. & Long, M. 2009. Particle breakage during cyclic triaxial loading of a carbonate sand. *Géotechnique*, 59, 477–482.

Hall, E. & Gordon, B. 1963. Triaxial testing with large-scale high pressure equipment. *Laboratory Shear Testing of Soils*, 361, 315–328.

Hardin, B. O. 1985. Crushing of soil particles. *Journal of Geotechnical Engineering*, 111, 1177–1192.

Ismail, M. A., Joer, H. A., Sim, W. H. & Randolph, M. F. 2002. Effect of cement type on shear behavior of cemented calcareous soil. *Journal of Geotechnical and Geoenvironmental Engineering*, 128, 520–529.

Lee, K. L. & Farhoomand, I. 1967. Compressibility and crushing of granular soil in anisotropic triaxial compression. *Canadian Geotechnical Journal*, 4, 68–86.

Luzzani, L. & Mr, C. 2002. On the relationship between particle breakage and the critical state of sands. *Soils and Foundations*, 42, 71–82.

Salem, M., Elmamlouk, H. & Agaiby, S. 2013. Static and cyclic behavior of North Coast calcareous sand in Egypt. *Soil Dynamics and Earthquake Engineering*, 55, 83–91.

Shahnazari, H. & Rezvani, R. 2013. Effective parameters for the particle breakage of calcareous sands: An experimental study. *Engineering Geology*, 159, 98–105.

Shaqour, F. M. 2007. Cone penetration resistance of calcareous sand. *Bulletin of Engineering Geology and the Environment*, 66, 59–70.

Sharma, S. S. & Ismail, M. A. 2006. Monotonic and cyclic behavior of two calcareous soils of different origins. *Journal of Geotechnical and Geoenvironmental Engineering*, 132, 1581–1591.

Jiang, M. J., Wu, D., Cao, P. & Ding, Z. J. 2017. Connected inner pore analysis of calcareous sands using SEM. *Chinese Journal of Geotechnical Engineering*, 39(S1), 1–5.

Jiang, M. J., Xu, Z, W., Liu, J., Wu, D., Wu, X, F. & Wang, J, F. 2019. Experimental study on single-particle crushing of calcareous sand under cyclic loading. *Journal of Tianjin University(Science and Technology)*, 52, 23–28.

Jiang, M. J., Yang, K. X., Chen, Y. L., Ding, Z. J. & Xie, Y. B. 2018. Experimental study on crushability of single calcareous sand obtained from South China sea. *Journal of Hunan University(Natural Sciences)*, 45(S1), 150–155.

Liu, C. Q. & Wang, R. 1998. Physical and Mechanical Properties of Calcareous Sand. *Rock and Soil Mechanics*, 19, 32–37.

Zhang, J. M., Wang, N., Shi, X. F., Li, J. G. & Chen, H. Y. 2005. Compression and Crushing Behavior of Calcareous Sand under Confined Compression. *Chinese Journal of Rock Mechanics and Engineering*, 24, 3327–3331.

Smart Geotechnics for Smart Societies – Zhussupbekov, Sarsembayeva & Kaliakin (Eds)
© 2023 The Author(s), ISBN 978-1-003-29912-7
Open Access: www.taylorfrancis.com, CC BY-NC-ND 4.0 license

Shear modulus (G_{max}) degradation of marine clay during recompression and swelling

Ramesh Gangisetti
Doctoral Scholar, Department of Civil Engineering, Indian Institute of Technology Hyderabad (IITH), Kandi, Sangareddy, Telangana, India

Sireesh Saride*
Professor, Department of Civil Engineering, Indian Institute of Technology Hyderabad (IITH), Kandi, Sangareddy, Telangana, India

C.R. Parthasarathy
CMD, Sarathy Geotech & Engineering Services Pvt Ltd, Bengaluru, Karnataka, India

ABSTRACT: This paper presents the secant shear modulus (G_{max}) response of a normally consolidated undisturbed marine clay cyclically loaded during recompression to the past effective overburden pressure and swelling stages after consolidating to a new pre-consolidation pressure. The strain-controlled undrained dynamic cyclic simple shear tests were performed on undisturbed marine clay obtained from offshore Indonesia. The clay samples were consolidated to OCR of 2.3 and 4.6 during the loading stage up to in-situ past effective stress of 230kPa and allowed to swell to the same OCR values after consolidating to new past effective stress of 700kPa. The cyclic shear loading was applied with shear strains ranging from 0.025% to 0.5% at 0.5Hz. The results revealed that for the same effective axial stress and OCR, the G_{max} in the swelling stage is more than in the recompression stage.

Keywords: Marine clay, G_{max}, Cyclic simple shear, Recompression, Pre-consolidation pressure, Swelling, OCR

1 INTRODUCTION

The marine soils are often over-consolidated due to the geologic history of glaciation, erosion, etc. (Lad et al. 1980, 1981: Loken 1976; Mishu et al. 1982). Also, the normally consolidated soils may become over-consolidated because of stress release due to the decommissioning of offshore structures after their service life. The marine soils are subjected to dynamic installation loads from pile driving and environmental loads from waves, wind, and seismic activity. Undrained cyclic loading on cohesive soils causes a decrease in effective stress and breaks the soil structure leading to degradation of strength and stiffness (Thiers and Seed, 1969, Brown et al., 1975, Andersen et al., 1975, Yasuhara et al., 1983b, 1992, Yasuhara 1985). The foundation soil response to dynamic loading in terms of shear modulus (G_{max}) degradation and damping (ζ) may be influenced by the number of loading cycles (N), frequency (f), shear strain (γ_c), OCR, effective confining stress (p') and plasticity index (PI). The shear modulus degradation was not influenced significantly by f and N, whereas damping values increase with increasing f and decrease at large γ_c with increasing N (Darendeli, 2001). The shear modulus degradation parameter(t) increases rapidly when γ_c exceeds 1% and decreases with increasing OCR (Vucetic and Dobry, 1988; Takaki Kagawa, 1992).

*Corresponding author: sireesh@ce.iith.ac.in

DOI: 10.1201/9781003299127-342

It may happen that an over-consolidated soil due to previous stress history might be loaded to a normally consolidated state and upon stress release, it might go back to an over-consolidated state again. This study aims to understand the G_{max} behavior of an undisturbed, normally consolidated marine clay when cyclically sheared initially, during the recompression stage, and later during the swelling stage after it is consolidated to new pre-consolidation pressure.

2 MATERIALS AND TESTING PROGRAM

The marine clay obtained from offshore Indonesia was tested for Atterberg limits and specific gravity (Table 1). The natural moisture content and the bulk density are 60% and 16.2kN/m^{3,} respectively. The liquid limit and plasticity index are 110% and 65%, respectively. The soil is classified as clay of high plasticity (CH) as per ASTM D2487-17 (ASTM 2017a).

Table 1. Soil index properties.

Test particulars	value	Reference	
Natural Moisture Content, %	60	ASTM D 2216-19	(ASTM 2019)
Liquid Limit, %	110	ASTM D 4318-17	(ASTM 2017b)
Plastic Limit, %	45	ASTM D 4318-17	(ASTM 2017b)
Plasticity Index, %	65	ASTM D 4318-17	(ASTM 2017b)
Specific gravity, (-)	2.7	ASTM D 854-14	(ASTM 2014)
Bulk unit weight, kN/m^3	16.2	ASTM D 7263-09	(ASTM 2009)
Initial void ratio (-)	2.93	-	

The undisturbed soil specimens of size 70mm diameter and 20mm height were cut from the soil core. The soil specimens were saturated by applying a 10kPa back pressure through PV controller and collected the backwater from the specimen top. The saturation was considered 100% if the backwater collected was three times the soil pore volume.

The testing program included a) An oedometer test for the consolidation characteristics, b) A static simple shear test to determine undrained shear strength at pre-consolidation pressure of 230kPa obtained from the oedometer test, c) Undrained cyclic simple shear test (loading stage) on specimens consolidated to effective axial stresses of 50kPa (OCR = 4.6), 100kPa (OCR = 2.3) and 230kPa (OCR = 1.0), 500kPa (OCR = 1.0) and 700kPa (OCR = 1.0) d) Undrained cyclic simple shear test (unloading stage) on specimens consolidated to effective axial stresses of 150kPa (OCR = 4.6), 304kPa (OCR = 2.3). The loading frequency and the number of cycles for each test were 0.5Hz and 5, respectively. For each effective axial stress, the cyclic shear amplitude ranged from ±0.025% to ±0.5%. The test program for undrained cyclic simple shear tests is shown in Table 2.

Table 2. Test program for undrained cyclic simple shear tests.

Test particulars	p′	p′$_c$	OCR
Loading Stage	50	230	4.6
	100	230	2.3
	230	230	1.0
	500	500	1.0
	700	700	1.0
Unloading Stage	304	700	2.3
	150	700	4.6

3 RESULTS AND DISCUSSION

The oedometer test was conducted with effective axial stresses varying from 10kPa to 900kPa. The duration of each stress increment was 24hrs. The recompression, compression, and swell indices determined from void ratio – effective stress [e -log(p')] curve are 0.04, 0.84, and 0.23, respectively. The pre-consolidation pressure obtained using Casagrande's graphical method is 230kPa (Figure 1).

The static simple shear test was conducted with pre-consolidation pressure of 230kPa. The shear strain rate was 5% per hour up to a shear strain of 20% (ASTM D6528-17). The active height control method was used to maintain constant volume conditions so that the change in effective axial stress could be considered as excess pore-pressure mobilized during shear. As shown in Figure 2, the peak static undrained shear strength is 110 kPa.

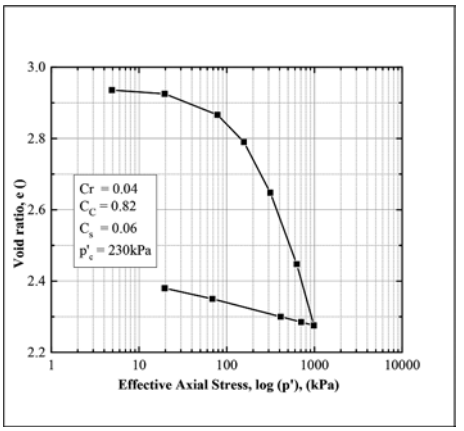

Figure 1. E-log (p′) curve.

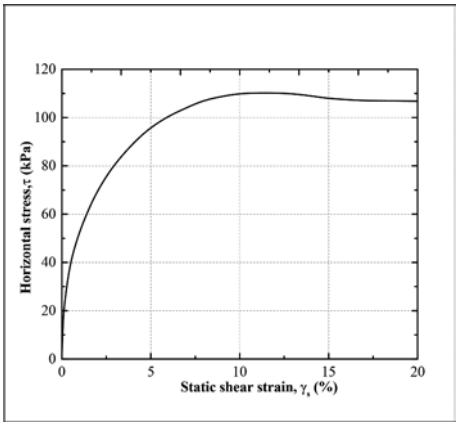

Figure 2. Horizontal stress, τ (kPa) vs static shear strain, γ_s (%).

The undrained cyclic simple shear tests were conducted as per the test program shown in Table 2 to determine the secant shear modulus of the first cycle (G_{max}) and its degradation with the increase in cyclic shear strain (γ_c) from ±0.025% to ±0.5% at a constant frequency of 5Hz and no. of cycles of 5. The cyclic shear stress vs. cyclic shear strain of the recompression stage from effective axial stress of 50 kPa to 230kPa, compression stage from 500kPa to 700 kPa, and swelling stage from 304 kPa to 50 kPa are shown in Figure 3. The G_{max}, at a very small shear strain of 0.025%, increased from 11.6MPa to 14.5MPa in recompression, 14.5MPa to 19.5MPa in compression, and 19.5MPa to 16.2MPa in swelling.

As shown in Figure 4, the G_{max} for the same effective axial stresses in recompression and swelling increased from 11.6MPa to 15.5MPa, 13.3MPa to 15.7MPa, and 14.5MPa to 16.2MPa, respectively, for 50kPa, 100kPa, and 230kPa. The increase in G_{max} in swelling compared to recompression can be attributed to the increase in soil stiffness due to the new pre-consolidation pressure of 700kPa. For any γc, the difference in G_{max} in the compression stage is more than in the swelling stage. At any $\gamma_c > 0.2\%$, the difference in G_{max} in the swelling stage is negligible.

As shown in Figure 5, the G_{max} for the same OCR of 2.3 increased from 13.3MPa in recompression to 16.5MPa in swelling and, for the same OCR of 4.6, increased from 11.6MPa to 15.9MPa. The increase in G_{max} in swelling compared to recompression could be due to the combined effect of new pre-consolidation pressure and effective axial stress to maintain the same OCR. The damping, ζ, in general, increased with the increase in γ_c for all P′. It varied from 1.7% at γ_c of 0.025% to 8.9% at γ_c of 0.5% in recompression and from 0.4% to 3.5% in swelling. The damping in swelling compared to recompression decreased by about 40%.

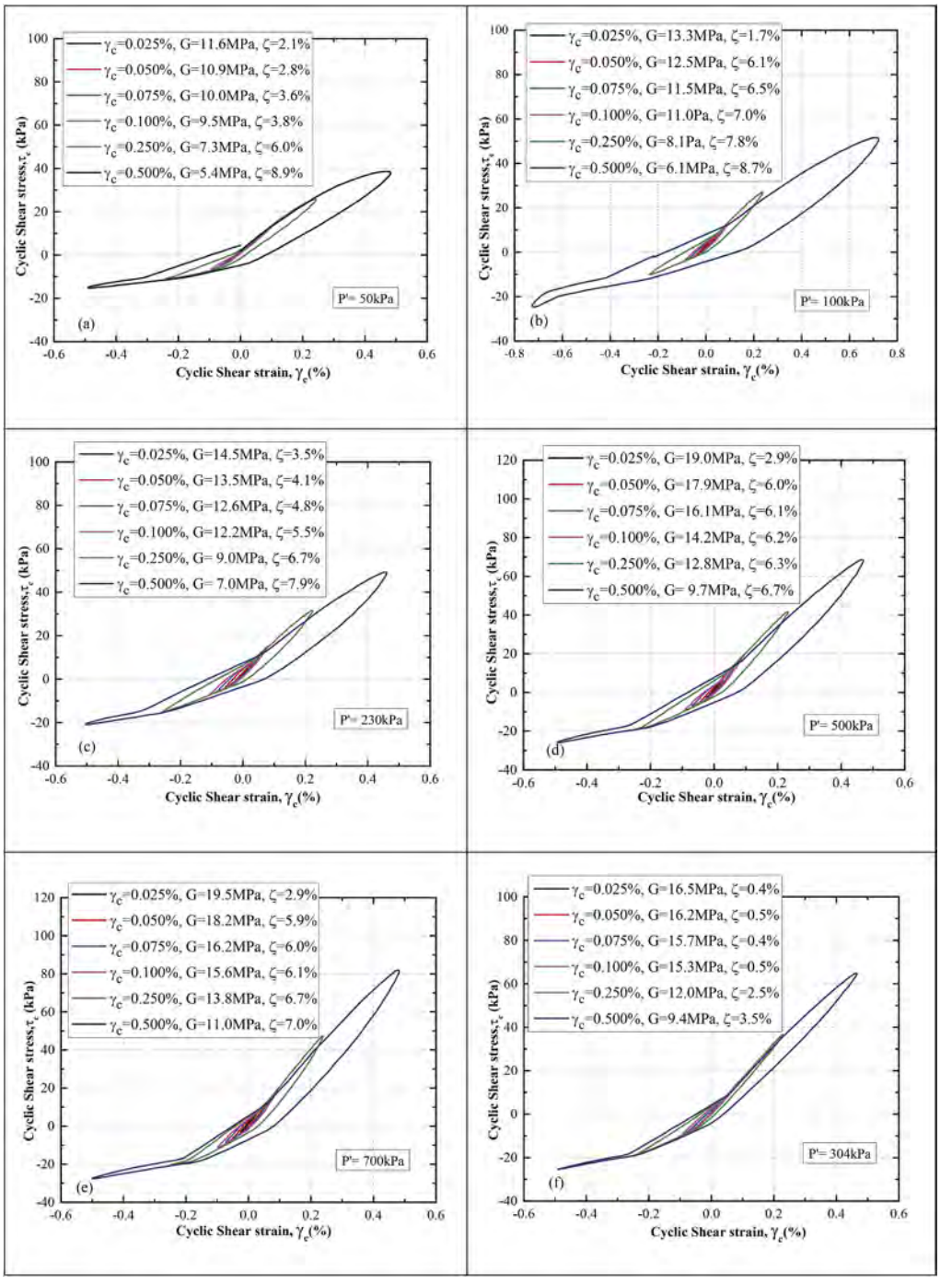
γc=0.025%, G=11.6MPa, ζ=2.1%
γc=0.050%, G=10.9MPa, ζ=2.8%
γc=0.075%, G=10.0MPa, ζ=3.6%
γc=0.100%, G=9.5MPa, ζ=3.8%
γc=0.250%, G=7.3MPa, ζ=6.0%
γc=0.500%, G=5.4MPa, ζ=8.9%
P'= 50kPa
(a)
γc=0.025%, G=13.3MPa, ζ=1.7%
γc=0.050%, G=12.5MPa, ζ=6.1%
γc=0.075%, G=11.5MPa, ζ=6.5%
γc=0.100%, G=11.0Pa, ζ=7.0%
γc=0.250%, G=8.1Pa, ζ=7.8%
γc=0.500%, G=6.1MPa, ζ=8.7%
P'= 100kPa
(b)
γc=0.025%, G=14.5MPa, ζ=3.5%
γc=0.050%, G=13.5MPa, ζ=4.1%
γc=0.075%, G=12.6MPa, ζ=4.8%
γc=0.100%, G=12.2MPa, ζ=5.5%
γc=0.250%, G= 9.0MPa, ζ=6.7%
γc=0.500%, G= 7.0MPa, ζ=7.9%
P'= 230kPa
(c)
γc=0.025%, G=19.0MPa, ζ=2.9%
γc=0.050%, G=17.9MPa, ζ=6.0%
γc=0.075%, G=16.1MPa, ζ=6.1%
γc=0.100%, G=14.2MPa, ζ=6.2%
γc=0.250%, G=12.8MPa, ζ=6.3%
γc=0.500%, G= 9.7MPa, ζ=6.7%
P'= 500kPa
(d)
γc=0.025%, G=19.5MPa, ζ=2.9%
γc=0.050%, G=18.2MPa, ζ=5.9%
γc=0.075%, G=16.2MPa, ζ=6.0%
γc=0.100%, G=15.6MPa, ζ=6.1%
γc=0.250%, G=13.8MPa, ζ=6.7%
γc=0.500%, G=11.0MPa, ζ=7.0%
P'= 700kPa
(e)
γc=0.025%, G=16.5MPa, ζ=0.4%
γc=0.050%, G=16.2MPa, ζ=0.5%
γc=0.075%, G=15.7MPa, ζ=0.4%
γc=0.100%, G=15.3MPa, ζ=0.5%
γc=0.250%, G=12.0MPa, ζ=2.5%
γc=0.500%, G=9.4MPa, ζ=3.5%
P'= 304kPa
(f)
Cyclic Shear stress,τc (kPa)
Cyclic Shear strain, γc(%)

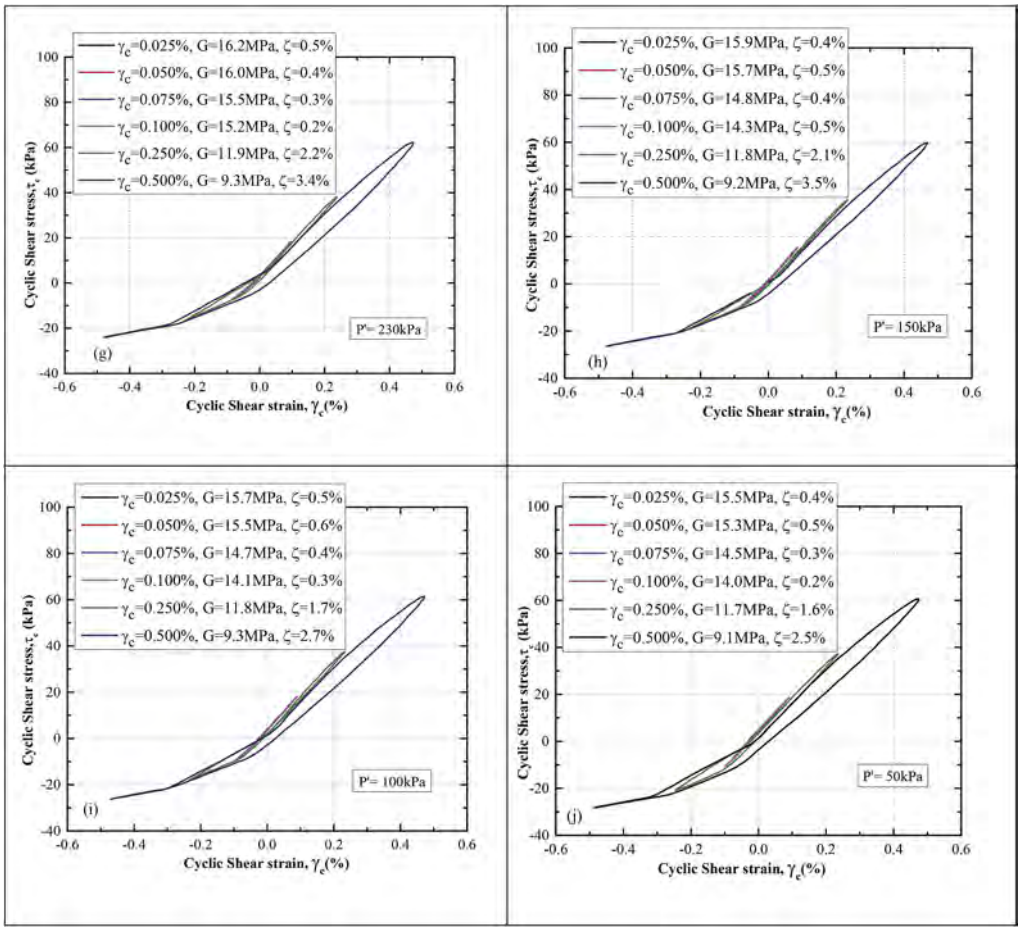

Figure 3. Cyclic shear stress, τ, vs. Cyclic shear strain, γ_c; (a-c) Recompression (50-230kPa), (d-e) Compression (500-700kPa) and (f-j) Swelling (304-50kPa).

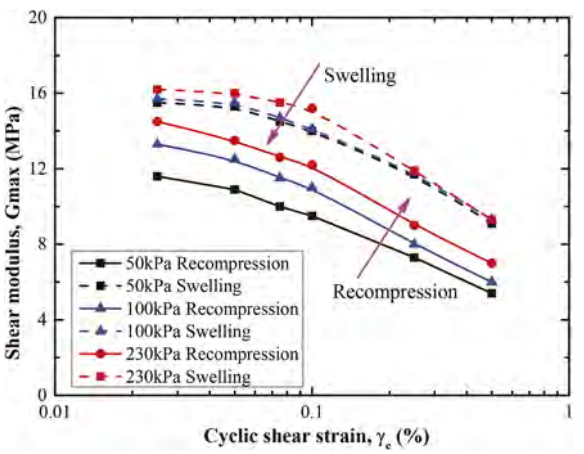

Figure 4. Shear modulus, G_{max}, vs. Cyclic shear strain, γ_c; Recompression & Swelling (50-230kPa).

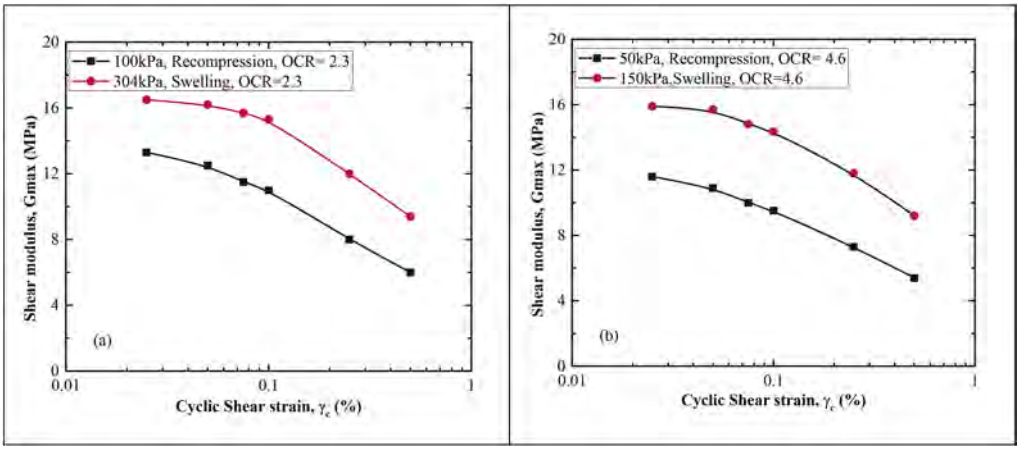

Figure 5. Shear modulus, G_{max} vs Cyclic shear strain, γ_c, (a) OCR=2.3, (b) OCR=4.6.

4 CONCLUSIONS

Dynamic cyclic simple shear tests were conducted to understand the G_{max} behavior during recompression, and swelling stages after the soil is consolidated to a new pre-consolidation pressure and stress release. The study's findings lead to the following conclusions.

1. The G_{max} increases in the recompression/compression stages and decreases in the swelling stage.
2. For the same effective axial stress, the G_{max} in the swelling stage is more than in the recompression stage due to the increase in soil stiffness when the soil is consolidated to a new pre-consolidation pressure. The difference in G_{max} in the compression stage, with the increase in P', is more than in the swelling stage. At any $\gamma_c > 0.2\%$, the difference in G_{max} in the swelling stage is negligible.
3. For the same OCR, the G_{max} in the swelling stage is more than in the recompression stage. This could be due to the combined effect of the new pre-consolidation pressure and the increase in effective axial stress in the swelling stage to maintain the same OCR.
4. The damping at a maximum γ_c of 0.5% examined in the current study decreased by 40% in the swelling compared to recompression.

REFERENCES

Andersen, K. H. (1975). Repeated loading of clay; summary and interpretation of test results. NGI Internal Rep. 74037-9, NGI, Oslo, Norway.

ASTM. 2009. Standard test methods for laboratory determination of density (unit weight) of soil specimens. ASTM D7263-09. West Conshohocken, PA: ASTM

ASTM. 2014. Standard test methods for specific gravity of soil solids by water pycnometer. ASTM D854-14. West Conshohocken, PA: ASTM.

ASTM. 2017a. Sandard practice for classification of soils for engineering purposes. (Unified Soil Classification System). ASTM D2487-17el. West Conshohocken, PA: ASTM.

ASTM. 2017b. Sandard test methods for liquid Limit, plastic Limit, and plasticity index of soils. ASTM D4318-17el. West Conshohocken, PA: ASTM.

ASTM. 2019. Sandard test methods for Laboratory determination of water (moisture) content of soil and rock by mass ASTM D2216-19. West Conshohocken, PA: ASTM.

Brown, S.F., Andersen, K.H., and McElvaney, J. (1977). The effect of cyclic loading of clays. Proc., 9th ICSMFE, Vol. 2, ICSMFE, Tokyo, Japan, 195–200.

Ladd, C.C., et al. (1980). Evaluation of compositional and engineering properties of offshore Venezuelan soils, Vol. 1: Orinoco clay (Gulf of Paria and Orincoco Delta). Research Report No. R80-14, Dept. of Civil Engineering, Massachusetts Institute of Technology, Boston, Mass.

Ladd, C.C., et al. (1981). Evaluation of compositional and engineering properties of offshore Venezuelan soils, Vol. 2: North of Paria stiff clays. Research Report No. R81-21, Dept. of Civil Engineering, Massachusetts Institute of Technology, Cambridge, Mass.

Loken, T. (1976). Geology of superficial sediments in the northern North Sea. Proceedings, International Conference on the Behavior of Offshore Structures, BOSS'76, Trondheim, Norway, Vol. 1, 501–515.

Mishu, R., et al. (1982). Evaluation of compositional and engineering properties of offshore Venezuelan soils, Vol. 3: Tuy Cariaco clays. Research Report No. R82-31, Dept. of Civil Engineering, Massachusetts Institute of Technology, Cambridge, Mass.

Thiers, G. R., and Seed, H.B. (1969). Strength and stress-strain characteristics of clays subjected to seismic loading conditions. Vibration effects of earthquakes on soils and foundations; STP 450, ASTM, Philadelphia, Pa., 3–56.

Vucetic, M., and R. Dobry. (1988). Degradation of marine clays under cyclic loading. J. Geotech. Eng. 114(2): 133–149.

Yasuhara, K., Fujiwara, H., Hirao, K., and Ue, S. (1983b). Undrained shear behavior of quasi-overconsolidated clay induced by cyclic loading. Proc., IUTAM Symp.; Seabed Mech., 17–24.

Yasuhara, K. (1985). Undrained and drained cyclic triaxial tests on marine clay. Proc., 11th ICSMFE, Vol. 2, Paris, France, 1095–1098.

Yasuhara, K., Hirao, K., and Hyde, A.F.L. (1992). Effects of cyclic loading on undrained strength and compressibility of clay. Soils and Found., 32(1), 100–116.

Smart Geotechnics for Smart Societies – Zhussupbekov, Sarsembayeva & Kaliakin (Eds)
© 2023 The Author(s), ISBN 978-1-003-29912-7
Open Access: www.taylorfrancis.com, CC BY-NC-ND 4.0 license

Appraisal of barge-ladden oil drilling rig stability in the mangrove swamp of southern Nigeria

W.I. Beresibo
University of Port Harcourt, Nigeria

ABSTRACT: Accomplished in this paper is the stability appraisal of a 43,620kN barge-ladden oil rig platform in the mangrove swamp of southern Nigeria. The rig is to be deployed to a dredged slot and while in place it is meant to be ballasted prior to the oil drilling exercise. The appraisal of the rig-soil system was carried out using analytical methods and based on the operational requirements of the rig, soil condition and tidal information. The ratio of the bearing resistance to the rig load was found to be greater than 20; indicating that ultimate limit state is ensured. Serviceability limit state checks gave 207mm consolidation settlement which was estimated to occur over 18years period. Within the 10 months period over which the oil drilling exercise is planned, only about 25% degree of consolidation is expected. The results suggest that the operational minimum freeboard of 0.61m will be not exceeded.

1 INTRODUCTION

The southern part of Nigeria especially the Niger Delta region is known for oil and gas exploration activities. Several of these activities take place nearshore within the mangrove swamps. For such locations, a barge-ladden oil rig platform is usually mobilized. These rigs are made up of high ship and deck loads, founded on a barge with a large surface area. The barge helps in the movement of the oil drilling rigs to locations and acts as the platform that bears directly on the soils during the oil drilling operations. Contact pressure from the rig is exacted on the underlying soils through the barge.

The mangrove swamp is one of the morphological units of the coastal environment of the Niger Delta (Short & Stable 1967). The formation of soils across this sub environment are known to be stratified in structure (Whiteman 1982). They are mostly of weak strength with high compressibility characteristics and can hardly support high loads without significant settlements (Abam & George 1997). Hence for projects that involves heavy and sensitive structures, proper soil investigation program and analysis is required in order to avoid failures. This is particularly important for the mangrove swamp sub-environment of southern Nigeria where the soils are known to exhibit high variability and poor strength.

Failures of oil drilling rig platforms are usually fatal and with attendant economic consequences and litigations. Hence, the analysis of the rig-soil system is a necessary requirement prior to the deployment of the rig platform for any drilling operations. In this paper, the stability of a 43,620 kN barge-ladden oil drilling rig has been appraised. This rig is to be deployed to one of the mangrove swamps of southern Nigeria. In the analysis, the operations requirements of the rig, the prevailing soil condition of the site as well as the behaviour of the nearby river were taken into consideration. Analytical methods were employed in the calculations. Both ultimate and serviceability limit state checks were carried out in the analysis. Part of the brief for the analysis is to decide on ground improvement measures in the event that the minimum freeboard is exceeded by the downward movement of the barge. Another aspect of the decision

DOI: 10.1201/9781003299127-343

making involved the determination of the depth of dredge of the top soil layer. This depth has to be adequate for the haulage of the barge into the slot both at low and high-water conditions.

1.1 *Study area*

The study area is located within the Ogbotobo marginal field in the Niger Delta region of Nigeria. It lies within the mangrove swamp vegetation morphological units with network of rivers and creeks. The underlying sediments consist of sand deposits with alternating layers of clay and sand deposits.

2 INVESTIGATION PROGRAM

The investigation program included both field investigation and laboratory testing. Soil borings and sampling were accomplished to a depth of 20 m using percussion drilling rig The field operations were in accordance to requirements of Eurocode 7; part 2. Soil samples retrieved from the boreholes were subjected to laboratory tests to determine their index, strength and compressibility characteristics using relevant sections of the code.

2.1 *Ground condition*

Information obtained from the field and laboratory tests showed that the site consists of a layer of sand occupying the top horizon up to an average depth of 5.25 m. This sand deposit is medium to dense in compact state and overlies a thick layer of soft greyish clay that extended to a depth of 18 m. Beneath clay layer is another layer medium sand layer that extended to the limit of geotechnical exploration. The summary of the soil profile is given in Table 1. The water levels were measured at 0.52 m and 1.45 m below ground surface at high tide and low tide respectively.

The range of value for relevant soil parameters considered as inputs for the analysis is presented in Table 2. Characteristic soil parameters were determined from statistical approach defined by Schneider (1997). In the case of the coefficient of volume compressibility and coefficient of consolidation, their values are not constant but stress level depended. Hence their design values are based on the stress level that corresponds to the load from the oil drilling rig.

Table 1. Subsoil profile of the site.

Soil	Depth to both of stratum (m)	Thickness (m)	Consistency/ Density
Sand	0.00 – 5.25	5.25	Medium to dense
Clay	5.25 – 18.0	12.75	Soft
Sand	18.0 – 20.0	2.00	Medium dense

Table 2. Engineering properties of soils.

Soil	Soil properties	Units	Range of values	Design Value
Sand	Unit weight, γ	kN/m^3	19.9 ~ 20.1	19.9
	Friction angle ϕ	°	35 ~ 43	36
	Soil modulus, E	MPa	41 ~ 90	55
Clay	Unit weight, γ	kN/m^3	15.4 ~ 17.6	15.7
	Undrained cohesion	kPa	10 ~ 12	11
	Soil modulus, E	MPa	5 ~ 6	5
	Coeff. of vol. comp. Mv	m^2/MN	0.77 ~ 1.54	
	Coeff. of consol. Cv	m^2/yr	2.56 ~ 7.19	
Sand	Unit weight, γ	kN/m^3	19.0 ~ 20.2	19.2
	Friction angle ϕ	°	32 ~ 33	32
	Soil modulus, E	MPa	24 ~ 27	25

3 STABILITY ANALYSIS

3.1 *Design situation*

The stability of the rig-soil system was appraised in terms of shear failure and vertical movement of the soil. The following design situations were considered in the analysis.

- The overall rig loads taken as 43,620 kN.
- The dimension of the barge given as 63.9 m x 21.95 m x 4.27 m.
- The condition of soil underlying the site which comprised of sand deposits underlain by clay which in turn overlies sand beds at depths.
- The low and high-water levels of the adjourning river which was measured at 0.52 m and 1.45 m respectively.
- The nature of the rig facilities is such that is to be considered sensitive.
- Loading condition are static in nature
- Short term design was adopted noting the geotechnical and loading conditions of the site.
- The specification of the barge-ladden rig requires that the freeboard of not less than 0.61 m should be maintained during operations.

3.2 *Dredging requirement for the barge-ladden rig*

Based on the topography of the site, rivel level and transit draft of the barge, it is proposed that the top horizon of the soil profile be dredged to a depth of 3.09m in order for the rig to be tugged unhindered to the location. While in place at the drilling location, the compartments of the barge will be ballasted with water in order for the base to have a direct contact with the soil for commencement of the oil drilling operations. Given the elevation of the ground with the proposed depth of the dredge and the soil profile, the barge is expected to rest directly on a 2.16 m thick sand. Based on the high-water level of 0.52 m below ground surface, the freeboard when the barge is in contact with slot bed prior to any vertical movement is 1.7 m. Schematic drawing of the rig-soil system is presented in Figure 1.

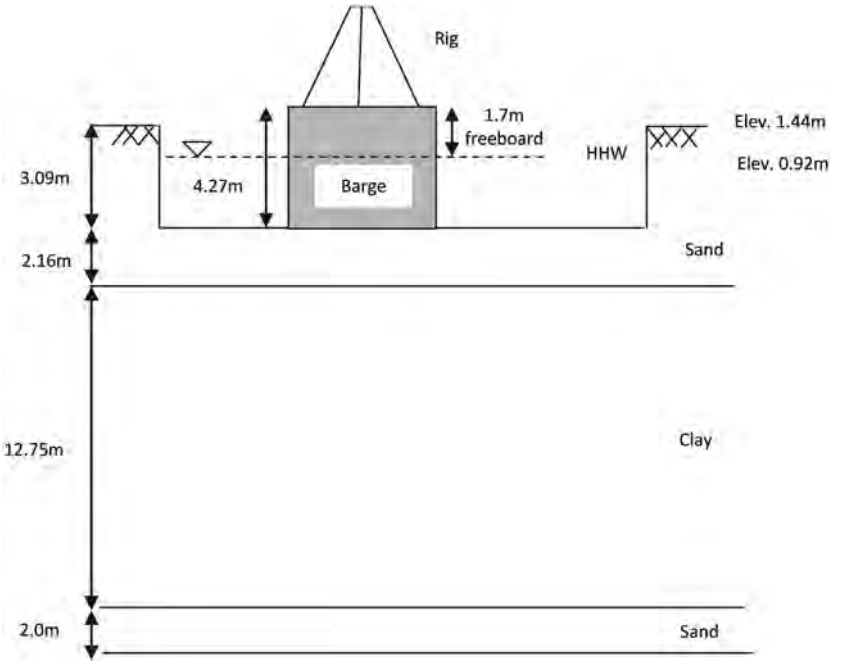

Figure 1. Schematic drawing of the soil-rig system.

3.3 *Analytical methods*

Stability of the barge-ladden rig was carried out with strict adherence to the provisions of relevant sections of part 1of Eurocode 7: Geotechnical Design - Part 1: General rules. Separate checks of ultimate limit states ULS and serviceability limit states SLS were conducted with well-established calculation procedures and reliable design models.

3.3.1 *Ultimate limit state check*

Given the profile of the site and the expected depth of excavation, it is expected that the rig will be resting directly on the medium to dense sand layers while in place. Hence, the effective stress parameters were considered for the stability analysis. The equation used is as given in Annex D, section 2.4 of the Eurocode 7. In the analysis, design approach 1; combination 2 was adopted. Appropriate partial factors were applied to the material properties, loads and bearing resistances. The analytical model used in the computation is expressed equation 1 below:

$$\frac{R}{A'} = C_u N_c S_c + q' N_q S_q + 0.5 B \gamma' N_\gamma S_\gamma \tag{1}$$

Where R = bearing resistance; A′ = effective area of the footing; C_u = undrained shear strength; q' = effective overburden pressure at the base level of the foundation; γ' = effective unit weight above the base level of foundation; N_γ N_q N_c = bearing capacity factors; and $S_c S_q$ S_γ = shape factors.

3.3.2 *Serviceability limit state check*

Serviceability was considered as the governing criteria for the stability appraisal of the rig-soil system. In the analysis, consolidation settlement was considered as the most critical given the condition of the soils at the site. Consolidation settlement analyses were performed using the equation given below:

$$S_c = \sum M_v \Delta_P H \tag{2}$$

Where Mv = coefficient of volume compressibility; H = thickness of the clay layer; and Δ_p is the increment in the vertical effective stress in the layer due to the net bearing pressure.

The rate of consolidation settlement was also estimated. The expression used to determine the time rate of settlement equation given below.

$$T_v = C_v \; t/H^2 \tag{3}$$

Where: Tv = time factor; Cv is coefficient of consolidation; and H is the thickness of the consolidating layer which is $H/2$ for double drainage situation. The characteristics values of the coefficient of consolidation used in the equation is based on the values obtained for the range of pressure that corresponds to the un-factored rig load.

4 DISCUSSION

Results from the ultimate limit state check returned bearing resistance values of 2271 kPa. The high value of the bearing resistance is attributed to the shearing resistance of the sand materials and the width of the barge. Given the 63.9 m x 21.95 m dimension of the barge, the rig is expected to exact a pressure 31 kPa on the soil. The ratio of the bearing resistance to the rig load is seen to be more than 20. This signifies that the ultimate limit state requirement is met. The serviceability limit state results indicated that the clay soils would undergo consolidation settlement of 207 mm when subjected to the rig load. The rate of consolidation of the clay layer is estimated at 18 years for 95 percent degree consolidation. It is planned that the entire oil drilling exercise would be concluded within 10 months period. In this case, only about 25%-degree consolidation would have been achieved. This would correspond to

a settlement of about 52 mm. The variation of the estimated consolidation settlement with time is shown in Figure 2. The freeboard that is achievable based on the estimated consolidation settlement and the observed high-high water level is 1.49 m; which is greater than the specified minimum value of 0.61 m. This shows that the serviceability limit state is also ensured and ground improvement is equally not necessary.

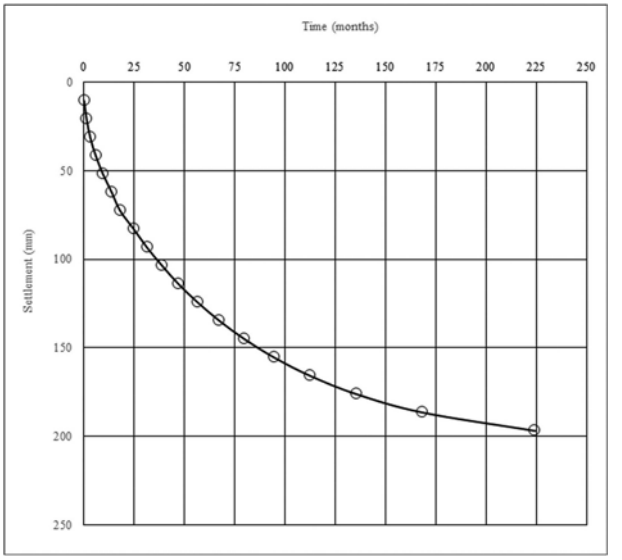

Figure 2. Variation of settlement with time.

5 CONCLUSION

The paper has been able to highlight some of the important geotechnical requirements in the determination of the stability of a barge-ladden oil drilling rig in mangrove swamps operations. The stability is accessed in terms of shear failure and vertical downward movement of the barge. For sites underlain by clay formations, consolidation settlement is considered the governing criteria. The limit of vertical movement is defined by the required minimum freeboard specified for the barge-ladden rig. The ballasting of the barge ought to be carried out in a manner that will ensure the entire barge base rest on the river bed at same time in order to avoid the occurrence of differential settlement.

REFERENCES

Abam, T. K. S. & George, E. A. J. 1997. Penetration testing in the highly stratified sediments of the Niger Delta. *Journal of Mining and Geology*, *33(1)*, 7–14.

Eurocode 7, Geotechnical Design Part 1: 2004. *General rules*. European Committee for Standardization: Brussels.

Eurocode 7, Geotechnical Design Part 2:2007. *Ground investigation and testing*. European Committee for Standardization: Brussels.

Schneider, H. R. 1999. Definition and determination of characteristic soil properties. *Proceedings of the fourteenth international conference on soil mechanics and foundation engineering, Hamburg*. 2271–2278.

Short, K. C & Stable, A. J. 1967. Outline of the geology of Niger Delta, *AAPG*, *51*, 761–779.

Whiteman, A. 1982. Nigeria, its petroleum geology, recent source and potential. *Graham and Trotman* 12, 166–168.

Smart Geotechnics for Smart Societies – Zhussupbekov, Sarsembayeva & Kaliakin (Eds)
© 2023 The Author(s), ISBN 978-1-003-29912-7
Open Access: www.taylorfrancis.com, CC BY-NC-ND 4.0 license

Study of the resistance on the side surface of the underwater vehicle's soil base

A.A. Ananiev
Saint-Petersburg State University of Architecture and Civil Engineering, Saint-Petersburg, Russia

ABSTRACT: The object is the soil of the ocean floor. The goal is to predict the resistance of the underwater vehicle's soil base. Tools - laboratory methods for studying the physical and mechanical properties of soils, physical modeling of the work of the soil base, statistical processing of measurement results. The approach is verification of the viscous fluid model. The main results are experimental values of physical, strength and rheological parameters of the bottom soil, mathematical description of the experimental results, normative values of the strength of the ocean soil.

1 INTRODUCTION

The concept of technology for the development of deposits of ferromanganese nodules (FMN) of the World Ocean provides for the creation of a mining vehicle (MV) (Alexandrov 1992, Jungmeister, Smirnov, Verzhansky 2015, Tetsuo 2017). In operating mode, the MV must reliably move on weak soils of the ocean floor at depths of 4000-5000 m at a speed of 0.5- 1.5 m/s. Separation of FMN *1* from the soil *2* is carried out using a «knife-comb» *3*. The estimated depth of entry of the working body into the ground base is 100 mm and a width of 3-4 m (Figure 1) (Egorov, Kondratenko, Grigortsuk 2020).

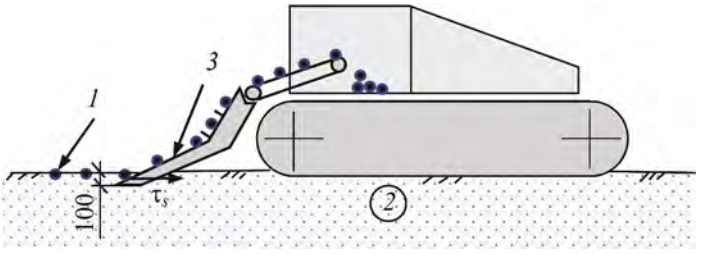

Figure 1. Scheme of separation of FMN: 1– FMN; 2 – ocean silt; 3 – knife-comb; τ_s – soil shear resistance.

To design the tractive forces of the MV, it is necessary to predict the resistance of the bottom soil on the side surface of the comb knives. To this end, experiments were conducted that made it possible to identify the features of the physical and mechanical properties of the bottom soil, and using the calculation model of the soil, a mathematical description of the results of the experiments was given.

DOI: 10.1201/9781003299127-344

2 PHYSICAL CHARACTERISTICS OF BOTTOM SOIL

Information on the characteristics of the physical properties of bottom soils in the ore province of Clarion-Clipperton of the Pacific Ocean was obtained by the Research Institute in the field of marine geology (VNIIOkeangeologia) together with the Saint Petersburg State University of Architecture and Civil Engineering (SPbGASU) (Neizvestnov, Kondratenko, Ananiev et al. 2004, Kondratenko 2012). Soils sampling of the ocean floor was carried out from the board of the research ship «Akademik Alexander Karpinsky» with the help of a grapple, a box-shaped sampler and a ground tube. The maximum stripped depth of the geological section was 4.15 m. The production of soil samples of undisturbed build was carried out by the cutting ring method. Samples were tested in laboratories on board and on land. The monoliths were isolated by the waxing method, the disturbed samples were placed in containers with hermetically sealed lids.

Physical characteristics – soil density ρ, water content w, solid particles density ρ_s, plasticity index I_P and liquidity index I_L were determined by standard methods of GOST 5180–2015 «Soils. Laboratory methods for determination of physical characteristics», by calculation method – dry soil density ρ_d, porosity n and void ratio e. All characteristics of water content were calculated with an adjustment for the mineralization of pore water. The areas of values of the physical characteristics of ocean soil are presented in Table 1.

Table 1. Physical characteristics of the ocean soil.

Soil characteristics	Indicators of soil characteristics
Soil density ρ, kg/m^3	(1.14–1.22)·10^3
Solid particles density ρ_s, kg/m^3	(2.41–2.42)·10^3
Dry soil density ρ_d, kg/m^3	(0.24–0.33)·10^3
Water content w, %	274–384
Porosity n, %	88–90
Void ratio e,	7.05–9.00
Plasticity index I_P, %	64–98
Liquidity index I_L	0,96–3,0

It has been established that in the active zone of interaction of the MV with the ground base, according to the classification of Neizvestnov, mainly weak clayey and siliceous-clayey bottom sediments of Holocene-Middle Miocene age lie. The mineral composition of the clay fraction is represented by hydromica, smectite and chlorite. The content of amorphous silica can reach 15-20%. Weakly compacted water sediments are characterized by a large aggregate structure, high dispersion. The most important distinctive features of the ocean soil are: high porosity, complete water saturation, absence of gases in free and dissolved form, fluid consistency. According to its state, the bottom soil can be considered as a solid-like viscoplastic medium.

3 MECHANICAL MODEL OF BOTTOM SOIL

Determination of the lateral resistance of the bottom soil was carried out at the stand for modeling the operation of soil bases (SMOB-1) (Dalmatov, Bronin, Ananiev et al. 1987). The closest analogue to the SMOB-1 design is a stand for studying the strength properties of ocean soils, developed at the University of San Diego (Noorany, Fuller 1982).

A sample of natural soil of ocean floor *1* with a total weight of 0.54 tons was loaded into tray *2* with overall dimensions: length – 6 m; width – 0,3 m; height – 0,3 m. The soil was mixed to a homogeneous state, the soil surface was leveled to a horizontal plane and covered with a layer of seawater 2-3 cm thick. Control of the uniformity of the bottom soil was carried out using an impeller. The tray was hermetically sealed with lids. The soil base prepared in this way was kept for 6 days before the start of the tests.

Models No. 1 and 2 were steel plates pointed from the end with a thickness of 2 mm with a height of 50 and 100 mm and a length of 200 and 400 mm, respectively, *3* buried in the ground vertically along the direction of movement. The models were moved in the ground base at constant speeds of 0.2 and 1.7 m/s using a drive mechanism. The pulling force was measured by a strain gauge rod *4* connecting the model to the trolley *5* and recorded on a paper recorder tape as the displacements of the model increased. A total of 20 experiments were performed: 6 with model No. 1; 5 and 3 with model No. 2 at shear speeds of 0.2 and 1.7 m/s, respectively. The number of experiments with the Model No. 2 was reduced to avoid the breakdown of the test machine due to its design flaws. The obtained data were processed in the form of graphs $T_i = f(U_i)$ (Figure 2).

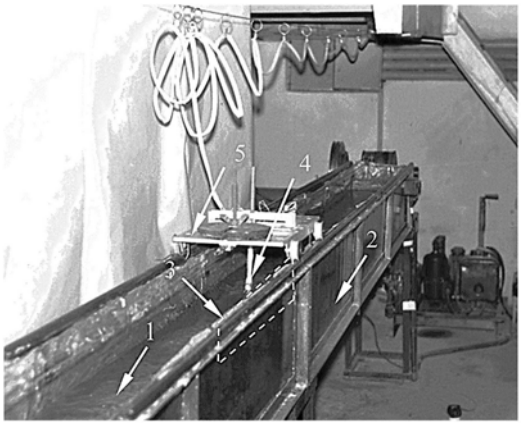

Figure 2. Testing machine SMBO-1: 1 – silt; 2 – tray; 3 – model; 4 – strain gauge; 5 – trolley.

During the experiments, T_i values were recorded on the paper tape of the recorder, depending on the horizontal movements U_i of the models. The characteristic graphs of the dependencies $T_i = f(U_i)$ are shown in Figure 3.

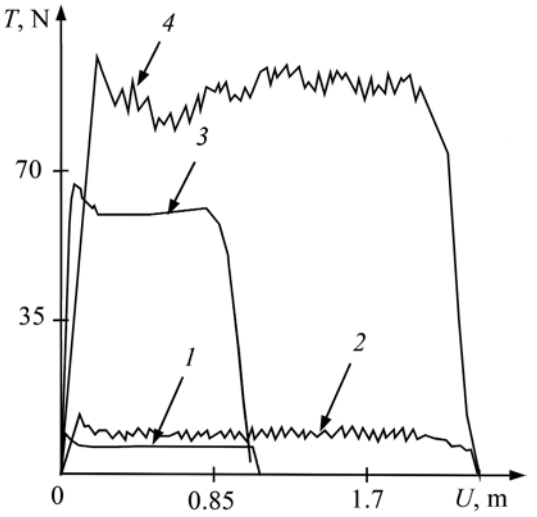

Figure 3. Graphs of the dependence of shear load T_i on horizontal deformation U_i: 1 – model No. 1, speed of movement V_1 = 0.2 m/s; 2 – the same V_2= 1.7 m/s; 3 – model No2, V_1=0,2 m/s; 4 – the same V_2 =1.7 m/s.

Graphs have a complex outline. Two characteristic criteria for the strength of the bottom soil, peak and residual shear resistance, were recorded. In the hardening section, the shear resistance increases linearly and reaches peak values, and in the softening section, the shear resistance decreases non-linearly to residual values. The process of reducing the strength of the bottom soil as the deformation increases can be explained by creep. Peak and residual strength increases with increasing deformation rate. The jagged sections of the graphs are explained by the vibration of the test machine at high shear speeds. During the experiments, a flow of the soil was recorded in a layer bordering with the models with a thickness of δ=20 (Figure 4).

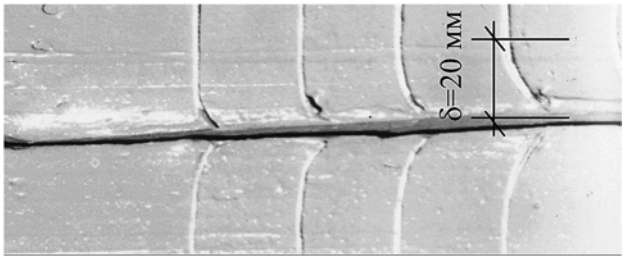

Figure 4. Boundary layer flow.

The values of peak and residual soil shear resistances were determined by the formula

$$\tau_i = T_i/A, \tag{1}$$

where T_i = the peak or residual shear load determined by the graphs $T_i = f(Ui)$; A = the side surface area of the model, $A = 0.02$ or 0.04 m^2.

Statistical verification of partial values of peak τ_i^{max} and residual τ_i^{min} of soil shear resistance showed the absence of possible erroneous values of characteristics (GOST 20522–2020 "Soils. Methods of statistical processing of test results"). As a result, the normative values of the parameters of the strength of the ocean soil are taken to be equal to their arithmetic means. (Table 2).

Table 2. Normative strength characteristics of ocean soil.

Model No1				Model No2			
Strain rate V m/s							
0.2		1.7		0.2		1.7	
Normative values of peak (max) and residual (min) shear resistances of the bottom soil, kPa							
τ_{n1}^{max}	τ_{n1}^{min}	τ_{n2}^{max}	τ_{n2}^{min}	τ_{n3}^{max}	τ_{n3}^{min}	τ_{n4}^{max}	τ_{n4}^{min}
0,59	0,42	0,67	0,51	1.48	1.35	2.5	2.2

Experiments have shown that with an increase in the size of the model object and a decrease in the time of exposure to the load, the strength of the ocean soil increases up to 80%.

The identified features of the deformation of ocean silt by mobile loads make it possible to choose a viscoplastic model, currently called the Bingham body, to describe the results of experiments. The flow equation of the Bingham body is written as follows:

$$\tau_i = \tau_l + \dot{\gamma}_i, \tag{2}$$

where τ_l = limiting shear stress; η = viscosity coefficient; $\dot{\gamma}_i$ = shear deformation rate.

Such a record of the equation of state of a solid means that at stresses less than the limit value τ_l of the soil is deformed elastic-plastically, and when this limit is reached, it begins to flow at a constant speed (Vyalov 1978).

The shear deformation rate $\dot{\gamma}_i$ let's define from the expressions:

$$\dot{\gamma}_1 = \gamma/t = U/(t \cdot \delta) = V_1/\delta = 0.2/0,02 = 101/\text{s}; \tag{3}$$

$$\dot{\gamma}_2 = V_2/\delta = 1.7/0,02 = 851/\text{s}. \tag{4}$$

4 RHEOLOGICAL CHARACTERISTICS OF BOTTOM SOIL

The rheological characteristics of the soil will be determined from the graph $\dot{\gamma} = (\tau_{ni}^{min})$: η_i – by the slope tangent of inclination of the straight line to the abscissa axis; τ_{li} – in scale, like a segment cut off by a straight line on the axis of the ordinate (Figure 5).

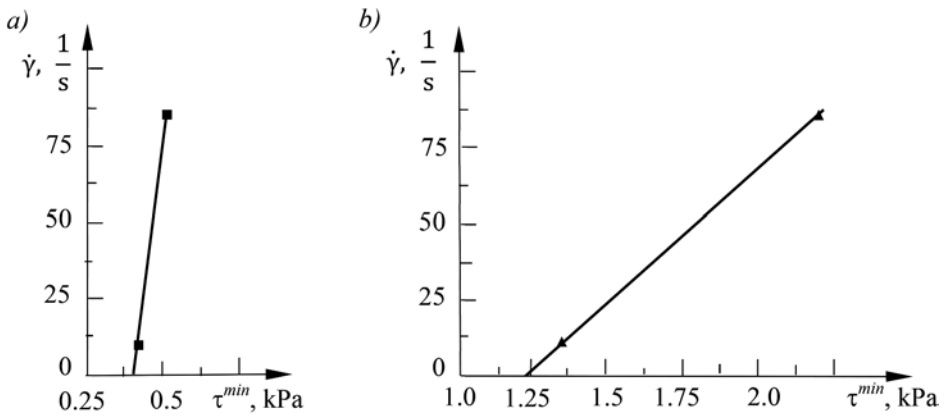

Figure 5. Rheological curves: *a)* – ocean silt creep in the boundary layer of Model No. 1; *b)* – same Model No. 2.

$$\eta_1 = (\tau_{n2}^{min} - \tau_{n1}^{min})/(\dot{\gamma}_2 - \dot{\gamma}_1) = (0.51 - 0.42)/(85 - 10) = 1.20 \cdot 10^{-3}\text{kPa} \cdot \text{s}; \tag{5}$$

$$\tau_{l1} = 0.25 + 6 \cdot 0.025 = 0.4\text{kPa}; \tag{6}$$

$$\eta_2 = (\tau_{n4}^{min} - \tau_{n3}^{min})/(\dot{\gamma}_2 - \dot{\gamma}_1) = (2.20 - 1.35)/(85 - 10) = 11.10^{-3}\text{kPa} \cdot \text{s}; \tag{7}$$

$$\tau_{l2} = 1.0 + 9 \cdot 0.025 = 1.23\ kPa. \tag{8}$$

The results of calculations according to the formulas (5) ÷ (8) show that with an increase in the lateral surface area of the model object by 4 times, the viscosity coefficient of the bottom soil increases by an order of magnitude, the liquidity strength increases by 3 times.

To compare the values of the rheological characteristics obtained during physical modeling, they were determined by the rotating cylinder method (Ananiev, Voznesenskaya 1988). Samples of bottom soils were tested on a rotational viscometer RV-4, Volarovich systems. The principle of operation of the device is based on the rotational shift relative to each other of the layers of a viscous body placed in the working space between the movable *1* and fixed *2* coaxial cylinders. Torque is created by a load mounted on thread suspensions 3 (Figure 6).

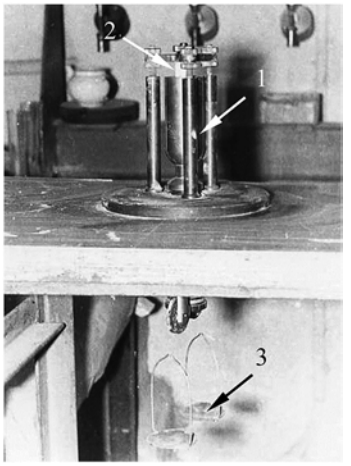

Figure 6. Viscometer RV-4: 1 – movable cylinder with silt; 2 – fixed cylinder; 3 – suspension for cargo.

Prior to the start of the experiments, the viscometer was calibrated for friction in the ball bearings. A soil sample was formed in the working space of the device using a rule. During the test, the load on the sample was transferred using a load of mass P_i, the angular velocity of the rotation cylinder N_i was measured using a stopwatch. A total of 5 soil samples with a multiplicity of 3 were tested.

Statistical verification of the partial values of the shear rate of the bottom soil N_i, performed in order to establish and exclude values sharply different from most values, showed the absence of possible erroneous measurements of the characteristic. A graphical representation of the test point polygon is shown in Figure 7.

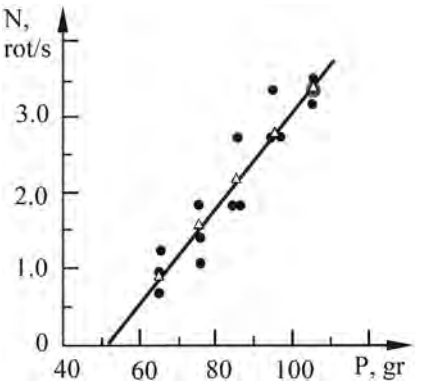

Figure 7. Graph $N=(fP)$.

Using the least squares method for a set of 15 pairs of experimental values of the parameters N_i and P_i, an approximating dependence was found

$$N_i = 61.2P_i - 3.08. \tag{9}$$

The normative angular velocity of the rotational shift N_{in}, calculated by the formula (9), are presented in Table 3.

Table 3. Results of determination of the viscosity coefficient of bottom soil.

Weight of the load rotating the cylinder with the ground adjusted for friction in bearings P, kg	Normative angular velocity of the rotational shift N_n, rot/s	Viscosity coefficient η, kPa ·s
0,066	0,959	$11{,}69\cdot10^{-3}$
0,076	1,57	$8{,}23\cdot10^{-3}$
0,086	2,183	$6{,}70\cdot10^{-3}$
0,096	2,795	$5{,}84\cdot10^{-3}$
0,106	3,4	$5{,}30\cdot10^{-3}$

The limiting shear stress τ_{sl} and the viscosity coefficient η of the bottom soil were calculated according to the formulas given in the instructions for the device PB-4:

$$\tau_{sl} = K_0 \cdot P_0 = 4191.01 \cdot 0.056 = 235\text{Pa} = 0.235\text{kPa}, \tag{10}$$

where K_0 is a constant, $K_0 = 4191.1$ 1/m·s^2; P_0 is the minimum weight of the load corresponding to the beginning of rotation of the cylinder with the ground adjusted for friction in the bearings, $P_0 = 0.056$ kg;

$$\eta = K \cdot \left(P_i - P_f\right)/N_{ni}, \tag{11}$$

where K is the constant, $K = 169.95$ 1/m·s^2; P_i is the mass of the load rotating the cylinder of the viscometer without adjusting for friction (Table 3); P_f is the friction of the bearings of the device, i.e. the minimum value of the load driving the empty cylinder, P_f = 9 g.

The results of determining the viscosity coefficient according to formula (11) are presented in Table 3. It is established that with an increase in the flow rate, the viscosity coefficient of the bottom soil decreases.

The viscosity coefficient defined as the tangent of the inclination angle of the graph $N = f(P)$ (Figure 6) turned out to be equal

$$\eta = K \cdot (P_5 - P_1)/(N_{n1} - N_{n5}) = 169.95 \cdot (0.106 - 0.066)/(3.4 - 0.959) = 2.785 \cdot 10^{-3}\text{kPa} \cdot \text{s}. \tag{12}$$

This viscosity value is close to the value $\eta_1 = 1.20 \cdot 10^{-3}$ kPa·s found in the conditions of testing the strength of ocean silt by Model No. 1.

5 CONCLUSION

Let's make a forecast of residual stresses τ_1^{min} and τ_2^{min} of bottom soil (see Table 2) on contact with Model No. 1. Rheological characteristics: τ_{sl} = 0,235 kPa (see Equation 10); $\eta_1 = 11{,}69\cdot10^{-3}$ kPa·s $\eta_2 = 5{,}30\cdot10^{-3}$ kPas (see Table 3) we will accept the results of their determination in a viscometer.

Using the Bingham body flow equation, we obtain:

$$\tau_1^{min} = \tau_{sl} + \eta_1 \dot{\gamma}_1 = 0.235 + 11.69 \cdot 10^{-3} \cdot 10 = 0.352\text{kPa}; \tag{13}$$

$$\tau_2^{min} = \tau_{sl} + \eta_{21} \dot{\gamma}_2 = 0.235 + 5.3 \cdot 10^{-3} \cdot 85 = 0.686\text{kPa}. \tag{14}$$

Comparison of the calculated values of shear stresses (see Equations 13 and 14) with the experimental ones $\tau_{n1}^{min} = 0.42$ kPa and $\tau_{n2}^{min} = 0.51$ kPa shows that their discrepancy is 16% and 26%, respectively. Since the discrepancy is less than 30%, the mathematical description of the

experimental results can be considered satisfactory. Experiments with Model No. 2 showed that a 4-fold increase in the lateral surface area of the model object caused a significant increase in shear resistance (see Table 2). The results obtained cannot be explained from the standpoint of the theory of viscous fluid, and, on the contrary, they may well be explained by the laws of solid-state mechanics. At the R&D stage, it is recommended to adopt the normative peak and residual shear resistance on the side surface of the comb knives respectively 2.5 and 2.2 kPa for the design of the MV mock-up sample (see Table 2). These strength values are in good agreement with the data of 12 measurements of rotational shear resistance, equal to 0.7-2.6 kPa, of samples of natural bottom soil containing nodules.

REFERENCES

Alexandrov I.L. 1992. Development of research into the technology of deep-sea mining of ferromanganese nodules in France and Japan. M.: Geoinformmark.

Ananiev A.A., Voznesenskaya E.S. 1988. Assessment of the rheological properties of silts in the Clarion-Clipperton and Wake-Necker regions. M.: OTSNTI VNII ekon. miner. raw materials 17.02.1988, 539–NG.

Dalmatov B.I., Bronin V.N., Ananiev A.A. et al. 1987. Stand for the study of mechanical properties of ocean soils. Copyright Certificate No. 1385798 A 1, ICI G0 1 No.33/24: No. 4054746 declared 11.04.1986; published 01.12.1987; applicants: Leningrad Institute of Civil Engineering and the Russian Research Institute of Oceanology.

Egorov, J.V, Kondratenko A.V., Grigortsuk A.V. et al. 2020. Prospects for Development of Deep-water Machinery for Exploration and Exploitation of Polimetallic Sulphides in Russion Exploration Area (the Mid-Atlantic Ridge). *Proc. of the Thirtieth Intern. Ocean and Polar Engineering Conf.* 11– 16 October 2020. Shanghai: 1–7.

Jungmeister D.A., Smirnov D.V., Verzhansky A.P. et al. 2015. Machines and equipment for the extraction of ferromanganese nodules. Jungmeister D.V. (ed.). Spb.: Polytechnic-service.

Kondratenko A.V. 2012. Physical and mechanical properties of bottom formations in deep-sea deposits of ferromanganese nodules. Gornyi Zhurnal 3: 37–41.

Neizvestnov Ya.V., Kondratenko A.V., Ananiev A.A. et al. 2004. The Engineering Geology of Ore Mining Province Clarion-Clipperton in the Pacific Ocean. Neizvestnov Ya.V. (ed.). *Proc. of RAS and RF Ministry of Natural Resources. Research Institute of Oceanology*. Vol.197. Spb.: Nauka.

Noorany J., Fuller J.T. 1982. Soil-machine interaction studies for manganese nodule mining. *Annual offshore Technology conference*. Houston, Texas: 445–446.

Tetsuo Y. 2017. Fundamental geotechnical consideration for design of deep-sea mining systems. Springer International Publishing, 259–295.

Vyalov S.S. 1978. Rheological Principles of Soil Mechanics. M.: Higher Schools Publishing House.

Megaprojects and transportation geotechnics

Taylor & Francis
Taylor & Francis Group
http://taylorandfrancis.com

Smart Geotechnics for Smart Societies – Zhussupbekov, Sarsembayeva & Kaliakin (Eds)
© 2023 The Author(s), ISBN 978-1-003-29912-7
Open Access: www.taylorfrancis.com, CC BY-NC-ND 4.0 license

Information systems in geotechnics

G.G. Boldyrev
LTD NPP-Geotek, Penza, Russia

ABSTRACT: The article discusses the application of building information modeling (BIM) technology to build a 3D geotechnical model. The workflow for building a 3D geotechnical model includes surface relief data, field and laboratory test data, soil lithology, geometric characteristics of the foundation structure and load. Automated systems with processing and interpretation of test data are used to determine the characteristics of soils. Mathematical modeling of the behavior of the foundations of the foundations with various input data is performed using analytical solutions and numerical methods. The natural heterogeneity of soil properties and its impact on the behavior of buildings is estimated by the sensitivity indicator of the foundation-foundation system by introducing virtual workings between the existing normative ones and the subsequent calculation of the precipitation and roll of the foundation.

1 INTRODUCTION

The widespread use of information modeling in construction (BIM-Building Information Modeling) is mainly due to the advantages in terms of saving costs and time for the implementation of the project, due to the reduction of unforeseen problems and easier updating of the digital model. Thanks to technical research conducted by universities and industry, useful tools have been developed to optimize digital models and improve interaction between various specialists involved in the design process (Morin et al. 2014).

Building information modeling is widely used by civil engineers and architects for designing structures of buildings. At the same time, it may sound paradoxical, geological and geotechnical data are not used at all in the BIM design process, although most of the risks and uncertainties of construction arise from unknown or incorrectly estimated engineering and geological conditions. At the moment, BIM technologies are being developed for many sections of the design and construction, with the exception of engineering-geological and geotechnical surveys.

Unfortunately, not so many geotechnical projects have yet been implemented using the BIM approach, and in most cases, it still consists only in archiving, storing and updating geological and geotechnical data (Xikui et al. 2016, Migilinskas et al. 2013). However, in the last two years, the situation has changed and there have been works that consider the methodology of building information systems in geotechnics (Nappa et al. 2019, Pan et al. 2019).

This article demonstrates the applicability of the developed technology to the entire process of designing the foundations of construction objects, starting with engineering-geological, engineering-geotechnical surveys and ending with the calculation of the foundations of foundations using appropriate sets of rules or numerical methods. The advantage of automated testing methods and mathematical modeling of foundation bases based on known values of physical and mechanical properties of soils at normative and virtual workings is emphasized.

2 BASIC CONCEPTS AND DEFINITIONS

Basic definitions. The initial data for the construction of a digital information geotechnical model is an engineering-geological model, which is a schematic spatial representation of

DOI: 10.1201/9781003299127-345

engineering-geological elements (IGE), groundwater, hazardous geological and engineering-geological processes in the field of interaction of the object with the geological environment. This definition is given in SP 446.1325800.2019 "Engineering and geological surveys for construction. General rules for the production of works" and is incomplete, so it does not include the properties of soils in the IGE, despite the fact that the survey results include data on the physical and mechanical properties of soils. The proposed geotechnical information System (BIMG) has a more extended definition:

1. BIMG (Building Information Model Geotechnical) is a digital information model with a set of components that characterize stratigraphy and lithology, physical and mechanical properties of soils and the construction of the foundation in three-dimensional space.
2. BIMG-contains the information necessary for the design of the foundations of buildings and structures according to the limit states and is one of the information models that make up the BIM of a construction object.
3. The development and development of BIMG is carried out in a shared data environment, which means that all interested parties have constant access to a model filled with information from surveys at the construction site.
4. BIMG uses three approaches to modeling: geostatistical, explicit and numerical modeling. For all approaches, data is collected, quality-controlled, transformed (if necessary), harmonized, classified and interpreted. Modeling begins only after the input data has successfully passed the processing and quality control processes.

In order to eliminate confusion in the concepts of "geological model" and "geotechnical model", we will introduce additional explanations.

The 3D geotechnical model is created by geostatistical methods based on workings, surface maps and engineering-geological sections. It is important that the source data used is uniformly classified and consistent. The choice of the geostatistical method, scale, and other parameters of the model depends on various criteria, such as the parameter to be modeled, the scale of the model, the complexity of engineering and geological conditions, and the distribution of input data. To validate the implemented 3D models, various checks are carried out: visual checks, variogram analysis and cross-validation. Automation of data processing and interpretation processes ensures the relevance of models and the ability to track their development. That is why it is extremely important to automate as many stages of the workflow as possible.

The 3D geotechnical model is created on the basis of a 3D geological model by introducing additional information about the design of the projected foundation, external loads on the foundation, as well as the parameters of soil models necessary for calculating the foundations of foundations by numerical and analytical methods.

3 METHODOLOGY

The procedure for creating a geotechnical information system (BIMG) is a workflow consisting of the following main stages:

1) the surface relief of the construction site under consideration is determined using GIS systems.
2) a complex of laboratory and field tests of soils is carried out using automated complexes at standard workings. Here and further in the text, mining is understood as a geological well with the selection of monoliths or a point of static or dynamic sounding;
3) the stratigraphy and lithology, physical and mechanical characteristics of soils are determined. In the case of using numerical methods, the parameters of soil models are determined;
4) a 3D geological model is being built;
5) a geotechnical 3D model is formed by dividing the geological model into finite elements of a given scale and the coordinates of their nodes X,Y,Z are determined;
6) using the interpolation functions (for example, Shepard, Delaunay, Kriging, etc.) and the values of soil characteristics at standard workings, the soil characteristics (parameters of soil models) are found in finite elements;

7) the foundation structure and loads are introduced into the 3D model;
8) the foundation is calculated using analytical solutions of the corresponding sets of rules or numerical calculation methods;
9) virtual workings are introduced and the influence of heterogeneity of soil properties on the results of analytical or numerical solutions is evaluated;
10) To transfer information to the external environment, a 3D digital geotechnical model is produced in the IFC4 format, which allows it to be used in 3D programs such as Civil 3D, Revit, Allplan, Flac, Plaxis, etc.

3.1 *Geotechnical data*

Engineering-geological and geotechnical studies performed by geotechnical engineers or geologists are the main way to obtain geotechnical data that carry information about stratigraphy, lithology, physical and mechanical properties of soils and rocks at the survey site. Geotechnical data are of crucial importance in the design of the foundations of buildings and structures and the construction of transport infrastructure facilities.

Standard geotechnical data is collected from three main sources: (1) wells and pits; (2) in situ tests, including geophysical surveys, static (CPT) and dynamic sounding (SPT) tests, etc.; and (3) laboratory tests conducted on samples taken from wells. Some geotechnical data can be collected from pits or tests at the bottom of pits. However, they make up a small percentage of the data compared to well data and are usually processed in the same way.

For laboratory testing of soils, the automated ASIS Lab system (www.npp-geotek.com) has been developed, which includes various devices for static and dynamic testing of unfrozen and frozen dispersed soils, rocks. Field tests are carried out using various methods, such as cone penetration test, standart penetration test, dilatometer test, pressiometer test, etc. The interpretation of field test data is automated and is performed using the «Geotek Field» program.

3.2 *Data maps*

Data maps in the form of a situational plan of engineering-geological and geotechnical studies (Figure 1) describe the type of data (geophysical studies, field tests with stamps, static and dynamic penetration, etc.) available for each IGE in the model. Although these maps do not convey the reliability of the geological model, they give a very clear idea of what type of data contributed to each IGE and what is the data density in this area of the model. Based on the information obtained from the data maps, the user can quickly recognize areas studied by mathematical modeling (virtual workings) and areas based on measured data (standard workings). For example, in Figure 1, at object 4A-8, drilling wells and static penetration were performed at four points (standard workings, cone penetration tests) and 13 virtual workings (V1-V13) were constructed using the interpolation functions, in which the lithology and soil properties were determined.

The scale and detail with which a geotechnical model can be built are inherently related to the density and detail of data obtained from engineering-geological and geotechnical investigations. The amount of data depends on the stage of surveys and the category of complexity of engineering and geological conditions, which are determined by the regulatory requirements of SP 47.13330.2012 “Engineering surveys for construction. Main provisions”: the stage of choosing a construction site; the stage of preparing project documentation; the stage of construction and reconstruction of buildings and structures; and three categories of complexity of engineering and geological conditions. For example, for the stage of preparation of project documentation, the distance between the normative workings depends on the complexity category of engineering and geological conditions and varies from 25 to 100 m. The total number of mine workings within the contour of each building and structure for category I is 1-2 workings; for category II-at least 3-4, for category III – the number of mine workings is determined by the design of a specific foundation, loads on the base and engineering and geological conditions, but not less than 4-5, taking into account the geometric dimensions of the object. With such a meager density of workings, it is quite difficult to assess the heterogeneity of soil properties and their influence on the behavior of the projected building or structure.

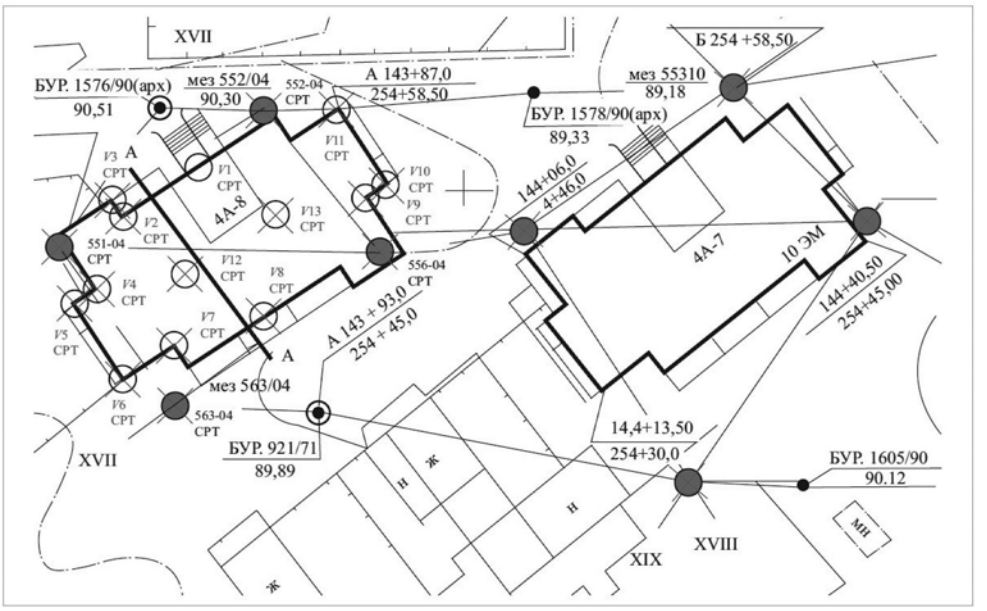

Figure 1. Survey data map with building plans.

3.3 *Data processing and interpretation*

The use of all available data from the workings involves the use of automated interpretation procedures due to the huge amount of available data. We have created a set of tools to provide a standard method for processing laboratory data, cone penetration test (CPT) and standard penetration test (SPT) data. With the help of this tool, we can interpret the lithology in the workings, using their position in the direction of the XY and Z coordinates of the three-dimensional soil array. The lithology inside the geotechnical model is determined by simple processing of CPT parameters (cone resistance, coefficient of friction, depth, see Figures 3 and 4) using P. Robertson diagrams (Lunne et al. 1997), and the physical and mechanical characteristics of soils are found from correlation equations connecting them with the parameters of static (CPT) and dynamic sounding (SPT). By applying automated procedures, we can use more data than ever before. This allows us to create more detailed geotechnical models.

Currently, BIMG includes data from laboratory tests, CPT, CPTU, SPT, DCPT in situ tests, performs a basic interpretation from the point of view of the behavior of the soil type (Lunne et al. 1997), determines the physical and mechanical characteristics of soils and calculates the foundations of buildings and structures in accordance with the requirements of the codes of regulations of the Russian Federation SP 47.13330-2012 "Engineering surveys for construction. Basic provisions", SP 24.13330.2011 "Pile foundations", SP 22.13330.2016 "Foundations of buildings and structures", SP 25.13330.2012 "Base and foundations on permafrost soils" or foreign regulatory technical documents EN 1997-1 "Eurocode 7-Geotechnical Design-Part 1: General rules", etc.

When determining the physical and mechanical characteristics of soils, correlation dependencies are used (for example, SP 446.1325800.2019) between the parameters measured during static and dynamic penetration and the data of laboratory tests of soils. Using the sounding parameters and correlation equations, the physical and mechanical characteristics of soils are determined.

The IFC4 format is used to transmit information to an external user. The IFC4 format was developed by building SMART in 2013 specifically for building information modeling, approved by the international standard ISO 16379 and recommended by GOST 10.0.02-2019 for use in the Russian Federation. The format file has a text structure corresponding to the STEP file (ISO 10303-21 international standard for CAD data exchange), which borrows a model of entity relationships from the EXPRESS data modeling language. Such entities are:

building elements, geometry, basic constructs. Entities form an object hierarchy with property inheritance. At the moment, there are more than 700 such entities. The format is extensible, if the required building element is not described, then it is possible to add your own.

No special entities have been created yet to create a digital geotechnical model. This is due to the lack of a format for the exchange of engineering and geological data in the Russian Federation at the moment. The authors use the entities IfcBuildingElementProxy and IfcPropertySet to build such a model. The first entity contains a geometric description of the surfaces, coordinates, color, and the name of the type of soil. The second one is responsible for storing the physical and mechanical characteristics of soils 2D and 3D visualization. An example of a three-dimensional visualization of a geological model is shown in Figure 2 (cross-section section A - A in Figure 1) together with the construction of a slab foundation. The 3D modeling and visualization provides a powerful tool for spatial analysis. The purpose of visualization is to use a 3D model that can receive different scales of information from different sides and in sections. Visualization includes standard and virtual workings, lithological columns, profiles of physical and mechanical characteristics of soils, the position of the groundwater level, the foundation structure.

Knowing the values of the soil characteristics in the standard workings, you can build virtual workings and then use the obtained values of the characteristics in calculations (for example, the calculation of the settlement and the tilt of the foundation according). You can build as many virtual workings as you want, and their impact can be estimated by the amount of the determined foundation precipitation. The main rule for choosing the number of virtual workings is determined by the rule for stabilizing the increment of the average foundation settlememnt as they are introduced. In Figure 3 shows an example of constructing a field of values of the deformation modulus for two standard workings and with the introduction of two virtual workings. In this example, the Kicking interpolation function is applied. As can be seen from the example considered, the use of the interpolation function allows you to build a digital array of the required soil characteristics.

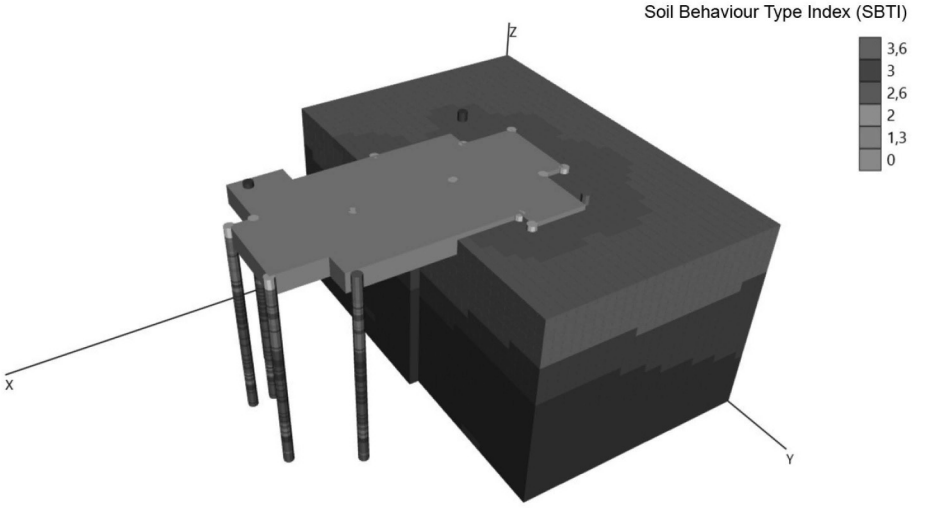

Figure 2. An example of 3D visualization of a geotechnical model with a foundation structure, virtual and standard workings.

It should be noted that the considered procedure is performed automatically, directly in the process of static sounding of soils, and since it is possible to perform sounding not in four, but in a larger number of points during a working shift, the accuracy of estimating the heterogeneity of engineering and geological conditions will be significantly higher.

Calculation of the foundation bases. Currently, the foundations of buildings and structures are designed using analytical and numerical solutions. Analytical solutions are simple, easily

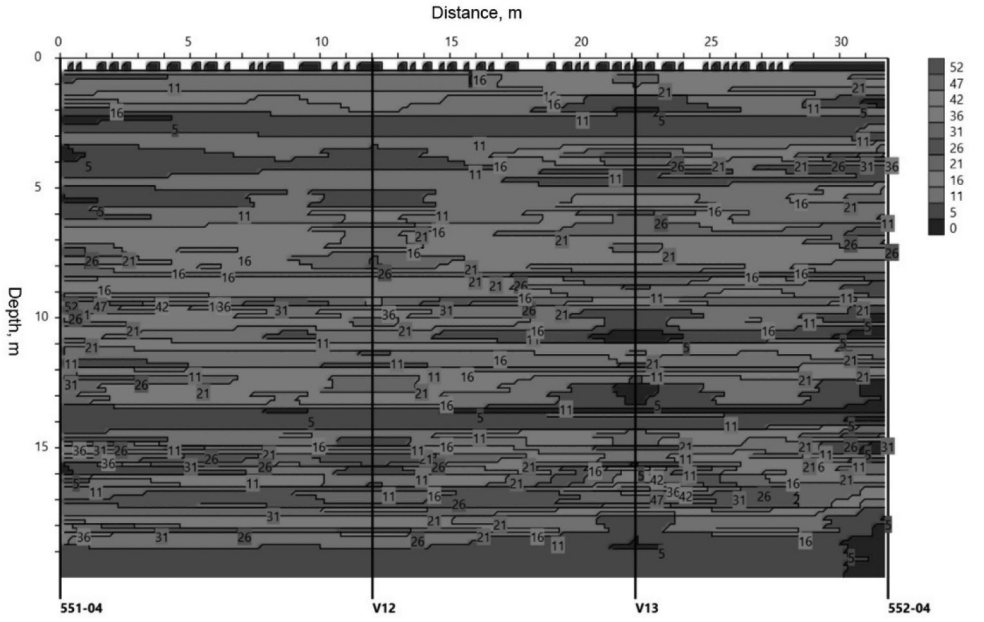

Figure 3. 2D distribution of the deformation modulus: 551-04, 552-04 - standard workings; V12, V13 - virtual workings.

programmable, require determining the minimum number of soil characteristics, and the long-term practice of their application testifies to the reliability of these solutions. Numerical methods for calculating the bases are much more complicated, in most cases it is necessary to determine a larger number of characteristics (model parameters) of soils during surveys, and often their reliability has to be checked using analytical solutions. Due to the fact that compliance with regulatory requirements is still mandatory in the Russian Federation, we suggest using the appropriate analytical solutions provided in regulatory documents to solve practical problems of designing buildings and structures. At the same time, the structure of the proposed information technology allows us to apply numerical methods of solutions implemented in various programs such as PLAXIS, FLAC, etc.

Thus, BIMG uses two procedures for calculating the foundations. Classical solutions given in the previously mentioned SP and the finite element method. These calculations allow us to model the behavior of the foundations using various defining equations (soil models), including elastic behavior (in the case of using SP) and nonlinear models in finite element calculations. The second modeling procedure was successfully tested for various engineering and geological conditions when solving problems of calculating the settlement of foundations, as well as the stability of the slopes. In both cases, the transition from the 3D model to the 2D model is used.

Estimation of the uncertainty of the properties of the 3D model. In geotechnical studies, it is generally accepted practice (or should be) to assess possible errors in determining the lithology, physical and mechanical properties of soils and the impact of these errors on a building or structure under construction. This is sometimes called a hazard and risk analysis (Shi 2014). Various methodologies, such as geostatic methods and probabilistic studies, are used to give a certain quantitative assessment of possible errors in the design of an engineering structure due to uncertainty about the properties of soils. However, two very important main points - the geological and geotechnical expertise used to create the model, and the division of the soil mass into IGE are considered in these analyses only very superficially or not at all.

In the existing estimates of the uncertainty of soil properties, the probability of distribution or innate error in estimating properties in a certain place of space is well determined if appropriate statistical procedures are used. However, much depends on the correctness of the data, which in itself is related to (1) the geology and (2) the variations allowed for each of the geotechnical characteristics of soils.

In the technology under consideration, it is proposed to evaluate the uncertainty of soil properties by modeling the behavior of the reference foundation for various input characteristics of soils (Barvashov & Boldyrev 2017). In this case, the sensitivity of the base-foundation-structure system (BFSS) is evaluated by introducing virtual workings between the existing standard ones and the subsequent calculation of settlement at the considered point of the foundation.

Such calculations can be performed on a variety of virtual workings with the determination of the average foundation settlement. If such variations lead to significant changes in the behavior of BFSS, then it is necessary to increase the volume of engineering and geological data due to additional workings, or to increase the reliability of the structure by increasing the strength of structures. This question is analyzed in the works (Barvashov & Boldyrev 2016, 2017) with the help of mathematical modeling and exact solutions for the standards (simplified models) of SOFS

Thus, the proposed approach of "sensitivity" analysis allows us to assess the degree of influence of each of the input parameters and the type of interpolation functions on the final result of the calculation. If traditional calculations gave only an average or pessimistic value, now you can find more information about possible variations in the results of calculations.

4 CONCLUSION

1. Digital processing of engineering-geological and geotechnical data leads to the fact that huge volumes of such data can be combined and analyzed, as well as imported and exported from databases and/or large spatial models in fractions of seconds. As a result, the assessment of the behavior of the designed buildings can be performed directly in the field during engineering and geological surveys.
2. Uniformity of data formats is important for the interoperability of data on various parameters and from various data sources. However, the use of large databases and the import of data sets into foundation calculation programs also require uniformity in the ways of structuring the description of geotechnical parameters and foundation structure
3. Time is almost never a parameter in 3D geotechnical models. If you enter time as a parameter of the model, then we are already talking about 4D modeling. This is fundamentally important when calculating the sediment of foundations in time and taking into account the creep of soils, as well as modeling the process of freezing and thawing of frozen and permafrost soils.

REFERENCES

Barvashov, V.A. & Boldyrev, G.G. 2016. Soil Data Inflation in Analysis of Settlements and Tilts of Structures. *5th International Conference on Geotechnical and Geophysical Site Characterisation*, 5-8 September, Australia*:*1–5.

Barvashov, V.A. & Boldyrev G.G. 2017. Sensitivity of structures and geological data. In M. Papadrakakis, M. Fragiadakis (eds.), *COMPDYN 20176th ECCOMAS Thematic Conference on Computational Methods in Structural Dynamics and Earthquake Engineering*: 1–11. Rhodes Island, Greece, 15–17 June 2017.

Lunne, T., Robertson, P.K., Powell, J.J.M. 1997. *Cone penetration testing in geotechnical practice*. Blackie Academic. Chapman-Hall Publishers.

Nappa, V., Ventini R., Ciotta, V., Domenico, A. 2019. A new frontier of BIM process: Geotechnical BIM. *Proceedings of the XVII ECSMGE-2019 Geotechnical engineering foundation of the future*: 1–7.

Migilinskas, D., Popov, V., Juocevicius, V., Ustinovichius, L. 2013. The Benefits, Obstacles and Problems of Practical Bim Implementation. *Procedia Engineering*. 57: 767–774.

Morin, G., Hassall, S., Chandler, R. 2014. Case study - The real life benefits of Geotechnical Building Information Modelling. In D.G. Toll et al. (eds.), *Proceedings of Information Technology in Geo-Engineering*: 95–102.

Pan, X., Chu, J., Aung, Z., Chiam, K., Wu, D. 2019. 3D Geological Modelling: A Case Study for Singapore. *ICITG 2019: Information Technology in Geo-Engineering*: 161–167.

Shi, G. 2014. *Data Mining and Knowledge Discovery for Geoscientists*.

Xikui, L., Li, Y., Sun, P. 2016. Study on Three Dimensional Modeling and Visualization in Geology. *The Open Civil Engineering Journal*. 10: 114–124.

Smart Geotechnics for Smart Societies – Zhussupbekov, Sarsembayeva & Kaliakin (Eds)
© 2023 The Author(s), ISBN 978-1-003-29912-7
Open Access: www.taylorfrancis.com, CC BY-NC-ND 4.0 license

Simulation of the operation of a composite wooden beam with a wall made of OSB and plywood in the SCAD program

G.T. Tleulenova
Eurasian National University, Nur-Sultan, Kazakhstan

K.T. Makashev
University of Nottingham, UK

Zh.M. Omarov & D.K. Orazova
Toraighyrov University, Pavlodar, Kazakhstan

ABSTRACT: The paper presented a wooden frame house is one of the best inventions of human architectural thought. Wooden and half-timbered houses were widespread in medieval Western Europe. They create a unique flavor of small towns in Switzerland, Germany, Belgium, the Netherlands. To date, this branch of construction is actively developing - frame housing construction of low-rise buildings with the use of wooden composite I-beams and racks. The paper presented model of a beam with an OSB wall in program SCAD. The paper presented result of isofields of longitudinal stresses in the elements of the beam model and comparison of the test results of beams with a plywood wall.

Keywords: wooden composite I-beams, SCAD, OSB wall

1 INTRODUCTION

A wooden frame house is one of the best inventions of human architectural thought. Wooden and half-timbered houses were widespread in medieval Western Europe. They create a unique flavor of small towns in Switzerland, Germany, Belgium, the Netherlands. To date, this branch of construction is actively developing - frame housing construction of low-rise buildings with the use of wooden composite I-beams and racks in Figure 1. In such design solutions, you can easily embody any design fantasies. It is easy to pick up furniture made of FWF.

Figure 1. Wooden composite I-beams.

DOI: 10.1201/9781003299127-346

The experience of using glued wooden beams shows that their reliability depends on the quality of gluing and careful observance of the manufacturing process in special workshops with the necessary expensive equipment for high-quality drying of lumber. One of the ways to reduce labor and material costs is the widespread use in low-rise construction of composite wooden structures with a wall made of OSB plate (Oriented Strand Board) with a nagel connection with shelves. Unlike other plate materials, OSB has the ability to hold fasteners not with a binder, but with the nature of laying the board, with numerous thin chips oriented in a plane perpendicular to the axis of the fasteners.

Classification of beams:

Made of solid wood:

- solid wood;
- composite beams on malleable ties.

Made of glued wood:

- board-glued (consisting of packages of boards glued together mainly along the plast).

Glued plywood:

- plywood walls;
- LVL walls
- OSB walls.

To determine the VAT of the elements of a composite wooden beam with an OSB wall and a nagel connection with wooden shelves, an engineering calculation method has been developed and numerical and experimental studies have been carried out.

2 RESEARCH METHOD

2.1 *Creation of computer models of composite beams of the PC "SCAD"*

The theory of numerical methods is an extensive science and is widely used in the calculations of structures. The most widely used methods in the calculations of building structures of buildings and structures are the finite difference method (FDM), finite element method (FEM), variation-difference method (VDM), curved grid method (CGM), etc. The finite difference method makes it possible to solve very complex problems with known approximations, for which analytical methods are ineffective. FDM differs from many methods in its simplicity and algorithmicity. It is well implemented on a computer. The advantage of this method is its weak dependence on the geometry of the shell, the nature of the initial stress state. FDM makes it possible to successfully solve problems of stability and dynamics on a computer under boundary conditions, with the exception of a free edge, an inhomogeneous stress field and variable stiffness of thin-walled structures. The disadvantage of FDM is the need to specify a large number of grid steps to obtain good results, which leads to a high order of the system of algebraic equations. Among the numerous methods of calculating complex thin-walled and continuous systems in recent years, the finite element method has stood out sharply. The idea of the method is that a continuous medium (the structure as a whole) is modeled by dividing it into regions (finite elements), in each of which the behavior of the medium is described using a group of selected functions representing stresses and displacements in this area. The advantage of FEM is the convenience of forming equations and the possibility of representing irregular and complex structures and loading conditions. One of the numerical methods for studying the stress-strain state is the method of boundary integral equations (MBIE), otherwise - the method of boundary elements. When calculating homogeneous bodies, the number of variables can be significantly reduced by reducing boundary value problems for differential equations to integral equations at the boundary of the domain.

To calculate the composite beam, use the SCAD program.

The SCAD complex is used in the calculation and design of structures of various types and purposes. Having in its composition developed means of data preparation, calculation and

analysis of results, it does not impose practical restrictions on the size and shape of the projected structures. At the same time, for a design engineer, «simple» tasks are no less important, the solution of which takes him a significant part of the time. Checking the sections of elementary beams, collecting loads on structural elements, determining the geometric characteristics of composite sections - this is not a complete list of such routine design tasks. These circumstances stimulated the development of a series of «small» SCAD satellite programs focused on solving mass design problems. Together with the computing complex, they make up a single SCAD Office package.

The main stages of calculating the stress-strain state of building structures in SCAD. Here are the main stages of work on the linear calculation of the stress state of the rod system using the example of the SCAD program.

Stage 1. Launching the SCAD program and preparing to create a calculation scheme

Stage 2. Creation of the design scheme of the core system for the FEM

The geometric representation of the design schemes of flat trusses, frames and beams found in the tasks specified in the preface in the SCAD program can be performed in two ways:

a) using standard schemes of flat rod systems;
b) by sequentially entering first the nodes of the elements of the calculation scheme, and then the image of the elements themselves. A combination of these methods is also possible.

Stage 3. Loading the calculation scheme of the FEM. Loading in the SCAD program is called a system of simultaneously operating loads. The same core system can be calculated from several loading options. Therefore, their numbering is provided. The SCAD program allows you to immediately perform calculations from several loading options and from any combination of them. In accordance with the type of loads that occur in educational works, the following are given: the assignment of concentrated forces and moments acting at the nodes of the design scheme and at any point along the length of the type 2 element, and a uniformly distributed load applied along the length of the type 2 element. The program provides a procedure for crushing rods into sections to select points (intervals) load applications. In general, the procedure for loading the design scheme includes: Setting the nodal load. Setting the load on the element. Saving the upload. Print or save the calculation scheme with the created upload.

Stage 4. Performing a linear calculation and presenting its results:

a) Performing a linear calculation in which an algorithm for solving the FEM problem is implemented to determine the movements of nodes (in the coordinate system common to the rod structure) and forces in the sections of elements intended for calculation (in the local coordinate system);
b) Presentation of the obtained results of the calculation of the core system in the form of diagrams of the forces in its elements and a picture of the movements of the nodes. Saving and printing them;
c) Presentation of the obtained results of the calculation of the core system in the form of a table with the efforts in the planned sections of the elements and a table of displacements of the nodes of the design scheme. Saving and printing them.

Launching the SCAD program and preparing to create a calculation scheme. Window - Program Download, sections - Project, Options, Help. Window - Creating a new project. Project tree – Initial data, Calculation, Results, Construction. Types of finite elements in SCAD. The general and local coordinate system, the rule of signs. Filters for displaying and visualizing the calculation scheme. Numbering of nodes and elements in the diagram.

Creation of the design scheme of the core system for the FEM. Graphical representation of the design scheme in a common coordinate system. The geometric representation of the design schemes of flat trusses, frames and beams found in the tasks specified in the preface in the SCAD program can be performed in two ways:

– using standard schemes of flat rod systems;
– sequential input of the nodes of the elements of the calculation scheme first, and then the image of the elements themselves (input of elements). A combination of these methods is also possible.

Characteristics of procedures for entering nodes and elements, assigning the type and rigidity of elements. Features of the assignment of the stiffness of elements in the calculations of statically definable and statically indeterminate systems, depending on the purposes of calculation – determination of forces and displacements. The purpose of the support links, hinges in the nodes of the elements.

Loading the calculation scheme. Printing or saving the calculation scheme.

4) Procedures for calculating statically definable beam systems in SCAD. Implementation of the general calculation procedure: launch of the program - creation of the calculation scheme of the core system - loading of the calculation scheme - execution of linear calculation and presentation of its results for single-span and multi-span beam structures. Calculation of beams on a ground base according to the Winkler model.

5) Procedures for calculating statically definable truss and frame systems in SCAD. Implementation of the general calculation procedure: launch of the program - creation of the calculation scheme of the rod system - loading of the calculation scheme - performing linear calculation and presentation of its results for truss and frame structures. Example.

Procedures for calculating static undetectable frame structures in SCAD. Implementation of the general calculation procedure: launch of the program - creation of the calculation scheme of the core system - loading of the calculation scheme - execution of linear calculation and presentation of its results for statically indeterminate frame structures in the conditions of flat and spatial tasks. Illustration of an example.

Calculation of planar systems under conditions of plane stressed and deformed states. This category includes flat structures (for example, a wall panel, a stiffness diaphragm, a retaining wall, fragments of external and internal walls, slopes of pits and embankments, etc.). When calculating flat elements, the structure is divided into a set of finite elements (rectangular, triangular) in which a continuous displacement function is approximated on each element by a polynomial, which is determined by using the nodal values of this function. Calculations are made taking into account the features of the graphical representation of the design scheme, procedures for entering nodes and elements, assigning the type and stiffness of elements, assigning the stiffness of elements, assigning support links. Loading the calculation scheme. Printing or saving the calculation scheme. Conclusion and analysis of the results of the calculation of the stress-strain state of the structure under the conditions of a planar problem (components of stresses and deformations). Illustration of an example of calculating a rectangular beam-wall on the action of an external load.

The design model of a composite beam with belts of wooden bars connected to an OSB wall on glue was made up of plate elements with stiffness characteristics corresponding to the belts - pine tree of the 2nd grade for the wall - OSB plate in accordance with Figure 2. The dimensions of the elements of the design model are taken along the axes of the structural elements.

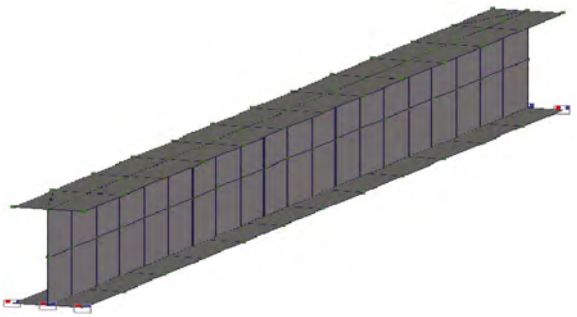

Figure 2. Model of a beam with an OSB wall.

2.2 *Creation of computer models of composite beams of the PC "SCAD"*

The design model of a composite beam with belts made of wooden bars connected to an OSB wall on glue, which is presented in accordance with Figure 1, was made up of plate elements with stiffness characteristics corresponding to the belts - a pine tree of the 2nd grade, for the wall – an OSB plate. The dimensions of the elements of the design model are taken along the axes of the structural elements.

The beam is fixed in three planes by a pivotally movable and pivotally fixed support located at the ends of the lower belt. The shelves are supposed to be glued. The beam is loaded with concentrated forces applied at the nodes of the upper tier. The beam elements are made of different materials (wood, plywood, OSB). The cross section of the beam is T-shaped.

For the proposed scheme of a loaded beam using the SCAD system, it is necessary to solve the problem: to form its plate finite element model.

Algorithm solution of the problem:

- Formation of the design scheme of structures;
- Creation of a calculation scheme;
- Setting the necessary parameters:
- Change the values of the units of measurement to m, mm, kN;
- Go to the calculation scheme Control tab, nodes and elements, node input, then enter the coordinates of the nodes along the x, y, z axes.

After entering the nodes, go to the nodes and elements tab adding plates, then go to the assignment tab, assign the stiffness of the plate. Since the SCAD PC library lacks these design characteristics, namely wood and other wood-based composites, we enter the characteristics of materials manually [21, p.4]. The process of entering design characteristics is presented in accordance with Figure 3.

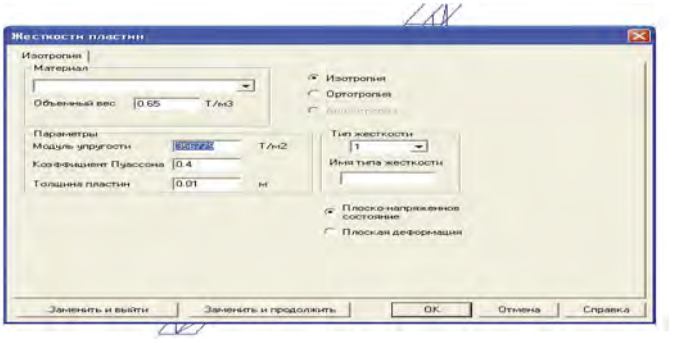

Figure 3. Plate stiffness assignments (OSB wall).

Next, go to the tab, the scheme is the generation of an arbitrary shape on the plane, the assignment of contours, automatic triangulation - stiffness, assign the stiffness of the materials of the shelves pine wood of the 2nd grade, since these materials are also not in the SCAD library, then assign them manually. Specify the triangulation step.

Next, we go into the nodes and elements of the crushing of 4 nodal plates, set the number of splits along the x-axis, along the y-axis.

The imposition of connections in the support nodes of the connection assignment beam, assign connections. After that, we set the loading of the beam.

All loads are applied in the global coordinate system of the calculation model. The following node movements are accepted as the main unknowns: X-linear on the X axis; Y-linear on the Y axis; Z-linear on the Z axis.

3 RESULT AND DISCUSSION

3.1 *Results of the calculation of the I-beam model*

The results of the numerical experiment are presented in the form of isofields of stress distribution in the elements and displacements of nodes of the calculated beam model in accordance with Figure 3.

According to the type of stress distribution in the beam elements, we can say the following:

– the level of longitudinal stresses in the wall elements has a maximum value of 1/3 of the span in the area of the transverse stiffeners and is close to the calculated tensile resistance-compression of the OSB plate with a thickness of 10 mm and further decreases in the middle of the beam span, and increases slightly to the supports;
– the level of transverse stresses in the wall elements is 4-5 times lower than the level of longitudinal stresses, and has a maximum value on supports and in places of load application;
– the level of displacement reaches an extreme in the middle of the span in the area of a clean bend.

As shown in Figure 4, the destruction of the beam is possible by the elements of the wall. At the same time, the greatest probability of destruction from tensile forces in 1/3 of the span in the area of the lower belt at the transverse ribs and further in the same sections from compressive forces at the upper belt.

The results of the numerical experiment are presented in the form of isofields of the stress distribution in the elements and displacements of the nodes of the calculated beam model.

According to the type of stress distribution in the beam elements, we can say the following:

– the level of longitudinal stresses has a maximum value in the girder belts in the middle compartment and is close to the calculated tensile resistance of the OSB plate with a thickness of 10 mm;
– the level of transverse stresses in the beam elements is an order of magnitude lower than the level of longitudinal stresses, and has a maximum value on supports and in places of load application.

Figure 4 shows the isofields of displacement, the maximum value at an external load of 1500 kg was 10 mm, which has sufficient similarity with the results of an experimental study, for a similar load – 8.56 mm. The discrepancy in the results was 14.4%.

Figure 5 shows the distribution of longitudinal stresses in the elements of a composite beam with belts of wooden bars connected to an OSB wall

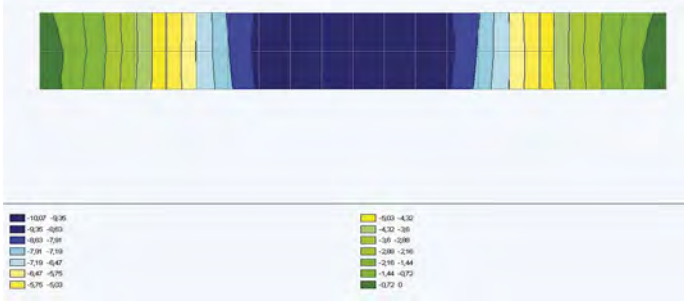

Figure 4. Isofields of longitudinal stresses in the elements of the beam model.

Comparison of the results of theoretical studies, experimental tests and modeling of the beams BDR-1, BDR-2, BDDSF-1 and BDDSF-2 in SCAD PC are presented in Figures 6 and 7.

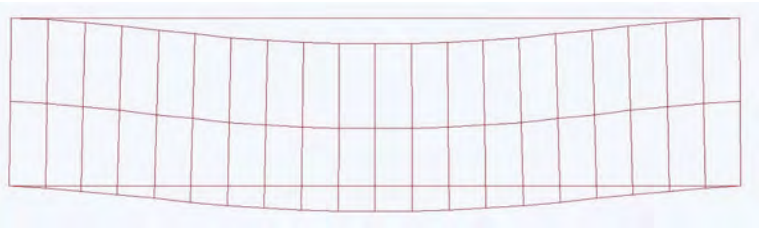

Figure 5. A picture of the possible destruction of the beam model.

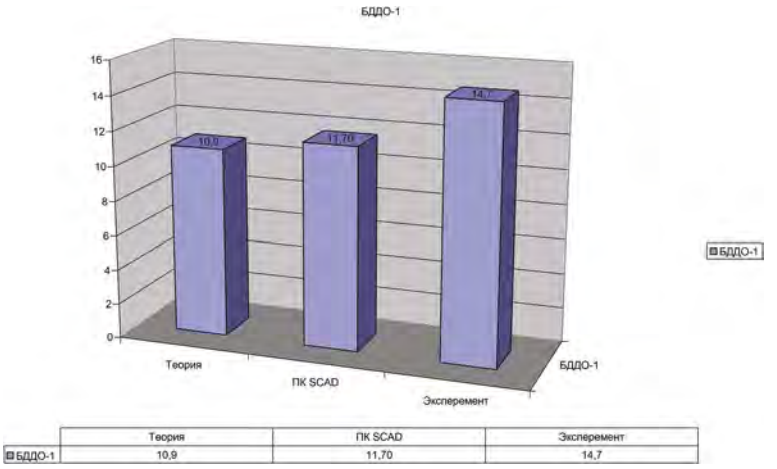

	Теория	ПК SCAD	Эксперемент
БДДО-1	10,9	11,70	14,7

Figure 6. Comparison of the test results of beams with a wall made of OSB.

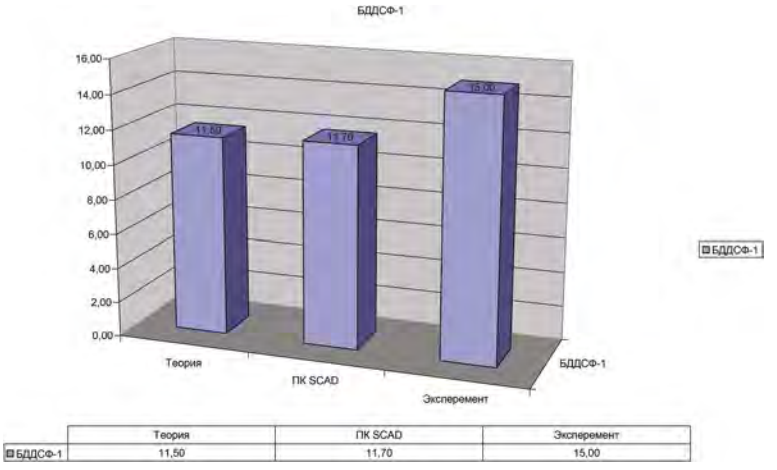

	Теория	ПК SCAD	Эксперемент
БДДСФ-1	11,50	11,70	15,00

Figure 7. Comparison of the test results of beams with a plywood wall.

4 CONCLUSION

Based on the results of the conducted research, the following conclusions can be drawn:

– Computer models of composite beams based on FEM have been developed, allowing to obtain the spatial distribution of stresses in the elements;

– Obtained isofields of stress distribution in the elements of beams, as well as pictures of possible destruction of beams in the nonlinear formulation of loading models;
– Comparisons of theoretical and experimental test results of wooden glued beams have been carried out, according to which the following inputs can be made when calculating according to the SNiP II-25-80 methodology, it is necessary to bring the materials of walls and shelves to the same material through elastic modules [22, 17 p.]. In the modeling of beams in the SCAD PC, this operation was not used, that is, the beams conditionally glued were not brought to the same material, and the shelves and the wall had their own characteristics. Simulations in the SCAD PC showed a discrepancy between the results and theoretical studies of 14.4% [23, 109 p.].

Belts of glued beams with a flat plywood wall should be made of vertically placed layers (boards). If the cross-section height of the belts exceeds 100 mm, horizontal cuts should be provided in them from the side of the walls. n. Plywood, LVL or OSB with a thickness of at least 8 mm should be used for the walls of the beams. In the plywood beams, it is advisable to place the plywood of the walls so that the fibers of the outer veneer sheets are directed along the axis of the beam, the connection of the plywood sheets is carried out «on the mustache». Flat-walled adhesive beams are recommended for spans up to 15 m. The height of the cross-section of such beams is taken from 1/5 to 1/12 of the span.

Calculation of board - glued beams . For a bent element provided against the loss of stability of a flat form of deformation, i.e. if there is no decrease in strength due to loss of stability in the transverse direction, the calculated strength will be determined by the strength of the material during bending. The loss of stability of an element bent relative to the y-y axis will occur if its compressed zone is not completely detached from the transverse displacement and the relative flexibility during bending relative to this axis is λ rel, $m > 0.75$.

Calculation of single-pitch glued beams. The calculation is based on the limiting states of the ability to determine:

– checking the carrier of the maximum values of shear stresses;
– maximum values of normal bending stresses.

When checking the limit states of operational suitability: deflections.

REFERENCES

Kireev, V.I., Panteleev, A.V. 2008. Numerical methods in examples and problems. 480. Moscow: *Higher School*.

Elmuratov, S.K. 2008. Numerical methods in calculations of structures. *Study guide*. 91. Pavlodar: Kereku.

Samarskiy, A. A. 2007. Introduction to numerical methods. *Textbook for universities*. 288.St. Petersburg: Lan

Kalitkin, N. N. 1978. Numerical methods. *Textbook*. Science. 512 Moscow: Science.

Kireev, V.I., Panteleev A.V. 2004. Numerical methods in examples and problems. *Textbook*. 512. Moscow: Scence.

Alexandrov, A.V., Potapov, V. D., Derzhavin B. P. 2009. Resistance of materials. *Textbook*.560. Moscow: Science.

Darkov, A.V., Shaposhnikov, N.N. 2010.Construction mechanics. *Textbook* 656. Russia: Moscow.

Konstantinov, I.A., Lalin, V.V., Lalina, I.I. 2011. Construction mechanics. *Textbook*.432. Russia: Moscow.

Karpilovsky, V.S., Kriksunov, E.Z., Malyarenko, A.A. et al. 2013. SCAD Office. Computing complex SCAD. *Textbook*. Russia: Moscow.

Trushin, S.I. 2008. Finite element method. Theory and tasks.256. *Textbook*. Russia: Moscow.

Varvak, P.M., Ryabov, A.F. 1971. Handbook of elasticity theory. 419. *Textbook*. Ukraina: Kiev.

Elmuratov, S.K. 2006. Practical methods of calculating structures. 109. *Study guide*. Kazakhstan: Pavlodar

Marchuk, G. I. 1977. Methods of computational mathematics.456. *Textbook*. Russia: Moscow.

Yudina, M.G. 2005. Mathematical package MathCAD. *Educational and methodical manual*. Berezniki: Perm State Technical University Berezniki branch.

Smart Geotechnics for Smart Societies – Zhussupbekov, Sarsembayeva & Kaliakin (Eds)
© 2023 The Author(s), ISBN 978-1-003-29912-7
Open Access: www.taylorfrancis.com, CC BY-NC-ND 4.0 license

Instrumentation and monitoring for KVMRT Line 2 tunnelling works (Bandar Malaysia North Station to Chan Sow Lin Station) in Kuala Lumpur

Y.C. Tan, C.L. Low, C.L. Tei & K.L. Teh
G&P Geotechnics Sdn. Bhd., Malaysia

ABSTRACT: Underground construction works for KVMRT Line 2 in Kuala Lumpur includes tunnel boring works, excavation works for shafts and stations, and mine tunnel works for cross-passage and adits. This paper will present the instrumentation and monitoring for tunnelling works from Bandar Malaysia North Station to Chan Sow Lin Station which tunnelling in Alluvium and Limestone formation. Generally, all above ground and underground structures (e.g. SMART tunnel and SBK Line 1) that located within minimum monitoring zone are to be instrumented especially the sensitive structures located on top or nearby to the tunnel alignment. Manual observation/surface monitoring by manpower is also adopted during tunnelling works in order to take immediate action and provide first-hand information to the respective parties in the case of excessive settlement/ sinkhole formation (especially tunnelling in Limestone formation). This paper will share the instrumentation monitoring methods and concepts of the proposed instrumentation monitoring works. The instrumentation results for ground and buildings along this tunnel alignment will be presented and discussed.

1 INTRODUCTION

Sungai Buloh-Serdang-Putrajaya (SSP) Klang Valley Mass Rapid Transit Line 2 (herein referred to as KVMRT Line 2) in Kuala Lumpur has begun its construction works in 2016. The entire length of tunneling section is 13.5km connecting 11 nos. of underground station from Sentul West Station(SWS) to Desa Water Park Portal(DEWP). Overall tunnelling work is divided into eight tunnelling section namely Tunnel Drive 1 (TU1) to Tunnel Drive 8 (TU8). Case study is carried out based on the completed tunneling section TU7 (From Bandar Malaysia North Station (BMNS) to Chan Sow Lin Station (CSLS).

This paper will present the effectiveness of the instrumentation monitoring works plan in monitoring of the ground movement by comparing to predicted ground movement from the numerical analysis. This paper will provide some recommendation to improve instrumentation monitoring plan.

2 SITE BACKGROUND

TU7 was the first started tunnel drive for KVMRT Line 2 line which begun on March 2018 and completed on April 2019. The tunnelling length for TU7 is about 1.8km which launched in BMNS (CH37460) and breakout at CSLS (CH35620). Other than bored tunnel, there are also mined tunnel in TU7 for the construction of cross-passage. Along the TU7, the existing building structure above ground including The Royal Malaysian Air Force (TUDM), low rise building, ramps, monsoon drain, and etc. The sensitive structure along TU7 including MEX

DOI: 10.1201/9781003299127-347

highways, Besraya highway (Pier Structure), ongoing construction DUKE highway and LRT tracks (On Bridge deck) which is close to the breakout at CSLS.

2.1 *Site geology*

Geological formation for TU7 is in limestone formation overlaid by alluvium layer of thickness 5m to 30m. The entire tunnelling works along TU7 is in deep rock where rock head is generally more than 1D (i.e. tunnel diameter, D=6.35m) ranging from 5mbgl to 30mbgl.

2.2 *Predicted ground movement*

Predicted ground movement due to the effect of both bored and mined tunneling works is presented in the form of settlement trough to show estimated surface movement on top of the tunnel alignment. Since the tunneling works are expected to be carried out in deep rock, generally negligible movement is predicted based on the numerical analysis. Nonetheless, a conservative assumption of 5mm was made for tunnelling in rock where the minimum rock cover above the tunnel crown is one time the tunnel diameter with the extent of 10m from the centreline of each tunnel alignment with reference to the earlier similar tunneling experiences in KVMRT Line 1.

3 INSTRUMENTATION MONITORING PLAN

3.1 *Instruments*

Monitoring of ground movement due to tunneling works are carried out by the installation of instruments in the form of array which arranged in fixed interval along the tunnel alignment. The monitoring array adopted for ground movement monitoring along TU7 as shown in Figure 1.

Monitoring arrays are arranged at maximum 100m spacing for T1 array, 200m for T3 array, and 1km for T5 array. Monitoring array consist of instruments such as surface settlement marker, inclinometer, extensometer, and vibrating wire piezometer. Value engineering had been carried out during the implementation of the instrumentation works. For instances, instruments such as inclinometer and extensometer are assigned whenever necessary for sensitive structures only.

Monitoring works for most of the existing building structures (EBS) are carried out by tiltmeter and building settlement markers to detect the changes in building distortion and movement. Other instruments such as optical prisms are installed for sensitive structures (which located immediate on top of tunnel alignment) such as viaduct piers with real-time monitoring (RTM) (reading taken at every 30 mins.).

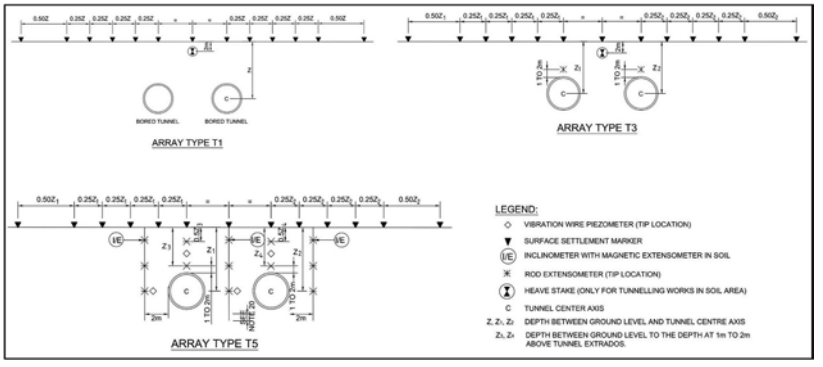

Figure 1. Instruments arrangement for Array Type 1, Type 3, and Type 5.

3.2 *Review level*

Review Level (Alert, Action, and Alarm) is established for the monitoring works based on respective predicted movement. Action is required to be taken when the monitoring results trigger the designed review level. Review level for different type of EBS were split into the 4 categories as shown in Table 1. Special category of review level will be provided for selected EBS based on building impact assessment or stakeholder's requirement.

Monitoring frequencies are based on tunnel activity and its relative distances to the EBS. Generally, monitoring frequencies increased when the distances from tunnel boring machine (TBM) to EBS is getting closer.

Table 1. Review levels.

		Alert Level		Action Level		Alarm Level	
Cat	Type of Structure/ Buildings	Building Settlement (mm)	Distortion Angle	Building Settlement (mm)	Distortion Angle	Building Settlement (mm)	Distortion Angle
1	Heritage Structure/ Building	7	1:1000	9	1:750	10	1:500
2A	Structure/Building on Deep Foundation Influenced by Tunnelling	11	1:750	13	1:500	15	1:300
2B	Structure/Building on Deep Foundation Influenced by Deep Excavation	11	1:750	13	1:500	15	1:300
3	Structures/Buildings on Shallow Foundation	18	1:750	21	1:500	25	1:300

3.3 *Case history for instrumentation monitoring and sinkholes – UG265 Sungai Besi Monsoon Drain*

GSMs monitoring nearby the Sungai Besi Monsoon Drain (UG-265-CH36920) showed first sudden drop on 18th July 2018 when NB TBM at about 5m away from the monsoon drain. GSMs were stable without showing any further movement until NB TBM passes the monsoon drain. Second sudden drop was observed on 25th August 2018 when SB TBM near to the monsoon drain as shown in Figure 2. The ground (2 to 3m) from monsoon drain was immediate found with sinkhole occurrence after the observation of sudden drop in GSMs.

For tiltmeter (TM) monitoring as shown in Figure 2, distortion of drain wall started to show increasing tilting trend and eventually breached Alert level (1.33mm/m) on 27th August 2018. It became stable when both north bound (NB) and south bound (SB) TBM passes for at least 300m away from the monsoon drain. Apart from instrumentation, whirlpool and air bubbles was observed when south bound (SB) TBM before reaching Sungai Besi Monsoon Drain (UG-265-CH36920). With all the monitoring results and observation, it is suspected sinkholes formed under the monsoon drain when NB TBM first arrive at this location. The sinkholes happened 2 to 3m away from the drain is suspected due to interconnected cavities which triggered by SB TBM (2nd TBM) when tunneling at this location.

Apart from instrumentation monitoring, the study on TBM parameters (i.e. the inlet and outlet slurry flow data), the slurry loss rate was found higher at about 150m^3/hour when south bound (SB) tunneling works was right below monsoon drain. Slurry was suspected to lose to the surrounding cavities which results in the monsoon drain movement.

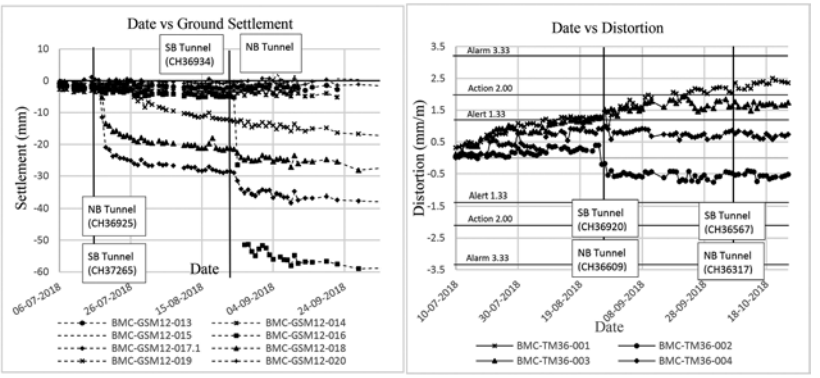

Figure 2. Ground settlements markers and tiltmeter monitoring results.

4 CONCLUSION AND RECOMMENDATION

4.1 *Conclusion*

Similar to the case history as discussed, ground settlement observed are mainly due ground depression caused by nearby sinkholes occurrences. Most of the monitoring results showed stable monitoring results during tunneling works in TU7. Exclude sinkholes, the findings from the instrumentation for ground movement is tally with the assumption that insignificant ground movement is expected for tunneling in deep rock area.

There was total 11 nos. different size sinkholes occurred along TU7 during tunneling works. 10 of out 11 nos. of the sinkholes were found located near to the tunnel alignment within 10m offset from tunnel centreline as mentioned in Section 2.2 predicted ground movement. As such, monitoring zone based on assumption of 5mm settlement contour for TBM impact zone is appropriated.

Instrumentation monitoring likely do not provide earlier warning for sinkhole occurrences when tunnelling at deep rock area. Nonetheless, the instrumentation monitoring is important to monitor the structure movements especially for sensitive structures.

4.2 *Recommendation*

TBM parameter is recommended to be reviewed as the changes in the parameter is good indication for possible ground movement/sinkholes occurrences caused during tunnelling works.

In order to minimize the occurrences of sinkholes or ground depression, pre-ground treatment such as grouting works is recommended to be carried out especially for tunnelling in high risk zone such as limestone formation or mixed soil condition.

Site team is recommended to provide close monitoring to standby for surface observation monitoring especially high risk activities such as unplanned cutterhead intervention.

REFERENCES

Fargnoli, V., Boldini, D., & Amorosi, A. 2013. TBM tunnelling-induced settlements in coarse-grained soils: the case of the new Milan underground line 5. *Tunnelling and Underground Space Technology*, vol. 38, pp. 336–347

Loganathan, N. & Poulos, H. G. 1998. Analytical Prediction for Tunnelling-induced Ground Movements in Clays. *Journal of Geotechnical and Geoenvironmental Engineering*, 124, 846–856.

Rankin, W. J. 1988. Ground Movement Resulting from Urban Tunnelling: Predictions and Effects. *Engineering Geology of Underground Movements*, pp. 79–92.

Smart Geotechnics for Smart Societies – Zhussupbekov, Sarsembayeva & Kaliakin (Eds)
© 2023 The Author(s), ISBN 978-1-003-29912-7
Open Access: www.taylorfrancis.com, CC BY-NC-ND 4.0 license

Deformation mechanism of existing underground structures in clay induced by deep construction disturbances

J.H. Zhang & A.X. Wang
Department of Hydraulic Engineering, State Key Laboratory of Hydroscience and Engineering, Tsinghua University, Beijing, China

X.S. Chen
College of Civil and Transportation Engineering, Shenzhen University, Shenzhen, China

ABSTRACT: This paper presents results of centrifuge tests investigating existing underground structures in a clay subjected to construction disturbance. A modelling technique was developed to simulate the failure of an excavation face in the ongoing construction. The effect of water was also simulated after the failure of the excavation. Deformations of the existing underground structures were measured by image analysis through tracing markers in the soil model. The centrifuge tests indicated that significant deformation developed in the soft clay resulted in great settlements of existing underground structures and bending of the existing tunnel. The maximum measured settlement of the existing tunnel was about 18% of tunnel diameter. The maximum settlements of the basement was 27.5% of tunnel diameter.

1 INTRODUCTION

Exploitation of the deep underground space results in a complex underground engineering system consisting of different functional structures. Soil–structure interaction design considerations are crucial for underground structures when subject to deep construction disturbance. The response behaviors of an underground system is influenced by the nonlinear soil/structure interaction, the failure pattern of the deep excavation, underground water, and the arrangement of the structures.

Numerous studies have been conducted using physical models to investigate the deformation and failure mechanism of structures due to excavation (e.g. Mair, 1979; Zhang et al., 2001; Ge, 2002; Son and Cording 2005; Zhang et al., 2007; Farrell and Mair 2010; Ng and Wong 2013; Sabagh and Ghalandarzadeh, 2020; Weng et al., 2020; Ritter et al. 2020; Xu et al., 2021).

In the present study, centrifuge model test was carried out to investigate the deformation mechanism of existing underground structures subjected to deep excavation failure in a clay. Effects of water discharge are also discussed.

2 CENTRIFUGE MODEL SETUP AND TESTING

Figure 1 shows the centrifuge model setup. A strong box accommodated existing underground structures in a clay of a building basement, a tunnel, two storage houses (Storage L and Storage R) and a sewer line (Sewer) above an ongoing deep construction. The model structures were boxes made from transparent acrylic plate. The deep construction was modeled by a rigid steel box at the bottom of the strong box, having an excavation face. A hydraulic actuator was connected to a steel plate simulating the excavation face. The actuator initially

DOI: 10.1201/9781003299127-348

supported the excavation face and later pushed the face at the centrifugal acceleration of 80 g to simulate excavation failure.

The centrifuge model test was carried out in the geotechnical centrifuge at Tsinghua University (Zhang et al., 2015). Soil models are scaled down to satisfy the principles of mechanical similitude between a model and its prototype (Taylor, 1995). The soil model, which was subjected to a centrifugal acceleration of 80 g, had internal dimensions 0.6 m long × 0.2 m wide × 0.5 m high, equivalent to 48 × 16 × 40 m in the prototype. A transparent side wall on one side of the strong box enabled the model to be monitored visually during the test.

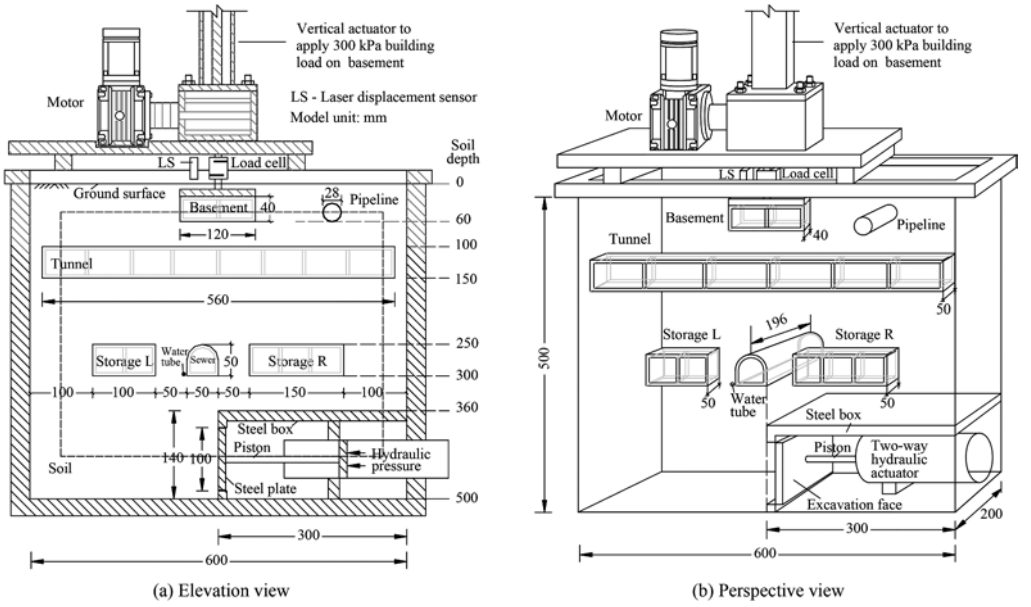

Figure 1. Centrifuge model setup in model scale: (a) elevation view, (b) perspective view.

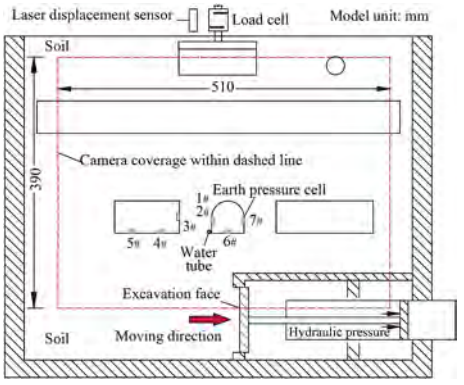

Figure 2. Instrument used in centrifuge model.

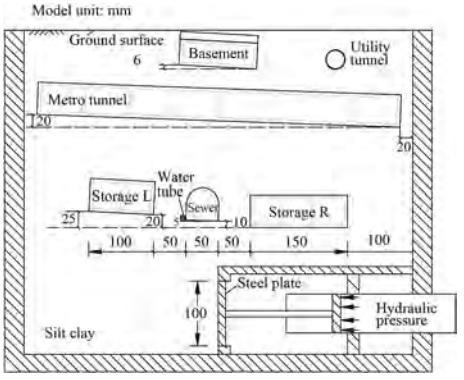

Figure 3. Positions of structures during preparation.

The clay had a plasticity index of 15.8, with a maximum dry density of 2287 kg/m^3 at a water content of 15% (ASTM D698). It was compacted into the strong box with a water content of 17% and a dry density of 1600 kg/m^3. The clay exhibited high plasticity and high compressibility. To compensate for significant deformation during consolidation, the model

structures were placed initially inclined as described in Figure 3. Markers of small white pebbles were placed on the side of the model to trace the deformations of the soil.

A surcharge loading of 300 kPa was applied by a vertical actuator on the basement to simulate the weight of the tall building. To measure the settlement of the ground surface, a non-contact laser displacement sensor was installed above the basement. Seven tiny earth pressure cells were used to monitor the change of earth pressures with time. A digital video camera was placed in front of the transparent side wall, covering an area as indicated by the dashed lines in Figure 2. A photo-imaging technique was used to accurately measure the displacements of the soil and the structures (Zhao and Zhang 2020). The soil model was consolidated at 80 g under self-weight and then consolidated again under the surcharge load. The excavation face then was pushed laterally to trigger soil and structure movement.

3 RESULTS AND DISCUSSIONS

Figure 4a shows the ground surface settled down 2.6 m due to consolidation. The positions of the structures after consolidation were taken as the initial positions for calculating the structure movement subject to excavation face displacement. Figure 4b presents displacement vectors of the clay toward the excavation face when it had moved 1.8 m. The maximum displacement of the clay of up to 0.9 m occurred ahead of the excavation face. A water discharge (0.84 kg in model scale) induced a crack and a muddy flow ahead of the excavation face (Figure 4c) and softened the clay. It thus resulted in more settlements of the structures with the increasing excavation face displacement from 3.0 m to 5.8 m (Figure 4d). The second water discharge (3.34 kg in model scale) was brought into the soil. It scoured the soil and widened the crack (Figure 4e). Eight minutes later after the water discharge was stopped, the settlements of the building basement, the metro tunnel, the left-hand storage and the sewer line were 1.1 m, 0.75 m, 0.97 m and 1.0 m, respectively (Figure 4f).

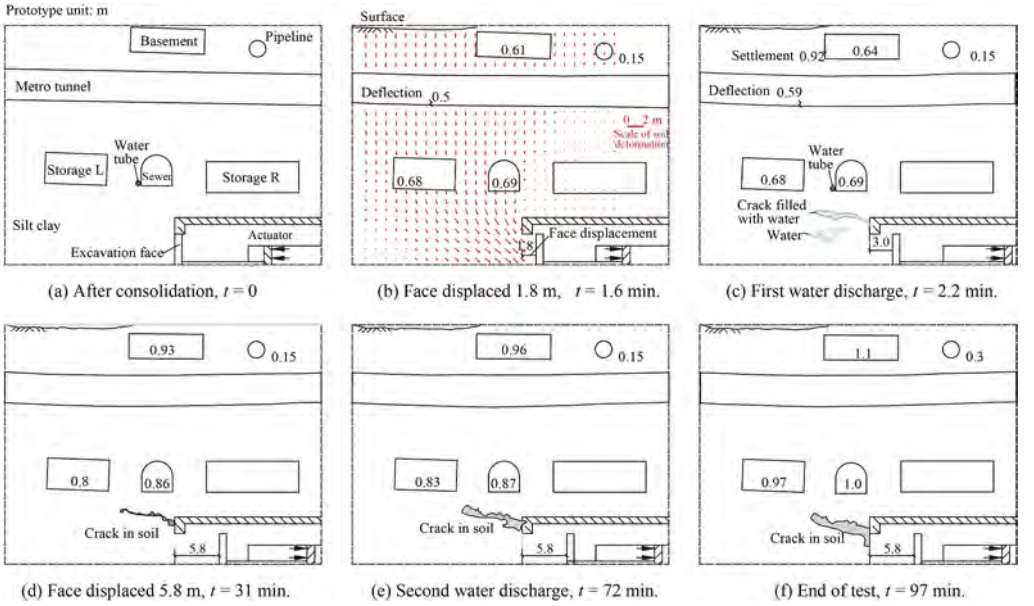

Figure 4. Deformation mechanism of underground structures in clay developed with excavation face displacement, underground water changes and time (model scale). Values in the figure indicate prototype settlements of the existing structures.

Figure 5 compares the settlements of the existing underground structures developed with time. The time is in model scale, originating from the point of when the tunnel face began to move. At about 2.2 minute, all the structures settled significantly consistent with the initial excavation face displacement of 0 – 3.0 m and the first water discharge. The basement experienced the most significant settlement. The maximum settlements of the basement was 1.1 m, 27.5% of tunnel diameter. Figure 6 shows deformations of the metro tunnel in the process of construction disturbance. The tunnel significantly bended at the middle part and lifted at the right side. The maximum measured settlement of the metro tunnel induced by soil-structure interactions was about 18% of tunnel diameter.

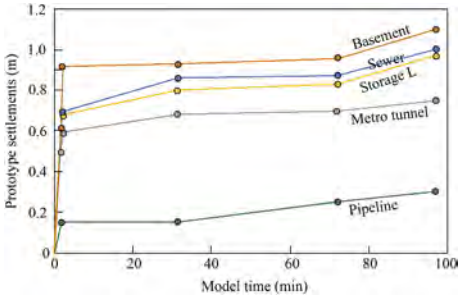

Figure 5. Structure settlements versus time.

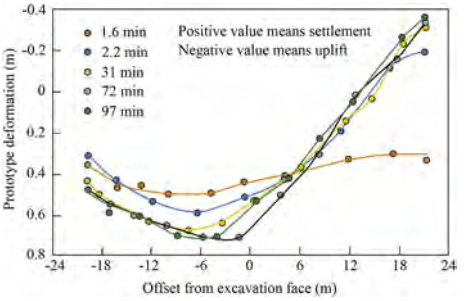

Figure 6. Deformations of tunnel versus time.

4 CONCLUSIONS

This paper presents results of centrifuge tests simulating existing underground structures in a clay subjected to deep construction disturbances. The results of centrifuge model tests indicated that significant deformation of the clay and existing underground structures developed when subject to the deep excavation failure. The maximum measured settlement of the existing tunnel induced by soil-structure interactions was about 18% of tunnel diameter. The maximum settlements of the basement was 27.5% of tunnel diameter.

ACKNOWLEDGEMENT

The authors would like to acknowledge financial support from the National Natural Science Foundation of China (No. 52279101 and 52090084).

REFERENCES

Farrell, R.P. & Mair, R.J. 2010. Centrifuge modelling of the response of buildings to tunnelling. 7th International Conference on Physical Modelling in Geotechnics, ETH Zurich, Switzerland, Jun 28-Jul 01, 2010 Vol. 1, pp.554–549 .

Franza, A. & Viggiani, G.M. 2021. Role of shear deformability on the response of tunnels and pipelines to single and twin tunneling. Journal of Geotechnical and Geoenvironmental Engineering, 147(12), 04021145.

Ge, X.W. 2002. Response of a shield-driven tunnel to deep excavations in soft clay. Ph.D. thesis, Department of Civil and Environmental Engineering, The University of Hong Kong Science and Technology, HKSAR.

Mair, R.J. 1979. Centrifugal modelling of tunnel construction in soft clay. Ph.D. thesis, University of Cambridge.

Ng, C.W.W. & Wong, K.S. 2013. Investigation of passive failure and deformation mechanisms due to tunnelling in clay. Can. Geotech. J. 50, 359–372.

Ritter, S., Giardina, G., Franza, A., DeJong, M.J., 2020. Building deformation caused by tunneling: centrifuge modeling. J. Geotech. Geoenviron. Eng., 146, 5. Article No. 04020017.
Sabagh, M., Ghalandarzadeh, A., 2020. Centrifugal modeling of continuous shallow tunnels at active normal faults intersection. Transportation Geotechnics, Vol 22, Article No. 100325.,
Son, M., Cording, E.J., 2005. Estimation of building damage due to excavation-induced ground movements. J. Geotech. Geoenviron. Eng., 131 (2), 162–177.
Taylor, R.N., 1995. Geotechnical centrifuge technology. Blackie Academic and Professional, London.
Weng, X.L., Sun, Y.F., Yan, B.H., Niu, H.S., Lin, R.A., Zhou, S.Q., 2020. Centrifuge testing and numerical modeling of tunnel face stability considering longitudinal slope angle and steady state seepage in soft clay. Tunnelling and Underground Space Technology, Vol 112, Article No. 103942.
Xu, J.M., Franza, A., Marshall, A.M., Losacco, N., Boldini, D., 2021. Tunnel-framed building interaction: comparison between raft and separate footing foundations. Géotechnique, 71 (7), 631–644.
Zhang, J.H., Chen, Z.Y., Wang, X.G., 2007. Centrifuge modelling of rock slopes susceptible to block toppling. Rock Mechanics and Rock Engineering, 40 (4), 363–382
Zhang, J.H., Pu, J., Zhang, M., Qiu, T., 2001. Model tests by centrifuge of soil nail reinforcements, Journal of Testing and Evaluation, 29 (4), 315–328.
Zhang, J.H., Lin, H.L., Wang, K.Z., 2015. Centrifuge modeling and analysis of submarine landslides triggered by elevated pore pressure. Ocean Engineering, 109 (11), 419–429.
Zhao, Y.Y., Zhang, G., 2020. Centrifuge modeling of soil slopes overlying bedrock under excavation conditions. Soils Found. 60 (2020), 886–897.

Smart Geotechnics for Smart Societies – Zhussupbekov, Sarsembayeva & Kaliakin (Eds)
© 2023 The Author(s), ISBN 978-1-003-29912-7
Open Access: www.taylorfrancis.com, CC BY-NC-ND 4.0 license

Analysis of the results of field tests and numerical modeling to determine the settlement of piles in astana city

A.Zh. Zhussupbekov & A.U. Yessentayev
L.N. Gumilyov Eurasian National University, Astana, Kazakhstan

E.N. Abdygaliyev
Karaganda Technical University, Karaganda, Kazakhstan

V.V. Konyushkov
Saint Petersburg State University of Architecture and Civil Engineering, Saint Petersburg, Russia

N.S. Nikitina
Moscow State Civil Engineering University, Moscow, Russia

ABSTRACT: A comparative analysis of the results of field tests and numerical modeling to determine the bearing capacity and settlement of a driven piles at medical facilitie at Astana are presented. The aim of the study was to carry out a comparative analysis of the results of numerical modeling and static tests in order to identify the difference in settlement of test pile under the design load. The results of settlement of the pile, determined by numerical modeling, is slightly lower than from static tests, with a difference in results being in 7%.

1 INTRODUCTION

An 800-bed Astana Medical University Hospital is being constructed on the right bank of the Esil River in the city of Astana, Kazakhstan. The total area of the hospital will be 140 thousand square meters. It will house a consultative and diagnostic center, round-the-clock and day facilities with 800 and 110 beds, respectively. Figure 1 shows an architectural rendering of the hospital complex.

Figure 1. Architectural rendering of hospital complex in Astana, Kazakhstan.

DOI: 10.1201/9781003299127-349

2 GEOLOGICAL AND GROUND CONDITION OF CONSTRUCTION SITE

At the time of the geologic survey, the building site was free of any previous development. A total of 22 exploratory borings were made at the site.

In all of the borings, the topmost soil layer was found to consist of dark brown top soil. The thickness of this layer ranged from 0.5 to 3.6 m.

In all 22 borings, the top soil was underlain by a layer of saturated, light brown loam with clay seams up to 20 cm in thickness. The consistency of the loam varied between hard to soft-plastic. The thickness of this layer ranged from 0.0 to 7.5 m.

In 5 borings, a layer of saturated, brown sandy loam of medium density was next encountered. The thickness of this later ranged from 2.9 to 4.6 m.

In 13 of the borings, a layer of saturated, grey fine sand was next encountered. The thickness of this layer ranged from 1.0 to 12.0 m.

In 19 of the borings, a layer of saturated, light brown gravelly sand was next detected at a depth of approximately 9.8 m. the thickness of this layer ranged from 0.6 to 5.2 m.

In 12 of the borings, the gravelly sand was underlain by a layer of saturated clayet loam that was violet in color. The thickness of this layer ranged from 9.5 to 18.0 m.

Table 1 summarizes the values of geotechnical parameters that were determined from the results of laboratory tests performed on undisturbed samples taken from the boreholes in conjunction with statistical analysis of test results.

Table 1. Summary of parameter values for soils at astana medical facility site.

Soil type	C (kPa)	φ (degrees)	E (MPa)
(EGE-1) Topsoil	–	–	–
(EGE-2) Loam	17.0	13.0	5.0
(EGE-3) Sandy loam	19.0	27.0	6.5
(EGE-4) Fine sand	1.0	33.0	27.0
(EGE-5) Gravelly sand	1.0	38.0	35.0
(EGE-6) Loam	38.0	11.7	12.2

Figure 2 shows an idealized soil profile at the site of the Astana medical facility.

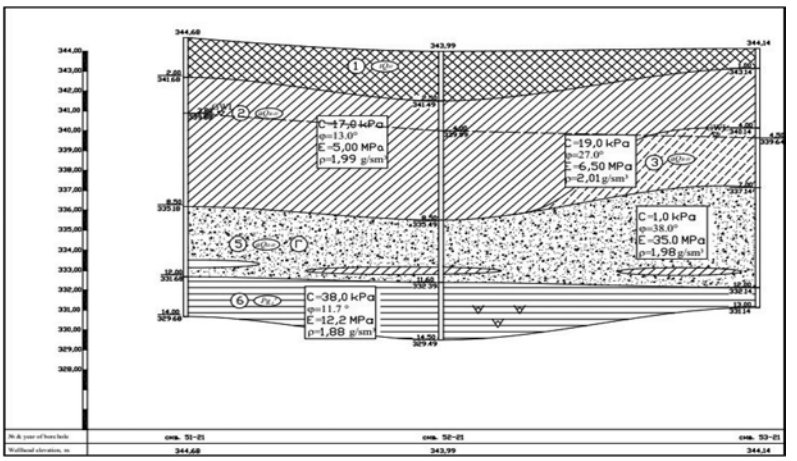

Figure 2. Soil profile at site of Astana medical facility.

3 NUMERICAL MODELING OF DRIVING PILE IN THE PLAXIS 3D

We will calculate the drilling pile using the solutions of the theory of the limit state of a granular medium (numerical methods). When using the numerical method - the finite element method and using the Plaxis application program.

According to the report of Engineering and geological surveys at the facility "800-bed Astana Medical University Hospital" was collected the calculation scheme of the engineering-geological well column No.53–21. Physical and mechanical properties of soils are presented in introduction. The Calculation model of driven test pile 10C-30 was showing in the picture.

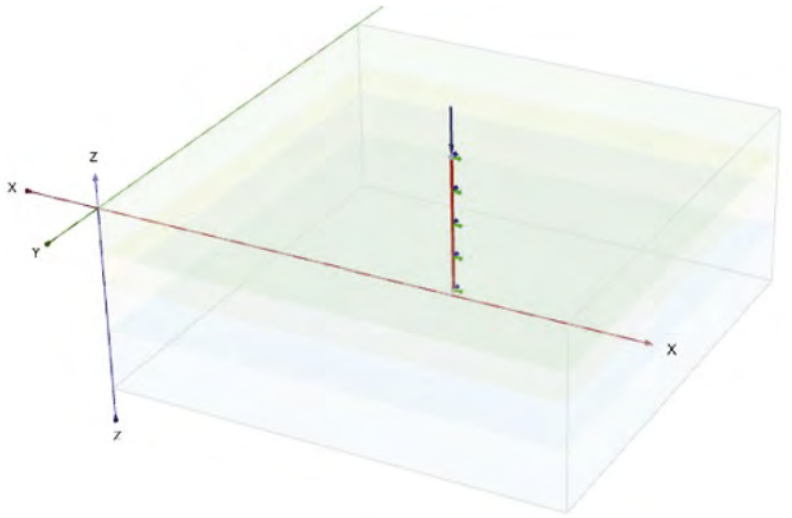

Figure 3. Calculation model of driven pile for Astana site.

To calculate pile, the Linear Elastic model and the Elastic-Plastic model with the Mohr-Coulomb strength criterion were used.

The analysis of the calculation results was performed according to:

- displacement of the pile are showing in the Figures 4–5;

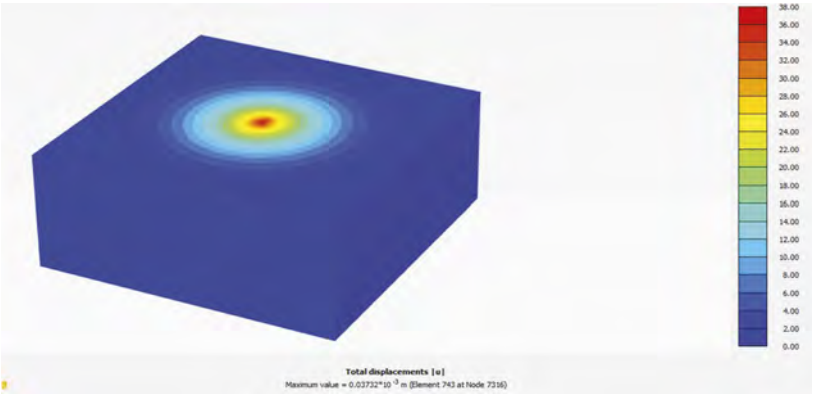

Figure 4. Total displacement of the pile.

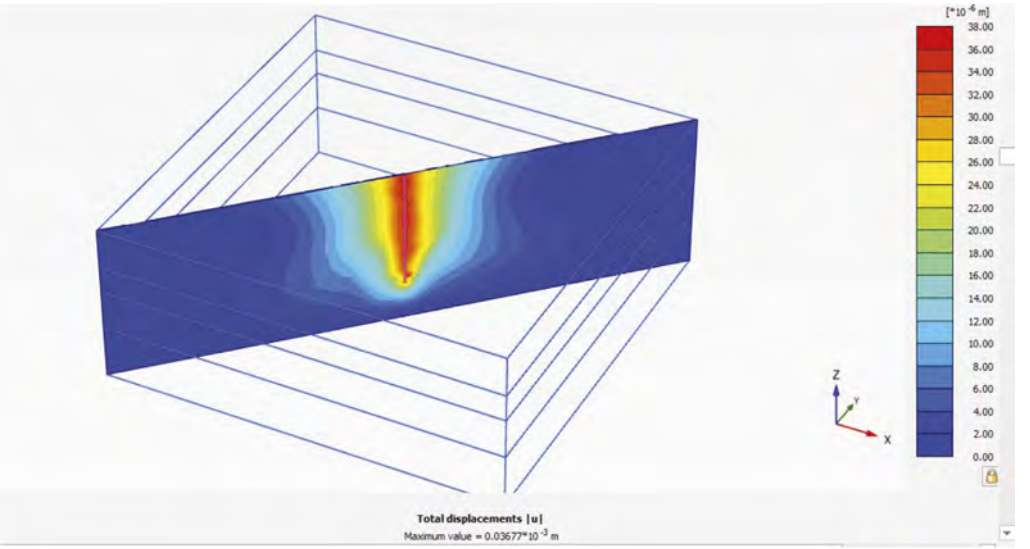

Figure 5. Total displacement of the pile.

The result of the numerical simulation of pile settlement with a design load of 940 kN in the Plaxis 3D software package is:

the settling of the driving pile C10-30 was 38 mm, which is within the normal range according to SP RK 5.01-103-2013. Pile foundations, 2015

4 STATIC PILE TESTS

Field tests of S10-30 driven piles with static, vertical-indentation loads were carried out from December 02, 2020 to January 08, 2021 at the construction site of the Main Building and the Parking lot of the Astana Medical University Hospital in Astana.

The tests were carried out on four driven test piles C10-30 numbered 29, 40 (Main building) and 62, 66 (Parking lot), as shown in Figure 6. The piles were driven to a depth of 9.5 m. Field

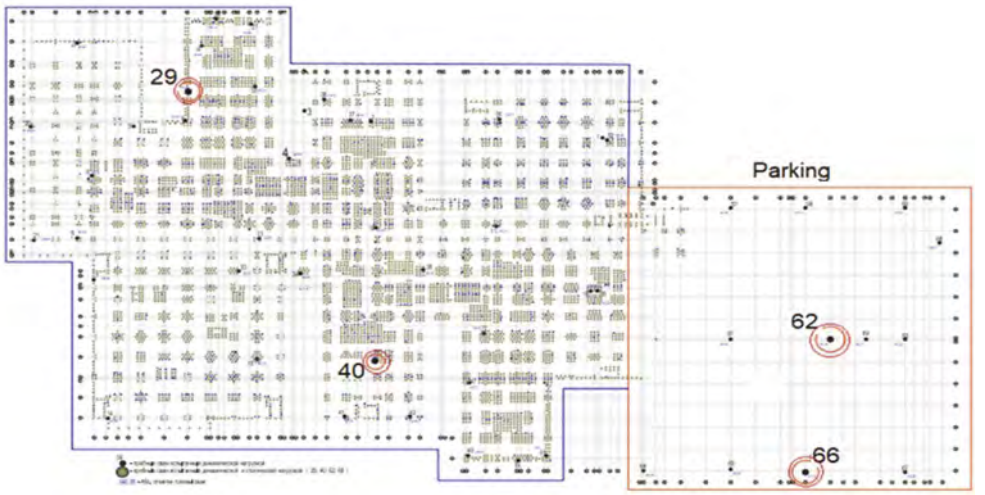

Figure 6. Plan view of static pile test layout at Astana site.

tests were carried out after a period of pile "rest" equal of 30 to 60 days after driving. The load on the pile was created using a 100-ton hydraulic jack "Enerpred DU100P150" with a pumping station "Enerpac P462", abutting against a test and loading stand, weighing 120.0 tons (Tulebekova, et al. 2012), (Zhussupbekov, et al. 2015).

The process is described in detail in the articles previously published. (Turashev, 2015, Yenkebayev, 2012, Tulebekova, 2021). Pile settlement curves are shown in Figure 7.

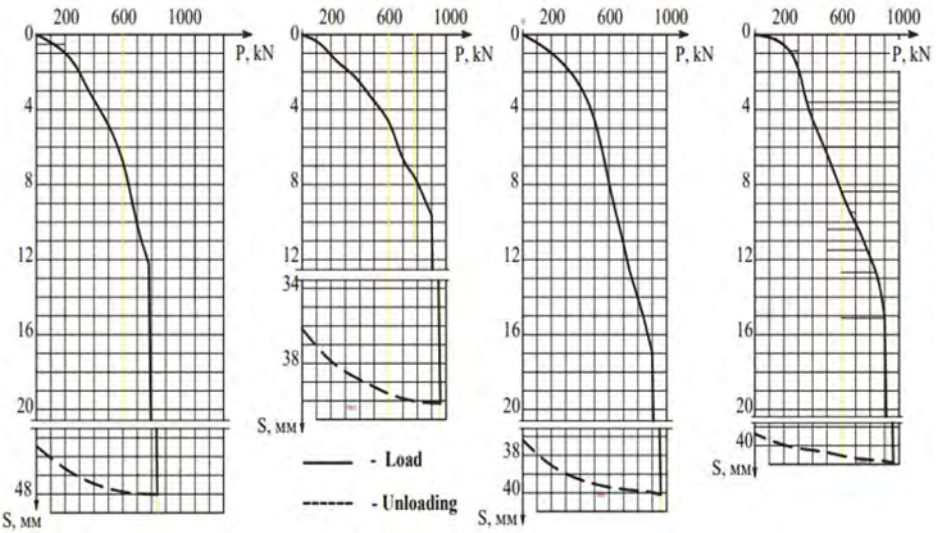

Figure 7. Pile settlement curves for Astana site.

The results of the static pile tests are summarized in Table 2. Some important points regarding the static pile tests at the Astana site are as follows: The bearing capacity of the pile tests at the locations of the main hospital building and the parking structure were 990 kN and 780 kN, respectively. The permissible pile load, taking into account the safety factor $\gamma_k = 1.2$ in accordance with clause 4.4.1.11. SP RK 5.01-103-2013 ("Pile foundations"), is equal to 750 kN and 650 kN for the main hospital building and parking structure locations, respectively.

Table 2. Summary of static test results for Astana site.

Pile №	Depth of immersion of piles in the ground, m	Maximum applied load, kN	Displacement at the highest applied load, mm	Partial value of ultimate resistance, kN	Bearing capacity of piles, kN
№ 62	9.5	840	48.01	780	780
№ 66	9.5	960	40.14	900	
№ 29	9.5	960	40.12	900	900
№ 40	9.5	960	40.91	900	

5 CONCLUSIONS

1. The result of the numerical simulation of pile settlement with a design load of 940 kN in the PLAXIS 3D software package is: the settling of the driving pile C10-30 was 38 mm
2. Static indentation test results must be considered when determining the correct pile length.
3. The results of settlement of the pile, determined by numerical modeling, is slightly lower than from static tests, with a difference in results being in 7%.

REFERENCES

Tulebekova, A. S., Zhusupbekov, A. Zh., Shakhmov, A., Yenkebayev, S. B. 2012. Experience of testing according to international standard ASTM on problematical soil ground of Astana. Vestnik Evraziiskogo natsional′nogo universiteta imeni L.N. Gumileva, publ. no. 2, pp. 126–131.

Zhussupbekov A. Zh., Syrlybaev M. K., Lukpanov R. E., Omarov A. R. 2015. The applications of dynamic and static piling tests of Astana. The 15th Asian Regional conference on soil mechanics and geotechnical engineering. Fukuoka, Japan, pp. 508–508.

Turashev A.S., Lukpanov R.E., Omarov A.R., Zhukenova G.A., Tanyrbergenova G.K. 2015. The applications of dynamic (PDA and traditional) and traditional static piling tests of Astana city. Vestnik Evraziiskogo natsional'nogo universiteta imeni L.N. Gumileva, publ. no. 6 (109), part 1, pp. 244–249.

Yenkebayev S.B., R.E. Lukpanov, A.Zh. Zhussupbekov. 2012. Comparison results of static and dynamic load test at the construction site of Astana. Proc. of Korea-Kazakhstan Joint Geotechnical Seminar. – Incheon, Korea. – P. 115–121.

Tulebekova A.S., and Zhussupbekov A.Zh. Geotechnical specificity of international requirements and traditional standards in pile testing: Monograph L.N. Gumilyov Eurasian National University.- Moscow: Moscow University Press, 2020, -111 P.

Smart Geotechnics for Smart Societies – Zhussupbekov, Sarsembayeva & Kaliakin (Eds)
© 2023 The Author(s), ISBN 978-1-003-29912-7
Open Access: www.taylorfrancis.com, CC BY-NC-ND 4.0 license

Digitalization and BIM in geotechnics – opportunities and challenges

C. Boley
Institute for Soil Mechanics and Geotechnical Engineering, Bundeswehr University Munich, Germany

L. Wilfing
Boley Geotechnik GmbH, Munich, Germany

ABSTRACT: The topic of BIM is also gaining enormous importance due to public requirements for current and future tenders for infrastructure projects. So far, the specifications, requirements and software programs are mainly based on the subject of structural engineering and infrastructure. But also in the field of geotechnics it is necessary to keep up with the progress and to transfer the ground structure from 2D sections into a 3D ground model.

For this purpose, the borehole profiles have to be implemented and the subsoil layers have to be connected to form a spatial 3D layer model. A multitude of attributes can be assigned to these solids (geotechnical parameters, homogeneous areas, etc.). In the article, several software programs available on the market were tested and the advantages and disadvantages of each were compiled. The 3D ground model can be integrated into the overall BIM model via the open data exchange format IFC, so that 4D or even 5D planning of large projects is possible.

Finally, the opportunities and challenges of BIM in geotechnics are explained and discussed using project examples from practice.

1 INTRODUCTION

For some years now, the BIM method has to be implemented for new construction projects. The core of the BIM method is the creation of three-dimensional building models, which contain predefined components and structural elements. Such predefined models do not exist in geotechnical modeling. In principle, a building structure model can be used at any location on earth, whereas a ground model is site-specific and, due to its natural formation, not generally reproducible and geometrically heterogeneous in nature.

So far, the requirements for the BIM model have been based on the fields of structural engineering and infrastructure planning. Thus, the "subject model ground" differs significantly from the other subject models (e.g. structural engineering, signal technology, buildings, etc.) in terms of its content structure.

On the one hand, the article is intended to show which challenges have to be met by the geotechnical sector due to the introduction of digital construction and, above all, due to the "subject model ground" with 3D ground modeling. On the other hand, the possibilities of the BIM methodology will also be explained on the basis of project examples.

2 SUBJECT MODEL GROUND – STATE OF THE ART

The ground model is an attributed and parameterized 3D soil model. The integration of the "subject model ground" into the overall BIM model is necessary in order to take the properties of the soil into account in the other trades during the planning phase and to evaluate the information for processes and cost forecasts.

The model contains all the information describing the ground (Figure 1). This includes, above all, terrain models, suspected contaminated sites and explosive ordnance, geological and hydrogeological fundamentals as well as the findings from project-specific ground investigations (e.g. thickness and composition of the ground layers, groundwater levels, homogeneous areas, etc.).

DOI: 10.1201/9781003299127-350

However, the specialized model is only valid in connection with the geotechnical report and is to be seen as a supplement to it. With completion of the geotechnical report the "subject model ground" has to be handed over and should consist of the following 3D sub-models:

- Sub-model "Outcrop"
- Sub-model "Ground layers"
- Sub-model "Homogeneous areas"
- Sub-model "Groundwater"

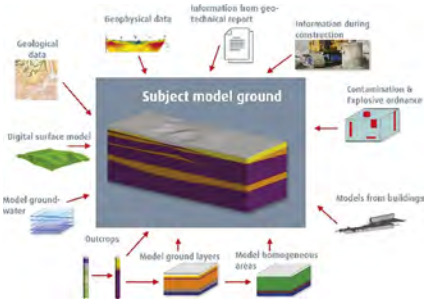

Figure 1. Information needed to build a 3D ground model.

3 APPLICATION EXAMPLES

There are many software packages available on the market, some with very different workflows and capabilities for basic 3D ground modeling. In the context of this article, application examples will be shown with two software solutions that differ significantly from each other in terms of their basic structure.

3.1 *3D ground model with Autodesk Civil 3D*

Autodesk programs have already been used for a long time to create plans, so the program is already available in many engineering companies and the step of acquisition or the decision for the Civil 3D add-on is made much easier.

Due to the individual programming of Dynamo scripts, importing and further editing of the specialist data in Civil 3D is very convenient. For example, investigation data can be automatically imported as 3D cylinders from a CSV or XLSX file. In principle, there are many possibilities for automated processing. However, the creation of dynamo scripts requires a significant amount of prior knowledge in programming as well as a high time requirement - especially for the first projects in which a 3D ground model is to be created.

The creation of solids or ground layers, on the other hand, is quite complicated and requires time-consuming post-processing (Figure 2). Attributes can be attached to the individual solids by creating individual property sets and exported to the IFC file format (openBIM) together with the geometry.

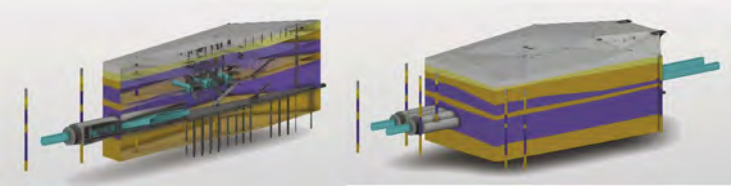

Figure 2. 3D ground model of a deep construction pit with Civil 3D.

A major advantage of Civil 3D is the possibility of automated coordinate transformation. Here, all the different basic and project data can be transferred into a uniform coordinate system specified by the employer. This enables the spatial representation of the ground-structure interaction as well as the early detection of possible collisions. The import of structures such as tunnels, station structures or bridges is easily possible using standard Autodesk formats (Figure 2). This aspect is a big plus especially with regard to public relations and the early involvement of the population in large projects.

Civil 3D is designed for the planning of infrastructure projects and is not specialized for the creation of 3D ground models. However, the software complements special ground modeling programs very well due to its additional functions (e.g. coordinate transformation).

It has been shown that Civil 3D is a good software alternative for spatially limited project areas. For larger projects with more complex layered structure (faults, geological lenses, etc.) and large project sections, it is advisable to work with a special software solutions for 3D ground modeling.

3.2 *3D ground model with Leapfrog*

Leapfrog Works is a software specialized in the construction of 3D ground models. With Leapfrog, complex and very large 3D ground models can be created. The software is probably not one of the standard programs used in medium-sized engineering companies. The field of application of the software is limited to the creation of 3D ground models, so that the economic efficiency must also be weighed up when purchasing the software.

The software is clearly and logically structured due to the project tree, so that the program can be used without much previous experience. The automatic modeling of individual bore profiles to form connecting ground layers is much easier than with Civil 3D, and the attribution of the solids is also intuitive (Figure 3). However, the flexibility in importing and attributing outcrop data is more limited than with Civil 3D and automatic coordinate transformation is not possible.

However, even this program has reached its limits in the case of complex geological conditions. If there are long tracks with a strong tectonic desintegration (e.g. up- & downdip, horst- & trench structures), the automated modeling of the ground layers works only conditionally. Here, for example, each individual tectonic plateau must be represented as a separate submodel, which ultimately significantly increases the amount of work involved in modeling but especially in attributing each individual layer (Figure 3). To minimize this effort, again the import of the ground layer model can be done in Civil 3D or Revit, in which the further steps like attribution and data export can be done in a more automated way.

Similar to Civil 3D, the 3D models of the planned structures can be integrated in the program in order to obtain a clear visualization at an early stage of the project and, if necessary, to identify critical collisions.

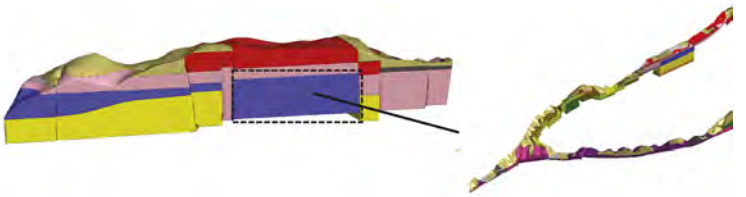

Figure 3. 3D ground model of a tunnel track with Leapfrog.

3.3 *Conclusion software programs (Advantages & Disadvantages)*

Basically, the programs mentioned are both suitable for the creation of a 3D ground model, whereby each software has its strengths in different areas. Which software is used most sensibly also depends to a large extent on the project conditions. Here, the size of the project area to be modeled and the complexity of the subsurface conditions are the most important factors.

In the case of long tracks, such as in large-scale infrastructure projects, the use of Leapfrog is the best option. If the ground model must include a large number of geological layers as well as tectonic structures, the use of software specially developed for ground modeling is recommended. This is often the case, for example, in tunnel construction projects, where the tunnel gradient is well below the ground surface and the complete layer structure from the ground level to the gradient must therefore be represented in the model.

The strengths of 3D construction modeling with Civil 3D lie in its high flexibility due to the programming of dynamo scripts for the automated import of technical data and the attribution of layers. It has been shown that especially complex construction projects with a limited project size, such as deep excavations, can be modeled optimally.

4 CONCLUSION AND OUTLOOK

The majority of projects that have to implement the BIM method and the 3D ground model in accordance with the requirements of the state, are in the preliminary planning stage or in an early phase of planning. In many cases, the planner has not yet been named, so that the continuous coordination process between the geotechnical expert and the planner cannot take place with regard to the required specialist data and, above all, their depth of detail and data format. Thus, the "subject model ground" is often created so far without knowing exactly whether the planner can continue to use the model in this form or which aspects should be worked on more intensively or less intensively. The issue of subsequent data exchange is also still unclear.

In addition, the requirements for BIM-supported planning are still strongly influenced by the areas of structural engineering and, in some cases, simply cannot be implemented, since the ground or ground layers cannot be predefined but are geometrically extremely heterogeneous volume elements.

The development of recommendations for 3D ground modeling within the framework of the BIM method and thus a standardization of the processing is decisive for the successful implementation of the BIM method.

The creation of the "subject model ground" can be accomplished in many ways and with a wide variety of software. There is a wide range of different software solutions, whereby each program still has its application limits and no model solution is available. Especially for medium-sized engineering companies, the aspect of economic efficiency must also be taken into account when using specialized software. Here, it must be weighed up whether sufficient BIM projects with the requirement of a 3D ground model can be acquired in the future to compensate for the partly very cost-intensive software.

Nevertheless, digitalization in geotechnical engineering offers many advantages that can simplify many processes. Anyone who does not want to loose the connection in the construction industry will inevitably have to deal with the topic of BIM and 3D ground modeling in the future.

REFERENCES

Bauer, J. 2022: Digitalisierung in der Geotechnik – Status Quo und aktuelle Entwicklungen. 13. Kolloquium Bauen in Boden und Fels, Technische Akademie Esslingen, 25–39.

Bundesministerium für Verkehr und Digitale Infrastruktur 2015: Stufenplan Digitales Planen und Bauen. Berlin.

Bundesministerium für Verkehr und Digitale Infrastruktur 2019: Handreichung und Leitfäden – Teil 1 : Grundlagen und BIM-Gesamtprozess. Berlin.

Deutsche Bahn AG 2022: BIM-Strategie: Implementierung von Building Information Modelling (BIM) im Vorstandsressort Infrastruktur der Deutschen Bahn AG. DB AG.- Digitales Planen und Bauen von Infrastrukturprojekten (KM).

Henkel, J., Möller, O. & Querfurth, T. 2021: BIM in der Geotechnik. Building Smart Deutschland.

Molzahn, M., Bauer, J., Henke, S. & Tilger, K. 2021: Das Fachmodell Baugrund – Empfehlung des Arbeitskreises 2.14 der DGGT "Digitalisierung in der Geotechnik". Geotechnik, 44, 1.

Stütz, D. & Herten, M. 2020: Evaluation von Software zur Generierung von Baugrundschichtenmodellen. Geotechnik, 43, 4.

Norwegian Geotechnical Institute 2020: BIM for GeoScience Webinars.

Schmitt, J., Cortese, C., Michael, J. & Meißner, S. 2022: Parametrisierung und Attribuierung von BIM-Fachmodellen für Aufgabenstellungen aus dem Bereich der Geotechnik und des Tunnelbaus. 13. Kolloquium Bauen in Boden und Fels, Technische Akademie Esslingen, 351–360.

Tawelian, L. & Mickovski, S. 2016: The implementation of geotechnical data into the BIM process. Procedia Engineering, 143.

Wilfing, L. & Hausperger, T. 2022: Digitalisierung in der Geotechnik – Möglichkeiten und Herausforderungen. 13. Kolloquium Bauen in Boden und Fels, Technische Akademie Esslingen, 25–39.

Smart Geotechnics for Smart Societies – Zhussupbekov, Sarsembayeva & Kaliakin (Eds)
© 2023 The Author(s), ISBN 978-1-003-29912-7
Open Access: www.taylorfrancis.com, CC BY-NC-ND 4.0 license

Laboratory study on soil properties of natural Iraqi clay

Rula Fuad Ibrahim, Mohammed Y. Fattah & Nahla M. Salim
Civil Engineering Department, University of Technology, Baghdad, Iraq

ABSTRACT: The aim of this research is to gain a more thorough understanding of how soft clays can be modeled and predicted more accurately with respect to primary consolidation settlements by using finite element analysis, and how to cope with uncertainties that follow the selection of soil parameters drawn from standard soil investigation reports. The natural soil used in this study is a brown soft clay soil brought from Al- Sadder site east of Baghdad city. Standard tests were performed to determine the physical and chemical properties of the soil. The grain size distribution of the soil used is which reveals that the soil is composed of (7%) sand, (38%) silt and (55 %) clay. The consistency limit tests include liquid limit and plastic limit tests of soil by using the Casagrande apparatus in accordance with ASTM D 4318 standard procedure. Soil classification was (CL) according to plasticity chart.

Keywords: Soft soil, properties, laboratory, material parameters

1 INTRODUCTION

Soft clays are defined as cohesive soils whose water content is higher than its liquid limit. Soft clays are well known for their low strength and high compressibility. Usually, due to sedimentary process on different environment, both physical and engineering properties of the clays (namely void ratio, water content, grain size distribution, compressibility, permeability and strength have been calculated. Furthermore, they exhibit high compressibility (including an important secondary consolidation), reduced strength, low permeability and compactness, and consequently low quality for construction. Terzaghi and Peck (1967), stated that clay is considered as very soft if its unconfined compressive strength is less than 25 kPa and as soft when the strength is in the range of 25 to 50 kPa.Brand and Brenner (1981), specified that the identification and classification of a soft clay should be based on the following type of information:

1. The geological history of the deposit.
2. The water content and the Atterberg limits.
3. A description based on a visual study of the fabric of clay in a wet and a partly dried out condition.
4. The results of one or several in-situ vane tests.
5. The results of consolidation tests for evaluation the shape of the e-log p curve.

The determination of soil properties of soft soils requires undisturbed samples of high quality. The quality of the samples depends on the sampling, storage and preparation techniques. All the apparatus so far developed for sampling from the surface are based on the same principle, which is to push a tube in the soft soil layer. When a soil is exposed to a certain amount of load, it tends deform in the direction of the application of the load. The type and value of deformation differ from one soil type to another. For instance, soft soil tends to deform in a different manner when compared to stiff soil

DOI: 10.1201/9781003299127-351

through application of the same amount of load. The deformation property of soil is dependent on the origin of the soil, the structure of the soil particles, the bond between particles, water content and so on. (Gustafsson, 2011). A field and laboratory evaluation of a soft clay southern Iraq was presented by Fattah et al. (2006). The study described the geotechnical properties of normally consolidated Garmat Ali clay located at the meeting of the Tigris and Euphrates rivers southern Iraq, to form Shatt Al–Arab River which flows southward entering the Arabian Gulf. They presented the data developed from the field investigations performed at the Garmat Ali site of the water injection project in Rumaila. Namely, the data of boring explorations which include the results of field tests such as Dutch cone tests, standard penetration tests, vane shear tests and field density tests, in addition to the results of laboratory tests on samples taken from the site. The subsurface conditions in this area indicated the presence of a deep layer 15 m of soft clay. Several correlations were obtained from the field and laboratory properties of the soil.. From these relationships, several correlations were obtained from which prediction for geotechnical properties of soft clays can be made.The engineering properties of surface layer on very soft clay of the south coast in Korea presented by Jung et al., (2006). They evaluated the undrained shear strength of very soft clay layer in the south coast area to investigate engineering characteristics of in situ clay and dredged-reclaimed clay by various test methods. Results obtained by standard penetration test, field vane test, piezocone penetration test and dynamic cone penetrometer test were compared.It was concluded that when undrained shear strengths depth are analyzed compared with penetration depth, in case of very soft grounds composed of cohesive soil, the strength of the upper surface layer was verified to be higher than that of the lower part. The strength of lower part is greater than that of upper part in the very soft grounds (Site D) composed of loose sandy soil.A Comparison between behavior of undisturbed and reconstituted Tunis soft clay was presented by Klai and Bouassida, (2009). A laboratory investigation was carried out on undisturbed specimens and remoulded specimens of Tunis soft clay preceded by initial consolidation under vertical stress of 50 kPa. Recorded laboratory data were collected from oedometric and triaxial tests. A comparison between characteristics of undisturbed and remoulded Tunis soft clay specimens was presented by Klai and Bouassida, (2009). A laboratory investigation was carried out on undisturbed specimens and remoulded specimens of Tunis soft clat preceded by intial consolidation under vertical stress of 50 kPa. Recorded laboratory data were collected from oedometric and triaxial tests. A comparision between characteristics of undisturbed and remoulded Tunis soft clay specimens was then discussed. Also the verification of well-known correlation between physical parameters and mechanical characteristics has been investigated. Back analysis of soft clay behavior under highway embankments was presented by Rémai, (2012), who discussed the most important goals of Hungary to develop high quality transportation links between different parts of the country, and (with special respect to the goals the European Union) between the surrounding countries. As early as the design phase the subsoil conditions must be taken into consideration (in some cases soil improvement techniques may be necessary), because proper embankment base is required to find a durable, safe, high quality, economical and environmentally friendly solution for highway embankment construction. Remai (2012) investidated the strength parameter determination of saturated, soft cohesive soils based on moder in situ test results. Investigation of recently used methods' reliability; proposal of new empirical relationship for soft clays in Hungary. Calculation possibilities of embankment settlements (i.e. the compression of the underlying soft clay layer) using analytical and finite element methods were also studied the objectives of the present paper is to determine the material properties for a sophisticated soil model called "Soft Soil Model" which is widely used in the software PLAXIS and other programs . A clayey soil from Baghdad city was selected. the objective of the present study to understand the geotechnical properties of clayey soil which are required to characterize the general relations among soil parameters.

2 EXPERIMENTAL WORK

The testing program includes determination of water content, specific gravity, particle size distribution by sieve analysis and hydrometer and Atterberg limits. The program also includes compaction test on soil samples, unconfined compression test, consolidation test and triaxial compression test on samples prepared at different water contents. The natural soil used in this study is a brown soft clay soil brought from Al-Sadder site east of Baghdad city. Standard tests were performed to determine the physical and chemical properties of the soil. The grain size distribution of the soil used is shown in Figure 1 which reveals that the soil is composed of (7%) sand, (38%) silt and (55 %) clay. The soils used in the study were classified in accordance with the AASHTO soil classification and the Unified Soil Classification System (USCS). These classifications are based on the consistency limits and the particle-size analysis. The consistency limit tests include liquid limit and plastic limit tests of soil by using the Casagrande apparatus in accordance with ASTM D 4318 standard procedure. Soil classification was (CL) according to plasticity chart. The classification according to the AASHTO system is A-7-5. Table 1 shows the results of these tests with physical properties of the soil used.The soil is classified as CL according to (USCS).

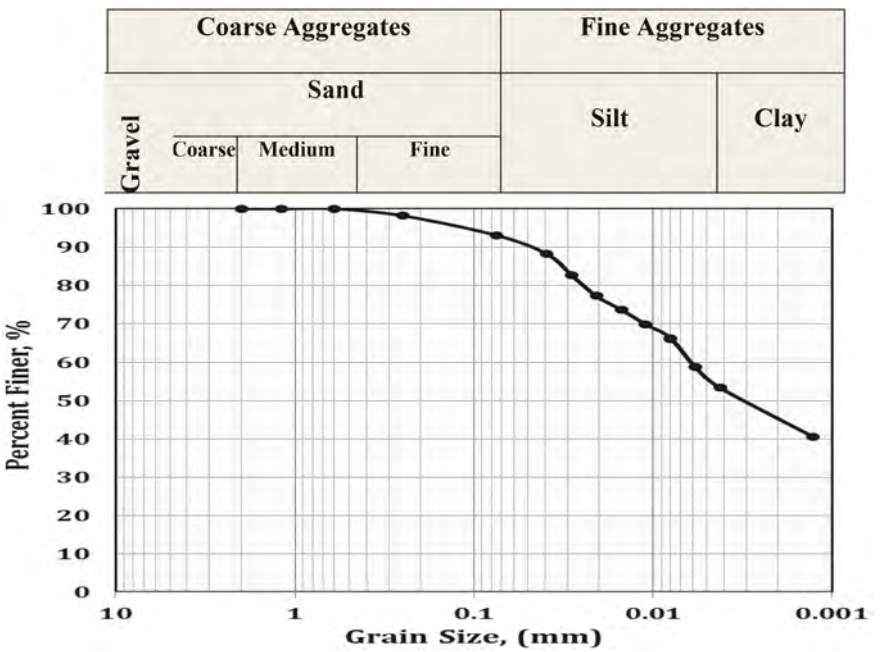

Figure 1. Grain size distribution of the soil tested.

Table 1. Physical properties of the soil used.

Physical properties	Index properties	Index values
Atterberg limits	Liquid limit, L.L (%)	33
	Plastic limit, P.L (%)	21
	Plasticity index P.I (%)	8
Grain size analysis	% sand (0.075-4.75) mm	6.9
	% silt (0.005-0.075) mm	38.1
	% clay (< 0.005) mm	55
Specific gravity G_s	----	2.723
Compaction test	Optimum moisture content	20 %
	Max γdry, kN/m^3	16.67

Regarding the standard Proctor test, the soil is compacted according to (ASTM D 698-00) in a mold of 4 in (101.6 mm) diameter and 4.584 in (116.43 mm) height in three layers with a hammer mass of 5.5 Ib (2.5 kg) dropped from a height of 12 in (305 mm) and the number of hammer blows for each layer is 25. The dry unit weight-moisture content relationship for the soil used is determined. Consolidation test was carried out on four samples with different water contents (15%, 20%, 25% and 33%) which represent dry side, optimum and wet side, respectirely. The last water contents 33% illustrates the layer of soil which is fully saturated. Consolidation test is very essential in soil mechanics for acquiring parameters in the calculation of consolidation settlements and evaluating stress history. The samples were performed at three water contents (dry, optimum and wet). According to NGI for equipment and procedure guidelines, it is possible to get reliable and credible parameters for very soft clays and other difficult parameters. The test was carried out according to ASTM D 2435 - Standard Test Method for One-Dimensional Consolidation properties of soils. Triaxial tests with the device have been one of the special equipment which is used to estimate reliable soil parameters to the maximum possible for an extensive range of geotechnical difficulties and soil types mainly for soft and quick clays, ASTM D2850:Standard Test Method for Unconsolidated Undrained Triaxial. Compression test on cohesive soils. When the deformation analysis of soil is performed by an advanced soil model in PLAXIS program, there is a need to a triaxial test. This is because advanced models require more input of material data, for instance hardening soil model requires input of three modules, such as Eoed obtained from consolidation test, E50 and Eur, which are obtained by performing a triaxial test. The triaxial test is a common test performed to determine the deformation properties, in this case compression modulus. In the test method, a cylindrical soil sample is placed into the test equipment, which is filled with water.Unconfined compressive strength tests (UCS) were performed according to (ASTM D 2166) on the raw soils at different moisture contents to draw the soil strength versus moisture content to evaluate the threshold moisture content at which soil strength treatment is required in the finite element model. All the samples for UCS tests were compacted in 3 layers with 25 number of blows/layer to achieve approximately uniform energy that is equivalent to standard Proctor test (12.4 ft.lb/ft^3). The number of blows per layer was determined by equating the compacting energy from 3 layers and 25 number of blows/layer of standard Proctor test with the energy produced by three layers of soils in 2.8 inch (71.12 mm) diameter and 5.6 inch (142.24 mm) high mold while keeping the hammer weight as well as drop height constant.

3 RESULTS AND DISCUSSION

The soil has predominately clay particles with mineralogy test indicating primarily kaolinite and halloysite. The moisture-dry unit weight relation showed high values for maximum dry unit weight in accordance to energy applied on the sample. The results can be shown in Table 2. The shape of compaction curves for standard Proctor compaction showed a single peak curve, Figure 2. The decrease in dry unit weight with increase in moisture content (at about 5%) can be attributed to the capillary tension effect. At lower moisture contents, the capillary tension in the pore water inhibits the tendency of the soil particles to move around and be densely compacted, (Das, 2002).

Table 2. Summary of compaction test results at water contents of 15%, 20%, 25% and 33%.

Water content, %	15%	20%	25%	33%
Maximum dry unit weight, (kN/m^3)	15.93	16.67	16.01	14.67

The maximum dry unit weight was found equal to 16.67 kN/m^3 at water content 20%. This method could be more accurate to determine the unit weight for soft soils with some fines.

Figure 3 and Table 3 present a summary of the results of consolidation test on samples prepared at different water contents. The coefficient of consolidation C_v was determined by Casagrandi method at a pressure of 200 kN/m^2.

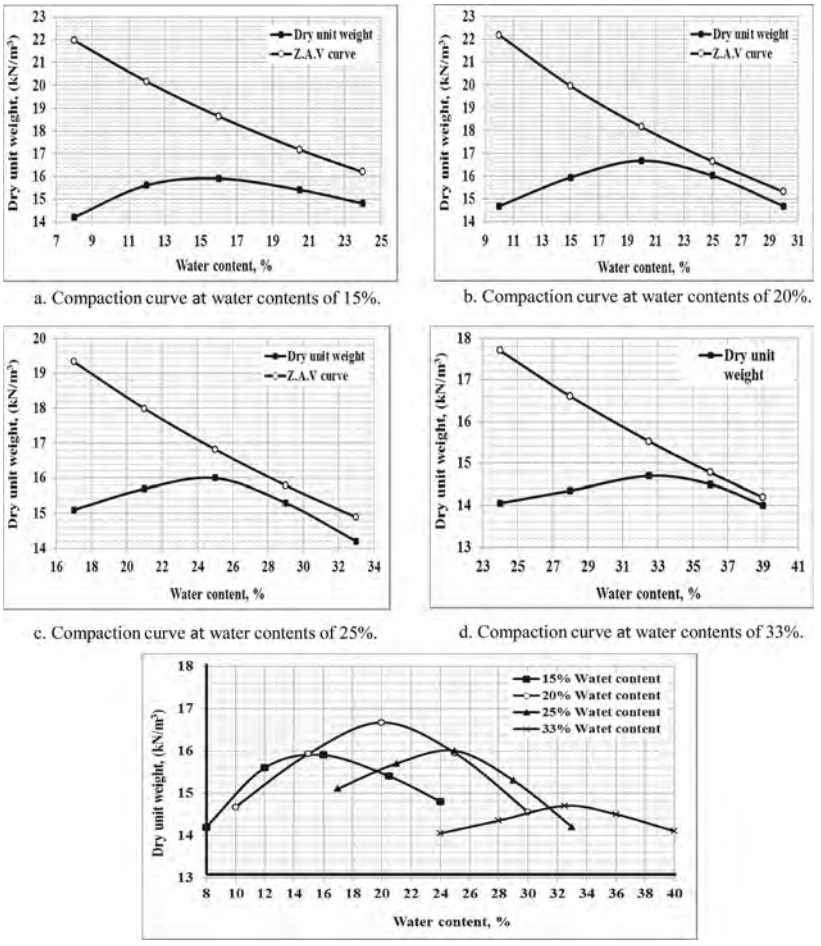

Figure 2. Compaction curves for all samples.

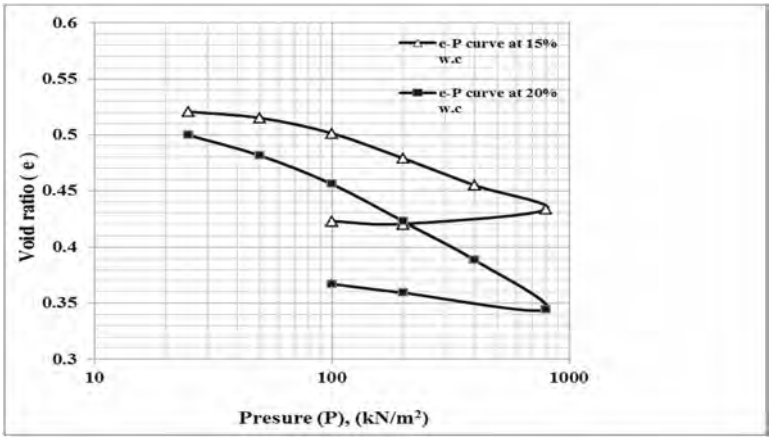

Figure 3. Void ratio versus effective stress curves from the consolidation test on samples prepared at different water contents.

Table 3. Summary of consolidation test results on samples at different initial water contents.

Properties	Water content, %			
	15%	20%	25%	33%
av, (m^2/kN)	0.0002	0.00023	0.0005	0.0003
mv, (m^2/kN)	0.0001	0.0002	0.0003	0.0002
C_c	0.077	0.112	0.199	0.128
C_r	0.008	0.026	0.038	0.032
C_v, (cm^2/min)	0.007	0.013	0.016	0.013
λ	0.034	0.049	0.087	0.056
λ*	0.022	0.032	0.057	0.037
κ	0.0695	0.023	0.033	0.027
κ*	0.0456	0.015	0.021	0.018
E_{oed}, (kPa)	18462	13750	8718	1000

Figures below from (4) to (7) present relationships between the dail reading and time at deffernt water contents:

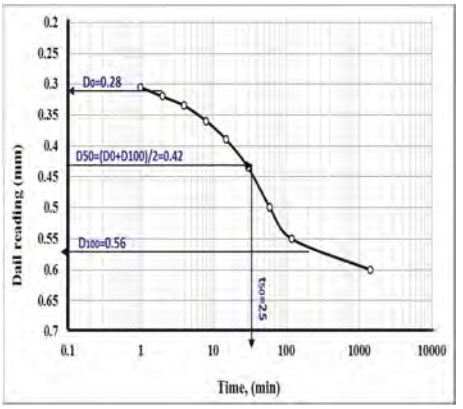

Figure 4. Dial reading versus time curve from the consolidation test at 15% initial water content.

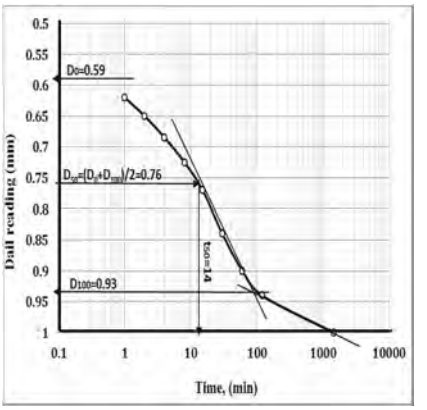

Figure 5. Dial reading versus time curve from the consolidation test at 20% initial water content.

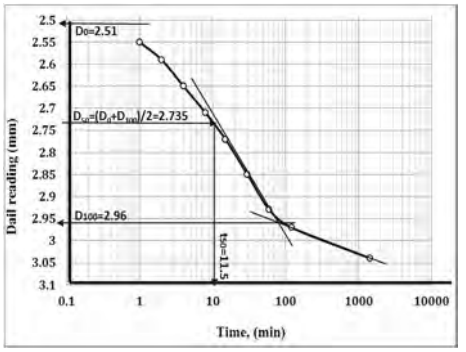

Figure 6. Dial reading versus time curve from the consolidation test at 25% initial water content.

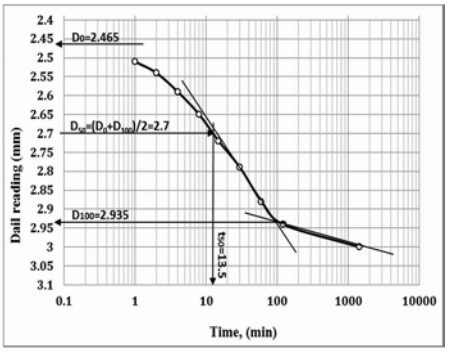

Figure 7. Dial reading versus time curve from the consolidation test at 33% initial water content.

Table 4 summarizes the results of unconfined compressive strength (UC test) at different water contents. The sample with an initial water content of 15% showed a maximum deviator stress value of 89 kN/m^2. The sample with 20% of water content failed at 64.6 kN/m^2. The sample with 25% of water content failed at 28.6 kN/m^2. These unconfined compressive strength values (28.6 and 89.0) kN/m^2 correspond to a soil soft consistency.

Table 4. Summary of unconfined compression strength test results for samples prepared at water contents of 15%, 20% and 25%.

	properties	
Water content	Qu (kpa)	Cu = Qu/2
15%	89	44.5
20%	64.6	32.3
25%	28.6	14.3

The Mohr-Coulomb failure criterion was used to establish the relation between shear strength parameters, as illustrated in Figures 10 to 12 at different water contents. From these values, higher strength can be achieved at water content is 15% (C_u = 88 kPa), and there was no change on angle of internal friction (ϕ_u = 0). Table 5 presents a summary of the results.

Figures 12 to 14 present the deviator stress – axial strain relationships for these samples, from these figures, the tangent elastic modulus is obtaine.

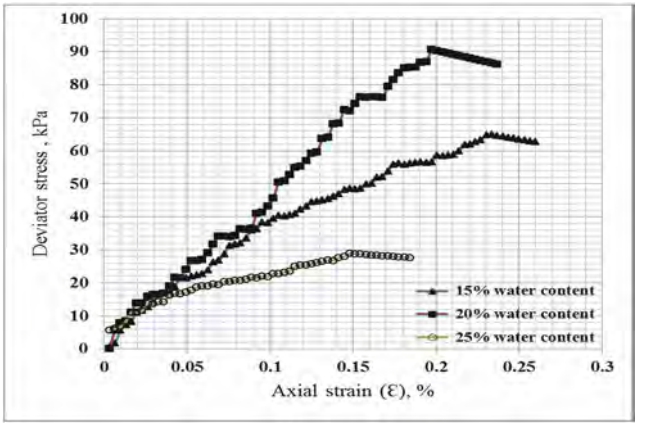

Figure 8. Present the deviator stress - strain relationships.

Table 5. Summary of traixial test results for samples prepared at initial water contents are 15%, 20% and 25%.

water content, %	C_u, kPa	ϕ_u
15%	88	0°
20%	63	0°
25%	43	0°

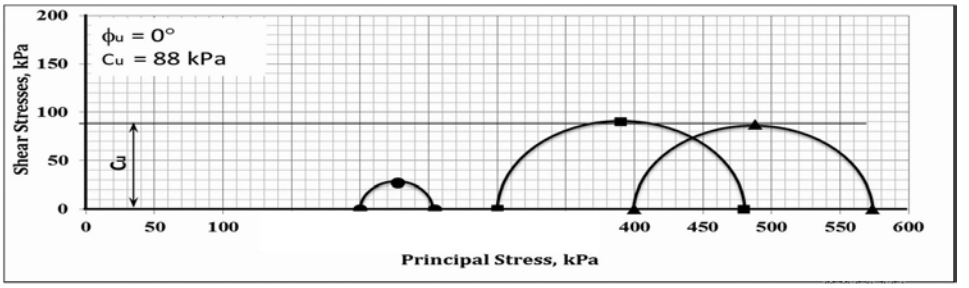

Figure 9. Total stress Mohr's circle and failure envelope ($\phi = 0$) obtained from triaxial UU test on soil prepared at water content of 15%.

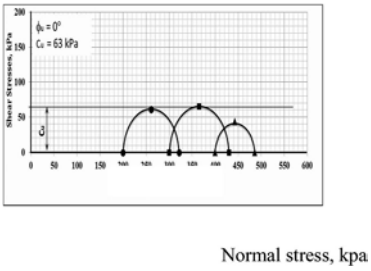

Figure 10. Total stress Mohr's circle and failure Envelope(ϕ=0) obtained from triaxial UU test On soil prepared at W.C of 20%.

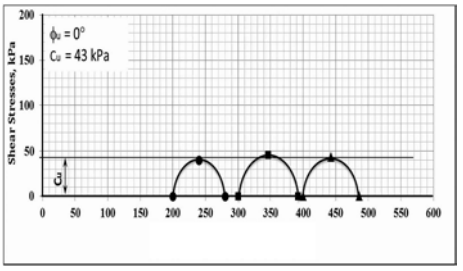

Figure 11. Total stress Mohr's circle Envelope (ϕ=0) obtained from triaxial test on soil prepared at W.C of 25%.

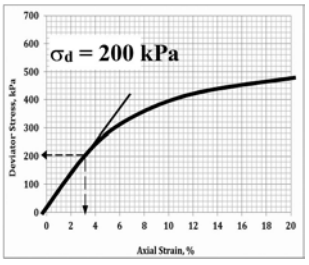

Figure 12. Deviator stress versus axial strain obtained from triaxial UU test on soil at water content of 20%.

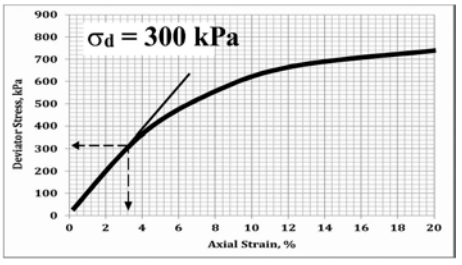

Figure 13. Deviator stress versus axial strain obtained from triaxial UU test on soil at water content of 15%.

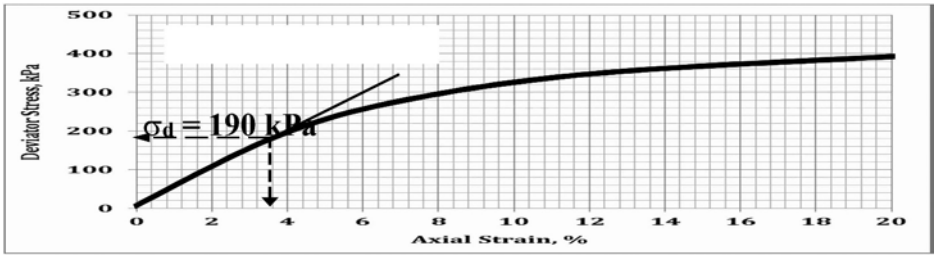

Figure 14. Deviator stress versus axial strain obtained from triaxial UU test on soil at water content of 25%.

4 CONCLUSIONS

1. Design parameters adopted by two failure criteria; Mohr-Coulomb and Soft Soil model were determined experimental for a soil from Baghdad city.
2. Initial water content of soil samples play controlling role in determination of soil strength and compressibility. As the water content is increased from 15% to 25%, the undrained cohesion is halved. On the other hand, the initial tanget modulus increases five times for same change in water content.

REFERENCES

American Association of State Highway and Transportation Officials. Standard method of test for resilient modulus of subgrade soils and untreated base/subbase materials, AASHTO designation 307, standard specifications for transportation materials and methods of sampling and testing, Part II Tests,2002.

ASTM D 2166-00, "Standard test method for laboratory determination of unconfined compressive strength of cohesive soil", American Society for Testing and Materials.

ASTM D 2435-04: "Standard test method for one-dimensional consolidation properties of soils using incremental loading", American Society for Testing and Materials.

ASTM D 2850-03: "Standard test method for unconsolidated-undrained triaxial compressiontest on cohesive soils", American Society for Testing and Materials.

ASTM D 4318-00, "Standard test methods for liquid limit, plastic limit, and plasticity index of soils", American Society for Testing and Materials.

ASTM D 698-00, "Standard test methods for laboratory compaction characteristics of using standard effort (600 kN-m/m^3)", American Society for Testing and Materials.

Brand, E. W. and Brenner, R. P., (1981), "Soft clay Engineering", Elsevier scientific publishing company, Amsterdam, pp.778.

Das, B.M., (2002), "Principles of geotechnical engineering", Fifth Edition, Australia; Brooks/Cole.

Fattah, M.Y., Baqir, H.H., and Al-Rawi, O.F., (2006), "Field and laboratory evaluation of a soft clay southern Iraq", Proceedings of the 4th Jordanian Civil Engineering Conference, 28-30 March 2006, Amman Jordan.

Jung, H. S., Cho, C. G. and Chun, B.S., (2006): "The engineering properties of surface layer on very soft clay of the south coast in Korea", Hanyang University, Seoul, South Korea.

Klai, M, and Bouassida, M., (2009), "Comparison between behaviour of undisturbed and reconstituted Tunis soft clay", Proc. 2nd Int. Conf. New Develop. In SMGE.Edit. Atalar et al. 28-30 May NEU Nicosia, pp. 414–419.

Plaxis, (2012): Plaxis 2D-Material Models Manual 2012. Plaxis B.V, Delft, Netherlands.

Rémai Zs., (2012), "Back analysis of soft clay behavior under highway embankments". Asian Journal of Civil Engineering – Building and Housing, Vol. 14, No. 1, pp. 31–47.

Terzaghi K., Peck R. B. (1967), "Soil mechanics in engineering practice", Second Edition, John Wiley and Sons, New York, USA.

Smart Geotechnics for Smart Societies – Zhussupbekov, Sarsembayeva & Kaliakin (Eds)
© 2023 The Author(s), ISBN 978-1-003-29912-7
Open Access: www.taylorfrancis.com, CC BY-NC-ND 4.0 license

Technology of geodetic works during modernization operating construction

M.Zh. Sagyndyk, Zh.M. Aukazhiyeva, M.Sh. Ishankulov & A.M. Sharapiev
L.N. Gumilyov Eurasian National University, Astana, Kazakhstan

ABSTRACT: The issues of application of laser scanning technology, tacheometry, satellite methods for obtaining information about underground and above-ground engineering structures on the example of operating oil producing enterprises are considered.

Keywords: Modernization of existing facilities, laser scanning, tacheometry, satellite methods

1 INTRODUCTION

It was planned to start the technical re-equipment of existing enterprises of the oil industry in Kazakhstan with a set of measures, ranging from the re-equipment of existing workshops in order to install new equipment necessary for the modernization of production to the modernization of existing facilities for launching information platforms that integrate the production and service sectors, while maintaining the existing functional purpose of the enterprise. At the same time, the technologies of geodetic works of are no small consequence.

2 METHODS

The area of the research object is about 2.5 km^2. As a result of the technical survey, the technically and technologically complex facilities of the enterprise were divided into three levels - low, medium and high complexity. The objects of low complexity included roads, trees, signposts, etc. Office and residential buildings, construction sites, etc. attributed to objects of medium complexity, and to objects of high complexity - various installations, pipes, valves, etc.

Geodetic monitoring of these objects, located in a remote and dangerous place for human life, consisted in the use of modern measuring instruments and in obtaining real-time information about the state of the entire object and its individual parts.

One of the important stages of geodetic monitoring in the study area was the reconstruction of the network. The network reconstruction was carried out not only to improve the accuracy of the network, the reliability of determining the parameters of the transformation between the global geocentric coordinate system, the state and local geodetic coordinate systems, but also to preserve the local coordinate system in which large-scale surveys were previously performed (Sysoeva, 2005).

Geodetic monitoring using modern measuring instruments to safely obtain information about an object located in a hard-to-reach place and dangerous to human life is currently widely used not only in the reconstruction of structures, but also in the modernization of production. Modern technologies have radically changed the conditions for conducting field and cameral.

DOI: 10.1201/9781003299127-352

At the same time, the density and conditions for fixing the points of the geodetic base, the error in the mutual position of the points in plan and in height ensure the subsequent thickening and development of the network to provide topographic surveys and solve other engineering and geodetic problems. And the use of satellite technologies and electronic total stations must correspond in accuracy to the terms of reference submitted by the customer.

The next important task is to identify areas of possible obstacles, distortions and radio interference. As a result of the reconnaissance, the position of the points planned earlier in the design process was clarified. Taking into account the clarifications, and also taking into account that geodetic observations will be carried out on the territory of the enterprise with objects of varying technical complexity, a rational method was chosen to create a geodetic base in the form of polygonometry moves. The constructed polygonometry passages will serve as a planned basis for the production of topographic and ground-based laser surveys.

Practical experience has shown that in places where the passage of radio signals from satellites is difficult, it is necessary to use the Leica TS10 total station. Points are fixed with temporary signs taking into account their safety at the time of filming. Satellite determinations were made by two (base and rover) GPS receivers Leica GPS1200. The measurement results are processed using the Credo software, which includes preprocessing, adjustment and correction of measurement errors.

Topographic and ground-based laser surveys based on the developed project were carried out to survey all above-ground and underground structures, marks, identification marks, installations and others. The result of the laser scanning process is shown in Figure 1.

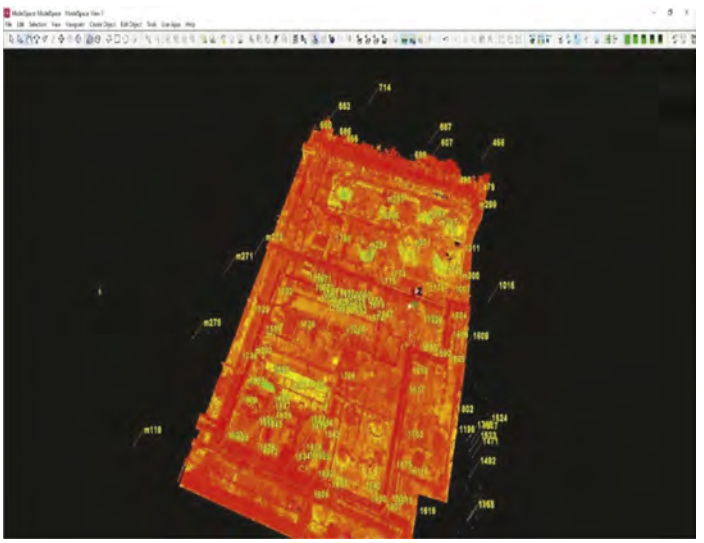

Figure 1. The result of the laser scanning process in intensity.

An electronic tacheometer is installed at the shooting point and, in sequence, special poles with reflectors are installed at the picket points. The measured data are processed using a special program to obtain the data necessary to build a digital terrain model or a topographic plan (Marfenko, 2004).

Scanning was performed by two scanners located close to each other, given that the scanning range of the RTC 360 (Figure 2) of 130 m is the maximum for equipment of this class.

One scanner was intended for scanning indoors, and the second for scanning outdoor installations. The location of the stations during scanning is shown in Figure 3.

Based on the developed technique, scanning inside the premises was carried out at medium density, and for scanning outdoor installations at high density. The measurement results were processed using the Leica Cyclone software package.

Figure 2. RTC 360 laser scanner.

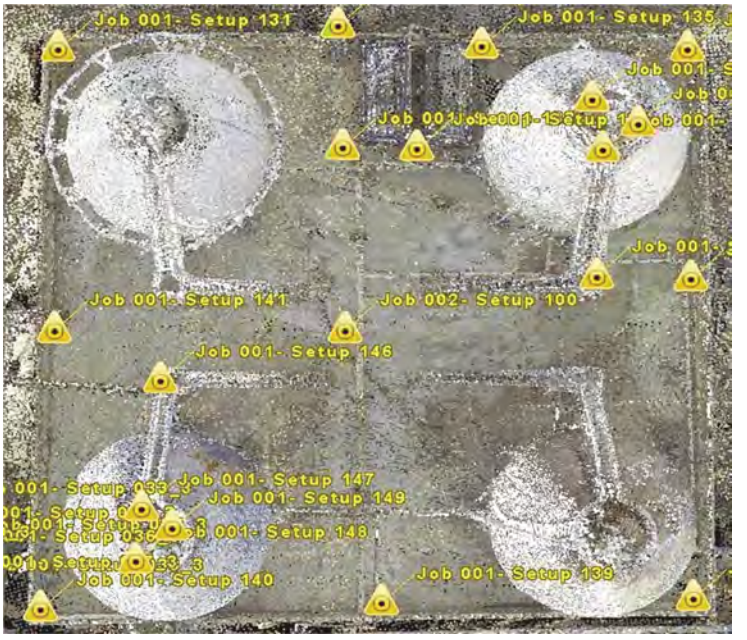

Figure 3. Location of scanner stations.

Control, stitching and binding of scans was carried out by marks, the centers of which were determined by the tacheometer.

3 RESULTS

The first stage of office work is data loading. The import is done via the Import RTC 360 data function. One of the main criteria for brand selection is brand display in the Leica Cyclone software. The brand display error occurs during the process of brand recognition by the program. Sometimes crosshairs in brick buildings can be recognized as a mark.

The next stage of in-office processing is cleaning the scans from noise and checking them for ghosting. Scans are cleaned in Model Space. Noise is a cloud of points that occur in various places. Noises also arise from hot fumes released by industrial facilities. Frequently encountered noises include noises located on power cables. Noise points are shown in Figure 4.

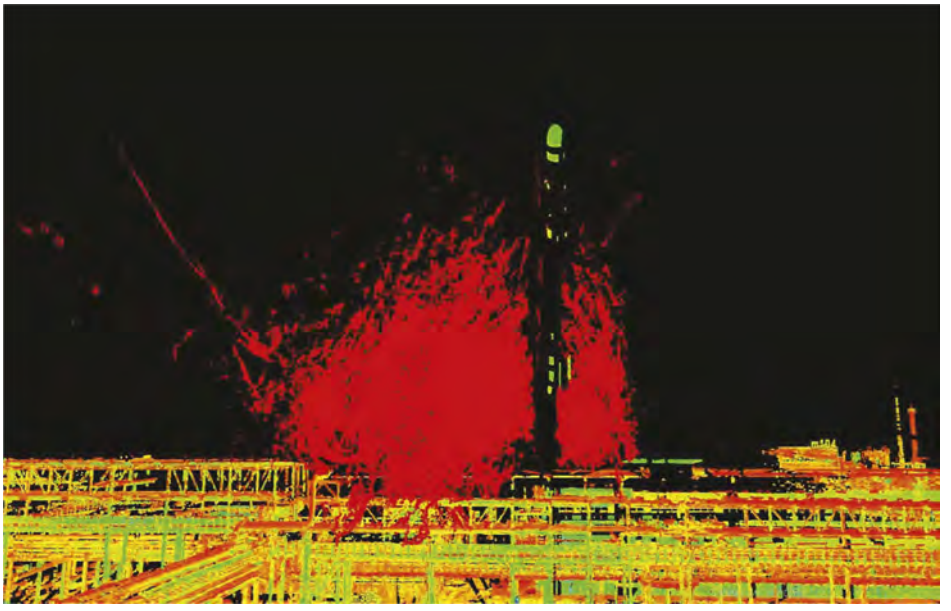

Figure 4. Noise points.

4 DISCUSSION

The shooting process depends on various external conditions that must be taken into account in the process of work. When conducting ground-based laser surveys in an industrial area, it is necessary to pay attention to three main factors that affect the final result of the survey.

4.1 *The content of vapors and dust in the air*

In industrial facilities, fumes and dust are often present in the air. When scanning, errors occur, the so-called noise, due to the fact that these particles have a density. Noise occurs, as a rule, when the scanner beams collide with particles of steam or dust. This is a big hindrance, because sometimes these particles do not allow you to get data about the object behind them. Therefore, there is a need to clarify the operating time of the structure, and minimize this factor.

4.2 *Inhomogeneous surfaces*

The presence of heterogeneous surfaces in the industrial zone is one of the main factors. An inhomogeneous surface is a surface that has the ability to reflect. Heterogeneous surfaces also occur after precipitation. They are most often represented on scans as noise covering objects or below the scanner horizon.

4.3 *Scanner stability and vibration*

The location of the scanner on the surface plays a huge role in the shooting process. At the slightest vibration, a systematic shift can occur, which will lead to errors in the overall system. This problem can be averaged during data processing, or duplicate scans can be eliminated.

It is possible to indicate in advance the areas where a large amount of noise and various errors may occur, taking into account these factors.

The most common type of noise occurs due to a weak signal when reflected from various metal structures. Usually, these noises appear at the edges of various objects, cables, pipes. These errors will appear on every scan. Elimination is done manually in the Leica Cyclone software, or by removing it by finding the noise intensity factor limit. In the course of the work, it was proved in a practical way that points in the intensity limit of 0.001 are noise points. This technique of eliminating noise within the one-hundredth limit is not correct when cleaning inside buildings, since the correct point clouds may be in this limit. Therefore, this method is used when cleaning the outside of buildings and on the street (Seredovich, 2009).

At an industrial facility, during the process of functioning of various structures, various pairs are emitted, which will be reflected on the scans as noise. This problem is solved by manually deleting a portion of the point cloud. In some cases, pairs can show the real location of the object, which should not be removed.

The considered noises arise due to a weak signal and the functioning of an industrial facility. Ambient type noise may also occur during the ground laser survey process. Noise can be a person caught in the frame, birds and other moving objects. This type of noise is removed manually by selecting them.

The next main work process is the stitching of scans. This operation is done through registration. Registration is a project that includes the functions of stitching, adding marks, and adjustment.

Stitching can be done using stamps, manual and automatic methods. Cross-linking can also be done using a visual method. These methods can be applied in different ways. At the beginning of work with registration and loading data into it, the stitching is performed by an automatic method. This method can be applied once for stitching a general contour. However, some scans may not be stitched together. To solve this problem, the manual stitching method is used. Thus, the main stitching of the network occurs when using two methods. At the same time, stitching using the visual method works much better inside buildings and structures.

The bonds obtained are evaluated by the quality of the crosslinking. The Error Vector indicator is responsible for this. It evaluates a single link between scans. Empirically, we decided to re-link all connections with an accuracy of more than 20 mm. These values allow you to say with what accuracy the scans were filed. The automatic stitching process ends after all inaccurate links have been corrected. Then the registration process starts. The registration process involves the adjustment and general stitching of the Model Space. Often, due to errors in scanning, there is a lack of links. The problem is solved by creating a single network of scans, which includes a serial network system. Further stitching is done using a manual method.

Manual stitching of scans is performed by finding scans with the same overlap. In this mode, 4 common points on two scans are selected, due to which the stitching is performed. In this case, the accuracy depends only on the performer.

The links created are passed through the optimization and registration operation. Links are created until registration is made. If the registration is successful, there is no need to add links. The performed registration stitches all scans and determines the mean square error of each connection relative to the total stitching by the least squares method. The error should be no more than 10 mm.

The network of scans must be adjusted if errors greater than 10 mm occur. Error reduction is achieved by creating additional links to the link that gives the error. The cause of the error may be double scans, or poor-quality communication. Thus, error reduction is achieved and equalization is performed

One effective method to control and verify links is to add tags. The marks serve as a control of the accuracy of the stitching, the accuracy of 10 mm, in case of exceeding, an error is searched for, and the erroneous connection is corrected. The next step is to create a general model that includes all the scans included in the registration. This process merges all Model Spaces into a single space. Thus, this model represents the result of the entire registration (Simonyan et al, 2019).

After obtaining the general model, it is landed on the coordinates. The coordinates are obtained by surveying marks located in different areas.

The final process for processing ground-based laser survey data in Leica Cyclone is the unification of the entire common point cloud. Unification is a process designed to average point clouds into a single one since there can be more than 7- or 8-point clouds per design. Unification averages all these clouds into one model. This results in one finished model for modeling.

5 CONCLUSION

The end result of the data was submitted for further modeling of the digital twin in the AVEVAEverything 3D program, the formation of a common plant database and the registration of obsolete equipment. The model is a single cloud of points of the entire plant, planted by coordinates in natural colors without errors and doubling. The resulting model will allow the integration of a digital twin system with PDM systems for full control of the plant, which will help simplify most of the work, as well as increase work efficiency and improve the quality of products.

REFERENCES

Sysoeva, O.I. 2005. Reconstruction of industrial facilities. Tutorial. Minsk: Belarusian National Technical University. 136 p.

Marfenko, S.V. 2004. Geodetic works during surveys and construction of industrial facilities. Tutorial. Moscow: MIGAC. 49 p.

Seredovich, V.A. 2009. Terrestrial laser scanning. Novosibirsk: SSGA. 261 p.

Simonyan, V.V., Shmelin, N.A., Zaitsev, A.K. 2015. Geodetic monitoring of buildings and structures. Moscow: MSCU.

Smart Geotechnics for Smart Societies – Zhussupbekov, Sarsembayeva & Kaliakin (Eds)
© 2023 The Author(s), ISBN 978-1-003-29912-7
Open Access: www.taylorfrancis.com, CC BY-NC-ND 4.0 license

Dynamic and spectral characteristics of the Kapchagay HPP dam

Vladimir Lapin, Yerken Aldachov, Nurakhmet Makish, Seric Aldachov & Alimzhan Ali
Kazakh Scientific Research and Design Institute of Civil Engineering and Architecture JSC, Almaty, Kazakhstan

ABSTRACT: For the first time, the instrumental records of accelerations at the Kapchagay HPP facilities (soil, HPP building and channel dam) are provided at two 5-magnitude earthquakes, the foci of which are located at different distances from these facilities. The task was set to study spectral characteristics of these earthquakes in the points of instrumental recordings and to determine the period of the dam channel vibrations. The β spectral curves have been constructed. It was found that the spectral curves are the least different for the case of the channel dam, the most– for the registration point on the soil. Dominant periods of soil vibrations under the influence of 2 earthquakes vary within the range of 0.15-0.55 sec.

The period of the spectrum maximum, approximately equal to the period of vibration of the dam -0.59-0.67 sec. Recommendations are provided for increasing the number of registration points.

Keywords: instrumental records, antiseismic construction, accelerograms, embankment dams, vibration period

1 INTRODUCTION

Ensuring the reliability of critical structures such as dams is an important and complex task. Especially it concerns the issues of seismic stability of dams of hydraulic structures made of earthen materials. Such structures can be erected from available and cheap local materials in almost any alignment and on any grounds. They can be of significant height up to 300 m and more, have good technical and economic indicators, high enough seismic stability and therefore are very common.

There is a sufficient number of works devoted to different aspects of investigation of dams of different types Biondi (2021), Wang (2018), Gu, (2015), Gu, (2021), Alibertia (2016), Valamenesh (2011), Zhong (2013), Cascone (2021), Bayraktar (2009). For example, Biondi (2021)] studies existing earth dams that were designed and constructed before the introduction of the seismic code, so it is of considerable interest to assess their seismic performance and operation conditions after seismic impacts. Probabilistic methods are used in Wang (2018) to estimate seismic stability of a 285.5 m high dam in China. Non-linear models and finite element schemes for calculating the dam in Italy are provided in Alibertia (2016) Topical issues of studying the effects of antiseismic strengthening with Fiber-Reinforced Poly/mer Material (FRP) attached to the surface of the dam in the design of dams are considered in Zhong (2013).

There are many HPP dams located in earthquake-prone areas in Kazakhstan. In East Kazakhstan, these are the Bukhtarma and Ust-Kamenogorsk HPPs, built in an area that was not previously considered earthquake-prone.

In Almaty region, the Kapchagay HPP with a capacity of 100 MW is located in the area of a seismicity of 7 MSK, supplying the entire region with cheap electricity. This Power Plant is an important element of Almaty's infrastructure, supplying it with electricity. The height of the channel dam is 49.0 m. It is the only Plant in the Republic of Kazakhstan that is equipped with a seismic engineering service station. The Plant was installed in 1977.

DOI: 10.1201/9781003299127-353

The Shardara HPP is located in an earthquake-prone area in the south of Kazakhstan.

The mud dam in Medeo mountain area near the city of Almaty is located in the 10-magnitude area.

Therefore, the field studies of the behavior of dams during earthquakes become important Krasnikov (1981).

A new Seismic Zoning Map has been introduced in the Republic of Kazakhstan, in which each territory corresponds to a seismic magnitude or peak acceleration value. These are the predicted amplitude characteristics in the territory of Hydroelectric Power Plants.

The actual task is to determine the spectral characteristics of seismic impacts on the territory of the Kapchagay HPP and dynamic characteristics of the 49 m high channel dam on the basis of the analysis of instrumental records of earthquakes. Such tasks were not solved earlier.

2 MATERIALS AND METHODS

The 49-meter-high Kapchagay Dam was built on the Ili River near the city of Kapshagay. In the area with a seismicity of 7 MSK. This Dam is the first dam in the world to be made of homogeneous fine-grained eolian sands (fractions less than 0.1 mm make up 80%). The upstream and downstream slopes base was determined by calculating their stability at constant accelerations along the height of the structure equal to $1.5K_{C7}$, where $K_{C7} = 0.025$ coefficient of seismicity, which characterizes the RMS of acceleration in fractions from the acceleration of free fall.

Laboratory and field (using explosions) studies of the stability of the structure of water-saturated eolian sands have shown that they are dynamically stable at vibration accelerations corresponding to a 7-magnitude earthquake Mikhailova (2013). However, this conclusion, due to lack of the critical acceleration method certainly needed to be clarified. Therefore, the instruments of the seismic engineering service station were installed to observe the dam.

Kazakh Scientific Research and Design Institute of Civil Engineering and Architecture JSC has the only engineering seismic service station in the Republic of Kazakhstan, which has 12 stations. Kapshagay Plant 15 was established in 1975 and is equipped with analog instruments.

In 2011, the well-known Kapshagay earthquake occurred, but due to specific location of the earthquake focus on the territory of the HPP the seismic vibrations were practically not felt. The earthquake has been registered on May 1, 2011 at 08 hours 31 minutes local time. Residents of Almaty felt the earthquake, the intensity of which was 4 - 5 MSK in the city. The earthquake magnitude is $m_b = 5.6$ and the focus depth is 20-23 km. Parameters of strong movements on the territory of Almaty according to the Geophysical Research Institute of the National Nuclear Center of the Republic of Kazakhstan demonstrated predominantly high-frequency seismic impacts with dominant periods of 0.13s. The intensity of impacts at the level of 8.4 cm/s^2 (KNDC plant was at a distance of 79 km from the epicenter) Mikhailova (2013).

Therefore, instrumental records of seismic Kapchagay HPP recorded in 1978 and 1979 were re-digitized for analysis.

On March 25, 1978 there was a strong Zhalanashtyup earthquake, which was felt on a large territory of Almaty region and Tyup district of Kyrgyzstan. Its epicenter was at a distance of 140 km from Almaty. This earthquake (magnitude about 6.5, the focues depth is 30-35 km) is the strongest for the last 40 years on the territory of Almaty region. In Kazakhstan it was strongest in Kegen (7-8 MSK), Narynkol (6-7 MSK) districts of Almaty Region. On the territory of Kyrgyzstan, the maximum intensity of the earthquake was observed in the Santash Collective Farm, Taldy-Su Settlement, etc. (about 7 MSK). (about 7 MSK) with gradual decrease to Tyup (about 6 MSK) and Przhevalsk (about 5 MSK) Zhunussov (1982).

A very strong earthquake on the territory of Kazakhstan occurred on September 25, 1979, 198 km north of Almaty (magnitude 5.6; intensity about 7 MSK; focus depth is 30-40 km), which was registered on the territory of the city of Almaty with a force of 4 MSK Zhunussov (1079). According to the results of MSK-64 scale macroseismic survey of damages of different building types the intensity of earthquake effect in Bakanas settlement (60 km from epicenter, the nearest settlement to the earthquake epicenter) made up 6-7 MSK. In Kapchagay city (120 km from the epicenter) the intensity of the earthquake according to the results of

macroseismic survey and instrumental data recorded at the Kapchagay seismic engineering service station reached 5 MSK. The Bakanas earthquake is peculiar in the location of the focues, which was located in a non-seismic area.

By the way, in Almaty and the surrounding areas, the Bakanas earthquake was recorded simultaneously by a large number of seismic engineering service stations installed on buildings of various design solutions and storeys erected on different soils.

3 RESULTS

Table 1 provides the maximum acceleration values for each of the components of the instrumental records for the case of the Zhalanashtyup earthquake, and– Bakanas in Table 2 (the accelerograms sample interval in Tables h). The soil registration points (fissured rocky soil), the HPP building (steel frame, second floor) and the channel dam crest (mark 49 m).

Instrumental recordings (accelerograms) were recorded on the soil, the HPP building and the channel dam.

Table 1. The maximum values of accelerations and parameters of accelerograms during an earthquake on March 23, 1978 (h=0.027 s).

	Acceleration	Effective duration		Spectrum maximum period
Component	cm/s^2	s	Spectral Coefficient	s
Soil-y	19	7.83	3.16	0.15
HPP	20	5.35	3.61	0.25
DAM	48	4.40	3.75	0.59

Table 2. The maximum values of accelerations and parameters of accelerograms during an earthquake on September 25, 1979 (h=0.028s).

	Acceleration	Effective duration		Spectrum maximum period
Component	cm/s^2	s	Spectral Coefficient	s
Soil-y	28.27	12.99	3.02	0.55
HPP	30.70	11.79	3.21	0.42
DAM	0.95	13.38	3.55	0.67

According to the current MSK-64(K) scale, a 5-magnitude earthquake corresponds to an acceleration interval of 16-35 cm/s^2 with a median value of 25 cm/s^2. Tables 1-2 show that the acceleration value on the soil falls within the specified interval. The same can be said about the registration point on the HPP building. The accelerations are very different on the dam crest. This is due to the fact that the dam is a structure with a rather complex spectrum. It should also be noted that the effective duration of the accelerogram of the Bakanas earthquake is 2-2.5 times higher than the similar characteristic of the Zhalanashtyup earthquake (the effective duration here is a period of time during which the acceleration amplitude is not less than half of the maximum value).

Attention should be paid to significant fluctuations of accelerations at the channel dam crest. At the same time, the foci are 120-135 km away from the Kapchagay HPP for both earthquakes. The acceleration maxima differ up to one and a half times for the other two registration points.

Figures 1 and 2 show the spectral curves of seismic events for three registration points (Figure 1 shows – Zhalanashtyup earthquake on March 23, 1978, Figure 2 shows– Bakanas earthquake on September 25, 1979). Spectral curves were determined for the magnitude of the vibration decrement equal to 0.3. The Figures 3-5 show spectral curves in pairs for each registration point for the convenience of comparison.

The smallest differences in the values of the spectral coefficient occur for the channel dam. The most spectral curves differ for the case of the registration point on the soil (Figure 3).

For the registration point on the channel dam, the values of the maximum period of the spectrum of 0.59-0.67 seconds are apparently close to the period of vibrations in the fundamental tone. The result was obtained for the first time.

The registration point in the HPP building is installed on a steel column of the 2nd floor, so the spread of the maximum values of the spectrum does not cause surprise (Figure 4).

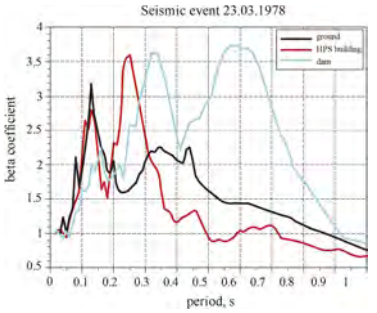

Figure 1. Zhalanashtyup earthquakeon March 23, 1978.

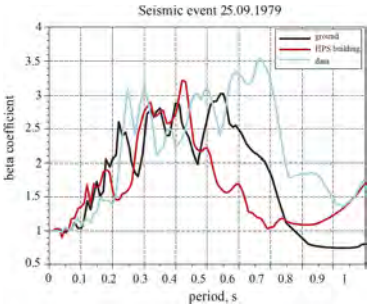

Figure 2. Bakanas earthquake on September 25, 1979.

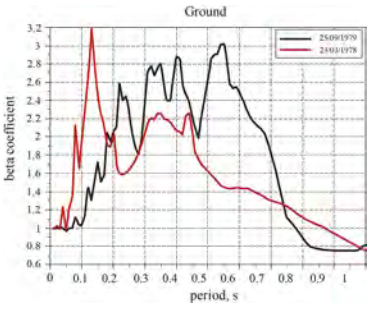

Figure 3. Spectral curves of seismic events, March 23, 1978 and September 25, 1979 (soil).

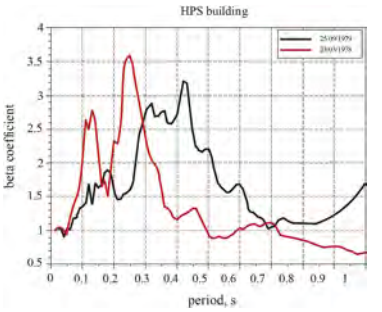

Figure 4. Spectral curves of seismic events, March 23, 1978 and September 25, 1979 (HPP building).

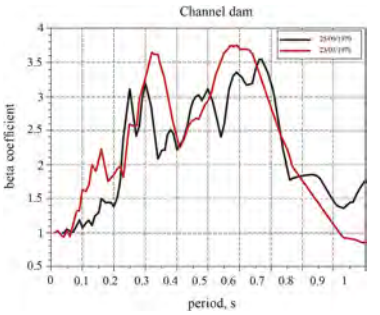

Figure 5. Spectral curves of seismic events, March 23, 1978 and September 25, 1979, (channel dam).

The maximum values of spectral curves for the registration point on the channel dam are the most stable. The same can be said about the maximum period of the spectrum. It is notable that the spectral curves for the two earthquakes here are generally similar in nature (Figure 5), although the maximum acceleration values differ by two orders of magnitude.

The spectrum of the recording on the soil for the case of the Bakanas earthquake are strongly indented (Figure 3). Instrumental recordings are quite different in spectral composition.

The greatest width of the spectrum occurs for accelerograms of the Bakanas and Zhalanashtyup earthquakes recorded on the channel dam crest.

According to accelerograms, it is hard to judge the influence of the water body on the amplitude and frequency composition of the impact. It is possible that the significant indentation of the spectrum is a consequence of the presence and impact of the water body.

Interesting results can also be obtained by decomposing instrumental records into Fourier series or by using classical correlation and spectral analysis.

4 DISCUSSION

It is interesting to assess the reliability of the estimation of the period of channel dam vibration. Lyamzina (1973) shows the results of experimental studies of the Orthokay rock-earth dam with a height of 54 meters. According to the results of the analysis of instrumental records of earthquakes, the vibration period was 0.45 seconds. Taking into account that at approximately the same height, a rock-earth dam is tougher than an embankment dam, the vibration period of an embankment dam of 0.59-0.67 seconds seems very reliable.

The results of the study can be used to perform calculations of this dam based on the application of a new regulatory framework in construction - according to Eurocode 8. At the same time, the peak acceleration value, taking into account the data of the Seismic Zoning Map of the Republic of Kazakhstan should be taken with a repeatability of 1 earthquake in 475 years – 0.15g, in 2475 years - 0.32g (g is the free fall acceleration).

5 CONCLUSIONS

1. For the first time the vibration periods of 0.59-0.67 sec were defined using instrumental records of seismic engineering service for the Kapchagay HPP channel dam.
2. The dominant periods of soil vibrations during the impact of 2 earthquakes vary within the range of 015-0.55 sec.
3. The seismic events of March 23, 1978 and September 25, 1979 represent 5-magnitude earthquakes in terms of acceleration on the soil.
4. The least spectral curves differ for the channel dam, the most - for the soil. Apparently, this is determined by spectral features of earthquakes.
5. For such a structure as the Kapchagay HPP the number of registration points should be doubled. It is necessary to add registration point on the middle of channel dam. It is necessary to set the registration point on the middle of the logging dam, where the hydraulic shock during seismic impact will be less noticeable. In addition, it is desirable to install recording devices on the water pipe – the underground tunnel.
6. In order to equip Hydroelectric Power Plants with seismic engineering service stations, it is advisable to develop a special normative and technical document (regulations) regulating the arrangement of devices (displacement, velocity and acceleration sensors) at such facilities.

REFERENCES

Alibertia, D., Casconea, E., Biondia, G. 2016. Seismic performance of the San Pietro dam Domenico, *Procedia Engineering* 158: 362–367 doi: 10.1016/j.proeng.2016.08.456

Bayraktar, A., Kartal, M. E., Basaga, H. B. 2009. Reservoir water effects on earthquake performance evaluation of Torul Concrete-Faced Rockfill Dam. *Water Science and Engineering*, 2(1): 43–57 doi:10.3882/j.issn.1674-2370.2009.01.005

Biondi, G., Cascone,E., Alibertia D., Rampello S. 2021. Screening-level analyses for the evaluation of the seismic performance of a zoned earth dam. *Engineering Geology* 280 105954 https://doi.org/10.1016/j.enggeo.2020.105954

Cascone, E., Biondi, G., Aliberti, D., Rampello, S. 2021. Effect of vertical input motion and excess pore pressures on the seismic performance of a zoned dam Soil Dynamics and Earthquake Engineering 142: 106566 https://doi.org/10.1016/j.soildyn.2020.106566

Gu, C. & Su,H. 2015. Review of research on long-term service and risk assessment of concrete dam engineering Scientific and Technological Progress in Water Conservancy and Hydropower, 35 (5); 1–12.
Gu, H, Yang, M, Gu, C, Huang, X. 2021. A factor mining model with optimized random forest for concrete dam deformation monitoring. *Water Science and Engine*ering 14(4): 330–336 https://doi.org/10.1016/j.wse.2021.10.004.
Krasnikov, N.D. 1981. Seismic stability of hydraulic structures made of earthen materials. Moscow: Energoizdat
Lyamzina, G.A. 1973. Dam influence on vibrations of gorge pit walls. *Proceedings of the Institute of Physics of the Earth, Academy of Sciences of the USSR* 15: 171–176.
Mikhailova, N.N. & Poleshko, N.N. 2013. Kapchagay earthquake on May 1, 2011. Vestnik (Newsletter) of the National Research Center of the Republic of Kazakhstan 1: 103–110.
Valamanesh, V., Estekanchi, H.E., Vafai, A., Ghaemian, M. 2011. Application of the endurance time method in seismic analysis of concrete gravity dams. *Scientia Iranica, Transactions A: Civil Engineering* 18: 326–337 doi:10.1016/j.scent.2011.05.039
Wang, R., Chen, L., Zhang, C. 2018. Seismic design of Xiluodu ultra-high arch dam. *Water Science and Engineering* 11(4): 288–301 https://doi.org/10.1016/j.wse.2019.01.002
Zhong, H., Wang, N., Lin, G. 2013. Seismic response of concrete gravity dam reinforced with FRP sheets on dam surface. Water Science and Engineering 6(4): 409–422 doi:10.3882/j.issn.1674-2370.2013.04.005
Zhunussov, T.Zh 1982 *Zhalanash-Tyup earthquake* Alma-Ata: Nauka
Zhunussov, T.Zh. & Vypryazhkin Yu.A. 1979. Instrumentation readings on the vibration of buildings in Alma-Ata during the Bakanas earthquake on September 25. *Sat. Structurs and onstructions earthquake stability research* 12(22): 87–93.

Smart Geotechnics for Smart Societies – Zhussupbekov, Sarsembayeva & Kaliakin (Eds)
© 2023 The Author(s), ISBN 978-1-003-29912-7
Open Access: www.taylorfrancis.com, CC BY-NC-ND 4.0 license

Geomonitoring of the foundation of a high-rise building applied fiber optics

A. Buranbayeva, A. Sarsembayeva & S.T. Mussakhanova
L.N. Gumilyov Eurasian National University, Astana, Kazakhstan

ABSTRACT: New technologies in building and high-rise monitoring make it possible to track damage and defects in existing structures and infrastructures. The need for timely detection of defects in building structures using fiber optic sensors is increasingly prompting planners, builders and facility managers to use the capabilities of a powerful system such as DFOSS. In addition to the well-known advantages, they are the most reliable in conveying the stress-strain state of the structure in the long term. The main objective of any construction project is safety for people, which can only be ensured by proper monitoring of the condition of the building, where the presentation and management of the resulting information on changes in the system and structure can be ensured with DFOSS.

1 INTRODUCTION

The condition may deteriorate over time, resulting in a serious and ongoing issue for the operating company. Evaluating the genuine state of crumbled structures is important for opportune distinguishing proof of deformities and settling on conclusions about suitable fixes.

Because of the enormous number of maturing frameworks, including noteworthy designs, observing the state of designs has started to assume a powerful part during the activity and upkeep period of the primary life cycle the board interaction.

SHM works with the observing and assessment of primary properties, which streamlines underlying upkeep costs and further develops underlying wellbeing [Buranbayeva, 2022].

Structures have various responses under various burdens during their life cycle, which can be estimated by utilizing SHM frameworks and sensors to acquire data about the changed boundaries and components. Observation and measurement of design, condition assessment, information management, planning and decision-making, repair execution, and evaluation of repair and maintenance performance are the primary stages of condition monitoring [Agdas, 2016], [Huston, 2016].

Utilizing a distributed fiber optic monitoring system will make structural condition assessment in sanitary monitoring more efficient and accurate. The construction sector can benefit greatly from DFOSS's use.

The limitation of a structure's deformations and/or stresses is frequently the foundation for engineering design standards. This is significant because deformation indicates the potential degree of damage that has occurred and is a measure of how close the construction material is to its strength capacity. This is significant on the grounds that disfigurement is a proportion of how close the material of development is to its solidarity limit, and hence shows the likely level of harm that has happened.

There is a long history of applying solid checking strategies to take care of structural designing issues. For instance, vibrating wire or metal foil strain checks are notable devices for estimating resist individual focuses in a construction. Because the strain distribution is a function of the end conditions and the applied load, they are typically suitable for determining the

DOI: 10.1201/9781003299127-354

complete strain profile within structural components like beams or columns. However, foundations, tunnels, and pipelines—all of which interact with the ground—are exempt from this.

Since the soil loads are dispersed in these situations, it is impossible to fully comprehend the structure's state without knowing the entire site strain profile [Soga, 2015]. Problems caused by soil heterogeneity, such as deformations, rotations, and unevenly distributed soil and structural force interaction forces, can be identified with the assistance of knowledge of the continuous deformation profile. Conventional pinpoint strain measurements can miss such problematic areas [Soga, 2014]. FO distributed strain sensing became a tool to provide continuous strain profiling and, as a result, enhance our comprehension of civil structures around the middle of the 2000s.

For more than a decade, DFOSS has been used to measure the strain in civil engineering structures. It is now used worldwide to monitor a variety of structures, including diaphragm walls, tunnels, bridges, piles, dams, embankments, and bridges.

DFOSS depends after backscattering when lights communicated along an optical fiber. One standard ticular part of the backscattered light is created by Brillouin dissipating. Anytime along a fiber, the recurrence of Brillouin backscattered light relies on the strain and temperature by then. Considering the impact of temperature thusly, the strain anyplace along a fiber can be reasoned by communicating beats of light down the fiber and dissecting the recurrence of backscattered light.

DFOSS presents a novel approach to strain measurement in comparison to the utilization of isolated strain gauges in that:

1. The continuous strain profile along a structural element is returned by DFOSS. It is possible for strain gauges to miss vital strain variations between gauges because they can only provide discrete pointwise readings.
2. Electromagnetic interference does not affect optical fiber backscattering.
3. Pure, inert and extremely stable silica forms the core of optical fibers. The filaments in this manner oppose consumption, don't taint the neighborhood climate and have a design life estimated regarding many years.

Optical filaments can work over a lot more extensive scope of temperatures than most electronic gadgets.

Because of their small size and lack of intrusion, optical fibers are simple to incorporate into both new and existing structures.

The total strain profile can be recuperated for a fiber extending a few kilometers, potentially supplanting a huge number of discrete sensors. Installation is greatly simplified by using a single cable.

Because of the continuous improvement of DFOSS read-out units, a DFOSS framework inslowed down presently can profit from potential upgraded estimation capacities later on.

2 ENGINEERING-GEOLOGICAL INVESTIGATION OF THE CONSTRUCTION SITE

The site of the experiment was in Astana city, in the basement of the tallest building complex in Central Asia - Abu Dhabi Plaza, 320 meters high. Abu Dhabi Plaza is a complex high-rise building with a retail and leisure podium and a hotel cluster at the base that rises to form a series of office and residential towers to the north – a creation of the famous British architect Norman Foster (Figure 1).

The raft construction process is shown in Figure 2, the complex consists of several buildings, where fiber optic cable monitoring was carried out in 3 of them, blocks R, Z, Y. Block R is the tallest building in the complex and is a 75-storey residential building with a 4-storey underground parking at the base. The foundation structure of the building consists of a pile raft including Auger Cast Piles 1,125 m and boring piles with a diameter of 1.2 to 1.5 meters (Figure 2).

The length of the piles varies depending on the height of blocks from 13 to 25 m from high-strength concrete with an exposure durability of 40 MPa. The raft is built form the C28/35 concrete. The maximum design excavation level for the construction of a raft for block R was 19.30 m. The basement floors consist of 4 levels from B1 to B4 of the lowest.

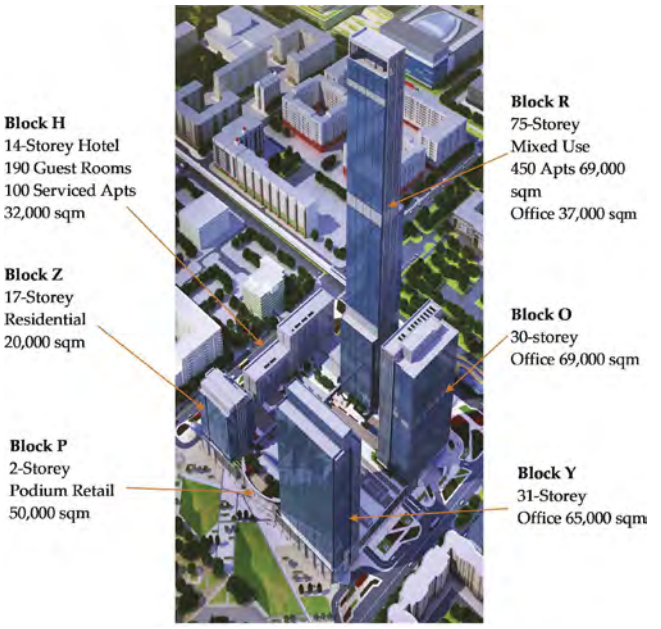

Figure 1. Abu Dhabi plaza building complex.

Figure 2. Construction site.

3 FIBER OPTIC MONITORING SYSTEM

3.1 *Design of distributed fiber optic strain sensing system (DFOSS)*

The proposed DFOSS system comprises a grid of fiber optic cable bonded to the B4 slab linked to an analyzer located in a temperature- and humidity-controlled room at B1 level.

On the B1 level, there is an analyzer of the monitoring system for temperature and strain data collected via distributed fiber optic strain sensing system (DFOSS) from B4 level (Figure 3). The applied DFOSS system transmits the signal via a grid of fiber optic cable to the B4 raft linked to an analyzer located in a temperature- and humidity-controlled room at B1 level.

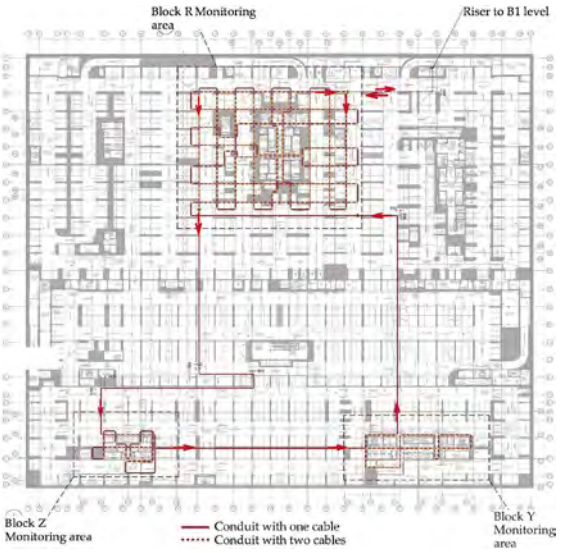

Figure 3. Part plan of cable routing in block R monitoring area on B4 raft.

3.2 *Analyzer and analyzer room*

The analyzer must operate within specified environmental conditions and so must be located inside a room whose temperature and humidity are controlled. The analyzer room will also accommodate the logging system and computer required to interface with the Internet and as such the room must be supplied with uninterrupted electrical power and a high-bandwidth Internet connection and must be sufficiently spacious for two operatives to work comfortably inside. A summary of the analyzer specification is presented in Table 1.

Table 1. Specification for analyser.

Parameter	Value
Spatial resolution	≤ 1.5 m
Optical budget	≥ 11 dB
Measurement resolution	≤ 22με
Distance range	≥ 2.09 km
Gauge length	≥ 2 m
Measurement range	≥ 1.5 %
Measurement interval	≤ 3hrs
Operational period	≥ 70 yrs
Data acquisition	Remote control and transmission via internet

Note – Optical budget includes both strain and temperature measurements cables configured in a loop

Particular consideration must be given to the routing of the fiber optic cables into the analyzer room from the riser used to route the cables to B4 level. The cables may be routed in channels cut into the B1 slab in a manner similar to the channels in the B4 slab. Running the channels through doorways instead of under walls would remove the need to demolish portions of blockwork wall to enable cable installation. Alternatively, the cables may be routed overhead via cable trays into the analyzer room (Figure 4); in this case blockwork at ceiling level will need to be removed for the cable to pass through any walls. Regardless of the routing method it is essential that the allowable curvature of the cable is not exceeded.

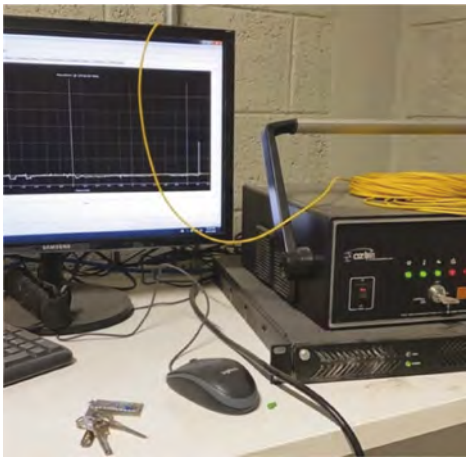

Figure 4. Monitoring room with typical analyser.

3.3 *Field results*

Emphasis in obtaining the results of the fiber optics was given to high-rise blocks, namely block R, where, as expected, the highest strain values of the fiber optic cable were obtained. C_T was found as 1.113MHz/°C, and Cε was equal to 0.054MHz/με. At the time of the measurements, the temperature field distribution was relatively stable and varied within + 4 +8°C over the entire area of the B4 level of block R (Figure 5). The location of areas with lower temperatures in the center of the building along the load-bearing walls of the core is explained by the greater thermal conductivity of reinforced concrete structures. Considering the depth of the raft -19 m and the allocation of the block R in the middle of the complex of buildings the ambient temperature did not affect to the results of the FO strain measurements during recording. Considering that the measurements were taken in February 2021, as well as the cold climate of Astana.

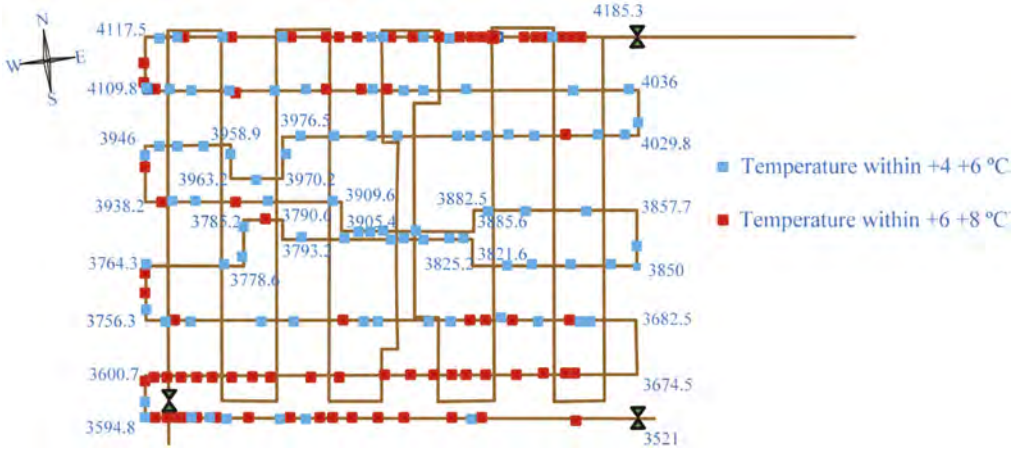

Figure 5. Temperature field distribution in block R.

As can be seen in Figure 6, the fiber optic results show alternating strain signs along the length of the fiber optic cable embedded in the raft of the lowest level B4 of block R. Compression deformations prevail in the central part of the building core, in the zone of

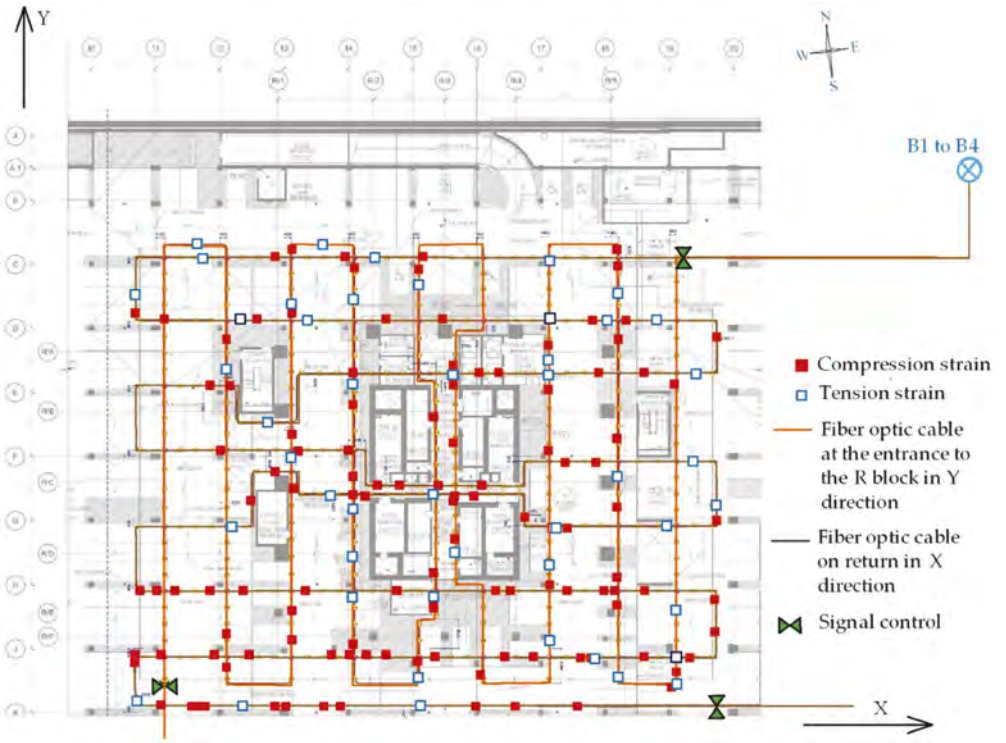

Figure 6. Fiber optic strain along the cable layout in the block R, level B4.

increased load from reinforced concrete load-bearing walls. Tensile deformations are most focused on the extreme axes, as well as near the joints of the columns. The interpretation of compression zones by values is shown in Figure 7 and tensile zones in Figure 8.

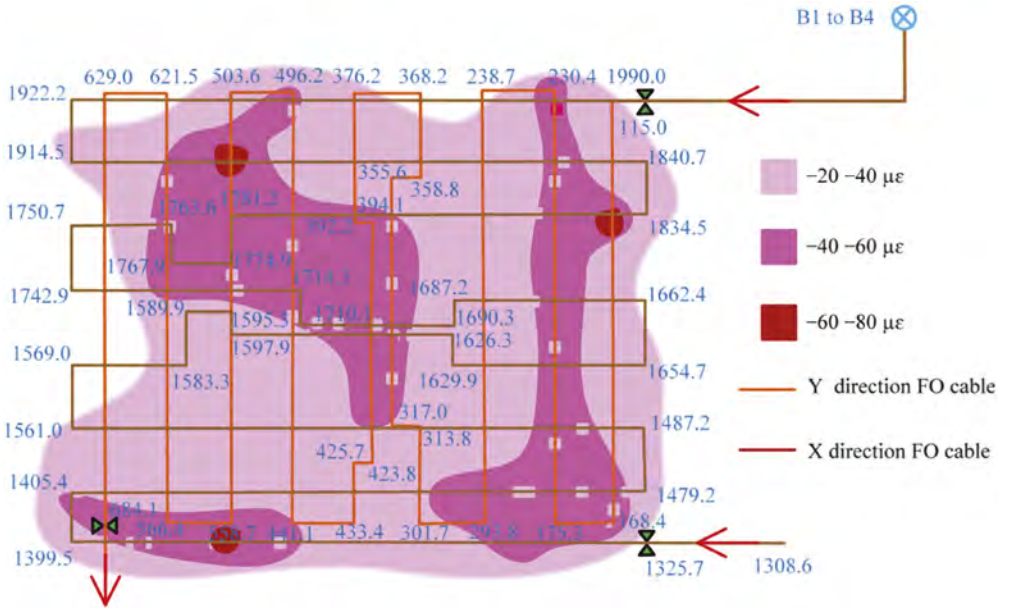

Figure 7. Zones subjected to compression strains.

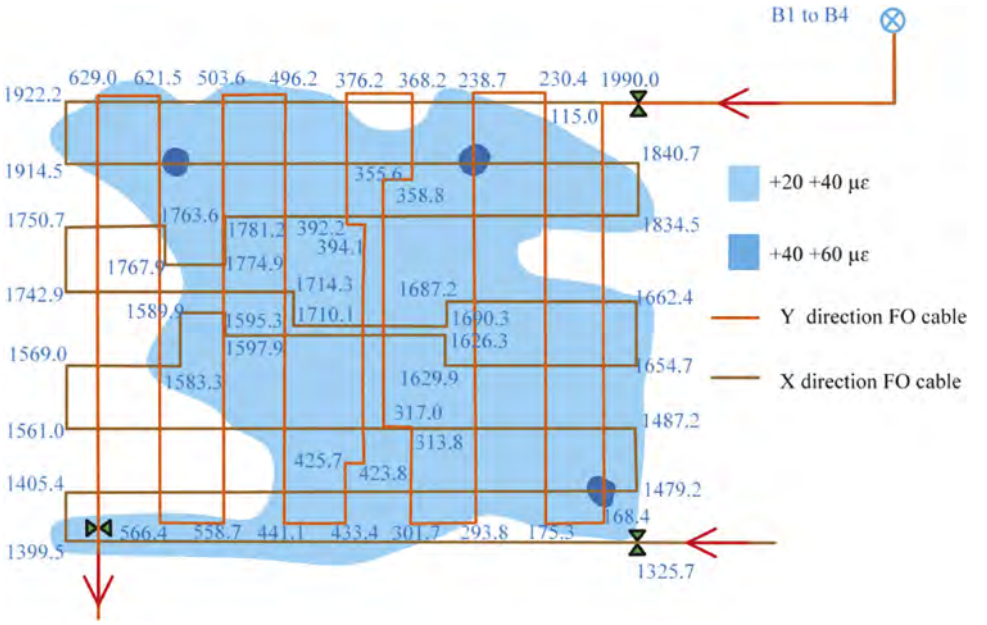

Figure 8. Zones subjected to tension strains.

Tension zones as indicated by Figure 8 are uniformly disseminated over values from −20 to −40 με, with a slight transcendence on the right (east) side of the structure. Individual spots of −40 to −60 με are once in a while situated along the external shape of the structure. Tensile stresses accumulate in more stable patterns in the building's center, north, and east [Buranbayeva, 2022].

4 CONCLUSION

The authors considered whether the distributed fiber optic strain sensing system technology could be used to monitor structures, using the Abu Dhabi Plaza complex's underground parking lot as an example in Astana's soil conditions. The technology enables you to evaluate the outcomes of geomonitoring in real time, ensuring the safe operation of underground buildings in the challenging engineering and geological conditions of Kazakhstan's capital.

The following conclusions were drawn as a result of the evaluation of the data used for structural health monitoring that was embedded in the raft plane of pile-raft foundations of a high-rise building at the beginning of its operation:

1. Fiber optic's monitoring made it possible to provide actual results of strains in the upper layer of the raft at the lowest level B4 of the high-rise 75-storey block of the Abu Dhabi Plaza building on multilayer soils of Astana city.
2. The compression strains were observed over the entire area of the building with values -20-40 με. A greater values of compression strain, -40-60 με, were registered in the center in the Y direction and along the eastern facade of the block R in the building core with some points up to - 60-80 με.
3. The tension strains are concentrated along the extreme axes of the building, with a predominance in the southern part of the R block, as well as in the immediate vicinity of the columns, in a range of + 20+40 με, with separate spots +40+60 με.
4. Individual patches of tension strains near the columns have been explained by the increased deflection of the raft under the application of a concentrated load (columns).

5. When a strain above 1000 με (1%) occurs, a basic structural analysis is recommended, above 1500 με (1.5%) a detailed structural analysis is required.
6. Fiber optic monitoring results at the time of testing did not exceed the permitted values for high-rise building operation; however, they characterized the general picture of the strain in the raft plane and make it possible to determine the initiation of cracks in concrete at an early stage.

ACKNOWLEDGEMENT

This work was funded by the Science Committee of the Ministry of Science and Higher Education of the Republic of Kazakhstan (Grant No. AP13268861).

REFERENCES

Buranbayeva, A. & Zhussupbekov, A. 2022. Design a Building Information Modeling (BIM) project concept in combination with foundation monitoring on the example of the Abu Dhabi Plaza construction project. BULLETIN of L.N. Gumilyov ENU. Technical Science and Technology Series, 1(138): 23–33.

Agdas, D. & Rice, J.A. & Martinez, J.R. 2016. Comparison of visual inspection and structural- health monitoring as bridge condition assessment methods. J. Perform. Constr. Facil., 30, 04015049.

Huston, D. & Burns, D. & Razinger, J. 2016. Structural health monitoring and maintenance aided by building information modelling and repair information tools. WIT Trans. Ecol. Environ., 204: 897–907.

Soga K. & Kwan V. & Pelecanos L. et al. 2015. The role of distributed sensing inunderstanding the engineering performance of geotechnical structures // Procced. 16th European conf. on Soil Mechanics and Geotechnical Engineering. – Edinburgh. – P. 13–48

Soga K. 2014. Understanding the realperformance of geotechnical structures using an innovativefibre optic distributed strain measurement technology // Rivista Italiana di Geotechnica. – Vol. 4: 7–48

Buranbayeva, A. 2022. Evaluation of the Structural Health Monitoring Results of the Applied Fiber Optics in the Pile-Raft Foundations of a High-Rise Building. Appl. Sci., 12, 11728. https://doi.org/10.3390/app122211728

Smart Geotechnics for Smart Societies – Zhussupbekov, Sarsembayeva & Kaliakin (Eds)
© 2023 The Author(s), ISBN 978-1-003-29912-7
Open Access: www.taylorfrancis.com, CC BY-NC-ND 4.0 license

BIM technologies - New design options in architecture

O.N. Semenyuk, U.D. Dyisebayev & V.S. Semenyuk
Gumilyov Eurasian National University, Kazakhstan

ABSTRACT: The difficulty and complexity of the problems solved in architectural design, the change in construction technologies, the development of new materials, require constant improvement of the methods of training in shaping, the widespread use of innovative systems for modeling buildings and structures, techniques and technical means in architectural creativity. The shaping of the future structure is of fundamental importance for the design. BIM is a comprehensive program that uses a common three-dimensional base for the model and tools, replenished and improved during the design process. BIM based on a parametric building model that combines 3D model and external data. Due to the interdependence of all elements, the model is correctly updated and allows you to automatically generate updated project documentation.

1 INTRODUCTION

Building Information Modeling (BIM) is a process that generates an information model of a building (structure), and for each stage there is a certain model that displays the amount of information processed (architectural, design, technological, economic) about a building or structure, to which all interested parties have access.

The conceptual model is a 3D sketch of the future building, which allows in the early stages of design to provide customers (investors, buyers) with a visually understandable concept of the future object (plans, facades, sections, bypasses).

This model quickly created and easily edited, which allows you quickly make changes at the initial stage of approval. BIM based on a parametric building model that combines 3D model and external data.

The ability to import the model into software packages (3ds Max and Lumion) allows you to quickly create high-quality photorealistic renders and animations.

The shaping of the future structure is of fundamental importance for the design. Traditional methods of solving this issue include the widest range of technical tools: manual sketch - clause, working layout, model in various 3D packages successfully imported into Revit.

In Revit Architecture, when searching for the shape of a building, you can immediately calculate very important characteristics for the project as areas and volumes, and their values will automatically change depending on the course of the simulation (Figure 1).

Mass elements allow you to perform tasks such as creating in-place or family-based instances of mass elements specific to individual project parameters, creating mass element families associated with commonly used building volumes.

You can change the materials, shapes, and relationships between the mass elements that represent the main components of a building, and design options.

Examine zoning mapping, both visually and numerically, by correlating the building's intended shape with its volume and floor area, and by composing complex mass elements from a library of standard families.

DOI: 10.1201/9781003299127-355

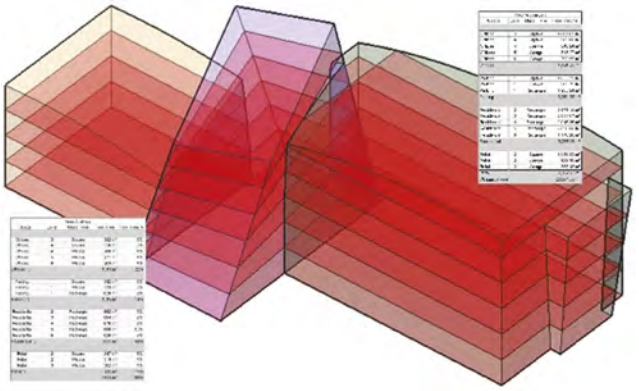

Figure 1. Model in Revit Architecture.

Creates floors, roofs, stained glass systems, and walls from mass instances when managing categories, types, and parameter values. When a mass element changes, the update of these elements is completely controlled [1]. BIM Technology helps to create a building project in a shorter time.

2 HISTORY OF BIM TECHNOLOGIES

The concept of computer modeling in construction began to develop back in the late 20th century. At that time, CAD technologies actively used, but the capabilities of technology did not yet allow us to move to a qualitatively new level.

The idea of BIM modeling takes its roots from the 1970s. In 1975, AIA (American Institute of Architects) published the work of Technology Institute professor Chuck Eastman, which first mentioned an information model of a building called the Building Description System. In parallel, similar work carried out in Europe. For example, in Finland in the early 1980s, the term Product Information Model came into use, and in the USA - Building Product Model. Both systems not focused on the design process, but on its object. Later, the general concept of Building Information Modeling formed.

In 1986, the creator of the RUCAPS program, English engineer Robert Aish, formulated the basic principles of the information approach to design:

- Automatic drawing;
- Creating 3D objects;
- Intelligent parameterization of buildings;
- Database rollup;
- Distribution of construction stages over time, etc.

The practical application of the technology demonstrated during the reconstruction of the third terminal of Heathrow Airport.

Since the early 2000s, the history of BIM technology has moved to a new round. The term has become one of the key in the global construction industry.

The concept of "building information model" was first mentioned in the current meaning in the article "Modeling multiple views on buildings" by G. A. van Nederwin and F. P. Tolman. This term came into wide use only in 2002 and began to use to name the digital representation of the construction process. The founders of modern BIM programs were the applications RUCAPS, Sonata and Reflex, ArchiCAD. Today, the key players in the global building information modeling market are Autodesk, Bentley Systems, Dassault Systemes, AECOM, Asite Solutions, Beck Technology, Nemetschek, Pentagon Solutions, Trimble Navigation, and Synchro Software [2].

In fact, the purpose of using information modeling technology is to embody numerical information in a form that is convenient for perception and analysis. The input data in the finished model is coordinated, coordinated and linked to each other. Each digit has a specific physical reference. It is can analyzed and calculated. Simplifies the procedure for making adjustments, updates.

3 OVERVIEW, APPLICATION

Preparation of architectural and construction projects in the BIM environment - a set of interconnected processes for creating an information model based on the customer's requirements. The technology of design, erection and operation of the object in BIM considered in the section of the life cycle (from the English product life cycle, PLM) of the product, in this case, the object of construction. The information model (IM), being a digital analogue, also experiences all stages of the LC: from the idea of creating an object to its reconstruction/dismantling (Figure 2).

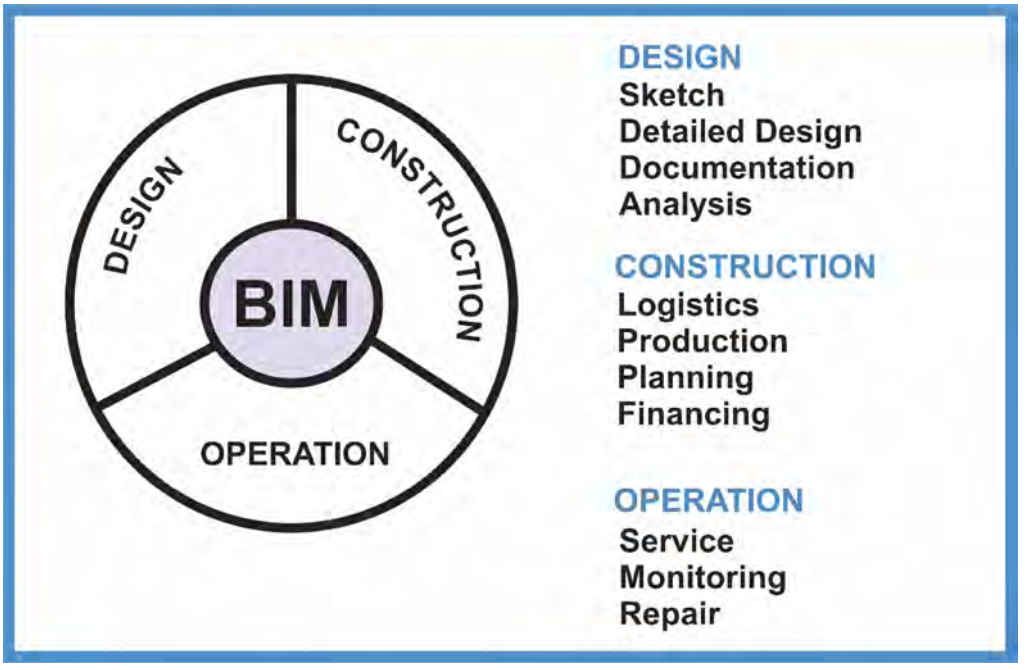

Figure 2. Preparation of architectural and construction projects in BIM environment.

BIM can considered both the process of building a model itself, and the finite model itself, saturated with information. An information model (IM) is information suitable for computer processing about a designed or existing construction site, while:

- Properly coordinated, coordinated and interconnected;
- Having a geometric reference;
- Suitable for calculations and analysis;
- Allowing the necessary updates;
- Interoperable [3].

BIM based on object-oriented design. This means that all programs working in this technology assume modeling based on a large number of pre-created objects, called families, the main design operations carried out with elements such as indivisible blocks, a kind of components. Each model element carries geometric and attribute information (Figure 3).

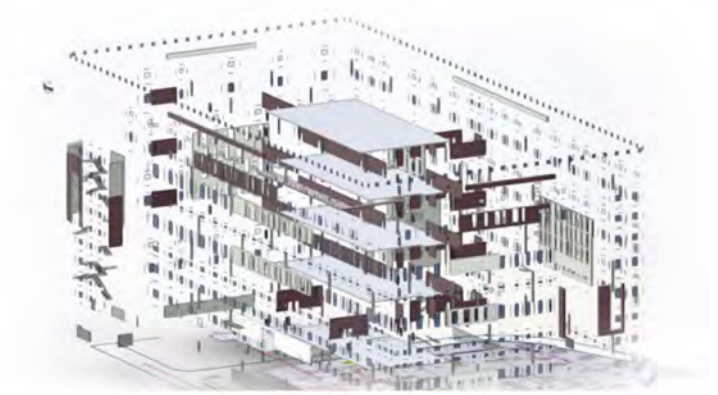

Figure 3. Each model element carries geometric and attribute information.

The unified information model involves collective work that brings together specialists from all design areas: technologists, architects, designers, engineers of internal and external networks, etc. Teamwork carried out in a single design environment, a pig (general data pig environment) and must comply with certain rules and interaction between the participants in the BIM modeling process, which are reflect in the BEP document.

The use of BIM technology in construction has many advantages:

- Visually inform contractors, investors, customers, controlling authorities about the state of the object using 3D visualization. Models can be demonstrated using special glasses;
- Centralized storage of the full range of data on the object under construction. When making changes to any one section, the designer can immediately follow the results and consequences in interconnected projections;
- Shortening project development time;
- Reducing the risk of errors, detecting inconsistencies at the design stage, and not during implementation;
- Quick and visual calculation of the main building structures. For the development of engineering complexes, already created bases of typical nodes and elements used;
- Real-time management. BIM design allows you to control the key indicators of the facility and the timing of the work;
- Automation of working equipment control processes;
- Quick unloading of information on the results of tests, surveys, data from design documentation, other information on request;
- Possibility of changing the financial parameters of the building, labor costs in individual specifications to adjust the total cost of construction;
- Centralized management of accounting, procurement, development programs;
- Easier and more efficient operation of buildings;
- Construction of a facility that meets the customer's requirements and desired characteristics as much as possible.

4 BIM MODEL CREATION PROCESS

The following algorithm can schematically display the process of creating a BIM model:

Creation Request (Sold-to Party)

- Formation of terms of reference, EIR;
- Development of the project implementation plan by the Contractor BEP;
- Pre-project, equipment layout;

– Design works;
– Approval;
– Development of detailed design documentation;
– Transferring the model to construction;
– Updating the model during LC;
– Archiving.

The information supplied to the BIM model stored and processed in this model and obtained from it for further use shown in (Figure 4).

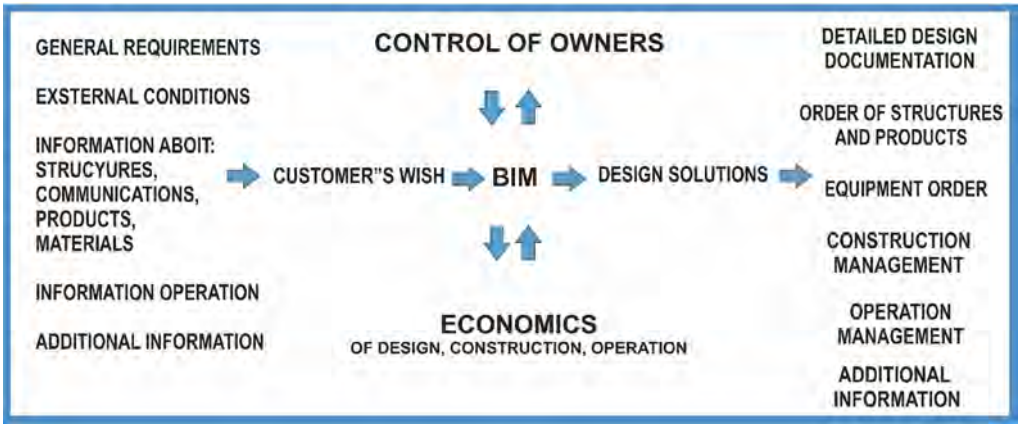

Figure 4. Information to and from the BIM model stored and processed in this model for further use.

The development and development of the model carried out in a common data environment (CDE), which means that all interested parties have constant access to the model filled with useful and up-to-date information: engineering, chronological, financial, and so on.

The delegation of access levels for a different circle of persons involved in the interaction process when creating an object ensures the clarity and relevance of the received data for each task. Thus, BIM covers all stages of the life cycle of a building or structure, continuously filling it with valuable information, which, in turn, significantly reduces the cost of its maintenance (OPEX), reduces the speed of construction, minimizes design errors, and allows all interested parties to have prompt access to information (Figure 5).

5 BIM DESIGN PHASES

The use of BIM technologies in design can conditionally divided into several stages.

Creates a 3D architectural model of the building. Visualize all sections, plans. The data required for the Architectural Solutions section is automatically loaded.

Calculation of parameters of the main elements of the building. The specialist enters the received model into a program that provides characteristics and simultaneously uploads drawings, specifications, lists, details of determining the estimated cost of construction.

Introduction of information about engineering networks. The 3D model determines the natural illumination level of areas, heat losses, and other important characteristics.

Development of WEP (Method Statement) and Construction Management Plan (Construction Management Plan). This step performed after the calculation of the scope of work obtained. The program automatically prepares the planning table.

Logistics. Enter information about the types of materials and the timing of their delivery to the object into the model.

Figure 5. Delegation of access levels for different groups of people involved in the interaction process when creating an object.

The process is as follows.

The program develops blocks that will manufactured outside the construction site and are not subject to division into parts, but are important components of the building: windows, doors, lighting and heating equipment, ventilation, floor slabs, etc.

They model the parts of the building that will erected directly on the site: walls, foundation, roof, facade system, etc.

At any stage, you can change one type of heating equipment to another, with different characteristics and costs, for example. The volumetric model is very flexible - this is one of the key advantages of BIM technology. You can change the modeling stages without performing large-scale additional work to adjust the project documentation.

When finished, the finished 3D model can used to operate the building. For this, a sensor system is used. The program monitors emergencies, operating modes of engineering communications, etc. The 3D model will automatically change its configuration and content according to the initial data throughout the life cycle of the building.

Information modeling of objects under construction does not replace traditional design, but is only one of the next stages of its development. It should understood that fundamental decisions still depend on the person, and the program only performs the work of finding, storing and analyzing the information provided. The difference lies in the quality and volume of processed data, which simply cannot handled manually and which brilliantly operated by the computer.

6 APPLYING BIM TO PROJECT PARTICIPANTS

Traditionally, building design involves working with separate two-dimensional projections: plans, drawings, technical documents. The BIM design technology allows you to collect and process data on all the main characteristics of the object in a single information field. The specialist gets the opportunity simultaneously analyze structural, architectural and planning, technological, economic, operational solutions in conjunction. The information rendered on a 3D virtual model with real physical properties.

However, the volumetric representation of the design data of the structure is not all the possibilities of BIM. The technology adds variables: cost, plans, timing. The parameters of the

building construction process can calculated even before the start of work. 3D Model Management enables you to find the best solutions to shorten project life and extend design life [4].

Using BIM for the customer allows you to solve the following problems:

- Visualization of the facility before the start of construction;
- Risk management in the implementation of the investment project;
- The ability to monitor the progress of design and construction based on the BIM model in real time with cloud services;
- Optimal technical solutions;
- Maximum accuracy of ICP cost calculation (according to AACEI);
- Control of compliance of design solutions and construction results;
- Obtaining a digital twin based on the results of construction (AS BUILD model for maintenance, reconstruction, dismantling).

Using BIM for the designer allows you to solve the following problems:

- Implementation of design with selection of options;
- Automation of routine operations;
- Reduction of time for making changes to the detailed design documentation;
- Reduce design errors with visualization;
- Interdisciplinary collaboration: collaboration of various specialists in 3D;
- Centralized document management on your server or in the cloud;
- Checking the project for collisions (intersection of engineering equipment with other elements) before the start of construction;
- Check for compliance with SP, GOST and SNiP in specialized software;
- Facilitating communication with the customer, expertise, builders;
- Protection of the process of transferring the design results to the customer.

Using BIM for builders allows you to solve the following problems:

- Clarity of technical solutions and the result of construction due to the presence of a BIM model;
- Visualization of the object erection in conjunction with the schedule;
- Setting tasks and deadlines for its execution with reference to the 2D- or BIM model;
- Introduction of electronic technical documentation of equipment and materials into the BIM model;
- Design documentation does not contain collisions, and therefore "surprises" at the construction site;
- Unloading of materials for PTD into one "click";
- Facilitated communication with project organizations due to the possibility of prompt introduction of changes and comments into the same BIM model;
- Introduction and approval of adjustments to the project directly at the construction site;
- The builder always has the latest version of the project documentation;
- Centralized document management on your server or in the cloud;
- Marking and notification of problems and/or changes clearly, with reference to the 2D- or BIM model;
- Unloading of as-built documentation from the BIM model.

BIM in operation:

- The BIM model corresponds to the constructed object;
- BIM-model building elements contain the necessary technical documentation;
- The presence of a BIM model allows you to quickly find and fix problems, carry out current maintenance of the object;
- Reception of text, audio and video applications about problems with reference to a specific location on the area and/or zone.

Market Compliance Challenge.

In-depth and comprehensive TEO analysis based on the LOD 200 BIM model variants; development of marketing materials.

– Resource and Risk Assessment Challenge.

Formation of primary requirements for equipment; assessment of technical specifications for connection to communications; options for the optimal location of the object on the ground.

– Database consistency Challenge.

All project participants have operational access to feedback information; modeling of calendar and network schedules of work performance based on IM.

– Deadline problem.

Modeling of calendar and network schedules based on IM.

– Budget savings.

Modeling of financial flows based on MI 4D.

– Reduction initial scope of work.

Through a clearly formulated budget, deadlines, compliance of the scope of work with the project.

– Project deviations.

Comprehensive analysis and approval of technical solutions during design check for collisions.

– Construction quality.

The materials and equipment used known in advance; the scope of work precisely defined; author's control based on MI.

– Labor protection.

By optimal arrangement and control of elements (fences, scaffolding, fire hydrants...) ensuring safety.

– The problem of operation.

Electronic passport of the facility, including all up-to-date information on equipment, materials, service life, monitoring and maintenance systems.

– The problem of transparency of the work process.

Data on the object and the progress of its implementation are available in the cloud (closed server);

Roles and responsibilities regulated by the requirements of EIR, BEP, etc...;

All changes promptly made to the model with the possibility of feedback;

Speed of decision-making and prompt monitoring of design/construction progress are available to all interested parties

VDC - we immediately predict based on the optimal decisions of them construction time, financial flows, minimized deviations, make operational management decisions.

8 DIGITALIZATION OF CONSTRUCTION IN KAZAKHSTAN

The size of the construction market of Kazakhstan in 2021 was estimated at $20.3 billion. The market was projected to grow at an AAGR of more than 5% between 2023-2026 [5].

Digitalization of construction in Kazakhstan is in full swing - thanks to an active state program - and this can called a feature of this market, which allocates Kazakhstan from many countries. Since the state program "Digital Kazakhstan" has been launched in Kazakhstan since 2018: now there are digital projects in the construction segment that are aimed at maximizing the digitization of many bureaucratic issues in construction and simplifying a number of procedures, contributing to the transparency of interaction between government agencies and end consumers. These include several innovative digital initiatives developed with government support.

Digital Construction Systems of Kazakhstan.

The E-Kurylys system is a single information system that is one of the digital tools for improving quality control and transparency of construction in the country. They are trying to lead with it state architectural and construction control in the Republic of Kazakhstan. All reports for each of the construction facilities are contained; the stages of acceptance and commissioning of the facilities recorded. There are more than 25,000 objects in the database.

E-PSD is a system for interaction between experts and customers. It stores all data on projects - from technical and economic indicators of the project and estimates, to standard projects.

Also in Kazakhstan, there is a single geoportal of infrastructure data (EGID). It designed to regulate urban planning and development of territories - it contains data on all general plans, planning and engineering nodes and infrastructure, as well as analytics of urban development. The database contains 63.7% of information about the engineering networks of the built-up area; the number of users in the system is about 2000.

E-SHANYRAQ. This system focused on the needs of housing and communal services. With its help, the effectiveness of the work of utilities monitored and analyzed - to ensure their transparency and productivity. This includes a water and heat metering instrumentation system, accounting and control of the operation of elevators, etc. The system helps quickly track the state of the communal infrastructure in order to make effective decisions.

As we can see, in fact, these systems took as a basis individual components of the information model, where the entire information on the project is located in one three-dimensional information model of a particular object.

With the introduction of BIM technology in Kazakhstan, things are also not bad - large construction companies-developers and private architectural bureaus offer design using BIM (more precisely, in Kazakhstan they prefer the abbreviation TIMSO- technology of information modeling of construction facilities).

That is, the maturity of BIM technology in Kazakhstan can defined as level 0, but the state is in every possible way interested in its development. In particular, Almaty General Plan has developed national standards for the use of BIM technologies taking into account international standards, in particular, the regulatory and technical framework for BIM: general provisions, design and construction, operation and information security).

Technologically complex facilities in the Republic of Kazakhstan used by TIMSO and experts at various specialized seminars and business conferences repeatedly voice support and the need to develop this technology.

The need for digitalization of construction and technology confirmed by such figures: in 2017-2019, it was spent on information and communication technologies (ICT) by 31% more than in 2014-2016. In 2020, 13.2 billion tenge was spent on ICT. In addition, in general, investments in technologies for construction demonstrate positive dynamics in the Republic of Kazakhstan. There is also a system "State Bank of Information Models," the purpose of which is to collect and provide all data on TIMSO facilities and for making decisions when implementing investment projects. 2023 is called the year when it is planned that the construction sector of Kazakhstan will switch to the widespread use of BIM technologies.

9 CONCLUSIONS

BIM is at the intersection of different disciplines. Using this modeling method in one project, you can combine comprehensive data on architecture, design, engineering, economic solutions and much more, which together allows you to avoid errors, increase the payback and efficiency of the project.

The data entered in accordance with the established standards, are accurate and updated regularly. One of the main advantages of the model is the reduction of time and costs on the part of the customer, as well as the ability to correct and improve the project at the first stages of its formation. Information modeling technology makes the customer a full participant in construction. It can visualize what the object will be like and make adjustments along the way. No 2D drawing will provide such a realistic picture of the future building as is possible with BIM modeling. It happens that the idea of an architect, designer or customer is not always feasible in practice, and only in the BIM model can this seen at the initial stages of design. With this type of design, a building that has not yet been built "comes to life" on the screen, making any shortcomings and possible problems noticeable.

For the model to work effectively, you need to create a single information environment that can provide instant access to the data of all project participants. A huge amount of data is tied to the digital BIM model, including work schedule, geolocation, and financial statements. Modern mobile applications are capable of reproducing virtual reality, which allows you to recreate a construction facility in real conditions and assess the progress of construction, while being anywhere in the world.

REFERENCES

[1] Revit: BIM software for designers, builders, and doers. //https://www.autodesk.com/products/revit/overview?term=1-YEAR&tab=subscription.

[2] Talapov, V.V. 2011. BIM Basics: Introduction to Building Information Modeling. *Moscow:* DMK Press, 392 p.

[3] Pakidov, O.I. 2014. Basics of BIM: information modeling for builders. *Naberezhnye Chelny*.

[4] Dobrynin, A.I., Tarasevich, L. S. 2004. Economic theory. - *St. Petersburg:* Ed. "Peter", 544 p.

[5] Romanova, O. May 20, 2022. Construction market of Kazakhstan 2022: technologies and digitalization. // https://www.planradar.com/ru/obzor-stroitelnogo-rynka-kazahstana.

Smart Geotechnics for Smart Societies – Zhussupbekov, Sarsembayeva & Kaliakin (Eds)
© 2023 The Author(s), ISBN 978-1-003-29912-7
Open Access: www.taylorfrancis.com, CC BY-NC-ND 4.0 license

Application of information modeling technology in geotechnics

A.Zh. Zhussupbekov, A. Kemerbayeva, T. Iskakova & A.E. Yeleusinova
L. N. Gumilyov Eurasian National University, Astana, Kazakhstan

I.O. Morev
LLP "KGS-Astana", Astana, Kazakhstan

ABSTRACT: Geotechnics is an essential component of construction and engineering that involves studying how rock and soil interact with structures. Borehole drilling and sample collections are traditional methods used to collect subsurface data, but they are time-consuming, expensive, and only cover a small area. Information modeling technology can address these challenges by building intricate digital models of subsurface conditions that are more accurately and effectively used to design and analyze structures such as buildings, bridges, tunnels, and dams. This article discusses the main stages of creating an information model of a geotechnical object, including preparatory work, preliminary tests and work volume determination, field tests, and laboratory tests. The resulting digital engineering-geological model should include the geometric dimensions of the investigated soil mass and the physical and mechanical characteristics of the soils in the IFC data format.

1 INTRODUCTION

Any building or structure is built on a soil foundation or is located directly in the thickness of the soil. Its strength, stability and normal operation are determined not only by the structural features of the structure, but also by the properties of the soil, the conditions of interaction between the structure and the foundation (Talapov, 2021 & Talapo, 2015).

The cost of foundations is on average 12% of the cost of the structure, labor costs often reach 15% or more of the total labor costs, and the duration of the construction of foundations reaches 20% of the total construction time of the structure. In difficult soil conditions, these figures increase significantly. Therefore, the improvement of design and technological solutions in the field of foundation engineering will lead to large savings in material and labor resources, and a reduction in the construction time for buildings and structures (*https://www.planradar.com/ru/bim-tekhnologii-v-stroitelstve*).

With the assignment to the city of Astana of the honorary title - the capital of the Republic of Kazakhstan, the development of its territory is being carried out at an accelerated pace. Under these conditions, the analysis and optimization of one or more factors that are repeatedly repeated in production can provide a significant economic effect, as well as significantly improve and increase the efficiency of this type of work.

The territory of Astana is due to rather complex engineering and geological conditions, which is confirmed by a large variety of stratification of relatively weak soils in the upper part of the base, but at the same time, the bearing layers of the soil turn out to be quite reliable (*https://www.planradar.com/ru/bim-tekhnologii-v-stroitelstve*).

Designers in these conditions, when choosing foundations, often use pile foundations, the bearing capacity of which is not fully used in projects, and in some cases its underutilization reaches 40%. This leads to unjustified expenditure of funds, material and labor resources, due to the incomplete use of the bearing capacity of piles in terms of soil and material.

DOI: 10.1201/9781003299127-356

The design and construction of economic structures of pile foundations is possible if there is sufficiently representative and reliable information about the conditions of occurrence and properties of soils at construction sites, which are obtained as a result of soil studies during engineering and geological studies.

The presence in the projects of excessive reserves of the bearing capacity of piles can be explained by the following reasons:

- inferior engineering and geological surveys.
- manifestation by designers of excessive caution due to the fact that the structures of pile foundations are assumed by them to be insufficiently reliable;
- the experience of previous construction, in similar soil conditions, is not taken into account.

Geotechnics is a crucial aspect of construction and engineering. It entails examining and comprehending how rock and soil behave and interact with structures. Construction projects might suffer from costly and deadly mistakes if subsurface conditions are not accurately or sufficiently disclosed. Borehole drilling and sample collection are two common traditional techniques for getting subsurface data, but they can be time-consuming, expensive, and only cover a small area.

These issues can be resolved using information modeling technology, which builds intricate digital models of subsurface conditions. These models can be used more accurately and effectively to build and analyze structures. This article examines the use of information modeling technology in geotechnics.

2 GEOTECHNICAL ENVIRONMENT OF ASTANA CITY

The mechanical composition of floodplain deposits is more or less uniform. This is unsorted gravel, sandy-clay and loamy material. The heaviest precipitation is observed in the floodplain of the Nura and in the narrowed sections of the Ishim valley. Floodplain deposits of Kulanutpes are usually sandy-loamy. The formation of spits and shoals is currently taking place. Deposit thickness up to 4m. In terms of studying the geological features of the territory of Astana, the results of studies obtained in the course of his work by Popov V. N. are also of particular interest (Zhussupbekov et al. 2023 & Zhussupbekov et al. 2021 & Zhussupbekov et al. 2019a & Zhussupbekov et al. 2019b & Zhussupbekov et al. 2020) and Alibekova N.T. (Alibekova et al. 2020 & Zhussupbekov and Alibekova. 2013).

Popov V.N. in his work (Zhussupbekov et al. 2023 & Zhussupbekov et al. 2021 & Zhussupbekov et al. 2019a & Zhussupbekov et al. 2019b & Zhussupbekov et al. 2020), conducted research to assess the geotechnical conditions of the territory of Astana, the results of which include:

- description of geomorphological characteristics, within the boundaries of the city, on the basis of which a geomorphological map was compiled at a scale of 1: 100,000;
- hydrological conditions were described and a hydrological map was drawn up at a scale of 1:100,000;
- the geological conditions were studied taking into account the influence of geotechnical loads and a geotechnical map of the scale 1:100000 was compiled, with an explanatory table to it;
- an assessment of the physical and mechanical properties of soils was made by conducting a complex of field and laboratory studies;
- an assessment of the geo-ecological state of the territory was given.

The predominant geomorphological type of terrain in the region of Astana and the adjacent territory is the watershed plain. The southwestern part of the territory is characterized by two types: high and low floodplains.

The floodplain terrace separates the high floodplain from the watershed plain, which can be classified as a river terrace (Figure 1).

In addition, on the basis of the geomorphological map, a geotechnical map (Figure 2) of the territory of Astana was compiled.

On the basis of the geophysical surveys and reference drilling with a depth of up to 40 m, Popov V.N. indicated that along the Astana-Rozhdestvenka highway there is a zone of a sharp

drop in the depth of the roof of sedimentary rock, extending in the meridional direction (Figure 1), which should be addressed attention when designing high-rise buildings in the area.

Alibekova N.T. (Zhussupbekov et al. 2023 & Zhussupbekov et al. 2021 & Zhussupbekov et al. 2019a & Zhussupbekov et al. 2019b & Zhussupbekov et al. 2020 & Alibekova et al. 2020 & Zhussupbekov and Alibekova. 2013), together with Japanese geotechnicians, for the first time created the Geoinformation Database program based on the materials of engineering and geological surveys to assess the engineering and geological conditions of the built-up area of the city.

This program, at the time of its creation, included data from 1200 boreholes, 402 static sounding points and 125 dynamic sounding points and static and dynamic load pile tests, which made it possible to analyze the regional soil conditions before a detailed study (Figure 2) (Buranbayeva et al. 2023 & Zhussupbekov et al. 2022 & Buranbayeva et al. 2021 & Omarov et al. 2021 & Zhussupbekov et al. 2021 & Zhussupbekov et al. 2020a & Zhussupbekov and Omarov 2020 & Zhussupbekov et al. 2020b & Zhussupbekov et al. 2019a & Zhussupbekov et al. 2019b & Zhussupbekov et al. 2019c & Zhussupbekov et al. 2018 & Zhussupbekov et al. 2015 & Zhussupbekov et al. 2016a & Zhussupbekov et al. 2016b).

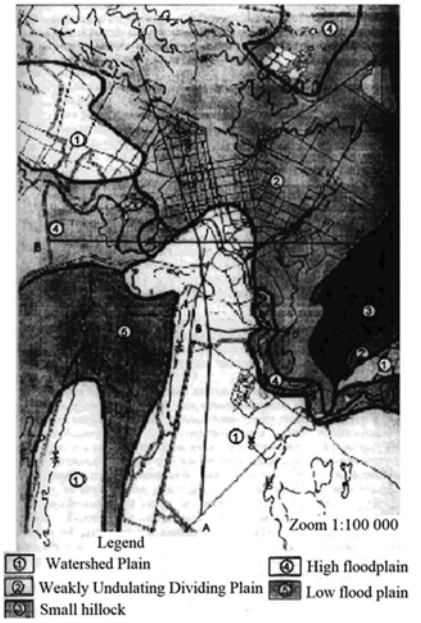

Figure 1. Geomorphological map. (Popov).

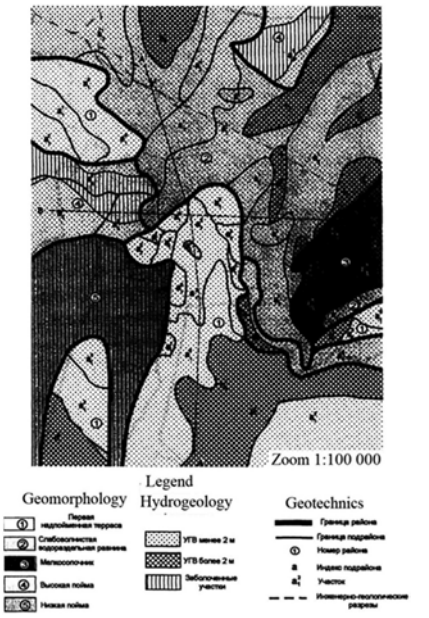

Figure 2. Geotechnical map of Astana.

With the help of the "Geoinformation Database" program, six main engineering-geological elements (EGE) of various origin and age were identified, and maps were built for them by thickness [9]:

- EGE-1 - technogenic deposits (tIV) are represented by a soil-vegetation layer (EGE-1a) and bulk soil (EGE-1b). The loamy soil-vegetation layer has a thickness of 0.2 to 0.5 m. Bulk soils are composed of Quaternary loams, construction and household waste, the thickness varies from 0.2 to 2.0 m.
- EGE-2 - alluvial mid-Quaternary modern deposits a (QII-IV) are represented by clayey soils, consisting mainly of loams (EGE-2a) with intercalation of sandy loams (IGE-2b), clays (IGE-2c) and silt (IGE-2g), throughout their thickness they have lenses and interlayers of sands of various sizes up to 1-3 cm, sometimes up to 10 cm. The thickness of these soils varies from 0.9 to 10.0 m.
- EGE-3 - alluvial mid-quaternary sand and gravel formations a (QII-IV) consist of sands of various sizes (EGE-3a), gravel sands (EGE-3b) and gravel soils (IGE-3c). The thickness of

sands of various sizes varies from 0.4 to 8.3 m, gravelly sands from 0.5 to 6.5 m, gravel soils from 1.0 to 9.2 m.

– EGE-4 - eluvial formations of the weathering crust e(C1) are presented in the form of loams and clays with lenses and interlayers of sandy loams and inclusions of gruss-rubble soils occurring at depths of 6.0-10.0 m.
– EGE-5 - eluvial formations in the form of gruss-rubble soils e(C1) are widespread in the study area and they were found at depths from 7.0 to 23.0 m.
– EGE-6 - sedimentary rocks of the Lower Carboniferous (C1) are represented mainly by sandstones, which are interbedded with siltstones and mudstones of the same age throughout their thickness. They occur at depths from 11.6 to 26.2 m.

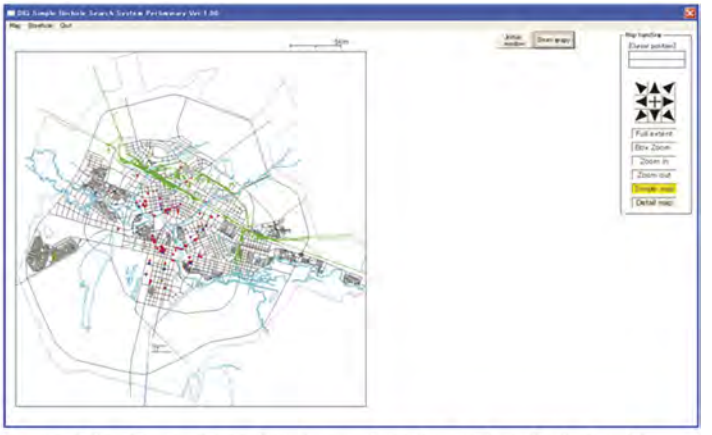

a) a map of the city territory showing engineering and geological wells

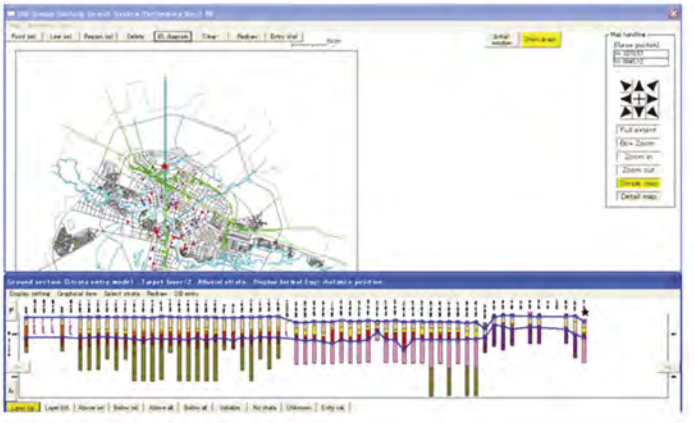

b) geological and lithological section South-West

Figure 3. General view of the program "Geoinformation database" (Alibekova et al. 2020).

In addition, with the help of the Geoinformation Database program, engineering-geological sections were built, which made it possible to assess the conditions of soil occurrence, on the basis of which it was revealed that these elements form about eight types of foundations up to bedrock (Figure 4).

The engineering-geological, geomorphological and hydrological description of the territory of Astana considered above by various authors in their works V.I. Dmitrovsky, Popov V.N. and Alibekova N.T. (Figure 4) provide a cartographic display of the construction characteristics of the geological environment and make visual results of engineering and geological surveys, and

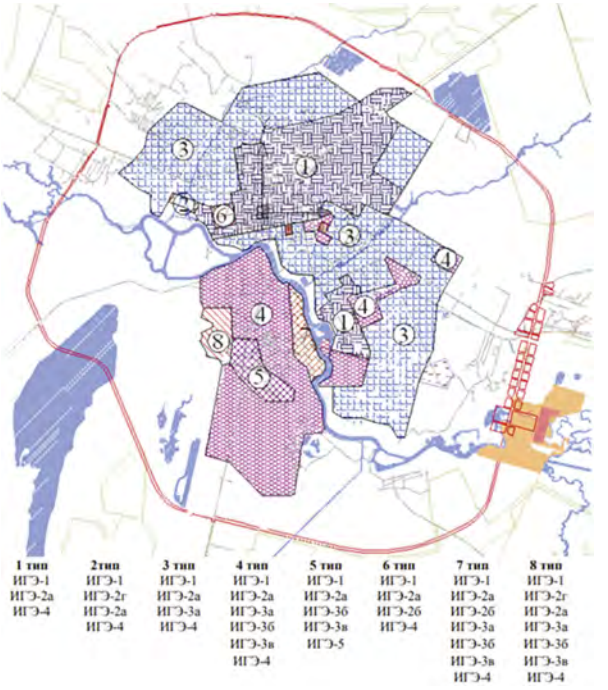

Figure 4. Zoning of the territory of the city of Astana by types of grounds (Zhussupbekov and Alibekova 2013).

can also serve as the basis for the analysis of the geological environment in order to optimize the length of the piles.

3 GEOTECHNICAL USE OF INFORMATION MODELING TECHNOLOGY

The creation of digital models of subsurface conditions is a step in the application of information modeling technology in geotechnics. The process includes collecting data on soil and rock layers, groundwater, and other geological features, and creating a three-dimensional digital model using specialized software. The digital model can then be used to design and analyze structures, such as buildings, bridges, tunnels, and dams.

The step of data collection entails boring holes, gathering samples, and performing laboratory tests. A three-dimensional model of the subsurface conditions, including soil and rock layers, groundwater, and other geological elements, can be made using the data gathered. To build a more complete model, this digital model might also include additional data, such as topographical and environmental data.

The digital model can be used to design and examine structures once it has been constructed (Liam et al. 2016). The behavior of the rock and soil layers and their interactions with the structure can be simulated by the software. This can assist identify potential problems before construction and offer insightful information on the structure's performance.

Let's consider the main stages of creating an information model of a geotechnical object:

1. Preparatory work.
   Create a project. Enter the site plan of the survey area. Enter the technical characteristics of the object. Enter the locations of the boreholes and field tests. Choose a method of field testing and enter equipment parameters. Choose the type of correlation equations.
2. Preliminary tests and determination of work volumes.
   Perform preliminary static penetration tests at four points at the corners of the survey area,

determine the type of soils (engineering-geological element), physical and mechanical properties of soils, and the depth of compressible strata. Refine the number of boreholes and field test locations, the volume of field and laboratory soil tests. Make changes to the site plan.

3. Field tests.
   Static probing. Dynamic probing. Testing with a flat or helical stamp.
4. Laboratory tests.
   Using the data from field and laboratory tests, develop a digital engineering-geological model (DEGM) of the survey area (in IFC data format). The model should include the geometric dimensions of the investigated soil mass and the physical and mechanical characteristics of the soils. An example of such a model created in the Geotek Field program is shown in Figure 5.

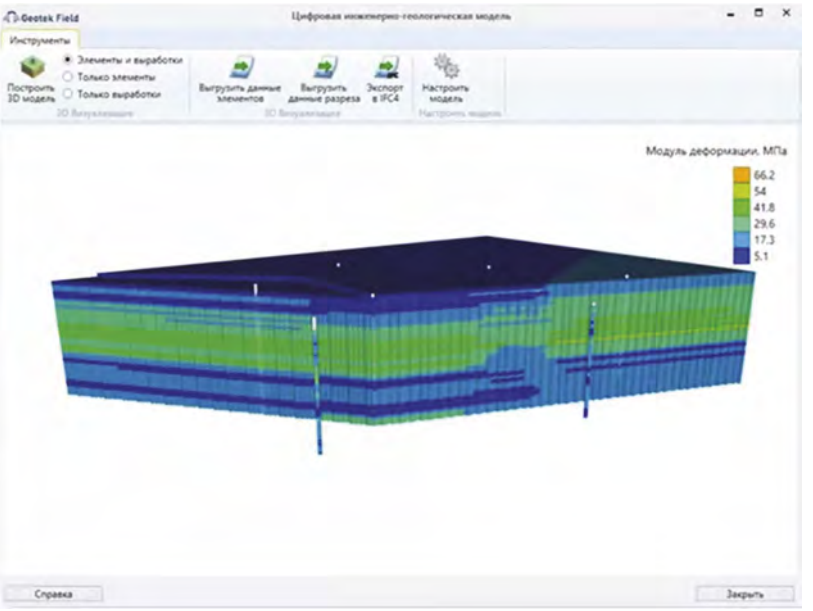

Figure 5. Digital engineering-geological model of the base of the building.

The file with the IFC extension contains an information model of a building or structure and is used to exchange model data between different computer-aided design systems that support the Building Information Modeling (BIM) standard. The file includes data on spatial elements, materials, and forms of the construction object model. Programs such as Graphisoft ArchiCAD, Autodesk AutoCAD, FreeCAD, and others support working with IFC files.

From the point of view of the authors of the article, which explores the potential use and benefits of BIM technologies in the construction sector (Bryde et al. 2013), a BIM model should include at least the following geotechnical information:

1. Information on geological workings.
2. Rules for constructing engineering-geological sections between wells.
3. A table of the main indicators of physical and mechanical properties of soils, determined in accordance with the current normative literature.

The following information may also be present:

1. Results of static probing performed directly at the construction site.
2. Results of soil testing with screw stamps or pressiometric tests.
3. Protocols for conducting soil tests, including triaxial tests.
4. Results of determining additional characteristics (RQD, OCR, data from dynamic probing, data from geophysical studies, etc.).

5. Data from hydrogeological studies.
6. Alternative data on the main indicators of physical and mechanical properties of foundation soils as a result of additional surveys.
7. Data on work performance (including ground freezing, excavation of the pit, discrepancies in the actual geological structure compared to the results of engineering-geological surveys, deviations of piles from design positions, presence of a sludge layer, defects in piles, results of concreting, lack of contact between the foundation and the base, defects in waterproofing, etc.).
8. Information about communications.

Note that the engineering digital terrain model usually includes information about communications that are located close to the surface. However, part of the communications on it cannot be shown for various reasons.

When constructing foundations, the possible number of adjustments to the design documentation is significantly higher than when constructing aboveground structures. This is due to the difference in the actual geological structure of the site from the results of surveys, the presence of hidden voids in the soil, and the impossibility of accessing all areas of the constructed structures (primarily this applies to piles and structures constructed using the "wall in the ground" method). From this perspective, the implementation of information technologies in the production of work on the construction of all types of foundations is a relevant task.

3.1 *Conclusions*

The analysis of the engineering-geological conditions of the territory of the city of Astana and the experience of building pile foundations in the territory of Astana in the conditions of a variety of building complexes and soil stratification made it possible to establish that the engineering-geological conditions of the construction area and the characteristic features of buildings and structures are not sufficiently taken into account when forming the development of quarters, choice of foundation designs and technology of their construction. These circumstances lead to a significant rise in the cost of foundations and lengthening the construction of buildings and structures.

The application of BIM technology in geotechnical engineering provides a collaborative platform for collaboration among all stakeholders, from the geotechnical engineer to the architect, contractor and owner. It provides a 3D model that can collect and visualize geotechnical data, including soil profiles, well logs, and geophysical surveys. This data can be used to make informed decisions during the design phase, such as choosing the best type of foundation or slope stabilization measures. Geotechnical engineers can model soil and structure behavior, analyze the effects of various loads, and optimize the structure accordingly. During the construction phase, BIM technologies can be used to create a virtual construction site that allows contractors to plan construction sequences, visualize earthworks and identify potential hazards. The use of BIM technology allows you to increase efficiency, as well as reduce the number of errors and rework. In conclusion, the use of information modeling in geotechnical engineering has revolutionized the industry by providing a collaborative platform for all stakeholders from the design phase to construction, maintenance and management. By incorporating geotechnical data into the BIM model, engineers can design more efficiently, reduce errors, and optimize designs for safety and sustainability.

REFERENCES

Alibekova, N., Zhussupbekov, A., Mimura, M., Akhazhanov, S. 2020. Geoinformation database for installation of driving and boring piles in Astana. *16th Asian Regional Conference on Soil Mechanics and Geotechnical Engineering, ARC 2019*.

BIM technologies in construction. Available at: https://www.planradar.com/ru/bim-tekhnologii-v-stroi telstve/ (accessed 20 February 2023).

Bryde D., Broquetas M., Volm J.M. 2013. The project benefits of building information modeling (BIM). *International Journal of Project Management*. 7. (31): 971–980.

Buranbayeva, A., Zhussupbekov, A., Sarsembayeva, A., Omarov, A. 2022. Evaluation of the Structural Health Monitoring Results of the Applied Fiber Optics in the Pile-Raft Foundations of a High-Rise Building. *Applied Sciences (Switzerland)*, 12(22), 11728

Buranbayeva, A.M., Zh Zhussupbekov, A., Omarov, A.R. 2021. Numerical analysis and geomonitoring of behaviour of foundation of Abu-Dhabi Plaza in Nur-Sultan. *Journal of Physics: Conference Series*, 1928(1), 012033

Liam R. Tawelian, Slobodan B. Mickovski. 2016. The Implementation of Geotechnical Data Into the BIM Process. *Proceedings Engineering The 3rd International Conference on Transportation Geotechnics* (ICTG 2016). Advances in Transportation Geotechnics 3. (143): 734–741.

Omarov, A.R., Kuderin, M., Zhussupbekov, A., Kaliakin, V.N., Iskakov, S. 2021. Vibration measurements at a new monument in NurSultan city. *International Journal of GEOMATE*, 21(85): 24–31.

Talapov V. V. 2015. BIM technology. The essence and features of the implementation of information modeling of buildings/V. V. Talapov. – M.: DMK-Press: 410.

Talapov V. V. 2021. The concept of BIM implementation in Kazakhstan: key facts. Available at: https://kazniisa.kz/index.php/component/k2/item/133-bim (accessed 2021).

Zhussupbekov, A.Zh., Alibekova, N.T. 2013. Geotechnical zoning territory of new capital Astana. *Geotechnical and Geophysical Site Characterization 4 - Proceedings of the 4th International Conference on Site Characterization* 4, ISC-4, (2): 1537–1542.

Zhussupbekov, A., Alibekova, N., Akhazhanov, S., Sarsembayeva, A. 2021. Development of a unified geotechnical database and data processing on the example of Nur-Sultan City. *Applied Sciences (Switzerland)*, 11(1): 1–20.

Zhussupbekov, A.Z., Alibekova, N.T., Akhazhanov, S.B., Shakirova, N.U., Alpyssova, A.B. 2019. Geotechnical Geo-Information System of Astana. *Soil Mechanics and Foundation Engineering*, 55(6): 420–424.

Zhussupbekov, A., Sarsembayeva, A., Alibekova, N. 2023. Preliminary Assessment of the Bearing Capacity of Soils Using a Geotechnical Database. *Lecture Notes in Networks and Systems*, 574 LNNS: 3065–3074.

Zhussupbekov, A., Alibekova, N., Kaliakin, V. 2019a. Geotechnical geoinformation data base for the new capital city of Astana, Kazakhstan. *17th European Conference on Soil Mechanics and Geotechnical Engineering, ECSMGE 2019 – Proceedings*.

Zhussupbekov, A., Chang, D.-W., Utepov, Y., Borgekova, K., Omarov, A. 2019a. Estimating the Driven Pile Capacities for COF Project in West Kazakhstan. *Soil Mechanics and Foundation Engineering*, 56(2): 121–127.

Zhussupbekov, A., Kaliakin, V., Chang, D.-W., Omarov, A. 2022. Investigation of Interaction of Piles at New Cargo Sea Transportation Route and LRT Projects with Problematic Soils of Kazakhstan. *Lecture Notes in Civil Engineering*, (164):945–957.

Zhussupbekov, A.Z., Lukpanov, R.E., Omarov, A.R. 2016a. Bi-Directional Static Load Testing. *Geotechnical Special Publication*, 2016-January(265 GSP): 35–42.

Zhussupbekov, A., Mangushev, R., Omarov, A. 2021. Geotechnical Piling Construction and Testing on Problematical Soil Ground of Kazakhstan and Russia. *Lecture Notes in Civil Engineering*, (112): 89–107.

Zhussupbekov, A., Morev, I., Omarov, A., Borgekova, K., Zhukenova, G. 2018. Geotechnical considerations of piling testing in problematical soils of West Kazakhstan. *International Journal of GEOMATE*, 15(47): 111–117.

Zhussupbekov, A.Zh., Omarov, A.R. 2020. Geotechnical considerations of piling construction and testing in problematical soils of Kazakhstan. *16th Asian Regional Conference on Soil Mechanics and Geotechnical Engineering*, ARC 2019.

Zhussupbekov, A., Omarov, A., Shakirova, N., Abdrakhmanova, B., Razueva, D. 2020a. The experience of piling tests on Astana LRT construction site. *16th Asian Regional Conference on Soil Mechanics and Geotechnical Engineering*, ARC 2019.

Zhussupbekov, A., Omarov, A., Shakirova, N., Razueva, D. 2020b. Complex analysis of bored piles on LRT construction site in Astana. *Lecture Notes in Civil Engineering*, (49):461–471.

Zhussupbekov, A., Omarov, A. 2016b. Modern Advances in the Field Geotechnical Testing Investigations of Pile Foundations. *Procedia Engineering*, (165): 88–95.

Zhussupbekov, A., Iwasaki, Y., Omarov, A., Tanyrbergenova, G., Akhazhanov, S. 2019b. Complex of static loading tests of bored piles. International Journal of GEOMATE, 16(58): 8–13.

Zhussupbekov, A., Omarov, A., Tanyrbergenova, G. 2019c. Design of anchored diaphragm wall for deep excavation. *International Journal of GEOMATE*, 16(58): 139–144.

Zhussupbekov, A.Zh., Syrlybaev, M.K., Lukpanov, R.E., Omarov, A.R. 2015. The applications of dynamic and static piling tests of Astana. *15th Asian Regional Conference on Soil Mechanics and Geotechnical Engineering, ARC 2015: New Innovations and Sustainability*,:2726–2729.

Zhussupbekov, A.Zh., Temirova, F.S., Riskulov, A.A., Omarov, A.R. 2020. Investigations of historical cities of Uzbekistan and Kazakhstan as objects of the silk way. *International Journal for Computational Civil and Structural Engineering*, 16(1): 147–155.

Smart Geotechnics for Smart Societies – Zhussupbekov, Sarsembayeva & Kaliakin (Eds)
© 2023 The Author(s), ISBN 978-1-003-29912-7
Open Access: www.taylorfrancis.com, CC BY-NC-ND 4.0 license

Modeling of geogrids in the analysis of the stability of reinforced soil structures with the finite element method

A.V. Kuznetsova
Tensar Innovative Solutions, Russia

ABSTRACT: Finite elements models (FEM) programs have become an integral part of geotechnical analysis. However, the inclusion of geosynthetics in the model often gives results that differ from the actual behavior of the structure. The classic way is the modeling of a geogrid in the form of a membrane with specified strength parameters. The list of these parameters and methods for their determination are not spelled out clearly enough in the design and test standards. The author proposes to investigate both the finite element and analytical models and estimate their cohesion with the monitoring results and ability to fully consider the effect of geogrids.

1 INTRODUCTION

Reinforced soil was used for retaining systems since ancient times. Ziggurat in Mesopotamia, Roman marinas, the Great Wall of China and a lot of other structures were built using this technology. But today's methodology of design and construction has started its development in 1960s by Henri Vidal. Until the two last decades of technology development mainly analytical design methods have been used by engineers. But today finite elements models (FEM) serve to check the validity of the design for complex geometry, geology or loading. The classic way is the modeling of a geogrid in the form of a membrane with specified strength parameters. The list of these parameters and methods for their determination are not spelled out clearly enough in the design and test standards. In this study author defines time and load dependent parameters for both analytical and FEM methods, provides comparison of results of both approaches and makes propositions for the further development of the model.

2 REINFORCED SOIL MODELING

2.1 *Analytical methods*

A number of analytical design methods have been developed since 1960s. All of them analyze the balance of forces and mainly differ in terms or partial factors and a degree of conservatism.

Reinforcing elements are described by their design strength calculated as short-term tensile strength reduced by a row of durability parameters including creep, installation damage and environmental influence. The purpose of the analysis is to check the balance between acting and resisting forces as shown in Figure 1.

Analytical methods have been widely used during the last three decades and are showing good correspondence with the actual structure behavior.

DOI: 10.1201/9781003299127-357

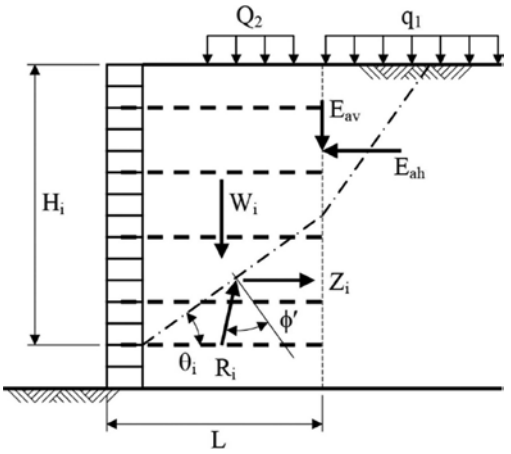

Figure 1. Scheme for calculating the internal stability of a reinforced soil retaining wall.

H – total height; H_i – distance from the top to the wedge base; L – length of geosynthetic material; φ' – fill angle of friction; θ – angle from horizontal to the failure surface; Q_2 and q_1 – surcharge; E_{ah} and E_{av} – horizontal and vertical components of active force and surcharge; W_i – failing wedge weight; Z_i - required resistance force; R_i – base resistance force.

2.2 *Finite element analysis (FEM)*

Firstly used for homogeneous soil structures, FEM now covers all types of reinforced soil applications, including retaining walls. Geogrids are implemented as membrane elements with given stiffness or modulus. Soil models are well calibrated with actual soil behavior, but geogrid models are far from that point. For that purpose, a number of real laboratory tests have been modeled with the use of FEM, like tensile strength test or pull-out test, shown in Figure 2 and others. But the behavior of a full structure still cannot be predicted accurately.

Figure 2. Geogrid model used for correlation.

FEM highly overestimates facing deformation due to the inability to model the actual grid influence on the fill material.

3 DESIGN STRENGTH AND STRAIN OF A GEOSINTETIC ELEMENT

3.1 *Design strength*

Design strength is described in a number of national standards and manuals for reinforcement soil design (BS8006, EBGEO and etc.) as a strength, guaranteed on the last year of service

after material was affected by creep, installation, aggressive environment, microbiology and UV. For polymer geogrids and geotextiles creep is the main reduction parameter and it could drop the strength to 30 – 60 % of quality control short-term strength. Figure 3 shows the difference in creep behavior of HDPE geogrid depending on the load applied. For this particular material creep test the long-term creep strength for 120 years is set as 24kN/m.

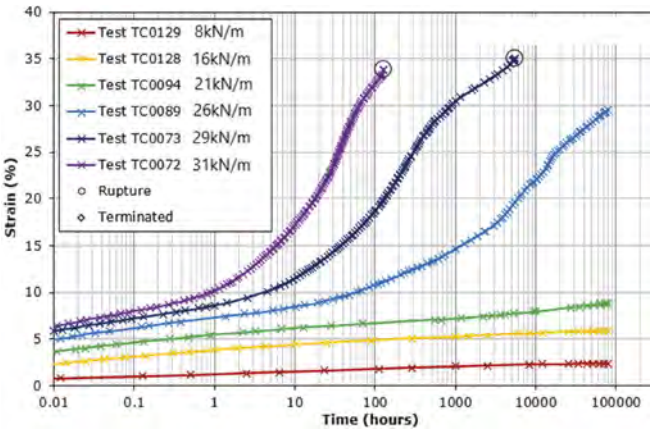

Figure 3. A series of creep test.

This number is used for ultimate limit state (ULS) analysis, that models a case where geogrid is ruptured. But for the serviceability limit state (SLS) that investigates geomaterial strain during the post-construction period, allowable load for geogrid should be limited even stricter. For reinforced soil retaining wall geogrid strain during the service life is limited by 1% only. Due to this design strength for the material above is set as 10kN/m for SLS analysis.

3.2 *Creep related stiffness*

FEA uses the stiffness of material that is generally obtained as load (strength) divided by strain. From geometry point of view stiffness could be compared looking at the degree of lines in Figure 3. First, it differs dramatically depending on the load applied, but Figure 4 indicates that even for the single load it changes during the test.

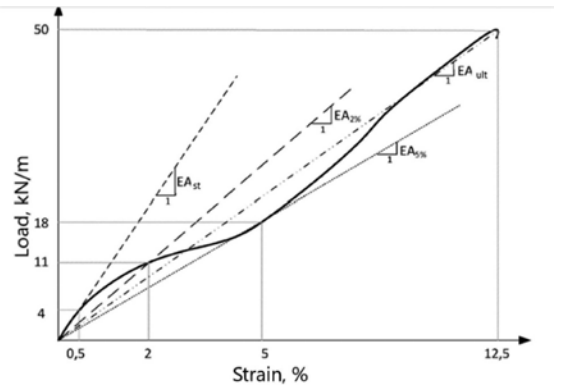

Figure 4. Stiffness deviation during the test.

In Russian design manual for geosynthetic materials FEM ODM 218.3.120-2020 short-term stiffness at 2 or 5% load is recommended as a performance related parameter. During the service life HDPE geogrid is subject to permanent load equal to 5 – 45% of its short-term strength. It could hardly be correlated with short-term 2% strain load recommended in ODM. For example, 50kN/m strong HDPE grid shows a short-term stiffness at 2% equals to 500kN/m but the 120 years creep test isochrone provides 262 kN/m for 2% strain.

Apart from loading speed and type there is one more significant factor for polymer geogrids – design temperature in the soil massive. ISO/TR 20432:2007 proposes to define it as the temperature which is halfway between the average yearly air temperature and the normal daily air temperature for the hottest month at the site. Creep behavior related to test speed and temperature is shown in Figure 5.

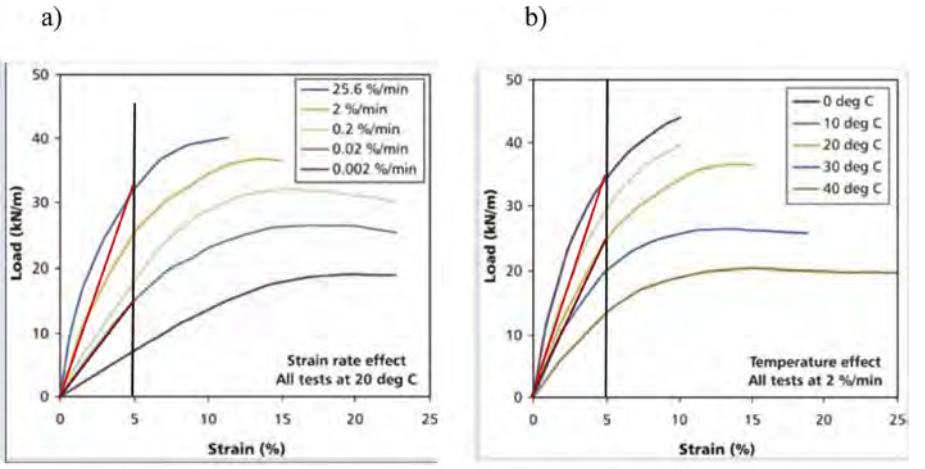

a) short- and long-term stiffness comparison; b) stiffness at various temperatures

Figure 5. Stiffness deviation due to loading speed and temperature.

Summarizing the above, the list of input data is the following:

- design life;
- design temperature;
- durability parameters;
- actual load in reinforcing element as partial from short-term strength.

To provide this data, geogrid should have been tested for creep at all range of loads from 5% to maximum creep related strength that differs from 40 to 70% depending on polymer type.

During a finite element analysis operator or software defines the actual load in reinforced element and uses the corresponded stiffness. For example, Plaxis includes Elastoplastic (N-e) geogrid model that requires stiffnesses at all load proportions and chooses the proper one automatically.

4 FINITE ELEMENT MODEL

4.1 *Soil slope model*

To highlight the difference between soil and reinforced soil models two structures are shown. First one is a Mohr-Coulomb simple soil 6m high embankment with no geosynthetic material. Main design properties are shown in Table 1.

Table 1. Design properties for soil slope.

Parameter	Fill	Foundation
Cohesion, kPa	1	-
Angle of friction, °	36	-
Su, kPa	-	125
Unit weight, kN/m3	19	18

Stability analysis shown in Figure 6 provides a factor of safety equal to 1,22.

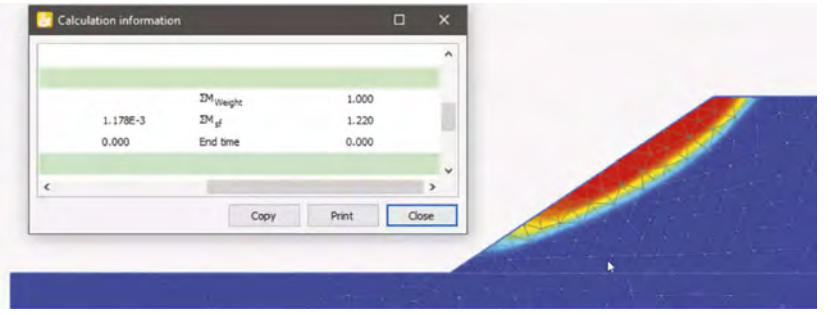

Figure 6. Simple slope FEM analysis.

The same slope modeled by analytical method shows a non-circular slip surface with quiet close nature and safety factor of 1,206 as per Figure 7.

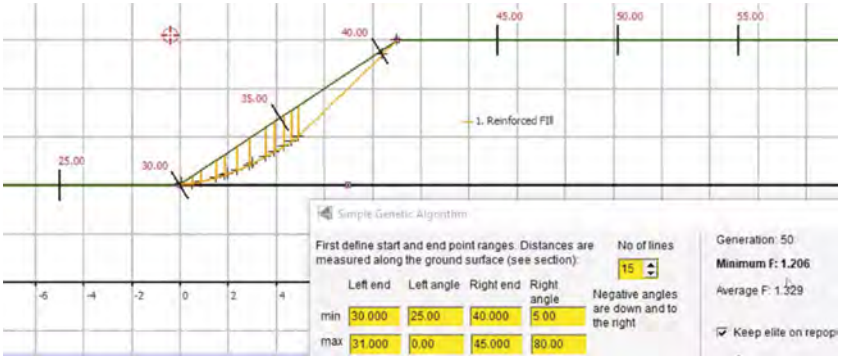

Figure 7. Simple slope analytical analysis.

Based on this, we can assert a high convergence of finite element and analytical modeling the results.

4.2 *Reinforced soil model*

Second model represents a 6m high reinforced soil structure with facing wrapped around sandbags. Main design properties are shown in Table 2, section is shown in Figure 8.

Table 2. Design properties for soil slope.

Parameter	Reinforced soil	Retained fill	Foundation	Soilbags
Material model	H-S (Drained)	H-S (Drained)	M-C	M-C
E_{50}^{ref}	25.000	20.000	-	-
E_{oed}^{ref}	25.000	20.000	-	-
E_{ur}^{ref}	75.000	60.000	-	-
m	0.5	0.5	-	-
E, kN/m^2	-	-	37.500	30.000
v	-	-	0.35	0.30
λ*	-	-	-	-
k*	-	-	-	-
c', kPa	1	0.1	-	10
s_u,kPa	-	-	125	-
Angle of friction, °	36	30	-	30
ψ, °	0	0	-	-
Unit weight sat, kN/m3	19	19	18	19
Unit weight sat, kN/m3	19	19	18	19

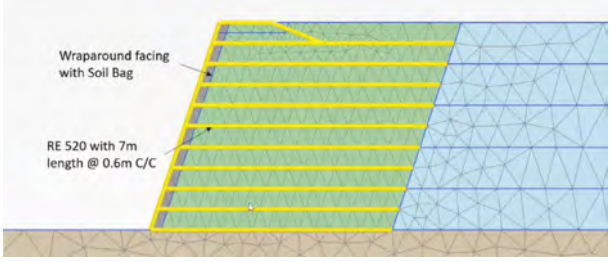

Figure 8. Reinforced soil structure FEM model.

For geogrid an elastoplastic model was obtained with secant stiffness EA_1 = 262kN/m and design strength $N_{p,1}$=23.5 kN/m that came from a set of creep tests under loads from 5 to 65% of short-term strength. No surcharge was used. Stability analysis shows factor of safety 2,11 and 10,5cm surface deformation as per Figure 9.

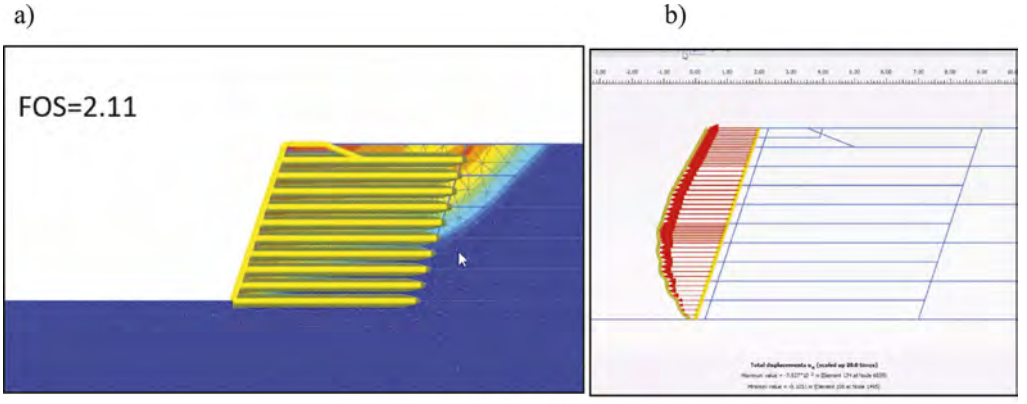

a) failure surfaces; b) deformations

Figure 9. Reinforced soil structure FEM stability and deformation analysis.

The same structure modeled in analytical software shows a different way of failure with much lower factor of safety (1,657) as per Figure 10. Grid strain is lower than 0,25% or 1,5cm.

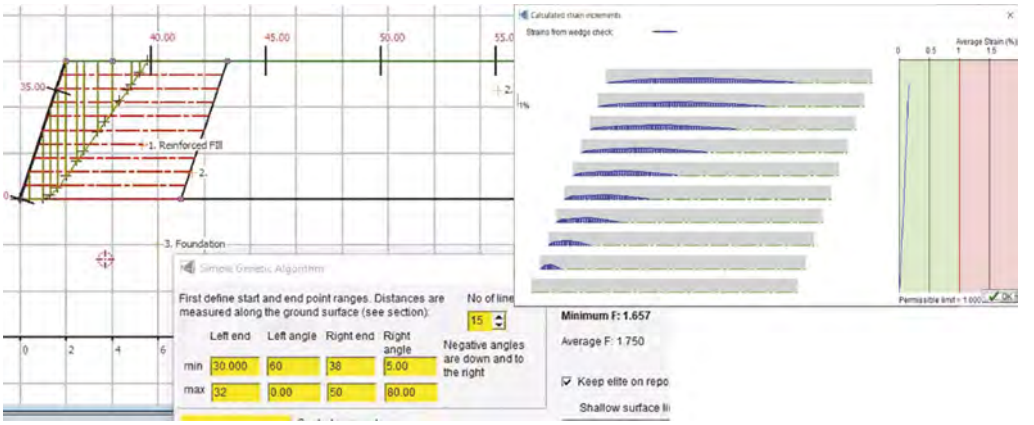

Figure 10. Reinforced soil structure stability and deformation analysis in analytical software.

Modeling a real reinforced soil structure on the automobile road "Perm - Berezniki" in Perm region of Russia under in-service load resulted in 25cm movement shown in Figure 11.

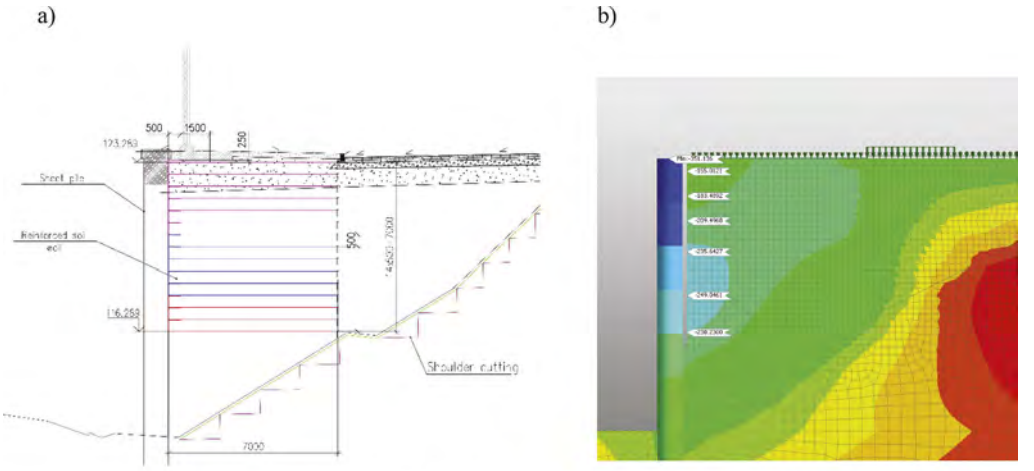

a) design section; b) FEA DX displacement result

Figure 11. Reinforced soil wall at "Perm - Berezniki".

Construction is going to start in the beginning of 2023 with accompanying monitoring. Further scientific work is being carried out to compare the results of modeling and monitoring.

5 ALTERNATIVE APPROACH

Lees & Dobie (2021) propose to include stabilisation effect of geogrid into the analysis. This effect was measured during biaxial testing in a unit cell as an ability to reduce the horizontal

stress and strain once loaded vertically. The biaxial test was then simulated by FEA using Plaxis 3D software followed by a back-calculation of existing trial wall behavior. It was recommended to add stabilisation effect as an additional 9° to an angle of friction for reinforced soil areas with σ_3 < 20kPa or 14kPa cohesion for reinforced soil areas with σ_3 > 20kPa.

This approach was proved to follow the actual reinforced wall behavior way more accurate than classic FEM modeling of a membrane elements. But stabilisation effect must be defined for each individual grid + fill combination during the specific and not standardized test.

6 DISCUSSIONS

This is an important finding in the understanding of the long-term creep related stiffness being the key design parameter together with classic service life design strength. The present study confirmed the findings about insufficiency of current FEM models. Previously this fact was not so evident because of wide usage of short-term stiffness.

7 CONCLUSION

At this moment, analytical modeling methods better correspond to the real life behavior of reinforced soil structures. Numerical modeling is used for complex geometry cases and is able to include reinforcement effect. To do this, a full range of creep tests is required for specifying long-term stiffness at design tension level in reinforcement. Secant stiffness EA_1 is obtained from a creep test isochrone for required service life and not from a short-term tensile test. Long-term stiffness is 50-100% lower than short-term one and this reveals a problem of FEM overestimating structure deformations when compared to either analytical designs or actual soil structure behavior. Discovering of stabilisation effect that geosynthetics provides to a fill material moves FEM models closer to actual monitored structure deformation but requires a series of specific and not standardized tests.

ACKNOWLEDGEMENT

The author would like to acknowledge Lau Joe Jiunn of Tensar International - Malaysia for providing a sensitivity FEM analysis and Mikhail Strapchuk of the JSC "Stroyproekt Institute" for project support.

REFERENCES

British Standards Institution. 2016. *BS8006-1:2010 +A1:2016 Code of practice for strengthened/reinforced soils and other fills*. London: BSI Standards Limited

German Geotechnical Society. 2012. *Recommendations for Design and Analysis of Earth Structures using Geosynthetic Reinforcements – EBGEO, Second Edition*. Germany: Wilhelm Ernst & Sohn

NTC GEOPROECT. 2012. *ODM 218.3.120-2020 Guidelines for the design of road embankments on soft foundation soils using geosynthetic materials*. Moscow: Rosavtodor

ISO/TR 20432:2007 Guidelines for the determination of the long-term strength of geosynthetics for soil reinforcement.

Lees A. & Dobie M. 2021 *Finite Element Modeling of a Mechanically Stabilized Earth Trial Wall*, Transportation Research Record Journal of the Transportation Research Board.

Smart Geotechnics for Smart Societies – Zhussupbekov, Sarsembayeva & Kaliakin (Eds)
© 2023 The Author(s), ISBN 978-1-003-29912-7
Open Access: www.taylorfrancis.com, CC BY-NC-ND 4.0 license

Modeling simultaneous transfer of soil water and heat in the evaporation process in unsaturated shallow ground

M. Sawada
Tokyo Institute of Technology, Tokyo, Japan

M. Mimura & K. Yoshikawa
Kyoto University, Kyoto, Japan

ABSTRACT: The accurate prediction of complex mechanical and hydrothermal soil behavior in shallow zones is necessary to mitigate geo-disasters. This study aimed to develop a numerical model for predicting soil water transfer in both liquid and vapor forms, involving heat transfer in the evaporation process in shallow zones. Parametric studies demonstrated that intensive surface desiccation occurs in soils with a low coefficient of permeability or low water retention. The numerical model was validated by comparing the numerical and experimental results of the evaporation tests, which showed that the evaporation rate can be predicted quantitatively. However, some modifications are required for both calculations and experiments to confirm the validity of local soil water transfer and temperature variation.

1 INTRODUCTION

Soil behavior in shallow zones is significantly affected by climate, which occasionally results in slope failure, collapse, desiccation cracks, and salinization. The occurrence of these phenomena affecting our lives can increase because of future extreme climates, such as heavy rainfall and drought. However, to predict these phenomena, the mechanical and hydraulic behavior unique to shallow zones must be considered. Tensile failure is prone to occur in shallow zones under unsaturated and low-confining-pressure conditions. Additionally, pore water transfers both in liquid and vapor forms, and the phase change involves heat transfer. Such complex behavior in shallow zones is not completely covered by conventional geotechnical engineering.

We aimed to develop a numerical model for predicting deformation and hydrothermal transfer in shallow zones. This paper discusses the numerical modeling of the simultaneous transfer of water and heat during evaporation. Predicting the evaporation process is difficult compared with the seepage process in terms of the boundary conditions between the atmosphere and ground surface, where the time-varying evaporation rate is governed by both atmospheric conditions and the hydraulic properties of soils. The temperature decrease due to the latent heat consumed during the phase change from liquid to vapor also contributes to the evaporation rate. We created a one-dimensional analysis code to predict the evaporation process and performed parametric studies to elucidate the effects of the soil permeability and water retention. Furthermore, the numerical model was validated by comparing the numerical and experimental results of evaporation tests.

2 METHODOLOGY

We used the governing equations proposed by Wilson et al. (1994) for the evaporation analysis. The equations for the water and heat transfer are expressed as follows:

$$\frac{\partial \theta}{\partial t} = \frac{\partial}{\partial z}\left\{k_w \cdot \frac{\partial(\psi + z)}{\partial z}\right\} + \frac{1}{\rho_w} \cdot \frac{\partial}{\partial z}\left(D_v \cdot \frac{\partial P_v}{\partial z}\right) \quad (1)$$

DOI: 10.1201/9781003299127-358

$$C_h \cdot \frac{\partial T}{\partial t} = \frac{\partial}{\partial z}\left(\lambda \cdot \frac{\partial T}{\partial z}\right) + L_v \cdot \left(\frac{P + P_v}{P}\right) \cdot \frac{\partial}{\partial z}\left(D_v \cdot \frac{\partial P_v}{\partial z}\right) \quad (2)$$

where θ is the volumetric water content, k_w is the coefficient of permeability [m/s], ψ is the pressure head [m], ρ_w is the water density [kg/m^3], D_v is the diffusion coefficient of water vapor [kg•m/kN•s], P_v is the pore air vapor pressure [kPa], P is the atmospheric pressure (101.325 kPa), C_h is the volumetric heat capacity [kJ/m^3•K], T is the temperature [K], λ is the thermal conductivity [W/m•K], and L_v is the latent heat (2557 kJ/kg). The functions referred to as the van Genuchten—Mualem model (van Genuchten 1980) were used to express the relationships between θ and ψ (i.e. SWCC) and $k_w - \psi$. A semi-empirical model (Wilson et al. 1994) was used to determine D_v, which is a function of the soil cross-sectional area occupied by pore air. The moisture dependency of λ was considered by applying an approximation formula given by Equation 3 to an experimentally obtained relationship between the degree of saturation, S_r, and λ (Sawada & Mimura 2017);

$$\lambda = \frac{\lambda_{max}}{1 + C_1 exp(-C_2 S_r)} \quad (3)$$

where λ_{max} [W/m•K], C_1, and C_2 are the fitting parameters. The evaporation rate E [m/s] at the ground surface was estimated using the Dalton-type equation:

$$E = f(u)(e_s - e_a) \quad (4)$$

where $f(u)$ is the turbulent exchange function [m/s•kPa], e_s is the vapor pressure at the ground surface [kPa], and e_a is the vapor pressure in the atmosphere [kPa]. In this study, $f(u)$ under hydrothermal conditions (i.e. 20 °C, 60%RH) was determined to be 6.489×10^{-7} m/s•kPa by measuring the evaporation rate from the free water surface (i.e. e_s=saturated vapor pressure). The heat transfer at the ground surface results from latent heat being proportional to E, and sensible heat q_u [W/m^3], which is estimated as follows (Hokoi et al. 2002):

$$q_u = \alpha_h \cdot (T_\infty - T_s) \quad (5)$$

where α_h is the heat transfer coefficient considering convection and radiation (23.0 W/m^3•K), T_∞ is the ambient temperature at a location well away from the ground surface [K], and T_s is the ground surface temperature [K]. Subsequently, the calculation results were obtained using the forward finite difference method.

3 PARAMETRIC STUDIES

Evaporation from a sandy soil column (sand: 58%, silt: 17.3%, clay: 24.8%) with a height of 0.45 m placed under a constant climatic condition of 20 °C and 60%RH was calculated. The bottom of the soil column was assumed to be impermeable to both water and heat. The parameters are listed in Table 1. Several additional experiments were performed to analyze the influence of the coefficient of permeability and SWCC on evaporation. In this study, two additional cases were compared with the original case (i.e. Case 1): Case 2, where the saturated coefficient of permeability, k_{sat} [m/s], was 1/10 of Case 1, and Case 3, where S_r at an arbitrary suction was lower than that of Case 1.

Figure 1a compares the evaporation rate and total evaporation for the three cases. The evaporation rate rapidly decreased after the start because the vapor pressure at the soil surface decreased with a decrease in temperature owing to latent heat, and then it was almost constant for several days. This potential evaporation rate in the first stage was governed only by atmospheric conditions. The decrease in the evaporation rate in the subsequent second stage was affected by the hydraulic properties of the soil. Figure 1 shows that in the additional cases, the transition to the second stage was early, which lowered the total evaporation. This was because of the clear difference in the water content profiles in the vertical direction between Case 1 and the other cases. A comparison between Cases 1 and 2 (Figure 1b) indicated that upward water transfer in the soil column lagged the potential evaporation rate as a demand from the atmosphere when the coefficient of permeability was

Table 1. Parameters used in Case 1.

Properties			Properties		Properties	
SWCC	θ_s	0.481	λ_{max}	1.258	void ratio	0.927
	θ_r	0.000	C_1	2.470	dry density [g/cm^3]	1.370
	α [1/m]	1.435*	C_2	0.026	initial water content [%]	29.0
	n	0.187	k_{sat}	1.04×10^{-5}**		

* α=5.000 in Case 3. ** k_{sat}=1.04×10^{-6} in Case 2.

low, which resulted in an early transition to the second stage and intensive surface desiccation with the remaining wet deep zone. Intensive surface desiccation was also observed in Case 3, although the water content and coefficient of permeability in Case 3 were initially equal to those in Case 1 (Figure 1c). In the evaporation process, the water transfer in the liquid phase in the upward and downward directions was caused by the pressure head gradient and gravity, respectively, as described in Equation 1. In Case 3, assuming a soil with low water retention, the intensive surface desiccation was caused by these opposite flow directions. The downward flow in Case 3 was significant compared with that in Case 1 because the initial suction was small and the suction gradient corresponding to the water content gradient was small.

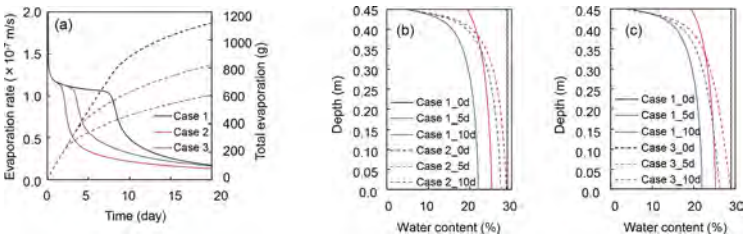

Figure 1. Results of parametric studies.

4 MODEL VALIDATION

Evaporation tests were conducted in a constant climate chamber in which the temperature and relative humidity were kept constant at 20 °C and 60%RH, respectively, using a rectangular soil column (0.10 m × 0.15 m × 0.45 m). The soil column with initial water content and dry density are listed in Table 1 was prepared by compacting sandy soil in an acrylic mold. The sides of the soil column were covered with a Rockwool sheet to cut off heat inflow from the atmosphere. The weight of the soil column was measured to determine the evaporation rate. Moisture sensors (TEROS 10, METER, Inc.) and potential sensors (TEROS 21, METER, Inc.) were installed at depths of 0.05, 0.15, 0.25, and 0.35 m. The potential sensors measured suction within a range of 9–2000 kPa and temperature.

The SWCCs obtained in the evaporation test were almost consistent with the results of the water retention tests during the drying process, although the suction near the surface reached the measurement upper limit during the test. The best-fit curve estimated using the least-squares method had fitting parameters of θ_s =0.481, θ_r =0.000, α = 3.167, and n = 1.184. The evaporation test was numerically simulated using the SWCC. The other parameters used for the simulation were the same as those listed in Table 1. Figure 2a compares the measured and calculated evaporation rates and total evaporation. The measured and calculated evaporation rates agreed well throughout the first and second stages until five days after the start, although a slight discrepancy was observed in the subsequent third stage with a constant evaporation rate. Figure 2b compares the measured and calculated time series of water content. The calculated water content was lower than the measured value throughout the test at the two lower measurement points. This tendency was observed at the upper two measurement points a few days after the start, and the calculated water content subsequently exceeded the measured value. These results indicated that the numerical model can quantitatively predict evaporation over the entire soil column; however, the actual local water transfer in the soil column differed from the numerically

predicted one. This discrepancy may have been due to the discontinuities in the non-homogeneously compacted soil column. Sandy soil with a high fine fracture content was difficult to compact homogeneously because it was aggregated at the initial water content. Fissures or voids above the two lower measurement points in the soil column may have restrained the upward liquid water flow from the lower zone and accelerated evaporation in the upper zone. To confirm the validity of local water transfer, evaporation tests should be modified to use homogenous soil columns of sandy soil prepared at lower water contents or other soils with lower fine fraction content.

Figure 2c compares the measured and calculated time series of the temperature. Temperature significantly decreased a few days after the start owing to latent heat and then gradually recovered with a decrease in the evaporation rate and heat inflow from the atmosphere through the soil surface. The calculated temperature qualitatively agreed with the measured temperature. However, the calculated temperature decrease was significant compared with the measured decrease, although the evaporation rate was underestimated. These conflicting results were owing to the heat inflow through the sides of the actual soil column, which was not considered in the one-dimensional analysis. This was supported by additional evaporation tests without the side Rockwool sheet, which measured a smaller decrease in temperature. It was impossible to completely cut off the heat inflow from the sides in the experiments. Thus, a three-dimensional analysis is necessary to confirm the validity of temperature variation.

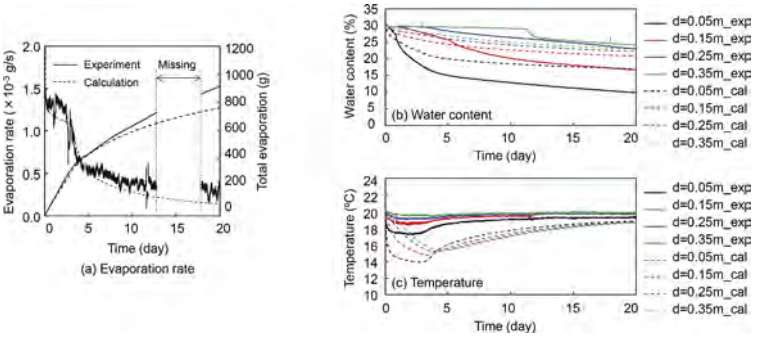

Figure 2. Comparison between calculated and measured results.

5 CONCLUSIONS

This paper presents a numerical analysis of the simultaneous transfer of soil water and heat during evaporation in shallow zones. Parametric studies showed that intensive surface desiccation occurs in soils with a low coefficient of permeability or low water retentivity. A comparison between the numerical and experimental results of evaporation tests showed that the numerical model is valid for predicting the evaporation rate; however, some modifications are required for both calculation and experiment to confirm the validity of local soil water transfer and temperature variation.

ACKNOWLEDGEMENTS

This work was supported by JSPS KAKENHI (grant number 21 K14240).

REFERENCES

Hokoi, S., Ikeda, T. & Nitta, K. 2002. *Environmental Engineering II.*: Asakura Publishing. [in Japanese]

Sawada, M. & Mimura, M. 2017. Environment control in a burial chamber by covering with an earth mound. *Journal of Japan Society of Civil Engineers, Ser. C*, 73(4): 368–361. [in Japanese]

van Genuchten, M. T. 1980. A closed-form equation for predicting the hydraulic conductivity of unsaturated soils. *Soil Science Society of America Journal*, 44(5): 892–898.

Wilson, G.W., Fredlund, D., & Barbour, S.L. 1994. Coupled soil-atmosphere modelling for soil evaporation. *Canadian Geotechnical Journal*, 31: 151–161.

Smart Geotechnics for Smart Societies – Zhussupbekov, Sarsembayeva & Kaliakin (Eds)
© 2023 The Author(s), ISBN 978-1-003-29912-7
Open Access: www.taylorfrancis.com, CC BY-NC-ND 4.0 license

Comprehensive engineering protection of the territory on the example of the sochi mountain cluster

I.S. Bogdanov
GEOIZOL Project LLC, St. Petersburg, Russia

ABSTRACT: Hosting the Winter Olympics 2014 became an incentive for an active development of the Sochi mountain cluster (Krasnodar Region, Russia). A set of engineering protection measures against dangerous geological phenomena and processes was taken on the territory where sports and recreational infrastructural facilities were to be constructed. The Sochi mountain cluster became a real testing ground for implementing advanced technical solutions in the area of engineering protection in really specific conditions when developing facilities in the national park on a steeply sloping terrain under the risk of high seismic activity (9 points). The article provides review of the measures taken. They include constructing flexible mudflow-retaining and snow-retaining barriers, ensuring the stability of slopes by soil nailing using the GEOIZOL-MP multifunctional geotechnical system, constructing retaining structures (retaining walls) of various designs: piled, corner monolithic on a piled base, reinforced soil, gabions.

Keywords: Engineering protection of the territory, Landslide, Mudflow, Snow avalanche, Rockfall, Erosion, Ground anchor, GEOIZOL-MP

1 GENERAL DESCRIPTION OF THE DESIGN OBJECT

The 2014 Winter Olympics became the starting point for creating one of the largest conglomerates of mountain climate resorts in Eastern Europe in the mountain cluster of Sochi (Krasnodar Region, Russia). Implementation of the large-scale construction project began in the national park, which required to minimize environmental impact and preserve the existing ecosystems. The construction sites of the recreational and sports infrastructural facilities were located in the hard-to-reach areas on steep slopes. There was a risk for the facilities to be exposed to the dangerous geological phenomena and processes such as soil erosion, landslide processes, mudflows, snow avalanches, and rockfalls. Another complicating condition is a high seismic activity of the region (9 points).

Under the given conditions, traditional methods of engineering protection of the territory with massive reinforced concrete structures, dirt fills, and dams were inapplicable. GEOIZOL Project analyzed the best international practices in engineering protection of the territory and introduced a wide range of advanced technical solutions to ensure the possibility of construction and subsequent safe operation of the facilities.

It is especially worth noting a comprehensive approach to engineering protection of the territory and facilities that included a use of combinations of various structures to improve reliability of structures and optimize financial costs. The mountain cluster of Sochi became a testing ground for implementing new methods of engineering protection of the territory. One of the outcomes of this work is development of the regulatory and technical base as well as adding new technologies and solutions to the standards.

DOI: 10.1201/9781003299127-359

2 MEASURES FOR COMPREHENSIVE ENGINEERING PROTECTION OF THE TERRITORY

2.1 *Drainage and protection against erosion*

Water is one of the main destructive factors in the mountains. When flowing downhill, running water accumulate significant energy, destroying ground cover and having a negative impact on engineering structures. Water soaks soil bodies, activating landslide processes. In this regard, during a design stage it should be given a priority to measures for draining water away from the facilities under construction: building drainages, intercepting and slope ditches, and capture chambers.

During construction work, an integrity of the soil cover is inevitably disturbed. Without additional protection, opened ground is subject to erosion – intensive destruction by wind and precipitation.

Cover systems of various designs are generally used for erosion control. Geosynthetic erosion control mats are installed to provide soil reinforcement and subsequent revegetation. A high-strength steel mesh fixed with ground anchors is additionally arranged on steep slopes.

Anti-erosion measures fully offset a negative effect of anthropogenic impact on soil and prevent the development of creep processes.

2.2 *Landslide protection without changing the relief*

When implementing the projects in the mountain cluster of Sochi, soil nailing of slopes was widely used as a landslide protection. The essence of the technology is to spatially reinforce a soil body with such geotechnical elements as injection-bored soil nails. Ground nails extend beyond the slope sliding surface, holding a soil body (landslide body), and they are fixed in the deeper stable layers. The cover system (high-strength steel mesh with anti-erosion mats) prevents displacements on the surface, it does not allow soil to fall out in the inter-nail space and protects against erosion.

The solution is used to ensure stability of natural and artificial slopes when there is a high risk of triggering landslide processes. It allows performing the work without vegetation destruction while maintaining the original relief. Soil nailing is also justified when locating facilities on a slope, for example, cableway supports.

The principle of such reinforcement is similar to how anchors fix concrete pressure plates. It is a proprietary design of GEOIZOL Project. The solution is a compact alternative to a counterweight berm. Plates fixed with anchors create additional pressure (counterweight) on the soil in the lower area of the landslide body and increase the holding forces, thus increasing stability of a potential landslide slope.

The multifunctional GOIZOL-MP system is used as ground anchors and nails (as well as bored micropiles). The GEOIZOL Group solution has better characteristics than the best European analogues. The production of GOIZOL-MP was deployed at the Pushkin Machine-Building Plant in St. Petersburg.

2.3 *Landslide protection with changing the relief*

Locating objects on steep mountain slopes inevitably leads to changing the relief for leveling construction sites or laying roads. It often requires installation of restraining structures of various designs. When cutting slopes, sheetpile or pile retaining walls are used. A pile retaining wall consists of one or more rows of bored piles, united along the top with a grillage. An additional stability of the structure is usually achieved by ground anchors. They are arranged in one or more horizontal rows through the distribution beams as the soil is excavated. At the final stage, a monolithic pressure wall is made on the front side.

When forming the relief by backfilling of the territory, it is possible to use various structures. They include corner walls on a natural or pile foundation, different reinforced ground embankments lined with gabions, prefabricated concrete elements, the Green Terramesh system or their combinations. To ensure even greater stability, the restraint structures may be supplemented with an uphill and downhill soil nailing.

2.4 *Mudflow protection*

Engineering protection measures against mudflows are chosen depending on the specifics of the protected facility. GEOIZOL Project applied various technical solutions and their combinations at the sites in Sochi. First of all, measures are provided to exclude mudflow triggering factors: stabilization of watercourses, installation of erosion protection in the mudflow basin, nailing of certain potentially unstable soil bodies.

A traditional solution to eliminate an impact of mudflows on the protected facility is constructing mudflow trapping reservoirs along with retaining dams and special drainage structures.

Traditional massive anti-mudflow dams were replaced with flexible mudflow-retaining barriers in the mountain cluster of Sochi. They are installed across the foreseeable mudflow bed to retain the solid part of the flow, which poses the greatest threat to the protected facilities. The barrier consists of a high-strength steel mesh stretched between posts and reinforced with steel ropes and buffers. The GEOIZOL-MP injection-bored ground anchors are used to fix the posts and guy ropes. The construction and operation of such structures is possible using compact vehicles, even in the hard-to-reach areas where laying access roads is impossible.

Only a section of the ski slope had to be protected at one of the facilities. A closed-type structure was built for this purpose. A box-shaped tunnel was built under the protected ski slope for the estimated volume of mudflow to go through. It ensures a normal regime of stream between mudflows.

2.5 *Avalanche protection*

Engineering protection methods are chosen depending on the avalanche type. Preventive measures should be taken in the areas with a high avalanche risk. One the most common measures is artificial triggering snow flows. To reduce the snow mass, it is possible to set up snow blowing structures or GAZEX avalanche-control systems in places where snow is accumulated.

When constructing facilities in the area characterized with high risk of channeled avalanches, it is possible to erect local protective structures. High reinforced soil embankment with gabion lining was made to provide avalanche protection for the Yunost ropeway station, located on the slope of the Aibga Ridge. The nearby cableway supports are protected by massive reinforced concrete avalanche breakers.

A natural method of controlling snow slides is forest restoration. Another effective control method is erecting flexible snow-retaining barriers. The barrier structures are installed across the slope in places where snow is accumulated. The barriers keep the snow mass in a static state, reducing the risks of snow slides. The structures are fixed with the GEOIZOL-MP ground anchors. In summer, the structures can function as rock barriers.First line of text or heading.

2.6 *Rockfall protection*

Before choosing rockfall protection solutions, it is necessary to determine dangerous areas and a type of the rock mass destruction. If the area where rocks can fall off is relatively small, it is fully covered with a high-strength steel mesh while large rock formations are reinforced. In some cases, an optimal solution to prevent landslide phenomena can be nailing. To protect the facilities against falling debris, including those having high energy of up to 10,000 kJ, installation of rock barriers is applicable. Such mesh structures can also be used to protect against associated risks such as avalanches and mudflows.

2.7 *Repair of emergency retaining structures*

Sometimes the company has to deal with cases where a customer needs to restore existing retaining walls. Increasing rigidity of such structures is one of the most difficult engineering tasks in the field of protection against landslide processes. When designing such measures, it is necessary to take into account an actual rigidity of emergency structures and how their functionality will be changed after reinforcement. An actual state of the structures is also taken into account, including a decrease or partial loss of the bearing capacity of the structural elements.

There are several approaches to reinforcing emergency retaining walls. The first one is improving stability of retaining structures by arranging rows of the GOIZOL-MP ground anchors inserted through the body of existing structures. Another one is installation of backup retaining walls to relieve additional load under special effects.

It should be noted that a comprehensive approach is required when designing repair of emergency structures. First of all, it is necessary to identify the reasons for reduced performance of the structures. This may be a change of the hydrogeological conditions. The essential parts of the design should be elimination of these causes and elimination of consequences of man-made impact during the repair: taking anti-erosion protection measures and providing drainage.

3 CONCLUSION

After having designed the engineering protection of the territory for the Olympic venues in Sochi, GEOIZOL Project Company gained a unique experience. This work demonstrated the obvious need for an integrated approach when designing safety engineering measures for the territory. Considering all the risk groups on the whole allows us to interconnect and optimize protective measures, which positively affects both the effectiveness of the measures adopted in the framework of the project, as well as the terms and cost of their implementation. An integrated approach to designing the engineering protection of the territory has become the standard for the Company.

In the Sochi mountain cluster, GEOIZOL Project Company has put into practice the methods for safety engineering for the territory proven their effectiveness, which allow ensuring the required level of safety with a minimal impact on the environment. Many of these technologies have never been used in Russia before. These include flexible barriers used to protect against mudflows, avalanches and rockfalls. Also in Sochi, the soil nailing of landslide hazard slopes is widely used.

The experience gained in the construction of Olympic venues has had a positive impact on the construction industry in Russia as a whole. The GEOIZOL Project Company has become one of the pioneers of the engineering protection of the territory as an independent trend in the construction industry of the country.

REFERENCES

Aleksandrov P.A. 2022. Experience in the design and operation of anti-mudflow structures // site of the company “GEOIZOL Project”. URL: https://geoizolproject.ru/library/publikacii/opyt-proektirovanija-i-jekspluatacii-protivoselevyh-sooruzhenij/ (date of access: 12/03/2023).

Dmitrieva N.V., Popov O.A., Stepanenko N.A. 2019. Analysis of landslide phenomena and ways to prevent them // EESJ. №4–3 (44).

Svalova V. 2016. Landslides modeling, monitoring, risk management and reduction // EESJ. №4.

Trofimov V. T., Korolev V. A. 2012. Engineering Protection of Territories and Buildings in the System of Engineering and Environmental Protection. Moscow University Geology Bulletin. Vol. 67, No. 1, pp. 52–57. DOI: 10.3103/S0145875212010103.

Zhuravlev P.A., Marukyan A.M. 2020. Engineering protection of buildings, structures and territories as a factor of innovative development of spatial planning. Vestnik MGSU [Monthly Journal on Construction and Architecture]. 15(10):1440–1449. DOI: 10.22227/1997-0935.2020.10.1440-1449.

SP 116.13330.2012. A set of rules. Engineering protection of territories, buildings and structures from dangerous geological processes. Basic principles// approved by Order of the Ministry of Regional Development of the Russian Federation No. 274/pr dated 30.06.2012 and put into effect from 01.01.2013.

SP 436.1325800.2018. A set of rules. Engineering protection of territories, buildings and structures from landslides and land-slides. Design rules // approved by Order of the Ministry of Construction and Housing and Communal Services of the Russian Federation No. 787/pr dated 5.12.2018 and put into effect from 6.06.2019.

Smart Geotechnics for Smart Societies – Zhussupbekov, Sarsembayeva & Kaliakin (Eds)
© 2023 The Author(s), ISBN 978-1-003-29912-7
Open Access: www.taylorfrancis.com, CC BY-NC-ND 4.0 license

Studying the state of stress parameters of stress intensity factors in reinforced concrete bending elements

Zh.S. Nuguzhinov
KazMIRR Institute of the NJC "KarTU named after Abylkas Saginov", Karaganda, Kazakhstan

M.Zh. Bakirov
NJC "KarTU named after Abylkas Saginov", Karaganda, Kazakhstan

D.T. Tokanov, O. Habidolda & I.A. Kurokhtina
KazMIRR Institute of the NJC "KarTU named after Abylkas Saginov", Karaganda, Kazakhstan

A.T. Mukhamejanova & D.K. Zhilkibayev
Eurasian National University, Nur-Sultan, Kazakhstan

ABSTRACT: The work determines the stress intensity factor (SIF) at the crack tip in bending reinforced concrete beams. The problem has been solved in a three-dimensional formulation using special elements that take into account peculiarities of the stress field at the crack tip.

Calculations have been carried out for beams of rectangular cross-section with pure bending to obtain analytical calculated dependences on variable factors. To obtain analytically calculated dependences on variable factors, a matrix of rational planning a multifactorial computer experiment has been compiled to determine the SIF and stress state parameters in bending rectangular reinforced concrete beams with a crack. Regression dependences for the SIF and the stress in the armature on the parameters of the beam and loading are obtained. The numerical calculation method is general and applies to beams of an arbitrary section under arbitrary loading. The obtained dependencies make it possible to evaluate the crack resistance of reinforced concrete beams according to the force criterion of fracture mechanics without the use of computer technology and expensive software complexes. In this paper, there is considered determining the SIF in bending reinforced concrete beams by the finite element method. The calculation results are presented in the form of the SIF regression dependences on the varied parameters.

1 INTRODUCTION

Cracks are a very common type of defect in reinforced concrete structures [1, 2]. They can appear both at the manufacturing stage and the stage of mounting and operation. Operational cracks appear in the tensile zone of concrete when the maximum stress exceeds the ultimate strength of concrete. Since concrete is a brittle material and has lower tensile strength than compressive strength, cracks appear even before the bearing capacity of the reinforced concrete element is exhausted.

It is necessary to determine the stress state in the section with a crack to assess the bearing capacity of a reinforced concrete element. To assess crack resistance, it is necessary to determine the parameters of fracture mechanics that correspond to the accepted fracture criterion. The brittle fracture force criterion is applied for concrete, expressed through the stress intensity factor (SIF). When bending, it is necessary to determine the SIF of the first type (a separation crack). It is necessary to know the nominal stresses at the crack tip to determine it.

In the general case, the calculation of the SIF is performed by the finite element method (FEM) in a linear formulation. Such a calculation for bending reinforced concrete elements is

DOI: 10.1201/9781003299127-360

rarely performed. The one is due to the complexity of the calculations associated with the above-mentioned character of crack development and the need for a volumetric formulation of the problem.

Since cracks exist in any reinforced concrete elements, determining the stress state in the section with a crack and calculating the SIF are very important for assessing the real state of the structure in operation.

In this paper, there is considered determining the SIF in bending reinforced concrete beams by the finite element method. The calculation results are presented in the form of the SIF regression dependences on the varied parameters.

2 METHODS

The finite element method is the main method of determining the parameters of fracture mechanics in metal structures. Because of the complexity of implementing the algorithm of determining the SIF in reinforced concrete structures, it is rarely used and has its characteristics. This calculation is carried out in a linear setting based on a three-dimensional model. The SIF is determined by the field of displacements or stresses at the crack tip. In the ANSYS software package, all the stages of calculations are automated, especially in the Workbench interactive mode.

A common disadvantage of numerical calculation methods is the difficulty of analyzing the final results to control the calculated value. It is not clear from the solution, which input parameters, in which direction, and how much is better to be changed to get the desired result. It is necessary to carry out multiple calculations with step-by-step changes in many variable parameters to catch the change trends. In addition, the results obtained cannot be used with a quantitative change in the properties of materials, structural parameters or loading.

For reasonable selecting of the parameters of reinforced concrete elements and controlling the loading parameters, it is necessary to have analytical dependences of the SIF on the varied parameters. A multifactorial computer experiment must be planned and performed to obtain these dependencies. By processing the results of such an experiment, the desired regression dependencies can be obtained.

3 RESULTS

The SIF in a flexible reinforced concrete beam was calculated by the finite element method in a linear formulation based on a three-dimensional model. The SIF was determined from the displacement or stress field at the crack tip. ANSYS (Ansys, Inc., Canonsburg, PA, USA) was used in Interactive Workbench mode. The main stages of solving the problem were as follows.

According to the above algorithm, there has been calculated a reinforced concrete beam of rectangular cross-section with the size of (15x30) cm of concrete grade B25 (Rbt=1.6 MPa, Rb=14.5 MPa, Eb=24000 MPa) with reinforcement made of AIII steel (Rs=370 MPa, E=200000 MPa). Figure 1 shows the scheme of fastening and loading the beam. In the middle section of the beam, a pure bending occurs with the moment M=Fa.

The beam has an initial crack l0=6 cm in the pure bending and reinforcement zone with the area of As=6.75 cm2 in the tension zone at a distance of 3 cm from the edge of this zone. The calculation of the beam has been carried out under the action of the torque of 8 kN·m. As a result of the calculation, there has been obtained KI=0.41 MN/m3/2.

4 PLANNING A COMPUTER EXPERIMENT

The purpose of the experiment is to obtain an analytical dependence of the SIF on the varied parameters. To assess the bearing capacity of a beam, one can simultaneously determine such dependences for the stress in the reinforcement and for the maximum compression stress in concrete. The analysis of numerous calculations to determine the stress state in reinforced

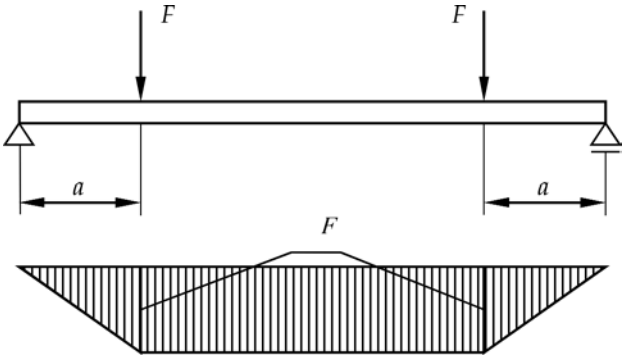

Figure 1. The calculation scheme with a moment diagram.

concrete beams with a bending crack shows that the stress in the reinforcement reaches standard resistance earlier than the stress in concrete. Therefore, alongside the SIF, regression dependences for the stress in the reinforcement σ_s are determined.

To obtain these dependencies, one first needs to select the parameters that significantly impact the output function. Then it is necessary to determine the real limits of changes in these parameters. Each argument's levels should be set so that they meet the requirements of the arithmetic progression (have the same intervals). These actions make it possible to plan the experiment properly and can reduce the required volume significantly.

When planning experiments, selecting the factor levels is important. It is made taking into account two conflicting requirements: the levels of factors should cover the entire possible range of its change, the total number of levels for all the factors should not lead to an excessive volume of tests.

For testing, we take a rectangular beam with reinforcement in the tension zone at a distance of 3 cm from the edge of this zone.

The main factors influencing the output values are the section dimensions h, b, the crack length l, the percentage of reinforcement μ, the elastic moduli of concrete E_b and reinforcement E_s, and the bending moment M. Since the calculation is performed in a linear formulation, the output values will vary linearly to the moment. Therefore, it can be excluded from the number of variable factors and taken fixed in the experiment. The performed test calculations and the analysis of analytical solutions [3, 4] show that the impact of the elastic moduli of materials can be taken into account by one parameter equal to their ratio $\alpha=E_s/E_b$. This leaves five variable factors: h, b, $z=l/h$, μ, α.

We will take the limits of changing these factors to most fully cover the entire range of their changes in real conditions:

$$h = (10 \ldots 50)\text{cm}, b = (5 \ldots 40)\text{cm}, z = 0.1 \ldots 0.7, \mu = (0, 5 \ldots 3)\%, \alpha = 6 \ldots 11.$$

There are no interrelationships between the factors of the model. Therefore, we will use rational planning of the experiment. Since there are five variable factors, we will change them at five equal levels. Table 1 shows the values of the varied parameters at different levels.

Table 1. Varied parameters values.

	Variable values				
Levels	h, cm	b, cm	z	μ, %	A
1	10	5	0.1	0.5	6
2	20	14	0.25	1.1	7.2
3	30	23	0.4	1.7	8.4
4	40	32	0.55	2.3	9.6
5	50	41	0.7	2.9	10.8

With few numbers of factors ($k > 4$) for obtaining an experiment plan, it is more rational to use numerical matrices. The number of rows in the matrix is equal to the number of experiments, and the number of columns is equal to the number of influencing factors. The combination of numbers in each line is a combination of the factor levels in the corresponding experiment. Such plans are based on Latin squares. Only orthogonal Latin squares are suitable to obtain an optimal plan [5]. The technique of constructing mutually orthogonal squares is described in detail in [6].

According to the planning matrix, the full experiment will consist of 25 experiments divided into five orthogonal squares. The first three squares are shown below:

1	1 2 3 4 5	6	1 3 5 2 4	11	1 4 2 5 3
2	2 3 4 5 1	7	2 4 1 3 5	12	2 5 3 1 4
3	3 4 5 1 2	8	3 5 2 4 1	13	3 1 4 2 5
4	4 5 1 2 3	9	4 1 3 5 2	14	4 2 5 3 1
5	5 1 2 3 4	10	5 2 4 1 3	15	5 3 1 4 2

Each row of the matrix represents one experiment, the number of which is indicated by the first digit, and the subsequent digits indicate the levels of the corresponding factor. These levels correspond to the values of the varied parameters shown in Table 1. The first row of the planning matrix shows all the levels in ascending order. The rest of the rows are obtained by incrementing the level number by one in the matrix column with the order from the last to the first number. The first line of the next square consists of the diagonal of the previous square.

5 NUMERICAL CALCULATION

To carry out a computer experiment, we use the structural design shown in Figure 1. The bending moment at pure bending is set equal to 10 kN·m.

The calculation of the SIF in the beam is performed using the ANSYS Software with the rational planning matrix. In each experiment, as a result of the calculation, the SIF (K_I) and the stress in the reinforcement σ_s have been displayed for viewing. A fragment of the experimental results is shown in Table 2.

Table 2. A fragment of the experiment results.

No.	h, cm	b, cm	z	μ	α	K_I, MN/m$^{3/2}$	σ_s, MPa
1	10	14	0.4	2.3	10.8	0.433	229
2	20	23	0.55	2.9	6	0.266	27
3	30	32	0.7	0.5	7.2	0.195	98
4	40	41	0.1	1.1	8.4	0.13	15.3
5	50	5	0.25	1.7	9.6	0.6	57

Based on the results of the computer experiment, regression dependences are constructed for the output parameters. To do this, we will use an unconventional regression analysis method, which is implemented in the ANETR program created at Karaganda Technical University.

The program first arranges the factors in order of decreasing the impact on the output parameter value. For each factor, it selects the corresponding equation from 15 types of equations included in the program. At the same time, to identify the impact of some factors, it may be necessary to neutralize the impact of potent factors. The program ends with selecting a certain combination of partial equations to form the general model. The dependences obtained in this way are valid in the range of variation of the variable parameters.

The adequacy of the general model is assessed by the standard deviation (SD) of the calculated and experimental values of the output quantity and the multiple correlation coefficient of the model. Note that the program developers evaluate the resulting regression model as "excellent" if the standard deviation is lower than 25% and "good" if the standard deviation is lower than 40%.

The initial data of each experiment are entered into the ANETR program in the form of a 25x5 matrix and the value of the analyzed output parameter (response function) in the form of a 25x1 column vector to obtain regression dependences.

Let us present the finally formed multidimensional models for the stress intensity factor:

$$K_I = (M/10)[1.415 \cdot 10^{-3}h^2 - 0.125h + 7.09/b - 1.086\lg z + \\ +0.537\mu^2 - 1.804\mu - 0.117\alpha + 4.209]\left(\mathrm{MN/m^{3/2}}\right). \quad (1)$$

In this expression, the variables must be substituted in the units in which they are indicated in Table 1. The results will also be in the units in which the output values are given in Table 2. The standard deviation of the model is 38.2 %, and the multiple correlation coefficient is $R = 0.82$.

Regression dependences for stress in reinforcement:

$$\sigma_s = (M/10)[25460/h^{1.718} + 1202.5/b + 1697z^2 - 1290z - 85.5\mu + \\ +310.9/\alpha + 185.7](\mathrm{MPa}). \quad (2)$$

The SD of the model makes 25.4%, and the coefficient of multiple correlation R=0.924.

To reduce the standard deviation, you can increase the number of levels of changing the factors, but this will increase the number of experiments. For example, for seven levels, there are needed 49 experiments

The SIF is a parameter of linear fracture mechanics. Therefore, its FEM calculation is carried out in a linear setting. With increasing the bending moment, there should be expected increasing the error in determining the SIF. This is due to the growing influence of physical nonlinearity at high stresses. Under these conditions, it is recommended to calculate the SIF only by the analytical method [4].

6 CONCLUSIONS

The technique and algorithm of determining the stress intensity factor in bending reinforced concrete beams with a crack by the finite element method are described. A matrix of rational planning of the multifactorial computer experiment to determine the SIF in bending rectangular reinforced concrete beams with a crack has been compiled. Based on this planning matrix, using the ANSYS software, machine experiments have been carried out for pure bending beams. By processing the experiment results using the program of unconventional regression analysis ANETR, dependencies have been obtained for determining the SIF and stress in reinforcement in reinforced concrete beams with cracks. The impact of the operational crack length on the SIF has been analyzed. It has been found that in a reinforced concrete beam, the SIF decreases with increasing the crack length. At the critical crack length, the SIF becomes zero and the effective moment is equal to the breaking moment. In reinforced concrete beams, unstable crack development does not lead to the rapid destruction of the beam. However, it reduces its bearing capacity due to increasing the crack length and increasing stresses in concrete and reinforcement. The obtained dependences make it possible to evaluate the crack resistance of reinforced concrete beams according to the force criterion of fracture mechanics without the use of computer technology and expensive software systems. They also make it possible to assess the real state of the beam depending on the reinforcement stress.

REFERENCES

[1] Kumar, S.; Barai, S. v *Concrete Fracture Models and Applications*; Springer Berlin Heidelberg: Berlin, Heidelberg, 2011; ISBN 978-3-642-16763-8. Concrete Fracture Models and Applications | SpringerLink.

[2] Guo, Z. *Principles of Reinforced Concrete*; Elsevier, 2014; ISBN 9780128008591. Principles of Reinforced Concrete (elsevier.com).

[3] Nuguzhinov, Z.; Vatin, N.; Bakirov, Z.; Khabidolda, O.; Zholmagambetov, S.; Kurokhtina, I. Stress-Strain State of Bending Reinforced Beams with Cracks. *Magazine of Civil Engineering* 2020, *97*, 9701–9701, doi:10.18720/MCE.97.1. Scopus - сведения о документе - Stress-strain state of bending reinforced beams with cracks.

[4] Nuguzhinov, Z.S.; Bakirov, Z.B.; Yu Kurokhtin, A.; Khabidolda, O.; Nuguzhinova, A. Assessment of Bending Reinforced Concrete Beams Crack Resistance. In Proceedings of the IOP Conference Series: Materials Science and Engineering; 2019; Vol. 690. Scopus - сведения о документе - Assessment of Bending Reinforced Concrete Beams Crack Resistance.

[5] Keedwell, A.D.; Dénes, J. *Latin Squares and Their Applications*; Elsevier, 2015; ISBN 9780444635556. Latin Squares and their Applications - 2nd Edition (elsevier.com).

[6] Draper, N.R.; Smith, H. *Applied Regression Analysis*; 2014; ISBN 9780471170822. Applied Regression Analysis, 3rd Edition | Wiley.

Smart Geotechnics for Smart Societies – Zhussupbekov, Sarsembayeva & Kaliakin (Eds)
© 2023 The Author(s), ISBN 978-1-003-29912-7
Open Access: www.taylorfrancis.com, CC BY-NC-ND 4.0 license

Assessment of the reliability of building structures based on probabilistic-statistical and deterministic approaches

Zh.S. Nuguzhinov
KazMIRR Institute of the NJC "KarTU named after Abylkas Saginov", Karaganda, Kazakhstan

S.K. Ahmediev
NJC "KarTU named after Abylkas Saginov", Karaganda, Kazakhstan

S.R. Zholmagambetov, D.K. Zhilkibayev & N.Zh. Zhumadilova
KazMIRR Institute of the NJC "KarTU named after Abylkas Saginov", Karaganda, Kazakhstan

ABSTRACT: In this paper, a theoretical study of the problems of reliability of building structures of buildings and structures is carried out. The deterministic (classical) and probably-statistical approach is considered; at the same time, it is established that the probabilistic calculation method with a small increase in material consumption (compared with the deterministic calculation method) gives higher reliability indicators. A methodology for determining the residual resource of buildings and structures based on the results of a technical survey (with an example of calculation) is also proposed.

1 INTRODUCTION

When designing new and operating existing construction structures of buildings and structures, along with deterministic methods of calculation and their bearing capacity (strength, rigidity, stability), probabilistic methods are also used, which take into account the statistical variability of the properties of materials and the magnitude of external influences, etc [1-3].

For practical calculations in building codes and regulations, such variability is indirectly (indirectly) taken into account through appropriate safety coefficients (for materials, for loads), which are based on a statistical, but deterministic essence. In these conditions, the reliability approaches of load-bearing capacity calculations are of actual importance, directly (directly) taking into account statistical variations of the entire complex of initial parameters, represented as random variables or random processes [4-6].

With such a dual approach (deterministic and probabilistic), a logical question arises - to what extent the obtained results of deterministic and probabilistic calculation methods differ, i.e. whether there is a similar difference in the margin of safety (reliability or safety), and also what kind of savings or overspending of construction materials designed during the operation of existing ones building structures of buildings and structures [7].

Since the method of deterministic calculation of building structures is well known, then we will consider in more detail the method of probabilistic calculation.

2 METHODOLOGY

The reliability of "H" structures (in the absence of failures) is determined by the following formula

$$H = P(R < S) \tag{1}$$

DOI: 10.1201/9781003299127-361

where P – probability of an event, R – random limit voltages, S – random design voltages.

To conduct a comparative analysis of the results of deterministic and probabilistic calculation of building structures, we calculated a single-span metal beam for transverse plane bending in two variants: the first - based on the probability approach; the second - based on the deterministic approach.

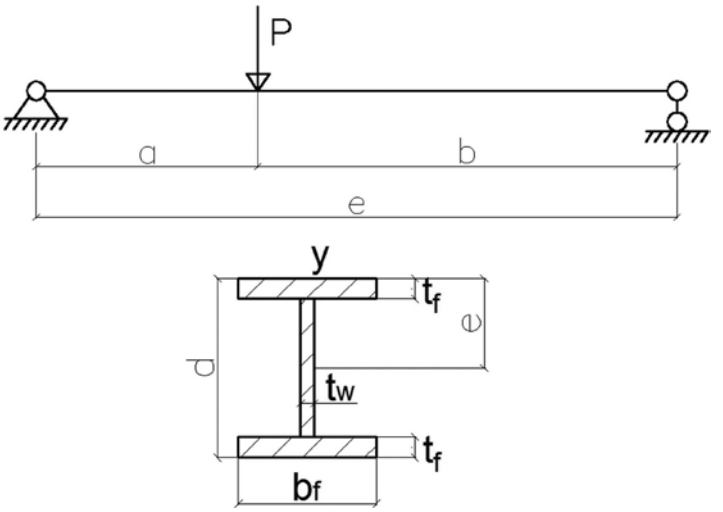

Figure.1. Calculation of a single-span beam for bending: a- girder geometry, b- cross-section.

Determine the dimensions of the cross section in a probabilistic and deterministic way.

Random variables:

a) dimensions a, b, l;
b) strength characteristics of "R";
c) the load value "P".

Comparison of the results (obtained):
(d=62.2 mm) – by the probabilistic method,
(d=59 mm) – by the deterministic method.

3 RESULTS

Thus, the probabilistic method of calculating the beam in comparison with the deterministic one leads to a slight increase in the consumption of materials (steel), but at the same time the reliability of its operation (or safety) increases in some way.

Next, we will consider the relationship between the stock ratio (laid down in building codes) and the reliability of structures:

The strength condition (in general) has the form:

$$S \leq R \tag{2}$$

where S- actual voltage; R- limit voltage; m_s- average mathematical expectations «S»; m_r- also for «R».

According to the probabilistic scheme, expression (2) can be written as follows:

$$S_p \leq R_p \tag{3}$$

S_p- quite rarely (probably) a possible occurring high value of the load parameter; R_p- also, but a low value of the carrying capacity; $S_н$, $R_н$ – normative values; S_p, R_p – calculated values; S_K, R_K – quantiles of the corresponding distributions f(S) and f(R).

Quantile is the value of the corresponding given probability, at which its distribution function is equal to the given probability.

Probability distribution parameters:

m_s, m_R – mathematical expectations

σ_s, σ_R – the same standards (or sko.-standard deviations)

$R_s = \sigma_s/m_s$; $K_R = \sigma_R/m_R$ – coefficients of variation.

a) For the average regulatory resistance, you can write:

$$1_R = 1 - \gamma_R K_R \tag{4}$$

probabilistic interpretation of the material reliability coefficient ($l_R = R_p/R_H$)

б) With some difference in the normative resistance from the average value, we have:

$$R_H = m_R(1 - \sigma_R{}^* K_R) \tag{5}$$

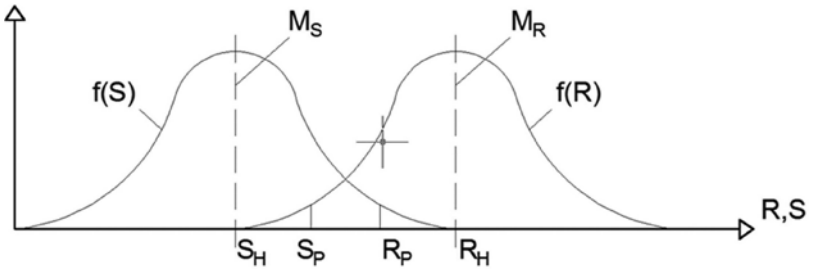

Figure.2. Ratio between (S) and (Rp).

Then (taking into account 5) expression (4) has the form:

$$1_R = \frac{1 - \gamma_R{}^* K_R}{1 - \gamma_R{}^* K_R} \tag{6}$$

With a normal distribution of ɤr=3 (3 sigma rule), n(ɤR=3) the probability of finding a smaller value of "R" will be 0.00135 (P=0.00135).

Similarly to (6), we can write an expression for the load reliability coefficient

$$1_s = \frac{1 + \gamma_s * K_s}{1 + \eta_s * K_s} \tag{7}$$

Thus, using the formulas (3,4,6), it is possible to express the value of the margin coefficient in terms of the probabilistic characteristics of loads and resistances:

$$n = \frac{1 + \gamma_s{}^* K_s}{1 + \eta_s{}^* K_s} * \frac{1 - \eta_R{}^* K_R}{1 + \gamma_R{}^* K_R} \tag{8}$$

that is, the relationship of the reserve coefficient "n" with the load reliability coefficient has a statistical nature.

Let 's introduce the notation:

(Ψ= R – S) – the function of indestructibility (reliability). Then the reliability of the "H" structures is defined as the ratio:

$$H = p(\Psi > 0) = \int_{-\infty}^{\infty} f(\Psi) d\Psi \tag{9}$$

where p=(Ψ>0)- probability; f(Ψ) – probability density of the magnitude distribution «Ψ»;

With a normal distribution law (for 9):

$m_\Psi = m_R - m_s$ - mathematical expectation

$$\sigma^2{}_\Psi = \sigma^2{}_R + \sigma^2{}_s \tag{10}$$

Then (by "9") (taking into account "10") we have:

$$H = \frac{1}{\sigma_\Psi \sqrt{2\pi}} \int_0^\infty \exp\left[-(\Psi - m_\Psi)^2/(2\sigma_\sigma)^2\right] d\Psi \tag{11}$$

Let's replace the variables:

$$t = (\Psi - m_\Psi)/\sigma_\Psi \tag{12}$$

Then, taking into account expression (12), expression (11) will take a different form:

$$H = \frac{1}{2\pi} \int_{-t_0}^{\infty} \ell^{-t^{2/2}} dt \tag{13}$$

$$t_0 = (m_R - m_s)/\sqrt{\Psi_R^2 + \Psi_s^2} \tag{14}$$

In this case, we have a special case: if the limiting voltage "R" is a deterministic value, then instead of expression (8) we have:

$$n = 1 + t_0 \, K_s \tag{15}$$

Consider the case when the probabilistic distribution of stress and strength is unknown, but the first two moments of these distributions are known. In this case, probabilistic reliability is determined by the formula:

$$H \geq 1 - \frac{n_c^2 \left(K_R^2 + K_s^2\right)}{n_c^2 \left(K_R^2 + K_s^2\right) + \left[n_c\left(1 + K_s^2\right) - 1\right]} 2 \tag{16}$$

The lower limit of reliability at the known two moments of stress distribution and strength

$$n_c \geq \left[1 + K_s^2 - \frac{\sqrt{\left(K_R^2 + K_s^2\right)} H}{1 - H}\right]^{-1} \tag{17}$$

$$K_n = \sqrt{K_R^2} + K_s^2 \,/\, \left(1 + K_s^2\right) \tag{18}$$

The calculation of the remaining resource is performed according to one or more criteria:

1) Calculation of the residual resource depending on physical wear and tear

$$\varepsilon = \frac{a_1 \, \varepsilon_1 + a_2 \varepsilon_2 + \ldots + a_i + \varepsilon_i}{a_1 + a_2 + \ldots a_i} \tag{19}$$

where, ε_1, ε_2, ε_i, – maximum damage to individual structures; a_1, a_2 … a_i – coefficient of significance of individual structures. a) Relative assessment of damage to the structure [8]

$$\lambda = 1 - \varepsilon \tag{20}$$

The constant of "wear" is determined by the results of surveys

$$\lambda = \frac{-\ell \, \mathrm{n}\, y}{t_{cp}} \tag{21}$$

where t_0 – service life in years at the time of the survey.

The service life of the first operation in years before the start of repair [9]

$$T = \frac{0.16}{\lambda} \tag{22}$$

2) Calculation of the residual resource with statistical strength. Residual life according to permissible voltages

$$\mathrm{T_R(T_Э)} = \frac{\sigma_{\varepsilon(t)} - [\sigma]}{\alpha_0} \tag{23}$$

where $\sigma_{\varepsilon(t)}$ - tensile strength at the time of examination; [σ] – tensile strength by calculation; α_0 – the rate of reduction of mechanical properties.

$$\alpha_0 = \frac{\sigma_\varepsilon - \sigma_{\varepsilon\,(t)}}{\mathrm{t}} \tag{24}$$

σ_ε- normal tensile strength; t– time from the start of operation to the moment of inspection; 3) Calculation of residual corrosion life (for metal)

$$\mathrm{T_K} = \frac{\mathrm{S_ф} - S_\mathrm{p}}{\lambda} \tag{25}$$

$\mathrm{S_ф}$– actual minimum thickness in mm; $\mathrm{S_p}$ – the calculated value of the degree, in mm; α – uniform corrosion rate, mm/year

$$\alpha = \frac{\mathrm{S_u} - \mathrm{S_ф}}{\mathrm{t}} \tag{26}$$

where $\mathrm{S_u}$- executive wall thickness of the element, mm; t- the time of the start of operation until the time of the survey, years.

4) Calculation of the residual resource for structural fatigue:

$$\mathrm{T_Ц} = \frac{\mathrm{T_Э} - [\mathrm{N}]}{\mathrm{N_Э}} \tag{27}$$

Тэ-operating time from the moment of operation, years; [N] – additional number of loading cycles; Nэ- the number of loading cycles during the period of operation; Next, we calculate the resource of residual performance:

$$\mathrm{T_{ОСТ(Ц)}} = T_ц - T_Э \tag{28}$$

4 CONCLUSIONS

In the process of analysis, it was established:

1. The results of deterministic and probabilistic calculation methods are quite close; at the same time, probabilistic calculation, compared with deterministic, leads to a small increase in material consumption with a simultaneous increase in the degree of reliability (safety).

The reliability coefficient of the structures "nc" statistically depends on the coefficients of variation in load and strength, which in turn statistically affects the probabilistic reliability of the structures "H".

2. The value of the residual life (in years) of the operated structure depends on the rate of change in mechanical properties and the rate of corrosion of materials and the number of loading cycles.
3. The probability of the presence of defective plates in the general population depends on the number of such plates in the corresponding sample, on the distribution laws of the probability function (the paper presents comparative results of two distribution laws: standard normal and Poisson distribution); In this case, the calculation according to the normal distribution law will give a lower probability.

REFERENCES

1. Raiser V.D. Calculation and rationing of reliability of building structures // Stroyizdat. 1995. C.349.
2. Poryvay G.A. Prevention of Premature Wear of Buildings//Stroizdat.1979.P.284.
3. Roitman A.G. Reliability of Structures of Buildings in Service // Stroyizdat. 1985.C.175.
4. Dobromyslov A.N. Estimation of reliability of buildings and constructions by external signs // ASV.2006. C.71
5. Lychev, A.S. Reliability of the building structures (in Russian) // ASV.2008. C.188.
6. Augusti G., Baratta A., Casciati F. Probabilistic Methods in Building Design // Stroyizdat. 1988. C.584.
7. Svetnitskiy V.A. Random fluctuations of mechanical systems // Reference book; Edited by I. A. Ushakov. I.A. Ushakova // Radio and Communications. 1985. C.606. (C.29).
8. Bakirov Zh.B. Probabilistic methods of calculation of structural elements // Manual. Karaganda. Karaganda State Technical University. 2001. P.180. (P.11.11–C.11.14).
9. Kochurov V.A., Novikov G.A. Examples of calculating the characteristics of aircraft // Samara. Samara State Aerospace University. C.48.

Smart Geotechnics for Smart Societies – Zhussupbekov, Sarsembayeva & Kaliakin (Eds)
© 2023 The Author(s), ISBN 978-1-003-29912-7
Open Access: www.taylorfrancis.com, CC BY-NC-ND 4.0 license

Developing a two-dimensional nonlinear vertical spring model for mat foundation in clays using hyperbolic function

D.W. Chang & T.M. Chou
Tamkang University, New Taipei City, Taiwan

ABSTRACT: A two-dimensional nonlinear soil spring model for mat foundation in clays is introduced in this paper. Hyperbolic function was used to model the nonlinear load-displacement relationships of the mat. The solutions from three-dimensional finite element analysis were analyzed to find the model parameters of the soil springs underneath the slab. Using the normalized functions of the model parameters across the mat, the two-dimensional modelling of the soil springs was suggested. The solutions from the proposed model with the finite difference analysis were found agreeable to the three-dimensional finite element analysis.

1 INTRODUCTION

The serviceability performance of the foundation has become more important in modern foundation design. It requires the structural deformation analysis to predict the load-displacement relations of the foundation. For nonlinear responses of mat foundation, three-dimensional finite element analysis can provide the most rigorous solution, and the approximate analyses have been often used in design practice with appropriate nonlinear soil springs. The former requires the explorations of the material Laws while the latter simply needs a few model parameters in applications. It should be noted that the soil springs are not the same due to the flexibility of the mat. Recently a two-dimensional soil spring model based on linearly elastic soils has been suggested by Chang et al (2021). The principles of the mat (raft) foundation analysis and design can be found in Bowles (1997) and Fellenius (2014).

The hyperbolic function used in geotechnical engineering can be found by Kondner (1963) in modeling the stress and strain behaviors of cohesive soils. Alternate form of such modeling for clays from the Tri-axial test was known as the Hyperbolic soil model (Duncan & Chang 1970). Until now, the hyperbolic soil model has been discussed frequently with the hardening soil model (Schanz et al 1999). It can be used as three-dimensional constitutive laws for the clays in both drained and undrained conditions. On the other hand, the application of the hyperbolic function in modeling the Plate Load test on gravels has been reported by Wrench (1984). The hyperbolic function of the soil reactions, q and foundation displacements, s can be expressed in Equation (1) with two parameters k and q_{ult}. The value k is defined as the initial tangent modulus of the curve, and q_{ult} is the ultimate strength revealed.

$$q = s/(1/k + s/q_{ult}) \tag{1}$$

The hyperbolic function shown in Equation (1) is adopted in this study. Through a number of numerical studies on the loaded mat foundations, the soil reactions and the foundation displacements from the three-dimensional finite element analysis were analyzed to obtain the parameters k and q_{ult} for each nonlinear soil spring. They are varying across the mat and dependent of soil stiffness and foundation width. The proposed modeling is discussed as follows.

DOI: 10.1201/9781003299127-362

2 NUMERICAL MODELLING

A square mat foundation with width varying at 16, 26 and 36 meters was assumed. The thickness of the mat was 1m. Homogeneous clays were assumed as the ground soil. The corresponding shear wave velocity, V_s of the soil was varying at 120, 140, 160, and 180 m/s, respectively. The study neglected the ground water table, and the Poisson's ratio of the soil was assumed at 0.4. The Young's modulus of the soil, E_s can be thus obtained. Empirical relations suggested by Hsieh et al (2003) between the Young's modulus E_s and the undrained shear strength of the clays, S_u in Taipei was used to obtain the value of the undrained shear strength. The Mohr-Coulomb soil model was adopted. The uniform load, p was applied until the foundation failure. It was decomposed into a series of load increments at 10kPa. Iterative procedure was carried out to ensure the equilibriums of the system. Table 1 summarizes the material properties and engineering parameters used in the analysis.

Table 1. Foundation geometries, material properties and parameters of the study.

Foundation dimensions and load	FE zone: 200m×200m×60m for Mat width (B): 16m, 26m FE zone: 300m×300m×60m for Mat width (B): 36m Thickness of mat: 1m Maximum load (p): 220kPa, 310kPa, 410kPa, 530kPa varied w/ soil stiffness
Concrete	γ_c =24 kN/m^3, E_c =30 GPa, ν_c = 0.15
Soil	γ_s=20 kN/m^3, ν_s= 0.4, V_s = 120m/s, 140ms, 160m/s, 180m/s E_s = 82Mpa, 112Mpa, 146Mpa, 184Mpa; S_u= 41kPa, 56kPa, 73kPa, 92kPa Note E_s/S_u =2000 is assumed for different clays

The 3D FE analysis was made using Midas GTX NX package (Midas, 2014). Three dimensional 8-node solid elements were used to model the concrete structure and the soils. The interface elements were implemented between the concrete and the soils. Normal and tangent stiffness of the interface elements, k_n and k_t were assigned as $10E_s$ and E_s, respectively. Ultimate adhesion of the interface elements was assumed as 2/3 of the undrained shear strength of the clay. The stability of the foundation displacements was ensured with the FE dimensions varied (see Figure 1). Essential boundaries such as the rollers were placed. Two- and three-dimensional hinges were resulted at the interfaces of these boundaries. Since the structural system and load symmetry, only 1/4 of the structural system was analyzed. The computation time required for the FE analysis approximates 0.5~2.5 hrs using PC with CPU: AMD Ryzen 7 3800X 8-Core Processor, GPU: NVIDIA GeForce GTX 1060 3GB, and RAM: 64GB.

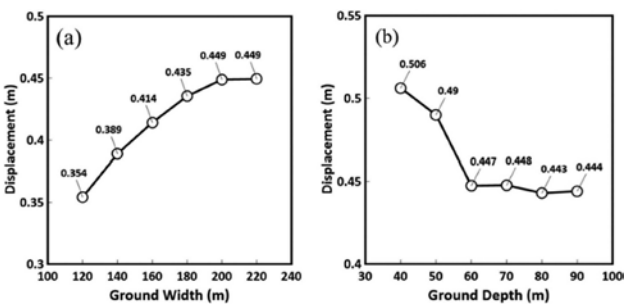

Figure 1. Stability of the solutions from 3D FE analysis (a) ground width (b) ground depth.

3 HYPERBOLIC MODEL PARAMETERS AND THEIR FUNCTIONS

The FE analysis was first conducted to obtain the load-displacement relationships of all the cases. The soil reactions, q obtained at the nodes across the central section of the mat foundation were plotted against the nodal displacements, s of the foundation. By doing so, the hyperbolic function can be used to model the curves found by q vs. s. Figure 2 reveals the modeling where the value of q_{max} was the maximum load pressure that can be applied before reaching the ultimate load, q_{ult}. The ratio of q_{ult}/q_{max} was assumed to obtain q_{ult} for the appropriate modeling. In the study, the ratios at 1.1~1.4 were suggested to yield rational predictions from the hyperbolic functions with those obtained from FE analysis. Figure 3 illustrates the matching results for mats with width at 26m on soils with shear wave velocity of 140m/s using q_{max} and q_{ult}. It can be observed that the modification of q_{max} is rather important. The values of k and q_{ult} for nodes at the center of the mat foundations studied can be found in the range of 1.2~10.8MN/m^3 (for k) and 264~681kPa (for q_{ult}). Detailed values can be found in Chou (2022).

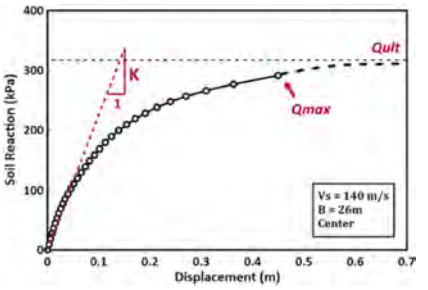

Figure 2. The relationships of soil reactions and foundation displacements.

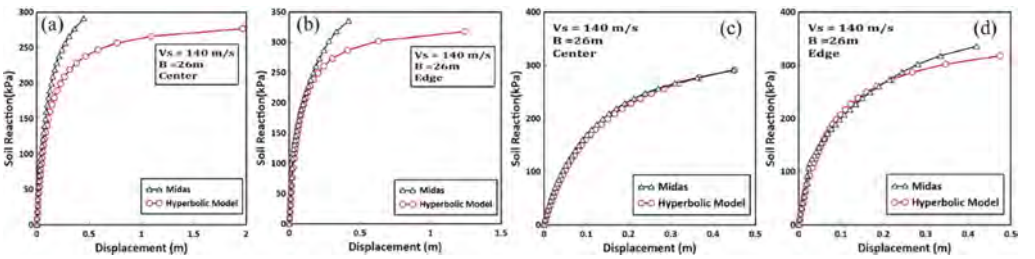

Figure 3. Hyperbolic modeling of soil reactions and foundation displacements (a) & (b) using q_{max} (c) & (d) using q_{ult}.

Plotting the values of k and q_{ult} obtained at the nodes across the central section of the foundation, the normalized functions of k and q_{ult} can be both achieved with respect to their values exerted at the center of the foundation. Figure 4 depict the variations of the normalized data for k and $q_{ult,}$. The normalized functions $f_k(x)$ for k and $f_q(x)$ for q_{ult} have been reported by Chou (2022) using the regression analysis. They are dependent of the soil stiffness and the mat width. As the results, the two-dimensional nonlinear soil model can be suggested by following equations in association with the use of Equation (1). Note that k_c and q_{ultc} are the parameters found at center of the foundation.

$$k = k_c \times f_k(x) \times g_k(y), \text{ where } g_k = f_k \tag{2}$$

$$q_{ult} = q_{ultc} \times f_q(x) \times g_q(y), \text{ where } g_q = f_q \tag{3}$$

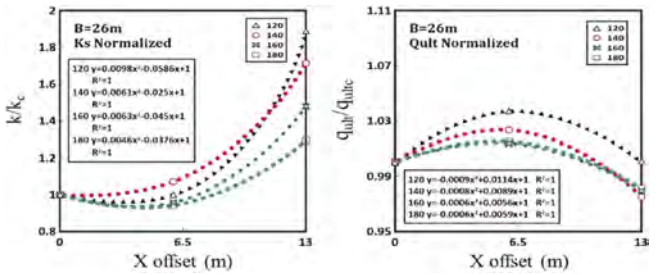

Figure 4. Variations of the normalized k and q_{ult} for mat with width of 26m.

4 VALIDATIONS

In order to verify the proposed model of the nonlinear soil springs, the finite difference analysis WERAFT (Chang et al 2018) for the mat foundation following the Thin-Plate theory was adopted. The soil springs underneath the mat foundations in WERAFT analysis were replaced by the newly proposed model. It is important to point out that the secant modulus of the sub-grade reactions at the nodes of the mat must be computed first in order to form the structural stiffness matrix for solving the foundation displacements. Thus the secant modulus of the sub-grade reactions is dependent of the foundation displacements. Therefore the equilibriums of the applied load with respect to the foundation displacements must be ensured by the iterative procedures. The solutions from the WERAFT analysis using the two-dimensional nonlinear soil springs suggested in this study were found agreeable with those obtained from 3D FE analysis. Figure 5 reveals their comparisons. They are applicable to mat foundation with thickness of 1m~2m (Chou, 2022). Note that the computational time required for the WERAFT analysis is much less than those found in the Midas analysis.

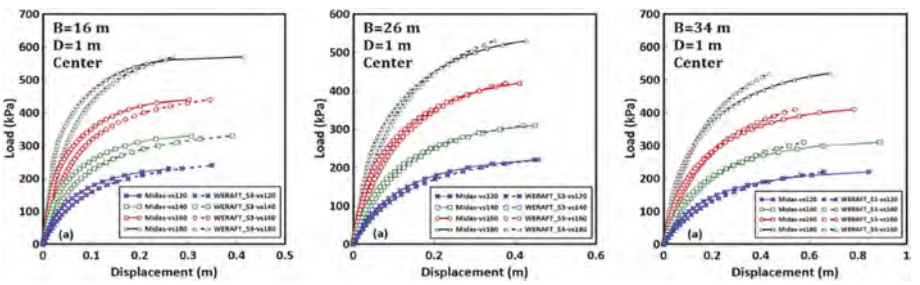

Figure 5. Comparison of the solutions from FD w/ the proposed soil springs and FE analyses.

5 CONCLUDING REMARKS

A two-dimensional nonlinear soil spring model is suggested in this study for vertically loaded mat foundation located in clays. Hyperbolic function is adopted to model the nonlinear relationships between soil reactions and foundation displacements. Model parameters k and Q_{ult} were back-analyzed from the solutions of 3D FE analysis. The variations of these parameters across the mat were calibrated with the normalized functions. The proposed modeling can be applied to the finite difference analysis of the mat foundation, and the results were found comparable with the 3D FE analysis.

ACKNOWLEDGEMENT

This paper presents a partial result of the research project sponsored by Ministry of Science and Technology (MOST) in Taiwan. Sincere gratitude is expressed towards the finance supports through research grant MOST109-2221-E-032-010-MY2.

REFERENCES

Bowles, J.E. (1997). Foundation Analysis and Design, McGraw-Hill Pub. 1175p.

Chang, D.W., Hung, M.H. & Jeong, S.S. (2021). Modified Lysmer's analog model for two dimensional mat settlements under vertically uniform load, *Int. J., Geomechanics and Engineering*, 25(3), 221–231.

Chang, D.W., Lien, H.W. & Wang, T. (2018). Finite difference analysis of vertically loaded raft foundation based on the plate theory with boundary concern, *Journal of GeoEngineering*, 13(3), 135–147

Chou, T.M. (2022). Development of nonlinear vertical springs for mat foundations in clays, Mater Thesis, Department of Civil Engineering, Tamkang University, Taiwan. (in Chinese)

Duncan, J.M. & Chang, C.M. (1970). Nonlinear analysis of stress and strain in soils. *Journal of Soil Mechanics and Foundations Division*, ASCE, 96(SM5), 1629–1653.

Fellenius, B. (2014). Basics of Foundation Design, electronic edition.

Kondner, R.L. (1963). Hyperbolic stress-strain response: cohesive soils. *Journal of Soil Mechanics and Foundation Engineering*, ASCE, 89(1), 115–143.

Hsieh, P.G., Kung, T.C., Ou, C.Y. & Tang, Y.G. (2003). Deep excavation analysis with consideration of small srain modulus and its degradation behavior of clay, *Procds*., The 12th Asian Regional Conference on Soil Mechanics and Geotechnical Engineering, Singapore, Vol.1, 785–733.

Midas (2014). Midas GTS NX User Manual; Midas Ltd., Co.: Tokyo, Japan.

Schanz, T., Vermeer, P.A. & Bonnier, P.G. (1999). The hardening soil model: Formulation and verification, *Beyond 2000 in Computational Geotechnics – 10 Years of PLAXIS*, Balkema, Rotterdam.

Wrench, B.P. (1984). Plate tests for the measurement of modulus and bearing capacity of gravels, DIE SIVIELE INGENIEUR in Suid-Afrika, September. 429–437.

Smart Geotechnics for Smart Societies – Zhussupbekov, Sarsembayeva & Kaliakin (Eds)
© 2023 The Author(s), ISBN 978-1-003-29912-7
Open Access: www.taylorfrancis.com, CC BY-NC-ND 4.0 license

Dimensionless modulus of subgrade reaction for embedded mat foundation in soft clay under vertical load

D.W. Chang & J.H. Lin
Tamkang University, New Taipei City, Taiwan

Y.K. Lin, F.C. Lu & C.J. Kuo
Ground Master Construction Co., Ltd., Taipei, Taiwan

ABSTRACT: The dimensionless modulus of the subgrade reaction for embedded mat foundation in soft clays under the vertical load is suggested in this paper using 3D FEM analysis and the Mohr-Coulomb soil model. Besides the soil stiffness, the embedded depth and width of the raft, the depth of diaphragm wall, and the total structural loads were considered as influence factors. For applications to routine designs, foundation displacement, soil reaction, and modulus of subgrade reaction were examined by their non-dimensional measures. The optimized correlations with the foundation geometries are suggested based on various soil stiffness and structural load.

1 INTRODUCTION

1.1 *Analysis of mat foundation*

The serviceability performance of the foundation has become more important in modern foundation design. It requires the structural deformation analysis besides the conventional ultimate capacity analysis of the foundation. For mat foundation, the deformation analysis can be simply made by treating the foundation as a one-dimensional beam or two-dimensional mat resting on a series of soil springs. For more rigorous analysis, the foundation and its surrounding soils can be modeled as a continuum discretizing by two- or three-dimensional finite elements. Despite that the finite element (FE) analysis has been widely used in modern foundation designs, the approximate numerical analyses are still adopted in many foundation designs due to its simplicity. The principles of the mat (raft) foundation analysis and design were discussed by Bowles (1997) and Fellenius (2014).

1.2 *Modulus of subgrade reactions*

If a simplified numerical tool was used to analyze a mat foundation, the modulus of subgrade reaction of the soils is important for engineers to know. The modulus of subgrade reaction for soils underneath the raft deforming vertically is denoted as k_v (units in F/L^3). It is defined as the ratio of the soil reactions to the foundation displacement. For foundation vibrations, the soil spring constant of a rigid disc foundation has been suggested by Lysmer & Richart (1966). Alternate spring models of the soils can be found either with the effects of foundation geometry and finite thickness of subgrade or with the embedment of foundation (Novak & Beredugo 1972, Kausel et al 1978, Gazetas 1991). By taking the load frequency as zero, static displacement of the foundation can be achieved. The modulus of subgrade reaction in above models is able to obtain by dividing the soil spring constant with the area of foundation. In addition, many researchers focused on analyzing the foundation settlements due to large static

DOI: 10.1201/9781003299127-363

loads following the Theory of Elasticity and/or consolidation hypothesis. In such case, the modulus of subgrade reaction, k_v of the foundation can be determined by dividing the load pressure with the calculated foundation settlement. Poulos (2018) has discussed the modulus of subgrade reaction for foundation analysis. It should be pointed out that the resulting strain level of the soil is important in different engineering problems. Engineers must use appropriate soil modulus to obtain rational predictions. In recent years, research studies conducted by advanced analytical and/or numerical analyses (Lee et al 2015, Chang et al 2019) had shown that the foundation settlements under vertical load are varying across the foundation, and affected by soil stiffness, foundation size, and the load applied to the foundation. Therefore, the soil spring constants underneath the mat should be dependent of these design factors. Chang et al (2021) have suggested a two-dimensional soil spring model for the surface mat foundation in soft clay. This study intends to discuss the modulus of subgrade reaction for mat foundation embedded in soft clays due to the vertical load. The modulus of subgrade reaction was calibrated to dimensionless measure, and their correlation with the dimensionless quantities representing the foundation geometry was suggested.

2 NUMERICAL MODELS

2.1 *Foundation modelling*

The numerical model of the embedded mat foundation is illustrated in Figure 1. A square mat foundation with the width varying at 16, 26 and 36 meters was assumed. The thickness of the mat was 1m. Embedded depth of the mat was varying at 8 and 12m. For more realistic modelling, the concrete diaphragm wall was around the mat. The depth of the diaphragm wall was kept as 2 and 2.5 times of the depth for foundation embedment. Homogeneous soft clay was assumed for the ground soil. The corresponding shear wave velocity, V_s of the soil was varying at 100, 120 and 140 m/s, respectively. Ground water table was not included whereas the Poisson's ratio of the soil was 0.4.

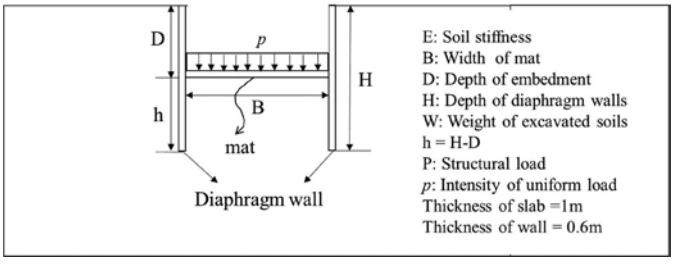

Figure 1. Foundation model of this study.

The Young's modulus of the soil, E_s can be thus obtained. Empirical relations suggested by Hsieh et al (2003) between the Young's modulus E_s and the undrained shear strength of the clays, S_u in Taipei was used to obtain the value of the undrained shear strength. The Mohr-Coulomb soil model was adopted. Notice that the structural load, P was taken approximately as 1 and 1.5 times the weight of excavated soils. In some studies, the total load was fixed and independent of embedment depth and size of the slab. The applied uniform load, p was decomposed into a series of incremental loads of 10kPa. Iterative procedure was carried out to ensure the equilibriums of the system. Table 1 summarizes the material properties and engineering parameters used in the analysis. Totally 72 numerical cases were analyzed.

Table 1. Foundation geometries, material properties and parameters of the study.

Foundation dimensions and load	FE zone: 200m×200m×60m, Mat width (B): 16m, 26m, 36m, Depth of embedment (D): 8m, 12m Depth of diaphragm (H): 2.D and 2.5D Thickness of mat: 1m, Thickness of wall: 0.6m Structural load (P): 1.0W, 1.5W, Weight of soils excavated (W): $\gamma_s \times B^2 \times D$
Concrete	γ_c =24 kN/m^3, E_c =30 GPa, ν_c = 0.15 γ_s=20 kN/m^3, ν_s= 0.4, V_s = 100m/s, 120ms, 140m/s,
Soil	E_s =57 MPa, 82Mpa, 112Mpa, S_u= 28.5kPa, 41kPa, 56kPa (E_s/S_u =2000) for soils denoted as E1, E2 and E3

2.2 *Discrete mesh and boundaries*

The 3D FE analysis was made using Midas GTX NX package (Midas, 2014). Three dimensional 8-node solid elements were used to model the concrete structure and the soils. The interface elements were implemented between the concrete and the soils. Normal and tangent stiffness of the interface elements, k_n and k_t were assigned as $10E_s$ and E_s, respectively. Ultimate adhesion of the interface elements was assumed as 2/3 of the undrained shear strength of the clay. Stage-construction feature available in Midas analysis was used. The stability of the foundation displacements was ensured with the FE dimensions at 200m×200m×60m. Essential boundaries such as the rollers were placed. Two- and three-dimensional hinges were resulted at the interfaces of these boundaries. The computation time required for the analysis are around 4~24 hours using PC with Processor 11th Gen Intel® Core™ i7-11700 @2.5 GHz.

3 FOUNDATION BEHAVIORS

3.1 *Foundation displacements*

The largest displacements of the foundations were found appeared at the center in the range of 15~310mm. They were mainly affected by soils stiffness. Large structural loads would increase the settlements. Nonlinear load-displacement relationship was able to find. For similar structural loads, increasing the depth of embedment and the size of the mat foundation will reduce the foundation settlements. The depth of diaphragm wall could slightly reduce the foundation settlements especially for the mat in very soft soil. Figure 2 presents the influences

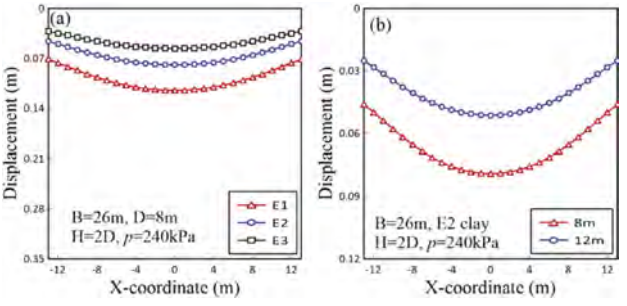

Figure 2. Foundation displacements affected by (a) soil stiffness (b) depth of embedment.

of soil stiffness and depth of embedment of the mat with width at 26m. The maximum foundation displacements occurred at different locations of the cases were reported by Lin (2022).

3.2 *Soil reactions*

The soil reactions underneath the mat foundation are generally distributed like the settlements. Nevertheless, in some cases where the structural load is equal to the weight of the excavated soils, i.e. compensated foundation, when the soil stiffness increased, the soil reactions at the foundation center became less than the soil reactions occurred near to the edge. The oscillations of the soil reactions were found in such cases. The largest soil reaction of the foundations were found in the range of 190~385 kPa. They will be affected by soil stiffness, depth of foundation embedment, and total structure load. Figure 3 indicates the corresponding soil reactions for those shown in Figure 2. Again, the largest soil reactions recorded in the study was discussed in Lin (2022).

3.3 *Modulus of subgrade reaction*

The modulus of subgrade reactions, k_s of the soils underneath the mat can be obtained as in the range of 3~26 MN/m^3 for compensated foundation (i.e. P=1W), and 1.5~12 MN/m^3 for the cases where the structural load is 1.5 times the weight of excavated soils. These moduli were found to be smaller for softer soils and larger structural loads. The distributions of the soil reactions along the foundation showed that the smaller k_s were found in the center.

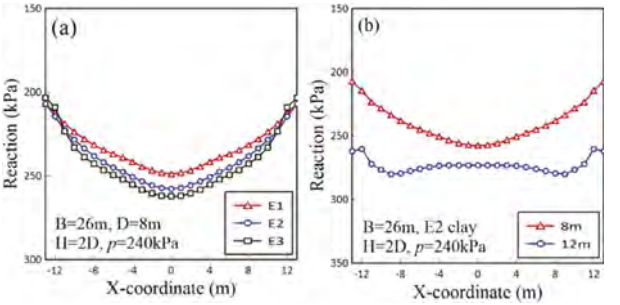

Figure 3. Soil reactions affected by (a) soil stiffness (b) depth of embedment.

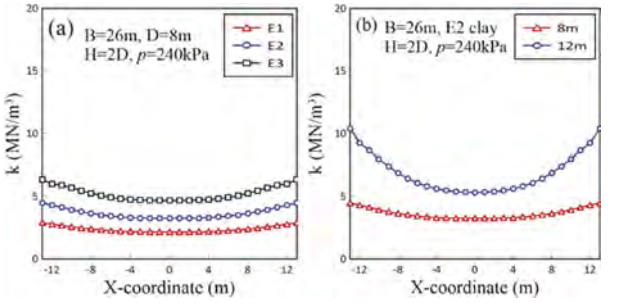

Figure 4. Modulus of subgrade reaction affected by (a) soil stiffness (b) depth of embedment.

Figure 4 reveals the corresponding results. The depths of the foundation embedment and the diaphragm wall would help to increase the modulus of subgrade reactions. For more information, please refer to Lin (2022).

4 DIMENSIONLESS MEASURES

4.1 *Foundation displacements*

In order to apply the study results, dimensionless measures of the maximum foundation displacements, s were defined as $\gamma_s s/E_s$, s/B, and $\gamma_s s/p$, whereas γ_s, E_s, B and p are the unit weight of the soil, Young's modulus of the soil, width of the mat, and the loading pressures applied to the mat, respectively. The dimensionless values representing for the foundation geometry were defined as 2D/B and 2h/B, whereas D is the embedded depth of foundation, h is defined as the length of the diaphragm wall underneath the embedment, which is equal to H-D. The relationships of the dimensionless foundation displacement with respect to the dimensionless values of the foundation geometries was evaluated respectively by plotting the data in x-y plane formed by non-dimensional displacements as the ordinate and the geometric values as the abscissa. Regression analysis was applied to examine the corresponding statistic efficiency of the correlations. The optimized correlations between the dimensionless foundation displacement and the dimensionless values of the foundation geometry was found to be $\gamma_s s/p$ vs. 2D/B. Figure 5 depicts their correlations with the dependence of soil stiffness and structural load applied at the foundation. Note that P1 is equal to the weight of excavated soil, W whereas P2 is equal to 1.5W.

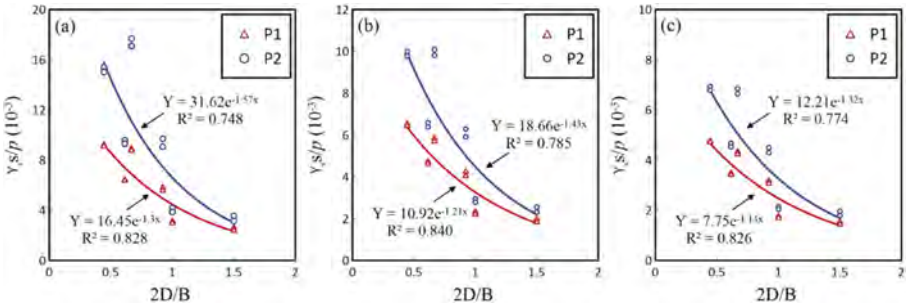

Figure 5. Optimized correlations of dimensionless foundation displacements versus 2D/B of mat (a) E1 clay (b) E2 clay (c) E3 clay.

4.2 *Soil reactions*

Similarly, dimensionless soil reactions in association with the above dimensionless foundation displacements were defined as q/E_s, $q/\gamma_s B$, q/p (where q is the soil reactions recorded at the center of foundation), respectively. These values were plotted against the values of dimensionless foundation geometry to verify their efficiency. Again, the optimized correlations formed by q/p and 2D/B can be shown in Figure 6.

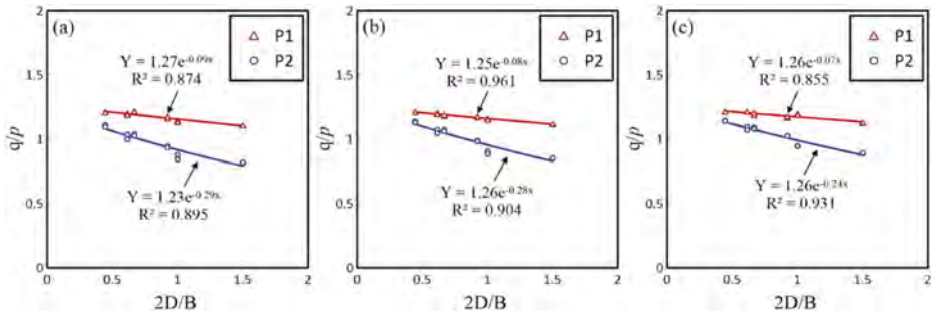

Figure 6. Optimized correlations of dimensionless soil reactions versus 2D/B of mat (a) E1 clay (b) E2 clay (c) E3 clay.

4.3 *Modulus of subgrade reaction*

The dimensionless modulus of subgrade reactions in association with all the dimensionless foundation displacements and their corresponding soil reactions was found as $q/\gamma_s s$. Their values were plotted against the values of dimensionless foundation geometry to determine the optimized correlation. As the results, the optimized correlations between $q/\gamma_s s$ and 2D/B can be shown in Figure 7. Notice that to obtain the value of k_s, one must compute the foundation settlement, s first from Figure 5. Then use Figure 7 or Figure 6 to obtain q. k_s is computed as q/s.

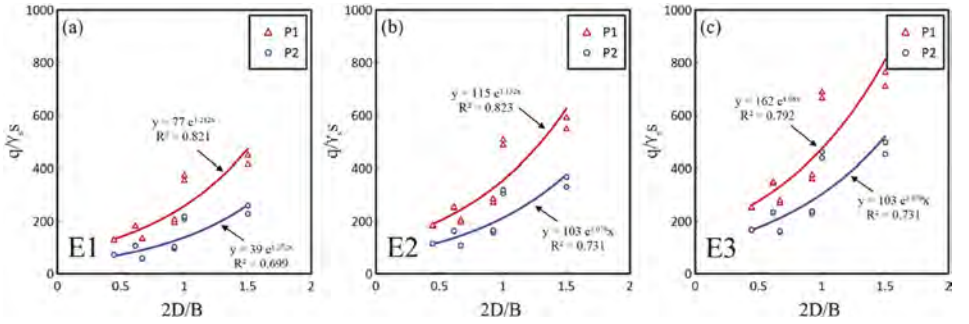

Figure 7. Optimized correlations of dimensionless modulus of subgrade reaction versus 2D/B of mat (a) E1 clay (b) E2 clay (c) E3 clay.

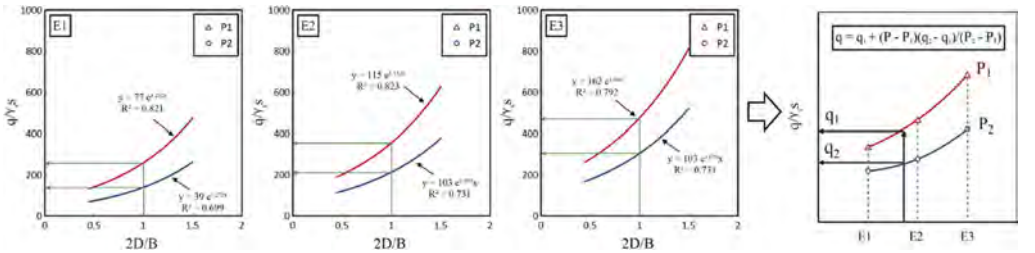

Figure 8. Soil reaction to be calculated from the interpolations.

4.4 *Applications*

The engineers can use the regression curves shown in Figures 5–7 to estimate the foundation displacement, the soil reactions and the modulus of subgrade reactions if the site soils and the structural loads are similar to the case studied. For soil stiffness and structural load different to the suggested quantities, interpolations should be used to obtain the approximated values. For example, the soil reaction, q can be found as the procedures shown in Figure 8. Foundation displacement can be found using the similar procedure. Once the foundation settlement, s and soil reactions, q are obtained, the modulus of subgrade reaction, k_s can be thus calculated.

5 CONCLUDING REMARKS

The foundation displacements, soil reactions, and the modulus of subgrade reactions of the embedded mat foundation located in soft clays subjected to vertical loads have been analyzed by 3D FE analysis. The influences of the soil stiffness, the foundation size, the depth of embedment, the depth of diaphragm wall, and the structural loads were studied by seventy-two cases. In order to use them in routine design, their values were first transformed to dimensionless quantities, and then correlated to dimensionless values of the foundation geometry. The correlations of $\gamma_s s/p$, q/p, and $q/\gamma_s s$ versus 2D/B was found to be the optimized one. They are suggested as a preliminary

design tool for mat foundations in soft clays. Further examination with the field measurements is encouraged.

ACKNOWLEDGEMENT

This paper presents a partial result of the technical project supported by Ground Master Construction Co. Ltd. In Taiwan. Sincere gratitude is expressed. The thankfulness is extended to Prof. C.H. Chen (NTU), Dr. C.D. Ou (SEAGS & AGSSEA) and R&D Director Mr. C.C. Ko (MAA) for their valuable comments/suggestions in reviewing the project.

REFERENCES

Bowles, J.E. (1997). Foundation Analysis and Design, McGraw-Hill Pub. 1175p.

Chang, D.W. Lien, H.W., Hu, G.Y. & Chuang, Y.A. (2019). Developing a three dimensional finite-difference analysis for piled raft foundation settlements under vertical loads, 4th Int. Bolivia Conference on Deep Foundation, May 23-24, Santa Cruz, Bolivia.

Chang, D.W., Hung, M.H. & Jeong, S.S. (2021). Modified Lysmer's analog model for two dimensional mat settlements under vertically uniform load, *Int. J., Geomechanics and Engineering*, KGS, 25(3), 221–231

Fellenius, B. (2014). Basics of Foundation Design, electronic edition.

Gazetas, G. (1991). Formulas and charts for impedance of surface and embedded foundations, *Journal of Geotechnical Engineering*, 117(9), 1363–1381.

Hsieh, P.G., Kung, T.C., Ou, C.Y. & Tang, Y.G. (2003). Deep excavation analysis with consideration of small srain modulus and its degradation behavior of clay, *Procds*., The 12th Asian Regional Conference on Soil Mechanics and Geotechnical Engineering, Singapore, Vol.1, 785–733.

Kausel, E., Whitman, R.V., Morray, J.P. & Elsabee, F. (1978). The spring method for embedded foundations, *Nuclear Engineering and Design*, 48(2-3), 377–392.

Lee, J., Jeong, S. & Lee, J.K. (2015). 3D analytical method for mat foundations considering coupled soil springs, *Geomechanics and Engineering*, 8(6), 845–867.

Lin, J.H. (2022). Study on coefficients of subgrade reactions and pile stiffness of piled raft foundations in clays subjected to vertical loads, Master Thesis, Department of Civil Engineering, Tamkang University (in Chinese)

Lysmer, J. & Richart, F.E. (1966). Dynamic responses of footings to vertical loading, *Journal of the soil mechanics and Foundation Division*, 92(1).

Midas (2014). Midas GTS NX User Manual; Midas Ltd., Co.: Tokyo, Japan.

Novak, M. & Beredugo, Y.O. (1972). Vertical vibration of embedded footings, *Journal of the Soil Mechanics and Foundation Division*, ASCE, 98 (12) 1291–31.

Poulos, H. (2018). Rational assessment of modulus of subgrade reaction, *Geotechnical Journal of the SEAGS & AGSSEA*, 49(1), 1–7.

Smart Geotechnics for Smart Societies – Zhussupbekov, Sarsembayeva & Kaliakin (Eds)
© 2023 The Author(s), ISBN 978-1-003-29912-7
Open Access: www.taylorfrancis.com, CC BY-NC-ND 4.0 license

Evolution of the foundation design methods for multi-storey and high-rise buildings in seismic regions

A.I. Polishchuk, M.B. Marinichev & I.G. Tkachev
Kuban State Agrarian University named after I.T. Trubilin, Krasnodar, Russian Federation

ABSTRACT: Methods for the construction of foundations for multi-storey and high-rise buildings in seismic areas are proposed, taking into account compound conditions, such as: slopes of the relief, heterogeneity of subsoil layers, the risk of landslide processes and others. A point system for assessing areas of territory by the convenience of its development for the construction of multi-storey and high-rise buildings (structures) has been developed. Effective solutions of the foundations for the projects in difficult soil conditions have been patented. Methods of calculation and design of foundations were developed and implemented during the construction and reconstruction of multi-storey and high-rise buildings in Krasnodar, Sochi, Novorossiysk, Anapa.

1 INTRODUCTION

Over the past decade, new methods of design for raft-pile foundations in particularly difficult soil conditions have been developed and implemented. Methods are divided into the following three groups: the implementation of foundations with a given initial settlement of the slab part; implementation of piles with different lengths and consequential inclusion in joint work with the slab part; technical solutions with the possibility of foundation settlements regulation during construction stages (Shadunts K.Sh. et al, 2007, 2008, 2010, 2012).

The proposed methods are the development of well-known methods of calculation and construction of pile and pile-raft foundations taking large vertical and horizontal loads (Mangushev and Osokin, 2010; Ilyichev et al., 2021; Katzenbach et al., 2020a; Katzenbach et al., 2020b; Gotman and Gotman, 2018; Mangushev et al., 2023; Zhussupbekov et al., 2022; Ter-Martirosyan and Ter-Martirosyan, 2020; Ter-Martirosyan et al., 2021). The main point of the studied methods is to find ways to greaterly include the foundation slab in joint work with piles, which is expressed in the ratio of the corresponding shares. When the desired result is achieved, the share of the load transferred to the foundation slab can be up to 40-50% of the total value.

A perspective direction in the use of the developed foundation design methods for the pile and raft-pile foundations is their consideration during preparations the master plans of territories with the presence of complex soil conditions. For this purpose, a classification of methods for calculating and constructing the foundations of multi-storey and high-rise buildings in particularly difficult ground conditions is proposed, which allows to avoid mistakes at the stage of choosing design solutions and, thereby, reduce the risks of investments in construction.

2 METHODS

2.1 *The implementation of raft-pile foundations with a given initial settlement of the slab part*

The method of execution of the foundation proposed in Figure 1 (RU patent No. 2379425) includes the execution of a pile field and a slab, where the piles are made along the perimeter of the foundation, and the slab is made of two parts - the external, which has ledges upwards, immediately resting on the piles, and the internal one - with ledges downwards, which rests on the outer

DOI: 10.1201/9781003299127-364

part of the slab. At the same time, after reaching the calculated settlement, the outer and inner parts of the slab are rigidly combined, ensuring the joint operation of the pile-slab foundation.

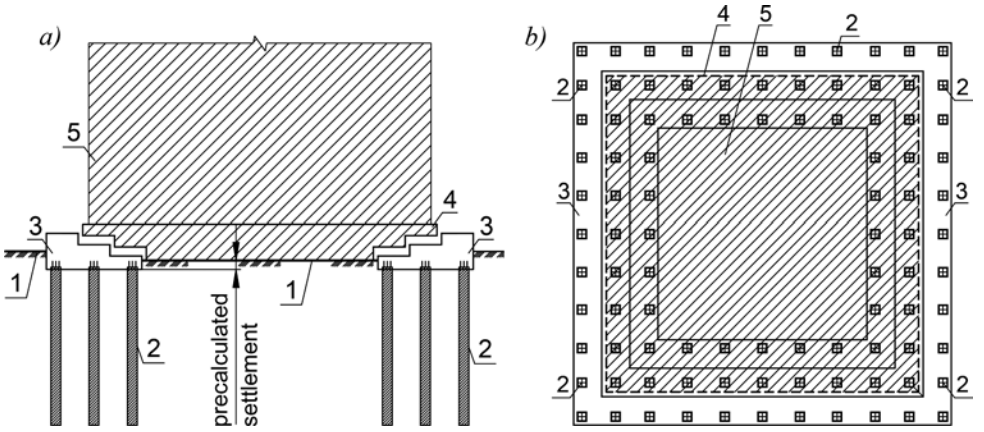

Figure 1. Scheme of construction of a raft-pile foundation: *1* – prepared soil surface; *2* – perimetral piles, united by a grillage; *3*; *4* – foundation slab with designed configuration; *5* – high-rise building (RU patent No 2379425).

The first group of methods also includes: construction method for a raft-pile foundation (RU patent No. 2378454); pile-slab foundation (RU patent No. 2331738).

2.2 *Implementation of piles with different lengths and consequential inclusion in joint work with the slab part*

A brief description of the methods included in the group is given below.

The method presented in Figure 2 (RU Patent No. 2300604) assumes that in order to increase the proportion of the load on the slab, it is necessary to make the slab with the opportunity to obtain a large amount of displacement at the initial stage of settlement development. This is possible if the interaction of the slab and the piles begins after the slab has undergone a certain predetermined initial settlement. The result is achieved if piles forming the raft-pile foundation have different lengths: the main ones - long piles - are located directly under the load-bearing elements of the building and are included in the joint work after the foundation slab receives a certain proportion of settlement, i.e., at a given (controlled) stage of including the piles in joint work with the slab part.

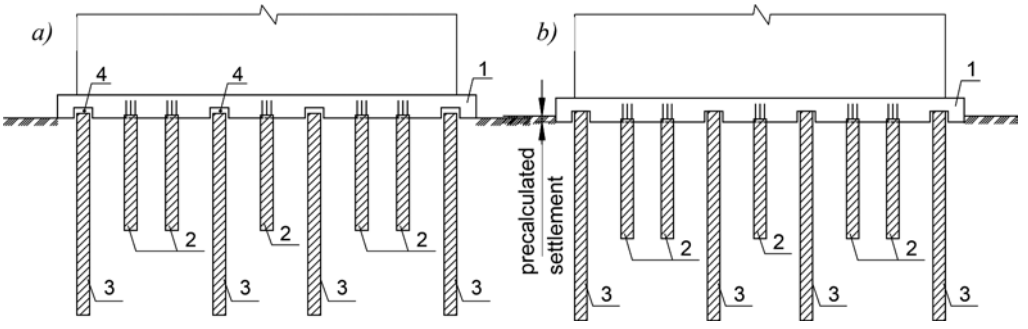

Figure 2. Method of construction of raft-pile foundations in seismic areas: *а)* the initial stage of deformation increment – the settlement of the slab rigidly combined with short piles: *1* – foundation slab; *2* –short piles rigidly joined with the slab; *3* – long piles separated from the slab by a design clearance *4*; *б)* the final stage of deformation development is the involvement of long piles in the work of the raft-pile foundation (RU patent No. 2300604).

The second group of methods also includes: method of a bored pile installation with increased bearing capacity for construction in seismic areas (RU patent No. 2761795); improved raft-pile foundation (RU patent No. 2320820).

2.3 *Technical solutions with the possibility of foundation settlements regulation during construction stages*

The methods included in the group are listed below.

The developed method of erecting a raft-pile foundation (Figure 3) allows to achieve the greatest efficiency due to the consequential inclusion of foundation elements in the joint work (RU patent No. 2513050). Often, in the construction of high-rise objects, cross-wall structural schemes are used due to their high spatial rigidity and bearing capacity. In particular, such a scheme allows within the framework of existing regulatory documents to provide for the largest number of storeys for seismic areas.

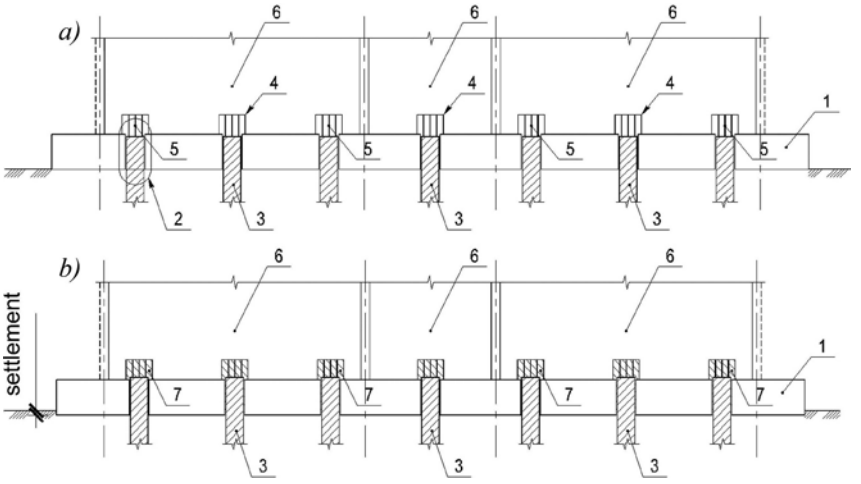

Figure 3. Method of construction of pile-slab foundation: *1* – foundation slab; *2* – through hole in the slab; *3* – projected piles; *4* – niches above pile heads in load-bearing walls; *5* – upper parts of pile reinforcment for the formation of rigid joints; *6* – load-bearing walls; *7* – concrete to fill niches in the walls when the specified value of the slab settlement is reached (RU patent No. 2513050).

The third group of methods also includes: a method for regulating the inclinations of the pile-slab foundation in seismic areas on unevenly compressible soils (RU patent No. 2734750); slab foundation on an unevenly compressible base with the possibility of regulation the inclinations (RU patent No. 2731969).

Based on the research and taking into account new methods of construction of pile and raft-pile foundations recommendations were prepared for the design and construction of foundations in particularly difficult soil conditions, taking into account the given stages of construction.

2.4 *Calculation and construction methods of foundations of multi-storey and high-rise buildings in particularly difficult soil conditions*

The developed methods for calculating and constructing the foundations of multi-storey and high-rise buildings in particularly difficult ground conditions include:

- The method of calculation and construction of foundations based on the studieded parameters of interaction between single pile and soil and between the pile group and soil
- The method of calculation and construction of pile foundations using an intermediate transfer layer
- The method for regulating uneven foundation settlements by increasing the spatial stiffness of the foundation structure

– The method of foundations design using adaptation of its form to the surface of steep relief
– The method of construction of foundations with constant and temporary deformation joints
– The method of construction of foundations with the consequential inclusion of foundation elements in the joint work

The implementation of the developed methods of calculation and construction of foundations in particularly difficult ground conditions was carried out at more than 50 objects of multi-storey and high-rise buildings (Figures 4-7).

3 RESULTS

3.1 *A complex of multi-storey residential buildings on a steep terrain on yesaulenko street in Sochi*

One of the objects in the implementation of the method of foundations design using adaptation of its form to the surface of steep relief is a complex of multi-storey residential buildings located on a slope steepness of up to 35 ° in Sochi (Figure 4).

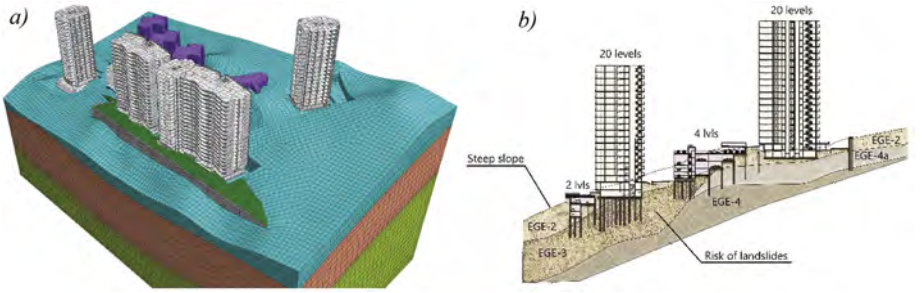

Figure 4. Multi-storey residential buildings located on a steep slope with a risk of landslides: *a* – spatial FEM model; *b* – geological section of the construction site, combined with the designed multy-storey buildings.

The construction was carried out in the conditions of adjoining new buildings to existing residential buildings located at a distance of 5 meters or more from the structures being built. The adjoining of the loaded foundations of existing buildings determined strict requirements for maintaining a minimum impact on existing facilities, so the deep excavation for the construction site was initially excluded. The solution was found by adapting the raft-pile foundation to the variable surface of the relief, which made it possible to minimally affect the slope and avoid

Figure 5. Stages of construction of multi-storey buildings on a landslide slope: *a* – general view of the construction site; *b* – the final stage of construction of section No. 1.

landslides. As a result of the application of a reasonable consequence the construction of the foundation became possible to achieve compliance with all the required parameters (Figure 5).

3.2 *Multi-storey multifunctional residential complex on a landslide slope in the Khosta district of Sochi*

In the process of implementing the method of construction of foundations with constant and temporary deformation joints, analyses were carried out to assess the forces arising in the completed piles of overlying blocks at each stage of the construction of the foundations of the complex, up to the moment of unification of the adjacent sections in the places of temporary deformation joints (Figure 6). After that the horizontal forces and bending moments in the piles were significantly reduced due to the inclusion in the joint work of the underlying structural block and its foundations.

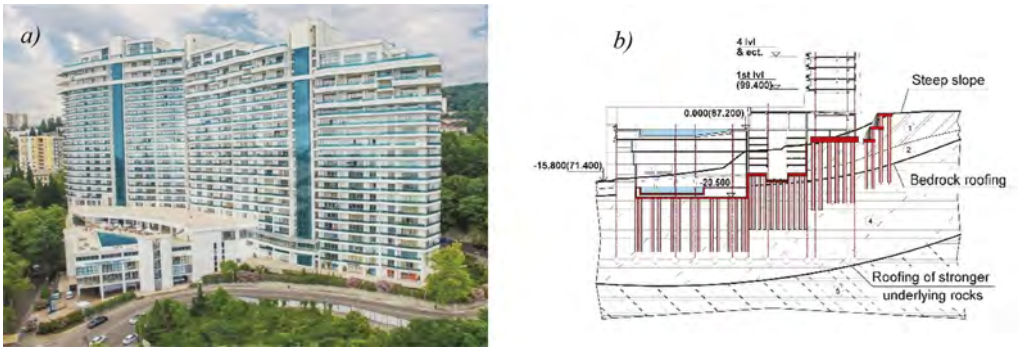

Figure 6. Multi-storey residential complex on a landslide slope in an area with 9-point seismicity: *a* – completed construction; *b* – scheme of a terraced foundation combined with the geological section.

The final scheme of the foundations, terraced from top to bottom, also let to achieve the required spatial stability of the landslide slope, which became possible due to the formed spatial stiffness of the completed foundations and upper structures, sequentially combined into a single scheme by modification of temporary deformation joints. The pile layout for each block (Figure 7) was determined by analyzing the worst combination of forces.

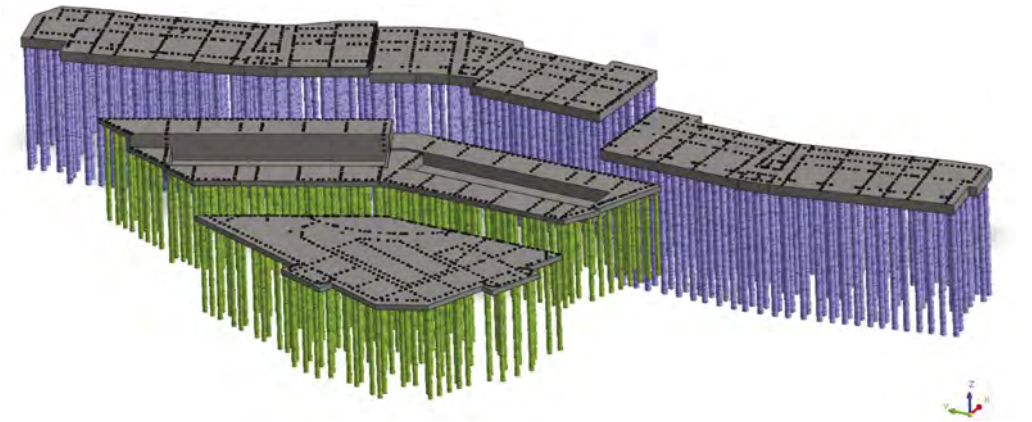

Figure 7. 3D scheme of the terraced raft-pile foundation of the neighboring high-rise blocks.

In general, more than 20 geotechnical and structural design stages were calculated and implemented, the most important were the stages of combining horizontal forces and displacements of adjacent foundations using temporary deformation joints.

Blocks work separately from each other when taking external influences. However, a solution to reduce the loads on the foundation of the high-rise part can be found by involving adjacent stylobate parts in the work of the foundation. Joints between adjacent blocks designed hinged - only for the transmission of horizontal forces. In combination with this, the terracing of adjacent foundations, taking into account the natural shape of the slope, allows to significantly reduce the amount of soil excavation. The overall stability of the entire scheme can be ensured after the properly integrated upper structures and the foundations of the underlying blocks in the joint work with the overlying blocks by combining them through horizontal temporary deformation joints.

4 DISCUSSION

The efficiency after the application of the developed methods is the greatest in conditions of dynamic and seismic influences, as it leads to a decrease of horizontal loads on piles. The reduction of moment loads and horizontal forces ensures the stability of the soil around the lateral surface of the upper part of the piles. That was confirmed in the series of numerical studies in a volumetric approach, taking into account the seismic intensity of 7, 8 and 9 points, described by accelerograms of real earthquakes of different years. With an intensity of seismic impact of 7-9 points, the maximum horizontal forces in the upper part of the piles, consequently included in joint work with the slab, are reduced by 2.5-3.0 times in comparison to standard schemes.

When constructing such foundations, attention should be paid to the rational layout of piles within the plot of the foundation: the distance between piles, it's length, diameter and total volume of the material, taking into account the shape and spatial stiffness of the aboveground structure (Marinichev, 2022).

As a result of the implementation of the developed methods, the reduction of vertical and horizontal loads on piles reasonably leads to a decrease in the volume of material for construction, a decrease in overall costs and a reduction in the time of construction stage.

5 CONCLUSION

New methods of design and construction of pile and raft-pile foundations in seismic areas are proposed: the implementation of foundations with a given initial settlement of the slab part; implementation of piles with different lengths and consequential inclusion in joint work with the slab part; technical solutions with the possibility of foundation settlements regulation during construction stages. The developed classification of methods for calculating and constructing the foundations of multi-storey and high-rise buildings in particularly difficult ground conditions helps to avoid mistakes at the stage of choosing design solutions and allows to ensure the safety of objects during the construction period and further operation, reduces the risks of investments.

REFERENCES

Aizhan, Zh. & Zhussupbekov, A.Zh. & Tulebekova, A.S. & Tleubayeva, A.K. (2022). Field tests of soils during the investigation works. *Bulletin of Kazakh Leading Academy of Architecture and Construction*. 85. 136–142. 10.51488/1680-080X/2022.3–13.

Buranbayeva, A. & Zhussupbekov, A.Zh. & Sarsembayeva, A. & Omarov, A.R. (2022). Evaluation of the structural health monitoring results of the applied fiber optics in the pile-raft foundations of a high-rise building. *Applied Sciences*. 12. 11728. 10.3390/app122211728.

Gotman, N.Z. & Gotman, A.L. (2018). *The karst protection foundations design*. ce/papers. 2. 877–882. 10.1002/cepa.781.

Ilyichev, V. A. & Nikiforova, N.S. & Konnov, A.V. (2021). Technological Soil Mechanics in Underground Construction. *IOP Conference Series: Materials Science and Engineering*. 1079. 042056. 10.1088/1757-899X/1079/4/042056.
Katzenbach, R. & Leppla, S. & Alzaylaie, M. (2020a). *Sustainable foundation systems of high-rise buildings*.
Katzenbach, R. & Arslan, U. & Reul, O. (2020b). *Soil-structure-interaction of a piled raft foundation of a 121 m high office building on loose sand in Berlin*. 10.1201/9781003078517-28.
Katzenbach, R. & Arslan, U. & Moormann, Chr. (2020c). *Design and safety concept for piled raft foundations*. 10.1201/9781003078517-62.
Marinichev, M.B. & Marshalka A.Ju. RU Patent No. 2 513 050, Byull. Izobret., No. 11 (2012).
Marinichev, M.B. RU Patent No. 2 734 750, Byull. Izobret., No. 30 (2020).
Marinichev, M.B. & Tkachev I.G. RU Patent No. 2 731 969, Byull. Izobret., No. 25 (2020).
Marinichev, M.B., Lyashenko P. A., Denisenko V. V., Tkachev I.G. & Azov I.G. RU Patent No. 2 761 796, Byull. Izobret., No. 3 (2022).
Marinichev, M.B. (2022). The influence of the shape of high-rise buildings on the design features and methods of making foundations in difficult soil conditions. *E3S Web of Conferences*. 363. 10.1051/e3sconf/202236302013.
Marinichev, M.B. & Tkachev, I.G. (2019). Some features of foundation stage in construction process of high-rise buildings located on steep slopes in areas with high seismicity. *Construction and Architecture*. 7. 20–27. 10.29039/article_5ca75f9b461354.57548169.
Marinichev, M.B. (2018). Features of subsoil behavior consideration in geotechnical design of high-rise buildings located on floodplain territories in seismic regions. *PNRPU Construction and Architecture Bulletin*. 9. 103–113. 10.15593/2224-9826/2018.1.10.
Mangushev, R.A. & Osokin A.I. (2010). *Geotechnics in Saint Petersburg*. Moskow: Publishing House ACB., p. 260
Mangushev, R.A., Igoshin, A.V., Oshurkov, N.V. et al. Slab-pile foundation for a high-rise building. Soil Mech Found Eng 45, 17–22 (2008). https://doi.org/10.1007/s11204-008-0004-y
Mangushev, R.A. & Rybnov, E.I. & Zhussupbekov, A.Zh. & Omarov, A.R. (2023). *Investigation of the work of the Lakhta Center in weak soil foundations of St. Petersburg*. 10.1007/978-3-031-21432-5_265.
Ter-Martirosyan, Z.G. & Ter-Martirosyan, A.Z. (2020). *Soil Mechanics in high-rise construction*. Moscow:ABC.
Ter-Martirosyan, Z.G. & Ter-Martirosyan, A.Z. & Akuleckiy, A. (2021). Interaction of large piles with a multilayer soil mass, taking into account hardening and softening. *International Journal for Computational Civil and Structural Engineering*. 17. 67–75. 10.22337/2587-9618-2021-17-2-67-75.
Ter-Martirosyan, A.Z. & Anh, Le. (2020). Calculation of the settlement of pile foundations taking into account the influence of soil liquefaction. *IOP Conference Series: Materials Science and Engineering*. 869. 052025. 10.1088/1757-899X/869/5/052025.
Shadunts K.Sh., Marinichev, M.B. & Demchenko V.A. RU Patent No. 2 300 604, Byull. Izobret., No. 16 (2007).
Shadunts K.Sh., Marinichev, M.B. & Demchenko V.A. RU Patent No. 2 320 820, Byull. Izobret., No. 9 (2008).
Shadunts K.Sh, & Marinichev, M.B. RU Patent No. 2 331 738, Byull. Izobret., No. 23 (2008).
Shadunts K.Sh, & Marinichev, M.B. RU Patent No. 2 378 454, Byull. Izobret., No. 1 (2010).
Shadunts K.Sh, & Marinichev, M.B. RU Patent No. 2 379 425, Byull. Izobret., No. 2 (2010).
Zhussupbekov, A.Zh. & Sarsembayeva, A. & Alibekova, N.T. (2023). *Preliminary assessment of the bearing capacity of soils using a geotechnical database*. 10.1007/978-3-031-21432-5_338.
Zhussupbekov, A.Zh. & Chunyuk, D. & Kaliakin, V. & Omarov, A.R. (2022). *Experimental assessment of bearing capacity on pile foundations of the new monument in Nur-Sultan City*. 10.1007/978-981-19-7358-1_21.

Smart Geotechnics for Smart Societies – Zhussupbekov, Sarsembayeva & Kaliakin (Eds)
© 2023 The Author(s), ISBN 978-1-003-29912-7
Open Access: www.taylorfrancis.com, CC BY-NC-ND 4.0 license

Ground modelling by MPS-CAE simulation under different influencing parameters

S. Shakya & S. Inazumi
Shibaura Institute of Technology, Tokyo, Japan

ABSTRACT: This study focuses on the application of the MPS (moving particle semi-implicit) - CAE (computer-aided engineering) method to simulate the unconfined compression test, from the planning and design stages, in an attempt to model the ground parameters under various influencing parameters. The best fitting ground model was designed for the primary parameters and is compared with the known soil data to justify the claim. Furthermore, the authors endeavored to find the secondary governing factors that will affect the accuracy of the ground modelling. The results show that the values of the primary parameters are influenced by the values of the secondary parameters, resulting in a different model. The influence of the secondary parameters is studied and the best fitting ground model is designed by incorporating both primary and secondary parameters. The resultant ground model is expected to provide more accurate results if firstly applied in various construction simulations.

1 INTRODUCTION

Research based on simulations has become popular for the study of soil-improvement methods and for the visualization of construction phenomena and evaluation methods. These studies are generally carried out from the design phase of the ground model. The accuracy of the studies mostly depends on the accuracy of the ground model. Unlike other participating materials, the governing parameters for the soil are difficult to measure; therefore, the ground modelling is carried out by conducting an unconfined compression test simulation to derive the values of the ground parameters. Inazumi et al. (2021) used an unconfined compression test simulation to check the validity of the ground parameters employed in the visualization and evaluation of jet grouting technology. Since the MPS-CAE method (Inazumi et al. 2020) is preferrable for the present study, the major governing parameters that define the ground models are the plastic viscosity, yield value, and yield parameter.

2 OUTLINE OF BINGHAM FLUID

A Bingham fluid is a fluid that flows when the shear stress exceeds a specified value. The model employed for this fluid is a bi-viscosity model (Nakao et al. 2021). It treats the fluid as a viscoplastic fluid in the fluid state, and as a highly-viscous fluid in a rigid state.

The apparent viscosity in the fluid state is reflected in Eq. 1.

$$\eta = \left(\eta_p + \frac{\tau_y}{\dot{\gamma}}\right) \quad \dot{\gamma} \geq \dot{\gamma}_c \tag{1}$$

The apparent viscosity in the rigid state is reflected in Eq. 2.

$$\eta = \left(\eta_p + \frac{\tau_y}{\dot{\gamma}}\right) \quad \dot{\gamma} < \dot{\gamma}_c \tag{2}$$

DOI: 10.1201/9781003299127-365

where τ_y is the yield value, η_p is the plastic viscosity, $\dot{\gamma}$ is the average shear velocity, and γ_c is the yield criterion of the fluid and rigid states, given by Eq. 3.

$$\dot{\gamma}_c = \frac{2C_y\tau_y}{\eta_p} \tag{3}$$

where C_y is the yield parameter.

During the design stage, the yield value (τ_y), plastic viscosity (η_p), and yield parameter (C_y) are presented as the model parameters.

3 ANALYSIS CONDITIONS

3.1 *Modelling and simulation specifications of sample*

A cylindrical soil sample, 50×100 mm, and an unconfined compression test simulation setup were modeled. The top plate was lowered such that the soil would deform at the uniform strain ratio of 1% per minute. It was simulated for a total time of 1200 seconds during which the soil was expected to exceed the yield value.

The effects of the yield value, plastic viscosity, and yield parameters were studied for soil with a strength level of 60 kPa and subjected to numerous trial-and-error simulations. In this way, the best fitting ground model was designed. It was observed that yield parameter values greater than 1/1000 resulted in the collapse of the structural composition during the simulation, leading to failure. The yield value was inputted as 60 kPa and the values of the other parameters, at which the input yield value became equal to the output yield value, were determined.

3.2 *Material parameters*

Table 1 shows the final values of the materials employed in the unconfined compression test that produced the best fitting ground model after incorporating the influence of the primary parameters. The values for these parameters were selected after the successful simulation of the unconfined compression test.

Table 1. Material parameters.

Material	Density (kg/m^3)	w/c	Yield value (Pa)	Plastic viscosity (Pa.s)	Yield parameter (-)	Surface tension (N/m)	Fluid model
Water	1000	-	-	-	-	0.10	Newtonian fluid
Ground	1600	-	60000	17000	0.0001	0.002	Bingham fluid

4 MPS-CAE SIMULATION RESULTS

4.1 *Comparison of results with known data*

Figure 1 shows the results of the simulated stress-strain curve for the Table 1 data compared with the known data. The soil yielded at the compressive strength of 61.24 kN/m^2 and strain value of 12.59%. The Aomori soil sample was silty soil with an avg. diameter of 0.0036 mm. It yielded at a compressive strength of 64.69 kN/m^2 and strain value of 4.73%. The Yamagata soil sample was sandy soil with an avg. soil diameter of 0.034 mm. It yielded at a compressive strength of 61.55 kN/m^2 and strain value of 0.55%. Although the simulation results and known data are approximately equal in terms of their peak strength, they all yielded at different strain values. In order to determine the cause of this discrepancy, further study is conducted with the intention of determining the secondary parameters.

4.2 *Studying the influence of density and soil particle size*

In this simulation, the water content of the test sample could not be defined clearly, but the input value for density was changed for different simulations, while all the other parameters

were kept constant. The results showed that the values for the output compressive strength and exerted strain were almost the same, implying that for samples with the same yield value, yield parameter, surface tension, and plastic viscosity, a change in density has no effect on the design of the ground model. Table 2 summarizes the overall simulation results for the changing density.

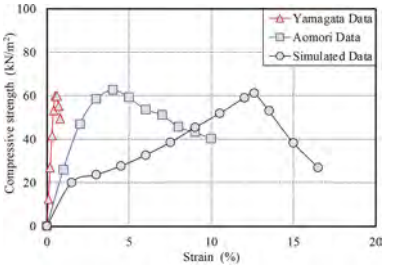

Figure 1. Simulation results compared to known data.

Table 2. Influence of density of ground modelling.

Yield value = 60 kPa, Plastic viscosity = 17000 Pa·s,	Density (kg/m^3)	Compressive strength (kN/m^2)	Strain (%)
Particle size = 3 mm,	1600	61.299	12.59
Yield parameter = 0.0001,	1172	61.559	12.49
Surface tension = 0.002 N/m	793	61.702	12.4

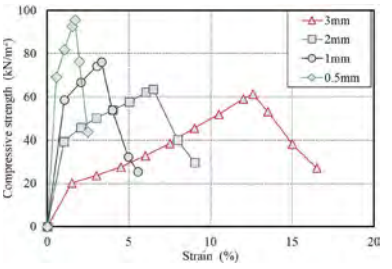

Figure 2. Comparison of simulated results for particles of various sizes.

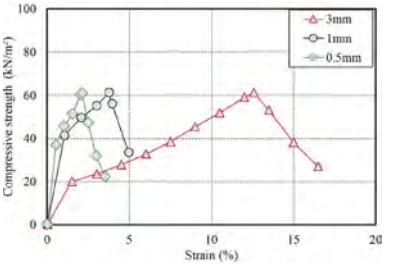

Figure 3. Correct output model for 0.5-mm and 1-mm soil particles.

As the known data have different particle sizes and different strain values, the study was conducted to find the influence of the particle size. Figure 2 shows the changes in the output yield value when the particle size in the simulation was changed to 2, 1, and 0.5 mm and was compared to that of 3-mm soil particles. All the other parameters were kept the same, but the results

Table 3. New material parameters and output results for each soil particle size.

Soil size (mm)	Input yield value (Pa)	Plastic viscosity (Pa·s)	Yield parameter (-)	Output yield value (kPa)	Strain (%)	Fluid model
3	60000	17000	0.0001	61.30	1.26	Bingham fluid
1	60000	10000	0.0001	61.30	0.38	Bingham fluid
0.5	60000	5500	0.0001	61.07	0.21	Bingham fluid

showed drastic changes in the output yield value and strain. The soil samples yielded at 63.43, 76.03, and 95.54 kN/m^2, respectively, and strain values of 6.48, 3.34, and 1.69%, respectively.

4.3 *Remodeling the ground for different soil particle sizes*

As the influence of the secondary parameters has been quantified, a correct model must be designed for each soil particle size. The process includes trial-and-error simulations to determine accurate values for the primary parameters that are similar to those of the initial phase.

Figure 3 shows the correct stress-strain relationship for soil particles of sizes 0.5 mm and 1 mm compared to the 3-mm soil particles. Since the results for the 2-mm soil particles did not largely deviate from those for the 3-mm soil particles, it was not remodeled in this study. However, if the situation demands, it can be remodeled too. For this study, the interest lies in remodeling for the minute particles which showed more deviation from the original 3-mm soil particles.

Table 3 shows the details of the new ground parameters and output values for each soil particle size. For the 0.5-mm soil particles, the output compressive strength of 61.07 kN/m^2 and strain value of 2.11% were obtained for the input plastic viscosity of 5500 Pa.s. For the 1-mm soil particles, the output yield value was recorded to be 61.30 kN/m^2 and it yielded at the strain value of 3.76%. These results were obtained for the plastic viscosity of 10000 Pa·s.

5 DISCUSSION

It was observed that the plastic viscosity and strain value for finer soil particles decreases if the yield value is kept constant. One probable reason is that the composition characteristics of the soil sample correspond to its yield value. And, since the bi-viscosity model was assumed, the value for the plastic viscosity itself is likely to be high. However, one can only speculate by the empirical method based on the simulation results. The influence of the surface tension, when simulated, was found to be low. Thus, its value was assumed to be approximately zero in order to reduce the calculation load. Moreover, since changes in density were seen to have a negligible influence, the soil samples were assumed to be in a dry state such that the value for the surface tension could be disregarded.

Simulations for finer soil particles involve an astronomical calculation load and may even fail to produce the results of the unconfined compression test simulation depending upon the calculation load. The objective should be to create as accurate a ground model as possible and it should be easily adoptable for future studies. The results of this study have suggested that soil particles of a smaller size provide the best fitting stress-strain curve characteristics when compared to the known data. However, due to the increased calculation load, the simulation might also fail. Thus, the optimum choice should be made regarding the adoption of a soil particle size.

6 CONCLUSIONS

In this study, the importance of the soil particle size during the simulation of the unconfined compression test under different parameters was confirmed. In addition, the model suitable for each soil particle size was successfully recreated. It was observed that the simulation tended to fail due to the heavy calculation load if the soil particles were very small. It was also found that the ground modelling had almost no relation to the density of the soil.

In conclusion, this study will be a helpful reference for future studies related to ground simulations and for creating more accurate ground models.

REFERENCES

Inazumi, S., Kuwahara, S., Jotisankasa, A. & Chaiprakaikeow, S. 2020. MPS-CAE simulation on dynamic interaction between steel casing and existing pile when pulling out existing piles, *International Journal of GEOMATE, Geotechnique, Construction Materials and Environment*, 18: 68–73.

Inazumi, S., Shakya, S., Komaki, T. & Nakanishi, Y. 2021. Numerical analysis on performance of middle-pressure jet grouting method for ground improvement, *Geosciences*, 11, 8: 313

Nakao, K., Inazumi, S., Takaue, T., Tanaka, S. & Shinoi, T. 2021. Evaluation of discharge surplus soils for relative stirred deep mixing methods by MPS-CAE analysis, *Sustainability*, 14, 1: 58

Smart Geotechnics for Smart Societies – Zhussupbekov, Sarsembayeva & Kaliakin (Eds)
© 2023 The Author(s), ISBN 978-1-003-29912-7
Open Access: www.taylorfrancis.com, CC BY-NC-ND 4.0 license

Investigation of the behavior of the spiral micropile in soil

Y.A. Pronozin, R.V. Melnikov, I.A. Zaboev & D.D. Muslova
Industrial University of Tyumen, Tyumen, Russia

E.P. Bragar
L.N. Gumilyov Eurasian National University, Nur-Sultan, Kazakhstan
Industrial University of Tyumen, Tyumen, Russia

ABSTRACT: The study of a new construction of a micropile are presented. The proposed vertical micropiles of a new construction has a large surface area due to the spiral shape and a bigger bearing capacity compared to the usual micropile. As a result, numerical modeling, the influence of the number of a pile spiral turn and the relative "elongation" of a spiral turn on the change in load capacity, as well as the features of its compressibility. Analysis of the results of the numerical modeling shows area of the effective constructive combinations of the spiral turns number along the length of pile and the "elongation" (width) of the turn. This area arranges the biggest load capacity of the spiral pile compared to the usual micropile. Additionally, restrictions on compressibility have been imposed to confine torsional tensions. At conclusion, the authors for-mulate the problems for continuation research.

1 INTRODUCTION

One of the areas of geotechnics, the development of which is most active, is pile foundations. This is promoted by the development of construction on areas with difficult unfavorable soils and the increasing in the technological level of execution the work.

The common goal in the development of all pile technologies is to maximize the bearing capacity of the piles. At the same time the pile must have a high technological effectiveness of the pile installation, a low unit cost and minimum settlements. Many new installation technologies for various types of piles have appeared in recent decades to solve this goal (Mangushev et al., 2015). The goal achievement is particular important during construction on soft soil, where the pile cannot be based upon hard or rock soil. Such soil conditions imply the using of friction piles only. These soils are common in Sedimentary and Residual Soils areas.

2 STATE OF THE RESEARCH

Many scientists have worked on the problem of increasing the bearing capacity of friction piles in soft soil (Xu et al., 2020). Studies were conducted on various ways to increase friction forces on the side surface of piles(Teixeira et al., 2012, Dai et al., 2007), determinate and clarify friction coefficients between soil and pile (Ivanova et al., 2016), clarify calculation assumptions and models (Basack et al., 2022), develop new pile designs (Vertynskii and Emel'yanova, 2013). Many studies have found application in civil engineering (Hajrullin et al., 2015).

One way to increase the bearing capacity of a friction pile is to increase the side surface area. Until now, this could be achieved in two ways: by increasing the cross-section of the pile or by increasing its length. However, there is another way, suggested by the authors, that does

DOI: 10.1201/9781003299127-366

not affect the cross-section and length of the pile. In this case pile length will be understood as the depth of the pile tip position.

In order to describe this method, it is first necessary to explain the stages that preceded its creation. The authors encountered a problem of ensuring the verticality of the borehole at depths greater than 10 meters - the borehole axis began to deflect. The first stage included this observation about the borehole, that was made for soil investigation or the micropile installation. The maximum deflection angle of the borehole or micropile axis reached 10 degrees during vertical drilling. This led to the conclusion that the probability of borehole deviation from the vertical increases with depth. The next step was a study based on previous findings: if random deviation from vertical is possible for a vertical micropile, how will it affect on the bearing capacity of the pile? Authors found out during a series of numerical modeling experiments that a small deviation of the micropile from the vertical has no effect on its bearing capacity. Then the angles of deviation from the vertical were larger, than the bearing capacity decreased.

Analyzing the conclusions at each of the steps, the author's team decided to apply the idea of "Conversion of harm into benefit" for the method of increasing the bearing capacity of the pile. The use of this idea is expressed in the following: 1 - there is always a probability of micropile deviation from the vertical during installation; 2 - the probability of micropile deviation increases through depth; 3 - minor deviations do not affect on the bearing capacity of micropile; 4 - deviation of micropile from the vertical reduces the depth of the pile tip position.

Therefore, if the micropile axis is bent, it is possible to increase the lateral surface area, compared to the vertical micropile, which have the same tip depth. If the micropile axis is not randomly bent, but rather, it is possible to obtain a micropile of a new design. All this can have a favorable effect on the bearing capacity of the pile.

3 MATERIALS AND METHODS

A new design of spiral micropile (SMP) is proposed. A spiral shape of micropile is described by equations (1). SMP can be created with different shapes. The study was conducted with different design solutions of SMP in order to identify the general laws of the shape influence on SMP behavior in the soil. The design dimensions are shown in Figure 1: D_1 is the overall diameter of SMP, D is the diameter of the spiral, d is the cross-sectional diameter of the micropile shaft, L is the overall height of SMP, l is the pitch of the spiral. The top of the SMP has a vertical section for coaxial accommodation of the vertical load.

$$\{x = (u)\ (cos\ cos\ (v) + B)\ y = A \cdot sin(u)(cos(v) + B)\ z = sin(v) + C \cdot u \tag{1}$$

if $u \in [-D{\cdot}\pi;\ D{\cdot}\ \pi]$ $v \in [-D{\cdot}\ \pi; D{\cdot}\pi]$

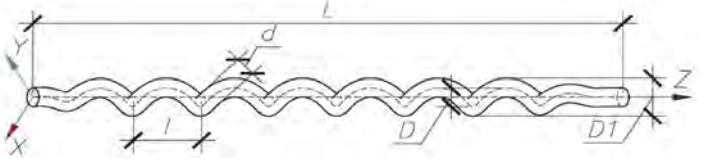

Figure 1. General design of the spiral micropile (SMP).

Taking into account different design types of SMP to study their behavior in the soil, it is necessary to introduce additional properties of SMP, allowing them to classify. Such properties will be: the relative elongation of the pitch of the spiral l/D (Figure 2) and the number of the pitch of the spiral L/l (Figure 3).

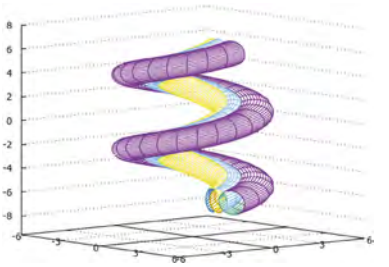

Figure 2. Influence of the relative elongation of the pitch of the spiral *l*/*D* at a constant value of *l*.

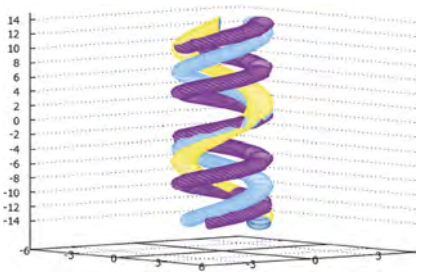

Figure 3. Influence of the number of the pitch of the spiral *L*/*l* at a constant value of *D*.

Using parameters *l*/*D* and *L*/*l*, it is possible to perform a simultaneous analysis of SMP of different shapes to identificate of trends of changes in bearing capacity and compressibility. Unfortunately, different mathematical forms of SMP cannot be reflected in reality. This is hindered by technological limitations and principles of reasonableness.

The design of the spiral micropile is new and implies many directions for its research. Given that the advantage of such piles has not yet been identified, the least time-consuming study would be numerical modeling.

4 NUMERICAL MODELING

To identify the influence of the SMP shape on its behavior in the soil, a numerical study was performed using Midas FEA NX 2022.1.1. Various SMP shapes with intersectional parameters *l*/*D* and *L*/*l* (Table 1, columns 1-7) with a constant cross-sectional diameter of the micropile shaft *d* were considered.

Table 1. Dimensions of the studied SMP.

№	*d*, m	*D*, m	*L*, m	*l*, m	*L*/*l*	*l*/*D*	IF_d, kN	$IF_{d,min}$, kN	IF_d	ε_i, %
1	2	3	4	5	6	7	8	9	10	11
1		0.45	4			2.67	547		1.31	0.022
2		0.6			3.33	2.00	617	419	1.47	0.068
3		0.9				1.33	607		1.45	0.263
4		0.45	7			2.67	846		1.36	0.038
5	0.3	0.6		1.2	5.83	2.00	895	622	1.44	0.090
6		0.9				1.33	641		1.03	0.214
7		0.45	10			2.67	1091		1.30	0.042
8		0.6			8.33	2.00	1020	841	1.21	0.097
9		0.9				1.33	646		0.77	0.171

The general view of the computational model is shown in Figure 4. The computational model has dimensions of 26,0x21,2x20,0 m. The structure is a pile cap measuring 6,0x1,2 m and two identical spiral micropiles (Table 1, columns 2-7) with a spacing of 4,0 m. A uniformly distributed load was applied to the pile cap to determine the bearing capacity of the piles. Transmission of pressure from the pile cap to the soil was prohibited.

Additionally, vertical micropile simulations were performed with the same tip depth to determine the effectiveness of SMP (Figure 5).

Mohr-Coulomb model was used to define soil behavior, Elastic model was used to define contruction behavior (Mirnyj and Ter-Martirosyan, 2017). The parameter values are presented in Table 2. Based on the geometric model, a finite element mesh was created (Karaulov et al., 2022). The size of the finite elements increased as they moved away from the study area. The interface elements were used for modeling SMP in the soil.

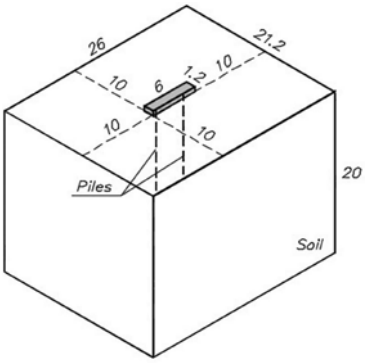

Figure 4. The general view of the computational model.

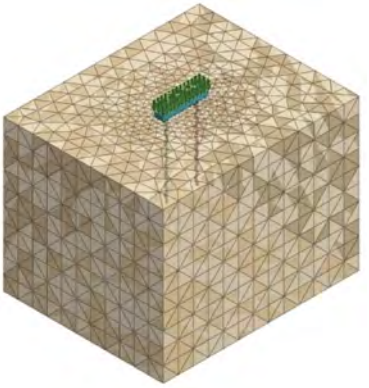

Figure 5. The computational model.

Table 2. Material models and their parameters.

Symbol	Parameter	Unit	Material model	
			Mohr-Coulomb	Elastic
E'	Young's modulus	MPa	15.2	38000
v	Poisson's ratio	-	0.39	0.2
c	Intercept cohesion	kPa	33	–
φ	Angle of internal friction	degree	17.5	–
ψ	Angle of dilatancy	degree	0	–
γ	Unit weigh	kN/m^3	18.7	25

5 ANALYSIS AND RESULTS

A series of numerical calculations with SMP of different shapes made it possible to determine their bearing capacity (Table 1, column 8). It was found that the increase of parameter *l*/*D* decreases the bearing capacity of the pile. The bearing capacity values of vertical micropiles were also obtained (Table 1, column 9). An the bearing capacity increase index $\boldsymbol{IF_d}$ for SMP was additionally determined to evaluate the obtained data (Table 1, column 10). It was defined as the ratio between the bearing capacity of the SMP of the selected shape and he bearing capacity of the vertical micropile at equal pile length *L* and pile cross-section *d*. This index allows us to evaluate the effectiveness of the SMP form, considering only the criterion of bearing capacity increase.

A polygonal surface was constructed to analyze the effectiveness of multiple SMP shapes simultaneously. Nodes of the surface were the values of the bearing capacity increase index IF_d (Figure 6), the relative elongation of the pitch of the spiral *l*/*D* and the number of the pitch of the spiral *L*/*l* of each investigated SMP shape. The polygonal surface has a delineated maximum $IF_d = 1.44$ (Figure 6, point 5), and a delineated minimum $IF_d = 0.77$ (Figure 6, point 9). This allows us to conclude that the shape of the SMP significantly affects on the bearing capacity.

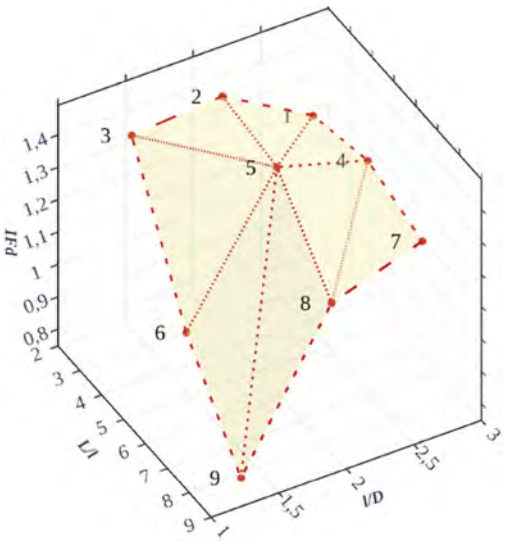

Figure 6. Polygonal surface IF_d for SMP.

For further analysis of the results, the complexity of the SMP shape compared to the vertical micropile should be considered. A reasonable application of the SMP should provide a significant increase in the bearing capacity compared to the vertical micropile (i.e., a significant increase in IF_d). In author's opinion, this would be a reasonable "price" for the increased complexity of the SMP shape. The condition $IF_d \geq 1.4$ is assigned as an area of reasonable SMP appliance. A horizontal cutting plane was drawn across the polygonal surface (Figure 6) at $IF_d \geq 1.4$ (Figure 7) to determine the many different SMP shapes that possess the accepted condition. A projection on the plane of the polygonal surface represents the outer boundaries of the effectiveness SMP forms area satisfying the condition $IF_d \geq 1.4$.

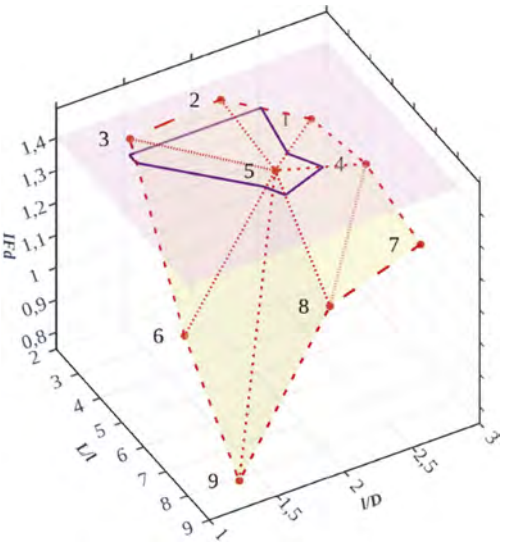

Figure 7. Polygonal surface IF_d for SMP and horizontal cutting plane.

The identified area (Figure 7) determines the effective shape of the SMP, based only on the accepted its bearing capacity increasing. At the same time, it should be taken into account that the shape of SMP is more susceptible to compression than vertical micropile due to helicity. Therefore, the SMP behavior in the soil should be evaluated by the compression of the pile shaft additionally.

The fulfilled series of SMP numerical calculations made it possible to determine the relative compression of the pile shaft ε under the load equal to the bearing capacity of the pile (Table 1, column 11). It was found that the SMP length has an insignificant effect on the compressibility of the pile (less than 15%). The greatest influence on the compressibility of the SMP shaft has the relative elongation of the pitch of the spiral l/D. The increasing of D at constant l increases the relative compressibility of the SMP particularly (Figure 8). For example, for a 7 m long SMP with $l/D = 2.67$, the relative compressibility of the pile shaft is $\varepsilon = 0.038\%$, and with $l/D = 1.33$ $\varepsilon = 0.214\%$, higher by 463%. Relative compressibility of the pile shaft ε decreases as the parameter l/D increases.

It is necessary to establish limit values to evaluate the relative compressibility of the pile shaft ε. If parameter ε is in excess of limit values the SMP material mode of operation changes significantly. In other words, the limit value of ε should indicate the elastic limit or the beginning of the cracking process. The actual value of the limit parameter ε should depend on the SMP material and the technology of its installation. Authors specified the value of the limit of the relative compressibility of the pile shaft ε as 0.1% (horizontal red dashed line in Figure 8). It intersects with the envelope functions of compressibility development for SMP with different length. The projection of the intersection point on the X-axis indicates the minimum allowable value of the parameter $l/D = 1.95$ that meets the compressibility criterion. Thus, the area of SMP design solutions according to the criterion of relative compressibility admissibility is highlighted (the green area in Figure 8).

Effective SMP shapes must meet the joint requirements of higher bearing capacity and low compressibility. Thus, it is necessary to combine the surface projection IF_d (effective SMP shapes) satisfying the condition $IF_d \geq 1.4$ (Figure 7) and the minimum allowable value of parameter $l/D = 1.95$ (Figure 8), assigned by the compressibility criterion $\varepsilon \leq 0.1\%$. The result is the highlighted area of the effective SMP shape, shown in Figure 9.

The coordinates of the point (l/D and L/l) inside the selected area describe the design solution of the SMP that simultaneously meets two conditions: $IF_d \geq 1.4$ and $\varepsilon \leq 0.1\%$.

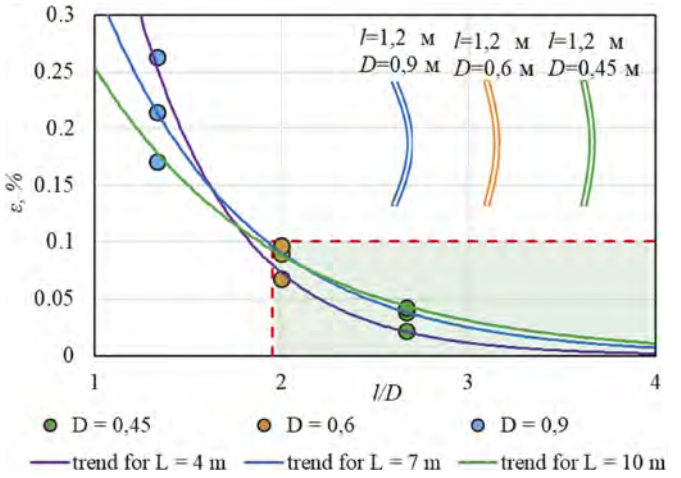

Figure 8. Analysis of change ε for SMP.

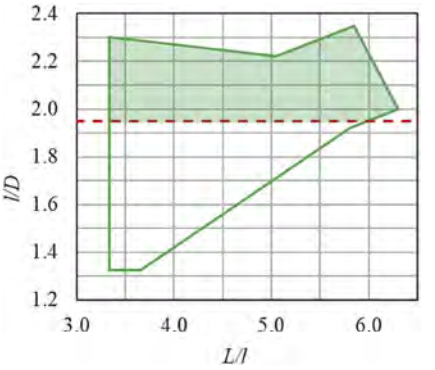

Figure 9. Surface projection IF_d for SMP that are limited by compressibility criteria.

6 CONCLUSIONS

It should be introduced a significant clarification that the spiral micropile (SMP), at the moment, is only an idea. Completed numerical simulation of its behavior with the soil is an effort to reveal the reasonableness of its more targeted research in future. The conditions adopted in the work $IF_d \geq 1.4$(and $\varepsilon \leq 0.1\%$) reflect only the way of such search and do not yet have the necessary justification. Nevertheless, taking all this into account, it is possible to draw general conclusions:

1. The spiral shape of micropile is the result to solve the problem of the verticality of boreholes at depths greater than 10 m. The way to find such a solution was to adopt one of the **TIPS** ideas "Conversion of harm into benefit". It allows to reinforce the main defect of micropile - random deviation from verticality.
2. Giving the micropile a regular spiral shape affects its bearing capacity. The bearing capacity of some SMP structural forms exceeds the vertical micropile bearing capacity with the same length by more than 40%. The bearing capacity of the SMP depends to a greater extent on the elongation of the pitch of the spiral.
3. The regular spiral shape of the micropile significantly effects on its compressibility. The elongation of the pitch of the spiral is more significant than the number of the pitch of the

spiral along its length. The compressibility of the SMP exceeds the compressibility of the vertical micropile. Therefore, the structural shape of SMP should be based on the condition of its ultimate compressibility.

The idea of the SMP is inherently revolutionary. The pile shaft was traditionally perceived only as straight, and its deviation (curvature) was considered as a defect. That was the inertia of thinking. SMP appeared by looking at this problem from a different angle and turning the disadvantage to the advantage. A wine corkscrew can be considered as the prototype of SMP in normal life. The bearing capacity of such "anchor pile" is very high. Research of the SMP behavior as an anchor will be conducted.

The material of SMP and the technology of its installation into the soil are a fair question. At this stage the authors see the implementation of SMP from metal or reinforced concrete. SMP can be screwed into the soil or arranged in the soil by directional drilling. Be that as it may, the questions of SMP material and technology have not been answered.

The authors are convinced that the idea of SMP should be protected. That is why a patent application has been filed for future research.

REFERENCES

Basack, S., Karami, M., Karakouzian, M., 2022. Pile-soil interaction under cyclic lateral load in loose sand: Experimental and numerical evaluations. Soil Dynamics and Earthquake Engineering 162, 107439.

Dai, Z., Su, M., Hu, C., 2007. Two numerical solutions of piles subjected to laterally parabolic distributed loads with biparameter method. Yanshilixue Yu Gongcheng Xuebao/Chinese Journal of Rock Mechanics and Engineering 26, 1463–1469.

Hajrullin, V.A., Zencov, V.N., Shakirova E. V., 2015. Ocenka ekonomicheskogo effekta ot vnedreniya novyh konstruktivnyh reshenij v stroitel'stve [WWW Document]. Izvestiya vysshih uchebnyh zavedenij. Sociologiya. Ekonomika. Politika. № 1.

Ivanova, T. v., Albert, I.U., Kaufman, B.D., Shulman, S.G., 2016. The load-bearing capacity of hanging piles by the strength criterion of a pile or soil material. Magazine of Civil Engineering 67, 3–12.

Karaulov, A.M., Korolev, K. v., Kuznetsov, A.O., 2022. Bearing Capacity Assessment of Soil Foundation. Soil Mechanics and Foundation Engineering 59, 111–118.

Mangushev, R.A., Gotman A. L., Znamenskij V. V., Ponomarev A. B., 2015. Svai i svajnye fundamenty. Konstrukcii, proektirovanie i tekhnologii [WWW Document]. Moscow. ASV.

Mirnyj, A.Yu., Ter-Martirosyan, A.Z., 2017. Oblast' primeneniya sovremennyh mekhanicheskih modelej gruntov [WWW Document]. Geotekhnika № 1.

Teixeira, A., Honjo, Y., Gomes Correia, A., Abel Henriques, A., 2012. Sensitivity analysis of vertically loaded pile reliability. Soils and Foundations 52, 1118–1129.

Vertynskii, O.S., Emel'yanova, T.A., 2013. Development and investigation of the performance of a new design of cast-in-place pile. Soil Mechanics and Foundation Engineering 50, 206–211.

Xu, X.B., Hu, M.Y., Zhang, T.Y., Chen, K.L., Wang, J.C., 2020. Model tests on the bearing capacity of precast open-ended micro pipe piles in soft soil. Proceedings of the Institution of Civil Engineers: Geotechnical Engineering 173, 500–518.

Smart Geotechnics for Smart Societies – Zhussupbekov, Sarsembayeva & Kaliakin (Eds)
© 2023 The Author(s), ISBN 978-1-003-29912-7
Open Access: www.taylorfrancis.com, CC BY-NC-ND 4.0 license

Mathematical equations for modelling soil-water characteristic curve

Nura Bello, Alfrendo Satyanaga*, Gerarldo Davin Aventian, Sung-Woo Moon & Jong Kim
Department of Civil and Environmental Engineering, Nazarbayev University, Kazakhstan

ABSTRACT: Climate change is continuously becoming a vivid global problem that needs to be tackled from every angle for the survival of our planet. Landslide is one of the fore-front phenomena attributed to climate change, claiming lives, and destroying the environment across the globe. To prevent the occurrences of those slides, a good understanding of unsaturated soil is necessary. Soil-water characteristic curve (SWCC) which describes the amount of water retained by a particular soil is an important hydraulic property of the soil, especially related to the soil's pores sizes and spaces connection within it. Modeling water distribution and flow in unsaturated soils requires knowledge of the SWCC which plays a critical role in water management and in prediction of its transport within the soil. There are many attempts to model SWCC mathematically, with the likes of the Satyanaga, Zhai, Fredlund and Xing, Van Genutchen, Brooks and Corey, and several other models for soils with unimodal and bimodal characteristics. Each equation has its own advantage and disadvantage which can model certain type of soil due to the variability of soil properties. It is however important to analyze the available models, study their best applicable scenario and limitations. This paper will therefore study and review several available mathematical equations for modelling SWCC.

1 INTRODUCTION

Soil slopes constitutes an inclined earth face that are either naturally occurring as in hills and cliffs, or artificially made, usually to carry transportation infrastructure such as in road and rail embankments. Those slopes are continuously facing a danger of slides in form of partial or total collapse, and when the slopes fail, it usually involves damage to such infrastructures they supported, deters daily economic activities and often even leads to loss of lives (Bello et al., 2019, Gariano and Guzzetti, 2016). Climate change is the fore-front phenomenon contributing to landslides and slope failures. It causes an escalation of rainfall, and the increases in the rainfall intensity yield a significant impact on groundwater changes and alter those parameters responsible for soil strength, such as suction, thereby causing various geotechnical problems such as excessive soil settlement and slope failures (Satyanaga et al., 2022a, Tamm et al., 2008, Jakob, 2022). As such, the need to quantify effects of climate variables on geohydrogical hazards is therefore becoming more necessary (Gariano and Guzzetti, 2016).

With the incorporation of the unsaturated soil mechanics principles, many of the geotechnical problems including slope instability could be attenuated. This is achieved by proper understanding of the soil's mechanisms and making appropriate designs using actual soil's condition and its variability. Whilst soils suction is highly dependent on soil types and its infiltration settings, understanding its mechanism plays a vital role in stabilising geotechnical structures, as it is a common knowledge that changes in soil's pore-water pressure is the top variable influencing a slope performance or failure (Satyanaga et al., 2022a, Griffiths and Lu, 2005). In fact, the variation in negative pore-water pressure (suction) and water content hugely influences the

*Corresponding author: Alfrendo.satyanaga@nu.edu.kz

DOI: 10.1201/9781003299127-367

unsaturated soil's shear strength as observed by (Rahardjo, 2009), and the two most distinct hydraulic properties related to unsaturated soil are its water-characteristic curve (SWCC) and permeability function (Satyanaga et al., 2022b).

SWCC signifies a relationship between soil suction (ψ) and its pore water content (either in gravitational or volumetric form). It is believed to be one of the most important soil parameters for geotechnical engineering operation involving unsaturated soil mechanics. Various important soil behaviour such as its shear strength, water volume storage, change in volume, thermal conductivity and specific heat could all be deduced using SWCC (Sillers, 1997, Sillers et al., 2001, Pan et al., 2021). SWCC could be measured directly in the laboratory, but the procedure is highly time consuming, coupled with high cost and results variability, due to its importance, various empirical equations were developed to calculate SWCC. Therefore, in doing that, a suitable mathematical equation that will clearly provide physical definitions of the SWCC variables must be sought and used (Ellithy, 2017, Pan et al., 2021, Satyanaga et al., 2017). The main objective of this paper is therefore to understand some important available mathematical equations for modelling SWCC and provide an informed review accordingly.

2 UNIMODAL SWCC

Plotting SWCC in respect of water content (θ_w) against soil suction (u_a-u_w) was first proposed by Fredlund (2006), the curve always having a sigmoidal shape have four main elements: the saturated volumetric water content (θ_s) residual volumetric water content (θ_r,) air entry value (ψ_a) and water-entry value (ψ_w). The curve are generally plotted on a logarithmic scale for whole abscissa range (Satyanaga et al., 2017).

There are a variety of fitting equations developed to model the relationship between quantity of water retained by a soil and its matric suction (Zhai and Rahardjo, 2013), the following are some of the best fit equations used for unimodal SWCC.

2.1 *Brooks and Corey, (1964)*

Brooks and Corey (1964) provided one of the earliest fitting models for drying SWCC at a suction lager than air entry value of the soil, in the form of equation (1) (Tinjum et al., 1997, Fredlund, 2006, Wang et al., 2021).

$$\Theta_n = \left[\frac{\psi}{\psi_{aeb}}\right]^{\lambda} for\ \psi > \psi_{aeb} \tag{1}$$

Where, Θ_n is dimensionless normalized volumetric water content, and it is equal to $\left[\frac{(\theta-\theta_r)}{(\theta_s-\theta_r)}\right]$

θ *and* θ_r are saturated and volumetric water contents respectively

ψ is soil suction at a point and ψ_{aeb} is air entry value of the soil

λ is a fitting parameter called pore size distribution index

Degree of Saturation (S) could replace the normalised water content Θ_n in the equation, while residual water content θ_r could be established on semi log plot of straight line by trial and error (Fredlund and Xing, 1994).

Brooks and Corey equation has been widely used by many researchers, but its main shortfall is it only describes SWCC between air entry value (AEV) and residual condition. In order to solve this, McKee and Bumb (1987) and Bumb (1987) presents a more fitting model for SWCC approximation in the area before AEV but unfortunately not useful in the high suction range (Gardner et al., 1970, Rogowski, 1971, Williams et al., 1983, Bumb, 1987, McKee and Bumb, 1987).

The McKee and Bumb equation is given by;

$$\Theta_n = \frac{1}{1 + exp[\frac{\psi - a_m}{n_m}]} \tag{2}$$

where a and n are fitting parameters.

2.2 *Van Genuchten (1980)*

Van Genuchten model is another popular relationship between water content and suction that was widely used among researchers.

$$\Theta = \left[\frac{1}{1+(p\psi)^n}\right]^m \tag{3}$$

p, n and m are soil parameters. The equation provides additional flexibility compared to Brooks and Corey, (1964) (Ellithy, 2017, Pan et al., 2021). However, as noted by Fredlund and Xing, 1994, "in trying to get a closed-form solution for hydraulic conductivity, Van Genuchten (1980) related m and n through the equation m = (1-1/n), and therefore reduced the added flexibility" and as shown by best fit analysis, identical quality fit could be equally be possible by simply taking the variable (m) as 1. (Fredlund and Xing, 1994, Fredlund, 2006).

2.3 *Gardner, (1958)*

Gardner (1958) presents permeability function equation that mirrored SWCC and could be seen as an extension of Van Genuchten model.

$$\Theta = \frac{1}{1+q\psi^n} \tag{4}$$

q and n are curve fitting parameters related to soil's AEV and the inflection point's slope of the SWCC, respectively.

2.4 *Fredlund and Xing, (1994)*

Fredlund and Xing, (1994) proposed a fitting model relating volumetric water content (θ) and soil suction (ψ) which complements the limitations of the previous fitting equations (i.e., this equation is valid for the entire suction range up to 10^6 kPa). The proposed equation was in the form of;

$$\theta = \theta_s\left[\frac{1}{In(e+\psi/a)^n}\right]^m \tag{5}$$

Equation (5) have three fitting parameters a, m and n, such that if m and n are fixed then a will have a value so close to the soil air entry value for albeit for a small value of m, otherwise the a is generally greater than aev.

$$a = \psi i,\ m = 3.6\ In(\theta_s/\theta_r),\ and\ n = \frac{1.31^{m+n}}{m\theta_s} 3.72s\ \psi i$$

and the slope to the tangent line of the curve (s) could be calculated using $s = \frac{\theta_i}{\psi p - \psi i}$ where ψp is an intercept of the tangent to the suction.

The equation (5) clearly indicated that (θ) equals (θ_s) when (ψ) is zero; as such it will be valid at the lower suction range, but it can be noted that θ becomes (0) when suction approach infinity, therefore still needing modification for fitting the upper limit of suction. As indicated in experimental data by (Croney and Coleman, 1961), that soil suction attains its peak value of 10^6 kPa when $\theta = 0$, thus the upper limit of the suction range needs to be taken care by the equation. In doing so, a correction factor C(ψ) was introduced into the equation (5).

$$\theta(\Psi, a, m, n) = C(\psi)\left[\frac{\theta_s}{In(e+\psi/a)^n}\right]^m \tag{6}$$

$$\text{Where } C(\psi) = \left[-\frac{In(1+\psi/\psi_r}{In(1+10^6/\psi_r)}\right] + 1$$

It could be seen that at the limiting value of $\psi = 10^6$ kPa, the C will be equals to 0, clearly indicating at that limiting value the corresponding water content (θ) calculated using equation (6) will now be equals to (0) (Fredlund and Xing, 1994). The equation (6) provided by Fredlund and Xing 1994, could safely be used for whole suction range (i.e., 0kPa -10^6 kPa) and has successfully taken care of the limitations of the previous fitting equations.

2.5 *Satyanaga Et Al., (2017)*

Although equation (6) could be used to fit SWCC for the entire suction range, it has one important disadvantage, in the sense that most of its parameters lacked a clear physical meaning, which refers to as "an ability of the equation parameters to clearly represents the variables in the SWCC" (Satyanaga et al., 2017).

So, for the fact that a convenient mathematical equation containing parameters that are able to represents the exact variables in the SWCC is needed, Satyanaga (2017) presents an efficient best fitting model for that;

$$\theta_w = C(\psi)\left[\theta_r + \left\{\theta_s - \theta_r\left(1 - (\beta)efrc\left(\frac{In\left(\frac{\psi_a - \psi}{\psi_a - \psi_m}\right)}{s}\right)\right)\right\}\right] \tag{7}$$

Where;
β is 0 at the suction range at or before aev, and 1 at any suction beyond aev
θ_w is calculated volumetric water content
θ_s is saturated volumetric water content
ψ is matric suction in view (kPa)
ψ_a is soil's air entry value (kPa)
ψ_m is the matric suction at inflection point of the SWCC (kPa)
S is representing standard deviation of the SWCC
θ_r soil's residual volumetric water content
ψ_r is matric suction corresponding to θ_r on the SWCC (kPa)

The good thing about equation (7) is, while it is valid for the entire suction range, its parameters equally have a clear physical meaning to represents the variables of soil water characteristics curve.

3 BIMODAL SWCC

Debris of weathered rocks found in an unsaturated zone are called residual soils, and in most cases, those residuals and colluvial soils are widely gap graded, exhibiting bimodal grain-size distribution (GSD). And usually, colluvial soils with bimodal characteristics GSD brings about bimodal characteristics of SWCC, the bimodal SWCC happens as a result of the soil containing two pore series (Kutílek, 2004, Rahardjo et al., 2004, Zhang and Chen, 2005, Satyanaga et al., 2013).

GSD and SWCC modelling using continuous function is very important, as the SWCC predicted using GSD could be used to establish various soil properties in very short duration, as compared to the time-consuming laboratory SWCC tests. Among many GSD equations developed Fredlund et al., is commonly used for fitting bimodal GSD, although the equation's parameters are unrelated to the soil's physical properties (Satyanaga et al., 2013).

3.1 *Zhang and Cheng (2005)*

Zhang and Cheng (2005) developed a method of predicting bimodal soil water characteristics curve for bimodal soil. They utilized the theoretical basis of estimating SWCC from a pore distribution as provided by Fredlund and Xing, 1994. The SWCC for the bimodal soil was

established as the sum of the two components of the soil with large pore series and small pore series. And the bimodal SWCC could be described using either Van Genuchten, 1980 function or Fredlund and Xing, (1994) function as follows.

$$\Theta(\psi) = p_i n_{p1}\left[\frac{1}{1+(a_i\psi)^{ni}}\right]^{mi} + p_s n_{ps}\left[\frac{1}{1+(a_s\psi)^{n}s}\right]^{m_s} \tag{8}$$

where,

a_l, n_l, and m_l are fitting parameters for the large-pore series component, and a_s, n_s, and m_s are fitting parameters for the small-pore series component.

p_l and p_s are respectively the volumetric percentages of the components with the large-pore series and the small-pore series in the soil mass and could be calculated easily based on the density values and the percentages by dry weight of the soil components.

n_{pl} and n_{ps} are porosities of the components with the large-pore series and the small-pore series when they are considered individually

and;

$$\begin{aligned}\theta(\psi) =& \mathrm{p_i n_{p1}}\left[\left[1-\frac{\mathrm{In}(1+\psi/\psi_\mathrm{r}}{\mathrm{In}(1+10^6/\psi_\mathrm{r}}\right]\right]\left\{\frac{1}{\mathrm{In}(\mathrm{e}+\psi/\mathrm{a_1})^{\mathrm{n1}}}\right\}^{\mathrm{m_l}} \\ &+\mathrm{p_s n_{ps}}\left[\left[1-\frac{\mathrm{In}(1+\psi/\psi_\mathrm{r}}{\mathrm{In}(1+10^6/\psi_\mathrm{r})}\right]\right]\left\{\frac{1}{\mathrm{In}(\mathrm{e}+\psi/\mathrm{a_s})^{\mathrm{n_s}}}\right\}^{\mathrm{m_s}}\end{aligned} \tag{9}$$

where,

e is the base of natural logarithm; and all other parameters as explained.

3.2 *Satyanaga Et Al., (2013)*

Although Zhang and Cheng (2005) present a model that could predicts a bimodal soil water characteristics curve for a bimodal soil, the equations where developed based on Van Genuchten 1980 and Fredlund and Xing (1994), whose some of the variables having no physical meaning in relation to the SWCC's parameters. Therefore Satyanaga et al. (2013) provide an equation to mitigate limitation of the Zhang and Cheng (2005) model.

"The equation was developed considering five important factors.

i. The equation parameters could be related to the soil's physical meaning
ii. The soil water content is set to zero as the soil's suction reached 10^6 and the Fredlund and Xing's correction function (C) is utilized
iii. The shape of SWCC is like lognormal distribution. Therefore, Kosugi (1994) equation is used as a basis for the development of the proposed equations.
iv. Water content when soil is fully saturated (saturated water content, w_{sat}) is known.
v. Since the bimodal characteristic of SWCC occurs if the percentage of coarse-grained soil is high, the total volume of soil is assumed to be constant during the SWCC tests (Satyanaga et al., 2013, Kosugi, 1994)."

$$\begin{aligned}\theta_w = \left(1-\frac{In(1+\psi/\psi_r)}{In(1+10^6/\psi_r)}\right)\Bigg[\theta_r + (\theta_{s_1}-\theta_{s_2})\left(1-efrc\left(\frac{In\left(\frac{\psi_{a_1}-\psi}{\psi_{a_1}-\psi_{m_1}}\right)}{s_1}\right)\right)+ \\ (\theta_{s_2}-\theta_r)\left(1-efrc\left(\frac{In\left(\frac{\psi_{a_2}-\psi}{\psi_{a_2}-\psi_{m_2}}\right)}{s_2}\right)\right)\Bigg]\end{aligned} \tag{10}$$

where,

θ_w is the calculated volumetric water content, θ_s the saturated volumetric water content (measured in the laboratory), ψ is the matric suction under consideration, ψ_a represents the air-entry value of soil, and ψ_m represents the matric suction at the inflection point of SWCC and S represents the geometric standard deviation of SWCC (Satyanaga et al., 2013).

4 CONCLUSION

Many SWCC equations were reviewed in this work, such as Brooked and Corey, (1964), Van Genuchten, (1980), Gardener, (1958), Fredlund and Xing, (1994) and Satyanaga et al., (2017) for unimodal SWCC, while Zhang and Cheng, (2015) and Satyanaga et al., (2013) were used for bimodal SWCC. And it could be concluded that Satyanaga, (2017) for unimodal SWCC (equation 7) and Satyanaga et al., (2013) for bimodal SWCC (equation 10) are best fit for the said purpose. This is for their unique ability of been valid for the entire soil suction range (up to 10^6kPa), also containing parameters that have physical meanings that best describe the soil variables.

REFERENCES

Bello, N., Rees, S. W. & Salisu, S. A. 2019. Influence of tree type to suction development and the stability of slope. *IOP Conference Series: Materials Science and Engineering*, 527, 012011.

Bumb, A. C. 1987. *Unsteady-state flow of methane and water in coalbeds*, University of Wyoming.

Croney, D. & Coleman, J. 1961. *Pore pressure and suction in soils*, London, Butterworths.

Ellithy, G. 2017. A spreadsheet for estimating soil water characteristic curves (SWCC). *ERDC/GSL TN-17-1*, 1.

Fredlund, D. G. 2006. Unsaturated Soil Mechanics in Engineering Practice. *Journal of Geotechnical and Geoenvironmental Engineering*, 132, 286–321.

Fredlund, D. G. & XING, A. 1994. Equations for the soil—water characteristic curve. *Canadian Geotechnical Journal*, 31.

Gardner, W., Hillel, D. & Benyamini, Y. 1970. Post-irrigation movement of soil water: 1. Redistribution. *Water Resources Research*, 6, 851–861.

Gariano, S. L. & Guzzetti, F. 2016. Landslides in a changing climate. *Earth-Science Reviews*, 162, 227–252.

Griffiths, D. V. & Lu, N. 2005. Unsaturated slope stability analysis with steady infiltration or evaporation using elasto-plastic finite elements. *International Journal for Numerical and Analytical Methods in Geomechanics*, 29, 249–267.

Jakob, M. 2022. Chapter 14 - Landslides in a changing climate. *In*: Davies, T., Rosser, N. & Shroder, J. F. (eds.) *Landslide Hazards, Risks, and Disasters (Second Edition)*. Elsevier.

Kosugi, K. 1994. The parameter lognormal distribution model for soil water retention. *Water Resource Research*, 30.

KutÍlek, M. 2004. Soil hydraulic properties as related to soil structure. *Soil and Tillage Research*, 79, 175–184.

Mckee, C. & Bumb, A. 1987. Flow-testing coalbed methane production wells in the presence of water and gas. *SPE formation Evaluation*, 2, 599–608.

Pan, D.-L., NI, W., Kang, C.-Y., LÜ, X. & Wang, H.-M. 2021. *A Mathematical Model for Soil-Water Characteristic Curve by Weibull Distribution*.

Rahardjo, H., Aung, K. K., Leong, E. C. & Rezaur, R. B. 2004. Characteristics of residual soils in Singapore as formed by weathering. *Engineering Geology*, 73, 157–169.

Rahardjo, I. 2009. Shear strength characteristics of a compacted soil under infiltration conditions. *Geomechanics and Engineering*, vol. 1, no. 1,, 35–52.

Rogowski, A. 1971. Watershed physics: Model of the soil moisture characteristic. *Water Resources Research*, 7, 1575–1582.

Satyanaga, A., Bairakhmetov, N., Kim, J. R. & Moon, S.-W. 2022a. Role of Bimodal Water Retention Curve on the Unsaturated Shear Strength. *Applied Sciences*, 12, 1266.

Satyanaga, A., Moon, S.-W. & KIM, J. 2022b. Stability analyses of dual porosity soil slope. *Geomechanics and Engineering*, 28, 77–87.

Satyanaga, A., Rahardjo, H., Leong, E.-C. & Wang, J.-Y. 2013. Water characteristic curve of soil with bimodal grain-size distribution. *Computers and Geotechnics*, 48, 51–61.
Satyanaga, A., Rahardjo, H. & Zhai, Q. 2017. Estimation of unimodal water characteristic curve for gap-graded soil. *Soils and Foundations*, 57, 789–801.
Sillers, W. 1997. *The mathematical representation of the soil—water characteristic curve. M.Sc. thesis*, Saskatoon, Canada, University of Saskatchewan.
Sillers, W. S., Fredlund, D. G. & Zakerzadeh, N. 2001. Mathematical attributes of some soil—water characteristic curve models. *In*: Toll, D. G. (ed.) *Unsaturated Soil Concepts and Their Application in Geotechnical Practice*. Dordrecht: Springer Netherlands.
Tamm, T., NÕges, T., JÄrvet, A. & Bouraoui, F. 2008. Contributions of DOC from surface and groundflow into Lake Võrtsjärv (Estonia). *In*: NÕges, T., eckmann, R., Kangur, K., NÕges, P., Reinart, A., Roll, G., Simola, H. & Viljanen, M. (eds.) *European Large Lakes Ecosystem changes and their ecological and socioeconomic impacts*. Dordrecht: Springer Netherlands.
Tinjum, J. M., Benson, C. H. & Blotz, L. R. 1997. Soil-Water Characteristic Curves for Compacted Clays. *Journal of Geotechnical and Geoenvironmental Engineering*, 123, 1060–1069.
Wang, S., Fan, W., Zhu, Y. & Zhang, J. 2021. The effects of fitting parameters in best fit equations in determination of soil-water characteristic curve and estimation of hydraulic conductivity function. *Rhizosphere*, 17, 100291.
Williams, J., Prebble, R., Williams, W. & Hignett, C. 1983. The influence of texture, structure and clay mineralogy on the soil moisture characteristic. *Soil Research*, 21, 15–32.
Zhai, Q. & Rahardjo, H. 2013. Quantification of uncertainties in soil–water characteristic curve associated with fitting parameters. *Engineering Geology*, 163, 144–152.
Zhang, L. & Chen, Q. 2005. Predicting Bimodal Soil–Water Characteristic Curves. *Journal of Geotechnical and Geoenvironmental Engineering*, 131, 666–670.

Smart Geotechnics for Smart Societies – Zhussupbekov, Sarsembayeva & Kaliakin (Eds)
© 2023 The Author(s), ISBN 978-1-003-29912-7
Open Access: www.taylorfrancis.com, CC BY-NC-ND 4.0 license

Assessing shallow landslide susceptibility using the random forest algorithm

M.L. Lin & P.H. Huang
Department of Civil Engineering, National Taiwan University, Taipei, Taiwan

ABSTRACT: Typhoon Morakot induced significant shallow landslide failures that spread widely in southern Taiwan causing severe property and infrastructure damages. This study adopted a Random Forest Algorithm to construct a shallow landslide susceptibility map for the Namasia study area in southern Taiwan. The landslide inventory was compiled using data from existing landslide inventory by Central Geological Survey in 2009, satellite images, and field investigations. Nine causal factors, namely: slope angle, lithology, aspect, terrain ruggedness index, curvature, distance to fault, distance to road, and distance to stream were examined in the analysis. The scale effect was studied using four different grid resolutions to generate landslide susceptibility map. The resulting susceptibility map was validated with satisfactory accuracy. Thus, the susceptibility map could provide vital references supporting hazard mitigation strategy.

1 INTRODUCTION

Being situated in the convergence zone of tectonic plates, Taiwan is prone to fragile geological conditions, and typhoons often carry heavy rainfall causing landslide hazard. Typhoon Morakot brought more than 3000 mm accumulated rainfall in 2009, and induced widely spread shallow landslides in southern Taiwan. The shallow landslides caused by Typhoon Morakot in the Namashia area, Kaoshiung City, south Taiwan, were identified by Soil and Water Conservation Bureau (Lin et al. 2013), and susceptibility assessment of the area was conducted in this study. The machine learning method has a good ability of event classifications, and can be used to discriminate landslide versus non-landslide units. We adopted Random Forest Algorithm for its capability of treating nonlinear multi-variates relation, and the susceptibility assessment model was constructed. The environment causal factors were selected and tested for independency and significancy. The model was then constructed and validated, and the regional susceptibility map of the study area was developed accordingly.

2 STUDY AREA AND MATERIALS

2.1 *Study area*

The study area is the Namashia area in Kaoshiung City, south Taiwan, which locates in the upstream area of the Chishan River Watershed with elevation ranging from 217 to 2480 m a.s.l. as shown in Figure 1. The Namashia study area locates in the Western Foothill Geological Zone and is composed mainly of sedimentary rock formations. The lithology of the area is unmetamorphic rock formations of the Miocene with sandstone, siltstone, shale, and sandstone/shale interlayer formations, that include mainly Changchihkeng Formation, which is a sandstone/shale interlayer, Hunghuatzu Formation, which is mainly a silty sandstone, and Sanmin Shale. A small area of Lushan formation was identified in the north part of the area, which is composed

DOI: 10.1201/9781003299127-368

of slate. The geological map of the study area modified from 1:50000 watershed geological map published by the Central Geological Survey (CGS) in 2000 is as shown in Figure 2.

2.2 *Inventory of shallow landslides and data*

The Central Geological Survey conducted mapping of debris avalanche of the southern Taiwan affected by Typhoon Morakot in 2009. The CGS defines the debris avalanche as the sliding of weathered top soil, rock fragment and debris, and colluvium, which can be considered as shallow landslide. Mapping was conducted using aerial photos taken after Typhoon Morakot for the slope area with slope angle smaller than 55°. The mapped results were verified using FORMOSAT-2 satellite images, and field investigation was conducted. The mapped shallow landslides were then compared to the deep-seated landslide inventory by National Science and Technology Center for Disaster Reduction. The mapped shallow landslide scars coincided with the deep-seated landslide scars were eliminated to avoid the possible errors (Lin & Chen 2016). A total of 1710 shallow landslides were identified after verification and data modification. Figure 3 shows the distribution of the mapped landslides.

Digital terrain model (DTM) with a 5m resolution produced by the Ministry of Interior in 2003 was adopted for derivation of topographic related causal factors in the Geographic Information System (GIS). The geological map in Figure 2 was used for derivation of the geology related causal factors.

3 RESEARCH METHOD

3.1 *Environmental causal factors*

A grid-based analysis was conducted, and grids enclosed in the landslide scars were considered as landslide units, while other grids were considered as non-landslide units. The environmental causal factors typically include geomorphology related factors, geology related factors, and hydrology related factors. Referring to factors adopted by previous researches (Dai & Lee 2002, Guzzetti et al. 1999), the slope angle, lithology, aspect, terrain roughness index, curvature, distance to fault, distance to road, and distance to stream were selected for this study. The geomorphological factors were derived from the DTM data, and geological factors were obtained from the digital geological map, while the hydrological factors werer derived by generating watershed and stream based on DTM in GIS. The factors for both landslide and non-landslide units were generated in the analysis. All factors were tested for independency and significancy.

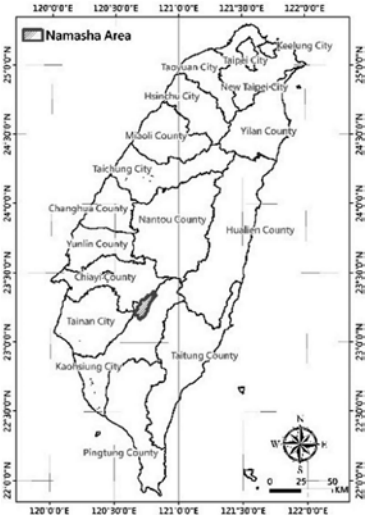

Figure 1. Location of study area.

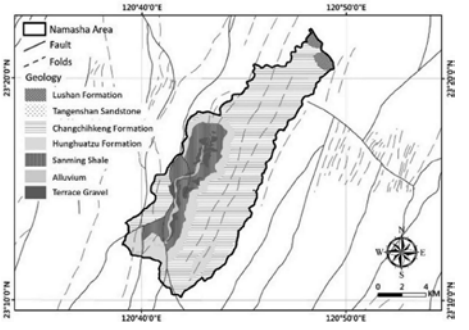

Figure 2. Geological map of the study area.

Figure 3. Distribution of mapped landslides in the study area.

3.2 *Random forest algorithm*

The random forest algorithm is a supervised machine learning method that has been used for classification. In this study, the random forest algorithm is used to identify landslide from non-landslide grids. The supervised learning process is conducted by input sets of factors and expected output values for training and thus a prediction model is constructed. The random forest is an ensemble of decision trees that can consider both the numerical and categorical factors without pre-process of unit or scale of factor. The tree randomly samples a subset training data to build the model through bootstrapping techniques, and data not included are referred to as out-of-bag, which account for about 30 % of the original sample subset (Breiman 2001). Each tree randomly selects variables to split each node to minimize classification errors. The error can be estimated through prediction errors of the out-of-bag data of each tree (Liaw &Wiener 2002). An overall error estimation can be presented as the average error of the out-of-bag errors of all the trees.

3.3 *Model test and verification*

To set up the over-all model of the random forest, the number of trees, settings of nodes of each tree, and the number of runs need to be determined. A series of tests were conducted to examine variations of the out-of-bag errors versus each variable set. The prediction model is expected to provide consistent and stable results from the causal factors with selected random components. The over-all accuracy of the prediction model is evaluated using the confusion matrix. For the confusion matrix, the accurately predicted instances are the sum of true positive and true negative classes, and the accuracy rate is represented by the ratio of the sum over the total number of instances. The receiver operating characteristic curve (ROC) is plotted as the true positive ratio versus the false positive ratio, and the area under the curve (AUC) was calculated to assess the performance of the prediction model. The AUC value of 0.5 suggests no prediction capability, and the larger the AUC value, the better the prediction performance.

4 RESULTS AND DISCUSSIONS

A series of test was conducted starting with 10 trees and gradually increased to 1500 trees, and the out-of-bag error decreased rapidly with increasing number of trees. The variations of out-of-bag error becomes stable with 500 trees. The number of nodes of each tree and number of runs were tested using the similar process, and 200 nodes and 100 runs were used to construct a stable prediction model. Due to the factors used in the model were derived on a grid-based analysis, the sensitivity of the factors and results could be significantly affected by the size of the grid, which has been discussed by several researchers (Catani et al. 2013). The effects were evaluated in this study by using grid sizes of 5m, 10m, 20m, 25m, and 40m resolution respectively, by combining the 5m resolution DEM into larger grids. In addition, the number of landslide data was much smaller than the number of non-landslide data as shown in Figure 3, which might induce sample bias problem. To avoid bias of sample sizes, two different measures were adopted. The first measure was to resample (up-sample) the landslide data, and the second measure was down-scale

sampling (down-sample) of non-landslide data to ensure an equivalent size of landslide and non-landslide data.

Comparing the results of up-sample to the down-sample sets, it was found that the up-sample set yields more stable results of ROC curve and higher AUC values. Figure 4 shows the ROC curves for different grid sizes using up-sampling data. It appears that the curves and AUC values for grid sizes of 5m, 10m, and 20m are about the same, however, the set with grid size of 5m has the best average accuracy rate of 75.65% from the confusion matrices. Thus, the landslide susceptibility map of the study area was developed according to the threshold on the ROC curve as shown in Figure 5. Close examination of the susceptibility map shows that most mapped landslides locate in the area with medium to high potential, and the prediction model provides satisfactory results.

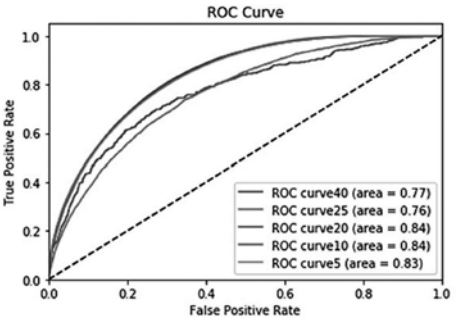

Figure 4. ROC curves for up-sampling of different grids.

Figure 5. Susceptibility map of the study area.

5 CONCLUSIONS

This study adopted a Random Forest Algorithm to construct a shallow landslide susceptibility map for the Namasia study area in southern Taiwan. The landslides caused by Typhoon Morakot were compiled and nine causal factors were adopted in the analysis. The model settings and scale effect were tested using four different grid resolutions. Equivalent sample sizes were warranted adopting up-sampling of landslide data. The resulting susceptibility map from 5m grid up-sampling data was validated with satisfactory accuracy. The susceptibility map could provide vital references supporting hazard mitigation strategy.

REFERENCES

Central Geological Survey, 2000. 1:50000 watershed geological map.

Breiman, L. 2001. Random forests. *Mach. Learn*. 45: 5–32

Catani, F. Lagomarsino, D. Segoni, S. & Tofani, V. 2013. Landslide susceptibility estimation by random forests technique: sensitivity and scaling issues. *Nat. Hazards Earth Syst. Sci*. 13: 2815–2831.

Dai, F.C. & Lee, C.F. 2002. Landslide characteristics and slope instability modeling using GIS, Lantau Island, Hong Kong. *Geomorphology* 42(3–4): 213–228.

Guzzetti, F. Carrara, A. Cardinali, M. & Reichenbach, P. 1999. Landslide hazard evaluation: a review of current techniques and their application in a multiscale study, Central Italy. *Geomorphology* 31: 181–216.

Liaw, A. & Wiener, M. 2002. Classification and regression by random forest, *R News*, 2: 18–22.

Lin, M.L. & Chen, Y.C. 2016. *Relationship of landslides and rainfall in the Kaoping River Watershed*, Report to the Soil and Water Conservation Bureau, Taiwan.

Lin, M.L. Chen, T.C. Wang, K.L. Chen, T.W. & Chen, Y.C. 2013. *Effects of landslide on debris flow hazard in watershed*, Report to the Soil and Water Conservation Bureau, Taiwan.

Smart Geotechnics for Smart Societies – Zhussupbekov, Sarsembayeva & Kaliakin (Eds)
© 2023 The Author(s), ISBN 978-1-003-29912-7
Open Access: www.taylorfrancis.com, CC BY-NC-ND 4.0 license

Global warming impact of drilled shafts

M. Lee & D. Basu
University of Waterloo, Waterloo, Canada

ABSTRACT: Incorporating sustainability considerations as early as in the design of pile foundations can help in reducing excessive use of construction materials, thereby reducing environmental impacts. This paper uses drilled shafts as an example to illustrate the importance of environmental impact assessment in the design phase of foundations. Life cycle assessment (LCA), a standardized method for quantifying environmental impacts, is applied to drilled shafts in this study. The global warming impact of drilled shaft, quantified using LCA, is compared with two reference values – global warming impact caused by a person annually and a passenger car throughout its entire twelve-year life cycle. The comparisons help in understanding how severe the global warming impact of drilled shaft is in relation to commonly perceived polluters. Plots are developed that may be used for quick estimation of global warming impact of drilled shafts without the use of specialized LCA software programs.

1 INTRODUCTION

Drilled shafts are one of the widely used deep foundations that provide support to bridges, high-rise buildings, excavations, retaining structures, and slopes (FHWA, 2010). Concrete and steel, known to be energy and carbon intensive materials, are the main materials used in constructing drilled shafts. These materials together are responsible for 16% of global carbon dioxide emissions that contribute significantly to global warming and climate change (Watts, 2019; World Steel Association, 2021). As the use of drilled shafts continually increases, it is important to understand their environmental impacts through quantitative methods.

Studies quantifying the environmental impacts of geotechnical structures are rather limited and mostly performed using life cycle-based tools. Life cycle assessment (LCA) has been particularly used for quantifying the environmental impacts of various geotechnical applications including pile foundations (Giri and Reddy, 2014; Luo et al., 2019; Misra, 2010). Although drilled shafts have been widely used for various applications, there is a lack of knowledge regarding their environmental impacts. There is no easy-to-use guideline available using which a designer can relate a particular design to its environmental impact without the use of specialized LCA software packages. In this study, the global warming impact of typical single drilled shafts are quantified using LCA considering different subsurface and loading conditions.

2 DRILLED SHAFT DESIGN

The drilled shafts in this study are designed by satisfying the ultimate limit state criterion of ultimate pile capacity corresponding to 10% relative settlement and the serviceability limit state criterion of allowable pile settlement. The ultimate capacity of drilled shafts is calculated as the summation of capacities developed at the base and along the shaft:

$$Q_{ult} = q_{b,ult}A_b + \sum_i q_{sL,i}A_{s,i} \quad (1)$$

where Q_{ult} is the total ultimate capacity (kN), $q_{b,ult}$ is the ultimate unit base resistance (kPa), A_b is the cross-sectional area of the pile base (m^2), $q_{sL,i}$ is the limit unit shaft resistance of the i^{th} soil

DOI: 10.1201/9781003299127-369

layer (kPa), and $A_{s,i}$ is the surface area of the pile in contact with the i^{th} layer (m^2). According to Salgado (2008), the ultimate unit base capacity of drilled shafts in sand is given by

$$q_{b,ult} = 0.38 p_A \exp(-0.0066 D_R) \exp[0.1041\phi_c + (0.0264 - 0.0002\phi_c) D_R] \left(\frac{\sigma'_h}{p_A}\right)^{0.841 - 0.0047 D_R} \quad (2)$$

where D_R is the relative density of sand (%), p_A is the atmospheric pressure (= 100 kPa), ϕ_c is the angle of friction at the critical state, and σ'_h is the effective horizontal stress (kPa) at the pile base. The limit unit shaft capacity of drilled shafts in sand is given by (Salgado 2008):

$$q_{sL} = \sigma'_z \left[0.7 K_0 \exp\left\{\left[0.0114 - 0.0022 \ln\left(\frac{\sigma'_z}{p_A}\right)\right] D_R\right\}\right] \tan\delta \quad (3)$$

where σ'_z is the effective vertical stress at a depth where q_{sL} is determined, K_0 is the coefficient of lateral earth pressure at rest, and δ is the friction angle at the interface of the pile and soil (= ϕ_c).

The total settlement of drilled shafts ΔH_p is calculated following the method by Bowles (1997):

$$\Delta H_p = \frac{P L_p}{A_b E_p} + \Delta q B_p \frac{1 - \mu_s^2}{E_s} m I_s I_F F_1 \quad (4)$$

where P is the axial force (kN), L_p is the length of pile (m), E_p is the Young's modulus of pile (kPa) (= 34,077,000 kPa in this study), Δq is the bearing pressure at the pile base (kN/m^2), B_p is the drilled shaft diameter (m), μ_s is Poisson's ratio of soil (= 0.35), E_s is the Young's modulus of soil below the pile base (kPa), mI_s is the shape factor (= 1.0), I_F is the Fox embedment factor = 0.55 if $L_p/B_p \le 5$ and = 0.50 if $L_p/B_p > 5$, and F_1 is the reduction factor (= 0.50 in this study).

The working stress design method is used to obtain the drilled shaft dimensions with a factor of safety (FS) ranging over 2-3. Hence, the allowable pile capacity Q_{all} is obtained by reducing Q_{ult} with a factor of safety (FS) — $Q_{all} = Q_{ult}$/FS. The allowable settlement of drilled shaft is assumed to be 30 mm, as recommended by Salgado (2008). The volume of steel reinforcement in the drilled shaft is assumed to be 2.5% of the volume of concrete shaft (FHWA, 2010).

Two sandy soil profiles are considered in this study, as described in Figures 1(a)-(b). For an applied load, the drilled shafts are designed assuming either (i) a fixed diameter or (ii) a fixed length. For example, if a fixed diameter of, say, 600 mm is assumed, the pile length that satisfies the ultimate limit capacity with a factor of safety is determined, and if a fixed length of, say, 10 m is assumed, the pile diameter is determined. In this study, the pile length L_p is varied from 5 m to 30 m, and pile diameter B_p is varied from 0. 3 m to 1.5 m.

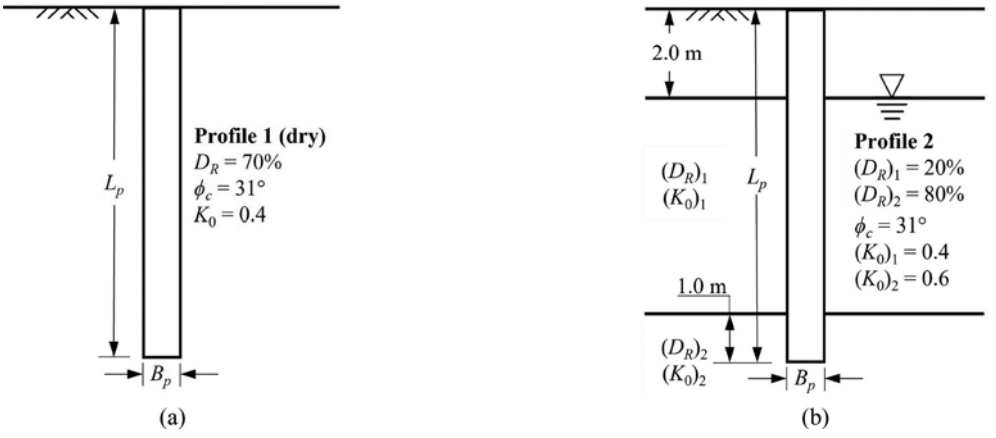

Figure 1. Soil profiles considered in this study.

For a given profile and applied load, the drilled shaft dimensions are determined as part of design. After the dimensions of the drilled shafts are finalized, the total volumes of concrete and

steel are computed and converted into their corresponding masses using the respective densities of 2400 kg/m^3 (Vieira, 2015) and 7850 kg/m3 (CEN, 2002), respectively. For example, for a single drilled shaft with 0.8 m diameter, 15 m length, and 2.5% steel reinforcement, the total masses of concrete and steel are 18096 kg and 1480 kg, respectively. These values are used as inputs to the LCA.

3 LIFE CYCLE ASSESSMENT OF DRILLED SHAFTS

LCA is a tool for quantifying the environmental impacts (e.g., global warming) that are caused throughout the life cycle of a product (drilled shaft in this case). Figure 2 shows the life cycle of typical drilled shafts based on which the LCA is performed in this study. LCA comprises four parts: (1) goal and scope definition, (2) life cycle inventory analysis (LCI), (3) life cycle impact assessment (LCIA), and (4) interpretation, as described in Figure 3. ISO 14040 and 14044 standards are followed and GaBi software program is used to conduct the LCA (ISO, 2006a; 2006b).

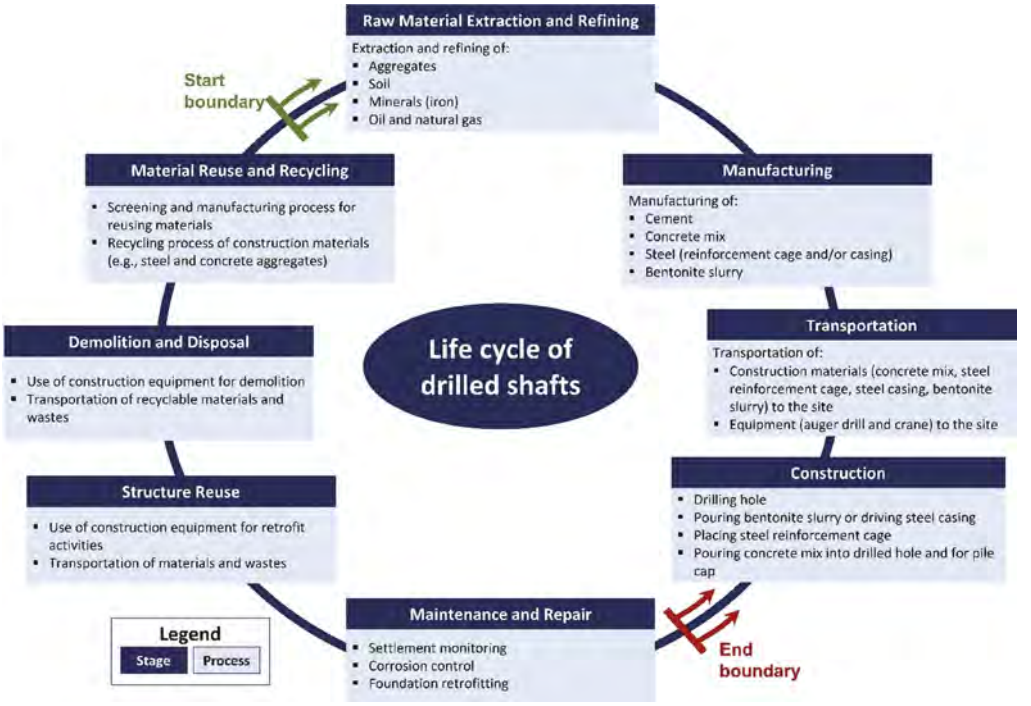

Figure 2. Typical life cycle of drilled shafts.

In this study, the system boundary starts from the extraction and refining of raw materials and ends with the completion of the construction stage, as shown in Figure 2. The functional unit is "the mass (in kg) of drilled shaft required to support the applied load in a given subsurface profile without bearing capacity failure (assuming FS = 2-3) and settlement exceeding 30 mm". Table 1 lists the assumptions used in conducting the LCA.

In LCI, the inputs (e.g., raw materials and energy) and outputs (e.g., emissions) for a product are compiled and quantified considering all the processes in its defined life cycle (ISO, 2006a). In this study, inventory databases by Thinkstep (Gabi, 2021), World Steel Association (Gabi, 2021), and National Renewable Energy Laboratory (NREL, 2012) are used to conduct the LCI. The LCIA characterizes the emissions (computed from the LCI) as global environmental impacts. LCIA is capable of quantifying various environmental impacts as shown in Figure 3. However, only global warming impact of drilled shaft is discussed in this paper because of space constraints. In this study, the ReciPe method by Goedkoop et al. (2013) is followed to conduct the LCIA.

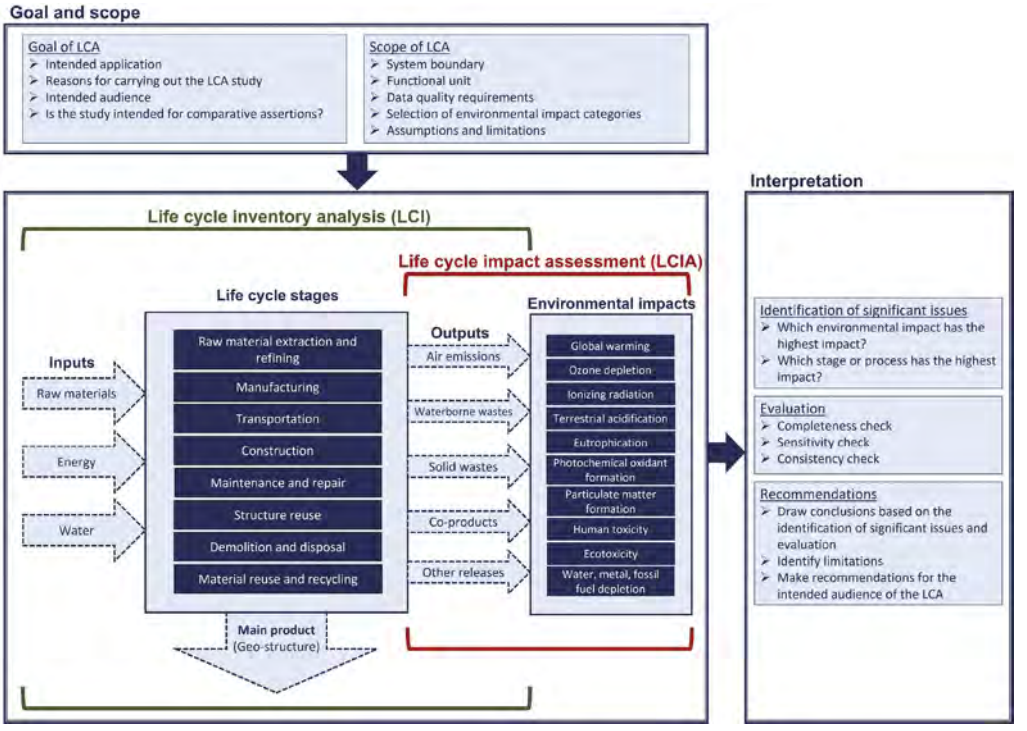

Figure 3. Framework of life cycle assessment.

Table 1. Assumptions used in LCA of drilled shaft.

LCA stage	Characteristics of materials or assumptions	
From raw material extraction to manufacturing	Strength class of concrete	C35/45 according to Eurocode 2 (CEN, 2004)
	Type of steel	Steel reinforcing bar rolled on a hot rolling mill
Transportation	Weight of the construction machinery	Auger drilling machine: 43000 kg (Bauer Maschinen GmbH, 2021) Hydraulic cane:12340 kg (Tadano, 2018)
	Hauling distance	From concrete manufacturing plant to site: 10 km From steel manufacturing plant to site: 50 km From machinery rental location to site: 50 km
	Type and payload capacity of hauling trucks	Diesel-driven 27-tonne capacity trucks
Construction	Operation time of the construction machinery	Calculated based on Zayed and Halpin (2005)
	Fuel consumption rate of the construction machinery	Auger drilling machine: 21.4 L/hr (Bauer Maschinen GmbH, 2021) Concrete mixer truck: 11.1 L/hr (Zagula et al., 2012) Hydraulic crane: 11.6 L/hr (Tadano, 2018)

4 GLOBAL WARMING IMPACT OF DRILLED SHAFTS

Table 2 summarizes a sample result of LCA for a drilled shaft (L_p = 15 m, B_p = 0.8 m, P = 1000 kN, and Profile 1). The actual values of global warming impact are compared with (i) the annual world impact per person in year 2010, obtained from Huijbregts et al. (2016) and (ii) a complete life cycle of a typical passenger vehicle with a lifespan of 12 years, obtained from European Commission (2008), as shown in Table 2. A typical drilled shaft with L_p = 15 m and B_p = 0.8 m, for

example, generates 4.2 tonnes of global warming potential (GWP), which is equivalent to 7.6% and 39% of the GWP of a typical passenger car and GWP of annual world impact per person, respectively. GWP is a measure of global warming impact that combines the contributions from different greenhouse gases such as carbon dioxide, methane, and nitrous oxide.

In order to investigate the relationship between GWP and pile dimensions for different applied loads, GWPs of drilled shaft designs with fixed pile length with L_p = 5-30 m and correspondingly B_p = 0.4-2.2 m are calculated for P = 1000, 2000, and 3000 kN in Profiles 1 and 2. Figure 4 shows designed pile length and diameter corresponding to the different applied loads. The GWP for each design is calculated and plotted on the same figure, and curves joining these points generate the GWP contours. For example, for a drilled shaft with L_p = 15 m and B_p = 0.8 m under P = 1000 kN in Profile 1, its GWP is slightly less than 5000 kg CO_2 equivalent according to Figure 4(a), which is consistent with the results in Table 2.

Table 2. Environmental impacts of a drilled shaft (L_p = 15 m, B_p = 0.8 m, P = 1000 kN, and Profile 1).

Global warming (kg of CO_2)	Drilled shaft impacts	Typical passenger vehicle impacts	Proportional drilled shaft impact with respect to passenger vehicle (%)	Annual world impact per person	Proportional drilled shaft impact with respect to annual world impact (%)
	4244	56200	7.6	10757	39

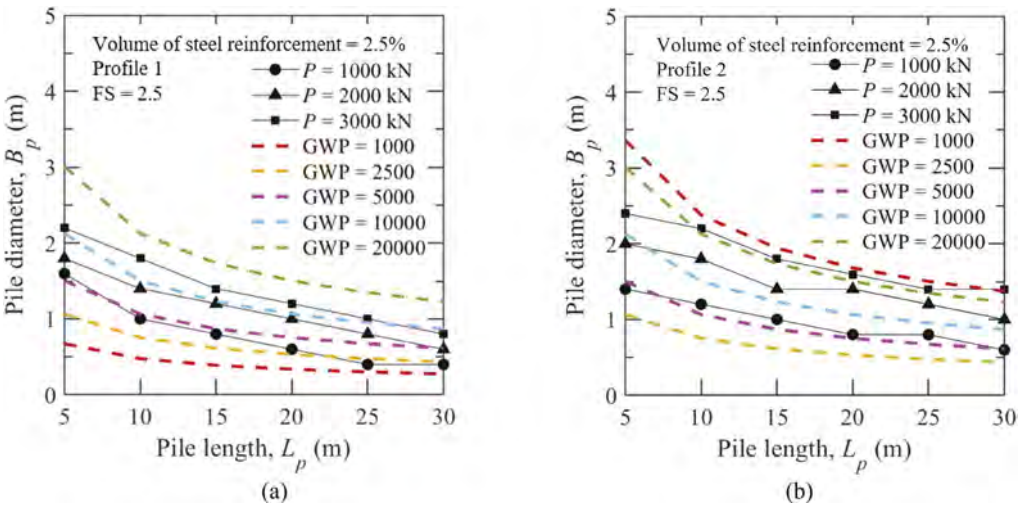

Figure 4. Relationship between dimensions of drilled shafts for different applied loads along with GWP contours (GWP in kg of CO_2 equivalent) for (a) soil profile 1 and (b) soil profile 2.

5 CONCLUSIONS

Concrete and steel – the two most used materials in geotechnical constructions – require large amount of fossil fuel in the production phase. Hence, minimizing the use of these materials is crucial in reducing global warming impact, and it can be practiced as early as in the design phase.

In this paper, life cycle assessment (LCA) is used to quantify the global warming impact of drilled shafts installed in two different sandy soil profiles. The relationship between pile diameter and length for different applied axial loads are plotted for two sandy soil profiles along with the contours of global warming potential (GWP). These figures can be used for quick initial estimate of GWPs by the designers without the use of sophisticated LCA software packages. Similar project-specific figures can be developed for ready reference of the designers in important projects. The GWPs of a typical drilled shaft are compared with the global warming impact caused by a typical passenger vehicle over its life span and the annual world impact per person. Global warming impact of a typical single drilled shaft is equivalent to

7.6% of impacts by a typical passenger vehicle and 39% of the annual world impact per person. Considering the large number of drilled shafts constructed all over the world, the global impact of drilled shaft constructions is significant.

The LCA results in this paper provide a sound basis for understanding the importance of environmental considerations in geotechnical designs. LCA can be applied to other types of foundations and geo-structures with appropriate considerations of life cycle processes, functional units, LCA databases, and other site-specific data.

REFERENCES

Bauer Maschinen GmbH. 2021. Bauer BH 15 H. Bauer. Retrieved from https://www.bauer.de/export/shared/documents/pdf/bma/datenblatter/BG_valueline/BG_15_H_BT_50_EN_905_786_2.pdf

Bowles, J. E. (1997). Foundation analysis and design (5th Ed.). Singapore: McGraw-Hill Companies.

CEN (European Committee for Standardization). 2002. Eurocode 1: Actions on structures – Part 1-1: General actions – Densities, self-weight, imposed loads for buildings (EN 1991-1-1:2002 E). European Committee for Standardization.

CEN (European Committee for Standardization). 2004. Eurocode 2: Design of concrete structures – Part 1-1: General rules and rules for buildings (EN 1992-1-1). European Committee for Standardization.

European Commission. 2018. European reference life cycle database. Retrieved from https://data.jrc.ec.europa.eu/dataset?collection=EPLCA

FHWA (Federal Highway Administration). 2010. Drilled shafts: Construction procedures and LRFD design methods (Publication No. FHWA-NHI-10-016).

GaBi. 2021. GaBi life cycle inventory data documentation. Retrieved from https://gabi.sphera.com/canada/support/gabi/gabi-database-2020-lci-documentation/

Giri, R. and Reddy, K. 2014. LCA and sustainability assessment for selecting deep foundation system for high-rise buildings. Proceedings of International Conference on Sustainable Infrastructure 2014, Long Beach, California, USA, 621–630.

Goedkoop, M., Heijungs, R., Huijbregts, M., Schryver, A., Struijs, J., & Zelm, R. 2013. Recipe 2008: A life cycle impact assessment method which comprises harmonised category indicators at the mid-point and endpoint Level (version 1.08). Retrieved from https://www.rivm.nl/documenten/a-lcia-method-which-comprises-harmonised-category-indicators-at-midpoint-and-endpoint

Huijbregts, M., Steinmann, Z., Elshout, P. et al. 2016. Normalization scores ReCiPe 2016. Ministry of Housing, Spatial Planning and Environment, Den Haag, Netherlands. Retrieved from https://www.rivm.nl/en/documenten/normalization-scores-recipe-2016

ISO (International Organization for Standardization). 2006a. ISO 14040: Environmental management – life cycle assessment – Principles and framework (ISO 14040:2006). ISO.

ISO (International Organization for Standardization). 2006b. ISO 14044: Environmental management - life cycle assessment - Requirements and guidelines. (ISO 14044:2006). ISO.

Luo, W., Sandanayake, M., & Zhang, G. 2019. Direct and indirect carbon emissions in foundation construction – Two case studies of driven precast and cast-in-situ piles. Journal of Cleaner Production, 211(1), 1517–1526.

Misra, A. 2010. A multicriteria based quantitative framework for assessing sustainability of pile foundations [Master's Thesis, University of Connecticut - Storrs].

NREL (National Renewable Energy Laboratory). 2012. U.S. life cycle inventory database. Retrieved from https://www.lcacommons.gov/nrel/search.

Salgado, R. 2008. The engineering of foundations. Boston, MA: McGraw Hill.

Tadano. 2018. GR-150XL. Retrieved from https://www.tadano.com/businesses/service/upload/docs/GR-150-1-00101_US-01.pdf

Vieira, M. 2015. Concrete. In M. C. Gonçalves, F. Margarido (Eds). Materials for construction and civil engineering: Science, processing, and design (pp. 185–236). Springer.

Watts, J. 2019. Concrete: the most destructive material on Earth. The Guardian. https://www.theguardian.com/cities/2019/feb/25/concrete-the-most-destructive-material-on-earth

World Steel Association. 2021. Climate change and the production of iron and steel. https://worldsteel.org/wp-content/uploads/ClimateChange_Policy-Paper-1.pdf?x98447

Zagula, M., Hinkle, J. Mobley, B. Williams, D., & Mullings, G.M. 2012. 2012 National ready mixed concrete association fleet benchmarking and costs survey. Silver Spring, MD: National Ready Mixed Concrete Association.

Zayed, T.M., & Halpin, D.W. 2005. Pile construction productivity assessment. Journal of Construction Engineering and Management, 131(6), 705–714.

Smart Geotechnics for Smart Societies – Zhussupbekov, Sarsembayeva & Kaliakin (Eds)
© 2023 The Author(s), ISBN 978-1-003-29912-7
Open Access: www.taylorfrancis.com, CC BY-NC-ND 4.0 license

Off-fault displacement distribution of dip-slip fault by analog experiment

N. Inoue & N. Kitada
Geo-Research Institute, Osaka, Japan

T. Watanabe & M. Tonagi
Kozo Keikaku Engineering Incorporated, Tokyo, Japan

N. Shibuya & M. Omata
Pasco Corporation, Tokyo, Japan

ABSTRACT: The ranges of distribution of off-fault displacement occurring apart from the main fault are very important threshold values for city planning, mitigating hazards, etc. Analog experiments using wheat flour examined the evolutions and distributions of dip-slip off-fault displacements (fault dip angles of 30° and 60°). The experiments have conducted repetitions of up or down movement of the basal fault, and surface displacements have been measured with a 3D scanner on every incremental displacement. Some off-faults show no displacement with the incremental main fault displacement. Most of the off-fault displacements occurred on the hanging-wall side. The off-fault distributions of analog experiments indicated a similar distribution compared with the off-fault displacement attenuation relation, which has been constructed from field observations compiled from reverse faulting earthquakes.

1 INTRODUCTION

Surface ruptures caused by an earthquake occur not only on previously mapped faults but also on unknown traces. Most of the former are main faults (principal faults), while some of the latter are off-faults (secondary or distributed faults). The off-fault may occur at a location distant from the principal fault. Recently detailed distributions of off-faults can be obtained through the progress of aerial photograph surveys and satellite data (e.g., Fujiwara et al., 2016; Omata et al., 2017). The displacement of the principal fault can be estimated from geological, geomorphological, and paleoseismological surveys. On the contrary, predicting off-fault displacements is difficult, because of previously unavailable mapping capability due to the small amount of displacement and discontinuity before an earthquake.

Ranges of distribution and displacement of off-faults are important threshold values considering fault displacement hazards of nuclear facilities and important structures and have been examined in many previous studies (e.g. Youngs et al., 2003; Petersen et al., 2011; Valentini et al., 2021). The range of distribution and displacement of off-faults of dip-slip faults were investigated by analog experiments with wheat flour.

2 METHOD

The analog model, which was enabled to simulate both reverse and normal faults, consists of a wheat flour layer deposited with a total thickness of about 2.5cm in an acrylic-sided experimental device (Figure 1). The height of the surface was measured with a high-resolution 3D scanner when the displacements of the basal fault were 0.5, 1, 2, 3, 5 and 8mm. The vertical and horizontal direction accuracies and measurement range are 5μm, 0.1mm, and

DOI: 10.1201/9781003299127-370

10cm×15cm, respectively. Wheat flour was densely packed pressing by a trowel. The final displacement of the basal fault was set to 8mm in the 30° experiments and up to 5mm in the 60° experiments. The final vertical displacement of both models was about 4mm.

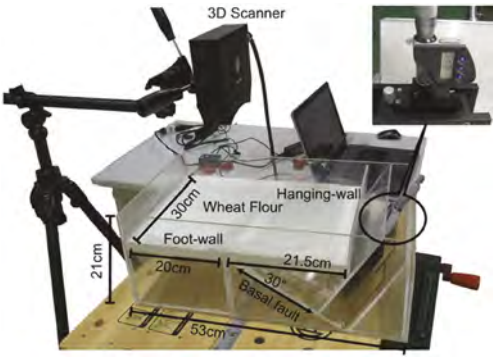

Figure 1. Experimental equipment (the dip angle of the basal fault is 30°).

3 RESULTS

In order to interpret the faults that occurred in the analog experiments, corresponding to the extension from the basal fault were treated as the principal fault and the other faults were classified as off-faults.

3.1 *Reverse fault experiment*

The principal fault propagated from the basal fault with a convex shape occurred around 40mm on the y-axis in Figures 2(a) and 2(b). In the cross section (Figure 2(c)), until 0.5mm of displacement of the basal fault, the fault occurred between 40mm and 45mm on the horizontal axis. After 1mm of displacement on the basal fault, the fault displacement was increased near 50mm on the horizontal axis, and the displacement of the previously formed fault did not seem to increase. In other words, the principal fault displacement that previously occurred shifted to the foot-wall side and was activated. The short fault, which was the principal fault at the initial stage, showed no displacement after the principal fault shifted to the foot-wall side. A fault is also formed on the hanging-wall side, which was considered to correspond to the back thrust (e.g. Lin et al., 2006).

In the result with the fault dip angle of 60°, the principal fault occurred 40 to 70mm away from the basal fault. An off-fault above the basal fault showed an opening displacement. There was no off-fault far from the basal fault on the hanging-wall side like in the results with 30° (Figure 2). In numerical simulations based on a Finite Element Method, the back thrust was formed on the hanging-wall side under low-angle reverse faults with strong ground strength (Lin et al., 2006).

3.2 *Normal fault experiment*

In the result with the fault dip angle of 30°, the principal fault propagated from the basal fault and occurred near 0mm on the y-axis as shown in Figures 3(a) and 3(b). The fault displacement was increased at 20mm away from the initial fault on the foot-wall side during the small basal fault displacements as shown in Figure 3(c). After 5mm displacement of the basal fault, much larger fault displacements were observed around 0mm on the y-axis. The fault that occurred on the foot-wall side seemed to be displaced as the principal fault at the initial stage. In the result with the fault dip angle of 60°, the principal fault occurred above the basal fault similar to the result of 30° normal fault experiments. The off-fault appeared around 30mm away from the principal fault on the hanging-wall side and showed wider distributions at the higher fault dip angle.

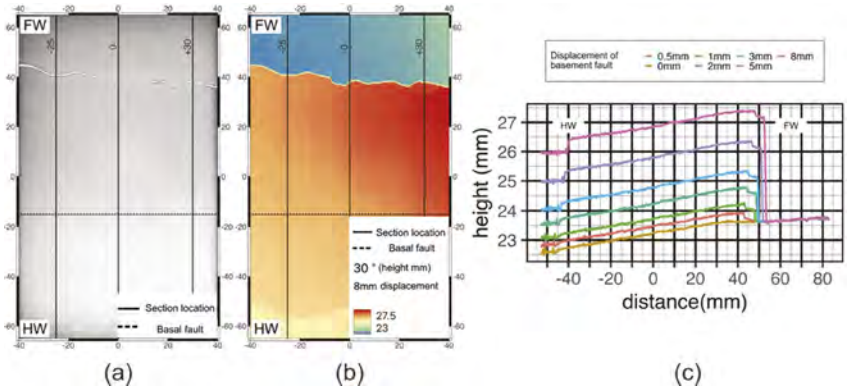

Figure 2. Experiment results of reverse fault (fault dip angle of 30°). (a) and (b) are the image and height of the wheat flour surface obtained by the 3D scanner, respectively when the displacement of the basal fault is 8mm. (c) Cross sections along 30mm on the x-axis of Figures 2(a) and 2(b). HW and FW are hanging-wall and foot-wall sides, respectively. The horizontal axis is shifted in the location of the basal fault to 0mm on the horizontal axis compared to Figures 2 (a) and 2 (b).

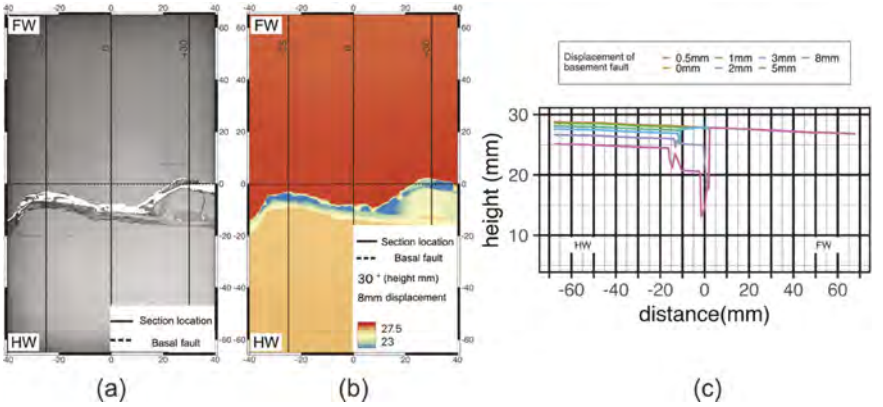

Figure 3. Experiment results of normal fault (fault dip angle of 30°). (a) and (b) are the image and height of the wheat flour surface obtained by the 3D scanner, respectively when the displacement of the basal fault is 8mm. (c) Cross sections along 30mm on the x-axis of Figures 3(a) and 3(b). HW and FW are hanging-wall and foot-wall sides, respectively. The basal fault is located at 0mm on the horizontal axis.

4 DISCUSSION

Previous Probabilistic Fault Displacement Hazard Analysis (PFDHA) studies provide off-fault displacement attenuation relations of various faulting types (e.g. Youngs et al., 2003; Petersen et al., 2011). Figure 4 indicates the off-fault displacement attenuation relation compiled by reverse faulting earthquakes with the experiment results considering the length scaling 1.7×10^{-4} (natural sedimentary rock, cohesion=50MPa and density=2.8g/cm^3; the dense deposited wheat flour, cohesion=2.5kPa and density=0.80 g/cm^3 derived from strength measurement). The attenuation relation of the analog experiments was in good agreement with the field observations.

The numerical simulation of the analog experiment was conducted using a discrete element method, to simulate the wheat flour layer. The simulation results indicated a similar fault distribution to that of the analog experiment.

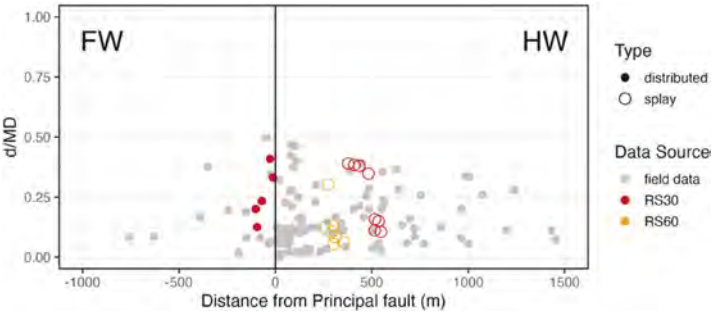

Figure 4. Comparison off-fault displacements between the field observation and the analog experiment for the results of reverse faulting. The vertical axis was normalized off-fault displacements (d) by the maximum displacement (MD).

5 CONCLUDING REMARKS

Analog experiments with wheat flour were conducted using pieces of equipment capable of simulating reverse faults and normal faults with high (60°) and low (30°) fault dips. In the case of reverse faults, the distribution range of off-faults tended to be wider in the low-angle experimental results. On the other hand, for normal faults, the principal fault tended to occur above the basement fault, regardless of the fault dip angle of the basal fault. In addition, the distribution of off-faults tended to be wider at higher angles in the case of the normal fault. Some off-faults show no displacement with the incremental basal fault displacement. Most of the off-fault displacements occurred on the hanging-wall side. The attenuation relation of the analog experiments was in good agreement with the field observations constructed from reverse faulting earthquakes.

ACKNOWLEDGEMENTS

Part of this study is due to the 2018 research project 'Acquisition of knowledge on fault displacement evaluation' and the 2021 research project 'Research on fault displacement evaluation' by the Secretariat of Nuclear Regulation Authority (NRA), Japan.

REFERENCES

Fujiwara, S., Yarai, H., Kobayashi, T., Morishita, Y., Nakano, T., Miyahara, B., Nakai, H., Miura, Y., Ueshiba, H., Kakiage, Y., & Une, H. 2016. Small-displacement linear surface ruptures of the 2016 kumamoto earthquake sequence detected by alos-2 SAR interferometry. *Earth, Planets and Space*, 68, 1: 160, DOI: 10.1186/s40623-016-0534-x.

Lin, M.-L., Chung, C.-F., & Jeng, F.-S. 2006. Deformation of overburden soil induced by thrust fault slip. *Engineering Geology*, 88, 1–2: 70–89, DOI: http://dx.doi.org/10.1016/j.enggeo.2006.08.004.

Omata, M., Kohriya, Y., Sango, D., Shibuya, N., & Taniguchi, K. 2017. Small ground deformations of the 2016 kumamoto earthquake detected by lc-insar analysis. *Japanese Society for Active Fault Studies 2017 annual meeting abstract*, P–4.

Petersen, M. D., Dawson, T. E., Chen, R., Cao, T., Wills, C. J., Schwartz, D. P., & Frankel, A. D. 2011. Fault displacement hazard for strike-slip faults. *Bulletin of the Seismological Society of America*, 101, 2: 805–825.

Valentini, A., Fukushima, Y., Contri, P., Ono, M., Sakai, T., Thompson, S. C., Viallet, E., Annaka, T., Chen, R., Moss, R. E. S., Petersen, M. D., Visini, F., & Youngs, R. R. 2021. Probabilistic Fault Displacement Hazard Assessment (PFDHA) for Nuclear Installations According to IAEA Safety Standards. *Bulletin of the Seismological Society of America*, DOI: 10.1785/0120210083.

Youngs, R. R., Arabasz, W. J., Anderson, R. E., Ramelli, A. R., Ake, J. P., Slemmons, D. B., McCalpin, J. P., Doser, D. I., Fridrich, C. J., Swan, F. H., Rogers, A. M., Yount, J. C., Anderson, L. W., Smith, K. D., Bruhn, R. L., Knuepfer, P. L. K., Smith, R. B., dePolo, C. M., O'Leary, D. W., Coppersmith, K. J., Pezzopane, S. K., Schwartz, D. P., Whitney, J. W., Olig, S. S., & Toro, G. R. 2003. A methodology for probabilistic fault displacement hazard analysis (pfdha). *Earthquake Spectra*, 19, 1: 191–219.

Smart Geotechnics for Smart Societies – Zhussupbekov, Sarsembayeva & Kaliakin (Eds)
© 2023 The Author(s), ISBN 978-1-003-29912-7
Open Access: www.taylorfrancis.com, CC BY-NC-ND 4.0 license

Comparison of small bridges and box culverts

Akira Hasegawa
Emeritus Professor, Hachinohe Institute of Technology, Hachinohe, Japan

Shinya Sukegawa
Technical Section Chief, GIKEN, Aomori, Japan

ABSTRACT: Aging of bridges is a common issue in the world. Bridges are one of important social infrastructures that is indispensable for living and industry, it is necessary for us to solve the problem of aging of Bridges. About 720,000 road bridges have been constructed in Japan, many of which are managed by local governments. Bridges managed by them are almost small bridges with narrow widths and short lengths. As structures for short bridges, two types are used: bridge type and box culvert type. Box culvert without the joints is effective in easing deterioration and simplifying inspection work. In addition, the precast box culvert, which is manufactured in advance at the factory, is excellent in that the material quality can be ensured and the construction period can be shortened. It is suitable for constructions with limited traffic restrictions and in winter of cold regions. In this paper, the comparison and discussion for two types are described.

1 INTRODUCTION

Aging of bridges is a common issue in the world. In Japan, the aging of bridges that have been constructed so far has become a major issue. Since bridges are important social infrastructures that are indispensable for living and industry, it is necessary for us to solve the problem of aging. About 720,000 road bridges have been constructed in Japan, many of which are managed by local governments. The bridges managed by the government are constructed for wide area transportation and include many large-scale bridges. On the other hand, the bridges managed by local governments are mainly constructed for the local transportation of the local governments, and many of them are small bridges with narrow widths and short lengths.

There are two types for small span bridges: bridge types such as slab bridges and girder bridges, and box culverts. The bridge type consists of abutments, bearings, girders and slabs, and the box culvert is an integrated structure as a rigid flame. Moisture and salt are the main causes of aging, and deterioration of member joints such as member ends is conspicuous. Box culvert with the joints removed is effective in mitigating deterioration and simplifying inspection work. In addition, the precast box culvert, which is manufactured in advance at the factory and joined at the site, is excellent in that the material quality can be ensured and the construction period can be shortened. It is suitable for erections with limited traffic restrictions and winter erections in cold regions. In this paper, we will consider the small-scale bridges used for road bridges in comparison with box culverts. In particular, the comparison will be made in consideration of the aging of bridges in cold regions that are damaged by frost and salt.

2 TWO TYPES: BRIDGE TYPE AND BOX CULVERT TYPE

Figures 1 and 2 show examples of two structures used to straddle the span. Different types of structures are used for similar short span lengths. Figure 1 is a girder bridge and Figure 2 is a box culvert. Here, the former type is called a bridge type and the latter is called a box culvert type.

DOI: 10.1201/9781003299127-371

Figure 1. Example of a bridge type.

Figure 2. Example of a box culvert type.

2.1 *Bridge type*

It is a structure in which a bearing is placed on the abutment, several bridge girders are hung on it, and a floor slab is placed on it. I girders, T girders, and box girders are used for bridge girders depending on the span length and materials used. If the span length is short, there is a slab bridge that omits the girder and puts it directly on the bearing. Both girder bridges and slab bridges are composed of abutments, bearings, bridge girders and decks, and joints of members are generated. If the span length is short, the road load is received only by the floor slab without installing a bridge girder.

2.2 *Box culvert type*

Box culvert is a structure integrated with reinforced concrete members which are called a top end, side wall, bottom slab, etc. depending on the position of the member. However, after the reinforced concrete is placed, it is an integrated structure. In the case of precast box culvert manufactured in advance at the factory, due to restrictions on the transportation dimensions from the factory to the erection position, it is divided into several parts,transported to the site, and united there. Lastly, the members become an integrated structure.

3 USING OF TWO TYPES

Figure 3 shows the completed years of the bridges managed by Aomori Prefecture (1418 bridges, excluding 827 bridges which completed year is unknown) among the bridges (2,245 bridges with a bridge length of 2 m or more) by every 10 years. Since World War II, new bridges have been constructed, with the largest number being in the 1970s. After 1970s, new construction has been carried out, however with the improvement of road maintenance, human resources and expenses have been shifting to the maintenance of bridges.

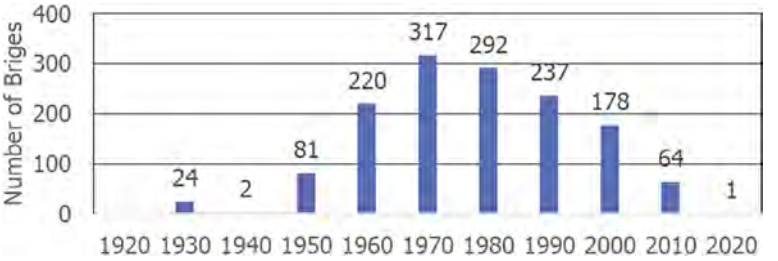

Figure 3. The completed year and the number of bridges managed by Aomori Prefecture.

A comparison was made by classifying bridges before 1979 and after 1980, with the 1970s, when the completed year was at its peak. The target bridges were 1406 bridges excluding 827 bridges of unknown construction year and 12 bridges of unknown type, 639 bridges before 1979, and 767 bridges after 1980. In Figure 4a, the number of bridges in which box culvert is used is shown every 5m in the average span lengths. Before 1979, box culvert was used to be less

than about 5 m, but since 1980 it has expanded to about 10 m. Figure 4b shows the number of bridges by average span length of bridges that also use slab bridges as the bridge type. Before 1979, it was often used under 5m, but since 1980, the range of use has expanded to around 15m.

A similar spread of the span length is seen in the girder bridge, and before 1979, the peak was 5-10 m and the use decreased as the span length became longer, but after 1980, it has been widely used around 30 m. The truss, arch, rigid frame bridge, and cable-stayed bridge were not compared because the number of bridges is small.

The fact that the range of span lengths adopted by various bridge types is expanding indicates that the technology of each bridge type has been developed and it has become possible to provide span lengths with a wide range.

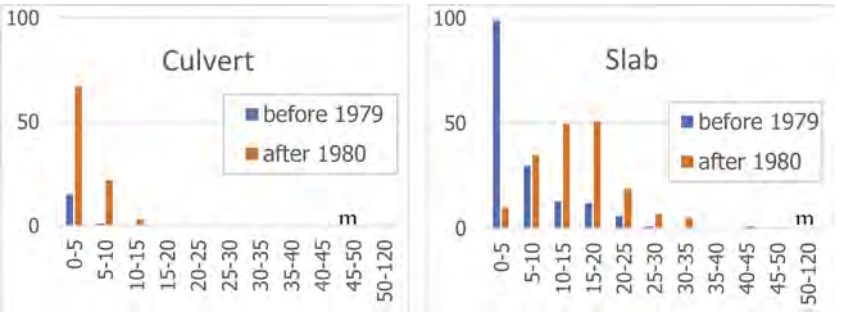

Figure 4. The number of bridges and average span length (left 4a: box culvert, right 4b slab).

4 DIFFERRENCES OF TWO TYPES

4.1 *Differences in construction*

In the girder bridge type, starting from the construction of the abutment with foundation work, after the abutment is prepared, the bearing is installed on it, and the bridge girder is erected on it. The bridge girder is pre-made in the factory or around the site, moved and installed in place.

On the other hand, in culvert box, especially in the precast box culvert, the parts are divided into parts in advance at the factory and manufactured, and then joined at the site to form an integrated structure. Depending on the size of the culvert cross section, it is divided into two or four parts. The maximum internal cross section is 13m wide and 9m high. In addition, by providing a partition wall in the middle, it is possible to connect two or three boxes. The appeal of precast box culvert is quality and construction period. Since the parts are manufactured under factory management, the quality of reinforced concrete is high, and the construction period can be shortened by about 70% compared to the culvert box constructed on site.

Figure 5. Construction site of girder bridge (left) and box-culvert (right).

4.2 *Differences in aging*

It can be said that the issue of aging bridges is worldwide. In Japan, various efforts have begun since the accident caused by aging in the tunnel in 2012. The concept of maintenance has changed

from the conventional post-maintenance that repairs after breaking to preventive maintenance that is inspected and repaired in advance. It is also obligatory to visually inspect every five years.

According to the observation results up to now, it is known that the deterioration at the member joint of the bridge is remarkable. Especially in cold regions, frost damage caused by hydration and salt damage caused by the salt content of the snow melting agent sprayed on the pavement surface occur. In addition, it may take time to inspect the bearings due to sediment accumulation and overgrowth of vegetation. In the case of bridges, efforts are being made to facilitate maintenance. For example, efforts are being made to reduce the number of girders that support the deck and reduce the number of member elements.

Comparing the two bridge types from the viewpoint of dealing with aging, it can be said that the box culvert, which is an integrated structure, is more advantageous than the bridge type having member joints such as bearings.

5 CONCLUSIONS

In this paper, we have compared and studied two types of small-scale bridges, the bridge girder type and the culvert. These two types are often used for short span bridges. As a result of comparing the features of both in consideration of cold regions and aging, the following conclusions were obtained.

(1) There are two types of bridges between small spans: deck type and culvert. The bridge type consists of abutments, bearings, and decks, and the box culvert is an integrated structure. Box culvert with few structural elements can simplify the work from manufacturing to inspection.
(2) Moisture and salt are the main causes of deterioration of aging, and most of them occur at the member ends and decks of member joints in girder bridges. Therefore, it can be said that removing the joint portion alleviates deterioration and is effective as a countermeasure against aging, and box culvert is excellent as a countermeasure against aging.
(3) In addition, the precast box culvert, which is manufactured in advance at the factory and united at the site, is excellent in that the material quality can be ensured and the construction period can be shortened. It is suitable for construction with limited traffic restrictions and winter erections in cold regions.
(4) However, there is a limit to the span length that can properly use box culvert. Therefore, it is expected that it will be applied to various span lengths by studying the structure of other chambers using partition walls.

Structural simplification simplifies work from construction to maintenance. Looking at the member force generated in the member, it changes smoothly as compared with the structure in which many members are combined. The fact that abrupt changes in stress do not occur is also excellent in terms of mechanical strength. However, we need inspection methods for deterioration of back surface faced to soil. Though we use the method such as tapping sound inspection, it is expected to develop a simple inspection method for a damage of back surface.

ACKNOWLEDGMENTS

In this paper, we referred to the documents of the Ministry of Land, Infrastructure, Transport and Tourism in Japan and Aomori Prefecture. In particular, we referred to Aomori Prefecture Longevity Repair Plan formulated by the Road Division of Department of Land and Infrastructure in Aomori Prefecture. we would like to express deep thanks everyone involved. And, we thank Prof. Takase (Associate Professor of HIT) and Mr. Goto (Senior Managing Director of GIKEN in Aomori) for their kind support.

REFERENCES

Ministry of Land, Infrastructure, Transport and Tourism in Japan: https://www.mlit.go.jp/
Aomori Prefecture: Longevity Repair Plan in Aomori Prefecture Japan, 2017.

Smart Geotechnics for Smart Societies – Zhussupbekov, Sarsembayeva & Kaliakin (Eds)
© 2023 The Author(s), ISBN 978-1-003-29912-7
Open Access: www.taylorfrancis.com, CC BY-NC-ND 4.0 license

Fundamental study on trench stability of diaphragm wall foundation with enlarged part

A. Iwata
Building Construction Division, Taisei Corporation, Japan

K. Watanabe
Department of Civil Engineering, Aichi Institute of Technology, Japan

M. Kato
Taisei Advanced Center of Technology, Japan

ABSTRACT: Significant compressive and tensile forces due to both ordinary and earthquake loads act on the foundations of ultrahigh-rise buildings with large aspect ratios, which are increasing in urban areas of Japan. A diaphragm wall foundation with an enlarged part has been developed to handle this issue; this is a diaphragm wall foundation with an increased width at a section of the foundation near the wall tip. It is important for the trench of diaphragm wall foundation to be stable in the construction process. The purpose of this study is to evaluate the trench stability for the diaphragm wall foundation with an enlarged part. The following studies were carried out to grasp this. 1) Centrifuge model tests to evaluate the trench stability of the diaphragm wall foundation with an enlarged part. 2) Numerical simulation using a shear strength reduction FEM to simulate the centrifuge model tests.

1 INTRODUCTION

Significant compressive and tensile forces due to both ordinary and earthquake loads act on the foundations of ultrahigh-rise buildings with large aspect ratios, which are increasing in urban areas of Japan. A diaphragm wall foundation with an enlarged part shown in Figure 1 has been developed to handle this issue; this is a diaphragm wall foundation with an increased width at a section of the foundation near the wall tip. It is important for the trench of diaphragm wall foundation to be stable in the construction process from the excavation to the concrete placing stage.

The trench stability of diaphragm wall has been studied previously in several researches, in which experimental and numerical approaches have been attempted. A concept that the diaphragm wall is generally stable is summarized in JGS(1988), since the fluid pressure such as the slurry in the trench supports the earth-pressure of ground around the trench. Katagiri et al. (2000) carried out centrifuge model tests to examine the trench stability of diaphragm wall. An analytical study of trench stability was performed by Ishii et al. (2001). They conducted an elasto-plastic FEM combined with a shear strength reduction method to estimate the global safety factor.

It is therefore necessary to evaluate the trench stability on the diaphragm wall foundation with an enlarged part because the failure mechanism and the applicability of analysis are still uncertain.

Thus, the purpose of this study is to evaluate the trench stability on the diaphragm wall foundation with an enlarged part. The following studies were carried out to grasp this:

DOI: 10.1201/9781003299127-372

1) The centrifuge model tests to evaluate the trench stability of the diaphragm wall foundation with or without an enlarged part in a sandy model ground.
2) Numerical simulation using a shear strength reduction FEM to evaluate the centrifuge model tests.

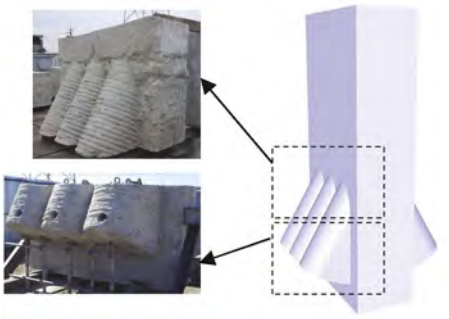

Figure 1. Diaphragm wall foundation with an enlarged part.

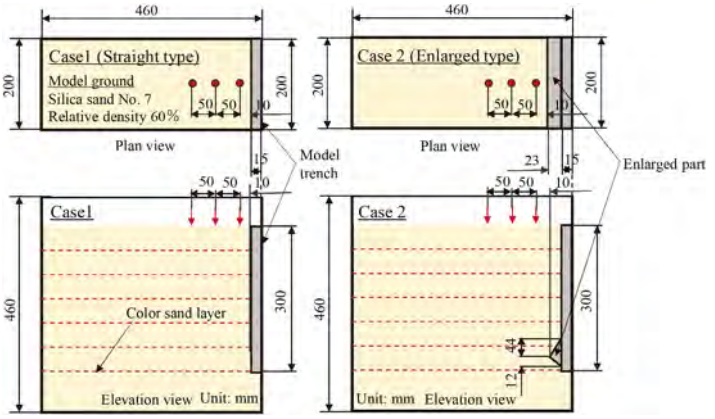

Figure 2. Schematic view of centrifuge model test apparatus.

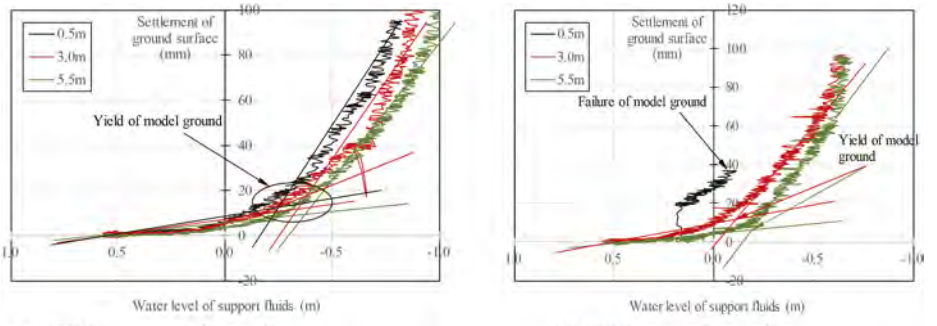

Figure 3. Relationships between settlement of model ground and water level of support fluid.

2 CENTRIFUGE MODEL TESTS

2.1 *Experimental condition*

The Aichi Institute of Technology Centrifuge (AIT Centrifuge) was used in the model test described in this paper. This centrifuge is a beam type with a pair of parallel arms that hold platforms on which the model container and a counterbalance weight are mounted. Effective radius of rotation is 1.36m, which is the distance from the rotating shaft to the platform base.

A schematic view of the test apparatus is shown in Figure 2. The dimensions of the steel container are width B=460mm, height h=460mm and length l=200mm. The model ground was prepared by air-pluviation method using Silica sand No. 7 which has the physical properties of $\rho_s = 2.645\text{g/cm}^3$, e_{max}=1.158 and e_{min}=0.692 to achieve a relative density of D_r=60%. The model ground is saturated after preparing the dry sand ground. All the tests were conducted in saturated sand conditions under 50G. The model diaphragm wall foundations are assumed in a two-dimensional condition considering symmetry of the prototype diaphragm wall foundation in the planar shape. The shape of model diaphragm wall is simulated by a thin plastic (thickness t=0.1mm). This thin plastic represents mud membrane inside the trench in the actual construction process.

The experiments progress in such a way that the support fluid in the model trench decreases when a target centrifuge acceleration of 50G is reached. Here, the support fluid used is

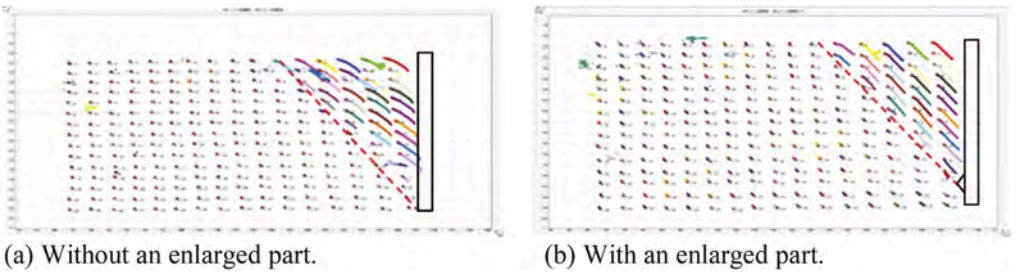

Figure 4. Results of image analysis.

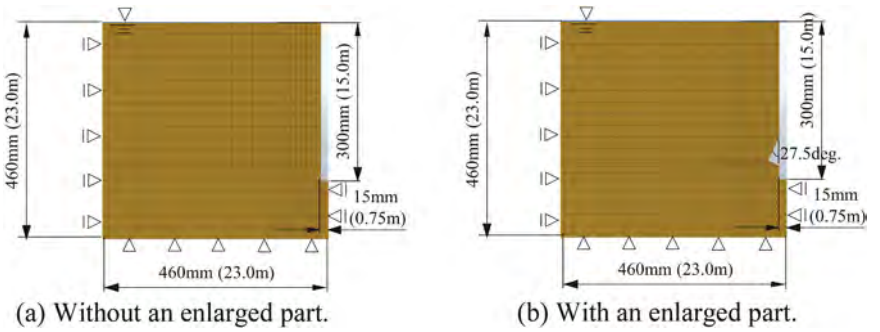

Figure 5. Schematic view of FEM analysis model.

a saline water (Specific gravity, 1.05) which is equivalent to actual support fluid such as bentonite and polymer fluid. The initial water level before the support fluid drainage is set 0.5m above the ground surface in the prototype scale. A low-flow type solenoid valve is used to drain the support fluid in the model trench of the diaphragm wall foundation.

2.2 *Results of centrifuge model tests*

Figure 3 indicates the relationships between settlement of model ground and water level of support fluid. The settlement of model ground increases as the water level of support fluid decreases. The model ground yields when the water level of support fluid is 0~-0.25m.

The failure modes obtained from the image analysis of the centrifuge model tests are shown in Figure 4. The deformation of the model ground progresses as the support fluid in the model trench decreases. It is seen in Figure 4 that a slip line occurs when the trench and the model ground fail. The shape of the slip lines is a straight line in both cases. The angle of slip line is 64 deg. for diaphragm wall foundation with and without an enlarged part. Here, the active failure angle is calculated as 63.4 deg. if an internal friction angle obtained from the triaxial compression test for silica sand No. 7 is used. It is said that the failure (*i.e,* slip line) occurs at a deeper depth for diaphragm wall foundation without an enlarged part (Figure 4 (a)). On the other hand, as shown in Figure 4(b),the failure progresses near the enlarged part for diaphragm wall foundation with an enlarged part.

3 SIMULATION OF CENTRIFUGE MODEL TESTS

3.1 *Numerical analysis method*

Shear Strength Reduction-FEM (SSR-FEM) is an elasto-plastic FEM simulation scheme including the shear strength reduction method and can evaluate the global safety factor that is defined by limit equilibrium methods without assuming a slip surface. In addition, when deformation problems have to be considered in elasto-plastic FEM simulations, it can deal with complicated conditions, taking into account the confining pressure which acts on a sliding earth mass.

The purpose of this analysis is to simulate the results of centrifuge model tests described in Section 2. The model trench is a quadrant of the prototype scale considering symmetry. It is assumed that the failure of soil is defined by the Mohr-Coulomb's failure criterion. The iteration process is based on the modified Newton Raphson method.

Figure 5 indicates a schematic view of the FEM analysis model. The model is divided into the model ground and the model trench. The parameters of ground and the support fluid used in the

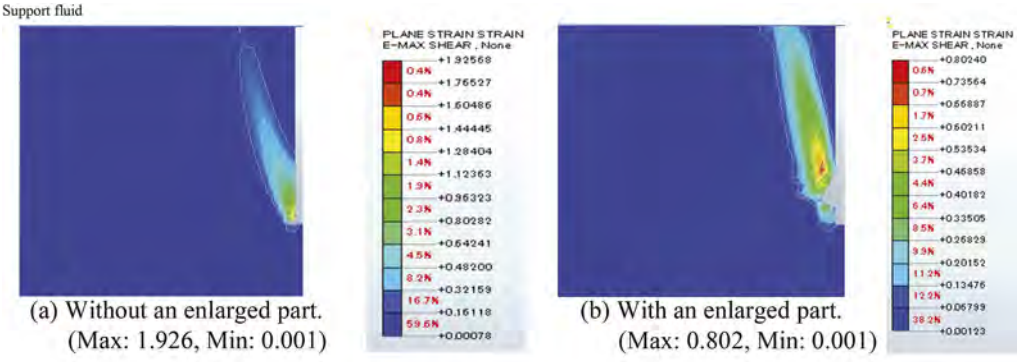

Figure 6. Distributions of maximum shear strain (Water level of support fluid: 0m).

analysis are shown in Table 1. The material parameters of cohesion c', internal friction angle φ' and deformation modules E_{50} are determined based on the results of triaxial compression tests. The Poisson's ratio is obtained from the result of K_0 consolidation test. As for the boundary

Table 1. Parameters of FEM analysis model.

Model ground	Saturated unit weight γ_{sat}	18.3	kN/m^3
	Deformation modulus E_{50}	4470	kN/m^3
	Poisson's ratio ν	0.28	
	Cohesion c	6.5	kN/m^2
	Internal friction angle ϕ	37.3	°
	Dilatancy angle Ψ	37.3	°
Support fluids	Unit weight γ_s	10.3	kN/m^3

conditions, the displacement on the bottom surface is fixed in all directions, while back and right-side surfaces are laterally confined.

3.2 *Results of numerical analysis*

Figure 6 presents the contour of maximum shear strain when the difference in water level ΔH is -0m. This means the support fluid level is equal to the ground water level at the ground surface. The figure shows the deformation immediately after the failure. According to the contour of maximum shear strain, deformation toward the ground surface was confirmed from the model diaphragm wall foundation. In addition, it is seen that the shape of indicated slip line is a straight line. This trend is consistent with the results of centrifuge model test shown in Figure 4. In case of diaphragm wall foundation with an enlarged part, it is observed that the maximum shear strain becomes large near the enlarged part. It is therefore clear that the deformation behavior for the centrifuged model test can be simulated by the SSR-FEM described in this section.

4 CONCLUSIONS

The purpose of this study is to evaluate the trench stability on the diaphragm wall foundation with an enlarged part. The following findings were obtained from this study.

1. The failure mode of diaphragm wall foundation with or without an enlarged part was exam- ined by the centrifuge model tests. It is suggested that the failure mode is in a straight slip line close to the active failure line.
2. The failure mode of FEM simulation is consistent with the centrifuge model test results, suggesting that can be simulated by the SSR-FEM.

REFERENCES

Ishii, T., Saitoh, K., Kuwabara, K. & Ugai, K. 2001. Stability analysis by 3-D elasto-plastic finite element method for slurry trenches constructed in sandy ground. *Journal of Japanese Society for Civil Engineering* No. 673: 1–14.

Japanese Geotechnical Society 1988. Diaphragm wall construction method, *Japanese Geotechnical Society*.

Katagiri, M., Ishii, T., Saitoh, K., Masuda, T., Aizawa, F. & Ugai, K. 2000. Observation and evaluation on failure mechanism of slurry trenches in sandy ground. *Journal of Japanese Society for Civil Engineering* No. 666: 127–143.

Smart Geotechnics for Smart Societies – Zhussupbekov, Sarsembayeva & Kaliakin (Eds)
© 2023 The Author(s), ISBN 978-1-003-29912-7
Open Access: www.taylorfrancis.com, CC BY-NC-ND 4.0 license

Strength and deformations of volume-blocks

Aliy Bespaev
Kazakh Research and Design Institute of Construction and Architecture

Ilya Teshev
MX-Engineering, Kazakhstan

U.S. Kuralov
Satbayev University, Astana, Kazakhstan
Kazakh Scientific Research and Design Institute of Civil Engineering and Architecture, Almaty, Kazakhstan

U.B. Altigenov
L.N. Gumilyov Eurasian National University, Astana, Kazakhstan
Kazakh Scientific Research and Design Institute of Civil Engineering and Architecture, Almaty, Kazakhstan

ABSTRACT: The results of experimental studies of the stress-strain state of reinforced concrete three-dimensional blocks under the action of vertical loads are presented. Information is given on the distribution of deformations, the formation and opening of cracks, horizontal displacements, strength and nature of destruction, and the influence of the type of concrete. Proposals are given for calculating the bearing capacity, taking into account damage.

Keywords: reinforced concrete volume blocks, strength, deformations, cracks and displacements, failure patterns.

1 INTRODUCTION

The ideas of volume-block construction originated in the USSR and abroad at the beginning of the 20th century. At the end of the fifties, the design of structural systems and the construction of residential buildings from reinforced concrete three-dimensional blocks began in the Soviet Union. Currently, in various cities of the CIS (Khabarovsk, Krasnodar, Gulkevichi, Volzhsk, Minsk, Voronezh, Moscow and Astana) there are factories for the manufacture of volumetric blocks and the construction of volumetric-block buildings up to 16 floors high. The most widely used volumetric blocks such as "cap" and "lying glass". In recent years, several countries have built a significant number of multi-storey buildings from reinforced concrete three-dimensional blocks (Weisman 1967, Drozdov 1969, Berezovsky 1973).

The advantages of volumetric-block construction are the transfer of the main construction processes to the factory, which makes it possible to improve the quality of construction (Toleubayeva 2020), automate production, use effective building materials, reduce the impact of seasonal work, drastically reduce construction time, and significantly reduce construction costs (Kirkorov 1975, Ilyenko 1979). The main features of a three-dimensional block building are associated with increased flexibility of wall elements, which leads to premature loss of wall stability (Zhussupbekov 2020). In addition, the extremely limited amount of experimental and theoretical studies of such constructive systems should be attributed to the disadvantages of using volume-block housing construction (Utepov 2022).

DOI: 10.1201/9781003299127-373

In the city of Astana (Kazakhstan), a house-building plant "ModeX Astana" was built, which manufactures reinforced concrete volumetric blocks of the "lying glass" type of enlarged sizes. The building is mounted from pillars of volumetric modules, leaning against each other through a layer of mortar. In the process of mastering the technology at the plant, control tests were carried out on the main load-bearing structures of volume-block multi-story buildings, which made it possible to improve their manufacturing technology and design solution, taking into account the use of modern materials.

2 EXPERIMENTAL STUDIES

This article presents the results of testing full-scale volumetric blocks that differ in the type and strength of concrete, as well as reinforcement. Volumetric blocks have two side walls of a ribbed design with a wall thickness of 50 mm and ribs 100 high, as well as a flat end wall 100 mm thick. The floor slab of the volumetric unit is ribbed with a shelf 80 mm thick and ribs 170 mm high. The ceiling slab of the volumetric unit is flat with a run-out, 80-97 mm thick. Volumetric blocks are reinforced with spatial frames and reinforcing meshes made of cold-drawn wire Ø4-Ø5 mm Y500C class, combined into a single spatial block, as well as additional bar reinforcement Ø12 S500. External insert wall panels are multi-layered with a bearing layer of concrete, effective insulation and a facing layer, installed as a facade system.

Three-dimensional blocks were tested on a test bench, which is a rigid rod system of adjustable vertical and horizontal frames (Guidelines 1977, Guidlens 1983). The loading of volumetric blocks was carried out using hydraulic jacks with a capacity of 200 tf through a distribution reinforced concrete slab. During the tests, the compressive deformations of concrete were measured using vertical strain gauges with a base of 50 mm, horizontal and vertical displacements of walls and ceilings - using digital deflection gages PA0-6, and the crack opening width - using an MPB-3 microscope (CP 501.1325800.2021).

Volumetric block No. 1 is made of concrete of axial compressive strength class LC20/22 and density grade D1800 using crushed expanded clay. At a vertical load of N = 728.4 tf, cracks were observed at the corners of the volumetric block, vertical cracks in the lintel above the window in the wall panel and in the lintel above the doorway in the end wall. At the same time, the opening width of existing technological cracks increased by 0.05 mm (CP RK EN 2011).

Figure 1 shows a plot of longitudinal deformations of concrete along the perimeter of the walls of a volumetric block with a vertical load N = 829.86 tf. The value of vertical deformations along the length of the longitudinal walls was within -(26-61) 10-5 relative units and averaged -(42-53)10-5 relative units. The concrete deformations in the end wall and wall panel were almost 20% less. Under this load, the crack opening width in the lintels reached 0.05-0.10 mm, and the crack opening width in the longitudinal walls was in the range of 0.10-0.25 mm.

The destruction of the volumetric block occurred at a vertical load N = 1083.88 tf and was caused by fragmentation of the upper part of the longitudinal wall in the area of adjacency to the wall panel with the continuous growth of horizontal deformations of the walls from the plane and the formation of new cracks. The crack opening width in the lintels reached cracks of 0.15-0.2 mm, and the crack opening width in the longitudinal walls was within 0.20-0.25 mm (Figure 2).

Figure 3 shows diagrams of horizontal displacements of walls from the plane of the volumetric block. The largest movements of the top of the longitudinal walls reached 2.1-2.45 mm, the movements of the end wall were 3.08 mm, and the wall panel - 4.24 mm. The increase in displacements almost linearly depended on the vertical load, and only at the last stage of loading was a sharp increase in horizontal displacements (deplanation) of the walls observed. (Figure 5). The average compressive stresses of concrete in the longitudinal walls were equal to 8.74 MPa, that is, they amounted to 43.7% of the concrete strength. The average compressive stresses in the concrete of the longitudinal walls were equal to 8.33 MPa, that is, they amounted to 41.7% of the concrete strength. The experimental breaking load exceeds the control breaking load for 16-storey buildings in Astana by 4%.

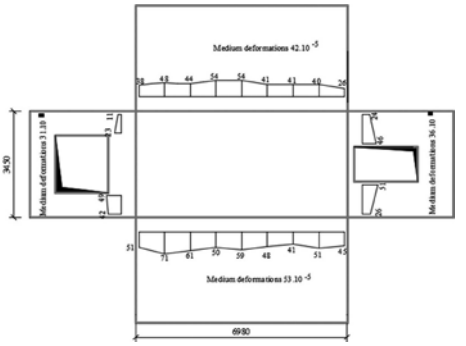

Figure 1. Distribution of concrete compression strains along the perimeter of the walls of block No. 1 at 76% of the breaking load.

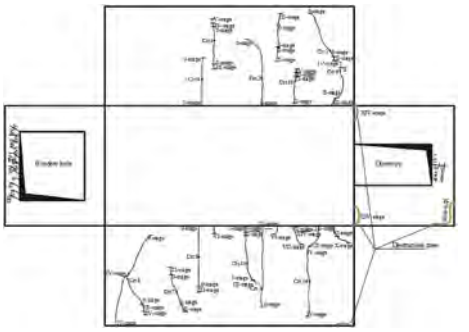

Figure 2. Scheme of the location of cracks on the development of the walls of block No. 1.

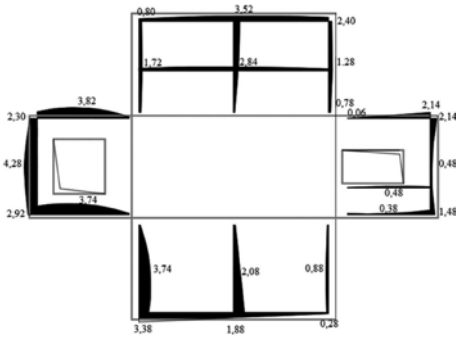

Figure 3. Horizontal displacements of walls under breaking load.

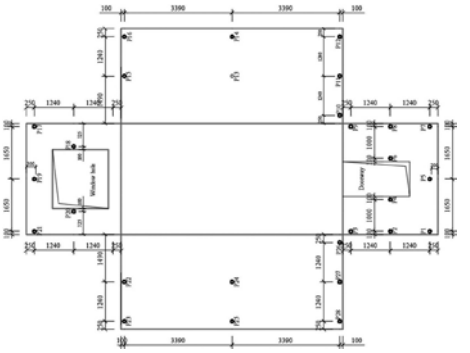

Figure 4. Scheme of the location of deflectometers.

Figure 5. Damage to the interface between walls and ceiling slabs.

Volumetric block No. 2 is similar in geometrical dimensions to block No. 1, however, it had less reinforcement of walls and floors, and was also made on crushed expanded clay from concrete of class LC16/18, density grade D1800. When loading the sample with a vertical load up to N = 652.4 tf, cracks formed at the corners of the volumetric block, vertical cracks in the lintel above the window in the wall panel and the lintel above the doorway in the end wall. With a vertical load N = 815.5 tf, the crack opening width in the lintels reached 0.05-0.10 mm, and the crack opening width in the longitudinal walls was in the range of 0.10-0.25 mm. The value of

vertical deformations of concrete along the length of the longitudinal walls was within -(22 - 49) 10-5 relative units, concrete deformations in the end wall were about 72% of the average deformations of the longitudinal walls, concrete deformations in the wall panel were about 52 % of these deformations. In this case, the largest displacements of the top of the longitudinal walls were 2.63 and 2.84 mm, deformations of the end wall - 3.29 mm, and the wall panel - 2.07 mm.

The destruction of the volume block occurred at a vertical load of N = 1002.33 tf (Figure 6) and was accompanied by the destruction of the concrete of the upper part of the longitudinal walls in the area of interface with the roof slab and the outer wall panel, the splitting of the roof slab and the end wall, as well as the continuous increase in the horizontal deformations of walls from the plane. The average compressive stresses in the longitudinal walls were equal to 7.93 MPa, that is, they amounted to 49.56% of the concrete strength. The experimental breaking load exceeds the control vertical load for 13-storey buildings in Astana by 30%.

Figure 6. Splitting of the block floor slab No. 2.

Block No. 3 was similar in terms of reinforcement and geometrical dimensions to block No. 1, but was made of heavy concrete of class C20/22. The first vertical cracks appeared in the lintel of the wall panel under a vertical load of N=850 tf, then vertical cracks appeared in the lintel of the doorway and vertical cracks in the window sill of the wall panel. During the stage before the destruction of the volume block, the largest crack opening width did not exceed 0.20-0.25 mm, the horizontal displacements of the walls from the plane of the volume block did not exceed 1.2 mm, and in the middle part of the window opening of the wall panel was 5.03 mm. The compressive deformations of concrete in the longitudinal walls were in the range of -(19 - 31)10-5, and in the area of adjacency to the wall panel they increased sharply, approaching the ultimate compressibility of concrete in axial compression. The deformations of concrete in the end wall and wall panel were two times less than the deformations of concrete in the longitudinal walls.

The destruction of the volumetric block occurred at a vertical load N = 1482.21 tf and was accompanied by the destruction of the upper part of the longitudinal walls in the area of interface with the floor slab, the opening of vertical seams between the wall panels, the formation of cracks in the lintels of the wall panel and the end wall, the formation of longitudinal cracks in the ceiling slab with an opening width of 0.10-0.15 mm. The average compressive stresses in the longitudinal walls were equal to 12.03 MPa, that is, they amounted to 57.8% of the concrete strength. The experimental breaking load exceeded the control breaking load for 16-storey buildings in Astana by 4%.

3 ANALYSIS OF RESEARCH RESULTS

The performed studies of the bearing capacity of three-dimensional blocks revealed their complex stress state under vertical loads, established the sequence of formation and width of cracks in walls and ceilings, the magnitude of the ultimate deformations of walls from the plane, the distribution of longitudinal deformations of concrete in the walls and the causes of destruction of

three-dimensional blocks. The main features of the behavior of volumetric blocks under vertical loads are associated with a small wall thickness compared to that required for buildings with load-bearing reinforced concrete walls, which, according to [18], should be at least 200 mm.

Increased flexibility of the walls of volumetric blocks at initial loads, an increase in the free length of walls in the process of significant damage to walls and ceilings, as well as significant displacements of walls from the plane of the building under high vertical loads, lead to premature destruction of volumetric blocks.

The destruction of the walls of expanded clay concrete volumetric blocks for the destructive stage of the work of the walls occurs at compressive stresses in the walls equal to 44.7-49.6% of the concrete strength. Thus, the strength of reinforced concrete walls should be determined by introducing the coefficient of reduction in the bearing capacity of flexible compressed elements φ=0.44-0.5. When designing the walls of the volume blocks of the lower tiers of buildings, damage to the volume blocks should be taken into account. Changes in the flexibility of walls in the calculation of serviceability limit states (SLS) can be ignored, and for critical states in terms of bearing capacity (ULS), the design length of the walls should be increased by 50-56%.

The rigidity and crack resistance of volumetric blocks made of heavy concrete is much higher than that of volumetric blocks made of expanded clay concrete. Therefore, when designing walls of bulk blocks made of heavy concrete for the action of vertical loads, taking into account damage to bulk blocks, the change in the flexibility of walls when calculating serviceability limit states (SLS) can also be ignored, and for critical states in terms of bearing capacity (ULS), the calculated length walls should be increased by 43%.

REFERENCES

Weisman E.P., Tuchnin A.A.1967 Statistic studies of the glass-type building block modules in Syzran./ Modular construction in the USSR. Central Research and Design Institute of Residential and Public Buildings, Moscow

Drozdov P.F. 1969. Calculation of multi-storey buildings consisting of building block modules./ "Concrete and reinforced concrete", Issue 12, Moscow

Berezovsky L.F., Kedich I.N., Smekh I.V., Furunzhiyev R.I., Mikhailovski D.A. 1973.About the work of monolithic building block modules used in the construc-tion of residential buildings./ "Building structures." Collected works of Institute of construction and architecture BSSR, issue 14, Minsk

Toleubayeva, Sh., Akhmetzhanov T., Danenova G., Tanirbergenova A., Yeleussinova, A. 2020. effect of complex additive on exothermic kinetics and hydration stages of cement systems. International Journal of Geomate, 19 (75). pp.184–192

Kirkorov S.S. Production and construction of buildings of building block modules for the settlements of power engineers (Review). Informenergo, Moscow, 1975;

Utepov Ye, Tulebekova A., Aldungarova A., Zharassov Sh., Sabitov Ye. 2022. Performance of a wireless sensor adopted in monitoring of concrete strength. International Journal of Geomate, 23 (95). pp.73–80

Ilyenko I.A. 1979. Production of reinforced concrete products for modular con-struction in the USSR./ Review information, All-Russian Research Institute of Metrological Service, Moscow

Zhussupbekov A., Tulebekova A., Jumabayev A., Zhumadilov I, 2020. Assessment of soils deformability under vertical load. International Journal of Geomate, 18 (70). pp. 221–228

Guidelines for statistical tests of reinforced concrete load-bearing building block modules, Research institute of building structures, Kyiv, 1977

Guidelines for the design of large-panel buildings with the use of load-bearing building block modules, Moscow, Research institute of building structures, 1983

Guidelines for the design, plant production, transportation, and assembly of building block modules of the Krasnodar technical direction, Moscow, Central Research and Design Institute of Residential and Public Buildings, 1983

CP 501.1325800.2021 Buildings made of large modules. Rules for the design and construction. General provisions, Moscow, 2021

CP RK EN 1992-1-1:2004/2011 "Design of reinforced concrete structures" Part 1-1 General rules and rules for buildings. Astana, 2016

Smart Geotechnics for Smart Societies – Zhussupbekov, Sarsembayeva & Kaliakin (Eds)
© 2023 The Author(s), ISBN 978-1-003-29912-7
Open Access: www.taylorfrancis.com, CC BY-NC-ND 4.0 license

Landscape science potentiality for the construction of buildings on megafans

M.Sh. Ishankulov, Zh. M. Aukazhiyeva & M.Z. Sagyndyk
L.N. Gumilyov Eurasian National University, Astana, Kazakhstan

ABSTRACT: The possibility of using the potential of landscape science for the construction of buildings is considered on the example of two unique natural formations of Kazakhstan - megafans of the Talass and Kon rivers. Landscape science as a synthetic natural science discipline can contribute to the design of foundations for buildings and structures. The presented materials testify to the variety of variants of megafans, their dissimilarity, which entails the need for an individual approach to their assessment. The megafans considered by us are complex and diverse in their structure and do not always correspond to traditional ideas about alluvial fans and inland deltas. Separate cone-shaped formations included in their composition are facultatively closed; they correspond to the time stages of mudflow or, in the case of inland deltas, flood process. The approach outlined in the article is considered by us as an addition to engineering and geological surveys, which are mandatory when designing the foundations of buildings and structures. It gives a systematic vision of the subject of research. The approach is applicable in the development of a strategy for large-scale design of the construction of buildings and structures in the volumes of the country's regions.

Synthetic physical-geographical discipline - The Science of Landscape - has been developing in Kazakhstan since the early 60s of the last centuries. Its foundations were laid in the 19th century by the outstanding Russian naturalist V.V. Dokuchaev. The subject of study of landscape science are natural formations of different hierarchical levels.

Landscape cartography serves as a source of new information about natural formations, the basis for creating thematic maps for various scientific purposes and theoretical generalizations. Two giant (more than 10^5 km^2) fan formations - alluvial fans and inland deltas in the basin of the Talass and Kon rivers were chosen by us for a closer acquaintance with the possibilities of landscape maps for the construction of buildings. These natural formations are the main arena for the life of the population in arid conditions and the objects of the construction boom that has unfolded in the country.

1 TALASS COMPOUND MEGAFAN

1.1 *Landscape map of the Talass river alluvial fans*

The landscape map of the Talass river megafan is shown in Figures 1 and 2).

a – Current lines of former water-ground flows drawn along watersheds (solid, dotted and dotted lines correspond to alluvial fans of landscape rank (Solntsev, 1948); b- corresponding to the tops of alluvial fans; c - branching nodes of current lines of former water-ground flows, corresponding to the tops of alluvial fans in the rank of morphological units of the landscape (tracts, facies) d – numbers of alluvial fans landscapes; e - the border of the Talass and Assa of alluvial fans systems; f – boundary of the Assa alluvial fans system of with fans superimposed on the Talass fans; g - boundary of the alluvial fans of the Ichkeletau mountains and the Talass system

DOI: 10.1201/9781003299127-374

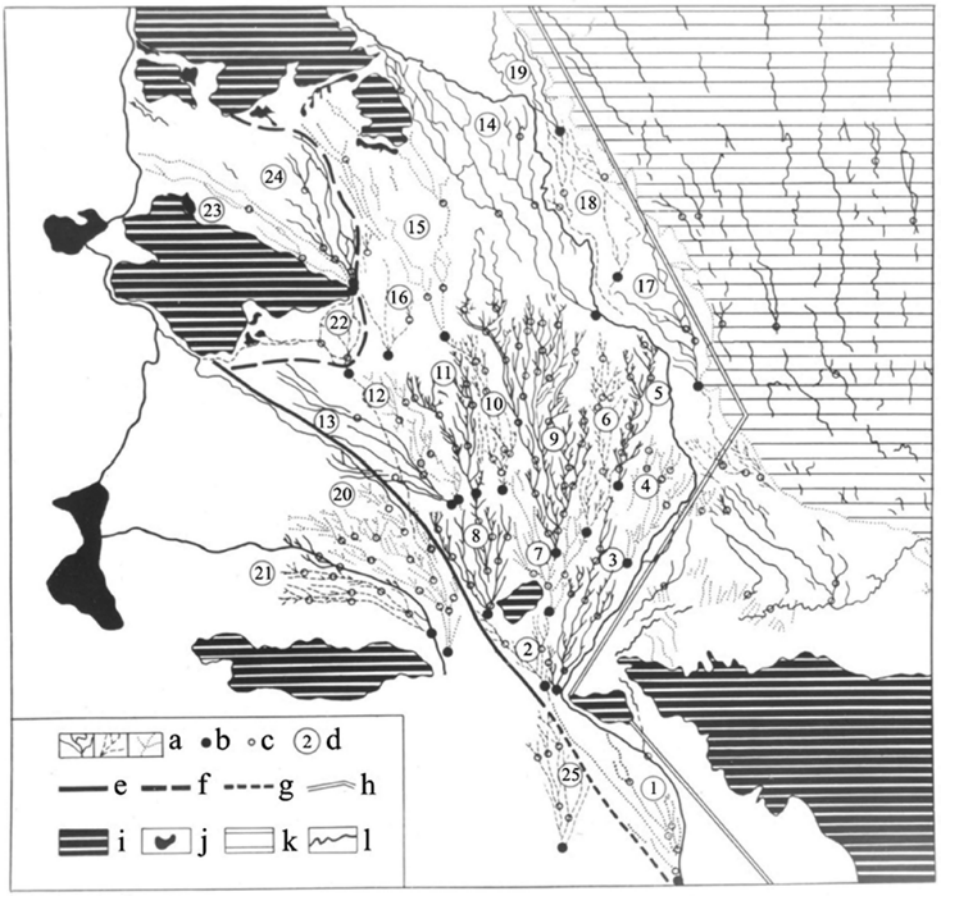

Figure 1. Talass system of alluvial fans landscapes (Ishankulov, Ropot, 1978, p.33).

of alluvial fans; h – boundary of the dead system of Talass alluvial fans, buried under eolian sediments of the Moyinkum and partially involved in the mountain uplift in the process of orogenization of the territory (restored by interpretation of aerial photographs); i - low mountains, remnant low mountain massifs and plateaus within the territory of the development of alluvial fans; j - lakes; k- sands; l – rivers-bed.

Talass alluvial fans landscapes system:

Active fans: 1 - Pokrovka, 2 - Dzhambul, 3 - Rovnoe, 4 - Karasu, 5 - Zylikha, 6 - Kosheni, 7 - Karatobekol, 8 - Zhanasaz.

Dying fans (transitional state from active to dead): 9 - Karashingil, 10 - Eshkilikbay, 11 – Kolkaynar, 12 – Shiyozek, 13 – Torangy.

Dead fans: 14 – Karabakyr, 15 – Dalazhailau, 16 – Kudeli, 17 – Upper Kokozek, 18 – Middle Kokozek, 19 – Lower Kokozek.

Assa river alluvial fans system: 20 – Karakemir, 21 – Kyrshandy.

Assa alluvial fans landscapes system superimposed on landscapes of alluvial fans of the Talass system: 22 – Karabuget, 23 – New Tasaryk, 24 – Old Tasaryk (Figure 2).

1.2 *Landscape map of the Talass river alluvial fans*

Tracts and their combinations:

1 – Delta streams, mostly sandy with a thin layer of silt, deposited during flood periods by undeveloped alluvial-meadow soils with succession changes of herbaceous communities.

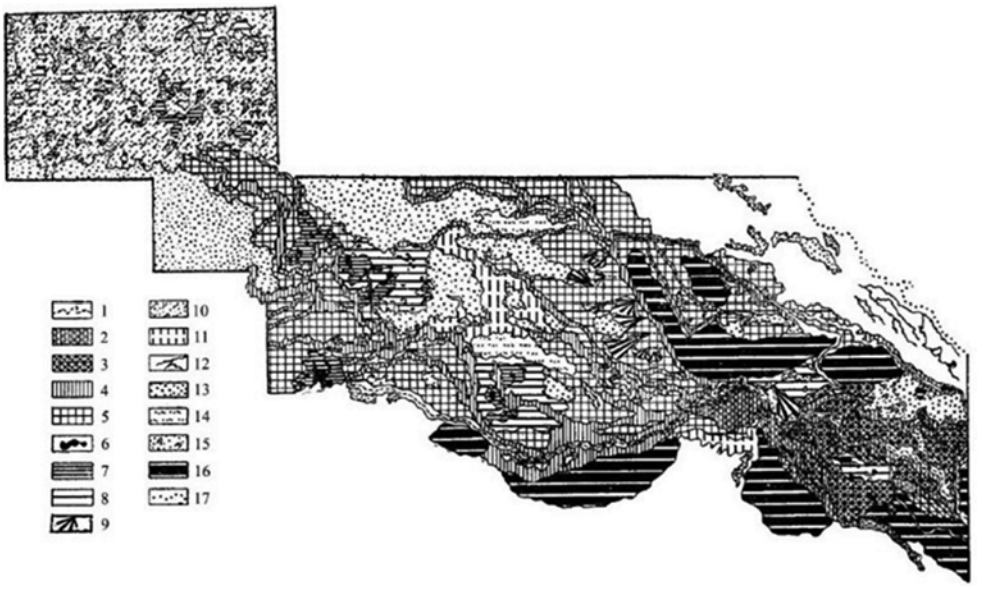

Figure 2. Landscape map of the Talass river inland deltas (Bogachev, Ishankulov, 1986, p. 22-23).
The map of inland deltas is a continuation in runoff of the map of Talass alluvial fans, presented in Figure 1.

2 – Embryonic levee, composed mainly of sands and sandy loams, washed out during floods with a multi-year periodicity; alluvial-meadow-tugai and alluvial-meadow soils under Salsola chingils.

3 – Embryonic interchannel depressions composed of medium and heavy loams during flooding for 10-40 days a year and groundwater at a depth of up to 2.5 m with meadow-bog and bog-meadow soils under reed-forb-reed, Climacopter-reed, Comba communities.

4 – Mature levee composed mainly of sandy loam and light loam when washed out during floods with annual or long-term periodicity with alluvial-meadow-tugai and alluvial-meadow soils under Elaeagnus angustifolia and Chingil tugai; in the absence of floods - with alluvial-meadow desertifying soils under Saltwort chingils, Aeluropus–limonium-Saltwort with Alhagi communis.

5-8 – Mature interchannel depressions composed of medium and heavy loams and clays (5) with year-round stagnation of waters entering the flood – deltaic lakes (6); with flooding 160-190 days a year and groundwater at a depth of up to 1 m with swamp soil under Typha angustifolia, Typha angustifolia-Phragmites communis, Aeluropus and Bolboschoenus communities (7); with flooding 100-110 days a year and groundwater at a depth of up to 2.5 m – with meadow boggy soils under Forb-read, Reed grass-Forb-Reed communities (8); with flooding 30-40 days a year and groundwater up to 5 m – with swampy-meadow and meadow-swampy decertifying soils under Elytrigia repens, Puccinellia, Tamarix and Halostachys communitis; in the absence of floods and occurrence of groundwater at depth of 5-10 m and deeper – with takyr-like soils under Artemisia-Anabasis salsa with Haloxylon aphyllum communities.

9 – Alluvial fans formed by temporary flows originating from the remnants surrounding land deltas, composed mainly of saline red-colored clays with gray-brown desert soils under Gramínea-Saltwort communities in the upper part and solonchaks along the periphery of alluvial fans.

10 – Eolian hilly-ridged sands processed by floods; with flooding 160-190 days a year and groundwater at a depth of 2.5 m with meadow boggy and swampy meadow soils under Forb-reed communities; with flooding 30-40 days a year and groundwater at a deep of 2.5-5.0 m – with alluvial-meadow soils under Forb grass-Calamagrostis communities.

11 – Runoff hollows filled with silty sands with alluvial-meadow soils under Artemisia- Puccinellia communities.

12 – Gully.
13 – Hilly-ridged sands with Agropyron fragile-Hordeum communities.
14 – Ridge sands with Artemisia-Agropyron repens-Eurotia ceratoides communities.
15 – Dune-hummocky sands with Artemisia-Agropyron repens communities.
16 – Monoclinal remnant ridges - local anticlines composed of red-colored clays, gray-brown desert soils under Artemisia pauciflora.
17 – The boundary of the sand massif Moyinkum.

2 KON COMPOUND MEGAFAN

2.1 *Proluvium of the North Kazakh Plain*

Five rivers of the basins of the Ob watershed of the Kazakh hills (Kon, Nura, Ishim, Olenty and Shiderty) created the North Kazakh plain. In the geographical literature, it is also called the Ishim plain, and sometimes the Ishim steppe. Each of the watercourses, upon exiting the drainage basin to the North Kazakh Plain, forms alluvial fans and inland deltas created by deposits of proluvial genesis (Figure 3).

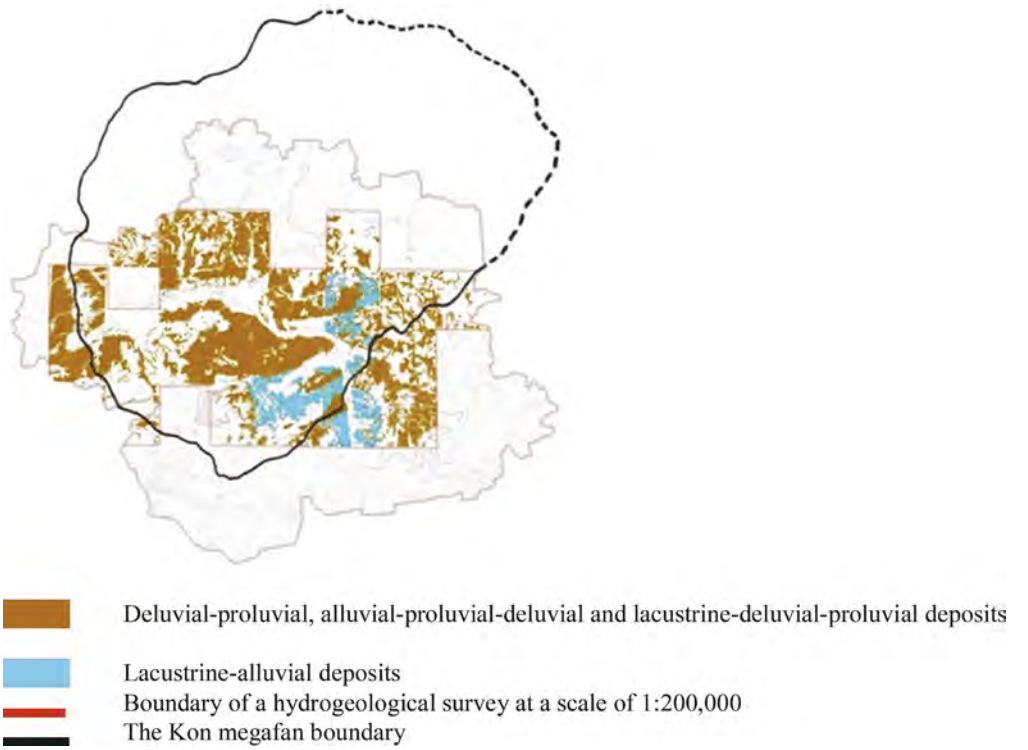

Figure 3. Proluvium of the North Kazakh Plain within the boundaries of the Akmola and Nurinsky districts of the Karaganda region (compiled by M.Sh. Ishankulov according to the hydrogeological maps of the USSR, m 1:200,000, surveyed in 1955-1979).

The alluvial fan of the Kon River stands out with gigantic dimensions against the background of all 5 alluvial fans of Kazakhstani rivers of the Ob watershed of the Kazakh hummocky terrain (Figure 4). Its area is estimated at 240,368 km^2; length from north to south – 586 km; from west to east – 587 km (Figure 4).

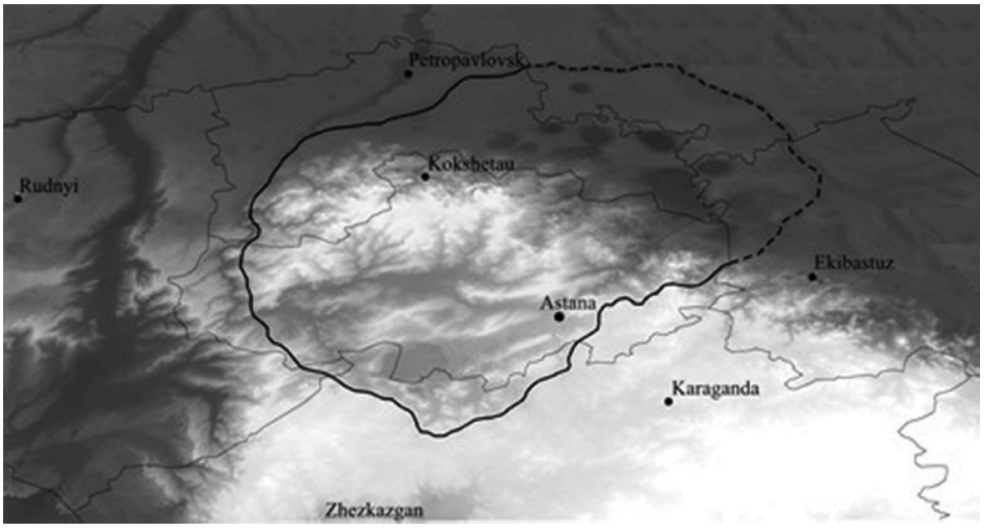

Figure 4. Proluvium of the North Kazakh Plain within the boundaries of the North-Kazakhstan, Akmola and Nura districts of the Karaganda region (compiled by M.Sh. Ishankulov according to the hydrogeological maps of the USSR, m 1:200,000, surveyed in 1955-1979). (The dotted line shows the proposed segment of the border. Thin lines inside the object of study are the boundaries of administrative regions).

The reason for such gigantism lies in the specifics of its origin and in the properties of the rocks of the catchment. The megafans arose due to the ultra-mud flow. Such flows are rare and represent one of the groups of mudflows and mudflows of the Earth, characterized by a grandiose scale of the process (Perov, 1996). As for the properties of rocks, it was found that the drainage basin of the Kon river is the only active river catchment area on the Ob watershed of the Kazakh hummocky terrain that can supply material with plastically viscous properties for in other watersheds mudflows - fatty Miocene clays. in other watersheds, such clays are absent or limited (Figure 5).

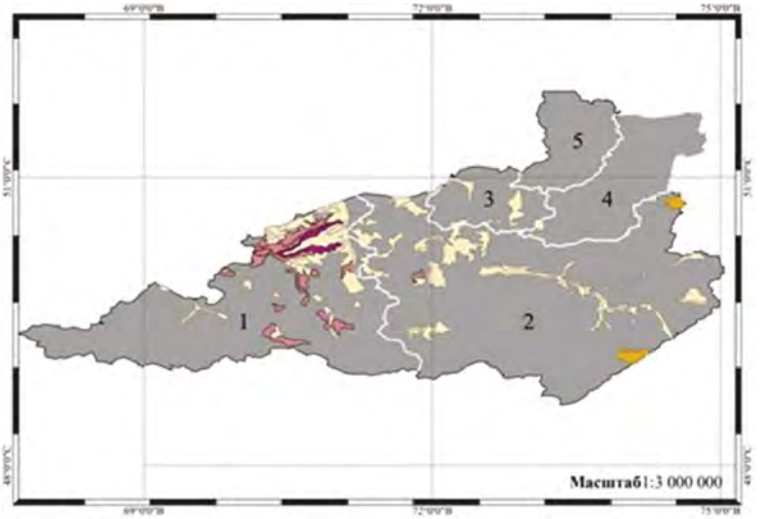

Figure 5. Resilience of rocks composing watersheds to displacement under conditions of extreme climatic situations. Drainage basins of the rivers: 1 – Kon, 2 – Nura, 3 – Ishim, 4 – Selety, 5 – Shiderty.

The object discovered in 2007 has not yet been studied with the same detail as the Talass compound megafan. However, the first results of the research say that the object is original and does not look like the Talass megafan at all. Its drainage basin is located not in the mountains, but in the hills of the Kazakh hummocky terrain.

Its top is composed not of coarse clastic material, but of red-colored saline clays, which led to the formation of saline deep-lying groundwater and soils of the saline series (Figure 6).

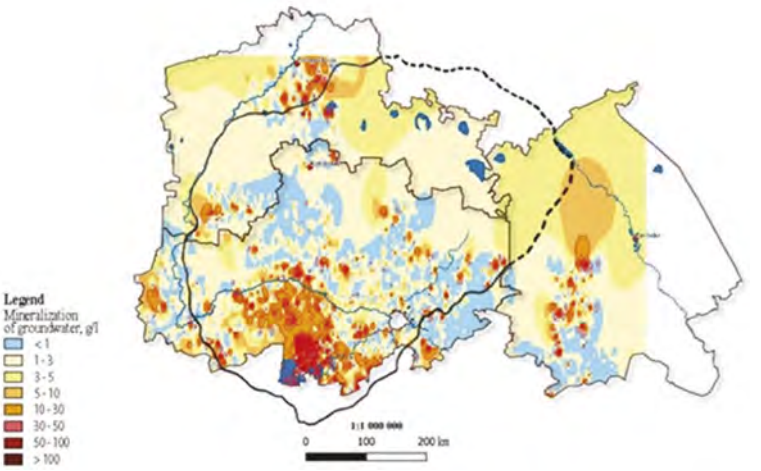

Figure 6. Mineralization of underground waters of the Kon megafan.

The issue of choosing a foundation for the construction of buildings is a key one and needs to be thoroughly considered. Construction objects in the cartographic material presented in the article are considered against a wide systemic natural background instead of the practiced point local consideration of specific objects that have little to do with the natural environment. The content of landscape maps testifies to the existence of a variety of options for megafans, their dissimilarity, optional isolation and the need for an individual approach to their assessment for construction purposes. They also contain specific detailed factual material in terms of soil characteristics, which is necessary when designing shallow foundations.

Practitioners-builders are little aware of the potential inherent in landscape maps and they are not used and for landscape specialists, familiarity with the subject of building construction can become a new area for the practical application of acquired knowledge.

REFERENCES

Ishankulov, M.Sh., Ropot B.M. 1978. Talass irrigation array: soil-reclamation study of the landscape level of the system of alluvial fans and continental deltas of Talass river, *Science of the Kazakhstan*. Alma-Ata.

Bogachev V.P., Ishankulov, M.Sh. 1986. Methods of spatial analysis of saline soils: (On the example of landscapes of alluvial fans and inland deltas), *Science of the Kazakhstan*. Alma-Ata.

Ishankulov, M.Sh. 2010. Landscapes of alluvial fans of arid territories, *KzHi-Tech LLP*. Astana.

Solntsev, N.A. 1948. Natural geographical landscape and some of its general patterns, *Proceedings of the II All-Union Geographical Congress 258-269*. Moscow.

Perov, V.F. 1996. Mudflow phenomena (Terminological dictionary), *Publishing House of Moscow State University*. Moscow.

Smart Geotechnics for Smart Societies – Zhussupbekov, Sarsembayeva & Kaliakin (Eds)
© 2023 The Author(s), ISBN 978-1-003-29912-7
Open Access: www.taylorfrancis.com, CC BY-NC-ND 4.0 license

Experimental study of reinforced concrete elements reinforced with fiber-reinforced plastics in inclined section under static loading

Ulan Altigenov
L.N. Gumilyov Eurasian National University, Astana, Kazakhstan
Kazakh Scientific Research and Design Institute of Civil Engineering and Architecture JSC, Almaty, Kazakhstan

Aliy Bespaev
Kazakh Scientific Research and Design Institute of Civil Engineering and Architecture JSC, Almaty, Kazakhstan

Ulan Kuralov & Birim Amanov
Satbayev University, Almaty, Kazakhstan
Kazakh Scientific Research and Design Institute of Civil Engineering and Architecture JSC, Almaty, Kazakhstan

ABSTRACT: The results of experimental studies of the strength of inclined sections of bent reinforced concrete elements with fiber-reinforced plastics are presented. Comparative data have been obtained on the use of new types of fiber-reinforced plastics for reinforcing reinforced concrete structures. Experimental studies have been obtained on the value taken into account in the calculations of the limiting deformations of fiber-reinforced plastics under various types of loads.

Keywords: Bending reinforced concrete elements, Beams, Strength of inclined sections, Deformations and cracks, Reinforcements, Fiber-reinforced plastics, Prototypes, Deflections, Tests

1 INTRODUCTION

The need to strengthen reinforced concrete structures during operation arises due to the long-term effect of operational loads or corrosive wear, when errors are eliminated in the design, manufacture, and transportation when the operating conditions become more complicated or not envisaged by the project, the scheme of action and magnitude of loads, the occurrence of various damages, as well as when reconstruction and renovation of the enterprise (EN 2004). An alternative to traditional methods of reinforcing reinforced concrete structures is the use of fiber-reinforced plastics (FRP) - polymers reinforced with fiberglass. Unlike traditional reinforcement methods using steel reinforcement, these methods have high reinforcement efficiency, and do not require overburden and welding, concreting of reinforced elements, they are distinguished by durability, corrosion resistance, low labor intensity, and economic feasibility.

The following types of fibers are commonly used as FRP reinforcement: basalt (B), carbon (C), aramid (A), glass (G), and polyester (Teng et al., 2002).

Reinforcement of reinforced concrete structures with fiber-reinforced plastics (FRP) can be used in the following cases:

– to reinforce undamaged reinforced concrete structures due to increasing loads during the reconstruction of the object (Shilin 2004);
– to strengthen reinforced concrete structures damaged during operation ("shooting off" of the protective layer of concrete, corrosion of reinforcement and concrete, formation and

DOI: 10.1201/9781003299127-375

development of cracks, excessive deflections, etc.) in order to restore the performance of the elements (Mander et al., 1988);
- to protect against corrosion, increase water resistance, and increase the durability of structures (Mochizuki 2020);
- fiber reinforcement (FAP) is produced by the following methods;
- by impregnation of concrete;
- external reinforcement with fiber-reinforced plastics (FRP)

Reinforcement systems for reinforced concrete structures are made in the form of unidirectional braided sheet coverings or woven unidirectional or bidirectional fibers produced on looms. The most widespread are the following types of fibrous fibers; carbon, aramid and glass. The most common method of reinforcement is external reinforcement with fiber-reinforced plastics (FRP), which is used for longitudinal and transverse reinforcement, as well as for creating reinforcing clips in compressed concrete elements, which prevent the transverse expansion of concrete, creating a triaxial stress state in concrete and can increase the strength of the latter in repeatedly (Samaan 1988, Awwad et al., 2019).

Wrapping reinforced concrete structures with polymer fiber fabrics (FFA) can increase the strength of compressed elements several times by limiting the transverse expansions of concrete and thereby creating a triaxial stress state. Sticking high-strength polymer-fiber tapes (laminate) with unidirectional fibers can significantly increase the strength of tensile reinforcement, and reduce the width of normal cracks (Saafi et al., 1999).

Sticking high-strength polymer-fiber tapes (laminate) with bilaterally directed fibers can significantly increase the strength of the transverse force, reduce the width of the opening of inclined cracks, or significantly increase the bearing capacity of reinforced concrete slabs supported along the contour.

However, comprehensive data on the operation of reinforced concrete structures reinforced in such ways under various operating conditions and the variety of influences of force, temperature, aggression and other factors have not yet been obtained (Miyauchi et al., 2000, Miyauchi et al., 2005).

The purpose of this work is to obtain experimental data on the strength of inclined sections of bent reinforced concrete structures reinforced with fiber-reinforced plastics (Katsumata et al., 1988) under static loading, as well as information on the stress-strain state, strength, stiffness and crack resistance of inclined sections of bent reinforced concrete elements reinforced with high-strength fiber-reinforced plastis.

The implementation of the proposed project will radically improve the technical support and implementation of the strengthening and restoration of building structures, increase the qualifications and potential of workers, reduce noise and environmental pollution due to the rejection of overburden, welding and labor-intensive work, increase the durability and aesthetic appearance of reinforced structures, reduce the time and cost of implementation works.

2 EXPERIMENTAL STUDIES

The strength of inclined sections in terms of the transverse force of bent reinforced concrete elements was tested on 3 batches of prototypes of reinforced concrete beams reinforced in the support zone with fiber-reinforced meshes. The batches of samples differed in the type of fiber-reinforced materials used for reinforcement. The prototypes were tested according to the scheme of a hinged beam with a span of 2.0 m, loaded in the span by two equal concentrated forces at a distance of 1.2 m. At the same time, the ratio between the size of the cut span and the height of the section was providedequallyl to lcp/h = 2.0.

The study of the work of inclined sections of bent reinforced concrete elements, reinforced in the support zone with fiber-reinforced mesh tapes, was carried out on experimental reinforced concrete beams of three batches, tested according to the scheme of a hinged beam with a span of 2.0 m, loaded in the span by two equal concentrated forces at a distance of 1.2 m. In this case, the ratio between the span of the cut and the height of the section lcp/h = 2 was provided.

Three batches of reinforced concrete beams were tested, and the reinforcement of the support zones of which differed in the type of reinforcing material:

- samples of the 1st batch were reinforced with meshes of the S&P C Sheet 240 series 50 mm wide (BASF, Germany);
- samples of the 2nd batch were reinforced with meshes of the FibArm Tape 530/300 series 300 mm wide (HK Composite, Russia);
- samples of batch III were strengthened with meshes of the MBRACE FIB CF 230/4900/530 g/5.100 m series (BASF, Germany).

The prototypes of the 1st batch in the support zone at one end of the beams were reinforced with bent double-shear clamps from Ø6 A-1, installed with a step of 100 mm, and the other end was reinforced in the support zone with vertical or inclined tapes from unidirectional meshes of the S & P C Sheet 240 series 50 mm wide. In addition, the stretched zone was reinforced with S&H Laminate CFR 150/200 50 x 1.2 mm.

Table 1 presents the following experimental data for testing beams of the BI series:

- bending moment at which normal cracks appeared;
- transverse force at which oblique cracks were formed;
- shear force that caused the destruction of the beam;
- bending moment at which the beam failed.

Table 1. Forces at which cracks were formed and the destruction of beams of the BQ-I series occurred.

Beam brand	Transverse reinforcement	$M_{crc,s}$ kNm	$Q_{crc,w}$ kN	M_u kNm	Q_u kN
BQ1-1c	Without clamps	6,38	36,79	15,94	45,53
BQ1-2c		6,87	36,70	18,67	53,44
BQ1-3c	Vertical hair mesh	5,15	31,88	31,76	90,74
BQ1-4c		5,15	41,69	38,63	110,36
BQ1-5c	Inclined mesh strips	5,15	39,24	35,19	100,55
BQ1-6c		6,87	39,24	28,33	80,93

Table 2 presents the following experimental data for testing beams of the BQ-I series:

- the greatest deformations in tension reinforcement;
- the greatest deformations in the compressed reinforcement;
- the greatest deformations in steel collars;
- the greatest deformations in fiber-reinforced meshes;
- the greatest width of opening of normal cracks;
- the largest width of the opening of inclined cracks in the zone of reinforcement with steel clamps;
- the largest crack opening width in the reinforcement zone with fiber-reinforced meshes;
- vertical deflections in the middle of the span of the beam.

Table 2. Deformation parameters of the operation of inclined sections of beams of the BQ-I series.

№	Transverse reinforcement	ε_s ‰	$\varepsilon_{s.1}$ ‰	$\varepsilon_{f,w}$ ‰	$w_{k,s}$ mm	$w_{k,w}$ mm	$w_{k,p}$ mm	a_k mm
1	Without clamps	1,4	0,4	–	0,2	3,5	–	5,82
2		0,96	0,5	1,1	0,16	3,4	–	6,66
3	Vertical stripes made of fiber-reinforced mesh	1,75	0,7	–	0,3	0,6	1,55	14,03
4		1,95	1,4	3,8	0,35	0,9	0,95	15,25
5	Inclined strips of fiber-reinforced mesh	2,0	0,7	2,3	0,3	0,65	0,95	11,12
6		1,9	0,7	2,6	0,25	0,4	1,5	11,14

Let us consider the features of the work of inclined sections in terms of transverse force with their various reinforcement. In beams that do not have transverse reinforcement at the support end, in the process of increasing the vertical load with a bending moment of about 15% of the breaking load, the formation of normal cracks in the zone of pure bending was observed, with an increase in the load by almost 5 times, oblique cracks formed in the support zones. With a further increase in the vertical load, accelerated opening of inclined cracks was observed, and after reaching a crack width of more than 3-3.5 mm, the concrete was destroyed along the inclined zone in the supporting unreinforced zone of the beam. The vertical deflections were about 6 mm, the deformations of the tensile longitudinal reinforcement were about 0,15%, the deformations of the compressed reinforcement were 0,05%, and the opening width of normal cracks was about 0.2 mm. At the opposite end of the beam, reinforced with clamps Ø6 A-1 with a pitch of 100 mm, the width of the opening of inclined cracks did not exceed 0.1 mm, and the deformations in the clamps were about 0,1%.

In beams reinforced in the supporting zone with strips of fiberglass mesh, the strength of inclined sections in terms of transverse force almost doubled. After the formation of normal cracks, which also appeared at a bending moment of about 15% of the breaking load, oblique cracks were formed at a transverse force of about 35-40% of the breaking load. The destruction of the beams was caused by the breaking off of the concrete layer under the glued mesh strips, the switching off of the transverse reinforcement, was accompanied by a loud sound and had a fragile character. At the stage before destruction, inclined cracks reached a value of 1.0–1.5 mm; clamps were about 0.2. The values of vertical deflections were about 11-15 mm, the deformations of the tensile longitudinal reinforcement were about 0.2% of the compressed reinforcement - 0.7-1.0, the opening width of normal cracks was about 0.35 mm.

Prototypes of the BQ-II series of the batch in the form of beams 2.2 m long, had a cross section of 120 × 200 mm and were reinforced with double reinforcement: in the lower zone 2Ø18 A-III and in the upper zone - 2Ø10 A-III. In the support zone, one end of the beams was reinforced with bent double-shear clamps made of Ø6 A-1, installed with a step of 100 mm, and the opposite end did not have transverse reinforcement.

The support zones of the beams of the BQ-II series were reinforced with a sticker of vertical unidirectional meshes of the FibArm Tape 530/300 series 300 mm wide, and the tension zone was reinforced with a FibArm Lamel 12/100 lamella.

The beams were loaded in stages not exceeding 5-8% of the breaking load.

Table 3 presents the following experimental test data for beams of the first batch:

- bending moment at which normal cracks appeared;
- transverse force at which oblique cracks were formed;
- shear force that caused the destruction of the beam;
- bending moment at which the beam failed.

Table 3. Results of testing beams of the second batch BQ-II.

Beam brand	$M_{crc,s}$ kNm	$Q_{crc,w}$ kN	M_u kNm	Q_u kN
BQII-1	13.3	73,3	48.0	120.0
BQII-2	12.0	80	58,0	145,0
BQI1-3	12,0	70	48,0	120,0

With an increase in the transverse load, normal cracks formed in the zone of pure bending, then oblique cracks appeared, after which the destruction of the support zone occurred, accompanied by separation of the concrete protective layer.

Table 4 presents the following experimental data for testing beams of the first batch:

- the greatest deformations in tension reinforcement;
- the greatest deformations in the compressed reinforcement;
- the greatest deformations in fiber-reinforced meshes;

– the greatest width of opening of normal cracks;
– the largest width of the opening of inclined cracks;
– vertical deflections in the middle of the span of the beam;
– vertical deflections under loads.

Table 4. Deformation parameters of inclined sections.

Beam brand	ε_s ‰	$\varepsilon_{s.1}$ ‰	$\varepsilon_{f,w}$ ‰	$w_{k,s}$ mm	$w_{k,w}$ mm	f_{max} mm	f_o mm
BQI1-1	1,76	–1,44	3,36	0,1	0,30	13,8	7,4
BQI1-1	2,4	–1,52	3,84	0,25	0,30	15,0	9,6
BQI1-1	1,76	–1,6	2,72	0,20	0,30	12,0	8,5

The distribution of tensile strains of fiber fibers along the length of the cut occurs along a convex curve, while the largest strains of mesh fibers reached values of 0,2-0,38%.

Prototypes of beams of the BQ-III series, 2.2 m long, had a cross section of 120 × 200 mm and were reinforced with double reinforcement: in the lower zone 2Ø18 A-III and in the upper zone - 2Ø10 A-III. The stretched area of the beams was reinforced with a sticker of MBRACE LAM CF 165/3000 100x1,4.100m laminate, and the support areas of the beams were reinforced with a sticker of vertical unidirectional meshes of the MBRACE FIB CF 230/ 4900.530g/5.100m series.

Table 3.10 presents the strength test data for BQ-III series beams:

– bending moment at which normal cracks appeared (Mcrc,s);
– bending moment at which the beam failed (Mu);
– shear force that caused the destruction of the beam (Qu).

Table 5. Forces at which normal cracks were formed and the destruction of BQIII series beams occurred.

Beam brand	$M_{crc,s}$ kNm	M_u kNm	Q_u kN
BQIII-1	5,53	38,2	95,5
BQIII-2	11,1	31,6	78,9
BQIII-3	11,1	34,3	85,8

With an increase in the transverse load, normal cracks were formed in the zone of pure bending, then the delamination of the upper corner of the grids near the zone of application of the transverse force and the separation of the protective layer of concrete began, after which the destruction of the support zone of the beam occurred, accompanied by crushing of the concrete along the inclined strip.

Table 6 presents the following deformation data based on the test results of BQIII series beams:

– the greatest deformations in tension reinforcement (εs);
– the greatest deformations in the compressed reinforcement (εs.1);
– the greatest deformations in the strips of the laminate (εf, lam);
– the largest deformations in the reinforcement grids (εf,w);
– maximum width of normal cracks (ak,s);
– vertical deflections in the middle of the span of the beam (fmax);
– vertical movements under loads (fo).

Thus, the experimental strength in terms of the transverse force of inclined sections of reinforced concrete beams, reinforced in the support zones with fiber-reinforced meshes, exceeds the design strength by an average of 16%.

Table 6. Deformation characteristics of BQIII series beams.

Beam brand	ε_s ‰	$\varepsilon_{s.1}$ ‰	$\varepsilon_{f,lam}$ ‰	$\varepsilon_{f,w}$ ‰	$a_{k,s}$ mm	$_{fmax}$ mm	f_o mm
BQIII-1	–	–1,79	2,62	1,5	0,20	9,2	5,9
BQIII-2	2,18	–1,38	2,51	1,39	0,10	9,1	6,3
BQIII-3	2,18	–1,62	4,05	4,53	0,20	8,9	7,7

Table 7. Comparison of the experimental and design strength of beams in terms of transverse force.

Beam brand	t_f. mm	E_f. GPA	α	s, cm	ε_f. ‰	Q_{design}, кN	$Q_{experimental}$, кN	$Q_{experimental}$/ Q_{design}
BQ1-1c					3,1	78,0	100,55	1,33
BQ1-2c	0,176		45°		3,8	80,0	80,93	1,01
BQ1-3c		240		11.2	3,1	77,85	90,74	1,18
BQ1-4c	0,176		90°		3,8	85,96	110,36	1,28
BQII-1c					3,36	108,81	120	1,1
BQII-2c	0.245	245			3,84	117,77	145	1,23
BQII-3c			90°	–	2,72	96,86	120	1,24
BQIII-1c					1,5	73,58	95,5	1,3
BQIII-2c	0,293	230			1,39	71,35	78,9	1,11
BQIII-3c					2,54	94,64	85,8	0,91

3 CONCLUSIONS

1. The results of tests on the transverse force of inclined sections of bent reinforced concrete structures reinforced by gluing in the support zone by surface gluing of various types using carbon fiber plastics showed that reinforcement of beams increases strength by 1.4-2.3 times.
2. The calculated strength of inclined sections of bent reinforced concrete structures reinforced with fiber-reinforced plastics showed a fairly close agreement with the experimental data.

REFERENCES

1. EN 1992-1-1:2004 Design of concrete structures: General rules and rules for buildings. Introduced. 2004. Technical Committee CENT/TC250. Brussels, 2004.
2. Teng, J.G. Chen J.F., Smith S.T., Lam I. 2002. FRP Strengthened RC Structures. John Wiley & Sons, Ltd. p. 245.
3. Shilin, A.A. 2004. External reinforcement of reinforced concrete structures. p. 139.
4. Mander, J.B., Priestly M.J.N., Park R. 1988. Theoretical stress-strain model for confined concrete. ASCE Journal of Structural Engineering. No 8. p. 1804–1826.
5. Mochizuki A, Zhussupbekov A., Fujisawa J., Tanyrbergenova G, Tulebekova A. 2021. Strength Anisotropy of Compacted Sandy Material. *Soil Mechanics and Foundation Engineering*, 57 (6), pp. 480–490
6. Samaan, M., Mirmiran A., Sahawy K. 1998. Model of Concrete Confined by Fiber Composites. Journal of Structural Engineering. ASCE. No 9. p. 1025–1031.
7. Awwad T., Mussabayev T., Tulebekova A., Jumabayev A. 2019. Development of the computer program of calculation of concrete bored piles in soil ground of Astana city.International Journal of Geomate, 17 (60). pp. 176–182
8. Saafi, M., Toutanji H.A., Li Z. 1999. Behavior of Concrete Confined with Fiber-Reinforced Polymer Tubes. ACI Material Journal. No 4. p. 500–509.
9. Miyauchi, K., Inouse S., Kuroda T., Kobayashi A. 2000. Strengthening Effects of concrete Columns with Carbon Fiber Sheet. Transactions of the Japan Concrete Institute V.21, p. 143–159.
10. Miyauchi K., Inouse S., Kuroda T., A. Kobayashi. 2005. Axial Load Behavior of Large-Scale Columns Confined with Fiber-Reinforced Polymer Composites. ACF Structural Journal. March-April. p. 258–267.
11. Katsumata, H., Katsumata A.H., Kobatake Y., Takeda A. 1988. Study of Strengthening with Carbon Fiber for Earthquake-Resistant Capacity of Exiting Reinforced Concrete Columns. Proceedings of the Ninth World Conference on Earthquake Engineering. Tokyo-Kyoto, Japan, V-VII. p. 517–522.

Smart Geotechnics for Smart Societies – Zhussupbekov, Sarsembayeva & Kaliakin (Eds)
© 2023 The Author(s), ISBN 978-1-003-29912-7
Open Access: www.taylorfrancis.com, CC BY-NC-ND 4.0 license

Reinforcement of compressed reinforced concrete structures with composite materials

U.S. Kuralov
PhD student of Satbayev University, Almaty, Kazakhstan
Kazakh Scientific Research and Design Institute of Civil Engineering and Architecture, Almaty, Kazakhstan

Z.T. Nashraliev
PhD, Associate Professor, Satbayev University, Almaty, Kazakhstan

U.B. Altigenov
PhD student of L.N. Gumilyov Eurasian National University, Astana, Kazakhstan
Kazakh Scientific Research and Design Institute of Civil Engineering and Architecture, Almaty, Kazakhstan

B.N. Amanov
Master's student of Satbayev University, Almaty, Kazakhsatn
Kazakh Scientific Research and Design Institute of Civil Engineering and Architecture, Almaty, Kazakhstan

ABSTRACT: There are presented the results of an experimental study of the strength of compressed reinforced concrete elements with polymer-reinforced plastics FIBARM TAPE 530/300. Reinforcement of compressed reinforced concrete elements with cages made of fiber-reinforced plastics causes triaxial compression in concrete, in which the strength of the elements can increase several times. Gluing clips of unidirectional vertical grids led to an increase in the strength of the compressed elements of a circular cross-section.

Keywords: Amplification, Fiber reinforced plastic, Carbon fiber, Composite, Static loading, Deformation

1 INTRODUCTION

In the process of operation, buildings and structures change their purpose, undergo reconstruction and renovation, they increase the requirements for reliability and comfort, they are subject to physical wear and tear and damage. Under these conditions, the need to strengthen building structures is becoming increasingly important. A special place is given to the strengthening and restoration of buildings and structures in seismic areas of construction (Zhussupbekov et al., 2020, Tulebekova et al., 2022), in areas of natural disasters, and after accidents and terrorist attacks.

Most of the load-bearing structures of buildings and structures of our time are made of concrete and reinforced concrete, so the problems of developing methods for strengthening reinforced concrete structures are becoming increasingly relevant. Traditional methods (SNIP 1991) of reinforcing reinforced concrete structures are very laborious, require overburden, welded and concrete work, and require considerable time to ensure the required strength. New, modern methods of reinforcing reinforced concrete structures are focused on the use of composite fiber-reinforced plastic materials for reinforcing, which are characterized by high strength, corrosion resistance and durability.

An alternative to traditional methods of reinforcing reinforced concrete structures is the use of fiber-reinforced plastics (FRP) - polymers reinforced with fiber fibers (Bakis et al., 2002). Unlike traditional reinforcement methods using steel reinforcement, these methods have high reinforcement efficiency, and do not require overburden and welding, or concreting of reinforced elements, they are distinguished by durability, corrosion resistance, low labor intensity, and economic

DOI: 10.1201/9781003299127-376

feasibility. The following types of fibers are commonly used as FRP reinforcement: carbon (C), aramid (A), glass (G), polyester.

2 METHODOLOGY

The study of the operation of compressed elements reinforced with fiber-reinforced plastics was carried out on samples of concrete cylinders and prisms of various sizes, differing in the number of layers of reinforcement meshes.

Some of the samples were tested under the axial action of quasi-static compression on hydraulic presses IPS-200 and ALPHA 3-3000S. To do this, the samples were subjected to axial compression with a gradual increase in the magnitude of the longitudinal compressive force at a rate of 0.3 MPa/s, up to the destruction of the sample. The magnitude of the stage of load increase did not exceed 5–8% of the breaking load.

During static loading, the longitudinal and transverse deformations of the prototypes were measured using strain gauges with a base of 50 mm, glued to all side faces of the samples, and an automatic strain gauge AID-4M (Figure 1).

Figure 1. General view of the test of reinforced samples for axial compression on hydraulic presses ALPHA 3-3000S and IPS-200.

3 RESULTS

JSC Kazakh Scientific Research Institute of Civil Engineering and Architecture conducted research on the behavior of reinforced concrete elements under static effects of compression, reinforced with layers of fiber-reinforced meshes FibArm Tape 530/300 (Modern Composite Materials of the Composite Holding Company), limiting transverse deformations of concrete and thereby creating triaxial compression of concrete.

Concrete cylinders of three sizes were used as prototypes: with a diameter of 100 mm and a height of 200 mm (K10), a diameter of 150 mm and a height of 300 mm (K15) and a diameter of 200 mm and a height of 400 mm (K20), made from one batch of concrete of natural hardening class B27.5. The prototypes were pasted over with layers of carbon unidirectional meshes (FibArm Tape 530/300), which had unidirectional fibers, a width of 300 mm, a surface density of 530 g/m2, a design thickness of 2.45 mm, with an elastic modulus Ef = 245 GPA and tensile strength fu =3.6 GPa.

Static tests of concrete cylinders were carried out under axial action of quasi-static compression on hydraulic presses IPS-200 and ALPHA 3-3000S. The samples were subjected to axial compression with a gradual increase in the magnitude of the longitudinal compressive force at a rate of 0.3 MPa/s, up to the destruction of the sample.

Tables 1-3 present data on the strength under static loading of concrete cylinders with a different number of reinforcement layers with FibArm Tape polymer meshes, the strength ratio of the series, ultimate longitudinal and transverse deformations.

Table 1. Static compressive strength of concrete cylinders with a section of 100x200 (dxh) mm.

Sample brand	Breaking force N. kN	Voltage, σ, MPa	Medium voltages σ_{mid}, MPa	Strength comparison	Deformations, 10^{-5}	
					ε_{long}	ε_{cross}
K10-0-1	235	25.4	26.6	1.0	190	50
K10-0-2	210	22.9			205	32
K10-0-3	290	31.4			200	32
K10-1-1	702	75.9	79.9	3.0	700	660
K10-1-2	701	75.1			415	310
K10-1-3	797	88.7			810	530
K10-2-1	900	98.3	86.2	3.24	410	215
K10-2-2	700	77.9			260	150
K10-2-3	740	82.3			415	160
K10-3-1	1246	138.6	147.1	5.53	302	375
K10-3-2	1500	163.8			500	435
K10-3-3	1250	139.0			450	335

Table 2. Static compressive strength of concrete cylinders with a section of 150x300 (dxh) mm.

Sample brand	Breaking force N. kN	Voltage, σ, MPa	Medium voltages σ_{mid}, MPa	Strength comparison	Deformations, 10^{-5}	
					ε_{long}	ε_{cross}
K15-0-1	510	28.1	25.1	1.0	128	66
K15-0-2	410	22,5			90	28
K15-0-3	444	24.8			133	22
K15-1-1	1200	69.8	65.9	2.62	310	330
K15-1-2	1000	58.1			320	194
K15-1-3	1249	69.9			300	270
K15-2-1	1450	83.4	94.1	3.75	650	440
K15-2-2	1797	100.4			350	380
K15-2-3	1899	108.9			310	300
K15-2-4	1500	83.8			340	356
K15-3-1	2299	130.1	131.1	5.22	300	436
K15-3-2	2400	135.2			320	425
K15-3-3	2200	127.9			340	330

Table 3. Static compressive strength of concrete cylinders with a section of 200x400 (dxh) mm.

Sample brand	Breaking force N. kN	Voltage, σ, MPa	Medium voltages σ_{mid}, MPa	Strength comparison	Deformations, 10^{-5}	
					ε_{long}	ε_{cross}
K20-0-1	853,5	26.9	26.4	1.0	110	22
K20-0-2	814,2	25.6			98	23
K20-0-3	833,9	26.6			105	20
K20-1-1	1570	39.2	37.2	1.41	320	275
K20-1-2	1619	40.5			400	270
K20-1-3	1275	31.9			312	170
K20-2-1	2500	59.5	64.3	2.43	480	430
K20-2-2	2900	69.0			435	434
K20-3-1*	3001	71.4	69.0	2.61	391	284
K20-3-2*	2700	64.2			363	302
K20-3-3*	3000	71.4			489	474

The destruction of samples reinforced with FibArm Tape carbon fiber meshes occurred gradually (Khayutin et al., 2002). At first, a crack appeared, caused by the rupture of individual fibers, with an increase in the load, the crack increased and a section of the mesh broke and the concrete was brittle crushed in this zone, accompanied by a sharp sound.

4 DISCUSSION

Analysis of the data shows that the strengthening of the samples by wrapping (pasting) with FibArm Tape 530/300 material led to a significant increase in the strength of the compressed samples, while the strengthening value almost linearly depended on the number of mesh layers. So, single-layer meshes caused an increase in strength by an average of 200% for samples (K10 series), by 162% for samples (K15 series), by 41% for samples (K20 series), two-layer meshes led to an increase in strength by 224% for samples (K10 series), by 275% for samples (K15 series), by 143% for samples (K20 series), and three-layer meshes - by 453% for samples (K10 series), by 422% for samples (K15 series), by 161% for samples (K20 series).

The presence of cages made of FibArm Tape meshes leads to a significant increase in the longitudinal deformations of concrete, which reach 4‰, as well as an increase in the transverse deformations of concrete, which can increase almost 10 times, reaching a value of 0.3-0.4%. In addition, there is an increase in the initial modulus of elasticity, which increased by 30%, 52% and 61% with one, two and three layers of reinforcement meshes.

In general, the effect of reinforcement with FibArm Tape meshes for 200x400 (bxh) mm samples is much less than for 100x200 mm and 150x300 (bxh) mm samples.

5 CONCLUSION

The destruction of concrete samples reinforced with carbon fibers of the FibArm Tape series occurs gradually under axial compression. First, a crack appears, caused by the rupture of individual fibers. With an increase in the load, the crack increases and then there is a brittle crushing of the concrete in the area of the mesh rupture, accompanied by a sharp sound. The more layers of reinforcement, the earlier the process of breaking the fibers of the grids begins.

Strengthening concrete samples by wrapping (pasting) FRP under axial compression led to a significant increase in the strength of the elements, while with an increase in the cross-sectional dimensions of the sample and the number of layers of reinforcement grids, the efficiency of using FRP decreases. So, for samples with dimensions of 100×200 (b×h) mm and 150×300 (b×h) mm, single-layer meshes caused an increase in strength on average by 200% and 162%, respectively, two-layer meshes led to an increase in strength by 224% and 275%. % and three-layer mesh increased strength by 443% and 422%. At the same time, for larger specimens (200×400 (b×h) mm), the corresponding increase in strength was much smaller.

The presence of meshes leads to a significant increase in the longitudinal deformations of concrete, however, with an increase in the number of layers of meshes, the intensity of strain growth decreases and, with three layers of meshes, the deformations of concrete differ little from the deformations of specimens with two layers of meshes. The ultimate compressibility of concrete is about 0.3%. The presence of meshes also causes an increase in transverse deformations of concrete. They increase from 30-40×10-5 to 300-400×10-5 relative units, i.e. in magnitude approach the limiting value of longitudinal deformations.

Increasing the cross-sectional dimensions of the compressed members reduces the effect of increasing the strength of the compressed members. An increase in the cross sections of compressed specimens from 100 × 200 (b×h) mm and 150 × 300 (b×h) mm to 200 × 400 (b×h) mm led to a decrease in relative strength by almost a factor of two.

REFERENCES

1. Zhussupbekov A., Tulebekova A., Jumabayev A., Zhumadilov I, 2020. Assessment of soils deformability under vertical load. International Journal of Geomate, 18 (70). pp. 221–228.
2. Tulebekova A.S., Jumabayev A.A., Aldungarova A., Zhankina A. 2022. The use of geosynthetics for strengthening the soil base: a laboratory experiment to develop practical skills of postgraduate students. World Transactions on Engineering and Technology Education, 20 (4), pp. 286–291.
3. SNiP 2. 03.01-84* 1991. Concrete and reinforced concrete structures. State Construction of the USSR, 1991

4. Bakis C.E., Bank L.C., Brown V.L., Cosenza E., Davalos J.F., Lesko J.J., Machida A., Rizkalla S.H., Triantifillou T.C. 2002. Fiber-Reinforced Polymer Composites for Construction-State-of-the-Art Review. Journal of Composites in Construction, 2002, V.6, No 2, pp. 73–87.
5. Khayutin Yu.G., Chernyavsky V.L., Axelrod E.Z. 2002. The use of carbon fiber to strengthen building structures//Concrete and reinforced concrete. - No. 6. - 2002. - p. 17-20; No. 1. - 2003. - p. 25–29.

Smart Geotechnics for Smart Societies – Zhussupbekov, Sarsembayeva & Kaliakin (Eds)
© 2023 The Author(s), ISBN 978-1-003-29912-7
Open Access: www.taylorfrancis.com, CC BY-NC-ND 4.0 license

Slope slip surface prediction using machine learning algorithms

Jeehoon Ma & Tae Sup Yun
Yonsei University, Seodaemun-gu, Seoul, Republic of Korea

ABSTRACT: In this study, the slip surface of the slope was predicted using several machine learning algorithms multilayer perceptron (MLP), XGBoost, and support vector machine (SVM). The slope used for the study is in the form of a simple finite slope, and the soil constituting the slope is sandy soil containing fine content. In performing the slope stability analysis, groundwater conditions were considered, and the influence of matric suction in unsaturated soils was also considered. The results of slope stability analysis using the limit equilibrium method were derived by applying the results of analysis on groundwater conditions using FEM. Using the Morgenstern-Price method, which can consider both force and moment equilibrium, a total of 42,000 data were produced and used for model training. In order to quantify the performance of the model in predicting the slip surface, the factor of safety of the slip surface obtained using the limit equilibrium method and the machine learning algorithm was compared.

1 INTRODUCTION

Slopes are widely distributed structures, including artificial and natural slopes. Since slope failure often occurs on a large scale, and cases of slope failure and its damage are also reported continuously, slope stability analysis has been a very important geotechnical design problem (Singh 2008; Wang 2013; Bünz 2005; Oh 2008; Song 2006). Therefore, the slope stability analysis started with the traditional method of slice, and then the strength reduction method through the finite element analysis (Dawson 1999; Matsui 1992; Kim 2004), numerical analysis considering rainfall infiltration (Cai 1998; Cai 2004; Duong 2019; Wei 2019; Cho 2019; Park & Ahn 2019), and slope stability analysis in earthquakes considering groundwater (Lu 2015) has also been developed. In the case of the conventional method using the finite element method, there is a disadvantage in that it is difficult to configure the domain conditions and mesh for analysis.

For this reason, recent attempts to apply a simple form of artificial intelligence to slope stability analysis and use it as an auxiliary means are steadily being made (Ma & Yun 2022). However, many attempts are limited to simply predicting the factor of safety of the slope, so information on the slip surface cannot be obtained, or the distribution of the groundwater level within the slope and the matric suction of the unsaturated soil are not considered by simply considering the groundwater level as the pore water pressure ratio.

Although it is known that the destruction of the slope is mainly affected by groundwater (Brönnimann 2011; Zhang 2012), the groundwater on the slope increases the shear strength through matric suction in the unsaturated soil. (Ng & Shi 1998). In fact, most of the ground in the natural state exists as unsaturated soil rather than completely dry or saturated, so the results of the stability analysis of the slope considering the mechanical characteristics of the unsaturated soil are highly applicable to the field.

Therefore, in this study, we trained to perform slope stability analysis using simple artificial intelligences multilayer perceptron (MLP), XGBoost, and support vector machine (SVM). A model for predicting the failure arc was trained, and to compare the results of the three models, a methodology to evaluate the performance of the model was presented. In order to

DOI: 10.1201/9781003299127-377

consider the matric suction of unsaturated soil due to the presence of groundwater in the modeling of the slope used for training, data were generated by analyzing both the dry slope and the slope in which the groundwater level was considered.

2 MATERIALS AND METHODS

2.1 *Finite element method*

In order to consider the groundwater condition of the slope, the seepage analysis using the commonly used finite element method was applied. In numerical analysis, the structure is actually divided into elements of finite size, and the structure is analyzed as an aggregate of these elements. In this study, the SEEP/W program of Geostudio 2012 software was used to analyze the steady-state seepage of groundwater. The soil composing the slope to be analyzed was assumed to be sandy soil containing fine particles widely distributed in the natural world by referring to the results of ground surveys in various regions of Korea (Park 2017; Jung 2014). The volumetric water content function was calculated and used in the program so that the matric suction has a maximum of 1,000 kPa and a minimum of 0.01 kPa in the range of the volumetric water content that the soil constituting the slope can have. Based on this volumetric water content function, the hydraulic conductivity function representing the relationship between the head (h) and the hydraulic conductivity ($K_r(h)$) was estimated by the van Ganuchten method (van Genuchten 1980). The form of the hydraulic conductivity function is expressed by Equation (1), where, *m, n,* and α are the van Genuchten model parameters.

$$K_r(h) = \frac{1 - (\alpha h)^{n-2}\left[1 + (\alpha h)^n\right]^{-m}}{\left[1 + (\alpha h)^n\right]^{2m}},\ (m = 1 - 1/n,\ 0 < m < 1) \tag{1}$$

2.2 *Limit equilibrium method*

To obtain the factor of safety of the slope, a slope stability analysis was performed using the limit equilibrium method. Using the SLOPE/W program of Geostudio 2012 software, the factor of safety and slip surface of the slope were obtained through the Morgenstern-Price method, which can consider both the force and moment equilibrium between the slices (Morgenstern & Price 1965). In this process, the groundwater conditions were analyzed using the analysis results of SEEP/W, considering the effect of matric suction on the effective stress of unsaturated soil. In addition, for comparison with the case where there is no groundwater, analysis was performed on the dry slope under the same conditions.

2.3 *Constitution of slope domain*

The geometry of slope used in slope stability analysis is a condition of 6 slope height (H: 10, 12, 14, 16, 18, 20 m) and 5 slope inclination conditions (β: 1:1.0, 1:1.2, 1:1.5, 1:1.8, 1:2.0) were combined. The normalized value of the groundwater level in each slope geometry to the slope height (H_w*: -1.0, 0, 0.2, 0.4, 0.6, 0.8, 1.0) were set for 7 groundwater level conditions. To set the soil conditions for the analysis section, the soil constant of sandy soil mixed with fine particles was given. In general, the porosity of sandy soil with fine particles is distributed between 0.145 and 0.495, and accordingly, the specific gravity (G_s) of the solid is considered as 2.65 and the dry unit weight (γ_d) range is set to 13.0 ~ 22.35 kN/m^3, friction angle (ϕ) and cohesion (c) were set to be uniformly distributed within the indicated range (Swiss Standard SN 670 010b, 1999) (Table 1).

2.4 *Training machine learning models*

In this paper, MLP, XGBoost, and SVM were used to predict the failure arc of the slope by using the slope geometry, soil properties, and groundwater level conditions as input

Table 1. Range and distribution of input parameters used in seepage and slope stability analysis.

	H (m)	β (-)	γ_d (kN/m^3)	c (kN/m^2)	ϕ (°)	H_w* (-)
Min	10	1	13.00	2	30	-1
Max	20	2	22.35	22	40	1
Mean	15	1.5	17.64	12.03	34.96	0.286
St. dev.	3.42	0.369	2.67	5.75	2.87	0.613

parameters. In order to predict the failure arc of the slope through regression model, it was expressed as the length of the radius of failure arc (R) and the abscissa on both sides of the point where the failure arc and the slope meet (x_{in}, x_{out}) (Figure 1).

In the case of the MLP model, it consists of one input layer with 6 nodes, four hidden layers with 800 nodes, and one output layer with 3 nodes. The training schedule of the MLP model consisted of learning rates of 0.00001 and 500,000 epochs, and the SGD optimizer was used as the optimizer. In the case of XGBoost, the learning rate was set to 0.05 and the maximum depth was set to 500. In the case of SVM, the order of the polynomial kernel function was set to 3 and the tolerance of the stopping criterion was set to 0.001.

Figure 2 Shows the training data configuration of the MLP model. A total of 42,000 data consisting of 6,000 slope domains and 7 groundwater conditions for each domain were randomly separated at a ratio of 6:1:3 for training, validation, and testing. In the training of the 3 models used in this study, a separate dataset was applied at the same rate. The validation data is to confirm that the model overfits the training data during the training process.

Figure 3 Describes the overall sequence of this study. In [Step A], seepage analysis was performed by inputting the slope height (H), slope inclination (β), groundwater level (H_w), and dry unit weight (γ_d) of the slope shape factors into SEEP/W. In [Step B], the SEEP/W analysis result obtained in [Step A] and the previously set friction angle (ϕ) and adhesive force (c) conditions were used as initial conditions, and these were entered into the SLOPE/W program. After that, slope stability analysis was performed. Failure arc parameters (Arc_{Geo}: x_{in}, x_{out}, R) calculated through slope stability analysis were obtained. In [Step C], three models (MLP, XGBoost,

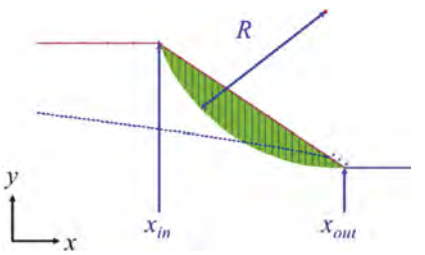

Figure 1. Expression of the slip surface with abscissa of both ends (x_{in}, x_{out}) and radius of the failure arc (R).

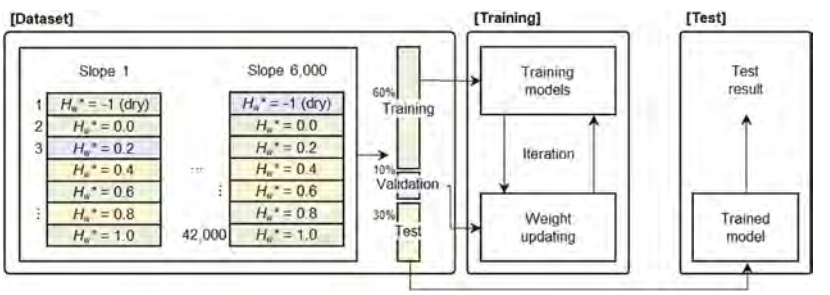

Figure 2. Data set configuration and MLP model training, validation, and test process.

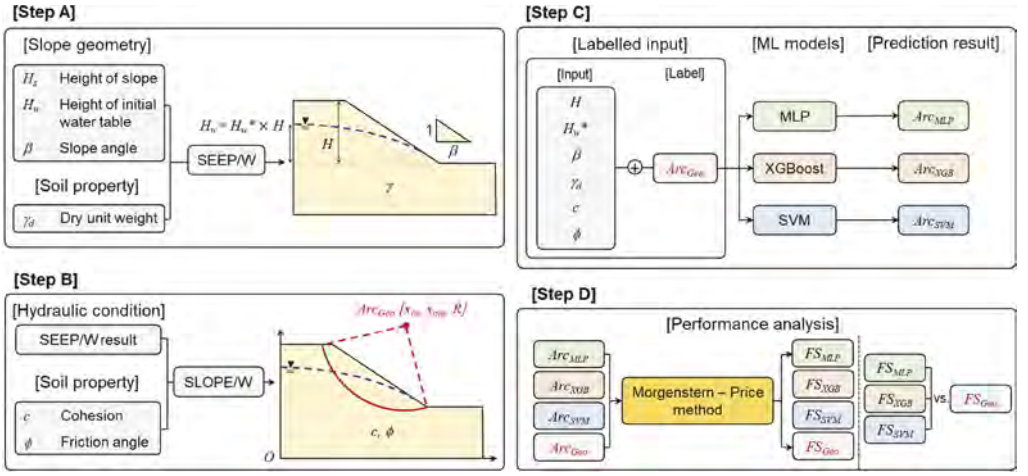

Figure 3. Overall sequence of data generation, MLP model training, and analysis.

SVM) were trained to predict the failure arc of the slope, respectively. Training is performed so that the failure arc predicted by the models for the input H, β, γ_d, c, ϕ, H_w* are approximated to the labels Arc_{Geo} (x_{in}, x_{out}, R) prepared in [Step B], respectively. Finally, in [Step D], the performances of the models were quantitatively evaluated by comparing the results of the slope stability analysis using SLOPE/W with the prediction results of the trained models. The FS_{Geo} was calculated by the Morgenstern-Price method from the failure arc Arc_{Geo} (x_{in}, x_{out}, R) obtained from the SLOPE/W analysis and FS_{MLP}, FS_{XGB}, and FS_{SVM} were calculated by failure arc Arc_{MLP}, Arc_{XGB}, and Arc_{SVM} (x_{in}, x_{out}, R) predicted by the three models, respectively. The performance of the model was evaluated by comparing FS_{MLP}, FS_{XGB}, FS_{SVM} and FS_{Geo}.

3 RESULT

To evaluate the performance of the model, the factor of safety of the failure arc predicted by the MLP, XGBoost, and SVM model was obtained using the method of slice and the values were compared. When performing the limit equilibrium analysis using the program the effective stress increase due to the matric suction in the unsaturated soil is considered, it is difficult to obtain the factor of safety by simply using the intercept method in the case of the groundwater exist. Therefore, using the Morgenstern-Price method for the analysis results of the dry slope among the test data, the factor of safety calculated by the failure arc predicted by models were compared with the factor of safety calculated by SLOPE/W in the same method.

Figure 4 Is the result of comparing the factor of safety (FS_{MLP}, FS_{XGB}, and FS_{SVM}) of the failure arc predicted by the trained model with the factor of safety (FS_{Geo}) of the failure arc calculated by SLOPE/W. Among the test data, 1,829 data on dry slopes were compared, and both safety factors were calculated from the failure arc. The coefficients of determination (R^2) were 0.999, 0.999, and 0.994 at MLP, XGBoost, SVM model respectively. Overall, the prediction performance was high, and the MLP and XGBoost models showed similar performance, but the performance of the SVM was slightly lower.

4 CONCLUSION

In this study, slope stability analysis was performed using simple machine learning algorithms such as MLP, XGBoost, and SVM. In training the model, a total of 42,000 data were generated using SEEP/W and SLOPE/W from various slope inclinations, distribution of groundwater, and soil properties. The slope used for data generation is a simple slope composed of

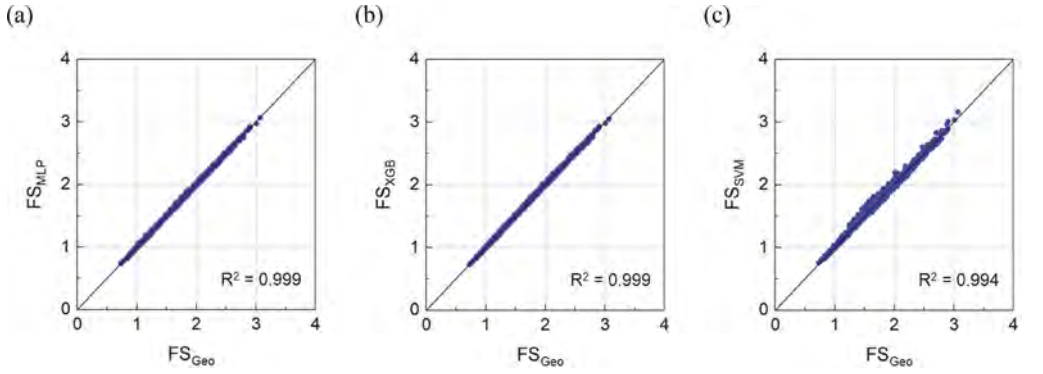

Figure 4. Failure arc prediction performance of (a) MLP, (b) XGBoost, and (c) SVM model through comparison of the factor of safety calculated from Arc_{Geo} and Arc_{MLP}, Arc_{XGB}, and Arc_{SVM}.

one layer, and the ground condition of the slope is assumed to be sandy soil containing fine particles, and the corresponding physical properties are given.

(1) In order to evaluate the performance of predicting the failure arc, the Morgenstern-Price method is used to calculate and compare the safety factor of the failure arc predicted by the machine learning model (FS_{MLP}, FS_{XGB}, and FS_{SVM}) and the safety factor of the failure arc derived from SLOPE/W (FS_{Geo}). Through this evaluation method, the performance of the model predicting the failure arc was good, and the coefficients of determination were 0.999, 0.999, and 0.994 in MLP, XGBoost, and SVM model respectively. This training method has a wider scope of application in that it can even obtain information on the failure arc than the result of training by simply targeting the factor of safety.
(2) The performance of the SVM model was the worst. It is considered that this is because multiple regression is not possible due to the characteristics of SVM regression analysis, so the predictions for x_{in}, x_{out}, and R are individually evaluated. Training took more than 2 hours for MLP model, tens of seconds for SVM, and several seconds for XGBoost. The MLP model has the advantage of having excellent performance and being able to easily change the structure of the model, but it has the disadvantage of taking a long time to train. XGBoost, which takes less time and has excellent performance, is concerned to be suitable for extending and applying to other later problems of slope stability.
(3) As a result of analyzing the results on the factor of safety and failure pattern, most of the fractures occurred were toe failure, and there were a few cases of base failure, and almost no case of slope failure. For the general application of the training model on the failure pattern, it is concerned that training based on the analysis results in a slope made of several layers of soil or in more diverse soil conditions is necessary.

In this study, slope stability analysis was trained using a machine learning algorithm. Due to the nature of machine learning, which requires a lot of learning data, a large number of data is required, and it is unreasonable to compose data with the physical properties of actual slopes through literature research and satisfy the number. Therefore, all the data used in the study are virtual slope data composed by arbitrarily inputting physical properties suitable for the conditions of the soil constituting the slope. In a follow-up study, these limitations can be compensated for by verifying the actual slope data using the test set of the machine learning algorithm.

ACKNOWLEDGEMENT

This work was supported by the Land and Housing Institute (LHI) grant funded by the Korea Land and Housing Corporation, and the National Research Foundation of Korea (NRF) Grant funded by the Korea government (MSIT) (Nos. 2020R1A2C1014815, NRF-2021R1A5A1032433).

REFERENCES

Brönnimann, C.S. 2011. Effect of groundwater on landslide triggering (No. THESIS): EPFL.

Bünz, S., Mienert, J., Bryn, P., & Berg, K. 2005. Fluid flow impact on slope failure from 3D seismic data: a case study in the Storegga Slide. *Basin Research*: 17(1), 109–122.

Cai, F., Ugai, K., Wakai, A., & Li, Q. 1998. Effects of horizontal drains on slope stability under rainfall by three-dimensional finite element analysis. *Computers and Geotechnics*: 23(4), 255–275.

Cai, F., & Ugai, K. 2004. Numerical analysis of rainfall effects on slope stability. *International Journal of Geomechanics*: 4(2), 69–78.

Cho, S.E. 2019. Probabilistic Failure-time Analysis of Soil Slope under Rainfall Infiltration by Numerical Analysis. *Journal of the Korean Geotechnical Society*: 35(12), 45–58.

Dawson, E.M., Roth, W.H., & Drescher, A. 1999. Slope stability analysis by strength reduction. *Geotechnique*: 49(6), 835–840.

Duong, T.T., Do, D.M., & Yasuhara, K. 2019. Assessing the effects of rainfall intensity and hydraulic conductivity on riverbank stability. *Water*: 11(4), 741.

Jung, Y.H., Kim, T., & Cho, W. 2014. Gmax of reclaimed ground on the western coast of Korea using various field and laboratory measurements. *Marine Georesources & Geotechnology*: 32(4), 351–367.

Kim, Y.M. 2004. Slope Stability Analysis Considering Seepage Conditions by FEM Using Strength Reduction Technique. *Journal of the Korean geotehnical society*: (20), 97–102.

Lu, L., Wang, Z.J., Song, M.L., & Arai, K. 2015. Stability analysis of slopes with ground water during earthquakes. *Engineering Geology*: 193, 288–296.

Ma, J., & Yun, T.S. 2022. Prediction of Slope Failure Arc Using Multilayer Perceptron. *Journal of the Korean Geotechnical Society*: 38(8), 39–52.

Matsui, T., & San, K.C. 1992. Finite element slope stability analysis by shear strength reduction technique. *Soils and foundations*: 32(1), 59–70.

Morgenstern, N.U., & Price, V.E. 1965. The analysis of the stability of general slip surfaces. *Geotechnique*: 15(1), 79–93.

Ng, C.W.W., & Shi, Q. 1998. A numerical investigation of the stability of unsaturated soil slopes subjected to transient seepage. *Computers and geotechnics*: 22(1), 1–28.

Oh, S., Mun, J.H., Kim, T.K., & Kim, Y.K. 2008. A case study of rainfall-induced slope failures on the effect of unsaturated soil characteristics. *KSCE Journal of Civil and Environmental Engineering Research*: 28(3C), 167–178.

Park, C.S., & Ahn, S.J. 2019. An Analytical Study on the Slope Safety Factor Considering Various Conditions. *Journal of the Korean Geotechnical Society*: 35(5), 31–41.

Park, K.H., Jung, Y.H., & Chung, C.K. 2017. Evolution of stiffness anisotropy during creep of engineered silty sand in South Korea. *KSCE Journal of Civil Engineering*: 21(6), 2168–2176.

Singh, T.N., Gulati, A., Dontha, L., & Bhardwaj, V. 2008. Evaluating cut slope failure by numerical analysis—a case study. *Natural hazards*: 47(2), 263–279.

Song, Y.S. 2006. A Case Study on the Reinforcement of Stabilizing Piles against Slope Failures in a Cut Slope. *The Journal of Engineering Geology*: 16(2), 189–199.

Swiss Standard SN 670 010b, Characteristic Coefficients of soils, Association of Swiss Road and Traffic Engineers

van Genuchten, M.T. 1980. A closed-form equation for predicting the hydraulic conductivity of unsaturated soils. *Soil science society of America journal*: 44(5), 892–898.

Wang, L., Hwang, J.H., Luo, Z., Juang, C.H., & Xiao, J. 2013. Probabilistic back analysis of slope failure–a case study in Taiwan. *Computers and Geotechnics*: 51, 12–23.

Wei, Z.L., Lü, Q., Sun, H.Y., & Shang, Y.Q. 2019. Estimating the rainfall threshold of a deep-seated landslide by integrating models for predicting the groundwater level and stability analysis of the slope. *Engineering Geology*: 253, 14–26.

Zhang, M., Dong, Y., & Sun, P. 2012. Impact of reservoir impoundment-caused groundwater level changes on regional slope stability: a case study in the Loess Plateau of Western China. *Environmental earth sciences*: 66(6), 1715–1725.

Smart Geotechnics for Smart Societies – Zhussupbekov, Sarsembayeva & Kaliakin (Eds)
© 2023 The Author(s), ISBN 978-1-003-29912-7
Open Access: www.taylorfrancis.com, CC BY-NC-ND 4.0 license

Study of the feasibility of compacting low-water soils in semi-arid and arid zones: Application to road infrastructures

O. Aiche, A. Medjnoun & R. Bahar
University of Sciences and Technology Houari Boumediene, Faculty of Civil Engineering, LEEGO, Algiers, Algeria

M. Khiatine
University of Yahia Farès Médéa, Faculty of Technology Department of Civil Engineering, Médéa, Algeria

ABSTRACT: In the arid and semi-arid zones, where about eighty of the area of Algeria is covered, the difficulties linked to the supply of water for watering these workings make it necessary to examine the solution of compaction with low water content. The proposed communication will be an experimental contribution on low water compaction of fill soils, in order to optimize the reuse of excavated soils and to minimize the amount of water needed to achieve optimum compaction. Its main objective is to better appreciate the role of water in compaction when the water content varies from the dry state to water content close to the Proctor optimum water content. In a first phase, three Algerian soils with different granular classes are investigated in laboratory to analyse the impact of soil nature and compaction energy on the soil's California Bearing Ratio value. The results show that a soil compacted at 56 blows at a water content of 2% had a higher bearing capacity than a soil compacted at the same speed under optimal water content. It concluded that compaction with low water content is possible on soils with well-graded grain size and high compaction energies. In the second phase, two section tests are performed on a local material enabled us to release that it is possible to compact materials with low water content if the aim is to obtain adequate properties for the construction embankments and subgrades. The compactness obtained varies between 86 and 93%.This experimental study on site lead to the conclusion that dry compaction does not make it possible to obtain the expected compactness for the upper layer of the earthworks and the foundation layer. Compaction to fifty percent of the optimum water content of the upper layer of the earthworks is achievable.

1 INTRODUCTION

Arid regions represent about eighty percent of the surface area of Algeria. The development of these regions, which contain oil and gas resources, requires the construction of a large number of road, rail and airport infrastructures. However, the construction of pavements in deserted areas is handicapped by the unavailability of water necessary for the compaction of materials. The scarcity of water makes compaction in these regions costly and difficult. Since the water points are very far away (about 100 to 300 km), the compaction operations (drilling wells, pumping water, spreading and mixing) require a sometimes constraining worksite organization, in particular to limit the rapid evaporation of water. Experience has shown that the cost of the water needed to compact materials can represent up to a third of the cost price of road infrastructure. Under these conditions, it is clear that the compaction of materials in their hydric state can represent a definite socio-economic potential for arid regions. Interest in the compaction of soils with low water content began with the Trans-Saharan project in the seventies. Due to socio-economic conditions the project was stopped. In recent years, as part of the implementation of the principles of sustainable development, efforts to promote local materials and the preservation of rare resources have revived the interest of researchers in redefining more efficient compaction methods that

DOI: 10.1201/9781003299127-378

allow achieve water savings. During the construction of earthworks, the compaction of soils and materials is traditionally carried out at an optimum water content defined in the laboratory by the Proctor test which should correspond to the best densification of the material. The choice of this water content, which saves compaction energy, is amply justified in temperate countries in which soils and materials are naturally in states of humidity close to optimal values. However, in sunny countries like Algeria, which suffer from severe water deficits, especially in arid areas, the soils have an almost dry water state and require considerable quantities of water to reach the optimum water content. This operation is all the more complicated as the hot and drying environment of these areas prevents the maintenance of this humidity until compaction is carried out due to evaporation during transport and the watering of the soil.

Many scientists have investigated compaction energy's impact on the engineering characteristics of both unstabilized and stabilized soils. Attom (1997) studied the effect of increasing compaction energy on shear strength, swelling pressure and permeability of compacted cohesive soils. Bahar et al. (2004) and Kenai et al. (2006) investigated the performance of three compaction methods (dynamic, static and vibro-static) on unstabilized and cement stabilized soil characteristics. Çokça et al. (2004) researched the influence of compaction with low water content on the shear strength of clay soils. Drew and White (2005) analysed the impact of compaction energy level on optimal moisture content, maximum dry and unconfined compression strength of soils. Ampadu (2007) and Vinod et al. (2015) investigated the effect of water content and compaction energy on the California Bearing Ratio (CBR) of local soils. Yusoff et al. (2017) analysed the effect of different compaction energy on geotechnical properties of Kaolin and Laterite soil. Loualbia et al. (2022) assessed the impact of the compaction water content on the mechanical behaviour of a lime-stone tuff under static loading. Sadek et al. (2022) investigated the impact of the combination (cement/energy) on soil behavior for pavement construction in arid areas. All authors agree that a higher compaction effort increases the dry density and, consequently, the stiffness and strength of the material.

The paper contributes to research efforts aimed at developing a practical method for compacting materials with low water content in arid areas. The compaction of soils with low water content and the impact of the nature of the soil and the energy of compaction on the value of the California Bearing Ratio (CBR) of the soil are analyzed in the laboratory. Three Algerian soils are studied.

2 MATERIALS AND TESTS

Three Algerian soils are studied. The first soil was extracted from the Chlef region, located in the north center of Algeria, characterized by a semi-arid climate. The second soil is from Oued-Souf and the third is from Bousaada, these two last soils are dune sand, located in the north of the Algerian desert. The two sand soils are very used in civil engineering buildings. The soils are subjected physical, standard Proctor and CBR tests following geotechnical French standards (NF P94-AFNOR). The previous materials are subsequently subjected to more intense compaction to increase their maximum density using the proctor normal/modified test. After having fixed the water content at 2% (climate arid condition), CBR tests are carried out on several samples in order to vary the energy of compaction. The compaction energies are calculated according to the height of fall, the mass and the number of blows. For this work, the increasing energies (E) correspond to 10 (E1), 25 (E2), 56 (E3) and 80 (E4) blows.

3 RESULTS AND DISCUSSION

3.1 *Soil characterisation and Proctor tests*

Figure 1 presents the grain size distribution curves of the three soils. Table 1 presents the results of the specific gravity, sieve analysis test, methylene blue test (VBS), Atterberg limits.

Figure 2 presents the conventional compaction curves obtained on the three soils for two different compaction energy level, normal (E1) and modified compaction test (E2). The maximum dry unit weight and the optimum moisture content are presented in Table 2.

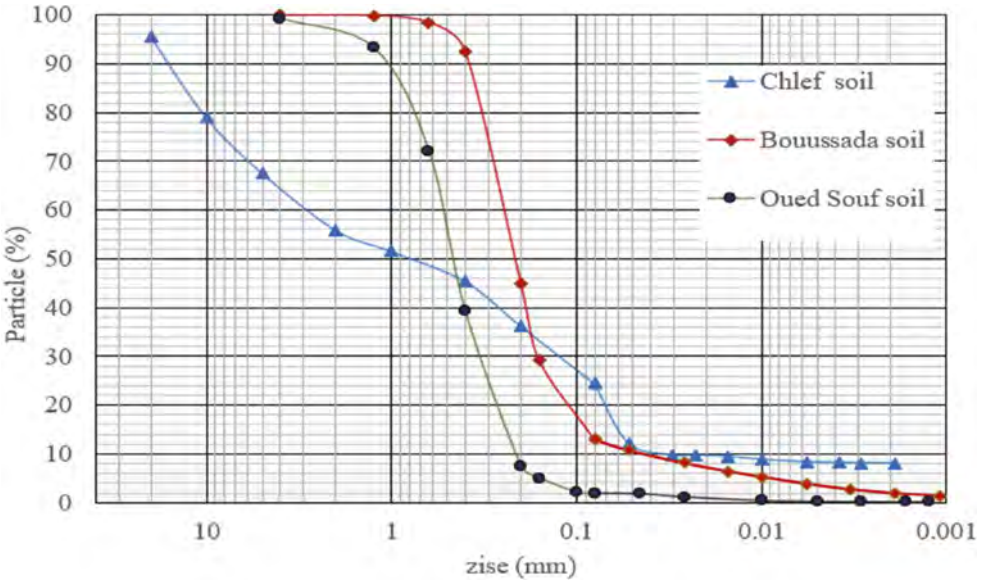

Figure 1. Particle size distribution curves.

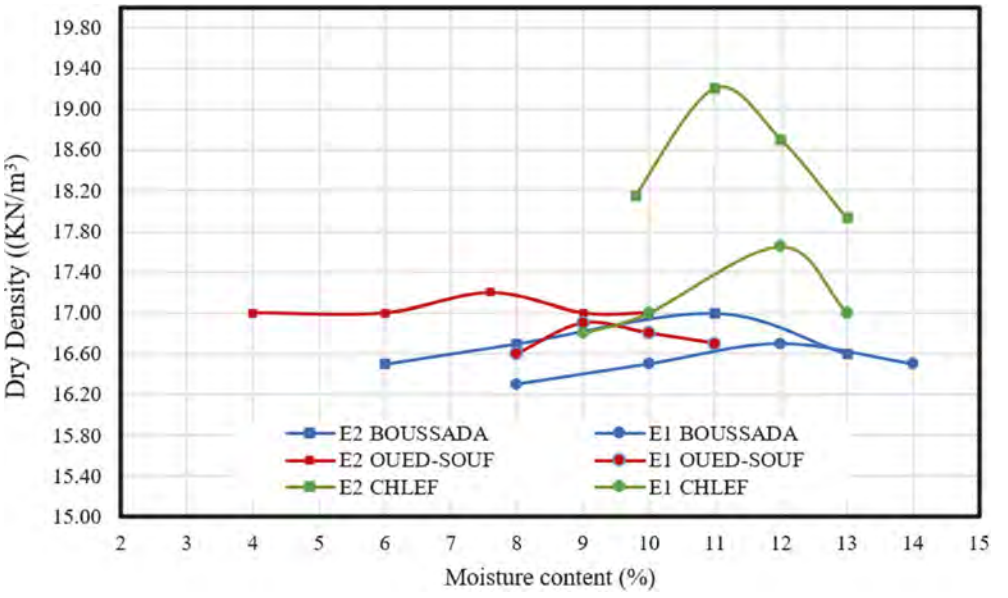

Figure 2. Normal and modified compaction test curves.

From the results of Table 1 and Figure 1, the used soils are classified as below: the Chlef soil is a well-graded silty sandy gravel soil with a spread particle size and low plasticity. By referring to the French Roadworks Guide (GTR) and LCPC classification, Chlef soil is classified silty sandy gravel (B5) and silty sand (SL) respectively. The Oued-Souf sand is poorly graded soil (94% of sand), tight particle size and it is not sensitive to water, classified (SM). The Bousaada

Table 1. Soil properties.

Parameter	Chlef Soil	Oued-Souf sand	Bousaada sand
Specific gravity	2.70	2.6	2.6
Gravel (%)	45	3	0
Sand (%)	31	94	87
Silt (%)	16	2.5	10
Clay (%)	8	0.5	3
Uniformity coefficient (Cu)	100	2.5	6.25
Coefficient of gradation (Cc)	1	0.9	3.24
VBS	0.4	-	0.1
Liquid Limit LL (%)	29.1	-	-
Plasticity Index PI(%)	5.21	-	-

Table 2. Normal and modified compaction results.

Soils	Chlef	Oued-Souf	Bousaada
Normal Proctor			
MDD (kN/m^3)	17.7	17.0	16.77
w_{OPT} (%)	11.9	9	12
Modified Proctor			
MDD (kN/m^3)	19.2	17.3	17
w_{OPT} (%)	11.2	7.5	11
CBR	50	13	13

soil is poorly graded silty sand (87 % of sand) tight particle size and not sensitive to water. It is classified (SL). By referring to the French GTR, The two sands are classified (B1).

Figure 2 indicates clearly the effect of soil nature on the compaction results. The high maximum dry density (MDD) obtained for the silty sandy gravel of Chlef soil are 17.7 kN/m^3 and 19.2 kN/m^3 for normal proctor energy (E1) and modified proctor energy (E2) respectively. Their optimal moisture content are 12.2 % and 11.3% respectively. The lower dry density is obtained for Bousaada soil (γ_d=16.7 KN/m^3) for normal and modified Proctor energy. The compaction curve of Oued-Souf soil is almost flat and the change in optimal moisture content doesn't affect the MDD because this soil is not sensitive to water. The increase of level compaction energy doesn't affect the state of soil compaction because of the grains size of the soil; the soil has a uniform grain size (0.1 ≤ sand diameter (mm) ≤1). The Boussaada soil almost behaves in the same way as the Oued-Souf. Despite the presence of silt in addition to sand, increasing compaction energy had no effect on maximum dry density. Contrary to the Boussaada and Oued-Souf soils the compaction curve of Chlef soil is well graded, and the effect of the compaction energy is well observed. This soil is silty sandy gravel with a presence of 8% of clay. Its composition gives the tested soil the lowest water sensitivity (low plastic) and also the ability to improve compactness when the compaction energy is increased. According to the CBR values obtained from the tested soil compacted with modified Proctor standard (Table 2), Chlef soil has a good bearing (CBR= 50). The other two sand soils have the same value of CBR around 13; this value is more than 10 indicating a good bearing.

3.2 *Compaction at low moisture content*

Since the compaction energy has no effect on the soils of Oued-souf and Boussaada, the study of the evolution of the maximum dry density as a function of the increase in the compaction energy level will be carried out only on the Chlef soil. The results of modified Proctor tests performed at different level of energy compaction and at the low moisture content (w=2%) are shown in Figure 3. The MDD increases with the increasing of number of blows; for ten (10) 84 blows the MDD is equal to 16.1 KN/m^3 and 18.6 kN/m^3 respectively. In the dry part of the compaction curve, the moisture contents are very low to saturate the soil. Therefore, the

reduction in void ratio volume can always be achieved by increasing the compaction energy. Figure 3 shows that the increase in maximum dry density as a function of compaction energy is non-linear and tends towards a limit value beyond 55 blows. Figures 4 and 5 show the results of CBR tests carried out on samples compacted at a water content of 2% with different compaction energies. The CBR value increases with the compaction energy and confirm the behavior observed with the modified Proctor tests. These results were observed by many researchers (Attom, 1997; Vinod et al., 2015; Masoud et al., 2015; Yusoff et al., 2017; Basack et al., 2021). They reported an increase in maximum density and a decrease in optimal moisture content when the compaction energy increased. It was also found that the higher CBR values were recorded with increase in compaction energy.

Soils compacted with 56 and 84 blows require high penetration energy to reach a depth of 2.5 mm, the compaction energy required to reach this depth is 497 and 746 kN.m/m^3 respectively (Table 3). For samples compacted with lower values, 10 to 25, the same penetration (2.5 mm) does not require great energy, it is 89 and 182 kN.m/m3 respectively. This result is consistent with that found by Ampadu (2007).

Soils compacted with low water content (2%) have a very high bearing capacity and a low density (MDD=18.6 kN/m^3) compared to that obtained at the optimum water content (MDD=19.2 kN/m^3). The CBR value obtained at optimal water content (w_{opt}= 11.2%) is 50 and that obtained for water content of 2 % under the same number of blows (56 blows) is about 91 (Figure 5). In the dry part of the compaction curve, the soil does not resist by its compactness but probably by the mobilization of friction forces between the grains which are not sufficiently lubricated, which justifies the increase in the CBR values.

Table 3. Energy of compaction value.

Energy of compaction (kN.m/m^3)	89	182	497	746
Number of blows	10	25	56	84
Weight of hammer (kN)	45.35	45.35	45.35	45.35
Number of layer	5	5	5	5
Height of drop (m)	0.457	0.457	0.457	0.457

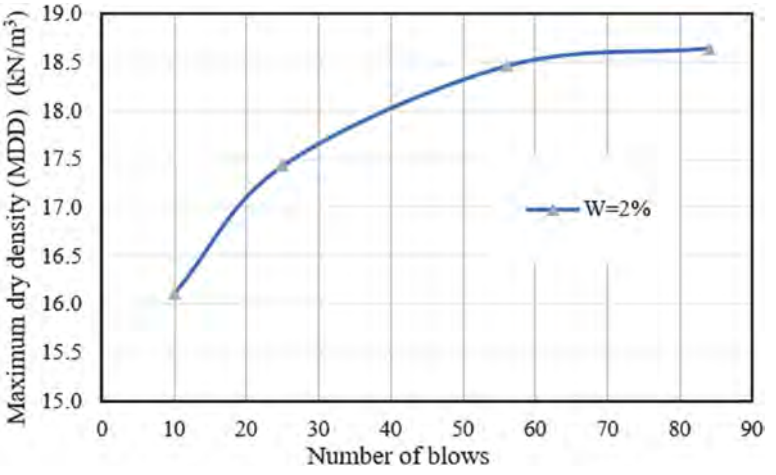

Figure 3. Evolution of the maximum dry density (MDD) with compaction energy.

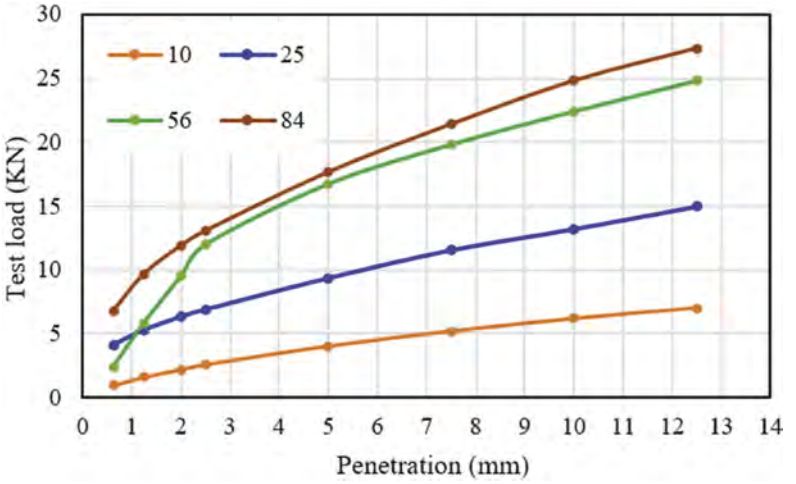

Figure 4. Standard force-penetration relationships assessment with compaction energy effect.

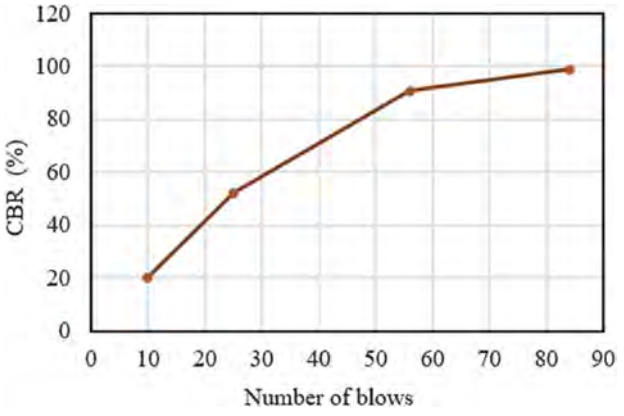

Figure 5. CBR index assessment under different compaction energy.

3.3 *Application*

As part of the construction of a road in the Algerian Sahara, a local material is subjected to laboratory tests and experiments on site. Two sections 250 m long, 10 m wide and 0.20 m thick, compacted dry or with low water content are carried out. The compaction of the first board is mixed, and the second is compacted with a vibrating compactor. The results of laboratory tests carried out on the material extracted from a site located approximately 0.50 km from the test sections are given in Table 4. The first section is compacted with a water content of 50% of the optimum Proctor (OPM), or 3%. The layer are leveled and moistened by a water tank after scarification of the surface of the platform, and compacted with 13 tons vibrating roller, and the finish is carried out with 27 tons heavy roller-tyred roller. The number of passes at any point is 6 passes for the vibrating compactor and 8 passes for the pneumatic compactor. the compactness ($\gamma_{d(lab)}/\gamma_{d(site)}$) reached at different points for maximum compaction energy of more than 2 t.m3/km varies between 93 and 97%. The dry compaction is assigned exclusively to the with 13 tons vibrating roller. The compactness measurements are performed every 3 passes on each measured point. the compactness obtained varies between 86 and 93%. The analysis of all the results obtained lead to the conclusion that dry compaction does not make it possible to obtain the expected compactness for the upper layer of the earthworks and the foundation

layer. Compaction to 50% of the optimal water content is achievable for the upper layer of earthworks and is possible for the foundation layer provided that the water content is well homogenized by effective mixing of the material and that compactnesses are accepted in the vicinity by 96% for the foundation layer which represents sufficient resistance (bearing capacity). These results are in agreement with the results of the researches carried out by Cisse (1982) and Ellis (1980). The two studies deals with the dry compaction of embankments and roadbases and subbases. Cisse (1982) conducted trials in Niger, two materials underwent laboratory testing and field experiments: a dune sand and ungraded gravel desert material. Ellis (1980) carried out trials in Sudan on black silty clay for use on a road embankment and subgrade. Tests in Morocco (Kabbaj 1979) using natural well graded gravels as fill material were reported to be successful but problems were experienced with dry sands.

Table 4. Soil properties.

Properties	Values	Compactness (%)
% passing 2 mm	32	-
% passing 0,08 mm	10	-
Plasticity Index PI	6,3	-
Maximum Dry Densiy (kN/m^3)	22,3	-
w_{OPM} (%)	6,0	-
Immediate CBR (55 blows)	108	100
Immediate CBR (25 blows)	66	96
Immediate CBR (10 blows)	31	92
Compression strength (MPa)	2,02	-

4 CONCLUSION

An experimental study was carried out in the laboratory on three types of soil with different granular classes to evaluate the feasibility of compaction at low water content and to identify the factors that influence compaction. It concluded that compaction with low water content is possible on soils with well-graded grain size and high compaction energies. Increasing the compaction energy offers the possibility of reducing the volume of voids and it will have no effect once saturation is reached. Soils with approximately uniform grain size are more difficult to compact. The results showed us that a soil compacted at 56 blows at a water content of 2% had a higher bearing capacity than a soil compacted at the same speed under optimal water content. The section tests carried out on a local material enabled us to release that it is possible to compact materials with low water content if the aim is to obtain adequate properties for the construction embankments. For the foundations, it is necessary to moisten the surface and couple two compactors, a vibrating roller and a heavy roller-tyred roller. The experimental study on site lead to the conclusion that dry compaction does not make it possible to obtain the expected compactness for the upper layer of the earthworks and the foundation layer. Compaction to 50% of the optimum water content of the upper layer of the earthworks is achievable. It is also possible for the foundation layer provided that the water content is well homogenized by effective mixing of the material, and that compactnesses around 96% are accepted. With these conditions, the foundation layer has sufficient bearing capacity. We propose to extend this research to other materials and other types of equipment.

ACKNOWLEDGEMENT

The authors greatly appreciate the assistance of the Department of Public Works, Public Works Ministry, in particular for some data available for scientific purposes.

REFERENCES

Attom, M.F. 1997. *The Effect of Compactive Energy Level on Some Soil Properties*. Applied Clay Science, 12, 61–72.

Ampadu, S.I.K. 2007. *A Laboratory Investigation into the Effect of Water Content on the CBR of a Subgrade soil*. In: Schanz, T. (eds) Experimental Unsaturated Soil Mechanics. Springer Proceedings in Physics, vol 112. Springer, Berlin, Heidelberg.

Bahar, R., Benazzoug, M. & Kenai, S. 2004. *Performance of Compacted Cement Stabilized Soil*. Cement and Concrete Composites, 25, 633–641

Basack, S., Goswami, G., Khabbaz, H., Karakouzian, M., Baruah, P., & Kalita, N. 2021. *A Comparative Study on Soil Stabilization Relevant to Transport Infrastructure using Bagasse Ash and Stone Dust and Cost Effectiveness*. Civil Engineering Journal, 7(11), 1947–1963.

Cisse, A. 1982. *Compactage à sec des remblais et assises de chaussées*. Rapport de Recherche des Laboratoires des Ponts et Chaussées, 112, 1–98.

Cokca, E., Erol, O. & Armangil, F. 2004. *Effects of compaction moisture content on the shear strength of an unsaturated clay*. Geotechnical and Geological Engineering, 22(2), 285–297.

Drew, I.R. 2005. *Influence of compaction energy on soil engineering properties*. Master Thesis. Iowa State University, Iowa USA 18909.

Ellis, C.I. 1980. *Soil compaction at low moisture content - field trials in Sudan*. 7th Regional Conference for Africa on Soil Mechanics and Foundation Engineering, Accra, Ghana, 331–340.

Kabbaj, M. 1979. *National report -Morocco - Question V Low cost and lowtraffic roads*. PIARC XVIth World Road Congress. Vienna.

Kenai, S., Bahar, R. & Benazzoug, M. 2006. *Experimental analysis of the effect of some compaction methods on mechanical properties and durability of cement stabilized soil*. Journal of Materials Science, 41(21), 6956–6964.

Loualbia, H., Duc, M., Demdoum, A. & Feia S. 2022. *Investigation of the water content effect on the mechanical behavior of a compacted limestone tuff*. Arabian Journal of Geosciences, 15(646): 1–9

Masoud, T., Alsharie, H. and Qasaimeh, A. 2015. *Energy Analysis for the Compaction of Jerash Cohesive Soil*. Computational Water, Energy, and Environmental Engineering, 4, 1–4.

Sadek, Y., Rikioui, T., Abdoun, T. & Dadi, A. 2022. *Influence of Compaction Energy on Cement Stabilized Soil for Road Construction*. Civil Engineering Journal, 8(3), 580–594

Yusoff, S.A.N.M., Bakar, I., Wijeyesekera, D., Zainorabidin, A., Azmi, M. & H. Ramli, H. 2017. *The effects of different compaction energy on geotechnical properties of kaolin and laterite*. AIP Conference Proceedings, AIP Publishing LLC

Vinod, P.P., Sridhran, A. & Soumya R.J. 2015. *Effect of compaction energy on CBR and compaction behaviour*. Proceedings of the Institution of Civil Engineers - Ground Improvement 168(2), 116–121.

Smart Geotechnics for Smart Societies – Zhussupbekov, Sarsembayeva & Kaliakin (Eds)
© 2023 The Author(s), ISBN 978-1-003-29912-7
Open Access: www.taylorfrancis.com, CC BY-NC-ND 4.0 license

Strength-ductility behavior of earthen block reinforced with vetiver shoot

M.S. Islam, S. Paul & S.M. Iqbal
Department of Civil Engineering, Bangladesh University of Engineering and Technology (BUET), Dhaka, Bangladesh

ABSTRACT: Buildings made of earthen blocks have gained popularity in recent years from the viewpoint of sustainability. But due to their brittleness and low tensile strength, earthen buildings are very prone to earthquakes. Recent studies have focused on improving the strength-ductility behavior of earthen blocks by incorporating natural and synthetic fibers. Vetiver grass is utilized to safeguard embankment slopes and riverbanks worldwide. But its effectiveness in reinforcing earthen blocks is missing in the literature. Work herein focuses on evaluating the strength and ductility characteristics of vetiver shoot reinforced earthen blocks through unconfined compression tests. Vetiver shoots in 1%, 2%, and 3% proportions are mixed with clay soil for the preparation of earthen blocks. Improvements of up to 38% in compressive strength and 202% in ductility index are obtained in reinforced samples compared to unreinforced samples. Microstructural investigation shows that clay particles sticking to the fiber surface contributed to such improvements.

1 INTRODUCTION

Many civilizations have employed earthen building materials for ages. About 30% of the world's population still resides in earthen houses, with that number rising to 50% in developing nations (Minke, 2013). But due to stability problems brought on by insufficient strength, ductility, and susceptibility to earthquakes, new building materials like concrete, steel, fired clay bricks, etc. have emerged (Islam & Iwashita, 2006; Paul et al., 2022). These new building materials are not considered sustainable, particularly for developing nations, due to their high cost and energy-intensive production processes (Sujatha & Selsia Devi, 2018). Stabilization of earthen structures can ensure sustainable earthen construction by improving the strength and ductility properties of raw earth. In earlier research, different natural and synthetic fibers were used to reinforce earthen blocks to increase their strength and ductility. Fibers like sugarcane bagasse, banana, jute, coconut, steel, plastic, polypropylene, etc. have been widely used in previous studies for reinforcing earthen blocks (Danso et al., 2015; Eko et al., 2012; Islam & Iwashita, 2010; Jiang et al., 2010; Kumar & Barbato, 2022; Prasad et al., 2012; Sujatha & Selsia Devi, 2018). Here, fibers can make the soil more resilient and ductile by preventing the cracks at the shear band from spreading and enlarging. Vetiver grass (*Chrysopogon zizanioides*) has a lengthy and bushy root system (Badhon, 2021). Its shoots have a height range of 0.5 to 1.5 meters and are heavily branched on stems that cluster together in big clumps. The usefulness of vetiver roots in increasing soil shear strength and lowering slope erosion potential has been widely studied in recent research (Aziz & Islam, 2022; Badhon, 2021). However, the effectiveness of vetiver shoots as earth reinforcement has not been studied previously. The current study focuses on investigating the suitability of vetiver shoots in enhancing the strength-ductility characteristics of earthen blocks. Unconfined compressive strength tests were conducted on un-reinforced and vetiver shoot-reinforced specimens to discern the strength and

DOI: 10.1201/9781003299127-379

ductility properties of earthen blocks. Moreover, microstructural analysis has been conducted to analyze the effectiveness of vetiver shoots in controlling the development and propagation of cracks and to understand the reinforcement mechanism.

2 MATERIALS: SOIL AND VETIVER SHOOT

The soil sample for the present study was collected from Gazipur, Dhaka. The grain size distribution of the soil was obtained by conducting a hydrometer analysis (as the soil particles were smaller than 0.075 mm) as per ASTM D 7928. For further characterization of soil, specific gravity tests, Atterberg limit tests, and standard proctor compaction tests were conducted as per ASTM D 4318, ASTM D 698, and ASTM D 854 respectively. The physical properties of soil are shown in Table 1. The soil is classified as lean clay (CL) according to the Unified Soil Classification System. Dry vetiver shoots were cut at 50 mm lengths, and the width of the shoots varied from 4-5 mm.

Table 1. Physical characteristics of the soil considered in this study.

Soil Property	Value
Specific gravity, G_S	2.72
Silt (%)	72
Clay (%)	28
Liquid Limit, LL (%)	30
Plastic Limit, PL (%)	18
Plasticity Index, PI (%)	12
Optimum moisture content (%)	11.3
Maximum dry density (kNm^{-3})	17.2
Soil classification (USCS)	CL

3 METHODS

3.1 *Production of earthen blocks*

Earthen blocks were manufactured by using the selected vetiver shoot content of 0%, 1%, 2%, and 3% by weight of dry soil. The size of the earthen blocks molded for this research is 241 mm × 114 mm × 70 mm. Firstly, the soil sample and fibers were mixed homogenously under dry conditions. Then the proper amount of water which is the optimum moisture content determined from the standard proctor test previously was added to the soil-fiber mixture. The mixture was kneaded again under wet conditions to prepare a homogenous mix. The mixture was then poured into the mold and compacted in three layers using the standard proctor hammer. Here, the compaction energy was kept equal to the standard proctor compaction energy (593.7 kJ/m^3). After preparing samples, the mold was kept undisturbed for 24 hours, and thereafter, the sample was taken out of the mold. The samples were dried in the shade for 7, 14 and 28 days.

3.2 *Experimental investigation*

Unconfined compression tests were performed on the prepared reinforced and unreinforced samples to assess the compressive strength and ductility behavior of earthen blocks as per ASTM D 5102.The samples were tested after 7, 14, and 28 days of drying. The loading device was set so that the upper platen just touched the prepared specimen after it had been centered on the bottom platen and loaded into it. Axial force and deformation readings were taken. The loading was continued up to the failure point. An axial deformation rate of 1%

per minute was maintained. For conducting scanning electron microscopy (SEM) tests on vetiver shoot-reinforced earthen blocks, some small portions measuring 2 cubic inches were cut from each sample using a sharp wire, which were mounted on a stud and placed in the chamber of a machine with SEM capabilities.

4 RESULTS AND DISCUSSIONS

Figure 1 Shows the axial stress-strain behavior of unreinforced clay and clay reinforced with various contents of vetiver shoots (0%, 1%, 2%, and 3% by weight of dry soil), over periods of 7 days, 14 days, and 28 days. The results reveal that there is a significant improvement in ductility (up to 202%) of earthen blocks when vetiver shoots are incorporated. Thus, vetiver shoot reinforcement improves the post-peak behavior by distributing the loads across the cracks. Moreover, the presence of shoots in the soil matrix prevents the propagation and widening of cracks. The SEM micrograph of vetiver shoot stabilized earthen blocks is depicted in Figure 2(a), which reveals that soil particles are strongly adhered to the surface of the vetiver shoot. This makes the soil matrix more homogenous and interconnected, which leads to better strength-ductility behavior of vetiver shoot reinforced earthen blocks. On the other hand, Figure 2(b) reveals the heterogeneity of the unreinforced specimen having a higher number of voids and fissures.

Table 2. Summary of unconfined compressive strength (UCS) test results.

Sample ID	Shoot Content (%)	Density (kNm^{-3})	UCS (MPa)	% Increase in UCS	Failure Strain (%)	Elastic Strain (%)	Ductility Index (D)	% Increase in Ductility
V0D7	0	17.2	0.866	×	3.81	0.912	4.177	×
V1D7	1	16.7	0.836	-3.5	6.35	1.145	5.546	32.8
V2D7	2	17.1	0.941	8.7	8.89	1.974	4.503	7.8
V3D7	3	16.6	1.100	26.9	20.32	3.134	6.484	55.2
V0D14	0	14.0	0.890	×	4.45	1.195	3.718	×
V1D14	1	13.4	0.995	11.9	10.16	1.953	5.202	39.9
V2D14	2	12.9	1.232	38.5	12.07	2.414	4.997	34.4
V3D14	3	12.6	1.068	20.1	19.05	2.075	9.181	146.9
V0D28	0	13.4	1.238	×	8.26	3.065	2.693	×
V1D28	1	13.1	1.437	16.1	8.26	2.437	3.387	25.8
V2D28	2	14.4	1.337	7.9	11.43	2.699	4.234	57.2
V3D28	3	12.6	0.965	-22.1	21.59	2.655	8.133	201.9

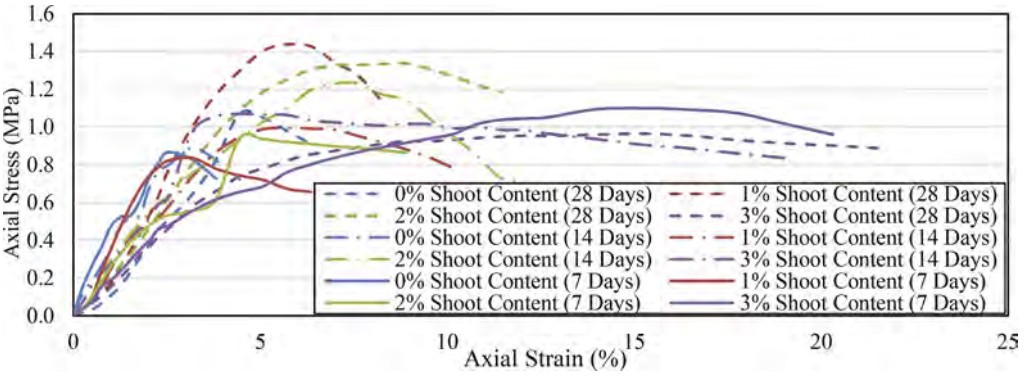

Figure 1. Axial stress-strain behavior of unreinforced and fiber reinforced earthen blocks.

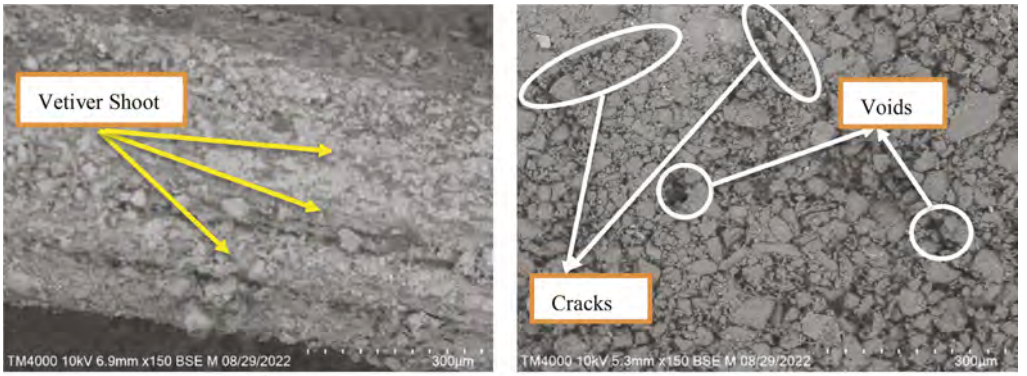

Figure 2. SEM micrographs of (a) fiber reinforced and (b) unreinforced earthen blocks.

Table 2 lists the unconfined compressive strength (q_u) and ductility index (D) of unreinforced and reinforced soil blocks. The specimens are designated as VxDy, where x denotes the vetiver shoot contents and y denotes the sample age in days. Here, the ratio of total elastoplastic response strain (failure strain) to strain at the elastic limit (strain at $q_u/2$) is known as the ductility index (Islam & Iwashita, 2010). The unconfined compressive strength of reinforced earthen blocks is increased with respect to the unreinforced ones, except for the V1D7 and V3D28 specimens. The increase in unconfined compressive strength is due to the creation of an isotropic matrix between the soil and the vetiver shoot, which prevents the movement of the soil particles. Considering both strength and ductility perspectives, a vetiver shoot content of 2% is recommended.

5 CONCLUSIONS

Unfired earthen blocks have significant economic and environmental advantages over fired clay bricks. Therefore, it is necessary to improve the mechanical properties of earthen blocks to overcome the limitations of raw earth. Based on the findings of this study, vetiver shoot reinforcement can effectively improve the strength-ductility behavior of earthen blocks. At 2% vetiver shoot content, significant increase in ductility was found with no reduction in compressive strength. Therefore, the optimum shoot content is recommended to be 2%.

ACKNOWLEDGEMENT

The authors acknowledge the infrastructural and financial support received from Bangladesh University of Engineering and Technology (BUET), Dhaka-1000, Bangladesh for carrying out the research work.

REFERENCES

Aziz, S., & Islam, M. S. (2022). Mechanical Effect of Vetiver Grass Root for Stabilization of Natural and Terraced Hill Slope. *Geotechnical and Geological Engineering*, *40*(6), 3267–3286.

Badhon, F. F. (2021). Contribution of Vetiver Root on the Improvement of Slope Stability. *Indian Geotechnical Journal*, *51*(4), 829–840.

Danso, H., Martinson, D. B., Ali, M., & Williams, J. (2015). Effect of fibre aspect ratio on mechanical properties of soil building blocks. *Construction and Building Materials*, *83*, 314–319.

Eko, R. M., Offa, E. D., Ngatcha, T. Y., & Minsili, L. S. (2012). Potential of salvaged steel fibers for reinforcement of unfired earth blocks. *Construction and Building Materials*, *35*, 340–346.

Islam, M. S., & Iwashita, K. (2010). Earthquake Resistance of Adobe Reinforced by Low Cost Traditional Materials. *Journal of Natural Disaster Science*, *32*(1), 1–21.
Islam, M. S., & Iwashita, K. (2006). Seismic Response of Fiber-Reinforced and Stabilized Adobe Structures. *Proceedings of the Getty Seismic Adobe Project 2006 Colloquium*, *11*(3), 13.
Jiang, H., Cai, Y., & Liu, J. (2010). Engineering Properties of Soils Reinforced by Short Discrete Polypropylene Fiber. *Journal of Materials in Civil Engineering*, *22*(12), 1315–1322.
Kumar, N., & Barbato, M. (2022). Effects of sugarcane bagasse fibers on the properties of compressed and stabilized earth blocks. *Construction and Building Materials*, *315*(December 2021), 125552.
Minke, G. (2013). Building with Earth: Design and Technology of a Sustainable Architecture. In *Building with Earth*.
Paul, S., Islam, M. S., & Elahi, T. E. (2022). Comparative effectiveness of fibers in enhancing engineering properties of Earth as a building Material: A review. *Construction and Building Materials*, *332*, 127366.
Prasad, C. K. S., Nambiar, E. K. K., & Abraham, B. M. (2012). Plastic Fibre Reinforced Soil Blocks as a Sustainable Building Material. *International Journal of Advancements in Research & Technology*, *1*(5), 3–6.
Sharma, V., Vinayak, H. K., & Marwaha, B. M. (2015). Enhancing compressive strength of soil using natural fibers. *Construction and Building Materials*, *93*, 943–949.
Sujatha, E. R., & Selsia Devi, S. (2018). Reinforced soil blocks: Viable option for low cost building units. *Construction and Building Materials*, *189*, 1124–1133.

Smart Geotechnics for Smart Societies – Zhussupbekov, Sarsembayeva & Kaliakin (Eds)
© 2023 The Author(s), ISBN 978-1-003-29912-7
Open Access: www.taylorfrancis.com, CC BY-NC-ND 4.0 license

Deformation analysis of the reclaimed submarine foundations with dredged materials in Osaka Bay by utilizing the geoinformatic database

M. Mimura, Y. Iseki & M. Imiya
Kyoto University, Kyoto, Japan

ABSTRACT: A series of elasto-viscoplastic finite element analyses is conducted to assess the long-term deformation of this reclaimed island with dredged materials at Yumeshima reclaimed island in Osaka Bay, Japan. The geoinformatic database has been utilized to develop the initial subsurface ground model together with the setting the geotechnical parameters for the individual Holocene and Pleistocene soils. The generation and dissipation process of excess pore water pressure as well as the related compression performance of the natural and reclaimed dredged materials are discussed. The calculated performance shows the remarkable long-term settlement even after the completion of reclamation, which can affect the superstructures on the reclaimed island.

1 INTRODUCTION

Osaka Bay is a heart of Kansai economy along which the urban business cities such as Osaka and Kobe are located. Urbanization has been progressed in Japan associated with the development of coastal area as well as offshore-reclaimed lands. Yumeshima Island is one of the largest reclaimed islands in Osaka Port. The world exposition will be held in 2025 followed by the development of the integrated resort facilities on this reclaimed island. A large and long-term settlement is generally expected to occur in such offshore reclaimed island on the marine soft ground. Because the Yumeshima Island is reclaimed with dredged clayey materials from the seabed, the superstructures constructed on this island will suffer from soft soil induced serious geotechnical problems such as a large and long-term settlement. Compared to general offshore islands, which are reclaimed with low-compressibility high-quality soils, Yumeshima has the serious problem that tremendous compression is expected to occur in the reclaimed soil itself.

In the present paper, a series of elasto-viscoplastic finite element analyses is conducted to assess the long-term deformation of this reclaimed island with dredged materials at Yumeshima reclaimed island in Osaka Bay, Japan. The Kansai Geoinformatics Database has been utilized to develop the subsoil ground model as well as setting the necessary material parameters that are required by the elasto-viscoplastic constitutive model. The construction sequence is modeled based on the Yumeshima construction reports. Stress and deformation of the reclaimed dredged layers together with the natural foundation ground in Osaka Bay is discussed on the basis of the calculated performance. Attention is focused on the long-term settlement of the deep Pleistocene clay layers that affects the stability of the superstructures constructed on the Yumeshima Reclaimed Island.

2 SUBSURFACE MODELING BASED ON THE GEOINFORMATIC DATABASE

Geometrical modeling of the foundation ground is indispensable to conduct the deformation analyses due to reclamation. Soil boring logs are the essential information of the subsoil structures. Usually, prior to construction work, a boring survey is carried out in the target area, and the profile of the soil classification from the ground surface to the required depth is shown in

DOI: 10.1201/9781003299127-380

the form of a soil boring log describing what kind of soil is deposited with depth. It is true the individual soil boring log has the advantage of showing the correct information of the subsurface structure of the site, but that they have the problem that the individual boring information does not give the spread of strata. Then it is effective to utilize a database that integrates soil boring information to know what kind of sedimentary structure the target area has, and the information such as lateral continuity and change in thickness of the individual layers. In the present paper, the Kansai Geoinformatics Database of Kansai Geoinformatics Network (KG-NET) is applied to construct the subsoil model of Yumeshima Reclaimed Island.

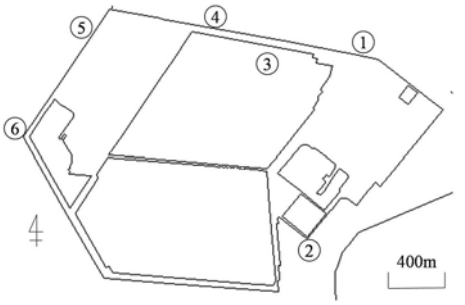

Figure 1. Location of the boreholes before construction at Yumeshima Reclaimed Island.

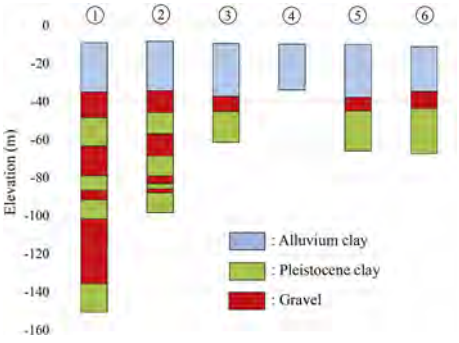

Figure 2. Stratigraphy of the 6 boreholes.

About 130 boring data for Yumeshima have been registered in the Kansai Geoinformatics database. Attention should however be paid to the fact that boring data before reclamation is necessary to develop the initial ground model without the effect of compression of clay layers due to reclamation. Screening under these conditions limits the number of borings that can be used to six as shown in Figure 1. The almost all borings were located near the border of Yumeshima Reclaimed Island because the soil investigation from the sea was conducted for the design of seawall of the reclaimed island. The selected 6 soil boring logs are shown in Figure 2. As shown in Figure 2, the survey depths of the six boreholes are different, but the overall stratigraphy is the same. The Holocene clay layer is underlain by the alternating Pleistocene gravel and clay layers. The representative soil profile model was developed based on those six boring data and the lower Pleistocene deposits were modeled by introducing the existing information from the adjacent reclamation islands in Osaka Bay. Then, Figure 3 shows the setup initial foundation ground model

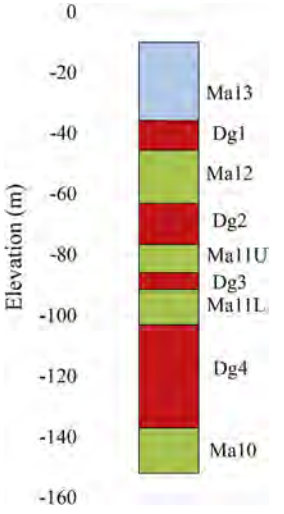

Figure 3. Representative sub soil ground model for the Yumeshima Reclaimed Island.

that is regarded as the representative one for Yumeshima Reclaimed Island. Based on the soil classification and clay content of the individual boring data, the boundary between the clay layer and the gravel layer is determined. As for the thickness of each layer, the average value of them was adopted. For example, the thickness of the Holocene clay, Ma13 was determined by averaging the data from six borehole data. The thickness of the gravel layer, Dg2 was determined with boring 1 and 2 that contain Dg2 in them. The deep Pleistocene layers were determined based on the information of boring 1. As shown in Figure 3, the elevation of the seabed is -10m and the bottom of the representative model is the Pleistocene clay called Ma10 because of the limitation of the deep deposits information.

3 ELAST-VISCOPLASTIC FINITE ELEMENT ANALYSIS

3.1 *Constitutive model and formulation*

The elasto-viscoplastic constitutive model used in this paper was proposed by Sekiguchi (1977). Sekiguchi (1982) et al. modified the model to a plane-strain version. The viscoplastic flow rule for the model is generally expressed as follows:

$$\dot{\varepsilon}_{ij}^{p} = \Lambda \frac{\partial F}{\partial \sigma'_{ij}} \tag{1}$$

in which F is the viscoplastic potential and Λ is the proportional constant. Viscoplastic potential F is defined as follows:

$$F = \alpha \cdot \ln\left[1 + \frac{\dot{v}_0 \cdot t}{\alpha} \exp\left(\frac{f}{\alpha}\right)\right] = v^{p} \tag{2}$$

in which α is a secondary compression index, $\dot{v}_0$ is the reference volumetric strain rate, f is the function in terms of the effective stress and v^{p} is the viscoplastic volumetric strain. The concrete form of the model is shown in the reference (Mimura and Sekiguchi, 1986). The resulting constitutive relations are implemented into the finite element analysis procedure through the following incremental form:

$$\{\Delta\sigma'\} = [C_{\mathrm{ep}}]\{\Delta\varepsilon\} - \{\Delta\sigma^{\mathrm{R}}\} \tag{3}$$

Where $\{\Delta\sigma'\}$ and $\{\Delta\varepsilon\}$ are the associated sets of the effective stress increments and the strain increments respectively, and $[C_{\mathrm{ep}}]$ stands for the elasto-viscoplastic coefficient matrix. The term $\{\sigma^{\mathrm{R}}\}$ represents a set of 'relaxation stress', which increases with time when the strain is held constant. The pore water flow is assumed to obey isotropic Darcy's law. In relation to this, it is further assumed that the coefficient of permeability, k, depends on the void ratio, e, in the following form:

$$k = k_0 \cdot \exp\left(\frac{e - e_0}{\lambda_k}\right) \tag{4}$$

in which k_0 is the initial value of k at e=e_0 and λ_{k} is a material constant governing the rate of change in permeability subjected to a change in the void ratio. Note that each quadrilateral element consists of four constant strain triangles and the nodal displacement increments and the element pore water pressure is taken as the primary unknowns of the problem. The finite element equations governing those unknowns are established on the basis of Biot's formulation (Christian, 1968, Akai and Tamura, 1976) and are solved numerically by using the semi-band method of Gaussian elimination.

3.2 *Determination of material parameters*

The soil parameters required for the input to the finite element code are determined rationally based on the prescribed procedure (Mimura et al., 1990). The necessary parameters for clays

are "compression index; λ", "swelling index; κ", "critical stress ratio; M", "initial void ratio; e_0", "elastic shear modulus; G", "secondary compression index: α" and "reference volumetric strain rate; $\dot{v}_0$". A due attention should be paid to the fact that the Pleistocene clays in Osaka Bay exhibit lightly overconsolidated performance although they are normally consolidated without any mechanical overconsolidated history (Mimura et al., 2003). In the present paper, the concept of quasi-overcosolidated clay reported by Mimura and Jang (2004) is applied to the Pleistocene clays in Osaka Bay. The compression less than p_c is assumed to be elasto-viscoplastic with the compression index, λ_{QOC} that is equivalent to κ. Time dependent behavior is also assumed to occur in the compression less than p_c with the secondary compression index α_{QOC}. See reference (Mimura and Jan, 2004) for more detail of the modeling concept of the quasi-overconsolidated Pleistocene clays in Osaka Bay. The material parameters are shown in Table 1.

Table 1. Material parameters for Holocene and Pleistocene clays.

	C_c	C_s	M	e_0	α	$\dot{v}0$ (/day)	k_0 (m/day)
Dredged materials	0.84	0.08	1.3	2.83	4.75×10^{-3}	2.50×10^{-7}	6.81×10^{-5}
Ma13U	1.03~1.45	0.10~0.15	1.3	2.21~2.76	5.95×10^{-3} ~8.76×10^{-3}	2.17×10^{-7} ~3.06×10^{-7}	4.64×10^{-5} ~9.03×10^{-5}
Ma13L	0.41~0.89	0.04~0.09	1.3	1.21~1.63	4.02×10^{-3} ~7.32×10^{-3}	5.73×10^{-7} ~2.57×10^{-6}	8.16×10^{-5} ~3.09×10^{-4}
Ma12U	1.37~1.60	0.14~0.16	1.3	1.91~2.10	1.02×10^{-2} ~1.12×10^{-2}	2.66×10^{-6} ~4.02×10^{-6}	5.33×10^{-5} ~9.32×10^{-5}
Ma12L	0.79~1.20	0.08~0.12	1.3	1.21~1.68	7.80×10^{-3} ~9.74×10^{-3}	1.78×10^{-6} ~2.77×10^{-6}	3.35×10^{-5} ~4.86×10^{-5}
Ma11U	0.44~1.15	0.04~0.11	1.3	0.96~1.44	4.83×10^{-3} ~1.02×10^{-2}	6.35×10^{-6} ~9.62×10^{-6}	1.74×10^{-5} ~2.37×10^{-5}
Ma11L	1.13~1.40	0.11~0.14	1.3	1.51~1.76	9.76×10^{-3} ~1.10×10^{-2}	3.04×10^{-6} ~4.76×10^{-6}	8.90×10^{-6} ~1.35×10^{-5}
Ma10	1.25~1.76	0.13~0.18	1.3	1.64~2.12	1.03×10^{-2} ~1.22×10^{-2}	1.44×10^{-6} ~5.41×10^{-6}	1.14×10^{-5} ~5.61×10^{-5}

3.3 *Loading sequence*

Unplanned damping was carried out from the sea before the start of development from the sea, followed by the official construction of the Yumeshima Reclaimed Island that was started in 1985 with the construction of seawalls. The official construction was conducted by dumping the channel dredged soils from the Osaka Port (Osaka Port Authority, 2016, 2017). Then, filling was carried out with good quality gravelly soils for the surface ground of the Yumeshima Reclaimed Island. Based on the unit weight of the corresponding materials, the stress increment Δp in terms of the reclamation loading is modeled with the elapsed time as shown in Figure 4.

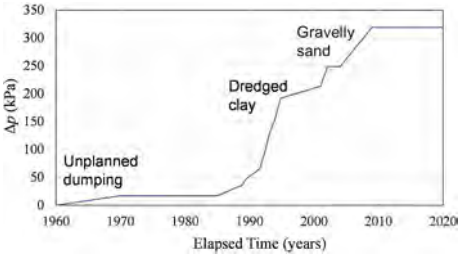

Figure 4. Loading stress history reflecting the reclamation work of Yumeshima.

4 RESUTS AND DISCUSSIONS

4.1 *Excess pore-water pressure generation and dissipation*

Reclamation stress loaded on the seabed causes the generation of excess pore water pressure particularly in the clay layers together with the dredged soil layer. The profile of excess pore water pressure with depth is shown in Figure 5. Here, Vertical drains are installed in the dredged soil layer and the alluvial clay layer sandwiching the sand mat. The macro-element method (Sekiguchi et al., 1986) is introduced to model the radial collection and drainage function in 1-D analysis. At the completion of reclamation in 2008, large amount of excess pore water pressure generated and remained in all dredged and natural clay layers. Because of the vertical drain effect, excess pore water pressure in the dredged soil and Ma13 layers, excess pore water pressure partly dissipated even during the loading period. At present in 2022, consolidation of these layers almost terminated whereas the excess pore water pressure still remains in the Pleistocene clay layers. It means that the long-term consolidation induced settlement will occur mainly in the Pleistocene clay layers in future. Almost all clay layers except Ma10, excess pore water pressure will dissipate in 2070. The relatively large amount of excess pore water pressure remains in Ma10 because Ma10 has a large thickness and high plasticity with low permeability. Vertical drains cannot be adopted for such deeply situated clay deposit. As is already pointed out, long-term settlement will occur not in the shallow Holocene and dredged soil layer but deep Pleistocene clay layers.

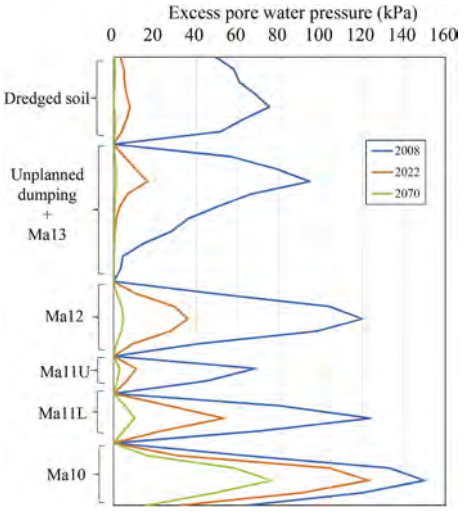

Figure 5. Calculated profile of excess pore water pressure with depth.

4.2 *Settlement*

Calculated compression with time for the individual clay layers is shown in Figure 6. The main reclamation was started in 1985. Drastic compression of the alluvial clay layer is attributed to the loading by the sand mat and drainage promotion effect of the vertical drain driven at the time. Compression of the reclaimed dredged soil is also tremendous because of its high water content and compressibility. Rapid progress in compression from 1989 to 2002 is attributed to the accumulation of dumped dredged soils with vertical drains. As for the Pleistocene clay layers, the progress in compression is milder compared to Ma13 and dredged soil layer and a larger settlement is found to occur in the upper Pleistocene clay layers. In 2022, the settlement of Ma13 and dredged soil layer is 6.5m and 5m respectively whereas .the one of Ma12 is about 1.85m. Long-term settlement is found to take place in all Pleistocene clay layers with time.

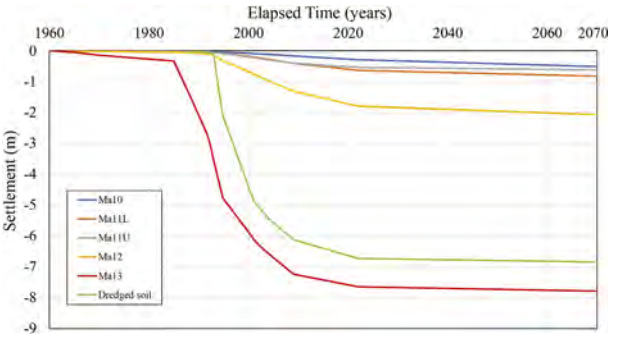

Figure 6. Time~settlement relations for the individual clay layers.

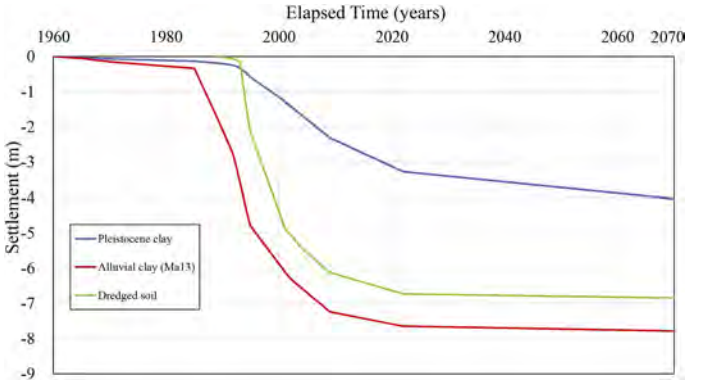

Figure 7. Contribution to the settlement for the dredged soil, alluvial and Pleistocene clay layers.

Contribution to the total settlement for the dredged soil, the alluvial clay (Ma13) and the Pleistocene clay layers is shown in Figure 7. Although the amount of settlement is occupied by the compression of alluvial clay and dredged soil, the long-term settlement such as the one after 2022 is found to occur mainly in the Pleistocene clays. This behavior is very consistent with the dissipation result of excess pore water pressure shown in Figure 5. The long-term compression of both Ma13 and dredged soil is regarded as a secondary consolidation without dissipation of excess pore water pressure and the amount of settlement of these layers remains limited. In contrast, the settlement of the Pleistocene clay layers is about 1m for the coming 50 years. A due consideration is necessary to the harmful effect on the stability of the pile foundations that will install to the bearing stratum in the Pleistocene deposits.

5 CONCLUSIONS

A series of one-dimensional elasto-viscoplastic finite element analyses was conducted to assess the stress and deformation of the reclaimed marine foundations at the Yumeshima Reclaimed Island in Osaka Bay, Japan. The sophisticated geoinformatic database was utilized to setup the subsoil geometrical model together with the determination of the required material parameters. The calculated performance showed that the steady excess pore water pressure dissipation due to the effect of the vertical drains both in the alluvial and dredged soil layers while the excess pore water pressure remains.in the Pleistocene clay layers for a long time and it may cause the long-term settlement of the reclaimed foundations. It is also found that the rapid and large settlement took place in the alluvial and dredged soil layers in the short period due to the effect of vertical drains. On the other hand, serious long-term settlement will occur in

the Pleistocene clay layers. After completion of reclamation, the high rise buildings and facilities for meeting, incentive travel, convention and exhibition/event (MICE) are planned to be constructed on the subsiding foundations. We have to pay attention to the effect of the long-term settlement on the stability of pile foundations driven into the Pleistocene bearing stratum to support those superstructures.

REFERENCES

Akai, K. and Tamura, T. 1976. An Application of Nonlinear Stress-strain Relations to Multi-dimensional Consolidation Problems. *Annuals DPRI, Kyoto University*, 21(B-2): 19–35 (in Japanese).

Christian, J.T. 1968. Undrained Stress Distribution by Numerical Method, *Journal of the Geotechincal Engineering Division, ASCE*. 94(SM6): 1333–1345.

Mimura, M. and Jang, W. 2004. Description of Time-dependent Behavior of Quasi- overconsolidated Osaka Pleistocene Clays Using Elasto-viscoplastic Finite Element Analyses, *Soil and Foundations*, 44 (4): 41–52.

Mimura, M. and Sekiguchi, H. 1986. Bearing Capacity and Plastic Flow of A Rate-sensitive Clay Under Strip Loading. *Bulletin of DPRI, Kyoto University*, 36(2): 99–111.

Mimura, M., Shibata, T., Nozu, M. and Kitazawa, M. 1990. Deformation Analysis of A Reclaimed Marine Foundation Subjected to Land Construction, *Soils and Foundations*, 3(4): 119–133.

Mimura, M., Takeda, K., Yamamoto, K. and Fujiwara, T. and Jang, W. 2003. Long-term Settlement of the Reclaimed Quasi-overconsolidated Pleistocene Clay Deposits in Osaka Bay. *Soils and Foundations*, 43(6): 141–153.

Osaka Port Authority. 2016. Report on the 2015 Work Consignment for Evaluation of the Ground Behavior and the Observation of Settlement at Yumeshima Reclaimed Island (in Japanese).

Osaka Port Authority. 2017. Report on the 2016 Work Consignment for Evaluation of the Ground Behavior and the Observation of Settlement at Yumeshima Reclaimed Island (in Japanese).

Sekiguchi, H. 1977. Rheological Characteristics of Clays. *Proc. 9th ICSMFE*, 1: 289–292.

Sekiguchi, H., Shibata, T., Fujimoto, A. and Yamaguchi, H. 1986. A Macro-element Approach to Analyzing the Plane-strain Behaviour of Soft Foundation with Vertical Drains, *Proc. 31th Symposium, JSSMFE*: 111–120 (in Japanese).

Sekiguchi, H., Nishida, Y. and Kanai, F. 1982. A Plane-strain Viscoplastic Constitutive Model for Clay. *Proc. 37th National Conf., JSCE*: 181–182 (in Japanese).

Smart Geotechnics for Smart Societies – Zhussupbekov, Sarsembayeva & Kaliakin (Eds)
© 2023 The Author(s), ISBN 978-1-003-29912-7
Open Access: www.taylorfrancis.com, CC BY-NC-ND 4.0 license

Architectural and historical value - The heritage of the people

K.K. Arynov, E.K. Duisebay, S.Sh. Sadykova, L.A. Zhakhsylykova & E.N. Khvan
Department of Architecture of the Faculty of Architecture and Construction, L.N.Gumilyov Eurasian National University, Astana, Kazakhstan

ABSTRACT: The article adresses the results of staged restoration of architectural and historical monuments of educational building of Kazakh Humanitarian Law Innovative University located at Abay street 94, in Semey city and the current state of other valuable historical monuments with spiritual values and historical significance to future generations of the country.

Keywords: monuments of architectural and historical value, restoration, major repairs, facade, building built in the style of Russian classicism

1 INTRODUCTION

The main focus of the article is devoted to the academic building of the university, which has architectural and historical significance and is distinguished by its cultural and spiritual values, located at Abay Street 94, in Semey city.

This building is notable for its uniqueness and historical value not only in the city of Semey, but also at the national level. (Figure 1).

Figure 1. The building of the Kazakh Humanitarian Law Innovative University, before restoration.

The building was built in 1872 and is a national historical and architectural monument. From 1894 to 1919the building was the educational building of the Pedagogical Institute of the Kazakh SSR (former male gymnasium), from 1919 to 1934 the Siberian district headquarters of the 11th White Guard Regiment. Since 1934 the facility served various educational institutions, and now the building is the educational building of the Kazakh Humanitarian Law Innovative

DOI: 10.1201/9781003299127-381

University. As it can be seen, over the existence of the mentioned building hid many mysterious twists and turns of fate [1,3,5].

The general plan of the building is a 2-storey U-shaped house, made in the style of Russian classics, decorated in a component of white and white-pink colors. The length of the main facade, located on the side of Abay Street, is 40,000 mm (40 m) (Fig. External surface of the building is plastered with a traditional lime-sand mortar. Technically, the building consists of three floors - the 1st and 2nd floors and basement. Height of 1st and 2nd floors from floor to ceiling is 3,90 m, basement's - 2,85 m. (its upper side above the ground level of 1.25 m, the lower side of 1.60 m from ground level).

The load-bearing structure of the building, i.e., the bearing walls are built of burnt red brick, wall thickness is 950 mm (3 bricks), the thickness of the walls in the basement is 1150 mm.

2 MATERIALS AND METHODS

The research method is based on a systematic analysis of research objects, compositional analysis of graphic measurements and scientific generalizations.

The work is based on the description of the material collected by the authors as a result of studying materials on architectural objects and an analytical review of scientific literature.

3 RESULTS AND DISCUSSION

The building has been in continuous use since its construction to the present day, that is, almost a century and a half of use. Up until yesterday no comprehensive research capital repair and restoration work was carried out.

Restoration is not an easy task that can be done in a short time, so research work and restoration work go hand in hand here. Because in reconstruction, namely in the modernization of historic buildings, other additional types of work of varying degrees of complexity is involved. Much of the work is done by hand, with great patience and precision, and requires not only professional skill, but also deep knowledge of history and architecture [1,3]. (Figure 2).

Figure 2. The building of the Kazakh Humanitarian Law Innovative University, after restoration.

As of today, with the support of the university administration, the overhaul and renovation work on the building has been successfully completed on schedule. Before proceeding to such a very important work, we had to step by step and systematically solve many problems. Especially these few concerns had to be addressed:

– conducting an overall integrated historical and architectural study of the building;
– review and analysis of extant archives and other historical sources;
– determining the suitability of the building's foundation, the basement fence and the load-bearing walls (resulting in a positive conclusion);
– the phased implementation of a series of rehabilitation measures to prevent further deterioration and deterioration of the building's roofing and covering structures such as beams, rafters and batten (due to the potential excessive drying out of wooden beams and rotting of rafters from moisture);
– testing the quality of the brick, which is the main building material, to determine the degree of deformation due to various external natural influences (resulting in a positive conclusion). (Figure 3);
– carrying out an inspection and corresponding comprehensive survey on the suitability of the building's exterior plaster layers to date.

As a result of site-specific investigations, it was found that the external surface of the facade plaster and paint layer has significant damage (abrasions, cracks) at various levels as a result of various external natural influences and long-term use.

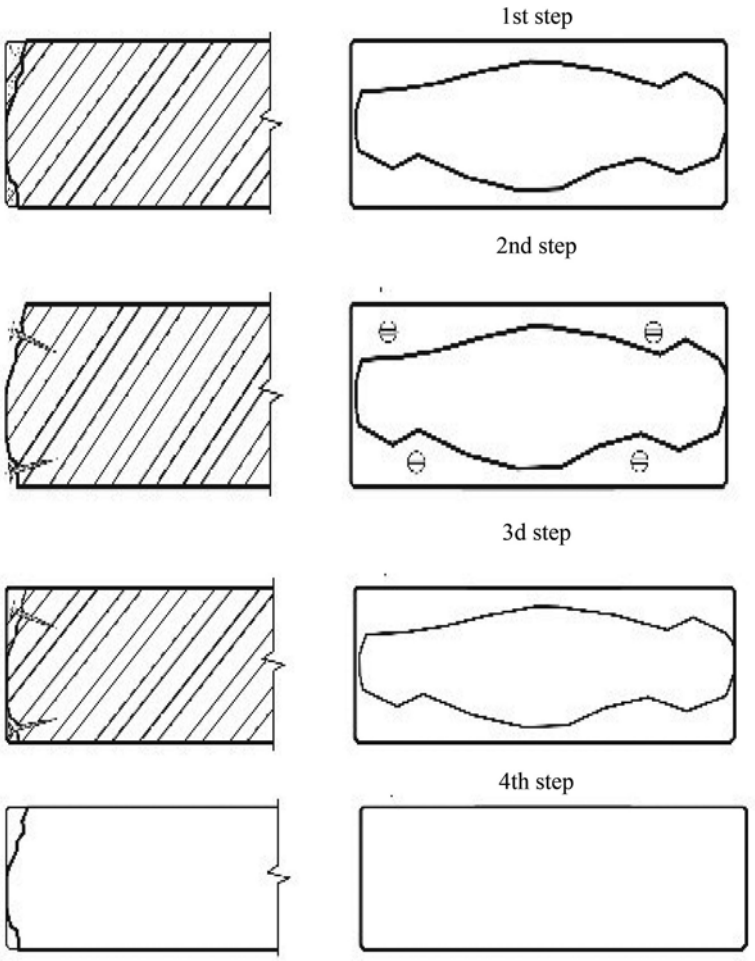

Figure 3. Steps of restoration of deformed parts of building bricks due to various external natural influences (in section and front view).

Subsequently, external plaster layers and brick surfaces deemed unsuitable are routinely removed (dismantled) and replaced with new plaster (4,5-drawings);

When the building was reconstructed, tiles of various shapes were made and used on the basis of previous architectural elements in order to preserve the artistic and stylistic features of its facade.(Figure 6) In spite of the long period of use, the building has survived to this day in reasonably good condition [1,5].

Figure 4. The building of the Kazakh Humanitarian Law Innovative University, after restoration (fragment).

Figure 5. The building of the Kazakh Humanitarian Law Innovative University, after restoration (fragment)

During the renovation and restoration work, the university administration fully understood the importance of the project, took great responsibility for it and contributed actively to the successful completion of the work.

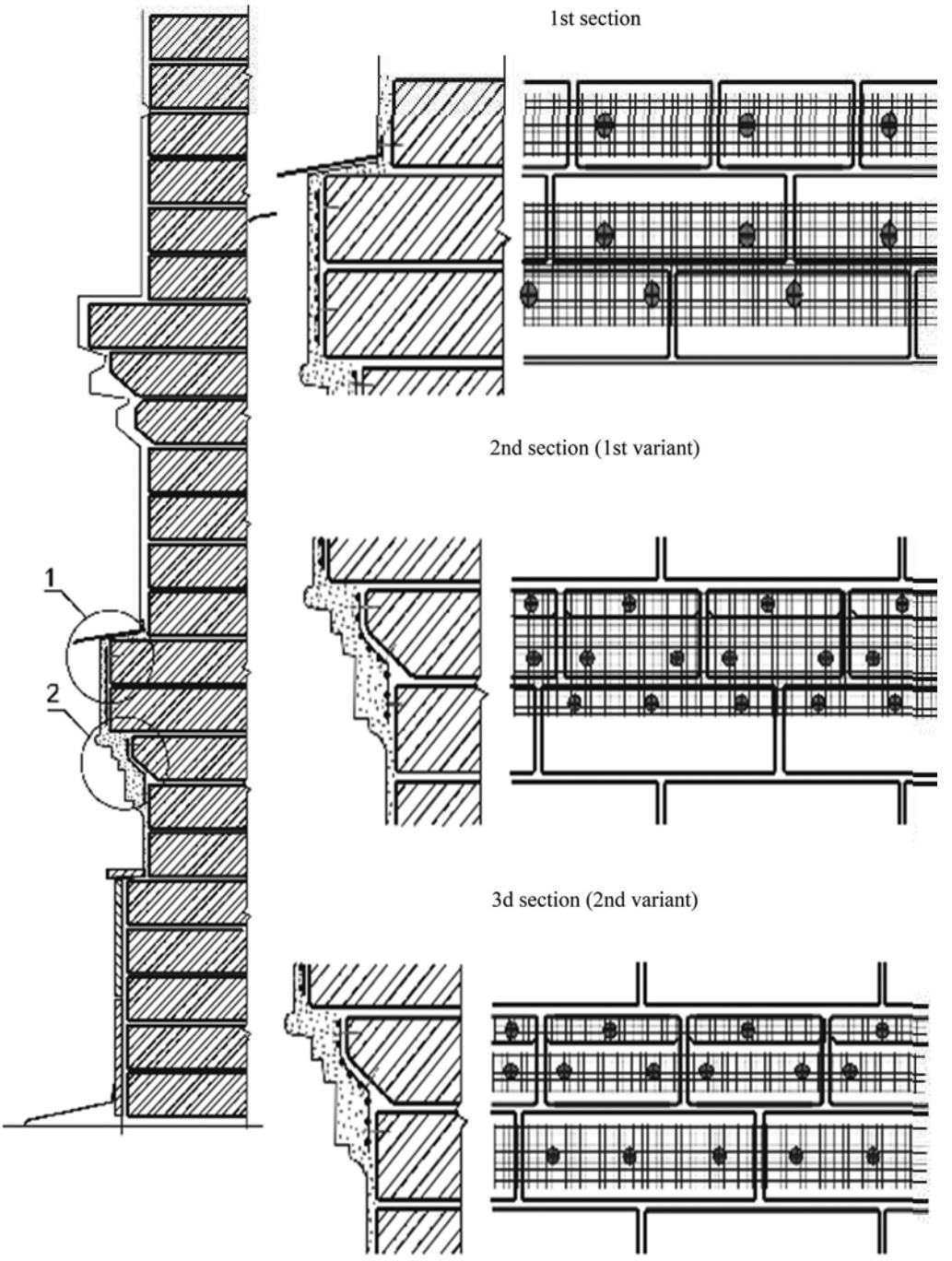

Figure 6. Measures to preserve artistic and stylistic features and external architectural elements of the exterior of buildings.

In the near future, in addition to continuing the exterior restoration of the building, there are plans to restore its interior historic finish, improve the quality of the wooden roof structures, and study and, if possible, run the interior natural ventilation, air purification and heating systems. This means going beyond the exterior architectural restoration of a building and trying to restore it to its original interior working condition in a comprehensive way [2].

On the basis of the research and restoration work carried out to date and the results of future work, there are plans to write digital catalogues and monographs on the restoration and reconstruction of architectural monuments in Semey.

It is worth noting that this is the first time such a positive initiative has been launched in Semey from a building belonging to this university. We hope that such activities will continue at the city level and Semey could, with its rich architectural and historical gems of the 18th-19th centuries, be counted among the number of cities such as Turkestan, Taraz, Sayram, having architectural and historical value of the world level. We believe that the restoration and preservation of such architectural and historical treasures should be one of the most pressing problems facing the citizens [3].

Currently, the state of architectural monuments with historical values in the city of Semey is critical. Suffice it to mention as an example the fate of the former Semey Veterinary Institute. This building is unique with its architectural and stylistic features and obviously a very valuable architectural object, that does not have got any analogues not only in Kazakhstan but also in other neighboring countries, including Russia [4,5].

Figure 7. Current view of the former Semey Veterinary Institute building.

The building, built before the revolution (at that time a female gymnasium) burned down for the first time in the assembly hall in the evening of December 10, 1917, and for the second time on December 9, 1986, 69 years later. Since then, 36 years have passed; now the walls of the magnificent building gradually crumble with each year, it is impossible to pass by such a deplorable appearance of buildings without sympathy. (Figure 7).

4 CONCLUSIONS

The fact that such buildings over the years are severely affected by nature and neglect by society is deeply troubling and saddening, another spiritual value «disappearing before our very eyes»!

High spiritual values, such as the architectural and historical heritage of the people, have always been and will remain one of the important aspects of the country's development. We want to believe that the preservation of architectural monuments will become one of the priority tasks of our republic.

REFERENCES

Arynov K. K. Architecture of buildings of craft centers: monograph. - Astana: IP "Dana" publishing house, 2018. - 271 p.: ill.

Kazakh SSR: a short encyclopedia/Ch. ed. R.N.Nurgaliev. - Alma-Ata: Ch.ed. Kazakh SovietEncyclopedia, 1991 .– Vol. 4: Language.Literature. Folklore. Art. Architecture. - P. 381.–31,300 copies.

Shuymerdenov K. TarikhieskertkishterrukhaniKazynabailyktar. Shymkent, 1981

Tasmaganbetov I. SuletOnerininasyltuyndysy. Almaty, 2005

Toқtabay A. Eskerkishter - eltarikhi: tarikhieskertkishterge restoration zhasau məseleleri. Kazakh Adebieti, 2003 mamyr

Smart Geotechnics for Smart Societies – Zhussupbekov, Sarsembayeva & Kaliakin (Eds)
© 2023 The Author(s), ISBN 978-1-003-29912-7
Open Access: www.taylorfrancis.com, CC BY-NC-ND 4.0 license

Geotechnical properties of combustion waste and its suitability for embankment constructions

A. Dąbska, P. Pytlak, B. Bednarz & Z. Bereda
Faculty of Building Services, Hydro and Environmental Engineering, Warsaw University of Technology, Warsaw, Poland

ABSTRACT: This paper presents research results on the geotechnical properties of the combustion by-products (fly ashes) from wet waste landfills "Jelnia" in Stalowa Wola. The fly ash's physical, mechanical, and permeability properties were determined in laboratory conditions. The possibility of using combustion waste to construct road and water engineering embankments was assessed regarding the applicable European standards and guidelines. Examples of fly ash usage in embankments construction are also presented.

1 INTRODUCTION

In recent years, there has been an intensive development of expressway and freeway networks as well as large-scale construction and modernization of flood banks in Poland. These activities require a high demand for soil materials necessary for the construction of transport and flood embankments. Limited resources of natural materials, more and more difficult to obtain concessions for the opening of new mines and high costs of transport of these materials are the reasons for looking for alternative materials of anthropogenic origin for the embankment constructions. Types of anthropogenic soils allowed for embankment construction are specified in the Regulation of the Minister of the Environment from the 11th of May 2015 (Dz. U. 2015 poz. 796).

Ashes and slags from coal combustion in power and heating plants, classified as Combustion By-products (CBs) are one of the anthropogenic materials (Szczygielski 2015). Various chemical and phase compositions as well as physical and mechanical properties of fly ashes force to analyze their parameters each time to select the most effective method of their transformation or utilization (Zabielska-Adamska 2019). Recycling ashes is also a part of the idea of sustainable development and a circular economy, implemented successfully in Poland (Kledyński et al. 2020). CPs storage generates significant financial and ecological problems and their rational use in the economy, especially in the construction industry, is more frequently recommended (Roszczynialski et al. 2012). The ash reuse reduces the amount of ash in landfills, limits the exploitation of natural resources and indirectly lowers carbon dioxide emissions, e.g. by partially replacing fly ash with Portland clinker, as it requires thermal treatment involving the emission of CO_2.

The paper presents the results of geotechnical properties tests of ashes deposited on the combustion waste landfill "Jelnia" and an analysis of the possibility of using these ashes for the transport and flood embankment bodies.

2 TESTED MATERIAL – FLY ASH

Investigated combustion waste was taken from the combustion waste landfill "Jelnia" in Stalowa Wola (Poland).

The tests were performed on four samples of combustion waste taken from quarters no. 4S-E (Figure 1), from about 2.0 m below the level of accumulated wastes. Two of them were taken

DOI: 10.1201/9781003299127-382

from the discharge zone (Z1, Z2) and two from the inlet zone, at the overflow well on the western side (U1) and on the eastern side (U2). The samples were characterized by a disturbing texture and were protected from moisture content and graining changes during transport and storage.

Figure 1. The combustion waste landfill "Jelnia"- view of the waste-filled quarters No. 4S-E (September 2018).

3 PROPERTIES OF COMBUSTION WASTE FROM "JELNIA"

3.1 *Test method*

Soil description by macroscopic analysis, grain size composition, moisture content, specific density of solids, compactibility, capillarity rise, permeability coefficient, swelling, compressibility and shear strength tests were performed at the Laboratory of Soil Mechanics and Geotechnics of the Department of Building Services, Hydro and Environmental Engineering at Warsaw University of Technology. Testing of specific density of solids was performed in accordance with PN EN 1097-7 standard, however other tests were carried out according to the PN-B-04481:1988 standard and the guidelines in the book (Pisarczyk & Rymsza 2003). Capillarity rise, permeability coefficient, swelling, compressibility and shear strength were determined at compaction with optimum water content assessed by the standard method I Proctor test.

Table 1. Properties of tested fly ash.

Parameter				Sample no.			
Name		Symbol	Unit	Z1	Z2	U1	U2
Fraction content	gravel	f_z	%	0.6	0.1	0.2	0.1
	sand	f_p	%	93.6	81.5	83.0	84.2
	silt	f_π	%	5.7	18.0	16.4	15.4
	clay	f_i	%	0.1	0.4	0.4	0.4
Uniformity coefficient		C_U	-	3.42	2.57	2.82	2.39
Natural moisture content		w_n	%	17.8	53.5	62.1	61.4
Specific density of solids		ρ_s	kg/m^3	2480	2150	2210	2160
Capillarity rise		H_{kc}	m	1.19	> 2.00	> 2.00	> 2.00
Permeability coefficient		k_{10}	m/s	$8.0*10^{-7}$	$4.3*10^{-10}$	$2.0*10^{-10}$	$5.6*10^{-10}$
Expansion index / swelling index		I_{hc}	%	0.9	13.4	12.8	12.2
Compactibility (I normal Proctor method)	optimum water content/optimal moisture content	w_{opt}	%	21.6	33.2	36.1	38.0
	maximum dry density	ρ_{ds}	kg/m^3	1430	1130	1130	1060
Oedometric modulus (primary consolidation) (0-0.2 MPa)		M_0	MPa	8.9	3.1	2.3	4.2
Shear strength (direct shear apparatus)	cohesion	c_u	kPa	13.6	50.2	42.5	50.4
	internal friction angle	φ_u	°	48.6	36.9	38.6	41.0

3.2 *Test results*

The results of fly ash laboratory tests are shown in Table 1. More detailed test results are included in the engineering thesis (Pytlak 2020).

4 ANALYSIS OF TEST RESULTS

4.1 *Assessment of combustion waste properties*

Wastes disposed in one section of the landfill are not homogeneous materials, and their properties change depending on the material storage zone. The grain size composition of the discharge zone waste corresponds to uniformly-grained fine sand and silty sand, whereas that of the waste from the intake zone corresponds only to silty sand (PN-B-02480:1986). The specific density of combustion waste is lower than the density in soils of natural origin. Considering physical properties, compactability, permeability and mechanical properties tested ashes do not correspond to natural soils of similar grain size (PN-B-03020:1981). Significant differences are noticed in the strength and compactibility parameter values. The combustion waste is characterized by lower maximum bulk densities of the skeleton at lower optimum moisture contents, higher cohesion and internal friction angles. The properties of the studied ashes do not differ from other hard coal ashes (Pisarczyk 2015).

4.2 *Assessment of applicability of ash for construction of embankments*

4.2.1 *Road embankments*

The soil for the construction of road embankments in Poland should be selected in accordance with the PN-S-02205:1998 standard which allows the usage of anthropogenic materials to construct road embankments, including fly ash and ash-slag mixtures. Tested ashes can be used in

Table 2. Properties of the tested ash according to the requirements for ash-slag mixtures for construction of road embankments based on the PN-S-02205:1998 standard.

Parameter	Value required for embankment body construction	Sample no.			
		Z1	Z2	U1	U2
Main conditions					
Grain size composition	≥ 35 %	94.2 %	81.6 %	83.2 %	84.3 %
- sand-gravel friction content	≤ 75 %	12.0 %	30.0 %	30.0 %	25.0 %
- grain smaller than 0.075 mm content					
Organic matter content (unburned carbon)	≤ 10 %	6.7 % (Dąbska et al. 2019)			
Maximum dry density after compaction according to Proctor (I or II method)	≥ 1 kg/m^3	1430 kg/m^3	1130 kg/m^3	1130 kg/m^3	1060 kg/m^3
California bearing ratio (CBR), after 4 days of soaking in water	≥ 10 %	n.d.	n.d.	n.d.	n.d.
Linear swelling					
- without load	≤ 2 %	0.9 %	13.4 %	12.8 %	12.2 %
- under 3 kN/m2 load	≤ 0,5 %	b.d.	b.d.	b.d.	b.d.
Additional conditions					
Internal friction angle φ	≥ 20°	48.6°	36.9°	38.6°	41.0°
Passive capillarity H_{kb}	≤ 2 m	n.d.	n.d.	n.d.	n.d.
Sulphate content (as SO_3)	< 3 %	0.07 % (Dąbska et al. 2019)			

n.d. – no data

lower layers of road embankments, below the frost zone, in dry or water-isolated areas, and after improvement with binders such as cement, lime, and active ash in upper layers of embankments in the frozen zone (Dabska et al. 2022). Requirements for ash-slag mixture application into road embankments according to the PN-S-02205:1998 and the comparison of tested ash properties are presented in Table 2.

Analysis of data presented in Table 2. shows that the tested wastes follow the requirements for ash-slag mixtures for road embankment construction, except for the linear swelling requirement for combustion waste with a grain size that corresponds to the grain size of silty sand. The combustion waste can be used in lower layers of road embankments below the frozen zone, under conditions of isolation from water, and in upper layers of embankments in the frozen zone, after improving it with binders. Combustion waste with a silty sand grain size requires previous mixing with coarser fractions in order to reduce their swelling properties.

The road embankments of the S19 expressway in Poland constructed with tested combustion waste are presented in Figures 2-3.

Figure 2. Forming a slope from ashes on the section Janów Lubelski – Łążek of the S19 expressway in Poland (May 2020) (GDDKiA).

Figure 3. View from above on the S19 expressway embankment, made of ashes from the combustion waste landfill "Jelnia" (May 2020) (GDDKiA).

4.2.2 *Flood embankments*

Ash-slag mixtures are not recommended for use in the earth dams in riverbeds and flood embankments. Ashes and slags are commonly used to construct subsequent phases of wet landfill embankments, functioning as water engineering structures (DGWiM 1973, Dąbska et al. 2019). Tested ash was used for the construction of the second, third and fourth phases of the embankment at the combustion waste landfill in Stalowa Wola (Figure 4).

Figure 4. Embankment of the combustion waste landfill "Jelnia" in Stalowa Wola (Poland) constructed from ashes (November 2020).

5 SUMMARY

According to the preliminary assessment, the tests of combustion waste properties and analysis of their results indicate that this material can be built-in in the bodies of transport embankments and used for the construction of embankments of combustion waste landfills under some restrictions. The main limitation of using ashes with finer grains is their swelling in direct contact with water. For this reason, ashes cannot be applied in layers where there is a possibility of contact with water in most water engineering constructions and transport embankments.

The presented results should be supplemented by testing the California bearing ratio CBR, soil swelling under load, and passive capillarity to fully evaluate the suitability of tested ashes from the wet landfill "Jelnia" for constructing the bodies of transport and flood embankments. These tests can significantly affect the preliminary assessment of their use as embankment soils.

Construction of the S19 expressway, the ring road of Stalowa Wola and Nisko towns with the use of ashes from the wet landfill "Jelnia", indicate that properly built waste can be a material for building the body of road embankments, and effectively limit the exploitation of local mines of natural resources. It is estimated that about 1.1 million tons of combustion waste from the "Jelnia" landfill have been applied to the road embankments, which effectively increased the storage capacity of the landfill. This investment is an excellent example of the idea of a circular economy implementation, bringing real economic benefits and a positive impact on the environment.

REFERENCES

Dąbska, A. 2019. *Nadzór naukowo-techniczny nad MMOP „Jelnia w Tauron Wytwarzanie S.A. Elektrownia Stalowa Wola w roku 2019*. Warszawa: Zakład Budownictwa Wodnego i Hydrauliki Politechniki Warszawskiej.

DGWiM, M. 1973. *Budownictwo specjalne w zakresie gospodarki wodnej. Zapory ziemne. Wytyczne projektowania*. Warszawa: Wydawnictwo katalogów i cenników.

Kledyński, Z. et al. 2020. Condition of Circular Economy in Poland. *Archives of Civil Engineering* 66(3): 37–80.

Pisarczyk, S. 2015. *Grunty nasypowe. Właściwości geotechniczne i metody ich badania*. Warszawa: Oficyna Wydawnicza Politechniki Warszawskiej.

Pisarczyk, S. & Rymsza, B. 2003. *Badania laboratoryjne i polowe gruntów*. Warszawa: Oficyna Wydawnicza Politechniki Warszawskiej.

PN-B-02480:1986 Grunty budowlane. Określenia, symbole, podział i opis gruntów.

PN-B-03020:1981 Grunty budowlane. Posadowienie bezpośrednie budowli.

PN-B-04481:1988 Grunty budowlane. Badania próbek gruntu.

PN EN 1097-7:2008 Badania mechanicznych i fizycznych właściwości kruszyw - Część 7: Oznaczanie gęstości wypełniacza - Metoda piknometryczna.

PN-S-02205:1998 Drogi samochodowe. Roboty ziemne - wymagania i badania.
Pytlak, P. 2020. *Badanie właściwości geotechnicznych odpadów paleniskowych MMOP "Jelnia" w aspekcie przydatności do budowy nasypów*. Praca inżynierska. Warszawa: Politechnika Warszawska. Wydział Instalacji Budowlanych Hydrotechniki i Inżynierii Środowiska.
Roszczynialski, W. et al. 2012. Uboczne produkty spalania jako podstawowe składniki spoiw hydraulicznych dla drogownictwa. *Prace Instytutu Ceramiki i Materiałów Budowlanych* 5(11): 101–111.
Rozporządzenie Ministra Środowiska z dnia 11 maja 2015 r. w sprawie odzysku odpadów poza instalacjami i urządzeniami (Dz. U. 2015 poz. 796).
Szczygielski, T. 2015. *Szanse i zagrożenia dla UPS w aspekcie strategii UE*. Warszawa: IBS Politechnika Warszawska.
Zabielska-Adamska, K. 2019. *Grunty antropogeniczne: zagęszczalność i właściwości gruntów zagęszczanych*. Studia z Zakresu Inżynierii 106. Warszawa: Polska Akademia Nauk.
https://s19-janowlubelski-lazek.pl/galeria/ (access date: May 2022)

Smart Geotechnics for Smart Societies – Zhussupbekov, Sarsembayeva & Kaliakin (Eds)
© 2023 The Author(s), ISBN 978-1-003-29912-7
Open Access: www.taylorfrancis.com, CC BY-NC-ND 4.0 license

Geotechnical forecast of the construction of structures in conditions of degrading permafrost soils

S.A. Kudryavtsev, T.Yu. Valtseva, A.V. Kazharsky, I.I. Gavrilov, I.I. Sakharov & V.N. Paramonov
Far Eastern State Transport University, Khabarovsk, Russia

ABSTRACT: The article summarizes the results of the operation of the roadbed for more than fifty years of operating experience on degraded permafrost soils. The modern technique of numerical modeling of the forecast of the process of degradation of frozen soils is considered, which allows the development of modern structures that reduce or exclude deformations of structures. The construction and operation of structures in permafrost conditions is associated with the degradation of the temperature state of the soil of structures due to the effects of solar radiation. Global climate change plays a crucial role in ensuring the reliability of railway infrastructure facilities. To prevent thawing of permafrost soils of the base, thermostabilizers are used - seasonal cooling devices and stone cooling sketches. The article considers predictive thermal engineering studies of permafrost foundations of railway bridges and pipes in order to substantiate regulatory design solutions. Numerical studies were carried out by the finite element method using a non-stationary and physically nonlinear thermophysical model of soils

Keywords: permafrost, degradation, soils, temperature, thawing

1 INTRODUCTION

The purpose of this work is to consider the methodology of numerical modeling of structures taking into account insolation and the use of modern devices that exclude deformation of the roadbed on permafrost soils. The embankment with a permafrost subgrade on swampy areas has undergone substantial processes of freezing, thawing and heaving during its 40-year exploitation period. The major defrosting factor for a permafrost subgrade is a water impact. In case the water runoff is absent, a consequent thawing of the permafrost subgrade takes place that results in thawing basin. To avoid this effect, it is reasonable to make drainage soil fills, rocky cooling structures and take other analytically proved effective measures [1,2].

Construction and operation in permafrost conditions is associated with many problems, the most urgent of which is the degradation of the frozen state of soils due to the effects of solar radiation on the process of thawing of permafrost foundations of buildings and structures.

Currently, considerable attention is being paid to the negative impact of natural impacts on railway infrastructure facilities and the level of train safety. It is noted that the greatest natural risks are directly or indirectly related to climate change in recent decades.

According to the materials of the Russian Hydrometeorological Service, the average rate of warming of permafrost soils in Russia is three times higher than the average for the globe and is 0.51 ° C/10 years. In 2020, the average annual air temperature anomaly left +3.22°C - more than 1 degree higher than the previous maximum in 2007 at a rate of 2.2% of the ten–year norm.

DOI: 10.1201/9781003299127-383

According to the data of the international program CALM (Circum Polar Active Layer Monitoring) for the period 2005-2020 in the zone of permafrost soils of Russia, the thickness of the seasonally thawed layer increased by an average of 5-15 cm [3–6].

The increase in air temperatures in recent decades in the Baikal-Amur Mainline zone strongly affects the temperature regime of the soil of the roadbed and its foundations. It was found that during the period 2010-2020, in areas without cooling structures, the permafrost roof at the base of the roadbed decreased to 0.5 m with an increase in soil temperatures of undisturbed landscapes and a decrease in the permafrost roof to 1.8 m on the southern slopes of positive relief forms, as well as in areas stacked with well-draining soils. The degradation of permafrost is accompanied by the disappearance of "ice-cement", which binds loose soils into a single, previously stable mass.

2 DESIGN-BASIS JUSTIFICATION

Design-basis justification is necessary for a variable development of the designing solutions for railway structures that keep the roadbed and its base at a less than maximum permissible values or even zero deformability.

In 2005 we developed for construction engineering organizations a unique software that makes numerical modeling by the method of finite elements. It simulates freezing, heaving and thawing processes in seasonally frozen and permafrost soils in a 3-dimentional perspective. This is the only programming product calculating not only temperature fields but also deformations in the embankment and the base. This complex uses the Cloud technologies. A wide circle of users enjoys a monograph that contains practical examples of thermo-physical and stress-strain calculations of the embankment, the roadbed, bridges pipes, waterworks, seasonally cooling structures for permafrost preserving and other structures.

In this research first of all a thermo-physical task should be solved as a basis for the study of a stress strain behavior of the railway embankment taking into account its perspective life-span on permafrost.

2.1 *The numerical modeling of thermo-physical design calculations*

The numerical modeling was carried out in the program complex FEM-models developed by the "Geoconstruction" Design Institute, St.Petersburg, Russia. As a part of this program complex, the "Termoground" program allows a 3D research of freezing, frost heaving and thawing processes in an annual cycle by the finite elements numerical modeling [7–11]. The calculation was performed for a fifty-year forecast period and, due to a universal solver, is performed with multimillion operations of unknowns with a finite element dimension of tens of centimeters within one hour. For the study, it is necessary to determine the thermophysical, physical and climatic properties.

The program calculations assume the researched area including the design is divided into the finite elements of the same temperature and soil characteristics. The design model is defined first by the initial and the boundary conditions, then the thermotechnical task is solved resulting in calculation of temperature and moisture areas for every time-period.

The initial conditions include the soil temperature defined by depth, while the boundary conditions include the surface temperature (under the rock fill) defined by time. The upper boundary is affected by a time-variant heat flow determined by the defined air temperatures and the heat-transfer coefficients.

General equation describing the freezing and thawing processes for a transient thermal regime in a three dimensional soil space can be expressed as following:

$$C_{th(f)}\rho\frac{\partial T}{\partial t} = \lambda_{th(f)}\left(\frac{\partial^2 T}{\partial x^2} + \frac{\partial^2 T}{\partial y^2} + \frac{\partial^2 T}{\partial z^2}\right) + q_V \tag{1}$$

where $C_{th(f)}$ - specific heat of soils (frozen or thawed), J/kgK; ρ - soil consistency, kg/m³; T – temperature, K; t – time, c; $\lambda_{th(f)}$ - thermal conductivity of soil (frozen and thawed), W/mK; x, y, z – coordinates, m; qv- internal heat source capacity, W/m³.

The core of a mathematical modeling of thermophysical processes in "Termoground" program is the model of high ice, thawed and frozen soils offered by N.A. Tsytovich, Y.A. Kronik and V.F. Kiselev.

The major factors determining the defined surface temperatures on the embankment elements and the adjacent territory are the atmospheric air temperature and the heat exchange conditions between the air and the structure surface that depend on the wind conditions, solar radiation, vaporation, and others.

The calculation value of the defined average monthly air temperature is determined from the formula:

$$T_{np.} = T_b + \Delta t_r - \Delta t_e \tag{2}$$

where T_b is average monthly air temperature; Δt_r and $\Delta t_e$are corrections to average monthly air temperatures due to solar radiation and evaporation, °C.

The correction to air temperature due to solar radiation (Δt) is calculated according to formula:

$$t_r = \frac{R}{0.073\alpha}, \tag{3}$$

where R is monthly sum of radiation balance for the considered element of the surface, kkal/см2 ×months; α is surface heat exchange coefficient, kkal/м2 ×h×°C, and its empirical-formula dependence is:

$$\alpha = 10\sqrt{V}, \tag{4}$$

where V is wind velocity.

The monthly sums of radiation balance for horizontal surfaces are determined from the formula:

$$R_o = Q_o \times k - 0.42, \tag{5}$$

where Q_o is average monthly sum of total solar radiation striking the horizontal surface, kkal/см2 ×months; k – empirical coefficient in terms of the surface reflecting capacity (albedo).

The monthly sums of radiation balance for bevel faces (subgrade embankments) are determined from the formula:

$$R_\beta = \left(m_\beta I_o + P_\beta D_o\right) \times k - 0.42, \tag{6}$$

where I_o and D_o – average monthly sums of direct and diffuse radiations striking the horizontal surface, kkal/см2 ×months, the values being taken from the climatological guide; m_β non-dimensional coefficient in terms of the bevel face angle to horizon and spatiolization of the face for beam radiation intake; P_β – coefficient in terms of the bevel face angle to the horizon and spatialization of the face for a sky radiation intake that is determined from the formula:

$$P_\beta = \cos^2\frac{\beta}{2}, \tag{7}$$

where β– angle of the bevel face to the horizon, degrees.

The thermophysiscal characteristics of the roadway and roadbed soils in thawed and frozen states are taken in accordance with the СП 25.13330.2012 – Permafrost Foundation Engineering Standards.

2.2 *The numerical modeling of the embankment stress strain behavior for the targeted time-period*

The relative thawing strains of permafrost are determined according to the results of the standard laboratory tests. In this case the relative stresses are calculated according to the formula:

$$\varepsilon_{th} = A_{th} + \delta_{ith} \tag{8}$$

where $A_{th}$is the relative strain of thaw thermal subsidence; $\delta_{ith}$is the relative strain of thaw loading subsidence.

$$\delta_{ith} = \mathrm{m_{0th}} \cdot \mathrm{p}_i, \tag{9}$$

where m_{0th} is the coefficient of compressibility of thaw soil (MPa-1); p_i is the compacting vertical stress (MPa).

3 DEVELOPING A RATIONAL DESIGN

Administratively, the work site is located in the Amur region of the Baikal-Amur Mainline in Russia. The embankment is built up to 9.0 m high. Part of the railway track runs along the swampy above-floodplain terrace of the river, composed of peat, sandy loam, sand and gravel-pebble deposits lying on the weathering crust of granite rocks of the early Archean. The distribution of permafrost soils and taliks is reflected in the normative geocryological data. According to engineering-geological and geocryological conditions, the railway track is laid on a section of the III (complex) category.

The climate of the area of the site location is of a sharply continental type, with monsoon features and is characterized by a harsh long winter and a short hot summer. Specific soils are widespread along the highway: peat, eluvial deposits, permafrost and technogenic soils. Of the unfavorable geological processes and phenomena in this area, it is possible to distinguish: the presence of permafrost soils; frost heaving, deformation of the roadbed.

Thermal engineering calculations were performed for various variants of cooling structures. The experience of operating the existing track, the latest achievements of research and development work were taken. The article presents the construction of the roadbed with measures to prevent further thawing of permafrost soils.

The article presents the results of the performed forecast calculation at the time of maximum thawing of soils - october of the calculated year. The calculation was made for the third, fifth, tenth year of operation of the roadbed. The results are presented for the tenth year of operation.

The stabilization of the roadbed in the areas of permafrost degradation will occur between the fifth and tenth years. The design of the cooling rock outline was selected individually, depending on the type of foundation, the established temperature field, engineering and geological features, etc. The article presents an optimal cooling stone structure that allows to raise the permafrost by more than one meter in ten years (Figures 1–2).In the studies, boundary conditions of the first kind were accepted, the essence of which is that the temperature is set at all points on the surface of the body for a given time.

Designs that did not provide the required reliability parameters were excluded from further consideration. The results of thermophysical calculations showed that under the existing embankments of the site, the temperature of permafrost soils increases with the formation of a thawing bowl, and the degradation of permafrost is observed.

When using cooling measures in the form of a rock outline, the permafrost boundary rises into the body of the embankment, ensuring reliable operation. Geometric dimensions (width, height) were selected individually taking into account the operation of the existing railway.

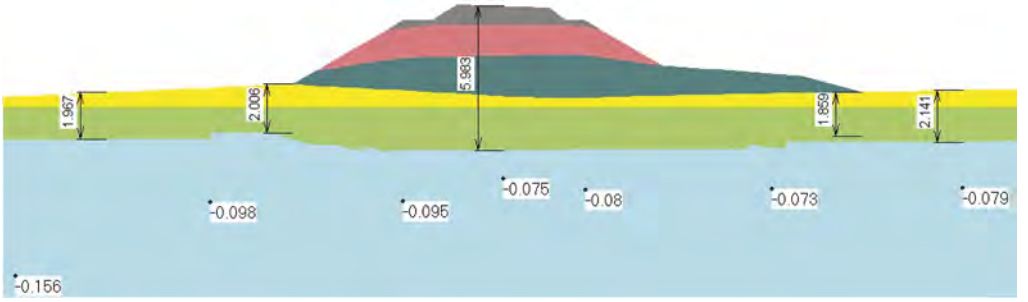

Figure 1. The results of determining the boundary of permafrost soils at the initial time. The blue color shows the ground in a frozen state.

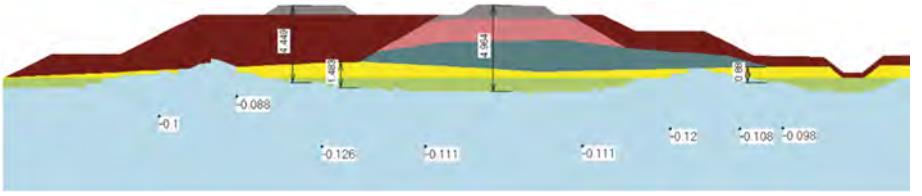

Figure 2. The results of determining the boundary of permafrost soils at the estimated time. The blue color shows the ground in a frozen state.

In Figures 3–4, a variant of the device of a cooling stone outline on the cones of the bridge abutment was considered. Thawing for ten is about five meters. The columnar foundation is located on frozen soils with sufficient bearing capacity and, accordingly, load capacity.

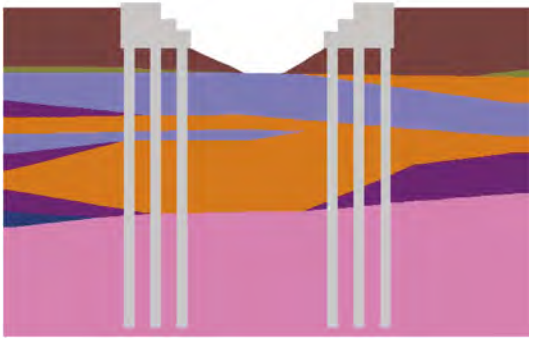

Figure 3. Design scheme of the bridge section.

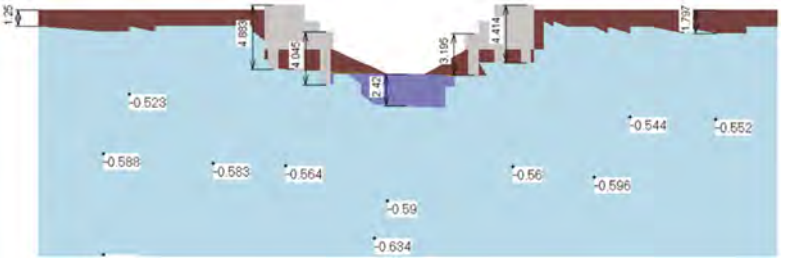

Figure 4. The results of determining the boundary of permafrost soils at the calculated time. The blue color shows the ground in a frozen state.

4 CONCLUSIONS

1. The detailed information of the study includes a set of measures that allow to give an objective forecast of the preservation of the permafrost base from the degradation process as a result of an increase in air and soil temperatures. The research was carried out on a section of the Baikal-Amur railway in Russia. Using the survey and the numerical modeling method for the calculation of quantitative and qualitative assessment of the railway structures on permafrost makes it possible to carry out thermo-technical designs of constructing and projected buildings and structures with the perspective to know their behavior in decades. This allows to assess stress and strain state of "base-embankment" system and provide a reliability of the projected structures when considering all the variants. The obtained forecast results of numerical modeling are in good agreement with the data of observations of the temperature and the processes of thawing of permafrost soils of the base of the railway embankment.
2. The program complex "FEM-models" having the "Termoground", a module for non-stationary heat flow calculation, allows to make calculations of freezing, thawing and frost heaving for seasonally freezing and permafrost soils.
3. If the lateral seepage through the embankment roadway and the subgrade takes place, the permafrost eventually gets thawed, and a thawing basin is formed under the embankment.
4. If the lateral seepage is not stopped, some cooling methods such as rock fills or ditches are not effective for keeping the permafrost in the subgrade.
5. When a geomembrane is installed along the rock fill toe, the infiltration of water due to warm precipitation and ground waters through gravel soils of the roadway and turf soils of the subgrade get reduced or disappear. This method provides a longer exploitation period of rock fill structures as well as lifts the permafrost line into the roadway and lessens deformations of the embankment to the accepted values.

REFERENCES

[1] Zhussupbekov A., Shakhmov Z., Lukpanov R., Tleulenova G., Kudryavtsev S. 2017. Frost depth monitoring of pavement and evaluation of frost susceptibility at soil ground of Kazakhstan. ICSMGE 2017-19th International Conference on Soil Mechanics and Geotechnical Engineering. 19, Unearth the Future, Connect Beyond. 2017. C. 1455-1458.

[2] Zhussupbekov, A., Alibekova, N., Akhazhanov, S., Sarsembayeva, A. 2021.'Development of a unified geotechnical database and data processing on the example of Nur-Sultan City. Applied Sciences (Switzerland), 2021, 11(1),pp. 1–20, 306.

[3] Sarsembayeva, A., Zhussupbekov, A. 2021. 'Experimental study of deicing chemical redistribution and moisture mass transfer in highway subsoils during the unidirectional freezing' Transportation Geotechnics, 2021, 26, 100426.

[4] Utepov, Y., Aniskin, A., Tulebekova, A., Zharassov, S., Sarsembayeva, A. 2021.'Complex maturity method for estimating the concrete strength based on curing temperature, ambient temperature and relative humidity' Applied Sciences (Switzerland), 2021, 11(16), 7712.

[5] Unaibayev, B.B., Unaibayev, B.Zh., Alibekova, N., Sarsembayeva, A. 2021. Installation of bored piles with a protective silicate shell of a new design in saline silty-clayey soils' Applied Sciences (Switzerland), 2021, 11(15), 6935.

[6] Assel Sarsembayeva; Askar Zhussupbekov; Philip E. F. Collins. 2022. Heat and Mass Transfer by Vapour in Freezing Soils. Energies 2022, 15, 1515.

[7] Kudryavtsev S.A., Kazharsky A.V.A.V., Goncharova E.D., Kotenko Z.I., Grigoriev D.O. 2017. Embankment on permafrost eastern polygon of Baikal-Amur Mainline. Procedia Engineering. 2017. P. 774–782.

[8] Kudryavtsev S., Borisova A. 2018. The research of the freezing and thawing process of the foundations with the use of season and cold-producing devices. MATEC Web of Conferences. 2018. P. 03040.

[9] Kudryavtsev S.A., Berestyanyy U.B, Goncharova E.D. 2013. Engineering and construction of geotechnical structures with geotechnical materials in coastal arctic zone of Russia. Proceedings of the

international offshore and polar engineering conference. «Proceedings of the 23rd international offshore and polar engineering conference». Proceedings of the ISOPE Ocean Mining Symposium. 2013. C. 562.
[10] Kudryavtcev S., Valtceva T., Kotenko Z., Kazharsrki A., Paramonov V., Saharov I., Sokolova N. 2021. Reinforcing a railway embankment on degrading permafrost subgrade soils. Advances in Intelligent Systems and Computing. 2021. T. 1258. C. 35-44.
[11] Kudryavtcev S.A., Ulitskii V.M., Paramonov V.N., Sakharov I.I. 2015. Bed – structure system analysis for soil freezing and thawing using the termoground program. Soil mechanics and foundation engineering. 2015. Springer New York Consultants Bureau, ISSN: 0038-0741. P.1–7.

Smart Geotechnics for Smart Societies – Zhussupbekov, Sarsembayeva & Kaliakin (Eds)
© 2023 The Author(s), ISBN 978-1-003-29912-7
Open Access: www.taylorfrancis.com, CC BY-NC-ND 4.0 license

Pile field numerical calculation method accounting load history

L.V. Nuzhdin
Department of Engineering Geology and Foundations, Novosibirsk State University of Architecture and Civil Engineering (Sibstrin), Russia
Department of Construction Operations and Geotechnics, Perm National Research Polytechnic University, Russia

V.S. Mikhailov
Department of Engineering Geology and Foundations, Novosibirsk State University of Architecture and Civil Engineering (Sibstrin), Russia

ABSTRACT: The authors propose a combined approach for a cylindrical geomechanical model of piles by numerical determination of shear rigidity of a multilayer soil cut by a pile. The rigidity of the subsoil under the tip of the pile is calculated analytically as for a stamp on an elastoplastic base. This approach is more visual in the analysis of the stress-strain state of piles and near pile soils. The finite element method simplifies the consideration of the non-linear properties of materials and the additional swelling or frost effects Dynamic impacts always affect the foundation, which is already experiencing deformations from dead loads. The approach proposed by the authors makes it possible to take into account the conditions of the formation of the stress-strain state of the pile foundation within universal model of the pile cell. After the perception of horizontal static horizontal loads by piles in the form of a beam on an elastic base, proceed to the integral dynamic rigidity of the large pile field.

1 SINGLE PILE MODELS

1.1 *Analytical cylindrical two-layer model of a pile*

A mathematical shear two-layer cylindrical model of a single pile or a group of up to 25 piles was introduced in 2010 in the Russian Code Design SP 24.13330.2011 "Pile foundations" (clause 7.4.2) instead of the method of «conditional foundation». The model is based on a significant amount of experimental data generalized by the research team of the NIIOSP (Fedorovsky et.al. 1972, 2003). However, a mathematical presentation with an excessive number of intermediate coefficients makes it difficult to perceive the physical meaning of the technique.

The authors would describe in the Fedorovsky model the condition that there is an influence of neighboring piles loads introducing the limiting radius a_{lim} (Formula 1). The limiting radius parameter of mutual piles influence is the radius of a cylindrical geomechanical model, with a height equal to the length of the pile L and with an underlying layer depth of $0.5L$ (Figure 1a). The exclusion of deformability of the concrete pile and the introduction of the radius of influence simplifies the formulas of SP 24.13330 for a homogeneous subsoil (Formulas 2, 3, 4).

$$a_{lim} = k_\nu \frac{G_1 L}{2G_2} = \left(2.82 - 3.78\nu + 2.18\nu^2\right)\frac{G_1 L}{2G_2} \tag{1}$$

$$S_i = 0.17\ln\left(\frac{a_{lim}}{2d}\right)\frac{N_i}{G_1 L} \tag{2}$$

DOI: 10.1201/9781003299127-384

$$S_{ad.ij} = 0.17 \ln\left(\frac{a_{lim}}{a_j}\right) \frac{N_j}{G_1 L} \tag{3}$$

$$S_{i.gr} = S_i + \sum\nolimits_{j \neq i} S_{ad.ij} \tag{4}$$

The obvious advantage of the single pile analytical shear model is the simplicity of application for automation of FEM numerical calculations (Shapiro 2016, Edigarov 2015, Nuzhdin & Mikhaylov 2018a). The two-layer concept was proposed for the first time in 1953 (Ter-Ovanesov 1956). Excluding the small compressibility of the pile body in comparison with the soil, the total settlement of the pile S is easily decomposed into the settlement of the subsoil along the lateral surface S_τ (Figure 1b), always equal to the settlement of the underlying soil S_0 from the pushing of the pile bottom (Figure 1c). Based on this concept the research team of the MSUCE developed alternative analytical geomechanical model of the pile taking into account rheological and elastoplastic processes in the soils (Ter-Martirosyan & Dinh, 2006).

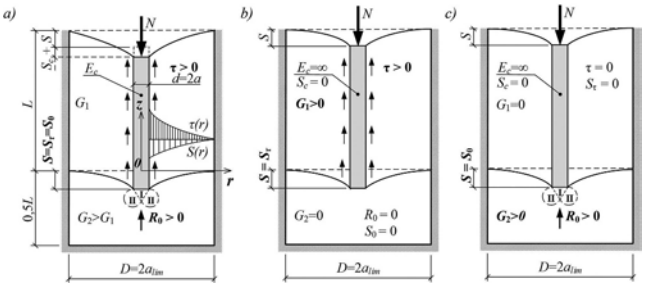

Figure 1. Diagram of a two-layer analytic cylindrical geomechanical pile model.

1.2 *Numerical cylindrical multilayer model of a pile*

The authors propose further development of the cylindrical model by replacing the analytical description for the area of shear linear deformations along the length of the pile with a multilayer axisymmetric numerical FEM solution. The method was verified in the Mathcad software (see Figure 2) with a spatial (see Figure 3a) and an axisymmetric (see Figure 3c) finite element models of a pile in SCAD software, considering a fragment of a cell with a height of 0.4 m and a radius of 0.57 m, and the pile of concrete B20 and 0.34 m in diameter is surrounded by loam with a deformation modulus of 10 MPa. A fragment of the numerical finite element method (FEM) solution in SCAD software with the definition of nodal displacements in the finite elements of an axisymmetric body and in spatial FEM model are presented below (see Figure 3b and d).

The settlement of a single pile of the 12 m length (L) in an elastic axisymmetric model in SCAD software is shown below (see Figure 4). Settlement with a depth of the underlying layer of $0.5L$ (see Figure 4a) is 24% less than the analytical solution (see Equation 1–4). An increase in the thickness of the elastic underlying layer to the depth of the compressible thickness of the conditional foundation H_c = 11.4 m is insufficient (see Figure 4b). The complete exclusion of the underlying layer leaves only the shear rigidity along the lateral surface with an excess of settlement S_τ = 6.41 mm by 4.8% over the analytical solution (see Figure 4c). Only at a double depth of $2xH_c$ = 22.8 m, the settlement corresponds to the analytical solution. This is due to the fact that nonlinear zones of compacted core and limit equilibrium are formed under the pile fifth (see Figure 4d) and should be found in elastoplastic or by the analytic solutions (Schleicher, 1928).

The numerical solution corresponding to the analytical method can be achieved by replacing the underlying layer with a spring with the rigidity of the base under a round stamp (see Figure 4d). The parameter of the spring under the fifth of the pile can be calculated by the analytic solution either from the inverse ratio G_2d/G_1L, indicating what proportion of the rigidity under the fifth is of the rigidity on the lateral surface, equal to 3.4% in the example under consideration.

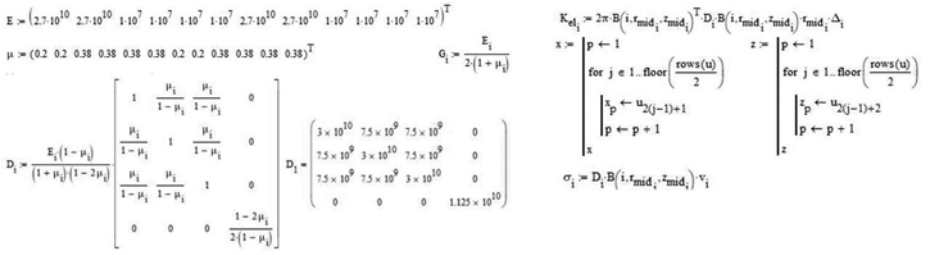

Figure 2. The FEM numerical solution in Mathcad for a pile as an axisymmetric body of rotation.

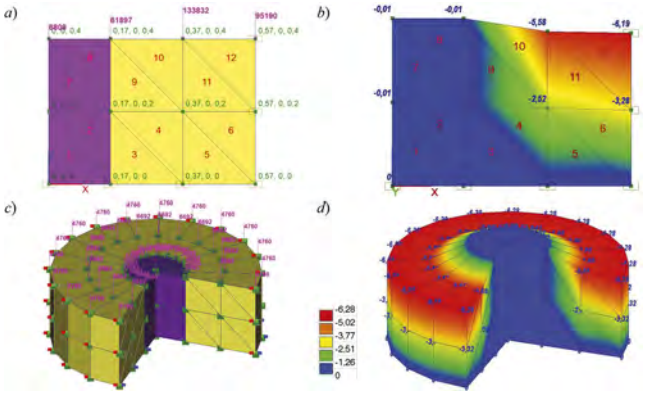

Figure 3. Axisymmetric (above) and spatial finite elements models. Deformations in axisymmetric and in spatial models in SCAD.

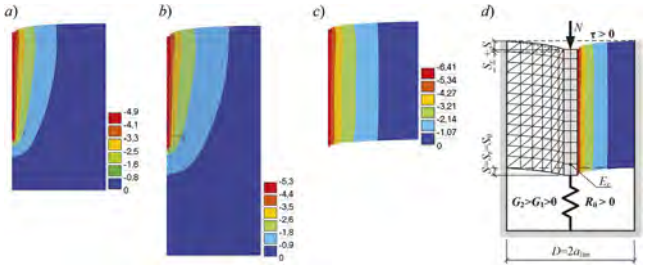

Figure 4. Deformations in axisymmetric single pile model (a, b, c) and diagram of the complex model (b).

2 LARGE PILE FOUNDATION MODELS

2.1 *Numerical model of a large pile foundation under impact of dynamic loads*

In the Figure 5 presented an example of a pile field foundation numerical model accounting on the effect of vertical and horizontal loads, which was considered in detail in the authors' previous publications (Nuzhdin & Mikhaylov 2018b, 2020). The given example of calculating piles in a group in accordance with analytical methods can be implemented by a single algorithm for foundations in the form of a single pile, a group of piles or a pile field with equivalent stiffness at various stages of the formation of the stress-strain state of structures.

At the first step of static numerical modelling in SCAD FEM software, bed coefficients are assigned along the lateral surface of the piles to set their horizontal stiffness, which increases in depth as soil weight increases. Taking into account the horizontal influence of piles in the group (Fedorovsky et.al. 1972, 2003), algorithm begins with the calculation of the reducing coefficient

α. Then the values of the coefficients of the bed C_z on the side faces of the pile are calculated in accordance with the table of stiffness for different types of soils (Zavriev et.al. 1970):

$$C_z = K \cdot z \cdot \frac{\alpha}{\gamma_c}. \tag{5}$$

At the second step of numerical calculation in SCAD, the initial boundary conditions are assigned vertically without taking into account the mutual influence of piles in the group. The calculation of the preliminary vertical rigidity of piles is carried out in accordance with analytical cylindrical two-layer model of a pile (see Equation 2). The shear modulus G_1 of the soil layers cut through by the pile is calculated on the basis of the averaged deformation modulus E_1 and the dimensionless Poisson's ratio ν_1 for the i layers cut through by the pile. Similarly, the shear modulus G_2 is calculated for the soil layers located under the lower ends of the piles. The modulus of deformation of the soil layers located under the pile, E_2, is taken averaged within a depth equal to half the length of the pile $0.5L$ or equal to $10d$ of the reduced pile diameters from the lower ends of the piles. The Poisson's ratio ν_2 is set directly on the layer below the pile tips.

Figure 5 shows a fragment of the algorithm for taking into account the mutual influence of piles in the pile field. The problem is solved using linear programming. An array with imported coordinates of pile nodes is converted into two numerical series with X and Y coordinates. The next step is to form a general matrix a_2 of the relative position of piles in the pile field in the form of calculated distances between piles.

Based on the matrix of mutual arrangement of piles, the δ_2 matrix of vertical mutual influence of piles in the pile field is calculated according to the theory of elastic half-space in the form of additional efforts or in the form of coefficients of reduction of the initial stiffness. This is ensured by performing multiple calculations of each member of the matrix in accordance with the analytical formulas (see Equations 1–4), which provides for zeroing the coefficient of mutual influence of one pile on another when a certain distance between them is exceeded. The limiting radius of influence a_{lim} (see Equation 1), is the radius beyond which there is no mutual influence between piles.

The last step is the calculation of the additional forces ΔN_h, which are the sum of the initial vertical reactions N_h in closely spaced piles, taking into account the coefficient of mutual influence δ. These efforts are necessary for the occurrence in the design scheme of additional deformations in the lower node of each pile and the formation of a common settlement funnel.

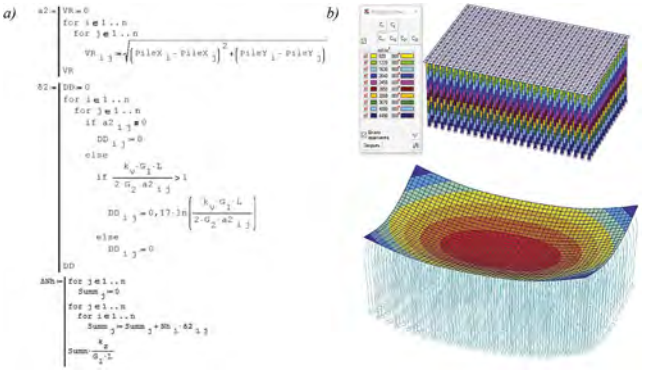

Figure 5. Algorithm of mutual influence of piles in the field (a) and resulting FEM model in SCAD (b).

2.2 *Numerical model of a large pile foundation under impact of static loads*

When performing dynamic calculations, the discrete model of a pile field is the most researched. The reduction in the bearing loads of piles for vertical loads is carried out by

reducing coefficients and by introducing the zone of partial loss of contact with the ground in the upper area of the pile along its side surface in accordance with (Ilyichev et.al. 1983).

For taking into account the horizontal dynamic rigidity of a wide pile field in conditions of seismic impacts the authors recommend methods, used in specialized software as SASSI. Difficulties in developing such a technique are associated with a number of features of the pile foundation (Tyapin A.G. 2000). The increased rigidity of the pile group in comparison with the initial soil in its natural state, as well as the possibility of loss of contact with the soil along the lateral surface of the piles, does not allow us to consider the pile field as a layered half-space with anisotropic properties. The dimensions of the pile sections are so small, and their number is so large that the applicability of discrete models is not feasible in practice.

A new approach is considered by the authors, which adapts the methodology for an impedance numerical-analytical model in the SASSI software for use in direct physical models of pile foundations, which can be implemented in the environment of the widespread FEM programs.

The method is based on the use of dynamic characteristics of soils (modulus of elasticity, shear modulus, Poisson's ratio), studied by seismic and microseismical methods before and after the completion of the pile field. The results of the seismic method on the velocities of elastic waves make it possible to identify soil layers with characteristic of dynamic stiffness, as well as to check their damping properties. If strong seismic movements of the soil are possible on the site, then further data processing for a given intensity of seismicity of the construction site is performed. The experimental data are applied to a foundation direct physical numerical model.

In accordance with (Ilyichev et.al. 1983), only the integral shear stiffness of concrete piles without soil stiffness is taken into account for the calculated depth to which the resistance of the soil on the side surface is not taken into account. The shear stiffness of this layer is defined as the sum of the moments of inertia of single bent piles without taking into account the contribution of the bending component according to Steiner, which is equal to the product of the moment of interference of the section of a single pile by the ratio of the cross-sectional area of the pile to the area of the elementary pile cell. At the same time, in the plane of the pile raft, in order to take into account, the effect of the separation of piles in the plan, an additional connection of the final torsional stiffness in two vertical planes is added to the head of each pile (see Figure 6):

$$C_{\varphi} = \frac{E(I_1 - I_2)}{B}, \tag{6}$$

where E is the elastic modulus of a concrete pile; B – the width of the pile cell; I_1, I_2 - the moments of inertia of a pile, group of piles, accounting the Steiner component and without it.

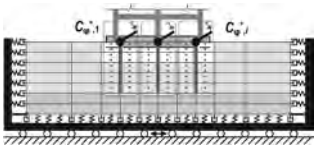

Figure 6. Diagram of a dynamic pile cell.

The following layers of the pile-reinforced soil mass along the perimeter of the pile raft are considered as reduced rigidity in accordance with the lithological structure of the base to the level of the bottom of the piles. The last underlying layer to a depth equal to half the length of the piles, by analogy with the circular cylindrical shear model according to (Fedorovsky V.G. et.al. 2003), is considered as a soil with dynamic modulus, determined by seismic methods.

It should be noted that not in all cases large direct physical models of the pile foundation are necessary (Nuzhdin, Mikhaylov, Yankovskaya, 2019a). If the analysis still indicates the need for the soil-structure interaction analysis, then the rules for constructing direct physical models of the foundation has been published earlier (Nuzhdin, Mikhaylov, Voskresenskiy, 2019b).

3 CONCLUSIONS

The considered complex numerically analytical model of a pile foundation make it possible to implement a universal finite super-element that changes its properties depending on the size of the foundation and the type of impact. The axisymmetric model of a volumetric body of rotation proposed by the authors allows displaying a detailed picture of the stress-strain state of a pile, both single, as part of a small group, and as part of a pile field or a combined pile-slab foundation.

Under static conditions, the rigidity of a horizontally loaded pile in any type of foundation can be represented as a beam on an elastic base. The solution of the differential equation can be performed both numerically and by the finite element method, with the determination of equivalent stiffness at the level of the pile head or at the corresponding nodes along the length of the shaft axis of a discrete pile.

Dynamic impacts always affect the foundation, which is already experiencing deformations from constant and prolonged loads. The approach proposed by the authors makes it possible to take into account the genetically nonlinear conditions of the formation of the stress-strain state of the pile foundation within the framework of the universal numerical-analytical model of the pile. After the perception of horizontal static horizontal loads by piles in the form of a beam on an elastic base, proceed to the integral dynamic rigidity of the pile field, determined on the basis of geophysical studies by seismic methods. This can be done both by uniformly lowering the horizontal coefficients of the bed along the lateral surface of discrete piles by changing the coefficient α, and by lowering the equivalent bending finite stiffness at the level of the pile heads.

REFERENCES

Fedorovsky V.G. 1972. Calculation of the stress-strain state of a multilayer half-space under the action of a concentrated load. *Subsoils, foundations and soil mechanics*, (5), 54–56.

Fedorovsky V.G. and others 2003. Piles in hydraulic engineering construction. Publishing House ASV, Moscow.

Ilyichev V.A., Mongolov Yu.V., Shaevich V.M. 1983. Pile foundations in seismic areas. Stroyizdat, Moscow.

Klovanich S.F. 2009. The finite element method in nonlinear problems of engineering mechanics. Publishing house Svit geotechniki, Zaporozhye.

Nuzhdin L.V. and Mikhailov V.S. 2018a. Models and calculation methods of the pile foundation in SCAD Office. *Proc. XVI DECGE*. Ernst & Sohn. Berlin.

Nuzhdin L.V. and Mikhailov V.S. 2018b. Numerical modeling of pile foundations in the computational and analytical complex SCAD Office. *Bulletin of PNRPU. Construction and Architecture* (8), 5–18.

Nuzhdin L.V., Mikhailov V.S., Yankovskaya I.D. 2019a. On criterion for considering dynamic Soil-Structure Interaction effects. *Proc. GFAC 2019*, 210–215.

Nuzhdin L.V., Mikhailov V.S., Voskresenskiy M.N. 2019b. Methods for subsoil modelling under dynamic impacts and multicomponent damping in SCAD FEA software with geophysical monitoring. Modelling and Methods of Structural Analysis. *J. Phys.: Conf. Ser*. (1). Moscow.

Nuzhdin L.V. and Mikhailov V.S. 2020. Methods of modelling and calculating the system Pile foundation - Ground subsoil in SCAD Office and SMath Studio. *Izv.vuzov*. (5) 42–52.

Schleicher F. Senkungsmittelwert und ahnlichkeitsbedingung fur platen und balken auf isotroper elastischer unterlage // Zeitschrift für Angewandte Mathematik und Mechanik, 1928. B.8. – S. 68-70.

Ter-Ovanesov G.S. 1956. Joint work of foundation slab, piles and soil in hanging pile foundations. *Candidate of Technical Sciences Thesis*. MISI, Moscow.

Ter-Martirosyan Z.G. and Dinh Hoang Nam 2006. Interaction of long piles with soil in the pile foundation. *Thesis of Candidate of Technical Sciences*. MSUCE, Moscow.

Tyapin A.G. 2000. Modeling of a pile field in calculations for seismic impacts. *Earthquake safety of structures* (2) 23–26.

Zavriev K.S. et.al. 1970. Calculation of the bridge foundations with deep laying of supports. Rotaprint, Moscow.

Smart Geotechnics for Smart Societies – Zhussupbekov, Sarsembayeva & Kaliakin (Eds)
© 2023 The Author(s), ISBN 978-1-003-29912-7
Open Access: www.taylorfrancis.com, CC BY-NC-ND 4.0 license

Segmental retaining wall monitoring technique using single camera system with various conditions

Y.S. Ha, M.V. Pham & Y.T Kim
Pukyong National University, Busan, Republic of Korea

ABSTRACT: Various types of Segmental Retaining Wall (SRW) are widely used worldwide for land use in slope areas. Inspections are periodically performed on the retaining wall, and various studies have been conducted to analyze the behavior of the retaining wall according to load and rainfall. However, the collapse of SRW continues to occur, and most collapses of SRW are attributed to facing displacement and settlement caused by water pressure and earth pressure. In this study, the behavior of SRW was monitored from a single camera system consisting of monocular vision and feature matching considering various conditions such as noise and brightness in the image. Performances of image registration and behavior calculation were evaluated from the results of several experiments. Behavior measurement error in controlled conditions was distributed within 1.89mm, and RMSE and MRE were 1.22 mm and 3.68%, respectively.

1 INTRODUCTION

In order to secure the stability of segmental retaining wall (SRW), the agency in charge manages SRW according to the maintenance guidelines. A general safety inspection is periodically carried out at least two times a year, and a precision safety inspection is conducted once every 1-3 years, according to the Special Act on the Safety and maintenance of Public Structures to inspect the physical condition of SRWs (KALIS, 2019). In addition, Koerner and Koerner (2018) investigated the collapses of 320 geosynthetic reinforced mechanically stabilized earth walls around the world, the primary causes of the collapses were inadequate or improper design and/or construction. The major design inadequacy appears to be the use of fine-grained soils in the backfill and the lack of proper drainage systems. The major construction inadequacy is the use of fine-grained silt and clay as backfill soils and inadequate placement and compaction. In addition, the collapse of SRW continues to occur owing to various causes such as poor drainage systems, inadequate compaction of backfill material, insufficient length of reinforcement, and problems in design and construction.

In this study, a single-camera monitoring system was developed to monitor displacements occurring in individual blocks within SRW under various conditions. And the monitoring performance for SRW in laboratory conditions was evaluated, and the monitoring performance for SRW was analyzed considering the illuminance change that may occur in the field.

2 EXPERIMENT

2.1 *Laboratory experiment*

The laboratory experiment was performed preferentially to evaluate the matching and displacement calculation performance under controlled conditions in a laboratory environment. Figure 1a shows an experimental SRW (width: 650 mm, height: 270 mm) made of 121 blocks. Figure 1b shows the experimental setup, consisting of SRW blocks, a camera, and a total

DOI: 10.1201/9781003299127-385

station. The camera was installed at a position (θ_x = 43°, D = 1267 mm) in the range of incident angles (20–70°) suggested through the pilot-phase experiment. Four steps of facing displacement and settlement were generated step by step using the displacement generator under the structure.

The displacements were calculated by matching and analyzing the images of the evenly distributed 10 target blocks (red boxes in Figure 1a) taken before and after the behaviors. The matching performance was evaluated based on repeatability, matching score, number of inlier matching features, and mTRE. The displacement calculation performance was evaluated by comparing the reference displacements of the 10 parts, which were measured from the total station. The correlation between the matching and displacement calculation performance for the 10 parts was also analyzed.

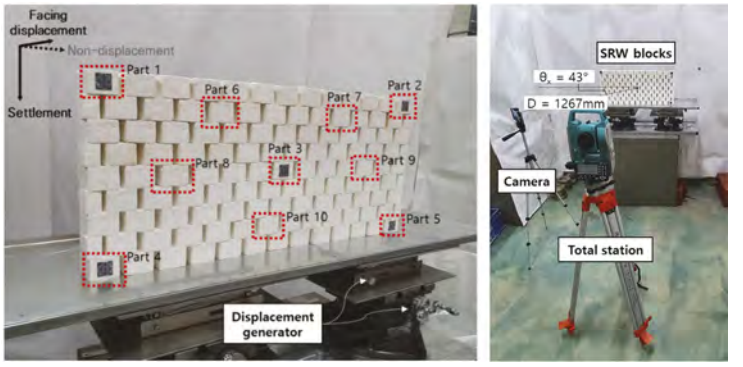

Figure 1. Laboratory experiments: (a) Monitoring targets for detection and tracking behavior, (b) experimental setup of camera and total station.

2.2 *Laboratory experiment with different illuminance*

In the case of short-time monitoring of SRW, there is no significant change in illuminance and position of the light source. However, when it is installed in the field and monitored for a long time, various changes in the SRW image occur, such as a change in illuminance and a change in the position of the light source according to the time change. The purpose of this study is to evaluate the performance of single-camera monitoring system matching and displacement calculation for illuminance change. Figure 2a shows the distribution of illuminance measured for one day in Busan in October. At noon when the sun rises vertically in the sky, it becomes bright up to 75,500 lx and maintains the brightness of over 50,000 lx even with obstacles such as clouds. In a location without illumination at night, it converges to 0 lx with or without moonlight. But SRWs have streetlights installed around them. Therefore, the illuminance was measured in the direction perpendicular to the ground, such as the facing of the retaining wall, at a distance of 5.5 m (2 lanes of road) from the street lamp. The illuminance of 36 lx was maintained in the state of the street lamp illuminating regardless of dawn and night. Figure 2b shows the experimental setup with different illuminances. The same block, total station, and camera were used in the laboratory experiment, and a floodlight was used for illuminance control. The camera was installed at a position (θ_x = 48°, D = 1, 160 mm). Facing displacement was generated using the displacement generator under the structure. In order to minimize the effect of changes in the position of the floodlight, the light on the front of the fixed floodlight was gradually blocked and the illuminance was adjusted. The detection and displacement calculation performance of the block was evaluated by generating a facing displacement for each illuminance. The displacements were calculated by matching and analyzing the images of the evenly distributed 10 target blocks taken before and after the behaviors.

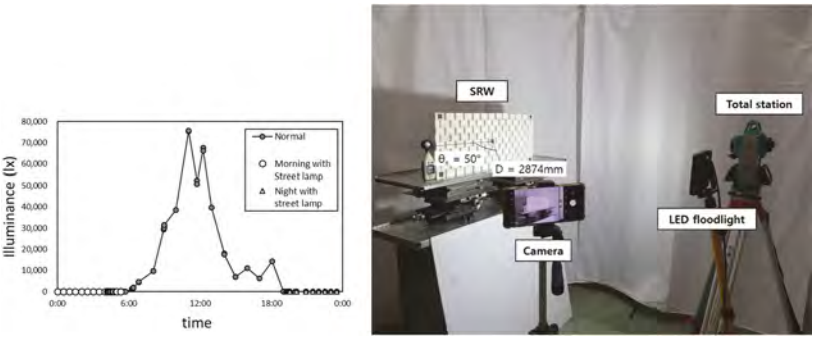

Figure 2. Experimental set up with different illuminance (a) daily illuminance distribution, (b) experimental setup.

3 RESULT AND DISCUSSION

3.1 *Laboratory experiment*

Figure 3 shows an example of the blocks trained and detected for the laboratory experiment. 9 images were used for validation, and 2 images are shown in the figure. Each column represents the original image, ground truth, and predicted mask. Although blocks could not be detected for some sections for each image, laboratory SRW blocks were detected with the precision of 92.28%, recall of 92.51%, and f1 score of 92.31%. Figure 4 shows the results of calculating the behavior based on the detected blocks. In the case of using mask R-CNN, since transformation by behavior is not considered, the error does not increase significantly for each behavior step. In addition, the performance is excellent with an error within 2.12mm. Figure 4b shows the MRE of ATs and NTs for the laboratory experiment. The MRE of NTs were smaller than those of ATs, sheet target was attached in front of ATs which was disturbed to detect the blocks.

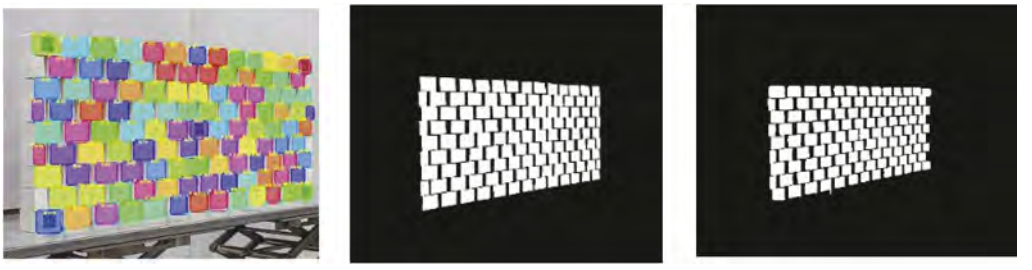

Figure 3. An example of the blocks trained and detected for the laboratory experiment: (a) detected image, (b) trained mask, (c) detected mask.

3.2 *Laboratory experiment with different illuminance*

Figure 5 shows an example of training and detection blocks for an experiment with different illuminance. Each column represents the original image, ground truth, and predicted mask, and the precision, recall, and f1 score for 9 images used for validation are shown in Table 4.6. In some cases, blocks could not be detected for some sections of each image, but laboratory SRW blocks were detected with the precision of 93.19%, recall of 95.10%, and f1 score of 94.08%. Figure 6 shows the results of calculating the behavior based on the detected blocks. Mask R-CNN shows similar performance in all illuminances because it detects blocks according to the trained target illuminance by changing the illuminance. However, in the case of the minimum value, it tends to gradually decrease as the illuminance increases, which means that detection performance can be excellent in images with high illuminance. The highest error for each illuminance occurs largely in part 1, 2, 4, and 5, and it is located at the corner of the

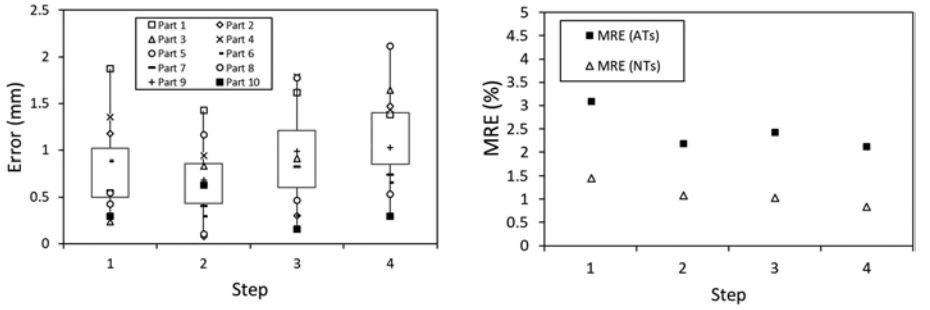

Figure 4. Results of displacement calculation error for laboratory experiment: (a) error, (b) MRE.

SRW structure, and detection performance is poor. MRE was distributed within 1.43 %. The block existing inside the structure, which is not at the edge of SRW, showed excellent performance with an error within 1.68mm despite the change in illuminance.

Figure 5. An example of training and detection blocks for an experiment with different illuminance: (a) detected image, (b) trained mask, (c) detected mask.

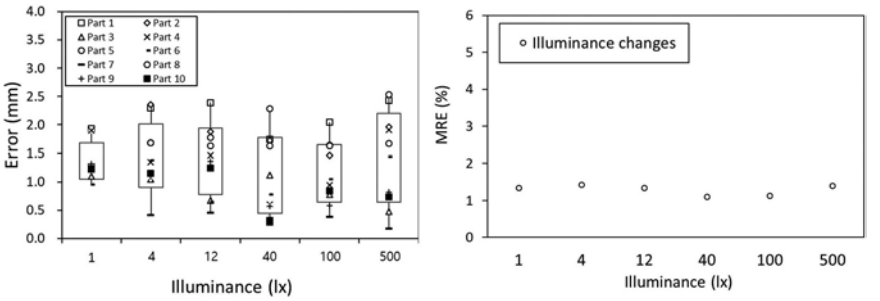

Figure 6. Results of displacement calculation error for experiment with different illuminance: (a) error, (b) MRE.

ACKNOWLEDGEMENT

This work was supported by a Technology Innovation Program (Grant K-G012001951201) funded by the Ministry of Trade, Industry & Energy (MOTIE, Korea).

REFERENCES

KALIS. Safety Inspection Manual for National Living Facilities, Korea Infrastructure Safety Corporation, Seoul, Korea, 2019, p. 6.

Koerner, R.M. and Koerner, G.R. An Extended Data Base and Recommendations Regarding 320 Failed Geosynthetic Reinforced Mechanically Stabilized Earth (MSE) Walls. Geotextiles and Geomembranes 2018, 46, 904–12.

Smart Geotechnics for Smart Societies – Zhussupbekov, Sarsembayeva & Kaliakin (Eds)
© 2023 The Author(s), ISBN 978-1-003-29912-7
Open Access: www.taylorfrancis.com, CC BY-NC-ND 4.0 license

Improvement of large-scale box shear apparatus by reducing interface friction

Sreng Sokkheang Suzuki
R&D Center, Nippon Koei Co. Ltd., Tsukuba, Japan

Hiroki Ishikawa
Osaka Branch, Nippon Koei Co. Ltd., Osaka, Japan

Kentaro Uemura
R&D Center, Nippon Koei Co. Ltd., Tsukuba, Japan

ABSTRACT: In this study, a large-scale box shear apparatus was improved to evaluate shear strength of coarse-grained materials. Interface friction problem occurred between specimen and inner side of shear box was successfully reduced by improvement of the box shear apparatus. The improved large-scale box shear apparatus was applied to evaluate shear strength of two different coarse-grained materials. Triaxial compression tests for both materials were also conducted in CD condition to compare with the box shear tests. It was found that the Interface friction caused by dilation of specimen affected shear strength of the coarse-grained materials and should not be ignored. The results (shear strength) obtained from the box shear tests are almost the same as the results of triaxial compression tests. It was revealed that the improved large-scale shear box apparatus can be used to evaluate accurately shear strength of coarse-grained materials.

1 INTRODUCTION

The box shear test is one of several direct shear test methods, and it is superior compared with the triaxial compression test because of the following reasons. (1) The structure of the apparatus is simple, and the test method is easy. (2) The stress state on the shear plane should be clear. (3) It is possible to perform tests under low confining pressure conditions. (4) There are no test restrictions, such as the self-sustaining limit of large specimens, even for coarse-grained materials. However, in the conventional large-scale direct shear test apparatus for coarse-grained materials such as rockfill dam materials, it has been reported that owing to structural problems of the test apparatus, the obtained shear strength shows an excessive value compared with the triaxial compression test result; for example, the internal friction angle ϕ shows a maximum difference of about 15° (JGS 1986). It has been proposed that the main reason for this is that because the vertical displacement of the shear box is constrained in the direct shear test (constant-pressure test), there is friction (interface friction) between the specimen and the inner surface of the shear box owing to positive dilatancy during shear test (Takada & Yunoki 1984, JGS 1986, Hongo et al. 1995). However, this problem has not been solved from a practical perspective, and the current situation is that the direct shear test is not actively used.

Many studies have been conducted to determine the effects of interface friction using small- and medium-sized single-shear tests (Takada & Yunoki 1984, Hongo et al. 1995, Shibuya 1995, Oshima et al. 1996, JGS 1997, Ishikawa et al. 2009). A summary of past research is as follows.

Takada & Yunoki (1984) developed a medium-sized box shear test (specimen (rectangular parallelepiped) dimensions: length 30 cm × width 20 cm × height 12 cm) for coarse-grained materials. This test apparatus is designed to move the upper shear box in the shear direction,

DOI: 10.1201/9781003299127-386

and it enables two types of tests: (1) the "pressure plate fixed-type" test that integrates the penetration shaft (loading plate) and the lower shear box; and (2) the "pressurized plate penetration type" test, in which the penetration axis penetrates the lower shear box. In the case of the pressure plate fixed-type test, because the shear box and the specimen move together, the effect of interface friction is negligible. By comparing the results for coarse-grained material (maximum grain size 15.9 mm) from both types of testers, it was noted that the shear strength is overestimated because of the effect of interface friction during specimen expansion, and that the shear strength is underestimated during specimen contraction.

Next, Oshima et al. (1996) installed two parallel plate load cells between the upper shear box and the vertical reaction roller, and they made improvements that enable the measurement of the change in upper vertical stress (σ_U) due to the occurrence of positive dilatancy (specimen (cylindrical) dimensions: diameter 12 cm × height 4 cm). Here, to consider the effect of interface friction, we conduct (1) a test in which the vertical stress σ_L at the bottom is constant in the conventional method while measuring σ_U (conventional constant pressure test), and (2) a test (true constant-pressure test) to control the vertical stress (σ_L) at the bottom so that σ_U is constant in order to verify that the strength constant of sand (maximum grain size 0.425 mm) could be obtained with good accuracy, and this was adopted in the Japanese Geotechnical Society Test Standard (JGS 1997) (Method for consolidated constant-pressure direct box shear test on soils JGS T 561-1997).

In addition, Ishikawa et al. (2009) improved the structure of a Mikasa-type direct shear test apparatus (Mikasa 1960) (size of specimen (cylinder): diameter 6 cm × height 2 cm) to prevent the generation of interface friction. This test apparatus is equipped with two independent air jacks and load cells between the upper surfaces of the upper shear box, and it has a structure that maintains a strictly constant pressure by slightly moving it up and down while keeping the upper shear box horizontal (the structure is the same as the "pressure plate fixed-type" test proposed by Takada & Yunoki (1984)). This test apparatus is capable of conducting tests under low confining pressure conditions. It is reported that the results of Toyoura sand (maximum grain size: 0.425 mm) and the results of the triaxial compression test obtained using this device were almost the same.

In this study, based on the above-mentioned previous studies, a large-scale box shear apparatus (specimen (cubic) dimension: length 30 cm × width 30 cm × height 20 cm) with reducing the interface friction was improved. Actual rock material and crushed stone material (maximum grain size 37.5 mm) were used in this study. Triaxial compression tests (CD test, specimen (cylindrical) dimensions: 15 cm in diameter × 30 cm in height) were also conducted. The effect of interface friction in a large-scale box shear test, the comparisons between results of box shear tests and triaxial compression tests were compared and discussed.

2 TEST MATERIALS

The materials used in the tests were two types of grain size adjustment materials (maximum grain size: 37.5 mm), rock material (referred to as Material No.1), and C-40 crushed stone (referred to as Material No.2). Figure 1 shows the grain size distribution curves of the materials.

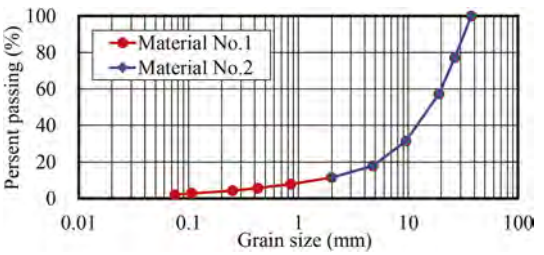

Figure 1. Grain size distribution curve.

3 IMPROVEMENT OF LARGE-SCALE BOX SHEAR TEST APPARATUS

Figure 2 shows the outline of the structure of the improved large-scale box shear test apparatus. This apparatus is a movable-type lower shear box. To prevent the generation of the interface friction, a vertical roller is installed between the upper shear box and the reaction plate, and the vertical movement of the upper shear box is made possible by following the volume change of the specimen that occurs during the shear test process.

In addition, hydraulic hand pumps (see Figure 2) are placed at both ends of the horizontal adjustment beams attached to the upper shear box to apply a moment in order to keep the upper shear box horizontal during shear test. Furthermore, in order to confirm the effect of interface friction on the shear strength evaluation of coarse-grained materials such as rock materials, we compared the conventional box shear test method in which the upper shear box is fixed in the vertical direction (see Figure 3, hereinafter referred to as "fixed-type") with the method in which the upper shear box can be moved vertically by using the test apparatus improved by the above method (hereinafter referred to as "movable-type"). With this test apparatus, it is possible to perform "fixed-type" or "movable-type" tests by respectively fixing or not fixing the upper shear box. Next, triaxial compression tests were performed under the same specimen conditions, and the shear strength characteristics were compared with the results of the movable-type large-scale box shear test.

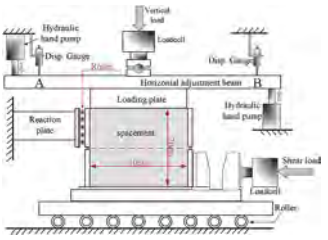

Figure 2. Schematic diagram of movable-type large-sized box shear test apparatus.

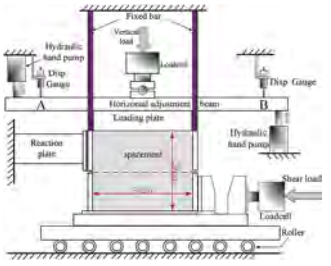

Figure 3. Fixed-type large-scale box shear test (conventional type).

4 TEST CASES AND CONDITIONS

The test conditions are as shown in Table 1. The specimens (cubic shape, dimensions: length 30 cm × width 30 cm × height 20 cm) for the large-scale box shear test were air-dried for both materials No.1 and No.2. The specimens were prepared by using compaction method in three layers so that the dry densities were ρ_d = 1.997 g/cm^3 and ρ_d = 2.004 g/cm^3 (both with degree of compaction (D_c) = 95%), and also so that the shear plane does not coincide with the joint plane.

For comparison, a medium-sized triaxial compression test (CD test) specimen (cylindrical with a diameter of 15 cm and a height of 30 cm) was also prepared by five-layer compaction with the same dry density as above.

5 HORIZONTAL AND VERTICAL STRESS CONTROL OF THE LOADING PLATE

The loading plate horizontal control of this test apparatus monitored the movement of the displacement gauge attached to the horizontal adjustment beam shown in Figure 2 and manually controlled the hydraulic hand pump. Figure 4 shows the relationship between the displacement error of the leveling beam and the shear displacement that was measured during the test. Here, the displacement error is the difference between the vertical displacement of point A and point B measured at both ends of the horizontal adjustment beam shown in Figure 2 (displacement error = point B displacement – point A displacement). When the value of the displacement error is positive, it means that point A falls and point B rises, and vice

Table 1. Test cases and conditions.

Test name	Movable-type large-scale box shear test	Fixed-type large-scale box shear test	Medium triaxial compression test
Specimen preparation	Compaction method	Compaction method	Compaction method
Specimen density (Dc = 95%)	Material No.1 ρ_d = 1.997 g/cm^3 Material No. 2: ρ_d = 2.004 g/cm^3	Material No.1 ρ_d = 1.997 g/cm^3 Material No. 2: ρ_d = 2.004 g/cm^3	Material No.1 ρ_d = 1.997 g/cm^3 Material No. 2: ρ_d = 2.004 g/cm^3
Test conditions	Constant pressure, unsaturated	Constant pressure, unsaturated	CD test, saturated
Shear rate	1.3 mm/min	1.3 mm/min	0.5%/min
Normal stress/Confining pressure (kN/m^2)	σ_n = 50, 100, 200, 300	σ_n = 50, 100, 200, 300	σ_3 = 50, 100, 200

versa when it is negative. The distance between the displacement gauges installed on the horizontal adjustment beam is 236 cm.

In some cases, the displacement error shown in Figure 4 momentarily reached ±0.8 mm, but it generally remained within ±0.5 mm (inclination angle is within ±0.005°), and it is determined that there is no problem with the accuracy of horizontal control. In addition, Figure 5 shows an example of the relationship between the controlled normal stress and shear displacement (Material No.2, unsaturated condition) in a movable-type large-scale box shear test under constant pressure conditions. The control of the normal stress is within the range of ±0.5 kN/m^2 to ±1 kN/m^2 (0.5% to 2%) of the set value of the normal stress, and it can be seen that a nearly constant pressure state is maintained.

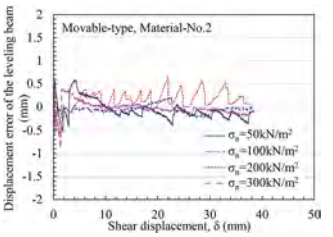

Figure 4. Result of horizontal control of loading plate (movable-type).

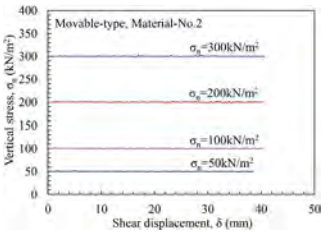

Figure 5. Relationship between controlled vertical stress and shear displacement (movable-type).

6 INFLUENCE OF INTERFACE FRICTION

In order to confirm the effect of interface friction, the movable-type large-scale box shear test and the conventional fixed-type large-scale box shear test were conducted under the same conditions using two materials, and a comparative study was carried out to determine parameters such as the condition of the specimen after the test, the shear strength characteristics, and the dilatancy characteristics.

Figure 6 shows the conditions of fixed-type and movable-type specimens after the large-scale box shear test.

For the fixed-type shown in Figure 6(a), it was confirmed that the gap between the upper and lower shear boxes remains unchanged, and that the upper surface of the specimen expanded beyond the top of the upper shear box owing to the volume change (positive dilatancy) on the expansion side that occurred during shear test. Therefore, as shown in Figure 7(a), it can be inferred that the occurrence of interface friction between the inner surface of the shear box and the specimen is the cause of the increase in vertical stress, which significantly affects the shear strength. However, Figure 6(b) shows the state of the specimen after shear test using the improved movable -type large-scale box shear test. Unlike the conventional fixed-type test, the upper surface of the

specimen after shear test did not expand beyond the upper edge of the upper shear box, and the shear gap opened with positive dilatancy. Therefore, it is clear that the part of the specimen above the shear zone was integrated with the upper shear box and floated in an upward direction.

Figure 8 shows a comparison of the relationship between shear stress and dilatancy for fixed-type and movable-type in the case where σ_n = 100 kN/m^2. From the figure, in the fixed-type test, the vertical displacement (positive dilatancy) generated during shear test is smaller than in the movable-type test because the specimen is constrained by interface friction. As a result, it can be interpreted that the shear stress of the fixed-type is larger than that of the movable-type test.

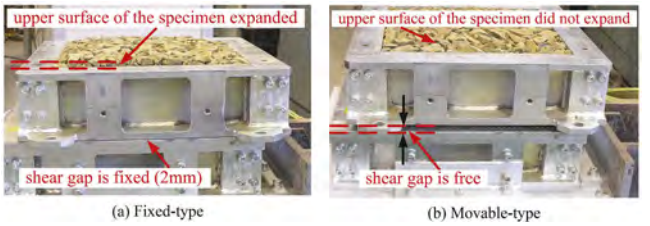

Figure 6. Comparison of specimen status after testing.

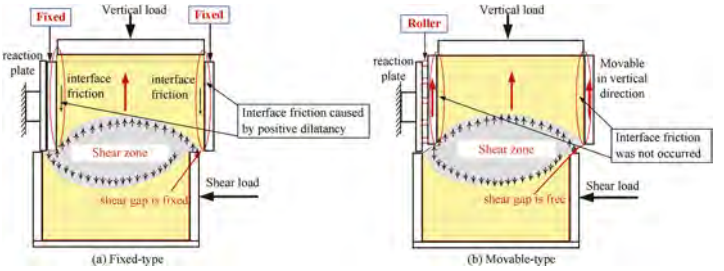

Figure 7. Mechanism of interface friction occurring during shearing.

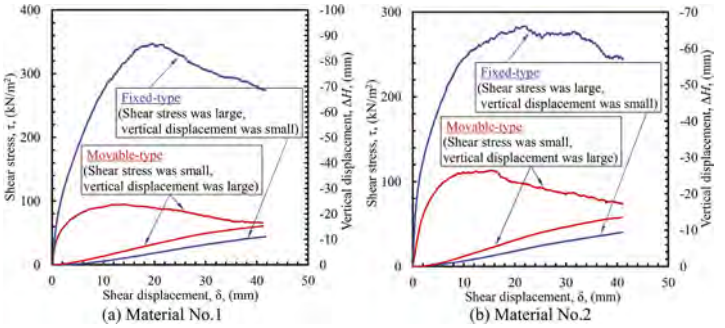

Figure 8. Comparison of shear processes.

7 COMPARISON OF TEST RESULTS

Figure 9 compares the shear strength for the fixed-type and movable-type tests. Figure 9(a) is the result of Material No.1, and Figure 9(b) is the result of the Material No.2. The results of the triaxial compression test are also plotted in the figure. The triaxial compression test results were organized as normal stress $\sigma_n = (\sigma_1+\sigma_3)/2 + (\sigma_1-\sigma_3) \times \cos 2\alpha/2$ and shear stress $\tau_n = (\sigma_1-\sigma_3) \times \sin 2\alpha/2$. Here, $\alpha = 45° + \phi_0/2$ and $\phi_0 = \sin^{-1}\{(\sigma_1-\sigma_3)/(\sigma_1+\sigma_3)\}$.

It can be seen that the proposed movable-type test results (shear strength) are almost the same as the triaxial test results. However, the fixed-type test results are considerably larger than those of the movable-type and triaxial tests (maximum c is about 10 times larger and ϕ is about 15° greater).

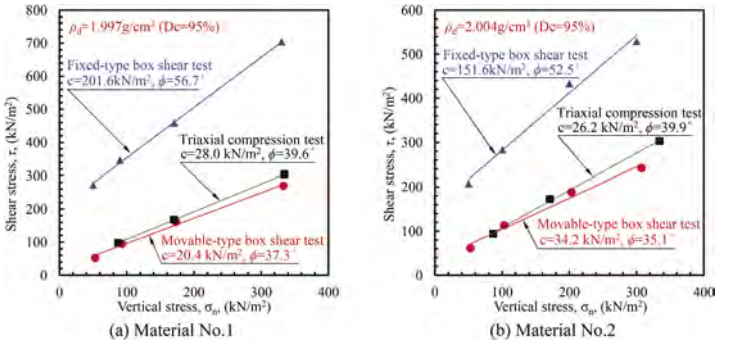

Figure 9. Comparison of test results.

8 CONCLUSION

Because the improved movable-type large-scale box shear test can obtain almost the same shear strength as the triaxial compression test, this test method was considered to be appropriate. In addition, the improved box shear test can be performed under low confining pressure, and it is possible to conduct the test using materials with a maximum grain size exceeding 63 mm. Therefore, the combination of uses of triaxial test and box shear test, it is expected that the evaluation of the shear strength of coarse-grained materials can be performed more rationally in the future. Furthermore, it is believed that it can also be used in some countries, where it is difficult to conduct large-scale triaxial tests.

REFERENCES

Hongo, T., Akai, T. & Ikeda, T. 1995. Automation and applicability of direct shear tester. *Symposium on Direct Shear Test Methods and Applications*: 135–140. Tokyo: Japanese Geotechnical Society.

Ishikawa, H., Liu, Y., Mochizuki, A., Okada, S., & Sreng, S. 2009. Development of new direct shear apparatus and discussion on its effectiveness. *Japanese Geotechnical Journal* 4(1): 11–19. Tokyo: Japanese Geotechnical Society.

Japanese Geotechnical Society 1986. *Deformation and strength of coarse-grained materials*: 132–167. Tokyo: Japanese Geotechnical Society.

Japanese Geotechnical Society 1997. *Japanese Geotechnical Society Standard and Commentary IV (FY1997 Edition)*: 15–49. Tokyo: Japanese Geotechnical Society.

Mikasa, M. 1960. New single shear tester. *Proceedings of the 15th Annual Conference of the Japan Society of Civil Engineers*: 45–48. Tokyo: Japan Society of Civil Engineers.

Oshima, A., Takada, N. & Sakamoto, K. 1996. Comparison of single shear conventional constant pressure test and true constant pressure test. *Proceedings of the 31st Japan National Conference on Geotechnical Engineering*: 665–666. Tokyo: Japanese Geotechnical Society.

Shibuya, S. 1995. Recent advances in direct shear testing of soils and interpretation of results. *Symposium on Direct Shear Test Methods and Applications*: 67–86. Tokyo: Japanese Geotechnical Society.

Takada, N. & Yunoki, Y. 1984. Comparison of simple and box shear of coarse grained soils. *Soil Mechanics and Foundation Engineering* 32(5): 17–22. Tokyo: Japanese Geotechnical Society.

Smart Geotechnics for Smart Societies – Zhussupbekov, Sarsembayeva & Kaliakin (Eds)
© 2023 The Author(s), ISBN 978-1-003-29912-7
Open Access: www.taylorfrancis.com, CC BY-NC-ND 4.0 license

Evaluation of the work of driving piles under dynamic loads

G.T. Tleulenova, A.R. Omarov, A.S. Tulebekova & G.K. Tanyrbergenova
L.N. Gumilyov Eurasian National University, Astana, Kazakhstan

R.K. Bazilov
LLP "KGS-Astana", Astana, Kazakhstan

ABSTRACT: The aim of the work is a complex of studies of the operation of driven piles in the presence of loads. To achieve this goal, the following tasks were set: to analyze theoretical and experimental data in the field of driven pile research; carrying out a calculated assessment of the capabilities of driven piles according to regulatory documents; comparison of comparative analyzes of indicators of bearing capacity of driven piles based on test results.

Keywords: pile, normative standard, tests, bearing capacity

1 INTRODUCTION

1.1 *Construction site*

The purpose of the tests is to determine the pile driving depth and the pile bearing capacity. The dynamic pile load tests on preliminary C70.30-8 driven piles and C70.30-6 working piles on the construction site of the Project "Construction of multifunctional family-entertainment and tourist area" in the city of Astana, were carried out by specialists of KGS-Astana LLP.

Driving of preliminary C70.30-8 piles in the amount of 21 pieces subjected to dynamic tests was carried out by KGS-Astana LLP on January 28 to February, 25, 2021. Driving of working C70.30-6 piles in the amount of 7 pieces, also subjected to dynamic tests, was carried out from January 16 to January 25, 2021.

When driving preliminary piles, a Junttan PM-20 pile-driving rig was used with an HHK-5A hydraulic hammer with a shock mass of 5000 kg with a cap, and a weight of 835 kg. When driving working piles, Junttan PM-25 pile-driving rigs were used with hydraulic hammers HHK-7A and HHK-9A with a shock mass of 7000 kg and 9000 kg, with caps weighing 990 kg and 1160 kg, respectively.

2 RESEARCH METHOD

2.1 *Dynamic pile load testing*

Characteristics of the tested piles: C70.30-8, 7.0 m long, section 30x30 cm. Absolute elevations: soil surface: 345.66m; the bottom of the piles according to the project: 336.325m.

Dynamic pile load tests are carried out in order to determine the possible depth of their penetration and changes in the value of refuses, as well as to assess the bearing capacity of the piles. Dynamic pile load tests should be performed in accordance with the requirements. The piles will be driven by a Junttan HHK-5A hydraulic hammer with a hammer weight of 5000kg and a cap with a weight of 835kg. Preliminarily, the pile surfaces are marked in graduations with paint every 1m, and every 0.1m on the last meter.

DOI: 10.1201/9781003299127-387

During the dynamic pile load testing the following types of work are carried out:

- delivery of piles to the point of driving,
- while observing measures that exclude breakages and cracks in the pile body;
- the customer defines and produces a geodetic breakdown of pile tests;
- test piles are driven to the design elevation or to their possible depth of penetration.

Testing of preliminary piles, stage 1:

- preliminary pile marking from the tip every 1m to 5m, then 10cm to the expected possible depth of penetration;
- moving the pile driving unit to the place of test pile driving;
- installation of piles at the point of their driving and driving piles with an impact energy that ensures penetration in dense soils, to the maximum depth;
- calculate the number of hammer blows for each meter of pile penetration, and on the last meters - for every 10 cm of penetration.

Testing of preliminary piles, stage 1: the 'rest' of the piles is maintained for 3 to 6 days; before after-driving, a millimeter measuring tape is attached to the driven piles;

- pile after-driving is carried out by single blows with the same equipment that was used during driving,
- the drop height of the striking part of the hammer during after-driving must be constant;
- after-driving is carried out with two consecutive counts of 3 and 5 blows.

The largest average refusal is taken as the estimated pile refusal; pile penetration is recorded using a measuring tape with an accuracy of 1 mm; in the process of pile driving, an observation log shall be kept, upon completion of the tests the pile test report shall be filled in.

3 TEST RESULTS AND DISCUSSION

Table 1 presented results of dynamic load test of construction site.

Table 1. Results of DLT.

	Pile number	Pile mark and section, cm	Abs. elevations of the soil surface near the pile, m	Depth of driving piles into the soil, m	Particular value of pile ultimate resistance, (t)	Bearing capacity of piles	Design allowable pile-bearing load, taking into account the reliability factor γ_k=1.4, (t)
1	P1 TP1	C7-30, 30x30	345.66	6.20	58.3	48.7	34.8
2	P1 TP2	C7-30, 30x30			58.3		
3	P1 TP3	C7-30, 30x30			-		
4	P1 TP5	C7-30, 30x30			36.4		
5	P1 TP6	C7-30, 30x30			60.8		
6	P1 TP7	C7-30, 30x30			64.8		
7	P1 TP9	C7-30, 30x30			68.2		
8	P1 P462	C7-30, 30x30			49.3		
9	P2 TP1	C7-30, 30x30			58.3	70.4	50.3
10	TP2	C7-30, 30x30			63.7		
11	TP5	C7-30, 30x30			65.9		
12	TP6	C7-30, 30x30			84.9		
13	TP7	C7-30, 30x30			80.7		
14	TP8	C7-30, 30x30			84.9		
15	P3 TP1	C7-30, 30x30			48.3	42.7	30.5
16	P3 TP3	C7-30, 30x30			30.6		

(*Continued*)

Table 1. (*Continued*)

	Pile number	Pile mark and section, cm	Abs. elevations of the soil surface near the pile, m	Depth of driving piles into the soil, m	Particular value of pile ultimate resistance, (t)	Bearing capacity of piles	Design allowable pile-bearing load, taking into account the reliability factor γ_k=1.4, (t)
17	P3 TP4	C7-30, 30x30			36.9		
18	P3 TP5	C7-30, 30x30			56.7		
19	P3 TP6	C7-30, 30x30			68.2		
20	P3 TP7	C7-30, 30x30			80.7		
21	P3 TP9	C7-30, 30x30			80.7		

The bearing capacity of the piles was determined on the basis of statistical processing of test results in accordance with GOST 20522-96.

4 CONCLUSION

The bearing capacity of the piles according to the results of dynamic tests was 48.7 tons for Parking Zone P1; 70.4 tons for Parking Zone P2; 42.7 tons for parking Zone P3. The design allowable pile-bearing load should be taken with consideration of the reliability factor γ_k = 1.4 SP RK 5.01-103-2013 Pile foundations should be taken equal to: 34.8 tons for Parking Zone P1; 50.3 tons for Parking Zone P2; 30.5 tons for parking Zone P3.

REFERENCES

Zhussupbekov, A., Eun Chul Shin, Shakhmov Zh & Tleulenova, G. 2018. Experimental study of model pile foundations in seasonally freezing soil ground. *International Journal of GEOMATE 15(51)*: 85–90.

Smart Geotechnics for Smart Societies – Zhussupbekov, Sarsembayeva & Kaliakin (Eds)
© 2023 The Author(s), ISBN 978-1-003-29912-7
Open Access: www.taylorfrancis.com, CC BY-NC-ND 4.0 license

Application of in-situ static load test of pile in Nur-Sultan

A.Zh. Zhussupbekov, G.T. Tleulenova, Zh.A. Shakhmov & A.A. Jumabayev
Eurasian National University, Nur-Sultan, Kazakhstan

R.K. Bazilov
LLP "KGS-Astana", Nur-Sultan, Kazakhstan

ABSTRACT: The paper presents discussions of the bearing capacities of precast concrete piles from construction site of the Construction of multifunctional family-entertainment and tourist area in the city of Nur-Sultan, Kazakhstan. According to the design drawings construction site was planned to be installed by precast concrete piles. PCPs were composed with cross-section of 30 cm × 30 cm with the length of bottom segment 7.0m. In paper presented in-situ static vertical loading tests on C7-30 driven piles were carried out on the construction site of the Parking Zone P1, P2 of the Project 'Construction of multifunctional family-entertainment and tourist area in the city of Nur-Sultan, from 05 to 13 February, 2021. The permissible load on the pile, taking into account the safety factor γ_k =1.2 in accordance with Standard should be taken equal to – 681 kN, 800 kN respectively.

Keywords: load-settlement, in-situ SLT tests, pile

1 INTRODUCTION

1.1 *Construction site*

In-situ static load tests on C7-30 driven piles on the construction site of the Project 'Construction of multifunctional family entertainment and tourist area in the city of Nur-Sultan, were carried out by specialists of KGS-Astana LLP according to the Agreement with Renaissance Construction JSC.

Characteristics of the tested piles: Driven pile C7-30, section 30x30 cm, length 7.0 m (Figure 1).

Figure 1. Mounting kentledge system.

DOI: 10.1201/9781003299127-388

Table 1 presented absolute elevations of piles P480, P1210.

Table 1. Absolute elevations.

Pile number	P480	P1210
- soil surface at the pile	345.66	345.66
- pile heads	346.36	346.36
- pile bottom	339.36	339.36

Transportation, installation of the test and loading stand and cargo was carried out from 04.02.2021 to 11.02.2021.

2 RESEARH METHODS

2.1 *Equipment and devices*

Testing and loading stand. Support structure for the reception of reactive forces: main beam, support platform and load piles. Hydraulic jack. Loading for testing with static vertical driving loads shall be performed with an Enerpac CLS2006 185 ton hydraulic jack. Pressure gauge. The pressure shall be recorded by a MA100VU100 type pressure gauge with a graduation rate of 20 bar (kgf/cm2) up to 1000 bar (kgf/cm2).

Displacement measuring sensors. Pile displacements shall be measured by four digital electronic converters of 028DG1, 028DG2 and 028DG3 type. Digital dynamometer. The load shall be recorded by a digital Load Cell type dynamometer connected to the SLT2 system. Pumping station. The hydraulic jacks are pressurized with a P462 hand pump. Reference system. A steel equal angle 63x63x5, 4 m long, fixed to the reinforcement, driven into the ground to a depth of at least 1.0 m shall be used for the reference system. SLT2 monitoring systems. The instruments of SLT2 static load test monitoring system are specially designed to monitor static load tests and report data in accordance with Eurocode 7.

Figure 2. Assembling loads during mounting kentledge system.

This system allows monitoring the static load tests from a distance of up to 25 m, without the need for personnel to approach potentially hazardous system components that are under high load. The pile load was created using an Enerpac CLS 2006 185-ton hydraulic jack with an Enerpac P462 pumping station, resting against a test and loading stand, weighing 120.0

tons. The load was recorded with a pressure gauge up to 1000 atm. (kgf/cm2) of the MA100VU100 type with a graduation rate of 20 atm. (kgf/cm2) and a digital dynamometer of the Load Cell type connected to the SLT2 monitoring system (Figure 2).

The movement of each pile was measured by four digital electronic displacement transducers of 028DG1, 028DG2, 028DG3, 028DG4 type working in conjunction with SLT2.

The SLT2 system monitoring devices are specifically designed to monitor static pile load tests for the purpose of obtaining results in accordance with Eurocode 7 standards. This system gives an opportunity for controlling the static pile load tests at a distance of up to 25m. This system allows personnel (testers) to remotely monitor the pile settlement and the actual load on the pile, without approaching the potentially dangerous area of the test site structure, where the system is under high pressure and load.

3 DISCUSSION

These pile tests shall be carried out with static loads to establish the actual bearing capacity of the pile. A pile shall be loaded with a static vertical-driving, stepwise-increasing load, in accordance with the Table 2.

Table 2. Program of pile test.

Load step number	Loading per step		Total load:	
	kgf/cm2	kN	kgf/cm2	kN
1	40	104	40	104
2	40	104	80	208
3	40	104	120	312
4	40	104	160	416
5	40	104	200	520
6	40	104	240	624
7	40	104	280	728
8	20	52	300	780
9	20	52	320	832
10	20	52	340	884
11	20	52	360	936
12	20	52	380	988

The vertical load shall be brought to a value that causes the pile to move by at least 40 mm or to the maximum load provided for by this program (Figures 3 and 4).

Figure 3. Reference system with displacement transducers, hydraulic jack Enerpac CLS 2006, Load cell Comp load 100t.

Unloading of the tested piles shall be carried out in steps equal to the double loading steps, in accordance with the Table 3.

Table 3. General unloading pile.

Unloading step number	Unloading per step		General unloading	
	kgf/cm2	kN	kgf/cm2	kN
Unloading				
1	40	104	340	884
2	40	104	300	780
3	60	156	240	624
4	80	208	160	416
5	80	208	80	208
6	80	208	0	0

Figure 4. General view of the kentledge system with a container for test.

Strain gauge readings shall be taken immediately after each unloading step and observed after 15 minutes. After complete unloading (to zero), elastic displacements shall be monitored for 1 hour, with readings taken every 15 minutes.

In the course of the tests, a log of the established form shall be maintained, according to the test results, graphs of the dependence of the pile settlement on the load $S = f(p)$ and the change in the settlement according to the load steps $S = f(t)$ in time shall be plotted.

In the process of testing, in parallel with the electronic data collection by the SLT2 static load test monitoring system, a log of in-situ pile tests shall be maintained in accordance with GOST 5686-2012.

Table 4. Results of SLT of pile.

Pile	Pile cross section	Max applied	Displacement, mm	Bearing capacity, kN	Permission design load, kN
P480	30*30	936	40.62	818	681
P1210		988	40.56		

Table 4, Figure 5 presented results of piles P480 and P1210.

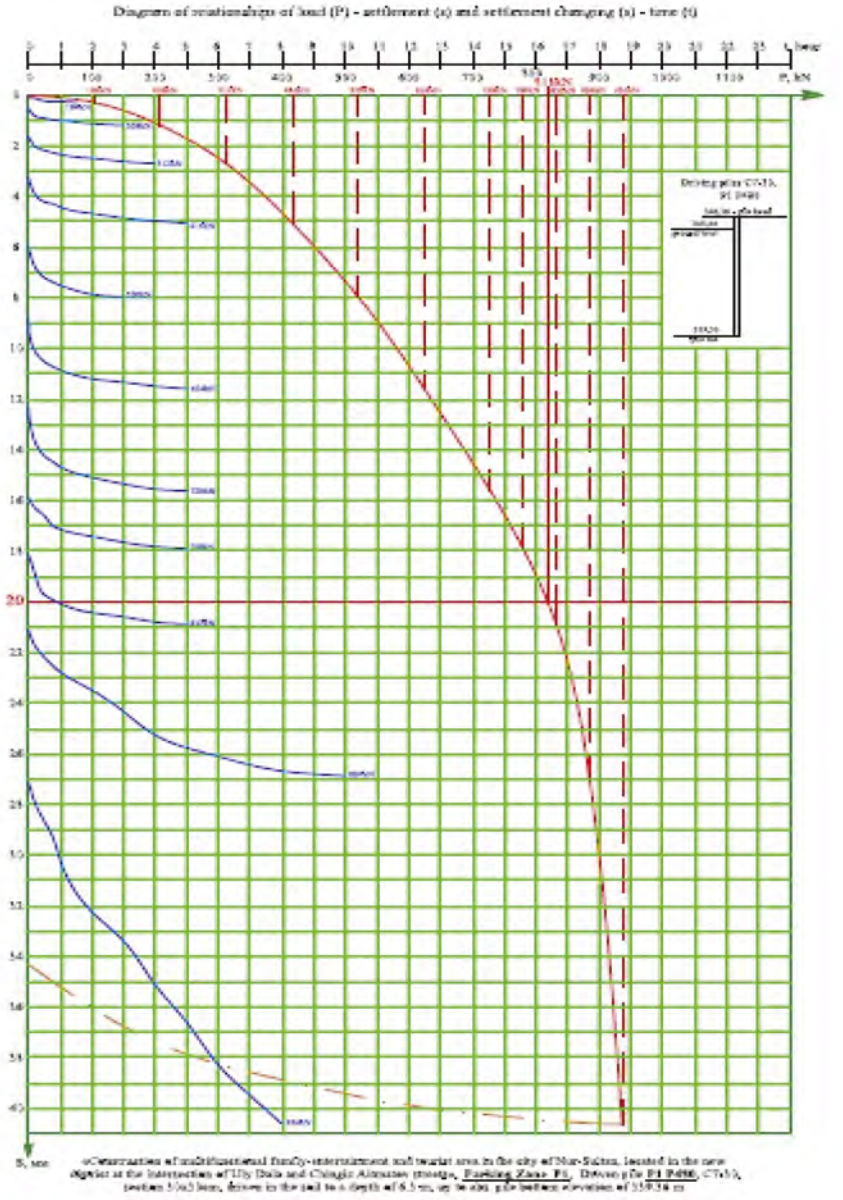

Figure 5. Results of SLT.

4 CONCLUSION

On the construction site of the Parking Zone P1 of the Project 'Construction of a multifunctional family-entertainment and tourist area in the city of Nur-Sultan, static tests of two C7-30 driven piles driven in the soil to a depth of 6.3m up to the abs. pile bottom elevation of 339.36 m were carried out from 05 to 13 February, 2021. The bearing capacity of the piles, according to the results of their static load tests at the above construction site, was 818 (Eight hundred and eighteen) kN. The permissible load on the pile, taking into account the safety factor γ_k =1.2 in accordance with Clause 4.4.1.11. SP RK 5.01-103-2013 'Pile foundations' should be taken equal to – 681 (Six hundred eighty-one) kN.

REFERENCES

Zhussupbekov, A.Zh., Omarov, A.R., Yergen, A., Borgekova K., Tleulenova, G. 2017. Piling Designing, Installation and Testing on Problematical Soil Ground of Kazakhstan. *SEAGS 50th Anniversary Symposium Proceedings,* 77–80.

Zhussupbekov, A., Omarov, A., Moldazhanova, A., Tulebekova, A., Borgekova, K., Tleulenova, G. 2017. Investigations of interaction of joint piles with problematical soil ground in Kazakhstan. *GEOMATE Geotechnique, Construction Materials & Environment Volume 7*. Tsu, Mie. Japan. 383–388.

Kiyalbayev, A., Kiyalbay, S., Tolkynbayev, T., Tleulenova, G. 2022. Theoretical model for anchoring a particle of preheated sand into an ice formation. International Journal of GEOMATE, 23(96). 112–120.

Zhussupbekov, A., Shin, E.C., Shakhmov, Z., Tleulenova, G. 2018. Experimental study of model pile foundations in seasonally freezing soil ground. International Journal of *GEOMATE*. 15 (51). Tsu, Mie. 85–90.

Smart Geotechnics for Smart Societies – Zhussupbekov, Sarsembayeva & Kaliakin (Eds)
© 2023 The Author(s), ISBN 978-1-003-29912-7
Open Access: www.taylorfrancis.com, CC BY-NC-ND 4.0 license

Application of the method of deep mixing in the hardening of soft bases in the regions of the south of Kazakhstan

Vitaliy Khomyakov*
Kazakhstan Department of the Civil Engineering, Kazakh Leading Academy of Architecture and Civil Engineering, Almaty, Kazakhstan

Eraly Shokbarov, Beybut Shelkaev & Yussuf Yemenov
Kazakh Scientific Research and Design Institute of Civil Engineering and Architecture JSC, Almaty, Kazakhstan

ABSTRACT: The natural climatic conditions of southern Kazakhstan are characterized by a geological structure, represented by deposits of macroporous and subsiding soils. Construction on these soils requires a set of measures to strengthen and improve mechanical properties. One of the hardening methods is deep mixing within the active compressible strata. However, the method is still limited in application. The main reason for the weak distribution of the method is the quality of the soil-cement column-column obtained by mixing and the effect of seismic action on its bearing capacity. It is the column that is the main element that increases the bearing capacity of the foundation soils. The article presents the results of a study of the physical and mechanical properties of columns obtained by deep mixing in subsidence loess soils in the south of Kazakhstan. The studies were carried out on samples taken from soil-cement columns from depths of 3 and 5 meters, in a natural and soaked state. The mechanical parameters were obtained by tests in uniaxial and triaxial compression devices. The dependences of the change in the mechanical parameters of the column material on the brand of cement, the degree of water saturation are obtained, and the properties of anisotropy are revealed. Based on the results of the research, calculations were made at the facilities of the city of Shymkent and recommendations were given on the use of reinforcing elements to increase the bearing capacity of weak foundations

1 INTRODUCTION

An important feature of the geological structure of the regions of the South of Kazakhstan is the distribution of weak macroporous soils. Such soils form mountain, foothill and counter surface deposits, which extend to a depth of 5 to 30 meters. Most often, by origin, such soils belong to alluvial deposits of the Middle Quaternary age, represented by loess-like sandy loams or loams. The latter belong to structurally unstable soils, especially in the case of active moisture and seismic loads. Both reasons are relevant for the regions of Kazakhstan, since in the foothill areas groundwater is distributed at a depth of 25-30 meters, but surface atmospheric and technogenic waters often weaken surface soils.

According to building codes, the use of subsidence soils as the foundations of structures is prohibited without the elimination of subsidence or special measures to strengthen and increase their bearing capacity. In some regions, there is a practice when soils are completely removed to eliminate subsidence, sometimes to a depth of 20-30 meters. Further, the pit was covered with the same soil with layer-by-layer compaction. However, when compacting such deep pits, compaction quality is very difficult to achieve.

Today, soil strengthening technologies, especially with the use of mechanization, have advanced far ahead (Nuzhdin,2000), (Mirsayapov,2017), (Shen,2008). Among them, the

*Corresponding author: khomyakov57@list.ru

DOI: 10.1201/9781003299127-389

direction of strengthening with reinforcing elements is developing most actively, among which it should be noted rolled wells filled with soil or concrete, jet-grauting technology, deep soil mixing, etc. In this article, we present some results of the application of deep mixing technology in Kazakhstan on the example of the city of Shymkent.

2 GEOLOGICAL CONDITIONS

In geomorphological terms, most of the territory of the city of Shymkent is represented by a hilly plain, crossed by river valleys and located within the ancient valley of the Sairamsu River. The surface of the site is relatively flat, with a slope to the northwest. The main natural waterways of the city of Shymkent is the river. Badam and Kochkarata with its branch - the Karasu rivers, as well as artificial watercourses-canals that cross the city of Shymkent in the general direction from east to west. Of the physical and geological processes in the region, a weak planar washout, erosional development of dens and subsidence phenomena are developed. The geological and lithological structure of the site involves alluvial deposits of the Middle Quaternary age, represented by loess-like loams and pebble deposits, overlain by a thin soil-vegetative layer and in places with bulk soil.

In the lower part of the geological profile, from a depth of 22.0-23.6 m, there is gravel soil with sand filler, with a content of up to 20-25%. The exposed thickness of gravel soil is 1.3-2.6 m. Table 1 shows a general view of the geological section and a selection of the main physical and mechanical properties of soils. 5 types of EGE have been identified.

EGE-1 - soil-vegetative layer; EGE-1a - bulk soil; EGE-2 - subsidence loam, occurring to a depth of 11.0-12.0 m; EGE-3 - subsidence loam, lying deeper than 11.0-12.0 m; EGE-4 - non-subsidence loam; EGE-5 - gravel soil with sandy aggregate.

Table 1. Geological profile and parameters of the physical and mechanical properties of soils.

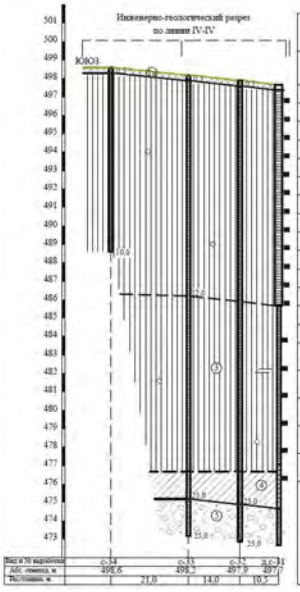

h	We	p	pd	e	Sr	Il	E МПа		Начальное просадочное давление	График изменения начального просадочного давления
м	%	г/см3	г/см3	д.е.	%	д.е.	ест.	зам.	кПа	50 100 150 200 250 300
1	0.066	1.58	1.48	0.822	0.217	>0	4.8	0,9	33	
2	0.071	1.52	1.42	0.904	0.213	>0	10.4	4,0	75	
3	0.065	1.57	1.48	0.830	0.211	>0	4.4	3,9	101	
4	0.060	1.54	1.45	0.864	0.188	>0	8,6	1,5	28	
5	0.062	1.45	1.37	0.978	0.171	>0	46,4	0,5	53	
6	0.068	1.51	1.41	0.911	0.202	>0	19,9	1,5	48	
7	0.071	1.62	1.51	0.784	0.245	>0	19,5	4,9	116	
8	0.104	1.68	1.52	0.771	0.364	<0	17,8	5,4	134	
9	0.107	1.64	1.48	0.825	0.350	<0	14,5	1,7	114	
10	0.108	1.56	1.41	0.916	0.318	<0	18,2	1,4	102	
11	0.107	1.59	1.44	0.880	0.328	<0	7,3	2,3	99	
12	0.107	1.58	1.43	0.888	0.325	<0	5,0	2,6	173	
14	0.155	1.75	1.51	0.785	0.533	<0	5,0	3,0	64	
15,5	0.158	1.89	1.64	0.650	0.656	<0	6,3	6,3	-	
17	0.131	1.78	1.57	0.720	0.491	<0	23,3	7,0	282	
18.5	0.141	1.85	1.62	0.669	0.569	<0	17,2	5,9	314	
20	0.158	1.82	1.57	0.722	0.590	<0	13,1	10,2	239	
21,5	0.183	1.86	1.57	0.717	0.689	<0	8.6	8.3	-	

3 MEASURES FOR STRENGTHENING THE SOIL OF THE BASE

The analysis of the geological profile allows us to say that the foundation soils have sufficient heterogeneity and weak physical and mechanical parameters. Over the entire thickness of EGE2 and EGE3, an almost chaotic change in depth of all parameters can be observed, and especially the

value of the initial settling pressure. There are large changes within the entire EGE2. There is some hardening towards the base of the layer, but then a decrease towards the top of the EGE3. The general trend of increasing the strength of the soil is observed only from a depth of 14-15 m from the surface. Starting from this depth, the value of the initial subsidence pressure steadily increases to 200-250 kPa and the value of the deformation modulus E increases to 7.0-10.2 MPa.

The recommended set of measures includes surface and deep hardening. Surface har dening includes the construction of a soil cushion, deep hardening - the use of wet deep mixing (DSM) technologies. Considering the above analysis of the geological structure, we believe that only the lower boundary of EGE3, EGE4 and EGE5 has sufficient bearing capacity. Since the thickness of the layer is small in terms of the geological structure in EGE3 and EGE4, then the strengthening elements of the overlying layers should be supported on EGE5.

The final constructive solution for the foundation of the buildings was adopted in the form of a soil cushion 1.5 meters thick from undrained soil. The pillow rests on an array, reinforced with DSM elements, 1.0 meters in diameter, made to a depth of 15 meters and supported by EGE5. Preliminary studies on the physical and mechanical properties of DSM are given below.

4 FIELD AND LABORATORY STUDIES TO DETERMINATE DSM PARAMETERS

DSM technology in Kazakhstan has a pioneer application. In this regard, studies were carried out to study the strength and deformation properties of soil-cement columns, arranged to strengthen the base. To obtain these data, experimental soil-cement columns were made in the city of Shymkent, from which, after gaining strength when reaching the age of 28 days from the moment of installation, test columns were excavated to a depth of 3 meters and cores with a diameter of 100mm, 50mm, 40mm were cut in horizontal and vertical direction for laboratory testing (Malinin, 2010).

Figure 1. General view of soil-cement column samples for core sampling .

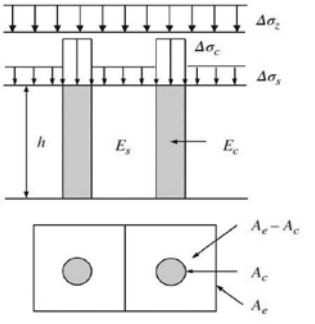

Figure 2. Scheme of the formation of a hardened soil array.

According to the test, cores taken in vertical and horizontal directions relative to the longitudinal axis of the column were examined to determine the physico-mechanical properties and possible anisotropy of the column material. The tests were carried out in accordance with the requirements of paragraphs 5.2 and 5.3 of GOST 12248-2010, Soils, "Methods for laboratory determination of strength and deformability characteristics." Uniaxial compression devices and a triaxial compression chamber were used for the tests.

The tests were carried out in the laboratory "Soil base and foundations" of KazNIISA and on the basis of the Faculty of General Construction of KazGASA. Core samples were taken at the facilities of Shymkent, Karatau district, Nursat residential area. Cores from experimental columns were taken in the vertical and horizontal directions, as shown in Figure 1. Vertical samples from the end of the columns, horizontal - with lateral drilling from a depth of up to 5.0m. The main purpose of the research is to determine the ultimate strength of the column material for uniaxial compression, the total deformation modulus and Poisson's ratio. The tests were carried out in the devices of uniaxial and triaxial compression, shown in Figure 3.

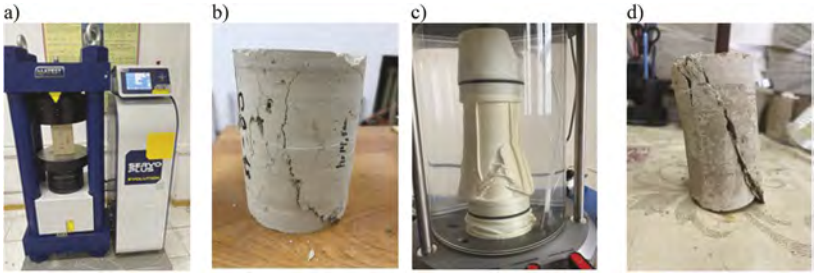

Figure 3. General view of the uniaxial compression device (a), the tested sample (b), the sample in the triaxial compression device (c) and the sample after destruction (d).

Tests were carried out separately for samples taken in the vertical and horizontal directions and for the natural and water-soaked states. The soaking of the samples was carried out by immersing the samples in water and keeping them for 2 weeks before the start of the tests. The main test results are given in Table 2.

Table 2. The results of determining the physical and mechanical parameters of soil-cement columns.

№	State	Core sampling direction	Density, kg/m^3	Ultimate strength for uniaxial compression, Rc, MPa		Deformation modulus,Eo, MPa	Poisson's ratio,ν
				normative	design		
1	Dry	Horizontal	1721	6,36	6,04	424,3	0,287
		vertical	1725	4,68	4,36		
2	Wet	Horizontal	1920,8	3,7	3,53	381,5	0,316
		vertical	1907,3	3,14	2,97		

5 METHOD OF CALCULATION OF BASES USING DSM

Currently, the method for calculating bases using DSM has its own features related to the working conditions of soil-cement columns in the soil base. It is known from international experience that when individual columns are subjected to vertical compressive load, crushing, shearing, failure or buckling failure may occur. Due to the difference in the modulus of elasticity of the DSM columns and the surrounding soil, higher stresses occur in the DSM columns than in the surrounding soil, then the composite soil foundation is loaded. This stress difference is often described as a stress concentration factor, which is defined as the ratio of the stress on the column to the stress on the surrounding soil. Field data show that the stress concentration factors generally range from 5.0 to 10.0 under design loads. It has been established by foreign experience that the constructive solution of foundations made by DSM can be considered as a composite foundation. Most of the theories developed to date for composite foundations are based on the condition of rigid load and equal strain. Under heavy load, the distribution of stresses on columns and soils can be simplified and, based on the balance of forces, the following relation can be established:

$$\Delta\sigma_z A_e = \Delta\sigma_s (A_e - A_c) + \Delta\sigma_c A_c \quad (1)$$

where $\Delta\sigma_z$ - is the average vertical stress applied to the composite foundation; A_e - area of influence (also called effective or working area) of one column; $\Delta\sigma_s$ - vertical stress on the ground; $\Delta\sigma_c$ - vertical stress on the column; A_c - column cross-sectional area, Figure 2;

Dividing Equation (1) by A_e on both sides and entering the value as $=A_c/A_e$ - area replacement factor, we get:

$$\Delta\sigma_z = \Delta\sigma_s\ (1 - a_s)\ +\ \Delta\sigma_c a_s \quad (2)$$

where $a_s = A_c/A_e$ is the area replacement factor, defined as the ratio of the cross-sectional area of the column to the area of the hardened array.

Based on the compatibility of soil deformations εs and columns εc, the following formula for determining the equivalent modulus for calculating base deformations is obtained:

$$E_{eq} = E_s(1-a_s)+E_c a_s \quad (3)$$

where E_{eq} is the equivalent modulus of the composite base; E_s = modulus of elasticity of the soil; E_c is the modulus of elasticity of the column. Further in the calculations, the value of E_{eq} will be used as the main deformation characteristic of the hardened array.

Knowing the total weight of the building and the bearing capacity of the columns, it is possible to determine the required amount of DSM. Columns are spaced within the contour of the foundation slab at certain intervals and critical condition and serviceability checks are performed (Liu 2012), (Khomyakov 2020, 2022).

6 CALCULATION SUBSTANTIATION OF THE HARDENED BASE

The subsequent calculation procedure was carried out using the PLAXIS 2D software package, specially designed for modeling the interactions between structures and the base soil using the finite element method. The calculation of the complex of buildings of 9, 12 and 16 floors has been performed. The pressure under the base of the foundation is accepted: for a 9-storey building -171 kPa, for a 12-storey building - 221 kPa, for a 16-storey building - 298 kPa.

The calculation procedure begins with determining the bearing capacity of the soil-cement column. The bearing capacity is determined taking into account the results of Table 2 and is equal to 1396kN. Based on this, a preliminary number of columns was calculated to strengthen the weak base. According to the method described above, the values of the equivalent module Eeq for each of the three EGEs through which the soil-cement column passes are determined.

Table 3. The results were obtained natural and water-saturated state of the base.

				Natural state				Water-saturated state		
№EGE	Average distance of columns, m	E_s MPa	E_c, MPa	E_{eq} equivalent modulus of massif deformation, MPa			E_c, MPa	E_{eq} equivalent modulus of massif deformation, MPa		
				9floor	12floor	16floor		9 floor	12 floor	16 floor
2	2,3	1,9	424,3	64,6	67,4	89,1	381,5	58,2	60,8	80,3
3	2,3	5,4	424,3	67,6	70,4	91,9	381,5	61,2	63,7	83,0
4	2,3	10,4	424,3	71,8	74,6	95,8	381,5	65,5	68,0	87,0

Note. Symbols in the table correspond to chapter 5.

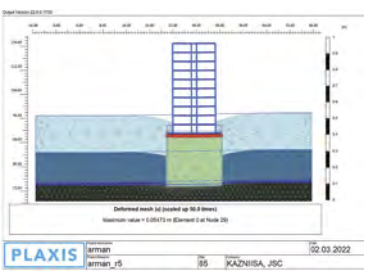

Figure 4. Deformations of the building during hardening of the base by the DSM method.

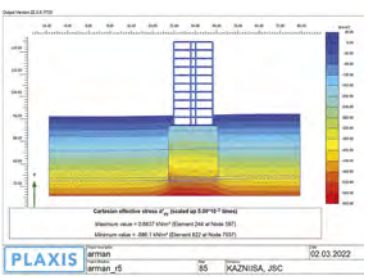

Figure 5. Effective stresses during hardening of the base by the DSM method.

Further calculations are aimed at optimizing the number of elements depending on the equivalent module and the required maximum settlement of the building. The results of calculations of

buildings for deformations and stresses are obtained in the form of mosaics and are shown in Figures 4 and 5. For all buildings, the final values of deformations are shown in Table 4.

Table 4. Calculation results in PC PLAXIS 2D.

Number of floors	Deformation modulus of columns, MPa	Number of DSMs, pieces	Stresses along the sole of the foundation, kPa	Settlement of the building after hardening, m	Coefficient of elastic base, kN/m3
9	424,3	86	171	0,054	3167
12	424,3	99	221	0,074	2987
16	424,3	126	298	0,16	1863

7 CONCLUSIONS

1. The geological conditions of southern Kazakhstan are different in that most of the territory is formed by soils with weak mechanical properties. These include subsidence, macroporous, swelling soils. In this connection, during the construction of buildings on these soils, measures are required to strengthen the base of the buildings.
2. At the present stage, for deep strengthening of soils, mechanical hardening methods based on mixing existing soils with cement mortar along the depth of the base are most actively used. Forming soil-cement columns have a strength much higher than natural soil. However, the properties of soil cement for the soil conditions of Kazakhstan have not been studied at all.
3. In KazNIISA, for the first time, studies of the properties of soil-cement columns on experimental sites were carried out. Samples were taken from the columns from a depth of 3-4 meters in the vertical and horizontal directions. The tests were carried out in the natural and water-soaked state in uniaxial and triaxial compression devices. The test results revealed anisotropy in the values of the compressive strength of about 20-28% and a decrease in strength at water saturation up to 10%.
4. Efficiency of foundation soil strengthening with the use of soil-cement columns is shown on the example of high-rise buildings of 9, 12 and 16 floors. According to the adopted method, the main parameter characterizing the hardened base and reducing its deformability is the equivalent reduced modulus of deformation. Its value was obtained with the optimal number of soil-cement columns and the allowable settlement of buildings. Calculations were performed in the PLAXIS 2D software package with checks on the bearing capacity of the foundation and the operational suitability of buildings.

REFERENCES

1. Nuzhdin, L.V. Reinforcement of foundation soils with vertical rods/L.V. Nuzhdin, A.A. Kuznetsov // *Proceedings of the international seminar on soil mechanics, foundation engineering and transport facilities. - M., 2000. - S. 204–206.*
2. Mirsayapov, I.T. Stress-strain state of the soil base, reinforced with vertical and horizontal elements/I. T. Mirsayapov, R.A. Sharafutdinov // *Izvestiya KGA-SU. - 2017. - No. 1 (39). - WITH . 153–158.*
3. Malinin, A.G. Jet cementation of soils/*A.G. Malinin. - M.: OJSC "Publishing house" Stroyizdat, 2010. - 226 p.*
4. Liu, S.-Y., Du, Y.-J., Li, Y.-L., and Puppala, A.J. (2012). "Field investi-gations on performance of T-shaped Deep Mixed (TDM) soil-cement columns supported embankment over soft ground." J. Geotech. Geoenvi-ron. Eng., 138(6), 718–727.
5. Shen, S.L., Han, J., and Du, Y.J. (2008). "Deep induced mixing property changes in sensitive marine clays." *J. Geotech. Geoenviron. Eng., 134(6): 845–854.*
6. Khomyakov V.A., Shalkaev B., Yemenov Yu.M. Application of various methods of soil reinforcement for slope stabilization in seismic areas. *"Foundations". Scientific and practical magazine for designers and builders., No. 1, 2020, pp. 11–14.*
7. Khomyakov V.A., Gumenyuk V.V., Dursynov S.B. Restoration of the operational suitability of buildings in areas of distribution of loess macroporous foundations. *In the journal "Industrial and civil construction", No. 8, 2022, p. 48–56.*

Smart Geotechnics for Smart Societies – Zhussupbekov, Sarsembayeva & Kaliakin (Eds)
© 2023 The Author(s), ISBN 978-1-003-29912-7
Open Access: www.taylorfrancis.com, CC BY-NC-ND 4.0 license

Concept based approach for geotechnical safety support of the high-rise building construction under complicating factors

F.F. Zekhniev, D.A. Vnukov, D.E. Razvodovsky & A.N. Nikolaev
Research Center of Construction - Gersevanov Research Institute of Bases and Underground Structures (NIIOSP), Moscow, Russia

ABSTRACT: A new design of a high-rise building exceeding 100 m in height is considered. The superstructure was planned to rest on a five-level underground structure, the construction of which was interrupted some years ago. The intermittent low reinforcement of the foundation slab, the uncertain mechanical behavior of the foundation slab and adjacent excavation enclosure, deflection of the foundation slab and defects of the previously erected underground structure, as well as areas of frozen soil affected the design and construction processes. It was decided to increase structural stiffness of the underground construction and apply corrective measures during the construction of the superstructure. An observational design method performed with using geotechnical monitoring instrumentation proved the efficiency of the adopted design solutions.

1 INTRODUCTION

The observational method in geotechnical engineering, which was first defined by Peck, now is well known technique presented in Eurocode 7 and SP 22.13330. This method is more favorable when construction work is performed under significant uncertainty. The essence of the method includes preparing a preliminary design based on favorable and unfavorable data, a monitoring plan for verifying that the structure behaves acceptably during construction and action plan that is put into operation if defined limits. Economic crises often lead to the suspension of construction and the subsequent modification of the project. In this case monitoring data can be used to evaluate how well the actual construction process is proceeding in relation to the predicted behavior of existing structures as well as to control the construction process and update the design. In Russia observational method may be favorable in the design after changing the project of numerous multistory building. The article provides an example of the application observational method for multistory building in Moscow.

In Moscow, close to Kutuzovski Avenue, a redesigned high-rise building has been constructed since 2019. The building rests on a five-level underground structure. Being constructed in 1995-1999, the underground structure was embedded to a depth of 18,5 m below the day surface, and it covered the area of 72 x 63 m.

The underground structure was constructed in an open excavation that was secured by a diaphragm wall reinforced with three levels of anchors. The structure rested on a 2.5m thick reinforced concrete foundation slab. Structurally, it was a reinforced concrete frame with a 9 m column grid.

Compressible subsoil continuum comprised loam and clay with deformation modulus E = 15÷27 MPa, and a thin sand layer in the middle of the cross-section. The sand deformation modulus was 45MPa. The compressible subsoil overlaid the limestone deposit occurring at a depth of 18 m below the bottom of the foundation slab.

To a depth of 1 m below the slab bottom, subsoil with poor deformation properties was met in places. This resulted from the impact of external environmental processes on the surface of soil foundation during construction and preservation of the building.

DOI: 10.1201/9781003299127-390

Figure 1. High-rise hotel and business complex - design (left) and present time (right).

A new design presented the skyscraper as a 33-storey H-shaped building. Three lower levels of the underground section were of a rectangular shape. All bearing structures were included in a reinforced concrete frame. Taking into account construction conditions and long-term preservation of the construction, the designers picked out some factors affecting the design of the new building. Those factors included:

- The intermittent low reinforcement of the foundation slab;
- Uncertain mechanical behavior of the foundation slab and adjacent excavation enclosure;
- Non-uniform deformation soil properties and frozen areas under the foundation slab;
- Defects and leakage in underground structures;
- A total lack of monitoring data;
- Numerous reports on violating requirements of construction Codes during the construction process;
- The 35 mm deflection of the foundation slab that appeared after the underground structure was erected in 1999.

As far as the main design principle, the increase in frame stiffness of the erected underground structure with the maximum reduction in the load transferred to the foundation was accepted. To increase frame stiffness, shear walls and transverse diaphragms should be added to four lower levels of the frame.

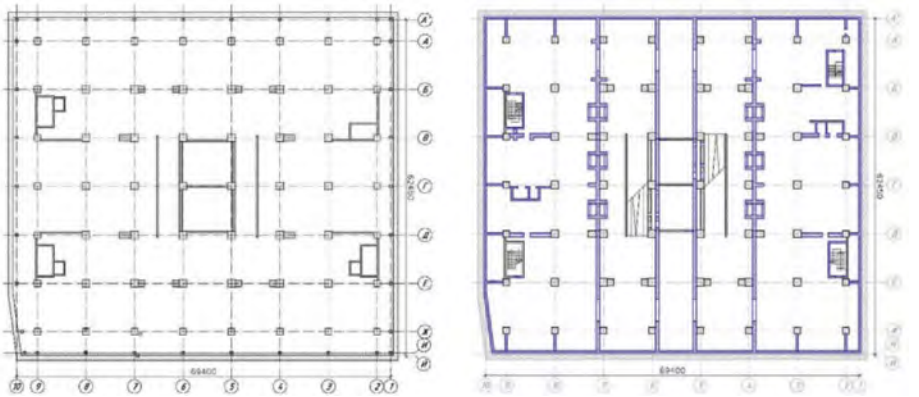

Figure 2. Scheme of the underground section before (left) and after (right) reinforcement with transverse diaphragms and shear walls along the section perimeter.

Diaphragms and shear walls changed spatial performance of the underground structure and limited deformations and stress in the foundation slab, produced by the erected superstructure. Another advantage of this design approach was a relatively low cost of the construction work performed without using specific equipment, but with opportunity to undertake visual quality control.

Considering uncertainties of the mechanical behavior of the underground section and soil foundation, an observational design method was applied. According to the method, the foundation design could be corrected on the base of monitoring results. If the foundation slab suffered significant deflection followed by the loss of its bearing capacity, a new foundation slab was proposed to replace the lower underground level [1].

2 GEOTECHNICAL MONITORING OF THE CONSTRUCTING BUILDING

Geotechnical monitoring was set up when the construction of a redesigned building was resumed in 2019, and it has still been in progress. The main bearing structures have been already erected and finishing work has been started by now.

To date, maximum additional settlement of the constructing building is 91 mm; maximum relative differential settlement is 0,0017. The average settlement of the foundation slab is 68 mm.

The measured deformation of the building foundation does not exceed regulation and predicted values, that is, mean settlement – 20 cm and 14,3 cm, relative differential settlement – 0,003 and 0,002 respectively.

Figure 3 shows the distribution of the measured deformations across the foundation slab area. In general, distribution of the foundation slab measured deformations qualitatively corresponds to the predicted distribution of deformations obtained during the design.

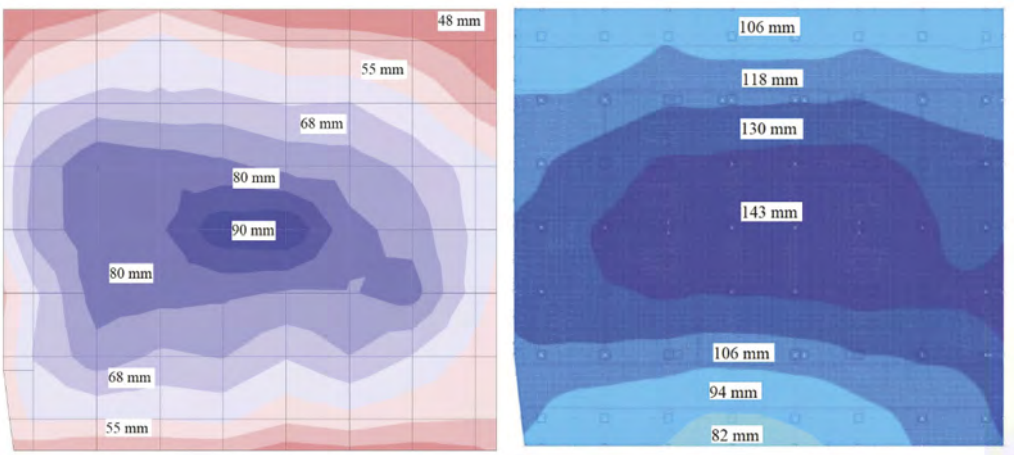

Figure 3. Distribution of the foundation slab settlements observed at 80% load (left) and settlements predicted from total loads (right).

The settlement values of the edge sections of the foundation slab are less than those of the central section are, because the diaphragm wall installed along the perimeter of the underground section constrains deformation of foundation edges. Another reason for that is underground structure and diaphragm wall interaction along the contact between them.

When the settlement rate of the slab central section was increasing against the edge sections, the authors recommended erecting the exterior sections of the aboveground structure prior to the central one. Currently, due to the recommended construction sequence, settlements uniformly develop across the area of foundation slab.

Geodetic monitoring of the "diaphragm wall" settlements confirmed its influence on the foundation deformation process. To date, the average settlement of the "diaphragm wall" is 18 mm, and the settlement of the edge section is 56 mm. Maximum settlement of the

"diaphragm wall" – 23 mm was observed along the A' - axis. Meanwhile, the average settlement of the edge section along the same direction was minimum, if compared with other edge sections, and amounted 50 mm (Figure 4).

The deformation measurement results indicate a significant effect of the "diaphragm wall" on the section of the underground structure, where crack appeared in the 2-nd floor framing beam to A'-directional protective wall connection (Figure 4 and 5). The crack width was up to 5 mm. It appeared when the reinforced beam of the second floor "caught" the edge of the "diaphragm wall".

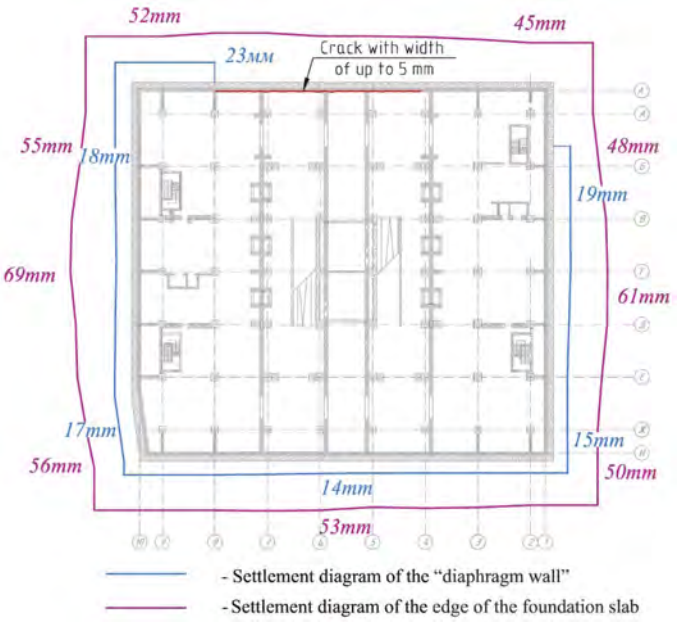

Figure 4. Deformation diagrams of the edge of the foundation slab of the constructing building and the adjacent "diaphragm wall".

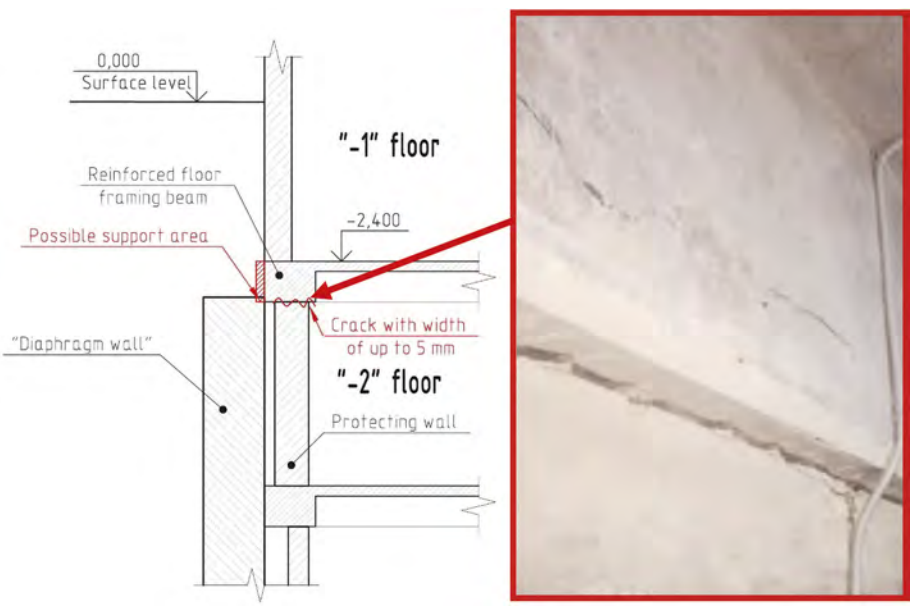

Figure 5. The crack observed in the 2-nd floor framing beam to A'- directional protective wall joint.

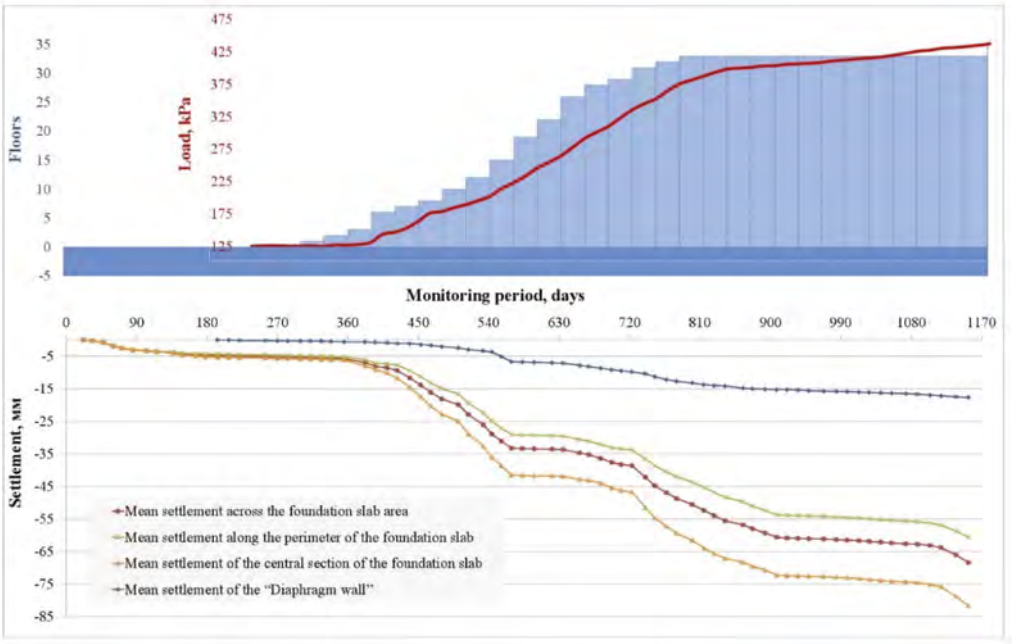

Figure 6. Diagram showing the development of foundation settlements and pressure on the foundation versus time.

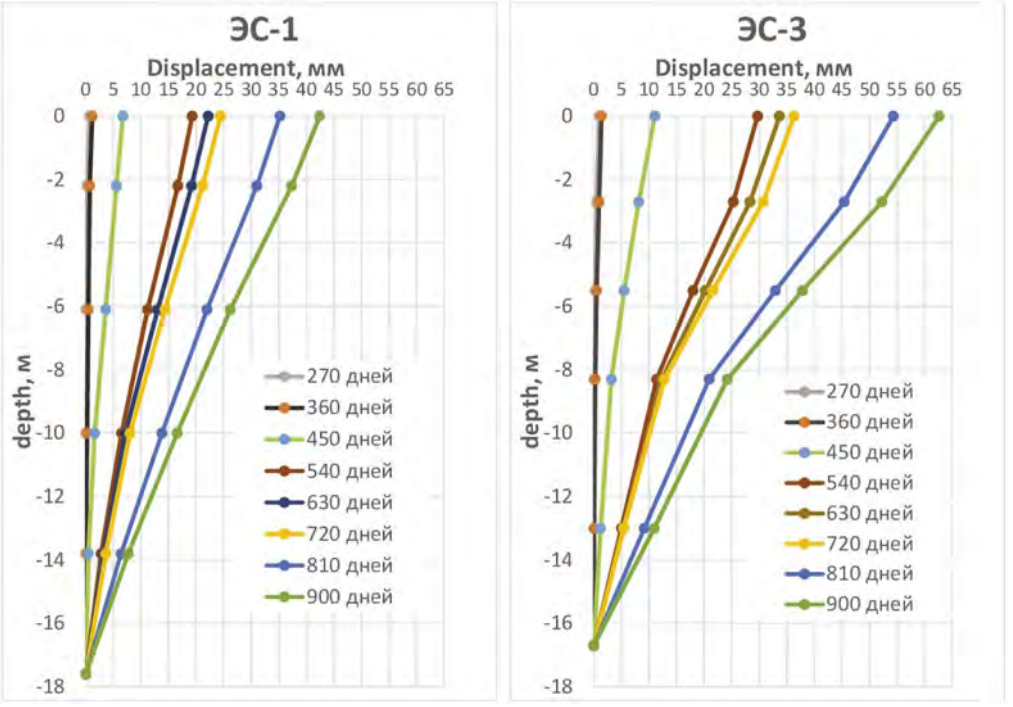

Figure 7. Changes in soil displacement in depth versus time, measured in extensometer wells (left – edge well, right – central well).

The foundation settlement incrementally develops in time with relatively even increase in load (Figure 6), which is largely due to the complex nature of the interaction of the underground structures with "diaphragm wall".

Analysis of the layer-by-layer soil foundation displacement measured using extensometer system shows that all soil continuum observed suffered deformation, wherein clayey layers occurring in the upper part of the compressible strata to the depth of 8 m possess relative compressibility.

3 CONCLUSIONS

Within the framework of the observational design method, instrumentation of geotechnical monitoring helps to assess building's behavior while the performance of the entire structure is uncertain.

Adopted design solutions and application of the corrective measures diminished the impact of hazardous geotechnical factors on the construction process. Those solutions and measures were as follows:

- Installation of the transverse diaphragms and shear walls, which increased stiffness of the underground structure, compensated the existed foundation for the lack of stiffness.
- Construction of the reinforced concrete frame and erection of the exterior structure sections prior to the central one minimized the difference of settlements between central

Presently, measured deformations of the foundation, as well as relative differential settlement, meet the required values.

REFERENCES

Peck, R. B. 1969. Advantages and limitations of the observational method in applied soil mechanics. Géotechnique, 19 2, 171–187.

Nicholson, D, Tse, C and Penny, C. (1999). The Observational Method in ground engineering – principles and applications. Report 185, CIRIA, London

Patel, D., Nicholson, D., Huybrechts, N. and Maertens, J. 2007. The Observational Method in Geotechnics. Proceedings of the 14th ECSMGE: Madrid, Spain. Vol. 2, 365–370.

M. Jamiolkowski Soil mechanics and the observational method: challenges at the Zelazny Most copper tailings disposal facility Géotechnique,Volume 64, Issue 8 June 2014, pages 590–619.

Razvodovsky D.E., Skorikov A.V., Zechniev F.F., Vnukov D.A. 2019. Geotechnical aspects of construction in case of unscheduled change of design decisions of aboveground structures. *Vestnik NIC Stroitel'stvo = Bulletin of Science and Research Center of Construction*. Russia.

Peck R.B. 1969. Advantages and limitations of the observational method in applied soil mechanics. *Geotechnique*. Russia.

Razvodovsky D.E., Kolybin I.V., Anisimov I.G., Fokin N.N. 2016. Overview of Possibilities and Prospects of the Use of Observational Method. *Promyshlennoe i Grazhdanskoe Stroitel'stvo = Industrial and Civil Engineering*. Russia.

Smart Geotechnics for Smart Societies – Zhussupbekov, Sarsembayeva & Kaliakin (Eds)
© 2023 The Author(s), ISBN 978-1-003-29912-7
Open Access: www.taylorfrancis.com, CC BY-NC-ND 4.0 license

Analytical and numerical solutions for temperature distribution in topsoil layers

T. Musabaev, T. Kayupov, D. Seilkhanova & G. Khafizova
Eurasian Institute of Technology at L.N. Gumilyov Eurasian National University, Astana, Kazakhstan

ABSTRACT: The article analyzes the analytical and numerical solutions of heat conduction under the theory of inhomogeneous bodies. The distribution of sub-zero temperature in an inhomogeneous half-space and accounting for the continuous inhomogeneity of the heat conduction rate and internal heat dissipation sources are given for the first time. The evaluation of the obtained results and the known solutions as per the European and national standards are reviewed. The comparison of numerical and analytical solutions for the test problems proves the accuracy of the obtained results. Given the availability of appropriate coefficients, these solutions are also correct for solving problems of chemical reactions with the release of heat, moisture transmission, diffusion, corrosion cracking, and other problems described by the equation of heat conduction.

1 INTRODUCTION

In winter, the atmospheric temperature in the northern regions of the country, in Nur-Sultan city, goes down to -40°C, but the depth of ground freezing is accepted to be 1,800 mm. At the same time, frosty days are changed to snowfall when the temperature rises to -10°C, and there is an alternation of day and night. Also, the ground is covered with snow. Is this standard depth of ground freezing sufficient?

The survey site is in the left-bank part of Astana, between the avenues of Kabanbay Batyr and Mangilik El, and is characterized by absolute levels (at the mouths of drilled wellbores) within the range of 348.33 - 348.74 m. This site has an embedded structure, next to which snow is not removed. The standard thickness of snow in the area of 100 cm will be taken as the thickness of the stale snow in the clearing. There is a 50 cm thick topsoil all around under the snow, consisting of interwoven plant roots and air pockets. We model this layer as peat heat insulating slabs per Table 1 SN RK [1] (Figure 1).

Table 1. Coefficient of heat conduction of materials.

Name of materials listed in [3]	Coefficient of heat conduction λ, W/moC	Isıl İletkenlik Hesap Değeri λ (W/mK)
Interior plaster (İÇ SIVA)	0.76	0.7
Brick wall (DOLGU DUVAR)	0.41	0.45
External plaster (DIŞ SIVA)	0.76	1.6
Waterproofing (SU YALITIMI)	-	0.19
Heat insulation (ISI YALITIM)	0.035	0.035
Heat insulating plaster (ISI YALITIM SIVASI)	-	0.35

DOI: 10.1201/9781003299127-391

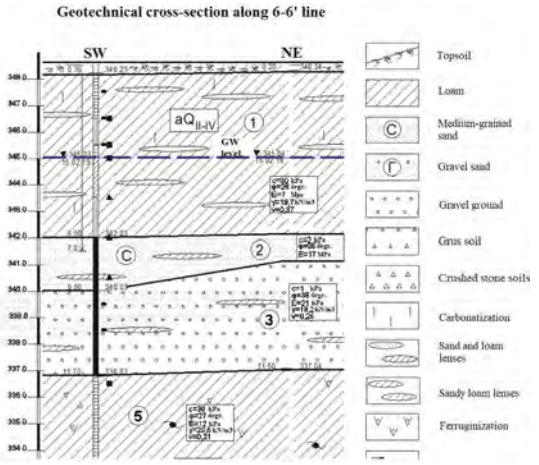

Figure 1. Geotechnical cross-section of the ground of the embedded structure on Mangilik El Avenue in Astana.

According to Eurocode 1, in case there are no internal sources of heat dissipation, the temperature distribution in layered structures shall be determined by the following formula (1) [2]:

$$T(x) = T_{in} - \frac{R(x)}{R_{tot}}(T_{in} - T_{out}) \tag{1}$$

where T_{in} is the indoor air temperature; T_{out} is the outside air temperature; R_{tot} is the total thermal resistance of an element, including the resistances of both surfaces (2); $R(x)$ is the thermal resistance from the inner surface and layers on the inner surface to the given point with coordinate x (Figure 1).

A similar formula can be found in formula (29) of SN RK [1], where the thermal resistance to heat transmission of layered structures can be determined by a similar one with (2) [2]:

$$R_0^{mp} = \frac{1}{\alpha_H} \cdot + \cdot \frac{h_1}{\lambda_1} \cdot + \cdot \frac{h_2}{\lambda_2} \cdot + \cdot \ldots \cdot + \cdot \frac{h_n}{\lambda_n} \cdot + \cdot \frac{1}{\alpha_B} \tag{2}$$

where α_B=8.7 is the coefficient of heat transfer from the inner surface of the land cover, taken according to Table 1 [1] as the coefficient of heat transfer from the inner surface of the walls; α_H=6 is the coefficient of heat transfer of the outer surface of the ground (snow cover), taken according to Table 1 [1] as the covering over the unheated basement; h_i is the thickness of the i-th layer, m; λ_i is the heat conduction of the material of the i-th layer, taken based on the results of tests in an accredited laboratory [1].

A comparison of the heat conduction values of the materials in the composition of the wall [3] as given in the Turkish and Kazakh national appendices to the Eurocode is listed in Table 1. As Table 1 shows, there is no significant difference in the numerical values of the heat conduction of materials, with the exception that in practice, the presence of some materials marked with the minus sign in Table 1 is not taken into account in thermo-technical calculations.

In the climatic conditions of Astana city, due to the presence of castle clay under the clay loam layer, the surface soils, except for the topsoil for the winter, are getting waterlogged and in some places are connected by an aquifer. The topsoil passes through the moisture like a sieve, supplies water to vegetation, and desiccates before the weather is cold. During waterlogging, all soil interstices are filled with water and freeze in winter, forming a monolith of soil and ice. Therefore, the thermal properties of the frozen soil layers can be equated with those

of ice [4]. It is seen from Figure 2 that the coefficient of heat conduction of ice is strongly dependent on temperature. For this reason, the value of the heat conduction coefficient of frozen ground is a function of temperature.

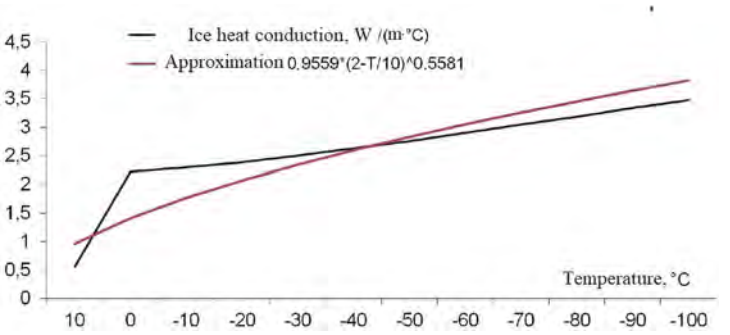

Figure 2. Ice heat conduction coefficient and the approximation of its graph by a power function.

As a rule, the depth of ground freezing does not reach the aquifer. Most likely that the aquifer is formed by the following processes such as ice formation, melting, ice surfacing in the water lens, raising and lowering of the surface soil layer due to the lunar attraction, as well as sand settlement to the bottom of the water lens.

Assume that the ground surface is covered with fresh snow with a heat conduction coefficient of λ_1 = 0.15 W/m °C [5] with a thickness of δ_1 = 0.2 m and a stale snow cover of λ_2 = 0.5 W/m °C [5] with a thickness of δ_2 = 0.8 m. The surface coating of the layered half-space is split into a topsoil layer (modeled as peat heat-insulating slabs of λ_3 = 0.064 W/m °C [1]) with a thickness of δ_3 = 0.5 m, frozen loam (as ice at -10°C λ_4 = 2 W/m °C [4]) with a thickness of δ_4 = 1.5 m, and other layers from Table 2. From [1] and [5], we will take the thermo-physical properties of other soil layers, as per the geotechnical cross-section (Figure 1).

Table 2. Heat transmission resistance in the multilayer land cover.

Layers	h, m	λ, W/m°C	Rlayer
Heat transfer coefficient of the outer snow surface	α_{out}=	6	0,17
Fresh snow	0.2	0.15	1.33
Stale snow cover	0.8	0.5	1.60
Topsoil: peat insulation	0.5	0.064	7.81
Frozen loam	1.5	2	0.75
Water saturated loam - aquifer	2	1.33	1.50
Clay	0.5	0.8	0.63
Dry loam	1.5	0.5	3.00
Coefficient of inner surface heat transfer	$\alpha_{in.}$=	8.7	0.11
Overall thickness of the concerned multilayer land cover	7	ΣR0 =	16.91

In establishing the thickness of the land cover, it is essential to identify the mark of the beginning of the temperature of 10°C for the considered region. Normally, the temperature of 10°C is observed at a depth of 10 m, 20 m, and 30 m as well. In this case, we accept the thickness of the land cover to be 7 m.

Figure 3 depicts plots of the distribution of coefficient of heat conduction of land cover layers by the depth and its approximation by a power function calculated using the least-squares method and a polynomial function, selected visually.

It is seen from Figure 3 that the standard values of the coefficient of heat conduction of land cover layers have a step pattern of distribution. With the polynomial approximation, it is possible to partially describe the ascending and descending branches of the normative graph

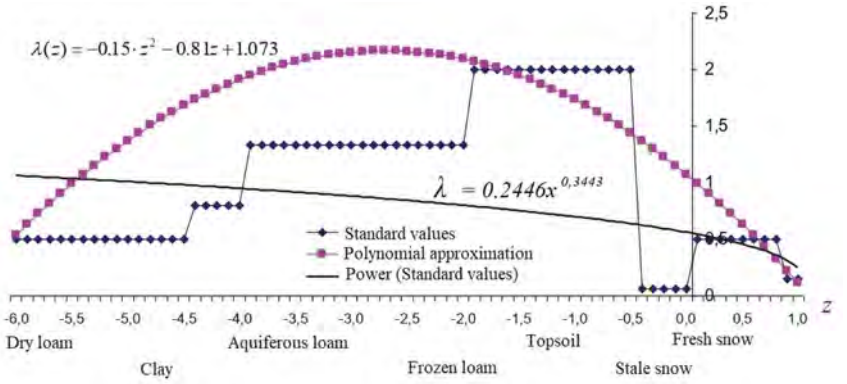

Figure 3. Graph of the variation of the coefficient of heat conduction of land cover layers by the depth and its approximation by the power and polynomial functions.

and the initial and final value. With the power approximation, it is possible to approach the standard values only on the surface layers. The efficiency of the approximation can be determined after plotting the temperature distribution with different methods, comparing and evaluating the obtained results.

The differential equation of heat conduction of one-dimensional problem (the properties of layers are given only along the z-axis which is perpendicular to the ground surface, and the properties and thickness do not change in each layer) in the orthogonal coordinates is written as follows:

$$\frac{\partial}{\partial r}\left(\lambda(r,z)\cdot\frac{\partial T}{\partial r}\right)+\frac{\partial}{\partial z}\left(\lambda(r,z)\cdot\frac{\partial T}{\partial z}\right)=\gamma\cdot c\cdot\frac{\partial T}{\partial \tau}-q(r,z) \tag{3}$$

where γ is the bulk weight, kg/m^3, c is the specific heat capacity, J/(kg °C), $\lambda(r,z)$is the heat conduction coefficient; $q(r,z)$ is the density of internal heat dissipation sources [6, 7, 8].

Let there are no internal heat dissipation sources, a steady-state problem of heat conduction ($\partial T/\partial\tau = 0$) is considered, and the coefficient of heat conduction of soils is changing in the following manner:

$$\lambda(z)=\lambda_0\cdot z^m \tag{4}$$

where λ_0=0.2446, m=0,3443 – approximation by power function, Figure 3.

By integrating (3) by z, we will get:

$$\lambda_0\cdot z^m\frac{\partial T}{\partial z}=C_1;\ T=C_1\cdot\frac{z^{1-m}}{1-m}+C_2 \tag{5}$$

where C_1 and C_2 are arbitrary constants determined from boundary conditions.

In this case, as boundary conditions, the laws of convective heat transfer of the medium with the wall surface are used [7]:

$$\lambda_0\cdot a^m\frac{\partial T}{\partial Z}=\alpha_B(T-T_B);\lambda_0\cdot b^m\frac{\partial T}{\partial Z}=-\alpha(T-T_H) \tag{6}$$

Here, a and b are, respectively, the coordinates of the outer and inner surfaces of the considered land cover; α_B, α_H are the heat transfer coefficients; T_B,T_H is the temperature of the environment near the inner and outer surfaces of the considered land cover.

We substitute the solution of (4) and (5) into (6), and then the solution of equation (3) is determined based on the solution of the system of equations:

$$C_1 \cdot \left(\frac{a^{1-m}}{1-m} - \frac{\lambda_0}{\alpha_B}\right) + C_2 = T_B; C_1 \cdot \left(\frac{b^{1-m}}{1-m} + \frac{\lambda_0}{\alpha_H}\right) + C_2 = T_H \tag{7}$$

$$C_1 = (T_H - T_B)/\left(\frac{b^{1-m} - a^{1-m}}{1-m} + \frac{\lambda_0}{\alpha_H} + \frac{\lambda_0}{\alpha_B}\right); C_2 = T_B - C_1 \cdot \leq \left(\frac{a^{1-m}}{1-m} - \frac{\lambda_0}{\alpha_B}\right) \tag{8}$$

Let the heat transfer coefficient of the wall change in the following manner:

$$\lambda(z) = -0,15 \cdot z^2 - 0.81z + 1,073 \tag{9}$$

By integrating (3) by z, we will get:

$$\frac{\partial T}{\partial z} = \frac{C_1}{-0,15 \cdot z^2 - 0.81z + 1,073};\ T = C_1\left(0,88ln\left|\frac{z+6,5}{z-1,1}\right|\right) + C_2 \tag{10}$$

By solving the quadratic equation (9), we get two roots: z_1 = 1.1 and z_2 = -6.5, which gives zero in the denominator. These points are beyond the range of consideration.

To solve the formulated boundary value problem (3) with boundary conditions (6) using the numerical method, the variation-difference method is applied. Following this method, the ground depth interval a ≤ z ≤ b of unit height and length is arbitrarily subdivided into M - 1 parts, i.e. an irregular rectangular mesh is introduced (Figure 4).

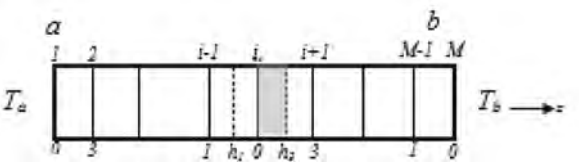

Figure 4. Difference mesh.

The numbering at the top refers to the difference mesh node number, and at the bottom - 0, 1, 3 - are the local numbers of the i-th node cells. The numbers in the cell number indicate which node the given cell is located near h1 and h3 are the mesh steps near the cells. The basic mesh is shown with solid lines, and the additional - with dotted lines, and the typical right cell 03 is shaded.

The equivalent functional of the Ritz method [9] is as follows:

$$I(T) = \int_V \left(\lambda(z) \cdot \frac{\partial T}{\partial z}\right)^2 dv - \alpha_n \oint_S \left(T^2 - 2T_n T\right) \cdot ds \tag{11}$$

where T is the temperature, °C, αn is the surface heat transfer coefficient; T_n is the ambient temperature near the surface with the outer normal n.

An approximate finite-difference expression of potential energy (11) is obtained under the assumption that all functions are constant in each cell. For instance, for a typical cell 03, derivatives are replaced by difference expressions, and the functions take the following values:

$$T = T_0, \frac{\partial T}{\partial Z} = \frac{T_3 - T_0}{h_3}, T_n = T_a, \alpha_n = -\alpha_a,\ \ dv = \frac{h_3}{2} \cdot 1 \cdot 1,\ \ ds = h_3 \cdot 1 \tag{12}$$

The values of the surface heat transfer coefficient αn for the cells where the direction of the outer normal n does not coincide with the direction of the z-axis are taken with the opposite sign. E.g., for cell 01:

$$\alpha_n = \alpha_b \tag{13}$$

The sum of potential energies of all cells will be the total potential energy of the whole body. The boundary integrals are calculated using the trapezoid formula. The minimum of this function is attained subject to the following conditions:

$$\frac{\partial I(T)}{\partial T_0} = 0 \tag{14}$$

By performing differentiation, one can obtain a difference approximation of the boundary value problem (3), (6), (11).

After reducing the constants, the equation for the right cell 03 has the following finite-difference expression:

$$(\lambda_0 + \lambda_3)\frac{T_3 - T_0}{2h_3} = \alpha_a(T_0 - T_a) \tag{15}$$

The equation is similar for the left cell 01:

$$(\lambda_0 + \lambda_1)\frac{T_1 - T_0}{2h_1} = -\alpha_b(T_0 - T_b) \tag{16}$$

The equations for the other cells are different in the absence of boundary elements and the presence of both right and left cells so that they are obtained by summing the summands of formulas (15) and (16)

$$(\lambda_0 + \lambda_1)\frac{T_1 - T_0}{h_1} + (\lambda_0 + \lambda_3)\frac{T_3 - T_0}{h_3} = 0. \tag{17}$$

The matrix of algebraic equations will be tridiagonal. That is why it is convenient to present the system of linear algebraic equations as follows [7]:

$$a_i T_{i-1} - c_i T_i + b_i T_{i+1} = -f_i \tag{18}$$

where a_i are the coefficients preceding T_1, c_i are the coefficients preceding T_0, b_i are the coefficients preceding T_3, fi is the product of coefficients preceding T_a and T_b and their values. The sweep method [10] is used to calculate the temperature.

The results of computing the temperature distribution in an inhomogeneous half-space under the snow cover, which are calculated by formulas: (1), (8), (10), and the numerical solution, are presented in Figure 5. The considered thickness of 7 m of the land cover is divided into 70 steps with a length of 0.1 m.

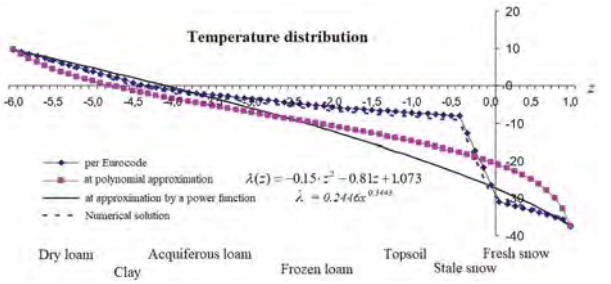

Figure 5. Temperature distribution in an inhomogeneous half-space under the snow cover.

It is seen from Figure 5 that formula (2) of Eurocode 1 [2] and formula (29) of SN RK [1] adequately describe the temperature distribution in the multilayer structure of the land cover formation. A linear law of temperature distribution is observed in each layer. The numerical calculation qualitatively repeats the temperature distribution result; quantitatively, there are differences of less than 2 % in some nodes.

The temperature determined using the power function qualitatively differs from other solutions, and the quantitatively adequate result is obtained at the point of temperature sign change. Such differences may be caused by the approximation of the heat conduction coefficient by a power function, which qualitatively differs from the set heat conduction coefficient variation law. The temperature distribution using formula (10) in the approximation of the heat conduction coefficient by a quadratic polynomial better conveys the behavior of the change in the Eurocode solution. But the dew point position by (8) is better compared to formula (10). Two analytical solutions based on the theory of inhomogeneous bodies, i.e., inhomogeneous models of the structure adequately describe the physical process of heat conduction in a multilayer half-space under the snow cover on the effect of sub-zero temperature.

2 CONCLUSION

1. As can be seen from the figure, all temperature distribution curves turn out to be qualitatively similar; in quantitative terms, there are differences near the surface layer.
2. The solutions of (8) and (10) types can be used as a test task to evaluate the results of physical and numerical experiments with complex boundaries or in two- and three-dimensional settings.
3. Based on the results of calculations in different models in a one-dimensional setting for Nur-Sultan city, the standard depth of ground freezing of 1,800 mm is not sufficient, as the dew point in Figure 5 goes down to 4 m.
4. The results obtained may change in case of using other models of soil, snow, ice, the thickness of the considered cover, heat transfer coefficients, as well as in case of two-dimensional or nonlinear non-steady solution taking into account heating pipe mains, sewerage systems, power supply networks as sources of heat and temperature fluctuations in the winter season.

REFERENCES

[1] SP RK 2.04-107-2013. 2015. Construction heat engineering. Astana.
[2] Eurocode 1. Actions on structures. Part 1-5. General influences. Temperature influences,https://www.phd.eng.br/wp-content/uploads/2015/12/en.1991.1.5.2003.pdf.
[3] https://docplayer.biz.tr/115084-Duvarlarda-isi-yalitimi.html.
[4] http://thermalinfo.ru/svojstva-materialov/materialy-raznye/plotnost-lda-i-snega-teploprovodnost-teploemkost-lda.
[5] http://thermalinfo.ru/svojstva-materialov/strojmaterialy/teploprovodnost-stroitelnyh-materialov-ih-plotnost-i-teploemkost.
[6] Musabaev T., Kayupov, T., Seilkhanova D. New methods for calculating nonlinear one-dimensional heat conduction problems for chemically inhomogeneous bodies.
[7] Kayupov, T. Seilkhanova, D. 2014. Solution of one-dimensional problems of heat conduction of inhomogeneous bodies. Concrete and reinforced concrete - a look into the future: scientific works of the III All-Russian (II International) conference on concrete and reinforced concrete, Moscow, May 12-16. Pp. 166–179.
[8] Bukhmirov, V. 2009. Theoretical foundations of heat engineering. Basics of heat and mass transfer/ GOU VPO "Ivanovo State Power Engineering University named after V.I. Lenin". – Ivanovo. - 102 p.
[9] Ritz's method for solving variational problems, https://scask.ru/i_book_calc2.php?id=92.
[10] Samarskiy, A., Nikolaev E. 1978. Methods for Solving Grid Equations. - M.: Nauka. - 589 p.

Smart Geotechnics for Smart Societies – Zhussupbekov, Sarsembayeva & Kaliakin (Eds)
© 2023 The Author(s), ISBN 978-1-003-29912-7
Open Access: www.taylorfrancis.com, CC BY-NC-ND 4.0 license

Characterization of stockpiled Basic Oxygen Furnace (BOF) slag for railway ballast material application

S. Olagunju, Z. Suleimen, D. Mukhtarkhan, T. Darbayeva, A. Muratova, J. Kim & S-W. Moon
Nazarbayev University, Nur-Sultan, Kazakhstan

ABSTRACT: Railway ballast usually uses natural crushed stone to transfer the load from the rails to the ground. However, the material has a detrimental impact on the environment as the extraction of it is a destructive process, and it is also prone to degradation and fouling in rail tracks. Therefore, this research evaluates the Basic Oxygen Furnace (BOF) slag as an alternative to traditional ballast material in the Kazakhstani railway industry. The tested BOF slags were grouped into top and bottom stockpiled with a mean age of 3–4 years and 10 years, respectively. GOST standards were mainly utilized to analyze the feasibility of the use of BOF slag in Kazakhstan. As a result, both types of BOF slag represented complete satisfaction with the proposed standards. Therefore, the potentiality of the application of stockpiled BOF slag for railway ballast material is verified.

1 INTRODUCTION

Continuous steelmaking, which generates massive waste, is a critical factor in human development; one of these wastes is BOF slag. However, BOF slag poses a severe environmental threat due to its limited potential for reuse and increasing production volume (Naidu et al., 2020). BOF slag has been used for different purposes in the developed countries such as USA, German, and France (Yi et al., 2012). For instance, it is utilized as a part of cement production process in China, as highway pavement in Japan and Australia. BOF slag is also currently used in some parts of Europe to improve agricultural soil condition (e.g., Gencel et al., 2021, Proctor et al., 2000). Another initiative that is being made worldwide to further reduce the amount of BOF slag in circulation is the use of BOF slag as a railway. BOF slag has been utilized as a railway ballast in Brazil, USA, Canada, and Iran (Hussain and Hussaini, 2022). Previous research on BOF slag concluded that BOF slag has higher resistance against lateral pressure and more resistance to breakage when compared with natural crushed stones that are currently utilized as railway ballast (Koh et al., 2018). Therefore, this study characterized the stockpiled BOF slags to apply them to railway ballast materials in Kazakhstan.

2 EXPERIMENTAL WORKS

2.1 *Sample preparation*

The BOF material used in this experimental work was collected from the steel plant located near Karaganda in Kazakhstan. A series of laboratory tests were conducted to investigate the chemical, physical, mechanical, and environmental properties of top and bottom stockpiled BOF slag. The top material has a mean age of 3-4 years, whereas the bottom material has been stored for 10 years in a stockpiled condition. Before starting the main experimental work, the material required preliminary treatment and sorting because the excessive water and

DOI: 10.1201/9781003299127-392

dirt on the aggregates could directly affect further tests. Thus, the first step was oven drying the samples for 48hours at 95°*C* and sieving them according to the GOST standard (GOST 7392, 2014). The sieve sizes were chosen according to the standard for category B materials (square-sized sieves). The samples were sieved through different sieve sizes by shaking the machine for 10 minutes.

2.2 *Experimental methods*

Multiple tests were chosen to assess the slag in an application as ballast material. The most significant ones were selected from physical property requirements, strength, and resistance to environmental conditions. The physical property of BOF slags was evaluated by the Specific Gravity test conducted according to GOST 7392 - 2014. Mechanical properties of the BOF were investigated by Los Angeles (LA) abrasion method using ASTM C535 and aggregate crushing value (ACV) test according to BS 812-110. LA abrasion test was carried out to determine the abrasion resistance and toughness of the aggregates, while ACV test was performed to relatively measure the strength of aggregates needed to resist gradual compressive loads and to crush resistance. Environmental properties were determined through freeze and thaw and organic impurity tests. The freeze and thaw testing was conducted to assess the durability of BOF slag and its resistance to weathering and disintegration by repeated freezing and thawing processes. Meanwhile, an organic impurity test was performed to check the presence of injurious organic impurities. Both tests were carried out according to the GOST 7392 - 2014.

3 RESULTS AND DISCUSSION

3.1 *Chemical property tests*

X-ray diffraction analysis (XRD) and scanning electron microscopy (SEM) were conducted to analyze the chemical property of the stockpiled BOF slags. According to the results presented in Figure 1, stockpiled BOF material has Portlandite ($Ca(OH)_2$), Silicon Oxide (SiO_2), Calcite ($CaCO_3$), Periclase (MgO), Lead Arsenate ($PbAs_2O_6$), Wurtzite (FeO) and others. Comparing both types of BOFS, it can be seen that the intensity of compounds like portlandite and lime is approximately the same, meanwhile, the intensity of SiO_2 (Silicon oxide) is larger in the bottom BOF rather than in the top BOF (Table 1) which indicates that the bottom BOF slag has weaker structure, therefore, is more likely to break. The results for top materials which have a mean age of 3 to 4 years are better than for bottom slag with a mean age of 10 years caused by differences in materials from batch to batch.

Table 1. RIR values of free-lime, portlandite and calcite in top and bottom BOF slag.

BOF type	f-CaO	Portlandite, $Ca(OH)_2$	Calcite, $CaCO_3$	SiO_2
Top	2.54	1.40	1.49	3.04
Bottom	2.54	1.40	2.00	3.31

Along with elemental composition, surface pictures displayed the information regarding the compound of BOFS. The hexagonal plate shape of stockpiled BOF is dictated by the aging of the material that is typical for $Ca(OH)_2$ which forms as long as the material ages and free lime reacts to form portlandite ($Ca(OH)_2$) and calcite ($CaCO_3$). Figure 2 shows the propagation of $Ca(OH)_2$ and $CaCO_3$ that explains the hexagonal shape formations on the surface of the BOF slag.

3.2 *Physical property tests*

According to the GOST specification, the specific gravity of the BOF should be more than 2.40. The top and bottom stockpiled BOF slags' specific gravities constitute 3.29 and 3.25,

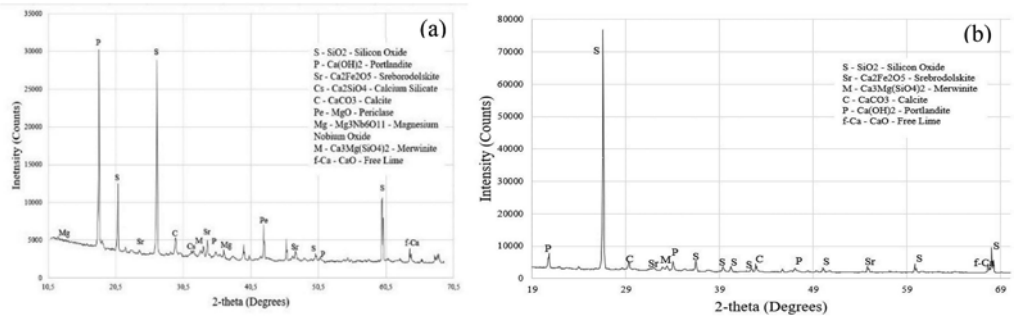

Figure 1. XRD for (a) Top and (b) Bottom BOF slags.

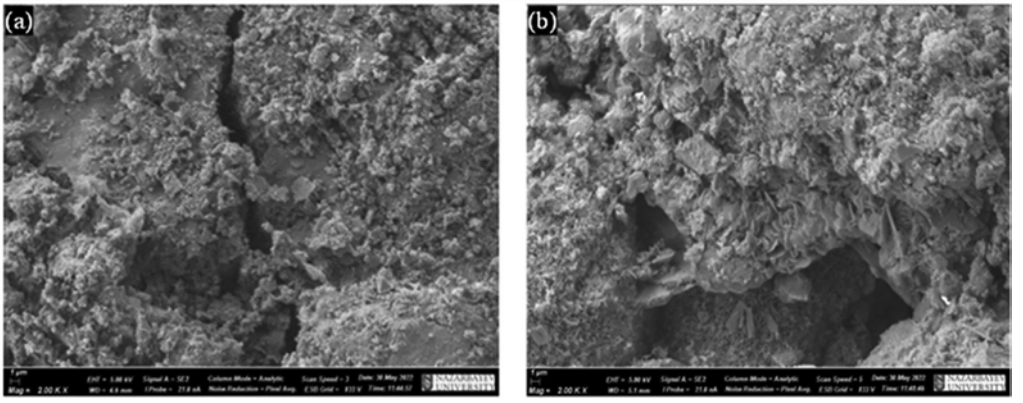

Figure 2. SEM images of (a) Top and (b) Bottom BOF slags.

respectively; satisfying the specification. As the aggregate's strength can be assessed by its specific gravity, the specific gravity that is more than the minimum required value signifies a strong aggregate, as in the case of the stockpiled BOF slag. As regards the absorption capacity, it is less than 2% required by British standards (BS EN 1097-6, 2022). The relatively low values for both stockpiled top (1.18%) and bottom BOF (1.15%) show low permeability of the BOF aggregates.

3.3 *Mechanical property tests*

Los Angeles abrasion and aggregate crushing value tests were performed to determine the strength properties of BOF slag. Both top and bottom stockpiled BOF slags satisfy the ASTM standard of railway ballast since their mass loss values of 22.8% and 23.9% respectively are less than 30% maximum mass loss standard set by AREMA. Therefore, BOF slag is strong enough to resist abrasion and wear and tear during usage. In terms of the aggregate crushing value test, the results have shown that aggregate crushing values for top and bottom stockpiled BOF slags are 19.3% and 20.5% respectively. According to the British Standard, the allowable value of the aggregate crushing value for railway ballast material should be less than 22% (BS EN 13450, 2020). The resulting values put the stockpiled BOF slags within the allowable limit as per the British Standard. Top stockpiled BOF slag provides a higher strength value in comparison to the bottom BOF slag, which makes top BOF slag more resistant to abrasion and crushing under the application of gradual compressive load.

3.3 *Environmental property tests (Freeze and Thaw test & Organic impurity test)*

Both stockpiled BOF slag satisfied the GOST requirement as their mass losses are 3.9% and 4.3% for top and bottom respectively and less than 5%. Therefore, the stockpiled BOF slag will provide great resistance to freeze and thaw in cold climate regions, where the freezing-thawing cycles occur constantly. As for the organic impurity test, it was observed that the sodium hydroxide solution that contains the samples was not colored, but there is a slight change in the turbidity of the solution. The solution colors do not match the reference colors of the ASTM color standard organic plate (ASTM C40M, 2020); this implies that there are no organic impurities present. It would be recommended to conduct preliminary treatment of aggregate by oven drying to burn out the undesirable organic impurity content.

4 CONCLUSIONS

The fast development of the railway industry in Kazakhstan leads to an increase in the extraction level of natural crushed stone for ballast application. The industry requires a sustainable solution that will be both economically and environmentally beneficial. Thus, the BOF slag stockpiled in the steelmaking industries could become a potential alternative to the traditional ballast material in Kazakhstan. Consequently, the sample BOF material was assessed by checking the compliance of its properties with the ballast requirements specified mainly in the GOST standard. As a result, the stockpiled BOF slag demonstrated complete compliance with the ballast material requirements of the obtained experimental program or testing standard. However, the superiority of top material over bottom could be noticed. According to the chemical analysis, the higher amount of SiO2 in the bottom BOF slag could lead to a comparable decrease in strength property. Nevertheless, the further assessment of BOF slag requires the practical investigation of performance in real-life scenarios.

REFERENCES

ASTM STANDARD C40/C40M, 2020, Standard Test Method for Organic Impurities in Fine Aggregates for Concrete, ASTM International, West Conshohocken, PA, 2016, DOI: 10.1520/C0033-03, www.astm.org.

ASTM STANDARD C535, 2016, Standard Test Method for Resistance to Degradation of Large-Size Coarse Aggregate by Abrasion and Impact in the Los Angeles Machine, ASTM International, West Conshohocken, PA, 2016, DOI: 10.1520/C0033-03, www.astm.org.

British Standards Institute, 2021. BS EN 13450-1: Aggregates for railway ballast, London: British Standards Institute.

British Standards Institute, 2022. BS EN ISO 1097-6: Tests for mechanical and physical properties of aggregates Determination of particle density and water absorption. London: British Standards Institute

British Standards Institute, 2020. BS 812-110: Methods for determination of aggregate crushing value - Testing aggregates. London: British Standards Institute.

Gencel, O., Karadağ, Ö., Oren, O. & Bilir, T. 2021. Steel slag and its applications in cement and concrete technology: A review. *Construction and Building Materials*, 283, 122783.

Hussain, A. & Hussaini, S.K.K. 2022. Use of steel slag as railway ballast: A review. *Transportation Geotechnics*, 35, 100779.

Koh, T., Moon, S.-W., Jung, H., Jeong, Y. & Pyo, S. 2018. A Feasibility Study on the Application of Basic Oxygen Furnace (BOF) Steel Slag for Railway Ballast Material. *Sustainability*, 10.

Naidu, T.S., Sheridan, C.M. & Van Dyk, L.D. 2020. Basic oxygen furnace slag: Review of current and potential uses. *Minerals Engineering*, 149, 106234.

Proctor, D., Fehling, K., Hynds, E., Wittenborn, J.L., Green, J.J., Avent, C., Bigham, R.D., Connolly, M., Lee, B., Shepker, T.O. & Zak, M.A. 2000. Physical and Chemical Characteristics of Blast Furnace, Basic Oxygen Furnace, and Electric Arc Furnace Steel Industry Slags. *Environmental Science & Technology*, 34, 1576–1582.

Yi, H., Xu, G., Cheng, H., Wang, J., Wan, Y. & Chen, H. 2012. An Overview of Utilization of Steel Slag. *Procedia Environmental Sciences*, 16, 791–801.

Smart Geotechnics for Smart Societies – Zhussupbekov, Sarsembayeva & Kaliakin (Eds)
© 2023 The Author(s), ISBN 978-1-003-29912-7
Open Access: www.taylorfrancis.com, CC BY-NC-ND 4.0 license

Features of road design in difficult soil conditions

A.K. Zhankina, A.Zh. Zhussupbekov & S. Nurakov
L.N.Gumilyov Eurasian National University, Astana, Kazakhstan

R.S. Imambayeva
Kazakh Leading Academy of Architecture and Civil Engineering, Almaty, Kazakhstan

D.T. Kurmanova
D. Serikbayev East Kazakhstan Technical University, Ust-Kamenogorsk, Kazakhstan

ABSTRACT: One of the most important tasks facing the road industry is to improve the methodology and technology of road design and construction. Road design is a complicated complex of research works, which includes geological studies, determination of technical parameters, selection of design, and technological solutions. Designing in difficult ground conditions is especially difficult. The paper presents the peculiarities of design and construction of auto roads, the results of laboratory and field soil tests, a choice of road design considering the requirements of normative documentation. The recommendations for the choice of measures to ensure the reliability and durability of road pavement and the high level of reliability are presented.

1 INTRODUCTION

Improving the quality and efficiency of construction on subsidence soils largely depends on properly assessing their properties. The choice of methods for improving subsidence foundations and making the appropriate structural and technological solution plays a key role in the design. Traditionally, in the construction of buildings and structures, as well as road structures on weak and collapsing soils, the priority belongs to pile foundations. The expediency of improving subsidence foundations with these foundations is due to the high load-bearing capacity, reliability, and economic and technological efficiency. The proper determination of the bearing capacity of piles is one of the most critical stages in the design of foundations on collapsing soil bases. This parameter is often set experimentally from the condition of the piles on the ground. It is also necessary to improve the mechanical properties of collapsible soils by reinforcing them with geotextile materials.

The development of reliable methods for improving soil foundations in subsidence areas is an urgent task today. A distinctive feature of collapsible soils is their ability when stressed by their weight or the foundation's external load, to give additional settlements, called collapses, when moisture increases – soaking (Houston, S.L. 2002). Collapsible soils include loess, loess-like sand – clays, loams, and clays, some types of head loams and sand–clays, as well as, in some cases, fine and dusty sands with high structural strength, bulk clay soils, industrial wastes (grate dust, ash, ash deposits, etc.) Loess rocks (synonym of the term "dusty rocks") occupy a place between sandy and clayey rocks in the series of uncemented sedimentary rocks and, like them, have a polygenetic origin. The term "loess rocks" has two notions: "loess" and "loess-like" rocks (Gaaver, 2012). Loess is a rock with collapsing under natural pressure and additional loads; it has a homogeneous (non-laminated) texture and weak water-resistant structural bonds; the structure is often dusty-filmy and granular-filmy (Jiang, M. 2012).

DOI: 10.1201/9781003299127-393

The main features of loess soils are (Opukumo, A.W. *et al.* 2022):

1. Yellow-brown and pale-yellow coloration.
2. High dustiness (the content of dusty fraction (0.05-0.005 mm) over 50% with a small number of clay particles.
3. The raised porosity (40-55%) with a network of macropores in size 1-3 mm visible to the naked eye caused by the presence of thin vertical tubules.
4. Low natural humidity from 0.04 to 0.18 (Sr = 0.5).
5. Ability to keep a vertical slope of considerable height in a dry condition.
6. High carbonate content.

Loess-like soils are brown and red-brown, with many fine-dust particles, fewer macropores, and granular-aggregate and aggregate structures.

Today the world practice different methods (Bellil, Abbeche and Bahloul, 2018) and ways of eliminating subsidence properties of soils by their compaction or consolidation; the device of soil cushions is used (Akbari Garakani *et al.* 2019). To consolidate the subsidence soils, use the methods of one-solution silicification or thermal firing. The device of ground cushions creates a layer of non-subsidence soil in the foundation base (Zhussupbekov,A.Zh. *et al.* 2019; Tulebekova *et al.*, 2022). Another practice presented the construction of fixed soil columns and piles in weak dusty-clayey soils when combinations of jetting and boring methods (Awwad, T. 2019; Zhussupbekov A.Zh., Utepov, Ye.B. 2015) or combination of jetting technology with the immersion of ready reinforced concrete elements are also promising (Akhazhanov,S. 2020; Yessentay,D. 2021). Also, one of the effective methods of designing structures on subsidence soils is the reinforcement of foundation soils. One of the basic concepts of soil reinforcement is reduced to the scheme when the weak soil mass is reinforced with high-strength elements and diaphragms placed in the ground. In this case, both vertical and horizontal reinforcement is possible, which in each case has a different effect on the stress-strain state of foundation soils and the operation of foundations. The improvement of ground and soil base reinforcement is directly related to the materials used for reinforcement (Zhussupbekov, A.Zh., Zhankina, A.2021).

2 INVESTIGATION CONSTRUCTION SITE

The planned section of the road (km 240 + 00-km 440 + 00) is in the Karasay and Ili districts of the Almaty region (Figure 1).

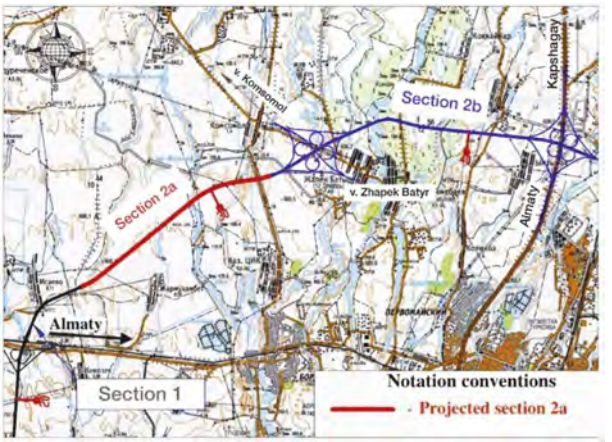

Figure 1. Section road for investigation.

2.1 *Engineering and geological conditions*

Geomorphologically, the construction site is located the foothills of the Zailiskiy Alatau (KGS 2019, 2020).

The climate of the district is sharply continental. The climate features of the region are determined by the latitude and presence of orographic elements on its surface. The combination of climate-forming factors causes the predominance of hot, dry weather with sharp seasonal and daily fluctuations in air temperatures. Summers are hot, and winters are moderately cold and mild. Heavy rains are noted in spring and summer.

The Tien Shan region is a complex mountain country formed due to repeated changes in tectonic conditions. The oldest geosyncline stage of tectonic development continued from the Archaea in places to the Ordovician. Orographically, the region is represented by a complex system of ridges and cavities. Precambrian and Caledonian fold structures form the Tien Shan region. Alpine folding began in the Upper Cretaceous era and continues intermittently to the present.

There is a general relief slope to the north. The relief was formed due to mudflows and the intense activity of river waters. It is a weakly hilly plain with river valleys. The remains of the I and II floodplain terraces are observed on it.

Hydrographically, the investigated section is located between the Kaskelen and Talgar rivers, including their feeders, and the planned route passes through them.

The planned route directly crosses the network of watercourses. Because the route of the designed road passes through these streams, they will directly affect the formation of engineering and geological conditions of the projected facility (Tulebekova,A.S. 2020; Zhussupbekov, A.Zh 2020).

The area's geological structure is characterized by loose Quaternary deposits lying on rocks of the Paleozoic bedrock. The indigenous sediments are represented by granitoid, granodiorite, and porphyrite intrusions in river basins crossing the Zailiskiy Alatau ridge. These rocks will not have a decisive impact on geotechnical profiteering, so a detailed description of the bedrock rocks is not given—soft deposits of medium- and modern-quaternary age form alluvial-proluvial complex of stones.

To detail the geological-lithological section along the axis of the route, 51 exploration wells were drilled to a depth of 6.0m. In total 199.0m were penetrated. Absolute elevations of wells are 631.59-680.70 m.

Route section from the surface is represented by topsoil with a thickness of 0.2 m. Lams from solid to fluid is penetrated with a thickness of up to 6.0 m below and sandy loams up to 1.5 m. There are layers of medium-grained sand and coarse penetrated with a thickness of 0.6 m below.

Filling soil is found on intersected existing roads. It is represented by semi-solid loam containing gravel and pebbles. Groundwater during the survey was penetrated at a depth of 1.0 - 7.8 m. The maximum penetrated power is 3.2 m.

The physical and mechanical properties of soils are given in Table 1.

2.2 *Field tests*

The tests of soil piles were carried out according to the requirements of GOST 5686-2020 (GOST 2012). The tests were carried out by the static pressing loads of 20 piles on this site (Figure 2). Loading the tested piles was made evenly, without blows, by loading steps whose size was no more than 1/10 estimated bearing capacity.

The loading and measuring devices consist of a power stand, DG200P250 jack, hydraulic pump, deflectometer 6PAO-0.01, roulette, and manometer.

The reading of each device was taken at each step of a pile loading, the first hour with an interval of 15 min., further with an interval of 30 min, before attenuation of movement of the pile called stabilization. Observations were accepted for the conditional stabilization of a pile.

Unloading of a pile was made by the steps equal to the doubled sizes of stages of loading, with the endurance of each step within 15 min. Counting on devices to measure deformations

Table 1. Physical and mechanical properties of soils.

Parameter name	EGE-2a	EGE-2b	EGE-2v	EGE-2d	EGE-3a	EGE-4v	EGE-4g
Liquid limit, %	26.9	26.3	27.1	27.3	20.7	-	-
Plastic limit, %	18.8	18.7	18.9	19.0	16.9	-	-
Plasticity index, %	8.1	7.6	8.2	8.3	3.8	-	-
Index of liquidity, %	<0	0.38	0.62	0.94	<0	-	-
Natural humidity, %	12.2	21.6	24.0	26.7	4.6	-	-
Soil particles density, g/sm3	2.71	2.70	2.71	2.71	2.69	-	-
Soil density, g/sm3	1.61	1.91	1.94	1.84	1.61	1.62	1.88
Dry soil density, g/sm3	1.45	1.57	1.57	1.45	1.54	-	-
Void ratio	0.86	0.72	0.73	0.87	0.74	-	-
Degree of humidity	-	-	-	0.97	-	-	-
Coefficient of permeability, m/d	-	-	-			7.4	-
The natural angle of slope in the dry state, deg.	-	-	-			35	38
Soil resistance, kPa	318.0	145	98	98	294	400	500

Figure 2. General view of the support prepared for static tests.

was removed after each unloading step and in 15 min observations. Observations of the movement of a pile were carried out within 60 min after complete unloading (to zero) with the removal of counting from devices every 15 min. According to the project, the movement speed in soil was no more than 0.1 mm in the last 60 min.

Stamp tests were carried out in Section 2 to study the bearing capacity of the artificial base soil for the pipe at km 43 + 225.

The bearing capacity of the base soil under the Overpass bridge was studied at 3 points of stamp testing. A stamping unit with a rotary console acting on the principle of a balance beam was used to carry out the tests.

3 RESULTS

The results of the tests are given in Table 2.

Results of the test showed that the pile during the test perceives the design load of the pile head to equal - 71.0 tf. By results of the carried-out static tests of pile No. 33 on support No. 1 (Overpass bridge through the Borolday river 2 on KM 31+265) at the tenth step of loading, the equal 106.5 tf recorded deformation (deposit) - 40.28 mm. Gain of deformations on 4.24 mm is recorded after additional endurance for 26 h. The total gain of deformations was 44.58 mm, while a stabilization deposit isn't recorded. They are objectively analyzing increment of

Table 2. Test results.

Location	No. of support	No. of pile	Design load, t	Maximum load, t	Average settlement, mm
1	2	3	4	5	6
km 24+477	3	g3	project-wise	239.0	1.48
km 29+240	1	33	project-wise	160.0	2.71
km 29+240	4	33	project-wise	135.15	2.58
km 31+245	3	43	project-wise	129.0	8.02
km 31+265	1	33	71.0	85.2	44.58
km 31+265	1	45	71.4	74.9	41.43
km 31+265	2	33	69.6	52.0	41,715
km 31+265	2	42	69.6	72.975	45.965
km 31+443	2	41	75.8	113.7	6.18
km 31+443	1	34	project-wise	83.0	24.78
km 32+730	1	67	55	83.0	29.8
km 32+730	2	33	100	102.0	38.32
km 34+169	3	56	71.7	107.6	16.49
km 34+650	1	158	109.8	165.0	6.31
km 35+622	2	5	168.3	252.5	0.96
km 35+622	4	10	167.1	250.7	3.37
km 40+100	1	24	118	177.0	5.16
km 40+131	2	9	117.8	176.7	1.33
km 40+620.37	2	11	115.8	174	6.20
km 40+620.37	1	19	115.8	174	5.22

Note – Compiled according to the source (Eurasian National University named after L.N. Gumilyov, Nur-Sultan, Kazakhstan et al., 2021; Zhankina et al., 2022)

deformations and overdue approach of stabilization to the 9th steps at the impact of efforts - 96.0 tf and schedules of the actual behavior of piles under loading perhaps reasonably to take for the extreme resistance of a pile of Fu at the pressing loadings the eighth step - 85.2 tf.

The carried-out static test of pile No. 42 on support No2 (Overpass bridge through the Borolday river 2 on personal computer 31+265), the pressing loadings showed that at the eighth step of loading, the equal 83.4 tf deformation - 45.965 mm was recorded that exceeds extreme size equal - 40 mm. According to SP RK 5.01–103–2013 (items 4.5.5), the pressing loadings take the loading of the seventh step for the extreme resistance of Fu pile- 72. 975 tf. The test results showed that the bearing capacity of pile No. 42 on support No2 on soil is sufficient to perceive design loading.

Static test of pile No33 of support No2 (Overpass bridge on personal computer 32+730) the pressing loading showed that at the eighth step of loading the equal 117 tf late stabilization (was recorded through - 34.5 hours) at the same time deformation was 38.32 mm. The seventh step loading for the extreme resistance of a pile of Fu - 102 tf is taken at the pressing loadings. The test results showed that the bearing capacity of pile No33 on support No2 on soil is sufficient to perceive a projected estimated pile load.

Test of pile No45 of support No1 (Overpass bridge through the Borolday river 2 on KM 31 +265), the following result was issued by the pressing loadings: at the eighth step of loading 85.6 tf, 41.43 mm settlement was recorded, at the same time stabilization of deformation didn't happen. The results showed that the bearing capacity of pile No45 on support No1 on soil is insufficient to perceive the maximum pressing design load. The actual bearing capacity doesn't exceed 74.9 tf, which is less than the projected capacity.

Static test of pile No. 33 of support No2 by the pressing loadings showed that the deformation - 41.715 mm was recorded at the sixth step of loading equal to 62.4 tf, at the same time, stabilization of deposit was not registered. The fifth step, 52.0 tf is taken for the extreme resistance of pile Fu at the pressing loadings. The tests showed that the bearing capacity of pile No. 33 on support No. 2 on soil is insufficient to perceive the maximum pressing design load. The actual bearing capacity doesn't exceed 52.0 tf, and there is less than the projected capacity.

The following conclusions can be drawn based on the results of stamp tests of artificial soil:
Point 1: Equivalent modulus of deformation of the structure E_d = 8.15 MPa.

The modulus of elasticity of the structure is not considered correctly due to extremely small elastic deformations and accumulation of residual deformations. No loss of bearing capacity occurs. Mean base modulus ratio Ee/E_d = 9.1 (Point1); Ee/Ed = 8.19 (Point 2); Ee/Ed = 6.85 (Point 3) presented in Figure 3.

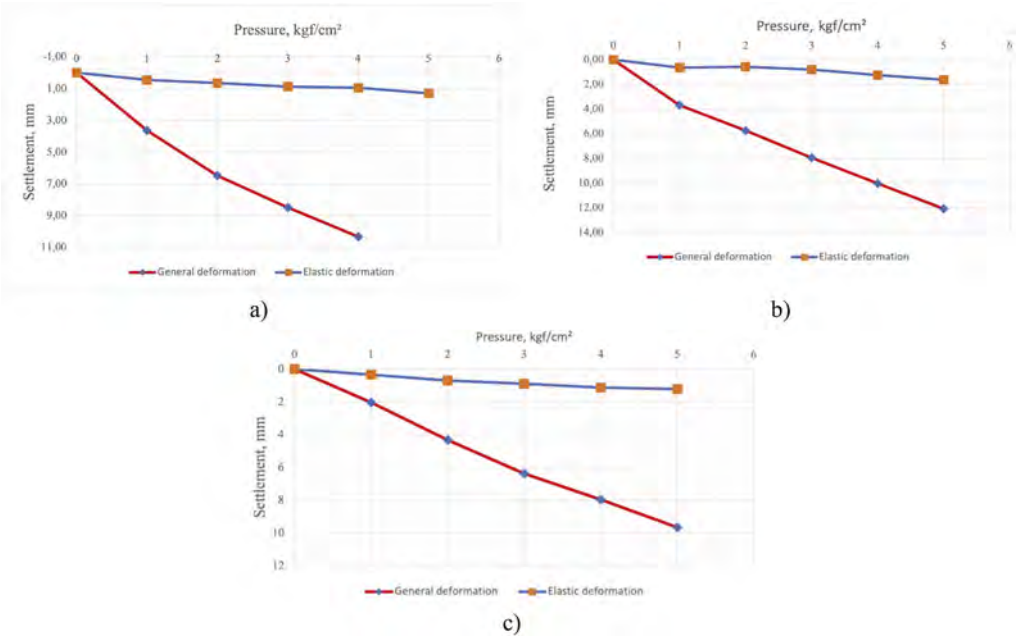

Figure 3. Stamping test results: a) Point 1; b) Point 2; c) Point 3.

4 CONCLUSIONS

According to the results of the study, it is concluded that:

1. The survey area is located within the IV road climatic zone.
2. Excavations with 25.0 m groundwater were penetrated at a depth from 0.4 m to 15.9 m from the day surface. The amplitude of seasonal variation of the groundwater level is + 1.0-1.2 m.
3. The standard depth of loam freezing is 0.79 m; loam, sandy, dusty and fine sands - 0.96 m; gravelly, coarse, and medium-grained sands - 1.03 m, coarse clastic sands - 1.17 m.
4. The area is in the zone with seismic hazard (according to SP RK 2.03-30-2017) [87] - 9 (nine) points.
5. The following conclusions can be drawn based on the results of the tests:

The average modulus of the structure deformation at 3 test points is following: E_d = 8.83 MPa. It is recommended to perform more thorough compaction, following the average ratio of the base modules Ee/E_d = 9.09 at the 1st point; Ee/E_d = 8.19 at the 2nd point; Ee/E_d = 6.85 at 3rd point.

REFERENCES

Houston, S. L., Houston, W. N. and Lawrence, C. A. 2002. Collapsible Soil Engineering in Highway Infrastructure Development. *Journal of Transportation Engineering* 128(3): 295–300. doi: 10.1061/(ASCE)0733-947X(2002)128:3(295).

Gaaver, K. E. 2012. Geotechnical properties of Egyptian collapsible soils. *Alexandria Engineering Journal* 51(3): 205–210. doi: 10.1016/j.aej.2012.05.002.

Jiang, M., Hu, H. and Liu, F. 2012. Summary of collapsible behaviour of artificially structured loess in oedometer and triaxial wetting tests. *Canadian Geotechnical Journal* 49(10): 1147–1157. doi: 10.1139/t2012-075.

Opukumo, A.W., Davie, C.T., Glendinning, S., Oborie, E. A. 2022. A review of the identification methods and types of collapsible soils. *Journal of Engineering and Applied Science* 69(1):17. doi: 10.1186/s44147-021-00064-2.

Bellil, S., Abbeche, K. and Bahloul, O. 2018. Treatment of a collapsible soil using a bentonite–cement mixture. *Studia Geotechnica et Mechanica* 40(4):233–243. doi: 10.2478/sgem-2018-0042.

Akbari Garakani, A. et al. 2019. Testing and Constitutive Modeling of Lime-Stabilized Collapsible Loess. II: Modeling and Validations. *International Journal of Geomechanics* 19(4). doi: 10.1061/(ASCE)GM.1943-5622.0001386.

Tulebekova, A.S., Jumabayev, A.A., Aldungarova, A.K., Zhankina, A.K. 2022. The use of geosynthetics for strengthening the soil base: a laboratory experiment to develop practical skills of postgraduate students. World Transactions on Engineering and Technology Education 20 (4):286–292.

Zhussupbekov, A., Tulebekova, A., Jumabayev, A., Zhumadilov, I. 2020. Assessment of soils deformability under vertical load. *International Journal of GEOMATE* 18(70):221–228. doi: 10.21660/2020.70.12174.

Awwad, T., Mussabayev, T., Tulebekova, A., Jumabayev, A. 2019. Development of the computer program of calculation of concrete bored piles in soil ground of Astana city. *International Journal of GEOMATE* 17(60):176–182. doi: 10.21660/2019.60.17339.

Zhussupbekov, A. Z., Utepov, Y. B. and Morev, I. O. 2015. Numerical and field analysis of interaction of piling foundations with soil ground in Computer Methods and Recent Advances in Geomechanics - *Proceedings of the 14th Int. Conference of International Association for Computer Methods and Recent Advances in Geomechanics*, IACMAG 2014: 519–522. doi: 10.1201/b17435-87.

Akhazhanov, S., Omarbekova N., Mergenbekova A., Zhunussova G., Abdykeshova D. 2020. Analytical solution of beams on elastic foundation. *International Journal of GEOMATE* 19(73):193–200. doi: 10.21660/2020.73.51487.

Yessentay, D., Sagybekova, A., Tulebekova, A., Muzdybayeva, T. 2021. Reliability criterion for calculation of the optimum driving speed on road in winter. *International Journal of GEOMATE* 21 (83):72–78. doi: 10.21660/2021.83.j2115.

Zhussupbekov, A. Zhankina, A., Tulebekova, A., Yessentayev, A., Zhumadilov, I. 2022. Features of the bearing capacity estimation of the collapsing soil bases. *International Journal of GEOMATE* 22(92): 32–40. doi: 10.21660/2022.92.1656.

KGS, LTD. 2020. Working Project «Big Almaty Ring Road Construction». Technical report.

«Research and Manufacturing Company Kazdorinnovaciya» LLP, Working Project «Big Almaty Ring Road Construction» Survey Materials, Geological Report.; 2019

Tulebekova, A., Zhussupbekov, A., Zhumadilov, I., Bukenbaeva, D., Drozdova, I. 2020. Laboratory tests of soils on triaxial compression apparatus. *in 16th Asian Regional Conference on Soil Mechanics and Geotechnical Engineering*, ARC 2019.

Zhussupbekov, A., Tulebekova, A., Zhumadilov, I., Zhankina, A. 2020. Tests of Soils on Triaxial Device. *Key Engineering Materials* 857: 228–233. doi: 10.4028/www.scientific.net/KEM.857.228.

State Standard GOST 5686-2012; Soils Field Test: Methods for Piles; Standartinform: Moscow, Russia, 2012. (In Russian).

Smart Geotechnics for Smart Societies – Zhussupbekov, Sarsembayeva & Kaliakin (Eds)
© 2023 The Author(s), ISBN 978-1-003-29912-7
Open Access: www.taylorfrancis.com, CC BY-NC-ND 4.0 license

The viability of using biopolymer-stabilized municipal solid waste fines in subgrade to enhance pavement performance

Abhay Kumar Verma
Research Scholar, Civil Engineering Department, Indian Institute of Technology, Banaras Hindu University, India

Abhishek Kumar
Masters Student, Civil Engineering Department, Indian Institute of Technology, Banaras Hindu University, India

Arun Prasad
Professor, Civil Engineering Department, Indian Institute of Technology, Banaras Hindu University, India

ABSTRACT: Chemical-based soil stabilization brings adverse effects to soil ecology; hence, bio-based soil stabilization is becoming popular nowadays. The present study analyzes the suitability of using different biopolymers s as additives in pavement subgrade. Two biopolymers, Xanthan gum, and Agar are used in 0-1.5% quantity in MSWF, and their CBR values are calculated. The improved biopolymer-based MSWF is deployed in the pavement subgrade, and the pavement is analyzed based on rutting and fatigue at various pavement conditions. The flexible pavement analysis is carried out through a computer-based application IIT-Pave. It is found that the subgrade made of modified MSWF with a high percentage of biopolymer shows the minimum strain on the subgrade and bituminous layer. Hence, the biopolymers can be successfully used in pavement subgrade to improve its performance.

1 INTRODUCTION

Utilization of municipal solid waste and using biomaterials in engineering applications are two critical activities in the row of sustainability. 1.15 lakh metric tons per day (TPD) or 42.0 million tons of municipal solid waste are produced in urban India each year, of which 83,378 TPD are produced in 423 Class-I cities (Sharma and Jain 2019). The landfills are rising day by day. It is therefore required to reduce the load of landfills, and landfill mining is the workable technique in this row (Frändegård et al. 2013; Yi 2019; Hogland, Marika, and Marques 2010). In landfill mining, the dumped MSW is mined from the landfill and utilized for various other applications (Kandpal and Datta). The previous study shows that the soil-like material of the MSW can be utilized in different civil engineering applications, such as in roads and embankments (Somani 2021; Somani et al. 2022). But in most cases, the share and the compressive strength of this soil-like material or MSW-Fines are not enough per the requirement. In that case, stabilization of that soil-like material is required (Chandana et al. 2021; Goli et al. 2022). At the same time, the technique of the stabilization should be eco-friendly. To realize sustainability in a complete sense, it is required that most of the engineering activities should be inspired by green technology. Using biopolymer for stabilization is an eco-friendly approach (Chang et al. 2020; Latifi et al. 2017). In the present study, an attempt has been made to stabilize the municipal solid waste fines (soil-like material in MSW) using two polymers, Xanthan gum, and Agar gum. It is seen that places in India are flooded during rainy seasons it is hence any civil engineering material that is used in pavement subgrade is required to have good performance in soaking conditions. But generally, it is found that biopolymers disintegrate in the presence of water. To assess the performance of biopolymers in water, the test is carried out in wet conditions.

DOI: 10.1201/9781003299127-394

2 MATERIAL USED

MSW is collected from an abandoned landfill in Varanasi, India. The sample is collected by removing the top 15 cm upper layer. The sample is then dried in the sun and sieved from the No-4 ASTM (4.75 mm) sieve. The soil-like material passed after sieving is used in the present study. The passing soil-like material is denoted as municipal solid waste fines (MSWF) later in the study. For the biotreatment of the MSWF, two biopolymers are chosen: Xanthan Gum (XG) and Agar Gum (AG). These biopolymers and microorganism-based and algae-based biopolymers consecutively. Xanthan gum has numerous industrial applications like in food and cosmetics. It gets its name from the kind of bacteria employed in the fermentation process, Xanthomonas campestris, and is made from simple sugars. Xanthan gum is a good thinker and stabilizer; its civil engineering application is recently explored (Chang et al. 2015; Dehghan et al. 2019). Agar consists of two substances: the linear polysaccharide agarose and a heterogeneous collection of smaller molecules termed agaropectin. It is released during the boiling process because it serves as the structural framework in the cell walls of some types of algae. Even a tiny quantity of Xanthan Gum creates so much emulsion. When combined with the soil particles with water, it forms hydrogel, and the interparticle bonds thicken on dehydration. The quality of Agar is that it comes in gel form when the temperature goes up to 80º C, which solidifies and becomes semi-solid while the temperature downsides to 30-40º C. Due to this vast temperature difference, when it combines with soil, it is easily mixed and then remains semi-solid, enhancing the soil's mechanical properties (Smitha, Rangaswamy, and Keerthi 2021; Smitha and Sachan 2016). The basic properties of the MSWF are given in Table 1.

Table 1. Basic properties of MSW-Fines.

Properties	Values
Maximum Dry Density (MDD) (Mg/m3)	1.71
Optimum Moisture Content (OMC) (%)	17.0
Specific Gravity	2.23
Clay and Silt Size Particles (%)	60.8
Sand Size Particles (%)	39.2
Unified soil classification system (USCS)	CL
Plasticity Index (PI)	11.09

3 METHOD OF STUDY

ASTM standards are followed to determine the basic properties of MSWF. Xanthan gum and Agar gum are mixed separately in MSWF in the varying percentage of 0, 0.25, 0.5, 1 & 1.5% by the weight of water mixed in MSWF (W_b/W_w) while maintaining its maximum dry density. Here W_b is the weight of biopolymer and W_w is the weight of water mixed in MSWF. The wet mixing method adopted by (Bonal et al., 2021) is used for the test. As per ASTM D1883, the soaked CBR tests are carried out for all the MSWF and biopolymer mixes. To carry out the CBR test, about 5 kg of oven-dried MSWF is taken, and then the water-based biopolymer solution is mixed thoroughly into the MSWF as per the OMC of the mix. The mix is compacted in the CBR mold in three layers; each layer is compacted with 56 blows. After compaction, the compacted MSWF is submerged in the water for 96 hours then the standard plunger is penetrated the compacted mix. The CBR ratio is then calculated w.r.t. the load required for the penetration in standard material. For designing flexible pavement, IRC 37 2019 is adopted. The natural MSWF and biopolymer-treated MSWF are considered to be borrowed and compacted in a 500 mm layer in the subgrade. The designed pavements contain subgrade, granular sub-base, and bituminous layer. As recommended in IRC-37, the bituminous pavement layer is optimized using the computer program IIT-Pave to reduce the cost of the pavement.

4 RESULTS AND DISCUSSION

The MSWF is mixed with biopolymer in varying percentages and compacted in a CBR mold. The soaked CBR values are measured for each mix, and the results are shown in Figures 1(a, b). It can be seen that the CBR value of Xanthan gum mixed MSWF is increased with an increasing percentage of Xanthan gum for up to 1% Wb/Ww; beyond 1% of xanthan gum, the soaked CBR value is decreased. It is because when the Xanthan gum comes in contact with water, it forms hydrogels, and it also has lubricating nature when it is in the form of a gel. As xanthan gum is in excess, it shows a lubrication effect, and the plunger penetrates the compacted MSWF relatively more easily. It is also evident from other studies that Xanthan gum makes interparticle bonds and increases the mechanical strength of the soil. In the case of Agar gum, the CBR value of the mix is increased consistently. As the agar gum solidifies at 30-40ºC, it remains semi-solid even when submerged in water. The Agar also forms an interparticle connection, and the mechanical strength increases when the bond between particles thickens. The maximum socked CBR is reported as % and % in the case of Xanthan gum and agar gum, which shows an increment of % from the soaked CBR of natural MSWF.

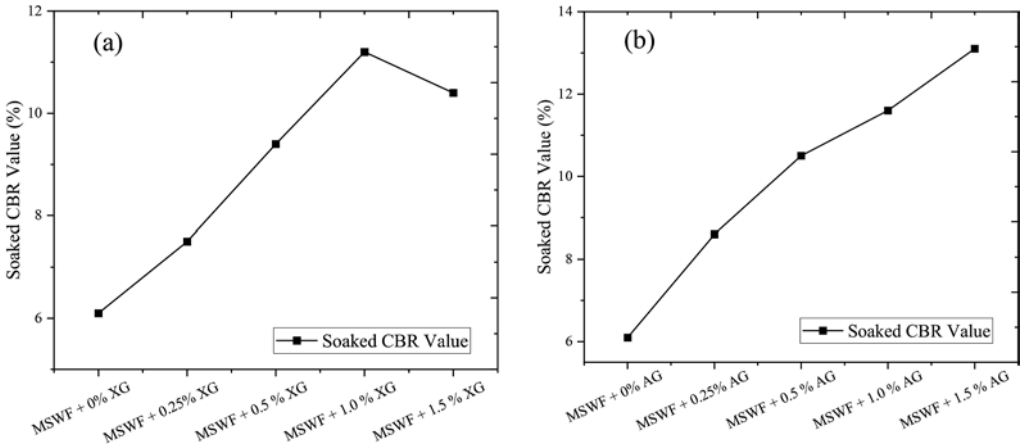

Figure 1. Variation of soaked CBR values (a) For Xanthan Gum (b) For Agar Gum.

Viability of the MSWF mixed with biopolymer in pavement subgrade: The CBR of the subgrade has a vital role in deciding the thickness of the upper layers of pavement. The CBR of the subgrade can be enhanced to optimize the sub-bases thickness, and the bituminous layer since the pavement rests over it. As recommended by IRC-37, the pavement subgrade can be strengthened by replacing the upper 500 mm of the weak soil with the borrowed high-strength soil in the subgrade. In the present study, the pavement will be designed over the subgrade modified with borrowed MSWF-Biopolymer mix. The bituminous layer's thickness is optimized to lower the cost of the pavement. The typical pavement layers are shown in Figure 2.

By following the procedure of designing pavement, the resilient modulus of the subgrade is calculated using Equation 1, and the resilient modulus of the granular subbase is calculated using 2. The present design is based on 90% reliability, meaning there are only 10% chances that the calculated strains will surpass the allowable strains. As per IRC-37, the pavement is tested for strain rutting over the subgrade layer and fatigue below the bituminous layer. The maximum allowable stain for rutting and fatigue criteria can be calculated using Equations 3 and 4. The pavement is designed considering two traffic cases: 50 MSA (Million standard axle) and 100 MSA. VG-40 bitumen grade is taken for the present bituminous layer, and the MR (Resilient modulus) of the VG-40 bitumen at 35° C is taken 3000 from IRC-37. Linear analysis-based software IIT-Pave calculates the flexible pavement system's actual strains.

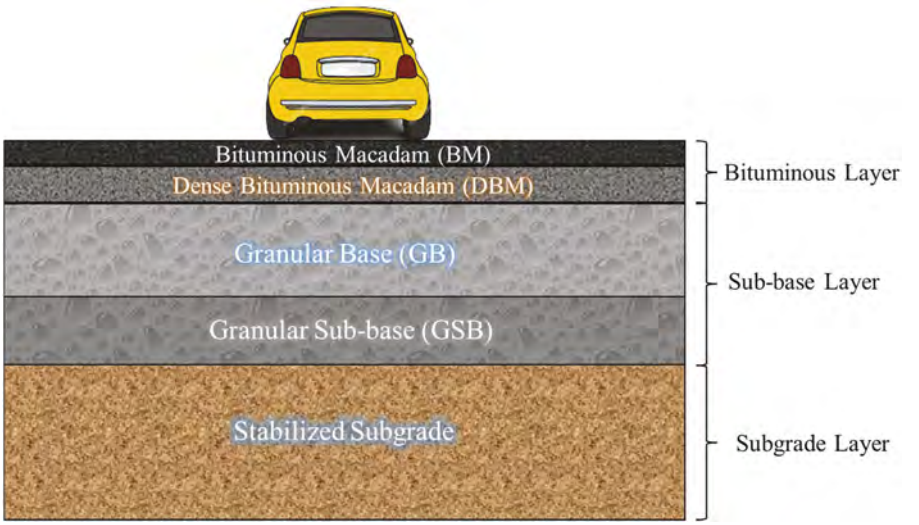

Figure 2. Details of pavement layers.

$$M_{RS} = 17.6\ x\ (CBR)^{0.64} \qquad \text{For CBR} > 5.00\% \tag{1}$$

$$M_{SB} = 0.2(h)^{0.45} x\ M_{RS} \tag{2}$$

Where M_{RS} = Resilient modulus of subgrade soil (in MPa).
CBR = California bearing ratio of subgrade soil (%)
M_{SB} = Resilient modulus of granular sub-base (in MPa)
Sub-grade rutting criteria

$$N_R = 1.4100\ x\ 10^{-08}\left[\frac{1}{\varepsilon_v}\right]^{4.5337} \qquad \text{For 90\% Reliability} \tag{3}$$

Where N_R = Subgrade rutting life
ε_v = Vertical compressive strain at the top of the subgrade
Fatigue cracking criteria for bituminous layer

$$N_f = 0.5161\ x\ C\ x\ 10^{-04}\ x\ \left[\frac{1}{\varepsilon_t}\right]^{3.39} x\ \left[\frac{1}{M_{Rm}}\right]^{0.854} \qquad \text{For 90\% Reliability} \tag{4}$$

Where N_f = Fatigue life of bituminous layer
C = Factor based on the % bitumen and % air voids in the bitumen layer
ε_t = maximum horizontal tensile strain at the bottom of bituminous layer (DBM)
M_{Rm} = Resilient modulus (MPa) of the bituminous mix
Allowable strain for rutting and cracking from equations 4 & 6
ε_v = 0.0003716 (rutting) | ε_t = 0.00017813 (cracking)

Table 2. Details of pavement for the MSWF subgrade stabilized with Xanthan gum (XG).

MSWF & Biopolymer mix	Soaked CBR Value (%)	MR subgrade (MPa)	MR of Sub-base (MPa)	Bituminous layer thickness (mm)
MSWF + 0% XG	6.1	56.0	175.0	175
MSWF + 0.25% XG	7.5	63.9	199.8	158
MSWF + 0.5 % XG	9.4	73.8	230.8	150
MSWF + 1.0 % XG	11.2	82.6	258.2	138
MSWF + 1.5 % XG	10.4	78.8	246.3	145

Table 3. Details of pavement for the MSWF subgrade stabilized with Agar gum (AG).

MSWF & Biopolymer mix	Soaked CBR Value (%)	MR subgrade (MPa)	MR of Sub-base (MPa)	Bituminous layer thickness (mm)
MSWF + 0% AG	6.1	56.0	175.0	175
MSWF + 0.25% AG	8.6	69.8	218.1	155
MSWF + 0.5 % AG	10.5	79.3	247.8	145
MSWF + 1.0 % AG	11.6	84.5	264.1	140
MSWF + 1.5 % AG	13.1	91.3	285.5	130

In the present analysis, the total sub-base thickness is taken as 450 mm, in which the granular sub-base and granular base are taken as 200 and 250 mm consecutively for all cases. The bituminous layer optimized thickness is given in Figure 3 and Tables 2–3. The bituminous layer consists two sub layer one is dense bituminous macadam (DBM) and bituminous macadam (BM), which is the surface course. The minimum thickness of BM is taken 40 mm. It can be seen that the bituminous layer thickness decreased for both cases of XG and AG, while for XG, the thickness reduced by up to 1% of XG. The maximum and minimum thickness of the bituminous layer is calculated at 175 mm, and 130 mm (for 1.5% W_b/W_wAG) for XG minimum thickness is analyzed as 138 mm.

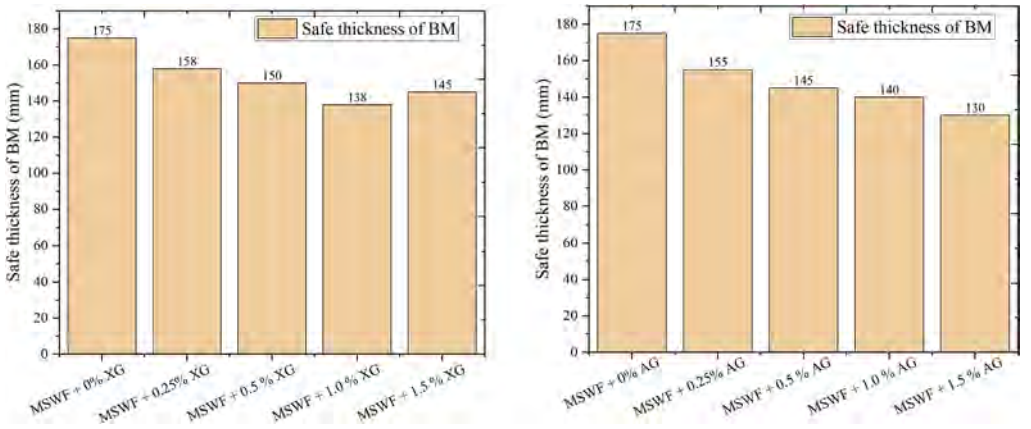

Figure 3. Bituminous layer thickness of pavement having biopolymer stabilized subgrade (a) Xanthan Gum (b) Agar Gum.

5 CONCLUSION

After performing the soaked CBR test, it is found that even after long-term soaking in water, the MSWF and biopolymer mix gives good resistance to penetration. For XG, the optimum percentage of biopolymer is observed at 1%, while for AG, the optimum percentage is reported at 1.5%. When the flexible pavement is designed while considering MSWF and biopolymer mix in the subgrade, it is observed that the bituminous layer thickness is reduced by as much as 25.7%, which is a significant reduction compared to the amount of biopolymer used for strengthening the subgrade. It is hence can be concluded that XG and AG stabilized MSWF can be used in pavement subgrade to reduce the thickness of pavement and also to optimize material cost.

REFERENCES

Chandana, N., V.S.N.S. Goli, A. Mohammad, and D.N. Singh. 2021. Characterization and Utilization of Landfill-Mined-Soil-Like-Fractions (LFMSF) for Sustainable Development: A Critical Appraisal. *Waste and Biomass Valorization*. Springer Science and Business Media B.V.

Chang, I., J. Im, A.K. Prasidhi, and G.C. Cho. 2015. Effects of Xanthan Gum Biopolymer on Soil Strengthening. *Construction and Building Materials* 74 (January 15): 65–72.

Chang, I., M. Lee, A.T.P. Tran, S. Lee, Y.-M. Kwon, J. Im, and G.-C. Cho. 2020. Review on Biopolymer-Based Soil Treatment (BPST) Technology in Geotechnical Engineering Practices. *Transportation Geotechnics* 24 (September): 100385.

Dehghan, H., A. Tabarsa, N. Latifi, and Y. Bagheri. 2019. Use of Xanthan and Guar Gums in Soil Strengthening. *Clean Technologies and Environmental Policy* 21, no. 1 (January 15): 155–165.

Frändegård, P., J. Krook, N. Svensson, and M. Eklund. 2013. A Novel Approach for Environmental Evaluation of Landfill Mining. *Journal of Cleaner Production* 55 (September 15): 24–34.

Goli, V.S.N.S., P. Singh, D.N. Singh, and L.K. Tak. 2022. Investigations on Characteristics of Landfill-Mined-Soil-like-Fractions and Their Dependency on Organic Matter. *Process Safety and Environmental Protection* 162 (June 1): 795–812.

Hogland, W., H. Marika, and M. Marques. 2010. Enhanced Landfill Mining: Material Recovery, Energy Utilization and Economics in the EU (Directive) Perspective. In.

Kandpal, L., and M. Datta. *Shear Strength Behavior of Soil-Sized Material Obtained from Landfill Mining, Waste-to-Energy Plants and C&D Processing Plants*.

Latifi, N., S. Horpibulsuk, C.L. Meehan, M.Z. Abd Majid, M.M. Tahir, and E.T. Mohamad. 2017. Improvement of Problematic Soils with Biopolymer—An Environmentally Friendly Soil Stabilizer. *Journal of Materials in Civil Engineering* 29, no. 2 (February): 04016204.

Sharma, K.D., and S. Jain. 2019. Overview of Municipal Solid Waste Generation, Composition, and Management in India. *Journal of Environmental Engineering* 145, no. 3 (March): 04018143.

Smitha, S., K. Rangaswamy, and D.S. Keerthi. 2021. Triaxial Test Behaviour of Silty Sands Treated with Agar Biopolymer. *International Journal of Geotechnical Engineering* 15, no. 4: 484–495.

Smitha, S., and A. Sachan. 2016. Use of Agar Biopolymer to Improve the Shear Strength Behavior of Sabarmati Sand. *International Journal of Geotechnical Engineering* 10, no. 4 (August 7): 387–400.

Somani, M. 2021. Landfill Mining: Characterization of Soil-Like Material (SLM) Reclaimed from Old MSW Dumpsites and Its Suitability for Geotechnical Re-Use. Delhi: Indian Institute of Technology-Delhi.

Somani, M., M. Datta, G. V. Ramana, I. Hölzle, R. Sundaram, and T.R. Sreekrishnan. 2022. Effect of Depth of Landfill on the Characteristics of Soil-like Material of Aged Waste: A Case Study of Bhalswa Dumpsite, India. *Journal of Material Cycles and Waste Management* (June 27). https://link.springer.com/10.1007/s10163-022-01447-0.

Yi, S. 2019. Resource Recovery Potentials by Landfill Mining and Reclamation in South Korea. *Journal of Environmental Management* 242 (July 15): 178–185.

Smart Geotechnics for Smart Societies – Zhussupbekov, Sarsembayeva & Kaliakin (Eds)
© 2023 The Author(s), ISBN 978-1-003-29912-7
Open Access: www.taylorfrancis.com, CC BY-NC-ND 4.0 license

Evaluation of resilient modulus of asphalt pavement in cold region with Thermo-Hydro-Mechanical coupling simulation

J. Si
Graduate School of Engineering, Hokkaido University, Sapporo, Japan

T. Ishikawa
Faculty of Engineering, Hokkaido University, Sapporo, Japan

ABSTRACT: To understand the actual response of asphalt pavement in cold regions, this study establishes a coupled thermo-hydro-mechanical (THM) Finite Element analysis of asphalt pavement incorporating a M_r-prediction model, which can adequately evaluate the influences of stress state, freeze-thaw, and water content on the resilient modulus (M_r). The FE analysis can not only obtain the changes in water content and temperature of the pavement, but also quantitatively reflect the synergistic effects on the resilient modulus. For this reason, the FE analysis can reproduce a typical Sandwich-Structure in the thawing season. This is of great significance to predict the mechanical properties and fatigue life of asphalt pavements in cold regions.

1 INTRODUCTION

Freeze-thaw action deteriorates the pavement in two ways as frost-heave and thaw-weakening. The frost heave induces the surface cracking in the asphalt mixture layer (hereafter referred to as "As layer"). On the other hand, the thaw-weakening means a drop of the bearing capacity for base and subgrade layers caused by rise in water content. Thus, it is necessary for precisely evaluating the fatigue life of the asphalt pavement to understand the variation mechanism of resilient modulus (M_r) influenced by the weather condition. Ishikawa et al. (2019) examined the effects of freeze-thaw actions and the concurrent seasonal fluctuations in water content on the resilient deformation characteristics of base course materials, while Lin et al. (2022) examined the climate effect on the resilient modulus of subgrade materials to evaluate the mechanical behavior of asphalt pavement. This study proposes a M_r-prediction model to replace the constant elastic modulus of base course and subgrade layer to the resilient modulus related to stress states and climate conditions. Besides, a two-dimensional (2D) FE model using the coupled Thermal-Hydro-Mechanical (THM) analysis is developed to study the behavior of asphalt pavement.

2 SIMULATION METHOD

2.1 *Pavement FE model*

The pavement FE model consists of the As layer, base course layer (C-40), anti-frost layer (C-80), and subgrade layer, as shown in Figure 1.

2.2 *Soil properties for unsaturated and freezing conditions*

For the water retention and unsaturated permeability characteristics, the VG model is adopted. Besides, VG model is combined with the Clapeyron equation to estimate the degree of saturation for liquid water in unsaturated soil subjected to freeze-thaw. The effective heat conductivity and volumetric heat capacity of the solid-fluid system is calculated as follows.

DOI: 10.1201/9781003299127-395

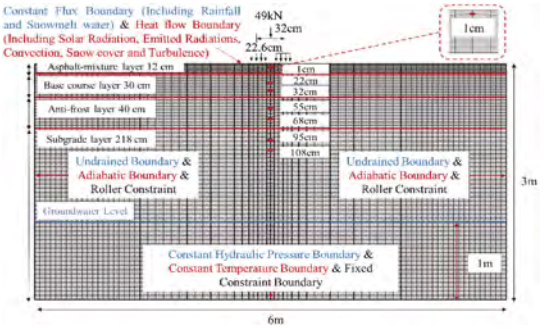

Figure 1. Pavement FE model.

$$\lambda_T = (\lambda_s)^{1-n}(\lambda_i)^{n-\theta_w}(\lambda_w)^{\theta_w} \tag{1}$$

$$C_{Ta} = (1-n)C_{Tp} + nS_wC_{Tw} + nS_iC_{Ti} \tag{2}$$

where λ_s, λ_i, λ_w is heat conductivity of soil particles, ice and water, respectively; θ_w is volumetric water content; C_{Tp}, C_{Ti} are volumetric heat capacity of soil particles and ice, respectively.

The elastic modulus (E_1) of As layer (Figure 2(a)) is obtained by the following equation.

$$E_1 = a \times \arctan(bT_1 + c) + d \tag{3}$$

where *a, b, c, d* are regression constants; T_1 is average temperature of As layer.

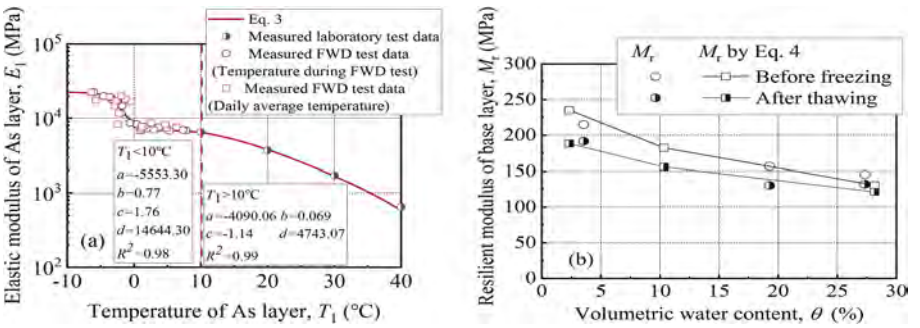

Figure 2. Estimated modulus of different layers (a. As layer; b. Base layer).

Lin et al. (2021) proposed a simple model to estimate the climate effect on the M_r (Figure 2 (b)), which capture the decreasing M_r with freeze-thaw and water content as follows.

$$M_r = F_{clim} \cdot k_1 p_a \left(\frac{\sigma_{ii}}{p_a}\right)^{F_{clim}\cdot k_2} \left(\frac{\tau_{oct}}{p_a}+1\right)^{F_{clim}\cdot k_3} \left(\frac{\psi}{\sigma_{net}}+1\right)^{F_{clim}\cdot k_4} \tag{4}$$

where F_{clim}, k_1, k_2, k_3, k_4 are regression constants; p_a is atmospheric pressure and set as 101 kPa in this study; σ_{ii} is bulk stress (kPa), defined as $\sigma_1+\sigma_2+\sigma_3$; τ_{oct} is octahedral shear stress (kPa); σ_{net} is net mean stress (kPa), defined as $[\sigma_{ii}/3\text{-}u_a]$; u_a is pore air pressure.

2.3 *Coupled THM analysis*

The THM coupled analysis is performed by considering the dependence of resilient modulus on temperature, water content and stress state, and obtaining the accurate M_r distribution through convergence analysis, as shown in Figure 3.

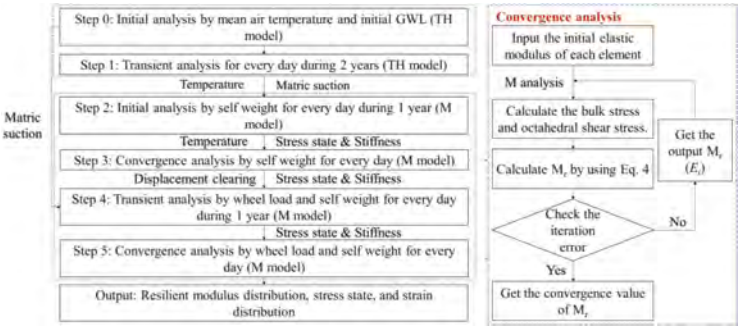

Figure 3. Flow chart of THM analysis and numerical simulation model.

3 RESULTS AND DISCUSSIONS

3.1 *Ground temperature and degree of saturation*

As shown in Figure 4, it is revealed that the fluctuation in ground temperature becomes remarkable at the shallow part of pavement structure. This indicates that the closer to the ground surface, the more significant the environmental impact on the ground temperature. Meanwhile, there is a tendency for the degree of saturation of base course layer to decrease rapidly after late December 2009, which was due to the freezing of pore water at a ground temperature lower than the frozen temperature. In thawing season on March, the thawing of frozen water and the snowmelt water infiltration contribute to high water content of the pavement structure. The change in water content, observed from the regular season to the thawing season, seriously influences the mechanical behavior of base course layer and subgrade layer. Besides, it is recognized that the annual change in the ground temperatures and the degree of saturation obtained from the proposed THM coupling simulation are al-most consistent with the measured results.

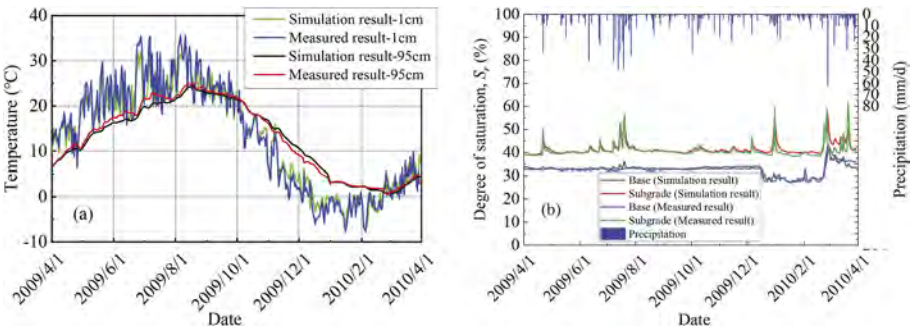

Figure 4. Distribution of temperature and water content (a. Ground temperature; b. Degree of saturation).

3.2 *Variation of resilient modulus distribution with time*

To separately evaluate the impact of weather conditions on resilient modulus, the distributions of resilient modulus are shown in Figure 5 under five different weather conditions (no rainfall and maximum rainfall in the regular season, the maximum frost-penetration depth state in the freezing season, and the full and partial thawing states in the thawing season). The resilient modulus increases as the depth increases, which is due to the bulk stress of soils increasing, and the octahedral shear stress is weakened along with the depth. Under the center of wheel loads, the resilient modulus at the surface of base course layer changes significantly, which is due to the stress concentration in this area. Besides, in the thawing season and rainy days, higher water content dramatically reduces the resilient modulus of base course layer and subgrade layer, and

freezing action improves the resilient modulus of base course layer. Moreover, the resilient modulus increases with increasing the matric suction away upward from the groundwater level, and the resilient modulus below the groundwater level increases with increasing the bulk stress as the matric suction keeps zero. Meanwhile, the resilient modulus dramatically decreases in the thawing season, which significantly impact the fatigue life of the pavement. Since the subgrade layer was not frozen in the winter, the resilient modulus was mainly affected by water content change. Importantly, the formation of a thin inside frozen layer in base layer forms a typical Sandwich-Structure of pavement in the thawing season. It significantly reduces the resilient modulus at the upper part of base layer, which seriously affects the safety of the pavement.

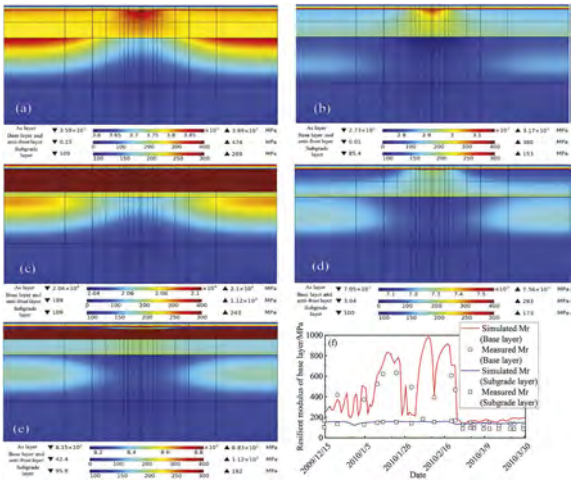

Figure 5. Distribution of resilient modulus (a. regular season-sunny day; b. regular season-rainy day; c. freezing season; d. thawing season; e. thawing season-partial; f. variation of average M_r with time).

4 CONCLUSIONS

- The proposed THM coupling simulation could reasonably reproduce the annual changes in temperature, water content and resilient modulus in the asphalt pavement. This indicates that it cannot only obtain the changes in water content and temperature of the pavement, but also quantitatively reflect the synergistic effects on the resilient modulus.
- The rise in water content leads to a significant decrease in the resilient modulus of pavement, while the freezing of pore water induces a dramatic increase. Therefore, the THM coupling simulation can reproduce a typical Sandwich-Structure in the thawing season.

ACKNOWLEDGMENTS

This research was supported in part by Grant-in-Aid for Scientific Research (B) (19H02234) and (A) (20H00266) from Japan Society for the Promotion of Science (JSPS) KA-KENHI. Special thanks should go to Dr. Maruyama and Dr. Ueno who have supported field measured data and put considerable efforts. A part of this study was conducted in collaboration with the CERI.

REFERENCES

Ishikawa, T. Lin, T. Kawabata, S. Kameyama, S. Tokoro, T. 2019. Effect evaluation of freeze-thaw on resilient modulus of unsaturated granular base course material in pavement. *Transportation Geotechnics* 21: 100284.

Lin, T. Ishikawa, T. Yang, J. Tokoro, T. 2022. Evaluation of climate effect on resilient modulus of granular subgrade material. *Cold Regions Science and Technology* 194: 103452.

Smart Geotechnics for Smart Societies – Zhussupbekov, Sarsembayeva & Kaliakin (Eds)
© 2023 The Author(s), ISBN 978-1-003-29912-7
Open Access: www.taylorfrancis.com, CC BY-NC-ND 4.0 license

Numerical analysis of embankments on soft clay supported with cement-mixed columns

Ashutosh Kumar Singh
Research Scholar, Indian Institute of Technology Roorkee, Roorkee, India

Anumita Mishra
Assistant Professor, Indian Institute of Technology Roorkee, Roorkee, India

ABSTRACT: Embankments constructed over soft soil are susceptible to bearing capacity failures, intolerable settlements and lateral stability problems. Therefore, columns supported with soil-cement mix (DCM) platform restrict the vertical deformation of the structure and lateral displacements. Soil arching has a significant effect on the behavior of columns-supported embankments. Therefore, the mixing of soil with cement as a load transfer platform enhances the performance of embankments. A numerical study is conducted to investigate the performance of soil-cement mix column supported embankment subjected to static loading. The effectiveness of the soil-cement mix is examined by comparing the lateral displacement and settlement for three cases: embankment on DCM columns with load-transfer platform, embankments on DCM columns only, and stone columns. Stress contours and stress variations are presented to show soil arching during the embankment construction. It is observed that the inclusion of soil-cement mix at the load platform and below the embankment reduces the settlement and lateral displacement by 73% and 38%, respectively, as compared to stone columns.

1 INTRODUCTION

The construction of embankments over soft soil is a challenging task for geotechnical engineers due to its low strength and high compressibility. Therefore, there are numerous methods available to improve the condition of soft soil, such as installation of stone columns, provision of drains to accelerate the rate of consolidation, reduction of weight of the embankment by using lightweight fill materials, stabilization of soft soil with cement, and bypassing the soft soil to the firm stratum with the help of rigid piles. Soil stabilized with binder provides an economical solution for the construction of roads and highway over soft soil (Chai et al., 2015; Yapage et al., 2014). The deep mixing technique stabilizes the soil by mechanically mixing it with dry or wet binder.

Several researchers have performed numerical studies to understand the performance of embankments on soft soil by ground improvement techniques. Most of the researchers have used granular columns below the embankment to reduce the settlement and increase consolidation (Mohapatra and Rajagopal, 2017; Xue et al., 2019).In the past, most studies focused on the performance of embankment supported over DCM columns (Yapage et al., 2014; Jamsawang et al., 2016; Ye et al., 2017; Venda et al., 2011; Huang et al., 2009). Dang et al. (2020) numerically studied the deformation characteristics of the fibre-reinforced load-transfer platform and columns-supported embankments. Past studies have also focused on geosynthetics reinforced and pile-supported embankments (Pham and Dias 2021). However, limited studies have been done on the use of soil-cement mixed as a load transfer platform (LTP). Soil-cement mixed as LTP would reduce the lateral displacement of the toe and would increase the load on the DCM columns. This LTP will act as a semi-rigid slab which will be an economical solution, and DCM columns will work effectively. It will also maintain continuity

DOI: 10.1201/9781003299127-396

between DCM columns and LTP. But in the case of GRPS embankments, geosynthetics are generally placed above the piles at a certain height to avoid mechanical failure.

The embankment fill between DCM columns tends to settle due to the presence of soft soil underneath it. The fill above the DCM columns will be partly restrained against this settlement. This resistance reduces the pressure on the soft soil but increases the pressure on the DCM columns. This mechanism is termed the 'soil arching effect' (Terzaghi 1943). The past researchers have proposed various parameters such as stress reduction ratio and stress concentration ratio, to predict the degree of arching (Liu et al., 2007; Han and Gabr, 2002). Stress concentration ratio (n) is defined as the ratio of stress on the DCM column (σ_p) to that on the soil (σ_s).

Based on past studies, this paper describes the effect of inclusions of soil-cement mixed as a LTP in the embankment supported with DCM columns and the degree of soil arching in DCM columns with LTP. The settlement, excess pore water pressure, lateral displacement at the toe, and stress distribution under construction and loading have been evaluated for embankments supported on stone columns and DCM columns with LTP. This study also compared the magnitudes of stress transfer in soil and columns for two cases, i.e., DCM columns with soil-mixed cement LTP and stone columns.

2 NUMERICAL MODELLING

Wijerathna and Liyanapathirana (2021) compared four different models (Plane strain with equivalent areas, plane strain with equivalent properties, axisymmetric unit cell, and three-dimensional unit cell). They confirmed that out of the four models, plane strain equivalent area model predicted better results. A two-dimensional plane strain analysis is performed using commercial finite element software PLAXIS 2D, by adopting the equivalent area method (Tan et al., 2008; Wijerathna and Liyanapathirana, 2021). The advantage of the 2D model is that it is less time-consuming and has better accuracy. The model is validated by a field study performed by tan and Oo (2008) to validate the developed numerical model. In the field study, the embankment is 20m wide at the crust, 1.8m high, and is filled with sandy material. The embankment is rested on a gravel layer of 1m thickness, underlain by soft soil of 5m thickness. The stone columns are 80cm in diameter and are placed at a square grid spacing of 2.4 m c/c to a depth of 6m. The ground water table is 1m below the ground or at the top of the soft soil.

In the present study, a plane strain analysis based on equivalent area approach is performed, in which the stone column diameter is converted into equivalent wall thickness. The properties will remain the same for soil and stone columns. For 2.4m spacing of stone columns and diameter of 0.8m, the equivalent wall thickness is 0.21m. The horizontal displacement is restrained at the left and right sides of the boundary, whereas the bottom boundary is restrained in both directions. The 15-noded triangular element is used for meshing to achieve better accuracy. The construction of the embankment is performed in 9 days, then consolidation is allowed until complete dissipation of excess pore water pressure. The height of the embankment is increased by 0.6 m in every 3 days, till it reaches a height of 1.8m. The numerical study is validated by comparing the settlement and excess pore water pressure with a field study performed by Tan et al. (2008). It is observed from Figure 1 that numerical results and field study show good agreement, and the error is about 3%for settlement and about 7% in the case of excess pore water pressure.

The validated model is further used for analysis to predict the behavior of the embankment supported on columns. Therefore, in the present study, stone columns are replaced by DCM columns, and a soil-cement mixed LTP is provided at the base of the embankment of 0.6m, as shown in Figure 2. In the Figure 2, the points SP-1, SP-2, and SP-3 are the stress points at the pile head, and SS-1, SS-2, and SS-2 are the stress points on the soil. The DCM columns or soil-cement mixed, fill material, soft clay, and stiff clay are modeled as a linear elastic-perfectly plastic material using Mohr-Coulomb (MC) model. The tensile strength of DCM or soil-cement mixed is considered using tension cutoff, i.e., $0.15q_u$. The properties of fill, soft

clay, stiff clay, and DCM or soil-cement mixed are shown in Table 1. Due to symmetry of the embankment, only half of the embankment is simulated. The purpose of providing crust over soft soil is to provide a drainage layer. Due to the relatively high permeability, the embankment fill and crust are assumed to behave in a drained condition. Due to the low permeability of DCM columns or soil-cement mixed, soft and stiff clay are assumed to be undrained.

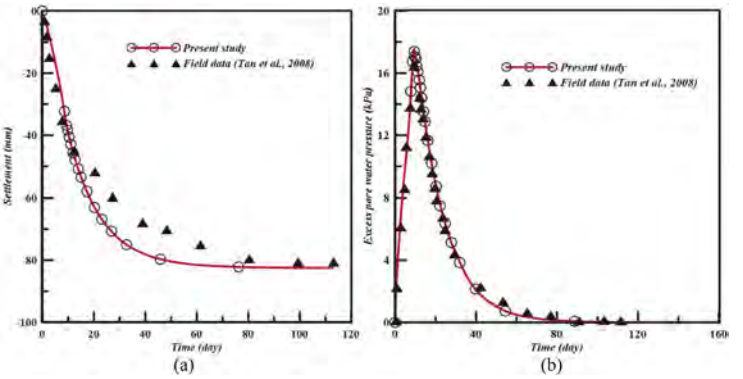

Figure 1. Comparison between Numerical study and Field data: (a) Settlement at point SP-1 (b) Excess pore water pressure at pore pressure measurement point.

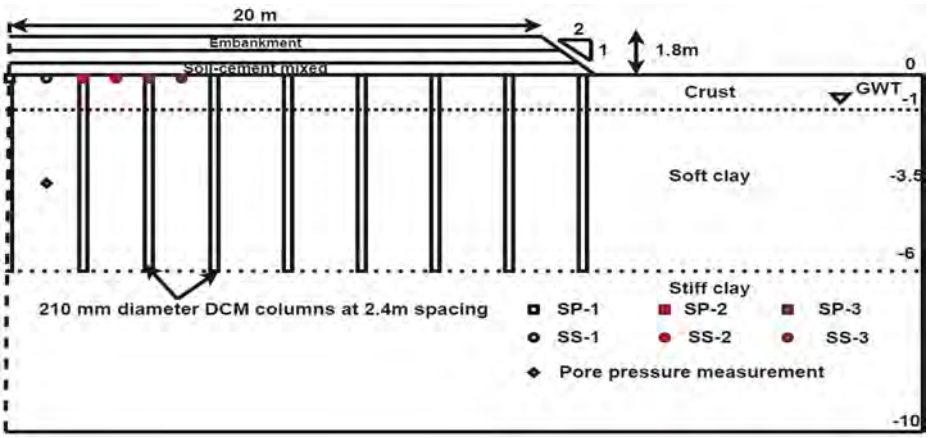

Figure 2. Two-dimensional plane strain model of the present study.

Table 1. Material properties of the embankment, DCM columns, and subgrade soil layers.

Parameters	Embankment Fill[b]	DCM Columns[a]	Crust layer [b]	Soft Clay [b]	Stiff Clay[b]	Units
Unit weight	20	15	18	15	19	kN/m^3
Cohesion	3.0	c_u= 450	3	1	3	kN/m^2
Frictional angle	33	0	28	20	30	Degrees
Permeability (k_v)	1.16×10^{-5}	5.78×10^{-9}	1.16×10^{-7}	1.16×10^{-9}	1.16×10^{-9}	m/s
(k_h)	1.16×10^{-5}		3.47×10^{-7}	3.47×10^{-9}	3.47×10^{-9}	
Poisson's ratio	0.3	0.33	0.3	0.3	0.3	N/A
Young's Modulus	15000	80000	15000	1100	40000	kN/m^2

[a] Jamsawang et al. (2016);
[b] Tan et al. (2008)

3 ANALYSIS OF RESULTS

3.1 *Settlement, excess pore pressure, and lateral displacement*

Figure 3(a) shows the variation of settlement at the center of the embankment with time. From the figure, it has been observed that the inclusion of DCM columns reduces the settlement as compared to the stone columns. The settlement for stone columns, DCM columns, and DCM columns with LTP are 83mm, 22.84mm, and 22.27mm, respectively. The presence of binder in soil stabilizes the soil, and the soil becomes more confined compared to stone columns. Because of it, stone columns settle more than the DCM columns. It has also been observed that the stone columns take less time to reach a constant settlement than the DCM columns. The stage loading generates higher excess pore water pressure in DCM with LTP as compared to stone columns, as shown in Figure 3(b), due to which it will take more time to dissipate from the soil. The effect of LTP with DCM causes an insignificant reduction of settlement as compared to DCM columns. The reason is that the excess pore water pressure is nearly the same in both the cases, i.e., DCM and LTP with DCM. However, DCM with LTP restricts the lateral settlement at the toe of the embankment, as shown in Figure 3(c). The lateral displacement for unreinforced, stone columns, DCM columns, and DCM columns with LTP are 29.8mm, 17mm, 22.31mm, and 10.42mm, respectively. The lateral displacement for DCM columns with LTP reduces by 38.7% as compared to the stone columns. The LTP located at the base of the embankment behaves like a semi-rigid slab which helps in reducing the lateral displacement.

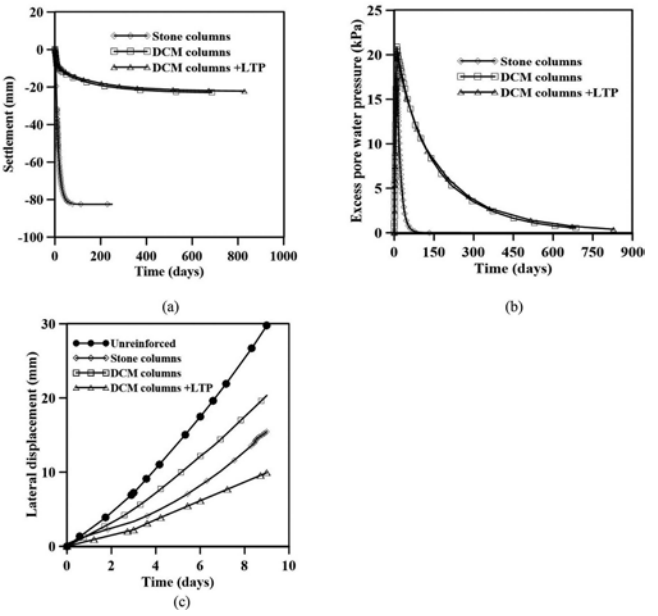

Figure 3. Comparison of (a) Settlement (b) Excess pore water pressure (c) Lateral displacement with time for different cases.

3.2 *Stress variation*

Figure 4(a) shows the variation of stresses for stone columns and LTP with DCM columns. The stresses for stone columns at the pile and soil are 19.2 kN/m^2 and 14.4 kN/m^2, respectively. In the case of stone columns, the stresses generated in columns and soil are nearly equal. The stresses for LTP with DCM columns at the pile and soil are 59.2 kN/m^2 and 11.3 kN/m^2, respectively. In the case of LTP with DCM columns, DCM columns take more load than the

surrounding soil. It means LTP with DCM columns is more effective than stone columns in terms of stress transfer.

Figure 4(b) shows the effect of static loading on developed stresses on piles and soil. The stress points under loading at the columns and soil are shown in Figure 2. The stresses on piles increase linearly with the increase in loading. The stress developed at the pile located at the center of the embankment (i.e., SP-1) is more than the other piles (SP-2 and SP-3). Similarly, the variation of stresses on the surrounding soil is the same, however, the rate of increase is slower, as evident from the slope of the line.

Soil arching occurs because of differences in the stiffness of the columns and surrounding soil. The stress concentration ratio for stone columns and DCM columns with LTP are determined as 1.33 and 5.24, respectively.

Figures 5(a) and (b) show the stress contour for stone columns and DCM with LTP. It is observed that stress concentration occurs at the soil and columns in the case of an embankment supported with stone columns. In the case of unreinforced embankments, stresses are distributed in the whole area. However, in the case of DCM columns and DCM columns with LTP, stress concentration is more at the columns as compared to the surrounding soil.

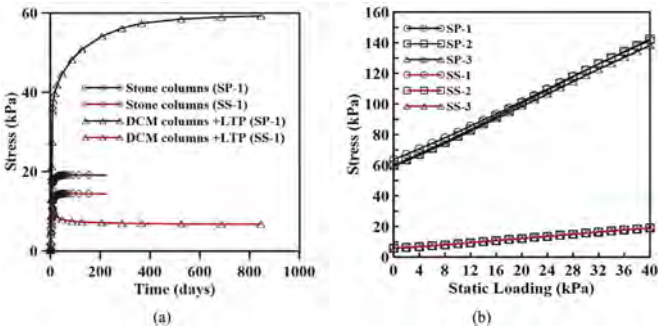

Figure 4. Comparison of stress with time for stone columns and LTP with DCM columns and under loading.

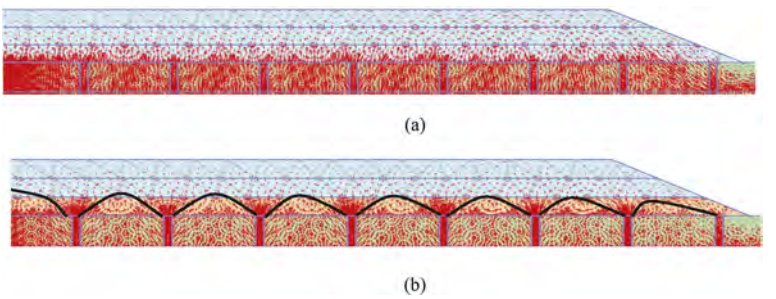

Figure 5. Stress contours for (a) Stone columns (b) DCM columns with LTP.

4 CONCLUSIONS

This paper presented a numerical investigation of embankment supported with DCM columns and soil-cement mixed as a load transfer platform. The comparison of embankment supported with DCM column with LTP and embankment supported with stone columns were also studied. The main findings of this numerical study are summarised below:

1. The effect of inclusion of LTP as soil-cement mixed is less in the case of settlement (at the center of the embankment), however, it helps in reducing the lateral displacement at the

toe of the embankment. A stiffer platform at the base of the embankment restricts the lateral displacement.
2. The dissipation of excess pore water pressure takes less time in the stone columns as compared to the DCM columns with LTP. The excess pore water pressure generated in the DCM with LTP (inside the soil shown in Figure 2) is higher than the stone column during the loading stage and, thus, takes additional time for dissipation.
3. The stresses on DCM columns are about five times higher than the stresses on surrounding soil. However, in the case of the stone columns, the stresses on stone columns are about 1.2 times more than the stresses on surrounding soil.
4. Soil arching is more effective in embankments supported with DCM columns with LTP in comparison to embankments supported with stone columns.

REFERENCES

Dang, L.C., Dang, C.C., Khabbaz, H., Sheng, D. (2020). Numerical study on deformation characteristics of fibre-reinforced load-transfer platform and columns-supported embankments. *Can. Geotech. J*., 58: 328–350.

Han, J., Gabr, M.A. (2002). Numerical analysis of geosynthetic-reinforced and pile-supported earth platforms over soft soil. *Journal of Geotechnical and Geoenvironmental Engineering*, vol. 128, no.1.

Huang, J., and Han, J. (2009). 3D coupled mechanical and hydraulic modeling of a geosynthetic-reinforced deep mixed column-supported embankment. J. *Geotextile Geomembr*., 27(4), 272–280.

Huang, J., Han, J., and Oztoprak, S. (2009). Coupled mechanical and hydraulic modeling of geosynthetic-reinforced column-supported embankments. J. *Geotech. Geoenviron. Eng*., 10.1061/(ASCE)GT.1943-5606.0000026, 1011–1021.

Huang, J. & Han, J. (2010). Two-dimensional parametric study of geosynthetic-reinforced column-supported embankments by coupled hydraulic and mechanical modeling. *Computers and Geotechnics*, vol. 37, no. 5, pp. 638–48.

Jamsawang, P., Yoobanpot, N., Thanasisathit, N., Voottipruex, P., and Jongpradist, P. (2016). Three-dimensional numerical analysis of a DCM column-supported highway embankment. *Computers and Geotechnics*. 72: 42–56. doi:10.1016/j.compgeo.2015.11.006.

Liu, H.L., Charles, W.W., Fei, K. (2007). Performance of a geogrid-reinforced and pile supported highway embankment over soft clay: case study. *Journal of Geotechnical and Geoenvironmental Engineering*, vol. 133, no.12, pp. 1483–1493.

Mohapatra SR, Rajagopal K (2017) Undrained stability analysis of embankments supported on geosynthetic encased granular columns. *Geosynthetics International* 24(5):465–479, DOI: 10.1680/jgein.17.00015

Pham, T.A., Dias, D. (2021). 3D numerical study of the performance of geosynthetic-reinforced and pile-supported embankments. *Geotextiles. Soils and Foundations* 61 (2021) 1319–1342.

Terzaghi, K., 1943. Theoretical soil mechanics. JohnWiley & Sons. New York, 11–15.

Venda Oliveira, P.J., Pinheiro, J.L.P. & Correia, A.A.S. (2011). Numerical analysis of an embankment built on soft soil reinforced with deep mixing columns: Parametric study, *Computers and Geotechnics*. vol. 38, no. 4, pp. 566–76.

Xue J, Liu Z, Chen J (2019) Triaxial compressive behaviour of geotextile encased stone columns. *Computers and Geotechnics*. 108:53–60, DOI: 10.1016/j.compgeo.2018.12.010

Yapage, N., Liyanapathirana, D., Kelly, R., Poulos, H. & Leo, C. (2014). Numerical Modeling of an Embankment over Soft Ground Improved with Deep Cement Mixed Columns: Case History. *Journal of Geotechnical and Geoenvironmental Engineering*, vol. 140, no. 11, p. 04014062.

Ye, G., Cai, Y., Zhang, Z. (2017). Numerical study on load transfer effect of stiffened deep mixed column-supported embankment over soft soil. *KSCE J. Civ. Eng*. 21 (3), 703–714.

Smart Geotechnics for Smart Societies – Zhussupbekov, Sarsembayeva & Kaliakin (Eds)
© 2023 The Author(s), ISBN 978-1-003-29912-7
Open Access: www.taylorfrancis.com, CC BY-NC-ND 4.0 license

Causes of water encroachment in open-cut tunnel structures and innovative waterproofing, and repair systems for its elimination

Dmitriy S. Konyukhov, Tengiz E. Kobidze & Oleg B. Krymov
JSC Mosinzhproekt, Moscow, Russia

ABSTRACT: One of the topical problem of underground construction is the protection of under-ground structures from water encroachment. The problem is based on the impossibility to apply traditional waterproofing materials for underground constructions (bituminous-polymer rolls, polymer sprayed compositions) on inaccessible exterior insulated surfaces of runway slabs and wall structures constructed in open pits without slots for backfilling. Before the erection of supporting structures, the waterproofing coating is laid on the accessible surfaces of the concrete preparation and "diaphragm wall". This eliminates the adhesion of the waterproofing coating on the outer surface of the protected structures and results in the formation of a gap between the waterproofing and the protected structure. In the case of damage or defect of the waterproofing coating, the seeping ground waters migrate uncontrollably along the formed joint and penetrate into the building. The report presents the results of scientific and practical work performed in the JSC 'Mosinzhproekt' to eliminate the mentioned problem, including the development of design and techno-logical solutions using the methods of voile injection and manufacture of a two-layer seamless waterproofing membrane in the building environment as well as making changes to the effective regulatory and technical documents of the Russian Federation.

1 INTRODUCTION

One of the urgent problems in modern tunnelling is the problem of preventing or eliminating water encroachment of underground transport structures, built by Cut and cover and semi-closed-cut methods, which in these conditions completely lose their waterproofing protection, lose their water resistance and repairability, thus violating the conditions of their safe operation.

2 MAIN ISSUE

2.1 *Regulatory requirements*

The problem arises from restrictions on the use of traditional waterproofing materials for tunnel construction. The most widely used among them, approved by regulatory documents for waterproofing of underground transport structures (subways, road and railway tunnels, underground car parks, etc.) by cut and cover and semi-closed-cut methods include bituminous-polymer fusible roll materials and, to a lesser extent, sprayable polymer compositions based on bituminous-polymer composites, polyurea, methyl methacrylate resin (CS 120.13330.2012, CS 122.13330.2012, PS NOSTROY 2.27.123-2013).

According to paragraph 7.1.2 of PS NOSTROY 2.27.123-2013, to ensure the device reliable waterproofing of underground structures coating of cladding and sprayed materials should be applied directly to the building envelope from the outside (the side of exposure to

DOI: 10.1201/9781003299127-397

groundwater). However, these materials can only adhere to the surface of a prefabricated and seasoned ('old') concrete basement. Consequently, a prerequisite for their application to the external surfaces of the structures to be protected is the accessibility of the surface to be insulated. In the case of underground structures for transport purposes, such structures include only the containment walls with backfill cavities and roof slabs (Figure 1).

This restriction excludes the possibility of laying these materials on the outer surfaces of protected structures, which are not accessible to the surface to be insulated. Such structures include buckle slabs of all types of underground structures, walls constructed without backfill cavities and retaining walls for load-bearing 'diaphragm walls'. Therefore:

- in accordance with paragraph 5.6.3.20 of CS 120.13330.2012 and paragraph 5.4.6.4 of CS 122.13330.2012 for buckle slab waterproofing, the waterproofing coating should be placed on a concrete foundation mattress;
- when constructing underground structures using the 'diaphragm walls' technology or without cavities for backfill according to paragraph 5.6.3.24 of SP 120.13330.2012 and paragraph 5.4.6.10 of SP 122.13330.2012 the waterproofing shall be arranged on the 'diaphragm wall' surface, and the 'pressure wall' or permanent wall shall be made tightly against the 'diaphragm wall' to absorb the expected hydrostatic pressure for the design of waterproofing in given conditions until the amendment of CS 120.13330.2012 No. 4 (2020), although they contradicted the requirement of paragraph 7.1.2 of PS NOSTROY 2.27.123-2013 that waterproofing coating should be placed directly on the outer surface of building envelopes.

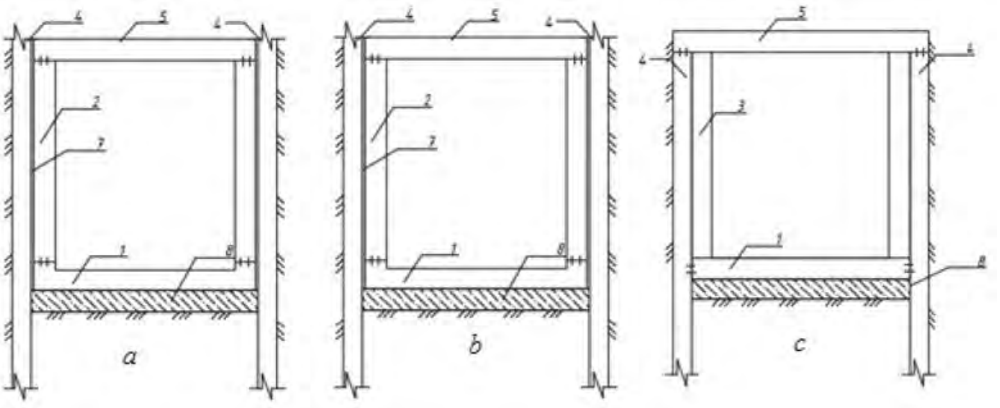

Figure 1. Variety of methods of construction of underground structures made of cast reinforced concrete: a – cut and cover method with backfill slots; b – cut and cover method without backfill slots; c – cut and cover and semi-closed-cut method with slab (cover) spacing discs, with a load-bearing 'diaphragm wall'; 1 – buckle (foundation) slab; 2 – bearing wall; 3 – pressure wall; 4 – excavation wall (in part b – bearing structure); 5 – floor slab (cover); 6 – cavities for backfilling; 7 – sliding plane (plane of mutual shift of the walls); 8 – concrete foundation mattress.

In the practical implementation of the above-mentioned design rules, the principle of waterproofing protection of building envelopes on the groundwater exposure side is observed, but the lack of adhesive bonding with the insulated surface deprives the waterproofing coating of the ability to localise seeping groundwater within the permeable damage and prevent uncontrolled groundwater migration across the outer surface of the protected structure (in violation of requirement CS 120.13330.2012 with Amendments No. 1-4, paragraph 5.5.3.18).

As practical experience shows, this leads to an unrepairable emergency situation, in particular:

- complete watering of the external surface of the structure being insulated and, as a rule, penetration of groundwater into the structure through filtering defects of concrete and

reinforced concrete structure itself (cracks, voids, weakened and highly porous areas of concrete, technological and expansion joints etc.) in the form of leaks of different intensity and damp spots on the internal surfaces of the structure;
– loss of repairability of the protected structure, because sealing one or a number of filtering defects (which would give a positive effect in the presence of a continuous adhesive bond of waterproofing with the concrete base) leads to an increase in the hydrostatic pressure of groundwater and, consequently, to the activation of 'sleeping' filtering defects and the appearance of new water appearing in other areas of the surface of the watered structure.

The loss of repairability requires costly and complex technological measures to restore the water tightness of a watertight structure, which include the use of water injection to provide a waterproofing coating on the outer surface of the protected structure or an impervious blanket in the surrounding soil mass.

In practice, the elimination of the possibility of such accidents required the elimination of contradictions between the considered normative rules for the design and waterproofing of building envelopes. For this purpose, the authors initiated amendments to paragraphs 5.6.3.17, 5.6.3.18 and 5.6.3.24 of CS 120.13330.2012 in order to establish uniform rules for the arrangement of a reliable and serviceable waterproofing of an underground structure based on the principle of a waterproofing coating to be installed by means of adhesive bonding directly onto the outer surface of the protected structure whether it has access to the insulated surface or not.

2.2 *Changes to the design rules in section 'Waterproofing of concrete lining' in CS 120.13330.2012*

Old Edition
5.6.3.17 The type and design of waterproofing of lining modes are determined by engineering and geological conditions of construction, magnitude of hydrostatic pressure, presence of aggressive effects of the environment, type of lining, possibilities to ensure water resistance of concrete under the accepted technology of construction works and other production conditions.
Revised version. Modification No. 2
5.6.3.17 The type and design of lining waterproofing of different modes are determined by the engineering and geological conditions of construction, magnitude of hydrostatic pressure, presence of aggressive environmental impacts, type of lining, possibilities to ensure water tightness of concrete under the accepted technology of construction works and repairability and other production conditions.
Old edition
5.6.3.18 Cut and cover tunnel structures shall have a continuous external waterproofing.
Revised edition. Modification No. 2 and 4
5.6.3.18 Cut and cover and semi-closed-cut tunnel structures should have a closed contour waterproofing to prevent uncontrolled migration of seeping groundwater to the surface of the isolated structures in case of damage.
Old edition
5.6.3.24 The flexible waterproofing, if necessary on the inside of the lining, should be protected by a reinforced concrete 'jacket' designed to withstand the expected hydrostatic pressure. It is necessary to ensure that the internal reinforced concrete structure is pressed tightly against the waterproofing.
Revised edition. Modification No. 4
5.6.3.24 The flexible waterproofing on the inside of the excavation enclosure 'diaphragm' wall or on the inside of the lining should be protected by an internal structure in the form of a pressure wall or secondary lining respectively designed to withstand the expected hydrostatic pressure. The waterproofing must have a continuous adhesive bond of at least 0.5 MPa between the waterproofing and the internal structure or, if an adhesive bond is not available, the waterproofing must be fitted with a sectional waterproofing control-injection system.

After the introduction of the new regulations, the use of traditional adhesive bonding materials and their laying techniques for waterproofing building envelopes with no access to the outside surface remains possible, but not a regulatory technical solution, leading to an unreliable and unrepairable waterproofing system. As a result, there is an urgent need to introduce a new generation of waterproofing materials into construction practice that can meet updated regulatory requirements.

The domestic market offers a number of innovative waterproofing materials, both domestic and foreign, which are capable of solving this problem. A distinctive feature of these materials is their ability to exhibit, in the form of pre-installed waterproofing coatings, a continuous adhesive bond to freshly poured concrete of protected underground structures with no access to the outside surface, such as buckle plates, wall structures constructed without backfill cavities and a pressure wall for a load-bearing 'diaphragm wall'.

2.3 *Innovative waterproofing, and repair systems*

These materials include the following.

1. The original waterproofing system based on the use of an innovative waterproofing composite material developed by the authors by combining the technical properties of two initial materials, which were selected (patent RU162638U1 16.12.2015, patent RU164721U1 14.01.2016):

- sprayable waterproofing polymer compositions with 'two-sided' adhesion, in particular, ethylene vinyl acetate polymer (EVA) and bitumen-polymer composite of 'Flexigum' brand, providing standard adhesion (≥ 0.5 MPa according to CS 120.13330.2012) not only with the 'old concrete' substrate covered with a layer of sprayed polymer, but also with the external surface of the concrete laid in the form of mortar on the ready-made waterproofing coating.
  The ability of long-term adhesion of bituminous-polymer waterproofing systems to concrete is confirmed by their traditional use in construction, and EVA polymer – by many years of experience in the construction of composite waterproofing lining of transport tunnels made of shotcrete, erected by mining method [6];
- geotextile nonwoven needle-punched material with a density of 250-500 g/m2 (GOST R 53225-2008) used as a reinforcing and strengthening element of the polymer coating, as well as an underlay - bedding for making a two-layer seamless waterproofing coating (polymer membrane with a base) in construction conditions by spraying a 4-6 mm thick layer of waterproofing composition on a ready-made geotextile underlay.

The application of the sprayed composition with double-sided adhesion and its modification in the form of a two-layer polymer seamless membrane with a reinforcing base, as well as the possibility of directional regulation of physical and mechanical properties of the waterproofing coating with a reinforcing web depending on the problem to be solved provide:

– the use of a waterproofing coating without a protective layer of fine-grained concrete when the reinforcement frame is tied and the buckle plate is subsequently concreted, due to the reinforcing geotextile fabric reinforcing the surface layer of the coating (Figures 2 and 3). This accelerates the waterproofing process, reduces the cost of waterproofing works and ensures a continuous adhesive bond between the waterproofing coating and the inaccessible exterior surface of the buckle plate;
– adhesion bonding of the sprayed polymer layer of the double-layer sprayed membrane to the inaccessible external wall surface of structures erected without backfill cavities. Preservation of this coating on the wall surface during subsidence of the underground structure, due to the free suspension of the double-layer membrane on the 'diaphragm wall' (Figure 4);
– the construction of a reliable waterproof three-layer sandwich wall structure by applying a sprayed waterproofing layer with double-sided adhesion to the levelled surface of the

'diaphragm wall' and the subsequent erection of a pressure wall of monolithic or shortcrete when building underground structures using the 'diaphragm wall'technology by 'top-down' method (Figure 5);

– reliability of waterproofing, safety of protected underground structures and their repairability due to:
  a) adhesive fixing of the seamless waterproofing coating directly on the outer surfaces of the protected structures with and without access to the outer surface according to the requirements of CS 120.13330.2012 with Amendments №1-4 and paragraph 7.1.2 of PS NOSTROY 2.27.123-2013;
  b) the local nature of water penetration due to the continuous adhesive bond between the waterproofing and the concrete substructure. Under these conditions, penetration of groundwater into an underground structure is possible if the location of the penetrating damage to the waterproofing coating or process joint and the filtering defect of the envelope structure coincide. The low probability of such coincidence increases the operational reliability and safety of underground structures. However, in the case of such a coincidence, the localization of groundwater within the pavement damage and its migration through the filtering concrete defect makes it easier to locate the site for local and relatively low-cost work to restore the waterproofing of the structure by injecting a sealing compound into the filtering concrete defect.

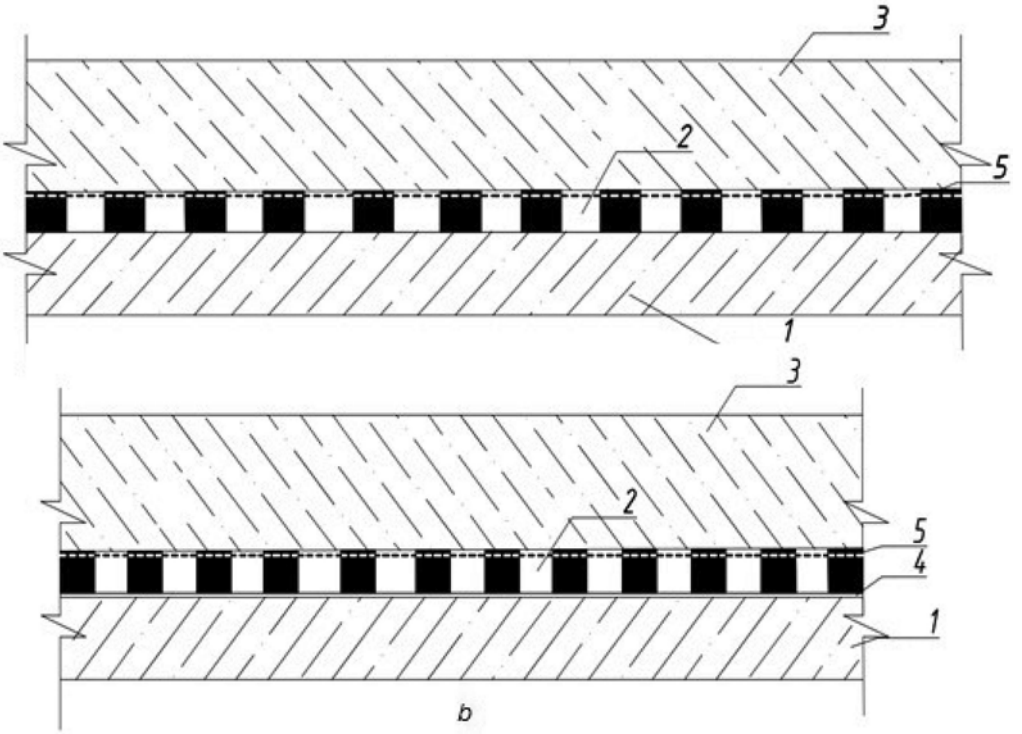

Figure 2. Seamless waterproofing of the buckle plate with sprayed compositions with double-sided adhesion: a – without underlay; b – with underlay of non-woven geotextile; 1 – concrete preparation; 2 – waterproofing layer; 3 – buckle plate; 4 – underlay of non-woven geotextile; 5 – non-woven geotextile, reinforcing the surface layer of waterproofing coating.

Technical characteristics of materials and structural and technological solutions for the installation of the developed waterproofing system under construction conditions were approved during bench tests and recommended for pilot application in the Moscow Metro facilities by an interdepartmental commission consisting of representatives of the Moscow

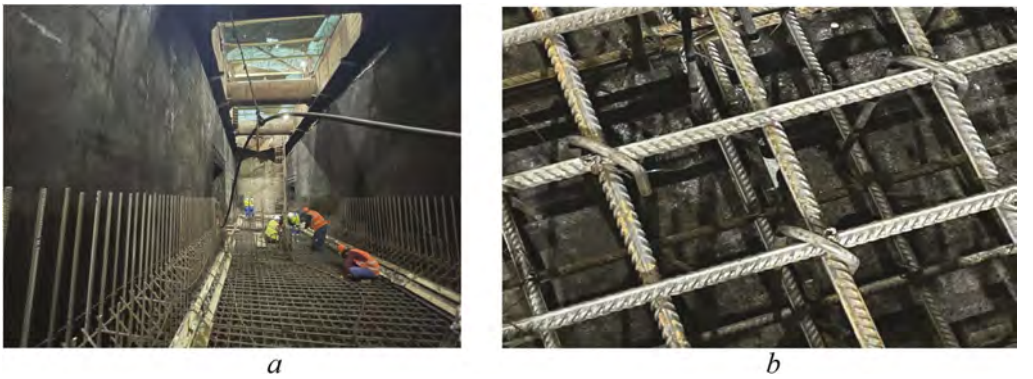

Figure 3. Seamless sprayed waterproofing membrane for cut-and-cover underground structures without backfill slots: a – sprayed waterproofing material with double-sided adhesion on the inner surface of the lining and installation of the reinforcement cage; b – binding of the reinforcement cage over the sprayed waterproofing membrane with double-sided adhesion with a reinforced surface layer of geotextile fabric and without a protection layer of fine-grained concrete.

Metro State Unitary Enterprise, Mosinzhproekt JSC, Mospromproekt JSC, Lenmetrogiprotrans JSC, Mosmetrostroy JSC and Tunnelling Research Centre LLC.

A number of Russian companies are suppliers of roll-fed polymeric waterproofing membranes from foreign manufacturers that provide adhesive bonding to the inaccessible external surface of the protected structures of underground structures.

These materials are rolls of waterproofing polymer with a thickness of 2 to 4.5 mm, depending on the initial raw material (polyethylene, PVC or bituminous-polymer composite, respectively) with a special thin and reinforced surface layer, which provides:

- adhesion (≥ 0.5 MPa) of the waterproofing coating to the surface of the freshly placed concrete of the reinforced concrete structures to be erected without access to the external surface;
- the fine-grained concrete waterproofing membrane is rejected, and the reinforcement is tied, and the buckle plate is concreted immediately after the waterproofing membrane has been laid. The waterproofing coating made of these materials is arranged by laying rolls with an overlap of 10-15 cm and sealing them with the formation of technological joints (Figure 6).

Factory-ready membranes guarantee consistency of quality characteristics, significantly reduce the time of waterproofing and general construction works, as well as labour and material and financial costs during their performance, but the presence of technological joints requires their qualitative performance to ensure the operational reliability of the waterproofing coating.

All materials are certified, meet the requirements of CS 120.13330.2012 and have test protocols of concrete base samples with waterproofing coatings for resistance to lateral water migration, which confirm the reliability and water resistance of the adhesive contact layer at hydrostatic pressure of at least 0.5 MPa.

Rules for design and execution of waterproofing works with application of the considered new generation waterproofing systems for underground constructions of cut-and-cover and semi-closed type for transport purposes are concentrated in PS 75-03 Mosinzhproekt JSC.

Figures 7 and 8 show the diagrams of waterproofing for underground structures constructed without and with backfill cavities, respectively, using the new-generation materials under consideration, which differ in their adhesive bonding ability with freshly poured concrete.

3 CONCLUSION

The existence of contradictory rules in national and industry standards for the design of waterproofing of underground transport structures using traditional waterproofing materials

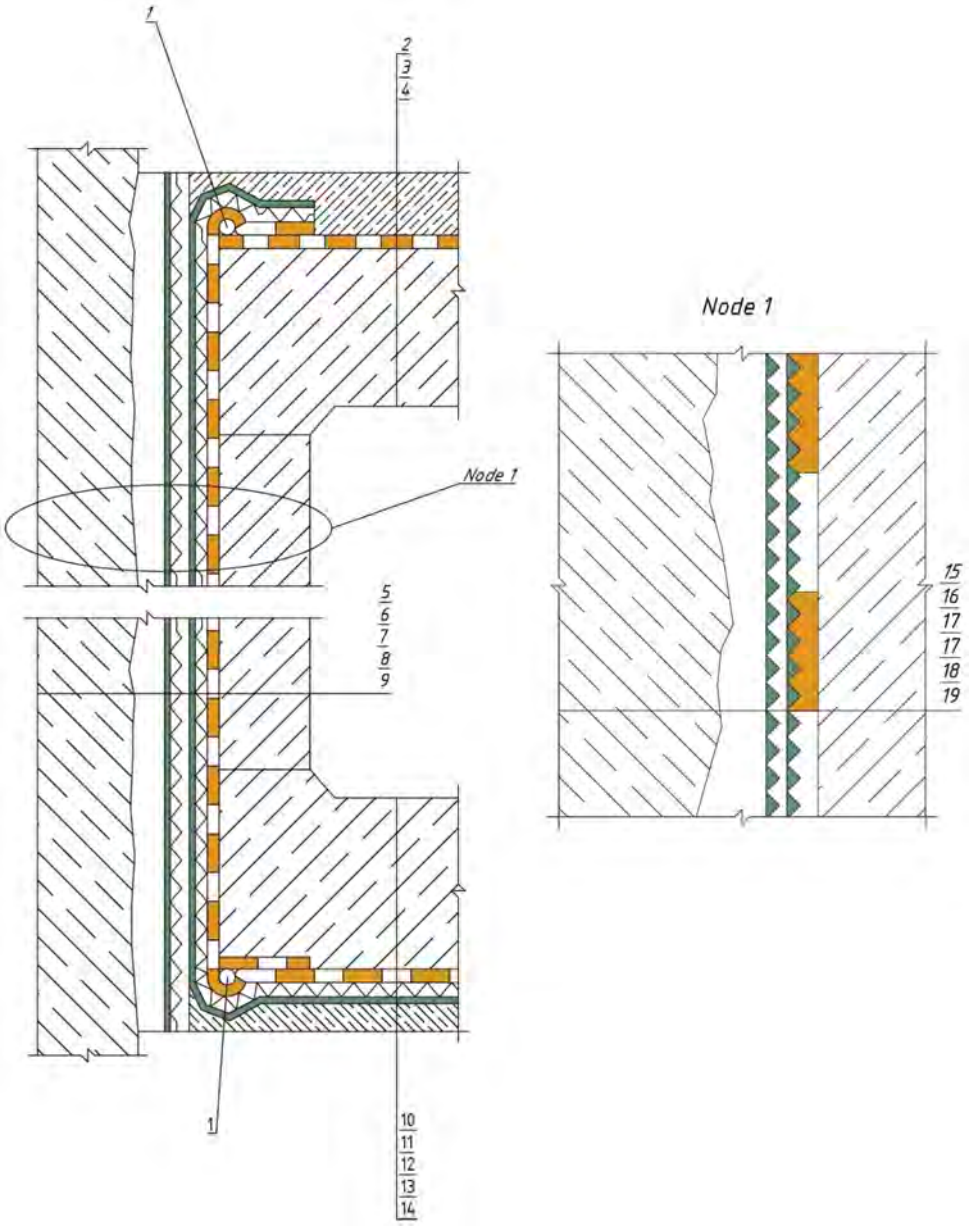

Figure 4. Waterproofing with two-layer sprayed waterproofing coatings with adhesion to freshly laid concrete of the monolithic wall construction of an underground structure without backfill cavities (Node 1): 1 – compensating loop; 2 – protective layer of concrete on mesh; 3 – sprayed waterproofing coating with primary and secondary adhesion; 4 – reinforced concrete floor; 5 – ditch sheeting – 'diaphragm wall'; 6, 11, 16 – levelling layer (if necessary); 7 – two layers of geocomposite material; 8 – waterproofing coating with primary and secondary adhesion applied to the geotextile of the geocomposite material; 9 – reinforced concrete wall; 10 – concrete buckle plate; 11 – protective sand cement screed; 12 – waterproofing coating with primary and secondary adhesion applied to the geotextile of the geocomposite material; sprayed waterproofing coating with primary and secondary adhesion; 13 – geocomposite material; 14 – concrete bedding; 15 – ditch sheeting - 'diaphragm wall'; 17 – geocomposite material (polyethylene film + geotextile, facing a layer of polyethylene film to the 'diaphragm wall'); 18 – sprayed waterproofing coating with primary and secondary adhesion applied to a geotextile geocomposite material; 19 – concrete load bearing wall.

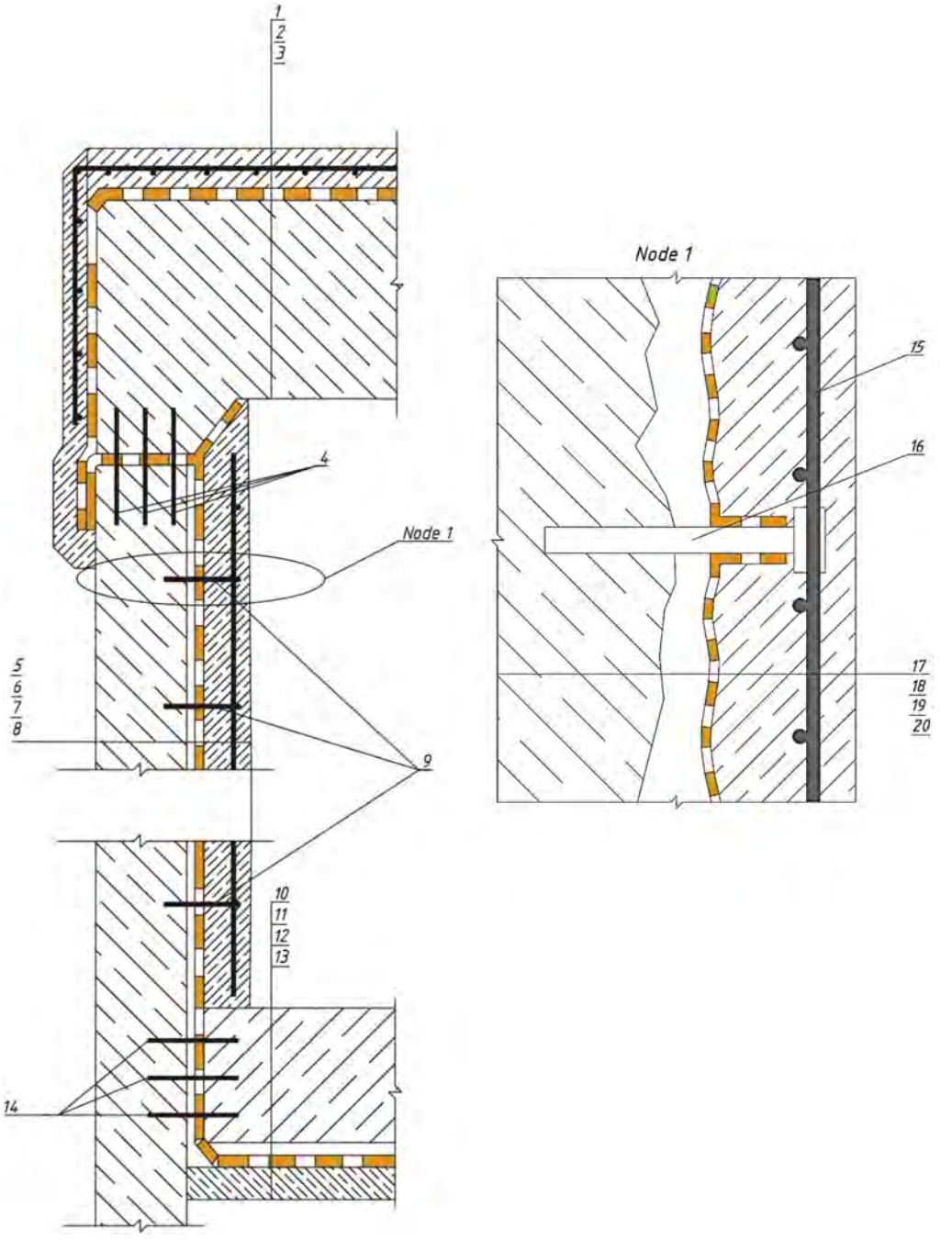

Figure 5. Waterproofing the load-bearing wall of an underground 'diaphragm wall' structure with sprayed polymer compound with two-sided adhesion: 1 – protective layer of concrete on mesh; 2, 7, 12 – sprayed waterproofing coating with primary and secondary adhesion; 3 – reinforced concrete floor; 4 – free length of 'diaphragm wall' reinforcement; 5 – load-bearing 'diaphragm wall'; 6 – levelling layer (if necessary); 8 – pressed wall of concrete on mesh; 9 – anchoring the pressure wall; 10 – buckle plate; 11 – protective sand cement screed; 13 – concrete bedding; 14 – anchoring the buckle plate; 15 – steel mesh; 16 – steel anchor; 17 – load bearing 'diaphragm wall'; 18 – levelling/smoothing layer (if necessary); 19 – sprayed waterproofing coating with primary and secondary adhesion; 20 – pressed wall on mesh.

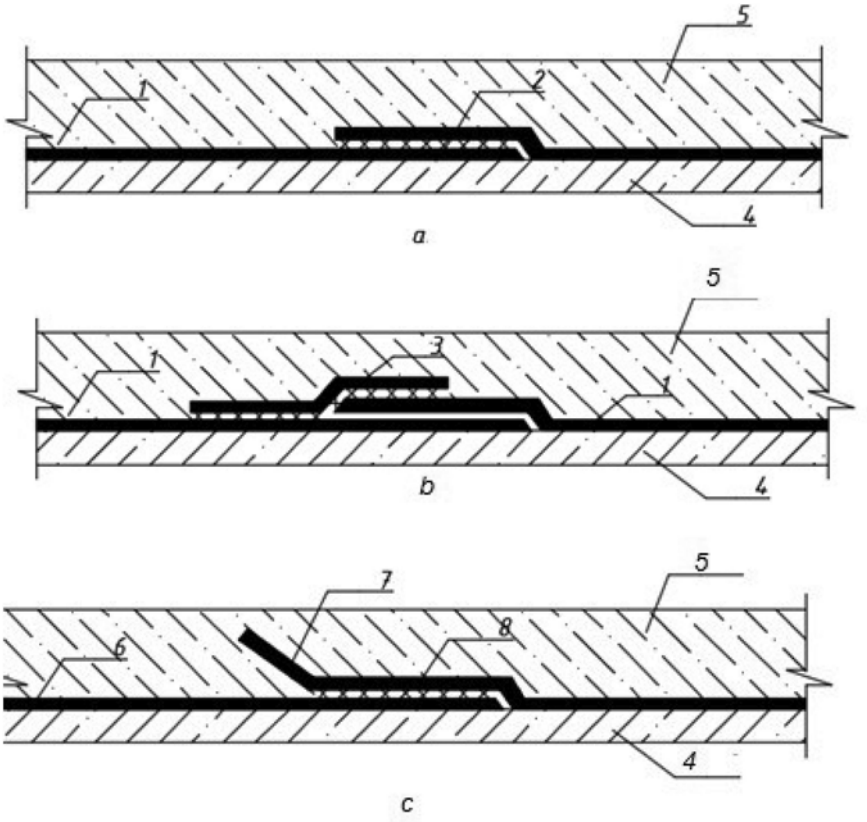

Figure 6. Waterproofing of the buckle (foundation) plate using factory-assembled 'free' laid three-layer sheet membranes and with adhesion to the freshly formed concrete. Laying diagram of three-layer sheet membranes with overlaps: a – self-adhesive longitudinal edge strips; b – transversal edges with overlapping adhesive sheets; c – Kolfen BSH bitumen-polymer-based membranes with overlapping longitudinal edges; 1 – three-layer sheet membrane; 2 – process joint of self-adhesive longitudinal edge strips; 3 – overlapping adhesive sheet; 4 – concrete surface; 5 – gutter board, laid on the waterproofing coating; 6 – rolls of Kolfen BSH; 7 – edge piece for welding; 8 – self-adhesive edge piece (joining of transversal edges of Kolfen BSH is made only with overlapping of the welding edge).

has led to incorrect technical solutions and to water leakage accidents in structures in operation. This has led to the necessity to:

– eliminate the contradictions in the current design rules;
– development of innovative waterproofing materials which meet the updated regulations.

The application of new generation waterproofing materials in the practice of tunnelling on the basis of the updated design rules guarantees:

– no possibility of making incorrect design decisions for waterproofing of underground transport structures;
– elimination of conditions for abnormal situations as a result of water encroachment of tunnel lining structures, which cannot be repaired and require costly rehabilitation work on the outside waterproofing of the structure or building;
– acceleration and reduction of the cost of repairable waterproofing works when constructing underground structures for transportation purposes, ensuring conditions for their durable, safe and low-cost operation.

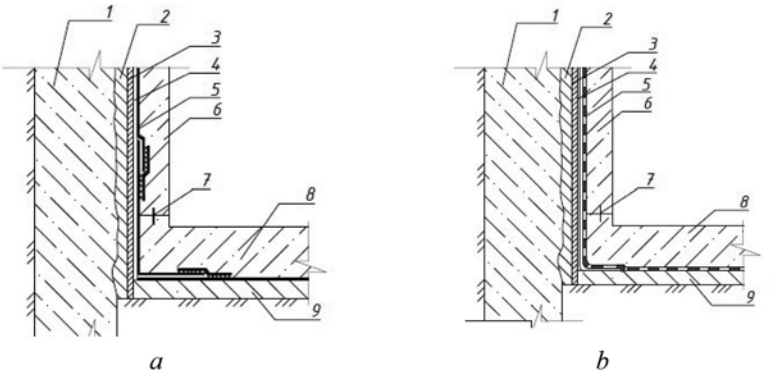

Figure 7. Waterproofing of structures without backfill cavities: a – using factory-made membranes; b – using sheet waterproofing with a surface layer of sprayed compositions with two-sided adhesion; 1 – enclosing 'diaphragm wall'; 2 – levelling layer of fine-grained concrete or false wall; 3 – layer of geotextile fabric, polyester foam boards or profiled membranes; 4 – slip plane; 5 – waterproofing coating; 6 – permanent wall; 7 – water stop; 8 – buckle plate; 9 – foundation mattress.

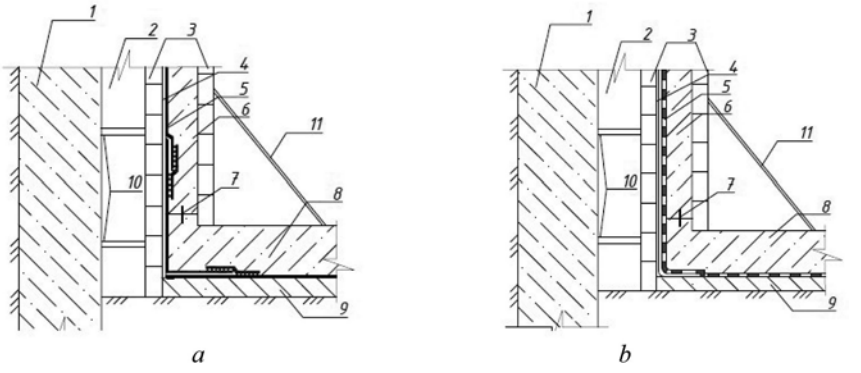

Figure 8. Waterproofing of structures with backfill cavities: a – factory-assembled roll-fed waterproofing coating, b – sprayed waterproofing coating; 1 – excavation protection; 2 – cavities; 3 – external and internal shuttering boards; 4 – geotextile fabric substrate; 5 – waterproofing coating; 6 – monolithic wall structure; 7 – water stop; 8 – buckle plate; 9 – foundation mattress; 10 – telescopic spindles; 11 – frame for single-sided concreting.

REFERENCES

CS 120.13330.2012 *Subways* (with Revisions No. 1-4). Updated edition of SNiP 32- 02-2003.

CS 122.13330.2012 *Railway and road tunnels* (as amended by the 1st Amendment), updated version of SNiP 32-04-97.

PS NOSTROY 2.27.*123-2013 Waterproofing of transport tunnels and open-cut subways*. Rules for designing, manufacturing.

Patent RU162638U1 16.12.2015.

Patent RU164721U1 14.01.2016.

PS TAR (Tunnel Association of Russia) 93.060-001-2012. *Waterproofing of underground structures with sprayed waterproofing of polymer cement-based MASTERSEAL series*. Design and workmanship rules.

GOST R 53225-2008 *Geotextile materials*.

PS 75-03 'Mosinzhproekt' JSC. *Waterproofing of underground structures of transport subways, erected by cut-and-cover and semi-closed methods of work*. Design and work execution rules.

Smart Geotechnics for Smart Societies – Zhussupbekov, Sarsembayeva & Kaliakin (Eds)
© 2023 The Author(s), ISBN 978-1-003-29912-7
Open Access: www.taylorfrancis.com, CC BY-NC-ND 4.0 license

Improvement of properties of black cotton soil subgrade through lime kiln dust and sand stabilization

A.A. Kibuka & S. Jjuuko
Makerere University, Kampala, Uganda

D. Kalumba
University of Cape Town, Cape Town, South Africa

ABSTRACT: The soil sample was blended with varying proportions of sand alone, and a combination of sand and Lime Kiln Dust (LKD). The laboratory results were analyzed based on the effect of the additives on the engineering properties of the soil sample. From the test results on neat soil sample, it was observed that black cotton soil had a high plasticity index, high swelling potential, and low bearing strength. The addition of sand-LKD to black cotton soil sample exhibited a significant improvement in strength, and reduction in the plasticity index and swelling potential. The application of 30% sand and 3% LKD increased the CBR value of the neat sample from 5% to 18%, reduced the PI value of the native soil from 49% to 10.2%. This combination satisfied all the Ministry of Works and Transport subgrade specification requirements and was considered as the optimum stabilizer content for black cotton subgrade soils.

1 INTRODUCTION

Black cotton (BC) soils are inorganic clays characterized by exceptionally low bearing capacity, high compressibility, low permeability, and high-volume change under changing moisture conditions (Amadi & Osu 2018, Kollaros & Athanasopoulou 2016). BC soils exhibit high swelling and shrinking due to changes in moisture content (Dalal et al. 2017). The soil is extremely hard when dry and loses its strength further upon wetting. The alternate wet and dry conditions in the soil bring about severe movements of the soil mass, thus structures built on BC soil experience recurring cracking and progressive damage in the form of settlement, unevenness, etc. (Dalal et al. 2017, Verma & Marv 2013). In Uganda, BC soils are mainly found in the semi-arid Karamoja subregion in the North East.

The high swelling and shrinkage properties of BC soil can be attributed to the presence of a considerable amount of montmorillonite clay mineral (Etim et al. 2017). It has an expanding lattice that easily adsorbs water, hence expanding. Montmorillonite is also associated with more surface area per unit mass than other clay minerals (Alshameri et al. 2014, Salima & Abdelhak 2013). Roads constructed on expansive subgrade soils have not fulfilled their intended functions of accessibility and mobility due to being in poor condition, to which the nature of the soil contributes to some extent (Ikeagwuani et al. 2019). At the same time, gravel roads with expansive subgrade soil, such as BC soil, have failed to perform their intended function of providing satisfactory ride quality due to deteriorations like cracks, bumps, slipperiness, and impassibility, especially in wet conditions (Verma & Marv 2013, Etim et al. 2017, Al Fouzan & Dafalla 2014). This is exactly the situation of the roads in North-Eastern Uganda, where most of the roads are almost impassable during rainy season, hence bringing businesses to a standstill. There is, therefore, a need for improvement of such problematic subgrade soil before it is built upon.

DOI: 10.1201/9781003299127-398

Different techniques have been adopted to enhance the engineering properties of black cotton soils and these include substitution and chemical stabilization, such as the use of lime. The optimal selection among the various methods is guided by various economic, practical, and environmental considerations. According to Ground Engineering Magazine (2009) & Edil et al. (2006), the reutilization of materials found on-site has proved to be more sustainable and environmentally positive than the conventional method of substitution (dig and dump) by dealing with unsuitable subgrade materials. Though stabilization is an economical and popular way of reusing on-site materials, the use of lime, either in isolation or with other stabilizing agents, has been found to be expensive, especially in third world countries (Zami & Lee 2009). Recent research has successfully utilized other effective and environmentally sustainable additives either in isolation or in combination with lime, including groundnut shell ash, bagasse ash, iron ore tailings, ground granulated blast furnace slag, and wood powder, to improve the properties of black cotton soil (Dalal et al. 2017, Ikeagwuani et al. 2019, Etim et al. 2017, Kang et al. 2015, Sreekrishnavilasam et al. 2007).

Research has shown that stabilization of locally available problematic soil by utilizing industrial and construction waste materials along with natural poorly graded river sand provides improved compaction and strength characteristics and reduces the cost of construction substantially (Kollaros & Athanasopoulou 2016, Kang et al. 2015, Gupta & Sharma 2016, Jjuuko et al. 2011, Schanz & Elsawy 2017). Lime kiln dust (LKD), a by-product from the manufacturing process of quick lime with high lime content, has potential in the stabilization of soils as a direct substitute for hydrated lime (Arulrajah et al. 2017).

This study investigated the potential use of lime kiln dust (LKD) and sand together as additives in the modification of BC soil in Uganda. Approximately, over 3600 kg of lime kiln waste dust is generated daily during lime production at Tororo Cement Limited. In addition, sand is naturally occurring and is one of the materials that are readily available in Uganda. Its constituents can easily be controlled. According to Adam & Agib (2001), in order to achieve higher quality and production cost reductions, proportions between soil, stabilizer, and compaction pressure need to be optimized, taking into consideration the specific characteristics of the soil. In spite of all this, little work has been done to determine the requirements of LKD and sand for stabilizing BC soil in Uganda to obtain optimum results. The work concentrated on the characteristics of BC soil, sand, and LKD samples, and on the effect of stabilizing BC soil by mixing it with dry sand and LKD.

2 MATERIALS AND METHODS

2.1 *Black Cotton (BC) soil*

Samples of black cotton soil were obtained from Nakapiripirit district (Namalu-Kaiku Road). The required amount of soil was obtained at depths of about 0.5 m below the ground level. Sufficient care was taken to ensure that the collected soil samples were fairly homogenous. The topsoil was ignored since it was more likely to contain organic matter and other foreign materials. The tests conducted on BC soil indicated a poorly graded material with a 99% proportion of fines passing sieve No. 200. It was classified as A-7-6 (55) according to AASHTO, an inorganic clay with a high plasticity index. A group index of 55 was greater than the required maximum of 20, indicating a poor subgrade material. The chemical constituents of the obtained BC soil sample were tested in Makerere University, Department of Geology and Petroleum Studies laboratory. The results obtained were CaO at 0.63%, MgO at 2.32%, Fe_2O_3 at 3.82%, Al_2O_3 at 17.29% and SiO_2 at 34.71%. Perkin Elmer Analyst 400 equipment was used in the analysis.

2.2 *Lime Kiln Dust (LKD)*

LKD is a waste product from the production process of quick lime. It is estimated that about 3600 kg of LKD is generated daily during lime production at the Tororo Cement Limited plant alone. LKD is suitable for stabilizing a wide range of soils, both cohesive and non-cohesive. This is also a cost-effective way of reusing it. LKD has been successfully used to

stabilize subgrade soils. It has been found to enhance values of the California Bearing Ratio, resilient modulus, and unconfined compressive strength, and lower the plasticity index (Kang et al. 2015, Heckel & Wahab 1996, Burnham et al. 1992, Daita et al. 2001, Solanki et al. 2010, Cetin et al. 2010). LKD used in the study was sourced from Tororo Lime Plant. It was packed in sacks and transported to the Geotechnical Engineering laboratory in Makerere University. The chemical constituents of LKD were determined in the laboratory of Tororo Lime Plant. Its chemical properties, as determined in the laboratory, included CaO at 71.52%, MgO at 2.66%, Fe_2O_3 at 1.47%, Al_2O_3 at 0.73% and SiO_2 at 2.38%. The values indicated high quantities of CaO, hence suitable for stabilization of BC soil with high amounts of SiO_2 and Al_2O_3.

2.3 *Sand*

Sand was obtained from River Lolachat in Nakapiripirit district. The grading curve for sand from the sieve analysis test was fitting in the grading envelope defined by the grading limits in the Ministry of Works and Transport (MoWT) specifications. The grading curve indicated uniformly graded sand with both coarse and fine particles. According to the Unified Soil Classification System (USCS), it was classified as Silty Sand, which bonds well with clay particles.

2.4 *Sample preparation*

The samples for laboratory testing were prepared in accordance with BS 1377 Part1:1990. It has been reported that some tropical soils are sensitive to pretest drying methods [44]. Therefore, all the samples of black cotton soil were air-dried. Other pretest sample preparation methods included pulverization using a rubber mallet, sieving, and sub-sampling (coning, quartering, and riffling)2. After air-drying, index property tests were carried out for classification.

In order to investigate the effect of sand and lime kiln dust on the properties of black cotton soil, specimens with specified amounts of sand, lime kiln dust, and soil were prepared in different mixes. The soil was blended with varying percentages of sand in the proportions of 0%, 20%, 30%, 40%, and 50%. Black cotton soil was further blended with lime kiln dust by keeping 30% sand constant and varying lime kiln dust in proportions of 3%, 4%, 5%, and 6% by mass. Most specifying bodies permit the use of recycled materials as a portion of the road improved subgrade. According to BS 6543 for waste materials and industrial by-products, a maximum of 50% LKD by weight of total mass could be used. The mixing was done mechanically on a metal tray. For consistency, soil was mechanically blended before mixing with sand and LKD. Tests of physical properties of the different blends/mixes were conducted.

2.5 *Initial consumption of lime kiln dust*

The method developed by Eades and Grim to measure the pH of soil stabilized with various percentages of lime or any other pozzolanic stabilizer was utilized. The quantity of lime kiln dust necessary to maintain the pH of 12.40 in the soil–LKD–water mix after one hour is considered to be the initial consumption of LKD of the material. It is the required minimum content of LKD that will stimulate the pozzolanic reactions to achieve a permanent gain in strength of the subgrade material. Samples of black cotton soil were mixed with distilled water and different proportions of LKD. The pH values for the different proportions of LKD were then read from the pH meter and recorded. The graph of pH against LKD content was then plotted and the minimum content of LKD needed to give a pH value of 12.40 was read from the graph. The initial consumption of lime kiln dust was determined as 5.6% at a pH value of 12.4. For adequate stabilization, an excess of lime kiln dust has to be added to black cotton soil.

2.6 *Laboratory tests*

Laboratory tests were carried out on the natural soil sample and blended soil mixtures. The tests were carried out to determine the index and strength properties of the native and blended soil samples. The results were analyzed based on the effect of the stabilizer in comparison with

the properties of the neat soil sample and stabilized soil samples. They were then compared against the MoWT specification requirements for subgrade construction. The tests were conducted in accordance with British Standards, Indian Standards, and American Society for Testing and Materials Standards, as shown in Table 1.

Table 1. Summary of laboratory tests.

Material to Be Tested	Tests	Standard Test and Designation
Black cotton soil	Particle size distribution (wet sieving and hydrometer)	BS 1377: Part 2: 1990
	Moisture content	BS 1377: Part 2: 1990
	Liquid limit	BS 1377: Part 2: 1990
	Plastic limit	BS 1377: Part 2: 1990
	Linear shrinkage	BS 1377: Part 2: 1990
	Compaction test	BS 1377: Part 4: 1990
	CBR Three-point method	BS 1377: Part 4: 1990
	Free swell test	IS 2720: Part 40: 1977
Sand	Particle size distribution	BS 1377: Part 2: 1990
Lime Kiln Dust	Optimum LKD Content	ASTM D6276
Blended mix of BC soil, Sand, and Lime Kiln Dust	Particle size distribution	BS 1377: Part 2: 1990
	Liquid limit	BS 1377: Part 2: 1990
	Plastic limit	BS 1377: Part 2: 1990
	Compaction test-stabilized materials	BS 1924: Part 2: 1990
	CBR Three-point method	BS 1377: Part 4: 1990

3 RESULTS

3.1 *Effect of sand on the index and strength properties of black cotton soil*

3.1.1 *Effect of sand on the gradation of black cotton soil*

The grading curves of the blended mixes improved with addition of sand. In addition, the group index of the blended mixes decreased with an increase in sand content. This was evidenced by an increase in the amount of particles retained on sieve No 200. The finer particles of BC soil were replaced with coarser particles of sand, resulting in uniform gradation of particles in the blended mixes (Kollaros & Athanasopoulou 2016).

3.1.2 *Effect of sand on atterberg limits of black cotton soil*

There was a reduction in the liquid limit, plastic limit, and shrinkage limit and plasticity index with increasing percentages of sand content in the black cotton soil as indicated in Table 2. The liquid limit decreased from 70.5% to 29.4% with increasing proportions of sand. The plastic limit slightly decreased from 21.5% to 12.4%, whereas the linear shrinkage decreased from 15% to 6.4%. There was also a general reduction in the plasticity index of the modified black cotton soil from 49% to 17.0%. These results agree with those of several researchers (Gupta & Sharma 2016, Jjuuko et al. 2011, Babu et al. 2016). This can be attributed to a reduction in the fine proportions needed for bonding of the clay particles, and the changes in soil texture on addition of sand from fine-grained clay to the increasingly coarse-grained nature of the black cotton soil–sand mix. Addition of more non-cohesive sand minimizes the binding ability of the mixes and their ability to retain moisture. The reducing plasticity automatically results in less swell ability, hence low susceptibility to cracking. All the blends were associated with liquid limits less than 50%. Such soil materials are suitable for pavement layers (Jjuuko et al. 2011).

3.1.3 *Effect of sand on the free swell ratio of black cotton soil*

From Table 2, it was observed that, as more sand was added to the soil, the free swell ratio of the blended mixes decreased and thus a reduction in the swell potential of the soil resulted. The same behavior was reported by Babu et al. (2016), and it follows the obtained results. This was due to

the reduction in the proportion of clay particles, which are responsible for its high swelling potential. This changed the nature of subgrade soil from swelling to non-swelling.

3.1.4 *Effect of sand on the Maximum Dry Density (MDD) and Optimum Moisture Content (OMC) of black cotton soil*

As more percentages of sand were added to black cotton soil, the maximum dry density slightly increased with increasing sand percentages. Similarly, the optimum moisture content decreased with increasing percentages of sand, Table 2. The same trend was reported by Gupta & Sharma (2016), Babu et al. (2016), Ningthoujam & Pramod (2018), and it is in accordance with obtained results. According to Jjuuko et al. (2011), soil type is a major variable in the resulting moisture density relationships. The alterations can be attributed to the variations in plasticity index and specific gravity of the mixes. Reduction in plasticity index minimizes the binding and moisture retention abilities of soil specimens. Well-graded soils exhibit higher MDDs than poorly graded soils, while finer soils exhibit higher OMCs and lower MDDs than coarser soils. Usually soils with MDDs greater than 2 Mg/m^3 and OMCs less than 15% are easier to compact.

The increase in the maximum dry density is attributed to the addition of the coarse sand particles into fine-grained black cotton soil. This is explained by the fact that addition of coarse-grained sand particles to fine-grained soil occupies the void spaces between the soil particles. Furthermore, the addition of sand particles to fine-grained clay results in a coarse-grained skeleton-like structure and the voids between the particles are filled with fine-grained or clay particles. This enhances the compaction properties of the material and hence results in higher densities. Therefore, an increase in sand content leads to a reduction in void spaces in the soil sample, thus resulting in an increased density.

The decrease in the optimum moisture content is due to the reduction in the volume of voids as more sand is added to fill the void spaces between black cotton soil particles. The fact that clay has a high voids ratio due to its high proportion of fines, means the addition of sand particles to it reduces its capacity to hold water. In addition, the sand particles have a coarse-grained texture with a less specific surface area and thus a lesser amount of water is required to slide the particles together to achieve the desired density.

Table 2. Laboratory test results of black cotton soil-sand mixes.

	Atterberg Limits						
Mix	LL	PL	PI	LS	Free Swell Ratio	MDD	OMC
Neat BC	70.5	21.5	49.0	15.0	2.3	1.571	18.6
20% SD	43.8	10.4	27.4	10.0	2.0	1.729	16.4
30% SD	39.4	14.3	25.1	8.6	1.8	1.796	14.2
40% SD	36.8	13.8	23.0	7.1	1.5	1.823	12.9
50% SD	29.4	12.4	17.0	6.4	1.3	1.905	11.4

3.1.5 *Effect of sand on the California Bearing Ratio (CBR) of black cotton soil*

The soaked CBR values increased appreciably with an increase in percentages of sand. The CBR value of neat black cotton soil increased from 5.0% to 23.0% with the addition of sand content. The modified soil samples had CBRs of 7.0%, 13.0%, 16.0%, and 23.0% with addition of 20%, 30%, 40%, and 50% of sand, respectively. The same behavior was reported by Babu et al. (2016). The CBR values increased with addition of sand content due to the rearrangement of the soil particles from fine-grained soil to an increasingly granular nature having an interlocked structure between the soil particles. This improves the strength properties of the material by increasing the density of the material. Replacement of fine particles of BC soil with coarser sand particles results in uniformly graded blends with enhanced cohesion and friction parameters. Therefore, the higher the density of the material, the greater resistance to penetration force, thus resulting in an increase in the CBR value. If properly mixed, placed, and compacted in the field, the composite mixes exhibit improved load-bearing capacity.

3.1.6 *Selection of the BC soil–sand optimum mix to be blended with LKD*

On the basis of the above results, the optimum mix for the BC soil–sand mix was decided based on:

- Plasticity index and CBR value in compliance with the MoWT specifications. A mix of 30% sand was considered as the optimum mix to be blended with varying proportions of lime kiln dust, as it proved to be the minimum mix and economical for use. This had a PI value of 25.1%, which was close to the required maximum of 25%, and a CBR value of 13.0%, which was above the required minimum CBR of G7. However, this did not satisfy all the MoWT requirements because of its swelling in nature, with a free swell ratio of 1.8 and plasticity index value that was greater than required. Therefore, further modification was necessary to satisfy all the required standards;
- Economic reasons. 30% sand may be more economical for use as it would require:
  - Less imported material,
  - Less in-situ material wastage,
  - Less energy consumed in site preparation (excavation to spoil),
  - Less site operation costs (transportation costs).

3.2 *Effect of Sand–Lime Kiln Dust (SD-LKD) combination on the physical and strength properties of black cotton soil*

3.2.1 *Effect of SD-LKD combination on the atterberg limits of black cotton soil*

The Atterberg limit results for the black cotton soil–sand–lime kiln dust (BCS-SD-LKD) mix are presented Figure 1. It can be seen that a slight increase in the plastic limit values was noticed with the addition of 3% and 4% LKD content, whereas the addition of 5% and 6% LKD content in BCS-SD mix altered the composite mix to a non-plastic condition. The results showed that the liquid limit values were not consistent with the increasing LKD content. The liquid limit gradually increased from 39.2% to 43.5% with the addition of 3% to 5% LKD content, respectively, and further addition of 6% LKD content slightly reduced the liquid limit to 42.6. The general reduction in the plasticity index of the composite mix was observed with the increasing LKD content. The plasticity index reduced from 10.2% to 0% with the addition of 3% to 6% LKD, respectively. The same trend was observed with the shrinkage limit values with the increasing percentage of LKD.

The reduction in the plasticity index may be attributed to the aggregation of clay particles from fine clay to an increasingly granular nature induced by cation exchange and flocculation and agglomeration reactions. The increase in liquid limit is attributed to flocculation and agglomeration of the clay soil particles due to the addition of lime kiln dust. This results in aggregation of the clay soil particles from a fine-grained nature to increasingly coarser aggregates (Bell 1996, Al-Rawas et al. 2005, Nalbantoglu & Tuncer 2001). These have the ability to increase the water-retaining capacity of the flocculated aggregated structure and hence increase the liquid limit as well as the plastic limit of the soil. The decrease in liquid limit is attributed to the effect of cation exchange reactions between the cations of the soil and those of lime kiln dust, which depress the thickness of the diffuse double layer due to the increase in cation concentration. The addition of 6% LKD induced a reduction in the water-holding capacity of the soil and hence a decrease in liquid limit. The same behavior was reported by Bessaim et al. (2018) and it follows the above results.

3.2.2 *Effect of SD-LKD combination on the MDD and OMC of black cotton soil*

From Figures 2 and 3, as higher percentages of LKD content were added to the BCS-SD mix, the maximum dry density slightly decreased, whereas the optimum moisture content increased. These results follow the results of several researchers (Makandar 2016, Achampong et al. 2013). The variations in the MDD and OMC of the soil are attributed to flocculation of the soil particles, as indicated by the Atterberg limits (Al-Rawas et al. 2005, Nalbantoglu & Tuncer 2001). The increase in the optimum moisture content is attributed to the increase in the shearing resistance of the soil particles. As more LKD content is added to the BCS-SD composite, the soil

particles are gradually cemented, increasing the particle resistance to compactive effort. This cementation of the soil particles induces a higher water-holding capacity and thus an increase in optimum moisture content and a corresponding decrease in the maximum dry density. In addition, the increase in OMC is due to the larger specific surface area of LKD particles and hence more water is required for sufficient lubrication of the blended mixture to obtain MDD. The increase in OMC may also be attributed to the flocculated and agglomerated clay particles, which tend to agglomerate, thus occupying larger spaces and leading to an increase in water content. The decrease in MDD is due to the fact that LKD has a lower specific gravity as compared to the BCS-SD composite. This is attributed to flocculated structure aggregation formed by the addition of LKD having a lower specific gravity and hence a reduction in MDD (Kang et al 2015). The MDD and OMC of all blends was greater than that of the neat soil sample. This can be attributed to the high lime content of LKD facilitating faster consumption of water in the mixes. Similarly, the higher specific area of LKD leads to higher water absorption and quicker reaction, hence dense matrix of hydrated LKD (Bernard et al. 2010).

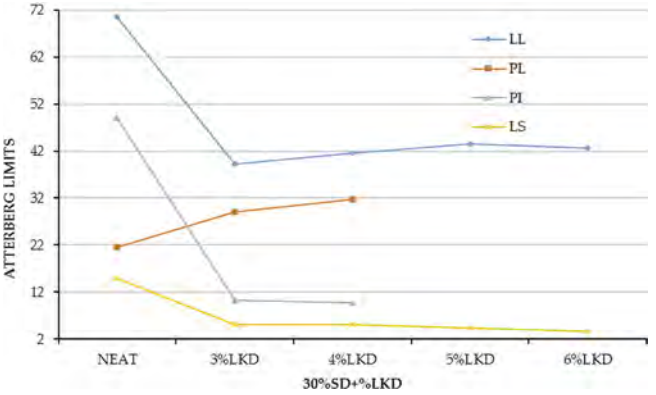

Figure 1. Variation of Atterberg limits with 30% Sand (SD) and LKD content.

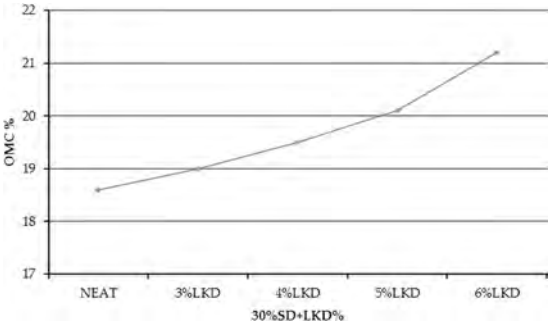

Figure 2. Variation of OMC with 30% SD and LKD content.

3.2.3 *Effect of SD-LKD combination on the CBR of black cotton soil*

The CBR results presented in Figure 4 show that the CBR value of the BCS-SD composite blended with LKD increased with addition of LKD content. The same trend was reported by Achampong et al. (2013). The increase in CBR values is attributed to the cation exchange reaction and flocculated structure aggregation of the soil particles (Bell 1996, Al-Rawas et al. 2005, Nalbantoglu & Tuncer 2001). In addition, the increase in CBR values may be related to the pozzolanic reactions, which are responsible for the strong cementing bond between the clay soil particles. These reactions resulted in the formation of cementitious compounds, i.e., calcium silicate hydrate

(CSH) and calcium aluminate hydrate (CAH) (Al-Rawas et al. 2005). The formed compounds crystalize with time and thus result in changes in clay plasticity, increase in shear strength, and changes in swelling properties. Therefore, addition of LKD to the BCS-SD composite resulted in the bonding of clay particles together, which increases the resistance to penetration and thus results in an increase in the CBR value.

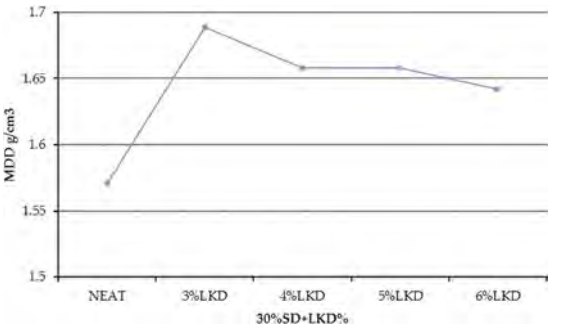

Figure 3. Variation of MDD with 30% SD and LKD content.

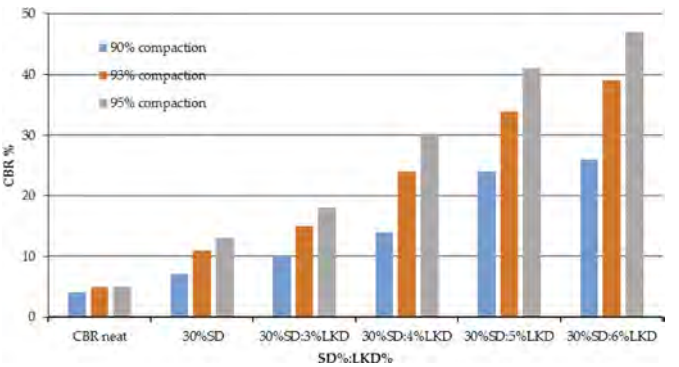

Figure 4. Variation of CBR with 30% SD and LKD content.

4 CONCLUSIONS

- The black cotton soil used in this study had the following physical properties: liquid limit of 70.5%, plastic limit of 21.5%, plasticity index of 49%, and free swell ratio of 2.3. For the strength properties: a CBR value of 5% at 95% compaction, MDD of 1.571 g/cm3 and OMC of 18.6%.
- There was a general reduction in the Atterberg limits with increasing percentages of sand. The liquid limit and plastic limit of the soil blended with sand decreased from 70.5% and 21.5% to 29.4% and 12.4%, respectively. The same trend was observed with plasticity index and linear shrinkage values from 49% and 15% to 17.0% and 6.4%, respectively.
- The variations in the free swell ratio of black cotton soil blended with sand show that black cotton soil had a free swell ratio of 2.3, which was reduced to 1.3. This implies that the black cotton soil changed from its swelling nature to a non-swelling nature after blending with sand.
- There was a reduction in OMC values and a corresponding increase in MDD with increasing proportions of sand. The maximum dry density of black cotton soil increased from

1.571 g/cm3 to 1.905 g/cm3 for the BCS-SD mix, whereas the optimum moisture content of the black cotton soil decreased from 18.6% to 11.4% of the blended mix. More so, the CBR of black cotton soil increased relative to increasing percentages of sand. The CBR values increased from 5% to 23% for sand content of 0% to 50%, respectively.

- BC soil treated with a combination of lime kiln dust and sand exhibited a general decrease in plasticity index and linear shrinkage values to levels lower than those achieved with sand content alone. The plastic limit values slightly increased with the addition of 3% and 4% LKD content, whereas further addition of 5% and 6% rendered the mix non-plastic. In addition, the liquid limit gradually increased from 39.2% to 43.5% with the addition of 3% to 5% LKD content, respectively, and furthermore, addition of 6% LKD slightly reduced the liquid limit to 42.6%.
- The compaction test results showed a reduction in the maximum dry density with a corresponding increase in the moisture content with the addition of LKD content. The MDD of black cotton soil increased from 1.571 g/cm3 to 1.689 g/cm3 for the final optimum mix, whereas the OMC of black cotton soil increased from 18.6% to 19.0% for the final optimum mix.
- The CBR results of the composite treated with LKD increased with the addition of various percentages of LKD. The soil treated with a combination of LKD and sand showed more strength gain than black cotton soil treated with sand alone. The CBR of black cotton soil increased from 5% to 18% for the final optimum mix. From the above results, the modified black cotton soil can be successfully used for subgrade construction.

REFERENCES

Achampong, F., Anum, R.A. and Boadu, F., 2013. Effect of lime on plasticity, compaction and compressive strength characteristics of synthetic Low Cohesive (CL) and High Cohesive (CH) clayey soils. *International Journal of Scientific & Engineering Research, 4*(11).

Adam, E. & Agib, A 2001. Compressed Stabilized Earth Block Manufacture in Sudan. Print. by Graphoprint United Nations Educ. *Sci. Cult. Organ*, *France, Pa*, p.101.

Al Fouzan, F. and Dafalla, M.A. 2014. Study of cracks and fissures phenomenon in Central Saudi Arabia by applying geotechnical and geophysical techniques. *Arabian Journal of Geosciences*, *7*(3), pp.1157–1164.

Al-Rawas, A.A., Hago, A.W. & Al-Sarmi, H. 2005. Effect of lime, cement and Sarooj (artificial pozzolan) on the swelling potential of an expansive soil from Oman. *Building and environment*, *40*(5), pp.681–687.

Alshameri, A., R Abood, A., Yan, C. & Muhammad, A.M. 2014. Characteristics, modification and environmental application of Yemen's natural bentonite. *Arabian Journal of Geosciences*, *7*(3), pp.841–853.

Amadi, A.A. & Osu, A.S. 2018. Effect of curing time on strength development in black cotton soil – Quarry fines composite stabilized with cement kiln dust (CKD). *J. King Saud Univ. Eng. Sci*. 30, 305–312.

Arulrajah, A., Mohammadinia, A., D'Amico, A. & Horpibulsuk, S. 2017. Effect of lime kiln dust as an alternative binder in the stabilization of construction and demolition materials. *Construction and Building Materials*, *152*, pp.999–1007.

Babu, V.R., Niveditha, K. & Babu, B.R. 2016. Stabilization of black cotton soil with sand and cement as a subgrade pavement. *Int J Civil Eng Technol*, *7*(2), pp.341–351.

Bahia, L. and Ramdane, B., 2012. Sand: an additive for stabilization of swelling clay soils. *International Journal of Geosciences, 2012*.

Bhatta, N. 2008. Engineering properties of pond ash and pond ash sand mixtures. *Indian Highways*, *36* (7), pp.49–59.

Bell, F.G., 1996. Lime stabilization of clay minerals and soils. *Engineering geology*, *42*(4), pp.223–237.

Bernal, S.A., De Gutierrez, R.M., Provis, J.L. and Rose, V., 2010. Effect of silicate modulus and metakaolin incorporation on the carbonation of alkali silicate-activated slags. *Cement and Concrete Research*, *40*(6), pp.898–907.

Bessaim, M.M., Bessaim, A., Missoum, H. & Bendani, K. 2018. Effect of quick lime on physicochemical properties of clay soil. In *MATEC Web of Conferences* (Vol. 149, p. 02065). EDP Sciences.

Burnham, J.C., Hatfield, N., Bennett, G.F. & Logan, T.J. 1992. Use of kiln dust with quicklime for effective municipal sludge pasteurization and stabilization with the N-Viro Soil process. *Innovations and uses for lime*, pp.128–141.

Cetin, B., Aydilek, A.H. & Guney, Y. 2010. Stabilization of recycled base materials with high carbon fly ash. *Resources, Conservation and Recycling*, *54*(11), pp.878–892.

Daita, R.K., Drnevich, V.P., Kim, D. & Chen, R. 2006. Assessing the quality of soils modified with lime kiln dust: Measuring electrical conductivity with time domain reflectometry. *Transportation research record*, *1952*(1), pp.101–109.

Dalal, S.P., Patel, R. & Dalal, P.D. 2017. Effect on engineering properties of black cotton soil treated with agricultural and industrial waste. *Materials Today: Proceedings*, *4(9)*, pp.9640–9644.

Das, B.M. 2015 *Principles of Foundation Engineering*, *7th ed.; Cengage Learning*: MA, USA.

Edil, T.B., Acosta, H.A. & Benson, C.H. 2006. Stabilizing soft fine-grained soils with fly ash. *Journal of materials in civil engineering*, *18*(2), pp.283–294.

Etim, R.K., Eberemu, A.O. & Osinubi, K.J. 2017. Stabilization of black cotton soil with lime and iron ore tailings admixture. *Transportation Geotechnics*, *10*, pp.85–95.

Gupta, C. and Sharma, R.K., 2016. Black cotton soil modification by the application of waste materials. *Periodica polytechnica civil engineering*, *60*(4), pp.479–490.

Heckel, G. & Wahab, R. 1996. Soil stabilization utilizing alternative waste materials. In *Materials for the New Millennium* (pp. 318–327). ASCE.

Ikeagwuani, C.C., Obeta, I.N. & Agunwamba, J.C. 2019. Stabilization of black cotton soil subgrade using sawdust ash and lime. *Soils and Foundations*, *59*(1), pp.162–175.

Jjuuko, S., Kalumba, D. & Bagampadde, U. 2011. The use of locally available sand in stabilization of Ugandan clayey soils: Case study of clayey soil from Busega area. In *Uganda Institution of Professional Engineers 16th National Technology Conference (NTC 2011)*; Kampala, Uganda.

Kang, X., Ge, L., Kang, G.C. & Mathews, C. 2015. Laboratory investigation of the strength, stiffness, and thermal conductivity of fly ash and lime kiln dust stabilized clay subgrade materials. *Road materials and pavement design*, *16*(4), pp.928–945.

Khemissa, M., Mahamedi, A. & Mekki, L. 2015. Problematic soil mechanics in the Algerian arid and semi-arid regions: Case of M'sila expansive clays. *Journal of Applied Engineering Science & Technology*, *1*(2), pp.37–41.

Kollaros, G. & Athanasopoulou, A. 2016. Sand as a Soil Stabilizer. *Bull. Geol. Soc. Greece*, 50, 770–777.

Nalbantoglu, Z. & Tuncer, E.R. 2001. Compressibility and hydraulic conductivity of a chemically treated expansive clay. *Canadian geotechnical journal*, *38*(1), pp.154–160.

Ningthoujam, R. & Pramod, K. 2018. Stabilization of Black Cotton Soil Using Additives. *International Journal of advance research in Science and Engineering, 7*(3).

Prasad, C.R.V. & Sharma, R.K. 2014. Influence of sand and fly ash on clayey soil stabilization. *IOSR Journal of Mechanical and Civil Engineering*, *334*, pp.36–40.

Roy, T.K. 2013. Influence of sand on strength characteristics of cohesive soil for using as subgrade of road. *Procedia-Social and Behavioral Sciences*, *104*, pp.218–224.

Salima, B. and Abdelhak, B. 2013. Geology, mineralogy, and chemistry of the M'zila bentonitic clay deposit (Mostaganem, NW Algeria). *Arabian Journal of Geosciences*, *6*(6), pp.2165–2172.

Schanz, T. & Elsawy, M.B. 2017. Stabilisation of highly swelling clay using lime–sand mixtures. *Proceedings of the Institution of Civil Engineers-Ground Improvement*, *170*(4), pp.218–230.

Solanki, P., Zaman, M.M. & Dean, J. 2010. Resilient modulus of clay subgrades stabilized with lime, class C fly ash, and cement kiln dust for pavement design. *Transportation research record*, *2186*(1), pp.101–110.

Sreekrishnavilasam, A., Rahardja, S., Kmetz, R. & Santagata, M. 2007. Soil treatment using fresh and landfilled cement kiln dust. *Construction and Building Materials*, *21*(2), pp.318–327.

The British Geotechnical Association. 2009. *Ground Engineering Magazine*. Hampstead Road: London, UK.

Tugume, B., Owani, I., Jjuuko, S. & Kalumba, D. 2018, October. Performance of lateritic soils stabilized with both crushed rock aggregates and carbon black as a pavement base layer. In *The international congress on environmental geotechnics* (pp. 382–388). Springer, Singapore.

Verma, S.K. and Maru, S., 2013. Behaviourial study of expansive soils and its effect on structures–A review. *International Journal of Innovations in Engineering and Technology*, *2*(2), pp.228–238.

Zami, M.S. & Lee, A. 2009. Contemporary Earth Construction in Urban Housing– Stabilized or Unstabilised? *School of the Built Environment, University of Salford.*

Smart Geotechnics for Smart Societies – Zhussupbekov, Sarsembayeva & Kaliakin (Eds)
© 2023 The Author(s), ISBN 978-1-003-29912-7
Open Access: www.taylorfrancis.com, CC BY-NC-ND 4.0 license

Use of waste rubber inclusions for ballasted railway construction – A real-life case study

Chathuri M.K. Arachchige, Buddhima Indraratna, Cholachat Rujikiakamjorn, Yujie Qi & Anees Raja Siddiqui
Transport Research Centre, University of Technology Sydney, Sydney, New South Wales, Australia

ABSTRACT: The rail track substructure is an essential element in ballasted embankment, transferring the train loadings to underlying subgrade soil. To enhance track performance and embrace circular economy, three different track formations modified with rubber waste additives were constructed at the Chullora Technology Precinct (near Sydney), Australia. A blended mix of ballast aggregates and recycled rubber granules, geogrids made of recycled rubber panels, and recycled tyres infilled with granular waste are the three innovative concepts used in this real-life application. This paper evaluates the vertical stress distribution of modified track sections compared to the conventional ballasted track substructure under train loads. Monitoring outcomes demonstrate that stress redistribution due to rubber inclusion can increase track longevity.

1 INTRODUCTION

A typical ballasted railway substructure includes a ballast bed, a subballast (capping) layer, and subgrade soil. The stability and durability of the rail track closely rely on the load distribution of these underneath subsequent layers. With the increased demand for rail transportation, the speed and loading intensity of trains are constantly growing, leading to faster track deterioration. However, considering the safety and passenger comfort, the maximum vertical stresses along the substructure should be well controlled in practice (Seed et al. (1962). It is proven that the change in confining pressure, degree of compaction of substructure layers, rail superstructure arrangement and the train loading conditions are the main factors affecting the vertical stress distribution within the track substructure (Indrarathna et al., 1998, Zhang et al, 2016). Overstressing the track components leads to track degradation and frequent maintenance. This paper discusses the application of three recycled rubber-based innovations and their performance, particularly on redistribution of vertical stresses compared to the conventional track section: (i) Rubber Intermixed Ballast System (RIBS) as an alternative material for bottom ballast where 10% of the weight consist of rubber granules derived from waste tyres; (ii) Energy-Absorbing Rubber Geogrids (EARS) as a special type of geogrid made from used rubber conveyor belts; and (iii) Tyre Cell Track Foundation (TCTF) as an assembly of recycled tyres filled with granular waste in lieu of traditional capping material. These three innovative techniques were applied along a 380 m ballasted railway track built at the Chullora Technology Precinct, New South Wales, Australia.

2 CHULLORA RAIL PRECINCT

2.1 *Project description*

The test track section constructed in Chullora Technology Precinct was divided into four sections (Figure 1), namely (i) Section F-G: TCTF section, (ii) Section E-F: Control track section, (iii) Section D-E: EARS section and (iv) Section B-C: RIBS section. As shown in Figure 1, three 20-m long instrumented track sections were constructed with intermediate standard track sections to avoid the

DOI: 10.1201/9781003299127-399

boundary effects and in all sections, materials, earthworks, and track components complied with Transport for New South Wales (TfNSW) standards except for the modifications associated with rubber inclusions. An 81 Class locomotive (21.5-ton axle load) was chosen to operate on all the test sections running at around 10-13 km/h, as per the train speed restrictions.

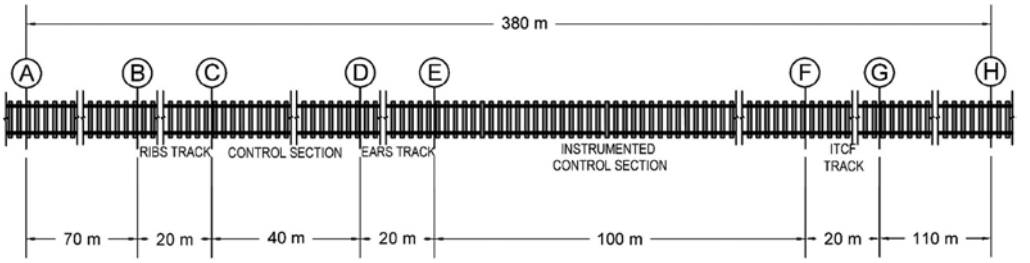

Figure 1. Plan view of the track.

2.2 *Rubber Intermixed Ballast System (RIBS)*

RIBS applied in the track was a blended mixture of conventional ballast material and 10% (by total weight) recycled granulated rubber in the size of 8-15 mm. More details on the properties and behaviour of RIBS can be found elsewhere (Arachchige et al. 2022). A calibrated volumetric mixer was used to mix rubber and ballast aggregates at the site. Figures 2a-b show a typical cross-section of the RIBS track in which a 150-mm thick bottom ballast layer was replaced with RIBS and the preparation of RIBS at the site.

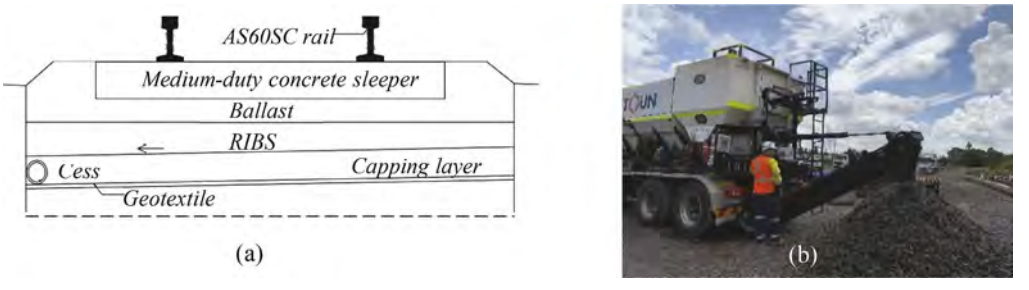

Figure 2. (a) Cross-section of RIBS track (b) Mixing materials at the site using a volumetric mixture. Energy-Absorbing Rubber Seam (EARS).

2.3 *Energy-Absorbing Rubber Seam (EARS)*

Rubber panels from end-of-life conveyor belts were utilized to manufacture EARS resembling geogrids with square apertures through water jet cutting. The aperture size of the rubber panel was 51×51 mm^2, while its thickness was 10 mm. The rubber geogrids were laid on top of the compacted capping layer of the EARS track section before placing the ballast layer (Figures 3a-b).

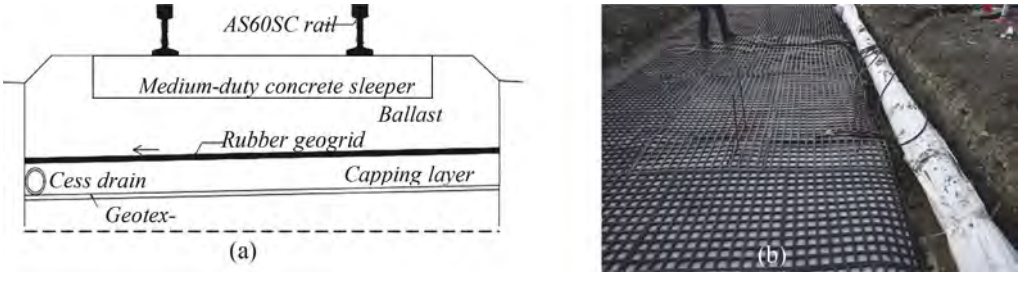

Figure 3. (a) Cross-section of EARS track (b) Rubber geogrids laid on top of the compacted capping.

2.4 *Tyre Cell Track Foundation (TCTF)*

Tyre Cell Track Foundation (TCTF) is an assembly of 200 mm thick, and 600mm diameter recycled tyres filled with granular materials placed on top of the subgrade, replacing the conventional capping layer (Indrarathna et al, 2022). A typical cross-section of a 20 m long TCTF track section and the tyre assembly during the construction are shown in Figures 4a-b.

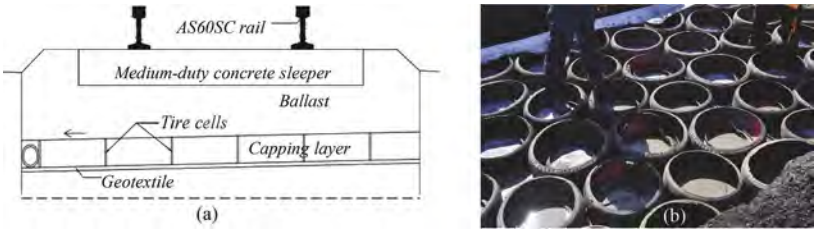

Figure 4. (a) Cross-section of ITCF track (b) Tyre cell assembly before granular filling.

3 PRESSURE DISTRIBUTION

Following Indraratna & Ngo (2018), the dynamic wheel load (P=112kN) applied on the rail was calculated using the formula, P=P$_s$$P = P_s \times IF$ where P_s was half of the axle load and IF was the dynamic amplification factor. Here, $IF = 1 + 5.21\ V/D$ where V was the train speed and D was the wheel diameter in km/h and mm, respectively. The applied loading on the rail from the locomotive is presented in Figure 5.

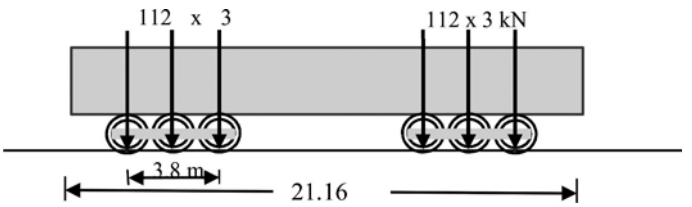

Figure 5. Applied loads from the locomotive.

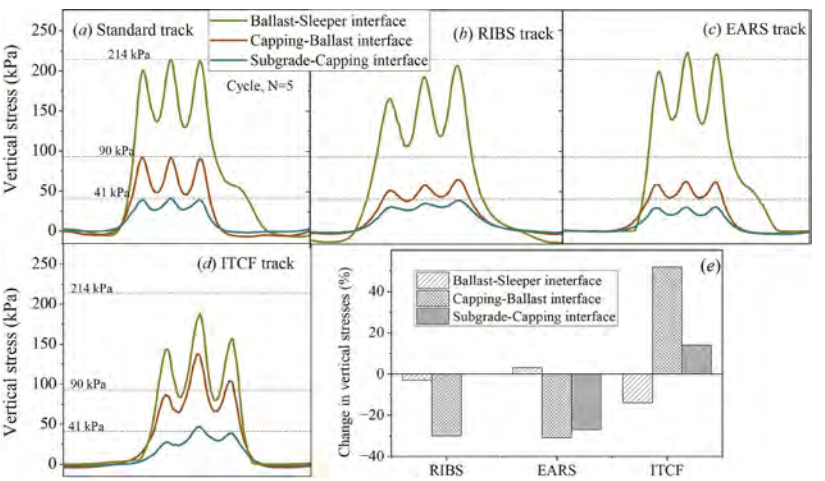

Figure 6. (a-d) Vertical stress distribution (e) Change in the vertical stress distribution at the interfaces.

In the analysis, a loading cycle represents the passing of one axle at a particular point in each track section, and the end of the axle is connected to a set of three wheels. At the initial stage of the loading, a few numbers of loading cycles were applied on the track, and Figures 6a-d show the vertical stress distribution of each track section subjected to the 5^{th} loading cycle (N=5), and Figure 6e shows the percentage of change in vertical stresses at the different interfaces of the substructure. At the ballast-sleeper interface, no significant change was observed in RIBS and EARS sections compared to the standard (conventional) track section; however, more than a 10% reduction was observed in the TCTF track section. On the other hand, significant stress reduction (around 30%) was observed at the capping-ballast interfaces of RIBS and EARS sections. Stresses at the capping-ballast and subgrade-capping interfaces of TCTF were increased by about 55% and 14%, respectively, due to the increased stiffness generated by the compacted granular materials in the confined tyre cells. Furthermore, in the EARS section, the vertical stress at the capping-subgrade interface was reduced by around 25% compared to the conventional track section. The reduced vertical stress distribution within the ballast layer is advantageous because it reduces particle breakage and related track degradation. Note that the stress relieving in RIBS and EARS sections is significant within the ballast layer and, in TCTF, the capping layer.

4 CONCLUSION

This paper discusses the three types of real-life applications of waste rubber-derived elements in rail infrastructure, namely rubber intermixed ballast system (RIBS), energy absorbing rubber seam (EARS) and infilled tyre cell foundation (TCTF). Manufacturing and the application procedure of RIBS, EARS and TCTF as a modification to the conventional ballasted track are briefly presented. The performance of each track section under typical train loading is further discussed in relation to vertical stress distribution along the subsurface profile. In general, RIBS and EARS reduced vertical stresses (by around 30%) in the ballast layer. In contrast, the tyre cell assembly adequately relieves increased vertical stresses at the capping-ballast interface of the TCTF section so that the stresses transfer into the subgrade is well controlled. Following the present results, this study confirms that substructure layers modified by rubber inclusions play a vital role in stress redistribution of the track. In addition, using waste rubber in infrastructure projects promotes sustainable construction applications by reusing non-biodegradable waste and reducing the carbon footprint.

ACKNOWLEDGEMENTS

Financial assistance provided by the Australian Research Council (ARC) ITTC-Rail, Linkage and Discovery Projects (DP220102862, LP200200915, IC170100006) and industry partners, including Transport for NSW (formerly Sydney Trains), Bridgestone Corporation, EcoFlex and Global Synthetics is gratefully acknowledged. Also, the assistance provided by Trung Ngo, Rakesh Malisetty, Fatima Mehmood, Mandeep Singh, Joseph Arivalagan, Courage Dzaklo, Aaron Eagleton, Shigeki Endo, Jim Grant, Dipendra Badu, and EngAnalysis in executing field trial tests is gratefully appreciated.

REFERENCES

Arachchige, C.M.K., Indraratna, B., Qi, Y., Vinod, J.S. & Rujikiatkamjorn, C. 2022. Geotechnical characteristics of a Rubber Intermixed Ballast System. *Acta Geotechnica* 17(5): 1847–1858.

Indraratna, B. & Ngo, T. 2018, *Ballast railroad design: smart-uow approach*. CRC Press: UK.

Indraratna, B., Mehmood, F., Mishra, S., Ngo, T. & Rujikiatkamjorn, C. 2022. The role of recycled rubber inclusions on increased confinement in track substructure. *Transportation Geotechnics* 36: 100829.

Indraratna, B., Ionescu, D. & Christie, H.D. 1998. Shear behaviour of railway ballast on large-scale triaxial tests. *Journal of Geotechnical and Geoenvironmental Engineering* 124(5): 439–449.

Seed, H.B., Chan, C.K. & Lee, C.E. 1962. Resilience characteristics of subgrade soils and their relation to fatigue failures in asphalt pavements. *In International Conference on the Structural Design of Asphalt Pavements. Supplement University of Michigan, Ann Arbor*.

Zhang, T.W., Cui, Y.J., Lamas, L.F., Calon, N. & D'Aguiar, S.C. 2016. Modelling stress distribution in substructure of French conventional railway tracks. *Construction and Building Materials* 116: 326–334.

Smart Geotechnics for Smart Societies – Zhussupbekov, Sarsembayeva & Kaliakin (Eds)
© 2023 The Author(s), ISBN 978-1-003-29912-7
Open Access: www.taylorfrancis.com, CC BY-NC-ND 4.0 license

An assessment of progress and challenges in modelling of railway track transition zones

Namrata Bhattacharjee
PhD Research Student, Indian Institute of Technology Delhi, India

Kirti Choudhary
Senior Project Scientist, Indian Institute of Technology Delhi, India

Bappaditya Manna
Professor, Indian Institute of Technology Delhi, India

Arnab Banerjee & Debayan Bhattacharya
Assistant Professor, Indian Institute of Technology Delhi, India

ABSTRACT: Abrupt stiffness changes encountered in the transition zone lead to an accelerated deterioration of track components and passenger discomfort, eventually leading to an increase in maintenance cost and hindering smooth railway functioning. This paper aims to understand the major causes and analyse countermeasures deployed at the railway transition zone. The present study covers the chronological advancement made in the study of transition zone using numerical, analytical, and experimental models. As field experiments require significant investments in terms of instrumentation and setup, the numerical and analytical approaches have become popular among practising engineers. Along with understanding the present state of work, this paper explores the various loading techniques simulated with the help of a Finite Element Model to understand the details of carrying out such numerical experiments. A simple bridge embankment system is modelled to understand the suitability of the method of loading serving a particular purpose.

1 INTRODUCTION

Transition zones are the structural solution aimed at attenuating the problems encountered due to the variation in vertical stiffness. In locations where there is a shift of track support from engineering structure to soil subgrade, there is an abrupt variation of stiffness. This sudden change in the vertical support system leads to the variation of wheel-rail interaction, eventually causing the degradation of the track system. Consequently, the problems associated with the variation require regular maintenance which not only sums up to a hefty amount annually but also hinders the smooth flow of traffic. (Li and Davis, 2005). To curb the high maintenance cost of the transition zone, proper analysis and mitigation techniques are implemented. Transition zones requires around 200 million dollars for annual maintenance (Qian et al.) The study aims at understanding the different models which have been formulated over time to analyse the problems encountered and the mitigation techniques implemented. A finite element model has been prepared to understand the loading technique of the moving vehicle and the time required for computation along with the soundness of the results.

2 PROBLEMS ENCOUNTERED

Locations near the engineering structures, such as bridges, viaducts, culverts etc., are prone to accelerated track geometry degradation and other negative impacts on the track and vehicle

DOI: 10.1201/9781003299127-400

components. The researchers have conducted a good number of studies to investigate the behaviour of the bridge embankment transition zone. Triaxial accelerometers, Strain gauges, geophones, LVDT etc., have been used to measure the real-time response of the transition zone under moving train loading. FEM-based numerical modelling approach has been used to simulate the scaled models to obtain the response under different boundary conditions and loading parameters. The present segment is organised into three sub-segments- problems encountered in the transition zone, prevention measures and conclusions.

The variation in stiffness at the junction of the bridge embankment transition zone may generate low-frequency random vibrations in the car body leading to the discomfort of the passengers (Dahlberg,2010). Another major issue faced in the junction of the bridge embankment transition zone is the differential settlement. The uneven displacement in the bridge and the embankment due to the difference in stiffness leads to geometric irregularity causing the differential settlement (Gallage, Chaminda et al. 2013). Differential settlement in the railway transition zone leads to the formation of dips and bumps which further causes the formation of hanging sleepers near the bridge embankment junction (Wang, 2015, Hunt 1997). Mauer (1995) observed that the differential settlement due to geometric irregularities also affects the dynamic wheel load and the wheel-rail interaction forces. The abrupt change in stiffness, differential settlement and track irregularity aggravates the deterioration of the transition zone.

3 COUNTERMEASURES

With the increasing development of the high-speed railway, there arises a need for improvement in the performance of the transition zone. Numerous precautionary measures have been taken up by researchers to improve the track transition system. The behaviour of the transition zones is still very unpredictable although, to mitigate the existing problems encountered in the transition zone, some countermeasures are implemented by various researchers over the last few decades. The countermeasures can be divided into corrective countermeasures and preventive countermeasures (Wang, Markine (2018a)). Li and Davis (2005a) compared the track performance of a UP standard to bridge approaches with geocell in the sub-ballast layer, HMA (hot mix asphalt) and cement stabilised backfill. It was seen that a granular layer infilled in geocell used for correcting the issues of soft soil deformation highly improved the performance of the track. Punetha et al., 2021 observed that the use of geogrids in the sub-ballast did not show any significant improvement in the performance, however, the use of wedge-shaped engineered backfill at the bridge embankment contributed well to the improvement of the bridge embankment transition zone. The decrease in sleeper spacing in the study showed a reduction in the deformation in the region near the bridge, which is because of the increased stiffness. However, the region beyond the modified segment showed excessive displacement (Punetha et al., 2021). The abrupt generation of force at the transition section due to the difference in stiffness can be reduced by the usage of under sleeper pads. Dahlberg (2010) believes that under sleeper pads attenuate the wheel-rail interaction force, decreasing the detrimental effects of dips, bumps and hanging sleeper. Nimbalkar and Indraratna (2016) suggested that using geogrids and geocomposites reduces ballast settlement by nearly 35%.

The abrupt change in stiffness, varying speed of the train, and soil parameters of the underlying soil affect the dynamic response of the railway bridge-embankment transition zone. The dynamic wheel-rail interaction force and the differential settlement at the junction are the prime causes which lead to the degradation of the track performance. In addition, the increasing speed of the train further accelerates the deterioration of the track performance. Hence, special design considerations have to be made for High-Speed Railways. Due to the participation of several structural components at the junction of the transition zone, the dynamic response at the location is unpredictable. The numerical models which have been studied are predominantly elastic, however, degradation at the transition zone takes place with multiple passages of trains over some time. Under actual conditions of train loading, the ballast and sub-ballast do not behave linearly or elastically, giving rise to plastic deformation over time. The plastic deformation is not considered in the numerically simulated models, which is why there is a discrepancy with the actual field response.

The behaviour of the transition zone under dynamic loading is unpredictable under the influence of several structural elements. The performance of the critical zone is improved with the modifications, resulting in a reduced degradation rate of the bridge-embankment transition system.

4 3D SIMULATION OF THE BALLAST-TRACK SYSTEM

A simple ballast track model has been simulated using FE software ABAQUS. The mass and cross-sectional properties of UIC60 have been used to model the rail. The track has been modelled, representing the Indian Broad Guage section. For the train body simulation, only the wheels have been modelled, on which the weight of the vehicle body, bogie and other subparts has been applied as a point load. The movement of the vehicle is considered from the embankment to the bridge section. The bottom of the bridge is considered to be fixed, representing a rigid body, while the ballast bottom allows a displacement in the z-direction. Absorbent vertical boundaries have been implemented to prevent the reflection of waves. Figure 1(a) and 1(b) show the 3D modelling of the ballast track system and the schematic representation of the bridge embankment transition zone, respectively.

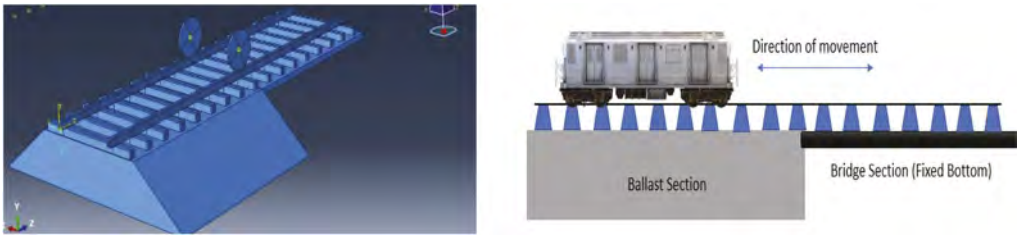

Figure 1. (a) 3D modelling of ballast track system; (b) Schematic diagram of the track transition zone.

5 DISCUSSION

This segment presents the differential settlement at the bridge-embankment transition zone. The current simulation assumes the train's movement from a softer stiffness region to a stiffer region. The sudden change in stiffness at the transition junction develops a differential settlement leading to the formation of hanging sleepers. In Figure 2, location zero represents the sleeper at the intersection of the bridge-embankment. There is a sudden displacement, when the train crosses the junction, however, the relative displacement ceases to exist at sleeper locations far from the intersection of the railway transition zone.

Figure 2. Relative settlement at sleeper location.

6 CONCLUSIONS

The representation of the vehicle in the current study is functional when the study's primary objective is from the perspective of geotechnical engineering. The computational time is reduced manifold for the simplicity of the model. However, the model needs to be modified to a full-scale car body to understand the impact of multiple subparts on the generation of dynamic force at the track level. The change in stiffness at the juncture leads to the generation of blunt wheel-rail interaction force, aggravating the deterioration of the track performance. Preventive and precautionary measures must be taken considering both the bridge-embankment junction's long-term and short-term behaviour and the local site conditions.

REFERENCES

Dahlberg, T. 2010. Railway track stiffness variations–consequences and countermeasures, International journal of civil engineering. 8, 1. 1–12.

Ford, R.2018. Differential ballast settlement, and consequent undulations in track, caused by vehicle-track interaction, Interaction of Railway Vehicles with the Track and its Substructure. 222–233.

Li, D.2000. Deformations and remedies for soft railroad subgrades subjected to heavy axle loads, Advances in transportation and geoenvironmental systems using geosynthetics. 307–321.

Li,D. Davis,D. 2005a.Transition of railroad bridge approaches, Journal of geotechnical and geoenvironmental engineering. 131,11. 1392–1398.

Li.D, Davis D. 2005b.Transition of railroad bridge approaches, Journal of geotechnical and geoenvironmental engineering. 131,11. 1392–1398.

Markine V, Wang H, Shevtsov I. 2004. Experimental analysis of the dynamic behaviour of a railway track in transition zones, Proceedings of theNinth International Conference on Engineering Computational Technology,Naples, Italy. 2–5.

Mauer, L.1995. An interactive track-train dynamic model for calculation of track error growth, Vehicle System Dynamics. 1995. 24, sup1. 209–221.

Punetha, P. Maharjan, K. Nimbalkar, S. 2021. Finite Element Modeling of the Dynamic Response of Critical Zones in a Ballasted Railway Track. Front, Built Environ. 7:660292. doi: 10.3389/fbuil.2021.660292

Shan,Y. Albers, B. Savidis, S. 2013. A. Influence of different transition zones on the dynamic response of track–subgrade systems, Computers and Geotechnics. 48. 21–28.

Wang, H., Markine,V. 2018b Modelling of the long-term behaviour of transition zones: Prediction of track settlement, Engineering Structures. 156. 294–304.

Wang, H., Markine, V. 2018a. Corrective countermeasure for track transition zones in railways:adjustable fastener, Engineering Structures. 169. 1–14.

Wang, H., Markine, V.L. Shevtsov, I.Y. Dollevoet, R.P.B.J. 2015. Analysis of the dynamic behaviour of a railway track in transition zones with differential settlement, ASME/IEEE Joint Rail Conference. 56451.V001T01A024.

Wang, H., Markine, V. 2019. Dynamic behaviour of the track in transitions zones considering the differential settlement, Journal of Sound and Vibration. 459. 114863.

Wang, H., Markine, V.L. 2017. Analysis and improvement of the dynamic track behaviour in transition zone, Bearing Capacity of Roads, Railways and Airfields.1827–1835.

Wang, H., Markine, V., Shevtsov, I. 2014 The analysis of degradation mechanism in track transition zones using 3D finite element model, Proceedings of the second international conference on railway technology: research, development and maintenance.

Zhao, C., Wang, P., Yi, Q., Meng, D. 2015. Application of polyurethane polymer and assistant rails to settling the abnormal vehicle track dynamic effects in transition zone between ballastless and ballasted track, Shock and vibration.

Smart Geotechnics for Smart Societies – Zhussupbekov, Sarsembayeva & Kaliakin (Eds)
© 2023 The Author(s), ISBN 978-1-003-29912-7
Open Access: www.taylorfrancis.com, CC BY-NC-ND 4.0 license

Field tests of railway ballast vibration

A.F. Kolos & A.A. Konon
Emperor Alexander I St. Petersburg State Transport University, St. Petersburg, Russia

ABSTRACT: The paper presents a review of authors work on railway ballast vibration testing on a few sites. The aim of testing is to get the level of vibration amplitude in terms of train speed and axle load. The rolling stock causes oscillations of track superstructure, which show up in the form of noise and vibration. The increase in loads and speeds of trains leads to a significant increase of dynamic vibration effects on the roadbed. Because of this exposure the intensity of uneven residual deformation accumulation of the railway track increases. It affects not only on the roadbed, but also on constructions of buildings and construction. The study of ballast vertical vibration displacement gives the following conclusions: 1. Displacement amplitudes and frequency range of ballast particles are derived. Both horizontal components increase linearly with approximately the same intensity with speed growth, and their values in the entire range of speeds do not exceed 225 μm in the transverse direction and 90 μm in the longitudinal direction. The vertical component also increases according to a nearly linear dependence up to 190 km/h, and at higher speed it stabilizes and even slightly decreases, which leads to almost the same values of the resulting vibration displacement amplitude up to 275 km/h. 2. No differences in the oscillatory process are revealed for different types of rail fastenings (KB-65, ARS-4 or Pandrol). 3. The obtained results can be used to simulate the vibrational dynamic effect in triaxial tests. Such modeling is necessary to study the sensitivity of crushed stone ballast to the loads, which is shown in a decrease in the strength and deformation properties of the ballast, to predict the bearing capacity and deformability of the ballast under various operating conditions.

1 INTRODUCTION

Stable ballast operation during the established overhaul period is possible only in case the ballast bearing capacity exceeds the loads occuring due to the movement of the rolling stock, and the resulting residual deformations and the rate of their accumulation do not lead to track damage. To assess ballast stability, it is necessary to determine the permissible stress in the ballast p_p, the permissible ballast deformation $[S]$ and operational loads from the rolling stock p, which, among other things, determine the residual deformation of the ballast S. Numerous studies prove the significant role of the vibrational dynamic impact of the rolling stock on the bearing capacity of soils (Butorina, M. et al. 2017, Kaewunruen, S. et al. 2008, Kolos, A. et al. 2017, Kolos, A. et al. 2020, Remennikov, A. et al. 2020, Serebryakov, D. et al. 2017, Konon, A. & Petriaev, A. 2018, Petriaev, A. et al. 2022), which fully applies to crushed stone. Thus, calculations of ballast strength and deformability should be performed concidering the action of inertial forces that arise in crushed stone under the influence of rolling stock, and the reduction under the influence of vibrodynamic load of the strength and deformation characteristics of crushed stone ballast.

To solve these problems, it is necessary to establish the relationship of oscillation propagation in the ballast. Oscillations of soil grains are characterized by displacement amplitudes (A), oscillation frequency (f), vibration velocity (V) and vibration acceleration (a). This article presents the results of railway ballast displacement amplitudes in different operation conditions.

DOI: 10.1201/9781003299127-401

2 MATERIALS AND METHODS

To study the vibrational dynamic effect of trains on the ballast in the period from 2000 to 2020, a group of authors conducted full-scale tests on different sections of the operated railway tracks, which differ in track structure and operating conditions. The description of the test sites is presented in Table 1.

All test sites had R-65 rails and reinforced concrete sleepers and were located at the straight section. Ballast layer was constructed using granite crushed stone of 25-60 mm grains.

The measurements were conducted with a set of equipment consisting of a digital seismic signal recorder ZET 048; a PC with licensed software; an amplifier; a 220 V power supply, a set of seismic sensors (seismometers). Devices for in-situ oscillation testing are shown in Figure 1.

Table 1. Characteristics of the test sites.

	Test site location						
	Moscow – Saint-Petersburg					Saint-Petersburg – Vyborg	Railway research institute of JSC Russian Railways test loop
Test site characteristics	№ 1	№ 2	№ 3	№ 4	№ 5	№ 6	№ 7
Superstructure	Continious welded rail						Jointed rail
Fastenings	KB-65	Pandrol	KB-65	KB-65	ARS-4	KB-65	KB-65
Ballast depth under the sleeper, cm	40	75	40	45	45	40	40
Subballast depth, cm	20	none	20	none	none	none	20
Subgrade soils	loam and cement composite (0,3 m), stiff loam	medium sand, geotextile (h=40 cm)	stiff loam	medium sand, geotextile (h= 45 cm)	medium sand	medium sand	stiff loam
Train operation conditions	passenger and freight trains with axle load up to 250 kN and 120 kmph speed	speed passenger trains (140 – 200 kmph)	freight trains with axle load 270-300 kN	speed passenger trains (140 – 200 kmph)	high-speed passenger trains (more than 200 kmph)	passenger and freight trains with axle load up to 250 kN and 120 kmph speed	freight trains with axle load 270-300 kN
Sensor placement: scheme A scheme B scheme C	+	+	+	+	+	+	+

Statistical processing of measurement results was carried out. The average value of vibration displacement, the standard deviation, the maximum probable value and the coefficient of variation were determined. The probability level was assumed 0.994.

Displacement was measured in three axes as shown in Figure 3.

Figure 1. Test devices set.

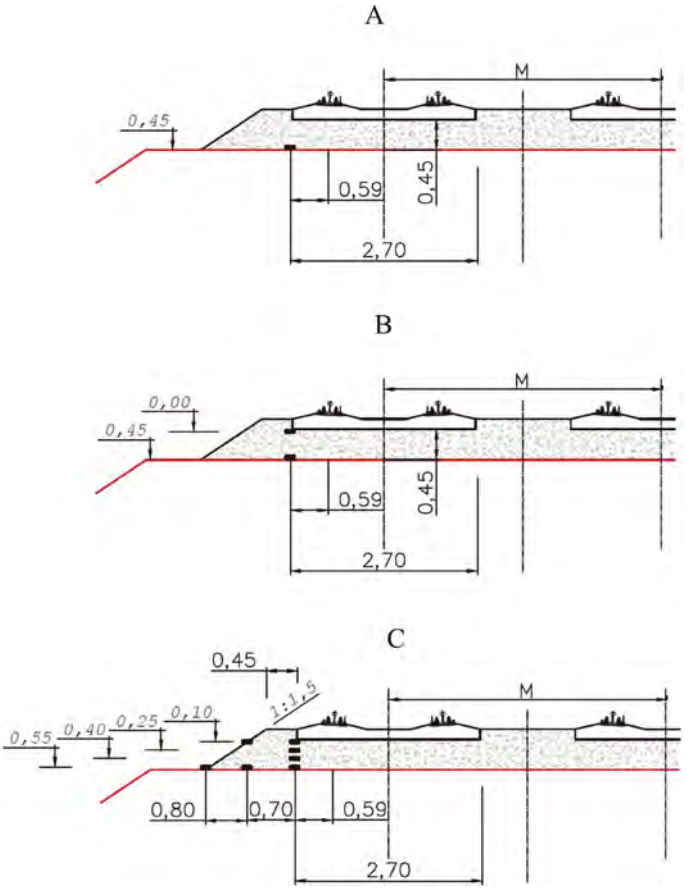

Figure 2. Seismometers installation schemes.

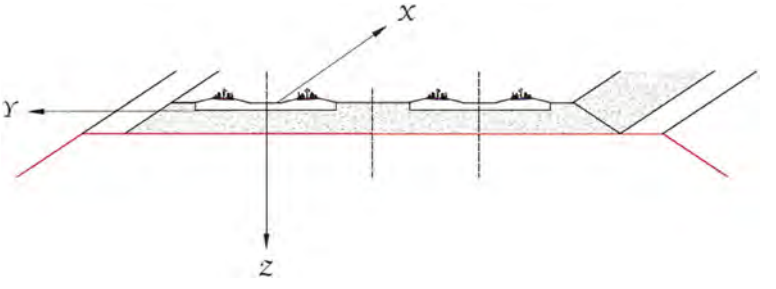

Figure 3. Axes of coordinates.

3 RESULTS AND DISCUSSION

Studying the amplitude-frequency characteristics of the ballast oscillation process is determined by the need to simulate the behaviour of crushed stone in triaxial tests when studying the mechanical properties of crushed stone ballast under the action of a vibration dynamic load.

Figure 4 shows the plots of the vibration displacement amplitudes registered under the sleeper when the high-speed 'Sapsan' train (Siemens Desiro RUS) is passing at a speed of 275 km/h, and Figure 5 shows similar data at a depth of 40–45 cm under the sleeper during the passage of a speed train "Aurora", moving at a speed of 141 km/h.

As Figures 4 and 5 show, the maximum amplitudes of vibration displacements are registered in the vertical plane along the Z axis (Figure 3, curves 2 in Figures 4 and 5) and coincide quite clearly with the rolling stock axles passage over the location of the seismometers. The vibration displacement amplitudes along the horizontal axis Y (curves 1 in Figures 5 and 5) have slightly lower values, and the lowest values are recorded along the X axis (curves 3 in Figures 4 and 5), This pattern is also typical for the movement of freight trains moving at speeds of 60–90 km/h.

Test data show that rather high ballast displacement amplitudes occur, reaching 420-450 μm at passenger train speeds of 200 km/h and higher. The features of the oscillation components growth with an increase in the speed of movement are distinctive. Both horizontal components increase linearly with approximately the same intensity with speed growth, and their values in the entire range of speeds do not exceed 225 μm in the transverse direction and 90 μm in the longitudinal direction. The vertical component also increases according to a nearly linear dependence up to 190 km/h, and at higher speed it stabilizes and even slightly decreases, which leads to almost the same values of the resulting vibration displacement amplitude up to 275 km/h (Figure 6).

Analysis of ballast vertical oscillations shows no differences in the oscillatory process are revealed for different types of rail fastenings (KB-65, ARS-4 or Pandrol). The obtained results provide the amplitude-frequency characteristics of the ballast oscillation process, shown in Table 2. These characteristics can be used to simulate the vibrational dynamic effect in triaxial tests. Such modeling is necessary to study the sensitivity of crushed stone ballast to the loads, which is shown in a decrease in the strength and deformation properties of the ballast, to predict the bearing capacity and deformability of the ballast under various operating conditions.

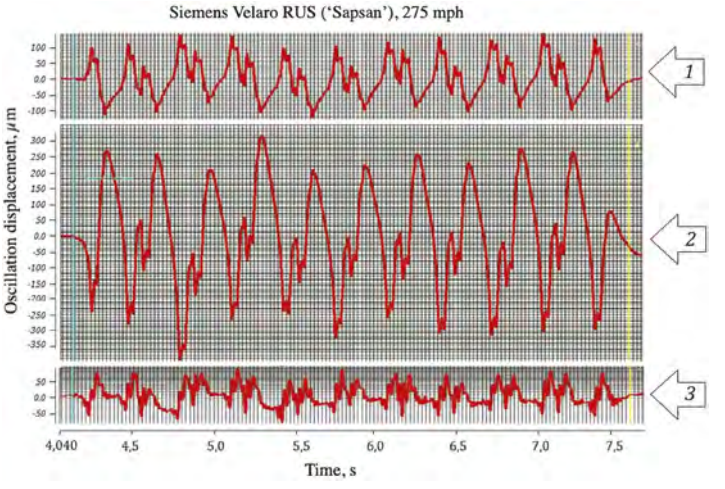

Figure 4. Amplitudes of vibration displacement under sleeper during the passage of the high-speed train "Sapsan" at a speed of 275 km/h: 1 – Y axis, 2 – Z axis, 3 – X axis.

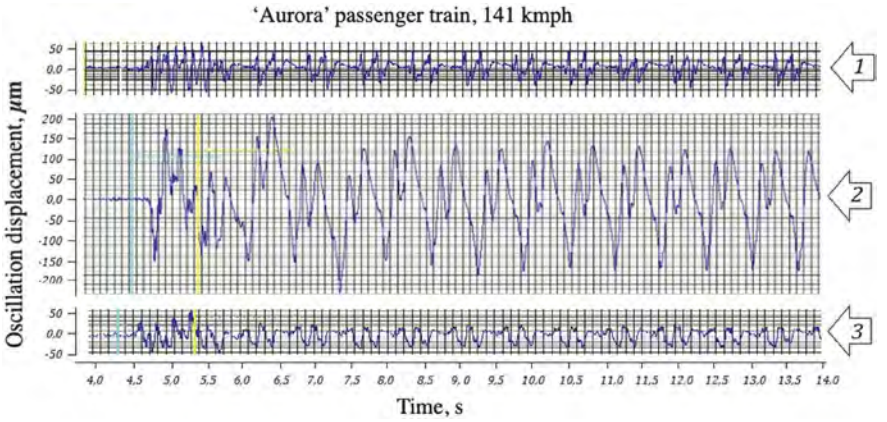

Figure 5. Amplitudes of vibration displacement under sleeper during the passage of the 'Aurora' passenger train at a speed of 141 km/h: 1 – Y axis, 2 – Z axis, 3 – X axis.

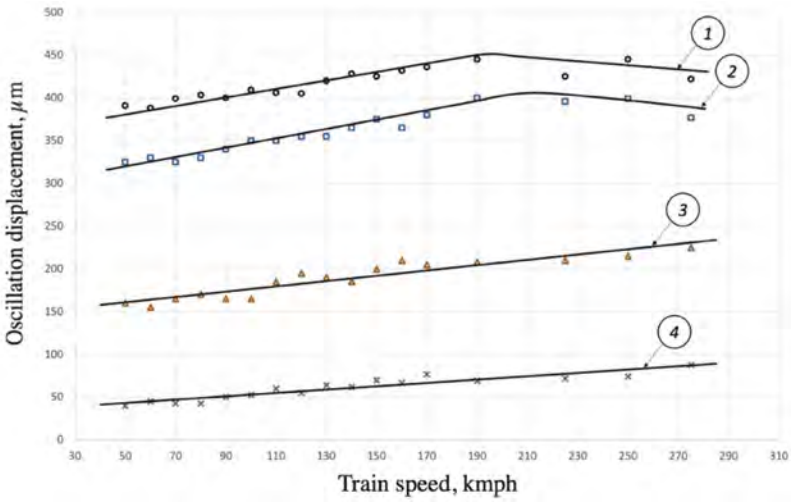

Figure 6. Amplitudes of ballast vibration displacement at passenger trains speed (under the sleeper): 1 - resulting; 2 - in the vertical direction (Z); 3 - in the horizontal direction perpendicular to the longitudinal axis of the track (Y); 4 - in a horizontal direction along the longitudinal axis of the track (X).

Table 2. The amplitude-frequency characteristics of the ballast.

Frequency component	Vibration displacement amplitude and frequency	Vibration components along the axes			Descruption
		X	Y	Z	
Low	f_l, Hz	1,7-4,6	2,0-5,0	1,5-5,2	Cumulative force impact caused by the passage of rolling stock bogies
	A_l, μm	25-45	80-120	200-360	
Medium	f_m, Hz	5-50	5-50	4-40	Force impact caused by the passage of wheelsets (individual axles in the bogie)
	A_m, μm	5-10	20-35	50-100	
High	f_h, Hz	40-120	50-150	40-600	Oscillations of unsprung masses of rolling stock
	A_h, μm	0-5	0-15	10-15	

4 CONCLUSIONS

The study of ballast vertical vibration displacement gives the following conclusions:

1. Displacement amplitudes and frequency range of ballast particles are derived. Both horizontal components increase linearly with approximately the same intensity with speed growth, and their values in the entire range of speeds do not exceed 225 μm in the transverse direction and 90 μm in the longitudinal direction. The vertical component also increases according to a nearly linear dependence up to 190 km/h, and at higher speed it stabilizes and even slightly decreases, which leads to almost the same values of the resulting vibration displacement amplitude up to 275 km/h.
2. No differences in the oscillatory process are revealed for different types of rail fastenings (KB-65, ARS-4 or Pandrol).
3. The obtained results can be used to simulate the vibrational dynamic effect in triaxial tests. Such modeling is necessary to study the sensitivity of crushed stone ballast to the loads, which is shown in a decrease in the strength and deformation properties of the ballast, to predict the bearing capacity and deformability of the ballast under various operating conditions.

REFERENCES

Butorina, M., Minina, N., Ivanov, P. & Petryaev, A. 2017. Reduction of vibroacoustic effect of high-speed trains. *Procedia Engineering* 189: 352–359.

Kaewunruen, S. & Remennikov, A.M. 2008. An alternative rail pad tester for measuring dynamic properties of rail pads under large preloads. *Experimental Mechanics* 48: 55–64.

Kolos, A.F., Ryzhov, V.S., Shmulevich, M.I. & Akkerman, G.L. 2017. Deformation properties of decomposed peat under vibration and dynamic load impact. *Procedia Engineering* 189: 792–799.

Kolos, A., Romanov, A., Govorov, V. & Konon, A. 2020. Railway subgrade stressed state under the impact of new-generation cars with 270 kN axle load. *Lecture Notes in Civil Engineering* 49: 343–351.

Remennikov, A. & Kaewunruen, S. & Ikaunieks, K. 2020. Deterioration of dynamic rail pad characteristics. Faculty of Engineering - Papers.

Serebryakov, D., Zaitsev, E. 2017.The study of subgrade operating conditions at bridge abutment approach. *Procedia Engineering* 189: 893–897.

Konon, A. & Petriaev, A. 2018. Influence of geosynthetics on the oscillations amplitude of railway subgrade. *11th International Conference on Geosynthetics 2018*, *ICG 2018*: Seoul, 16–21 September 2018. – P. 990–998.

Petriaev, A. & Konon, A. & Muhammadiyev, N. 2022. Parameters of the Rail Sleeper Base Oscillatory Process in the Rail Joint Area When Using Elastic Elements. *Lecture Notes in Networks and Systems*. 402: 493–502.

Smart Geotechnics for Smart Societies – Zhussupbekov, Sarsembayeva & Kaliakin (Eds)
© 2023 The Author(s), ISBN 978-1-003-29912-7
Open Access: www.taylorfrancis.com, CC BY-NC-ND 4.0 license

The elastic dampers effect on the vibrodynamic impact of rolling stock in the rail track junction zone

A.F. Kolos, A.A. Konon & A.V. Petriaev
Emperor Alexander I St. Petersburg State Transport University, St. Petersburg, Russia

N.R. Muhammadiyev
Tashkent State Transport Universityy, Tashkent, Uzbekistan

ABSTRACT: The paper presents the results of sub-rail pads field tests to assess the effect of the stiffness and number of standard and prototype sub-rail pads on the level of vibration transmitted to the track when trains pass in the rail junction area. In order to achieve this goal, vertical vibration accelerations arising from trains passing in the rail joint area were measured with different numbers of standard sub-rail pads and high elasticity pads. At all investigated types of rolling stock (passenger train, Lastochka, Sapsan) with standard vibration damping pads before their replacement in the area of the rail joint on the subgrade top 2-3 times higher amplitudes of vertical vibration accelerations were fixed than at the distance of 7 sleepers from the joint. Comparison of vibration acceleration amplitudes in the rail joint area with different numbers of dampers showed that 7 dampers installed on each side of the rail joint are most effective. A comparison of vibration-dynamic impact level of on the ballast in the area of the rail joint depending on the type of rolling stock with different axle load and speed has shown, that Lastochka and Sapsan have a greater impact on the track than passenger trains with a speed of 90 km/h and a load of 150-160 kN per axle. Vibration acceleration amplitudes in the ballast layer with 7 pads of increased elasticity Sylodyn NF (experimental) are 1.4-2 times smaller than those of standard - CP-204-M-ARS (standard).

1 INTRODUCTION

The railway track is experiencing increased dynamic loads due to the global trend of increasing the traffic, train speeds and axial loads. The increase in loads leads to accelerated track deterioration. The railway operation world experience and the field experiments results have indicated that the ballast layer is the element with the smallest margin of safety. The stability of the track geometric parameters depend on the state of the ballast. The shock-dynamic impact of rolling stock on the track is significantly enhanced in the rail joint area, which is a node with particularly difficult working conditions (Kolos 2020). Despite the fact that by far the most common is the long-welded rails, expansion joints of rails and switches (Petriaev 2020) require optimization of the design. In the rail joint area and adjacent sleepers, the rolling stock increased impact significantly affects the track stability. To solve this problem, elastic sub-rail pads are used (Petriaev 2017, Kaewunruen 2008, Sol-Sánchez 2015). The pads are made of various materials: high-strength polyethylene (HDPE), various elastomers, including natural rubber, polyurethane (Remennikov 2020), recycled rubber (Sol-Sánchez 2014), reinforced rubber (Carrascal 2018, Sol-Sánchez 2014). Optimization of their stiffness, thickness and the placement location choice is the important problem.

This article presents the results of sub-rail pads full-scale tests in order to assess the impact of their number and stiffness in the rail junction area on the vibration level transmitted to the railway track due to trains pass.

DOI: 10.1201/9781003299127-402

The measurement of vertical vibration accelerations occurring during the trains passage on the rail junction area with a different number of standard sub-rail pads of increased elasticity has been carried out.

2 MATERIALS AND METHODS

The study was carried out on the high-speed railway line St. Petersburg - Moscow. The test site was located on a straight track section. The roadbed was represented by a zero level. The characteristics of the upper structure of the railway track are presented in Table 1.

Table 1. Characteristics of the upper structure.

Parameter	Unit of measurement	Value
Type of rails		R65
Type of sleepers		IIIC-ARC
The ballast thickness	m	0.45
Track gauge	m	1.523
Rail level	mm	0-3
Space allowance	mm	12
The force of pressing the rails with the terminal	kN	7.7–9.7

The characteristics of standard CP-204-M-ARS (standard) sub–rail pad are presented in Table 2.

Table 2. Characteristics of CP-204-M-ARS pad.

Parameter	Unit of measurement	Value
Category		II
Execution		D
Thickness	mm	14
Weight	kg	0.46
Tensile strength at break	MPa	10
Elongation at break	%	300
Static compression stiffness	kN/mm	80

The appearance of the standard and experimental pad is shown in Figure 1.

Figure 1. Standard CP-204-M-APC gasket (standard, top) and Sylodyn NF high-elasticity gasket (experimental, bottom).

Sylodyn NF (experimental) high-elasticity under-rail pad are made of a material whose characteristics are given in Table 3.

Table 3. Characteristics of pad with increased elasticity Sylodyn NF (experimental).

Parameter	Unit of measurement	Value
Static scope of application	N/mm^2	1.5
Peak loads	N/mm^2	8.0
Mechanical loss factor		0.1
Rebound elasticity	%	70
Residual deformation during compression	%	<5
Static modulus of elasticity	N/mm^2	11.95
Dynamic modulus of elasticity	N/mm^2	16.85
Static shift modulus	N/mm^2	0.8
Dynamic shift modulus	N/mm^2	1.18
Min. breaking tensile stress	N/mm^2	7.0
Min. elongation at break	%	500
Abrasion	mm^3	90
Coefficient of friction (steel)		>0.7
Coefficient of friction (concrete)		>0.7
Specific volumetric resistance	Ω*cm	$>10^{11}$
Thermal conductivity	Wt/mK	0.15
Operating temperature range	°C	-30 - 70
Peak temperatures	°C	120
Flammability	class	E/EN 13501-1

Measurements were performed with integrated circuit piezoelectric accelerometers (type 393B04) by PCB Piezotronics. The sensors were installed at sleeper bearing level and 40 cm below. The placement of the sensors is shown in Figure 2. The seismic receivers were installed on a leveled platform with precise observance of the three directions measurement (vertical, horizontal across and along the track).

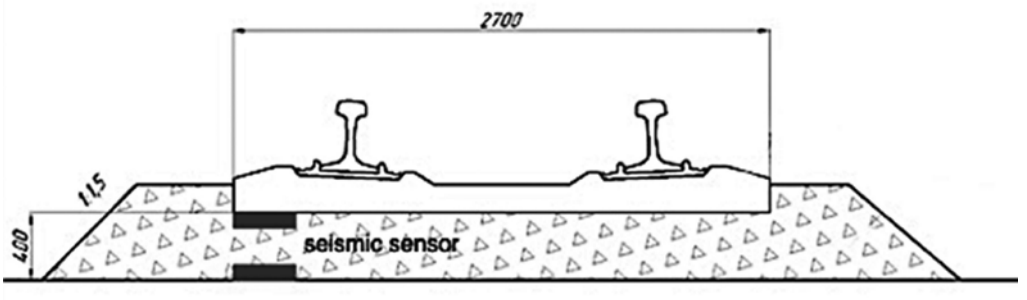

Figure 2. Layout of vibration sensors in the experimental section (cross section).

Passenger trains moved along the experimental section at speeds of 85-95 km/h, high-speed electric trains "Lastochka" (Siemens Desiro RUS) - 170 km/h, high-speed electric train "Sapsan" (Siemens Velaro RUS) - 190 km/h.

The measured parameters are vertical vibration accelerations in the area of the rail joint, in units of *g*.

The measurements were carried out using a set of equipment consisting of a digital seismic signal recorder ZET 048; a laptop computer with licensed software; a signal amplifier; a 220 V power supply, a set of vibration sensors (accelerometers and seismic sensors).

There were 30-40 train passages registered at in the joint area and at a distance of 7 sleepers from the joint for standard sub-rail pads and experimental ones.

The equipment scheme for registering vibration accelerations is shown in Figure 3.

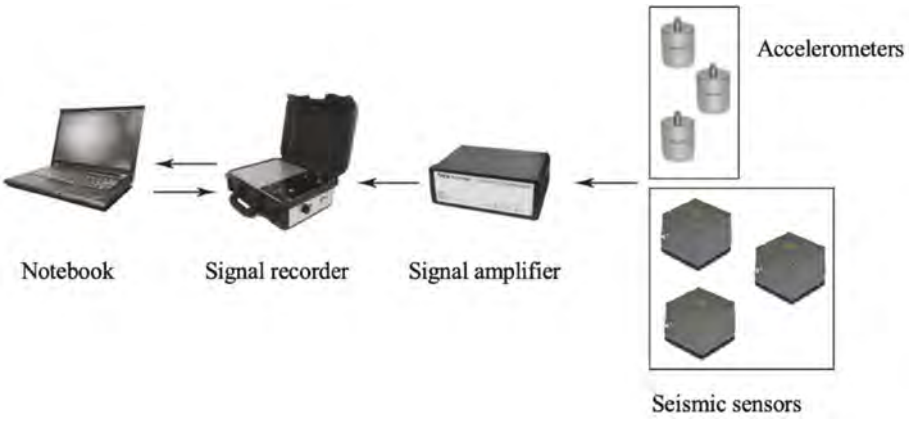

Figure 3. Oscillation amplitudes registration scheme.

The measurement results were statistically processed taking into account the following factors:

1. The statistical series included the measurement results during the movement of various types of rolling stock.
2. From each car, the maximum value of vibration accelerations is included in the statistical series.
3. Statistical processing of measurement results was carried out by methods based on the theory of mathematical statistics. In the course of statistical processing, the average value of vibration accelerations, the standard deviation, the maximum probable value and the coefficient of variation were determined. The probability level was assumed 0.994 due to "The methodology for assessing the impact of rolling stock on the track in terms of ensuring reliability" (order of Russian Railways No. 2706r, December 22, 2017).

3 RESULTS AND ANALYSIS

Comparative diagrams were plotted based on the results of the vibration accelerations measurement which occurs during train passage in the area of the rail junction. The results of the study are presented in Figures 4–6.

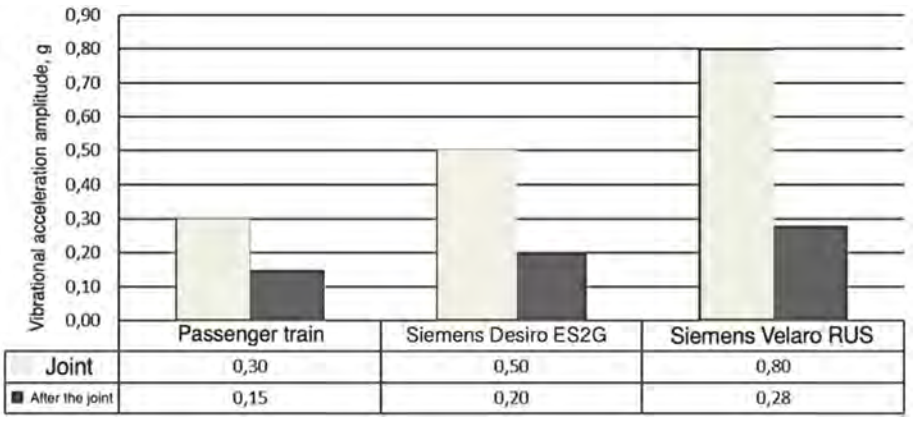

Figure 4. Amplitudes of vertical vibration accelerations on the subgrade top in the joint area and at a distance of 7 sleepers from the joint, with standard pads.

During the investigation, 2-3 times greater amplitudes of vibration accelerations were recorded near joint area compared with the point at the distance of 7 sleepers from the joint for the all types of rolling stock. The results obtained indicate an increased level of vibrodynamic impact on the sub-rail base in the joint zone.

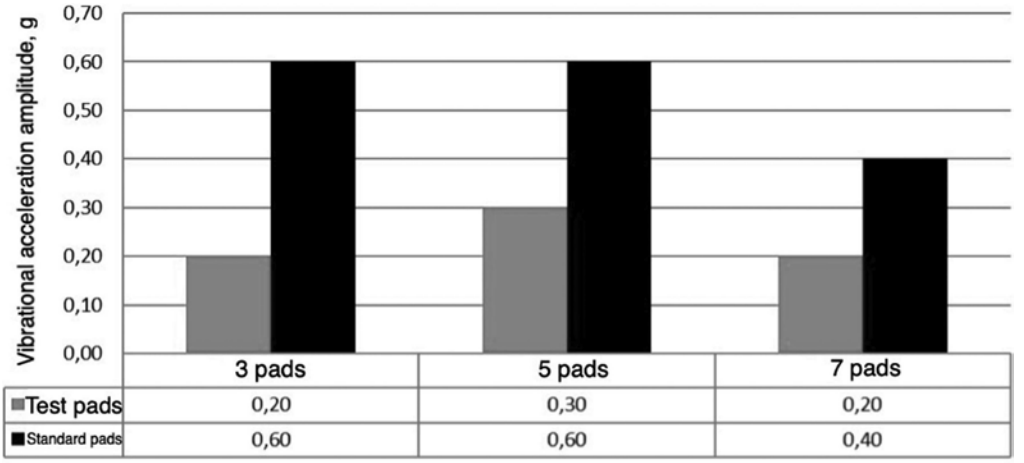

Figure 5. Amplitudes of vertical vibration accelerations on the subgrade top in the joint area and at a distance of 7 sleepers from the joint, with standard pads.

The vibration acceleration study results on the number of elastic pads are shown in Figure 6. A comparison of the amplitudes of vibration accelerations in the area of the rail joint with a different number of pads (both high elasticity and standard) showed that 7 shock absorber pads installed on each side of the rail joint work most effectively.

Analysis of the vibrodynamic impact level on the ballast in the area of the rail junction, showed that the Desiro and Velaro have a greater impact on the track than passenger trains with a speed of 90 km/h and a load of 150-160 kN per axle. At the same time, the level of the Desiro and Velaro impact is approximately the same. It is explained by the fact that despite the higher speed of the Velaro (190 km /h), it has a load of 170-180 kN per axle, and the Desiro, moving slower (170 km /h), has a load of 190-200 kN per axle (Figure 6). The amplitudes of vibration

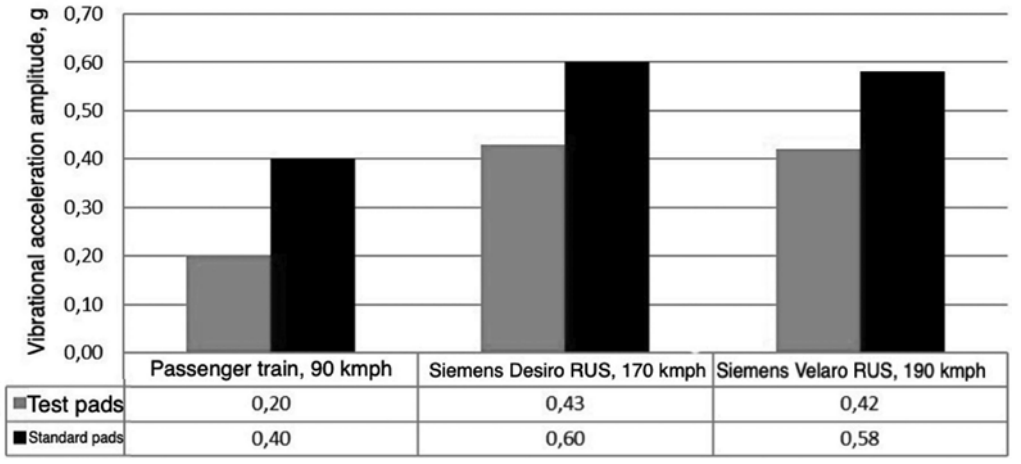

Figure 6. Vertical vibration accelerations amplitudes in the ballast at the sleeper bearing level in the sub-rail section in the area of the rail joint with 7 new standard and experimental sub-rail pads.

accelerations in the ballast layer with 7 increased elasticity pads of Sylodyn NF (experimental) are 1.4-2 times less than with standard CP-204-M-APC (standard).

This is primarily because experimental pads have less stiffness than standard ones and better dampen the vibrodynamic effect transmitted from rails to sleepers and further to the ballast, which inevitably leads to an increase in the track stability (Butorina 2017, Serebryakov 2017, Boronenko 2020, Blazhko 2017, Kolos 2017, Sakharova 2017, Sakharova 2018).

4 CONCLUSIONS

The study of ballast vertical vibration accelerations in the area of the rail joint with a different number of standard pads CP-204-M-APC and Sylodyn NF allow us to draw the following conclusions:

1. For all types of rolling stock studied with standard elastic pads, 2-3 times greater amplitudes of vertical vibration accelerations were recorded in the area of the rail joint than at the distance of 7 sleepers from the joint.
2. Comparison of vibration acceleration amplitudes in the rail joint area with a different number of pads showed that 7 pads installed on each side of the rail joint are the most effective solution.
3. Comparison of vibrodynamic impact level on the ballast in the area of the rail junction, depending on the type of rolling stock having different axle loads and speeds, showed that the Desiro and Velaro have a greater impact on the track than passenger trains with a speed of 90 km/ h and a load of 150-160 kN per axle. At the same time, the impact level of the Desiro and Velaro is approximately the same. This fact is explained by the fact that despite the higher speed of the Velaro (190 km /h), it has a load of 170-180 kN per axle, and the Desiro, moving slower (170 km/h), has a load of 190-200 kN per axle.
4. Vibration accelerations amplitudes in the ballast layer with seven pads of increased elasticity Sylodyn NF (experimental) are 1.4-2 times less than with standard - CP-204-M-APC (standard). This fact is explained primarily by the fact that the experienced elastic pads have less stiffness than the regular ones, and better dampen the vibrodynamic effect transmitted from the rails to the sleepers and further to the ballast.

REFERENCES

Blazhko, L.S., Shtykov, V.I. & Chernyaev, E.V. 2017. Enhancement of subgrade's bearing capacity in low water permeable (clay) soils. *Procedia Engineering* 189: 710–715.

Boronenko, Yu.P, Rahimov, R.V., Lafta, W.M., Dmitriev, S.V., Belyankin, A.V. & Sergeev, D.A. 2020. Continuous monitoring of the wheel-rail contact vertical forces by using a variable measurement scale. *2020 Joint Rail Conference, JRC 2020*.

Butorina, M., Minina, N., Ivanov, P. & Petryaev, A. 2017. Reduction of vibroacoustic effect of high-speed trains. *Procedia Engineering* 189: 352–359.

Carrascal, Isidro & Núñez, Alejandro & Casado, José & Diego, Soraya & Polanco, Juan & Martin, Juan. 2018. Development of metal rubber pads for high-speed railways. *WIT Transactions on The Built Environment* 181: 487–498. https://doi.org/10.2495/CR180431.

Kaewunruen, S. & Remennikov, A.M. 2008. An alternative rail pad tester for measuring dynamic properties of rail pads under large preloads. *Experimental Mechanics* 48: 55–64.

Kolos, A.F., Ryzhov, V.S., Shmulevich, M.I. & Akkerman, G.L. 2017. Deformation properties of decomposed peat under vibration and dynamic load impact. *Procedia Engineering* 189: 792–799.

Kolos, A., Romanov, A., Govorov, V. & Konon, A. 2020. Railway subgrade stressed state under the impact of new-generation cars with 270 kN axle load. *Lecture Notes in Civil Engineering* 49: 343–351.

Petriaev, A. 2017. Stress response analyses of ballasted rail tracks, reinforced by geosynthetics. *Procedia Engineering* 189: 660–665.

Petriaev, A. 2020. Modeling of a railway roadbed reinforcement. *Lecture Notes in Civil Engineering* 50: 27–35.

Remennikov, A. & Kaewunruen, S. & Ikaunieks, K. 2020. Deterioration of dynamic rail pad characteristics. Faculty of Engineering - Papers.

Sakharova, A.S., Svatovskaya, L.B. & Baidarashvili, M.M. 2018. Construction wastes application for environmental protection. *WASTES - Solutions, Treatments and Opportunities II - Selected papers from the 4th edition of the International Conference Wastes: Solutions, Treatments and Opportunities, 2017*: 345–350.

Sakharova, A.S., Petriaev, A.V. & Kozlov, I.S. 2019. New construction solutions for geoenvironment protection of transport infrastructure. *IOP Conference Series: Earth and Environmental Science* 272 (2): 022220.

Serebryakov, D., Zaitsev, E. 2017. The study of subgrade operating conditions at bridge abutment approach. *Procedia Engineering* 189: 893–897.

Sol-Sánchez, M. & Moreno-Navarro, Fernando & Gámez, Ma. 2014. The use of deconstructed tire rail pads in railroad tracks: Impact of pad thickness. *Materials and Design* 58: 198–203.

Sol-Sánchez, M. & Moreno-Navarro, Fernando & Gámez, Ma. 2014. Viability analysis of deconstructed tires as material for rail pads in high-speed railways. *Materials and Design* 64: 407–414.

Smart Geotechnics for Smart Societies – Zhussupbekov, Sarsembayeva & Kaliakin (Eds)
© 2023 The Author(s), ISBN 978-1-003-29912-7
Open Access: www.taylorfrancis.com, CC BY-NC-ND 4.0 license

Many years consolidation of soils under cyclic load at the base of shipping locks

O.P. Minaev
Military Academy of Logistics named Army General A.V. Chrulev, The Russian Federation

ABSTRACT: For the first time ever, the author of the paper considers the effect caused by cyclic navigational load on the long-term settlement of soils at the base of shipping locks during their operation. Ships go through a lock when it is filled with water and the level in the upstream and downstream waterways decreases, which results in cyclic load that has an impact on the foundation soils. Long-term monitoring of the Gorodets and Volga hydroelectric complex gives evidence that the final settlement of some sections of locks under operational load varies from 25 to 65 mm and 10 - 12 cm (plus 14 - 18 cm during the construction period) while the settlement lasted for 52 and 31 years respectively. The value of the residual settlement caused by static and cyclic loading decreases if the initial density of the foundation soil is higher, the same as the number of loading cycles for achieving it at given stresses from the external load. The author suggests effective vibrodynamic methods of compaction that should be applied in order to decrease the values of settlements from static and cyclic loads and reduce the consolidation time of water-saturated sandy soils under cyclic load.

1 INTRODUCTION

Most locks on the waterways of Russia are built on sandy subsoils of considerable thick mass (up to 12 m and over) and solid main bottom (Figure 1); with the sandy layer frequently varying in thickness within the limits of the structure.

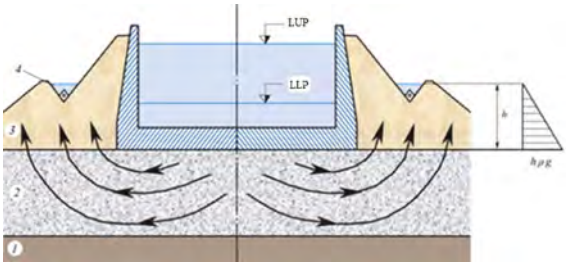

Figure 1. The diagram of the filtration consolidation in the foundation of the lock chamber: 1 – confining layer; 2 – filtration subsoil layer; 3 – chamber backfill; 4 – drainage.

Many years of monitoring the Gorodetz and Volga hydroelectric complex esprovide evidence, that the final settlement of individual lock sections under operational load varies from 25 to 65 mm and 10-12 cm (plus 14-18 cm during construction) while the settlements lasted 52 and 31 years respectively.

Unbalanced settlements and deformations in the design structures cause cracks, obliqueness and other defects, which affect normal operation. The experience in the operation of locks shows that if we analyze the outcomes and causes of the lasting lock deformations without considering the soil consolidation in the foundation area, obtain erroneous results.

DOI: 10.1201/9781003299127-403

When structures are built on sandy subsoils of thick mass (10-20 m), their settlements under static and especially dynamic loads can achieve considerable values amounting to several dozens of centimeters. However, the process of fading these settlements go through is relatively fast due to a higher coefficient of sandy soil filtration, which is several orders of magnitude higher than in the case of clay soils.

Given these conditions, the data below may seem paradoxical even though they are based on many years of monitoring of some locks built on sandy subsoils and operating since the 1950-60s.

Thus, the author of this paper was the first to raise a question about the effect that cyclic navigation load has on lasting settlements of locks during their operation (Figure 2).

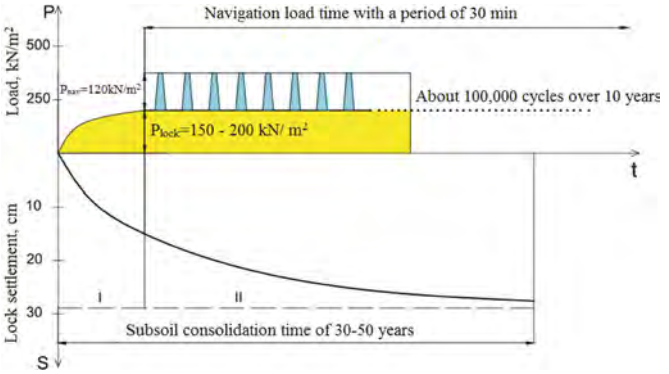

Figure 2. The "load-settlement" graph of the lock under: I –construction load; II –operational load.

Vessels go via a lock after it is filled with water and its level is lowered upstream and downstream the waterway, which results in the impact of cyclic load on the subsoils, according to what the author claims.

The paper provides the results of theoretical studies of sandy soil consolidation and laboratory tests of soil deformations under cyclic load, as well as field observations of the operating locks built on sandy subsoils. Benchmarking proves that in case loose soils are compacted to firm consistence in the foundation area of the lock, the settlements and the soil consolidation time reduce a lot.

2 THEORETICAL DEPENDENCES

The main consolidation equation worked out by V.A. Florin (Florin 1959) can be integrated only in the simplest cases of a one-dimensional problem. In this case, if there is no trapped gas, instantaneous soil load and instantaneous deformation of the soil skeleton, the main consolidation expression takes the following form according to Equation 1:

$$\frac{\partial H}{\partial t} = C_v \frac{\partial^2 H}{\partial z^2}, \tag{1}$$

where $Cv = (1 + e)\ K_f\ /\gamma w \times a$ is the consolidation coefficient, m^2/s; e is the soil porosity coefficient, K_f is the soil filtration coefficient, cm/s; γ_w is the specific gravity of water, kN/m^3; $a = 1 / E$ is the soil compaction coefficient, 1/MPa, E is the subsoil deformation modulus, MPa.

If the soil layer is compacted by evenly distributed load q, instantly applied at the point of time $t = 0$, it can be assumed that q causes the depth stabilized stress $\sigma * z = const$. Then $\sigma * z = q$, while $H = H\ (z,\ t)$.

The solution to Equation 1 will be the expression according to Equation 2:

$$H_{z,t} = \frac{4q}{\pi\gamma_w} \sum_{i=1,3}^{\infty} \frac{1}{i} \left(e^{-\frac{c_v i^2 \pi^2}{h^2} t} \right) \sin \frac{i\pi z}{h}. \tag{2}$$

The expression in Equation 2 can be used for determining the hydraulic pressures $H(z,t)$, obtaining stresses in the soil skeleton for any point of time t and measuring the settlement for the same points of time $S(t)$.

The solution to Equation 1 obtained for determining the settlements has the following form according to Equation 3:

$$S_t = \frac{a}{1+e} q \int_0^h [1 - \frac{4q}{\pi\gamma_w} \sum_{i=1,3}^{\infty} \frac{1}{i} (e^{-\frac{C_v i^2 \pi^2}{h^2} t}) \sin\frac{i\pi z}{h}] dz = \frac{aqh}{1+e} [1 - \frac{8}{\pi^2} \sum_{i=1,3}^{\infty} \frac{1}{i^2} e^{-\frac{C_v i^2 \pi^2}{h^2} t}] \quad (3)$$

$$= S_{consol} \times \mu,$$

where $\cos\frac{i\pi z}{h} \int_0^h dz = \cos i\pi - \cos 0 = -2$, μ is the degree of consolidation.

For the case under consideration we find the solution for the sandy soil layer with thickness h_1, lying on a water impermeable foundation (Figure 3), for the boundary conditions at $z = 0$ $H = 0$, at $z = h$ $\partial H/\partial z = 0$.

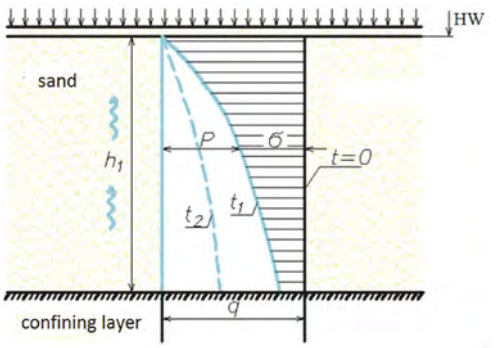

Figure 3. Pressure p in water and stresses in the soil skeleton upon consolidation affected by q of evenly distributed load of the soil layer on water-permeable foundation.

The expression for finding the heads $H(z,t)$ and settlement S_t can be obtained from to Equations 2 and 3 by substituting h for $2h_1$ in them.

Value μ varies from 0 at t = 0 to 1 at $t = \infty$ and is found according to the ratio

$$\mu = S_t / S_{consoll}, \quad (4)$$

The final settlement of the soil layer is found according to the dependence

$$S_{consol} = \frac{aqh}{1+e}. \quad (5)$$

Figure 3 shows the nature of the curves reflecting the excessive pressure in water ($pz = \gamma w \times H$) and stresses in the soil skeleton $\sigma z = q - p$ for various points of time t_1 and t_2 according to Equation 2. At t = 0 along the entire height of the soil layer, the heads $Ho = q/\gamma w = const$ According to Figure 3 the time of consolidation of the water-saturated soil layer $t_o > t_2 > t_1$. You can learn about the solution to this equation in more detail by referring to (Ivanov 1991) or the original source (Florin 1959).

We found the final lock settlements S_{final} and soil consolidation time t using Equation 3 for small and medium-sized sands, which the author obtained in his studies on dynamic soil compaction, as referred to below. For the two extreme cases of loose and dense fine and medium-

sized sands with the skeleton porosity coefficient after backfill e = 0.75 and after dynamic compaction e = 0.61, deformation modulus E of fine and medium-sized sands is taken to be 9 and 40 MPa, respectively.

It is known that the filtration coefficient K_f of fine and medium-sized sands varies from $0.5x10^{-2}$ to $0.5x10^{-3}$.Increases by an order of magnitude along with the growing density. The calculations consider the thickness of the sandy soil layer in the foundation area of the lock h_1 = 12 m and the filtration path length of the forced-out water estimated at a given vessel width b_{vessel} = 30 m.

The resulting calculations for the degree of consolidation $\mu = 0.96$ show that the final settlement of the lock on loose water-saturated sandy soils caused by instantly applied load with intensity of 320 kN/m^2, is 23.4 cm, having reduced to 5.7 cm. In addition, the consolidation time of the fine and medium-sized water-saturated sands in the foundation area of the lock under the instantly applied load does not exceed 6.0 hours.

3 ANALYSIS OF LABORATORY TEST RESULTS

According to Professor P.L. Ivanov (Ivanov 1991), the compression equipment under cyclic load and unload and at the same stresses shows that the accumulated residual deformation sattenuate. Gradually the load and unload curves merge and the soil behaves as an ideal elastic body. In slightly wet soils, load and unload curves sometimes merge after 20. . .30 loading cycles.

We may conclude that the soil porosity coefficient reduces from e_0 to e_1, and then progressively goes down to e_1,e_2... e_n with the increasing load cycles for stresses given. It means that during cyclic load, the residual settlement S_{resid} consists of the final settlement S_{fin} from the applied static load and additional settlement S_{cyclic} under cyclic load. Moreover, in the case of a higher initial density of the soil (e_o>e_1>e_2...e_n), not only does the value of the final settlement S_{fin} from the applied statistic settlement reduce, but so does the additional settlement S_{cyclic} from the cyclic load, the same as the number of load cycles needed for achieving the complete residual settlement S_{res} for the given stresses from external load.

The author obtained similar in the compression tests of slightly wet medium-sized sand for cyclic load in the laboratory of the Department of Ports, Bases and Foundations of the Institute of Water Transport, Admiral Makarov SUMIS.

4 RESULTS OF THE OBSERVED SOIL SETTLEMENTS IN THE FOUNDATION AREA OF THE LOCK

Throughout the operation of the locks, the services of the hydroelectric complexes constantly observe the deformations in the bases of the structures and regularly measure the settlements of the lock chambers. The table below presents the results of the observations.

Table 1. Results of field observations of locks settlement.

Navigable hydroelectric complex	Consolidation period, years	Consolidation term, years
Gorodetz – locks No. 15 – 16	1953 – 2005	52
Volga – locks No. 30 – 31	1962 – 1993	31

As seen from the table, the process of soil consolidation under the bottom of the lock can take several decades. Thus, the soil consolidation in the foundation area of the Gorodetz locks (according to the FBU "Administration of the Volga Basin") lasted about 50 years, while the period of consolidation in the foundation area of the Volga locks (according to the FBU "Volgo-Don") lasted about 30 years.

As an example, Figure 4 shows the settlement graph of the Volga hydroelectric complex.

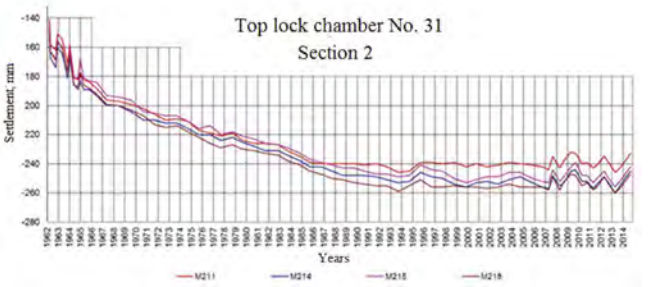

Figure 4. The settlement graph of the Volga lock sections.

From the settlement graph of the Gorodets and Volga hydroelectric complexes it has been found that the rate of the consolidation process curve has a dying form, close to an exponential curve.

For the Gorodets locks, the most intensive stage of filtration consolidation took place in 1953-1958 (5 years), while for the Volga locks it was in 1962-1967 (6 years). In this very period the intensity of settlements was 8 mm a year for the Gorodets locks, and 10 mm a year for the Volga locks. In later years the intensity of settlements reduces by 2-3 times. After fifty (thirty) years' period, the settlements virtually stopped.

5 THE CAUSE OF LONG-LASTING LOCK SETTLEMENTS

On the whole, the deformations of lock structures are caused by the long-lasting consolidation of loose sand subsoils being quite slow due to a navigation cyclic load on subsoils, which was noted for the first time ever by the author of this article. Let us clarify the above-said with the chronometric observations presented on Figure 5. This chronometric graph was drawn up from experience in operation of navigable locks.

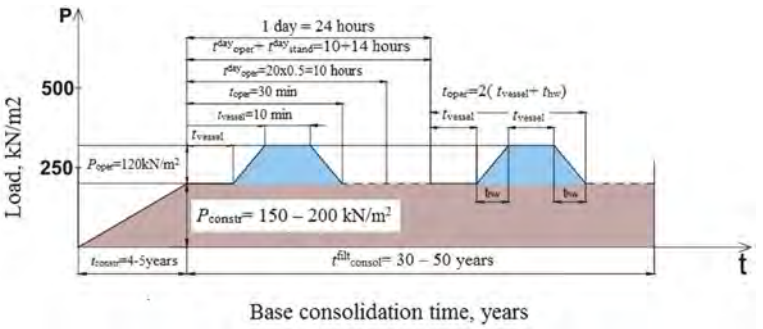

Figure 5. Chronometrical graph of base soil consolidation.

Designations: t_{constr} is the construction period of the lock, years; t^{filt}_{consol} is the term of filtration consolidation, years; t_{oper} is the operation time for the passage of a vessel, min; t_{vessel} is the net time of movement of a vessel in the lock, min; t_{hw} is the time of filling the lock with water or lowering the water level in the lock, min; t^{day}_{oper} is the total operation time of the lock per day, hours; t^{day}_{stand} is the standstill time of the lock per day, hours

We see from the graph on Figure 5 that the process of soil consolidation begins in the period t_{constr} of the lock construction, which lasts at least 4-5 years. According to the author's estimates, the maximum static load P_{constr} from the weight of the structure on the lock subsoils is 150 – 200 kN/m^2.

Under the effect of this load that was growing during the construction, the lock obtained a certain fixed settlement, which, in case of the Volga hydroelectric complex, amounted to 14-18 cm (See Figure 5).

In the operation of the locks, the subsoils are affected by the cyclic load P_{oper} for the time t_{oper} of the lock operating as a vessel passes it. Besides, the maximum intensity of this load, equal to 120 kN/m^2, occurs during the net time t_{vessel} within which the vessel passes upstream. The cyclic load increases for the time t_{hw} within which the water level rises in the lock up to 12 m and goes down to the initial value for the time t_{hw} within which the water level reduces to the upstream and downstream elevations, respectively.

The total time $t^{day}{}_{oper}$ of the impact of the load P_{oper} upon passage of 20 vessels through the lock is 10 hours a day, while the standstill time $t^{day}{}_{stand}$ of the lock is, correspondingly, 14 hours a day; the time of the impact of the maximum load P_{oper} does not exceed 3-4 hours a day.

The temporary cyclic load affects the subsoils many times. According to the estimates, the number of these impacts can vary from several tens of thousands to several hundred thousand times over 10–20 years of operation of the hydroelectric complexes. During the period of complete consolidation of the subsoils, which lasted for 31 years for the Volga hydroelectric complex,, the additional settlement was due to the effect of this cyclic load was 10–12 cm. Thus, the total settlement of the Volga hydroelectric complex achieved the values of 24 to 30 cm throughout the entire period of filtration consolidation of the sandy soils in the foundation area of the lock.

Figure 1 presents the resulting "load-settlement" graph of the lock.

The experience obtained during operation of locks shows that not only does this cyclic load act as a pump can cause long-lasting deformations and settlements, especially in the case of loose sandy subsoils, but it also results in the filtration flow of sandy subsoils throughout the operation of the navigable locks provided that the sealing of the water stop in the bottom of the lock. The latter can lead to dangerous local voids and extensive cavities under the bottom of the lock is damaged or totally destroyed.

In order to compact the subsoils of locks, it is necessary to use effective vibro-dynamic ways for compacting sandy soils that have been developed by the author and become widely used (Minaev 2011, Minaev 2014).

The measurement of the required degree of compaction of sandy soils shows that the compaction of sandy soils makes it possible to considerably decrease the final settlements and reduce the time of soil consolidation in the base of navigable river locks resulting from navigable cyclic load.

6 CONCLUSION

1. The author of this paper was the first to raise the question about the effect of the cyclic navigation load on the long-lasting settlements observed during operation of navigable locks built on sandy water-saturated subsoils.
2. In order to increase the resistance of the sandy soil structure to the process of liquefaction (Ishihara 1996, Idriss and Boulanger 2008, Kolosov and Morgunov 2021) under dynamic (seismic) load, reduce the values of settlements from static and cyclic loads and reduce the consolidation time of water-saturated sandy soils under cyclic load, we recommend that effective vibro-dynamic methods of soil compaction should be used.

REFERENCES

Coste, J. 1981. Soil mechanics. Moscow: Stroyizdat.

Florin, V.A. 1959-1961. Fundamentals of soil mechanics. Leningrad - Moscow: Gosstroyizdat.

Idriss, I.M., Boulanger, R.W. 2008. Soil liquefaction during earthquakes. USA, California: EERI.

Ivanov, P.L. 1991. Soils and foundations of hydraulic structures. Soil mechanics. Moscow: Higher School.

Ishihara, K. 1996. Soil Behaviour in Earthquake Geotechnic. USA, Oxford: Clarendon Press.

Kolosov, M.A., Morgunov, K.P. 2021. The phenomena of soil liquefience in the bases of hydraulic structures. IOP Conference Series: Earth and Environmental Science 868(1): 012081.

Minaev, O.P. 2011. Development of vibratory method for soil compaction during construction. Soil Mechanics and Foundation Engineering 48(5): 190–195.

Minaev, O P. 2014. Development of Dynamic Methods for Deep Compaction of Slightly Cohesive Bed Soils. Soil Mechanics and Foundation Engineering 50(6): 251–254.

Smart Geotechnics for Smart Societies – Zhussupbekov, Sarsembayeva & Kaliakin (Eds)
© 2023 The Author(s), ISBN 978-1-003-29912-7
Open Access: www.taylorfrancis.com, CC BY-NC-ND 4.0 license

Effect of traffic loads on drainage capacity of geocomposite embedded pavement layers

Huchegowda BK
Doctoral Scholar, Department of Civil Engineering, Indian Institute of Technology Hyderabad (IITH), Kandi, Sangareddy, India

Sireesh S*
Professor, Department of Civil Engineering, Indian Institute of Technology Hyderabad (IITH), Kandi, Sangareddy, India

ABSTRACT: It is a general practice to recommend high-permeable granular subbase layers in pavements to avoid moisture infiltration into subgrade. In this study, a three-layered pavement was prepared in a large-scale permeameter to estimate the drainage capacity of controlled and geocomposite-embedded subbase layers under realistic traffic loading. Preliminary studies indicate that the measured permeability of subbase layer was 4 m/day, which do not meet the design criteria of 300 m/day. Two types of geocomposites (GCs) viz., bi-planar (2D-GC) and tri-planar (3D-GC) were used to enhance the drainage capabilities. Results indicated that the improved permeability of the subbase was 410 and 725 m/day, respectively, for bi- and tri-planar GCs. The compression of GCs in the subbase layer decreased the permeability up to 40% for 2D-GC and 20% for 3D-GCs for a given load equivalency factors of 0.63 to 2.54. In addition, PLAXIS-2D analysis was performed to confirm the reinforcement function of GCs.

Keywords: Geocomposite, Permeability, subbase layer, Compressibility, PLAXIS 2D

1 INTRODUCTION

A typical flexible pavement includes the surface course/bituminous layers, base, and subbase courses. The bituminous layers improve the ride quality and enhance the stability of the pavement system. While the base and subbase courses provide structural support to the asphalt layers, and especially subbase layer enhances the drainage properties. However, the availability of good quality aggregates meeting the gradation requirements of granular subbase (GSB) material is becoming scarce. Hence, at times inferior-grade subbase materials are used in the pavement considering the cost-effectiveness and proximity of the materials (Saltan and Findik, 2008). It is essential to design the subbase in such a way that it drains off the infiltrated rainwater quickly to protect the subgrade. Besides, good drainage materials can improve the load-carrying capacity by reducing the pore pressure in the base and subbase layers (Kumar et al., 2006). When replacing poor-quality drainage materials, it is necessary to check the materials' drainage and structural capacity. Notable studies reported lower permeability of the pavement materials, less than the required for two lanes pavement (300 m/day) (Jones and Jones, 1989; Grover and Veeraragavan, 2010; Singh et al., 2020; Koohmishi and Azarhoosh, 2021).

Recently, practitioners are extensively using geosynthetic materials in the pavement to improve the structural stability. The geogrids are majorly used in the base and subbase layers to improve the structural capacity of the layers (Baadiga et al., 2021(a); Saride et al., 2022a). Few studies reported that the geocomposite (GCs) made of geonet and geotextile

*Corresponding author: sireesh@ce.iith.ac.in

DOI: 10.1201/9781003299127-404

combination could enhance the drainage and structural capacity of the pavement (Bilodeau et al., 2015; Zornberg et al., 2017; Li et al., 2017). However, the compressible nature of GCs can influence the drainage capability of the pavement system. Hence, it is also important to understand the effect of wheel load on the drainage characteristics of the GSB layer when GC's are considered. In the design, an equvalent single axle wheel load of 560 kPa pressure is considerd. A load equivalency factor (LEFs) is generally considerd to represent the mixed-axle loads in terms of a single-axle load. LEF multiplied by the number of axle loads within a given weight category and axle configuration gives the number of single-axle load applications that will have an equivalent effect on the performance of the pavement structures.

Pavement performance is also influenced by mechanical properties such as the thickness of each layer, properties of geosynthetics, load characteristics, and the interaction between geosynthetic and granular layers (Taherkhani and Jalali., 2017). The performance evaluation through large-scale experiments gives enough evidence of particular behavior of a limited combination of many parameters. Thus, examining the boundary conditions, geometric parameters on the behavior of geocomposites in pavements is possible through numerical analysis. Several studies tried to understand the reinforcement mechanism, influence of boundary, and geometrical parameters for different problems in pavements (Ling and Liu, 2003; Correia et al., 2018). Therefore, in this study, a series of large-scale permeability tests were carried out for GC-reinforced granular layers to improve the permeability through bi-planar (2D) and triplanar (3D) geocomposites. Further permeability corresponding to the traffic load on the pavement in terms of load equivalency factors (LEF) was studied. Finally, numerical analyses were conducted to understand the reinforcement effect of GC-embedded in the subbase layer.

2 MATERIALS

In this study, a granular material was used to simulate the subbase (GSB) layer between the subgrade and the wet mix macadam (WMM) (base) layer. The GSB and WMM materials were sourced from a near byquarry. The locally available red soil was used for subgrade preparation. Figure 1(a) shows the grain size distribution of all the pavement materials used in the study. The basic material properties were determined per the American Society for Testing Materials (ASTM), as seen in Table 1. The liquid and plastic limits of the soil were 50 % and 24 %, respectively, and the soil was classified as clayey sand (SC). The standard proctor compaction test resulted in the maximum dry unit weight (MDU) of 18.95 kN/m^3 and the optimum moisture content (OMC) of 14.2 %. The corresponding California bearing ratio (CBR) value was observed as 7 %.

The two different GCs were used in this study are 2D-GC and 3D-GC, as shown in Figures 1(b) and 1(c). The GC comprises a medium-weight non-woven, needle-punched,

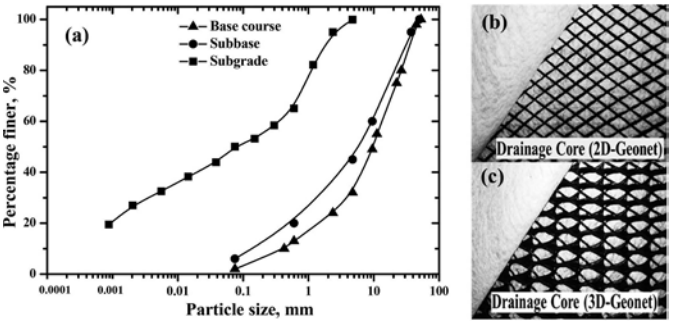

Figure 1. The grain size distribution of material used and geocomposite (a) grain size distribution curve, (b) 2D GC used in the study, and (c) 3D GC used in the study.

polypropylene geotextile filter on both sides of a polyethylene drainage core. The GC ultimate tensile strength in machine direction is 21 kN/m and 20 kN/m for 2D and 3D-GC, respectively.

Table 1. Engineering properties of aggregate materials.

Test particulars	GSB	WMM	Reference
Specific Gravity (CA)	2.62	2.66	ASTM C 127
Specific Gravity (FA)	2.61	2.65	ASTM C 128
Specific Gravity of filler	2.62	2.67	ASTM C 128
Flat & Elongated Particles (%)	24	16	ASTM D4791
Los Angeles Abrasion (%)	32	35	ASTM C 131
Water absorption (%)	0.28	0.4	ASTM C 127
Impact Value (%)	14	15	IS 2366-4
Compaction: OMC, %	4.94	5.45	
: MDU kN/m^3	23.25	22.62	

3 TEST METHODOLOGY

The permeability of pavement materials was determined using a large-scale permeameter of 600 x 300 x 450 mm in size. The loading arrangement was made on the permeameter to find pavement permeability for various LEFs. The permeability tests were carried out for subbase material sandwiched between the subgrade and WMM layers. The subbase layer is 200 mm thick, and the GC is located 50 mm below from the bottom of base layer. The detailed test bed preparation and aggregate layer construction are reported in Saride et al. (2022b). The schematic of the large-scale permeameter is shown in Figure 2. The following section details the results obtained based on the large-scale testing and numerical analysis performed through PLAXIS 2D finite element method.

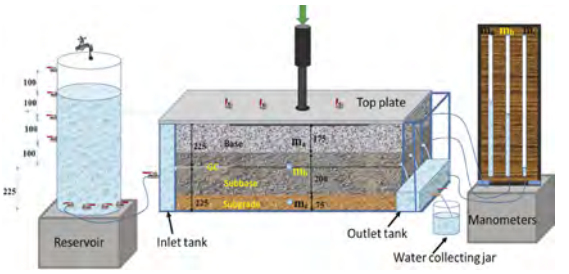

Figure 2. Schematic of the permeability test setup.

4 RESULTS AND DISCUSSION

Pavement performance highly depends on the thickness of layers, material properties, and drainage quality. In this study, a well graded subbase material was used to maintain the structural strength of the pavement, which means that the drainage characteristics of the layer are low. Hence, two different GCs were used to improve the drainage quality of the GSB layer. The single axle load with a dual wheel carrying an 80 kN load is considered as the equivalent single axle load in the design of pavement. However, in practice, the pavement layers experience much different stress conditions due to different class of vehicles. In this study, a single axle type H-10 (LEF = 0.63), type 3 heavy tandem axle (LEF = 1.9), and school bus (LEF = 2.54) were considered, and corresponding stresses were replicated on the pavement surface.

The permeability of the subbase without GC is measured to be less than 4 m/day, indicating a poor drainage quality. The same section, reinforced with the 2D-GC, the permeability is

improved to 410 m/day. At the same time, the permeability was reduced by 7 %, 15 %, 30 %, and 40 %, corresponding to the LEF of 0.63, 1.0, 1.9, and 2.54, respectively (Figure 3a). This observation suggested that under the typical wheel load conditions, GC undergoes compression resulting in lower permeability. Further, the permeability was reduced to 50 % by increasing the hydraulic gradient from 0.16 to 1.0. This permeability reduction corresponds to turbulent flow in the pavement layer (Bourgès-Gastaud et al., 2013). For the subbase layer with 3D-GC, the permeability was 725 m/day without traffic load. With increasing the wheel load on the pavement, the permeability was reduced by 6 %, 10 %, 18 %, and 22 %, corresponding to LEF of 0.63, 1.0, 1.9, and 2.54, respectively (Figure 3b). The permeability corresponding to equivalent single axle load for 2D and 3D-GC is 350 m/day and 651 m/day, respectively. The minimum permeability required for a two-lane pavement is 300 m/day (IRC:37, 2018), hence, the GC-embedded GSB layer under equivalent single axle wheel load satisfied this requirement. Besides, the permeability considering the LEF of 2.54 was, respectively, 245 m/day and 560 m/day for 2D and 3D GCs. The 2D-GC permeability is slightly lower than the permissible value, besides, 3D-GC meets the drainage criteria even with LEF = 2.54. Compared to equivalent single axle wheel load (LEF = 1) to LEF = 2.54, the permeability reduction is 29 % and 14 % for 2D and 3D-GC, respectively.

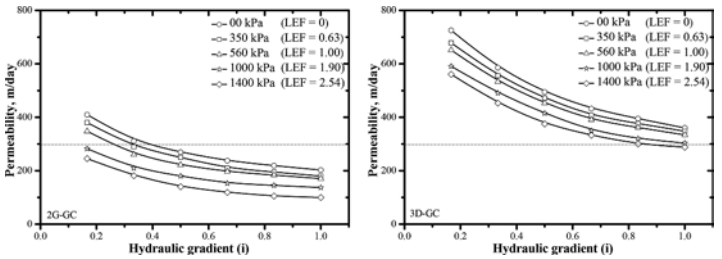

Figure 3. Permeability corresponding to hydraulic gradient for various LEF for (a) 2D- and (b) 3D-GC.

5 NUMERICAL MODELING

A numerical model was developed using PLAXIS 2D finite element software to analyze the reinforcement function of the geocomposite-embedded pavements. The model size was chosen to avoid interfering with the pavement boundary, which should be at least 15 times the size of the loading area. An axisymmetric model with 15-noded structural solid elements was chosen for the analysis. The subgrade thickness of 500 mm was maintained in all models, and the reinforcement was located 50 mm below from the bottom of base layer. Two different subgrade CBRs, equal to 4 % and 7 %, were considered to understand the effect of reinforcement on the weak subgrade corresponding to their calibrated density and moisture contents. The bulk unit weight for CBR 4 % and 7 % are 16.18 and 16.57 kN/m^3, respectively. The granular material properties from the present study, as reported in Table 1 were used. Unconfined compression tests for subgrade materials and large-scale direct shear tests were conducted for aggregate layers to get the shear strength parameters. The reinforcement was modeled using a linear elastic model with a stiffness of 500 kN/m.

A two-layered pavement with a 200 mm thick GSB layer over a 500 mm thick subgrade was modeled. Figure 4 depicts a deformed contour after applying 560 kPa contact pressure on a 150 mm radius plate for a subgrade CBR of 4 %. The vertical deformation corresponding to 560 kPa for 200 mm GSB is 14 mm for subgrade CBR of 4 %. When the subgrade CBR was increased to 7 %, the vertical deformation was reduced to 11.5 mm. With the inclusion of the GC layer, the surface deformation redused to 8.8 mm and 7.0 mm for CBR 4 % and 7 %, respectively. The stress distribution on the subgrade below the loading area for the 200 mm thick subbase layer was 125 kPa and 148 kPa for CBR 4 % and 7 %, respectively.

Further, it was reduced to 85 kPa and 104 kPa for GC embedded in the GSB layer. The contact pressure beneath the loading area will be more for stiffer subgrades. Baadiga et al.

(2021b) have observed similar results. The reinforcement can reduce the stresses on the subgrade by increasing the stress distribution area. It is observed that the reinforcement is more effective in weak subgrade layers. This is because the tensile strength of GC will render excellent support as deformation increases.

According to Ueshita and Meyerhof (1967), the elastic modulus was calculated corresponding to the pressure at 1.25 mm deformation. A modulus improvement factor (MIF) was defined as a ratio of an elastic modulus of the pavement with geocomposite to the elastic modulus of pavement without reinforcement at an elastic deformation of 1.25 mm. When comparing the CBR of 4% and 7% pavement sections, it is observed that in the reinforced sections, the MIF is higher when a weaker subgrade is considered due to more effectiveness of the GC. The MIF is observed to be 1.70 and 1.60 for 200 mm thick subbase overlying CBR 4 % and 7 %, respectively.

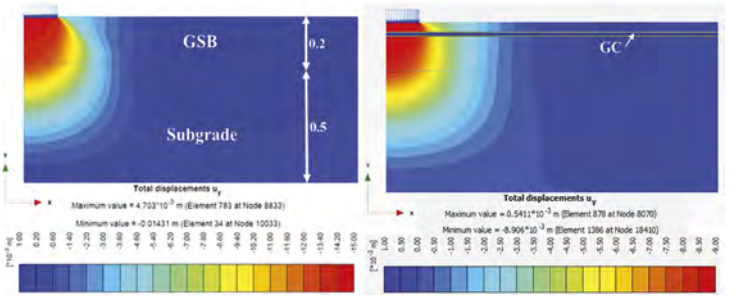

Figure 4. Displacement contour for unreinforced and reinforced modeled section using PLAXIS 2D.

6 CONCLUSIONS

To understand the drainage capabilities and effect of the load equivalency factor on the permeability of GC embedded pavement layers, large-scale permeameter tests were conducted by varying the wheel load on the pavement. Further, numerical analysis was conducted to understand the improvement of the pavement layers' structural capacity due to the GC's reinforcement effect. The study's findings lead to the following conclusions.

1. The permeability of the subbase materials without reinforcement was observed to be 4 m/day which does not meet the design criteria of 300 m/day.
2. Including 2D- and 3D-GC in the granular subbase layer the permeability improved to 410 m/day and 725 m/day, respectively, indicating excellent drainage capability of the geocomposites.
3. With the application of wheel contact pressure on the pavement, the permeability is reduced by 15 % and 10 % for 2D and 3D-GC, respectively.
4. Effects of various LEF on the permeability of GC-embedded pavement were conducted. An increase in the LEF from 1 to 2.54 reduces the permeability by 29 % and 14 % in 2D- and 3D-GC, respectively.
5. Numerical analyses showed that the reinforcement function is highly effective in weak subgrade conditions.
6. With the inclusion of reinforcement, the MIF increased to 1.70 and 1.60 for CBR 4% and 7% subgrade conditions.

REFERENCES

Baadiga, R., Saride, S., Balunaini, U., Madhira, M.R., 2021(a). Influence of tensile strength of geogrid and subgrade modulus on layer coefficients of granular bases. Transp. Geotech. 29, 100557. https://doi.org/10.1016/j.trgeo.2021.100557

Baadiga, R., Balunaini, U., Saride, S. and Madhav, M.R., 2021(b). Influence of geogrid properties on rutting and stress distribution in reinforced flexible pavements under repetitive wheel loading. Journal of Materials in Civil Engineering, 33(12), p.04021338.

Bilodeau, J.P., Doré, G., Savoie, C., 2015. Laboratory evaluation of flexible pavement structures containing geocomposite drainage layers using light weight deflectometer. Geotext. Geomembranes 43(2), 162–170. https://doi.org/10.1016/j.geotexmem.2015.02.002

Bourgès-Gastaud, S., Blond, E., Touze-Foltz, N., 2013. Multiscale transmissivity study of drain-tube planar geocomposites: effect of experimental device on test representativeness. Geosynth. Int. 20(3), 119–128. https://doi.org/10.1680/gein.13.00006

Correia, N.S., Esquivel, E.R. and Zornberg, J.G., 2018. Finite-element evaluations of geogrid-reinforced asphalt overlays over flexible pavements. Journal of Transportation Engineering, Part B: Pavements, 144(2), p.04018020.

Grover, S., Veeraragavan, A., 2010. Quantification of benefits of improved pavement performance due to good drainage. In Journal of the Indian Roads Congress 71(1), 77–99.

IRC 37, 2018. Guidelines for the design of flexible pavements. Indian Road Congress (Fourth Revision). New Delhi, India.

Jones, H.A. and Jones, R., 1989. Horizontal permeability of compacted aggregates. unbound aggregates in roads. Proceedings of the 3rd international symposium, university of nottingham, 70–77.

Koohmishi, M., Azarhoosh, A., 2021. Assessment of permeability of granular drainage layer considering particle size and air void distribution. Construct. Build. Mater. 270, 121373. https://doi.org/10.1016/j.conbuildmat.2020.121373

Kumar, P., Chandra, S. and Vishal, R., 2006. Comparative study of different subbase materials. Journal of Materials in Civil Engineering, 18(4), pp.576–580.

Li, C., Ashlock, J., White, D., Vennapusa, P., 2017. Permeability and stiffness assessment of paved and unpaved roads with geocomposite drainage layers. Appl. Sci. 7(7), 718. https://doi.org/10.3390/app7070718

Ling, H.I. and Liu, H., 2003. Finite element studies of asphalt concrete pavement reinforced with geogrid. Journal of engineering mechanics, 129(7), pp.801–811.

Saltan, M. and Fındık, F.S., 2008. Stabilization of subbase layer materials with waste pumice in flexible pavement. Building and Environment, 43(4), pp.415–421.

Saride, S., Baadiga, R., Balunaini, U. and Madhira, M.R., 2022(a). Modulus Improvement Factor-Based Design Coefficients for Geogrid-and Geocell-Reinforced Bases. Journal of Transportation Engineering, Part B: Pavements, 148(3), p.04022037.

Saride, S., Huchegowda, B.K. and Vyas, S., 2022(b). Evaluation of drainage coefficients for 2D and 3D−geocomposite embedded subbase layers. Geotextiles and Geomembranes. https://doi.org/10.1016/j.geotexmem.2022.07.003

Singh, S., Monu, K., Ransinchung RN, G.D., 2020. Laboratory investigation of RAP for various layers of flexible and concrete pavement. Int. J. Pavement Eng. 21(14), 1780–1793. https://doi.org/10.1080/10298436.2019.1567920

Taherkhani, H. and Jalali, M., 2017. Investigating the performance of geosynthetic-reinforced asphaltic pavement under various axle loads using finite-element method. Road Materials and Pavement Design, 18(5), pp.1200–1217.

Ueshita, K. and Meyerhof, G.G., 1967. Deflection of multilayer soil systems. Journal of the Soil Mechanics and Foundations Division, 93(5), pp.257–282.

Zornberg, J.G., Azevedo, M., Sikkema, M., Odgers, B., 2017. Geosynthetics with enhanced lateral drainage capabilities in roadway systems. Transp. Geotech. 12, 85–100. https://doi.org/10.1016/j.trgeo.2017.08.008

Smart Geotechnics for Smart Societies – Zhussupbekov, Sarsembayeva & Kaliakin (Eds)
© 2023 The Author(s), ISBN 978-1-003-29912-7
Open Access: www.taylorfrancis.com, CC BY-NC-ND 4.0 license

Retaining walls made of infilled blocks in civil engineering

N.Ya. Tsimbelman, I.V. Kuzovatkin & T.I. Chernova
Far Eastern Federal University, Vladivostok, Russia
Branch FGBU TSNIIP Russian Ministry of Construction DalNIIS, Vladivostok, Russia

Ya.I. Kotik
Zakhar Ltd, Vladivostok, Russia

D.Iu. Ivannikov & V.N. Babkin
Corbet Ltd, Moscow, Russia

ABSTRACT: The article deals with a calculation method and examples of application of a rapidly erected retaining wall design. The retaining wall has an increased resistance to dynamic loads, aesthetic appeal, and relatively low cost. The retaining structure is a stepped semi-gravitational structure made of blocks filled with soil. The joint work of the blocks is ensured by the forces of dry friction due to the dense placement of the filler soil inside each block, as well as due to the formation of a compacted wall base on the slope being strengthened. The task of constructing a simulation method of retaining structures consisting of blocks having no rigid structural connection and filled with a granular body is set. The given technique can be applied to any retaining walls of a similar design solution. Examples of constructing such walls in the climatic conditions of the Russian Far East are given.

1 INTRODUCTION

The specificities of solving the problem of protecting a soil massive from collapse (the main functional purpose of retaining structures) determine the range of application for a particular constructive solution. At present there exists a wide array of constructive solutions for retaining structures, such as solid (gravity), semi-solid (semi-gravity), piling, and reinforced soil structures (Anderson, 2012, Tsimbelman, 2009), among which are beneficially standing out retaining walls comprised of separate blocks with granular infill which can be classified as semi-gravity retaining walls. The walls of this type have received rather widespread use in regions with increased seismic activity, including Japan (Civil Engineering Research Centre, Japan, 2016).

The known positive aspects of prefabricated structure technology compared to monolithic structures, such as rapid installation and dismantlement, the lack of «wet» processes during construction, superior aesthetics, structural flexibility and comparatively high dynamic load resistance, can be attributed to advantages of such structures. The use of rubble (or other drainage material) as infill allows, in the majority of cases, to omit the installation of wall-adjacent drainage. The described conceptual constructive solution of retaining walls comprised of separate blocks with soil infill can be used in industrial, civil and road construction practices (Figure 1a).

Despite the mentioned advantages, the use of retaining structures of such constructive solution in Russian construction practice (Tsimbelman, Estrin, 2009) has yet to become widespread due to historically established dominance of traditional constructive solutions as well as certain issues of theoretical nature, which the work examined in this article aims to solve.

The primary goal of this work lies in identifying the constructive specificities inherent to retaining structures of the described type which significantly affect their calculation method, suggesting a formula for determining active ground pressure on the pressure face of the

DOI: 10.1201/9781003299127-405

retaining structure, as well as denoting tasks for future research of retaining walls comprised of soil-infilled blocks.

2 CALCULATION METHOD AND SPECIFICITIES

In essence, the calculation method for retaining walls comprised of separate soil-infilled blocks corresponds to the general calculation algorithm for similar structures regimented by existing Russian norms. The principal constructive specificity of the described structure lies in the fact that the levels of blocks making up the wall are not structurally tied to one another: soil-infilled blocks are held in the designated position due to the friction forces formed by the weight of the structure itself (Figure 1a).

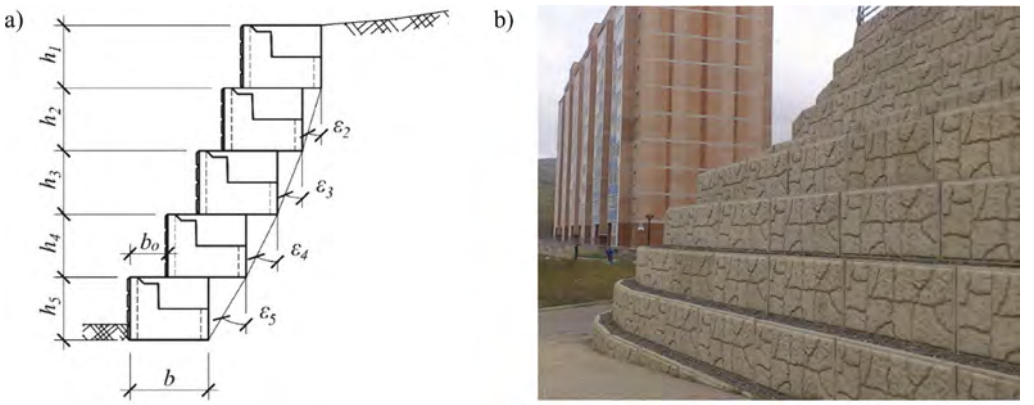

Figure 1. Retaining wall: a – infilled block layout scheme; b – retaining wall comprised of infilled blocks with height of up to 9 m (Vladivostok, Russia).

As a result, the first and foremost specificity of the calculation procedure consists of sequential (from top to bottom) determination of lateral earth pressure with simultaneous monitoring of the possibility of block-on-block displacement. During this process, the pressure face inclination angle will be changing from level to level, and the force of the overlaying block level and the earth load it receives will be transferred to the underlaying level with a cumulative total.

When determining active earth pressure on retaining walls with complex shape pressure face, generally employed methods are either approximate methods which do not consider the pressure face change with the height of the structure (Klein, 1964, Snitko, 1963) or the method of enumerating possible slide angles of the soil collapse prism (Civil Engineering Research Centre, Japan, 2016). Employing methods based on considerable tolerances does not consistently provide results with the required level of accuracy while the consequent enumeration method is exceedingly difficult to implement without the use of specialized computer software due to the bulkiness of the method.

The prerequisites to the method of determining earth pressure on retaining walls of the described design generally match classic solutions for which the balance of forces applied to the prism of soil collapse arising behind the pressure face of the wall is considered. The sliding prism is at an equilibrium by the forces of its own weight, the reaction of the retaining wall and the reaction of the rest of the granular body (Klein, 1964, Snitko, 1963, Brooks, 2018, Braja M. Das, 2007). Next, by expressing the reaction of the retaining wall from the equation and differentiating this expression by the soil collapse angle, a condition is found where earth pressure takes the maximum value. At the same time, determination of active earth pressure on each level of the wall must include taking into account the shape of the pressure face of the overlaying wall level, since ignoring this parameter can lead to significant discrepancies in calculations.

In the case of flat backfill surface under evenly distributed load and «polygonal» surface of the pressure face of the retaining wall, the value of active earth pressure E_a (kN/m) should be calculated using the formula proposed by the author (1).

$$Ea_i=\frac{\gamma}{2}\left(\sum_{j=1}^{i-1}\frac{h_j}{\cos(\varepsilon_j)}\frac{\cos(\varepsilon_j+\rho)}{\cos(\varepsilon_i+\rho)}+\frac{h_i}{\cos(\varepsilon_i)}\right)^2\frac{1}{\cos(\varepsilon_i-\varphi_s)}\lambda_i^2\left(1+\frac{2p\cos\rho}{\gamma\left(\sum_{j=1}^{i}\frac{h_j}{\cos(\varepsilon_j)}\cos(\varepsilon_j+\rho)\right)}\right)-\sum_{j=1}^{i-1}\frac{Ea_j\cos(\varepsilon_j-\varphi_s)}{\cos(\varepsilon_i-\varphi_s)} \quad (1)$$

where γ = specific gravity of soil (kN/m^3); ε = pressure face inclination angle (°); ρ = backfill surface inclination angle (°); φ_s = angle of internal soil friction on pressure face (°); h = retaining block height (m); λ_i = lateral earth pressure coefficient; p = load on original ground surface (kN/m^2); φ = internal soil friction angle (°); E_a = active earth pressure value (kN/m); i = number of the block for which active pressure is being calculated; j = sequence number of the block.

The lateral earth pressure coefficient in this case is calculated using the formula (2).

$$\lambda_i=\frac{\cos(\varepsilon_i+\rho)\cos(\varepsilon_i+\varphi-\alpha_i)}{\cos(\varepsilon_i+\rho-\alpha_i)\left(1+\sqrt{\frac{\sin(\varphi+\varphi_s-\alpha_i)\sin(\varphi-\rho)}{\cos(\varepsilon_i-\varphi_s)\cos(\varepsilon_i+\rho-\alpha_i)}}\right)} \quad (2)$$

where α_i = angle providing the transition from factual prism of collapse (with polygonal base) to arbitrary (with triangular base) (°).

This problem is directly connected to the question of determining the self-weight of the wall, since the volume of soil involved in the work of the wall (block infill and wall-adjacent prisms – Figure 1a) is separated from external surrounding soil by an arbitrary pressure face, for which active earth pressure is calculated and which is polygonal since for each row of blocks it has its own angle of deviation.

As an example, a retaining structure simple in configuration and small in height will be considered with height h = 3 m and flat horizontal infill surface (ρ = 0) upon which a load with an intensity of p = 10 kN/m^2 is evenly distributed. Specific gravity of soil γ = 19 kN/m^3, internal soil friction angle φ = 30°, angle of internal soil friction on pressure face φ_s = 20°, pressure face inclination angle of the first two blocks $\varepsilon_{1,2}$ = 11.31°, pressure face inclination angle of the third block ε_3 = 21.8° (Figure 2).

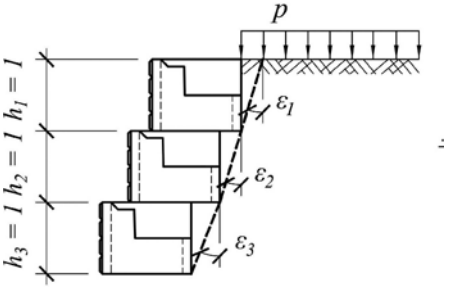

Figure 2. Retaining wall calculation scheme.

The calculation results using the formulae (1) and (2) are as follows: value of active earth pressure on the first block of the retaining structure E_{a1} = 4.36 kN/m; value of active earth pressure on the second block of the retaining structure E_{a2} = 8.62 kN/m; value of active earth pressure on the third block of the retaining structure E_{a3} = 9.32 kN/m.

A comparison of the received results and the solution obtained via the in-progress enumeration method (Civil Engineering Research Centre, Japan, 2016) proves the validity of the derived analytical expression for calculating active earth pressure value on each of the blocks of the retaining structure. The discrepancy between the received results and the results described in (Civil Engineering Research Centre, Japan, 2016) amounts to less than 1%, which

allows the use of the proposed formulae in calculating tall retaining structures of more complex configuration when the enumeration method calculation becomes irrational.

Due to the cyclicity of the procedure of determining earth pressure on the wall and the accompanying calculations it would be reasonable to form a software package allowing to automate the procedure of by-level load gathering and sequential calculations via a certain algorithm. The software must offer the selection of optimal form of the cross section of the retaining wall (number of rows, wall inclination, the presence and magnitude of recesses from row to row) depending on calculation conditions. The calculation procedure is implemented for a limited set of initial conditions in a pilot computer program (Kotik et al., 2019) for which interfacing modules are currently being developed.

3 APPLICATION PRACTICE

During the 2010-2022 period twenty-five retaining facilities implementing the described structure have been erected in the Russian Far East with the total area of 40 000 m^2 in six cities of federal and district significance, as well as a range of minor structures in the landscaping sector. The largest retaining structure built to date in Russia within city limits and comprised of infilled blocks using the proposed technology is situated in Vladivostok (Figure 1b).

The retaining wall was erected in December of the year 2010 with a maximum height of 9 m and a total area of 7668 m^2. During the more than nine-year lifetime the structure has not generated any criticism from maintenance services and supervising entities, no maintenance work on the structure is required. High operational reliability and aesthetic appeal of the structure, including greening potential and great integration into the surrounding landscape, allow the facilities of described structure to be used in low-rise and private real estate areas (Figures 3).

4 RESEARCH OBJECTIVES

Numerical modeling of retaining walls of similar constructive solutions was previously done predominantly in the plane formulation (Civil Engineering Research Centre, Japan, 2014). Taking into consideration the contemporary recommendations to calculation modeling of structures (cl. 6.1.9 SP 381.1325800.2018, cl. 5.1.10 SP 22.13330.2016, cl. 8.1.7 SP 248.1325800.2016), the task of creating a method of numerical modeling of retaining walls comprised of soil-infilled blocks in the spatial formulation with experimental verification according to the results of natural and semi-natural testing, or small-scale model testing in a laboratory environment on condition of following the provisions of similarity theory, is established. At the same time, special attention must be paid to the relevant question of delineating the conditions of medium interaction on the contact surface between the infill (representing a fundamental constructive material of the structure) and the block walls. This problem can be solved following the example of thin-walled soil-

Figure 3. Retaining structures comprised of infilled blocks with greening (Vladivostok, Russia).

infilled shell research (Bekker et al., 2015) since the hollow box represents a shell holding the infill (compacted rubble) in its designated position.

A justified numerical model will allow, first of all, to solve the problem of assessing the stress-strain state of the components of a retaining structure comprised of blocks with granular infill, and second, to create the algorithm of selecting the optimal form of the diameter (and form a set of standard solutions) depending on the purpose of the structure (technological and other loads) as well as the properties of infill, backfill and foundation soils.

5 CONCLUSIONS

The retaining structure comprised of separate thin-walled blocks with soil infill represents a promising constructive solution for civil, industrial and road construction purposes. The structure possesses an array of significant advantages which allow to shorten the construction period, avoid labor-intensive technological operations during installation, and, as a result, provide economic efficiency of the structure. It should be individually noted that the structure is well predisposed to withstanding dynamic loads (transportation vibration, impacts, seismic influences).

Despite the affirmative usage experience of erected retaining structures comprised of soil-infilled blocks (during the period from the year 2000 and onwards approximately 10 000 meters of retaining structures of this type have been erected in the Russian Far East), the scope of application is restricted by the difficulties of calculational and theoretical justification.

This article proposes a calculation formula for determining the value of active earth pressure on a retaining structure possessing a complex pressure face shape in the form of a polyline. Preliminary results of calculating active earth pressure on each of the blocks of the retaining structure have shown high convergence with results received via the enumeration method (the discrepancy value amounts to approximately 1%). Thus, the formulae suggested in this work can be used in determining active pressure on comparatively tall retaining walls with complex outline of the pressure face when employing approximate methods and methods based on value enumeration proves irrational due to their increased laboriousness.

Among the primary questions the need for forming an algorithm and an adaptation of the calculation method for Russian criteria is denoted. The research task of creating a method of numerical modeling of structures comprised of soil-infilled blocks in the spatial formulation is also established. Research must include calibration and verification of numerical models based on experimental data. The task of developing automatization means for the cyclical calculation procedure typical for this type of structure, as well as the task of forming an algorithm of selecting the optimal form of the cross section of the structure, are also established.

REFERENCES

Anderson, S 2012 Chapter 62, Types of retaining wall. In ICE Manual. London: ICE Publishing.

Tsimbelman, N Ya 2009 Hope and support. *Science and life* №8:60–65.

Construction method "Box type retaining wall". Engineering manual. – *Civil Engineering Research Centre*. Japan, August 2016 (Jap.).

Tsimbelman, N Ya, Estrin, L Z 2009 Utility model patent № 85502. Retaining wall. Publ. 10.08.2009. Bull. № 22.

Klein, G K 1964 Calculation of retaining walls. Moscow: Vishaya shkola.

Snitko, N K 1963 Static and dynamic soil pressure and calculation of retaining walls. Moscow: Gosstroyizdat.

Brooks, H 2018 Basics of retaining wall design. A design guide for earth retaining structures. 11th edition. California: HBA Publications, Inc.

Braja, M Das 2007 Fundamentals of geotechnical engineering. 3rd edition. Madrid: CL Engineering.

Kotik, Ya I, Voronov, A Iu, Zhirkov, M A, Stas, M S 2019. Computer software certificate № 2019612433 from 19.02.2019 «Calculation of retaining walls constructed with AZConcrete box-blocks».

Construction technology inspection report. Building materials/ products/ technologies, road maintenance technologies. Construction and technical inspection act №0327. Angled retaining wall with contact capability "Box retaining wall". - Civil Engineering Research Centre. Japan, March 2014 (Jap.).

Bekker, A T, Tsimbelman, N Y, Chernova, T I, Bruss, V D, Bilgin, Ö 2015 Interface Friction Parameters for the Mathematical Modeling of Shell Structures with Infill. The Proceedings of the Twenty-fifth *International Ocean and Polar Engineering Conference* (ISOPE -2015) Kona, Big Island, Hawaii, USA.

Smart Geotechnics for Smart Societies – Zhussupbekov, Sarsembayeva & Kaliakin (Eds)
© 2023 The Author(s), ISBN 978-1-003-29912-7
Open Access: www.taylorfrancis.com, CC BY-NC-ND 4.0 license

Compaction characteristics of coarse post-glacial soil improved by fiber-reinforcement and cement addition

K. Zabielska-Adamska, P. Dobrzycki & M. Wasil
Bialystok University of Technology, Bialystok, Poland

ABSTRACT: Stabilization with cement is an effective way to increase the stiffness of base and subbase layers and to improve the rutting of subgrade. Another way to improve the soil properties is to use fiber-reinforcement. The aim of the study is to investigate the effect of various percentages of cement additives: 1.5 and 3.0% and polypropylene fibers of various percentages: 0-0.3% on the compaction of post-glacial non-cohesive soil. The influence of the compaction method, the standard Proctor and the modified, was also analyzed. Problems with sample preparation were described too. The increase in the fiber and cement content resulted in an increase in the maximum dry density and a reduction in the optimum water content. The method of mixing the samples with fibers can have a significant effect on compaction parameters causing the maximum value of dry density to be underestimated.

1 INTRODUCTION

Soil compaction is characterized as the ability to achieve the maximum possible dry density, $\rho_{d\ max}$. The compaction depends on the compaction effort, the way it is used, and the type of soil and its water content. The laboratory test of soil compaction consists in its compaction in a standardized manner at different water contents and plotting the obtained results on a graph of the dependence of the soil dry density on the water content $\rho_d = f(w)$. The moisture at which compacted soil reaches its maximum dry density is called optimum water content, w_{opt}. The curves $\rho_d = f(w)$ of well-grained non-cohesive soils as well as sandy clays and clayey sands always have a well-defined peak value. The uniform sands and clays are characterized by gently sloping arches. The generally flat compaction curve applies to uniform soils, while the well-grained soil curve shows a clear maximum value.

The impact methods are the most common methods used for fine-grained soils: the standard Proctor test and the modified Proctor test, with energies corresponding to field compaction by lightweight soil compactors or heavy compactors, respectively. In the case of coarse-grained soils, the grains can be displaced instead of compacting, so according to the United States Bureau of Reclamation (USBR 5500-89), impact compaction can only take place on soils containing more than 15% of fine particles.

Cement addition influences non-cohesive soil compaction. With increasing cement percentage in the soil and cement mix, the maximum dry density increases and optimum water content decreases (Zabielska-Adamska 2008, Shooshpasha & Shirvani 2014, Choobbasti et al. 2015). Changes in compaction parameters, $\rho_{d\ max}$ and w_{opt}, after cement addition, are caused by an increase in solid particle density, a moisture content decrease, and a change in the grain-size distribution of the mix. The compaction characteristics of fiber reinforced non-cohesive soils are rather poorly presented in the literature. Silveira et al. (2021) tested the compaction of lateritic clayey sand with 0.1% and 0.25% fiber content, compared to the natural soil. The behavior of the maximum dry unit weight did slightly reduce with the fiber addition into the sandy soil, while the optimum water content did not change. The addition of 0.5% by weight of

DOI: 10.1201/9781003299127-406

fibers to fly ash resulted in decrease in maximum dry density and optimum water content (Kumar & Singh 2008). For comparison, after huge − 1-5% addition of fibers to clay a continuous reduction in the maximum dry unit weight along with an increase in the optimum moisture content was observed. This was explained by replacement of soil grains with fibers, which have less specific gravity compared with that of soil grains and the lubricating effect of absorbed water by fibers, which reduces the compaction impact (Mirzababaei et al. 2013).

Many references consider the effect of the addition of fibers or fibers and cement on the shear or tensile strength of the compacted mixture but take no notice of their impact on the compactibility, often referring only to the compaction curves of natural soils, for example (Consoli et al. 1998) or (Tang et al. 2016). The aim of the study was to explore the effect of various percentage cement additives: 1.5 and 3.0% and polypropylene fibers of 12 mm length and percentages: 0-0.3% on the compaction of post-glacial gravelly sand and show that addition strongly influenced the compaction parameters. The previous research of the authors (Zabielska-Adamska et al. 2021, 2023) has revealed the necessity of soil improvement in the case of cyclic tests. Consequently, the studies were conducted on two research samples of non-cohesive soil, cement-stabilized soils, and their mixes with different quantities of polypropylene fibers. The influence of the compaction Proctor method, the standard and modified, were also shown.

2 MATERIALS AND METHODS

The tested soil is a Pleistocene glaciofluvial soil consisting of well-rounded quartz crumbles, as well as angular grains, with a considerable addition of lytic particles and feldspars (Zabielska-Adamska et al. 2021). According to EN ISO 14688-1 standard the tested soil is gravelly sand (grSa) with the primary fraction as sand, and the secondary as gravel. Figure 1 shows the grain size distribution curve of tested soil based on the sieve analysis. The tested soil based on uniformity and curvature coefficients (Table 1) can be assessed as a material responding poorly to compaction.

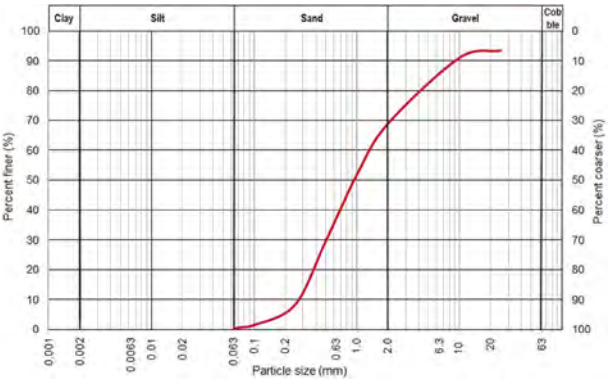

Figure 1. The gravelly sand grain-size distribution.

Table 1. Graining parameters of tested soil.

	Grain diameters (mm)			Coefficient of uniformity (−)	Coefficient of curvature (−)
Material	D_{10}	D_{30}	D_{60}	C_U	C_C
grSa	0.28	0.51	1.41	5.04	0.66

Compaction parameters, maximum dry density, $\rho_{d\ max}$, and optimum water content, w_{opt}, were founded according to the standard Proctor (SP) and modified Proctor (MP) tests, following EN

13286-2 standard. The compaction curves of gravelly sand with saturation lines are presented in Figure 2. The samples were compacted by the impact methods despite the absence of fines.

The soil and cement mix was produced with the addition of 42.5R Portland cement in the quantity of 1.5% and 3.0% of the dry mass of cement to the dry mass of soil in a tested sample. The soil and soil-cement mix with polypropylene fibers of 12 mm longest were also used. The fibers were added in amounts of 0.1%, 0.2% and 0.3% in relation to the dry mass of compacted soil. The soil or soil and cement were mixed with polypropylene fibers using a laboratory mechanical stirrer, which is of great importance for the homogeneity of the tested samples. The change in the mixing method of the samples from manual to mechanical mixing resulted in approx. 6% difference in the maximum dry density value for both compaction methods, reducing this value in the case of manual mixing (Figure 3), which is especially important for future conclusions. The polypropylene fibers are shown in Figure 4.

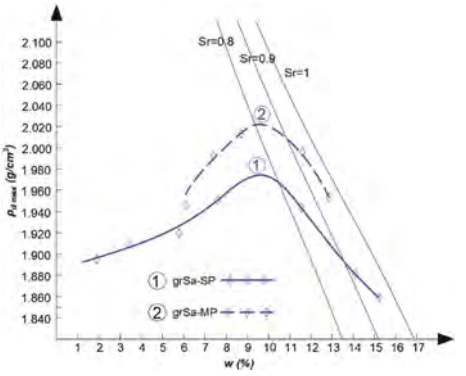

Figure 2. Compaction curves of gravelly sand by the standard (SP) and modified (MP) Proctor methods.

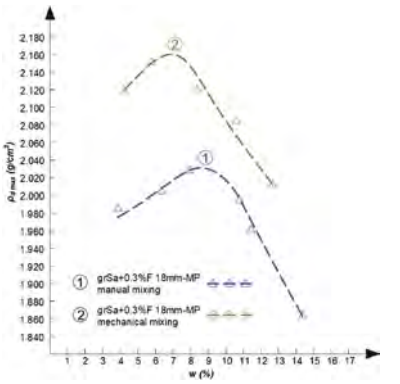

Figure 3. Compaction curves (MP) for manually and mechanically mixed soil with 0.3% fibers.

Figure 4. The polypropylene fibers with 12 mm longest added to the soil in a mass ratio of 0.1%, 0.2% and 0.3% to the dry mass of the compacted soil.

3 RESULTS AND DISCUSSION

The compaction parameters, $\rho_{d\,max}$ and w_{opt}, and specific dry density, ρ_s, of all tested materials are presented in Table 2. Figures 5−8 show the compaction curves obtained for all data set.

The cement addition to the gravelly sand increases the maximum dry densities of soil/cement mixes, while decreasing optimum water content values (Figure 5). Points ($\rho_{d\,max}$, w_{opt}) lie approximately along a line, more vertically for standard compaction than for modified.

The cement addition results in a moisture decrease by about 0.5% with a 3% addition of cement for standard compaction, and about 1% for modified. The $\rho_{d\ max}$ values increase with 3% cement addition by about 3.5% for both compaction methods.

Table 2. Compaction parameters of tested materials.

Material	ρ_s (g/cm^3)	Compaction method			
		Standard Proctor		Modified Proctor	
		w_{opt} (%)	$\rho_{d\ max}$ (g/cm^3)	w_{opt} (%)	$\rho_{d\ max}$ (g/cm^3)
grSa	2.65	9.70	1.974	9.60	2.022
grSa+1.5%C	2.66	9.50	2.010	9.50	2.070
grSa+3.0%C	2.66	9.20	2.046	8.70	2.090
grSa+0.1%F 12 mm	2.65	9.90	1.999	8.00	2.092
grSa+0.2%F 12 mm	2.85	9.60	2.020	7.70	2.134
grSa+0.3%F 12 mm	2.65	9.40	2.027	6.50	2.157
grSa+1.5%C+0.2%F 12 mm	2.66	9.40	2.075	7.90	2.150
grSa+1.5%C+0.3%F 12 mm	2.66	8.90	2.103	6.80	2.170
grSa+3.0%C+0.2%F 12 mm	2.66	8.80	2.151	8.10	2.167
grSa+3.0%C+0.3%F 12 mm	2.66	8.30	2.179	7.00	2.190

C – cement addition, F – fiber addition.

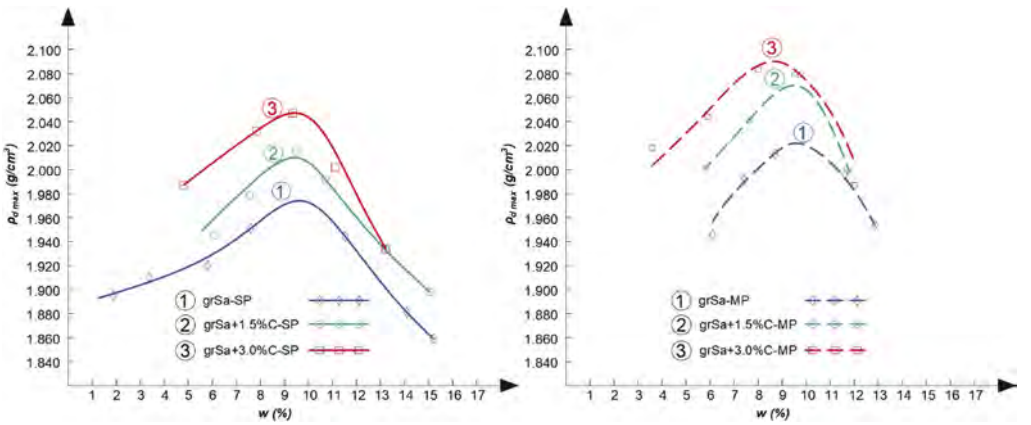

Figure 5. Compaction curves of gravelly sand with 0-3.0% cement addition: a) the SP test, b) MP test.

The fiber addition to the gravelly sand (Figure 6) influences the compaction parameters even more, especially in the case of the modified compaction. The maximum dry densities of mixes slightly increase, while reducing optimum water content values. The fiber addition results in a moisture decrease only by 0.3% with a 0.3% addition of fibers for standard compaction, and over 3% for modified. The $\rho_{d\ max}$ values increase with 0.3% fiber addition by about 3% in standard compaction, and about 7% in modified. In the case of the standard compaction of the mixture with the addition of 0.2% and 0.3% fibers, no increase in $\rho_{d\ max}$ was found. A similar relationship was found in the authors' own research of soil mixtures with 18 mm long fibers (Zabielska-Adamska et al. 2023). Probably more fibers make it difficult to move the soil when compacted with less energy. Therefore, the compaction of a soil-fiber mixture is more effective with the modified Proctor method.

The effect of the increase in compaction in the case of a mixture of soil, cement and fibers is much greater than in the case of each of the factors separately for both compaction methods. The addition of 0.3% of fibers and 1.5% of cement raises the maximum dry density by about 7% (Figure 7). Increasing the cement to 3% enhances the maximum density by about 10% (Figure 8).

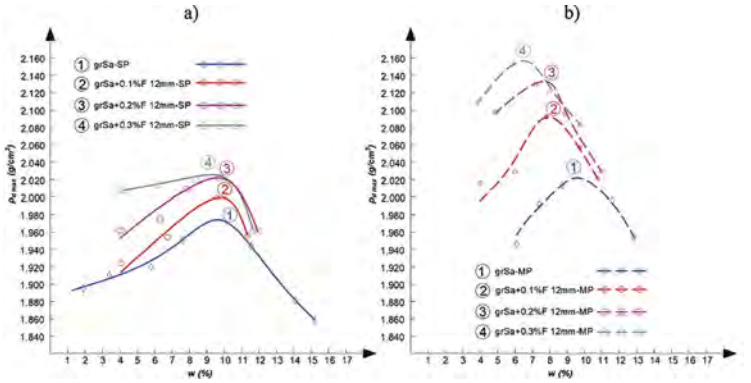

Figure 6. Compaction curves of gravelly sand with 0-0.3% fiber addition: a) the SP test, b) the MP test.

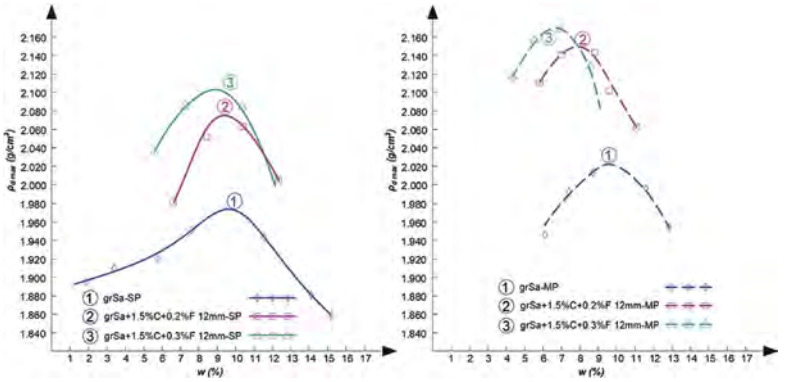

Figure 7. Compaction curves of gravelly sand with 1.5% cement and 0.2-0.3% fiber addition compared to natural soil: a) the SP test, b) the MP test.

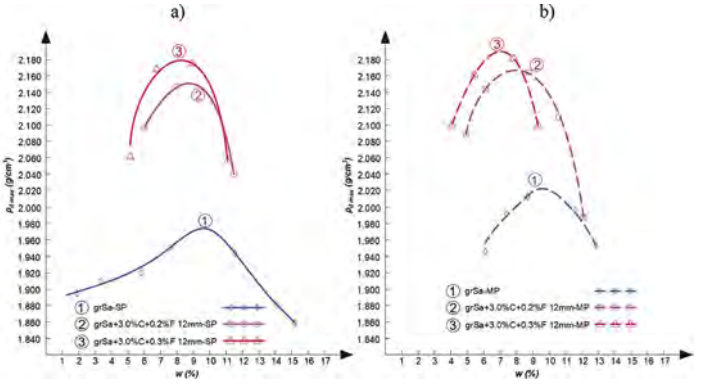

Figure 8. Compaction curves of gravelly sand with 3.0% cement and 0.2-0.3% fiber addition compared to natural soil: a) the SP test, b) the MP test.

Therefore, one cannot agree with the literature reports that the addition of fibers or fibers and cement slightly influences the compaction parameters or even lowers them. The reduction in maximum dry density after the addition of fibers may have been due to insufficient homogenization of the samples. Inaccurate mixing of samples with fibers causes the maximum value of dry density to be underestimated (Figure 3), which eliminates the effect of the additive on density.

4 CONCLUSIONS

Based on the compaction results of gravelly sand in a natural state and improved by polypropylene fiber and/or cement addition, the following conclusions are made:

1. The cement addition influences the compactibility of the gravelly sand. With increasing cement percentage in the mix, the maximum dry density increases and optimum water content decreases. Changes in compaction parameters are caused, among others, by increasing the solid particle density and adding fines to the mixture.
2. The fiber addition increases the maximum dry density and reduces the optimum water content, which is more evident in the modified Proctor compaction. With standard compaction energy, more fibers make it difficult to compact the mixture.
3. The effect of increasing compaction in the case of the mixture of soil, cement and fibers is far greater than for each of the factors separately for both methods of compaction.
4. The method of mixing the samples with fibers can have a significant impact on the compaction parameters. Manual mixing causes insufficient homogenization of the sample, which leads to an underestimation of the maximum dry density value.

REFERENCES

Choobbasti, A.J, Vafaei, A., Kutanaei, S.S. 2015. Mechanical properties of sandy soil improved with cement and nanosilica. *Open Engineering* 5: 111–116.

Consoli, N.C., Prietto, P.D.M., Ulbrich, L.A. 1998. Influence of fiber and cement addition on behavior of sandy soil. *Journal of Geotechnical and Geoenvironmental Engineering* 124: 1211–1214.

Kumar, P., Singh, S.P. 2008. Fiber-reinforced fly ash subbases in rural roads. *Journal of Transportation Engineering* 134: 171–180.

Mirzababaei, M., Miraftab, M., Mohamed, M., McMahon, P. 2013. Unconfined compression strength of reinforced clays with carpet waste fibers. *Journal of Geotechnical and Geoenvironmental Engineering* 139: 483–493.

Silveira, M.R., Rocha, S.A., Correia, N.D.S., Rodrigues, R.A., Giacheti, H.L., Lodi, P.C. 2021. Effect of polypropylene fibers on the shear strength–dilation behavior of compacted lateritic soils. *Sustainability* 13: 12603.

Shooshpasha, I., Shirvani, R.A. 2014. Effect of cement stabilization on geotechnical properties of sandy soils. *Geomechanics and Engineering* 8: 17–31.

Tang, C.S., Wang, D.Y., Cui, Y.J., Shi, B., Li, J. 2016. Tensile strength of fiber-reinforced soil. *Journal of Materials in Civil Engineering* 28: 04016031.

USBR 5500-89. 1990. *Performing laboratory compaction of soils—5.5-lbm rammer and 18-in drop*. Bureau of Reclamation Earth Manual, Part 2, 3rd Edition.

Zabielska-Adamska, K. 2008. Laboratory compaction of fly ash and fly ash with cement addition. *Journal of Hazardous Material* 151: 48–489.

Zabielska-Adamska, K., Wasil, M., Dobrzycki, P. 2021. Resilient response of cement-treated coarse post-glacial soil to cyclic load. *Materials* 14: 6495.

Zabielska-Adamska, K., Dobrzycki, P., Wasil, M. 2023. Estimation of stiffness of non-cohesive soil in natural state and improved by fiber and/or cement addition in different load conditions. *Materials* 15: 417.

Smart Geotechnics for Smart Societies – Zhussupbekov, Sarsembayeva & Kaliakin (Eds)
© 2023 The Author(s), ISBN 978-1-003-29912-7
Open Access: www.taylorfrancis.com, CC BY-NC-ND 4.0 license

Experimental test and numerical simulation on static and dynamic characteristics of new pile-supported slab subgrade structure in high-speed railway

Xiao Hong, Jin Feng & Fang Jia
Beijing Jiaotong University, Beijing, China

Hu Fei
CIECC Overseas Consulting Company Limited, Beijing, China

ABSTRACT: Pile-supported slab is a new type of subgrade structure, its working characteristics are still unclear. Based on the model similarity theory, the static horizontal loading model experiments and dynamic vertical excitation experiments of two spans were carried out. The characteristics of pile-supported slab are analyzed through the coupling model of train and pile-supported slab. The results show that: (1) The subgrade soil has an obvious horizontal restraint effect on the pile, and the variation of pile-soil interaction along the pile is different from bridge pile foundation. (2) Under the vertical excitation load, the supporting effect of the lower soil on the supported slab is obvious. (3) The pile, slab and soil of pile-supported slab have complex interaction, and the state equilibrium achieved after a certain number of dynamic actions. In general, the design of pile-supported slab adopted by high-speed railway is redundant, which has a lot of optimization space.

1 INTRODUCTION

The pile-supported slab is a new type of track substructure, which is mainly used in special sections such as transition zones between subgrade and rigid structures(Li et al. 2020), soft soil sections (Huang et al. 2015), etc. to provide better stability(Chen et al. 2014) and control the foundation differential settlement(Shan et al. 2021). The schematic diagram of the structure is shown in Figure 1. Currently, there are some engineering applications in several countries, such as Germany(Wang et al. 2006), Netherlands (Woldringh et al. 1999, Bachmann et al. 2003), China(Wei 2008, Wang et al. 2012), Korea (Lee et al.e 2013) and Africa (Messioud et al. 2017). However, due to the complexity of its working mechanism, the pile-slab structure is often designed based on field conditions with empirical design or based on experimental results (Wang et al. 2012). For example, the pile-slab structure of the Dutch high-speed railway is designed based on the experimental results of the Technical University Munich. In China, engineers mostly adopt a conservative design, without considering the supporting effect of the soil under the slab and the lateral restriction effect of subgrade soil the same as the design of the bridge. These restrict the popularization and application of pile-slab structure seriously. In fact, pile-slab structure differs from bridge structure and subgrade structure. Its resistance comes from the interaction between the pile, slab, and subgrade soil, which meets the engineering requirements.

For pile-slab structure, the key factors are the supporting effect on infrastructure slab and lateral restriction on pile foundation from subgrade soil. To find pile-soil and slab-soil interaction mechanisms, static horizontal loading tests and dynamic vertical exciter tests were designed. We intended to identify the law of pile-soil and slab-soil interaction under loading

DOI: 10.1201/9781003299127-407

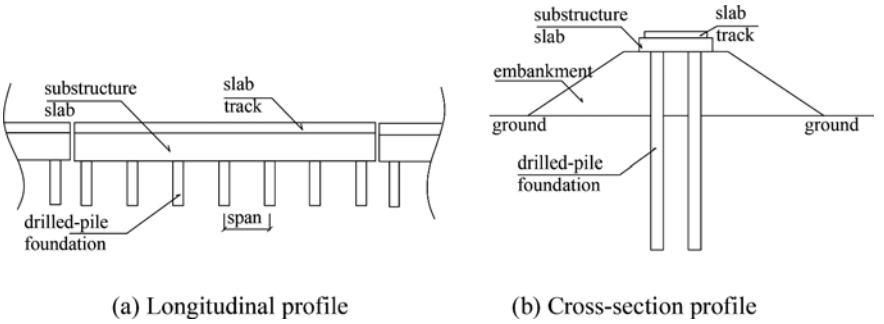

Figure 1. Sketch of pile-slab structure.

action by model testing, to provide theoretical guidance for the rational design of the pile-slab structure.

2 SCHEME OF MODEL TESTING

2.1 *Testing purposes*

The main purposes of these model testing are: ①mechanical behaviors of slab-soil interaction, including variation tendency of the supporting performance of soil under various loads; ②mechanical properties of pile-soil interaction, including pile-soil contact force variation with pile depth; ③effect of different spans on infrastructure slab; ④mechanical properties of slab with soil support under the slab and without soil; ⑤distribution of stress and of slab and pile.

2.2 *Similarity ratio of model*

After comprehensively considering the economy, model dimension size, the performance of loading equipment, and maneuverability, we chose 1:20 as the similarity ratio of the model. To satisfy the similarity of main parameters, such as actual stiffness and surface roughness of pile-soil, cohesive strength, and internal friction angle of soil in the embankment, we used prototype materials of pile and soil in the model testing. To be specific, we used a reinforced concrete grouting pile, whose strength grade is C30. Because the parameters of sand are clear, we chose sand as model soil. Taking compactness of subgrade and engineering practice into consideration, we chose the parameters of sand in the model testing as follows: moisture content is 11%, compactness is 93%, and dry density is 1.836 g/cm^3, so the calculated density $\rho = \rho_d(1+w) = 1.836\times(1+11\%) = 2.038$ g/cm^3.

2.3 *Model dimensions and manufacture*

2.3.1 *Model dimensions*

Considering the actual structure used in engineering practice, we chose a pile-slab structure with spans of 5.0m and 7.5m as the prototype, and designed two groups of model testing correspondingly, as shown in Figure 2.

2.3.2 *Model manufacture*

The track structure is the double-block ballastless track, and dimensions are as follows: length is 4.856m, width is 2.80m, thickness is 0.35m, and strength grade of concrete is C40. The sizes of infrastructure slab of the pile-slab structure are: length is 30.0m, width is 4.40m, height is 0.60m, strength grade of concrete is C40.

For convenience and rational reinforcement when making models, the ballastless track and infrastructure slab were poured together. ①Length: according to the pile-slab structure of 5m

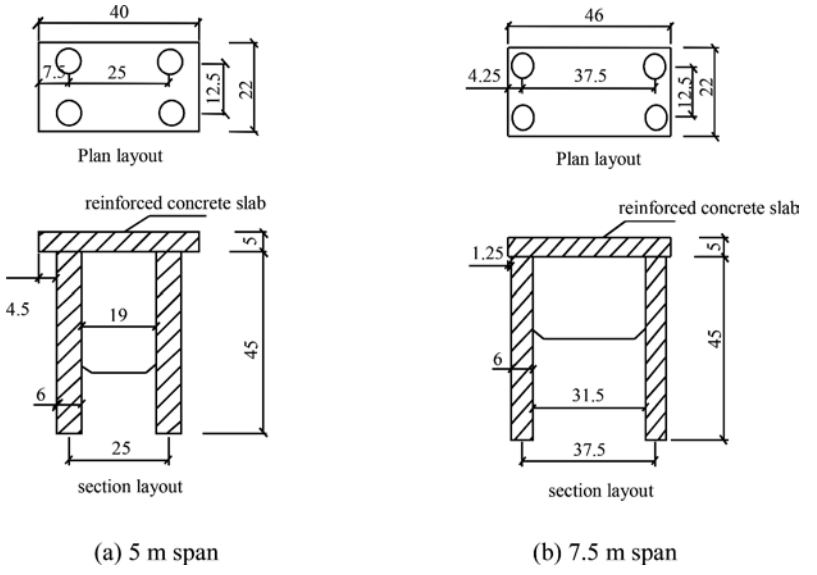

Figure 2. Sketch of pile-slab structural model (unit: cm).

and 7.5m spans, model spans are 500/20=25cm and 750/20=37.5cm. ②Width: width of the infrastructure slab is 4.4m, so the model width is 440/20=22cm. ③Thickness: the total thickness of the track and infrastructure slab is 0.35+0.6=0.95m, so the model thickness is 95/20 = 4.75cm ≈5cm. ④Gauge is 1500mm/20=75mm.

3 STATIC HORIZONTAL LOADING TEST

3.1 *Experiment scheme*

To eliminate the boundary effect under horizontal loading, these experiments were conducted on a horizontal ground of a natural foundation. Firstly, place the model into an empty hole and fill it with sand, ensuring the density of the soil body near the hole is consistent with the actual situation, then apply horizontal load. There are five levels of loading forces that are 1.15kN, 1.47kN, 1.96kN, 2.33kN, and 2.77kN. The following experimental data is obtained after stabilization of the structures, which are all applied load until 2.77kN. The sketch of loading and layout of measuring points are shown in Figure 3.

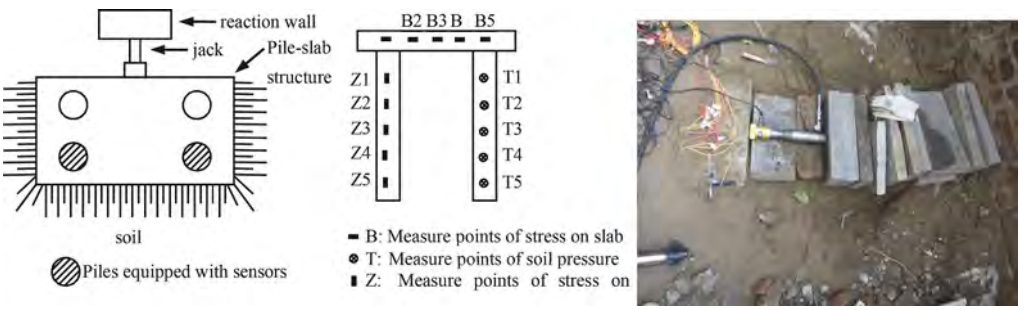

Figure 3. Layout of sensors for lateral loading.

3.2 *Analysis of experimental data*

3.2.1 *Pile-soil interaction forces*

The pile-soil interaction stresses of the two experimental models are shown in Figure 4. As is shown in Figure 4, pile-soil interaction of pile-slab structure with 5.0m and 7.5m spans both decreases rapidly with increasing depth, variation tendency of two spans is basically the same and influenced range is mainly the upper half of the pile. It can also be seen that the interaction stress of a 7.5m span is 4.275% more than the stress of a 5m span, which shows that span has little effect on pile-soil interaction under lateral loads.

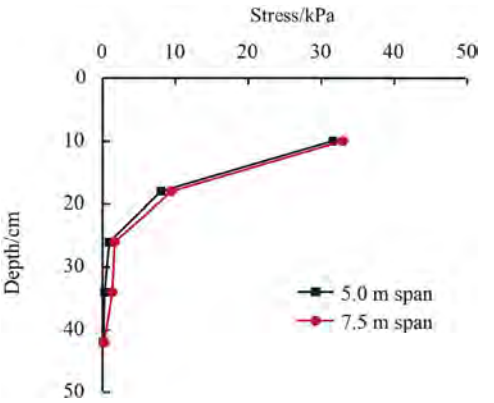

Figure 4. Variation tendency of pile-soil interaction forces with pile depth.

3.2.2 *Stresses of infrastructure slab*

The measured stresses infrastructure slabs are shown in Figure 5.

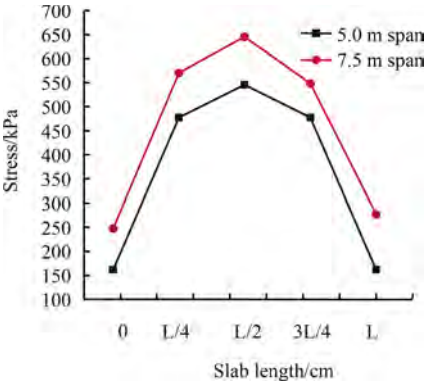

Figure 5. Variation tendency between lateral stress and length.

As can be seen from Figure 5, the variation tendency between lateral stress and length of these two spans under lateral load is basically the same, which likes a parabolic curve, and the maximum stress occurs in mid-span. It can be seen that the stress of slab with a 7.5m span is 19.266% more than the stress of a 5m span. It clears that the larger the span of pile-slab structure is, the greater the bending-tensile stress of the slab under lateral load. Obviously, in the design of the pile-slab structure at the curve section, if the unbalanced centrifugal force is very large, the stress of the infrastructure slab at mid-span should be checked.

3.2.3 *Bending stress of pile*

Measured bending stresses of piles under lateral load are shown in Figure 6. As can be seen from the figure, under lateral load, pile bending stresses of two spans both increase at first and then decrease, and their variation tendency is the same. This curve shape shows that the pile-soil interaction of pile-slab structure is obvious, and horizontal resistance is significant. Its mechanical behaviors are different from those of pile foundation in bridge and influenced range is mainly the upper half of the pile. As can be seen from the experimental data in Figure 6, pile stresses of the two spans have little difference, which means the spans of the pile-slab structure have little effect on the bending stress of the pile under lateral load.

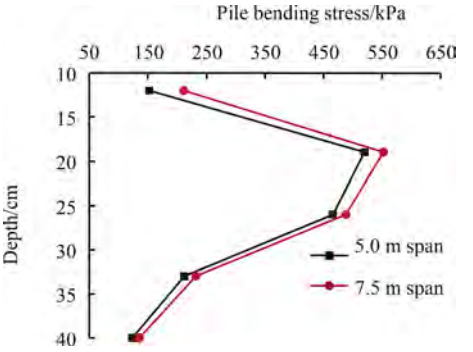

Figure 6. Relationship between pile bending stress and depth.

4 DYNAMIC VERTICAL EXCITATION TEST

4.1 *Experiment scheme*

Spans of corresponding prototypes of model testing were 5.0m and 7.5m, and loading frequency was 5Hz, using sinusoidal load with a dynamic amplitude of 2.97kN. Firstly, model testing with soil supporting was conducted, then soil under the slab was excavated (hereinafter called soilless supporting), making the slab separate from the soil, then a soilless supporting experiment was conducted. The layout of the sensors is shown in Figure 7.

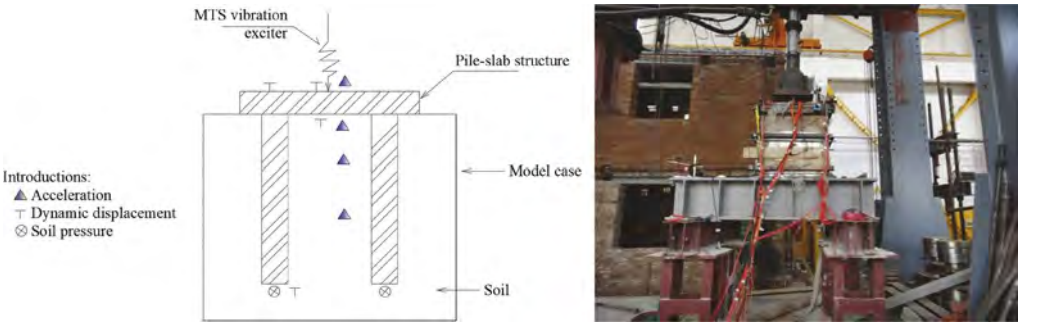

Figure 7. Layout of sensors for vertical excitation test.

4.2 *Analysis of experimental data*

4.2.1 *Acceleration of slab*

As the acceleration sensors buried in model soil were damaged when filling the soil, only the acceleration on the up of slab can be analyzed, which is shown in Figure 8.

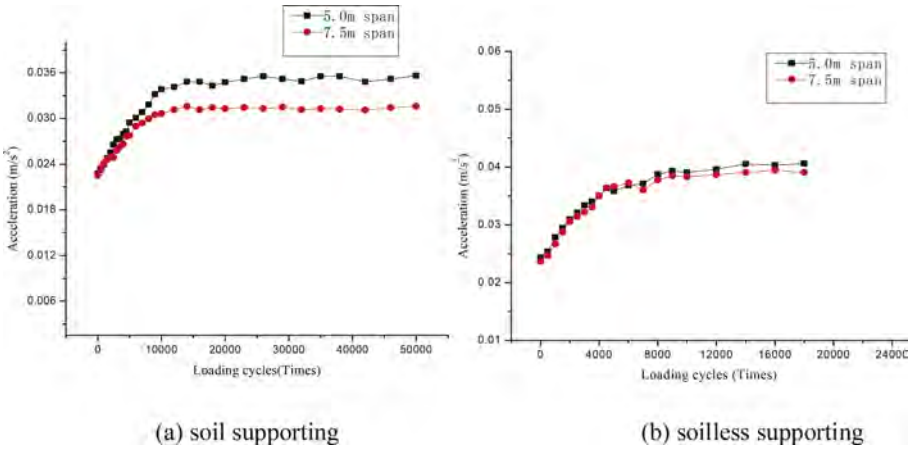

Figure 8. Relationship between acceleration of slab and loading cycles.

As can be seen from Figure 8, the relationship between acceleration and loading cycles of a 5.0m span is like that of a 7.5m span. They both have an early stage where acceleration increases with the increase of loading cycles, and it stabilizes after a certain number of loading times. In the case of soil supporting, 5.0m span stabilizes after 12000 loading times, and 7.5m span stabilizes after 14000 loading times. For the condition without soil support, the two models both stabilize after 6000 loading times. There is an obvious interaction between pile and soil under soil supporting conditions, and this structure needs more loading cycles to reach equilibrium.

It can be seen from the experimental data that, the acceleration of a 5.0m span is larger than that of a 7.5m span. Comparing the data after stabilization, it is not hard to find that, under soil supporting conditions, acceleration of 5.0m span is 12.0% larger than that of 7.5m span; under soilless supporting condition, acceleration of 5m span is 2.2% larger than that of 7.5m span. This is because the smaller the span is, the larger the stiffness of the structure, then the acceleration will be larger when other conditions are the same.

4.2.2 *Dynamic displacement of mid-span*
Measured data is shown in Figure 9.

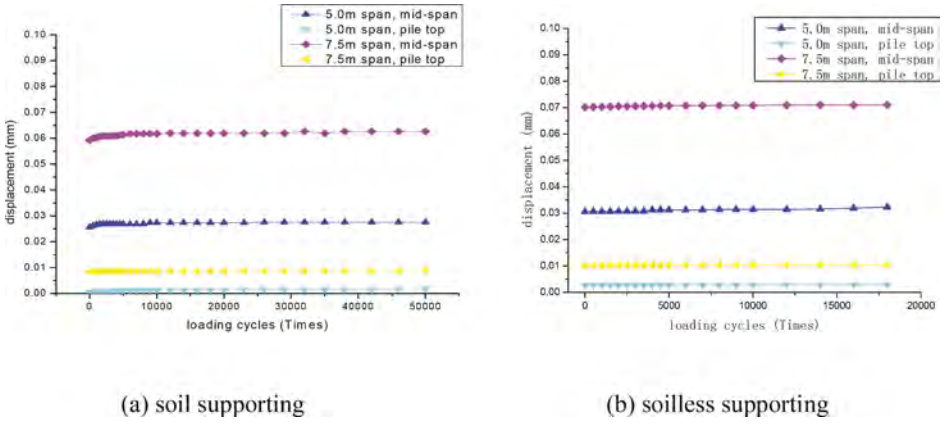

Figure 9. Relationships between loading cycles and dynamic displacement of pile top and mid-span of infrastructure slab.

As can be seen from Figure 9, the relationship between dynamic displacement and loading cycles of a 5.0m span is similar to that of a 7.5m span, the displacement of mid-span is larger than that of pile top.

It can also be seen that dynamic displacement of mid-span of 5.0m span is larger than that of 7.5m span. Comparing the data after 50000 loading cycles, under soil supporting conditions, dynamic displacement of mid-span of 7.5m span is 1.3 times larger than that of 5.0m span. Comparing the data after 20000 loading cycles, under soilless supporting condition, dynamic displacement of mid-span of 7.5m span is 1.2 times larger than that of 5.0m span. This is because the larger the span is, the smaller the stiffness of the structure, then the dynamic displacement will be larger when other conditions are the same. Moreover, comparing soilless supporting with soil supporting, the former stabilizes more quickly.

In addition, comparing two supporting conditions, the results show that the dynamic displacement of a 5.0 m span of soil supporting is 0.0048mm less than that of soilless support. The soil under the slab has an obvious supporting effect on the pile-slab structure and decreases the dynamic displacement of the slab effectively, and the larger the span is, the more obvious the supporting effect. Obviously, as for train ride comfort, the supporting effect of soil under the slab is beneficial to high-speed rail running.

4.2.3 *Soil pressure at the bottom of pile*

Measured data of soil pressure under pile bottom is shown in Figure 10.

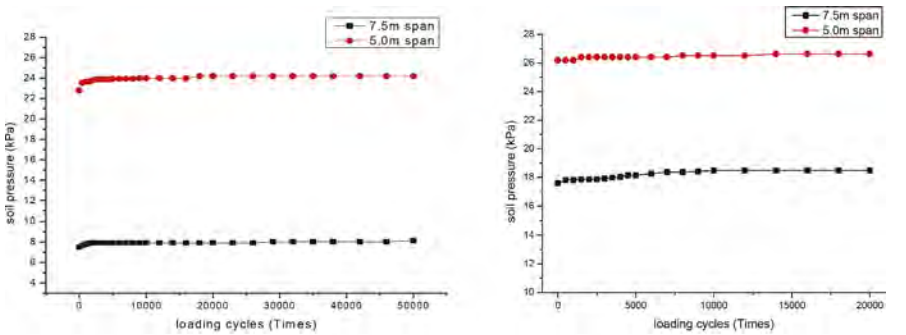

Figure 10. Relationship between loading cycles and soil pressure under pile bottom.

As can be seen from Figure 10, the relationship between loading cycles and soil pressure under pile bottom of 5.0m span is like that of 7.5m span. Both have an early stage that soil pressure increases with the increase of loading cycles, and they stabilize after a certain number of loading times.

It shows from the measured data that, soil pressure of mid-span of 5.0m span is obviously larger than that of 7.5m span. Comparing the data of stabilization after 50000 loading cycles, under soil supporting conditions, soil pressure of mid-span of 5.0m span is 2.08 times larger than that of 7.5m span. Comparing the data after 20000 loading cycles, under soilless supporting conditions, soil pressure of mid-span of 5.0m span is 39.08% larger than that of 7.5m span. This is because the larger the span is, the smaller the stiffness of the structure, and the more significant pile-soil interaction, the soil pressure under the pile is smaller when other conditions are the same.

In addition, comparing soil supporting with soilless supporting, for a 5.0m span, soil pressure of soilless supporting is 10% larger than that of soil supporting; for a 7.5m span, soil pressure of soilless supporting is about 1.42 times larger than that of soil support. The soil under the slab has an obvious supporting effect on the infrastructure slab, and the larger the span is,

the more obvious the supporting effect. The spans of engineering practices are as follows, the span of the Dutch high-speed railway is 5m(Bachmann et al. 2003), the spans of the Sui-Yu railway in China are 5m and 10m(Wei 2008), and the span of the Zhengzhou-Xi'an high-speed railway is 7m(Wang et al. 2012). Because the soil has an obvious supporting effect on structures with such spans, pile-slab structures with such spans should be considered in engineering design.

5 CONCLUSIONS

(1) Under the horizontal load, the pile-soil interaction is obvious. The test data show that the subgrade soil has an obvious horizontal restraint effect on the pile foundation, the bending stress of the pile shows a trend of first increasing and then decreasing, and the main action area is within the upper half of the pile, which is different from bridge structures.

(2) Under the action of horizontal load, the force and deformation laws of pile-slab structures with different spans are basically the same. The interaction stress of a 7.5m span is 4.275% more than the stress of a 5m span, and the stress of slab with a 7.5m span is 19.266% more than the stress of a 5m span. The span size has little effect on the force of the pile but has a great influence on the force of the slab. According to the test results, it is suggested that when designing the pile-slab structure in the curved section, if the centrifugal force of the uneven horizontal is large, the transverse bending stress at the mid-span position of the bearing slab should be checked.

(3) Under the vertical cyclic load, the acceleration, dynamic displacement, and pile subsoil pressure of the pile-supported slab have certain changes at the initial stage of loading, and the test values tend to be stable with the increase of loading times. Among them, the number of stabilization required by soil bearing is obviously larger than that without soil bearing. The results show that there is a complex interaction between pile, slab and soil in the pile-supported slab under dynamic load, and the state equilibrium will be reached after a certain number of dynamic cycles.

(4) The span of the slab has an obvious influence on pile-supported slab under the vertical cyclic load. The acceleration value of the 5m span is 12.0% larger than that of the 7.5m span. The mid-span displacement of the pile of 7.5m span is 1.3 times larger than that of a 5m span. The bottom stress of a 5m span is 2.08 times higher than a 7.5m span. It can be concluded from the results that the larger the span, the smaller the stiffness of the structure, and the more significant the interaction between the slab and the lower soil. From the economic point of view of engineering design, the bearing resistance of soil under pile slab structure should be considered in the design.

(5) The supporting with or without soil has an obvious effect on the pile-slab structure under the vertical cyclic load. The acceleration in the case of soilless supporting is apparently larger than that of soil support. The acceleration value of the 5m bearing slab span is 16.5% larger when without the soil supporting while the 7.5m bearing slab span is 25.3% larger. The mid-span dynamic displacement of the bearing slab increases significantly. In the unsupported state, it increases by 17.4% when the bearing slab span is 5m, and increases by 13.4% when the bearing slab span is 7.5m. The soil pressure at the bottom of the pile increases significantly, with an increase of 10% when the span of the bearing slab is 5m, and an increase of 1.42 times when the span is 7.5m. The soil under the slab has an obvious supporting effect on the bearing slab, and the larger the span is, the more obvious the supporting effect is. It is suggested that the structure should adopt a pile-slab structure with a larger span as far as possible under the condition of meeting the resistance, to give full play to the supporting effect of the soil.

ACKNOWLEDGEMENTS

This work was financially supported by the Fundamental Research Funds for the Central Universities (Science and technology leading talent team project) No. 2022JBXT010 and

Science and technology project of Shandong Railway Investment Holding Group Co.,Ltd. (grant number TTKJ2021-07).

REFERENCES

Bachmann, H., Mohr, W. & Kowalski, M. 2003. The Rheda 2000 ballastless track system. *European Railway Review* (1).

Chen, H., Xu, S. H. & Zhang, B. Q. 2014. Reinforcement Effectiveness Analysis of Road Pile-Plank Structure in Soft Soil Area. *In Applied Mechanics and Materials* Trans Tech Publications Ltd. 482: 227–232.

Huang, J., Su, Q., Liu, T. & Wang, X. 2015. Vibration and long-term performance analysis of pile-plank-supported low subgrade of ballastless track under excitation loads. *Shock and Vibration* (2015).

Lee, I. W., Lee, S. J., Lee, S. H. & Lee, K. M. 2013. Wave propagation on a high-speed railway embankment using a pile-slab structure. *Journal of the Korean society for railway* 16(4): 278–285.

Li, S., Wei, L., Chen, X. & He, Q. 2020. Numerical investigation on dynamic performance of a bridge-tunnel transition section with a deep buried pile-plank structure. *Advances in Civil Engineering* (2020).

Messioud, S., Sbartai, B. & Dias, D. 2017. Estimation of dynamic impedance of the soil–pile–slab and soil–pile–mattress–slab systems. *International journal of structural stability and dynamics* 17(6): 1750057.

Shan, Y., Zhou, X. & Zhou, S. 2021. One-dimensional semi-analytical model on longitudinal thermal loads of a tram track pile-plank structure buried beneath the pavement. *Archives of Civil and Mechanical Engineering* 21(1): 1–18.

Wang, X., Su, Q. & Xiao, H. 2012. Field Test Research of Pile-Plank Structure on Zhengzhou-Xi'an High-Speed Rail. *In Advanced Materials Research* Trans Tech Publications Ltd. 354: 109–113.

Wang, Z.W. & Xu, H.S. 2006. Ballastless Track on Nuremberg——Ingolstadt Germany New Line [J]. *Chinese Railways* (6): 21–24

Wei, Y.X. 2008. Study on pile-slab structure subgrade for ballastless track of passenger dedicated line. *Journal of Railway Engineering Society* 4: 19–22.

Woldringh, R. F. & New, B. M. 1999. Embankment design for high speed trains on soft soils Conception de remblais sur sols meubles pour les chemins de fer à grande vitesse. *Geotechnical Engineering for Transportation Infrastructure*, Barends et al. (eds).

Smart Geotechnics for Smart Societies – Zhussupbekov, Sarsembayeva & Kaliakin (Eds)
© 2023 The Author(s), ISBN 978-1-003-29912-7
Open Access: www.taylorfrancis.com, CC BY-NC-ND 4.0 license

Numerical investigation of the ultimate bearing capacity of geosynthetic-reinforced soil abutments

Chongxi Zhao
Department of Geotechnical Engineering, Tongji University, Shanghai, China

Chao Xu
Key Laboratory of Geotechnical and Underground Engineering of Ministry of Education, Tongji University, Shanghai, China

Qingming Wang
Department of Geotechnical Engineering, Tongji University, Shanghai, China

ABSTRACT: In this work, a series of 2D numerical models of geosynthetic-reinforced soil (GRS) abutment based on centrifugal model test were established to study the characteristics of GRS abutment ultimate bearing capacity and related influencing factors. Firstly, the numerical model was calibrated and verified against the test results of centrifugal model test. Subsequently, parametric studies were carried out to investigate the influence of reinforcement strength, setback distance and beam seat width on the ultimate bearing capacity of the GRS abutment. The results show that reducing the reinforcement strength or increasing the beam seat width weakened the ultimate bearing capacity. While, increasing the setback distance within 0.3 times of abutment height increased the ultimate bearing capacity of GRS abutment. In addition, the response of stress distribution, lateral displacement and max tension of reinforcement to above factors was also discussed based on numerical results.

1 INTRODUCTION

Geosynthetic reinforced soil integrated bridge system (GRS-IBS) is an effective scheme to reduce the bump at the intersection of approach and bridge beam and prolong the service life of abutment (Adams et al. 2011; Adams & Nicks 2018). As the structure bearing the load of the bridge superstructure, it is of great significance to understand the bearing performance of GRS abutments. Previous field tests and laboratory tests have confirmed that the GRS abutments have a relatively high ultimate bearing capacity (Wu et al. 2006, 2008). Researches showed that the high bearing capacity of GRS abutments mainly attributes to the closely arrangement, usually less than 0.3m, of geosynthetics (Wu & Pham 2013). The field test results of mini-pier tests showed that the setback distance, the dimension of abutment bearing area, the height of reinforced soil abutment and other dimensional factors have a certain impact on the bearing capacity of GRS abutments (Adams et al. 2007; Nicks et al. 2016). However, due to the mini-pier tests were carried out under uniform axial load, further research on the above influence factors still needs to be conducted concentrating on GRS abutment under local load. Researchers have carried out many reduced-scale model tests of GRS abutments, and results indicate that the effect of reinforcement spacing on the stability of abutment is more significant (Xu et al. 2019). Increasing the setback distance will also increase the ultimate bearing capacity of the GRS abutment, but no longer impact when the setback distance increases to a certain threshold (Xiao et al. 2016). Through both reduced-scale model and large-scale

DOI: 10.1201/9781003299127-408

model tests, it was clarified that the GRS abutments adopting large facing block have obviously strong bearing capacity (Hatami & Doger 2021a, b). And the abutments adopting full height panel facing have stronger bearing capacity than the abutments adopting modular facing or wrapped facing (Zhang et al. 2022). The numerical simulation study showed that the reinforcement spacing and the fill properties have a great impact on the ultimate bearing capacity of GRS abutments (Helwany et al. 1999; Zheng & Fox 2017; Zheng et al. 2018). Although plenty of factors have been considered to study their influence on the ultimate bearing capacity of GRS abutments, the influence of the geometric characteristics of the abutments has not been clearly explored. In this study, FLAC 2D software was used to establish the numerical model of GRS abutment in plane strain state to study its ultimate bearing capacity and the distribution of earth pressure under the limit state. The baseline case was compared with centrifugal model test to verify the rationality of the model. Subsequent parameter studies included the effects of reinforcement strength and abutment geometry. The results obtained in this research are expected to enhance the understandings of bearing capacity of GRS abutments.

2 NUMERICAL MODEL

2.1 *Model geometry*

A centrifuge model of a GRS abutment which was tested at 10g (Figure 1a) was amplified in 10 times and used as the model of the numerical simulation baseline group. The centrifugal test model includes Concrete Masonry Unit (CMU) facing blocks, backfill and reinforcement. The baseline model had a total wall height of H = 6 m, and 30 modular facing blocks with 0.2 m in length and 0.2 m in height. A beam seat with a thickness of 0.2 m and a length of 1 m was set on the top of the GRS fill. The horizontal distance between the beam seat and the wall facing, that is, the setback distance, was 0.2 m. Linear Variable Displacement Transducer (LVDT), strain gauges and earth pressure gauges were set in the model as shown in Figure 1a to monitor the lateral displacement of the facing block, reinforcement strain and earth pressure respectively. Figure 1b shows the mesh of the numerical model. The numerical model adopted uniform reinforcement length of 4.2 m (0.7H), and the vertical spacing was 0.2 m. The lateral boundaries of the model were set with horizontal constraints, but allowed to move in the vertical direction. The bottom boundary was fixed in both horizontal and vertical directions.

2.2 *Constitutive models and properties*

A linearly-elastic perfectly-plastic Mohr-Coulomb (MC) constitutive model was adopted to define the backfill soil and retained soil in numerical model. According to centrifuge test and laboratory test results, a dry density of 1750 kg/m^3, a friction angle ϕ of 38° and a cohesion c of 0 kPa were adopted in the numerical models. Recommended by Coduto (2015), An elastic modulus of 20 MPa and a Poisson's ratio of 0.25 were used. The value of the dilatancy angle ψ was determined as 8° according to the empirical relationship of $\psi = \phi$ - 30° recommended by Bolton (1986).

Reinforcements were modeled using different linearly elastic structural elements depending on their location. For reinforcements between two CMU blocks, the beam structural elements with zero moment of inertia were used, while for reinforcements embedded in backfill, the cable structural elements were used. There were two types of reinforcement used in this study. Amplifying the wide-width tensile test results of the geotextile used in centrifugal test in 10 times, the reinforcement used in baseline group, recorded as G1, had a tensile stiffness of 850 kN/m at a tensile strain of 2% and an ultimate tensile strength of T_{ult} = 63 kN/m. The other reinforcement used in parameter study, recorded as WS, was a type of window screen and had a tensile stiffness of 160 kN/m at a tensile strain of 2% and an ultimate tensile strength of T_{ult} = 20 kN/m based on wide-width tensile test. Assuming that the thickness of

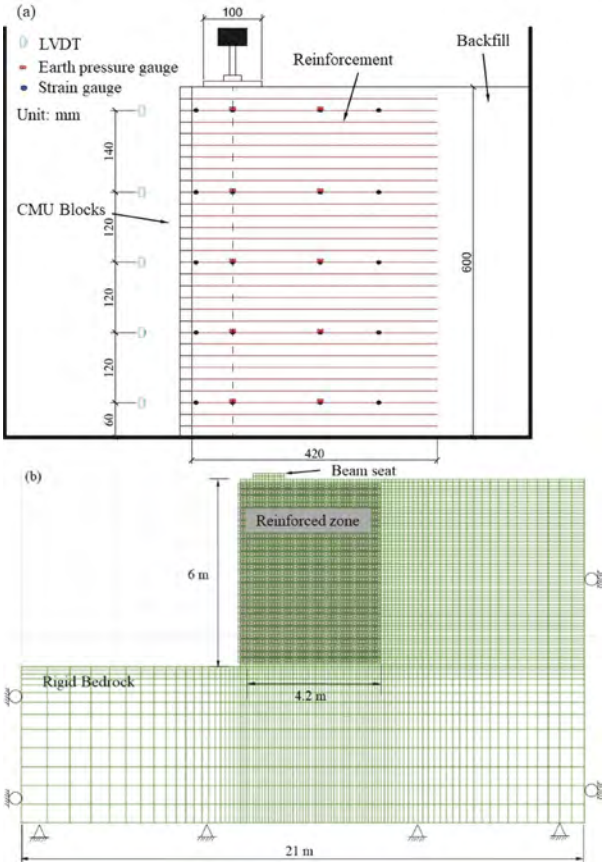

Figure 1. Layouts of the GRS abutment model: (a) cross-section and monitoring arrangement of the centrifuge model; (b) numerical model mesh for the baseline case.

the structural elements is 1 mm and the width were 1 m, the elastic modulus of the two kinds of reinforcement were 850 MPa and 160MPa respectively, calculated by dividing tensile stiffness by the sectional area.

The bedrock, CMU blocks and beam seat slab were all modeled by linear-elastic constitutive. Their input parameters are listed in the Table 1.

Table 1. Input parameters for bedrock, CMU blocks and beam seat slab.

Components	Density (kg/m^3)	Elastic modulus (MPa)	Poisson's ratio
Bedrock	2000	2000	0.2
CMU block	1800	20000	0.15
Beam seat slab	9600*	2000	0.15

*Calculated according to the dead load stress of the beam seat slab of 20 kPa.

2.3 *Interfaces*

The reinforcement-soil interaction was simulated by the embedded grout annulus around the cable structural elements, while the reinforcement-block interaction was simulated by linearly-elastic perfectly plastic interface elements on both upper and lower sides of beam structural elements. These interface elements were also adopted to model the soil-block interface or block-block interface. The properties of the reinforcement-soil interface and the soil-block

interface were determined by direct shear test. The reinforcement and the block were connected by friction; hence the reinforcement-block interaction properties were determined according to pullout test results of Awad & Tanyu (2014). Table 2 summarizes the types and parameters of interfaces in this work.

Table 2. Input parameters for different interfaces.

Interface	Modeling method	Friction angle (°)	Cohesion (kPa)	interaction coefficient
Reinforcement-soil* G1 (WS)	embedded grout annulus	28.3 (33.2)	0 (0)	0.69 (0.84)
Reinforcement-block**	interface elements	16.2	9.5	/
Soil-block and soil- beam seat*	interface elements	28.8	0	0.71
Block-bedrock***	interface elements	31	0	/

*Determined by direct shear test.
**Based on Awad & Tanyu (2014) and parameters of two types of reinforcement were assumed the same.
***Based on ACI 318-02 (ACI, 2002).

2.4 *Modelling procedure and load settings*

Before the construction of the abutment model, the bedrock element and corresponding constraints were activated first, and then an equilibrium were reached under gravity. A layer of the facing block, the backfill, the retained soil, and the reinforcement were installed, and then the interfaces were activated. The above steps were repeated until the installation of topmost layer was finished. At last, the beam seat was installed and interfaces were activated. In order to simulate the compaction effect during construction, a vertical stress of 8 kPa was applied on the top of each layer of the reinforced area and removed before the installation of next layer (Hatami & Bathurst 2005; Shen et al. 2020).

A vertical stress of 20 kPa from the end of the beam seat to the rightmost boundary of the model was applied to simulate the dead load of the approach. As the first stage of loading, the self-weight load stress of beam seat slab was also 20 kPa. The subsequent bridge load was achieved by applying vertical stress on the beam seat slab in an increment of 25 kPa before 400 kPa, and in an increment of 50 kPa after 400 kPa. During the loading process, the axial forces of reinforcements were monitored. When the axial force of any reinforcement reached its ultimate tensile strength, or the safety factor of the model is equal to 1, it could be considered that the abutment had reached the ultimate bearing capacity.

2.5 *Validation of the model*

To verify the accuracy of the numerical model, the simulation results of baseline were compared with the results of the centrifugal test. In order to facilitate the validation of the full-scale numerical model, the monitoring data obtained from the centrifugal model test had been converted according to the model similarity scale (n=10 g) and similarity principle of centrifugal test (Viswanadham, 2019). Figure 2a shows the lateral displacement profile of the facing block along the height of the abutment obtained from both centrifugal test and the baseline group. Although there are some discrepancies in magnitude, the measured and simulated lateral displacement of the facing block still show similar distribution trends. The measured and simulated additional vertical stresses below the centerline of the beam seat induced by the bridge slab load are shown in Figure 2b. It can be found that the simulation values match well with the measured results under different applied vertical stresses. Figure 2c shows comparison of measured and simulation reinforcement strain profile along abutment height below the centerline of the beam seat. Also, there are some acceptable deviations in magnitude, but the distribution trends of measured and simulated strains show consistency. In terms of the lateral

displacement of facing block, additional vertical stress and reinforcement strain, the numerical model established in this work can reasonably reflect the performance of the abutment in the centrifugal test. Therefore, the numerical model established in this section can be used for subsequent parametric study.

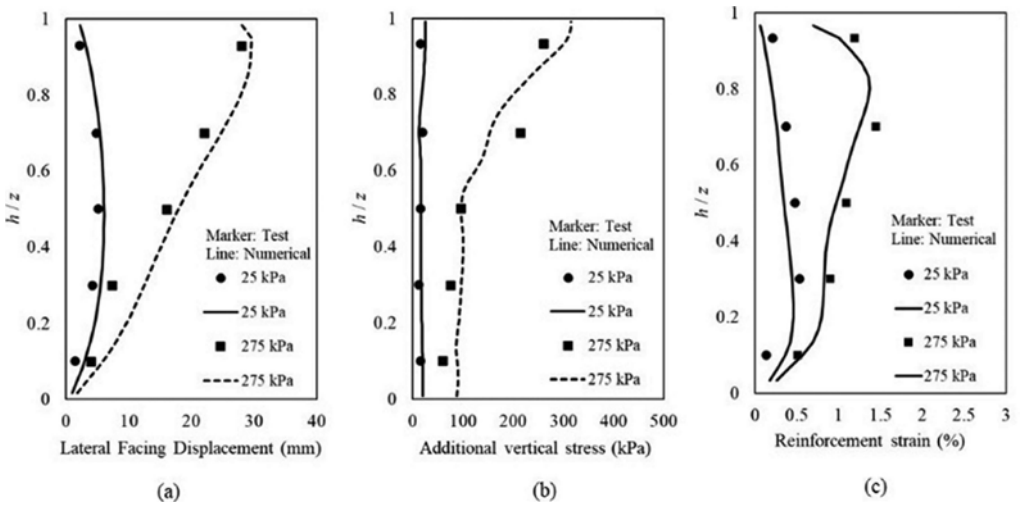

Figure 2. Comparison of centrifugal test results (converted according to the model similarity scale) and numerical results: (a) Lateral displacement of the facing block; (b) additional vertical stresses below the centerline of the beam seat; (c) reinforcement strain below the centerline of the beam seat.

3 PARAMETRIC STUDY

After the validation of the numerical models, parametric study was carried out to study the influence of some key factors on the ultimate bearing capacity of the GRS abutments and the performance of GRS abutments in the limit state. The factors included reinforcement tensile strength, setback distance and beam seat width.

3.1 *Ultimate bearing capacity*

Parametric study settings and corresponding simulation results of ultimate bearing capacity are drawn in Table 3. It should be mentioned that for all groups of simulation, the strength limit of reinforcement had been reached before the safety factor of the model was equal to 1. Hence, for all groups, the ultimate bearing capacity of the GRS abutment is defined according to the vertical load when any reinforcement reached its ultimate tensile strength. The simulation results show that weakening the reinforcement strength or increasing the beam seat width both have a negative impact on the ultimate bearing capacity of GRS abutments. It should be noted that although increasing the beam seat width reduces the bearing capacity per unit area, the total load that GRS abutments can bear increases due to the increase of the total bearing area. It indicates that GRS abutments can bear heavier bridge beams by increasing the beam seat width when space allows. The lengthening of setback distance increases the ultimate bearing capacity of GRS abutments until the setback distance is extended to 1.8 m (0.3H). Then, until the beam seat is close to the right boundary of the reinforced area, that is, when the setback is 3 m (0.5 H) in length, ultimate bearing capacity remains stable and does not increase with the lengthening of setback distance. It indicates that the bearing capacity of GRS abutments is improved most effectively when the beam seat is located in the middle of the reinforced area.

Table 3. Parametric study setting and ultimate bearing capacity results.

Model	Reinforcement type	Ultimate tensile strength of reinforcement (kN/m)	Beam seat dimension b (m)	Setback distance a_b (m)	Ultimate bearing capacity (kPa)
Baseline	G1	63	1	0.2	1500
Group 1	WS	20	1	0.2	478
Group 2	WS	20	1.5	0.2	438
Group 3	WS	20	2	0.2	419
Group 4	WS	20	1	0.4	501
Group 5	WS	20	1	0.8	522
Group 6	WS	20	1	1.2	545
Group 7	WS	20	1	1.8	575
Group 8	WS	20	1	2.4	579
Group 9	WS	20	1	3	575

3.2 *Additional vertical stress and lateral earth pressure*

The distribution of additional vertical stress under the center line of beam seat along the height at limit state is shown in Figures 3. It can be observed that the change of the tensile strength of the reinforcement has no obvious effect on the distribution trend of the additional vertical stress (Figure 3a). Similar to the response of the ultimate bearing capacity to the setback distance, the lengthening of setback distance moves the position where the maximum additional vertical stress value appears upward, and when the setback distance reaches 1.8 m (0.3H), the position no longer change (Figure 3b). Increasing the beam seat width makes the distribution of the additional vertical stress more uniform along the height, and the position where the maximum value appears moves downward (Figure 3c).

The distribution of additional lateral earth pressures behind the abutment facing along the height at limit state is drawn in Figures 4. Same as additional vertical stress, the tensile strength of the reinforcement does not have a significant effect on the distribution of the additional lateral earth pressures behind the abutment facing (Figure 4a). The increasing of setback distance leads to the continuous decrease of the peak value of the additional lateral earth pressure. And when the setback distance increases to 1.8 m (0.3H), the additional lateral earth pressure eventually no longer presents a single peak distribution (Figure 4b). It indicates that as the beam seat is far away from the abutment facing, the influence of the bridge slab load near the free facing is gradually weakened, especially at the higher position. Increasing the beam seat width has no obvious effect on the location of the peak additional lateral earth pressure, but the lateral earth pressure increases at the lower part of the abutment (Figure 4c).

Also, the calculated results using the Boussinesq solution for an area transmitting a uniform surcharge recommended by the FHWA for the GRS-IBS (Adams and Nicks, 2018) is drawn in Figures 3 and 4 with solid lines. When the bridge slab load is large, the basal earth pressure of the rigid beam seat cannot be simply approximated to the average distribution. Therefore, the calculation results of additional vertical stress according to the Boussinesq solution for an area transmitting a uniform surcharge are smaller than numerical result. It indicates that in order to accurately analyze the internal vertical stress distribution of GRS abutment under relatively large bridge load, firstly it is necessary to clarify the basal earth pressure of the beam seat, and then use the integral method to solve according to the Boussinesq solution for concentrated vertical force. The Boussinesq solution is to solve the internal stress distribution in the semi-infinite space, and cannot correctly consider the reduction of the additional lateral earth pressure due to the lateral displacement of the abutment facing. Therefore, the calculation results overestimate the additional lateral earth pressure behind the abutment facing. Although, in magnitude, the theoretical calculation results significantly underestimate the additional vertical stress and overestimate the additional lateral earth pressure, the distribution trends of numerical results and the calculation results of the Boussinesq solution are in good agreement.

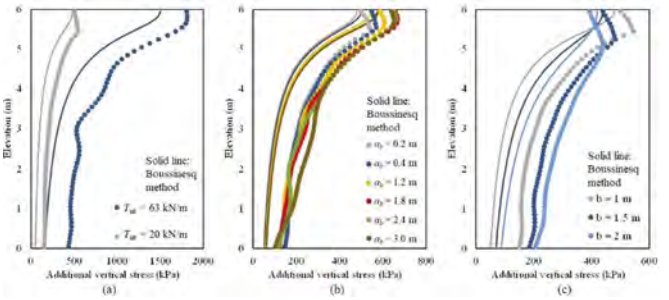

Figure 3. Distribution of additional vertical stresses under the beam seat centerline (a) effect of different reinforcement strength T_{ult}; (b) effect of setback distance a_b; (c) effect of beam seat width b.

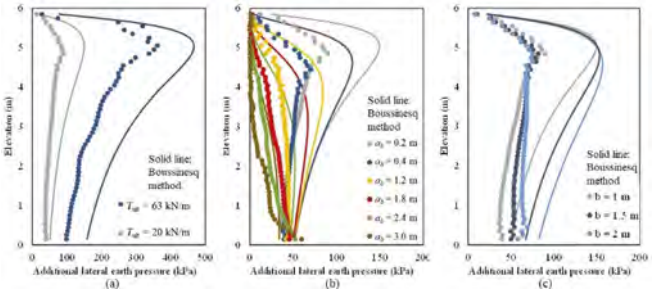

Figure 4. Distribution of additional lateral earth pressures behind the abutment facing (a) effect of different reinforcement strength T_{ult}; (b) effect of setback distance a_b; (c) effect of beam seat width b.

3.3 *Lateral displacement of facing block*

The profiles of lateral displacement of facing block are shown in Figure 5. As shown in Figure 5a, Due to the difference in the stiffness of the reinforcement, the lateral displacement of the cases with different reinforcement is slightly different in magnitude. However, the lateral displacement distribution trends of the two cases are not affected. With the increase of setback distance, the lateral displacement of the upper facing decreases, while the lateral displacement of the bottom facing slightly increases. At the same time, the peak lateral displacement of facing decreases, and its appearance position also moves downward (Figure 5b). This is because the father the beam seat is away from the free facing of abutment, the lower the height when the stress induced by bridge slab loading diffuses to the facing. Increasing the beam seat width results in a larger lateral displacement of facing block, and a lower position of the peak lateral displacement (Figure 5c). This phenomenon is consistent with the increase of the total load of the abutment when the beam seat width increases.

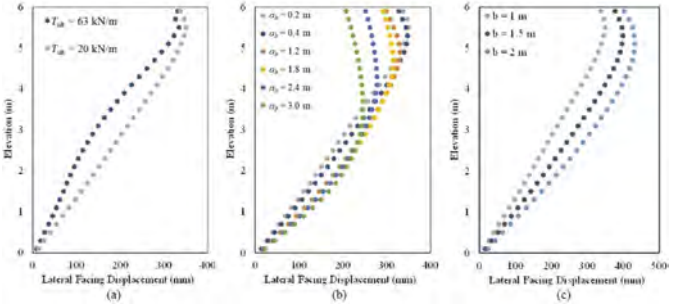

Figure 5. Distributions of lateral displacement of facing block (a) effect of different reinforcement strength T_{ult}; (b) effect of setback distance a_b; (c) effect of beam seat width b.

3.4 *Max tension of reinforcement*

Figures 6 shows the distribution of the maximum tension (T_{max}) in the reinforcement. Since the difference in the reinforcement strength, the maximum tension is normalized by the ultimate strength of the reinforcements. As shown in the Figure 6a, the effect of reinforcement strength is insignificant for the distribution of the maximum tension. With the increase of setback distance, longer reinforcements between the beam seat and the facing are mobilized to confine the backfill. Hence, the increase of setback distance leads to the decrease of the maximum tension of reinforcement (Figure 6b). Increasing the beam seat width results in smaller T_{max} in the upper reinforcement layers while larger in the bottom reinforcement layers. And the position of the reinforcement reaching the ultimate strength moves downward since the increase of the beam seat width (Figure 6c).

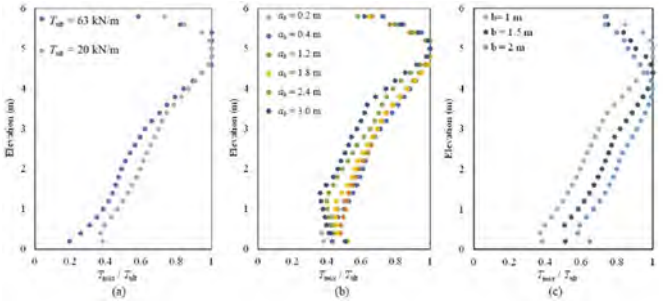

Figure 6. Distributions of maximum tension in the reinforcement T_{max} (a) effect of different reinforcement strength T_{ult}; (b) effect of setback distance a_b; (c) effect of beam seat width b.

4 CONCLUSION

In this work, the responses of GRS abutment subjected to bridge slab loading under ultimate stress condition state were evaluated by two-dimensional numerical simulation. A series of parametric studies were carried out to investigate the response of stress distribution, lateral displacement and max tension of reinforcement to various factors, including reinforcement strength, setback distance and beam seat width. The following conclusions are reached in this work:

1. The reinforcement strength only has an obvious effect on the ultimate bearing capacity of the abutment, while shows less effect on stress distribution, lateral displacement and max tension of reinforcement.
2. Increasing the setback distance within a certain range ($0.3H$) results in the increase of ultimate bearing capacity of the abutment and change the additional vertical stress distribution under the beam seat centerline. As the beam seat moves away from the abutment facing, the T_{max} of each reinforcement layer, the additional lateral earth pressure and lateral displacement of facing gradually decrease.
3. Larger beam seat width results in lower ultimate bearing capacity. And the increase of the beam seat width results larger stress distribution, lateral displacement of facing and T_{max} of reinforcement below the position where corresponding peak appears.
4. The Boussinesq solution for uniform surcharge results in a smaller calculated additional vertical stress distribution under the beam seat centerline and a larger calculated additional lateral earth pressure behind the abutment facing. The Boussinesq solution dose not consider the uneven distribution of the basal earth pressure under the rigid beam seat and the effect of the abutment facing at ultimate state.

REFERENCES

Adams, M., Ketchart, K., Wu, J.T. 2007. Mini pier experiments: geosynthetic rein-forcement spacing and strength as related to performance. Geosynthetics in reinforcement and hydraulic applications 165: 1–9.

Adams, M., Nicks, J., Stabile, T., Wu, J.T., Schlatter, W., Hartmann, J. 2011. Geosynthetic Reinforced Soil Integrated Bridge System Synthesis Report. Report No. FHWA-HRT- 11-027. Federal Highway Administration, Washington, D.C., USA.

Adams, M. & Nicks, J. 2018. Design and Construction Guidelines for Geosynthetic Reinforced Soil Abutments and Integrated Bridge Systems. FHWA Publication No: FHWA-HRT-17-080. Federal Highway Administration, Washington, D.C., USA.

American Concrete Institute (ACI) 2002. Building Code Requirements for Structural Concrete (ACI 318-02) and Commentary (ACI 318R-02). Farmington Hills, MI.

Bolton, M.D. 1986. The strength and dilatancy of sands. Geotechnique 36(1): 65–78.

Coduto, D.P., Kitch, W.A., Yeung, M.R. 2015. Foundation Design: Principles and Practices.

Hatami K. & Bathurst R.J. 2005. Development and verification of a numerical model for the analysis of geosynthetic-reinforced soil segmental walls under working stress conditions. Canadian Geotechnical Journal 42(4): 1066–1085.

Hatami, K. & Doger, R. 2021a. Load-bearing performance of GRS abutments with different facing alternatives. In: Geosynthetics Conference 2021, Kansas City, MO,February 2021 .

Hatami, K. & Doger, R. 2021b. Load-bearing performance of model GRS bridge abutments with different facing and reinforcement spacing configurations. Geotextiles and Geomembranes 49(5): 1139–1148.

Helwany, S.M.B., Reardon, G., Wu, J.T. 1999. Effects of backfill on the performance of GRS retaining walls. Geotextiles and Geomembranes 17(1): 1–16.

Nicks, J., Esmaili, D., Adams, M. 2016. Deformations of geosynthetic reinforced soil under bridge service loads. Geotextiles and Geomembranes 44(4): 641–653.

Shen, P., Han, J., Zornberg, J.G., Tanyu, B.F., Christopher, B.R., Leshchinsky, D. 2020. Responses of geosynthetic-reinforced soil (GRS) abutments under bridge slab loading: Numerical investigation. Computers and Geotechnics 123: 103566.

Viswanadham, B.V.S. 2019. Centrifuge Model Studies on the Performance of Geosynthetic-Reinforced Soil Structures. In Frontiers in Geotechnical Engineering: 157–182. Springer, Singapore.

Wu, J.T., Lee, K.Z.Z., Pham, T. 2006. Allowable bearing pressures of bridge sills on GRS abutments with flexible facing. Journal of Geotechnical and Geoenvironmental Engineering 132(7): 830–841.

Wu, J.T., Ketchart, K., Adams, M. 2008. Two full-scale loading experiments of geosynthetic-reinforced soil (GRS) abutment wall. International Journal of Geotechnical Engineering 2(4): 305–317.

Wu, J.T.H. & Pham, T.Q. 2013. Load-carrying capacity and required reinforcement strength of closely spaced soil-geosynthetic composites. Journal of Geotechnical and Geoenvironmental Engineering 139(9): 1468–1476.

Xiao, C., Han, J., Zhang, Z. 2016. Experimental study on performance of geosynthetic-reinforced soil model walls on rigid foundations subjected to static footing loading. Geotextiles and Geomembranes 44(1): 81–94.

Xu, C., Mei, X.S., Han, J. 2019. Model tests investigating the behavior of geosynthetic-reinforced soil (GRS) abutments subjected to static footing load. In Proceedings of geosynthetics conference: 368–378.

Zhang, J., Jia, Y., Guo, W., Zhao, J., Ling, J., Zheng, Y. 2022. Experimental study on the load bearing behavior of geosynthetic reinforced soil bridge abutments with different facing conditions. Geotextiles and Geomembranes.

Zheng, Y. & Fox, P.J. 2017. Numerical investigation of the geosynthetic reinforced soil–integrated bridge system under static loading. Journal of Geotechnical and Geoenvironmental Engineering 143(6): 04017008.

Zheng, Y., Fox, P.J., McCartney, J.S. 2018. Numerical study on maximum reinforcement tensile forces in geosynthetic reinforced soil bridge abutments. Geotextiles and Geomembranes 46(5): 634–645.

Smart Geotechnics for Smart Societies – Zhussupbekov, Sarsembayeva & Kaliakin (Eds)
© 2023 The Author(s), ISBN 978-1-003-29912-7
Open Access: www.taylorfrancis.com, CC BY-NC-ND 4.0 license

Accumulation of moisture in winter at the base of the road due to the forces of cryosuction on the example of monitoring a highway in Astana, Kazakhstan

A. Sarsembayeva
Department of "Civil Engineering" of the L.N. Gumilyov ENU, Astana, Kazakhstan

Z. Saginov
RSE on REM "National Center for the Quality of Road Assets" of the Ministry of Industry and Infrastructure Development of the Republic of Kazakhstan, Astana, Kazakhstan

T. Tolkynbayev & S.T. Mussakhanova
Department of "Civil Engineering" of the L.N. Gumilyov ENU, Astana, Kazakhstan

ABSTRACT: This paper presents a calculation of the mass transfer of water and its accumulation in the soils of the base of the road, considering the engineering-geological zoning on the example of the city of Astana, Kazakhstan. A detailed analysis of the physical and mechanical properties of the foundation soils of the highway in the geoclimatic conditions of the city of Astana was carried out. The temperature fluctuations of the layers of the pavement and the base of the subgrade in the winter period were monitored by installing sensors in the layers of pavement and subgrade of the road. The depth of freezing in winter was determined, and the distribution of temperature in the depth of the pavement and base soils was analyzed. It has been established that the soil foundations of roads, as well as the layers of pavement, remain in a stably frozen state due to sub compensation of heat transfer of the underlying layers and have a sufficient margin of safety. It was determined that the mass transfer of water in gaseous state was 1.44 10^{-4} g/h per 1 dm³ of soil volume at a temperature of -5-8 °C at a depth of -60 cm under the road. To prevent negative impact and uneven deformation of the subgrade in zones 1-8 in Astana city, it was recommended to provide additional vapour barrier at a depth of 57-60 cm, before the construction of the underlying layer of gravel-sand mixture.

1 INTRODUCTION

The location of Kazakhstan in a sharply continental climate entails a pronounced effect of temperature fluctuations on the road structure (Teltayev et al. 2022). Moreover, not only the upper layers of asphalt concrete fall under the influence, but also the soil bases, which in winter freeze to a depth of 2 meters. The new capital of Kazakhstan, Astana, is a territory of active urban development. According to the Geoinformation Database (Zhussupbekov et al. 2021), the territory of Astana city can be subdivided into 8 subzones according to the composition of the soils, consisting of 6 main engineering-geological elements and the occurrence of soil subtypes. Subzones 4, 5, 7, 8 belong to the left bank of Yesil River or to the territory of new development (Figure 1).

The topsoil (EGE-1a) with the thickness less than 1 m does not serve as a foundation soil for highway construction and most often cut off or replaced with bulk soil. Beneath there are sandy clay loams $a(Q_{II\text{-}IV})$ designated as EGE-2a, with interlayering loamy sands and sandy

DOI: 10.1201/9781003299127-409

loam soils (EGE-2b), clays (EGE-2c) and silty soils (EGE – 2d). Horizontal layers of sands of various sizes (EGE-3a), gravelly sands (EGE-3b) and gravel soils (EGE-3c), belong to alluvial medium-Quaternary sand and gravel formations $a(Q_{II\text{-}IV})$. Below the alluvial layer there is eluvia layer of sandy clay loams $e(C_1)$ (EGE-4). Gravelly, gruss and rubble soils of eluvial formations of the weathering crust e(C1) of EGE-5 is widespread on the site and have been found at a depth of 7.0 to 23.0 m. Sedimentary rocks of the Lower Carboniferous (C1) that are represented mainly by sandstones, which are inter bedded with siltstones and mudstones of the same age throughout their entire thickness and serve as a reliable basis for the development of urban construction projects. The highway base soils in zones 1, 2, 3, 5, 6, and 7 are alluvial clayey soils represented by the engineering-geological element EGE 2a, in zone 4 sand layers with the engineering-geological element EGE 3a, and in 8 silty clay zone including alluvial deposits EGE 2d.

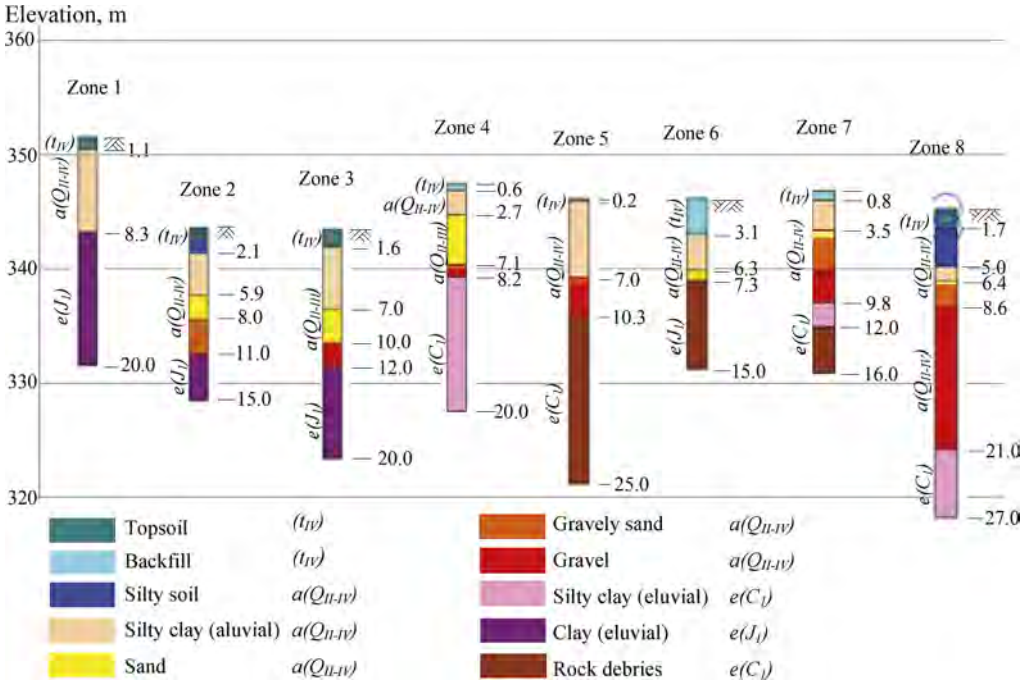

Figure 1. Geotechnical zoning of Astana city.

The constant impact of heavy vehicles and construction equipment further exacerbates the negative impact on the soil base of roads, especially in spring, when the bearing capacity drops tenfold due to the intensive melting of ice in the soil and an increase in its moisture content (Sarsembayeva & Zhussupbekov 2021, Teltayev, & Suppes, 2019). As it became known from previous studies, mass transfer in axially freezing soil significantly depends on the density of dry soil, namely on the porosity coefficient, as well as on the temperature difference between the layers along the height of the soil (Sarsembayeva et al. 2022). And the soils under the road are characterized by greater mass transfer due to lower temperatures in the dense upper layers of asphalt concrete, which are characterized by high thermal conductivity (Sarsembayeva & Collins 2017), and the leveling temperature isoline of the transition through 0° C degrees with soils on both sides of the road (Figure 2).

In order to study in more detail, the changes in the temperature field and also to find a preventive method for steam transfer in soils under the road, field observations of the temperature field in the construction of highways were carried out, and also determined the physical and mechanical properties of soils in the laboratory for further calculation of the volume of water transfer due to cryosuction forces.

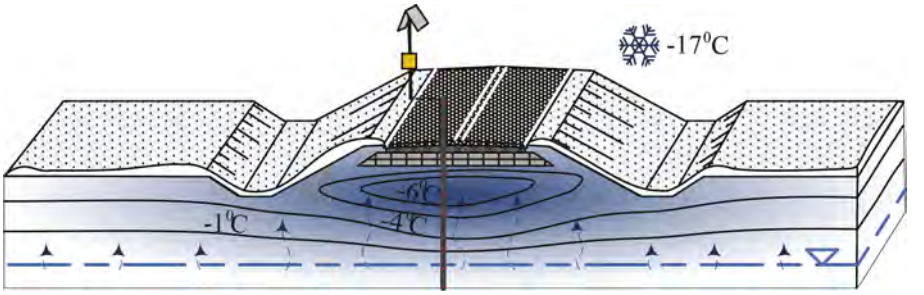

Figure 2. Moisture distribution due to cryosuction forces.

2 METHOD

2.1 *Testing site*

On the section of the road located near the airport of Astana, in the area of the Karkaraly highway, 8 km from the bypass road towards the town of Koshy, sensors were installed at a depth of 3 meters from the road surface to constantly monitor temperature and humidity changes (Figure 3).

Figure 3. Temperature and humidity monitoring station along the road.

The road is located in the 4th zone according to the type of soil in Astana. This means that alluvial loam deposits $a(Q_{II\text{-}IV})$ serve as the sub bases for the road foundation To assess the state of the subgrade and subbase soils, soil samples were taken near the roadside in winter period. According to the results of a laboratory study, the density of the loamy soil was 2.0 g/cm³, the

moisture in the natural state was 20.2%, the soil filtration coefficient for Quaternary loams was 0.01-0.13 m/day. The groundwater level was found at a depth of 2.0 m. Groundwater in this area is assessed as sodium chloride, very hard, slightly alkaline, brackish. In relation to concrete grade B4 on Portland cement, groundwater is non-aggressive and slightly aggressive, in relation to reinforced concrete structures it is moderately aggressive.

Table 1. The physical and mechanical characteristics of foundation soils.

Characteristic	Units	Value at 2 m depth
Moisture content	%	20.2
Liquid Limit	%	27.0
Plastic Limit	%	15.0
Plasticity Index	%	12.0
Consistency index	-	0.5
Bulk density	g/cm³	2.0
Particle density	g/cm³	2.7
Void ratio	-	0.7
Degree of saturation	-	0.8
Deformation modulus	MPa	6.5
Cohesion	kPa	23.5
Angle of internal friction degree	-	22

The road structure is a non-rigid pavement consisting of a 5 cm layer of hot mix asphalt, a bottom layer of a 10 cm thick hot mix porous asphalt concrete pavement, a 12 cm thick top layer of a hot high-porosity asphalt concrete mix, a bottom layer of a gravel-sand mixture 15 cm thick, an underlying layer of gravel-sand mixture 15 cm thick on the compacted base soil (Figure 4).

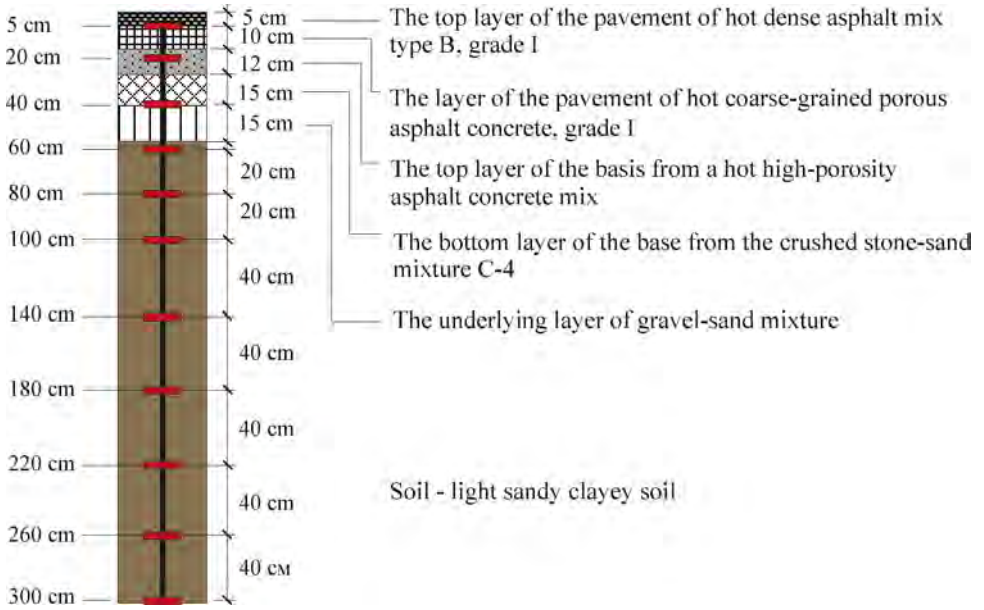

Figure 4. Highway structure and sensors allocation.

Temperature and moisture observations were carried out by automatic measurement by sensors embedded in metal capsules installed at a depth of 0.05; 0.2; 0.4; 0.6; 0.8; 1; 1.4; 1.8; 2.2; 2.6 and 3.0 m from the ground (Figure 2). The frequency of measurements was 1 time per hour.

2.2 *Calculation of mass transfer*

Calculation of the moisture transfer from the base layers upwards the freezing front is based on the measurement of temperature, density and moisture content, and detailed in ENERGIES. The volume of voids in soils is considered a decisive parameter for calculating the volume of steam in each gap and is assumed to be filled with saturated vapour under stable conditions or tending to such a state by sublimation or solidification at negative temperatures. The vapour speed is calculated as a heat transfer over cumulative void channel dimensions, vapour flow density corresponding to the temperature and time:

$$v_{vapour} = \frac{Q}{C \cdot \rho_{vapour} \cdot A_{air} \cdot \Delta T \cdot t} \tag{1}$$

where, – average speed of vapour, cm/h; – heat transfer in a gaseous state, – measured temperature difference, ºC; - C – specific heat of vapour passing through the cumulative air voids cross section, $J/kg \cdot ^oC$; - vapour density corresponding to the temperature, g/cm³; - cumulative cross section of the air voids, cm², corresponding to the porosity coefficient and moisture content; – time, h.

$$m_{ice} = \rho_{vapour} \cdot V_{air\ voids} = \rho_{vapour} \cdot v \cdot t \cdot A_{air} \tag{2}$$

where, - mass of built ice in grams; - is taken as an average density value of the vapour densities at the start and end time point, g/cm³.

3 RESULTS AND DISCUSSION

3.1 *Temperature monitoring*

The results of temperature monitoring showed large amplitude jumps during the day in the upper layers of asphalt concrete (Figure 4). The results are considered on the example of observation in February 2022. During February 13 transitions over 0°C were recorded, but the underlying layers of the gravel sand mixture remained frozen, apparently by compensating for the heat transfer of the underlying cooler layers. In contrast to the asphalt concrete layers,

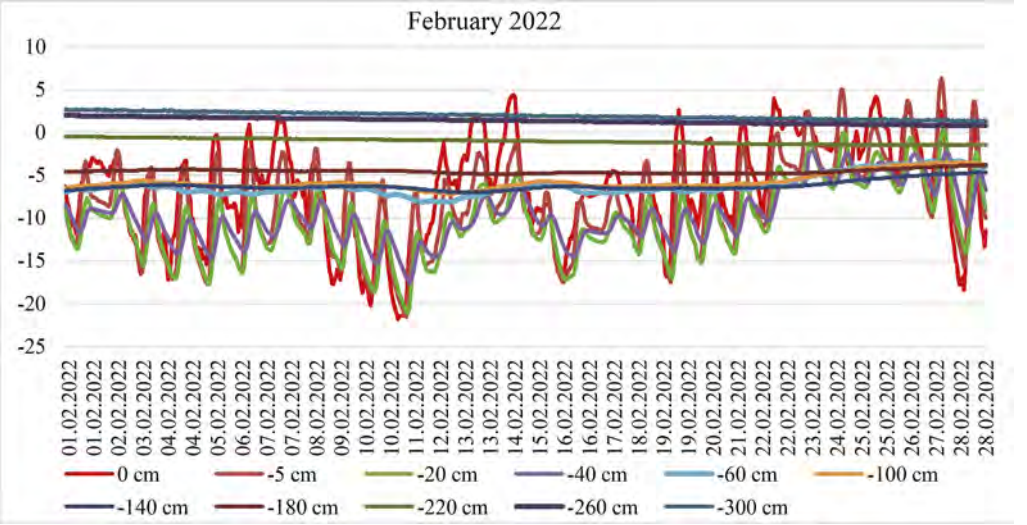

Figure 5. Temperature distribution in Kosshy road, Astana city, Kazakhstan.

which have sharp temperature fluctuations during the day, the temperature of the base soil maintained stable temperature ranges over the month. The relative stabilization of the foundation soils reached from a depth of -0.6 m at negative temperatures in the range of -6 -4°C. The freezing depth continues to steadily increase from 2.20m at the beginning of the month and 2.50 m at the end of February. Minimum air temperature dropped to -21.8 °C, while average temperature was -6.46°C.

3.2 *Moisture change*

Moisture content remained relatively steady in the soil bases except for places of phase transition: freezing and thawing. The decrease in saturated vapor pressure in the pore space in the frozen part caused the migration of moisture in the gaseous state towards the freezing front. The lack of pore pressure (negative pressure) is compensated by vapour migration from the warm part from below.

During the winter months the freezing front fell lower in depth, reaching the greatest freezing point in February (Figure 5). The difference from 21 to 11 % between the layers of 60 cm and 100 cm in November indicated freezing and an urgent solidification of moisture in the frozen part. In December freezing front occured at a depth of 100 cm and is accompanied by a drop in humidity in the pore space from 19 to 15%. And in January, freezing occurs at a depth of 140 cm and 180 cm, as evidenced by a drop in humidity from 21 and 23%, respectively, to 17% in a frozen state. During February, there is a decrease in humidity at a depth of 2.20 m, which means freezing of this layer.

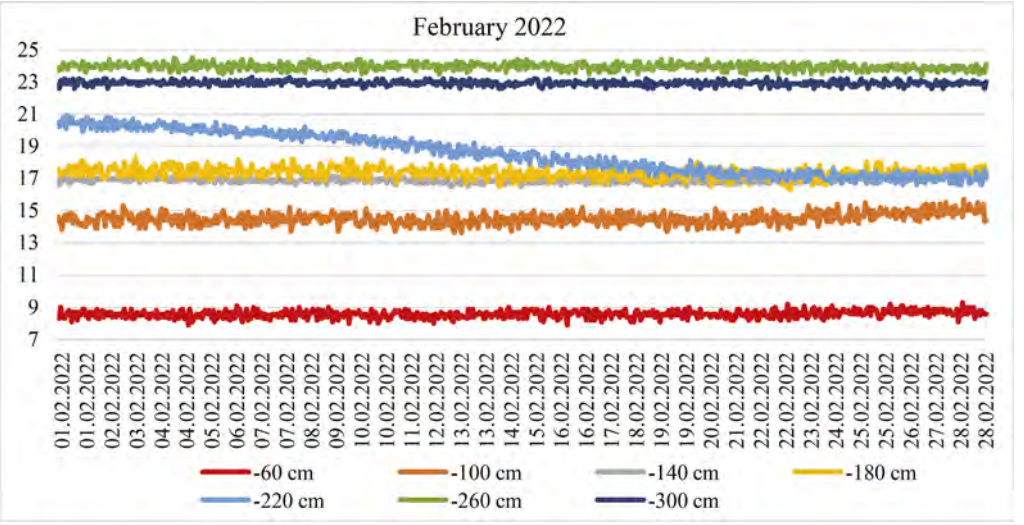

Figure 6. Temperature distribution in Kosshy.

Calculation of vapor migration from warmer to frozen layers according to the method described in (Sarsembayeva et al. 2022), defined that water mass transfer in a form of vapour is $1.44 \cdot 10^{-4}$ g/h per 1 dm3 of soil at with temperature fluctuations -5-8 °C. The rate of passage of vapour towards the freezing front in the light sandy clayey soil was 0.467 m/h. So, for 1 hour in 1 m³ of subgrade at a temperature of -5-8°C at a depth of -60-160 cm from the road surface due to the transfer of moisture from warmer soil layers, 0.144 g of ice is formed, and per day this amount is 3.46 g of ice. And since the freezing of the ground base in winter in Astana lasted 132 days, it can be assumed that during this time only due to the migration of water in a gaseous state, each 1 cubic meter of the road base in zone 4 collected 456.72 g of ice, which increases the moisture content of the soil up to 40% or more, which will significantly reduce the bearing capacity of the road during the spring thaw (Sarsembayeva & Collins 2017).

4 CONCLUSIONS

Thus, considering the above results of the study conducted in the 4th zone of the city of Astana, it was found that the effect of water transfer in frozen soils is greatly underestimated, and an additional layer of vapor barrier is needed to prevent the accumulation of ice lenses under the pavement structure.

1. The upper layers of asphalt concrete were subjected to 8 to 14 transitions through 0°C per month, while the temperature of the crushed stone-sand mixture at a depth of -37 cm remained stably frozen.
2. The base soils, located at a depth of -60 cm, consisting of light sandy loamy clay soils at a temperature of -5-8 ° C were the main zone of moisture accumulation in the form of ice.
3. The freezing of the clayey soil layer at the base of the highway was accompanied by a sharp drop in the humidity of the pore space from 21-23 to 11-14 %, due to the fact that part of the water in the gaseous state was sublimated, forming a negative cryosuction pressure in these layers.
4. Taking into account the physical and mechanical characteristics and the state of the soil base of this particular road it is proposed to lay an additional layer of vapor barrier over the soil base at a depth of -60 cm to prevent a migration in the form of vapour. Such isolation would decrease the heat conductivity in the soil subgrade but also prevent a water mass transfer from the adjacent soils to the highway subbase, thus the loss of bearing capacity during the spring thaw will be reduced.
5. The calculation of the mass transfer of water in the form of steam determined that 1.44 10^{-4} g/h is formed in the frozen layer per 1 dm3 of soil at temperature fluctuations of -5-8 °C. The rate of vapor transfer towards the freezing front in the soil was 0.467 m/h.
6. Freezing of the ground base during 132 days of the winter period in Astana leads to the formation of 456.72 g of ice due to the migration of water in the gaseous state in each 1 m3 of soil, which increases the humidity by 40% or more and significantly reduces the bearing capacity of the road during the spring thaw.
7. As a solution to the problem of water migration in the form of vapour, it is proposed to lay an additional layer of vapor barrier over the soil base at a depth of -60 cm.

ACKNOWLEDGMENTS

This work was supported by the Science Committee of the Ministry of Science and Higher Education of the Republic of Kazakhstan (Grant No. AP13268861). The team of authors would like to thank the RSE on REM "National Center for the Quality of Road Assets" of the Ministry of Industry and Infrastructure Development of the Republic of Kazakhstan for organizing the monitoring of the temperature and humidity condition of the highway in 2022.

REFERENCES

Sarsembayeva, A. & Collins, P.E.F. 2017. Evaluation of frost heave and moisture/chemical migration mechanisms in highway subsoil using a laboratory simulation method. *Cold Regions Science and Technology*. 133: 26–35. https://doi.org/10.1016/j.coldregions.2016.10.003.

Sarsembayeva A. & Zhussupbekov A. 2021. Experimental study of deicing chemical redistribu-tion and moisture mass transfer in highway subsoils during the unidirectional freezing. *Transportation Geotechnics*, 26: 100426 https://doi.org/10.1016/j.trgeo.2020.100426.

Sarsembayeva, A. Zhussupbekov, A. Collins P.E.F. 2022. Heat and Mass Transfer by Vapour in Freezing Soils. *Energies*. 15(4):1515. https://doi.org/10.3390/en15041515.

Teltayev, B.B. & Suppes, E.A. 2019.Temperature in pavement and subgrade and its effect on moisture. *Case Studies in Thermal Engineering*. 13:100363. https://doi.org/10.1016/j.csite.2018.11.014.

Teltayev, B. Oliviero Rossi, C. Aitbayev, K. Suppes, E. Yelshibayev, A. Nugmanova, A. 2022. Freezing and Thawing Processes of Highways in Kazakhstan. Applied Sciences. 12(23): 11938. https://doi.org/10.3390/app122311938.

Zhussupbekov, A. Alibekova, N. Akhazhanov, S. Sarsembayeva, A. 2021. Development of a unified geotechnical database and data processing on the example of Nur-Sultan City. *Applied Sciences*, 11(1): 306. https://doi.org/10.3390/app11010306.

Smart Geotechnics for Smart Societies – Zhussupbekov, Sarsembayeva & Kaliakin (Eds)
© 2023 The Author(s), ISBN 978-1-003-29912-7
Open Access: www.taylorfrancis.com, CC BY-NC-ND 4.0 license

Peculiarities of temperature and moisturechanges in a highway pavement and subgrade in Western Kazakhstan

B.B. Teltayev
Joldasbekov Institute of Mechanics and Engineering, Almaty, Kazakhstan
LLP "Road Research and Production Center", Almaty, Kazakhstan

E.E. Aitbayev & A.S. Zhaisanbayev
LLP "Road Research and Production Center", Almaty, Kazakhstan

ABSTRACT: The temperature and moisture at the points of a highway pavement and subgrade were measured by means of a special measurement system. By analyzing the results obtained, the peculiarities of temperature and moisture changes at different depths in the summer warmest and winter coldest days of years were established. The rates of freezing and thawing, the depth of freezing were determined. A comparative analysis of changes in air, the pavement and subgrade temperatures has been carried out.

1 INTRODUCTION

Main structural parts of a highway - pavement and subgrade for a very long period (for several decades) continuously operate under difficult conditions of the combined effects of mechanical, hydrological, weather-climatic and other factors (Ivanov et al. 1973, Yoder & Witczak 1975, Zolotar et al 1971, Huang 2004). In our opinion, the influence of weather-climatic and hydrological factors on the state, and therefore on the strength and durability of highways, has not been studied enough. This problem is especially relevant for many countries of the world, including Kazakhstan, which have a large territory with a wide variety of weather, climate and hydrological conditions.

Properties of many road materials and soils are highly dependent on temperature and moisture (Papagiannakis & Masad 2008, Teltayev & Radovskiy 2016). Their characteristics can change significantly during the cold period (Tsytovich 1973, Teltayev & Radovskiy 2016, Sarsembayeva & Zhussupbekov 2021, Sarsembayeva et al. 2022). These features of the behavior of road materials and soils should be taken into account when designing pavements for highways (SP RK 2015).

In Kazakhstan, since 2009, studies of temperature and humidity in pavements and subgrade of highways have begun (Teltayev & Aitbayev 2015, Teltayev et al. 2015, Teltayev & Suppes 2017a, Teltayev & Suppes 2017b, Teltayev et al. 2018, Teltayev & Suppes 2019a, Teltayev & Suppes 2019b, Teltayev et al. 2020, Teltayev et al. 2022).

This article is a continuation of these works and contains some results of temperature and moisture monitoring in pavement and subgrade of a highway located in Western Kazakhstan.

2 EXPERIMENTAL

2.1 *Test section of highway*

The site where the measuring system for long-term monitoring of temperature and moisture is installed is located at the 5th kilometer (km 4+700) of the "Zhetibai-Zhanaozen" highway

DOI: 10.1201/9781003299127-410

(Mangistau region). The highway has four traffic lanes. The width of the carriageway is 15 m (4x3.75 m). Shoulder width: 2x3.75 m. Reconstruction of the highway completed in 2020.

The pavement structure on the site consists of the following layers: stone mastic asphalt concrete (SMA) - 5.5 cm; coarse-grained porous asphalt concrete - 10 cm; coarse-grained highly porous asphalt concrete - 14.5 cm; a mixture of crushed stone and sand - 18 cm; a mixture of gravel and sand -20 cm. The total thickness of the pavement is 68 cm.

The highwaysubgrade and its natural soil base consists of the following soils: dusty sandy loam - 0.55 m; sandy loam - 1.20 m; sandy loam silty gruss - 1.80 m.

On the experimental section, the highway passes through an embankment with height 1.52 m. Groundwater is located deep (below 4 m).

2.2 *System for measuring temperature and moisture*

The system used for temperature and moisture was invented and assembled at the Kazakhstan Highway Research Institute. It consists of above-ground and underground parts. Its above-ground part is a vertical mast, on which are located electronic units for storing and transmitting measured values of temperature and moisture, two solar panels and a battery; the underground part of the measuring system includes temperature and moisture sensors, cables for transmitting measured temperature and moisture values to the electronic storage and transmission units.

Temperature and moisture sensors are installed at the points of the pavement, subgrade and natural soil base at the following depths from the SMA surface: 3 cm; 12 cm; 20 cm; 45 cm; 60 cm; 90 cm; 130 cm; 180 cm; 240 cm; 300 cm and at a height of 200 cm from the SMA surface.

3 RESULTS AND DISCUSSION

3.1 *Temperature on a hot day*

Figure 1 shows graphs for changes air temperature and temperature at points of the pavement and subgrade on the hottest summer day in 2022 (July 18-19, 2022). Analysis of the graphs revealed that:

- daily temperature fluctuations occur only in the upper part of the pavement (45 cm); at points located below the temperature practically does not change in the daily cycle;
- in the asphalt concrete layers (up to 20 cm) the daily temperature fluctuation is almost harmonic; the nature of the daily change in air temperature is also harmonic;
- about 11 o'clock in the morning air temperature and temperature of the asphalt concrete layers (up to 20 cm) are approximately the same and equal to 36-37 °C;
- the maximum temperature of the pavement of SMA (at a depth of 3 cm), equal to 54.5 °C and taking place at 17-18 hours in the afternoon, is noticeably higher than the maximum air temperature, equal to 44.3 °C;
- as expected, in the daily cycle the highest values of air temperature and temperature in the asphalt concrete layers occur from the second half of the day to midnight, and the lowest temperatures are noted from midnight to morning; the minimum daily values of air temperature and temperature of SMA (3 cm) are 24.5 °C and 32.1 °C respectively; changes in air temperature and temperature of SMA layer on the hottest day equal to 18.1 °C and 22.4 °C respectively.

3.2 *Temperature on a cold day*

Figure 2 shows graphs of changes in air temperature and temperature at the points of the pavement and subgrade on the coldest winter days of 2021 and 2022 (December 26-27, 2021).

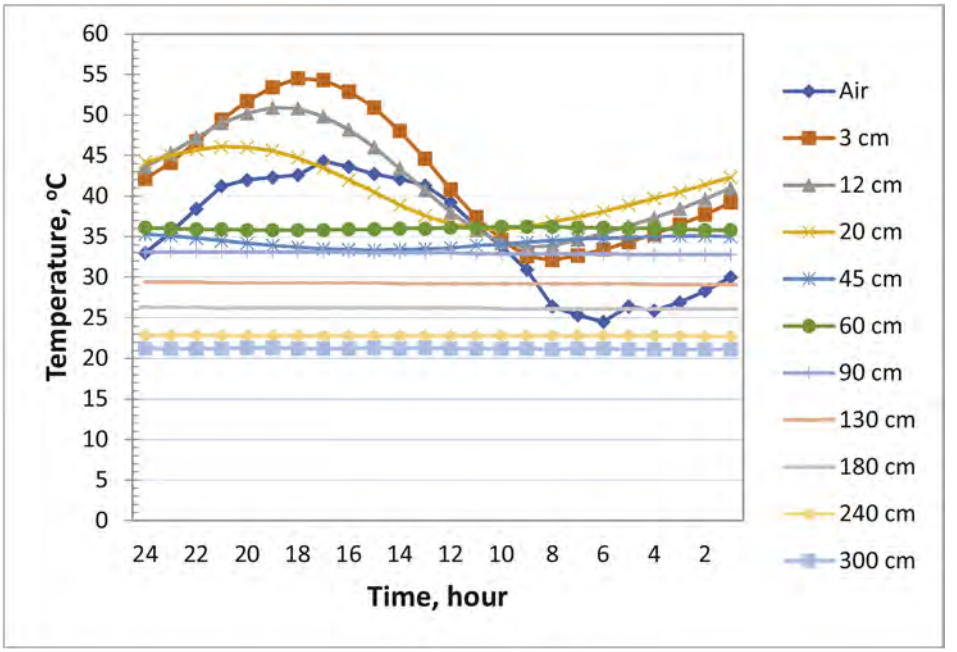

Figure 1. Graphs for changes air temperature and temperature at points of the pavement and subgrade on the hottest summer day in 2022 (July 18-19, 2022).

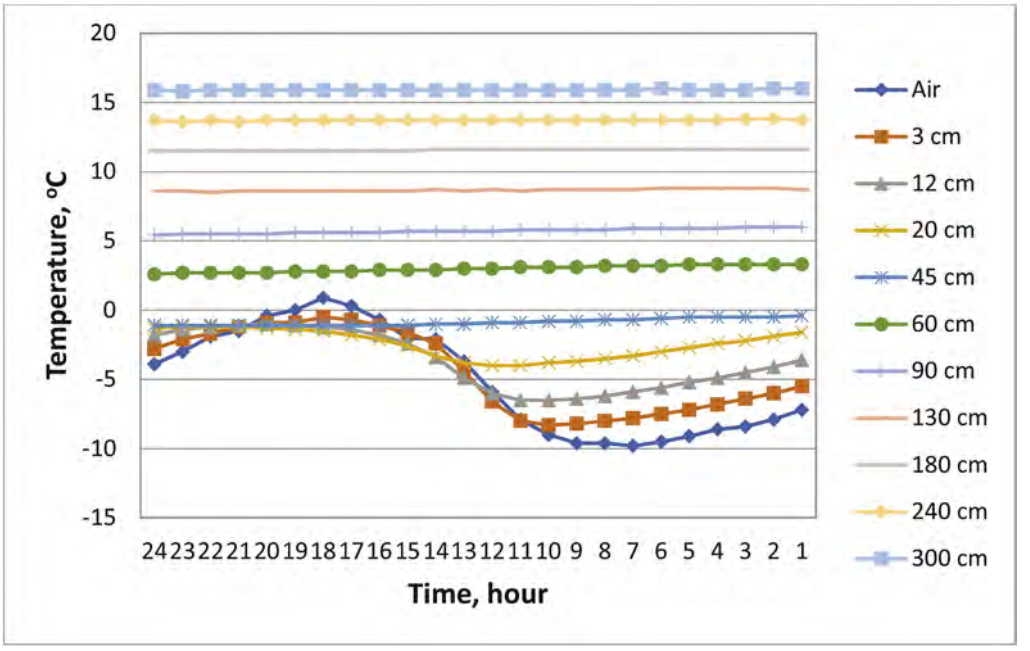

Figure 2. Graphs for changes air temperature and temperature at points of the pavement and subgrade on the coldest winter day in 2021 and 2022 December 26-27, 2021).

It can be seen from this figure that on the highway section under consideration, on the coldest winter days, the temperature in the pavement changes only in its upper part; at depths of

45 cm and 20 cm the daily temperature change was only 0.7 °C and 2.8 °C respectively. It has been established that:

– from 13:00 to 24:00 air temperatures and temperature in the asphalt concrete layers (up to 20 cm) are very close and range from 0.9 °C to -3.9 °C; At 7 o'clock in the morning the air temperature dropped to -9.8 °C; the lowest temperature of the asphalt concrete layers at depths of 3 cm, 12 cm and 20 cm was -8.3 °C (at 10 a.m.), -6.5 °C (at 10 a.m.) and -4.0 °C (at 11 a.m.), respectively; Thus, it can be assumed that in the daytime air temperatures and temperature in the upper part of the asphalt concrete layers are the same, and at night the upper part of the asphalt concrete layers is 2-6 °C warmer than the air.

3.3 *Freezing depth*

Information on freezing and thawing of the pavement on the site is presented in Table 1. Analyzing these data, it was found that:

– freezing started approximately in the middle of the first decade of November;
– the maximum freezing depth was 46 cm, which was reached at the end of January; it is important to note here that the maximum freezing depth does not exceed the thickness of the pavement layers of stable materials (asphalt concretes, a mixture of crushed stone and sand);
– average freezing rate was 1.16 cm/day;
– bottom-up thawing began approximately at the end of the second decade of January, and downward thawing began approximately in the middle of the third decade of March;
– the average thawing rate was 0.49 cm/day.

In the observed cold period, freezing of pavement occurred almost 2.5 times faster than thawing. This fact can be explained by the rapid onset of the cold period and slow warming in the spring.

Table 1. Freezing and thawing depth.

Freezing and thawing depth			
freezing		thawing	
date	depth, cm	date	depth, cm
November 6, 2021	3	January 20, 2022	45
November 17, 2021	12	February 10, 2022	20
December 14, 2021	20	March 29, 2022	12
December 25, 2021	46	March 23, 2022	3

3.4 *Moisture*

Graphs of changes in air moisture and moisture in the points of the pavement, subgrade and natural soil base in the hottest summer day of 2022 (July 18-19, 2022) and in the coldest winter day of 2021 and 2022 (December 26-27, 2021) are shown in Figures 3 and 4 respectively. It turned out that inthe hot summer day air moisture varies greatly in the daily cycle (from 22.1% at 17:00 in the afternoon to 52.6% at 6:00 in the morning, i.e., almost 2.5 times); the lowest moisture occurred in the period from 13:00 to 17:00, i.e. during the hottest period of the day, and the highest moisture was noted in the period from 2 to 8 hours, i.e. in the second half of the night and in the morning, when the air is relatively cool. Despite the strong change in air moisture in the hot summer day, its maximum daily value was only 52.6%.

In contrast to the hot summer day, in the cold winter day the air is saturated with moisture, the maximum value of air moisture reaches 100%. During most of the day air moisture has

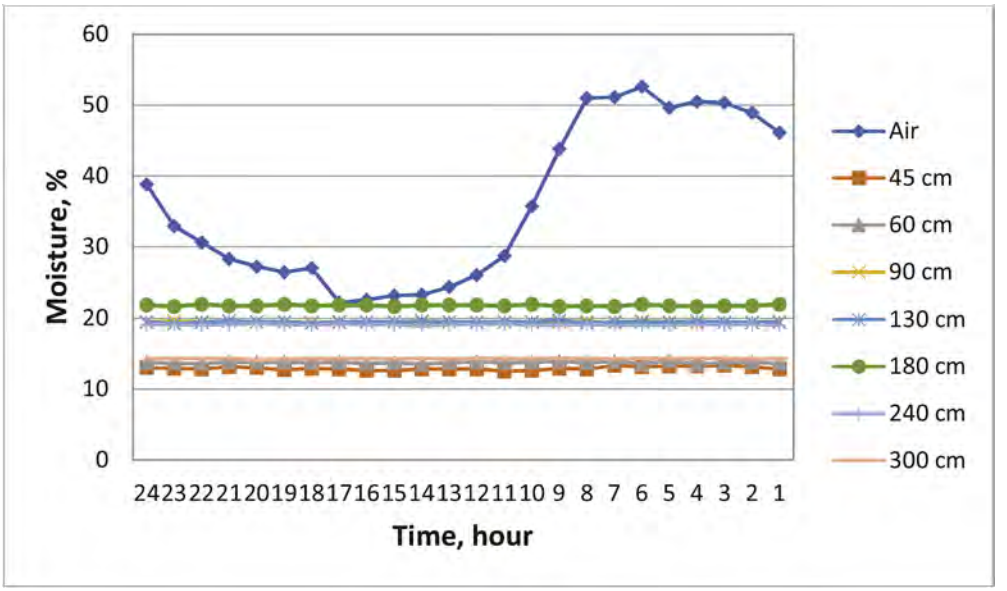

Figure 3. Graphs for changes air moisture and moisture at points of the pavement and subgrade on the hottest summer day in 2022 (July 18-19, 2022).

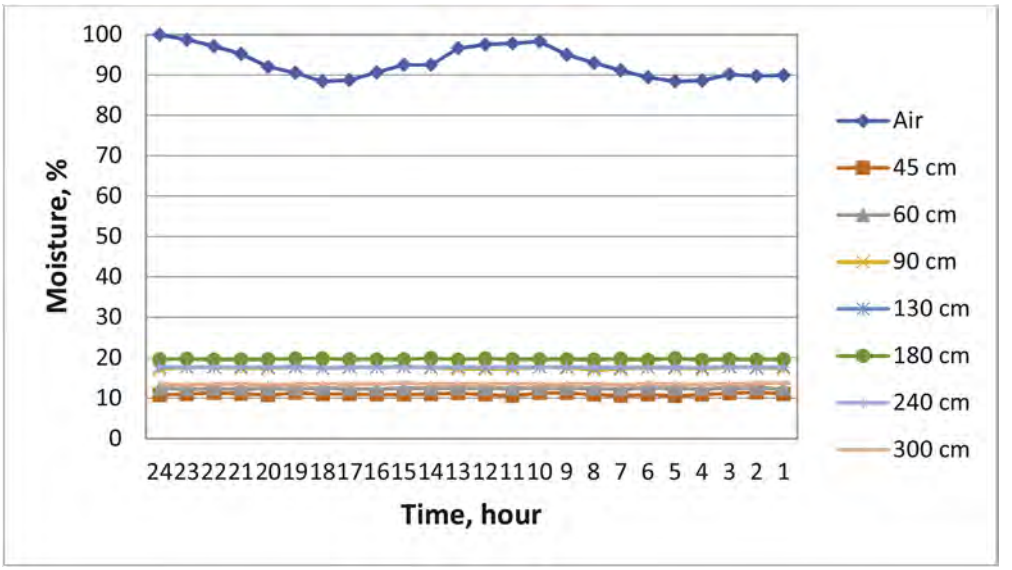

Figure 4. Graphs for changes air moisture and moisture at points of the pavement and subgrade on the coldest winter day in 2021 and 2022 December 26-27, 2021).

a value ranging from 90 to 100% and changes slightly during the day (from 88.4% to 100%, i.e. 11-12%).

The values of moisture at the points of the pavement, subgrade and soil base in the considered summer and winter days are given in Table 2.

Figures 3 and 4 and Table 2 show that:

– moisture in the points of the pavement, subgrade and soil base in the summer and winter days does not change in daily cycles;

Table 2. The values of moisture at the points of the pavement, subgrade and soil base in the considered summer and winter days.

Depth, cm	Moisture,%	
	summer	winter
45	12,8	10,9
60	13,9	12,4
90	19,4	17,2
130	19,4	17,7
180	21,8	19,6
240	19,1	17,7
300	14,3	13,5

- character of moisture distribution by depth in summer and winter is the same: the lowest values (11-14%) occur at depths of 45-60 cm (in pavement layers) and 300 cm, and the highest values (18-22%) are noted at depths of 90 -240 cm (subgrade and soil base);
- in the all points the moisture in winter is only 1.5-2.0% less than in summer;
- at a depth of 300 cm the summer and winter moisture values are almost equal: 14.3% and 13.5% respectively, i.e. the difference is only 0.8%; this shows that groundwater does not affect the distribution of moisture in the structural parts of the highway.

4 CONCLUSION

1. In the hot summer day in asphalt concrete layers of the pavement (up to 20 cm) temperature changes harmonically; the maximum values of air temperatureand temperature inthe upper asphalt concrete layer (depth of 3 cm) reached 44.3 °C and 54.5 °C respectively; daily temperature fluctuations occur only in the upper part of the pavement (up to 45 cm); 1n points located below the temperature does not change in the daily cycle.
2. In a cold winter day a noticeable temperature change occurs only in the upper part of the pavement (up to 20 cm); the minimum temperatures of air and in the upper asphalt concrete layer (depth of 3 cm) reached -9.8 °C and -8.3 °C, respectively.
3. The maximum freezing depth is 46 cm, i.e. 22 cm less than the total thickness of the pavement; the average freezing and thawing rates are 1.16 cm/day and 0.49 cm/day, respectively.
4. In the hot summer and cold winter days the moisture in the points of the pavement, subgrade and natural soil base does not change in daily cycle; distribution of moisture on depth in the summer and winter is qualitatively and practically quantitatively the same: moisture in the pavement base layers(45-60 cm) and in subgrade and soil base (90-240 cm) is in the range of 11-14% and 18-22% respectively.

REFERENCES

Ivanov, N.N. et al. 1973. *Design and Calculation of Flexible Pavement*. Moscow: Transport.

Yoder, E.J. & Witczak, M.W. 1975. *Principles of Pavement Design*. 1975. New Jersey: John Willey & Sons.

Zolotar, I.A. et al. 1971. *Water and Thermal Regime of Subgrade and Pavements*. Moscow: Transport.

Huang, Y.H. 2004. *Pavement Analysis and Design*. New Jersey: Pearson Education.

Papagiannakis, A.T. & Masad, E.A. 2008. *Pavement Design and Materials*. New Jersey: John Wiley & Sons.

Teltayev, B. & Radovskiy, B. 2016. *Low temperature cracking problem for asphalt pavements in Kazakhstan*. Proc.8 RILEM Int. conf.m ech. crack. debond. pavem.
Tsytovich, N.A. 1973. *Mechanics of Frozen Soils*. Moscow: Higher School.
Sarsembayeva, A. & Zhussupbekov, A. 2021. *Experimental study of deicing chemical redistribution and moisture mass transfer in highway subsoil during the unidirectional freezing*. Transp. Geotechn 26: 100426–100439.
Sarsembayeva, A., Zhussupbekov, A. & Collins, P.E.F. 2022. *Heat and mass transfer by vapour in freezing soils*. Energies 15 (4): 1515–1531.
SP RK 3.03-104-2014. 2015. *Flexible Pavement Design*. Astana.
Teltayev, B. & Aitbayev, K. 2015. *Modeling of temperature field in flexible pavement*. Indian Geotechnical Journal 45 (4): 371–377.
Teltayev, B., Baibatyrov, A. & Suppes E. 2015. *Characteristics of highway subgrade frost penetration in regions of the Kazakhstan*. Proc. 15 Asian region. conf. soil mech. geotech. eng., Fukuoka.
Teltayev, B.B. & Suppes, E.A. 2017a. *Regularities for temperature variation in subgrade of highway*. Geomechanics and Engineering 13(5): 793–807.
Teltayev, B. & Suppes, E. 2017b. *Freezing characteristics of a highway subgrade*. Sciences in Cold and Arid Regions 9(3): 325–330.
Teltayev, B.B., Liu, J. & Suppes E.A. 2018. *Distribution of temperature, moisture, stress and strain in the highway*. Magazine of Civil Engineering 7: 102–113.
Teltayev, B.B. & Suppes, E.A. 2019a. *Temperature in pavement and subgrade and its effect on moisture*. Case studies in Thermal Engineering 13: 1–11.
Teltayev, B.B. & Suppes, E.A. 2019b. *Temperature and moisture in a highway in the south Kazakhstan*. Transportation Geotechnics 21: 1–11.
Teltayev, B.B., Zhussupbekov, A.Zh., Shakhmov & Suppes E.A. 2020. *Field experimental investigations of freezing and thawing of highway subgrade*. Lect. notes civ. eng. Proc. TRANSOILCOLD 2019. Transport.soil eng.cold reg. Vol.1. St Petersburg,2019. Singapore: Springer Nature.
Teltayev, B., Suppes, E., Sarsembayeva, A. & Tileu, K. 2022. *Freezing and thawing characteristics in highway pavements and subgrade in conditions of Kazakhstan*. Proc. 20 int. conf. soil mech. geotech. eng., Sydney.

Smart Geotechnics for Smart Societies – Zhussupbekov, Sarsembayeva & Kaliakin (Eds)
© 2023 The Author(s), ISBN 978-1-003-29912-7
Open Access: www.taylorfrancis.com, CC BY-NC-ND 4.0 license

Enhancing road infrastructure in Kazakhstan with modified sulfur and low-strength inert materials

A.U. Nugmanova & A.O. Yelshibayev
JSC Kazakhstan Highway Research Institute, Astana, Kazakhstan

ABSTRACT: The Republic of Kazakhstan has been working to improve its road infrastructure by using modified sulfur to strengthen low-strength inert materials, such as limestone-shell rock. This study aims to provide an overview of the existing research on this topic, highlighting the chemical modification of sulfur, the properties of low strength inert materials, and the potential applications of sulphurous stone in the construction industry.

Sulfur has been identified as a promising binder for composite materials due to its abundance, low cost, and unique physical properties (Youssef et al., 2015). However, in its elemental form, sulfur exhibits poor mechanical properties and low resistance to environmental factors, which limits its applications in construction materials (Yildirim & Şimşek, 2019). To overcome these limitations, researchers have focused on the chemical modification of sulfur using various organic modifiers, such as epoxy resins and unsaturated compounds (Zhang et al., 2017; Xie et al., 2018). These modifications have been found to improve the physical and mechanical characteristics of sulfur, resulting in a binder with increased strength, durability, and resistance to external factors (Youssef et al., 2015; Yildirim & Şimşek, 2019). Limestone and shell rock are examples of low strength inert materials that have been explored as potential substrates for sulfur-based binders. These materials are characterized by their low strength and porosity, which can be advantageous when combined with a sulfur binder due to the impregnation of the sulfur into the porous structure, resulting in improved strength and durability (Youssef et al., 2015). Additionally, limestone and shell rock are abundant and inexpensive, making them an attractive option for large-scale construction applications (Yildirim & Şimşek, 2019).

The combination of modified sulfur and low strength inert materials has been shown to produce a high-strength composite material, referred to as "sulphurous stone" (Youssef et al., 2015). The impregnation of sulfur into the porous structure of limestone or shell rock, along with the chemical modification of sulfur, results in a composite material with improved mechanical properties, such as increased compressive strength, flexural strength, and resistance to external factors (Yildirim & Şimşek, 2019; Zhang et al., 2017). Additionally, sulphurous stone has been shown to exhibit low water absorption and excellent resistance to freeze-thaw cycles, making it a suitable material for use in various construction applications (Youssef et al., 2015).

1 ADVANTAGES OF USING MODIFIED SULFUR IN ROAD CONSTRUCTION

1. Enhances the strength of low-strength inert materials: Modified sulfur has the potential to increase the strength of materials like limestone-shell rock, making them more suitable for road construction.
2. Environmental benefits: Sulfur is a byproduct of the petroleum industry, and utilizing it in road construction can help to reduce waste and improve the environmental situation.

DOI: 10.1201/9781003299127-411

3. Economic benefits: The use of modified sulfur in road construction can lead to an increase in the service life of pavements and a more efficient use of funds allocated for road maintenance.

2 SAMPLING OF ROAD BUILDING MATERIALS

Limestone-Shell Rock: This environmentally friendly, natural, low-cost material is abundant in the West Kazakhstan region. The characteristics and prevalence make it an ideal choice for road infrastructure. Sampling was carried out at a quarry in Aktau, Karakiya district, Zhetybai village (Figure 1). Tests were carried out in accordance with ST RK 1213-2003 to determine grain composition, crushability, abrasion, water absorption, frost resistance, and compressive strength.". The material, shell rock, was sampled at an air temperature of 35°C, in clear weather, in the amount of 140 kg.

Figure 1. Quarry LLP "Zhetybay-Dostyk".

Modified Sulfur: This material was sampled at the Tengiz oil field in the west of Kazakhstan, following GOST 127.3-93 guidelines for sampling and preparation of samples. It was provided to JSC "KazdorNII" in two bags of 50 kg each for determining physical and mechanical properties. With a low melting point and melt viscosity, solid crystalline sulfur has sufficient mechanical strength, hydrophobicity, and water resistance. The sulfur melt can penetrate deeply into the capillaries of materials and form a new material with an interpenetrating structure upon crystallization. Sampling of modified sulfur is carried out from vehicles, gondola cars, barges (Figure 2).

Figure 2. Sampling of modified sulphur.

3 DETERMINATION OF STANDARD PHYSICAL AND MECHANICAL CHARACTERISTICS OF ROAD BUILDING MATERIALS

Tests to determine the physical and mechanical properties of limestone-shell rock were carried out in accordance with ST RK 1213-2003 "Crushed stone from gravel from dense rocks and industrial waste for construction work. Methods of physical and mechanical tests". The following tests have been carried out in accordance with this standard:

1) Determination of the grain composition - by sieving the sample on a standard set of sieves. The results of this test are shown in Table 1.

Table 1. Grain composition of limestone - shell rock, fr. 5-20 mm.

	Sieve size, mm						
	20	15	12.5	10	7.5	5	< 5
Retained mass, g	742	668	526	368	1072	1064	560
Retained mass, g	14.8	13.4	10.5	7.4	21.4	21.3	11.2
Total total mass, %	14.8	28.2	38.7	46.1	67.5	88.8	100
Full passes, %	85.2	71.8	61.3	53.9	32.5	11.2	

2) Determining the crushability of crushed stone according to the degree of grain destruction during compression (crushing) in the cylinder. The crushability was determined with an accuracy of 1%. The results of this test are shown below:
   - Weight loss of crushed stone when tested in a dry state -34.2%, grade - 200.
   - Mass loss of crushed stone when tested in a water-saturated state - 43.5%, grade - 200.
3) The determination of crushed stone abrasion by grain mass loss was carried out in a shelf drum with balls. For crushed stone with a fraction of 10-20 mm, the number of cast-iron balls required for testing is 11 pcs, the number of revolutions of the shelf drum is 500 s. The weight loss during the test is 56.7% by weight, which corresponds to the I-4 type.
4) Determination of water absorption by comparing the mass of crushed stone samples in a state saturated with water and after drying. Crushed stone samples were placed in a vessel with water at room temperature so that the water level in the vessel was at least 20 mm higher than the top of the crushed stone sample. Water absorption is determined by the formula specified in ST RK 1213-2003 (section 4.18). The result obtained is 7.1% by weight.
5) Determination of frost resistance of crushed stone by weight loss of the sample during alternate freezing and thawing.
   The duration of the crushed stone freezing cycle in the chamber at a steady temperature of minus 18°C is 4 hours. After that, the vessel with crushed stone, placed in a bath with running water with a temperature of (20 ± 5) ° C, was kept in it until the crushed stone was completely thawed. The following results were obtained from this test: number of cycles 25; weight loss 5.6%; the corresponding grade for this limestone - shell rock F 25.
6) Determination of the compressive strength of the rock and bringing samples (cubes or cylinders) to destruction on a press. From the selected rock sample, using a stone-cutting machine, two samples were made in the form of a cube with an edge of 40–50 mm. The results of this test are shown in Table 2.

Table 2. Results of determining the compressive strength of shell rock.

Name	a, mm	b, mm	P, N (kgf)	R_f, MPa
Porous	5.82	5.75	565	1.7
Dense	5.67	5.67	1782	5.5
The arithmetic mean value of the shell rock				3.6

The sample was placed in the center of the press base plate. The load on the sample during testing should increase continuously and evenly at a rate of 0.5 MPa (5 kgf / cm ^{2}) per second, the destruction of the sample is shown in Figure 3.

Sulfur has low melting point (112.8-119.3°C) and melt viscosity ($6.5 \cdot 10^{-3}$ Pa·s). In solid crystalline form, sulfur has sufficient mechanical strength, hydrophobicity, water resistance (Table 3).

Figure 3. Destruction of the sample when determining the ultimate compressive strength.

Table 3. Physical and mechanical properties of sulfur.

The amount of sulfur, wt.%	Density, kg/m ^{3}	Water absorption, wt.%	Compressive strength, MPa
99.99	1.73	0.15	12.00

The sulfur melt is able to penetrate deeply into the capillaries of materials and, in the process of crystallization upon cooling, is firmly connected to the matrix, forming a new material with an interpenetrating structure.

Development of a technology for the impregnation of substandard inert materials with a melt and/or solution of sulfur to obtain high-strength "sulphurous stone"

Over the past few decades, there have been numerous advances in the synthesis of new types of sulfur-containing polymers and the modification of the properties of some important classes of polymers by adding sulfur moieties or polysulfides to polymer compositions. To obtain sulfur composite materials, stabilized polymeric sulfur is required. There are a large number of developments of methods for stabilizing polymeric sulfur. The use of sulfur as a binder in composite materials requires giving it a number of additional properties due to chemical modification. Chemical modification is carried out by reacting sulfur in the melt with various organic modifiers.

To modify sulfur, first, elemental sulfur was heated to 150-190 °C while stirring with a stirrer, then 0.5-1.5 g of sodium sulfate was added to the sulfur solution, the solution was stirred for 10 minutes. Next, epoxy resin was added, heated to a temperature of 170-180 °C, after stirring for 30 minutes, the first sample was taken, after 60 minutes - the second sample.

The reason for preheating the epoxy resin to 170-180 ºC is to increase the reactivity, this starts the boiling process and the formation of steam on the surface layer, which is able to react with the melt containing sulfur and sodium sulfate. This whole mixture is heated to 150 ºC and stirred, samples are taken after 30 and 60 minutes, the samples are shown in Figure 4. The resulting melt, as shown in the figure, is a non-contact polymerized mass of bright yellow color.

Figure 4. Sulfur modified with epoxy and sodium sulphate.

Structural (microscopic) analysis of sulfur melts.

To study the surface structure of the sulfur melt, the FLU.02.3201LED4 epifluorescence microscopy method was used.

Figure 5 shows an image of sulfur and its modified melt under the same conditions and on the same scale for comparison with each other. Figure 5(A) shows an image of elemental

Figure 5. Microscopic image of elemental sulfur (A) and its melt (B).

sulfur as a starting material. The structure of its surface showed that the particle size is small, large particles are marked with circles and an ellipse. Figure 5(B) shows a sulfur melt modified at 150 °C and, as can be seen from the figure, the melt particles are larger in size than in elemental sulfur. They are marked with elliptical and circular lines. Due to the addition of modifiers, the particle size becomes larger because of crosslinking and polymerization of sulfur.

Chemical modification is carried out by reacting sulfur in the melt with various organic modifiers. Unsaturated compounds, such as cyclic diene hydrocarbons, oleic acid, epoxy resin, and their oligomers, are the most widely used as modifiers.

To accelerate the process of interaction of elemental sulfur with the modifier, it is necessary to use initiating additives. Since sulfur reacts with epoxy resin under rather harsh conditions (170-180 °C), it is necessary to use physical and chemical methods of initiation. For the preparation of crushed sulfur, pre-washed and heated shell rocks in an oven at 160-200 °C for about 1 hour are introduced into the finished melt of modified sulfur and mixed for up to 30 and 60 minutes. The obtained samples of sulfur stone are dried for 24 hours at room temperature.

Laboratory study of crushed sulfur from industrial waste. Determination of the physical and mechanical properties of the obtained sulfur stone

Impregnation of limestone-shell rock with a melt or a solution of modified sulfur makes it possible to improve the physical and mechanical properties of substandard inert materials. Modified sulfur with resin and styrene was used to process crushed stone (Figure 6).

Figure 6. Crushed stone modified with resin (a); crushed sulfur stone modified with styrene (b).

In accordance with ST RK 1213-2003, the following results were obtained:

1) Determination of grain composition. The results are shown in Table 4 - for resin-modified crushed stone and in Table 5 - for modified sulfur stone styrene.
2) Determination of crushability of crushed stone by the degree of destruction of grains during compression (crushing) in the cylinder. The crushability was determined with an accuracy of 1%. The test results are shown below: the mass loss of crushed stone modified with resin, when tested in a dry state, is 17.65%, which corresponds to the grade - 600; the weight loss of crushed stone modified with styrene, when tested in a dry state, is 13.66%, which corresponds to a grade of 800.
3) The determination of the abrasion of crushed stone by the loss of mass of grains was carried out in a shelf drum with balls. According to this test, the weight loss for crushed sulfur stone modified with resin is -32%, which corresponds to grade I-2, the weight loss for crushed sulfur stone modified with styrene is -25%, corresponds to grade I-1.

Table 4. Grain composition of crushed stone modified with resin, fr. 5-20 mm.

	Sieve size, mm						
	20	15	12.5	10	7.5	5	< 5
Retained mass, g	784	611	535	388	1140	1137	405
Retained mass, g	15.7	12.2	10.7	7.8	22.8	22.7	8.1
Total mass, %	15.7	27.9	38.6	46.4	69.2	91.9	100.0
Full passes, %	84.3	72.1	61.4	53.6	30.8	8.1	0

Table 5. Grain composition of crushed stone modified with styrene, fr. 5-20 mm.

	Sieve size, mm						
	20	15	12.5	10	7.5	5	< 5
Retained mass, g	815	620	558	401	1109	1026	471
Retained mass, %	16.3	12.4	11.2	8.0	22.2	20.5	9.4
Total mass, %	16.3	28.7	39.9	47.9	70.1	90.6	100.0
Full passes, %	83.7	71.3	60.1	52.1	29.9	9.4	0

4) Determination of water absorption by comparing the mass of samples of sulfur stone in a state saturated with water and after drying. By determining the water absorption of sulfur stone, the following results were obtained: water absorption of crushed stone modified with resin - 4.9% by weight; water absorption of crushed stone modified with styrene - 1% by weight.
5) Determination of frost resistance of crushed stone by weight loss of the sample during alternate freezing and thawing. According to this test, the following results were obtained for resin-modified crushed stone: number of cycles - 25; weight loss - 8.5%; the corresponding grade for this sulfur stone is F 25, whereas for crushed stone modified with styrene: number of cycles - 50; weight loss - 4.9%; the corresponding grade for this sulfur stone is F 50.
6) Determination of the compressive strength of crushed stone and bringing samples (cubes) to destruction on a press. The results of this test are shown in Table 6.

Table 6. Results for determining the compressive strength of crushed stone.

Name	a, mm	b, mm	P, N (kgf)	$R_{f,}$ MPa
Crushed stone modified with resin	50	50	16.42	6.6
	50	50	14.50	5.8
Arithmetic mean				6.2
Crushed stone modified with styrene	50	50	21.31	8.5
	50	50	20.85	8.3
Arithmetic mean				8.4

To determine the physical and mechanical properties of raw and processed substandard low-strength limestone-shell rock (crushed stone), tests were carried out to determine the indicators of crushability, abrasion, water absorption, frost resistance and tensile strength of cubic samples. Based on the test results, when treating limestone-shell rock with modified sulfur, the indicators of physical and mechanical properties improve. The test results are shown in comparative Table 7.

Determination of radioactivity, chemical composition and harmful impurities in mineral materials.

Table 7. Comparative analysis of the test results of untreated and processed substandard low-strength shell limestone modified with sulfur.

The name of indicators	In original state	treated with modified sulfur	
Breakability of crushed stone according to the degree of destruction of grains during compression (crushing) in the cylinder, brand	200	resin 600	styrene 800
Abrasion of crushed stone according to the loss of mass of grains in the shelf drum with balls, brand	I-4	AND 2	I-1
Water absorption by comparing the mass of crushed stone samples in a state saturated with water and after drying, %	7.1	4.9	1
Frost resistance of crushed stone in terms of sample mass loss during alternate freezing and thawing, grade	F 25	F 25	F 50
Ultimate strength of the rock in compression and bringing samples to failure, MPa	3.6	6.2	8.5

In order to compare the chemical compositions of sulfur melts modified with epoxy resin with sulfur melts modified with styrene, the elemental composition of modified sulfur was determined by XRF, the results of which are presented in Table 8.

Table 8. Results of X-ray fluorescence analysis of the sulfur melt modified with epoxy resin.

Element	Relative concentration, %
Al	0.201
P	0.179
S	77.97
Ca	0.235
Fe	0.002

As can be seen from the table, the sulfur content in the sulfur melt modified with epoxy resin was 77.97%. In addition, elements such as Al, P, Ca, Fe can be present in a very small amount in the melt. Basically, this sulfur melt contained 98.0% pure sulfur, which decreased to 77.97% due to its polymerization. An x-ray of this sulfur melt can be seen in the following Figure 7.

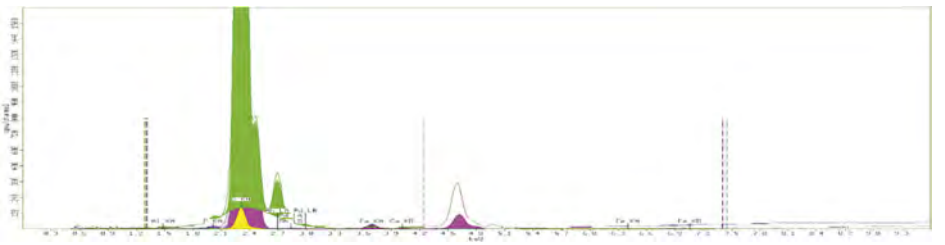

Figure 7. X-ray pattern of the molten sulfur modified with epoxy resin.

Together with the sulfur melt modified with epoxy resin, an X-ray phase analysis of the sulfur melt modified with styrene was carried out. The results of X-ray fluorescence analysis of the styrene-modified sulfur melt are shown in Table 9.

Table 9. Results of X-ray phase analysis of sulfur melt modified with styrene.

Element	Relative concentration, %
Al	0.178
P	0.177
S	63.938
K	0
Ca	0.242
Fe	0.002
Pd	0
Ag	0.019
CD	0
In	0.006

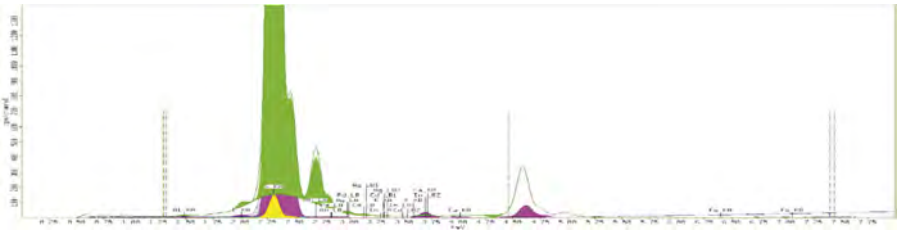

Figure 8. X-ray pattern of styrene-modified sulfur melt.

The sulfur content in the styrene-modified sulfur melt was 63.938%. This is less than the amount of sulfur that was in the sulfur melt modified with epoxy resin. Basically, the composition of this sulfur melt consisted of 97.5% pure sulfur, the amount of which decreased to 63.938% due to the fact that most of it is involved in polymerization. This melt also contains a small amount of the elements Al, P, Ca, Fe, Ag, and In. An x-ray of this sulfur melt can be seen in the following Figure 8. Before measuring radioactivity, samples are monitored at a temperature of 23 °C, air humidity 61% (sulfur, modified sulfur, shell rock, sulfur gravel) using a dosimeter-radiometer MKS-AT6130. All samples showed 0.12 μSv/h (Figure 9), which does not exceed the value of the natural natural gamma background (Limit from 0.07 to 0.20 μSv/h in Kazakhstan).

Figure 9. Dosimetric control of samples.
a- sulfur, b - modified sulfur, c - shell rock, d - crushed stone

4 DISCUSSION

According to the results of tests of limestone-shell rock, the following indicators were obtained: the grain composition of limestone - shell rock corresponds to a fraction of

5-20 mm; crushing strength in compression in the cylinder of a fraction of 10-20 mm in the dry state - 34.2% (weight loss), in the water-saturated state -43.5%, which correspond to the -200 grade; abrasion in the shelf drum was -56.7%, which corresponds to the brand - I1; water absorption by weight was 7.1%; frost resistance (freeze-thaw method), weight loss after 25 cycles is 5.6%, which corresponds to the F 25 brand; compressive strength: porous structure of the shell rock - 1.7 MPa; the dense structure of the shell rock is 5.5 MPa.

The main physical and mechanical properties of sulfur according to the test data obtained showed that the sulfur content is 99.99%, the color is yellow, the density is 1.73 kg/m 3, water absorption is 0.15% by weight, compressive strength is 12 MPa.After stirring the mixture for 30 minutes, the first sample was taken, after 60 minutes - the second sample. As the melting point of sulfur rises, it can be seen that the color of its modified melt changes from light yellow to burgundy. Analysis of the structure of sulfur and its modified melt showed that the particle size in the melt modified at 150°C is larger than in elemental sulfur. Due to the addition of modifiers, the particle size in the melts becomes larger as a result of crosslinking and polymerization of sulfur. Additional introduction together with epoxy resin of sodium sulfate in the amount of 0.5-1.0% made it possible: reduction of the reaction temperature to 150°C; the reaction time is reduced to 30 minutes; alkali resistance and resistance to sulfuric bacteria are provided; the adhesive properties of the modified sulfur to the shell rock are increased.

During the work on this topic, the results showed that the abrasion grade for limestone-shell rock before treatment with modified sulfur is I-4, after treatment -I-1; water absorption before treatment with modified sulfur is 7.1%, after treatment -1%, i.e. water absorption after treatment with modified sulfur decreased by 7 times; frost resistance grade for limestone-shell rock before treatment with modified sulfur F25, after treatment -F50 (but the weight loss after the test was 4.9% (at the limit) with a requirement of not more than 5% for grade F50 according to ST RK 1284); the ultimate strength of cubic samples of raw crushed stone corresponds to 3.6 MPa, after treatment with modified sulfur - 8.5 MPa, i.e. due to the modification of limestone-shell rock with gray, the tensile strength index increased by 2.4 times.

5 CONCLUSION

In conclusion, the use of modified sulfur and low-strength inert materials such as limestone-shell rock can result in the production of high-strength "sulphurous stone". The combination of these materials not only increases the strength of the resulting product but also provides a more sustainable alternative to traditional building materials.

REFERENCES

Youssef, M. A., Abdel-Hamed, M. O., El-Sayed, S. M., & El-Sayed, A. A. (2015). *Sulfur as a promising binder for composite materials: A review*. Materials Science and Engineering: A, 644, 112–120.

Yildirim, H., & Şimşek, M. (2019). *Chemical modification of sulfur for the development of high-performance materials:* A review. Polymers, 11(2), 276.

Zhang, S., Li, Z., Chen, L., Li, Q., Wang, D., & Wu, G. (2017). *Toughening and reinforcing of sulfur-based composites by epoxy resin*. Journal of Materials Science, 52(2), 808–820.

Xie, J., Cui, W., Chen, W., Guo, Y., & Wu, D. (2018). *Improvement of mechanical properties of sulfur-based composites by modification with an unsaturated compound*. Journal of Materials Science, 53 (2), 1541–1552.

Smart Geotechnics for Smart Societies – Zhussupbekov, Sarsembayeva & Kaliakin (Eds)
© 2023 The Author(s), ISBN 978-1-003-29912-7
Open Access: www.taylorfrancis.com, CC BY-NC-ND 4.0 license

Modernization of the tramway infrastructure with the use of vibroisolation elements within track structure

A.A. Zaytsev, A.V. Kendyuk & A.A. Sidrakov
Russian University of Transport, Moscow, Russia

D.A. Basovsky
Emperor Alexander I St. Petersburg State Transport University, Sankt Petersburg, Russia

M.A. Papaev
JCC "GK-Techstroy, Moscow, Russia

ABSTRACT: The analysis of buildings and structures falling within the zone of influence of the projected tram line was carried out. Mathematical analysis of the level of vibrations occurring in buildings and structures were performed, taking into account the actual values of loads from rolling stock, engineering and geological surveys in the construction area and the results of the survey of buildings and structures falling into the zone of influence - an assessment of the technical characteristics of the sub-regions selected for the design of the tram line was carried out. Thus, the use of vibration-proofing sub-ballast mats in compliance with the laying technology allows us to bring the vibration indicators generated during the passage of tramcars to the normalized values for administrative and administrative premises of buildings, including taking into account the correction for non-constant vibration for residential premises.

1 INTRODUCTION

Investigations for the development of effective solutions for vibration-proof structures for the infrastructure of railways and urban rail transport is carried out in the CIS countries (SP 98.13330.2018, Methodology 2019, GOST 14837-1-2007, Tram car model 2017, Lakusic et al 2008, 2011, Weisemann et al 2012), Europe and Asia (Zou et al 2017). The series of reseaches and projections has been carried out In order to develop the tramway infrastructure in capitals for the purpose of the measuring the vibration impact generated by the passage of tram cars in order to assess the effectiveness of the vibration-proof structure of the tramway with the use of ballast mats during the implementation of the project of complex improvement of streets and public spaces and ensuring the preservation of cultural heritage objects Figure 1.

At the experimental site, during the measurement period, tramcars of the Vityaz project passed. Vibration parameters were measured within the existing tram routes to measure the vibration effect exerted by the passage of tramcars on the surrounding buildings. A program of experimental work has been implemented to measure the vibration effects generated by a tramcar within a 15-meter zone from the axis of the tramway and on the basement of a building falling into the previously estimated zone of influence - Figure 1.

Also, calculation schemes have been prepared with the application of the geological structure, physical and mechanical parameters of soils, existing and projected structures; the analysis of loads from tram cars, physical and mechanical parameters of soils (according to engineering-geological and geophysical surveys); the substantiation of the theoretical provisions of the

DOI: 10.1201/9781003299127-412

calculation in the form of an assessment of the impact of vibration effects of tram, parameters of materials, sub-ballast mats and modelling of the system.

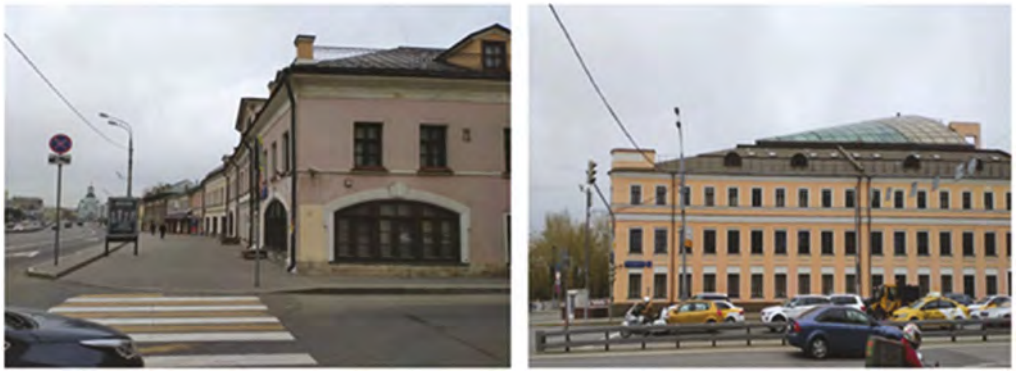

Figure 1. Heritage two-storey and three-storey buildings.

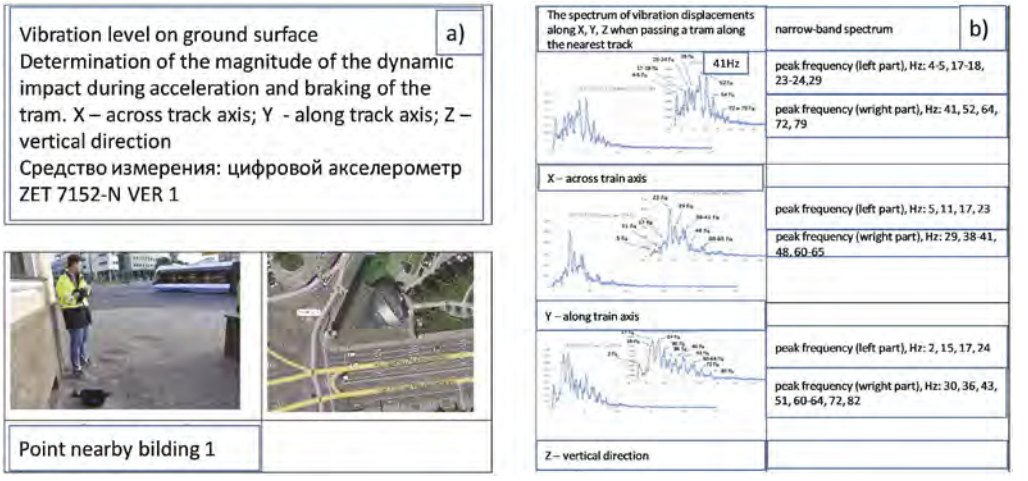

Figure 2. Results of field measurements.

2 SELECTION OF OBJECTS-ANALOGUES ON THE TRAMWAY INFRASTRUCTURE

The design area of the new tramway and the location of cultural heritage objects on this site. Thus, analogous objects were selected on the basis of full-scale inspections of the design object (Sergiy Radonezhsky Street), analysis of regulatory design documentation and previously implemented projects for the reconstruction of tram tracks, as well as from the condition of similarity of the location of buildings, track design (without vibration protection and with vibration protection) and density of urban development.

At this site, during the measurement period, tramcars of the «Vityaz» project are operated. Characteristics of the rolling stock - tram cars planned for circulation on the site: a six-axle three-section low-floor tram (tramcar) is produced, according to the characteristics meets the requirements of SP 98.133330.2012. The tram is designed to transport passengers on city lines

along a tram track with a gauge of 1524mm. Three traction trolleys, two of which are rotary - Figure 2, support the tramcar.

Tramway 71-931M

Track width	1524 mm
length	27,5 m
Height	3,5 m

Base wagon	8,994 m
Base bogie	1,8 m
Maximum velocity	75 km/h
Mass	37 t
Doors	6
Nominal capacity	188 (5 passenger / m2)
Full capacity	265 (8 passenger / m2)
Seats	60(64)

Figure 3. General view of the tram car and its characteristics.

The tramcar consists of two rotary and one non-rotating trolley (the structural difference in them lies in the performance of the pivot beam), specially designed for a low-floor car. When passing curved sections of the railway track, smooth running is ensured by two-stage springing and other equipment installed on trolleys, including a wheelset with a gearbox, traction motor, gear clutch and electromechanical braking system.

As initial data for dynamic calculation from tramcars, it is customary to use the values of vertical and horizontal loads. In the calculations of vibration-proof (vibration-insulated) VSP structures with the use of ballast mats, a design scheme is considered where the track structure is represented as a beam of infinite length lying on a solid elastic base loaded with a system of concentrated wheel loads replaced by equivalent single loads, respectively, when determining bending moments and stresses in rails and track plate using the function and when determining bending moments and stresses in rails – using the function, fasteners, on sleepers, on ballast and its base.

A probabilistic character was assigned for the calculations when determining the maximum values of loads.

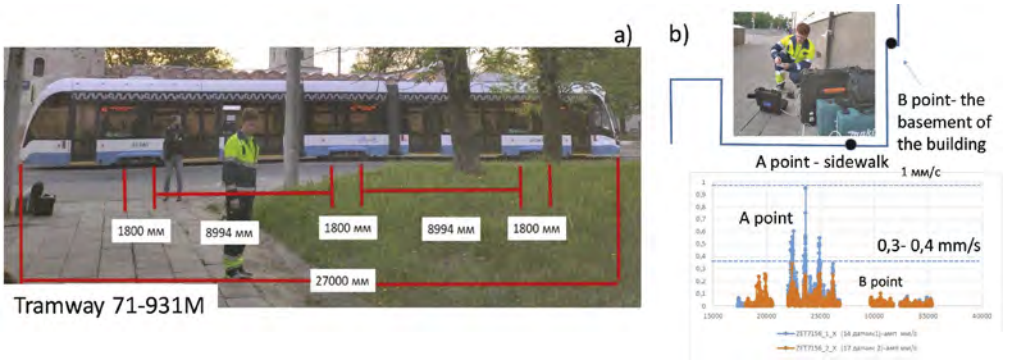

Figure 4. Tram car 71-931 Vityaz-M on Andronyevsky passage a) and spectrum of acceleration on two points nearby building.

Vibration-proofing mats PM-011 (development from 2018) are designed for laying on the site designed for use on railway, tram and subway tracks in order to reduce vibration effects that are transmitted from rolling stock to infrastructure facilities. The mat material is rubber from the upper and lower sides bonded with geotextile material.

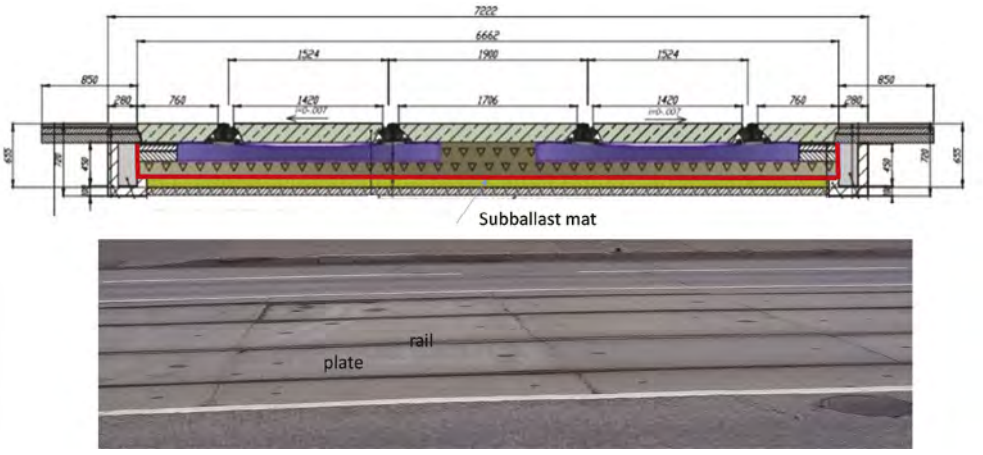

Figure 5. Tram track type with large size concrete plates.

According to the design experience for the specified parameters, the elastic draft of the rail at the speed of the tramcar 20km per hour is no more than 3 mm.

3 MAIN PROVISIONS OF THE CALCULATION METHODOLOGY

Vibration-insulating sub-ballasted mats PM-011 TU 22.21.42-004-02488336-2018 it is intended for use on railway, tram and subway tracks in order to reduce vibration effects that are transmitted from rolling stock to infrastructure facilities. Vibration-proofing mats are used as: sub-ballast gaskets on sections of railway and tram tracks exposed to increased axial loads, in places of exposure to increased dynamic loads (switches, artificial structures, transitional sections, small radius curves, etc.); sub-ballast mats on sections of railway and tram tracks both on the roadbed and on artificial structures.

Vibration-insulating mats are manufactured for the purpose of their application to solve the following tasks: isolation from mechanical noise in populated areas; protection of vibration-sensitive structures and buildings with increased requirements; sound insulation; reduction of static and dynamic pressures caused by the movement of trains and allow more evenly distributing loads at the base of the sub-track; increasing the stability of the track and reducing the (alternating) compression of crushed stone ballast.

Figure 6. Installation of tram tracks with vibration-proof mats, monitoring.

In buildings remote from the source of the vibro-dynamic impact, the levels of vibration acceleration at the main frequencies range from 25 dB to 27 dB. The use of vibration-isolating mats reduces this indicator from 5 to 7 dB. Vibration-proofing mats PM-011 are available in thickness

from 10 mm to 30 mm (in the project, the thickness of the mat is 20 mm). The upper and lower layer of the mat are made of synthetic geotextile material reinforced with surface firing.

The mat is filled with a granular composite material based on rubbers 5 or 5 EV 5 (the size of the granules ranges from 0.58 mm to 4 mm).

Dynamic parameters of the path without the use of vibration-proof mats. One of the main dynamic parameters of a system with one degree of freedom is its natural frequency.

To calculate the effective mass of the system, we calculate the length of an absolutely rigid beam *l* lying on an elastic base with an elastic modulus and a total stiffness. In this case, the deviation of the rail from the unit force will be equal to the deviation of an equivalent absolutely rigid beam of length.

We will take as the effective mass of the system the mass of rails, sleepers, ballast and the mass of wheel pairs on a section of length d. If the length d is less than the base of the trolley, then only one wheelset is taken into account. To calculate the mass of the ballast, the cross-sectional area of the ballast along the trapezoid is taken, taking into account the distribution of pressure in the ballast from the side of the sleeper at an angle of 45°. With a sleeper length of 270 cm and a ballast height of 40 cm, the cross-sectional area of the ballast (per rail thread) is calculated as follows: (2,7+0,4) ×0,40/2 = 0,62 m^2.

Results of calculating the natural frequency of a system with one degree of freedom for a track with sub-ballast mats (one rail thread): mat thickness = 42 mm; modulus of elasticity of the path, U=47800000 MPa; rigidity of the path, β=18211412 MN/m; length of the equivalent beam (support) 1.75 m; effective total mass of the system, m=3217.8 kg; the natural frequency of the system, f_0=11.20 Hz.

The vibration transmission coefficient K, represented as a logarithm of the ratio of oscillation amplitudes in decibels, shows how many times the vibration level of one structural element is less or more than the vibration level of another.

Using the vibration transmission coefficient, it is possible to evaluate the effectiveness of both individual structural elements and the entire structure as a whole. In this case, the vibration transmission coefficient from the rail to the ground was determined. In accordance with this, Figure 6 shows the curves of the vibration transmission function for the track structures under consideration.

Figure 6 show a comparison of the effectiveness of the upper structure of the path with sub-ballast mats compared with the upper structure of the path without sub-ballast mats.

In accordance with the manufacturer's data for the proposed vibration-insulating sub-ballast mats PM-011 TU 22.21.42-004- 02488336-2018 It is assumed that the vibration isolation efficiency is equal to 5 dB for the considered geometric mean frequencies of the octave range.

On Figure 7 shows the curves of the vibration transfer function for the track structures under consideration and the calculation results comparing the efficiencies of tramway structures with sub-ballast mats compared to the upper structure of the track without sub-ballast mats.

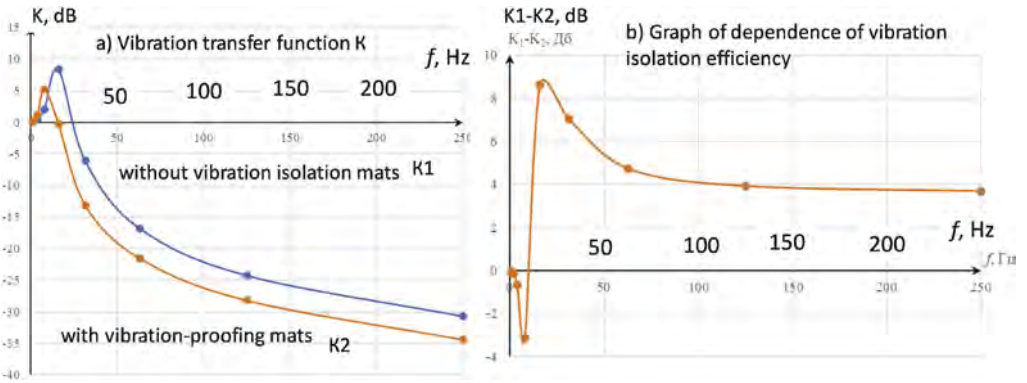

Figure 7. The results of calculation vibro - isolation efiiciency.

4 CONCLUSION

At the article presents the results of work on experimental and calculated determination of vibration velocities, vibration accelerations and prediction of vibration levels on existing buildings and structures near the projected tramway line.. Variants of technically feasible ways to reduce vibration levels to acceptable values in the premises of buildings located near the reconstructed tram line have shown that the main effective way to reduce vibrations is the use of vibration-proofing ballast mats, which is aimed at reducing the rigidity of the track structure and the implementation of a vibration-proof function. Indeed, to ensure the preservation of cultural heritage sites. It is necessary to use a vibration isolation system of the upper structure of the path. Strongly recommended to use a vibration-proof structure of the upper structure of the track with vibration-noise insulation sub-ballast mats, which reduce the level of vibration and structural noise to acceptable parameters. The prediction of the vibration level for existing buildings (without vibration isolation mats) revealed an excess of the permissible vibration level at the average geometric frequencies of the octave ranges: 8, 16 and 31.5 Hz. Thus, the condition of structures and buildings, objects of cultural heritage does not allow to accept the traditional design of tram tracks, without vibration-proof structures. Vibration-proofing sub- ballasted mats PM-011 were adopted for analysis with vibration isolation efficiency equal to 5 dB. The option of using sub-ballast mats along the contour of the pit (the base and side walls of the pit) for the device of tramway elements is a necessary technical solution to reduce the vibration effect to an acceptable level. The use of vibration-proofing sub-ballast mats, with the use of appropriate laying technology, will ensure the requirements for permissible values of vibration levels. The prediction of the vibration level for existing buildings, with the traditional version of the construction (without vibration isolation mats) revealed an excess of the permissible vibration level at the average geometric frequencies of the octave ranges: 8, 16 and 31.5 Hz. Thus, the condition of structures and buildings, objects of cultural heritage does not allow accepting the traditional design of tram tracks, without vibration-proof structures, without sub-ballasted mats.

REFERENCES

SP 98.13330.2018 Tram and trolleybus lines. SNiP 2. 05.09-90.

Methodology for measuring and evaluating vibrations in predicting the vibroacoustic impact on the surrounding buildings arising from the movement of rolling stock, including high-speed and high-speed types, on land railways, *RUT (MIIT)*, 2019, manuscript

Tram car model 71-931M. User Manual, *PC Transport Systems LLC*, Moscow 2017, 128 p.

Noise and vibrations at tram track intersection; Stjepan Lakusic, Marijan Bogut and Visnja Tkalcevic Lakusic - University of Zagreb, Faculty of Civil Engineering, Croatia, *Acoustics'08 Paris June 29-July* 4, 2008 www.acoustics08-paris.org

Weisemann, U., Großmann S., Ehrenberg H., Ewert, W.F. (2012): Development of a Geocomposite to Improve the Bed Support Conditions of Railway Track Gravel for Railroad Tracks, *5. European Geosynthetics Congress*, Valencia, 16.- 19. 09.2012.

GOST 14837-1-2007 Vibration. Noise and vibration generated by the movement of rail.

Zaytsev Andrey, Petriaev Andrey, Cerniauskaite Laura. Track structure reconstruction practice for the subgrade on weak foundation soils, *Proceedings CETRA 2018: 5th International Conference on Road and Rail Infrastructure*, 17-19 May, Zadar, Croatia, 739–745 p.p. DOI.

Zou C., Wang YM., Moore J.A., Sanayei M. Train-induced field vibration measurements of ground and over-track buildings. *Sci Total Environ 2017*; 575:1339–51.

Lakušić Stjepan, Brčić Davor, Tkalčević, Lakušić Višnja Analysis of Vehicle Vibrations – New Approach to Rating Pavement Condition of Urban Roads, *Promet - Traffic & Transportation, Scientific Journal on Traffic and Transportation Research*, 23 (2011), 6; 485–494.

Smart Geotechnics for Smart Societies – Zhussupbekov, Sarsembayeva & Kaliakin (Eds)
© 2023 The Author(s), ISBN 978-1-003-29912-7
Open Access: www.taylorfrancis.com, CC BY-NC-ND 4.0 license

Water and thermal regimes of road structures in Kazakhstan seasonal freezing regions

B.B. Teltayev
Joldasbekov Institute of Mechanics and Engineering, Almaty, Kazakhstan
LLP "Road Research and Production Center", Almaty, Kazakhstan

K. Aitbayev
JSC "Kazakhstan Highway Research Institute", Almaty Branch, Almaty, Kazakhstan

K.B. Tileu
JSC "Kazakhstan Highway Research Institute", Astana, Kazakhstan

ABSTRACT: The article describes the results of the water-temperature regime analysis in road structures in the cold regions of the Republic of Kazakhstan based on experimental studies. The types of extreme situations that reduce the strength and durability of road structures are listed. The freezing maps of the soil base of the road pavement, formed in different winter periods, are given. A relationship between the level of soil moisture and the value of negative temperature in it during the periods of winter freezing and spring thawing has been established.

Keywords: water-temperature regime, freezing map, winter freezing, spring thawing, humidity level

1 INTRODUCTION

Yang, et al. (2022) studied extreme thermal conditions of the soil are the main factors contributing to premature wear and destruction of road structures, including pavements built in regions with seasonal freezing and thawing.

During winter freezing, the pavement will be subjected to swelling pressure and a possible "frost heave" phenomenon. In addition, the pavement may even crack due to excessive tensile stresses caused by extremely low freezing temperatures in winter.

With the approach of summer, starting from May, the frozen soil will begin to thaw. This spring thaw of the soil can cause significant damage to the upper asphalt concrete layers of the road structure. Abundantly moistened by the thawed part of the moisture, the soil loses its bearing capacity, and the pavement seems to sag over it. If the melting is also accompanied by a spring, seasonal increase in traffic activity, then the risk of pavement failures increases many times over.

During transitional periods between extreme temperatures, before complete freezing and before intense thawing, so-called periods of uncertain freezing and thawing occur, when the temperature on the coating will fluctuate between plus temperatures during the day and minus temperatures at night. During this period, the pavement will be subjected to the "thermal fatigue" test, when thermal expansion is repeatedly replaced by low-temperature contraction.

Since in this paper we consider mainly cold regions of the country with seasonal freezing of the soil, we will not touch on another negative phenomenon, such as the formation of ruts on pavements caused by excessive overheating of the asphalt concrete pavement on summer days in the south.

DOI: 10.1201/9781003299127-413

In foreign scientific literature, considerable attention is paid to the issues of "thermal fatigue" of the road surface. Although everyone understands that freeze-thaw cycles have a great influence on the properties of asphalt pavement, the quantitative side of this effect is still poorly understood. In a detailed study of this issue, air voids, high temperature stability, low temperature cracking resistance and moisture sensitivity and other issues of the microstructure of the asphalt concrete pavement mix are analyzed. The micromorphology and chemical composition of the cement-asphalt mortar were observed using scanning electron microscopy by Ayar, (2018). Freeze-thaw cycles reduce the durability of asphalt pavement in areas that experience seasonal frost. According to Xu, et al. (2015), the destructive effects of freeze-thaw cycles are caused by the expansion of water in the asphalt mix when the temperature is below 0°C. The degree of damage caused by foamed water to the asphalt mix during multiple freeze-thaw cycles has been assessed. The results showed that freeze-thaw cycles accelerate internal damage to the asphalt mix and lead to an increase in air voids and a decrease in adhesive strength. The influence of freeze-thaw cycles on the fatigue characteristics of asphalt concrete mixture was studied by You, et al. (2018). Here it is shown that the fatigue life decreases as the saturation and freeze-thaw cycles increase. And the fatigue life was significantly reduced at high stress levels. Duoji, et al. (2021) demonstrated the flexural tensile properties of blends using freeze-thaw bending tests. It was shown that the bending tensile strength and strain decreased with increasing freeze-thaw cycles. The deterioration of flexural tensile properties decreased significantly at the beginning of freeze-thaw cycles, but became smooth after freeze-thaw cycles. It should be noted that all the above-mentioned works were carried out with the help of modern high-precision installations and devices.

2 KAZAKHSTAN EXPERIENCE IN STUDYING ROAD WATER-THERMAL REGIME

Based on the methodology for determining the freezing depth proposed by Teltayev, for the first time Teltayev and Sakanov (2004) created a separate map of the depth of freezing of roads in Kazakhstan. The map was subsequently included in the main state standards for the design of road structures. For the development of the mapping methodology, data on the actual frost penetration depths of roads and on air temperatures in the points of road pavement and subgrade were used. The number of data sources was limited.

In the development of this topic in the works Teltayev et al. (2015,2017,2019), studies were carried out to improve methods for determining the depth of freezing.

Starting from 2019, Kazakhstan has taken a course to strengthen the experimental base for research on the water-thermal regimes of roads.

Measuring stations equipped with temperature and humidity sensors, operating in automatic mode, and transmitting measured values to a database via the Internet, began to be equipped throughout Kazakhstan. In 2021, the number of such stations was increased to 28 units, which makes it possible to build maps of freezing depths with more accurate data.

3 WATER-THERMAL REGIMES OF ROADS IN KAZAKHSTAN COLD REGIONS

The cold regions include Kostanay, North Kazakhstan, Akmola, Pavlodar and East Kazakhstan regions of the Republic of Kazakhstan. They are united by a harsh, snowy and long winter. The depth of freezing in some years approaches 3 meters.

The chronological freeze-thaw map is one of the most effective tools for studying the patterns of formation of the water-thermal regime on a specific section of the road for a specific period of time. In terms of time, the map covers the period, including the moment of the beginning of the freezing of the road structure and the end of the thawing process. To demonstrate the methodology for constructing a freezing map, consider a road section near the city of Kostanay (section of the Karabutak-Kostanay-Yekaterinburg-Almaty, Kostanay city, km 1), Figure 1.

Table 1. Road pavement structure.

№	Layer material, soil	Layer thickness
1.	Asphalt concrete, type B	h_1=5 cm
2.	Coarse-grained porous asphalt concrete	h_2=13 cm
3.	Coarse-grained highly porous asphalt concrete	h_3=9 cm
4.	mixture	h_4=35 cm
5.	Soil - sand	h_5=90 cm
6.	Soil - black earth	h_6=148 cm

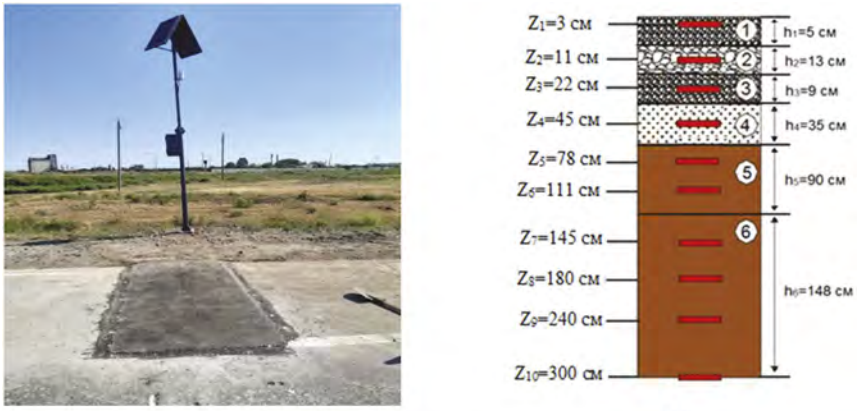

Figure 1. Measuring station near Kostanai. a) External view of the transmitting antenna of the measuring station near Kostanai. b) Schematic view of the road structure.

Table 2. Location depths of sensors.

Vertical coordinate of sensor	Z_1	Z_2	Z_3	Z_4	Z_5	Z_6	Z_7	Z_8	Z_9	Z_{10}
Value, cm	3	11	22	45	78	111	145	180	240	300

The mathematical model of the problem of the temperature regime in the considered multilayer road structure is a one-dimensional composite well with a unit cross-sectional area (Figure 1b).

The chronological freeze-thaw map (CFTM) of a multilayer road structure is the locus of points with zero temperature on the (n, z) plane, where n is an integer coordinate in hours, z is the vertical coordinate of a point on the mathematical model.

To build a map of freezing and thawing of a section of the road near Kostanay in winter, according to the data of an experimental study of the water-thermal regime, first, the moment of occurrence of negative temperatures at the points of the road pavement and the subgrade is established, and at the end, the completion of the thawing process is recorded, when at the points road construction everywhere only positive temperature.

At the measuring station in Kostanay in the winter period 2021-2022 the following dates are set: for the first time, the front of negative temperatures (zero line) crosses the sensor located at a depth of 3 cm at 18:58 on November 2, 2021. In turn, the negative temperature was last recorded by a sensor located at a depth of 180 cm at 5:58 on April 30, 2022. Thus, the process of freezing and thawing of a section of the road near the city of Kostanay will need to be monitored for all 180 days - from November 2, 2021 to April 30, 2023.

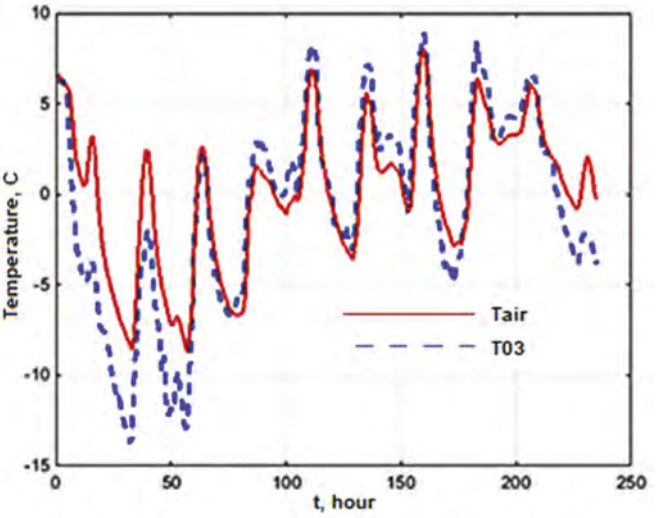

Figure 2. Temperature variations at a depth of 3 cm (T03) in comparison with air temperature (Tair) variations in the period from 0:58 AM on November 1 to 18:58 PM on November 11, 2021 (n=1: 234).

However, the processes of freezing and thawing do not always occur with the same intensity. At the initial stage, in the period from 0:58 on November 1 to 18:58 on November 11, 2021, which corresponds to the interval of change in the time coordinate 'n' from 1 hour to 234 hours, there is an unsteady process of formation of the temperature regime with frequent zero crossings (Figure 2).

The picture of temperature change at a depth of 3 cm, shown in Figure 3, is of interest from the point of view of the fatigue strength of the asphalt concrete pavement, when alternating compression and tension occur under the influence of temperature.

It is easy to see that this period of freezing does not affect the maximum depth of freezing of the soil base, which is the main subject of research. The physical processes occurring in this period of time (n=1:234) will be singled out as a separate problem, where the influence of a cyclic process caused by thermal forces of compression or tension will be studied.

Since n=235, the actual process of freezing of the road structure begins, when the temperature at its points is stably negative. It should be noted that the readings of the temperature sensors cannot be strictly equal to zero at any point of the integer time coordinate n. Therefore, if necessary, interpolation methods are used to determine the coordinates of the front of negative temperatures.

For the winter period of 2021-2022, the hodograph of the vector of negative temperatures runs through the time interval from n=235 to n=4302. At the last moment, the freezing depth is H=195 cm. Moreover, the maximum freezing depth is reached much earlier. The greatest freezing depth in the road structure of the section of the Karabutak-Kostanai-Yekaterinburg-Almaty, Kostanai highway, km 1 for the winter period of 2021-2022 was 225 cm. This depth was achieved at n=3783, which corresponds to 14:58 hours on April 8, 2022. Later, under the influence of heat from the bowels of the Earth, the ground base begins to melt, since at this time of the year the intensity of the negative temperature directed from top to bottom weakens. The process of soil thawing from bottom to top will be completed at the time n=4302, or at 5:58 on April 30, 2022 at a depth of Z=195 cm, when thawing from above reaches the same depth.

With the onset of spring, the frozen road structure begins to melt from above. The defrosting process starts at 15:58 hours on February 21, 2022. But, as in the initial period of freezing, this process is unstable, and frequent transitions through '0′ will continue until 08:58 hours on April 6th.

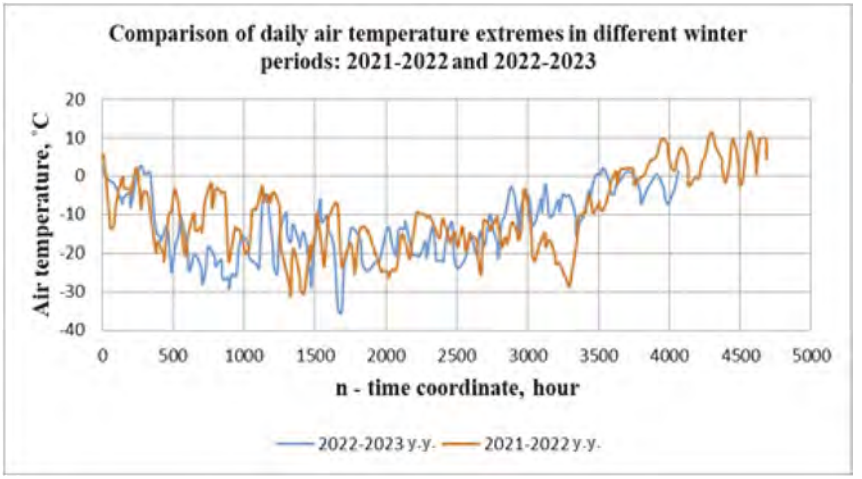

Figure 3. Comparison of daily air temperature extremes in different winter periods: 2021-2022 and 2022-2023.

It is clear that in order to assign the calculated values of individual parameters of the water-thermal regime, it is necessary to take into account the variability over the years of the weather in a given area. In this paper, such variability is demonstrated using the winter periods of 2021-2022 and 2022-2023 as an example. Figure 3 compares daily air temperature extremes in different winter periods: 2021-2022 and 2022-2023. Here, daily extremes were considered only to increase the visibility of graphic materials, since with an hourly demonstration, due to the high frequency of data, it will not be possible to discern individual features of the results.

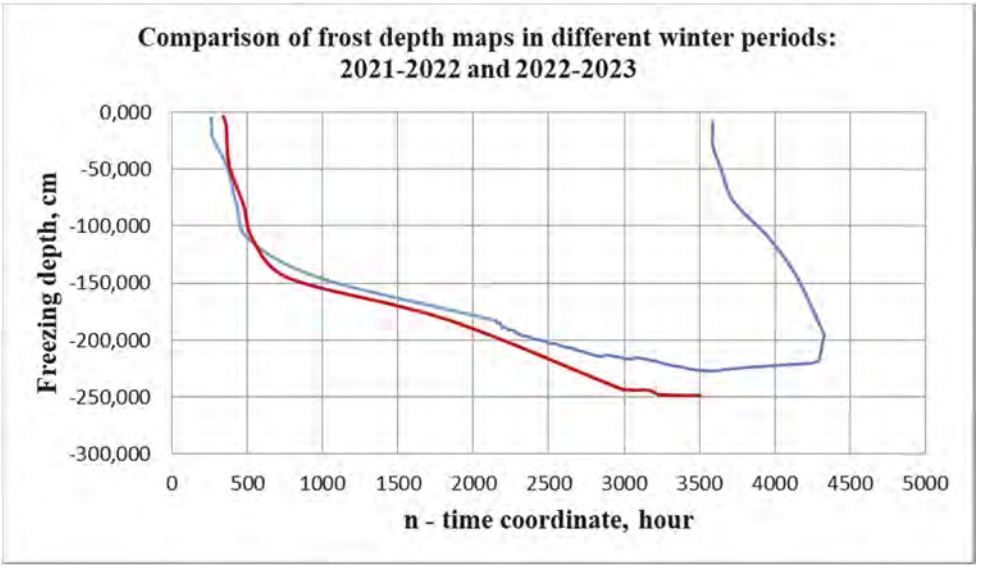

Figure 4. Comparison of freezing depths in different winter periods:2021-2022 and 2022-2023.

From the analysis of the experimental results, we conclude that during the winter period2021-2022 the minimum air temperature reached Tmin=-31.0°C, while for the winter period of 2022-2023. it was equal to Tmin=-35.5°C. However, such a slight difference of -4.5°C in air temperature will lead to a noticeable increase in the freezing depth (Figure 4).

An analysis of the numerical data of the graphs in Figure 4 shows that for the winter period 2021-2022. Freezing depth reached H=225.0 cm, while this parameter for the winter period of 2022-2023. Reached H=250.2 cm. It is clear that an increase in the freezing depth by as much as 25 centimeters or more can lead to a noticeable increase in soil waterlogging during the spring thaw. It follows that the change in weather conditions in the area where the road passes from year to year is a factor that should not be taken into account.

REFERENCES

Ayar, P. 2018. Effects of additives on the mechanical performance in recycled mixtures with bitumen emulsion: An overview. Constr. Build. Mater., 178: 551–561.

Duojie, C., Si, W., Ma, B., Hu, Y., & Wang, X. 2021. Assessment of freeze-thaw cycles impact on flexural tensile characteristics of asphalt mixture in cold regions. Math. Probl. Eng., 2021: 6697693.

Fan, Z., Xu, H., Xiao, J., & Tan, Y. 2020. Effects of freeze-thaw cycles on fatigue performance of asphalt mixture and development of fatigue-freeze-thaw (FFT) uniform equation. Constr. Build. Mater., 242: 118043.

RK 218-38-04. 2004. Recommendations on accounting for the zoning of the territory of Kazakhstan according to the estimated depth of freezing of subgrade soils of highways. Astana: 43 p.

SN RK 3.03-19-2006. 2007. Design of non-rigid pavements. Astana: 87 p.

SN RK 3.03-34-2006. 2005. Instructions for the design of rigid pavements. Astana: 89 p.

Teltaev, B., Baibatyrov, A., & Suppes, E. 2015. Characteristics of highway subgrade frost penetration in regions of the Kazakhstan. The 15th Asian Regional Conference on Soil Mechanics and Geotechnical Engineering, Fukuoka, Japan: 1664–1668.

Teltayev, B.B., & Suppes, E.A. 2017. Regularities for temperature variation in subgrade of highway. Geomechanics and Engineering, 13(5): 793–807.

Teltayev, B., Aitbayev, K., & Suppes, E. 2019a. Temperature and moisture distribution in a highway in south Kazakhstan. Procds. of the 16th Asian Regional Conference on Soil Mechanics and Geotechnical Engineering, Taipei, Taiwan: 1–4.

Tileu, K., Teltayev, B., Aitbayev, K., & Suppes, E. 2019b. Mapping of frost penetration depth for highways in Kazakhstan. Procds. of the 16th Asian Regional Conference on Soil Mechanics and Geotechnical Engineering, Taipei, Taiwan: 1–4.

Xu, H., Guo, W., & Tan, Y. 2015. Internal structure evolution of asphalt mixtures during freeze-thaw cycles. Mater. Des., 86: 436–446.

Xu, H., Guo, W., & Tan, Y. 2016. Permeability of asphalt mixtures exposed to freeze-thaw cycles. Cold Reg. Sci. Technol., 123: 99–106.

Yang, Y., Sun, Z., Yang, Y., Yue, L., & Chen, G. 2022. Effects of Freeze–Thaw Cycles on Performance and Microstructure of Cold Recycled Mixtures with Asphalt Emulsion. Coatings, 12(8): 802. https://doi.org/10.3390/coatings12060802.

Yan, K., Ge, D., You, L., & Wang, X. 2015. Laboratory investigation of the characteristics of SMA mixtures under freeze-thaw cycles. Cold Reg. Sci. Technol., 119: 68–74.

You, L., You, Z., Dai, Q., Guo, S., Wang, J., & Schultz, M. 2018. Characteristics of water-foamed asphalt mixture under multiple freeze-thaw cycles, Laboratory evaluation. J. Mater. Civ. Eng., 30: 0401827021: 48.

Smart Geotechnics for Smart Societies – Zhussupbekov, Sarsembayeva & Kaliakin (Eds)
© 2023 The Author(s), ISBN 978-1-003-29912-7
Open Access: www.taylorfrancis.com, CC BY-NC-ND 4.0 license

Author Index